VIII Gruppo Nazionale di Bioingegneria

EIGHTH NATIONAL CONGRESS OF BIOENGINEERING

Proceedings

Organized by

Università degli Studi di Padova
(Dipartimento di Ingegneria dell'Informazione,
Dipartimento di Ingegneria Industriale,
Dipartimento di Neuroscienze,
Dipartimento di Ingegneria Civile, Edile e Ambientale)
and Consiglio Nazionale delle Ricerche
(Istituto di Neuroscienze)

Pàtron editore

ISSN 2724-2129
ISBN 9788855580113



800 1222·2022 ANNI

UNIVERSITÀ DEGLI STUDI DI PADOVA

Consiglio Nazionale delle Ricerche

Gruppo Nazionale di Bioingegneria

DIPARTIMENTO DI INGEGNERIA DELL'INFORMAZIONE

DIPARTIMENTO DI INGEGNERIA INDUSTRIALE

ICEA DIPARTIMENTO DI INGEGNERIA CIVILE, EDILE E AMBIENTALE
DEPARTMENT OF CIVIL, ARCHITECTURAL AND ENVIRONMENTAL ENGINEERING

DNS DIPARTIMENTO DI NEUROSCIENZE

PATROCINIO
REGIONE DEL VENETO

dexcom

Telea MEDICAL

sanofi

20 ANNI 2003-2023 MP strumenti

exemplar Solutions for Complexity

natus micromed

BIOMOMENTUM

inventis Audiology & Balance

Gruppo Nazionale di Bioingegneria

GNB 2023

Organizing Committee

Sponsor and awards

Emanuele Luigi Carniel, Dipartimento di Ingegneria dell'Informazione, Università degli Studi di Padova
Chiara Dalla Man, Dipartimento di Ingegneria dell'Informazione, Università degli Studi di Padova
Roberto Bizzotto, Istituto di Neuroscienze, Consiglio Nazionale delle Ricerche

Finance

Mattia Veronese, Dipartimento di Ingegneria dell'Informazione, Università degli Studi di Padova
Chiara Giulia Fontanella, Dipartimento di Ingegneria Industriale, Università degli Studi di Padova
Morten Gram Pedersen, Dipartimento di Ingegneria dell'Informazione, Università degli Studi di Padova
Zimi Sawacha, Dipartimento di Ingegneria dell'Informazione, Università degli Studi di Padova
Francesca Maria Susin, Dipartimento di Ingegneria Civile, Edile e Ambientale, Università degli Studi di Padova

Venue

Andrea Bagno, Dipartimento di Ingegneria Industriale, Università degli Studi di Padova
Fabio Scarpa, Dipartimento di Ingegneria dell'Informazione, Università degli Studi di Padova
Martina Vettoretti, Dipartimento di Ingegneria dell'Informazione, Università degli Studi di Padova

Event

Emanuela Formaggio, Dipartimento di Neuroscienze, Università degli Studi di Padova
Alice Berardo, Dipartimento di Ingegneria Civile, Edile e Ambientale, Università degli Studi di Padova
Monica Dettin, Dipartimento di Ingegneria Industriale, Università degli Studi di Padova
Michele Schiavon, Dipartimento di Ingegneria dell'Informazione, Università degli Studi di Padova

Abstracts and contributions

Simone Del Favero, Dipartimento di Ingegneria dell'Informazione, Università degli Studi di Padova
Manfredo Atzori, Dipartimento di Neuroscienze, Università degli Studi di Padova
Alessandro Gandin, Dipartimento di Ingegneria Industriale, Università degli Studi di Padova
Camillo Porcaro, Dipartimento di Neuroscienze, Università degli Studi di Padova
Silvia Todros, Dipartimento di Ingegneria Industriale, Università degli Studi di Padova

Publicity, web and social media

Andrea Facchinetti, Dipartimento di Ingegneria dell'Informazione, Università degli Studi di Padova
Giacomo Baruzzo, Dipartimento di Ingegneria dell'Informazione, Università degli Studi di Padova
Marco Castellaro, Dipartimento di Ingegneria dell'Informazione, Università degli Studi di Padova
Maria Rubega, Dipartimento di Neuroscienze, Università degli Studi di Padova
Roberto Visentin, Dipartimento di Ingegneria dell'Informazione, Università degli Studi di Padova

Coordination

Alessandra Bertoldo, Dipartimento di Ingegneria dell'Informazione, Università degli Studi di Padova
Giovanna Brusatin, Dipartimento di Ingegneria Industriale, Università degli Studi di Padova
Piero Pavan, Dipartimento di Ingegneria Industriale, Università degli Studi di Padova
Giovanni Sparacino, Dipartimento di Ingegneria dell'Informazione, Università degli Studi di Padova

Scientific Committee

Track 1 - E-health and Clinical Engineering

Miloš Ajčević, Università degli Studi di Trieste
Sergio Casciaro, Consiglio Nazionale delle Ricerche
Danilo Pani, Università degli Studi di Cagliari
Pierangelo Veltri, Università della Calabria

Track 2 - Physiological and Neural System Modelling

Leonardo Bocchi, Università degli Studi di Firenze
Cristiano Cuppini, Alma Mater Studiorum - Università di Bologna
Chiara Dalla Man, Università degli Studi di Padova
Alessandra Sciutti, Istituto Italiano di Tecnologia

Track 3 - Biomechanics and prosthetics
Maria Cristina Bisi, Alma Mater Studiorum - Università di Bologna
Emanuele Luigi Carniel, Università degli Studi di Padova
Michele Conti, Università degli Studi di Pavia
Luigi La Barbera, Politecnico di Milano
Giuseppe Vannozzi, Università degli Studi di Roma "Foro Italico"
Track 4 - Biomaterials, Cell & Tissue Engineering, Biofabrication
Irene Carmagnola, Politecnico di Torino
Carmelo De Maria, Università di Pisa
Silvia Farè, Politecnico di Milano
Laura Pastorino, Università degli Studi di Genova
Marco Rasponi, Politecnico di Milano
Leonardo Ricotti, Scuola Superiore Sant'Anna
Chiara Tonda Turo, Politecnico di Torino
Enza Torino, Università degli Studi di Napoli Federico II
Francesco Urciuolo, Università degli Studi di Napoli Federico II
Track 5 - Biomedical Signal and Image Processing
Emilia Ambrosini, Politecnico di Milano
Gabriele Arnulfo, Università degli Studi di Genova
Laura Astolfi, Sapienza Università di Roma
Laura Burattini, Politecnica delle Marche
Cristiano De Marchis, Università degli Studi di Messina
Luca Faes, Università di Palermo
Manuela Ferrario, Politecnico di Milano
Alberto Greco, Università di Pisa
Giulia Matrone, Università degli Studi di Pavia
Kristen Meiburger, Politecnico di Torino
Micaela Morettini, Università Politecnica delle Marche
Giandomenico Nollo, Università di Trento
Mario Sansone, Università degli Studi di Napoli Federico II
Roberto Sassi, Università degli Studi di Milano
Silvia Francesca Storti, Università di Verona
Track 6 - Neural Engineering and Micro and Nano-technologies
Alfonso Gautieri, Politecnico di Milano
Alberto Mazzoni, Scuola Superiore Sant'Anna
Marta Parazzini, Consiglio Nazionale delle Ricerche
Track 7 - Biorobotics, rehabilitation & Assistive Technologies
Andrea Canessa, Università degli Studi di Genova
Gastone Ciuti, Scuola Superiore Sant'Anna
Francesca Cordella, Università Campus Bio-Medico di Roma
Taian Martins, Politecnico di Torino
Track 8 - Design and Validation of Biomedical Devices
Giovanni Calcagnini, Istituto Superiore di Sanità
Gianni Pedrizzetti, Università degli Studi di Trieste
Mara Terzini, Politecnico di Torino
Tommaso Villa, Politecnico di Milano

Gruppo Nazionale di Bioingegneria

GNB 2023

Organizing Committee

Sponsor and awards

Emanuele Luigi Carniel, Dipartimento di Ingegneria dell'Informazione, Università degli Studi di Padova
Chiara Dalla Man, Dipartimento di Ingegneria dell'Informazione, Università degli Studi di Padova
Roberto Bizzotto, Istituto di Neuroscienze, Consiglio Nazionale delle Ricerche

Finance

Mattia Veronese, Dipartimento di Ingegneria dell'Informazione, Università degli Studi di Padova
Chiara Giulia Fontanella, Dipartimento di Ingegneria Industriale, Università degli Studi di Padova
Morten Gram Pedersen, Dipartimento di Ingegneria dell'Informazione, Università degli Studi di Padova
Zimi Sawacha, Dipartimento di Ingegneria dell'Informazione, Università degli Studi di Padova
Francesca Maria Susin, Dipartimento di Ingegneria Civile, Edile e Ambientale, Università degli Studi di Padova

Venue

Andrea Bagno, Dipartimento di Ingegneria Industriale, Università degli Studi di Padova
Fabio Scarpa, Dipartimento di Ingegneria dell'Informazione, Università degli Studi di Padova
Martina Vettoretti, Dipartimento di Ingegneria dell'Informazione, Università degli Studi di Padova

Event

Emanuela Formaggio, Dipartimento di Neuroscienze, Università degli Studi di Padova
Alice Berardo, Dipartimento di Ingegneria Civile, Edile e Ambientale, Università degli Studi di Padova
Monica Dettin, Dipartimento di Ingegneria Industriale, Università degli Studi di Padova
Michele Schiavon, Dipartimento di Ingegneria dell'Informazione, Università degli Studi di Padova

Abstracts and contributions

Simone Del Favero, Dipartimento di Ingegneria dell'Informazione, Università degli Studi di Padova
Manfredo Atzori, Dipartimento di Neuroscienze, Università degli Studi di Padova
Alessandro Gandin, Dipartimento di Ingegneria Industriale, Università degli Studi di Padova
Camillo Porcaro, Dipartimento di Neuroscienze, Università degli Studi di Padova
Silvia Todros, Dipartimento di Ingegneria Industriale, Università degli Studi di Padova

Publicity, web and social media

Andrea Facchinetti, Dipartimento di Ingegneria dell'Informazione, Università degli Studi di Padova
Giacomo Baruzzo, Dipartimento di Ingegneria dell'Informazione, Università degli Studi di Padova
Marco Castellaro, Dipartimento di Ingegneria dell'Informazione, Università degli Studi di Padova
Maria Rubega, Dipartimento di Neuroscienze, Università degli Studi di Padova
Roberto Visentin, Dipartimento di Ingegneria dell'Informazione, Università degli Studi di Padova

Coordination

Alessandra Bertoldo, Dipartimento di Ingegneria dell'Informazione, Università degli Studi di Padova
Giovanna Brusatin, Dipartimento di Ingegneria Industriale, Università degli Studi di Padova
Piero Pavan, Dipartimento di Ingegneria Industriale, Università degli Studi di Padova
Giovanni Sparacino, Dipartimento di Ingegneria dell'Informazione, Università degli Studi di Padova

Scientific Committee

Track 1 - E-health and Clinical Engineering

Miloš Ajčević, Università degli Studi di Trieste
Sergio Casciaro, Consiglio Nazionale delle Ricerche
Danilo Pani, Università degli Studi di Cagliari
Pierangelo Veltri, Università della Calabria

Track 2 - Physiological and Neural System Modelling

Leonardo Bocchi, Università degli Studi di Firenze
Cristiano Cuppini, Alma Mater Studiorum - Università di Bologna
Chiara Dalla Man, Università degli Studi di Padova
Alessandra Sciutti, Istituto Italiano di Tecnologia

Track 3 - Biomechanics and prosthetics
Maria Cristina Bisi, Alma Mater Studiorum - Università di Bologna
Emanuele Luigi Carniel, Università degli Studi di Padova
Michele Conti, Università degli Studi di Pavia
Luigi La Barbera, Politecnico di Milano
Giuseppe Vannozzi, Università degli Studi di Roma "Foro Italico"
Track 4 - Biomaterials, Cell & Tissue Engineering, Biofabrication
Irene Carmagnola, Politecnico di Torino
Carmelo De Maria, Università di Pisa
Silvia Farè, Politecnico di Milano
Laura Pastorino, Università degli Studi di Genova
Marco Rasponi, Politecnico di Milano
Leonardo Ricotti, Scuola Superiore Sant'Anna
Chiara Tonda Turo, Politecnico di Torino
Enza Torino, Università degli Studi di Napoli Federico II
Francesco Urciuolo, Università degli Studi di Napoli Federico II
Track 5 - Biomedical Signal and Image Processing
Emilia Ambrosini, Politecnico di Milano
Gabriele Arnulfo, Università degli Studi di Genova
Laura Astolfi, Sapienza Università di Roma
Laura Burattini, Politecnica delle Marche
Cristiano De Marchis, Università degli Studi di Messina
Luca Faes, Università di Palermo
Manuela Ferrario, Politecnico di Milano
Alberto Greco, Università di Pisa
Giulia Matrone, Università degli Studi di Pavia
Kristen Meiburger, Politecnico di Torino
Micaela Morettini, Università Politecnica delle Marche
Giandomenico Nollo, Università di Trento
Mario Sansone, Università degli Studi di Napoli Federico II
Roberto Sassi, Università degli Studi di Milano
Silvia Francesca Storti, Università di Verona
Track 6 - Neural Engineering and Micro and Nano-technologies
Alfonso Gautieri, Politecnico di Milano
Alberto Mazzoni, Scuola Superiore Sant'Anna
Marta Parazzini, Consiglio Nazionale delle Ricerche
Track 7 - Biorobotics, rehabilitation & Assistive Technologies
Andrea Canessa, Università degli Studi di Genova
Gastone Ciuti, Scuola Superiore Sant'Anna
Francesca Cordella, Università Campus Bio-Medico di Roma
Taian Martins, Politecnico di Torino
Track 8 - Design and Validation of Biomedical Devices
Giovanni Calcagnini, Istituto Superiore di Sanità
Gianni Pedrizzetti, Università degli Studi di Trieste
Mara Terzini, Politecnico di Torino
Tommaso Villa, Politecnico di Milano

DAY 1

Podium session

Track 1 - E-health and Clinical Engineering

Health Information Technology Adverse Events Identification and Classification with Natural Language Processing and Deep Learning
Alessio Luschi, Paolo Nesi and Ernesto Iadanza

Dynamic Bayesian Networks and Transfer Learning Enable the Development of Deep Sequence-Based Models on Small-Sample Data
Enrico Longato, Erica Tavazzi, Adriano Chiò, Giovanni Sparacino and Barbara Di Camillo

EyeLab: a user-friendly Matlab tool for real-time monitoring of eye movements
Giulia Olla, Giulia Sedda, Annalisa Bonfiglio, Sebastiano Traccis and Danilo Pani

Track 2 - Physiological and Neural System Modelling

Multi-Input Multi-Output Model Predictive Control for Drugs Delivery in Clinical Anesthesia
Eleonora Manzoni, Jacopo Pavan, Mirco Rampazzo and Simone Del Favero

Non-linear analysis of HRV reveal lower signal complexity in patients with a prolonged Disorder of Consciousness
Piergiuseppe Liuzzi, Bahia Hakiki, Antonello Grippo, Francesca Cecchi and Andrea Mannini

Track 9 - Bioinformatics and Synthetic Biology

Study and characterization of bile acid biosensors in engineered probiotic bacteria
Daniele Pastorelli, Debora Dallera, Emanuele Persico, Massimo Bellato, Gabriella Cusella Maria, Lorenzo Pasotti and Paolo Magni

Modeling metabolic overload effects in bacterial growth rate in synthetic biology
Elisa Gaetan, Chiara Cimolato, Luca Schenato and Massimo Bellato

The long story of SWIM methodology: from grapevine to personalised medicine
Paola Paci

Poster session 1

Track 1 - E-health and Clinical Engineering

Wearable-based Sit-to-Stand transfers in Older Adults: context differences between in-lab and home-based assessments
Jose Albites-Sanabria, Pierpaolo Palumbo, Jorunn L. Helbostad, Luca Palmerini and Lorenzo Chiari

A novel tool for the annotation of bipolar electrograms for cardiac electrophysiology
Marco Orrù, Elisa Pitzalis, Giulia Baldazzi, Graziana Viola and Danilo Pani

Design and Evaluation of an Intuitive Administration Dashboard for a Platform used to Monitor Clinical Trials
Luca Cossu, Lorenzo Carlo Causin, Andrea Facchinetti and Giacomo Cappon

Automatic extraction of acoustic features to predict Alzheimer's disease among English-speaking subjects
Chiara Giangregorio, Emilia Ambrosini and Simona Ferrante

Development of an Integrated Software System for Medical Equipment Management: the experience of the Spedali Civili Hospital
Paola Picozzi, Gian Luca Viganò, Matteo Verga, Martina Capuzzo, Claudia Duri, Lucia Maria Ignoti, Sara De Paola and Veronica Cimolin

A tool to perform semi-supervised anomaly detection and annotation on 15 lead ECG signals
Ugo Lomoio, Patrizia Vizza, Raffaele Giancotti, Giuseppe Tradigo, Salvatore Petrolo, Sergio Flesca, Pietro Hiram Guzzi and Pierangelo Veltri

Identifying Extreme Profiles in Amyotrophic Lateral Sclerosis Patients at Diagnosis through Archetypal Analysis
Isotta Trescato, Erica Tavazzi, Martina Vettoretti, Rosario Vasta, Adriano Chiò and Barbara Di Camillo

Assessing Personal Exposure to Airborne Particulate Matter with Wearable Sensors and Ventilation Rate Models
Michele Atzeni, Caterina Grisi, Giacomo Cappon and Martina Vettoretti

Key points to design the MDs Library of a National implant Registry: lesson learned from the Italian experience
Simona Pascucci, Michela Franzò, Veronica Mari, Alessia Biondi, Stefania Ceccarelli, Fabiano Bini, Franco Marinozzi, Enrico Ciminello, Paola Ciccarelli, Paola Laricchiuta, Eugenio Carrani and Marina Torre

Improving data quality in healthcare: medical informatics tools and standards
Mauro Giacomini, Sara Mora, Elena Lazarova, Norbert Maggi and Carmelina Ruggiero

Commercial Smart Virtual Assistants to support medication adherence in chronic patients: a preliminary usability study
Emanuele Tauro, Enrico Gianluca Caiani, Giacomo Galuzzi, Margot Mazziotti, Fosco Cancelliere and Grzegorz Bilo

Prediction of Atrial Fibrillation using Deep Learning techniques
Francesco Goretti, Alberto Vassia Marzullo, Massimo Milli and Ernesto Iadanza

3D upper limbs tracking through inertial sensors: calibration, methodology, and validation
Elena Bardi, Carola Butera, Luca Pozzi, Marta Gandolla, Francesco Braghin and Emilia Ambrosini

Manual and automatic identification of ACMG evidence in scientific papers
Francesca Longhin, Alessandro Guazzo, Enrico Longato, Diego Boscarino, Dino Paladin, Nicola Ferro and Barbara Di Camillo

Development of predictive models for short-term prediction of disability progression in multiple sclerosis
Erica Tavazzi, Davide Albertini and Martina Vettoretti

A Distributed Multi-Centric Application for the Analysis of Cardiac Biomarkers
Nicola Cortese, Anna Procopio, Salvatore De Rosa, Giovanni Canino, Alessio Merola, Jolanda Sabatino, Claudia Critelli, Ciro Indolfi, Francesco Amato and Carlo Cosentino

Quantifying the contribution of single joint kinematics to the overall ergonomic discomfort
Emilia Scalona, Doriana De Marco, Gianluca Rossetto, Martina Mosso, Pietro Avanzini, Maddalena Fabbri-Destro, Giuseppe Andreoni and Nicola Francesco Lopomo

Co-design of a points-based reward system to boost motivation in children and improve adherence to learning serious games
Chiara Piazzalunga, Alice Donati and Simona Ferrante

Risk management in a medical device software: evaluation of the usability characteristics of a 3D viewer for reporting
Alessio Luschi, Laura Gatti, Eleonora Tiribilli, Elena Denisova, Leonardo Manetti, Leonardo Bocchi and Ernesto Iadanza

Track 2 - Physiological and Neural System Modelling

A computational platform to assess the metabolic-electrophysiological behaviour of neurons cultured in monolayers
Rachele Fabbri, Arti Ahluwalia and Chiara Magliaro

Full-scale point-neuron model of the mouse hippocampal microcircuits
Giulia Maria Boiani, Sergio Solinas, Giacomo Preti, Aurora Manini, Michele Migliore, Jonathan Mapelli and Daniela Gandolfi

A neural model of sensory interactions in young neurotypical and ASD children
Melissa Monti, Sophie Molholm and Cristiano Cuppini

Functional Connectivity of the EEG in epilepsy: a single case study
Giovanni Chiarion and Luca Mesin

The prediction of the patient's response to hemodialysis treatment: DialysIS vs InterACTIVE-HD 2.0 experience
Carlo Balsamello, Silvio Pianca, Antonio Bellasi, Carla Colturi, Gianvincenzo Melfa, Giuseppe Rombolà, Reto Venzin, Pietro Cippà, Giustina Casagrande and Maria Laura Costantino

Smart Titration of Long-Acting Insulin in Insulin-Naïve Type 2 Diabetic Subjects
Jacopo Bonet, Roberto Visentin, Martina Vettoretti, Andrea Facchinetti and Chiara Dalla Man

Toward Implicit Communication of Object Properties for Human-Robot Interaction
Linda Lastrico, Alessandro Carfì, Francesco Rea, Fulvio Mastrogiovanni and Alessandra Sciutti

Brain-heart interaction: an ECG-fMRI integrated study in physiology and major depressive disorder
Federica Goffi, Pierluigi Reali, Adele Ferro, Viviana Pescuma, Giandomenico Schiena, Ylenia Barone, Paolo Enrico, Yvan Torrente, Fabio Triulzi, Anna Maria Bianchi, Paolo Brambilla and Eleonora Maggioni

Modelling cerebral blood flow and neuroreceptor occupancy in dopamine blocking studies
Mario Severino, Pierluigi Selvaggi, Martin Osugo, Ottavia Dipasquale, Uzma Zahid, Thomas Whitehurst, Ellis Onwordi, Ben Statton, Tiago Reis Marques, Robin Murray, Mitul Mehta, Oliver Howes and Mattia Veronese

Modeling Doxorubicin Treatment Effect in Multiple Myeloma
Daniele Andrean, Francesco Da Ros, Mario Mazzucato, Morten Gram Pedersen and Roberto Visentin

Single region contribution to the brain dynamic (in)stability
Danilo Benozzo, Giorgia Baron, Giacomo Baggio, Alessandro Gozzi, Maurizio Corbetta, Alessandro Chiuso, Sandro Zampieri and Alessandra Bertoldo

A multiscale computational approach to replicate the full-scale mouse striatum model
Alberto Antonietti, Paolla Furquim Daud and Alessandra Pedrocchi

A Comprehensive Nonlinear Mixed Effects Model of Glucose, Insulin, and C-Peptide Interaction during IVGTT
Edoardo Faggionato, Paolo Denti, Anna Largajolli, Alessandra Bertoldo and Chiara Dalla Man

Model Assessment of Doxorubicin Pharmacokinetics in Multiple Myeloma
Matteo Baldan, Francesco Da Ros, Mario Mazzucato, Morten Gram Pedersen and Roberto Visentin

Numerical simulations of the cerebrospinal flow through the Sylvius aqueduct modeled as a diffuser/nozzle pump.
Paolo Peruzzo and Francesca Maria Susin

Mathematical model of glucagon kinetics during an oral glucose tolerance test based on a dual regulation mechanism
Micaela Morettini, Agnese Piersanti, Christian Göbl, Laura Burattini and Andrea Tura

Network model accounts for evolution of EEG functional connectivity in patients with cognitive decline
Lorenzo Gaetano Amato, Alberto Arturo Vergani, Michael Lassi, Riccardo Mannella, Valentina Bessi, Antonello Grippo and Alberto Mazzoni

Noise-Induced Dynamics and Stochastic Slow Manifolds in the Bistable Xiong-Ferrell Model
Matteo Martin and Morten Gram Pedersen

From data to knowledge: definition of an exploratory dataset for deep brain stimulation
Marco Prenassi, Manuel Ellero, Annamaria Caruso and Sara Marceglia

How to assess vascular dysfunction during septic shock and resuscitation
Marta Carrara, Pietro Antenucci and Manuela Ferrario

Track 3 - Biomechanics and prosthetics

A novel artificial urinary sphincter and comparison with reference device
Maria Vittoria Mascolini, Joseph Vannel Fotso Fogang, Valentina Salomoni, Chiara Giulia Fontanella, Emanuele Luigi Carniel and Arturo Nicola Natali

A dexterous hand prosthesis based on additive manufacturing
Manfredo Atzori, Henning Müller, Alessandro Buosi, Franco Reggiani, Jacopo Lazzaro, Giosuè Alberti, Cesare Tiengo, Franco Bassetto and Nicola Petrone

Adaptation of cardiac deformation pattern during exercise in children
Dario Collia and Gianni Pedrizzetti

Development of novel computational tool to support surgical planning for the treatment of Anomalous Aortic Origin of the Coronary Arteries (AAOCA)
Serena Anglese, Mauro Lo Rito, Antonio Rosato, Valentina Ceserani, Giovanni Maria Formato, Ariel Fernando Pascaner and Michele Conti

3D Finite Element Analysis of a Percolating Cluster inside the Mineralized Collagen Fibril
Andrada Pica, Andrea Marinozzi, Franco Marinozzi and Fabiano Bini

The effect of CFR-PEEK cross-link in short fixation for the stabilisation of lumbar metastasis: an in-vitro comparative study.
Simone Borrelli, Giovanni Putame, Alberto Audenino, Andrea Ferro, Stefano Marone and Mara Terzini

Inertial measurements unit validation for countermovement jump (CMJ) tests in athletes
Federica Camuncoli, Luca Barni, Sebastiano Nutarelli, Jacopo Emanuele Rocchi, Matteo Barcillesi, Irene Di Dio, Andrea Sambruni and Manuela Galli

Advances in the development of a instrumented head surrogate for brain injury investigation
Giuseppe Zullo, Elisa Baldoin, Andrey Koptyug, Mikael Bäckström and Nicola Petrone

Towards a Wearable System for Complete Collection of Clamp Loads in Transfemoral Paralympic Sprinters
Giacomo Fabris, Mattia Scapinello, Samira Breban, Sara Barbacane, Gianluca Migliore, Andrea Cutti and Nicola Petrone

Face mobility analysis in Spinal Muscular Atrophy
Elena Pegolo, Elena Carraro, Federica Cibin, Fabiola Spolaor, Francesca Salmin, Andrea Lizio, Maria Chiara Frisoni, Stefano Becchiati, Valeria Sansone and Zimi Sawacha

Structural Simulation of Transcatheter Heart Valve in Transcatheter Heart Valve
Roberta Scuoppo, Stefano Cannata, Caterina Gandolfo and Salvatore Pasta

A Workflow for Biomechanical Simulation of Patient-specific Atherosclerotic Carotid Artery
Nicoletta Curcio, Antonio Rosato, Daniela Mazzaccaro, Michele Conti and Giulia Matrone

Experimental Analysis of the biomechanics of healthy porcine corneas
Ilaria Toniolo, Maria Vittoria Mascolini, Simona Neri, Antonella Peruffo, Anna Perazzi and Chiara Giulia Fontanella

Numerical Analysis of the Bicaval Transcatheter System for the Treatment of Severe Tricuspid Regurgitation
Fabrizio Crascì, Stefano Cannata, Caterina Gandolfo and Salvatore Pasta

Biomechanical characterization of human plantar fascia through experimental tests
Sofia Pettenuzzo, Alice Berardo, Elisa Belluzzi, Assunta Pozzuoli, Pietro Ruggieri, Emanuele Luigi Carniel and Chiara Giulia Fontanella

Static strength of lower-limb prosthetic sockets for the activities of daily living
Francesca Gariboldi, Mattia Scapinello, Nicola Petrone, Gian Luca Migliore, Gregorio Teti and Andrea Giovanni Cutti

Computational modelling of the contractile behavior of cardiomyocytes on hydrogel scaffolds for cardiac tissue regeneration
Silvia Spadoni, Silvia Todros, Michael Magnussen, Dominique Scaglioni, Anna Urciuolo, Nicola Elvassore and Piero Pavan

The biomechanical behaviour of fascial system: Superficial VS Deep Fascia
Lorenza Bonaldi, Chiara Giulia Fontanella, Carmelo Pirri, Carla Stecco and Alice Berardo

Analysis of an Elite Amputee Paralympic Sprinter in Track Running Pilot Tests
Sara Barbacane, Samira Giuliana Breban, Giacomo Fabris, Mattia Scapinello, Roberto Di Marco, Giuseppe Marcolin, Gian Luca Migliore, Andrea Giovanni Cutti and Nicola Petrone

Lumped-parameter hemodynamic model as a non-invasive tool to assess coronary blood flow in AAOCA
Valentina Ceserani, Mauro Lo Rito, Giovanni Maria Formato, Mauro Luca Agnifili, Antonio Rosato, Ariel Fernando Pascaner and Michele Conti

Comparative Analysis of Steady and Resisted Accelerated Treadmill Running of an Elite Amputee Paralympic Sprinter
Samira Giuliana Breban, Sara Barbacane, Valerio Pelusi, Roberto Di Marco, Giuseppe Marcolin, Andrea Giovanni Cutti and Nicola Petrone

Integrated Protocol for Multidimensional In Vivo Assessment of Glenohumeral Joint Function during Dynamic Tasks
Emilia Scalona, Gianluca Rossetto, Martina Mosso, Maristella Francesca Saccomanno, Giuseppe Milano and Nicola Francesco Lopomo

Motor performances evaluation of female soccer players from AC Trento Women
Giacomo Villa, Marta Galeotti, Foivos Papaioannou, Veronica Cimolin and Manuela Galli

Development of a contrast-enhanced micro tomography protocol for human meniscus: a pilot study
Chiara Falsina, Melania Maglio, Nicola Francesco Lopomo, Gianluca Giavaresi, Alberto Grassi, Stefano Zaffagnini, Massimiliano Baleani, Gregorio Marchiori and Matteo Berni

Biomechanical assessment of the anomalous coronary compression by patient-specific finite element analysis
Antonio Rosato, Mauro Lo Rito, Giovanni Maria Formato, Serena Anglese, Valentina Ceserani, Ariel Fernando Pascaner and Michele Conti

Mechanical evaluation of synthetic meshes: definition and verification of a rigorous test protocol
Vittoria Civilini, Vincenzo Giacalone, Alberto L. Audenino and Mara Terzini

An Inverse Analysis for the Assessment of Material Properties of TAVI Patients
Chiara Catalano, Stefano Cannata, Caterina Gandolfo and Salvatore Pasta

Mechanical characterization of hybrid membrane suitable for biomedical application
Roberto Gemelli, Martina Todesco, Emanuele Luigi Carniel, Gino Gerosa and Andrea Bagno

Track 9 - Bioinformatics and Synthetic Biology

Exploring heterogeneity in lymphoid malignancies from mouse to human gene expression profiles
Martina Vescio, Matteo Bulloni, Andrea Brendolan and Linda Pattini

Network-based integration of clinical, imaging and molecular biomarkers of dementia
Caterina Alfano, Lorenzo Farina and Manuela Petti

Genetic Algorithms for the identification and design of physiologically relevant 3D constructs
Flavio Fontana, Piera Mancini, Ermes Botte, Chiara Magliaro and Arti Ahluwalia

A preliminary version of a Genome-Scale Metabolic Model for Induced Human Pluripotent Stem Cells (hiPSCs)
Anna Procopio, Elvira Parrotta, Stefania Scalise, Nicola Cortese, Alessio Merola, Francesco Amato, Giovanni Cuda and Carlo Cosentino

Giving new life to seafood waste: in silico engineering of a chitinolytic LPMO enzyme
Andrea Ricci, Alfonso Gautieri, Giulia Di Rocco and Carlo Augusto Bortolotti

Oxygen metabolism in in vitro ecosystems
Ermes Botte, Piera Mancini, Chiara Magliaro and Arti Ahluwalia

A bioinformatic pipeline for identifying bacterial constitutive promoters based on transcriptomic data analysis
Debora Dallera, Stefano Quaranta, Davide De Marchi, Giovanni Cipriano, Paolo Magni and Lorenzo Pasotti

Longitudinal Relationships Between Proteomics and Beta-Cell Dysfunction in Type 2 Diabetes: An Imi Direct Study
Carlo Alberto Rossi, Ana Vinuela, Jochen M. Schwenk, Ewan R. Pearson, Andrea Mari and Roberto Bizzotto

Lipid Droplets associated genes link HSV-1 infection to neurodegeneration pathways
Veronica Zatta, Massimo Bellato, Alice Pegoraro, Giulia Bernabè, Sara Letrari, Astghik Stepanyan, Barbara Di Camillo, Paola Brun and Ignazio Castagliuolo

Simulating microbial communities' evolution via Agent base modelling: a Python tool
Massimo Bellato, Marco Cappellato, Andrea Calzavara, Alessandro Lucchiari, Sara Rebecca and Barbara Di Camillo

Automated control of bioreactors: An hardware-in-the-loop proof of concept test towards an experimental facility
Alessandro Bernardi, Massimo Bellato, Riccardo Antonello, Barbara Di Camillo, Luca Schenato and Simone Del Favero

A workflow for the construction of reproducible living biosensors built by printing bacterial materials
Francesca Usai, Giada Loi, Franca Scocozza, Massimo Bellato, Paolo Magni, Michele Conti and Lorenzo Pasotti

Uncovering quorum sensing and quenching structural properties: a systems biology approach
Chiara Cimolato, Gianluca Selvaggio, Massimo Bellato, Luca Marchetti and Luca Schenato

Bioinformatics analyses to identify molecular gene signatures associated with breast cancer phenotypes
Federica Conte, Giulia Fiscon and Paola Paci

A network-based algorithm for identifying drug repurposing opportunities for complex diseases
Giulia Fiscon, Federica Conte and Paola Paci

Day 2

Podium session

Track 3 - Biomechanics and prosthetics

Assessment of a parametric thoracic spine model for the generation of in silico cohorts
Alice Perego, Alice Pezzinga, Emilia Bellina and Luigi La Barbera

Synergy-dependent patterns of reaction forces in sit-to-stand movements
Simone Ranaldi, Leonardo Gizzi, Giacomo Severini and Cristiano De Marchis

A numerical finite element methodology of the EVAR procedure
Anna Ramella, Francesco Migliavacca, Jose Felix Rodriguez Matas, Erica Mariani, Tim J. Mandigers, Daniele Bissacco, Antonio Freyrie, Santi Trimarchi and Giulia Luraghi

Track 6 - Neural Engineering and Micro and Nano-technologies

Coupled Hydrodynamic Flow Focusing to design Lipid-Polymer NPs (LiPoNs) for theranostics
Felicia Roffo, Alfonso Maria Ponsiglione, Paolo Antonio Netti and Enza Torino

Development of a microfluidic system for impedance-based cell sorting
Cristian Brandi, Sergio Spanò, Gian Carlo Cardarilli, Enrico Verona, Luca Businaro, Paolo Bisegna, Adele De Ninno and Federica Caselli

Magnetoelectric nanoparticles as promising tools for motor nerve stimulation
Valentina Galletta, Emma Chiaramello, Serena Fiocchi, Alessandra Marrella, Giulia Suarato, Marta Bonato, Marta Parazzini and Paolo Ravazzani

Track 8 - Design and Validation of Biomedical Devices

Reducing bone plates standard fatigue test time with an analytical runout load prediction
Federico Bologna, Alberto Audenino and Mara Terzini

Zwitterionic coatings for an implantable artificial pancreas
Erika Roventini, Giulia Ballardini, Aliria Poliziani, Lorenzo Arrico and Leonardo Ricotti

Track 5 - Biomedical Signal and Image Processing

Development of a novel surface-based approach to quantify fNIRS-fMRI spatial correspondence
Augusto Bonilauri, Alice Pirastru, Francesca Sangiuliano Intra, Sara Isernia, Marta Cazzoli, Valeria Blasi, Giuseppe Baselli and Francesca Baglio

Discriminatory power of Global Longitudinal Strain and Left Ventricular Ejection Fraction for Identification of Dilated Cardiomyopathy
Katerina Iscra, Aleksander Miladinovic, Milos Ajcevic, Laura Munaretto, Jacopo Giulio Rizzi, Marco Merlo and Agostino Accardo

Autonomic response to virtual reality in oncological patients in real-world context
Serena Moscato, Silvia Orlandi, Andrea Giannelli, Rita Ostan, Silvia Varani and Lorenzo Chiari

Supervised Learning-based Detection of Pressure-induced Failures in Continuous Glucose Sensors
Elena Idi, Eleonora Manzoni, Andrea Facchinetti, Giovanni Sparacino and Simone Del Favero

Quantitative validation of an automatic videoPPG technique during autonomic elicitations
Andrea Costanzo Palmisciano, Maximiliano Mollura, Riccardo Barbieri and Luca Mainardi

Assessment of cerebral autoregulation in patients undergoing anaesthesia with propofol: a comparison among spontaneous variability methods
Roberta Saputo, Laura Sparacino, Riccardo Pernice, Francesca Gelpi, Vlasta Bari, Alberto Porta and Luca Faes

Early stages of cognitive decline are characterized by different EEG microstates dynamics
Michael Lassi, Carlo Fabbiani, Salvatore Mazzeo, Rachele Burali, Alberto Arturo Vergani, Giulia Giacomucci, Valentina Moschini, Filippo Emiliani, Maenia Scarpino, Silvia Bagnoli, Assunta Ingannato, Benedetta Nacmias, Sonia Padiglioni, Silvestro Micera, Sandro Sorbi, Antonello Grippo, Valentina Bessi and Alberto Mazzoni

Hessian-based neck tracing of dendritic spines: a preliminary study on confocal images
Ester Bruno, Simone Cauzzo, Alejandro Callara, Arti Ahluwalia, Chiara Magliaro and Nicola Vanello

Quality enhancement of dermatological images using GANs: a proof of concept
Francesco Branciforti, Kristen Meiburger, Elisa Zavattaro, Federica Veronese, Vanessa Tarantino, Paola Savoia and Massimo Salvi

Poster session

Track 5 - Biomedical Signal and Image Processing

Associations between fatigue and functional connectivity of dopamine and noradrenaline circuits in Parkinson's disease
Manuela Moretto, Ilaria Di Vico, Agnese Tamanti, Giovanni Tomelleri, Daniel Martins, Ottavia Dipasquale, Mattia Veronese, Alessandra Bertoldo, Sarah Ottaviani, Francesca Benedetta Pizzini, Michele Tinazzi and Marco Castellaro

Breast Cancer Detection via Two-dimensional Ultrasound Tomography
Stefano Franceschini, Michele Ambrosanio, Maria Maddalena Autorino, Vito Pascazio and Fabio Baselice

Computer Vision and Deep Learning for Human Motion Analysis
Matteo Moro, Vito Paolo Pastore, Giorgia Marchesi, Luca Garello, Chiara Tacchino, Paolo Moretti, Matilde Inglese, Francesca Odone and Maura Casadio

fMRI characterization of intrinsic brain networks relevant for motor control with and without visual feedback by fractal dimension
Camilla Sala, Camillo Porcaro, Stephen D. Mayhew and Andrew Bagshaw

Radiofrequency Echographic Multi Spectromery for Fragility Fracture prediction through Fragility Score
Fiorella Anna Lombardi, Paola Pisani, Alessandra Natale, Ernesto Casciaro, Fabiola Rosa Contaldo, Roberto Franchini, Maurizio Muratore, Francesco Conversano and Sergio Casciaro

Towards 3D Virtual Histology of melanoma tissue by means of lab-based X-ray Phase Contrast Computed Micro-Tomography
Giulia Saccomano, Francesco Brun, Diego Dreossi, Giuliana Tromba, Luca Brombal and Maurizio Pinamonti

Comparison of autonomic signals between healthy subjects and chronic low back pain patients at rest and during noxious stimulation
Serena Moscato, Wenchao Zhu, Yikang Guo, Sagar Kamarthi, Carin Ann Colebaugh, Kristin L. Schreiber, Robert Randolph Edwards, Richard D. Urman, Yan Xiao, Lorenzo Chiari and Yingzi Lin

XGBoost vs. TabPFN in Neuroimaging Machine Learning-based analysis
Alessandro Pasquale De Rosa, Alessandro d'Ambrosio, Chiara Marzi, Mario Cirillo, Alvino Bisecco, Manuela Altieri, Stefano Diciotti, Maria Assunta Rocca, Nicola De Stefano, Patrizia Pantano, Massimo Filippi, Gioacchino Tedeschi, Antonio Gallo and Fabrizio Esposito

Effect of EDA-driven sympathetic responses on the central processing of faces cued by hedonic odors: a preliminary ERP study
Gianluca Rho, Alejandro Luis Callara, Cinzia Cecchetto, Roberto Garofalo, Tommaso Lomonaco, Enzo Pasquale Scilingo and Alberto Greco

Comparative analysis of EMG-based classifiers for recognizing hand/wrist gestures and forces
Roberto Billardello, Francesca Cordella, Francesca Leone, Federico Mereu, Emanuele Gruppioni and Loredana Zollo

Osteoporosis Identification at Lumbar Vertebrae through a Neural Network Classifier
Manuel Maggio, Tommaso De Marco, Francesco Conversano, Giulia Macchia, Ivan Primitivo, Fiorella Lombardi, Paola Pisani and Sergio Casciaro

Cardiotocography in antenatal fetal monitoring of diabetes-complicated pregnancies
Giulio Steyde, Edoardo Spairani, Beniamino Daniele, Giovanni Magenes and Maria Gabriella Signorini

Control Theory Measures for Dynamic Analyses of Human Functional Connectome Data
Simone Papallo, Ester Riccio, Alessandro Pasquale De Rosa, Mario Cirillo, Francesco Amato, Mario Sansone and Fabrizio Esposito

EEG-based quantitative measures to support the clinical diagnosis of disorders of consciousness
Ilaria Quattrociocchi, Donatella Mattia, Angela Riccio, Mariagrazia D'Ippolito, Marta Aloisi, Rita Formisano and Jlenia Toppi

A Novel Authentication System Based on Hand Gesture Ultrasound Signatures
Stefano Franceschini, Maria Maddalena Autorino, Michele Ambrosanio, Vito Pascazio and Fabio Baselice

A comparative study of Super-Resolution methods in fetal MRI
Tommaso Ciceri, Letizia Squarcina, Adele Ferro, Florian Montano, Alessandra Bertoldo, Nicola Persico, Simona Boito, Fabio Triulzi, Giorgio Conte, Paolo Brambilla and Denis Peruzzo

Brugada Syndrome: Characterization of QT Interval Components and Correction
Agnese Sbrollini, Sofia Romagnoli, Emanuela Teresina Locati, Micaela Morettini and Laura Burattini

Interhemispheric functional connectivity: an fMRI study in two split-brain patients
Ilaria Marcantoni, Giusi Piccolantonio, Elena Vitti, Gabriele Polonara, Mojgan Ghoushi, Marco Valenti, Luca Reversi, Nicoletta Foschi, Simona Lattanzi, Laura Burattini and Mara Fabri

A convolutional neural network to identify osteoporosis from femoral echographic scans: a preliminary study
Antonio Colucci, Giusy Peluso, Fiorella Anna Lombardi, Mauro Bellone, Francesco Conversano, Roberto Franchini, Paola Pisani, Italo Epicoco, Massimo Cafaro and Sergio Casciaro

Comparison of Machine Learning Approaches for Physiological States Classification Using Heart Rate and Pulse Rate Variability Indices
Marta Iovino, Michal Javorka, Luca Faes and Riccardo Pernice

Bayesian Surprise from a Deep Learning Model of Italian Language to Model Neural Activity
Andrea Gerardo Russo, Assunta Ciarlo, Francesco Di Salle, Mario Sansone, Gioacchino Tedeschi and Fabrizio Esposito

The role of hemodynamics in arteriovenous fistula remodelling and failure. A CFD longitudinal study
Luca Soliveri, Michela Bozzetto, Paolo Brambilla, Anna Caroli and Andrea Remuzzi

Abnormal Ventricular Potentials Identification Using a Siamese Neural Network
Andrea Pitzus, Giulia Baldazzi, Graziana Viola, Luigi Raffo and Danilo Pani

Evaluation of breast density variability between right and left breasts
Francesca Angelone, Alfonso Maria Ponsiglione, Maria Paola Belfiore, Gianluca Gatta, Roberto Grassi, Francesco Amato and Mario Sansone

Estimating the degree of Non-Alcoholic Fatty Live Disease (NAFLD) from ultrasound images: preliminary results
Simone Kresevic, Milos Ajcevic, Mauro Giuffrè, Pierpaolo Pupa, Carlo Moretto, Simone Pennini, Lory Saveria Crocè and Agostino Accardo

Soft-tissue alterations identified with a CNN trained with simulated ultrasound images integrating expert knowledge
Luigi Antelmi, Antonio Colucci, Fiorella Anna Lombardi, Alessia Centonze, Tommaso De Marco, Francesco Conversano, Paola Pisani and Sergio Casciaro

Exploring the potential of MCVAE for patients stratification and skewed data compensation across the AD continuum
Federica Cruciani, Ettore Cinquetti, Lorenza Brusini, Anonino Aparo, Carlo Combi, Ilaria Boscolo Galazzo and Gloria Menegaz

A deep learning network from downsampled diffusion-weighted MRI k-space to image-space
Marta Gaviraghi, Baris Kanber, Antonio Ricciardi, Fulvia Palesi, Francesco Grussu, Carmen Tur, Alberto Calvi, Rebecca Samson and Claudia Angela Michela Gandini Wheeler-Kingshott

Distinguishing lymph nodes in head and neck cancer patients using MRI-based radiomics
Jiaying Liu, Anna Corti, Giuseppina Calareso, Valentina Corino and Luca Mainardi

A deep learning approach for the analysis of voxel composition in magnetic resonance imaging
Maria Maddalena Autorino, Stefano Franceschini, Michele Ambrosanio, Fabio Baselice and Vito Pascazio

Association between inflammation and brain microstructure in First Episode Psychosis investigated with DTI
Letizia Squarcina, Giuseppe Delvecchio, Matilde Pavan, Cinzia Perlini, Marcella Bellani, Antonio Lasalvia, Annamaria Finardi, Mirella Ruggeri, Roberto Furlan and Paolo Brambilla

Analysis of muscular activity of a cashier during different modalities of human robot collaboration
Giovanni Corvini, Silvia Conforto, Simone Ranaldi, Maurizio Schmid and Daniele Bibbo

Machine learning-based classification of cortical response to visual stimuli recorded with an ECoG array in mice: a case study
Daniela De Luca, Sara Moccia, Raffaele Mazziotti, Leonardo Lupori, Tommaso Pizzorusso and Silvestro Micera

Effects of State Representation on a Reinforcement Learning Based Decision Support System
Cristian Drudi, Maximiliano Mollura and Riccardo Barbieri

Driver drowsiness detection relying on infrared thermal imaging: a machine learning approach
Daniela Cardone, David Perpetuini, Michele Tritto, Sergio Nocco, Alessandro Tiberio and Arcangelo Merla

Decoding Emotions through Music: A Physiological Analysis of Emotion Recognition
Edoardo Maria Polo, Maximiliano Mollura, Alessia Paglialonga and Riccardo Barbieri

Assessing Multisite PET Neuroimaging Harmonisation for Normative Modelling
Alessio Giacomel, Daniel Martins, Giovanna Nordio, Rubaida Easmin, Oliver Howes, Steven C.R. Williams, Federico Turkheimer, Marius de Groot, Ottavia Dipasquale and Mattia Veronese

A Multiparameter Statistical Approach for Cardiotocographic Signals Analysis
Alfonso Maria Ponsiglione, Annarita Tedesco, Noemi Pisani, Leandro Donisi, Carlo Ricciardi, Maria Romano and Francesco Amato

Disclosing brain functional connections with multi-dimensional approaches
Laura Marzetti, Alessio Basti, Roberto Guidotti, Guido Nolte and Vittorio Pizzella

Enhancing Safety in Industry 4.0: The Use of Passive Brain Computer Interfaces for Vigilance Monitoring
Ettore Cinquetti, Ilaria Siviero, Silvia Francesca Storti and Gloria Menegaz

Optimization of a cardiac tissue segmentation pipeline in murine whole-heart reconstructions
Francesco Giardini, Eleonora Barcali, Martino De Santis, Benedetta Olmi, Erica Lazzeri, Cosimo Nardi and Leonardo Bocchi

Combining high-density electromyography and ultrafast ultrasound to assess individual motor unit properties in vivo
Marco Carbonaro, Robin Rohlén, Silvia Seoni, Kristen Meiburger, Taian Vieira, Christer Grönlund and Alberto Botter

Tensor-based morphometry of T1 weighted brain images reveals subtle volume enlargement of temporalis muscles
Assunta Ciarlo, Andrea G. Russo, Andrea Viggiano, Carmine Secondulfo, Francesco Di Salle, Fabrizio Esposito and Antonietta Canna

Pseudo resting-state investigation from task-evoked functional MRI signals
Alice Giubergia, Sara Mascheretti, Valentina Lampis, Tommaso Ciceri, Francesca Maccarone, Martina Villa, Chiara Andreola, Filippo Arrigoni, Alessandra Bertoldo and Denis Peruzzo

Phase synchronization between breathing and ppg signals in sleep events recordings of adult subjects
Alberto Morelli, Leonardo Bocchi and Piergiorgio Francia

Impact of diffusion connectivity metrics on white matter abnormalities in glioma
Maria Colpo, Erica Silvestri, Umberto Villani, Mariagiulia Anglani, Diego Cecchin, Maurizio Corbetta and Alessandra Bertoldo

Millimeter-Waves Imaging for Breast Cancer Detection: Development of Analytical Models
Simona Di Meo, Giulia Bertuzzi, Giulia Matrone, Giovanni Magenes and Marco Pasian

mmWave Radars Data Processing for Gait Parameters Extraction
Antonio Nocera, Federica Verdini, Sandro Fioretti, Gianluca Ciattaglia, Michela Raimondi, Laura Burattini, Linda Senigagliesi and Ennio Gambi

Synthesis of ultrasound images from semantic labels with controllable texture features
Francesco Marzola, Nens van Alfen, Massimo Salvi, Jonne Doorduin and Kristen Meiburger

Myelin quantification in Magnetic Resonance Imaging
Eleonora Lupi, Marta Gaviraghi, Simone Rancati, Fulvia Palesi, Francesco Grussu, Marco Battiston, Carmen Tur, Alberto Calvi, Sara Collorone, Antonio Ricciardi, Ferran Padros, Baris Kanber, Egidio D'Angelo, Rebecca Samson and Claudia Am Gandini Wheeler-Kingshott

Automated quantification of FDOPA PET using XNAT
Giovanna Nordio, Rubaida Easmin, Alessio Giacomel, Ottavia Dipasquale, Daniel Martins, Astrid Schiulaz, Steven Williams, Federico Turkheimer, Oliver Howes and Mattia Veronese

Experimental Microwave Imaging of Human Forearm
Michele Ambrosanio, Martina Teresa Bevacqua, Tommaso Isernia, Joe Lo Vetri and Vito Pascazio

K-medoid clustering of premotor firing patterns supports fine decoding of macaque reach-and-grasp
Elena Hilary Rondoni, Matteo Pizzinga, Francesca Lanzarini, Monica Maranesi, Davide Albertini, Luca Bonini and Alberto Mazzoni

Impact of model selection procedure on Deep Neural Networks ensemble for the Choroid Plexus segmentation in Multiple Sclerosis
Valentina Visani, Valerio Natale, Annalisa Colombi, Agnese Tamanti, Alessandra Bertoldo, Corina Marjin, Giuseppe Kenneth Ricciardi, Francesca Benedetta Pizzini, Massimiliano Calabrese and Marco Castellaro

3D moles mapping and analysis for automatic melanoma detection
Giulia Nanto, Alexa Berto, Luigi Dall'Olmo, Christian Ciolfi, Filippo Scolaro, Mauro Alaibac, Simone Mocellin, Antonio Galgaro and Fabio Scarpa

Error perception in different environments: Monitor vs Augmented Reality
Andrea Farabbi, Luigi Pizzulli, Eleonora Sala, Letizia Santini and Luca Mainardi

Time-frequency analysis of brain response to 3D slant texture and stereo cues
Francesca Peveri, Gabriele Arnulfo, Silvio Paolo Sabatini and Andrea Canessa

Breast Cancer Imaging at Microwave Frequencies via Neural Networks
Michele Ambrosanio, Stefano Franceschini, Maria Maddalena Autorino, Fabio Baselice and Vito Pascazio

On the use of PARAFAC algorithm in group network analysis: a simulation study
Andrea Ranieri, Floriana Pichiorri, Emma Colamarino, Valeria de Seta, Donatella Mattia and Jlenia Toppi

Hidden Markov Models for the identification of fetal phases in CTG recordings
Edoardo Spairani, Giulio Steyde, Beniamino Daniele, Maria Gabriella Signorini and Giovanni Magenes

P300 event-related potential in patients with cognitive decline correlates with task performance
Alberto Arturo Vergani, Carlo Fabbiani, Salvatore Mazzeo, Rachele Burali, Michael Lassi, Giulia Giacomucci, Valentina Moschini, Filippo Emiliani, Maenia Scarpino, Silvia Bagnoli, Assunta Ingannato, Benedetta Nacmias, Sonia Padiglioni, Sandro Sorbi, Antonello Grippo, Valentina Bessi and Alberto Mazzoni

Cortical correlates in upright static balance in adolescent idiopathic scoliosis
Maria Rubega, Matilde Paramento, Stefano Masiero and Emanuela Formaggio

Decoding the interplay between brain structural and functional connectivity in Alzheimer's disease
Virginia Filippi, Edoardo Paolini, Federica Cruciani, Lorenza Brusini, Francesco Dal Santo, Gloria Menegaz, Ilaria Boscolo Galazzo and Silvia Francesca Storti

Closing the loop between neurostimulation and control theory
Roberto Guidotti, Alessio Basti, Giulia Pieramico, Antea D'Andrea, Gian Luca Romani, Vittorio Pizzella and Laura Marzetti

A machine learning approach for stride speed estimation based on a head-mounted IMU
Paolo Tasca, Francesca Salis, Samanta Rosati, Gabriella Balestra and Andrea Cereatti

Differences in cortical reorganization during visuo-motor tasks executed with the dominant and non-dominant hands
Alessandra Calcagno, Stefania Coelli, Federico Temporiti, Manuela Galli, Roberto Gatti and Anna Maria Bianchi

Alteration of muscle recruitment in Parkinson's disease assessed by EMG-based occurrence frequency
Marco Romanato, Francesco Di Nardo, Fabiola Spolaor, Daniele Volpe, Sandro Fioretti and Zimi Sawacha

Altered EEG amplitude coupling correlates to cognitive dysfunction in iRBD patients
Monica Roascio, Rosella Trò, Dario Arnaldi, Francesco Famà, Pietro Mattioli, Ki-Young Jung and Gabriele Arnulfo

Validating biomedical and clinical data via an annotations based framework: experiences within the PON VQA project
Barbara Puccio, Ugo Lomoio, Raffaele Giancotti, Mattia Cannistrà, Sergio Flesca, Francesco Scala, Giuseppe Tradigo, Pietro Hiram Guzzi, Pierangelo Veltri and Patrizia Vizza

Drivers' mental workload assessment based on machine learning applied to multimodal physiological data
David Perpetuini, Daniela Cardone, Michele Tritto, Sergio Nocco, Alessandro Tiberio and Arcangelo Merla

Algorithm based on the "dynamic risk" concept allows ahead-of-time suggestion of corrective insulin boluses in type 1 diabetes therapies employing continuous glucose monitors
Elisa Pellizzari, Francesco Prendin, Giacomo Cappon, Giovanni Sparacino and Andrea Facchinetti

Assessing the impact of brain gliomas on effective connectivity gradients
Giulia Pagnin, Giorgia Baron, Erica Silvestri, Alessandro Chiuso, Diego Cecchin, Maurizio Corbetta and Alessandra Bertoldo

Assessment of the effects of parcellation and frequency band on the definition of functional hubs in rsfMRI
Giulia Vallini, Erica Silvestri, Alessandro Panciera, Marco Aiello and Alessandra Bertoldo

Radiomic analysis of Epicardial Adipose Tissue in cardiac MRI for hospitalization risk assessment
Francesca Lo Iacono, Martina Minotti, Marco Gugliemo, Marco Penso, Maria Ludovica Carerj, Gianluca Pontone and Valentina D.A. Corino

Augmented Reality to Evaluate Temporo-Mandibular Joint Alterations in Orthognathic Patients
Nicolas Emiliani, Federico Babini, Chiara Gulotta, Giovanni Badiali, Emanuela Marcelli and Laura Cercenelli

Transfer learning approaches to classify foetal occiput positions on transperineal ultrasound images
Rocco Morello, Maria Giovanna Di Trani, Andrea Dall'Asta, Francesco Conversano, Paola Pisani, Marco Di Paola, Tullio Ghi and Sergio Casciaro

The hidden structural complexity of the human cerebral cortex
Federica Giorgini, Stefano Diciotti and Chiara Marzi

Track 6 - Neural Engineering and Micro and Nano-technologies

Prediction of injectables' stability leveraging inline analysis and machine learning
Samuele Fiorenza, Paolo Antonio Netti and Enza Torino

A testbed for mechanical and thermal stimulation in studies of somatosensory functions
Marika Sperduti, Nevio Luigi Tagliamonte, Costantino Casale, Paolo Antonio Netti and Loredana Zollo

Engineering of biological entities through dynamic perturbations of lipidic membranes.
Simona Silvestri, Eugenia Romano, Paolo Antonio Netti and Enza Torino

Mechanical validation of an innovative intrafascicular neural interface to restore urinary bladder dysfunctions
Elena Aprea, Alice Giannotti, Outman Akouissi and Silvestro Micera

Development of excitatory neuronal networks derived from human induced pluripotent stem cells
Giulia Parodi, Michela Chiappalone and Sergio Martinoia

A novel microfluidic-based approach to study protein stability behavior in highly concentrated and viscous (HCV) systems
Osvaldo Bortone, Paolo A. Netti and Enza Torino

Towards personalized electroceutical therapy: electrophysiological investigations in a pre-clinical model of ischemic lesion
Marta Carè, Federico Barban, Mattia Di Florio, Rosaria Greco, Cristina Tassorelli and Michela Chiappalone

Boosted transport of Theranostic Angiopep-2 engineered crosslinked Hyaluronic Acid NanoParticles (Thera-ANG-cHANPs) in glioblastoma cells
Angela Costagliola Di Polidoro, Joost Haeck, Laura Mezzanotte, Martine Lamfers and Enza Torino

Integrated sensors for real-time monitoring of biological barriers in engineered cell culture dynamic in vitro models
Simone Perottoni, Alessandro Bonacina, Ruben Dell'Oro, Francesca Donnaloja, Lucia Boeri, Luca Magagnin, Diego Albani and Carmen Giordano

PEDOT:PSS ink-jet printed microelectrodes on paper: towards low-cost and green MEA devices
Fabio Terranova, Andrea Spanu, Annalisa Bonfiglio and Sergio Martinoia

Photosensitive pattern to control geometry and activity of a neural network
Andrea Andolfi, Pietro Arnaldi, Donatella Di Lisa, Monica Frega, Sergio Martinoia and Laura Pastorino

Exposure Assessment of Young People to Wearable Antennas at 5G frequencies
Silvia Gallucci, Martina Benini, Marta Bonato, Emma Chiaramello, Serena Fiocchi, Gabriella Tognola and Marta Parazzini

Interconnected brain regions-on-a-chip: role of connectivity and heterogeneity in the electrophysiological activity
Martina Brofiga, Francesca Callegari, Fabio Poggio, Ilaria Donati della Lunga, Letizia Cerutti, Mariateresa Tedesco and Paolo Massobrio

Comparison of RF exposure levels in 5G-V2X and ITS-5.9 GHz vehicular connectivity
Martina Benini, Marta Bonato, Silvia Gallucci, Serena Fiocchi, Emma Chiaramello, Marta Parazzini and Gabriella Tognola

Profiling of phase-amplitude couplings across sleep for personalized neuroengineering systems
Vinícius Cota, Gianluca Federici, Gabriele Arnulfo and Michela Chiappalone

Day 3

Podium session

Track 4 - Biomaterials, Cell & Tissue Engineering, Biofabrication

Peptide-functionalized chitosan sponges for bone tissue regeneration
Elena Zeni, Paola Brun, Leonardo Cassari, Giovanna Iucci, Antonio Gloria, Annj Zamuner and Monica Dettin

Innovation in neuronal cell culture: from adhesion to maturation, chitosan promotes developing nervous system
Donatella Di Lisa, Lorenzo Muzzi, Elena Dellacasa, Monica Frega, Sergio Martinoia and Laura Pastorino

Development of analytical models to predict self-folding of 4D bioprinted scaffold
Alessio Esposito, Irene Chiesa, Claudia Dell'Amico, Marco Onorati and Carmelo De Maria

Dose-controlled low-intensity pulsed ultrasound and pulsed electromagnetic fields stimulations modulate inflammation in human macrophages
Francesco Iacoponi, Fabio Orlando, Soria Gasparini, Tiziano Pratellesi, Andrea Cafarelli and Leonardo Ricotti

In vitro exposure of endothelial cells to mechanical vibrations
Elena Carrara, Sofia Poloni, Chiara Emma Campiglio, Elisa Riceputi, Michela Bozzetto and Andrea Remuzzi

Vibropolyfection: boosting polymer-mediated gene delivery by mechanical cell loading
Nina Bono, Federica Ponti, Luca Russo, Paolo Bigini, Diego Mantovani and Gabriele Candiani

Track 7 - Biorobotics, rehabilitation & Assistive Technologies

A Reliable User-Independent Motion Intent Detection from Transient EMG Data for Shoulder Joint
Mara Scattolini, Andrea Tigrini, Federica Verdini, Sandro Fioretti, Laura Burattini, Micaela Morettini and Alessandro Mengarelli

Performance Evaluation of the Gloreha Sinfonia Device in Bimanual Modality
Martina Lapresa, Emilio Maria Romano, Loredana Zollo and Francesca Cordella

Poster session

Track 4 - Biomaterials, Cell & Tissue Engineering, Biofabrication

Composite scaffolds based on polyvinyl alcohol and acellular cartilage matrix for hemophilic arthropathy treatment
Marta Confalonieri, Silvia Barbon, Elena Stocco, Veronica Macchi, Raffaele De Caro, Silvia Todros, Andrea Porzionato and Piero Giovanni Pavan

Micropatterned PDMS substrates for cellular mechanotransduction modelling
Elena Bianchi, Cecilia Crescioli, Paola De Stefano, Gabriele Dubini and Alessandro F. M. Pellegata

Cell encapsulation into silk fibroin microgels
Giovanni Perotto, Federica Ponti, Giulio Saroglia, Stefania Marcuzzo, Eleonora Giagnorio, Giuseppe Lauria Pinter, Elena Rosini, Luigi De Nardo, Athanassia Athanassiou, Gabriele Candiani and Nina Bono

Tuning the features of microphysiological systems for biomimetic intestinal in vitro models
Alessandra Maria Anna Rando, Lorenzo Pietro Coppadoro, Sabrina Nicolò, Maria Lombardi, Chiara Foglieni, Gianfranco Beniamino Fiore and Monica Soncini

Injectable gelatin-based photocurable fiber-reinforced hydrogel for the treatment of osteochondral defects
Ignazio Niosi, Lorenzo Vannozzi, Diego Trucco, Silvia Farè and Leonardo Ricotti

Green-Based Anti-Biofilm Nanoformulations Against Bacterial Contaminations In Nosocomial Environments
Giovanni Lo Bello, Roberto Raiteri, Elena Dellacasa, Orietta Monticelli, Maria Luisa Cristina and Laura Pastorino

Near Field Electrospinning Process Using a Multi-Axis Robot
Salvatore D'Alessandro, Andrada Pica, Franco Marinozzi, Fabiano Bini and Gianluca Cidonio

Biological evaluation in vitro and in vivo of hybrid membrane to assess biomedical application
Martina Todesco, Roberto Luisetto, Martina Casarin, Saima Jalil Imran, Gino Gerosa, Chiara Giulia Fontanella and Andrea Bagno

Bio-fabrication of in vitro tissues possessing organ-specific endogenous extracellular matrices
Francesco Urciuolo, Giorgia Imparato, Vincenza de Gregorio and Paolo Antonio Netti

Hydrogel-based photopolymers for 3D printing of scaffolds by bench-top stereolithography
Chiara Merli, Claudia Capitini, Martino Calamai, Gabriele Frediani, Federico Carpi and Caterina Credi

Assessment of printability on autoclaved biomaterial inks for extrusion bioprinting
Eugenia Spessot, Aurora Battistella, Antonella Motta and Devid Maniglio

Intestinal epithelium on chip for absorption studies
Alessandro Cordiale, Mattia Ballerini, Luigi Nezi, Paola Occhetta and Marco Rasponi

Effect of Chitosan coating on PLA electrospun scaffolds for bone tissue engineering
Francesco Lopresti, Vincenzo La Carrubba, Simona Campora and Giulio Ghersi

Microgels as a Biosensing Platform
Edmondo Battista, Sabrina Napoletano, Maria Isabella Maremonti, David Dannahuser, Paolo Antonio Netti and Filippo Causa

Experimental and computational pipeline for identifying oxygen metabolic rate parameters in 2D and 3D in vitro constructs
Ermes Botte, Piera Mancini, Chiara Magliaro and Arti Ahluwalia

Antibacterial activity of bacterial cellulose based wound care paste
Stefania Villani, Sanosh Kunjalukkal Padmanabhan, Mariangela Stoppa, Rossella Nisi, Antonio Licciulli, Pietro Alifano and Christian Demitri

Microfluidic system for a label-free, real-time functional assessment of thrombotic risk
Tatiana Mencarini, Eleonora Puce, Mariagrazia Calogiuri, Mariangela Scavone, Silvia Bozzi and Alberto Redaelli

In-flow viscoelastic compression to probe single-cell biomechanical properties
Maria Isabella Maremonti, David Dannhauser, Valeria Panzetta, Paolo Antonio Netti and Filippo Causa

Mesenchymal Stem Cell Response to Micropatterns and Dynamic Topographies
Chiara Cimmino, Paolo Antonio Netti and Maurizio Ventre

Cell-aware optimization of the extrusion-based bioprinting process
Amedeo Franco Bonatti, Irene Chiesa, Gabriele Maria Fortunato, Aurora De Acutis, Giovanni Vozzi and Carmelo De Maria

3D bioprinting as a tool for the early correction of leather defects in the tanning industry
Costanza Daddi, Matteo Baggiani, Matteo Nicoletta, Simone Micalizzi, Gabriele Maria Fortunato, Aurora De Acutis, Carmelo De Maria, Marco Onorati and Giovanni Vozzi

An engineered breast cancer model on chip for personalized and multiple drug therapy
Giorgia Imparato, Claudia Mazio, Francesco Urciuolo and Paolo Antonio Netti

RNA Sequencing analysis to study Duchenne dilated cardiomyopathy in patient-derived 3D organoid models
Vittoria Marini, Fabiola Marino, Flaminia Aliberti, Maurilio Sampaolesi and Yoke Chin Chai

Hydrogels scaffolds as 2D in vitro models to explore the impact of microenvironmental stiffness on lung adenocarcinoma cells
Valeria Panzetta, Crescenzo Frascogna, Claudia Mazio, Francesco Catuogno, Giorgia Imparato, Francesco Urciuolo and Paolo Antonio Netti

A microfluidic platform to unravel immune cells cross-talk in rheumatoid arthritis
Cecilia Palma, Bianca Aterini, Carlotta Catozzi, Luigi Nezi, Silvia Lopa, Teresa Manzo, Marco Rasponi and Paola Occhetta

Valve-jet technology for robotic-based in situ bioprinting applications
Elisa Batoni, Gabriele Maria Fortunato, Andrea Guerra, Giovanni Vozzi and Carmelo De Maria

Cryopreservation effects on biological tissues: histological and mechanical assessments
Martina Casarin, Martina Todesco, Chiara Giulia Fontanella, Alessandro Morlacco, Fabrizio Dal Moro and Andrea Bagno

Design and fabrication of a novel bioreactor for the engineering of tendon/ligament-to-bone interfaces
Ginevra Pegollo, Simone Micalizzi, Aurora De Acutis, Carmelo De Maria and Giovanni Vozzi

Biological validation of thiolated food grade secondary oil in water nanoemulsions with enhanced mucus-adhesion properties in Intestine-on-a-chip model
Elena Lagreca, Raffaele Vecchione, Raffaele Crispino and Paolo Antonio Netti

Design and fabrication of a micro-dialyser for the study of the gut microbiota-tissues cross-talk
Aurora De Acutis, Costanza Daddi, Francesco Biagini, Emanuele Russello, Marco Calvigioni, Emilia Ghelardi, Carmelo De Maria and Giovanni Vozzi

Natural polymer-based bioinks exploiting internal gelation mechanism for cardiac tissue engineering
Giovanni Paolo Stola, Elena Marcello, Camilla Paoletti, Letizia Nicoletti and Valeria Chiono

Design and fabrication of an intestinal phantom to mimic intestinal tone and motility
Paolo Signorello, Ludovica Cacopardo, Nicole Guazzelli, Irene Nicolai, Federica Viti, Paolo Gandullia, Robert Heuckeroth and Arti Ahluwalia

Nanostructured coatings with bacteria-triggered antimicrobial response for medical devices
Maria Antonia Cassa, Gianluca Ciardelli, Piergiorgio Gentile and Irene Carmagnola

An advanced culture system to investigate electrospun graft biomechanisms for vascular tissue engineering
Elia Pederzani, Chiara Emma Campiglio, Marta Ripamonti, Maichael Esposito, Angela Rizzo, Alice Caldiroli, Stefania Adele Riboldi, Andrea Remuzzi, Gianfranco Beniamino Fiore and Monica Soncini

3D printing of a nanomaterials-embedded gelatin/pectin hydrogel for the development of an in vitro drug testing platform
Lorenzo Guidi, Elisabetta Rosellini, Giovanni Vozzi, Luigi Lazzeri, Maria Grazia Cascone, Carmelo De Maria, Gabriele Maria Fortunato and Anna Lapomarda

Optimization of advanced setups with integrated readouts for evaluation of cardiac toxicity in a heart on chip device
Giacomo Cretti, Marco Rasponi, Roberta Visone, Udo Kraushaar and Paola Occhetta

Peptide anchoring methods for PEEK surfaces
Leonardo Cassari, Annj Zamuner, Grazia Maria Lucia Messina, Martina Marsotto, Hao-Chen Chang, Trevor Coward, Chiara Battocchio, Giovanni Marletta, Lucy Di Silvio and Monica Dettin

Design and validation of a microfluidic cartridge to prepare non-viral gene delivery complexes
Giovanni Protopapa, Nina Bono, Roberta Visone, Fabio D'Alessandro, Marco Rasponi and Gabriele Candiani

Biomimetic platform for investigating in vitro the cell biological response to mechanical stretching – periodontal ligament stem cell application
Beatrice Masante, Giovanni Putame, Andrea Tancredi Lugas, Marta Tosini, Ilaria Roato, Federico Mussano, Mara Terzini, Alberto Audenino and Diana Massai

Evaluation of the optimal pore size for 3D printed bone scaffolds in a perfusion bioreactor
Elisa Batoni, Carmelo De Maria and Giovanni Vozzi

Extrusion control strategy for robotic-based in situ bioprinting
Gabriele Maria Fortunato, Michele Molisani, Giovanni Vozzi and Carmelo De Maria

Effects of different degumming methods on the quality of sericin samples
Ivana Dragojlov, Simone Vesentini and Elisa Fasoli

Engineering the tumor environment in vitro using peptide-enriched, hyaluronic acid-based hydrogels
Annj Zamuner, Leonardo Cassari, Monica Dettin, Maria Teresa Conconi and Elisabetta Sieni

Multiscale computational models for predicting hydrogel viscoelastic properties
Nicole Guazzelli, Ludovica Cacopardo, Valentina Inghirami and Arti Ahluwalia

Engineering of poly(urethane)-based porous constructs for cardiac tissue model design
Andrea Alliaud, Monica Boffito, Rosella Laurano, Susanna Sartori and Gianluca Ciardelli

FRESH approach for the development of 3D channel network in 3D in vitro models
Matteo Pitton, Chiara Liguori and Silvia Farè

Mathematical model of nutrients transport and cell growth in a bioprinted hydrogel
Ilaria Parodi, Silvia Scaglione, Marco Massimo Fato and Rodolfo Repetto

Rapid prototyping of a microfluidic platform for nasal mucosa models
Maria Testa, Francesco Lopresti, Olga Manna, Stefano Burgio, Giorgia Intilli, Alberto Fucarino and Vincenzo La Carrubba

Track 7 - Biorobotics, rehabilitation & Assistive Technologies

Brain-Computer Interface assisted Motor Imagery training in post-stroke rehabilitation: longitudinal study of the EEG sensorimotor rhythms
Elena Mongiardini, Emma Colamarino, Floriana Pichiorri, Andrea Ranieri, Jlenia Toppi, Donatella Mattia and Febo Cincotti

A multimodal wearable system for Human Activity Recognition during daily activities
Pietro Benvenuti, Erika Rovini, Laura Fiorini and Filippo Cavallo

Effectiveness of a home-based tele-rehabilitation program for post-Covid patients: preliminary results
Serena Cerfoglio, Paolo Capodaglio, Paolo Rossi, Federica Verme, Gabriele Boldini, Viktoria Cvetkova, Manuela Galli and Veronica Cimolin

Virtual prototyping of a robotic chess player for play therapy
Mattia Pesenti, Roberto Schinelli, Alberto Antonietti, Marta Gandolla and Alessandra Pedrocchi

A hydraulic implantable artificial detrusor for controlled bladder voiding
Simone Onorati, Federica Semproni, Linda Paternò, Giada Casagrande, Veronica Iacovacci and Arianna Menciassi

Brain signals in semi-immersive and immersive VR environments: a feasibility study
Valerio Antonio Arcobelli, Kevin Marcaccini, Poula Hassaballah, Luca Tonin, Stefano Tortora and Silvia Orlandi

Wearable tactile display of softness for virtual reality
Gabriele Frediani and Federico Carpi

Computational joint action: dynamical models to understand the development of joint coordination
Cecilia De Vicariis, Laura Bandini, Vinil T. Chackochan and Vittorio Sanguineti

Fast path replanning in a dynamic environment in percutaneous cardiac interventions
Angela Peloso, Rossella Damiano, Emiliano Votta and Elena De Momi

An attention classifier for the evaluation of a robotic therapy in children with Autism Spectrum Disorder
Laura Santos, Martina Murgo, Bárbara Silva, Alice Geminiani, Arianna Caglio, Silvia Annunziata, Catarina Barata, José Santos-Victor and Alessandra Pedrocchi

A safe robot control for semi-autonomous pedicle tapping
Clemente Lauretti, Francesca Cordella, Ilenia Saltarelli and Loredana Zollo

Evaluating Spatial Hearing in Virtual Reality Environment
Fulvio Missoni and Andrea Canessa

A cloud-based mobile platform to monitor and counteract cognitive decline
Laura Bandini, Cecilia De Vicariis, Maria Cristina Novello, Carlo Chiorri and Vittorio Sanguineti

Non-linear dimensionality-reduction approach for powered wheelchair control
Elisa Misley, Fabio Rizzoglio, Amy Bellitto, Antonino Massone, Davide Russo, Giorgio Carlini, Maura Casadio and Camilla Pierella

A preliminary test of a novel method for the real time estimation of foot displacement using MIMUs attached to the foot
Ilaria Giuseppina Porco, Sergio Mauro Gavino Solinas, Aldo Lazich and Ugo Della Croce

Understanding user needs for robotics assisted cognitive and physical rehabilitation
Ludovico Ferreri, Enea Parimbelli, Irene Aprile and Silvana Quaglini

Assessment of Balance disorder and vestibular dysfunction using Mixed Reality
Simona Pascucci, Valerio Margani, Michela Franzò, Matteo Curcio, Alberto Polsinelli, Rita Talamonti, Maurizio Barbara, Franco Marinozzi and Fabiano Bini

A Safe Reinforcement Learning platform for Autonomous Robotic Tissue Approaching
Ke Fan, Giancarlo Ferrigno and Elena De Momi

Sensor-based Assessment of Gross and Fine Motor Development in Primary School Children
Maria Cristina Bisi, Alice Masini, Stefania Toselli, Sofia Marini, Laura Bragonzoni, Andrea Ceciliani, Marcello Lanari, Alessandra Sansavini, Alessia Tessari, Davide Gori, Laura Dallolio and Rita Stagni

Personality Traits Influence the Perception of a Robotic Arm endowed with Social Cues
Carlo La Viola, Laura Fiorini, Gianmaria Mancioppi and Filippo Cavallo

A motor-assisted recumbent trike for cycling training in neurological patients
Federica Ferrari, Davide Savona, Eleonora Guanziroli, Franco Molteni, Alessandra Pedrocchi and Emilia Ambrosini

An improved method for the characterization of infants' general movements using a RGB-Depth sensor and a deep neural network tracking processing tool
Diletta Balta, Ilaria Giuseppina Porco, Hsinhung Kuo, Jing Wang, Olga Morozova, Manon Schladen, Andrea Cereatti, Peter Lum and Ugo Della Croce

Track 8 - Design and Validation of Biomedical Devices

Ex Vivo Animal Evaluation of IntraValvular Impedance Sensing Applied to Biological Heart Valve Prostheses
Camilla Gironi, Laura Cercenelli, Barbara Bortolani, Nicolas Emiliani, Lorenzo Tartarini and Emanuela Marcelli

Wearable sensor for in-vivo skin hydration monitoring
Andrea Cataldo, Raissa Schiavoni, Antonio Masciullo and Christian Demitri

Establishing Computational Modeling Credibility in Patients Undergoing TAVI
Chiara Catalano, Stefano Cannata, Caterina Gandolfo and Salvatore Pasta

Mechanical Properties of Polyamide 12 for the use in Balloon-Expandable Transcatheter Heart Valves
Omar Zahalka, Chiara Catalano, Tahir Turgut, Nils Gotzen, Stefano Cannata, Caterina Gandolfo and Salvatore Pasta

Patient-specific phantom for home haemodialysis
Gabriele Maria Fortunato, Francesca Tonelli, Alberto Greco, Nicola Carbonaro, Aldo Casani and Carmelo De Maria

A response surface-based approach to predict spinal rod contouring parameters
Francesca Berti, Linda Carpenedo, Camilla Boldrin and Luigi La Barbera

Highly controlled ultrasound-mediated drug delivery experiments: an in vitro set-up
Sofia Sirolli, Leonardo Ricotti and Andrea Cafarelli

Exposure set-up for assessing the far-field electromagnetic immunity levels of active implantable medical devices
Cecilia Vivarelli, Rosaria Falsaperla, Giancarlo Burriesci, Federica Censi, Giovanni Calcagnini and Eugenio Mattei

Temperature influence on reflectance photometers for bilirubin measurement
Lorenzo Zucchini, Milos Ajcevic and Agostino Accardo

Combination of VR and manikins to improve medical training
Mara Coduri, Andrea Calandrino, Giulia Addiego Mobilio, Elisa Grasso, Matteo Pescio, Paolo Rossi, Giorgio Carlini, Marco Chirico, Fabio Solari, Manuela Chessa, Maura Casadio and Serena Ricci

Usability of a multi-sensor array for the application of electro-phonocardiography in home care
Noemi Giordano, Gabriella Balestra, Samanta Rosati and Marco Knaflitz

Physiologically relevant in vitro experiments: degradation kinetics of a pool of enzymes
Cristina Oldani, Nina Bono, Alice Caldiroli, Stefania Adele Riboldi and Gabriele Candiani

Multiscale Modelling of Platelet Activation in Membrane Oxygenation Systems
Marta Baccarella and Salvatore Pasta

Engineering a smart intrauterine device based on pH-controlled copper release.
Greta Bertola, Ludovica Cacopardo, Florinda Coro, Carmelo De Maria and Arti Ahluwalia

Circulating tumour cells deformability measurement in microfluidics
Maria Isabella Maremonti, David Dannhauser, Paolo Antonio Netti and Filippo Causa

Open-source as an enabling approach for the introduction of artificial intelligence in healthcare
Florinda Coro, Amedeo Franco Bonatti, Gabriele Maria Fortunato, Ilenia Gulino, Lucia Arcarisi, Maria Elena Lippi, Valentina Calderai, Gionatan Gallo, Maurizio Palmieri, Pietro Ducange, Cinzia Bernardeschi, Gabriele Tomei, Paolo De Simone, Arti Devi Ahluwalia and Carmelo De Maria

A method for the evaluation of cervical surgical instrumentation reliability through a computational and experimental approach
Luca Ciriello, Alessandro Belluzzo, Andrea Grassi and Tomaso Villa

Microfluidic platform for cell classification from optical signatures via machine learning
David Dannhauser, Maria Isabella Maremonti, Paolo Antonio Netti and Filippo Causa

Remote In-Bed Monitoring of Vital Signs Using Radar Technology
Marco Mercuri, Ilde Lorato, Tom Torfs and Felice Crupi

A novel concept of steerable catheters actuated by muscle cells: the BioMeld project
Carlotta Salvatori, Leonardo Ricotti and Lorenzo Vannozzi

Development of a computational model to estimate the hemolysis risk associated with hemodialysis catheters
Ilaria Guidetti, Francesco De Gaetano, Diego Gallo, Umberto Morbiducci and Maria Laura Costantino

Author Index

Accardo Agostino	Discriminatory power of Global Longitudinal Strain and Left Ventricular Ejection Fraction for Identification of Dilated Cardiomyopathy
–	Estimating the degree of Non-Alcoholic Fatty Live Disease (NAFLD) from ultrasound images: preliminary results
–	Temperature influence on reflectance photometers for bilirubin measurement
Agnifili Mauro Luca	Lumped-parameter hemodynamic model as a non-invasive tool to assess coronary blood flow in AAOCA
Ahluwalia Arti Devi	A computational platform to assess the metabolic-electrophysiological behaviour of neurons cultured in monolayers
–	Design and fabrication of an intestinal phantom to mimic intestinal tone and motility
–	Early stages of cognitive decline are characterized by different EEG microstates dynamics
–	Engineering a smart intrauterine device based on pH-controlled copper release.
–	Experimental and computational pipeline for identifying oxygen metabolic rate parameters in 2D and 3D in vitro constructs
–	Genetic Algorithms for the identification and design of physiologically relevant 3D constructs
–	Multiscale computational models for predicting hydrogel viscoelastic properties
–	Open-source as an enabling approach for the introduction of artificial intelligence in healthcare
–	Oxygen metabolism in in vitro ecosystems
Aiello Marco	Assessment of the effects of parcellation and frequency band on the definition of functional hubs in rsfMRI
Ajcevic Milos	Discriminatory power of Global Longitudinal Strain and Left Ventricular Ejection Fraction for Identification of Dilated Cardiomyopathy
–	Estimating the degree of Non-Alcoholic Fatty Live Disease (NAFLD) from ultrasound images: preliminary results
–	Temperature influence on reflectance photometers for bilirubin measurement
Akouissi Outman	Mechanical validation of an innovative intrafascicular neural interface to restore urinary bladder dysfunctions
Alaibac Mauro	3D moles mapping and analysis for automatic melanoma detection
Albani Diego	Integrated sensors for real-time monitoring of biological barriers in engineered cell culture dynamic in vitro models
Alberti Giosuè	A dexterous hand prosthesis based on additive manufacturing
Albertini Davide	Development of predictive models for short-term prediction of disability progression in multiple sclerosis
–	K-medoid clustering of premotor firing patterns supports fine decoding of macaque reach-and-grasp
Albites-Sanabria Jose	Wearable-based Sit-to-Stand transfers in Older Adults: context differences between in-lab and home-based assessments
Alfano Caterina	Network-based integration of clinical, imaging and molecular biomarkers of dementia

Aliberti Flaminia	RNA Sequencing analysis to study Duchenne dilated cardiomyopathy in patient-derived 3D organoid models
Alifano Pietro	Antibacterial activity of bacterial cellulose based wound care paste
Alliaud Andrea	Engineering of poly(urethane)-based porous constructs for cardiac tissue model design
Aloisi Marta	EEG-based quantitative measures to support the clinical diagnosis of disorders of consciousness
Altieri Manuela	XGBoost vs. TabPFN in Neuroimaging Machine Learning-based analysis
Amato Francesco	A Distributed Multi-Centric Application for the Analysis of Cardiac Biomarkers
–	A Multiparameter Statistical Approach for Cardiotocographic Signals Analysis
–	A preliminary version of a Genome-Scale Metabolic Model for Induced Human Pluripotent Stem Cells (hiPSCs)
–	Control Theory Measures for Dynamic Analyses of Human Functional Connectome Data
–	Evaluation of breast density variability between right and left breasts
Amato Lorenzo Gaetano	Network model accounts for evolution of EEG functional connectivity in patients with cognitive decline
Ambrosanio Michele	A Novel Authentication System Based on Hand Gesture Ultrasound Signatures
–	Breast Cancer Detection via Two-dimensional Ultrasound Tomography
–	Breast Cancer Imaging at Microwave Frequencies via Neural Networks
–	Experimental Microwave Imaging of Human Forearm
–	A deep learning approach for the analysis of voxel composition in magnetic resonance imaging
Ambrosini Emilia	3D upper limbs tracking through inertial sensors: calibration, methodology, and validation
–	A motor-assisted recumbent trike for cycling training in neurological patients
–	Automatic extraction of acoustic features to predict Alzheimer's disease among English-speaking subjects
Andolfi Andrea	Photosensitive pattern to control geometry and activity of a neural network
Andrean Daniele	Modeling Doxorubicin Treatment Effect in Multiple Myeloma
Andreola Chiara	Pseudo resting-state investigation from task-evoked functional MRI signals
Andreoni Giuseppe	Quantifying the contribution of single joint kinematics to the overall ergonomic discomfort
Angelone Francesca	Evaluation of breast density variability between right and left breasts
Anglani Mariagiulia	Impact of diffusion connectivity metrics on white matter abnormalities in glioma
Anglese Serena	Biomechanical assessment of the anomalous coronary compression by patient-specific finite element analysis
–	Development of novel computational tool to support surgical planning for the treatment of Anomalous Aortic Origin of the Coronary Arteries (AAOCA)
Annunziata Silvia	An attention classifier for the evaluation of a robotic therapy in children with Autism Spectrum Disorder

Antelmi Luigi	**Soft-tissue alterations identified with a CNN trained with simulated ultrasound images integrating expert knowledge**
Antenucci Pietro	**How to assess vascular dysfunction during septic shock and resuscitation**
Antonello Riccardo	**Automated control of bioreactors: An hardware-in-the-loop proof of concept test towards an experimental facility**
Antonietti Alberto	**A multiscale computational approach to replicate the full-scale mouse striatum model**
–	**Virtual prototyping of a robotic chess player for play therapy**
Aparo Anonino	**Exploring the potential of MCVAE for patients stratification and skewed data compensation across the AD continuum**
Aprea Elena	**Mechanical validation of an innovative intrafascicular neural interface to restore urinary bladder dysfunctions**
Aprile Irene	**Understanding user needs for robotics assisted cognitive and physical rehabilitation**
Arcarisi Lucia	**Open-source as an enabling approach for the introduction of artificial intelligence in healthcare**
Arcobelli Valerio Antonio	**Brain signals in semi-immersive and immersive VR environments: a feasibility study**
Arnaldi Dario	**Altered EEG amplitude coupling correlates to cognitive dysfunction in iRBD patients**
Arnaldi Pietro	**Photosensitive pattern to control geometry and activity of a neural network**
Arnulfo Gabriele	**Altered EEG amplitude coupling correlates to cognitive dysfunction in iRBD patients**
–	**Profiling of phase-amplitude couplings across sleep for personalized neuroengineering systems**
–	**Time-frequency analysis of brain response to 3D slant texture and stereo cues**
Arrico Lorenzo	**Zwitterionic coatings for an implantable artificial pancreas**
Arrigoni Filippo	**Pseudo resting-state investigation from task-evoked functional MRI signals**
Aterini Bianca	**A microfluidic platform to unravel immune cells cross-talk in rheumatoid arthritis**
Athanassiou Athanassia	**Cell encapsulation into silk fibroin microgels**
Atzeni Michele	**Assessing Personal Exposure to Airborne Particulate Matter with Wearable Sensors and Ventilation Rate Models**
Atzori Manfredo	**A dexterous hand prosthesis based on additive manufacturing**
Audenino Alberto L.	**Biomimetic platform for investigating in vitro the cell biological response to mechanical stretching – periodontal ligament stem cell application**
–	**Mechanical evaluation of synthetic meshes: definition and verification of a rigorous test protocol**
–	**Reducing bone plates standard fatigue test time with an analytical runout load prediction**
–	**The effect of CFR-PEEK cross-link in short fixation for the stabilisation of lumbar metastasis: an in-vitro comparative study**.
Autorino Maria Maddalena	**A Novel Authentication System Based on Hand Gesture Ultrasound Signatures**
–	**Breast Cancer Detection via Two-dimensional Ultrasound Tomography**
–	**Breast Cancer Imaging at Microwave Frequencies via Neural Networks**

–	**A deep learning approach for the analysis of voxel composition in magnetic resonance imaging**
Avanzini Pietro	**Quantifying the contribution of single joint kinematics to the overall ergonomic discomfort**
Babini Federico	**Augmented Reality to Evaluate Temporo-Mandibular Joint Alterations in Orthognathic Patients**
Baccarella Marta	**Multiscale Modelling of Platelet Activation in Membrane Oxygenation Systems**
Bäckström Mikael	**Advances in the development of a instrumented head surrogate for brain injury investigation**
Badiali Giovanni	**Augmented Reality to Evaluate Temporo-Mandibular Joint Alterations in Orthognathic Patients**
Baggiani Matteo	**3D bioprinting as a tool for the early correction of leather defects in the tanning industry**
Baggio Giacomo	**Single region contribution to the brain dynamic (in)stability**
Baglio Francesca	**Development of a novel surface-based approach to quantify fNIRS-fMRI spatial correspondence**
Bagno Andrea	**Biological evaluation in vitro and in vivo of hybrid membrane to assess biomedical application**
–	**Cryopreservation effects on biological tissues: histological and mechanical assessments**
–	**Mechanical characterization of hybrid membrane suitable for biomedical application**
Bagnoli Silvia	**Early stages of cognitive decline are characterized by different EEG microstates dynamics**
–	**P300 event-related potential in patients with cognitive decline correlates with task performance**
Bagshaw Andrew	**fMRI characterization of intrinsic brain networks relevant for motor control with and without visual feedback by fractal dimension**
Baldan Matteo	**Model Assessment of Doxorubicin Pharmacokinetics in Multiple Myeloma**
Baldazzi Giulia	**A novel tool for the annotation of bipolar electrograms for cardiac electrophysiology**
–	**Abnormal Ventricular Potentials Identification Using a Siamese Neural Network**
Baldoin Elisa	**Advances in the development of a instrumented head surrogate for brain injury investigation**
Baleani Massimiliano	**Development of a contrast-enhanced micro tomography protocol for human meniscus: a pilot study**
Balestra Gabriella	**A machine learning approach for stride speed estimation based on a head-mounted IMU**
–	**Usability of a multi-sensor array for the application of electro-phonocardiography in home care**
Ballardini Giulia	**Zwitterionic coatings for an implantable artificial pancreas**
Ballerini Mattia	**Intestinal epithelium on chip for absorption studies**
Balsamello Carlo	**The prediction of the patient's response to hemodialysis treatment: DialysIS vs InterACTIVE-HD 2.0 experience**

Balta Diletta	An improved method for the characterization of infants' general movements using a RGB-Depth sensor and a deep neural network tracking processing tool
Bandini Laura	A cloud-based mobile platform to monitor and counteract cognitive decline
–	Computational joint action: dynamical models to understand the development of joint coordination
Barata Catarina	An attention classifier for the evaluation of a robotic therapy in children with Autism Spectrum Disorder
Barbacane Sara	Analysis of an Elite Amputee Paralympic Sprinter in Track Running Pilot Tests
–	Comparative Analysis of Steady and Resisted Accelerated Treadmill Running of an Elite Amputee Paralympic Sprinter
–	Towards a Wearable System for Complete Collection of Clamp Loads in Transfemoral Paralympic Sprinters
Barban Federico	Towards personalized electroceutical therapy: electrophysiological investigations in a pre-clinical model of ischemic lesion
Barbara Maurizio	Assessment of Balance disorder and vestibular dysfunction using Mixed Reality
Barbieri Riccardo	Decoding Emotions through Music: A Physiological Analysis of Emotion Recognition
–	Effects of State Representation on a Reinforcement Learning Based Decision Support System
–	Quantitative validation of an automatic videoPPG technique during autonomic elicitations
Barbon Silvia	Composite scaffolds based on polyvinyl alcohol and acellular cartilage matrix for hemophilic arthropathy treatment
Barcali Eleonora	Optimization of a cardiac tissue segmentation pipeline in murine whole-heart reconstructions
Barcillesi Matteo	Inertial measurements unit validation for countermovement jump (CMJ) tests in athletes
Bardi Elena	3D upper limbs tracking through inertial sensors: calibration, methodology, and validation
Bari Vlasta	Assessment of cerebral autoregulation in patients undergoing anaesthesia with propofol: a comparison among spontaneous variability methods
Barni Luca	Inertial measurements unit validation for countermovement jump (CMJ) tests in athletes
Baron Giorgia	Assessing the impact of brain gliomas on effective connectivity gradients
–	Single region contribution to the brain dynamic (in)stability
Barone Ylenia	Brain-heart interaction: an ECG-fMRI integrated study in physiology and major depressive disorder
Baselice Fabio	A Novel Authentication System Based on Hand Gesture Ultrasound Signatures
–	Breast Cancer Detection via Two-dimensional Ultrasound Tomography
–	Breast Cancer Imaging at Microwave Frequencies via Neural Networks
–	A deep learning approach for the analysis of voxel composition in magnetic resonance imaging
Baselli Giuseppe	Development of a novel surface-based approach to quantify fNIRS-fMRI spatial correspondence
Bassetto Franco	A dexterous hand prosthesis based on additive manufacturing

Basti Alessio	Closing the loop between neurostimulation and control theory
–	Disclosing brain functional connections with multi-dimensional approaches
Batoni Elisa	Evaluation of the optimal pore size for 3D printed bone scaffolds in a perfusion bioreactor
–	Valve-jet technology for robotic-based in situ bioprinting applications
Battista Edmondo	Microgels as a Biosensing Platform
Battistella Aurora	Assessment of printability on autoclaved biomaterial inks for extrusion bioprinting
Battiston Marco	Myelin quantification in Magnetic Resonance Imaging
Battocchio Chiara	Peptide anchoring methods for PEEK surfaces
Becchiati Stefano	Face mobility analysis in Spinal Muscular Atrophy
Belfiore Maria Paola	Evaluation of breast density variability between right and left breasts
Bellani Marcella	Association between inflammation and brain microstructure in First Episode Psychosis investigated with DTI
Bellasi Antonio	The prediction of the patient's response to hemodialysis treatment: DialysIS vs InterACTIVE-HD 2.0 experience
Bellato Massimo	A workflow for the construction of reproducible living biosensors built by printing bacterial materials
–	Automated control of bioreactors: An hardware-in-the-loop proof of concept test towards an experimental facility
–	Lipid Droplets associated genes link HSV-1 infection to neurodegeneration pathways
–	Modeling metabolic overload effects in bacterial growth rate in synthetic biology
–	Simulating microbial communities' evolution via Agent base modelling: a Python tool
–	Study and characterization of bile acid biosensors in engineered probiotic bacteria
–	Uncovering quorum sensing and quenching structural properties: a systems biology approach
Bellina Emilia	Assessment of a parametric thoracic spine model for the generation of in silico cohorts
Bellitto Amy	Non-linear dimensionality-reduction approach for powered wheelchair control
Bello Giovanni Lo	Green-Based Anti-Biofilm Nanoformulations Against Bacterial Contaminations In Nosocomial Environments
Bellone Mauro	A convolutional neural network to identify osteoporosis from femoral echographic scans: a preliminary study
Belluzzi Elisa	Biomechanical characterization of human plantar fascia through experimental tests
Belluzzo Alessandro	A method for the evaluation of cervical surgical instrumentation reliability through a computational and experimental approach
Benini Martina	Comparison of RF exposure levels in 5G-V2X and ITS-5.9 GHz vehicular connectivity
–	Exposure Assessment of Young People to Wearable Antennas at 5G frequencies
Benozzo Danilo	Single region contribution to the brain dynamic (in)stability
Benvenuti Pietro	A multimodal wearable system for Human Activity Recognition during daily activities

Berardo Alice	**Biomechanical characterization of human plantar fascia through experimental tests**
–	**The biomechanical behaviour of fascial system: Superficial VS Deep Fascia**
Bernabè Giulia	**Lipid Droplets associated genes link HSV-1 infection to neurodegeneration pathways**
Bernardeschi Cinzia	**Open-source as an enabling approach for the introduction of artificial intelligence in healthcare**
Bernardi Alessandro	**Automated control of bioreactors: An hardware-in-the-loop proof of concept test towards an experimental facility**
Berni Matteo	**Development of a contrast-enhanced micro tomography protocol for human meniscus: a pilot study**
Berti Francesca	**A response surface-based approach to predict spinal rod contouring parameters**
Berto Alexa	**3D moles mapping and analysis for automatic melanoma detection**
Bertola Greta	**Engineering a smart intrauterine device based on pH-controlled copper release.**
Bertoldo Alessandra	**A comparative study of Super-Resolution reconstruction methods in fetal MRI**
–	**A Comprehensive Nonlinear Mixed Effects Model of Glucose, Insulin, and C-Peptide Interaction during IVGTT**
–	**Assessing the impact of brain gliomas on effective connectivity gradients**
–	**Assessment of the effects of parcellation and frequency band on the definition of functional hubs in rsfMRI**
–	**Associations between fatigue and functional connectivity of dopamine and noradrenaline circuits in Parkinson's disease**
–	**Impact of model selection procedure on Deep Neural Networks ensemble for the Choroid Plexus segmentation in Multiple Sclerosis**
–	**Impact of diffusion connectivity metrics on white matter abnormalities in glioma**
–	**Pseudo resting-state investigation from task-evoked functional MRI signals**
–	**Single region contribution to the brain dynamic (in)stability**
Bertuzzi Giulia	**Millimeter-Waves Imaging for Breast Cancer Detection: Development of Analytical Models**
Bessi Valentina	**Early stages of cognitive decline are characterized by different EEG microstates dynamics**
–	**Network model accounts for evolution of EEG functional connectivity in patients with cognitive decline**
–	**P300 event-related potential in patients with cognitive decline correlates with task performance**
Bevacqua Martina Teresa	**Experimental Microwave Imaging of Human Forearm**
Biagini Francesco	**Design and fabrication of a micro-dialyser for the study of the gut microbiota-tissues cross-talk**
Bianchi Anna Maria	**Brain-heart interaction: an ECG-fMRI integrated study in physiology and major depressive disorder**
–	**Differences in cortical reorganization during visuo-motor tasks executed with the dominant and non-dominant hands**
Bianchi Elena	**Micropatterned PDMS substrates for cellular mechanotransduction modelling**

Bibbo Daniele	Analysis of muscular activity of a cashier during different modalities of human robot collaboration
Bigini Paolo	Vibropolyfection: boosting polymer-mediated gene delivery by mechanical cell loading
Billardello Roberto	Comparative analysis of EMG-based classifiers for recognizing hand/wrist gestures and forces
Bilo Grzegorz	Commercial Smart Virtual Assistants to support medication adherence in chronic patients: a preliminary usability study
Bini Fabiano	3D Finite Element Analysis of a Percolating Cluster inside the Mineralized Collagen Fibril
–	Assessment of Balance disorder and vestibular dysfunction using Mixed Reality
–	Key points to design the MDs Library of a National implant Registry: lesson learned from the Italian experience
–	Near Field Electrospinning Process Using a Multi-Axis Robot
Biondi Alessia	Key points to design the MDs Library of a National implant Registry: lesson learned from the Italian experience
Bisecco Alvino	XGBoost vs. TabPFN in Neuroimaging Machine Learning-based analysis
Bisegna Paolo	Development of a microfluidic system for impedance-based cell sorting
Bisi Maria Cristina	Sensor-based Assessment of Gross and Fine Motor Development in Primary School Children
Bissacco Daniele	A numerical finite element methodology of the EVAR procedure
Bizzotto Roberto	Longitudinal Relationships Between Proteomics and Beta-Cell Dysfunction in Type 2 Diabetes: An Imi Direct Study
Blasi Valeria	Development of a novel surface-based approach to quantify fNIRS-fMRI spatial correspondence
Bocchi Leonardo	Optimization of a cardiac tissue segmentation pipeline in murine whole-heart reconstructions
–	Phase synchronization between breathing and ppg signals in sleep events recordings of adult subjects
–	Risk management in a medical device software: evaluation of the usability characteristics of a 3D viewer for reporting
Boeri Lucia	Integrated sensors for real-time monitoring of biological barriers in engineered cell culture dynamic in vitro models
Boffito Monica	Engineering of poly(urethane)-based porous constructs for cardiac tissue model design
Boiani Giulia Maria	Full-scale point-neuron model of the mouse hippocampal microcircuits
Boito Simona	A comparative study of Super-Resolution reconstruction methods in fetal MRI
Boldini Gabriele	Effectiveness of a home-based tele-rehabilitation program for post-Covid patients: preliminary results
Boldrin Camilla	A response surface-based approach to predict spinal rod contouring parameters
Bologna Federico	Reducing bone plates standard fatigue test time with an analytical runout load prediction
Bonacina Alessandro	Integrated sensors for real-time monitoring of biological barriers in engineered cell culture dynamic in vitro models

Bonaldi Lorenza	The biomechanical behaviour of fascial system: Superficial VS Deep Fascia
Bonato Marta	Comparison of RF exposure levels in 5G-V2X and ITS-5.9 GHz vehicular connectivity
–	Exposure Assessment of Young People to Wearable Antennas at 5G frequencies
–	Magnetoelectric nanoparticles as promising tools for motor nerve stimulation
Bonatti Amedeo Franco	Cell-aware optimization of the extrusion-based bioprinting process
–	Open-source as an enabling approach for the introduction of artificial intelligence in healthcare
Bonet Jacopo	Smart Titration of Long-Acting Insulin in Insulin-Naïve Type 2 Diabetic Subjects
Bonfiglio Annalisa	EyeLab: a user-friendly Matlab tool for real-time monitoring of eye movements
–	PEDOT:PSS ink-jet printed microelectrodes on paper: towards low-cost and green MEA devices
Bonilauri Augusto	Development of a novel surface-based approach to quantify fNIRS-fMRI spatial correspondence
Bonini Luca	K-medoid clustering of premotor firing patterns supports fine decoding of macaque reach-and-grasp
Bono Nina	Cell encapsulation into silk fibroin microgels
–	Design and validation of a microfluidic cartridge to prepare non-viral gene delivery complexes
–	Physiologically relevant in vitro experiments: degradation kinetics of a pool of enzymes
–	Vibropolyfection: boosting polymer-mediated gene delivery by mechanical cell loading
Borrelli Simone	The effect of CFR-PEEK cross-link in short fixation for the stabilisation of lumbar metastasis: an in-vitro comparative study.
Bortolani Barbara	Ex Vivo Animal Evaluation of IntraValvular Impedance Sensing Applied to Biological Heart Valve Prostheses
Bortolotti Carlo Augusto	Giving new life to seafood waste: in silico engineering of a chitinolytic LPMO enzyme
Bortone Osvaldo	A novel microfluidic-based approach to study protein stability behavior in highly concentrated and viscous (HCV) systems
Boscarino Diego	Manual and automatic identification of ACMG evidence in scientific papers
Boscolo Galazzo Ilaria	Decoding the interplay between brain structural and functional connectivity in Alzheimer's disease
–	Exploring the potential of MCVAE for patients stratification and skewed data compensation across the AD continuum
Botte Ermes	Experimental and computational pipeline for identifying oxygen metabolic rate parameters in 2D and 3D in vitro constructs
–	Genetic Algorithms for the identification and design of physiologically relevant 3D constructs
–	Oxygen metabolism in in vitro ecosystems
Botter Alberto	Combining high-density electromyography and ultrafast ultrasound to assess individual motor unit properties in vivo
Bozzetto Michela	In vitro exposure of endothelial cells to mechanical vibrations

–	The role of hemodynamics in arteriovenous fistula remodelling and failure. A CFD longitudinal study
Bozzi Silvia	Microfluidic system for a label-free, real-time functional assessment of thrombotic risk
Braghin Francesco	3D upper limbs tracking through inertial sensors: calibration, methodology, and validation
Bragonzoni Laura	Sensor-based Assessment of Gross and Fine Motor Development in Primary School Children
Brambilla Paolo	A comparative study of Super-Resolution reconstruction methods in fetal MRI
–	Association between inflammation and brain microstructure in First Episode Psychosis investigated with DTI
–	Brain-heart interaction: an ECG-fMRI integrated study in physiology and major depressive disorder
–	The role of hemodynamics in arteriovenous fistula remodelling and failure. A CFD longitudinal study
Branciforti Francesco	Quality enhancement of dermatological images using GANs: a proof of concept
Brandi Cristian	Development of a microfluidic system for impedance-based cell sorting
Breban Samira Giuliana	Analysis of an Elite Amputee Paralympic Sprinter in Track Running Pilot Tests
–	Comparative Analysis of Steady and Resisted Accelerated Treadmill Running of an Elite Amputee Paralympic Sprinter
–	Towards a Wearable System for Complete Collection of Clamp Loads in Transfemoral Paralympic Sprinters
Brendolan Andrea	Exploring heterogeneity in lymphoid malignancies from mouse to human gene expression profiles
Brofiga Martina	Interconnected brain regions-on-a-chip: role of connectivity and heterogeneity in the electrophysiological activity
Brombal Luca	Towards 3D Virtual Histology of melanoma tissue by means of lab-based X-ray Phase Contrast Computed Micro-Tomography
Brun Francesco	Towards 3D Virtual Histology of melanoma tissue by means of lab-based X-ray Phase Contrast Computed Micro-Tomography
Brun Paola	Lipid Droplets associated genes link HSV-1 infection to neurodegeneration pathways
–	Peptide-functionalized chitosan sponges for bone tissue regeneration
Bruno Ester	Early stages of cognitive decline are characterized by different EEG microstates dynamics
Brusini Lorenza	Decoding the interplay between brain structural and functional connectivity in Alzheimer's disease
–	Exploring the potential of MCVAE for patients stratification and skewed data compensation across the AD continuum
Bulloni Matteo	Exploring heterogeneity in lymphoid malignancies from mouse to human gene expression profiles
Buosi Alessandro	A dexterous hand prosthesis based on additive manufacturing
Burali Rachele	Early stages of cognitive decline are characterized by different EEG microstates dynamics

–	P300 event-related potential in patients with cognitive decline correlates with task performance
Burattini Laura	A Reliable User-Independent Motion Intent Detection from Transient EMG Data for Shoulder Joint
–	Brugada Syndrome: Characterization of QT Interval Components and Correction
–	Interhemispheric functional connectivity: an fMRI study in two split-brain patients
–	Mathematical model of glucagon kinetics during an oral glucose tolerance test based on a dual regulation mechanism
–	mmWave Radars Data Processing for Gait Parameters Extraction
Burgio Stefano	Rapid prototyping of a microfluidic platform for nasal mucosa models
Burriesci Giancarlo	Exposure set-up for assessing the far-field electromagnetic immunity levels of active implantable medical devices
Businaro Luca	Development of a microfluidic system for impedance-based cell sorting
Butera Carola	3D upper limbs tracking through inertial sensors: calibration, methodology, and validation
Cacopardo Ludovica	Design and fabrication of an intestinal phantom to mimic intestinal tone and motility
–	Engineering a smart intrauterine device based on pH-controlled copper release.
–	Multiscale computational models for predicting hydrogel viscoelastic properties
Cafarelli Andrea	Dose-controlled low-intensity pulsed ultrasound and pulsed electromagnetic fields stimulations modulate inflammation in human macrophages
–	Highly controlled ultrasound-mediated drug delivery experiments: an in vitro set-up
Cafaro Massimo	A convolutional neural network to identify osteoporosis from femoral echographic scans: a preliminary study
Caglio Arianna	An attention classifier for the evaluation of a robotic therapy in children with Autism Spectrum Disorder
Caiani Enrico Gianluca	Commercial Smart Virtual Assistants to support medication adherence in chronic patients: a preliminary usability study
Calabrese Massimiliano	Impact of model selection procedure on Deep Neural Networks ensemble for the Choroid Plexus segmentation in Multiple Sclerosis
Calamai Martino	Hydrogel-based photopolymers for 3D printing of scaffolds by bench-top stereolithography
Calandrino Andrea	Combination of VR and manikins to improve medical training
Calareso Giuseppina	Distinguishing lymph nodes in head and neck cancer patients using MRI-based radiomics
Calcagnini Giovanni	Exposure set-up for assessing the far-field electromagnetic immunity levels of active implantable medical devices
Calcagno Alessandra	Differences in cortical reorganization during visuo-motor tasks executed with the dominant and non-dominant hands
Calderai Valentina	Open-source as an enabling approach for the introduction of artificial intelligence in healthcare
Caldiroli Alice	An advanced culture system to investigate electrospun graft biomechanisms for vascular tissue engineering

–	Physiologically relevant in vitro experiments: degradation kinetics of a pool of enzymes
Callara Alejandro	Early stages of cognitive decline are characterized by different EEG microstates dynamics
Callara Alejandro Luis	Effect of EDA-driven sympathetic responses on the central processing of faces cued by hedonic odors: a preliminary ERP study
Callegari Francesca	Interconnected brain regions-on-a-chip: role of connectivity and heterogeneity in the electrophysiological activity
Calogiuri Mariagrazia	Microfluidic system for a label-free, real-time functional assessment of thrombotic risk
Calvi Alberto	A deep learning network from downsampled diffusion-weighted MRI k-space to image-space
–	Myelin quantification in Magnetic Resonance Imaging
Calvigioni Marco	Design and fabrication of a micro-dialyser for the study of the gut microbiota-tissues cross-talk
Calzavara Andrea	Simulating microbial communities' evolution via Agent base modelling: a Python tool
Campiglio Chiara Emma	An advanced culture system to investigate electrospun graft biomechanisms for vascular tissue engineering
–	In vitro exposure of endothelial cells to mechanical vibrations
Campora Simona	Effect of Chitosan coating on PLA electrospun scaffolds for bone tissue engineering
Camuncoli Federica	Inertial measurements unit validation for countermovement jump (CMJ) tests in athletes
Cancelliere Fosco	Commercial Smart Virtual Assistants to support medication adherence in chronic patients: a preliminary usability study
Candiani Gabriele	Cell encapsulation into silk fibroin microgels
–	Design and validation of a microfluidic cartridge to prepare non-viral gene delivery complexes
–	Physiologically relevant in vitro experiments: degradation kinetics of a pool of enzymes
–	Vibropolyfection: boosting polymer-mediated gene delivery by mechanical cell loading
Canessa Andrea	Evaluating Spatial Hearing in Virtual Reality Environment
–	Time-frequency analysis of brain response to 3D slant texture and stereo cues
Canino Giovanni	A Distributed Multi-Centric Application for the Analysis of Cardiac Biomarkers
Canna Antonietta	Tensor-based morphometry of T1 weighted brain images reveals subtle volume enlargement of temporalis muscles
Cannata Stefano	An Inverse Analysis for the Assessment of Material Properties of TAVI Patients
–	Establishing Computational Modeling Credibility in Patients Undergoing TAVI
–	Mechanical Properties of Polyamide 12 for the use in Balloon-Expandable Transcatheter Heart Valves
–	Numerical Analysis of the Bicaval Transcatheter System for the Treatment of Severe Tricuspid Regurgitation
–	Structural Simulation of Transcatheter Heart Valve in Transcatheter Heart Valve

Cannistrà Mattia	Validating biomedical and clinical data via an annotations based framework: experiences within the PON VQA project
Capitini Claudia	Hydrogel-based photopolymers for 3D printing of scaffolds by bench-top stereolithography
Capodaglio Paolo	Effectiveness of a home-based tele-rehabilitation program for post-Covid patients: preliminary results
Cappellato Marco	Simulating microbial communities' evolution via Agent base modelling: a Python tool
Cappon Giacomo	Algorithm based on the "dynamic risk" concept allows ahead-of-time suggestion of corrective insulin boluses in type 1 diabetes therapies employing continuous glucose monitors
–	Assessing Personal Exposure to Airborne Particulate Matter with Wearable Sensors and Ventilation Rate Models
–	Design and Evaluation of an Intuitive Administration Dashboard for a Platform used to Monitor Clinical Trials
Capuzzo Martina	Development of an Integrated Software System for Medical Equipment Management: the experience of the Spedali Civili Hospital
Carbonaro Marco	Combining high-density electromyography and ultrafast ultrasound to assess individual motor unit properties in vivo
Carbonaro Nicola	Patient-specific phantom for home haemodialysis
Cardarilli Gian Carlo	Development of a microfluidic system for impedance-based cell sorting
Cardone Daniela	Driver drowsiness detection relying on infrared thermal imaging: a machine learning approach
–	Drivers' mental workload assessment based on machine learning applied to multimodal physiological data
Carè Marta	Towards personalized electroceutical therapy: electrophysiological investigations in a pre-clinical model of ischemic lesion
Carerj Maria Ludovica	Radiomic analysis of Epicardial Adipose Tissue in cardiac MRI for hospitalization risk assessment
Carfi Alessandro	Toward Implicit Communication of Object Properties for Human-Robot Interaction
Carlini Giorgio	Combination of VR and manikins to improve medical training
–	Non-linear dimensionality-reduction approach for powered wheelchair control
Carmagnola Irene	Nanostructured coatings with bacteria-triggered antimicrobial response for medical devices
Carniel Emanuele Luigi	A novel artificial urinary sphincter and comparison with reference device
–	Biomechanical characterization of human plantar fascia through experimental tests
–	Mechanical characterization of hybrid membrane suitable for biomedical application
Caroli Anna	The role of hemodynamics in arteriovenous fistula remodelling and failure. A CFD longitudinal study
Carpenedo Linda	A response surface-based approach to predict spinal rod contouring parameters
Carpi Federico	Hydrogel-based photopolymers for 3D printing of scaffolds by bench-top stereolithography
–	Wearable tactile display of softness for virtual reality

Carrani Eugenio	Key points to design the MDs Library of a National implant Registry: lesson learned from the Italian experience
Carrara Elena	In vitro exposure of endothelial cells to mechanical vibrations
Carrara Marta	How to assess vascular dysfunction during septic shock and resuscitation
Carraro Elena	Face mobility analysis in Spinal Muscular Atrophy
Caruso Annamaria	From data to knowledge: definition of an exploratory dataset for deep brain stimulation
Casadio Maura	Combination of VR and manikins to improve medical training
–	Computer Vision and Deep Learning for Human Motion Analysis
–	Non-linear dimensionality-reduction approach for powered wheelchair control
Casagrande Giada	A hydraulic implantable artificial detrusor for controlled bladder voiding
Casagrande Giustina	The prediction of the patient's response to hemodialysis treatment: DialysIS vs InterACTIVE-HD 2.0 experience
Casale Costantino	A testbed for mechanical and thermal stimulation in studies of somatosensory functions
Casani Aldo	Patient-specific phantom for home haemodialysis
Casarin Martina	Biological evaluation in vitro and in vivo of hybrid membrane to assess biomedical application
–	Cryopreservation effects on biological tissues: histological and mechanical assessments
Casciaro Ernesto	Radiofrequency Echographic Multi Spectromery for Fragility Fracture prediction through Fragility Score
Casciaro Sergio	A convolutional neural network to identify osteoporosis from femoral echographic scans: a preliminary study
–	Osteoporosis Identification at Lumbar Vertebrae through a Neural Network Classifier
–	Radiofrequency Echographic Multi Spectromery for Fragility Fracture prediction through Fragility Score
–	Soft-tissue alterations identified with a CNN trained with simulated ultrasound images integrating expert knowledge
–	Transfer learning approaches to classify foetal occiput positions on transperineal ultrasound images
Cascone Maria Grazia	3D printing of a nanomaterials-embedded gelatin/pectin hydrogel for the development of an in vitro drug testing platform
Caselli Federica	Development of a microfluidic system for impedance-based cell sorting
Cassa Maria Antonia	Nanostructured coatings with bacteria-triggered antimicrobial response for medical devices
Cassari Leonardo	Engineering the tumor environment in vitro using peptide-enriched, hyaluronic acid-based hydrogels
–	Peptide anchoring methods for PEEK surfaces
–	Peptide-functionalized chitosan sponges for bone tissue regeneration
Castagliuolo Ignazio	Lipid Droplets associated genes link HSV-1 infection to neurodegeneration pathways

Castellaro Marco	**Associations between fatigue and functional connectivity of dopamine and noradrenaline circuits in Parkinson's disease**
–	**Impact of model selection procedure on Deep Neural Networks ensemble for the Choroid Plexus segmentation in Multiple Sclerosis**
Catalano Chiara	**An Inverse Analysis for the Assessment of Material Properties of TAVI Patients**
–	**Establishing Computational Modeling Credibility in Patients Undergoing TAVI**
–	**Mechanical Properties of Polyamide 12 for the use in Balloon-Expandable Transcatheter Heart Valves**
Cataldo Andrea	**Wearable sensor for in-vivo skin hydration monitoring**
Catozzi Carlotta	**A microfluidic platform to unravel immune cells cross-talk in rheumatoid arthritis**
Catuogno Francesco	**Hydrogels scaffolds as 2D in vitro models to explore the impact of microenvironmental stiffness on lung adenocarcinoma cells**
Causa Filippo	**Circulating tumour cells deformability measurement in microfluidics**
–	**In-flow viscoelastic compression to probe single-cell biomechanical properties**
–	**Microfluidic platform for cell classification from optical signatures via machine learning**
–	**Microgels as a Biosensing Platform**
Causin Lorenzo Carlo	**Design and Evaluation of an Intuitive Administration Dashboard for a Platform used to Monitor Clinical Trials**
Cauzzo Simone	**Early stages of cognitive decline are characterized by different EEG microstates dynamics**
Cavallo Filippo	**A multimodal wearable system for Human Activity Recognition during daily activities**
–	**Personality Traits Influence the Perception of a Robotic Arm endowed with Social Cues**
Cazzoli Marta	**Development of a novel surface-based approach to quantify fNIRS-fMRI spatial correspondence**
Ceccarelli Stefania	**Key points to design the MDs Library of a National implant Registry: lesson learned from the Italian experience**
Cecchetto Cinzia	**Effect of EDA-driven sympathetic responses on the central processing of faces cued by hedonic odors: a preliminary ERP study**
Cecchi Francesca	**Non-linear analysis of HRV reveal lower signal complexity in patients with a prolonged Disorder of Consciousness**
Cecchin Diego	**Assessing the impact of brain gliomas on effective connectivity gradients**
–	**Impact of diffusion connectivity metrics on white matter abnormalities in glioma**
Ceciliani Andrea	**Sensor-based Assessment of Gross and Fine Motor Development in Primary School Children**
Censi Federica	**Exposure set-up for assessing the far-field electromagnetic immunity levels of active implantable medical devices**
Centonze Alessia	**Soft-tissue alterations identified with a CNN trained with simulated ultrasound images integrating expert knowledge**
Cercenelli Laura	**Augmented Reality to Evaluate Temporo-Mandibular Joint Alterations in Orthognathic Patients**

–	Ex Vivo Animal Evaluation of IntraValvular Impedance Sensing Applied to Biological Heart Valve Prostheses
Cereatti Andrea	A machine learning approach for stride speed estimation based on a head-mounted IMU
–	An improved method for the characterization of infants' general movements using a RGB-Depth sensor and a deep neural network tracking processing tool
Cerfoglio Serena	Effectiveness of a home-based tele-rehabilitation program for post-Covid patients: preliminary results
Cerutti Letizia	Interconnected brain regions-on-a-chip: role of connectivity and heterogeneity in the electrophysiological activity
Ceserani Valentina	Biomechanical assessment of the anomalous coronary compression by patient-specific finite element analysis
–	Development of novel computational tool to support surgical planning for the treatment of Anomalous Aortic Origin of the Coronary Arteries (AAOCA)
–	Lumped-parameter hemodynamic model as a non-invasive tool to assess coronary blood flow in AAOCA
Chackochan Vinil T.	Computational joint action: dynamical models to understand the development of joint coordination
Chai Yoke Chin	RNA Sequencing analysis to study Duchenne dilated cardiomyopathy in patient-derived 3D organoid models
Chang Hao-Chen	Peptide anchoring methods for PEEK surfaces
Chessa Manuela	Combination of VR and manikins to improve medical training
Chiappalone Michela	Development of excitatory neuronal networks derived from human induced pluripotent stem cells
–	Profiling of phase-amplitude couplings across sleep for personalized neuroengineering systems
–	Towards personalized electroceutical therapy: electrophysiological investigations in a pre-clinical model of ischemic lesion
Chiaramello Emma	Comparison of RF exposure levels in 5G-V2X and ITS-5.9 GHz vehicular connectivity
–	Exposure Assessment of Young People to Wearable Antennas at 5G frequencies
–	Magnetoelectric nanoparticles as promising tools for motor nerve stimulation
Chiari Lorenzo	Autonomic response to virtual reality in oncological patients in real-world context
–	Comparison of autonomic signals between healthy subjects and chronic low back pain patients at rest and during noxious stimulation
–	Wearable-based Sit-to-Stand transfers in Older Adults: context differences between in-lab and home-based assessments
Chiarion Giovanni	Functional Connectivity of the EEG in epilepsy: a single case study
Chiesa Irene	Cell-aware optimization of the extrusion-based bioprinting process
–	Development of analytical models to predict self-folding of 4D bioprinted scaffold
Chiò Adriano	Dynamic Bayesian Networks and Transfer Learning Enable the Development of Deep Sequence-Based Models on Small-Sample Data
–	Identifying Extreme Profiles in Amyotrophic Lateral Sclerosis Patients at Diagnosis through Archetypal Analysis

Chiono Valeria	Natural polymer-based bioinks exploiting internal gelation mechanism for cardiac tissue engineering
Chiorri Carlo	A cloud-based mobile platform to monitor and counteract cognitive decline
Chirico Marco	Combination of VR and manikins to improve medical training
Chiuso Alessandro	Assessing the impact of brain gliomas on effective connectivity gradients
–	Single region contribution to the brain dynamic (in)stability
Ciardelli Gianluca	Engineering of poly(urethane)-based porous constructs for cardiac tissue model design
–	Nanostructured coatings with bacteria-triggered antimicrobial response for medical devices
Ciarlo Assunta	Bayesian Surprise from a Deep Learning Model of Italian Language to Model Neural Activity
–	Tensor-based morphometry of T1 weighted brain images reveals subtle volume enlargement of temporalis muscles
Ciattaglia Gianluca	mmWave Radars Data Processing for Gait Parameters Extraction
Cibin Federica	Face mobility analysis in Spinal Muscular Atrophy
Ciccarelli Paola	Key points to design the MDs Library of a National implant Registry: lesson learned from the Italian experience
Ciceri Tommaso	A comparative study of Super-Resolution reconstruction methods in fetal MRI
–	Pseudo resting-state investigation from task-evoked functional MRI signals
Cidonio Gianluca	Near Field Electrospinning Process Using a Multi-Axis Robot
Ciminello Enrico	Key points to design the MDs Library of a National implant Registry: lesson learned from the Italian experience
Cimmino Chiara	Mesenchymal Stem Cell Response to Micropatterns and Dynamic Topographies
Cimolato Chiara	Modeling metabolic overload effects in bacterial growth rate in synthetic biology
–	Uncovering quorum sensing and quenching structural properties: a systems biology approach
Cimolin Veronica	Development of an Integrated Software System for Medical Equipment Management: the experience of the Spedali Civili Hospital
–	Effectiveness of a home-based tele-rehabilitation program for post-Covid patients: preliminary results
–	Motor performances evaluation of female soccer players from AC Trento Women
Cincotti Febo	Brain-Computer Interface assisted Motor Imagery training in post-stroke rehabilitation: longitudinal study of the EEG sensorimotor rhythms
Cinquetti Ettore	Enhancing Safety in Industry 4.0: The Use of Passive Brain Computer Interfaces for Vigilance Monitoring
–	Exploring the potential of MCVAE for patients stratification and skewed data compensation across the AD continuum
Ciolfi Christian	3D moles mapping and analysis for automatic melanoma detection
Cippà Pietro	The prediction of the patient's response to hemodialysis treatment: DialysIS vs InterACTIVE-HD 2.0 experience
Cipriano Giovanni	A bioinformatic pipeline for identifying bacterial constitutive promoters based on transcriptomic data analysis

Ciriello Luca	**A method for the evaluation of cervical surgical instrumentation reliability through a computational and experimental approach**
Cirillo Mario	**Control Theory Measures for Dynamic Analyses of Human Functional Connectome Data**
–	**XGBoost vs. TabPFN in Neuroimaging Machine Learning-based analysis**
Civilini Vittoria	**Mechanical evaluation of synthetic meshes: definition and verification of a rigorous test protocol**
Coduri Mara	**Combination of VR and manikins to improve medical training**
Coelli Stefania	**Differences in cortical reorganization during visuo-motor tasks executed with the dominant and non-dominant hands**
Colamarino Emma	**Brain-Computer Interface assisted Motor Imagery training in post-stroke rehabilitation: longitudinal study of the EEG sensorimotor rhythms**
–	**On the use of PARAFAC algorithm in group network analysis: a simulation study**
Colebaugh Carin Ann	**Comparison of autonomic signals between healthy subjects and chronic low back pain patients at rest and during noxious stimulation**
Collia Dario	**Adaptation of cardiac deformation pattern during exercise in children**
Collorone Sara	**Myelin quantification in Magnetic Resonance Imaging**
Colombi Annalisa	**Impact of model selection procedure on Deep Neural Networks ensemble for the Choroid Plexus segmentation in Multiple Sclerosis**
Colpo Maria	**Impact of diffusion connectivity metrics on white matter abnormalities in glioma**
Colturi Carla	**The prediction of the patient's response to hemodialysis treatment: DialysIS vs InterACTIVE-HD 2.0 experience**
Colucci Antonio	**A convolutional neural network to identify osteoporosis from femoral echographic scans: a preliminary study**
–	**Soft-tissue alterations identified with a CNN trained with simulated ultrasound images integrating expert knowledge**
Combi Carlo	**Exploring the potential of MCVAE for patients stratification and skewed data compensation across the AD continuum**
Conconi Maria Teresa	**Engineering the tumor environment in vitro using peptide-enriched, hyaluronic acid-based hydrogels**
Confalonieri Marta	**Composite scaffolds based on polyvinyl alcohol and acellular cartilage matrix for hemophilic arthropathy treatment**
Conforto Silvia	**Analysis of muscular activity of a cashier during different modalities of human robot collaboration**
Contaldo Fabiola Rosa	**Radiofrequency Echographic Multi Spectromery for Fragility Fracture prediction through Fragility Score**
Conte Federica	**A network-based algorithm for identifying drug repurposing opportunities for complex diseases**
–	**Bioinformatics analyses to identify molecular gene signatures associated with breast cancer phenotypes**
Conte Giorgio	**A comparative study of Super-Resolution reconstruction methods in fetal MRI**
Conti Michele	**A Workflow for Biomechanical Simulation of Patient-specific Atherosclerotic Carotid Artery**

–	A workflow for the construction of reproducible living biosensors built by printing bacterial materials
–	Biomechanical assessment of the anomalous coronary compression by patient-specific finite element analysis
–	Development of novel computational tool to support surgical planning for the treatment of Anomalous Aortic Origin of the Coronary Arteries (AAOCA)
–	Lumped-parameter hemodynamic model as a non-invasive tool to assess coronary blood flow in AAOCA
Conversano Francesco	A convolutional neural network to identify osteoporosis from femoral echographic scans: a preliminary study
–	Osteoporosis Identification at Lumbar Vertebrae through a Neural Network Classifier
–	Radiofrequency Echographic Multi Spectromery for Fragility Fracture prediction through Fragility Score
–	Soft-tissue alterations identified with a CNN trained with simulated ultrasound images integrating expert knowledge
–	Transfer learning approaches to classify foetal occiput positions on transperineal ultrasound images
Coppadoro Lorenzo Pietro	Tuning the features of microphysiological systems for biomimetic intestinal in vitro models
Corbetta Maurizio	Assessing the impact of brain gliomas on effective connectivity gradients
–	Impact of diffusion connectivity metrics on white matter abnormalities in glioma
–	Single region contribution to the brain dynamic (in)stability
Cordella Francesca	A safe robot control for semi-autonomous pedicle tapping
–	Comparative analysis of EMG-based classifiers for recognizing hand/wrist gestures and forces
–	Performance Evaluation of the Gloreha Sinfonia Device in Bimanual Modality
Cordiale Alessandro	Intestinal epithelium on chip for absorption studies
Corino Valentina	Distinguishing lymph nodes in head and neck cancer patients using MRI-based radiomics
–	Radiomic analysis of Epicardial Adipose Tissue in cardiac MRI for hospitalization risk assessment
Coro Florinda	Engineering a smart intrauterine device based on pH-controlled copper release.
–	Open-source as an enabling approach for the introduction of artificial intelligence in healthcare
Cortese Nicola	A Distributed Multi-Centric Application for the Analysis of Cardiac Biomarkers
–	A preliminary version of a Genome-Scale Metabolic Model for Induced Human Pluripotent Stem Cells (hiPSCs)
Corti Anna	Distinguishing lymph nodes in head and neck cancer patients using MRI-based radiomics
Corvini Giovanni	Analysis of muscular activity of a cashier during different modalities of human robot collaboration
Cosentino Carlo	A Distributed Multi-Centric Application for the Analysis of Cardiac Biomarkers

–	A preliminary version of a Genome-Scale Metabolic Model for Induced Human Pluripotent Stem Cells (hiPSCs)
Cossu Luca	Design and Evaluation of an Intuitive Administration Dashboard for a Platform used to Monitor Clinical Trials
Costantino Maria Laura	Development of a computational model to estimate the hemolysis risk associated with hemodialysis catheters
–	The prediction of the patient's response to hemodialysis treatment: DialysIS vs InterACTIVE-HD 2.0 experience
Cota Vinícius	Profiling of phase-amplitude couplings across sleep for personalized neuroengineering systems
Coward Trevor	Peptide anchoring methods for PEEK surfaces
Crascì Fabrizio	Numerical Analysis of the Bicaval Transcatheter System for the Treatment of Severe Tricuspid Regurgitation
Credi Caterina	Hydrogel-based photopolymers for 3D printing of scaffolds by bench-top stereolithography
Crescioli Cecilia	Micropatterned PDMS substrates for cellular mechanotransduction modelling
Cretti Giacomo	Optimization of advanced setups with integrated readouts for evaluation of cardiac toxicity in a heart on chip device
Crispino Raffaele	Biological validation of thiolated food grade secondary oil in water nanoemulsions with enhanced mucus-adhesion properties in Intestine-on-a-chip model
Cristina Maria Luisa	Green-Based Anti-Biofilm Nanoformulations Against Bacterial Contaminations In Nosocomial Environments
Critelli Claudia	A Distributed Multi-Centric Application for the Analysis of Cardiac Biomarkers
Crocè Lory Saveria	Estimating the degree of Non-Alcoholic Fatty Live Disease (NAFLD) from ultrasound images: preliminary results
Cruciani Federica	Decoding the interplay between brain structural and functional connectivity in Alzheimer's disease
–	Exploring the potential of MCVAE for patients stratification and skewed data compensation across the AD continuum
Crupi Felice	Remote In-Bed Monitoring of Vital Signs Using Radar Technology
Cuda Giovanni	A preliminary version of a Genome-Scale Metabolic Model for Induced Human Pluripotent Stem Cells (hiPSCs)
Cuppini Cristiano	A neural model of sensory interactions in young neurotypical and ASD children
Curcio Matteo	Assessment of Balance disorder and vestibular dysfunction using Mixed Reality
Curcio Nicoletta	A Workflow for Biomechanical Simulation of Patient-specific Atherosclerotic Carotid Artery
Cusella Maria Gabriella	Study and characterization of bile acid biosensors in engineered probiotic bacteria
Cutti Andrea Giovanni	Analysis of an Elite Amputee Paralympic Sprinter in Track Running Pilot Tests
–	Comparative Analysis of Steady and Resisted Accelerated Treadmill Running of an Elite Amputee Paralympic Sprinter
–	Static strength of lower-limb prosthetic sockets for the activities of daily living
–	Towards a Wearable System for Complete Collection of Clamp Loads in Transfemoral Paralympic Sprinters

Cvetkova Viktoria	**Effectiveness of a home-based tele-rehabilitation program for post-Covid patients: preliminary results**
Da Ros Francesco	**Model Assessment of Doxorubicin Pharmacokinetics in Multiple Myeloma**
–	**Modeling Doxorubicin Treatment Effect in Multiple Myeloma**
Daddi Costanza	**3D bioprinting as a tool for the early correction of leather defects in the tanning industry**
–	**Design and fabrication of a micro-dialyser for the study of the gut microbiota-tissues cross-talk**
Dal Santo Francesco	**Decoding the interplay between brain structural and functional connectivity in Alzheimer's disease**
D'Alessandro Fabio	**Design and validation of a microfluidic cartridge to prepare non-viral gene delivery complexes**
D'Alessandro Salvatore	**Near Field Electrospinning Process Using a Multi-Axis Robot**
Dalla Man Chiara	**A Comprehensive Nonlinear Mixed Effects Model of Glucose, Insulin, and C-Peptide Interaction during IVGTT**
–	**Smart Titration of Long-Acting Insulin in Insulin-Naïve Type 2 Diabetic Subjects**
Dall'Asta Andrea	**Transfer learning approaches to classify foetal occiput positions on transperineal ultrasound images**
Dallera Debora	**A bioinformatic pipeline for identifying bacterial constitutive promoters based on transcriptomic data analysis**
–	**Study and characterization of bile acid biosensors in engineered probiotic bacteria**
Dallolio Laura	**Sensor-based Assessment of Gross and Fine Motor Development in Primary School Children**
Dall'Olmo Luigi	**3D moles mapping and analysis for automatic melanoma detection**
d'Ambrosio Alessandro	**XGBoost vs. TabPFN in Neuroimaging Machine Learning-based analysis**
Damiano Rossella	**Fast path replanning in a dynamic environment in percutaneous cardiac interventions**
D'Andrea Antea	**Closing the loop between neurostimulation and control theory**
D'Angelo Egidio	**Myelin quantification in Magnetic Resonance Imaging**
Daniele Beniamino	**Cardiotocography in antenatal fetal monitoring of diabetes-complicated pregnancies**
–	**Hidden Markov Models for the identification of fetal phases in CTG recordings**
Dannhauser David	**Circulating tumour cells deformability measurement in microfluidics**
–	**In-flow viscoelastic compression to probe single-cell biomechanical properties**
–	**Microfluidic platform for cell classification from optical signatures via machine learning**
–	**Microgels as a Biosenardibocchiminottiminottinsing Platform**
Daud Paolla Furquim	**A multiscale computational approach to replicate the full-scale mouse striatum model**
De Acutis Aurora	**3D bioprinting as a tool for the early correction of leather defects in the tanning industry**
–	**Cell-aware optimization of the extrusion-based bioprinting process**

–	**Design and fabrication of a micro-dialyser for the study of the gut microbiota-tissues cross-talk**
–	**Design and fabrication of a novel bioreactor for the engineering of tendon/ligament-to-bone interfaces**
De Caro Raffaele	**Composite scaffolds based on polyvinyl alcohol and acellular cartilage matrix for hemophilic arthropathy treatment**
De Gaetano Francesco	**Development of a computational model to estimate the hemolysis risk associated with hemodialysis catheters**
De Gregorio Vincenza	**Bio-fabrication of in vitro tissues possessing organ-specific endogenous extracellular matrices**
de Groot Marius	**Assessing Multisite PET Neuroimaging Harmonisation for Normative Modelling**
De Luca Daniela	**Machine learning-based classification of cortical response to visual stimuli recorded with an ECoG array in mice: a case study**
Della Croce Ugo	**A preliminary test of a novel method for the real time estimation of foot displacement using MIMUs attached to the foot**
–	**An improved method for the characterization of infants' general movements using a RGB-Depth sensor and a deep neural network tracking processing tool**
De Marchi Davide	**A bioinformatic pipeline for identifying bacterial constitutive promoters based on transcriptomic data analysis**
De Marchis Cristiano	**Synergy-dependent patterns of reaction forces in sit-to-stand movements**
De Marco Doriana	**Quantifying the contribution of single joint kinematics to the overall ergonomic discomfort**
De Marco Tommaso	**Osteoporosis Identification at Lumbar Vertebrae through a Neural Network Classifier**
–	**Soft-tissue alterations identified with a CNN trained with simulated ultrasound images integrating expert knowledge**
De Maria Carmelo	**3D bioprinting as a tool for the early correction of leather defects in the tanning industry**
–	**3D printing of a nanomaterials-embedded gelatin/pectin hydrogel for the development of an in vitro drug testing platform**
–	**Cell-aware optimization of the extrusion-based bioprinting process**
–	**Design and fabrication of a micro-dialyser for the study of the gut microbiota-tissues cross-talk**
–	**Design and fabrication of a novel bioreactor for the engineering of tendon/ligament-to-bone interfaces**
–	**Development of analytical models to predict self-folding of 4D bioprinted scaffold**
–	**Engineering a smart intrauterine device based on pH-controlled copper release.**
–	**Evaluation of the optimal pore size for 3D printed bone scaffolds in a perfusion bioreactor**
–	**Extrusion control strategy for robotic-based in situ bioprinting**
–	**Open-source as an enabling approach for the introduction of artificial intelligence in healthcare**
–	**Patient-specific phantom for home haemodialysis**
–	**Valve-jet technology for robotic-based in situ bioprinting applications**

De Momi Elena	A Safe Reinforcement Learning platform for Autonomous Robotic Tissue Approaching
–	Fast path replanning in a dynamic environment in percutaneous cardiac interventions
De Nardo Luigi	Cell encapsulation into silk fibroin microgels
De Ninno Adele	Development of a microfluidic system for impedance-based cell sorting
De Paola Sara	Development of an Integrated Software System for Medical Equipment Management: the experience of the Spedali Civili Hospital
De Rosa Alessandro Pasquale	Control Theory Measures for Dynamic Analyses of Human Functional Connectome Data
–	XGBoost vs. TabPFN in Neuroimaging Machine Learning-based analysis
De Rosa Salvatore	A Distributed Multi-Centric Application for the Analysis of Cardiac Biomarkers
De Santis Martino	Optimization of a cardiac tissue segmentation pipeline in murine whole-heart reconstructions
de Seta Valeria	On the use of PARAFAC algorithm in group network analysis: a simulation study
De Simone Paolo	Open-source as an enabling approach for the introduction of artificial intelligence in healthcare
De Stefano Nicola	XGBoost vs. TabPFN in Neuroimaging Machine Learning-based analysis
De Stefano Paola	Micropatterned PDMS substrates for cellular mechanotransduction modelling
De Vicariis Cecilia	A cloud-based mobile platform to monitor and counteract cognitive decline
–	Computational joint action: dynamical models to understand the development of joint coordination
Del Favero Simone	Automated control of bioreactors: An hardware-in-the-loop proof of concept test towards an experimental facility
–	Multi-Input Multi-Output Model Predictive Control for Drugs Delivery in Clinical Anesthesia
–	Supervised Learning-based Detection of Pressure-induced Failures in Continuous Glucose Sensors
Della Croce Ugo	An improved method for the characterization of infants' general movements using a RGB-Depth sensor and a deep neural network tracking processing tool
Dellacasa Elena	Green-Based Anti-Biofilm Nanoformulations Against Bacterial Contaminations In Nosocomial Environments
–	Innovation in neuronal cell culture: from adhesion to maturation, chitosan promotes developing nervous system
Dell'Amico Claudia	Development of analytical models to predict self-folding of 4D bioprinted scaffold
Dell'Oro Ruben	Integrated sensors for real-time monitoring of biological barriers in engineered cell culture dynamic in vitro models
Delvecchio Giuseppe	Association between inflammation and brain microstructure in First Episode Psychosis investigated with DTI
Demitri Christian	Antibacterial activity of bacterial cellulose based wound care paste
–	Wearable sensor for in-vivo skin hydration monitoring
Denisova Elena	Risk management in a medical device software: evaluation of the usability characteristics of a 3D viewer for reporting

Denti Paolo	A Comprehensive Nonlinear Mixed Effects Model of Glucose, Insulin, and C-Peptide Interaction during IVGTT
Dettin Monica	Engineering the tumor environment in vitro using peptide-enriched, hyaluronic acid-based hydrogels
–	Peptide anchoring methods for PEEK surfaces
–	Peptide-functionalized chitosan sponges for bone tissue regeneration
Di Camillo Barbara	Automated control of bioreactors: An hardware-in-the-loop proof of concept test towards an experimental facility
–	Dynamic Bayesian Networks and Transfer Learning Enable the Development of Deep Sequence-Based Models on Small-Sample Data
–	Identifying Extreme Profiles in Amyotrophic Lateral Sclerosis Patients at Diagnosis through Archetypal Analysis
–	Lipid Droplets associated genes link HSV-1 infection to neurodegeneration pathways
–	Manual and automatic identification of ACMG evidence in scientific papers
–	Simulating microbial communities' evolution via Agent base modelling: a Python tool
Di Dio Irene	Inertial measurements unit validation for countermovement jump (CMJ) tests in athletes
Di Florio Mattia	Towards personalized electroceutical therapy: electrophysiological investigations in a pre-clinical model of ischemic lesion
Di Lisa Donatella	Innovation in neuronal cell culture: from adhesion to maturation, chitosan promotes developing nervous system
–	Photosensitive pattern to control geometry and activity of a neural network
Di Marco Roberto	Analysis of an Elite Amputee Paralympic Sprinter in Track Running Pilot Tests
–	Comparative Analysis of Steady and Resisted Accelerated Treadmill Running of an Elite Amputee Paralympic Sprinter
Di Meo Simona	Millimeter-Waves Imaging for Breast Cancer Detection: Development of Analytical Models
Di Nardo Francesco	Alteration of muscle recruitment in Parkinson's disease assessed by EMG-based occurrence frequency
Di Paola Marco	Transfer learning approaches to classify foetal occiput positions on transperineal ultrasound images
Di Polidoro Angela Costagliola	Boosted transport of Theranostic Angiopep-2 engineered crosslinked Hyaluronic Acid NanoParticles (Thera-ANG-cHANPs) in glioblastoma cells
Di Rocco Giulia	Giving new life to seafood waste: in silico engineering of a chitinolytic LPMO enzyme
Di Salle Francesco	Bayesian Surprise from a Deep Learning Model of Italian Language to Model Neural Activity
–	Tensor-based morphometry of T1 weighted brain images reveals subtle volume enlargement of temporalis muscles
Di Silvio Lucy	Peptide anchoring methods for PEEK surfaces
Di Trani Maria Giovanna	Transfer learning approaches to classify foetal occiput positions on transperineal ultrasound images

Di Vico Ilaria	**Associations between fatigue and functional connectivity of dopamine and noradrenaline circuits in Parkinson's disease**
Diciotti Stefano	**The hidden structural complexity of the human cerebral cortex**
–	**XGBoost vs. TabPFN in Neuroimaging Machine Learning-based analysis**
Dipasquale Ottavia	**Assessing Multisite PET Neuroimaging Harmonisation for Normative Modelling**
–	**Associations between fatigue and functional connectivity of dopamine and noradrenaline circuits in Parkinson's disease**
–	**Automated quantification of FDOPA PET using XNAT**
–	**Modelling cerebral blood flow and neuroreceptor occupancy in dopamine blocking studies**
D'Ippolito Mariagrazia	**EEG-based quantitative measures to support the clinical diagnosis of disorders of consciousness**
Donati Alice	**Co-design of a points-based reward system to boost motivation in children and improve adherence to learning serious games**
Donati della Lunga Ilaria	**Interconnected brain regions-on-a-chip: role of connectivity and heterogeneity in the electrophysiological activity**
Donisi Leandro	**A Multiparameter Statistical Approach for Cardiotocographic Signals Analysis**
Donnaloja Francesca	**Integrated sensors for real-time monitoring of biological barriers in engineered cell culture dynamic in vitro models**
Doorduin Jonne	**Synthesis of ultrasound images from semantic labels with controllable texture features**
Dragojlov Ivana	**Effects of different degumming methods on the quality of sericin samples**
Dreossi Diego	**Towards 3D Virtual Histology of melanoma tissue by means of lab-based X-ray Phase Contrast Computed Micro-Tomography**
Drudi Cristian	**Effects of State Representation on a Reinforcement Learning Based Decision Support System**
Dubini Gabriele	**Micropatterned PDMS substrates for cellular mechanotransduction modelling**
Ducange Pietro	**Open-source as an enabling approach for the introduction of artificial intelligence in healthcare**
Duri Claudia	**Development of an Integrated Software System for Medical Equipment Management: the experience of the Spedali Civili Hospital**
Easmin Rubaida	**Assessing Multisite PET Neuroimaging Harmonisation for Normative Modelling**
–	**Automated quantification of FDOPA PET using XNAT**
Edwards Robert Randolph	**Comparison of autonomic signals between healthy subjects and chronic low back pain patients at rest and during noxious stimulation**
Ellero Manuel	**From data to knowledge: definition of an exploratory dataset for deep brain stimulation**
Elvassore Nicola	**Computational modelling of the contractile behavior of cardiomyocytes on hydrogel scaffolds for cardiac tissue regeneration**
Emiliani Filippo	**Early stages of cognitive decline are characterized by different EEG microstates dynamics**
–	**P300 event-related potential in patients with cognitive decline correlates with task performance**

Emiliani Nicolas	Augmented Reality to Evaluate Temporo-Mandibular Joint Alterations in Orthognathic Patients
–	Ex Vivo Animal Evaluation of IntraValvular Impedance Sensing Applied to Biological Heart Valve Prostheses
Enrico Paolo	Brain-heart interaction: an ECG-fMRI integrated study in physiology and major depressive disorder
Epicoco Italo	A convolutional neural network to identify osteoporosis from femoral echographic scans: a preliminary study
Esposito Alessio	Development of analytical models to predict self-folding of 4D bioprinted scaffold
Esposito Fabrizio	Bayesian Surprise from a Deep Learning Model of Italian Language to Model Neural Activity
–	Control Theory Measures for Dynamic Analyses of Human Functional Connectome Data
–	Tensor-based morphometry of T1 weighted brain images reveals subtle volume enlargement of temporalis muscles
–	XGBoost vs. TabPFN in Neuroimaging Machine Learning-based analysis
Esposito Maichael	An advanced culture system to investigate electrospun graft biomechanisms for vascular tissue engineering
Fabbiani Carlo	Early stages of cognitive decline are characterized by different EEG microstates dynamics
–	P300 event-related potential in patients with cognitive decline correlates with task performance
Fabbri Rachele	A computational platform to assess the metabolic-electrophysiological behaviour of neurons cultured in monolayers
Fabbri-Destro Maddalena	Quantifying the contribution of single joint kinematics to the overall ergonomic discomfort
Fabri Mara	Interhemispheric functional connectivity: an fMRI study in two split-brain patients
Fabris Giacomo	Analysis of an Elite Amputee Paralympic Sprinter in Track Running Pilot Tests
–	Towards a Wearable System for Complete Collection of Clamp Loads in Transfemoral Paralympic Sprinters
Facchinetti Andrea	Algorithm based on the "dynamic risk" concept allows ahead-of-time suggestion of corrective insulin boluses in type 1 diabetes therapies employing continuous glucose monitors
–	Design and Evaluation of an Intuitive Administration Dashboard for a Platform used to Monitor Clinical Trials
–	Smart Titration of Long-Acting Insulin in Insulin-Naïve Type 2 Diabetic Subjects
–	Supervised Learning-based Detection of Pressure-induced Failures in Continuous Glucose Sensors
Faes Luca	Assessment of cerebral autoregulation in patients undergoing anaesthesia with propofol: a comparison among spontaneous variability methods
–	Comparison of Machine Learning Approaches for Physiological States Classification Using Heart Rate and Pulse Rate Variability Indices
Faggionato Edoardo	A Comprehensive Nonlinear Mixed Effects Model of Glucose, Insulin, and C-Peptide Interaction during IVGTT

Falsaperla Rosaria	**Exposure set-up for assessing the far-field electromagnetic immunity levels of active implantable medical devices**
Falsina Chiara	**Development of a contrast-enhanced micro tomography protocol for human meniscus: a pilot study**
Famà Francesco	**Altered EEG amplitude coupling correlates to cognitive dysfunction in iRBD patients**
Fan Ke	**A Safe Reinforcement Learning platform for Autonomous Robotic Tissue Approaching**
Farabbi Andrea	**Error perception in different environments: Monitor vs Augmented Reality**
Farè Silvia	**FRESH approach for the development of 3D channel network in 3D in vitro models**
–	**Injectable gelatin-based photocurable fiber-reinforced hydrogel for the treatment of osteochondral defects**
Farina Lorenzo	**Network-based integration of clinical, imaging and molecular biomarkers of dementia**
Fasoli Elisa	**Effects of different degumming methods on the quality of sericin samples**
Fato Marco Massimo	**Mathematical model of nutrients transport and cell growth in a bioprinted hydrogel**
Federici Gianluca	**Profiling of phase-amplitude couplings across sleep for personalized neuroengineering systems**
Ferrante Simona	**Automatic extraction of acoustic features to predict Alzheimer's disease among English-speaking subjects**
–	**Co-design of a points-based reward system to boost motivation in children and improve adherence to learning serious games**
Ferrari Federica	**A motor-assisted recumbent trike for cycling training in neurological patients**
Ferrario Manuela	**How to assess vascular dysfunction during septic shock and resuscitation**
Ferreri Ludovico	**Understanding user needs for robotics assisted cognitive and physical rehabilitation**
Ferrigno Giancarlo	**A Safe Reinforcement Learning platform for Autonomous Robotic Tissue Approaching**
Ferro Adele	**A comparative study of Super-Resolution reconstruction methods in fetal MRI**
–	**Brain-heart interaction: an ECG-fMRI integrated study in physiology and major depressive disorder**
Ferro Andrea	**The effect of CFR-PEEK cross-link in short fixation for the stabilisation of lumbar metastasis: an in-vitro comparative study**
Ferro Nicola	**Manual and automatic identification of ACMG evidence in scientific papers**
Filippi Massimo	**XGBoost vs. TabPFN in Neuroimaging Machine Learning-based analysis**
Filippi Virginia	**Decoding the interplay between brain structural and functional connectivity in Alzheimer's disease**
Finardi Annamaria	**Association between inflammation and brain microstructure in First Episode Psychosis investigated with DTI**
Fiocchi Serena	**Comparison of RF exposure levels in 5G-V2X and ITS-5.9 GHz vehicular connectivity**
–	**Exposure Assessment of Young People to Wearable Antennas at 5G frequencies**
–	**Magnetoelectric nanoparticles as promising tools for motor nerve stimulation**

Fiore Gianfranco Beniamino	**An advanced culture system to investigate electrospun graft biomechanisms for vascular tissue engineering**
–	**Tuning the features of microphysiological systems for biomimetic intestinal in vitro models**
Fiorenza Samuele	**Prediction of injectables' stability leveraging inline analysis and machine learning**
Fioretti Sandro	**A Reliable User-Independent Motion Intent Detection from Transient EMG Data for Shoulder Joint**
–	**Alteration of muscle recruitment in Parkinson's disease assessed by EMG-based occurrence frequency**
–	**mmWave Radars Data Processing for Gait Parameters Extraction**
Fiorini Laura	**A multimodal wearable system for Human Activity Recognition during daily activities**
–	**Personality Traits Influence the Perception of a Robotic Arm endowed with Social Cues**
Fiscon Giulia	**A network-based algorithm for identifying drug repurposing opportunities for complex diseases**
–	**Bioinformatics analyses to identify molecular gene signatures associated with breast cancer phenotypes**
Flesca Sergio	**A tool to perform semi-supervised anomaly detection and annotation on 15 lead ECG signals**
–	**Validating biomedical and clinical data via an annotations based framework: experiences within the PON VQA project**
Foglieni Chiara	**Tuning the features of microphysiological systems for biomimetic intestinal in vitro models**
Fontana Flavio	**Genetic Algorithms for the identification and design of physiologically relevant 3D constructs**
Fontanella Chiara Giulia	**A novel artificial urinary sphincter and comparison with reference device**
–	**Biological evaluation in vitro and in vivo of hybrid membrane to assess biomedical application**
–	**Biomechanical characterization of human plantar fascia through experimental tests**
–	**Cryopreservation effects on biological tissues: histological and mechanical assessments**
–	**Experimental Analysis of the biomechanics of healthy porcine corneas**
–	**The biomechanical behaviour of fascial system: Superficial VS Deep Fascia**
Formaggio Emanuela	**Cortical correlates in upright static balance in adolescent idiopathic scoliosis**
Formato Giovanni Maria	**Biomechanical assessment of the anomalous coronary compression by patient-specific finite element analysis**
–	**Development of novel computational tool to support surgical planning for the treatment of Anomalous Aortic Origin of the Coronary Arteries (AAOCA)**
–	**Lumped-parameter hemodynamic model as a non-invasive tool to assess coronary blood flow in AAOCA**
Formisano Rita	**EEG-based quantitative measures to support the clinical diagnosis of disorders of consciousness**

Fortunato Gabriele Maria	3D bioprinting as a tool for the early correction of leather defects in the tanning industry
–	3D printing of a nanomaterials-embedded gelatin/pectin hydrogel for the development of an in vitro drug testing platform
–	Cell-aware optimization of the extrusion-based bioprinting process
–	Extrusion control strategy for robotic-based in situ bioprinting
–	Open-source as an enabling approach for the introduction of artificial intelligence in healthcare
–	Patient-specific phantom for home haemodialysis
–	Valve-jet technology for robotic-based in situ bioprinting applications
Foschi Nicoletta	Interhemispheric functional connectivity: an fMRI study in two split-brain patients
Fotso Fogang Joseph Vannel	A novel artificial urinary sphincter and comparison with reference device
Franceschini Stefano	A Novel Authentication System Based on Hand Gesture Ultrasound Signatures
–	Breast Cancer Detection via Two-dimensional Ultrasound Tomography
–	Breast Cancer Imaging at Microwave Frequencies via Neural Networks
–	A deep learning approach for the analysis of voxel composition in magnetic resonance imaging
Franchini Roberto	A convolutional neural network to identify osteoporosis from femoral echographic scans: a preliminary study
–	Radiofrequency Echographic Multi Spectromery for Fragility Fracture prediction through Fragility Score
Francia Piergiorgio	Phase synchronization between breathing and ppg signals in sleep events recordings of adult subjects
Franzò Michela	Assessment of Balance disorder and vestibular dysfunction using Mixed Reality
–	Key points to design the MDs Library of a National implant Registry: lesson learned from the Italian experience
Frascogna Crescenzo	Hydrogels scaffolds as 2D in vitro models to explore the impact of microenvironmental stiffness on lung adenocarcinoma cells
Frediani Gabriele	Hydrogel-based photopolymers for 3D printing of scaffolds by bench-top stereolithography
–	Wearable tactile display of softness for virtual reality
Frega Monica	Innovation in neuronal cell culture: from adhesion to maturation, chitosan promotes developing nervous system
–	Photosensitive pattern to control geometry and activity of a neural network
Freyrie Antonio	A numerical finite element methodology of the EVAR procedure
Frisoni Maria Chiara	Face mobility analysis in Spinal Muscular Atrophy
Fucarino Alberto	Rapid prototyping of a microfluidic platform for nasal mucosa models
Furlan Roberto	Association between inflammation and brain microstructure in First Episode Psychosis investigated with DTI
Gaetan Elisa	Modeling metabolic overload effects in bacterial growth rate in synthetic biology
Galeotti Marta	Motor performances evaluation of female soccer players from AC Trento Women

Galgaro Antonio	3D moles mapping and analysis for automatic melanoma detection
Galletta Valentina	Magnetoelectric nanoparticles as promising tools for motor nerve stimulation
Galli Manuela	Differences in cortical reorganization during visuo-motor tasks executed with the dominant and non-dominant hands
–	Effectiveness of a home-based tele-rehabilitation program for post-Covid patients: preliminary results
–	Inertial measurements unit validation for countermovement jump (CMJ) tests in athletes
–	Motor performances evaluation of female soccer players from AC Trento Women
Gallo Antonio	XGBoost vs. TabPFN in Neuroimaging Machine Learning-based analysis
Gallo Diego	Development of a computational model to estimate the hemolysis risk associated with hemodialysis catheters
Gallo Gionatan	Open-source as an enabling approach for the introduction of artificial intelligence in healthcare
Gallucci Silvia	Comparison of RF exposure levels in 5G-V2X and ITS-5.9 GHz vehicular connectivity
–	Exposure Assessment of Young People to Wearable Antennas at 5G frequencies
Galuzzi Giacomo	Commercial Smart Virtual Assistants to support medication adherence in chronic patients: a preliminary usability study
Gambi Ennio	mmWave Radars Data Processing for Gait Parameters Extraction
Gandini Wheeler-Kingshott Claudia Angela Michela	A deep learning network from downsampled diffusion-weighted MRI k-space to image-space
–	Myelin quantification in Magnetic Resonance Imaging
Gandolfi Daniela	Full-scale point-neuron model of the mouse hippocampal microcircuits
Gandolfo Caterina	An Inverse Analysis for the Assessment of Material Properties of TAVI Patients
–	Establishing Computational Modeling Credibility in Patients Undergoing TAVI
–	Mechanical Properties of Polyamide 12 for the use in Balloon-Expandable Transcatheter Heart Valves
–	Numerical Analysis of the Bicaval Transcatheter System for the Treatment of Severe Tricuspid Regurgitation
–	Structural Simulation of Transcatheter Heart Valve in Transcatheter Heart Valve
Gandolla Marta	3D upper limbs tracking through inertial sensors: calibration, methodology, and validation
–	Virtual prototyping of a robotic chess player for play therapy
Gandullia Paolo	Design and fabrication of an intestinal phantom to mimic intestinal tone and motility
Garello Luca	Computer Vision and Deep Learning for Human Motion Analysis
Gariboldi Francesca	Static strength of lower-limb prosthetic sockets for the activities of daily living
Garofalo Roberto	Effect of EDA-driven sympathetic responses on the central processing of faces cued by hedonic odors: a preliminary ERP study
Gasparini Soria	Dose-controlled low-intensity pulsed ultrasound and pulsed electromagnetic fields stimulations modulate inflammation in human macrophages
Gatta Gianluca	Evaluation of breast density variability between right and left breasts

Gatti Laura	Risk management in a medical device software: evaluation of the usability characteristics of a 3D viewer for reporting
Gatti Roberto	Differences in cortical reorganization during visuo-motor tasks executed with the dominant and non-dominant hands
Gautieri Alfonso	Giving new life to seafood waste: in silico engineering of a chitinolytic LPMO enzyme
Gaviraghi Marta	A deep learning network from downsampled diffusion-weighted MRI k-space to image-space
–	Myelin quantification in Magnetic Resonance Imaging
Gelpi Francesca	Assessment of cerebral autoregulation in patients undergoing anaesthesia with propofol: a comparison among spontaneous variability methods
Gemelli Roberto	Mechanical characterization of hybrid membrane suitable for biomedical application
Geminiani Alice	An attention classifier for the evaluation of a robotic therapy in children with Autism Spectrum Disorder
Gentile Piergiorgio	Nanostructured coatings with bacteria-triggered antimicrobial response for medical devices
Gerosa Gino	Biological evaluation in vitro and in vivo of hybrid membrane to assess biomedical application
–	Mechanical characterization of hybrid membrane suitable for biomedical application
Ghelardi Emilia	Design and fabrication of a micro-dialyser for the study of the gut microbiota-tissues cross-talk
Ghersi Giulio	Effect of Chitosan coating on PLA electrospun scaffolds for bone tissue engineering
Ghi Tullio	Transfer learning approaches to classify foetal occiput positions on transperineal ultrasound images
Ghoushi Mojgan	Interhemispheric functional connectivity: an fMRI study in two split-brain patients
Giacalone Vincenzo	Mechanical evaluation of synthetic meshes: definition and verification of a rigorous test protocol
Giacomel Alessio	Assessing Multisite PET Neuroimaging Harmonisation for Normative Modelling
–	Automated quantification of FDOPA PET using XNAT
Giacomini Mauro	Improving data quality in healthcare: medical informatics tools and standards
Giacomucci Giulia	Early stages of cognitive decline are characterized by different EEG microstates dynamics
–	P300 event-related potential in patients with cognitive decline correlates with task performance
Giagnorio Eleonora	Cell encapsulation into silk fibroin microgels
–	A tool to perform semi-supervised anomaly detection and annotation on 15 lead ECG signals
Giancotti Raffaele	A tool to perform semi-supervised anomaly detection and annotation on 15 lead ECG signals
	Validating biomedical and clinical data via an annotations based framework: experiences within the PON VQA project

Giangregorio Chiara	**Automatic extraction of acoustic features to predict Alzheimer's disease among English-speaking subjects**
Giannelli Andrea	**Autonomic response to virtual reality in oncological patients in real-world context**
Giannotti Alice	**Mechanical validation of an innovative intrafascicular neural interface to restore urinary bladder dysfunctions**
Giardini Francesco	**Optimization of a cardiac tissue segmentation pipeline in murine whole-heart reconstructions**
Giavaresi Gianluca	**Development of a contrast-enhanced micro tomography protocol for human meniscus: a pilot study**
Giordano Carmen	**Integrated sensors for real-time monitoring of biological barriers in engineered cell culture dynamic in vitro models**
Giordano Noemi	**Usability of a multi-sensor array for the application of electro-phonocardiography in home care**
Giorgini Federica	**The hidden structural complexity of the human cerebral cortex**
Gironi Camilla	**Ex Vivo Animal Evaluation of IntraValvular Impedance Sensing Applied to Biological Heart Valve Prostheses**
Giubergia Alice	**Pseudo resting-state investigation from task-evoked functional MRI signals**
Giuffrè Mauro	**Estimating the degree of Non-Alcoholic Fatty Live Disease (NAFLD) from ultrasound images: preliminary results**
Gizzi Leonardo	**Synergy-dependent patterns of reaction forces in sit-to-stand movements**
Gloria Antonio	**Peptide-functionalized chitosan sponges for bone tissue regeneration**
Göbl Christian	**Mathematical model of glucagon kinetics during an oral glucose tolerance test based on a dual regulation mechanism**
Goffi Federica	**Brain-heart interaction: an ECG-fMRI integrated study in physiology and major depressive disorder**
Goretti Francesco	**Prediction of Atrial Fibrillation using Deep Learning techniques**
Gori Davide	**Sensor-based Assessment of Gross and Fine Motor Development in Primary School Children**
Gotzen Nils	**Mechanical Properties of Polyamide 12 for the use in Balloon-Expandable Transcatheter Heart Valves**
Gozzi Alessandro	**Single region contribution to the brain dynamic (in)stability**
Grassi Alberto	**Development of a contrast-enhanced micro tomography protocol for human meniscus: a pilot study**
Grassi Andrea	**A method for the evaluation of cervical surgical instrumentation reliability through a computational and experimental approach**
Grassi Roberto	**Evaluation of breast density variability between right and left breasts**
Grasso Elisa	**Combination of VR and manikins to improve medical training**
Greco Alberto	**Effect of EDA-driven sympathetic responses on the central processing of faces cued by hedonic odors: a preliminary ERP study**
–	**Patient-specific phantom for home haemodialysis**
Greco Rosaria	**Towards personalized electroceutical therapy: electrophysiological investigations in a pre-clinical model of ischemic lesion**
Grippo Antonello	**Early stages of cognitive decline are characterized by different EEG microstates dynamics**

–	**Network model accounts for evolution of EEG functional connectivity in patients with cognitive decline**
–	**Non-linear analysis of HRV reveal lower signal complexity in patients with a prolonged Disorder of Consciousness**
–	**P300 event-related potential in patients with cognitive decline correlates with task performance**
Grisi Caterina	**Assessing Personal Exposure to Airborne Particulate Matter with Wearable Sensors and Ventilation Rate Models**
Grönlund Christer	**Combining high-density electromyography and ultrafast ultrasound to assess individual motor unit properties in vivo**
Gruppioni Emanuele	**Comparative analysis of EMG-based classifiers for recognizing hand/wrist gestures and forces**
Grussu Francesco	**A deep learning network from downsampled diffusion-weighted MRI k-space to image-space**
–	**Myelin quantification in Magnetic Resonance Imaging**
Guanziroli Eleonora	**A motor-assisted recumbent trike for cycling training in neurological patients**
Guazzelli Nicole	**Design and fabrication of an intestinal phantom to mimic intestinal tone and motility**
–	**Multiscale computational models for predicting hydrogel viscoelastic properties**
Guazzo Alessandro	**Manual and automatic identification of ACMG evidence in scientific papers**
Guerra Andrea	**Valve-jet technology for robotic-based in situ bioprinting applications**
Gugliemo Marco	**Radiomic analysis of Epicardial Adipose Tissue in cardiac MRI for hospitalization risk assessment**
Guidetti Ilaria	**Development of a computational model to estimate the hemolysis risk associated with hemodialysis catheters**
Guidi Lorenzo	**3D printing of a nanomaterials-embedded gelatin/pectin hydrogel for the development of an in vitro drug testing platform**
Guidotti Roberto	**Closing the loop between neurostimulation and control theory**
–	**Disclosing brain functional connections with multi-dimensional approaches**
Gulino Ilenia	**Open-source as an enabling approach for the introduction of artificial intelligence in healthcare**
Gulotta Chiara	**Augmented Reality to Evaluate Temporo-Mandibular Joint Alterations in Orthognathic Patients**
Guo Yikang	**Comparison of autonomic signals between healthy subjects and chronic low back pain patients at rest and during noxious stimulation**
Guzzi Pietro Hiram	**A tool to perform semi-supervised anomaly detection and annotation on 15 lead ECG signals**
–	**Validating biomedical and clinical data via an annotations based framework: experiences within the PON VQA project**
Haeck Joost	**Boosted transport of Theranostic Angiopep-2 engineered crosslinked Hyaluronic Acid NanoParticles (Thera-ANG-cHANPs) in glioblastoma cells**
Hakiki Bahia	**Non-linear analysis of HRV reveal lower signal complexity in patients with a prolonged Disorder of Consciousness**
Hassaballah Poula	**Brain signals in semi-immersive and immersive VR environments: a feasibility study**

Helbostad Jorunn L.	**Wearable-based Sit-to-Stand transfers in Older Adults: context differences between in-lab and home-based assessments**
Heuckeroth Robert	**Design and fabrication of an intestinal phantom to mimic intestinal tone and motility**
Howes Oliver	**Assessing Multisite PET Neuroimaging Harmonisation for Normative Modelling**
–	**Automated quantification of FDOPA PET using XNAT**
–	**Modelling cerebral blood flow and neuroreceptor occupancy in dopamine blocking studies**
Iacoponi Francesco	**Dose-controlled low-intensity pulsed ultrasound and pulsed electromagnetic fields stimulations modulate inflammation in human macrophages**
Iacovacci Veronica	**A hydraulic implantable artificial detrusor for controlled bladder voiding**
Iadanza Ernesto	**Health Information Technology Adverse Events Identification and Classification with Natural Language Processing and Deep Learning**
–	**Prediction of Atrial Fibrillation using Deep Learning techniques**
–	**Risk management in a medical device software: evaluation of the usability characteristics of a 3D viewer for reporting**
Idi Elena	**Supervised Learning-based Detection of Pressure-induced Failures in Continuous Glucose Sensors**
Ignoti Lucia Maria	**Development of an Integrated Software System for Medical Equipment Management: the experience of the Spedali Civili Hospital**
Imparato Giorgia	**An engineered breast cancer model on chip for personalized and multiple drug therapy**
–	**Bio-fabrication of in vitro tissues possessing organ-specific endogenous extracellular matrices**
–	**Hydrogels scaffolds as 2D in vitro models to explore the impact of microenvironmental stiffness on lung adenocarcinoma cells**
Imran Saima Jalil	**Biological evaluation in vitro and in vivo of hybrid membrane to assess biomedical application**
Indolfi Ciro	**A Distributed Multi-Centric Application for the Analysis of Cardiac Biomarkers**
Ingannato Assunta	**Early stages of cognitive decline are characterized by different EEG microstates dynamics**
–	**P300 event-related potential in patients with cognitive decline correlates with task performance**
Inghirami Valentina	**Multiscale computational models for predicting hydrogel viscoelastic properties**
Inglese Matilde	**Computer Vision and Deep Learning for Human Motion Analysis**
Intilli Giorgia	**Rapid prototyping of a microfluidic platform for nasal mucosa models**
Iovino Marta	**Comparison of Machine Learning Approaches for Physiological States Classification Using Heart Rate and Pulse Rate Variability Indices**
Iscra Katerina	**Discriminatory power of Global Longitudinal Strain and Left Ventricular Ejection Fraction for Identification of Dilated Cardiomyopathy**
Isernia Sara	**Development of a novel surface-based approach to quantify fNIRS-fMRI spatial correspondence**
Isernia Tommaso	**Experimental Microwave Imaging of Human Forearm**

Iucci Giovanna	**Peptide-functionalized chitosan sponges for bone tissue regeneration**
Javorka Michal	**Comparison of Machine Learning Approaches for Physiological States Classification Using Heart Rate and Pulse Rate Variability Indices**
Jung Ki-Young	**Altered EEG amplitude coupling correlates to cognitive dysfunction in iRBD patients**
Kamarthi Sagar	**Comparison of autonomic signals between healthy subjects and chronic low back pain patients at rest and during noxious stimulation**
Kanber Baris	**A deep learning network from downsampled diffusion-weighted MRI k-space to image-space**
–	**Myelin quantification in Magnetic Resonance Imaging**
Knaflitz Marco	**Usability of a multi-sensor array for the application of electro-phonocardiography in home care**
Koptyug Andrey	**Advances in the development of a instrumented head surrogate for brain injury investigation**
Kraushaar Udo	**Optimization of advanced setups with integrated readouts for evaluation of cardiac toxicity in a heart on chip device**
Kresevic Simone	**Estimating the degree of Non-Alcoholic Fatty Live Disease (NAFLD) from ultrasound images: preliminary results**
Kuo Hsinhung	**An improved method for the characterization of infants' general movements using a RGB-Depth sensor and a deep neural network tracking processing tool**
La Barbera Luigi	**A response surface-based approach to predict spinal rod contouring parameters**
–	**Assessment of a parametric thoracic spine model for the generation of in silico cohorts**
La Carrubba Vincenzo	**Effect of Chitosan coating on PLA electrospun scaffolds for bone tissue engineering**
–	**Rapid prototyping of a microfluidic platform for nasal mucosa models**
La Viola Carlo	**Personality Traits Influence the Perception of a Robotic Arm endowed with Social Cues**
Lagreca Elena	**Biological validation of thiolated food grade secondary oil in water nanoemulsions with enhanced mucus-adhesion properties in Intestine-on-a-chip model**
Lamfers Martine	**Boosted transport of Theranostic Angiopep-2 engineered crosslinked Hyaluronic Acid NanoParticles (Thera-ANG-cHANPs) in glioblastoma cells**
Lampis Valentina	**Pseudo resting-state investigation from task-evoked functional MRI signals**
Lanari Marcello	**Sensor-based Assessment of Gross and Fine Motor Development in Primary School Children**
Lanzarini Francesca	**K-medoid clustering of premotor firing patterns supports fine decoding of macaque reach-and-grasp**
Lapresa Martina	**Performance Evaluation of the Gloreha Sinfonia Device in Bimanual Modality**
Largajolli Anna	**A Comprehensive Nonlinear Mixed Effects Model of Glucose, Insulin, and C-Peptide Interaction during IVGTT**
Laricchiuta Paola	**Key points to design the MDs Library of a National implant Registry: lesson learned from the Italian experience**
Lasalvia Antonio	**Association between inflammation and brain microstructure in First Episode Psychosis investigated with DTI**

Lassi Michael	Early stages of cognitive decline are characterized by different EEG microstates dynamics
–	Network model accounts for evolution of EEG functional connectivity in patients with cognitive decline
–	P300 event-related potential in patients with cognitive decline correlates with task performance
Lastrico Linda	Toward Implicit Communication of Object Properties for Human-Robot Interaction
Lattanzi Simona	Interhemispheric functional connectivity: an fMRI study in two split-brain patients
Laurano Rosella	Engineering of poly(urethane)-based porous constructs for cardiac tissue model design
Lauretti Clemente	A safe robot control for semi-autonomous pedicle tapping
Lazarova Elena	Improving data quality in healthcare: medical informatics tools and standards
Lazich Aldo	A preliminary test of a novel method for the real time estimation of foot displacement using MIMUs attached to the foot
Lazzaro Jacopo	A dexterous hand prosthesis based on additive manufacturing
Lazzeri Erica	Optimization of a cardiac tissue segmentation pipeline in murine whole-heart reconstructions
Lazzeri Luigi	3D printing of a nanomaterials-embedded gelatin/pectin hydrogel for the development of an in vitro drug testing platform
Leone Francesca	Comparative analysis of EMG-based classifiers for recognizing hand/wrist gestures and forces
Letrari Sara	Lipid Droplets associated genes link HSV-1 infection to neurodegeneration pathways
Licciulli Antonio	Antibacterial activity of bacterial cellulose based wound care paste
Liguori Chiara	FRESH approach for the development of 3D channel network in 3D in vitro models
Lin Yingzi	Comparison of autonomic signals between healthy subjects and chronic low back pain patients at rest and during noxious stimulation
Lippi Maria Elena	Open-source as an enabling approach for the introduction of artificial intelligence in healthcare
Liu Jiaying	Distinguishing lymph nodes in head and neck cancer patients using MRI-based radiomics
Liuzzi Piergiuseppe	Non-linear analysis of HRV reveal lower signal complexity in patients with a prolonged Disorder of Consciousness
Lizio Andrea	Face mobility analysis in Spinal Muscular Atrophy
Lo Iacono Francesca	Radiomic analysis of Epicardial Adipose Tissue in cardiac MRI for hospitalization risk assessment
Lo Rito Mauro	Biomechanical assessment of the anomalous coronary compression by patient-specific finite element analysis
–	Development of novel computational tool to support surgical planning for the treatment of Anomalous Aortic Origin of the Coronary Arteries (AAOCA)
–	Lumped-parameter hemodynamic model as a non-invasive tool to assess coronary blood flow in AAOCA
Lo Vetri Joe	Experimental Microwave Imaging of Human Forearm
Locati Emanuela Teresina	Brugada Syndrome: Characterization of QT Interval Components and Correction

Loi Giada	A workflow for the construction of reproducible living biosensors built by printing bacterial materials
Lombardi Fiorella Anna	A convolutional neural network to identify osteoporosis from femoral echographic scans: a preliminary study
–	Osteoporosis Identification at Lumbar Vertebrae through a Neural Network Classifier
–	Radiofrequency Echographic Multi Spectromery for Fragility Fracture prediction through Fragility Score
–	Soft-tissue alterations identified with a CNN trained with simulated ultrasound images integrating expert knowledge
Lombardi Maria	Tuning the features of microphysiological systems for biomimetic intestinal in vitro models
Lomoio Ugo	A tool to perform semi-supervised anomaly detection and annotation on 15 lead ECG signals
–	Validating biomedical and clinical data via an annotations based framework: experiences within the PON VQA project
Lomonaco Tommaso	Effect of EDA-driven sympathetic responses on the central processing of faces cued by hedonic odors: a preliminary ERP study
Longato Enrico	Dynamic Bayesian Networks and Transfer Learning Enable the Development of Deep Sequence-Based Models on Small-Sample Data
–	Manual and automatic identification of ACMG evidence in scientific papers
Longhin Francesca	Manual and automatic identification of ACMG evidence in scientific papers
Lopa Silvia	A microfluidic platform to unravel immune cells cross-talk in rheumatoid arthritis
Lapomarda Anna	3D printing of a nanomaterials-embedded gelatin/pectin hydrogel for the development of an in vitro drug testing platform
Lopomo Nicola Francesco	Development of a contrast-enhanced micro tomography protocol for human meniscus: a pilot study
–	Integrated Protocol for Multidimensional In Vivo Assessment of Glenohumeral Joint Function during Dynamic Tasks
–	Quantifying the contribution of single joint kinematics to the overall ergonomic discomfort
Lopresti Francesco	Effect of Chitosan coating on PLA electrospun scaffolds for bone tissue engineering
–	Rapid prototyping of a microfluidic platform for nasal mucosa models
Lorato Ilde	Remote In-Bed Monitoring of Vital Signs Using Radar Technology
Lucchiari Alessandro	Simulating microbial communities' evolution via Agent base modelling: a Python tool
Lugas Andrea Tancredi	Biomimetic platform for investigating in vitro the cell biological response to mechanical stretching – periodontal ligament stem cell application
Luisetto Roberto	Biological evaluation in vitro and in vivo of hybrid membrane to assess biomedical application
Lum Peter	An improved method for the characterization of infants' general movements using a RGB-Depth sensor and a deep neural network tracking processing tool
Lupi Eleonora	Myelin quantification in Magnetic Resonance Imaging

Lupori Leonardo	**Machine learning-based classification of cortical response to visual stimuli recorded with an ECoG array in mice: a case study**
Luraghi Giulia	**A numerical finite element methodology of the EVAR procedure**
Luschi Alessio	**Health Information Technology Adverse Events Identification and Classification with Natural Language Processing and Deep Learning**
–	**Risk management in a medical device software: evaluation of the usability characteristics of a 3D viewer for reporting**
Maccarone Francesca	**Pseudo resting-state investigation from task-evoked functional MRI signals**
Macchi Veronica	**Composite scaffolds based on polyvinyl alcohol and acellular cartilage matrix for hemophilic arthropathy treatment**
Macchia Giulia	**Osteoporosis Identification at Lumbar Vertebrae through a Neural Network Classifier**
Magagnin Luca	**Integrated sensors for real-time monitoring of biological barriers in engineered cell culture dynamic in vitro models**
Magenes Giovanni	**Cardiotocography in antenatal fetal monitoring of diabetes-complicated pregnancies**
–	**Hidden Markov Models for the identification of fetal phases in CTG recordings**
–	**Millimeter-Waves Imaging for Breast Cancer Detection: Development of Analytical Models**
Maggi Norbert	**Improving data quality in healthcare: medical informatics tools and standards**
Maggio Manuel	**Osteoporosis Identification at Lumbar Vertebrae through a Neural Network Classifier**
Maggioni Eleonora	**Brain-heart interaction: an ECG-fMRI integrated study in physiology and major depressive disorder**
Magliaro Chiara	**A computational platform to assess the metabolic-electrophysiological behaviour of neurons cultured in monolayers**
–	**Early stages of cognitive decline are characterized by different EEG microstates dynamics**
–	**Experimental and computational pipeline for identifying oxygen metabolic rate parameters in 2D and 3D in vitro constructs**
–	**Genetic Algorithms for the identification and design of physiologically relevant 3D constructs**
–	**Oxygen metabolism in in vitro ecosystems**
Maglio Melania	**Development of a contrast-enhanced micro tomography protocol for human meniscus: a pilot study**
Magni Paolo	**A bioinformatic pipeline for identifying bacterial constitutive promoters based on transcriptomic data analysis**
–	**A workflow for the construction of reproducible living biosensors built by printing bacterial materials**
–	**Study and characterization of bile acid biosensors in engineered probiotic bacteria**
Magnussen Michael	**Computational modelling of the contractile behavior of cardiomyocytes on hydrogel scaffolds for cardiac tissue regeneration**
Mainardi Luca	**Distinguishing lymph nodes in head and neck cancer patients using MRI-based radiomics**

–	**Error perception in different environments: Monitor vs Augmented Reality**
–	**Quantitative validation of an automatic videoPPG technique during autonomic elicitations**
Mancini Piera	**Experimental and computational pipeline for identifying oxygen metabolic rate parameters in 2D and 3D in vitro constructs**
–	**Genetic Algorithms for the identification and design of physiologically relevant 3D constructs**
–	**Oxygen metabolism in in vitro ecosystems**
Mancioppi Gianmaria	**Personality Traits Influence the Perception of a Robotic Arm endowed with Social Cues**
Mandigers Tim J.	**A numerical finite element methodology of the EVAR procedure**
Manetti Leonardo	**Risk management in a medical device software: evaluation of the usability characteristics of a 3D viewer for reporting**
Maniglio Devid	**Assessment of printability on autoclaved biomaterial inks for extrusion bioprinting**
Manini Aurora	**Full-scale point-neuron model of the mouse hippocampal microcircuits**
Manna Olga	**Rapid prototyping of a microfluidic platform for nasal mucosa models**
Mannella Riccardo	**Network model accounts for evolution of EEG functional connectivity in patients with cognitive decline**
Mannini Andrea	**Non-linear analysis of HRV reveal lower signal complexity in patients with a prolonged Disorder of Consciousness**
Mantovani Diego	**Vibropolyfection: boosting polymer-mediated gene delivery by mechanical cell loading**
Manzo Teresa	**A microfluidic platform to unravel immune cells cross-talk in rheumatoid arthritis**
Manzoni Eleonora	**Multi-Input Multi-Output Model Predictive Control for Drugs Delivery in Clinical Anesthesia**
–	**Supervised Learning-based Detection of Pressure-induced Failures in Continuous Glucose Sensors**
Mapelli Jonathan	**Full-scale point-neuron model of the mouse hippocampal microcircuits**
Maranesi Monica	**K-medoid clustering of premotor firing patterns supports fine decoding of macaque reach-and-grasp**
Marcaccini Kevin	**Brain signals in semi-immersive and immersive VR environments: a feasibility study**
Marcantoni Ilaria	**Interhemispheric functional connectivity: an fMRI study in two split-brain patients**
Marceglia Sara	**From data to knowledge: definition of an exploratory dataset for deep brain stimulation**
Marcelli Emanuela	**Augmented Reality to Evaluate Temporo-Mandibular Joint Alterations in Orthognathic Patients**
–	**Ex Vivo Animal Evaluation of IntraValvular Impedance Sensing Applied to Biological Heart Valve Prostheses**
Marcello Elena	**Natural polymer-based bioinks exploiting internal gelation mechanism for cardiac tissue engineering**
Marchesi Giorgia	**Computer Vision and Deep Learning for Human Motion Analysis**
Marchetti Luca	**Uncovering quorum sensing and quenching structural properties: a systems biology approach**

Marchiori Gregorio	Development of a contrast-enhanced micro tomography protocol for human meniscus: a pilot study
Marcolin Giuseppe	Analysis of an Elite Amputee Paralympic Sprinter in Track Running Pilot Tests
–	Comparative Analysis of Steady and Resisted Accelerated Treadmill Running of an Elite Amputee Paralympic Sprinter
Marcuzzo Stefania	Cell encapsulation into silk fibroin microgels
Maremonti Maria Isabella	Circulating tumour cells deformability measurement in microfluidics
–	In-flow viscoelastic compression to probe single-cell biomechanical properties
–	Microfluidic platform for cell classification from optical signatures via machine learning
–	Microgels as a Biosensing Platform
Margani Valerio	Assessment of Balance disorder and vestibular dysfunction using Mixed Reality
Mari Andrea	Longitudinal Relationships Between Proteomics and Beta-Cell Dysfunction in Type 2 Diabetes: An Imi Direct Study
Mari Veronica	Key points to design the MDs Library of a National implant Registry: lesson learned from the Italian experience
Mariani Erica	A numerical finite element methodology of the EVAR procedure
Marini Sofia	Sensor-based Assessment of Gross and Fine Motor Development in Primary School Children
Marini Vittoria	RNA Sequencing analysis to study Duchenne dilated cardiomyopathy in patient-derived 3D organoid models
Marino Fabiola	RNA Sequencing analysis to study Duchenne dilated cardiomyopathy in patient-derived 3D organoid models
Marinozzi Andrea	3D Finite Element Analysis of a Percolating Cluster inside the Mineralized Collagen Fibril
Marinozzi Franco	3D Finite Element Analysis of a Percolating Cluster inside the Mineralized Collagen Fibril
–	Assessment of Balance disorder and vestibular dysfunction using Mixed Reality
–	Key points to design the MDs Library of a National implant Registry: lesson learned from the Italian experience
–	Near Field Electrospinning Process Using a Multi-Axis Robot
Marjin Corina	Impact of model selection procedure on Deep Neural Networks ensemble for the Choroid Plexus segmentation in Multiple Sclerosis
Marletta Giovanni	Peptide anchoring methods for PEEK surfaces
Marone Stefano	The effect of CFR-PEEK cross-link in short fixation for the stabilisation of lumbar metastasis: an in-vitro comparative study.
Marques Tiago Reis	Modelling cerebral blood flow and neuroreceptor occupancy in dopamine blocking studies
Marrella Alessandra	Magnetoelectric nanoparticles as promising tools for motor nerve stimulation
Marsotto Martina	Peptide anchoring methods for PEEK surfaces
Martin Matteo	Noise-Induced Dynamics and Stochastic Slow Manifolds in the Bistable Xiong-Ferrell Model

Martinoia Sergio	Development of excitatory neuronal networks derived from human induced pluripotent stem cells
–	Innovation in neuronal cell culture: from adhesion to maturation, chitosan promotes developing nervous system
–	PEDOT:PSS ink-jet printed microelectrodes on paper: towards low-cost and green MEA devices
–	Photosensitive pattern to control geometry and activity of a neural network
Martins Daniel	Assessing Multisite PET Neuroimaging Harmonisation for Normative Modelling
–	Associations between fatigue and functional connectivity of dopamine and noradrenaline circuits in Parkinson's disease
–	Automated quantification of FDOPA PET using XNAT
Marzetti Laura	Closing the loop between neurostimulation and control theory
–	Disclosing brain functional connections with multi-dimensional approaches
Marzi Chiara	The hidden structural complexity of the human cerebral cortex
–	XGBoost vs. TabPFN in Neuroimaging Machine Learning-based analysis
Marzola Francesco	Synthesis of ultrasound images from semantic labels with controllable texture features
Masante Beatrice	Biomimetic platform for investigating in vitro the cell biological response to mechanical stretching – periodontal ligament stem cell application
Mascheretti Sara	Pseudo resting-state investigation from task-evoked functional MRI signals
Masciullo Antonio	Wearable sensor for in-vivo skin hydration monitoring
Mascolini Maria Vittoria	A novel artificial urinary sphincter and comparison with reference device
–	Experimental Analysis of the biomechanics of healthy porcine corneas
Masiero Stefano	Cortical correlates in upright static balance in adolescent idiopathic scoliosis
Masini Alice	Sensor-based Assessment of Gross and Fine Motor Development in Primary School Children
Massai Diana	Biomimetic platform for investigating in vitro the cell biological response to mechanical stretching – periodontal ligament stem cell application
Massobrio Paolo	Interconnected brain regions-on-a-chip: role of connectivity and heterogeneity in the electrophysiological activity
Massone Antonino	Non-linear dimensionality-reduction approach for powered wheelchair control
Mastrogiovanni Fulvio	Toward Implicit Communication of Object Properties for Human-Robot Interaction
Matrone Giulia	A Workflow for Biomechanical Simulation of Patient-specific Atherosclerotic Carotid Artery
–	Millimeter-Waves Imaging for Breast Cancer Detection: Development of Analytical Models
Mattei Eugenio	Exposure set-up for assessing the far-field electromagnetic immunity levels of active implantable medical devices
Mattia Donatella	Brain-Computer Interface assisted Motor Imagery training in post-stroke rehabilitation: longitudinal study of the EEG sensorimotor rhythms
–	EEG-based quantitative measures to support the clinical diagnosis of disorders of consciousness

–	On the use of PARAFAC algorithm in group network analysis: a simulation study
Mattioli Pietro	Altered EEG amplitude coupling correlates to cognitive dysfunction in iRBD patients
Mayhew Stephen D.	fMRI characterization of intrinsic brain networks relevant for motor control with and without visual feedback by fractal dimension
Mazio Claudia	An engineered breast cancer model on chip for personalized and multiple drug therapy
–	Hydrogels scaffolds as 2D in vitro models to explore the impact of microenvironmental stiffness on lung adenocarcinoma cells
Mazzaccaro Daniela	A Workflow for Biomechanical Simulation of Patient-specific Atherosclerotic Carotid Artery
Mazzeo Salvatore	Early stages of cognitive decline are characterized by different EEG microstates dynamics
–	P300 event-related potential in patients with cognitive decline correlates with task performance
Mazziotti Margot	Commercial Smart Virtual Assistants to support medication adherence in chronic patients: a preliminary usability study
Mazziotti Raffaele	Machine learning-based classification of cortical response to visual stimuli recorded with an ECoG array in mice: a case study
Mazzoni Alberto	Early stages of cognitive decline are characterized by different EEG microstates dynamics
–	K-medoid clustering of premotor firing patterns supports fine decoding of macaque reach-and-grasp
–	Network model accounts for evolution of EEG functional connectivity in patients with cognitive decline
–	P300 event-related potential in patients with cognitive decline correlates with task performance
Mazzucato Mario	Model Assessment of Doxorubicin Pharmacokinetics in Multiple Myeloma
–	Modeling Doxorubicin Treatment Effect in Multiple Myeloma
Mehta Mitul	Modelling cerebral blood flow and neuroreceptor occupancy in dopamine blocking studies
Meiburger Kristen	Combining high-density electromyography and ultrafast ultrasound to assess individual motor unit properties in vivo
–	Quality enhancement of dermatological images using GANs: a proof of concept
–	Synthesis of ultrasound images from semantic labels with controllable texture features
Melfa Gianvincenzo	The prediction of the patient's response to hemodialysis treatment: DialysIS vs InterACTIVE-HD 2.0 experience
Mencarini Tatiana	Microfluidic system for a label-free, real-time functional assessment of thrombotic risk
Menciassi Arianna	A hydraulic implantable artificial detrusor for controlled bladder voiding
Menegaz Gloria	Decoding the interplay between brain structural and functional connectivity in Alzheimer's disease
–	Enhancing Safety in Industry 4.0: The Use of Passive Brain Computer Interfaces for Vigilance Monitoring

–	Exploring the potential of MCVAE for patients stratification and skewed data compensation across the AD continuum
Mengarelli Alessandro	A Reliable User-Independent Motion Intent Detection from Transient EMG Data for Shoulder Joint
Mercuri Marco	Remote In-Bed Monitoring of Vital Signs Using Radar Technology
Mereu Federico	Comparative analysis of EMG-based classifiers for recognizing hand/wrist gestures and forces
Merla Arcangelo	Driver drowsiness detection relying on infrared thermal imaging: a machine learning approach
–	Drivers' mental workload assessment based on machine learning applied to multimodal physiological data
Merli Chiara	Hydrogel-based photopolymers for 3D printing of scaffolds by bench-top stereolithography
Merlo Marco	Discriminatory power of Global Longitudinal Strain and Left Ventricular Ejection Fraction for Identification of Dilated Cardiomyopathy
Merola Alessio	A Distributed Multi-Centric Application for the Analysis of Cardiac Biomarkers
–	A preliminary version of a Genome-Scale Metabolic Model for Induced Human Pluripotent Stem Cells (hiPSCs)
Mesin Luca	Functional Connectivity of the EEG in epilepsy: a single case study
Messina Grazia Maria Lucia	Peptide anchoring methods for PEEK surfaces
Mezzanotte Laura	Boosted transport of Theranostic Angiopep-2 engineered crosslinked Hyaluronic Acid NanoParticles (Thera-ANG-cHANPs) in glioblastoma cells
Micalizzi Simone	3D bioprinting as a tool for the early correction of leather defects in the tanning industry
–	Design and fabrication of a novel bioreactor for the engineering of tendon/ligament-to-bone interfaces
Micera Silvestro	Early stages of cognitive decline are characterized by different EEG microstates dynamics
–	Machine learning-based classification of cortical response to visual stimuli recorded with an ECoG array in mice: a case study
–	Mechanical validation of an innovative intrafascicular neural interface to restore urinary bladder dysfunctions
Migliavacca Francesco	A numerical finite element methodology of the EVAR procedure
Migliore Gian Luca	Analysis of an Elite Amputee Paralympic Sprinter in Track Running Pilot Tests
–	Static strength of lower-limb prosthetic sockets for the activities of daily living
Migliore Gianluca	Towards a Wearable System for Complete Collection of Clamp Loads in Transfemoral Paralympic Sprinters
Migliori Michele	Full-scale point-neuron model of the mouse hippocampal microcircuits
Miladinovic Aleksander	Discriminatory power of Global Longitudinal Strain and Left Ventricular Ejection Fraction for Identification of Dilated Cardiomyopathy
Milano Giuseppe	Integrated Protocol for Multidimensional In Vivo Assessment of Glenohumeral Joint Function during Dynamic Tasks
Milli Massimo	Prediction of Atrial Fibrillation using Deep Learning techniques

Minotti Martina	Radiomic analysis of Epicardial Adipose Tissue in cardiac MRI for hospitalization risk assessment
Misley Elisa	Non-linear dimensionality-reduction approach for powered wheelchair control
Missoni Fulvio	Evaluating Spatial Hearing in Virtual Reality Environment
Mobilio Giulia Addiego	Combination of VR and manikins to improve medical training
Moccia Sara	Machine learning-based classification of cortical response to visual stimuli recorded with an ECoG array in mice: a case study
Mocellin Simone	3D moles mapping and analysis for automatic melanoma detection
Molholm Sophie	A neural model of sensory interactions in young neurotypical and ASD children
Molisani Michele	Extrusion control strategy for robotic-based in situ bioprinting
Mollura Maximiliano	Decoding Emotions through Music: A Physiological Analysis of Emotion Recognition
–	Effects of State Representation on a Reinforcement Learning Based Decision Support System
–	Quantitative validation of an automatic videoPPG technique during autonomic elicitations
Molteni Franco	A motor-assisted recumbent trike for cycling training in neurological patients
Mongiardini Elena	Brain-Computer Interface assisted Motor Imagery training in post-stroke rehabilitation: longitudinal study of the EEG sensorimotor rhythms
Montano Florian	A comparative study of Super-Resolution reconstruction methods in fetal MRI
Monti Melissa	A neural model of sensory interactions in young neurotypical and ASD children
Monticelli Orietta	Green-Based Anti-Biofilm Nanoformulations Against Bacterial Contaminations In Nosocomial Environments
Mora Sara	Improving data quality in healthcare: medical informatics tools and standards
Morbiducci Umberto	Development of a computational model to estimate the hemolysis risk associated with hemodialysis catheters
Morelli Alberto	Phase synchronization between breathing and ppg signals in sleep events recordings of adult subjects
Morello Rocco	Transfer learning approaches to classify foetal occiput positions on transperineal ultrasound images
Moretti Paolo	Computer Vision and Deep Learning for Human Motion Analysis
Morettini Micaela	A Reliable User-Independent Motion Intent Detection from Transient EMG Data for Shoulder Joint
–	Brugada Syndrome: Characterization of QT Interval Components and Correction
–	Mathematical model of glucagon kinetics during an oral glucose tolerance test based on a dual regulation mechanism
Moretto Carlo	Estimating the degree of Non-Alcoholic Fatty Live Disease (NAFLD) from ultrasound images: preliminary results
Moretto Manuela	Associations between fatigue and functional connectivity of dopamine and noradrenaline circuits in Parkinson's disease
Morlacco Alessandro	Cryopreservation effects on biological tissues: histological and mechanical assessments
Moro Fabrizio Dal	Cryopreservation effects on biological tissues: histological and mechanical assessments

Moro Matteo	**Computer Vision and Deep Learning for Human Motion Analysis**
Morozova Olga	**An improved method for the characterization of infants' general movements using a RGB-Depth sensor and a deep neural network tracking processing tool**
Moscato Serena	**Autonomic response to virtual reality in oncological patients in real-world context**
–	**Comparison of autonomic signals between healthy subjects and chronic low back pain patients at rest and during noxious stimulation**
Moschini Valentina	**Early stages of cognitive decline are characterized by different EEG microstates dynamics**
–	**P300 event-related potential in patients with cognitive decline correlates with task performance**
Mosso Martina	**Integrated Protocol for Multidimensional In Vivo Assessment of Glenohumeral Joint Function during Dynamic Tasks**
–	**Quantifying the contribution of single joint kinematics to the overall ergonomic discomfort**
Motta Antonella	**Assessment of printability on autoclaved biomaterial inks for extrusion bioprinting**
Müller Henning	**A dexterous hand prosthesis based on additive manufacturing**
Munaretto Laura	**Discriminatory power of Global Longitudinal Strain and Left Ventricular Ejection Fraction for Identification of Dilated Cardiomyopathy**
Muratore Maurizio	**Radiofrequency Echographic Multi Spectromery for Fragility Fracture prediction through Fragility Score**
Murgo Martina	**An attention classifier for the evaluation of a robotic therapy in children with Autism Spectrum Disorder**
Murray Robin	**Modelling cerebral blood flow and neuroreceptor occupancy in dopamine blocking studies**
Mussano Federico	**Biomimetic platform for investigating in vitro the cell biological response to mechanical stretching – periodontal ligament stem cell application**
Muzzi Lorenzo	**Innovation in neuronal cell culture: from adhesion to maturation, chitosan promotes developing nervous system**
Nacmias Benedetta	**Early stages of cognitive decline are characterized by different EEG microstates dynamics**
–	**P300 event-related potential in patients with cognitive decline correlates with task performance**
Nanto Giulia	**3D moles mapping and analysis for automatic melanoma detection**
Napoletano Sabrina	**Microgels as a Biosensing Platform**
Nardi Cosimo	**Optimization of a cardiac tissue segmentation pipeline in murine whole-heart reconstructions**
Natale Alessandra	**Radiofrequency Echographic Multi Spectromery for Fragility Fracture prediction through Fragility Score**
Natale Valerio	**Impact of model selection procedure on Deep Neural Networks ensemble for the Choroid Plexus segmentation in Multiple Sclerosis**
Natali Arturo Nicola	**A novel artificial urinary sphincter and comparison with reference device**
Neri Simona	**Experimental Analysis of the biomechanics of healthy porcine corneas**
Nesi Paolo	**Health Information Technology Adverse Events Identification and Classification with Natural Language Processing and Deep Learning**

Netti Paolo Antonio	A novel microfluidic-based approach to study protein stability behavior in highly concentrated and viscous (HCV) systems
–	A testbed for mechanical and thermal stimulation in studies of somatosensory functions
–	An engineered breast cancer model on chip for personalized and multiple drug therapy
–	Bio-fabrication of in vitro tissues possessing organ-specific endogenous extracellular matrices
–	Biological validation of thiolated food grade secondary oil in water nanoemulsions with enhanced mucus-adhesion properties in Intestine-on-a-chip model
–	Circulating tumour cells deformability measurement in microfluidics
–	Coupled Hydrodynamic Flow Focusing to design Lipid-Polymer NPs (LiPoNs) for theranostics
–	Engineering of biological entities through dynamic perturbations of lipidic membranes.
–	In-flow viscoelastic compression to probe single-cell biomechanical properties
–	Hydrogels scaffolds as 2D in vitro models to explore the impact of microenvironmental stiffness on lung adenocarcinoma cells
–	Mesenchymal Stem Cell Response to Micropatterns and Dynamic Topographies
–	Microfluidic platform for cell classification from optical signatures via machine learning
–	Microgels as a Biosensing Platform
–	Prediction of injectables' stability leveraging inline analysis and machine learning
Nezi Luigi	A microfluidic platform to unravel immune cells cross-talk in rheumatoid arthritis
–	Intestinal epithelium on chip for absorption studies
Nicolai Irene	Design and fabrication of an intestinal phantom to mimic intestinal tone and motility
Nicoletta Matteo	3D bioprinting as a tool for the early correction of leather defects in the tanning industry
Nicoletti Letizia	Natural polymer-based bioinks exploiting internal gelation mechanism for cardiac tissue engineering
Nicolò Sabrina	Tuning the features of microphysiological systems for biomimetic intestinal in vitro models
Niosi Ignazio	Injectable gelatin-based photocurable fiber-reinforced hydrogel for the treatment of osteochondral defects
Nisi Rossella	Antibacterial activity of bacterial cellulose based wound care paste
Nocco Sergio	Driver drowsiness detection relying on infrared thermal imaging: a machine learning approach
–	Drivers' mental workload assessment based on machine learning applied to multimodal physiological data
Nocera Antonio	mmWave Radars Data Processing for Gait Parameters Extraction
Nolte Guido	Disclosing brain functional connections with multi-dimensional approaches
Nordio Giovanna	Assessing Multisite PET Neuroimaging Harmonisation for Normative Modelling

–	**Automated quantification of FDOPA PET using XNAT**
Novello Maria Cristina	**A cloud-based mobile platform to monitor and counteract cognitive decline**
Nutarelli Sebastiano	**Inertial measurements unit validation for countermovement jump (CMJ) tests in athletes**
Occhetta Paola	**A microfluidic platform to unravel immune cells cross-talk in rheumatoid arthritis**
–	**Intestinal epithelium on chip for absorption studies**
–	**Optimization of advanced setups with integrated readouts for evaluation of cardiac toxicity in a heart on chip device**
Odone Francesca	**Computer Vision and Deep Learning for Human Motion Analysis**
Oldani Cristina	**Physiologically relevant in vitro experiments: degradation kinetics of a pool of enzymes**
Olla Giulia	**EyeLab: a user-friendly Matlab tool for real-time monitoring of eye movements**
Olmi Benedetta	**Optimization of a cardiac tissue segmentation pipeline in murine whole-heart reconstructions**
Onorati Marco	**3D bioprinting as a tool for the early correction of leather defects in the tanning industry**
–	**Development of analytical models to predict self-folding of 4D bioprinted scaffold**
Onorati Simone	**A hydraulic implantable artificial detrusor for controlled bladder voiding**
Onwordi Ellis	**Modelling cerebral blood flow and neuroreceptor occupancy in dopamine blocking studies**
Orlandi Silvia	**Autonomic response to virtual reality in oncological patients in real-world context**
–	**Brain signals in semi-immersive and immersive VR environments: a feasibility study**
Orlando Fabio	**Dose-controlled low-intensity pulsed ultrasound and pulsed electromagnetic fields stimulations modulate inflammation in human macrophages**
Orrù Marco	**A novel tool for the annotation of bipolar electrograms for cardiac electrophysiology**
Ostan Rita	**Autonomic response to virtual reality in oncological patients in real-world context**
Osugo Martin	**Modelling cerebral blood flow and neuroreceptor occupancy in dopamine blocking studies**
Ottaviani Sarah	**Associations between fatigue and functional connectivity of dopamine and noradrenaline circuits in Parkinson's disease**
Paci Paola	**A network-based algorithm for identifying drug repurposing opportunities for complex diseases**
–	**Bioinformatics analyses to identify molecular gene signatures associated with breast cancer phenotypes**
–	**The long story of SWIM methodology: from grapevine to personalised medicine**
Padiglioni Sonia	**Early stages of cognitive decline are characterized by different EEG microstates dynamics**
–	**P300 event-related potential in patients with cognitive decline correlates with task performance**
Padmanabhan Sanosh Kunjalukkal	**Antibacterial activity of bacterial cellulose based wound care paste**
Padros Ferran	**Myelin quantification in Magnetic Resonance Imaging**

Paglialonga Alessia	**Decoding Emotions through Music: A Physiological Analysis of Emotion Recognition**
Pagnin Giulia	**Assessing the impact of brain gliomas on effective connectivity gradients**
Paladin Dino	**Manual and automatic identification of ACMG evidence in scientific papers**
Palesi Fulvia	**A deep learning network from downsampled diffusion-weighted MRI k-space to image-space**
–	**Myelin quantification in Magnetic Resonance Imaging**
Palma Cecilia	**A microfluidic platform to unravel immune cells cross-talk in rheumatoid arthritis**
Palmerini Luca	**Wearable-based Sit-to-Stand transfers in Older Adults: context differences between in-lab and home-based assessments**
Palmieri Maurizio	**Open-source as an enabling approach for the introduction of artificial intelligence in healthcare**
Palmisciano Andrea Costanzo	**Quantitative validation of an automatic videoPPG technique during autonomic elicitations**
Palumbo Pierpaolo	**Wearable-based Sit-to-Stand transfers in Older Adults: context differences between in-lab and home-based assessments**
Panciera Alessandro	**Assessment of the effects of parcellation and frequency band on the definition of functional hubs in rsfMRI**
Pani Danilo	**A novel tool for the annotation of bipolar electrograms for cardiac electrophysiology**
–	**Abnormal Ventricular Potentials Identification Using a Siamese Neural Network**
–	**EyeLab: a user-friendly Matlab tool for real-time monitoring of eye movements**
Pantano Patrizia	**XGBoost vs. TabPFN in Neuroimaging Machine Learning-based analysis**
Panzetta Valeria	**In-flow viscoelastic compression to probe single-cell biomechanical properties**
–	**Hydrogels scaffolds as 2D in vitro models to explore the impact of microenvironmental stiffness on lung adenocarcinoma cells**
Paoletti Camilla	**Natural polymer-based bioinks exploiting internal gelation mechanism for cardiac tissue engineering**
Paolini Edoardo	**Decoding the interplay between brain structural and functional connectivity in Alzheimer's disease**
Papaioannou Foivos	**Motor performances evaluation of female soccer players from AC Trento Women**
Papallo Simone	**Control Theory Measures for Dynamic Analyses of Human Functional Connectome Data**
Paramento Matilde	**Cortical correlates in upright static balance in adolescent idiopathic scoliosis**
Parazzini Marta	**Comparison of RF exposure levels in 5G-V2X and ITS-5.9 GHz vehicular connectivity**
–	**Exposure Assessment of Young People to Wearable Antennas at 5G frequencies**
–	**Magnetoelectric nanoparticles as promising tools for motor nerve stimulation**
Parimbelli Enea	**Understanding user needs for robotics assisted cognitive and physical rehabilitation**
Parodi Giulia	**Development of excitatory neuronal networks derived from human induced pluripotent stem cells**
Parodi Ilaria	**Mathematical model of nutrients transport and cell growth in a bioprinted hydrogel**

Parrotta Elvira	A preliminary version of a Genome-Scale Metabolic Model for Induced Human Pluripotent Stem Cells (hiPSCs)
Pascaner Ariel Fernando	Biomechanical assessment of the anomalous coronary compression by patient-specific finite element analysis
–	Development of novel computational tool to support surgical planning for the treatment of Anomalous Aortic Origin of the Coronary Arteries (AAOCA)
–	Lumped-parameter hemodynamic model as a non-invasive tool to assess coronary blood flow in AAOCA
Pascazio Vito	A Novel Authentication System Based on Hand Gesture Ultrasound Signatures
–	Breast Cancer Detection via Two-dimensional Ultrasound Tomography
–	Breast Cancer Imaging at Microwave Frequencies via Neural Networks
–	Experimental Microwave Imaging of Human Forearm
–	A deep learning approach for the analysis of voxel composition in magnetic resonance imaging
Pascucci Simona	Assessment of Balance disorder and vestibular dysfunction using Mixed Reality
–	Key points to design the MDs Library of a National implant Registry: lesson learned from the Italian experience
Pasian Marco	Millimeter-Waves Imaging for Breast Cancer Detection: Development of Analytical Models
Pasotti Lorenzo	A bioinformatic pipeline for identifying bacterial constitutive promoters based on transcriptomic data analysis
–	A workflow for the construction of reproducible living biosensors built by printing bacterial materials
–	Study and characterization of bile acid biosensors in engineered probiotic bacteria
Pasta Salvatore	An Inverse Analysis for the Assessment of Material Properties of TAVI Patients
–	Establishing Computational Modeling Credibility in Patients Undergoing TAVI
–	Mechanical Properties of Polyamide 12 for the use in Balloon-Expandable Transcatheter Heart Valves
–	Multiscale Modelling of Platelet Activation in Membrane Oxygenation Systems
–	Numerical Analysis of the Bicaval Transcatheter System for the Treatment of Severe Tricuspid Regurgitation
–	Structural Simulation of Transcatheter Heart Valve in Transcatheter Heart Valve
Pastore Vito Paolo	Computer Vision and Deep Learning for Human Motion Analysis
Pastorelli Daniele	Study and characterization of bile acid biosensors in engineered probiotic bacteria
Pastorino Laura	Green-Based Anti-Biofilm Nanoformulations Against Bacterial Contaminations In Nosocomial Environments
–	Innovation in neuronal cell culture: from adhesion to maturation, chitosan promotes developing nervous system
–	Photosensitive pattern to control geometry and activity of a neural network
Paternò Linda	A hydraulic implantable artificial detrusor for controlled bladder voiding
Pattini Linda	Exploring heterogeneity in lymphoid malignancies from mouse to human gene expression profiles

Pavan Jacopo	**Multi-Input Multi-Output Model Predictive Control for Drugs Delivery in Clinical Anesthesia**
Pavan Matilde	**Association between inflammation and brain microstructure in First Episode Psychosis investigated with DTI**
Pavan Piero Giovanni	**Composite scaffolds based on polyvinyl alcohol and acellular cartilage matrix for hemophilic arthropathy treatment**
–	**Computational modelling of the contractile behavior of cardiomyocytes on hydrogel scaffolds for cardiac tissue regeneration**
Pearson Ewan R.	**Longitudinal Relationships Between Proteomics and Beta-Cell Dysfunction in Type 2 Diabetes: An Imi Direct Study**
Pedersen Morten Gram	**Model Assessment of Doxorubicin Pharmacokinetics in Multiple Myeloma**
–	**Modeling Doxorubicin Treatment Effect in Multiple Myeloma**
–	**Noise-Induced Dynamics and Stochastic Slow Manifolds in the Bistable Xiong-Ferrell Model**
Pederzani Elia	**An advanced culture system to investigate electrospun graft biomechanisms for vascular tissue engineering**
Pedrizzetti Gianni	**Adaptation of cardiac deformation pattern during exercise in children**
Pedrocchi Alessandra	**A motor-assisted recumbent trike for cycling training in neurological patients**
–	**A multiscale computational approach to replicate the full-scale mouse striatum model**
–	**An attention classifier for the evaluation of a robotic therapy in children with Autism Spectrum Disorder**
–	**Virtual prototyping of a robotic chess player for play therapy**
Pegollo Ginevra	**Design and fabrication of a novel bioreactor for the engineering of tendon/ligament-to-bone interfaces**
Pegolo Elena	**Face mobility analysis in Spinal Muscular Atrophy**
Pegoraro Alice	**Lipid Droplets associated genes link HSV-1 infection to neurodegeneration pathways**
Pellegata Alessandro F. M.	**Micropatterned PDMS substrates for cellular mechanotransduction modelling**
Pellizzari Elisa	**Algorithm based on the "dynamic risk" concept allows ahead-of-time suggestion of corrective insulin boluses in type 1 diabetes therapies employing continuous glucose monitors**
Peloso Angela	**Fast path replanning in a dynamic environment in percutaneous cardiac interventions**
Pelusi Valerio	**Comparative Analysis of Steady and Resisted Accelerated Treadmill Running of an Elite Amputee Paralympic Sprinter**
Peluso Giusy	**A convolutional neural network to identify osteoporosis from femoral echographic scans: a preliminary study**
Pennini Simone	**Estimating the degree of Non-Alcoholic Fatty Live Disease (NAFLD) from ultrasound images: preliminary results**
Penso Marco	**Radiomic analysis of Epicardial Adipose Tissue in cardiac MRI for hospitalization risk assessment**
Perazzi Anna	**Experimental Analysis of the biomechanics of healthy porcine corneas**

Perego Alice	**Assessment of a parametric thoracic spine model for the generation of in silico cohorts**
Perlini Cinzia	**Association between inflammation and brain microstructure in First Episode Psychosis investigated with DTI**
Pernice Riccardo	**Assessment of cerebral autoregulation in patients undergoing anaesthesia with propofol: a comparison among spontaneous variability methods**
–	**Comparison of Machine Learning Approaches for Physiological States Classification Using Heart Rate and Pulse Rate Variability Indices**
Perotto Giovanni	**Cell encapsulation into silk fibroin microgels**
Perottoni Simone	**Integrated sensors for real-time monitoring of biological barriers in engineered cell culture dynamic in vitro models**
Perpetuini David	**Driver drowsiness detection relying on infrared thermal imaging: a machine learning approach**
–	**Drivers' mental workload assessment based on machine learning applied to multimodal physiological data**
Persico Emanuele	**Study and characterization of bile acid biosensors in engineered probiotic bacteria**
Persico Nicola	**A comparative study of Super-Resolution reconstruction methods in fetal MRI**
Peruffo Antonella	**Experimental Analysis of the biomechanics of healthy porcine corneas**
Peruzzo Denis	**A comparative study of Super-Resolution reconstruction methods in fetal MRI**
–	**Pseudo resting-state investigation from task-evoked functional MRI signals**
Peruzzo Paolo	**Numerical simulations of the cerebrospinal flow through the Sylvius aqueduct modeled as a diffuser/nozzle pump.**
Pescio Matteo	**Combination of VR and manikins to improve medical training**
Pescuma Viviana	**Brain-heart interaction: an ECG-fMRI integrated study in physiology and major depressive disorder**
Pesenti Mattia	**Virtual prototyping of a robotic chess player for play therapy**
Petrolo Salvatore	**A tool to perform semi-supervised anomaly detection and annotation on 15 lead ECG signals**
Petrone Nicola	**A dexterous hand prosthesis based on additive manufacturing**
–	**Advances in the development of a instrumented head surrogate for brain injury investigation**
–	**Analysis of an Elite Amputee Paralympic Sprinter in Track Running Pilot Tests**
–	**Comparative Analysis of Steady and Resisted Accelerated Treadmill Running of an Elite Amputee Paralympic Sprinter**
–	**Static strength of lower-limb prosthetic sockets for the activities of daily living**
–	**Towards a Wearable System for Complete Collection of Clamp Loads in Transfemoral Paralympic Sprinters**
Pettenuzzo Sofia	**Biomechanical characterization of human plantar fascia through experimental tests**
Petti Manuela	**Network-based integration of clinical, imaging and molecular biomarkers of dementia**
Peveri Francesca	**Time-frequency analysis of brain response to 3D slant texture and stereo cues**
Pezzinga Alice	**Assessment of a parametric thoracic spine model for the generation of in silico cohorts**

Pianca Silvio	The prediction of the patient's response to hemodialysis treatment: DialysIS vs InterACTIVE-HD 2.0 experience
Piazzalunga Chiara	Co-design of a points-based reward system to boost motivation in children and improve adherence to learning serious games
Pica Andrada	3D Finite Element Analysis of a Percolating Cluster inside the Mineralized Collagen Fibril
–	Near Field Electrospinning Process Using a Multi-Axis Robot
Piccolantonio Giusi	Interhemispheric functional connectivity: an fMRI study in two split-brain patients
Pichiorri Floriana	Brain-Computer Interface assisted Motor Imagery training in post-stroke rehabilitation: longitudinal study of the EEG sensorimotor rhythms
–	On the use of PARAFAC algorithm in group network analysis: a simulation study
Picozzi Paola	Development of an Integrated Software System for Medical Equipment Management: the experience of the Spedali Civili Hospital
Pieramico Giulia	Closing the loop between neurostimulation and control theory
Pierella Camilla	Non-linear dimensionality-reduction approach for powered wheelchair control
Piersanti Agnese	Mathematical model of glucagon kinetics during an oral glucose tolerance test based on a dual regulation mechanism
Pinamonti Maurizio	Towards 3D Virtual Histology of melanoma tissue by means of lab-based X-ray Phase Contrast Computed Micro-Tomography
Pinter Giuseppe Lauria	Cell encapsulation into silk fibroin microgels
Pirastru Alice	Development of a novel surface-based approach to quantify fNIRS-fMRI spatial correspondence
Pirri Carmelo	The biomechanical behaviour of fascial system: Superficial VS Deep Fascia
Pisani Noemi	A Multiparameter Statistical Approach for Cardiotocographic Signals Analysis
Pisani Paola	A convolutional neural network to identify osteoporosis from femoral echographic scans: a preliminary study
–	Osteoporosis Identification at Lumbar Vertebrae through a Neural Network Classifier
–	Radiofrequency Echographic Multi Spectromery for Fragility Fracture prediction through Fragility Score
–	Soft-tissue alterations identified with a CNN trained with simulated ultrasound images integrating expert knowledge
–	Transfer learning approaches to classify foetal occiput positions on transperineal ultrasound images
Pitton Matteo	FRESH approach for the development of 3D channel network in 3D in vitro models
Pitzalis Elisa	A novel tool for the annotation of bipolar electrograms for cardiac electrophysiology
Pitzus Andrea	Abnormal Ventricular Potentials Identification Using a Siamese Neural Network
Pizzella Vittorio	Closing the loop between neurostimulation and control theory
–	Disclosing brain functional connections with multi-dimensional approaches
Pizzinga Matteo	K-medoid clustering of premotor firing patterns supports fine decoding of macaque reach-and-grasp

Pizzini Francesca Benedetta	**Associations between fatigue and functional connectivity of dopamine and noradrenaline circuits in Parkinson's disease**
–	**Impact of model selection procedure on Deep Neural Networks ensemble for the Choroid Plexus segmentation in Multiple Sclerosis**
Pizzorusso Tommaso	**Machine learning-based classification of cortical response to visual stimuli recorded with an ECoG array in mice: a case study**
Pizzulli Luigi	**Error perception in different environments: Monitor vs Augmented Reality**
Poggio Fabio	**Interconnected brain regions-on-a-chip: role of connectivity and heterogeneity in the electrophysiological activity**
Poliziani Aliria	**Zwitterionic coatings for an implantable artificial pancreas**
Polo Edoardo Maria	**Decoding Emotions through Music: A Physiological Analysis of Emotion Recognition**
Polonara Gabriele	**Interhemispheric functional connectivity: an fMRI study in two split-brain patients**
Poloni Sofia	**In vitro exposure of endothelial cells to mechanical vibrations**
Polsinelli Alberto	**Assessment of Balance disorder and vestibular dysfunction using Mixed Reality**
Ponsiglione Alfonso Maria	**A Multiparameter Statistical Approach for Cardiotocographic Signals Analysis**
–	**Coupled Hydrodynamic Flow Focusing to design Lipid-Polymer NPs (LiPoNs) for theranostics**
–	**Evaluation of breast density variability between right and left breasts**
Ponti Federica	**Cell encapsulation into silk fibroin microgels**
–	**Vibropolyfection: boosting polymer-mediated gene delivery by mechanical cell loading**
Pontone Gianluca	**Radiomic analysis of Epicardial Adipose Tissue in cardiac MRI for hospitalization risk assessment**
Porcaro Camillo	**fMRI characterization of intrinsic brain networks relevant for motor control with and without visual feedback by fractal dimension**
Porco Ilaria	**A preliminary test of a novel method for the real time estimation of foot displacement using MIMUs attached to the foot**
–	**An improved method for the characterization of infants' general movements using a RGB-Depth sensor and a deep neural network tracking processing tool**
Porta Alberto	**Assessment of cerebral autoregulation in patients undergoing anaesthesia with propofol: a comparison among spontaneous variability methods**
Porzionato Andrea	**Composite scaffolds based on polyvinyl alcohol and acellular cartilage matrix for hemophilic arthropathy treatment**
Pozzi Luca	**3D upper limbs tracking through inertial sensors: calibration, methodology, and validation**
Pozzuoli Assunta	**Biomechanical characterization of human plantar fascia through experimental tests**
Pratellesi Tiziano	**Dose-controlled low-intensity pulsed ultrasound and pulsed electromagnetic fields stimulations modulate inflammation in human macrophages**
Prenassi Marco	**From data to knowledge: definition of an exploratory dataset for deep brain stimulation**
Prendin Francesco	**Algorithm based on the "dynamic risk" concept allows ahead-of-time suggestion of corrective insulin boluses in type 1 diabetes therapies employing continuous glucose monitors**

Preti Giacomo	**Full-scale point-neuron model of the mouse hippocampal microcircuits**
Primitivo Ivan	**Osteoporosis Identification at Lumbar Vertebrae through a Neural Network Classifier**
Procopio Anna	**A Distributed Multi-Centric Application for the Analysis of Cardiac Biomarkers**
–	**A preliminary version of a Genome-Scale Metabolic Model for Induced Human Pluripotent Stem Cells (hiPSCs)**
Protopapa Giovanni	**Design and validation of a microfluidic cartridge to prepare non-viral gene delivery complexes**
Puccio Barbara	**Validating biomedical and clinical data via an annotations based framework: experiences within the PON VQA project**
Puce Eleonora	**Microfluidic system for a label-free, real-time functional assessment of thrombotic risk**
Pupa Pierpaolo	**Estimating the degree of Non-Alcoholic Fatty Live Disease (NAFLD) from ultrasound images: preliminary results**
Putame Giovanni	**Biomimetic platform for investigating in vitro the cell biological response to mechanical stretching – periodontal ligament stem cell application**
–	**The effect of CFR-PEEK cross-link in short fixation for the stabilisation of lumbar metastasis: an in-vitro comparative study**.
Quaglini Silvana	**Understanding user needs for robotics assisted cognitive and physical rehabilitation**
Quaranta Stefano	**A bioinformatic pipeline for identifying bacterial constitutive promoters based on transcriptomic data analysis**
Quattrociocchi Ilaria	**EEG-based quantitative measures to support the clinical diagnosis of disorders of consciousness**
Raffo Luigi	**Abnormal Ventricular Potentials Identification Using a Siamese Neural Network**
Raimondi Michela	**mmWave Radars Data Processing for Gait Parameters Extraction**
Raiteri Roberto	**Green-Based Anti-Biofilm Nanoformulations Against Bacterial Contaminations In Nosocomial Environments**
Ramella Anna	**A numerical finite element methodology of the EVAR procedure**
Rampazzo Mirco	**Multi-Input Multi-Output Model Predictive Control for Drugs Delivery in Clinical Anesthesia**
Ranaldi Simone	**Analysis of muscular activity of a cashier during different modalities of human robot collaboration**
–	**Synergy-dependent patterns of reaction forces in sit-to-stand movements**
Rancati Simone	**Myelin quantification in Magnetic Resonance Imaging**
Rando Alessandra Maria Anna	**Tuning the features of microphysiological systems for biomimetic intestinal in vitro models**
Ranieri Andrea	**Brain-Computer Interface assisted Motor Imagery training in post-stroke rehabilitation: longitudinal study of the EEG sensorimotor rhythms**
–	**On the use of PARAFAC algorithm in group network analysis: a simulation study**
Rasponi Marco	**A microfluidic platform to unravel immune cells cross-talk in rheumatoid arthritis**
–	**Design and validation of a microfluidic cartridge to prepare non-viral gene delivery complexes**

–	Intestinal epithelium on chip for absorption studies
–	Optimization of advanced setups with integrated readouts for evaluation of cardiac toxicity in a heart on chip device
Ravazzani Paolo	Magnetoelectric nanoparticles as promising tools for motor nerve stimulation
Rea Francesco	Toward Implicit Communication of Object Properties for Human-Robot Interaction
Reali Pierluigi	Brain-heart interaction: an ECG-fMRI integrated study in physiology and major depressive disorder
Rebecca Sara	Simulating microbial communities' evolution via Agent base modelling: a Python tool
Redaelli Alberto	Microfluidic system for a label-free, real-time functional assessment of thrombotic risk
Reggiani Franco	A dexterous hand prosthesis based on additive manufacturing
Remuzzi Andrea	An advanced culture system to investigate electrospun graft biomechanisms for vascular tissue engineering
–	In vitro exposure of endothelial cells to mechanical vibrations
–	The role of hemodynamics in arteriovenous fistula remodelling and failure. A CFD longitudinal study
Repetto Rodolfo	Mathematical model of nutrients transport and cell growth in a bioprinted hydrogel
Reversi Luca	Interhemispheric functional connectivity: an fMRI study in two split-brain patients
Rho Gianluca	Effect of EDA-driven sympathetic responses on the central processing of faces cued by hedonic odors: a preliminary ERP study
Riboldi Stefania Adele	An advanced culture system to investigate electrospun graft biomechanisms for vascular tissue engineering
–	Physiologically relevant in vitro experiments: degradation kinetics of a pool of enzymes
Ricci Andrea	Giving new life to seafood waste: in silico engineering of a chitinolytic LPMO enzyme
Ricci Serena	Combination of VR and manikins to improve medical training
Ricciardi Antonio	A deep learning network from downsampled diffusion-weighted MRI k-space to image-space
–	Myelin quantification in Magnetic Resonance Imaging
Ricciardi Carlo	A Multiparameter Statistical Approach for Cardiotocographic Signals Analysis
Ricciardi Giuseppe Kenneth	Impact of model selection procedure on Deep Neural Networks ensemble for the Choroid Plexus segmentation in Multiple Sclerosis
Riccio Angela	EEG-based quantitative measures to support the clinical diagnosis of disorders of consciousness
Riccio Ester	Control Theory Measures for Dynamic Analyses of Human Functional Connectome Data
Riceputi Elisa	In vitro exposure of endothelial cells to mechanical vibrations
Ricotti Leonardo	A novel concept of steerable catheters actuated by muscle cells: the BioMeld project

–	Dose-controlled low-intensity pulsed ultrasound and pulsed electromagnetic fields stimulations modulate inflammation in human macrophages
–	Highly controlled ultrasound-mediated drug delivery experiments: an in vitro set-up
–	Injectable gelatin-based photocurable fiber-reinforced hydrogel for the treatment of osteochondral defects
–	Zwitterionic coatings for an implantable artificial pancreas
Ripamonti Marta	An advanced culture system to investigate electrospun graft biomechanisms for vascular tissue engineering
Rizzi Jacopo Giulio	Discriminatory power of Global Longitudinal Strain and Left Ventricular Ejection Fraction for Identification of Dilated Cardiomyopathy
Rizzo Angela	An advanced culture system to investigate electrospun graft biomechanisms for vascular tissue engineering
Rizzoglio Fabio	Non-linear dimensionality-reduction approach for powered wheelchair control
Roascio Monica	Altered EEG amplitude coupling correlates to cognitive dysfunction in iRBD patients
Roato Ilaria	Biomimetic platform for investigating in vitro the cell biological response to mechanical stretching – periodontal ligament stem cell application
Rocca Maria Assunta	XGBoost vs. TabPFN in Neuroimaging Machine Learning-based analysis
Rocchi Jacopo Emanuele	Inertial measurements unit validation for countermovement jump (CMJ) tests in athletes
Rodriguez Matas Jose Felix	A numerical finite element methodology of the EVAR procedure
Roffo Felicia	Coupled Hydrodynamic Flow Focusing to design Lipid-Polymer NPs (LiPoNs) for theranostics
Rohlén Robin	Combining high-density electromyography and ultrafast ultrasound to assess individual motor unit properties in vivo
Romagnoli Sofia	Brugada Syndrome: Characterization of QT Interval Components and Correction
Romanato Marco	Alteration of muscle recruitment in Parkinson's disease assessed by EMG-based occurrence frequency
Romani Gian Luca	Closing the loop between neurostimulation and control theory
Romano Emilio Maria	Performance Evaluation of the Gloreha Sinfonia Device in Bimanual Modality
Romano Eugenia	Engineering of biological entities through dynamic perturbations of lipidic membranes.
Romano Maria	A Multiparameter Statistical Approach for Cardiotocographic Signals Analysis
Rombolà Giuseppe	The prediction of the patient's response to hemodialysis treatment: DialysIS vs InterACTIVE-HD 2.0 experience
Rondoni Elena Hilary	K-medoid clustering of premotor firing patterns supports fine decoding of macaque reach-and-grasp
Rosati Samanta	A machine learning approach for stride speed estimation based on a head-mounted IMU
–	Usability of a multi-sensor array for the application of electro-phonocardiography in home care
Rosato Antonio	A Workflow for Biomechanical Simulation of Patient-specific Atherosclerotic Carotid Artery

–	Biomechanical assessment of the anomalous coronary compression by patient-specific finite element analysis
–	Development of novel computational tool to support surgical planning for the treatment of Anomalous Aortic Origin of the Coronary Arteries (AAOCA)
–	Lumped-parameter hemodynamic model as a non-invasive tool to assess coronary blood flow in AAOCA
Rosellini Elisabetta	3D printing of a nanomaterials-embedded gelatin/pectin hydrogel for the development of an in vitro drug testing platform
Rosini Elena	Cell encapsulation into silk fibroin microgels
Rossetto Gianluca	Integrated Protocol for Multidimensional In Vivo Assessment of Glenohumeral Joint Function during Dynamic Tasks
–	Quantifying the contribution of single joint kinematics to the overall ergonomic discomfort
Rossi Carlo Alberto	Longitudinal Relationships Between Proteomics and Beta-Cell Dysfunction in Type 2 Diabetes: An Imi Direct Study
Rossi Paolo	Combination of VR and manikins to improve medical training
–	Effectiveness of a home-based tele-rehabilitation program for post-Covid patients: preliminary results
Roventini Erika	Zwitterionic coatings for an implantable artificial pancreas
Rovini Erika	A multimodal wearable system for Human Activity Recognition during daily activities
Rubega Maria	Cortical correlates in upright static balance in adolescent idiopathic scoliosis
Ruggeri Mirella	Association between inflammation and brain microstructure in First Episode Psychosis investigated with DTI
Ruggieri Pietro	Biomechanical characterization of human plantar fascia through experimental tests
Ruggiero Carmelina	Improving data quality in healthcare: medical informatics tools and standards
Russello Emanuele	Design and fabrication of a micro-dialyser for the study of the gut microbiota-tissues cross-talk
Russo Andrea Gerardo	Bayesian Surprise from a Deep Learning Model of Italian Language to Model Neural Activity
–	Tensor-based morphometry of T1 weighted brain images reveals subtle volume enlargement of temporalis muscles
Russo Davide	Non-linear dimensionality-reduction approach for powered wheelchair control
Russo Luca	Vibropolyfection: boosting polymer-mediated gene delivery by mechanical cell loading
Sabatini Silvio Paolo	Time-frequency analysis of brain response to 3D slant texture and stereo cues
Sabatino Jolanda	A Distributed Multi-Centric Application for the Analysis of Cardiac Biomarkers
Saccomanno Maristella Francesca	Integrated Protocol for Multidimensional In Vivo Assessment of Glenohumeral Joint Function during Dynamic Tasks
Saccomano Giulia	Towards 3D Virtual Histology of melanoma tissue by means of lab-based X-ray Phase Contrast Computed Micro-Tomography
Sala Camilla	fMRI characterization of intrinsic brain networks relevant for motor control with and without visual feedback by fractal dimension

Sala Eleonora	Error perception in different environments: Monitor vs Augmented Reality
Salis Francesca	A machine learning approach for stride speed estimation based on a head-mounted IMU
Salmin Francesca	Face mobility analysis in Spinal Muscular Atrophy
Salomoni Valentina	A novel artificial urinary sphincter and comparison with reference device
Saltarelli Ilenia	A safe robot control for semi-autonomous pedicle tapping
Salvatori Carlotta	A novel concept of steerable catheters actuated by muscle cells: the BioMeld project
Salvi Massimo	Quality enhancement of dermatological images using GANs: a proof of concept
–	Synthesis of ultrasound images from semantic labels with controllable texture features
Sambruni Andrea	Inertial measurements unit validation for countermovement jump (CMJ) tests in athletes
Sampaolesi Maurilio	RNA Sequencing analysis to study Duchenne dilated cardiomyopathy in patient-derived 3D organoid models
Samson Rebecca	A deep learning network from downsampled diffusion-weighted MRI k-space to image-space
–	Myelin quantification in Magnetic Resonance Imaging
Sangiuliano Intra Francesca	Development of a novel surface-based approach to quantify fNIRS-fMRI spatial correspondence
Sanguineti Vittorio	A cloud-based mobile platform to monitor and counteract cognitive decline
–	Computational joint action: dynamical models to understand the development of joint coordination
Sansavini Alessandra	Sensor-based Assessment of Gross and Fine Motor Development in Primary School Children
Sansone Mario	Bayesian Surprise from a Deep Learning Model of Italian Language to Model Neural Activity
–	Control Theory Measures for Dynamic Analyses of Human Functional Connectome Data
–	Evaluation of breast density variability between right and left breasts
Sansone Valeria	Face mobility analysis in Spinal Muscular Atrophy
Santini Letizia	Error perception in different environments: Monitor vs Augmented Reality
Santos Laura	An attention classifier for the evaluation of a robotic therapy in children with Autism Spectrum Disorder
Santos-Victor José	An attention classifier for the evaluation of a robotic therapy in children with Autism Spectrum Disorder
Saputo Roberta	Assessment of cerebral autoregulation in patients undergoing anaesthesia with propofol: a comparison among spontaneous variability methods
Saroglia Giulio	Cell encapsulation into silk fibroin microgels
Sartori Susanna	Engineering of poly(urethane)-based porous constructs for cardiac tissue model design
Savoia Paola	Quality enhancement of dermatological images using GANs: a proof of concept
Savona Davide	A motor-assisted recumbent trike for cycling training in neurological patients

Sawacha Zimi	**Alteration of muscle recruitment in Parkinson's disease assessed by EMG-based occurrence frequency**
–	**Face mobility analysis in Spinal Muscular Atrophy**
Sbrollini Agnese	**Brugada Syndrome: Characterization of QT Interval Components and Correction**
Scaglione Silvia	**Mathematical model of nutrients transport and cell growth in a bioprinted hydrogel**
Scaglioni Dominique	**Computational modelling of the contractile behavior of cardiomyocytes on hydrogel scaffolds for cardiac tissue regeneration**
Scala Francesco	**Validating biomedical and clinical data via an annotations based framework: experiences within the PON VQA project**
Scalise Stefania	**A preliminary version of a Genome-Scale Metabolic Model for Induced Human Pluripotent Stem Cells (hiPSCs)**
Scalona Emilia	**Integrated Protocol for Multidimensional In Vivo Assessment of Glenohumeral Joint Function during Dynamic Tasks**
–	**Quantifying the contribution of single joint kinematics to the overall ergonomic discomfort**
Scapinello Mattia	**Analysis of an Elite Amputee Paralympic Sprinter in Track Running Pilot Tests**
–	**Static strength of lower-limb prosthetic sockets for the activities of daily living**
–	**Towards a Wearable System for Complete Collection of Clamp Loads in Transfemoral Paralympic Sprinters**
Scarpa Fabio	**3D moles mapping and analysis for automatic melanoma detection**
Scarpino Maenia	**Early stages of cognitive decline are characterized by different EEG microstates dynamics**
–	**P300 event-related potential in patients with cognitive decline correlates with task performance**
Scattolini Mara	**A Reliable User-Independent Motion Intent Detection from Transient EMG Data for Shoulder Joint**
Scavone Mariangela	**Microfluidic system for a label-free, real-time functional assessment of thrombotic risk**
Schenato Luca	**Automated control of bioreactors: An hardware-in-the-loop proof of concept test towards an experimental facility**
–	**Modeling metabolic overload effects in bacterial growth rate in synthetic biology**
–	**Uncovering quorum sensing and quenching structural properties: a systems biology approach**
Schiavoni Raissa	**Wearable sensor for in-vivo skin hydration monitoring**
Schiena Giandomenico	**Brain-heart interaction: an ECG-fMRI integrated study in physiology and major depressive disorder**
Schinelli Roberto	**Virtual prototyping of a robotic chess player for play therapy**
Schiulaz Astrid	**Automated quantification of FDOPA PET using XNAT**
Schladen Manon	**An improved method for the characterization of infants' general movements using a RGB-Depth sensor and a deep neural network tracking processing tool**
Schmid Maurizio	**Analysis of muscular activity of a cashier during different modalities of human robot collaboration**

Schreiber Kristin L.	Comparison of autonomic signals between healthy subjects and chronic low back pain patients at rest and during noxious stimulation
Schwenk Jochen M.	Longitudinal Relationships Between Proteomics and Beta-Cell Dysfunction in Type 2 Diabetes: An Imi Direct Study
Scilingo Enzo Pasquale	Effect of EDA-driven sympathetic responses on the central processing of faces cued by hedonic odors: a preliminary ERP study
Sciutti Alessandra	Toward Implicit Communication of Object Properties for Human-Robot Interaction
Scocozza Franca	A workflow for the construction of reproducible living biosensors built by printing bacterial materials
Scolaro Filippo	3D moles mapping and analysis for automatic melanoma detection
Scuoppo Roberta	Structural Simulation of Transcatheter Heart Valve in Transcatheter Heart Valve
Secondulfo Carmine	Tensor-based morphometry of T1 weighted brain images reveals subtle volume enlargement of temporalis muscles
Sedda Giulia	EyeLab: a user-friendly Matlab tool for real-time monitoring of eye movements
Selvaggi Pierluigi	Modelling cerebral blood flow and neuroreceptor occupancy in dopamine blocking studies
Selvaggio Gianluca	Uncovering quorum sensing and quenching structural properties: a systems biology approach
Semproni Federica	A hydraulic implantable artificial detrusor for controlled bladder voiding
Senigagliesi Linda	mmWave Radars Data Processing for Gait Parameters Extraction
Seoni Silvia	Combining high-density electromyography and ultrafast ultrasound to assess individual motor unit properties in vivo
Severini Giacomo	Synergy-dependent patterns of reaction forces in sit-to-stand movements
Severino Mario	Modelling cerebral blood flow and neuroreceptor occupancy in dopamine blocking studies
Sieni Elisabetta	Engineering the tumor environment in vitro using peptide-enriched, hyaluronic acid-based hydrogels
Signorello Paolo	Design and fabrication of an intestinal phantom to mimic intestinal tone and motility
Signorini Maria Gabriella	Cardiotocography in antenatal fetal monitoring of diabetes-complicated pregnancies
–	Hidden Markov Models for the identification of fetal phases in CTG recordings
Silva Bárbara	An attention classifier for the evaluation of a robotic therapy in children with Autism Spectrum Disorder
Silvestri Erica	Assessing the impact of brain gliomas on effective connectivity gradients
–	Assessment of the effects of parcellation and frequency band on the definition of functional hubs in rsfMRI
–	Impact of diffusion connectivity metrics on white matter abnormalities in glioma
Silvestri Simona	Engineering of biological entities through dynamic perturbations of lipidic membranes.
Sirolli Sofia	Highly controlled ultrasound-mediated drug delivery experiments: an in vitro set-up
Siviero Ilaria	Enhancing Safety in Industry 4.0: The Use of Passive Brain Computer Interfaces for Vigilance Monitoring

Solari Fabio	**Combination of VR and manikins to improve medical training**
Solinas Sergio	**Full-scale point-neuron model of the mouse hippocampal microcircuits**
Solinas Sergio Mauro Gavino	**A preliminary test of a novel method for the real time estimation of foot displacement using MIMUs attached to the foot**
Soliveri Luca	**The role of hemodynamics in arteriovenous fistula remodelling and failure. A CFD longitudinal study**
Soncini Monica	**An advanced culture system to investigate electrospun graft biomechanisms for vascular tissue engineering**
–	**Tuning the features of microphysiological systems for biomimetic intestinal in vitro models**
Sorbi Sandro	**Early stages of cognitive decline are characterized by different EEG microstates dynamics**
–	**P300 event-related potential in patients with cognitive decline correlates with task performance**
Spadoni Silvia	**Computational modelling of the contractile behavior of cardiomyocytes on hydrogel scaffolds for cardiac tissue regeneration**
Spairani Edoardo	**Cardiotocography in antenatal fetal monitoring of diabetes-complicated pregnancies**
–	**Hidden Markov Models for the identification of fetal phases in CTG recordings**
Spanò Sergio	**Development of a microfluidic system for impedance-based cell sorting**
Spanu Andrea	**PEDOT:PSS ink-jet printed microelectrodes on paper: towards low-cost and green MEA devices**
Sparacino Giovanni	**Algorithm based on the "dynamic risk" concept allows ahead-of-time suggestion of corrective insulin boluses in type 1 diabetes therapies employing continuous glucose monitors**
–	**Dynamic Bayesian Networks and Transfer Learning Enable the Development of Deep Sequence-Based Models on Small-Sample Data**
–	**Supervised Learning-based Detection of Pressure-induced Failures in Continuous Glucose Sensors**
Sparacino Laura	**Assessment of cerebral autoregulation in patients undergoing anaesthesia with propofol: a comparison among spontaneous variability methods**
Sperduti Marika	**A testbed for mechanical and thermal stimulation in studies of somatosensory functions**
Spessot Eugenia	**Assessment of printability on autoclaved biomaterial inks for extrusion bioprinting**
Spolaor Fabiola	**Alteration of muscle recruitment in Parkinson's disease assessed by EMG-based occurrence frequency**
–	**Face mobility analysis in Spinal Muscular Atrophy**
Squarcina Letizia	**A comparative study of Super-Resolution reconstruction methods in fetal MRI**
–	**Association between inflammation and brain microstructure in First Episode Psychosis investigated with DTI**
Stagni Rita	**Sensor-based Assessment of Gross and Fine Motor Development in Primary School Children**
Statton Ben	**Modelling cerebral blood flow and neuroreceptor occupancy in dopamine blocking studies**

Stecco Carla	The biomechanical behaviour of fascial system: Superficial VS Deep Fascia
Stepanyan Astghik	Lipid Droplets associated genes link HSV-1 infection to neurodegeneration pathways
Steyde Giulio	Cardiotocography in antenatal fetal monitoring of diabetes-complicated pregnancies
–	Hidden Markov Models for the identification of fetal phases in CTG recordings
Stocco Elena	Composite scaffolds based on polyvinyl alcohol and acellular cartilage matrix for hemophilic arthropathy treatment
Stola Giovanni Paolo	Natural polymer-based bioinks exploiting internal gelation mechanism for cardiac tissue engineering
Stoppa Mariangela	Antibacterial activity of bacterial cellulose based wound care paste
Storti Silvia Francesca	Decoding the interplay between brain structural and functional connectivity in Alzheimer's disease
–	Enhancing Safety in Industry 4.0: The Use of Passive Brain Computer Interfaces for Vigilance Monitoring
Suarato Giulia	Magnetoelectric nanoparticles as promising tools for motor nerve stimulation
Susin Francesca Maria	Numerical simulations of the cerebrospinal flow through the Sylvius aqueduct modeled as a diffuser/nozzle pump.
Tacchino Chiara	Computer Vision and Deep Learning for Human Motion Analysis
Tagliamonte Nevio Luigi	A testbed for mechanical and thermal stimulation in studies of somatosensory functions
Talamonti Rita	Assessment of Balance disorder and vestibular dysfunction using Mixed Reality
Tamanti Agnese	Associations between fatigue and functional connectivity of dopamine and noradrenaline circuits in Parkinson's disease
–	Impact of model selection procedure on Deep Neural Networks ensemble for the Choroid Plexus segmentation in Multiple Sclerosis
Tarantino Vanessa	Quality enhancement of dermatological images using GANs: a proof of concept
Tartarini Lorenzo	Ex Vivo Animal Evaluation of IntraValvular Impedance Sensing Applied to Biological Heart Valve Prostheses
Tasca Paolo	A machine learning approach for stride speed estimation based on a head-mounted IMU
Tassorelli Cristina	Towards personalized electroceutical therapy: electrophysiological investigations in a pre-clinical model of ischemic lesion
Tauro Emanuele	Commercial Smart Virtual Assistants to support medication adherence in chronic patients: a preliminary usability study
Tavazzi Erica	Development of predictive models for short-term prediction of disability progression in multiple sclerosis
–	Dynamic Bayesian Networks and Transfer Learning Enable the Development of Deep Sequence-Based Models on Small-Sample Data
–	Identifying Extreme Profiles in Amyotrophic Lateral Sclerosis Patients at Diagnosis through Archetypal Analysis
Tedeschi Gioacchino	Bayesian Surprise from a Deep Learning Model of Italian Language to Model Neural Activity
–	XGBoost vs. TabPFN in Neuroimaging Machine Learning-based analysis

Tedesco Annarita	**A Multiparameter Statistical Approach for Cardiotocographic Signals Analysis**
Tedesco Mariateresa	**Interconnected brain regions-on-a-chip: role of connectivity and heterogeneity in the electrophysiological activity**
Temporiti Federico	**Differences in cortical reorganization during visuo-motor tasks executed with the dominant and non-dominant hands**
Terranova Fabio	**PEDOT:PSS ink-jet printed microelectrodes on paper: towards low-cost and green MEA devices**
Terzini Mara	**Biomimetic platform for investigating in vitro the cell biological response to mechanical stretching – periodontal ligament stem cell application**
–	**Mechanical evaluation of synthetic meshes: definition and verification of a rigorous test protocol**
–	**Reducing bone plates standard fatigue test time with an analytical runout load prediction**
–	**The effect of CFR-PEEK cross-link in short fixation for the stabilisation of lumbar metastasis: an in-vitro comparative study**.
Tessari Alessia	**Sensor-based Assessment of Gross and Fine Motor Development in Primary School Children**
Testa Maria	**Rapid prototyping of a microfluidic platform for nasal mucosa models**
Teti Gregorio	**Static strength of lower-limb prosthetic sockets for the activities of daily living**
Tiberio Alessandro	**Driver drowsiness detection relying on infrared thermal imaging: a machine learning approach**
–	**Drivers' mental workload assessment based on machine learning applied to multimodal physiological data**
Tiengo Cesare	**A dexterous hand prosthesis based on additive manufacturing**
Tigrini Andrea	**A Reliable User-Independent Motion Intent Detection from Transient EMG Data for Shoulder Joint**
Tinazzi Michele	**Associations between fatigue and functional connectivity of dopamine and noradrenaline circuits in Parkinson's disease**
Tiribilli Eleonora	**Risk management in a medical device software: evaluation of the usability characteristics of a 3D viewer for reporting**
Todesco Martina	**Biological evaluation in vitro and in vivo of hybrid membrane to assess biomedical application**
–	**Cryopreservation effects on biological tissues: histological and mechanical assessments**
–	**Mechanical characterization of hybrid membrane suitable for biomedical application**
Todros Silvia	**Composite scaffolds based on polyvinyl alcohol and acellular cartilage matrix for hemophilic arthropathy treatment**
–	**Computational modelling of the contractile behavior of cardiomyocytes on hydrogel scaffolds for cardiac tissue regeneration**
Tognola Gabriella	**Comparison of RF exposure levels in 5G-V2X and ITS-5.9 GHz vehicular connectivity**
–	**Exposure Assessment of Young People to Wearable Antennas at 5G frequencies**
Tomei Gabriele	**Open-source as an enabling approach for the introduction of artificial intelligence in healthcare**

Tomelleri Giovanni	**Associations between fatigue and functional connectivity of dopamine and noradrenaline circuits in Parkinson's disease**
Tonelli Francesca	**Patient-specific phantom for home haemodialysis**
Tonin Luca	**Brain signals in semi-immersive and immersive VR environments: a feasibility study**
Toniolo Ilaria	**Experimental Analysis of the biomechanics of healthy porcine corneas**
Toppi Jlenia	**Brain-Computer Interface assisted Motor Imagery training in post-stroke rehabilitation: longitudinal study of the EEG sensorimotor rhythms**
–	**EEG-based quantitative measures to support the clinical diagnosis of disorders of consciousness**
–	**On the use of PARAFAC algorithm in group network analysis: a simulation study**
Torfs Tom	**Remote In-Bed Monitoring of Vital Signs Using Radar Technology**
Torino Enza	**A novel microfluidic-based approach to study protein stability behavior in highly concentrated and viscous (HCV) systems**
–	**Boosted transport of Theranostic Angiopep-2 engineered crosslinked Hyaluronic Acid NanoParticles (Thera-ANG-cHANPs) in glioblastoma cells**
–	**Coupled Hydrodynamic Flow Focusing to design Lipid-Polymer NPs (LiPoNs) for theranostics**
–	**Engineering of biological entities through dynamic perturbations of lipidic membranes.**
–	**Prediction of injectables' stability leveraging inline analysis and machine learning**
Torre Marina	**Key points to design the MDs Library of a National implant Registry: lesson learned from the Italian experience**
Torrente Yvan	**Brain-heart interaction: an ECG-fMRI integrated study in physiology and major depressive disorder**
Tortora Stefano	**Brain signals in semi-immersive and immersive VR environments: a feasibility study**
Toselli Stefania	**Sensor-based Assessment of Gross and Fine Motor Development in Primary School Children**
Tosini Marta	**Biomimetic platform for investigating in vitro the cell biological response to mechanical stretching – periodontal ligament stem cell application**
Traccis Sebastiano	**EyeLab: a user-friendly Matlab tool for real-time monitoring of eye movements**
Tradigo Giuseppe	**A tool to perform semi-supervised anomaly detection and annotation on 15 lead ECG signals**
–	**Validating biomedical and clinical data via an annotations based framework: experiences within the PON VQA project**
Trescato Isotta	**Identifying Extreme Profiles in Amyotrophic Lateral Sclerosis Patients at Diagnosis through Archetypal Analysis**
Trimarchi Santi	**A numerical finite element methodology of the EVAR procedure**
Tritto Michele	**Driver drowsiness detection relying on infrared thermal imaging: a machine learning approach**
–	**Drivers' mental workload assessment based on machine learning applied to multimodal physiological data**
Triulzi Fabio	**A comparative study of Super-Resolution reconstruction methods in fetal MRI**
–	**Brain-heart interaction: an ECG-fMRI integrated study in physiology and major depressive disorder**

Trò Rosella	**Altered EEG amplitude coupling correlates to cognitive dysfunction in iRBD patients**
Tromba Giuliana	**Towards 3D Virtual Histology of melanoma tissue by means of lab-based X-ray Phase Contrast Computed Micro-Tomography**
Trucco Diego	**Injectable gelatin-based photocurable fiber-reinforced hydrogel for the treatment of osteochondral defects**
Tur Carmen	**A deep learning network from downsampled diffusion-weighted MRI k-space to image-space**
–	**Myelin quantification in Magnetic Resonance Imaging**
Tura Andrea	**Mathematical model of glucagon kinetics during an oral glucose tolerance test based on a dual regulation mechanism**
Turgut Tahir	**Mechanical Properties of Polyamide 12 for the use in Balloon-Expandable Transcatheter Heart Valves**
Turkheimer Federico	**Assessing Multisite PET Neuroimaging Harmonisation for Normative Modelling**
–	**Automated quantification of FDOPA PET using XNAT**
Urciuolo Anna	**Computational modelling of the contractile behavior of cardiomyocytes on hydrogel scaffolds for cardiac tissue regeneration**
Urciuolo Francesco	**An engineered breast cancer model on chip for personalized and multiple drug therapy**
–	**Bio-fabrication of in vitro tissues possessing organ-specific endogenous extracellular matrices**
–	**Hydrogels scaffolds as 2D in vitro models to explore the impact of microenvironmental stiffness on lung adenocarcinoma cells**
Urman Richard D.	**Comparison of autonomic signals between healthy subjects and chronic low back pain patients at rest and during noxious stimulation**
Usai Francesca	**A workflow for the construction of reproducible living biosensors built by printing bacterial materials**
Valenti Marco	**Interhemispheric functional connectivity: an fMRI study in two split-brain patients**
Vallini Giulia	**Assessment of the effects of parcellation and frequency band on the definition of functional hubs in rsfMRI**
van Alfen Nens	**Synthesis of ultrasound images from semantic labels with controllable texture features**
Vanello Nicola	**Early stages of cognitive decline are characterized by different EEG microstates dynamics**
Vannozzi Lorenzo	**A novel concept of steerable catheters actuated by muscle cells: the BioMeld project**
–	**Injectable gelatin-based photocurable fiber-reinforced hydrogel for the treatment of osteochondral defects**
Varani Silvia	**Autonomic response to virtual reality in oncological patients in real-world context**
Vassia Marzullo Alberto	**Prediction of Atrial Fibrillation using Deep Learning techniques**
Vasta Rosario	**Identifying Extreme Profiles in Amyotrophic Lateral Sclerosis Patients at Diagnosis through Archetypal Analysis**
Vecchione Raffaele	**Biological validation of thiolated food grade secondary oil in water nanoemulsions with enhanced mucus-adhesion properties in Intestine-on-a-chip model**

Veltri Pierangelo	A tool to perform semi-supervised anomaly detection and annotation on 15 lead ECG signals
–	Validating biomedical and clinical data via an annotations based framework: experiences within the PON VQA project
Ventre Maurizio	Mesenchymal Stem Cell Response to Micropatterns and Dynamic Topographies
Venzin Reto	The prediction of the patient's response to hemodialysis treatment: DialysIS vs InterACTIVE-HD 2.0 experience
Verdini Federica	A Reliable User-Independent Motion Intent Detection from Transient EMG Data for Shoulder Joint
–	mmWave Radars Data Processing for Gait Parameters Extraction
Verga Matteo	Development of an Integrated Software System for Medical Equipment Management: the experience of the Spedali Civili Hospital
Vergani Alberto Arturo	Early stages of cognitive decline are characterized by different EEG microstates dynamics
–	Network model accounts for evolution of EEG functional connectivity in patients with cognitive decline
–	P300 event-related potential in patients with cognitive decline correlates with task performance
Verme Federica	Effectiveness of a home-based tele-rehabilitation program for post-Covid patients: preliminary results
Verona Enrico	Development of a microfluidic system for impedance-based cell sorting
Veronese Federica	Quality enhancement of dermatological images using GANs: a proof of concept
Veronese Mattia	Assessing Multisite PET Neuroimaging Harmonisation for Normative Modelling
–	Associations between fatigue and functional connectivity of dopamine and noradrenaline circuits in Parkinson's disease
–	Automated quantification of FDOPA PET using XNAT
–	Modelling cerebral blood flow and neuroreceptor occupancy in dopamine blocking studies
Vescio Martina	Exploring heterogeneity in lymphoid malignancies from mouse to human gene expression profiles
Vesentini Simone	Effects of different degumming methods on the quality of sericin samples
Vettoretti Martina	Assessing Personal Exposure to Airborne Particulate Matter with Wearable Sensors and Ventilation Rate Models
–	Development of predictive models for short-term prediction of disability progression in multiple sclerosis
–	Identifying Extreme Profiles in Amyotrophic Lateral Sclerosis Patients at Diagnosis through Archetypal Analysis
–	Smart Titration of Long-Acting Insulin in Insulin-Naïve Type 2 Diabetic Subjects
Vieira Taian	Combining high-density electromyography and ultrafast ultrasound to assess individual motor unit properties in vivo
Viganò Gian Luca	Development of an Integrated Software System for Medical Equipment Management: the experience of the Spedali Civili Hospital
Viggiano Andrea	Tensor-based morphometry of T1 weighted brain images reveals subtle volume enlargement of temporalis muscles

Villa Giacomo	**Motor performances evaluation of female soccer players from AC Trento Women**
Villa Martina	**Pseudo resting-state investigation from task-evoked functional MRI signals**
Villa Tomaso	**A method for the evaluation of cervical surgical instrumentation reliability through a computational and experimental approach**
Villani Stefania	**Antibacterial activity of bacterial cellulose based wound care paste**
Villani Umberto	**Impact of diffusion connectivity metrics on white matter abnormalities in glioma**
Vinuela Ana	**Longitudinal Relationships Between Proteomics and Beta-Cell Dysfunction in Type 2 Diabetes: An Imi Direct Study**
Viola Graziana	**A novel tool for the annotation of bipolar electrograms for cardiac electrophysiology**
–	**Abnormal Ventricular Potentials Identification Using a Siamese Neural Network**
Visani Valentina	**Impact of model selection procedure on Deep Neural Networks ensemble for the Choroid Plexus segmentation in Multiple Sclerosis**
Visentin Roberto	**Model Assessment of Doxorubicin Pharmacokinetics in Multiple Myeloma**
–	**Modeling Doxorubicin Treatment Effect in Multiple Myeloma**
–	**Smart Titration of Long-Acting Insulin in Insulin-Naïve Type 2 Diabetic Subjects**
Visone Roberta	**Design and validation of a microfluidic cartridge to prepare non-viral gene delivery complexes**
–	**Optimization of advanced setups with integrated readouts for evaluation of cardiac toxicity in a heart on chip device**
Viti Federica	**Design and fabrication of an intestinal phantom to mimic intestinal tone and motility**
Vitti Elena	**Interhemispheric functional connectivity: an fMRI study in two split-brain patients**
Vivarelli Cecilia	**Exposure set-up for assessing the far-field electromagnetic immunity levels of active implantable medical devices**
Vizza Patrizia	**A tool to perform semi-supervised anomaly detection and annotation on 15 lead ECG signals**
–	**Validating biomedical and clinical data via an annotations based framework: experiences within the PON VQA project**
Volpe Daniele	**Alteration of muscle recruitment in Parkinson's disease assessed by EMG-based occurrence frequency**
Votta Emiliano	**Fast path replanning in a dynamic environment in percutaneous cardiac interventions**
Vozzi Giovanni	**3D bioprinting as a tool for the early correction of leather defects in the tanning industry**
–	**3D printing of a nanomaterials-embedded gelatin/pectin hydrogel for the development of an in vitro drug testing platform**
–	**Cell-aware optimization of the extrusion-based bioprinting process**
–	**Design and fabrication of a micro-dialyser for the study of the gut microbiota-tissues cross-talk**
–	**Design and fabrication of a novel bioreactor for the engineering of tendon/ligament-to-bone interfaces**

–	Evaluation of the optimal pore size for 3D printed bone scaffolds in a perfusion bioreactor
–	Extrusion control strategy for robotic-based in situ bioprinting
–	Valve-jet technology for robotic-based in situ bioprinting applications
Wang Jing	An improved method for the characterization of infants' general movements using a RGB-Depth sensor and a deep neural network tracking processing tool
Whitehurst Thomas	Modelling cerebral blood flow and neuroreceptor occupancy in dopamine blocking studies
Williams Steven	Automated quantification of FDOPA PET using XNAT
Williams Steven C.R.	Assessing Multisite PET Neuroimaging Harmonisation for Normative Modelling
Xiao Yan	Comparison of autonomic signals between healthy subjects and chronic low back pain patients at rest and during noxious stimulation
Zaffagnini Stefano	Development of a contrast-enhanced micro tomography protocol for human meniscus: a pilot study
Zahalka Omar	Mechanical Properties of Polyamide 12 for the use in Balloon-Expandable Transcatheter Heart Valves
Zahid Uzma	Modelling cerebral blood flow and neuroreceptor occupancy in dopamine blocking studies
Zampieri Sandro	Single region contribution to the brain dynamic (in)stability
Zamuner Annj	Engineering the tumor environment in vitro using peptide-enriched, hyaluronic acid-based hydrogels
–	Peptide anchoring methods for PEEK surfaces
–	Peptide-functionalized chitosan sponges for bone tissue regeneration
Zatta Veronica	Lipid Droplets associated genes link HSV-1 infection to neurodegeneration pathways
Zavattaro Elisa	Quality enhancement of dermatological images using GANs: a proof of concept
Zeni Elena	Peptide-functionalized chitosan sponges for bone tissue regeneration
Zhu Wenchao	Comparison of autonomic signals between healthy subjects and chronic low back pain patients at rest and during noxious stimulation
Zollo Loredana	A safe robot control for semi-autonomous pedicle tapping
–	A testbed for mechanical and thermal stimulation in studies of somatosensory functions
–	Comparative analysis of EMG-based classifiers for recognizing hand/wrist gestures and forces
–	Performance Evaluation of the Gloreha Sinfonia Device in Bimanual Modality
Zucchini Lorenzo	Temperature influence on reflectance photometers for bilirubin measurement
Zullo Giuseppe	Advances in the development of a instrumented head surrogate for brain injury investigation

Wearable-based Sit-to-Stand transfers in Older Adults: in-lab and home-based assessments

Jose Albites-Sanabria[1,2], Pierpaolo Palumbo[1], Jorunn L. Helbostad[3], Luca Palmerini[1,4] and Lorenzo Chiari[1,4]
[1] *Department of Electrical, Electronic, and Information Engineering – DEI, University of Bologna*
[2] *Institute of Advanced Studies, University of Bologna, Italy*
[3] *The Norwegian University of Science and Technology, NTNU, Trondheim, Norway*
[4] *Health Sciences and Technologies-Interdepartmental Center for Industrial Research, University of Bologna, Italy*

***Abstract*— The ability to complete sit-to-stand (STS) transfers has a significant impact on a person's functional mobility. Wearable sensors allows for objective, long-term monitoring of STS transfers under home-based conditions. However, despite some recent initiatives assessing STS transfers in home-based settings, the majority of STS transfer algorithms have primarily been used for assessment during the execution of prescribed activities in a lab setting. More research is also required to comprehend the distinctions between in-lab and home-based measurements, as well as their relationship to clinical outcomes. The current study compared STS features identified in 20 older adults performing activities in-lab and at home. Our results showed that duration, peak acceleration, and smoothness of STS transfers performed in the lab versus at home differed significantly. The duration of STS transfers at home was 30% longer on average than in the lab. Furthermore, because they are natural rather than instructed actions as in lab settings, the number of STS per hour was significantly lower in home-based conditions. Understanding the distinctions highlighted is critical for the successful incorporation of home-based mobility assessments into prospective clinical trials.**

***Keywords*—wearable sensors, sit-to-stand, home-based, in-lab.**

I. Introduction

Wearable sensing technology advancements have increased interest in objective, home-based measurement of health and well-being [1]. Because they can be packaged into small, power-efficient devices that can be discretely worn at various locations on the body, inertial measurement units (IMUs) are particularly well-suited for continuous movement measurements. Recent research has shown that IMUs can be used to identify sit-to-stand (STS) transfers. Approaches that use multiple IMUs across multiple body locations [2], [3] can detect STS transfers and measure STS kinematics with reasonable accuracy. However, because of the poor wearability and high patient burden associated with the use of these multi-sensor systems, they are unsuitable for long-term monitoring in home-based conditions and have limited application in clinical research. To address these limitations, several attempts have been made to detect and assess STS transfers using a single IMU located somewhere on the torso (typical locations: chest, waist, lower back) or thigh/upper leg [2]–[5].

While the majority of the research to date has focused on the evaluation of prescribed STS transfers performed in the lab, some recent efforts [6], [7] have examined data collected under home-based conditions. The findings show that STS transfer features derived from IMU data collected during home-based conditions can detect differences in age, fall risk, and disease severity (e.g., mild vs. severe Parkinson's disease). Furthermore, multi-parametric approaches [7] that rely on features extracted from STS transfers such as duration, smoothness, variability or peak acceleration have been shown to be more sensitive for detecting clinically meaningful differences than single-parametric approaches.

The research presented herein focuses on evaluating quantity and quality features extracted from STS transfers in lab and home-based settings using data from a single inertial unit worn on the lower back. To understand the contextual differences between in-lab and home-based assessments, descriptive analysis, correlations, and percentual changes on identified STS transfers were performed.

II. Methods

A. Study Participants

The current study is based on the ADAPT study dataset, which included 20 older adult participants recruited from a senior citizen center in Norway's Trondheim area [8]. Participants included in this study were over the age of 65, able to walk 100 meters without a walking aid, and able to follow oral instructions, and living independently.

The ADAPT study was approved by the Regional Committee on Ethics in Medical Research in Central Norway. Table I displays the participants main characteristics.

TABLE I: Cohort characteristics

	Participants (N=20)
Gender (M/F)	5/15
Age (years)	76.4 ± 5.6
Height (cm)	167 ± 7.2
Weight (kg)	73.7 ± 11.4

B. Wearable sensor characteristics and setup

The ADAPT dataset includes a diverse set of sensors on various body locations, motivated by the potential for algorithm development from popular activity monitoring device attachment locations [3], [9]–[11] and existing large datasets recorded from independent living older adults in previous projects focused on fall detection and risk assessment. In our research, we focused the analysis on a single wearable sensor located on the lower back. The sensor was a tri-axial accelerometer and gyroscope sensor with a sampling frequency of 100 Hz and a measurement range of

±2g.

C. *In-lab and Home-based protocol*

All subjects in the ADAPT study completed two task-based protocols: a supervised semi-structured protocol (in-lab) and a home-based unsupervised protocol (home-based). Walking, shuffling, stairs (ascending/descending), standing, postural transfer, sitting, lying, leaning, picking, and kneeling were the general purpose categories for all activities.

The in-lab protocol was carried out in a smart-home environment in the Usability Laboratory at the Norwegian University of Science and Technology's Faculty of Medicine in Trondheim, Norway. This laboratory is made up of three rooms and an observation room. The three rooms featured various types of furniture as well as ceiling-mounted cameras that were monitored and controlled from an observation room. The subjects were given a task-based protocol to follow in a specific order [8].

The home-based protocol was recorded in the participant's home environment with inertial sensors and a GoPro Hero3+ (GoPro, Inc., San Mateo, CA, USA) body-worn camera at the chest and pointed towards the feet. The performed activities were identified using video data, and the sensor data was labelled accordingly. Five experts labelled the data according to the general activity categories.

D. *Sit-to-stand identification*

To identify STS transfers, a previously validated algorithm [6] was implemented in Python 3.8.

The method relies on a single 3-axis accelerometer data and works in any device orientation, performing a calibration step each time the device is worn. The method is divided into two parts: (1) acceleration filtering with potential STS identification, and (2) STS transfer confirmation.

The first step starts by removing high frequency components. The acceleration vector magnitude is first zero-phase filtered with a fourth order Butterworth filter with a cutoff frequency of 5 Hz. The resulting signal is smoothed by taking a rolling mean (RM) with a 0.25 s window and equal weighting, resulting in the RM acceleration. The RM acceleration is subjected to a continuous wavelet transform (CWT), with coefficients in the 0-0.5 Hz band summed at each time point to yield the CWT 'power'. Potential STS transfer time points are identified as peaks in the CWT power with a minimum time difference of one second and a minimum amplitude greater than the standard deviation of the power.

Following what was defined in previous studies, we calculated quantity and quality sit-to-stand parameters associated with movement disorders and the risk of falling [3], [6], [7]. Sit-to-stand quantity was characterized by the number of sit-to-stand transfers per hour (SPH). Sit-to-stand quality was characterized by the duration (s), maximum and minimum acceleration (m/s^2), spectral arc length (SPARC) and jerk (associated with smoothness), and vertical displacement (m).

For each parameter, the average from all sit-to-stand transfers was computed for each participant.

E. *Statistical analysis*

Correlation matrices were computed during laboratory and home-based assessments to investigate the relationships between the different features. Wilcoxon signed-rank test was performed to analyse differences between lab and home-based assessments, adjusted p-values (Benjamini-Hochberg) were computed to account for false discovery rate. Analyses were performed using the SciPy and Scikit-learn libraries in Python 3.8.

III. Results

A. *Sit-to-stand transfers*

A total of 8.9 and 36.3 hours of recording were analysed, allowing the identification of 416 and 318 STS transfers for all participants during in-lab and home-based conditions, respectively. To account for the differences in the number of recording hours, the number of sit-to-stands was divided by the number of recording hours (Sits per hour, SPH). Figure 1 shows the distribution of SPH under both settings. In-lab recordings show a higher number of SPH. The logic behind this is that in lab settings, a specific number of STS transfers must be completed by a participant which is dependent on the specific laboratory protocol, whereas in home-based settings, a person's day-to-day pace may reflect a more natural number of STS transfers.

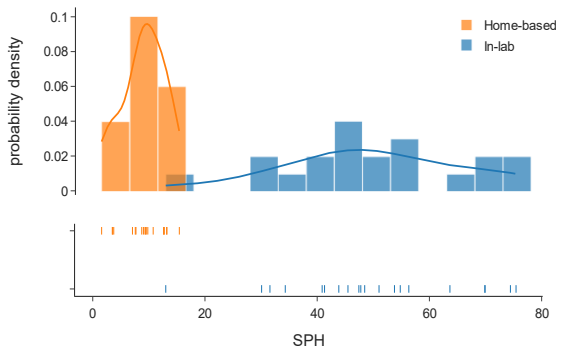


Fig. 1: Histogram distribution of the identified sit-to-stand per hour (SPH) during in-lab and home-based recordings per participant

A similar trend was observed when analysing subgroups based on gender. Participants performed less sit-to-stand transfers ($p<0.05$) in home-based conditions for both subgroups (Figure 2).

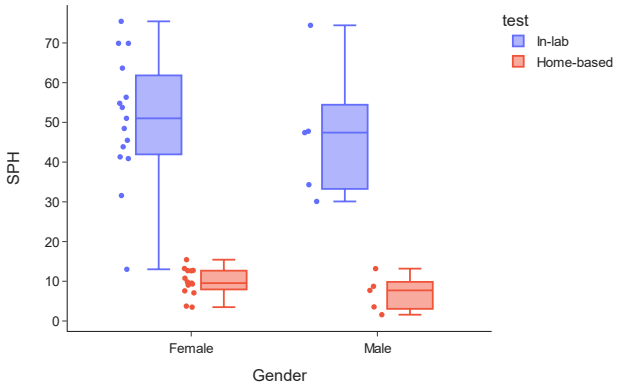


Fig. 2: Lab and home-based SPH differences by subgroups

Figures 3 shows a moderate correlation (r=0.6) for sit-to-stand per hour computed for lab and home-based assessments.

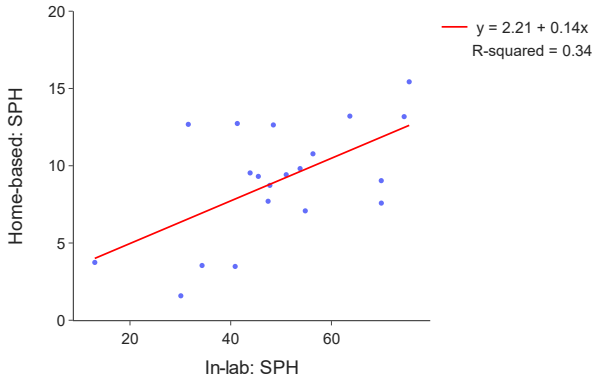


Fig. 3: SPH correlation identified in in-lab and home-based settings

Despite the fact that more SPH were performed under in-lab conditions than under home-based transfers, a moderate correlation was observed. However, no significant correlations were found for some quality features (e.g. Duration, Figure 4).

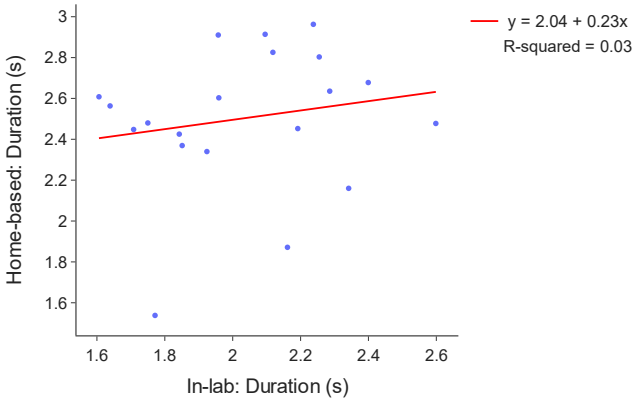


Fig. 4: STS duration correlation identified in lab and home-based settings

Table II shows the mean and standard deviation (SD) for all extracted features under in-lab and home-based assessments. Only SPH (p=0.007) and Max Acc. (p=0.02) were found to be significantly correlated.

TABLE II: SIT-TO-STAND BASED MEASURES

	In-lab		*Home-based*		*Correlation*	
	Mean	*SD*	*Mean*	*SD*	*r*	*p*
SPH	49.7	15.6	9.1	3.7	0.6	0.007
Duration	2.03	0.27	2.5	0.3	0.18	0.44
Max Acc.	11.8	0.5	11.4	0.5	0.52	0.02
Min Acc.	7.53	0.46	8.13	0.5	0.36	0.12
SPARC	-2.3	0.05	-2.38	0.04	0.39	0.09
Jerk	-3.8	0.56	-3.81	0.53	0.21	0.36
Vertical Disp.	0.63	0.16	0.55	0.12	0.38	0.1

To assess the differences between in-lab and home-based measurements, the percentage change from home-based parameters was calculated from the mean values obtained from in-lab assessments (Figure 5). The number of sit-to-stand transfers performed during home-based assessments was 80% lower than the number of sit-to-stand transfers performed during in-lab assessments. Furthermore, the duration of STS transfers at home was 30% longer on average than in the lab. Finally, the Wilcoxon signed-rank test (p-values adjusted) showed significant differences between lab and home-based measurements for SPH (p<0.0001), duration (p=0.0003), max. Accel. (p=0.004), min. Accel. (p=0.0004), SPARC (p=0.0003), and vertical displacement (p=0.025). No significant differences were found for jerk.

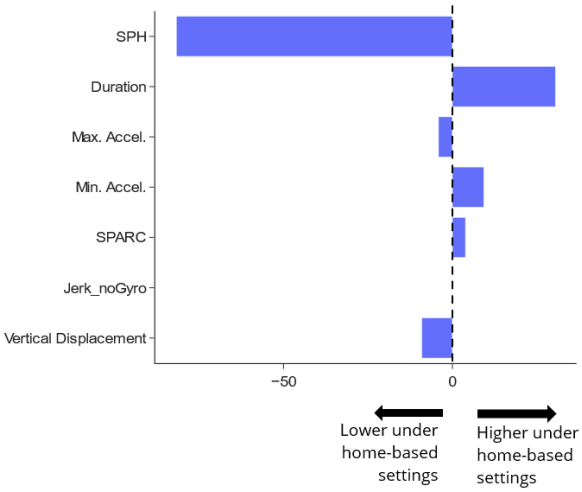


Fig. 5: Percentage change from parameters measured under home-based conditions compared with in-lab conditions

IV. CONCLUSION

The present study aimed to assess the differences between in-lab and home-based sitting transfer measurements. Our results showed that features extracted from home-based measurements significantly differ from in-lab measurements. The duration of sitting transfers was longer under home-based conditions, suggesting that home-based STS transfers may be more demanding than in-lab assessments. Several factors could explain the significant differences in the analysed. Home-based behaviours are usually self-initiated, embedded in a rich behavioural context, and goal directed. In contrast, actions in a more supervised setting, are typically triggered by a command and performed in an isolated, standardised setting with limited ecological validity. Performance can be influenced by a variety of psychological and physiological processes that vary depending on the context. These include attentiveness, motivation, fatigue, pain, and stress.

On the other hand, while in our study the number of sitting transfers per hour was lower under home-based assessments, wearable-based monitoring at home opens the possibility to extend the recordings for days/weeks allowing to potentially identify a greater number of sitting transfers than in laboratory assessments.

A current limitation of the present study, lies in the number of participants and recording hours. In addition, the home-based assessments were not completely unsupervised as there were some tasks that participants had to complete, though at their own choice of order and preference. We must note that to better evaluate home-based events reliably, future studies need to measure patients inconspicuously and for longer periods of

time, while they move freely and fully unsupervised in their daily living environment.

Overall, the differences found in lab and home-based assessments in this study aims to raise the attention on the need to move from traditional laboratory assessments. Clinicians and researchers should consider these disparities and the multiple factors that contribute to them in order to successfully integrate home-based mobility assessments into clinical practice.

ACKNOWLEDGEMENT

This study was partially funded by the Innovative Medicines Initiative 2 Joint Undertaking under grant agreement No 820820 (Mobilise-D). This Joint Undertaking receives support from the European Union's Horizon 2020 research and innovation programme and EFPIA.

REFERENCES

[1] E. Warmerdam *et al.*, "Personal View Long-term unsupervised mobility assessment in movement disorders," *Lancet Neurol.*, vol. 19, no. 5, pp. 462–470, 2020, doi: 10.1016/S1474-4422(19)30397-7.

[2] E. P. Doheny, C. W. Fan, T. Foran, B. R. Greene, C. Cunningham, and R. A. Kenny, "An instrumented sit-to-stand test used to examine differences between older fallers and non-fallers," in *2011 Annual International Conference of the IEEE Engineering in Medicine and Biology Society*, 2011, pp. 3063–3066. doi: 10.1109/IEMBS.2011.6090837.

[3] L. Montesinos, R. Castaldo, and L. Pecchia, "Wearable inertial sensors for fall risk assessment and prediction in older adults: A systematic review and meta-analysis," *IEEE Trans. Neural Syst. Rehabil. Eng.*, vol. 26, no. 3, pp. 573–582, 2018, doi: 10.1109/TNSRE.2017.2771383.

[4] A. Ejupi, M. Brodie, S. R. Lord, J. Annegarn, S. J. Redmond, and K. Delbaere, "Wavelet-based sit-to-stand detection and assessment of fall risk in older people using a wearable pendant device," *IEEE Trans. Biomed. Eng.*, vol. 64, no. 7, pp. 1602–1607, Jul. 2017.

[5] T. Pozaic, U. Lindemann, A.-K. Grebe, and W. Stork, "Sit-to-Stand Transition Reveals Acute Fall Risk in Activities of Daily Living," *IEEE J. Transl. Eng. Heal. Med.*, vol. 4, pp. 1–11, 2016, doi: 10.1109/JTEHM.2016.2620177.

[6] L. Adamowicz *et al.*, "Assessment of Sit-to-Stand Transfers during Daily Life Using an Accelerometer on the Lower Back," 2020, doi: 10.3390/s20226618.

[7] M. H. Pham, "Validation of a Lower Back ' Wearable ' -Based Sit-to-Stand and Stand-to-Sit Algorithm for Patients With Parkinson ' s Disease and Older Adults in a Home-Like Environment," vol. 9, no. August, pp. 1–11, 2018, doi: 10.3389/fneur.2018.00652.

[8] A. K. Bourke, E. A. F. Ihlen, R. Bergquist, P. B. Wik, B. Vereijken, and J. L. Helbostad, "A physical activity reference data-set recorded from older adults using body-worn inertial sensors and video technology—The ADAPT study data-set," *Sensors (Switzerland)*, vol. 17, no. 3, 2017, doi: 10.3390/s17030559.

[9] L. Donath, O. Faude, E. Lichtenstein, G. Pagenstert, C. Nüesch, and A. Mündermann, "Mobile inertial sensor based gait analysis: Validity and reliability of spatiotemporal gait characteristics in healthy seniors," *Gait Posture*, vol. 49, pp. 371–374, Sep. 2016.

[10] P. Bet, P. C. Castro, and M. A. Ponti, "Foreseeing future falls with accelerometer features in active community-dwelling older persons with no recent history of falls," *Exp. Gerontol.*, vol. 143, no. October 2020, p. 111139, 2021, doi: 10.1016/j.exger.2020.111139.

[11] A. Soltani, N. Abolhassani, P. Marques-Vidal, K. Aminian, P. Vollenweider, and A. Paraschiv-Ionescu, "Real-world gait speed estimation, frailty and handgrip strength: a cohort-based study," *Sci. Rep.*, vol. 11, no. 1, pp. 1–11, 2021, doi: 10.1038/s41598-021-98359-0.

A novel tool for the annotation of bipolar electrograms for cardiac electrophysiology

M. Orrù[1,2], E. Pitzalis[2], G. Baldazzi[2], G. Viola[3] and D. Pani[2]
[1]Department of Informatics, Bioengineering, Robotics and Systems Engineering (DIBRIS), University of Geno, Genoa, Italy
[2]Department of Electrical and Electronic Engineering (DIEE), University of Cagliari, Cagliari, Italy.
[3]Department of Cardiology, Santissima Annunziata Hospital Sassari, Sassari, Italy.

***Abstract*—Nowadays, some solutions based on automatic approaches to identify, characterize, and delineate abnormal potentials in post-ischemic ventricular tachycardia bipolar electrograms have been proposed in the literature. However, while a significant amount of annotated data is required for these purposes, no open annotated dataset is currently available. Furthermore, there is also a lack of freely available and open-source software to enable collaborative clinical annotation. In particular, for post-ischemic ventricular tachycardia electrograms, the presence of such tools and dataset could significantly foster the research in the field of computer-aided minimally disruptive ablation procedures.**

This paper proposes a tool entirely developed in MATLAB, which allows clinical experts to annotate post-ischemic ventricular bipolar electrograms by labelling them as physiological or not and delineating the abnormal potentials. The proposed interface embeds several features, beyond the annotation options, such as the electroanatomic map display, electrogram spatial localisation, the twelve surface ECG representation and QRS delineation, and several graphical facilities.

In upcoming works, we aim to use the proposed graphical user interface to conduct intra- and inter-annotator studies and produce a validated and trustworthy annotated dataset to be publicly released according to the open data initiative.

***Keywords*—Ventricular tachycardia, cardiac electrophysiology, open data, dataset annotation**

I. Introduction

THE most widely used approach for the treatment of post-ischemic ventricular tachycardias is trans-catheter radiofrequency ablation [1], [2]. This technology is mainly based on the identification of target areas to be ablated in order to completely suppress the arrhythmia. Such areas are commonly characterized by local bipolar electrograms (EGMs), also known as abnormal ventricular potentials (AVPs), that exhibit late activations with high-frequency fractionated components [3]–[5].

Nowadays, the process of identifying AVPs and, consequently, targeting ablation zones, is performed during substrate mapping by the electrophysiologists, who visually analyse the morphology of each recorded EGM, in a very time-consuming procedure. Some solutions based on automatic approaches to identify ablation sites are being proposed in the literature [6], [7], with the aim of shortening the procedure time and possibly improve its effectiveness.

In addition to the use of substrate maps to distinguish physiological EGMs and AVPs, the characterization of the late activations in the AVPs is also of great interest to better understand the behaviour of wavefronts activation in correspondence with the post-ischemic scar, as also the re-entry circuit pathways. The latency identification, often investigated in the literature [8]–[10], actually represents a signal delineation problem.

Unfortunately, the data from post-ischemic ventricular tachycardia procedures that can be collected in a single hospital are often limited and not readily available. However, solutions based on supervised learning for the development of accurate AVP identification and delineation, require large and annotated datasets for a proper training.

To the best of the authors' knowledge, no such kind of public dataset currently exists. Moreover, there is also a lack of freely available and open-source software tools enabling collaborative clinical annotation of post-ischemic VT EGMs.

On these premises, this research was aimed at designing and developing a graphical user interface (GUI) that allows clinical experts to annotate post-ischemic ventricular bipolar EGMs, with the final aim of creating a reliable multi-annotated dataset to be released. Specifically, the dataset will contain information regarding both the type of each EGM and the delineation of the late activation in the case of AVP. This solution could solve the lack of a public dataset in the field of post-ischemic VT, thus enabling the effective development and benchmarking of algorithms for arrhythmogenic sites detection and characterisation, as also to facilitate collaboration across the research community.

II. Methods

The GUI has been entirely developed in MATLAB R2022b (MathWorks Inc., MA, USA) and provides a user-friendly tool for the annotation of post-ischemic VT bipolar EGMs. For the time being, the development of the tool is directed at reading export files of mapping procedures performed using the CARTO®3 system (Biosense Webster, Inc., Diamond Bar, California), but it will be further extended in next versions.

The tool consists of two windows: the **Start Window**, which is the initial window used to launch the annotation while providing a summary of the annotation progress, and the **Annotation Window**, which includes all the functionality to fulfil the annotation. The tool analyses each procedure independently and provides a .mat file as output.

A. Data loading

The software loads the data from a folder containing all the procedures that the user must annotate, each one contained into a dedicated folder. The folders do not report any personal data of the patient they refer to, but only the procedure data useful

to perform the annotation. The four types of files used by the software are described in Table 1.

TABLE I: FILES USED BY THE ANNOTATION GUI

Files	*Content*
[MapIndex-MapName]_car.txt	Summary of values recorded for each point
[StudyName]_[StudyDate].xml	Summary of the entire mapping study
[MapIndex-MapName].mesh	Geometry data of 3D images
[MapIndex-MapName]_P[Point#]_ECG_Export.txt	2.5 seconds of intracardiac and body surface ECG signals

On the left, the format of file contained in each procedure folder; on the right, the content of each file type.

In particular, the .mesh file is the main file used for the reconstruction of the ventricle map with the corresponding voltage or local activation time (LAT) information. The .xml and car.txt files are used for data extraction to locate the bipolar EGM on the map. Finally, the folder contains multiple ECG_Export.txt files, one for each recorded bipolar EGM. These files are taken as input for the extraction of all the recorded signals, both the EGM and the 12-lead superficial ECG. The procedure file also contains other types of data that are not used by the current version of the annotation tool.

B. *Start window*

The "Start window" it's the first window that is displayed every time that to tool is launched. When a user runs the tool for the first time, the system requests the name and surname initials, which will be used as a reference to save the output data and keep track of who performed that annotation. This information is then stored and is no longer requested. Finally, as shown in Figure 1, the "Start Window" contains the start button and a counter that displays the progress made in the annotation by the user.

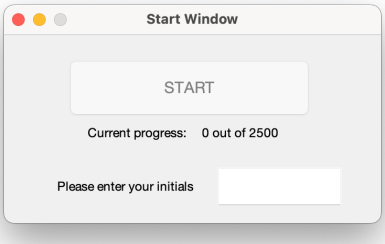


Fig. 1: Start window of the developed annotation GUI for post-ischemic VT bipolar EGMs. Here the current number of annotated EGMs with respect to the overall dataset is displayed, along with an editable text field for input of annotator initials.

C. *Annotation window*

The main window of the GUI is designed to be an intuitive, user-friendly environment that provides simple tools for the visualization, annotation, and delineation of physiological EGMs and AVPs. The window can be conceptually divided

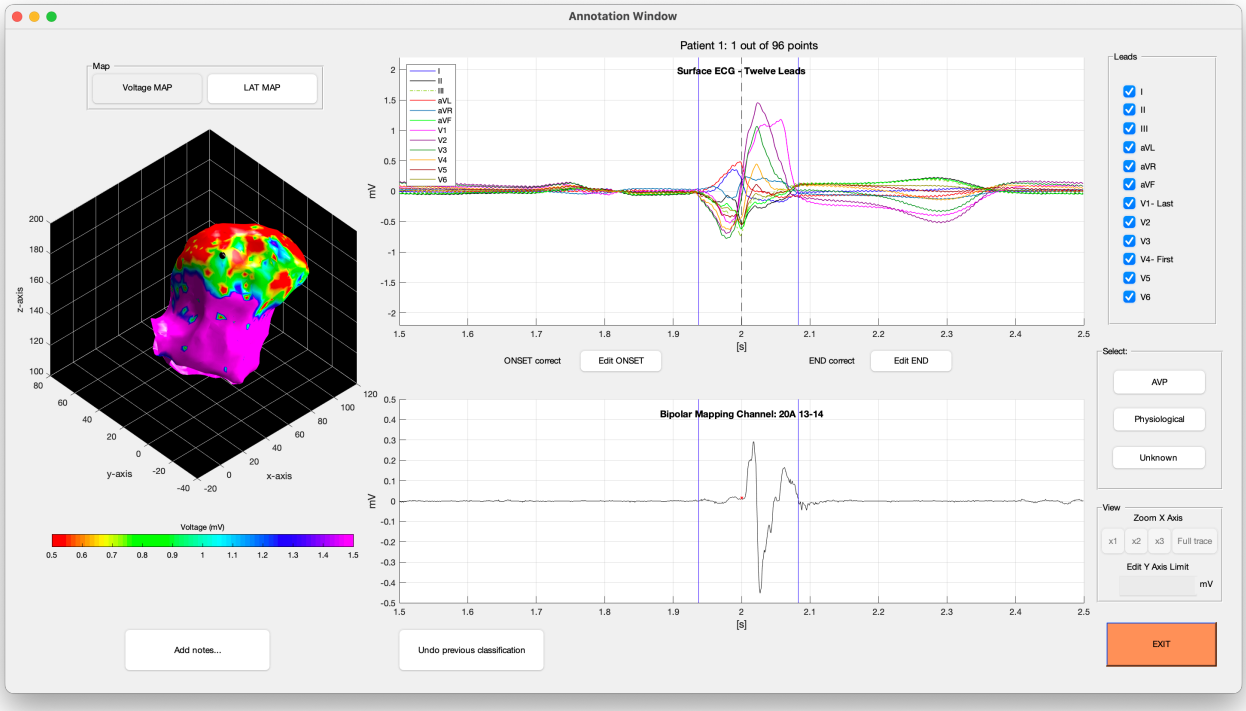


Fig. 2: Annotation window of the GUI developed for the annotation of post-ischemic VT bipolar EGMs. The plot on the left represents the bipolar voltage/LAT map which the current bipolar EGM refers to. On the right, the 12-lead surface ECG (on top) and the bipolar EGM (on bottom) to be annotated. Below the plot of the 12-lead surface ECG, the "Edit ONSET" and "Edit END" buttons enable the editing of the onset and end of the QRS complex automatically detected by the system. On the right side of the ECG plot, the "Leads" panel is available, which contains a check box for the selection of the surface leads to be plotted; below, the "Select" panel is introduced to annotate the bipolar EGM, along with the "View" panel, in which the user can modify the zoom settings on the bipolar EGM plot both on the x and y axis. Finally, at the bottom, there are the buttons to add notes and go back to the previous point, and, in orange, the button to close the tool.

into three plots: a 12-lead ECG plot, a bipolar mapping channel EGM plot, and a 3D colour-coded cardiac chamber map.

The ECG and EGM signals from the dataset are automatically and sequentially loaded onto the window to be displayed on the two 2D plots, as shown in Figure 2. Their default view displays only a segment of the signal, centred on the recorded beat.

An underlying algorithm detects the two superficial ECG leads that exhibit the earliest activation and the latest end of the QRS complex. These fiducial points are indicated by the two blue lines in the upper plot; if needed, the user can change their location simply through the dedicated buttons (i.e., the **Edit ONSET** and **Edit END**) and by clicking on the graph for repositioning. Any edit is saved, thus allowing for further statistical analysis and annotation validation. The user can also choose which of the 12-lead surface ECG wants to display, using the checkboxes in the **Leads** panel.

The lower section is the one aimed at the EGM classification and delineation. After observing the bipolar signal morphology, the user is expected to choose among the three classes in the **Select** panel: AVP, Physiological and Unknown. The last two options automatically save the selection, whereas the AVP class requires the user to mark both the onset and end of the abnormal potential in the current signal. The AVP button also enables the tool on the **View** panel, allowing the user to access the zoom option and modify the view, freely switching from the default focus view to the full view (i.e., the entire 2.5 s long EGM recording) or to focused views on x and y axis, and vice versa. Once the selection is performed the annotation automatically moves to the next signal annotation.

Furthermore, the user is presented with another information to further enhance task performance: the 3D colour-coded cardiac chamber map. This remarkable feature is based on the data from the CARTO®3 mapping system procedure, which contains both the voltage map and the LAT map. By simply clicking on the dedicated upper buttons (i.e., **Voltage MAP** and **LAT MAP**), the user can switch between these two representations, displayed on the left side of the window. In Figure 3, an example of the two maps is proposed. In addition to the information given by the colour coding, the localization of the current point is also shown to the user, marked on the ventricle map by a black sphere.

Additional features are the option to add notes, which will be later saved into an additional file, the **UNDO** button, which allows the user to delete the previous signal annotation, and the **EXIT** button, which allows the annotation process to be stopped and to resume it later.

Furthermore, to avoid affecting any reliability of data gathering, some strategies have been implemented to prevent users from altering the desired running condition, such as granting full view accessibility only during the AVP delineation and enabling the undo action no more than once in a row.

D. Data saving

During the annotation process, a cell array named "datamatrix" is updated in all its fields by adding an item each time a new annotation is carried out. Once the annotation is completed on the entire procedure, the interface returns a .mat file containing the datamatrix. In addition, the .mat file reports in its name the initials of the annotator, so that this information can be used for future analyses, label voting and annotation validation. The saved cell array consists of nine fields, one per column, labelled as follows:

- Folder Name: the path of the patient folder.
- File Name: the name of the analysed .txt file is

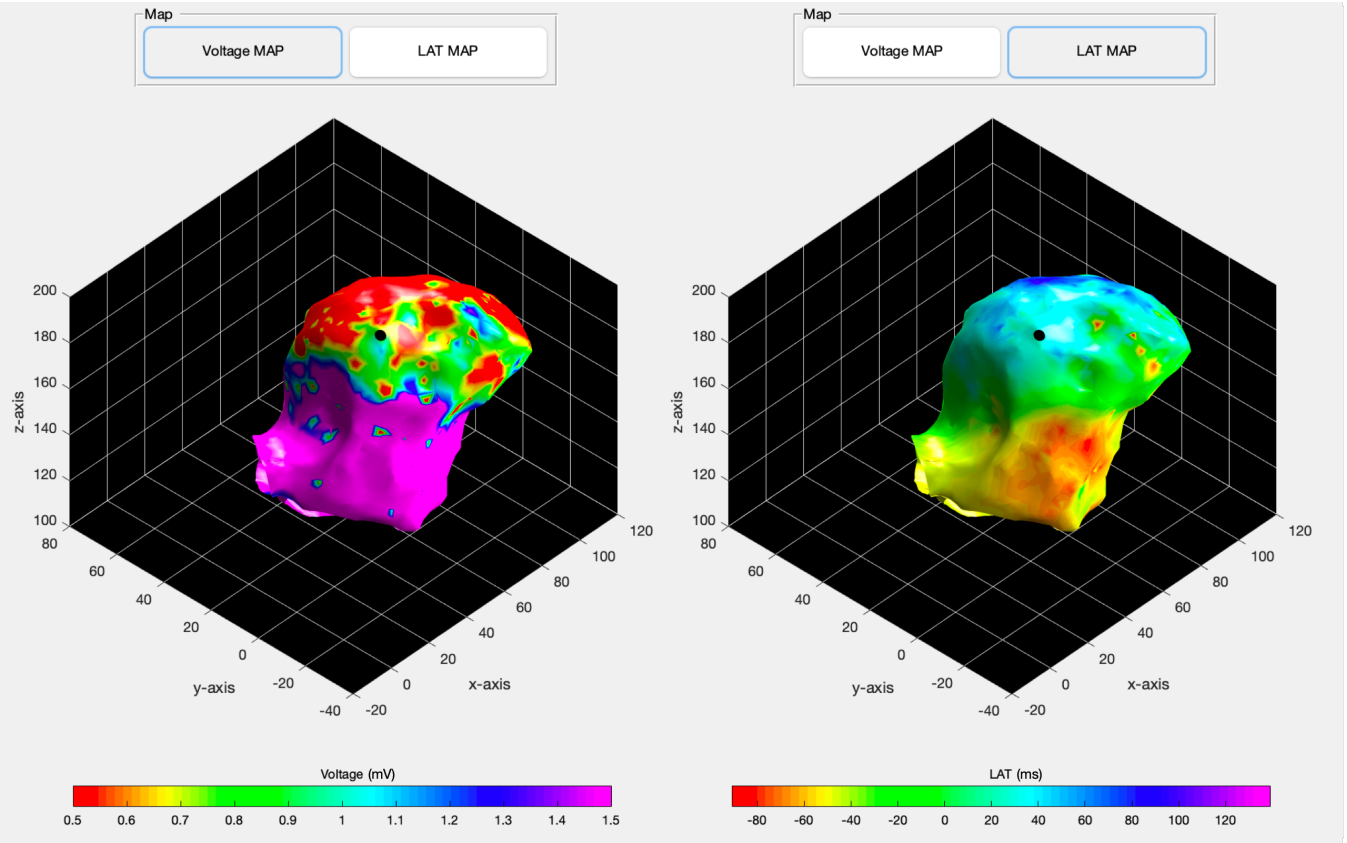


Fig. 3: The 3D color-coded ventricle maps. On the left, the voltage map, and on the right, the LAT map representation of the same ventricle.

saved.

- Onset/End Number: the samples that the annotator marked as the onset and end points of the AVP. For the “Physiological” and “Unknow” classes, this value is set to NaN.
- Class: the manual annotation. To facilitate the creation and subsequent management of the datamatrix, each class has been saved as a number: 2 for AVP, 1 for Physiological, and 0 for Unknown.
- QRS Onset/End: the samples corresponding to the onset and end of the QRS complex automatically computed by the algorithm embedded in the annotation tool.
- QRS Onset/End Modified: the samples selected by the annotator as the actual QRS onset and end points, if the expert needs to modify the ones proposed by the system; in case of no modification, these values are set to NaN.

In addition to the datamatrix, eventually, the interface also returns .txt files that carry notes entered by the operator during the annotation phase.

III. Discussion and conclusions

This work proposes the first tool for the annotation of post-ischemic ventricular bipolar EGMs and the delineation of AVPs. The proposed solution is a user-friendly GUI currently dedicated exclusively to procedures performed and exported through the CARTO®3 mapping system (Biosense Webster, Inc., Diamond Bar, California). However, future versions will also allow annotating data from multiple electroanatomic mapping systems.

This tool is currently being used to present the same dataset to multiple expert electrophysiologists to investigate inter-annotator variability in the manual annotations, and for the construction of a validated annotated dataset to be released as open data. This would fill the gap in the literature about the existence of freely accessible and public datasets of AVPs and physiological post-ischemic VT electrograms. In addition, because of the interface input structure required, it is also possible to create mini-batch of a repeated set of data to be submitted to the same annotator to conduct intra-annotator variability analyses, useful to identify the expected precision of the automatic tools.

Currently, multiple expert annotators are being enrolled to access to a multi-procedure dataset containing a mini-batch of repeated signals. From this, we aim to conduct intra- and inter-annotator analysis and produce a validated and trustworthy annotated dataset that may be exploited to design automated classification and annotation systems in order to develop and benchmark computer-aided systems to support clinicians during such electroanatomic mapping and ablation procedures.

Acknowledgement

The authors wish to thank Giorgia Ibba for her important contribution to the preliminary development of the MATLAB graphical user interface.

This work was conducted within the project "ARGO study: Ablation Reinforcement by computer-aided Guidance and Optimization" approved by Azienda Tutela Salute Sardegna (ATSSardenga).

References

[1] G. S. Guandalini, J. J. Liang, and F. E. Marchlinski, “Ventricular Tachycardia Ablation: Past, Present, and Future Perspectives,” JACC: Clinical Electrophysiology, vol. 5, no. 12. Elsevier Inc, pp. 1363–1383, Dec. 01, 2019. doi: 10.1016/j.jacep.2019.09.015.

[2] J. W. Cheung, “Targeting Abnormal Electrograms for Substrate-Based Ablation of Ventricular Tachycardia: Can We Ablate Smarter?,” JACC: Clinical Electrophysiology, vol. 6, no. 7. Elsevier Inc, pp. 812–814, Jul. 01, 2020. doi: 10.1016/j.jacep.2020.04.013.

[3] G. Baldazzi, M. Orrù, G. Solinas, M. Matraxia, G. Viola, and D. Pani, “Spectral characterisation of ventricular intracardiac potentials in human post-ischaemic bipolar electrograms,” Sci Rep, vol. 12, no. 1, p. 4782, 2022, doi: 10.1038/s41598-022-08743-7.

[4] P. Jaïs et al., “Elimination of local abnormal ventricular activities : A new end point for substrate modification in patients with scar-related ventricular tachycardia,” Circulation, vol. 125, no. 18, pp. 2184–2196, May 2012, doi: 10.1161/CIRCULATIONAHA.111.043216.

[5] S. K. S. Huang and J. M. Miller, Catheter ablation of cardiac arrhythmias e-book. Elsevier Health Sciences, 2019.

[6] G. Baldazzi, M. Orru, M. Matraxia, G. Viola, and D. Pani, “Supervised Classification of Ventricular Abnormal Potentials in Intracardiac Electrograms,” in Computing in Cardiology, Sep. 2020, vol. 2020-September. doi: 10.22489/CinC.2020.397.

[7] A. Pitzus et al., “Exploring Transfer Learning for Ventricular Tachycardia Electrophysiology Studies,” in Computing in Cardiology (CinC), Sep. 2022.

[8] A. Alcaine et al., “A wavelet-based electrogram onset delineator for automatic ventricular activation mapping,” IEEE Trans Biomed Eng, vol. 61, no. 12, pp. 2830–2839, 2014.

[9] N. Cortez-Dias et al., “Novel ‘late potential map’ algorithm: Abnormal potentials and scar channels detection for ventricular tachycardia ablation,” J Cardiovasc Electrophysiol, 2022.

[10] G. Lima da Silva et al., “Impact of different activation wavefronts on ischemic myocardial scar electrophysiological properties during high-density ventricular tachycardia mapping and ablation,” J Cardiovasc Electrophysiol, 2022.

Design and Evaluation of an Intuitive Administration Dashboard for a Platform used to Monitor Clinical Trials

L. Cossu[1], L.C. Causin[1], A. Facchinetti [1] and G. Cappon[1]
[1] *Department of Information Engineering, University of Padova*

***Abstract*—The IMPACT platform, an integrated mobile solution for simplifying the conduct of clinical trials, has recently been developed. To enhance the platform, a new administrative dashboard was designed and developed with the goal of ensuring the quality of data collected during the trial and facilitating the necessary actions for its conduction. To improve accessibility, a role-based access policy was implemented during the design and development of the dashboard, with different roles such as data and study administrators granted access to the newly developed dashboard. Usability of the dashboard was evaluated through task-based sessions with 14 participants, and the results were analyzed using custom-defined metrics. The analysis revealed that the dashboard was well-received and highly usable, as participants were able to complete tasks with minimal errors and a reasonable amount of time, after an initial period of acclimation to the layout of the dashboard.**

***Keywords*—Administrative dashboard, clinical trial management, platform, usability**

I. INTRODUCTION

Clinical trials play a vital role in advancing medical technology by providing a means to evaluate the effectiveness of new therapies and technologies in real-world conditions. However, these trials come with a host of challenges, one of which is effective subject and data management. Data collection from various sources such as sensors, questionnaires and patient diaries can be in various formats and must be effectively integrated into the trial framework. This data may also need to be made available to clinicians and other trial operators to monitor patients' conditions and ensure safety during the trial.

To address the challenges of clinical trial management, we have indeed developed IMPACT [1], an Integrated Mobile Platform for Automated Clinical Trials. This mobile platform automates the processes of data collection, organization, and display for monitoring, allowing for a predefined and modular approach. Currently, IMPACT consists of three components that communicate via a secure ad-hoc web API: a mobile application for use by trial participants to collect data during the trial, a website for clinicians to monitor all enrolled patients in real time, and a cloud database that stores all collected data and allows remote monitoring via the website. The schema of the platform structure and components is illustrated in Figure 1.

The mobile application component of IMPACT is designed to function as an electronic diary for trial participants, allowing them to log and track all events relevant to the study.

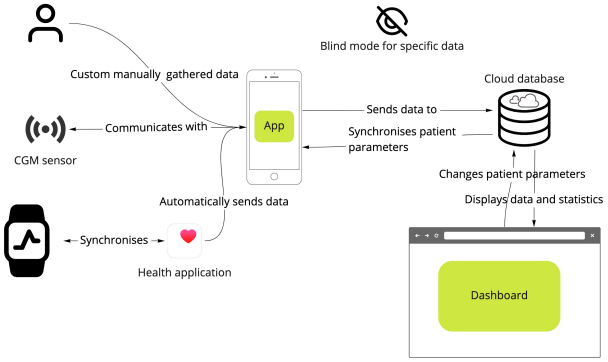


Fig. 1: Overview of the current structure of the IMPACT platform, illustrating the main components and data flow.

The application is able to automatically collect data without requiring any input from the user, reducing the burden of manual data entry. The modular approach of the application allows it to be adapted to the specific requirements of each trial, implementing solutions to collect all necessary data in the most reliable and least burdensome way for the patient.

The web application component of IMPACT is intended for use by clinicians to monitor patients' status and data in real-time, ensuring their safety and enabling them to make adjustments to trial parameters as needed.

Currently, the only way to verify the status of data collection and address potential issues is through the clinical web application, this method however is not ideal as it requires clinicians and data managers to share login credentials, which can lead to exposing personal information to data managers who may unintentionally modify data parameters. A more efficient approach is to clearly differentiate the responsibilities of data management and clinical tasks, ensuring that clinicians are only responsible for clinical duties and data managers are responsible for verifying the integrity of the data.

In this work, we present how we have implemented a solution to address this issue by implementing role-based access to the data and dividing tasks among different roles. This approach allows us to thoroughly verify the integrity of the trial conduction while also safeguarding the privacy of participants by clearly differentiating the responsibilities of data management and clinical tasks, and ensuring that only

authorized personnel have access to sensitive data.

II. MATERIAL AND METHODS

On the IMPACT platform, several new roles have been implemented, each with specific functions and permissions. These roles are:

- Superuser
- Data administrator
- Study administrator
- Researcher

The superuser role serves as the primary system administrator and is responsible for the technical management of the platform. This role has the authority to carry out any action within the system, including accessing all system data, registering any type of user, and creating new studies. Below the superuser in terms of privileges and permissions are the data administrator and the study administrator. The data administrator has almost the same privileges as the superuser, including access to all system data and the ability to register any type of user except for the superuser. However, the data administrator is not able to delete another data administrator or a superuser. This role is responsible for managing the data and ensuring its integrity. The study administrator, who is ranked below the data administrator, has access to all data related to a specific study. However, its authority is limited to only registering new clinicians. Overall, the study administrator has similar privileges to the data administrator, including the ability to create and modify details for patients, clinicians, and clinical centers within the study, as well as delete them. However, the main limitation for both the study administrator and the data administrator is their inability to enroll patients, a task that is reserved for clinicians. The researcher role has access to all data related to the specific study they are a part of, but cannot access data from other studies. A researcher is able to view the complete list of patients within their study, but can only see the clinicians who have access to the data of the study and are considered active, rather than those who do not have access and are inactive. Only data administrators have the ability to create a researcher and give it access to a study.

Access rules for the platform are directly implemented and can be managed through an administrative interface. This interface allows the study and data administrator to view all relevant information for their role and perform all actions they are authorized to take. The access rules are deeply integrated into the platform server, ensuring that all requests and actions made by each user are authorized by the platform based on their role. In this way, the system ensures that all access and permissions are granted to the right person and with clear limits and responsibilities, thus allowing for a thoughtfully secure, efficient and user-friendly management of the clinical trial data.

The mobile application and clinician dashboard have been developed using Flutter [2], a cross-platform framework that allows for the creation of a single codebase that can be deployed on mobile, desktop, and web platforms. This capability enabled the reuse of most features and design elements from the clinician dashboard for the administrative interface.

The administrative dashboard allows study and data administrators to log in and access a version of the dashboard that is tailored to their privileges i.e., the study administrator does not have access to the researchers and administrators management pages. The other main pages of the dashboard include the study overview, enrolments, clinicians, patients, and clinical centers management pages. These pages provide an overview of the trial characteristics and personnel and allow for various actions such as adding, modifying, or deleting users. For example, the patients page, shown in Figure 2, lists all patients in the study with their study-related information such as the clinical center responsible for their care and whether the patient has requested to be removed from the system in accordance with GDPR [4] regulations. Each row also includes buttons to perform relevant actions for each patient, such as modifying their information, transferring them to a new clinical center, deleting the patient from the system, and accessing a page with information on the patient's data quality and details.

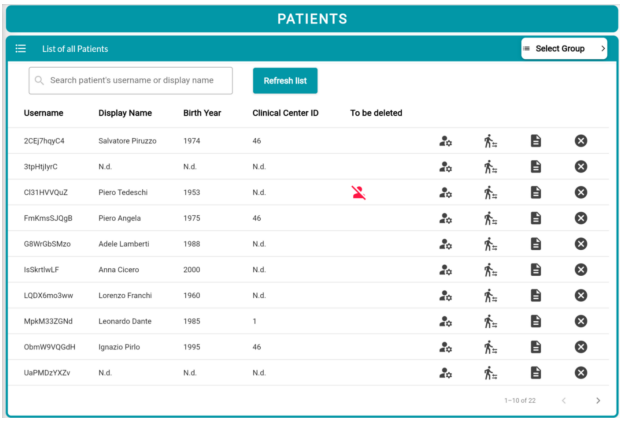


Fig. 2: Patients page of the administrative dashboard.

III. USABILITY ASSESSMENT

Usability is a crucial aspect of any tool as it directly impacts the effectiveness and efficiency with which tasks can be completed. A user-friendly dashboard that allows administrators to easily navigate and access the necessary features and functions can significantly reduce the time and effort required to perform their duties. Therefore, ensuring the usability of an administrative tool is crucial for its success and widespread adoption.

To assess the usability and ease of use of the IMPACT platform's administrative dashboard, we conducted a task-based testing session. Participants were asked to perform 10 different tasks, designed to simulate common actions that an administrator would take on the dashboard. These tasks were carefully crafted to evaluate the usability of the tool and identify any potential issues or areas for improvement. This task-based testing approach allows for an in-depth evaluation of the tool's usability, by providing insights on the participants'

experience and perception of the interface, and providing valuable feedback on how to improve it. Furthermore, this methodology is a trustable and efficient way to evaluate the user interface usability as it allows to measure the performance, satisfaction, and error rate of the tasks assigned to the participants. The 10 different tasks have been designed as follows:

1) Starting from the "Log In" screen, perform the log in and read the clinical study report on the main page, called "Study Overview." On this page, the user must then change the name of the clinical study to "Type 2 Diabetes Study," save the preferences, and log out.
2) Starting from the "Log In" screen: perform the log in and go to the "Enrollments" section. Here, the user must pause enrollment number X and then terminate enrollment number Y, entering a date of their choice and the end-of-enrollment reason "Adverse event."
3) Starting from the homepage, find the identification number (ID) of the Clinical Center associated with Padova.
4) Starting from the homepage, find the clinician "USERNAME," assign them the name "Mario Rossi" and the ID of the Clinical Center in Padova, and save the changes.
5) Starting from the homepage, the user has to find the patient "USERNAME," change their Display Name to "Mario Rossi" and their date of birth to "DATE OF BIRTH".
6) Starting from the homepage, the user must transfer patient "USERNAME" to the Clinical Center in Padova.
7) Starting from the homepage, grant researcher "USERNAME" access to study data until December 15, 2023.
8) Starting from the homepage, the user must find and view all patients enrolled with clinician "USERNAME."
9) Starting from the homepage, the user must create a new study administrator, find it, and delete it. The user must then log out.
10) Log in as a study administrator. Starting from the homepage, the user must create a new clinician and assign them to the center in Padova, giving them the Display Name "FIRST AND LAST NAME." The user must then delete the clinician.

To evaluate the ease of use, efficiency, and subjective satisfaction with the administrative dashboard, we considered a comprehensive set of evaluation metrics. These metrics, including the Task Success Rate (TSR), Time on Task (ToT), Number of Clicks, Difficulty Rating and Errors, were carefully selected to provide a thorough understanding of the performance of the dashboard from various perspective.

- Task Success Rate (TSR): Defined as the normal rate of task completion, TSR is calculated by dividing the number of users who successfully completed a task by the total number of subjects who attempted the task. A high TSR indicates that most users were able to complete the task successfully. Additionally, to evaluate the number of errors made during the task completion, the error-free task success rate (ef-TSR) was also calculated, which is defined as the number of people who completed the task without making errors divided by the total number of people who attempted the task.
- τ: the normalized increase in percentage of time required to complete the task in relation to the minimum task time (MTT)
- χ: percentage increase in clicks compared to the minimum number of clicks required to complete the specific task. Similarly to the previous metric, after defining the minimum number of clicks (MC), we have normalized the number of click done above the minimum by the minimum number of cliks.
- Difficulty: at the end of each task, users were asked to rate the difficulty of the task as low, medium, or high (corresponding to values 1, 2, and 3, respectively). The average rating was then calculated using the arithmetic mean.
- Errors: these are defined as the number of incorrect clicks made per task (as opposed to clicks, which refer to the total number of clicks made per task). The number of critical errors, or errors that resulted in the failure of a task, was also taken into account. The average number of errors and critical errors per task was also calculated using the arithmetic mean.

Furthermore, to evaluate the overall satisfaction with the administrative dashboard, participants were asked to complete the System Usability Scale (SUS) questionnaire [3] at the end of the tasks. The SUS is a widely-used tool for efficiently evaluating the usability of websites and other systems. The SUS provides a single score between 0 and 100, the higher the score, the more usable is considered the system.

IV. Results

The usability and ease of use of the administrative dashboard were rigorously evaluated through a task-based testing session with 14 volunteers (8 males, with an average age of 33 ± 13.5 years). The participants were selected to ensure a diverse range of expertise and familiarity with telemedicine, with 9 of the participants reporting low levels of knowledge, and half reporting some prior experience with telemedicine platforms.

The tests were conducted using the Zoom online video conference software, with the participants sharing their screens as they logged into the administrative interface with provided credentials and completed the tasks. Table I shows the reference values for the τ and χ metrics, which are the minimum time (MTT) and minimum number of clicks (MC) required to complete each task.

The findings of the experiments are documented in Tables II and III. The results of the task-based testing session indicate that the administrative dashboard has a high level of usability and ease of use.

TABLE I: Reference values for each task in minimum number of clicks and time of task

Task	MTT [s]	MC
1	25	8
2	27	13
3	11	3
4	19	5
5	29	5
6	13	4
7	23	7
8	19	5
9	36	12
10	51	19

The overall success rate for completing tasks was high, with the exception of one participant who made an unintentional error in one task, which resulted in a critical failure and prevented the completion of the task. Despite this, the overall success rate is commendable, particularly in light of the fact that many of the participants reported minimal prior experience with telemedicine and a significant proportion had not previously utilized a telemedicine interface.

TABLE II: Numeric results on the average success rate, time on task and clicks

Task	TSR	ef-TSR	τ	χ
1	100%	79%	195,90%	12,14%
2	93%	79%	262,50%	27,32%
3	100%	71%	332,47%	63,31%
4	100%	100%	196,70%	26,20%
5	100%	100%	59,93%	30,25%
6	100%	71%	201,25%	47,19%
7	100%	79%	240,51%	57,54%
8	100%	29%	496,17%	116,81%
9	100%	43%	360,62%	82,13%
10	100%	100%	94,18%	8,58%

TABLE III: Numeric results on average self-reported difficulty, errors and critical errors for each task

Task	Difficulty	Errors	Critical errors
1	1,00	1,00	0
2	1,50	1,79	1
3	1,50	1,36	0
4	1,14	0,50	0
5	1,00	0,43	0
6	1,21	0,93	0
7	1,64	2,50	0
8	2,21	3,21	0
9	2,36	4,93	0
10	1,21	2,36	0

From the results, it can be concluded that the dashboard is characterized by high usability and great intuitive use. Test users, who did not have much familiarity or expertise with similar sites, needed more time to become familiar with the interface. This is evident from the results presented in the τ and χ columns of Table II. While these metrics show that participants required more time and clicks than the minimum needed to complete the tasks, they also demonstrate that once participants were familiar with the interface, they were able to complete tasks with ease. However, it is worth noting that, notwithstanding the aforementioned results, only two tasks (8 and 9) presented more challenges for participants in terms of time taken, clicks, difficulty and errors. Specifically, the τ parameter shows a time increase of 500% and 360% respectively for tasks 8 and 9, compared to the minimum time required to complete the same tasks. The χ parameter also reports an increase, respectively for tasks 8 and 9, of 116% and 82% of clicks compared to the minimum number of clicks necessary to complete them. Moreover, these tasks were rated by participants as harder than the others. These results indicate that there may be room for improvement in these specific tasks, devising ways to make them less cumbersome for users and making them more trustworthy.

Nevertheless, aside from these two tasks, the metrics used to evaluate the usability of the dashboard, such as task success rate, time on task, number of clicks, and user ratings of task difficulty, generally showed low levels of difficulty and errors for the majority of tasks. Notwithstanding this, the results of the System Usability Scale (SUS) questionnaire were favorable, with a mean score of 89.3 and a standard deviation of 5.5, which indicates that the dashboard is considered to be highly usable, versatile, and user-friendly.

V. Conclusion

In conclusion, this study has presented the results of a usability evaluation of a telemedicine administration interface, which was developed to support a real clinical study. Overall, the findings of the experiments indicate that the dashboard is an easy-to-use, intuitive and reliable tool. Nonetheless, the difficulties encountered in tasks 8 and 9 should be taken into account and further research could be done to address any seasonality issues with the use of the platform, in order to ensure a thorough user experience.

Acknowledgement

This work was partially supported also by MIUR under the initiative “PRIN: Programmi di Ricerca Scientifica di Rilevante Interesse Nazionale (2020),” project ID: 2020X7XX2P, project title: “A noninvasive tattoo-based continuous GLUCOse Monitoring electronic system FOR Type-1 diabetes individuals (GLUCOMFORT)

References

[1] G. Cappon, L. Cossu, F. Boscari, D. Bruttomesso, G. Sparacino, A. Facchinetti. An Integrated Mobile Platform for Automated Data Collection and Real-Time Patient Monitoring in Diabetes Clinical Trials. Journal of Diabetes Science and Technology. 2022;16(6):1555-1559. doi:10.1177/19322968211024620

[2] Flutter: open source framework for building applications. https://flutter.dev. Last accessed on Jan 10, 2023

[3] Brooke, John. (1995). SUS: A quick and dirty usability scale. Usability Eval. Ind.. 189.

[4] General Data Protection Regulation (EU) 2016/679. Available at: https://gdpr-info.eu. Last accessed on Jan 10, 2023

Automatic extraction of acoustic features to predict Alzheimer's disease among English-speaking subjects

C. Giangregorio[1], E. Ambrosini[1], and S. Ferrante[1]
[1] *Department of Electronics, Information and Bioengineering, Politecnico di Milano, Milan, Italy*

***Abstract*—Dementia is a disease characterized by the decline of cognitive function. Previous studies have shown that speech conveys information about health and cognitive status. The current work aims at validating the capability of a set of acoustic features automatically extracted from voice recordings to classify the level of cognitive decline. To reach this aim, the Pitt Corpus, a dataset of 458 recordings of English-speaking subjects, has been exploited. A Support Vector Machine classifier achieved the best classification performance, with an F1-score of 78% to distinguish people with a diagnosis of Alzheimer's Disease (AD) from non-AD subjects. An improvement of the classification performance was achieved by two gender-based classifiers, which obtained an F1-score of 83% and 88% for female-based and male-based classifiers, respectively. The results of this study confirmed the possibility to predict AD based on acoustic features automatically extracted from voice recordings. Since no manual intervention was required in data processing, the proposed algorithm is a good candidate for being implemented on a mobile application so as to implement an ecological momentary assessment of people at risk of cognitive decline.**

***Keywords*—Alzheimer's Disease, speech processing, machine learning**

I. INTRODUCTION

Dementia is a category of neurodegenerative diseases defined by a gradual long-term decrease in cognitive function. It is characterized by a set of symptoms including memory loss, poor executive functions (e.g. problem-solving, decision-making), language impairment, motor problems, and emotional distress. This category comprises different forms, the most common one being Alzheimer's disease (AD) which represents up to 75% of total cases [1]. It is important to stress that this pathology starts silently for up to 20 years before there are clear and observable cognitive symptoms, thus there is a need to find strategies to detect the problem as early as possible, to enhance therapy effectiveness and quality of life. Since speech and language capacity is a well-established early indicator of cognitive deficits, speech-processing methods may offer the possibility of automatically screening for prototypical indicators in real-time. Indeed, in recent years, voice has been one of the most studied digital biomarkers [2], being widely employed since it allows an ecological and rapid assessment of several aspects linked to the health status of a subject that would usually be assessed in presence of clinicians.

The use of voice to detect cognitive decline from the analysis of acoustic features has been eased by the advent of artificial intelligence. Indeed, several studies have been reported in the literature on the recognition of cognitive decline from spontaneous speech, thanks to the availability of already existing datasets such as the Pitt Corpus, the largest public corpus of speech tasks from elderly subjects and those with dementia (AD). For example, Fraser et al. exploited the Pitt Corpus to distinguish healthy control and AD, based on linguistic variables derived from transcripts, achieving an accuracy of 81% [3]. Other studies have used linguistic features derived from the manual transcriptions to classify the recordings: Ammar et al. obtained 79% of accuracy [4] by considering linguistic, syntactic and pragmatic features; while Orimaye et al. considered n-grams, i.e. collections of *n* successive words, along with the linguistic and syntactic features, reaching an AUC of 0.93 [5]. Nevertheless, the main disadvantage of transcription-derived features is that they are language-dependent and rely on the information content. Therefore, to comply with the privacy issue, they could be employed only when the recordings do not involve sensible data, making them not suitable for ecological assessment in a domestic environment. Other works have focused on the prediction of AD subjects relying only on acoustic features [6–10]. Warnita et al. for example used the features extracted through OpenSMILE, an open-source toolkit for audio feature extraction, usually employed in speech emotion recognition, to distinguish controls from AD subjects using a gated Convolutional Neural Network, obtaining an overall accuracy of 73.6% [7].

The aim of this work is to develop a classification model based only on automatically extracted acoustic features for the prediction of AD in English-speaking subjects. In a previous study, currently under evaluation, the same acoustic features have been employed in Latin-derived-language speaking subjects, Italian and Spanish; in that work, an overall accuracy of about 70% has been achieved in distinguishing people with mild impairment of cognitive function from healthy controls. This study aims therefore at validating the transferability of these features on subjects with a diagnosis of AD and on a different language.

II. METHODS

A. Dataset

The current work was developed by exploiting the recordings contained in the Pitt Corpus, an existing dataset of 458

TABLE I: Demographic characteristics of the two groups of the dataset. (*): mean (standard deviation); (†): median (interquartile range).

	AD (n=237)	non-AD (n=180)
Age, years*	71.6 (8.4)	64 (7.8)
Gender (Female / Male)	163 / 74	113 / 67
YoE, years†	12 (3)	13 (4)
MMSE†	19 (8)	30 (1)

recordings of English-speaking subjects, a part of which with a diagnosis of Alzheimer's Disease (AD) [11]. Each recording, acquired through an air microphone, contains the description of the *Cookie Theft picture* of the Boston Diagnostic Aphasia Examination [12]. From the AD group, MCI subjects and those that were not classified as probable or possible AD were discarded. In particular, 180 non-AD and 237 AD recordings were selected for the purpose of this work, maintaining the classes unbalanced. The demographic characteristics of the selected subjects are described in Table I.

B. Feature extraction

Features extraction was performed via an automatic algorithm implemented in MATLAB, which has been previously described in detail in [13]. A summary of these features, grouped by domain, is reported in Table II. Before the extraction, recordings were standardized by removing the mean value for each recording and by dividing them by their standard deviation. To evaluate the robustness of the features in an uncontrolled environment, no manual pre-processing was performed to clean the recordings from possible interruptions by the interviewer. Features extraction was repeated three times for voice segments lasting respectively 5s, 10s, and 15s to assess whether specific patterns can be captured by different time lengths. Moreover, to reduce noise among the segments, each feature with a normal distribution has been substituted by its mean and standard deviation, while the remaining ones with their median and interquartile range, thus extracting a total of 138 features.

TABLE II: Summary table of extracted features

Domain	Feature	
Voice periodicity	Unvoiced percentage	F1
	Unvoiced and voiced parts (and related statistics)	F2-F9
	Total voice breaks	F10
Shimmer	Shimmer	F11
Syllables	Speech Rate	F12
	Phonation Percentage	F13
	Articulation Rate	F14
	Intersyllabic time	F15
	Intrasyllabic time	F16
	Pauses	F17
	Duration of pauses	F18
Spectral features	Pitch (mean, standard deviation)	F19, F20
	Standard deviation of the 3rd formant	F21
	Speech Temporal Regularity	F22
	Centroid	F23

C. Feature selection and classification

Binary classification was performed on the selected recordings of the Pitt Corpus, to discriminate between healthy control (non-AD) and Alzheimer's disease (AD).
Moreover, classification was also carried out on two separate subsets, composed by Female-only and Male-only subjects, respectively, since it has been shown how some acoustic features, such as pitch, are highly affected by gender [14].

1) Classifiers: To perform the classification, support vector machines (SVM), CatBoost classifier (CAT), and Logistic Regression (LR) were compared. The first two classifiers were chosen since SVM is robust to noise in training data, while CatBoost is the state of the art of boosting algorithms, and it has been proven to be effective with small datasets. Finally, LR was taken into account for its simplicity and computational speed. Each classifier was implemented in Python using the Scikit-learn libraries and the Catboost library. In order to achieve robust estimations the performance of each classifier was evaluated using repeated 10-fold cross-validation. Indeed, for each model, cross-validation was repeated 10 times, each time with a different random seed and the reported performances are the overall mean and standard deviation. Due to the unbalanced nature of the dataset, Precision, Recall and F1-score were computed as performance metrics. The choice of the best model was based on the F1-score.
Since the number of features is high with respect to the dimension of the dataset, it was decided to reduce the computational cost of the problem, by carrying out the analysis and selection of the most informing features through SHAP [15].

2) Model explainability: To understand the impact of the acoustic features in the prediction of AD, a ranking of the most informing features has been implemented by summing up the unweighted mean of the Shapley values obtained at each cross-validation.

III. RESULTS

Results obtained on the whole Pitt Corpus dataset are reported in Table III. The best model, chosen in terms of the highest F1-score, is support vector machine which yields a mean F1-score of 78% and both Precision and Recall of 79%. Table IV reports instead the classification performance of the gender-based classifiers. In this task, the classification performances highly improve for all the machine learning models. In particular, support vector machine achieves a mean F1-score of 83% and 88%, respectively for the Female-only and the Male-only dataset.
To analyze the impact of features, the rankings for the overall dataset and the two subsets are reported in Figure 1 and 2, respectively. The features have been grouped in the four domains defined in Table II, according to their information content: spectral (in red), syllabic (in blue), those related to voice periodicity (in green), and shimmer (in yellow). Figure 1 shows that features related to the periodic nature of the voice hold great relevance in the prediction of cognitive decline, with the unvoiced percentage and the voice breaks in the first positions, followed by the syllabic and spectral features, such

TABLE III: Performance of the classification models obtained on the whole dataset

Model	Precision	Recall	F1-score
CAT	0.77 (0.02)	0.79 (0.02)	0.77 (0.01)
SVC	0.79 (0.01)	0.79 (0.01)	0.78 (0.01)
LR	0.73 (0.01)	0.80 (0.01)	0.76 (0.01)

TABLE IV: Performance of the classification models obtained on the Female-only (F) and Male-only (M) dataset

Model	Gender	Precision	Recall	F1-score
CAT	F	0.81 (0.02)	0.84 (0.02)	0.82 (0.01)
	M	0.83 (0.02)	0.80 (0.02)	0.81 (0.02)
SVC	F	0.82 (0.02)	0.85 (0.02)	**0.83 (0.01)**
	M	0.90 (0.02)	0.87 (0.01)	**0.88 (0.02)**
LR	F	0.75 (0.01)	0.85 (0.02)	0.79 (0.01)
	M	0.77 (0.02)	0.75 (0.02)	0.75 (0.01)

as the duration between syllables and pitch. The importance of the voice periodicity is confirmed in Figure 2a and 2b, although some differences can be observed. Indeed, for the Female-only dataset, shimmer is shown to have an important role in the prediction of AD, being in the top 5 features after the features related to the unvoiced parts of speech, whereas for the Male-only dataset, spectral features, i.e. pitch and the standard deviation of the 3^{rd} formant, are in the first positions of the ranking along with those related to voice periodicity.

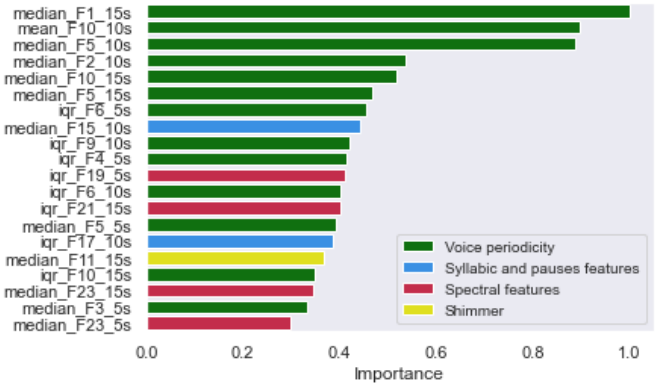


Fig. 1: Feature ranking of the complete dataset

IV. DISCUSSION

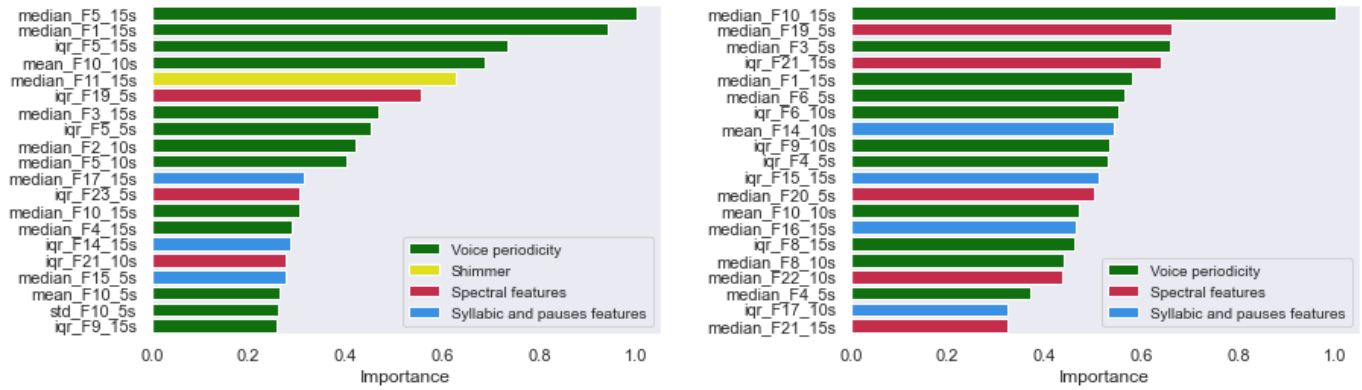
An automatic classification algorithm has been implemented for the detection of AD among English-speaking subjects of the Pitt Corpus, by considering it all together and then dividing the subjects by the reported gender. For the overall dataset, the best performance of the classification model was 78% with support vector machine, whereas for the Female-only and Male-only subsets an F1-score of 83% and 88% was achieved, respectively. The metrics obtained in the classification task of the complete dataset are slightly lower than those obtained with the gender-based classifiers, probably due to the intrinsic different acoustic characteristics of the two genders that may act as confounding factors in the prediction. Nevertheless, the feature ranking obtained from the overall classification in Figure 1 showed in the first places voice periodicity features, which are strictly correlated with cognitive decline. Indeed, in past studies, it has been shown that unvoiced percentage and number of voice breaks tend to increase with AD [16]. However, the feature rankings of the gender-specific classifiers highlighted that also different sets of features are relevant for AD detection, depending on gender. For example, shimmer appeared among the top features of the female-based classifier whereas spectral features, such as pitch and the third formant, highly contribute to the prediction of AD in the male-based classifier.

These performances were obtained by considering only acoustic features, to determine whether the identified features can be used to define a screening tool, with the possible aim of longitudinal monitoring of cognitive decline among elderly people. Other studies have classified the Pitt Corpus dataset by considering only speech features. Kumar et al. achieved an F1-score of 87.5% by computing acoustic features such as MFCCs, and formants [8]. Triapthi et al. obtained an F1-score of 85.7% by employing acoustic features derived from subsampled signals [9]. Finally, Liu et al. achieved an F1-score of 82.9% after data augmentation [10]. The aforementioned classification performances have all been obtained after a manual cleaning of the recordings in which silences and the possible interruptions of the interviewer were removed. In the current work, this step was ignored since the objective was to validate the features in a context as similar as possible to real life, in which it is highly probable that the speaker is interrupted by other people or has long periods of silence. Nevertheless, the performances obtained when building the two different gender-based classifiers were comparable with those obtained in literature, with the male-based classifier even reaching a higher F1-score with respect to the aforementioned works, suggesting that our automatic feature extractor and classifier can be robust in monitoring elderly people in an uncontrolled environment.

The same starting set of features was previously successfully employed to classify Italian and Spanish people with the earliest symptoms of cognitive decline, defined in the previous study by a low Mini-Mental State Examination score, i.e. less than 26. The good performances obtained in a non-Latin-derived language prove the cross-language potential of this set, which might be exploited for a mass screening of symptoms of cognitive decline in elderly people.

V. CONCLUSION

The Pitt Corpus was analyzed to distinguish AD subjects from the control subjects, by automatically extracting acoustic features. The analysis was fully automatic, without further manual cleaning of the recordings to test the robustness of the features in a completely uncontrolled scenario. The good performances achieved, mainly on gender-based classifiers, are promising for the employment of this set of features in the development of a cross-language screening tool for symptoms



(a) Female-only dataset

(b) Male-only dataset

Fig. 2: Feature ranking of the two subsets

of cognitive decline and more specifically of Alzheimer's Disease.

Acknowledgement

This research was funded by European Union's Horizon 2020 research and innovation programme under the call SC1-PHE-CORONAVIRUS-2020-2B grant number 101016112.
We acknowledge B. MacWhinney (DementiaBank) for hosting and sharing the Pitt Corpus database.

References

[1] C. A. Lane, J. Hardy, and J. M. Schott. "Alzheimer's disease". In: *European Journal of Neurology* 25.1 (2018), pp. 59–70.

[2] J. Robin et al. "Evaluation of Speech-Based Digital Biomarkers: Review and Recommendations". In: *Digit Biomark* 4.3 (2020), pp. 99–108.

[3] Kathleen C. Fraser, Jed A. Meltzer, and Frank Rudzicz. "Linguistic Features Identify Alzheimer's Disease in Narrative Speech". In: *Journal of Alzheimer's Disease* 49 (2016), pp. 407–422.

[4] Randa Ben Ammar and Yassine Ben Ayed. "Speech Processing for Early Alzheimer Disease Diagnosis: Machine Learning Based Approach". In: *2018 IEEE/ACS*. 2018, pp. 1–8.

[5] S. O. Orimaye, J. S. Wong, K. J. Golden, C. P. Wong, and I. N. Soyiri. "Predicting probable Alzheimer's disease using linguistic deficits and biomarkers". In: *BMC Bioinformatics* 18.1 (Jan. 2017), p. 34.

[6] Sofia de la Fuente Garcia, Fasih Haider, and Saturnino Luz. "Cross-corpus Feature Learning between Spontaneous Monologue and Dialogue for Automatic Classification of Alzheimer's Dementia Speech". In: *2020 42nd Annual IEEE EMBC*. 2020, pp. 5851–5855.

[7] Tifani Warnita, Nakamasa Inoue, and Koichi Shinoda. "Detecting Alzheimer's Disease Using Gated Convolutional Neural Network from Audio Data". In: *Proc. Interspeech 2018*. 2018, pp. 1706–1710.

[8] M. Kumar et al. "Dementia Detection from Speech Using Machine Learning and Deep Learning Architectures". In: *Sensors* 22 (Nov. 2022), p. 9311.

[9] Ayush Triapthi, Rupayan Chakraborty, and Sunil Kumar Kopparapu. "Dementia Classification using Acoustic Descriptors Derived from Subsampled Signals". In: *2020 28th EUSIPCO*. 2021, pp. 91–95.

[10] Zhaoci Liu, Zhiqiang Guo, Zhenhua Ling, and Yunxia Li. "Detecting Alzheimer's Disease from Speech Using Neural Networks with Bottleneck Features and Data Augmentation". In: *ICASSP 2021*. 2021, pp. 7323–7327.

[11] J. T. Becker, F. Boller, O. L. Lopez, J. Saxton, and K. L. McGonigle. "The natural history of Alzheimer's disease. Description of study cohort and accuracy of diagnosis". In: *Arch Neurol* 51.6 (June 1994), pp. 585–594.

[12] Elaine Giles and Karalyn Patterson. "Performance on the Boston Cookie Theft picture description task in patients with early dementia of the Alzheimer's type: Missing information". In: *Aphasiology* 10 (May 1996), pp. 395–408.

[13] E. Ambrosini et al. "Automatic speech analysis to early detect functional cognitive decline in elderly population". In: *IEEE EMBC* 2019 (July 2019), pp. 212–216.

[14] I. R. Titze. "Physiologic and acoustic differences between male and female voices". In: *J Acoust Soc Am* 85.4 (Apr. 1989), pp. 1699–1707.

[15] Scott M Lundberg and Su-In Lee. "A Unified Approach to Interpreting Model Predictions". In: *Advances in Neural Information Processing Systems 30*. Curran Associates, Inc., 2017, pp. 4765–4774.

[16] Juan Meilán, Francisco Martínez-Sánchez, Juan Carro, Nuria Carcavilla, and Olga Ivanova. "Voice Markers of Lexical Access in Mild Cognitive Impairment and Alzheimer's Disease". In: *Current Alzheimer research* 15 (Jan. 2018), pp. 111–119.

Development of an Integrated Software System for Medical Equipment Management: the experience of the Spedali Civili Hospital

Paola Picozzi[1,2], Gian Luca Viganò[1], Matteo Verga[1,2], Martina Capuzzo[1], Claudia Duri[1], Lucia Ignoti[1], Sara De Paola[2], Veronica Cimolin[2,3]

[1]*ASST Spedali Civili di Brescia - SC Ingegneria Clinica, 25123 Brescia, Italy*

[2]*Department of Electronics, Information and Bioengineering, Politecnico di Milano, 20133 Milano, Italy*

[3]*Istituto Auxologico Italiano, IRCCS, S. Giuseppe Hospital, 28824 Piancavallo, Oggebbio (Verbania), Italy*

***Abstract*— In recent years, the increasingly widespread use of medical equipment has revolutionized the way in which clinical practice is performed and made their management increasingly complex. The Clinical Engineering of the Spedali Civili Hospital in Brescia decided to develop a medical equipment management software with the aim of digitalize and optimize its own processes. The objective of the present study is to share the methodology used for the implementation of a tailor-made software for medical equipment management throughout the entire device's life cycle.**

***Keywords*— Clinical Engineering, digitalization, Medical Equipment Management Software**

I. INTRODUCTION

Nowadays, health technology is an integral part of clinical workflow and play a central role in everyday practice. However, the complexity of electromedical equipment, in terms of number and differentiation, is reflected in the complexity of managing these medical devices [1].

To satisfy this increasing need, clinical engineering departments (CEDs) adopts management software systems that enable safe and optimized management of the hospital's medical equipment [2].

Many benefits are provided by the use of Medical Equipment Management Software (MEMS), compared to paper-based management: easier storage and faster retrieval of information, more efficient maintenance management, greater patient safety [2], reduction in working time and workload [3], minimize human error [4], facilitate the tracking of medical equipment during the entire life-cycle [5].

The idea of using management software also responds to the need, increasingly common in all sectors, to collect structured data that can be processed, analyzed and exchanged between operational units. [6,7]. To understand this necessity in CEDs it is important to consider the quality ISO 9001 standard - which requires that the main actions performed within a complex structure (CS) have to be tracked - and the Medical Device Regulation 2017/745 which states that the recalls of devices from the market have to be done using the UDI or serial number. So, it is important to have this data available and to be able to retrieve them in a quick and easy way.

According to literature [3, 5], since 90s CEDs has been developed or adopted different modalities of MEMS: Integrated Software System for Medical Equipment Management (ISSMEM) that provides useful tools for all the management activities range; Computerized Maintenance Management System which operates for gathering, storing and analyzing data on the maintenance performed on the medical devices; discrete component that targets one function of the health technology management.

The ready-made software already available in the market are solutions that concentrate on only equipment maintenance management. For this reason, most of these software systems have been designated based on the specified needs of the CEDs [3].

In this pilot study it is presented the pathway elaborated by the CS[1] Clinical Engineering of the Spedali Civili Hospital in Brescia to develop an ISSMEM. The final aim of this system is to digitalize and optimize all the processes managed by this CS. Furthermore, the MEMS offer to the CS Clinical Engineering the possibility to monitor the quality and the cost-effectiveness of the service through the use of quality and cost KPIs.

Another objective of this work is to compare the new software to the previous situation in which the CS Clinical Engineering of the Spedali Civili Hospital had a software (provided by the global service), that doesn't allow the management of all the activities, so part of the tasks was done using paper.

Lastly, the aim of this study is to share the methods and the preliminar results about the work done by CED of the Spedali Civili Hospital to develop a tailor-made software for medical equipment management throughout the entire device's life cycle.

II. MATERIALS AND METHODS

For the realization of the software the CS Clinical Engineering of the Spedali Civili Hospital selected, through open tender procedure, a technological partner identified in the company ELLF S.r.l. This partner is involved in the project for the development of the coding part of the software. Additionally, it was deemed appropriate to form a multidisciplinary team involving the research university Politecnico of Milan and the CS ICT of the Hospital, required

[1] A complex structure is an operational unit, endowed with autonomous resources, which performs major functions in support of corporate management and performs activities primarily related to the planning and organizational growth of the company.

for the integration with other application tools and for IT security problems.

With this team a series of multidisciplinary working meetings have been carried on for one year in which the software system development follows the phases of *requirement analysis, analysis* and *optimization of processes, software design, implementation* and *evaluation*.

To understand the general requirements and specifications to be developed within the portal, the technology partner asked a series of questions to the CS Clinical Engineers. In addition, to find a solution to these requirements, a number of solutions were proposed by all team members and discussed and selected through common brainstorming techniques.

Regarding process analysis, Clinical Engineering described in detail all phases and steps of the current procedures carried out within the CS. Each step was examined to understand how the software could be used within the flow of activities, with the aim of simplifying and optimizing them. Then the functions that the application must perform within the procedure were identified. Subsequently, the data involved within a given process and their flow between the different functions were defined: each function was matched with the data that it uses as input and the data it produces as output. To carry forward this process analysis, User Stories and Use Cases Diagrams were developed.

The software evaluation was conducted as a Beta Testing activity developed through two different operations:

- The use and the test of the software by the final user with the goal to determine the proper functioning of the system, to monitor problems and to find bugs.
- The distribution of a questionnaire that could assess the first use of the Beta version of the software. The questionnaire was designed by the authors following the steps described below. The decision to implement a questionnaire and not to use an already validated one is due to the consequent possibility of greater customization of the questions. Initially, the Clinical Engineers of the CS were identified as the recipients of the survey, because they are professionals with significant knowledge of the software structure. In a second moment the questionnaire was deliver also to the Technicians as external end-users that didn't participate to the development phase.

  After this step, investigation areas were defined: they correspond to the different sections of the software and an additional section for the general evaluation of the usability.

  Then questions and rating scale have been defined. Lastly, the questionnaire was implemented online with *Google Forms* and then it was distributed to the recipients through a link shared via e-mail.

III. Results

In this paragraph it is reported the result obtained for each development phase.

A. Requirements analysis

The fundamental objective of a ISSMEM is to support the CEDs in the management activities of the entire medical equipment's life cycle. The discussion led to the definition of the needs of the Clinical Engineering and to the drafting of general technical specifications that the software must have or allow to do. The following are the main ones:

- ability to use the core functionality of the platform without the need for installation/setup on users' computers;
- user friendly interface;
- user authentication and user profiling;
- modular access permission management;
- management of users and user licenses;
- storage management;
- system configuration managed by the user;
- management of the device entry process;
- creation of a tender documents' repository;
- portals monitoring of external companies;
- calculation of ISO 9001 process indicators;
- importing data from Excel;
- modular dashboards;
- generation of reports;
- alerts and notifications;
- computerization of backup equipment management;
- monitoring of effectiveness and efficiency indicators through the creation of a management dashboard;
- management of requests for action by business units through a prioritization algorithm;
- monitoring of major maintenance activities;
- monitoring of equipment utilization and development of indicators to support HTA;
- compilation by suppliers of a dedicated form to collect input data for all equipment;
- tracking of major actions carried out using the software.

B. Analysis and optimization of the process

At this stage, the different types of software users were defined. They are shown below:

- manager of the CS Clinical Engineering;
- clinical engineers;
- clinical engineering technicians;
- clinical engineering warehouse workers;
- clinical engineering secretaries;
- coordinators of hospital departments;
- clinical engineering suppliers.

Next, all processes to be digitized were identified:

- Scheduling of technology equipment purchases, in collaboration with the corporate biomedical technology committee;
- Tenders for maintenance services and technology purchases, in coordination with the Procurement Unit;
- Definition of the technical specifications of biomedical and technical-economic technologies, verifying with departmental referents the specific needs to be met.
- Installation, testing, inventory of new equipment;
- Preventive maintenance;
- Corrective maintenance in case of failure, with backup equipment inventory management;
- Electrical and functional safety controls according to current CEI standards;
- Decommissioning of medical equipment;

- Development of HTA studies, in connection with regional organization.

Each of these processes was analysed and digitalized through the use of the software.
Using the Uses Cases Diagram (one example reported in Fig. 1), it is possible to observe all the actors involved and the main activities that will be carried out with the new management software.

In particular, some elements that have been derived from this analysis are the simplification and optimization of processes due to automatic actions and controls performed by the software. This results in significant time savings, and in a higher efficiency compared to the current situation where CS Clinical Engineering has to perform these tasks.

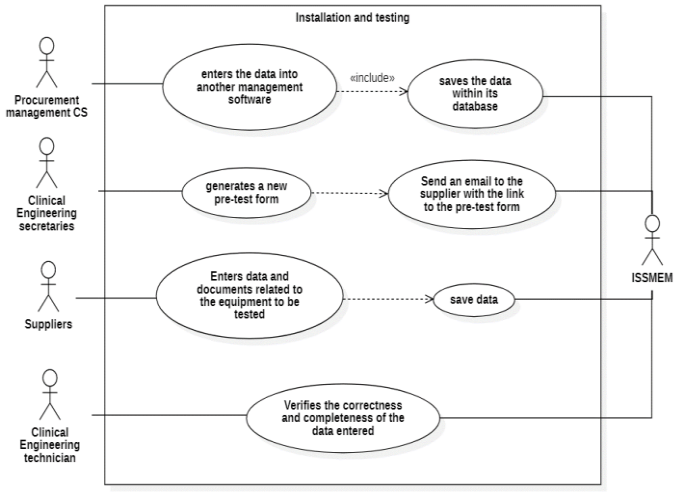


Fig. 1: Use Case Diagram Installation and Testing process

C. Software design

First of all, a modular design has been chosen because it offers many advantages in terms of upgradability, system efficiency, and the ease of maintenance. The system architecture is based on a central module which carries out the main tasks of the CS Clinical Engineering, while each peripheral module performs a more specific function.
Other design characteristics are defined by the multidisciplinary group: single page application usable through all modern browsers, both PC and mobile, cloud hosting that ensures data security and scalability, integrated authentication with enterprise Active Directory on Premise, simplified software update process that does not require desktop client installation and upgrade, user friendly and customizable interface.

The programming language used is C# associated with Angular and NodeJS for the web interface part; the DB used is SQL Server on Microsoft Azure cloud.

D. Software implementation

This system has been implemented to manage all the aspects related with Clinical Engineering technical management, so the main modules developed in the Beta-version are:

- Contract management section;
- Testing and installation section;
- Medical equipment section that contains inventory, classification, technical specification, warranty (Fig. 2)
- Personnel management section;
- Maintenance management section (in which is possible to manage the preventive and corrective maintenance);
- Biomedical gas management section;
- Master data and element type tables management section;
- Modular dashboards to set the KPIs.

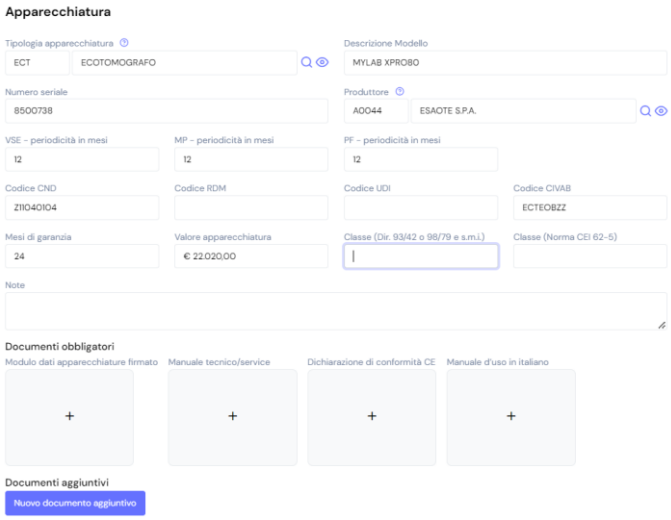


Fig. 2: Screen showing the registry of an equipment

E. Evaluation

Initially, the Beta testing activity was characterized by performing several operations on the software to test the Beta version and check for bugs. In this version, a database extrapolated from the previous management software was used, so test operations were carried out using real data.
Problems were found about the user access to the software and related to what different types of users can edit and fill out in the different modules.
The critical issues were discussed and resolved with the technology partner, and then the satisfaction questionnaire was developed and distributed.

Submitting the questionnaire to the clinical engineers who participated in the design of the software itself certainly poses a very high risk of bias, but it was necessary to involve them in this evaluation as experienced users who were in a position to determine whether what was required was implemented correctly by the developers.
In a second step, the questionnaire was submitted to the clinical engineering engineers, who reported ratings in line with those of the engineers.

All respondents felt that the software was extremely simple and intuitive. 100% of users think that the new Software is intuitive, user-friendly, and comprehensive, and that not many steps are needed to achieve the goal.
Concerning the comparison with the previous software, all engineers agreed that the new management software was more efficient and user-friendly.
Lastly, on a scale of one to five all users are more than satisfied

with the overall use of the new software, as shown in the chart below (Fig. 3).

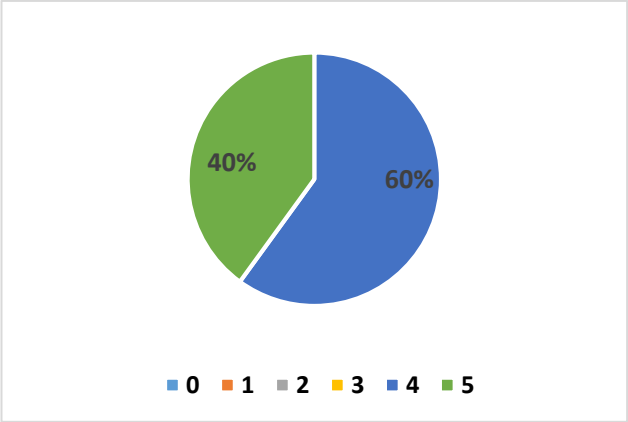


Fig. 3: answers to the question: "How much satisfied are you with the overall use of the new management software?"

IV. Discussion and conclusion

The results reported in the previous paragraph are preliminar and the pathway to obtain the final version is still long and complicated, but many advantages are already appreciated by the final user.

An important element is the constant monitoring of the progressive implementation status of the software in order to supervise the functional and coordinated integration of the final system into the operational reality.

In any case, having defined the technical specifications in detail at the beginning made possible to develop software that fully reflected the needs of the Clinical Engineering. With the flow analysis, it was possible to think in depth about the processes in place in the CS: this activity allowed not only to implement the paper forms in digital format, but also to revise the processes in order to make the most of digitization as a tool for simplification and data analysis.

The entire specification and flow analysis phase led to the development of the most important sections of the new software. From the first use of the Beta version and subsequently from the positive feedback gathered from the analysis of the questionnaire data, it was found that the new software is more simple, intuitive and functional than the one in use.

The latter considerations lead to the possibility of conducting a constructive reasoning about the contextualization of development technology in the hospital setting. On the one hand, the innovation brought by software brings to a change in work mentality, revolutionizing the current method of parceled work, reorganizing and facilitating the ordinary activities of the Clinical Engineering into a single digitized working solution. However, on the other hand, it is also true that this aspect has to be accompanied by the development of an appropriate digital culture in the system in which it is integrated. In this sense, the business managements effort in appropriate digital training plays a role of primary importance.

Consequently, process digitalization must be flexible and able to modulate itself to the needs of the realities in which it is structured, and not vice versa. Only in this way it is possible to create value for the citizen.

In this context, the software developed by CED of Spedali Civili Hospital has the greatest strength of being a customized platform, which adapts to the needs of the specific context, in a simple and intuitive way.

References

[1] E. Iadanza, V. Gonnelli, F. Satta, M. Gherardelli, *Evidence-based medical equipment management: a convenient implementation*, Medical & Biological Engineering & Computing, vol 57, pp. 2215–2230, 2019.

[2] Z. Bliznakov, G. Pappous, K. Bliznakova, N. Pallikarakis, *Integrated software system for improving medical equipment management*, Biomed Instrum Technol vol 37, pp. 25–33, 2003.

[3] A. Abayazeed SidAhmed, O. Hamza Alnazier, *Software applications in healthcare technology management: a review*, Journal of Clinical Engineering vol 35(2), pp. 88-92, 2010.

[4] I. Mobarek, W. Tarawneh, F. Langevin, M. Ibbini, *Fully automated clinical engineering technical management system*, Journal of Clinical Engineering, vol 31, pp. 46-60, 2006.

[5] S. Neven; S. A. Rahman, *An Automated Medical Equipment Management System Proposed for Small-Scale Hospitals*, Journal of Clinical Engineering, vol 42(4), pp. E1-E8, 10/12, 2017.

[6] N. Kanga, C. Zhaob, J. Lib, J. Horst, *A hierarchical structure of key performance indicators for operation management and continuous improvement in production systems*, Int J Prod Res, vol. 54(21), pp. 6333–6350, 2016.

[7] D. Rodrigues, R. Godina, P.E. da Cruz, *Key performance indicators selection through an analytic network process model for tooling and die Industry*, Sustainability, vol. 13, 2021.

A tool to perform semi-supervised anomaly detection and annotation on 15 lead ECG signals

Ugo Lomoio[1], Patrizia Vizza[1], Raffaele Giancotti[1], Giuseppe Tradigo[3], Salvatore Petrolo[2], Sergio Flesca[2], Pietro Hiram Guzzi[1], Pierangelo Veltri[1,2]

[1] *Department of Surgical and Medical Sciences, Magna Græcia University of Catanzaro*

[2] *Department of Computer, Modeling, Electronics and System Engineering, University of Calabria, Rende, Italy*

[3] *SMARTEST Laboratory, eCampus University*

***Abstract*—Measuring both electrical and mechanical activities of the heart has gained success thanks to technologies able to measure them. Heart electrical activity is measured by means of Electrocardiography which generate Electrocardiographic (ECG) signals. The automatic analysis of ECG signals by means of algorithms and tools may help to detect anomalies and automatically annotate them. Recently, a particular type of network architecture, referred to as Autoencoder (AE), has been used for similar tasks in many fields, both biomedical and not. Nevertheless, using an AE for the analysis of ECG signals can still provide improvements to clinicians. We here present a tool that can be used by clinicians for the semi-automatic identification of anomalous windows in ECG signals. Moreover, the tool allows signal visualization, manual annotation, and measuring.**

***Keywords*—ECG, anomaly detection, signal annotation, autoencoder**

I. INTRODUCTION

Biomedical signals are related to the investigation of neural activity, cardiac rhythm and other physiological activities. Biomedical signal processing involves the acquisition, management and analysis of such signals to extract meaningful information to identify patterns and trends within the signals.

ECG signals measure the rhythmic electric activity of the heart and can be composed of one up to fifteen channels. The standard number of channels of an ECG signal is typically twelve.

One ECG signal has a variable duration ranging from 10 seconds for a standard clinical ECG up to 24/72 hours for a cardiac holter.

Cardiac diseases, such as arrhythmia, represent a disturbance in the normal heart rhythm resulting in an irregular heartbeat, which is responsible for the addition of irregular patterns to the ECG signal. Visual inspection of ECG signals with the aim of annotating possible cardiac arrhythmias events is time-consuming, thus software tools able to automatically analyze heart-related signals could be a valuable help as a clinical decision support system.

AEs are relatively new types of neural network architectures that have increasingly been used to detect anomalies in signals. An AE uses a feedforward approach to reconstruct its input in the output. The comparison between the reconstructed output and input data allows to detect possible anomalies in the input. [6]

AE is usually trained on data without anomalies. After the training phase, an AE model is able to reconstruct signals without anomalies but fails to perform well with signals containing anomalies. The reconstruction error, which is the error measured between the input signal and its low dimensional reconstruction is used to detect anomalies. We used root mean square error (RMSE) as the reconstruction error metric.

We here describe the development of a tool, based on an AE model, able to perform the unsupervised anomaly detection task on 15 lead ECG signals.[5] The proposed system is able to perform semiautomatic identification and annotation of anomalies on ECG signals having 15 channels, 12 standard ECG leads and 3 Frank leads.[2]

II. Methods

The proposed tool has been implemented in the Python 3 programming language and it uses the following Python libraries:

- *Tkinter*, a library used to build the Graphical User Interface;
- *Pytorch*, a largely adopted library for creating and training deep learning models;
- *dash* and *plotly*, used for plotting signals;
- *neurokit2*, an open-source library for the analysis of biomedical signals, used in our tool to perform R-peaks detection in ECG signals.

A. Dataset

Synthetic ECG signals were generated using the SIMARR3 arrhythmia simulator [3]. This software can simulate both normal signals and signals with atrial fibrillation, tachycardia, and bradycardia events at a given sam-

pling rate. It is also possible to generate signals containing one or a mix of the most common types of artifacts in ECG signals such for example, electromyography (EMG) noise, baseline wander caused by respiration, and electrode movement artifacts.

We generated:

- 500 ECG signals with no arrhythmia events (labelled as *normal*) sampled at 500 Hz and with a duration of at least 60 seconds;
- 290 ECG signals with atrial fibrillation events (labelled as *anomaly*), sampled at 500 Hz and with a duration of at least 60 seconds.

For each signal, a windowing algorithm has been applied to extract 281 three-seconds windows of the signal.

We split the windows data into training and test set like the following:

- the training set contains 100500 normal windows with no atrial fibrillation events;
- the test set contains 81490 windows with atrial fibrillation event and 40000 normal windows.

B. Tool

Our tool is composed of a Graphical User Interface (GUI), depicted in Figure 1, for signal loading, visualization, manual annotation, and semiautomatic annotation performed by our AE.

The proposed AE, called DPNet depicted in Figure 2, is a convolutional autoencoder (CAE), i.e an AE composed only of convolutional 2-dimensional layers. The model input consists of a 3-second signal window of 15 lead ECG sampled at 500 Hz. The workflow used to perform the anomaly detection is depicted in Figure 3, the overall workflow of our tool represented in Figure 4. By using this software, the clinician is able to:

- identify, visualize and annotate abnormal portions of the signal;
- visualize a single channel or all 15 channels of the signal;
- zoom on the signal;
- visualize singularly each heart beats;
- visualize a specific time window of the signal;
- visualize the distance between two successive R peaks of the ECG signal;
- click on a specific point of the signal to insert a text annotation;
- visualize the heart rate, in beats per minute;
- make textual and/or geometric (rectangles, lines) annotations on the signal.

C. RESULTS

For the evaluation of the AE model, we computed the reconstruction error on the test set. Then, the model has been evaluated in terms of the AUC metric score (Area Under Curve) on the test set. AUC is the area under the ROC (Receiver Operating Characteristic) curve

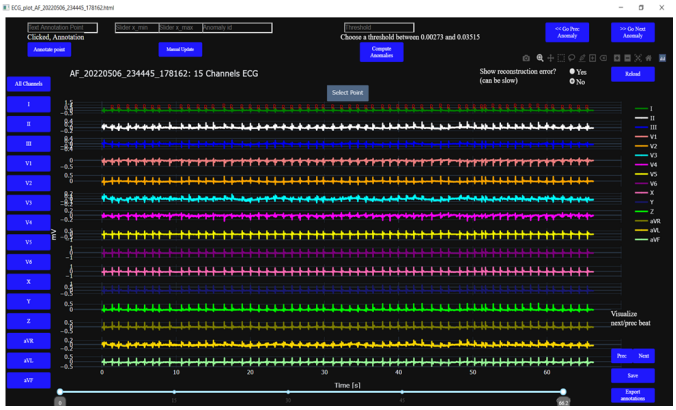


Fig. 1: ECG anomaly detector and annotator tool initial interface.

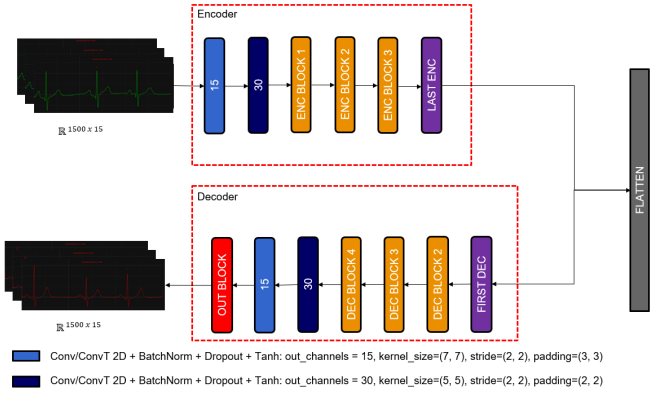


Fig. 2: The DPNet architecture.

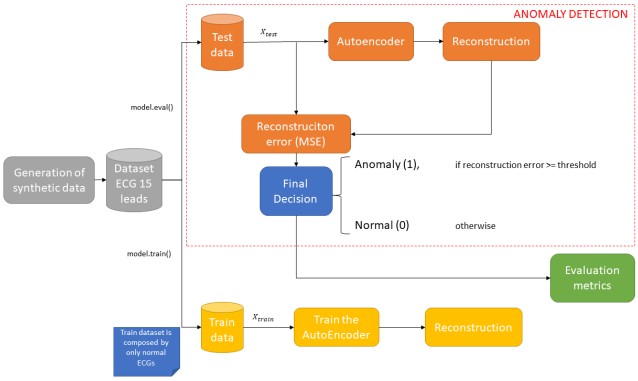


Fig. 3: Workflow for anomaly detection.

and represents the degree of separability between the two classes, i.e. normal and abnormal, providing an indicator of how well the model is able to distinguish between two classes. The model marked an AUC score equal to 0.925 on the test set. In figure 5 we show an example of a real window with a cardiac arrhythmia event correctly detected using our tool.

In table I we report some classification performance

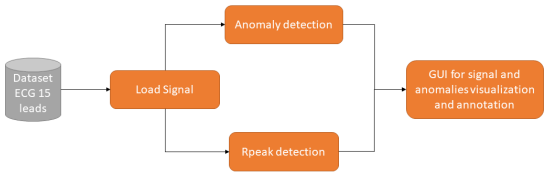


Fig. 4: Workflow of our proposed tool.

Metric name	Metric value
Accuracy	0.9257
F1 score	0.9204
Sensitivity	0.9124
Specificity	0.9376
ROC AUC	0.925

TABLE I: Performance metrics of our AE in the anomaly detection task with a threshold parameter equal to 0.0073 (optimized).

metrics of our AE in the task of anomaly detection. Those metrics were obtained using only the test set of our dataset and by optimizing the threshold parameter for the anomaly detection task. The optimized threshold found is equal to 0.0073.



Fig. 5: An example of a corrected identified atrial fibrillation event found using our tool with a threshold of 0.0073.

III. Conclusion

In this work, we presented an AE model that can be used to automatically identify anomalies in ECG signals. We trained the AE using synthetic normal ECG windows, then we evaluated the model using synthetic normal and abnormal ECG windows (with atrial fibrillation events). In these steps, synthetic signals were generated using the SIMARR3 software. We measured the performance of the AE in the anomaly detection tasks obtaining an AUC score of 0.925.

We then developed a tool for the loading, analysis, visualization, manual and semi-automatic annotation of ECG signals.

Our tool can, with good precision, automatically identify and send to the clinician the portions of the signal that are considered anomalous because correlated, for example, with atrial fibrillation events, cardiac arrhythmias, or noise presence.

The main problem with the AE is due to the fact that it has been trained using 15 lead ECG signals. In clinical reality, however, there are few hospital centers that perform this type of measurement (12 lead ECG is the standard). Also, the signals used to train and test the model are synthetically generated and not real human signals.

One possible future work can be, for example, retraining the model using only the 12 channels related to the ECG signal.

ACKNOWLEDGEMENTS

PNG, PV and UL were partially funded by the MISE PON-VQA project. UL Ph.D. fellow is partially supported by Relatech S.p.A. Authors thanks Elena Succurro for suggestions on ECG signals.

References

[1] Fikri, Muhammad Soesanti, Indah Nugroho, Hanung Adi. (2021). ECG Signal Classification Review. IJITEE (International Journal of Information Technology and Electrical Engineering). 10.22146/ijitee.60295.

[2] Pengfei Liu, Xiaoming Sun, Yang Han, Zhishuai He, Weifeng Zhang, Chenxu Wu (2022). Arrhythmia classification of LSTM autoencoder based on time series anomaly detection, Biomedical Signal Processing and Control, Volume 71, Part B, 2022, 103228. 10.1016/j.bspc.2021.103228.

[3] Soloenko, Andrius Petrnas, Andrius Paliakait, Birut Sörnmo, Leif Marozas, Vaidotas. (2021). Model for Simulating ECG and PPG Signals with Arrhythmia Episodes. 10.13026/c5qq-2g72.

[4] Shchetinin, E.Y., Glushkova, A.G., Sevastianov, L.A. (2022). Anomaly Electrocardiograms Automatic Detection with Unsupervised Deep Learning Methods. Distributed Computer and Communication Networks: Control, Computation, Communications. DCCN 2022. Lecture Notes in Computer Science, vol 13766. Springer, Cham. 10.1007/978-3-031-23207-7n_10

[5] R. Giancotti, U. Lomoio, P. Veltri, P. H. Guzzi and P. Vizza, "A machine-learning based tool for bioimages managing and annotation," 2022 IEEE International Conference on Bioinformatics and Biomedicine (BIBM), Las Vegas, NV, USA, 2022, pp. 2589-2594, doi: 10.1109/BIBM55620.2022.9995608.

[6] Bank D., Koenigstein N., Giryes R. (2020). Autoencoders. arXiv. https://doi.org/10.48550/arXiv.2003.05991

Identifying Extreme Profiles in Amyotrophic Lateral Sclerosis Patients at Diagnosis through Archetypal Analysis

I. Trescato[1], E. Tavazzi[1], M. Vettoretti[1], R. Vasta[2], A. Chiò[2], B. Di Camillo[1,3*]
[1] *Department of Information Engineering, University of Padova, Padova, Italy.*
[2] *Neuroscience Department "Rita Levi Montalcini", University of Torino, Torino, Italy.*
[3] *Department of Comparative Biomedicine and Food Science, University of Padova, Padova, Italy.*
[*] *Corresponding author: barbara.dicamillo@unipd.it.*

***Abstract*—The clinical heterogeneity that characterizes Amyotrophic Lateral Sclerosis (ALS) makes its diagnosis, prognosis, and care difficult. In this context, characterizing patients based on their clinical features or progression patterns is crucial, allowing a deeper understanding of the disease and the planning of more effective treatments. In this work, we employ Archetypal Analysis for studying a real-world ALS population based on their characteristics at diagnosis. First, we derive a set of extreme clinical types (archetypes) whose combination describes the study population, and analyze their differences in terms of clinical characteristics. Then, we cluster patients according to their similarity to the archetypes and we investigate how the so-obtained groups differ in terms of time to life-support interventions and survival.**

***Keywords*—Amyotrophic Lateral Sclerosis, Archetypal Analysis, patient stratification, unsupervised clustering.**

I. Introduction

Amyotrophic lateral sclerosis (ALS) is a progressive and degenerative disease that affects the nerve cells that control voluntary muscle movement. ALS progression impairs motor neurons in the brain and spinal cord, wasting the muscles and leading to the inability to control movements; sometimes it is also accompanied by cognitive and behavioural symptoms. ALS aetiology is still unknown, with some genetic and environmental factors possibly triggering the disease onset. The mean life expectancy is 3-5 years from onset, with death usually occurring from respiratory failure. Despite a relative uniformity during the late stages of the disease, the symptoms at the onset and the timing of the clinical manifestations are highly variable among the patients [1].

Related to this heterogeneity, one of the major needs is the identification of groups of patients with similar characteristics (*i.e.*, patient stratification), to be able to effectively predict the course of the disease in terms of speed of worsening, symptom occurrence, and the need for life-supporting interventions. For a deep understanding of this rare and incurable disease, it is also essential to investigate which are the main markers that determine its different manifestations. Clinically, patients can be stratified into phenotypes based on their characteristics or by observing their clinical progression. Alternatively, it is possible to automatically stratify patients using a data-driven approach: recently, clustering algorithms such as k-means, dimensionality reduction methods such as Uniform Manifold Approximation and Projection (UMAP), and network-based approaches were employed for this purpose [2], [3].

Archetypal Analysis (AA) is an alternative unsupervised computational approach that allows to discern a specific number of extreme and not necessarily observed points called archetypes (i.e. ideal, prototype patients), such that each archetype is constrained to be a mixture of points in the dataset and such that each point can be well represented as convex mixtures of the archetypes [4]. AA can be used on multivariate datasets as an exploratory tool since, analyzing the characteristics of each archetype, allows for highlighting the differences among groups of patients.

In this work, we aim at stratifying ALS patients by employing AA and considering the variables collected at the diagnosis of a real-world ALS cohort. First, we derive the archetypes and analyze their differences in terms of clinical features. Then, we associate each patient with their closest archetype. Finally, we investigate how the identified patients' groups differ in terms of clinical outcomes, considering: the need for non-invasive ventilation (NIV), percutaneous endoscopic gastrostomy (PEG), tracheostomy, and death.

II. Materials and methods

A. Dataset

The dataset used in this work was extracted from the Piemonte and Valle d'Aosta ALS register (PARALS) [5]: selecting the patients with the first visit from January 1st, 2007 to December 31st, 2015, we identified 924 ALS subjects. For each patient, we collected features to characterize their condition at the time of diagnosis, including:

- demographics and lifestyle: sex, marital status, educational level, smoke habits;
- dates of: birth, onset, diagnosis, PEG, NIV, tracheostomy, death;
- ALS-related variables: onset site, phenotype, mutation in ALS-linked genes (C9orf72, SOD1, TARDBP, FUS, OPT, TUB);

- comorbidities: psoriasis, epilepsy, stroke, rheumatic diseases, poliomyelitis, obstructive sleep apnea syndrome, monoclonal gammopathy of undetermined significance;
- other health-related variables: frontotemporal dementia (FTD), forced vital capacity (FVC), first/second tumour, thyroid impairments, psychiatric diseases, hypertension, diabetes, chronic obstructive pulmonary disease (COPD);
- a panel of 39 different blood exams, covering general health analysis, heart problems, and organ function.

B. Data preprocessing

A preprocessing phase was necessary to solve some typical issues that may arise with real-world data. First, we aggregated the variables presenting low occurrences and belonging to the same category, creating the binary variables: "genetics", which indicates if a mutation occurs in at least one tested gene; "comorbidities", indicating that at least one of the concurrent conditions listed above occurs; "tumour", which indicates that the patient had at least one cancer. Other more frequent and already binary conditions, such as hypertension or diabetes, were not aggregated. Variables assuming multiple possible values were either converted into binary features, if their occurrence had low frequency in the data (such as psychiatric diseases, that were transformed into new features indicating the presence/absence of at least one psychiatric disease), or coded as dummy features (such as FTD and smoke habits).

Then, we derived some variables coding the time passed from the ALS onset to the other clinical events for which a date was available, obtaining the following new features: age at onset, diagnostic delay, and time to PEG/NIV/tracheostomy/death. Next, we filtered out the blood test variables presenting more than 30% of missing values. In total, 16 of the 39 available tests were removed, 10 of which had more than 50% missing values. We imputed the remaining missing values in the preprocessed data using the *mice* R package [6] with default parameters. To check the robustness of the imputation process, we compared the distribution of each variable before and after the imputation.

Tables I and II provide an overview of the data after these preprocessing steps. Lastly, we scaled all variables in the range [0,1] to balance the contribution of features to the analysis.

C. Method

The goal of the analysis is the unsupervised stratification of the patients according to their clinical characteristics at diagnosis and the comparison of the obtained groups in terms of clinical outcomes, namely time to NIV, time to PEG, time to tracheostomy, and time to death. The analysis consists of three steps: (1) the identification of a number of archetypes from the data, using all the available variables except those corresponding to the outcomes; (2) the unsupervised classification of the subjects into different clusters according to their similarity to the archetypes; (3) the comparison of the clusters in terms of the four outcomes of interest.

1) *Archetypal Analysis.* Given an $n \times m$ matrix X representing a multivariate dataset, where n is the number of observations, m is the number of variables, and k is the number of archetypes chosen by the user, AA allows determining a $k \times m$ matrix Z of archetypes such that:

a) the data are best approximated by convex combinations of the archetypes Z, *i.e.*, they minimize the residual sum of squares (RSS):

$$RSS = ||X - \alpha Z^T||_2, \quad \alpha_i \geq 0, \quad \sum\nolimits_i \alpha_i = 1 \qquad (1)$$

b) the archetypes are convex combinations of the data points:

$$Z = X^T \beta, \quad \beta_i \geq 0, \quad \sum\nolimits_i \beta_i = 1 \qquad (2)$$

where α are the coefficients of the archetypes and β are those of the dataset, respectively.

Since the identification of the archetypes is based on an iterative process that, starting from a set of *k* randomly chosen points in the features' space, minimizes the approximation error between the original data points and those reconstructed as a combination of the archetypes, it is recommended to repeat the identification algorithm several times to avoid falling into local minima [4]. Here, we tested a number of archetypes *k* from 2 to 8, repeating the procedure 15 times for each *k*. The optimal number of archetypes was chosen by detecting the elbow in the scree plot reporting on the x-axis the value of *k* and on the y-axis the RSS. To reinforce the choice of the best *k*, we also analyzed the minimum, mean and standard deviation of the RSS over the 15 repetitions for each *k* [7].

The archetypes, by construction, lie on the boundary of the convex hull of the data and can be therefore easily influenced by outliers. Thus, to avoid incorrect or skewed results, we employed the identification method of *robust archetypes*, which reduces the influence of outliers by using M-estimators instead of least squares estimators when performing the optimization procedure [8]. All analyses were performed using the *archetypes* R package [9].

For the sole purpose of visualizing the data and archetypes in two dimensions, principal component analysis (PCA) was used. The two-dimensional representation allows to easily check the position of the archetypes with respect to the data and to verify that they are actually on the convex hull. Radar plots were used to investigate the characteristics of each archetype individually; for a more effective rendering, we computed for each variable its standard deviation (sd) across the *k* archetypes and then only included in the radar plots those with sd>0.13 (sd_{min}=0.00004679, sd_{max}=0.4158768), i.e. those variables that differentiate the most among archetypes.

2) *Subject clustering based on archetypes.* As mentioned, AA allows representing the data as a linear combination of archetypes, each multiplied by a non-negative coefficient α_i. We decided to assign each subject to the archetype with higher α_i, following the rationale of the nearest prototype classifier [7], to inspect how patients cluster based on their extreme behaviours, obtaining *k* distinct clusters.

3) *Comparison of the cluster in terms of clinical outcomes.* Finally, we compared the different clusters using the Wilcoxon test to assess any statistically significant differences in terms of

TABLE I: Preprocessed categorical variables.

Feature	Levels	% of subjects
sex	0: male	52 %
	1: female	48 %
marital status	0: combined	77 %
	1: living alone	23 %
education	0: illiterate	3 %
	1: primary school	35 %
	2: 8th grade	32 %
	3: short diploma	7 %
	4: high school	16 %
	5: graduated	7 %
smoke habits *	0: never	48 %
	1: ex	35 %
	2: current	17 %
genetics	0: no gene mutations	89 %
	1: gene mutation	11 %
onset site	0: bulbar	33 %
	1: not bulbar	67 %
FTD *	0: ftd	18 %
	1: cognitive	20 %
	2: behavioral	16 %
	3: non-executive	3 %
	4: healthy	49 %
tumour	0: never	95 %
	1: at least one	5 %
comorbidities	0: none	88 %
	1: at least one	12 %
thyroid	0: healthy	88 %
	1: impairment	12 %
psychiatric dis.	0: healthy	95 %
	1: impairment	5 %
hypertension	0: healthy	49 %
	1: impairment	51 %
diabetes	0: healthy	89 %
	1: impairment	11 %
COPD	0: healthy	93 %
	1: impairment	7 %

TABLE II: Preprocessed continuous variables.

Feature	25^{th}-50^{th}-75^{th} percentile
age at onset [years]	60 - 67 - 74
diagnostic delay [months]	5 - 9 - 14
time to PEG ◇ [months]	16 - 24 - 33
time to NIV ◇ [months]	14 - 23 - 34
time to tracheo ◇ [months]	21 - 27 - 43
time to death ◇ [months]	19 - 30 - 47
FVC at diagnosis [L]	70 - 87 - 104
white blood cells [10^9/L]	5.2 - 6.2 - 7.5
neutrophils [10^9/L]	2.8 - 3.6 - 4.6
lymphocytes [10^9/L]	1.4 - 1.7 - 2.2
monocytes [10^9/L]	0.4 - 0.5 - 0.6
ESR [1] [mm/h]	4 - 9 - 19
creatinine [mg/dL]	0.6 - 0.7 - 0.9
uric acid [mg/dL]	3.8 - 4.7 - 5.6
albumin [g/dl]	4 - 4.3 - 4.6
glucose [mg/dL]	81 - 88 - 99
triglycerides [mg/dL]	73 - 94 - 128
$\text{cholesterol}_{\text{tot}}$ [mg/dL]	174 - 199 - 230
$\text{cholesterol}_{\text{hdl}}$ [mg/dL]	49 - 58 - 70
$\text{cholesterol}_{\text{ldl}}$ [mg/dL]	96 - 117 - 144
$\text{cholesterol}_{\text{ldl/hdl}}$	1.5 - 2 - 2.7
$\text{bilirubin}_{\text{tot}}$ [mg/dL]	0.5 - 0.7 - 0.9
$\text{bilirubin}_{\text{dir}}$ [mg/dL]	0.2 - 0.2 - 0.3
$\text{bilirubin}_{\text{indir}}$ [mg/dL]	0.3 - 0.5 - 0.6
alkaline phosphatase [U/L]	56 - 68 - 86
creatine phosphokinase [U/L]	90 - 153 - 251
sodium [mEq/L]	140 - 142 - 143
potassium [mmol/L]	3.9 - 4.2 - 4.4
chlorine [mmol/L]	101 - 103 - 105
TSH [2] [mU/L]	0.9 - 1.6 - 2.5

* categorical variables coded as dummy
◇ outcome variables
[1] erythrocyte sedimentation rate
[2] thyroid stimulating hormone

the time of occurrence of the clinical outcomes, by performing a multiple pairwise comparison between groups.

III. Results

Fig. 1 shows the scree plot for the tested k, while Tab. III shows the minimum, average and standard deviation value of the RSS calculated over the 15 repetitions for each k. These methods identify $k = 7$ as the optimal number of archetypes.

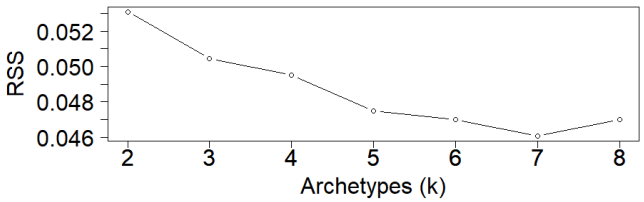


Fig. 1: Scree plot for a number of archetypes k from 2 to 8. The RSS value displayed for each k is the minimum RSS obtained over the 15 repetitions of the algorithm.

TABLE III: Minimum, mean, and sd of the RSS computed over 15 repetitions, for a number of archetypes k from 2 to 8.

Archetypes	k=2	k=3	k=4	k=5	k=6	k=7	k=8
min	0.0531	0.0504	0.0495	0.0475	0.0470	**0.0461**	0.0470
mean	0.0531	0.0511	0.0502	0.0482	0.0479	**0.0474**	0.0476
sd	<0.0001	0.000642	0.00045	0.001264	0.000715	**0.00064**	0.000426

Fig. 2 shows how the archetypes (in red) are positioned amongst the subjects (in green): as expected, they position

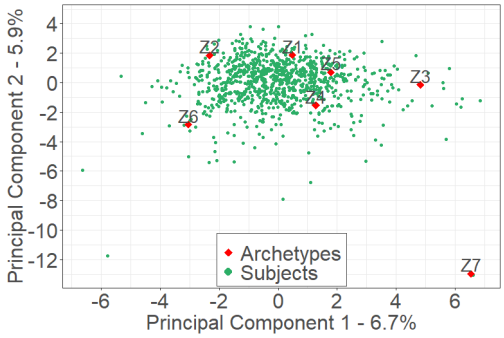


Fig. 2: Two-dimensional representation of the subjects (green dots) and archetypes (red diamonds) using PCA.

on the borders of the dataset, identifying types who are not necessarily observed in the data but who are extreme in their characteristics.

The 7 mined archetypes are reported in Fig. 3 as radar plots. The variables were filtered according to their standard deviation, ultimately retaining 24 features out of a total of 44.

By analyzing the resulting archetypes Z_i, we can describe the extreme behaviors characterizing the data. Z_1 represents a male subject with non-bulbar onset and medial age at onset, as well as Z_2, which is a female subject almost free of other diseases. Z_3 delineates an individual who is living alone, with mainly no FTD issues and high bilirubin values. Z_4 represents a subject with rather advanced age at onset and FTD at diagnosis. Z_5 outlines an ex-smoker subject, with older age at onset and affected by hypertension; this is, in general, also the

archetype placing greater emphasis on the presence of other comorbidities, such as diabetes. Z_6 is mainly similar to Z_1, presenting in addition relatively high values of triglycerides and cholesterol. Finally, Z_7 describes a female subject, ex-smoker, with pronounced cognitive FTD impairment and with high ESR and albumin values; this is also the only archetype with a low chlorine value.

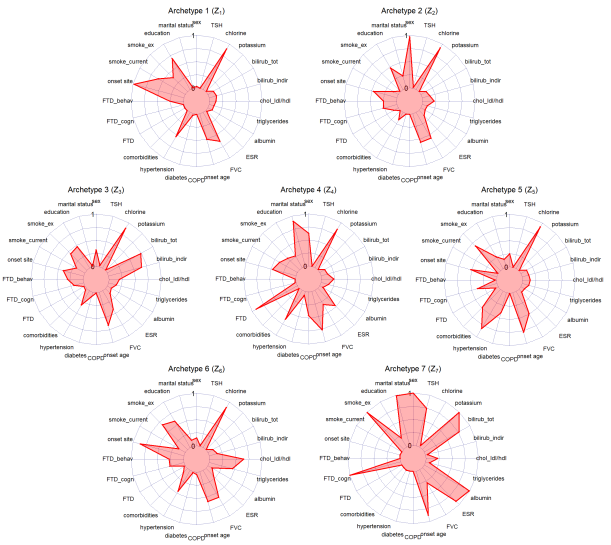


Fig. 3: Radar plots representing the archetypes, including the 24 variables with sd>0.13 only. For each variable, the innermost circle represents a standardised value equal to 0, the outermost circle equal to 1. The levels of the categorical variables correspond to those of Tab. I, then normalized in the range [0,1].

We then assigned each subject to their most representative archetype, getting seven clusters C_i with 60 subjects in C_1, 286 in C_2, 59 in C_3, 79 in C_4, 259 in C_5, 180 in C_6, and only 1 subject in C_7. Based on this, we decided to perform the following analysis only considering clusters C_1-C_6.

Fig. 4 reports the comparison of the time of occurrence of the four considered outcomes in the different clusters. The clusters differ in terms of mean time as well as in the order of occurrence of the outcomes. Clusters C_1 and C_3 have time-to-event values comparable with those of the other clusters, for all outcomes but tracheostomy, where C_3 has the shortest time of occurrence among all clusters. Statistically significant differences are observed in C_2 vs C_4, C_2 vs C_5, and C_4 vs C_6 for PEG, NIV and death (all p-values<0.015). This confirms that archetypes-based clustering can be a useful tool to identify groups of patients with different characteristics both in terms of covariates at diagnosis and clinical outcomes.

IV. Conclusion

In this work, we applied AA to a multivariate dataset of ALS patients to study disease heterogeneity and outline extreme behaviors at diagnosis. We identified 7 archetypes that were first compared in terms of clinical characteristics, and then used to define 7 clusters of patients. By analyzing their distributions in terms of time to PEG, NIV, tracheostomy, and death, we assessed how stratifying patients based on their similarity to the mined archetypes can be a valid criterion to identify groups characterized by different progression timing and patterns. In future works, we aim to further characterize the identified clusters to explore intra-cluster variability (e.g. by comparing the characteristics of the subjects belonging to the same cluster) and inter-cluster variability (e.g. considering the differences in progression patterns and comparing the archetypes with the clinical phenotypes described in the literature).

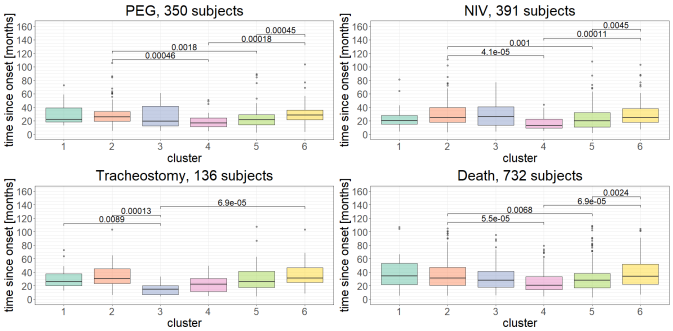


Fig. 4: Box plots comparing the times of occurrence of the outcomes (PEG, NIV, tracheostomy, and death) among the clusters. For each outcome, the number of subjects who experienced the event and statistically different p-values (Wilcoxon test, threshold = 0.01) are reported.

Acknowledgement

This research was supported by the University of Padova project C94I19001730001, by the Italian Ministry of Health (Ricerca Finalizzata) grant RF-2016-02362405, and by the Italian Ministry of Education, University and Research (PRIN) grant 2017SNW5MB, and by the BRAINTEASER project (contract n. GA101017598), as a part of the European Union's Horizon 2020 research and innovation programme. ET was founded by the Department of Information Engineering, University of Padova (Research Grant B junior).

References

[1] Chiò, A., Calvo, A., Moglia, C., Mazzini, L. & Others Phenotypic heterogeneity of amyotrophic lateral sclerosis: a population based study. *Journal Of Neurology, Neurosurgery & Psychiatry*. **82**, 740-746 (2011)

[2] Tang, M., Gao, C., Goutman, S. & Others Model-based and model-free techniques for amyotrophic lateral sclerosis diagnostic prediction and patient clustering. *Neuroinformatics*. **17** pp. 407-421 (2019)

[3] Tavazzi, E., Daberdaku, S., Zandonà, A., Vasta, R. & Others Predicting functional impairment trajectories in amyotrophic lateral sclerosis: a probabilistic, multifactorial model of disease progression. *Journal Of Neurology*. **269**, 3858-3878 (2022)

[4] Cutler, A. & Breiman, L. Archetypal analysis. *Technometrics*. **36**, 338-347 (1994)

[5] Chiò, A., Mora, G., Moglia, C., Manera, U., Canosa, A. & Others Secular trends of amyotrophic lateral sclerosis: the Piemonte and Valle d'Aosta register. *JAMA Neurology*. **74**, 1097-1104 (2017)

[6] Van Buuren, S. & Groothuis-Oudshoorn, K. mice: Multivariate imputation by chained equations in R. *Journal Of Statistical Software*. **45** pp. 1-67 (2011)

[7] Ragozini, G., Palumbo, F. & D'Esposito, M. Archetypal analysis for data-driven prototype identification. *Statistical Analysis And Data Mining: The ASA Data Science Journal*. **10**, 6-20 (2017)

[8] Eugster, M. & Leisch, F. Weighted and robust archetypal analysis. *Computational Statistics & Data Analysis*. **55**, 1215-1225 (2011)

[9] Eugster, M. & Leisch, F. From spider-man to hero-archetypal analysis in R. (2009)

Assessing Personal Exposure to Airborne Particulate Matter with Wearable Sensors and Ventilation Rate Models

M. Atzeni[1], C. Grisi[1], G. Cappon[1], M. Vettoretti[1*]
[1] *Department of Information Engineering, University of Padova, Padova, 35131, Italy*
* Corresponding Author

***Abstract*—Air pollution is a major contributor to global morbidity and mortality. Accurate assessment of individual's exposure to air pollution is important to quantify the impact of air pollution on human health. Historically, human exposure to air pollution has been quantified using pollutant concentrations from fixed air quality monitoring stations. This approach does not consider the subject's activities and the differences between indoor and outdoor air pollution; however, these limitations can be overcome using wearable sensors.**

In this work, we propose a new approach to measure personal exposure to airborne Particulate Matter (PM) that consists in using a wearable/portable air quality sensor to measure air quality at the subject's location, a wearable Heart Rate (HR) sensor to collect HR timeseries, and a ventilation rate (VE) model to estimate the volume of inhaled air per minute (L/min) based on HR and other subject's covariates. Finally, VE and PM timeseries are combined to estimate the inhaled pollutant doses over time, as a measure of personal exposure. To model VE as a function of HR, 4 literature models are considered. The estimates obtained with the 4 models are compared in 3 representative subjects. Initial data analysis showed that the 4 models may drive to statistically significant differences in exposure estimates, thus the choice of the model can be a critical aspect of this approach. Regardless of the model used, timeseries of inhaled PM revealed significant daily variations in pollutant exposure, highlighting the importance of methodologies for accurate personal exposure assessment.

***Keywords*—Personal Exposure, Air Pollution, Wearable Sensors, Respiratory Rate Estimation.**

I. Introduction

Air pollution is a significant contributor to global morbidity and mortality. Nearly 90% of the global population is exposed to air that exceeds the WHO's guideline limits for pollutants [1]. One of the major air pollutants is particulate matter (PM), i.e., a mixture of solid particles and liquid droplets in the air generated by sources such as road dust, construction debris and fuels burned in automobiles. The small size (1, 2.5 and 10 μg) of PM allows it to penetrate the lungs upon inhalation, leading to respiratory illnesses [2].

Air pollution is not solely an outdoor phenomenon, as indoor air quality can also be affected by the infiltration of outdoor air into buildings. This means that indoor air quality can have a significant impact on human health. As a result, it is essential to accurately quantify total exposure to poor-quality air, which has been identified as a major health hazard.

Exposure assessment refers to the process of estimating or measuring the magnitude, frequency, and duration of an individual's exposure to a particular agent. Accurate quantification of everyday human exposure to air pollution is necessary for health risk assessments. However, exposure is the result of complex interactions between environmental and human systems, making it challenging to assess. Ideally, the assessment has to be based on measuring the concentration of a pollutant within the person's breathing zone for a defined time. Historically, approaches to quantify human exposure have relied on pollutant concentrations from fixed outdoor air quality monitoring stations linked to subject's residence or workplace. Fixed sensors generally give accurate measurements, but, because air quality monitoring sites are often spaced far apart, their location rarely coincides with the places where people experience the majority of their exposure (e.g., at home, work, or school). As a result, it is necessary to use spatial interpolation techniques or statistical methods to indirectly measure a subject's exposure to air pollution.

Environmental parameters, such as pollution, can vary significantly over short distances (e.g., a few meters) [3] and short time intervals [4]. Given the rapid proliferation of mobile devices, as well as the different types of advanced sensors being embedded, there is high interest in exploring the feasibility of using wearable sensors to quantitatively define an individual's exposure to environmental pollution.

Numerous research studies have been conducted to investigate the feasibility of assessing exposure levels in various circumstances by integrating air quality data with wearable devices and/or location data, the latter of which can be obtained through Global Positioning System (GPS) or Time Activity Diary (TAD) [5][6]. For instance, a study [7] compared residence-based monitoring station assessment, mobility-based monitoring station assessment, and mobility-based real-time sensing assessment. The findings revealed that monitoring station assessment may lead to substantially biased estimates due to potential under- or overestimation of individual exposure levels at indoor locations. However, these methods lack precision in measuring the inhaled pollutant dose, which is crucial in transit environments where physical activity can rise inhalation rates.

In this work, we propose a new approach for monitoring

the personal exposure to air pollution using wearable sensors of air quality and activity, and some literature models for the estimation of ventilation rate to compute the inhaled pollutant dose. For estimating ventilation rate, 4 candidate models are considered. The feasibility of the proposed approach is tested on 3 healthy subjects. The exposure estimates obtained with the 4 candidate models on the 3 subjects are finally compared.

II. Estimation of Personal Exposure to Airborne PM using Wearable Sensors

A. Overview of the proposed approach

The proposed approach integrates the measurements collected by a wearable/portable air quality sensor and a wearable heart rate sensor, using a ventilation rate model and an inhalation model. Wearable/portable air quality sensors can measure pollutant concentration (e.g., PM) at the subject's location at almost continuous time (e.g., every 1-5 min).

It is well established that the pollutant amount inhaled is not only influenced by an individual's location (i.e., the level of pollution they are exposed to) but also by their activity level (as the intensity of activities affects the respiration rate and, therefore, the amount of contaminants ingested).

According to Borghi et al. [8], the amount of inhaled dose over a certain time of exposure can be estimated as:

$$I_{pollutant} = C_{pollutant} * VE * t \tag{1}$$

where $I_{pollutant}$ is the dose of pollutant inhaled by a subject in μg; $C_{pollutant}$ is the concentration of pollutant measured in μg/m^3; VE is the ventilation rate in m^3/min and t the time of exposure in minutes.

Measuring Ventilation Rate (VE) in daily life is challenging, because it requires the use of a face mask with an airflow sensor, which can obstruct the intake of air pollution and obstacle the daily activities. Therefore, VE estimation methods are often used in field studies. In some cases, the VE of the subject is derived from literature population values and adjusted based on physical effort intensity during measurements.

In the proposed approach, VE timeseries are estimated starting from almost continuous-time heart rate (HR) timeseries collected by a wearable smartwatch, using some literature models of VE that have HR as main predictor. In particular, the 4 candidate models described below are considered.

B. Ventilation rate models

Several solutions were proposed in the literature for the estimation of VE starting from HR, which is easy to measure in the field using portable and inexpensive equipment. Although HR is affected by various factors, it is mainly influenced by oxygen consumption, which is strongly correlated with respiration. The following subsections describe some literature models to estimate VE starting from HR.

a) Model A

Zuurbier et al. [9] proposed 3 different models for estimating VE in individuals, one for both males and females, one for males, and one for females. Volunteer subjects (N = 34) performed submaximal tests on bicycle ergometers. HR was recorded every second and VE was measured using a pneumotach. Regression equations between HR and the natural log-transformed VE were calculated:

$$VE_{overall} = e^{0.89+(0.022*HR)} \tag{2}$$

$$VE_{men} = e^{1.03+(0.021*HR)} \tag{3}$$

$$VE_{women} = e^{0.57+(0.023*HR)} \tag{4}$$

b) Model B

In a study published by Guo et al. [10], 80 volunteers underwent incremental tests on a bicycle ergometer. HR was continuously measured with a chest strap and VE was measured with a facial mask and a portable gas analyzer. The investigators proposed 3 exponential models, one for both men and women, one for men, and one for women, in which the exponent is a regression of HR:

$$VE_{overall} = 10^{0.585+(0.007*HR)} \tag{5}$$

$$VE_{men} = 10^{0.559+(0.007*HR)} \tag{6}$$

$$VE_{women} = 10^{0.647+(0.006*HR)} \tag{7}$$

c) Model C

In a study conducted by Good et al. [11], 35 volunteers were provided with an Oxycon Mobile indirect calorimetry system that measured breath-to-breath VE and HR in a laboratory setting. The volunteers performed 9 or 11 prescribed tasks (6 min each). Predictive models for VE were developed based on multiple linear regression. The resulting model equation is:

$$\begin{aligned} VE = {} & 0.99 - 27.41 * sex + 50.24 * \frac{HR}{100} \\ & + 15.73 * \frac{age}{100} - 43.65 * \frac{HR_{rest}}{100} \\ & - 7.02 * \frac{hip}{100} + 23.02 * sex * \frac{HR}{100} - 10.34 * sex * \frac{age}{100} \\ & - 26.21 * sex * \frac{HR_{rest}}{100} + 38.78 * sex * \frac{hip}{100} \end{aligned} \tag{8}$$

where HR_{rest} is resting HR and hip is the hip circumference.

d) Model D

Greenwald et al. [12] conducted a pooled-data analysis that included 8 datasets for a total of 471 individuals. The study protocols included measures of Forced Vital Capacity (FVC), VE, HR and physical activity. The data analyzed included subjects performing sport or routine activities. The models developed in this study were based on log-transformed generalized linear mixed models. The resulting model equation is:

$$VE = e^{-9.59} * HR^{2.39} * age^{0.274} * sex^{-0.204} * FVC^{0.520} \tag{9}$$

Three models out of four (A, B, D) were not validated, except from the model C which has been validated on the same subjects performing different physical tasks.

III. Feasibility Study of the Proposed Approach

A. Data collection

The feasibility of the proposed approach was tested with data collected from 3 healthy volunteers. Upon recruitment, each volunteer completed a questionnaire that included information about their gender, age, hip circumference, FVC, and resting HR. Each participant was provided with a personal air quality monitor, i.e., the Atmotube PRO (Atmotech Inc., San Francisco, CA), and a smartwatch, i.e., either a Fitbit Charge 5 (Fitbit Inc., San Francisco, CA) or an Apple Watch (Apple Inc., Cupertino, CA) to gather HR data.

The Atmotube PRO is a wearable/portable air quality monitoring device. It is equipped with sensors that measure the concentrations of PM of different sizes (PM1, PM2.5, PM10), total volatile organic compounds (VOCs), temperature, humidity, and pressure. The sensors are calibrated automatically and do not require any input from the user beyond placing the device in its charger as needed and synchronizing data through the proprietary app installed on the user's smartphone. Participants in this study were asked to wear the Atmotube PRO and the smartwatch continuously for a period of 4 weeks.

B. Statistical analysis

The inhaled doses of PM1 were estimated using the 4 models of VE (Eq. 3-6-8-9) presented in subsection II-B combined with Eq. 1. Descriptive statistics, such as mean and standard deviation (SD), maximum and minimum values, median and percentiles (5% - 95%), were calculated for each inhaled dose timeseries to provide a comprehensive overview of the data. Moreover, the average daily sum of inhaled dose was computed for each signal, to obtain an index of the average daily exposure over the 4-week period.

To determine if there were significant differences between the daily sum of inhaled dose estimated with the different VE models, a Kruskal-Wallis H Test (1% significance level) and multiple pairwise Wilcoxon test were conducted for each subject independently, after checking the normality assumption (Lilliefors test) and the homogeneity of variance (Levene test).

IV. Results

The mean age of the study participants at the time of recruitment was 27.7 years, and all subjects were male. The average resting HR and hip circumference were 55.7 beats/min and 98.5 cm, respectively. The FVC of all participants was set to 5 L, based on the normal range for healthy males between the ages of 20-60 (4.75-5.5 L). The study dataset included 94 person-days of data collected from May to December 2022, with an average follow-up period of 31.5 days. Figure 1 shows the average daily VE timeseries provided by the 4 VE models (top panel), the average daily PM1 concentration timeseries (middle panel), and the daily mean profiles of inhaled PM1 dose (bottom panel), for Subject 1. We can observe that the estimates of Model C (Good, violet curve) are systematically higher than those of the other models, while the other three models provide estimates closer to each other.

TABLE I: Descriptive statistics of PM1 inhaled doses [μg] estimated with the 4 VE models.

	Subject 1	*Subject 2*	*Subject 3*
Model A			
Mean±SD	0.88±1.33	1.08±2.38	0.54±0.56
min-max	0.04-20.14	0.04-69.4	0.09-17.7
median (5^{th} - 95^{th})	0.55 (0.08-2.37)	0.67 (0.1-3)	0.41 (0.17-1.3)
Model B			
Mean±SD	0.78±0.93	0.97±2	0.34±0.4
min-max	0.04-12.77	0.04-61.1	0.04-15.5
median (5^{th} - 95^{th})	0.53 (0.07-2.14)	0.63 (0.09-2.6)	0.24 (0.06-0.88)
Model C			
Mean±SD	1.44±1.92	1.25±3.2	0.46±0.75
min-max	0.02-26.41	0.05-98.1	0.5-22.7
median (5^{th} - 95^{th})	0.85 (0.12-4.42)	0.63 (0.08-3.9)	0.23 (0.01-1.56)
Model D			
Mean±SD	0.72±1.25	0.9±2.1	0.29±0.44
min-max	0.02-20.01	0.02-61.5	0.01-12.5
median (5^{th} - 95^{th})	0.4 (0.06-2.10)	0.51 (0.09-2.67)	0.17 (0.04-0.9)

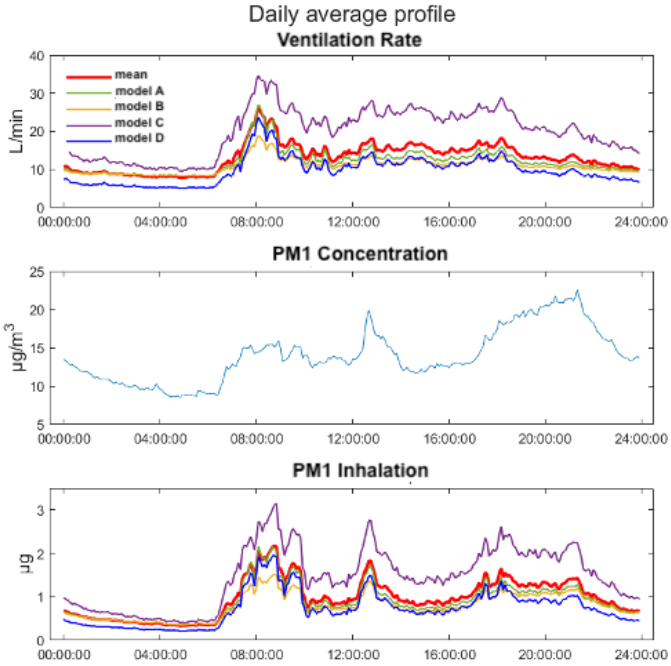


Fig. 1: Subject 1 daily average profile. From the top: VE computed using all the models (A - Zuurbier, B - Guo, C - Good, D - Greenwald), PM1 concentration measurements, Inhalation rate computed using each VE estimations. In the top and bottom panels, the red profile represents the mean of the profiles obtained with the 4 models.

The descriptive statistics calculated for each timeseries of PM1 inhaled dose are reported in Table I. The Model D estimation is typically lower, while Model C results in higher PM1 inhaled dose estimates. SD and the minimum-to-maximum interval show that Model C has a larger level of variability than the other models. Then, Model C appears to overestimate the inhalation of pollutants and to be more

sensitive to changes in the independent variables. Regarding the differences among subjects, we shall consider that the measurements of Subjects 1 and 2 were collected in the autumn, while the measurements of Subject 3 were collected during the spring. While air pollution is a problem throughout the year, some pollutants tend to be more prevalent during certain seasons due to a variety of factors like temperature, environment, and human activity. Pollution levels generally decline during the warmer and more sunny seasons, with consequent lower individual exposure. This likely explains the lower inhaled doses of Subject 3 compared to the others.

TABLE II: Average daily sum of inhalation [μg].

Model	*Subject 1*	*Subject 2*	*Subject 3*
A	245.7 $\pm$144.6	244.8$\pm$170.7	76.8$\pm$45.4
B	217.9 $\pm$121.6	217.8$\pm$150.3	70.2$\pm$40.5
C	399.5 $\pm$224.8	280.7$\pm$214.8	93.9$\pm$57.5
D	200.6 $\pm$124	203.4$\pm$146.4	59.7$\pm$36.6

TABLE III: Kruskal-Wallis H and Multiple Comparison Tests for the daily sum of inhalations timeseries.

	Subject 1	*Subject 2*	*Subject 3*
Kruskal-Wallis H Test (p-value < 0.01)			
P-Value	<0.01	0.54	0.1
Multiple Comparison Test (p-value < 0.05)			
P-Value (Model A vs B)	0.91	0.93	0.94
P-Value (Model A vs C)	<0.05	0.99	0.77
P-Value (Model A vs D)	0.54	0.7	0.45
P-Value (Model B vs C)	<0.05	0.82	0.42
P-Value (Model B vs D)	0.9	0.97	0.8
P-Value (Model C vs D)	<0.05	0.54	0.07

Table II shows the average daily sum of inhalation. In accordance with Table I results, the average daily sum of PM1 inhalation calculated using Model C has generally higher values, whereas that calculated using Model D has generally lower values. Regardless of the model used, the inhalation time series showed a large daily variation in exposure to contaminants to which subjects may be exposed.

The Lilliefors and Levene tests indicated that the assumptions of normality and homogeneity of variance were not met. Therefore, a Kruskal-Wallis H Test and subsequent Multiple Comparison Test were conducted. The findings from the Kruskal-Wallis analysis (Table III) revealed a statistically significant difference in the average daily sum of inhalation estimates among the four models (p-value < 0.01) for Subject 1, but not for Subjects 2 and 3 (with p-values of 0.54 and 0.1 respectively). Further pairwise comparison tests showed that Model C was significantly different from the other models for Subject 1. As expected, there were no significant differences between the models for Subjects 2 and 3. These results are consistent with the mean values presented in Table II. This behavior could be attributed to the inherent characteristics of Model C, which uses a linear regression model with a greater number of factors and interaction terms compared to simpler exponential models.

V. Conclusion

We proposed a new approach to assess the personal exposure to airborne PM using wearable sensors of air quality and HR, and models of VE and inhalation. Four literature models for estimating VE starting from HR were used for this purpose in a feasibility study conducted in 3 subjects.

A preliminary data analysis revealed that there might be significant differences between the inhalation estimates obtained by the 4 models. This suggests that the choice of the VE model may be a critical aspect of the proposed approach. Regardless of the model used, inhalation timeseries revealed significant daily variations in exposure to pollutants that a subject may experience, which cannot be captured by traditional approaches based on fixed monitoring stations. This encourage future research studies to enhance approaches, like the one proposed in this study, to assess personal exposure using wearable sensors.

Future work includes the assessment of the proposed approach on a larger population. Moreover, given the significant differences between the estimates obtained in this study, a benchmark study to validate VE models against standard methods (e.g., pneumotach) on a large population is needed to enable robust choice of VE models for future projects.

Acknowledgement

Michele Atzeni acknowledges the support of MUR (Italian Ministry of University and Research) under the PON initiative ex DM 1061.

References

[1] World Health Organization, et al. WHO global air quality guidelines: particulate matter (PM2. 5 and PM10), ozone, nitrogen dioxide, sulfur dioxide and carbon monoxide. World Health Organization, 2021.

[2] Singla, Savina, et al. "Towards an integrated framework for air quality monitoring and exposure estimation—A review." Environmental monitoring and assessment 190.9 (2018): 1-21.

[3] Santamouris, Matheos. Energy and climate in the urban built environment. Routledge, 2013.

[4] Ramachandran, Gurumurthy, et al. "Characterizing indoor and outdoor 15 minute average PM 2.5 concentrations in urban neighborhoods." Aerosol Science & Technology 37.1 (2003): 33-45.

[5] V. Casella, et al, “Dynamic Assessment of Personal Exposure to Air Pollution for Everyone: a Smartphone-Based Approach,” ISPRS – International Archives of the Photograppetry, Remote Sensing and Spatial Information Sciences, vol. XLIII-B4-2020, pp. 655-663, (2020).

[6] Liang, L., Gong, P., Cong, N. et al. Assessment of personal exposure to particulate air pollution: the first result of City Health Outlook (CHO) project. BMC Public Health 19, 711 (2019).

[7] Ma, Jing, et al. "Assessing mobility-based real-time air pollution exposure in space and time using smart sensors and GPS trajectories in Beijing." Annals of the American Association of Geographers 110.2 (2020): 434-448.

[8] Borghi, Francesca, et al. "Estimation of the inhaled dose of pollutants in different micro-environments: a systematic review of the literature." Toxics 9.6 (2021): 140.

[9] Zuurbier, Moniek, et al. "Minute ventilation of cyclists, car and bus passengers: an experimental study." Environmental health 8.1 (2009): 1-10. interfaces(Translation Journals style),Ó IEEE Transl. J. Magn.Jpn., vol. 2, Aug. 1987, pp. 740Ð741.

[10] Guo, Qian, et al. "Using heart rate to estimate the minute ventilation and inhaled load of air pollutants." Science of The Total Environment 763 (2021): 143011.

[11] Good, N., et al. "Development and validation of models to predict personal ventilation rate for air pollution research." Journal of exposure science & environmental epidemiology 29.4 (2019): 568-577.

[12] Greenwald, Roby, et al. "Estimating minute ventilation and air pollution inhaled dose using heart rate, breath frequency, age, sex and forced vital capacity: A pooled-data analysis." PloS one 14.7 (2019): e0218673.

Key points to design the MDs Library of a National implant Registry: lesson learned from the Italian experience

S. Pascucci[1,2], M. Franzò[1], V. Mari[2], A. Biondi[2], S. Ceccarelli[2], F. Bini[1], F. Marinozzi[1], E. Ciminello[2], P. Ciccarelli[2], P. Laricchiuta[2], E. Carrani[2] and M. Torre[2]

[1] *Department of Mechanical and Aerospace Engineering, "Sapienza" University of Rome, Rome (Italy)*
[2] *Scientific Secretariat of the Presidency, Italian National Institute of Health, Rome (Italy)*

***Abstract*— In 2017, the European Medical Device Regulation 2017/745 made official and effective the implementation of a unified European database on medical devices, EUDAMED, and stated the need to adopt a medical device (MD) nomenclature to support its functioning. Registries are a fundamental tool to evaluate MD long-term safety and to contribute to its traceability. To achieve these goals, the MD Library embedded in the Registry framework plays an important role as it contains all information useful to identify the implanted medical devices and to compare their performance. Similarly to EUDAMED, MD Registry Libraries are based on a detailed and defined MD taxonomy that allows a correct MD categorisation on the basis of a selected set of technical features. The aim of this study is to propose a generalised approach to build a MD taxonomy to be implemented in a MD Registry Library starting from the experience gathered in the implementation of the MD Registries included in the Italian Implantable Prostheses Registry (RIPI).**

***Keywords*— medical devices, nomenclatures, registry, RIPI**

I. INTRODUCTION

IN 2017, the European Medical Device Regulation (MDR) 2017/745 made official the implementation of a unified European database on medical devices, EUDAMED, and stated that a medical device (MD) nomenclature should be made available to facilitate the functioning of EUDAMED [1]. In 2021, the Regulation (EU) 2021/2078 was issued providing all the rules for EUDAMED implementation and use [2]. Accordingly, all medical devices marketed in Europe should be collected in the single database EUDAMED and identified by a unique number, the Unique Device Identifier (UDI).

The selection of a MD nomenclature was fundamental to the functioning of EUDAMED in order to classify all medical devices into macroscopic and homogeneous classes. The European Medical Device Nomenclature (EMDN) was adopted by the European Commission (EC) on March 4th, 2019 taking as a reference the Italian national MD classification (Classificazione Nazionale dei Dispositivi medici, CND) [3],[4]. In 2021, WHO analysed different nomenclatures concluding that CND was the one that complies with the WHO principles for international classification, coding and nomenclature of medical devices. [5]. Moreover, WHO and EC have recently been collaborating in view of adopting an international standardised nomenclature [6].

Besides its role in EUDAMED, EMDN is also a useful tool for other purposes, representing a 'classification root' from which other systems can be developed [4]. Among them, MD Registries can benefit from more detailed and specific classifications, or taxonomies, to classify the implanted devices [7]. Indeed, in depth device knowledge allows a more complete, consistent and informative interpretation of the clinical data collected from the Registry, helping to obtain information on device usage and performance and to compare similar devices [8]. A medical device Registry is defined as an "organized system that continuously and consistently collects relevant data in conjunction with routine clinical care, evaluates meaningful outcomes, and comprehensively covers the population defined by exposure to particular device(s) at a reasonably generalizable scale (e.g. international, national, regional, and health system) with a primary aim to improve the quality of patient care" [9]. Since it represents a fundamental tool to contribute to the traceability of the device and to improve patient safety [10], its establishment is encouraged by MDR especially for class III MDs [1]. Certainly, a Registry should rely on a MD Library based on a defined taxonomy, classification or nomenclature to ensure MD traceability and monitoring,[11]-[13].

The aim of this study is to describe the methodology set up by the Italian Implantable Prostheses Registry (RIPI) [14] to design a taxonomy specific for a class of medical devices. The final scope of the taxonomy design is to complement the existing nomenclature, providing more detailed technical features of the device, and to set up the basis for the development of a dedicated MD Registry Library, essential to promptly identify and characterise the implanted device [8], [15], [16].

This work has been conducted for the purposes of the development of the MD Libraries for the Italian National Registries of spinal implants (RIDIS) and of cardiac devices, defibrillators and pacemakers, (RIDEP). Both RIDEP and RIDIS are included into RIPI.

II. STATE-OF-THE ART

A. The Italian Implantable Prostheses Registry (RIPI)

RIPI was established by law at the Italian National Institute of Health in 2017 (Istituto Superiore di Sanità, ISS) (DPCM 03/03/2017). It is organised as a cross coordination structure of individual registries of implantable devices divided by subject: joint prostheses like hip, knee, shoulder, and ankle (Italian Arthroplasty Registry, RIAP); spinal implants (Italian Spinal Implants Registry, RIDIS); implantable cardioverter defibrillator and pacemaker (Italian Implantable Cardioverter-defibrillator and Pacemaker Registry (RIDEP); artificial heart valves (Italian Heart Valves Registry, RIVAC) and implantable hearing devices (Italian Implantable Hearing

Device Registry, RIDIU) (https://ripi.iss.it/ripi/en/). Currently, RIAP is already active and collects data routinely; RIDIS and RIDEP have been completely designed while design of RIVAC and RIDIU is ongoing.

B. The MD Library

The Library is the database of all implantable devices collected by a specific Registry included in RIPI. Each device contained in the Library is described by a set of technical features. The Library is designed to be directly fed by manufacturers, according to the rules stated by a high-specific taxonomy.

C. The agreement with NJR to adopt the NJR-EPRD classification and share the MD Library

Most of the existing implant registries collect only the device ID or its barcode, which provide only market data for traceability but not specific device information [17]-[19]. However, the Dutch registry LROI [8], the English National Joint Registry (NJR) (https://www.njrcentre.org.uk/njr-annual-report-2022/) and the Endoprothesen Register Deutschland (EPRD) (https://www.eprd.de/de/downloads-1/berichte) have defined their detailed taxonomies to classify the registered devices. Remarkably, in 2018, NJR and EPRD, in the absence of a universally recognised and shared nomenclature for joint prostheses, agreed in developing and continuously updating over the years an internationally shared taxonomy [13],[16],[20]. This collaboration is the first example of an inter-registry international cooperation for classifying medical devices. For joint prostheses, ISS has recently signed an agreement with NJR in order to adopt the already defined NJR-EPRD classification and set up a shared international MD database linking both RIAP and NJR Libraries.

III. Materials and Methods

1) Materials

The taxonomy is a structured list including device-specific variables, properly grouped and described by a minimum core set of technical and identification features.

To set up the RIDIS and RIDEP taxonomies, the following sources of information were considered:

- CND nomenclature: a hierarchical classification organised in 22 anatomical/functional categories that characterise devices by homogeneous properties. Each category is organised in groups and sub-groups structured in different levels (up to 7) and identified by a correspondent alphanumeric code [21];
- Medical Devices Database of the Italian Ministry of Health (BDRDM): a database that contains all medical devices marketed in Italy, together with their technical datasheets (the registration is mandatory) [22];
- Medical Devices datasheets: technical documents available on the manufacturers websites;
- Literature review: analysis of studies concerning survival and/or failure of the specific implantable devices;
- Opinions of experts: clinicians and specialists, members of the registry technical panel.

In particular, the following CND classes (version 2022, January 26) were considered:

- RIDIS:
  i. “P0907. Prostheses and Stabilisation Systems of the Vertebral Column”, i.e., systems for interbody fusion, cages or cages and disc prostheses;
  ii. “K0103. Devices for Minimally Invasive Spinal Surgery”, i.e., devices used for kyphoplasty, vertebroplasty and products for cementation;
  iii. “J020202 Totally implantable spinal neurostimulators”;
- RIDEP:
  i. “J01. Cardiac Function Devices”, i.e., pacemakers, implantable defibrillators and leads;
  ii. “C02Devices for Arrhythmology”, i.e., leads and cardioversion devices.

2) Methods

A technical expert panel composed by clinicians nominated by the involved scientific societies and by researchers of ISS was established to define a first draft of the taxonomy structure, organised in groups and sub-groups. Both engineering and clinical aspects were considered to define the taxonomy: the first ones due to the fact that they are more closely related to the technical features of the devices, the last ones as they are associated to the device intended purpose.

The items included in the first structure were then weighed by associating the number of devices registered in BDRDM in order to have an overview of all specific devices actually marketed in Italy, selected on the basis of the proper CND code.

A set of technical features was then selected from the technical sheets, the manufacturers' manuals and catalogues, and associated to each item included in the first version of the taxonomy. To ensure device identification and traceability, the following information were selected and included in the taxonomy for each device: CND, manufacturer, product catalogue code, lot, barcode, UDI, ID registration in BDRDM.

The taxonomy was then shared and discussed with the clinical experts: only the technical features deemed as most useful to characterise the device and to carry out future analyses were retained. Subsequently, the taxonomy was shared with the manufacturers covering the highest portion of the spinal device market in Italy and was then finalised in a consensus meeting aimed at refining and making the taxonomy feasible and functional.

The final version of the taxonomy was then made suitable to fit into formal XML (eXtensible Markup Language, lit. “extensible markup language”) and XSD (“XML Schema Definition”) schemas, useful for the subsequent implementation of the MD Library in the RIPI platform. To perform this step, the names of the identified variables were translated into English, according to the specifications provided by RIPI-IT group. Moreover, specific business rules were introduced, namely syntactical and semantic rules providing a set of variable combinations which help avoid mistakes in compilation and ensure data coherency.

IV. Results

The designed methodology is structured in the following six steps (reported in Table I):

1. The CND (EMDN) codes of medical devices matching the registry area of interest are identified;
2. The first minimum core set of technical and functional features essential to assess the MD performance is defined on the basis of the information available from different sources (technical datasheets, institutional MD Database, EUDAMED, commercial catalogues, scientific publications);
3. The draft of the core set is discussed with the clinicians in order to check completeness of the list of variables useful to assess the performance of the devices from the clinical perspective;
4. The taxonomy is shared with the representatives of the industries to verify its feasibility and functionality at industrial level. To quantify the characteristics that they could easily routinely upload in the Library, manufacturers are required to classify the information requested on the taxonomy as "available", "not available" and "searchable". To ensure the consideration of all crucial technical features of the selected devices, it is advisable to include the highest number of manufacturers, if possible all, in this process;
5. Specific business rules are introduced to enter only valid combinations of values into the web-based platform in order to reduce compilation errors. The rules are defined using both manufacturers' datasheets and surgeons' opinions;
6. The taxonomy is converted into XML and XSD schemas to allow its implementation in the Registry Library. When feeding the MD Library, manufacturers are required to structure their data by using the XML format in accordance with the XSD schemas.

TABLE I
SUMMARY OF THE METHODOLOGY TO SET UP A MD TAXONOMY

step	*description*
1	*Identification of CND classes of Medical Devices that match Registry area*
2	*Definition of a first core-set of technical features*
3	*Proactive discussion of taxonomy draft within the multidisciplinary team of the Registry technical panel*
4	*Sharing of the taxonomy draft with the leading industries to verify its feasibility*
5	*Definition of business rules*
6	*Adaptation of taxonomy in XML and XSD schemas for subsequent implementation of the Registry MD Library*

Table II shows the macro categories of the taxonomies developed for the RIDIS and RIDEP registries.

V. Discussion

The methodology to design a taxonomy for a specific MD registry was abstracted from the processes developed in the implementation of two Italian implantable prostheses registries: RIDIS and RIDEP.

TABLE II
MACRO CATEGORIES OF MD TAXONOMIES DEVELOPED FOR RIDIS AND RIDEP REGISTRIES

categories	*RIDEP*	*RIDIS*
MD Identification	*Manufacturer, product code, CND/EMDN, UDI, lot number*	
Type of device	*Defibrillator, Pacemaker, catheters and loop recorder*	*Spinal fixation system, cages, disc prostheses, cements*
Technical and functional features	*Chambers connector, remote control, MRI conditional, sensors*	*Geometry, type, materials, spine level, mechanics or physics properties*

Implantable prostheses registries have become increasingly widespread in recent decades [10],[23] because of the highest economic impact on healthcare and invasiveness for the patient (risk class III) of the devices they monitor [24],[25].

This study highlighted some essential features that should be accomplished when designing a specific MD taxonomy: 1) to select only properties actually bringing information and knowledge when comparing devices' performance and their effects on patients, avoiding excessive details unnecessary to reach registry's aims; 2) to involve all actors (clinicians and manufacturers) dealing with the device within the Registry to collect their opinion and retain only the essential characteristics. Indeed, it is crucial to consider all the stakeholder perspectives in the decision-making process of inclusion and exclusion criteria; 3) to share the design of the taxonomy with the largest number of manufacturers to verify that they are able to provide all the selected information because are either available or collectable and not confidential, thus making the feeding of the Library feasible.

The availability of BDRDM was very helpful to draft a first list of medical devices marketed in Italy. However, the integration with other sources, such as literature and catalogues, was necessary to have a global perspective by including also the devices not marketed in Italy.

Hopefully in the near future, EUDAMED could fulfil at least at European level the same role BDRDM has at the Italian level; indeed, it includes information relating both to the economic operator and to the device (Annex VI, Part A) [1].

However, Registries need more specific information regarding the implanted medical devices to perform statistical analyses on their performance. Therefore, MD Libraries represent an important source of long-term data when the Registry goes live [11]. By following the methodology presented in this study, it is possible to implement a MD Registry Library and support health operators in data collection, without asking them to manually input MD codes, thus dramatically reducing identification errors. Moreover, each device is described by a set of technical features useful to conduct analyses on its use and performance over time according to the diseases or conditions of the patients [26]. Accordingly, manufacturers can also receive valuable information on how their devices are performing and they might possibly correct the focus for a safer device design.

A limit of the proposed methodology is related to the possible biased exclusion of selected MD properties in the taxonomy.

Indeed, some technical information characterising the device, that might be important to be studied, may be confidential as protected by patents and therefore not sharable by the manufacturers, thus preventing the Registry to perform subsequent complete statistical analyses.

VI. Conclusion

In this paper, starting from the experience gathered in Italy in the framework of RIPI, a methodology to implement a MD Library functional to achieve the MD Registry goals is presented. In a worldwide context, where safety and traceability of medical devices are considered a priority and data exchange and statistical results are crucial for social and scientific growth, the implementation of MD Libraries and MD taxonomies might be an essential step. Due to its generalisation and its easy use, the presented methodology might represent a first useful reference to set up taxonomies not only for other implantable prostheses, but also for other categories of devices.

Acknowledgements

This study was coordinated by the Italian National Institute of Health and supported by the General Directorate of Medical Devices and the Pharmaceutical Service at the Ministry of Health. We acknowledge the RIPI team (M. Masciocchi and A. Cornacchia) for the administrative management and for the preparation of the database. Also, we acknowledge the experts participating in the RIDIS (G. Barbagallo, P. Berjano, A. Piazzolla, L. Sampaolo, V. Vitiello, G. Zanoli) and RIDEP (G. Calcagnini, F. Censi, M. Ghidina, A. Proclemer, G. Zanotto, M. Zecchin) technical panels.

References

[1] *Regulation (EU) 2017/745 of the European Parliament and of the Council of 5 April 2017 on medical devices, amending Directive 2001/83/EC, Regulation (EC) No 178/2002 and Regulation (EC) No 1223/2009 and repealing Council Directives 90/385/EEC and 93/42/EEC*. Official Journal of the European Union L117/1, 5.5.2017. Available: https://eur-lex.europa.eu/legal-content/EN/TXT/PDF/?uri=CELEX:32017R0745

[2] *Commission Implementing Regulation (EU) 2021/2078 of 26 November 2021 laying down rules for the application of Regulation (EU) 2017/745 of the European Parliament and of the Council as regards the European Database on Medical Devices (Eudamed)*. Official Journal of the European Union L426/9, 29.11.2021. Available: https://eur-lex.europa.eu/eli/reg_impl/2021/2078

[3] EU Commission, GROW.DDG1. D.4. (2019, March 4). Medical Devices Nomenclature [Online]. Available: https://ec.europa.eu/docsroom/documents/34264

[4] M.Franzò, F. D'Agostino, C. Chierchia, K. Cucchiara, E. Carrani, *et al*., "Does a medical device nomenclature suitable for all purposes exist? Twenty years of Italian experience with the CND and its adoption in EUDAMED at European level", *in 2020 Proc. 7th Congress of Bioengineering GNB.*

[5] World Health Organization, Executive board 145. (2019, April 30). Standardization of medical devices nomenclature: International classification, coding and nomenclature of medical devices: report by the Director-General [Online]. Available: https://apps.who.int/iris/handle/10665/328220

[6] EU Commission, DG Health and Food Safety, Directorate Health systems, medical products and innovation, Unit Medical Devices. (January 2020). The European Medical Device Nomenclature (EMDN) [Online]. Available: https://health.ec.europa.eu/medical-devices-sector/new-regulations/guidance-mdcg-endorsed-documents-and-other-guidance_en

[7] M. Franzò, E. Carrani, M. Asaro, E. Caton, K. Tucker, *et al*,. "Harmonisation of medical devices classification systems: development of a generalised approach starting from hip prostheses. A first example of an international and standardised nomenclature to be integrated within the European Medical Device Nomenclature*", in 2020 Proc. 7th Congress of Bioengineering GNB.*

[8] G. A. W. Denissen, L. N. van Steenbergen, W. T. Lollinga, N. J. J. Verdonschot, B. W. Schreurs, and R. G. H. H. Nelissen, "Generic implant classification enables comparison across implant designs: the Dutch Arthroplasty Register implant library", *EFORT Open Rev*, vol. 4, pp 345-350, 2019.

[9] *Essential Principles of Safety and Performance of Medical Devices and IVD Medical Devices*, International Medical Device Regulators Forum (IMDRF), IMDRF Good Regulatory Review Practices Group 31.10.2018. Available: https://www.imdrf.org/documents/essential-principles-safety-and-performance-medical-devices-and-ivd-medical-devices

[10] E. Romanini, I. Schettini, M. Torre, M. Venosa, A. Tarantino, *et al*., "The rise of registry-based research: a bibliometric analysis", *Acta Orthopaedica*, vol. 92, pp. 628-632, June 2021.

[11] C. Henschke, D. Panteli, M. Perleth, and R. Busse, "Taxonomy of medical devices in the logic of health technology assessment", *International Journal of Technology Assessment in Health Care*, vol. 31, pp. 324-330, 2015.

[12] S. Challa, M. Wazid, A. K: Das, and M. K. Khan, "Authentication Protocols for Implantable Medical Devices: Taxonomy, Analysis and Future Directions", *IEEE Consumer Electronics Magazine*, vol. 7, pp. 57-65, 2018.

[13] W. Blömer, A. Steinbrück, C. Schröder, F.J. Grothaus, O. Melsheimer, *et al*., "A new universal, standardized implant database for product identification: a unique tool for arthroplasty registries", *Arch Orthop Trauma Surg*, vol. 135, pp. 919–926, 2015.

[14] M. Torre, E. Carrani, M. Franzò, E. Ciminello, I. Urakcheeva, *et al*.,. "Il Registro Italiano delle Protesi Impiantabili: una nuova realtà per la sicurezza del paziente", *Boll Epidemiol Naz*, vol. 2, pp. 16-23, 2021.

[15] M. Torre, E. Romanini, G. Zanoli, E. Carrani, I. Luzi, *et al*., "Monitoring Outcome of Joint Arthroplasty in Italy: Implementation of the National Registry", *Joints*, vol. 5, pp. 70-78, 2017.

[16] V. Jansson, A. Grimberg, O. Melsheimer, C. Perka, and A. Steinbrück. "Orthopaedic registries: the German experience". *EFORT Open Reviews*, vol. 4, pp. 401-408, 2019.

[17] V. J. Hansen, M. E. Greene, M. A. Bragdon, A. K. Nebergall, C. J. Barr, *et al*., "Registries Collecting Level-I through IV Data: Institutional and Multicenter Use", *Journal of Bone and Joint Surgery – American Volume*, vol. 96, pp. e160, 2014.

[18] C. Röder, A. El.Kerdi, A. Frigg, C. Kolling, L. P. Staub, *et al*., "The Swiss Orthopaedic Registry", *Bull Hosp Jt Dis*, vol. 63, pp. 15-19, 2005.

[19] M. L. Van Hooff, W. C. H. Jacobs, P. C. Willems, M. W. J. M Wouters, M. de Kleuver, *et al*., "Evidence and practice in spine registries", *Acta Orthopaedica*, vol. 86, pp. 534-544, 2015.

[20] J. White and G. Carolan-Rees, "Current state of medical device nomenclature and taxonomy systems in the UK: spotlight on GMDN and SNOMED CT.", *JRSM Short Rep*., vol. 4, pp. 1-7, 2013.

[21] *Decreto del Ministro della salute 20 febbraio 2007. Approvazione della Classificazione Nazionale dei Dispositivi Medici (CND).* Gazzetta Ufficiale Serie Generale N. 63, 16.03.2007. Available: https://www.gazzettaufficiale.it/eli/id/2007/03/16/07A92230/sg

[22] *Decreto del Ministro della salute 20 febbraio 2007. Nuove modalità per gli adempimenti previsti dall'articolo 13 del decreto legislativo 24 febbraio 1997, n. 46 e successive modificazioni e per la registrazione dei dispositivi impiantabili attivi nonché per l'iscrizione nel Repertorio dei dispositivi medici.* Gazzetta Ufficiale Serie Generale N. 63, 16.03.2007. Available: https://www.gazzettaufficiale.it/eli/id/2007/03/16/07A92230/sg

[23] H. Mauch, J. Kaur, C. Irwin, and J. Wyss. "Design, implementation, and management of an international medical device registry", *Trials*, vol. 22, pp. 1-12, 2021.

[24] E. W. Paxton, M. C. S. Inacio, and M. L. Kiley, "The Kaiser Permanente Implant Registries: Effect on Patient Safety, Quality Improvement, Cost Effectiveness, and Research Opportunities", *Perm J*, vol. 16, pp. 36-44, 2012.

[25] MedTech Europe. (2021, June 21) The European Medical Technology Industry in figures [Online]. Available: https://www.medtecheurope.org/resource-library/medtech-europes-facts-and-figures-2021/

[26] B. Pop, B. Fetica, M. L. Blaga, A. P. Trifa, P. Achimas-Cadariu, *et al*., "The role of medical registries potential application and limitation", *Medicine and Pharmacy Reports*, vol. 92, pp. 7-14, 2019.

Improving data quality in healthcare: medical informatics tools and standards

M. Giacomini[1,2], S. Mora[1], E. Lazarova[1,3], N. Maggi[1,2], and C. Ruggiero[1,2]
[1] *Dept. of Informatics, Bioengineering, Robotics and System Engineering, Univ. of Genoa, Italy*
[2] *Healthropy s.r.l., Savona, Italy*
[3] *Local Health Care Authority 3, Genoa, Italy*

***Abstract*— This paper relates to projects that are being carried out at the Health Informatics section of the Bioengineering laboratory of the DIBRIS (University of Genoa). The main and unifying aspect of the work in this section is the treatment of clinical data in order to achieve data sets characterized by high quality to support medical research. Specifically, the presented examples are about: an infectious disease network, a natural language processing based pipeline for microbiology and an electronic health record system for cardiology. Methodologically, an attempt has been made to make extensive use of specific standards in order to collect data already widely available the digital format on various platforms, both those already analytically organized and those dispersed in natural language pieces.**

***Keywords*— Standards, Interoperability, Natural language processing, Electronic Health Record.**

I. Introduction

THE work described here relates to projects that are being carried out at the Health Informatics section of the Bioengineering laboratory of the DIBRIS (University of Genoa). The main and unifying aspect of the work in this section is the treatment of clinical data in order to achieve data sets characterized by high quality to support medical research. Specifically, the presented examples are about: an infectious disease network [1], a natural language processing based pipeline for microbiology [2] and an electronic health record system for cardiology [3].

In the last decades evidence-based medicine has emerged as an important aspect of clinical practice and scientific research. Electronic health information collected during health care delivery can help address the need for evidence about effectiveness, safety, and quality of medical care. In order to manage the great amount of data from health facilities and to build clinical pathways research systems and public health management policies software systems play a key role. Often distributed networks that combine information from multiple sources are needed in this respect [4].

A. The Liguria Infectious Disease Network (LIDN)

Clinical data collection - both manual and automatic - from diverse data sets by software systems can support patient care, clinical trials, and secondary use of health records [5]. Web based systems have been set up in order to support data exchange in a great number of fields. Data storing and management systems in many medical domains have been set up by multicentric research networks and management systems [6]. In the last few years many health-related networks have been established [7]–[10].

An integrated system of ad hoc interfaces and tools has been set up for clinical data collection, both manually and automatically, to support patient care, research and clinical trials in the Liguria region in Italy. The initial objective was to develop a web-based tool to allow clinicians to collect and manage data of HIV infected patients for patient care and for research. Subsequently, an automatic data transfer system from the hospitals electronic health records (HER)s towards the LIDN and then from the LIDN towards the national health system.

B. A natural language processing pipeline for microorganisms' data

The COVID-19 pandemic has highlighted to a great extent the widespread increasing circulation of pathogenic microorganisms in hospitals and assisted residences. Hospital acquired infections (HAI) are most frequent and serious problems in healthcare. The identification of a pathogenic microorganism causing HAI allows antibiotic treatment and the adoption of infection-control measures. This information is obtained from culture of specimens from infected body sites, and the outcomes are normally reported in laboratory exams. Multidrug resistant (MDR) organisms are a great problem worldwide [11]. Laboratory information systems (LIS)s have managed laboratory analyses for many years, and individual centres set up their own vocabularies. The need to make results from different laboratories comparable brought about the development of coding systems and standards for terminology management. An international vocabulary which can be applied to clinical and laboratory observations is the Logical Observations Identifiers Names and Codes (LOINC), which is the most widely used terminology standard for health observations, measurements, and documents [12]. The common Terminology Service Release 2 (CTS2) standard [13] is focused on terminology management and originates from the Object Management Group (OMG) and Health Level 7 (HL7).

Microbiology is a highly variable discipline and habits of laboratories are quite different. This originated a contrast between the need for great variability of this field and the mandatory use of LISs, which is imposed by national laws, whose structure may be regarded as too stiff. Therefore, to represent and manage microbiology-related information it is often preferred to use clinical notes written as natural text. Such clinical notes have become an important source of information for patient care and research. On the other hand, the need for manual inspection makes their use expensive in terms of personnel effort and time. The limitations of

information collection in LIS and the advantages of concept representation by domain-specific languages can be addressed by artificial intelligence (AI) tools for natural language processing [14].

An NLP pipeline for automatic information extraction from microbiological notes has been set up.

C. An interoperable EHR system for cardiology

Healthcare is currently changing, and its many features require the availability of a wide range of tools to improve aspects of the professional activity of clinicians by contributing to the achievement of optimal diagnose and therapeutic decisions. The EHR is an essential technology for healthcare [4]. Information and communication technology for health e-Health is being increasingly adopted worldwide. In 2013 a resolution on e-Health standardization and interoperability was adopted, and member states of the World Health Assembly were invited to set up strategic plans for the development of e-health services and infrastructures [5]. Traditional patient records were mostly illness focused, but healthcare is increasingly focused on health from wellness to illness and recovery. EHRs are going to increasingly carry health related information, including images and genomic data [15]. Advantages of EHRs are availability of information, entry controls and increase in data quality by validity checks and conditional data entry [16]. Relevant benefits for care quality have been found. Moreover, HER systems affect costs and efficiency of healthcare systems [17]. Their adoption automates data management and supports care related activities, integrating data for different aspects, including treatment effectiveness, adverse condition reporting and research. Adoption of EHRs can improve quality, safety, and efficiency, even though several challenges still need to be overcome. EHRs represent a great data resource for biomedical research and clinical care [18], [19]. Secondary use of EHRs has been carried out in many areas.

The standardization of medical information is receiving increasing attention. To support the development of interoperable and reliable medical systems several medical standards are used, mainly developed by HL7, such as Clinical Document Architecture (CDA) and others. In 2011 HL7 introduced Fast Healthcare Interoperability Resources (FHIR), which extended the previous HL7 specifications to web technologies. FHIR is being increasingly adopted and is regarded as an emerging standard for health data exchange in many domains, including EHRs.

An interoperable EHR system has been developed for the cardiology wards of two hospitals and has been integrated into the hospital information systems (HIS)s to exchange data with the regional health information infrastructure (RHII). The system has been set up according to HL7 specifications.

II. Methods

A. The LIDN

The architectural development of the LIDN is described in [20]. From a technical point of view the approach is similar to the ones described in [21], [22].

According to the General Data Protection Regulation Requirements only minimal sensitive information was collected (such as for example year of birth, gender and nationality). Moreover, the patient hospital code has been collected, in order to track the patient through different hospitals. If this is the case explicit coordination among clinicians is needed, since the LIDN does not contain any personal information that identifies the patient. The platform has been designed to allow the storage of different types of clinical data by specific entities called events. Each event consists of different categories and each category consists of several parameters. The platform's database has been developed on a Microsoft SQL server, which allows for easy addition of new parameters, categories, and event types. The web – user interface has been developed by the Microsoft.NET framework and page visualization uses Microsoft.ascx templates, which allows dynamical loading of the web pages, achieving a fast personalization of the interfaces. The Clinical Data management system is essential to handle the great amount of data in multicentre networks. For the LIDN laboratory data have been considered in the first place because they are the largest dataset which is used for clinical trials. Two possible scenarios have been considered, taking into account the level of the hospitals that were involved:

1 hospital in which data are not stored in digital format or in which data are stored in digital form but external agents cannot obtain access to data.
2 hospital in which data are stored in digital format and external authorized agents can access specific data subsets.

Hospitals belonging to scenario 1 can manually insert data by a web user interface, while hospitals belonging to scenario 2 can exploit a data reuse paradigm. An automatic transfer of clinical data from each hospital has been set up, according to the availability of services for patients' data and according to national regulations. Laboratory data have been organized in standard documents according to the HL7 Clinical Document Architecture (HL7 v3 CDA r2) guidelines.

An additional feature of the LIDN is the univocal interpretation of clinical data. Each code identifying a laboratory result from the local coding system is mapped to the international vocabulary LOINC. A terminology service supports the mapping between coding systems.

B. A NLP pipeline for microorganisms' data

The pipeline consists of 4 main sections: data preparation, pattern recognition, pattern removal and microorganism detection.

The data preparation section prepares the input values, describes the vocabulary database, and loads and pre-processes the clinical notes. The pattern recognition section converts the textual data into numerical representations and builds three models that foresee if a specific pattern is contained in a clinical note. The pattern removal section considers the sentences that have been identified as containing a specific pattern and removes it. The microorganism detection section extracts from the clinical notes meaningful information, such as for example the microorganism name and whether a microorganism belongs to the dangerous microorganism group).

The sample that was considered derived from LIS of the main hospital of Pescara in Abruzzo region in Italy and was

collected from clinical notes extracted from a one-month collection of anonymized laboratory referrals. It contained 499 texts from culture reports.

The pipeline has been developed in Python language using the Pandas library for data analysis and manipulation[1], the Pyodbc open-source model for accessing databases and the Natural Language Toolkit to perform text analysis [23]. The open-source library SpaCy [24], and the Python module Re, which provides operations for work with regular expressions, have been used. Moreover, Scikit-learn, containing several machine learning algorithms have been also included.

C. An interoperable HER system for cardiology

A modular EHRs has been set up to replace the paper-based system in two hospitals in Genova, in Liguria region in Italy.

Specific aspects of the system that have been developed relate to therapy, referrals, and discharge letter.

As relates to therapy, the hospitals' requirements include ensuring the identity of the prescribing doctor the prescribed drug and the identity of the administering nurse. Moreover, the occurred administration has to be confirmed with a high certainty level.

As relates to referrals, the hospitals' requirements included the availability on a platform of results and diagnostics from other platforms.

As relates to the discharge letter the hospitals required that the main data stored during hospitalization are easily transferred to the discharge letter. The letter must comply with the standards by the Italian government.

The architecture of the EHRS is based is based on central federated databases (one per hospital) and on an interactive web-based platform. The databases have been developed using Microsoft SQL server as Management system, implemented with Visual Studio through NET framework, and deployed on the internet information system. A corporate regional/national health information infrastructure (HII) provides timely health information and facilitates communication mostly among healthcare professionals and public health professionals. To warrant interoperability the HII uses standards and integrates systems, applications and technologies for personalised health. Italian regions have developed their own HIIs, but they adopted architectures based on an institutional centred approach. Since the health records are not centrally stored, at least one central index is needed, by which the information on a particular patient can be extracted. When a patient data is requested, the index is used to query the repository where the stored information is located, and the complete patient record data is produced.

An architecture has been developed to integrate a routinely used cardiology EHRS into the RHII system of Liguria region. All documents of the RHII are given as HL7 CDA and messages are sent as HL7 v2 and / or HL7 FHIR. All external interfaces of the CEHRS have been designed according to a service-oriented approach on the Healthcare Services Specification project that uses CDA, v2 and FHIR [25]. In order to obtain a fully interoperable system as defined by the Clinical Data Interchange Standards Consortium the CEHRS can be interfaced with a terminology service [20].

[1] https://pandas.pydata.org/

III. Results

A. The LIDN

At present the LIDN involves the infectious diseases departments of six hospitals and is open to extra regional collaborations on specific projects. Currently data coming from two hospitals in Piemonte region are also present. In the LIDN three hospitals belong to scenario 2, the others belong to scenario 1. These three hospitals have different types of information systems, so three solutions have been developed to enable the sharing of clinical data. Currently, more than 8000 patients have been or are under treatment for at least one infectious disease among human immunodeficiency virus (HIV), hepatitis C virus, severe acute respiratory syndrome coronavirus 2 and tuberculosis. Automatic data transfer has had a great impact on the presence of laboratory tests in the three hospitals belonging to scenario 2. The differences between automatic and manual scoring have been quantitatively evaluated considering the cumulative number of laboratory tests per year and the mean number of parameters collected per single laboratory.

B. A NLP pipeline for microorganisms' data.

The main results relate to the identification and removal of a specific pattern, to the Genus extraction and to the microorganism detection. As relates to the identification and removal of a specific pattern. The best results that have been obtained are in terms of mean accuracy across classifiers (99.06 %). The SVM classifier with a Gaussian kernel obtained a mean accuracy of 98,99 %, the LR classifier obtained a mean accuracy of 98,99 %, and the RF classifier obtained a mean accuracy of 99,19 %. Therefore, the pattern was completely identified using all classifiers, and can be securely removed from the clinical notes.

As relates to genus extension the sample of clinical notes contained a total number of 107 abbreviated genera followed by their species. Processing of the notes has shown that all 107 genera were extended. This completely matched with the expert indications.

As relates to microorganism detection, the sample of clinical notes was composed of 499 texts and 276 of them presented the name of a microorganism. Two tests were carried out. First the entire sample was introduced into the module for microorganism extraction, then only the notes that contained the names of the microorganisms have been introduced. The system correctly identified all microorganism names in both cases.

C. An interoperable EHR system for cardiology

The CEHRS has been adopted in two hospitals in Genova: Villa Scassi (VS) since 2018 and Padre Antero Micone (PAM)since May 2021.

The specific needs of the cardiology staff as relates to storage stability and responsibility attribution have been taken into account, while retaining the confidence of the staff in the paper system, which has been used for many years. The system that has been set up satisfies these needs using the database systems and the authentication systems of both hospitals. The

design features of the EHR guarantee both storage stability and v responsibility attribution. For any stored information the staff member who stored or modified or cancelled it can be known. These features have been obtained by an architecture that is commonly adopted in many hospitals. An additional need has been interoperability with other hospitals and local medical informatics applications – a feature which is present only to a small extent in commercial EHRSs.

The development of the CEHRS has started at the beginning of 2018 with a very close. interaction between software developers and physicians. In December 2018 the CEHRS has been adopted on an experimental basis but has immediately become the only software support of the cardiology ward. In October 2020 the experimental phase has been completed, the CEHRS has been adopted has become the only official health record of the cardiology ward. In May 2021 the CEHRS has also been adopted in the cardiology ward of PAM.

IV. Conclusion

A. The LIDN

This work has involved professionals form various fields for more than 10 years, with the main aim to support patient care, clinical trials and research on infectious diseases. A modular system has been developed to respond to specific needs for infectious diseases, such as for example the COVID-19 pandemics.

B. A NLP pipeline for microorganisms' data

The main result of this work is the development of an NLP pipeline to support the automatic extraction of microorganisms' names and relevant information which is contained in microbiological notes of culture reports. A future step will be the automatic extraction of the antibiogram data from the clinical notes. In this respect, key information is the sensitivity of each microorganism to each antibiotic.

C. An interoperable EHR system for cardiology

In the future the high analytical capacity of the CEHRS will enable the secondary use of EHRs for clinical trials, for clinical studies and for the development of clinical decision support systems. The ability to use all EHR parts based on natural language (anamnesis, clinical diary and hospital discharge letter) for research is an important aspect. In this respect, the interoperability features of the EHR can interface effectively with terminology management systems and with natural language processing systems.

References

[1] S. Mora *et al.*, "Ten Years of Medical Informatics and Standards Support for Clinical Research in an Infectious Diseases Network," *Appl. Clin. Inform.*, vol. 14, no. 01, pp. 16–27, 2023.

[2] S. Mora *et al.*, "A NLP Pipeline for the Automatic Extraction of a Complete Microorganism's Picture from Microbiological Notes," *J. Pers. Med.*, vol. 12, no. 9, p. 1424, 2022.

[3] E. Lazarova *et al.*, "An Interoperable Electronic Health Record System for Clinical Cardiology," in *Informatics*, 2022, vol. 9, no. 2, p. 47.

[4] M. Tsiknakis, D. G. Katehakis, and S. C. Orphanoudakis, "An open, component-based information infrastructure for integrated health information networks," *Int. J. Med. Inform.*, vol. 68, no. 1–3, pp. 3–26, 2002.

[5] W. H. Organization, "Global Strategy on Digital Health 2020–2025," Geneva, Switzerland, 2021.

[6] K. El Emam, E. Jonker, M. Sampson, K. Krleža-Jerić, and A. Neisa, "The use of electronic data capture tools in clinical trials: Web-survey of 259 Canadian trials," *J. Med. Internet Res.*, vol. 11, no. 1, p. e8, 2009.

[7] J. Demotes-Mainard and C. Kubiak, "A European perspective–the European clinical research infrastructures network," *Ann. Oncol.*, vol. 22, no. Suppl 7, pp. vii44–vii49, 2011.

[8] A. Dagliati *et al.*, "A data gathering framework to collect type 2 diabetes patients data," in *IEEE-EMBS International Conference on Biomedical and Health Informatics (BHI)*, 2014, pp. 244–247.

[9] L. C. Crosswell and J. M. Thornton, "ELIXIR: a distributed infrastructure for European biological data," *Trends Biotechnol.*, 2012, doi: 10.1016/j.tibtech.2012.02.002.

[10] M. Gencturk *et al.*, "End User Evaluation of the FAIR4Health Data Curation Tool," *Public Heal. Informatics Proc. MIE 2021*, pp. 8–12, Jul. 2021, doi: 10.3233/SHTI210110.

[11] Available: "https://www.epicentro.iss.it/." .

[12] J. Y. Adamu, A. I. Raufu, F. C. Chimaroke, and J. A. Ameh, "Antimicrobial susceptibility testing of Staphylococcus aureus isolated from apparently healthy humans and animals in Maiduguri, Nigeria," *Int. J. Biomed. Heal. Sci.*, vol. 6, no. 4, 2021.

[13] R. Gazzarata *et al.*, "A Terminology Service Compliant to CTS2 to Manage Semanticswithin the Regional HIE," *Eur. J. Biomed. Informatics*, vol. 13, no. 1, pp. 43–50, Oct. 2017, doi: 10.24105/EJBI.2017.13.1.7.

[14] M. E. Matheny *et al.*, "Detection of Blood Culture Bacterial Contamination using Natural Language Processing," *AMIA Annu. Symp. Proc.*, vol. 2009, p. 411, 2009, Accessed: Sep. 21, 2021. [Online]. Available: /pmc/articles/PMC2815455/.

[15] P. C. McMullen *et al.*, "Electronic medical records and electronic health records: overview for nurse practitioners," *J. Nurse Pract.*, vol. 10, no. 9, pp. 660–665, 2014.

[16] A. Uslu and J. Stausberg, "Value of the electronic medical record for hospital care: update from the literature," *J. Med. Internet Res.*, vol. 23, no. 12, p. e26323, 2021.

[17] G. B. Melton, C. J. McDonald, P. C. Tang, and G. Hripcsak, "Electronic Health Records BT - Biomedical Informatics: Computer Applications in Health Care and Biomedicine," E. H. Shortliffe and J. J. Cimino, Eds. Cham: Springer International Publishing, 2021, pp. 467–509.

[18] H. Atasoy, B. N. Greenwood, and J. S. McCullough, "The digitization of patient care: a review of the effects of electronic health records on health care quality and utilization," *Annu. Rev. Public Health*, vol. 40, pp. 487–500, 2019.

[19] P. B. Jensen, L. J. Jensen, and S. Brunak, "Mining electronic health records: towards better research applications and clinical care," *Nat. Rev. Genet.*, vol. 13, no. 6, pp. 395–405, 2012.

[20] R. Gazzarata, B. Giannini, and M. Giacomini, "A SOA-based platform to support clinical data sharing," *J. Healthc. Eng.*, no. In press, 2017.

[21] R. Gazzarata, F. Vergari, T. S. Cinotti, and M. Giacomini, "A standardized SOA for clinical data interchange in a cardiac telemonitoring environment," *IEEE J. Biomed. Heal. Informatics*, vol. 18, no. 6, pp. 1764–1774, Nov. 2014, doi: 10.1109/JBHI.2014.2334372.

[22] M. Bonetto *et al.*, "I-Maculaweb: A Tool to Support Data Reuse in Ophthalmology," *IEEE J. Transl. Eng. Heal. Med.*, vol. 4, pp. 1–10, 2016.

[23] E. Loper and S. Bird, "NLTK: The Natural Language Toolkit," May 2002, Accessed: Sep. 21, 2021. [Online]. Available: https://arxiv.org/abs/cs/0205028v1.

[24] M. Honnibal and I. Montani, "spaCy 2: Natural language understanding with Bloom embeddings, convolutional neural networks and incremental parsing," *To Appear*, vol. 7, no. 1, pp. 411–420, 2017.

[25] N. G. Weiskopf, G. Hripcsak, S. Swaminathan, and C. Weng, "Defining and measuring completeness of electronic health records for secondary use," *J. Biomed. Inform.*, vol. 46, no. 5, pp. 830–836, 2013.

Commercial Smart Virtual Assistants to support medication adherence in chronic patients: a preliminary usability study

E. Tauro[1,2], G. Galuzzi[1], M. Mazziotti[1], F. Cancelliere[1], G. Bilo[2], E.G. Caiani[1,2]
[1] *Dipartimento di Elettronica, Informazione e Bioingegneria, Politecnico di Milano, Milan, Italy*
[2]*Istituto Auxologico Italiano, IRCCS, Milan, Italy*

***Abstract*— Low medication adherence is identified as one of the main issues for increased morbidity and mortality in chronic patients. Smart Virtual Assistants (SVA) devices are becoming increasingly common in households, enabling the possibility of using vocal commands to interact with active solutions to non-adherence. Thus, the aim of this study was to evaluate the usability of commercially available SVA devices to support medication adherence in chronic patients. A skill was developed for the most common commercially available SVA environment (Amazon Alexa), together with a cloud database and a connected online dashboard. Each enrolled participant answered the eHealth Literacy Scale (IT-eHEALS) questionnaire and to a question on perceived adherence, then the prescribed medications were inserted into the online dashboard and linked to their SVA device account at home, thus automatically setting reminders at the proper time and 25 minutes later. A 30-minute interval after each reminder was allowed to vocally confirm to the SVA the medicine intake. After seven days, participants participated in a semi-structured interview including the System Usability Scale (SUS) questionnaire. Eleven subjects (7M, 4F, median age 52 (IQR = 13.5) years old) participated in the study. IT-eHEALS scores ranged from 20 to 40. Overall, low adherence to therapy was identified before the experiment. Post-experiment SUS questionnaire resulted in median score of 77.5 (IQR = 11.25).**

Participants were very satisfied with the usability of the developed skill. The high SUS score demonstrates how SVA devices could be perceived as effective, interactive and easy-to-use tools to support medication adherence. Further studies are required to improve the developed skill and quantify its ability to effectively increase adherence in chronic patients.

***Keywords*—Medication adherence, Smart Virtual Assistants, eHealth, mHealth, Telemedicine.**

I. Introduction

The World Health Organization (WHO) has identified low medication adherence as a global concern that poses a significant challenge to the healthcare system. This issue results in increased morbidity and mortality among patients suffering from chronic illnesses [1]. Studies have demonstrated that medication adherence in chronic patients in developed countries averages around 50% after one year of treatment. Furthermore, low medication adherence is a leading factor to hospital admissions and elevated healthcare costs [2], and requires techniques and solutions tailored towards patients to be overcome [3]. Forgetfulness and polypharmacy, defined as the administration of multiple drugs at the same time, are associated with lower quality of life and are some of the main factors in low adherence in chronic patients [4].

Smart Voice Assistants (SVA) are artificial intelligence (AI) systems that allow users to interact with them using voice commands. Examples of such devices include Amazon Alexa and Google Assistant, which can perform a variety of tasks, including setting reminders, playing music, answering questions, and controlling smart home devices. Their popularity has been increasing in recent years, with 30 million units sold in the United States alone by the end of 2020 and a market that continues to grow rapidly [5]. In the healthcare context, SVA devices have the potential to support medication adherence by providing reminders, tracking medication intake, and offering personalized feedback and support. Recent studies have also demonstrated that these devices can effectively streamline data collection across various contexts and could be used to diagnose and monitor chronic conditions, greatly reducing time and cost requirements [6].

Thus, the aim of this preliminary work was to evaluate the usability of the most common SVA device commercially available on the market (Amazon Alexa) to support medication adherence in chronic patients.

II. Materials and Methods

A. Platform structure

The developed platform was based on a three-tier architecture (data – application – presentation) [7], used to identify and separate the various components, as well as to follow the single responsibility principle [8]. Figure 1 presents the elements and frameworks used to create the platform.

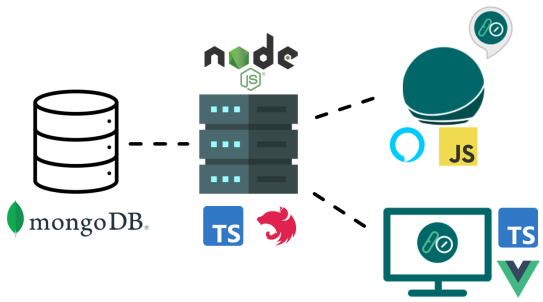


Fig. 1: Three tier architecture of the developed platform. On the left the data tier, in the center the application tier and on the right the two modules concerning the presentation tier. Logos around each element represent languages and frameworks used for their development.

In the data tier, a cloud server was established using a NoSQL database management system. This approach was chosen due to the inherent capabilities of non-relational databases., that do not necessitate strict constraints and schemas, thus enabling greater flexibility in data structure, augmented scalability of the developed system, and improved efficiency in executing queries. [9]

The application tier was developed using the NodeJS and NEST frameworks. It was composed of a series of modular, independent components, including providers and controllers, that receive input from the presentation tier applications, perform logical operations, and facilitate communications with the underlying data tier.

Regarding the presentation tier (i.e., all applications that allow users to interact with the system), two modules were developed: an online dashboard and a skill for the Amazon Alexa environment.

The online dashboard was developed using the VUE framework, defining a single-page interactive application for patients. It allowed users to log in using private credentials and enter their own prescriptions. Prescriptions were formulated by the medication's name, the corresponding dosage, the designated time of intake, and any relevant instructions (i.e,, before, during, after meals). The system allowed programming for all types of therapies: daily, weekly, only on specific days or for a set number of intakes. Users could also access their own data and adherence statistics, both global or associated with only one medication. Through the online dashboard, data was sent to the cloud database via secure HTTPS communication.

The skill was developed for the Amazon Alexa environment, with the aim of providing an interface for patients to assist them in managing their treatment plan. The online dashboard generated a temporary One Time Password (OTP) to securely connect a user's Alexa device with their cloud-stored data. Reminders on the device were configured according to the prescriptions entered into the online dashboard.

The skill included a vocal reminder feature which prompted the user to confirm medication intake when activated. The reminder was designed to verbally state the medication name, dosage, and any associated instructions regarding meals. It also provided a 30-minute window around the scheduled medication intake time: if the medication was taken before the designated time, but not earlier than 30 minutes prior, the corresponding reminder was not sent to the user. Additionally, a second reminder was issued 25 minutes after the first one, in case of no confirmation. These timeframes were decided with the aid of domain experts. Once the medication intake was vocally confirmed, the information was transmitted to the cloud database, along with the time of intake. If no confirmation was received within 30 minutes of the initial reminder, the intake was recorded as missed and could not be modified.

Users could communicate with the skill through set phrases, and their response, or lack thereof, was stored in the database and used to update adherence statistics, accessible either through the online dashboard or the Alexa device.

B. *Study protocol*

The initial usability of the developed skill was tested through a protocol approved by the ethical committee of Politecnico di Milano (45/2021). Participants were enrolled on a voluntary basis, with the requirements of having a stable WiFi connection at home, being previously diagnosed with a chronic disease and taking at least one medication per day. They were asked to install the skill on their own devices, or were provided with a device if they did not have one. Additionally, before the experiment, they were then asked to input their therapies in the online dashboard, complete the Italian version of the eHealth Literacy Scale (IT-eHEALS) [10, 11] questionnaire, which measures health and digital literacy, and answer a question related to their perceived adherence (low, medium or high). Personal data of participants was pseudonymised and kept in a separate server from the cloud database. Volunteers were guided step-by-step through the configuration of the skill and were given instructions on how to operate with it.

During the 7-days test, participants were able to explore all the functionalities of the skill and monitor their own adherence. At the end of the 7-days, they were asked to complete the Italian version of the System Usability Scale (SUS) [12, 13] questionnaire and participate to a semi-structured interview developed ad-hoc for this study to assess the perceived usability, performance, strong and weak points of the skill. The study population consisted of 11 volunteers, 7 (64%) men and 4 (36%) women, with a median age of 52 (IQR = 13.5) years old, that met all predetermined inclusion criteria and gave informed consent for the use of their data.

III. RESULTS

A. *IT-eHEALS and adherence*

Table 1 presents the results concerning all the participants involved in the study of the IT-eHEALS questionnaire, perceived adherence and the percentage of adherence registered by the system computed over all therapies, for the 7-days experiment. As regards the IT-eHEALTS, five participants reached the maximum level or one point below, two scored in the 30-32 range, and four scored in the 20-23 range. Perceived adherence was low for eight subjects (73%), medium in two, and high in one.

TABLE I: AGE, IT-EHEALS, PERCEIVED ADHERENCE BEFORE THE EXPERIMENT AND PERCENTAGE OF ADHERENCE DURING THE EXPERIMENT REGARDING THE 11 PARTICIPANTS IN THE STUDY.

Participant	*Age*	*IT-eHEALS (min: 8; max: 40)*	*Perceived adherence (low, medium, high)*	*Adherence during the experiment (%)*
A	47	40	Low	85.71 %
B	66	20	Medium	100%
C	61	22	Low	100%
D	43	21	Low	85.71%
E	75	40	Low	75%
F	31	40	Low	57.14%
G	46	39	Low	90.65%
H	52	39	High	100%
I	56	31	Medium	75%
J	56	32	Low	71.42%
K	44	23	Low	70.83%

During the experiment, adherence was calculated separately for each therapy and defined as the % of confirmed intakes over the total number of prescribed doses over the 7-day period. If the participant had more than one therapy, the final score was obtained by averaging the adherence % of all

TABLE 2: SYSTEM USABILITY SCALE SCORES REGARDING THE 11 PARTICIPANTS IN THE STUDY. EACH ROW REPRESENTS A QUESTION IN THE QUESTIONNAIRE, WHILE EACH COLUMN REPRESENTS A PARTICIPANT AND THE FINAL ROW IS THE SUS TOTAL SCORE FOR EACH PARTICIPANT. ALL QUESTIONS RANGE FROM 1 (STRONGLY DISAGREE) TO 5 (STRONGLY AGREE), WHILE THE TOTAL SCORE RANGES FROM 0 TO 100.

Participant	*A*	*B*	*C*	*D*	*E*	*F*	*G*	*H*	*I*	*J*	*K*	*Question median value*
1. I think that I would like to use this system frequently	5	4	4	5	2	5	5	4	4	4	4	4
2. I found the system unnecessarily complex	2	1	1	1	1	1	4	4	2	1	1	1
3. I thought the system was easy to use	4	4	5	5	3	4	2	3	4	4	5	4
4. I think that I would need the support of a technical person to be able to use the system	1	3	2	1	1	1	1	2	1	4	1	1
5. I found the various functions in the system were well integrated	4	3	5	5	3	4	4	3	3	3	3	3
6. I thought there was too much inconsistency in the system.	2	1	1	1	2	1	2	1	4	1	1	1
7. I would imagine that most people would learn to use this system very quickly	5	4	5	4	4	4	3	3	5	5	4	4
8. I found the system very cumbersome to use	3	1	2	1	2	1	1	2	2	1	1	1
9. I felt very confident using the system	4	3	5	5	5	5	5	4	4	4	3	4
10. I needed to learn a lot of things before I could get going with this system	2	1	1	1	1	1	1	2	2	3	3	1
SUS Total Score	80	77.5	92.5	97.5	75	92.5	75	65	72.5	75	80	

therapies. The resulting median adherence among the eleven participants was 80.35% (IQR = 21.72%), which indicates an improvement compared to the perceived adherence initially reported in the questionnaire.

B. System Usability Scale

The results of the SUS questionnaire are presented in Table 2. The median score was 77.5 (IQR = 11.25). Only 1/11 participants reported a value below 68, defined in literature as the threshold defining the positive usability of a system [14]. Scores for SUS questions range from 1 (strongly disagree) to 5 (strongly agree), with questions formulated alternatively with a positive and negative connotation to reduce bias in responses [12]. For questions 1, 3, 7, and 9 (i.e., positively formulated), the median value of the answers was 4, one point below the maximum value attainable. Only for the positively formulated question 5, to assess whether the user found the various functions in the system well-integrated, the median value across all participants was 3. For questions 2, 4, 6, 8, and 10 (i.e, negatively formulated), the median value aligned with the minimum score, representing the ideal answer for such questions. The final score was calculated using the formulae defined in current literature [12].

The results of the semi-structured interview can be divided into four macro-groups, according to the questions' theme: setup configuration, skill usage, Alexa device and perceived adherence.

Concerning setup configuration, 9/11 participants reported that the initial configuration was easy to perform. The setup included verbally inputting the OTP and completing the step-by-step vocal confirmations required by the Alexa device to configure the therapies.

Regarding skill usage, only 2/11 participants reported partial dissatisfaction with the skill, while all other participants reported partial or complete satisfaction. Seven participants felt the proposed system as not intrusive into their personal lives. One participant suggested that there was no need to repeat the dosage with every notification, while two found the notifications to be too repetitive. Positive aspects of the system included the automated reminder setting, the ability to communicate via voice, and the ability to use the skill from the Alexa application on smartphones, when out of home. The repetition of the notification 25 minutes after the first one was positively received by 8/11 participants, while two found it not required and one found it intrusive. Four participants felt that the 30-minute range around the set time for the intake was too short. Finally, 8/11 participants reported some initial difficulties in communicating with the skill due to the complexity of the sentences that needed to be used.

Regarding the usage of the Alexa device in general, both participants who were already using the device and those who did not use it previously reported interest in using it as a support for adherence, with10/11 participants stating that they would also be interested in using it for other purposes. With respect to perceived adherence, 7/11 participants reported perceiving increased medication adherence thanks to the skill, while 4/11 reported no perceived improvement.

IV. DISCUSSION

In this study an initial usability test was performed to assess the feasibility of using SVA devices, such as Amazon Alexa, to support medication adherence in chronic patients.

The developed skill is designed to align with and to incorporate certain strategies from the persuasive system design model [15]: specifically, the emphasis was placed on ensuring unobtrusiveness in daily activities and transparency of intent. Additionally, other strategies such as complexity reduction, implemented through fast and secure configuration, tunnelling, customization and self-monitoring, were incorporated into the development of the skill [16].

The population studied, ranging from 32 to 75 years old with a prevalence in the 40-60 years old range, is a good representation of what would be the target users of the skill, where the prevalence of chronic illnesses increases with age [17].

The results of the IT-eHEALS questionnaire indicate that most participants considered themselves capable of using

digital technology for their healthcare needs, while others reported some difficulties in usage of such technology for health or lack of trust in the information received through such means. No correlation (Spearman's correlation) was found between the initial results of IT-eHEALS and the results of the SUS questionnaire (s = -0.232, p = 0.4913) [18].

The obtained scores in the SUS questionnaire indicate that the skill was considered usable, unobtrusive, and not interfering with everyday life. Based on the median responses to each question, participants expressed interest in frequently using the skill, found it easy to use and not complex, and did not feel that technical assistance was necessary for its use. They also considered the skill consistent and easy to learn. However, the worst score (3 out of 5) was obtained for question 5, suggesting that improvements are needed in the implementation of certain features of the skill. Similar concerns were also raised in the semi-structured interview, where participants expressed doubts about specific features and functionalities that should be modified or improved: in particular, participants reported that the adherence information obtained through the skill was not particularly useful or engaging. However, it is worth noting that the limited duration of the 7-day usability test may have contributed to this perception.

Nevertheless, medication adherence estimated through the system showed improvements over the initial perceived adherence by the participants. In fact, the median adherence over the eleven participants (80.35%) is larger when compared to the average adherence in chronic patients in developed countries reported by WHO (50%) [2], confirming the constant participation throughout the test period for most participants and a potential positive effect in increasing adherence throughout the use of such SVA technology. The concordance between the estimated adherence and the SUS scores confirmed further the usability of the skill to support medication adherence.

The trial period of 7 days was too short to draw definitive conclusions about the skill's ability to increase medication adherence, even though preliminary results suggest a positive trend. The main concerns raised by participants in the semi-structured interview were related to the activation phrases required by Amazon Alexa, which were perceived as being too complex in Italian. This limitation can only be partially addressed as it conflicts with Amazon Alexa's guidelines for skill design, suggesting that other voice assistant devices should also be explored. Furthermore, the 30-minute window around the set time to confirm medication intake was considered too narrow by the participants. In future developments, it is suggested that this window could be tailored for each medication in consultation with the healthcare practitioner. However, it is important to note that in this test no doctor was involved and the configuration was standardized for all subjects, while in the final version the central role of the physicians in the configuration phase is expected.

V. CONCLUSIONS

The aim of this study is to assess the usability of a skill developed for the Amazon Alexa SVA to support medication adherence in chronic patients. Very high SUS results and patient satisfaction showed that the developed skill can be used to such objective, without requiring particularly high eHealth literacy or technical knowledge. Further studies are required to assess the effects of the skill in increasing medication adherence, to improve features deemed not interesting and to further simplify its usage.

ACKNOWLEDGMENTS

We acknowledge support to this study by the Ministry of Health (Bando Ricerca finalizzata 2022, project "Intake Care").

REFERENCES

[1] Bosworth, Hayden B et al. "Medication adherence: a call for action." *American heart journal* vol. 162,3 (2011): 412-24. doi:10.1016/j.ahj.2011.06.007

[2] Lam, Wai Yin, and Paula Fresco. "Medication Adherence Measures: An Overview." *BioMed research international* vol. 2015 (2015): 217047. doi:10.1155/2015/217047

[3] Jimmy, Beena, and Jimmy Jose. "Patient medication adherence: measures in daily practice." *Oman medical journal* vol. 26,3 (2011): 155-9. doi:10.5001/omj.2011.38

[4] Souliotis, Kyriakos et al. "Assessing forgetfulness and polypharmacy and their impact on health-related quality of life among patients with hypertension and dyslipidemia in Greece during the COVID-19 pandemic." *Quality of life research : an international journal of quality of life aspects of treatment, care and rehabilitation* vol. 31,1 (2022): 193-204. doi:10.1007/s11136-021-02917-y

[5] Fortune Business Insight, "The global smart speaker market is projected to grow from $9.04 billion in 2021 to $34.24 billion in 2028 at a CAGR of 21.0% in forecast period, 2021-2028", Market Research Report (2022).

[6] Gouda, Pishoy et al. "Feasibility of Incorporating Voice Technology and Virtual Assistants in Cardiovascular Care and Clinical Trials." *Current cardiovascular risk reports vol. 15*,8 (2021): 13. doi:10.1007/s12170-021-00673-9

[7] Buschmann, Frank. "Pattern-Oriented Software Architecture, Volume 1, a System of Patterns". John Wiley & Sons, 1996.

[8] Fowler, Martin. "Patterns of Enterprise Application Architecture". Addison-Wesley, 2015.

[9] Gyorodi, Cornelia, et al. "A Comparative Study: Mongodb vs. Mysql." *2015 13th International Conference on Engineering of Modern Electric Systems (EMES)*, 2015, https://doi.org/10.1109/emes.2015.7158433.

[10] Norman, Cameron D, and Harvey A Skinner. "eHEALS: The eHealth Literacy Scale." *Journal of medical Internet research* vol. 8,4 e27. 14 Nov. 2006, doi:10.2196/jmir.8.4.e27

[11] Bravo, Giovanni, et al. "Validazione della versione italiana del questionario di alfabetizzazione sanitaria digitale (IT-eHEALS)" *Istituto Superiore di Sanità* (2018).

[12] Brooke, John. "SUS: A quick and dirty usability scale". CRC Press, 1996.

[13] Borsci, Simone et al. "On the dimensionality of the System Usability Scale: a test of alternative measurement models." *Cognitive processing* vol. 10,3 (2009): 193-7. doi:10.1007/s10339-009-0268-9

[14] Sauro, Jeff, and Lewis, James R. "When designing usability questionnaires, does it hurt to be positive?" *Proceedings of the SIGCHI Conference on human factors in computing systems* (2011): 2215-2224. doi: 10.1145/1978942.1979266

[15] Win, Khin Than et al. "Persuasive system features in computer-mediated lifestyle modification interventions for physical activity." *Informatics for health & social care* vol. 44,4 (2019): 376-404. doi:10.1080/17538157.2018.1511565

[16] Oinas-Kukkonen, Harri, and Harjumaa, Marja. "Persuasive Systems Design: Key Issues, Process Model, and System Features" *Communications of the Association for Information Systems*, vol. 24, (2009) pp. 28-500. doi:10.17705/1CAIS.02428

[17] Atella, Vincenzo et al. "Trends in age-related disease burden and healthcare utilization." Aging cell vol. 18,1 (2019): e12861. doi:10.1111/acel.12861

[18] Sedgwick, Philip M. "Spearman's rank correlation coefficient", *BMJ (Online)*, vol. 349: pp. g7327 (2015).

Prediction of Atrial Fibrillation using Deep Learning techniques

F. Goretti[1†], A. V. Marzullo[2†], M. Milli[3], and E. Iadanza[4]
[1] *European Laboratory for Nonlinear Spectroscopy/Unifi, Via Nello Carrara 1, 50019 Sesto Fiorentino, Italy*
[2] *School of Information Engineering, University of Florence, via di Santa Marta, 3, Florence, 50139, Italy*
[3] *USL Toscana Centro, Department of Cardiology, Ospedale S. Maria Nuova, 50122 Firenze, Italy*
[4] *Department of Medical Biotechnologies, University of Siena, Via Aldo Moro, 2, 53100 Siena Tuscany, Italy*
[†] These authors contributed equally to the realization of this paper.

***Abstract*—Atrial fibrillation (AF) is one of the most prevalent arrhythmias encountered in cardiological practice; it is a leading cause of stroke and heart failure and has a growing financial impact on the healthcare system. The aim of this study is to test the efficacy of deep learning in predicting AF. Early diagnosis can improve patients quality of life, reduce hospitalizations and minimize the financial impact on the health care system. Two methods for automatically predicting AF based on Convolutional Neural Networks (CNN) are proposed. The first model is characterized by a one-dimensional (1D) CNN network that takes, directly, electrocardiogram (ECG) signals as input, while the second model consists of a two dimensional (2D) CNN network that inputs image data corresponding to the numerical values of the most important events associated with each ECG waveform. The 1D-CNN model achieved an accuracy of 71.69%, while the 2D-CNN model reached 76.19%. The second method, in addition of being a novel approach to classification problem, reached a good score in predicting the outcome of atrial fibrillation.**

***Keywords*—Prediction, Atrial Fibrillation, Deep Learning, Decision Support System.**

I. INTRODUCTION

An arrhythmia is an alteration of the regularity of heartbeat. one of the most common types of arrhythmia is AF, it is characterized by the lack of atrial synchronization that make atrial contraction ineffective[1]. The incidence increases exponentially with age and the effects increase the risk of developing other cardiac problems[1], [2], [3]. This condition is caused by an abnormal sinus rhythm which results in an irregular heartbeat. The presence of AF can produce, often, several important adverse health outcomes including stroke and heart failure[4], [5]. The economic and clinical burden of AF is mainly due to repeated hospitalizations and healthcare service utilization. Therefore, the prediction of AF is significant clinically and economically[6], [7]. As reported by *'Velleca et al.'* [8], in Italy, France, Germany and England alone, more than 11 million patients are affected by this disease, with an average annual cost between 660 and 3,286 million euros.

The visual representation of the heart activity is fundamental to highlight eventual abnormalities in the cardiac rhythm and stimulus propagation. The diagnosis is usually carried out by mean of a long-term ECG that is collected using cardiac monitoring devices, such as the Holter monitor[1]. An ECG waveform characterized by the absence of a clear P wave and an abnormal pattern of the R-R interval shows the presence of AF (Fig.1). Traditionally, abnormalities in an ECG waveform are identified through visual inspection by expert cardiologists. This process is effective only if executed by trained personnel[1] and can be time consuming. The aim of this study is to realize an automated method that provide a prediction of AF, in order to reduce the time required for the diagnosis and the dependence from expert personnel. To achieve this objective, deep learning models based on CNNs were developed. CNNs are widely used both in the analysis of ECG signals[9], [10], for the detection[11], [12], [13] and prediction[14], [15] of AF. In this work, two CNN models were developed. The first model is a 1D-CNN that takes ECG signals as input. In the second model, the numerical values of the most relevant features of the ECG signal were transformed and used as input to a 2D-CNN[16]. In both cases the output is a binary output, where one value represent the risk of developing AF, while the other suggest the absence of such a risk.

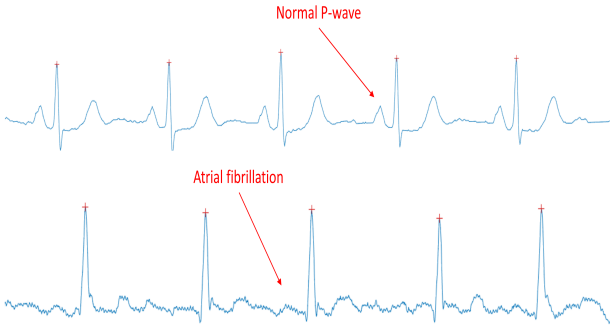


Fig. 1: Normal ECG vs AF ECG

II. METHODS

For the realization of the models, we developed, starting from a database of holter recordings, two pipelines for the pre-processing of data, the realization of CNNs structure and, finally, for the test phase. The overall process was carried out using Python as programming language.

A. Creation of database

The creation of the dataset was made possible thanks to an established collaboration with "USL Toscana centro", in particular with the department of cardiology at the Santa Maria Nuova Hospital (Florence). The clinicians of the structure provided us with the requested, anonymized, database. Summarily, 608 patients who underwent a Holter examination were analyzed. Of these initial number, eligible patients were selected based on:

- Development of at least one episode of AF within three years of the Holter examination.
- Absence of AF within three years of the Holter examination.

Ineligible subjects were those who:

- Had AF during the Holter examination.
- Did not have enough follow-up.
- Had developed AF following surgery.

After the application of the selection criteria, a new database of 134 subjects was created, consisting of 52 patients who developed AF in the three years following the Holter examination, and 82 subjects who did not develop AF in the three years following the analysis. Ethical review and approval were waived for this study due to the fact that there was no deviation from the patient's "normal care" who had provided consent for the management of personal data.

B. 1D-CNN model

The first model proposed for the prediction of AF consists of a 1D-CNN that takes directly the ECG signals as input. The labels associated with each subject were binary, where a 1 represent the future development of AF and 0 the opposite. This model architecture is shown in Table I. Next, The model was trained using K-fold cross validation, with the training parameters shown in Table II.

TABLE I: Structure of the 1D-CNN model.

Layers	Parameters	Activation
Conv1D	Filters 32 / Kernel 5	ReLu
MaxPooling	2	
Conv1D	Filters 64 / Kernel 5	ReLu
MaxPooling	2	
Conv1D	Filters 64 / Kernel 5	ReLu
MaxPooling	2	
Conv1D	Filters 128 / Kernel 5	ReLu
MaxPooling	2	
Dropout	0.5	
Flatten		
Dense	128	ReLu
Dropout	0.5	
Dense	32	ReLu
Dense	2	SoftMax

The flowchart followed for the data processing and the testing phase of the 1D-CNN model is reported in Fig.2.
For each patient, three-lead Holter ECG signals with a sampling rate of 200Hz and a duration of three minutes were selected. The selection was done manually paying attention to select good quality signal that belongs to the same time span.

TABLE II: Training parameters of the 1D-CNN.

Training parameters	Values
Number of K-fold	10
Epochs	200
Early stopping	30
Optimizer	Adam
Learning rate	0.001
Loss function	Categorical crossentropy

The selected ECG signals were divided into five seconds windows, allowing to increase the dimension of the dataset which, after this process, was composed of 4,068 records.

Of the whole dataset, 85% was used as the training set while the remaining 15% was used for the test set. During the splitting process care has been taken in keeping data from the same patient in the same division to avoid a bias in the model. Among the iterations of k-fold validation we selected the best model that has been, then, evaluated on the test set.

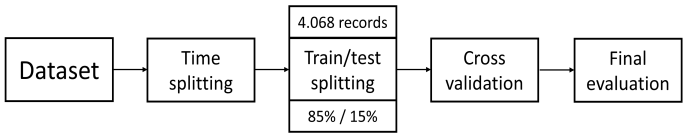


Fig. 2: Flow chart of data processing and testing of the 1D-CNN model.

C. 2D-CNN model

For the creation of the second model, we took inspiration from the work done in[16] in which the authors describe a method that allows numerical features to be transformed into images, for the purpose of serving as inputs for 2D-CNN networks. In this particular implementation, the model architecture is reported in Table III. The training phase was carried out with the parameters shown in Table IV.

TABLE III: Structure of the 2D-CNN model.

layers	Parameters	Activation
Conv2D	Filters 32 / Kernel 5	ReLu
MaxPooling	2	
Conv2D	Filters 64 / Kernel 5	ReLu
MaxPooling	2	
Conv2D	Filters 64 / Kernel 5	ReLu
MaxPooling	2	
Conv2D	Filters 128 / Kernel 5	ReLu
MaxPooling	2	
Dropout	0.5	
Conv2D	Filters 128 / Kernel 5	ReLu
MaxPooling	2	
Flatten		
Dense	128	ReLu
Dropout	0.5	
Dense	32	ReLu
Dense	2	SoftMax

Respect to the one applied in the first phase, the flowchart for the second phase, reported in Fig.3, has more preprocessing operations and data manipulation, moreover the starting data was composed by vectors of features instead of ECG signals.

1) The dataset:

TABLE IV: Training parameters of the 2D-CNN.

Training parameters	Values
Epochs	200
Early stopping	30
Optimizer	Adam
Learning rate	0.001
Loss function	Categorical crossentropy

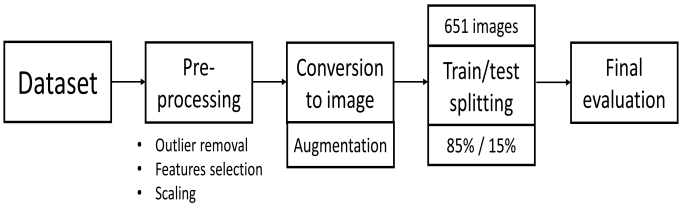


Fig. 3: Flow chart of data processing and testing of the 2D-CNN model

The second dataset was composed by numeric features, representative of the most important characteristic of the considered ECG track. Heart rate-related values and RR interval features were selected to represent each subject.

2) Data pre-processing:
Subject removal based on the absence of one or more of the following parameters:
   - Maximum, average and minimum heart rate during the whole recording.
   - Average heart rate.
   - Minimum and maximum value of the RR interval.

   Secondly, the most relevant features, i.e. those most frequently reported for each patient, were selected. These include all aforementioned parameters as well as the Ventricular (BEV) and supraventricular extrasystoles (BESV). Finally, the values of selected fundamental parameters were scaled between zero and one in order to prepare for the next stage of greyscale image creation.
3) Feature transformation:
The selected, and scaled, feature was transformed into an image. A grid composed of nine sections was created and filled with the selected features. Consequently, a black and white image was created from the grid, with the intensity of each portion depending on the value of each specific feature, as reported in Fig.4
4) Data augmentation:
The data augmentation phase was characterized by rotation operations and various small translations, in order to increase the number of images present in the dataset.
5) Training and test sets:
A final dataset of 651 images was obtained. As previously stated, the whole dataset were splitted in train and test set, whilst also ensuring that the subjects present in the training set were different from those in the test set.
6) Evaluation:
The 2D-CNN model was trained and then evaluated on the test set to check its performance.

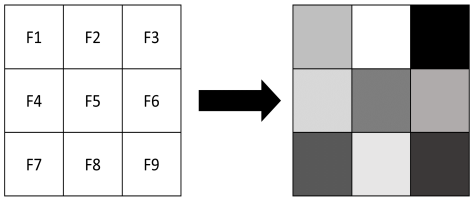


Fig. 4: Schematic representation of the process of transforming features into images

III. Results

The results obtained from the two proposed models have been evaluated using confusion matrices. For the 1D-CNN model, a good convergent behaviour is observed throughout the training, showing an increase in accuracy and a decrease in loss over time. The results on the test set are shown in the confusion matrix in Fig.5. The system showed 71.693% accuracy, 61.077% precision, 70.833% sensitivity, and 72.222% specificity.

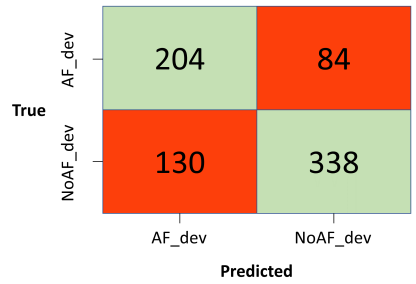


Fig. 5: Confusion Matrix of 1D-CNN model classification on test set

Similarly for the 2D-CNN model, a good behavior characterized by an increase in accuracy and a decrease in loss was observed throughout the training. The results of the test set are displayed in the corresponding confusion matrix in Fig.6. Here, the system achieved an accuracy of 76.190%, 68.627% precision, 71.428% sensitivity, and 79.221% specificity. Comparison of obtained results for the two models is shown in Table V.

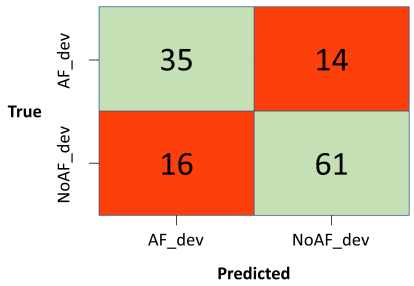


Fig. 6: Confusion Matrix of 2D-CNN model classification on test set

IV. Discussion

In this work, two methods are proposed to provide an early prediction of AF, in order to improve the quality of life of

TABLE V: Comparison between the two proposed models.

Model	Accuracy	Precision	Sensitivity	Specificity
1D-CNN	71.693	61,077	70.833	72.222
2D-CNN	76.190	68.627	71.428	79.221

subjects, reduce hospitalizations and decrease the economic impact on the health system. In particular, for this task, two new datasets were created: the first one was composed of ECG signals obtained from individual patients, while the second one was characterized by a numerical dataset containing the values of the most relevant events occurring during a Holter analysis. These datasets were tested with various models in varying configurations. Specifically, a 1D-CNN network for the dataset composed of ECG signals and a 2D-CNN network for the other composed of numerical features. Respect to similar works, the presented results are comparable to many recent papers and have the potential to grow even more. In [14] the authors obtained a less smaller sensitivity, but using a way bigger dataset and limiting the event time at one year. Using a 1D-CNN the authors of [15] reached more than 98% of accuracy, but with a smaller number of instances. The topic of AF prediction is a growing field of interest given the importance of anticipating such events. A recent review reports that machine learning is a good tool to be exploited[17]; however, the high variability between the size, type and processing of data, makes hard to compare different models directly. It is certain that the direction of the literature push toward the realization of more studies dealing with this problem.

The main contribution of our proposed models is that they showed good accuracy, comparable with other approaches from the literature, with the following pros:

1) Using a small fraction of an ECG Holter.
2) Exploiting an unconventional model by means of a novel technique.

The limitations of the study are represented by the size of data, which needs to be improved to confirm the quality of the models, and the limited amount of computing power that reduced the potential pool of testable models. The selection criteria restricted the pool of available data, but was mandatory due to the defined objectives. Given these reasons, one of the future goals is to increase the number of patients present in the current datasets. In this way, more robust and generalizable results could be achieved. Moreover, different type of networks and a higher number of parameters could be tested and optimized, exploiting also techniques like transfer learning.

The exploration of novel techniques in growing, important, fields like the prediction of AF development, is fundamental to improve the quality and quantity of available tools that have the potential of reducing the burden of disabling disease, both in terms of life quality, for the patients, and in terms of expenses charged on the healthcare system.

REFERENCES

[1] G. Hindricks, T. Potpara, N. Dagres, E. Arbelo, J. J. Bax, C. Blomström-Lundqvist, G. Boriani, M. Castella, G.-A. Dan, P. E. Dilaveris, L. Fauchier, G. Filippatos, J. M. Kalman, M. La Meir, D. A. Lane, J.-P. Lebeau, M. Lettino, G. Y. H. Lip, F. J. Pinto, G. N. Thomas, M. Valgimigli, I. C. Van Gelder, B. P. Van Putte, C. L. Watkins, and E. S. D. Group, "2020 ESC Guidelines for the diagnosis and management of atrial fibrillation developed in collaboration with the European Association for Cardio-Thoracic Surgery (EACTS): The Task Force for the diagnosis and management of atrial fibrillation of the European Society of Cardiology (ESC) Developed with the special contribution of the European Heart Rhythm Association (EHRA) of the ESC," *European Heart Journal*, vol. 42, pp. 373–498, 08 2020.

[2] E. Vizzardi, A. Curnis, M. G. Latini, F. Salghetti, E. Rocco, L. Lupi, R. Rovetta, F. Quinzani, I. Bonadei, L. Bontempi, *et al.*, "Risk factors for atrial fibrillation recurrence: a literature review," *Journal of cardiovascular medicine*, vol. 15, no. 3, pp. 235–253, 2014.

[3] D. M. Lloyd-Jones, T. J. Wang, E. P. Leip, M. G. Larson, D. Levy, R. S. Vasan, R. B. D'Agostino, J. M. Massaro, A. Beiser, P. A. Wolf, *et al.*, "Lifetime risk for development of atrial fibrillation: the framingham heart study," *Circulation*, vol. 110, no. 9, pp. 1042–1046, 2004.

[4] S. Stewart, C. L. Hart, D. J. Hole, and J. J. McMurray, "A population-based study of the long-term risks associated with atrial fibrillation: 20-year follow-up of the renfrew/paisley study," *The American journal of medicine*, vol. 113, no. 5, pp. 359–364, 2002.

[5] R. Gopinathannair, S. P. Etheridge, F. E. Marchlinski, F. G. Spinale, D. Lakkireddy, and B. Olshansky, "Arrhythmia-induced cardiomyopathies: mechanisms, recognition, and management," *Journal of the American College of Cardiology*, vol. 66, no. 15, pp. 1714–1728, 2015.

[6] C. T. January, L. S. Wann, H. Calkins, L. Y. Chen, J. E. Cigarroa, J. C. Cleveland, P. T. Ellinor, M. D. Ezekowitz, M. E. Field, K. L. Furie, *et al.*, "2019 aha/acc/hrs focused update of the 2014 aha/acc/hrs guideline for the management of patients with atrial fibrillation: a report of the american college of cardiology/american heart association task force on clinical practice guidelines and the heart rhythm society," *Journal of the American College of Cardiology*, vol. 74, no. 1, pp. 104–132, 2019.

[7] J. H. Jeong, "Prevalence of and risk factors for atrial fibrillation in korean adults older than 40 years," *Journal of Korean medical science*, vol. 20, no. 1, p. 26, 2005.

[8] M. Velleca, G. Costa, L. Goldstein, M. Bishara, and L. Ming, "A review of the burden of atrial fibrillation: understanding the impact of the new millennium epidemic across europe," *CARDIOLOGY*, 2019.

[9] F. Murat, O. Yildirim, M. Talo, U. B. Baloglu, Y. Demir, and U. R. Acharya, "Application of deep learning techniques for heartbeats detection using ecg signals-analysis and review," *Computers in biology and medicine*, p. 103726, 2020.

[10] S. Hong, Y. Zhou, J. Shang, C. Xiao, and J. Sun, "Opportunities and challenges of deep learning methods for electrocardiogram data: A systematic review," *Computers in Biology and Medicine*, p. 103801, 2020.

[11] C.-H. Hsieh, Y.-S. Li, B.-J. Hwang, and C.-H. Hsiao, "Detection of atrial fibrillation using 1d convolutional neural network," *Sensors*, vol. 20, no. 7, p. 2136, 2020.

[12] A. Rizwan, A. Zoha, I. Mabrouk, H. Sabbour, A. Al-Sumaiti, A. Alomaniy, M. Imran, and Q. Abbasi, "A review on the state of the art in atrial fibrillation detection enabled by machine learning," *IEEE reviews in biomedical engineering*, 2020.

[13] J. Wang, "A deep learning approach for atrial fibrillation signals classification based on convolutional and modified elman neural network," *Future Generation Computer Systems*, vol. 102, pp. 670–679, 2020.

[14] S. Raghunath, J. M. Pfeifer, A. E. Ulloa-Cerna, A. Nemani, T. Carbonati, L. Jing, D. P. vanMaanen, D. N. Hartzel, J. A. Ruhl, B. F. Lagerman, *et al.*, "Deep neural networks can predict new-onset atrial fibrillation from the 12-lead ecg and help identify those at risk of atrial fibrillation–related stroke," *Circulation*, vol. 143, no. 13, pp. 1287–1298, 2021.

[15] U. Erdenebayar, H. Kim, J.-U. Park, D. Kang, and K.-J. Lee, "Automatic prediction of atrial fibrillation based on convolutional neural network using a short-term normal electrocardiogram signal," *Journal of Korean medical science*, vol. 34, no. 7, 2019.

[16] M. F. Aslan, K. Sabanci, and A. Durdu, "A cnn-based novel solution for determining the survival status of heart failure patients with clinical record data: numeric to image," *Biomedical Signal Processing and Control*, vol. 68, p. 102716, 2021.

[17] I. Matias, N. Garcia, S. Pirbhulal, V. Felizardo, N. Pombo, H. Zacarias, M. Sousa, and E. Zdravevski, "Prediction of atrial fibrillation using artificial intelligence on electrocardiograms: A systematic review," *Computer Science Review*, vol. 39, p. 100334, 2021.

Health Information Technology Adverse Events Identification and Classification with Natural Language Processing and Deep Learning

A. Luschi[1], P. Nesi[1], and E. Iadanza[2]
[1] *Department of Information Engineering, University of Florence, Italy*
[2] *Department of Medical Biotechnologies, University of Siena, Italy*

***Abstract*—The main topic of this work is to develop a framework to extract Real-World Evidence through Natural Language Processing (NLP) and Neural Networks. An initial literature analysis has been performed, from which it clearly emerges that adverse events concerning Health Information Technology (HIT) are gradually growing over time. The goal of the proposed framework is to automatically identify adverse event reports related to HIT, aiming to support Health Technology Assessment and Post Market Surveillance as outlined in European Regulation 2017/745 on Medical Devices. The designed model uses a pre-trained version of ClinicalBERT, additionally fine-tuned on 3,705 adverse events reports extracted from the FDA MAUDE database, which had been previously manually labelled by experts. Results show better metrics than other existing HIT adverse events reports text classifiers based on non-BERT models, performing with an accuracy of 0.9906, precision of 0.9840, recall of 0.9973, and F1 score of 0.9906.**

***Keywords*—natural language processing, deep learning, HTA, medical devices.**

I. INTRODUCTION

Lexicon-based approaches are not well suited for capturing the meanings in medical texts and ML methods have been shown to be more effective [1], [2]. The majority of the studies reviewed used ML methods such as Support Vector Machines (SVM), Naive-Bayes, and regression trees, and features such as POS tagging, TD-IDF, BTO, and Word2Vec [3], [4]. Recent works have demonstrated the effectiveness of deep learning models such as Transformers, specifically BERT (Bidirectional Encoder Representations from Transformers) [5] and GPT (Generative Pre-trained Transformer) [6], in solving NLP and biomedical causal relation extraction tasks. Additionally, these models have been fine-tuned to improve performance on specific language tasks and biomedical and clinical text information. BERT-based models, such as SciBERT [7], BioBERT [8], and ClinicalBERT [9], that have been proposed by biomedical and clinical NLP community researchers, process biomedical and clinical text information more effectively and efficiently. This work aims to develop a framework to support Health Technology Assessment (HTA) through the use of Natural Language Processing (NLP) and Neural Networks. HTA is used to provide reliable and timely information on developed devices, medicines, vaccines, procedures and systems to solve health problems and improve quality of life. Real-World Data (RWD) can be used to generate Real-World Evidence (RWE) to assess the effectiveness and safety of a given health technology in a real-world setting. Medical RWD can come from various sources, such as Electronic Health Records (EHR), Computerized Maintenance Management Systems (CMMS) [10], Spontaneous Reporting Systems (SRS), and other clinical sources [11]. Studies have found that computer-related recalls, particularly software faults, have been a significant contributor to medical device recalls and have resulted in serious injury or death [12]. Studies on Health Information Technologies (HIT) failure [13] show that from January 2008 to July 2010, there were 678 reports of 436 different adverse medical device events associated with HIT. Most of the 46 events associated with patient harm were related to the computerized physician order entry and picture archiving and communication systems. Studies have also reported a constant increase in software failure in HIT over the years (Figure 1) [14].

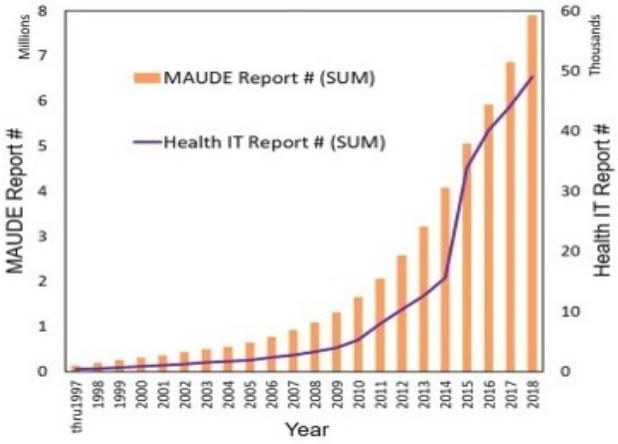


Fig. 1: HIT-related adverse events extracted from MAUDE database up to 2018 [14].

NLP and Machine Learning/Deep Learning techniques are used to extract structured data from SRS databases, which is significant for fulfilling legal obligations regarding Post Market Surveillance (PMS) as outlined in European Regulation 2017/745 on Medical Devices. This includes the continuous analysis of safety signals that emerge from the adverse events of medical devices available on the market. RWE is also useful for market evaluations, analysing faults, planning updates and

interventions, and avoiding recalls by authorities. Decision support techniques such as Multi-Criteria Decision Analysis (MCDA) or Analytic Hierarchy Process (AHP) can also be applied to obtain RWE on different aspects of different health technologies, in order to provide innovation in assessment for public international institutions and authorities, such as the World Health Organization or public health. To achieve this goal, data from the FDA MAUDE database was used and labelled by experts in HIT/non-HIT adverse events. The data was used to fine-tune a pre-trained ClinicalBERT model for binary text classification, which was then validated through a 10-fold validation process and tested against a subset of records to assess its performance.

II. MATERIALS AND METHODS

A. Proposed framework

The proposed framework is illustrated in Figure 2. Input data can originate from different sources (CMMS, SRS, EHR), even though at the moment the only analysed domain is the FDA MAUDE database of adverse event reports. HitBERT module is a ClinicalBERT model fine-tuned with adverse events reports originating from the MAUDE database, which had been manual-labelled by experts [15]. Text classification performs binary classification between HIT and non-HIT reports.

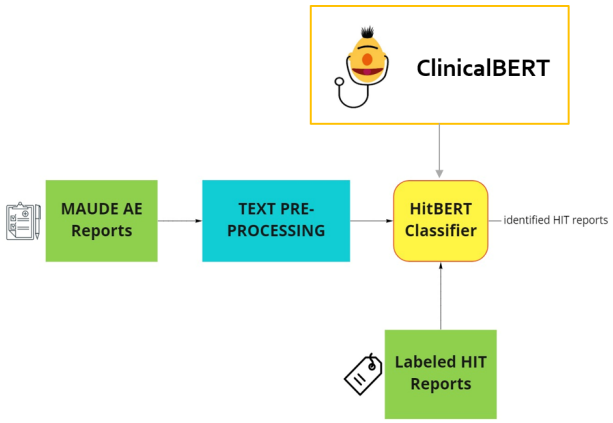


Fig. 2: Proposed framework.

B. Dataset

1,857 reports extracted from the FDA MAUDE were labelled as HIT-related between January, 1st 2008 and June, 30th 2010. The remaining 513,183 reports were identified as non-HIT in the same period. 1,848 reports have been randomly sampled from the non-HIT dataset in order to build a balanced training dataset for the BERT classifier. The combined 3,705 reports have been used for training, evaluation and testing. 20% of the whole dataset has been used for testing, while the remains rows have been split respectively into 80% for training and 20% for validation. Dropout hyper-parameters have been set to 0.5 for the attention layer and 0.1 for the hidden layer [16]. Texts longer than 512 words (0.86% of the whole dataset) have been truncated as the majority of records are between 0 and 200 words in length so no meaningful information was lost (Fig. 3).

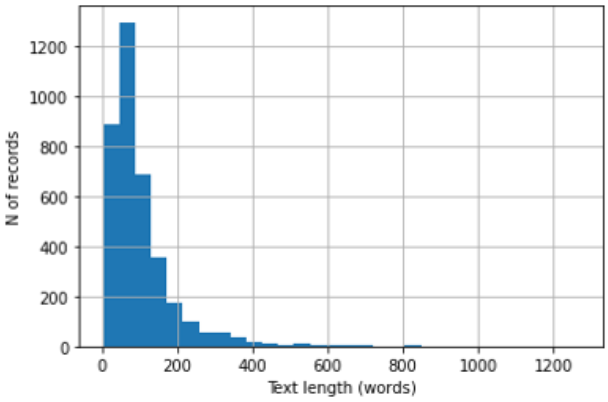


Fig. 3: Number of words for analysed records. The majority of records present a text length which is shorter than 512 words.

Padded texts have been tokenized with a generic class instantiated with a BERT tokenizer. BERT uses special tokens [CLS] and [SEP] to understand input properly. [SEP] token has to be inserted at the end of a single input, while [CLS] is a special classification token and the last hidden state of BERT corresponding to this token is used for classification tasks. Classification performance has been evaluated by comparing training and validation losses, accuracy, precision, recall, and F1-score. Validation of the final model has been performed with 10-fold cross-validation. The best-performing fold has finally been tested and evaluated with the same metrics.

III. RESULTS

Various experiments have been conducted in order to tweak model parameters such as activation function (Sigmoid linear unit – SiLU, Rectifier linear unit – ReLU, and Gaussian Error Linear Unit – GELU), learning rate (5e-5, 3e-5 and 2e-5) [17] for the optimization algorithm, batch size and the number of epochs (2, 3 or 4) [17]. The best performance was achieved with the GELU activation function, a batch size of 16, AdamW optimizer with a learning rate of 5e-5 and 4 epochs (0.9764 accuracy, 0.9609 precision, 0.9933 recall and 0.9768 F1 score). Tuned parameters have been then used for training a new model with k-fold cross-validation (10 folds). Results are shown in Table I.

TABLE I: Results of 10-fold validation on 2,964 records.

Fold	*Train loss*	*Validation loss*	*Accuracy*	*Precision*	*Recall*	*F1 score*
1	0.0216	0.0773	0.9764	0.9797	0.9732	0.9764
2	0.0140	0.0348	0.9966	1.0000	0.9933	0.9966
3	0.0027	0.0001	1.0000	1.0000	1.0000	1.0000
4	0.0115	0.0923	0.9865	0.9932	0.9799	0.9865
5	0.250	0.0547	0.9865	0.9866	0.9866	0.9866
6	0.0028	0.0502	1.0000	1.0000	1.0000	1.0000
7	0.0196	0.0885	0.9730	0.9795	0.9662	0.9728
8	0.0020	0.0059	0.9966	0.9933	1.0000	0.9966
9	0.0204	0.0913	0.9730	0.9667	0.9797	0.9732
10	0.0021	0.0001	1.0000	1.0000	1.0000	1.0000

The best-performing model (fold number 10) has finally been tested on the testing dataset, performing with an accuracy

of 0.9906, precision of 0.9840, recall of 0.9973, F1 score of 0.9906, and a Matthews Correlation Coefficient (MCC) of 98.12%. Receiver Operating Characteristic (ROC) curve and confusion matrix for testing results are shown in Fig. 4.

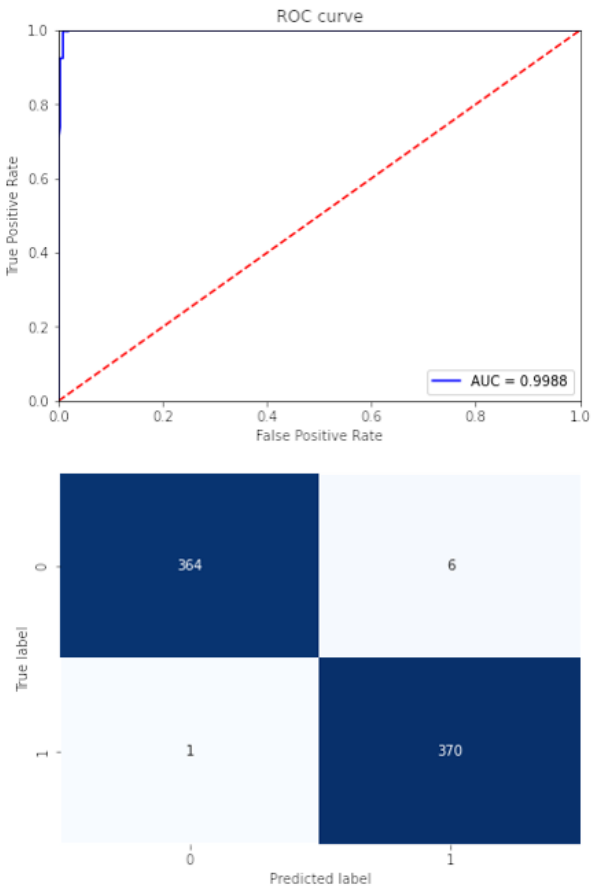


Fig. 4: ROC curve and confusion matrix for Fold #10 tested on 741 records (20% of the whole dataset).

IV. CONCLUSION

The proposed framework employs Natural Language Process techniques and models, such as BERT, to automatically identify adverse event reports related to Health Information Technologies. The framework aims to support Health Technology Assessment, as well as Post Market Surveillance and Post Market Clinical Follow-up as outlined in European Regulation 2017/745 on Medical Devices. The designed model uses a pre-trained version of ClinicalBERT, additionally fine-tuned on 3,705 adverse events reports extracted from the FDA MAUDE database, which had been previously manually labelled by experts. Further connections could be soon available to access data of local hospitals' CMMS and Computer-Aided Facility Management systems (CAFM) [18], [19]. Results show better metrics than other existing NLP HIT adverse events reports text classifiers based on non-BERT models [14], [15], [20], [21] (Table II).

TABLE II: Comparison of performances of the proposed NLP model (fine-tuned ClinicalBERT) and other non-BERT models.

Model	*Accuracy*	*Precision*	*Recall*	*F1 score*
ClinicalBERT	**0.9906**	**0.9840**	**0.9973**	**0.9906**
LR [15]	-	0.9670	0.9420	0.9540
LR [20]	-	0.6940	0.8040	0.7450
SVM+LR+CNN [21]	0.9012	0.8796	0.8606	0.8700
LR+CNN+HRNN[14]	0.9030	-	-	0.8760

REFERENCES

[1] J. Polisena, M. Andellini, P. Salerno, S. Borsci, L. Pecchia, and E. Iadanza, "Case studies on the use of sentiment analysis to assess the effectiveness and safety of health technologies: A scoping review," *IEEE Access*, vol. 9, pp. 66043–66051, 2021.

[2] X. Luo, G. Zimet, and S. Shah, "A natural language processing framework to analyse the opinions on hpv vaccination reflected in twitter over 10 years (2008 - 2017)," *Human Vaccines & Immunotherapeutics*, vol. 15, no. 7-8, pp. 1496–1504, 2019.

[3] S. M. Jiménez-Zafra, M. T. Martín-Valdivia, M. D. Molina-González, and L. A. Ureña-López, "How do we talk about doctors and drugs? sentiment analysis in forums expressing opinions for medical domain," *Artificial Intelligence in Medicine*, vol. 93, pp. 50–57, 2019. Extracting and Processing of Rich Semantics from Medical Texts.

[4] J. Du, J. Xu, H. yi Song, X. Liu, and C. Tao, "Optimization on machine learning based approaches for sentiment analysis on hpv vaccines related tweets," *Journal of Biomedical Semantics*, vol. 8, 2017.

[5] T. Wolf, L. Debut, V. Sanh, J. Chaumond, C. Delangue, A. Moi, P. Cistac, T. Rault, R. Louf, and M. Funtowicz, "Transformers : State-ofthe-art natural language processing," 2019.

[6] A. Radford and K. Narasimhan, "Improving language understanding by generative pre-training," 2018.

[7] I. Beltagy, K. Lo, and A. Cohan, "Scibert: A pretrained language model for scientific text," in *EMNLP*, 2019.

[8] J. Lee, W. Yoon, S. Kim, D. Kim, S. Kim, C. H. So, and J. Kang, "Biobert: a pre-trained biomedical language representation model for biomedical text mining," *Bioinformatics*, vol. 36, pp. 1234 – 1240, 2020.

[9] K. Huang, J. Altosaar, and R. Ranganath, "Clinicalbert: Modeling clinical notes and predicting hospital readmission," *ArXiv*, vol. abs/1904.05342, 2019.

[10] L. Mascii, A. Luschi, and E. Iadanza, "Sentiment analysis for performance evaluation of maintenance in healthcare," in *IFMBE Proceedings*, vol. 84, pp. 359–367, 2021.

[11] E. Iadanza, R. Fabbri, A. Luschi, P. Melillo, and F. Simonelli, "A collaborative restful cloud-based tool for management of chromatic pupillometry in a clinical trial," *Health and Technology*, vol. 10, no. 1, pp. 25–38, 2019.

[12] H. Alemzadeh, R. K. Iyer, Z. Kalbarczyk, and J. Raman, "Analysis of safety-critical computer failures in medical devices," *IEEE Security Privacy*, vol. 11, no. 4, pp. 14–26, 2013.

[13] F. Magrabi, M.-S. Ong, W. B. Runciman, and E. W. Coiera, "Patient safety problems associated with heathcare information technology: an analysis of adverse events reported to the us food and drug administration.," *AMIA ... Annual Symposium proceedings. AMIA Symposium*, vol. 2011, pp. 853–7, 2011.

[14] H. Kang and Y. Gong, "Creating a database for health it events via a hybrid deep learning model," *Journal of Biomedical Informatics*, vol. 110, p. 103556, 2020.

[15] K. Chai, S. Anthony, E. Coiera, and F. Magrabi, "Using statistical text classification to identify health information technology incidents," *Journal of the American Medical Informatics Association : JAMIA*, vol. 20, 05 2013.

[16] S. El Anigri, M. Himmi, and A. Mahmoudi, *How BERT's Dropout Fine-Tuning Affects Text Classification?*, pp. 130–139. 05 2021.

[17] J. Devlin, M.-W. Chang, K. Lee, and K. Toutanova, *BERT: Pre-training of Deep Bidirectional Transformers for Language Understanding*, vol. 1, pp. 4171–4186. 2019.

[18] E. Iadanza and A. Luschi, "An integrated custom decision-support computer aided facility management informative system for healthcare facilities and analysis," *Health and Technology*, vol. 10, no. 1, pp. 135–145, 2019.

[19] E. Iadanza, A. Luschi, R. Gusinu, and F. Terzaghi, "Designing a healthcare computer aided facility management system: A new approach," in *IFMBE Proceedings*, vol. 73, pp. 407–411, 2020.

[20] A. Fong, K. Adams, M. Gaunt, J. Howe, K. Kellogg, and R. Ratwani, "Identifying health information technology related safety event reports from patient safety event report databases," *Journal of Biomedical Informatics*, vol. 86, 09 2018.

[21] E. Wang, H. Kang, and Y. Gong, "Generating a health information technology event database from fda maude reports," *Studies in health technology and informatics*, vol. 264, pp. 883–887, 08 2019.

3D upper limbs tracking through inertial sensors: calibration, methodology, and validation

E. Bardi[1,3], C. Butera[2], L. Pozzi[1,3], M. Gandolla[1,3], F. Braghin[1,3], and E. Ambrosini[1,2]
[1] *WE-COBOT Lab, Polo territoriale di Lecco, Politecnico di Milano, Lecco, Italy*
[2] *NEARLab, Department of electronics, information and bioengineering, Politecnico di Milano, Milano, Italy*
[3]*Department of mechanical engineering, Politecnico di Milano, Milano, Italy*

***Abstract*—In home-based motor rehabilitation, bio-feedback and remote monitoring are essential to maintain patient motivation and ensure appropriate monitoring of training effects. Wearable sensors can be exploited to provide this feedback both to the patient and to the therapist. This paper presents an algorithm for the real-time extraction of shoulder and elbow joint angles from three inertial measurement units (IMUs). The five angles extracted are defined according to the International Society of Biomechanics (ISB) convention. The algorithm includes a two-step calibration procedure (N-pose and T-pose), which allows placing the IMUs on the limbs freely, without the need to use the magnetometer, and the real-time computation of the joint angles. The algorithm was validated on the arm of the TIAGo robot by comparing the joint angles measured by the robot encoders against the joint angles derived from the IMU sensors. Results show that the presented method is accurate (the maximum RMSE is 4.96° for the pronation-supination angle) and robust to different IMUs positioning.**

***Keywords*—upper limb joint angles, ISB convention, IMU, home-based training**

I. INTRODUCTION

Disabilities of the upper limb, resulting both from neurological or neuromuscular pathologies and traumatic injuries, can greatly impact the ability to conduct activities of daily living. Rehabilitation is, therefore, fundamental to promote motor recovery and improve the quality of life of those affected by upper limb motor impairment.

Some key ingredients leading to the success of a rehabilitation program are motivation, dose, intensity, and personalization of the treatment [1]. These factors should be guaranteed not only in the clinic, but also at home to maintain and enhance the obtained progresses.

Wearable robots, such as exosuits, have been developed to support at-home therapy both for the lower and the upper limbs. However, the adoption of these devices is still limited and not fully exploited [2]. This is due to the immature state of the technology that has limitations, but also to a lack of motivation [3].

When it comes to home-based rehabilitation, it is necessary to encourage the patients and inspire their enthusiasm whether they are using a wearable robot or not. This could be addressed by providing daily feedback on their motor performance by exploiting wearable sensors, such as IMUs (Inertial Measurement Units). At the same time, the metrics extracted could be sent to the therapist to remotely monitor the patient's progress and tailor the treatment to their needs [4].

II. STATE OF THE ART

To extract performance metrics from the IMUs, the first step is to compute the upper limb joint angles. Several studies addressed the challenge of computing the upper limb angles [5]–[7], but they did not follow the ISB (International Society of Biomechanics) convention, recognized as the standard for reporting joint motions in a clinically relevant way [8].

A recent study aimed at providing bio-feedback during aquatic exercises proposed a method to extract upper limb joint angles according to the ISB convention. The proposed algorithm does not employ the magnetometer and does not constrain the position of the IMUs thanks to a two-step calibration procedure [9]. However, the group only validated shoulder abduction/adduction and elbow flexion/extension angles.

The aim of this work is to provide a complete mathematical explanation of the magnetometer-free algorithm to extract upper limb joint angles according to the ISB convention, and to validate it for all the angles on a robotic arm.

III. MATERIALS AND METHODS

A. Reference frames definition

The reference frames that will be used in the following sections are defined as shown in Fig. 1 and are:

- Global reference frame (G);
- IMU reference frame (I);
- Body segment reference frame (B);
- ISB convention reference frame (ISB).

When left joints are concerned, we used the same reference frame and we applied, when needed, a term that is defined as:

$$\kappa = \begin{cases} +1, & \text{if right arm} \\ -1, & \text{if left arm} \end{cases} \tag{1}$$

B. ISB upper limb angles definition

According to the ISB convention, the rotation matrix describing the orientation of the upper arm body segment (ISB,UA) with respect to the ground reference frame (G) can be defined as:

$$R^G_{ISB,UA} = R^G_{ISB,TH} R_y(\kappa POE) R_x(-\kappa AOE) R_y(\kappa HR) \tag{2}$$

where $R^G_{ISB,TH}$ is the rotation matrix of the thorax body segment with respect to G, POE is the Plane of Elevation angle

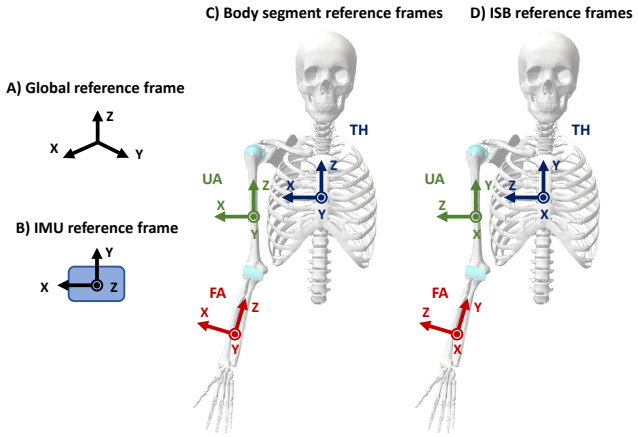


Fig. 1: A) Global, B) IMU, C) Body segment, D) ISB reference frames. TH indicates the thorax, UA indicates the upper arm, FA indicates the forearm.

(positive when moving the arm frontally), AOE is the Angle of Elevation (positive when elevating), HR is the Humeral Rotation angle (positive when the rotation is internal), and R_x, R_y represent the rotation matrices deriving from the rotation respectively around the x and y-axis of the angles indicated between parenthesis.

The rotation matrix describing the orientation of the forearm body segment with respect to G can be defined as:

$$R^G_{ISB,FA} = R^G_{ISB,UA} R_z(FE) R_y(\kappa PS) \tag{3}$$

where FE is the elbow Flexion-Extension angle (positive when flexing), and PS is the forearm Pronation-Supination angle (positive when pronating).

The ISB angles are null when the user is standing with the arms resting and the palms of the hands pointing forward (N-pose).

C. IMUs calibration

Since the magnetometer is not used, in order to make the IMUs share the same G, they are aligned on a rigid surface and the yaw is reset: the G z-axis points up in the direction of gravity, while x-axis and y-axis match the IMU x and y axis at time of reset. The IMUs are then placed on the thorax, upper arm, and forearm.

When placing the IMUs on the limbs, the IMUs axes and the body segments axes are usually not coincident. The calibration procedure is needed to align the IMUs reference frames (I) and the body segments reference frames (B). Calibration is performed by acquiring data from two different poses: i) the N-pose and ii) the T-pose. During the N-pose the user stands still with the arms resting and the palms of the hands pointing forward. In this configuration, the ISB joint angles are ideally null.

The orientation of each IMU with respect to G is expressed by the rotation matrix estimated by the IMU and can be expressed as:

$$R^G_{I_i} = R^G_{I_{i,0}} R^{I_{i,0}}_{I_i} \tag{4}$$

where $R^G_{I_{i,0}}$ is the rotation matrix of the i-th IMU during the N-pose, and $R^{I_{i,0}}_{I_i}$ is the rotation matrix of the i-th IMU calibrated with respect to the N-pose. Inverting Eq. (4), we obtain:

$$R^{I_{i,0}}_{I_i} = (R^G_{I_{i,0}})^T R^G_{I_i} \tag{5}$$

The orientation of each IMU with respect to G is also expressed as:

$$R^G_{I_i} = R^G_{B_i} R^{B_i}_{I_i} \tag{6}$$

where $R^G_{B_i}$ is the rotation matrix describing the orientation of the i-th body segment with respect to G, and $R^{B_i}_{I_i}$ is the rotation matrix describing the orientation of the i-th IMU with respect to the i-th body segment. This rotation matrix is assumed to be constant during the subsequent use of the sensors, such that $R^{B_i}_{I_i} = R^{B_{i,0}}_{I_{i,0}}$, where 0 indicates the N-pose configuration. If the sensors are moved relative to the body segments, the calibration procedure should be performed again.

The rotation matrix describing the orientation of the body segment with respect to G can be expressed as:

$$R^G_{B_i} = R^G_{B_{i,0}} R^{B_{i,0}}_{B_i} \tag{7}$$

where $R^G_{B_{i,0}}$ is the rotation matrix of the i-th body segment with respect to G in the N-pose and is unknown, and $R^{B_{i,0}}_{B_i}$ is the rotation matrix describing the orientation of i-th body segment at the current time instant with respect to the N-pose.

Using Eq. (7), Eq. (6) can be rewritten as:

$$R^G_{I_i} = R^G_{B_{i,0}} R^{B_{i,0}}_{B_i} R^{B_i}_{I_i} \tag{8}$$

During the T-pose the arms are rotated by 90° in the coronal plane. In this configuration, the ISB joint angles are ideally null except for AOE which is equal to 90°.

Assuming that in the N-pose the z-axes of the body segments are aligned with the z-axes of the IMUs calibrated as in Eq. (5) and the z-axis of G, the rotation matrices expressing the orientation of the body segments with respect to G in the N-pose can be expressed as a rotation around the z-axis of an angle θ:

$$R^G_{B_{i,0}} = R_z(\theta) \tag{9}$$

$$\theta = \angle(X_G, -\kappa Z_{I,calib_{UA}}) \tag{10}$$

where X_G is the x-axis of G (namely $[1,0,0]$), and $Z_{I,calib_{UA}}$ is the z-axis of the IMU placed on the upper arm and calibrated with respect to the N-pose. Eq. (6) can be rewritten for the N-pose as:

$$R^G_{I_{i,0}} = R_z(\theta) R^{B_i}_{I_i} \tag{11}$$

The expression of $R^{B_i}_{I_i}$ is then obtained reversing Eq. (11):

$$R^{B_i}_{I_i} = R_z(\theta)^T R^G_{I_{i,0}} \tag{12}$$

Substituting Eq. (9) and Eq. (12) in Eq. (8) we obtain:

$$R^G_{I_i} = R_z(\theta) R^{B_{i,0}}_{B_i} (R_z(\theta)^T R^G_{I_{i,0}}) \tag{13}$$

Finally, inverting Eq. (13) we obtain the following expression:

$$R_{B_i}^{B_i,0} = R_z(\theta)^T R_{I_i}^G (R_z(\theta)^T R_{I_i,0}^G)^T \quad (14)$$

Once this matrix is obtained for each body segment, it must be rotated to be expressed in the ISB reference frame:

$$R_{ISB_i}^{ISB_i,0} = R_{B_i}^{B_i,0} R_x\left(\frac{\pi}{2}\right) R_y\left(\frac{\pi}{2}\right) \quad (15)$$

D. Upper limb joint angles computation

For the sake of clarity, we will refer to $R_{ISB_i}^{ISB_i,0}$ for each body segment as TH for the thorax, UA for the upper arm, and FA for the forearm.

The POE can be computed as:

$$POE = \angle(proj_{XZ_{TH}}(Y_{UA}), -\kappa Z_{TH}) \quad (16)$$

that is the relative angle between the projection of the y-axis of UA (Y_{UA}) onto the plane defined by the x-axis and the z-axis of TH (XZ_{TH}), and the z-axis of TH. It is worth remarking that, in the particular case of a null AOE, Y_{UA} is orthogonal to XZ_{TH}, thus the projection $proj_{XZ_{TH}}(Y_{UA}$ degenerates to a point, and Eq. (16) loses its significance. This means that the POE is ill-defined when AOE is null. Indeed, if AOE is null, POE and HR coincide.

The AOE can be computed as:

$$AOE = \angle(Y_{UA}, Y_{TH}) \quad (17)$$

that is the relative angle between the y-axis of TH and the y-axis of UA.

Inverting Eq. (2), we can compute HR as:

$$R_y(HR) = (R_x(-\kappa AOE))^T (R_y(POE))^T (TH)^T UA \quad (18)$$

$$HR = tan^{-1}([R_y(HR)]_{1,3}, [R_y(HR)]_{1,1}) \quad (19)$$

where $[A]_{i,j}$ indicates the element of the matrix at the i-th row and j-th column.

FE can be computed as:

$$FE = \angle(Y_{FA}, Y_{UA}) \quad (20)$$

that is the relative angle between the y-axis of UA and the y-axis of FA.

Inverting Eq. (3), we can compute PS as:

$$R_y(PS) = (R_z(FE))^T (UA)^T FA \quad (21)$$

$$PS = tan^{-1}([R_y(PS)]_{1,3}, [Ry(PS)]_{1,1}) \quad (22)$$

E. Experimental Validation

Three IMUs (NGIMU, x-io Technologies Limited Bristol, UK) were placed on the TIAGo robot (PAL Robotics Barcelona, Spain) on its thorax, upper arm, and forearm as shown in Fig. 2. The TIAGo robot is a mobile manipulator with a 7-DOFs (degrees of freedom) actuated arm that allows reading the angle values by means of the encoders [10]. Each DOF of the TIAGo robot arm corresponds to one of the angles defined by the ISB convention for the upper limb.

The TIAGo robot was controlled to move its arm in the N-pose, in the T-pose, and then in multiple configurations. During the experiments, both the encoders signals and the IMUs rotation matrices were acquired and saved. The experiment was repeated twice changing the IMUs orientation to better support the validity of the results.

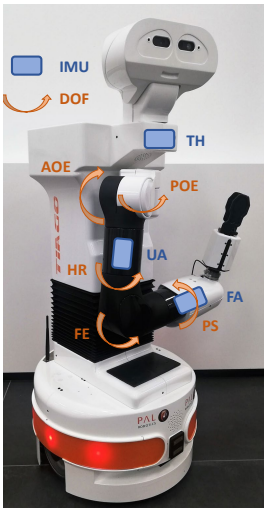


Fig. 2: IMUs (in blue) position on TIAGo robot and DOFs (in orange).

A comparison between the angles computed by the algorithm and those measured by the TIAGo robot, considered as the ground truth, was conducted.

IV. Results and Discussion

The experimental results in terms of root-mean-square error (RMSE) and correlation coefficient are summarized in Table I. The mean RMSE values between the two trials for the POE, AOE, HR, FE, and PS are respectively 4.87°, 2.75°, 2.76°, 4.93°, and 4.96° whereas the mean correlation coefficients r are 0.998, 0.998, 0.999, 0.996, and 0.995. The RMSE values differ slightly between the two experimental sessions showing that the positioning of the IMUs on the arm does not significantly influence the accuracy of the results.

The temporal history of one of the two repetitions is shown in Fig. 3. The error spike that can be observed in the POE, can be traced back to the ill-posed definition of POE when AOE is equal or close to 0°. We hypothesize that the other errors are mainly due to imprecisions during the three-phase calibration procedure (i.e., IMU alignment, N-pose, T-pose).

TABLE I: Correlation coefficient r and RMSE between the upper limb joint angles measured by the encoders and estimated with the proposed method during the two runs.

	Run 1		Run 2		Mean	
	r	RMSE [°]	r	RMSE [°]	r	RMSE [°]
POE	0.998	3.99	0.998	5.75	0.998	4.87
AOE	0.998	3.16	0.999	2.33	0.998	2.75
HR	0.999	3.23	0.999	2.27	0.999	2.76
FE	0.997	4.57	0.995	5.28	0.996	4.93
PS	0.997	2.54	0.993	7.37	0.995	4.96

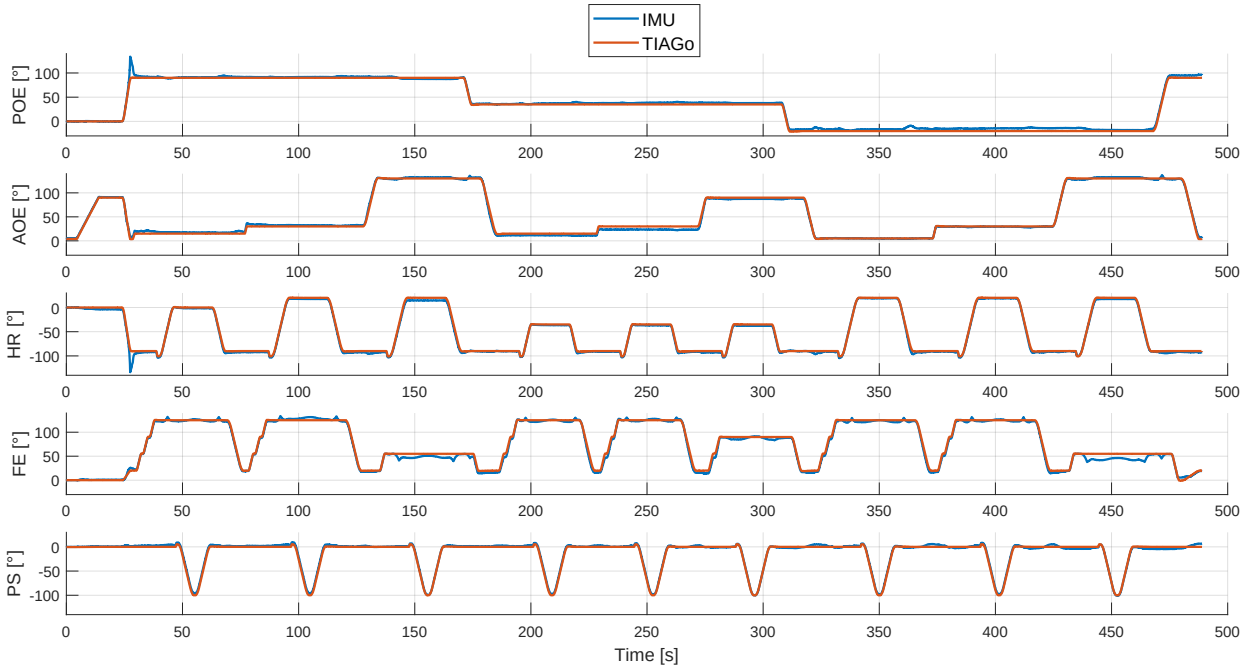


Fig. 3: Comparison between joint angles measured by TIAGo encoders (in orange) and computed by the IMUs (in blue) during run 1.

We acknowledge that the errors derived from the calibration might grow more significant when the calibration is performed on humans since the N-pose and T-pose configurations will be less precise. Moreover, since the muscles and the skin do not move rigidly with the bones, we expect higher errors in humans, especially in HR estimation.

V. Conclusion

The presented algorithm effectively estimated the upper limb joint angles according to the ISB convention on a robot arm. The algorithm does not need the magnetometer, and it allows for free positioning in terms of the orientation of the IMUs on the segments. Nevertheless, since the human body is not rigid, future works must include the validation of the whole algorithm on human participants. Moreover, the angle accuracy should be evaluated over a long period of time (i.e., a day). The extraction of meaningful metrics on motor performance could be finally carried out to compile a report.

References

[1] R. Gassert and V. Dietz, "Rehabilitation robots for the treatment of sensorimotor deficits: A neurophysiological perspective," *J. Neuroeng. Rehabil.*, vol. 15, pp. 1–15, 2018.

[2] E. Bardi, M. Gandolla, F. Braghin, F. Resta, A. L. Pedrocchi, and E. Ambrosini, "Upper limb soft robotic wearable devices: a systematic review," *J. Neuroeng. Rehabil.*, vol. 19, no. 1, pp. 1–17, 2022, ISSN: 17430003.

[3] C. Basla, I. Hungerbühler, J. T. Meyer, P. Wolf, R. Riener, and M. Xiloyannis, "Usability of an exosuit in domestic and community environments," *J. Neuroeng. Rehabil.*, vol. 19, no. 1, pp. 1–13, 2022.

[4] C. R. Forman, J. B. Nielsen, and J. Lorentzen, "Neuroplasticity at Home: Improving Home-Based Motor Learning Through Technological Solutions. A Review," *Front. Rehabil. Sci.*, vol. 2, no. December, pp. 1–7, 2021.

[5] M. El-Gohary and J. McNames, "Human Joint Angle Estimation with Inertial Sensors and Validation with A Robot Arm," *IEEE Trans. Biomed. Eng.*, vol. 62, no. 7, pp. 1759–1767, 2015.

[6] M. Lapresa, C. Tamantini, F. S. Di Luzio, *et al.*, "Validation of Magneto-Inertial Measurement Units for Upper-Limb Motion Analysis through an Anthropomorphic Robot," vol. 22, no. 17, pp. 16 920–16 928, 2022.

[7] D. Laidig, I. Weygers, and T. Seel, "Self-Calibrating Magnetometer-Free Inertial Motion Tracking of 2-DoF Joints," *Sensors (Basel)*, vol. 22, no. 24, pp. 1–28, 2022.

[8] G. Wu, F. C. Van Der Helm, H. E. Veeger, *et al.*, "ISB recommendation on definitions of joint coordinate systems of various joints for the reporting of human joint motion - Part II: Shoulder, elbow, wrist and hand," *J. Biomech.*, vol. 38, no. 5, pp. 981–992, 2005.

[9] M. Gandolla, A. Pedrocchi, S. Ferrante, *et al.*, "Wearable Biofeedback Suit to Promote and Monitor Aquatic Exercises: A Feasibility Study," *IEEE Trans. Instrum. Meas.*, vol. 69, no. 4, pp. 1219–1231, 2020.

[10] L. Pozzi, M. Gandolla, F. Pura, *et al.*, "Grasping learning, optimization, and knowledge transfer in the robotics field," *Sci. Rep.*, vol. 12, no. 1, p. 4481, 2022.

Manual and automatic identification of ACMG evidence in scientific papers

F. Longhin[1], A. Guazzo[1], E. Longato[1], D. Boscarino[2], D. Paladin[2], N. Ferro[1], and B. Di Camillo[1,3]
[1] University of Padova, Department of Information Engineering, Padova, 35131, Italy
[2] AB ANALITICA Srl, Padova, 35127, Italy
[3] University of Padova, Department of Comparative Biomedicine and Food Science, Legnaro (PD), 35020, Italy

***Abstract*—Next-generation sequencing technologies have been producing a growing volume of genomic data, increasing the challenge of clinical sequence variant interpretation. Identifying disease-causing mutations within millions of variants relies on the research of evidence in support of or against variant pathogenicity, a process regulated by specific American College of Medical Genetics and Genomics (ACMG) guidelines, which leverages data from biological databases and scientific literature. Despite recent improvements towards automation, searching shreds of evidence for pathogenicity in the literature still requires manual curation, a time-consuming process, due to the ever-growing number of published papers.**

As a first step towards automatic annotation, with this work we provided a reliable manually curated dataset of articles which activate two types of ACMG evidence code, namely PS3 and BS3, (positive articles) and articles which do not activate any of the above evidence code (negative articles). Moreover, we demonstrated that such dataset can be used to train a predictive model that automatically identifies positive articles.

We started from analysing PS3/BS3 evidence codes collected by ClinGen expert curators and then we performed our own manual curation on 132 articles retrieved from EuropePMC: 71 positives and 61 negatives. We used a combination of bag-of-words encoding and logistic regression to efficiently identify positive articles, with an F1-score of 0.85.

The model' performance constitutes a clear proof of concept for automatic PS3/BS3 evidence identification. Our dataset represents a useful resource to train further models.

***Keywords*—Variant Annotation, Clinical Genetics, Pathogenicity Assessment, ACMG guidelines**

I. Introduction

RECENTLY, Next Generation Sequencing (NGS) of whole exomes or genomes has become a widely accessible and relatively inexpensive practice, resulting in its increased use in clinical diagnostics for precision medicine. Indeed, NGS approaches can identify most of a person's genetic variants, thus allowing clinicians to provide suitable therapies to patients or assess disease risk [1].

Variant identification is followed by variant interpretation and prioritisation, which are crucial steps in the clinic, as they deeply impact healthcare decisions. To correctly assign a variant to its pathogenicity class, a biocurator firstly needs to perform a complete variant annotation, a process which consists in gathering all relevant information about the nature and the effect of the specific variant from databases and literature [2].

In 2015 the American College of Medical Genetics and Genomics (ACMG) published recommended standards and guidelines for variant interpretation [3]. The guidelines defined 28 criteria, each identified by an evidence code representing evidence in support of variant benignity or pathogenicity [4]. Criteria are applied on the basis of evidence contained in biological databases (variant frequencies, pathogenicity prediction scores, etc.) while others require information contained in scientific literature (variant functional studies, analysis of the pattern of inheritance of a particular trait throughout a family, etc.).

Specifically, the task of mining evidences of a variant malignity/benignity from the literature, a process known as manual curation, is extremely complex and time-consuming as it requires highly qualified curators that analyse all relevant papers and combine information coming from different resources. Typically, the curator queries literature search engines with "*Variant_Name* AND *Gene_Name*" and proceeds by reading all retrieved articles, searching for relevant information in figures, tables, sentences which contain the name of the variant and those nearby (e.g. the previous or next sentence) [5].

As a result of such a lengthy annotation process, currently there is the lack of a complete and constantly updated database containing papers curated following the ACMG guidelines for each variant and for each criterion. Several automatic tools have been proposed to speed up variant annotation, such as the Ensembl Variant Effect Predictor [6], that associates each variant to its transcripts and regulatory regions, or ANNOVAR [7], that predicts variant functional consequences. However, none of them can perform a comprehensive screening of the extensive and ever-growing literature, nor automatically extract from papers the information needed for the assignment of ACMG criteria.

With this work, we want to provide a reliable, manually curated dataset of articles, which activate, for a specific variant, one of two opposing ACMG criteria, named PS3 and BS3, (positive articles) or which activate neither (negative articles). PS3 and BS3 are alternatively assigned to a specific pair (variant, article) when the article describes a well-established functional test (in vitro or in vivo), carried out on the variant, that is supportive of a damaging or null effect on protein function, respectively. Moreover, we demonstrated the utility of our dataset as training set by performing a preliminary exploratory analysis concerning the development of an automatic, machine learning based predictive model to perform automatic positive (variant, article) evidence identification. This can be thought as a first step before a second classification step in PS3 vs. BS3.

II. METHODS

A. Retrieval of articles to be included in the curated dataset

To build our dataset, we started from the ClinGen Evidence Repository [8], an expert-curated registry that provides the evidence codes of each variant in the database, accordingly to the ACMG standards. In particular, ClinGen contains information about 4581 curated genetic variants, which can be distributed across 78 genes of interest. Each curated variant is reported with its standard nomenclature and the associated ACMG evidence codes. Also, ClinGen provides a summary of the variant interpretation where each ACMG evidence code is briefly explained, specifying the source of evidence, which can be a database or one or more scientific papers, identified by PubMed [9] identification codes (PMIDs). PubMed is a free search engine for retrieval of biomedical literature abstracts, indexed through their PMIDs. Also, PubMed provides links to articles' full-texts, when these are available from other sources, such as PubMed Central [10] (PMC), in which full-texts are indexed through PMCIDs.

As mentioned before, we decided to focus only on variant curations where either PS3 or BS3 evidence codes are assigned, given that the evidence needed for these assignments is often contained in papers plain texts. ClinGen contains 385 genetic variants (*ClinGen variants*) with PS3 or BS3 criteria for which we extracted the corresponding PMIDs (*ClinGen articles*). As we want to analyse papers full-texts, we converted PMIDs to PMCIDs. *ClinGen articles* with no PMCID were ignored. We choose to use EuropePMC as literature search engine, for it has a very convenient R interface, provided by the package *europepmc* [11]. Specifically, the user can define a query through the function *epmc_search* and obtain PMCIDs of retrieved articles.

Given that *ClinGen articles* are curated by expert biocurators, we expect querying of EuropePMC by *ClinGen variant* specific nomenclatures to produce a pool of retrieved articles which contains at least one already curated positive article, the so called *ClinGen article*, and, eventually, some other positive articles (not identified by ClinGen curators) and some negative articles, which have to be manually curated in order to build the dataset.

As we want to mimic the same procedure followed by manual curators, our queries contain "*Variant_Name* AND *Gene_Name* AND *Keywords*". Given the great variety of nomenclatures commonly used for genetic variants such as: i) nucleotide change (e.g. c.1A>G); ii) one-letter amino acid change (e.g. p.M1V); iii) three-letters amino acid change (e.g. p.Met1Val); iv) rsID (e.g. rs786204467), etc., we choose to consider as *Variant_Name* for each *ClinGen variant* only the specific one used in all of its *ClinGen articles*.

Keywords is a set of 113 words we added to the query syntax in order to retrieve articles containing at least one of these terms, thus slightly narrowing the research. We extracted *Keywords* from two resources: Mastermind [12], which is a commercial search engine that allows paid users to rank retrieved articles according to ACMG relevance through criteria-specific keywords, and *ClinGen articles*. In particular, Mastermind contains 68 keywords for PS3/BS3, while the other 45 keywords were words recurrently found in *ClinGen articles*, which are known to be positive for PS3/BS3. For example, *Keywords* contains names of functional tests (ELISA, FISH, etc.), experimental materials (in vivo, in vitro, human cells, animal model, etc.), and species (drosophila, mouse, zebrafish, etc.). Considering that the aim of functional tests is typically the functional comparison between one or more mutants with the wild-type, i.e., the non-mutated genomic sequence (often referred to as wild type, control, mock, water, etc.), or with other mutants known to cause functional alterations (e.g., activating/inactivating mutations) these latter words were included as well in *Keywords*.

Furthermore, we refined the query syntax by adding the following flags:

- BODY: query terms are searched within the body of full-text articles. Sections such as "References" and "Acknowledgements" are not considered.
- OPEN_ACCESS: it limits search results to articles that are Open Access in EuropePMC. This is needed as we need access to the full-text.
- PUB_TYPE: filter by publication type. Only journal articles were considered.

These customised queries produced lists of retrieved articles, identified by their PMCIDs, for each *ClinGen variant*. As some *ClinGen articles* are not Open Access, some queries do not contain any *ClinGen articles* and thus they were discarded in the current analysis.

Finally, 1466 distinct articles were retrieved using queries related to 47 *ClinGen variants*: 31 *ClinGen articles* and 1435 articles not included in *ClinGen articles*.

B. Manual curation of retrieved articles

Manual curation is needed to distinguish between positive articles (assigned to the label 1), i.e., articles that contain sentences that activate either PS3 or BS3 evidence codes and, negative articles (assigned to the label 0), which do not contain any of these sentences. The presence of at least one positive sentence inside an article confers positivity to the whole article itself. It is worth noting that the positive or negative label also depends on the specific variant considered, thus, more specifically, it is assigned to each (variant, article) pair.

We selected for manual curation only *target sentences*, i.e., sentences containing *ClinGen variants* specific name concatenated to the ones immediately adjacent (the previous and next sentences). In this way, we considered only textual information, easily interpretable for an automatic algorithm (tables and figures are excluded, as they would require additional, specialised modules). We performed sentences extraction through the R package *tidypmc* [13].

For each *ClinGen variant*, we read all *target sentences* extracted from its *ClinGen articles* and, for sake of time parsimony, given the burden of human curation in terms of time, from a random subset of articles not included in *ClinGen articles* but retrieved by our queries.

We performed manual curation considering the following rules and ensuring consistencies with the Genomic Variant Analysis & Clinical Interpretation [5] procedure. We assigned to each article the label negative (0) if:

- None of *target sentences* contains sufficient information for assigning PS3 or BS3 as defined by ACMG guidelines (i.e., all *target sentences* are negative), regardless of the content of tables or figures (which could contain information for assigning PS3 or BS3).

Instead, the positive (1) label was assigned to papers for which:

- At least one *target sentence* contains information for assigning PS3 or BS3 (i.e., at least one *target sentence* is positive). Positive *target sentences* include sentences that refer to other papers or sentences where the comparison to wild-type is implicit.

We excluded articles for which there were no *target sentences* (the name of the variant only appears in tables).

C. Preprocessing and Train, Test and Validation set

We trained the automatic classification model on this dataset according to a by-sentence perspective, where we considered each sentence as an independent entry. For performance evaluation only, we considered also a by-paper perspective by only distinguishing between positive and negative papers according to the classification of each of their target sentences (the paper is positive if it contains at least one positive sentence). We pre-processed the sentences included in the dataset according to the following typical steps [14]:

- Deletion of English stop words;
- Word stemming;
- Deletion of the 10% least frequent words;
- Exclusion of sentences consisting of less than 3 words.

Finally, the pre-processed dataset was split into training-set, test-set and validation-set (70%, 15%, 15%), making sure that proportions of positive and negative articles and sentences are similar in the 3 subsets.

D. Model and hyperparameter optimisation

We performed a preliminary exploratory analysis on automatic PS3/BS3 evidence identification using a simple logistic regression (LR) trained after applying the bag-of-words (BOW) [15] approach to transform the original dataset into a version where each sentence was represented by the number of occurrences of each word within it. For this model, we considered a L2 regularisation loss-function with a single hyperparameter that needed optimisation, the inverse of the regularisation strength C.

We performed hyperparameter optimisation considering only the training set using a 5-fold cross validation [16] and a random search approach [17] accounting for 10,000 values of C, randomly sampled from a log uniform distribution ranging from 10^{-4} to 10^{2}. We selected the best hyperparameter as the one that led to the minimum average binary cross-entropy across the 5 folds.

To transform the model from a ranker into a classifier useable in practice for automatic PS3/BS3 evidence identification, we implemented a thresholding approach by identifying one probability threshold (th) to discriminate between sentences that would activate PS3 or BS3 (1, if predicted probability $p \geq th$) and negative (0, if $p < th$) predictions. We selected the optimal threshold by using each probability value predicted for sentences in the validation set as a threshold and choosing the one associated to the maximum geometric mean between true positive and true negative rate.

E. Performance evaluation

In the by-sentence perspective, we evaluated the discrimination performance of the model via five metrics: area under the receiver operating characteristic (AUROC) and area under the precision-recall curve (AUPRC) [18] for the continuous probability output; as well as precision, recall, and F1-score after applying the aforementioned thresholding approach. In the by-paper perspective, we did not consider AUROC and AUPRC as predicted labels were assigned by conglomerating by-sentence outputs after thresholding.

III. Results

A. Manually curated dataset

Manual curation was actually carried out on 755 sentences belonging to 196 articles. However, as 64 articles were discarded (see Section II.B), the manually curated dataset finally comprises 649 sentences belonging to 132 articles. Table I and Table II provide a comparison of assigned labels in *ClinGen articles* and non-*ClinGen articles* and among train, test and validation sets, respectively.

TABLE I: ClinGen Articles VS Non-ClinGen Articles

		Total	Positive	Negative
ClinGen articles	**Sentences**	281	162	119
	Articles	23	22	1
Non-*Clingen articles*	**Sentences**	368	167	201
	Articles	109	49	60

TABLE II: Train Set VS Test Set VS Validation Set

		Total	Positive	Negative
Training	**Sentences**	477	241	236
	Articles	92	50	42
Testing	**Sentences**	109	56	53
	Articles	20	11	9
Validation	**Sentences**	63	32	31
	Articles	20	10	10

The dataset contains almost the same amount of positive and negative sentences, respectively 329 and 320. The same goes for positive and negative articles, which are respectively 71 and 61.

B. Classification results

The performance metrics obtained in both considered perspectives (by-sentence where we considered each sentence independently from the others, and by paper where we conglomerated sentences according to the paper they belonged to) are shown in Table III. As explained above (Section II.D), AUROC and AUPRC are not reported in by-paper perspective.

TABLE III: Classification results

Perspective	AUROC	AUPRC	F1-score	Precision	Recall
By-sentence	0.822	0.821	0.741	0.769	0.714
By-paper			0.857	0.900	0.818

BOW+LR model performance evaluation metrics computed on the test set for the by-sentence and by-paper perspectives. N_sentences = 109, N_papers = 20.

The BOW+LR model performed well in both perspectives according to all considered metrics with AUROC and AUPRC well above 0.8. As the number of false negatives was higher than the one of false positives, precision was higher than recall. This result suggests that correctly identifying negative

sentences and papers was slightly more challenging than correctly identifying positive cases. While not directly comparable, performance was overall better in the by-paper setting than in the by-sentence one, which was expected as it is easier to obtain a correct classification looking at multiple sentences for each paper rather than classifying each sentence independently.

IV. Discussion And Conclusions

The main aim of this work was to define a reliable manually-curated dataset that associates each variant to its PS3/BS3 evidence code associated articles (positive set) and not associated articles (negative set), and to demonstrate its utility by developing a predictive model to perform automatic positive article identification.

The manually curated dataset comprises 649 sentences of 132 articles. In order to be sure enough to have a sufficient number of positive examples, we included in the dataset 23 *ClinGen articles* and, to consider a more representative sample of the entire corpus of articles retrieved when querying for a specific variant, 109 non-*ClinGen articles*. As expected, most of *ClinGen articles* were positives (only 1 was reclassified as negative, as we analysed only textual information). Overall, about half extracted sentences contained sufficient evidence for PS3 or BS3 evidence code, and same for the articles. A positivity offset is given by the elevated number of positive sentences extracted from few *ClinGen articles*, but generally positive sentences and articles are respectively less than negative ones (167 vs. 201 sentences extracted from 49 vs. 60 non-*ClinGen articles*). However, we found a significant number of positive articles in non-*ClinGen articles* (49 out of 109), suggesting that manually curated information contained in ClinGen is incomplete and/or not updated frequently enough.

Despite the limited size of the dataset and the relatively simple methodological approach that we decided to consider for a preliminary exploratory analysis, discrimination performance concerning automatic identification of PS3 or BS3 evidence code vs. negative articles was good both in the by-sentence and by-paper perspective, with F1-scores above 0.7 and 0.8 respectively. This result suggests that reliable tools could be developed in support of manual curation, providing to clinicians all information needed for a complete and correct variant interpretation.

Future developments include increasing the dataset sample size, i.e., the number of curated articles, considering all possible variant synonyms, and optimising the workflow for automatic sentences extraction. Moreover, we will focus on a more specific classification for the (variant, article) pair. The solid manual curation procedure described in this work may be applied to variants which are not included in ClinGen and expanded to the evaluation of other evidence codes among the 28 covered by ACMG guidelines.

Data Availability

The dataset will be available upon reasonable request to the corresponding author.

Acknowledgement

This work was supported in part by MIUR (Italian Ministry for Education) under the initiative “Department of Excellence” (Law 232/2016) and by Fondazione Cassa di Risparmio di Padova e Rovigo and AB ANALITICA under the initiative “Smart PhD – Dottorati in Azienda!”.

References

[1] M. Morash, H. Mitchell, H. Beltran, O. Elemento, e J. Pathak, «The Role of Next-Generation Sequencing in Precision Medicine: A Review of Outcomes in Oncology», *Journal of Personalized Medicine*, vol. 8, fasc. 3, set. 2018, doi: 10.3390/jpm8030030.

[2] L. M. Amendola *et al.*, «Performance of ACMG-AMP Variant-Interpretation Guidelines among Nine Laboratories in the Clinical Sequencing Exploratory Research Consortium», *Am J Hum Genet*, vol. 98, fasc. 6, pp. 1067–1076, giu. 2016, doi: 10.1016/j.ajhg.2016.03.024.

[3] S. Richards *et al.*, «Standards and Guidelines for the Interpretation of Sequence Variants: A Joint Consensus Recommendation of the American College of Medical Genetics and Genomics and the Association for Molecular Pathology», *Genet Med*, vol. 17, fasc. 5, pp. 405–424, mag. 2015, doi: 10.1038/gim.2015.30.

[4] S. M. Harrison, L. G. Biesecker, e H. L. Rehm, «Overview of specifications to the ACMG/AMP variant interpretation guidelines», *Curr Protoc Hum Genet*, vol. 103, fasc. 1, p. e93, set. 2019, doi: 10.1002/cphg.93.

[5] «GVACI Course 2022». https://gvaci.genomes.in/home

[6] W. McLaren *et al.*, «The Ensembl Variant Effect Predictor», *Genome Biol*, vol. 17, p. 122, giu. 2016, doi: 10.1186/s13059-016-0974-4.

[7] K. Wang, M. Li, e H. Hakonarson, «ANNOVAR: functional annotation of genetic variants from high-throughput sequencing data», *Nucleic Acids Res*, vol. 38, fasc. 16, p. e164, set. 2010, doi: 10.1093/nar/gkq603.

[8] «Evidence Repository - Clinical Genome Resources». https://erepo.clinicalgenome.org/evrepo/

[9] «PubMed», *PubMed*. https://pubmed.ncbi.nlm.nih.gov/

[10] «Home - PMC - NCBI». https://www.ncbi.nlm.nih.gov/pmc/

[11] N. Jahn e M. Salmon, «europepmc: R Interface to the Europe PubMed Central RESTful Web Service». https://CRAN.R-project.org/package=europepmc

[12] L. M. Chunn *et al.*, «Mastermind: A Comprehensive Genomic Association Search Engine for Empirical Evidence Curation and Genetic Variant Interpretation», *Front Genet*, vol. 11, p. 577152, nov. 2020, doi: 10.3389/fgene.2020.577152.

[13] C. Stubben, «tidypmc: Parse Full Text XML Documents from PubMed Central». https://CRAN.R-project.org/package=tidypmc

[14] A. Kathuria, A. Gupta, e R. K. Singla, «A Review of Tools and Techniques for Preprocessing of Textual Data», in *Computational Methods and Data Engineering*, V. Singh, V. K. Asari, S. Kumar, e R. B. Patel, A c. di, in Advances in Intelligent Systems and Computing. Singapore: Springer, 2021, pp. 407–422. doi: 10.1007/978-981-15-6876-3_31.

[15] W. A. Qader, M. M. Ameen, e B. I. Ahmed, «An Overview of Bag of Words;Importance, Implementation, Applications, and Challenges», in *2019 International Engineering Conference (IEC)*, giu. 2019, pp. 200–204. doi: 10.1109/IEC47844.2019.8950616.

[16] D. Berrar, «Cross-Validation», in *Encyclopedia of Bioinformatics and Computational Biology*, S. Ranganathan, M. Gribskov, K. Nakai, e C. Schönbach, A c. di, Oxford: Academic Press, 2019, pp. 542–545. doi: 10.1016/B978-0-12-809633-8.20349-X.

[17] J. Bergstra e Y. Bengio, «Random Search for Hyper-Parameter Optimization», *Journal of Machine Learning Research*, vol. 13, fasc. 10, pp. 281–305, 2012.

[18] K. Boyd, K. H. Eng, e C. D. Page, «Area under the Precision-Recall Curve: Point Estimates and Confidence Intervals», in *Machine Learning and Knowledge Discovery in Databases*, H. Blockeel, K. Kersting, S. Nijssen, e F. Železný, A c. di, in Lecture Notes in Computer Science. Berlin, Heidelberg: Springer, 2013, pp. 451–466. doi: 10.1007/978-3-642-40994-3_29.

Development of predictive models for short-term prediction of disability progression in multiple sclerosis

E. Tavazzi[1], D. Albertini[1], and M. Vettoretti[1*], for MSOAC[†]
[1] *Department of Information Engineering, University of Padova, Padova, Italy*
[*] *Corresponding author: martina.vettoretti@unipd.it.*

***Abstract*—Multiple Sclerosis (MS) is an autoimmune degenerative disease of the central nervous system, in which chronic inflammation leads to demyelination with transient or permanent axon damage. Symptoms of MS include problems with vision, movement, sensation and balance, which can be intermittent or progressively increasing over time until bringing to permanent disability. Predictive models of MS disability progression can be very useful to support the clinician in choosing the best care for each patient.**

The aim of this work is to develop predictive models of short-term MS disability progression. Data are part of the Multiple Sclerosis Outcome Assessments Consortium (MSOAC) Placebo database, which includes longitudinal demographic and clinical data of 2465 MS patients who were enrolled in the control arm of different MS clinical trials. Variables collected in the first visit were used to predict a binary outcome of disability progression at 6 months and 18 months from the baseline, using a logistic regression model. Disability progression was defined as a 1.5 increase in the Expanded Disability Status Scale (EDSS) value compared to the baseline time. 20 input variables were considered in each model, including demographics, medical history, functional tests, questionnaires, and MS phenotype. Preprocessed data were split into a training and a test set with an 80%-20% proportion. Logistic regression models were trained on the training set, using over-/undersampling techniques for balancing the classes. The identified models were tested on the test set by assessing the area under the receiver operating characteristic curve (AUC).

Prediction performance on the test set was satisfactory, although not optimal, with AUC equal to 0.74 at 6 months and 0.71 at 18 months. These prediction performances are comparable with results obtained by other literature studies on smaller cohorts.

Future developments of this work include the use of other machine learning techniques for model training, the application of feature selection and variable ranking techniques, the incorporation of new variables (e.g., imaging variables), and the external validation of the models on new populations.

***Keywords*—Predictive Model, Multiple Sclerosis, Expanded Disability Status Scale, Disability Progression**

I. Introduction

Multiple Sclerosis (MS) is a chronic autoimmune and inflammatory disease involving the central nervous system, characterised by demyelination and transient or permanent damage to axons [1]. MS is a multifactorial disease whose causes are still not fully determined. Probable underlying causes include genetics, environmental factors, as well as viral infections [2]. MS causes a variety of physical and cognitive symptoms. The course of the disease can consist of isolated recurring attacks, named relapses, that characterise the relapsing-remitting MS (RRMS) phenotype, or of a progressive decline of the subject's functionalities, that can either occur since the first phases of the disease (Primary Progressive Multiple Sclerosis, PPMS) or in a second phase only (Secondary Progressive Multiple Sclerosis, SPMS). The care for MS mainly consists of pharmacological treatments administered to delay disease progression or mitigate the symptoms.

In this context, the employment of prognostic predictive models would lead to many advantages, including promoting the understanding of the mechanisms of MS, anticipating treatments for patients in need of preventive therapies, thereby improving the risk/benefit ratio and the quality of life of these individuals, as well as informing patients and caregivers about the future evolution of the disease. Several literature studies have investigated the prediction of progression in terms of different outcomes, such as the values of functional tests performed by the patients or a related score [3], [4], the increase of fatigue [5], the shift from one MS phenotype to another [6], [7], or the time/chance of occurrence of a relapse [8], [9]. To this end, various classical machine learning methodologies have been used, adopting regression, classification, or survival analysis approaches.

In this work, we focused on modelling the progression of MS in terms of the worsening of the patient's disabilities. We considered as the outcome the Expanded Disability Status Scale (EDSS) [10], a score that is used in clinical practice for monitoring the status and capacities of MS patients and whose variation over time is typically used to define an exacerbation of the disease. The EDSS ranges from 0 (normal status) to 10 (death due to MS), with increasing values as the disability progresses. This score incorporates the status of eight functional systems (pyramidal, cerebellar, brain stem, sensory, bowel and bladder, visual, mental, and other functions), which together express all possible neurological alterations induced by the disease. After defining a threshold on EDSS variations and a prediction horizon, i.e., a temporal time-window in

[†]Data used in the preparation of this article were obtained from the Multiple Sclerosis Outcome Assessments Consortium (MSOAC). As such, the investigators within MSOAC contributed to the design and implementation of the MSOAC Placebo database and/or provided placebo data, but did not participate in the analysis of the data or the writing of this report.

which the subject is observed, each subject can be associated with a binary outcome (progression of disability occurred or not), and the prediction can be approached as a classification task.

This approach mimics the ones proposed in the literature by Zhao et al. [11], [12], by Law et al. [3], by Tommasin et al. [13], and by Yperman et al. [14]. In that literature studies, however, we observed that the cardinality of the cohorts used for model development was often limited to only a few hundred patients, which clashes with the requirements of machine learning to have a sufficiently large number of instances to learn models appropriately. To overcome this issue, in this work we employed the Multiple Sclerosis Outcome Assessments Consortium (MSOAC) Placebo database [15], [16], which includes demographic and clinical data of 2465 MS patients who were involved in clinical trials of MS treatments as the control groups. Starting from the first recorded visit (baseline), we identified two prediction horizons, namely 6 and 18 months after the baseline, computed the outcomes, and developed a logistic regression model for each setting using as input the variables collected during the first trial visit. We then assessed the prediction performance of the model on an independent test set.

II. Materials and Methods

A. Dataset and preprocessing

The MSOAC Placebo Database includes fully anonymized longitudinal data of 2465 MS patients from 9 clinical trials [15], [16]. The database contains data on demographics, medical history, performance outcome measures (e.g., Timed 25 Foot Walk (T25FW), 9-Hole Peg Test (NHPT), Paced Auditory Serial Addition Test (PASAT)), clinician-reported outcome measures (e.g., EDSS, Kurtzke Functional Systems Scores (KFSS)), patient-reported outcome measures (e.g., 36-Item Short Form Health Survey (SF-36)), relapse information, and MS phenotype (e.g., relapsing-remitting), for a total of 104 longitudinally-collected variables. The MSOAC database does not include imaging data. Due to the nature of the dataset, enrollment time and follow-up duration may vary for subjects participating in different clinical trials.

We extracted the information collected at the first visit of each patient to be used as input for the predictive models and preprocessed it as follows. After removing the data that referred to an under-represented MS phenotype (Progressive-Relapsing MS, 2 patients only), we filtered the variables to remove the ones with too much missing information. By excluding the variables with more than 30% of missing values, the total number of features was reduced to 23. We then filtered out three more boolean features – namely the one indicating the need for more than 2 attempts to perform the T25FW test, the NHPT with the dominant hand, or with the non-dominant hand – that were excluded since the occurrence of positive cases was extremely limited. This brought the final number of features to 20. Table I reports a description of the included variables, with the percentage of their missing values (fourth column), the mean and interquartile range (IQR) of numerical variables or the levels of categorical variables (fifth column).

B. Model development pipeline

Data collected at the first visit of each subject, referred to as baseline, were used to predict subject's disease progression at two prediction horizons (PH), i.e., at 6 and 18 months after the time of the baseline visit (t_B). For each subject, the EDSS value at baseline, $EDSS_{t_B}$, was defined as the first available EDSS value. The EDSS at PH, $EDSS_{t_B+PH}$, was defined as the EDSS value recorded at $t_B + PH$. Subjects with no EDSS value recorded at $t_B + PH$ were excluded from the analysis. For each PH value, a binary outcome of disability progression was defined as follows. A subject was provided label "1", i.e., progression of disability, if $EDSS_{t_B+PH} - EDSS_{t_B} \geq 1.5$ in accordance with the work by Zhao et al. [12]. Conversely, a subject was assigned label "0", i.e., no progression of disability, if $EDSS_{t_B+PH} - EDSS_{t_B} < 1.5$.

A different predictive model was developed for each PH using logistic regression as a binary classification model. Labelled data were randomly split into a training set, with 80% of the subjects, and a test set, with the remaining 20% of the subjects. The training-test split was stratified by model outcome in order to maintain the same proportion of classes in the two sets. Missing values in the input variables were imputed using the Multiple Imputation by Chained Equations (MICE) method [17]. The parameters of the imputation algorithm were learned from the training set, and used to impute both the training and the test set. Then, categorical variables were encoded using dummy variables. Finally, numerical variables were scaled in the range 0-1, by subtracting to each variable its minimum value in the training set, and then dividing the result by the range of the variable values in the training set. In order to manage the strong class unbalance, two strategies were adopted for balancing the classes on the training set. The first one consisted in oversampling the less frequent class, until the two classes are balanced ("Oversampling"). The second one consisted in oversampling the less frequent class, and undersampling the more frequent class, until the two classes are balanced ("Both Over-/Under-sampling").

A logistic regression model was trained on the balanced training set. The logistic regression equation is:

$$ln(\frac{P}{1-P}) = \beta_0 + \beta_1 \cdot X_1 + ... + \beta_n \cdot X_n) \qquad (1)$$

where P is the probability of the class "1", X_i, i = 1,..., n are the input variables, β_i, i = 1,...,n are the model parameters associated with the input variables, and β_0 is the intercept parameter. Model parameters were estimated on the training set by maximum likelihood. Variables significantly associated with the outcome were identified by the Wald test (significance level 5%).

In total 4 models were developed (2 PH values x 2 strategies for balancing the training set).

TABLE I: BASELINE VARIABLES SELECTED AS INPUT FOR THE PREDICTIVE MODEL AFTER DATA PREPROCESSING.

Domain	Name	Description	NA (%)	Mean [IQR] / Levels
Demographics	AGE	Age at first visit (in years)	3.37	41.77 [18, 72]
	SEX	Sex	0	Male / Female
Findings about Medical History	P1Y_RELAPSES	Number of relapses experienced in the year previous to the first visit	27.75	1.376 [0, 7]
	T25_FW_first	First T25FW test performed: time taken to cover a straight stretch of 25 feet (in seconds)	0.81	9.217 [0.7, 218.2]
	T25_FW_second	Second T25FW test performed: time taken to cover a straight stretch of 25 feet (in seconds)	0.85	9.095 [0.7, 232.1]
	PASAT_tc_3s	PASAT: number of correct answers (out of 60) presented every 3 seconds each	3.41	47.24 [0, 60]
Functional Tests	NHPT01_DH1	First NHPT performed with the dominant hand: time taken to complete the test (in seconds)	3.41	25.1 [1, 300]
	NHPT01_DH2	Second NHPT performed with the dominant hand: time taken to complete the test (in seconds)	3.45	23.88 [8.5, 300]
	NHPT01_NDH1	First NHPT performed with the non-dominant hand: time taken to complete the test (in seconds)	3.77	26.87 [1.4, 312.7]
	NHPT01_NDH2	Second NHPT performed with the non-dominant hand: time taken to complete the test (in seconds)	3.85	26.16 [1.2, 356.7]
	EDSS	EDSS score value (in the 1-10 range)	3.29	3.406 [0, 6.5]
	KFSS101	KFSS score value on pyramidal functions (in the 0-9 range)	15.62	1.853 [0, 5]
	KFSS102	KFSS score value on cerebellar functions (in the 0-9 range)	13.35	1.29 [0, 9]
	KFSS103	KFSS score value on brain stem functions (in the 0-9 range)	15.62	0.6351 [0, 4]
Questionnaires	KFSS104	KFSS score value on sensory functions (in the 0-9 range)	15.62	1.178 [0, 5]
	KFSS105	KFSS score value on bowel and bladder functions (in the 0-9 range)	15.62	0.8322 [0, 6]
	KFSS106	KFSS score value on visual functions (in the 0-9 range)	15.62	0.7543 [0, 6]
	KFSS107	KFSS score value on cerebral (or mental) functions (in the 0-9 range)	15.62	0.5827 [0, 3]
	DH	Dominant hand	3.25	Left / Right
Medical History	PHENOTYPE	MS phenotype at first visit	0	RRMS / SPMS / PPMS

C. Performance metrics

Each model was applied to the test set to assess its performance. As performance metrics, we considered the receiver-operating-characteristic (ROC) curve, i.e., the plot of sensitivity vs. 1-specificity for different classification thresholds on the predicted probability of class "progression of disability" (P in eq. 1), and the area under the ROC curve (AUC). The AUC varies between 0 and 1, with 0.5 corresponding to the model that randomly assigns the classes, 1 corresponding to the model that perfectly classifies the data, and 0 to the model that perfectly divides the two classes but switches them.

III. Results

There were a total of 2232 subjects with a definite outcome at 6 months after baseline, of whom 103 had a progression of disability (i.e., EDSS worsening $\geq$ 1.5) and the other 2129 have no progression of disability (i.e., EDSS worsening $<$ 1.5). At the 18-month PH, 1605 subjects have a definite outcome, of whom 164 are in the "progression of disability" class and 1441 in the "no progression of disability" class. After splitting the data, the training and the test sets for the prediction of disability progression at 6 months include 1786 and 446 subjects, respectively. For the 18-month PH, the number of subjects in the training and the test sets is 1284 and 321, respectively.

The AUC values obtained on the test set are reported in Table II. At 6 months, the models achieve satisfactory, though not optimal, prediction performance, with the best results obtained by the model trained with oversampling of the training set. The ROC curve for this model is shown in Fig. 1. At 18 months, the model prediction performance is slightly lower than those at 6 months. At 18 months, the technique that performs both over- and undersampling of the training set achieves a slightly higher prediction performance. The ROC curve for this model is shown in Fig. 2.

In Table III we report for each final model the list of variables that resulted significantly associated with the outcome according to the Wald test (significance level 5%) and the corresponding p-values.

TABLE II: AUC VALUES ON THE TEST SET

Prediction horizon	*Sampling strategy*	*AUC value*
6 months	Oversampling	0.7404
6 months	Both over-/undersampling	0.7284
18 months	Oversampling	0.6969
18 months	Both over-/undersampling	0.7101

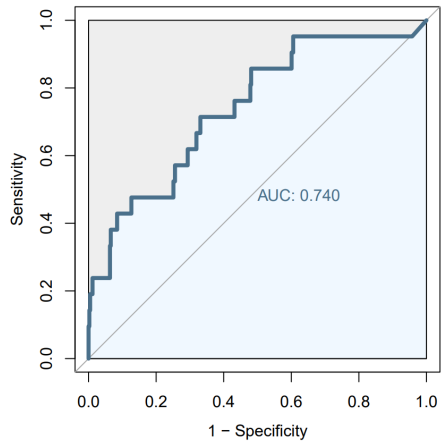


Fig. 1: ROC curve on the test set of the logistic regression model that predicts disease progression at 6 months, using the oversampling technique for balancing classes on the training set.

TABLE III: P-VALUES OF THE VARIABLES ASSOCIATED WITH MODEL OUTCOME ACCORDING TO THE WALD TEST IN AT LEAST ONE MODEL

Variable	*Model PH=6*	*Model PH=18*
AGE	4.95e-15	
SEX	0.033533	
P1Y_RELAPSES	< 2e-16	0.026148
T25FW_first	7.97e-05	
T25FW_second	9.14e-06	
PASAT_tc_3s	< 2e-16	
NHPT01_DH1	4.72e-06	0.012367
NHPT01_DH2	0.001201	
EDSS	8.70e-12	7.33e-11
KFSS101		0.000386
KFSS105		0.006603
DH		0.030788
PHENOTYPE	0.000287	2.11e-05

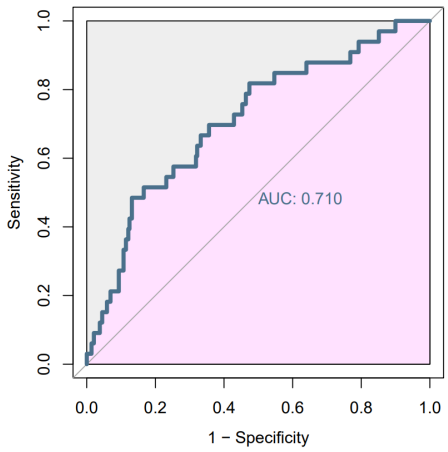


Fig. 2: ROC curve on the test set of the logistic regression model that predicts disease progression at 18 months, using both over-/undersampling techniques for balancing classes on the training set.

IV. Conclusion

In this work, we used the data of the MSOAC Placebo Database to develop logistic regression models of short-term disability progression, defined as an increase of the EDSS score larger than 1.5, with a PH of 6 months and 18 months. The developed models achieved satisfactory prediction performance on an independent test set, with AUC values of 0.74 at 6 months and 0.71 at 18 months. The slight deterioration of prediction performance at 18 months is somehow expected because, given the large variability among disease progression profiles observed in MS, the larger the PH the more difficult is to predict with confidence the progression of disability. These prediction performances are comparable with results obtained by other literature studies on smaller cohorts (AUC=0.62 at 6 months in Law et al. [3] using a cohort of 485 patients; AUC=0.79 at 24 months in Tommasin et al. [13] using a cohort of 163 patients; AUC=0.75 at 24 months in Yperman et al. [14] using a cohort of 642 patients), confirming the feasibility of MS progression prediction.

By comparing the variables most significant for outcome prediction at different PH (Table III), we can observe that some variables are significantly associated to progression of disability at both 6 and 18 months (i.e., number of relapses in the last year, EDSS, NHPT01_DH1, and MS phenotype). Interestingly, the role of other variables varies with the PH, with demographic variables (i.e., age and sex) being not significantly associated to progression of disability at 18 month.

The prediction performance is still not optimal, but several margins for improvement exist. Although the dataset used in this study is larger than those used by studies in the literature, indeed, this dataset poses some major challenges, such as significant class imbalance, absence of imaging data, short follow-up period, and possibly different enrollment times. Class imbalance can significantly affect model training, although in this study we mitigated its effect by using over/undersampling techniques. Magnetic resonance imaging (MRI) of the central nervous system is the main diagnostic test to quantify the effects of demyelination, and it is routinely performed to monitor MS progression. Therefore, the inclusion of MRI-derived variables in the models could bring some important information to improve the prediction of disease progression. Finally, datasets with longer follow-up periods could allow the development of predictive models of long-term disease progression.

Future developments of this work include the use of other machine learning techniques for model development (e.g., support vector machines or random forest), application of feature selection and variable ranking techniques, incorporation of new variables (e.g., MRI variables if available), and external validation of the models on new patient populations.

Acknowledgement

This work was supported by MIUR (Italian Ministry for Education) under the initiative "Departments of Excellence" (Law 232/2016), the Department of Information Engineering of the University of Padova, Padova, Italy ("Dotazione Ordinaria per la Ricerca" 2019, and "Research Grant (type B) – junior initiative" 2021.)

References

[1] Compston, A. & Coles, A. Multiple sclerosis. *Lancet* **372**, 1502–17 (2008).
[2] Kamm, C. P. *et al.* Multiple sclerosis: current knowledge and future outlook. *European neurology* **72**, 132–141 (2014).
[3] Law, M. T. *et al.* Machine learning in secondary progressive multiple sclerosis: an improved predictive model for short-term disability progression. *Multiple Sclerosis Journal–Experimental, Translational and Clinical* **5**, 2055217319885983 (2019).
[4] Tsagkas, C. *et al.* Central nervous system atrophy predicts future dynamics of disability progression in a real-world multiple sclerosis cohort. *European Journal of Neurology* **28**, 4153–4166 (2021).
[5] Ibrahim, A. A. *et al.* Inertial sensor-based gait parameters reflect patient-reported fatigue in multiple sclerosis. *Journal of neuroengineering and rehabilitation* **17**, 1–9 (2020).
[6] Manouchehrinia, A. *et al.* Predicting risk of secondary progression in multiple sclerosis: a nomogram. *Multiple Sclerosis Journal* **25**, 1102–1112 (2019).
[7] Pisani, A. I. *et al.* A novel prognostic score to assess the risk of progression in relapsing- remitting multiple sclerosis patients. *European journal of neurology* **28**, 2503–2512 (2021).
[8] Chalkou, K. *et al.* A two-stage prediction model for heterogeneous effects of treatments. *Statistics in medicine* **40**, 4362–4375 (2021).
[9] Ahuja, Y. *et al.* Leveraging electronic health records data to predict multiple sclerosis disease activity. *Annals of clinical and translational neurology* **8**, 800–810 (2021).
[10] Kurtzke, J. F. Rating neurologic impairment in multiple sclerosis: an expanded disability status scale (edss). *Neurology* **33**, 1444–1444 (1983).
[11] Zhao, Y. *et al.* Exploration of machine learning techniques in predicting multiple sclerosis disease course. *PloS one* **12**, e0174866 (2017).
[12] Zhao, Y. *et al.* Ensemble learning predicts multiple sclerosis disease course in the summit study. *NPJ digital medicine* **3**, 1–8 (2020).
[13] Tommasin, S. *et al.* Machine learning classifier to identify clinical and radiological features relevant to disability progression in multiple sclerosis. *Journal of neurology* **268**, 4834–4845 (2021).
[14] Yperman, J. *et al.* Machine learning analysis of motor evoked potential time series to predict disability progression in multiple sclerosis. *BMC neurology* **20**, 1–15 (2020).
[15] Rudick, R. A., LaRocca, N., Hudson, L. D. & Msoac. Multiple sclerosis outcome assessments consortium: genesis and initial project plan. *Multiple Sclerosis Journal* **20**, 12–17 (2014).
[16] Multiple Sclerosis Outcome Assessments Consortium. Msoac - critical path institute. URL: https://c-path.org/programs/msoac/ URL visited on 16th January 2023.
[17] Van Buuren, S. & Groothuis-Oudshoorn, K. mice: Multivariate imputation by chained equations in R. *Journal of statistical software* **45**, 1–67 (2011).

Dynamic Bayesian Networks and Transfer Learning Enable the Development of Deep Sequence-Based Models on Small-Sample Data

Enrico Longato[1], Erica Tavazzi[1], Adriano Chiò[2], Giovanni Sparacino[1], Barbara Di Camillo[1,3]
[1] *Department of Information Engineering, University of Padova, Padova, Italy.*
[2] *Neuroscience Department "Rita Levi Montalcini", University of Torino, Torino, Italy.*
[3] *Department of Comparative Biomedicine and Food Science, University of Padova, Padova, Italy.*

***Abstract*—The development of prognostic models for rare diseases is often limited by the latter's extremely low prevalence, which, in turn, affects the breadth of modelling techniques that may be applied. Notably, a severe lack of training data may hinder or prevent the implementation of high-capacity models, such as deep neural networks, despite their known effectiveness in predicting adverse outcomes and efficiency in making use of longitudinal data. To address this issue, in the present work, we propose a novel methodological pipeline where we first train a dynamic Bayesian network (DBN) on the few available data to simulate an adequate number of virtual patients whose variables are linked by the same probabilistic relationship over time as in the original data; then, we train a deep learning model based on recurrent neural networks on the simulated data; and, finally, we apply finetuning, a transfer learning (TL) technique, to adapt the model to the real data. To demonstrate the potential usefulness of our approach, we apply it to the prediction of 3-year mortality in amyotrophic lateral sclerosis (ALS), a rare (<0.01% prevalence), fatal neurodegenerative disease, starting from a population of 985 patients from the Piemonte and Valle d'Aosta ALS (PARALS) register. We show that our pipeline of DBN and TL effectively combines the simulated data it is able to generate and the few available real data, leading to an 8.2% AUROC improvement over a reference deep learning model trained only on the real data.**

***Keywords*—Data Augmentation, Deep Learning, Dynamic Bayesian Networks, Rare Diseases, Transfer Learning.**

I. Introduction

Prognostic model development for rare diseases presents an additional set of challenges compared to more frequent conditions. Notably, whereas, for many clinical applications, data scarcity can partially be remedied by extending the study to different types and sources of data (e.g., by making a secondary use of administrative or routinely acquired data), the inherently small number of people affected by rare diseases sets a hard limit to data availability. In turn, this reflects on the breadth of modelling approaches that can be applied with the reasonable expectation of obtaining robust results. Particularly, the usage of high-capacity models such as deep neural networks, which have been successful in tackling complex modelling tasks, especially using longitudinal data [7], seems difficult to justify in light of the disproportionately limited sample size of many rare-disease databases.

To address this issue, one possibility might be resorting to standard data augmentation techniques to artificially increase the number of available training examples via transformations of the data [8]. However, while some domains, such as image analysis, naturally lend themselves to the application of data augmentation techniques, the best way to augment typical clinical data, including patient characteristics, vital parameters, and, possibly, longitudinally-acquired timeseries, is still unclear. An alternative approach would be to leverage data generation techniques [16] to produce a sufficient number of virtual patients, and, then, train a model using the simulated data. Dynamic Bayesian networks (DBNs) are an effective tool to perform purely data-driven simulation of clinical data by, first, learning the joint probability distribution of patient covariates over time, and, then, resampling from the trained DBN to simulate the static and longitudinal data of an arbitrary number of virtual patients. While these simulated data can be (and have successfully been [14]) used for model training as if they were real patient data, there is no guarantee that the resulting model would then translate directly to real-life individuals. Challenges such as this are the focus of transfer learning (TL), a range of techniques aiming at transferring knowledge across tasks. A typical transfer learning workflow starts from a model that is known to solve a task on a given domain, the *source* domain, which is then adapted to solve a similar task on an adjacent domain, the *target* domain. This approach has shown great promise in different fields, especially in image recognition where, e.g., a deep neural network developed on generic image data (source domain) can be successfully adapted to radiology applications (target domain) without full retraining [5].

In the present work, we propose a novel approach combining DBNs and TL to develop deep, sequence-based models despite low data availability. Briefly, we first train a DBN on the training data and use it to simulate a large number of virtual patients, complete with their longitudinal data; then, we train a deep learning model based on recurrent neural networks on the simulated data (source domain); finally, we apply finetuning, a TL technique, to adapt the network trained on the simulated data to the target domain, i.e., the original, real data. Specifically, we focus on the case study of predicting 3-year mortality in amyotrophic lateral sclerosis (ALS), a rare (<0.01% prevalence) but fatal neurodegenerative

disease, based on the longitudinal data of 985 patients from the Piemonte and Valle d'Aosta ALS (PARALS) register [3], and show that our approach leads to a 8.2% performance improvement relative to an equivalent model trained from scratch on the real data only.

II. Data description and preparation

A. Database

We studied the data of a real-world cohort of 985 ALS patients extracted from the PARALS register. The data consisted of demographic and clinical information collected during routine screening visits, outlining the patients' status from diagnosis onwards. The information collected at diagnosis included sex, age at onset, site of onset (spinal or bulbar), diagnostic delay, body-mass index (BMI) both premorbid and at diagnosis, forced vital capacity (FVC) at diagnosis, the result of a genetic test on the main ALS-related genes (namely C9orf72, FUS, SOD1, and TARDBP), ALS familiality, and presence of frontotemporal dementia (FTD). Additionally, longitudinal information was also available both at the time of diagnosis and at each follow-up visit: namely, the use/administration of non-invasive ventilation (NIV) and percutaneous endoscopic gastrostomy (PEG), and the values of the Milano-Torino staging (MiToS) system [2], a scale comprising four binary variables reflecting impairment (or lack thereof) in the following four functional domains: breathing, walking/self-care, swallowing, and communicating. Finally, the date of death or tracheostomy (henceforth referred to simply as death, as tracheostomy-free survival is a conventional endpoint in ALS clinical trials) is also reported, if applicable.

B. Outcome definition and exclusion criteria

The prediction outcome for this study was 3-year mortality, i.e., the occurrence of death within 3 years after the 9-month longitudinal baseline that served as the input to the predictive model (see Section III-B).

Starting from the initial cohort of 985 patients, we applied the following exclusion criteria.

a) Subjects whose date of death preceded their first recorded visit.
b) Subjects with fewer than 2 visits before and 1 after the 9-month mark (the baseline length for prediction), to help the convergence of the DBN and ensure that all subjects had at least some longitudinal data.
c) Subjects for whom it was impossible to determine the prediction outcome, i.e., survivors censored before the 3-year mark.

This process resulted in the selection of 626 subjects, for a total of 7241 visits.

C. Data split and imputation

We split the data into a training, a validation, and a test sets, comprising 64%, 16%, and 20% of the subjects, respectively. The data characteristics are shown in Table I, with the continuous and categorical variables reported as means $\pm$ SD, and frequencies and proportions, respectively.

We then imputed the missing data by chained equations using the *mice* R package [15] with default parameters. To fit our modelling pipeline (see Section III) and avoid information leakage, we trained two imputers, one on the training data to impute missing values on the training and validation sets, and another on the union of the training and validation data to impute missing values on the entire database, including the test set. These steps resulted in a training set of 399 subjects and 4640 visits, a validation set of 98 subjects and 1128 visits, and a test set of 129 subjects and 1473 visits with no missing values.

TABLE I: DEMOGRAPHIC AND CLINICAL FEATURES OF THE STUDY POPULATION AFTER PREPROCESSING.

	Levels	**Training (n=399)**	**Validation (n=98)**	**Test (n=129)**
Sex	Female	197 (49.4%)	39 (39.8%)	60 (46.5%)
Familiality	Yes	44 (11.0%)	4 (4.1%)	10 (7.8%)
	<NA>	1 (0.3%)	0 (0%)	2 (1.6%)
Genetics	Mutated	44 (11.0%)	9 (9.2%)	8 (6.2%)
	<NA>	17 (4.3%)	6 (6.1%)	17 (13.2%)
FTD	Yes	42 (10.5%)	7 (7.1%)	19 (14.7%)
	<NA>	141 (35.3%)	31 (31.6%)	44 (34.1%)
Onset site	Bulbar	122 (30.6%)	26 (26.5%)	48 (37.2%)
Age at onset (years)		62.67 ± 11.17	62.78 ± 10.79	62.56 ± 10.34
Diagnostic delay (months)		12.00 ± 10.06	11.04 ± 10.28	12.00 ± 13.56
BMI premorbid (kg/m^2)		26.14 ± 4.39	26.17 ± 4.22	25.80 ± 3.73
BMI at diagnosis (kg/m^2)		25.19 ± 4.40	25.09 ± 4.71	24.32 ± 3.73
FVC at diagnosis (%)		93.41 ± 22.00	93.66 ± 23.13	90.69 ± 24.21
NIV	Administered	164 (41.1%)	42 (42.9%)	51 (39.5%)
PEG	Administered	134 (33.6%)	31 (31.6%)	49 (38.0%)
MiToS walking/self-care	Impaired	319 (79.9%)	77 (78.6%)	94 (72.9%)
MiToS swallowing	Impaired	142 (35.6%)	33 (33.7%)	50 (38.8%)
MiToS communication	Impaired	109 (27.3%)	31 (31.6%)	35 (27.1%)
MiToS breathing	Impaired	184 (46.1%)	44 (44.9%)	55 (42.6%)
Cumulative incidence of 36-month mortality		70.90%	68.40%	76.60%

III. Methodology

The proposed methodological pipeline is based on the cascade of a DBN and a TL approach known as finetuning [12]. Briefly, we performed the following sequence of actions.

i) Train a DBN on the training set and use it to simulate data from the training and validation sets.
ii) Develop a deep learning model based on recurrent neural networks on the simulated training data and use the simulated validation data for early stopping and hyperparameter optimisation. We call this model the encoder.
iii) Remove the output neuron from the encoder and attach a fully-connected subnetwork in its place to obtain the TL model.
iv) Train the TL model as per Section III-B on the real training data and use the real validation data for hyperparameter optimisation.

Finally, we compared the predictive performance of the TL model to that of a model with the same architecture as the encoder, but trained and optimised on the real data, on the real test set. The target metric was the cumulative/dynamic area under the receiver-operating characteristic curve (AUROC) [1] at 3 years.

A. DBN

DBNs are probabilistic graphical models capable of encoding the joint conditional probability distributions (CPDs) over time of a set of longitudinally-collected variables [10]. DBNs are well suited to modelling the evolution of diseases for descriptive and prognostic purposes (e.g., [13]). After a DBN has been trained, the probability relationships over time that it has encoded in the learning phase can be used to simulate,

starting from an initial (clinical) condition, the evolution over time of a population of subjects, thus obtaining an in silico population that preserves the trends seen in the real training population.

Here, we learnt a DBN starting from the training set using the *bnstruct* R package [4]. First, in order to better model the temporal evolution of ALS, we computed two derived variables for each visit: the distances of each visit from the onset (time since onset, TSO) and from the following visit (time between visits, TBV). Then, to allow the DBN to observe a more balanced occurrence of the death outcome, we coded survival at each visit as a binary variable answering the question "Will the subject die within the next 9 months?" We set the layering for the DBN, i.e., the rules that govern forbidden relationships, in accordance with literature knowledge (e.g., MiToS score values must depend on TSO, as they are expected to change as the disease progresses) and common sense (e.g., sex cannot depend on clinical values). The DBN structure was inferred using the Max-Min Hill-Climbing algorithm, using the Bayesian information criterion as the score function, while the CPDs' parameters were computed via maximum a posteriori estimation.

After learning the DBN on the training set, we simulated 100 synthetic repetitions of each real patient of both the training and validation sets starting from their first recorded visit, and ending after 40 virtual visits or on (simulated) death.

B. Transfer learning

1) Input data coding: The TL part of the proposed pipeline was based on recurrent neural networks. We considered a baseline window of 9 months to predict subsequent 3-year mortality. To leverage longitudinal information on the MiToS scores during the first 9 months, we used an input coding scheme that had previously proved successful for other applications [6]. Specifically, we built a (17×10) matrix where each row represented a variable and each column a visit within the 9-month baseline (up a maximum to 10). The first 6 rows were dedicated to dynamic data (the four MiToS scores, NIV, and PEG), while the remaining 11 to static variables (sex, age, familiality, genetics, onset site, FTD, diagnostic delay, time since onset, premorbid BMI, BMI at diagnosis, FVC at diagnosis). The data were right-aligned such that the latest visit within the baseline was in the tenth column. Static data were only reported on the tenth column as well. We used a masking value of "-1" to signal that either a visit was missing (which resulted in the 6 dynamic columns being masked at the missing row) or that the column referred to a static variable (which resulted in all rows except the tenth one being masked). Masked values were ignored during training.

2) Encoder and reference model: Developing an encoder is the first step to applying finetuning-based TL. In this context, an encoder is simply a model trained on the source domain (simulated data), which we will then extend to the target domain (real data) by attaching a fully-connected subnetwork to it and performing a second round of training on the real data. Particularly, for the encoder, we implemented a deep learning architecture based on recurrent layers as follows: the masked input matrix described in Section III-B1 enters a recurrent layer, possibly with dropout; then, the transformed sequence passes through a series of fully-connected layers with ReLU activation, of progressively halving size, finishing on a single output neuron with a sigmoid activation function, representing the predicted outcome, i.e., 3-year mortality. The hyperparameters of the architecture were: the type of recurrent layer (GRU or LSTM), its size (16, 32, or 64), its dropout (0 or 0.1) and recurrent dropout (0 or 0.1) levels, its activation function (ReLU or tanh), the number of fully-connected layers (2 or 3), and the number of nodes in the first fully-connected layer (16, 32, or 64). We used the simulated training data to tune the weights of the encoder via the ADAM algorithm (0.0001 learning rate) and the binary cross-entropy loss function. We used the simulated validation data to perform early stopping when the loss function on the simulated validation set stopped improving, and also to select the best hyperparameters as the ones maximising the (simulated) validation AUROC.

We followed the same procedure to train a reference model on the real data, i.e., a deep neural network with the same architecture, but trained and optimised on the real training and validation data, respectively. This model served as a comparison for the TL model.

3) Finetuned transfer learning model: To turn the encoder, i.e., the model able to solve the 3-year mortality prediction task on the source domain of simulated data, into the full TL model, we proceeded as follows. First, we removed the output neuron and retained the model, with its pre-trained weights, up until the last fully-connected layer, and we attached an untrained fully-connected subnetwork (hyperparameters: 2 or 3 progressively half-sized layers; 16, 32, or 64 nodes in the first layer) ending with a sigmoid-activated output neuron; then, keeping the encoder weights fixed for a number of pretraining epochs (0, 10, or 20), we trained only the newly-added fully-connected layers with the ADAM algorithm (learning rate 0.00005) on the real training set; finally, we finetuned the entire network, including the encoder weights, with a 100 times smaller learning rate. We used the real validation set to perform early stopping and hyperparameter optimisation. This procedure yielded the final TL model.

IV. Results and discussion

Figure 1 shows the DBN obtained on the training set, with nodes representing the variables and directed edges entering a node corresponding to the conditional dependency effect of the child node on its parents. Self-loops on the dynamic variables (blue nodes in the figure) represent the dependence of the variable at a time point from itself at the previous time point. Analysing the resulting relationships, we can see that the DBN effectively integrates the imposed literature relationships with others directly learned from the data. Numerous known relationships emerge, such as the relationship between ALS familiarity and age of onset [9], or the dependence of diagnostic delay on gender and site of onset [11]. The fact that the credibility of the relationships learnt by the DBN can

be checked via inspection of the graphical model allows for greater control over the expected quality of the simulated data compared to generic data augmentation techniques.

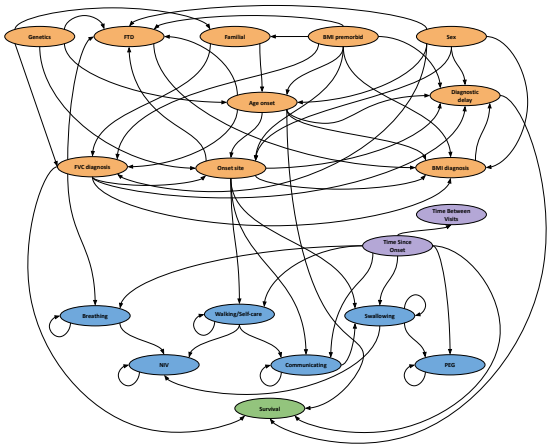


Fig. 1: DBN obtained on the training set. Dynamic variables are reported in blue (MiToS scores, NIV, and PEG), purple (TBV and TSO), and green (survival), while static variables are in orange.

Hyperparameter optimisation yielded the following results. The optimal reference model was made up of a size-32 ReLU-activated GRU with 0.1 dropout and 0.1 recurrent dropout, and two fully-connected layers of 32 and 16 neurons. The optimal TL model was the cascade of the optimal encoder (similar hyperparameters to the reference model, but different weights: size-32 GRU, ReLU activation, no dropout; two fully-connected layers of 32 and 16 neurons) and an optimal subnetwork of two fully-connected layers of sizes 16 and 8; the optimal number of pretraining epochs during which the encoder weights were fixed was 20.

TABLE II: PERFORMANCE EVALUATION ON THE REAL TEST SET (n=129).

Model	Training data	AUROC
Reference model	Real	0.649
Finetuned TL model	Real and simulated	0.702

Table II compares the reference model and the TL model on the task of predicting 3-year mortality after a 9-month baseline on the real data. The difference between the two was that the former only used the real data, whereas the latter was finetuned starting from an encoder learnt only on the data simulated by the DBN. We observed a substantial relative performance improvement of 8.2% between the reference model's AUROC of 0.649 and the TL model's AUROC of 0.702.

These results support the hypothesis that, while small-sample datasets might be insufficient, on their own, to develop deep sequence-based models, the opportune application of a cascade of DBNs (to simulate an adequate number of virtual subjects retaining the same conditional probability relationships over time as the original, real subjects) and TL (to adapt the model from the source domain of simulated data to the target domain of real data) may allow deep recurrent neural networks to learn a robust temporal representation of the data regardless of the original sample size. Having learnt such representation, a very limited number of real data are sufficient to finetune the model's parameters and improve on the reference model's performance. Future developments will pertain to the optimisation of the trade-off between the number of simulated data (computationally expensive) and model performance. This preliminary result is especially encouraging in the field of rare diseases, as it presents a novel, but effective way to implement high-capacity, sequence-based models despite the inevitably low cardinality of the available data.

Acknowledgement

This research was supported by the University of Padova project C94I19001730001, by the Italian Ministry of Health grant RF-2016-02362405, and by the Italian Ministry of Education, University and Research (PRIN) grant 2017SNW5MB. EL and ET were founded by the Department of Information Engineering, University of Padova (Research Grant B junior).

References

[1] Aasthaa Bansal and Patrick J Heagerty. A tutorial on evaluating the time-varying discrimination accuracy of survival models used in dynamic decision making. *Medical Decision Making*, 38(8):904–916, 2018.

[2] Adriano Chiò, Edward R Hammond, et al. Development and evaluation of a clinical staging system for amyotrophic lateral sclerosis. *Journal of Neurology, Neurosurgery & Psychiatry*, 86(1):38–44, 2015.

[3] Adriano Chiò, Gabriele Mora, et al. Secular Trends of Amyotrophic Lateral Sclerosis: The Piemonte and Valle d'Aosta Register. *JAMA Neurology*, 74(9):1097–1104, 2017.

[4] Alberto Franzin, Francesco Sambo, and Barbara Di Camillo. bnstruct: an R package for Bayesian Network structure learning in the presence of missing data. *Bioinformatics*, 33(8):1250–1252, 2017.

[5] Belal Hossain, SM Hasan Sazzad Iqbal, et al. Transfer learning with fine-tuned deep CNN ResNet50 model for classifying COVID-19 from chest X-ray images. *Informatics in Medicine Unlocked*, 30:100916, 2022.

[6] Enrico Longato, Barbara Di Camillo, et al. Time-resolved trajectory of glucose lowering medications and cardiovascular outcomes in type 2 diabetes: a recurrent neural network analysis. *Cardiovascular Diabetology*, 21(1):159, 2022.

[7] Enrico Longato, Gian Paolo Fadini, Giovanni Sparacino, Angelo Avogaro, et al. A deep learning approach to predict diabetes' cardiovascular complications from administrative claims. *IEEE Journal of Biomedical and Health Informatics*, 25(9):3608–3617, 2021.

[8] Kiran Maharana, Surajit Mondal, and Bhushankumar Nemade. A review: Data pre-processing and data augmentation techniques. *Global Transitions Proceedings*, 2022.

[9] Puja R Mehta, Ashley R Jones, Sarah Opie-Martin, et al. Younger age of onset in familial amyotrophic lateral sclerosis is a result of pathogenic gene variants, rather than ascertainment bias. *Journal of Neurology, Neurosurgery & Psychiatry*, 90(3):268–271, 2019.

[10] Kevin Patrick Murphy and Stuart Russell. Dynamic bayesian networks: representation, inference and learning. 2002.

[11] Hipolito Nzwalo, Daisy de Abreu, Michael Swash, Susana Pinto, and Mamede de Carvalho. Delayed diagnosis in als: the problem continues. *Journal of the Neurological Sciences*, 343(1-2):173–175, 2014.

[12] Maxime Oquab, Leon Bottou, Ivan Laptev, and Josef Sivic. Learning and transferring mid-level image representations using convolutional neural networks. In *Proceedings of the IEEE conference on computer vision and pattern recognition*, pages 1717–1724, 2014.

[13] Chiara Roversi, Erica Tavazzi, Martina Vettoretti, et al. A dynamic bayesian network model for simulating the progression to diabetes onset in the ageing population. In *2021 IEEE EMBS International Conference on Biomedical and Health Informatics (BHI)*, pages 1–4. IEEE, 2021.

[14] Erica Tavazzi, Sebastian Daberdaku, et al. Predicting functional impairment trajectories in als: a probabilistic, multifactorial model of disease progression. *Journal of neurology*, pages 1–21, 2022.

[15] Stef van Buuren and Karin Groothuis-Oudshoorn. mice: Multivariate Imputation by Chained Equations in R. *Journal of Statistical Software, Articles*, 45(3):1–67, 2011.

[16] Marco Viceconti, Adriano Henney, and Edwin Morley-Fletcher. In silico clinical trials: how computer simulation will transform the biomedical industry. *International Journal of Clinical Trials*, 3(2):37–46, 2016.

A Distributed Multi-Centric Application for the Analysis of Cardiac Troponin Profiles

N. Cortese[1,&], A. Procopio[1,&], S. De Rosa[2,&], G. Canino[2], A. Merola[1], J. Sabatino[2], C. Critelli[2], C. Indolfi[2,3], F. Amato[4], C. Cosentino[1,*]

[1] *Biomechatronics Lab, Dept. of Experimental and Clinical Medicine, Università Magna Graecia di Catanzaro*

[2] *Interventional Cardiology Unit, Dept. of Medical and Surgical Sciences, Università Magna Graecia di Catanzaro*

[3] *Mediterranea Cardiocentro-Napoli, Naples, Italy*

[4] *Dept. of Electrical Engineering and Information Technology, Università degli Studi Federico II di Napoli*

[&] Equal contribution, * Corrisponding author: carlo.cosentino@unicz.it

***Abstract*—Interaction between the clinical and engineering worlds is essential for the development of new medical technologies, as well as the maintenance of medical advancements. In this context, software applications represent the potent, user-friendly, and highly analytical bridge between the two disciplines. In this research, we have developed a distributed web application whose computational core consists of a compartimental model of cardiac troponin release following acute myocardial infarction. This system allows reconstruction of the cardiac troponin release curve in patients with ST-Elevation Myocardial Infarction. The developed software represents an innovative platform geared toward personalized medicine, aming to simplify and expedite patient triage, as well as to support physicians during the diagnostic and prognostic phases. The application is also a valuable research tool since it enables for the structured and reliable collection and retrieval of clinical data to support further studies.**

***Keywords*—eHealth, multi-centric system, cardiac biomarkers, biological models**

I. INTRODUCTION

Cooperation between the information technologies (IT) world and the clinical sector is becoming increasingly cohesive and enables a significant reduction in the time and cost of diagnosis, the production of large volumes of data for research, and their classification and analysis in order to generate knowledge. In the literature, there are many examples of IT that can be used in the medical field. These range from simple toolboxes to computer programs with online or desktop interfaces. These software programs are typically used to analyze and/or extract information from experimental evidence transferred to computer data [1], [2], [3]. This type of applications are only a few instances of how small stand-alone programs may streamline healthcare operations and help research. However, designs that expand the reachability of such tools and systems that enable the gathering and handling of massive volumes of data (e.g. client-server, peer-to-peer) are frequently required. In this paper, we present a distributed web application for the reconstruction of the cardiac biomarkers release curves in patients with ST-Elevation acute Myocardial Infarction (STEMI), and that retains the core concept of the previously developed Cardiac Biomarker Release Analyzer (CBRA) [4]. The software consists of several interfaces, realized in MATLAB App Designer. These allow the definition of a customized flow of operations for each type of intended user, in an effort to simplify data entry and analysis. The development of a user-friendly interface for the implementation of the model-based algorithm for the reconstruction of the troponin curve was given special consideration. In fact, this allows for both the dynamic visualization of the curve and the modification of model resolution parameters. Finally, a system for anonymizing and recognizing shared data was developed, allowing the export of sensitive data to be omitted while still retrieving the patient's identity in response to a formal request containing the unique code. A distributed infrastructure was implemented to manage the workload and large quantities of data generated by multiple centres. The proposed distributed system is comprised of one datapoint per centre, with each datapoint consisting of a single machine with client-server architecture to make the software easily reachable. This serves to have a common data scheme for the various centres, and makes the workload and quantity of data easier to handle. As a result, the program adds a system for obtaining and analysing patients data, comparing the release curves of various patients, and providing large datasets, a hint for future research, to its fundamental role.

This article is structured as follows: Section II is dedicated to providing basic knowledge on the clinical aspect treated. All the information about the methodologies, development and deployment of the software platform are presented in the Section III, while Section IV is dedicated to the conclusions and future developments.

II. BACKGROUND

Acute myocardial infarction (AMI) represents the most frequent acute coronary syndromes as well as the primary cause of mortality in the world. An AMI occurs as a consequence of a coronary obstruction inducing necrosis of tissue due to insufficient perfusion of oxygen and nutrients [5]. The diagnosis is based on the analysis of the ECG trace, to monitor the electrical activity of the heart, and on the investigation of the presence of specific biomarkers for cardiac damage in the blood of patients. About the last point, the

gold standard biomarker for AMI detection is represented by cardiac troponin (cTn), a protein involved in the contraction of myocardial muscle cells, and composed of three constituent parts, C, I, and T. While the cTnC is similar to its skeletal isoforms, cTnT and cTnI are extremely specific for the necrosis of the heart tissue, [6], and they are commonly exploited in clinical practice.

Two types of AMI patients are distinguished: STEMI and NSTEMI. Due to complete coronary obstruction, STEMI patients exhibit the characteristic ST-tract elevation on the electrocardiogram. For NSTEMI patients, often with a non-complete obstruction, biomarker release curve analysis is essential at this point to assess their clinical situation [7]. Procopio et al., in [8], presented an ad-hoc mathematical model describing the variation of the concentration of cTnT among the cellular compartments of the sarcomere, cytosol, and plasma. Under physiologic conditions, cTnT is undetectable in the plasma: following an AMI, as a result of cell dismantling, the concentration of cTnT in this compartment rapidly increases. The mathematical model was derived from these physiological observations; specifically, it consisted of three differential equations that exploit Fick's first law of diffusion. The purpose of this model, [8], [9], integrated into CBRA, is therefore to reconstruct the missing data, beginning with those obtained from highly specific assays during the patient's hospitalization. Therefore, analyze the specific patient response and extract diagnostically useful information, such as the values and times of maximum concentration points or the time of AMI onset.

III. MATERIALS AND METHODS

A. Data management system

To prepare the application for workload management and maximise data acquisition from multiple centres, a distributed system was chosen. Each data centre consists of a database and application server running on a client-server architecture. Although the use of a single centralized server implementation allows for greater control, particularly in terms of version control over the entirety of the data, it is currently regarded as posing critical issues. The distributed implementation seeks to eliminate the need for a big data centre capable of storing a potentially large quantity of data over time. It also significantly improves client-server response times by having clients report to various independent server, due to the fact that each server can manage fewer simultaneous connections and, consequently, fewer tasks. Therefore, the entire amount of work performed by a single client-server architecture can be divided into as many tiny, independent same architectures. Because of the distributed and multi-center character, information acquired by several centres may be combined and conveyed into the same database structure. The data sharing system, on the other hand, enables for the download and import of a dataset built over time in one centre into another, as well as analysis between patient curves. Furthermore, once a substantial dataset has been produced, its export provides an ideal foundation not just for developing the model itself, but also for performing additional research on the data, using techniques such as machine learning.

In order to provide the capability of collecting and organizing data in a consistent way, a new database was designed. In the database composition, all the data have been organized in order to correctly identify their source (origin center and physician's data) as well as the related patient. The sensitive data have been differentiated from the clinical ones to establish a degree of separation between two different entities, which allows a convenient extraction of shareable data. The information required to reconstruct the release curve has been separated into two distinct classes: hospitalizations and acquisitions. Hospitalization serves to store data relating

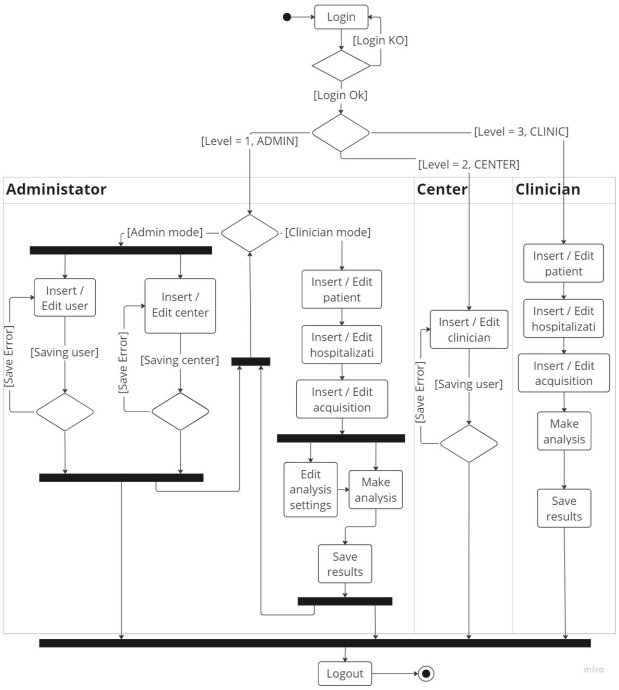


Fig. 1: Activity diagram outlining the available pathways of functionalities based on user types that logs in.

to the AMI, including the date and time of the event and admission, along with other patient clinical information. Acquisitions, on the other hand, are used to record data regarding experimental measurements, taking execution date-time and instant biomarker concentration. Due to these factors, it have been considered the following constraint rules:

1) Each user must be associated with a type that defines its functions and views within the system;
2) Users and patients must be limited to one center membership;
3) Access to all the system functions and the data must be available to admin users;
4) Clinicians users can only access to data of their patients;
5) A patient may be hospitalized more than once and each new admission may be associated with new acquisitions and simulations;
6) Each hospitalization must be associated with the patient, as well as the clinician user who inserts it;

7) Any acquisition must be associated with the current hospitalization.

B. User types and security system

The architecture of the security system starts with the login. To avoid unauthorized access, each user has a unique username and a password encrypted through a SHA-256 algorithm. The system validates these credentials and then determines level of access privileges granted to the user who is attempting to log in. To conduct the preceding check, the system refers to the external key in the user table, which contains the user type identifier. Three different types of users (ADMIN, CENTER, and CLINICIAN) are defined hierarchically, as a consequence, as shown in Figure 1, each has access to distinct functions. The ADMIN user has complete control over the system, including managing the centers on the same server and their user accounts as well as the personal and medical information of patients. In summary, an ADMIN can insert and modify centers, users, and patients, and he/she is able to manage clinical data related to experimental acquisitions or admissions and perform analysis for each patient. CENTER user is constrained to the simple management of the accounts associated with the reference center. Lastly, CLINICIAN user is limited to the management of patients with which he is affiliated, as well as performing standard analyses. Different user interface pathways, which direct the available functions depend on each user's security level, define these boundaries. To prevent cyberattacks, especially SQL injection, each text field is under the supervision of a function that scans the input field to ensure that no MySQL keywords are contained. This prevents the unexpected retrieval of data through the interface by attempting to send commands directly to the DBMS and provides an additional layer of protection between the user and the database. To significantly enhance the network security aspect, it is reasonable to equip the host server with a firewall that restricts access to the software to IP addresses that have been authorised. To preserve anonymity in the sharing system, clinical data is maintained as a distinct entity from personal data. Each patient is associated with a unique code to enable the tracing of any anomalous data about the patient. This code is generated upon insertion and identifies the patient individually. As described in Figure 2, it is composed of 24 alphanumeric characters made up of database source data. In order to reduce user input mistakes, a check system analyzes and reports indications of any empty fields.

C. Interfaces and scenarios

The entire software was written in MATLAB, with heavy reliance on App Designer for the user interface (UI) development. This section describes the different functions provided by the UI, and how the sequence of these produces a specific path of tasks for each type of user. Starting from the activities of the clinician, this user can enter all the information related to the personal and clinical data of his related center patients, as well as conduct analysis on the cardiac troponin release curves. The home page for clinicians users is composed of i) a navigation menu, ii) a summary table of patients, iii) a panel for the modification of personal data, and iv) a pop-up menu to select the collected patients, and access their hospitalizations and acquisitions data. Clinicians can access the page "Hospitalization", dedicated to the patient's clinical data through the navigation menu. The hospitalizations list for chosen patients, the time-series of cTnT based on related acquisitions, and a panel for adding or changing data can all be found on this page. Information about potential thrombolysis and subsequent revascularization in addition to the temporal data related to the hospitalization and the AMI occurrence are also stored. Additionally, there are clinical data for the TIMI Score calculation, used to gauge the risk of death in STEMI patients 30 days after the event: age, systolic blood pressure, heart rate (HR), weight, Killip classification, anterior ST elevation (STE), left bundle branch block (LBBB), diabetes mellitus, hypertension, angina, and time to thrombolytic treatment, [10]. The data relating to the concentrations of cTnT could be added using the same navigation menu to access the page "Acquisitions". The analysis interface presents commonly an output plot in the upper left corner, along with a patient summary. To perform a good analysis, the selected patient must have at least one hospitalization and 5 acquisitions. The Analysis page for clinicians consists of a panel showing a summary of the selected patient, the run button for the simulation start, and the axes where the curve will be plotted. Once the simulation is complete, the graph is plotted, and the results and time was taken are displayed in the relevant panel at the bottom. Regarding the user center, it was designed to have an intermediate level of security that would allow an administrator to manage the utilities of the center. Therefore, it consists of one interface that allows one to insert new users and navigate between those already present. The creation of new users is limited to the inclusion of clinical users. The admin view is designed to act as both a profile to manage the entire system of centers that are placed on the same server, as well as to perform more advanced analysis of the data. To reach this aim, the admin user can switch between the Admin and Clinician Advanced modes. Through the clinician mode, all the clinician interfaces, with some additional features, are available to the admin. The main difference between an Administrator and a Clinician user is present in the analysis interface: whereas the clinical user has the exclusive ability to run a simulation and check the results, an admin can change the initial configuration of the analysis, such as upper and lower bounds, initial values, and optimization algorithms. Once the simulation is complete, the graph is plotted, and the results and time was taken are displayed in the relevant panel at the bottom. Both the admin and the clinician users have also access to the sharing system: on the Home Page of the patient data management system, there are two buttons labeled Import and Export Data, which allow, respectively, the import, and export of clinical data through .csv or .xlsx files. In particular, to flavor the import of data, an ad hoc excel standard has been developed with database table-compatible fields, as well as a system that

automates and checks file loading. In compliance with patient privacy, the resulting CSV/XLSX can be utilized with third-party analytic tools in addition to serving as data exchange material between the centers.

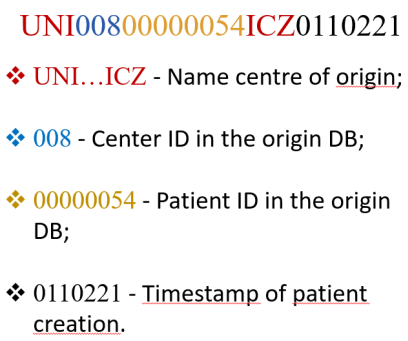


Fig. 2: Composition of the patient's identifying code, which includes i) the name, and id of the center, ii) the id of the patient, and iii) the creation time in the database of the origin center.

D. Deployment

MATLAB Web App Server and MATLAB Runtime v912 are required for software deployment. The minimum hardware requirements for running MATLAB Web App Server with a MATLAB Runtime are an x86-64 based CPU with at least one core, 1 GB of RAM, as well as an SSD of at least 60 GB. More precisely, the number of MATLAB server sessions that could be started at once, determines how many CPU cores and GB of RAM are needed. As a result, each center, that wants to utilize the program on a local server, can customize it to correspond to its requirements, and available resources based on the maximum number of concurrent users it wishes to support. For instance, the MATLAB server has to create 4 workers in order to support 4 concurrent sessions, hence at least 4 CPU cores and 4 GB of RAM must be accessible. All the tests are performed on a server with an Intel i7 octa-core CPU with 16 GB of RAM.

IV. CONCLUSION

The developed software, implementing the model-based core in a web-based application, provides a distributed platform for reconstructing the cTnT release curve, and for managing all collected patients data. The combination of the model-based approach and the capabilities of the web has enabled the development of a software with an intuitive UI that can improve data input and management operations. The remote connection to the server via network facilitates the clinician's ability to enter and retrieve data from any connected device. The new database associated enables data collection in a consistent and robust way and provides the doctor with an instant and comprehensive overview of the clinical status of the patients. The multi-centric architecture paired with the data-sharing system represents a further strength of this new software. This association reduces costs by constructing an ad hoc server with features specific to the requirements of the individual center, while the sharing system works as a bridge between the centers. In this manner, meaningful data for both clinical and scientific reasons may be acquired in large quantities and with minimal effort and enables the use of comprehensive software for collecting and analyzing measurements data of cardiac biomarkers. This application was developed in collaboration with the Interventional Cardiology unit of the University of Magna Graecia of Catanzaro, where it's currently being tested. As demonstrated by previous research, the model has also been extended to another cardiac biomarker, creatine kinase isoenzymes (CK-MB) [11]. The subsequent phases of development will therefore concentrate on supplying a system for analysing this and other biomarkers in future, as well as enhancing the software's performance and safety. Other potential future advances might be based on the integration of machine learning techniques for patient classification, and new clinical knowledge generation. Finally, the future goal will be to take advantage of the developed distributed platform for the implementation of a federated learning framework, to avoid privacy concerns and automate the process of model refinement.

REFERENCES

[1] T. Karhu, T. Leppänen, J. Töyräs, A. Oksenberg, S. Myllymaa, and S. Nikkonen, "Abosa–freely available automatic blood oxygen saturation signal analysis software: Structure and validation," *Computer Methods and Programs in Biomedicine*, vol. 226, p. 107120, 2022.

[2] P. Perakakis, M. Joffily, M. Taylor, P. Guerra, and J. Vila, "Kardia: A matlab software for the analysis of cardiac interbeat intervals," *Computer methods and programs in biomedicine*, vol. 98, no. 1, pp. 83–89, 2010.

[3] D. Palomino-Fernández, A. Gómez-Grande, M. Fernández-Igarza, P. Pilkington, A. P. Seiffert, H. Bueno, E. J. Gómez, and P. Sánchez-González, "Cassia (cardiology software suite for image analysis): a potential new tool for the evaluation of [18f] fdg pet/ct in the setting of infective endocarditis," *International Journal of Computer Assisted Radiology and Surgery*, pp. 1–13, 2022.

[4] A. Procopio, S. De Rosa, F. Montefusco, G. Canino, A. Merola, J. Sabatino, J. Ielapi, C. Indolfi, F. Amato, and C. Cosentino, "Cbra: Cardiac biomarkers release analyzer," *Computer Methods and Programs in Biomedicine*, vol. 204, p. 106037, 2021.

[5] J. Kingma *et al.*, "Myocardial infarction: An overview of stemi and nstemi physiopathology and treatment," *World Journal of Cardiovascular Diseases*, vol. 8, no. 11, p. 498, 2018.

[6] S. Mythili and N. Malathi, "Diagnostic markers of acute myocardial infarction," *Biomedical reports*, vol. 3, no. 6, pp. 743–748, 2015.

[7] D. D. McManus, J. Gore, J. Yarzebski, F. Spencer, D. Lessard, and R. J. Goldberg, "Recent trends in the incidence, treatment, and outcomes of patients with stemi and nstemi," *The American journal of medicine*, vol. 124, no. 1, pp. 40–47, 2011.

[8] A. Procopio, M. Bilotta, A. Merola, F. Amato, C. Cosentino, S. De Rosa, C. Covello, J. Sabatino, A. De Luca, and C. Indolfi, "Predictive mathematical model of cardiac troponin release following acute myocardial infarction," in *2017 IEEE 14th International Conference on Networking, Sensing and Control (ICNSC)*, pp. 643–648, IEEE, 2017.

[9] A. Procopio, S. De Rosa, C. Covello, A. Merola, J. Sabatino, A. De Luca, C. Liebetrau, C. W. Hamm, C. Indolfi, F. Amato, *et al.*, "Estimation of the acute myocardial infarction onset time based on time-course acquisitions," *Annals of Biomedical Engineering*, vol. 49, pp. 477–486, 2021.

[10] D. A. Morrow, E. M. Antman, A. Charlesworth, R. Cairns, S. A. Murphy, J. A. de Lemos, R. P. Giugliano, C. H. McCabe, and E. Braunwald, "Timi risk score for st-elevation myocardial infarction: a convenient, bedside, clinical score for risk assessment at presentation: an intravenous npa for treatment of infarcting myocardium early ii trial substudy," *Circulation*, vol. 102, no. 17, pp. 2031–2037, 2000.

[11] A. Procopio, S. De Rosa, C. Covello, A. Merola, J. Sabatino, A. De Luca, C. Indolfi, F. Amato, and C. Cosentino, "Mathematical model of the release of the ctnt and ck-mb cardiac biomarkers in patients with acute myocardial infarction," in *2019 18th European Control Conference (ECC)*, pp. 1653–1658, IEEE, 2019.

Quantifying the contribution of single joint kinematics to the overall ergonomic discomfort

E. Scalona[1], D. De Marco[2], G. Rossetto[4], M. Mosso[4], P. Avanzini[2], M. Fabbri-Destro[2], G. Andreoni[3] and N.F. Lopomo[4]

[1] *Dipartimento di Specialità Medico-Chirurgiche, Scienze Radiologiche e Sanità Pubblica, Università degli Studi di Brescia*
[2] *Istituto di Neuroscienze, Consiglio Nazionale delle Ricerche, Parma*
[3] *Dipartimento di Design, Politecnico di Milano*
[4] *Dipartimento di Ingegneria dell'Informazione, Università degli Studi di Brescia*

***Abstract*—Work-related musculoskeletal disorders (WMSDs) represent one of the major issues concerning the occupational safety and health of workers. Thus, a reliable evaluation of workers' exposure to the risk factors that may contribute to WMSDs development is mandatory, above all, within an industrial context. At present, standard synthetic indices are widely used in this frame, presenting – however - several limitations due to poor reliability and time efficiency. The aim of this work was to investigate the contribution of the displacement quantified for each single joint during the execution of simple reaching tasks, to the overall discomfort of the worker evaluated by means of standard observational methods.**

Forty-five healthy volunteers were included in the analysis; each subject was asked to reach and rotate 2 spheres placed on a custom-made rack in standardized positions, i.e., above the head and one at floor level at centre side. Whole-body kinematics was acquired via a system based on wearable inertial measurement units. Standard ergonomic scales including RULA (Rapid Upper Limb Assessment), REBA (Rapid Entire Body Assessment), and MMGA (Method for Movement and Gesture Assessment), were assessed for each subject and each sphere position. Moreover, a quantitative index based on actual joint kinematics, i.e., W_1 index, was computed for each joint angle involved in the task. Correlation analysis was performed for W_1 relative to each joint with respect to RULA, REBA, and MMGA scores.

Considering REBA and MMGA scores, the most comfortable reaching areas were the ones in which the sphere was positioned at the top; in contrast, the lowest positions evidenced the most increased discomfort indexes. The RULA did not result sensitive to the different positions, while REBA and MMGA seemed to be more influenced by the range of motion of the lower limb joint angles than the upper limb ones.

This study underlines the necessity to focus on multiple potential contributors to WMSDs and underlines the importance of subject-specific approaches toward risk assessment by exploiting quantitative measurements and wearable technologies, which indeed represent key enabling approaches even in consideration of the novel "Industry 5.0" perspective.

***Keywords*—Ergonomics assessment, wearable technologies, kinematic monitoring, risk assessment, standard scales, RULA, REBA, MMGA.**

I. Introduction

Work-related musculoskeletal disorders (WMSDs) have been widely reported to be a leading cause of sick leave in many occupational contexts [1]. Indeed, within working environments, it is still common to suffer from repetitive arm movements, and awkward postures are widely adopted despite very recent improvements also due to the introduction of several enabling technologies, including exoskeletons and robots [2]. Indeed, within the actual context defined by "Industry 4.0", work intensity has been growing because of the presence of "hybrid" manufacturing lines which can involve workers in increasingly complex activities. For these reasons, very recently, "Industry 5.0" human-centric approach has been proposed also to mitigate these problems and promote the concepts of overall occupational well-being.

From a general perspective, health and welfare costs for workers must be considered when applying policies aimed at minimizing WMSDs risks. At present, to prevent WMSDs, the best practice is to properly evaluate the exposure to risk factors of a class of workers in a defined working environment during the realization of specific tasks characterizing their working shift; following this analysis it is mandatory to plan ergonomic interventions, as – for instance - a workplace redesign [3]. In this picture, a large number of observational methods, which are widely used in industry, have been presented in the last decades, most of which involve direct visual observation of workers during their activities [4,5]; this approach supports the need to assess the risk of developing WMSDs, which led to the definition of ergonomic scales addressing overall discomfort. In particular, RULA (Rapid Upper Limb Assessment) [6], and REBA (Rapid Entire Body Assessment)[7] represent the main applied methods during ergonomic risk assessment. On the other hand, these two scales present several limitations and have the main disadvantage to require a field expert who performs a time-consuming analysis of the postures.

Over the years some progress has been made to overcome the limits of these methods, leading - for example - to the definition of the MMGA (Method for Movement and Gesture Assessment) [8] and the introduction of wearable technologies, as inertial measurement units (IMUs) which allow for quantitative assessment [9].

However, the use of discrete parameters could be a limitation considering the inherent variability that exists in the ways individuals can complete a specific working task; in fact, most of the movements we perform during daily life activities involve different muscles and multiple joint coordination.

Recently, Lorenzini *et al.* designed a multi-index framework based on kinematic and dynamic parameters estimated via wearable technologies [9]. In particular, the authors proposed a kinematic-based displacement index (W_1) for each joint and degrees of freedom. However, the authors did not provide cues concerning possible relations between standard assessment methodologies and joint-specific metrics.

Therefore, this work aimed at investigating the contribution of the displacement quantified for each single joint (W_1)

during the execution of simple reaching tasks, to the overall discomfort of the worker evaluated by means of standard observational methods and scores. In fact, we hypothesized that W_1 represented a paradigmatic kinematic index able to better highlight the multi-factorial aspects that affect the overall discomfort of the worker and – vice versa – we focused on the need to introduce specific quantitative and subject-specific approaches able to better characterize the occupational risks and, thence, guide the mitigating strategies.

II. Materials and Methods

A. Participants

Forty-five healthy volunteers (33 females, 12 males, mean age 25.1 years old) were enrolled in the study. All the subjects reported no previous history of neurological disorders or recent orthopedic injuries. All subjects were right-handed according to the Edinburgh Handedness Inventory [10]. All the subjects were instructed with respect to the assessment procedure and signed informed consent. The study was approved by the local institutional review board (Comitato Etico dell' Area Vasta Emilia Nord, 10084, 12.03.2018).

B. Experimental setup and Testing procedure

Subjects were asked to perform motor tasks which consists of reaching and manipulating 2 soft spheres (6 cm diameter) placed on a 2x1 meters rack, adapting the experimental paradigm proposed by Andreoni et al. [8]. In particular, the 2 spheres were positioned according to the anthropometric measures of the subject and centered on the midline; the one in the lower position was placed 6 cm above the floor, whereas the one in the top position was moved in correspondence to the participant's height plus 10 cm. The subjects stand still in front of the rack with the feet behind a reference cross placed considering the length of the forearm plus 30 cm, to make the task more challenging. Each movement started from a static standing position with the arms by their side and the subject was asked to perform the task without crossing the reference line and without lifting their feet completely off the ground. From the starting position, participants reach and grasp the sphere addressing the manipulation of each sphere, i.e., three times clockwise rotations with the right hand. The task was repeated five times for each position of the spheres (i.e. the upper and lower ones). The experimental setup and task execution are reported in Figure 1.

C. Motion tracking

Whole-body kinematics was acquired by using a full-body motion tracking system based on IMUs (MVN Link and Biomech Awinda, XSens, The Netherlands). The motion trackers were positioned within the suit according to the protocol required by the manufacturer; in particular, 17 sensors were positioned on the subject to capture the movement of the following 23 body segments, which included the head, neck, eighth and tenth thoracic vertebra, third and fifth lumbar vertebra, right and left shoulder, right and left arm, right and left forearm, right and left hand, pelvis, right and left thigh, right and left shank, right and left foot, and right and left forefoot. Before starting the recording session, a calibration procedure was performed to align the motion trackers to the anatomical segments of the subject. The movement were acquired by using a sampling frequency of 240 Hz.

D. Data analysis

Data acquired by IMUs were first exported by using the Xsens MVN-Analyze software (XSens, The Netherlands). From the kinematic variables provided by the software, we selected three-dimensional joint angles which were exported via custom routines developed in a numerical computing environment (Matlab2018a; MathWorks Inc.). Before additional data processing, the start and end frames for each trial were determined. In particular, we focused only on the reaching phase which was segmented according to the tangential velocity of the hand [11]; the temporal boundaries of the reaching phase were identified as the times at which the hand velocity surpasses and returns below 5% of the peak velocity (reaching start and end, respectively).

Once defined the overall repetition, RULA and REBA indices were estimated and MMGA scores were calculated for each subject, each sphere position, and each trial and then averaged among trials. Moreover, the kinematic-based displacement index W_1 was computed for paradigmatic joints, including pelvis-trunk, right shoulder, right elbow, right wrist, right and left hips, right and left knees, and right and left ankle; W_1 was averaged among trials as well. We decided to not consider the joint angles relative to the left upper limb since all subjects were right-handed.

To evaluate the difference between lower and upper conditions, paired t-tests were conducted for RULA, REBA, and MMGA. Pearson's correlation analysis was performed for the values of W_1 relative to each joint with respect to the obtained, REBA, and MMGA scores, and Spearman correlation with RULA scores to assess their sensitivity with respect to the contribution of each individual joint.

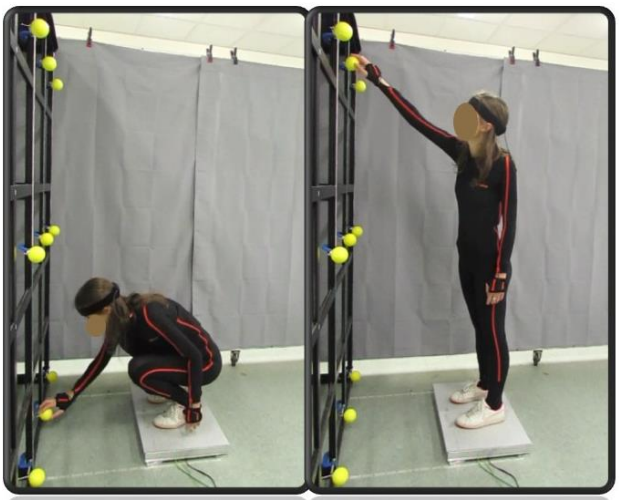


Fig. 1: Experimental setup; spheres on right, left sides and in the middle line were not used for this study.

III. Results and Discussions

Concerning the lowest and highest positions, the average scores of RULA were 6.08 (±0.56) and 5.97 (±0.33) ($t(44) = 1.56$, $p = 0.12$), whereas focusing on REBA we obtained a score of 10.04 (±0.72) and 7.46 (±0.71) ($t(44) = 22.73$, $p < 0.01$), respectively; from the analysis of

MMGA, the score was 424.75 (±44.62) for the lower and 190.42 (±21.72) for the highest position ($t(44) = 39.8$, $p < 0.01$).

Considering both REBA and MMGA scores, the reaching areas presenting less discomfort were the ones in which the sphere was positioned at the highest level; on the other hand, the lowest position evidenced the most increased discomfort indexes. Surprisingly, the RULA index did not highlight any difference between the tasks devoted to reaching the sphere positioned at the highest level with respect to that placed at the lowest one, highlighting a lack of sensitivity towards this kind of task.

Focusing on the correlation analysis, the main results are reported in Table 1.

TABLE 1 – SPEARMAN AND PEARSON'S CORRELATION COEFFICIENT AMONG W1 RELATIVE TO EACH JOINT WITH RESPECT TO RULA, REBA, AND MMGA SCORES. (*) INDICATES P < 0.05.

W_1	RULA	REBA	MMGA
Pelvis_trunk bend	*0,03*	*-0.64**	*-0.64**
Pelvis_trunk rot	*0,16*	*0.37**	*0.51**
Pelvis-trunk tilt	*0,29**	*0.92**	*0.95**
RShoulder Ab	*0,00*	*-0.72**	*-0.75**
RShoulder Rot	*-0,09*	*-0.76**	*-0.86**
RShoulder Flex	*-0,06*	*-0.61**	*-0.76**
RElbow prono	*0,02*	*0.11*	*0.10*
RElbow Flex	*-0,18*	*-0.79**	*-0.87**
RWrist Flex	*0,19*	*0.61**	*0.63**
RHip Ab	*0,18*	*0.72**	*0.85**
RHip Rot	*0,30**	*0.65**	*0.74**
RHip Flex	*0,16*	*0.90**	*0.96**
RKnee Flex	*0,13*	*0.89**	*0.97**
RAnkleFlex	*0,23**	*0.86**	*0.91**
LHip Ab	*0,21**	*0.71**	*0.81**
LHip Rot	*0,20**	*0.70**	*0.77**
LHip Flex	*0,17*	*0.90**	*0.96**
LKnee Flex	*0,06*	*0.88**	*0.96**
LAnkleFlex	*0,17*	*0.87**	*0.91**

In this frame, the RULA index significantly correlate with any W_1 of trunk bending, right and left hip rotation, right ankle flexion and left hip abduction. However, the correlation coefficient does not exceed 0.30 ,further underling the lack of sensitivity of this assessment method with respect to these specific tasks. On the other hand, both REBA and MMGA negatively correlate with trunk bending, all shoulder rotations, and elbow flexion ($r < -0.65$, $p < 0.01$); further, both indices positively correlate with trunk tilt and all rotations of the lower limbs' joint angles ($r > 0.65$, $p < 0.01$).

As we expected, and as it was confirmed by the analysis of W_1, the movements toward the highest vs lowest positions recruited body segments differently. Figure 2 shows, as a paradigmatic example, the difference in terms of joint angles curves. It is possible to notice that participants expressed higher shoulder flexion in movement toward the upside with respect to the ones in the low side. On the contrary, higher grades of knee flexion characterize the movement in the lower part of the rack. Finally, RULA seemed to be not sensitive to the different positions, whereas REBA and MMGA seem to be more influenced by the range of motion of the lower limbs' joint angles than the upper limbs' ones.

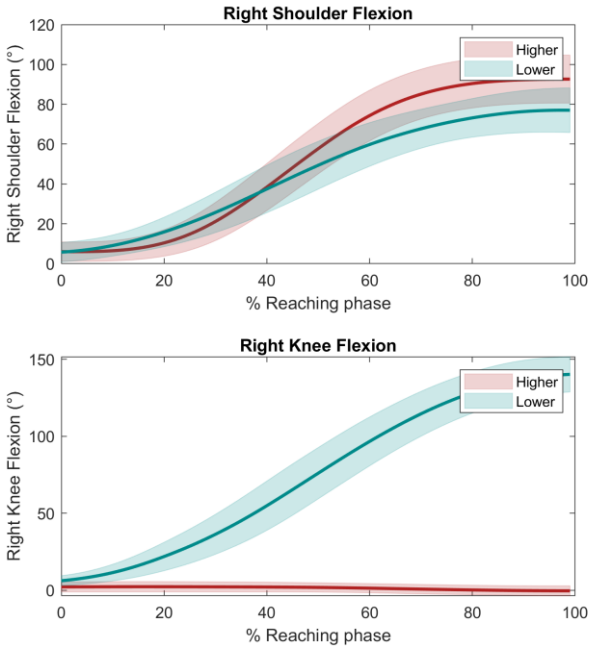


Fig. 2: Mean and standard deviation among subject of the normalized joint angle curves. Right shoulder flexion curves relative to task in the higher and lower position is depicted on the top. Right knee flexion is depicted in the bottom of the figure.

IV. CONCLUSION

The aim of this work was to investigate the contribution of each single joint, in terms of overall joint displacement (W_1) to the overall discomfort of the worker during the execution of manipulative tasks evaluated by means of standard observational methods and scores. In fact, we focused on the need for assessing which standard ergonomic index is more sensitive to the variations of the position of individual body districts.

From the main findings obtained in this study emerged that RULA index was indeed not sensitive to the different tasks required to reach the sphere placed at different positions; on the other hands both REBA and MMGA seemed to be more suitable to underline the ergonomic difference emerging from the two tasks. The reaching areas presenting less discomfort were the ones in which the sphere was positioned at the highest level, while the lowest position evidenced the most increased discomfort indexes.

Moreover, the REBA and MMGA seem to be mainly influenced by the range of motion of the lower limb joint angles than the upper limb ones.

Further studies should be conducted considering different tasks combining different body positions and applying different loads.

These findings suggest the need to focus on multiple potential contributors to WMSDs and underline the importance of subject-specific approaches toward risk assessment by exploiting quantitative measurements and wearable technologies, which indeed represent key enabling approaches within "Industry 5.0" perspective.

REFERENCES

1. Eurofound First findings: Sixth European working conditions survey 2015.
2. Manghisi, V.M.; Uva, A.E.; Fiorentino, M.; Bevilacqua, V.; Trotta, G.F.; Monno, G. Real time RULA assessment using Kinect v2 sensor. Appl. Ergon. 2017, 65, 481–491, doi:https://doi.org/10.1016/j.apergo.2017.02.015.
3. Bortolini, M.; Gamberi, M.; Pilati, F.; Regattieri, A. Automatic assessment of the ergonomic risk for manual manufacturing and assembly activities through optical motion capture technology. Procedia CIRP 2018, 72, 81–86, doi:https://doi.org/10.1016/j.procir.2018.03.198.
4. LI, G.; BUCKLE, P. Current techniques for assessing physical exposure to work-related musculoskeletal risks, with emphasis on posture-based methods. Ergonomics 1999, 42, 674–695, doi:10.1080/001401399185388.
5. David, G.C. Ergonomic methods for assessing exposure to risk factors for work-related musculoskeletal disorders. Occup. Med. (Chic. Ill). 2005, 55, 190–199, doi:10.1093/occmed/kqi082.
6. McAtamney, L.; Nigel Corlett, E. RULA: a survey method for the investigation of work-related upper limb disorders. Appl. Ergon. 1993, 24, 91–99, doi:https://doi.org/10.1016/0003-6870(93)90080-S.
7. Hignett, S.; McAtamney, L. Rapid Entire Body Assessment (REBA). Appl. Ergon. 2000, 31, 201–205, doi:https://doi.org/10.1016/S0003-6870(99)00039-3.
8. Andreoni, G.; Mazzola, M.; Ciani, O.; Zambetti, M.; Romero, M.; Costa, F.; Preatoni, E. Method for Movement and Gesture Assessment (MMGA) in Ergonomics BT - Digital Human Modeling.; Duffy, V.G., Ed.; Springer Berlin Heidelberg: Berlin, Heidelberg, 2009; pp. 591–598.
9. Lorenzini, M.; Kim, W.; Ajoudani, A. An Online Multi-Index Approach to Human Ergonomics Assessment in the Workplace. IEEE Trans. Human-Machine Syst. 2022, 52, 812–823, doi:10.1109/THMS.2021.3133807.
10. Oldfielf, R.C. The assesment and analysis of handedness: the Edimburgh inventory. Neuropsychologia 1971, 9, 97–113, doi:10.1007/978-0-387-79948-3_6053.
11. Michaelsen, S.M.; Jacobs, S.; Roby-Brami, A.; Levin, M.F. Compensation for distal impairments of grasping in adults with hemiparesis. Exp. Brain Res. 2004, 157, 162–173, doi:10.1007/s00221-004-1829-x.

EyeLab: a user-friendly Matlab tool for real-time monitoring of eye movements

G. Olla[1], G. Sedda[1], A. Bonfiglio[1], S. Traccis[2], and D. Pani[1]
[1] *DIEE - Dept. Electrical and Electronic Engineering, University of Cagliari (Italy)*
[2] *Dept. of Neurology, Ospedale Antonio Segni, Ozieri (Italy)*

***Abstract*—Despite the advantages of objective analysis of oculomotor behaviour and the continuous progresses in eye-tracking technologies, eye-movement studies are likely confined to research laboratories and seldom applied in the clinical practice. The neurologist's expertise in reading the traces from eye-trackers, along with the specialized technical knowledge required to manage, program and use such tools, hampered their widespread adoption.**

Recently, many open-source software tools have been developed to expand the usability of eye tracking systems to study oculomotor functioning, but none of these allows the experimenter to simultaneously control the trial and visualize and monitor eye movements in real-time.

In this work, we present EyeLab, a new MATLAB graphical user interface developed for the analysis of both saccadic and smooth pursuit eye movements while using the video-based Eye Link II eye-tracker by SR Research. Developed by exploiting the Psychophysics Toolbox, it extends the functionalities of EyeLink II by introducing and managing an intuitive real-time monitoring user-friendly interface on a third screen, which also allows personalizing the experimental procedure and managing data acquisition, visualization, processing, and storage, without requiring programming skills to the user. The real-time features enable the prompt adaptation of the experimental protocol to the ongoing results and the correction of any setup problem that could affect the correct acquisition of a whole set of tests.

***Keywords*—eye tracking, graphical user interface, real-time monitoring.**

I. Introduction

EYE movements are excellent markers for predicting, documenting and diagnosing multiple neurological abnormalities. For example, reduction in pursuit gain has been reported in patients with schizophrenia [1] and with mild traumatic brain injuries, the latter in conjunction with a decrease in vergence velocity and an increase in the trial-to-trial variability of eye movements [2, 3]. In addition, an increase in the number of errors on anti-saccade tasks and prolongation of the saccadic latency have been documented in patients with dementia or with Parkinson disease [4, 5].

Although these changes in eye movements are large enough to produce disturbances in patients, at the same time they are often too small to be detected by direct qualitative observation by the doctor, typically representing the standard approach during a clinical examination [6, 7]. The quantitative study of eye movements allows the ophthalmologist or the neurologist obtaining oculomotor measurements with very high spatial and temporal resolution, to permanently record the data and access them during the post-processing phase, in order to calculate quantitative indicators of eye movement such as the response gain, which corresponds to the speed of the eye relative to the speed of the objective, the speed of the head, and so on.

Despite the obvious advantages of objective and quantitative analysis of oculomotor functioning and the continuous advances in eye-tracking technologies, they remain relatively rare in current clinical practice compared to subjective evaluation [8]. Specialty clinics often have devices that are dedicated to particular kinds of eye movement testing, such as video-oculography for the evaluation of vestibular function [9], or limbal trackers for recording eye movements during reading [10].

In comparison, video-based eye tracking systems are more confined to research applications [11, 9], because they are more expensive and require high programming skills to the user in order to be integrated in custom experimental protocols [12, 13]. They generally are stand-alone devices with proprietary software and have the advantage of being portable, lightweight and optionally head-mounted, which makes them ideal for tracking the eyes in natural head-free condition and for vestibular testing. For many applications this is enough to make accurate clinical judgments, because of the richness of relevant features of eye movements.

The current rapid rate of technological improvement should ensure that systems with integrated sophisticated eye-tracking capabilities will be deployed more commonly in the clinic, for example by providing appropriate and user-friendly interfaces to allow for eye movement signals to be sampled, stored, and visualized and possibly exploited to the best clinical advantage.

In the present study, we introduce EyeLab, a novel open-source MATLAB graphical user interface that leverages on the features provided by Psychtoolbox-3 f to allow both clinicians and researchers to use the commercial EyeLink II eye-tracking system by SR Research with intuitive and novel intuitive features, without requiring users to have programming skills and with the aim to encourage the introduction of this technology in the clinical practice.

II. Materials and Methods

EyeLab is a new open-source tool provided with a user-friendly graphical user interface (GUI), which substantially extends the conventional capabilities of the EyeLink II eye-tracker by SR Research, providing a real-time control interface on an additional screen to configure and personalize the experimental procedure and manage data acquisition, visualization, processing, and storage.

The EyeLab GUI is intuitive and does not require users to have programming skills; it consists of three main processing

modules:
1. the Real Time Analysis Interface, for real-time monitoring the binocular oculomotor signals during the experiment, while the participant is performing the task. Figure 1 shows the panel of the interface where the signals acquired and processed in real-time (position and velocity of both eyes) are displayed.

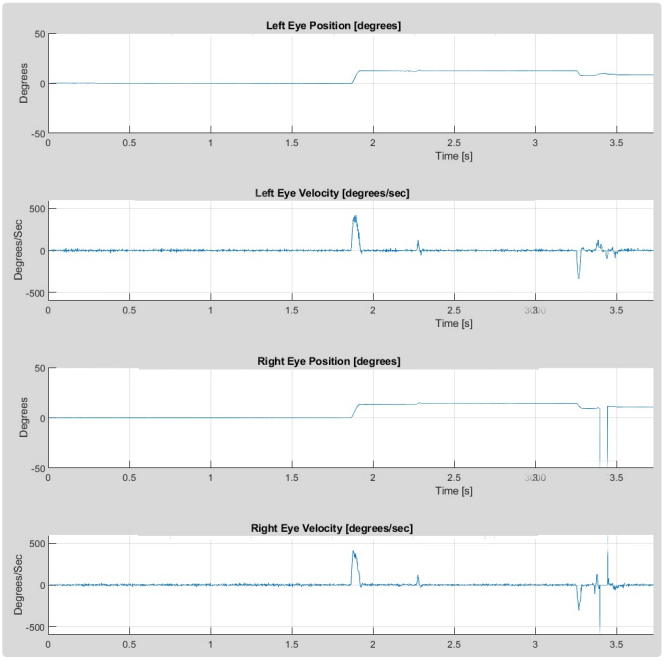


Figure 1. Visualization of eyes' position and velocity in the Real-Time Analysis Interface.

2. the OffLine Analysis Interface, which allows the experimenter to offline post-process the acquired signals (eye position and velocity),and provides several tools for performing the quantification and analysis of saccadic and smooth pursuit eye movements and fixations. For instance, the 'Show Saccades' panel displays one saccade at a time, specifying which eye it refers to, the temporal and spatial position and the duration (see Figure 2). This analysis can be performed using different algorithms [14] and setting constraints to filter the saccade search, such as the minimum temporal interval between two consecutive saccades, the latency interval, the window width, the minimum duration of the saccade or the velocity threshold.

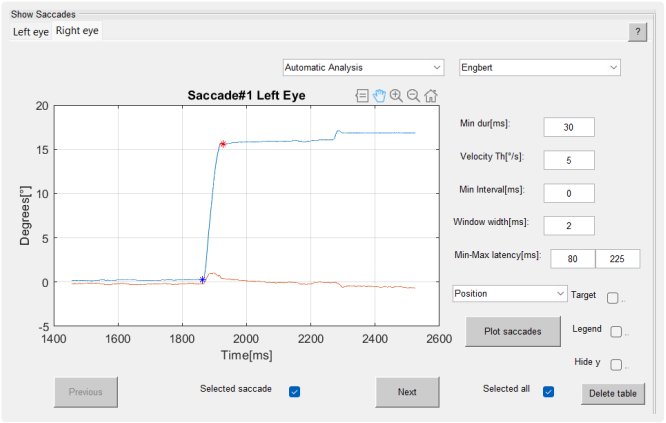


Figure 2. The 'Show Saccades' panel allows both post-processing and visualization of each saccade in the Offline Analysis Interface.

3. the Protocol-based Settings Interface (see Figure 3), which supply many functionalities to create and customize new experimental protocols, for example by generating automatic target movements in specific positions, for the study of saccadic movements.

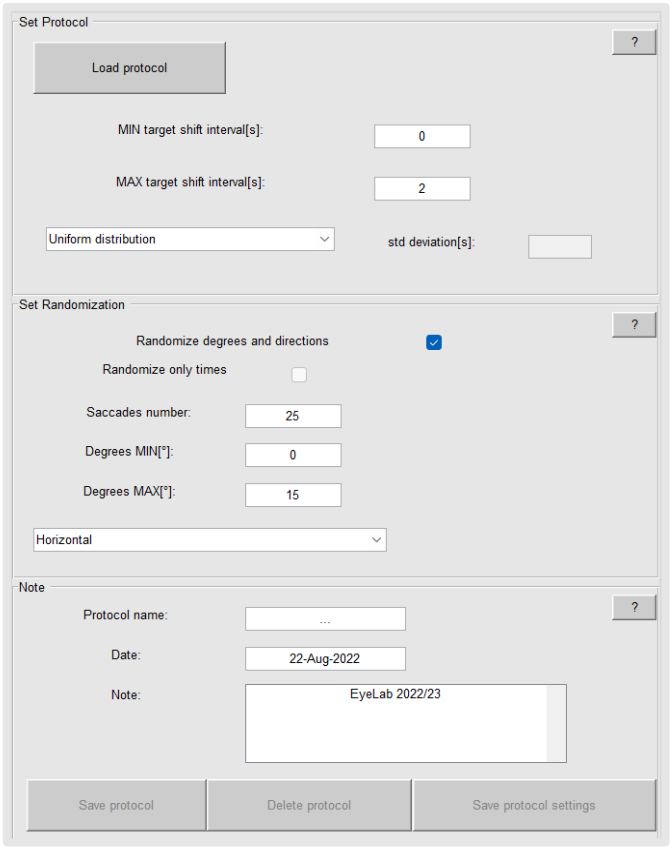


Figure 3. The Protocol-based Settings Interface

The 'Set Protocol' panel allows the experimenter to load a previously designed protocol or to create a new one, defining the visualization interval of the stimuli, which can be fixed or variable, and in this second case they can follow a certain statistical distribution (for example, a uniform distribution). Other panels of the same interface define the randomization protocol, the position of the targets, the pattern (for inducing, for example, saccades), repetitions and more.

Moreover, EyeLab can be installed on different operating systems (Windows, Linux, MacOS) as it is based on the Eyelink Toolbox functions, which provide an interface between the Psychophysics Toolbox Version 3 (PTB-3) for Matlab and the Eyelink II system. These functions work on raw data collected by EyeLink II, in particular the binocular time series of the participant's gaze on the screen on a normalized scale (using the screen size and the distance from the observer as reference). The application is standalone, so it does not require a Matlab license to function properly, but since it was developed under an academic license, it can currently only be released for educational purposes.

In summary, Eyelab is an intuitive and user-friendly GUI, allowing even less experienced users to better exploit the high potential and performance of the Eye Link II system, in order to encourage the introduction and diffusion of this type of

technology in the clinical ophthalmology practice and in research.

Integration with the EyeLink II system

The EyeLink II is the head-mounted video-based eye tracker with high resolution (less than 0.01°) and fast data rate (500 Hz). It is equipped with the Host Computer, which hosts the system application and is connected to the EyeLink II monitor, and the Display Computer, with its monitor surrounded by four active infrared markers in the corners, to track head movements, and adopted for displaying the visual stimuli.

The head-mounted system is composed of three miniature cameras mounted on a padded headband: one head-tracking camera is used to detect the infrared markers, while two eye cameras focus respectively on the left and right eye, providing high-quality computer-based eye tracking.

The Host Computer is used for performing the setup, the calibration and the validation procedures by using its proprietary GUI. The setup interface allows the experimenter to adjust the focus and position of the cameras relative to the pupils, in order to correctly place the headband on the subject's head; moreover, the user can choose many settings, including the number of points for calibration, the sampling frequency (250Hz or 500Hz), the tracking mode (Pupil-Corneal or Pupil Only Reflection mode), and others. The EyeLink GUI provides also two optional tools: the Experiment Builder function to set up a new experiment, and the Data Viewer, which allows the offline displaying, filtering, extraction and manipulation of EyeLink data.

On the Display PC, the experimenter can run the experimental applications by using the EyeLink API. With EyeLab it is possible to use a second monitor connected to the Display Computer, to provide the control interface that allows the experimenter to customize the experimental protocols, visualize the data acquired during the experiments in real-time, monitor, process and store the recorded signals, by disruptively widening the standard functionalities of the EyeLink II eye-tracker (see Figure 4).

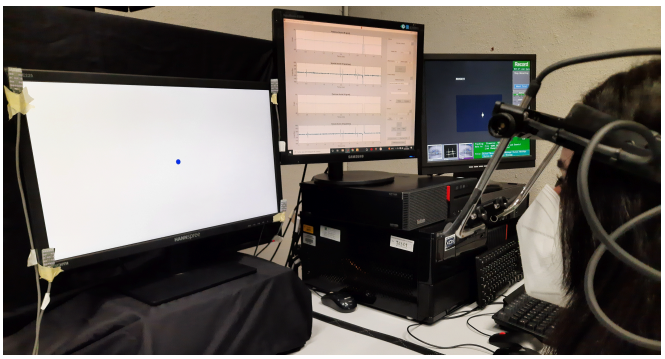


Figure 5. The EyeLab setup, with one monitor connected to the Host Computer (on the right) and two monitors connected to the Display Computer.

III. Preliminary Results

EyeLab allows the user to visualize, record, store and process the oculomotor signals of both eyes, such as saccades, smooth pursuit movements, fixations, and blinks.

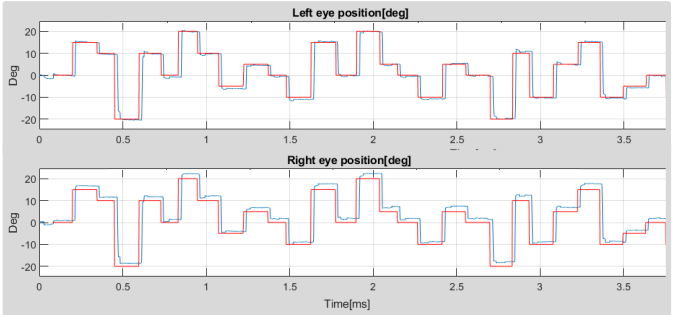


Figure 4. Binocular eye positions (see blue traces) recorded during a test for studying saccades, where the target (red traces) changes position quickly in the horizontal direction only.

For example, Figure 5 shows the binocular traces (in blue) of the right and left eye during a test for the study of saccades, carried out through the protocol-based interface. The exercise involves a single target (in red), initially placed in the center of the screen. Subsequently, the target moves by a pre/selected position, between ±20 deg in the horizontal direction only, with a random time interval between 125-135 ms. The experimenter can decide to pre-assign a test duration or to end the exercise by pressing a key on the keyboard.

Another example is reported in Figure 6, which reports the binocular traces (in blue) of the right and left eye during a sinusoidal smooth-pursuit exercise. In this case the target (in red), initially placed in the center of the screen, moves with harmonic motion only in the horizontal direction, with an excursion of ±20 deg.

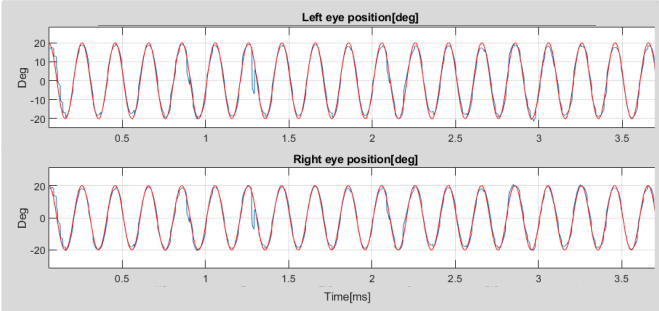


Figure 6. Binocular eye positions (in blue) recorded during harmonic smooth pursuit test (the target is in red).

IV. Conclusions

The benefits of objective analysis of oculomotor functioning and continuous advances in eye-tracking technologies are likely confined to research laboratories. EyeLab is a simple and intuitive interface for the study and assessment of eye movements, whose real-time features enable the adaptation of the experimental protocol to the ongoing results.

EyeLab was developed with neurologists longing for a usable tool that could go beyond neurological research, to enter the clinical practice. Tool validations are currently being performed.

Acknowledgement

The authors acknowledge funding from Sardegna Ricerche, Bando “PROOF of CONCEPT - Valorizzazione dei risultati

della ricerca in biomedicina" - PO FESR 2014-2020 – RiPARTO project.

REFERENCES

[1] M. E. Calkins, W. G. Iacono, and D. S. Ones, "Eye movement dysfunction in first-degree relatives of patients with schizophrenia: A meta-analytic evaluation of candidate endophenotypes," *Brain Cogn*, vol. 68, no. 3, pp. 436–461, Dec. 2008, doi: 10.1016/J.BANDC.2008.09.001.

[2] J. Maruta, M. Suh, S. N. Niogi, P. Mukherjee, and J. Ghajar, "Visual tracking synchronization as a metric for concussion screening," *Journal of Head Trauma Rehabilitation*, vol. 25, no. 4, pp. 293–305, 2010, doi: 10.1097/HTR.0B013E3181E67936.

[3] P. Thiagarajan, K. J. Ciuffreda, and D. P. Ludlam, "Vergence dysfunction in mild traumatic brain injury (mTBI): a review," *Ophthalmic Physiol Opt*, vol. 31, pp. 456–468, 2011, doi: 10.1111/j.1475-1313.2011.00831.x.

[4] A. J. Hood, S. C. Amador, A. E. Cain, K. A. Briand, A. H. Al-Refai, and M. C. Schiess, "Levodopa slows prosaccades and improves antisaccades: an eye movement study in Parkinson's disease," *J Neurol Neurosurg Psychiatry*, vol. 78, pp. 565–570, 2007, doi: 10.1136/jnnp.2006.099754.

[5] U. P. Mosimann, R. M. Müri, D. J. Burn, J. Felblinger, J. T. O'Brien, and I. G. McKeith, "Saccadic eye movement changes in Parkinson's disease dementia and dementia with Lewy bodies," *Brain*, vol. 128, no. 6, pp. 1267–1276, Jun. 2005, doi: 10.1093/BRAIN/AWH484.

[6] C. D. Pensyl and W. J. Benjamin, "Ocular Motility," *Borish's Clinical Refraction*, pp. 356–399, 2006, doi: 10.1016/B978-0-7506-7524-6.50015-6.

[7] N. J. Wade, "Pioneers of Eye Movement Research," *https://doi.org/10.1068/i0389*, vol. 1, no. 2, pp. 33–68, Jan. 2010, doi: 10.1068/I0389.

[8] H. E. Bedell and S. B. Stevenson, "Eye movement testing in clinical examination," *Vision Res*, vol. 90, pp. 32–37, Sep. 2013, doi: 10.1016/J.VISRES.2013.02.001.

[9] "The Neurology of Eye Movements - R. John Leigh, David S. Zee - Google Libri." https://books.google.it/books?hl=it&lr=&id=v2s0BwAAQBAJ&oi=fnd&pg=PP1&ots=4rwl-aCKwH&sig=NxhzdmFdRJOMHheLwZMS4LX_RDs&redir_esc=y#v=onepage&q&f=false (accessed Jan. 26, 2023).

[10] P. Quaid and T. Simpson, "Association between reading speed, cycloplegic refractive error, and oculomotor function in reading disabled children versus controls," *Graefe's Archive for Clinical and Experimental Ophthalmology*, vol. 251, no. 1, pp. 169–187, Jan. 2013, doi: 10.1007/S00417-012-2135-0/FIGURES/14.

[11] T. Eggert, "Eye Movement Recordings: Methods," *Dev Ophthalmol*, vol. 40, pp. 15–34, 2007, doi: 10.1159/000100347.

[12] D. A. Chernyak, "Iris-based cyclotorsional image alignment method for wavefront registration," *IEEE Trans Biomed Eng*, vol. 52, no. 12, pp. 2032–2040, Dec. 2005, doi: 10.1109/TBME.2005.857674.

[13] J. Narváez, M. Brucks, G. Zimmerman, P. Bekendam, G. Bacon, and K. Schmid, "Intraoperative cyclorotation and pupil centroid shift during LASIK and PRK," *Journal of Refractive Surgery*, vol. 28, no. 5, pp. 353–357, May 2012, doi: 10.3928/1081597X-20120124-03.

[14] R. Engbert and K. Mergenthaler, "Microsaccades are triggered by low retinal image slip," *Proc Natl Acad Sci U S A*, vol. 103, no. 18, pp. 7192–7197, May 2006, doi: 10.1073/PNAS.0509557103/ASSET/FE70BFAA-0256-41BD-BFAC-D9FB33E8126B/ASSETS/GRAPHIC/ZPQ01806-1988-M02.JPEG.

Co-design of a points-based reward system to boost motivation in children and improve adherence to learning serious games

C. Piazzalunga[1], A. Donati[1], S. Ferrante[1]
[1] *Department of Electronics, Information and Bioengineering, Politecnico di Milano, Milan, Italy*

***Abstract*—Specific Learning Disorders are disabilities that impair the ability to learn, which can be mitigated through timely training. However, administering such training can be challenging due to screening difficulties, including teachers' inadequate training and clinicians' lengthy waiting lists, and to challenges posed by distance modalities and children's low compliance. To improve adherence and motivation, gamification techniques should be used. After a co-design process carried out with clinicians, teachers, and children, we thus added a coin-collection system and an in-game shop to the learning games of the ESSENCE project, and analyzed the trend of the usage and of the performance in the games to verify its impact. 66 children participated in the testing, for a total of 6822 serious games uses. Weekly usage increased after the introduction of both coins and shop (84.0 before, 145.6 after coins, 403.2 after shop), while performance improved significantly after the introduction of the coins, but not of the shop (0.66±0.24 before, 0.86±0.16 after coins, 0.87±0.13 after shop), suggesting that the presence of rewards was enough to improve adherence and lead to better results.**

***Keywords*—serious games, learning, gamification, adherence**

I. INTRODUCTION

Specific Learning Disorders (SLDs) are conditions that cause difficulties comprehending or processing information, and lead to subpar academic performance given proper conditions like age, intelligence, the absence of sensory-motor problems, and an adequate opportunity to learn. As of now, these disorders cannot be cured, but adequate training can alleviate their effects to lessen the impact of the disability on the subject's life. These training activities are especially effective if carried out early in a child's life. Thus, it is important that children are screened from a young age to allow for a timely intervention. To guarantee this, the 170/2010 Italian law [1] mandates that during the first years of primary school teachers are supposed to observe students to check if their evolution in reading, writing, and calculation skills are in line with their peers. If teachers notice that a student's development is subpar, they must try to compensate their difficulties with additional training; if the gap is not filled after the skills enhancement attempt it is likely they have a SLD, and teachers must report the case to the child's family and, eventually, to clinical professionals for further evaluation. This process presents several criticalities, like the teachers' lack of training or the length of waiting lists [2]. In addition to these problems, the lockdowns related to the COVID-19 pandemic impacted not only children's performance and mental health [3], but also SLD management [4]. The screening process, in fact, is much more difficult to carry out remotely, since the observation may not be as effective as in-presence, making it harder for teachers to exploit the benefits of personalized plans without adequate inspection upstream. Moreover, adherence to this kind of training is not guaranteed, as, without enough motivation and the control of a school environment, students may just ignore the proposed exercises, particularly if they find them challenging [5].

The pandemic was, however, a catalyst for technological development to cope with these new challenges, even leading the Italian Ministry of Education to include technological tools in their SLD managament guideline [2]. A recent European project, ESSENCE (Empathic platform to personally monitor, Stimulate, enrich, and aSsist Elders aNd Children in their Environment), is aimed at designing and developing a platform to support vulnerable populations (children and elders) through home-based care. In particular, the portion of the system catered to children includes several modules that strive to enrich every step of the SLD screening. In this work, we focus on ESSENCE's training tools, a set of serious games covering the three areas of learning: writing, reading and mathematics. The games were co-designed with psychologists, child neuropsychiatrists, teachers, and children by gamifying existing exercises.

The gamification process consists in the insertion of game design elements to exploit engagement, human competitiveness and ambition as strategies to make the user accomplish the task [6]. Some examples of gamification techniques are game elements, like points, badges, levels and scoreboards or leaderboards, game dynamics, with interactive elements and decision-making processes, parasocial relationships [7], and rewards [8].

However, gamifying reading, writing, or calculation exercises without distorting the rationale behind them is not an easy task; it means that the gamification features used can barely act on the mechanics and the stimuli, but have to focus on other aspects. To boost motivation in ESSENCE's users, we thus added an element which was external to the games: a system of rewards based on the collection of coins, which can be spent in an in-game shop to customize the main character, Bianchetto.

The central aim of this work is therefore to analyze the impact of the coins system and, later, of the shop, on the usage frequency of the games and on the children's performances in the games.

II. MATERIALS AND METHODS

A. Co-design of the rewards system

The target users of the ESSENCE platform are children attending the first and second year of primary school. One of the main principles adopted in the creation of the platform was that of co-design, which consists in the involvement of the relevant stakeholders in the design process. For the development of the shop, we involved clinicians, teachers, and children that were participating in the pilot testing of ESSENCE and were thus already acquainted with the platform and the games. Firstly, we organized focus groups (FGs) with clinicians and teachers, to identify which gamification factors were, in their experience, the most effective to boost adherence and motivation in primary school children. Then, we organized an in-presence FG with children, during which they were asked questions to investigate their opinions about a system of rewards, their preferences in terms of items to buy in an hypothetical shop, and the way in which they would have liked to customize the serious games experience.

Finally, the shop was developed using Unity 2021.3.8f1 (https://unity.com/).

B. Pilot testing

The ESSENCE project's platform was tested during a pilot testing phase which started in December 2021, and lasted until December 2022, whose protocol was approved by Politecnico di Milano's Ethical Committee n. 04/2021, date of approval March 23, 2021. 66 children participated, 30 females and 36 males; 21 of them were attending first grade, while 45 were in second grade. During the pilot testing, children were given a tablet (Samsung S6 Lite with the Samsung S-Pen) on which we gradually released 21 serious games, which implemented gamified exercises in the domains of reading, writing, and calculation. Even though access to the games was unrestricted, the families of the participants were instructed to monitor the children to avoid excessive usage and to encourage them to use the games once a week under the guidance of a teacher. The coins system was introduced on May 26, 2022, while the shop was introduced on October 24, 2022. For every element of the platform, from the shop to the games themselves, low-fidelity prototypes were used to gather feedback and refine the designs accordingly.

During the pilot testing phase, the serious games logged their results on the ESSENCE servers, recording the children's performances along with the number of coins they earned and the items they bought.

At the end of the pilot testing, the activities in the ESSENCE project were evaluated. Among other questions regarding the project, we asked:

- What did you like the most about the serious games?
- Do you have any suggestions to improve the serious games?
- What did you like the most about the ESSENCE project?
- Do you have any suggestions to improve the ESSENCE project?

C. Data analysis

Data analysis was performed offline in Python 3.8 (https://www.python.org/).

Our hypothesis aimed to test whether the utilization of serious games increased following the implementation of both the coins system and the shop. We thus extracted the number of entries from the database to compare the frequency of usage before the introduction of the coins, between the introduction of the coins and the introduction of the shop, and after the introduction of the shop.

It is not enough to simply increase the usage of a tool, but its increased usage should lead to an improvement of performances. We thus chose the game that was played the most and which had some sort of quantitative measurement of performance, then computed the Moving Average of its results. We used a Friedman test to compare the distributions of the accuracy in each phase, identifying the phases that differ significantly with a Nemenyi post hoc test. Finally, we used the `ruptures` library [9] to locate change points in the time series. We used the Dynamic programming algorithm in the library, which needs to know in advance how many points to find. We firstly set this parameter to 1 to identify the most relevant change point, then we increased it up to 3 to locate other interesting dates.

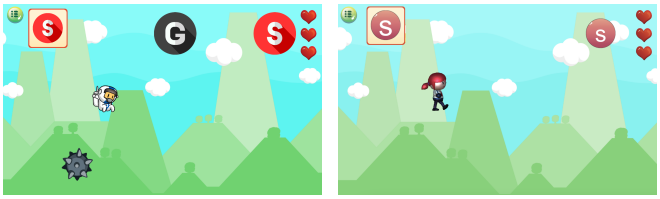
III. RESULTS

A. Co-design of the rewards system

The FG with clincians highlighted the impossibility to distort the serious games' mechanics in favor of gamification. Because of this, the techniques chosen were rewards and customization, which act on factors that are external to the games themselves.

Regarding the children FG, the vast majority of the suggestions that emerged regard clothing, while the remaining ones concern the appearance of Bianchetto (shape of facial features, color of skin). It was thus decided to allow the customization of the character in these two aspects, while ignoring other popular customization options, such as animations, or voices.

The results from the FG were also used to define how to structure the collection of currency. To encourage children to explore all of the games, we introduced three different currencies, one of each learning domain, instead of having just one type of coins. The type of coin is determined by the domain to which the game belongs and is symbolized by an icon coherent with its setting: leaves for reading, which is set in the forest; suns for writing, set in the savannah; droplets for calculation, set in the pond. The number of coins that games grant ranges from 1 to 10, proportional to the child's performance, but never amounting to zero. This was done in accord with the advice of clinicians and teachers, to



(a) (b)

Fig. 1: A screenshot of the game Quick catch **(a)** without the customized character and **(b)** with the customized character.

encourage children who may struggle with some games and avoid feelings of mortification.

Regarding the way in which children wanted to make use of the items bought in the shop, during the FG the idea of seeing the customized character inside the game themselves emerged. Therefore, after the introduction of the shop, we included a dressed-up version of Bianchetto in some of the games. This can be observed in Figure 1.

B. Description of the shop

The final version of the shop can be observed in Figure 2. The coins' values are retrieved from the user's profile, which is stored in ESSENCE's database. We included a tutorial, which is loaded automatically the first time the shop is open and can be then accessed through a button.



Fig. 2: Final shop implementation

C. Pilot testing

By the end of the pilot testing, 3 first-grade children and 2 second-grade children had dropped out of the study because they had changed schools. Because of this, the final questionnaire was filled by 59 children. Regarding the unstructured questions about preferences, we reported the answers in Figure 3. Regarding the suggestions, most children wished either for more games or for more customization options.

D. Impact of the reward system on the adherence and the performance

1) Game usage: The total number of usages of the serious games was 6822. Table I reports the number of usages and the weekly frequency of usage in the corresponding period.

TABLE I: Usage of serious games.

Period	*N. of usages*	*N. of usages / week*
Before coins	1462	84.0
Between coins and shop	3112	145.6
After shop	2248	403.2



(a) (b)

Fig. 3: Word clouds of the preferences of the children regarding **(a)** the serious games and **(b)** the whole project.

2) Game performance: To check if the introduction of the rewards had any impact on the performance in the game, we chose to analyze the results of "Quick catch", a reading game, which was the one that children appreciated the most. It was the second most played game, at 1258 times. We discarded the most played game, "Tunnels", as it did not have an objective quantitative measure of performance, while "Quick catch" had a numerical outcome, namely the accuracy. The average accuracy values can be found in Table II. The results are shown in Figure 4, while the Moving Average of the accuracy can be observed in Figure 4..

TABLE II: Average performance of Quick catch.

Period	*Accuracy*
Before coins	0.66 ± 0.24
Between coins and shop	0.86 ± 0.16
After shop	0.87 ± 0.13

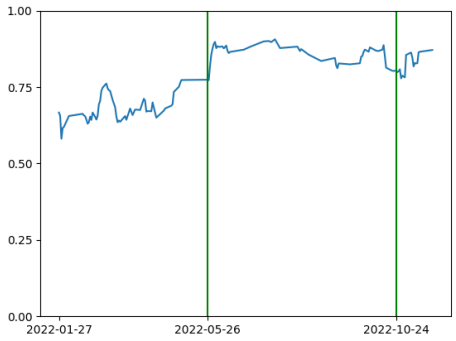


Fig. 4: Plot showing the Moving Average of the Quick catch accuracy, along with the date of introduction of the coins and of the shop.

The Friedman test found the averages of the accuracy were different in the three considered periods (t: 39.18, p-value < 0.001). The post hoc test located differences between the period before the introduction of the coins and the other two (p-value < 0.001), while the introduction of the shop did not generate a significant difference. The `ruptures` library detected the day of the introduction of the coins as a breakpoint in the trend of the accuracy. Conversely, the day of the introduction of the shop was not detected as a change point, not even when increasing the number of breakpoints to look for.

IV. DISCUSSION

Specific Learning Disorders (SLDs) are conditions that impair the ability to process information and cause difficulties during schooling. To strengthen the training, which is necessary to alleviate their effects, we co-designed with teachers, clinicians and children some gamification elements to enrich the serious games of the ESSENCE project. We identified rewards and customization, in the form of coins and of a shop, as adequate techniques. Children tested the serious games during a year-long pilot, at the end of which they filled a satisfaction questionnaire. To verify whether the aforementioned gamification elements contributed to an increment in usage and an improvement in performances, we compared the weekly usages of the games before and after the introduction of the coins and of the shop, along with the average accuracy obtained by users in the most relevant game. We then used the `ruptures` package to identify changes in the trend in this game's accuracy.

The pilot testing included 66 first- and second-grade children, who played the serious games for a total of 6822 times. Looking at the number of uses per week (84.0 before coins, 145.6 between coins and shop, 403.2 after coins) it is apparent that the introduction of the rewards caused an increase in usage frequency, which grew even more after the introduction of the shop.

Accuracy was then taken into consideration, comparing the average results in the three different periods. It emerged that the average accuracy increased over time (0.66 ± 0.24 before coins, 0.86 ± 0.16 after coins, 0.87 ± 0.13 after the shop), although the starkest difference is the one consequent to the introduction of coins. The Friedman test and the Nemenyi post hoc test confirm this, since it emerged that the three periods have different averages of the accuracy (t: 39.18, p-value $<$ 0.001), but only the differences between the first period and the other two were significant ($p < 0.001$). The increasing of performances by itself is surely not enough to impute credit to the gamification elements, since other confounding factors, such as the increasing familiarity with the games and the age of the children, may have influenced this increment. However, when looking for breakpoints in the trend of accuracy, the first point that was detected was exactly the introduction of the coins. This suggests that the impact of the rewards on the performance was strong, and that their introduction was not the sole cause, but a driving force that brought children to engage more with the games, acquiring more familiarity, and achieving better results. Conversely, the introduction of the shop was not relevant. This may be explained by its late introduction, or may mean that children did not necessarily need a way to employ the rewards that they earned during the games, since the satisfaction of collecting the coins was, in itself, a sufficient reason to engage with the games more. However, the shop was particularly appreciated by children, as emerged from the questionnaire, so its importance should not be undermined, particularly because it is plausible that the appeal of the coins' collection came from the knowledge that they would have a way to spend them. It is also important to note that some children stopped caring about the collection of coins after they had acquired the items they were interested in. Consequently, the shop could be a source of further engagement if enriched with more customization options.

ACKNOWLEDGEMENT

This research was funded by European Union's Horizon 2020 research and innovation programme under the call SC1-PHE-CORONAVIRUS-2020-2B grant number 101016112.

The authors wish to thank the schools in which the subjects were recruited and in which the data acquisition was carried out, primary schools "Risorgimento" and "San Benedetto", from Gavirate, province of Varese.

REFERENCES

[1] Italian Ministry of Instruction University and Research. Law october 8th, 2020, n. 170. new rules on specific learning disabilities in schools. In *Gazzetta Ufficiale n. 244, October 18th, 2010*, Rome, Italy, 2010.

[2] Istituto Superiore di Sanità. Linee guida alla gestione dei disturbi specifici dell'apprendimento, 2012. https://snlg.iss.it/wp-content/uploads/2022/03/LG-389-AIP_DSA.pdf, Last accessed on 2023-01-25.

[3] C. Termine, L. G. Dui, L. Borzaga, V. Galli, R. Lipari et al. Investigating the effects of covid-19 lockdown on italian children and adolescents with and without neurodevelopmental disorders: a cross-sectional study. *Current Psychology*, 2021.

[4] Flavia Marchese, Assunta Grillo, Massimo Pettoello Mantovani, Giulia Gargano, Pierpaolo Limone, and Flavia Indrio. Specific learning disorders and special educational needs during covid-19 pandemic; pilot survey study performed in local district schools in italy. *Children*, 9(6), 2022.

[5] T. Y. Gao, J. M. Black, R. J. Babu, W. R. Bobier, A. Chakraborty et al. Adherence to home-based videogame treatment for amblyopia in children and adults. *Clinical and Experimental Optometry*, 104(7):773–779, 2021.

[6] S. Radovick, E. Hershkovitz, A. Kalisvaart, M. Koning, K. Paridaens et al. Gamification concepts to promote and maintain therapy adherence in children with growth hormone deficiency. *Feature Papers for J-Multidisciplinary Scientific Journal*, 2018.

[7] K. L. Brunick, M. M. Putnam, L. E. McGarry, M. N. Richards, S. L. Calvert. Children's future parasocial relationships with media characters: the age of intelligent characters. *Journal of Children and Media*, 2016.

[8] Ahn SJ (Grace), K. Johnsen, C. Ball. Points-based reward systems in gamification impact children's physical activity strategies and psychological needs. *Health Education & Behavior*, 2019.

[9] C. Truong, L. Oudre, N. Vayatis. Selective review of offline change point detection methods. *Signal Processing*, 167, 2020.

Risk management in a medical device software: evaluation of the usability characteristics of a 3D viewer for reporting

A. Luschi[1], L. Gatti[1], E. Tiribilli[1,2], E. Denisova[1,2], L. Manetti[2] L. Bocchi[1], and E. Iadanza[3]
[1] *Department of Information Engineering, University of Florence, Italy*
[2] *Epica Imaginalis, Sesto Fiorentino, Italy*
[3] *Department of Medical Biotechnologies, University of Siena, Italy*

***Abstract*—The theme of usability in the medical field is becoming of vital importance for the development of new software and medical devices that can meet users' needs. The main purpose of this work is to design a usability test of a 3D viewer for biomedical images, by following the guidelines for the development of usable software, and then to define the procedures that should be used for future usability evaluation. In our specific purpose, the fastest access to all basic functionalities of the viewer was identified as the goal. The entire usability evaluation was designed to test the software from this perspective. The test environment was setup with all equipment necessary to conduct the test, specific and exploratory tasks were defined, test administration and collection of results have been planned. Finally, participants have been recruited and a pilot test was successfully conducted, validating the designed usability test.**

***Keywords*—usability, 3d viewer, healthcare, medical device.**

I. INTRODUCTION

Usability, according to the international standard ISO 9241, is "the extent to which a system, product, or service can be used by specified users to achieve specified goals with effectiveness, efficiency, and satisfaction in a specified context of use" [1]. Assessing usability means evaluating the ease of an interface to be used by a group of users to perform a given operation. This assessment can be performed via usability testing, defined as "an evaluation that involves representative users performing specific tasks with the system to enable the measurement of efficiency, effectiveness, and/or user satisfaction" [2]. To fulfil the goals of improving the delivery of health care and increasing patient safety, the technologies must be demonstrated as not being error-prone. Usability evaluation, part of the whole process of risk management for medical devices [3], is one way of ensuring that interactive systems are adapted to the users, to their tasks and that there are no negative outcomes of their usage [4]. In this sense, it is part of a process of health technology design management based on evidence [5], [6] which can be also applied to several other aspects of the healthcare environment [7], [8], [9]. Human Factors Engineering (HFE) is a discipline concerned with the design of tools, machines, and systems that take into account human capabilities, limitations, and characteristics. The goals are to design for safe, comfortable, and effective human use. Ergonomics, usability engineering, and user-centred design are considered synonymous [10]. "User-centered design" is built on an HFE process. The human-machine interface design approach here emphasizes user requirements, user characteristics, and end-user testing. The idea of iterative design and testing is another crucial aspect of this user-centred design methodology. Simply said, the design is iteratively improved throughout the design cycle based on the results of user testing (also known as usability testing), which is repeated at the very beginning of the design cycle [11]. ISO 26800 describes the ergonomics principles for interfaces, in order to improve safety, performance and usability by analysing the population target, the environment, the goals and the expected results [12]. ISO 9241-11 describes users, environment, resources, goals and tasks as different aspects of the context of the use of the analysed system, product or service, whose usability evaluation outcomes its effectiveness, efficiency and user's satisfaction [1] (Fig. 1).

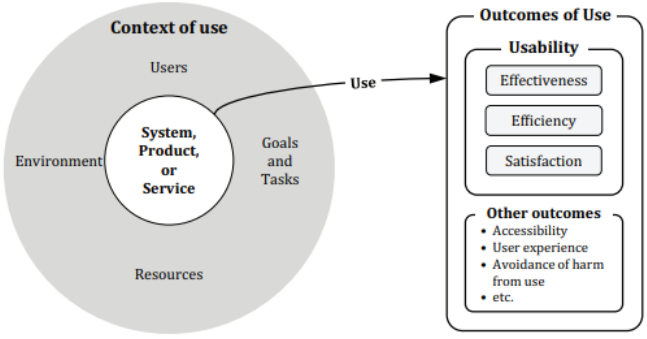


Fig. 1: Schematic representation of the different aspects of the context of the use of the analysed system according to the standard ISO 9241-11.

Finally, ISO 25066 examines different existing usability testing approaches: inspection and heuristics review of the interface, tests and post-market surveys [13]. Usability testing is a highly effective methodology for identifying barriers to use and for finding opportunities for making products, services and systems more effective, efficient and satisfying to use [14]. Usability tests can be conducted in a variety of environments

with varying degrees of formality, collecting various types of qualitative and quantitative data, and with different types of teams working with the end-users. Usability tests can be conducted both in a preliminary developing phase so that possible problems can be immediately identified and solved and after the distribution of the product. In the latter case, tests can reveal criticalities which may lead to updates with the aim of improving the user experience [15]. Tests must be thoroughly designed and planned by defining the number and the type of involved users, the methods of implementation, the measurements and the tasks to be verified. In this paper, the design of a test for the usability evaluation of a multi-modal medical imaging viewer platform, developed by Epica Imaginalis (Sesto Fiorentino, Italy), is presented. The software is a complex image viewer platform conceived to be used in diagnosis and planning, allowing visualization, exploration, measurement, comparison of multiple studies and planning of surgical procedures in compliance with the DICOM (Digital Imaging and COmmunications in Medicine) standard. The paper presents the methods employed to design and administer the tests.

II. METHODS

The designed usability test is structured to be performed as moderated in-lab testing (Fig. 2) with three well-defined phases so that a linear and homogeneous path could be followed. The main phases are:

- Preparation: in this phase, the questionnaires and the task lists have been designed according to the previous heuristic evaluation performed on the interface [16], together with the consultations of experts. Moreover, the typologies of users have also been defined, together with the location where the test will be administrated, and the tools needed.
- Execution: the real administration of the tests to the selected users. Testers have been monitored with specific tools (chosen in the previous phase) while interacting with the interface. In this phase, the two figures of the "observer" and the "moderator" are introduced. The former verifies the correct execution of the tasks, while the latter talks to the user, forcing him to "think aloud" so that every faced complexity can be addressed and noted.
- Analysis and Report: collected data are analysed, errors are pinning-out, and possible restyling of the interface is proposed according to the obtained results.

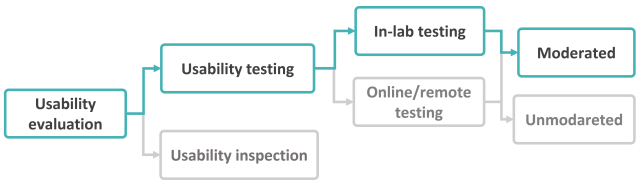


Fig. 2: Chosen structure of test administration.

In this paper, the authors focus on the technical choices made on preparation phase.

First of all, the goal of usability test was identified, as suggested by ISO 9241-11, 5.3.3. As the time the physicians spend for image exploration is critical, the focus of the preparation phase was to design the usability test, specifying as a goal the fastest access to all basic functionalities of the viewer platform. Analysing the heuristic evaluation previously performed on the interface, the total amount of 55 exploratory tasks and 4 specific tasks (Table I) was designed for each test: the former consist of tasks designed to explore the various functionalities of the viewer, while the latter are based upon hypothetical use cases which can include more than one exploratory task.

Next, the environment for the text execution was setup. Tests were thought to be conducted within two adjacent rooms, one for the user, and the other one for the moderator and the observer. Both a front and an external camera should be used to allow the moderator and the observer to look at the user's facial expression and his interaction with the interface (Fig. 3).

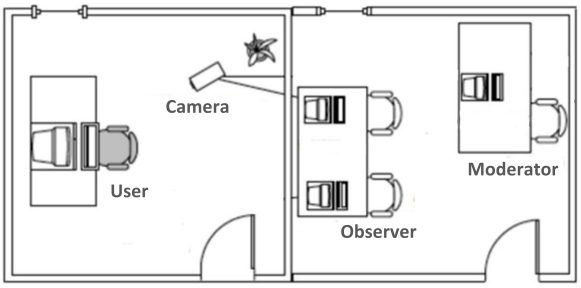


Fig. 3: Implemented environment for test administration.

Finally, the test was validated by the administration of the pilot session, that confirmed the reasonableness of the proposed methods.

III. RESULTS

Nielsen claims that five people are sufficient to identify more than 80% of the usability issues [17]. The intricacy of the study must be taken into account, though, because the harder the activities are, the more complex the study should be and the more volunteers would be needed. The complexity of the study is effectively decreased, enabling you to use fewer participants, if the same training is provided to the entire intended user population. Context and complexity have a major impact on the ideal participant count. According to Virzi, three to twenty people are the appropriate amount of participants for many studies [18]. Faulkner estimated that ten persons would likely identify at least 82% of the flaws [19]. Turner thinks that seven people is the ideal amount, even for challenging studies [20]. According to research, between three and twenty people can yield trustworthy results, with five to 10 being a good place to start. Generally speaking, more volunteers are needed for more difficult, risky initiatives, but fewer volunteers are needed to test more creative ideas. At the moment of writing this paper, 11 participants have been recruited for composing the testing population, which

is a satisfactory participants number according to the above statements. Four of the participants are biomedical engineers, two radiographers, two radiologists, one electronic engineer, one software developer, and one application specialist. They are mostly women (73%), with a working experience between 0 and 10 years (82%).

To assess the results of the usability tests, efficacy, efficiency, and user satisfaction will be evaluated. Efficacy is scored with the degree of completion of each task: 0 is for a failed task, 1 is an indirect success (a success accomplished within an easy task or with little help by the moderator), 2 is for a partly-corrected task, and 3 for a completed task, achieve without any help by the moderator and also without inspecting out-of-context functionalities. Efficiency is scored with the average time employed to complete each task. In case of failure, the maximum time defined for the task will be noted. Finally, user satisfaction will be evaluated with a post-test questionnaire.

In order to validate the designed test a pilot test was conducted on an external volunteer. The pilot test allows to verify all the technical choices made on preparation phase, such as the use of "transparent" screen recording software, camera position, and recording quality. Moreover, pilot test allowed to test the moderator and performer roles during the execution phase and evaluate the overall duration of the test to plan its administration. The results of the pilot test allowed to confirm the goodness of the overall design of the usability test, in term of location, tools and roles. The pilot user took 40 minutes to conduct the pilot test.

IV. CONCLUSIONS

The examination of a product's usability is advised as a crucial step in both its creation and enhancement. Nevertheless, many businesses still struggle to include usability assessment in their design and development processes, despite the practice's widely acknowledged benefits. The lack of research based on actual user contact with any program might result in the creation of a product that is sometimes dangerous or does not meet the needs of the user. This paper presents the design of a usability test following the best-practice guidelines and standards observed from the literature. The test will be administered to a group of recruited users, assessing efficacy, efficiency, and user satisfaction in relation to a multi-modal medical imaging viewer platform. Future works will analyse the whole method, presenting both quantitative and qualitative results emerging from the assessment. Moreover, a possible user-interface redesign to mitigate the observed criticalities will be also taken into account.

REFERENCES

[1] "EN ISO 9241-11:2018. Ergonomics of human-system interaction - Part 11: Usability: Definitions and concepts," standard, International Organization for Standardization, 2018.

[2] "ISO/IEC TR 25060:2017. Systems and software engineering - Systems and software product Quality Requirements and Evaluation (SQuaRE) - Common Industry Format (CIF) for usability: General framework for usability-related information ," standard, International Organization for Standardization, 2017.

[3] "ISO 14971:2019. Medical devices — Application of risk management to medical devices ," standard, International Organization for Standardization, 2019.

[4] J. Bastien, "Usability testing: A review of some methodological and technical aspects of the method," *International journal of medical informatics*, vol. 79, pp. e18–23, 05 2009.

[5] E. Iadanza, V. Gonnelli, F. Satta, and M. Gherardelli, "Evidence-based medical equipment management: a convenient implementation," *Medical & biological engineering & computing*, vol. 57, no. 10, pp. 2215–2230, 2019.

[6] R. Miniati, F. Dori, E. Iadanza, M. M. Fregonara, and G. B. Gentili, "Health technology management: A database analysis as support of technology managers in hospitals," *Technology and Health Care*, vol. 19, no. 6, pp. 445–454, 2011.

[7] E. Iadanza, A. Luschi, T. Merli, and F. Terzaghi, "Navigation algorithm for the evacuation of hospitalized patients," vol. 68, p. 317 – 320, 2019.

[8] E. Iadanza, L. Ottaviani, G. Guidi, A. Luschi, and F. Terzaghi, "License: Web application for monitoring and controlling hospitals' status with respect to legislative standards," in *IFMBE Proceedings*, vol. 41, pp. 1887–1890, 2014.

[9] A. Luschi, M. Monti, and E. Iadanza, "Assisted reproductive technology center design with quality function deployment approach," pp. 1587–1590, 2015.

[10] J. Gosbee, "Human factors engineering and patient safety," *Quality & safety in health care*, vol. 11, pp. 352–4, 01 2003.

[11] E. Denisova, E. Tiribilli, L. Manetti, L. Bocchi, and E. Iadanza, "Multimodal biomedical imaging platform all-in-one," in *IFMBE Proceedings*, 2022 In Press.

[12] "EN ISO 26800:2011. Ergonomics - General approach, principles and concepts," standard, International Organization for Standardization, 2011.

[13] "EN ISO/IEC 25066:2019. Systems and software engineering - Systems and software Quality Requirements and Evaluation (SQuaRE) - Common Industry Format (CIF) for Usability - Evaluation Report," standard, International Organization for Standardization, 2019.

[14] C. Hass, *A Practical Guide to Usability Testing*, pp. 107–124. 2019.

[15] J. F. Dumas and J. Redish, *A Practical Guide to Usability Testing*. Intellect Books, 1999.

[16] E. Tiribilli, E. Denisova, A. Luschi, L. Manetti, L. Bocchi, and E. Iadanza, "Heuristic evaluation of a medical imaging platform," in *IFMBE Proceedings*, 2022 In Press.

[17] J. Nielsen, "Why you only need to test with 5 users, March 19, 2000." https://www.nngroup.com/articles/why-you-only-need-to-test-with-5-users, Last accessed on 2022-03-24.

[18] R. A. Virzi, "Refining the test phase of usability evaluation: How many subjects is enough?," *Human Factors*, vol. 34, pp. 457–468, 1992.

[19] L. Faulkner, "Beyond the five-user assumption: Benefits of increased sample sizes in usability testing," *Behavior research methods, instruments, & computers*, vol. 35, pp. 379–83, 09 2003.

[20] C. Turner, J. Lewis, and J. Nielsen, *Determining Usability Test Sample Size*. International Encyclopedia of Ergonomics and Human Factors, 2nd Ed., Vol. 3, 01 2006.

TABLE I: List of 55 exploratory tasks and 4 specific tasks.

Task Number	*Type*	*Task*
1	Exploratory	Open CAT CT on the desktop.
2	Exploratory	Open Settings and explore the various layout options and overlays. Chose the preferred one.
3	Exploratory	Test the layout for left-handed people. If you are not left-handed, go back to the default setting.
4	Exploratory	Test zoom, rotation, and panning. Edit window width and intensity level.
5	Exploratory	Switch to 2D modality in axial view and test again zoom, rotation, and panning.
6	Exploratory	Reset the geometry of the axial view.
7	Exploratory	Switch to 3D modality. Reset the volume to the initial state.
8	Exploratory	Make a screenshot and save it as "screenshot1" on the desktop. Do not anonymise the screenshot.
9	Exploratory	Anonymise the current study and hide all objects from the scene but the volume.
10	Exploratory	Open and then close DICOM tags.
11	Exploratory	Make objects visible on the scene again. Open the histogram.
12	Exploratory	Edit the current intensity with the histogram: set the value of width to about 2500 and the intensity to 1000.
13	Exploratory	Save the preset as "Preset1".
14	Exploratory	Open filter settings and change luminosity to 70. Apply the filter.
15	Exploratory	Open filter settings again and bring back luminosity to 50. Apply the filter.
16	Exploratory	Apply filter settings and undo the last setting.
17	Exploratory	Apply colour inversion. Reset the whole volume to its initial state.
18	Exploratory	Open the "Intensity Preset" menu and choose the "CT Cardiac" preset.
19	Exploratory	Move the histogram and set the values between 200 and 2500.
20	Exploratory	Save the preset as "Preset2".
21	Exploratory	Open "Transfer Function" and select "CT Lung Transfer Function".
22	Exploratory	Change the colour of some points to taste.
23	Exploratory	Add a new point.
24	Exploratory	Add a new tissue.
25	Exploratory	Remove a point to taste.
26	Exploratory	Save the preset as "Transfer1".
27	Exploratory	Open the coronal view in widescreen.
28	Exploratory	Measure a length and an angle.
29	Exploratory	Perform a measurement with the ellipse tool.
30	Exploratory	Change the colour of the ellipse measurement, then delete it.
31	Exploratory	Reset the layout to its initial state.
32	Exploratory	Browse through the slices of the coronal view, open the list of performed measurements, and select the angular one.
33	Exploratory	Open the list of performed measurements, hide the one referred to length.
34	Exploratory	Hide all the measurements only in the 3D view.
35	Exploratory	Delete the length measurement, and then delete all the measurements.
36	Exploratory	Open "Slab Thickness" function.
37	Exploratory	Edit the thickness to 46mm. Test the following functions: maximum, averaging, and minimum projection. Unselect the "Slab Thickness" function.
38	Exploratory	Cut the 3D series with the cube tool.
39	Exploratory	Hide the cube tool.
40	Exploratory	Try the "axial cut" modality.
41	Exploratory	Choose the "ISO Surface" visualization algorithm, then reset the volume to its initial state.
42	Exploratory	Try the "Play" modality. Set the frame rate to 20fps and then stop it.
43	Exploratory	Open SIMBA Single Stack CT on the desktop.
44	Exploratory	Open advanced menu and select "compare".
45	Exploratory	Inspect the volumes to taste, then lock them and continue the exploration.
46	Exploratory	Reset the geometry of both volumes to their locked states.
47	Exploratory	Unlock and reset the geometry of both volumes to their initial state.
48	Exploratory	Exit the "compare" modality.
49	Exploratory	Open "planning" modality.
50	Exploratory	Plan an intervention with the cannula: place it to taste.
51	Exploratory	Open the list of performed planning, hide the planning and then delete it.
52	Exploratory	Try the "scalpel" tool, save the planning and exit the modality.
53	Exploratory	Select the axial view and try the "multislices" modality.
54	Exploratory	Change the layout and edit the space between slices.
55	Exploratory	Switch to the sagittal view and then exit the "multislices" modality.
1	Specific	Locate the post-traumatic fracture by performing the appropriate reconstructions.
2	Specific	Locate the screw, and calculate the inclination between it and the vertebrae in relation to the vertical axe. Then check the correct placement.
3	Specific	Locate the dental cavity and perform a comparison between the current and the past state of the tooth acquired with a CT.
4	Specific	Make the 2D views visible and locate the spine calcification.

A computational platform to assess the metabolic-electrophysiological behaviour of neurons cultured in monolayers

R. Fabbri[1, 2], A. Ahluwalia[1,2], and C. Magliaro[1,2]
[1] *Department of Information Engineering, University of Pisa*
[2] *Research Center "Enrico Piaggio", University of Pisa*

***Abstract*—Current computational models of biological neural networks do not include oxygen concentration as an input variable influencing neuron electrophysiological activity. However, oxygen concentration constitutes a limiting factor for cell viability and function in vitro. The aim of this work is to develop a platform to model the oxygen dependent electrophysiology of neurons cultured in monolayers. The model accounts for oxygen diffusion and consumption to supply metabolic energy for the electrical firing of a neuron. The platform is built to be modular: each block simulating a neuron can be connected to create neuronal network models with different layouts. Preliminary results show the expected oxygen-dependent behaviour of the model. The platform can be a powerful tool in the field of neuronal models, allowing different types of neurons, synapses and networks to be implemented.**

***Keywords*—neuronal cultures, computational platform, firing, oxygen.**

I. Introduction

In vitro models of neural tissues represent invaluable tools for the study of the human brain in both its physiological and diseased conditions. Different cell sources, substrate materials and architectures can be adopted to obtain in vitro models with controlled and tailored features [1].

Traditional cellular models of the brain are represented by two-dimensional (2D) monolayers, where neurons are seeded on Petri dishes or culture flasks either directly or after coating them with a substrate for promoting cell adhesion. Then, the well is filled with a medium, containing substances allowing cells to survive and maintain their viability. The presence of medium also enables the diffusion of ambient oxygen to the neuron monolayer. Thus, the availability of oxygen is a crucial factor affecting cell viability and functioning, as well as their electrophysiological behaviour. Indeed, since neuron firing is an ATP-dependent process, and local oxygen concentration plays a key role in determining how the neuronal networks behaves [2], [3].

However, generating and maintaining neural constructs is expensive due to low-throughput technology and costly reagents, especially if stem cell-derived neurons or primary neurons are involved [4]. Moreover, their lack of reproducibility limits their applicability in research (e.g., neurotoxicity) and regulatory testing [5]. Finally, the technologies currently available for characterizing the electrophysiological activity *in vitro* (e.g., patch clamp, micro-electrode array technology) do not enable a faithful characterization of the 3D electrophysiological activity at the single-cell level [6], [7]. In this scenario, computational model-based solutions can support the understanding of *in vitro* neural network behaviour. However, current computational models of biological neuronal networks do not include the local oxygen concentration as a variable.

To this end, we developed a novel computational platform for assessing the electrophysiological and metabolic behaviour of neurons in monolayer cultures. The platform embeds a model of neuron firing activity over time, considering its dependency on the local oxygen concentration. In Section II the mathematical model of the single neuron metabolism and electrophysiology is described, together with the neuronal network layouts and the development of the computational platform. Section III reports the results where the dependency of the simulation outputs on the local oxygen concentration is shown. Finally, Section IV summarises the main findings of the work and describes future developments.

II. Materials and Methods

A. Computational model of the single neuron

The model comprises neurons arranged on a culture plate filled with medium. Since oxygen is consumed by the cells for fuelling both their metabolic and electrophysiological functions, three phenomena occur: i) diffusion of oxygen from the outer environment through the medium, ii) neuron oxygen consumption and iii) their electrophysiological activity.

Since diffusion happens along the vertical direction (i.e., from the outside to the bottom of the culture plate), the system can be simplified and 1D geometry can be adopted. Thus, each neuron of the monolayer is modelled as a cube of edge 50 μm and a column of medium of height 1mm (h) which allows oxygen to diffuse along the z axis and reach the cell for fuelling its metabolic and electrophysiological activities (Fig. 1).

The governing equation of the single neuron behaviour is a modified version of the reaction diffusion equation where a term for oxygen dependent firing is introduced:

$$\frac{\partial C}{\partial t} = D\nabla^2 C + R(C) + F(C) \quad (1)$$

Eq. (1) states that the local oxygen concentration (C) over time depends on the diffusion of oxygen governed by the diffusion coefficient D, but also on its metabolic rate $R(C)$ and electrophysiological $F(C)$ consumption.

The consumption of oxygen is modelled using Michaelis-Menten kinetics:

$$R(C) = -\frac{OCR\ \rho\ C}{k_m + C} \quad (2)$$

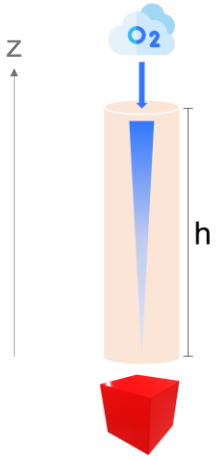


Fig. 1: Model of the single neuron within the monolayer

Where OCR is the maximum Oxygen Consumption Rate of a single neuron and k_m is the Michaelis-Menten constant.

The electrophysiological activity of the neurons is described by a modified version of the Hodgkin-Huxley model [8], where the dependency on oxygen is introduced:

$$F(C) = -\alpha\lambda\left(I_{pump}(C) + I_{gliapump}(C)\right) \quad (3)$$

I_{pump} and $I_{gliapump}$ are respectively the ionic current of the Na-K-ATP and Na-K glial pumps, both of which depend on the local O_2 concentration [8]. All the parameters of the model are listed in Table I.

TABLE I: PARAMETERS OF THE COMPUTATIONAL MODEL

Symbol	*Model parameter*	*Value*
D	Oxygen diffusion coefficient	1.75 e-12 m^2/ms
OCR	Oxygen Consumption Rate	8.6 e-16 g/s
ρ	Cell density	8 e12 cell/m^3
k_m	Michaelis-Menten constant	0.03 mM
α	Conversion factor	5.3 g/mol
λ	Relative cell density	1

B. *Neuronal network models*

Neurons arranged in monolayers can form synaptic connections [9], [10]. Thus, the single neuron model is exploited for implementing networks of neurons, to analyse the influence of oxygen on their collective electrophysiological output. The connections were modelled as electrical synapses, i.e., gap junctions, with conductance gain following a log-normal distribution with values from 0.1 to 1 mS/cm^2 [11].

For studying the electrophysiological behaviour of neurons when connected in a network, three different layouts were defined. Two topologies reproduce the arrangement of the electrodes of microelectrode arrays (MEA), the technology usually used to measure the electrophysiological activity in vitro [12]. The grid arrangement of the 60 electrodes in the MEA layout and the corresponding neuronal network models are depicted in the first line of Fig. 2. The first network model comprises 60 neurons and the other one 256. Although the MEA-like grid arrangements do not reproduce the actual distribution of neurons, these layouts facilitate the comparison of the model outputs with experimental data from neurons cultured on MEA chips. In the network with 256 neurons the outputs of four cells were mediated to simulate the real setting acquisition of electrophysiological signals where each MEA electrode records the activity of about four adjacent neurons. In both the MEA-like layouts, connections between neuron blocks were randomly generated [13], [14].

The third network layout reproduces the so-called Small World (SW) networks [15]. SW networks have been reported to mimic the functional graphs of neural networks both in the brain and in vitro [16]–[18]. They are characterised by highly connected clusters of neighbour nodes. The SW network implemented in this work is made up of 60 neurons and 120 connections (Fig. 2, second line).

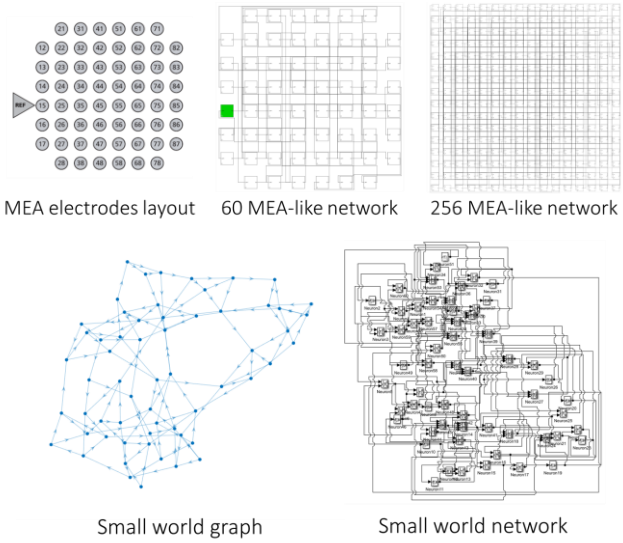


Fig. 2: Representations of the MEA-like and small world networks

C. *Computational platform*

The computational platform was developed in Matlab (The Mathworks Inc.) exploiting the Simulink toolbox. Specifically, the platform is constituted by a Simulink library where the functions describing the single neuron behaviour of Eq. 1 are embedded. Matlab scripts are used for the creation of the neuronal network layouts.

The output of each simulation is the membrane potential over time of each neuron of the network and the oxygen concentration in the medium above the cell, discretized into six intervals. The membrane potential signals are collected and processed to detect spikes and calculate the mean firing rate (i.e., number of spikes per second). The workflow is depicted in Fig. 3.

Statistical analysis of the firing rate of the models was performed in GraphPad Prism 8.0. The Mann-Whitney test with a significance level equal to 0.05 was adopted.

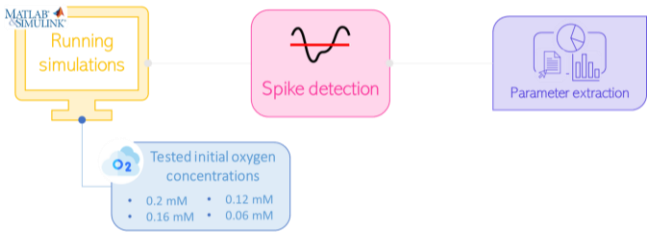


Fig. 3: Workflow

III. Results

The single neuron block as well as each network layout was simulated varying the initial oxygen concentration in the medium (0.2 mM, 0.16 mM, 0.12 mM and 0.06 mM) to analyse the dependency of the outputs of the platform on this variable.

A. *Single neuron*

The single neuron block was simulated for ten minutes for the four initial media O_2 concentrations. The outcomes of the single neuron model show that the electrophysiological behavior of the neuron is consistent with the expected dependency on the local oxygen concentration. Specifically, Fig. 3 shows the membrane potential over time in blue, while the orange plot describes the variations of the oxygen concentration at the boundary between the medium and the neuron. Potential is expressed in mV and concentration in mM.

As expected, the neuron has an intense firing activity when a higher concentration of oxygen is available, and it decreases its electrophysiological activity as O2 levels decrease.

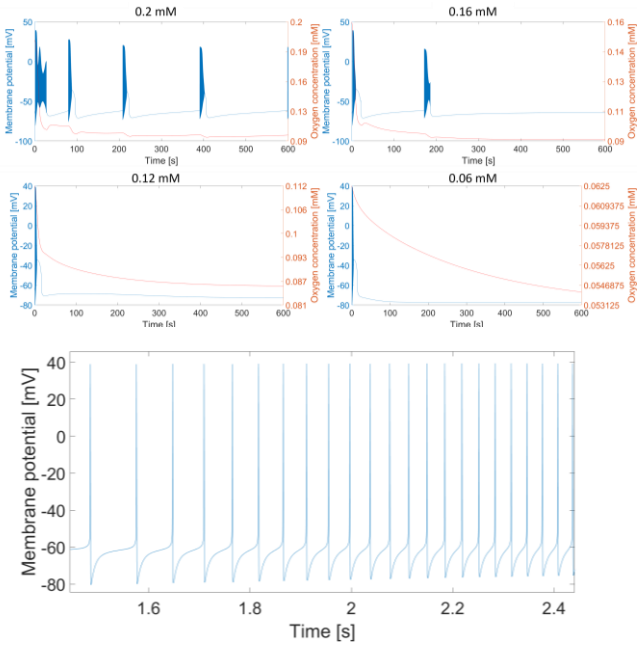


Fig. 4: Output of the single neuron block with different initial oxygen concentrations and detail of the membrane potential

Moreover, during intense firing activities (i.e., the close action potentials in the insert in Fig. 4) oxygen concentration rapidly drops off. On the other hand, Fig. 4 also shows that during the recovery time after a period of intense firing, the neuron does not produce action potentials and the oxygen concentration increases.

The cell consumes O2 for fueling its metabolism and for sustaining the activity of its Na-K-ATP pumps, responsible for the depolarization and repolarization of the membrane potential. In fact, the oxygen concentration, starting from the set initial value, rapidly decreases at the beginning of the simulation since it diffuses within the medium and reaches the neuron.

B. *Networks firing rate*

The networks generated according to Section II were simulated for ten seconds, and the membrane potential signals obtained were processed for identifying spikes (i.e., the membrane potential overcoming a threshold) and calculating the mean firing rate of each network as the number of spikes divided by the time of simulation.

The results of the statistical analysis of the mean firing rate calculated for each network layout simulated with the four initial O2 concentrations are shown in Fig. 5. Interestingly, although the values of the mean firing rates are different among network layouts, no significances were identified between the initial oxygen concentrations of 0.2 mM and 0.16 mM, while a significant difference (i.e., p-value≤0.001) is identified between all the other initial concentrations.

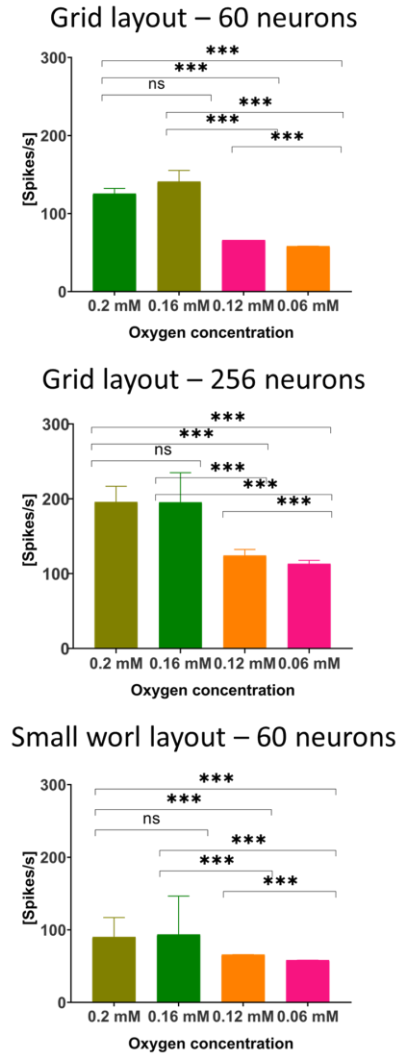


Fig. 5: Firing rate of the three network models as a function of initial O2 level (ns: non-significant; ***: p-value ≤ 0.001)

IV. Conclusion

In this work, a novel computational platform for mimicking the oxygen-dependent firing activity of neurons in monolayers is described. Ambient oxygen diffuses through the medium filling the culture plate, reaching the neurons. Each neuron is modelled as a unit that consumes the available local oxygen. The outputs of the simulations show the oxygen dependency of the electrophysiological activity of the neuron. In particular, neurons start to experience an hypoxic environment when the oxygen drops to the lowest levels used in the simulations.

The computational platform was developed with a modular and scalable architecture, allowing for further analyses and for the tuning of other desired parameters.

Future improvements of the work are ongoing and regard the validation of the platform using experimental data obtained from neuronal cultures seeded on MEA chips (e.g. publicly available datasets [19]). Such data will be analysed for extracting the local firing rate of the in vitro neural networks, to be compared with ones extracted from the platform. Also, a connectivity analysis will be conducted, assessing a correlation coefficient (e.g., the Spike Time Tiling Coefficient [20]) between the channels of the MEA. This will allow the identification of functional connectivity patterns that could be reproduced in a neuronal network within the computational platform. Once validated the platform will be improved for modelling 3D geometries, and in particular brain organoids [21]–[23], which are vessel-free, thus particularly O2 limited, which in turns limits cell viability and electrophysiological behaviour. Future improvements will consider also to increase the number of neurons within networks, to integrate a model of the glial cells and to implement neuron plasticity mechanisms.

The platform represents a powerful tool for the simulation of different models of neurons, synapses and neuronal networks and for studying the effects of the local oxygen concentration and other modulators (e.g., neurotoxins) on the output signals.

References

[1] J. Gordon and S. Amini, “General Overview of Neuronal Cell Culture,” *Methods in Molecular Biology*, vol. 2311, pp. 1–8, 2021, doi: 10.1007/978-1-0716-1437-2_1/COVER.

[2] J. Ingram *et al.*, “Oxygen and seizure dynamics: I. experiments,” *J Neurophysiol*, vol. 112, no. 2, pp. 205–212, Jul. 2014, doi: 10.1152/JN.00540.2013/ASSET/IMAGES/LARGE/Z9K01114243200003.JPEG.

[3] S. Özugur, L. Kunz, and H. Straka, “Relationship between oxygen consumption and neuronal activity in a defined neural circuit,” *BMC Biol*, vol. 18, no. 1, pp. 1–16, Jul. 2020, doi: 10.1186/S12915-020-00811-6/FIGURES/5.

[4] D. V LaBarbera, B. G. Reid, and B. H. Yoo, “The multicellular tumor spheroid model for high-throughput cancer drug discovery,” *Expert Opin Drug Discov*, vol. 7, no. 9, pp. 819–830, 2012.

[5] C. Hirsch and S. Schildknecht, “In vitro research reproducibility: Keeping up high standards,” *Front Pharmacol*, p. 1484, 2019.

[6] D. Poli, C. Magliaro, and A. Ahluwalia, “Experimental and Computational Methods for the Study of Cerebral Organoids: A Review,” *Front Neurosci*, vol. 13, Mar. 2019, doi: 10.3389/fnins.2019.00162.

[7] J. Pas *et al.*, “Neurospheres on patterned PEDOT: PSS microelectrode arrays enhance electrophysiology recordings,” *Adv Biosyst*, vol. 2, no. 1, p. 1700164, 2018.

[8] Y. Wei, G. Ullah, J. Ingram, and S. J. Schiff, “Oxygen and seizure dynamics: II. Computational modeling,” *J Neurophysiol*, vol. 112, no. 2, pp. 213–223, Jul. 2014, doi: 10.1152/JN.00541.2013/SUPPL_FILE/SUPPLEMENTARY_MATERIAL_CODE_ARCHIVE.ZIP.

[9] D. Sulzer *et al.*, “Dopamine Neurons Make Glutamatergic Synapses In Vitro,” *Journal of Neuroscience*, vol. 18, no. 12, pp. 4588–4602, Jun. 1998, doi: 10.1523/JNEUROSCI.18-12-04588.1998.

[10] P. Massobrio, J. Tessadori, M. Chiappalone, and M. Ghirardi, “In vitro studies of neuronal networks and synaptic plasticity in invertebrates and in mammals using multielectrode arrays,” *Neural Plast*, vol. 2015, 2015, doi: 10.1155/2015/196195.

[11] R. M. Hasani, V. Beneder, M. Fuchs, D. Lung, and R. Grosu, “SIM-CE: An Advanced Simulink Platform for Studying the Brain of Caenorhabditis elegans”.

[12] Y. Nam and B. C. Wheeler, “In Vitro Microelectrode Array Technology and Neural Recordings,” *Critical Reviews™ in Biomedical Engineering*, vol. 39, no. 1, pp. 45–61, 2011, doi: 10.1615/CRITREVBIOMEDENG.V39.I1.40.

[13] S. Marom and G. Shahaf, “Development, learning and memory in large random networks of cortical neurons: lessons beyond anatomy,” *Q Rev Biophys*, vol. 35, no. 1, pp. 63–87, 2002, doi: 10.1017/S0033583501003742.

[14] M. Chiappalone, P. Massobrio, and S. Martinoia, “Network plasticity in cortical assemblies,” *European Journal of Neuroscience*, vol. 28, pp. 221–23728, 2008, doi: 10.1111/j.1460-9568.2008.06259.x.

[15] D. J. Watts and S. H. Strogatz, “Collective dynamics of ‘small-world’ networks,” *Nature*, vol. 393, no. 6684, pp. 440–442, Jun. 1998, doi: 10.1038/30918.

[16] D. S. Bassett and E. Bullmore, “Small-World Brain Networks,” *The neuroscientist*, vol. 12, no. 6, pp. 512–523, Jun. 2016, doi: 10.1177/1073858406293182.

[17] J. H. Downes *et al.*, “Emergence of a Small-World Functional Network in Cultured Neurons,” *PLoS Comput Biol*, vol. 8, no. 5, p. e1002522, 2012, doi: 10.1371/JOURNAL.PCBI.1002522.

[18] D. de Santos-Sierra *et al.*, “Emergence of Small-World Anatomical Networks in Self-Organizing Clustered Neuronal Cultures,” *PLoS One*, vol. 9, no. 1, p. e85828, Jan. 2014, doi: 10.1371/JOURNAL.PONE.0085828.

[19] F. Emre Kapucu, andrey Vinogradov, tanja Hyvärinen, L. Ylä-Outinen, and S. Narkilahti, “Comparative microelectrode array data of the functional development of hPSC-derived and rat neuronal networks”, doi: 10.1038/s41597-022-01242-4.

[20] C. S. Cutts and X. S. J. Eglen, “Detecting Pairwise Correlations in Spike Trains: An Objective Comparison of Methods and Application to the Study of Retinal Waves,” *Journal of Neuroscience*, vol. 34, no. 43, pp. 14288–14303, Oct. 2014, doi: 10.1523/JNEUROSCI.2767-14.2014.

[21] M. Hofer and M. P. Lutolf, “Engineering organoids,” *Nat Rev Mater*, vol. 6, no. 5, pp. 402–420, 2021, doi: 10.1038/s41578-021-00279-y.

[22] M. A. Lancaster and J. A. Knoblich, “Organogenesisin a dish: Modeling development and disease using organoid technologies,” *Science (1979)*, vol. 345, no. 6194, 2014, doi: 10.1126/science.1247125.

[23] T. Sharf *et al.*, “Intrinsic Network Activity in Human Brain Organoids,” *SSRN Electronic Journal*, no. January, 2021, doi: 10.2139/ssrn.3797268.

Multi-Input Multi-Output Model Predictive Control for Drugs Delivery in Clinical Anesthesia

E. Manzoni[1], J. Pavan[1], M. Rampazzo[1,2], and S. Del Favero[1]
[1] *Department of Information Engineering, University of Padova, Via Gradenigo 6/B, 35131, Padova, Italy.*
[2] *Department of Industrial Engineering, University of Padova, Via Gradenigo 6/A, 35131, Padova, Italy*

***Abstract*—Automatic drugs delivery during anesthesia can lead to faster sedation, increase patient's safety, and reduce the burden on anesthesiologists. This preliminary study proposes a Model Predictive Control (MPC) algorithm to control the induction and maintenance of the states of hypnosis, analgesia and neuromuscular blockade by means of automatic infusion of three drugs: Propofol, Remifentanil, and Atracurium. The study is conducted in a simulated environment based on a non-linear model describing the patient physiology that includes synergic effects among drugs and interpatient variability, as well as measurement noise and a variable surgical stimulation disturbance. Simulations on 24 virtual subjects show fast and safe induction of anesthesia. In terms of median [5th, 95th] percentiles, the MPC algorithm maintained hypnosis in a suitable range for 98.9 [93.7, 99.3]% of the time, analgesia for 100 [65.4, 100]% of the time, and neuromuscular blockade for 100 [100, 100]% of the time.**

***Keywords*—Automatic drug delivery, Clinical anesthesia, Closed-loop control, Model Predictive Control.**

I. INTRODUCTION

Automatic control of general anesthesia during surgeries has attracted attention due to its potential benefits to patients and for the medical personnel. It improves patients' safety by continuously monitoring vital signs and by modulating drug injections consequently, which may speed up the recovery process and reduce side effects, [1]; additionally, it helps the reduction of the workload of the anesthesiologist, although their presence in the operative room is still a necessity.

General anesthesia has three main effects: hypnosis, analgesia, and neuromuscular blockade (NMB). Hypnosis is the loss of consciousness required to prevent intraoperative awareness and memorization; analgesia is the suppression of physiological responses to nociceptive stimulation to prevent the perception of pain; NMB is the blockage of neuromuscular activity that results in paralysis. These outcomes are attained by the use of certain medications that the anesthesiologist carefully administers throughout the procedure. Propofol, in particular, is frequently used as a hypnotic. Remifentanil, a regularly used analgesic, is popular due to its quick onset of action, which reduces unfavorable opioid-induced side effects. When used together, Remifentanil and Propofol have a synergic impact on the patient's depth of hypnosis (DoH). Furthermore, curare-based drugs like Atracurium are frequently utilized for NMB.

The anesthesia procedure can be divided into three distinct stages: induction, maintenance, and emergence. The patient is brought from consciousness to the necessary hypnotic condition during the induction phase, which usually lasts 4-5 minutes. During the maintenance phase the surgery procedures take place. In this phase, it is necessary to maintain an adequate depth of anesthesia (DoA) despite the occurrence of disturbances, mainly due to nociceptive stimulation during the surgery. The final phase of anesthesia consists in awakening the patient by suspending drugs infusion.

Due to the intrinsic system complexity brought on by multiple inputs and outputs, non-linearities, noise effects, and coupling effects, the design of a closed-loop control system is a non-trivial task. Several solutions have been proposed for automatic single-input single-output DoH regulation, ranging from PID control [2], to machine learning based approaches, such as q-learning control, [3].

Among these different approaches, model predictive control (MPC) has emerged as a promising solution [4], [5], [6], [7]. MPC, that uses a model of the process, can handle multi-input multi-output (MIMO) systems, while satisfying a set of constraints, e.g. on system inputs and outputs. This is particularly useful in drug-delivery problems, in which the input variables (drug infusions) are constrained to be non-negative (as drugs cannot be "extracted" from the body). When an accurate model of the plant is available, MPC can reduce the impact of absorption delays or disturbances by embedding this information in the controller logic.

In this preliminary work, we designed a MPC algorithm, validated trough simulations, to simultaneously regulate the states of hypnosis, analgesia and neuromuscular blockade, by manipulating the infusion rates of Propofol, Remifentanil and Atracurium. The block-scheme of the control approach is shown in Fig. 1.

II. PATIENT SIMULATOR

In this work we use a state-of-the-art simulator of anesthesia that closely mimics the clinical and physiological body response to various drug dosing infusions [8]. The proposed patient simulator includes synergic interaction elements of general anesthesia. It considers three drug infusion rates input variables – i.e., Propofol $u_P(t)$, Remifentanil $u_R(t)$, and Atracurium $u_A(t)$ – and three output variables – i.e., bispectral index scale (BIS) linked to the DoH, Richmond Agitation Sedation Scale (RASS) linked to the analgesic state, and the NMB index – in 24 virtual subjects [8], i.e., 24 different set of parameters for the model.

Pharmacokinetic (PK) and pharmacodynamic (PD) models are used to characterize the link between drug infusion rate and

drug effect. The model for Propofol and Remifentanil includes a three compartments describing the distribution of the drug among blood, fast- and slow- exchanging tissues. Moreover, a further compartment is introduced to describe the drug transportation to the effect site. The effect site concentration is related to the drug effect by a nonlinear sigmoidal dose-effect response. Furthermore, Propofol and Remifentanil, have a synergic effect on the BIS level, lowering it in a non-linear way. The expression of BIS, a dimensionless index normalized between 0 (isoline) and 100 (patient fully awake and alert), as a function both Propofol and Remifentanil concentration in the effect site, is the following:

$$\text{BIS(t)} = E_{0_{BIS}} - E_{max_{BIS}} \frac{\left(\frac{U_P(t)+U_R(t)}{U_{50}(\Phi)}\right)^{\gamma}}{1+\left(\frac{U_P(t)+U_R(t)}{U_{50}(\Phi)}\right)^{\gamma}}, \quad (1)$$

where $E_{0_{BIS}} \approx 100$ is the baseline value representing the initial drug-free state of the patient, $E_{0_{BIS}} - E_{max_{BIS}}$ is the maximum reachable effect, γ determines the maximum steepness of the curve (i.e., the receptiveness of the patient to the drug), and C_{e50_P} and C_{e50_R} are the Propofol and Remifentanil concentrations necessary to reach half of the BIS maximal effect, respectively. Finally, $U_P(t)$, $U_R(t)$ are related to the effect site concentration of Propofol $C_{e_P}(t)$, and of Remifentanil $C_{e_R}(t)$ by means of the following equations: $U_P(t) = C_{e_P}(t)/C_{e50_P}$, $U_R(t) = C_{e_R}(t)/C_{e50_R}$. Finally $U_{50}(\Phi) = 1 - \beta\Phi + \beta\Phi^2$ where $\Phi = U_P(t)/(U_P(t)+U_R(t))$. Specifically, β describes the synergic effect of Propofol and Remifentanil: as β increases, the mixture of drugs becomes more powerful and induces a stronger hypnotic effect. The RASS metric, ranging from 0, patient calm and alert, to -5, unresponsive to voice and stimulation, is just influenced by the Remifentanil infusion as follows:

$$\text{RASS(t)} = E_{0_{RASS}} - E_{max_{RASS}} \frac{C^{\gamma}_{e_R}(t)}{C^{\gamma}_{e50_R} + C^{\gamma}_{e_R}(t)}. \quad (2)$$

The Atracurium PK-PD model has been developed in [9]. Its PK structure can be seen as a two-compartmental model and the PD model includes a second-order transfer function and nonlinear Hill function in series. Specifically, the NMB is normalised between 0 and 100, where 0 corresponds to full paralysis and 100 to full muscular activity:

$$\text{NMB(t)} = 100 \frac{C^{\gamma}_{e50_A}(t)}{C^{\gamma}_{e50_A} + C^{\gamma}_{e_A}(t)}, \quad (3)$$

where C_{e50_A} is the Atracurium concentration necessary to reach half of the NMB maximal effect, while C_{e_A} is the effect-site concentration of Atracurium. Every of the previously introduced parameters is patient-specific. Further details can be found in [8].

In order to increase the realism of the simulated scenario, further sources of complexity have been introduced into the simulations. Measurement noises affecting BIS and NMB have been modeled as in [10] and [11], respectively. Since RASS is an integer number estimated by the anesthesiologist, RASS measurements were rounded to the closest integer value. The measurement error introduced in this way is more realistic that a zero-mean Gaussian noise. The sampling period of these measurements is $T_s = 20$s.

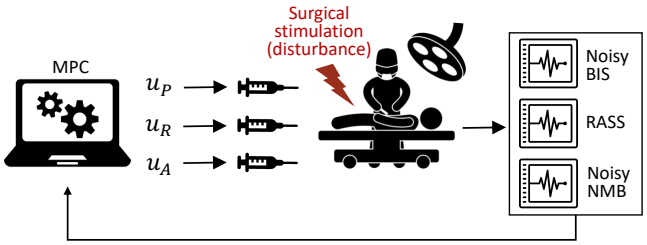


Fig. 1: Closed-loop control scheme.

Surgical stimulation has been added to the simulated scenario as an additive unmeasured disturbance on hypnotic state's output, that instantaneously increases the BIS level. Its shape has been taken from [12] and is common for all subjects, but its duration (linked to the surgical procedure duration) and magnitude (that depends on patient sensitivity) are patient-dependent. The shape, illustrated in Fig. 2, describes the three typical stages of a surgical intervention: a first arousal due to the surgical incision, a persistent phase associated to the surgical operation, and the final descending phase during the skin-closing procedure. Stimulation length is uniformly drawn in the range $[25,\ 35]$min while the maximum magnitude of the stimulation is uniformly drawn in the range $[+16,\ +24\%]$.

III. Methods

A. Control algorithm

At each control instant T_s, MPC finds the sequence of control actions that is predicted to achieve the "best system behavior" in a finite prediction horizon. Predictions are computed using a model of the process, whereas the "best system behavior" is assessed by minimizing a desired cost functional. According to the principle of the receding horizon, only the first action of this sequence is actuated; then, a new sequence is computed in the following control instant, using the new available measurements. This policy reduces the effect of

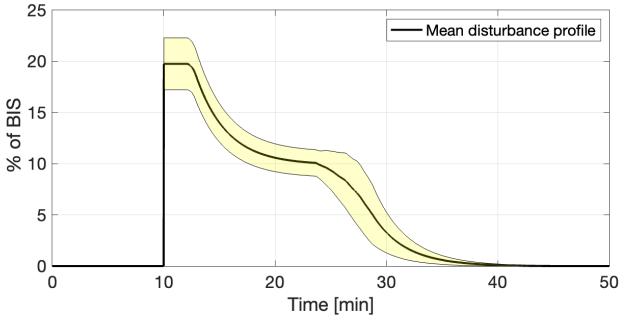


Fig. 2: Simulated disturbance profile variability due to surgical stimulation. The nominal curve is reported as the black line, while the variability interval of one standard deviation is reported as the yellow band.

errors due to model mismatches and the impact of unexpected disturbances affecting the system.

We employed a linear MPC formulation by relying on a linearized, averaged and discretized version of the model described in Section II. The model has been linearized around a suitable equilibrium operating point (x_{eq}, u_{eq}) that permits to maintain steady-state the desired output values: $\text{BIS}_{eq} = 50$, $\text{RASS}_{eq} = -4$ and $\text{NMB}_{eq} = 15\%$. Such equilibrium point has been computed using the trimming procedure implemented in the "Model Analyzer" application in Simulink.

The so-derived linearized model can be represented in state-space form as:

$$\begin{cases} \bar{x}(k+1) = A\bar{x}(k) + B\bar{u}(k), \\ \bar{y}(k) = C\bar{x}(k) + Md(k), \end{cases} \tag{4}$$

where:

- $\bar{x}(k)$ is the deviation of the state vector from the equilibrium state x_{eq};
- $\bar{u}(k)$ is the deviation of the input vector $u(k) = [u_P(k), u_R(k), u_A(k)]'$ from the inputs u_{eq} that guarantees the steady-state;
- $\bar{y}(k)$ is the deviation of the output vector $y(k) = [\text{BIS}(k), \text{RASS}(k), \text{NMB}(k)]'$ from the steady-state vector $y_{eq} = [\text{BIS}_{eq}, \text{RASS}_{eq}, \text{NMB}_{eq}]'$;
- $d(k)$ represents the output disturbance (i.e., surgical stimulation).

The optimization problem in MPC consists in minimizing, at each control instant, the following quadratic cost function:

$$J(k, y(\cdot), u(\cdot)) = \sum_{i=0}^{N-1} ||y(k+i) - y_0||_Q^2 + ||u(k+i) - u_0||_R^2. \tag{5}$$

It consists of two terms. The first penalizes the ℓ_2-norm of the difference between the future outputs of the model and the reference set-point $y_0 = y_{eq}$. The second term penalizes the ℓ_2-norm of the difference between future drugs infusion rates and a target set-point $u_0 = u_{eq}$. The matrices $Q \in \mathbb{R}^{3\times3}$ and $R \in \mathbb{R}^{3\times3}$ are non-negative weight matrices setting the trade-off between the two penalty terms in (5). They were set by trial and error on an average virtual patient to $Q = diag(10, 1, 5\%)$ and $R = diag(0.1\ [\text{min/kg/mg}]^2, 0.01\ [\text{min/kg/}\mu\text{g}]^2, 100\ [\text{min/kg/}\mu\text{g}]^2)$. The prediction horizon, N, is here set to 100.

System outputs are predicted via forward simulation from an estimate of the current system state, $\hat{x}(k)$. This estimate is obtained by means of a Kalman Filter, with the measurement noise modeled as in Section II.

Let $\mathcal{U}(k) = [u(k), \ldots, u(k+N-1)]'$ be the sequence of control actions that the MPC has to compute and $\mathcal{D}(k) = [d(k), \ldots, d(k+N-1)]'$ be the predicted disturbance profile. The optimal control problem solved by MPC is:

$$\min_{\mathcal{U}(k) \text{ s.t. } \mathcal{U}(k) \geq 0} J(k, \hat{x}(k), \mathcal{U}(k), \mathcal{D}(k)). \tag{6}$$

Drugs infusion rates are constrained to be non-negative. The constrained optimization problem is solved by using an interior-point algorithm. Once the optimal sequence $\mathcal{U}(k)$ is computed, only the first control action of this sequence is applied, following the receding horizon policy. The optimization problem is then repeatedly solved to compute the control actions to be applied.

B. Disturbance detection

Surgical stimulation is a challenging disturbance as it increases instantaneously the BIS level. To improve the rejection of this disturbance, we assumed to know its shape and its average length, while the magnitude of this disturbance, that depends on the patient sensitivity to the stimulus, is estimated in real-time. When a sudden change of slope (i.e., at least 15% BIS in 20s) is inferred, confirmation of the start of the surgery is requested to clinical staff. Assuming that the information is verified, the nominal disturbance profile shown in Fig. 2 (black line) is announced to the MPC algorithm ($d(k)$ in (4)) with amplitude scaled so that its maximal height is set equal to the measured change in BIS.

IV. Performance assessment

Our ultimate objective is to keep BIS, RASS and NMB indices within their clinical safe range by automatically adjusting Propofol, Remifentanil and Atracurium infusion rates achieving a proper degree of DoA. Moreover, according to [13], the adequate interval of the BIS index for anesthesia is [40, 60], the desired RASS is [-4, -5] and the NMB is to be maintained in the interval [10, 20]%. To evaluate the performance of the closed-loop control of DoA, a suitable set of performance indices is proposed:

- Time to Target (T2T): time required to reach the target range for the first time;
- BIS-NADIR: the lowest value of BIS observed during the induction phase;
- Time in Range (TIR): percentage of time spent in target range during the maintenance phase for BIS, RASS and NMB.

Results will be reported as median [5^{th}, 95^{th}] percentiles.

V. Results and Discussions

Fig. 3 reports the medians (blue lines) and interquartile ranges (black dotted lines) of the trajectories of drugs infusions, along with the trajectories of BIS, RASS and NMB, obtained in simulation on the 24 virtual patients.

The general guideline for the induction phase recommend to reach a good anesthetic state (i.e., the output variables within their safe range) in less than 4-5 minutes. It is also important to avoid drug over-dosing in this phase, as undershoots in the BIS index may be responsible for life-threatening hypotension. We achieved a T2T of 1.3 [1.3, 2.1]min for BIS, 1.3 [0.9, 1.3]min for RASS and 1 [1, 1]min for NMB, meaning that a good anesthetic state is generally reached in less than 5 minutes. Fig. 3 shows that proper induction of anesthesia is achieved safely, with a BIS-NADIR value of 47 [42.7, 51.5] (i.e., inside target range). Moreover, the disturbance rejection is satisfactory, the control response is fast and the indices stay

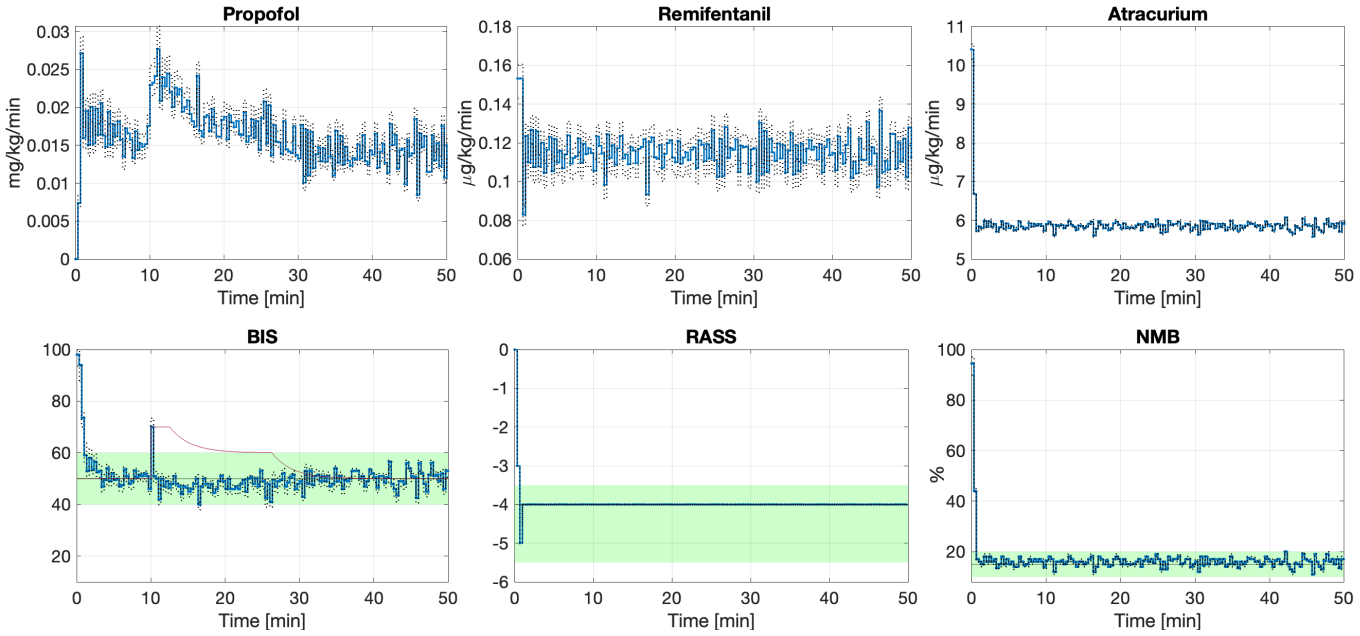


Fig. 3: Simulations of the MPC algorithm for the regulation of BIS, RASS and NMB by manipulating the infusion rates of Propofol, Remifentanil and Atracurium, respectively in the simulated patients. The green bands represent the target ranges for the three outputs. The red line on the BIS panel is the nominal disturbance profile. In each panel are reported the medians (blue lines) and interquartile ranges (black dotted lines).

inside the appropriate interval highlighted in green. TIR is 98.9 [93.7, 99.3]% for BIS, 100.0 [65.4, 100.0]% for RASS and 100.0 [100.0, 100.0]% for NMB. Disturbance on BIS was effectively detected and rejected. This was possible thanks to the a priori information on this disturbance (i.e., the nominal disturbance profile).

VI. Conclusions

In this article, a MIMO MPC algorithm is developed to accomplish the automatic control of the depth of anesthesia. The algorithm is developed and tested in silico. The simulated scenario is realistic, thanks to non-linearities introduced by the pharmacodynamics of the drugs, noise effects on BIS and NMB signals, differences in intra- and inter-patient parameters, and surgical stimulation disturbances. The approach proves to achieve accurate and safe control in both the induction and maintenance phases. Satisfactory disturbance rejection is achieved by using a priori knowledge on the surgical stimulus. The achieved control performance, as well as the infusion rates, are consistent with what has been reported in previous literature, [6], [7]. Future developments will involve the use of specialized infusion drugs to control various output variables associated with hemodynamics, while also accounting for other system factors like delays in the BIS signal.

References

[1] M. Ghita, M. Neckebroek, C. Muresan, and D. Copot, "Closed-loop control of anesthesia: Survey on actual trends, challenges and perspectives," *IEEE Access*, vol. 8, pp. 206264–206279, 2020.

[2] L. Merigo, F. Padula, N. Latronico, M. Paltenghi, and A. Visioli, "Optimized pid control of propofol and remifentanil coadministration for general anesthesia," *Communications in nonlinear science and numerical simulation*, vol. 72, pp. 194–212, 2019.

[3] G. Calvi, E. Manzoni, and M. Rampazzo, "Reinforcement q-learning for closed-loop hypnosis depth control in anesthesia," in *2022 30th Mediterranean Conference on Control and Automation (MED)*, pp. 164–169, IEEE, 2022.

[4] S. Ntouskas and H. Sarimveis, "A robust model predictive control framework for the regulation of anesthesia process with propofol," *Optimal Control Applications and Methods*, vol. 42, no. 4, pp. 965–986, 2021.

[5] N. Eskandari, K. van Heusden, and G. A. Dumont, "Extended habituating model predictive control of propofol and remifentanil anesthesia," *Biomedical Signal Processing and Control*, vol. 55, p. 101656, 2020.

[6] A. Maxim and D. Copot, "Closed-loop control of anesthesia and hemodynamic system: a model predictive control approach," *IFAC-PapersOnLine*, vol. 54, no. 15, pp. 37–42, 2021.

[7] A. Pawłowski, M. Schiavo, N. Latronico, M. Paltenghi, and A. Visioli, "Model predictive control using miso approach for drug co-administration in anesthesia," *Journal of Process Control*, vol. 117, pp. 98–111, 2022.

[8] C. M. Ionescu, M. Neckebroek, M. Ghita, and D. Copot, "An open source patient simulator for design and evaluation of computer based multiple drug dosing control for anesthetic and hemodynamic variables," *IEEE Access*, vol. 9, pp. 8680–8694, 2021.

[9] B. Weatherley, S. Williams, and E. Neill, "Pharmacokinetics, pharmacodynamics and dose-response relationships of atracurium administered iv," *British Journal of Anaesthesia*, vol. 55, pp. 39S–45S, 1983.

[10] F. Padula, C. Ionescu, N. Latronico, M. Paltenghi, A. Visioli, and G. Vivacqua, "Optimized pid control of depth of hypnosis in anesthesia," *Computer Methods and Programs in Biomedicine*, vol. 144, pp. 21–35, 2017.

[11] J. M. Lemos, H. Magalhães, T. Mendonça, and R. Dionísio, "Control of neuromuscular blockade in the presence of sensor faults," *IEEE Transactions on Biomedical Engineering*, vol. 52, no. 11, pp. 1902–1911, 2005.

[12] G. A. Dumont, A. Martinez, and J. M. Ansermino, "Robust control of depth of anesthesia," *International Journal of Adaptive Control and Signal Processing*, vol. 23, no. 5, pp. 435–454, 2009.

[13] S. D. Kelley, "Monitoring consciousness," *Using the Bispectral IndexTM during anesthesia*, 2007.

Non-linear analysis of HRV reveal lower signal complexity in patients with a prolonged Disorder of Consciousness

P. Liuzzi[1,2], B. Hakiki[1], A. Grippo[1], F. Cecchi[1,3] and A. Mannini[1]
[1] *IRCCS Fondazione Don Carlo Gnocchi ONLUS, Firenze*
[2] *Scuola Superiore Sant'Anna, Istituto di BioRobotica, Pontedera*
[3] *Università di Firenze, Dipartimento di Medicina Clinica e Sperimentale, Firenze*

***Abstract*— Detecting residual awareness in patients in a prolonged Disorder of Consciousness (pDoC) is a crucial issue in neurorehabilitation. Autonomic functions have been shown to correlate to the severity of brain injuries. Thus, we investigated whether metrics derived from non-linear Heart Rate Variability (HRV) analysis could be used to differentially diagnose patients with a pDoC. A prospective observational study was performed consecutively enrolling 209 patients with a severe brain injury. Resting-state ECG recordings were collected and nine metrics related to HRV complexity were correlated with the presence/absence of a pDoC. Then, the discriminatory capabilities of HRV complexity were evaluated. Lower HRV complexity was found to be associated with pDoC and SampEn, FuzzyEn, MultiScaleEn and Katz Fractal Dimension resulted capable of discrimination between patients with and without a pDoC. Complexity of HR, viewed as change in HRV at different time-scales, was found to be associated with presence of consciousness. With this work, we confirmed the mutual correlation between autonomic functions and consciousness alterations, providing complementary information for the implementation of low-cost clinical decision support tools in patients with a pDoC.**

***Keywords*—Disorder of Consciousness; Heart Rate Variability; NeuroRehabilitation.**

I. Introduction

Consciousness detection in patients with a severe Acquired Brain Injury (sABI) is challenging. These patients, after the coma phase, can transit to a state of prolonged Disorder of Consciousness (pDoC) which includes the Unresponsive Wakefulness State (UWS) and the Minimal Conscious State (MCS) [1]. This condition may persist or cease achieving a full recovery emerging from the MCS (E- MCS). Such heterogenous conditions, combined with consciousness fluctuations in the short or long term, can make neurological diagnosis complex and prone to misclassification. Nevertheless, the Coma Recovery Scale- Revised [2] with appropriate staff training and repetitive assessments lowers the cumulative misdiagnosis rate, even if falling under specific clinical conditions. To cope with such issue, the latest international guidelines for diagnosis of patients with pDoC have recommended the use of both clinical and instrumental evaluations to minimize the risk of misdiagnosis [3].

Within the possible instrumental evaluations, electrocardiography (ECG) provides a non-invasive way to investigate the functioning of the Autonomic Nervous System (ANS). Specifically in patients with a pDoC, it has been proposed that ANS may modulate large-scale brain patterns, attempting to balance sympathetic/parasympathetic homeostatic balance and to restore consciousness levels [4]–[6]. This two-way functional link between central nervous system (CNS) and ANS has been hypothesized in the Central Autonomic Network (CAN) model [7]. Currently, the work of Riganello et al. provided evidence of how heart rate variability (HRV), and in particular its complexity, can be used as a diagnostic marker of patients' neurological outcomes [5], [6], [8]. Similarly, complexity indexes of HRV have been shown to distinguish with a 90% accuracy UWS from MCS in a dataset of 30 acute sABI patients (16 MCS, 14 UWS) [8].

Given the aforementioned findings, our hypothesis, was that HRV complexity may be relevant also within rehabilitative contexts in non-sedated pDoC patients. Moreover, considering that the cardiac system works on multiple time scales (e.g., short time-responses, emotional influence, circadian rhythms) non-linear measures of HRV (NL-HRV) are among the most appropriate technique to analyse such signals. Such measures, compared to classical frequency or time-domain metrics, define the complexity of the signal at different time scales, instead than focussing on specific frequency ranges or time intervals. For these reasons, we extracted different complexity measures from ECG signals at admission to an Intensive Rehabilitation Unit (IRU) and correlated with the presence of a pDoC.

II. Materials and Methods

A. Study design and data collection

This analysis was performed in the framework of the PRABI study [9]. Inclusion criteria were: patients admitted to IRCCS Fondazione Don Carlo Gnocchi (FI) IRU from 06-01-2021 to 12-01-2022; diagnosis of a sABI; adults (age > 18). Approval from the local Ethical Committee was obtained (N. 16606OSS) and enrolment was done following the Helsinki Declaration. Patients have been included after obtaining a written consent signed by a legal guardian. Based on five consecutive CRS-R administration, the best evaluation was adopted to formulate a clinical diagnosis of consciousness (UWS, MCS or e-MCS). Twenty minutes of ECG recording was performed by electrodes applied to the chest at a sample rate of 128 Hz. Tachogram was extracted using the Python library NeuroKit2 and it was visually inspected for missing beaks [10]. After extraction of R-peaks, ectopic beats were interpolated.

B. HRV and entropy

Approximate entropy adopts non-negative numbers to define the complexity of a time series. In particular given a time series $S(i) = \{s(1), s(2), s(N)\}$, take m consecutive points to form $S(i) = \{s(i), s(i+1), \dots s(i+m-1)\}$ and define the distance between $S(i), S(j)$ as follows

$$d[S(i), S(j)] = max_{k=0,1,\dots,m-1} |s(i+k) - s(j+k)|$$

Then, for a given threshold r, evaluate the number of distances smaller than r divided by the total number of distances (N-m+1) recorded as $C_m^r(i)$.

After taking the natural logarithm of $C_m^r(i)$ and calculating the average across all I, the quantity $\phi_m(r)$ can be defined. Then the dimension of the m coefficient is increased to $m+1$ and the approximate entropy is computed as follows:

$$ApEn(m, r, N) = \phi_m(r) - \phi_{m+1}(r)$$

Improvements on the concept of ApEn derive from the enforcement of the condition $i \neq j$ in the calculation of the ApEn. The latter results in the calculation of the Sample Entropy (SampEn) as follows

$$SampEn(m, r, N) = ln(\phi_m(r)/\phi_{m+1}(r))$$

In this work, the m and r parameters are set to m = 2 and r = 0.2 as in [11]. In order to perform a more robust phase-space reconstruction, a fuzzy membership function is used to measure similarity of vectors. In particular, the phase-space reconstruction performed was on the time series $S(i)$ by creating a set of f-dimensional ($f \leq N-2$) vectors as follows

$$X_i^f = s(1), s(2), \dots, s(i+f-1) - u_f(i) \quad with \quad i = 1,2, \dots . N-f+1$$

and $u_f(i)$ the average of the f-dimensional vector. Then, after calculating the maximal Euclidean distance between X_i^f and X_j^f defined as D_{ij}^f, the degree of similarity A_{ij}^f can be derived using the fuzzy membership.

$$A_{ij}^f = e^{\left(-\frac{\left(d_{ij}^f\right)^n}{r}\right)}$$

The fuzzy entropy can be then computed via

$$FuEn(f, r, n, N) = ln\phi^f(n, r) - ln\phi^{m+1}(n, r)$$

with, $\phi^f(n, r)$ defined as follows

$$\phi^f(n, r) = \frac{1}{N-f} \sum_{i=1}^{N-f} \left[\frac{1}{N-f-1} \sum_{j=1, j\neq i}^{N-f} A_{ij}^f \right].$$

Shannon's entropy can be easily defined by

$$ShanEn(n) = -S^{2(n)} log_2\left(S^{2(n)}\right).$$

Lastly, Multi Scale Entropy (MSE) generalizes the entropy concept to different time-scales by including an initial coarse graining step [14]. Via a scale factor τ, ranging from 1 to *s*, the initial time-series S is under sampled following,

$$y_i^\tau = \frac{1}{\tau} \sum_{i=(j-1)\tau+1}^{j\tau} s(j) \quad with \quad j = 1,2, \dots ., round(N/\tau)$$

to then compute the SampEn for each coarse-grained time series at different scale factors

$$MSE(\tau, m, r) = SampEn_{y_j^\tau}(m, r, N) \quad with \quad \tau = 1,2, \dots, s$$

Then the composite (CMSE) and refined (RMSE) version of the MSE are computed following Azami et al. [15] and the open-source implementation of the Neurokit2 Python toolbox as well as the Higuchi and Katz fractal dimension (HFD, KFD respectively, [16]).

C. Statistical analysis

Outcome was set as presence/absence of a pDoC. HRV complexity metrics entered multivariate logistic regressions adjusted by age and sex, given the known influence of such factors on cardiac cycles [17]. All analyses were performed on SPSS (Vs 26, Chicago, SPSS Inc.) and a p-value <0.05 was considered as statistically significant.

TABLE I: LOGISTIC REGRESSION DOC/NODOC

Variable	*OR*	*95%CI*	*p-value*
ApEN	0.328	0.168-0.640	**0.001**
SampEn	0.448	0.266-0.754	**0.002**
FuzzyEn	0.353	0.169-0.736	**0.005**
MSE	0.368	0.178-0.763	**0.007**
KFD	0.696	0.533-0.908	**0.008**

Multivariate analysis of NL-HRV measures corrected by age and gender
Legend. Reference is set to absence of a DoC (e.g. OR<1 indicates that an increasing independent variable correlates with absence of a DoC).

III. RESULTS

Two hundred fifteen patients (112 males) were included in the study with median age of 65 years [interquartile range, IQR = 21]. Seven patients were excluded from the analysis due to missing data. Out of 208, 122 patients were diagnosed with a pDoC via the CRS-R scale (median CRS-R value of 9 points [IQR = 8]). The patients' aetiologies resulted distributed as follows: 62 patients with a traumatic brain injury, 18 anoxic, 39 ischemic, and 89 patients suffering from a haemorrhagic lesion. Univariate analysis on the NL-HRV entropy features resulted in higher entropies indicating a better consciousness state (Table 1).

Approximate entropy (odds ratio, OR = 0.327, p = 0.001, median pDoC = 0.82 [IQR = 0.81], No-Doc = 1.12 [IQR = 0.79]), Sample Entropy (OR =0.456, p = 0.003, median pDoC = 0.65 [IQR = 0.93], No-DoC = 1.05 [IQR = 1.04]), Fuzzy entropy (OR = 0.349, p = 0.005, median pDoC = 0.54 [IQR = 0.56], No-DoC = 0.75 [IQR = 0.85]) and Multiscale Entropy (OR = 0.382, p = 0.009, median pDoC = 0.57 [IQR = 0.79], No-DoC = 0.88 [IQR = 0.67]) were all found to be negatively associated with the presence of a pDoC (Table 1 and Fig. 1). Also, a higher Katz fractal dimension was found to be significantly correlated with a favourable diagnosis with a median of 2.68 [IQR = 1.62] for the No-DoC group and a of 2.11 [IQR = 0.89] for the pDoC group.

Approximate Entropy was found to be the one with the

TABLE II: AREA UNDER THE CURVE

Variable	*AuC*	*Asymp. Sig.*	*Lower bound*	*Upper bound*
ApEN	0.647	0.001	0.565	0.720
SampEn	0.632	0.003	0.549	0.715
FuzzyEn	0.623	0.005	0.540	0.707
MSE	0.617	0.008	0.533	0.701
KFD	0.625	0.005	0.540	0.709

Metrics derived from the RoC curve for the complexity estimators found to be significant correlating with DoC occurrence.
Legend. AuC: Area under the Curve.

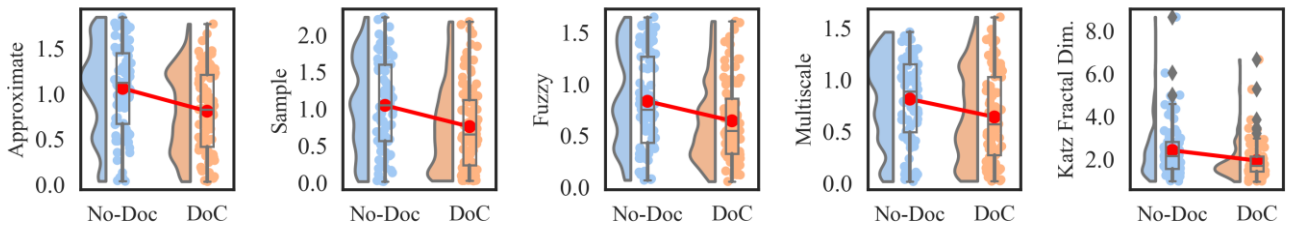


Figure 1. Box-plots of significant entropy measures across the two outcome groups.
Legend. DoC: Disorders of Consciousness

strongest odds ratio (OR = 0.328, 95%CI=0.168-0.640, p=0.001). Discrimination capability of the occurrence of a pDoC has been reported via Receiver Operating Characteristic (ROC) curves (Fig. 2). In particular, ApEn resulted the feature better identifying patients with a DoC with an AuC = 0.647 (Fig. 2, Table 2). Nevertheless, SampEn, FuzzyEn, MSE and KFD all resulted capable of providing significant information on the discrimination between patients with and without a pDoC (p<0.01, Table 2).

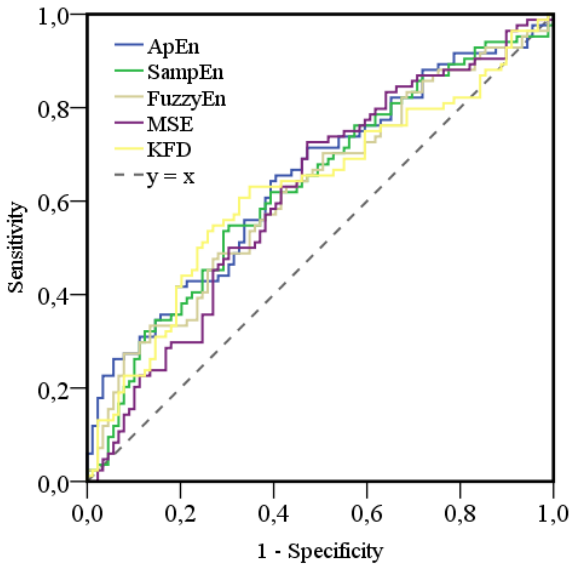


Figure 2. Receiver Operating Characteristic (ROC) curve for the complexity estimators which were found to be significant in univariate and with respect to pDoC/No-DoC.

IV. Discussion

Complementing consciousness diagnosis with instrumental evaluations would allow for a precise individualized rehabilitation management. To discriminate among patients with UWS and MCS, multifactorial approaches, including different instrumental evaluations, have been proposed [15]–[18]. The ECG signal, a non-invasive and inexpensive technique, is a proxy of the residual functionality of the ANS-CNS interplay. In particular, in patients with a brain injury it has been reported how HRV measures differentiate TBIs with elevated autonomic activity. Also, reduced HRV [19] and HRV MSE [20] were found to be predictors of mortality in TBI patients. The connection between consciousness, attention and HRV has been documented in a seminal study by Riganello et al., in which the likelihood of responding to visual/auditory stimuli was increased when the HRV low-frequency peak is around 0.1 Hz [21]. Specifically for the diagnosis of consciousness levels, complexity indexes were found to be capable of discriminating two groups of 16 MCS patients and 14 UWS patients sedated [8]. Furthermore, positive correlations were suggested between HRV entropy indexes, computed for long- and short-time scales, and fMRI-derived activation of brain areas involved in the CAN.

We extended on previous literature by providing a screening of different entropy measures in a notably larger cohort of sABI patients. Such bigger sample size enabled us to derive multivariate correlations of entropy measures with respect to the presence of a pDoC. Furthermore, given the importance of the assumptions made when performing each entropy estimates, we provide a comparison between different techniques together with the evaluation of typical fractal measures. Furthermore, entropy measures are strongly dependent on developmental parameters, calling for an aware choice of parameters when deriving such measures. Lastly, non-stationarities can either be due to artifacts or due to actual brain functioning. Among the different entropy measures adopted, Shannon entropy is the one most affected metrics by non-gaussian probability distribution function (PDF) of a time-series x(t), given the Jim-Paradigm mentioned in the work of Petty [22]. In our case, HRV being an absolute quantity and being affected by long-term non-stationarity is a candidate for a misleading use of Shannon entropy. Coherently, it is the one entropy measure with lowest significance with respect to the occurrence of a DoC. Moreover, the presence of long-term non-stationarities in HRV measures can affect the estimation of Shannon entropy given that the latter does not include any concept of distance (spread) in the x-space, measuring only the amount of information in the amount of information in the y-space of the PDF of x(t) [23]. ApEn, SampEn and FuzzyEn are known to decrease with increasing r, but in our case was kept fixed as in Riganello et al. to minimize such effect. ApEn values resulted higher in absolute value with respect to SampEn and FuzzyEn, common when investigating long signals [24].

Katz's algorithm is known to be less sensitive to noise with respect to Higuchi's method [13], coherent with the better performances obtained by KFD compared to HFD. Beyond, up to our knowledge this is the first study which, with such a large sample size, allows for multivariate correlations with the outcome, including known HRV confounding factors as age and sex [14]. Surely, the AuC achieved in this work is moderate. However, one has to take into account that each

variable is considered univariately as a predictor, without training any Machine Learning model and that the aim of the work was to specifically investigate the discrimination capability of HRV complexity. Coherently with a larger sample size and the inclusion of neurophysiological and neurobehavioral predictors, the AuC of a multivariate predictive model is expected to increase. With this work, we provided evidence that HRV complexity can be of fundamental help to complement a multifactorial diagnosis of consciousness. Such autonomic markers of consciousness may be used in absence of clear behavioural responses to improve consciousness diagnosis in patients with pDoC. Furthermore, HRV-derived markers, integrated with centrally derived neural correlates of consciousness and clinical assessments could be used to deploy decision support tools for diagnostic and prognostic purposes in patients with pDoC. Lastly, by providing a systematic evaluation of different complexity metrics, a preliminary insight on the best performing variables for the estimation of HRV complexity in patients with a pDoC was obtained.

REFERENCES

[1] J. Giacino, J. Fins, S. Laureys, e N. Schiff, «Disorders of consciousness after acquired brain injury: The state of the science», *Nature Reviews Neurology*, vol. 10, gen. 2014, doi: 10.1038/nrneurol.2013.279.

[2] J. Giacino, K. Kalmar, e J. Whyte, «The JFK Coma Recovery Scale-Revised: Measurement characteristics and diagnostic utility», *Archives of physical medicine and rehabilitation*, vol. 85, pp. 2020–9, gen. 2005, doi:10.1016/j.apmr.2004.02.033.

[3] D. Kondziella *et al.*, «European Academy of Neurology guideline on the diagnosis of coma and other disorders of consciousness», *European Journalof Neurology*, vol. 27, feb. 2020, doi: 10.1111/ene.14151.

[4] C. Di Perri *et al.*, «Limbic hyperconnectivity in thevegetative state», *Neurology*, vol. 81, fasc. 16, pp. 1417–1424, ott. 2013, doi: 10.1212/WNL.0b013e3182a43b78.

[5] F. Riganello, F. Zubler, M. Haenggi, e M. Lucia, «Heart rate complexity: An early prognostic marker of patient outcome after cardiac arrest», *Clinical Neurophysiology*, vol. 134, dic. 2021, doi: 10.1016/j.clinph.2021.10.019.

[6] F. Riganello, M. D. Cortese, G. Dolce, L. F. Lucca, e W. G. Sannita, «The Autonomic System Functional State Predicts Responsiveness in Disorder of Consciousness», *J Neurotrauma*, vol. 32, fasc. 14, pp. 1071–1077, lug. 2015, doi: 10.1089/neu.2014.3539.

[7] J.-A. Palma e E. Benarroch, «Neural control of the heart: Recent concepts and clinical correlations», *Neurology*, vol. 83, giu. 2014, doi: 10.1212/WNL.0000000000000605.

[8] F. Riganello *et al.*, «A Heartbeat Away From Consciousness: Heart Rate Variability Entropy Can Discriminate Disorders of Consciousness and Is Correlated With Resting-State fMRI Brain Connectivity of the Central Autonomic Network», *Frontiers in Neurology*, vol. 9, 2018, Consultato: 28 febbraio 2022. [Online]. Disponibile su: https://www.frontiersin.org/article/10.3389/fneur.2018. 00769

[9] B. Hakiki *et al.*, «Clinical, Neurophysiological, and Genetic Predictors of Recovery in Patients With Severe Acquired Brain Injuries (PRABI): A Study Protocol for a Longitudinal Observational Study», *Frontiers in Neurology*, vol. 13, feb. 2022, doi: 10.3389/fneur.2022.711312.

[10] D. Makowski *et al.*, «NeuroKit2: A Python toolbox for neurophysiological signal processing», *Behavior Research Methods*, vol. 53, fasc. 4, pp. 1689–1696, 2021, doi: 10.3758/s13428-020-01516-y.

[11] M. Costa e A. L. Goldberger, «Multiscale EntropyAnalysis (MSE)», p. 8.

[12] H. Azami, M. Rostaghi, D. Abasolo, e J. Escudero, «Refined Composite Multiscale Dispersion Entropy and its Application to Biomedical Signals», *IEEE Trans. Biomed. Eng.*, vol. 64, fasc. 12, pp. 2872–2879, dic. 2017, doi: 10.1109/TBME.2017.2679136.

[13] C. K. Loo, A. Samraj, e G. C. Lee, «Evaluation of Methods for Estimating Fractal Dimension in Motor Imagery-Based Brain Computer Interface», *DiscreteDynamics in Nature and Society*, p. 9.

[14] I. Antelmi, R. S. De Paula, A. R. Shinzato, C. A. Peres, A. J. Mansur, e C. J. Grupi, «Influence of age, gender, body mass index, and functional capacity on heart rate variability in a cohort of subjects without heart disease», *The American Journal of Cardiology*, vol. 93,fasc. 3, pp. 381–385, feb. 2004, doi: 10.1016/j.amjcard.2003.09.065.

[15] P. Liuzzi, A. Magliacano, F. De Bellis, A. Estraneo, e A. Mannini, «Predicting outcome of patients with prolonged disorders of consciousness using machine learning models based on medical complexity», *Scientific Reports*, vol. 12, fasc. 1, 2022, doi: 10.1038/s41598-022-17561-w.

[16] P. Liuzzi *et al.*, «Merging Clinical and EEG Biomarkers in an Elastic-Net Regression for Disorder of Consciousness Prognosis Prediction», *IEEE Transactions on Neural Systems and Rehabilitation Engineering*, vol. 30, pp. 1504–1513, 2022, doi: 10.1109/TNSRE.2022.3178801.

[17] J. Sitt *et al.*, «Large scale screening of neural signatures of consciousness in patients in a vegetative or minimally conscious state», *Brain : a journal of neurology*, vol. 137, giu. 2014, doi: 10.1093/brain/awu141.

[18] F. Raimondo *et al.*, «Brain-heart interactions reveal consciousness in non-communicating patients», *Annals of Neurology*, vol. 82, set. 2017, doi: 10.1002/ana.25045.

[19] W. P. Riordan, B. A. Cotton, P. R. Norris, L. R. Waitman, J. M. Jenkins, e J. A. Morris, «Beta-blockerexposure in patients with severe traumatic brain injury (TBI) and cardiac uncoupling», *J Trauma*, vol. 63, fasc. 3, pp. 503–510; discussion 510-511, set. 2007, doi: 10.1097/TA.0b013e3181271c34.

[20] W. P. Riordan, P. R. Norris, J. M. Jenkins, e J. A. Morris, «Early loss of heart rate complexity predicts mortality regardless of mechanism, anatomic location,or severity of injury in 2178 trauma patients», *J Surg Res*, vol. 156, fasc. 2, pp. 283–289, ott. 2009, doi: 10.1016/j.jss.2009.03.086.

[21] F. Riganello, M. D. Cortese, G. Dolce, e W. G. Sannita, «Visual pursuit response in the severe disorder of consciousness: modulation by the central autonomic system and a predictive model», *BMC Neurol*, vol. 13, p. 164, nov. 2013, doi: 10.1186/1471-2377-13-164.

[22] G. Petty, «On Some Shortcomings of Shannon Entropyas a Measure of Information Content in Indirect Measurements of Continuous Variables», *Journal of Atmospheric and Oceanic Technology*, vol. 35, mar. 2018, doi: 10.1175/JTECH-D-17-0056.1.

[23] J. K. Kanters, M. V. Højgaard, E. Agner, e N. H. Holstein-Rathlou, «Short- and long-term variations in non-linear dynamics of heart rate variability», *Cardiovasc Res*, vol. 31, fasc. 3, pp. 400–409, mar. 1996.

[24] C. González, E. Jensen, P. Gambús, e M. Vallverdú, «Entropy Measures as Descriptors to Identify Apneas in Rheoencephalographic Signals», *Entropy (Basel)*, vol. 21, fasc. 6, p. 605, giu. 2019, doi: 10.3390/e21060605.

Full-scale point-neuron model of the mouse hippocampal microcircuits

G.M. Boiani [1*], S. Solinas [3*], G. Preti [1], A. Manini [1], M. Migliore [4], J. Mapelli [1,2] and D. Gandolfi [1,2]

[1] *Department of Biomedical, Metabolic and Neural Sciences, University of Modena, Italy*

[2] *Center for Neuroscience and Neurotechnology, University of Modena and Reggio Emilia, Italy*

[3] *Department of Biomedical Sciences, University of Sassari, Sassari, Italy*

[4] *Institute of Biophysics, National Research Council, Palermo, Italy*

[*] *These authors contributed equally*

***Abstract*—The modelling of neural circuits with single cell resolution is progressively becoming a reliable benchmark to simulate the neurophysiological correlates of brain activity and to investigate brain dysfunctions. The physiological and pathological conditions in fact can be explored through single neuron models that can simulate the salient electrophysiological properties of biological neurons. One of the main issues of the realistic modelling of brain circuits is related to the connection strategy: to properly define the network connectome it is of utmost importance to take into account morpho-anatomical constraints dictated by neuronal cito-architecture. We have developed a strategy to generate realistic neuronal networks with single-cell resolution based on the creation of geometrical probability density functions mimicking extension and orientation of neuronal axons and dendrites. The first benchmark of the modelling pipeline allowed to create a full-scale point neuron model of the mouse CA1 hippocampus. The modelling strategy has been applied to the CA3 region of the mouse hippocampus allowing to generate a full network with limited computational costs suggesting that the present approach can be reliably translated to other brain areas.**

***Keywords*—Hippocampus, CA3, CA1, network activity, neuronal modelling.**

I. INTRODUCTION

THE research on computational models of brain circuits has increased tremendously and the implementations of large-scale brain circuits at single neuron resolution is becoming instrumental for Neuroscience research [1,2]. The use of such technologies could in fact lead to innovative therapeutics and diagnostic tools for in silico medicine [3,4]. In the last decades, a significant number of mathematical models has been proposed to explore different spatio-temporal scales of neuronal microcircuits. The construction of these models is bound to a series of approximations which scale up with the size of the network. The major factor is the size of the connectome [5], which affects the computational performance and shapes the input-output relationship of the circuit. Although single cell properties have been tailored and refined for several neuronal classes, the strategy adopted to generate the network connectome is still a critical issue [6,7]. According to i) data availability, ii) computational effort and iii) level of biological realism, different connection strategies have been proposed and tested: from statistical algorithms [8] to sophisticated methods strictly adhering to morphological and anatomical constraints [9]. The choice of the connectivity strategy strongly depends on the computational effort especially when more than hundreds of thousands of neurons must be connected. The estimation of connection probability through isotropic or distance-based probability clouds provides remarkable results especially when combined with some morphological rule [10]. Unfortunately, the use of realistic morphologies in large networks can be hardly sustained given the limited number of available data, which in turn requires to replicate randomly individual morphologies to reproduce biological variability. Here, we present a connection strategy based on the generation of probability density functions for neuronal processes. The strategy has been benchmarked on the mouse hippocampus by developing a statistical/geometric approach to customize local connectivity. Starting from morpho-anatomical constraints obtained from morphological data, the proposed method allowed to generate a network connectivity of the CA1 and CA3 regions of the mouse hippocampus that are consistent with experimental findings on real circuits at single cell resolution [11].

II. RESULTS

Here, we propose a strategy for modelling full-scale networks based on morpho-anatomical constraints. The algorithm has been validated on CA1 and CA3 mouse hippocampal regions and is organized in sequential steps that are detailed below.

A. Cell placement

The 3D neuronal coordinates for both CA1 and CA3 regions have been downloaded from the Blue Brain Cell Atlas database (https://bbp.epfl.ch/nexus/cell-atlas/). The repository provides annotated references in the Common Coordinated Framework (CCF) for all the layers of both regions divided in excitatory and inhibitory populations without further classification of neuronal subtypes. We have therefore extensively analyzed the literature on hippocampal single cell morphologies to identify the excitatory and inhibitory subclasses and to provide a strategy to generate a connectivity matrix. The neurons were divided into 13 classes (2 exc, 11 inh) for CA1 and 14 for CA3 (2 exc, 12 inh) [12,13]; Table1. The resulting scaffolds were obtained with the BSB (Brain Scaffold Builder) framework [14] and their graphical representation are shown in Figure 1 [https://pypi.org/project/mayavi].

B. Neuronal morphologies and orientation

The activity of large-scale neuronal network comprising several hundred thousands of cells and millions or billions of synapses can only be simulated by using “point neurons”, Integrate-and-Fire neuronal models with single compartment. Point neurons preserve most of the electrophysiological properties while discarding detailed morphological descriptions to reproduce the electrotonic response of the

neuronal membrane. Here, geometrical shapes have been created only to compute the connectivity matrix. Given the simplified nature of this approach, we have assumed that neurons belonging to the same class share similar geometrical features. We have analyzed single cell morphologies from public repositories (neuromorpho.org, http://mouselight.janelia.org/, https://portal.brain-map.org) to identify an average shape to represent neuronal subtypes.

TABLE I: NEURONAL POPULATION

Excitatory neurons

CA1			***CA3***		
Stratum	*Cell type*	*Count*	*Stratum*	*Cell type*	*Count*
SO	Deep Pyr	45408	*SO*	Deep Pyr	38512
SP	Superficial Pyr	216435	*SP*	Superficial Pyr	359885
	Total	261843		*Total*	398397

Inhibitory neurons

CA1			***CA3***		
Stratum	*Cell type*	*Count*	*Stratum*	*Cell type*	*Count*
SO	OLM, Tri, BP	1979	*SO*	OLM, Tri	4076
SP	CCKBC, PVBC, AA	1661	*SP*	CCKBC, PVBC, AA, BS, Ivy	5254
SR	Ivy, BS, SCA, PPA	10147	*SL*	Spiny, MFA	693
SLM	NGF	12397	*SR*	RC, PPA	3718
			SLM	NGF	168
	Total	26184		*Total*	13909

SO, Stratum Oriens; SP, Stratum Pyramidale; SR, Stratum Radiatum, SLM, Stratum Lacunosum-Molecolare, SL, Stratum Lucidum; Pyr, Pyramidal cell; OLM, Oriens-Lacunosum Molecolare cell; Tri, Trilaminar cell; BP, Bipolar cell; CCKBC, CCK+ Basket cell; PVBC, PV+ Basket cell; AA, Axo-axonic cell; BS, Bistratified cell; Ivy, Ivy cell; SCA, Schaffer's collateral-associated cell; PPA, Perforant path-associated cell; Spiny, Spiny lucidum cell; MFA, Mossy fibers-associated cell; RC, Radiatum cell; NGF, Neurogliaform cell.

The geometrical shapes associated to each neuron represent a probabilistic density function that mimic the volume occupancy of axons and dendrites. In our approach, we have assumed that neurites could be represented as a combination of ellipsoids and cones, whose parametrization were obtained from the average axonal and dendritic extensions derived from data analysis (see Fig. 2,3). To maintain cell-to-cell variability preserving the desired parametrization, normal distributions for all the geometric descriptors were created and the ellipsoids and cones dimensions were randomly sampled within the distributions.

The orientation of geometrical probability density functions was performed by measuring, through an iterative scanning algorithm, the relative distances between soma position, inner layers, and outer regions (CA3 and Subiculum for CA1 neurons; CA1 and Dentate Gyrus for CA3 neurons) and tilting the ellipsoids and cones according to their relative position within hippocampal layers and respecting the morpho-anatomical constraints derived from the literature. For example, basal and apical dendrites of Pyramidal Cells (PC) are oriented towards SO and SLM, respectively, while axons of CA3 PC run along SO and SR (see Fig. 2).

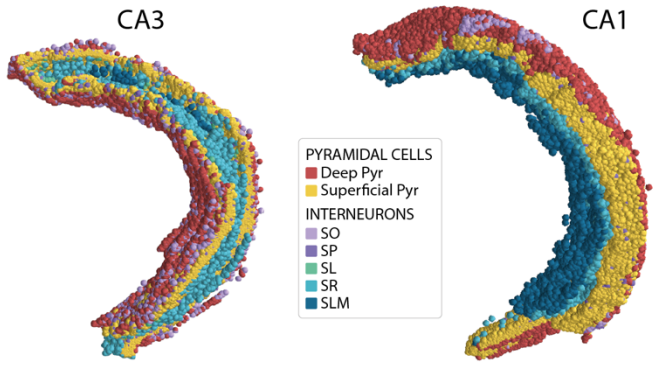


Fig. 1: Neuronal placement. Excitatory and inhibitory cell positioning according to the CA3 (left) and CA1 (right) region layer subdivision provided by the Blue Brain cell Atlas. Colored dots represent excitatory or inhibitory neurons that were divided according to their positioning within the CA1 and CA3 layers.

Geometrical morphologies mimicked the cross-section volumes of pre-synaptic axons and post-synaptic dendrites depending on the desired shape. The ellipsoids were modelled by assuming an orthonormal system of eigenvectors $\mathbf{v_1}$,$\mathbf{v_2}$,$\mathbf{v_3}$ associated with the eigenvalues λ_1, λ_2, λ_3 of a 3x3 symmetric positive matrix M.

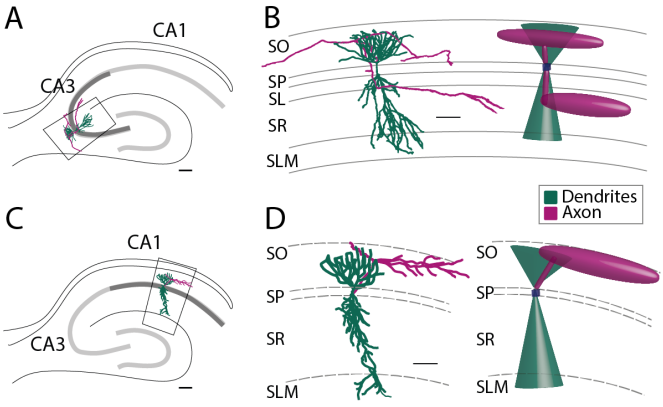


Fig. 2: Pyramidal neurons. (A) Scheme of a transversal section of the mouse hippocampus. Thick gray line represents the Pyramidal layer of CA3 area. (B). *Left.* Realistic morphology of a PC (dendrites in green, and axon in violet), oriented within a region of a transversal CA1 hippocampal slice (inset of A). *Right*. The probability density functions are represented as two cones and four ellipsoids (color code matches the colors of realistic morphology). (C) Similarly to A, scheme of a transversal section of the mouse hippocampus. The thick gray line represents the Pyramidal layer of CA1 area. (D). Similarly to B, a realistic morphology of a PC (dendrites in green and axon in violet) oriented within a region of a transversal CA1 hippocampal slice (inset of panel C). The corresponding probability density functions are represented on the right respecting the color code. Scale bars in μm (100 in A and C, 50 in B and D).

Considering $V = [v_1, v_2, v_3]$ then

$$V^T M V = \begin{bmatrix} \lambda_1 & 0 & 0 \\ 0 & \lambda_2 & 0 \\ 0 & 0 & \lambda_3 \end{bmatrix} = D[\lambda_1, \lambda_2, \lambda_3]; \qquad \text{Eq. 1}$$

is a diagonal matrix with the eigenvalues of M and the normalized vectors $\mathbf{v_1}$, $\mathbf{v_2}$, $\mathbf{v_3}$ are called the principal axis of M. Given an arbitrary base of orthonormal vectors $\mathbf{u_1}$, $\mathbf{u_2}$, $\mathbf{u_3}$ (the ellipsoid orientation vectors) forming the matrix U and a diagonal matrix of arbitrary eigenvalues D (semiaxis lengths), it is possible to obtain the symmetric matrix Q with

$$Q = UDU^T \qquad \text{Eq. 2}$$

The orientation vectors were selected according to the morpho-anatomical landmarks derived from the analysis of experimental morphologies in public repositories. The probability density function could then be modelled as tridimensional points scattered according to the following parametric equations:

$x = \lambda_1 cos\vartheta sin\varphi,\ y = \lambda_2 cos\vartheta sin\varphi,\ z = \lambda_3 cos\varphi$ Eq. 3

where $0 \leq \vartheta \leq 2\pi$ and $-\pi \leq \varphi \leq 0$.

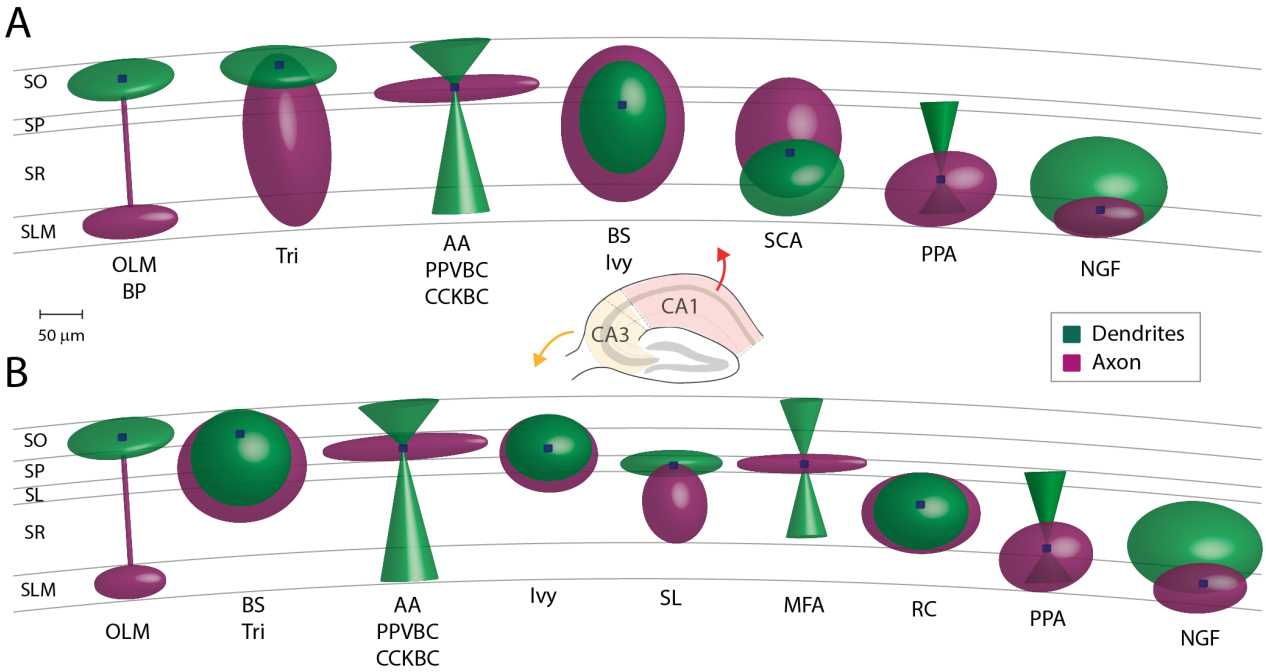


Fig. 3: Probability density functions of GABAergic interneurons. A. The 11 classes of CA1 interneurons described in table 1 have been represented with 7 shapes. B. The 12 classes of CA3 interneurons described in Table 1 have been represented with 9 shapes. Black squares indicate the preferential position of the cell soma while green and violet shades represent dendrites and axons respectively.

Conical probability density functions have been modeled as point cloud volumes with extent and orientation determined by parametric features and morpho-anatomical constraints. Assuming **u** and **v** are orthogonal vectors lying in the plane of the base, the scattered points in a conical volume are calculated with the following equation:

$$\begin{bmatrix} x \\ y \\ z \end{bmatrix} = \begin{pmatrix} O_x + \frac{h}{H}dx \\ O_y + \frac{h}{H}dy \\ O_z + \frac{h}{H}dz \end{pmatrix} + \begin{pmatrix} r \cdot \frac{h}{H} \cdot cos\vartheta \cdot u_x \\ r \cdot \frac{h}{H} \cdot cos\vartheta \cdot u_y \\ r \cdot \frac{h}{H} \cdot cos\vartheta \cdot u_z \end{pmatrix} + \begin{pmatrix} r \cdot \frac{h}{H} \cdot sin\vartheta \cdot v_x \\ r \cdot \frac{h}{H} \cdot sin\vartheta \cdot v_y \\ r \cdot \frac{h}{H} \cdot sin\vartheta \cdot v_z \end{pmatrix} 0 \leq h \leq H, 0 \leq \vartheta \leq 2\pi, 0 \leq r \leq R$$

Eq. 4

where $H = |P - O|$ is the height of the cone, O is the apex, P is the center point of the base, R is the radius of the cone base, [*dx,dy,dz*] are the vector component of H. The scattered points of the cone were created by randomly sampling h, theta and r in their respective ranges.

C. Neuronal connectivity

The geometrical morphologies were converted into axonal convex hulls and dendritic point clouds and an iterative algorithm intersected a single presynaptic axonal hull with all dendritic point clouds belonging to a particular neuronal class. Given the size of the benchmarked network (see Table 1) which could lead to an intensive computational load, the range of possible intersections was limited to axon and dendrites sharing putative volumes. This dimensional reduction was performed by calculating the bounding boxes for all geometric shapes and running the intersection algorithm to neurites with overlapping bounding boxes. The pairs of connected neurons were obtained by computing whether at least one dendritic point was included in an axonal convex hull. All neuronal pairs sharing one or more dendritic points were included in the empirical calculation of potential connection pairs. This initial evaluation was then reduced by estimating the putative number of connection pairs combining the number of pre and post synaptic neurons in both classes with the synaptic connection probabilities obtained from the public repository Hippocampome.org.

D. Benchmark of the modeling strategy

The proposed strategy has been benchmarked by generating two of the main regions of the mouse hippocampus, CA1 and CA3, each containing about 300'000 neurons. All the algorithms to the identify landmarks, to generate neuronal morphology and to intersect probability density functions were custom developed in Matlab (The Mathworks inc.) and then converted to python language. The time required to calculate the network connectivity depended i) on the number of points in each cloud, ii) the number of potential intersections and iii) the numerosity of each neuronal class. The codes were parallelized on a supercomputer (http://www.labcsai.unimore.it) equipped with an Intel Xeon

20 core 6230 2.1 GHz with 40 processors) to create the CA1 and CA3 circuits (each one with ~300k neurons and ~1 billion synapses).

.

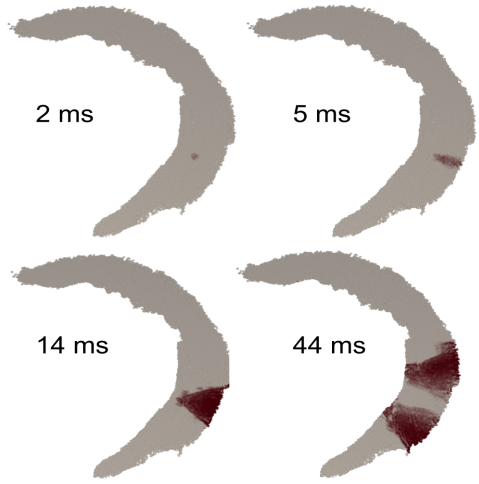


Fig. 4: HPC simulation results. The CA1 network model was stimulated to activate 240 neurons at time 2 ms after stimulation onset (upper left panel). All neurons are shown in grey. The neurons that fired an action potential within a 1 ms time window were plotted in dark red. The panels show the progression of the activation wave through the network at 5, 14 and 44 ms after stimulus onset.

E. Network simulation

The present connectivity strategy has been tested on the CA1 region by verifying the correct implementation of the directionality in Pyramidal-to-pyramidal activity propagation along transversal hippocampal slices. The CA1 simulation including PCs and inhibitory interneurons was set up on the supercomputer Piz-Daint of the Swiss HPC CSCS facility using the Cray X40 Compute nodes. Each node has two Intel® Xeon® E5-2695 v4 @ 2.10GHz (18 cores) and 64GB of RAM. The neuronal placement and connection matrices were loaded on the NEST simulator with Python API. All neuronal types were modeled as point neurons using the Hill & Tononi [15] neuron model available in NEST as it offers the possibility to receive AMPA, NMDA, and GABA mediated synaptic models. Synapses were endowed with short-term dynamics properly tuned according to the available literature using Tsodyks & Markram model. Neuronal models were not calibrated and tests were only performed to assess the technical feasibility of the overall implementation. To speed up the network setup, the neuronal placement and connection matrices were loaded into compressed datasets in a single HDF5 data file of 388 Mb. For these initial tests, we run simulations on a single HPC node. A simulation was set to use a single processor for the network setup and 18 threads to run the simulation. The network setup time was 65 secs and it took 373 secs to simulate 500 ms of network activity. Figure 4 shows the simulation results for the CA1 network model. After the stimulus onset, a front of active neurons spreads along the CA1 in both directions.

III. CONCLUSION

We have presented a generalized bottom-up strategy to generate networks of point neurons based on morpho-anatomical constraints that has been benchmarked on two mouse hippocampal regions. This data-driven method based on the construction of geometrical probability density functions mimicking axonal and dendritic shapes and extension, is particularly suitable in conditions of poor or absent data on cell morphologies which hamper the possibility to adopt more realistic strategies like touch algorithms requiring complete morphologies for all neurons. At the same time, connection strategies like random connectivity have been shown to produce networks connectivity with homogeneous distance connectivity and number of connections per neuron uniformly distributed, which has been shown to be unrealistic [8,11]. The proposed strategy will be integrated as a function of the BSB as a method to connect neuronal classes in a custom created circuit, providing an additional tool to generate network connectivity of large-scale circuits.

IV. ACKNOWLEDGMENTS

This work was supported by: FAR-DIP 2022 to DG, Bando Fondazione Sardegna 22-23 and “progetti di ricerca di base” to SS, FLAG-ERA JTC2019 SMARTBRAIN to JM.

REFERENCES

[1] Poirazi, P. & Papoutsi, A. “Illuminating dendritic function with computational models”. *Nat. Rev. Neurosci*.2020 21(6), 303–321.

[2] Gandolfi, D et al. “Modeling neurotransmission: Computational tools to investigate neurological disorders”. *Int. J. Mol. Sci*. 2021. 22(9), 4565.

[3] Jirsa VK et al. “The Virtual Epileptic Patient: Individualized whole-brain models of epilepsy spread. *Neuroimage.* 2017 Jan 15;145(Pt B):377-388.

[4] Lytton WW. “Computer modelling of epilepsy”. *Nat Rev Neurosci*. 2008 Aug;9(8):626-37. doi: 10.1038/nrn2416. Epub 2008 Jul 2. PMID: 18594562; PMCID: PMC2739976.

[5] Glasser MFet al. “The Human Connectome Project's neuroimaging approach”. *Nat Neurosci*. 2016 Aug 26;19(9):1175-87. PMID: 27571196; PMCID: PMC6172654.

[6] Markram H et al. “Reconstruction and Simulation of Neocortical Microcircuitry”. *Cell*. 2015 Oct 8;163(2):456-92. PMID: 26451489.

[7] Billeh YN et al. “Systematic Integration of Structural and Functional Data into Multi-scale Models of Mouse Primary Visual Cortex”. *Neuron*. 2020 May 6;106(3):388-403.e18. Epub 2020 Mar 5. PMID: 32142648.

[8] Giacopelli G et al. “On the structural connectivity of large-scale models of brain networks at cellular level.” *Sci Rep.* 2021 Feb 23;11(1):4345. PMID: 33623053; PMCID: PMC7902637.

[9] Reimann MW et al. “An algorithm to predict the connectome of neural microcircuits”. *Front Comput Neurosci*. 2015 Oct 8;9:120. PMID: 26500529; PMCID: PMC4597796.

[10] Udvary D et al. “The impact of neuron morphology on cortical network architecture”. *Cell Rep*. 2022 Apr 12;39(2):110677. doi: 10.1016/j.celrep.2022.110677. PMID: 35417720; PMCID: PMC9035680.

[11] D. Gandolfi et al. “A realistic morpho-anatomical connection strategy for modelling full-scale point-neuron microcircuits. *Sci Rep.* 2022 Aug 16;12(1):13864.

[12] Booker, S.A., & Vida, I. (2018). Morphological diversity and connectivity of hippocampal interneurons. Cell and Tissue Research, 373, 619 - 641.

[13] Le Duigou, C. et al. (2014). Recurrent synapses and circuits in the CA3 region of the hippocampus: an associative network. Front Cell Neurosci

[14] De Schepper, RS. *et al.* Model simulations unveil the structure-function-dynamics relationship of the cerebellar cortical microcircuit. *Commun Biol* **5**, 1240 (2022).

[15] S. Hill, G. Tononi (2005). Modeling sleep and wakefulness in the thalamocortical system. Journal of Neurophysiology. 93:1671-1698.

A neural model of sensory interactions in young neurotypical and ASD children

M. Monti[1], S. Molholm[2], and C. Cuppini[1]
[1] *Department of Electrical, Electronic, and Information Engineering Guglielmo Marconi, University of Bologna, Italy*
[2] *The Cognitive Neurophysiology Laboratory, Albert Einstein College of Medicine, New York, USA*

***Abstract*— The brain at birth is characterized by a default state of competition among the senses [1], and integrative abilities are acquired only later in life, based on experience. Recently, Crosse and colleagues [2] in a bisensory reaction time task, with auditory (A) and visual (V) stimuli, presented alone or together (AV), in a random sequence, showed that children's reaction times (RTs) to congruent AV stimuli did not differ significantly from unisensory RTs, but differences emerged between ASD and neurotypical (NT) subjects. In this work, we implemented a neurocomputational model to simulate the RTs and analyse the behavioural responses of ASD children (6-7 years of age) and their NT counterpart. The model suggests that the comparable RTs found in unisensory and multisensory conditions could be interpreted by the default competition among the senses; this default state can be implemented via mutual inhibition between primary sensory areas; and the shift toward the classical multisensory facilitation, observed in adults, is the result of the inhibitory cross-modal connections becoming excitatory after an extended multisensory experience. Moreover, model results suggest that differences between ASD and NT children are due to a stronger cross-modal inhibition in 6-7 year-old ASD children. Finally, this neurocomputational model allowed investigation of the temporal profile of interactions among stimuli of different sensory modalities. These findings link the perceptual framework delineated by several empirical results to a plausible neural implementation.**

***Keywords*—Neural Modelling, Autism, Sensory Interactions.**

I. Introduction

MULTISENSORY integration (MSI) is the mechanism exploited by the brain to deal with information from different sensory systems, and optimizing its responses in case of redundant multimodal cues compared to the individual unisensory components, when presented separately. The principles ruling MSI in the spatial domain, like the inverse effectiveness and the multisensory enhancement in case of congruent multisensory stimuli, have been known for a long time [3], [4]. In the temporal domain great effort has been dedicated to identify the conditions for a multisensory facilitation (the so-called temporal binding window, TBW) [5], [6], but only recently the competition among stimuli incongruent in time has been analysed: Cuppini et al. [7] addressed MSI in the temporal domain for healthy adult subjects. Additionally, MSI is not innate: the brain at birth is characterized by a default state of competition among the senses, and integrative abilities are acquired only later in life, based on sensory experience [1].

In the last decade, numerous studies dealing with MSI focused on its alterations in subjects with neurodevelopmental disorders. Among these, individuals with Autism Spectrum Disorders (ASD) have shown a lack of benefit from multiple sources of information as their neurotypical (NT) peers do [8]–[12]. These deficits have been observed in case of simple AV detection task, involving low-level stimuli [2], [13], but also with audiovisual (AV) speech stimuli, thus suggesting that perceptual deficits may be responsible for higher order core symptoms characterizing ASD [12].

Recently, Crosse and colleagues [2] implemented a bisensory reaction time task to characterize the MSI maturation, in NT and ASD, from childhood to the adult age, and analyse the switch cost (the difference between RTs in case of stimuli preceded by a different sensory modality, switch trials, and RTs in repeat trials, when the preceding stimuli are of the same modality). In their experimental setup, auditory (A) and visual (V) stimuli were presented in random sequence, alone or together (AV), and subjects were required to respond (pressing a button) as soon as they perceived a stimulus. They showed that children's reaction times (RTs) to congruent AV stimuli did not differ significantly from unisensory RTs. Similarly to [1], also these authors suggested that this behaviour could be ascribed to a default competitive interaction among sensory modalities. Postnatal multisensory experience is thought to craft cross-sensory projections between sensory cortices, promoting the maturation of integrative abilities and shift the competition to facilitative cross-modal interactions. Authors highlighted that this shift is delayed in ASD children.

Despite the numerous developmental studies, reporting reduced multisensory abilities in younger children, there is little evidence of such competitive cross-modal architecture. Moreover, to our knowledge, there is no study investigating the mechanisms underlying MSI in the temporal domain for children and/or for any pathological condition. Therefore, here, we used a computational modelling framework to reproduce the data of Crosse et al. [2], investigating the nature of cross-modal interactions in the youngest subjects (6-7 years of age), characterizing the differences between NT and ASD children, and the mechanisms underlying MSI in the temporal domain.

A. Data analysis

To identify the neural mechanisms to be implemented in the network, first we analysed the empirical results of [2], based on the age group, in the case of unisensory and multisensory stimulations.

As it can be seen in Fig. 1, data of 6-7 year-old subjects do not show a multisensory behavioural facilitation. Indeed, responses (RTs) were not significantly faster in the multisensory condition compared to the unisensory ones: in NT children (Fig. 1A), RTs in AV repeat trials were comparable with RTs in the visual repeat condition; in ASD children (Fig. 1B), RTs in AV repeat trials were comparable with RTs in the auditory repeat condition. Moreover, RTs in case of multisensory switch trials, do not differ neither from

AV repeat, nor from unisensory repeat condition. This pattern of behaviour not only denotes the absence of a multisensory facilitation, but it suggests an active competition between the two sensory modalities: the fact that behavioural responses in the multisensory repeat condition are comparable with RTs in the fastest unisensory repeat condition, suggests that in case of AV stimulation, the two sensory channels compete, and only one of them can drive the response and determine the RTs. In agreement with [1], [2], these results strongly suggest the existence of an initial cross-modal competition between the sensory modalities. During the development, this competition should be superseded by the classical multisensory facilitation, as the result of the multisensory experience a subject was exposed to.

In our model, this default cross-modal competition was implemented via inhibitory cross-modal projections, as shown in Fig. 2. These synapses produce a fast competition between sensory modalities, and, balancing the integration occurring in the M region (due to the excitatory feedforward connections projecting on it), nullify any multisensory facilitation.

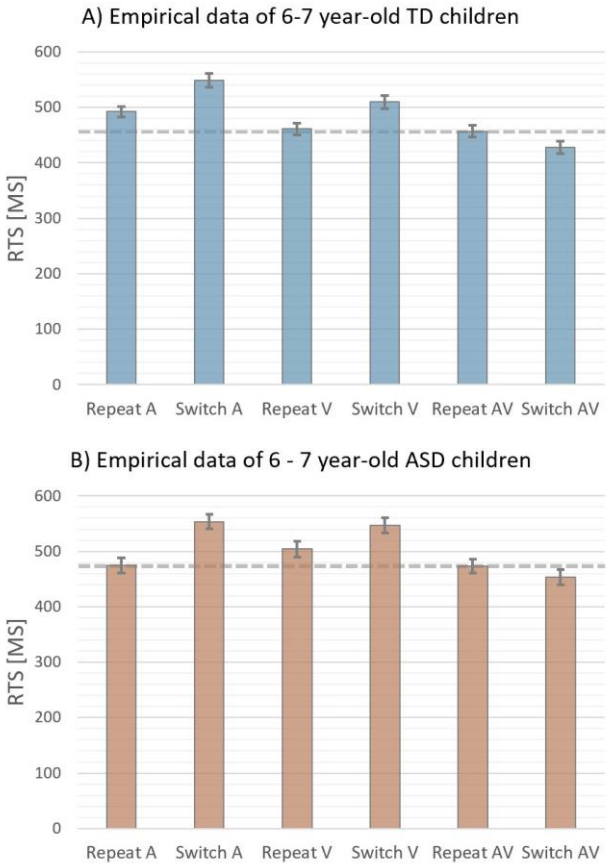


Fig. 1: Analysis of unisensory and multisensory RTs for both NT and ASD children of 6-7 years of age. A) In NT children of 6-7 years of age, RTs in the multisensory repeat trials were comparable with RTs in the visual repeat condition. B) In ASD children of 6-7 years of age, RTs in the multisensory repeat trials were comparable with RTs in the auditory repeat condition. It is evident that multisensory RTs were not faster than the faster of the unisensory conditions, but exactly comparable to it. This behavioural data could only be explained by a competition between the two sensory modalities.

II. Methods

A. Model architecture

The model has been realized to simulate the behavioural task implemented by [2], which focuses on multisensory interactions in the temporal domain: subjects (either adults or children, NT or ASD) were required to respond to auditory and visual stimuli, alone or combined, presented in a random sequence, with an inter-stimulus-interval (ISI) varying between 1 s and 3 s. Given the experimental set-up in [2], we do not require either multiple units sensitive to different spatial positions in each sensory area, nor do we need multiple sensory regions sensitive to different input features.

The model we developed is represented in Fig. 2. The network is composed of three layers.

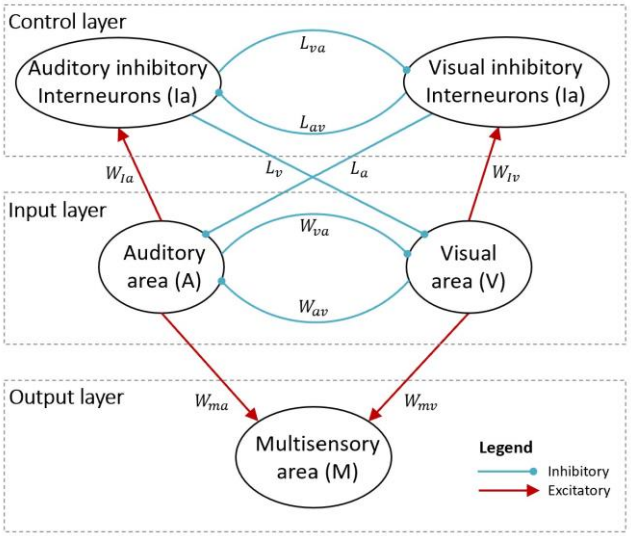


Fig. 2: Model structure. A and V represent the auditory and visual regions, responsible for the first sensory processing, and implementing the input layer. They exchange direct inhibitory synapses (W_{va} and W_{av}), implementing a cross-modal competition. M is the multisensory output region, excited by the input layer, through feedforward connections (W_{ma} and W_{mv}). It is responsible for generating the simulated reaction times (RTs) to the external stimuli. I_a and I_v are unimodal inhibitory areas, excited by the input layer (through W_{Ia} and W_{Iv}) and implementing a control mechanism via feedback inhibitory synapses (L_a and L_v) and a winner-takes-all mechanism (L_{va} and L_{av}).

A and V represent the auditory and visual regions, respectively, responsible for the first sensory processing of external stimuli, and implementing the "input layer". A and V exchange reciprocal inhibitory synapses, W_{va} and W_{av}, with a fast dynamic, implementing the default cross-modal competition.

M is the multisensory output region ("output layer"), responsible for generating the simulated reaction times (RTs) to the external stimuli. M, which receives the converging excitatory projections (W_{ma} and W_{mv},) from the two areas in the input layer, may correspond to multisensory associative cortices, including, for example, the Posterior Parietal Cortex (PPC).

Ia and Iv are unisensory inhibitory areas representing a "control layer". They are excited by the input layer (through W_{Ia} and W_{Iv}) and implement a cross-sensory competition between the two sensory modalities, characterized by a slow dynamics: if stimulated by an input of the corresponding sensory modality, these modality-specific inhibitory interneurons produce a long lasting inhibition of the input region processing external stimuli of the other sensory modality, via the inhibitory feedback projections (L_a and L_v), and the winner-takes-all mechanism (L_{va} and L_{av}). It is worth noting that, since the dynamics of this mechanism is slow, the processing of the current stimulus is affected by the previous

one, when of the opposite sensory modality. This competitive layer can be implemented through higher order regions, for example located in the medial Prefrontal Cortex (mPFC) or the Posterior Cingulate Cortex (PCC).

B. *Assessment of network performance*

First, as described above, to discriminate between alternative architectures for the network, we performed an analysis of the data collected by [2], based on the age group, in the case of unisensory and multisensory stimulation.

Once we identified the cross-modal inhibition as the more plausible neural architecture to explain these behavioural data, we performed several simulations to test the network behaviour. To this end, we presented sequences of unisensory (A or V) and congruent AV stimuli, in randomized order. The onset, duration, and presentation rate (ISI) of the stimuli were chosen to mimic the experimental setup of [2], whose data are compared to our results. Specifically, external stimuli are excitatory inputs with a duration of 60ms, presented at a rate of every 2s (the mean ISI in [2]). The activity elicited in the output region was compared with a fixed threshold, φ (10% of the maximum neurons' activity), to evaluate the simulated RTs, computed as the time interval between the instant of input presentation, and the instant when the evoked activity in the output area reaches the threshold. These results were analysed separately based on the respective input modality.

III. Results

In the following we present our results, critically analysing the model behaviour. This allows us to understand (i) what mechanisms are responsible for behavioural data in children and (ii) how such mechanisms differ in ASD.

TABLE I: Synaptic weights

NT children			
$L = 3$	$L_{a_NT} = 0.09$	$W_{av_NT} = -0.45$	$W_{ma_NT} = 1$
$WI = 1.4$	$L_{v_NT} = 0.07$	$W_{va_NT} = -0.45$	$W_{mv_NT} = 1.72$
ASD children			
$L = 3$	$L_{a_ASD} = 0.13$	$W_{av_ASD} = -0.8$	$W_{ma_ASD} = 1.1$
$WI = 1.4$	$L_{v_ASD} = 0.05$	$W_{va_ASD} = -0.8$	$W_{mv_ASD} = 1.3$

A. *Testing model simulations against empirical data*

Once we identified the cross-modal inhibition as the main mechanism to be implemented, the next step was to determine the exact parameters' values that allow to reproduce RTs reported in [2], for both ASD and NT children at 6-7 years of age. To this aim, several sets of parameters were tested, and the simulated RTs were compared with the experimental median RTs extracted from the population of real subjects.

Fig. 3 illustrates the comparison between simulated and real RTs, obtained with the best set of parameters for all the six input configurations, for both ASD and NT children. It is worth noting that, among all the parameters, only the synaptic weights differ between the two groups, and are reported in Table I.

In particular, model results suggest that differences between ASD and NT children can be explained by a stronger cross-modal inhibition in 6-7 year-old ASD children, as can be noted from the more negative value assumed by W_{va} and W_{av} in the ASD simulations (Table I). We made this assumption based on the delayed maturational trajectories characterizing ASD abilities [9], [14]: since the maturation of perceptual abilities is delayed in ASD, we could assume that cross-modal connections are more negative in ASD children of 6-7 years of age compared to their NT peers.

As it is evident from Fig. 3, the model provides a good fit with empirical data of [2].

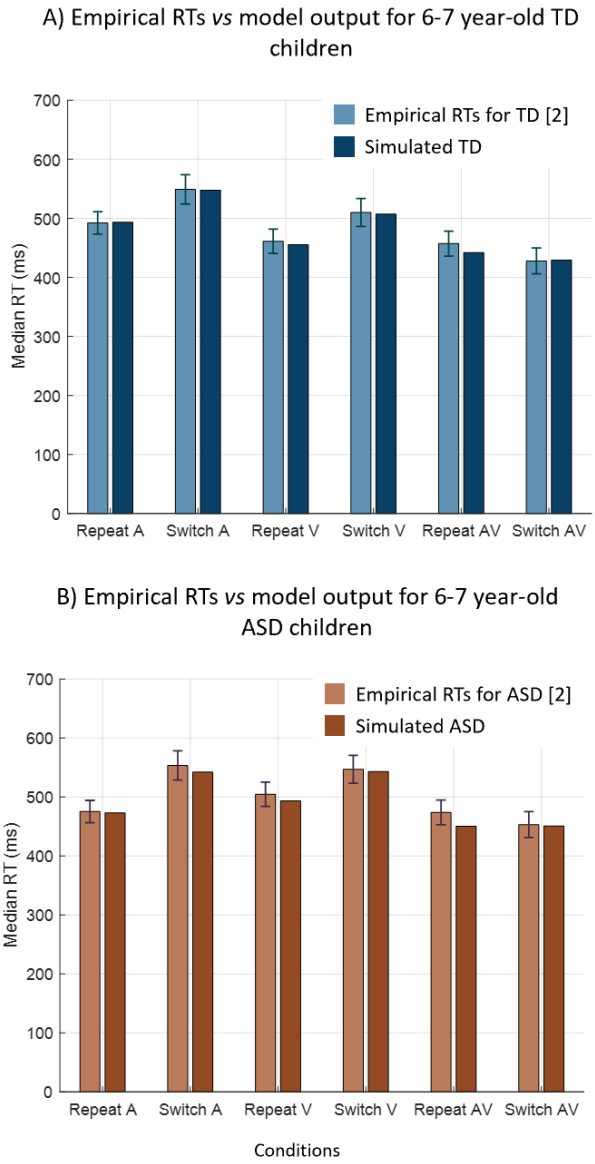


Fig. 3: Simulated RTs vs Median RTs of the subjects' population. For each stimulus configuration (A and V Repeat, A and V Switch, AV Repeat and Switch) RTs obtained with the model were compared with the experimental median RTs extracted from the population of real subjects. To set the basal configuration of parameters, no noise was added (neither on the input, nor on the synapses).

B. *Model's behaviour*

To clarify how each implemented mechanism contributes to the model's behaviour, in Fig. 4 we report the activities elicited in the NT network's regions in four exemplary conditions of unisensory (A) and multisensory (AV) repeat and switch.

Comparing the auditory repeat and switch conditions (Fig. 4A and 4B), we can notice that the activation elicited in the model by the second stimulus (A) is lower in the switch case. This is due to the inhibitory effect exerted by the prior input (V): the visual inhibitory interneuron, excited by the preceding visual stimulus, inhibits the auditory input region through the

feedback projections, characterized by a slow dynamic (i.e. the effect acts over a long period of time). The consequent lower activity produces a delayed activation of the multisensory region, resulting in longer RT.

Similar results were found for visual repeat/switch trials.

In case of multisensory stimulation, in addition to this slow inhibition that the prior input exerts on the processing of the current AV stimulus, the A and V components of the AV input reciprocally compete, by means of the direct inhibitory cross-modal synapses. This results in a lower activity elicited by an AV stimulus in the input layer (Fig. 4C and D) compared to the case of unisensory stimulation. This inhibition counterbalances the integration occurring in the M region, mediated by the excitatory feedforward projections. The presence of cross-modal inhibitory synapses is critical to explain the behavioural data. Indeed, without this mechanism a cross-modal input would produce RTs much faster than those found in [2].

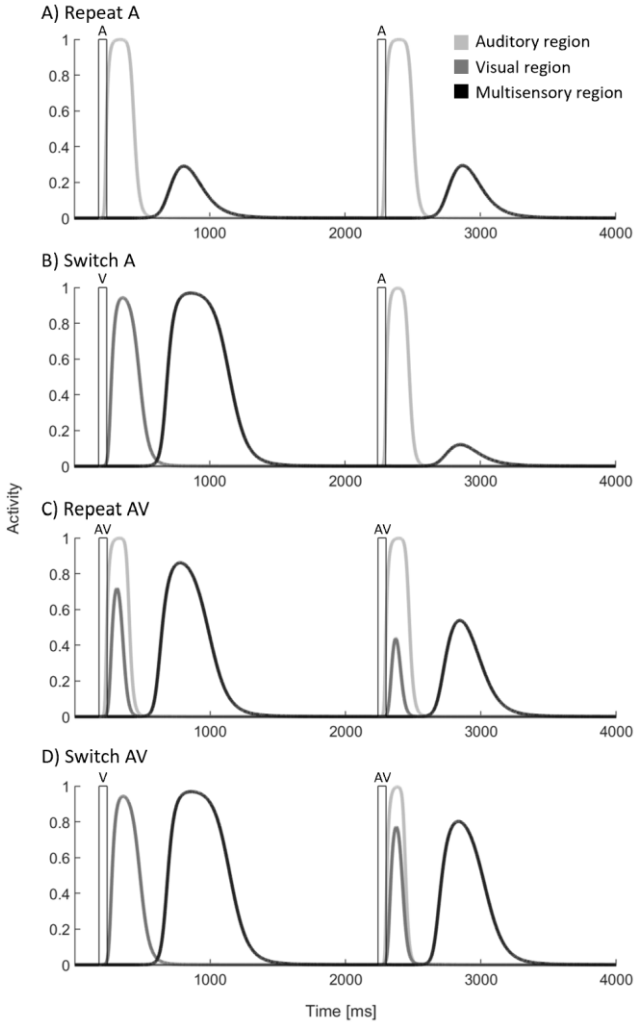


Fig. 4: Example of the network behavior, in the case of a A) Repeat A, B) Switch A, C) Repeat AV and D) Switch AV conditions, for NT children. Rectangular wave represents the external visual stimuli presented with an ISI of 2000ms. Light grey lines describe the activation of the auditory region, dark grey lines describe the activation of the visual area. Black lines represent the activity elicited in the output region in response to this stimulation.

IV. Conclusion

In this work, we developed a biologically plausible neurocomputational model of perceptual abilities and sensory interactions in children. This model should be thought of as a "engineering" tool, to test and interpret current empirical knowledge, elucidating the neural mechanisms in play.

In the first part of our work, we investigated the nature of cross-modal interactions in children. Empirical evidence [1] identified a default state of cross-modal competition in kittens, which could potentially represent a mechanism preserved also in human brain. Indeed, recent children's behavioural data [2] are consistent with such a competitive architecture. In our model, we linked these empirical results with a plausible neural implementation, in which the default competition is realized via inhibitory cross-modal projections.

In the second part, we tested how altered perceptual mechanisms could contribute to ASD phenotype and we suggested that the slower maturation of perceptual abilities in ASD would result in a stronger cross-modal competition in these children compared to their NT peers.

Overall, the importance of this work is that it provides with a deeper insight into perceptual function, dysfunction and behaviour in children. One field expected to benefit from this in the near future is the neurorehabilitation: by elucidating the underlying neural mechanisms, plausible neural networks will allow to make predictions, design specific interventions and explain their effects.

References

[1] L. Yu, C. Cuppini, J. Xu, B A. Rowland, and B. E. Stein, "Cross-modal competition: the default computation for multisensory processing", *J Neurosci.*, vol. 39(8), pp. 1374–1385, 2019.

[2] M. J. Crosse, J. J. Foxe, K. Tarrit, E. G. Freedman, and S. Molholm, "Resolution of impaired multisensory processing in autism and the cost of switching sensory modality", *Commun Biol.*, vol. 5(1), pp. 601, 2022.

[3] M. A. Meredith and B. E. Stein, "Visual, auditory, and somatosensory convergence on cells in superior colliculus results in multisensory integration", *J Neurophysiol*., vol. 56(3), pp. 640–662, 1986.

[4] B.E. Stein and M.A. Meredith, *The merging of the senses*. Cambridge, MA: Massachusetts Institute of Technology, 1993.

[5] M. A. Meredith, J. W. Nemitz, and B. E. Stein, "Determinants of multisensory integration in superior colliculus neurons. I. Temporal factors", *J Neurosci.*, vol. 7(10), pp. 3215–3229, 1987.

[6] M. T. Wallace, T. J. Jr Perrault, W. D. Hairston, and B. E. Stein, "Visual experience is necessary for the development of multisensory integration", *J Neurosci.*, vol. 24(43), pp. 9580–9584, 2004.

[7] C. Cuppini, M. Ursino, E. Magosso, M. J. Crosse, J. J. Foxe, and S. Molholm, "Cross-sensory inhibition or unisensory facilitation: A potential neural architecture of modality switch effects", *J. Math. Psychol*., vol. 99, pp. 102438, 2020.

[8] B. de Gelder, L. Vroomen, and L. Van der Heide, "Face recognition and lipreading in autism", *Eur. J. Cogn. Psychol*., vol. 3, pp. 69–86, 1991.

[9] J. J. Foxe et al., "Severe multisensory speech integration deficits in high functioning school-aged children with autism spectrum disorder (ASD) and their resolution during early adolescence", *Cereb Cortex*., vol. 25(2), pp. 298–312, 2015.

[10] R. A. Stevenson et al., "Multisensory temporal integration in autism spectrum disorders", *J. Neurosci*., vol. 34, pp. 691–697, 2014.

[11] R. A. Stevenson et al., "Evidence for diminished multisensory integration in autism spectrum disorders", *J Autism Dev Disord*., vol. 44, pp. 3161–3167, 2014.

[12] R. A. Stevenson et al., "The cascading influence of multisensory processing on speech perception in autism", *Autism*, vol. 22, pp. 609–624, 2018.

[13] A. B. Brandwein et al., "The development of multisensory integration in high functioning autism: high-density electrical mapping and psychophysical measures reveal impairments in the processing of audiovisual inputs", *Cereb Cortex*, vol. 23, pp. 1329–1341, 2013.

[14] N. Taylor, C. Isaac, and E. Milne, "A comparison of the development of audiovisual integration in children with autism spectrum disorders and typically developing children", *J Autism Dev Disord*., vol. 40, pp. 1403–1411, 2010.

Functional Connectivity of the EEG in epilepsy: a single case study

G. Chiarion[1], L. Mesin[1]
[1] *Mathematical Biology & Physiology, Dept. Electronics and Communications, Politecnico di Torino, Turin, Italy*

***Abstract*—This paper introduces some of the most used methods in the literature to explore network connections in the brain from electroencephalogram (EEG), based on functional connectivity (FC) metrics and topological indexes from graph theory. A publicly available dataset of EEG of epileptic children is studied. We trace in a single case all fundamental steps required to develop an adapted method for seizure prediction: extraction of FC indices, topological analysis by graph theory and prediction by machine learning. Specifically, some FC indexes (cross-correlation, phase-locking value and mutual information) are estimated to explore the information flow. Then, topological measurements (i.e., strength, clustering coefficient, characteristic path length and efficiency) are used to characterize the resulting connections. To discriminate inter-ictal and pre-ictal EEG epochs, we processed these topological indexes with different classifiers (k-Nearest-Neighbor, Support Vector Machine and Discriminant Analysis). Pseudo-Quadratic Discriminant Analysis classifier performed best to predict an epileptic seizure, with a mean accuracy up to 75% and a True Negative Rate of 80% suggesting, at least for the specific patient considered, a variation of brain connectivity before the onset of a seizure.**

***Keywords*—EEG, Connectivity, machine learning, seizure prediction.**

I. INTRODUCTION

Recent neuro-scientific studies, mostly based on functional magnetic resonance imaging (fMRI), had disproved the hypothesis that each human brain function is only associated to a specific area, evidencing that most of them result from coordinated activity between separated regions. Thus, spatially distant brain regions may share functional properties [1]. This is the focus of functional connectivity (FC), which explores the interconnections of spatially distant regions of the brain. It is defined as a statistical dependence among remote neurophysiological events [2] and accounts for determining which sets of neurons are appointed to carry out a precise function. Many efforts are devoted to deepen this research path. Indeed, neuronal interactions and their inter-dependence are fundamental for cognition [3] and the accomplishment of different tasks, e.g., in movement coordination [4]. Deficits in FC are associated to different diseases. For example, in autism, they reflect into a lack of social interaction and empathy [5]. Global changes to the functional organization of the brain network were found following stroke [6]. Moreover, connectivity between hippocampus and prefrontal cortex was found disrupted in psychiatric and neurodegenerative disorders [7].

The most known technique used so far in this context is fMRI, which allows to map the anatomical connectivity of a neural network by means of diffusion tensor imaging [8], [9]. However, fMRI lacks in time resolution and therefore cannot be entrusted with detecting short time events, which can instead be investigated by electroencephalography (EEG), which is a low-cost technique allowing to study FC among cortical brain regions and providing different information with respect to fMRI [10]. Many applications of EEG have been documented, e.g., in the study of schizophrenia and bipolar disorder [11], investigation of the level of consciousness [12], dyslexia [13], encephalitis [14], epilepsy [15]. Specifically, an epileptic seizure is a transient manifestation of abnormally high or synchronous activity of neurons in the brain [16], with symptoms like cognitive, emotional, affective, autonomic or motor problems.

To assess FC, different bivariate metrics can be used; indeed, a common practice is to combine different metrics to assess FC and draw a more meaningful scene of the network [17], [18].
Once obtained a network of connections, a key for understanding its topology is given by graph theory, providing different methods to post-process FC indexes, very useful in many applications [11], [19]. Different topological indexes are then introduced and applied. Here, we explore the topological structure of functional connections in an example application to the prediction of epileptic seizures, in which inter-ictal and pre-ictal time windows are discriminated by a machine learning approach applied to the indexes extracted from them.

II. FC METRICS

In neuroscience, there is a rich and evolving literature about the methods to quantify neuronal interactions [1].

In the following paragraphs, some popular FC metrics are described. The FC indexes estimated between pairs of EEG channels are collected in an adjacency matrix (AM). It has dimensions $N_{ch} \times N_{ch}$ and can be written as $A = \{a_{ij}\}_{i,j=1,\dots,N_{ch}}$, where a_{ij} is the FC index between channels i and j and N_{ch} are the total number of channels.

a) Cross-correlation: The simplest measure of synchronization between two discrete univariate time series x_n and y_n is ***cross-correlation***, defined as:

$$c_{x,y}(\tau) = \frac{1}{N-\tau} \sum_{i=1}^{N-\tau} \left(\frac{x_i - \overline{x}}{\sigma_x} \right) \left(\frac{y_{i+\tau} - \overline{y}}{\sigma_y} \right) \qquad (1)$$

where the time series are assumed to be real, i labels the i^{th} sample, x_i and y_i are the i^{th} samples of the two time series, $\bar{x}$

and $\bar{y}$ are their means, σ_x and σ_y are their standard deviations, N is the number of samples of the two time series and τ is the delay.

b) Mutual information: ***Mutual information*** is based on information-theoretic concepts [20], specifically on *Shannon entropy* [21]. It measures how much one random variable tells us about another one. A high mutual information indicates a large reduction in uncertainty on a variable once another is known, and zero mutual information between two random variables means that they are independent.
Mutual information between two random variables X and Y is defined as

$$I(X,Y) = H(X) + H(Y) - H(X,Y) \tag{2}$$

where $H(X)$ and $H(Y)$ are the entropies of X and Y, respectively, and $H(X,Y)$ is the joint entropy:

$$\begin{aligned} H(X) &= -\sum_{i=1}^{M_x} p_x(i) \log(p_x(i)) \\ H(Y) &= -\sum_{i=1}^{M_y} p_y(i) \log(p_y(i)) \\ H(X,Y) &= -\sum_{i=1}^{M_x} \sum_{j=1}^{M_y} p_{x,y}(i,j) \log(p_{x,y}(i,j)) \end{aligned} \tag{3}$$

p_x and p_y represent marginal probabilities, $p_{x,y}$ is the joint probability; M_x and M_y are the numbers of the states of X and Y, respectively.

c) Phase Locking Value: Phase synchronization problem has first been taken into account in [22] and [23] to surmount some limitations of linear methods, which are not able to separate amplitudes and phases in the interrelations between two signals.

The phase synchronization can be measured using the ***Phase Locking Value*** (PLV) which is defined as

$$PLV(t) = \left\| \frac{1}{n} \sum_{t=1}^{n} e^{i[\Phi_1(t) - \Phi_2(t)]} \right\| \tag{4}$$

where n is the number of samples, $i = \sqrt{-1}$ and $\Phi_k(t)$ is the instantaneous phase of the k^{th} signal.
The value of PLV ranges from 0 (i.e., the signals are completely decoupled) to 1 (i.e., the signals have constant phase lag and are coupled).

III. Indexes of the network patterns

Many indexes have been proposed to characterize the topological organization of networks represented by a graph [24], finding many applications in the interpretation of EEG [25]. The following topological indexes are considered in this paper. They are defined in terms of the coefficients

a) Global Strength (S): it is the sum of the weighted connections to a node:

$$\begin{aligned} S &= \tfrac{1}{N_{ch}} \textstyle\sum_{i \in N} S_i \\ S_i &= \textstyle\sum_{i \in N} w_{ij} \end{aligned} \tag{5}$$

where $N = \{1, 2, \ldots, N_{ch}\}$ and w_{ij} is the weight of the edge from node i to node j. It provides an overall characterization of how much the network is connected.

b) Clustering coefficient (CC): The global weighted CC of the network [26] is defined as:

$$\begin{aligned} C &= \tfrac{1}{N_{ch}} \textstyle\sum_{i \in N} C_i \\ C_i &= \tfrac{2}{k_i(k_i-1)} \textstyle\sum_{j,k} (w_{ij} w_{jk} w_{ki})^{1/3} \end{aligned} \tag{6}$$

where the triangle weights w are scaled by the largest weight in the network

$$w_{ij} = w_{ij} / \max(w_{ij}) \tag{7}$$

and C_i is the clustering coefficient of the i^{th} node. It is a measure of the degree to which nodes in a graph cluster together [27].

c) Global efficiency (GE): It is defined as [28]

$$E = \frac{1}{N} \sum_{i \in N} E_i = \frac{1}{n} \sum_{i \in N} \frac{\sum_{j \in N, j \neq i} d_{ij}^{-1}}{N_{ch} - 1} \tag{8}$$

where E_i is the efficiency of node i and d_{ij} is the shortest path length between nodes i and j

$$d_{ij} = \sum_{w_{uv} \in g_{i \leftrightarrow j}} w_{uv} \tag{9}$$

where $g_{i \leftrightarrow j}$ is the geodesic path between nodes i and j (with $d_{ij} = \infty$ for disconnected pairs). It measures the efficiency of the network to exchange information.

d) Characteristic path length (PL): The PL is defined as

$$\lambda = \frac{1}{N_{ch}} \sum_{i \in N} L_i = \frac{1}{N_{ch}} \sum_{i \in N} \frac{\sum_{j \in N, j \neq i} d_{i,j}}{N_{ch} - 1} \tag{10}$$

where L_i is the average distance between the node i and all other nodes. As for the previous index, it is also a measure of information transport in the network (with opposite trend with respect to the efficiency), as a short average path length between nodes indicates a better overall connection.

IV. Case study

Tests on real data were made using the *CHB-MIT Scalp EEG Database*, publicly available in Physionet [29]. The dataset is a list of 1 hour scalp EEG signals (sometimes the duration of the recordings can vary), grouped by patients (22 subjects from 1.5 to 22 years old). Not all the recordings nor the patients present ictal phases. Our tests were focused on one subject: the number 3, a 14 years old female patient. Four signals showing one seizure each were analyzed: recordings chb03_04, chb03_34, chb03_35 and chb03_36. In the following, we refer to these EEG traces as Signal 1, Signal 2, Signal 3 and Signal 4, respectively.

A. Pre-processing: filtering and artifact removal

A preliminary processing was applied on our data to attenuate the effect of noise. A portion of data centered on each seizure was selected: specifically, we included EEG traces from 15 minutes before to 10 minutes after the seizure. A broad 5^{th} order IIR Chebychev band-pass filter 0.1 - 80 Hz was applied. Anticausal double pass filtering was used to avoid any phase distortion. To remove EOG artifacts, as eye blink and eyeball movements, data have been pre-processed using

the Automatic Artifact Removal (AAR) toolbox [30]. Specifically, Second Order Blind-source Identification (SOBI) [31] algorithm was applied to decompose EEG into components [32] and the one with the lowest fractal dimension (computed by the Sevcik's method [33]) was removed.
At last, data have been segmented in epochs 5s long, overlapped by 80%. FC metrics has been computed on each of these epochs.

B. FC metrics evaluation

All the metrics have been evaluated in different frequency bands: δ: 0.5-4 Hz, θ: 4-8 Hz, α: 8-12 Hz, $\beta 1$: 12-20 Hz and also in a broad frequency band M1 (0.5-20 Hz). Once computed the metrics and obtained the correspondent weighted AMs, topological properties were measured. Since there is no consensus in literature on the optimal threshold to extract the significant connections [34], no threshold (absolute or proportional) was applied to the AMs. Indeed, the application of a different arbitrary threshold could lead to ambiguous and different results, also when the same metric is used [35].

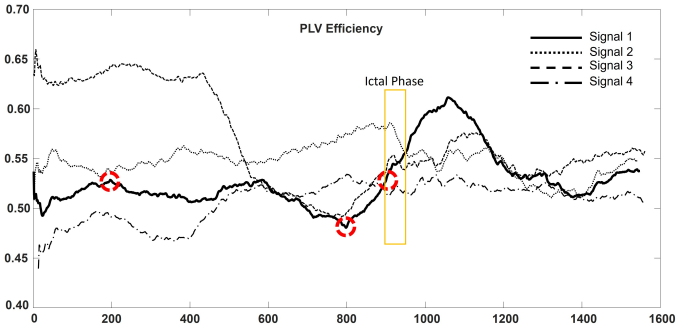


Fig. 1: Trend of efficiency applied to the adjacency matrix of the phase-locking value (PLV) calculated for 4 registrations of the same patient from 15 minutes before to 10 minutes after the seizure. The values are evaluated in windows of 5 s each with a 80% overlap, and then filtered by a causal moving average of 2 minutes.

C. Prediction of seizure onset

a) Dataset definition: The topological indexes described above were used to predict the onset of a seizure through a classifier. The dataset used for the classification was organized as a matrix $N \times M$, where the rows correspond to the 5 s epochs in which the signal was split (with 80% overlap, as explained before) and each column M_j represents a global topological metric. For each of the four signals, a moving average window of 30 s was applied, and two parts were extracted: the first 5 minutes, far from the seizure, considered as inter-ictal and labelled as "0"; the last 5 minutes before the seizure, considered as pre-ictal and labelled as "1". The final dataset had 2400 rows (600 elements for each signal) and 61 columns (3 Metrics, 4 Topological Indices, 5 Frequency Bands and the last column is the ground truth).

b) Classification methodology: All the available machine learning classifiers implemented in Matlab were trained using 5-fold cross-validation and default parameters. The classifiers were then sorted by validation accuracy and the top 3 were chosen to be tested and optimized: Support Vector Machine (SVM), k-Nearest Neighbor (kNN) and Discriminant Analysis (DA).

Leave-One-Trace-Out approach was chosen to train and test the classifier performance, using each time the data from 3 out of 4 signals (1800×61 dataset) to train the classifiers and the remaining to test the generalization of the model (600×60 dataset).

For SVM, different kernels have been tried: linear, Gaussian radial basis function and polynomial. Based on accuracy, the best results were achieved using a polynomial kernel with a mean accuracy of 64%. It's important to notice that the mean performances are heavily degraded by the first signal as test. In fact, the accuracy in this particular case is only of 46% and True Negative Rate (TNR) of 9%. Excluding this signal as test set brings the mean accuracy to 70% and TNR to 77%.

When using kNN, different distance metrics have been tried: Euclidean, Chebychev and cityblock. Based on accuracy, the best results were achieved using cityblock metric, with a mean accuracy of 59%. Also with this classifier, the average performance degraded due to the test on the first signal; excluding it, the mean accuracy was 62% and TNR increased to 72%.

Concerning DA, different types of analysis have been tried: linear, pseudo-quadratic and diag-quadratic. Based on accuracy, the best results were achieved using pseudo-quadratic DA, with a mean accuracy of 70%. The first signal had poor performance in the test, and excluding it made the mean accuracy increase to 75% and TNR to 80%. This classifier was the best in terms of performance with respect to the others tested.

Finally, an analysis of the distribution of the outputs of the classifiers was performed, considering our Leave-One-Trace-Out approach. Also in this analysis it is evident how the first signal behaves differently, since the vast majority of its predictions as test set are ones. By using the DA classifier, a 30 samples long uninterrupted true positive consensus region between signals is found, from 300 s to 270 s before the seizure onset. By choosing 50 predicted positive events in a 1 minute window as threshold, the classifier would uniquely recognize the ictal phase in all the signals, with the exception of the first.

V. Conclusion

FC and topological metrics can be useful tools to explore brain network connection in different conditions. Epilepsy is a neurological disorder characterized by the emergence of seizures, in which the brain activity becomes abnormal. The seizure is characterized by high or synchronous activity of neurons [16], which could be triggered by an anomalous connectivity pattern. Thus, comparing the functional connections in normal conditions and close to the seizure onset could be of relevance for the prediction of an incoming seizure [36]. We explored the possible variation of global topological indexes in the pre-ictal with respect to the

inter-ictal phase, by considering EEG epochs close (up to 5 minutes before) and far (10 to 15 minutes before) from the seizure, respectively. A single patient was considered, with a view to developing a method adapted to the specific subject. Discriminant Analysis can distinguish fairly well epochs recorded during the two phases, using topological indexes of different FC metrics. Thus, the evaluated topological indexes contain some information about the modification of brain activity in preparation to the onset of the seizure. Moreover, these results are consistent in different signals of the same subject, as the classifier was trained on data including some seizures and then applied on those concerning a different one. The classification performance were quite low for the first signal, regardless of the type of classifier used. Notice that, according to the author of the dataset, the first signal was acquired in the afternoon, while the other three were recorded in the late night. We can presume that the patient was awake during the acquisition of the first signal, while she was sleeping during the other recordings, thus affecting the characteristics of the signals.

REFERENCES

[1] A. Bastos and J. Schoffelen, "A tutorial review of functional connectivity analysis methods and their interpretational pitfalls," *Front Syst Neurosci.*, vol. 9, p. 175, 2016.

[2] K. Friston, "Functional and effective connectivity: a review," *Brain Connect.*, vol. 1, no. 1, pp. 13–36, 2011.

[3] S. Petersen and O. Sporns, "Brain networks and cognitive architectures," *Neuron*, vol. 88, no. 1, pp. 207–219, 2015.

[4] I. de Vries, A. Daffertshofer, D. Stegeman, and B. TW., "Functional connectivity in the neuromuscular system underlying bimanual coordination," *J Neurophysiol.*, vol. 116, no. 6, pp. 2576–2585, 2016.

[5] C. Cox, L. Uddin, A. Di Martino, F. Castellanos, M. Milham, and C. Kelly, "The balance between feeling and knowing: affective and cognitive empathy are reflected in the brain's intrinsic functional dynamics," *Soc Cogn Affect Neurosci.*, vol. 7, no. 6, pp. 727–37, 2012.

[6] T. Mima, K. Toma, B. Koshy, and M. Hallett, "Coherence between cortical and muscular activities after subcortical stroke," *Stroke*, vol. 32, no. 11, pp. 2597–2601, 2001.

[7] M. Li, C. Long, and Y. L., "Hippocampal-prefrontal circuit and disrupted functional connectivity in psychiatric and neurodegenerative disorders," *Biomed Res Int.*, p. 810548, 2015.

[8] D. Le Bihan, J. F. Mangin, C. Poupon, C. A. Clark, S. Pappata, N. Molko, and H. Chabriat, "Diffusion tensor imaging: concepts and applications," *J. Magn. Reson. Imaging*, vol. 13, pp. 534–546, Apr. 2001.

[9] H. Huang and M. Ding, "Linking functional connectivity and structural connectivity quantitatively: A comparison of methods," *Brain Connect.*, vol. 6, no. 2, pp. 99–108, 2016.

[10] J. Rizkallah, H. Amoud, M. Fraschini, F. Wendling, and M. Hassan, "Exploring the correlation between M/EEG source-space and fMRI networks at rest," *Brain Topogr.*, vol. 33, pp. 151–160, Mar. 2020.

[11] B. Cea-Cañas, J. Gomez-Pilar, P. Nùñez, E. Rodríguez-Vàzquez, N. de Uribe, A. Dìez, A. Pèrez-Escudero, and V. Molina, "Connectivity strength of the eeg functional network in schizophrenia and bipolar disorder," *Prog Neuropsychopharmacol Biol Psychiatry*, vol. 98, p. 109801, 2020.

[12] L. Imperatori, M. Betta, L. Cecchetti, A. Canales-Johnson, E. Ricciardi, F. Siclari, P. Pietrini, S. Chennu, and G. Bernardi, "Eeg functional connectivity metrics wpli and wsmi account for distinct types of brain functional interactions," *Sci Rep.*, vol. 9, no. 1, p. 8894, 2019.

[13] G. Fraga González, D. Smit, M. van der Molen, J. Tijms, C. Stam, E. de Geus, and M. van der Molen, "Eeg resting state functional connectivity in adult dyslexics using phase lag index and graph analysis," *Front Hum Neurosci.*, vol. 12, p. 341, 2018.

[14] G. Chiarion and L. Mesin, "Functional connectivity of eeg in encephalitis during slow biphasic complexes," *Electronics*, vol. 10, no. 2978, 2021.

[15] Y. Liang, C. Chen, F. Li, D. Yao, P. Xu, and L. Yu, "Altered functional connectivity after epileptic seizure revealed by scalp eeg," *Neural Plast.*, vol. 2020, p. 8851415, 2020.

[16] R. Fisher, W. van Emde Boas, W. Blume, C. Elger, P. Genton, P. Lee, and J. J. Engel, "Epileptic seizures and epilepsy: definitions proposed by the international league against epilepsy (ilae) and the international bureau for epilepsy (ibe)," *Epilepsia*, vol. 46, p. 470–472, 2005.

[17] I. Pirovano, A. Mastropietro, Y. Antonacci, C. Barà, E. Guanziroli, F. Molteni, L. Faes, and G. Rizzo, "Resting state EEG directed functional connectivity unveils changes in motor network organization in subacute stroke patients after rehabilitation," *Front. Physiol.*, vol. 13, p. 862207, Apr. 2022.

[18] G. Chiarion, L. Sparacino, Y. Antonacci, L. Faes, and L. Mesin, "Connectivity Analysis in EEG Data: A Tutorial Review of the State of the Art and Emerging Trends," *Bioengineering*, vol. 10, p. 372, Mar. 2023. Number: 3 Publisher: Multidisciplinary Digital Publishing Institute.

[19] G. Tomagra, C. Franchino, F. Cesano, G. Chiarion, A. de Iure, E. Carbone, P. Calabresi, L. Mesin, B. Picconi, A. Marcantoni, and V. Carabelli, "Alpha-synuclein oligomers alter the spontaneous firing discharge of cultured midbrain neurons," *Frontiers in Cellular Neuroscience*, vol. 17, p. 1078550, 2023.

[20] A. K. Seth, "A matlab toolbox for granger causal connectivity analysis," *Journal of Neuroscience Methods*, vol. 186, no. 2, pp. 262–273, 2010.

[21] C. E. Shannon, "A mathematical theory of communication," *Bell Syst. tech. j.*, vol. 27, pp. 379–423, July 1948.

[22] J. Lachaux, E. Rodriguez, J. Martinerie, and F. Varela, "Measuring phase synchrony in brain signals," *Hum Brain Mapp.*, vol. 8, no. 4, pp. 194–208, 1999.

[23] P. Tass, M. G. Rosenblum, J. Weule, J. Kurths, A. Pikovsky, J. Volkmann, A. Schnitzler, and H.-J. Freund, "Detection of $n : m$ phase locking from noisy data: Application to magnetoencephalography," *Phys. Rev. Lett.*, vol. 81, pp. 3291–3294, 1998.

[24] M. Rubinov and O. Sporns, "Complex network measures of brain connectivity: Uses and interpretations," *NeuroImage*, vol. 52, no. 3, p. 1059–1069, 2010.

[25] L. E. Ismail and W. Karwowski, "A graph theory-based modeling of functional brain connectivity based on eeg: A systematic review in the context of neuroergonomics," *IEEE Access*, vol. 8, p. 155103–155135, 2020.

[26] D. Watts and S. Strogatz, "Collective dynamics of 'small-world' networks," *Nature*, vol. 393, pp. 440–442, 1998.

[27] J.-P. Onnela, J. Saramäki, J. Kertész, and K. Kaski, "Intensity and coherence of motifs in weighted complex networks," *Physical Review E*, vol. 71, no. 6, p. 065103, 2005. Publisher: American Physical Society.

[28] V. Latora and M. Marchiori, "Efficient behavior of small-world networks," *Physical Review Letters*, vol. 87, no. 19, 2001.

[29] A. Shoeb, "Chb-mit scalp eeg database," 2010. Available from Physionet in https://physionet.org/content/chbmit/1.0.0/.

[30] G. Gomez, "Automatic artifact removal (aar) toolbox v 1 . 3 (release 09 . 12 . 2007) for matlab," 2007.

[31] L. De Lathauwer and J. Castaing, "Second-order blind identification of underdetermined mixtures. independent component analysis and blind signal separation," *Ed. by Justinian Rosca, Deniz Erdogmus, José C. Príncipe, Simon Haykin. Berlin, Heidelberg: Springer Berlin Heidelberg*, pp. 40–47, 2006.

[32] G. Gomez-Herrero, W. Clercq, H. Anwar, K. Kara, O. Egiazarian, S. Huffel, and W. Paesschen, "Automatic removal of ocular artifacts in the eeg without an eog reference channel," *Proceedings of the 7th Nordic Signal Processing Symposium*, pp. 130–133, 2006.

[33] C. Sevcik, "A procedure to estimate the fractal dimension of waveforms," *Complexity International*, vol. 5, 2018.

[34] K. Garrison, D. Scheinost, E. Finn, X. Shen, and R. Constable, "The (in)stability of functional brain network measures across thresholds," *NeuroImage*, vol. 118, pp. 651–661, 5 2015.

[35] S. Sun, X. Li, J. Zhu, Y. Wang, R. La, X. Zhang, L. Wei, and B. Hu, "Graph theory analysis of functional connectivity in major depression disorder with high-density resting state eeg data," *IEEE Transactions on Neural Systems and Rehabilitation Engineering*, vol. 27, pp. 429–439, 1 2019.

[36] K. Gadhoumi, J. Lina, F. Mormann, and J. Gotman, "Seizure prediction for therapeutic devices: A review," *Journal of neuroscience methods*, vol. 260, p. 270–282, 2016.

The prediction of the patient's response to hemodialysis treatment: DialysIS vs InterACTIVE-HD 2.0 experience

C. Balsamello[1], S. Pianca[2], A. Bellasi[2], C. Colturi[3], G. Melfa[4], G. Rombolà[5], R. Venzin[6], P. Cippà[2], G. Casagrande[1*], ML. Costantino[1*]

[1] *Department of Chemistry, Materials and Chemical Engineering, Politecnico di Milano, Milan, Italy*
[2] *Division of Nephrology, Ente Ospedaliero Cantonale, Lugano, Switzerland*
[3] *Nephrology and Dialysis UOC, ASST Valtellina e Alto Lario, Sondrio, Italy*
[4] *Department of Nephrology and Dialysis, Sant'Anna Hospital, ASST Lariana, Como, Italy*
[5] *Nephrology Dialysis and Kidney Transplant Unit, ASST Settelaghi, Varese, Italy*
[6] *Department of Nephrology, Kantonsspital Graubünden, Chur, Switzerland*
[*] *Co-last authors*

***Abstract*—In recent years, computational models have been clinically used for the prediction of the exchanges of main electrolytes, breakdown products, and body fluids during haemodialysis. If correctly trained, such models can lead to a therapy customization, mainly needed for ESRD patients characterized by multiple comorbidities. The multi-compartmental, multi-solute model developed during DialysIS and InterACTIVE-HD 2.0 frameworks allows to accurately predict the patient's response in the same sessions used for the model training but also in independent sessions, using only the clinical data recorded at the beginning of the session. Here, the reported results refer only to the centre of Lugano: hence, a comparison of the DialysIS and InterACTIVE-HD 2.0 datasets in terms of characteristics and predictive performance has been performed. The stable model's performance over time confirms the correctness of the path, even if further investigations are needed.**

***Keywords*—Hemodialysis, Patient-specific model, Predictive model, Clinical decision support systems.**

I. Introduction

In recent years, computational models have been used to predict the clinically observed trends of the main electrolytes, breakdown products, and body fluids volumes during haemodialysis. Either one, two or three-compartmental models have been developed, focused on the description of either a single (accurately but ignoring its complexity) or multiple solutes (for a limited dataset) [1]–[7]. Now, the use of models based on patients' characteristics is gaining ground, in order to customize the treatment, in particular for elderly ESRD patients that are characterized by multiple comorbidities [8]. According to this objective, a patient-specific model has been developed, improved, and optimized over the course of two projects (DialysIS first and InterACTIVE-HD 2.0 later) involving several patients in treatment in Italian and Swiss centres. More in detail it is a multi-solute three-compartmental model whose customization is achieved through the identification of parameters modulating – specifically on the basis of patient's characteristics – mass and fluid balance across dialyzer, capillary, and cell membranes [9]. This model, after being trained with three sessions, allows a proper simulation of each patient's response to the treatment, in terms of mass and fluids distributions within modelled compartments (intracellular, interstitial, and intravascular). Input were the initial clinical data and the output generation require less than a minute. A so performing tool could support the clinical decisions, improving the treatment efficiency as well as the patients' quality of life. Hence, a comparison of the DialysIS and InterACTIVE-HD 2.0 datasets in terms of characteristics and predictive performance has been performed.

II. Methods

A. Inclusion criteria

DialysIS project (2013–2016): enrolled patients are 18 or older, with a dialysis vintage higher than three months, and arteriovenous fistula as vascular access. They undergo standard HD (SHD) or hemodiafiltration (HDF). No further non-inclusion criteria were defined.

142 patients were enrolled from Nephrology and Dialysis Units of the Sant'Anna Hospital (Como, Italy), A. Manzoni Hospital (Lecco, Italy), Regional Hospital of Lugano (Lugano, Switzerland), and Circolo Hospital and Macchi Foundation (Varese, Italy).

InterACTIVE-HD 2.0 project (2020–2023): as for DialysIS for the age and then:

- dialysis vintage higher than 6 months;
- arteriovenous fistula or central catheter as access in a ratio similar to 7:3;
- residual renal function less than 10ml/min;
- patients with pacemakers less than 15% of the whole.

Moreover, it is suggested that at least one third be diabetic patients and that a balanced male/female ratio be maintained. Patients who have undergone major surgery or trauma in the three months preceding the beginning of the project were excluded a priori.

145 patients were enrolled from Nephrology and Dialysis Units of the Kantonsspital Graubünden (Chur, Switzerland), Sant'Anna Hospital (Como, Italy), Regional Hospital of Lugano (Lugano, Switzerland), ASST Valtellina e Alto Lario (Sondrio, Italy), and Circolo Hospital and Macchi Foundation (Varese, Italy).

B. Data acquisition

The data were acquired in accordance with the guidelines

approved by the ethics committees.

DialysIS data acquisition was performed over a two-week span of treatments (i.e., 6 HD sessions for each patient), while for InterACTIVE-HD 2.0 project the acquisitions were carried out either in 3 consecutive phases for the centres of Lugano and Como, and in 2 consecutive phases for the centres of Chur, Sondrio, and Varese. Each set of acquisitions last at least 1 month form the previous one.

Both projects' data acquisition integrates the clinical records, collected by means of hospital information system (HIS), patient-specific parameters measurements, and plasmatic electrolyte and catabolites concentrations.

The clinical records, allowing stratified analyses, included:

- gender and age;
- height and weight (at start and at the end of the session);
- pathologies leading to Chronic Kidney Disease;
- existing comorbidities and eventual drug doses (if taken) to control it;
- dialysis therapy (i.e., SHD or HDF);
- dialysis vintage;
- prescribed dry weight and weight loss;
- dialysis duration.

On the other hand, other parameters have been directly measured by machine sensors for each session, with different frequencies, as reported below:

- every minute: effective treatment time, ultrafiltration flow rate and ultrafiltration volume, dialysate flow rate and temperature, blood flow rate, dilution flow rate, body temperature, relative blood volume, pressures of arterial and venous lines, and trans-membrane pressure;
- every 15/20 minutes by using the machine' blood pressure cuff: systolic and diastolic blood pressure, and heart rate;
- every 30 minutes: plasma and dialysate conductivity.

For InterACTIVE-HD 2.0 project, the simultaneous use of smart devices (i.e., smartwatch ASUS VivoWatch SP and L.I.F.E Italia S.r.l. sensorized garment) was also planned for a more continuous and less invasive measurement of certain parameters, such as systolic and diastolic blood pressure, heart rate, and saturation, with the final aim of also predicting hypotensive episodes.

Blood composition instead has been analysed by means of either hemogasanalysis or central laboratory, at different time-steps, as reported in Table I.

The dialysate composition has been measured at the beginning of every session in DialysIS framework, while also at the end of every session for InterACTIVE-HD 2.0 project.

Moreover, patient hydration status has been analysed at the beginning of the first and the last sessions by using a Bio-Impedence-Analysis (BIA) in DialysIS framework, while also at the end but only of the first session for InterACTIVE-HD 2.0 project.

Moreover, during each session, for both projects, any complication has been registered.

C. Data transmission

Differently from DialysIS project, during InterACTIVE-HD 2.0, all the data recorded from the dialysis machine have been digitalized and stored in a Dialysis Unit DB, where integrated with clinical record, BIA, and laboratory data. Collected data were then anonymized and transferred in a .json file to be transmitted to the project online DB. The anonymous DB is accessible to the registered users through the project platform.

D. Proposed approach for the clinical use of the model

The developed model can be trained with 3 consecutive sessions (ID). In the training phase, the model needs as inputs all the data reported in the Sub-section B, returning the set of patient specific parameters that allow to minimize the overall error during the considered session. This first step takes only few minutes per session.

Hence, 3 different sets of patient-specific parameters are obtained and each one differently modulates mass and fluid balance across dialyzer, capillary, and cell membranes, according to the patient's characteristics during each session.

The next step is to average these 3 sets in order to obtain a set of parameters representative of the patient, avoiding peculiar values related to a single altered session. In this manner, it is possible to run the model in predictive mode (PRED), giving in input the patient parameters and the patient's conditions at the beginning of the session to be simulated. In less than 30s, the model gives as output the patient's response to the treatment, in terms of mass and fluids trends and distributions within modelled compartments.

TABLE I: BLOOD COMPOSITION – ACQUISITION FREQUENCY

Parameter	*DialysIS*	*InterACTIVE-HD 2.0*
pH	∀hour	∀hour
pO2	∀hour	not planned
pCO2	∀hour	∀hour
Hematocrit	∀hour	∀hour
Hemoglobin	∀hour	∀hour
[Electrolytes]	∀hour	∀hour
Glycemia	∀hour	∀hour
[Urea]	∀hour	∀hour
[Mg^{2+}]	start + end	∀hour
[Phosphates]	start + end	∀hour
[Albumine]	start + end	∀hour
$Calcemia_{TOT}$	start + end	start + end
[PTH]	(start + end)^{1st}	(start + end)^{1st}
[B2M]	(start + end)^{1st}	(start + end)^{1st}
[Creatinine]	(start + end)^{1st}	∀hour
BNP dosage	not planned	(start + end)^{1st}

Electrolytes stand for Na^+, K^+, Cl^-, Ca^{2+}, and HCO_3^-. ∀ stands for every session, while 1st for the only first session of each acquisition phase.

E. Performance evaluation

Hence, it will be firstly performed a comparison of baseline characteristics of the 2 sets of patients undergoing SHD/HDF, enrolled for the two frameworks. For Lugano, Como, and Varese centres, involved in both the project a direct comparison is possible.

Dataset were compared in term of gender, age, dialysis age, therapy distributions, initial electrolytes and urea concentration, as well as in term of presence of either cardiopathy or diabetes or hypertension.

The performances of the model are evaluated in terms of normalized Root Mean Squared Error (nRMSE), as in Eq. (1).

$$nRMSE = \sqrt{\frac{1}{N} \times \sum \left(\frac{y^2_{i,mod} - y^2_{i,cl}}{y^2_{i,cl}} \right)^2} \quad (1)$$

The subscript i stands for the i[th] of N acquisition time-points, while CL and MOD refer to the clinically measured data of interest and to the model simulated ones, respectively; y is the variable of interest, i.e., electrolytes' hematic concentrations.

F. Statistical analysis

DialysIS and InterACTIVE-HD 2.0 patients' baseline characteristics and nRMSEs have been compared via a Wilcoxon rank sum test.

Moreover, InterACTIVE-HD 2.0 inter-phase performance variability has been evaluated via a Kruskal-Wallis test.

III. Results

Being the InterACTIVE-HD 2.0 project still running, the preliminary results were here presented for the Lugano centre, involved in both the projects and having already completed all the acquisitions.

A. Baseline characteristics

The baseline characteristics of the enrolled patients for DialysIS and InterACTIVE-HD 2.0 projects in Lugano are shown in Table II, where quantitative values are reported as median (IQR). Statistical differences have been highlighted in InterACTIVE-HD 2.0 column: * when $0.01<p\leq0.05$, ** when $0.001<p\leq0.01$, and *** when $p\leq0.001$.

TABLE II: Baseline characteristics

Parameter	*DialysIS*	*InterACTIVE-HD 2.0*
Gender	13 M – 7 F	15 M – 10 F
Age	73 (58, 80)	81 (68, 85)
Dialysis age	49 (38, 61)	73 (49, 110) *
Therapy	120 HDF	209 HDF – 81 SHD ***
$[Na^+]_{in}$	137 (135, 138)	139 (137, 138) ***
$[K^+]_{in}$	4.70 (4.40, 5.30)	4.80 (4.40, 5.30)
$[Cl^-]_{in}$	105 (103, 106)	102 (99, 106) ***
$[Ca^{2+}]_{in}$	1.13 (1.09, 1.17)	1.10 (1.04, 1.17)
$[HCO_3^-]_{in}$	22.6 (21.0, 23.8)	21.4 (19.5, 23.0) **
$[Urea]_{in}$	17.5 (13.9, 20.9)	16.9 (12.7, 21.2)
Cardiopathy	85%	92%
Diabetes	35%	56%
Hypertension	85%	88%

Age is reported in years, while dialysis age in months; concentrations are reported in mmol/L.

B. Performances of the model

Relatively to DialysIS project, it was possible to run PRED model on 16 patients (out of 20 enrolled in Lugano).

Instead, for InterACTIVE-HD 2.0 project, PRED model successfully runs for 242 sessions out of 290 monitored, excluding only 2 patients on the 25 enrolled in Lugano.

The performances of the model ($nRMSE_{\%}$) are reported as boxplots in Figure 1. A distinction is made between ID mode (i.e., the first 3 sessions used for model training by the minimization of the deviation of model outputs from the clinical data – ID_{123}), PRED mode in the same sessions the model has been trained ($PRED_{123}$), and PRED mode in independent sessions ($PRED_{456}$).

In ID mode, the model simulates accurately all the electrolytes and urea plasmatic concentrations, with an average median nRMSE of 2.66% related to DialysIS and 4.49% related to InterACTIVE-HD 2.0 ($p\leq0.01$, except for HCO_3^-). In general, a greater dispersion is observed for InterACTIVE-HD 2.0.

In PRED mode, the model maintains its predictive accuracy, with no differences between the training sessions and independent ones: regarding DialysIS project, the nRMSE average increase with respect to ID mode is equal to +2.50 and +2.87 percentage points, respectively; instead, in the case of InterACTIVE-HD 2.0 project, this increase is equal to +3.31 and +4.81 percentage points, respectively.

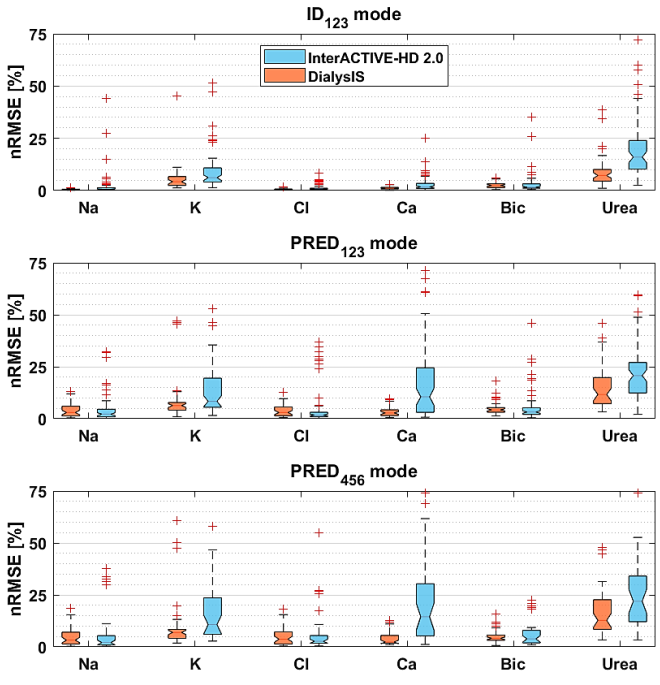


Fig. 1: nRMSE boxplots

Along the InterACTIVE-HD 2.0 project, the protocol included multiple acquisitions over time; specifically, in the

case of Lugano centre, clinical data acquisitions have been done on a 7-month span. The performances of the model in this timeframe are reported as nRMSE% boxplots in Figure 2.

It can be observed that for Na^+ predictive performances are maintained in this time span, and the same can be said for Ca^{2+} but at a higher level of error. For, Cl^- and HCO_3^- there's a gradual but constant loss of predictive performances, particularly evident at two months ($p \leq 0.01$). Finally, in spite of their high variability, K^+ and urea is predicted in an almost stable manner over time.

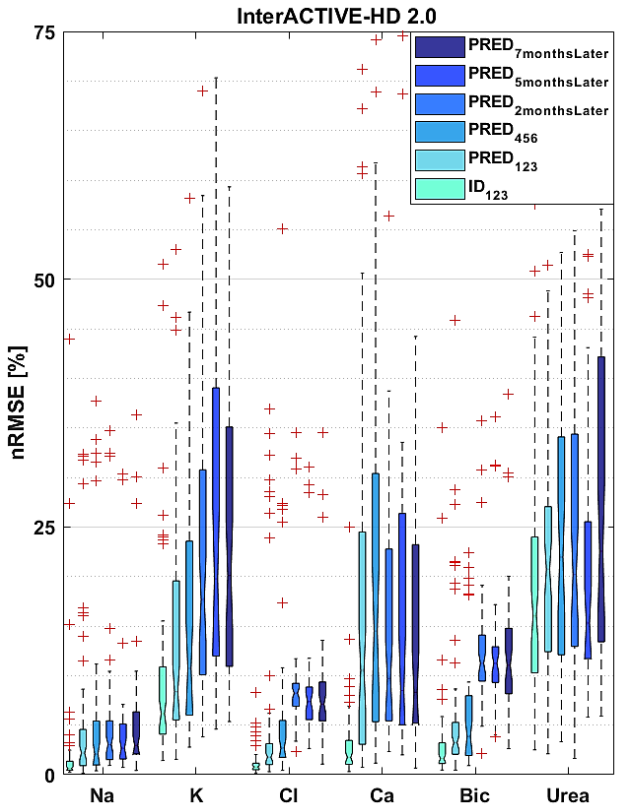


Fig. 2: InterACTIVE-HD 2.0 nRMSE boxplots – Performance over time

IV. Discussion

The two populations of patients enrolled for DialysIS and InterACTIVE-HD 2.0 in Lugano are in general superimposable in terms of baseline characteristics; however, some differences have been evidenced by the statistical analysis:

- InterACTIVE-HD 2.0 dialysis age distribution is much higher than DialysIS one ($0.01 < p \leq 0.05$), with some patients undergoing dialysis for at least 21 up to 243 months (against 3 up to 95 months);
- for InterACTIVE-HD 2.0, also SHD patients have been included, while before there were only HDF ones ($p \leq 0.001$);
- $[Na^+]_{in}$ distribution for InterACTIVE-HD 2.0 results shifted to higher values with respect to DialysIS ($p \leq 0.001$);
- $[Cl^-]_{in}$ distributions for InterACTIVE-HD 2.0 results more variable, particularly downwards, with respect to DialysIS ($p \leq 0.001$);
- $[HCO_3^-]_{in}$ measured values have similar values, but differently distributed ($0.01 < p \leq 0.05$).

The performance evaluation highlighted that:

- the dispersion observed for InterACTIVE-HD 2.0 ID nRMSEs seems to be not correlated to the differences of initial clinical data, but is attributable to a sub-set of patients probably characterised by greater intra-patient variability that the model cannot track; a different training approach should be used.
- in the case of $PRED_{123}$ and $PRED_{456}$ modes, the prediction of Na^+, Cl^- and HCO_3^- is better for InterACTIVE-HD 2.0, while for K^+, Ca^{2+} and urea there's a loss in accuracy: this loss is greater where there were observed already high errors in ID mode.

Finally, the predictive performances over a 7-month span in the InterACTIVE-HD 2.0 framework, suggest a recalibration of patient-specific parameters at least every two months to obtain even better results.

V. Conclusion

It is necessary to expand the set of patients on which to run the predictive model in order to obtain consistent results, as well as to stratify the results so as to identify that subset of patients simulated worse and thus suggesting specific model improvement.

Acknowledgement

The used data were recorded during DialysIS (Dialysis therapy between Italy and Switzerland) project funded by the cross-border cooperation program INTERREG IT/CH 2007-2013, Grant ID 33570710. Two of the authors (C.B. and G.C.) have been financed by the INTERACTIVE-HD2.0 project funded by the cross-border cooperation program INTERREG IT/CH 2014-2020, Grant ID 1441882.

References

[1] S.F.F. Santos, A.J. Peixoto, "Sodium balance in maintenance hemodialysis," *Semin Dial.* 2010; 23(6): pp. 549–555.

[2] B.U. Agar, B.F. Culleton, R. Fluck, J.K. Leypoldt, "Potassium kinetics during hemodialysis," *Hemodial Int.* 2015; 19(1): pp. 23–32.

[3] M. Prado, L. Roa, A. Palma, J.A. Milán, "A novel mathematical method based on urea kinetic modeling for computing the dialysis dose," *Comput Methods Programs Biomed.* 2004; 74(2): pp. 109–128.

[4] J.K. Leypoldt, B.U. Agar, A. Akonur, M.E. Gellens, B.F. Culleton, "Steady state phosphorus mass balance model during hemodialysis based on a pseudo one-compartment kinetic model," *Int J Artif Organs.* 2012; 35(11): pp. 969–980.

[5] M. Ursino, L. Colí, C. Brighenti, L. Chiari, A. De Pascalis, et al., "Prediction of solute kinetics, acid-base status, and blood volume changes during profiled hemodialysis." *Ann Biomed Eng.* 2000; 28(2): pp. 204–216.

[6] M. Ursino, L. Colí, E. Magosso, P. Capriotti, A. Fiorenzi, et al., "A mathematical model for the prediction of solute kinetics, osmolarity and fluid volume changes during hemodiafiltration with on-line regeneration of ultrafiltrate (HFR)," *Int J Artif Organs.* 2006; 29(11): pp. 1031–1041.

[7] M. Pietribiasi, J. Waniewski, A. Wójcik-Załuska, W. Załuska, B. Lindholm, "Model of fluid and solute shifts during hemodialysis with active transport of sodium and potassium," *PLoS One.* 2018; 13(12): pp. 1–22.

[8] M.L. Neal, R. Kerckhoffs, "Current progress in patient-specific modelling," *Brief Bioinform.* 2009; 11(1): pp. 111–126.

[9] G. Casagrande, C. Bianchi, C. Vito, F. Carfagna, C. Minoretti, et al., "Patient-specific modeling of multicompartmental fluid and mass exchange during dialysis," *Int J Artif Organs.* 2016; 39(5): pp. 220–227.

Smart Titration of Long-Acting Insulin in Insulin-Naïve Type 2 Diabetic Subjects

J. Bonet[1], R. Visentin[1], M. Vettoretti[1], A. Facchinetti[1] and C. Dalla Man[1]
[1]*Department of Information Engineering, University of Padova, Padova, Italy*

***Abstract*: Insulin-naïve subjects with type 2 diabetes (T2D) begin their therapy with a low initial insulin dose (IID) which is gradually increased to reach the optimal insulin dose (OID) and optimal blood glucose target (OBG). However, for those individuals with a high insulin need (HIN), the STANDARD IID recommended by American Diabetes Association (ADA) guidelines may not be sufficient for achieving OBG in a timely manner. To address this limitation, we propose a SMART IID strategy and assess its possible benefits and risks on blood glucose control during the insulin titration period.**

A 52-week basal insulin titration trial was performed on 300 in-silico insulin-naïve subjects of the T2D Padova simulator, to determine their subject-specific OID. Based on the final OID, subjects were classified as having HIN or low insulin need (LIN).

A logistic regression model was developed to classify subjects as HIN or LIN based on certain characteristics available at the start of the trial. The subjects classified as HIN by the model were then assigned to a higher IID (SMART). A second 52-week titration trial was conducted using the SMART IID on the subjects classified as HIN. To assess effectiveness and safety of SMART IID, we compared time above 180 mg/dL (T_a), time in target 70-180 mg/dL (T_t), time below 70 mg/dL (T_b), and cumulative number of hypoglycemic events (NH) in the two experiments at 90, 124, 180, 270 and 365 days, with 124 being the time to reach the OBG.

Results found that T_a was always significantly lower and T_t was always significantly higher with SMART IID than STANDARD titration ($p<0.001$). Although statistically significant, the differences in T_b at 3 months and in NH at 90 and 124 days were considered to be clinically negligible.

***Keywords*— logistic-regression model, machine-learning, simulation, diabetes therapy.**

I. Introduction

Type 2 diabetes (T2D) is a chronic disease characterized by high blood glucose levels (hyperglycemia) due to both an impaired pancreatic insulin secretion and a concomitant inability of insulin to properly control glucose utilization and production, known as insulin resistance.

With the progression of the disease (advance-stage T2D), patients may need exogenous insulin to control glucose metabolism: rapid-acting insulin (e.g., lispro [1]) before and after meals to prevent post-prandial hyperglycemic events, and long-acting insulin (e.g., degludec [2]) to keep plasma glucose level within the normal range between meals and overnight.

According to American Diabetes Association (ADA) standards of care [3], T2D insulin-naïve patients (i.e., subjects that start using exogenous insulin to treat diabetes) are usually initiated to basal insulin therapy with a low initial insulin dose (IID), typically 10 U (STANDARD), which is then adjusted weekly or twice a week, depending on fasting plasma glucose (FPG), to reach the optimal blood glucose (OBG) while avoiding hypoglycemia.

The procedure of determining the optimal insulin dose (OID), called insulin titration, is time consuming, particularly for individuals with high insulin resistance that results in a high insulin need (HIN). To speed up this phase, we developed a logistic regression model to predict the insulin need for insulin-naïve T2D subjects based on measurable characteristics. Then, a SMART titration rule, applied to HIN individuals, was proposed to rapidly achieve OBG.

To validate this method, the Padova T2D Simulator [5] was modified to create a population of insulin-naïve T2D subjects [6]. Then, the modified simulator was used to simulate both the STANDARD and SMART therapies, and the outcomes were compared in terms of common used glucose control metrics.

II. Methods

A. Subjects and Protocol

The data used in this study were generated using the University of Padova T2D Simulator (T2DS) [5], which consists of a sophisticated nonlinear model describing the glucose–insulin–C-peptide system dynamics and a population of *in silico* T2D subjects, each one represented by a different realization of the model parameter vector.

The T2DS was originally equipped with early-stage T2D virtual subjects (resembling those described in [7]-[9]) and, therefore, was not able to reliably predict the system dynamics in subjects with advanced-stage T2D. To overcome this issue, the T2DS was tailored on inulin-naïve T2D subjects, using the population tuning method presented in [6] and the data reported in [10].

The resulting *in silico* population consisted in 300 *in silico* insulin-naïve subjects (102 females) with body weight (BW) of 86 [77-97] kg (median [25th-75th] percentile), age of 51 [37-65] years and body mass index (BMI) of 31 [29-34] kg/m^2.

The *in silico* subjects underwent two experiments. The first one was a standard oral glucose tolerance test (OGTT), in which subjects ingested a 75g of glucose and plasma glucose, insulin and C-peptide concentrations were measured at fasting (t=0 min) and both 120 and 180 minutes after the glucose intake (Table I). The second experiment was a STANDARD 52-week basal insulin titration trial to find the subject-specific optimal insulin dose (OID) of degludec, starting with an IID of 10 U. In particular, the insulin dose was adjusted twice per week (+2U or -2/-4U) depending on the deviation of measured FPG from the target range of [70-90] mg/dL. The OID was defined as the degludec dose administered at week 52. Once OID was estimated in each subject, we labelled the subjects based of their insulin needs: high (HIN) if OID ≥44U, corresponding to the median value of OID distribution, and

TABLE I
BASELINE CHARACTERISTICS

G_0 (mg/dL)	G_{120} (mg/dL)	G_{180} (mg/dL)
159 [142-179]	234 [215-270]	224 [203-252]
I_0 (µU/mL)	I_{120} (µU/mL)	I_{180} (µU/mL)
59 [25-88]	258 [182-355]	210 ([152-305]
Cp_0 (pmol/L)	Cp_{120} (pmol/L)	Cp_{180} (pmol/L)
839 [629-1106]	1870 [1586-2176]	1823 [1563-2134]

Median [25th-75th] percentile of fasting (subscript 0) and postprandial (subscripts 120 and 180, i.e., 120 and 180 minutes after glucose intake) plasma glucose (G), insulin (I) and C-peptide (Cp) concentrations.

low (LIN), otherwise. Time in target [70-90] mg/dL (T_t), time above 180 mg/dL (T_a), time below 70 mg/dL (T_b) and cumulative number of hypoglycaemic events (NH) were also calculated both in HIN and LIN.

B. The Logistic Regression Model

We developed a logistic regression model to classify insulin naïve T2D subjects as HIN or LIN, based on some measurable features. Model equation is:

$$logit(P) = ln\left(\frac{P}{1-P}\right) = \beta_0 + \sum_{j=1}^{N} \beta_j X_j \quad (1)$$

where P is the probability that a subject is classified as HIN, $\beta = [\beta_0\ \beta_1 \ldots . \beta_N]$ is the vector of model coefficient with β_0 the intercept and β_j the coefficient related to the specific *j*-th feature and X_j are the input features. For our purpose, we considered as input features sex, BW, BMI, age, and the baseline plasma glucose, insulin and C-peptide concentrations measured at fasting (subscript 0), 120 minutes (subscript 120) and 180 minutes (subscript 180) after glucose intake (Table I).

Once the model is identified, the estimated probability of HIN was obtained as:

$$\hat{P} = \frac{\exp(logit(P))}{1+\exp(logit(P))} \quad (2)$$

Then, a subject was classified as HIN or LIN accordingly to the following decision rule:

$$\begin{cases} \text{HIN} & if\ \hat{P} > P_{th} \\ \text{LIN} & if\ \hat{P} \le P_{th} \end{cases} \quad (3)$$

where P_{th} is the threshold probability, optimally determined during model training as detailed in the next section. For each subject was also determined the lower bound (l_b) of the 95% CI of the estimated probability ($\hat{P}$), which was then used to determine an intermediate starting dose for HIN subjects (see *Clinical Assessment* section equation 10).

C. Model Training

We first split the dataset into training (70%) and test sets (30%) (Figure 1).

Model parameters were determined using the maximum-likelihood estimator on the training set [11].

In order to select an optimal feature set, an exhaustive feature selection was performed (i.e., all the possible feature combinations were evaluated, so that a total of 8191 models were considered) using a 100-bootstrap-resampling of the training-set. This strategy consisted in generating, at each iteration, an "internal training set" obtained by sampling with replacement from the training set, so that the cardinality remains the same, and an "internal test set" made up by the non-sampled data (*out of bag set*).

All the candidate models were trained on the 100 internal training sets. Then, we discarded models that did not satisfy the following conditions:

1) all the features being statistically significant (based on the Wald-Test [12]) in at least 70% of the internal training sets;
2) the average deviance being significantly different from that provided by the null model (based on the likelihood ratio test [13]).

Subsequently, for those models who passed the previous selection step, the area under the receiver operating characteristic curve (AUC-ROC) was computed on the internal test set. The best model was selected as the one with the highest average AUC-ROC value.

Finally, we used a *grid-search* approach to determine the best P_{th}, defined in (3), as:

$$P_{th} = argmax_P(mean(Sensitivity) * mean(Specificity)) \quad (4)$$

with *Sensitivity* and *Specificity* calculated in each internal test set as:

$$Sensitivity = \frac{TP}{TP+FN} \quad (5)$$

$$Specificity = \frac{TN}{(TN+FP)} \quad (6)$$

with *TP* the number of true positive, *FN* the number of false negative, *TN* the number of true negative and *FP* the number of false positive.

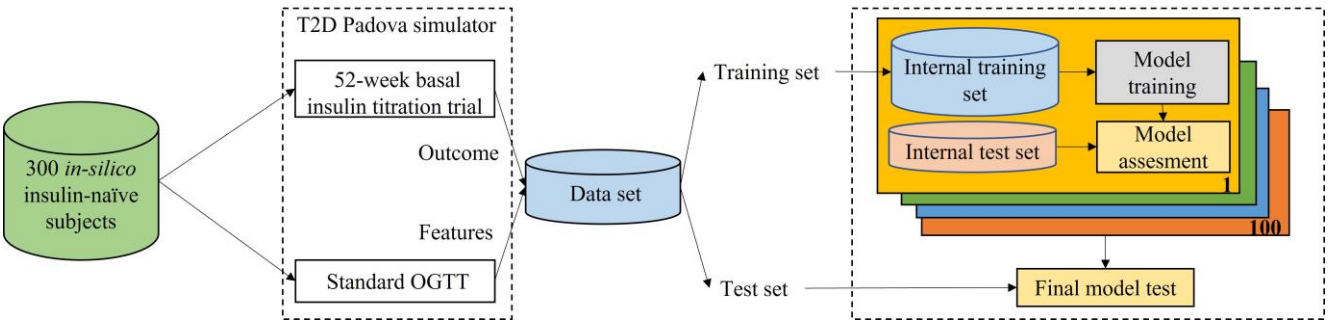


Fig. 1. Schematic representation of the training and test algorithm.

D. Model Testing

The selected model was then applied to the test set and, in addition to AUC-ROC, *Sensitivity* and *Specificity*, defined in (5) and (6), the following performance metrics were calculated:

$$Precision = \frac{TP}{TP+FP} \quad (7)$$

$$Accuracy = \frac{TP+TN}{TP+FP+TN+FN} \quad (8)$$

$$F1-score = \frac{2TP}{2TP+FP+FN} \quad (9)$$

E. Clinical Assessment

To assess the clinical impact of the classification model on glucose control optimization, the subjects classified as HIN underwent a SMART 52-week basal insulin titration trial. In particular, for each HIN subject, IID was set to:

$$IID = \begin{cases} 44U \ if \ l_b > P_{th} \\ 20U \ otherwise \end{cases} \quad (10)$$

As anticipated in the Methods, section B, the second equation was used to guarantee patient's safety whenever the uncertainty of the estimate was not negligible. The titration scheme and the target glucose range were the same used in the STANDARD protocol.

T_t, T_a, T_b, NH were calculated after 3-6-9-12 months and when OID is reached (TOBG, equal to 124 days in median during the SMART titration) and compared with those obtained in HIN subjects following the STANDARD titration (i.e., with IID of 10U), to assess the benefit and possible risk of the proposed titration rule.

F. Statistical Analysis

The comparisons were done using the paired Student T-test [14], for normally distributed metrics, and the paired Wilcoxon test [15]. Normality of distributions was assessed with Shapiro-Wilk test [16]. The significance level was set to α=0.05. Results are reported as mean ± standard deviation (SD), in case of normally distributed variables, and median [25^{th}, 75^{th}] percentile, otherwise.

III. Results

A. Model Performance

Among the candidate logistic models, the selected one predicts the insulin need based on subject's glucose and C-peptide measurements:

$$logit(P) = -5.2351 + 0.0742 \cdot G_0 - 0.0389 \cdot G_{180} + 0.003 \cdot Cp_0 - 0.0038 \cdot Cp_{120} + 0.0036 \cdot Cp_{180} \quad (9)$$

It classified the *in silico* subjects with a sensitivity of 87%, specificity of 91%, precision of 91%, accuracy of 89%, F1-score of 0.89 and AUC-ROC of 0.94.

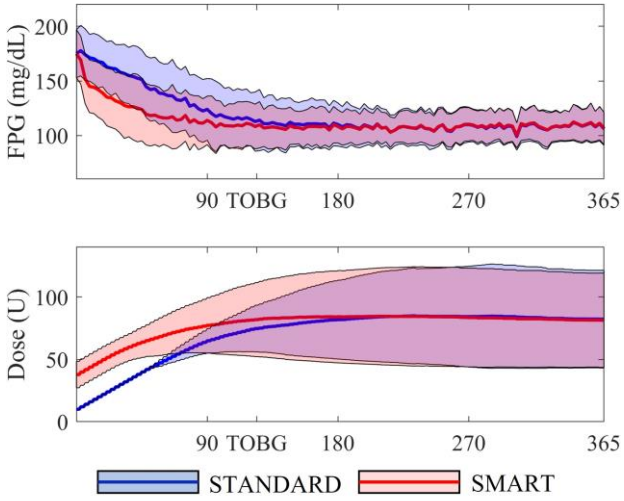


Fig. 2. Mean ± SD time courses of FPG (upper) and insulin dose (lower panel) during STANDARD (blue) and SMART titration (red).

B. Clinical Assessment

Figure 2 shows the simulated FPG and the administered insulin doses during the titration period. As expected, with the SMART titration scheme, the OBG is achieved 30 [0-86] days earlier than with the STANDARD algorithm, thanks to the higher IID. The performance metrics of the SMART vs. STANDARD algorithms, calculated as cumulative measurements at 3-6-9-12 months after the start of insulin titration and when OID is achieved, are compared in Figure 3. For all the considered time intervals, T_a was significantly lower and T_t was significantly higher during SMART than STANDARD titration ($p<0.001$) [17]. On the other hand, SMART titration led to significantly higher T_b ($p=0.001$) and NH ($p=0.005$) in the first 3 and 6 months of the trials, respectively. However, despite statistically significant, the difference in T_b at 3 months was clinically negligible (0% [0-0.08]%), with only one subject showing T_b during SMART higher than 1% with respect to the same metric calculated during the STANDARD therapy [18].

Similarly, the differences in NH at 90 and 124 days (TOBG), despite statistically significant, were 0 [0-1] and 0 [0-1.8].

IV. Conclusions

To achieve the OBG in a timely manner even in HIN subjects, we developed a logistic regression to predict the subject-specific OID as high or low before starting insulin titration, using glucose and C-peptide measurements obtained from an OGTT conducted before the titration. The model exhibited high specificity and precision and had a low number of false positives. This allowed for classification of subjects as HIN or LIN, enabling the initiation of insulin therapy with the most appropriate IID based on the subject's insulin needs. Specifically, this study shows that the SMART therapy in HIN subjects allows reaching the OID about one month in advance compared to the STANDARD method and shows a statistically significant improvement of T_t and reduction of T_a during the trial, with no relevant increase of T_b and NH in the first few months [18][3].

The main limitation of the proposed classification method is the need of plasma glucose and C-peptide measurements obtained before and after a standard OGTT, which requires subject's hospitalization. In the future, it is intended to refine

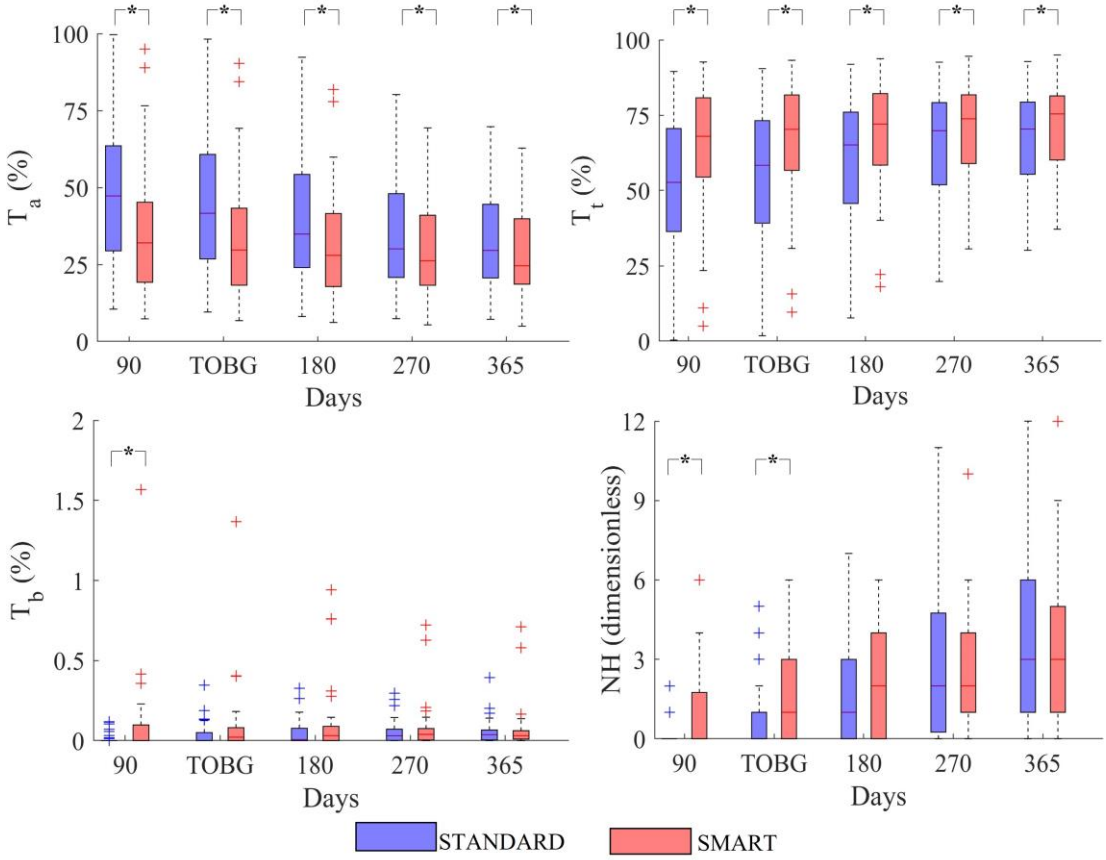


Fig. 3. Boxplot of T_a, T_t, T_b and NH during the STANDARD (blue) and SMART titration (red boxes) at 90, 180, 270, 365 days and TOBG. Asterisks denote statistically significant differences between STANDARD and SMART titration, according to either paired T-Student test or paired Wilcoxon test.

the model to achieve the same classification performance using data from wearable or minimally invasive devices. Another limitation is that the method uses a binary classification (LIN vs HIN) which is relatively coarse and could be refined by incorporating a multi-class classification algorithm to further personalize the IID.

Nevertheless, this study demonstrated that, in principle, IID of an insulin naïve T2D subject can be optimized based on a limited number of measurable characteristics, reducing the duration of the insulin titration phase without increasing the risk of hypoglycemia.

REFERENCES

[1] SL. Noble, E. Johnston, B. Walton.. “Insulin lispro: a fast-acting insulin analog”. Am Fam Physician. 1998 Jan 15;57(2):279-86, 289-92. PMID: 9456992.

[2] S. Kalra, Y. Gupta. “Clinical use of Insulin Degludec: Practical Experience and Pragmatic Suggestions”. N Am J Med Sci. 2015;7(3):81-85. doi:10.4103/1947-2714.153918

[3] American Diabetes Association “Standards of Medical Care in Diabetes - 2020,” Diabetes Care, vol. 43, no. Supplement 1, pp. S66–S76, Jan. 2020, doi: 10.2337/dc20-S006.

[4] B. Zinman, et al. “Insulin degludec versus insulin glargine in insulin-naive patients with type 2 diabetes: a 1-year, randomized, treat-to-target trial (BEGIN Once Long)”. Diabetes Care. 2012;35(12):2464-2471. doi:10.2337/dc12-1205

[5] R. Visentin, C. Cobelli, C. Dalla Man. “The Padova type 2 diabetes simulator from triple-tracre single-meal studies: in silico trials also possible in rare but not-so-rare individuals”, Diabtes Technol Ther, 2020 Dec; 22(12):892-903

[6] R. Visentin, M. Schiavon, C. Dalla Man. “In Silico Cloning of Target Type 2 Diabetes Population for Treatments Development and Decision Support,” Annu. Int. Conf. IEEE Eng. Med. Biol. Soc. IEEE Eng. Med. Biol. Soc. Annu. Int. Conf., vol. 2020, pp. 5111–5114, Jul. 2020, doi: 10.1109/EMBC44109.2020.9175271.

[7] G. Bock et al., “Pathogenesis of pre-diabetes: Mechanisms of fasting and postprandial hyperglycemia in people with impaired fasting glucose and/or impaired glucose tolerance,” Diabetes, 2006, vol. 55, no. 12, pp. 3536–3549

[8] A. Vella et al., “Effects of Dipeptidyl Peptidase-4 Inhibition on Gastro intestinal Function, Meal Appearance, and Glucose Metabolism in Type 2 Diabetes,” Diabetes, 2007 May, vol. 56, no. 5, pp. 1475 LP – 1480,

[9] A. Basu, et al., “Effects of type 2 diabetes on insulin secretion, insulin action, glucose effectiveness, and postprandial glucose metabolism,” Diabetes Care, 2009, vol. 32, no. 5, pp. 866–872,.

[10] J. Holst et al., “IDegLira Improves Both Fasting and Postprandial Glucose Control as Demonstrated Using Continuous Glucose Monitoring and a Standardized Meal Test.,” J. Diabetes Sci. Technol., vol. 10, no. 2, pp. 389–397, Oct. 2015, doi: 10.1177/1932296815610124.

[11] T. Hastie, R. Tibshirani, J. Friedman, ”The elements of statistical learning: data mining, inference and prediction”. Springer 2009.

[12] M.D. Ward, J.S. Ahlquist, “Maximum Likelihood for Social Science: Strategies for Analysis”. Cambridge University Press 2018. p. 36. ISBN 978-1-316-63682-4.

[13] B. Li, G.J. Babu (2019). A Graduate Course on Statistical Inference. Springer. p. 331. ISBN 978-1-4939-9759-6.F.

[14] H.A. David, J. L. Gunnink. "The Paired t Test Under Artificial Pairing". The American Statistician. 1977, 51 (1): 9–12.

[15] F. Wilcoxon "Individual comparisons by ranking methods" Biometrics Bulletin. 1945, 1 (6): 80–83.

[16] S. S. Shapiro, M. B. Wilk, "An analysis of variance test for normality (complete samples)". Biometrika. 1965, 52 (3–4): 591–611.

[17] T. Battelino, T. Danne, R. M. Bergenstal, et.al Clinical Targets for Continuous Glucose Monitoring Data Interpretation: Recommendations From the International Consensus on Time in Range. Diabetes Care 1 August 2019; 42 (8): 1593–1603. https://doi.org/10.2337/dci19-0028

[18] M.A.L. Gabbay, M. Rodacki, L.E. Calliari et al. “Time in range: a new parameter to evaluate blood glucose control in patients with diabetes“. Diabetol Metab Syndr 12, 22 (2020). https://doi.org/10.1186/s13098-020-00529-z

Toward Implicit Communication of Object Properties for Human-Robot Interaction

L. Lastrico[1,*], A. Carfì[2], F. Rea[1], F. Mastrogiovanni[2], and A. Sciutti[1]
[1] *Cognitive Architecture for Collaborative Technologies Unit (CONTACT), Italian Institute of Technology, Genoa, Italy*
[2] *Department of Informatics, Bioengineering, Robotics, and Systems Engineering (DIBRIS), University of Genoa, Italy*
*corresponding author, email: linda.lastrico@iit.it

***Abstract*—As humans, being sociable is fundamental to our existence, and communication underpins all of our interactions. Implicit communication accounts for a large portion of the information flow, and humans are adept at interpreting the unspoken from the actions of others. In the last three years, we studied the kinematics modulations that naturally occur when transporting objects and how they can reveal item characteristics to an external observer. The findings on human behavior guided us into developing robotic applications to automatically detect some features of the carried objects from the motion and, on the other hand, communicate the same information by exploiting the robot embodiment. In the current publication, we present a critical review of the state-of-the-art along with a description of the open issues and challenges.**

***Keywords*—Human-robot interaction, motion kinematics, implicit communication, object properties detection**

I. INTRODUCTION

In recent years, the use of robots in different fields, including industry, healthcare, and education, has increased. However, challenging barriers remain in place for integrating robots into our society. The difficulties in having direct and clear communication with an artificial agent stand out among the others. Standard communication mediums in robotics are based on speech [1], or explicit gestures [2], [3], while more recent approaches investigate new technologies such as augmented reality headsets [4], [5]. Nevertheless, an often overlooked channel of communication is the implicit one. Indeed, as humans, we communicate only partially through words; we heavily rely on subtle cues to collect from our peers a spectrum of information, ranging from internal status to intentions or needs [6]. Coordination emerges from the interaction precisely because of the implicit signals [7], giving rise to a series of mutual synchronization and anticipation phenomena that drastically reduce the need for complex verbal instructions and the resulting delays [8]. More precisely, implicit communication refers to all those modulations that occur in our gestures independently of our will or consciousness. In the presence of another person, these signals may be emphasized with a social purpose to make the action even more predictable and readable by a collaborator: this is called signaling [9]. Within our research, we have chosen to investigate a scenario where robots and humans often need to work together: the handling and transport of objects. In these situations, nonverbal communication plays a crucial role in conveying information about the transported object [10], such as its weight, fragility, spillability, potential danger, or assembly state. Through various methodologies and perspectives, we aim to explore ways in which the implicit communication associated with object handling can be applied to interaction with robots, drawing inspiration from natural human behaviors.

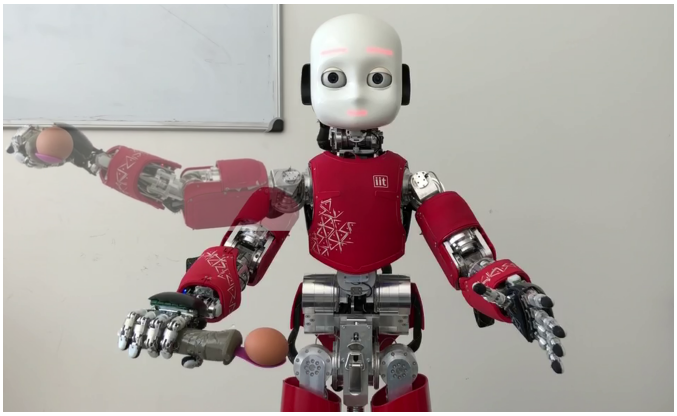


Fig. 1: Example of a careful action performed by the robot iCub, which is able to transport an egg by modulating appropriately the velocity profile during the motion

In Section II, we present the strategies humans adopt to handle objects which differ in weight or delicacy required by analyzing and modeling human motion. These observations guided us in exploring methods to infer properties relying on human kinematics. In Section III, we expose the dual challenge of generating expressive movements on a robot while being task-oriented (see Figure 1 for a motion proof of concept). Finally, in Section IV are gathered insights on how implicit modulation influence and affect the interaction. Conclusions follow.

II. RECOGNIZING OBJECT PROPERTIES FROM HUMAN MANIPULATION

Previous literature addressed implicit communication referred to objects, focusing on the intention of the action [11], the position and the timing of the handover [12], the carefulness in the motion [13], the spillability of containers [10] or more extensively on the weight [14], [15], [16], [10]. To study the strategies adopted by humans to transport

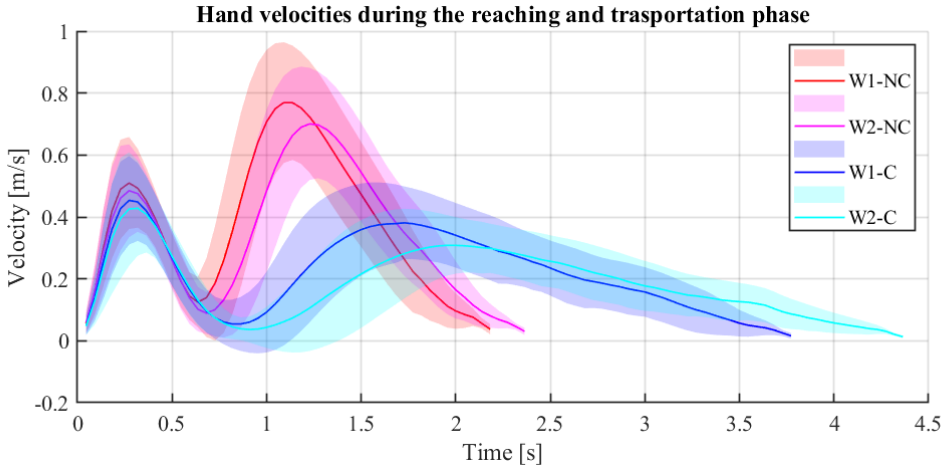


Fig. 2: Hand mean velocities and standard deviation, in transparency, are associated with reaching (first peak) and transportation movements (second peak) of four different glasses. The two cups containing water (W1-C and W2-C) are in blue, while the other coups not requiring care in their motion (W1-NC and W2-NC) are in red. The weight difference between W1 and W2 was 500 grams.

objects with different characteristics, we exploited a multimodal dataset involving four transparent plastic cups with two possible levels of weight (*W1:* 167 or *W2:* 667 grams) and associated carefulness. The carefulness was characterized by the presence of water to the brim or by its absence, leading to the definition of Careful (*C*) and Not Careful (*NC*) manipulations. Figure 2 summarizes the findings relative to human kinematics, measured with a motion capture system, during the transportation of the four objects typologies. While reaching the object, represented by the first peak of velocity, humans' motion is uniform for all the glasses, either full, empty, heavy, or light. The strongest modulation appears instead during the transport of the glasses. We can notice how the velocity peak is lower when transporting the *W1-C* and *W2-C* glasses, and the velocity profile follows a different shape. Indeed, the velocity is bell-shaped for glasses without water, while the careful transport movements present an anticipated peak with a prolonged deceleration phase, especially for the full, heavy container. Participants were especially cautious in the final phase of the movement, gently leaning the glass so as not to spill the content. In the initial phase of the movement, the velocity derivative is significantly steeper for empty glasses, indicating higher acceleration in moving the object only slightly modulated by the weight.

These results confirmed the hypothesis that human motion is strongly affected by the item's characteristics, particularly for the care adopted, and this modulation could be exploited for an automatic inference process. Therefore, we investigated which sensor could extract accurate kinematic features and which classifier could enable an online implementation of the architecture; details on this research are described in [17], [18]. As a critical summary of the results, motion descriptors could be extracted online with the iCub robot camera computing the optical flow of the scene. This approach allows for the most spontaneous interaction with the robot, but it presents some limitations that may need to be considered, depending on the application scenario. In particular, the perception of human motion with the robot camera, even if robust to some occlusions, should take place as much as possible in robot view sight. In addition, the proposed approach assumes that object transportation is the main motion in the scene and therefore is well described by the optical flow; if the person is walking in the room while handling objects, then an additional segmentation of the arm is required. We could mitigate these limitations by integrating data from an inertial sensor worn at the wrist, which was available in the dataset and gave good results in the offline classification of the carefulness using a simple Long Short Term Memory (LSTM) neural network. The same model was exploited for classifying online the carefulness using the camera alone, with modified transportation tasks with respect to those in the training set, with an accuracy that reached up to 81.3%. Duarte et al. [13] achieved similar accuracy levels by modeling the motion carefulness with a Gaussian Mixture Model and tracking the object with a motion capture system.

We did not pursue the online weight classification, given the poor performances obtained offline with all the possible sensors. This result can be ascribed to the characteristics of the data. As shown in Figure 2, the difference between the two levels of weight is not striking and is overridden by water presence. However, we are optimistic that with a more weight-oriented training set, such classification could be achievable with the same approach.

III. GENERATING COMMUNICATIVE ROBOT MOVEMENTS

The problem of generating human-like movements has been addressed from different perspectives. Some strategies resort to optimizing motion primitives such as the jerk [19], [20]; others make use of animation techniques or exploit learning from demonstration (see respectively [21] and [22] for a review). Coming to implicit communication through robot actions, Venture and Kulić proposed a recent and complete survey

on expressive robot motions [23]; other studies explored the possibility of conveying the goal of the action [24], or the weight of the handled object [16]. As pointed out by Sandini et al. [6], the challenge of generating plausible motions with a humanoid robot can be even greater: from one hand, their shape can solicit the same coordination mechanisms emerging in humans, but it also creates an expectation of competency that may be easily disrupted. We questioned then the possibility of creating robotic actions, human-inspired without being a replica, able to convey a specific attitude in the gesture - in this case, the carefulness - with a strategy that could be reproduced easily on different platforms, even not humanoid. From the recognition of the action patterns presented in Section II, we saw how the velocity of the motion is relevant in its whole dynamic. Therefore, adopting equivalent velocity profiles for the robot end-effector could effectively express the carefulness of a specific action without undermining its effectiveness and instead make it more closely fitting the object properties. With these goals in mind, we resorted to Generative Adversarial Networks [25], [26] to generate velocity profiles belonging to *C* or *NC* classes. Indeed, these networks can produce synthetic data capturing the distribution of the training set and therefore accounting for the natural variance that affects human actions [27]. An advantage of this approach is the applicability to different robotic platforms, as only the end-effector velocity is controlled, without applying constraints to the rest of the kinematic chain; of course, this may also lead to a sense of uneasiness depending on the dynamic of the secondary joints. Another point to be stressed is that resorting to velocity norms, they are detached from any particular trajectory. Therefore, to be applied to transport movement from point A to point B, each profile needs to be appropriately rescaled. Since in the literature, there are proofs of time-invariance in the upper limb movements [28], [29], we opted to maintain the duration of the action over the magnitude of the velocity reached. In any case, we should assess the effect on the interaction of the velocity modulation.

IV. THE EFFECT OF IMPLICIT COMMUNICATION OF OBJECT PROPERTIES: TOWARD THE INTERACTION

In the previous Sections, we presented different perspectives and studies on implicit communication applied to robotics for the expression and detection of object properties. However, the effect of such approaches on the interaction has been investigated only to a limited extent. For instance, it has been shown that, provided a well-thought robot's action, humans use the estimated weight of the object for planning their lifting action [16]. Another study considered a handover scenario where a robotic manipulator adapted its grasping strategy depending on the object being passed and was positively evaluated through questionnaires [30]. Indeed, the evaluation of interaction outcomes is commonly performed with questionnaires, even though implicit measures to estimate motor contagion may be preferable since they allow measuring spontaneous adaptations [31]. Physiological measures such as skin conductance or electromyogram can be useful to estimate the level of ease of the participants but require a more invasive framework [32]. We conducted two studies to assess if the attitude of transport actions with different robotic platforms - humanoid and not - were perceived as careful or not as intended [33], [34]. Findings showed that participants perceived the care in the action when explicitly questioned about it. Moreover, there was significant coordination with the robot even if was not made necessary by the task; when the robot executed a careful action, participants slowed down their reaching or transport actions, taking more time to complete them. Interestingly, this also happened with a robotic manipulator having a kinematic chain significantly different from the human arm. Bisio et al. [31] showed proof of how motor contagion appears as long as a humanoid robot respects biological laws of motion. In our case, the motion plausibility was granted using human-inspired velocity profiles. Even with a robotic manipulator, participants could match their motor repertoire to the motions of the observed agent, showing emerging coordination.

V. CONCLUSIONS

We showed several methods and strategies to open an additional communication channel to interact with robots, exploiting implicit cues embedded in the movements. In our research, as the area of designated application, we focused on the innovative one of perceiving and transmitting the properties of objects involved in transport actions, focusing particularly on motion carefulness. This feature, as in other works [13], [10], was achieved with the modulation of a single physical characteristic: through the manipulation of glasses full of water. Future studies should assess which other factors contribute to making an item delicate to handle and how they affect the kinematics. In this regard, preliminary evaluations were pursued in [33].

The leading idea and the whole framework are inspired by human behavior and interaction abilities. This approach could be seen as a limitation for application areas with a more functional focus, such as pre-defined assembly tasks, where the speed of execution and strength of robots reach levels unimaginable for a human being. However, if we want to build robots able to share the social sphere with us, there is no other way but to be inspired by what happens on the biological level. Knowing how human-human interaction works should guide us in designing better artificial agents: coordination can emerge only from mutual understanding.

ACKNOWLEDGEMENT

This work was carried out within the framework of the project "RAISE - Robotics and AI for Socio-economic Empowerment" and has been supported by European Union - NextGenerationEU. AS is supported by a Starting Grant from the European Research Council (ERC) under the European Union's Horizon 2020 research and innovation programme. G.A. No 804388, wHiSPER.

REFERENCES

[1] A. Cangelosi and T. Ogata, *Speech and Language in Humanoid Robots*. Dordrecht: Springer Netherlands, 2019, pp. 2261–2292.

[2] K. S. Lohan, H. Lehmann, C. Dondrup, F. Broz, and H. Kose, *Enriching the Human-Robot Interaction Loop with Natural, Semantic, and Symbolic Gestures*. Dordrecht: Springer Netherlands, 2019, pp. 2199–2219.

[3] H. Liu and L. Wang, "Gesture recognition for human-robot collaboration: A review," *International Journal of Industrial Ergonomics*, vol. 68, pp. 355–367, 2018.

[4] S. Macciò;, A. Carfì, and F. Mastrogiovanni, "Mixed reality as communication medium for human-robot collaboration," in *2022 International Conference on Robotics and Automation (ICRA)*, 2022, pp. 2796–2802.

[5] E. Rosen, D. Whitney, E. Phillips, G. Chien, J. Tompkin, G. Konidaris, and S. Tellex, "Communicating and controlling robot arm motion intent through mixed-reality head-mounted displays," *The International Journal of Robotics Research*, vol. 38, no. 12-13, pp. 1513–1526, Oct. 2019.

[6] G. Sandini, A. Sciutti, and F. Rea, *Movement-Based Communication for Humanoid-Human Interaction*. Dordrecht: Springer Netherlands, 2018, pp. 1–29.

[7] G. Knoblich, Butterfill, Stephen, and N. Sebanz, "Psychological research on joint action: Theory and data," in *Advances in Research and Theory*, ser. Psychology of Learning and Motivation. Academic Press, 2011, vol. 54, pp. 59–101.

[8] E. Bicho, L. Louro, and W. Erlhagen, "Integrating verbal and nonverbal communication in a dynamic neural field architecture for human–robot interaction," *Frontiers in neurorobotics*, vol. 4, 05 2010.

[9] G. Pezzulo, F. Donnarumma, and H. Dindo, "Human sensorimotor communication: A theory of signaling in online social interactions," *PloS One*, vol. 8, pp. 1–11, 2013.

[10] Q. Zheng, W. Wu, H. Pan, N. Mitra, D. Cohen-Or, and H. Huang, "Inferring object properties from human interaction and transferring them to new motions," *Computational Visual Media*, vol. 7, 04 2021.

[11] A. Cavallo, A. Koul, C. Ansuini, F. Capozzi, and C. Becchio, "Decoding intentions from movement kinematics," *Scientific Reports*, vol. 6, p. 37036, 11 2016.

[12] K. Strabala, M. K. Lee, A. Dragan, J. Forlizzi, S. S. Srinivasa, M. Cakmak, and V. Micelli, "Toward seamless human-robot handovers," *J. Hum.-Robot Interact.*, vol. 2, no. 1, p. 112–132, feb 2013.

[13] N. F. Duarte, K. Chatzilygeroudis, J. Santos-Victor, and A. Billard, "From human action understanding to robot action execution: how the physical properties of handled objects modulate non-verbal cues," in *2020 Joint IEEE 10th International Conference on Development and Learning and Epigenetic Robotics (ICDL-EpiRob)*, 2020, pp. 1–6.

[14] S. Runeson and G. Frykholm, "Visual-perception of lifted weight," *Journal of experimental psychology. Human perception and performance*, vol. 7, pp. 733–40, 09 1981.

[15] L. Schmitz, C. Vesper, N. Sebanz, and G. Knoblich, "When height carries weight: Communicating hidden object properties for joint action," *Cognitive Science*, vol. 42, no. 6, pp. 2021–2059, 2018.

[16] A. Sciutti, L. Patanè, F. Nori, and G. Sandini, "Understanding object weight from human and humanoid lifting actions," *IEEE Transactions on Autonomous Mental Development*, vol. 6, no. 2, pp. 80–92, 2014.

[17] L. Lastrico, A. Carfì, A. Vignolo, A. Sciutti, F. Mastrogiovanni, and F. Rea, "Careful with that! observation of human movements to estimate objects properties," in *Human-Friendly Robotics 2020*. Springer International Publishing, 2021, pp. 127–141.

[18] L. Lastrico, A. Carfì, F. Rea, A. Sciutti, and F. Mastrogiovanni, "From movement kinematics to object properties: Online recognition of human carefulness," in *Social Robotics*, vol. 13086. Springer International Publishing, 2021, pp. 61–72.

[19] K. Harada, K. Hauser, T. Bretl, and J.-c. Latombe, "Natural motion generation for humanoid robots," in *2006 IEEE/RSJ International Conference on Intelligent Robots and Systems*, 2006, pp. 833–839.

[20] T. Flash and N. Hogan, "The coordination of arm movements: an experimentally confirmed mathematical model," *Journal of Neuroscience*, vol. 5, no. 7, pp. 1688–1703, 1985.

[21] T. Schulz, J. Torresen, and J. Herstad, "Animation techniques in human-robot interaction user studies: A systematic literature review," *J. Hum.-Robot Interact.*, vol. 8, no. 2, jun 2019.

[22] H. Ravichandar, A. S. Polydoros, S. Chernova, and A. Billard, "Recent advances in robot learning from demonstration," *Annual Review of Control, Robotics, and Autonomous Systems*, vol. 3, no. 1, pp. 297–330, 2020.

[23] G. Venture and D. Kulić, "Robot expressive motions: A survey of generation and evaluation methods," *J. Hum.-Robot Interact.*, vol. 8, no. 4, nov 2019.

[24] A. D. Dragan, K. C. T. Lee, and S. S. Srinivasa, "Legibility and predictability of robot motion," in *Proceedings of the 8th ACM/IEEE International Conference on Human-Robot Interaction*, Tokyo, Japan, Mar 2013, pp. 301–308.

[25] J. Yoon, D. Jarrett, and M. van der Schaar, "Time-series generative adversarial networks," in *Proceedings of 33rd Conference on Neural Information Processing Systems*, Vancouver, Canada, Oct 2019.

[26] L. Garello, L. Lastrico, F. Rea, F. Mastrogiovanni, N. Noceti, and A. Sciutti, "Property-aware robot object manipulation: a generative approach," in *2021 IEEE International Conference on Development and Learning (ICDL)*, 2021, pp. 1–7, garello and Lastrico equally share the authorship.

[27] M. J. Gielniak, C. K. Liu, and A. L. Thomaz, "Generating human-like motion for robots," *The International Journal of Robotics Research*, vol. 32, no. 11, pp. 1275–1301, 2013.

[28] G. Averta, G. Valenza, V. Catrambone, F. Barontini, E. Scilingo, A. Bicchi, and M. Bianchi, "On the time-invariance properties of upper limb synergies," *IEEE Transactions on Neural Systems and Rehabilitation Engineering*, vol. PP, pp. 1–1, 05 2019.

[29] S. Ambike and J. P. Schmiedeler, *Time-Invariant Strategies in Coordination of Human Reaching*. Dordrecht: Springer Netherlands, 2008, pp. 205–214.

[30] W. Yang, C. Paxton, A. Mousavian, Y.-W. Chao, M. Cakmak, and D. Fox, "Reactive human-to-robot handovers of arbitrary objects," in *2021 IEEE International Conference on Robotics and Automation (ICRA)*, 2021, pp. 3118–3124.

[31] A. Bisio, A. Sciutti, F. Nori, G. Metta, L. Fadiga, G. Sandini, and T. Pozzo, "Motor contagion during human-human and human-robot interaction," *PLOS ONE*, vol. 9, no. 8, pp. 1–10, 08 2014.

[32] F. Dehais, E. A. Sisbot, R. Alami, and M. Causse, "Physiological and subjective evaluation of a human–robot object hand-over task," *Applied Ergonomics*, vol. 42, no. 6, pp. 785–791, 2011.

[33] L. Lastrico, L. Garello, F. Rea, N. Noceti, F. Mastrogiovanni, A. Sciutti, and A. Carfì, "Robots with different embodiments can express and influence carefulness in object manipulation," in *2022 IEEE International Conference on Development and Learning (ICDL)*, 2022, pp. 280–286.

[34] L. Lastrico, N. Ferreira Duarte, A. Carfì, F. Rea, F. Mastrogiovanni, A. Sciutti, and J. Santos-Victor, "Robots with different embodiments can express and influence carefulness in object manipulation," in *Social Robotics*. Springer International Publishing, 2022.

Brain-heart interaction: an ECG-fMRI integrated study in physiology and major depressive disorder

F. Goffi[1], P. Reali[1], A. Ferro[2], V.R. Pescuma[2], G. Schiena[2], Y. Barone[2], P. Enrico[3], Y. Torrente[2,3], F.M. Triulzi[4], A.M. Bianchi[1], P. Brambilla[2,3]*, and E. Maggioni[1]*

[1] *Department of Electronics, Information and Bioengineering, Politecnico di Milano, Milan, Italy.*
[2] *Dept. of Neurosciences and Mental Health, Fondazione IRCCS Ca' Granda Ospedale Maggiore Policlinico, Milan.*
[3] *Department of Pathophysiology and Transplantation, University of Milan, Milan, Italy.*
[4] *Neuroradiology Unit, Fondazione IRCCS Ca' Granda Ospedale Maggiore Policlinico, Milan, Italy.*
* These authors have contributed equally to this work.

***Abstract*—*Introduction.* The connection between brain activity and cardiac variability, through the modulation of the autonomic nervous system, is a well-established phenomenon. However, the studies that have addressed the reciprocal influences between central and autonomic nervous system during resting state are still limited, especially in the context of pathophysiology.**
***Aim.* In the present work, the main objective was to explore the relationship between the central nervous system and cardiac variability at rest in an integrated multimodal analysis thanks to simultaneously acquired ECG and fMRI data.**
Moreover, we evaluated possible differences in adult-onset major depressive disorder (MDD), in which both brain function and cardiac variability alterations are evident, but in which there is still no idea of their reciprocal effects.
***Methods.* Thirty-three participants were included in the study (67.33 ± 9.63 years, 58% females), 16 diagnosed with adult-onset MDD and 17 healthy controls (HC) with comparable age and sex. fMRI analysis was integrated with the analysis of the heart rate variability through an HRV-driven fMRI analysis to study the BOLD responses to sympathetic and vagal autonomic changes.**
***Results.* Our findings allowed to identify activations and deactivations in brain regions that are some of the key nodes of the central autonomic network (CAN), a network of brain structures that are involved in the regulation of autonomic processes at high central level. The comparison between patients affected by MDD and HC subjects revealed that differences in brain correlates of cardiac variability are present in brain regions of the CAN.**
***Conclusions.* Combined HRV-fMRI analyses provided new findings on physiological brain-heart interactions and allowed to characterize the autonomic and central neurobiological bases of depression from a wider and more comprehensive prospective.**

***Keywords*—fMRI, HRV, central autonomic network, major depressive disorder**

I. INTRODUCTION

The connection between the brain and the heart is a well-established phenomenon and, according to the neurovisceral integration model, central-level neural circuits are involved in the regulation of peripheral cardiac activity, through the modulation of the autonomic nervous system (ANS) [1].
Among the studies that have identified direct and indirect pathways by which neural networks are linked to autonomic circuits, of relevance is the work of Benarroch, who described the existence of the central autonomic network (CAN) [2], which is a network of brain structures involved in control mechanisms essential for adaptation and survival, among which baseline ANS function and its modulation in response to changing environment. The most acknowledged forebrain structures of the CAN include the hypothalamus, insula, and amygdala, whereas recent functional neuroimaging studies have shown that also the medial prefrontal cortex (mPFC), thalamus, anterior cingulate cortex (ACC), hippocampus, precuneus and cerebellum are involved in ANS functions [3].
Although neuroimaging techniques alone have allowed to understand the human brain and its complex functions, unprecedented findings on brain functioning are being achieved more recently thanks to the integration of multiple modalities that allow to explore also the links of the brain with other systems of the human body.
However, the studies that have investigated the brain regions involved in the dynamics of heart rate variability (HRV), which indexes autonomic modulation, are still limited.
A deeper knowledge of this complex interaction both in physiology and in pathology can be obtained by integrating electrocardiography (ECG) with functional magnetic resonance imaging (fMRI).
fMRI is a very powerful tool that allows to study brain function, mapping both brain activity and the network of connections among regions in the entire brain. The basic concept underlying fMRI measurements is that an increase in neuronal activity, stimulating both higher energy consumption and increased blood flow, can be detected by measuring changes in oxygenation concentration (Blood Oxygen Level Dependent, or BOLD contrast).
Instead, ECG recordings enable to extract information on the HRV, which is the physiological phenomenon that consists in changes in the time intervals between consecutive heartbeats

to rapidly adjust to physical and psychological stimuli to maintain homeostasis. Heart rate is largely under the control of the ANS, composed by two constantly interacting branches, the sympathetic activity, which has an excitatory role, and the parasympathetic or vagal activity, which mostly performs an inhibitory control.

The various oscillators generate rhythmic fluctuations at different frequency ranges, which are divided into four bands: ultra-low frequency and very low frequency that are related to slow circadian rhythms, low frequency (LF) (0.04-0.15 Hz) and high frequency (HF) (0.15-0.4 Hz) [4]. The efferent vagal activity is the major contributor to the HF component, while more controversial is the interpretation of the LF component, which is considered a parameter that includes both sympathetic and vagal influences.

HRV has considerable potential to assess the role of ANS in healthy individuals and in patients with various cardiovascular and non-cardiovascular disorders, including psychiatric illnesses.

In this respect, major depressive disorder (MDD) is a disabling psychiatric pathology that, besides being a brain disorder, is often characterized by autonomic neural dysfunction, reflected in reduced HRV [5].

Within this context, the main objective of this study was to provide deeper insights on the relationship between brain activity and cardiac autonomic-modulated activity through simultaneous ECG and fMRI techniques, via an HRV-driven fMRI analysis.

Since this relationship is even less explored in the context of psychopathology, our second aim was to explore possible differences in patients diagnosed with MDD with respect to the control group. Indeed, MDD is a heterogeneous disease, in which both brain function and HRV alterations have been shown, but there is less idea of their reciprocal effects. Therefore, the study of the interaction between the brain and heart could provide new findings about the disorder itself.

II. METHODS

A. Participants and study protocol

The dataset analyzed was extracted from the clinical study conducted in the RADAR project, "Role of LSD1 in aging-dependent epigenetic drift leading to frailty-associated mood disorders", which was coordinated by Fondazione IRCCS Ca' Granda Ospedale Maggiore Policlinico of Milan [6].

Thirty-three participants were included in the present analysis (67.33 ± 9.63 years, 58% females), 16 diagnosed with adult-onset MDD and 17 healthy controls (HC) with comparable age and sex. Clinical diagnoses were assessed using the Italian version of the Structured Clinical Interview for DMS-5 (SCID) and only subjects with MDD onset at age greater than 45 years were included in the patient group.

All subjects provided a written informed consent to the study protocol, which was conducted in accordance with the Declaration of Helsinki and approved by the Ethical Committee of Fondazione IRCSS Ca' Granda Ospedale Maggiore Policlinico, Milan, Italy.

The participants underwent a multimodal 3T MRI session including a simultaneous ECG-fMRI acquisition of 500 seconds during eyes-closed resting state condition.

B. fMRI preprocessing

Starting from raw fMRI data, fMRI preprocessing was performed by using HALFpipe standardized workflow, proposed by the ENIGMA Consortium for the elaboration of task-based and resting-state fMRI data [7]. Preprocessing implemented a consensus of preprocessing steps required for any fMRI study: re-aligment of fMRI volumes, coregistration with the anatomical image, segmentation, normalization and spatial smoothing.

As BOLD signals are generally noisy, we implemented an additional set of denoising pipelines with the aim of comparing them according to some quantitative metrics to identify which could be the more effective in both noise removal, resting-state networks identifiability and signal enhancement. Besides the minimal steps, according to the results of this comparison analysis, the mean signals from white matter and cerebrospinal fluid, and the mean global signal were regressed out.

C. HRV

In parallel to fMRI preprocessing, the ECG signal was pre-elaborated. The gradient artifact, which is due to ECG acquisition in fMRI environment, was removed through the artifact subtraction method and, next, ECG signals were filtered with a band-pass Hamming windowed sinc FIR filter with cut-off frequencies of 0.1-120 Hz, and a notch filter at 50 Hz to remove powerline interference.

R peaks were semi-automatically identified and HRV time series was computed as their difference in time. Moreover, an ECG-derived respiration signal was estimated by low-pass filtering the ECG at 1 Hz. The respirogram was extracted by sampling the respiration at each R peak time.

D. HRV-driven fMRI analysis

fMRI and HRV data were combined together to perform an HRV-driven fMRI analysis with the objective of studying the BOLD response corresponding to changes in HRV, due to both sympathetic and parasympathetic actions of the ANS.

We extracted time-varying HRV parameters that could represent sympathetic and parasympathetic activities, and their balance, to be used within a general linear model (GLM) in order to explain fMRI data. These regressors were computed starting from the tachogram and the ECG-derived respirogram that were inserted in a time-varying bivariate autoregressive model, which is a cross-spectral analysis used to highlight linear frequency relationships between the two different signals in input [8]-[9].

The explaining variable that corresponds to the sympathetic activity was computed as the time-varying power in the LF range of the power spectrum estimated from the tachogram alone, hence removing spectral contribution driven by respiration.

As regards vagal modulation, the corresponding regressor was

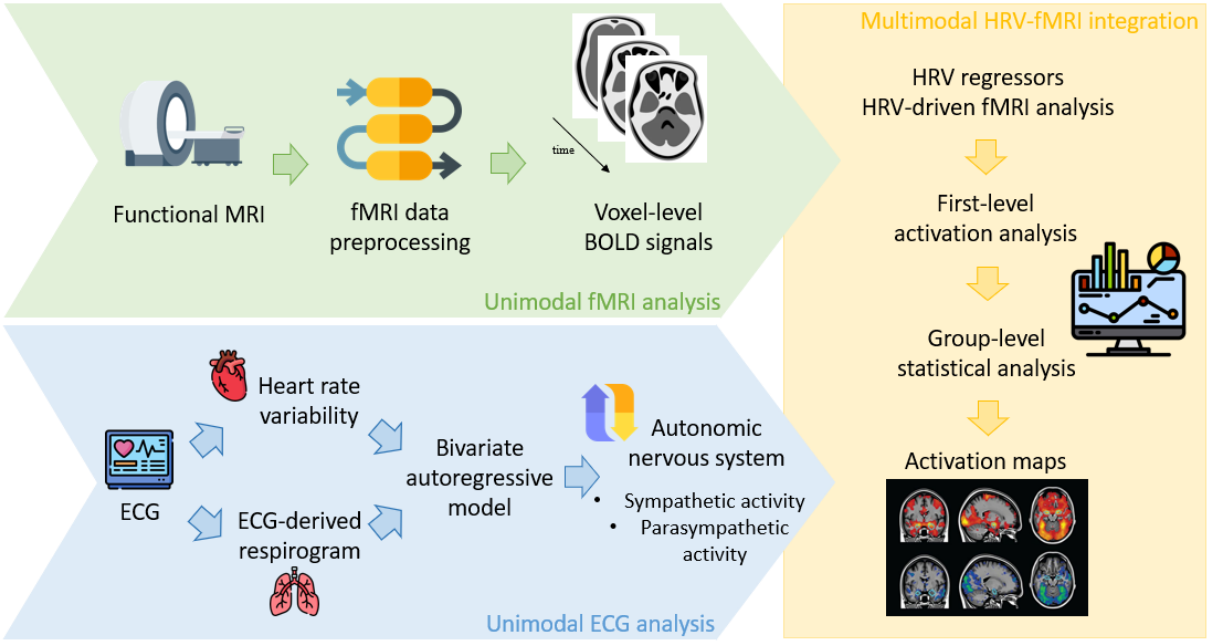


Fig. 1: Workflow.

calculated as the time-varying power in the spectrum that explains the respiration influence on cardiac variability. In resting state condition, this interaction is mainly related to respiratory sinus arrhythmia processes, hence it reflects the contribution of vagal activity at the respiratory rate (usually, falling in the HF range) [9].

Also the ratio between LF and HF power estimated time series was computed as regressor representing the sympathovagal balance of the autonomic nervous system.

The convolution with the canonical hemodynamical response function was applied to each regressor to take into account the intrinsic delay of the neurovascular coupling.

We performed subject-level HRV-fMRI activation analysis to identify cortical and subcortical brain regions with a significant BOLD response to different spectral changes in HRV, represented by the previously defined regressors. The design matrix was composed by the three HRV regressors and by six non-interest regressors that are the movement parameters estimated during fMRI volumes realignment phase.

After estimation of the GLM coefficients, inference on fMRI responses to LF, HF and LF/HF fluctuations was performed by creating contrasts that assess the contribution of the regressors of interest, alone or in combination, to the overall BOLD signal.

Group-level HRV-fMRI analysis was performed by making inference on the subject-level contrast maps representing the fMRI correlates of HRV analysis. Three group-level GLM analyses (for LF, HF and LF/HF) were performed. The GLM design matrix included age, sex, and diagnosis as covariates, plus a constant term used to evaluate the activation for the entire group. Inference on group-level fMRI responses and on diagnosis effects was based on T-tests on the corresponding regressor ($p \leq 0.001$). The clusters of voxels were then labeled according to AAL Atlas.

III. RESULTS

The HRV-driven fMRI analysis enabled the identification of brain regions with a BOLD response significantly correlated with ANS modulation.

Considering cardiac variability due to LF fluctuations, a group-level positive BOLD response was found in brain regions that belong to the CAN, such as left *precuneus* and bilateral *insula*, meaning that they have a positive hemodynamical correlation with LF power at group level. Instead, deactivation was found in left *middle frontal gyrus* and *inferior frontal gyrus* triangular part areas (see figure 2).

In the same condition, a higher BOLD response was discovered in the right *hippocampus/parahippocampus* in MDD patients than in healthy subjects, as shown in figure 3.

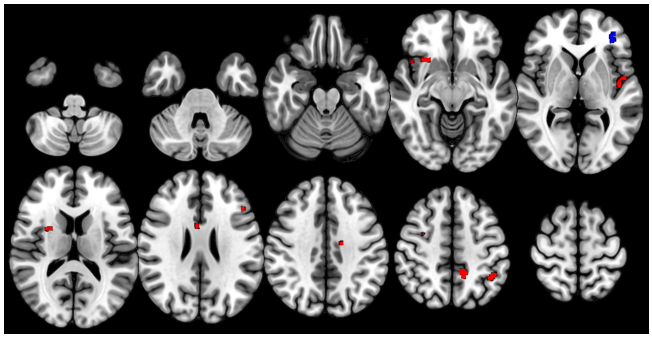


Fig. 2: LF: group-level positive (red) and negative (blue) BOLD responses.

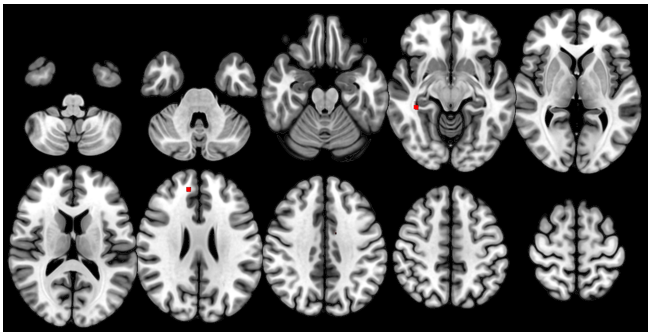


Fig. 3: LF: higher BOLD response in MDD group (red).

HF modulation induced a deactivation in the right *middle cingulate cortex*, right *lingual/precuneus/hippocampus* in the entire group at the net of age, sex and diagnosis effects, meaning that oxygenation, which is assumed to reflect neuronal activity, in these brain regions decreases in relation to an increase in vagal activity (see figure 4).
Bilateral *hippocampus*, bilateral *precuneus*, and right *parahippocampus* resulted to have a higher BOLD response associated to vagal activity variations in MDD group than in HC group, as shown in figure 5.

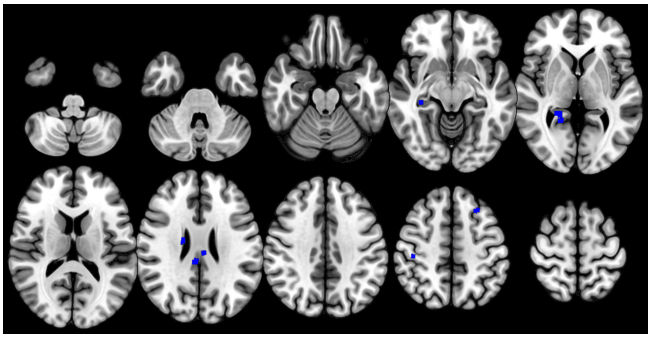


Fig. 4: HF: group-level negative (blue) BOLD response.

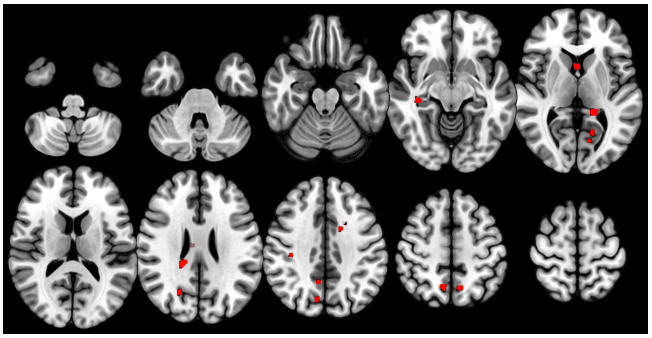


Fig. 5: HF: higher BOLD response in MDD group (red).

IV. CONCLUSIONS

In the present study, we have adopted a novel sophisticated multimodal methodological approach for the investigation of the resting state brain-heart interaction in healthy subjects and in individuals affected by adult-onset MDD.
The HRV-driven fMRI analysis allowed, using an entirely data-driven approach, to identify activation and deactivations of brain regions that have been shown to play a role within the CAN, involved in high central level autonomic processes.
Besides providing useful information on the physiology of central and peripheral nervous systems, we found alterations in their relationships in subjects affected by MDD.
The results suggest an overlap among brain circuits related to limbic, affective, cognitive, and autonomic dysregulations, supporting the idea of a common neurobiological source of multiple disease dimensions.
Further integrated HRV-fMRI analyses will provide a more comprehensive overview on the autonomic and central neural bases of MDD, bridging the gaps among its heterogeneous clinical features and allowing to characterize this disabling disorder from a new and different point of view.

ACKNOWLEDGEMENT

This study was partially funded by the Fondazione Cariplo (grant n° 2016-0908) and by the Italian Ministry of Health – Current research IRCCS 2023.

REFERENCES

[1] Thayer, J. F., & Lane, R. D. (2009). Claude Bernard and the heart-brain connection: further elaboration of a model of neurovisceral integration. Neuroscience and biobehavioral reviews, 33(2), 81–88. https://doi.org/10.1016/j.neubiorev.2008.08.004
[2] Benarroch E. E. (1993). The central autonomic network: functional organization, dysfunction, and perspective. Mayo Clinic proceedings, 68(10), 988–1001. https://doi.org/10.1016/s0025-6196(12)62272-1
[3] Sklerov, M., Dayan, E., & Browner, N. (2019). Functional neuroimaging of the central autonomic network: recent developments and clinical implications. Clinical autonomic research : official journal of the Clinical Autonomic Research Society, 29(6), 555–566. https://doi.org/10.1007/s10286-018-0577-0
[4] Heart rate variability: standards of measurement, physiological interpretation and clinical use. Task Force of the European Society of Cardiology and the North American Society of Pacing and Electrophysiology. (1996). Circulation, 93(5), 1043–1065.
[5] Koch, C., Wilhelm, M., Salzmann, S., Rief, W., & Euteneuer, F. (2019). A meta-analysis of heart rate variability in major depression. Psychological medicine, 49(12), 1948–1957. https://doi.org/10.1017/S0033291719001351
[6] Piani, M. C., Maggioni, E., Delvecchio, G., Ferro, A., Gritti, D., Pozzoli, S. M., Fontana, E., Enrico, P., Cinnante, C. M., Triulzi, F. M., Stanley, J. A., Battaglioli, E., & Brambilla, P. (2022). Sexual Dimorphism in the Brain Correlates of Adult-Onset Depression: A Pilot Structural and Functional 3T MRI Study. Frontiers in psychiatry, 12, 683912. https://doi.org/10.3389/fpsyt.2021.683912
[7] Waller, L., Erk, S., Pozzi, E., Toenders, Y. J., Haswell, C. C., Büttner, M., Thompson, P. M., Schmaal, L., Morey, R. A., Walter, H., & Veer, I. M. (2022). ENIGMA HALFpipe: Interactive, reproducible, and efficient analysis for resting-state and task-based fMRI data. Human brain mapping, 43(9), 2727–2742. https://doi.org/10.1002/hbm.25829
[8] Bianchi, A., Bontempi, B., Cerutti, S., Gianoglio, P., Comi, G., & Natali Sora, M. G. (1990). Spectral analysis of heart rate variability signal and respiration in diabetic subjects. Medical & biological engineering & computing, 28(3), 205–211. https://doi.org/10.1007/BF02442668
[9] Reali, P., Piazza, C., Tacchino, G., Songia, L., Nazzari, S., Reni, G., Frigerio, A., & Bianchi, A. M. (2021). Assessing stress variations in children during the strange situation procedure: comparison of three widely used respiratory sinus arrhythmia estimation methods. Physiological measurement, 42(8), 10.1088/1361-6579/ac18ff. https://doi.org/10.1088/1361-6579/ac18ff

Modelling cerebral blood flow and neuroreceptor occupancy in dopamine blocking studies

M. Severino[1], P. Selvaggi[2,3], M. Osugo[4,5], O. Dipasquale[2], U. Zahid[4], T. Whitehurst[5], E. Onwordi[5], B. Statton[5], T.R. Marques[4,5], R. Murray[4], M. Mehta[2], O. Howes[4,5] and M. Veronese[1,2]

1. Department of Information Engineering, University of Padua, Italy

2. Department of Neuroimaging, Institute of Psychiatry, Psychology and Neuroscience, King's College London, United Kingdom

3. Department of Basic Medical Sciences, Neuroscience and Sense Organs, University of Bari 'Aldo Moro', Bari, Italy

4. King's College London, Department of Psychosis Studies, London, United Kingdom

5. Imperial College London, MRC London Institute of Medical Sciences, London, United Kingdom

***Abstract*— As a result of neuro-vascular coupling, the functional effects of antipsychotics in human brain have been investigated using hemodynamic markers such as Cerebral Blood Flow (CBF) and Cerebral Blood Volume (CBV). However, the relationship between observed hemodynamic effects and the pharmacological action of antipsychotics has not been fully established. Here we wanted to investigate the relationship between the administered repeated dose of amisulpride, an atypical antipsychotic, and the changes in cerebral blood flow in the striatum. To investigate this relationship, we linked the plasma concentration to PET receptor occupancy and ultimately to the Arterial Spin Labelling's (ASL) CBF data from a placebo-controlled study in healthy volunteers, who received a repeated dose of amisulpride. To link the data, we developed a PK/PD framework which, starting from the dose administered, was able to predict the plasma drug concentration after a repeated dose, to predict the receptor occupancy (RO) in the targeted regions of the brain, and finally to link it with changes in cerebral blood flow in the striatum. The results showed a statistically significant monotonically increasing relationship between changes in relative to global CBF and receptor occupancies in the putamen (p-value < 0.001) and caudate regions of the brain (p-value < 0.01). These findings suggest that antipsychotics increase striatal perfusion, with a mechanism possibly mediated by D_2 receptors and represent further evidence supporting the hypothesized PK/PD model of antipsychotic effects on CBF measures founded on macaques by 'Sander et al, 2013'.**

***Keywords*—antipsychotics, amisulpride, receptor occupancy, dopamine**

I. Introduction

Antipsychotics are the preferred choice for the treatment of conditions such as schizophrenia and other psychiatric disorders with psychotic features. The main target of most of these compounds is the dopamine D_2 receptor where they act as antagonists or partial agonists [1]. The effects of antipsychotics in the brain have been investigated using different tools but their impact and mechanism of action on brain physiology is still not well understood. In this report we examine the effects of amisulpride, a second-generation antipsychotic and highly selective antagonist of dopamine D_2 and D_3 receptors [2]. Amisulpride has a dual range of applicability. At high doses (from about 400 to 600 mg/day) it is an effective neuroleptic [3] while at low doses (50–200 mg/day), amisulpride has been shown to have antidepressant properties [4]. Clinical effective doses and affinities of D_2 antagonists suggest that the antipsychotic effect arises when at least 60–70 % of these receptors is occupied by a drug of this class, whereas occupancies of more than 80% are associated with extrapyramidal side-effects [1]. The levels of striatal D_2 occupancy of amisulpride at higher doses (from 400 to 600 mg/day) are consistent with this model of antipsychotic action [5], [6]. The effect of D_2 blockade on resting perfusion levels or metabolism has been investigated in several studies, using PET and ASL [7], [8]. Results consistently show a rise of perfusion or metabolism in the basal ganglia, especially in the putamen. This effect can be attributed to an enhanced neurotransmitter turnover in the dopaminergic synapses inducing metabolic activity. However, since MRI does not measure neuronal activity directly, the neurochemical mechanisms underlying CBF changes after antipsychotics administration remain unclear. Up to date the only evidences linking hemodynamic changes induced by these drugs with dopamine receptors occupancy comes from animal literature, where a monotonic increase in regional Cerebral Blood Volume (rCBV) has been observed following injection of an increasing dose of the D_2/D_3 antagonist radiotracer [11C]raclopride in the striatum of two male rhesus macaques [9]. This result suggests that vascular responses to D_2R-like antagonists are coupled to changes in neuroreceptor occupancy.

The aim of the present work is to replicate this relation in human by developing a PK/PD framework capable to quantitively model the dose of amisulpride in plasma, the dopamine blockage (measured with PET imaging) and CBF changes (measured with MRI).

II. Materials and methods

A. Participants and study design

The data used for the current thesis were collected as part of a project organized by the Imperial College London in collaboration with King's College London, called 'Neuroreceptor regulation of brain structure and function'.

The aim of the project was to investigate the role of neuroreceptor agonism/antagonism on the brain, and it was approved by the West London & GTAC Research Ethics Committee. The experimental protocol consisted in a within-subject, cross-over, single-blinded placebo-controlled study design where healthy individuals received amisulpride or placebo. Healthy individuals were pseudo-randomized to receive the drug for a period of up to one week followed by placebo or to start with placebo and then receive the drug. A washout period of at least 10 days (or > 5 half-lives of the drug/active metabolites) was included in between interventions, in order to minimize any carry-over effects. The dose used for the study for the purpose of better tolerability was gradually raised: first day 200 mg, second day 300mg, and third to seventh day 400 mg. During the study the following assessments were made at several time-points:

- MRI (structural, MRS, ASL, fMRI) at baseline, after the first week of treatment and after the second week of treatment.
- PET [11C]-PHNO imaging at baseline and after the week of active treatment.
- Dopamine agonist/antagonist plasma levels after the first week of treatment and after the second week of treatment.
- Physical examination including weight, hip circumference, waist circumference at screening, baseline, after the first week of treatment and after the second week of treatment.

B. Pharmacokinetic analysis

In this study, sparse PK sampling was used; therefore, it was not possible to fully characterize the PK model on the basis of these data. In the literature, amisulpride PKs have been well described using a one-compartment open model with first-order absorption and elimination [10], [11]:

$$C_p(t) = \frac{Dose \cdot k_a}{V/_F \cdot (k_a - CL/_V)} \cdot \left(e^{\frac{CL}{V} t} - e^{k_a \cdot t} \right) \quad (1)$$

where Dose is the amount of drug, F the bioavailability, V/F (L) the apparent central volume, ka (1/h) the absorption rate constant, CL/V (L/h) the elimination constant rate defined as the ratio between oral clearance CL/F (L/h) and the apparent central volume. Since we had only one blood sample per subject it was not possible to directly estimate parameters for the population under study. To model the pharmacokinetic of amisulpride after a repeated dose administration we used as starting point, model parameters taken from previous studies conducted using amisulpride doses comparable with the one in our study [10], [11]. The simulation was implemented in order to model a repeated dose administration, with an oral administration every 24 hour for seven days. With a dose of 200mg for the first day, 300 mg for the second day and 400 from the third to the seventh day.

The results obtained by the simulation were compared with the measured data and those reported in literature by experiments with similar doses. The simulation was carried out using the MATLAB toolbox Simbiology®.

C. Direct Pharmacokinetic/Receptor occupancy model

The classical Hill equation was used to describe the relationship between drug plasma concentration and receptor occupancy. This equation is a direct model and assumes that free drug concentration equilibrates rapidly between the plasma, free brain, and target-bound compartments:

$$E = \frac{E_{max} \cdot C_p}{EC_{50} + C_p} \quad (2)$$

where C_p is the plasma concentration of the drug and EC_{50} the drug plasma concentration that achieves 50% of RO.
The PET RO occupancy data were available for only four subjects, so the model was firstly used to estimate the population EC_{50} parameters using the RO measured with PET and the plasma concentration at the time of PET scan. Once the model parameters were estimated, Eq. 2 was used to predict the RO for all the other subjects who did not perform the PET scans, by using measured plasma drug concentration.

D. Relationship between occupancies and CBF

Considering the ΔCBV/RO model proposed by Sander et al, 2013 [9]:

$$\Delta CBV = -N_2 \cdot B_{max,2} \cdot \vartheta(0)_{DA} \cdot \vartheta_{AM} \quad (3)$$

We tried to replicate this model but linking relative to global CBF changes (ΔCBF) to changes in receptor occupancies ($\Delta\theta$). We substituted the CBF to CBV inside the model using the relationship proposed by Grubb et al [12] which suggests a power law relationship between CBF and CBV:

$$CBV = c \cdot CBF^{\beta} \quad (4)$$

Combining Eq. 3 with Eq. 4, the final relationship between CBF changes and receptor occupancy:

$$\Delta CBF = \alpha \cdot \vartheta_{AM}^{b} \quad (5)$$

where $\alpha = \frac{-N_2 \cdot B_{max,2} \cdot \vartheta(0)_{DA}}{c}$ is a parameter that includes all the constant values inside the model of Sander, b is the inverse of the parameter β and ϑ_{AM} is the amisulpride RO.

III. Results

A. Statistical analysis

The mean drug plasma concentration was 291 ± 187 (234 ±114 *for male*, 343 ± 229 for female*)* the average age was 26

± 7.8, the average weight was 71 ± 14 kg. T-test revealed that there was no statistical difference in plasma concentration between female and male, even though female showed higher plasma concentration. Spearman rank correlation revealed that there was no statistical correlation of both weight and age with plasma concentration while it revealed a positive statistical correlation between relative CBF changes in putamen and plasma concentration ($R = 0.24$, $p\text{-value} < 0.05$) but this correlation was not significant for caudate.

B. PK/RO/CBF model

The pharmacokinetic simulation results showed that the model was able to correctly predict the kinetics of amisulpride after a repeated doses with the concentration being in line with the literature's results [13], [14], [15], [16]. Moreover, the majority of our subjects fall inside the simulated concentration curves showing that our data were in agreement with the

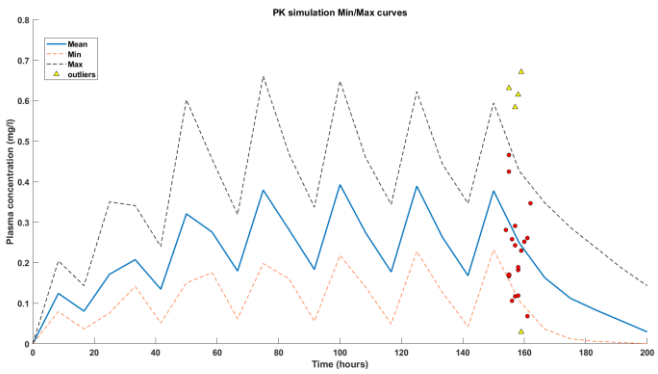


Fig. 1: Max, min and mean curves obtained with PK simulation

plasma concentration measured in previous studies (Fig.1). The subjects outside the range were considered as outliers and not considered for further analysis.

The fitting of PET RO data returned a EC_{50} value of 182.1 ng/ml for putamen and 117.7 ng/ml for caudate, both these values are in line with previous findings [5]. Given the plasma concentration of amisulpride across the subject, simulated RO ranged from 16.9 to 91.1% for caudate and from 11.6 to 86.9% for putamen. The *mean+/-SD* of amisulpride receptor occupancy was 62.3+/-17.2% for caudate and 52.9+/-17.7% for putamen and in agreement with expected D_2/D_3 occupancy of the drug with the given dosage.

Fig. 2 and Fig. 3 show the relationship between amisulpride receptor occupancies and ΔCBF changes for putamen and caudate. The models were statistically significant *(F-statistics = 19.2, p-value < 0.001)* for putamen and *(F-statistics = 8.25, p-value < 0.01)* for caudate. The exponent b of the power law model (Eq. 5) was 1.66 and 1.82 in putamen and caudate, respectively.

These results were concordant with the one founded by Sander et al on macaques [9] which returned a b = 1.7 for putamen and b = 1.4 for caudate in group 1 and b = 1.4 for putamen and b = 1.6 for caudate in group 2.

Thus, also in our case the data showed a monotonically increasing relationship between receptor occupancy and CBF changes and also in our case this relationship was regional dependent within the striatum, showing that the model better explained the putamen data compared to caudate.

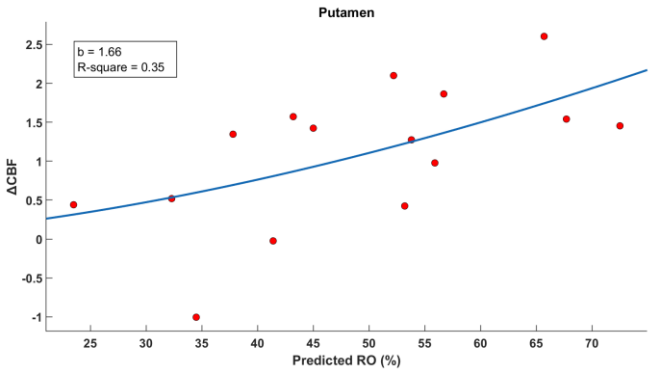


Fig. 2: ΔCBF vs amisulpride receptor occupancy for putamen, Data show a monotonically increasing relationship *(p-value < 0.001)*

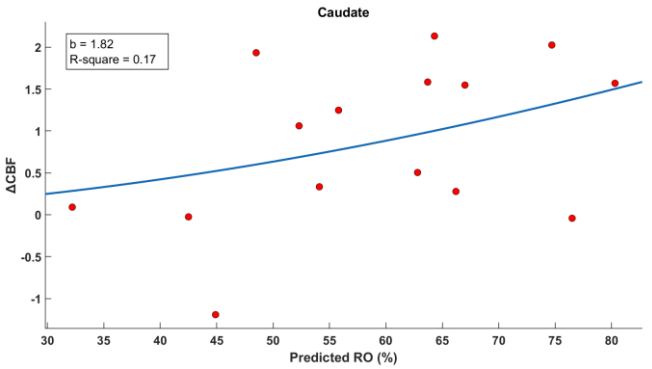


Fig. 3: ΔCBF vs amisulpride receptor occupancy for caudate, Data show a monotonically increasing relationship *(p-value < 0.01)*

IV. Discussion

In this study, we developed a PK/PD predictive framework to investigate the relationship between repeated clinical effective dose of amisulpride and cerebral blood flow of healthy volunteers in striatum. Results showed that the model accurately predicted the kinetics plasma drug concentrations after seven days of repeated administration. The ranges of concentrations obtained were in line with previous findings in literature [14], [15], [16], [17]. These results allowed us to evaluate the compliance of our subjects according to their plasma concentration data and to consider as outliers those subjects with a plasma concentration outside of the range Confounding variables such as gender, height, weight, and adverse events scores did not show a statistically significant effect on PK levels, even though mean plasma concentration of females has been reported higher than males [6]. Although it might a matter of statistical power, given the small sample.

The RO predictions obtained using the Hill equation model with the population EC_{50} parameter estimated were in line with expected value of RO given the corresponding plasma concentration [6]. The small number of PET scans limited the ability to conduct a more comprehensive analysis, such as

evaluating the relationship between the RO and dopamine receptors density distribution.

The results of the $\Delta CBF/RO$ model obtained integrating the CBF data inside the model proposed by Sander using the power law relationship between CBF and CBV, showed a monotonically increasing relationship between changes in CBF and amisulpride occupancies in caudate and putamen. The association between CBF changes induced by amisulpride and percentage of receptor occupancy matches earlier evidence in non-human primates showing large CBF increases after injection of the D_2 antagonist PET tracer [11C]raclopride in the same regions as the one investigated in this study [9]. These results suggest that the relationship between the physiological response to D_2 antagonist and D_2 availability described by 'Sander et al., 2013' in preclinical models also exists in humans.

To the best of our knowledge this is the very first time that this relationship has been detected in vivo in humans.

V. Conclusion

Understanding the link between neurochemical changes and brain function is crucial to uncover mechanisms underlying the effects of psychopharmacological treatment. In this work we investigated the case of amisulpride whose functional effect suggests a monotonic coupling relationship between neurovascular responses and dopamine D_2/D_3 occupancy in basal ganglia. We conclude that the perfusion changes in the basal ganglia uncovered by ASL under the administration of amisulpride were consistent with previous reports describing similar changes [17], [18]. This contributes into accumulating evidence that antipsychotics have similar effects on basal ganglia perfusion. However, the present findings were obtained using a combination of real and simulated data and we cannot exclude direct actions of dopamine on the vasculature that are uncoupled with neural activity. Therefore, the degree to which these non-neuronal effects contribute to the associations described here is not known.

References

[1] Farde, L., Hall, H., Pauli, S., Halldin, C., *Variability in D2-dopamine receptor density and affinity: a PET study with [11C]raclopride in man*. Synapse, 1995, 20, 200–208. https://doi.org/10.1002/syn.890200303.

[2] Perrault GH, Depoortere R, Morel E, Sanger DJ, Scatton B (1997) *Psychopharmacological profile of amisulpride: An antipsychotic drug with presynaptic D2/D3 dopamine receptor antagonist activity and limbic selectivity*. J Pharmacol Exp Ther, 1997, 280:73-120.

[3] Freeman HL (1997) *Amisulpride compared with standard neuroleptics in acute exacerbations of schizophrenia: Three efficacy studie*s. Int Clin Psychopharmacol 12(suppl 2):S11–S17.

[4] Racagni G, Canonico PL, Ravizza L, Pani L, Amore M (2004) *Consensus on the use of substituted benzamides in psychiatric patients*. Neuropsychobiology 50:134–143J.

[5] Vernaleken I, Siessmeier T, Buchholz HG, Härtter S, Hiemke C, Stoeter P, Rösch F, Bartenstein P, Gründer G (2004*) High striatal occupancy of D2-like dopamine receptors by amisulpride in the brain of patients with schizophrenia*. Int J Neuropsychopharmacol 7:421–430W.

[6] Sparshatt A, Taylor D, Paterl MX, Kapur S (2009) *Amisulpride - Dose, plasma concentration, occupancy and response: Implications for therapeutic drug monitoring*. Acta Psychiatr Scand 120:416–428.

[7] Miller DD, Rezai K, Alliger R, Andreasen NC (1997b) *The effect of antipsychotic medication on relative cerebral blood perfusion in schizophrenia: Assessment with Technetium-99 m HexamethylPropyleneamine Oxime single photon emission computer tomography*. Biol Psychiatry 41:550–559.

[8] *Handley R, Zelaya FO, Reinders AATS, Reis Marques T, Mehta MA, O'Gorman R, Alsop DC, Taylor H, Johnston A, Williams S, McGuire P, Pariante CM, Kapur S, Dazzan P (2013) Acute effects of single-dose aripiprazole and haloperidol on resting cerebral blood flow (rCBF) in the human brain. Hum Br Mapping 34:272–282*.

[9] Sander, C.Y., Hooker, J.M., Catana, C., Normandin, M.D., Alpert, N.M., Knudsen, G.M., Vanduffel, W., Rosen, B.R., Mandeville, J.B., 2013. *Neurovascular coupling to D2/D3 dopamine receptor occupancy using simultaneous PET/functional MRI*. Proc. Natl. Acad. Sci. U.S.A. 110, 11169–11174. https://doi.org/10.1073/pnas.1220512110.

[10] Huang, S., Lu Li, Xiao T., Li X., Liu S, … Shang D. (2021). *Modeling and Simulation for Individualized Therapy of Amisulpride in Chinese Patients with Schizophrenia: Focus on Interindividual Variability, Therapeutic Reference Range and the Laboratory Alert Level*. Drug Design, Development and Therapy 2021:15 3903–3913.

[11] Glatard A., Guidi M., Delacrétaz A., ... Csajka C. (2020). *Amisulpride: Real-World Evidence of Dose Adaptation and Effect on Prolactin concentrations and Body Weight Gain by Pharmacokinetics-Pharmacodynamics Analyses*, Clinical Pharmacokinetics 59:371–382.

[12] Grubb RL, Raichle ME, Eichling JO, et al. *The effects of changes in PaCO2 cerebral blood volume, blood flow, and vascular mean transit time.* Stroke 1974; 5: 630–639.

[13] Bressan R., "*Is Regionally Selective D2/D3 Dopamine Occupancy Sufficient for Atypical Antipsychotic Effect? An In Vivo Quantitative [123I]Epidepride SPET Study of Amisulpride-Treated Patients*", (Am J Psychiatry 2003; 160:1413–1420.

[14] Puech A, Fleurot O, Rein W. *Amisulpride, and atypical antipsychotic, in the treatment of acute episodes of schizophrenia: a dose-ranging study vs. haloperidol*. The Amisulpride Study Group. Acta Psychiatr Scand 1998; 98:65–72.

[15] Meisenzahl EM, Schmitt G, Grunder G et al. *Striatal D2 / D3 receptor occupancy, clinical response and side effects with amisulpride: an iodine-123-iodobenzamide SPET study*. Pharmacopsychiatry 2008; 41:169–175.

[16] Bowskill S., Patel M., Handley S., Flanagan R. (2012). *Plasma amisulpride in relation to prescribed dose, clozapine augmentation, and other factors: data from a therapeutic drug monitoring service*, 2002–2010. Hum. Psychopharmacol Clin Exp 2012; 27: 507–513.

[17] Viviani, R., Graf, H., Wiegers, M., Abler, B., 2013. *Effects of amisulpride on human resting cerebral perfusion*. Psychopharmacology 229, 95–103. https://doi.org/10.1007/s00213-013-3091-z

[18] Selvaggi, P., Hawkins, P. C. T., Dipasquale, O., Rizzo, G., Bertolino, A., Dukart, J., … Mehta, M. A. (2019). *Increased cerebral blood flow after single dose of antipsychotics in healthy volunteers depends on dopamine D2 receptor density profiles*. NeuroImage,188,774–784. doi: 10.1016/j.neuroimage.2018.12.028

Modeling Doxorubicin Treatment Effect in Multiple Myeloma

D. Andrean[1], F. Da Ros[2], M. Mazzucato[2], M.G. Pedersen[1], and R.Visentin[1]
[1] *Department of Information Engineering, University of Padova, Padova, Italy*[2]
[2] *Aviano National Cancer Institute, Aviano, Italy*

***Abstract*—Doxorubicin (DOXO) is commonly employed as chemotherapy drug to treat several kinds of cancer, including multiple myeloma (MM). Hence, a full characterization of DOXO pharmacokinetics/pharmacodynamics (PK/PD) is essential to maximize its efficacy while minimizing possible side effects. We recently proposed a mathematical model of DOXO PK in MM cells. Thus, as a natural succession, here we aim at modeling DOXO PD to describe its effects on MM cells.**

We monitored *in vitro* the MM cell proliferation in eight 2-week experiments, one under untreated conditions (control) and seven after a 3-h administration of DOXO at different concentrations (from 15 nM to 900 nM). A logistic growth and treatment response model, accounting for both cell proliferation and death rates, was developed and identified on each experiment to fit the collected cell count time series.

Results show that the proposed model is able to describe cellular growth both in untreated conditions and after DOXO treatment. We also propose a simple model to characterize the relationship between the administered DOXO amount and the corresponding drug-induced cell death rate parameter.

The proposed model is perfectly scalable to obtain a more precise descriptive implementation but also to develop a predictive framework that could lead to advancements in the current MM treatment paradigms.

***Keywords*—mathematical modeling, pharmacodynamics, in vitro, cancer.**

I. Introduction

MULTIPLE MYELOMA (MM) represents one of the most common types of blood cancer, affecting thousands of patients each year [1]. To this date it remains a treatable but not curable disease with a high death rate [2].

Chemotherapy drugs are common for tratment of MM, and, among them, Doxorubicin (DOXO) is well established and represents an effective MM therapy, often in combination with other drugs [3]. Mathematical modeling of pharmacokinetics (PK) and pharmacodynamics (PD) have proven a fundamental tool to guide new therapeutic protocols and to enlighten important phenomena regarding drug's effect [4], [5]. Moreover, coupled experimental/modelling approaches to study DOXO PK/PD have already proven useful, e.g., in breast cancer [5]. A similar approach was recently applied in MM too, with the development of a DOXO PK model [4]. To the best of our knowledge, this was the first attempt in the MM context.

In order to carry on the research in the field and to describe DOXO effects in MM cells, here we aim at modeling DOXO PD on a MM cell population.

Specifically, we start from an available model developed for breast cancer treatment [5], and properly modify it in order to describe the DOXO-induced cell death in a specific MM cell line.

II. Methods

A. Data description

Data used in the present work were collected at the Aviano National Cancer Institute, Aviano, Italy during *in vitro* experiments on MM cells.

MM1r cell lines (ATCC, http://www.atcc.or) were cultured in RPMI 1640 medium, supplemented with 10% fetal bovine serum (FBS) and penicillin/streptomycin. Cell cultures were subjected to different DOXO doses to observe the drug effect on vitality and cell growth. In particular, $5{,}6\times10^5$ cells were treated with different concentration of DOXO, i.e., 0 (control), 15, 20, 40, 50, 200, 450, 900 nM, for three hours. After 3 hours of drug exposure (t = 0 h), DOXO was removed and cells were seeded 10^4 cells/well in 96 well plate.

To monitor cell number, fluorescent CFDA-SE dye was used. In brief, cells were labeled with CFDA-SE 5 μM for 10 min and the emitted fluorescence was measured with TECAN. Fluorescence signal of each well was then converted in cell number taking advantage of a standard curve generated previously. This procedure was repeated every 24 h for 14 days.

Each experiment was repeated three times, starting on a different day of the week in order to possibly reduce the lack of measurement during the weekends, and to grant multiple samplings of the same relative time after DOXO removal (from 4 to 8).

Mean and standard deviation of cell count at each sampling time were calculated for each experiment and successively used as datapoints for model identification.

It is worth noting that, during each experiment, fresh culture media was added several times due to its consumption by the cells. This caused abnormal fluctuations and high uncertainty in some of the cell counts. An example of this phenomenon can be observed in Fig. 1 in the two measurements immediately before 300 h. Indeed, adding fresh media provided cells with a bolus of nutrients, thus likely promoting proliferation even in areas where the resource consumption was high enough to inhibit it. As such, this aspect, together with the known complex behaviors of MM cells when cultured *in vitro* [6], introduced some measurement uncertainty in time.

B. Doxorubicin response model

The PD model describing the MM cell response to DOXO administration is a simplified version of an available logistic

growth and treatment response model previously developed to describe DOXO effects on breast cancer [5].

The model assumes that the variation of cell count in time (*N*) is described by a single differential equation that includes a saturation term to account for the finite dimension of the culture well, which imposes an upper limit to the cell numerosity:

$$\frac{dN}{dt} = (k_p - k_d) * N * \left(1 - \frac{N}{\theta}\right) \quad N(0) = N_0 \qquad (1)$$

where k_p represents the proliferation rate, which determines how fast cells replicate, k_d is the drug induced death rate which models the drug effect on the population dynamics, θ is the maximum number of cells, and N_0 is the initial cell amount. The model assumes that k_p and θ are drug-independent parameters, while k_d depends on the DOXO dose.

C. Model identification

Model a priori global identifiability has been assessed using the Structural Identifiability Analyser (SIAN) software [7]. All the model parameters (k_p, k_d, θ) resulted globally identifiable since the proliferation and death rates are estimated separately.

The model of equation (1) was identified via nonlinear least squares estimator implemented in MATALB R2022a [8] using the *lsqnonlin* function.

The DOXO response model was identified on cell count datapoints, assumed affected by known standard deviation, empirically calculated from data as reported in section II-A. In particular, model parameters k_p, k_d, and θ were estimated in two separate steps.

The first step consisted in identifying the model on control experiment data (i.e., without DOXO administration). Since the proliferation rate is unaffected by the death rate in untreated conditions, only k_p and θ were estimated, while k_d was fixed to zero. Hence, the following cost function for nonlinear least squares estimation was minimized:

$$\hat{p}_{NLS} = argmin_p([y - G(p)]^T \sum_v^{-1} [y - G(p)]) \qquad (2)$$

where $p = [\theta, k_p]'$ is the parameter vector, y is the data vector containing the control experiment measures, $G(p)$ represents the model prediction and $\sum_v$ is the data covariance matrix, containing the sampled variances on the diagonal and zero elsewhere.

The second step consisted in identifying the model on treatment experiment data. In particular, a DOXO dose-dependent k_d was estimated for each treatment condition, while a unique θ was estimated by a Bayesian Maximum a Posteriori, with the statistical prior information taken from the previous θ estimated from control experiment data. Parameter k_p was fixed at the respective value estimated in the previous step. Therefore, model identification in this second phase was realized by considering the following cost function:

$$\hat{p}_{MAP} = argmin_p \Big([y - G(p)]^T \sum_v^{-1} [y - G(p)] + (p - \mu_p)^T \sum_p^{-1} (p - \mu_p) \Big) \qquad (3)$$

where $p = [\theta, k_d]'$ is the parameter vector, y is the data vector containing all the seven treatment experiment data time series, $G(p)$ represents the model prediction, $\sum_v$ is the data covariance matrix, and μ_p and $\sum_p$ are the a priori average vector and covariance matrix of model parameters.

It was observed that some experiments exhibited a cell count at time zero (N_0) unexpectedly higher than the following one at t=24 h (N_{24}). Thus, in order to improve model prediction, N_0 also was estimated in both control and treatment experiments. To note, including N_0 as additional model parameter to be estimated did not compromise a priori identifiability.

For each model identification, the estimated model parameters and the predicted cellular proliferation time course were analyzed. In addition, the model prediction 95% confidence intervals were calculated by bootstrapping data. For every experiment, each sample mean was randomly replaced by one of the single measurements used to calculate it. A new model identification was then performed on this resampled dataset. This process was repeated 500 times, for each experiment, to obtain a reliable confidence interval. It is worth noting that this procedure done in the control experiment also generated the mean and variance of the θ parameter that have been used as *a priori* information during the second-step of identification.

D. Death rate parameter fit

Model identification on different experiments led to a set of drug-induced death rate parameters k_d, one for each different DOXO concentration administered in a specific experiment.

As it will be shown in the Results section V, plotting the estimated k_d values as a function of DOXO concentrations suggests that death rate is linked to the applied drug dose following a saturation pattern. In particular, we described this relationship with a simple exponential model:

$$k_d = A * \left(1 - e^{-dose/B}\right) \qquad (4)$$

where $dose$ denotes the DOXO amount used in a specific experiment, A represents the maximum value of the death rate and B modulates the shape of the curve.

III. Results

A. Control experiment identification

Fig. 1 shows the model fit on control experiment data. In absence of DOXO treatment, the logistic model generally predicts the cellular growth well, except for the two samples before 300 h. To note, the experimental protocol required multiple refreshments of the culture media; in this regard, the immediate availability of nutrients caused the proliferation rate to increase rapidly and suddenly decrease the day after, due to the fast media consumption, thus causing the oscillation observed between 200 and 260 h.

All model parameters (θ, N_0, k_p) are estimated with good precision (Table 1), described in terms of percent coefficient of variation (CV). Interestingly, the k_p value is comparable with estimates obtained from breast cancer experiments [5].

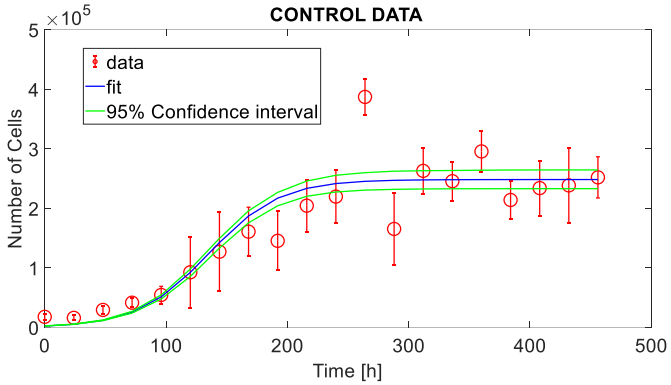


Fig. 1: Model fit on control experiment data. Cell count data are reported with red circles, with vertical bars representing the 95% confidence interval. Continuous blue line indicates model prediction, while green lines represent the 95% confidence intervals of the estimation, calculated with a bootstrap approach.

TABLE II: TREATMENT PARAMETER ESTIMATES

DOXO dose [nM]	θ [dimensionless]	N_0 [dimensionless]	k_d [h^{-1}]
15	236202 (3.99 %)	25657 (11.44%)	0.0179 (8.92%)
20	"	6355 (16.80%)	0.0208 (5.72%)
40	"	23722 (2.80%)	0.0317 (1.48%)
50	"	5726 (19.91%)	0.0330 (2.59%)
200	"	8039 (12.91%)	0.0482 (3.76%)
450	"	3684 (5.07%)	0.0479 (6.19%)
900	"	4579 (31.86%)	0.0549 (11.41%)

For each model parameter, the estimated value is provided together with its precision in terms of percent coefficient of variation (CV). Parameter θ is assumed independent from drug dose, i.e., a unique value is estimated, common to all the experiments. Parameter k_p is assumed fixed and equal to 0.0342, i.e. the estimate obtained from control experiment data.

B. *Treatment experiments identification*

Fig. 2 shows the model fit on treatment experiment data. In particular, the model is able to correctly describe the cell proliferation under DOXO treatment, also capturing the fact that any DOXO dose above 50 nM leads to a permanent stop of cellular proliferation.

Model parameters (θ, N_0, k_d) are estimated with good precision (Table 2). In particular, the estimated θ, common to all treatment experiments, is similar to the respective one obtained from control data; N_0 varies among experiments, accordingly with the respective data point at t = 0 h; k_d values are compatible with the expected saturation trend [5].

C. *Death rate model*

As shown in Fig. 3, the exponential model (4) is able to fit the k_d values estimated in the seven DOXO treatment experiments well. Model estimates suggest a maximum k_d value (i.e., parameter A) equal to 0.05 h^{-1}. The estimated parameter B is equal to 41.65 nM. Both parameters were estimated with good precision: CV(A) = 3.02%, CV(B) = 9.41%.

IV. CONCLUSION

In the present work, we aimed at modeling the effect of DOXO treatment in MM cells. Towards this end, a logistic growth and treatment response model was developed and identified on cell proliferation data of MM1r treated with seven different DOXO doses. This model proved to capture the observed dynamics well, both when the administered DOXO dose allows cell populations to regrow and when higher drug amounts lead to most of the cells dying. In particular, this was possible by accounting for a dose dependent drug induced death rate (k_d).

Some comments about the obtained results can be discussed. First, it is worth noting that the estimated k_d after administration of DOXO 50 nM resulted very close to the estimated proliferation rate (k_p). This would suggest that a cellular regrowth, even if not occurring in our experiment, may be observable for longer time periods. However, this is compatible with data coming from that of specific experiments in which some of the traces seemed to indicate cellular regrowth and some others did not. This could be also caused by instrumental errors leading to slightly different DOXO

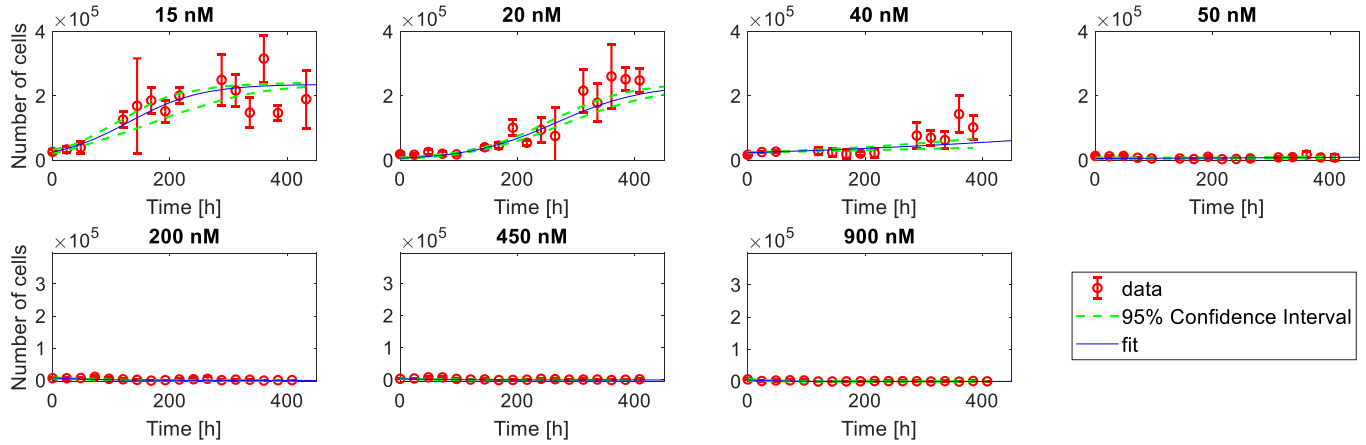


Fig. 2 Model fit on treatment experiment data obtained after administration of DOXO 15 nM, 20 nM, 40 nM, 50 nM, 200 nM, 450 nM, 900 nM. Cell count data are reported with red circles, with vertical bars representing the 95% confidence interval. Continuous blue line indicates model prediction, while green lines represent the 95% confidence intervals of the estimation, calculated with a bootstrap approach.

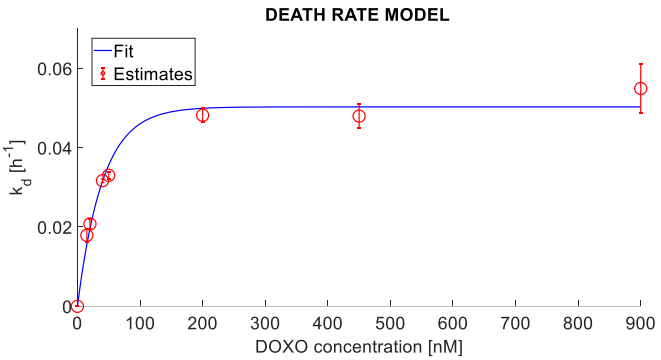


Fig. 3: Model fit describing relationship between DOXO amount and estimated cellular death rate (k_d). k_d values are plotted as red circles, with vertical bars indicating the estimated standard deviation. Continuous blue line indicates model prediction.

concentrations. In addition, we could model k_d as a function of the administered DOXO. Looking at the fitted death rate curve (Fig.3) can be enlightening; the curve around 50 nM is still steep, thus indicating that slight changes in the drug concentration may lead to sharp changes in the death rate value.

Given these considerations, longer experiments with DOXO doses around 50 nM will clarify this issue.

The k_d value estimated from experiment with DOXO 900 nM is the most uncertain and the highest among all the estimates. This is probably due to the fact that above a certain level of drug dose, cells rapidly die, and the resulting cell count remains constantly low for all the timepoints. This causes uncertainty in the death rate estimation, since, in principle, any value above saturation threshold ($A = 0.05$) grants a good fit. The same does not apply for the experiments with DOXO 200 nM and 450 nM, since cells start dying slightly later compared to what is observed during the experiment with DOXO 900 nM; higher k_d values would cause cell counts to decrease too sharply to properly fit these little delays.

It is important to underline that the present work is preliminary, and possible model refinements will be investigated in the future. In fact, the current version of the model does not account for any delay in the DOXO action, as k_d is assumed constant and always acting. This denies the ability to account for small initial fluctuations due to cellular growth followed by a gradual increase in the death rate, which causes the cell number to revert its trend and fall [5]. This behavior was noted in the experiments with the high administered DOXO, even if it was neglected since it involves low values of cell count (Fig. 2). Future works may include this feature to better describe small fluctuations.

DOXO effect fading should also be taken into consideration for future model refinements as it is likely that the drug loses its effect over time due to its half-life and dilution in the cells' nucleus after cellular replication.

These model improvements are currently under development.

In addition, in the current implementation, the maximum number of cells (θ) has been estimated from all data. However, to include the traces that remain flat at a low cell count is arguably useful, as these traces never approach the saturation values. Therefore, despite the precision of estimated θ was good, in future implementations it could be worth estimating this parameter only from saturating data and using this estimate as a fixed parameter on flat data.

It is also worth mentioning that the current experiments involved a single cell line, i.e., MM1r cells. Adding further cell lines would be greatly interesting and supportive as their pharmacodynamics could differ significantly, as already observed in other cancer types [5].

A final aspect to discuss is that cells had to be cultivated for unusual long times, requiring the administration of new culture media several times when needed, without a fixed refreshment protocol. As already mentioned, this caused fluctuations in the cell number that may or may not be synchronized among the single traces, possibly leading to refreshment-related patterns that are uninformative for the problem at hand (Fig. 1).

We chose to implement a simplified version of the model and we showed that it is nonetheless perfectly suitable to describe the evolution of cell populations for many different treatment conditions. It is to say however that our data had sensibly lower dose resolution due to the limited number of experiments if compared to other works [5].

In summary, here we proposed a simple yet effective model that summarizes the effect of DOXO with a single parameter, the drug-induced death rate (k_d) and we also propose a simple exponential law to characterize the relation between k_d and the applied DOXO dose.

ACKNOWLEDGEMENT

This work was supported by Department of Information Engineering, University of Padova, under the project SID 2020.

REFERENCES

[1] B. Sirohi and R. Powles, "Multiple myeloma," in The Lancet vol. 363, pp. 875–887, 2004, doi: 10.1016/S0140-6736(04)15736-X

[2] D. Kazandjian, "Multiple myeloma epidemiology and survival: A unique malignancy" in Seminars in Oncology, vol. 43, pp. 676-681, 2016, doi: 10.1053/j.seminoncol.2016.11.004.

[3] P.S. Becker, T.A. Gooley, D.J. Green, N. Burwick, T.Y. Kim, K. Kojouri, Y. Inoue, D.J. Moore, E. Nelli, T. Dennie, W.I. Bensinger, "A phase 2 study of bortezomib, cyclophosphamide, pegylated liposomal doxorubicin and dexamethasone for newly diagnosed multiple myeloma," in Blood Cancer Journal, vol. 6, no. e422, 2016, doi: 10.1038/bcj.2016.31.

[4] A. Giaretta, F. Da Ros, M. Mazzucato, M. G. Pedersen, R. Visentin "Modeling Pharmacokinetics of Doxorubicin in Multiple Myeloma Cells" in 43rd Annual International Conference of the IEEE Engineering in Medicine & Biology Society (EMBC), pp. 4374-4378, 2021, doi: 10.1109/EMBC46164.2021.9629493

[5] M. T. McKenna, J. A. Weis, S. L. Barnes, D. R. Tyson, M. I. Miga, V. Quaranta & T. E. Yankeelov, "A Predictive Mathematical Modeling Approach for the Study of Doxorubicin Treatment in Triple Negative Breast Cancer" in Scientific Reports, vol. 7, no. 5725, 2017, doi: 10.1038/s41598-017-05902-z

[6] Zlei M, Egert S, Wider D, Ihorst G, Wäsch R, Engelhardt M. "Characterization of in vitro growth of multiple myeloma" in Experimental Hematology, vol. 35, pp. 1550-1561, 2007, doi: 10.1016/j.exphem.2007.06.016

[7] H. Hong, A. Ovchinnikov, G. Pogudin, Chee Yap "Global Identifiability of Differential Models" in Communications on Pure and Applied Mathematics, Volume 73, Pages 1831-1879, 2020, available at https://maple.cloud/app/6509768948056064

[8] MATLAB, 9.12.0.1975300 (R2022a) Update 3, Natick, Massachusetts: The MathWorks Inc., 2022

Single region contribution to the brain dynamic (in)stability

D. Benozzo[1], G. Baron[1], G. Baggio[1], A. Gozzi[2], M. Corbetta[3,4], A. Chiuso[1], S. Zampieri[1], and A. Bertoldo[1,3]
[1] *Department of Information Engineering, University of Padova, Padova, Italy*
[2] *Functional Neuroimaging Laboratory, Center for Neuroscience and Cognitive Systems UniTn, Istituto Italiano di Tecnologia, Rovereto, Italy*
[3] *Padova Neuroscience Center, Padova, Italy*
[4] *Department of Neuroscience, University of Padova, Padova, Italy*

***Abstract*—An open question in neuroscience regards the origin of the flexible and heterogeneous spatio-temporal patterns of neural correlations assessed with fMRI. Model-based approaches are commonly used to shed light on this problem with the aim to reproduce the same dynamical richness observed in the empirical recordings. In particular, dynamic causal models are generative top-down models commonly used in this field based on a state-space representation where the state refers to the hidden neural dynamic. The corresponding state matrix is the so-called effective connectivity that is interpreted as a representation of the causal interactions between each ordered brain region pair. By looking at the effective connectivity in the context of linear system theory, we can derive a rich characterization of the dynamics of the system. In this work we propose a method for studying how each brain region participate in defining the global stability of the system and its application to both mouse and human resting-state fMRI datasets. In detail, this analysis is based on a decomposition of the state matrix into two components: a dissipative symmetric gradient flow, and a solenoidal component which accounts for the asymmetric, i.e. directional, coupling. By acting on the solenoidal part, we can simulate the segregation of a single region and evaluate its effect on the eigenvalues of the state matrix, specifically those related to the slower dynamics.**

***Keywords*—Dynamic causal modelling, resting-state fMRI, asymmetric coupling, stability**

I. INTRODUCTION

In the last decades, network science has changed the way neuroscience looks at the brain. Much more attention has been paid to how brain units interact with each other rather than their isolated behavior. This has been possible due to technological advancements in the mapping and recording of large-scale neuronal system, on one side. And on the other, by the need of understanding two fundamental neuroscience principles: the brain functional integration and segregation. One way to pursue this goal is through a model-based (mechanistic) approach, and specifically top-down models are the most suitable for this type of studies at the macroscale level. They aim to solve the inverse problem, thus searching for the model parameters that better explain the empirical data. There are two main groups of top-down models: the brain network models (BNMs) and the dynamic causal models (DCMs). BNMs rely on the idea of placing local neural models on top of the structural connectivity (SC) which encodes (symmetric) anatomical information [1]. While DCMs are generative top-down models that characterize the dynamics of the system by fitting a state-space model: the state represents the hidden neural activity and the state matrix is the so-called effective connectivity (EC) [2]. Given a brain region, the related row of the EC matrix tells how the whole network participates in modelling its dynamics. In case of no a priori constraints, EC is an asymmetric matrix, thus it encodes directional information that are commonly interpreted as the causal interactions between each ordered brain region pair. Moreover, since DCM is defined as a state-space model, EC can be seen as its Jacobian matrix. This means that we can take advantage of the linear system theory to provide a detailed characterization of the temporal brain dynamics.

These motivated our choice to focus on DCMs for studying the dynamical richness that we observe in the empirical brain recordings. Recently, variants of DCM have been proposed to be applied on resting-state whole-brain fMRI data [3]–[5], showing the possibility of overcoming some limitations: the scalability to whole-brain data and the original task-based implementation that prevented its application to resting-state data. Here, we propose a method for studying how each brain region participates in defining the global stability of the system and show its application in both mouse and human resting-state fMRI datasets. Stability and closeness to instability boundary are topics that are supported by a rich literature in the field of neuroscience. In particular, it has been shown that a metastable regime is the optimal one to reproduce brain dynamics [6] and that the intrinsic brain timescales are mainly defined by the real and imaginary parts of the slower eigenmodes, i.e. the closer to the vertical axis, [7].

II. MATERIALS AND METHODS

We applied a recently developed method for estimating whole-brain effective connectivity (sparse DCM, [5]) to resting-state fMRI BOLD recorded from the following mouse and human datasets. Concerning mouse data, BOLD time series were acquired using functional echo-planar imaging (TR/TE=1000/15 ms, 2.3x2.3 cm, 1920 volumes) [8]. rs-fMRI preprocessing steps were carried out including motion correction, volume despiking, temporal filtering (0.01-0.1 Hz) and spatial registration to a common anatomical reference template (74 ROIs, 37+37). Concerning human data, resting-state fMRI scans (TR=1.400 ms, TE=39.4 ms, flip

angle=69°, FOV=202x202 mm, voxel size=2.3x2.3x.2.3 mm, volumes=657, MBAccFactor=4) of 107 healthy subjects (age range: 20-40 yo) were retrieved from the publicly available MPI-Leipzig Mind-Brain-Body dataset [9]. We extracted subject-level time series data from a 100-area parcellation scheme of the cortex provided by the Schaefer atlas [10], which maps to 7 resting-state functional networks. We also defined a set of 12 subcortical and cerebellar regions based on the AAL3 segmentation [11]: for each hemisphere, 6 regions consisting of thalamus, caudate, putamen, pallidum, hippocampus and cerebellum. The temporal traces were motion-corrected, volume-despiked and band-pass filtered in the same frequency range employed for murine data. In addition, a consensus clustering procedure was also applied to reduce the number of cortical parcels [12]. The resulting clustering procedure provided 62 cortical clusters, from which demeaned fMRI time courses were extracted and supplied as inputs to sparse DCM together with the BOLD signals from subcortical nodes. It follows that the application of DCM resulted in the estimation of the EC between 74 ROIs (referring to 62 cortical and 12 subcortical parcels) at the individual level.

Regarding sparse DCM, it incorporates a prior that induces sparsity in the EC estimation and a statistical linearization of the HRF model to address the high-dimensional solution space. In terms of dynamical systems, the EC matrix represents the state matrix of a linear state-space model, where the state component, solution of a linear differential equation, represents the neural response, whereas the output a transformation from the neural activity to the BOLD signal through the haemodynamic function. Importantly, EC can be decomposed such that:

$$EC = \left(-\frac{\sigma^2}{2}I + S\right)\Sigma^{-1} \tag{1}$$

where σ^2 is the variance of each brain endogenous fluctuation, assumed to be the same across regions, Σ is the covariance matrix of the state (i.e. the functional connectivity matrix), and $S = -S^\top$ is a skew-symmetric matrix. S embodies the asymmetric part of EC and allows the interpretation of its entries as directed causal interactions. Eq.1 parametrizes all EC matrices that give the same Σ, i.e. the covariance matrix of the state, for any S. Thanks to this parametrization, the symmetric and asymmetric parts of EC are disentangled, so we can separately intervene on them. For example, by deleting or enhancing some entries of S we can manipulate the pattern of causal interactions and then derive the related EC that ensures the same functional pattern. Following the terminology in [7], $\frac{-\sigma^2}{2}I\Sigma^{-1}$ is the (symmetric) dissipative gradient flow determined by the real eigenvalues of the system, while $S\Sigma^{-1}$ is the non-dissipative solenoidal flow defined by the complex eigenvalues which are responsible for the sinusoidal component.

III. RESULTS

On each mouse and human rs-fMRI data, we applied sparse DCM and decomposed the related EC in S and Σ. Fig.1a shows a scatter plot of the imaginary vs. real eigenvalues of each single-subject EC of the mouse dataset (the color identifies the subject). Each dot represents a mode of the system. All modes are stable by construction, meaning that the real part is negative. Concerning the imaginary part it can be either zero, i.e. real mode with exponential decay, or not, i.e. exponentially damped oscillatory mode. For each subject, the complex mode with the highest imaginary part and its conjugate are marked with a square, i.e. mode of the principal frequency. In general, these modes are not the dominant ones, i.e. the closest to the stability boundary, but they become so if we globally increase the contribution of S in Eq.1. Note that the frequencies of these oscillatory modes are very slow, about 0.03 Hz. These are the so-called ultra-slow frequencies, a key feature of the resting-state fMRI [13]. Fig.1b shows the modes for each subject computed by replacing S with αS in Eq.1 (α=100 in Fig.1b), thus α is a global scaling factor that tunes the strength of the asymmetric component. By increasing α, all modes tend to vertically align to a unique real value, except for the ones with highest imaginary parts which are the least sensitive to changes in α. For a representative mouse, Fig.2a shows the effect on the system stability of isolating each node by setting to 0 its column and row in S. In particular, it shows the real part of the complex eigenvalue with the maximum imaginary part. The horizontal straight line refers to the corresponding value in the original EC, i.e. with no intervention on S, and square markers highlight the regions that strongly affect the system stability by reducing the real part of the principal frequency mode, i.e. by making its decay faster. Similarly, in Fig.2b the regions that are most responsible for the stability regime of the system are shown for each mouse. Fig.2c shows the global results across mice, in particular it reports the frequency histogram for each brain region and it highlights those that have been selected in more than 50% of mice. Similarly, Fig.3 shows the rate of selection computed on the human dataset.

IV. DISCUSSION

In the present study, we have analyzed how the pattern of directed causal links exhibited by each brain region contributes to the global stability of the system. In particular, through the proposed factorization of the EC matrix, we can simulate the segregation of a given node from the rest, while preserving its own endogenous activity and its similarity, i.e. function connectivity, with the rest of the network. Across mice and coherently between hemispheres, the secondary motor area (MOs), the primary somatosensory area (SSp), the anterior cingulate area (ACA) and part of the retrosplenial area (RSP) have shown to play an important role in keeping the system closer to the stability boundary, i.e. a condition that can be associated with a metastable regime, thus the optimal regime to emulate the brain dynamics [14]. From their structural properties, they have all been characterized as hubs in [15]. Regarding human subjects, lower-order regions (i.e., visual and somatosensory-motor) seem to be the most involved in determining system metastability. Interestingly, these parcels include regions that are usually implicated in auditory and

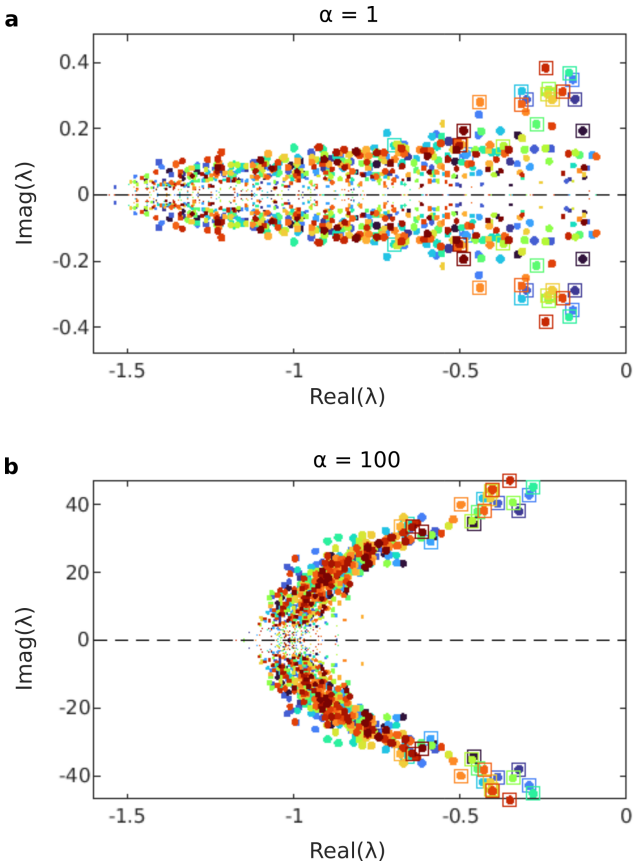


Fig. 1: Scatter plot of the imaginary vs. real eigenvalues of each single-subject EC of the mouse dataset. Each dot represents a mode of the system. **a**: modes of each EC. **b**: modes computed by replacing S with αS, α is a global scaling factor that tunes the strength of the asymmetric component.

motor-hand processing, which may be involved in the integration of information over different timescales performed by the dynamical core of the brain [14]. In addition, over-threshold visual ROIs are peripheral parcels in the visual system [16] that incorporate a fraction of the superior parietal lobule, which plays an important role in attention tasks [17]. On the other hand, attentive areas (referring to dorsal and salience ventral attention networks) and some right control ROIs are the highest-level cognitive nodes to unveil significant stability properties. These regions are mainly devoted to cognitive control and novel problem solving, whose high metastability was shown to be predictive of task-based reasoning [18]. Regarding subcortical nodes, cerebellar parcels play a key crucial role in the definition of network metastability. This is consistent with previous studies suggesting that cerebellum has an important synchronization effect across motor and cognitive tasks [19].

Acknowledgement

This research was supported by the DEI Proactive grant "Personalized whole brain models for neuroscience: inference and validation" of the Department of Information Engineering of the University of Padova.

References

[1] G. Deco, V. K. Jirsa, P. A. Robinson, M. Breakspear, and K. Friston, "The dynamic brain: from spiking neurons to neural masses and cortical fields," *PLoS computational biology*, vol. 4, 2008.
[2] K. J. Friston, L. Harrison, and W. Penny, "Dynamic causal modelling.," *NeuroImage*, vol. 19, pp. 1273–1302, 8 2003.
[3] A. Razi, M. L. Seghier, Y. Zhou, P. McColgan, P. Zeidman, *et al.*, "Large-scale dcms for resting-state fmri," *Network neuroscience (Cambridge, Mass.)*, vol. 1, pp. 222–241, 1 2017.
[4] S. Frässle, S. J. Harrison, J. Heinzle, B. A. Clementz, C. A. Tamminga, *et al.*, "Regression dynamic causal modeling for resting-state fmri," *Human brain mapping*, vol. 42, pp. 2159–2180, 5 2021.
[5] G. Prando, M. Zorzi, A. Bertoldo, M. Corbetta, M. Zorzi, and A. Chiuso, "Sparse dcm for whole-brain effective connectivity from resting-state fmri data," *NeuroImage*, vol. 208, 2020.
[6] G. Deco and M. L. Kringelbach, "Metastability and coherence: Extending the communication through coherence hypothesis using a whole-brain computational perspective," *Trends in Neurosciences*, vol. 39, pp. 125–135, 3 2016.
[7] K. J. Friston, E. D. Fagerholm, T. S. Zarghami, T. Parr, I. Hipólito, *et al.*, "Parcels and particles: Markov blankets in the brain," *Network Neuroscience*, vol. 5, pp. 211–251, 2 2021.
[8] D. Gutierrez-Barragan, M. A. Basson, S. Panzeri, and A. Gozzi, "Infraslow state fluctuations govern spontaneous fmri network dynamics," *Current Biology*, vol. 29, 2019.
[9] A. Babayan, M. Erbey, D. Kumral, J. D. Reinelt, A. M. Reiter, *et al.*, "A mind-brain-body dataset of mri, eeg, cognition, emotion, and peripheral physiology in young and old adults," *Scientific Data 2019 6:1*, vol. 6, pp. 1–21, 2 2019.
[10] A. Schaefer, R. Kong, E. M. Gordon, T. O. Laumann, X.-N. Zuo, *et al.*, "Local-global parcellation of the human cerebral cortex from intrinsic functional connectivity mri," *Cerebral Cortex*, vol. 28, pp. 3095–3114, 9 2018.
[11] E. T. Rolls, C. C. Huang, C. P. Lin, J. Feng, and M. Joliot, "Automated anatomical labelling atlas 3," *NeuroImage*, vol. 206, 2 2020.
[12] S. Ryali, T. Chen, A. Padmanabhan, W. Cai, and V. Menon, "Development and validation of consensus clustering-based framework for brain segmentation using resting fmri," *Journal of neuroscience methods*, vol. 240, pp. 128–140, 1 2015.
[13] R. Liégeois, J. Li, R. Kong, C. Orban, D. V. D. Ville, *et al.*, "Resting brain dynamics at different timescales capture distinct aspects of human behavior," *Nature Communications 2019 10:1*, vol. 10, pp. 1–9, 5 2019.
[14] G. Deco, M. L. Kringelbach, V. K. Jirsa, and P. Ritter, "The dynamics of resting fluctuations in the brain: metastability and its dynamical cortical core," *Scientific Reports 2017 7:1*, vol. 7, pp. 1–14, 6 2017.
[15] L. Coletta, M. Pagani, J. D. Whitesell, J. A. Harris, B. Bernhardt, and A. Gozzi, "Network structure of the mouse brain connectome with voxel resolution," *Science advances*, vol. 6, 12 2020.
[16] P. beim Graben, A. Jimenez-Marin, I. Diez, J. M. Cortes, M. Desroches, and S. Rodrigues, "Metastable resting state brain dynamics," *Frontiers in computational neuroscience*, vol. 13, 9 2019.
[17] A. Lanssens, G. Pizzamiglio, D. Mantini, and C. R. Gillebert, "Role of the dorsal attention network in distracter suppression based on features," *Cognitive neuroscience*, vol. 11, pp. 37–46, 4 2020.
[18] T. H. Alderson, A. L. Bokde, J. A. Kelso, L. Maguire, and D. Coyle, "Metastable neural dynamics underlies cognitive performance across multiple behavioural paradigms," *Human Brain Mapping*, vol. 41, pp. 3212–3234, 8 2020.
[19] F. Hancock, J. Cabral, A. I. Luppi, F. E. Rosas, P. A. Mediano, *et al.*, "Metastability, fractal scaling, and synergistic information processing: What phase relationships reveal about intrinsic brain activity," *NeuroImage*, vol. 259, 10 2022.

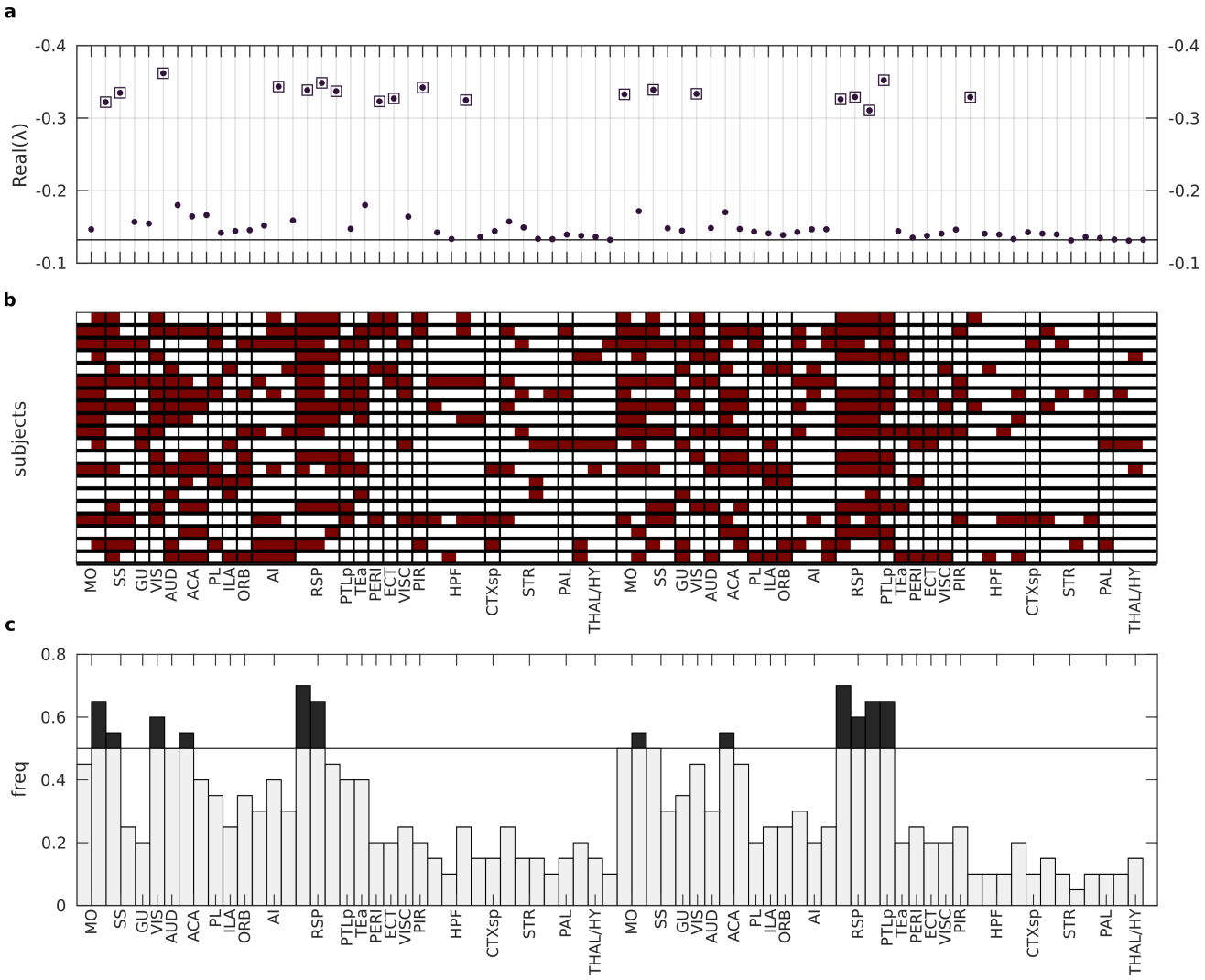


Fig. 2: How each brain regions contributes to defining the stability regime at the single-mouse level. **a**: for a representative mouse, the effect on the system stability of segregating each node by changing S. More specifically, it shows how the real part of the largest complex eigenvalue changes compared to the non-intervention case (horizontal straight line); square markers highlight the regions that strongly affected the system stability. **b**: as in **a** for each subject of the mouse dataset. **c**: selection rate across mice of each region to highlight those selected in more than 50% of subjects.

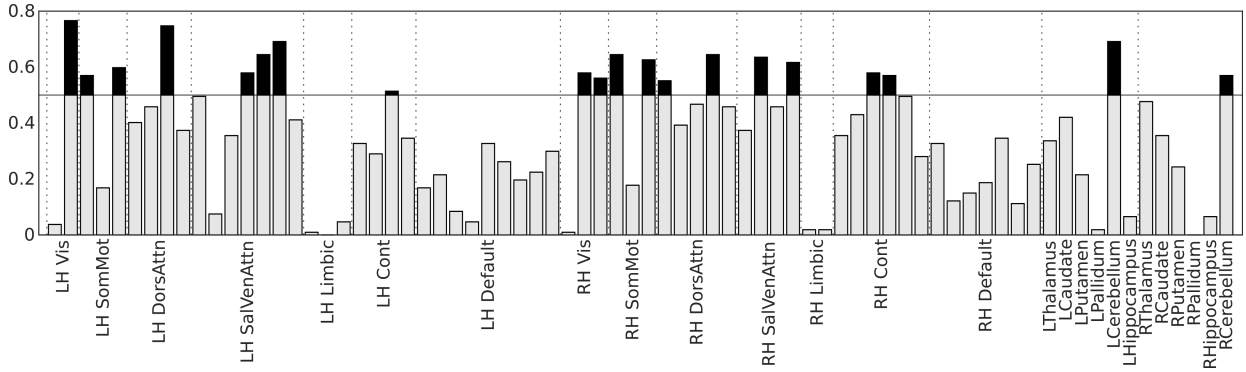


Fig. 3: Similarly to Fig.2c, the selection rate across human subjects of each region to highlight those selected in more than 50% of subjects.

A multiscale computational approach to replicate the full-scale mouse *striatum* model

A. Antonietti[1], P. Furquim Daud[1,2], and A. Pedrocchi[1]
[1] *Nearlab, Department of Electronics, Information and Bioengineering, Politecnico di Milano, Milano, Italy*
[2] *Artefact, São Paulo, Brazil*

***Abstract*—The present work aims to reproduce and replicate the results of a prominent study in the computational neuroscience field. The objectives of this reproduction are verifying the original claims and results and assessing the research's degree of replicability. In the original study, the authors presented a detailed neural network model of the *striatum*, a nucleus in the subcortical basal ganglia of the forebrain. The methodology employed for the replication focuses on two scopes: the influence of network size and model complexity on the observed dynamics in the neural circuit. Different combinations of scale and complexity reduction have been performed and compared. The results show similar qualitative behavior, considering the limitations and simplifications adopted. Reducing the size primarily impacted the overall network mean activity and firing rates while simplifying the single-neuron models affected the network responses to cortico-thalamic inputs. Lastly, some recommendations are made for future works: improvements that can be implemented on the replicated models and evaluation and feedback on the documentation and accessibility of the original research.**

***Keywords*—Computational neuroscience, replicability, neural circuits, basal ganglia**

I. Introduction

One of the most important keystones in science is the idea of researchers being able to reproduce each other's experiments in order to assess the results and further study the same subjects. Based on this idea, the description of methodology in reports became extremely important, given that the level of detail and instructions should be enough so that other scientists could follow the published steps and obtain the same results as the original authors.

In this work, we have adopted the Association for Computing Machinery definitions of reproducibility and replicability: Reproducibility (different team, same experimental setup), for computational experiments, this means that an independent group can obtain the same results using the author's own artifacts; Replicability (different team, different experimental setup), this means that an independent group can obtain the same results using artifacts that they develop independently [1].

The computerization of scientific research brought new challenges to the ability to replicate and reproduce research findings. Other study formats, which have been established for a longer time, already have a good consensus about how the methodology should be shared in order to allow verification. However, it seems that the computational science fields are still working towards discovering how to publish a work's methodology to guarantee that it can be reproduced [2].

While publishing the related code is already a good starting point [3] to increase the research's transparency, it still does not guarantee that it is replicable. Over 70% of the researchers who participated in a survey [4] have tried and failed to reproduce a peer's work. From this same source, there's an even more striking result that over half of the surveyed scientists have already failed to reproduce their own research at some point.

The aim of the present work is to reproduce and replicate a prominent study of the computational neuroscience field. In this effort, the objective can be divided into two main parts: firstly, achieving the reproduction in itself - and therefore aiming to validate and increase the reliability and robustness of the original work. Secondly, assessing the replicability of the original research with a reductionist approach, testing to which degree network size and model complexity contribute to the model's behavior.

II. The original study

Hjorth and colleagues have reconstructed a full-scale model of the mouse *striatum* at a cellular level [5]. The population of the network matches the real-life physiological system and the level of detail is very high, giving each cell its fully complex behavioral model.

While the simulation results are already very interesting alone, another main appeal that made this work a good candidate for the replicability process presented here is the fact that the authors developed a tool to assist this task. Moreover, this software tool was designed in the format of an easy-to-use platform, which can then be adopted by other scientists in the community.

The methodology employed in the research can be structured into multiple steps that can be managed using software developed by the authors called *Snudda*, a tool that facilitates the modeling phase of neural networks. The user specifies the desired configurations of the network through a series of JSON files, which are read by the framework to result in the final model.

According to the network size specified, each cell is instantiated with its respective model. Analyzing the generated circuit, it is possible to attest that the overall neuron type distribution agrees with the data available in the literature. Spiny Projection Neurons (the direct and indirect pathways, dSPN and iSPN) make up about 95% of the *striatum* population, and this percentage is equally divided amongst them. The remaining

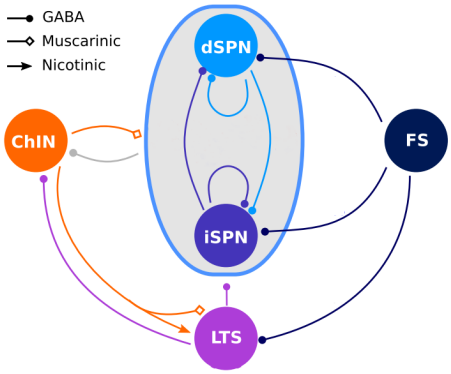


Fig. 1: Schematic connectivity within the dorsal *striatum* involving dSPN, iSPN, FS, LTS, and ChIN. Different arrows show the connectivity with GABAergic (inhibitory) connections and cholinergic ones (muscarinic and nicotinic). Adapted from [5]

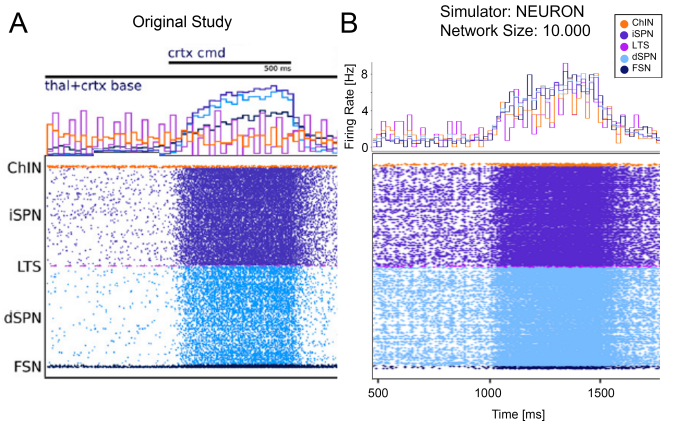


Fig. 2: Raster plots (lower panels) and firing rates (upper panels) from the original article [5] and the reproduction with our simulation (NEURON, 10'000 neurons network). *thal+crtx base* indicates the baseline thalamic and cortical input, while *crtx cmd* indicates the command signal from the cortex. The bin size of firing rates was set to 20 ms, as in [5]. Note that the vertical scale was not indicated for the firing rates of the original article.

5% are interneurons. The network only includes models of the three most frequent interneurons of the *striatum*: Low-Threshold Spiking (LTS), Cholinergic Interneurons (ChIN), and Fast Spiking Neurons (FSN). They represent, respectively, 1.3%, 1.1%, and 0.8% of the total neuronal population.

Each generated cell has a set of coordinates, indicating its position on the network. This information is fed into a touch-detection algorithm that signalizes any time there is enough proximity between two neurons. Combining the aforementioned values with the prescribed rules for synaptic connections, a realistic connection probability is set for each case, which can finally be used to obtain the connected network (Fig. 1).

Finally, with both the network model ready and the extrinsic input signals generated, the network is simulated with NEURON, a widely used simulator for biophysical neuron models [6].

III. Reproducibility and Replicability Studies

In this work, we not only attempted to reproduce the selected research but also to add insight and novelty by changing some aspects of it and analyzing the repercussions. Evidently, the original simulation involves many independent variables, which interact amongst themselves, contributing to the model, and assessing the impact of all of them would be infeasible.

Hence, two main scopes were chosen to be evaluated: the influence of network size and model complexity. Both of these aspects largely influence the computational power that a simulation demands, which in turn can determine whether it is feasible to replicate it. Consequently, the aforementioned dimensions were deemed interesting focuses for the framework.

Network size influence was assessed by generating three network structures of varying population numbers. In order to produce different enough structures, starting from the size of 10'000 neurons used in the original simulation, two reductions of one order of magnitude each were applied, resulting in additional neural networks of sizes 1'000 and 100 neurons.

The simplification of the model is implemented through a simulation tool change. While the *Snudda* software relies on the NEURON simulator, the simpler adaptation presented in this work was set on the NEST simulator for spiking neural networks that use point-neuron models such as leaky integrate-and-fire [7], [8].

The work can be therefore separated into three parts:

1) **Original study reproduction**. Using the 10'000 neuron network simulated with NEURON;
2) **Network size comparisons**. Studying how the network size (10'000 vs. 1'000 vs. 100 neurons) influences the output. All simulations were performed in NEURON.
3) **Model complexity comparison**. Studying how the simplification of neuron and synapse models, passing from biophysical multicompartmental (NEURON) to point-neuron (NEST) models, impacts the output. All simulations were performed with the 10'000 neurons network.

IV. Original Study Reproduction

With minor adaptations to the codes provided by the original paper's authors, we successfully generated and simulated through *Snudda* the 10'000 neuron network with NEURON. The network is driven by cortical and thalamic input. The two inputs represent 1) baseline activation of cortical and thalamic input from the beginning of the experiment and 2) a cortical command signal, starting at 1000 ms, during which the cortical activation is increased for 500 ms (given to all cells except the ChINs). We could therefore compare the simulation's output in terms of spikes patterns and the computation of firing rates for each population of neurons. Figure 2 shows that firing patterns and firing rates, divided per neuron type, are qualitatively similar to the original results.

There was a clear limitation due to the lack of information about the input that was used in the article's simulation.

Furthermore, the information shared about the inputs was primarily qualitative. Therefore, although it was clear that the sources of input spikes were the same as the ones provided in the example (Cortex and Thalamus), there was no confirmation that the frequencies of these spikes were the same as the ones observed in the original experiment. Furthermore, the authors deployed dopamine modulation for 300 ms in the original article. Unfortunately, this option was not available in the code provided to the public at the time of this project. Therefore, that part of the original results had no means of being reproduced. Another barrier that adds a challenge to the proper comparison of results is the absence of firing rate values. The original work features a figure with the firing rates for each cell type, but a scale is not present. For this reason, we focussed mainly on a visual analysis of the scatter plot and the qualitative aspects of the network's behavior.

Considering all these concerns, many relevant comparative results remain to be analyzed. Overall, the network's dynamic behavior is similar to the original simulation, most evidently in response to the addition of the cortex command. Even though the replication's projection neurons seem to have a higher basal activity level, the relative increase in the firing rates seems comparable to the one observed in Fig. 2A.

The opposite phenomenon can be detected in the FSNs' behavior. In the reproduction, this population has a lower basal activity rate. Nonetheless, the increase in firing with the cortical command is still present and considerably similar.

A notable distinction lies in the other interneurons' activity levels. In the original simulation, ChIN and LTS cells show a very constant and rhythmic firing rate pattern that suffers almost no alteration with the deployment of the cortical command. The replication results, on the other hand, exhibit different behavior. There is still a cyclic component to their dynamic, but the additional cortical input interferes with it, increasing the cells' activities.

A hypothesis for this discrepancy lies in one of the aforementioned limitations. Since the exact input configurations used on the original simulation are not available, it is speculated that it might be different from the one generated in the script made available for testing. One simple cause could be just that the frequency or weight of the inputs are not the same value. Another possibility is the existence of constant current injections in the original simulation, which might explain the interneurons' indifference toward the increase in input spikes. Unfortunately, we could not test this hypothesis because of the lack of data from the original paper and from the shared repository, too.

V. Network size comparisons

Having completed the first step, the reproduction of the original work, we continue our replication study by exploring variations in the striatal model. Using the same methodologies used for the 10'000 network, we have generated two smaller versions, with 1'000 and 100 neurons, respectively. It becomes evident in Fig. 3 that the reduction in network size interferes with the scale of the computed firing rates. Therefore, here we represent the firing rate plots both separately and together to allow better data visibility.

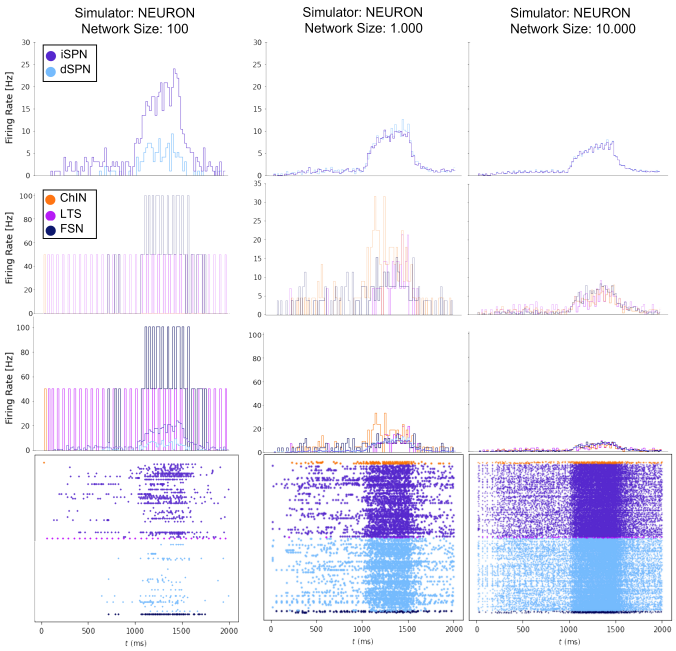


Fig. 3: Raster plots and firing rates of NEURON simulations with three network sizes: 100, 1'000, and 10'000 neurons. The first two rows show the firing rates of dSPN and iSPN (first row) and the other interneurons, i.e., ChIN, LTS, and FSN (second row), separately. The third row shows all the firing rates combined together.

The primary consideration to be made in this analysis regards the activity of the interneurons. The scale reduction of the network has a more significant effect on the interneurons since they represent a small percentage of striatal cells. This provokes a distortion in their behavior, which is most prominent in the firing rate values for the smaller network simulation. Furthermore, since the 100 neurons network has only one single interneuron of each type, the possible values of their firing rates are binary.

A phenomenon revealed by comparing neuronal firing rates is the consistency in the LTS firing rate. While the activity of the ChIN neuron is extinct in the 100 neurons network, and the FSN also suffers a reduction, the low threshold neuron continues to spike rhythmically.

Another interesting observation is the difference in the iSPN and dSPN behaviors under the cortical control signal. Observing the top row of Fig. 3, it is clear that the leftmost column has an increase in iSPN activity about 2 to 4 times higher than the dSPN. This discrepancy is only present on the smallest scale. In contrast, the middle and large-scale networks have a seemingly balanced response from the two projection neuron populations. This result suggests that the size reduction potentially caused too big of a change to the model, which in turn lost some of its dynamic properties.

On the other hand, the outline of the firing rate curves for the projection neurons on the 1'000 neuron network and the 10'000 neuron network are very similar. Both the rise and fall

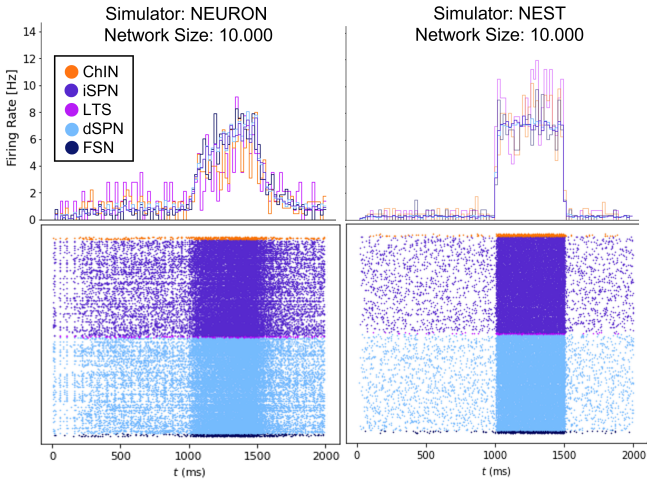


Fig. 4: Raster plots and firing rates of NEURON and NEST simulations of the 10'000 neurons network model.

patterns match really well, signaling that some fundamental characteristics were maintained with this change.

VI. Model complexity comparison

This section presents the results of the simulation obtained on NEST against the NEURON benchmark, using the 10'000 neurons network.

The results of the simulator change and model simplification have considerably good performance (Fig. 4), especially considering how simple the NEST model is. Furthermore, the observed range of firing rate values is almost the same as the NEURON benchmark, with peak values for the projection neurons reaching about 8 Hz.

One of the main divergences between the two simulations is the rise and decay behavior, which is much steeper in all cell types on NEST. This occurrence can be traced back to the fact that the neuronal models used on the simpler model, a leaky integrate-and-fire, have no active mechanisms. Therefore they purely respond to the input they are given, with no damping, attenuation, or other altering effects. Also, the synapse model is the same for every source and target combination, with only a change in the weight, but all with a fixed delay of 1 ms. Thus, all transmissions respond instantly to the input variations without any added gap in their transmissions. Both these factors can contribute to the almost immediate step-like change in the firing rates.

Lastly, there is a bigger contrast between the low firing rate values and the high ones. Simply put, the basal activity is somewhat lower for all the cell types, while the excited state is also slightly higher than the benchmark.

As previously discussed, the verification that a simpler model can generate consistent results is very compelling. The main advantage is that it allows for easier creation of similar work whenever the research objectives allow a more generalized overview of the results. Indeed, the simpler model cannot capture the dynamic nuances of each neuron, a task that is feasible with the complex biophysical model simulated in NEURON. But at the same time, this different approach admits more accessibility to the simulation by loosening the necessity of heavy computational power availability.

Another scenario where this framework can greatly benefit is on initial exploration steps of a research project. In hindsight, the work presented here actually used a similar tactic to allow faster testing. The learning process was facilitated by starting on a smaller scale since the temporal cost of trial-and-errors was minimized. The same logic can be applied when speaking of model complexity: before executing time-consuming and computational power-demanding simulations, it can be advantageous to perform simpler versions. Consequently, primary trials about configuration setting and parameter tuning are much quicker.

VII. Conclusion

In summary, there are two main conclusions about the work conducted in this project. The first one highlights the essential role in documenting and making available as much as possible the code, data, and software used in one's research. It becomes clear that this was, in different moments of this work, both the factor driving its feasibility and the one limiting and hindering the reproduction. Thus, it is fair to say that the thorough sharing of all that relates to a research's methodology is a decisive factor in its replicability and, by extension, its reliability. For this reason, we made publicly available all the codes and detailed descriptions of software versions and requirements to replicate our work at https://github.com/alberto-antonietti/BasalGanglia.

The second conclusion speaks of the intensive work and particular challenges that replication researches entail. Fully comprehending another author's work is extremely time-consuming, but at the same time, it fuels ideas for how to build on what was published and test new hypotheses. This is especially true in computational neuroscience, where models have endless applications and can be used to explore untested theories.

References

[1] H. E. Plesser, "Reproducibility vs. replicability: A brief history of a confused terminology," *Frontiers in Neuroinformatics*, vol. 11, p. 76, 2018.

[2] V. Stodden, P. Guo, and Z. Ma, "Toward reproducible computational research: An empirical analysis of data and code policy adoption by journals," *PLOS ONE*, vol. 8, pp. 1–8, 06 2013.

[3] N. Barnes, "Publish your computer code: it is good enough," *Nature*, vol. 467, no. 7317, pp. 753–753, 2010.

[4] M. Baker, "1,500 scientists lift the lid on reproducibility," *Nature*, vol. 533, no. 7604, pp. 452–454, 2016.

[5] J. Hjorth, A. Kozlov, I. Carannante, J. Frost Nylén, R. Lindroos, Y. Johansson, A. Tokarska, M. C. Dorst, S. M. Suryanarayana, G. Silberberg, J. Hellgren Kotaleski, and S. Grillner, "The microcircuits of striatum in silico," *Proceedings of the National Academy of Sciences*, vol. 117, no. 17, pp. 9554–9565, 2020.

[6] N. T. Carnevale and M. L. Hines, *The NEURON book*. Cambridge University Press, 2006.

[7] R. Deepu, S. Spreizer, G. Trensch, D. Terhorst, S. B. Vennemo, J. Mitchell, C. Linssen, H. Mørk, A. Morrison, J. M. Eppler, N. L. Kamiji, R. de Schepper, I. Kitayama, A. Kurth, A. Morales-Gregorio, P. Nagendra Babu, and H. E. Plesser, "Nest 3.1," Sept. 2021.

[8] M.-O. Gewaltig and M. Diesmann, "Nest (neural simulation tool)," *Scholarpedia*, vol. 2, no. 4, p. 1430, 2007.

A Comprehensive Nonlinear Mixed Effects Model of Glucose, Insulin, and C-Peptide Interaction during IVGTT

E. Faggionato[1], P. Denti[2], A. Largajolli[3], A. Bertoldo[1], and C. Dalla Man[1]
[1] *Department of Information Engineering, Università degli Studi di Padova, Padova, Italy*
[2] *Division of Clinical Pharmacology, University of Cape Town, Cape Town, South Africa*
[3] *Certara, Princeton, New Jersey, USA*

***Abstract*—Glucose-insulin interaction during an intravenous glucose tolerance test (IVGTT) has been widely investigated through the use of the glucose (GMM) and the insulin and C-peptide minimal model (IMM, CMM). The identification of these models usually employs a *forcing function* strategy (i.e., one measured profile is assumed to be an input of the system, known without error) to avoid compensation among model parameters. This approach may lead to the underestimation of concentration peaks and to an incorrect propagation of the measurement error, which in turn, may provide biased estimates of model parameters. Moreover, the separate identification of the system sub-models precludes a robust estimation of correlations among model parameters, which may rather be physiologically relevant. To overcome these limitations, here we aimed to build a comprehensive glucose – insulin – C-peptide MM, using nonlinear mixed effects (NLME) modeling, able to simultaneously describe glucose, insulin, and C-peptide concentrations during an IVGTT, and their inter-subject variability in a healthy population.**

Results showed that assuming a two-compartment model for both glucose, insulin, and C-peptide kinetics and log-normally distributed parameters best fitted the data and provided precise estimates of model parameters. Intriguingly, with the NLME approach, we highlighted significant positive correlations between parameters of the IMM and CMM and a significant negative correlation between insulin sensitivity and beta-cell function. In conclusion, with this study, we proved that is possible and worth applying the NLME approach to the simultaneous identification of a glucose, insulin, and C-peptide MM during IVGTT.

***Keywords*—Diabetes, NONMEM, parameter estimation, population modeling**

I. Introduction

The intravenous glucose tolerance test (IVGTT) is a clinical experiment used to assess insulin sensitivity, glucose effectiveness, and pancreatic beta-cell function, three clinical indices useful to summarize the metabolic portrait of a subject, possibly predicting the development of pre-diabetes and diabetes. This test consists of a rapid intravenous injection of glucose, sometimes followed by a rapid injection of insulin (insulin-modified IVGTT, IM-IVGTT), and the frequent collection of plasma samples for measuring glucose and insulin concentrations. When possible, also C-peptide concentration is measured, since C-peptide is a better marker of insulin secretion than insulin itself, given that insulin and C-peptide are secreted in a 1:1 ratio but, while insulin is partially extracted by the liver, C-peptide is not. Data collected during an IVGTT can be interpreted with the so-called minimal models (MMs) [1], [2], whose identification provides estimates of the aforementioned indices. The identification of these models usually employs a *forcing function* strategy to avoid compensation among model parameters, i.e., one measured profile is assumed to be an input of the system, ignoring that those measurements are affected by noise. For instance, when identifying the glucose MM [1], plasma glucose is considered the measured output while the interpolated insulin profile is used as known input. Vice-versa, when identifying insulin and C-peptide MMs (IMM and CMM) [2], the glucose profile is the one assumed as known. The most used method for identifying these models is the weighted nonlinear least squares approach [1]–[3], but examples exist of using more sophisticated Bayesian methods [4], [5]. In both cases, the identification problem was tackled at a single individual level. Therefore, any statistical moment or covariate analysis was performed *a posteriori* on the estimated parameters without considering the uncertainty that affects estimates, thus, leading to upwardly biased results [6].

Alternative approaches have been developed over the years trying to overcome such limitations. Among them, the nonlinear mixed effects (NLME) modeling has been shown to bring interesting advantages [6]. This technique consists in the simultaneous fitting of the model to the data of all individuals while allowing a hierarchical description of the variability present in the system. This is of particular importance, especially when modeling biological systems where a typical behavior is shared between individuals, but several factors (from demographic characteristics to seasonal fluctuations) contribute to the between-subject (BSV) and between-occasion variability. Hence, parameters describing the variability are estimated together with all other model parameters, allowing propagating measurement uncertainty, and avoiding biased results. In addition, covariates of the subjects can potentially be incorporated into the model leading to a better description of the BSV. The list of advantages of NLME propagates further with the possibility to employ measures fallen below or above the limits of detectability (often discarded from the analysis), the usability of the model in the case of sparse data, and the possibility to simultaneously identify the model on datasets

coming from different studies. NLME has already shown its potential when applied to the MMs [7]–[10]. However, to the best of our knowledge, the simultaneous identification of GMM, IMM, and CMM has never been attempted on glucose, insulin, and C-peptide data. In this study, we filled this gap and developed a comprehensive NLME model of glucose, insulin, and C-peptide interaction during IVGTT, able to describe the parameter distribution of a healthy population.

II. Methods

A. Database

An IM-IVGTT was performed on 204 non-diabetic subjects (118 males and 86 females, age = 55.5 $\pm$ 21.7 years, weight = 77.9 $\pm$ 13.3 kg) at the Mayo General Clinical Research Center (Mayo Clinic, Rochester, MN, USA). The protocol consisted of a constant intravenous injection of glucose (0.330 g per kg of body weight) for 2 minutes starting at time 0 followed by a constant insulin infusion (0.02 U per kg of body weight) for 5 minutes starting at time 20 min. Blood samples were collected at 0, 2, 4, 6, 8, 10, 15, 20, 22, 25, 26, 28, 31, 35, 45, 60, 75, 90, 120, 180, and 240 min for measurement of plasma glucose, insulin, and C-peptide concentrations. Median, 5th, and 95th percentiles of the data are visible later in this manuscript, in Fig. 2 in the *Results* section (continuous black lines). A complete description of the protocol is available in [11].

B. Nonlinear Mixed Effects Model

A series of models of increasing complexity were tested: one- vs two-compartment structures, including or not correlations between model parameters. All were made of three components: i) a structural model describing kinetics and interactions of glucose, insulin, and C-peptide, ii) a model describing the BSV of the structural model parameters, and iii) an error model for the residual unexplained variability.

1) Structural model: The tested structural models integrated and possibly expanded, the GMM [1], the IMM, and the CMM [2]. The main difference with respect to the original ones was that model equations were re-parameterized so that state variables represented amounts, instead of concentrations, and clearances (CL and BCL) were estimated instead of rate constants (k). Moreover, as already anticipated, at variance with the original works, here we assessed the performance of both a one- and a two-compartment description for glucose and insulin kinetics, to test if the NLME framework favored the identification of the peripheral compartments, which were difficult to identify in [1] and [2]. Below, the differential equations of the model are reported separately for each submodel, where two-compartment kinetics were assumed for the GMM and IMM. Equations for GMM are

$$\begin{cases} \dot{G}_1(t) = -[S_G + k_{G1} + A(t)]G_1(t) + S_G G_b V_{G1} \\ \qquad\qquad +k_{G2}G_2(t) + u_G(t) \\ \dot{G}_2(t) = -k_{G2}G_2(t) + k_{G1}G_1(t) \\ \dot{A}(t) = p_2 S_I[I(t)/V_{I1} - I_b] - p_2 A(t) \end{cases} \tag{1}$$

for the IMM

$$\begin{cases} \dot{I}_1(t) = -(k_{I0} + k_{I1})I_1(t) + k_{I2}I_2(t) + \\ \qquad\qquad m_I X_I(t) + u_I(t) \\ \dot{I}_2(t) = -k_{I2}I_2(t) + k_{I1}(t) \\ \dot{X}_I(t) = -m_I X_I(t) + Y_I(t) \\ \dot{Y}_I(t) = -\alpha_I Y_I(t) + \alpha_I\{\beta_I[G_1(t)/V_{G1} - G_b] \\ \qquad\qquad +k_{0I}I_b\}V_{I1} \end{cases} \tag{2}$$

and for the CMM

$$\begin{cases} \dot{C}_1(t) = -(k_{C0} + k_{C1})C_1(t) + k_{C2}C_2(t) + \\ \qquad\qquad m_C X_C(t) \\ \dot{C}_2(t) = -k_{C2}C_2(t) + k_{C1}(t) \\ \dot{X}_C(t) = -m_C X_C(t) + Y_C(t) \\ \dot{Y}_C(t) = -\alpha_C Y_C(t) + \alpha_C\{\beta_C[G_1(t)/V_{G1} - G_b] \\ \qquad\qquad +k_{0C}I_b\}V_{C1} \end{cases} \tag{3}$$

where $G(t)$, $I(t)$, and $C(t)$ are amounts of glucose, insulin, and C-peptide, respectively. Subscripts G, I, and C stand for glucose, insulin, and C-peptide sub-model, respectively; subscripts 1 and 2 for plasma and peripheral compartments, respectively, and subscript b for basal concentration. Exogenous infusions are represented by $u(t)$. V represents the volume of distribution. S_G is the glucose effectiveness, S_I the insulin sensitivity and p_2 is the rate constant describing the insulin action, $A(t)$. $X(t)$ is the amount of insulin or C-peptide (depending on the subscript) ready to be delivered in the circulation after the hepatic extraction or to be secreted by the beta-cells, respectively. $Y(t)$ is the insulin or C-peptide provision. α, β, and m are the parameters describing post-hepatic insulin delivery and C-peptide secretion. The model is assumed at steady state at time 0, except for $X_I(0) = X_{I0}$ and $X_C(0) = X_{C0}$ that represents insulin and C-peptide delivered right after the glucose injection (the so-called "first-phase insulin secretion"). For a detailed description of the model, we refer to the original works of [1] and [2].

Re-parametrization of transfer rates k was done according to

$$CL_l = k_{l,0} \cdot V_{l,1} \quad \text{and} \quad BCL_l = k_{l,n} \cdot V_{l,n} \tag{4}$$

where CL is the elimination clearance from the central compartment and BCL is the between-compartment clearance. Subscript l indicates the sub-model of glucose (G), insulin (I) or C-peptide (C), and n indicates central (1) or peripheral (2) compartments.

2) Model of the between-subject variability: The stochastic model assumes a log-normal distribution for all model parameters

$$\boldsymbol{\psi}_j = \boldsymbol{\theta}\exp(\boldsymbol{\eta}_j) \tag{5}$$

where $\boldsymbol{\psi}$ is the vector of model parameters for the jth subject, $\boldsymbol{\theta}$ is the vector of population parameters (fixed effects), and $\boldsymbol{\eta}$ is a vector of Gaussian random variables (random effects) with zero mean and covariance matrix Ω, which can be full or not, depending on whether the model does or does not account for correlation among parameters. This description of parameter

TABLE I: ESTIMATES AND PRECISION OF MODEL PARAMETERS

Glucose submodel			Insulin submodel			C-peptide submodel		
Parameter	*Value* [RSE]	*Unit*	*Parameter*	*Value* [RSE]	*Unit*	*Parameter*	*Value* [RSE]	*Unit*
S_G	0.0273 [1.8%]	min^{-1}	CL_I	1.62 [3.9%]	L/min	CL_C	0.214 [0.9%]	L/min
V_{G1}	81.5 [0.5%]	dL	V_{I1}	6.89 [0.9%]	L	V_{C1}	3.60 [1.3%]	L
V_{G2}	57.4 [0.5%]	dL	V_{I2}	4.81 [1.4%]	L	V_{C2}	5.00 [1.2%]	L
BCL_G	17.81 [0.8%]	dL/min	BCL_I	0.503 [8.9%]	L/min	BCL_C	0.413 [5.1%]	L/min
G_b	89.1 [0.1%]	mg/dL	I_b	23.6 [1.1%]	pmol/L	C_b	424 [0.4%]	pmol/L
p_2	0.0193 [1.4%]	min^{-1}	m_I	0.891 [28.5%]	min^{-1}	m_C	1.30 [15.2%]	min^{-1}
S_I	$1.72{\cdot}10^{-4}$ [0.8%]	$\frac{\text{L}}{\text{pmol}\cdot\text{min}}$	α_I	0.169 [3.3%]	min^{-1}	α_C	0.131 [2.8%]	min^{-1}
-	-	-	β_I	0.128 [1.7%]	$\frac{\text{dL}}{\text{mg}}\frac{\text{pmol}}{\text{L}\cdot\text{min}}$	β_C	0.518 [3.5%]	$\frac{\text{dL}}{\text{mg}}\frac{\text{pmol}}{\text{L}\cdot\text{min}}$
-	-	-	X_{0I}	513 [0.8%]	pmol	X_{0C}	1465 [0.5%]	pmol

RSE = Relative Standard Error.

variability is the most used since it allows a flexible description of parameter distribution with only two degrees of freedom, and it assumes non-negativity of physiological parameters.

3) Residual error model: Residual variability was assumed to be normally distributed with zero mean and standard deviation which is a combination of a constant component and a component proportional to the measured concentrations. The resulting six parameters of the error model (two for each measured concentration) were collected in the vector $\boldsymbol{\epsilon}$ and estimated along with the other model parameters.

C. Model Identification and Validation

During the identification of each model, the vector of population parameters $\boldsymbol{\theta} = [S_G, V_{G1}, V_{G2}, BCL_G, G_b, p_2, S_I, CL_I, V_{I1}, V_{I2}, BCL_I, I_b, m_I, \alpha_I, \beta_I, X_{I0}, CL_C, V_{C1}, V_{C2}, BCL_C, C_b, m_C, \alpha_C, \beta_C, X_{C0}]$, the covariance matrix of the random effects, Ω, and the vector of error parameters $\boldsymbol{\epsilon}$ were all estimated in a one-step procedure.

Model identification was performed in NONMEM [12] using the stochastic approximation of expectation maximization algorithm for parameter estimation, and an importance sampling algorithm to compute the exact maximum likelihood (ML). The best model was selected based on its ability to fit individual profiles, the physiological plausibility of its parameter estimates, and their precision. In particular, the objective function to be minimized was $\text{OF} = -2\ln(\text{ML})$, where a reduction in the OF greater than 3.84 units for each degree of freedom added to the model was considered statistically significant (p-value < 0.05), and therefore worth including in the model. Finally, a visual predictive check (VPC) plot was used to assess the predictive capability of the model visually.

III. RESULTS

The best model assumed that both glucose and insulin kinetics was described by a two-compartment model. Parameters of the structural model were estimated with good precision and lay within physiological ranges, as reported in Table I. Elements of ϵ and Ω were estimated with good precision as well (not reported). Relevant correlations among parameters were $\rho_{I_b,C_b} = 0.74$, $\rho_{m_I,m_C} = 0.65$, $\rho_{\alpha_I,\alpha_C} = 0.95$, $\rho_{\beta_I,\beta_C} = 0.51$, $\rho_{X_{0,I},X_{0,C}} = 0.91$, all related to insulin and C-peptide provision and secretion (as expected, since the two processes are physiologically and strongly related to each other), $\rho_{\beta_I,I_b} = 0.74$, as previously found in [10], and $\rho_{\beta_I,S_I} = -0.59$ as in [13]. The model was able to well fit individual profiles, as shown in Fig. 1, where observations are compared with individual predictions. Finally, the VPC (Fig. 2) showed that the model was able to reproduce both the average trend (95% prediction interval of the 50th percentile, red areas) and the variability (95% prediction interval of the 5th and 95th percentiles, blue areas) of the observed data well.

IV. CONCLUSIONS

In this work, we integrated the widely used GMM, IMM, and CMM in an NLME framework. The resulting model was able to simultaneously fit glucose, insulin, and C-peptide measured in 204 healthy subjects during an IM-IVGTT and provided precise and reliable estimates of insulin sensitivity, glucose effectiveness, and beta-cell function. This was done without resorting to the *forcing function* strategy, avoiding the risk of missing concentration peaks, and likely correctly propagating the uncertainty of measurements on model parameters. It is worth noting that the selected model included peripheral compartments for both glucose and insulin kinetics, which were not easily identifiable in a single-individual identification framework. The model also allowed estimating the kinetics parameters of C-peptide, which are usually fixed to population values [2], [14]. The integrated model provided a complete characterization of the joint parameter distribution of a healthy population. Further studies are needed to assess the possible covariate effects on model parameters and the usability of the model in prediabetic and diabetic populations.

REFERENCES

[1] R. N. Bergman, Y. Z. Ider, C. R. Bowden, and C. Cobelli, "Quantitative estimation of insulin sensitivity," *Am J Physiol*, vol.236, no. 6, pp. E667–77, Jun 1979.

[2] G. Toffolo, M. Campioni, R. Basu, R. A. Rizza, and C. Cobelli, "A minimal model of insulin secretion and kinetics to assess hepatic insulin extraction," *Am J Physiol Endocrinol Metab*. vol. 290, no. 1, pp. E169–76, Jan 2006.

[3] E. R. Carson, C. Cobelli, and L. Finkelstein, "The Mathematical Modeling of Metabolic and Endocrine Systems," John Wiley and Sons, New York, 1983.

[4] C. Cobelli, A. Caumo, and M. Omenetto, "Minimal model SG overestimation and SI underestimation: improved accuracy by a Bayesian two-compartment model." *Am J Physiol*, vol. 277, no. 3, pp. E481–8, Sep 1999.

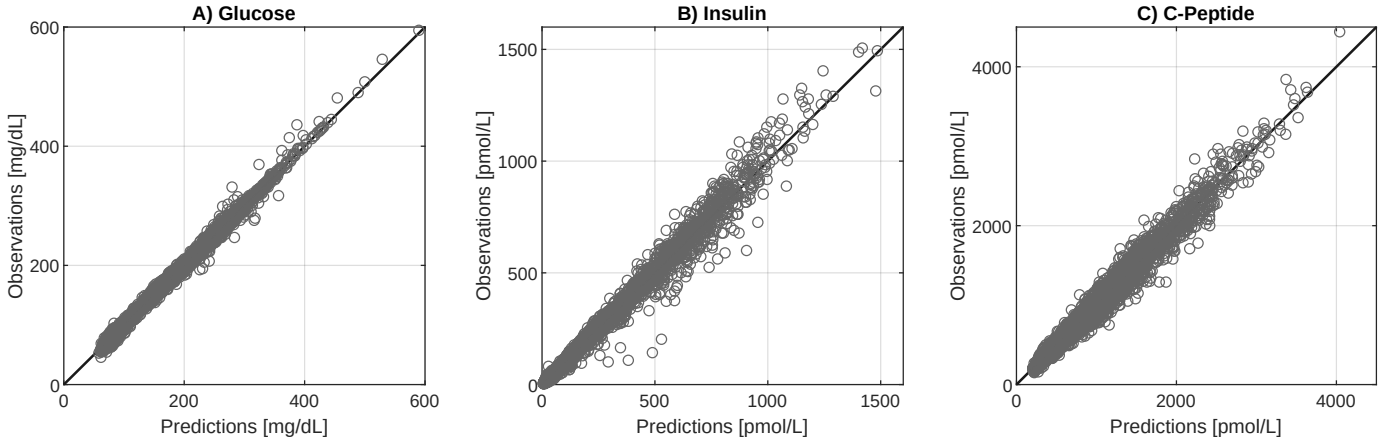


Fig. 1: Observation versus prediction plot. Concentration measurements, on the y-axis, are compared with individual predictions, on the x-axis (gray circles). The line x=y (continuous black line) is also displayed. *Panel A*: plasma glucose concentration. *Panel B*: plasma insulin concentration. *Panel C*: plasma C-peptide concentration.

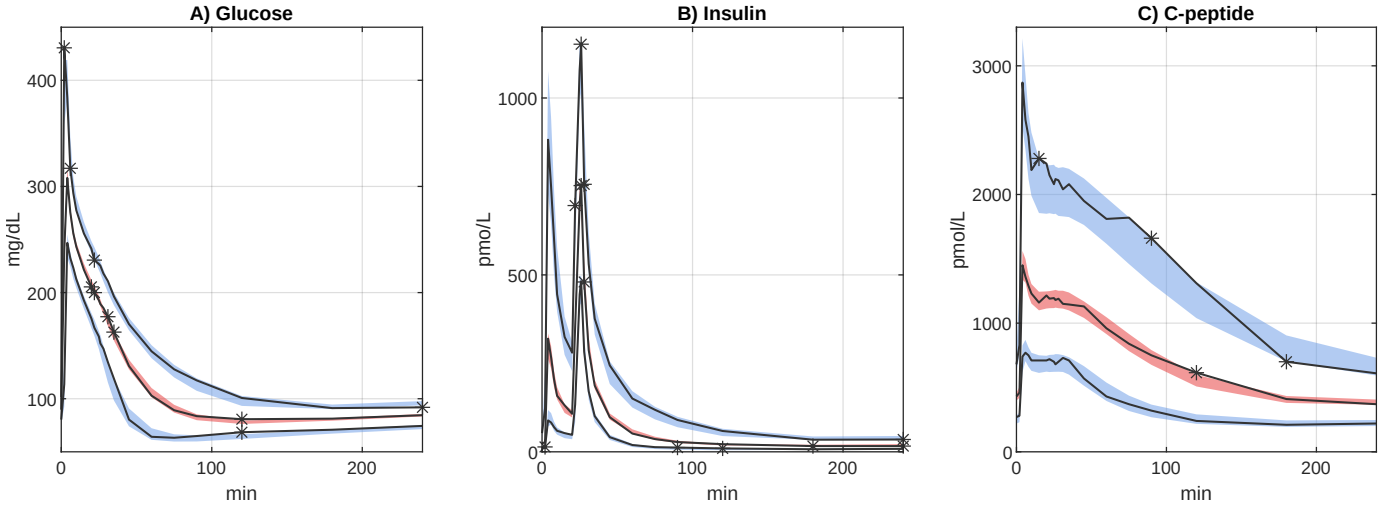


Fig. 2: Visual predictive check of the model. Ninety-five percent prediction intervals of 5th (blue lower areas), 50th (red central areas), and 95th (blue upper areas) percentiles are compared with 5th, 50th, and 95th empirical percentiles (continuous black lines). Observations outside the prediction intervals are marked with an asterisk. *Panel A*: plasma glucose concentration. *Panel B*: plasma insulin concentration. *Panel C*: plasma C-peptide concentration.

[5] G. Pillonetto, G. Sparacino, and C. Cobelli, "Numerical non-identifiability regions of the minimal model of glucose kinetics: superiority of Bayesian estimation," *Math Biosci*, vol. 184, no. 1, pp. 53–67, Jul 2003.

[6] M. Davidian and D. M. Giltinan, "Nonlinear Models for Repeated Measurement Data," in *Monograph on Statistics and Applied Probability*, 1st ed., vol. 62, Chapman & Hall, London, 1995.

[7] A. De Gaetano, G. Mingrone, and M. Castageneto, "NONMEM improves group parameter estimation for the minimal model of glucose kinetics," *Am J Physiol*, vol. 271, no. 5, pp. E932–7, Nov 1996.

[8] P. Denti, A. Bertoldo, P. Vicini, and C. Cobelli, "Nonlinear mixed effects to improve glucose minimal model parameter estimation: a simulation study in intensive and sparse sampling," *IEEE Trans Biomed Eng*, vol. 56, no. 9, pp. 2156–66, Sep 2009.

[9] P. Denti, A. Bertoldo, P. Vicini, and C. Cobelli, "IVGTT glucose minimal model covariate selection by nonlinear mixed-effects approach," *Am J Physiol Endocrinol Metab*, vol. 298, no. 5, pp. E950–60, May 2010.

[10] M. M. A. Ibrahim, A. Largajolli, M. O. Karlsson, and M. C. Kjellsson, "The integrated glucose insulin minimal model: An improved version," *Eur J Pharm Sci*, vol. 15, n. 134, pp. 7–19, Jun 2019.

[11] R. Basu et al., "Mechanisms of the age-associated deterioration in glucose tolerance: contribution of alterations in insulin secretion, action, and clearance," *Diabetes*, vol. 52, no. 7, pp. 1738–48, Jul 2003.

[12] R. J. Bauer, "NONMEM users guide. Introduction to NONMEM 7.5.0," ICON plc. Gaithersburg, MD, USA, 2017–2020.

[13] C. Cobelli et al., "Assessment of beta-cell function in humans, simultaneously with insulin sensitivity and hepatic extraction, from intravenous and oral glucose tests." *Am J Physiol Endocrinol Metab*, vol. 293, no. 1, pp E1–E15, Jul 2007.

[14] E. Van Cauter F. Mestrez, J. Sturis, and K. S. Polonsky, "Estimation of insulin secretion rates from C-peptide levels: Comparison of individual and standard kinetic parameters for C-peptide clearance," *Diabetes*, vol. 41, pp. 368–77, Mar 1992.

Model Assessment of Doxorubicin Pharmacokinetics in Multiple Myeloma

M. Baldan[1], F. Da Ros[2], M. Mazzucato[2], M.G. Pedersen[1], and R. Visentin[1]
[1] *Department of Information Engineering, University of Padova, Padova, Italy*
[2] *Aviano National Cancer Institute, Aviano, Italy*

***Abstract*—Multiple myeloma (MM) is a plasma cell neoplasm that is usually treated with chemotherapeutic drugs such as doxorubicin (DOXO). During treatment, drug administration must be optimized according to the patient's needs to reduce the side effects of therapy and increase its efficacy. To support the study of DOXO and treatment optimization, we have recently developed a pharmacokinetics (PK) model of DOXO in MM cells. Here we aim to evaluate the robustness of the PK model by assessing its performance in the context of a population-based approach.**

A series of *in vitro* experiments in MM1R cells treated with DOXO at 200 nM and 450 nM was performed. The measured intracellular DOXO concentrations have been organized to generate three different population datasets: a naive average dataset (NAD), obtained by averaging all cell readings and two datasets obtained by averaging the cell readings within the same experiment well or the same image field, respectively. The PK model has been identified on each population dataset, and the resulting model predictions and estimated parameters were compared across populations.

Model fit was satisfactory in all combinations, and the estimated model parameters were precise and comparable across population datasets. Although slight differences were found between results obtained with NAD and field-population dataset, they were mainly attributable to the expected different intrinsic dataset variability. On the other hand, the population approach based on the within-well cellular data provided almost superimposable results to those obtained with NAD, proving the model's ability to reliably describe DOXO PK in MM cells.

***Keywords*—compartmental modeling, system identification, cancer treatment, chemotherapy drug.**

I. INTRODUCTION

Multiple Myeloma (MM) is a malignancy of monoclonal plasma cells in the bone marrow. It has a 126% global incidence increase from 1990 to 2016 and can target several areas of the body. Its risk factors include chronic inflammation, inherited genetic variants, and exposure to radiation or chemicals [1].

MM does not show any evident symptoms in the early stages, which produces a process of diagnosis that is long, complicated, and discouraging for the patients. The most common treatment adopts chemotherapy drugs, with doxorubicin (DOXO) as a well-established treatment in MM, as well as breast cancer. [2], though it has serious side effects. Therefore, treatment with DOXO has to be optimized in terms of dose regimen to maximize drug efficacy and reduce side effects.

In this regard, mathematical modeling of pharmacokinetic (PK) and pharmacodynamic (PD) represents a valid approach to investigating the cellular response to the drug. A preliminary study explored which model could be more suitable to describe DOXO PK in MM cells. Here we aim to assess the robustness of the most promising model by evaluating its performance with a cell population approach that increases the variability in the available data. In particular, we will consider three different possible assumptions that could be made regarding the measurement error of the MM1R cell line data collection.

The paper is structured as follows: Section II describes the data collection, cell population setup, and the compartmental PK model, Section III outlines the model identification setup, Section IV reports the results and Section V provides a discussion about the closing remarks and future research development.

II. METHODS

A. Data collection

The dataset consists of *in vitro* experiments performed on MM1R human cell line (American Type Culture Collection (ATCC), http://www.atcc.org). Cells were cultured with a density of 5 x 10^5 cells/mL in Roswell Park Memorial Institute (RPMI) 1641 medium supplemented with 1% penicillin/streptomycin and 10% fetal bovine serum (FBS). The MM1R cell line is used to study DOXO cellular uptake and release by exploiting its autofluorescence property (i.e., it excites at 470 nm and emits light at 570 nm of wavelength [3]), measured using a fluorescence microscope (Nikon® Eclipse T1-U). The experiment is designed in two different phases. During the first phase (uptake), the cell line is treated with DOXO for 3 hrs at two concentrations, 200 nM or 450 nM. Immediately after DOXO administration at $t = 0$, hr 200 μL containing 10^5 cells are drawn and seeded in duplicate (i.e., 100 μL with 5 x 10^4 cells each) within two μ-Slide VI$^{0.4}$ wells (ibidi GmbH, Gräfelfing). For each well 4/5 images (fields) are then acquired every 20 minutes for 3 hrs at 40x magnitude for both bright-field and fluorescence. At $t = 3$ hrs, coinciding with the uptake end, the remaining cells are centrifuged for extracellular DOXO removal and resuspended in 300 μL of PBS, 20% FBS obtaining a density of 5 x 10^4 cells/100 μL. During this second phase (release), the cells are drawn and seeded in triplicate (i.e., 100 μL with 5 x 10^4 cells each) within three μ-Slide VI$^{0.4}$ wells. Analogously to the uptake phase, 4/5 images/well are then acquired at $t = [3.5, 4, 4.5, 5, 5.5, 6, 7, 8]$ hrs at 40x. Each acquired image is processed by ImageJ software and is related to a different frame of the well. Within every frame, it could be detected

a different amount of independent cells, which are measured to obtain their intracellular fluorescence intensity (*Int*). The latter is then removed of the background signal and mapped to DOXO concentration (*C*) values in nM. The mapping function is estimated empirically by a linear regression model fit to *C-Int* data, produced by serially administering known DOXO concentrations to a μ-Slide VI$^{0.4}$ well.

$$Int = 15.26 \cdot C + 508.66 \tag{1}$$

B. Data preprocessing

In order to remove possible outliers, for each time sample, only 95% of data measurements were maintained, while the remaining 5% was uniformly removed from both tails of data distributions. Moreover, an inconsistent increase in raw intracellular concentration after the end of the uptake phase was observed, likely due to the rewashing of the extracellular environment. Thus, data normalization was proposed to correct all the observations acquired in the release phase:

$$f = \frac{0.5 \cdot \left(\bar{C}_{1,\ t=3} + \bar{C}_{2,\ t=3}\right)}{max\left(\bar{C}_{1,\ t=3.5}, \bar{C}_{2,\ t=3.5}, \bar{C}_{3,\ t=3.5}\right)} \tag{2}$$

$$C_{j,t=i} = f \cdot C_{j,t=i} \tag{3}$$

where $j = 1, \ldots, 3$ and $i = 3, 3.5, \ldots, 8$ represent the well and time sample (hrs), respectively.

C. Datasets design

The data collection opens for considering different datasets containing distinct aggregated data. This feature is exploited for a population approach, i.e., by considering three possible datasets: 1) a naive average dataset (NAD), 2) a second dataset consisting of three well-dependent average data, and 3) a third one consisting of up to fifteen field-dependent average data.

Dataset 1: The first dataset, corresponding to a naive average data (NAD) approach, considers the average C across all detected cells at each time instant t (18 x 1) by considering all wells.

Dataset 2: The second dataset considers each experimental series as independent from the other ones and averages all detected cells at each time instant t within the same experiment. As such, this configuration implies that each time sample accounts for two or three data points, for uptake or release phase, respectively. Each experimental series is related to a different μ-Slide VI$^{0.4}$ well.

Dataset 3: The third dataset considers each acquired field, sorted by order of acquisition, as independent from the other ones and averages all detected cells at each time instant t within the same field.

D. Modeling Doxorubicin PK

Administering DOXO to a cell culture causes cells to absorb it and increase their intracellular concentration following certain kinetics. On the other hand, by removing the DOXO, the cells release the drug if it is not bound to DNA. Such a description has been modeled in breast cancer [4] and very recently in MM [5]. In the latter study, three different models were compared, and the following one resulted in the most suitable to describe DOXO PK in MM1R cells.

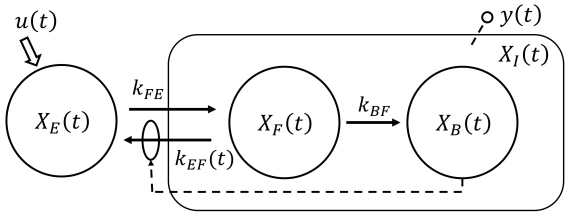


Fig. 1: DOXO PK model scheme

The model, schematized in Fig. 1, is described by three compartmental equations representing DOXO concentration in the extracellular space (X_E), in the cell cytoplasm (X_F) and bound to DNA (X_B):

$$\begin{cases} \dot{X}_E(t) = k_{EF}\frac{V_I}{V_E}X_F(t) - k_{FE}X_E(t) + u(t) \\ \dot{X}_F(t) = k_{FE}\frac{V_E}{V_I}X_E(t) - k_{EF}X_F(t) - k_{BF}X_F(t) \\ \dot{X}_B(t) = k_{BF}X_F(t) \end{cases} \tag{4}$$

where k_{FE}, k_{BF}, k_{EF} (hr^{-1}) are rate parameters describing transit from extracellular space to free intracellular, from free intracellular to bound to DNA, and from free intracellular back to extracellular space. In particular, k_{FE} and k_{BF} are constant and assumed being independent form drug dosage and exposure time, while k_{EF} is modeled with a Hill-like equation of order $q = 2$ dependent on the bounded DOXO concentration:

$$k_{EF} = V_{max}\frac{X_B^{q-1}(t)}{K_{th}^q + X_B^q(t)} \tag{5}$$

where K_{th} (nM) denote the X_B concentration at which $k_{EF}(t)$ is equal to its maximum value $V_{max}/2K_{th}$ and where V_{max} has units (nM/hr). This formula is aimed at implementing a cellular drug resistance mechanism that might be a consequence of DOXO binding to DNA in the cell nucleus, causing an increment in the outflow from the free intracellular towards the extracellular compartment.

Model input $u(t)$ is defined as:

$$u(t) = \begin{cases} D \cdot \delta(t) & if\ t = 0 \\ 0 & otherwise \end{cases} \tag{6}$$

where D denotes the amount of DOXO administered at $t = 0$. The accessible measurement site is represented by the intracellular concentration $X_I(t)$, which is given by the sum of free and bound DOXO concentration:

$$X_I(t) = X_F(t) + X_B(t) \tag{7}$$

III. MODEL IDENTIFICATION

A. A priori identifiability

In the present work, the a priori identifiability of model eq. (4-7) has been assessed by the Differential Algebra for Identifiability of Systems (DAISY) software, a tool developed to check for global identifiability of biological and physiological

systems [6]. It is assumed that the volumes $\{V_E, V_I\}$ are equal to 100 μL and 0.0703 μL.

B. System identification

Model identification is designed to estimate a unique set of model parameters based on the available observations of each one of the aggregated datasets described in section II-C. In our problem, the model of equations (4-7) has been identified on intracellular DOXO concentration X_I. In order to generalize the optimization problem to the dataset dimensions, the available observations are reshaped to be in the form of a column vector and maintaining the temporal order:

$$X_I(t) \qquad X_I(t) = \begin{bmatrix} X_{I,1}(t) \\ X_{I,2}(t) \\ X_{I,ne}(t) \end{bmatrix} \quad X_I(t) = \begin{bmatrix} X_{I,1}(t) \\ \vdots \\ X_{I,nf}(t) \end{bmatrix},$$

where X_I relates to datasets 1,2, and 3, from left to right, respectively, and ne, nf are the total number of experimental series and image fields.

Furthermore, both the observations acquired in 200 nM and 450 nM administered DOXO are merged together in one single vector *y(t)* in order to make the identification dosage-independent:

$$y(t) = X_I(t) = \begin{bmatrix} X_I^{200}(t) \\ X_I^{450}(t) \end{bmatrix} \tag{8}$$

Then, the measurement model is defined as:

$$\hat{y}(t) = \hat{X}_I(t, \theta) + v(t) \tag{9}$$

where $\hat{X}_I(t, \theta)$ represents the model prediction of the total intracellular concentration, function of the parameter vector $\theta = [k_{FE}, V_{max}, K_{th}, k_{BF}]$, and $v(t)$ is the DOXO measurement error, assumed as known and described by sampled standard deviation calculated from each population dataset. The model forcing-function is the DOXO amount (200 nM or 450 nM) administered at $t = 0$ hrs. At $t = 3$ hrs, X_E was forced to zero, in order to simulate DOXO removal and medium replacement occurring at the end of the uptake phase.

Model identification was done by using a Bayesian Maximum a Posteriori (MAP) estimator implemented in MATLAB 2022b (Natick, MA) [7] and solved by using the $lsqnonlin$ function. Specifically, for each population dataset, the optimal set of model parameters is obtained by solving the following problem,

$$\hat{\theta} = \underset{\theta}{argmin} \left[||y - \hat{X}_I(t, \theta)||^2_{\Sigma_v} + (\theta - \mu_\theta)' \Sigma_\theta^{-1} (\theta - \mu_\theta) \right] \tag{10}$$

where $\hat{X}_I$ is repeated according to the dimension of y.

Equation (10) accounts for both the weighted residual sum of squares (WRSS) and the distance from the estimated parameters and their joint prior distribution, i.e., the parameter average vector μ_θ and the covariance matrix Σ_θ. In particular, *a priori* information was considered for V_{max} and K_{th}, based on a previous study [8].

C. Model assessment

Model performance was assessed both graphically, by evaluating model's ability to predict the data, and numerically, in terms of plausibility of estimated model parameters and their precision described by percent coefficient of variation (CV).

The robustness of the model across the datasets was then evaluated by comparing the predicted cellular model compartments (X_I, X_F and X_B) and calculating the percent difference (Δ) between the same *i*-th model parameter estimated from dataset 2 ($p_{i,2}$) or 3 ($p_{i,3}$) and the corresponding one obtained from dataset 1 ($p_{i,1}$):

$$\Delta(p_i) = \frac{p_{i,n} - p_{i,1}}{p_{i,1}} \cdot 100 \ , \quad n = \{2, 3\}. \tag{11}$$

IV. RESULTS

A. Model performance

Figure 2 shows the model fit on MM1R intracellular DOXO concentration data. It is shown that the model predicts DOXO data by distinguishing between free DOXO in the cytoplasm and DNA-bound DOXO (Figure 3). In particular, the model well describes data measured during the experiment with DOXO 200 nM, while it underestimates three data points collected between 40 and 80 min after DOXO 450 nM administration. In this regard, dose dependent model identification was already conducted and not showing any significant improvement (results are not shown) [5].

Table I reports the model parameter estimated from each dataset. For all model identifications, all the model parameters have comparable values across the population datasets and are estimated with good precision, as proved by the low CV. Overall, the identification shows consistency and good reliability between all parameters and population datasets.

	k_{FE} (10^{-4} hr^{-1})	V_{max} (10^5 nM/hr)	K_{th} (10^3 nM)	k_{BF} (hr^{-1})
NAD	7.72 (2.63%)	2.10 (10.5%)	1.44 (4.91%)	1.48 (4.36%)
wells	9.45 (12.3%)	2.30 (12.7%)	1.40 (5.55%)	1.43 (8.63%)
fields	8.54 (14.0%)	2.38 (13.2%)	1.38 (5.86%)	1.33 (12.4%)

TABLE I: Model parameter estimates and their precision (described by coefficient of variation CV between parenthesis) for datasets 1 (NAD), 2 (wells) and 3 (fields).

B. Model robustness

Figure 3 shows the comparison between the model prediction of X_I, X_F and X_B for each population dataset. It can be observed how all the cell model states resulting from model identification on datasets 1 (NAD) and 2 (well population) are almost superimposable, while a different X_I predicted from dataset 3 (field population) is more evident, and mainly attributable to a different X_B. This is reflected by the numerical comparison of estimated model parameters (Table II), which shows that k_{BF} estimated from the field population data is about 10% slower than the respective counterpart

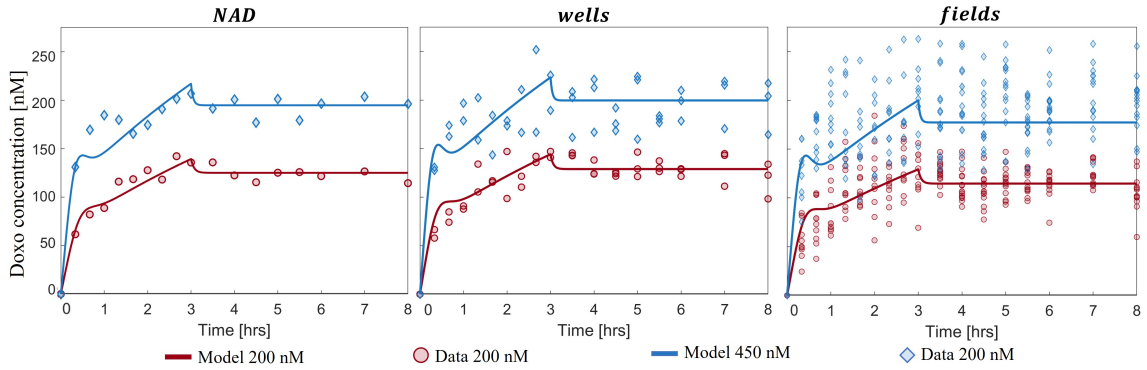


Fig. 2: Model fit on DOXO 200 nM and 450 nM intracellular data for each population dataset: NAD (left), wells (middle), fields (right).

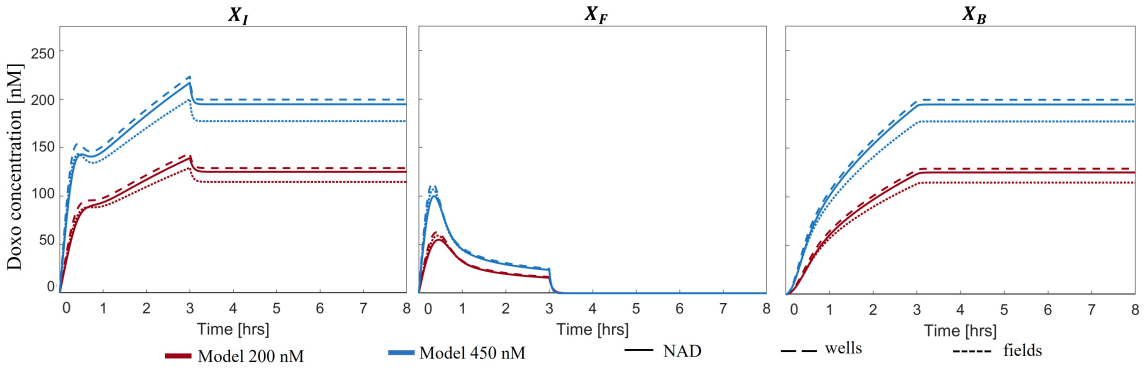


Fig. 3: Predicted model states across population datasets: total intracellular (X_I, left), free (X_F, middle) and DNA-bound (X_B, right).

obtained from NAD. Similarly, about 22% difference results by comparing k_{FE} estimated datasets 1 vs. 2. This translates into a slightly higher peak in X_F around 30 min.

%	$\Delta(k_{FE})$	$\Delta(V_{max})$	$\Delta(K_{th})$	$\Delta(k_{BF})$
wells	22.3	9.52	-2.37	-3.78
fields	10.6	13.1	-3.92	-10.4

TABLE II: Parameters percent difference between population datasets 2 (wells) or 3 (fields) vs. 1 (NAD).

V. CONCLUSION

The DOXO PK model is able to satisfactorily predict drug concentration data, irrespective of the population dataset subject of the analysis, thus strengthening the reliability of its identification in the case of the NAD approach. Some differences between estimated model parameters across population datasets have been found. However, they were expected since the population datasets show different shapes compared to the NAD approach, which substantially averages possible differences. It is worth mentioning that the proposed population approach yields promising results, particularly in the case of the well's population dataset, which intuitively might better represent independent experiments.

Future works will include the analysis of a second set of experiments administering DOXO in a different MM cell line in order to further strengthen the model assessment. In addition, since the estimated Hill function describing the DOXO efflux rate (k_{EF}) is only partially explored by the range of the current DOXO concentrations, it would be interesting to study DOXO PK with higher dosages. Alternatively, further possible models of the DOXO efflux rate could be evaluated.

ACKNOWLEDGEMENT

This work was supported by project SID 2020, Department of Information Engineering, University of Padova, and CARIPARO.

REFERENCES

[1] A. J. Cowan *et al.*, Global burden of multiple myeloma: a systematic analysis for the global burden of disease study 2016, JAMA oncology, vol. 4, no. 9, pp. 1221–1227, 2018.
[2] A. Shafei *et al.*, A review on the efficacy and toxicity of different doxorubicin nanoparticles for targeted therapy in metastatic breast cancer, Biomed Pharmacother, vol. 95, pp. 1209–1218, Nov 2017.
[3] K. K. Kakukstis, E. H. Thompson, J. A. Whiles, R. J. Rosenfeld, "Deciphering the fluorescence signature of daunomycin and doxorubicin", Biophysical chemistry, vol. 73, no. 3, pp. 249-263, 1998.
[4] M. T. McKenna *et al.*, "A predictive mathematical modeling approach for the study of doxorubicin treatment in triple negative breast cancer", Scientific reports, vol. 7. no. 1, pp. 1-14, 2017.
[5] A. Giaretta, F. Da Ros, M. Mazzucato, M. G. Pedersen, R. Visentin, "Modeling Pharmacokinetics of doxorubicin in multiple myeloma cells", 2021 43rd Annual International Conference of the IEEE Engineering in Medicine & Biology Society (EMBC). IEEE, 2021, pp. 4374-4378.
[6] G. Bellu, M. P. Saccomani, S. Audoly, L. D'angiò, "Daisy: A new software tool to test global identifiability of biological and physiological systems", Computer methods and programs in biomedicine, vol. 88, no. 1, pp. 52–61, 2007.
[7] MATLAB, 9.11.0.1769968 (R2021b), The MathWorks Inc., 2021
[8] J. Kopecka *et al.*, "Insights into P-Glycoprotein Inhibitors: New Inducers of Immunogenic Cell Death, Cells", vol. 9., no. 4, 2020

Numerical simulations of the cerebrospinal flow through the Sylvius aqueduct modeled as a diffuser/nozzle pump

P. Peruzzo[1] and F.M. Susin[1]
[1] *HER Lab, Department of Civil, Environmental and Architectural Engineering, University of Padova, Italy*

***Abstract*—The circulation of the cerebrospinal fluid is rhythmic with a preferential flow direction. In the present study, we performed a series of numerical simulations demonstrating that the shape of the Sylvius aqueduct is functional to this characteristic circulation acting as a diffuser/nozzle pump.**

***Keywords*—Cerebrospinal fluid, Diffuser/nozzle pump, CFD.**

I. Introduction

The cerebrospinal fluid (CSF) is a clear, colorless fluid that is part of the central nervous system (CNS). It belongs to the cerebral extracellular matrix and contains both inorganic and organic substances, including glucose, lactic acid, proteins, urea, sodium, potassium, magnesium, calcium, and lymphocytes [1]. CSF preserves brain functionalities since it damps mechanical stress, compensates for blood volume variations during the heartbeat, guarantees the transport of nutrients, and removes the toxins produced [2].

Precisely, the CSF is actively produced by both plexuses and brain parenchyma. It circulates through the ventricles of the brain (lateral ventricles of each hemisphere, third and fourth ventricles), the subarachnoid space, and the central canal of the spine. Finally, it is reabsorbed into the venous system, with a net volume daily exchanged of about 500 mL. The observed transport of species by the CSF is owing to a rhythmic oscillation of the fluid within the CNS promoted by the pressure variation in the surrounding cerebral cardiovascular circulation [3]. Therefore the resulting flow dynamics are rather complex, and not all the mechanisms that determine the observed net flux are fully understood yet.

Longatti et al. [4] recently argued that the trumpet shape of the Sylvius aqueduct connecting the third and fourth ventricles acts as a diffuser/nozzle pump, promoting a pulsatile flow with a net flow toward the craniocaudal direction. A 1D hydrodynamic model was applied to a simplified geometry of the anatomical district of interest obtained by magnetic resonance images (MRI) of a cohort of 10 volunteers. The analysis showed that the expected flow rate by the modeled diffuser/nozzle pump compared favorably with the flow rate measured within the aqueduct. Nevertheless, the theoretical model proposed by Longatti et al. was based on the mechanical energy conservation principle applied to a quasi-stationary flow through a standard conical diffuser/nozzle, i.e., a geometry fitting not perfectly to the aqueduct. Accordingly, the model was able to capture only the essential interactions among the geometric shape of the complex, the forcing pressure, and the CSF net flow.

In the present work, to have a more reliable picture of the relevance of the anatomy of the Sylvius aqueduct, we analyze numerically the hydrodynamics in the third ventricle-Sylvius aqueduct-fourth ventricle for the cohort of patients schematized in [4].

II. Materials and Methods

A. Numerical model

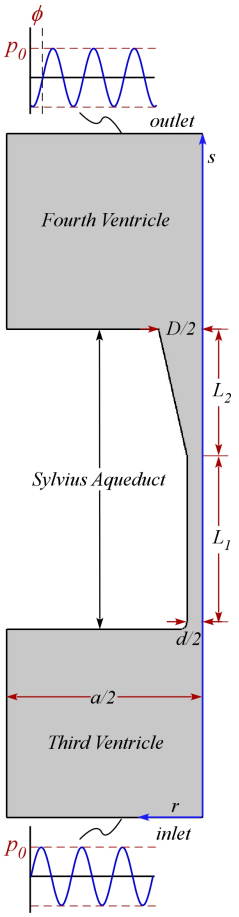


Fig. 1: Sketch of the geometry and boundary conditions of the simulations. s and r are the axial and radial directions, respectively.

TABLE I: The geometrical configurations of the third ventricle-Sylvius aqueduct- fourth ventricle system of the cohort of volunteers in [4]. RC is the reference case of the sample.

Case	d [mm]	D [mm]	L_1 [mm]	L_2 [mm]
1	2.49	5.29	14.86	14.10
2	1.55	4.06	16.53	13.67
3	1.94	5.33	14.89	17.78
4	2.12	5.04	16.88	13.56
5	1.40	4.73	16.37	13.64
6	1.65	3.27	19.20	10.48
7	2.07	3.97	16.83	12.39
8	1.78	4.65	17.85	11.56
9	1.77	3.85	10.50	10.36
10	2.40	6.77	8.22	14.90
RC	1.60	4.50	17.00	13.00

The flow through the Sylvius aqueduct has been computed numerically. The hydrodynamics has been solved in a parametrized 2D axisymmetric domain where two oscillating pressures act on both the inlet and outlet. The numerical model has been built in the CFD module of COMSOL Multiphysics 5.3 (Comsol Inc., Stockholm), which solves the Navier-Stokes equations for an uncompressible Newtonian as the CSF, and assumes laminar flow conditions in the entire domain since the physiological Reynolds number is not larger than some hundreds.

Fig. 1 shows the computational domain consisting of a cylindrical pipe and a conical diffuser in series (both schematizing the Sylvius aqueduct) that connect two cylindrical chambers of diameter a (the ventricles). The cylindrical stretch has a length L_1 and diameter d, whereas the conical portion has a length L_2 and a minimum and maximum diameter equal to d and D, respectively. In both chambers, the diameter was set $a = 10\,D$. The inlet between the third ventricle and the aqueduct was tapered with a fillet, whereas the connection with the outlet chamber (the fourth ventricle) was sharp. Such inlet/outlet geometry should have favored the asymmetrical behavior of the flow in the diffuser/nozzle phases [5].

The domain is discretized with indicatively 30,000 elements and consisted of an unstructured triangular grid in the bulk region and a structured quadrangular grid near the rigid wall.

B. Simulations

Two sinusoidal pressure waves of amplitude $p_0 = 1.0$ mm_{Hg} ($\approx$ 133 Pa) and frequency $f = 1$ Hz phased by ϕ were imposed at the inlet and outlet. The phase between the two pressures results from the delay of the pressure wave propagation along the aqueduct and is equal to $\phi = 2\pi\, f\,(L_1 + L_2)/c$, with $c = 5.0$ m/s the speed of the pressure perturbation [6]. Initially, the system was at rest and reached a steady periodic state in about ten cycles. The results of the last cycle were used in the analysis.

We performed a series of numerical experiments to evaluate the effectiveness of the theoretical solution using the configurations of the Sylvius aqueduct gathered from the magnetic resonance images of the volunteers population in Longatti et al. [4]. The total runs analyzed counts 11 experiments (10 volunteers and one configuration inferred as reference case of the cohort). The geometry details of the studied configurations are summarized in Table I. Fluid properties were constant, and in all tests, we prescribed for the CSF the density and kinematic viscosity equal to ρ=1000 kg/m^3 and ν=1.0$\times$10^{-6} m^2/s, respectively.

III. Results and Discussion

Fig. 2 shows some examples of the flow rate computed during the last cycle of the simulations. The flow rate in Reference Case (RC) shown in Panel a varies from 12.18 (toward the fourth ventricle) to -11.59 mL/min (toward the third ventricle), i.e., within the values of 10÷20 mL/min estimated in other studies [7], [8]. The computed net flow results in $Q_{net} \approx 0.34$ mL/min, equivalent to a daily volume of 483 mL. These results are thus in agreement with the physiological flows and confirm that the shape of the Sylvius aqueduct can facilitate CNS circulation.

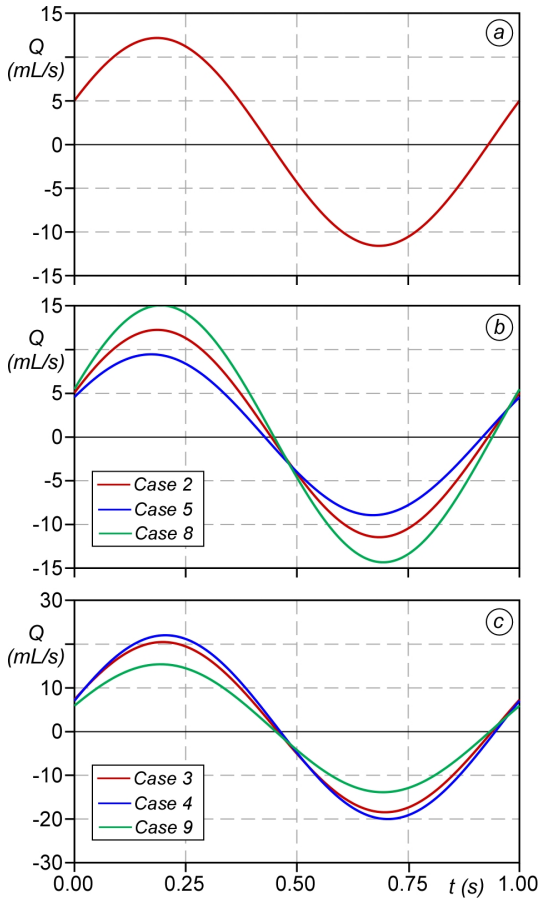


Fig. 2: Time-varying flow rate computed in the Sylvius aqueduct. a) Solution of RC; b) solutions for Cases 2, 5, and 8; and c) solutions for Cases 3, 4, and 9.

The variation of the Aqueduct shape inherently affects the hydrodynamics and the capability of the conduit to convey the CSF, as shown in Panels b and c, where we reported some of the simulations based on aqueduct geometries directly

measured by MRIs. Most cases have the peak flow in the physiological range (9.38÷21.87 mL/min), and, albeit the daily volume turns out to be in some runs overestimated (303÷1322 mL), the results seem coherent with RC. In contrast, two configurations (Cases 1 and 10) exhibit anomalous values of peak flow (31.62 and 36.00 mL/min) and significantly large exchanged volumes (2383 and 3267 mL). However, the presence of these outliers, rather than questioning the role of the Sylvius aqueduct as a pump, highlights the limits of the simplified anatomy used to model the CSF circulation accurately.

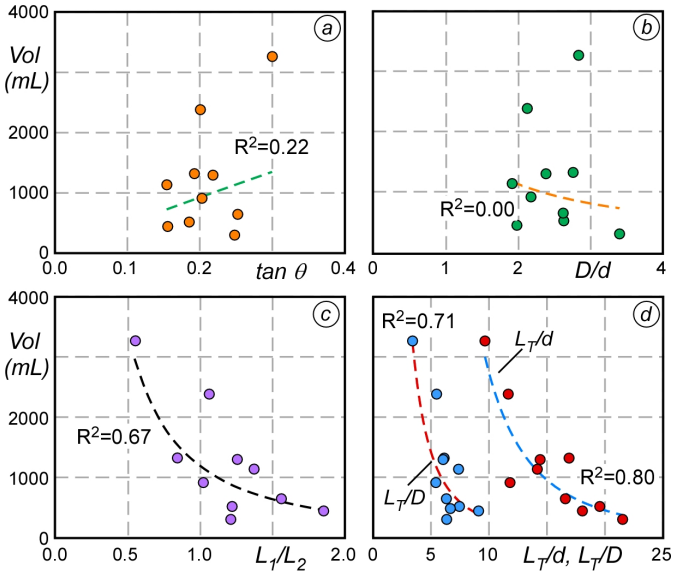


Fig. 3: Dependency of the daily net volume on $a)$ θ, $b)$ D/d, $c)$ L_1/L_2, and $d)$ L_T/d and L_T/D. Dashed lines are the best-fit power law regression of the experiments, and R^2 is the determination coefficient associated.

To get an insight into the relevance of the parameters and hence identify the potential drivers of the flow rate through the Sylvius aqueduct in the investigated population, we analyzed the total daily volume flowing through the system as a function of some non-dimensional quantities. Fig. 3 shows the model response considering the diffuser cone angle, θ, which is defined as $\theta = 2\arctan(D-d)/L_2$, the diameters ratio D/d, the length ratio L_1/L_2, and the tube slenderness L_T/d (or L_T/D), with $L_T = L_1 + L_2$.

Although the standard diffuser/nozzle pump varies its efficiency with θ [9], in the present configuration, the increase of the opening of the diffuser shows only a weak positive effect on the performance ($R^2 = 0.22$, Panel a), whereas is substantially unaffected by D/d ($R^2 = 0.00$, Panel b). This indicates that the diffuser/nozzle element is not *di per se* sufficient to explain the flow in the proposed Sylvius aqueduct schematization. The results reported in Panel c and d confirm this conclusion. Indeed, the cylindrical portion strongly limits the asymmetry of the pumping action, as evidenced by the inverse correlation between the volume and L_1/L_2 ($R^2 = 0.67$, Panel c). A similar trend is also observed in Panel d for the total slenderness of the aqueduct ($R^2 = 0.71$ for L/D and $R^2 = 0.80$ for L/d).

Further analyses, here not reported for brevity, aimed at investigating the role of the phased, ϕ, show that the present results are independent on this parameter (R^2 =0.12).

We can conclude that, in the cohort of investigated patients, the channel length is the primary factor influencing the flow rate since it is directly related to the flow dissipation. In addition, a relatively short straight channel portion facilitates the flow asymmetry that the diffuser/nozzle element promotes. However, the essential geometric modeling of the third ventricle-Sylvius aqueduct-fourth ventricle system adopted in the analysis suggests some caution in the generalization of these results and their direct application to the clinical setting.

IV. Conclusions

In the present work, we proposed a series of numerical simulations of the hydrodynamics through a channel consisting of a cylindrical pipe and a conical diffuser/nozzle element, which mimics the Sylvius aqueduct.

The results showed that $i)$ the trumpet shape of the aqueduct is functional to promote a preferential flow direction from the third ventricle toward the fourth ventricle of the central nervous system, and $ii)$ the key parameters influencing such net flow rate are the channel slenderness and the ratio between the straight and the diffuser/nozzle elements.

An exhaustive frame of the complex flow dynamics in the CSF circulation deserves further analyses based on more realistic models of the apparatus and possibly comparing the results model not only to population- but also to patient-specific flow data. A detailed sensitivity analysis of the model with respect to any single parameter is also required to further corroborate the presented results. This work represents the first step toward the realization of this numerical tool.

Acknowledgement

We wish to acknowledge Federica Victoria Romor for her contribution to the model realization.

References

[1] S. B. Hladky, and Barrand M. A. Mechanisms of fluid movement into, through and out of the brain: evaluation of the evidence. Fluids and Barriers of the CNS, Vol. 11 (1), 2014, pp. 1-32.
[2] M. K. Rasmussen, Mestre H., and Nedergaard M. Fluid transport in the brain. Physiological Reviews, Vol. 102 (2), 2022, pp. 1025-1051.
[3] Mestre H. et al. Flow of cerebrospinal fluid is driven by arterial pulsations and is reduced in hypertension. Nature communications, Vol. 9 (1), 2018, pp. 1-9.
[4] Longatti L, Fiorindi A., Peruzzo P., Basaldella L, and Susin F. M. Form follows function: estimation of CSF flow in the third ventricle-aqueduct-fourth ventricle complex modeled as a diffuser/nozzle pump. Journal of Neurosurgery, Vol. 133 (3), 2019, pp. 894-901.
[5] Olsson A., Stemme G., and Stemme E. Numerical and experimental studies of flat-walled diffuser elements for valve-less micropumps. Sensors and Actuators A: Physical, Vol. 84 (1-2), 2000, pp. 165-175.
[6] Figueroa C. A., and Humphrey J. D. Pressure wave propagation in full-body arterial models: a gateway to exploring aging and hypertension. Procedia IUTAM, Vol. 10, 2014, pp. 382-39.
[7] Wagshul M. E. et al. Amplitude and phase of cerebrospinal fluid pulsations: experimental studies and review of the literature. Journal of neurosurgery, Vol. 104 (5), 2006, pp. 810-819.

[8] Wagshul M. E., Eide P. K., and Madsen J. R. The pulsating brain: a review of experimental and clinical studies of intracranial pulsatility. Fluids and Barriers of the CNS, Vol. 8 (1), 2011, pp. 1-23.
[9] Jiang X. N. et al. Micronozzle/diffuser flow and its application in micro valveless pumps. Sensors and Actuators A: Physical, Vol. 70 (1-2), 1998, pp. 81-87.

Mathematical model of glucagon kinetics during an oral glucose tolerance test based on a dual regulation mechanism

M. Morettini[1,*], A. Piersanti[1], C. Göbl[2], L. Burattini[1], and A. Tura[3]
[1] *Department of Information Engineering, Università Politecnica delle Marche, Ancona, Italy*
[2] *Department of Obstetrics and Gynaecology, Medical University of Vienna, Vienna, Austria*
[3] *CNR Institute of Neuroscience, Padova, Italy*

Abstract*—Glucagon is a hormone secreted by the pancreatic alpha cells and plays a key role in glucose homeostasis and in the pathophysiology of type 2 diabetes (T2D). Different mechanisms are involved in its regulation, but exact mechanisms are still largely unknown. This study aimed to propose a model describing glucagon inhibition during an oral glucose tolerance test (OGTT), accounting for a double regulation mechanism. The model has been developed starting from a model previously proposed by our group that includes two differential equations, one for plasma glucagon and one for C-peptide (marker of insulin at pancreatic level). In the new model, in addition to plasma C-peptide, plasma glucose is included as model input. The model provides two parameters of possible clinical relevance, namely S_{GLUCA} and k_G (alpha-cell insulin and glucose sensitivity, respectively) and has been validated on mean literature data of healthy subjects and subjects affected by T2D (CNT and T2D, respectively). Model analysis yielded S_{GLUCA} estimates ranging from -0.1515 to 0.7629 and from -5.5602 to 1.1067 (ng of glucagon·nmol of C-peptide^{-1}) in CNT and T2D groups, respectively; according to the 95% confidence intervals (CIs), S_{GLUCA} was significantly different from zero in 4 and in 0 out of 8 time points, in CNT and T2D. Estimates for k_G were equal to 2.8302 (95% CIs: 1.1973 – 4.4632) and 0.9913 (95% CIs: -0.5559 – 2.5386) ng of glucagon·mmol of glucose^{-1}. Thus, results suggest both insulin (represented by C-peptide) and glucose significantly contributes to glucagon inhibition in healthy subjects, but not in T2D. In conclusion, the proposed model may help to describe different mechanisms acting on glucagon inhibition in the single individuals.

***Keywords*—Mathematical model, Parameter estimation, Glucose challenge test, Type 2 diabetes.**

I. Introduction

GLUCAGON is a hormone secreted by the alpha cells of the pancreas and it has the effect of elevating blood glucose level when it drops under normal values. Thus, in maintaining the glucose homeostasis glucagon appears to have an opposite action with respect to that of insulin (secreted instead by the beta cells of the pancreas). However, in recent years a more complex role has been ascribed for it beyond simple counterregulation of insulin especially in postprandial conditions [1]. Glucagon has also been given a role in pathophysiology of type 2 diabetes (T2D), but this is still controversial [2]. Indeed, in people with T2D, secretory defects of glucagon exist, resulting in inappropriately high glucagon levels in both fasting and postprandial states; however, also beneficial effects have been observed [3].

Remarkable evidence suggested that the regulation of glucagon secretion is achieved mainly through alpha-cell paracrine control by insulin (the so-called "intra-islet interaction"), but the role of other determinants of glucagon secretion or inhibition is not fully elucidated yet [4]. Especially, glucose may play a not-negligible role. Indeed, previous studies performed considering different macronutrients ingestion in healthy and in T2D subjects demonstrated that glucagon time patterns are highly heterogeneous, and the relationship with glucose and insulin strongly depends on the class of nutrients ingested [5].

Mathematical models may help to gain a deeper knowledge on the mechanisms relating glucagon kinetics to insulin and glucose. To date, a significant number of mathematical models accounting for glucagon contribution have been proposed, but just a few of them was designed to have potential applications to the clinical practice [6]–[12]. Among these models, those referring to glucose challenge tests are particularly suitable for this purpose [6], [7], [12]. In particular, the models by Kelly et al. [6] and Subramanian et al [7] were based on intravenous tests, which however are more difficult to perform compared to an oral glucose tolerance test (OGTT). In fact, our group proposed a mathematical model for the description of glucagon kinetics during an OGTT, providing the opportunity to individually estimate alpha-cell insulin sensitivity [12]. The aim of this study was to formulate an improved version of the previously proposed mathematical model to describe glucagon kinetics (especially, its inhibition) during an OGTT, by accounting for both mechanisms.

II. Materials and methods

A. Model formulation

The proposed model has been designed starting from the formulation previously proposed by our group [12] and considering inhibition of glucagon secretion during an OGTT as controlled by both insulin (C-peptide) and glucose-based mechanisms.

The latter, being the novelty of the present study, accounted for glucokinase activity [13], and were modelled considering glucagon inhibition controlled by the rate of change in plasma glucose. The former, as already done in the previous formulation [12], exploited plasma C-peptide as a marker of insulin secreted by the pancreatic beta cells (being C-peptide secreted equimolarly to insulin but not affected by clearance carried out by the liver).

The compartmental description of the model is depicted in Figure 1.

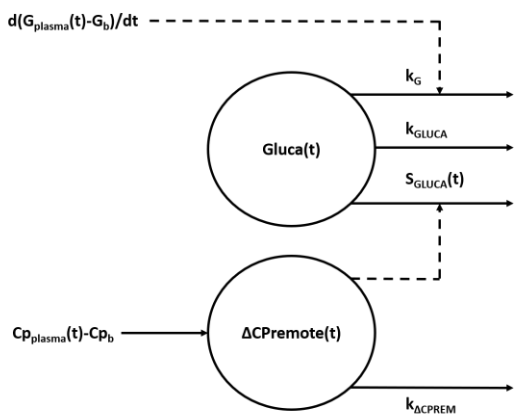


Fig. 1: Schematic representation of the compartmental model. The two compartments of the model are the plasma glucagon compartment, Gluca(t), and a delayed version of remote (from plasma) C-peptide, $\Delta CP_{remote}(t)$; the suprabasal C-peptide concentration in the remote compartment ($Cp_{plasma}(t)$-Cp_b) and the rate of change of suprabasal plasma glucose concentration ($G_{plasma}(t)$-G_b) exert a control action on Gluca(t) through the parameters $S_{GLUCA}(t)$ and k_G, respectively. k_{GLUCA} denotes glucagon elimination rate from plasma and $k_{\Delta CPREM}$ is the C-peptide elimination rate from the remote compartment.

The model is represented by two compartments, one for plasma glucagon and one for remote (from plasma) C-peptide, described by the following two differential equations:

$$\frac{dGluca(t)}{dt} = -k_{GLUCA}(t) \cdot Gluca(t) - k_G \cdot \frac{dG_{plasma}(t)}{dt} - S_{GLUCA}(t) \cdot \frac{d\Delta CP_{remote}(t)}{dt} \qquad Gluca(t) = Gluca_b \tag{1}$$

$$\frac{d\Delta CP_{remote}(t)}{dt} = -k_{\Delta CPREM} \cdot \Delta CP_{remote}(t) + \left(CP_{plasma}(t) - CP_b\right) \qquad \Delta CP_{remote}(0) = 0 \tag{2}$$

where Gluca(t) ($ng \cdot L^{-1}$) and $\Delta CP_{remote}(t)$ ($nmol \cdot L^{-1}$) represents the glucagon concentration in the plasma compartment and the suprabasal C-peptide concentration in a compartment remote from plasma, respectively. The first term on the right-hand side of Eq. (1) accounts for glucagon elimination from plasma due to clearance, through the clearance-rate parameter k_{GLUCA} (min^{-1}); the second term accounts for glucagon inhibition due to mechanisms controlled by the rate of change in plasma glucose (G_{plasma}, $mmol \cdot L^{-1}$) through the parameter k_G, representing the glucagon-inhibition sensitivity to glucose (*i.e.*, alpha-cell glucose sensitivity); eventually the third term accounts for glucagon inhibition due to paracrine mechanisms controlled by suprabasal C-peptide in a compartment remote from plasma through the time-varying parameter $S_{GLUCA}(t)$ (ng of glucagon·nmol of C-$peptide^{-1}$) representing glucagon-inhibition sensitivity to glucose-induced insulin secretion (*i.e.*, alpha-cell insulin sensitivity). Parameter $k_{\Delta CPREM}$ (min^{-1}) in Eq. (2) represents the C-peptide elimination rate from the remote compartment; CP_{plasma} represents plasma C-peptide concentration (CP_b being its basal value). G_{plasma} e CP_{plasma} are the model inputs.

B. Model implementation

The model has been implemented using Simulink and the parameter estimation procedure was set up on Matlab® R2022b. Values for the unknown model parameter vector $p=[k_{GLUCA}, k_{\Delta CPREM}, k_G, S_{GLUCA}(t)]$ have been estimated using the lsqnonlin function, providing a solution for the following nonlinear least-squares curve fitting problem:

$$\min_p \|f(p)\|_2^2 = \min_p \left[\text{RSS} + k_{GLUCA} + \frac{1}{k_G} + w1 \cdot S''_{GLUCA}(t) + w2 \cdot \text{count}(S_{GLUCA}(t) < 0)\right] \tag{3}$$

where RSS is the residual sum of squares, with residuals being the differences between model response and glucagon experimental measurements, and the other terms are added constraints that have been used to introduce further information to the problem. k_{GLUCA} denotes glucagon clearance and it should be small during an OGTT, during which the main contribution to glucagon suppression is given by insulin and glucose-based mechanisms. The term $1/k_G$ is included in equation (3) to prevent excessively small parameter values. $S_{GLUCA}''(t)$ is the second derivative of the parameter $S_{GLUCA}(t)$, and it is used to discourage abrupt changes of the parameter during the test. Similarly, including count($S_{GLUCA}(t)<0$) term allows limiting the number of samples where the parameter assumes negative values. Value for w1 and w2 weights has been manually adjusted. Using the lsqnonlin function, the trust-region-reflective algorithm has been selected, and the function and step-size tolerances have been set to 10^{-6}. Lower and upper bounds of parameter ranges have been set as follows: (0,1) for k_{GLUCA} and $k_{\Delta CPREM}$; ($-\infty$, $+\infty$) for k_G and $S_{GLUCA}(t)$; 95% confidence intervals (CIs) for all the model parameter estimates have been computed by using the nlparci function.

C. Model validation on reported mean experimental data

Mean experimental data used to validate the model are those reported in a recent study by Sonne et al. [14] involving 15 subjects having T2D and 15 healthy control subjects (CNT). All subjects underwent a 75 g OGTT, and blood samples were drawn 20, 10 and 0 min before and 15, 30, 45, 60, 90, 120, 180 and 240 min after glucose ingestion. The glucagon assay was directed against the C-terminal of the glucagon molecule and, thus, measures glucagon of pancreatic origin. In the present study, mean plasma glucose, C-peptide and glucagon concentrations in the two groups of the study by Sonne et al. [14] have been considered. Results are expressed as means±S.D. unless otherwise stated.

III. RESULTS

The best fit on mean experimental data reported by Sonne et al. [14] for CNT and T2D groups are shown in Figure 2, and the parameter estimates with related confidence intervals are reported in Table I. Trends of $S_{GLUCA}(t)$ for CNT and T2D during the whole OGTT is reported in Figure 3. According to the 95% CIs, estimates of $S_{GLUCA}(t)$ was significantly different from zero in 4 out of 8 time points in the CNT group, whereas in the T2D group $S_{GLUCA}(t)$ did not showed values significantly different from 0 throughout the whole OGTT. As regards k_G, lower values were found in T2D with respect to CNT; in the former value was not significantly different from 0, whereas in the latter a significant difference from 0 was found.

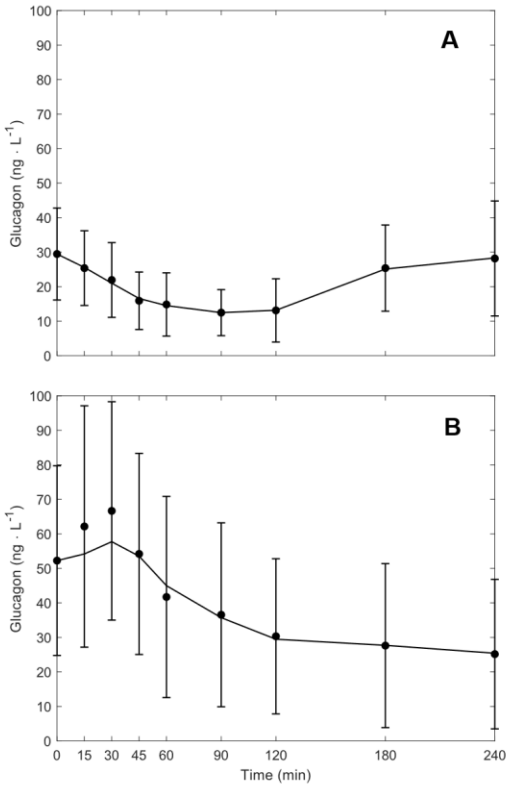


Fig. 2: Best fit of the model validated on mean experimental data by Sonne et al for the control group (panel A) and for the T2D group (panel B). Closed circles are the reference experimental values (mean ± SD); the continuous line is the model prediction.

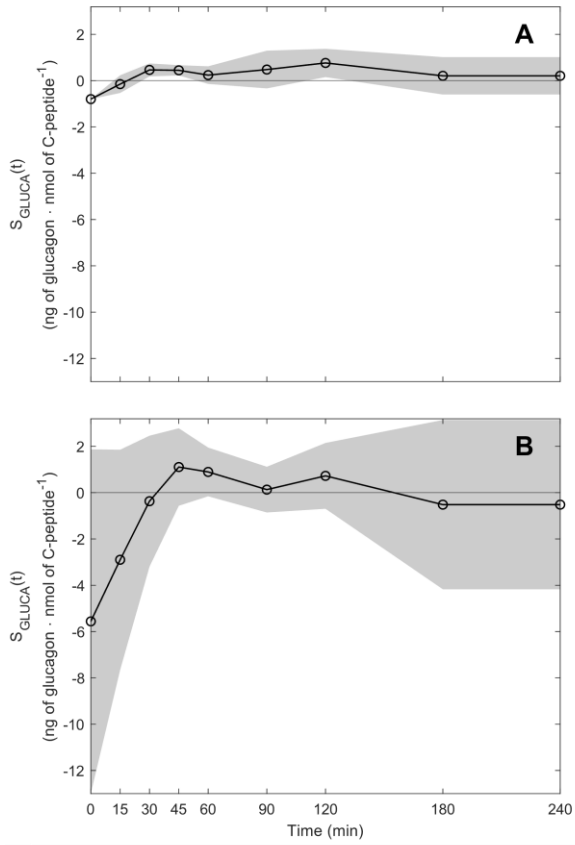


Fig. 3: $S_{GLUCA}(t)$ temporal estimates on reference mean experimental data for the control group (panel A) and for the T2D group (panel B) are shown with open circles and continuous line. Dashed lines represent related 95% CIs.

TABLE I: VALUES AND 95% CIS FOR THE ESTIMATES OF K_{GLUCA} (MIN^{-1}), $K_{\Delta CPREM}$ (MIN^{-1}), K_G (MIN^{-1}), S_{GLUCA} ($NG_{GLUCAGON}\cdot NMOL_{C\text{-}PEPTIDE}^{-1}$) ON REFERENCE MEAN EXPERIMENTAL DATA BY SONNE ET AL. [14] FOR THE CONTROL GROUP AND FOR THE T2D GROUP.

Estimated parameter	*Value*	*95% CI* [a]
	CNT [b] ***Group***	
k_{GLUCA}	$4.6673\ 10^{-6}$	-0.0073 – 0.0073
$k_{\Delta CPREM}$	0.0342	0.0290 – 0.03945
k_G	2.8302	1.1973 – 4.4632
S_{GLUCA1}	-0.7993	-0.7994 – -0.7993
S_{GLUCA2}	-0.1515	-0.5332 – 0.2302
S_{GLUCA3}	0.4620	0.1819 – 0.7420
S_{GLUCA4}	0.4449	0.2228 – 0.6670
S_{GLUCA5}	0.2375	-0.1428 – 0.6177
S_{GLUCA6}	0.4780	-0.3364 – 1.2924
S_{GLUCA7}	0.7629	0.1537 – 1.3720
S_{GLUCA8}	0.2069	-0.6035 – 1.0174
	T2D [c] ***Group***	
k_{GLUCA}	$9.1763\ 10^{-6}$	-0.0139 – 0.0139
$k_{\Delta CPREM}$	0.0096	-0.0078 – 0.0270
k_G	0.9913	-0.5559 – 2.5386
S_{GLUCA1}	-5.5602	-12.9854 – 1.8651
S_{GLUCA2}	-2.8988	-7.6482 – 1.8506
S_{GLUCA3}	-0.3694	-3.1971 – 2.4583
S_{GLUCA4}	1.1067	-0.5668 – 2.7802
S_{GLUCA5}	0.8949	-0.1576 – 1.9473
S_{GLUCA6}	0.1305	-0.8600 – 1.1210
S_{GLUCA7}	0.7260	-0.6903 – 2.1423
S_{GLUCA8}	0.2069	-4.1746 – 3.1374

[a] CI: Confidence Interval;
[b] CNT: Control;
[c] T2D: Type 2 Diabetes.

IV. DISCUSSION

This study proposed a mathematical model able to describe sensitivity of the alpha cell to insulin and glucose in the single individual during an OGTT. The new model has been derived from a former formulation proposed by our group [12]. Such former model was designed to account for paracrine mechanisms that lead to glucagon secretion/inhibition, and in particular it accounts for the control exerted by neighbouring beta cells secreting insulin according to the hypothesis called "intra-islet interaction". Thus, the main improvement of this new model formulation, was to include the contribution of mechanisms related to alpha-cell glucose sensing, under the consideration that the relationship linking glucagon to glucose and insulin is highly heterogenous and a model including different contributors of glucagon secretion may be important in capturing and elucidating such a high heterogeneity. Moreover, this may be of impact in understanding how

mechanisms and postprandial response change in relation to T2D state and/or to different macronutrients ingestion. Indeed, paracrine control of glucagon secretion is compromised in T2D state [15], resulting in a V-shaped non-physiological dose response to glucose with maximal exocytosis at hyperglycaemia.

Results of model validation on mean data of healthy and T2D subjects demonstrated that the proposed model provides results that are consistent with physiological and clinical observations. Indeed, both insulin and glucose-based mechanisms may play a remarkable role in determining glucagon secretion or inhibition (and thus, glucagon time course), as demonstrated by k_G and $S_{GLUCA}(t)$ values significantly different from zero in the healthy group. In contrast, in the T2D group, both glucagon regulation controls are impaired (S_{GLUCA} (t) and k_G not significantly different from zero), resulting in a defective glucagon inhibition.

Similarly to the previous model formulation, the new one was conceived to allow individual estimation of all model parameters and thus, it was maintained as simple as possible. No additional compartment was added to account for glucose contribution, which was represented as an input to the model. In more detail, the glucose regulation mechanism was modelled as dependent on glucose-concentration rate of change rather than the absolute value, consistently with results of studies on animal models showing that in the alpha cell the regulation of glucose sensing is operated by glucokinase [13], whose activity is driven by changes in plasma glucose [16].

Considering the postulated model structure, the addition of penalties in the form of constraints in the parameter estimation procedure was necessary to overcome the problem of ill-posedness and prevent overfitting. In particular, constraints on $S_{GLUCA}(t)$ were already included in the former model formulation with the aim of preventing excessively rapid variations and favouring the occurrence of positive rather than negative values (considering that suppression during OGTT is more likely than stimulation). In this new study, one further constraint has been added, related to k_G, to avoid the contribution of the glucose-based mechanism being excessively small, and possibly collapsing into other parameters. In addition, k_G was allowed to assume positive and negative values, indicating that, in principle, glucose may either inhibit or stimulate glucagon secretion.

Several others factors have been shown to possibly modulate glucagon secretion from alpha cells, including nutritional as well as chemical and ambient factors [17], [18]. As a fact, there are aspects of glucagon contribution to glucose homeostasis that still need clarification. Future models may consider the role of these other factors that, as for its intended purpose, the present model has disregarded.

V. Conclusion

In conclusion, the proposed model allows estimation of alpha-cell sensitivity to insulin and glucose in the single individual, and thus it may help to characterize distinct mechanisms acting on glucagon inhibition on different individuals and conditions.

References

[1] M. E. Capozzi *et al.*, "Glucagon lowers glycemia when β cells are active," *JCI Insight*, vol. 4, no. 16, Aug. 2019, doi: 10.1172/jci.insight.129954.

[2] I. Caruso *et al.*, "Glucagon in type 2 diabetes: Friend or foe?," *Diabetes. Metab. Res. Rev.*, Jan. 2023, doi: 10.1002/dmrr.3609.

[3] A. Lund, J. I. Bagger, M. Christensen, F. K. Knop, and T. Vilsbøll, "Glucagon and Type 2 Diabetes: the Return of the Alpha Cell," *Curr. Diab. Rep.*, vol. 14, no. 12, p. 555, Dec. 2014, doi: 10.1007/s11892-014-0555-4.

[4] J. W. Hughes, A. Ustione, Z. Lavagnino, and D. W. Piston, "Regulation of islet glucagon secretion: Beyond calcium," *Diabetes, Obes. Metab.*, vol. 20, pp. 127–136, Sep. 2018, doi: 10.1111/dom.13381.

[5] C. Göbl *et al.*, "Temporal Patterns of Glucagon and Its Relationships with Glucose and Insulin following Ingestion of Different Classes of Macronutrients," *Nutrients*, vol. 14, no. 2, p. 376, Jan. 2022, doi: 10.3390/nu14020376.

[6] R. A. Kelly, M. J. Fitches, S. D. Webb, S. R. Pop, and S. J. Chidlow, "Modelling the effects of glucagon during glucose tolerance testing," *Theor. Biol. Med. Model.*, vol. 16, no. 1, p. 21, Dec. 2019, doi: 10.1186/s12976-019-0115-3.

[7] V. Subramanian, J. I. Bagger, J. J. Holst, F. K. Knop, and T. Vilsbøll, "A glucose-insulin-glucagon coupled model of the isoglycemic intravenous glucose infusion experiment," *Front. Physiol.*, vol. 13, Sep. 2022, doi: 10.3389/fphys.2022.911616.

[8] V. Mojto, Z. Rausova, J. Chrenova, and L. Dedik, "Short-term glucagon stimulation test of C-peptide effect on glucose utilization in patients with type 1 diabetes mellitus," *Med. Biol. Eng. Comput.*, vol. 53, no. 12, pp. 1361–1369, Dec. 2015, doi: 10.1007/s11517-015-1416-2.

[9] D. Lv, M. D. Breton, and L. S. Farhy, "Pharmacokinetics Modeling of Exogenous Glucagon in Type 1 Diabetes Mellitus Patients," *Diabetes Technol. Ther.*, vol. 15, no. 11, pp. 935–941, Nov. 2013, doi: 10.1089/dia.2013.0150.

[10] A. Shirin, F. Della Rossa, I. Klickstein, J. Russell, and F. Sorrentino, "Optimal regulation of blood glucose level in Type I diabetes using insulin and glucagon," *PLoS One*, vol. 14, no. 3, p. e0213665, Mar. 2019, doi: 10.1371/journal.pone.0213665.

[11] S. Masroor, M. G. J. van Dongen, R. Alvarez-Jimenez, K. Burggraaf, L. A. Peletier, and M. A. Peletier, "Mathematical modeling of the glucagon challenge test," *J. Pharmacokinet. Pharmacodyn.*, vol. 46, no. 6, pp. 553–564, Dec. 2019, doi: 10.1007/s10928-019-09655-2.

[12] M. Morettini, L. Burattini, C. Göbl, G. Pacini, B. Ahrén, and A. Tura, "Mathematical Model of Glucagon Kinetics for the Assessment of Insulin-Mediated Glucagon Inhibition During an Oral Glucose Tolerance Test," *Front. Endocrinol. (Lausanne).*, vol. 12, Mar. 2021, doi: 10.3389/fendo.2021.611147.

[13] T. Moede *et al.*, "Glucokinase intrinsically regulates glucose sensing and glucagon secretion in pancreatic alpha cells," *Sci. Rep.*, vol. 10, no. 1, p. 20145, Nov. 2020, doi: 10.1038/s41598-020-76863-z.

[14] D. P. Sonne, J. F. Rehfeld, J. J. Holst, T. Vilsbøll, and F. K. Knop, "Postprandial gallbladder emptying in patients with type 2 diabetes: potential implications for bile-induced secretion of glucagon-like peptide 1," *Eur. J. Endocrinol.*, vol. 171, no. 4, pp. 407–419, Oct. 2014, doi: 10.1530/EJE-14-0309.

[15] M. Omar-Hmeadi, P.-E. Lund, N. R. Gandasi, A. Tengholm, and S. Barg, "Paracrine control of α-cell glucagon exocytosis is compromised in human type-2 diabetes," *Nat. Commun.*, vol. 11, no. 1, p. 1896, Apr. 2020, doi: 10.1038/s41467-020-15717-8.

[16] E. Van Schaftingen, "Energy Metabolism | Hexokinase/Glucokinase," in *Encyclopedia of Biological Chemistry III*, 3rd ed. vol. 1, E. Jez, Ed. Oxford: Elsevier, 2021, pp. 149–161.

[17] S. Hædersdal, A. Lund, F. K. Knop, and T. Vilsbøll, "The Role of Glucagon in the Pathophysiology and Treatment of Type 2 Diabetes," *Mayo Clin. Proc.*, vol. 93, no. 2, pp. 217–239, Feb. 2018, doi: 10.1016/j.mayocp.2017.12.003.

[18] G. C. Mannino, E. Mancuso, S. Sbrignadello, M. Morettini, F. Andreozzi, and A. Tura, "Chemical Compounds and Ambient Factors Affecting Pancreatic Alpha-Cells Mass and Function: What Evidence?," *Int. J. Environ. Res. Public Health*, vol. 19, no. 24, p. 16489, Dec. 2022, doi: 10.3390/ijerph192416489.

Network model accounts for evolution of EEG functional connectivity in patients with cognitive decline

L. G. Amato[1,2], A. V. Vergani[1,2], M. Lassi[1,2], R. Mannella[3], V. Bessi[4], A. Grippo[5] and A. Mazzoni[1,2]
[1] *The BioRobotics Institute, Scuola Superiore Sant'Anna (Pisa)*
[2] *Dept. of Excellence in Robotics and AI, Scuola Superiore Sant'Anna (Pisa)*
[3] *Dipartimento di Fisica, Università di Pisa (Pisa)*
[4] *Dept. of Neuroscience, Psychology, Drug Research and Child Health, Careggi University Hospital (Firenze)*
[5] *IRCCS Fondazione Don Carlo Gnocchi (Firenze)*

***Abstract*—Aggressive forms of dementia like Alzheimer's disease (AD) are known to cause deep structural alterations in the brain of affected subjects. The state of these alterations is nowadays deduced from invasive and/or expensive imaging techniques such as Magnetic Resonance Imaging and Positron Emission Tomography. Herein, we present a novel biophysically-inspired multi-scale cortical network model of disease progression enabling the reconstruction of AD-related structural alterations from resting state electroencephalography (EEG). The model, based on the The Virtual Brain platform, reproduced EEG features (power spectral alterations and changes in functional connectivity) of subjects in prodromic states of AD, i.e., subjective cognitive decline (SCD) and mild cognitive impairment (MCI). In particular, the model accounts for the counter-intuitive finding that subjects with SCD display a stronger functional connectivity than both MCI subjects and healthy controls. This model paves the way for an EEG-based reconstruction of patient-specific structural alterations.**

***Keywords*—Dementia, EEG, Computational models.**

I. INTRODUCTION

The diagnosis of Alzheimer's disease is an extremely difficult task. The only certain diagnostic method nowadays known is the autoptic exam [1], nonetheless, there are many imaging techniques that can determine the presence and even the severity of the disease in the human brain such as MRI, PET, and extraction of cerebrospinal fluid (CSF). However, these techniques are either very demanding for the dispensing facility, or stressful for the patient receiving it, or both. The evident drawbacks of such imaging techniques cause the clinicians to usually prescribe these tests when there are already evident signs of the disease. Moreover, in the last years, great attention has been paid to pre-AD states such as mild cognitive impairment [2] (MCI), and in cognitive complaints in people without evident symptoms of dementia, a condition called subjective cognitive decline [3] (SCD). People falling in these categories show a high probability of transition to AD [3], and would benefit the most from an early diagnosis of the disease, but are often excluded from imaging techniques with high discriminating power, for the reasons beforehand stated. On the other hand, EEG is a fast and cheap screening exam, that has been used reliably as a diagnostic tools for diseases such as epilepsy and stroke. EEG recordings in the resting state have also been used to discriminate AD patients from healthy subjects [4], and there are known EEG biomarkers of AD, mostly related to the spectral content and the functional connectivity (FC) computed from the recorded signals. However, when it comes to AD diagnosis, EEG is a far inferior tool when compared to more invasive and demanding tests such as MRI [5]. In the past years, along with standard imaging techniques, several computational tools have seen widespread use in modelling both physiological and pathological conditions. Many computational models have been able to capture salient features of AD such as the spreading of the disease in the human cortex and the alteration of brain waves [6], but there is no model nowadays able to describe local and global alterations of Alzheimer's in a biophysically realistic fashion. We here propose a hybrid clinical and computational pipeline, in which a multi-scale network model of disease progression - implemented in the The Virtual Brain software [7] - is used alongside experimentally recorded resting state EEG signals to determine the state of AD-related structural alterations. This constitutes the first example of a personalized, computational model of disease progression that doesn't rely on structural data (e.g. MRI or PET scans) to obtain a high fidelity to experimental recordings while also providing viable explanations for the experimentally observed alterations.

II. METHODS

A. Subjects recruiting and diagnosis

We collected EEG signals from 30 subjects sitting in a chair with eyes closed in a comfortable position for 30 minutes. The recorded signals were preprocessed according to the PREP pipeline [8] with subsequent ICA analysis in order to remove artifacts from the signals. The subjects were divided into three groups, healthy control group (HC, n = 9), SCD (n = 9) and MCI (n = 12) subjects. The assignment of subjects to these groups was based on extensive neurophysiological

assessments of cognitive performance and complaints of the subjects, along with an analysis of peripheral blood samples, to determine the presence of molecular hallmarks of the disease such Apolipoptrotein E and BDNF gentoypes.

B. EEG features

We then performed a quantitative analysis on the recorded signals, to assess the presence of significant difference between the EEG recordings of the three groups. We analyzed power spectral density (PSD) and functional connectivity between electrodes. We computed the average PSD for each group, comparing the results to assess the presence of significant differences between groups. PSD was computed with Welch method with Hanning windowing. We analyzed FC by computing the average FC matrices for each group, that we then thresholded and binarized to assess the differences in the number of significant functional connections between groups. FC was computed in all frequency bands except for gamma, whose values are too small to be used to deduce functional connections between electrodes. We also computed the time-domain FC, as envelope correlation between electrodes. We used one-way ANOVA f-test as statistical test to assess differences between groups.

C. Personalized network model of dementia progression

We developed a multi-scale cortical network model by using the TVB platform. This model is able to describe the electrophysiological activity of n=76 cortical regions by means of a network of neural masses. Connections between these masses are determined by a structural connectivity matrix that assigns to each pair of regions i and j a connective weight $C_{i,j}$; this matrix is a mathematical representation of the human connectome [9]. The masses capture in a mean-filed approximation the extracellular voltage fluctuations due to neuronal activity. We utilized the Jansen-Rit model [10] to describe the activity of each mass. The Jansen-Rit is a neural mass model that depicts every cortical region as a sum of three neuronal subpopulations (pyramidal and stellate cells along with inhibitory interneurons); we chose this model because it produces waves with the same spectral and dynamical features of the resting state EEG [10]. Parameters of the model are reported in Table 1. We then implemented AD-related circuital anomalies by changing the parameters of our model in both the meso (neural mass model) and macro (structural connectivity) scale. We altered the characteristic times of inhibitory and excitatory synapses [11] in the neural mass model, and the connective weights in the structural connectivity matrix, to introduce known AD-related alterations such as excitatory/inhibitory imbalance [11], hyperexcitation [12], white matter atrophy [13]. We also considered neuroplasticity [14] when altering the $C_{i,j}$ of the structural connectivity matrix. These alterations were introduced in the regions that are usually initially affected by the disease, according to the well-known Braak staging [15]. We condensed the meso-scale alterations of the neural mass models in a single local parameter lp, and the structural macro-scale alterations of the connectome in a connectivity parameter cp. Both parameters range from 0 to 1, with their value increasing with the severity of the condition.

TABLE I: Model Parameters

Parameter	*Description*	*Value*
A	Maximum Excitatory post-synaptic potential	3.25 mV
B	Maximum Inhibitory post-synaptic potential	22.0 mV
τ_e	**Excitatory time constant**	10 ms
τ_i	**Inhibitory time constant**	20 ms
v_0	Voltage threshold for which a 50 % firing rate is achieved	6.0 mV
ν_{max}	Maximum firing rate of neural population	0.0025 s^{-1}
r	Steepness of sigmoidal transfer function	0.56 mV^{-1}
C_1	Average probability of synaptic contacts in the feedback excitatory loop	1.0
C_2	Average probability of synaptic contacts in the slow feedback excitatory loop	0.8
C_3	Average probability of synaptic contacts in the feedback inhibitory loop	0.25
C_4	Average probability of synaptic contacts in the slow feedback inhibitory loop	0.25
η	Mean input noise	0.22 s^{-1}

We simulated brain waves with this model for various combinations of the parameters describing the disease progression, and we computed PSD and FC from these simulated signals with the same methods discussed in the previous subsection. We then compared the PSD and FC obtained from simulated signals with those computed from experimental EEG recordings, looking for the combination of lp and cp that best fitted the value of both quantities. We thus obtained three combinations of parameters that describe the structural alterations operated by the disease, one per group. These combinations should describe the average level of synaptic and connectomic degeneration for each group.

III. RESULTS

The PSD displayed significant differences between groups in the alpha (f = 6.87, p = 0.011) and theta (p = 4.88, p = 0.37) bands. In both delta and theta bands, average spectral power was higher for MCI subjects than for SCD, and for SCD than HC. A precise ordering is also present in the alpha band, where power is higher in HC than in SCD subjects, and in SCD than in MCI ones, see Figure 1a.

A non-linearity in the number of significant connections emerged from FC analysis (Figure 1b-c). In particular, we found that the HC group had an average of 26.4 % of significant connections, while the SCD group had 28.3 % and the MCI had 23.5 %. Overall, these findings are coherent with the known literature on AD biomarkers in EEG [4]

The quantitative analysis of EEG allowed us to fit the model parameters to describe both the spectral and FC features computed from experimental signals. We found three combinations of parameters, one per group, whose ordering is consistent with the severity of the diagnosed condition. In particular, we

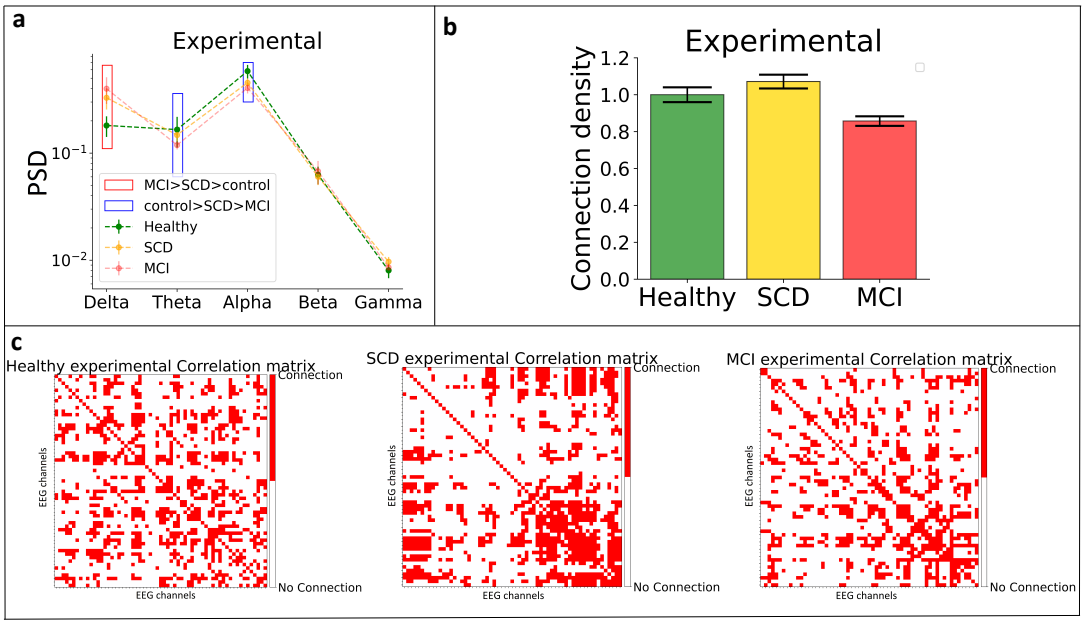


Fig. 1: FC and PSD features computed from experimental recordings: **a**: Band-wise PSD for each group. (* = p < 0.05) **b**: Barplot of the average FC density for each group **c**: Average thresholded FC matrix for each group

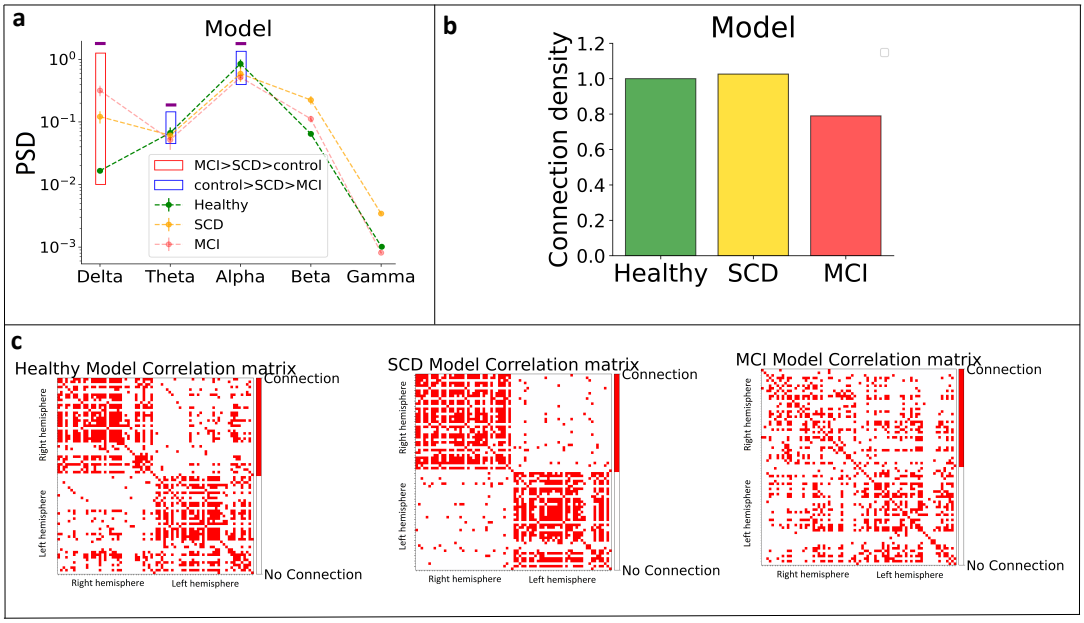


Fig. 2: FC and PSD features computed from simulated signals: **a**: Band-wise PSD for each group. (* = p < 0.05) **b**: Barplot of the average FC density for each group **c**: Average thresholded FC matrix for each group

found, for HC: lp = 0.52, cp = 0.24; for SCD: lp = 0.64, cp = 0.46; for MCI: lp = 0.74, cp = 0.90.

These combinations of model parameters were able to reproduce the ordering of PSD observed in experimental recordings in delta, theta and alpha bands, although difference were significant in the theta band only (f = 3.82, p = 0.04 in the theta band, f = 3.38, p = 0.063 in delta and f = 1.69, p = 0.22 in alpha, see Figure 2a). We reproduced also the non-linearity of FC values (24.0 % relevant functional connections in the modeled HC network, 24.8 % in the SCD, and 19.1 %

in the MCI one, Figure 2b-c). Furthermore, the model allows us to propose an explanation for the non-linearity observed in the FC. In fact, we found a quantity of the network, computed from the structural connectivity matrix, to also display a non-linear evolution during disease progression (Figure 3a) highly similar to that of FC connections. This quantity, called the Randic index [16] that is linked with network assortativity and the rich-club phenomenon [9], by bridging between the state of structural and functional connections, could explain why we observed a transient FC increase. Interestingly, in fact, when we computed the evolution of the Randic index in a network where all the dementia-related structural alterations were present, but with no neuroplastic effects, we found the Randic to evolve monotonously (Figure 3b). This would suggest that neuroplastic adjustments could explain the experimentally observed FC-nonlinearity.

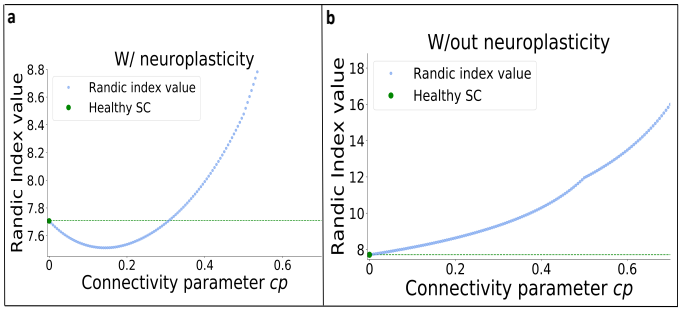


Fig. 3: **a**: Randic index evolution according to *cp* in the model with neuroplastic adjustments **b**:Randic index evolution according to *cp* in the model with no neuroplastic adjustments

IV. CONCLUSIONS

We presented a novel model of local synaptic degradation and global connectivity alterations due to the progression of cognitive decline. The model was validated comparing simulated neurophysiological features to EEG recorded in patients in healthy, SCD and MCI condition, and highlighted the mechanisms underlying non-monotonous evolution of functional connectivity. We plan to apply this approach to develop a personalized model of structural alterations underlying cognitive decline.

ACKNOWLEDGEMENTS

This project is funded by Tuscany Region - PRedicting the EVolution of SubjectIvE Cognitive Decline to Alzheimer's Disease With machine learning - PREVIEW - CUP. D18D20001300002.

REFERENCES

[1] Stefanovski et al. "Bridging Scales in Alzheimer's Disease: Biological Framework for Brain Simulation With The Virtual Brain". In: *Frontiers in Neuroinformatics* 15 (2021), p. 630172.

[2] Albert et al. "The diagnosis of mild cognitive impairment due to Alzheimer's disease: recommendations from the National Institute on Aging-Alzheimer's Association workgroups on diagnostic guidelines for Alzheimer's disease". In: *Alzheimer's & dementia* 7.3 (2011), pp. 270–279.

[3] Jessen et al. "A conceptual framework for research on subjective cognitive decline in preclinical Alzheimer's disease". In: *Alzheimer's & dementia* 10.6 (2014), pp. 844–852.

[4] Horvath et al. "EEG and ERP biomarkers of Alzheimer's disease: a critical review." In: *Frontiers in bioscience (Landmark edition)* 23 (2018), pp. 183–220.

[5] Farina et al. "A comparison of resting state EEG and structural MRI for classifying Alzheimer's disease and mild cognitive impairment". In: *NeuroImage* 215 (2020), p. 116795.

[6] Stefanovski et al. "Linking molecular pathways and large-scale computational modeling to assess candidate disease mechanisms and pharmacodynamics in Alzheimer's disease". In: *Frontiers in computational neuroscience* 13 (2019), p. 54.

[7] Sanz Leon et al. "The Virtual Brain: a simulator of primate brain network dynamics". In: *Frontiers in neuroinformatics* 7 (2013), p. 10.

[8] Bigdely-Shamlo et al. "The PREP pipeline: standardized preprocessing for large-scale EEG analysis". In: *Frontiers in neuroinformatics* 9 (2015), p. 16.

[9] Olaf Sporns. *Networks of the Brain*. MIT press, 2016.

[10] Ben H Jansen and Vincent G Rit. "Electroencephalogram and visual evoked potential generation in a mathematical model of coupled cortical columns". In: *Biological cybernetics* 73.4 (1995), pp. 357–366.

[11] Fernando Maestú et al. "Neuronal excitation/inhibition imbalance: core element of a translational perspective on Alzheimer pathophysiology". In: *Ageing Research Reviews* 69 (2021), p. 101372.

[12] Matthew R Hynd, Heather L Scott, and Peter R Dodd. "Glutamate-mediated excitotoxicity and neurodegeneration in Alzheimer's disease". In: *Neurochemistry international* 45.5 (2004), pp. 583–595.

[13] Agosta et al. "White matter damage in Alzheimer disease and its relationship to gray matter atrophy". In: *Radiology* 258.3 (2011), pp. 853–863.

[14] Bruce Teter and J Wesson Ashford. "Neuroplasticity in Alzheimer's disease". In: *Journal of neuroscience research* 70.3 (2002), pp. 402–437.

[15] Heiko Braak, Eva Braak, and Jürgen Bohl. "Staging of Alzheimer-related cortical destruction". In: *European neurology* 33.6 (1993), pp. 403–408.

[16] Xueliang Li and Yongtang Shi. "A survey on the Randic index". In: *MATCH Commun. Math. Comput. Chem* 59.1 (2008), pp. 127–156.

Noise-Induced Dynamics and Stochastic Slow Manifolds in the Bistable Xiong-Ferrell Model

M. Martin[1] and M.G. Pedersen[1]
[1] *University of Padova, Department of Information Engineering*

***Abstract* — In biology many phenomena involve noise and multiple time scales. Noise may be constructive and induce dynamics not seen in the deterministic version of the system of interest. The aim of this work is to give an explanation to the noise-induce dynamics observed in a polynomial simplification of the Xiong-Ferrell model as the noise variance (γ) and stimulation intensity (S) are changed. To understand this behaviour, the Stochastic Differential Equation (SDE) system is analysed with the use of a slow manifold statistical description and converted into an Ordinary Differential Equation (ODE) system via the G method, to investigate the location of saddle-node bifurcations in the (S, γ) plane. Our results explain why, due to and depending on the delocalization of these latter bifurcations, the system might present fluctuations around a stable equilibrium or exhibit noise-induced transitions and oscillations.**

***Keywords* — Modelling, Stochastic Dynamics, Bistability, Slow-fast dynamics, Bifurcation**

I. Introduction

Noise influences biological processes at all scales. In cellular systems, noise reduces the duration of beta cell's burst [8] and alters the behaviour of single neurons and neuronal network [3], [4] and [9]. In genetics, noise is an intrinsic property of the system due to the low copy number in genetic networks [10], [11]. Noise-induced phenomena that cannot be explained with the features of the corresponding deterministic model are known as noise-induced effects [6].

In dynamical systems theory, qualitative changes of the model's behaviour when varying parameters are known as bifurcations. For deterministic models, bifurcations occur in general for discrete values of some parameter. On the other hand, in stochastic models, bifurcations can occur smoothly in a parameter range, and moreover may be classified as phenomenological or dynamical [7], where the former are linked to changes in the stationary probability distribution.

The main aim of this work consists in analysing a simplified formulation of the Xiong-Ferrell model [1] under the perturbation by coloured noise. This model was developed to explain how positive feedback loops in complex gene networks may irreversibly alter biological functions, as experimentally observed in the p42 MAPK/Cdc2 system during Xenopus oocytes maturation. The analysis will be done via the extended Rodriguez and Tuckwell approximation [4] known as the G method [3], which shares the same rationale presented in [12]. The motivation behind this approach is to simplify the analysis of the stochastic system to a set of ODEs that describe the evolution of the averages, variances and covariances of the stochastic variables. This approach assumes that variables are normally distributed, which turns the approximation into an exact computation for polynomial models [3], [4].

The remainder of the paper is divided into three sections. In the first, model and methodologies are introduced. The second section outlines the main results by focusing on the stochastic slow manifold and, finally, conclusions are presented.

II. Methods

A. Reference Model and Simplification

In the present work the reference model, which was initially proposed in [1], is

$$\frac{dA}{dt} = S + f\frac{A^n}{A^n + K^n} - k_i A = S + G(A),$$

where A is the protein expressed concentration, S the external applied stimulus, f the positive feedback strength and k_i the degradation rate.

To apply the G method without introducing truncation errors, we approximate the cubic-shaped function $G(A)$ with a third-order polynomial $P(A)$ via a least-square procedure. The obtained estimates are reported in Table I. The considered deterministic model is therefore

$$\frac{dA}{dt} = S + p_3A^3 + p_2A^2 + p_1A + p_0 = S + P(A).$$

To understand the role of the noise, the external stimulus S is perturbed by coloured noise modelled via an Ornstein Uhlenbeck random process (OU process), leading to the following SDE system,

$$\frac{dA}{dt} = S + y_t + P(A),$$
$$dy_t = -\frac{1}{\tau}y_t dt + \frac{\gamma}{\tau}dW_t.$$

Here, dW_t is a white noise term with mutually uncorrelated samples and null expected value. Hence, y_t is an OU process, which acts on the stimulus applied to the model. The statistical properties of the OU process are:

$$\mathbb{E}[y_t] = y_0 e^{-\frac{t}{\tau}},$$
$$\mathbb{E}[(y_t - \mathbb{E}[y_t])^2] = \frac{\gamma^2}{2\tau}\left(1 - e^{-\frac{2t}{\tau}}\right). \quad (1)$$

Therefore, the parameters γ and τ act on the variance and on the convergence time. For sake of simplicity, in all simulations, the Initial Condition (IC) for y_t was $y_0 = 0$ yielding $\mathbb{E}[y_t] = 0$.

The parameters chosen for the reference model and the ones derived for the simplified version are reported in Table I, where p_3, p_2, p_1 and p_0 have no direct physiological meaning. The parameters S and γ are varied to understand how they influence the model dynamics.

TABLE I: MODEL PARAMETERS

f	K	n	k_i	τ
0.5	0.5	5	0.8	500
p_3	p_2	p_1	p_0	τ
-8.206	11.799	-5.189	0.514	500

B. Numerics

Computations were done with XPPAUT [2], and Matlab [5] was used for data post processing steps and visualisations. The SDE system was solved with a forward Euler method with time step equal to 0.01 time units. The ODE system was solved with an adaptive step-size, fourth order Runge-Kutta method.

C. Stochastic Analysis via G Method

Consider the SDE system with the polynomial approximation. We wish to evaluate and analyse how variations of γ and S change the model dynamics. The system is reduced to a set of ODEs using the approximations introduced by Rodriguez and Tuckwell [4] and its further development known as the G method [3]. To apply this latter, we assume that the dynamical variables are normally distributed. This assumption is perfectly satisfied for the variable y_t thanks to the statistical steady-state properties of the OU process. By applying the G method, the following ODE model can be derived,

$$\frac{d\mu_A}{dt} = S + p_3\mu_A^3 + p_2\mu_A^2 + (p_1 + 3p_3\sigma_A)\mu_A + (p_0 + p_2\sigma_A),$$

$$\frac{d\sigma_A}{dt} = 2\Sigma_{AY} + 2[3p_3\mu_A^2 + 2p_2\mu_A + p_1]\sigma_A + 6p_3\sigma_A^2,$$

$$\frac{d\Sigma_{AY}}{dt} = \frac{\gamma^2}{2\tau} + \left[3p_3\mu_A^2 + 2p_2\mu_A + p_1 + 3p_3\sigma_A - \frac{1}{\tau}\right]\Sigma_{AY}.$$

Here, the terms μ_A and σ_A represent, respectively, the mean and variance of A, whereas Σ_{AY} denotes the covariance between the protein concentration and the OU process. In the ODE system above, the mean and variance of the OU process are assumed to be in steady state, $\mathbb{E}[y_t] = 0$, $\mathbb{E}[y_t^2] = \gamma^2/2\tau$. These ODEs are analysed to infer the behaviour of the SDE system.

To illustrate how these equations are obtained, we present the derivation of the first equation. We have

$$\frac{d\mu_A}{dt} = \mathbb{E}\left[\frac{dA}{dt}\right] = S + \mathbb{E}[y_t] + \mathbb{E}[P(A)] = S + \mathbb{E}[P(A)],$$

where the right-hand-side can be computed by applying a Taylor series expansion around the mean, μ_A, of $P(A)$ and then the relationship is reduced by exploiting properties of higher order moments of the normal distribution. The Taylor expansion is

$$\mathbb{E}\left[P(A)|_{A=\mu_A}\right] = P(\mu_A) + \sum_{k=1}^{\infty}\frac{1}{k!}P^{(k)}(\mu_A)\mathbb{E}[(A-\mu_A)^k].$$

The derivatives of order higher than the degree of $P(A)$, as well as odd order moments, vanish. Therefore,

$$\mathbb{E}\left[P(A)|_{A=\mu_A}\right] = P(\mu_A) + 3p_3\mu_A\sigma_A + p_2\sigma_A.$$

We will denote this expression by $\mathcal{F}(\mu_A, \sigma_A)$.

III. RESULTS

A. Simulations

Depending on the values of the parameters S and γ, the system exhibits different kinds of behaviour. These resemble fluctuations around a stable equilibrium point (Figure 1a), simple transitions (Figure 1b), or oscillations (Figure 1c).

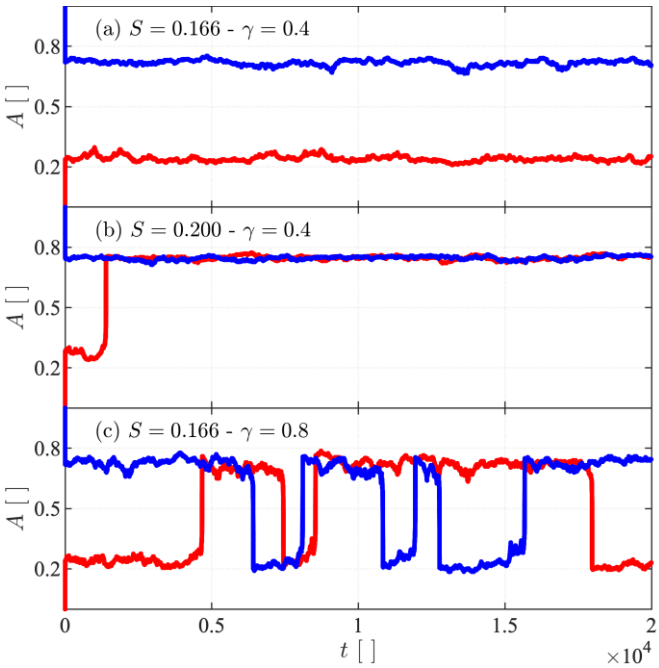


Fig. 1: Simulations of the stochastic polynomial model with parameters as in Table I and as specified. The red and blue traces indicate, respectively, simulations with $A(0) = 0$ and $A(0) = 1$.

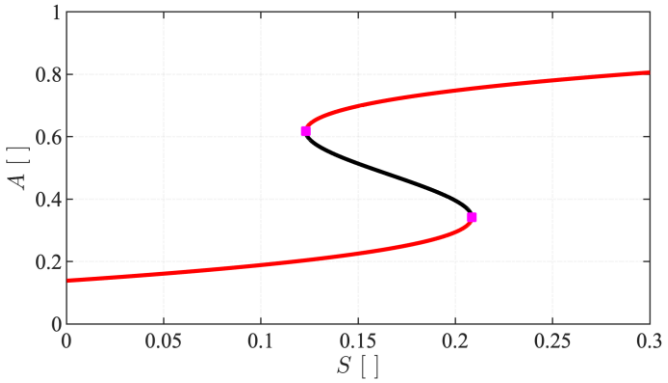


Fig. 2: Polynomial Xiong-Ferrell model bifurcation diagram. Two saddle node bifurcations are highlighted by the magenta squares. The right and left knees coordinates are respectively (0.123, 0.617) and (0.208, 0.342). The red and black branches indicate stable and unstable equilibrium points, respectively.

B. Deterministic Analyses

The bifurcation diagram associated to the deterministic polynomial model is shown in Figure 2. The model presents bistability for a range of the externally applied stimulus S. Therefore, for S in this interval the deterministic model evolves towards the upper or lower equilibrium point depending on the IC. The interval is limited by the values of S where the unstable and stable equilibria meet in saddle-node bifurcations. For values of S outside the bistable interval the trajectory evolves towards the unique stable equilibrium point admitted by the system. The s-shaped curve describing the equilibria can be found in closed form directly from the model's definition,

$$S = -p_3A^3 - p_2A^2 - p_1A - p_0 = -P(A).$$

C. Stochastic Analyses

1) Multiple Time Scale Interpretation

Consider now the SDE system and notice that the two variables evolve on different time scales. In fact, denoting the inverse of τ by ε, the system can be rewritten as

$$\frac{dA}{dt} = S + y_t + P(A),$$
$$dy_t = \epsilon[-y_t dt + \gamma dW_t].$$

Here, $\epsilon = 0.002 \ll 1$. Consequently, the variable y_t can be classified as slow while A as fast. This fact allows us to interpret the stochastic model as a multiple time-scale dynamical system.

The critical manifold $\mathcal{C}_0$ is obtained by setting $dA/dt = 0$ for $\epsilon = 0$. In this case, y_t can be treated as a parameter, which shifts the deterministic bifurcation diagram horizontally. Indeed, on average (over y_t) $\mathcal{C}_0$ coincides with the deterministic equilibrium curve. Moreover, its division into repelling and attracting submanifolds coincides with the stable and unstable branches shown in Figure 2.

This slow-fast interpretation of the model allows us to predict geometrically the evolution of the system in the presence of stochastic fluctuations, similarly to the analysis for deterministic slow-fast systems [6]. The trajectory rapidly approaches the attracting $\mathcal{C}_0$ submanifolds. Here, the dynamics is governed through its slow variable, thus noise-driven, and the system moves along $\mathcal{C}_0$ until it reaches a saddle-node bifurcation. Here, it may jump to the other attracting branch, and these large excursions are explained through the model's fast dynamics. See Figure 3 for examples of stochastic simulations starting from different ICs and for different parameters (corresponding to the traces in Figure 1) resulting in different types of behaviour.

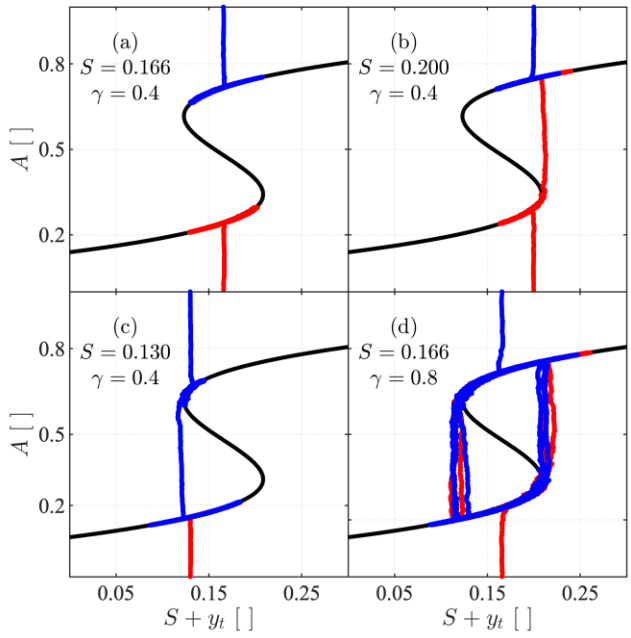


Fig. 3: Model simulations are started from $A(0) = 0$ (in red) or $A(0) = 1$ (blue). The black curve represents the average $\mathcal{C}_0$ in the singular limit, i.e., $S = -P(A)$. In (a) the system's trajectory fluctuates around a stable steady state. In (b) and in (c) only the right or the left SN is crossed, therefore single transitions are detected. In (d) the system's evolution crosses alternatively the two SNs, activating oscillations.

2) Critical Manifold Delocalization

The above reasoning is correct in the limit $\epsilon \to 0$. By relaxing this constraint, we expect that the system will evolve on a stochastic, slow manifold lying close to $\mathcal{C}_0$, i.e.,

$$S = -y_t - P(A) + O(\epsilon),$$

where the external stimulation S associated to an equilibrium point is stochastic and inherits A's random properties in addition to direct influence from the OU process.

From the previous relationship both the expected value and the variance of S, and hence of the stochastic slow manifold, can be derived. By applying the expectation operator and using $\mathbb{E}[y_t] = 0$ we get

$$\mathbb{E}[S] = -\mathbb{E}[P(A)],$$

where the right-hand-side was calculated in Section II.C. Thus,

$$\mu_S := \mathbb{E}[S] = -\mathcal{F}(\mu_A, \sigma_A),$$

and it follows that on average the slow manifold coincides with the manifold of equilibrium points of μ_A in the ODE system obtained with the G method.

By using the same approach, the variance of the external stimulus intensity S can be derived. We only outline the result as it is quite cumbersome.

$$\sigma_S = \mathbb{E}\left[\left(S - \mathbb{E}(S)\right)^2\right] = \mathbb{E}\left[\left(P(A) + y_t - \mathcal{F}(\mu_A, \sigma_A)\right)^2\right]$$
$$= \mathbb{E}[P^2(A)] - \mathcal{F}^2(\mu_A, \sigma_A) + \frac{\gamma^2}{2\tau} - 2\mathbb{E}[y_t P(A)],$$

where the first term is polynomial since $P(A)$ is polynomial, and hence its mean value can be computed exactly using the G method. The last term involves the covariance between A and y_t, Σ_{AY}, which is calculated using the G method as outlined in Section II.C. Therefore, both the variance and the expected value of a generic equilibrium point in the stochastic $\mathcal{C}_0$ can be computed from the ODE system obtained with the G method in Section II.C. This latter system can be analysed with bifurcation software such as the AUTO package in XPPAUT.

3) Two-Parameters Bifurcation Diagram

Intuitively, the system might jump to the other stable branch before reaching a saddle-node due to noise "pushing" the trajectory on the other side of the separating, unstable equilibrium. Such events correspond to a "translation" of the saddle-node point due to noise. Using the G-method ODE system and AUTO, we therefore follow the location of the saddle-node bifurcations when varying the noise strength γ. In Figure 4 we show the resulting two-parameters bifurcation diagram. As mentioned above, the result from the G method corresponds to the location of the average stochastic slow manifold. The chart shows how the saddle-node bifurcations move in the two-parameter plane by displaying both their average location and a centred symmetrical interval,

$$\left[\mu_S - \sqrt{\sigma_S}, \mu_S + \sqrt{\sigma_S}\right], \quad (2)$$

for each noise intensity level γ.

The background probability heatmap is generated from post processed data retrieved from Poincaré maps of 60 simulations executed for each (S, γ) combination, of the polynomial model. For each combination, half of the simulations were started at $A(0) = 0$ while the remaining ones had IC $A(0) = 1$. The total simulation windows were 10000- and 20000-time units, where the former was used for simulations with γ lower than 0.5, and the latter for γ above this value.

From Figure 4 the changes in model behaviour can be directly seen. In fact, a crucial point can be recognized. At the

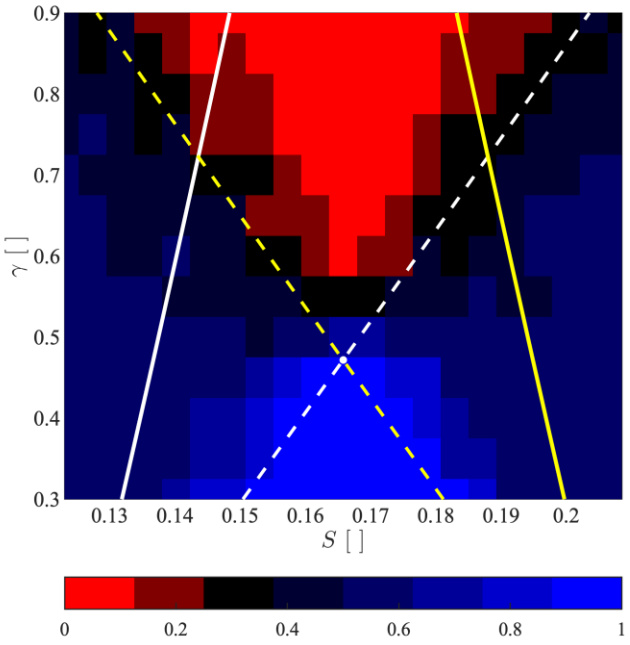


Fig. 4: Two-parameter bifurcation diagram of the G-method dynamical system with γ and S as bifurcation parameters. The continuous lines indicate the SN locations; the dashed lines the left-SN-upper and right-SN-lower boundary of the interval specified in (2). Right- and left-SN are colour-coded yellow and white, respectively.

cross between the two dashed curves, we observe a large increase probability of transition. This intersection separates the (S, γ) plane into four regions, which are discussed below.

The first section considered is the one in which the probability of observing a fluctuation around a steady state equilibrium point, with no large transition occurring, is great; this is the triangular zone below the crossing point. Indeed, the system behaviour is expected to evolve close to the upper or lower branch depending on the system's IC. An example is shown in Figure 3a.

The second and the third zones are located on the right and on the left of the dashed lines crossing point. In these areas, the empirical probability that an event will occur is ~50%. However, the only detected phenomenon are stochastic transitions. Deep in the right/left regions, the observable transitions are the one associated to the simulations that starts from, respectively low/high IC for A. This explains why a 50% probability of transition occurrence is detected. In fact, by considering the right region, only transitions in simulations that are started from the lower initial value will be activated. In contrast, for high initial value of A the noise does not present sufficiently large variance to make the system jumps back to the lower stable branch, so no transition is detected. The opposite rationale can be applied for the left zone. Examples of the system's evolution are given in Figure 3b and 3c.

The fourth section is the one associated to the upper triangular zone. In this region the SNs intervals specified in Eq. (2) overlaps and for these combinations of (S, γ) parameters the system has a higher propensity of generating stochastic oscillations due to model bistability, and not related to a Hopf bifurcation, as showed in Figure 3d.

These results reflect how the system is expected to evolve as the parameters are changed. In fact, increasing γ, which directly affects the steady state noise variance, as reported in Eq. (1), increases the noise-strength leading to a higher expectation of generating transition and stochastic oscillation. On the other hand, the activation of such phenomenon depends, once selected γ, also on the stimulus S since this latter defines, in the deterministic framework, the system's equilibrium points and therefore the nature of the evolution.

To conclude, note that the two-parameter bifurcation diagram of the ODE system is not enough to understand the SDE behaviour. This fact is because the information displayed is associated to $\mathbb{E}[S]$, which overestimates the value of γ at the crossing point. However, with additional information on the saddle-node standard deviation, the degree to which our analysis explains the results of the SDE model increases dramatically.

IV. Conclusion

Our method of analysing the model based on estimating the variance of the S coordinate of $\mathcal{C}_0$ in the stochastic system provides the basis to understand the underlaying dynamics by identifying the stochastic system's phenomenological bifurcation. In fact, as showed in Figure 4, the analytical results predict how to tune the parameter values of the system in order to maximise the probability of activating a given model activity, e.g., noise-induced oscillations. In synthetic biology, this method may play an important role. In fact, the coloured noise variance may be controlled via the introduction of new gene circuits that acts on the overall interfering network reducing or amplifying the noise strength.

In further studies, this methodology should be applied directly to the reference model in [1] and understand if, even in presence of error due to truncations of the Taylor expansion, the noise-induced activity maps may be sufficiently accurate and reliable.

References

[1] W. Xiong and J.E. Ferrell Jr, "A positive-feedback-based bistable 'memory module' that governs a cell fate decision", *Nature*, Vol. 426, 1983, pp. 460 – 465.

[2] B. Ermentrout, "Simulating, analyzing, and animating dynamical systems: a guide to XPPAUT for researchers and students", *SIAM*, Software Environ. Tools 14, 2002.

[3] S. Tanabe and K. Pakdaman, "Dynamics of moments of FitzHugh-Nagumo neuronal models and stochastic bifurcations", *Physical Review E*, Vol. 63, 2001, 031911.

[4] R. Rodriguez and H.C. Tuckwell, "Statistical properties of stochastic nonlinear dynamical models of single spiking neurons and neural networks", *Physical Review E,* Vol. 54, 1996, pp. 5585 – 5590.

[5] Matlab, Version 9.11.0.1837725 (R2021b).

[6] C. Kuehn, "Multiple time scale dynamics", *Applied Mathematical Sciences,* Vol. 191, *Springer,* 2015, pp. 447 – 524.

[7] L. Arnold, "Random Dynamical Systems", *Springer*, 2013

[8] M.G. Pedersen and M.P. Sorensen, "The effect of noise on β-cell burst period", *SIAM Journal on Applied Mathematics,* Vol. 67(2), 2007, pp. 530 – 542.

[9] M.E. Yamakou, T.D. Tran, and L.H. Duc, "The stochastic FitzHugh-Nagumo neuron model in the excitable regime embeds a leaky integrate- and fire model", *Journal of Mathematical Biology,* Vol. 79(2), 2019, pp. 509 – 532.

[10] D. Frigola, L. Casanellas, J.M. Sancho, and M. Ibañes, "Asymmetric stochastic switching driven by intrinsic molecular noise", *PLoS ONE,* Vol. 7(2), 2012, e31407.

[11] J.E. Ladbury and S.T. Arold, "Noise in cellular signaling pathways: causes and effects", *Trends in Biochemical Sciences,* Vol. 37(5), 2012, pp. 173 – 178.

[12] P. Whittle, "On the use of normal approximation in the treatment of stochastic processes", *Journal of the Royal Statistical Society,* Vol. 19(2), 1957, pp. 268 – 281.

From data to knowledge: definition of an exploratory dataset for deep brain stimulation

M. Prenassi[1], M. Ellero[1], A. Caruso[1], and S. Marceglia[1,2]
[1] *Department of Architecture and Engineering, Università degli studi di Trieste, Trieste, Italy*
[2] *U.O. Fisiopatologia, Fondazione IRCCS Ca' Granda Ospedale Maggiore Policlinico, Milano, Italy*

***Abstract*—Local Field Potentials from the basal ganglia are currently used in state-of-the art closed loop deep brain stimulation devices to guide automatic adaptation of DBS parameters. However, algorithms and methodologies for LFP-based closed loop DBS are still under investigation, especially to define reliable strategies to detect patient's clinical state. To support this research process, in this paper we describe the development of a LFP feature dataset that can be used in classification studies, and three different applications of the dataset. The dataset includes three types of LFP features: power spectral density estimates, burst features and spectral entropy. Relevant clinical and technical features were included to allow supervised learning. The dataset was created using data from 34 patients, for a total of 314 minutes of recording that resulted in a dataset of 21765 lines and 45 columns. The three applications showed that the dataset can be used to study classification algorithms, and that some positive results can be achieved with the present implementation. However, it requires to be further enhanced with more patient's data and conditions.**

***Keywords*—LFP, DBS, Machine Learning, Closed Loop DBS.**

I. Introduction

DEEP Brain Stimulation (DBS) is a neurosurgical procedure that involves the implantation of electrodes into the basal ganglia of the brain connected to an implantable pulse generator that provides a pulsed current to stimulate a target area. DBS is used to treat the symptoms of advanced Parkinson's Disease (PD), Tourette's Syndrome and other neurological disorders [1]. In Parkinson's disease, the target of election is the subthalamic nucleus (STN) [1]. New closed loop techniques [2]–[4] are capable of using the implanted electrode to record Local Field Potentials (LFPs) in the targeted area of the brain, and adapt the stimulation to the patient status. While closed-loop DBS devices are already tested in humans [3], there is increasing scientific enthusiasm on the possibility to record LFPs in a 24/7 fashion from implantable devices in chronic patients. Considering the large amount of data expected in the next year, machine learning techniques were proposed to analyze LFP data in order to better understand and regulate the effects of DBS stimulation [5], [6]. To do so, reliable datasets including characteristic features should be made available.

In this study we create a dataset based on LFP signals taken after a few days from the surgical implantation of DBS electrodes in PD patients in stable and replicable condition. As a proof-of-concept, the dataset will be used to model fast machine learning algorithms to classify various characteristics of the LFPs, aimed to 1) identify the patient, 2) identify the contacts from which the signal is acquired (See Figure 1) and 3) identify the hemisphere in which these signals were generated. These three cases were chosen because they could be of interest for closed-loop applications. More specifically, the first one is related to patient's data protection, and, in turn, assist in deidentification or normalization procedures. The second one could help the automatic definition of the best stimulation contact or it could be useful during electrode implantation to define the best implantation site. The third objective is a generalization of 2) but could be useful to assert the laterality of the brain to further improve the research in the field.

II. Methods

The dataset was created using retrospective data from 34 rigid-akinetic patients with advanced PD who underwent DBS electrode implantation surgery. The procedure and the experiments were carried out at the Neurosurgery Unit at Fondazione IRCCS Ca' Granda Ospedale Maggiore Policlinico Hospital in Milan, Italy. The patients were selected during three deep brain stimulation clinical studies [2], [3], [7]. All studies were approved by the institutional review board of the Policlinico Hospital and conformed with the Declaration of Helsinki. All patients provided written informed consent to the experimental procedures. Of the 34 patients here considered, 12 were included in the first study [7], 12 in the second one [3], and 10 in the third study [2]. No surgical complication was experienced by the patients selected.

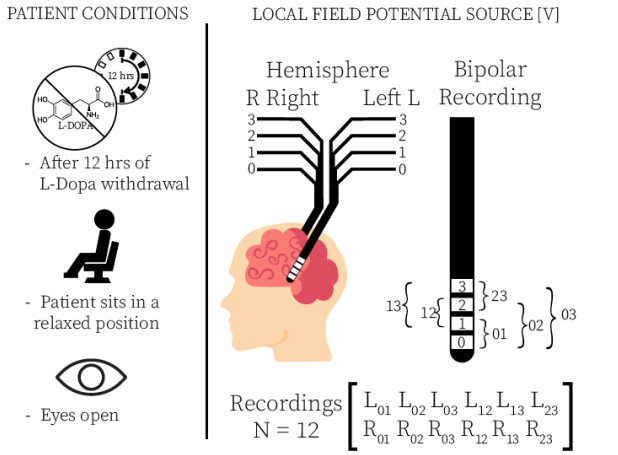


Figure 1: on the left the patients conditions, on the right the contact pair denominations and the electrode geometry.

A. Study Protocol:

The experimental sessions took place 5 days after the surgery, during normal hospital stay; all the experimental sessions took place with the contacts externalized before the connection to the subcutaneous pulse generator. The recordings used in this paper were collected in the morning after 12 hours withdrawal

of L-Dopa in a true "OFF" clinical status. Subjects sit on a chair in a relaxed position and with their eyes open during the recording sessions (Figure 1). The OFF recording lasted approximately 3 minutes. Immediately after the recording, the patients were disconnected from the acquisition amplifier and a UPDRS part III (UPDRSIII) evaluation was administered by a neurologist to quantitatively assess the clinical status. Normal therapy procedures were resumed soon after.

B. *Signal acquisition and pre-processing:*

Signal Acquisition: bipolar signals were recorded from a pair of contacts belonging to the same electrode (see Figure 1). LFPs were recorded using a standard amplifier (Model Grass ICP511, Astromed, USA) with gain 80 db, passband 1-100 Hz, 50Hz notch filter on. They were digitalized by a Micro1401-3 Analog to Digital converter (Cambridge Electronic Design, UK) at 256 samples/s and 16-bit resolution. The signals were displayed and saved using the Spike 2 software (Cambridge Electronic Design, UK) and the Matlab Software (The MathWorks, Inc., version 7.10.0, R2010a) was used to post-process the signals and to extract the features. The patients were included only if satisfactory multi-contact data were recorded (i.e. at least two recordings from at least two contact pairs from each hemisphere).

Pre-processing: this phase was divided in three steps: inspection, filtering, and normalization.

All the signals were manually inspected to remove initial dc drifts, when found. These artefacts duration was no more than 2 seconds. After the manual inspection, all signals were filtered by a bandpass FIR filter, Kaiser window, with a 3-dB cutoff between 1 Hz and 45 Hz.

Normalization: after filtering, each signal was normalized using a modified Min-Max procedure, designed to avoid offset, as shown in equation (1).

$$Min-Max: n_{MM}(t) = \frac{s(t)-\min(s(t))}{\max(s(t))-\min(s(t))} - \bar{s} \quad (1)$$

$n_{MM}(t)$: normalized signal, min-max

s(t): LFP signal

$\bar{s}$: the mean of s(t), this was subtracted to the Min-Max normalization to ensure a true zero offset of the signal.

Epoch subdivision: LFPs were then divided into overlapping (90%) 10 s epochs. The epochs therefore overlap themselves by 9 seconds, with one second offset.

The normalization was carried out using the entire signal to preserve the total power ratio between epochs making the PSD feature comparable between windows.

C. *Feature selection and estimation*:

To create the dataset, we selected the three main groups of features used in LFP research: (1) Power Spectral Density estimate (PSD) features, related to the mean power of physiological spectral bands of human brain, which is one of the classical approaches to study LFPs, (2) Burst features, that characterize LFP signals in PD patients [8] and are related to short-time increases in signal amplitude, and (3) Spectral Entropy features, which gives indications on the actual chaotic status of the system, used in [9], [10].

PSD features: for each 10-s epoch we obtained the signal periodogram using the Welch's Method (windows size: 256 samples, overlap 50%, spectral resolution: 1 Hz) [11]. The frequency space was divided in the classical physiological bands (see TABLE I) and the single bin values were summed to estimate the power spectral density in each band, thus obtaining a single feature for each band in each epoch.

Burst Features: in STN-LFPs, rapid amplitude changes in specific bands (e.g., the beta band 13-35 Hz) are very common, and their presence is an important pathological indicator [8]. The burst extraction process adapts the methodology presented in [12], and was conducted on each LFP epoch in each frequency band. The procedure consisted in calculating the root mean square of the upper envelope of the epoch with 64 samples sliding window. If the upper envelope exceeded the 65th percentile of the mean of the epoch and there were at least two consecutive peaks of the original signal crossing the threshold, then a "burst" was identified (see FIGURE 2).

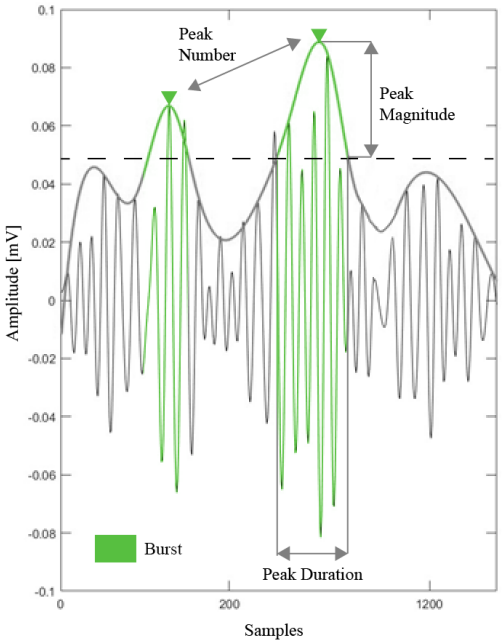


Figure 2: Burst features. The black bold line represents the upper Hilbert envelope of the signal. The dotted line represents the 65th percentile of the signal. The burst feature includes the mean and standard deviation of peak magnitude and peak duration of every epoch.

After obtaining and counting the bursts of every epoch of each frequency band, we calculated the mean and standard deviation of the peak amplitude, of the burst duration in seconds and of the area between the envelope curve exceeding the threshold. These five features plus the number of burst for every epoch were added to the dataset (see TABLE I).

Spectral Entropy features:

These features were calculated epoch by epoch based on the Shannon Entropy concept, as in equation (3):

$$H_{sp} = -\frac{\sum_{m=1}^{N} P(m)\log_2 P(m)}{\log_2 N} \quad (2)$$

Where P(m) is the probability distribution defined as

$$P(m) = |X(m)^2| / \sum_i |X(i)^2| \quad (3)$$

X(m) is the discrete Fourier transform of the sampled signal filtered by the physiological band. The function used to calculate these features is Matlab's "pentropy".

The total entropy features per epoch are 7, one for each physiological band (see TABLE I).

TABLE I
DATASET FEATURES

Physiological bands	PSD estimate features	Burst features*	Spectral Entropy features	Total
δ (1-4 Hz)	1	5	1	7
θ (4-8 Hz)	1	5	1	7
α (8-11 Hz)	1	5	1	7
Low β (11-25 Hz)	1	5	1	7
High β (25-35 Hz)	1	5	1	7
γ (35-45 Hz)	1	5	1	7
Categorical Features				
Patient Index				1
Contact Pair				1
Hemisphere				1
Total	6	30	6	**45**

Burst

* Burst features include epoch mean and standard deviation of peak magnitude, epoch mean and standard deviation of peak duration and epoch peak number.

Dataset creation: the final dataset was created aggregating all the three groups of features (14 features for each frequency band, 42 features for each epoch) and adding the categorical patient index, the DBS contact (see FIGURE 1) and the source hemisphere (right or left) in total, the dataset contains 45 columns.

D. *Training and testing*:

Categorization objectives: as a proof-of-concept regarding the use of the dataset for the definition of algorithms useful for closed-loop DBS, in this study we created 3 different machine learning categorizers: 1) capable of distinguishing the signal between different patients, 2) capable of distinguishing the signal from different contacts pairs (see Figure 1) and 3) capable of distinguishing the LFPs from different brain hemispheres. The first objective has 30 different categories (number of patients), the second one has 6 categories (not all the combination of the contacts where used, see Figure 1) and the third one only 2 (right or left hemisphere). After some qualitative tests we decided to use the Random Forest Classifier (RFC) with 42 estimators, implemented in Jasp (JASP Team, Version 0.16.4. 202. https://jasp-stats.org/) and in Python using the Sci-kit Learn library (version 1.2, https://scikit-learn.org/).

Training features: To train the algorithm, due to the relatively large and correlated dataset, we used a randomized 20% holdout validation. To train 1) and 2) we used all the 44 features without the objectives (Patient or Contact Pair respectively). To train 3) we excluded the also the Contact Pair as it is strictly correlated with the Hemisphere.

Testing the machine learning algorithms: algorithm 1) was tested with an additional randomized 20% holdout test data. Algorithms 2) and 3) were tested against a single holdout patient, in two different tests. The first test consisted of holding out 100% of the signals from the patient; the second test fed 25% of the initial signal data (about 10 seconds) of the holdout patient to the training algorithm and holds out the latter 75% to test against the response of trained algorithm. These two tests (100% patient holdout and 75-25% patient holdout) were used to simulate a machine working on a completely new patient or an algorithm trained on the spot with his/her LFP data. Due to this self-training nature of the 75-25% test, on-the-spot training time were also reported. Due to the simplicity of the algorithms we used only a single thread of the CPU of a single machine. The processor used is an Intel(R) Core i9-10900X CPU @ 3.70GHz, 3696 MHz with 64 GB of RAM.

TABLE II
TEST RESULTS – RANDOM FOREST CLASSIFICATION

1) IDENTIFY THE PATIENT

Number of rows			Accuracy		
Train set	Validation set	Test set	Validation	Test	OOB
13932	2806	4353	0.976	0.975	0.932

2) IDENTIFY THE CONTACT PAIR

		Mean rows		Mean accuracy	
		Train set	Test set	Validation set	Test set
100% Patient Holdout	Mean	21135	362	0.921	0.338
	St.D.	472	74	0.007	0.22
75-25% Patient Holdout	Mean	21278	152	0.920	0.530
	St.D.	381	98	0.006	0.200

3) IDENTIFY THE HEMISPHERE

		Mean rows		Mean accuracy	
		Train set	Test set	Validation set	Test set
100% Patient Holdout	Mean	21135	362	0.958	0.567
	St.D.	472	74	0.004	0.225
75-25% Patient Holdout	Mean	21278	152	0.958	0.771
	St.D.	381	98	0.003	0.162

OOB = Out-of-bag; St.D. = Standard Deviation.

III. RESULTS

The final dataset was created using 188 signals from 6 contact pairs in 34 patients. The average number of epochs per patients was 603.9 epochs with a standard deviation of 470.5 epochs.

. Using the pre-processing and feature estimation procedures previously described, we obtained a dataset of 21765 rows and 45 columns. Using this dataset as input, As shown in Table II the three algorithms perform within various degrees of accuracy.

1) Identify the patient:

The task to identify the patient given a random epoch of a signal was relatively easy for the algorithm, scoring 0.932 of Out-of-the-bag accuracy and 0.975 on the holdout test accuracy. The most prominent features were the mean of the peaks in the γ frequency (with a 0.201 total increase in node purity) followed by category features that indicates the contact pair from which the signal is recorded (0.168 total increase in node purity). Other important features for the classification reside in the β band (total increase in node purity, mean peak in high β: 0.152; power spectrum in high β: 0.143 spectral entropy in low β: 0.111).

2) Identify the contact pair:

The algorithm did not perform well given a completely new patient, albeit supplying the training even with a small (about

ten seconds) of a signal from the patient improved the classification behavior. Both 100% and 75-25% holdout showed anyway low scores (100% patient holdout: 0.338 ± 0.22 and 75-25% patient holdout: 0.530 ± 0.200.

3) Identify the hemisphere:

Whereas the 100% patient holdout still fails (0.576 ± 0.225), in the 75-25% holdout the mean accuracy is 0.771 ± 0.162 (see Figure 2). The training time of the RFC for this last test in the 75-25% test is 3.26 ± 0.16 seconds using a single CPU thread. Thus, it is feasible to train the algorithm during the data acquisition as it adds only a small delay.

IV. Discussion and Conclusions

In this paper, we described the implementation of a LFP-based dataset, composed of relevant features calculated from signals belonging to 34 patients in the medication OFF state. These allowed to obtain a dataset of 45 features and 21765 lines which was subsequently used to train three Random Forest algorithms dedicated to three classification tasks, one for the identification of the patient to which the signal belongs, one to identify the contact pair from which the signal was recorded, and one to identify the hemisphere.

Our results, even though limited by the small number of patients and by the use of a single condition (OFF medication), showed that the approach is feasible and can be applied to improve the knowledge coming from LFPs recorded in DBS patients to classify characterizes relevant either for closed-loop systems or for automatic programming.

However, while the results of the first task (patient's identification) were positive, the results of the other two highlight the challenges to work with LFPs. First, LFPs, even when normalized, remain heterogeneous between patients. This of course allows identifying signals belonging to a specific patient (as in task 1). This possibility could be exploited in a useful way, as a digital imprint, or, on the other hand, it could represent a threat to the privacy of the individual. As a further challenge, the inter-patient signal heterogeneity is also detrimental when trying to find common feature patterns across signals belonging to different patients. One of the reasons behind inter-patient variability is the precise targeting of the electrode, that it could vary not only from patient to patient, but also from hemisphere to hemisphere.

In addition, the use of an overlapping moving window introduced correlation between features. Also, only a min-max normalization was applied while future studies could consider z-scores or other normalization. Furthermore, LFPs length spans only 30 seconds, to record only a static patient status, whereas prolonging this acquisition time could open the possibility of study a time-evolving signal.

Despite these limitations, the third algorithm was able, albeit with some uncertainty, to distinguish between left and right hemispheres, indicating a possible lateralization of the STN activity, thus providing new insights into basal ganglia neural circuitry. This suggests that building datasets of known features from available LFPs in different patient conditions could support not only the research on signal classification and, in turn, on closed-loop DBS but also on deep brain structure neurophysiology.

In the future, including more data on such dataset it would be possible to apply not only simple and fast machine learning algorithms, but also other machine learning methods, including deep learning techniques.

V. References

[1] P. Krack, R. Martinez-Fernandez, M. Del Alamo, e J. A. Obeso, «Current applications and limitations of surgical treatments for movement disorders», *Movement Disorders*, vol. 32, fasc. 1, pp. 36–52, 2017.

[2] T. Bocci *et al.*, «Eight-hours conventional versus adaptive deep brain stimulation of the subthalamic nucleus in Parkinson's disease», *npj Parkinsons Dis.*, vol. 7, fasc. 1, Art. fasc. 1, set. 2021, doi: 10.1038/s41531-021-00229-z.

[3] M. Arlotti *et al.*, «Eight-hours adaptive deep brain stimulation in patients with Parkinson disease», *Neurology*, vol. 90, fasc. 11, Art. fasc. 11, 2018.

[4] S. Little *et al.*, «Bilateral adaptive deep brain stimulation is effective in Parkinson's disease», *Journal of Neurology, Neurosurgery & Psychiatry*, vol. 87, fasc. 7, Art. fasc. 7, 2016.

[5] T. Merk, V. Peterson, R. Köhler, S. Haufe, R. M. Richardson, e W.-J. Neumann, «Machine learning based brain signal decoding for intelligent adaptive deep brain stimulation», *Experimental Neurology*, vol. 351, p. 113993, mag. 2022, doi: 10.1016/j.expneurol.2022.113993.

[6] M. Peralta, P. Jannin, e J. S. H. Baxter, «Machine learning in deep brain stimulation: A systematic review», *Artificial Intelligence in Medicine*, vol. 122, p. 102198, dic. 2021, doi: 10.1016/j.artmed.2021.102198.

[7] M. Rosa *et al.*, «Adaptive deep brain stimulation in a freely moving Parkinsonian patient», *Movement Disorders*, vol. 30, fasc. 7, Art. fasc. 7, 2015.

[8] G. Tinkhauser *et al.*, «The modulatory effect of adaptive deep brain stimulation on beta bursts in Parkinson's disease», *Brain*, vol. 140, fasc. 4, Art. fasc. 4, 2017.

[9] S. Velasco, L. Branco, A. Abosch, e N. F. Ince, «The Entropy of Adaptively Segmented Beta Oscillations Predict Motor Improvement in Patients With Parkinson's Disease», *IEEE Transactions on Biomedical Engineering*, vol. 69, fasc. 7, pp. 2333–2341, lug. 2022, doi: 10.1109/TBME.2022.3142716.

[10] T. Wang, M. Shoaran, e A. Emami, «Towards Adaptive Deep Brain Stimulation in Parkinson'S Disease: Lfp-Based Feature Analysis and Classification», in *2018 IEEE International Conference on Acoustics, Speech and Signal Processing (ICASSP)*, apr. 2018, pp. 2536–2540. doi: 10.1109/ICASSP.2018.8462472.

[11] P. Welch, «The use of fast Fourier transform for the estimation of power spectra: a method based on time averaging over short, modified periodograms», *IEEE Transactions on audio and electroacoustics*, vol. 15, fasc. 2, pp. 70–73, 1967.

[12] D. Sand *et al.*, «Machine learning-based personalized subthalamic biomarkers predict ON-OFF levodopa states in Parkinson patients», *J. Neural Eng.*, vol. 18, fasc. 4, p. 046058, mag. 2021, doi: 10.1088/1741-2552/abfc1d.

How to assess vascular dysfunction during septic shock and resuscitation

M. Carrara[1], P. Antenucci[1] and M. Ferrario[1]
[1] *Politecnico di Milano, Department of Electronics, Information and Bioengineering*

***Abstract*— Septic shock is known to induce a severe vascular dysfunction which could also persist after hospital discharge and have long term sequela, increasing the cardiovascular complications and the mortality risk of survived patients. Typically, this vascular dysfunction consists in stiffening of large vessels (e.g., the aorta) and a loss of peripheral resistance, which can finally lead to a condition of peripheral vascular decoupling. These alterations are commonly overlooked during resuscitation, although they can be easily derived from routinely acquired signals such as invasive blood pressure. Several techniques to estimate arterial properties such as arterial compliance, total peripheral resistance, and time constant τ based on the Windkessel model of the cardiovascular system will be discussed and results obtained from different data and experiments will be presented to show the feasibility and the effectiveness of the proposed indices.**

***Keywords*—arterial compliance, peripheral resistance, Windkessel cardiovascular model, vascular decoupling.**

I. Introduction

SEPSIS and septic shock remain the main causes of mortality in intensive care, despite continuous efforts to improve the therapeutic protocols. Survived patients typically cohabit with a critical cardiovascular condition which determine a higher risk of fatal and non-fatal cardiovascular events [1]. The vascular endothelium is highly deteriorated by sepsis, leading to a dysfunction of arterial properties and the related vasodilatory and vasoconstrictive mechanisms [2]. Specifically, a stiffening of large vessels, such as the aorta [3], and a loss of peripheral resistance are often observed during septic shock, and these vascular alterations can lead to a condition of peripheral vascular decoupling [4], i.e., an inversion of the physiological amplification of pulse pressure from central to peripheral sites. Moreover, the blood pressure waveform has been shown to be profoundly altered by sepsis [5], hinting that blood flow transmission and reflection are also impaired.

Current clinical guidelines are mainly concerned to recover septic shock patients from hypotension and hypovolemia and global hemodynamic indices, such as mean arterial pressure, are still the key therapy targets [6]. However, even subtle changes occurring in the arterial pressure waveform can give insight on peripheral vascular tone, backward pressure waves, and large arteries compliance, but they are not addressed in current clinical guidelines and no therapy recommendations are available.

Our hypothesis is that invasive blood pressure, which is routinely collected in intensive care unit (ICU), contains dynamic signatures of the cardiovascular status that can give insights on vascular function and blood flow propagation, adding important information to average hemodynamic indices typically measured. Lumped-parameters models, such as the Windkessel model, can be used to extract these dynamic indices.

The aim of this paper is to describe some techniques useful to study the alterations in vascular properties and arterial waveform induced by sepsis/septic shock during different experimental protocols. The results presented were obtained from different data and experiments to show the feasibility and the effectiveness of the proposed indices.

II. Methods

A. The arterial Windkessel model

The two-element Windkessel model [7], reported in Fig. 1, describes the hemodynamics of the arterial system in terms of total peripheral resistance (TPR), mainly accounted by the smallest arteries and arterioles, and total arterial compliance (AC), mainly determined by the elasticity of the large arteries.

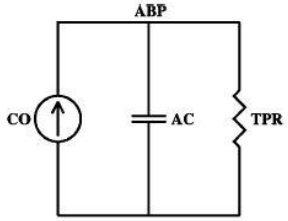


Fig. 1: The two-element Windkessel model of arterial tree. CO, cardiac output; ABP, arterial blood pressure; TPR, total peripheral resistance; AC, arterial compliance.

According to the model, TPR can be estimated as

$$TPR = \frac{P_{ao,mean} - P_{ven,mean}}{CO} \approx \frac{P_{ao,mean}}{CO} \quad (1)$$

where $P_{ao,mean}$ and $P_{ven,mean}$ are the mean value of aortic and venous arterial blood pressure (ABP), respectively, and CO the cardiac output. The compliance is defined as the ratio of a volume change, ΔV, and the resulting pressure change ΔP; the total arterial compliance (AC) is assessed as follows when ABP is measured in aorta:

$$AC = \frac{\Delta V}{\Delta P} = \frac{SV}{PP} \quad (2)$$

where SV is the stroke volume and PP is the pulse pressure, obtained as the difference between the systolic and the diastolic values within a pulse. According to the model, the time constant τ of the arterial tree, representing the time constant of the exponential diastolic decay, can be computed by the following equation:

$$\tau = AC \cdot TPR \quad (3)$$

This relationship holds on a beat-to-beat basis if we consider the ABP waveform measured centrally where the cumulative effects of wave reflections are attenuated [8]; in this case, ABP should decay like a pure exponential during each diastolic interval with a time constant τ. However, this relationship is also consistent if we consider a time scale sufficiently long such that the wavelengths of the propagating waves are much larger than the dimension of the arterial tree. At such time scales, the arterial tree acts as a single blood reservoir, and the Windkessel model is therefore valid. So, for example, if pulsatile activity abruptly ceased, then peripheral ABP may eventually decay like a pure exponential as soon as the faster wave reflections died out [9]. Based on this concept, we computed the time constant τ on long time intervals (6-min windows) of the measured ABP waveforms according to the method proposed by Mukkamala *et al*. [9]: i) a cardiac contraction signal $x(t)$ is created by placing impulses at the time instants of the onsets of ABP upstroke with an area equal to the ensuing PP; ii) a relationship between the cardiac contraction signal $x(t)$ and the ABP waveform named $y(t)$ is assessed by computing the impulse response function $h(t)$, which minimizes in the least squares sense the convolution with $x(t)$ in order to best fit $y(t)$. By mathematical definition, the estimated $h(t)$ represents the ABP response to a single cardiac contraction (normalized approximately by the average PP); iii) the Windkessel time constant τ is finally determined by fitting the portion of the estimated $h(t)$ after its maximum value with an exponential decay. This optimization problem is solved via linear least squares estimation by log-transforming $h(t)$.

B. *Peripheral pulse pressure amplification*

In physiological conditions the amplitude of arterial pulse, i.e., the PP, has increasing values from central to peripheral sites due to waves reflection. Indeed, since blood pressure measured in the periphery is close to the reflection sites, the backward wave has to travel back a shorter distance before summing up to the forward wave; moreover, the lower compliance of peripheral arteries leads to higher PP values. Generally, this phenomenon is called *peripheral amplification of the pulse pressure*.

C. *Datasets*

The first dataset analyzed includes 6 pigs undergoing to an experimental protocol of polymicrobial septic shock and standard resuscitation performed at *Université Libre de Bruxelles.* More details about the experimental protocol can be found in [5]. Briefly, the animals were analysed at baseline (T1), after severe septic shock development (T2), and after resuscitation with fluids and noradrenaline according to standard guidelines (T4, ~5/6h after T2). The time point after fluids only (T3) was skipped as some animals required immediately administration of noradrenaline. Moreover, the phase of sepsis development, i.e., from the insult, consisting in autologous feces inoculation into the peritoneum, until time point T2, was analysed and indices were computed every 5 minutes. ABP were continuously recorded in central aorta (sampling frequency 500Hz) and in peripheral femoral (sampling frequency 500Hz) and radial artery (sampling frequency 250Hz).

The second dataset consists of 9 pigs undergoing polymicrobial sepsis and resuscitation up to 74h after sepsis development; this allowed to disentangle the early and late response to the therapy. Seven pigs were treated as sham controls, i.e., monitored for the same time window allowing to appreciate the sepsis effects excluding confounding factors related to the experimental setups. The experiments were performed at *Insespital, University Hospital of Bern*, and more details about the experimental protocol can be found in [10]. ABP was continuously recorded in carotid artery at a sampling rate of 100 Hz. The animals were analyzed at baseline (T1), after sepsis development (T2), after 24h (T3), 48h (T4) and 72h (T5) of resuscitation according to clinical guidelines.

III. Results and Discussion

The results obtained from the first dataset are presented below. Fig. 2 shows the trend of central and peripheral PP and vascular properties, such as AC and TPR. Septic shock induced a profound dysfunction of the vascular system with stiffening of central vessels (reduced AC), peripheral vasodilation (decreased TPR), and alteration of PP amplification; indeed, the baseline condition of peripheral PP higher than central PP is lost after septic shock development.

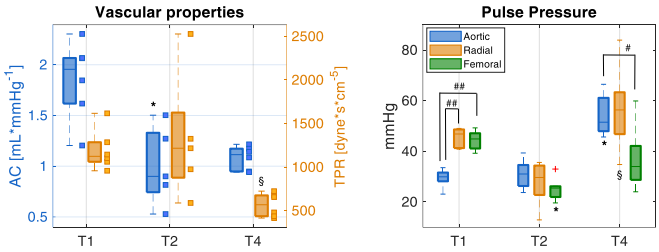


Fig. 2. Left panel: distributions of total arterial compliance (AC) and total peripheral resistance (TPR) values. The values relating each pig are marked by the little squares. Right panel: distribution of central and peripheral PP values. Wilcoxon signed test: ∗p-value < 0.05 with respect to T1, § p-value < 0.05 with respect to T2 (Friedman test p-value < 0.05). Mann–Whitney U-test: #p-value < 0.05, ##p-value < 0.01 between the specified variables.

This vascular dysfunction progressively develops during sepsis progression, as shown in Fig. 3 reporting the trend of aortic and femoral PP values at baseline (T1), and from the insult until full development of septic shock (T2). The different duration of each pig's trend highlights the heterogeneity of the response to sepsis induction. However, it is possible to observe in all animals the "crossover" between the two PP trends (i.e., femoral PP becoming lower than aortic PP), supporting the evidence that the peripheral vascular decoupling is a hallmark phenomenon occurring during sepsis development. The main responsible for this PP reversal is a decrease in peripheral PP, whereas the aortic PP maintains approximately constant values throughout the entire phase. Fig. 4 shows the trend of aortic PP and time constant τ at baseline (T1) and from the insult until T2. It is interesting to notice that the same "crossover" described before is still visible, driven by a reduction in the τ values. A decrease in the Windkessel constant could be due to vasodilation, i.e., a decrease in TPR, or stiffening of large arteries, i.e., a decrease in AC, or both phenomena.

This compromised vascular condition was not relieved by therapy administration, although the clinical hemodynamic targets were achieved in all animals, e.g., mean arterial pressure (MAP) >65mmHg. At this time point the aortic PP has significantly increased compared to T1 or T2, whereas the femoral PP has not been restored.

This can be macroscopically appreciated from the changes in morphology of aortic ABP waveforms, as shown in Fig 5: the shape of the aortic waveform mostly at T4 resembles the typical pressure waveform of a high cardiovascular risk subject, such as aged people [11], although these changes were developed only in a few hours of experiment.

These results were confirmed in the second dataset, where the resuscitation phase was longer, up to 74h after sepsis development.

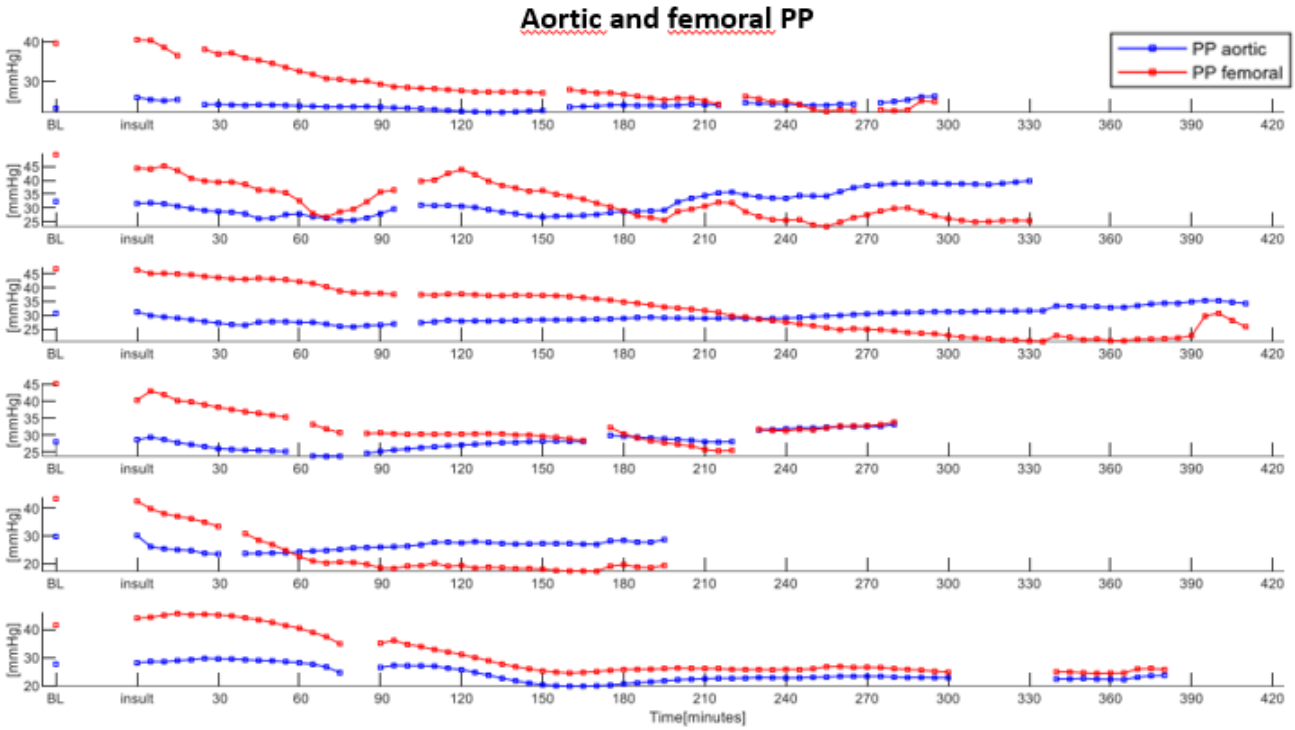


Fig. 3. Trend of aortic PP (blue squares) and femoral PP (red squares) for each animal at baseline (BL), which corresponds to T1, and from the inoculation of the feces (insult) and onwards until T2.

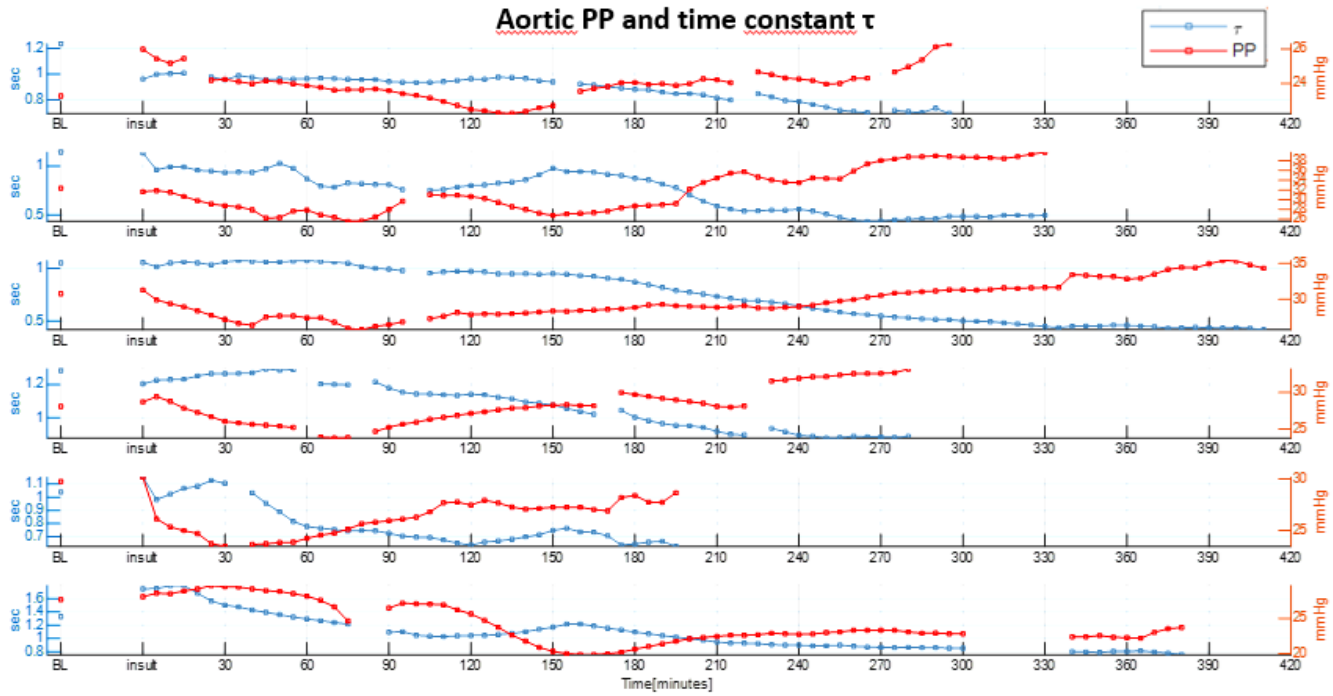


Fig. 4. Trend of aortic PP and time constant Windkessel τ for each animal at baseline (BL), which corresponds to T1, and from the inoculation of the feces (insult) and onwards.

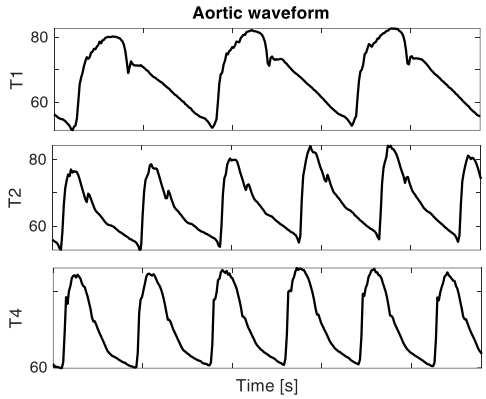


Fig. 5. Example of few beats extracted from aortic waveform at each time point for one animal from the experiments performed at *Université Libre de Bruxelles.*

Fig. 6 shows how the vascular alterations occurring in the early phase of sepsis development characterize not only the first hours of therapy administration, when recovery from hypotension is of primary importance and massive fluids and vasopressors infusion are crucial for survival, but they persist also after days, when hemodynamic stabilization has been optimized.

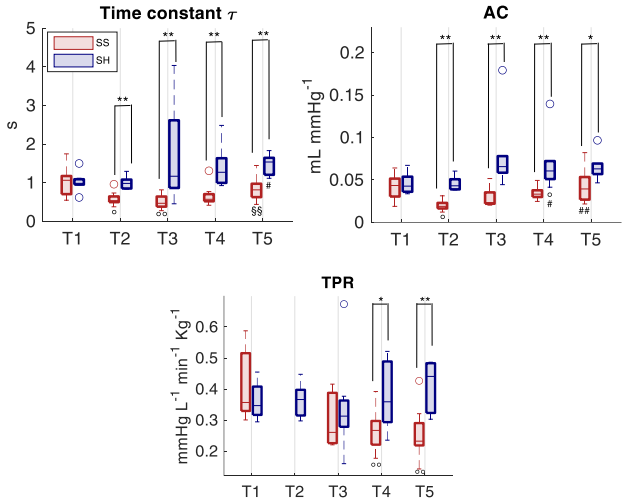


Fig. 6. Distributions of values of vascular indices for the two groups Comparison between Sepsis and Sham: *p-value < 0.05, **p-value < 0.01, ***p-value < 0.001 (Wilcoxon rank sum test). Wilcoxon signed test: °p-value < 0.05, °°p-value < 0.01 with respect to T1, #p-value < 0.05, ##p-value < 0.01 with respect to T2, §p-value < 0.05, §§p-value < 0.01 with respect to T3 (Friedman test p-value < 0.05).

These vascular alterations can be observed from the graph of carotid ABP waveform (Fig. 6). The ABP morphological characteristics in a sham pig at T5 are similar to baseline (T1), on the contrary, the ABP waveform in a septic pig is completely different from baseline and sham pig; in particular, a much steeper decay of the diastolic phase can be observed, consistently with the lower values of τ and AC previously described.

I. Conclusion

The indices described proved to be highly informative in the study of therapy response in septic shock, providing important insights into the cardiovascular status, not achieved by standard hemodynamic measures commonly used according to international guidelines. The results were confirmed both in short-term (~5/6h after resuscitation) and long-term experiments (up to 72 h of continuous resuscitation). Indeed, the same mean ABP value in two different subjects can hide two different cardiovascular conditions or can be achieved by very different therapeutic strategies. A complex pathological condition like septic shock needs an extensive monitoring without neglecting important information from commonly measured signals like arterial blood pressure.

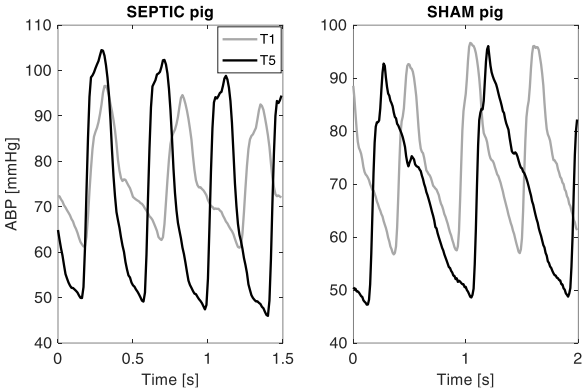


Fig. 6. Example of carotid arterial blood pressure waveform of a septic pig and a sham pig, at T1 (baseline) and T5 (72 h after the start of resuscitation) from the experiments performed at *University Hospital of Bern.*

References

[1] D. M. Musher, M. S. Abers, and V. F. Corrales-Medina, "Acute Infection and Myocardial Infarction," *N. Engl. J. Med.*, vol. 380, no. 2, pp. 171–176, 2019, doi: 10.1056/nejmra1808137.

[2] J. Joffre, J. Hellman, C. Ince, and H. Ait-Oufella, "Endothelial responses in sepsis," *Am. J. Respir. Crit. Care Med.*, vol. 202, no. 3, pp. 361–370, 2020, doi: 10.1164/rccm.201910-1911TR.

[3] S. Kazune, A. Grabovskis, C. Cescon, E. Strike, and I. Vanags, "Association between increased arterial stiffness and clinical outcomes in patients with early sepsis: a prospective observational cohort study," *Intensive Care Med. Exp.*, vol. 7, no. 1, 2019, doi: 10.1186/s40635-019-0252-3.

[4] F. Hatib, J. R. C. Jansen, and M. R. Pinsky, "Peripheral vascular decoupling in porcine endotoxic shock," *J. Appl. Physiol.*, vol. 111, no. 3, pp. 853–860, 2011, doi: 10.1152/japplphysiol.00066.2011.

[5] M. Carrara, A. Herpain, G. Baselli, and M. Ferrario, "Vascular Decoupling in Septic Shock: The Combined Role of Autonomic Nervous System, Arterial Stiffness, and Peripheral Vascular Tone," *Front. Physiol.*, vol. 11, no. July, pp. 1–13, 2020, doi: 10.3389/fphys.2020.00594.

[6] L. Evans *et al.*, "Surviving sepsis campaign: international guidelines for management of sepsis and septic shock 2021," *Intensive Care Med.*, vol. 47, no. 11, pp. 1181–1247, 2021, doi: 10.1007/s00134-021-06506-y.

[7] N. Westerhof, J. Lankhaar, and B. Westerhof, "The arterial Windkessel," *Med Biol Eng Comput.*, vol. 47, no. 2, pp. 131–41, 2009.

[8] M. J. Bourgeois, B. K. Gilbert, D. E. Donald, and E. H. Wood, "Characteristics of aortic diastolic pressure decay with application to the continuous monitoring of changes in peripheral vascular resistance," *Circ. Res.*, vol. 35, no. 1, pp. 56–66, 1974, doi: 10.1161/01.RES.35.1.56.

[9] R. Mukkamala, A. T. Reisner, H. M. Hojman, R. G. Mark, and R. J. Cohen, "Continuous cardiac output monitoring by peripheral blood pressure waveform analysis," *IEEE Trans. Biomed. Eng.*, vol. 53, no. 3, pp. 459–467, 2006, doi: 10.1152/japplphysiol.00951.2006.

[10] M. Carrara *et al.*, "Autonomic and circulatory alterations persist despite adequate resuscitation in a 5-day sepsis swine experiment," *Sci. Rep.*, vol. 12, no. 1, pp. 1–14, 2022, doi: 10.1038/s41598-022-23516-y.

[11] J. L. Izzo, "Aging, Arterial Stiffness, and Systolic Hypertension," *Hypertens. Elder.*, pp. 23–34, 2007, doi: 10.1007/978-1-59259-911-0_3.

A novel artificial urinary sphincter and comparison with reference device

M.V. Mascolini[1,§], J.V. Fotso Fogang[2,§], V. Salomoni[3], C.G. Fontanella[1], E.L. Carniel[1] and A.N. Natali[1]
[1] *Department of Industrial Engineering, University of Padova, Italy*
[2] *Department of Civil, Environmental and Architectural Engineering, University of Padova, Italy*
[3] *Department of Management and Engineering, University of Padua, Italy*
[§] *These authors contributed equally to this work*

Abstract **- Among all the available managements for the stress urinary incontinence, the Artificial Urinary Sphincter (AUS) is clinically considered the first-line treatment by inducing the lumen occlusion through a fluid-inflatable cuff applying a permanent pressure around the urethra.**

Over the decades of worldwide implantation of AUS, the success rate has emerged as deeply influenced by the mechanical stimulation of urethral tissues, which may be susceptible to potential degenerative phenomena, to urethral damage, with incontinence and necessary surgical revision.

To minimize the risk of urethral damage, this research work proposes a novel in silico strategy for AUS design, aiming to provide a device that is capable to apply a more uniform and appropriate occlusive action around the urethra.

Computational mechanics analyses are developed to evaluate the interaction between the urethra and the AUS device during the lumen occlusion and its subsequent opening because of bladder induced pressure, aiming to define the design parameters required for the continence condition, according to the tissue tolerability. The functionality of the novel device is compared with the reference AUS AMS800.

Keywords **- Stress urinary incontinence, artificial urinary sphincter, finite element method, computational structural mechanics**

I. INTRODUCTION

STRESS Urinary Incontinence (SUI) is a widespread pathological condition implying the involuntary leakage of urine in response to increasing intraabdominal pressure (e.g. coughing, sneezing or exercising), due to the deficiency of the urinary sphincteric mechanism. Nowadays, about 400 million people worldwide are affected by urinary incontinence, with SUI accounting for 24% to 45% in women [1] and about 10% in men [2], impacting significantly on quality of life and financial burden.

Since the 1970s, Artificial Urinary Sphincters (AUSs) have been developed for the SUI treatment as prosthetic devices which mimic the functionality of a natural urethral sphincter inducing the lumen occlusion during the storage phase of micturition. The operating principle consists generally in applying a pressure by means of a cuff inflated by saline solution, placed around the bulbar urethra or the bladder neck. Several variants of AUS are on the market and under experimental evaluation, distinguished in terms of control mechanism, pressure transmission and cuff shape and size.

In most cases, the pressure is set in the range 50-80 cmH_2O [3] and it is defined as a constant value by surgeons during the implantation. The pressure values are based on clinical experience in order to guarantee continence condition in daily situations. To date, despite successful post-surgery outcomes, the recurrent incontinence following the implantation of AUS is still an open clinical question [4]-[6]. High rates of surgical revision have been reported due to AUS failure because of the reaction of urethral tissues to pressure loading [3], [7]-[9].

In detail, the resulting negative outcome is twofold. First of all, urethral tissue in correspondence to the AUS cuff may undergo degenerative processes in terms of infection, atrophy and/or erosion. In some regions of interaction, tissue could be pinched during the inflation of the cuff and compressive action may cause a hypoxia condition [10]. In case of damaged tissue, the AUS may no longer guarantee the continence condition, even if it was initially adequate. All these complications involve pain and discomfort for the patient that should undergo a new surgery, unless significant tissue damage compromises the implantation of another device. Hence, the application of an artificial urinary sphincter requires a careful evaluation of the interaction phenomena between the device and the biological structures and tissues in contact.

The sphincter is permanently placed around the urethra by continuously applying an occlusive pressure, often higher than what is actually needed, in order to always guarantee continence, even in case of increased abdominal and bladder pressure. Only during voiding phase of micturition, typically around 6-7 times a day, the urethral duct is not exposed to the pressure load. In addition, the AUS is generally placed in urethral regions other than where the natural urethral sphincter is anatomically located and thus the tissues are not physiologically designed to be subjected to such occlusive stress and strain conditions. Therefore, as an essential requirement for the AUS reliability and durability, the biological tissue tolerability has to be necessarily considered in terms of compressive strain, compressive stress and hydrostatic pressure intensity and distribution.

For all these reasons, a novel in silico approach to the design of the AUS device is developed. A computational modelling strategy was defined, allowing to analyse the interaction phenomena between AUS and urethra, and thus to evaluate the device functionality. In detail, the cuff pressure that is required to ensure continence and the mechanical stimulation of urethral tissues, which may induce damage and/or vaso-constriction phenomena, can be evaluated. This approach was exploited to analyse a new AUS, which has been conceived introducing a novel conformation of the cuff as a fluid-inflatable cylindrical chamber to be placed circumferentially around the bulbar urethra.

The in silico procedure required the development of computational models of the male bulbar urethra and the AUS.

Models exploitation made it possible to investigate the urethral mechanical response under different occlusion conditions and intraurethral actions, by varying the material properties of the prosthetic device.

II. Materials and Methods

Over the years, the bioengineering methods provided valid support tools, in a wide range of medical fields, to study the functionality of biological tissues, plan surgical procedures and evaluate the efficacy and reliability of therapies and prosthetic devices. These methods are based on a tight coupling of experimental investigations, including the histo-morphometrical and mechanical characterization of biological systems and computational techniques. These latter allow to extend the experimental results to a wider scenario, simulating multiple situations and providing information on relevant aspects that are not accessible by clinical investigation. In this sense, the Computational Structural Mechanics (CSM) approach allowed to interpret the mechanical response of urethral tissue to the lumen occlusion process induced by the artificial sphincter, aiming to evaluate the reliability of the novel device.

A. Numerical model of the urethral duct

The bulbar urethral model was developed as a fully three-dimensional 50 mm length and 5 mm radius cylinder, with an elliptical lumen defined by internal major and minor axis of 8 and 1.6 mm, respectively (UGS NX3, Siemens PLM Software, Plano, Texas, USA). Lumen shape was previously investigated [10] according to the complex configuration in the bulbar area and here simplified by a regular elliptic shape, as it appears in other urethral regions, and also in consideration of a major pressure requirement for occlusion. Moreover, this shape minimizes the computational effort, suggesting the feasibility of real-time simulations for the surgical practice.

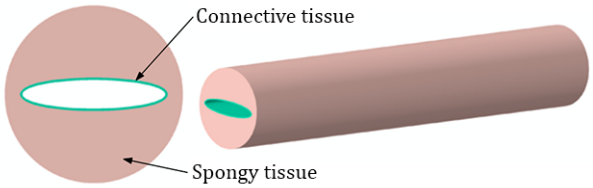


Fig. 1: Geometrical model of the urethral duct as a bi-layered structure.

The urethral wall was assumed to be composed by a thin layer of dense connective tissue that surrounds the lumen and an outer thick layer of spongy tissue all around (Figure 1). The mechanical behaviour of biological tissues was described by a specifically developed hyperelastic formulation [10]. The constitutive parameters were defined on the basis of inverse analysis of experimental data from uni-axial tensile tests and structural inflation tests performed on urethral samples [11].

A tie contact condition on the interfacing surfaces between the two layers and fixed-end constraints on cross-sectional surfaces at the two extremities of the urethral model were imposed to prevent relative and rigid body motion, respectively. The self-contact interaction between lumen surfaces was defined by a hard contact formulation with friction coefficient of 0.02 [10], [12], [13], considering that the tissue is physiologically wet. The urethral model was finite element discretized assuming different seeds for the two layers, by means of 145,920 and 200,640 linear hexahedral elements, corresponding to 184,000 and 213,440 nodes, respectively for the connective tissue and spongy tissue layers. Discretization was performed in the framework of Abaqus/CAE 6.14 (Dassault Systèmes, Vélizy-Villacoublay, France). To prevent mesh instability, the enhanced hourglass control formulation was adopted [14], [15].

B. Numerical model of the novel artificial urinary sphincter

The novel prototype of AUS has been conceived with an operating principle based on a hydraulic mechanism, as the majority actually on the market. The inflation of a fluid-filled cuff around the urethra provides for the lumen occlusion. However, on the basis of the current critical issues reported in literature, the novelty lies in the shape of the urethral cuff designed to improve the distribution of the pressure action by wrapping the duct more uniformly and safely, without pinching the tissue. In detail, as a matter of example, a 3D CAD model of the cuff was developed by assembling an inflatable chamber and an external supporting band. Both models were designed as a hollow cylinder with a constant curvature (Figure 2).

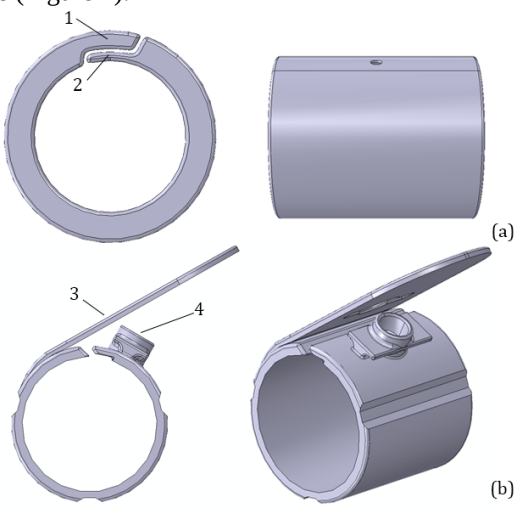


Fig. 2: Geometrical model of the novel artificial urinary sphincter composed by an inflatable chamber (a) and a supporting band (b).

The chamber and the circular band dimensions can be defined on the basis of the specific urethra requirements. In the initial configuration, the chamber end parts, labelled as 1 and 2, are detached and so the cuff is open, as shown in the Figure 2a. In the operative configuration, the band parts, labelled as 3 and 4 in Figure 2b, are intended to come into contact, inducing the closing of the cuff. In this manner, and according to wall stiffness distribution, it is expected that the inner wall of the chamber ensures a circular configuration around the urethra.

Regarding the design of the novel device, a relevant aspect was assumed by the mechanical characterization of its components. An elastomeric material was assumed for both the inflatable chamber and the supporting band, by considering an hyperelastic formulation defined in terms of the strain energy potential as:

$$W(\mathbf{C}) = K_v(J-1)^2 + C_1(\tilde{I}_1 - 3) \qquad (1)$$

where J is the deformation Jacobian, $\tilde{I}_1$ is the first invariant of the iso-volumetric part of the right Cauchy-Green strain tensor $\mathbf{C}$, K_v is a parameter related to the bulk modulus, C_1 is the material parameter related to the initial shear stiffness as $\mu_0 = 2C_1$. Different shear moduli were considered (Material 1, 2 and 3), as reported in Table I. The Material 3 was set to the same stiffness of the most used AUS worldwide, the AMS800 (Boston Scientific, Boston, USA) [10].

TABLE I: CONSTITUTIVE PARAMETERS

Material	*C_1 [MPa]*	*K_v [MPa]*
1	0.20	3.87
2	0.30	5.80
3	0.43	8.31

The contact interaction between the chamber and the band and also between each part was imposed in the normal direction by means of a hard contact formulation, and in the tangential direction with a friction coefficient of 0.1.

The finite element mesh of the supporting band was developed by means of 373,911 four-nodes tetrahedral elements having a mean size of 0.25 mm and a total of 79,182 nodes. On the other hand, the inflatable chamber was meshed by 51,503 three-nodes triangular shell elements, due to its small thickness to area ratio, and a total of 25,759 nodes. The enhanced hourglass control formulation was considered [13], [14].

C. Computational analyses of lumen occlusion

The two developed models were assembled together by positioning the sphincteric model around the middle region of the urethral duct, as shown in the Figure 3.

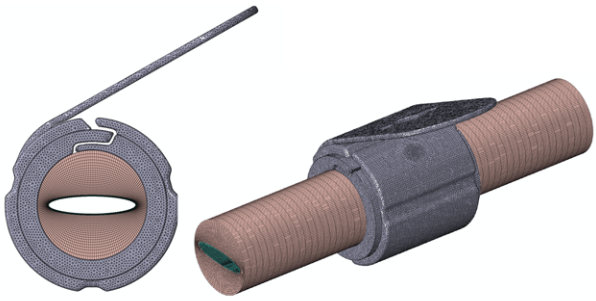


Fig. 3: Application of the novel device on the central zone of urethra.

In terms of contact property, a tangential behaviour was defined on the device regions in interaction with the urethral duct by means of friction coefficient of 0.02 [10],[12]. In addition, hard contact was considered in the normal direction on all the surfaces to prevent potential penetration phenomena.

To evaluate the minimum pressure that the novel AUS has to apply on the urethral duct for ensuring the continence, the lumen occlusion induced by the sphincter and the subsequent lumen opening due to the urine action were simulated for different constitutive parameters characterizing the device components. In detail, CSM analyses were performed by a three-step procedure. The first step simulated the cuff closing by applying a displacement boundary condition to carry the band tab portion in the operative positioning. Subsequently, during the second step, the chamber was inflated to a target pressure. Holding constant the occlusive action, during the third step, a radial pressure on the lumen inner surface was progressively increased up to the lumen opening.

The occlusive and intraluminal pressures were applied by means of hydrostatic pressure conditions. Load uniform distribution and velocity of 400 cmH_2O/s were assumed. Different target values of cuff pressure were considered in the range between 0 and 80 cmH_2O, on the basis of the occlusive pressure applied by the current AUSs. With regards to the urine action, the intraluminal pressure was considered within the physiological range during the voiding phase of micturition [16]. Since geometrical non-linearity effects and complex contact and self-contact conditions were expected during the analysis, the Abaqus/Explicit 6.14 (Dassault Systèmes, Vélizy-Villacoublay, France) non-linear dynamic explicit solver was adopted. The analyses were performed using a HPC server equipped with four Intel Xeon E7-8890 v4 and 512 GB RAM, allocating 30 to 50 threads for each target cuff pressure's simulation, resulting in an average analysis duration of 72 hours for each simulation.

III. RESULTS

The in silico approach to AUS design was exploited to investigate a novel device.

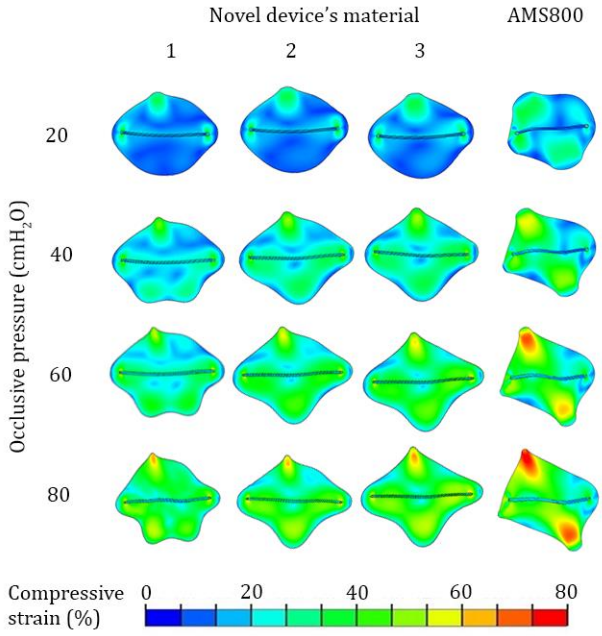


Fig. 4: Contours of compressive strain field at different level of cuff pressure for the different materials of the novel AUS and for the AMS800.

Numerical results of interaction phenomena between the urethral duct and the novel AUS were analysed during the lumen occlusion and opening processes considering different material parameters characterizing the device's components.

In particular, the compressive strain fields on the section of maximum stimulation of urethral model are reported for different occlusive pressures, as 20, 40, 60 and 80 cmH_2O, in relation with the three materials considered (Figure 4). In

comparison, the same mechanical fields for the AMS800 device are reported [10]. The results highlight an increase of compressive strain, proportional to the value of the applied cuff pressure and dependent on cuff material.

While minor difference emerges between the different materials of the novel device, it can be noted that, comparing them to the AMS800, less extensive areas are subjected to high values of compressive strain for occlusive pressures higher than 60 cmH_2O. This is an important aspect to consider because high values of compressive strain (and so of compressive stress) entail a risk of tissue degenerative phenomena. Moreover, for an occlusive action of 80 cmH_2O, the AMS800 involves more regions of urethra under hydrostatic pressures above 70 cmH_2O, which can obstruct most of the urethral vessels, where the blood flow reaches pressures between 13 and 105 cmH_2O [10].

For each material, the analyses allowed studying the relationship between sphincteric loading and urine action required to open the lumen. In particular, for each cuff material and each cuff pressure the corresponding lumen opening pressure was defined as the minimum intraluminal pressure needed to open the urethra. The resulting curves for the novel device are reported in Figure 5, in comparison to AMS800.

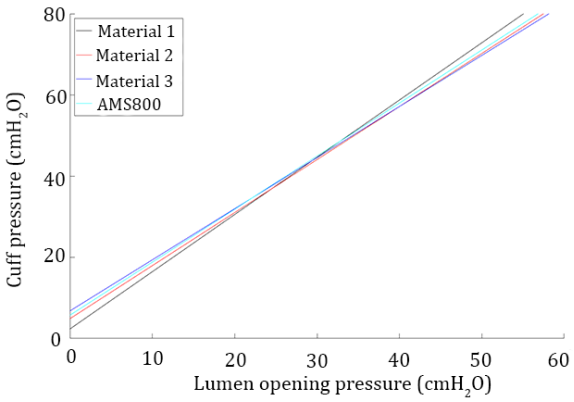


Fig. 5: Relation between lumen opening pressure and cuff pressure.

IV. Conclusion

AUS device is the gold standard treatment for severe SUI, with particular regard to male subjects. Nonetheless, the non-physiological mechanical effects on urethral tissues frequently entails complications. Aiming to a more reliable approach, a novel AUS has been defined by means of in silico methods, also supported by experimental tests. The methodology allows analysing interaction phenomena between AUS and urethral tissues and structure. The main outputs of the investigation consist in: i) the trend of cuff pressure that is required to ensure continence depending on bladder induced pressure, as a measure of functionality of the device, ii) the mechanical stimulation of urethral tissues depending on cuff pressure, in relation with the potential damage and/or vaso-constriction phenomena. The analysis shows that all the material configurations of the novel device have almost the same continence performance as the AMS800 (Figure 5). On the other side, it appears that the novel AUS device improves the distribution of the mechanical action on urethral tissues compared to the reference AUS case (Figure 4).

Even if supported by specific experimental tests, economic and time costs of the computational approach appears affordable and reliable, also overcoming ethical tasks. It represents a relevant support for clinical-surgical practice in the evaluation of the most appropriate solution to be adopted. The flexibility of the approach also leads to the possibility of prompt analysis of specific cases proposed for surgery.

Acknowledgement

This work was supported by University of Padova, Project FONT_BIRD2020_01 “Characterization of Artificial Urinary Sphincters for the identification of new DEVices (AUS-DEV)”.

References

[1] L. N. Tran and Y. Puckett, “Urinary incontinence”, *StatPearls* [Online], Treasure Island FL, 2022 Available: https://www.ncbi.nlm.nih.gov/books/NBK559095/

[2] R. Bientinesi, S. M. Recupero, G. Palermo, D. D’Agostino, P. F. Bassi et al., “Surgery for Male Urinary Incontinence: Where are we now and what is in the Pipeline?”, *Urologia Journal*, vol. 82, pp. 139-150, December 2014

[3] I. Toniolo, M. V. Mascolini, E. L. Carniel and C. G. Fontanella, “Artificial sphincters: An overview from existing devices to novel technologies”, *Artificial Organs*, November 2022

[4] A. Srivastava, G. A. Joice, H. D. Patel, M. G. Manka, N. A. Sopko et al., “Causes of Artificial Urinary Sphincter Failure and Strategies for Surgical Revision: Implications of Device Component Survival”, *European Urology Focus*, vol. 5, pp. 887-893, September 2019

[5] B. J. Linder, L. J. Rangel and D. S. Elliott, “Evaluating Success Rates After Artificial Urinary Sphincter Placement: A Comparison of Clinical Definitions”, *Urology*, vol. 113, pp. 220-224, March 2018

[6] S. Bugeja, S. L. Ivaz, A. Frost, D. E. Andrich and A. R. Mundy, “Urethral atrophy after implantation of an artificial urinary sphincter: fact or fiction?”, *BJU International*, vol. 117, pp.669-676, April 2016

[7] L. Marziale, G. Lucarini, T. Mazzocchi, E. Gruppioni, S. Castellano et al., “Artificial sphincters to manage urinary incontinence: a review”, *Artificial Organs*, vol. 42, pp 215-233, August 2018

[8] D. K. Agarwal, B. J. Linder and D. S. Elliott, “Artificial urinary sphincter urethral erosions: Temporal patterns, management, and incidence of preventable erosions”, *Indian Journal of Urology*, vol. 33, pp. 26-29, January 2017

[9] N. A. Chertack, K. M. Caldwell, G. A. Joice, M. Kavoussi, B. M. Dropkin et al., “Long-term lower urinary tract sequelae following AUS cuff erosion”, *Neurourology and Urodynamics*, vol. 41, pp. 229-236, September 2021

[10] A. N. Natali, E. L. Carniel and C. G. Fontanella, “Investigation of interaction phenomena between lower urinary tract and artificial urinary sphincter in consideration of urethral tissues degeneration”, *Biomechanics and Modeling in Mechanobiology*, vol. 19, pp. 2099-2109, May 2020

[11] A. N. Natali, E. L. Carniel, A. Frigo, P. G. Pavan, S. Todros et al., “Experimental investigation of the biomechanics of urethral tissues and structures”, *Experimental Physiology*, vol. 101, pp. 641-656, May 2016.

[12] C. G. Fontanella and E. L. Carniel, “Computational Tools for the Investigation of the Male Lower Urinary Tract Functionality in Health and Disease”, *Journal of Medical and Biological Engineering*, vol. 41, pp. 203-215, March 2021

[13] J. F. Prinz, R. A. de Wijk and L. Huntjens, “Load dependency of the coefficient of friction of oral mucosa”, *Food Hydrocolloids*, vol. 21, pp. 402-408, May 2007

[14] T. Belytschko and L. P. Bindeman, “Assumed strain stabilization of the eight node hexahedral element”, *Computer Methods in Applied Mechanics and Engineering*, vol.105, pp. 225-260, June 1993

[15] M. A. Puso, “A highly efficient enhanced assumed strain physically stabilized hexahedral element”, *International Journal for Numerical Methods in Engineering*, vol. 49, pp. 1029-1064, September 2000

[16] S. Zheng, D. Carugo, A. Mosayyebi, B. Turney, F. Burkhard et al., “Fluid mechanical modeling of the upper urinary tract”, *WIREs Mechanism of Disease*, vol.13, November 2021

A dexterous hand prosthesis based on additive manufacturing

M. Atzori[1,2], H. Müller[2,3], A. Buosi[2,7], F. Reggiani[4], J. Lazzaro[5], G. Alberti[5], C. Tiengo[1,6], F. Bassetto[1,6], N. Petrone[7]

[1]*Department of Neuroscience, University of Padova, Padova, Italy*
[2]*Information Systems Institute, University of Applied Sciences Western Switzerland (HES-SO Valais), Sierre, Switzerland*
[3]*Medical Faculty, University of Geneva, Geneva, Switzerland*
[4]*Dynatec Studio, Padova, Italy*
[5]*Playcast srl, Padova, Italy*
[6]*Clinic of Plastic Surgery, Padova University Hospital, Padova, italy.*
[7]*Department of Industrial Engineering, University of Padova, Padova, Italy*

***Abstract*—Upper limb amputation is a major injury that can strongly affect the daily life of a person. Prosthetic hands that can execute multiple movements are available, but they are expensive and difficult to control. Natural control via pattern recognition is promising but it is applied in real life prosthetics only in limited ways. Additive manufacturing and machine learning can revolutionize prosthetics with affordable and open-source solutions that can include 3D printed prosthetic hands, sockets and dexterous highly functional control. Nevertheless there are still intermediate steps to do into this direction. The objective of this paper is to introduce an ongoing project aimed at the development of low cost and dexterous prosthetic hands to be used in real life conditions based on open 3D models, additive manufacturing and machine learning. The results at the current state of advancement of the project include several versions of the prosthetic hand (powered by six servomotors and based on open design), of the control system (based on open electronic prototyping platforms) and of the socket. Preliminary tests of the hand demonstrate its dexterity, its potential and requirements to improve force. Once fully completed and released, the presented 3D printed, dexterous, open-source prosthetic hand has the potential to improve the life of hand amputees worldwide and to foster improvements in research and for future commercial prosthetic hands.**

***Keywords*—Electromyography, prosthetics, additive manufacturing, machine learning.**

I. Introduction

Upper limb amputation is a serious injury that can have a significant impact on a person's everyday life. According to estimates, 41,000 Americans were thought to have lost most of their upper limbs due to amputations above or below the elbow in 2005 [1].

Hand prosthetics is rapidly advancing, also thanks to machine learning and 3D printing. The combination of these solutions may revolutionize the domain if it is demonstrated to properly work on real life tasks and in a robust way. Although surface Electromyography (sEMG) commercial dexterous prosthetic hands (i.e., prosthesis that can do several movements) do exist, they are quite expensive and frequently difficult to control [2]. Their usage is thus often limited, because the control is frequently not sufficiently easy for usage in practical situations. Over the past ten years, a number of open models for 3D printed hand prosthetic hands have been created. Although 3D printing is one of the key technologies expected to revolutionize prosthetics in the future, open-source strong and dexterous prostheses have been limitedly developed.

Particularly if the amputation is bilateral, hand amputations are among the most physically and mentally debilitating injuries. At the moment, there are three types of hand prostheses: myoelectric, kinematic, and aesthetic. Cosmetic prosthetics provide psychological and esthetic support. Kinematic prostheses also have functional capabilities, since the user may control the opening and shutting of a gripper hand by the motion of the shoulder. In most myoelectric prostheses, two electrodes on the forearm allow the user to control a battery-operated hand using an electrical signal produced by the remaining muscles [2]. Prosthetic hands that can execute multiple movements are available, however they are frequently quite expensive. Few myoelectric hand prosthetics that are now on the market have the ability to replicate a variety of actions, e.g. Touch Bionics i-limb Quantum; Otto Bock Michelangelo; Steeper Bebionic v3; Vincent hand Evolution 2 [2]. Such prostheses are typically priced between $50,000 to $75,000, and the cost can further increase when pattern-recognition-based control systems are included. In such, still relatively rare, systems, typically, two or three sEMG electrodes are placed in the socket in relation to particular muscles to regulate them. The prosthetic hand opens and closes using myoelectric impulses, or a rise in the amplitude of the electrical signal released by the muscles. By using particular (for example, sequential) control procedures, the number of motions can be enhanced. Controlling prostheses needs a high level of competence and a dedicaterd training process, making such control tactics still far from being identifiable as natural.

The limited capabilities and acceptance of sEMG prostheses are a result of control issues among other challenges [3], but there are the premises for improvements in a near future. Effective tools for prosthesis control, pattern recognition and machine learning are primarily used in scientific studies [4] and there are currently not many commercially available systems. These techniques typically usually employ a higher number of sEMG electrodes to capture the myoelectric signals produced by the muscles. Utilizing algorithms for pattern recognition, the sEMG activity is examined to categorize the

movement that the subject intends to make in real time [5],[6]. Since 2013, Coapt-engineering[1] made a brand-new real-time pattern recognition-based hand prosthesis control system commercially available. Despite the incredible advancement for the domain, this system still does not replicate a biological hand's natural control and allows controlling usually a limited number of movements [2].

In recent research works, additional sources of information [6]–[8] have been suggested to be incorporated into the conventional myoelectric control, enhancing the controller with autonomous decision-making. Cognolato et al. enriched sEMG with eye tracking and computer vision data [9], [10].

A number of 3D printed hand prostheses have been developed in recent years thanks to 3D modeling and printing [11]. Numerous websites offer open designs that enable users to build their own 3D printed prosthesis[2]. Additive manufacturing processes and rapid prototyping techniques provide many options to quickly design, develop, build, and test functional prosthetic hands in a reasonable amount of time. In comparison to current commercial prostheses, 3D printed prosthetic hands may offer benefits like lower costs and patient-specific size adaptation. Additionally, an open-source architecture enables quick adaption to technological and scientific breakthroughs. An excellent example of the capabilities of this kind of approaches is provided by the HANDi HAND, which was created at the University of Alberta (Canada) [12], which has a number of actuators and a range of sensors (including pressure and positioning sensors) and that was tested in real life conditions by our group [13]. However, the majority of open hand prosthesis designs have only limited functionality (open-close), they are not robust enough to be used in real-world situations often having limitations in stiffness, grasp strength, assembly precision or structural strength and they have only received sporadic testing when combined with pattern recognition on practical tasks [13].

II. Methods

The prosthetic hand presented in this work was designed to allow for the most common hand movements for activities of daily living, with particular focus on the most used movement macro-classes [14]. The prosthetic hand was designed following the requirements of patients and it is composed of a dexterous robotic hand, a socket including eight sEMG electrodes and a control system.

A. Dexterous hand prosthesis

In most cases the available open source hand prostheses designs have limited functionality (open-close), they are not sufficiently robust to be used in real life conditions and they have been limitedly tested in combination with pattern recognition on real life tasks. The prosthetic hand presented in this work was designed to facilitate daily tasks as much as possible.

It is based on previous 3D printed open source hand prosthesis, the HANDi HAND, designed at the University of Alberta (Canada) [12], that includes six actuators and a variety of sensors (including pressure sensors and encoders for finger positioning). However, following a set of real life tasks tests [13], the hand was strongly redesigned to increase ergonomics, functionality for activities of daily living and usability: limitations such as the finger orientation, the zip-tie return spring, surface grasp friction and strength were addressed and intentionally improved.

The prosthetic hand includes six servomotors: five for finger flexion, one for thumb ab-adduction. The fingers are positioned to be similar to real prostheses and to allow functionally grasping objects and they are designed to allow the user predicting their positioning more intuitively. The internal transmission and gear systems were designed from scratch with a desmodromic transmission to reduce friction and to increase grasp force and mechanic life. Several servomotor models were tested as well with the aim of increasing strength. The prosthesis was produced through SLS (Selective Laser Sintering) technique, which allowed the use of complex and detailed geometry. The material used for the dorsal part of the hand is Nylon (PA 12), which provides good mechanical properties and strength. SLS (Selective Laser Sintering) technology uses a laser to sinter and fuse together layer after layer of powdered material, thus creating more robust components compared to the more commonly known FDM (Fused Deposition Modeling). Another advantage is that the non-sintered powdered material acts as support during the 3D-printing process. This allows to produce more complex shapes and eliminates the need for physical supports during the production of the component. The design of the hand will be released open-source as soon as it is finalised.

B. Socket

The socket was designed and made by Playcast Srl[3]. The design of the virtual model of the socket was made on the basis of real data using an innovative 3D scanning technique which was applied to the patient's amputated forearm. The obtained 3D reconstruction is very accurate and in high resolution, allowing limited changes to create the socket using proprietary design tools of the company. Among the changes, adaptation to include eight sEMG electrodes was required to allow empowering machine learning based algorithms and to include the prono-supination mechanism. The socket was then printed with additive manufacturing using the FDM technique and using recycled plastic, with low impact on the environment and it is fully recyclable. The socket is composed of three pieces: one is adherent to the distal stump and activates the hand pronosupination; two make up the outer shell of the socket, facilitate the wearing process and transmit the loads to the elbow epicondyles, by means of low shore paddings. The two pieces are held together by velcro straps.

C. Control system

The prosthetic hand is controlled via eight Otto Bock

[1] http://www.coaptengineering.com/

[2] E.g. http:// openbionics.org/ ; http://enablingthefuture.org/

[3] https://www.playcast.it/

13E200 EMG sensors, which detect the contraction of the remnant muscles in the proximal stump. The signal is transmitted to an open-source electronic prototyping platform (Arduino Mega).

The various possible movements associated with different patterns of contraction of the muscles in the forearm are then analysed to control the prosthesis. Custom made classification algorithms (developed by Dynatec studio[4]) classify the signal associated to four hand postures (fist, wrist flexion, wrist extension, fingers spread, rest) on the Arduino, which is also used for controlling the servomotors for positioning the hand prosthesis. Among the possible grasps performed by the prosthesis, the following ones were tested in different sessions: cylindrical, tripod, index finger extension, rest, lateral, tip pinch.

III. Results

A. *Dexterous hand prosthesis*

The developed hand prosthesis represents an effective application of additive manufacturing to the development of dexterous and high functionality prosthesis controlled via machine learning (Fig. 1).

The prosthetic hand was designed to allow for the most common hand movements for activities of daily living, to facilitate daily tasks as much as possible.

The design and the positioning of the fingers allow a functional and effective grasping of objects of different shapes, including bottles, balls, credit cards, pens. Moreover, the ongoing process of redesigning the fingers has allowed to increase the predictability of their positioning during grasps. The desmodromic design of the internal transmission and gear systems allowed to control actively both the flexion and extension of fingers and allowed to reduce friction and to increase the life of the components.

Among the servomotor models that were tested, six Hitec HS-65MG provided the best compromise between component durability and strength. More powerful servomotors were tested though. Those would likely benefit the usability of the prosthetic hand, but at the current status the authors could not find more powerful components able to provide sufficient durability and reliability.

In general, the 3D printed prosthetic hand showed very good usability in terms of ergonomics, usability and capability to interact with the environment for grasping objects (Fig. 2). It costs less than 600 €, weights 350 grams and it is capable of performing the most useful grasps for activities of daily living and to effectively grasp objects. The current challenge for the team is to improve the grasp strength, to satisfy the requirements of everyday life. According to users, the prosthesis represents an important step in the direction for future prosthetics.

B. *Socket*

The socket was designed by Playcast Srl and offers high adaptability, low making times and costs, relatively good usability and the possibility to include several sEMG electrodes to empower machine learning based control algorithms.

The socket was designed and made with 3D scanning and printing, which allowed to strongly reduce the time required to make it. The obtained 3D reconstruction is very accurate and in high resolution, leading to a good fit to the forearm of the patient. It allows to include eight surface electromyography electrodes and it can be easily connected to the robotic hand prosthesis. The socket includes a wrist rotation system and demonstrated good usability in preliminary tests, it is easier to wear than traditional ones and it offers sufficient comfort for experimental tests. In order to improve the electrode contact with the skin, an elastic armband was used provide pressure on the top of the electrodes.

The socket offers several advantages over traditional ones due to Voronoi holes pattern. First, it is breathable and fully washable; second, it does not require qualified personnel to be made; lastly, it is cheaper than a traditional system and it is made of 100% recyclable plastic, with positive outcomes for the environment). In addition the production cost is limited (less than 600 €) and it weighs only 350 grams.

Improvements are currently being implemented aiming at extending the usability, which is currently limited, for allowing everyday life usage.

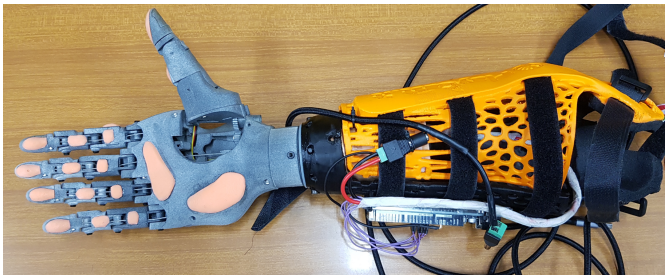


Fig. 1: 3D printed robotic hand and socket.



Fig. 2: Examples of hand grasp tests.

C. *Control system*

The control system is based on eight Otto Bock 13E200 EMG sensors (weight 4.5 g each), one Arduino Mega (cost less than 50 €, weight less than 50 g), one battery and custom-made machine learning algorithms. It demonstrated to perform well in practical tests, allowing to easily open and close the prosthesis in 3 different movements selected among the

[4] https://www.dynatecstudio.it/

taxonomy of hand movements [14]. The control system employed in this study experiments used a gesture recognition approach that made it possible to swiftly and automatically identify the required grasp. In addition to controlling the gesture used to open the prosthetic hand, the system was tailored to the characteristics and demands of the patients, enabling them to grip objects.

Controlling the prosthesis in the different movements was very fast and reliable, making its usage almost instantaneous, smooth and pleasant according to the users. The authors are current working to solve challenges mainly related to forearm positioning issues, which are well known in the domain of dexterous prosthetics.

IV. Discussion & Conclusion

The promising findings presented in this paper point to the viability of flexible robotic prosthetic hands based on additive manufacturing, 3D scanning and machine learning based control systems. These technologies are currently more widely available than in the past due to the components' and devices' rising affordability.

Despite the requirement to improve the socket usability and the prosthesis strength, the system demonstrates high usability capabilities and well represents the capabilities of the forementioned modern technologies for the future of prosthetics.

The whole system weighs less than 900 g plus the battery and costs less than 1’400 € excluding the electrodes. The electrodes currently represent the most expensive part of the system, but those could be replaced with open-source low cost solutions in the future. These facts suggest that the experimental setting can be successfully replicated and applied in situations where cost is a major concern, such as in the pediatric population, in underdeveloped nations, and in research teams with limited resources.

Acknowledgement

This project was partially supported this work via the SNSF Sinergia project # 410160837 MeganePro and by the Hasler Foundation via the ProHand project. The authors would like to thank Matteo Cognolato for his fundamental support at the beginning of the project, D. J. A. Brenneis, M. R. Dawson and P. M. Pilarski for the development and release of the HANDi Hand.

References

[1] K. Ziegler-Graham, E. J. MacKenzie, P. L. Ephraim, T. G. Travison, and R. Brookmeyer, “Estimating the prevalence of limb loss in the United States: 2005 to 2050,” *Arch Phys Med Rehabil*, vol. 89, no. 3, pp. 422–429, 2008.

[2] M. Atzori and H. Müller, “Control Capabilities of Myoelectric Robotic Prostheses by Hand Amputees: A Scientific Research and Market Overview,” *Front Syst Neurosci*, vol. 9, no. 162, 2015, doi: 10.3389/fnsys.2015.00162.

[3] D. J. Atkins, D. C. Y. Heard, and W. H. Donovan, “Epidemiologic overview of individuals with upper-limb loss and their reported research priorities,” *Journal of Prosthetics & Orthotics*, vol. 8, no. 1, pp. 2–11, 1996.

[4] D. Farina *et al.*, “The extraction of neural information from the surface EMG for the control of upper-limb prostheses: Emerging avenues and challenges,” 2014.

[5] E. Scheme and K. Englehart, “Electromyogram pattern recognition for control of powered upper-limb prostheses: State of the art and challenges for clinical use,” *The Journal of Rehabilitation Research and Development*, vol. 48, no. 6, p. 643, 2011, doi: 10.1682/JRRD.2010.09.0177.

[6] E. A. Corbett, K. P. Kording, and E. J. Perreault, “Real-Time evaluation of a noninvasive neuroprosthetic interface for control of reach,” *Neural Systems and Rehabilitation Engineering, IEEE Transactions on*, vol. 21, no. 4, pp. 674–683, 2013.

[7] M. Markovic, S. Dosen, D. Popovic, B. Graimann, and D. Farina, “Sensor fusion and computer vision for context-aware control of a multi degree-of-freedom prosthesis.,” *J Neural Eng*, vol. 12, no. 6, p. 66022, 2015, doi: 10.1088/1741-2560/12/6/066022.

[8] M. Markovic, S. Dosen, C. Cipriani, D. Popovic, and D. Farina, “Stereovision and augmented reality for closed-loop control of grasping in hand prostheses,” *J Neural Eng*, vol. 11, no. 4, p. 46001, Aug. 2014, doi: 10.1088/1741-2560/11/4/046001.

[9] M. Cognolato, M. Atzori, R. Gassert, and H. Müller, “Improving Robotic Hand Prosthesis Control With Eye Tracking and Computer Vision: A Multimodal Approach Based on the Visuomotor Behavior of Grasping,” *Front Artif Intell*, p. 199, 2022.

[10] M. Cognolato *et al.*, “Gaze, visual, myoelectric, and inertial data of grasps for intelligent prosthetics,” *Sci Data*, vol. 7, no. 1, pp. 1–15, 2020.

[11] J. Ten Kate, G. Smit, and P. Breedveld, “3D-printed upper limb prostheses: a review,” *Disabil Rehabil Assist Technol*, vol. 12, no. 3, pp. 300–314, 2017.

[12] D. J. A. Brenneis, M. R. Dawson, and P. M. Pilarski, “Development of the HANDi Hand: an inexpensive, multi-articulating, sensorized, hand for machine learning research in myoelectric control”.

[13] M. Cognolato *et al.*, “Multifunction control and evaluation of a 3D printed hand prosthesis with the Myo armband by hand amputees,” *bioRxiv*, p. 445460, 2018.

[14] F. Stival, S. Michieletto, M. Cognolato, E. Pagello, H. Müller, and M. Atzori, “A quantitative taxonomy of human hand grasps,” *J Neuroeng Rehabil*, 2019, doi: 10.1186/s12984-019-0488-x.

Adaptation of cardiac deformation pattern during exercise in children

D. Collia[1], and G. Pedrizzetti[1]
[1] *Department of Engineering and Architecture, University of Trieste, Italy.*

***Abstract*—In the cardiovascular system, the geometric remodeling of the cardiac chambers is the main mechanism allowing increased performance of athletes during exercise as well as underlying the pathological progression leading to heart failure. In this study we analyze cardiac mechanics in healthy children during four phases of physical exercise, *Rest*, *Mid*, *Peak* and *Recovery*, by 3D echocardiography. The analysis is performed in comparison with a set of normal children with the objective to identify the modifications induced by exercise that lay at the basis of cardiac remodeling induced by physical exercise. The ventricular functional performance is analyzed in terms of tissue deformation with the aim of verifying the activation of cardiac fibers through the response in terms of strain tensor its principal strain values and directions. This evaluation brings indications for identifying clinical markers that anticipate exercise-induced remodeling and that can also be useful for a deeper understanding of remodeling in cardiovascular pathologies or during therapeutic protocols.**

***Keywords*—Strain, cardiac mechanics, left ventricle, cardiac fibers, myocardial deformation.**

I. INTRODUCTION

The function of the human heart is that of a mechanical pump that creates and sustains blood motion through a sequence of passive relaxations and active contractions of the cardiac tissue. In particular, the left ventricle (LV), which represents the most important chamber according to the pumping purpose, fills with low pressure blood flowing from the left atrium (diastole) and contracts vigorously to eject blood at high pressure into the aorta (systole). This process is characterized by an intense dynamic interaction between the flowing fluids and the surrounding tissue; minor alterations to such a dynamic balance affect the reciprocal adaptive behaviors and can induce long-term progressive geometric changes [1], [2].

Progressive modifications of cardiac geometry are accompanied by an alteration of its functional parameters along a process known as cardiac remodeling. Typically, cardiac remodeling develops as a adverse consequence of almost all cardiac dysfunctions and leads to the syndrome of heart failure, the principal social threatening cardiac dysfunction [3], [4]. However, cardiac remodeling mechanism can also develops favorably as a result of virtuous factors like physical exercise. This type of remodeling is characterized by a structural and functional adaptations that facilitates the performance of the heart related to increased demand of blood flow like, at the extreme end, those found in the athlete's heart [5], [6]. Understanding the primary causes leading to either pathological or favourable cardiac remodeling is of paramount importance in multiple aspects of cardiology like anticipating disease progression, supervise healing response to physical exercise, monitor athletes during extreme performance, or even children during growth. At the present time, reliable models of remodeling are still largely unsatisfactory are not consistently predictive [7].

Within this general picture, the present study analyzes the structural adaptation of the left ventricles in a pediatric population during physical exercise. The LV function is analyzed from geometry extracted from three-dimensional (3D) echocardiography during four phases of exercise (*Rest*, *Mid*, *Peak* and *Recovery*). The study is performed through the evaluation of the strain tensor that permits evaluating both the entity and the direction of contraction and provides a comprehensive description of LV dynamics during the various cardiac phases of physical exercise in response to an adaptive effort.

This study aims to identify the alterations of LV function associated with exercise, which underlay the longer-term macroscopic adaptations induced by physical exercise therapy or found in athletes' heart. Results are also expected to be informative on the general phenomena associated to remodeling.

II. MATERIALS AND METHODS

The analysis is performed in a group of healthy children undergoing physical exercise test, it also includes an independent large group of age-matched subjects as control reference. All participants had normal cardiac function and absence of any identified disease. All subjects underwent three-dimensional (3D) echocardiography following a non-invasive protocol performed in collaborating clinical institutions for screening purpose. The 3D echocardiography requires that recordings are spatially focused on the LV to get high time resolution. The recorded 3D imaging datasets were analyzed by the same clinical institutions by a dedicated software (4D LV Analysis, TomTec Imaging System GmbH, Unterschleissheim, Germany) to extract the moving ventricular geometry. In that software, the boundary (endocardium) between ventricular tissue and blood pool is first drawn manually through the graphical user interface at one instant, then the software tracks the anatomical features over the entire heartbeat by an optical flow method. This analysis produces a triangulated surface of the moving endocardial geometry where vertices identify material points. The present study is dedicated to the

preliminary, blind analysis of these endocardial surfaces as provided by the clinical institutions in anonymous form.

Each subject enrolled in the study was recorded at four time phases during physical exercise: *Rest*, *Mid*, *Peak* and *Recovery*. The control reference group used for comparison was recorded at rest. All recordings are analyzed individually, then the modifications during physical exercise as well as the comparison with the reference normal group are performed statistically in terms of synthetic parameters of volumes, ejection fraction (EF) and strain. In addition, to improve the statistical comparison between the different phases in terms of spatially extended pattern, the geometries were averaged among the group during each phase of the physical exercise. To perform this averaging procedure, all ventricles in a set are translated to a common center, then anatomical landmarks (mitral annulus, center of aortic outlet, and apex) are identified and a 3D rotation is performed to bring all ventricles to a common axis and with the valve position aligned.

The dynamic properties of the cardiac tissue are principally studied in terms of tissue deformation or strain. Strain during cardiac deformation is described mathematically by the machinery of finite deformation [8], [9], which is briefly recalled here. Consider an initial state, say at a reference time $t = 0$ typically taken at end-diastole, where the material points in the tissue are described by their coordinates $\mathbf{X}$, and a deformed state at a second time t where each material point has moved to a new position $\mathbf{x}(\mathbf{X}, t)$, such that evidently $\mathbf{x}(\mathbf{X}, 0) = \mathbf{X}$. The transformation from $\mathbf{X}$ to $\mathbf{x}$ is described by the deformation gradient $\boldsymbol{\mathcal{F}}$ defined as

$$\mathcal{F}_{ij} = \frac{\partial \mathrm{x}_i}{\partial \mathrm{X}_j}. \tag{1}$$

Tensor $\boldsymbol{\mathcal{F}}$ can be separated through the polar decomposition in rotation and deformation

$$\boldsymbol{\mathcal{F}} = \boldsymbol{\mathcal{R}}\boldsymbol{\mathcal{U}}; \tag{2}$$

where $\boldsymbol{\mathcal{R}}$ is the rotation matrix, and $\boldsymbol{\mathcal{U}}$ is the right stretch tensor that contains the information about the deformation occurred during the time interval $(0, t)$. Along this approach, the straightforward definition for a *strain tensor* is

$$\boldsymbol{\mathcal{S}t} = \boldsymbol{\mathcal{U}} - \boldsymbol{\mathcal{I}}; \tag{3}$$

which is known as the Lagrangian strain, because it is computed following the material points identified in the original configuration. The strain tensor defined by (3) is also known as *Biot strain tensor* and as engineering strain, because this definition is commonly used in engineering for small deformation. This definition corresponds to the most intuitive description of deformation. For example, in one-dimensional (1D) deformation, a segment of length L_0 is stretched (compressed) to a deformed length $L_1 = L_0 + \Delta L$ and the strain measures the relative change of length $\mathcal{S}t = \frac{\Delta L}{L_0}$, which is a measure of the effective elongation (shortening) of an originally undeformed fiber. This definition of strain is that considered as a standard in cardiology at least for 1D strain in clinical imaging [10].

Several other definitions of strain based on the knowledge of the general transformation (1) are present in literature [9], [11], [12]; they may be less intuitive for the description of strain while they may present some other theoretical advantages; however, they are not common in clinical cardiology. In any case, results obtained with different definitions are comparable and interchangeable because all standard definitions of strain tensor associated to a common $\boldsymbol{\mathcal{F}}$ present the same eigenvectors while the eigenvalues are mathematically related one to the other.

Cardiac contraction starts at $t = 0$ from an undeformed reference configuration taken at the end of diastole, the instant in which the volume is maximum, and ends at the end of systole, when the volume is minimum and strain eigenvalues are negative. LV deformation is evaluated in terms of principal strain (PS), the most negative eigenvalue of the strain tensor (3), and secondary strain (SS), which is the second eigenvalue. The principal direction of contraction is obtained by the eigenvector corresponding to the PS. Evaluations are reported in terms of spatial pattern of PS value and direction evaluated at end-systole, and in terms of global (spatially-averaged) strain values (GPS, GSS) during tuime along the heatbeat. For comparability with existing studies, the global longitudinal and circumferential strain values (GLS, GCS) are also computed.

III. Results

The population is first compared during the rest phase with respect to the reference control group. Results confirm that the analyzed population is representative for normal children in terms of geometry (volumes) and contraction properties (EF and strain).

During exercise, the ventricle must pump a greater amount of blood per minute to the body, this objective is achieved by increasing the heart rate and by increasing muscular contraction resulting to a smaller LV volume at the end of systole. Overall, the increase of contraction is associated with an increase (more negative) PS as exercise progresses. This increased contraction corresponds to a spatial distribution of PS that becomes more uniform. The spatial distribution of PS during the four phases of the physical exercise is shown in figure 1, for one representative subject. The color map is drawn above *strain-lines* everywhere tangent to the corresponding eigenvector.

At the *Rest* phase, the LV strain directions range from circumferential to right-handed or left-handed helical directions in the various regions of the ventricle. This pattern is the result of the contraction of myocardial fibers whose arrangement vary from helical in the inner layer (sub-endocardium) through circumferential (mid-myocardium) to counter-rotating helix at the outer layer (sup-epicardium) [13], [14]. Subsequently, increasing the workload (*Mid* and *Peak* phases) the direction of deformation tends to become more circumferential; this is the result of the activation of multiple myocardial layers with different fiber directions across the entire thickness to achieve higher performance. In other terms, the concurrent contraction along multiple directions results in a strain tensor whose PS is

approximately aligned with the circumferential direction and a SS that is more longitudinal. This picture can be reinforced by the analysis of the time course of GPS and GSS: immediately at the onset of contraction the former presents a sharp decrease, such a strong contraction in the dominant direction provokes an initial stretch in the perpendicular direction and GSS increase to a positive peak; soon afterwards, all fibers become active for the contraction, both GPS and GSS decrease and reach, at end systole, their stronger exercise-induced value. Finally, in the *Recovery* phase it is interesting to note that although global contractile values return similar to those at rest, this normal degree of contraction is achieved with a different pattern of contraction that witnesses the persistent modification to LV function induced by exercise.

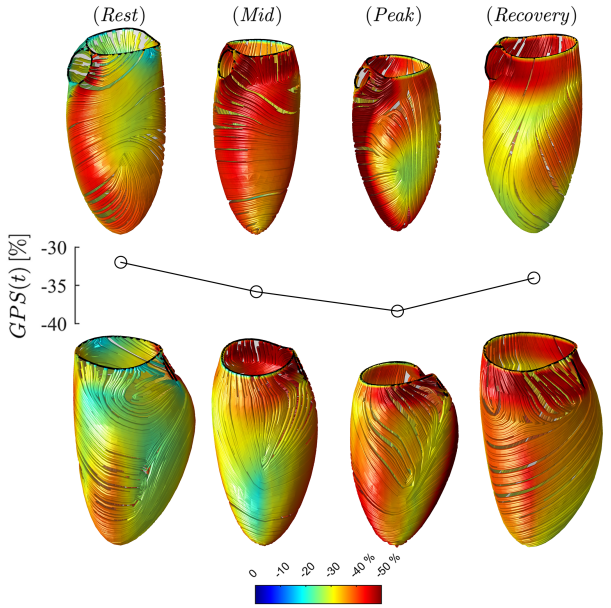


Fig. 1: Color map of the first principal strain (most-negative eigenvalue of the strain tensor) at the end of systolic contraction. Colors are drawn over the strain-lines (tangent to the corresponding eigenvector) for (*Rest*), (*Mid*), (*Peak*) and (*Recovery*), each one shown in two opposite facing views.

IV. Conclusions

The study of LV strain during physical exercise allows to identify the mechanical response induced by this type of stress and the likely longer-term remodeling that can be induced by its continuous application.

The present results, although preliminary, show evidence of modification in the cardiac deformation pattern induced by physical exercise. This modification is characterized by an increase of cardiac deformation along all directions with principal direction of contraction that becomes approximately circumferential.

The interpretation of strain results suggest that physical exercise stimulates the activation of myocardial fibers across the entire thickness [15]. This result is consistent with the increased myocardial thickness observed in athlete's heart and indicates that such an increase corresponds to increased muscular mass that is fully reversible and well different from a pathological hypertrophy. This result also supports therapies based on physical exercise indicating how they train the myocardium over the thickness and improves its efficiency [16].

On the methodological perspective, the present approach appears promising to evaluate the presence of early alterations of cardiac function that may be informative on the possible progression of remodeling during healing or disease.

Acknowledgement

DC and GP acknowledge partial support by Italian Ministry of Education, University and Research under project PRIN 2017A889FP_ 006.

References

[1] L. Andrés-Delgado and N. Mercader, Interplay between cardiac function and heart development, Biochim. Biophys. Acta – Mol. Cell. Res., 2016, 1863, 1707.

[2] G. Pedrizzetti, G. L. Canna, O. Alfieri, and G. Tonti, The vortex – an early predictor of cardiovascular outcome? Nat. Rev. Cardiol., 2014, 11, 545.

[3] D. Levy, S. Kenchaiah, M. G. Larson, E. J. Benjamin, M. J. Kupka,K. K. L. Ho, J. M. Murabito, and R. S. Vasan, Long-Term Trends in the Incidence of and Survival with Heart Failure. N. Engl. J. Med. 2002;347:1397-1402

[4] P. P. Sengupta, and J. Narula, Reclassifying heart failure: predominantly subendocardial, subepicardial, and transmural. Heart Fail Clin. 2008;4:379-82.

[5] A. La Gerche, G. Pedrizzetti, B. Ranieri, A. D'andrea, and E. Bossone, On the characterization of athlete's heart using 3D echocardiography, European Journal of Preventive Cardiology, 2022, 29, 1592–1593.

[6] T. W. Churchill, E. Groezinger, G. Loomer, J. S. Guseh, R. B. Weiner, M. M. Wasfy, B. D. Levine, and A. L. Baggish. Training-associated changes in ventricular volumes and function in elite female runners. Circ Cardiovasc Imaging 2020;13:e010567.

[7] L. H. Opie, P. J. Commerford, B. J. Gersh, and M. A. Pfeffer, Controversies in ventricular remodelling. Lancet, 2006, 367, 356.

[8] R. Ogden, Non-linear Elastic Deformations, Dover, 1997, New York.

[9] D. Collia, G. Pedrizzetti, T. Sato, D. Matsubara, L. Zovatto, M. Gei, A. Banerjee, and G. Pedrizzetti, Interplay between Geometry, Fluid Dynamics, and Structure in the Ventricles of the Human Heart, 2023, Phys. Rev. Applied, 19, 014006.

[10] J. Voigt, G. Pedrizzetti, P. Lysyansky, T. Marwick, H. Houle, R. Baumann, S. Pedri, Y. Ito, Y. Abe, S. Metz, J. Song, J. Hamilton, P. Sengupta, T. Kolias, J. d'Hooge, G. Aurigemma, J. Thomas, and L. Badano, Definitions for a common standard for 2d speckle tracking echocardiography: consensus document of the eacvi/ase/industry task force to standardize deformation imaging, Eur. Heart J., Cardiovasc. Imag., 2015, 16, 1.

[11] G. Pedrizzetti, E. Kraigher-Krainer, A. DeLuca, G. Caracciolo, J. Mangual, A. Shah, L. Toncelli, F. Domenichini, G. Tonti, G. Galanti, P. Sengupta, J. Narula, and S. Solomon, Functional Strain-Line Pattern in the Human Left Ventricle, Phys. Rev. Lett. 109, 048103, 2012.

[12] A. Satriano, P. Pournazari, N. Hirani, D. Helmersen, M. Thakrar, J. Weatherald, J. White, and N. Fine, Characterization of right ventricular deformation in pulmonary arterial hypertension using three-dimensional principal strain analysis, J. Am. Soc. Echocardiogr. 32, 385, 2018.

[13] G. Pedrizzetti, S. Sengupta, G. Caracciolo, C. Park, M. Amaki, G. Goliash, P. Sengupta, and J. Narula, Three-dimensional principal strain analysis for characterizing subclinical changes in left ventricular function, J. Am. Soc. Echocardiogr., 2014, 27, 1041.

[14] G. Buckberg, J. Hoffman, A. Mahajan, S. Saleh, and C. Coghlan., Cardiac mechanics revisited: the relationship of cardiac architecture to ventricular function, Circulation, 2008, 118, 2571.

[15] L. Stefani, A. D. Luca, L. Toncelli, G. Pedrizzetti, and G. Galanti, 3d strain helps relating lv function to lv and structure in athletes, Cardiovasc. Ultrasound, 2014, 2, 33.

[16] Caselli S, Maron MS, Urbano-Moral JA, Urbano-Moral JA, Pandian NG, Maron BJ, Pelliccia A. Differentiating left ventricular hypertrophy in athletes from that in patients with hypertrophic cardiomyopathy. Am J Cardiol 2014;114:1383–1389.

Development of novel computational tool to support surgical planning for the treatment of Anomalous Aortic Origin of the Coronary Arteries (AAOCA)

S. Anglese[1*], M. Lo Rito[2*], A. Rosato[1], V. Ceserani[3], G. M. Formato[1], A. F. Pascaner[3], M. Conti[3]
[1] *3D and Computer Simulation Laboratory, IRCCS Policlinico San Donato, San Donato Milanese, Italy*
[2] *Department of Congenital Cardiac Surgery, IRCCS Policlinico San Donato, San Donato Milanese, Italy*
[3] *DICAr, University of Pavia, Italy*
[*] *These authors (S.A, M.L.R) have contributed equally to this work.*

Abstract **– Anomalous Aortic Origin of the Coronary Artery (AAOCA) is a rare congenital heart disease and is a major cause of sudden cardiac death (SCD). Surgical operation is indicated for symptomatic forms or in the case of ischemic signs. Surgery aims to relieve the site of coronary compression along the anomalous segment. Several surgical techniques are available to resolve the coronary compression causing myocardial ischemia.**

This study aims to develop and create a computational tool to support surgeons when planning which technique to adopt to obtain the best fluid dynamic result.

We created a model based on Computational Fluid Dynamics (CFD) to compute post-operative coronary flow based on pre-operative data.

Although limited to preliminary investigation, the proposed model can replicate the three surgical modalities used in the clinical practice to treat AAOCA, computing the post-operative flow.

Future developments will target the fine-tuning of the model towards a patient-specific analysis, including clinical measurements, and the model validation to enhance its credibility.

Keywords **– anomalous coronary, computational fluid dynamics, surgical planning, decision support.**

I. Introduction

AAOCA is a rare congenital heart disease and is one of the leading causes of SCD in athletes and young subjects. It can remain silent for life for most of the sedentary and non-sports population [1] but the occurrence of SCD is unpredictive and not directly related to the amount of effort.

Surgical treatment aims to remove or resolve lumen reduction along the anomalous segment of the coronary artery. There are several surgical techniques (e.g., unroofing, reimplantation, patch osteoplasty) [2]–[6] adopted to treat such peculiar coronary compression [1], [7]. The unroofing consists of the longitudinal opening of the intramural segment up to the coronary take-off (Fig. 1a). Patch osteoplasty requires an extensive incision of the coronary artery and aorta on the anterior surface and the placement of a pericardial patch to recreate the roof and continuity of both structures (Fig. 1b). Reimplantation consists of a section of the anomalous coronary artery that is detached from the aorta at take-off; the coronary is re-implanted in another region of the aorta that is not subject to compression (Fig. 1c).

Due to the rarity of the disease and the impossibility to perform randomization based on the surgical operation a systematic comparison of techniques has not yet been conducted. The impossibility to determine which intervention is the most appropriate to recreate the physiological condition surgical planning still carries a degree of uncertainty.

Based on these considerations, our goal is to create a patient-specific computational tool that supports the surgeon in outlining the most appropriate surgical plan to restore normal coronary flow.

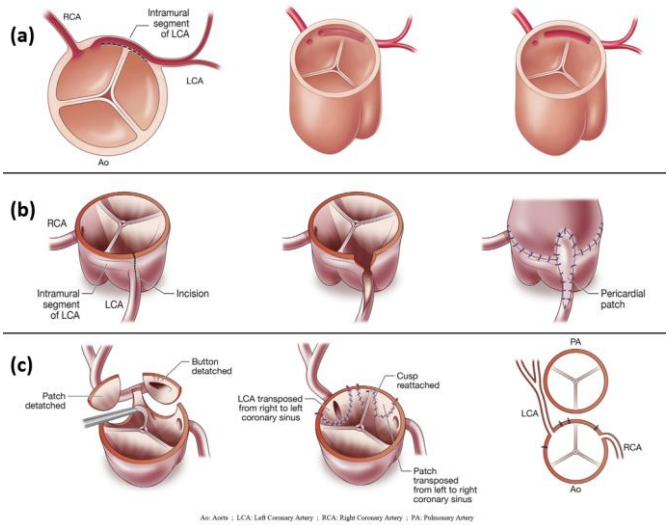


Fig. 1: Surgical techniques available to resolve the coronary compression causing myocardial ischemia: (a) unroofing, (b) patch osteoplasty, (c) reimplantation [8],[9].

II. Materials and Methods

We have divided the process into three steps (Fig. 2). In the pre-processing step the geometric models, i.e. the 3D computational domain, were created starting from the segmentation of the preoperative Computed Tomography (CT) images. The preoperative and healthy models were created using the Rhinoceros 6 software; the three different postoperative parametric models were built using Grasshopper (a Rhinoceros 6 plug-in).

In the processing step, the Navier-Stokes equations have been resolved using SimVascular software. The blood was

assumed to be a Newtonian fluid with a viscosity of 0.04 g/cm and a density of 1.06 g/cm^3 [13]. Boundaries conditions (BC) consisted of a 0D model to recreate peripheral circulation: the aorta outlet was modeled with a Windkessel 3-element circuit [10], and the coronary outlet was modeled with a 6-element circuit with an intramyocardial pressure generator [11].

Finally, in the post-processing step, the results were extracted, and we analyzed coronary flow (Q), pressure drop (ΔP), and wall shear stress (WSS) of the anomalous segment to evaluate all the techniques and find the one that provides the best result.

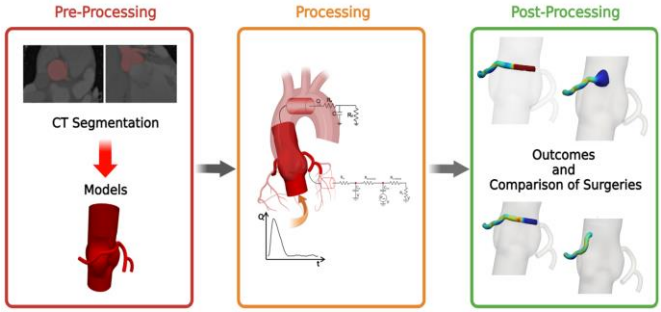


Fig. 2: Implemented Computer-Aided Engineering (CAE) process composed of three steps: pre-processing i.e. models creation, processing i.e. computational problem solving, post-processing, and comparison of results.

III. Results

A. Simulation results

We compared the preoperative model and the healthy model. This comparison makes the reduction in Q and P due to the anomalous segment evident (Fig. 4a-4b). The figures show a distance of ≈ 41 mmHg between healthy and preoperative models in the pressure plot and a distance of ≈ 1.08 mL/s in the flow plot (Table I).

We also compared the three different surgical models with healthy and preoperative cases. A comparison of flow rate and pressure is shown in Table I and Fig. 4c-4d. A flow rate improvement of ≈ 86% in the patch model, ≈ 83% in the reimplantation model, and ≈ 80% in the unroofing model can be observed. Instead, for pressure, the increase is ≈ 92%, ≈ 88%, and ≈ 83% respectively. All these values are supported by the Euclidean distance between the healthy and postoperative models (Table I).

In Fig. 3 we can observe shear stress. The preoperative model shows WSS > 44 dyne/cm^2, and that in all postoperative models decreases (10 < WSS < 25 dyne/cm^2). We have considered low, middle, and high WSS 5.7±2.3, 18±4.7, and 43.9±21.4 dyne/cm^2 respectively [12]. Low values cause increased vessel wall thickness, while high values cause inflammation and calcific plaque formation. Both compromise coronary flow. Instead, middle values are physiological values.

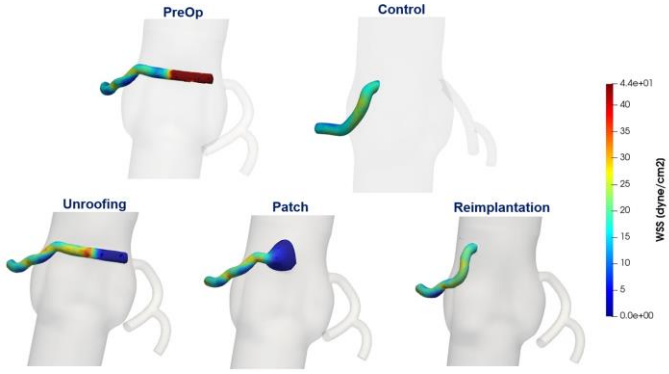


Fig. 2: Heatmap of time average WSS.

TABLE I: POSTOPERATIVE RESULTS FROM IDEAL MODELS

	$Q_{Eu.Dist.}$	$P_{Eu.Dist.}$	$Q_{Diff.\%}$	$P_{Diff.\%}$
PreOp	1.076	40.997	///	///
Unroofing	0.215	6.987	-79.985	-82,958
Patch	0.149	3.310	-86.164	-91,927
Reimplantation	0.185	4.862	-82.856	-88,140

Euclidean distances between health flow and pressure and pre- or postoperative flow and pressure, and quantification of improvements through difference of Euclidean distance flow and Euclidean distance pressure $(((PostOp\text{-}PreOp)/PreOp)*100)$.

B. Patient-specific example

We have also tested the ideal model in a patient-specific case. The preoperative simulation shows a pressure drop of 30 mmHg. We obtained a ΔP of 1.8 mmHg in unroofing simulation, 4.2 mmHg in patch simulation, and 1.8 mmHg in reimplantation simulation. We can observe a flow improvement in all the investigated post-operative scenarios; in particular, the model suggests for the reimplantation case that the flow is almost doubled when compared to the pre-operative condition.

IV. Discussion

Several intervention techniques exist to treat AAOCA, and this study aims to develop a novel computational tool to support surgical planning.

We created an ideal model to test the feasibility of the project and the possibility of correctly replicating the surgical intervention. The tool can distinguish the healthy model from the pathological model (Figs. 4a-4b) in which it replicates a restricted coronary flow pattern. The three surgical models were able to recreate unrestricted coronary flow with characteristics like the healthy model (Fig. 4c-4d). In this preliminary analysis, we can observe that all techniques restore adequate coronary flow although the characteristics of each postoperative flow suggest that the patch osteoplasty gives the best results by achieving the most unrestrictive and less turbulent flow.

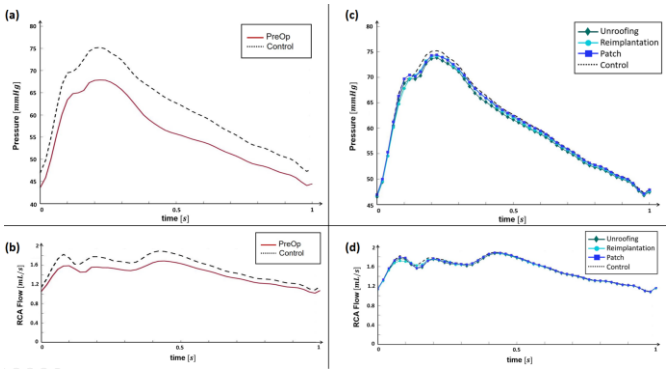


Fig. 4: Comparison of health model and preoperative model in terms of pressure (a) and flow (b); comparison of health model and all three postoperative models in terms of pressure (c) and flow (d).

In the second part, we tested the tool with patient-specific data. Again, we can distinguish the preoperative model from the postoperative model and the different types of surgery (Fig. 5). We can observe that patch osteoplasty and unroofing are better than the reimplantation technique. Clinically, unroofing is less difficult than patch osteoplasty, so unroofing is the treatment suggested.

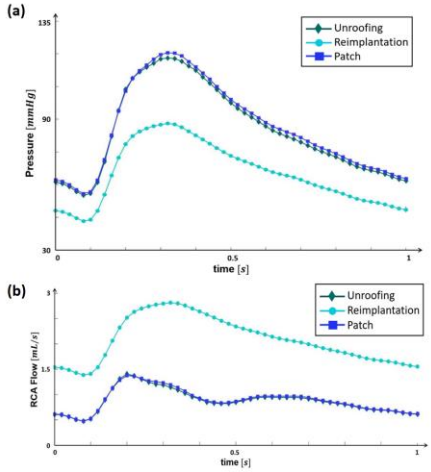


Fig. 5: Pressure (a) and flow (b) patterns of the three different surgical treatments.

V. Limitation and Conclusion

The study contains several limitations mainly related to the assumption and simplification adopted to replicate the complex physical phenomenon: we assume that the wall compliance is negligible imposing rigid wall conditions [13].

Finally, AAOCA concerning the right coronary (R-AAOCA) with intramural (IM) segment is more frequent than left coronary anomalies and the no-IM segment [14]. For this reason, the ideal model and patient-specific model concerning an R-AAOCA whit IM segment case.

This study provides the first biomechanical tool based on computational simulations to highlight the coronary flow differences when adopting different surgical techniques. So, the study is propaedeutic to predict hemodynamic indicators to support the surgeon in the choice of AAOCA surgery and identify which one can return the best fluid dynamic results in a patient-specific scenario.

As a future development, the results of the computational tool will be compared with data from post-operative AAOCA patients. A validation plan will be created; specifically, the study will be extended to all types of AAOCA.

Acknowledgment

The development of this study was possible through the collaboration of Università degli Studi di Pavia with IRCCS Policlinico San Donato. The IRCCS Policlinico San Donato is a Clinical Research Hospital recognized and the study was partially supported by the Italian Ministry of Health.

References

[1] G. M. Formato, M. Lo Rito, F. Auricchio, A. Frigiola, and M. Conti, "Aortic Expansion Induces Lumen Narrowing in Anomalous Coronary Arteries: A Parametric Structural Finite Element Analysis," J. Biomech. Eng., vol. 140, no. 11, Aug. 2018, doi: 10.1115/1.4040941.

[2] A. Jegatheeswaran et al., "Outcomes after anomalous aortic origin of a coronary artery repair: A Congenital Heart Surgeons' Society Study," J. Thorac. Cardiovasc. Surg., vol. 160, no. 3, pp. 757-771.e5, Sep. 2020, doi: 10.1016/j.jtcvs.2020.01.114.

[3] M. A. Padalino, A. Jegatheeswaran, D. Blitzer, G. Ricciardi, and A. Guariento, "Surgery for Anomalous Aortic Origin of Coronary Arteries: Technical Safeguards and Pitfalls," Front. Cardiovasc. Med., vol. 8, 2021, Accessed: May 18, 2022. [Online]. Available: https://www.frontiersin.org/article/10.3389/fcvm.2021.626108

[4] M. A. Padalino et al., "Surgery for anomalous aortic origin of coronary arteries: a multicentre study from the European Congenital Heart Surgeons Association†," Eur. J. Cardio-Thorac. Surg. Off. J. Eur. Assoc. Cardio-Thorac. Surg., vol. 56, no. 4, pp. 696–703, Oct. 2019, doi: 10.1093/ejcts/ezz080.

[5] M. Gaillard et al., "Anomalous aortic origin of coronary arteries: an alternative to the unroofing strategy," Eur. J. Cardiothorac. Surg., vol. 58, no. 5, pp. 975–982, Nov. 2020, doi: 10.1093/ejcts/ezaa129.

[6] A. C. Mills et al., "Surgical approach for anomalous aortic origin of a coronary artery: A comparison of two techniques," J. Card. Surg., vol. 36, no. 12, pp. 4546–4550, 2021, doi: 10.1111/jocs.16033.

[7] M. Lo Rito, R. M. Romarowski, A. Rosato, S. Pica, F. Secchi, A. Giamberti, F. Auricchio, A. Frigiola and M. Conti, "Anomalous aortic origin of coronary artery biomechanical modeling: Toward clinical application," Journal of Thoracic and Cardiovascular Surgery, vol. 161, no. 1, pp. 191-201, 2021.

[8] Agarwal, Prachi & Dennie, Carole & Pena, Elena & Nguyen, Elsie & LaBounty, Troy & Yang, Bo & Patel, Smita. (2017). Anomalous Coronary Arteries That Need Intervention: Review of Pre- and Postoperative Imaging Appearances. Radiographics : a review publication of the Radiological Society of North America, Inc. 37. 160124. 10.1148/rg.2017160124.

[9] Buratto E, Konstantinov IE. ''Current surgical management of anomalous aortic origin of a coronary artery.'' J Thorac Cardiovasc Surg. 2020 Sep 3:S0022-5223(20)32488-0. doi: 10.1016/j.jtcvs.2020.07.118

[10] Romarowski, R. M., Lefieux, A., Morganti, S., Veneziani, A., & Auricchio, F. (2018). Patient-specific CFD modelling in the thoracic aorta with PC-MRI–based boundary conditions: A least-square three-element Windkessel approach. International journal for numerical methods in biomedical engineering, 34(11), e3134.

[11] S. Sankaran, M. Esmaily Moghadam, A. M. Kahn, E. E. Tseng, J. M. Guccione, and A. L. Marsden, "Patient-specific multiscale modeling of blood flow for coronary artery bypass graft surgery," Ann. Biomed. Eng., vol. 40, no. 10, pp. 2228–2242, Oct. 2012, doi: 10.1007/s10439-012-0579-3.

[12] H. Samady et al., "Coronary Artery Wall Shear Stress Is Associated With Progression and Transformation of Atherosclerotic Plaque and Arterial Remodeling in Patients With Coronary Artery Disease," Circulation, vol. 124, no. 7, pp. 779–788, Aug. 2011, doi: 10.1161/CIRCULATIONAHA.111.021824.

[13] M. Conti et al., "Patient-specific computational fluid dynamics analysis of transcatheter aortic root replacement with chimney coronary grafts," Interactive CardioVascular and Thoracic Surgery, vol. 32, no. 3, pp. 408–416, Mar. 2021, doi: 10.1093/icvts/ivaa288.

[14] M. K. Cheezum et al., "Anomalous Aortic Origin of a Coronary Artery From the Inappropriate Sinus of Valsalva," J. Am. Coll. Cardiol., vol. 69, no. 12, pp. 1592–1608, Mar. 2017, doi: 10.1016/j.jacc.2017.01.031.

3D Finite Element Analysis of a Percolating Cluster inside the Mineralized Collagen Fibril

A. Pica[1], A. Marinozzi[2], F. Marinozzi[1], and F. Bini[1]
[1]*Department of Mechanical and Aerospace Engineering, "Sapienza" University of Rome, Rome (Italy)*
[2]*Orthopedy and Traumatology Area, "Campus Bio-Medico" University, Rome (Italy)*

***Abstract*—Bone is characterized at the nanoscale by the mineralized collagen fibril (MCF), mainly composed of apatite minerals and collagen. Among several factors, the 3D architecture of the nanostructure affects the tissue mechanical performance. In the present study, we developed a structural analysis of a model of apatite embedded in the collagen matrix, characterized by a percolating cluster, i.e. a spanning network of connected apatite minerals within the MCF. The geometric model is obtained after applying $6 \cdot 10^6$ translational and rotational perturbations to an ordered arrangement of mineral. The mechanical behaviour of the percolating cluster is compared with a model characterized by an ordered arrangement of mineral. The 3D Finite Element models are analysed under tensile and compressive simulation conditions. Normal and shear stresses are compared among the models. The outcomes suggest that the presence of a percolating cluster causes a general stiffening of the model, representing a condition of high susceptibility to fracture.**

***Keywords*—3D FEM, percolation theory, bone nanostructure.**

I. Introduction

BONE exhibits a hierarchical organization from the nano- to the macro-scale [1]. The nanoscale building unit of bone is the mineralized collagen fibril (MCF) that is composed of inorganic apatite minerals, type I collagen fibril, water and a small percentage of non-collagenous proteins (NCP) [2]. The highly organized embedded nanometric building blocks of collagen molecules and apatite crystals lead to enhanced features of the MCF with respect to the characteristics of the single constituents. The collagen component provides elasticity to the structure, while the apatite minerals contribute to the MCF stiffness and strength. In addition, water diffusion has a crucial role to bone mineralization ensuring the maintenance of an adequate supply of nutrients, growth factors and ions [3]. Water also mediates the interactions between apatite minerals and collagen [4]. Among several factors, the 3D architecture of the nanostructure affects the tissue mechanical performance.

Collagen molecules self-assemble in a staggered manner into fibrils with diameters ranging from 50 to 200 nm and length of about 1000 nm [5]. The arrangement of apatite crystals at the length scale of the MCF is still a subject of debate, although improvements concerning the techniques of visualization have been made [1], [6]. Apatite crystals are located both within and between collagen fibrils, i.e. intra and interfibrillar mineralization respectively. The organization of these crystals is usually illustrated in literature according to the model of 3D deck of cards arrangement in which the platelets lie almost parallel throughout the collagen fibril [7]. According to [8], [9], the mineral arrangement has a staggered structure in the longitudinal direction of the collagen fibril and parallel layers in the equatorial plane of the MCF. Recently, tomographic investigations highlighted that the mineral phase is present as individual crystallites and also as aggregates [1], [6]. For instance, Xu et al. [6] identified stacks of up to 8 apatite platelets at the length scale of single MCF. In this context, Landis et al. [10] also suggested that apatite crystal fusion can influence the biomechanical properties of bone.

In addition to experimental investigations, computational and numerical modelling based on probabilistic methods [11]–[13], molecular dynamics simulations [5] and finite element (FE) methods [14]–[17] have been developed to assess the contribution of the nanoscale components to the mechanical performance of bone. For instance, FE studies of Vercher-Martinez [15] have outlined that the arrangement of apatite minerals, the distance between apatite crystals and the mineral overlapping have considerable influence on the mechanical behaviour of the MCF.

Recently, Bini et al. [18] analysed the mineral network within the MCF applying the percolation theory. The percolation phenomenon is characterized by the onset of connected networks that span the domain of interest from one side to another. Applying the Monte Carlo technique, Bini and co-workers [18] investigated the formation of spanning networks of apatite crystals for different mineral volume fractions characteristic of the human bone tissue. In this framework, we aim to analyse here the mechanical behaviour of a percolating cluster of apatite platelets by means of FE analysis. The outcomes are then compared with the mechanical behaviour predicted for apatite platelets arranged in an ideal staggered configuration.

II. Methods

The mechanical behaviour is investigated by considering a geometrical model of the apatite cluster. The mineral configuration is generated by applying the Metropolis algorithm [19] to better mimic the mineral arrangement within the MCF. Apatite crystals start in an ordered, aligned configuration according to the model proposed by Hodge-Petruska [8] and Jäger and Fratzl [9]. Subsequently, each platelet is displaced and inclined by random amounts. The method is described in detail in a previous study of Bini et al. [18]. In the present work, we considered a cluster of apatite minerals (Fig. 1) spanning the equatorial plane of the MCF, specifically in the width (w) direction (see Fig. 4 of [18]). We assume all random values for the geometrical parameters that describe the apatite minerals within the ranges indicated in Literature [2]. Namely, the average width, thickness and length dimensions of the apatite platelets involved in this model are 43.5 nm, 3.65 nm and 101.8 nm, respectively. In this

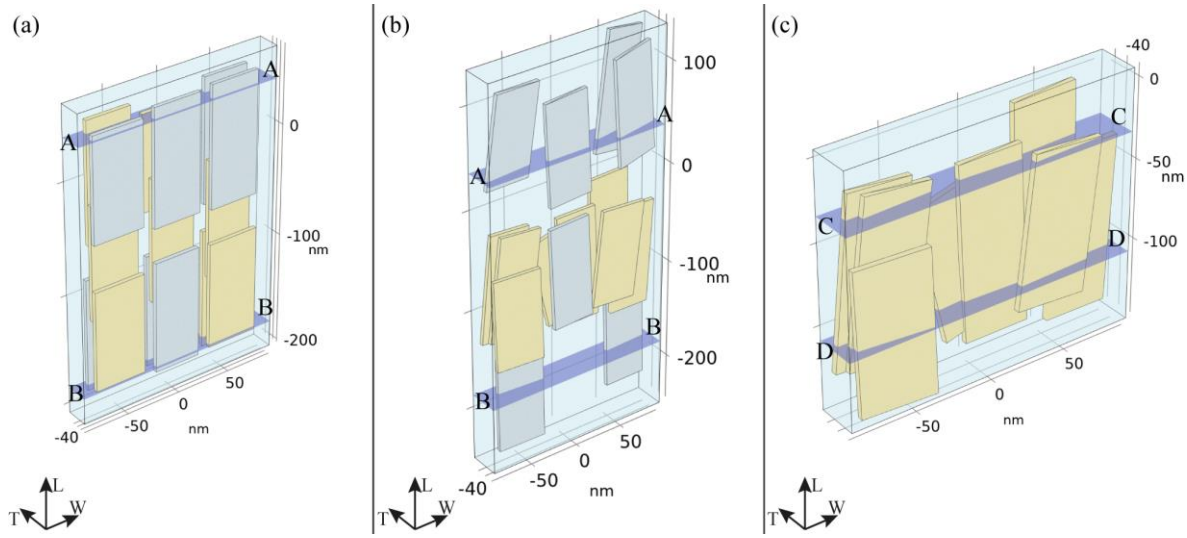


Fig. 1: 3D geometric model. In (a) starting configuration of apatite minerals (light grey and light yellow) embedded in the collagen matrix (light blue) aligned with the axis of the coordinate system. In (b) configuration of minerals after roughly $6 \cdot 10^6$ moves and rotations. In (c) percolating cluster. Light yellow platelets represent components of the percolating cluster.

study, the cluster was individuated in a MCF with a diameter of 200 nm and a mineral volume fraction of 37 percent [18], and it was generated after roughly $6 \cdot 10^6$ inclinations and rotations of the platelets [18].

The model with ordered apatite platelets (Fig. 1a) is determined considering the initial configuration of the mineral platelets that compose the percolating cluster. Analysing the initial arrangement, it was observed that these minerals are part of three repeating unit cells, each composed of 5 apatite crystals [9] (Fig. 1a). In Fig. 1b, we depict the platelets composing the three unit cells after the roughly $6 \cdot 10^6$ inclinations and rotations of the platelets. Given the variable dimensions of the apatite minerals, we considered two section planes (AA and BB in Fig.1) in order to obtain the maximum cross section of mineral on which the external stimulus is acting. Thus, sections at a distance of 10 nm from the superior and inferior boundaries have been performed in the ordered module (Fig. 1a). For visualization purposes, the section planes AA and BB at the same longitudinal coordinates were reported also in Fig. 1b. Finally, we determined the geometrical model that takes into account only the cluster of apatite minerals (Fig. 1c). Two sections (CC and DD) at the superior and inferior boundaries, respectively, are considered in order to obtain the maximum cross section of mineral on which the external stimulus is applied. In addition, according to [15]–[17], the collagen is represented as a continuum matrix between the mineral platelets. The generated geometry is converted into a non-uniform tetrahedral mesh. In Table 1 we indicate the corresponding number of degrees of freedom achieved for each model.

The apatite mineral is modelled assuming linear elastic, isotropic and homogeneous material behaviour. The collagen matrix is assumed to act as a nonlinear, homogeneous, hyperelastic material. Specifically, we considered a Neo-Hookean nearly incompressible constitutive model for collagen with the following strain energy ($W_{collagen}$) [20], [21]:

$$W_{collagen} = \frac{1}{2}\mu(I_1 - 3) + \frac{k}{2}(J_{el} - 1)^2 \quad (1)$$

where J_{el} is the elastic volume ratio calculated as the determinant of the elastic deformation gradient, I_1 is the first invariant of elastic right Cauchy-Green deformation tensor. The parameters μ and k represent the Lamé parameter and the material bulk modulus respectively, and are calculated as follows [22]:

$$\mu = \frac{E}{2(1+\nu)} \quad (2)$$

$$k = \frac{E}{3(1-2\nu)} \quad (3)$$

where E indicates the Young's modulus and ν is the Poisson's ratio. Tissues properties are defined within the range available from literature. As typical values to perform the mechanical analysis, we assume Young's modulus of 1 GPa [23] and 114 GPa [24] for the collagen and apatite mineral, respectively. Concerning the Poisson's ratio, it is attributed a value of 0.23 to the apatite [23] and 0.35 for the collagen matrix [25]. In addition, we assume a critical energy release rate of 1 J/m^2 [24] for the apatite mineral and of 0.2 J/m^2 [24] for the collagen.

To analyse the mechanical behaviour, uniaxial tension and compression simulations are performed for both 3D models. Appropriate boundary conditions (Fig. 2) are applied to simulate tensile and compressive loading.

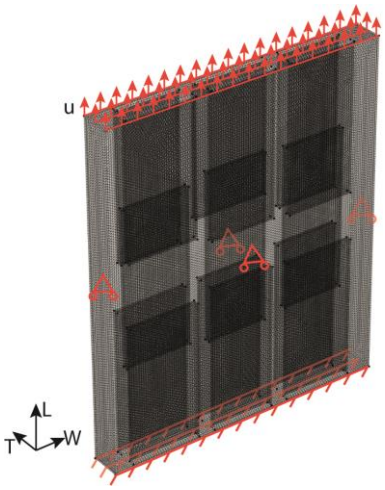


Fig. 2: Mesh and boundary conditions applied for the model considering the ordered configuration of apatite platelets.

TABLE I
FE MODEL STATISTICS

Model	*Number of mesh elements*	*Degrees of freedom*
Ordered configuration	1 411 586	21 887 053
Percolating Cluster	540 864	8 405 739

Displacements and rotations of the bottom surface are constrained [16], [23]. A roller condition is applied on the lateral surface of the collagen matrix [23]. The simulation is performed using monotonic displacement control with increments set in the order of 10^{-3} times lower than the average apatite length [26], until failure occurs. The same boundary conditions are implemented in both 3D models of ordered and disordered apatite platelets embedded in the collagen matrix.

The mechanical behaviour is investigated considering the phase field model. Further details of the phase field method can be found in [26], [27]. The phase field determines the damage through the minimization of an energy functional [26]:

$$E(u,\Phi) = \int_\Omega (1-\phi)^2 W d\Omega + \int_\Omega G_c \left(\frac{1}{2\ell_{int}}\phi^2 + \frac{\ell_{int}}{2}|\nabla\phi|^2\right) d\Omega \quad (4)$$

with u is the displacement field, G_c is the critical energy release rate, W is the strain energy density and ϕ is the phase field variable that varies smoothly from 0, i.e. undamaged material to 1, i.e. totally broken. The width of the transition zone of ϕ is controlled by the internal length scale ℓ_{int}. In this study, the parameter ℓ_{int} is chosen to be small relative to the apatite length, namely 3 percent of average apatite length, as in [28]. The phase field variable ϕ is solution of the differential equation:

$$\frac{\partial(1-\phi)^2}{\partial\phi} H_d - (\phi - \ell_{int}^2 \nabla^2\phi) = 0 \quad (5)$$

$$H_d = \max W \quad (6)$$

The function $(1-\phi)^2$ represents the degradation function that penalizes the material stiffness according to the value of ϕ. The governing equations for structural mechanics are reported in the following:

$$\nabla \cdot \sigma_d = 0 \quad (7)$$

$$\sigma_d = (1-\phi)^2 \sigma \quad (8)$$

where σ_d is the stress tensor of the damaged material, and σ is the undamaged stress tensor. For the linear elastic material the stress tensor follows the Hooke law:

$$\sigma = C : \varepsilon(u) \quad (9)$$

where C is the stiffness tensor and ε is the strain tensor.

For the hyperelastic material, the stress tensor follows from the definition of the second Piola-Kirchoff stress [29]:

$$\sigma = 2\frac{\partial W}{\partial C_{CG}} \quad (10)$$

where C_{CG} is the right Cauchy-Green deformation tensor.

To optimize the computational cost, the system of equations is solved using the Generalised Minimal Residual (GMRES) method by employing a geometric multigrid left preconditioner.

In Fig. 3 we represent the generated force in function of the prescribed displacement.

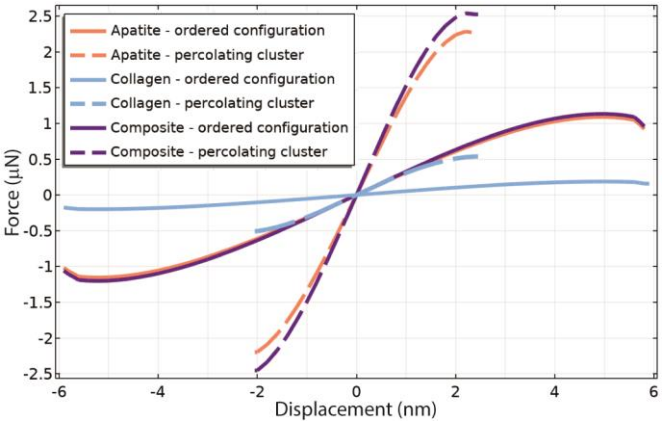


Fig. 3: Force-displacement curves for each component, i.e. apatite platelets and collagen matrix, and for the overall apatite – collagen composite of both models, i.e. ordered configuration and percolating cluster.

III. RESULTS AND DISCUSSIONS

In this study, we focused on the analysis of the mechanical behaviour of a percolating cluster of apatite within the MCF comparing it with an ordered configuration of minerals. Simulations were developed with different loading conditions, i.e. tension and compression, in order to capture variations in the stress distribution induced by the onset of the percolating cluster.

For the ordered apatite configuration, we calculate the normal and shear stresses (Fig. 4) and perform a comparison with earlier results reported in [17], where a FE analysis has been developed concerning one unit cell of MCF. The highest normal stress occurs in the mineral platelets, while maximum values of shear stress emerged in the collagen matrix in agreement with [7], [9]. The mechanical behaviour of the ordered configuration of apatite is consistent with previous data [15]–[17], thus supporting the efficacy of the model.

In the percolating cluster, for both tensile and compressive simulation, the normal and shear stresses (Fig. 5) show higher values than in the ordered configuration. As expected, the percolating cluster causes a general stiffening of the model. The peak values of stress occur in the region of

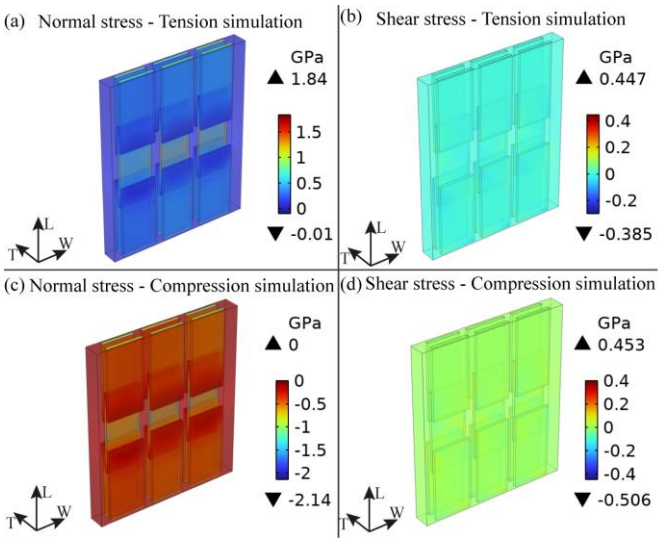


Fig. 4: Maximum normal (a, c) and shear (b, d) stress distributions achieved for the model with aligned apatite minerals during tensile (a, b) and compressive (c, d) simulation.

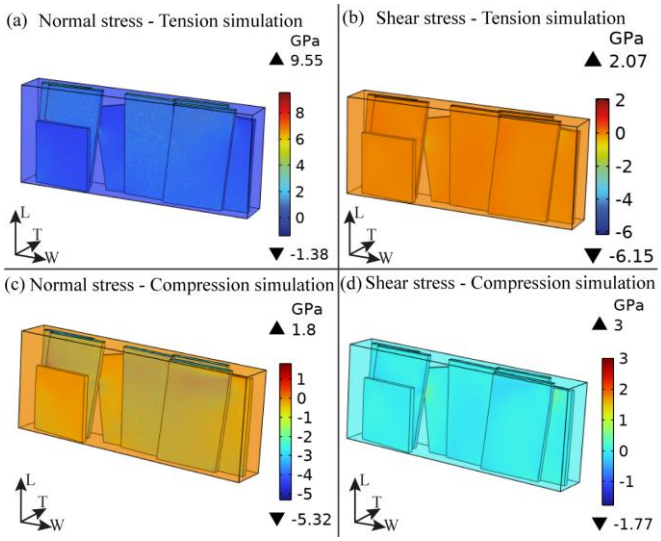


Fig. 5: Maximum normal (a, c) and shear (b, d) stress distributions achieved for the percolating cluster during tensile (a, b) and compressive (c, d) simulation.

interpenetration between apatite platelets [18].

Although highly consistent with available literature, the present FE analysis has some limitations. Since non collagenous proteins (NCP) represent less than 10% of the total organic components, these proteins were omitted here, following the study of [15], [23], [30]. Further studies will take into account also the NCP contribution to the mechanical behaviour of abnormal configurations of apatite, e.g. percolating clusters.

IV. Conclusion

In this study, we developed a FE analysis of an abnormal configuration of apatite platelets within MCF, namely a percolating cluster. We assessed the variations in the stress distributions that occur in the percolating condition. The 3D FE model represents a basis for further investigations concerning pathological conditions of bone tissue, characterized by increased mineral content and high probability of mineral fusion, as occurs in osteoporosis [31].

References

[1] N. Reznikov, M. Bilton, L. Lari, M. M. Stevens, and R. Kröger, "Fractal-like hierarchical organization of bone begins at the nanoscale," *Science*, vol. 360, no. 6388:eaao2189, 2018.

[2] M. J. Olszta *et al.*, "Bone structure and formation: A new perspective," *Mater. Sci. Eng. R Reports*, vol. 58, no. 3–5, pp. 77–116, 2007.

[3] F. Marinozzi, F. Bini, and A. Marinozzi, "Water uptake and swelling in single trabeculæ from human femur head," *Biomatter*, vol. 4: e28237, 2014.

[4] Y. Wang *et al.*, "Water-mediated structuring of bone apatite," *Nat. Mater.*, vol. 12, no. 12, pp. 1144–1153, 2013.

[5] B. Depalle, Z. Qin, S. J. Shefelbine, and M. J. Buehler, "Large Deformation Mechanisms, Plasticity, and Failure of an Individual Collagen Fibril with Different Mineral Content," *J. Bone Miner. Res.*, vol. 31, no. 2, pp. 380–390, 2016.

[6] Y. F. Xu *et al.*, "Intermolecular channels direct crystal orientation in mineralized collagen," *Nat. Commun.*, vol. 11, no. 1: 5068, 2020.

[7] P. Fratzl, H. S. Gupta, E. P. Paschalis, and P. Roschger, "Structure and mechanical quality of the collagen-mineral nano-composite in bone," *J. Mater. Chem.*, vol. 14, no. 14, pp. 2115–2123, 2004.

[8] A. J. Hodge and J. A. Petruska, "Recent studies with the electron microscope on ordered aggregates of the tropocollagen molecule BT - Aspects of Protein Structure," *Asp. Protein Struct.*, pp. 289–300, 1963.

[9] I. Jäger and P. Fratzl, "Mineralized collagen fibrils: A mechanical model with a staggered arrangement of mineral particles," *Biophys. J.*, vol. 79, no. 4, pp. 1737–1746, 2000.

[10] W. J. Landis, M. J. Song, A. Leith, L. McEwen, and B. F. McEwen, "Mineral and organic matrix interaction in normally calcifying tendon visualized in three dimensions by high-voltage electron microscopic tomography and graphic image reconstruction," *J. Struct. Biol.*, vol. 110, no. 1, pp. 39–54, 1993.

[11] F. Bini, A. Pica, A. Marinozzi, and F. Marinozzi, "3D random walk model of diffusion in human Hypo- and Hyper- mineralized collagen fibrils," *J. Biomech.*, vol. 125, 110586, 2021.

[12] F. Bini, A. Pica, A. Marinozzi, and F. Marinozzi, "A 3D Model of the Effect of Tortuosity and Constrictivity on the Diffusion in Mineralized Collagen Fibril," *Sci. Rep.*, vol. 9, no 1:2658, 2019.

[13] F. Bini, A. Pica, A. Marinozzi, and F. Marinozzi, "A nanostructured look of collagen apatite porosity into human mineralized collagen fibril," *Biocell*, vol. 46, no. 10, pp. 2225–2229, 2022.

[14] F. Bini *et al.*, "3D FEM model to simulate Brownian motion inside trabecular tissue from human femoral head," *Comput. Methods Biomech. Biomed. Eng. Imaging Vis.*, vol. 10, no. 5, pp. 500–507, 2022.

[15] A. Vercher-Martínez, E. Giner, C. Arango, and F. Javier Fuenmayor, "Influence of the mineral staggering on the elastic properties of the mineralized collagen fibril in lamellar bone," *J. Mech. Behav. Biomed. Mater.*, vol. 42, pp. 243–256, 2015.

[16] F. Yuan, S. R. Stock, D. R. Haeffner, J. D. Almer, D. C. Dunand, and L. C. Brinson, "A new model to simulate the elastic properties of mineralized collagen fibril," *Biomech. Model. Mechanobiol.*, vol. 10, pp. 147–160, 2011.

[17] E. Alizadeh, M. Dehestani, and P. Zysset, "An efficient two-scale 3D FE model of the bone fibril array: comparison of anisotropic elastic properties with analytical methods and micro-sample testing," *Biomech. Model. Mechanobiol.*, vol. 19, pp. 2127–2147, 2020.

[18] F. Bini, A. Pica, A. Marinozzi, and F. Marinozzi, "Percolation networks inside 3D model of the mineralized collagen fibril," *Sci. Rep.*, vol. 11, 11398, 2021.

[19] S. Torquato, *Random Heterogeneous Materials: Microstructure and Macroscopic Properties*, Springer New York LLC, 2002.

[20] C. Miller and T. C. Gasser, "A bottom-up approach to model collagen fiber damage and failure in soft biological tissues," *J. Mech. Phys. Solids*, vol. 169, 105086, 2022.

[21] A. Raina and C. Miehe, "A phase-field model for fracture in biological tissues," *Biomech. Model. Mechanobiol.*, vol. 15, pp. 479–496, 2016.

[22] G. A. Holzapfel, *Nonlinear Solid Mechanics A Continuum Approach for Engineering*. John Wiley & Sons Ltd, Chichester, 2000.

[23] D. W. Abueidda, F. A. Sabet, and I. M. Jasiuk, "Modeling of Stiffness and Strength of Bone at Nanoscale," *J. Biomech. Eng.*, vol. 139, no. 5, pp. 1–10, 2017.

[24] E. Hamed and I. Jasiuk, "Multiscale damage and strength of lamellar bone modeled by cohesive finite elements," *J. Mech. Behav. Biomed. Mater.*, vol. 28, pp. 94–110, 2013.

[25] H. Alijani and T. J. Vaughan, "A multiscale finite element investigation on the role of intra- and extra-fibrillar mineralisation on the elastic properties of bone tissue," *J. Mech. Behav. Biomed. Mater.*, vol. 129, 105139, 2022.

[26] J. M. Sargado, E. Keilegavlen, I. Berre, and J. M. Nordbotten, "High-accuracy phase-field models for brittle fracture based on a new family of degradation functions," *J. Mech. Phys. Solids*, vol. 111, pp. 458–489, 2018.

[27] C. Miehe, L. M. Schänzel, and H. Ulmer, "Phase field modeling of fracture in multi-physics problems. Part I. Balance of crack surface and failure criteria for brittle crack propagation in thermo-elastic solids," *Comput. Methods Appl. Mech. Eng.*, vol. 294, pp. 449–485, 2015.

[28] P. K. Kristensen, C. F. Niordson, and E. Martínez-Pañeda, "An assessment of phase field fracture: Crack initiation and growth," *Philos. Trans. R. Soc. A Math. Phys. Eng. Sci.*, vol. 379, 20210021, 2021.

[29] T. C. Gasser, R. W. Ogden, and G. A. Holzapfel, "Hyperelastic modelling of arterial layers with distributed collagen fibre orientations," *J. R. Soc. Interface*, vol. 3, no. 6, pp. 15–35, 2006.

[30] S. Nikolov and D. Raabe, "Hierarchical modeling of the elastic properties of bone at submicron scales: The role of extrafibrillar mineralization," *Biophys. J.*, vol. 94, no. 11, pp. 4220–4232, 2008.

[31] L. M. McNamara, P. J. Prendergast, and M. B. Schaffler, "Bone tissue material properties are altered during osteoporosis," *J. Musculoskelet. Neuronal Interact.*, vol. 5, no. 4, pp. 342–343, 2005.

THE EFFECT OF CFR-PEEK CROSS-LINK IN SHORT FIXATION FOR THE STABILIZATION OF LUMBAR METASTASIS: AN IN-VITRO COMPARATIVE STUDY.

S. Borrelli[1,2], G. Putame[1,2], A.L. Audenino[1,2], A. Ferro[3], S. Marone[3], M. Terzini[1,2]
[1] *Polito[BIO]Med Lab, Politecnico di Torino, Turin, Italy.*
[2] *Department of Mechanical and Aerospace Engineering, Politecnico di Torino, Turin, Italy.*
[3] *Oncologic Orthopaedic Surgery Division, CTO Hospital – Città della Salute e della Scienza di Torino, Turin, Italy.*

***Abstract*— The stabilization of the spine after the orthopaedic management of vertebral bone metastasis is a crucial step for the success of the surgery. Carbon fiber reinforced PEEK (CFR-PEEK) is being widely adopted for fixation instruments thanks to its good biomechanical performances and radio transparency. The study investigates whether the integration of a CFR-PEEK cross link in a short fixation could become a viable alternative to long gold standard fixation. An experimental *in-vitro* study was then conducted, comparing different surgical CFR-PEEK stabilizations by characterizing their kinetic (i.e., Moment vs ROM curves and long-chain stiffness) and kinematic (i.e., segmental angular contribution) responses in flexion-extension, lateral bending and axial rotation. To provide additional insights on long-term applicability, the event of a pedicle screw loosening was also replicated. The experimental results suggest that a CFR-PEEK short fixation augmented with cross-link can be a promising conservative strategy. This unprecedent biomechanical quantitative comparison of CFR-PEEK stabilizations could support future clinical studies.**

Keywords* — spinal instrumentation, lumbar spine, CFR-PEEK, short fixation, short stabilization, cross-link, vertebral metastasis, *in-vitro spine testing.

I. Introduction

VERTEBRAL metastases occur in more than the 5% of all patients with systemic cancer, and the lumbar segment is the most affected site of the spine [1]. In case of surgical treatment, spinal stabilization plays a crucial role in the success of the intervention. Gold standard spinal stabilization is established as a long posterior instrumentation fixing multiple levels above and below the metastasis [2], [3]. However, this practice has proved many drawbacks in terms of high invasiveness, excessive adjacent-level overloading and mobility reduction. Recently, carbon fiber reinforced (CFR-) PEEK has been introduced in spinal fixation instrumentations in place of metallic alloys, integrating good biomechanical performances with radio transparency property (which is of particular interest in oncologic surgery) [4]-[6].

To reduce the number of fixed vertebrae and the corresponding side-effects of current lumbar metastasis stabilization, this study explores the biomechanical effects of the combined use of CFR-PEEK cross-link and short fixation on the lumbar segment. Therefore, in the light of understanding the biomechanical applicability of this alternative, authors considered worthy to compare its kinematic and kinetic responses and those of the simple CFR-PEEK long and short fixations, with respect to control healthy and pathologic conditions, and to assess the effect of pedicle-screw loosening, which is the most common risks in short fixation. Hence, an experimental study was designed by recurring to a synthetic phantom loaded under flexion-extension, lateral bending and axial rotation. Hereby, this study presents for the first time a comparative biomechanical analysis of CFR-PEEK stabilizations for the management of lumbar vertebral metastasis and could support future clinical studies in oncological spinal surgery.

II. Materials and methods

A. Experimental setup

The study recurred to a Sawbones biomimetic phantom (SKU340) which replicated the lumbar segment and its adjacent vertebrae T12 and S1. The phantom presents all the passive elements of the spine, intervertebral discs, facet joints and the main ligaments (i.e., the anterior and posterior longitudinal ligaments, ligamenta flava, intertransverse ligaments, supraspinal and interspinal ligaments). The experimental set up is shown in Fig. 1. The phantom was disposed so as to have the L3 inferior endplate parallel to the global horizontal plane [7].

The loads were applied to the phantom through the linear-torsion test machine InstronE3000. The sacrum was always kept fixed to the machine and the loads were applied to the cranial vertebra through an already validated spine-loading apparatus [8]. In the case of axial rotation, the load was applied directly to the vertebra through a specific 3D printed coupling, while the bending along the sagittal and frontal planes were generated through an eccentric vertical load transmitted to the phantom through the combination of frictionless spherical and translational joints. The moment was calculated by assuming a constant arm with respect to the caudal constraint (flexion: 12.8±0.1cm, extension: 3.3±0.4cm, right lateral bending: 8.7±0.3cm, left lateral bending: 7.6±0.4cm). Loads were applied in slow-rate displacement-control to reduce any viscoelastic effect. Small range of motion was considered to prevent overloading. For sagittal and frontal bending, the

linear displacement rate was set at 20 mm/min up to 10mm, whereas for axial rotation the angular rate was set at 0.5°/s up to 3°. Three replicas were performed for each test; the initial position was always set to guarantee a slight contact with the machine, without introducing any relevant initial pre-stressed condition. Finally, adhesive reflective markers were positioned on the vertebral bodies and on the transverse process, and their displacements were recorded through a marker tracking system, synchronous with the tests. Markers were integrated with the load-displacement curves of the test machine to compute the moment at the S1 fixed joint.

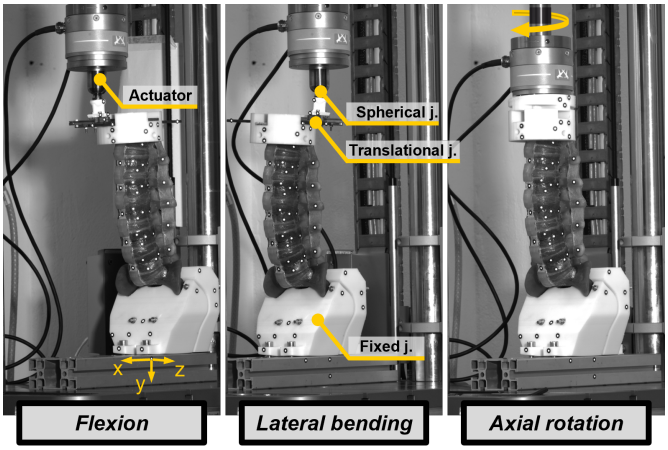


Fig. 1: The Sawbones mounted on the loading apparatus. The images are taken from one marker-tracking camera. The global reference system is also shown.

B. *Fixation layouts*

All the fixation layouts tested in this study were reproduced by experienced orthopaedic surgeons. The layouts were tested following a sequence which minimized the risk of phantom breakage (which did not occur). Hence, the tests started with the integral, non-instrumented phantom, considered as a 'healthy' control (*Ch*). Then, a metastatic lesion was mimicked in L3 by resecting the right half of its vertebral body. The posterior decompression performed surgically was also replicated by removing L3 pedicle and the posterior arch and taking care that no extra elements were affected. At that point, pedicle screws from Carboclear system (CarboFix Orthopaedic Ltd) were posteriorly inserted in L1, L2, L4 and L5 following anatomical trajectories. Dimensional consistency between pedicles and screws, as well as their mutual orientation, were confirmed by the surgeons by direct visualisation. From this condition, considered as a 'pathologic' control (*Cp*, Fig. 2), all the fixation layouts were tested: the long fixation (*L*, Fig. 2) was realised with bilateral CFR-PEEK rods connecting two spinal levels above and below the lesion in accordance with current clinical standard; the short fixation (*S*) connected only the spinal adjacent levels above and below L3, leaving L1 and L5 free to move. Then, a transversal rod-rod CFR-PEEK cross-link was added to the short fixation in correspondence of the metastasis, in a 'H' shape layout (*Scl,* Fig. 2). Finally, both short fixations were tested after the event of a pedicle screw loosening. When the screw anchorage in the vertebral bone fails, the load transmission through the screw between the vertebra and the rod is lost; a biomechanical equivalent mobilization was replicated experimentally by disconnecting the right rod-screw joint above the lesion (*S-m* and *Scl-m*).

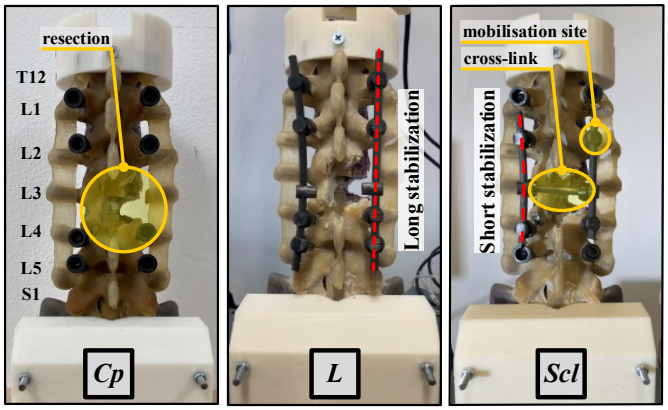


Fig. 2: Left - the Sawbones after the insertion of the pedicle screws, the reproduction of the posterior decompression and L3 vertebral body resection. Middle – Long fixation layout; the CFR-PEEK rods connect L1, L2, L4 and L5 vertebrae. Right: Short fixation layout with cross-link augmentation. The CFR-PEEK rods connect L2 and L4 vertebrae. The pedicle screw-rod joint detached to mimic the mobilization is also highlighted.

III. RESULTS

A. *Kinetic perspective*

Fig. 4 summarizes the Moment-Range of Motion (RoM) behaviour of all the layouts in flexion/extension and lateral bending. The experimental curves were realigned at 0.4Nm. Overall, the 'pathologic' control is always more flexible than the 'healthy' one, and the implementation of any fixation offers a stiffening of the phantom. The responses of short fixations (*S*, *Scl*) are always positioned in-between the other curves, thus permitting both a less marked stiffening compared to the long fixation and the restoration of a more favourable mobility. In accordance with literature, along the sagittal plane, either cross-link augmentation or mobilization influence the short construct behaviour. As far as the investigated small loads are concerned, symmetrical behaviour in lateral bending is maintained in all short layouts. In lateral bending, cross-link addition enables a stiffened response at parity of load. In the range of ±5Nm, the total range of motion is reduced of the 10.8% with respect to the *S* layout. Moreover, cross-link also contributes to the stability preservation in the case of pedicle-screw loosening, since it holds back the drop of stability by half, from +27% (*S-m*) to +13% (*Scl-m*).

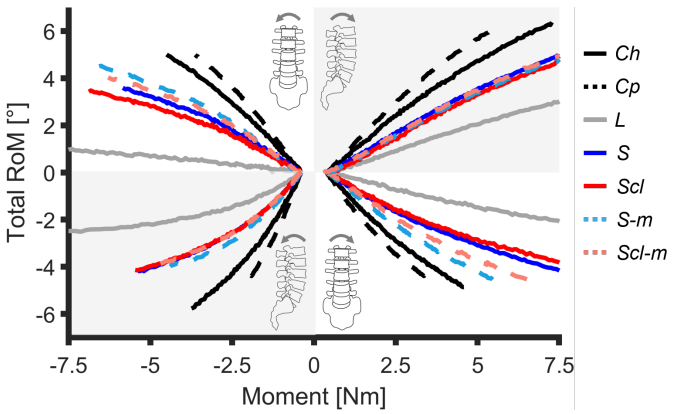


Fig. 3: Moment vs Total ROM curves of all the studied layouts. Mean values of the three replicas are represented. Each quadrant describes one different bending load: I and III flexion/extension; II and IV lateral bending on the resected and intact side, respectively.

In Fig. 4 is reported the torsional stiffness (K_T) calculated for each layout with a linear regression between the cranial vertebra rotation and the applied torque moment after having realigned the experimental curves at 0.6 Nm. The graph shows the results of all the constructs when rotated both on the intact and on the resected side. The symmetrical behaviour reported in the 'healthy' control is lost after the realization of the resection. Moreover, the 'pathological' control shows a stiffer response when rotated towards the resected side with an unbalanced deviation ΔK_T of 0.19Nm, and a significant drop of the torsional stiffness with respect to *Ch*.

If the simple short fixation doesn't succeed in recovering this gap, the addition of the cross-link makes the short fixation comparable to the intact phantom like the long fixation. Indeed, only these two layouts deviates less than the 8% from the values obtained with the *Ch.* The enhancement of cross-link augmentation in the short fixation is suggested also by the one-way ANOVA test which informs of a non-statistical difference between *S* and *Scl-m* layouts. That is to say that, in the case of pedicle screw loosening, if the simple short fixation becomes insufficient to guarantee an acceptable stability, on the other hand the addition of the crosslink makes the construct as stiff as the unimpaired short layout.

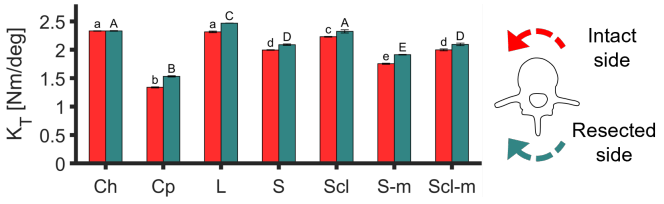


Fig. 4: Torsional stiffness of all the studied layouts. Labels indicate statistical significance among the stiffnesses along the intact (lower case labels) and resected (upper case labels) sides, according to Bonferroni post-hoc test.

B. Kinematic perspective

In order to quantify how the motion of vertebral joints across the lumbosacral segment varies with respect to the fixation layouts, the hybrid protocol [9] was adopted. The reference total RoM corresponded to the RoM achieved by the *Ch* layout under the following moments: 3Nm in flexion, 1.5Nm in extension, 1Nm in lateral bending. TABLE 1 describes the load necessary to reach the defined RoM, whereas Fig. 5 reports the motion contribution of each intervertebral joint. Negative values correspond to registered discord rotations with respect to the imposed motions.

TABLE 1: For each configuration, the table reports the applied moment necessary to achieve the RoM obtained by *Ch* at the indicated loads. Then, all the stabilizations were compared at parity of total rotation.

	Flexion	**Extension**	**Lat. bending resected side**	**Lat. bending intact side**
Ch	**3 Nm**	**1.5 Nm**	**1 Nm**	**1 Nm**
Cp	2.4 ± 0.05	1.2 ± 0.01	0.8 ± 0.02	0.9 ± 0.04
L	7.1 ±0.08	10.0 ± 0.09	3.0 ± 0.11	6.6 ± 0.70
S	4.1 ±0.09	2.5 ± 0.09	1.4 ± 0.09	1.4 ± 0.06
Scl	4.4 ±0.01	2.6 ±0.04	1.6 ± 0.10	1.6 ± 0.09
S-m	4.2 ±0.08	2.2 ± 0.10	1.2 ± 0.08	1.3 ± 0.05
Scl-m	4.1 ±0.07	2.5 ± 0.08	1.4 ± 0.07	1.3 ± 0.03

From a kinematic perspective, the introduction of the lesion mainly impacts on the joints below the lesioned vertebra (i.e., L3-L4 and L4-L5). Generally, the adjacent L3-L4 joint is less stiff, shielding the cranio-caudal motion distribution; for instance, in the case of flexion/extension L3-L4 contribution doubles, whereas L4-L5 one reduces from 20% to 3.2%. All the fixations (*L, S* and *Scl*) succeed in stabilizing the metastasis; nonetheless, the motion of the adjacent free joints is dependent on the fixation length: in the case of long fixation, L5-S1 is overinvolved with a bending contribution greater up to 5 times than *Ch* response. Conversely, in short layouts, L1-L2 and L5-S1 share more than the 80% of the total ROM; interestingly, although L4-L5 is not involved in fixation, its contribution remains extremely small, i.e., flexion: 5.7±2.5%, extension: 3.0±1.3%, lateral bending on the resected side: 4.0±3.1%, lateral bending on the intact side: -1.9±2.9%. Finally, L2 pedicle screw loosening doesn't provide evident effects during sagittal motion, while in lateral bending, a slight increased mobility is enregistered both at L2-L3 and at L3-L4 levels, revealing an increase of the relative rotations of the instrumented vertebrae and a reduced shielding effect on L4-L5 level.

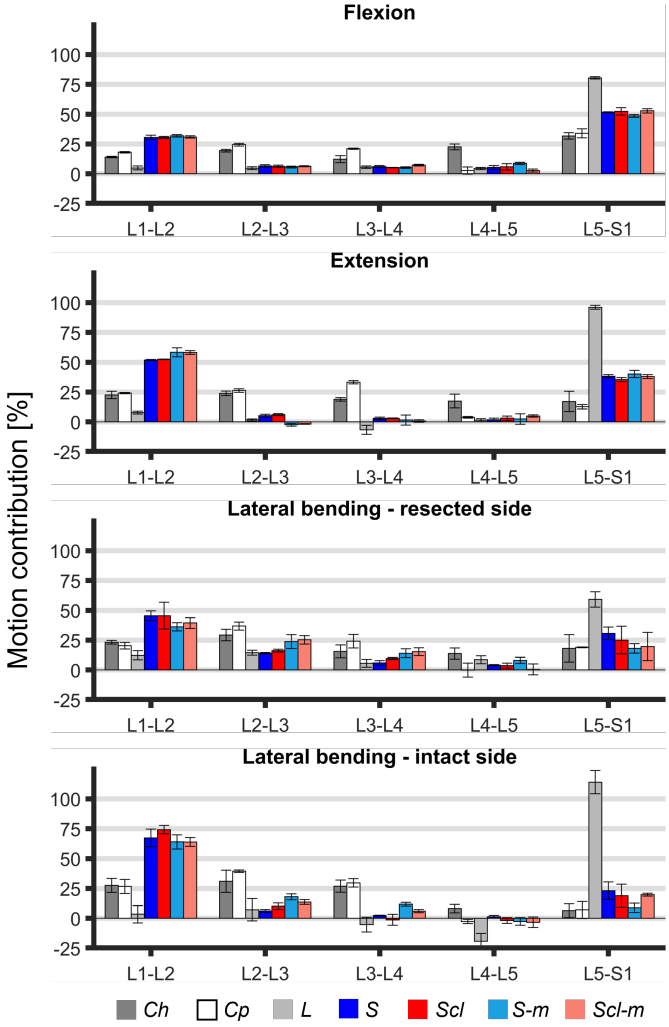


Fig. 5: Motion contribution of each vertebral joint, reported as percentage of the total L1-S1 range of motion (100%).

IV. DISCUSSION

This *in vitro* study aimed to compare different CFR-PEEK stabilization strategies from a kinetic and kinematic perspective, revealing that addition of a cross-link at the metastasis level could make short fixation a valid alternative.

Aware of the large spread of the use of synthetic phantoms in biomechanical studies [10], the authors recurred to a T12-S1 spinal segment Sawbones to conduct this study. Although this material doesn't replicate the diversity of real human specimen and doesn't permit to consider the local mechanical properties of pathologic bones, the differences expressed in the study can only be attributed to the relative differences of the fixation layouts, without any hardly controllable contribution such as disc degradation or the heterogeneity among samples.

In accordance with the literature referred to metallic cross-link use [11]-[13], *Scl* response in flexion/extension was analogous with *S* layout, both in terms of long-chain stiffness and in terms of segmental motion distribution pattern. Fig. 3 shows that cross-link in CFR-PEEK short fixation improves the frontal bending, by restoring a symmetrical behaviour on the two sides (thus, compensating the vertebral bone resection) and by limiting the effect of pedicle-screw loosening [14]. Fig. 4 puts light on the primary effect of cross-link in axial rotation. Indeed, if the K_T of simple short fixation is significantly reduced with respect to the 'healthy' control, the cross-link makes the construct comparable with long fixation and more conservative in terms of stability once mobilized. While rotating, the two longitudinal rods would get skewed, but the cross-link, that connects them transversally, counters this relative motion, making the whole construct stiffer.

Interestingly, Fig. 5 reports that in long fixation, vertebral levels below the resection had negative ROM contributions, that corresponded to vertebral rotations opposed to the main motion. These results suggest that the long fixation leads to local instabilities given by the altered distribution of the compressive loads and the over constrain of the construct [15]. The application of an eccentric load provoked a compressive stress state on the spinal segment, especially for the long fixation where the secondary effect of the compression summed to the moment was more pronounced (being stiffer, a higher load was necessary to reach the same ROM at parity of arm, TABLE 1).

Although the experimental test didn't apply a pure moment, the recorded maximum linear force applied to the phantom was less than 100N (except for the *L* layout which reached ~220N): these magnitudes are consistent with the compressive loads applied in lumbar *in vitro* studies, which range from 100N to 400N [16], [17].

Finally, since this study focused on small displacements range, eventual major deviations could have been hided; however, the spinal stability is strictly correlated to the neutral posture [18], [19], and it is only in this range that the activation of muscles can be neglected.

V. CONCLUSION

To conclude, in the framework of oncologic surgery, this work compares CFR-PEEK posterior stabilizations by recurring to a biomimetic lumbosacral phantom. Particular attention was paid on the effect of cross-link augmentation on a less invasive short segment fixation. Results quantitatively demonstrated that short fixations permit a less marked stiffening compared to the long one, restoring a more favourable mobility and less unbalance responses among lumbar vertebral joints. The most imputed drawback to short fixations is the loss of stability in case of pedicle screw loosening which can put dramatically at risk the surgical outcome. The study highlighted that cross-link could limit this crucial aspect. The *Scl* layout proved to be a promising conservative strategy, worthy to be further investigated also in *in silico* modelling and to be considered in future clinical studies in the ambit of oncologic spinal surgery.

VI. ACKNOWLEDGMENT

This work was supported by "Fondazione per la ricerca sui tumori dell'apparato muscoloscheletrico e rari Onlus".

REFERENCES

[1] A. Amelot, et al., "Approaching spinal metastases spread profile", *Surgical Oncology,* vol. *31,* pp. 61-66, 2019.

[2] A. Leone, et al., "Instability and impending instability in patients with vertebral metastatic disease", *Skeletal Radiol,* vol 48(2), pp. 195-207, 2019.

[3] A. Wagner, et al., "Comprehensive surgical treatment strategy for spinal metastases", *Sci Rep*, vol. 11(1), pp.1-11, 2021.

[4] F. Ringel, et al., "Radiolucent carbon fiber–reinforced pedicle screws for treatment of spinal tumors: advantages for radiation planning and follow-up imaging", *World Neurosurg.*, vol. 105, pp. 294-301, 2017.

[5] C. J. Laux, S. M. Hodel, M. Farshad, D. A. Müller, "Carbon fibre/polyether ether ketone (CF/PEEK) implants in orthopaedic oncology", *World J Surg Oncol*, vol. 16(1), pp.1–6, 2018.

[6] S. Oikonomidis, et al., "Biomechanical effects of posterior pedicle screw-based instrumentation using titanium versus carbon fiber reinforced PEEK in an osteoporotic spine human cadaver model", *Clin Biomech*, vol. 80 (August):105153, 2020.

[7] H. J. Wilke, K. Wenger, L. Claes, "Testing criteria for spinal implants: Recommendations for the standardization of in vitro stability testing of spinal implants", *Eur Spine J*, vol. 7(2), pp. 148-154, 1998.

[8] S. Borrelli, A. Formaggio, V. Civilini, A. T. Lugas, "Phantom-based lumbar spine experimental investigation and validation of a multibody model", *Int J Comput Methods Exp Meas*, vol. 9(3), pp. 226-238, 2021.

[9] M. M. Panjabi, "Hybrid multidirectional test method to evaluate spinal adjacent-level effects", *Clin Biomech*, vol. 22(3), pp. 257-265, 2007.

[10] D. J. DiAngelo, D. S. Hoyer, C. L. Chung, "Biomechanical evaluation of a full-length (T12-S) synthetic lumbar spine model", *MOJ Appl Bionics Biomech*, vol. 25(2), pp.170-179, 2000.

[11] F. Cornaz, J. Widmer, J. G. Snedeker, J. M. Spirig, M. Farshad, "Cross-link in posterior pedicle screw-rod instrumentation of the spine: a systematic review on mechanical, biomechanical, numerical and clinical studies", *Eur Spine J,* vol.30(1), pp.34-49, 2021.

[12] O. Uri, Y. Folman, G. Laufer, E. Behrbalk, "A novel spine fixation system made entirely of carbon-fiber-reinforced PEEK composite: an in vitro mechanical evaluation", *Adv Orthop*, 2020.

[13] G. Lynn, D. P. Mukherjee, R.N. Kruse, K. K. Sasasivan, J. A. Albright, "Mechanical stability of thoracolumbar pedicle screw fixation. The effect of crosslinks". *Spine (Phila Pa 1976)*, vol. 22(14), pp. 1568–1573, 1997.

[14] S. M. Kurtz, et al. "Retrieval analysis of PEEK rods for posterior fusion and motion preservation", *Eur Spine J*, vol. 22(12), pp. 2752–2759, 2013.

[15] S. Borrelli, G. Putame G. Pascoletti, M. Terzini, E. Zanetti, "In silico meta-analysis of boundary conditions for experimental tests on the lumbar spine", *Annals of Biomedical Engineering*, vol. 50, pp. 1243-1254, 2022.

[16] M. M. Panjabi, T. R. Oxland, I. Yamamoto, J. J. Crisco, "Mechanical behavior of the human lumbar and lumbosacral spine as shown by three-dimensional load-displacement curves" *Clinical. J Bone Jt Surg Am*, vol. 76(3), pp. 413–424, 1994.

[17] P. A. Cripton, S. B. Bruehlmann, T. E Orr, T. R. Oxland, L. P. Nolte, "In vitro axial preload application during spine flexibility testing: towards reduced apparatus-related artefacts". *J Biomech*, vol. 33(12), pp. 1559–1568, 2000.

[18] G. Tedesco, A. Gasbarrini, S. Bandiera, R. Ghermandi, S. Boriani, "Composite PEEK/Carbon fiber implants can increase the effectiveness of radiotherapy in the management of spine tumors", *J Spine Surg*, vol. 3(3), pp. 323–329, 2017.

[19] T. Di Pauli von Treuheim, O. M. Torre, G. E. Mosley, P. Nasser, J. C. Iatridis, "Measuring the neutral zone of spinal motion segments: Comparison of multiple analysis methods to quantify spinal instability", *JOR Spine*, vol. 3(2), pp.1–11, 2020.

Inertial measurements unit validation for countermovement jump (CMJ) tests in athletes

F. Camuncoli[1,2], L. Barni[3], S. Nutarelli[4,5], J.E. Rocchi[6,7], M. Barcillesi[1], I. Di Dio[1], A. Sambruni[8] and M. Galli[1,2]
[1] *Department of Electronics Information Technology and Bioengineering, Politecnico di Milano, 20133 Milan, Italy*
[2] *E4Sport Lab, Politecnico di Milano, 23900 Lecco, Italy*
[3] *Department of Physiotherapy, Faculty of Health Sciences, University of Malaga, 29071 Malaga, Spain*
[4] *Service of Orthopaedics and Traumatology, Department of Surgery, EOC, 6900 Lugano, Switzerland*
[5] *School of Public Health, Physiotherapy and Sports Science, University College Dublin, D04 V1W8 Dublin, Ireland*
[6] *Department of Movement, Human and Health Sciences, University of Rome Foro Italico, 00135 Rome, Italy*
[7] *Villa Stuart Sport Clinic—FIFA Medical Centre of Excellence, 00136 Rome, Italy*
[8] *Department of Medicine, Surgery and Neuroscience, Università degli Studi di Siena, 53100 Siena, Italy*

***Abstract*—In many sports, including soccer, basketball, and volleyball, the vertical jump is considered a valid test to evaluate the performance of an athlete during the season or to assess the possibility of returning to training. A reliable measurement method is therefore required. The validity of countermovement jump (CMJ) heights made with inertial sensors is a prerequisite for the reliable implementation of their use in clinical practice. Twenty-seven athletes (20 M / 7 F, age: 27 ± 7 years) after a 5-minute warm-up performed five double-leg CMJ, with the hands on hips. The jump height was computed with Baiobit inertial measurement unit placed at waist level and with an *ad hoc* Matlab® script using force platforms data. An excellent reliability (ICC = 0.92, 95% CI 0.89-0.94), a positive correlation (r = 0.93, p <0.001), and a positive bias of 3.7 cm were found. The Baiobit sensor underestimates the CMJ flight heights.**

***Keywords*—Baiobit, countermovement jump, inertial sensors, validation.**

I. Introduction

Vertical jumps such as the double-leg countermovement jumps (CMJ) are jumps that allow measuring the power of the lower limbs and the reactivity of an athlete [1].
In many sports, including soccer, basketball, and volleyball, the vertical jump is considered a valid test to evaluate the performance of an athlete during the season or to assess the possibility of returning to training.

Although the golden standard for assessing vertical jumps is the use of force platforms in conjunction with optoelectronics, nowadays there is an increasing need to be able to assess the athlete in the field outside of the laboratory through the use of wearable sensors.

Coaches and physiotherapists often evaluate performance qualitatively, without the use of a valid and repeatable quantitative assessment. Therefore, an integration of engineering knowledge into the clinical sports application is required to better assess sports performance [2].

Wearable sensors are lightweight and practical to handle, so there is a need to verify that the measured variables are as reliable as those detected by the golden standard.
At the state of the art, numerous wearable systems have been validated [3]–[9], among which we can name Gyko [3], G-WALK [4], but only our previous study has validated the Baiobit sensor [6]. This work is therefore intended as a continuation of the previously conducted one which aims to validate this device.

II. Material and Method

A. Population

All the participants have read and signed the informed consent to participate in the study approved by the Ethical Committee of the Politecnico di Milano (submission no. 22/2021). All the tests were performed at the "Luigi Divieti Posture and Movement analysis laboratory".

The study inclusion criteria were as follows: (i) athletes trained for a minimum of 4 h per week, (ii) were aged between 18 and 40 years, (iii) had a BMI between 18.5 and 24.9 kg/m^2, and (iv) had no self-reported neurological or musculoskeletal disorder. The population included in the study, therefore, consisted of 27 athletes 20 males and 7 females (age: 27 ± 7 years, height: 1.86 ± 0.09 m, weight: 75 ± 12 kg, body mass index (BMI): 21.7 ± 2.0 kg/m^2) performing beach volley (4), triathlon (3), volleyball (11), basket (4), swimming (1), athletics (1), tennis (2) and jiu-jitsu (1) (Table I).

B. Equipment

A wearable sensor (Baiobit Rivelo Srl — BTS bioengineering Group, Milan, Italy, sampling rate = 100 Hz), two three-dimensional force platforms (AMTI, Wetertown, MA, USA, dimensions: 464 × 508 × 82.5 mm; sampling rate = 200 Hz) synchronized with two video cameras (BTS Bioengineering, Garbagnate, Italy) framing the sagittal and frontal planes and a laptop (Notebook HP EliteBook 840 G3) were used for data collection.

C. Procedures

Before the tests, data on participants were entered into the software of the wearable sensor (baiobit v1.2.6).

First of all, the subject was asked to put on sneakers and clothing appropriate for the test. A short 5-minute warm-up consisting of this exercise sequence was performed: (i) 10 squats with hands at the hips × 2 repetitions (ii) 6 forward lunges 3 on each side × 2 repetitions (iii) low skip for 7 meters × 2 repetitions. A 5 meters distance was walked between each repetition.

Then, using an adhesive clip, the sensor was fixed at the level of the S1 and S2 vertebrae on the subject's waist.

This was followed by a familiarisation phase in which the

subject was explained the type of test to be performed. Two trial jumps were executed before the actual protocol, which consisted of 5 double-leg CMJs with the hands on hips (Akimbo technique) to minimize arm swinging and each foot placed on one force platform. The execution technique was evaluated by the clinicians included in the study. In case of an incorrect jump, the test was repeated.

After the acquisition, the athletes underwent the international physical activity questionnaire (IPAQ) [10], [11].

TABLE I: SUBJECTS' DEMOGRAPHIC AND ANTHROPOMETRIC MEASUREMENTS, SPORT PRACTICED AND IPAQ SCORE CLASSIFICATION.

Sex	*Age* (*years*)	*Weight (kg)*	*Height (m)*	*Sport*	*IPAQ*
F	36	73	1.85	beach volley	VA
M	26	77	1.82	triathlon	SA
M	27	86	1.91	volleyball	VA
M	22	81	1.92	basket	VA
M	27	85	1.92	basket	VA
M	23	80	1.91	swimming	SA
M	28	97	1.91	jiu- jitsu	SA
M	28	65	1.78	triathlon	SA
F	24	47	1.64	athletics	VA
M	23	92	2.02	volleyball	SA
M	21	62	1.85	volleyball	VA
M	21	69	1.81	tennis	VA
M	20	83	1.94	basket	VA
M	37	93	1.95	beach volley	VA
M	24	71	1.76	tennis	VA
M	36	76	1.89	volleyball	VA
F	19	69	1.86	volleyball	VA
F	31	76	1.90	volleyball	SA
M	41	80	1.83	triathlon	VA
M	38	75	1.83	beach volley	VA
F	22	59	1.74	volleyball	SA
F	19	68	1.82	volleyball	VA
M	24	87	1.97	volleyball	SA
M	39	72	1.82	beach volley	VA
M	21	70	1.86	volleyball	VA
F	21	54	1.68	volleyball	SA
M	23	85	1.92	basket	VA
20M 7 F	27 ±7	75 ±12	1.86 ± 0.09		18 VA 9 SA

VA = very active; SA = sufficiently active.

D. Data analysis

Using Baiobit, the CMJ heights were recorded and manually imported from the Baiobit software into an Excel worksheet. The ground reaction forces were recorded from the force platforms in .tdf files.

Using open source Matlab® code developed by Harry et al. [12], it was possible to derive the height of the CMJs from the force data.

E. Statistical analysis

Before statistical analysis 5 jumps were removed. The Shapiro-Wilk test was used to assess the data normality (α = 0.05). As the data have a normal distribution, they are reported as mean and standard deviation. A paired t-test was applied to assess the difference between the CMJ heights calculated in the Matlab® script and from the sensor's software.

To define the correlation and level of agreement between the gold standard (the force platforms) and the Baiobit inertial sensor system, Pearson's correlation coefficient and Winer's adjusted intra-class correlation coefficient (ICC; 2.1) with an absolute agreement and a 95% confidence interval (CI) were used respectively. Table II shown the ICC criteria classification.

TABLE II: INTRACLASS CORRELATION COEFFICIENT CLASSIFICATION.

ICC < 0.50	poor reliability
0.50 < ICC < 0.75	moderate reliability
0.75 < ICC < 0.90	good reliability
ICC > 0.90	excellent reliability

Fig. 1 shows the Bland-Altman plot of the CMJ heights. On the x-axis is the average between the gold standard (forces platforms) and Baiobit and on the y-axis is the difference between the two measurement methods [1].

The statistical analysis was performed in SPSS (IBM Statistic 26).

III. RESULTS

From the results of the IPAQ (Table I) 9 out of 27 participants have a sufficiently active lifestyle (SA) while 18 out of 27 have a very active lifestyle (VA). No one had an inactive life.

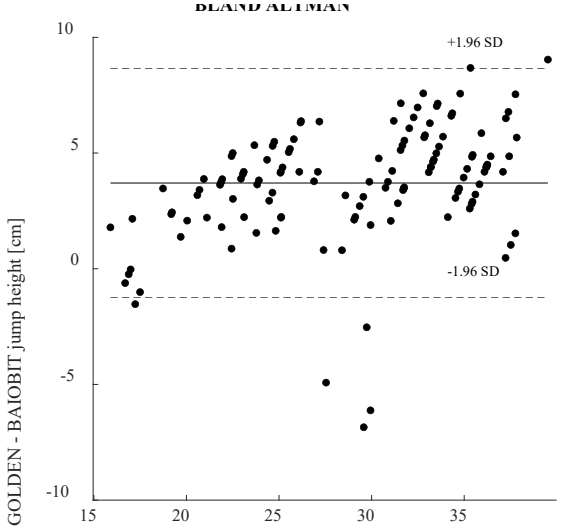


Fig. 1: Bland Altman plot comparing the Golden standard vs the Baiobit

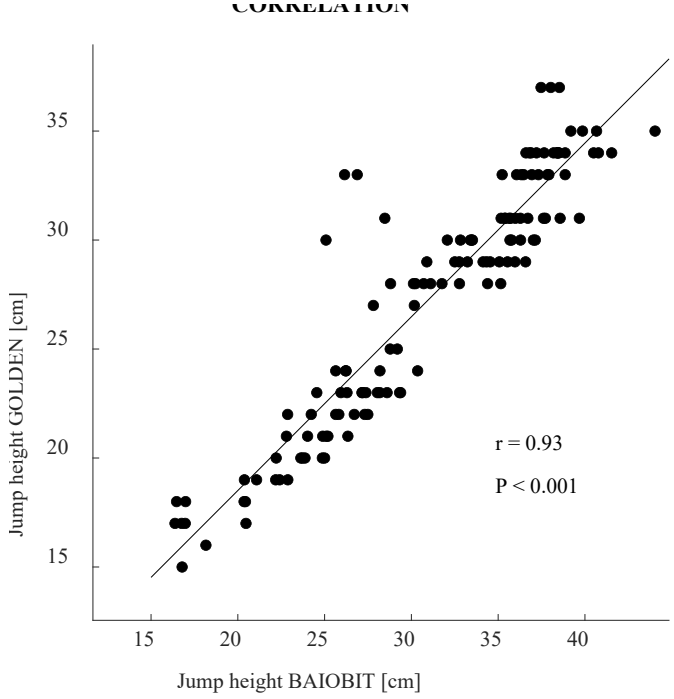


Fig. 2: Correlation plot between the Golden standard (force plates) and the Baiobit

Bland-Altman and correlation plots are shown in Figg. 1 and 2, whereas in Table III are represented the obtained results. The mean and the standard deviation of the CMJ height recorded by force platforms were equal to 30.9 ± 6.7 cm, while the height measured by the Baiobit sensor had a mean of 27.2 ± 5.7 cm. The difference between the two measurement methods is equal to 3.7 cm. Therefore, it can be stated that Baiobit underestimates the CMJ height.

In addition, a positive correlation was found between the Golden standard and Baiobit with a Pearson's coefficient equal to r = 0.93 (p <0.01). The ICC was rated as excellent (ICC = 0.92, 95% CI = 0.89-0.94).

TABLE III: VALIDITY OF THE AMTI FORCE PLATES AND BAIOBIT SENSOR FOR JUMP HEIGHT.

AMTI force plates [cm]	30.9 ± 6.7
Baiobit sensor [cm]	27.2 ±5.7
Systematic bias [cm]	3.7
Random error [cm]	±4.9
Lower LOA	-1.2
Upper LOA	8.6
ICC (95% CI)	0.92 (0.89 – 0.94)

ICC = Intraclass Correlation Coefficient; CI = Confidence Interval

The validation of wearable systems has already been addressed in numerous studies [3]–[9]. This analysis is in agreement with Edward R. Brooks et al. [9] who evaluated the repeatability and validity of an inertial measurement unit with respect to force platforms (r = 0.95, ICC = 0.91).

The study is not without its limitations, among which we find the inhomogeneity of the sample analyzed; athletes from different sports were recruited, with a predominance of male ones (20M vs 7F).

A possible future development of the project is to evenly distribute the number of males and females and select only one sport practiced.

IV. CONCLUSION

The study validated the Baiobit wearable system against the use of AMTI force platforms (Golden standard). An excellent reliability (ICC = 0.92), a positive correlation (r = 0.93), and a positive bias of 3.7 cm were found.

The Baiobit sensor underestimates the CMJ flight heights.

ACKNOWLEDGMENT

We thank Rivelo Srl—BTS Bioengineering Group for providing us with the Baiobit inertial measurement unit.

REFERENCES

[1] T. Rantalainen, T. Finni, and S. Walker, “Jump height from inertial recordings: A tutorial for a sports scientist,” *Scand. J. Med. Sci. Sport.*, vol. 30, no. 1, pp. 38–45, 2020, doi: 10.1111/sms.13546.

[2] T. W. Lu and C. F. Chang, “Biomechanics of human movement and its clinical applications,” *Kaohsiung J. Med. Sci.*, vol. 28, no. 2 SUPPL., 2012, doi: 10.1016/j.kjms.2011.08.004.

[3] M. Lesinski, T. Muehlbauer, and U. Granacher, “Concurrent validity of the Gyko inertial sensor system for the assessment of vertical jump height in female sub-elite youth soccer players,” *BMC Sports Sci. Med. Rehabil.*, vol. 8, no. 1, pp. 1–9, 2016, doi: 10.1186/s13102-016-0061-x.

[4] G. Yazici *et al.*, “The reliability of a wearable movement analysis system (G-walk) on gait and jump assessment in healthy adults,” *J Exerc Ther Rehabil*, vol. 7, no. 2, pp. 159–167, 2020, [Online]. Available: www.jetr.org.tr.

[5] E. T. Nielsen, P. B. Jørgensen, I. Mechlenburg, and H. Sørensen, “Validation of an inertial measurement unit to determine countermovement jump height,” *Asia-Pacific J. Sport. Med. Arthrosc. Rehabil. Technol.*, vol. 16, pp. 8–13, 2019, doi: 10.1016/j.asmart.2018.09.002.

[6] F. Camuncoli *et al.*, “Validity of the Baiobit Inertial Measurements Unit for the Assessment of Vertical Double- and Single-Leg Countermovement Jumps in Athletes,” *Int. J. Environ. Res. Public Health*, vol. 19, no. 22, p. 14720, 2022, doi: 10.3390/ijerph192214720.

[7] M. Gadev, P. Peev, and O. Hristov, “Agreeement Between Measurement of Jump Height in Different Vertical Jump Tests Executed By Young Football Players,” *J. Appl. Sport. Sci.*, vol. 2, no. 2020, pp. 51–63, 2020, doi: 10.37393/jass.2020.02.4.

[8] P. Picerno, V. Camomilla, and L. Capranica, “Countermovement jump performance assessment using a wearable 3D inertial measurement unit,” *J. Sports Sci.*, vol. 29, no. 2, pp. 139–146, 2011, doi: 10.1080/02640414.2010.523089.

[9] E. R. Brooks, A. C. Benson, and L. M. Bruce, “Novel technologies found to be valid and reliable for the measurement of vertical jump height with jump-and-reach testing,” *J. Strength Cond. Res.*, vol. 32, no. 10, pp. 2838–2845, 2018, doi: 10.1519/JSC.0000000000002790.

[10] A. Mannocci *et al.*, “International Physical Activity Questionnaire: Validation and assessment in an Italian sample,” *Ital. J. Public Health*, vol. 7, no. 4, pp. 369–376, 2010.

[11] M. Hagströmer, P. Oja, and M. Sjöström, “The International Physical Activity Questionnaire (IPAQ): a study of concurrent and construct validity,” *Public Health Nutr.*, vol. 9, no. 6, pp. 755–762, 2006, doi: 10.1079/phn2005898.

[12] J. R. Harry, “MATLAB Guide for Analyzing Countermovement Jump Strategies and Performance Over Time,” *Strength Cond. J.*, vol. 43, no. 5, pp. 44–53, 2021, doi: 10.1519/ssc.0000000000000624.

Advances in the development of a instrumented head surrogate for brain injury investigation

G. Zullo[1], E. Baldoin[1], A. Koptyug[2], M. Bäckström[2], and N. Petrone[1]
[1] *Department of Industrial Engineering, University of Padova, Padova, Italy*
[2] *Department of Engineering, Mathematics and Science Education, Mid Sweden University, Ostersund, Sweden*

***Abstract*—Acquiring knowledge on head traumas is useful since they represent a dangerous outcome of traumatic events. Injury criteria aim to link clinical evidence of injury with experimentally measurable physical quantities, however, recent studies based on numerical methods have pointed out that also other factors could be key contributors to brain injury probability and severity. Providing an experimental measure of more advanced injury criteria is challenging, and only few research groups have started to address the problem. Starting from an existing and validated biofidelic dummy head, advances in the mechanical components and sensors embedded inside the model have been carried out, aiming to improve both bio-fidelity and to address the measure of more advanced criteria. After realizing the prototype, preliminary drop tests were performed impacting the helmeted head over an anvil. Data collected showed increase of injury criteria values with the impact force. Results proved the possibility of using the surrogate for investigating simple and advanced injury criteria, and future works will aim to set test parameters to levels compatible with helmet standards.**

***Keywords*—head injury, protective headgear, surrogate head, impact test.**

I. Introduction

HEAD traumas represent a critical issue to society and are one of the most frequent consequences of severe injury or death after traumatic events [1]. Such traumas could include skull fracture and Traumatic Brain Injuries (TBI) and are caused by different mechanical stresses happening to the head, such as blunt, ballistic, penetrating, and concussive impacts. Aiming to reduce the incidence and severity of these harms, head protective gear has been developed and its usage encouraged or regulated. The causes lying underneath TBIs have been investigated through the years by taking advantage of cadaveric studies and more recently of numerical models of the human head [2], [3]. This led to the introduction of injury criteria to assess likelihood of injury based on global and measurable quantities such as accelerations and angular velocities. On this matter, Peak Linear Acceleration (PLA) was one of the first criteria to be introduced in the past [4]. Then, to account also for the duration of the impact. Head Injury Criterion (HIC) was defined as the integral of the acceleration inside a defined time window and proposed as a standard by the National Highway Traffic Safety Administration (NHTSA) in 1972. Only recently, thanks to advances in the numerical modelling of the head, scientists acknowledged the importance of angular acceleration in the likeability of brain trauma. This led to the introduction of criteria based on angular velocity such as the BrIC [5]. However, while the above criteria could be computed from quantities collected during experimental tests, more advanced criteria, based on internal stresses and strain of the brain, only exist in the numerical domain [2], [6].

To improve the quality of experimental tests, some research groups have started to develop more biofidelic surrogate heads, accounting for soft tissues such as brain and skin. Ouellet et al. developed a surrogate composed of a plastic skull, a soft brain, and a scalp to study blast injuries [7].

Petrone et al. started the development of their surrogate, which was assembled and validated in impact tests [8], [9]. Despite the novelty of the work, major improvements could still be made to increase the bio-fidelity, robustness, and sensor capabilities of their dummy head.

The aim of the present work is to improve the above surrogate [9] with the redesign of some mechanical components, and the inclusion of more advanced sensors to allow the measurement of brain stresses during impact tests [10]. The improved surrogate will be subjected to preliminary drop tests to test the response of its sensors.

II. Methods

A. Mechanical design

Models of the components of the head surrogate were obtained by MRI scans of a male human adult. Scans were imported in MeshMixer (Autodesk, USA) and simplified for manufacturing the prototype. More in detail, the skull model was divided into two halves, and a matching indent was designed to provide a robust mechanical coupling. Then, to secure the two parts of the skull, a set of screws were secured to brass inserts fixed in the superior part. To manufacture the skull, the model was printed in Polyamide 12 using selective laser sintering technique.

To produce the soft tissues, instead, we produced a set of plastic moulds in which we could pour our surrogate material.

The brain was manufactured in PlatsilGel OO30 silicone rubber (Polytek, USA). The rubber was furtherly softened by adding Smith's Prosthetic Deadener (Polytek, USA) to the mixture. After the curing process was completed a layer of open-cell foam was wrapped and glued around the brain to mimic the sub-arachnoidid space of the human meninges. The scalp was casted in PlatsilGel 10 silicone rubber (Polytek, USA).

Once assembled, the surrogate was filled with distilled water, acting as a surrogate for the Cerebral-Spinal Fluid (CSF). Figure 1 shows the three main elements composing the surrogate.

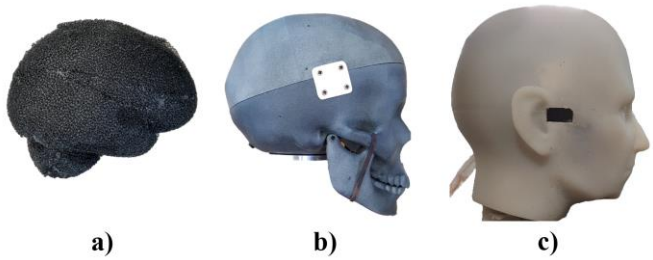


Fig. 1: surrogate head assembly: a) brain with meninges; b) skull; c) scalp

B. Sensors

The head was instrumented with several sensors positioned on the different parts of the surrogate. A triaxial accelerometer was positioned on the side of the skull of the surrogate, coincident to the sagittal projection of the Centre of Mass (COM). Inside the brain, a triaxial accelerometer and a gyro were embedded during the casting process in the brain COM. Moreover, next to the inertial sensors we positioned a Multi-Axial Pressure Sensors (MAPS) which provided a measure of normal and shear stresses in the brain COM, as well as the Von Mises Stress [10]. Figure 2 shows sensors on the head components.

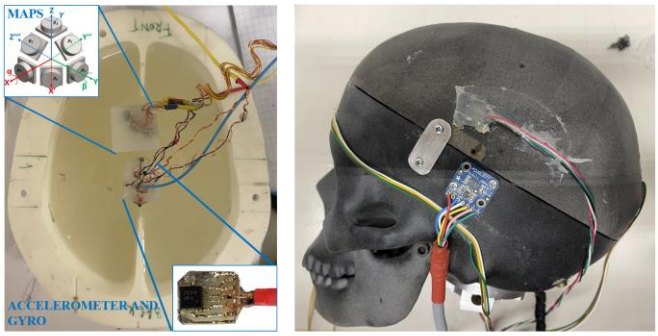


Fig. 2: head sensors: a) sensors casted inside the brain; b) accelerometer positioned on the skull

C. Drop tests

The dummy head was subjected to drop tests, impacting over an instrumented anvil equipped with a 44 kN load cell (FUTEK, USA). Drop tests were performed both with and without the CSF inside the skull/brain cavity. A Vega mountaineering helmet (Salewa, Italy) was fit on the head. The helmeted head was suspended with a thin rope and released from different heights to impact with increasing energies of 10, 13, and 16.7 J. Data of the anvil and head sensors were synchronously collected with a SoMat eDAQ lite (HBM, Germany) at 5 kHz.

D. Data Analysis

Data of the impact test were analysed in MATLAB R2022a (MathWorks, USA). First, data were low-pass filtered using a zero-phase Butterworth filter (2nd order, 500 Hz cut-off frequency). Then, we cut collected data from the first increase in force on the anvil to the subsequent 25 ms.

Raw data from the accelerometer of the brain was combined to obtain the resultant acceleration from its three cartesian components. From the resultant signal we computed the peak (PLA) and the HIC with a 15 ms window. Data from the six channels of the MAPS were combined and shear and normal components of stress, plus Von Mises stress, were computed.

III. RESULTS

Results of drop tests are reported in Table 1 and in Figure 3 and 4. Figure 5 shows injury criteria with respect to the impact force on the anvil, for the CSF test conditions.

We could observe that injury probability increases with the impact force for each of the mentioned criteria. Maximum values of force and VM stress were observed for the 13.3 J, CSF impact conditon, while PLA and HIC were maximum for the 16.7J, Dry condition.

TABLE I: RESULTS OF THE DROP TESTS

Test	*Peak Force [N]*	*PLA [g]*	*HIC [g]*	*Peak Von Mises Stress [kPa]*
10 J, CSF	2352	55.59	39.6	37.5
13.3 J, CSF	3393	79.57	60.2	64.8
16.7 J, CSF	2750	76.04	68.0	47.7
10 J, Dry	2253	59.07	94.3	22.5
13.3 J, Dry	2948	79.82	104.2	28.2
16.7 J, Dry	2774	99.87	140.2	34.4

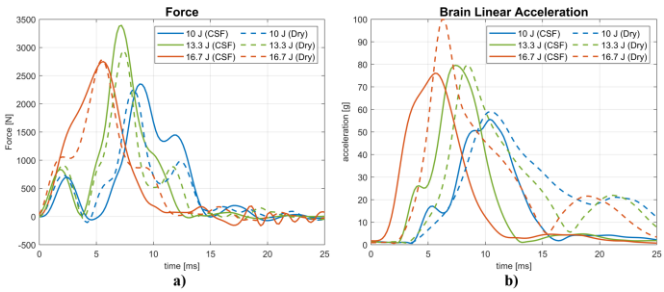


Fig. 3: global results of the impact tests: a) force on the anvil; b) brain peak linear acceleration

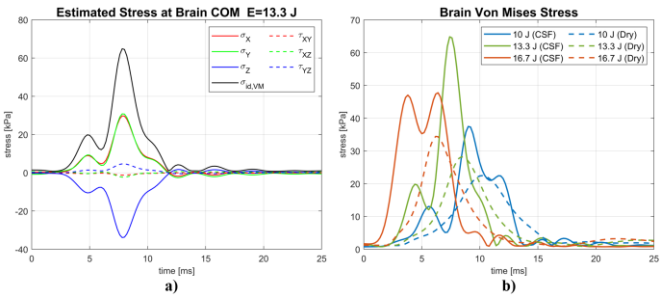


Fig. 4: brain stresses measured with MAPS: a) example of the six components of stress; b) Von Mises stress for the different tests performed

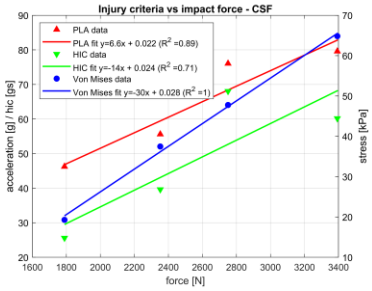


Fig. 5: injury criteria values with respect to impact force on the anvil of the head filled with CSF

IV. DISCUSSION

Advances coming from modelling new structures of this head surrogate are pulling towards an increased bio fidelity, as consequence of the newly introduced components and their interaction. However, its validation needs further and more advanced studies that will be addressed by either replicating cadaveric tests or by a numerical modelling of the surrogate.

Results of drop tests gave a first glance of the capabilities of the new head. Indeed, the presence of accelerometric sensors inside the brain allowed to compute its PLA and HIC [4]. Usually not possible when dealing with rigid head forms.

About the measure of Von Mises stress which was previously peculiar to numerical models [2], [6], we observed little or no shear components, which is compatible with the position of the sensor inside the brain and with the test performed without rotational components. Normal stress showed a high compressive load in the direction of the impact, and a consequent expansion in the orthogonal directions.

Interestingly, impact energy and measured quantities didn't grow together, but a maximum of force and Von Mises was observed for the intermediate energy impact (13.3 J). Instead, injury criteria were observed to increase with respect to the impact force, fitting well a linear trend, with peak Von Mises stress having the best fit.

When CSF was removed from the skull cavity, HIC and PLA increased. Instead, impact force and peak Von Mises stress reduced with respect to the trials with CSF. Although this phenomenon needs further investigation, tests carried out with CSF are more physiologically representative and of more interest to our study.

This preliminary work showed a possible application of this surrogate head for studying impacts and investigating the protective performances of head protective gear. Nevertheless, further tests will need to explore much higher energies and impact locations/conditions to comply with helmet standards.

REFERENCES

[1] M. Faul, L. Xu, M. M. Wald, and V. G. Coronado, "Traumatic Brain Injury in the United States: Emergency Department Visits, Hospitalizations and Deaths 2002–2006," 2010.

[2] D. Sahoo, C. Deck, and R. Willinger, "Brain injury tolerance limit based on computation of axonal strain," *Accid. Anal. Prev.*, vol. 92, pp. 53–70, 2016, doi: 10.1016/j.aap.2016.03.013.

[3] S. Kleiven, "Why Most Traumatic Brain Injuries are Not Caused by Linear Acceleration but Skull Fractures are," *Front. Bioeng. Biotechnol.*, vol. 1, no. November, pp. 1–5, 2013, doi: 10.3389/fbioe.2013.00015.

[4] W. N. Hardy *et al.*, "A study of the response of the human cadaver head to impact.," *Stapp Car Crash J.*, vol. 51, pp. 17–80, 2007.

[5] E. G. Takhounts, M. J. Craig, K. Moorhouse, J. McFadden, and V. Hasija, "Development of Brain Injury Criteria (BrIC)," *SAE Tech. Pap.*, vol. 2013-Novem, no. November, pp. 243–266, 2013, doi: 10.4271/2013-22-0010.

[6] C. Deck and R. Willinger, "Improved head injury criteria based on head FE model," *Int. J. Crashworthiness*, vol. 13, no. 6, pp. 667–678, 2008, doi: 10.1080/13588260802411523.

[7] S. Ouellet and M. Philippens, "The multi-modal responses of a physical head model subjected to various blast exposure conditions," *Shock Waves*, vol. 28, no. 1, pp. 19–36, 2018, doi: 10.1007/s00193-017-0771-3.

[8] N. Petrone, G. Carraro, S. D. Castello, L. Broggio, A. Koptyug, and M. Bäckström, "A Novel Instrumented Human Head Surrogate for the Impact Evaluation of Helmets," *Proceedings*, vol. 2, no. 6, p. 269, 2018, doi: 10.3390/proceedings2060269.

[9] N. Petrone *et al.*, "Feasibility of using a novel instrumented human head surrogate to measure helmet, head and brain kinematics and intracranial pressure during multidirectional impact tests," *J. Sci. Med. Sport*, pp. 4–10, 2019, doi: 10.1016/j.jsams.2019.05.015.

[10] G. Zullo, A. L. Silvestroni, G. Candiotto, A. Koptyug, and N. Petrone, "A Novel Multi-Axial Pressure Sensor Probe for Measuring Triaxial Stress States Inside Soft Materials," *Sensors*, 2021.

Towards a Wearable System for Complete Collection of Clamp Loads in Transfemoral Paralympic Sprinters

G. Fabris[1], M. Scapinello[1], S. G. Breban[1], S. Barbacane[1], G. Migliore[2], A.G. Cutti[2] and N. Petrone[1]
[1] *Department of Industrial Engineering, University of Padova, Padova, Italy*
[2] *INAIL Prosthetic Centre, Vigorso di Budrio (BO), Italy*

***Abstract*—Biomechanical analysis of paralympic amputee sprinters has implications for the design of prosthetic components and for the improvement of the athletic performance. Thus, the purpose of this study was to carry out the kinetic analysis of a unilateral transfemoral amputee sprinter running on track through measurement of reaction forces and inertial data with a wearable acquisition system. The outcomes here presented find agreement with literature findings and, on top of that, add new information that strengthen knowledge in the prosthetic field and can be used for future works.**

***Keywords*—Running Biomechanics, Paralympic Sprinters, Transfemoral, In vivo tests, Ground Reaction Force, Wearable system.**

I. INTRODUCTION

THE last few decades saw huge technological advancements in the field of running specific prostheses (RSP), assistive technologies specifically designed to help athletes with lower limb amputation reaching their maximal performance in sprinting competitions. Running prosthetic feet (RPF), carbon fibre blades with a spring-like function, have been introduced since the ‘90s and their design has been improved in order to better compensate for replacement of an active ankle foot complex. Researchers focused not only on the RPF properties, but also on the nature of loads that the ground applies through the foot to the leg and eventually to athlete’s body, named ground reaction force (GRF). The knowledge of the acting loads is crucial for evaluating athletes’ technique, designing safe feet, and for biomechanical modelling.

It has been observed [1] that laboratory measurements with subjects running on a treadmill are not fully realistic, as athletes are often not used to perform in such artificial environment on the limited running surface of the treadmill. On the contrary, several studies dealing with measurement of GRFs during overground running make use of force platforms placed on the running track [2][3]. Except in cases where the number of platforms is very high [4], the results of this type of studies depend to a large extent on the probability of obtaining good steps (athlete hitting the plate and whole foot placed on the plate).

Coming from these considerations, a previous study of the research group [5] aimed to develop an instrumented RPF, equipped with strain gauges bending bridges, capable of measuring GRFs without the force platforms. The advantages of this method were the collection of multiple steps and the minimum impact of the wearable system. On the contrary, strain gauges applied directly to the carbon blade made the RPF not interchangeable, requiring the prior instrumentation and calibration of each foot to be tested.

The purpose of the present study was to describe an alternative wearable acquisition system that represent the evolution of the previous work, allowing both the high precision data collection of multiple steps, coupled with the efficiency in the foot interchangeability and the athlete comfort, who could run on a familiar running surface.

II. MATERIALS AND METHODS

A. Participants

An elite Paralympic female athlete (55 Kg, 1.60 m) with left unilateral transfemoral amputation, gold medallist in the 100 m race of the Paralympic Games, voluntarily participated in this study. The RSP comprise of a custom-made socket, the mono axial Ottobock 3S80 prosthetic knee, and the Ottobock 1E91 standard RPF, category 3.5.

B. Instrumentation

The RSP was instrumented with a 6-axis ultra-thin load cell (diameter 65mm, thickness 9mm, mass 0.19kg), mounted in between the prosthetic knee and the clamp of the Running Prosthetic Foot (RPF), and a high-shock tolerant six degrees of freedom inertial sensor (DTS, CA, USA), taped to the inner surface of the proximal straight portion of the RPF, almost under the clamp (Fig. 1). Both sensors were connected through wires to an ultra-small, standalone acquisition system (DTS, CA, USA), which was placed inside a small running backpack, together with its Lithium-Polymer battery, which supplied 9V DC power to the acquisition system and a power bank used to power the load cell. The load cell allowed the measurement of reaction forces and torques, while the inertial sensor was used to measure the triaxial linear acceleration and triaxial angular rate at the clamp of the RPF.

Tests were performed in the indoor athletics track located in Padova Palaindoor. In order to validate the inertial sensors, the installation comprised of a total of 28 motion capture cameras (Vicon Motion System, Oxford, UK). 22 of them mounted on tripods placed all along the runway, covering approximately 20-metres-long acquisition volume, and 6 cameras installed on a double portal structure, placed in the centre of the runway, made of aluminium trusses with an overall size of 2.5 x 3 x 3.5 metres (length x width x height).

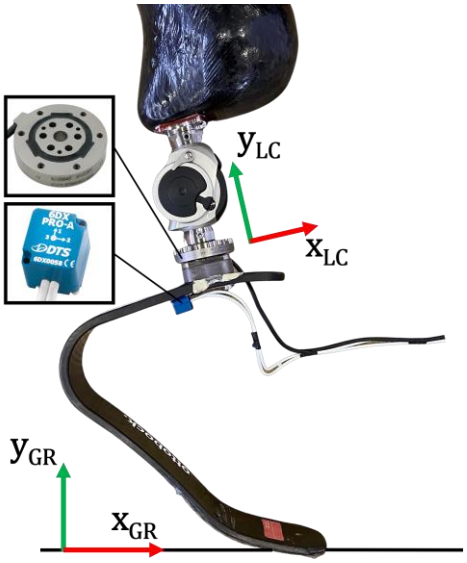


Fig. 1: Instrumented prosthesis: 6-axis load cell and inertial sensor set up. The coordinate systems LC and GR are represented by the longitudinal and shear directions and by the vertical and horizontal directions, respectively.

C. *Experimental protocol*

The inclination of the socket with respect to the vertical line passing through the greater trochanter and the centre of the prosthetic knee was regulated by the orthopaedic technician. The alignment adopted in the tests was A3 [6] which consists in a hip pre-flexion angle equal to 15°. Sixty-five retroreflective markers (14mm diameter) were attached to the subject on significative anatomical landmarks and specific locations of the prosthetic components, according to the established protocol. The athlete wore the running backpack and warmed up to familiarize with the track and the prosthesis setup. A push button panel, placed inside the backpack, was implemented to trigger and stop the DTS recording mode, while the Vicon was controlled from the software.

Two types of trials were performed: Steady State Running (TSSR) and Start (START). In TSSR trials the athlete sprinted from the start line, maintained a constant speed of approximately 60% of personal maximal speed while running across the Vicon acquisition volume, and finally decelerated towards the lane end. The start line and the lane end were positioned outside the acquisition volume. In START trials starting blocks were included and placed inside the acquisition volume. The athlete again sprinted to reach 60% of maximal speed, maintained a constant speed and slowed down towards the lane end. The participant performed three TSSR and three START trials. Kinematic data were collected at 300 Hz, whereas kinetic and inertial data were collected at 2000 Hz.

D. *Data analysis*

Reaction Forces and angular velocities were collected in the Loadcell Coordinate System (*LC* in Fig. 1), i.e., an orthogonal triad composed of the *x*, *y*, and *z* axes. The x-axis of the CS represented the anterior-posterior Shear direction (+ forward), y-axis the Longitudinal direction (+ upward) and the z-axis the medial-lateral direction (+ rightward). In order to synchronize data collected with Vicon system, it was first necessary to downsample the DTS acquisition frequency from 2000Hz to 300Hz, and then calculate the cross-correlation between signals. The angular rate signal of the RPF, obtained from Vicon as the first derivative of the angle of its reference system with respect to the global reference system, was aligned with the angular rate signal recorded with the DTS inertial sensor, until the maximum cross-correlation was observed and the time shift between the two systems was measured. Since per protocol the DTS recording was the first triggered, and therefore signals were longer than Vicon, it was trimmed accordingly. Subsequently, kinetic data were filtered using a zero-lag 4th order, low pass Butterworth filter with cut-off frequency of 52 Hz, which resulted the optimal value from the spectral analysis. Running cycle events (touch down and take-off) employed in the step segmentation were detected from the filtered Longitudinal force data using a 5 N threshold. As a result, loadcell and inertial data were segmented into the different individual steps the test consisted of, and the ground reaction force (GRF) components were computed using the clamp orientation matrix, calculated from the Vicon data. Alternatively, the angle between the longitudinal axis of the loadcell and the vertical axis in the global CS on the sagittal plane, named the loadcell angle (θ_{LC}), was calculated as the integration of the angular rate measured from the inertial sensor. Approximating methods, such as the trapezoidal method, imply an increasing error when estimating an integral. The initial and final value retrieved from Vicon, however, allowed to identify the error trendline and compensate the calculations. Finally, only in TSSR tests the steps were averaged, because in START tests high standard deviation levels were considered to be not representative.

Kinematic data labelling, on the other hand, was realized using Vicon Nexus 2.12.1 software. In order to smooth the data and remove noisy trajectory oscillations, data were low-pass filtered using a Butterworth fourth-order filter. The data analysis was then carried out in MATLAB.

III. RESULTS AND DISCUSSION

The MoCap acquisition volume is bound to the number and disposition of cameras deployed. Extensive installations can be rarely afforded, as they are expensive, and require large amount of space and time for the preparation. As a result, the acquisition volume could not be moved and did not cover the full track length. Data recorded with Vicon during START and TSSR tests only included the acceleration phase from starting blocks and the steady state phase of a sprint, respectively, cutting off the rest of the performance.

The wearable system, on the contrary, is only limited by the battery duration. Moreover, the measurements are no longer related to an acquisition volume, enabling to record the trial in its entirety. The analysis of the instrumented RPF kinetic and inertial data provided an explanatory overview of the trial performance (Fig. 2). By looking at the reaction forces signals, each step was easy to discern from the others and allowed to differentiate the three stages of a sprint, i.e., the accelerating, the steady state, and the breaking phase.

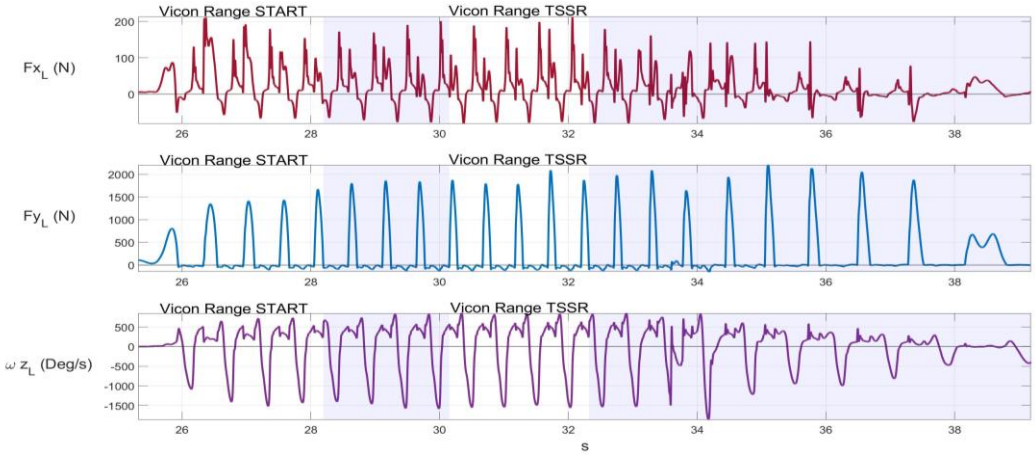


Fig. 2: Overview of an entire running test in the CS LC. Starting from the top the Shear force is depicted, then the Longitudinal force and the angular rate with respect to the z axis. The Vicon acquisition volumes are delimited in the white boxes.

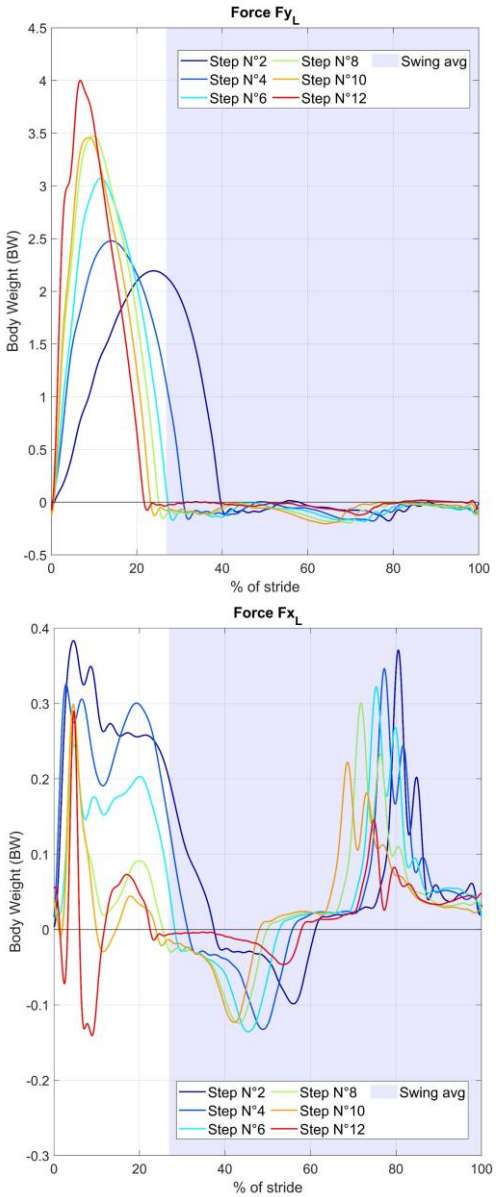


Fig. 3: step progression of the first 6 steps of the affected limb (AL) in a START test, from the reaction forces point of view. Only the AL is presented as the system cannot measure data of the unaffected limb (UL).

In Fig. 3, the step progression during a START trial is displayed in terms of reaction forces in the *LC CS*. Only the steps of the affected limb (AL) are represented, with colours varying from blue to red, as the system is not suitable for measuring loads on the unaffected limb (UL). While the Longitudinal force (F_y) increased progressively in magnitude and decreased in contact time, the Shear force (F_x) decreased both in magnitude and contact time simultaneously. An interesting data was provided by the Shear force measured during the swing phase of a running cycle, where two opposite peaks were detected. The first negative peak, at around 45% of the stride, was consistent with the maximum knee flexion that occur after the take-off event. The second, positive, happened at around 80% of the stride in correspondence with the full knee extension, in preparation to the following touch down event. The Shear force generated at this moment is equivalent in magnitude to the force generated during the stance phase.

The loadcell angle θ_{LC}, achieved through the integration of the angular rate, measured with the inertial sensor, and the error compensation, result of the approximating method in the integral calculation, was compared to the same angle obtained with Vicon. The comparison necessarily regarded the portion of the angle within the Vicon acquisition volume. The RMSE found value of 2.8° validated the angle measurement using the wearable system inertial data. This angle allowed to express the reaction forces from the *LC* into the Ground Coordinate System (*GR*). The GRF behavior at the 4th step (Fig. 4) differed from the literature because, at the present state, there is no evidence of reaction forces measured while the athlete was still accelerating. The literature behaviour, denoted by the change in the horizontal force from braking to propulsive, found agreement with the GRFs measured when running at constant speed (TSSR test in Fig. 5). The analysis of the reaction forces evidenced that the F_y did not show relevant dissimilarities when looking at the same stage of the test, but in different *CS*. Conversely, the magnitude peak was increased and reached faster during the steady state stage, which is consistent with the aforementioned progression. Concerning the F_x force, from

acceleration to steady state stage, the overall magnitude decreased in both *CS*, as the force became less propulsive coherently with the acceleration decrease. Eventually, the horizontal GRF became negative in the first half and positive in the second.

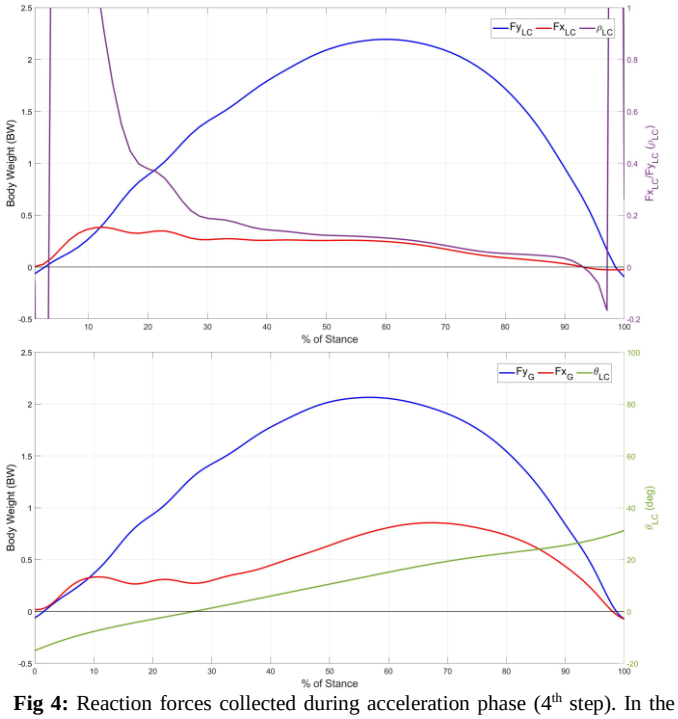


Fig 4: Reaction forces collected during acceleration phase (4th step). In the top graph the forces and the ρ_{LC} are measured in *CS LC*, in the bottom graph the forces and the loadcell angle θ_{LC} are measured in *CS GR*.

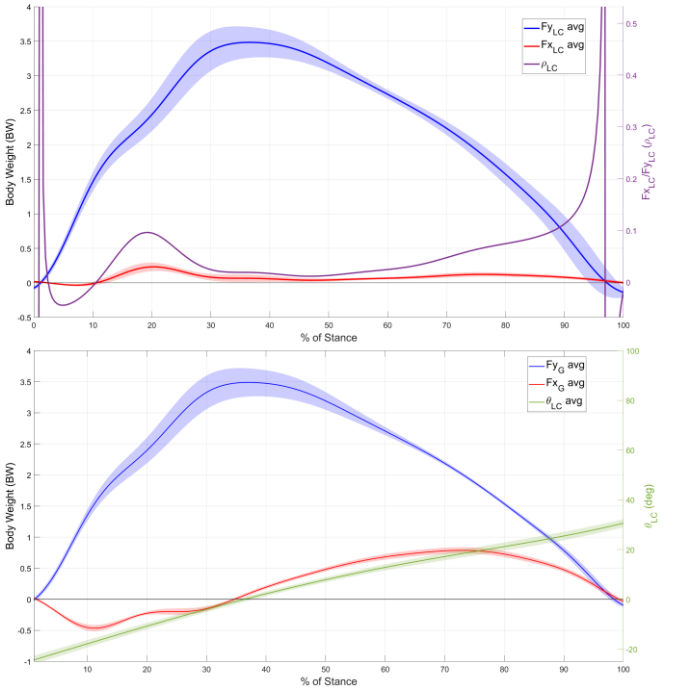


Fig. 5: Average reaction forces in the AL step range 18th – 26th measured both in the *CS LC* and *CS GR*, *in* the top and bottom graph respectively, combined with the ρ_{LC} and the θ_{LC}.

The change of sign in the Shear force can also be noted in the ratio of Fx_{LC} over Fy_{LC}, named ρ_{LC}. This ratio is an indicator of the Shear forward force component with respect to the Longitudinal force. It is a fundamental parameter when replicating the reaction forces on a test bench for RPF characterization. As a matter of fact, several studies [7][9] suggested that the foot stiffness is related to the ρ, and this correlation varies at different inclinations of the foot with respect to the ground [8]. In figures 4 and 5, the initial and final values of ρ are not representative, as the filtering of the foot resonance frequency resulted into negative values of the Longitudinal reaction force at the touch down event, which may seem not realistic. For the same reason, the spikes towards + and – infinity are the result of a non-null Shear force divided by a Longitudinal force equal to 0, which again is not meaningful when considering the instant of contact between the foot and the ground.

IV. CONCLUSIONS

The present work described a wearable system for collection of clamp loads for transfemoral paralympic sprinters. In addition, the inertial sensor allowed to measure the ground reaction forces, proving the system is capable of measuring loads acting from the ground without force platforms implementation. Finally, the Vicon system acted solely as a validation tool, demonstration that the wearable acquisition system can be used independently to measure reaction force and inertial data.

ACKNOWLEDGEMENT

The authors intend to thank the athlete and FISPES for their involvement in the study, INAIL for funding the OLIMPIA project PR19-PAI-P4.

REFERENCES

[1] Williams, K.R. The Dynamics of Running. In Zatsiorsky V.M. (Ed.) *Biomechanics in sport performance enhancement and injury prevention*. Blackwell Science Publisher, 2000. Available: https://doi.org/10.1002/9780470693797.ch8

[2] H. Hobara et al. (2013, Sept). Amputee locomotion: Spring-like leg behaviour and stiffness regulation using running-specific prostheses, *Journal of Biomechanics*, 46(14), 2483–2489. Available: https://doi.org/10.1016/j.jbiomech.2013.07.009

[3] Makimoto, A., et al. (2017, Dec). Ground reaction forces during sprinting in unilateral transfemoral amputees. *Journal of Applied Biomechanics*, 33(6), 406-409, Available: https://doi.org/10.1123/jab.2017-0008

[4] Nagahara, R., et al. (2018, Apr). Association of sprint performance with ground reaction forces during acceleration and maximal speed Phases in a Single Sprint. *Journal of applied biomechanics*, 34(2), 104–110. Available: https://doi.org/10.1123/jab.2016-0356

[5] Petrone, N., et al. (2020, Oct). Development of instrumented running prosthetic feet for the collection of track loads on elite athletes. *Sensors*, 20(20), 5758. Available: https://doi.org/10.3390/s20205758

[6] Migliore, G. L., et al. (2021, Feb). Innovative alignment of sprinting prostheses for persons with transfemoral amputation: Exploratory study on a gold medal Paralympic athlete. *Prosthetics and orthotics international*, 45(1), 46–53. Available: https://doi.org/10.1177/0309364620946910

[7] Petrone, N., et al. (2022, July). Stiffness comparison of running prosthetic feet of different categories after bench testing. *ISBS Proceedings Archive*, 40(1). Available: https://commons.nmu.edu/isbs/vol40/iss1/136

[8] Petrone, N., et al. (2020,June). Conceptual design of a new multi-component test bench for dynamic characterization of running specific prostheses. *Proceedings 2020*, 49(1),75. Available: https://doi.org/10.3390/proceedings2020049075

[9] Sano, Y., Makimoto, A., Hashizume, S., Murai, A., Kobayashi, Y., Takemura, H., & Hobara, H. (2017). Leg stiffness during sprinting in transfemoral amputees with running-specific prosthesis. *Gait and Posture*, 56, 65-67. Available: https://doi.org/10.1016/j.gaitpost.2017.04.038

Face mobility analysis in Spinal Muscular Atrophy

E. Pegolo[1], E. Carraro[2], F. Cibin[3], F. Spolaor[1], F. Salmin[2], A. Lizio[2], M. C. Frisoni[2], S. Becchiati[2], V. Sansone[2], and Z. Sawacha[1]

[1] *Department of Information Engineering, University of Padova, Padova, Italy*

[2] *Neurorehabilitation Unit, NeMO Clinical Center, University of Milan, Milano, Italy*

[3] *BBSoF S.r.l., Padova, Italy*

***Abstract*—Spinal muscular atrophy (SMA) is a neurodegenerative genetic disorder affecting motor neurons in the spinal cord. Depending on the different SMA classifications, symptoms can vary significantly among subjects and they usually include progressive muscle atrophy, weakness, and paralysis affecting the whole body. While impairments in trunk and limbs have been widely investigated, there is a paucity of research on oro-facial and bulbar functions. Since face analysis tools are gaining interest in the clinical context this study aims to verify the potential benefits of adopting them to assess symptoms in SMA. In this study, a face mobility index (FMI), previously developed by the authors for applications in Parkinson's disease, is proposed in a modified version adapted to SMA impairments. Fifty subjects affected by SMA at different stages of the disease (types and functions) and twenty healthy controls (HC) were evaluated and compared in different forced and relaxed tasks. A cluster analysis was applied to the obtained FMIs in order to highlight possible biomarkers of SMA. Results showed that FMI was able to better characterize SMA from HC while subjects were performing tight-lipped smile. Furthermore, this task was found to be related to the lip strength clinical variable. This innovative approach could be used by clinicians as a new non-invasive measure of face mobility. However, future analyses are needed to validate the metric and to increase the sample size.**

***Keywords*—Spinal Muscular Atrophy, Face Mobility, Cluster Analysis**

I. INTRODUCTION

Spinal Muscular Atrophy (SMA) is a severe neurodegenerative disease caused by the deletion of the Survival Motor Neuron (SMN1) gene on chromosome 5. The clinical spectrum of SMA is multifarious and individuals affected by this disease are usually classified into different SMA types on the basis of age of onset and maximum motor function achieved (i.e., non sitters, sitters, and walkers). Types 1, 2, and 3 are the most common ones appearing in the infantile $0-6$ months and $6-18$ months, and juvenile ages ($>$ 12 months), respectively. SMA symptoms are mostly related to the motor system causing progressive muscle atrophy, weakness, and paralysis [1]. Motor function assessment in SMA is therefore essential to describe the disease burden, assess motor impairment, and track disease progression. General consensus has been achieved regarding clinical scales to be employed in muscle strength and functional assessment for testing upper and lower limbs' muscles. However, little is known concerning the evaluation of bulbar functions. Some studies investigated the mandibular range of motion, including the maximal mouth opening, bite force, masticatory functions, and swallowing but, especially in adult patients, these metrics have not been validated and standardized yet [2], [3]. Consequently, there is a need for a better definition of outcome measures to improve the clinical assessment of oro-facial and bulbar functions in SMA.

Recently, face analysis software employed as clinical tools is gaining more and more interest in different pathologies affecting the oro-facial district such as endocrine and metabolic diseases, genetic and chromosome abnormalities, and neuromuscular diseases [4]. This type of technology is non-invasive and contact-free, thus offering a substantial advantage for applications in a wide range of pathologies. In the present study, a measure of face mobility previously validated on subjects with Parkinson's Disease will be employed (Face mobility index FMI, [5]). The index will be adjusted in order to be employed with specific facial tasks designed by the clinicians involved in the study. The aim of this work is to investigate SMA orofacial muscle impairments through this specific metric. Firstly, a comparison between SMA with different types and functions and healthy subjects will be performed. Then, an unsupervised classification technique will be employed as a tool to investigate whether any clinical variable is highlighted among the obtained clusters.

II. MATERIALS AND METHODS

A. Participants

Data of 50 subjects affected by SMA and 20 healthy controls (HC) were evaluated. Subjects were enrolled at the NeMO clinical center in Milan. Written informed consent was obtained from all participants and the study protocol was approved by the local ethics committee (number: 290-27052020). The study complied with the Declaration of Helsinki. Demographic and clinical data of the participants can be found in Table I. SMA subjects underwent clinical evaluations of type, function, and bulbar functions, i.e., active maximum mouth opening (AMMO) defined as the distance between the central incisal edges of the upper and lower central incisors plus the overbite [6], and lip strength (LS), and tongue strength (TS) measured using the validated Iowa Oral Performance Instrument (IOPI) [7].

TABLE I: DEMOGRAPHIC DATA

Characteristic	*SMA subjects*	*HC subjects*
Number	50	20
Age (years mean ± SD)	28.48 ± 18.89	19.0 ± 9.62
Gender	29 M, 21 F	12 M, 8 F
SMA Type	6 SMA 1 21 SMA 2 23 SMA 3 18 non sitters	–
SMA function	24 sitters 8 walkers	–
Lip strength (kPa mean ± SD)	14.19 ± 7.08	–
Tongue strength (kPa mean ± SD)	26.48 ± 16.43	–
Active maximum mouth opening (mm mean ± SD)	19 ± 8.9	–

Demographic data of SMA and HC participants.

B. Data acquisition

Frontal face videos (commercial cameras, 30 fps) of participants were recorded while subjects were comfortably seated with a neutral background behind them. They were instructed to perform the following tasks: (1) frowning, (2) eye closure without exertion, (3) eye closure with exertion, (4) tight-lipped smile, (5) smile, (6) kiss, (7) cheeks inflation. A neutral face expression was acquired as reference.

C. Data elaboration

Face mobility index (FMI) [5] was computed per each task and subject. FMI is obtained by tracking a set of landmarks on the designated frames per each expression and the consequent computation of 40 Euclidean distances, related to specific facial muscles, between these points. Normalization between each distance in the specific expression and the corresponding one in the neutral expression is performed in order to obtain an intra-subject measure of mobility. FMI represents a summary metric determined by the sum of all the mobility deviations from the neutral expression in each expression defined as follows:

$$FMI_j = \frac{\sum_{i=1}^{n_{dist}} |1 - ratio_i| \cdot 100\%}{n_{dist}} \quad (1)$$

where $ratio$ represents the normalized distance over the neutral expression, n_{dist} is the number of available distances and j is the specific expression under analysis.

Both a total FMI and three sub-indexes related to different parts of the face (FMI_up for the upper region, FMI_mid for the middle region, and FMI_low for the lower one) were calculated (Figure 1).

Data of FMIs in SMA individuals were divided into groups considering the two most commonly used clinical classifications, i.e., SMA type and SMA function. Wilcoxon rank sum test was used to compare FMIs in SMA subjects and HC.

Then, k-means clustering technique was applied to FMIs of SMA participants in order to verify the potential of this metrics

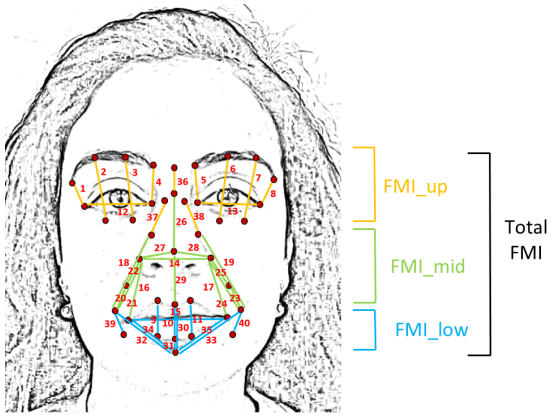


Fig. 1: Distances corresponding to the total FMI, and the FMIs per face regions: FMI_up, FMI_mid, and FMI_low

to characterize SMA impairments. The total FMI and the three subindexes per each task were used as inputs for the cluster analyses. Silhouette score was adopted as the optimum cluster criterion [8]. The results of the clustering were evaluated when they obtained an optimal number of clusters lower than 5. In order to interpret the obtained solutions, Wilkoxon rank sum test was employed to compare the continuous variables (AMMO, LS, TS) across clusters, whereas Fisher's exact test was used for the categorical ones (gender, SMA type, SMA function). A significance level of $p < 0.05$ was adopted for all the statistical analyses.

III. RESULTS

A. SMA type and function analysis

Results of the analysis according to SMA types and functions are reported in Figures 2 and 3, respectively, for only the total FMI per each task (the face region subindexes are not shown for space reasons). Higher values of FMI indicate greater variation from the neutral expression. As regards the SMA type analysis, it can be noted how lower FMI values are present in SMA subjects with more severe impairments, i.e. SMA 1, in some specific tasks. SMA 2 and SMA 3 subjects depict higher values of FMIs in almost all the tasks with respect to HC individuals. Statistically significant differences are found in Task 4 (tight-lipped smile) and Task 7 (cheeks inflation). In particular, Task 4 is able to distinguish both between HC and SMA subjects and within some types of SMA. Whereas, in Task 7 statistically significant differences are present among SMA groups.

The SMA function analysis highlights fewer differences among groups. However, Task 4 and 5 present statistically significant differences between HC subjects and the group of SMA sitters. Additionally, high variability is present in all the obtained data, especially in the SMA population, notwithstanding the clinical classification.

B. Cluster analysis

The cluster analysis considering either the total FMI or the subindexes per face region (FMI_up, FMI_mid, and FMI_low)

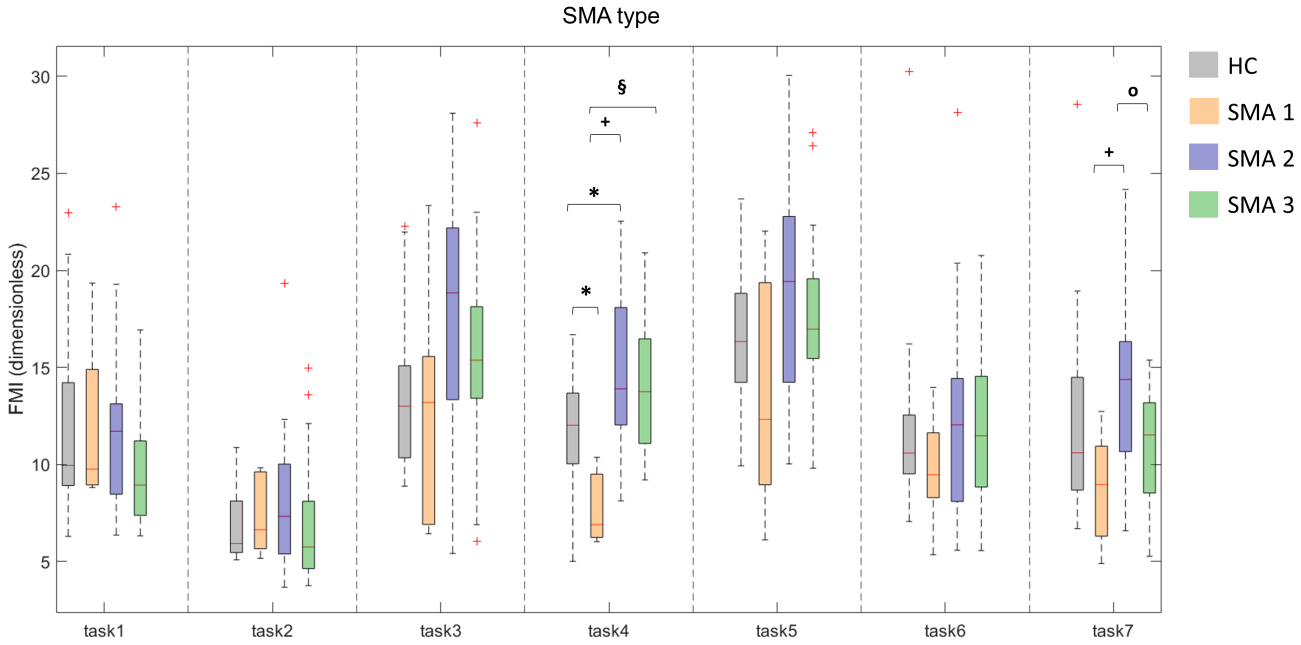


Fig. 2: Boxplot of total FMI per each task in HC and SMA according to their types: SMA 1, SMA 2, and SMA 3. (*) indicates statistically significant differences between HC and SMA subjects. (+), (§), and (o) indicate statistically significant differences between SMA 1 and SMA 2, SMA 1 and SMA 3, and SMA 2 and SMA 3, respectively. All statistically significant differences are considered at the 0.05 confidence level.

led to the definition of a different number of clusters per task. Hereinafter, only clusters that obtained statistically significant differences among clusters are reported. Figure 4 reports the description of the selected ones. FMI_low (Figure 4 (a)) and FMI_mid (Figure 4 (b)) evaluated in Task 4 produced two clusters. In both cases, the clusters include SMA subjects with varying variables. However, they are characterized by LS which is statistically significant between the two clusters in both situations.

IV. DISCUSSION

In this study, a face mobility analysis in SMA subjects was proposed. It represents an innovative approach to assessing oro-facial functions in these individuals. The methodology is easy-to-interpret by physicians and less cumbersome than the commonly used clinical tests (e.g., electromyography, nerve conduction study). Different facial tasks including forced and relaxed movements have been investigated. Generally, except for SMA 1 subjects and non sitters individuals, FMIs are higher than the ones of HC. These findings suggest that in order to perform the same task, compensatory movements recruiting more muscles, are required in these patients with respect to HC ones.

Nevertheless, Task 4 (tight-lipped smile) appears to play a key role in the evaluation of face mobility and it is able to distinguish between HC and SMA subjects and among different classes of SMA types. Moreover, it is the only task that led to a clear distinction of clusters in the FMI_mid and FMI_low with respect to the clinical variable of LS. Higher values of face mobility are related to higher values of LS thus confirming the relationship between impairment in LS and middle and lower face mobility.

The generalizability of these results is subjected to certain limitations. The number of participants is restricted resulting in unbalanced groups of SMA. SMA 1 and walker groups are the less numerous ones with six and eight individuals each. Furthermore, high variability is present in all the analyzed data leading to a need for increasing numerosity in all the considered classes, healthy subjects included. Moreover, the age of participants was not formerly discussed but SMA is known to be partially featured by it. Thereby, age-matched controls should be in included in the study, and classification by age in SMA could be addressed. Finally, formal validation of this approach in SMA subjects should be considered in future developments. Comparison with standardized techniques such as electromyography could be used as a reference tool.

V. CONCLUSION

In conclusion, this contribution proposes a novel potential approach to quantify face mobility in SMA. Results showed that the task that was most revealing was the tight-lipped smile. Clinicians could employ this face analysis tool focusing

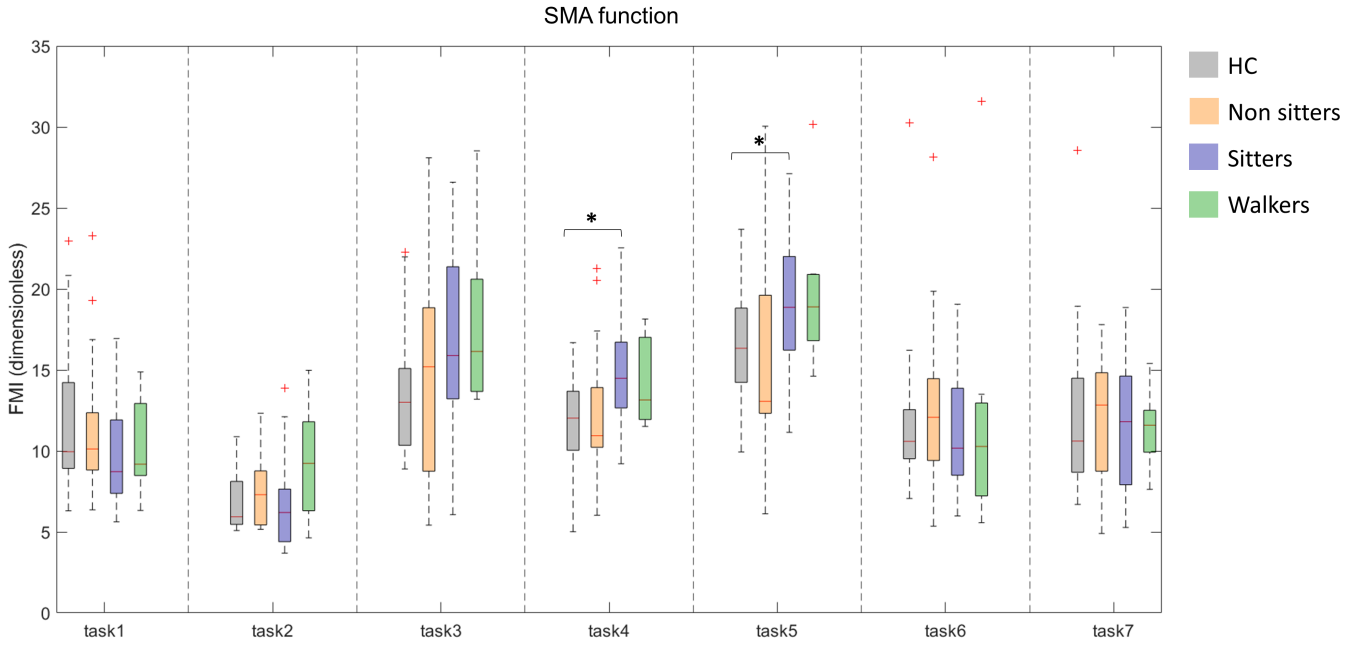


Fig. 3: Boxplot of total FMI per each task in HC and SMA according to their functions: non sitters, sitters, and walkers. (*) indicates statistically significant differences between HC and SMA subjects at the 0.05 confidence level.

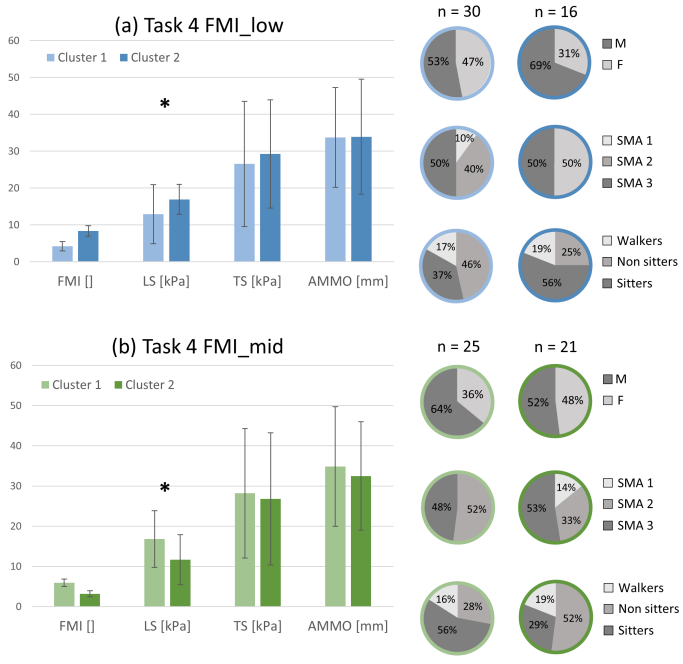


Fig. 4: Results of the cluster analysis in Task 4 FMI_low and FMI_mid in panels (a) and (b) respectively. Numerical variables are depicted as mean ± SD; categorical variables are represented as pie charts. (*) highlights statistically significant differences between clusters at the 0.05 confidence level.

on this expression as an indicator of disease impairment and progression. This easy-to-interpret metric may be employed to track possible alterations in oro-facial muscles mobility associated with the disease and to investigate the impact of different treatments aiming at restoring face mobility.

REFERENCES

[1] E. Mercuri, et al. "Diagnosis and management of spinal muscular atrophy: Part 1: Recommendations for diagnosis, rehabilitation, orthopedic and nutritional care" Neuromuscular Disorders, vol. 28, no. 2, pp. 103-115, 2018

[2] H. W. van Bruggen, et al., "Mandibular dysfunction as a reflection of bulbar involvement in SMA type 2 and 3" Neurology, vol. 86, no. 6 pp. 552-559, 2016

[3] R. I. Wadman, et al., "Bulbar muscle MRI changes in patients with SMA with reduced mouth opening and dysphagia" Neurology, vol. 83, n. 12, pp. 1060-1066, 2014

[4] J. Qiang at al., "Review on Facial-Recognition-Based Applications in Disease Diagnosis" Bioengineering, vol. 9, n. 7 p. 273, 2022

[5] E. Pegolo, D. Volpe, A. Cucca, L. Ricciardi and Z. Sawacha, "Quantitative Evaluation of Hypomimia in Parkinson's Disease: A Face Tracking Approach" Sensors, vol. 22, n. 4, p. 1358, 2022

[6] F. A. Sawair, Y. M. Hassoneh, B. M. Al-Zawawi, Z. H. Baqain, "Maximum mouth opening: Associated factors and dental significance", Saudi Med J, vol. 31 pp. 369-73, 2010

[7] V. Adams, B. Mathisen, S. Baines, C. Lazarus, and R. Callister "Reliability of measurements of tongue and hand strength and endurance using the Iowa Oral Performance Instrument with healthy adults" Dysphagia, vol. 29 n.1, pp. 83-95, 2014

[8] L. Kaufman and P. J. Rousseeuw, "Finding groups in data: an introduction to cluster analysis", John Wiley & Sons, 2009

Structural Simulation of Transcatheter Heart Valve in Transcatheter Heart Valve

R. Scuoppo[1], S. Cannata[2], C. Gandolfo[2], and S. Pasta[1,3]
[1]*Dipartimento di Ingegneria, viale delle Scienze Ed.8, University of Palermo, Italy*
[2]*Interventional Cardiology Unit, IRCCS ISMETT via Tricomi, 5, Italy*
[3]*Department of Research, IRCCS ISMETT via Tricomi, 5, Italy*

***Abstract*— The durability of transcatheter heart valves (THV) remains the main disadvantage of transcatheter heart valve implantation (TAVI) for treating aortic valve stenosis. In this study, we assessed the structural mechanics of TAV-in-TAVI using patient-specific modeling. A parametric analysis highlighted that the outcome of TAV-in-TAV depends on the implanted device position and the planned device to be implanted. Contact pressure evinced the impact of different implantation depth and device size on the TAV-in-TAV. This study may bring new insight in the biomechanical performance of TAV to evaluate options for future interventions when the current TAVs experience device failure.**

***Keywords*—finite-element analysis, transcatheter heart valves, redo-TAVI**

I. Introduction

Transcatheter aortic valve implantation (TAVI) is increasingly used to treat patients with severe aortic (AS) stenosis who are deemed inoperable or at high risk for surgical aortic valve repair [1]. After the publication of positive outcomes in inoperable patients with conventional surgery and in operable patients at high surgical risk, TAVI was included for the first time in the 2012 ESC/EACTS (European Society of Cardiology/European Association for Cardio-Thoracic Surgery) guidelines [2]. These guidelines specifically recommend TAVI for inoperable patients with severe symptomatic AS. Ongoing clinal trials are investigating the feasibility and safety of TAVI in low-risk patients and bicuspid aortic valve as these conditions were considered exclusion criteria in past trials [3].

Transcatheter heart valve (TAV) employed in TAVI is typically comprised of a biological valve mounted on a metal stent frame. The balloon-expandable SAPIEN 3 Ultra device (Edwards, Lifescience, Inc., Irvine, CA, USA) is composed of a metal stent in chrome-cobalt alloy, skirt in polyethylene terephthalate, three valve leaflets made of bovine pericardium, while the Evolut (Medtronic, Minneapolis, MN, USA) is made of porcine pericardium, and mounted on a self-expandable nitinol stent frame and sealing skirt [4].

An increasing number of younger patients with longer life-expectancy receive transcatheter aortic valve implantation (TAVI). Thus, even in the absence of concerns about TAV durability, a substantial proportion of contemporary TAVI patients are expected to live sufficiently long to experience the degeneration and failure of TAV. Indeed, the key disadvantage of TAVs is the limited durability as the chemically treated valve leaflets are not immune to structural degeneration from calcification and thrombosis. For instance, thrombosis was occurred within 3-year from TAVI procedure. The therapeutic option for the treatment of structural TAV degeneration are limited to open-heart surgery and redo-TAVI (or TAV-in-TAV) [5]. While the feasibility of TAV-in-TAV was recently demonstrated, the risk of coronary obstruction due to sinus sequestration is high [6].

In this context, computational modelling may allow to determine the biomechanical interaction of redo-TAVI. This study aimed to develop a computational framework to simulate TAV-in-TAV as clinically performed in one patient with early failure of the implanted device. Patient-specific computational modelling was carried out to determine structural metrics of delivered devices while a parametric analysis of the implantation depth of the second TAVI procedure was performed to assess the impact of the relative device position.

II. Materials and Methods

A. Patient Study Case

A 68-years old gentleman with severe AS was initially treated with a 23-mm SAPIEN 3 Ultra TAV at IRCCS ISMETT in 2019. After 3-year from TAVI, the device failure was treated by redo-TAVI with a 29-mm Evolut Pro device. The patient was discharged and is currently monitored with echocardiography. CT imaging was performed prior the first TAVI procedure for annulus size evaluation, after the TAVI and redo-TAVI.

B. 3D Reconstruction

Pre-TAVI CT images were processed in Mimics (v.21, Materialize, Belgium) to reconstruct the aortic root anatomy and calcific plaques using semi-automatic thresholding of the contrast-enhanced images [7]. Once segmented regions were obtained, the aortic wall and calcific plaques were exported as stereolithographic files for meshing. Since native valve leaflet were not clearly visible at CT scan, a parametric modelling approach was adopted generate the leaflet geometry using anatomic measurements and the CAD tool Rhinoceros (Rhinoceros v.7, McNeel & associates, USA). In brief, two 3rd-order NURBS curves interpolating commissures were delineated to model the free edge of valve leaflets, while the belly of each leaflet was considered using one control points. To model the leaflet-to-sinus attachments, a second set of 3rd-order NURBS curves were developed using Rhino software (v.7.1, McNeel & associates, USA). The NURBS curves were constrained to the aortic root surface by curve-to-surface projection, and then native valve leaflets were developed by a

multi-patch network of NURBS surfaces [8, 9].

Using ICEM meshing software (v2021, ANSYS Inc., USA), the aortic root luminal surface was discretized with unstructured triangular shell elements with size of 0.6 mm. Calcifications were meshed with tetrahedral solid elements with size of 0.5 mm. Native valve leaflets were initially discretized with triangular shell elements (element size of 0.6 mm) and then solid elements were obtained by element protrusion with thickness of 0.5 mm and 4 layers. Figure 1 shows the anatomic model parts of the patient model.

For the sake of simplicity, neo-Hookean models were adopted for both the aortic root and native valve leaflets. Specifically, the aortic root had C1=1.05 MPa and D=0.048 MPa^{-1} while the AS valve had C1=2.29 MPa and D=0.022 MPa^{-1}[10]. The neo-Hookean model allows to imitate the characteristics of the native tissue of aortic root in according to literature investigations [11].The calcification had a linear-elastic model with Young modulus of 400 MPa and Poisson coefficient of 0.475 [12]. Tie contact conditions were used to constraint anatomic parts while the proximal and distal ends of the aortic root was fixed in all directions.

C. *TAV Models*

Geometrical models of 23-mm SAPIEN 3 Ultra and 29-mm Evolut PRO device frames were obtained by reverse engineering of micro-CT images as described in a previous study from our group [13]. For the 23-mm SAPIEN 3 device, the metallic frame was meshed with nearly 60,000 structured-hexahedral solid elements with reduced integration (C3D8R). The Cobalt-Chromium alloy of stent frame was modeled with Von Mises plasticity and isotropic hardening [12]. The Evolut Pro device was meshed with 315,653 structured-hexahedral solid elements with reduced integration and hourglass control. The stent frame was modelled with nitinol alloy material properties as proposed by Auricchio et al [11]. In both cases, the sealing skirt is obtained closing the struct cell geometries with several surfaces modelled at mid-thickness of the device frame. For the SAPIEN 3, the sealing skirt was modelled at crimped stage of TAVI and after the redo-TAVI for the Evolut Pro. Skirts were simulated using surfaces with triangular shell elements assuming thickness of 0.1 mm and were then connected to the device frames using tie contact conditions. Elastic-plastic material properties were assumed for sealing skirt materials [13]. To include the SAPIEN 3 valve leaflets after TAVI, we closed all cell-struct frame to mimic the leaflet displaced by the TAV-in-TAV. For the Evolut Pro, the device leaflets were mapped after redo-TAVI. Figure 1 shows the device models.

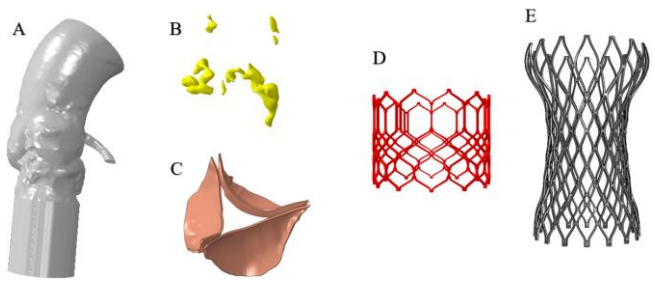


Figure 1: (A) patient model, (B) calcific plaques, (C) native valve leaflets, (D) SAPIEN 3 frame and (E) Evolut Pro frame

D. *Finite-element Analysis*

Numerical analysis of the redo-TAVI procedure was developed in Abaqus/Explicit (v2021hf7, Dassault Systèmes, USA) using a quasi-static approach and thus monitoring energy and ensuring the ratio of kinetic energy to internal energy remained less than 10%. Mass scaling was applied with an element-by-element stable time increment of 10^{-6} every 100 increments to reduce the computational cost.

The SAPIEN 3 stent frame was crimped by a rigid cylindrical surface gradually moved along the radial direction from the initial diameter of S3 (23 mm) to the final diameter of 6 mm. Frictionless contact condition was defined between the crimping surface and the device stent. Using a restart analysis, the crimped device was placed in the human host considering the stress state resulting from the crimping simulation (Fig. 2A). The SAPIEN device was positioned with an implantation depth of 5 mm. Expansion of S3 stent frame was simulated by the radial displacement of a rigid cylindrical surface representing the wall of the expanding balloon. The cylindrical surface is enlarged from the initial diameter of 6 mm to the nominal diameter of 23 mm. Frictionless contact was enabled between the cylindrical expanding surface and the S3 stent frame, which was allowed to be in contact with other anatomic parts. After expansion, an elastic recoil was allowed by the release of the cylindrical surface [5]. After TAVI simulation, the Evolut Pro was crimped using a cylindrical surface gradually moved along the radial direction from the initial device diameter to the final diameter of 6 mm using frictionless contact conditions. Both the stent and sleeve were positioned in the TAVI model with an implantation depth of 9 mm. By pulling the sleeve towards the distal ascending aorta and releasing the stent, because of its residual stresses, the Evolut Pro stent was gradually deployed into the TAV. The pull out of the rigid sleeve was performed by a uniform displacement of 75 mm.

Four different TAV-in-TAV scenarios were simulated varying the implantation depth or device size. The following parametric analysis were therefore performed:

1. 5-mm implantation depth for SAPIEN 3 and 9-mm implantation dept for Evolut Pro (reference configuration)
2. 5-mm implantation depth for SAPIEN 3 and 16-mm implantation dept for Evolut Pro (low redo-TAVI implantation depth)
3. 3-mm implantation depth for SAPIEN 3 and 9-mm implantation dept for Evolut Pro (high TAVI implantation depth)
4. 26-mm Evolut Pro in 23-mm SAPIEN 3 device (redo-TAVI overexpansion).

E. *TAV-in-TAV Analysis*

Eccentricity and expansion indexes were calculated from both TAVI CT and redo-TAVI CT images and then compared to those predicted by computational analysis. For each finite-element simulation the eccentricity index was calculated as follows: [1 − (minimum external THV diameter/maximum external THV diameter)] × 100 while the expansion index was expressed in relation to nominal prosthesis size as follows: (observed THV external area/ device area nominal size) × 100

[5]. Measurements were performed at 4 different anatomic levels (see Figure 6). For each simulation, the contact pressure exerted by the devices on the aortic wall was extracted. Distributions of contact pressure after redo-TAVI were mapped for the different scenarios.

III. RESULTS

Comparison between numerical and CT-based structural indices showed that numerical expansion indices remain lower than CT measurement at different anatomic levels (ie, 120.8 ± 10% for CT-based measured of S3 versus 96.5 ± 14% for numerical-based measured of S3, while 90.6 ± 13% for CT-based measured of Evolut Pro versus 79.2 ± 21% for numerical-based measured of Evolut Pro). In a different way, the eccentricity index shows that numerical simulations slightly underestimate frame-related elliptical deformed shapes.

Figure 2 shows the delivering phases of SAPIEN 3 device and Mises stress distribution at the end of crimping phase. Similarly, Figure 3 displays the deployment of Evolut Pro in the previous SAPIEN 3 TAV as well as the Mises stress distribution for self-expandable device.

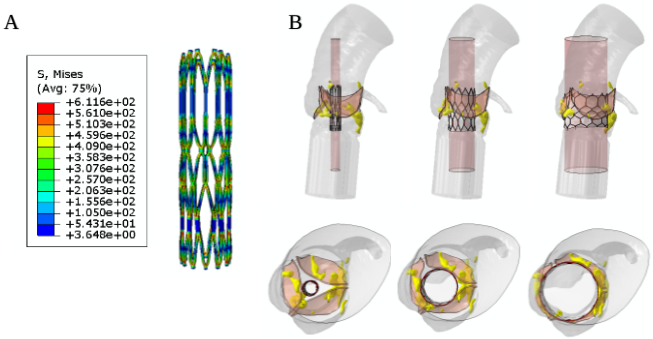


Figure 2: Deployment of SAPIEN 3 Ultra device simulating the TAVI

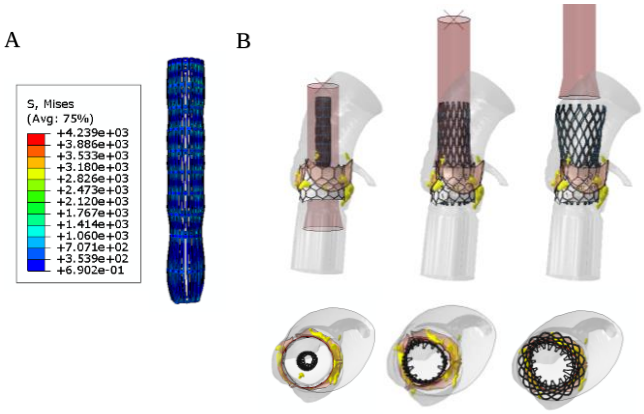


Figure 3: Deployment of Evolut Pro device simulating the redo-TAVI

Figure 4 illustrates the TAV-in-TAV deformed configurations for the four scenarios with different implantation depth or device overexpansion.

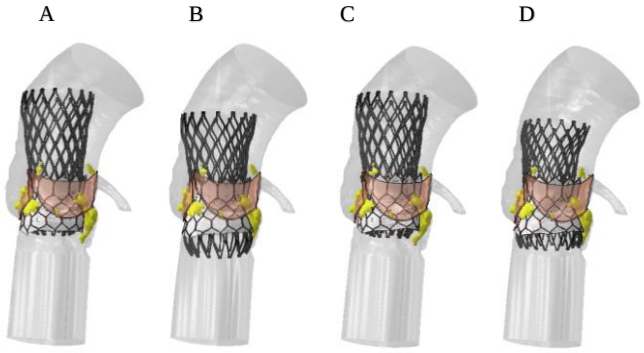


Figure 4: (A) reference TAV-in-TAV as done clinically, (B) low redo-TAVI, (C) high redo-TAVI and (D) TAV-in-TAV overexpansion

Figure 5 shows the Mises stress distribution and deformed shapes of each device.

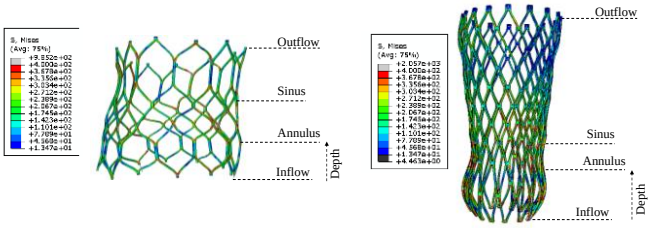


Figure 6: Mises stress distribution of each device for TAV-in-TAV

Figure 7 shows the contact pressure distribution among device frames (SAPIEN 3 and Evolut Pro) and aortic root for each TAV-in-TAV scenario. It is possible to observe a lower contact pressure in the fourth scenario (redo-TAVI overexpansion).

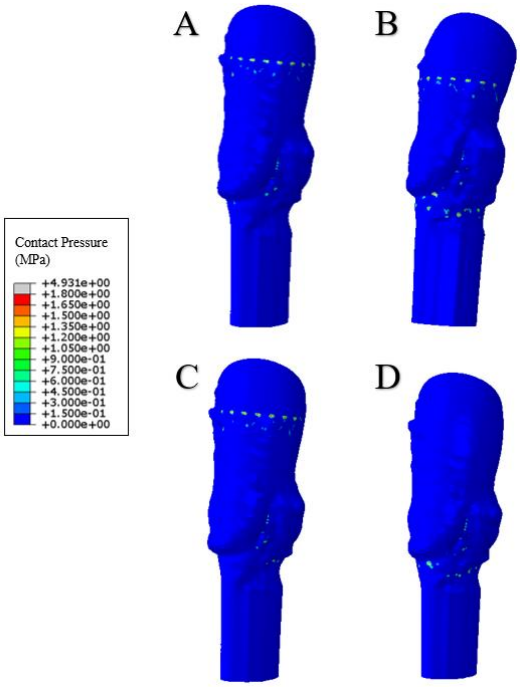


Figure 7: Contact pressure for (A) reference TAV-in-TAV as done clinically, (B) low redo-TAVI, (C) high redo-TAVI and (D) TAV-in-TAV overexpansion

IV. Discussion

To the best of our knowledge, this is the first computational study evaluating the structural mechanics of TAV-in-TAV. We first simulated the TAV-in-TAV according to the implantation depth and device size indicated by the Heart Team, and then carried out a parametric analysis varying these device parameters. The tendency of Evolut Pro devices to expand asymmetrically in the previous SAPIEN 3 device was observed and quantified at several anatomic levels. The utilize of a larger device size than that used by the Heart teams has increased the contact pressure on the aortic wall. We also found that the high implantation depth of Evolut Pro can lead to a final skirt position likely closing the coronary ostia. Future computational flow studies will be undertaken to explore whether the parametrically-derived TAV-in-TAV shapes may lead to coronary flow obstruction and thus adverse events.

Computational analyses of the structural mechanics of TAVI demonstrated that an overexpansion of the implanted device can lead to a high risk of the aortic annulus rupture [9, 13-17]. The impact of aortic root anatomy and tilt angle of the device [18], calcification patterns [19] and native leaflet morphology [20] on the device deployment were also investigated. Fluid-solid interaction was also proposed to simultaneously simulate the structural mechanics and hemodynamics [21]. Moreover, simulations were used to explore the efficacy and safety of TAVI in young and high-risk patients, which are not conventionally treated with THVs. With regards to bicuspid patients, Brouwer et al. [22] carried out computational flow analyses to assess the paravalvular leakage in bicuspid patients, and thus demonstrate the feasibility of TAVI with the newest generation of THVs. Similarly, Pasta et al. [16] investigated stenotic bicuspid patients and found a good agreement between computer and post-TAVI CT-based measurements of the device conformation to the bicuspid anatomy. Recently, the hemodynamic of TAV-in-TAV was investigated using particle image velocimetry by Hatoum and collaborators [23]. They performed a parametric analysis to investigate different device-size combination of TAV-in-TAV with both the SAPIEN 3 and Evolut THVs. They also found more turbulence for the TAV-in-TAV procedure as compared to that of traditional TAVI. In a different way, this study provided more insights on the structural mechanics of TAV-in-TAV to evaluate options for future indications when performing redo-TAVI. The material modeling of vessel wall using a neo-Hookean can be considered a limitation of the current study. However, the study documented by Bosi et al [12] has reported evidence that a linear elastic material model for the vessel is a valid approach to account the stiffen behavior of the diseased vessel.

V. Conclusion

We conclude that computational simulations can reveal important insights into the deployment of THVs when current devices experience structural valve failure. The outcome of TAV-in-TAV depends on both the original implant and the device to be implanted. Future flow studies are needed to assess whether the predicted TAV-in-TAV configurations can lead to coronary flow obstruction.

Acknowledgement

This project has received funding from the European Union's Horizon 2020 research and innovation programme under grant agreement No 101017523.

References

[1] Mylotte D, et al. Transcatheter heart valve failure: a systematic review. Eur Heart J 2015; 36(21): 1306-27.
[2] Arai T, et al. The feasibility of transcatheter aortic valve implantation using the Edwards SAPIEN 3 for patients with severe bicuspid aortic stenosis. J Cardiol 2017; 70(3-4): 220-24.
[3] Braghiroli J, et al. Transcatheter aortic valve replacement in low risk patients: a review of PARTNER 3 and Evolut low risk trials. Cardiovascular diagnosis and therapy 2020; 10(1): 59-71.
[4] Lifesciences E. 2015.
[5] Gallo M, et al. Transcatheter aortic valve replacement for structural degeneration of previously implanted transcatheter valves (TAVR-in-TAVR): a systematic review. European Journal of Cardio-Thoracic Surgery 2022; 61(5): 967-76.
[6] Ochiai T, et al. Risk of Coronary Obstruction Due to Sinus Sequestration in Redo Transcatheter Aortic Valve Replacement. Jacc-Cardiovasc Inte 2020; 13(22): 2617-27.
[7] Pasta S, et al. Three-dimensional parametric modeling of bicuspid aortopathy and comparison with computational flow predictions. Artif Organs 2017; 41(9): E92-E102.
[8] Pasta S, et al. Three-dimensional parametric modeling of bicuspid aortopathy and comparison with computational flow predictions. Artif Organs 2017.
[9] Scardulla F, et al. Shear stress alterations in the celiac trunk of patients with a continuous-flow left ventricular assist device as shown by in-silico and in-vitro flow analyses. J Heart Lung Transplant 2017; 36(8): 906-13.
[10] Di Giuseppe M, et al. Identification of circumferential regional heterogeneity of ascending thoracic aneurysmal aorta by biaxial mechanical testing. J Mol Cell Cardiol 2019; 130: 205-15.
[11] Cosentino F, et al. On the role of material properties in ascending thoracic aortic aneurysms. Computers in biology and medicine 2019; 109: 70-78.
[12] Bosi GM, et al. Population-specific material properties of the implantation site for transcatheter aortic valve replacement finite element simulations. Journal of biomechanics 2018; 71: 236-44.
[13] Pasta S, et al. Computational Analysis of Self-Expanding and Balloon-Expandable Transcatheter Heart Valves. Biomechanics 2021; 1(1): 43-52.
[14] La Grutta L, et al. TAVI imaging: over the echocardiography. La radiologia medica 2020: 1-19.
[15] Pasta S, et al. Transcatheter Heart Valve Implantation in Bicuspid Patients with Self-Expanding Device. Bioengineering 2021; 8(7): 91.
[16] Pasta S, et al. Simulation study of transcatheter heart valve implantation in patients with stenotic bicuspid aortic valve. Med Biol Eng Comput 2020.
[17] Pasta S, et al. Numerical simulation of transcatheter mitral valve replacement: The dynamic implication of LVOT obstruction in the valve-in-ring case. Journal of Biomechanics 2022; 144.
[18] Finotello A, et al. Finite element analysis of TAVI: Impact of native aortic root computational modeling strategies on simulation outcomes. Medical Engineering & Physics 2017; 47: 2-12.
[19] Sturla F, et al. Impact of different aortic valve calcification patterns on the outcome of transcatheter aortic valve implantation: A finite element study. J Biomech 2016; 49(12): 2520-30.
[20] Bailey J, et al. Assessing the impact of including leaflets in the simulation of TAVI deployment into a patient-specific aortic root. Computer methods in biomechanics and biomedical engineering 2016; 19(7): 733-44.
[21] Luraghi G, et al. The impact of calcification patterns in transcatheter aortic valve performance: a fluid-structure interaction analysis. Computer methods in biomechanics and biomedical engineering 2020: 1-9.
[22] Brouwer J, et al. Insight on patient specific computer modeling of transcatheter aortic valve implantation in patients with bicuspid aortic valve disease. Catheter Cardiovasc Interv 2018.
[23] Hatoum H, et al. The hemodynamics of transcatheter aortic valves in transcatheter aortic valves. J Thorac Cardiovasc Surg 2021; 161(2): 565-76 e2.

A Workflow for Biomechanical Simulation of Patient-specific Atherosclerotic Carotid Artery

N. Curcio[1], A. Rosato[2], D. Mazzaccaro[3], M. Conti[4], G. Matrone[1]
[1]*Dept. of Electrical, Computer and Biomedical Engineering, University of Pavia, Pavia, Italy*
[2]*3D and Computer Simulation Laboratory, IRCCS Policlinico San Donato, San Donato Milanese, Italy*
[3]*Operative Unit of Vascular Surgery, IRCCS Policlinico San Donato, San Donato Milanese, Italy*
[4]*Dept. of Civil Engineering and Architecture, University of Pavia, Pavia, Italy*

Abstract—**Atherosclerosis is a systemic pathology that leads to the development of plaques within the walls of vessels. Three types of plaque can be distinguished within the wall structure: soft, calcific and fibrous. The rupture of the plaque could cause thrombo-embolic events; thus, the assessment of plaque vulnerability is fundamental for their prevention. Our goal is to propose a workflow to model the atherosclerotic carotid wall and evaluate the stress distribution in the plaque region through finite element analyses. The segmentation of computed tomography angiography images of a patient was used to derive the geometries of the carotid lumen, calcific and lipid plaque components, while the fibrous component was reconstructed (together with the vessel wall) using purposely developed procedures. The resulting 3D patient-specific model of the vessel, including all plaque components, was used for structural simulations. Pressure load values were instead obtained from an ultrasound modality. The results were used to evaluate how mechanical and geometrical factors affect the stress in the atherosclerotic wall. In the paper, results from the analysis of a heterogeneous plaque with a lipid core surrounded by a thin fibrous cap, which could represent a potentially vulnerable plaque case, will be presented.**

***Keywords*— carotid plaque, image-based modelling, computational analysis.**

I. Introduction

CAROTID artery (CA) represent a common site for the development of atherosclerotic plaques [1]. The presence of the atheromatic plaque in carotid arteries is associated to acute cardiovascular consequences [2] and accounts for a major cause of all ischemic strokes [3]. Indeed, atherosclerosis involves the accumulation of deposits in the inner layer of artery walls (intima), that leads to the formation of an atheromatic plaque, whose development and progress depend on the influence of mechanical forces exerted on vessel walls. The earliest vascular change is the intimate thickening, which consists of layers of smooth muscle cells and extracellular matrix [4]. Some lesions with pathological thickening are characterized by the presence of varying degrees of cholesterol within lipid pools covered by a thick fibrous cap (FC) that begins to thin over time [5]. The FC thickness is critical for the maintenance of the integrity of the lesion and is subject to thinning, prior to rupture. The plaque that is prone to rupture is defined as "vulnerable". A calcified nodule could be present in the advanced stage of a lesion too, however it is the least frequent cause of thrombosis.

The rupture of the plaque is a mechanical event that occurs when the carotid wall loading exceeds the tissue strength and it is regulated by the cellular and molecular composition of plaques [6] [7]. Identifying patients with vulnerable plaques represents an important step to prevent acute and adverse cardiovascular events which could lead to complications [8].

Computational studies provide the three-dimensional (3D) stress/strain distributions in patient-specific diseased arteries with different plaque types and morphologies, so they could have the potential to give valuable information for the plaque vulnerability assessment. By combining clinical imaging methods, like e.g. computed tomography angiography (CTA), with computational analyses, several groups studied the structural stresses of diseased carotid arteries obtained from different modelling strategies. However, usually in CTA scans the fibrous component of the plaque and artery walls are not clearly distinguishable. For this reason, the reconstruction of these structures is challenging. Some works proposed the manual segmentation of clinical images to reconstruct the plaque components and wall structure geometries, such as [9], [10]; other studies performed a semi-automatic segmentation of lipid and calcific plaque components only [11] or modeled these ones as idealized geometries [12], while the fibrous and healthy wall tissues surrounding them were again reconstructed manually.

This work aims at providing a workflow that allows to model a patient-specific atherosclerotic CA and to perform 3D finite element analyses (FEA) in order to evaluate its structural behaviour, considering different plaque compositions (including both calcific, lipid and fibrous components) and biomechanical vessel loads. Concerning the atherosclerotic vessel modelling, we propose an *ad-hoc* developed semi-automatic procedure to reconstruct the carotid walls starting from CTA images. Since fibrous structures, such as the healthy wall and plaque fibrous component, are challenging to highlight in CTA images, we firstly segmented the plaque calcific and lipid components only and subsequently reconstructed the model of the plaque fibrous component and wall by applying the proposed automatic procedure. Indeed, modelling also the plaque fibrous component allows to represent more accurately the composition and morphology of the atherosclerotic vessel. Finally, for what concerns the vessel biomechanical load conditions to be set in FEA, we considered pressure values obtained from a specific ultrasound (US)-based wall-tracking modality, thus also exploiting different imaging techniques to derive patient-specific data.

II. Materials and Methods

A. *Image Acquisition*

Two different image acquisitions were performed on the considered patient before undergoing endarterectomy: 1) neck-head CTA scans, which were used to segment the different vessel structures in the DICOM sequences; 2) US

scans employing a dedicated software package that implements a radiofrequency (RF)-echo-based arterial-wall tracking procedure to derive carotid pressure waveforms. Further details are provided in [13], [14]. The software provided the local CA diastolic and systolic pressure values that were used in FEA analysis. The patient gave written informed consent and the study was approved by the IRCCS Ospedale San Raffaele ethical committee (record number 110/int/2019, 20 June 2019).

B. Proposed CA Modelling Methodology and Biomechanical Simulations

The atherosclerotic CA wall was reconstructed starting from the CTA segmentation (Fig. 1a). The segmentation of the CA lumen, calcific and lipid plaque components was performed using the ITK-Snap software [15]. The segmentation was confirmed by the vascular surgeon (D.M).

Since a semi-automatic segmentation of the CA wall and plaque fibrous component is not possible in CTA images, such structures were generated as computer aided design (CAD) models through a purposely-developed procedure using the Rhinoceros software (McNeel and Associates, Seattle, WA, USA) and the Grasshopper plug-in.

Firstly, the procedure started with the processing of the lumen STL (Fig. 1b) to generate the vessel wall inner surface; then, equally spaced sections were selected from the lumen surface and these latter were enlarged to obtain the vessel wall outer surface, keeping the plaque surface STL enclosed between the inner and outer walls (Fig. 1c). The final CA wall solid geometry was created by Boolean difference of the inner and outer walls.

Secondly, filling the stenotic area of the lumen between the inner and outer surfaces of the wall surrounding the other plaque components provided the plaque fibrous component (Fig. 1d).

3D FEA were then carried out using the commercial finite element package Abaqus CAE (Simulia, Providence, RI, USA). The solid domain was discretized with tetrahedral elements. The mesh was thickened with a local refinement in the plaque region, choosing a local mesh size of 0.3 mm, after a mesh convergence analysis. The global mesh size, out of the plaque region, was set to 0.8 mm.

The materials assigned to both the vessel wall and plaque components were set as incompressible, isotropic, linear elastic, with a 0.49 Poisson's ratio; instead, a different Young's Modulus was considered for each of them. The used material properties were chosen after a literature review [12], [16]–[21].

The load conditions of the CA wall were defined as follows: the distal and the proximal ends of the carotid bifurcation were constrained in the longitudinal and circumferential directions; also, the inner wall was loaded with a constant uniform pressure (i.e., 68.5 mmHg, as this was the patient-specific pressure value obtained from US acquisitions).

III. Results

In this section, results relative to one patient selected to test the developed procedures are presented.

First, the model resulting from the procedure previously described is shown in Fig. 1e. The model represents an heterogeneous plaque within CA walls with all the three plaque components mentioned before.

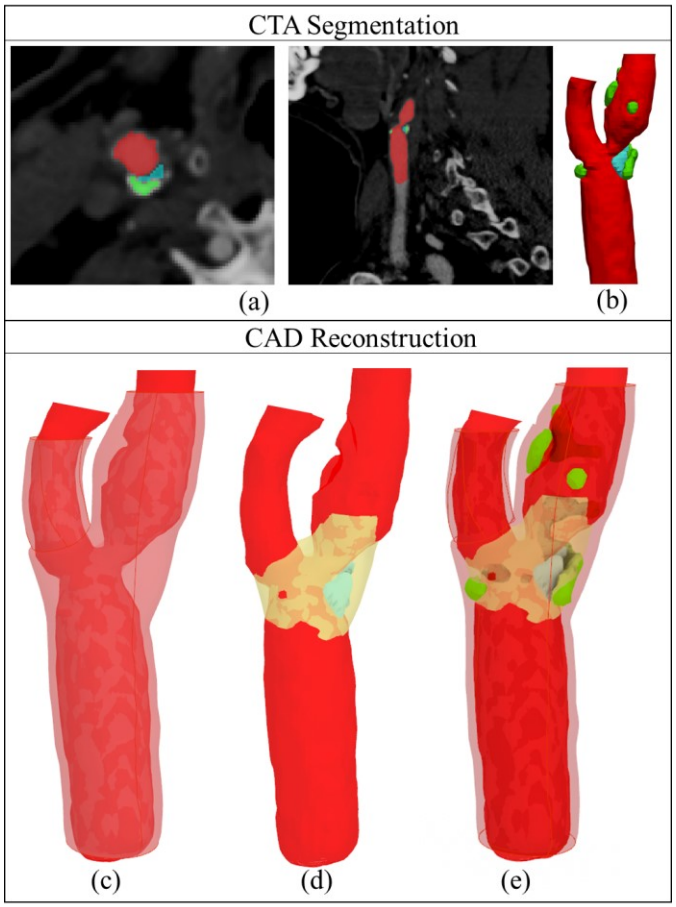


Fig. 1. Atherosclerotic carotid reconstruction workflow. CTA axial and sagittal views with overlapped segmentation (a) and the corresponding STL (b): the lumen is labelled in red, the lipid content of plaque is represented in blue and the calcific content in green. The CAD reconstruction provides: the final atherosclerotic wall geometry (e), obtained through a lumen enlargement procedure used to include the calcific and lipid components of the plaque (c), and the fibrous plaque component (in yellow in (d-e)) filling the stenotic lumen areas.

The obtained von Mises (VM) stresses were then analyzed as the simulation output. From a qualitative point of view, the contour plot of the stress distributions allows to check the localization of the highest stresses. In Fig. 2, the VM stresses distribution in the fibrous plaque and the CA healthy wall elements is provided. High VM stress regions (colored in red in Fig. 2) could appear both in the fibrous plaque and in non-pathological areas. In the plaque region, the highest stresses were located in the region of the FC, at the interface between the lipidic component and the lumen.

To perform a comparative analysis and validate the proposed procedure, the vascular surgeon provided the manual segmentation of the plaque fibrous component from CTA scans. Subsequently, two structural simulations were performed using, in one case, the fibrous plaque CAD model automatically generated using the proposed approach, and in the second one the STL file obtained from the manual segmentation of this component, performed by surgeon. The results of the two simulations are reported in Fig. 3. To analyze the stress distributions, we selected the same cross-sectional

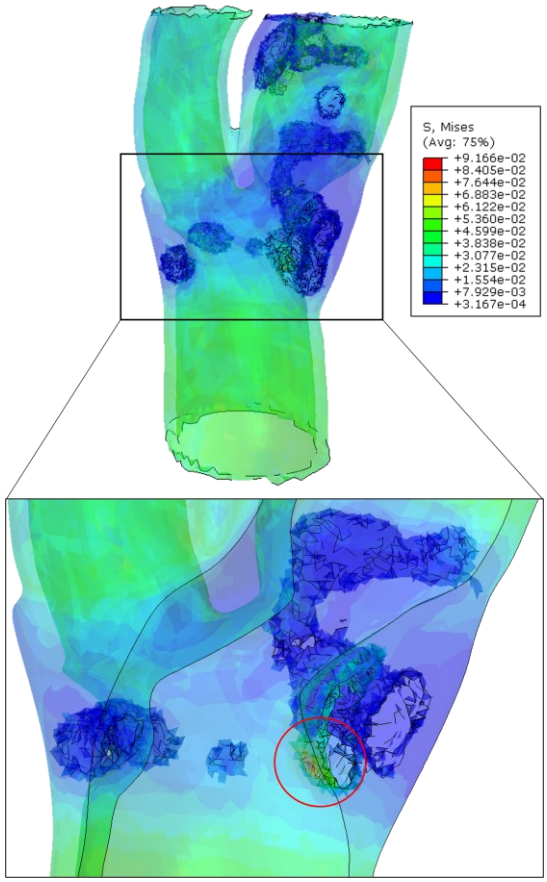


Fig. 2. Contour plots of the VM stress distribution, both in the CA healthy wall ad fibrous plaque regions, in 3D views. The highest stress regions in the fibrous subset are displayed in red (see color scales) and highlighted by the red circle.

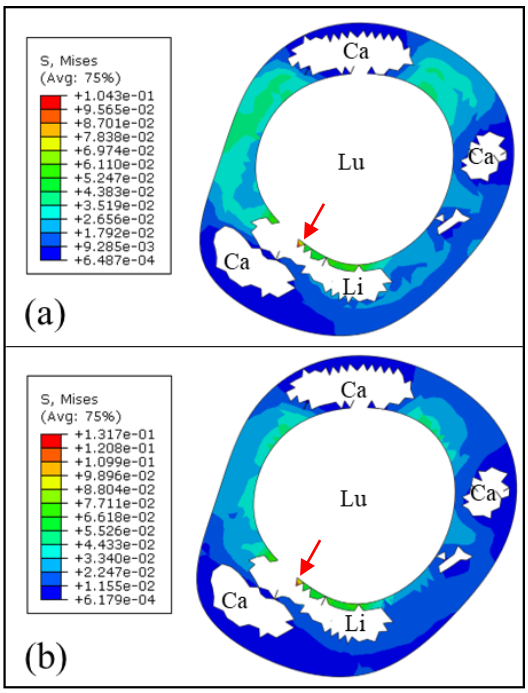


Fig. 3. Results of the comparative analysis. The figure shows the cross-sectional contour plots of VM stress distributions (colour scale in MPa) in the CA healthy wall and fibrous plaque, obtained from simulations with the proposed CAD model (a) and with the manually segmented model of the fibrous component (b). The slice including the maximum VM stress (highlighted by the arrow) has been selected. The lumen is denoted as Lu, while the lipid and calcific subsets are denoted as Li and Ca, respectively.

slice in both simulation outputs. In Fig. 3 a-b, the contour plots of the obtained VM distributions are compared: the simulated VM stress distributions and the location of the highest stress concentration look qualitatively similar in both models.

IV. Discussion and Conclusion

The aim of this work was to propose a new methodology to model an atherosclerotic carotid wall and different plaque components from CTA images, and to perform a computational analysis of stress distributions, including also data derived from an US-based modality. The advantage brought about by this method is that it generates models that are patient-specific and models the fibrous content of the plaque in an automatic way as a further plaque component, differently from other works that did not make any distinction between the fibrous plaque and vessel wall [22], [23] or in which these structures were manually segmented [11]. Modelling the plaque fibrous component allows to have a more accurate representation of the FC in plaques at different stages, that could be prone to rupture. Furthermore, different mechanical properties can be assigned to each region for a more accurate representation of the actual plaque composition.

On the other hand, the workflow here proposed also shows some limitations. First, the modelling procedure is not completely automatized, so the reconstruction is time-consuming because of the complexity of geometries; the settings of simulation are based on some simplifying hypotheses [12], [16], [17] concerning the material properties, even if it is well known that arterial soft tissues are non-linear hyperelastic materials. The simulations did not account for pre-stresses or specific CA loading conditions (i.e. blood pressure, residual stresses and axial pre-stretch) due to missing information on the cardiac cycle phase corresponding to CTA scan acquisitions. Finally, VM stresses were considered in these analyses, since they are suitable to describe the distribution of loads among different subsets of the simulation, and were used also in several other works in the literature [11], [12], [17], [22], [24]. These limitations will be addressed in future works, together with the inclusion of a higher number of cases in the analysis.

Acknowledgement

The research was funded by the Italian Ministry of Health with the financial contribution from the project of Ricerca Finalizzata 2018 (GR-2018-12366862).

References

[1] U. G. Schulz and P. M. Rothwell, “Major variation in carotid bifurcation anatomy: a possible risk factor for plaque development?,” *Stroke*, vol. 32, no. 11, pp. 2522–2529, Nov. 2001, doi: 10.1161/hs1101.097391.

[2] P. D. Richardson, “Biomechanics of Plaque Rupture: Progress, Problems, and New Frontiers,” *Ann Biomed Eng*, vol 30, no. 4, pp. 524–536. doi: 10.1114/1.1482781. PMID: 12086003.

[3] C. Banerjee and M. I. Chimowitz, “Stroke Caused by Atherosclerosis of the Major Intracranial Arteries,” *Circ Res*, vol. 120, no. 3, pp. 502–513, Feb. 2017, doi: 10.1161/CIRCRESAHA.116.308441.

[4] K. Sakakura, M. Nakano, F. Otsuka, E. Ladich, F. D. Kolodgie, and R. Virmani, “Pathophysiology of Atherosclerosis Plaque Progression,” *Heart, Lung and Circulation*, vol. 22, no. 6, pp. 399–411, Jun. 2013, doi: 10.1016/j.hlc.2013.03.001.

[5] Y. Wang, T. Wang, Y. Luo, and L. Jiao, "Identification Markers of Carotid Vulnerable Plaques: An Update," *Biomolecules*, vol. 12, no. 9, Art. no. 9, Sep. 2022, doi: 10.3390/biom12091192.

[6] B. R. Kwak *et al.*, "Biomechanical factors in atherosclerosis: mechanisms and clinical implications," *Eur Heart J*, vol. 35, no. 43, pp. 3013–3020, Nov. 2014, doi: 10.1093/eurheartj/ehu353.

[7] Z. Teng *et al.*, "A uni-extension study on the ultimate material strength and extreme extensibility of atherosclerotic tissue in human carotid plaques," *Journal of Biomechanics*, vol. 48, no. 14, pp. 3859–3867, Nov. 2015, doi: 10.1016/j.jbiomech.2015.09.037.

[8] M. M. Mughal, M. K. Khan, J. K. DeMarco, A. Majid, F. Shamoun, and G. S. Abela, "Symptomatic and asymptomatic carotid artery plaque," *Expert Rev Cardiovasc Ther*, vol. 9, no. 10, pp. 1315–1330, Oct. 2011, doi: 10.1586/erc.11.120.

[9] Z. Teng *et al.*, "3D Critical Plaque Wall Stress Is a Better Predictor of Carotid Plaque Rupture Sites Than Flow Shear Stress: An In Vivo MRI-Based 3D FSI Study," *J Biomech Eng*, vol. 132, no. 3, p. 031007, Mar. 2010, doi: 10.1115/1.4001028.

[10] U. Sadat *et al.*, "Association between Biomechanical Structural Stresses of Atherosclerotic Carotid Plaques and Subsequent Ischaemic Cerebrovascular Events – A Longitudinal in Vivo Magnetic Resonance Imaging-based Finite element Study," *European Journal of Vascular and Endovascular Surgery*, vol. 40, no. 4, pp. 485–491, Oct. 2010, doi: 10.1016/j.ejvs.2010.07.015.

[11] J. R. Leach, V. L. Rayz, B. Soares, M. Wintermark, M. R. K. Mofrad, and D. Saloner, "Carotid Atheroma Rupture Observed In Vivo and FSI-Predicted Stress Distribution Based on Pre-rupture Imaging," *Ann Biomed Eng*, vol. 38, no. 8, pp. 2748–2765, Aug. 2010, doi: 10.1007/s10439-010-0004-8.

[12] L. Bennati *et al.*, "A Computational Fluid–Structure Interaction Study for Carotids With Different Atherosclerotic Plaques," *Journal of Biomechanical Engineering*, vol. 143, no. 9, May 2021, doi: 10.1115/1.4050910.

[13] Esaote, MyLab, Advanced Operations. (2018). https://eifu.esaote.com/fileadmin/Manuals/F090101/italian/optional_sections/QASSection_I_R02.pdf.

[14] J. M. Meinders and A. P. G. Hoeks, "Simultaneous assessment of diameter and pressure waveforms in the carotid artery," *Ultrasound Med Biol*, vol. 30, no. 2, pp. 147–154, Feb. 2004, doi: 10.1016/j.ultrasmedbio.2003.10.014.

[15] P. A. Yushkevich *et al.*, "User-guided 3D active contour segmentation of anatomical structures: significantly improved efficiency and reliability," *Neuroimage*, vol. 31, no. 3, pp. 1116–1128, Jul. 2006, doi: 10.1016/j.neuroimage.2006.01.015.

[16] J. Benitez *et al.*, "Evaluating the Impact of Calcification on Plaque Vulnerability from the Aspect of Mechanical Interaction Between Blood Flow and Artery Based on MRI," *Ann Biomed Eng*, vol. 49, no. 4, pp. 1169–1182, Apr. 2021, doi: 10.1007/s10439-020-02655-1.

[17] H. Gao and Q. Long, "Effects of varied lipid core volume and fibrous cap thickness on stress distribution in carotid arterial plaques," *J Biomech*, vol. 41, no. 14, pp. 3053–3059, Oct. 2008, doi: 10.1016/j.jbiomech.2008.07.011.

[18] R. T. Lee, A. J. Grodzinsky, E. H. Frank, R. D. Kamm, and F. J. Schoen, "Structure-dependent dynamic mechanical behavior of fibrous caps from human atherosclerotic plaques," *Circulation*, vol. 83, no. 5, pp. 1764–1770, May 1991, doi: 10.1161/01.cir.83.5.1764.

[19] S. R. H. Barrett, M. P. F. Sutcliffe, S. Howarth, Z.-Y. Li, and J. H. Gillard, "Experimental measurement of the mechanical properties of carotid atherothrombotic plaque fibrous cap," *J Biomech*, vol. 42, no. 11, pp. 1650–1655, Aug. 2009, doi: 10.1016/j.jbiomech.2009.04.025.

[20] Z. Teng, U. Sadat, A. J. Brown, and J. H. Gillard, "Plaque hemorrhage in carotid artery disease: Pathogenesis, clinical and biomechanical considerations," *Journal of Biomechanics*, vol. 47, no. 4, pp. 847–858, Mar. 2014, doi: 10.1016/j.jbiomech.2014.01.013.

[21] H. E. Barrett, K. Van der Heiden, E. Farrell, F. J. H. Gijsen, and A. C. Akyildiz, "Calcifications in atherosclerotic plaques and impact on plaque biomechanics," *J Biomech*, vol. 87, pp. 1–12, Apr. 2019, doi: 10.1016/j.jbiomech.2019.03.005.

[22] H. Gao, Q. Long, M. Graves, J. H. Gillard, and Z.-Y. Li, "Carotid arterial plaque stress analysis using fluid–structure interactive simulation based on in-vivo magnetic resonance images of four patients," *Journal of Biomechanics*, vol. 42, no. 10, pp. 1416–1423, Jul. 2009, doi: 10.1016/j.jbiomech.2009.04.010.

[23] A. Creane, E. Maher, S. Sultan, N. Hynes, D. J. Kelly, and C. Lally, "Finite element modelling of diseased carotid bifurcations generated from in vivo computerised tomographic angiography," *Comput Biol Med*, vol. 40, no. 4, pp. 419–429, Apr. 2010, doi: 10.1016/j.compbiomed.2010.02.006.

[24] G. A. Holzapfel, G. Sommer, and P. Regitnig, "Anisotropic mechanical properties of tissue components in human atherosclerotic plaques," *J Biomech Eng*, vol. 126, no. 5, pp. 657–665, Oct. 2004, doi: 10.1115/1.1800557.

Experimental Analysis of the biomechanics of healthy porcine corneas

I. Toniolo[1, §], M.V. Mascolini[2, §], S. Neri[3], A. Peruffo[4], A. Perazzi[3], C. G. Fontanella[2]
[1] *Civil, Environmental and Architectural Engineering Department, University of Padova, Italy*
[2] *Industrial Engineering Department, University of Padova, Italy*
[3] *Department of Animal Medicine, Production and Health, University of Padua, Italy*
[4] *Department of Comparative Biomedicine and Food Science*
[§] *These authors equally contributed to the present study*

***Abstract*— Cornea is a composite tissue that exhibits nonlinear and time-dependent mechanical properties. Ulcers are one of the main pathologies affecting corneal tissue, leading to a structural non-integrity, and worsening the performance due to impaired functions. For this reason, assessing the mechanical behavior of the cornea is crucial not only to reveal the alterations induced by pathologies and lesions that could induce further damages, jeopardizing the mechanical response and performances of cornea, but also to evaluate treatments aimed at contrasting the corneal weakening.**

This study aimed at mechanically characterizing the healthy porcine corneas, as a suitable model to replace the lack of human samples, by performing sub-structural (uniaxial tensile) and structural (saline solution inflation) tests to reveal the mechanical behavior and the deformability of the corneal tissue. In detail, failure, cyclic and stress-relaxation tests were carried out on fresh corneas while structural tests were performed also on frozen corneas, to assess if the storing process alters the mechanical properties. The inflation tests were performed after having designed and printed a corneal support device, conceived to guarantee an adequate grip and a sealing system.

The results of tensile tests revealed that the failure was in average reached at a strain of 0.79 (± 0.14), relative to a mean stress of 1.274 (± 0.368) MPa. In cyclic tests, the two tested velocities seemed not to influence the results, while stress relaxation tests confirmed the viscoelastic behavior of the tissue. The inflation test results showed a non-significant difference in pressure-volume behavior between fresh and frozen corneas.

This work gave an overview of the mechanical properties of the healthy porcine corneas, also for large deformation, that in the past was not analyzed. Once the corneal tissues are proper characterized, a complete and validated computational model can be developed. Computational analysis could be a starting point to evaluate in silico the mechanical behaviour of cornea both in healthy status and simulated pathological conditions, without collecting biological samples.

In future, the same tests will be performed on treated corneas, for example via plasma treatment for cellular proliferation (used to treat wounds) or cross-linking, and on corneas subjected to a simulated lesion, to quantify the induced changes in mechanical proprieties.

***Keywords*—stress relaxation, corneal tissues, failure, cyclic test, inflation test**

I. Introduction

THE cornea is the outermost transparent tissue and the essential refractive component of the eye. Among the most common corneal pathologies, the ulcerative melting keratitis alters the microstructural organization of the tissue, impairing its mechanical and functional behaviour and, in the most severe cases, leading to blindness. Nowadays, considerable research efforts in regenerative medicine are focusing on the development of reliable alternatives to keratoplasty, due to the limited availability of healthy donated corneas. One of the main aspects to identify an adequate treatment is the restoration of the mechanical properties that have been modified due to the pathologies.

The mechanical behaviour of the corneal tissues has been studied largely in the last years and still numerous publications on the subject are emerging. Uniaxial tensile and inflation tests are the most frequent kind of experimental tests performed to evaluate the mechanical response of ex vivo corneas, revealing the nonlinear elastic, anisotropic and quasi-linear viscoelastic mechanical behaviour of the cornea [1]–[8]. Such mechanical response depends on the intricate, multi-scale structures with distinct patterns of fiber organization disposed on different layers [9]. Brillouin microscopy has been also applied for mapping the mechanical properties of the cornea as the elastic modulus in three dimensions with a high spatial resolution [10]. Because the difficulties in collecting human corneal tissues, porcine corneas are frequently used to replace them in assessing the biomechanical properties. However, despite some differences in corneal thickness, porcine cornea is largely accepted as a suitable model because exhibits similar stress-strain behaviour under short- and long-term loading and reacts likewise to sustained loading, although the creep is higher in human than in porcine corneas [3].

A mechanical overview of the corneal tissues could be crucial in the framework of biomechanics. In fact, several studies reported the finite element analyses on the corneal structure that, initially, were used to simulate the corneal mechanical response to refractive surgery. They provided a useful starting point for surgical planning and demonstrated how mechanical modeling could explain the refractive effects achieved by modulating the length and depth of surgical incisions. More recently, models have become more advanced by considering also patient-specific geometry, alignment and distribution of collagen fibrils, the aging and cornea transplant surgery [9].

In this study, several tests on healthy porcine corneas were performed, such as failure, cyclic and stress relaxation uniaxial tensile tests at large deformation that lacked in literature. Moreover, the saline solution inflation test was performed on fresh and frozen healthy corneas, highlighting if significant differences due to the storing process were detectable. Finally, a preliminary computational model simulating the inflation test was implemented with a view to implement in the future a model that has a robust constitutive formulation that can

correctly interpret corneal behavior, useful for simulations of surgical procedures.

II. Materials and Methods

A. Sample collection and preparation

A total number of 38 porcine corneal samples were tested. The samples were wastes of a local slaughterhouse and derived from animals intended for food consumption. All corneas were found to be clear, with no presence of corneal scarring or opacities, and transported under sterile condition to the laboratory inside a container with betadine, an antiseptic solution at 10%. The eyeballs were rinsed with phosphate buffered saline concentration to reduce contamination. The samples were split in two main groups: 20 corneas used for tensile tests and 18 for inflation tests.

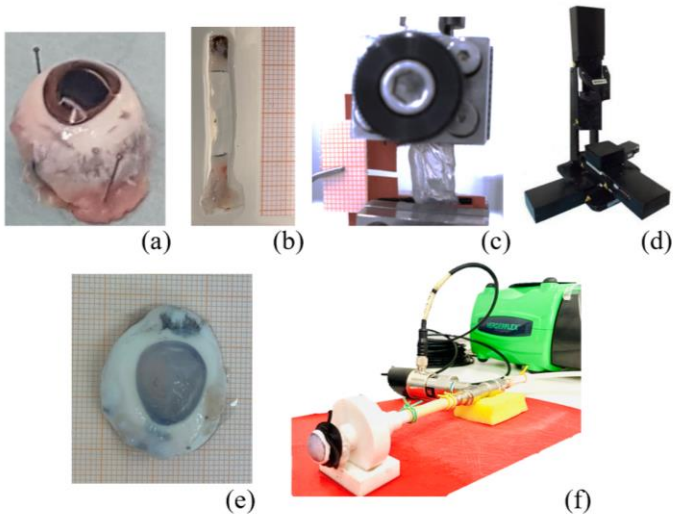


Fig. 1: Healthy eyeball sample (a). Corneal strip (b) and set up of the tensile tests (c). Biomomentum Mach-1 v500csst Machine (d). Whole corneal sample for inflation test (e) and linking of the artificial chamber to the pressure transmitter and peristaltic pump (f).

B. Experimental Set up – Tensile test

All the measurements were performed at the Biomomentum Mach-1 v500csst Machine (linear motion resolution 0.5 um, max acceleration 500 mm/s², single-axis load cell up to 250 N, resolution 12.5 mN) (Fig. 1d).

20 samples were used tensile tests and divided as follows: 7 samples for failure, 5 for cyclic and 8 samples for stress-relaxation tests. The corneal samples were cut into strips (Fig. 1b), ancored to the grips (Fig. 1c) and then preconditioned by the application of 10 loading-unloading cycles imposing a sinusoidal displacement to the tensile machine. The strain reached a maximum of 8%, the frequency was fixed at 0.5 Hz. Then, the samples were submitted to failure tensile tests by applying a progressive strain at a constant strain rate of 1%/s or 0.1 %/s and stopped when a null force was visualized at user interface.

The cyclic test consisted of two sets of three consecutive loading-unloading cycles with different strain rates, 1%/s and 10%/s. Between the sets, a pause of 360 s was imposed.

Also, stress relaxation test was performed and the protocol was composed by four steps of 8% of axial deformation (up to 32%), and a relaxation time of 400 s was waited at the end of each step to permitt the almost complete development of the relaxation phenomena. During tests, saline solution hydrated the surface's sample to prevent tissue dryness.

C. Experimental Set-up – Inflation test

The experimental equipment consisted of a peristaltic pump (VerderFlex Vantage 5000, Verder Ltd, UK), a Verdeprene 3.8mm-diameter tube, a pressure transmitter (range 0-200 mbar, current output, 0.5% precision, Trafag), a National Instruments chassis (NI cDAQ-9189 CompactDAQ), a current input NI module (NI-9253, 8-Ch, +/- 20 mA, 50kS/s/ch, 24-Bit filtered C Series), a laptop pc with installed LabView 2022. A specific LabView code was designed to collect the pressure data and control the pump. 18 corneas were used for inflation test and were split in two groups: 9 tested fresh and 9 stored in the freezer and tested the day after. The lens and iris were removed, while a part of sclera was retained to fix the specimen during the test (Fig. 1e). An *ad hoc* anterior artificial chamber was designed and printed in PA-GF blends polyamide powder and glass beads by Materialize to avoid the pressure leakages that were verified with standard anterior artificial chamber due to a bad grip. The cornea was gripped to the anterior chamber thanks to a gasket and a rubber band and connected both to the pressure transmitter and to the tube of the pump (Fig. 1f).

The protocol on the inflation test consisted in inflating three or four doses in order not to damage the pressure transmitter. Between doses, a relaxation time of 10 minutes was waited to permit the almost complete achievement of the equilibrium.

The equilibrium points after each dose were considered to obtain the pressure-volume curve at the equilibrium, while the relaxation parts of the curve were normalized and processed with a two-branches Prony model to get the viscous parameters (Tab. I).

TABLE I:
MEAN VISCOUS PARAMETERS

Test	*First Viscous Branch*	*Second Viscous Branch*
Inflation relaxation test	$p^{norm} = 1 - \sum_{i=1}^{2} \gamma^i \left(1 - \exp\left[-\frac{t}{\tau^i}\right]\right)$	
Frozen corneas	$\gamma_1 = 0.1555$ $\tau_1 = 28.31$ s	$\gamma_2 = 0.39$ $\tau_2 = 344.90$ s
Fresh corneas	$\gamma_1 = 0.12$ $\tau_1 = 20.12$ s	$\gamma_2 = 0.43$ $\tau_2 = 287.25$ s

D. Computational Analysis

A first preliminary computational model of the cornea was developed in Abaqus/CAE 2022 (Dassault Systémes Simulia Corp., Providence, RI) to simulate the inflation test and validate the constitutive models. The geometry comprehended a hollow spherical cap considering the application of 40° inclined supports at the marginal nodes of the cornea [11]. The thickness was not uniform: the central thickness of 0.833 mm, the side thickness of 1.033 mm, the front and rear base diameters of 13.81 mm and 12.228 mm respectively, the total

height of 2.4 mm [12]. A first-degree hyperelastic Ogden model was chosen for the corneal tissues and defined by inserting the stress relaxation data at equilibrium as Test Data. The evaluation of the material resulted stable for all strains. A fluid cavity pressure was defined, and a pressure ramp imposed.

III. Results

Results showed the nonlinear and time-dependent behavior of the cornea.

A. *Failure test*

In the failure test, no statistical difference was recorded by considering the two strain rates, hence for the elaboration of the results the data were considered as a single dataset. The slope of the curve changes for almost all specimens after a strain of 40 %, before the effective failure. Two Young's moduli were calculated to quantify the stiffness of the corneal tissues, at the initial portion of the curve, approximately up to a strain of 5 %, and at the central linear portion of the curve, ranging from 15 and 40 % of strain. The median moduli were 0.33 (±0.074) and 2.15 (±0.587) MPa. The failure was in average reached at a strain of 0.79 (± 0.14) %, relative to a stress of 1.274 (± 0.368) MPa.

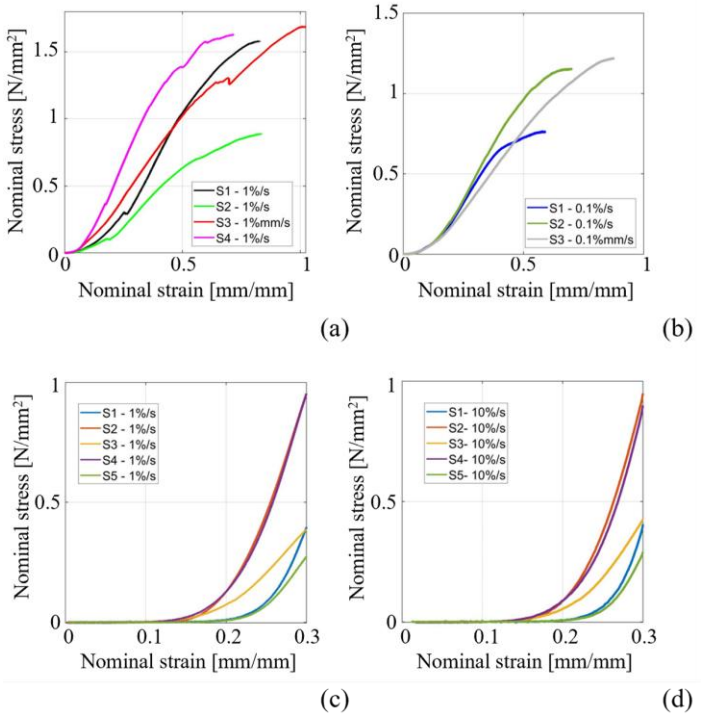


Fig. 2: Results of the failure test performed on 7 samples at 1%/s (a) and 0.1%/s strain rates (b). Results of the third loading ramp of the cyclic test for the 5 samples, at 1%/s (d) and 10%/s (e) strain rates.

B. *Cyclic test*

In the cyclic tests, the first cycle showed the highest hysteresis, while the others almost overlapped. To compare the action of the velocities, only the loading curve of the last cycle was considered in Figure 2 (c and d).

C. *Stress- and pressure- relaxation*

The results related to the stress- and pressure relaxation test for tensile and inflation test are proposed in Figure 3. The data are proposed in terms of equilibrium behavior, normalized stress and pressure over time.

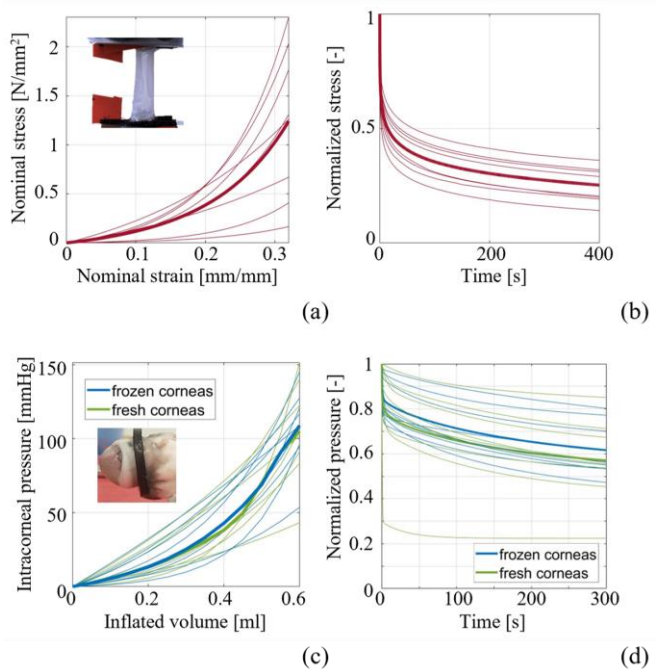


Fig. 3: Results of stress (a and b) and pressure- (c and d) relaxation after tensile and inflation test, in terms of equilibrium behaviour (a and c) and normalized relaxation over time (b and d). The ticker lines are the means, while the others the results of each sample.

IV. Discussion

The values resulting from the failure tests differed from those reported in the literature by Boschetti et al., which presented a significantly lower average failure strain (0.192 compared to 0.794) and a higher average failure stress (4.763 MPa compared to 1.274 MPa) [13], while much agreement was found by comparing the results to Tonsomboon's ones [14]. These failure tests assured the application of the stress relaxation protocol adopted in this work, ensuring that the tissue behaved smoothly at a strain of 32%.

The cyclic test results revealed the almost independence in the mechanical response from the strain velocity, confirmed by studies in literature [14], [15]. In fact, only a significant increase in stiffness at low strain rates, specifically going from 0.01 to 0.42 %/s, was recorded, while the effects of successive increases in strain rate were found to be statistically insignificant.

Figure 3 reported all the curves of the tested samples (thin lines) and the mean curves (thick lines). The results showed the high variability that characterized biological tissues, especially in relaxation over time graph. The results obtained from the computational model are reported in Figure 4. The good agreement between experimental and computational results revealed the reliability of the model in describing the inflation test.

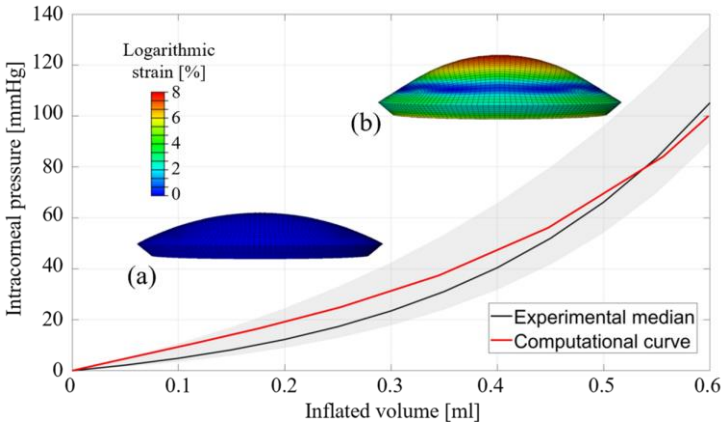


Fig. 4: Comparison between experimental (grey band) and computational (red curve) pressure-volume response for inflation test. The results must be intended at the equilibrium, after the almost complete relaxation of the tissue. Contours of the distribution of the logarithmic strain of the cornea at the beginning of the simulation (a) and 0.6ml of inflated volume (b).

V. Conclusions

The use of porcine corneas in mechanical property studies as an approximate model of human corneas is mainly due to the difficulty of obtaining in large quantities of corneas from human donors [16]. Both porcine and human corneas are characterized by a marked anisotropy and a nonlinear stress-strain relationship, and they exhibit a similar mechanical response to both short and prolonged loads. However, uniaxial tensile and inflation tests have shown a more pronounced viscoelasticity in the case of porcine corneas, putting more emphasis on the bilinear behavior of the tissue, and a lower overall stiffness than in human corneal samples [13]. The anisotropy of the tissues is, in this case, neglected because the low number of samples, preferring to propose different and independent mechanical tests.

The results presented in this work highlighted the time-dependency of the mechanical response of the corneal tissues, delineating the behavior of healthy porcine samples, at a sub-structural (uniaxial tensile test) and structural level (inflation test), at high level of deformation, which lacked in literature.

In future, further tests will be carried out to populate the limited number of samples and to analyze the corneal anisotropy. Furthermore, tests on corneas preserved in culture, treated with plasma or cross-linking and alkali-lesioned corneas will be included to analyze the influence of corneal modification on the tissue mechanical behavior.

Acknowledgements

This work was supported by MIUR, FISR 2019, Project n° FISR2019_03221, titled CECOMES: CEntro di studi sperimentali e COmputazionali per la ModElliStica applicata alla chirurgia

A special thanks to the master thesis students, Matteo Segato, Dario Zuin and Andrea Russo, for the help in acquiring the experimental data and post-processing.

References

[1] F. Boschetti, V. Triacca, L. Spinelli, and A. Pandolfi, “Mechanical characterization of porcine corneas,” *J. Biomech. Eng.*, vol. 134, pp. 1–9, 2012.

[2] M. Arsalan Khan, A. Elsheikh, and I. Ahmad Khan, “Biomechanical behaviour - Anisotropy of eye cornea through experimental strip tests,” *IOP Conf. Ser. Mater. Sci. Eng.*, vol. 310, 2018.

[3] S. Kling, L. Remon, A. Pérez-Escudero, J. Merayo-Lloves, and S. Marcos, “Corneal biomechanical changes after collagen cross-linking from porcine eye inflation experiments,” *Investig. Ophthalmol. Vis. Sci.*, vol. 51, pp. 3961–3968, 2010.

[4] S. Matteoli, A. Virga, I. Paladini, R. Mencucci, and A. Corvi, “Investigation into the elastic properties of ex vivo porcine corneas subjected to inflation test after cross-linking treatment,” *J. Appl. Biomater. Funct. Mater.*, vol. 14, pp. e163–e170, 2016.

[5] C. Whitford, A. Joda, S. Jones, F. Bao, P. Rama, et a., “Ex vivo testing of intact eye globes under inflation conditions to determine regional variation of mechanical stiffness,” *Eye Vis.*, vol. 3, pp. 1–12, 2016.

[6] G. Wollensak, E. Spoerl, and T. Seiler, “Stress-strain measurements of human and porcine corneas after riboflavin-ultraviolet-A-induced cross-linking,” *J. Cataract Refract. Surg.*, vol. 29, pp. 1780–1785, 2003.

[7] A. Elsheikh and K. Anderson, “Comparative study of corneal strip extensometry and inflation tests,” *J. R. Soc. Interface*, vol. 2, pp. 177–185, 2005.

[8] C. G. Fontanella , E. L. Carniel, L. Corain, A. Peruffo, I. Iacopetti, et al., “Mechanical behaviour of healthy versus alkali-lesioned corneas by a porcine organ culture model,” *BMC Vet. Res.*, vol. 17, pp. 1–14, 2021.

[9] B. J. Blackburn, M. W. Jenkins, A. M. Rollins, and W. J. Dupps, “A review of structural and biomechanical changes in the cornea in aging, disease, and photochemical crosslinking,” *Front. Bioeng. Biotechnol.*, vol. 7, 2019.

[10] G. Scarcelli, S. Kling, E. Quijano, R. Pineda, S. Marcos, et al., “Brillouin microscopy of collagen crosslinking: Noncontact depth-dependent analysis of corneal elastic modulus,” *Investig. Ophthalmol. Vis. Sci.*, vol. 54, pp. 1418–1425, 2013.

[11] K. Anderson, A. El-Sheikh, and T. Newson, “Application of structural analysis to the mechanical behaviour of the cornea,” *J. R. Soc. Interface*, vol. 1, pp. 3–15, 2004.

[12] J. Heichel, F. Wilhelm, K. S. Kunert, and T. Hammer, “Topographic Findings of the Porcine Cornea.,” *Med. hypothesis, Discov. Innov. Ophthalmol. J.*, vol. 5, pp. 125–131, 2016.

[13] F. Boschetti, V. Triacca, L. Spinelli, and A. Pandolfi, “Mechanical characterization of porcine corneas,” *J. Biomech. Eng.*, vol. 134, 2012.

[14] K. Tonsomboon, C. T. Koh, and M. L. Oyen, “Time-dependent fracture toughness of cornea,” *J. Mech. Behav. Biomed. Mater.*, vol. 34, pp. 116–123, 2014.

[15] A. Elsheikh, W. Kassem, and S. W. Jones, “Strain-rate sensitivity of porcine and ovine corneas,” *Acta Bioeng. Biomech.*, vol. 13, pp. 25–36, 2011.

[16] A. Elsheikh, D. Alhasso, and P. Rama, “Assessment of the epithelium’s contribution to corneal biomechanics,” *Exp. Eye Res.*, vol. 86, pp. 445–451, 2008.

Numerical Analysis of the Bicaval Transcatheter System for the Treatment of Severe Tricuspid Regurgitation

F. Crasci[1,3], S. Cannata[2], C. Gandolfo[2], and S. Pasta[1,3]
[1]*Dipartimento di Ingegneria, viale delle Scienze Ed.8, University of Palermo, Italy*
[2]*Interventional Cardiology Unit, IRCCS ISMETT via Tricomi, 5, Italy*
[3]*Department of Research, IRCCS ISMETT via Tricomi, 5, Italy*

***Abstract*— Tricuspid regurgitation (TR), also called tricuspid insufficiency, is a relatively common valvular diseases that can result from structural abnormalities of any anatomic part of the tricuspid valve apparatus. While trivial and moderate TR are compensated by the right atrial compliance, severe regurgitation conditions can result in congestive heart failure and hemodynamic impairment. We aim to model the non-invasive caval implantation treatment of TR seen in one patient using the novel bicaval transcatheter system (TricValve). Geometric models of TricValve devices were obtained from manufacturing guidelines and photography of devices. Then, the TricValve was simulated in a patient-specific model to assess the device structural performance. Computational fluid dynamics was also used to evaluate the pre- and post-TricValve haemodynamic. Ultimately, this study has the potential to better understanding the biomechanical performance of the novel TricValve system and may improve the way we design the next-generation of transcatheter therapies for severe TR.**

***Keywords*—finite-element analysis, computational fluid dynamic, transcatheter bicaval valves, tricuspid valve**

I. Introduction

Tricuspid regurgitation (TR) is a type of heart valve disease in which the valve between right ventricle and right atrium does not close properly [1]. As a result, blood leaks backward into the right atrium, ultimately increasing atrial pressure and leading to heart dilatation. Blood flowing back into the right atrium increases blood volume within the right atrium and results in a decrease in the proportion of blood pumped into the heart and to the body. Consequentially, the right atrium thickness and blood pressure increases in the right atrium and the large veins that flow into it. If the atrium is extremely dilated, the heartbeat becomes accelerated and irregular (resulting in what is known as atrial fibrillation), leading to a reduction in the heart's ability to pump, as the atrium in fibrillation trembles instead of pumping [2].

No major hemodynamic disturbances occur for trivial and moderate TR since the increase in blood pressure is compensated by the compliant nature of the right atrium. In case of severe TR, the haemodynamic impairment can lead to in right-sided congestive heart failure and thus fatal events. The incidence of TR is to be 0.9% in United States [3]. However, the medical management of patients with severe TR lead to a 5-year mortality rate as high as 50% [3]. The optimal timing of surgical repair or replacement of the TV still remains an open challenge.

II. Transcatheter Bicaval Valves

The development of non-invasive therapeutic strategies of the replacement of the TR has gained a remarkable attention.

Edge-to-edge tricuspid valve repair with the TriClip device (Abbott Cardiovascular, Plymouth, MN, USA), the PASCAL Repair system (Edwards Lifesciences, Irvine, CA, USA) have been developed to repair the regurgitant tricuspid valve [4]. Among tricuspid valve replacement, the first clinical applications were based on the utilize of devices not specifically designed for the tricuspid valve anatomy. For the first time, in 2011, transcatheter valve-in-valve was carried out to replace the tricuspid valve as an “off-label” application of the SAPIEN 3 devices (Edwards Lifesciences, Irvine, CA, USA) [5]. Later, a clinical study demonstrated the feasibility of this procedure [6]. The first use of a device specifically designed for the tricuspid valve anatomy was reported in 2020 using the self-expanding EVOQUE tricuspid valve replacement system [7].

Outside the implantation of devices in the diseased tricuspid valve, the TR can be indirectly treated by caval valve implantation using device implanted in the caval anatomy to alleviate congestive signs of heart failure and the hemodynamic impairment [8]. To perform caval valve implantation, the transcatheter bicaval system (TricValve) is the first type clinically-used device to treat TR by reducing caval pressure and improve the functional status at the 8-week follow-up [9, 10]. The TricValve does not substitute the tricuspid valve but it is composed of two valves, one implanted in the superior vena cava (SVC) and the other one in the inferior vena cava (IVC). The TricValve system is composed of self-expanding devices made of bovine pericardial tissue mounted on nitinol stents. The SVC valve has a long skirt designed to minimize paravalvular leakage, while the IVC valve has a short skirt to prevent occlusion of the hepatic vein flow. Device placement prevents regurgitant flow in the IVC and SVC, reducing liver congestion, increasing right ventricle stroke volume into the pulmonary system and improving cardiac output. Since the system does not alter the native tricuspid valve anatomy, the procedure allows for all future tricuspid valve surgical and procedural options, including transcatheter edge-to-edge repair, transcatheter tricuspid valve repair and transseptal puncture. Currently, the TricValve is the only caval implantation device with CE mark approval

obtained in May 2021.

The aim of the study is to carry out a computational analysis of the structural and hemodynamic performance of the TricValve system in patient-specific model. After developing the geometrical models of TricValve, the deployment was simulated to quantify the contact pressure exerted on the caval wall. A computational fluid dynamic study of the pre-TricValve scenario and the short-term follow-up period was also carried out.

III. Materials and Methods

A. Patient Study Case

The case of a 72-yrs old gentlemen with severe TR and sings of heart failure was investigated. The patient had a past history of both aortic and mitral valve repairs as well as pacemaker implantation in the right heart side. Conventional surgery was highly contraindicated.

Using the Materialise Mimics (v21.0; Materialise, Leuven, Belgium) and Rhinoceros 7 (McNeel & Associates, Seattle, WA, USA) software, a 3D model was created from the patient's computed tomography (CT) images [11]. The patient IVC and SVC and right atrium were segmented using semi-automatic segmentation followed by manual editing and smoothing of the anatomic mask. Using the Ansys ICEM program (v2021 Ansys Inc, Canonsburg, PA, USA), the patient geometry was then meshed with triangular shell element (S3) and uniform thickness of 1.5 mm. Given the lack of material parameters, we used an incompressible Neo-Hookean model with C1=0.6 MPa and D=0.074 MPa^{-1} for the vena cava wall [12].

B. TricValve Models

TricValve system are made of nitinol structure with leaflets made of the bovine pericardium. In the absence of device demo, the device geometries were obtained using photographic images acquired prior the clinical procedure. Dimensions from manufacturer manual were integrated for device modeling.

Using Grasshopper application, the model of the two valves was developed from a single wire replicated in polar series and then wrapped on a primitive surface. Specifically, the stent wire was generated from a spline curves interpolating several point representing the stent wire curvature. A rectangular cross section (0.300 x 0.135 mm) was used and then the stent wire was modeled with a surface in the unfolded configuration. After replicas and polar series, the IVC-related device was composed of six cells in the longitudinal direction and sixteen cells in the circumferential direction. The SVC-related device was modeled with seven cells in the longitudinal direction and eighteen cells in the circumferential direction. The unfolded device geometry was then wrapped on the primitive surface shape with varying diameter along the device axis to obtain the final TricValve geometry. The devices were then positioned in the patient vena cava anatomy with the support of CT images.

Both SVC and IVC devices were meshed with size 0.5 mm resulting in 149939 and 167729 hexahedral-structured elements, respectively (C3D8). The constitutive model proposed by Auricchio et al. [13] was used to simulate the biomechanical response of TricValve nitinol material. A Rayleigh damping of 200 was adopted to regulate the dynamic material response while a density of 6590 kg/m^3 was adopted.

C. Finite-Element Analysis

The simulation consisted of a) delivering both the IVC and SVC devices in the human host, followed by an elastic recoil, b) computational fluid dynamic analysis of post-TricValve deployment.

The crimping phase (0.5 s) was carried out using a cylindrical surface gradually moved along the radial direction (displacement of 18 mm) as done previously in similar studies. Frictionless contact conditions were used to model contact between devices and crimper. Once the device are crimped, a sleeve is moved along the device longitudinal axis to gradually deploy the device in the human host. A penalty formulation with factor of 0.1 and tangential behavior conditions were defined among parts in contact during the deployment phase (0.5 s). For boundary conditions, the distal ends of the patient model were fixed in all directions. After elastic recoil (0.1 s), the skirt and device leaflets were mapped in the deformed TricValve frame.

D. Computational Fluid Dynamic

The pre- and post-TricValve hemodynamic were investigated using Ansys Fluent code (v2021 Ansys Inc, Canonsburg, PA, USA). The fluid domain was meshed with unstructured tetrahedral elements with size of 0.5 mm. Laminar flow condition and non-Newtonian viscosity as modeled with the Carreau model were adopted as done in previous studies [14]. As boundary conditions, we imposed flow velocity profile at hepatic veins, IVC and SVC using literature data [15]. Specifically, the total inflow of 6 L/min was split among inlets with division proportional to each inlet area [16, 17]. For the outlet, the pressure waveform was obtained transforming and scaling the velocity profile to match the Cath-lab pressure of 27 mmHg. The so-obtained pressure waveform was imposed at tricuspid valve. As the leaflets of TricValve system are closed during systole, for the, the flow velocity and pressure were set to null values to mimic the systolic phase of post-TricValve hemodynamic.

IV. Results

Fig. 1 shows several steps of the crimping and deployment of the SVC device in the human host. The device is implanted in position in the IVC wall with device belly at the level of the innominate vein and without obstruction of the branch ostium. This reduces the risk of device migration induced by the oscillatory flow forces exerted on the device stent frame during the cardiac cycle.

Figure 2 shows the comparison of deformed shape of SVC device with the post-TricValve CT image. A good qualitative agreement between predicted and CT images can be observed.

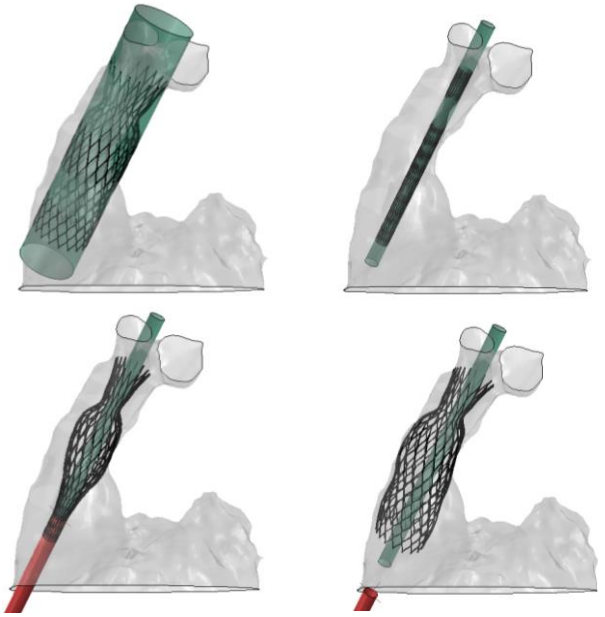


Figure 1. SVC simulation of crimping and release phases

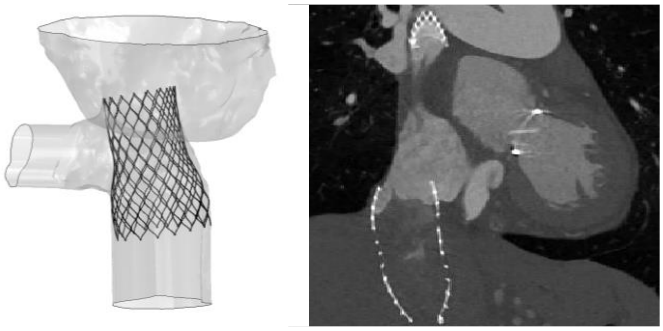


Figure 2. Comparison between the SVC-related TricValve and post-TricValve CT imaging.

Figure 3 shows the map of contact pressure for both the IVC and SVC part.

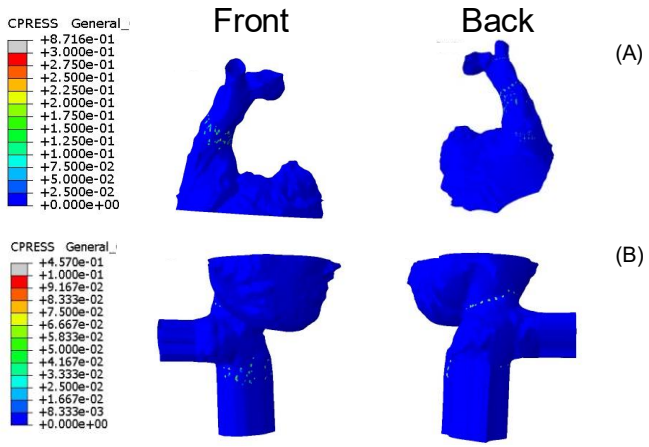


Figure 3. Map of contact pressure for both (A) SVC and (B) IVC devices.

Figure 4 shows the velocity distribution at a crosse section of patient model for both pre- and post-TricValve flow analysis. We found high velocities magnitude at the two systolic peaks rather than the diastole. During diastole (0.44 s), when the valve leaflets of both SVC and IVC devices are closed, the velocity drastically reduces as compared to that of pre-procedural scenario.

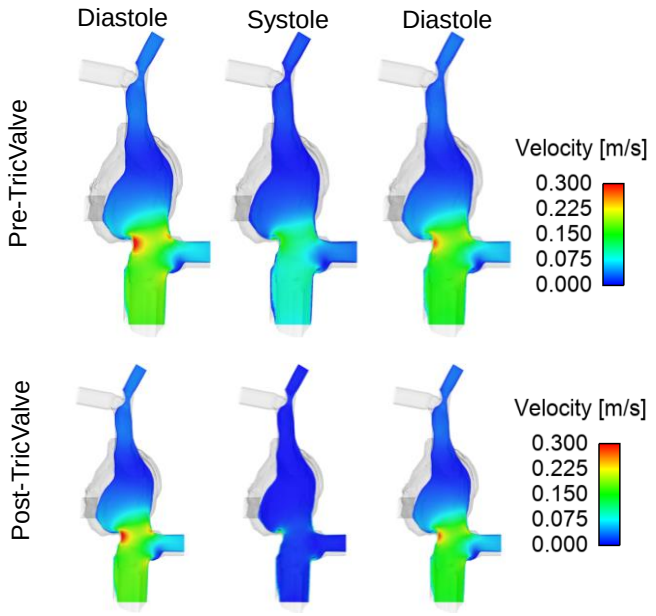


Fig. 4 Velocity map distribution for both pre- and post-TricValve during first diastolic peak, trough systole and then second diastolic peak

V. Discussion

To the best of our knowledge, this is first study describing the biomechanical performance of the new TricValve system to treat severe TR. The TricValve system deployment in the patient-specific anatomy was analyzed using both structural and flow simulation. The most striking findings are the contact pressure as indicator of the risk of stent frame migration and the low flow velocity alleviating the hemodynamic impairment during diastole. This study may provide new insight in the pre-procedural planning of TricValve implantation in the context of a complex clinical conditions.

In transcatheter aortic valve implantation, structural simulations of transcatheter heart valves have been proposed to understand the optimal device size, implantation depth and risk of annulus rupture [18-24]. Analysis of intramural stress at annulus may be used to assess the risk of aortic valve rupture [25]. Different studies have reported the distribution of contact pressure between the device and aortic wall as indicator of device anchorage [25, 26]. Using contact pressure, in the superior vena cava, the resulting device forces were found high in the region in contact between the wall vein and the device belly. The SVC device of TricValve system is designed with a belly in the upper frame region to reduce the risk of obstruction of flow circulating in the innominate vein. The device skirt is below the ostia of innominate vein so that migration into the right atrium may occur if not enough contact pressure are generated. On the other hand, in the inferior vena cava, the contact pressure was found high in the bottom region of the IVC device because of the pronounced area of the device in contact with the vena caval wall. This is because the inferior region of the prosthesis has highest radial force and larger

diameter than the upper region. The upper portion of the IVC-device is implanted in the right atrium as the bird-beak seen in thoracic endograft [27].

The computational flow analysis has allowed us to quantify the flow velocity during the cardiac beating. It should be however noted that the TricValve system ameliorates the right atrial blood pressure after 8-week from the implant. Therefore, the beneficial effect of the device deployment cannot be seen in our computational studies. We speculate that the low flow velocity seen in diastole may allow to outflow the cardiac flow in a larger time period with respect to the pre-TricValve hemodynamic conditions. This may reduce the hemodynamic impairment with the left heart and then the pressure into the right atrium, thereby portending remodeling of the right atrial chamber.

There are several limitations in this study. The material properties of the inferior and superior vena cava were from *ex-vivo* data on animal model because of the lack in human material characterization. In the post-TricValve flow analysis, the motion of the device leaflets was not considered. Fluid-solid interaction analysis are therefore recommended.

VI. Conclusion

This study can bring new insights on the biomechanics of the TricValve system to better understand device positioning and flow hemodynamic. Findings may also used to improve the design of novel transcatheter heart valve for the treatment of severe TR in the context of complex clinical conditions

Acknowledgement

Fabrizio Crascì thanks the IRCCS ISMETT and the PNRR for supporting his research.

References

[1] Kadri AN, *et al*. Outcomes of patients with severe tricuspid regurgitation and congestive heart failure. *Heart* 2019; 105(23): 1813-17.
[2] Dahou A, *et al*. Anatomy and Physiology of the Tricuspid Valve. *Jacc-Cardiovasc Imag* 2019; 12(3): 458-68.
[3] Fender EA, *et al.* Prognostic Importance and Predictors of Survival in Isolated Tricuspid Regurgitation: A Growing Problem. *Mayo Clinic proceedings* 2019; 94(10): 2032-39.
[4] Romeo JD, *et al*. Current Status of Transcatheter Tricuspid Valve Therapies. *Heart Int* 2022; 16(1): 49-58.
[5] Van Garsse LAFM, *et al.* Percutaneous Transcatheter Valve-in-Valve Implantation in Stenosed Tricuspid Valve Bioprosthesis. *Circulation* 2011; 123(5): E219-E21.
[6] McElhinney DB, *et al.* Transcatheter Tricuspid Valve-in-Valve Implantation for the Treatment of Dysfunctional Surgical Bioprosthetic Valves An International, Multicenter Registry Study. *Circulation* 2016; 133(16): 1582-+.
[7] Fam NP, *et al.* Transfemoral Transcatheter Tricuspid Valve Replacement. *Jacc-Cardiovasc Inte* 2020; 13(10): E92-E93.
[8] Altisent OAJ, *et al.* Caval Valve Implantation (CAVI): An Emerging Therapy for Treating Severe Tricuspid Regurgitation. *Journal of clinical medicine* 2021; 10(19).
[9] Lauten A, *et al.* Interventional Perspective of Tricuspid Regurgitation - Caval Valve Implantation from Preclinical Trials to First Human Application. *Journal of the American College of Cardiology* 2012; 59(13): E2046-E46.
[10] Lauten A, *et al*. Percutaneous caval stent valve implantation: investigation of an interventional approach for treatment of tricuspid regurgitation. *Eur Heart J* 2010; 31(10): 1274-81.
[11] D'Ancona G, *et al.* Haemodynamic predictors of a penetrating atherosclerotic ulcer rupture using fluid-structure interaction analysis. *Interactive cardiovascular and thoracic surgery* 2013; 17(3): 576-8.
[12] Di Giuseppe M, *et al.* Identification of circumferential regional heterogeneity of ascending thoracic aneurysmal aorta by biaxial mechanical testing. *J Mol Cell Cardiol* 2019; 130: 205-15.
[13] Auricchio F, *et al.* Patient-specific aortic endografting simulation: from diagnosis to prediction. *Computers in biology and medicine* 2013; 43(4): 386-94.
[14] Rinaudo A, *et al.* Biomechanical implications of excessive endograft protrusion into the aortic arch after thoracic endovascular repair. *Computers in biology and medicine* 2015; 66: 235-41.
[15] de Oliveira DC, *et al.* Computational fluid dynamics of the right atrium: Assessment of modelling criteria for the evaluation of dialysis catheters. *Plos One* 2021; 16(2).
[16] Scardulla F, *et al*. Shear stress alterations in the celiac trunk of patients with a continuous-flow left ventricular assist device as shown by in-silico and in-vitro flow analyses. *J Heart Lung Transplant* 2017; 36(8): 906-13.
[17] Pasta S, *et al*. Shear Stress and Aortic Strain Associations With Biomarkers of Ascending Thoracic Aortic Aneurysm. *Annals of Thoracic Surgery* 2020; 110(5): 1595-604.
[18] Pasta S, *et al.* Simulation of left ventricular outflow tract (LVOT) obstruction in transcatheter mitral valve-in-ring replacement. *Med Eng Phys* 2020; 82: 40-48.
[19] Pasta S, *et al.* Transcatheter Heart Valve Implantation in Bicuspid Patients with Self-Expanding Device. *Bioengineering* 2021; 8(7): 91.
[20] Pasta S, *et al.* Simulation study of transcatheter heart valve implantation in patients with stenotic bicuspid aortic valve. *Med Biol Eng Comput* 2020.
[21] Pasta S, *et al.* Numerical simulation of transcatheter mitral valve replacement: The dynamic implication of LVOT obstruction in the valve-in-ring case. *Journal of Biomechanics* 2022; 144.
[22] Pasta S, *et al.* Computational Analysis of Self-Expanding and Balloon-Expandable Transcatheter Heart Valves. *Biomechanics* 2021; 1(1): 43-52.
[23] Morganti S, *et al.* Prediction of patient-specific post-operative outcomes of TAVI procedure: The impact of the positioning strategy on valve performance. *J Biomech* 2016; 49(12): 2513-9.
[24] Morganti S, *et al.* Simulation of transcatheter aortic valve implantation through patient-specific finite element analysis: Two clinical cases. *Journal of Biomechanics* 2014; 47(11): 2547-55.
[25] Luraghi G, *et al*. The impact of calcification patterns in transcatheter aortic valve performance: a fluid-structure interaction analysis. *Computer methods in biomechanics and biomedical engineering* 2020: 1-9.
[26] Finotello A, *et al.* Finite element analysis of transcatheter aortic valve implantation: Insights on the modelling of self-expandable devices. *Journal of the mechanical behavior of biomedical materials* 2021; 123: 104772.
[27] Pasta S, *et al*. An In Vitro Phantom Study on the Role of the Bird-Beak Configuration in Endograft Infolding in the Aortic Arch. *Journal of Endovascular Therapy* 2016; 23(1): 172-81.

Assessment of a parametric thoracic spine model for the generation of *in silico* cohorts

A. Perego[1], A. Pezzinga[1], E. Bellina[1], and L. La Barbera[1,2]
[1] *Laboratory of Biological Structure Mechanics, Dept. Chemistry, Materials and Chemical Engineering, Politecnico di Milano, Italy*
[2] *IRCCS Istituto Ortopedico Galeazzi*

***Abstract*— *In silico* digital twins of spine segments are a valuable technology with the potential to generate biomechanically relevant information, not always obtainable with expensive *in vitro* measurements and invasive *in vivo* techniques. The present study introduces a novel strategy to generate a parametric CAD model of the thoraco-lumbar spine representative of the healthy adult population in standing posture. The CAD model requires few independent input parameters (VBHP, TK, LL, SS) to be completely defined. Regression equations obtained by fitting anatomical literature data were generate and implemented. The model was furtherly refined with the addition of the rib cage, modelled on the base of mean anatomical data inserted as inputs. To demonstrate the capability of the CAD model to be used for relevant biomechanical analyses, a representative thoracic functional spinal unit T6-T7-R7 functional unit was isolated and the material properties of each sub-structure (annulus fibrosus, nucleus pulposus, neural arch, facet joints, ligaments, ribs and sternum) were calibrated following a step-by-step backward stepwise reduction procedure.**

***Keywords*— Spine, biomechanics, finite element model, digital twin, calibration.**

I. Introduction

The human spine is a complex structure made up of interconnected hard and soft tissues, which contribute in supporting external loadings and maintaining the upright posture and sagittal human balance.

Spine pathophysiology is often studied using detailed patient-specific finite element models (FEMs) built using clinical diagnostic data (e.g. CTs, MRIs), which can be hardly generalized. Parametric spine models could be a more efficient strategy to generate whole cohorts of digital twins of patients with desired features and to virtually test *in silico* the biomechanical effects of a variety of treatment options.

Moreover, the potential of using digital twin technology to study any patient, to explore literally any clinical or virtual scenario and the potential for obtaining intrinsic quantities (stress and strain fields), which could never be assessed with traditional testing methods *in vitro* and *in vivo*, would be of fundamental aid in surgical planning and in basic spine biomechanics.

The goals of the present study were:

i) the development of a thoraco-lumbar parametric CAD model, comprehensive of ribs and sternum, based on regression equations allowing to predict a number of relevant morphometrical measurements starting from few input parameters only;

ii) the calibration of the mechanical properties of different soft and hard tissues materials of a representative thoracic functional spinal unit (T6-T7-R7) by comparison with published in vitro kinematic data (range of motion).

II. Materials and Methods

A. Regression equations + Parametric CAD model

Regression equations were built in order to compute 38 morphological quantities needed to describe the vertebral body (VB) and vertebral arch (VA) using the posterior height of the vertebral bodies (VBHP) as a single independent parameter. Mean anatomical data describing different dependent parameters were taken from Panjabi et al. [1, 2], plotted as a function of VBHP and then best-fitted with a third order polynomial regression functions [3]. The validity of these equations in predicting the 38 dependent parameters the coefficient of determination (R^2) and the Root Mean Square Error (RMSE) were quantified.

The parametric model of the thoraco-lumbar spine was created in Solidworks 2020 (SolidWorks Corporation, Waltham, MA, USA), where all parameters were defined as global variables and the regression equations were implemented.

Single parts representing each vertebra and the intervertebral disc (IVD) above, were drawn reducing each component in elementary geometrical parts. The vertebral body and the cranial disc, divided into annulus fibrosus and nucleus pulposus, were represented as cylindroids with elliptical section. The vertebral arch, the pedicles, the transverse processes and the articular processes were drawn as cylindroids with elliptical section; the spinous process was represented as a solid with rectangular section, whereas the laminae had rectangular section in the thoracic region and trapezoidal section in the lumbar one. The T1-T12 thoracic kyphosis (TK) and the L1-L5 lumbar lordosis (LL) were added as additional independent parameters describing the sagittal profile. At each level, a specific percentage of these angles, which defined the physiological curvatures, was assigned based on literature data. The single parts were then added to the same assembly and the sacral slope (SS) was used as an additional independent parameter to tilt the L5-S1 disc. The ribs and the sternum were modelled and all the needed geometrical quantities were set as global variables where the mean literature values were inserted. The ribs were represented as cylindroids with elliptical section, whereas the sternum was T-shaped and had a quadrilateral section (Fig. 1).

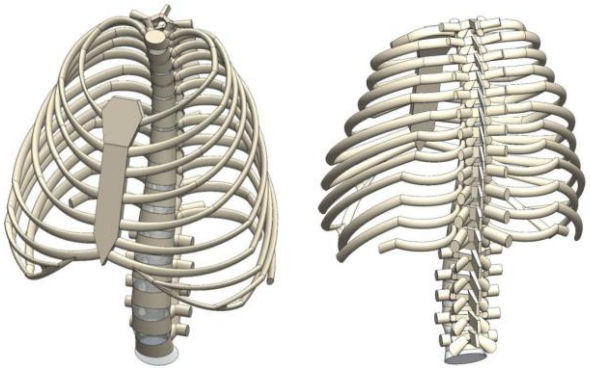


Fig. 1: Assembled thoraco-lumbar spine model: anterior (left) and posterior (right) views.

B. T6-T7-R7 FEM calibration

To demonstrate the feasibility of the presented approach to generate an average model ready to be used for FE analysis, average anatomical measurements were implemented for VBHP, TK, LL and SS, generating one representative average CAD model of a thoracic functional spinal unit.

The CAD model of T6-T7-R7, as a representative thoracic functional spinal unit (FSU) consisting of two vertebrae, the intermediate IVD and the rib, was imported from SolidWorks and assembled in Abaqus 2021 (Dassault Systemes, Simulia, Johnston, RI, USA). In particular, the cortical and the trabecular bone in the vertebral body were modelled using a transversally isotropic elastic constitutive model. The cartilage and the bone of the arch and of the rib, instead, were represented by an isotropic elastic model. For the annulus, the hyperelastic anisotropic formulation for the strain energy potential introduced by Holzapfel-Gasser-Ogden was used. The nucleus pulposus was considered hyperelastic isotropic following the Mooney-Rivlin model. Lastly, all the ligaments were represented as springs defined by their Stiffness (K). The parameters used for the calibration were taken from literature ranges, except for the costovertebral joint ligaments' stiffness where a single value, which was slightly arbitrarily modified to obtain a range, was found. The material parameters needed to define the constitutive equations of each hard and soft tissue were selected using a backward stepwise reduction strategy (Table I).

While the *in vitro* range of motion (RoM) of the FSU was evaluated following gradual resections of all the different structures of the FSU (ligaments, arch and nucleus), in the present study the *in silico* RoM was evaluated in a backward fashion quantifying at each step the biomechanical contribution that the addition of each spinal structure had on the kinematics of the FSU. The predicted *in silico* results, obtained under the same loading and reduction steps, were compared with the corresponding *in vitro* data. For the analysis on the FSU without ribs, the work by Wilke et al. [4] was considered, for the costovertebral joint the results by Lemosse et al. [5] was used, whereas for the intact T6-T7-R7 FSU including the sternum the data by Liebsch et al. [6] were used.

The CAD model was discretized assuming an average mesh size of1 mm (Fig. 2). Linear hexaedral elements were used for the vertebral bodies, the intervertebral disc, the endplates and the facet cartilage, while linear tetrahedral elements were used for the vertebral arch and the ribs, ligaments were modelled with non-linear spring elements.

TABLE I: Calibrated material constitutive parameters and mean error vs. kinematic *in vitro* data.

Material	*Constitutive parameters*	*Mean error (vs. experimental dispersion)*
Cortical bone	E_3=22 GPa, E_1=E_2= 11.3 GPa, G_{12}=3.8 GPa, G_{13}=G_{23}=5.4 GPa, ν_{12}=0.48, ν_{23}=ν_{13}=0.2	-
Trabecular bone	E_3=200 MPa, E_1=E_2= 140 MPa, G_{12}=48.3 MPa, G_{13}=G_{23}=48.3 MPa, ν_{12}=0.45, ν_{23}=ν_{13}=0.32	-
Endplates	E=26 MPa, ν_{13}=0.4	-
Annulus fibrosus (AF)	C_{10}=0.43MPa D=0.3MPa-1 k_1=1.08MPa k_2=11, k=0	20% (vs. 46%)
Nucleus (NUC)	C_{10}=0.64MPa C_{01}=0.09MPa D=0.022MPa-1	20% (vs. 62%)
Anterior longitudinal ligament (ALL)	K=61 N/mm	17% (vs. 58%)
Posterior longitudinal ligament (PLL)	K=25 N/mm	18% (vs. 70%)
Vertebral arch (VA)	E=6 GPa ν=0.25	19% (vs. 83%)
Facet joint capsules (FC)	E=4 GPa ν=0.25 K=45 N/mm	14% (vs. 81%)
Flaval ligament (FL)	K=25 N/mm	16% (vs. 84%)
Interspinous ligament (ISL)	K=8 N/mm	15% (vs. 87%)
Supraspinous ligament (SSL)	K=77 N/mm	12% (vs. 90%)
Rib (left)	E=6 GPa, ν =0.25	-
Costovertebral ligament (CVL)	K= 50 N/mm	41 % (vs. 60%)
Interosseous costotransverse ligament (ICT)	K= 60 N/mm	30% (vs. 51%)
Lateral costotransverse ligament (LCT)	K= 60 N/mm	26% (vs. 50%)
Superior costotransverse ligament (SCT)	K=40 N/mm	31% (vs. 40%)
Ribs (right)+Sternum	E=6 GPa, ν=0.25	-

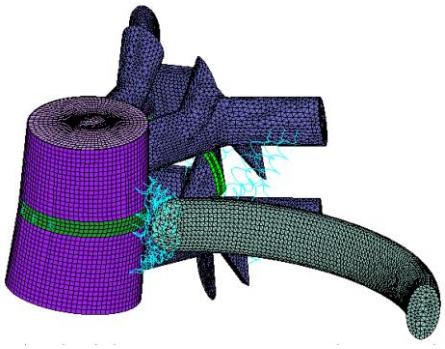


Fig. 2: Meshed T6-T7-R7 FSU including the first part of the left rib.

For the calibration of the FSU, the assembled unit, at each step comprehensive of the structures that were not resected in vitro only, was fixed in space by blocking all degrees of freedom on the bottom surface of the T7 vertebra. A bending moment of 1 Nm and 2.5 Nm was applied in flexion, extension, right lateral bending and left axial rotation on a reference point that was coupled with the upper surface of the T6 vertebra.

For the costovertebral joint calibration, instead, the boundary conditions limiting all the degrees of freedom were extended to the lower articular facets surfaces and to the previously described reference point. A local coordinate system was defined along or about which the loads were applied and the rotational displacements were evaluated in torsion, cranial/caudal and ventral/dorsal flexion. Two new reference points, which were coupled to a 10mm wide rib segment, were created for the loads' application according to Lemosse et al. [5]. Each of these loading conditions, replicating the ones implemented in the experimental set-ups, were simulated and the resulting rotational displacements were computed and compared with the expected values. The combination of parameters that provided the lowest mean total error, with respect to the in vitro data, was assigned to the material under analysis.

III. Results

A. *Regression equations + Parametric CAD model*

The relative error of the predicted values with respect to the anatomical measures (mean RMSE value: 8%) resulted always lower than the mean experimental dispersion (mean value: 20%). Fig.3 summarizes the predition error for all morphological parameters, by comparison with the average measurement error by Panjabi et al. [1, 2].

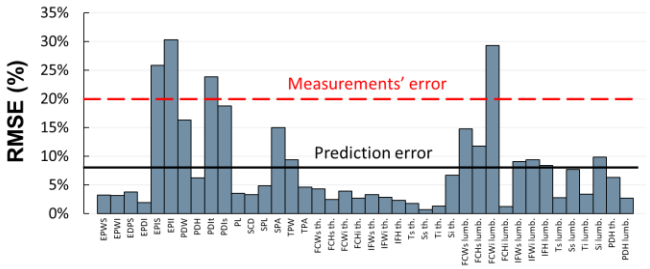


Fig. 4: RMSE of the prediction error for each anatomical parameters. The dashed line indicate the average measurements error on experimental data [1,2] .

B. *T6-T7-R7 FEM calibration*

At each calibration setp, the combination of material parameters minimizing the error or the difference vs. the experimental *in vitro* data was kept for each subsequent calibration step. Table I collects all the calibrated constitutive parameters and the mean final error obtained in all the performed calibration steps.

Each loading condition implemented in the referenced experimental set-ups [4, 5, 6] was replicated and the predicted RoM values were compared with the experimental data (Fig. 4, 5, 6).

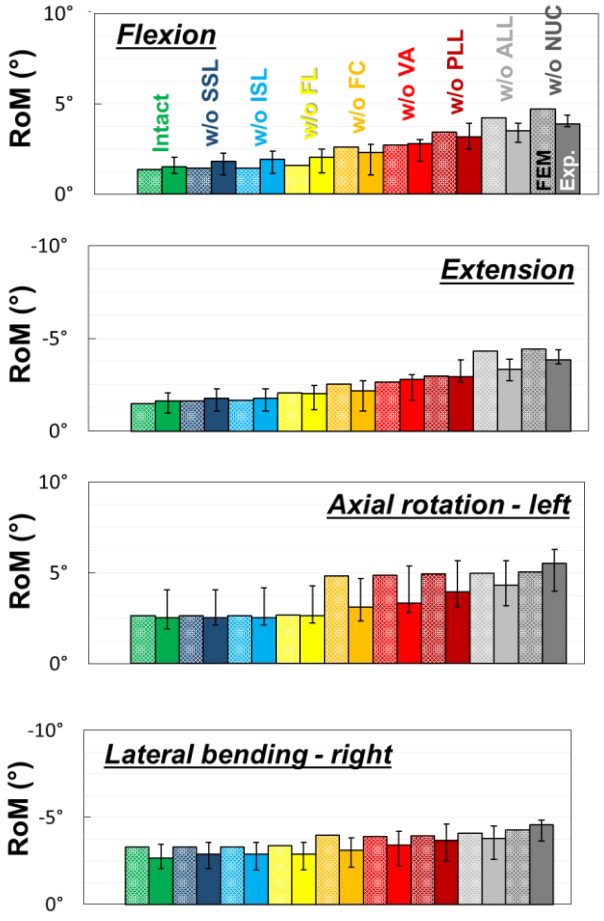


Fig. 4: RoMs comparison for the T6-T7 FSU during subsequent simulations (applied bending moment 2.5 Nm). For each colour, the left bar represents the *in silico* results (FEM), the right one the *in vitro* data (Exp.) [4].

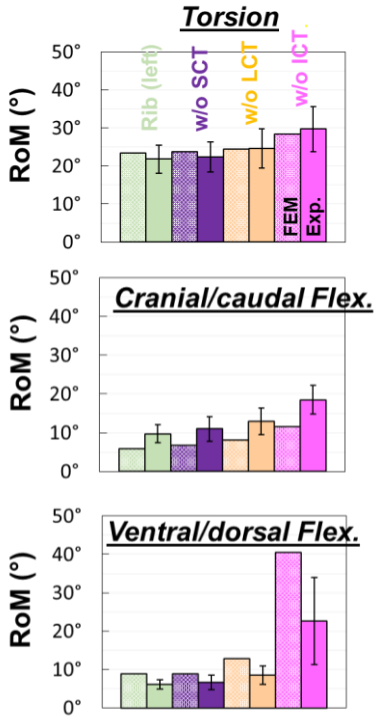


Fig. 5: RoMs comparison for the costovertebral joint (T6-T7-R7left) during subsequent simulations (applied bending moment 0.6 Nm). For each colour, the left bar represents the in silico results, the right one the in vitro data [5].

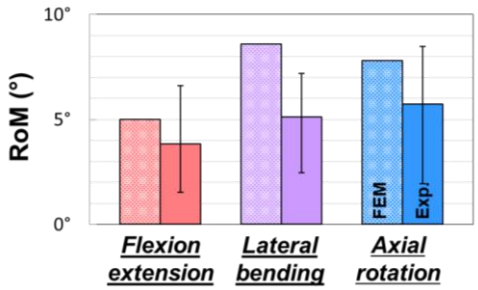


Fig. 6: RoMs comparison for the intact T6-T7-R7 FSU (applied bending moment 5 Nm). For each colour, the left bar represents the in silico results, the right one the in vitro data [6].

IV. Discussion

Several parametric models of the spine are already present in the literature, but the majority focus only on the lumbar segment. Models including the whole thoraco-lumbar spine, maybe including the rib cage, are mainly patient-specific or built based on CT or MRI diagnostic images.

The strength of the presented approach resides in the fact that by changing few independent parameters (1 per vertebra), like the posterior height of the vertebral bodies and the sagittal spinal curvatures (SS, LL and TK), the thoraco-lumbar CAD model can be easily updated to generate a variety of patients cohort. These parameters are easy to measure on traditional clinical images, therefore even an unexperienced user may generate patient-specific models within just few seconds. In the future, this model could be extended by including also the cervical region as well, by simply implementing regression equations specific for this spinal region.

During the calibration procedure it was observed that the model provided a good representation of the T6-T7 FSU kinematic behavior. During subsequent calibration steps, the mean error ranged from 12% to 20%, whereas the mean experimental dispersion ranged from 46% to 90%.

When calibrating the ribs, instead, the results were not as good, probably because no literature data on the ligaments' attachment points or stiffness ranges were found. Indeed, the mean error ranged from 26% to 41%, whereas the mean experimental dispersion ranged from 40% to 60%. When adding also both ribs nad the sternum the kinematic behavior of the intact T6-T7-R7 model was overall satisfactory, as it was always within one standard deviation of the experimental *in vitro* data. Therefore, besides capturing the general anatomical features of the spine, the model well replicated the kinematic behaviour of the FSU following different resection steps.

In the future, the whole thoraco-lumbar spine model could be fully calibrated also monitoring other relevant biomechanical data in more relevant functional loading conditions.

V. Conclusion

The developed parametric CAD model accurately describes the overall morphometric characteristics of an average healthy adult thoraco-lumbar spine. Furthermore, the material properties assigned to the representative thoracic FSU provide reliable kinematics data. Continuing with the calibration process, it could become useful for computing additional relevant biomechanical outputs and clinical values, such as intradiscal pressures, stress and strain fields on different FSU components with specific loading conditions.

Acknowledgement

This research was partially supported by MIUR FISR—FISR2019_03221 CECOMES.

References

[1] M. Panjabi, K. Takata, V. Goel, D. Federico, T. Oxland, J. Duranceau and M. Krag, "Thoracic human vertebrae. Quantitative three-dimensional anatomy," Spine, vol. 16, no. 8, pp. 888-901, 1991.

[2] M. Panjabi, V. Goel, T. Oxland, K. Takata, J. Duranceau, M. Krag and M. Price, "Human lumbar vertebrae. Quantitative three-dimensional anatomy," Spine, vol. 17, no. 3, pp. 299-306, 1992.

[3] M. Kunkel, H. Schmidt and H. Wilke, "Prediction equations for human thoracic and lumbar vertebral morphometry," J Anat., vol. 216, no. 3, pp. 320-328, 2010.

[4] H. Wilke, S. Grundler, C. Ottardi, C. Mathew, B. Schlager and C. Liebsch, "In vitro analysis of thoracic spinal motion segment flexibility during stepwise reduction of all functional structures," Eur Spine J., vol. 29, no. 1, pp. 179-185, 2020.

[5] D. Lemosse, O. Le Rue, A. Diop, W. Skalli, P. Marec and F. Lavaste, "Characterization of the Mechanical Behaviour Parameters of the Costo-Vertebral Joint," Eur Spine J, no. 18, pp. 16-23, 1998.

[6] C. Liebsch, R. Jonas and H. Wilke, "Thoracic spinal kinematics is affected by the grade of intervertebral disc degeneration, but not by the presence of the ribs: An in vitro study.," Spine J., vol. 20, no. 3, pp. 488-498, 2020.

Biomechanical characterization of human plantar fascia through experimental tests

S. Pettenuzzo[1], A. Berardo[1,2,3], E. Belluzzi[3,4], A. Pozzuoli[3,4], P. Ruggieri[3,4], E.L. Carniel[3,5] and C.G. Fontanella[3,5]

[1] *Department of Civil, Environmental and Architectural Engineering, University of Padova, Italy*
[2] *Department of Biomedical Sciences, University of Padova, Italy*
[3] *Centre for Mechanics of Biological Materials, University of Padova, Italy*
[4] *Orthopedics and Orthopedic Oncology, DiSCOG, University of Padova, Italy*
[5] *Department of Industrial Engineering, University of Padova, Italy*

***Abstract*—Plantar fascia is a complex structure, which stands between the calcaneus and the forefoot region of the foot. It plays a key role in foot biomechanics and its functionality can be compromised by different pathologies (*e.g.* plantar fasciitis). For these reasons, the aim of this study is the investigation of the plantar fascia's mechanical properties through experimental tensile tests.**

Mechanical tests have been performed on samples obtained from human plantar fascia considering different regions and directions. From failure tests, the ultimate tensile stress and the corresponding failure strain were obtained, while stress-relaxation tests were performed to compute the viscoelastic tissue parameters. Initial and final Young's moduli were determined for stress-strain curves from both failure and stress-relaxation tests. Experimental results showed a similar behaviour between proximal and distal plantar fascia regions, while it was different considering the proximal-distal and lateral-medial directions. Furthermore, the results highlighted the non-linear time-dependent behaviour and the anisotropy of the plantar fascia.

As further steps, these results could be implemented in a computational model of the entire foot region to investigate the mechanical response of tissues in both healthy and pathological conditions.

***Keywords*— Plantar fascia, tensile tests, biomechanics, anisotropy.**

I. Introduction

THE foot plantar fascia, also called plantar aponeurosis, is a connective tissue which spans between the calcaneal tuberosity and the forefoot. It is mainly composed of type I collagen fibres, elastic fibres and an extracellular matrix rich in hyaluronan [1]. Collagen fibres show a variable thickness, and are arranged along the proximal-distal direction but also along the transversal and oblique directions [2]. Plantar fascia plays a key role during propulsion in the gait cycle, it supports the medial and longitudinal arch of the foot [3], and permits the transmission of forces from the rear to the forefoot region and vice-versa.

Its mechanical functionality can be compromised by different pathologies such as plantar fasciitis, plantar fibromatosis (also called Ledderhose disease), and systemic pathologies such as type I diabetes. Plantar fasciitis is one of the most common diseases and usually affects runners or workers, whose activities require walking for a long time on hard surfaces [4]. Therefore, a better understanding of the plantar fascia's mechanical properties is of great interest in order to facilitate the treatment of its diseases.

Over the years, some studies analysed and tested plantar fascia's biomechanical behaviour, both in healthy and pathological conditions [5], [6], [7], reporting its visco-hyperelastic behaviour. However, tissue samples tested in these studies were taken only from the proximal-distal direction of a limited number of patients [5], [8]. Moreover, plantar fascia's behaviour was considered to be isotropic [9], [10], even if its collagen fibres are not only arranged in the proximal-distal direction.

In this context, the aim of this work is to fully describe the mechanical behaviour of the plantar fascia, in relation to its microstructure, by performing multiple experimental tests on samples taken from different fascia regions and orientations, with the future purpose to develop a computational model able to mimic its real mechanical behaviour.

II. Materials and Methods

A. Sample collection and dissection

Experimental tests were performed on plantar fascia collected from four human donors (male; age 56±18 years; BMI: 26.1±2.1) undergoing amputation due to cancer in other regions of the leg, at the Orthopedics and Orthopedic Oncology Unit, University Hospital of Padova (CESC Code: AOP2649). Plantar fasciae were not affected by musculoskeletal degeneration or pathology. After the dissection, the samples were frozen without additional treatments and kept at -20°C until the day of testing.

Each plantar fascia was cut into strips of approximately 13.2 (±3.2) mm in length, 8.6 (±2.7) mm in width, with 1.8 (±0.6) mm thickness, this latter measured with a manual calliper. Samples were obtained from all plantar fascia regions, *i.e.* distal, central and proximal, and they were cut according to longitudinal (proximal-distal, PD) and transversal (lateral-medial, LM) directions (Fig. 1 a-c). More precisely, samples collected from the central region were cut according to the LM direction, while those from distal and proximal regions were cut along the PD one. For simplicity, samples were named proximal-PD and distal-PD for specimens harvested according to the PD directions from the proximal and distal region respectively, and all-PD and all-LM for samples collected from different plantar fascia regions but cut along the PD and LM directions, respectively.

B. Mechanical tests

Uniaxial tensile tests were performed with the

Biomomentum testing machine (Model Mach-1 v500c, ©Biomomentum Inc.) using the uniaxial load cell with a capacity of 250 N and resolution of 0.0125 N. Specimens were tested at room temperature adopting two testing protocol types: (i) application of a constant strain rate until failure, and (ii) stress relaxation ramps. Samples were glued using cyanoacrylate to c-shaped specimen holders made of cardboard and Velcro to prevent sample slip from grips during testing.

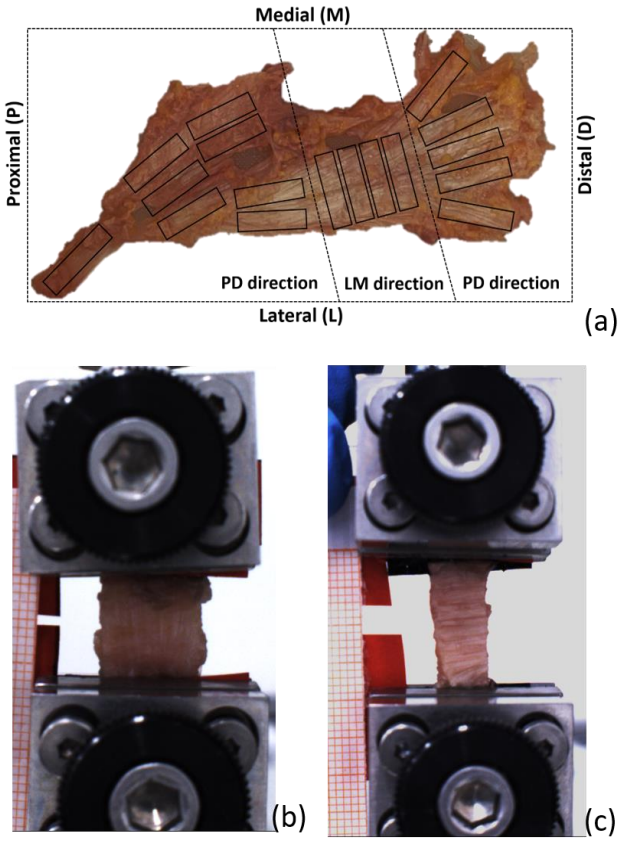


Fig. 1: Plantar fascia samples subdivision according to direction (a): PD and LM; an example of a tensile test on a sample cut according to PD (b) and LM directions (c).

Each sample was preconditioned by applying 10 loading-unloading cycles at 0.25 Hz with a maximum tensile strain equal to 4%. Sample preconditioning was applied to both types of tests as it allows repeatable and comparable results when investigating biological tissue properties [9]. In failure tests, samples were tightened at a 1%/s strain rate until rupture. Regarding stress relaxation protocol, five ramps composed of 2.5% strain at 100%/s strain rate and a subsequent 300s of resting, to allow the almost complete development of relaxation phenomena, were performed.

The experimental results were analyzed with Matlab 2021b (The MathWorks, Inc., MATLAB and Statistics Toolbox Release 2021b, Natick, Massachusetts, United States).

C. *Statistical Analysis*

The results of experimental tests were reported as mean ± standard deviation. Comparisons between groups (proximal-PD vs distal-PD and all-LM vs all-PD) were evaluated using a 2-sample T-test. All analyses were conducted with the statistical software Minitab 20 (Minitab, 2020). Significance was set at $p<0.05$.

TABLE I: FAILURE PARAMETERS

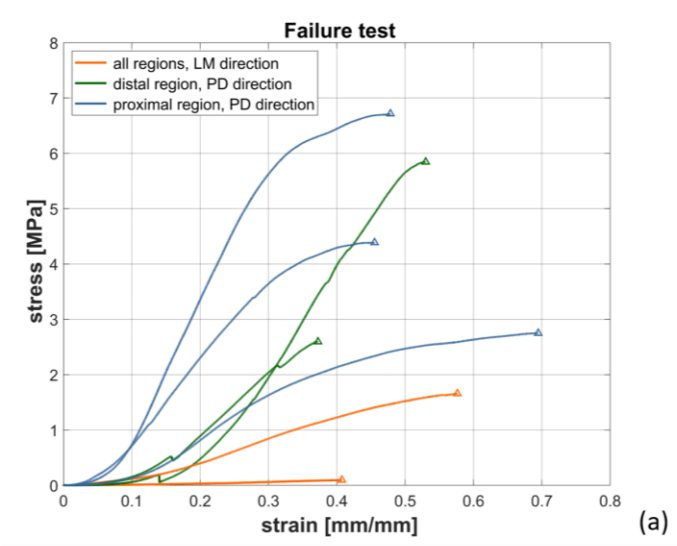
	UTS (MPa)	*p-value*	*Failure strain (%)*	*p-value*
proximal - PD	3.29±1.59	0.273	47.29±15.24	0.657
distal-PD	4.53±3.01		51.12±21.97	
all-PD	3.91±2.43	0.001*	49.21±18.51	0.875
all-LM	0.79±0.79		50.27±8.66	

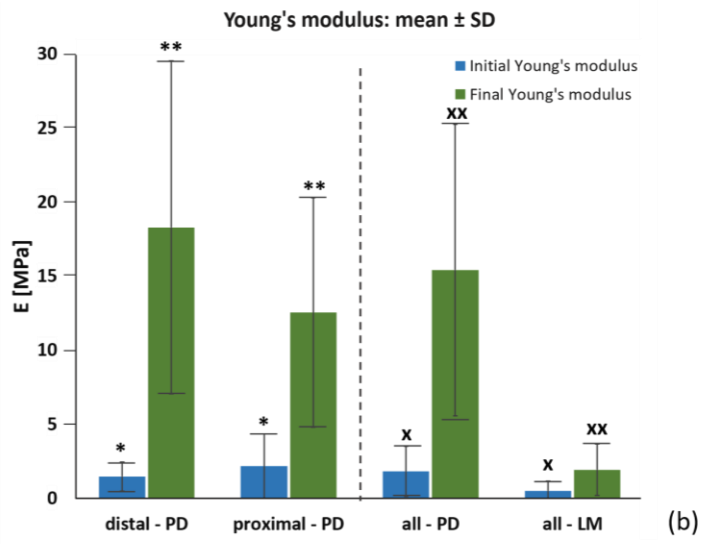
UTS (Ultimate Tensile Test) and Failure strain measured during failure tests. Mean value ± SD (*p-value < 0.05).

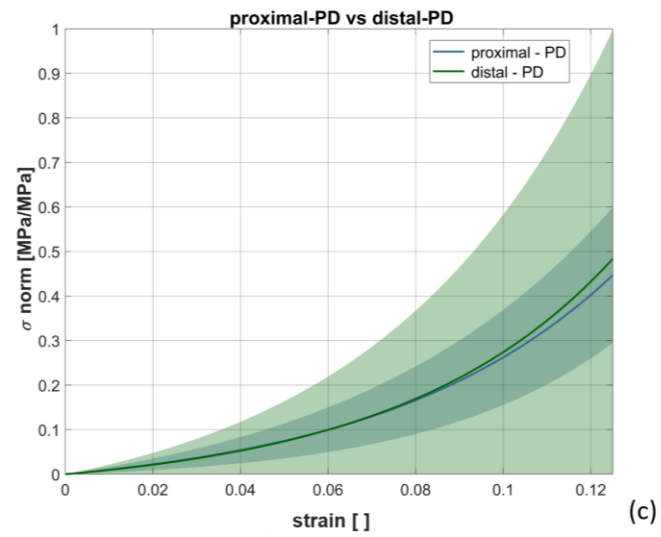
TABLE I: STRESS RELAXATION PARAMETERS

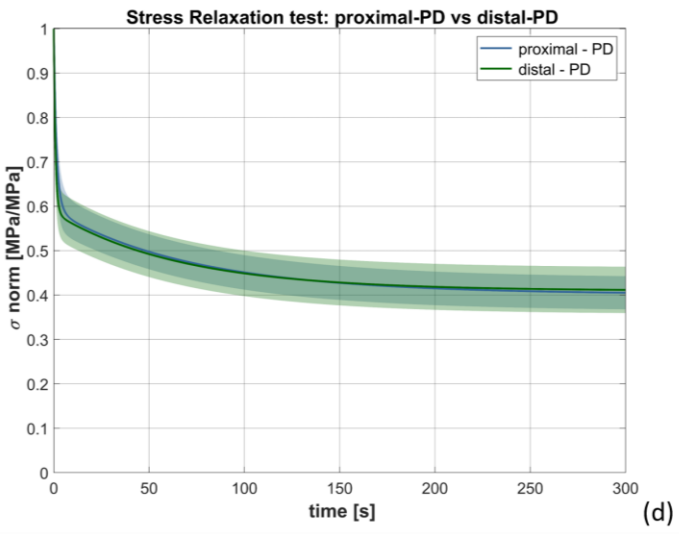
Parameter		*mean ±SD*	*p-value*		*mean ±SD*	*p-value*
E_i *(MPa)*	*proximal - PD*	1.14±0.62	0.929	*all-PD*	1.11±1.04	0.010*
	distal-PD	1.08±1.36		*all-LM*	0.12±0.09	
E_f *(MPa)*	*proximal - PD*	7.36±1.87	0.784	*all-PD*	7.90±5.92	0.003*
	distal-PD	8.35±8.18		*all-LM*	0.84±0.39	
γ_1	*proximal - PD*	0.19±0.01	0.110	*all-PD*	0.18±0.01	0.010*
	distal-PD	0.18±0.01		*all-LM*	0.15±0.01	
γ_2	*proximal - PD*	0.41±0.04	0.863	*all-PD*	0.41±0.05	0.004*
	distal-PD	67.19±6.66		*all-LM*	0.28±0.05	
τ_1 *(s)*	*proximal - PD*	76.56±16.07	0.277	*all-PD*	71.45±12.21	0.001*
	distal-PD	67.19±6.66		*all-LM*	131.36±12.21	
τ_2 *(s)*	*proximal - PD*	1.49±0.66	0.102	*all-PD*	1.15±0.57	0.048*
	distal-PD	0.87±0.27		*all-LM*	1.60±0.13	
% relax	*proximal - PD*	59.75±3.56	0.877	*all-PD*	59.53±4.04	0.157
	distal-PD	59.35±4.74		*all-LM*	41.12±6.32	

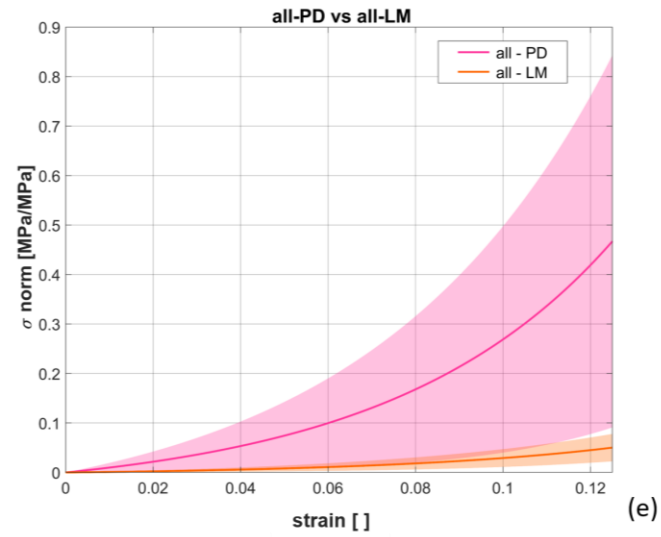
Initial (E_i) and final (E_f) moduli of equilibrium stress-strain and viscous parameters for the two different regions (proximal-PD and distal-PD) and the two different directions (all-PD and all- LM). Mean value ± SD (*p-value < 0.05).











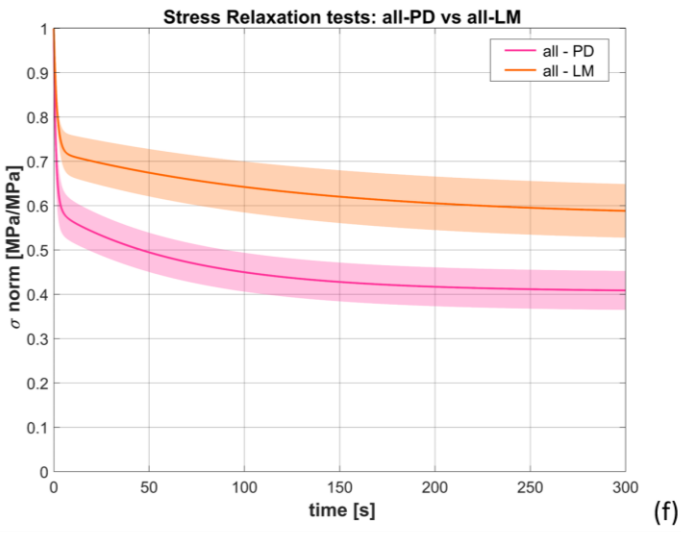


Fig. 2 A representative stress-strain curve obtained during failure tests for Subject 1 (a), initial and final Young's moduli obtained by failure curves (b) (* p-value = 0.371, ** p-value = 0.201, x p-value = 0.042, xx p-value = 0.001), stress-strain equilibrium curves (c) and normalized stress-time results (d) from tests performed on proximal-PD and distal-PD samples, stress-strain equilibrium curves (e) and normalized stress-time results (f) from tests performed on all-PD and all-LM samples. Mean value ± SD.

III. Results

Stress-strain curves obtained from failure tests are reported in Fig. 2 a. The mean value of ultimate tensile stress (UTS) and the corresponding failure strain, were computed for each region, proximal-PD and distal-PD, and for both directions, all-PD and all-LM (Table I). The initial and final Young's moduli of the failure curves were calculated (Fig. 2 b), *i.e.* the slope of the stress-strain curve in the toe region and in the quasi-linear region, respectively. UTS resulted statistically significant different ($p = 0.001$) when comparing PD and LM directions (all-PD: 3.91 MPa vs all-LM: 0.79 MPa), while failure strain was almost the same in all the plantar fascia (between 47.29% and 51.12%). Regarding the initial and final Young's moduli, distal and proximal regions showed similar values, while they were statistically different ($p = 0.042$ for E_i and $p = 0.001$ for E*f*) considering the orientation of the fibres (the all-PD final Young modulus is 15.42 MPa, seven times higher than the all-LM Young modulus, which is 1.93 MPa). These results demonstrate the plantar fascia anisotropic behaviour, which was also observed in the stress-strain equilibrium curves obtained from the stress-relaxation tests (Fig. 2 c, e). These curves were achieved by interpolating the stress and strain data obtained at the end of the holding phase of each ramp with an exponential formulation. A statistically significant difference was found for the initial ($p = 0.010$) and final elastic moduli ($p = 0.003$) between PD and LM directions, whose values are reported in Table II. The normalized stress-time curves (Fig. 2 d, f) highlighted the time-dependent behaviour of the tissue and the viscoelastic parameters (Table II), obtained by interpolating these curves with a typical exponential formulation using Matlab curve fitting tools [11], showed similar values for all regions except for the samples taken according to the LM direction.

IV. Conclusion

The results of the experimental tests highlighted a similar behaviour among the different plantar regions (proximal and distal), while a different one was observed considering longitudinal and transversal directions, supporting that the anisotropic behaviour of plantar fascia is due to its high component in collagen fibres. To the best of the authors' knowledge, this is the first study in which the plantar fascia anisotropy was analyzed and observed in detail. Indeed, in the literature, different studies assessed the viscoelastic and visco-hyperelastic plantar fascia behaviour till now [6], [7], [12], but none of them has considered the tissue anisotropy, due to the lack of mechanical tests on samples along the transversal direction.

Regarding the viscoelastic behaviour, slightly different results were observed comparing our fitted viscous parameters values with those of previous studies. For instance, the reduced percentage of stress at the end of the stress relaxation phenomena in both proximal and distal regions was 59% after 300 s in this study, while Pavan et al. [6] reported a stress decay of 35-40% in a time interval of 120 s. Results are comparable considering that, in the present study, samples were let to develop the relaxation phenomena for a higher time interval. Regarding the viscous parameters (γ_1, γ_2, τ_1 and τ_2), their values were confirmed by other studies except for the τ_1, which corresponds to double that of another work [12].

The data of this study suggest that human plantar fascia can be characterized as a non-linear anisotropic and viscoelastic material. The achieved experimental results will be therefore used, to define and develop a complete constitutive model able to describe the real mechanical behaviour of the plantar fascia.

The future goal is to introduce the complete plantar fascia mechanical characterization in the computational model of the foot, in order to investigate and compare the mechanical response of tissues in both healthy and pathological conditions. The numerical model of the foot could be a valuable tool to gain information on the mechanical behaviour of tissues that cannot be obtained through experimental tests. Furthermore, it could also be useful for clinicians in planning and simulating surgery, *e.g.* to repair pathological plantar fascia.

Acknowledgement

This work was supported by MIUR, FISR 2019, Project n° FISR2019_03221, titled CECOMES: CEntro di studi sperimentali e COmputazionali per la ModElliStica applicate alla chirurgia.

The authors would like to thank the MSc student Noemi Finco, University of Padua, for her contribution to experimental tests and data processing.

References

[1] C. Stecco et al., "Plantar fascia anatomy and its relationship with Achilles tendon and paratenon," *J. Anat.*, vol. 223, pp. 665–676, September 2013.

[2] A. Aquino, and C. Payne, "Function of the plantar fascia," *Foot*, vol. 9, pp. 73–78, 1999.

[3] J. Pontious, K. P. Flanigan, and H. J. Hillstrom, "Role of the plantar fascia in digital stabilization: A case report," *J. Am. Podiatr. Med. Assoc.*, vol. 86, pp. 43–47, January 1996.

[4] B. L. Warren, "Plantar Fasciitis in Runners: Treatment and Prevention," *Sport. Med.*, vol. 10, pp. 338–345, 1990.

[5] A. N. Natali, P. G. Pavan, and C. Stecco, "A constitutive model for the mechanical characterization of the plantar fascia," *Connect. Tissue Res.*, vol. 51, pp. 337–346, 2010.

[6] P. G. Pavan, C. Stecco, S. Darwish, A. N. Natali, and R. De Caro, "Investigation of the mechanical properties of the plantar aponeurosis," *Surg. Radiol. Anat.*, vol. 33, pp. 905–911, September 2011.

[7] S. Todros, C. Biz, P. Ruggieri, and P. G. Pavan, "Experimental analysis of plantar fascia mechanical properties in subjects with foot pathologies," *Appl. Sci.*, vol. 11, pp. 1–11, February 2021.

[8] J. Guo, X. Liu, X. Ding, L. Wang, and Y. Fan, "Biomechanical and mechanical behavior of the plantar fascia in macro and micro structures," *J. Biomech.*, vol. 76, pp. 160–166, 2018.

[9] A. Gefen, "The in vivo elastic properties of the plantar fascia during the contact phase of walking," *Foot Ankle Int.*, vol. 24, pp. 238–244, March 2003.

[10] J. T. M. Cheung, M. Zhang, A. K. L. Leung, and Y. B. Fan, "Three-dimensional finite element analysis of the foot during standing - A material sensitivity study," *J. Biomech.*, vol. 38, pp. 1045–1054, 2005.

[11] E. L. Carniel et al., "Biomechanics of stomach tissues and structure in patients with obesity," *J. Mech. Behav. Biomed. Mater.*, vol. 110, pp. 1-11, May 2020.

[12] P. G. Pavan, P. Pachera, C. Stecco, and A. N. Natali, "Constitutive modeling of time-dependent response of human plantar aponeurosis," *Comput. Math. Methods Med.*, vol. 2014, pp 1-8, February 2014.

Synergy-dependent patterns of reaction forces in sit-to-stand movements

S. Ranaldi[1], L. Gizzi[2], G. Severini[3] and C. De Marchis[4]
[1] *Roma Tre University, Rome, Italy*
[2] *University of Stuttgart, Stuttgart, Germany*
[3] *University College Dublin, Dublin, Ireland*
[4] *University of Messina, Messina, Italy*

***Abstract*—Sit-to-stand is a widely studied clinical test; however, despite its importance in the characterization of motor performance, the neuromechanical processes underlying its control are rarely characterized. One of the most used tools for neuromechanical characterization is the analysis of the ground reaction forces; moreover, muscle activations are often characterized in terms of coactivation structures, or muscle synergies. In this work, we analysed the reaction forces, both on the chair and on the ground, in a group of healthy subjects during sit-to-stand movement. Using an information-based model selection criterion, we divided participants based on the number of muscle synergies underlying movement generation, and analysed the inter-group differences in terms of the aforementioned reaction forces. Results show how it is indeed possible to isolate force characteristics that are dependent on the number of muscle synergies, especially in the management of body inertia and symmetry.**

***Keywords*—sit-to-stand, muscle synergies, reaction forces, neuromechanics**

I. INTRODUCTION

Sit-to-stand test is a widespread clinical test for assessing the alterations of human movement due to aging or neurological pathologies, and it has been shown to unveil an important relationship between the speed of repeated movements and the subjects' independence during activities of daily living [1]. This test is typically administered to obtain semi-quantitative information, such as the time needed for executing 5 times the movement (5 times sit to stand) or the number of sit-to-stand cycles completed in a 30 seconds time frame (30 seconds sit to stand); more recently, some instrumented versions of the sit-to-stand test have been proposed in the literature [2], aiming at increasing the amount of extracted clinically relevant information. To ensure a fast and simple execution of the test in clinical scenarios, these implementations typically foresee the use of wearable sensors or conventional cameras coupled with algorithms for extracting information from a short test. These implementations typically aim at adding insights on the motor control strategies adopted by the subjects during the task. Other approaches rely on a more complex setup, such as motion capture systems, to measure more detailed kinematic or muscle activity quantities. Regarding the latter, studying how muscles coordinate during sit-to-stand has gained the attention of the scientific community during the last few years [3]; these studies exploit the muscle synergy model [4] to identify muscle coordination patterns that are related to specific biomechanical functions, shifting the focus onto a neuromechanical characterization of sit-to-stand in healthy and pathological conditions [3], [5]–[7]. In all these applications, the correct identification of the underlying synergistic structure is of key importance. The accurate and thorough extraction of muscle synergies from multi-muscle surface electromyography (sEMG) requires a precise tuning of the methodologies that process and factorize the raw signals [8]–[10], to have a reliable and ecological neuromechanical assessment of sit-to-stand in clinical settings. It is thus important to understand how using relatively short signals coming from sit-to-stand standard clinical trials can yield relevant neuromechanical information. In this study, we use a dataset of sEMG and kinetic data recorded from a population of healthy subjects for studying the feasibility of standard sit-to-stand tests to characterize the adopted motor control strategies through an optimized muscle synergy analysis. The data have been recorded on the BENCH device, an instrumented chair for the biomechanical assessment of sit-to-stand maneuvers.

II. METHODS

A. Experimental protocol

The experimental protocol has been carried out using the BENCH instrumented chair [11] (Figure 1). This chair is equipped with two force platforms (*BTS P6000, BTS Bioengineering, Milan, Italy*, sampling frequency: 1 kHz), placed one at ground level and one on the seating plane. These two platforms have been used for the recording of the ground reaction forces during movement, in a synchronous fashion with respect to an 8-channels surface electromyography system (*BTS FreeEMG, BTS Bioengineering, Milan, Italy*, sampling frequency: 1 kHz) and a stereophotogrammetric system (*BTS SMARTDX, BTS Bioengineering, Milan, Italy*, sampling frequency: 250 Hz). EMG signals were acquired from the following muscles of the dominant leg: *soleus*, *gastrocnemius medialis*, *peroneus longus*, *tibialis anterior*, *biceps femoris long head*, *vastus lateralis*, *rectus femoris* and *gluteus maximus*, electrode positioning has been selected according to the SENIAM protocol. A reflective marker, placed in correspondence of the *sacrum* has been used as a kinematic reference for segmenting the sit-to-stand cycle; each cycle is

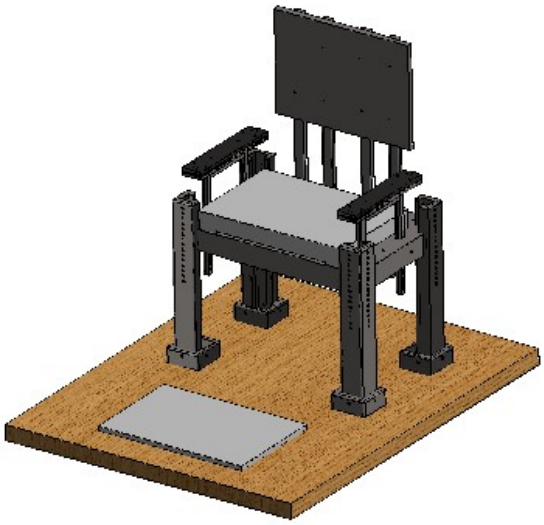


Fig. 1: A representation of the BENCH apparatus

defined as the portion of the signal between two subsequent maxima of the antero-posterior component of the 3D trajectory of this aforementioned marker.

In total, 12 healthy subjects (37 ± 10 years old, range 24-55 years old, 177.2 ± 6.6cm, 79 ± 11.7kg) participated to the experiment. The experimental protocol was approved by the ethics committee of the Roma Tre University, and was carried out according to the principles of the Declaration of Helsinki. The subjects were asked to perform a *30 seconds sit-to-stand* trial with their arms folded across the chest, and without moving the feet. The trial started in a seated position. At the *go* signal, the subject seamlessly performed sit-to-stand and stand-to-sit movements until the *stop* signal. The subjects were instructed to execute the test in a fast yet comfortable and clean way, reaching the full standing position at the end of every sit-to-stand movement.

B. Synergy Extraction

For synergy extraction, the envelope of the sEMG signal has been extracted through rectification and low-pass filtering at 10Hz. Prior to envelope extraction, sEMG signals have been filtered with a band pass filter between 30 and 450 Hz. Factorization of the multi-muscle signals has been realized through Non-negative Matrix Factorization [12] and the optimal number of synergies has then been selected using the adjusted Akaike Information Criterion presented in [9].

The analysis of the synergistic control strategies has been carried out by focusing on the temporal components alone, during the whole sit-to-stand-to-sit cycle. In order to do so, the H profiles coming from each cycle have been time-normalized on 100 samples, and an average cycle profile has been defined for each subject. Subsequently, subjects were categorized with respect to their number of synergies, and an inter-subject average profile has been defined for each N_{syn}.

In addition, all the average H profiles have been fed to a K-Means clustering algorithm ($K = 4$) to extract the four main waveform that can describe the coordination structure of all the subjects. Before the K-Means algorithm, some basic features describing the waveform have been extracted, namely the position of the first peak, the area under the waveform, the peak value, the time spent at a level higher than the 50% of the maximum and the centre of activity.

C. Force computation

Forces have been analysed in the vertical (z) and antero-posterior (x) directions for the platform on the chair, and for all direction for the ground sensors.

Force profiles have then been time-normalized following the same procedure described for the synergy activations, and an average behaviour for subjects characterized by each of the identified N_{syn} has been computed from the subject-specific average force profiles.

III. Results

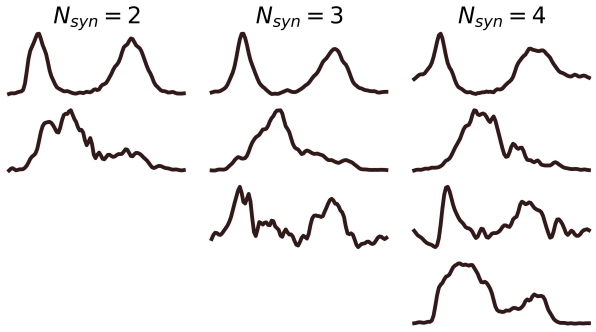


Fig. 2: Average profiles coming from the subjects exhibiting different N_{syn} values

The study population completed the *30 seconds sit-to-stand* trial executing 13.1 ± 1.66 cycles across subjects, with a complete sit-to-stand-to-sit cycle duration of 2.42 ± 0.32s across subjects.

A. Synergy results

The optimal number of synergies selection criterion resulted in the 25% of the subjects requiring two synergies for reconstructing the movement, while the 42 % and 33 % of the participants required three or four modules, respectively.

The average synergy activation profiles for the different N_{syn} are shown in Figure 2. The first biphasic shape (*cluster1*) appears to be consistent across all the identified groups; moreover, all the sets of waveform are characterized by only one mono-phasic activity (*cluster2*), while additional two-bursts activations are present for N_{syn} higher than two.

In Figure 3, the centroids coming from the K-Means procedure are presented, together with the waveforms composing the clusters. Cluster 1 is identified in the 83% of the subjects, while cluster 2, 3 and 4 in the 67, 25 and 50 %, respectively. The shapes identified in this procedure are coherent with the ones presented in Figure 2.

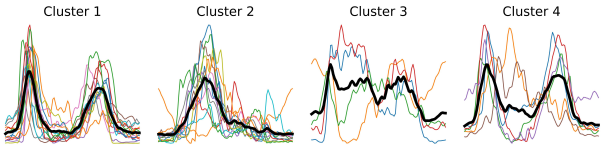


Fig. 3: Clustering results from the subject-specific H profiles

B. Force profiles

The force profiles related to the subject requiring different N_{syn} for movement generation are shown in Figure 4. The waveforms qualitatively show how subjects requiring different synergy sets are characterized also by different force profiles, especially in the management of the contact with the ground after standing and before seating. Differences are more evident for the subjects requiring 4 synergies, especially in the transverse plane.

IV. Discussions

The results presented here show how, in a population of healthy people performing a standard sit-to-stand test, the complexity of the motor control strategies may substantially differ. In this work, the number of muscle synergies required for the control of the sit-to-stand movement has been used as a key feature of motor control, investigating how people that differ in this parameter also differ in their biomechanical output (*i.e.* the reaction forces). At the same time, the biomechanical correlate that has been qualitatively identified here can be seen as the proof that optimal synergy analysis methods might pave the way for new interpretation of their outcomes, improving the ability of such analyses to identify neuromechanical relationship from multimodal measurements.

The activation profiles that have been presented here show that a complete sit-to-stand-to-sit cycle is composed at least of two alternating modules, one working in both the standing and sitting phase, and one stabilizing the movement when approaching the full standing posture. Additional modules are required by some subjects; these modules typically work in the same phases as the first module, while being characterized by generally longer activations. These features suggest that those synergies may act as stabilizing mechanisms that are functional to the activity of the two main modules. Clusters shown in Figure 3 support this hypothesis of two main modules (that are identified in a very stable way) and two support modules (that present higher variability).

The force profiles shown in Figure 4 are coherent with this hypothesis, showing that there is an increasing trend on the ground forces when the number of synergies is higher. This might indicate that people that tend to relate more to the inertia of the body (thus generating higher reaction forces during standing and sitting) require additional modules for managing the acceleration and deceleration of the body weight. Moreover, both small (*i.e.* 2) and large (*i.e.* 4) numbers of synergies correspond to an asymmetrical pattern in the medio-lateral ground reaction force around the full standing position, while the solution with three modules seems to represent a smoother and more symmetrical strategy; this latter characteristic might indicate that the presence of a third module stabilizes the body in the ML direction, with any additional module (on the dominant side) shifting the symmetry with respect to the 2 synergies solution, thus generating the out-of-phase pattern in the ML ground reaction force around the full standing phase (Figure 4).

These results are presented here in a qualitative way, but still they highlight a dependence of the biomechanical characteristics of the sit-to-stand movement on the number of motor modules required for the execution of the task. While the causal relationship between these two quantities is still to be unraveled, as well as the complete quantification of the mathematical relationship between those two characteristics, the presence of optimal methods for the investigation of modular motor control strategies yields fine information that typically remains hidden when common patterns (*e.g.* a common number of synergies for all the subjects) are imposed during the analyses.

Acknowledgement

This work has been supported by the FTSP1 EUROBENCH project "BENCH".

References

[1] G. E. Frykberg and C. K. Häger, "Movement analysis of sit-to-stand – research informing clinical practice," *Physical Therapy Reviews*, vol. 20, no. 3, pp. 156–167, Jun. 2015.

[2] M. Galli, V. Cimolin, M. Crivellini, and I. Campanini, "Quantitative analysis of sit to stand movement: Experimental set-up definition and application to healthy and hemiplegic adults," *Gait & Posture*, vol. 28, no. 1, pp. 80–85, Jul. 2008.

[3] H. Hanawa, K. Hirata, T. Miyazawa, K. Kubota, M. Yokoyama, Y. Matsumoto, T. Fujino, and N. Kanemura, "Classification of abnormal muscle synergies during sit-to-stand motion in individuals with acute stroke," *Measurement: Sensors*, vol. 16, p. 100055, Aug. 2021.

[4] E. Bizzi and V. C. Cheung, "The neural origin of muscle synergies," *Frontiers in Computational Neuroscience*, vol. 7, 2013.

[5] K. Yoshida, Q. An, A. Yozu, R. Chiba, K. Takakusaki, H. Yamakawa, Y. Tamura, A. Yamashita, and H. Asama, "Visual and Vestibular Inputs Affect Muscle Synergies Responsible for Body Extension and Stabilization in Sit-to-Stand Motion," *Frontiers in Neuroscience*, vol. 12, 2019.

[6] H. Kogami, Q. An, N. Yang, H. Yamakawa, Y. Tamura, A. Yamashita, H. Asama, S. Shimoda, H. Yamasaki, M. Itkonen, F. Shibata-Alnajjar, N. Hattori, M. Kinomoto, K. Takahashi, T. Fujii, H. Otomune, and I. Miyai, "Effect of Physical Therapy on Muscle Synergy Structure During Standing-Up Motion of Hemiplegic Patients," *IEEE Robotics and Automation Letters*, vol. 3, no. 3, pp. 2229–2236, Jul. 2018.

[7] R. Wang, Q. An, N. Yang, H. Kogami, K. Yoshida, H. Yamakawa, H. Hamada, S. Shimoda, H. R. Yamasaki, M. Yokoyama, F. Alnajjar, N. Hattori, K. Takahashi, T. Fujii, H. Otomune, I. Miyai, A. Yamashita, and H. Asama, "Clarify Sit-to-Stand Muscle Synergy and Tension Changes in Subacute Stroke Rehabilitation by Musculoskeletal Modeling," *Frontiers in Systems Neuroscience*, vol. 16, 2022.

[8] A. S. Oliveira, L. Gizzi, D. Farina, and U. G. Kersting, "Motor modules of human locomotion: Influence of EMG averaging, concatenation, and number of step cycles," *Frontiers in Human Neuroscience*, vol. 8, 2014.

[9] S. Ranaldi, C. De Marchis, G. Severini, and S. Conforto, "An objective, information-based approach for selecting the number of muscle synergies to be extracted via non-negative matrix factorization," *IEEE Transactions on Neural Systems and Rehabilitation Engineering*, vol. 29, pp. 2676–2683, 2021.

[10] R. Ballarini, M. Ghislieri, M. Knaflitz, and V. Agostini, "An Algorithm for Choosing the Optimal Number of Muscle Synergies during Walking," *Sensors*, vol. 21, no. 10, p. 3311, Jan. 2021.

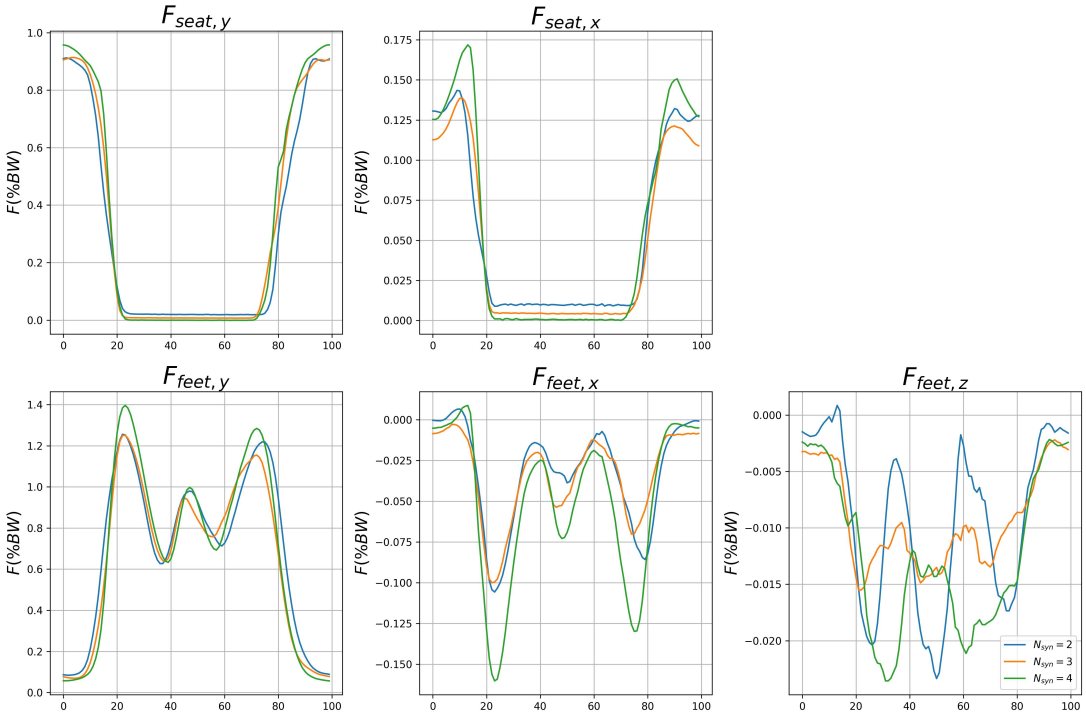


Fig. 4: Force profiles for the subjects exhibiting different N_{syn} values

[11] D. Muñoz, C. De Marchis, L. Gizzi, and G. Severini, "Predictive simulation of sit-to-stand based on reflexive-controllers," *Plos one*, vol. 17, no. 12, p. e0279300, 2022.

[12] D. Lee and H. S. Seung, "Algorithms for non-negative matrix factorization," *Advances in neural information processing systems*, vol. 13, 2000.

Static strength of lower-limb prosthetic sockets for the activities of daily living

Francesca Gariboldi[1], Mattia Scapinello[1], Nicola Petrone[1], Gian Luca Migliore[2], Gregorio Teti[2] and Andrea Giovanni Cutti[2]

[1] *Università degli Studi di Padova, Padova (PD), Italy*
[2] *Centro Protesi INAIL, Vigorso di Budrio (BO), Italy*

***Abstract*—Despite the central role that a prosthetic socket plays as the link between the patient and their prosthesis, yet no common guidelines or standardized methods exist to test their mechanical strength. Consequently, the socket structural properties remain largely unknown. The absence of a method to quantify socket structural strength has negative consequences, such as: the tendency to over-fabricate the socket, a general limitation in the introduction of innovative materials and techniques, and a challenge in complying with the current European regulatory requirements. To overcome these limitations, the authors defined a five-step plan intended to serve as a groundwork in the prosthetic field for the definition of a standardized testing method for prosthetic sockets. This plan includes the systematic analysis and organization of the available literature into key domains, the proposal of recommendations to address the current gaps in knowledge, the design, implementation and application of a test bench system based on the available evidence and on a worst-case approach and, finally, the definition of manufacturing guidelines based on quantitative data to be included in the production process of the INAIL Prosthetic Center. The activities described in this manuscript should guide other researchers of the prosthetic community to take coordinate action in the definition of a standardized method for socket testing.**

***Keywords*—Prosthetic sockets, structural testing, ISO 10328, lower-limb.**

I. Introduction

A PROSTHETIC socket is the custom element that serves as interface between the residual limb of a person with lower-limb amputation and the off-the-shelf mass-produced components of the prosthesis (e.g. prosthetic foot and possibly knee). The socket transfers load between the person and the rest of the prosthesis and allows control of the prosthetic limb. For this reason, it has to conform to the anatomy and clinical presentation of each unique limb, ensuring comfort and safeguarding its soft tissues.

Despite the central role of the socket in the prosthesis, no standards or common guidelines exist to test its structural strength, which therefore remains unknown. The current standard for structural testing of prosthetic components (ISO 10328 [1]) does not encompass custom-made devices, such as the socket, but only off-the-shelf mass-produced components (e.g. foot, knee). The traditional manufacturing techniques for sockets, such as lamination with composite materials and vacuum-bagging, are based on manual and highly operator-dependant processes that, to make up for the absence of quantitative data, tend to rely on over-fabrication to ensure safety. Despite having several downsides in terms of increased weight, rigidity and ultimately patient discomfort, this approach has higher risk of failure when experimenting with new materials and fabrication methods, for which training and clinical rules of thumb are not yet established. Finally, the absence of standardized test methods challenge the compliance with the current European Medical Device Regulation (MDR 745/2017) that requires documenting the expected performance of custom-made medical devices, such as sockets [2].

To overcome the current limitations associated to the absence of a standardized test method, meet the current regulatory requirements and improve the present manufacturing procedure of the INAIL Prosthetic Center, the authors have laid the foundation for the definition of a unified testing method based on the available evidence by drafting the following five-step plan:

A. Analyse and compare the current methods for socket testing available in literature;
B. Initiate a collaboration with other international scientists to take action in a coordinate manner;
C. Design and implement a test bench for socket testing based on literature findings;
D. Perform a socket testing campaign to analyse the mechanical strength of prosthetic sockets manufactured at the INAIL Prosthetic Center (Vigorso di Budrio, BO, Italy);
E. Draft internal guidelines for socket manufacturing based on quantitative data.

II. Methods

A. Review of the literature

A systematic review of the literature was conducted in 2021 to collect information about available socket mechanical testing methods. The review had the objective of analyzing the methods used for structural testing of lower-limb prosthetic sockets and among them identifying and analyzing the ones based on ISO 10328:2016 [3]. The review was conducted using the PRIMA process [4] and the findings were organized in key categories, such as socket information (amputation level, shape, fabrication technique and material), test characteristics (reference used, test setup, test sample, mock residual limb, alignment between sample components) and load characteristics (alignment of load line, type of loading, passing condition) [3].

B. Collaboration with the AOPA Socket Guidance Workgroup

In 2020 an international and multidisciplinary group of experts hosted by the American Orthotic & Prosthetic

Association (AOPA Socket Guidance Workgroup) was formed to provide the prosthetic community with evidence-based recommendations regarding socket structural testing methods to meet the emerging regulatory requirements. Using a systematic approach similar to the Delphi process, the first activity of the workgroup was the drafting of a discussion paper meant to highlight the problem of socket testing and call the stakeholders to action.

Starting from the findings of the systematic review [3], the aim of the paper was to describe the current state of knowledge available in literature regarding structural testing of transtibial prosthetic sockets, identify the knowledge gaps in this field and provide recommendations for how to address them. The possible recommendations were chosen from a pool of three options: 1) application of the exiting evidence from the literature, 2) group consensus, motivated by evidence in literature and/or knowledge of experts, 3) formation of a study group to assess the problem and find a way to address it. The paper was submitted and accepted for publication in *Prosthetics & Orthotics International* and is currently in the process of publication.

C. Design and implementation of a test bench for sockets

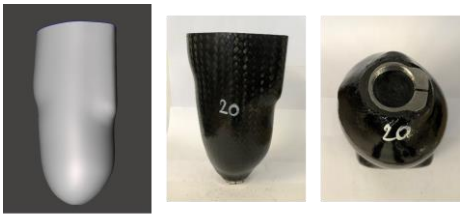
Based on the evidence collected from the Systematic Review and on the discussions in the workgroup technical meetings, a test bench system for lower-limb prosthetic sockets was designed and implemented at the Laboratory of Machine Design of the University of Padua (Padua, Italy) [5]. The test bench was designed to adapt the testing methods of ISO 10328:2016 to socket testing. Decisions about the modes of adaptations were made using a worst-case approach.

D. Socket testing

Thanks to the design and implementation of a test bench, an exploratory study was conducted at the University of Padua, aimed to analyse the effect of fiber layup, matrix and distal adapter on socket strength [6]. Twenty-three sockets were manufactured at the INAIL Prosthetic Center (Vigorso di Budrio, BO, Italy) from the same identical plaster model, using the traditional lamination technique with composite materials and resin infusion under vacuum-bagging. Each socket had a different combination of stratigraphy, distal adapter and resin. The shape of the limb represented the 98th percentile American male model of transtibial amputees, with a circumference at the patellar tendon bar of 52.4 cm and a length from the patellar tendon bar to distal end of 19.2 cm [7]. The different combinations of fiber layup, lamination resin and distal adapter were taken from the current production line of the INAIL Prosthetic Center.

The sockets were tested using the test bench designed and implemented at the University of Padua.

This study was described more extensively in a manuscript that was submitted and accepted with minor revision to *Medical Engineering & Physics*, and that is currently under review.



(a) (b) (c)

Fig. 1: Limb shape (a), example of test socket (b, c).

E. Guidelines for socket manufacturing

The test results allowed drafting lamination guidelines to be used in production at the INAIL Prosthetic Center (Vigorso di Budrio, BO, Italy). For each family of distal adapter, the guidelines were defined based on the sockets that reached the highest ultimate load at failure with lowest weight and with the simpler layup.

III. Results

A. Review of the literature

According to the results of the systematic review [3], only 16 peer-reviewed articles exist in literature that describe socket testing. The same result was also confirmed by recent a scoping review [8]. Given the absence of a standardized test method, most of the articles (13) are based on ISO 10328, each presenting different adaptation modes that were systematically summarized and organized in the review [3].

In particular, the socket was either tested alone or in combination with off-the-shelf components (e.g. prosthetic pylon, foot). Only transtibial sockets were tested, with the shape of the limb varying across studies (subject-specific vs. generalized). Three alignment modes were identified: a neutral and two worst-case alignments (with and without a prosthetic pylon). Among the two possible test conditions described in ISO 10328 (condition I, heel loading and condition II, forefoot loading), forefoot test condition was the most used across studies. Most of the articles performed static testing using the ISO 10328 passing conditions, which depend on test condition (I or II) and on loading level (P3 to P8), associated to different ranges of body weight.

B. Collaboration with the AOPA Socket Guidance Workgroup

The discussion paper of the AOPA Socket Guidance Workgroup identified knowledge gaps and solution approaches for four key domains: 1) mock residual limb shape and composition; 2) prosthetic socket coordinate system and alignment; 3) components and requirements of test samples; 4) test conditions, loading parameters and passing conditions.

All four knowledge gaps were deemed to lack sufficient high-quality literature for resolving via literature review alone. The group concluded that six of the gaps within these domains may be resolved adequately by expert consensus combined with existing literature, but three knowledge gaps will require new research studies to adequately address.

C. Design and implementation of a test bench for sockets

The test bench was designed starting from one of the adaptations of ISO 10328 described in the reviewed literature [7]. The test bench allowed to reproduce heel loading and

forefoot loading, i.e. the two most critical events during the stance phase according to ISO 10328 [1].

In the bench, the load was applied vertically through a uniaxial hydraulic cylinder used in force control. Load was then applied to the socket through a mock residual limb made of hard PU resin with the interposition of a soft styrene liner (Shore A 30) and cotton socks to ensure proper press fit. The load was transferred from the machine to the mock limb-socket system using rigid mounting elements (loading plates) that allowed applying the lever arms prescribed by ISO 10328 in forefoot loading for a patient weighing more than 100 kg (P5 to P8 condition). The bench could be used to perform both static and cyclic testing, according to the test procedures specified in ISO 10328.



(a) (b)

Fig. 2: Test bench for testing of lower-limb prosthetic sockets for the activity of daily living, CAD model (a) and implementation (b).

D. Socket testing

Among the twenty-three sockets tested, 50% weighted more than 600g and were therefore deemed too heavy for the size of the limb. 30% of all sockets did not reach the required strength (4500 N). Altogether, only 26% met the required strength (>4500 N) with acceptable weight (<600g) [6].

E. Guidelines for socket manufacturing

Among the sockets with required strength (>4500 N) and acceptable weight (<600g), five sockets were identified, one per type of distal adapter, and were used to define the lamination guidelines for the INAIL Prosthetic Center (Vigorso di Budrio, BO, Italy).

It was quantified that these new lamination guidelines allowed reducing material waste of manufacturing by 50%.

IV. Discussion

The aim of this study was to define a well-structured plan that should serve as a groundwork in the prosthetic field for the definition of a unified testing method for prosthetic sockets and thus help overcome the current limitations derived from the absence of a dedicated standard.

The systematic review of the literature [3] was the first element in this plan and highlighted that the literature regarding socket testing is very limited. ISO 10328 was commonly used as a guide for socket testing, but details of its adaptation to sockets varied considerably among articles. The main reason for this heterogeneity is that ISO 10328 was not designed for socket testing and consequently it is missing specific definitions and recommendations that would allow unambiguous implementation of such a testing.

Nevertheless, the findings of the systematic review were very valuable in the drafting of the discussion paper by the AOPA Socket Guidance Workgroup. The available evidence was organized in key domains, and for each of them the authors highlighted the knowledge gaps and proposed recommendations to address them. The discussion paper confirms that establishing a unified testing method for sockets is not an easy task. In fact, none of the knowledge gaps can be solved by simple application of the available evidence, and most of them will require the formation of study groups to carefully assess the problem. Nevertheless, it is the hope of the authors that the discussion paper will help spur the prosthetic field and serve as a roadmap for stakeholders to take coordinate action in their respective field of interest.

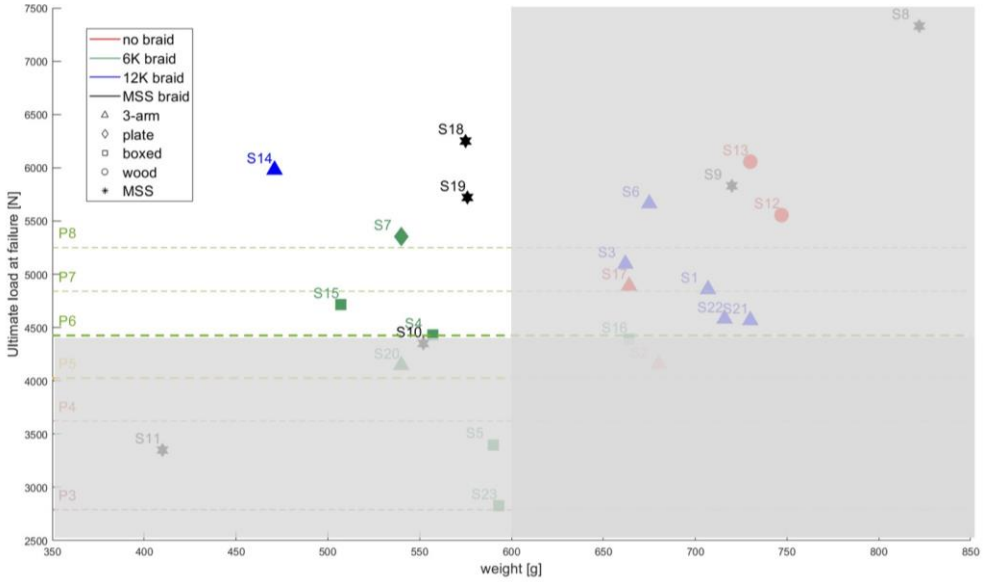


Fig. 3: Distribution of tested sockets according to ultimate load at failure and weight.

The systematic review and the discussion paper allowed to identify the topic areas that should be considered when defining a testing method for sockets. For each topic area the authors had to make decisions when evidence did not provide sufficient guidance. In the design of the test bench, the authors chose to adopt a worst-case approach that tended to maximize the bending moment at the socket distal end. We did so by implementing the adaptation of ISO 10328 proposed by Gerschutz et al. [7], which described testing the socket in isolation, in forefoot loading condition and P6 loading level. In addition, the limb increased dimensions represented a worst-case condition for pulled sockets and contributed to making the test more conservative. Even though it was the intent of the authors to establish a conservative testing system, the actual effect of different adaptations is unknown, and the decisions made on certain knowledge gaps will need to be confirmed once study groups are formed and/or consensus in the prosthetic community is reached.

Even with the limitations described above, the implementation of a test bench allowed to carry out a first test campaign with the objective of exploring existing combinations of layup-adapter-resin and establishing a benchmark based on the current practice of the INAIL Prosthetic Center (Vigorso di Budrio, BO, Italy). The study showed that the absence of an established method to quantify socket strength leads to a tendency of over-dimensioning. Half of the sockets were in fact deemed too heavy for the size of the limb. Overall, only 26% displayed sufficient strength (> 4500N) and acceptable weight (<600g).

Despite its limitations, this exploratory study allowed to identify correlations between certain combinations of layup resin and distal adapter and socket strength and/or weight. In addition, based on the sockets that produced the best output, it was possible to draft manufacturing guidelines for the INAIL Prosthetic Center, aimed at reducing material waste, unnecessary weight and maximize strength. The introduction of these guidelines in the production line of the Center has in fact allowed reducing the material waste by 50%, creating sockets that are lighter and stronger.

Overall, the path to the definition of a standardized method for socket testing is still long. Nevertheless, thanks to the activities described in this manuscript, the foundations have been laid and hopefully will guide other researchers of the prosthetic community to take coordinate in the definition of a unified method for socket testing.

V. Conclusion

The current manuscript outlines a possible approach to lay the foundation in the definition of a standardized method to test prosthetic sockets. This approach was intended to guide other researchers of the prosthetic community to take coordinate action in pursuing this objective.

Acknowledgement

Authors kindly acknowledge INAIL for funding the study through the OLYMPIA Project.

References

[1] ISO. BSI Standards Publication Prosthetics — Structural testing of lower-limb prostheses — Requirements and test methods (ISO 10328 : 2016). International Organization for Standardization. 2016;10328:2016.

[2] Official Journal of the European Union. Regulation (EU) 2017/745 of the European Parliament and of the Council of 5 April 2017 on medical devices, amending Directive 2001/83/EC, Regulation (EC) No 178/2002 and Regulation (EC) No 1223/2009 and repealing Council Directives 90/385/EEC and 93/42/EE. Official Journal of the European Union. http://data.europa.eu/eli/reg/2017/745/oj. Published 2017.

[3] Gariboldi F, Pasquarelli D, Cutti AG. Structural testing of lower-limb prosthetic sockets: a systematic review. Med Eng Phys. 2021;99:103742. doi:10.1016/j.medengphy.2021.103742

[4] Page MJ, et al. The PRISMA 2020 statement: an updated guideline for reporting systematic reviews. BMJ 2021;372. https://doi.org/10.1136/bmj.n71.

[5] Gariboldi F, Scapinello M, Sanchez Salazar PA, et al. TOWARDS THE DEVELOPMENT OF BENCH TESTING FOR LOWER-LIMB PROSTHETIC SOCKETS FOR SPORT APPLICATIONS. In: International Society of Biomechanics in Sports. 2022.

[6] Gariboldi F, Scapinello M, Petrone N, Migliore GL, Teti G, Cutti AG. TOWARDS THE DEVELOPMENT OF BENCH TESTING FOR LOWER-LIMB PROSTHETIC SOCKETS. In: American Orthotic & Prosthetic Association National Assembly; 2022.

[7] Gerschutz MJ, Haynes ML, Nixon D, Colvin JM. Strength evaluation of prosthetic check sockets, copolymer sockets, and definitive laminated sockets. The Journal of Rehabilitation Research and Development. 2012;49(3):405. doi:10.1682/JRRD.2011.05.0091

[8] G. Baer and S. Fatone, “Scoping Review of Mechanical Testing of the Structural and Material Properties of Lower-Limb Prosthetic Sockets,” 2022. [Online]. Available: http://journals.lww.com/jpojournal

Computational modelling of the contractile behavior of cardiomyocytes on hydrogel scaffolds for cardiac tissue regeneration

S. Spadoni[1], S. Todros[1], M. Magnussen[2], D. Scaglioni[2], A. Urciuolo[3,4], N. Elvassore[1,2], P.G. Pavan[1,4]
[1] *Department of Industrial Engineering, University of Padova, Italy*
[2] *University College London Great Ormond Street Institute of Child Health, London, United Kingdom*
[3] *Department of Molecular Medicine, University of Padova, Italy*
[4] *Fondazione Istituto di Ricerca Pediatrica Città della Speranza, Padova, Italy*

***Abstract*—In order to compare different approaches for cardiac tissue regeneration, it is fundamental to estimate the contractile behavior of cardiomyocytes interacting with hydrogel scaffolds. Direct measurement of specific mechanical parameters is difficult due to the small size of the treated samples and the complex mechanical behavior of tissues and scaffolds. Finite Element Method (FEM) models can be usefully adopted to estimate these parameters, as shown in this work. We have developed a constitutive model to describe the mechanical response of cardiomyocytes (CMs) and we are using this constitutive model in numerical models aimed at *in silico* analysis of original experimental tests involving human pluripotent stem cell–derived cardiomyocytes (hPSC-CMs).**

***Keywords*—cardiomyocyte, contractile behavior, constitutive modelling, Finite Element Analysis.**

I. Introduction

The heart is the first organ to be formed during embryonal development and this is the reason why cardiac abnormalities represent a massive cause of fetal death [1]. At week 3, the embryo consists of three layers, i.e. the endoderm, the ectoderm and the mesoderm, from which the cardiac tissue originates [2].

Embryonic cardiomyocytes (CMs) develop into a linear heart tube that eventually undergoes rightward looping and forms a primitive heart structure. Afterwards, the septal development and the formation of the valves provide the separation of the pulmonary and systemic circulations [1]. The human heart is a muscular organ and consists of several types of cells such as CMs, endothelial cells, fibroblasts and smooth muscle cells [3].

The main function of the newly formed heart is to pump blood during the contraction–relaxation cycle of the working myocytes, which represent the fundamental contractile cell of the heart. CMs are made of groups of myofibrils containing sarcomeres, consisting of myosin and actin proteins, which appear respectively as thick and thin myofilaments.

Human pluripotent stem cell–derived cardiomyocytes (hPSC-CMs) are an inexhaustible source of CMs for potential therapeutic applications and are very promising for the investigation of early developmental processes in human cardiomyogenesis and future cell replacement strategies.

Congenital heart defects (CHDs) are the most common type of birth defect and bring a huge life burden, since babies with a critical CHD need to undergo several surgical procedures in the first year of life.

Regenerative medicine may be an alternative approach to treat CHDs, based on the development of functional models of the heart muscle *in vitro*. These models can be based on different scaffolds in combination with hPSC-CMs. Scaffold biomaterials are required to actively support tissue reconstruction and regeneration by promoting cell-cell adhesion, proliferation and differentiation [4]. Cellular viability and contractile ability of hPSC-CMs on scaffolds shall be evaluated to assess the feasibility of different tissue engineering platforms to support the formation of the heart muscle. Therefore, using numerical methods to analyze the contractile force, mechanical properties and dynamic beating behavior of hPSC-CMs could be of great significance for the design of innovative therapeutic approaches.

A quantitative analysis of CMs and hPSC-CMs contractility can be carried out *in silico* to properly select the best scaffold biomaterial or structural shape to support cells growth and differentiation.

In this work, we propose a constitutive model to simulate the mechanical behavior of CMs and hPSC-CMs. The model is implemented in a general-purpose FEM software and adopted to simulate *in silico* different experimental assays involving the mechanical interactions of hPSC-CMs with structures made of different biomaterials, such as hydrogels. We show the general capabilities of the numerical procedures developed and how the contractile forces of hPSC-CMs adopted in original experimental tests can be assessed by means of FEM modeling.

II. Materials and Methods

A. Constitutive modeling

To describe the phenomenology of CMs and hPSC-CMs we have modified a constitutive model previously proposed for skeletal muscle tissue [5] and based on Hill's three-element model [6], composed of a contractile element (CE), an elastic element (SE), in series with CE and an elastic element (PE) in parallel with CE and SE. This model is a simplified version of the actual structure of the sarcomeres, where both SE and CE are affected by the cross-bridge properties. The tension on SE is equal to the one on CE, since the two elements are placed in series, while the element PE is responsible for passive elasticity. The stress response of contractile fibers is assumed as the sum of a passive term P_p and an active term P_a. The passive term is defined as:

$$P_p = \begin{cases} 0 & \lambda_f \le 1 \\ E_f \left(\lambda_f - 1\right)^2 & \lambda_f > 1 \end{cases} \quad (1)$$

where λ_f is the stretch of the fibers and E_f a parameter with stress-like dimension. The active stress is defined as:

$$P_a = P_0 \, f_a(t) \, f_l(\lambda_m) \, f_v(\dot{\lambda}_m) \quad (2)$$

where the scalar P_0 is the maximum isometric stress, f_a the activation function, f_l the force-length function and f_v the force-velocity function. The activation function depends on time t and is assumed in the following form [7]:

$$f_a(t) = (t/t_0)^2 \, exp\left[1 - (t/t_0)^2\right] \quad (3)$$

where the constant t_0 determines the time of contraction. The force-length function depends on the stretch λ_m of contractile element CE:

$$f_l(\lambda_m) = \begin{cases} \dfrac{\lambda_m - \lambda_{min}}{\lambda_{opt} - \lambda_{min}} \cdot \\ \cdot exp\left[\dfrac{\left(2\lambda_{min} - \lambda_m - \lambda_{opt}\right)\left(\lambda_m - \lambda_{opt}\right)}{2\left(\lambda_{min} - \lambda_{opt}\right)}\right] & \lambda_m > \lambda_{min} \\ 0 & \lambda_m \le \lambda_{min} \end{cases} \quad (4)$$

The function is fitted to experimental data by setting the values for the minimum λ_{min} and optimal λ_{opt} stretch. Finally, the force-velocity function depends on the stretch rate $\dot{\lambda}_m$ of the contractile element:

$$f_l(\lambda_m) = \begin{cases} \dfrac{1 - \dot{\lambda}_m / \dot{\lambda}_{max}}{1 + 1 - k_c \, \dot{\lambda}_m / \dot{\lambda}_{max}} & \dot{\lambda}_{max} < \dot{\lambda}_m < 0 \\ 0 & \dot{\lambda}_m \le \dot{\lambda}_{max} \end{cases} \quad (5)$$

The previous function is fit to experimental data by setting the parameters $\dot{\lambda}_{max}$ and k_c.

The mechanical response of a three-dimensional construct of CMs with contractile fibers aligned to a specified direction $\boldsymbol{a}_0$ is described as an isotropic fiber-reinforced material and, in terms of the first Piola-Kirchhoff stress tensor $\boldsymbol{P}$, it is written:

$$\boldsymbol{P} = \boldsymbol{P}_{iso} + \left(P_p + P_a\right) \boldsymbol{F} \cdot \left(\boldsymbol{a}_0 \otimes \boldsymbol{a}_0\right) \quad (6)$$

where $\boldsymbol{F}$ is the deformation gradient. Since for these constructs it is usually accepted and almost-incompressible behavior, the elastic response associated to $\boldsymbol{P}_{iso}$ is deduced via a standard derivative from a strain energy function of the type:

$$w_{iso} = \alpha_{m1} \, exp\left[\alpha_{m2}\left(\tilde{I}_1 - 3\right)\right] + \frac{k_{mv}}{4}\left[J^2 - 1 - 2\,ln(J)\right] \quad (7)$$

where J is the Jacobian of the deformation and $\tilde{I}_1$ the first invariant of the iso-volumetric part of the right Cauchy–Green strain tensor $\tilde{\boldsymbol{C}} = J^{-2/3}\boldsymbol{F}^T\boldsymbol{F}$. The scalars α_{m1} and α_{m2} are constitutive parameters related to the iso-volumetric response, while represents the bulk modulus**.** Finally, the stretch of contractile fibers λ_f is deduced as:

$$\lambda_f = \sqrt{\tilde{\boldsymbol{C}} : \left(\boldsymbol{a}_0 \otimes \boldsymbol{a}_0\right)} \quad (8)$$

A relevant aspect of muscle tissues and muscle-like construct obtained in tissue engineering pertains to the spatial orientation of the fibers, which can follow a statistical distribution respect to specific directions, according to the level of maturation and the mechanical stimulus applied [8].

This results in a different level of anisotropy that is described in this model by assuming a 2D Von Mises distribution, as proposed for connective tissues [9]. This is suitable for modeling the experimental assays where hPSC-CMs are disposed in thin layers, therefore, with a local planar disposition. The local 2D Von Mises distribution of a group of fibers with respect to a specified direction $\boldsymbol{a}_0$ is considered by a modified structural invariant:

$$\tilde{I}_4 = \kappa \tilde{\boldsymbol{C}} : \left(\boldsymbol{I} - \boldsymbol{t}_0 \otimes \boldsymbol{t}_0\right) + \left(1 - 2\kappa\right) \tilde{\boldsymbol{C}} : \left(\boldsymbol{a}_0 \otimes \boldsymbol{a}_0\right) \quad (9)$$

where $\boldsymbol{I}$ is the second rank identity tensor, $\boldsymbol{t}_0$ the local normal to the plane of the fibers in the undeformed configuration and κ a fiber dispersion factor that is deduced from the density function of the fibers [9]. Fibers are totally aligned to $\boldsymbol{a}_0$ with $\kappa = 0$, while they are randomly disposed in the plane normal to $\boldsymbol{t}_0$ if $\kappa = ⅓$. The density distribution of the fibers around the reference direction $\boldsymbol{a}_0$ for different values of the dispersion factor κ is represented in Figure 1.

The constitutive model has been implemented through FORTRAN subroutines in the general-purpose FEM software ABAQUS (SIMULIA™, Dassault Systèms, France). The subroutines allow the use in nonlinear static, implicit dynamic, as well as explicit dynamic procedures. Continuum 3D and plane-strain elements can be used with the constitutive model, also for hybrid formulation – when available – to overcome numerical instabilities due the almost-incompressible behavior, that is typical of tissues and materials considered in this study. Additional capabilities of the subroutines are represented by the possibility to provide 3D Von Mises distribution of the fibers and statistical distribution of other constitutive parameters, such as the maximum isometric tension of the fiber, which can be defined with spatial distribution at the level of Gauss points.

Since the numerical approach is aimed at evaluating specific constitutive parameters based on experimental data, it is helpful to have an inverse iterative procedure of model fitting. This has been obtained by linking ABAQUS and MATLAB (MathWorks, USA). A user script [10] is adopted to optimize the constitutive parameters by defining an objective function of error between numerical results and experimental data and by using a built-in MATLAB function to find the minimum of constrained nonlinear multivariable functions.

B. FEM models

FEM models were developed using ABAQUS CAE software (SIMULIA, Dassàult Systems, France) to test the general capability of the constitutive model and to simulate a specific experimental assay involving hPSC-CMs.

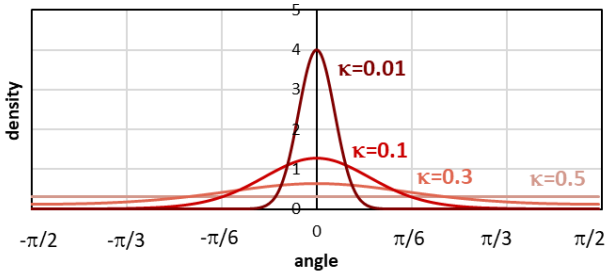


Fig. 1 Density distribution of the fibers around the reference direction $\boldsymbol{a}_o$ according to different values of the dispersion factor κ. For κ = 0 the fibers are totally aligned to $\boldsymbol{a}_o$.

To test the effect of fiber angular dispersion (parameter κ), a model with simple geometry was conceived, consisting of a free flat disc with 1 mm diameter and 0.1 mm thickness, and assuming the constitutive model described in section A. The reference direction for the fibers $\boldsymbol{a}_0$ is aligned with a diameter of the disc and different levels of fiber angle dispersion are considered, corresponding to the parameter κ equal to 0, 0.1, 0.3 and 0.5, while all the other constitutive parameters are considered fixed. The disc is free to deform under contraction of the fibers and the deformation is compared for the four conditions. Moreover, to test the capability of our numerical procedures to simulate large deflection problems we were inspired by the work of Shim et al. [7], modelling a composite flat rectangular sheet (2 mm × 4 mm) made of two overlapping layers: the upper layer (4 μm thickness) consists of cardiomyocytes while the lower layer (14 μm thickness) is made of hydrogel. The two layers are perfectly bounded at their interface and fixed at one of the short edges (Figure 2a). The sheet deflects under contraction of cardiomyocytes that are considered with two different spatial orientation in the plane of the sheet, lengthwise fibers, or oblique fibers with angle of 45°, with total alignment to the reference direction (κ = 0). The hydrogel is considered as an almost-incompressible neo-Hookean hyperelastic material with initial longitudinal elastic modulus of 10 kPa.

In addition, original experimental assays have been developed using tubular shape scaffolds with length of about 0.4 mm, made of hydrogel coated with an external layer of hPSC-CMs. The contraction of hPSC-CMs generates a deformation of the scaffold, which is analyzed by experiment specific models. Confocal microscope images of the tubular scaffold (Figure 2b) are used to reconstruct a model that consists of the hydrogel tube covered by a layer of cardiomyocytes. The transversal section of the hydrogel tube is roughly ellipsoidal with external diameters of about 200 μm and 170 μm, and internal diameters of about 150 μm and 70 μm.

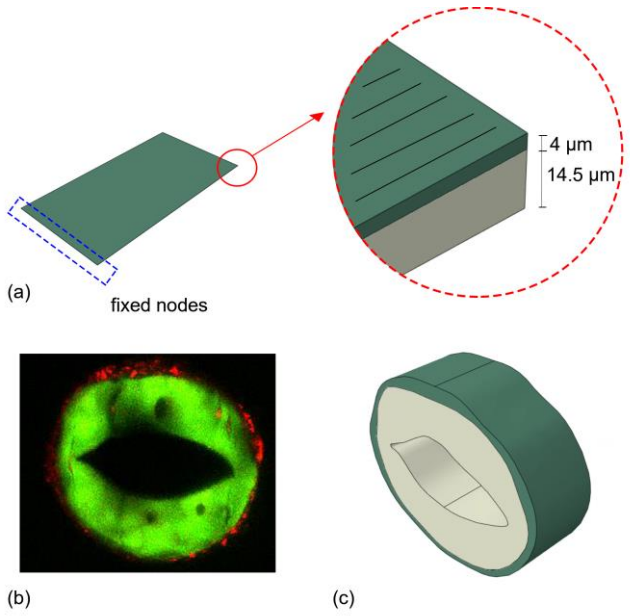


Fig. 2 Geometric reconstruction of a hydrogel sheet covered by a layer of cardiomyocytes (a); Confocal microscope image of a hydrogel tube coated by an external layer of cardiomyocytes (b); Geometric reconstruction of the structure of a tube slice and layer of cardiomyocytes (c).

The layer of hPSC-CMs has a thickness of about 5 μm (Figure 2c). The fibers are assumed to be aligned circumferentially to the external boundary of the tube.

The hydrogel is described as adopting an almost-incompressible neo-Hookean hyperelastic constitutive model with an initial longitudinal elastic modulus of 10 kPa (value deduced from experimental indentation). The contractile force of hPSC-CMs and the characteristic time of contraction are estimated via an inverse method based on the deformation of the transversal section of the scaffold.

In the three proposed examples, the models are discretized using linear hybrid hexahedral finite elements. A static non-linear procedure is adopted, according to the low value of the mass and the consequent negligible value of inertial forces.

III. Results

The numerical analyses performed using the flat disk and the flat sheet models allow to evaluate the effect of the fiber dispersion and orientation in the contractile response of cardiomyocytes. Figure 3 shows that the deformation at the same level of activation is different based on the dispersion level of fibers, where κ = 0 corresponds to fibers totally aligned to $\boldsymbol{a}_0$ and κ = 0.5 to fibers totally dispersed around $\boldsymbol{a}_0$.

Figure 4 shows the large folding of the sheet due to CMs contraction and the different resulting deformation according to the fiber orientation. A lateral component of displacement emerges in the case of fibers with a non-zero angle with respect to the lengthwise direction.

Regarding the tubular shape scaffold, the deformation induced by hPSC-CMs contraction is evaluated through the length change of the pseudo-diameters the internal cavity (Figure 5a). The maximum stress value (3.5 kPa) and time of contraction (about 0.45 s) in the constitutive model of cardiomyocytes are estimated through the fitting of the numerical model deformation to experimental data (Figure 5b).

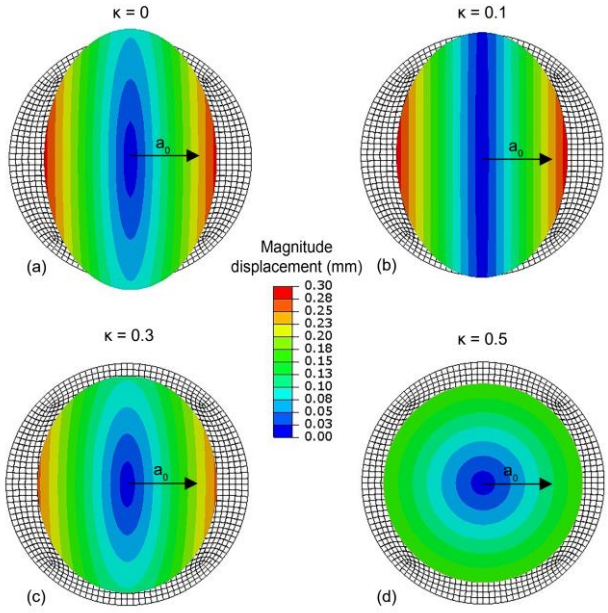


Fig. 3 Deformed configuration and magnitude displacement field (mm) for the flat disc, at the same level of contraction, according to the different angular distribution of the fibers around the direction represented by the vector $\boldsymbol{a}_0$. The value κ = 0 corresponds to the total alignment of the fibers along $\boldsymbol{a}_0$, while κ = 0.5 to the totally random dispersion of the fibers in the plane of the disc.

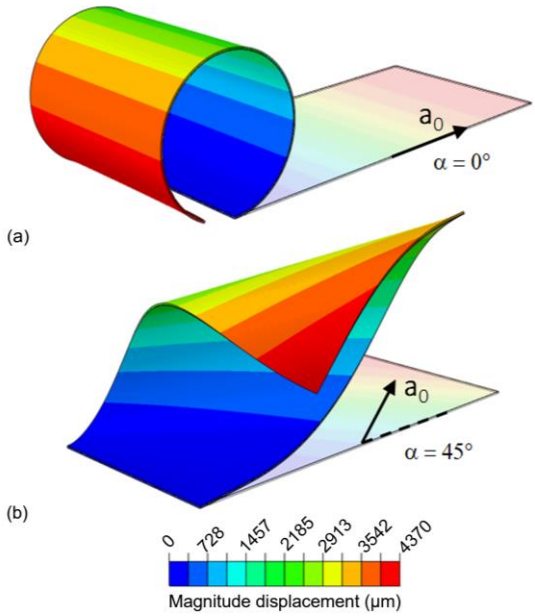


Fig. 4 Sheet folding at the same level of activation for a different spatial orientation of the fibers in the plane of the sheet. In both models, it is set $\kappa = 0$ (fibers perfectly aligned to $\boldsymbol{a}_0$).

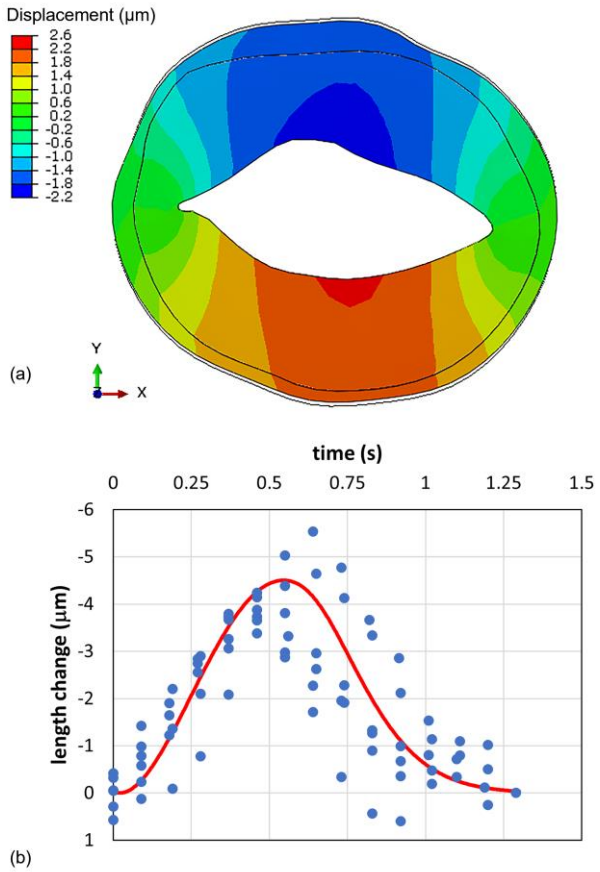


Fig. 5 Displacements field (μm) in Y direction in a specific transversal section of the tubular scaffold under cardiomyocytes contraction, compared to undeformed configuration (a); length change of the shorter internal diameter vs. time (b): numerical results (solid line) are compared with experimental data taken from 6 contraction cycles (dots).

IV. Conclusion

The proposed models allow to evaluate contraction capability of cardiomyocytes in different situations, and are also able to numerically reproduce experimental analyses on human embryonic stem cell-derived cardiomyocytes.

The development of such models is essential to study the relationship between cardiomyocytes mechanical behavior and cardiac pathologies, since many cellular alterations caused by cardiovascular diseases may induce a variation in the activation or the force generation processes of CMs.

However, there are still several aspects of these models that could be improved, for example, by considering that the hydrogel microtubes with hPSC-CMs layers are immersed in saline solution in the experimental set-up. Therefore, an improved model may also take into consideration the liquid flow through the microtube and its effect on cardiomyocytes contraction and on the microtube occlusion.

Despite some limitations, these models represent the first step towards the analysis of the active mechanical behavior of hPSC-CMs on hydrogel scaffolds and their future developments will enable to assess how CMs can organize on scaffolds to properly mimic the cardiac muscular tissue for tissue engineering applications.

References

[1] E.A. Woodcock and S.J. Matkovich, “Cardiomyocytes structure, function and associated pathologies”, *Int J Biochem Cell Biol.*, vol. 37, pp. 1746-1751, Sept. 2005

[2] A. Sizarov, J. Ya, B.A. de Boer, W.H. Lamers, V.M. Christoffels and A.F.M. Moorman, “Formation of the building plan of the human heart morphogenesis, growth, and differentiation”, *Circulation*, vol. 123, pp. 1125–1135, March 2011

[3] C.C. Kartha, “Cardiomyocytes in Health and Disease”, *Springer, Cham.*, Sept. 2021

[4] A.H. Nguyen, P. Marsh, L. Schmiess-Heine, P.J. Burke, A. Lee, J. Lee and H. Cao, “Cardiac tissue engineering: state-of-the-art methods and outlook”, *J. Biol. Eng.*, vol. 13, June 2019

[5] L. Marcucci, C. Reggiani, A.N. Natali and P.G. Pavan, "From single muscle fiber to whole muscle mechanics: a finite element model of a muscle bundle with fast and slow fibers", *Biomech. Model. Mechanobiol.*, vol. 16, pp. 1833-1843, Dec. 2017

[6] A.V. Hill, "The heat of shortening and the dynamic constants of muscle", *Proc. R. Soc. Lond. B. Biol. Sci.*, vol. 126, pp.136–195, Oct. 1938

[7] J. Shim, A. Grosberg, J.C. Nawroth, K.K. Parker and K. Bertoldi, "Modeling of cardiac muscle thin films: Pre-stretch, passive and active behavior", *J. Biomech.*, vol. 45, pp. 832–841, Oct. 2011

[8] E. Maghin, E. Carraro, D. Boso, A. Dedja, M. Giagante, P. Caccin, R.A. Barna, S. Bresolin, A. Cani, G. Borile, D. Sandrin, F. Romanato, F. Cecchinato, A. Urciuolo, D. Sandonà, P. De Coppi, P.G. Pavan and M. Piccoli, "Customized dynamic bioreactor system enables the production of radially aligned 3D diaphragmatic muscle constructs by promoting ECM remodeling and inhibiting fibroblasts overgrowth", *NPJ Regen. Med.*, vol. 7, Apr. 2022

[9] Y. Wang, S. Son, S.M. Swartz and N.C. Goulbourne, "A mixed Von Mises distribution for modeling soft biological tissues with two distributed fiber properties", *Int. J. Sol. Struct.*, vol. 49, pp. 2914-2923, May 2012

[10] S. Todros, S. Spadoni, S. Barbon, E. Stocco, M. Confalonieri, A. Porzionato and P.G. Pavan, "Compressive mechanical behavior of partially oxidized polyvinyl alcohol hydrogels for cartilage tissue repair", *Bioengineering*, vol. 9, Dec. 2022

The biomechanical behaviour of fascial system: Superficial VS Deep Fascia

L. Bonaldi[1], C.G. Fontanella[2,3], C. Pirri[4], C. Stecco[2,4], and A. Berardo[1,2,5]
[1] *Department of Civil, Environmental and Architectural Engineering, Via F. Marzolo 9, 35131 - Padova, Italy;*
[2] *Centre for Mechanics of Biological Material (CMBM), Via F. Marzolo 9, 35131 - Padova, Italy;*
[3] *Italy Department of Industrial Engineering, Via Venezia 1, 35121 - Padova, Italy;*
[4] *Department of Neuroscience, Via A. Gabelli 65, 35121 - Padova, Italy;*
[5] *Department of Biomedical Sciences, Via U. Bassi 58/B, 35131 – Padova.*

***Abstract*— The proper connective tissue, which defines the fascial system, plays a central role in supporting the biomechanics of the body. Fasciae can be classified between superficial and deep according to their anatomical structures and bodily functions. However, despite the importance of fascial alterations in different clinical conditions, the literature is still lacking in evidence comparing superficial and deep fasciae in terms of biomechanical properties. The present work, therefore, aims to offer an in-depth study on this topic. The experimental results showed a site-dependent anisotropy and a viscoelastic behavior of the fascial tissues. Mechanical comparison between fasciae is the key to tailor and target the most appropriate clinical intervention.**

***Keywords*— connective tissue, musculoskeletal system, fascial system, biomechanical properties.**

I. Introduction

THE PROPER CONNECTIVE TISSUE (CT) has many roles in body functioning such as structural support and connection of musculoskeletal system. In daily life, it is subjected to in vivo loads that arrange its structure according to multi-axial movement directions. Thus, the mechanical response of connective components (cells, collagen and elastin fibres, ground substance) is key for mechanotransduction. These properties are expressed by dense and loose connective substrates, which, between the skin and the deep muscle layers, are organized at several levels to slide over each other. The proper gliding between layers allows forces transmission between body structures and it could be altered in case of clinical conditions [1]. This specific arrangement of CT defines the fascial system made by a) Epidermis and Dermis, b) SAT with retinaculum cutis superficialis, c) Superficial Fascia (SF), d) DAT with retinaculum cutis profundus e) Deep Fascia (DF) f) Muscle [2]. Therefore, the continuity between skin layers and deep muscles is ensured through the retinacula that connect to SF and DF (Fig. 1). SF and DF have been shown to have different anatomy and are implicated in different disorders [3]. Despite the clinical implications of fasciae in several musculoskeletal diseases, literature is still poor of evidence that compares the structural characterization of SF and DF through mechanical tests. Therefore, in this research work we have investigated this open topic. Our contribution could guide the clinician in planning the most appropriate treatment modality according to the mechanical response of the fascial tissues.

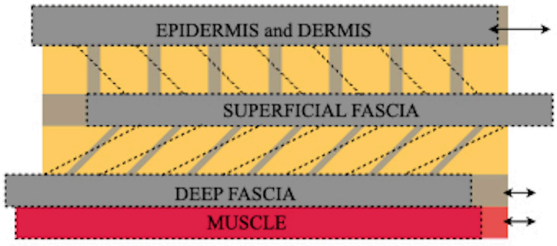


Fig. 1: Fascial system continuity from skin to muscles and gliding between layers.

II. Material and Methods

A. Samples collection

Fascia patches have been harvested from fresh-frozen human donors (Table I) according to Body Donation Program of the Institute of Anatomy of the University of Padua [4]-[6]. From the clinical history of the subjects, no alterations of the fascial tissue were reported.

TABLE I: Human Donors Information

Subject	*Gender*	*Age*	*Site*	*Patch*
1	1 Male	76 y/o	Fascia Lata	DF
2	1 Male	87 y/o	Abdomen	SF
3	1 Male	76 y/o	Thorax	

Table I: Harvested tissues and donors' information. Sites were selected based on donors' availability.

B. Micro and macrostructure of SF and DF

Samples of SF can be macroscopically isolated as a well-defined membrane but microscopically SF shows a multilamellar structure, where the various sublayers are interconnected to each other's and interspersed with irregular islets of fat cells.

Meanwhile, DF (in this case as aponeurotic fascia of the thigh) both macroscopically and microscopically shows a double-layer organization of dense connective tissue (well-separated by loose connective tissue), where collagen bundles follow specific directions, forming an inter-layer angle of 85° (Fig. 2).

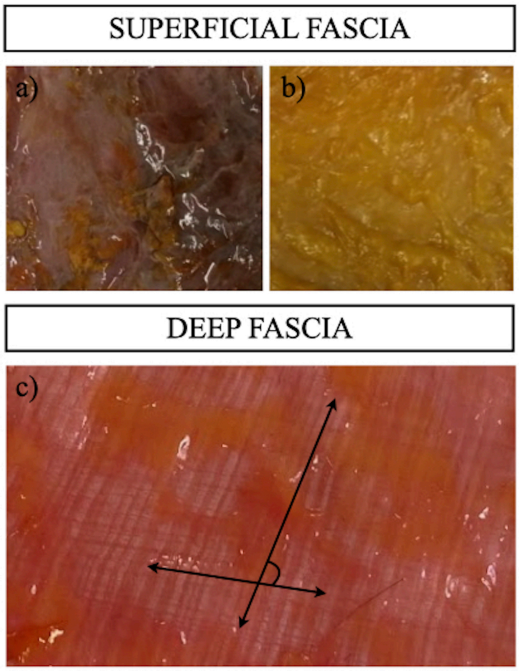


Fig. 2: Samples from donors a) thorax b) abdomen c) fascia lata, examples of collagen fibres directionality. The directions of the DF fibers form an inter-layers angle, while the SF samples do not show a specific orientation of the bundles.

C. *Experimental tests*

After thawing, the samples were cut into rectangular strips in two orthogonal directions (D1 and D2). The temperature and dimensionality of the strips were acquired at multiple points of the samples and recorded. Samples were kept moist with saline solution for the overall testing procedure. Then, each specimen was mounted on a mechanical tester (Model Mach-1, ©Biomomentum, with a load cell capacity of 250N and accuracy ±0.0125N) and loaded for uniaxial tensile tests. Preconditioning (10 cycles of loading-unloading) was performed before two different protocols of Failure and Stress-Relaxation (Table II), to evince potential tissues anisotropy and viscoelastic behaviours.

TABLE II: EXPERIMENTAL PROTOCOLS

Patch	*Preconditioning*	*Failure*	*Stress-Relaxation*
SF	10 cycles, 0.25 Hz, 4% strain	1%/s strain rate	15%/s strain rate, 5 ramps, 5% strain each, 300s resting time
DF	10 cycles, 0.125 Hz, 3% strain		1%/s strain rate, 5 ramps, 2% strain each, 300s resting time

Table II: Failure and stress-relaxation protocols information, designed and tuned based on experimental evidence.

D. *Statistical Analysis*

Mechanical results have been analysed with MATLAB 2021b (The MathWorks, Inc., MATLAB and Statistics, Natick, Massachusetts, United States). To compare the potential difference according to sites and directions, a statistical analysis was performed with Minitab Statistical Software (Software, Minitab, State College, Pennsylvania 2010 Minitab, Inc.). Inferential statistics compared the results for different sites (Two-sample t-test, two-tail, level of significance 0.05) and loading directions (Paired-sample, two-tail t-test, level of significance 0.05).

III. RESULTS

In the current section, the results for different sites and loading directions have been detailed. Specifically, the comparison of ultimate tensile strength (UTS)/strain at break/Young's Modulus (linear region) was reported for failure tests, while % stress decay was discussed for stress-relaxation curves.

A. *Failure test*

The comparison between SF and DF for different sites and directions was summarized in Table III and in Fig. 3.

TABLE III: FAILURE RESULTS

Patch	*Site*	*Direction*	*UTS (MPa)*	*Strain at break (%)*	*Young's Modulus (MPa)*
SF	*Abdomen*	*D1*	0.34 ± 0.12	47.0 ± 9.00	1.32 ± 0.82
		D2	0.66 ± 0.37	50.0 ± 11.0	2.25 ± 1.04
	Thorax	*D1*	8.86 ± 2.44	39.0 ± 5.00	37.76 ± 11.19
		D2	3.66 ± 0.92	34.0 ± 3.00	17.39 ± 4.43
DF	*Fascia Lata*	*D1*	10.53 ± 2.60	17.0 ± 8.00	155.88 ± 66.91
		D2	1.45 ± 0.76	16.0 ± 5.00	8.47 ± 6.47

Table III: Experimental results (mean ± SD) from failure curves for different sites and directions.

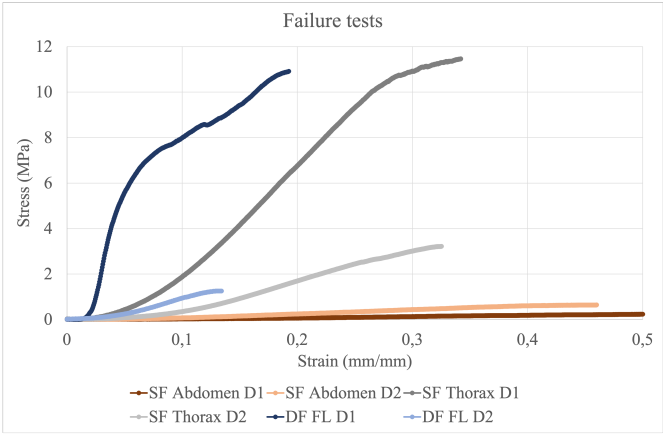


Fig. 3: Examples of stress-strain curves for different sites and directions.

Both SF and DF exhibited a non-linear stress-strain behaviour.

TABLE IV: INFERENTIAL STATISTICS, FAILURE RESULTS - COMPARISON BETWEEN DIRECTIONS

Patch	*Site*	*Direction*	*UTS*	*Strain at break*	*Young's Modulus*
SF	*Abdomen*	*D1* / *D2*	0.199	0.593	0.295
	Thorax	*D1* / *D2*	**0.014***	0.119	**0.030***
DF	*Fascia Lata*	*D1* / *D2*	**0.001***	0.845	**0.002***

Table IV: Statistical results (p-value) from failure curves for different sites between loading directions (*p-value < 0.05).

SF of thoracic region and DF showed an anisotropic behaviour between directions in terms of UTS and Young's Modulus values. Meanwhile, there are no specific differences between loading directions for all districts in terms of strain at break values (Table IV). In any case, from the statistical tests, the strain at break values between the sites were found to be significantly different (p-values < 0.05) and higher for SF than for DF. In general, in one direction, DF was stiffer and stronger than SF, meanwhile, the SF of the abdominal region was less stiff and strong than the other districts.

B. Stress-Relaxation test

The comparison between SF and DF for different sites and directions was summarized in Fig. 4, Table V and Fig. 5.

Normalized stress was obtained as the ratio of stress to the peak value recorded at the beginning of each relaxation curve. A two-term Prony series Eq. (1) was used to fit the normalized stress-relaxation curves:

$$\sigma_{norm} = 1 - \gamma_1 \left(1 - e^{\frac{t}{\tau_1}}\right) - \gamma_2 \left(1 - e^{\frac{t}{\tau_2}}\right) \quad (1)$$

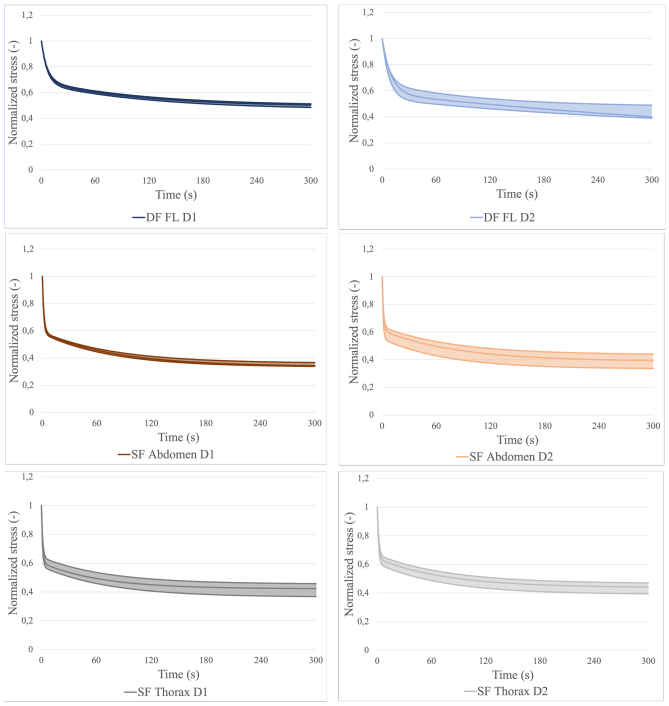


Fig. 4: Experimental results (median values) from stress-relaxation curves for different sites and directions. Color bands depicted the first and third percentiles.

TABLE V: STRESS-RELAXATION RESULTS

Patch	*Site*	*Direction*	*Residual stress*			
			After 10s	*After 30s*	*After 120s*	*After 240s*
SF	*Abdomen*	*D1*	0.56	0.51	0.40	0.35
		D2	0.59	0.54	0.44	0.40
	Thorax	*D1*	0.58	0.54	0.45	0.43
		D2	0.62	0.57	0.48	0.45
DF	*Fascia Lata*	*D1*	0.73	0.64	0.56	0.51
		D2	0.72	0.57	0.50	0.43

Table V: Median values of normalized residual stress (% of the peak, which is equal to 100%) from stress-relaxation curves for different sites and directions.

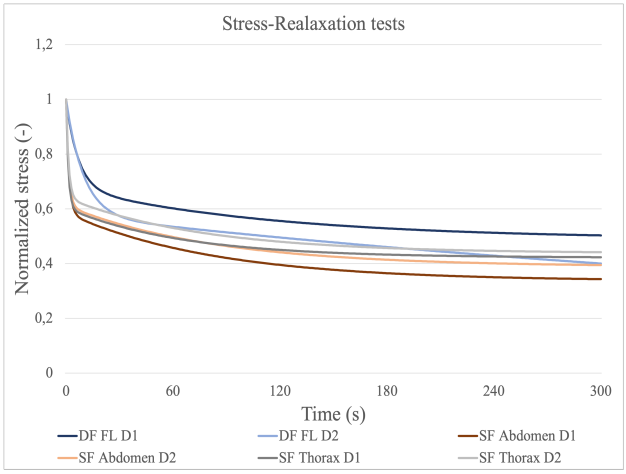


Fig. 5: Experimental results (median values) from stress-relaxation curves for different sites and directions.

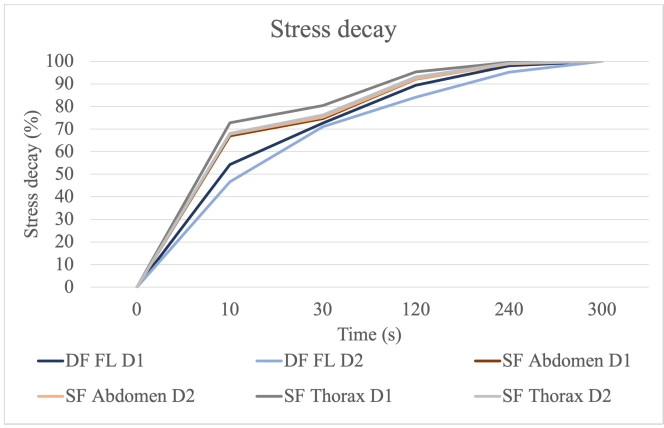


Fig. 6: Experimental results (stress-decay, % of the total relaxation which is equal to 100%) from stress-relaxation curves for different sites and directions.

Both SF and DF exhibited a viscoelastic response. SF of the abdominal region relaxed at lower levels of initial stress than other sites. A difference for stress decay was found in the early 30s between SF and DF. After 30s the stress decay is at least 64% of the initial stress for all specimens. In fact, most of the stress relaxed in the early 30s (at least 70% of total relaxation). Between 240s and 300s the stress decay reached a plateau (steady state) for all the samples. Fig. 6.

IV. DISCUSSION

The results of mechanical tests conducted on human SF and DF helped highlight the variability between the layers of the fascial system, as potential evidence of their structural differences and roles.

The stress-strain curves for both SF and DF showed a nonlinear behavior as for connective tissue [7]. At the beginning of each curve, in the so-called "toe" region, the collagen fibers of the fascia were in a crimped conformation, then reached a progressive uncrimping in the linear region until they broke.

Regardless of the direction of loading, the SF districts resisted greater strain before failure than DF, and in particular the abdominal region greater than the thoracic one. One hypothesis could be justified by the presence of a higher percentage of elastin fibres in SF than in DF, as characterized by reference [8]. This difference could also be explained in

terms of deformation changes of these body sites during activities of daily living.

In terms of UTS and Young's Modulus, anisotropy between loading directions was confirmed for the thoracic and fascia lata sites, but for the abdominal fascia, thus, increasing the importance in tissue placement (i.e., orientation), for example during the surgical procedure. Furthermore, in one direction the DF was stiffer and stronger than the SF, where the abdominal region showed lower values than the thoracic one. This confirmed the results concerning fascia lata anistotropy, as constituted by parallel layers of collagen fibers which contribute differently with reference to tissue strength and stiffness, in accordance with inter-layer angle. This fact reflects the ability of the fascia lata not only to adapt to muscle contraction but also to transmit the mechanical forces of in vivo loads along specific anatomical lines. As the literature still lacks evidence on the mechanical behavior of the SF of the abdominal and thoracic sites, we cannot compare our results. Explanatory hypotheses for the difference in tissue anisotropy could be found in the presence of anatomical connection between superficial fascia and different superficial veins/lymphatic vessels [3] and muscle groups. In fact, reference [9] already demonstrated SF variability in accordance with body location and gender.

The viscoelastic nature of connective tissues has been confirmed for both SF and DF by the results of stress relaxation. In general, for all the samples, at least 70% of the total stress decay occurred in the first 30s, while 300s could be considered sufficient for the completion of the stress relaxation phenomena (as rearrangement of tissue components for body optimization strategy), thus, potentially providing a reference for stretching practitioners in terms of maintaining a position for the aforementioned time intervals during their exercise (see [10] for further comparison with DF of the leg). In particular, the abdominal SF final stress (plateau) relaxed to lower levels than the other districts. Otherwise, the relaxation of the DF tissue in the early 30s behaved differently than that of the SF. The composite nature of DF with loose and dense layers of connective tissue could potentially account for this finding, as well as the different strain rates used to test the samples could impacted the results.

The challenges of the current work were the lack of data from literature in terms of protocol design and study comparison. A limitation of the present study is the low number of donors. As further proof of the concept, more studies should be performed on a larger sample size (i.e., additional sites of the same subjects and more subjects) to overcome the limitations of subject variability (i.e., gender, clinical history, BMI, age and so on) and with different protocols/parameters (i.e., strain rate).

In the future, the collection of additional data could permit the modelling of the overall fascial system in different clinical scenarios as physiological (such as pregnancy, aging) or pathological (such as musculoskeletal disorders) conditions. For example, it has been demonstrated that the functional role of SF in supporting the integrity of subcutaneous structures through stress adaptation could be modified with aging or in pathological conditions (e.g., as scar formation), thus leading to an alteration in nerve/vascular patency as well as in sliding/transmission of the forces between the muscles and the skin [1].

V. Conclusions

This work primarily helps to compare the superficial and deep fascia of different body regions as well as characterize the superficial fascia of the abdominal and thoracic sites.

The fascial system has demonstrated different mechanical properties according to site and directions.

The mechanical characterization of the different layers of the fascial system represents a fundamental information to deepen the knowledge of its arrangement, as a key connection for the transmission of mechanical loads. These findings have practical clinical implications such as in tissue engineering, graft surgery and rehabilitation planning.

Acknowledgement

This work was supported by MIUR, FISR 2019, Project n° FISR2019_03221, titled CECOMES (CEntro di studi sperimentali e COmputazionali per la ModElliStica applicata alla chirurgia).

References

[1] C. Stecco, *Functional Atlas of the human fascial system*. Churchill Livingstone, 2015.

[2] C. Stecco, V. Macchi, A. Porzionato, F. Duparc and R. De Caro, "The fascia: the forgotten structure", *Ital J Anat Embryol*, vol. 116, pp. 127-138, 2011.

[3] A. Stecco, R. Stern, I. Fantoni, R. De Caro and C. Stecco, "Fascial Disorders: Implications for Treatment", *PM & R: the journal of injury, function, and rehabilitation*, vol. 8, pp. 161-168, 2016.

[4] A. Porzionato, V. Macchi, C. Stecco, A. Mazzi, A. Rambaldo et al., "Quality management of Body Donation Program at the University of Padova", *Anat Sci Educ*, vol. 5, pp. 264-272, 2012.

[5] R. De Caro, R. Boscolo-Berto, M. Artico, E. Bertelli, M. Cannas et al, "The Italian law on body donation: A position paper of the Italian College of Anatomists", *ANNALS OF ANATOMY*, vol. 238, 2021.

[6] R. De Caro, M. Veronica and A. Porzionato, "Promotion of body donation and use of cadavers in anatomical education at the University of Padova", *Anat Sci Educ,* vol. 2, pp- 91-92, 2009.

[7] A. J. Threlkeld, "The effects of manual therapy on connective tissue", *Physical therapy*, vol. 72, pp. 893–902, 1992.

[8] C. Pirri, C. Fede, L. Petrelli, D. Guidolin, C. Fan et al, "Elastic Fibres in the subcutaneous tissue: Is there a difference between superficial and muscular fascia? A cadaver study", *Skin Res Technol*, vol. 28, pp. 21-27, 2022.

[9] M. F. Abu-Hijleh, A. L. Roshier, Q. Al-Shboul, A. S. Dharap and P. F. Harris, "The membranous layer of superficial fascia: evidence for its widespread distribution in the body", *Surgical and radiologic anatomy: SRA*, vol. 28, pp. 606–619, 2006.

[10] P. G. Pavan, A. Stecco, R. Stern and C. Stecco, "Painful connections: densification versus fibrosis of fascia", *Current pain and headache reports*, vol. 18, pp. 441, 2014.

Analysis of an Elite Amputee Paralympic Sprinter in Track Running Pilot Tests

S. Barbacane[1], S. G. Breban[1], G. Fabris[1], M. Scapinello[1], R. Di Marco[2], G. Marcolin[3], G. L. Migliore[4], A.G. Cutti[4] and N. Petrone[1]

[1] *Department of Industrial Engineering, University of Padova, Padova, Italy*
[2] *Department of Computer Science, University of Verona, Verona, Italy*
[3] *Department of Biomedical Sciences, University of Padova, Padova, Italy*
[4] *INAIL Prosthetic Centre, Vigorso di Budrio (BO), Italy*

***Abstract* — Biomechanical analysis of Paralympic amputee sprinters has implications for the design of prosthetic components and for the improvement of the athletic performance. Field measurements are the optimal condition to collect data for this purpose. Therefore, the aim of this study was to complete a kinematic and kinetic analysis of a unilateral transfemoral amputee sprinter running on track. Data were gathered with a 28-camera motion capture (mocap) system and wearable kinetic sensors. Joint kinematics of the prosthetic limb and the intact limb were compared. The results presented here provide an example of outcomes which can support the improvement of athletes' safety and performance.**

***Keywords*—Running Biomechanics, Paralympic Sprinters, Load Cell, Motion Capture.**

I. INTRODUCTION

IN the last decades there has been growing interest in the running biomechanics of individuals with lower limb amputation [1]. Research has allowed to gain greater insight into how lower-extremity amputees regain running capacity. Running Prosthetic Foot (RPF), carbon fibre blade with a spring-like function, has been introduced since the '90s and over the years its design has been improved in order to better compensate for the replacement of an active leg.

It has been observed that laboratory measurements with subjects running on a treadmill, despite having high precision and resolution, cannot be entirely realistic, because sprinters are not used to running in such an artificial environment and at a constant speed [2]. In contrast, overground running tests can reproduce sprints very close to those performed during races. Thus, the results obtained from these tests better correlate with the actual athletic performance and are more useful for the structural optimization of running prosthesis. However, data collected in indoor or outdoor tracks are challenging for the cost of instrumentation, which should cover kinematics and kinetics over a convenient portion of the track.

Several studies make use of force platforms placed on the running track to measure Ground Reaction Forces (GRFs) during overground running [3], [4]. Except in cases where the number of platforms is very large [5], the results of this type of studies depend to a large extent on the probability of obtaining valid steps for the analysis (athlete hitting the plate and whole foot placed on the plate). Instrumented prosthesis have been demonstrated to overcome this issue by allowing realistic and numerous performance data to be obtained [6]. Various attempts have been made at kinematic analysis using inertial sensors attached to the athlete's body, but results are less accurate than those obtained with the mocap system, considered the gold standard [7].

The purpose of the present study was to present kinematic and kinetic in-field collected data, obtained through an integrated motion capture and kinetic acquisition system, of a world-class athlete running unrestrained on a familiar track surface. These data will form the basis for a more in-depth analysis of the effects of the prosthesis configuration on running strategy and the minimization of injury risk.

II. MATERIALS AND METHODS

A. Participants

One elite, gold medallist, Paralympic female athlete (mass: 55 kg; height: 1.60 m) with left unilateral transfemoral amputation, participated in this study. She wore the Ottobock 1E91 standard RPF, category 3.5, and she used the mono-axial Ottobock 3S80 prosthetic knee.

B. Instrumentation

Tests were performed in a 60m indoor athletics track (Palaindoor, Padova). In detail, the athlete ran on the eighth lane of the central straight runway.

Motion capture cameras (25 *Vero* (fs = 300 Hz) and 3 *Vantage* (fs = 300 Hz) - Vicon Motion System, Oxford, UK) were placed in the central part of the runway, covering an approximated 20-metres-long acquisition volume. 22 cameras were mounted on tripods placed along the runway, while the remaining 6 were installed on a double portal structure made of aluminium trusses with an overall size of 2.5 x 3 x 3.5 metres (length x width x height) positioned in the midpoint of the runway (Figure 1).

The Running-Specific Prosthesis (RSP) was instrumented with a 6-axis ultra-thin load cell mounted in between the prosthetic knee and the clamp of the RPF, and connected through wires to an ultra-small, standalone acquisition system (*DTS SLICE NANO* (fs= 2000 Hz) - DTS, Seal Beach, USA). The acquisition system was placed inside a small running backpack, together with its battery and a power bank for the load cell power supply.

C. Experimental protocol

The subject wore the prosthesis and the orthopaedic technician set the inclination of the socket with respect to the vertical line passing through the greater trochanter and the centre of the prosthetic knee. Specifically, the alignment adopted in the tests consisted in a socket pre-flexion angle equal to 15°[8]. The athlete then warmed up to familiarize with the track and the prosthesis setup.

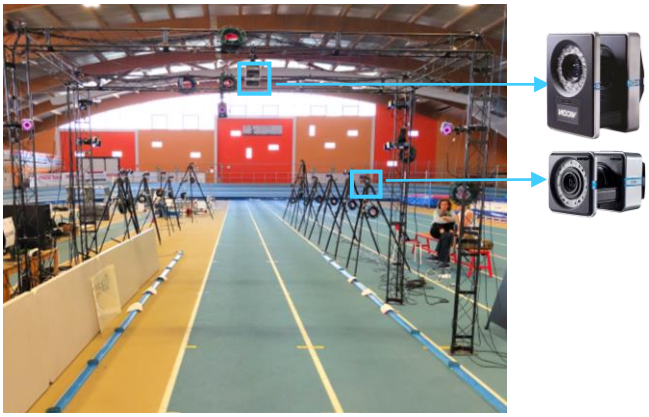


Fig. 1: Motion Capture system installed in the indoor athletics track. 28 Optoelectronic cameras (Vicon, fs = 300 Hz) placed on tripods and on the double portal structure.

Sixty-five retroreflective markers (14 mm diameter) were attached to the subject at specific anatomical landmarks and locations of the prosthetic components (Figure 2a, 2b), such as on the proximal and distal tip of the RPF, on the clamp, on the mechanical knee and on the socket. A wand calibration procedure was employed to identify 12 additional points, including four reference points on the loadcell, relative to technical clusters of markers. After the static acquisition, the calibrated markers, both placed medially on body segments (medial femoral epicondyle, medial malleolus, first metatarsal head, medial side of the prosthetic knee) and on the neck, thorax and posterior iliac spines were removed, because the former would have been likely to fall during the subsequent running trials and the latter would have been obstructed by the backpack and its straps.

The tests consisted of a series of sprints where the athlete started running from a line outside of the acquisition volume, accelerated to approximately 60% of her maximal speed (self-reported) and maintained this constant speed along the acquisition volume located 25 m from the start line. To avoid fatigue, the participant performed only three Steady State Running on track tests (TSSR).

D. Data analysis

Kinematic data were collected at 300 Hz. The labelling procedure was performed using Vicon Nexus 2.12 through an automatic algorithm. Subsequently, labelling was revised through careful frame-by-frame manual inspection to correct possible label swapping and gaps in the trajectories. Data were then low-pass filtered using a zero-lag fourth-order Butterworth filter with cut-off frequency equal to 10 Hz. Kinematic analysis was then carried out in MATLAB, with each body segment identified by a coordinate system (CS), i.e. an orthogonal triad defined through markers relative to that segment. The x-axis of the CS represented the anterior-posterior direction (pointing forward), y-axis the longitudinal direction (pointing upward) and the z-axis the medial-lateral direction (pointing rightward).

Ankle, knee and hip joint kinematics, as well as the prosthetic knee joint kinematics, were described by the orientation of the distal CS with regard to proximal CS using the Cardan angles. The sequence adopted was 'ZXY', except for the ankle angles, for which the 'ZYX' sequence was chosen instead. Trunk inclination in the sagittal plane was calculated as the angle – with respect to the vertical – of the vector joining

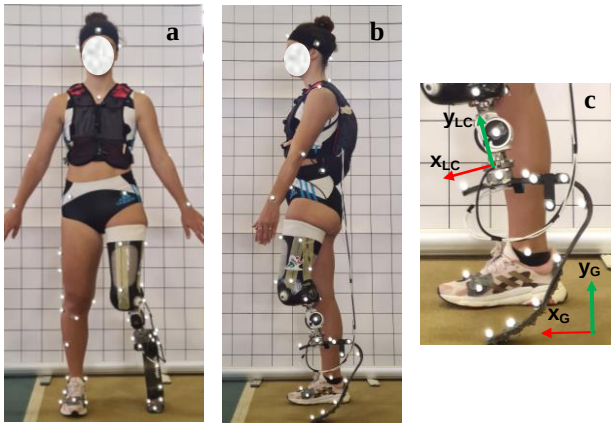


Fig. 2: 2a-b) Markerset adopted during the experimental session. Markers were applied on a headband worn by the subject, on arms, trunk, pelvis and right leg bony prominences and on the prosthetic components (socket, prosthetic knee, clamp and RPF). 2c) Detail of Load Cell coordinate system and ground coordinate system (sagittal view).

the centroid of the markers placed on the posterior iliac spines and the marker placed on the seventh cervical vertebra. The inclination in the sagittal plane of the unaffected shank (Theta Shank θ_S) and of the load cell installed in the prosthesis (Theta Load Cell θ_{LC}) were likewise calculated as the angle between the longitudinal axis of the segment and the vertical global axis. As far as shank is concerned, longitudinal axis corresponded to the anatomical axis, while for the load cell it was the normal to the sensor surface.

Reaction Forces at the load cell were collected at 2000 Hz, therefore they were downsampled to 300 Hz and synchronized to correspond to kinematic data. Next, kinetic data were filtered using a zero-lag fourth order low-pass Butterworth filter with cut-off frequency equal to 52 Hz, which was the optimal value chosen from the spectral analysis. Eventually, vertical and horizontal forces expressed in the reference system of the load cell (Fy_{LC} and Fx_{LC}) were resolved in the Ground reference system (Fy_G and Fx_G), by using the instantaneous orientation matrix of the load cell (Figure 2c).

Gait cycle events for the left leg were detected from filtered vertical force data, using a 5 N threshold, whereas for the right leg they were detected from the trajectory of the marker placed on the second metatarsal head, by identification of its minimum regions. Kinematic and kinetic data of each test were segmented into steps, averaged and normalized over the time of the right and left stride respectively.

Forward velocity was calculated as the distance divided by the elapsed time that the centroid of the pelvic cluster passed across the acquisition volume.

III. RESULTS

The results here provided are relative to the third test performed. Average speed over strides during this trial was 6.58 ± 1.12 m/s. Kinematic data are referred to both limbs, while kinetic data to the affected limb (AL) only, because in the unaffected limb (UL) neither force nor pressure sensors were used, and force platforms were not available.

A. Kinematics

The mean and standard deviation of lower-limb joint angles in the sagittal plane over stride time (5 strides AL, 4 strides UL) are reported in Figure 3, and analogous graphics were

obtained for joint kinematics in the transverse and frontal plane.

During stance phase (0-25% of stride time) UL hip extended from 40° until reaching maximum extension of -10° at toe off. During swing phase it flexed up to 90° and then extended rapidly in the terminal part of swing. AL hip behaved similarly to the UL hip, but at foot contact it was 55° flexed, then it extended until foot off, reaching 12° as maximum extension angle.

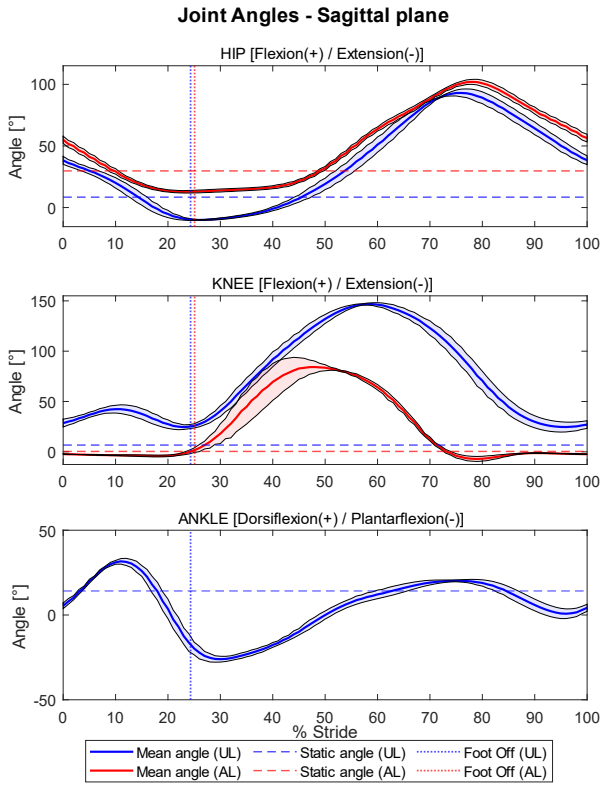


Fig. 3: Joint angles in the sagittal plane for hip, knee and ankle joint. Unaffected limb angles (mean ± 1 SD) are represented in blue and affected limb angles in red (mean ± 1 SD). Dashed horizontal lines represent the static angle (blue for UL, red for AL) and dotted vertical lines represent the average foot off instants (blue for UL, red for AL).

UL knee showed two periods of flexion, one during support and one during swing. Conversely, AL knee was completely extended during stance. The maximum flexion angle of the UL knee was nearly 60° higher than that of the prosthetic knee and it also happened later in swing.

The ankle joint was analysed for the UL only. Ankle was about 5° dorsiflexed upon foot contact, and then continued dorsiflexing rapidly to 31°. After midstance it plantarflexed and reached a maximum extension of -26° immediately after toe off. During the swing phase, ankle again dorsiflexed to 20°, and slightly extended prior to the next foot contact.

Figure 4a shows the trunk absolute inclination (positive forward). During AL support time the subject leaned forward, while during UL support time the trunk reduced its inclination. The total oscillation ranged from 3° to 18 °.

Figure 4b shows θ_S and θ_{LC}, i.e. the inclination of the shank (UL) and of the load cell (AL) normalized to the AL stride time. Despite the offset, the two angles had a similar trend and similar ranges. Both angles had an average excursion of 50° from foot contact to foot off, but while θ_{LC} (AL) increased from -25° to +25°, θ_S (UL) increased from +5° to +55°.

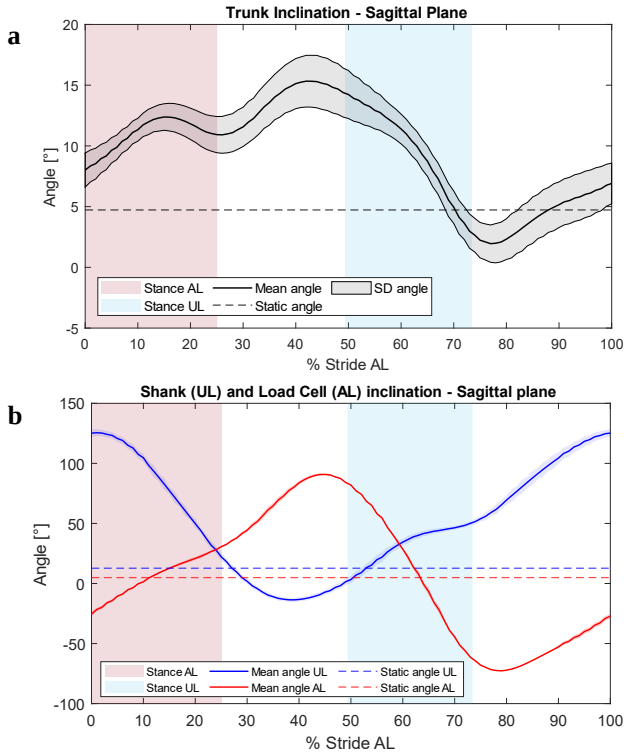


Fig. 4: Absolute angles in the sagittal plane of trunk (4a), shank and loadcell (4b) averaged and normalized over left stride time. Solid lines are the average angle during the running trial, horizontal dashed lines are the segments inclination in the static acquisition (black: trunk, blue: shank UL; red: load cell AL). Black shade in Fig. 4a is ±1SD relative to trunk average inclination. Red and blue vertical stripes represent the left and right stance time respectively.

B. *Kinetics*

Analysis of Reaction Forces (Figure 5) gave in output the average vertical and horizontal forces either in the Load Cell and in the Ground reference system. Vertical Forces, $F_{y_{LC}}$ and F_{y_G}, showed no relevant differences. They both peaked at nearly 3.5 N/BW, but in the second portion of the stance (40%-100%) F_{y_G} decreased more rapidly than $F_{y_{LC}}$. While horizontal Force $F_{x_{LC}}$ was always positive, F_{x_G} was negative until 50% of stance and then became positive. Just before the horizontal GRF changed from braking to propulsive, θ_{LC} turned from negative to positive.

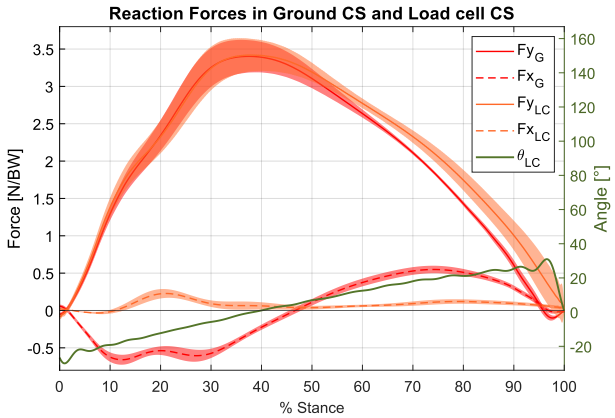


Fig. 5: Reaction forces measured by load cell averaged over 5 AL steps. Red lines represent the vertical (solid) and horizontal (dashed) forces in the Load Cell reference system (mean ± 1 SD). Orange lines depict the same forces projected onto the Ground reference system (mean ± 1 SD). Force values can be read in the left y axis, while the load cell inclination angle θ_{LC} (solid green) can be read in the right y-axis.

IV. DISCUSSION

With regard to sprinting kinematics, in literature there is little information on the joint kinematics of para-athletes with unilateral transfemoral amputation. The present work showed that AL hip is expectedly more flexed than UL hip during the entire stride: this is related to the alignment of the prosthesis adopted, which allowed AL hip to work in a more comfortable range [8]. Substantial differences can be highlighted by comparing the joint angles of UL and AL knee, as the former is a biological knee, while the latter is a mechanical knee. In fact, due to its intrinsic functioning principle, AL knee did not flex during the stance phase, whereas UL knee did.

Many studies in the literature report the asymmetry between the GRFs exerted by AL and UL, pointing out that the GRFs in AL are lower than that of UL [3],[4],[6],[9]. Although inter-limb GRFs comparisons cannot be made in the present work, as no information on forces on the UL is available, we can observe that vertical peak force for the AL approached 3.5 N/BW, which is consistent with AL values presented elsewhere [6]. However, these values are much higher than the AL peaks reported in previous studies [3],[4],[9], but differences could be ascribed to inter-subject variability and the higher running speed reached by the athlete during the present pilot test. Kinetic results also differ from those obtained during tests with the same athlete running on a treadmill. This could be due not only to the fact that the athlete ran at a higher running speed (6.6 m/s vs 5 m/s), but also to the better confidence of running on track compared to running on the treadmill [10].

In the next months, the athletics track used in the present pilot test will be equipped with nine force platforms installed on the sprint track and on the long jump track, and with ten motion capture cameras hanging from a moving support structure [11]. This configuration will allow for a more extensive data collection and subsequent comparison of multiple subjects.

V. CONCLUSIONS

This paper illustrated an experimental procedure to collect in vivo-indoor data during a pilot test of an elite Paralympic athlete running on a track. Mocap cameras and a wearable kinetic sensor installed in the RPF were used. Biomechanical analysis revealed differences between AL and UL joint kinematics and revealed high GRF values. These results could be useful for athletes and trainers in the fine-tuning of running strategy. However, it should be noted that this is a single case study, so the results will have to be confirmed by a larger analysis including more trials and more subjects, which will be carried out in the forthcoming months.

ACKNOWLEDGEMENT

The authors intend to thank the athlete and FISPES for their involvement in the study, INAIL for funding through the OLIMPIA project PR19-PAI-P4 and Comune of Padova for hosting the tests.

REFERENCES

[1] Hadj-Moussa F., Ngan C. C., Andrysek J., Biomechanical factors affecting individuals with lower limb amputations running using running-specific prostheses: A systematic review. (2022, Feb) *Gait & Posture*, 92. 83-95. Available: https://doi.org/10.1016/j.gaitpost.2021.10.044

[2] Williams, K.R. The Dynamics of Running. In Zatsiorsky V.M. (Ed.) *Biomechanics in sport performance enhancement and injury prevention*. Blackwell Science Publisher, 2000. Available: https://doi.org/10.1002/9780470693797.ch8

[3] Hobara, H., Baum, B. S., Kwon, H. J., Miller, R. H., Ogata, et al., (2013, Sept). Amputee locomotion: Spring-like leg behavior and stiffness regulation using running-specific prostheses. *Journal of biomechanics*, 46(14), 2483-2489. Available: https://doi.org/10.1016/j.jbiomech.2013.07.009

[4] Makimoto, A., Sano, Y., Hashizume, S., Murai, A., Kobayashi, et al., (2017, Dec). Ground reaction forces during sprinting in unilateral transfemoral amputees. *Journal of applied biomechanics*, 33(6), 406-409 Available: https://doi.org/10.1123/jab.2017-0008

[5] Nagahara, R., Mizutani, M., Matsuo, A., Kanehisa, H., & Fukunaga, T. (2018). Association of sprint performance with ground reaction forces during acceleration and maximal speed phases in a single sprint. *Journal of Applied Biomechanics*, 34(2), 104-110. Available: https://doi.org/10.1123/jab.2016-0356

[6] Petrone, N., Costa, G., Foscan, G., Gri, A., Mazzanti, L., Migliore, G., & Cutti, A. G. (2020). Development of instrumented running prosthetic feet for the collection of track loads on elite athletes. *Sensors*, 20(20), 5758. Available: https://doi.org/10.3390/s20205758

[7] Park S, Yoon S. (2012, May). Validity Evaluation of an Inertial Measurement Unit (IMU) in Gait Analysis Using Statistical Parametric Mapping (SPM). *Sensors* (Basel). 21(11):3667. DOI: 10.3390/s21113667

[8] Migliore, G. L., Petrone, N., Hobara, H., Nagahara, R., Miyashiro, K., et al., (2020). Innovative alignment of sprinting prostheses for persons with transfemoral amputation: Exploratory study on a gold medal Paralympic athlete. *Prosthetics and orthotics international*, 45(1), 46–53. Available: https://doi.org/10.1177/0309364620946910

[9] Sano, Y., Makimoto, A., Hashizume, S., Murai, A., Kobayashi, et al., (2017). Leg stiffness during sprinting in transfemoral amputees with running-specific prosthesis. *Gait and Posture*, 56, 65-67. Available: https://doi.org/10.1016/j.gaitpost.2017.04.038

[10] Breban, S. G., Bettella, F., Di Marco, R., Migliore, G. L., Cutti, A. G. & Petrone, N., (2022). GRF analysis of two elite Paralympic sprinters in steady and resisted accelerated treadmill running. *ISBS Proceedings*, 40 (1). Available: https://commons.nmu.edu/isbs/vol40/iss1/22

[11] Mistretta, P., Scapinello, M., Breban, S., Cutti, A. G., & Petrone, N. (2022). Instrumentation of sprint and long jump tracks of an indoor athletics field to study athletes' performances. ISEA 2022. DOI: 10.5703/1288284317522

Lumped-parameter hemodynamic model as a non-invasive tool to assess coronary blood flow in AAOCA

V. Ceserani*[1], M. Lo Rito*[3], G. M. Formato[2], M. L. Agnifili[4], A. Rosato[2], A. F. Pascaner[1] and M. Conti[1]
[1] *DICAr, University of Pavia,Italy*
[2] *3D and Computer Simulation Laboratory, IRCCS Policlinico San Donato, San Donato Milanese, Italy*
[3] *Department of Congenital Cardiac Surgery, IRCCS Policlinico San Donato, San Donato Milanese, Italy*
[4] *Department of Clinical and Interventional Cardiology, IRCCS Policlinico San Donato, San Donato Milanese, Italy*
* *These authors (V.C., M.L.R) have contributed equally to this work*

Abstract— Anomalous aortic origin of the coronary artery (AAOCA) can be associated with sudden cardiac death (SCD) usually related to physical effort. We aim to develop a patient-specific (PS) hemodynamic non-invasive tool based on clinical data to assess the coronary blood flow (CBF) in AAOCA and understand how the disease affects myocardial perfusion. A good correlation between CBF simulated and in-vivo measurements is demonstrated. Physiological changes will be integrated into the model to simulate different degrees of effort.

Keywords— AAOCA, coronary flow, lumped-parameter model, effort.

I. Introduction

AAOCA is a rare congenital disease that can cause sudden cardiac death (SCD) during physical effort. Our group has already developed a structural model that showed a limited expansion of the anomalous coronary artery (CA) during intense effort, particularly within the intramural tract [1]. Starting from this encouraging result our project aims to understand how this phenomenon affects myocardial perfusion computing coronary blood flow (CBF) at different effort conditions. Using multi-patient clinical data our goal is to develop a non-invasive computational tool to simulate CBF. We currently use a lumped-parameter model, its design, definition and first results are described in the following sections. A schematic representation of the work is presented in Fig.1.

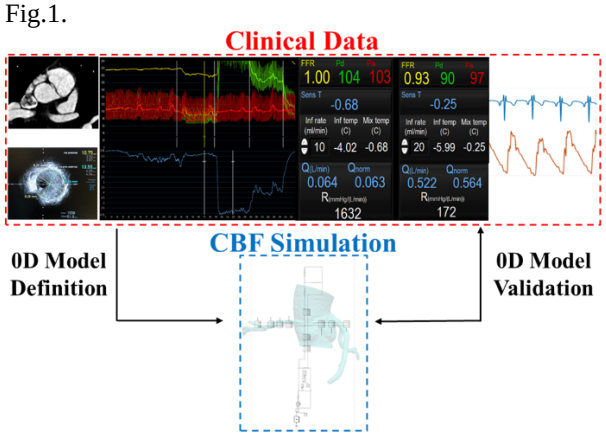


Fig. 1: Clinical data are used to define a PS 0D Model in order to assess the CBF. In-vivo measurements are used to validate the results of the model.

II. Materials and Methods

A. Clinical data and model definition

Multimodal diagnostic data are integrated to define a patient-specific (PS) lumped-parameter model to evaluate CBF under different hemodynamic conditions. The model describes each arterial segment as an electrical circuit (Fig. 2 A) whose components depend on the geometry of the vessel, its material, and blood properties [2]. Geometrical data to define electric parameters value is carried out from medical images. One of the project aims is to reduce the number of data retrieved from invasive procedures, for this reason, we test the model using both invasive and non-invasive imaging technique data. The aortic model and its parameters are calibrated using the measurements of computational tomography (CT) data, while the models of CAs are defined using both CT and intravascular ultrasound (IVUS) images, since our aim is to compare the accuracy of the model using different data sources.

B. Boudary conditions (BCs)

A PS pressure waveform is used as inlet condition (Fig 2 B). The aorta outlet is modeled with a Windkessel circuit (Fig. 2 C), whereas the CAs outlet is defined by a 6-elements circuit (Fig. 2 D) with an intramyocardial pressure source (Fig. 2 E). The total resistance of each outlet is split among circuit resistive parameters following the algorithm proposed by Sankaran et al. [3]. The total aortic resistance is evaluated with the patient's cardiac output (CO) and mean arterial pressure [3]. The total coronary resistance is defined during catheterization measurements under resting and hyperemic conditions. The left ventricular pressure (LVP) waveform is rescaled based on the PS data, the right one is evaluated as 20% of LVP [3].

To simulate effort, it will be required to integrate into the model changes related to coronary vasodilation mechanisms, increasing arterial pressure and heart rate. The first aspect we considered is related to vasodilator mechanisms that reduce peripheral coronary resistances. This variation is measured in vivo by inducing the condition of maximum hyperemia.

C. Statistical analysis

The CBF simulated values obtained with IVUS and CT images are compared with the Wilcoxon signed-rank test for paired data. Continue variables are expressed as median and interquartile range (IQR).

To study the correlation between CBF computed by the model and in-vivo measurements is used Kendall's τ coefficient. For

each comparison, the coefficient correlation value and the corresponding p-value are shown.

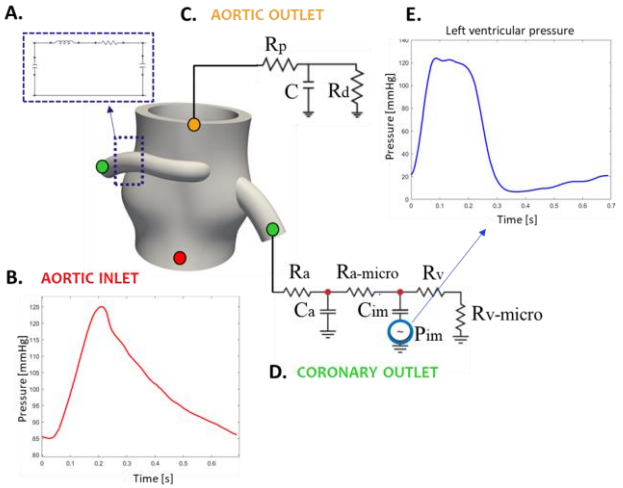


***Fig. 2*:** Schematic representation of the model: A) arterial segment circuit, B) aortic inlet pressure wave, C) aortic BC, D) coronary BC, E) LVP wave.

III. RESULTS

Resting and hyperemic conditions are simulated using data from 9 and 12 patients respectively. The simulated CBF are compared with in-vivo data to validate the numerical tool.

Considering in-vivo data the right median CBF value is 1.02(0.62) ml/s, the left one is 1.37(0.98) ml/s. Inducing vasodilatation hyperemic right and left CBF rise to 4.27(3.08) ml/s and 6.19(3.63) ml/s respectively. Considering the CBF simulated using IVUS to size the coronary circuits, results for resting condition are 0.92(0.62) ml/s at rest and 4.27(2.73) ml/s at hyperemia for right CA (RCA), 1.08(0.96) ml/s at rest and 6.27(3.62) ml/s at hyperemia for left CA (LCA). Using all geometrical data taken from CT, the CBF simulated results are 0.91(0.61) ml/s at rest and 4.39(2.84) ml/s at hyperemia for RCA, 1.08(0.99) ml/s at rest and 6.27(4.19) ml/s at hyperemia for LCA.

The results related to the two methodologies used to define the geometrical characterization of CAs are comparable (Fig. 3) and do not show significant differences (rest RCA p = 0.6523; rest LCA p = 0.3008; hyperemic RCA p = 0.7910; hyperemic LCA p = 0.6772). Both results are also well correlated with in-vivo measurements with statistical significance ($p<0.001$). The τ coefficient correlation values for the RCA and LCA are shown in Table I.

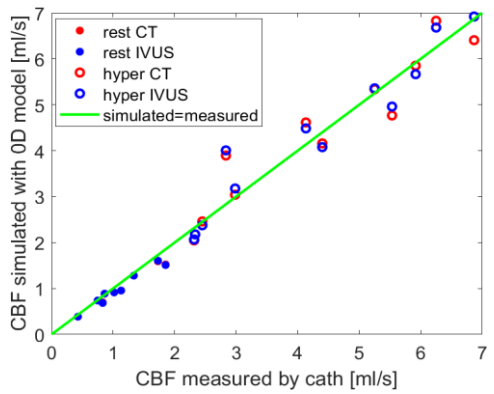


Fig. 3: 0D model results vs in-vivo measurements.

TABLE I: CORRELATION BETWEEN MODEL RESULTS AND IN-VIVO MEASUREMENTS

Hemodynamic condition	*comparison*	*side*	*τ*
Rest	In-vivo vs IVUS	RCA	0.8889
		LCA	0.7778
	In-vivo vs CT	RCA	0.8889
		LCA	0.8333
Hyperemia	In-vivo vs IVUS	RCA	0.9091
		LCA	0.8182
	In-vivo vs CT	RCA	0.8788
		LCA	0.7273

τ coefficient correlation value is presented for each comparison.

IV. CONCLUSION

The model is able to compute CBF in a non-invasive way with good accuracy. The results show a good correlation with in-vivo measurements in both hemodynamic conditions simulated: rest and maximum hyperemia. These first results suggest that our computational model could be a valuable tool to quantify myocardial perfusion in AAOCA allowing us to replicate conditions that cannot be reproduced during catheterization or clinical exams.

We plan to include physiological changes for stress simulation. We aim to define a relation between the coronary peripheral resistance changes and the magnitude of effort simulated. Furthermore, we want to integrate this relation with an algorithm to analytically calculate the rest values of coronary resistances. In-vivo measurements will allow us to validate the tool. In this way, we will reduce the number of PS data to have a non-invasive model to assess CBF in AAOCA without losing accuracy.

To study the impact of IM tract in effort simulation we will use the results of corresponding structural analysis to include in the model the percentage of IM tract narrowing at each degree of effort.

In future work, we could study a more complex and realistic fluid-structural interaction (FSI) between the IM tract and CBF through a PS 3D FSI simulation.

ACKNOWLEDGMENT

The project was supported and funded by the Italian Ministry of Health (GR-2019-12369166).

REFERENCES

[1] M. Lo Rito, R. M. Romarowski, A. Rosato, S. Pica, F. Secchi, A. Giamberti, F. Auricchio, A. Frigiola and M. Conti, "Anomalous aortic origin of coronary artery biomechanical modeling: Toward clinical application," Journal of Thoracic and Cardiovascular Surgery, vol. 161, no. 1, pp. 191-201, 2021.

[2] N. Westerhof, F. Bosman, C. J. De Vries and A. Noordergraaf, "Analog studies of the human systemic arterial tree," Journal of Biomechanics, vol. 2, no. 2, pp. 121-143, 1969.

[3] S. Sankaran, M. E. Moghadam, A. M. Kahn, E. E. Tseng, J. M. Guccione and A. L. Marsden, "Patient-specific multiscale modeling of blood flow for coronary artery bypass graft surgery," Annals of Biomedical Engineering, vol. 40, no. 10, pp. 2228-2242, 2012.

A numerical finite element methodology of the EVAR procedure

A. Ramella[1], F. Migliavacca[1], J. F. Rodriguez Matas[1], E. Mariani[2], T. J. Mandigers[3], D. Bissacco[3], A. Freyrie[2], S. Trimarchi [3,4], and G. Luraghi[1]

[1]*Department of Chemistry, Materials and Chemical Engineering "G. Natta", Politecnico di Milano (Italy)*

[2] *Vascular Surgery Unit, Department of Medicine and Surgery, University of Parma (Italy)*

[3]*Department of Clinical and Community Sciences, University of Milan (Italy)*

[4] *Fondazione IRCCS Ca' Granda Ospedale Maggiore Policlinico di Milano (Italy)*

***Abstract* — The abdominal aortic aneurysm (AAA) is one of the most frequent aortic wall pathologies and it is defined as a local dilation of the vessel, typically more than 50% of the physiological diameter. When surgical intervention is needed, AAA can be treated by a minimally invasive technique, endovascular aortic repair (EVAR). EVAR is becoming established as the primary treatment for AAA, given the high short-term success of the procedure. EVAR consists of placing a self-expandable device - called stent-graft (SG) - into the diseased aorta to restore the original lumen. In particular, the device is crimped and placed into a catheter; the catheter is inserted through the femoral artery into the patient and is delivered to the aorta; once the correct position is reached, the catheter is withdrawn, and the SG expands.**

Some studies are present in the literature adopting the finite element analysis to predict the SG behaviour after implantation and its interaction with the aortic wall.

This work aims at recreating stent-graft models similar to commercial ones including both the SGs main body and additional limb extensions and developing a methodology to replicate the EVAR procedure in patient-specific anatomy.

***Keywords* — stent-graft, in silico, FEA, AAA.**

I. INTRODUCTION

THE abdominal aortic aneurysm (AAA) is a localized enlargement of the abdominal aorta such that the diameter is greater than 3 cm or more than 50% larger than nominal. It is a potentially life-threatening condition, as it usually causes no symptoms, except during rupture [1]–[3]. Surgical intervention should be considered when the aneurysm diameter 55 mm, or in the case of rapid growth (>10 mm per year) [2], [4]. In that case, aneurysms can be treated either by open surgery or by an endovascular minimally invasive technique. The minimally invasive technique, called EVAR (endovascular aortic repair), is becoming the primary treatment choice for AAA and consists of placing a self-expandable stent-graft (SG) into the diseased aorta to restore the original lumen [5]. [6]. In particular, the device is crimped and placed into a small delivery system, the catheter. The catheter is then inserted through the femoral artery of the patient, and it is delivered to the aorta; once the correct position is reached, the catheter is withdrawn, and the SG expands [7]. The SG is composed of the stent, a metallic structure, usually made of Nitinol (Nickel-Titanium alloy) or Stainless steel, sutured to the graft, a fabric typically made with either polytetrafluoroethylene (ePTFE) or polyethylene terephthalate (PET)

Despite the high short-term success, the risk of late-onset complications (16-30% of cases [8]) is still present. When a persistent blood flow perfuses the pathological region, endoleaks occur, increasing the risk of rupture of the vessel. Endograft migration is another complication, defined as a SG displacement of 5-10 mm from its original fixation. This could result in endoleaks, and eventually aneurysmal rupture [8].

The Finite Element Analysis (FEA) is largely adopted in the literature to predict the structural behaviour of the SG and the aorta after the EVAR procedure and different approaches are present [9]. In the *virtual shell method* [10], [11] a tubular shell is placed around the device and then morphed to reach the vessel anatomy of the patient. In the *direct placement method* [12], [13] the stent-graft is placed within the patient's aortic lumen through a 3D morphing algorithm. Other studies [14], [15] followed the *virtual catheter method* in which the stent-graft is crimped, deformed by a cylindrical catheter, placed along the vessel centerline and then expanded by removing the catheter. Ramella et al. [16] developed the *tracking method* for the thoracic endovascular aortic repair, in which the stent-graft is crimped into a catheter, displaced along the vessel centerline and then gradually released in the desired aorta landing zone.

In this study CAD models of typical commercial SGs are recreated including both the main bodies and iliac extensions. Then, the *tracking method* is applied to model the EVAR procedure in a patient-specific abdominal aorta replicating both the main body and iliac extension insertion and deployment.

II. MATERIALS AND METHODS

A. Stent-graft CAD models and discretization

For the purpose of the study, two SGs were considered. The SGs are composed of a main body with two leg bifurcations and additional iliac components. The main body in SG1 has a longer ipsilateral leg with respect to SG2. Also, while for SG1 only a straight iliac extension was considered, the SG2 comprised two iliac extensions, a straight and a tapered one. They are suprarenal fixating as the proximal suprarenal stent ring extends above the graft proximally, ensuring the device fixation at the level of the suprarenal arteries.

The CAD modelling procedure to create the SGs main bodies and iliac extensions was performed in SolidWorks (Dassault Systèmes). Considering the stent struts, four types of shapes were identified: Suprarenal, V-type, W-type and

Regular W-type (Fig. 1.a). All the measurements related to the SGs such as diameters, lengths and cross-sections and graft thickness were collected from the literature [17]+(A). Complete models of the two SGs are reported in Fig. 1.b.

The SGs discretization process was performed in ANSA (BETA CAE). The stent rings were discretized using linear two-node beam elements. After a mesh sensitivity, an element size of 0.8 mm was selected. As regards the graft, a free mesh was constructed in ANSA using triangular shell elements with an average length of 0.8 mm and thickness of 0.1 mm (Fig. 2.a). The total number of nodes in the stent and graft for both SG main bodies and iliac extensions is reported in Table I.

The stent and graft in the real device are joined together by some suture points. As they were not directly included in the model, a node-to-node connection between the stent and graft meshes was defined to model the sutures between the two.

Nitinol shape memory material formulation for the stent and a fabric material formulation for the graft were adopted. Details on material parameters can be found in Ramella et al. [16].

TABLE I: NUMBER OF NODES IN THE STENT AND GRAFT FOR EACH STENT-GRAFT COMPONENT

SG component	*#nodes in the STENT*	*#nodes in the GRAFT*
Main body SG1	2464	13297
Main body SG2	2885	10797
Straight iliac extension	1296	7480
Tapered iliac extension	1296	7982

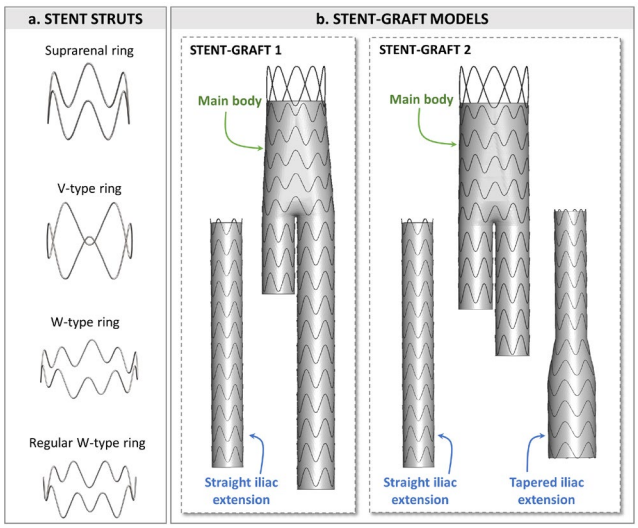


Fig. 1: (a) Different stent struts geometries in the considered stent-grafts; (b) stent-graft 1 (SG1) and stent-graft 2 (SG2) main bodies and limbic extension models recreated for the study.

B. *Aortic model*

Starting from clinical CTA images provided by Azienda Ospedaliera Universitaria di Parma (Italy), a patient-specific model of the aorta was reconstructed through an image segmentation process using the software VMTK (Orobix srl.). The aorta presents an aneurysm in the abdominal region.

The vessel model was discretized using triangular shell elements, with an average target length of 0.8 mm and a thickness of 1.8 mm was assigned [18] (Fig. 2.b). It was modelled as a rigid material as the focus of the methodology is on the SG deployment steps.

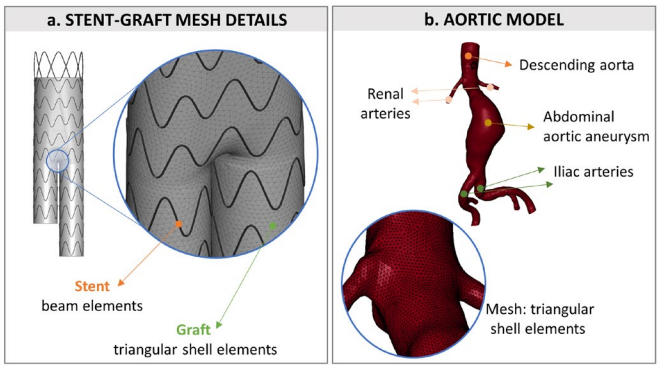


Fig. 2: (a) stent-graft mesh detail; (b) aortic model and mesh detail.

C. *EVAR Finite Element simulation set-up*

During the clinical procedure, the SG is crimped inside a catheter, inserted into the patient through the femoral artery and released into the aorta. As the numerical simulation has to mimic the surgery, these three main steps were simulated starting from the *tracking method* [16] and modifying it for the category of SGs used in the abdominal EVAR procedure.

The EVAR tracking simulation comprises three steps: (1) SG crimping, (2) SG tracking, and (3) SG deployment. In particular, as the SGs included two (SG1) or three parts (SG2), firstly the SG main body was implanted and then the iliac extensions. However, for each component, the simulations follow the three steps listed above.

The two input files (one for SG1 and one for SG2) were created in LsDyna (ANSYS) and included the following parts, as depicted in Fig. 3.a:

- SGs main body and iliac extension meshes;
- SG crimping cylinder was used to perform the device component crimping before the insertion into the femoral arteries.
- Patient-specific rigid aortic model fixed in space.
- Aortic centerlines, which represent the paths for the SGs and extensions displacement in the tracking phase.
- SG catheter, which maintained the SG crimped during the tracking into the aorta. The catheter was modelled as a rigid cylinder morphed on the aortic centerline.

Steps of the simulations for one main body and one iliac extension were reported in Fig. 3.b. In particular, in the first step of the simulation (*crimping phase*), the device was crimped by a cylinder up to a diameter of 10mm. Then, during the *tracking phase*, displacement boundary conditions were imposed on the most proximal stent ring (e.g., suprarenal ring in the case of the SG main body) to displace the device along the vessel centerline within the catheter until the desired landing zone is reached. Lastly, in the *deployment phase*, the SG was gradually released and expanded into the vessel lumen.

During the simulations, soft penalty-based contacts were defined between the SGs and the catheters, between the SGs and the aorta, between the main body legs and between the main body leg and iliac extensions.

For all the simulations, damping was imposed on the stent and graft with a factor equal to 1 ms^{-1} during the crimping, to 0 ms^{-1} during the displacement, and to 5 ms^{-1} during the deployment [16].

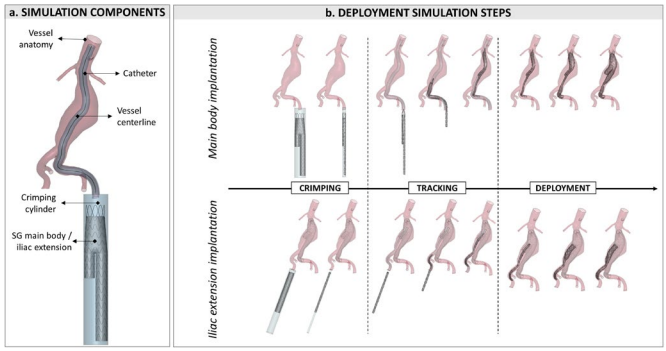


Fig. 3: (a) lists of components involved for the FE simulation; (b) three main steps of the EVAR simulation for the main body and one iliac extension of SG1.

Simulations were run on 20 CPUs with 120 GB of RAM, with a timestep equal to 0.009 ms.

The simulation results were analysed in terms of qualitative deployed configurations, the distance between the SGs and aorta, the maximum principal strain on the graft, and von Mises (VM) stress distribution in the stent and graft.

III. RESULTS

Fig. 4 reports the SGs main bodies and iliac extension deployed configurations.

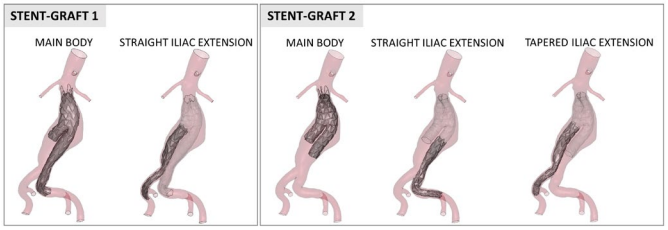


Fig. 4: Main bodies and iliac extensions deployed configurations for the two stent-grafts models

The distance between the device and the vessel is plotted on the aorta (Fig. 5) blue means the SG is completely in contact with the aorta. The distance increases in the aneurysmatic region.

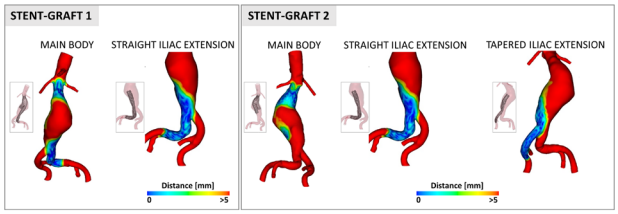


Fig. 5: Distances between the aorta and the main bodies and iliac extensions for both stent-grafts plotted for the vessel.

Maximum Principal Strains are shown in Fig. 6.a. The grafts (both the main body and iliac components) do not fully recover their initial configuration: some folds are present as the vessel has a lower diameter with respect to the initial configuration of the SGs due to the device oversizing. The strains reach higher values in the proximal aortic neck and in the two iliac bifurcations where the vessel is more tortuous and narrower.

Fig. 6.b report the VM Stress distribution on the grafts. The stress is higher in the regions where the grafts are in contact with the vessel, and in the portion of the graft close to the connection with the stent struts. Stresses and strains increase in the main bodies legs after the iliac extension implantation in the overlapped regions (not shown in the figures).

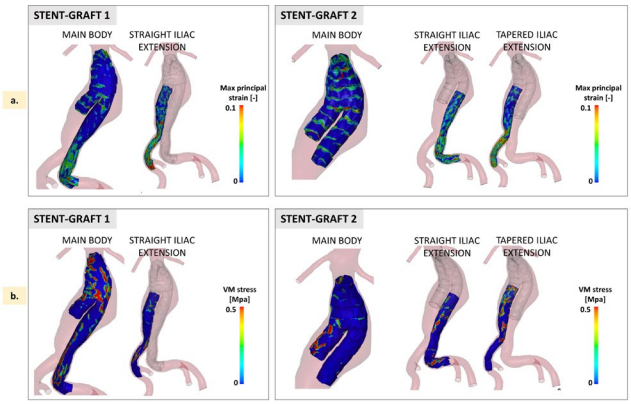


Fig. 6: (a) Maximum principal strain [-] and (b) Von Mises stress [MPa] in the graft of the main bodies (before iliac implantation) and iliac extensions for both stent-grafts.

Fig. 7 reports the VM Stress distribution in the stent struts. In all the configurations, stresses are higher in the regions where the stents are in contact with the vessel (abdominal aortic neck and iliac bifurcations) and in more tortuous regions (e.g., iliac bifurcations). In the aneurysmatic region, stresses are close to zero, as the stent struts have almost completely recovered their original stress-free configuration.

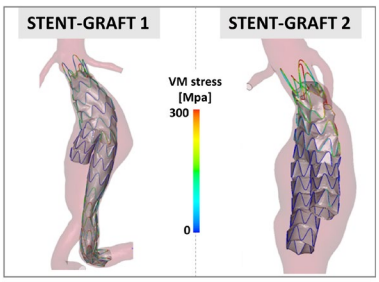


Fig. 7: Von Mises stress distribution in the stent struts for both stent-grafts main bodies.

IV. CONCLUSION

The developed numerical methodology allows simulating the EVAR procedure for the treatment of abdominal aortic pathologies, such as aneurysms. EVAR is a minimally invasive procedure that aims at restoring the physiological fluid dynamics in a pathological vessel by introducing a SG in the interested region [8].

Numerical simulations play an important role in pre-clinical planning to predict the biomechanical interaction between the SG and the aorta [19]. For example, in a pre-procedural patient-specific planning phase, the correct model and size of the device, as well as its positioning into the patient's vessel, can be optimized through FEA.

The present study aims at applying a previously validated methodology – specifically developed for the TEVAR technique – to model the EVAR procedure. Different from other literature methods [9], [11]–[13], the proposed strategy replicate the steps of the real clinical procedure considering also the crimping and gradual release phase for both the main bodies and iliac extensions implantations which could have a major impact on the success of EVAR.

The modelled devices are similar to two commercially available SGs. Both are composed of Nitinol stent rings sutured to a PET graft. To simulate the procedure, finite element domains of the devices were created. A patient-specific aortic model was segmented from clinical CTA images and then discretized. The structural simulation consisted of the following phases: crimping, tracking, deployment of the main body SG into the aorta, and iliac extension implantation. In the first two phases, the main body is crimped and displaced in the correct position of the vessel. During the deployment, the main body is gradually released, entering into contact with the abdominal aorta. During the iliac extension implantation phase, the previous three steps are replicated to implant the additional iliac components within the corresponding main body legs.

This study is not free from limitations. The SGs used in this work were similar to commercial ones but do not include all the peculiarities often found in abdominal SGs as the anchoring hooks, and they were modelled with geometries and materials taken from the literature. More accurate models of commercial SGs can be realized and validated with experimental tests. Also, a rigid aortic model was considered as the focus of the work was on the SGs implantation during EVAR. The EVAR simulation itself might be validated with an ad-hoc experimental set-up as proposed in Ramella et al. [16].

Despite the simplifications, after proper validation, the obtained results can be generalized to any size of a stent-graft and patient-specific deformable anatomies reconstructed from clinical images can be easily adopted for pre-procedural planning, device optimization or, in the future, in-silico clinical trials.

ACKNOWLEDGEMENT

This study has received funding from the MIUR FISR-FISR2019_03221 CECOMES.

REFERENCES

[1] A. Mathur, V. Mohan, D. Ameta, B. Gaurav, and P. Haranahalli, "Aortic aneurysm," *J. Transl. Intern. Med.*, vol. 4, no. 1, p. 35, Apr. 2016, doi: 10.1515/JTIM-2016-0008.

[2] C. Pratesi *et al.*, "Guidelines on the management of abdominal aortic aneurysms: updates from the Italian Society of Vascular and Endovascular Surgery (SICVE)," *J. Cardiovasc. Surg. (Torino).*, vol. 63, no. 3, pp. 328–352, Jun. 2022, doi: 10.23736/S0021-9509.22.12330-X.

[3] A. Wanhainen *et al.*, "Editor's Choice - European Society for Vascular Surgery (ESVS) 2019 Clinical Practice Guidelines on the Management of Abdominal Aorto-iliac Artery Aneurysms," *Eur. J. Vasc. Endovasc. Surg.*, vol. 57, no. 1, pp. 8–93, Jan. 2019, doi: 10.1016/J.EJVS.2018.09.020.

[4] D. K. Owens *et al.*, "Screening for Abdominal Aortic Aneurysm: US Preventive Services Task Force Recommendation Statement," *JAMA*, vol. 322, no. 22, pp. 2211–2218, Dec. 2019, doi: 10.1001/JAMA.2019.18928.

[5] H. O. Kim, N. Y. Yim, J. K. Kim, Y. J. Kang, and B. C. Lee, "Endovascular Aneurysm Repair for Abdominal Aortic Aneurysm: A Comprehensive Review," *Korean J. Radiol.*, vol. 20, no. 8, pp. 1247–1265, Aug. 2019, doi: 10.3348/KJR.2018.0927.

[6] I. C. T. Santos, A. Rodrigues, L. Figueiredo, L. A. Rocha, and J. M. R. S. Tavares, "Mechanical properties of stent-graft materials," *J. Mater. Des. Appl.*, vol. 226, no. 4, pp. 330–341, Oct. 2012, doi: 10.1177/1464420712451065.

[7] "Comparison of endovascular aneurysm repair with open repair in patients with abdominal aortic aneurysm (EVAR trial 1), 30-day operative mortality results: Randomised controlled trial," *Lancet*, vol. 364, no. 9437, pp. 843–848, Sep. 2004, doi: 10.1016/S0140-6736(04)16979-1.

[8] D. D. and T. G. Walker., "Complications of endovascular aneurysm repair of the thoracic and abdominal aorta: evaluation and management. Cardiovascular Diagnosis and Therapy, 8:S138, 4 2018."

[9] S. Avril, M. W. Gee, A. Hemmler, and S. Rugonyi, "Patient-specific computational modeling of endovascular aneurysm repair: State of the art and future directions," *Int. j. numer. method. biomed. eng.*, vol. 37, no. 12, p. e3529, Dec. 2021, doi: 10.1002/CNM.3529.

[10] D. Perrin *et al.*, "Patient-specific simulation of endovascular repair surgery with tortuous aneurysms requiring flexible stent-grafts," *J. Mech. Behav. Biomed. Mater.*, vol. 63, pp. 86–99, Oct. 2016, doi: 10.1016/J.JMBBM.2016.06.013.

[11] D. Perrin *et al.*, "Patient-specific numerical simulation of stent-graft deployment: Validation on three clinical cases," *J. Biomech.*, vol. 48, no. 10, pp. 1868–1875, Jul. 2015, doi: 10.1016/J.JBIOMECH.2015.04.031.

[12] A. Hemmler, B. Lutz, C. Reeps, G. Kalender, and M. W. Gee, "A methodology for in silico endovascular repair of abdominal aortic aneurysms," *Biomech. Model. Mechanobiol.*, vol. 17, no. 4, pp. 1139–1164, Aug. 2018, doi: 10.1007/S10237-018-1020-0/FIGURES/12.

[13] A. Hemmler, B. Lutz, G. Kalender, C. Reeps, and M. W. Gee, "Patient-specific in silico endovascular repair of abdominal aortic aneurysms: application and validation," *Biomech. Model. Mechanobiol.*, vol. 18, no. 4, pp. 983–1004, Aug. 2019, doi: 10.1007/S10237-019-01125-5/TABLES/6.

[14] R. M. Romarowski, E. Faggiano, M. Conti, A. Reali, S. Morganti, and F. Auricchio, "A novel computational framework to predict patient-specific hemodynamics after TEVAR: Integration of structural and fluid-dynamics analysis by image elaboration," *Comput. Fluids*, vol. 179, pp. 806–819, Jan. 2019, doi: 10.1016/J.COMPFLUID.2018.06.002.

[15] X. Kan, T. Ma, J. Lin, W. Lu, and X. Y. Xu, "Patient-specific simulation of stent-graft deployment in type B aortic dissection model development and validation.pdf," *Biomech. Model. Mechanobiol.*, vol. 20, pp. 2247–2258, 2021.

[16] A. Ramella *et al.*, "Validation and Verification of High-Fidelity Simulations of Thoracic Stent-Graft Implantation," *Ann. Biomed. Eng. 2022*, pp. 1–13, Jul. 2022, doi: 10.1007/S10439-022-03014-Y.

[17] X. C. Zhou, F. Yang, X. Y. Gong, M. Zhao, Y. F. Zheng, and Z. L. Sun, "New nitinol endovascular stent-graft system for abdominal aortic aneurysm with finite element analysis and experimental verification," *Rare Met.*, vol. 38, no. 6, pp. 495–502, Jun. 2019, doi: 10.1007/S12598-019-01250-1/FIGURES/10.

[18] M. L. Raghavan, J. Kratzberg, E. M. Castro de Tolosa, M. M. Hanaoka, P. Walker, and E. S. da Silva, "Regional distribution of wall thickness and failure properties of human abdominal aortic aneurysm," *J. Biomech.*, vol. 39, no. 16, pp. 3010–3016, Jan. 2006, doi: 10.1016/J.JBIOMECH.2005.10.021.

[19] G. H. W. van Bogerijen *et al.*, "Contemporary Role of Computational Analysis in Endovascular Treatment for Thoracic Aortic Disease," *Aorta*, vol. 1, no. 3, pp. 171–181, 2013, doi: 10.12945/j.aorta.2013.13-003.

Comparative Analysis of Steady and Resisted Accelerated Treadmill Running of an Elite Amputee Paralympic Sprinter

S.G. Breban[1], S. Barbacane[1], V. Pelusi[1], R. Di Marco[2], G. Marcolin[3], A.G. Cutti[4], and N. Petrone[1]
[1] *Department of Industrial Engineering, University of Padova, Padova, Italy*
[2] *Department of Computer Science, University of Verona, Verona, Italy*
[3] *Department of Biomedical Sciences, University of Padova, Padova, Italy*
[4] *INAIL Prosthetic Center, Budrio, Vigorso BO, Italy*

Abstract- Running Prosthetic Feet (RPF) enable athletes with lower limb amputation to compete in track races. Both Ground Reaction Forces (GRFs) and kinematics analyses allow evaluating running performance but they are seldom measured together. This work aims to compare kinematic and kinetic biomechanical parameters of an elite amputee Paralympic sprinter in a pilot feasibility study. Tests were performed on a commercial treadmill placed on four force platforms. Two conditions were tested: Steady State Running (SSR) and Resisted Accelerated Running (RAR). SSR results show that unaffected limb (UL) vertical GRF was 70% higher than affected limb (AL). Differences in trunk, hip, knee, and ankle angles were observed both between AL and UL sides (e.g., knee extension during stance), and between SSR and RAR tests (e.g., trunk inclination). Results obtained could be helpful to trainers to improve overall sprinting performance.

***Keywords*— running prosthetic feet, ground reaction forces, kinematics, treadmill.**

I. INTRODUCTION

Since the introduction of Running Prosthetic Feet (RPF) the interest in studying sprinting biomechanics of Paralympic athletes has grown. Indeed, RPFs enabled many athletes with leg amputations to compete with nonamputees in track races [1] On this matter, some authors speculated about a possible advantage in performance when using RPF vs biological legs. However, a debate is still open about this possibility [2], and further studies regarding amputee's sprinting biomechanics and adaptations are ongoing. This knowledge will allow specific rehabilitation and training strategies, as well as developments in prosthetic devices to be objectively evaluated. Kinematic alterations between sound and prosthetic limbs result from using RPF. Findings suggest that in case of transtibial amputation prosthetic could have similar behaviour of the intact one [3]. Conversely, in case of transfemoral amputations affected limb is considerably different compared to the sound limb or able-body subjects [3].

About Ground Reaction Forces (GRFs) authors reported a significant difference in average vertical GRF production between intact and prosthetic limbs among elite sprinters with lower limb amputations [4], [5]. In the above studies, affected side has lower GRFs than the intact one.

Differences in force production and joint kinematics between prosthetic and intact limbs in sprinters with unilateral transtibial amputations are due to the lack of the ankle joint [6].

The current research aims to better understand sprinting biomechanics and improve racing performance. As well known, during sprinting athlete accelerate their body forward to develop velocity in the shortest possible time. Speed is dependent upon a number of factors which include technique and force production capability, in particular lower limb musculature. Moreover, sport scientists have observed that one the most effective way to improve the overall performance is through resisted sprinting training which is usually done on track [7]. Pairing instrumented treadmill and motion capture system allows to measure GRFs and kinematics. However, treadmill was usually used to perform SSR only, while little was done to implement RAR tests.

The aim of this work is to perform a feasibility study on an elite amputee Paralympic sprinter, comparing GRFs and kinematics during SSR and RAR tests performed on treadmill.

II. METHODS

A. Participants

A female, gold medallist, elite Paralympic sprinter with unilateral transfemoral amputation was recruited for this study. The athlete (mass: 55 kg, height: 1.60 m) used Ottobock 1E91 standard RPF Cat. 3.5, mono-axial Ottobock 3S80 knee, and a specific alignment of the socket and the foot [8]. In this case the angle between socket axis and the axis passing through grand trochanter and knee joint centre was 15°.

During all tests the subject wore a safety harness.

B. Experimental Procedure

Tests were performed in a laboratory using a commercial treadmill (SkillRun Technogym) placed on four force platforms (BTS P6000- acquisition rate 1000 Hz). Kinematics was measured using a BTS motion capture system composed of eight infrared cameras (DX-6000, acquisition rate 250 Hz). This setup, as evaluated in [9] could give reliable results as concern SSR GRFs measurements compared with literature.

In this session two type of conditions were studied: Steady State Running (SSR) and Resisted Accelerated Running (RAR).

SSR was performed on the treadmill and consisted in reaching a self-selected constant speed and maintaining it for 7 seconds, time necessary to acquire at least six consecutive steps of each limb. The speed reached during this session was 5 m/s.

As regards RAR, athlete reached a steady speed of 3.11 m/s starting from zero. During RAR the treadmill motor was switched off to simulate passive inertial and air resistance. A load cell (FS 1000 N, acquisition rate 1000 Hz) was fixed to athlete's back through a pre-loaded elastic band with elastic constant K=120 N/m to measure the instantaneous resistance applied to the harness at the sacrum bone. In Figure 1 a schematic representation of both configurations is shown.

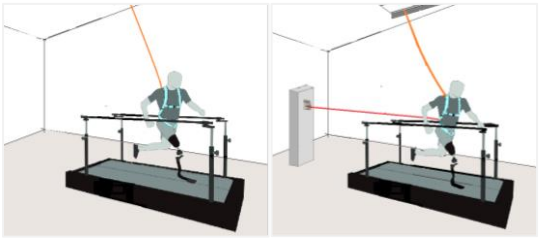


Fig. 1: Schematic representation of SSR (left) and RAR (right).

GRFs analysis

GRFs were collected at 1000 Hz and filtered to remove noise in input. After a spectral analysis of the GRF signal, a zero-phase low-pass Butterworth filter (15 Hz cut-off frequency, second order) was applied to data. Foot-contact and toe-off were detected using a threshold of 100 N on the filtered vertical GRF. For both SSR and RAR tests, GRFs obtained are in ground coordinate system: X- anterior posterior axis pointing forward; Y- vertical axis pointing upward; Z- medial lateral axis pointing rightward.

In the SSR test average curves of GRF_X and GRF_Y of the last 6 consecutives steps for each limb were collected.

In the RAR test, we focused on the acceleration phase and only the first 10 consecutive steps for each limb were considered, starting from the first ground contact of the prosthetic side at the beginning of the running phase. Therefore, to analyse acceleration phase we have considered for each limb 3 steps: one at the start, one during the acceleration, and one at the end. Indeed, from the 10th step onwards, the acceleration became considerably lower and a steady state running was achieved.

C. Kinematics analysis

During tests passive markers were applied to athlete's anatomical landmarks. The full marker set was composed of 56 markers: 23 applied on the upper part of the body, 4 on the pelvis and 33 on the lower part of the body.

The goal of the kinematics analysis was the calculation of Cardan Angles of hip, knee and ankle joints. The sequence used was *'ZXY'* for hip and knee, while *'ZYX'* for foot, considering X- anterior posterior axis pointing forward, Y- longitudinal axis pointing upward, Z- medial lateral axis pointing rightward. For the sound limb hip, knee and ankle Cardan angles were calculated after defining each relative coordinate system. Conversely, for the prosthetic limb, hip and knee joint angles only were calculated. Hip angles were obtained considering the rotation between pelvis and socket, while knee angles were calculated from rotation between socket and foot.

In the SSR test average curve of joint angles of the last 6 consecutive steps for each limb were calculated. In the RAR test, joint angles of the first 10 steps were presented for both limbs.

Finally, to better understand sprinting technique and athlete position during tests, trunk angle was calculated. This angle was obtained considering inclination in the sagittal plane of the segment joining 7th cervical vertebra to midpoint of posterior superior iliac spines with respect to global vertical axis.

III. Results

A. GRFs results

In Figure 3, GRFs average curves of affected (AL) and unaffected (UL) limbs are shown as percentage of stance for SSR test. GRF_Y peak values are of 4.43 N/BW and of 2.60 N/BW for UL and AL, respectively. As concern $GRFs_X$ UL has mainly a braking effect, while AL is mostly propulsive.

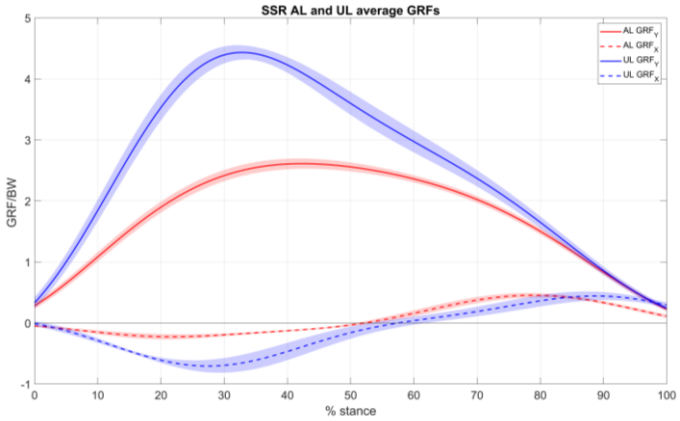


Fig. 3: Average GRFs curves for AL and UL during SSR test

In Figure 4, GRFs from RAR test are shown for three steps of the acceleration phase: 1st, 5th and 9th for AL and 2nd, 6th and 10th for UL. GRF_Y peak values are greater for UL, rather than AL. It could be observed that UL GRF_Y peak values increase from 2nd to 10th step. As regards GRF_X, during the acceleration phase: the braking phase is almost zero for both limbs, and the athlete was pulling an average of 0.185 N/BW on the rope.

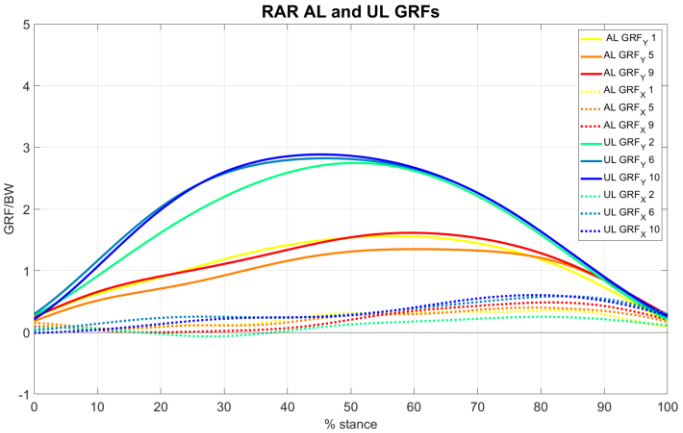


Fig. 4: GRFs curves of three steps for AL and UL limbs during RAR

Table 1 reports spatial-temporal parameters during the acceleration phase for all the steps analysed. The athlete started to run at 1.00 m/s and at the 10th step she reached a speed equal to 80 % of her maximum velocity. As concerns stance time, it could be observed that for both limbs it decreased at increasing speed. AL stance times were higher

than those of a consecutive UL step (51 %, 40% and 27 %, respectively).

TABLE I: SPATIAL-TEMPORAL PARAMETERS DURING ACCELERATION PHASE

Step	*Side*	*Speed [m/s]*	*Stance time [s]*
1	AL	1.00	0.236
2	UL	1.15	0.156
5	AL	1.69	0.216
6	UL	1.82	0.152
9	AL	2.19	0.188
10	UL	2.29	0.148

B. Kinematics results

In Figure 5, joint angles of both limbs are presented as percentage of stride. For what concern hip angles, it could be observed that AL has a greater flexion angle during stance, rather than UL. At foot off AL hip angle is slightly extended, but considering the initial contact angle, the range of motion varies during stance. Regarding knee angles, differently than UL, the prosthetic knee keeps in extension during the whole stance phase. Indeed, if otherwise, the sprinter would have fallen. Conversely, biological knee is in flexion along the entire stride. Trend shows two flexion peaks: one during stance and one during swing. For the ankle joint only the unaffected limb is presented. During the initial contact with the ground the foot is in plantarflexion and then changes
into dorsiflexion until foot off, where it is again in dorsiflexion.

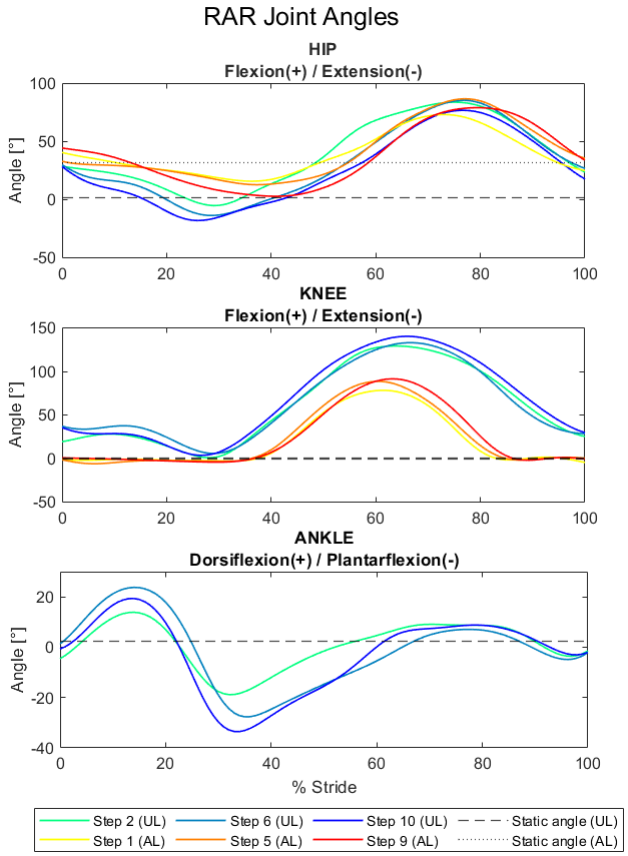


Fig. 5: Joint angles of AL and UL during SSR

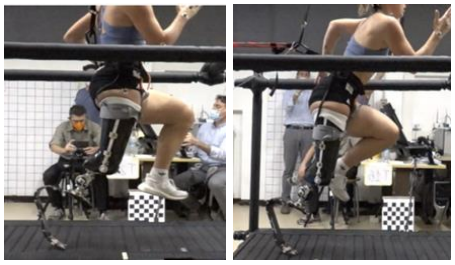


Fig. 7: Trunk inclination during SSR (left) and RAR (right)

Figure 6 presents joint angles of RAR test. As for GRF analysis, we have focused on some steps of the acceleration phase. Regarding hip angles, it could be seen that moving from the first step to the last one, for each limb the range of motion increases. Angles become more and more flexed during the acceleration phase. With reference to knee angles, it is possible to observe that the mechanical knee shows little variability between steps. Its range of motion is different from that of the unaffected one. During swing phase mean values of knee flexion are about 130° and 83° for UL and AL, respectively. Ankle angles presented are referred only to the UL. Ankle range of motion varies from step 2nd to 10th: it increases both in swing and stance phases.

Finally, trunk angle is calculated for both configurations: SSR and RAR. For SSR trunk angle is about 10.92°±2.8°, while for RAR is about 36.5°±2.63°. During RAR trunk is more inclined as shown in Figure 7. Indeed, it is well known that to reach higher speeds athlete propels the body forward.

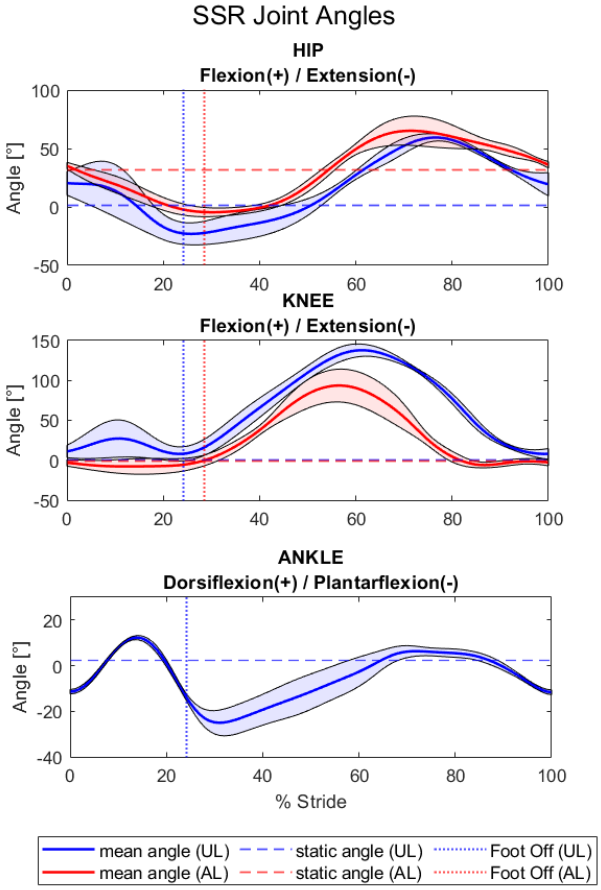


Fig. 6: Joint angles of AL and UL during RAR

IV. Discussion

Biomechanical analysis of GRFs and kinematics is necessary to better understand running technique and help trainers to improve athletes' performance. Concerning differences in GRFs between RAR and SSR, it could be observed that for both limbs vertical GRFs are higher for UL, consistently to previous findings[10], [11]. About horizontal GRF, in RAR no braking phase was present. As expected, during the acceleration phase the athlete needs propulsion to increase the running speed. In RAR test, stance time decreases as speed increases, accordingly with literature [6].

As regards kinematics, the main difference between AL and UL is knee angle. For both tests, during stance, prosthetic knee is always extended, unlike a biological knee where a small flexion occurs [3]. When comparing RAR and SSR tests, main difference regarding knee joint, is that the angle at foot contact is higher in the former case. This different behavior that we measured, agrees with literature which states that knee flexion at foot strike is greater during acceleration rather than maximum velocity sprinting [7]. We would like to verify with further tests if the two conditions are ideally represented by RAR and SSR performed on our instrumented treadmill.

In both tests performed, AL hip is almost entirely in flexion. Indeed, during sprinting as body's center of mass lowers, hip, knee and ankle flexion increases [3]. As observed during RAR trial, hip angles at foot strike keeps constant as speed changes [7].

About differences in kinematics found between SSR and RAR tests, a noticeable change was found in trunk inclination. Coaching observations suggest that during the initial stages of acceleration the body should be at an angle of 45°, compared to 36.5° that were measured in the present work. Then, as sprinter's velocity increases, the body become more upright [7]. Another difference regarded ankle joint, it could be observed that during SSR and RAR ankle angle has different values at foot strike. In SSR foot is more plantarflexed than in RAR. This may be related to trunk position; the more the trunk is inclined the more the foot is dorsiflexed. Results obtained during treadmill session will be compared with those obtained in track [12].

V. Conclusions

The aim of the present work was to compare GRFs and kinematics during SSR and RAR tests of an elite amputee Paralympic sprinter. Results confirmed that in both tests AL and UL have different behaviour. At the same time, analysis evidenced differences between the two configurations studied: SSR and RAR. However, the presented work is a case study and further tests are needed to perform an inferential statistical analysis and draw general conclusions on the observed data.

Acknowledgement

The authors intend to thank the athlete and FISPES for their involvement in the study, INAIL for funding through the OLIMPIA project PR19-PAI-P4.

References

[1] Beck, O. N. & Grabowski, A. M. (2018). The biomechanics of the fastest sprinter with a unilateral transtibial amputation. *J Appl Physiol*, 124, 641–645, doi: 10.1152/jappl.

[2] Beck, O. N., Taboga, P. & Grabowski, A. M. (2022). Sprinting with prosthetic versus biological legs: insight from experimental data. *R Soc Open Sci*, vol. 9(1), doi: 10.1098/rsos.211799.

[3] Buckley, J. G. (1999). Sprint kinematics of athletes with lower-limb amputations, *Arch Phys Med Rehabil*, 80, 501-508.

[4] Grabowski, A. M., McGowan, C. P., McDermott, W. J., Beale, M. T., Kram, R & Herr, H. M. (2010). Running-specific prostheses limit ground-force during sprinting, *Biol Lett*, 6(2), 201–204, doi: 10.1098/rsbl.2009.0729.

[5] Hobara, H., Baum, B. S., Kwon, H., Linberg, A., Wolf, E., Miller, R. H., & Shim, J., (2014). Amputee locomotion: Lower extremity loading using running-specific prostheses, *Gait Posture*, 39(1), 386–390, doi: 10.1016/j.gaitpost.2013.08.010.

[6] Hadj-Moussa, F., Ngan, C. C., & Andrysek, J. (2022). Biomechanical factors affecting individuals with lower limb amputations running using running-specific prostheses: A systematic review, *Gait Posture*, 92, 83–95, doi: 10.1016/j.gaitpost.2021.10.044.

[7] Cronin, J. (2006). Resisted sprint training for the acceleration phase of sprinting, *National Strength and Conditioning Association*, 28(4), 42-51.

[8] Migliore, G., Petrone, N., Hobara, H., Nagahara, R., Miyashiro, K., Costa, G. F., Gri, A., & Cutti, A. G. (2021). An innovative alignment for the sprinting prosthesis of above-knee amputees: Exploratory study on a gold-medal Paralympic athlete, *Prosthet Orthot Int*, 45(1), 46-53, doi:10.1177/0309364620946910.

[9] Breban, S. G., Bettella, F., Di Marco, R., Migliore, G., Cutti, A. G., & Petrone, N. (2022). GRF analysis of two elite Paralympic sprinters in steady and resisted accelerated treadmill running, *ISBS Proceedings Archive*, 40(1), 22.

[10] Sakata, H., Hashizume, S., Kobayashi, Y., Takemura, H., & Hobara, H. (2017). Running mechanics in unilateral transfemoral amputees across a range of speeds, *ISBS Proceedings Archive*, 36(1), 236.

[11] Makimoto, A., Sano, Y., Hashizume, S., Murai, A., Kobayashi, Y., Takemura, H., Hobara, H. (2017). Ground reaction forces during sprinting in unilateral transfemoral amputees, *J Appl Biomech*, 33(6), 406–409, doi: 10.1123/jab.2017-0008.

[12] Mistretta, P., Scapinello, M., Breban, S. G., Cutti, A. G., & Petrone, N. (2022). Instrumentation of sprint and long jump tracks of an indoor athletics field to study athletes'' performance. *ISEA 2022*, doi: 10.5703/1288284317522.

Integrated Protocol for Multidimensional *In Vivo* Assessment of Glenohumeral Joint Function during Dynamic Tasks

E. Scalona[1], G. Rossetto[2], M. Mosso[2], M.F. Saccomanno[1], G. Milano[1], and N.F. Lopomo[2]
[1] *Dipartimento di Specialità Medico-Chirurgiche, Scienze Radiologiche e Sanità Pubblica, Università degli Studi di Brescia*
[2] *Dipartimento di Ingegneria dell'Informazione, Università degli Studi di Brescia*

***Abstract*—The shoulder is widely considered as a complex system characterized by peculiar biomechanics and involving different joints, including glenohumeral one. Indeed, the inherent shoulder structure allows for high mobility, but at the same time - in case of injuries, traumatic events, or pathologies – the overall structure is easily exposed to articular and periarticular problems.**

Scientific literature presents several procedures devoted to the functional evaluation of shoulder complex, including - above all - movement analysis and assessment of muscular contribution. In the last years, ultrasonography has been also proposed to quantitatively assess anterior humeral head displacement, which represents an important metrics for shoulder dislocation.

The aim of this study was to present a non-invasive multidimensional testing procedure aiming at assessing the function of the shoulder complex, specifically focusing on the glenohumeral joint.

The proposed setting included the integration of marker-based optoelectronic stereophotogrammetric system, surface electromyography, and ultrasonography, so as to allow an instrumental evaluation able to provide information about overall kinematics, muscular activations and synergies, and joint tissues constraining behaviour in terms of humeral head displacement. In this feasibility analysis the subjects were asked to execute two specific dynamic tasks, which overall covered glenohumeral joint movements.

From this feasibility study, the proposed protocol allowed indeed to have information about the overall joint kinematics in terms of flexion/extension, abduction/adduction, and intra/extra-rotation, the corresponding muscular activations and, above all, the possibility of tracking the humeral head displacement.

All the available information record may enhance the possibility to identify altered patterns in shoulder biomechanics. This multidimensional approach may be used to help clinicians characterizing the glenohumeral joint during defined motor tasks and thus designing tailored rehabilitative interventions for the shoulder joint complex.

***Keywords* — Human motion analysis, surface EMG, Ultrasonography, Shoulder complex, Glenohumeral joint**

I. Introduction

The global range of motion of the arm is the result of a coordinated motion of the shoulder complex including glenohumeral (GH), scapulothoracic, sternoclavicular and acromioclavicular joints [1]. Evidence suggested that individuals with shoulder disorders present abnormal kinematic patterns and weakness in muscles activations [2]. As reported by Lucas et al. [3], shoulder pain presents an important incidence in the general population, up to 55.2%, and a prevalence of from 7.7 to 62 per 1000/persons year.

In general, to track the movement of the humerus and scapular joint angles, marker-based optoelectronic stereophotogrammetric systems are the most adopted [4,5]; indeed, this technology – by exploiting infrared reflective markers applied directly on the skin of the subjects – represents the state-of-the-art for non-invasive investigations of shoulder kinematics [6]. However, kinematics reflects only a part of the shoulder biomechanics. In this frame, surface electromyography (EMG) has been demonstrated to be an accurate, reliable, and non-invasive method to measure muscle activity and muscle timing of superficial muscles as, for instance, in the scapulothoracic joint [7].

However, the clinical evaluation of shoulder function is challenging because of the complex three-dimensional (3D) movement realized and the presence of surrounding soft tissues, which prevent – for instance - a reliable measurement of glenohumeral joint behaviour.

To overcome these limitations, shoulder biomechanics has been explored by in vitro cadaveric studies and in vivo magnetic resonance imaging (MRI), fluoroscopy, and computed tomography (CT) [8–10]. In these contexts, the imaging technique allows the accurate estimation of the translation of humeral head in different arm positions, which is indeed important to support clinicians in the functional evaluation. Furthermore, ultrasonography has been reported to enable the assessment of glenohumeral joint, without any invasion or radiation exposure; for instance, Inoue et al. [11], measured the translation of the anterior humeral head by ultrasound measurements, statically, at various shoulder abduction angles.

Although most of the realized imaging studies on GH joint provided accurate assessment of bone-bone relationships, they were not focused on depicting the overall movement characteristics, being mostly static techniques with a limited volume of acquisition [12]. On the other hand, most of the shoulder pathologies present important dynamic components, which must be highlighted during clinical examination [13].

Therefore, in this paper we preliminary presented an original evaluation protocol addressing shoulder function in a multidimensional perspective through the integration of different technologies, i.e., marker-based stereophotogrammetry, surface electromyography and ultrasound imaging; in this way, we hypothesized to obtain reliable information related to different characteristics of shoulder biomechanics during the execution of dynamic tasks, including kinematics, muscular activations and humeral head displacement.

II. MATERIALS AND METHODS

The proposed protocol included the exploitation of different technologies able to provide information about joint kinematics, muscular activations, and humeral head displacement.

A. Kinematics

In our feasibility study, the kinematics of the glenohumeral joint were acquired by using a marker-based stereophotogrammetric optoelectronic system (SMART DX 400; BTS Bioengineering), which consisted of 10 infrared cameras detecting the position of thirteen reflective spherical markers placed on subject's skin at a sampling rate of 100 Hz. The proposed protocol contemplates that the markers are positioned on the subject's dominant arm following the recommendations of the International Society of Biomechanics (ISB) [14], in particular: one marker on the incisa jugularis; one on the processus xiphoidus, one on the seventh cervical vertebra; one on the spinous process of the eight thoracic vertebra; one on the most ventral point on the sternoclavicular joint; one on the most dorsal point of the acromioclavicular joint; one on trigonum scapulae; one on the angulus inferior of the scapula; one on the angulus acromialis of the scapula; two markers on the elbow in the lateral and medial humerus epicondyle, respectively; and two markers on the wrist in the radius and ulnar styloid process, respectively.

After reconstructing the 3D positions of the markers during the movement, their raw trajectories undergo standard post-processing, including low-pass filtering and interpolation. Subsequently, we calculated shoulder joint angles following the ISB recommendations for the upper limbs [14]. The kinematic outcome parameters of the humerus and scapula, in particular, are be: i) humeral elevation angle; ii) arm abduction angle; iii) glenohumeral angle (angle between humerus and scapula); iv) scapulothoracic angle (angles reflecting upward rotation of the scapula); v) the ratio between the glenohumeral angle and the humeral elevation angle; vi) the ratio between the scapulothoracic angle and the humeral elevation angle; vii) the ratio between the glenohumeral and scapulothoracic angle [15].

B. Electromyography

The proposed protocol defines that surface electromyography (EMG) signals are recorded using ten bipolar surface probes obtained from ten muscle groups of the dominant arm, following the SENIAM (Surface ElectroMyoGraphy for the Non-Invasive Assessment of Muscles) guidelines [16], covering – in particular – the activities of: trapezius descens, trapezius trasversalis, deltoideus anterior, deltoideus medius, deltoideus posterior, biceps brachii, triceps brachii, pectoralis major, latissimus and sternocleidomastoid. In our preliminary analysis, EMG signals were collected via wireless system (Free EMG, BTS Bioengineering) with a sampling frequency of 1 kHz.

Before the execution of the required tasks, for each muscle, maximum voluntary contraction is recorded in order to normalize the amplitude of the signals. The raw EMG signals will be filtered with a fifth order high-pass Butterworth filter with 20 Hz cut-off frequency and then rectified and smoothed with a 20 ms moving window average. Then, muscle activity expressed as a percentage of the activity during maximal voluntary isometric contraction, muscle activity length, time broadness, and the onset of muscle activity are computed [15].

C. Ultrasound

In order to reliably acquire the behaviour of glenohumeral joint, we propose to follow the ESSR (European Society of MusculoSkeletal Radiology) guidelines [17], and the modified positions proposed by Vincenzo and Levent [18] for the dynamic measurement of the posterior capsule view. To focus better on the behaviour of the inferior joint capsule, we introduce also the reference proposed by Lee et al [19]. These projections can support the clinicians in the evaluation of the movement of the humeral head and, further, estimate the stiffness of the capsule joint.

In our feasibility analysis, we used an ultrasound system (Mindray M9GI, Mindray Medical international limited, China) in B-mode configuration; this system was specifically also equipped three different probes, i.e., two linear array (L14 – 6Ns, and L12 – 4s) and a convex one (C5 – 1s), and allowed also to perform strain elastography analysis. The ultrasound evaluation is recorded and video data is used to calculate the translation of the humeral head, following the procedure proposed in [11].

D. Experimental protocol

An expert operator is required to perform marker and surface EMG electrodes placement on subjects' skin. In order to minimize the impedance due to skin and sweating, the selected areas are initially rubbed with alcohol. After sensors placing, subjects were asked to perform isometric contractions to have the reference values of maximum voluntary contractions of EMG signals.

Subjects are required to seat on a stool, which is positioned oblique with respect to the absolute reference system to avoid occlusion due to the placement of the ultrasound probe. Each subject is required to perform two tasks characterizing glenohumeral function and described as follows:

- *Task 1*: the starting position is 40° of shoulder abduction in the scapular plane and subjects should perform intra/extra rotation movement of gleno/humeral joint with the elbow flexed at 90°. The ultrasound probe is located in front of the subject with the probes L12 – 4s and or C5 – 1s placed around the anterior axillary line, to visualize in longitudinal plane the cortex of the humeral head and its capsular joint.
- *Task 2*: the starting position is 90° of shoulder abduction in the scapular plane and subjects should perform shoulder flexion in the horizontal plane. Sonographer is located behind the subject with L14 – 6Ns probe placed on the posterior aspect of the shoulder, to visualize the posterior part of the humeral head in transverse oblique plane (close to the scapulae spine).

Each subject should perform ten repetitions of each task. The experimental setup is depicted in figure 1. Figure 2 shows two examples of images of the glenohumeral joint acquired via ultrasonography.

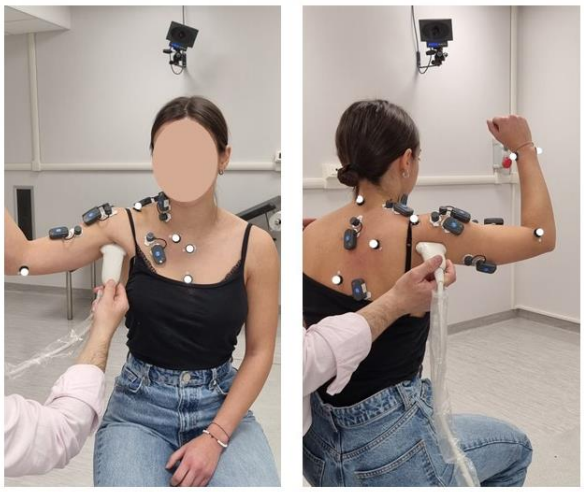


Fig. 1: Experimental setup. In the left side the ultrasound probe is placed around the anterior axillary line; in the right side the ultrasound probe is placed on the posterior aspect of the shoulder.

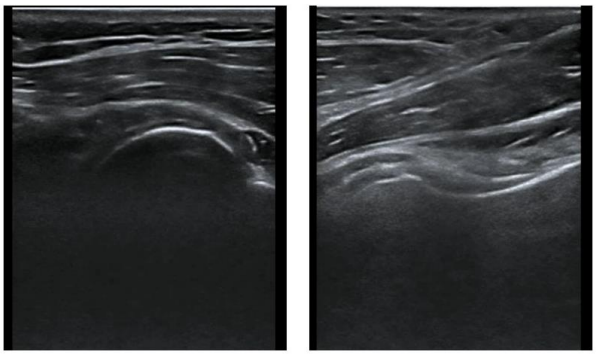


Fig. 2: Ultrasonography images of the humeral head. On the left side, the posterior capsule of the right shoulder in a posterior projection is shown; on the right side, the inferior capsular of the left shoulder in an anterior-inferior projection is shown. On both sides, the L14_6Ns probe is used.

III. Conclusion and Future Works

In this paper, we proposed an experimental setting which was designed to obtain multidimensional information concerning glenohumeral joint during dynamic tasks by integrating different technologies including marker-based stereophotogrammetric optoelectronic system, surface EMG and ultrasonography.

This work represents a preliminary feasibility analysis of the protocol, but further studies will involve a cohort of subject affected by shoulder disorders in order to characterize their movement patterns in terms of shoulder joint kinematics, muscles activation, and humeral head displacement (supporting diagnosis of shoulder instability) and compare them with respect to a control group of healthy subjects.

Therefore, the main purpose of this work is to analyse in depth the complexity of shoulder joint and define reliable features and characteristics for the identification of altered patterns of function by exploiting non-invasive approaches for in vivo assessment in inpatient settings. This protocol was designed to support clinicians to better understand the aetiology of the shoulder disorders and develop tailored treatment for the patients who suffering of shoulder pain.

References

1. Seth, A.; Matias, R.; Veloso, A.P.; Delp, S.L. A Biomechanical Model of the Scapulothoracic Joint to Accurately Capture Scapular Kinematics during Shoulder Movements. PLoS One 2016, 11, e0141028.
2. Huang, T.-S.; Ou, H.-L.; Huang, C.-Y.; Lin, J.-J. Specific kinematics and associated muscle activation in individuals with scapular dyskinesis. J. Shoulder Elb. Surg. 2015, 24, 1227–1234, doi:https://doi.org/10.1016/j.jse.2014.12.022.
3. Lucas, J.; van Doorn, P.; Hegedus, E.; Lewis, J.; van der Windt, D. A systematic review of the global prevalence and incidence of shoulder pain. BMC Musculoskelet. Disord. 2022, 23, 1–11, doi:10.1186/s12891-022-05973-8.
4. Garofalo, P.; Cutti, A.G.; Filippi, M.V.; Cavazza, S.; Ferrari, A.; Cappello, A.; Davalli, A. Inter-operator reliability and prediction bands of a novel protocol to measure the coordinated movements of shoulder-girdle and humerus in clinical settings. Med. Biol. Eng. Comput. 2009, 47, 475–486, doi:10.1007/s11517-009-0454-z.
5. Kontaxis, A.; Cutti, A.G.; Johnson, G.R.; Veeger, H.E.J. A framework for the definition of standardized protocols for measuring upper-extremity kinematics. Clin. Biomech. 2009, 24, 246–253, doi:https://doi.org/10.1016/j.clinbiomech.2008.12.009.
6. Charbonnier, C.; Chagué, S.; Kolo, F.C.; Chow, J.C.K.; Lädermann, A. A patient-specific measurement technique to model shoulder joint kinematics. Orthop. Traumatol. Surg. Res. 2014, 100, 715–719, doi:https://doi.org/10.1016/j.otsr.2014.06.015.
7. Illyés, Á.; Kiss, J.; Kiss, R.M. Electromyographic analysis during pull, forward punch, elevation and overhead throw after conservative treatment or capsular shift at patient with multidirectional shoulder joint instability. J. Electromyogr. Kinesiol. 2009, 19, e438–e447, doi:https://doi.org/10.1016/j.jelekin.2008.09.008.
8. Massimini, D.F.; Boyer, P.J.; Papannagari, R.; Gill, T.J.; Warner, J.P.; Li, G. In-vivo glenohumeral translation and ligament elongation during abduction and abduction with internal and external rotation. J. Orthop. Surg. Res. 2012, 7, 29, doi:10.1186/1749-799X-7-29.
9. Graichen, H.; Hinterwimmer, S.; Eisenhart-Rothe, R. vo.; Vogl, T.; Englmeier, K.-H.; Eckstein, F. Effect of abducting and adducting muscle acitivity on glenohumeral translation, scapular kinematics and subacromial space width in vivo. J. Biomech. 2005, 38, 755–760, doi:https://doi.org/10.1016/j.jbiomech.2004.05.020.
10. Bishop, J.L.; Kline, S.K.; Aalderink, K.J.; Zauel, R.; Bey, M.J. Glenoid inclination: In vivo measures in rotator cuff tear patients and associations with superior glenohumeral joint translation. J. Shoulder Elb. Surg. 2009, 18, 231–236, doi:https://doi.org/10.1016/j.jse.2008.08.002.
11. Inoue, J.; Takenaga, T.; Tsuchiya, A.; Okubo, N.; Takeuchi, S.; Takaba, K.; Nozaki, M.; Kobayashi, M.; Fukushima, H.; Kato, J.; et al. Ultrasound Assessment of Anterior Humeral Head Translation in Patients With Anterior Shoulder Instability: Correlation With Demographic, Radiographic, and Clinical Data. Orthop. J. Sport. Med. 2022, 10, 1–7, doi:10.1177/23259671221101924.
12. Dal Maso, F.; Raison, M.; Lundberg, A.; Arndt, A.; Begon, M. Coupling between 3D displacements and rotations at the glenohumeral joint during dynamic tasks in healthy participants. Clin. Biomech. 2014, 29, 1048–1055, doi:https://doi.org/10.1016/j.clinbiomech.2014.08.006.
13. Lefèvre-Colau, M.-M.; Nguyen, C.; Palazzo, C.; Srour, F.; Paris, G.; Vuillemin, V.; Poiraudeau, S.; Roby-Brami, A.; Roren, A. Kinematic patterns in normal and degenerative shoulders. Part II: Review of 3-D scapular kinematic patterns in patients with shoulder pain, and clinical implications. Ann. Phys. Rehabil. Med. 2018, 61, 46–53, doi:https://doi.org/10.1016/j.rehab.2017.09.002.
14. Wu, G.; Van Der Helm, F.C.T.; Veeger, H.E.J.; Makhsous, M.; Van Roy, P.; Anglin, C.; Nagels, J.; Karduna, A.R.; McQuade, K.; Wang, X.; et al. ISB recommendation on definitions of joint coordinate systems of various joints for the reporting of human joint motion - Part II: Shoulder, elbow, wrist and hand. J. Biomech. 2005, 38, 981–992, doi:10.1016/j.jbiomech.2004.05.042.
15. Spanhove, V.; Van Daele, M.; Van den Abeele, A.; Rombaut, L.; Castelein, B.; Calders, P.; Malfait, F.; Cools, A.; De Wandele, I. Muscle activity and scapular kinematics in individuals with multidirectional shoulder instability: A systematic review. Ann. Phys. Rehabil. Med. 2021, 64, 101457, doi:https://doi.org/10.1016/j.rehab.2020.10.008.
16. Stegeman, D.; Hermens, H. Standards for surface electromyography: The European project Surface EMG for non-invasive assessment of muscles (SENIAM). Línea). Dispon. en http//www. med. … 2007, 108–112.

17. Klauser, A.S.; Tagliafico, A.; Allen, G.M.; Boutry, N.; Campbell, R.; Court-Payen, M.; Grainger, A.; Guerini, H.; McNally, E.; O'Connor, P.J.; et al. Clinical indications for musculoskeletal ultrasound: A Delphi-based consensus paper of the European society of musculoskeletal radiology. Eur. Radiol. 2012, 22, 1140–1148, doi:10.1007/s00330-011-2356-3.
18. Vincenzo, R.; Levent, Ö. Dynamic ultrasound imaging of the posterior capsule in the shoulder: Tips and tricks. Kaohsiung J. Med. Sci. 2020, 36, 471–472, doi:10.1002/kjm2.12190.
19. Lee, J.-G.; Peo, H.; Cho, J.-H.; Cho, C.-H.; Kim, D.-K.; Kim, D.-H. Dynamic Ultrasonographic Measurement of Inferior Joint Capsule Thickness in Patients with Unilateral Frozen Shoulder. Diagnostics 2021, 11.

Motor performances evaluation of female soccer players from AC Trento Women

Giacomo Villa [1,2], Marta Galeotti [2], Foivos Papaioannou [2], Manuela Galli [1] and Veronica Cimolin [1,3]
[1] *Department of Electronics, Information and Bioengineering, Politecnico di Milano, Milano, Italy*
[2] *Euleria Health srl Società Benefit, Rovereto, Trento, Italy*
[3] *Istituto Auxologico Italiano, IRCCS, S.Giuseppe Hospital, 28824 Piancavallo, Oggebbio (Verbania), Italy*

***Abstract*— The aim of the study was to provide a quantitative evaluation of the motor performances of female athletes through a standardized test battery to create a normality dataset.**

Seventy-six female soccer players from AC Trento Women were assessed during the pre-season period (September 2021) through the test battery included in the Riablo™ medical device (Euleria Health, Rovereto (TN), Italy). The evaluations comprised stability test (ST) (two-leg and one-leg), countermovement jump (CMJ) test (two-leg and one-leg), plyometric jumps (PJ) test, parkour (PK) test (one-leg) and quick feet (QF) test. After verifying normal data distribution, for the test characterized by one-leg experimental set-up (one-leg test), the statistically significant differences between the two limbs are highlighted through the paired samples t-test ($\alpha = 0.05$). The normality values of the tested female athletes were obtained. In the one-leg test, the comparison between the performances of the two limbs showed no statistically significant differences.

The present study represents an attempt to identify a standardized test battery that can be used to evaluate the female soccer players performance. The data collected in this study can be used by the stakeholders involved in the female performance evaluation as normative reference data or to conduct further comparative analysis.

***Keywords*— Women's soccer, female performance evaluation, test battery, normative data**

I. Introduction

SOCCER is widely recognised as the most popular sport in the world [1]. One of the main aspects, especially when considering young soccer players, is to provide an adequate performance evaluation (PE) [2]. It can be conducted considering a myriad of factors such as physical, physiological, technical, tactical, and psychological aspects [3] and it requires a large amount of data to be carried out correctly.

The increasing of the financial support from the Union of European Football Associations (UEFA) [4] and of the participation rates over the last 10 years [5], shows a growing interest in women's soccer in the last years. Nevertheless, according to the FIFA executives (2019), there is still potential for further improvements in the quality women's soccer competition through the fundamental passage from "grassroots to elite" [6]. However, to date, the lack of information available on female soccer players limits the predictability of the future female players careers [7]. Consequently, there is a need to provide coaches and others stakeholder with relevant information that allows them to optimally support young athletes as they progress from the youth to elite level [6].

The aim of this study is to analyse the performance of seventy-six female soccer player through a standardized test battery. The data collected in this study can be used by the stakeholders involved in the female performance evaluation as normative reference data or to conduct further comparative analysis.

II. Methods

A. Participants

A group of female soccer players was recruited accordingly to the following criteria:

I. No injuries at the time of the evaluations.
II. No injuries in the two weeks prior the evaluations.

Following the inclusion criteria, 76 female soccer players from AC Trento Women (between 12 and 19 years old) were enrolled for the study and subjected to the test battery before the beginning of the sport season, in September 2021 (T0).

The tests were conducted at the Euleria Health headquarters (Rovereto (TN), Italy) in an indoor environment, on a tiled surface and making athletes wear sneakers.

Written informed consent was obtained from all participants or by their parents.

B. Experimental set-up

After a 10-minute standardized warm-up, all the athletes were subjected to the physical evaluation which included firstly an anthropometry evaluation and then the actual performance assessment.

1) Anthropometry

Height (cm) and weight (kg) were measured for each player before the beginning of the physical test, and the BMI (Body Mass Index, Kg/m^2) was calculated. Height was measured to the nearest 0.1 cm using a stadiometer and body weight was measured to the nearest 0.1 kg using a calibrated analogue scale. The athletes were wearing light indoor clothing, without shoes.

2) Physical tests

The test battery, used to perform the PE, is part of the Riablo™ medical device (Euleria Health, Rovereto, TN, Italy) and includes five different tests that allows to derive eight metrics which allow to assess different aspects of the physical performance:

I. Stability test (ST) performed on a MFT Challenge Disc (TST - Trend Sport Trading, Grosshöflein, Austria) free to move in all directions and connected to a PC. It is performed both with two-leg and with one-leg, and the subjects were expected to maintain their balance for 30 seconds. In case of a loss of balance, the test was restarted. The variable obtained from this test is named level of stability (LoS, index) and can assume values

between 1 and 5 where low values indicate a better postural control.

II. Countermovement jumps (CMJ) test performed placing a wireless IMU (EXL-S3, Exel, Bologna, Italy) above the greater hip trochanter through a waistband. In the case of the two-leg test, it was placed above the dominant leg while, in the case of the one-leg test, it was placed above the tested leg. After the calibration phase, the athletes had to perform a CMJ maintaining their arms on the hips trying to jump as high as possible. The variables obtained were the jump height (in cm) and the power developed (in W/kg).

III. In the plyometric jump (PJ) test, the athletes had to complete four consecutive vertical two-leg jumps focusing on maximizing the jump height minimizing the ground contact time between two consecutive jumps. The variables obtained from the wireless IMU were the ground contact time (in ms) and the reactivity (in mm/ms).

IV. Parkour test (PK) performed using the Speedy Basic Jump Set (TST Trendsport, Grosshöflein, Austria) to create a jump coordination path (as shown in **Errore. L'origine riferimento non è stata trovata.**a) in which the athletes had to perform 16 consecutive one-footed jumps. Double jumps without overcoming an obstacle, twisting of the hip or the touch of the raised leg on the ground were not allowed. The variable obtained was the time needed to fully complete the coordination path.

V. Quick-feet (QF) test performed with the Speedy Basic Jump Set (TST Trendsport, Grosshöflein, Austria) to create an obstacle (as shown in **Errore. L'origine riferimento non è stata trovata.**1b) used by the athletes to step in and out with one foot after the other until the completion of 15 repetitions. Also, in this test, the variable obtained is the time spent to complete all the repetitions.

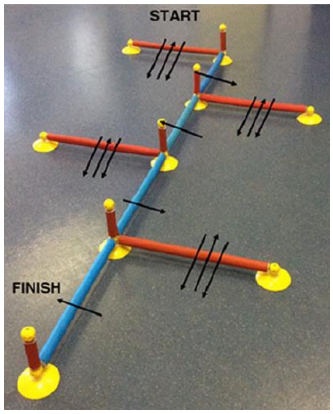




Figure 1a - Coordination path set-up for the PK test (sx)
Figure 1b – Obstacle set-up for the QF test (dx)
Source [8]

C. Statistical analysis

Data normality was verified using the Shapiro-Wilk test. The statistics were computed and reported in terms of mean and standard deviation (SD).

For the tests characterized by a one-leg experimental set-up, the statistically significant differences between the two limbs are highlighted through the paired samples t-test ($\alpha = 0.05$).

The data were analyzed and represented using Microsoft Excel® and MATLAB R2022a.

III. Results

The results for each variable are expressed as mean ± SD and reported in **Errore. L'origine riferimento non è stata trovata.**.

Data obtained from the tests conducted in both two-leg and one-leg modality has been represented through the boxplots (**Errore. L'origine riferimento non è stata trovata.** 2-5). To highlight statistically significant differences between the limbs, the results concerning the one-leg tests (ST; CMJ-Height, CMJ-Power and PK) have been compared.

TABLE I: Performance assessment results

Test	*Modality*	*Mean (± SD)*
Body mass (Kg)	-	56,04 (±8,29)
Height (cm)	-	162,84 (±7,09)
BMI (Kg/m^2)	-	21,09 (±2,62)
ST (LoS, Index)	Two-leg	2,87 (±0,68)
	One-leg-right	2,77 (±0,62)
	One-leg-left	2,76 (±0,60)
CMJ_Height (cm)	Two-leg	29,34 (±4,98)
	One-leg-right	17,15 (±3,65)
	One-leg-left	16,78 (±3,38)
CMJ_Power (W/Kg)	Two-leg	40,16 (±5,53)
	One-leg-right	26,77 (±5,35)
	One-leg-left	26,39 (±5,13)
PJ_Height (cm)	Two-leg	26,41 (±6,84)
PJ_ContactTime (ms)	Two-leg	174,4 (±39,15)
PJ_BIA (mm/ms)	Two-leg	1,58 (±0,40)
PK (s)	One-leg-right	6,80 (±2,28)
	One-leg-left	7,28 (±2,98)
QF (s)	Two-leg	9,21 (±1,86)

Table 1 - Mean (±SD) calculated in each test for the seventy-seven female athletes enrolled.

The evaluations obtained from this test battery, could highlight the characteristics in which the athletes are lacking and could give a hint on the performance area that have to be improved during the sport season.

For example, the mean value obtained in the two-leg ST (2,87 (±0,68)) is located almost in the middle of the evaluation scale (between 1 and 5) and this highlights a good, but not excellent, postural control by the female athletes that should be improved through specific training programmes.

The results in the CMJ test (both for the jump height and for the jump power) shows values that are double in the two-leg versus the one-leg tests.

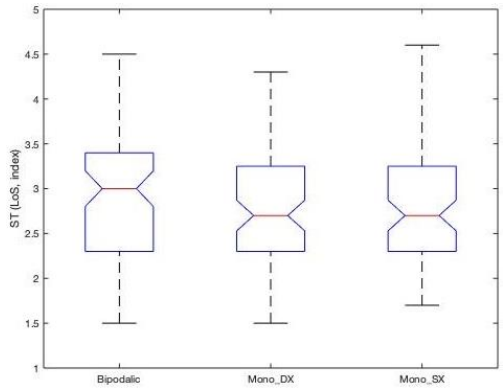


Figure 2 - Boxplot with the comparison of the results obtained in the ST (two-leg and one-leg)

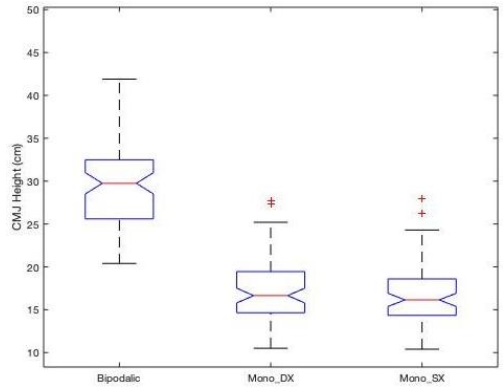


Figure 3 - Boxplot with the comparison of the height reached in the CMJ (two-leg and one-leg)

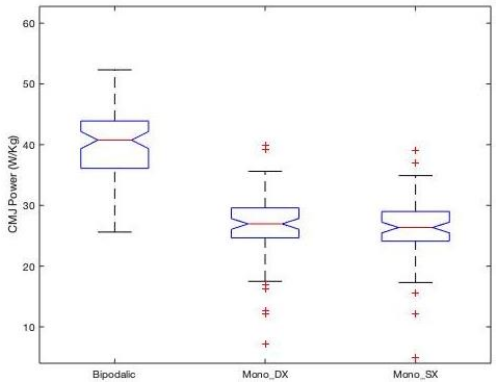


Figure 4 - Boxplot with the comparison of the power developed in the CMJ (one-leg and two-leg)

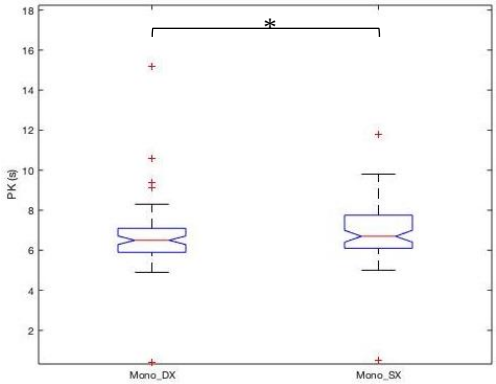


*Figure 5 - Boxplot with the comparison of the execution time in the PK test. * = p < 0.05*

TABLE II: T-TEST RESULTS

Test	*Comparison*	*P-value*
ST (LoS, Index)	DX vs SX	0.933
CMJ_Height (cm)	DX vs SX	0.204
CMJ_Power (W/Kg)	DX vs SX	0.259
PK (s)	**DX vs SX**	**0.017**

*Table 2 - P-values obtained from the limbs' comparison in the one-leg tests. In **bold** is reported the test correspondent to the statistically significant p-value.*

From presented data, the results of the LoS index and of the CMJ height and power seem to be not influenced by the change of the evaluated limb ($p > 0.05$) with the exclusion of the PK test ($p < 0.05$).

IV. DISCUSSION

The aim of the study was to introduce a standardized test battery, used to assess the female soccer players physical performance. When designing a study, the usage of an easy-to-use and standardized test battery is fundamental: in this way, the data collection is faster and easier, and provides to the stakeholders involved in the PE a large quantity of data.

In this study, the assessment of 76 athletes allows the creation of normative data that can be used as comparative data to assess if an athlete who has suffered an injury is able to safely return-to-sport because the performance returned to pre-injuries values. Moreover, with the addition of another test session, the collected data can be used to evaluate the effectiveness of training programs focused on the improvement of the deficient characteristics.

The symmetry between the two limbs is an important aspect to be assessed especially when considering the injuries risk [9]. Eventual asymmetries, in fact, have been described as one of the possible internal injuries risk factors: athletes may perform tasks in an efficient manner, causing fatigue or micro-trauma that can increase the probability of an injury [10]. In this case, while the stability and jumps performance shows no differences between the two limbs, the PK test highlights a significant difference that has to be monitored and constantly assessed in order to decrease the risk of injuries.

ACKNOWLEDGEMENT

The authors would like to acknowledge the staff of Euleria Health in particular David Tacconi, Ilaria Conforti, Gabriele Cera and Paolo Errico for their valuable contribution to the project. Moreover, we would like to thank the staff and the athletes of AC Trento Women involved in the project.

REFERENCES

[1] A. Mark Williams, Paul R. Ford & Barry Drust (2020) Talent identification and development in soccer since the millennium, Journal of Sports Sciences, 38:11-12, 1199-1210, DOI: 10.1080/02640414.2020.1766647

[2] Viswanath Unnithan, Jordan White, Andreas Georgiou, John Iga & Barry Drust (2012) Talent identification in youth soccer, Journal of Sports Sciences, 30:15, 1719-1726, DOI: 10.1080/02640414.2012.731515

[3] Lehance, C., Binet, J., Bury, T. and Croisier, J.L. (2009), Muscular strength, functional performances and injury risk in professional and junior elite soccer players. Scandinavian Journal of Medicine &

Science in Sports, 19: 243-251. https://doi.org/10.1111/j.1600-0838.2008.00780.x

[4] UEFA. (2015). Women's football across the national associations, 2014-2015. Retrieved from https://www.uefa.com/MultimediaFiles/Download/Women/General/02/03/27/84/2032784_DOWNLOAD.pdf

[5] Manson SA, Brughelli M, Harris NK. Physiological characteristics of international female soccer players. J Strength Cond Res. 2014 Feb;28(2):308-18. doi: 10.1519/JSC.0b013e31829b56b1. PMID: 24476742.

[6] Daniel Leyhr, Johannes Raabe, Florian Schultz, Augustin Kelava & Oliver Höner (2020) The adolescent motor performance development of elite female soccer players: A study of prognostic relevance for future success in adulthood using multilevel modelling, Journal of Sports Sciences, 38:11-12, 1342-1351, DOI: 10.1080/02640414.2019.1686940

[7] Naomi Datson, Matthew Weston, Barry Drust, Warren Gregson & Lorenzo Lolli (2020) High-intensity endurance capacity assessment as a tool for talent identification in elite youth female soccer, Journal of Sports Sciences, 38:11-12, 1313-1319, DOI: 10.1080/02640414.2019.1656323

[8] Hildebrandt, C., Müller, L., Zisch, B. et al. Functional assessments for decision-making regarding return to sports following ACL reconstruction. Part I: development of a new test battery. Knee Surg Sports Traumatol Arthrosc 23, 1273–1281 (2015). https://doi.org/10.1007/s00167-015-3529-4

[9] Helme, M., Tee, J., Emmonds, S., and Low, C. (2021). Does lower-limb asymmetry increase injury risk in sport? A systematic review. Physical Therapy in Sport, 204–213, DOI: https://doi.org/10.1016/j.ptsp.2021.03.001

[10] Murphy DF, Connolly DAJ, Beynnon BDRisk factors for lower extremity injury: a review of the literatureBritish Journal of Sports Medicine 2003;37:13-29.

Development of a contrast-enhanced micro tomography protocol for human meniscus: a pilot study

C. Falsina[1], M. Maglio[2], M. Berni[1,2], N. F. Lopomo[1], G. Giavaresi[2], A. Grassi[2], S. Zaffagnini[2], M. Baleani[2], G. Marchiori[1,2]

[1] *University of Brescia, Italy*

[2] *Rizzoli Orthopaedic Institute, Italy*

***Abstract*—Aiming to promote comprehensive imaging approaches integrating information about the microstructure of mineralized and soft tissues, because the latter are transparent to X-ray, the use of contrast-enhanced micro tomography (CE-µCT) is increasing significantly. In the present work, two tissue preparations – with PTA as contrast agent and by HMDS chemical drying – were tested on human meniscal tissue to evaluate their effectiveness in enhancing µCT tissue contrast. Eventual macroscopic alterations induced by such approaches were investigated through size/weight measures and mechanical testing, i.e., unconfined compression. Preliminary results showed that both strategies were able to enhance the µCT material contrast, albeit with different efficacy in tissue quote revealed and in highlighting microstructure; despite the promising evidence, alterations in the mechanics of the sample – in comparison with non-contrasted tissue – occurred.**

***Keywords*—contrast-enhanced µCT, phosphotungstic acid, hexamethyldisilazane, meniscus.**

I. INTRODUCTION

CONTRAST-ENHANCED micro tomography (CE-µCT) is an emerging tool for quantitative virtual 3D anatomical analysis of tissues in healthy conditions and, above all, when affected by a pathology. This approach aims at enhancing X-ray contrast of originally low-density materials, such as soft tissues. Before promoting CE-µCT as a standard technique complementary to immuno-histomorphometry, several limitations must be overcome: 1) operating procedures for sample preparation and imaging should be optimized and standardized; 2) contrast agent diffusion within the sample should be maximized together with minimizing tissue shrinkage; 3) tissue alteration due to the protocol should be minimized to ensure a not biased structural analysis and the complementarity with other assays and functional testing [1].

In this field, very few works are reported on human meniscus, a biphasic fibro-cartilaginous tissue present within the knee joint, despite its important role in knee biomechanics and homeostasis [2]. Phosphotungstic acid (PTA) was used to preferentially reveal collagenous structures [3], which are abundant in the meniscus; in fact, this approach was tested as contrast agent on animal models [4].

In this study, PTA for CE-µCT was investigated on human meniscal tissue and compared with chemical drying, a common procedure to enhance contrast in biological wet samples, already experimented on human meniscus [5]. Dimensional and weight measures served to reveal eventual tissue alterations due to the CE-µCT protocol. Moreover, the protocol was evaluated for complementarity with mechanical characterization, i.e., functional testing.

II. MATERIALS AND METHODS

Cubic samples were extracted from human menisci (ethical approval 952/2021/Sper/IOR), as needed by unconfined compression mechanical test [2].

For PTA CE-µCT, three adjacent samples were extracted from the central part of a same meniscus, and fixed in 4% formalin. Subsequently, a sample was contrasted with 1% (w/v) PTA in 70% ethanol (EtOH) solution [4] for 84 hours, a sample was contrasted with 1% (w/v) PTA in phosphate buffered saline (PBS) solution [6] for 84 hours, a sample was not contrasted (reference control). Samples were µCT scanned with source voltage 70 kV and current 250 µA, without metal filter (*Skyscan 1172, Bruker*, Belgium).

As for µCE-CT by chemical drying, two adjacent samples were extracted from the central part of a same meniscus and fixed in 4% formalin: one sample was dehydrated in ascending ethanol concentrations (1 hour each), treated with HMDS (1 hour) and air-dried in a fume hood overnight; a sample was not dehydrated (reference control). Samples were µCT scanned with source voltage 40 kV and current 250 µA, without metal filter.

After CE-µCT, samples contrasted with PTA were rehydrated with PBS immersion for 84 hours, while HMDS dried samples were rehydrated with immersion in decreasing alcohol concentrations up to water.

Samples' volume and weight were measured respectively by caliper and microbalance, before CE-µCT (PRE), before (INTERM) and after rehydration (POST). Unconfined compression tests (*Mach-1, Biomomentum*, Canada) were performed with the same schedule, in strain control, with a sequence of five incremental ramp-stress relaxations, loading along the sample vertical direction [2].

III. RESULTS

PTA resulted important for contrasting human meniscal tissue, otherwise transparent in µCT imaging. Nevertheless, staining concentration and time were not enough to reach a full tissue contrast, both in EtOH and PBS solution (Fig. 1A). After rehydration, samples appeared diffusely contrasted (Fig. 1B).

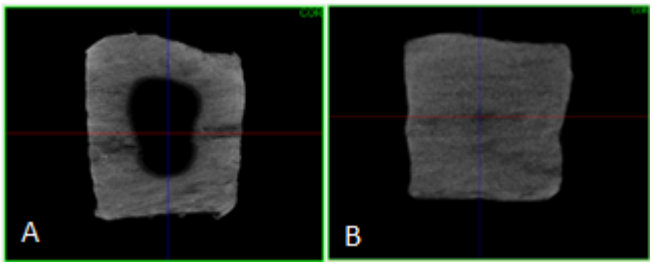


Fig. 1: µCT section of the sample (A) contrasted by PTA in PBS and (B) rehydrated.

Instead, HMDS treatment permitted full drying and imaging contrast.

Dimensionally, PTA in EtOH solution caused a tissue shrinking, not recovered by rehydration; conversely, PTA in PBS resulted more stable (Table I). Volume and weight loss, i.e., shrinking, was evident for chemical drying by HMDS, it was partially recovered by rehydration (Table II).

Mechanically, compression test highlighted a macroscopic change – overall stiffening – in the tissues entering µCT. Rehydration was effective in reversing the impact of sample preparation only in case of HMDS treatment (Fig. 2), while it even increased the stiffness of samples subjected to PTA treatments (Fig. 3,4). Indeed, after rehydration these samples showed a full µCT image contrast (Fig. 1B), even if with lower intensity, suggesting a complete diffusion of the PTA, that could increase tissue resistance to deformation.

TABLE I: DIMENSIONAL MEASURES ON SAMPLES CONTRASTED WITH PTA

Sample	*Volume (mm3)*	*Weight (mg)*
PTA-EtOH (PRE)	95	151
PTA-EtOH (INTERM)	74	96
PTA-EtOH (POST)	87	105
PTA-PBS (PRE)	164	227
PTA-PBS (INTERM)	166	207
PTA-PBS (POST)	172	204
CONTROL (PRE)	123	166
CONTROL (INTERM)	151	161
CONTROL (POST)	150	168

TABLE II: DIMENSIONAL MEASURES ON SAMPLES DRIED WITH HMDS

Sample	*Volume (mm3)*	*Weight (mg)*
HMDS (PRE)	69	111
HMDS (INTERM)	56	32
HMDS (POST)	72	91
CONTROL (PRE)	105	141
CONTROL (INTERM)	132	141
CONTROL (POST)	126	143

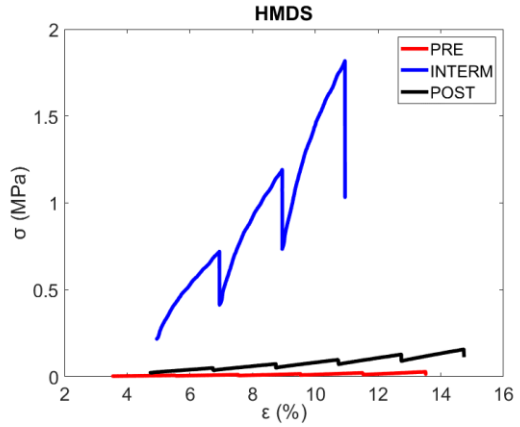


Fig. 2: stress (σ, MPa)-strain (ε, %) graph from unconfined compression on HMDS dried sample, before CE-µCT (PRE), after CE-µCT (INTERM) and after rehydration (POST).

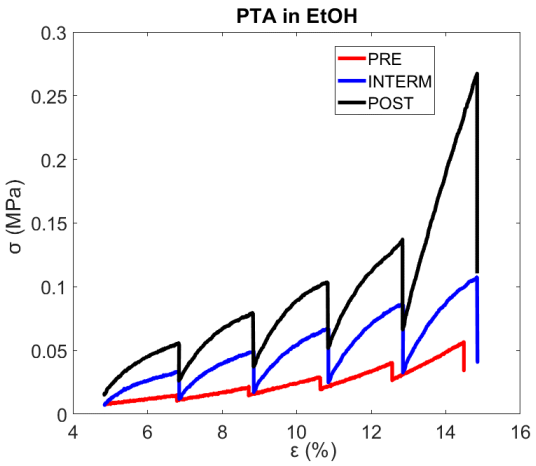


Fig. 3: stress (σ, MPa)-strain (ε, %) graph from unconfined compression on PTA in EtOH sample, before CE-µCT (PRE), after CE-µCT (INTERM) and after rehydration (POST).

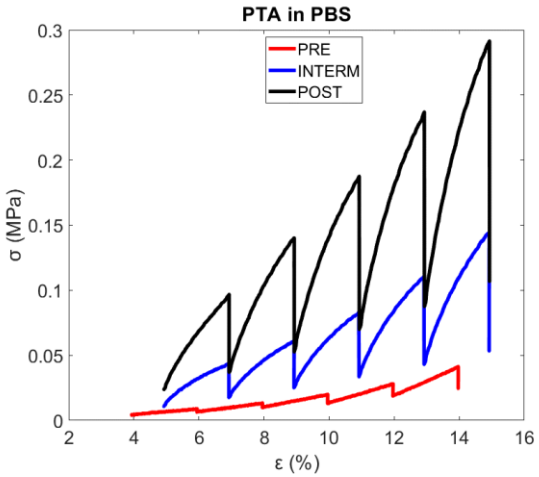


Fig. 4: stress (σ, MPa)-strain (ε, %) graph from unconfined compression on PTA in PBS sample, before CE-µCT (PRE), after CE-µCT (INTERM) and after rehydration (POST).

IV. DISCUSSION

This pilot study supported the development of reliable and repeatable CE-µCT protocols on human meniscal tissue, pointing out important aspects still not properly rated. Indeed, both the reference approaches [4,5] described several correspondence between µCT and histological imaging, validating their CE-µCT protocols, but only in a partial way; in fact, eventual tissue alterations, e.g., shrinking, were not discussed. Moreover, the complementarity with methods other than histology – such as the mechanical characterization – was not investigated.

The protocol with PTA as contrast agent in EtOH solution on equine meniscus described in [4] was here replicated on human meniscus: PTA may not reach the innermost parts of the tissue; PBS instead of EtOH as solvent could avoid shrinking, but not PTA partial diffusion and tissue stiffening. Moreover, an attempt to recover the original status of the meniscal tissue was here added, even if failed.

Overall, chemical drying appears as more effective in revealing tissue microstructure than PTA; however, PTA is a collagen-specific marker, can characterize collagen distribution and indirect interpretations could potentially be made based on the alignment of the extracellular matrix [6]. For this reason, our intent is the optimization of the PTA strategy, e.g. by increasing its concentration in solution and/or exposition time and by trying a different solvent, e.g. water [7]. Shrinking and stiffening phenomena in input to µCT will be always analysed for verifying if alterations are only compositional (e.g. dehydration), or even structural producing a bias. Finally, other strategies for washing out PTA after CE-µCT will be tested, in analogy with experiences on cartilage [8].

V. CONCLUSION

The evidence collected in this pilot study paves the way for further investigations aiming to develop an optimal CE-µCT protocol, capable of enhancing the detection of meniscus microstructure and preserving its main features. Integrating this approach with complementarity techniques would represent a comprehensive framework to face the complexity of soft articular tissues, crucial in validating advanced tissue models and regenerative medicine studies.

ACKNOWLEDGEMENT

We acknowledge the Italian Ministry of Health 5x1000 2019 (2018 incomes) “Medicina rigenerativa e riparativa personalizzata per le patologie dei tessuti muscolo-scheletrici e la chirurgia ricostruttiva ortopedica" project for the financial support.

REFERENCES

[1] S. de Bournonville, S. Vangrunderbeeck, and G. Kerckhofs, “Contrast-Enhanced MicroCT for Virtual 3D Anatomical Pathology of Biological Tissues: A Literature Review” *Contrast Media Mol Imaging*, February 2019.

[2] M. Berni, G. Marchiori, G. Cassiolas, A. Grassi, S. Zaffagnini, M. Fini, N. F. Lopomo, M. Maglio, “Anisotropy and inhomogeneity of permeability and fibrous network response in the pars intermedia of the human lateral meniscus” *Acta Biomater* 135:393-402, November 2021.

[3] P. Das Neves Borges, A. E. Forte, T. L. Vincent, D. Dini, M. Marenzana, “Rapid, automated imaging of mouse articular cartilage by microCT for early detection of osteoarthritis and finite element modelling of joint mechanics” *Osteoarthritis cartilage*, 22(10):1419-28, October 2022.

[4] I. Ribitsch, C. Peham, N. Ade, J. Dürr, S. Handschuh, J. P. Schramel, C. Vogl, H. Walles, M. Egerbacher, F. Jenner “Structure-Function relationships of equine menisci*” Plos One,* 13(3):e0194052, March 2018.

[5] I. Kestilä, E. Folkesson, M. A. Finnilä, A. Turkiewicz, P. Önnerfjord, V. Hughes, J. Tjörnstrand, M. Englund, S. Saarakkala “Three-dimensional microstructure of human meniscus posterior horn in health and osteoarthritis” *Osteoarthritis cartilage* 27(12):1790-1799, December 2019.

[6] H. J. Nieminen,T. Y. Yilitalo, S. Karhula, J-P. Suuronen, S. Kauppinen, R. Serimaa, E. Haeggström, K. P. H. Pritzker, M. Valkealahti, P. Lehenkari, M. Finnilä, S Saarakkala “Determining collagen distribution in articular cartilage using contrast-enhanced micro-computed tomography” *Osteoarthritis cartilage* 23(9):1613-1621, September 2015.

[7] G. Marchiori, A. Parrilli, N. Sancisi, M. Berni, M. Conconi, L. Luzi, G. Cassiolas, S. Zaffagnini, N. F. Lopomo “Integration of micro-CT and uniaxial loading to analyse the evolution of 3D microstructure under increasing strain: application to the Anterior Cruciate Ligament”, *materialstoday PROCEEDINGS* 7(1):501-507, March 2019.

[8] J. N.Clark, A. Garbout, S. A. Ferreira, B. Javaheri, A. A. Pitsillides, S. M. Rankin, J. R. T. Jeffers, U. Hansen “Propagation phase-contrast micro-computed tomography allows laboratory-based three-dimensional imaging of articular cartilage down to the cellular level” *Osteoarthritis cartilage* 28(1):102-111, January 2020.

Biomechanical assessment of the anomalous coronary compression by patient-specific finite element analysis

A. Rosato[1*], M. Lo Rito[2*], G. M. Formato[1], S. Anglese[1], V. Ceserani[3], A. F. Pascaner[3] and M. Conti[3]
[1] *3D and Computer Simulation Laboratory, IRCCS Policlinico San Donato, San Donato Milanese, Italy*
[2] *Department of Congenital Cardiac Surgery, IRCCS Policlinico San Donato, San Donato Milanese, Italy*
[3] *DICAr, University of Pavia,Italy*
** These authors (A.R., M.L.R.) have contributed equally to this work*

***Abstract*— Anomalous Aortic Origin of Coronary Arteries (AAOCA) with intramural course could represent a life-threatening pathology that leads to ischemia due to compression of the anomalous vessel. We developed a computational workflow to investigate variations in the coronary lumen cross-sectional area under simulated effort conditions. Preliminary results appear to confirm the clinical hypothesis of the intramural segment compression. Our pipeline is proposed as a tool that can provide useful information on the pathological mechanism of AAOCA.**

***Keywords*— AAOCA, intramural course, finite element analysis, cross-sectional area.**

I. Introduction

Anomalous Aortic Origin of Coronary Arteries (AAOCA) is a congenital condition where one or more coronary vessels originate from an ectopic site within the aorta and may take different courses [1]. Among these variants, the presence of an intramural segment (IM) is associated with the risk of ischemia and sudden cardiac death [2] probably related to lumen compression caused by the aorta expansion [3]. In this work, we propose a pipeline to assess changes in the coronary cross-sectional areas during simulated effort conditions using patient-specific finite element analyses (FEA).

II. Materials and Methods

A. Reconstruction of the patient's anatomy

The aortic and coronary lumen were segmented from the diastolic sequences of coronary computed tomography angiography (CCTA) scans of patients with AAOCA. The cross sections along the aortic and coronaric centerlines were then extracted from the STL reconstruction to build a three-dimensional computer-aided design (CAD) model of the anatomy of interest with vessel walls (Fig.1, panels A-B-C-D).

B. Simulation settings and analysis

FEA simulations were carried out through the commercial finite element package Abaqus/Standard 2019 (Dassault Systemès, Providence, RI). Static analyses were performed assuming that the geometric model, i.e., the computational domain, is subjected to an initial pressure equal to the patient's mean intraluminal pressure measured during catheterization. Incremental pressure loads were applied to the aortic lumen to simulate systolic peaks under normal and stress conditions, in a range between 120 and 250 mmHg. The coronary lumen was uniformly pressurized with an increment of 10 mmHg, with reference to the patient's initial pressure, and this value was kept constant throughout the simulation. A neo-Hookean model was used for the aorta and coronary arteries [4]. The models were discretized using hybrid 4-node tetrahedral

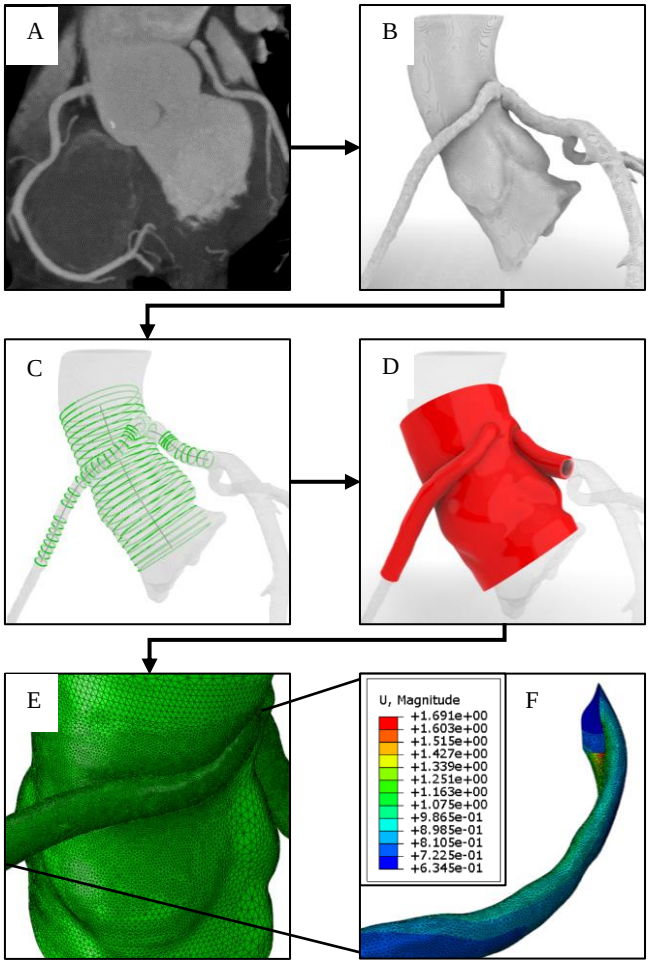


Fig. 1. Pipeline for AAOCA patient-specific simulation. Panel A: CCTA scan. Panel B: STL reconstruction of the aorta with coronary arteries. Panel C: slicing of the STL reconstruction and extraction of the profile curves (Vmtk v1.4 software, Orobix, Bergamo, Italy). Panel D: CAD model of the aortic root with healthy left coronary and anomalous right coronary with intramural course originating from the opposite sinus (Rhinoceros v6.0 software, McNeel and Associates, Seattle, Wash). Panel E: tetrahedral mesh with local refinement. Panel F: extraction of the anomalous luminal surface in its deformed configuration; legend: magnitude of nodal displacements.

elements with local refinements in the IM regions (Fig. 1, panel E). Boundary conditions were applied as done in our previous work [5].

C. *Post-processing of Simulation Results*

The deformed configuration of the coronary lumen was processed for each defined pressure increment (Fig. 1, panel F). The cross-sectional areas of the vessel were calculated from the ostium along the entire length of the coronary arteries and used to assess potential enlargement/narrowing. The anomalous coronaries were divided into three zones to better localize the phenomenon: the ostial zone (OST), from the origin up to a length of 1.5 mm; the intramural or middle zone (MID), from the end of the ostial zone to the end of the IM segment; and the distal zone (DIS), from the end of the intramural zone to the end of the coronary model. In the case of AAOCA without an intramural course, the length of the middle zone was considered equal to the average length of the intramural segments. Healthy coronaries were divided into two zones: the ostial zone, defined as above, and the distal zone, from the end of the ostial zone to the end of the coronary model.

D. *Statistical Analysis*

Comparison between homologous segments was made by Mann-Whitney U tests to assess whether there are differences in behavior between healthy and anomalous coronaries and between anomalous coronaries with and without IM segment.

III. Results

Our preliminary analysis was carried out on a group of 22 subjects with AAOCA, including 17 with the IM segment and 5 without the IM segment. The mean luminal areas of OST, MID, and DIS zones in the anomalous and healthy coronary arteries are summarized as median and interquartile range (IQR) in Table I for three aortic pressures: the basal value, i.e., the patients' mean intraluminal pressure at rest (90 ± 15 mmHg); 180 mmHg (effort condition); 240 mmHg (intense effort condition).

TABLE I: MEAN LUMINAL AREA

	Basal		180 mmHg		240 mmHg	
	median	IQR	median	IQR	median	IQR
OST						
NO-IM	8.45	5.37	8.84	5.35	8.83	5.51
IM	5.76	3.53	5.14	2.38	4.67	1.89
HEALTHY	13.02	8.64	13.86	9.17	14.42	9.17
MID						
NO-IM	5.37	2.76	5.29	2.67	5.19	2.56
IM	6.23	1.98	5.89	1.81	5.63	1.67
DIS						
NO-IM	2.91	2.85	2.92	2.76	2.92	2.66
IM	8.65	5.98	8.70	6.00	8.70	6.01
HEALTHY	13.37	9.28	13.62	9.60	13.74	9.79

Mean luminal areas (in mm^2) expressed as median and IQR. OST: ostial zone; MID: intramural or middle zone; DIS: distal zone. NO-IM: anomalous coronary without intramural segment; IM: anomalous coronary with intramural segment; HEALTHY: healthy coronary.

Variations in the MLA of coronary vessels, with reference to the undeformed configuration at the basal pressure value, were calculated at the OST, MID and DIS levels of the anomalous coronaries and at the OST and DIS level of the healthy ones (Fig. 2). Anomalous coronary arteries with the IM segment show a degree of narrowing in the OST and MID zones that increased in severity with increasing pressure loads. The

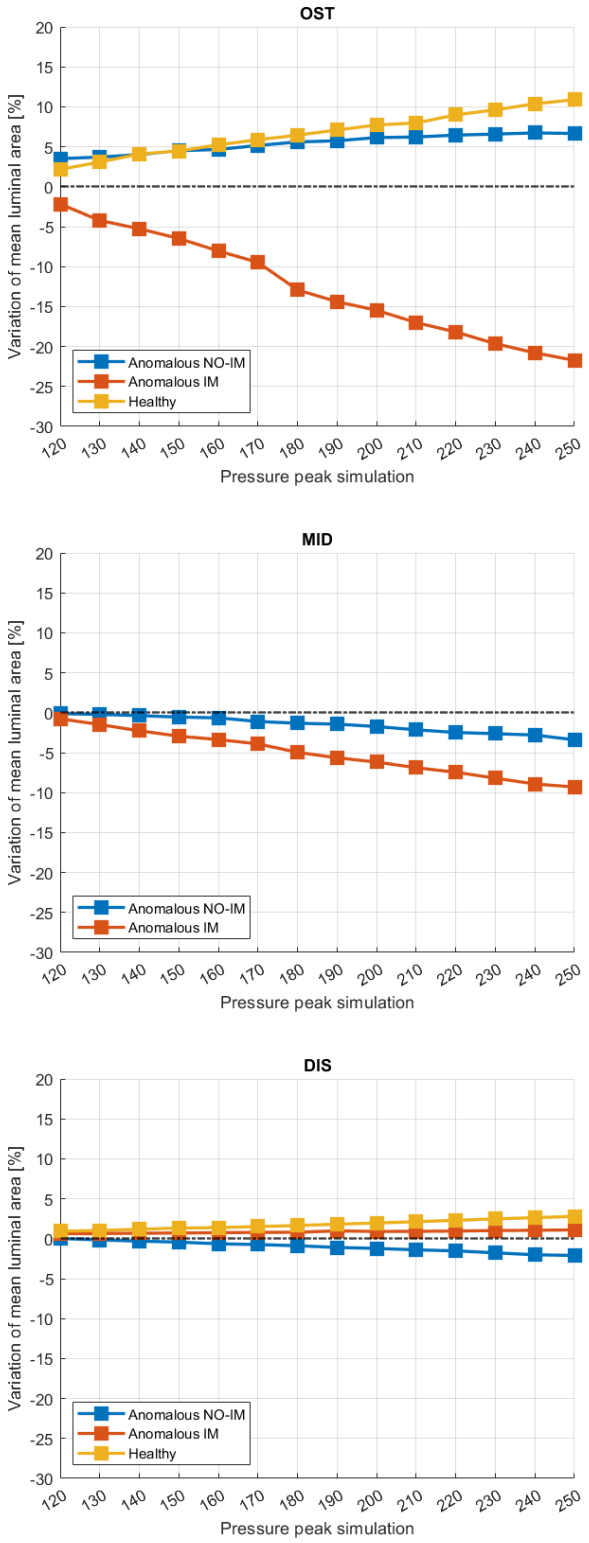


Fig. 2. Variations of the mean luminal area in the OST, MID and DIS zones for: healthy coronaries (yellow), in anomalous coronaries with intramural segment (red) and in anomalous coronaries without intramural segment (blue).

reduction in ostium caliber at 120 mmHg is -2.16% and increases to -21.7% at 250 mmHg. The anomalous coronaries without IM segment have a similar, though less pronounced, trend in the MID tract, while the ostial zone shows an expansion as the healthy ostium. No reduction in the caliber of healthy coronary arteries is observed. In the ostial zone, at all simulated pressures, MLA variations in anomalous coronaries with IM segment are significantly different from variations in anomalous coronaries without IM segment and substantially different from those in healthy coronaries. In the MID zone, at all simulated pressures except for 120 mmHg, variations of the MLA in anomalous coronaries with IM segment are significantly different than variations in anomalous coronaries without IM segment. Regarding the distal zone there are significant differences between the various types of coronary arteries at all simulated pressures.

IV. Discussion

In basal conditions the anomalous coronary with intramural segment has a mean luminal area of 5.76 and 6.23 mm^2, respectively at the OST and MID level, and a reference mean luminal area, in the distal zone, of 8.65 mm^2. Although the latter remains almost unchanged during effort conditions, the MLA in the OST and MID zones decreases, respectively, to 4.67 and 5.36 mm^2 applying a simulated aortic pressure of 240 mmHg. Therefore, the severity of stenosis of the anomalous lumen increases. Our preliminary results corroborate the clinical hypothesis that the expansion of the aortic root compresses the IM segment in systole, a mechanism that can lead to adverse events during physical exertion when the demand for oxygenated blood to the heart increases.

Limitations. The model does not account for vessel pre-stress; consequently, the unloaded, initial configuration of the arterial model resembles the geometry extracted from the diastolic phase of the CT scan that is paired to the mean pressure measured during catheterization. Then this configuration is updated to reach the corresponding 120 mmHg configuration and subsequently, progressively pressurized. Regarding the constitutive model, the assumption of a neo-Hookean formulation does not take into account the highly nonlinear, anisotropic and viscoelastic behavior of the aortic wall. Further development of the study should target these approximations and include comparisons with clinical data.

V. Conclusion

Our pipeline, based on patient-specific structural simulations, may allow retrieving the degree of narrowing and the critical locations of the phenomenon in AAOCA, which might be indicators for surgical planning.

Acknowledgement

The project was funded by the Italian Ministry of Health (GR-2019-12369166).

References

[1] M. K. Cheezum et al., “Anomalous Aortic Origin of a Coronary Artery From the Inappropriate Sinus of Valsalva,” J. Am. Coll. Cardiol., vol. 69, no. 12, pp. 1592–1608, 2017, doi: 10.1016/j.jacc.2017.01.031.

[2] A. Jegatheeswaran et al., “Features associated with myocardial ischemia in anomalous aortic origin of a coronary artery: A Congenital Heart Surgeons’ Society study.,” J. Thorac. Cardiovasc. Surg., vol. 158, no. 3, pp. 822-834.e3, 2019, doi: 10.1016/j.jtcvs.2019.02.122.

[3] M. Lo Rito et al., “Anomalous aortic origin of coronary artery biomechanical modeling: Toward clinical application,” J. Thorac. Cardiovasc. Surg., vol. 161, no. 1, pp. 191-201.e1, 2021, doi: 10.1016/j.jtcvs.2020.06.150.

[4] M. X. Jiang et al., “Patient-specific fluid–structure simulations of anomalous aortic origin of right coronary arteries,” JTCVS Tech., vol. 13, no. June, pp. 144–162, 2022, doi: 10.1016/j.xjtc.2022.02.022.

[5] Formato GM, Lo Rito M, Auricchio F, Frigiola A, Conti M. Aortic Expansion Induces Lumen Narrowing in Anomalous Coronary Arteries: A Parametric Structural Finite Element Analysis. J Biomech Eng. 2018 Nov 1;140(11):111008. doi: 10.1115/1.4040941.

Mechanical evaluation of synthetic meshes: definition and verification of a rigorous test protocol

V. Civilini[1,2], V. Giacalone[1,2], A.L. Audenino[1,2] and M. Terzini[1,2]
[1] *Department of Mechanical and Aerospace Engineering, Politecnico di Torino, 10129 Turin, Italy*
[2] *Polito[BIO]Med Lab, Politecnico di Torino, 10129 Turin, Italy*

***Abstract* — The definition of consistent experimental test benches for the estimation of mechanical characteristics of surgical meshes is still challenging due to the absence of specific standards for mechanical characterization of synthetic meshes. A meticulous test protocol for the mechanical comparison between surgical meshes having the same intended use is hereby proposed. The test protocol comprised three quasi-static test methods: (1) ball burst test, (2) uniaxial tensile test, and (3) suture retention test. For each test, the computation of relevant mechanical properties is detailed. The proposed test protocol was applied on 14 polypropylene meshes, 3 composite meshes (Comp), and 6 urogynecologic devices (UD) to verify its universal applicability towards meshes of different types and intended uses. The repeatability of the test methods is assessed in terms of coefficient of variation. The test protocol, easily performed to all the selected surgical meshes, exhibited an intra-subject variability characterized by coefficient of variations settled around 0.05. Its use within other laboratories could allow the determination of the inter-subject variability assessing its repeatability among users of alternative universal testing machines.**

***Keywords* — surgical meshes, urogynecologic devices, standard test protocol, mechanical characterization**

I. Introduction

SURGICAL meshes represent at present the gold standard for the repair of herniated abdominal wall and for the treatment of pelvic floor disorder (i.e., pelvic organ prolapse and stress urinary incontinence). Nevertheless, no specific standard regulates the functionality and the effectiveness assessment of these implantable devices. For this reason, a plurality of test methods arose to assess the mechanical characteristics of surgical meshes and urogynecologic devices [1], [2]. International or National Standards developed for textile industry are often adapted in terms of specimens dimensions and other test parameters (e.g., strain rate, ratio between the clamped region and the sphere diameter in ball burst test) [3]–[6]. In addition, the post-processing of raw data is reported with different methods in literature [7]. The aim of the post-processing is mainly the computation of the mechanical properties of the mesh. Some properties (e.g., anisotropy, membranal tension, and strain) can indeed lead to a better knowledge of implant acceptability, while others (e.g., maximum uniaxial tensile force and tension, uniaxial stiffness) are mainly useful for mechanical comparison [8], [9]. Differences in raw data manipulation can be found, for examples, considering the stiffness of the meshes computed from the uniaxial tensile test data [10]–[12] or the anisotropy between the two main directions of the knitted patches [4], [13]. The issues described above impact the repeatability and reliability of the results and are the main cause of the meaningful variability founded in literature [1], [12], [14]–[17]. Therefore, this study fits in this panorama proposing a comprehensive test protocol comprising: (1) a set of mechanical testing methods adapted from the International Standards and (2) the post-processing algorithms used to extract from the raw data the mechanical parameters useful to compare different devices. The defined test protocol is tested on 23 different devices to confirm its repeatability on devices having different knitted structures and different intended use.

II. Materials and Methods

The test protocol was designed selecting three quasi-static test methods characterized by ease of implementation and adaptability in terms of specimens dimensions. In detail, given its in vivo-like solicitation pattern, the static ball burst test was selected for performance assessment, to evaluate rupture behaviour at high loads and deformability behaviour under physiological or pathological stresses (Fig. 1a). The static uniaxial test represents the most performed mechanical test and was therefore chosen to provide basic mechanical characteristics (Fig. 1b). Finally, a static suture retention test completes the mechanical characterization of surgical meshes providing parameters related to the mesh positioning procedure (Fig. 1c). For each test method and configuration five specimens are tested in order to give statistical consistency of results. Specimens from the two principal knitting direction of each mesh type are tested in uniaxial tensile test and in suture retention test.

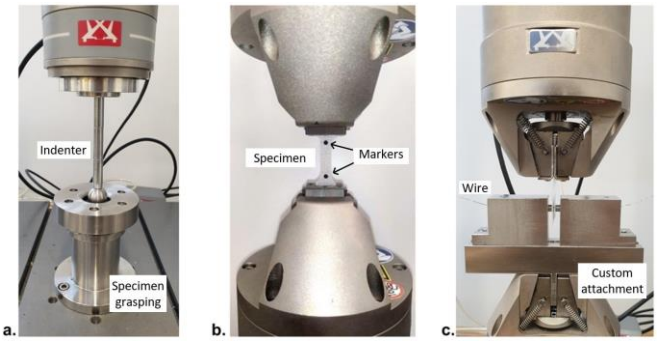


***Fig 1:** Test benches: a) Ball burst test; b) Uniaxial tensile test; c) Suture retention test*

A. Ball Burst test protocol and parameters computation

ASTM D6797-15 is used as reference standard for this test. Given the small and variable size of commercial products, reduced circular specimens (diameter = 55 mm) and ball-burst attachment dimensions (ring clamp internal diameter (aperture) = 35 mm and polished steel sphere diameter = 20 mm) are used in place of the recommended ones. The new dimensions were selected taking care of maintaining the same

ratio between the aperture and the ball diameter suggested by the standard (44.45 mm / 25.4 mm = 1.75).

After specimen positioning in the custom test grasping shown in Fig 1a, the spherical indenter is moved towards the mesh at 300 mm/min as the standard prescribes, while recording the force and the displacement.

The bursting strength is then computed as the maximum force value from the raw data. The dependency of the maximum force by the ratio between sphere and aperture diameter makes mandatory the computation of maximum membrane tension and dilatational strain for comparison purposes. These parameters are computed through an analytical method developed by [18], [19]. The true membrane tension depends on the radius in the truncated cone portion of the specimen free from the ball, decreasing as the considered radius increases. The true tension in the portion of the mesh in contact with the sphere, T, is indeed the greatest tension that the specimen stands and is therefore used to compute the maximum membrane tension and the corresponding dilatational strain.

On the other hand, the true membrane tension at the aperture, T_a, is the tension that affects the entire area of the specimen and can be thus considered to assess the dilatational strain of the graft corresponding to a membrane tension of 16 N/cm and at 32 N/cm, that correspond to the most reported tension requirements for surgical meshes [20], [21].

A one-way ANOVA analysis, followed by a Tukey-Kramer post-hoc test was implemented to compare inter material variability for the meshes grouped by density.

B. Uniaxial tensile test protocol and parameters computation

The ISO 13934-1:2013 international standard for textile fabrics is adapted in order to test medical devices in terms of specimen shape and dimension. The actual specimen design (Fig 1b) was selected in order to avoid specimens rupture within 5 mm from the grip, as prescribed by the standard. The choice of dogbone specimens compels the use of an optical measurement system to record the displacement of the narrow zone of the specimen. To that end, two markers are sewn at a distance of 20 mm on the mesh without interfering with yarns movements. The specimens are then mounted using pneumatic grips on the testing machine without applying a preload, and the upper grip is moved vertically at 20 mm/min while a Digital Image Correlation (DIC) system is used to acquire and analyse markers displacements. The force and the displacement data as well as images are acquired at 5 Hz.

The tension is computed from the force F acquired during the test as in Eq. (1):

$$T = \frac{F}{w_0} \tag{1}$$

where w_0 is the specimen width at rest, equal to 8 mm in the dogbone geometry defined.

Marker coordinates are computed using the acquired images. Hence, the deformation in the central portion of the specimen is computed as in Eq. (2):

$$\varepsilon = \frac{l - l_0}{l_0} \times 100 \tag{2}$$

where l is the incremental marker distance along the motion axis, and l_0 is the initial marker distance at rest along the motion axis.

The tension at rupture and the corresponding strain are reported as meaningful parameters. From the tension vs. deformation curve, the slope of the initial portion, named secant stiffness (k), is computed as the slope of secant line at 10% deformation. The anisotropy of the meshes is thus computed starting from the secant stiffness in the two perpendicular directions as in Eq. (3):

$$\alpha = \left|\log \frac{k_s}{k_w}\right| \tag{3}$$

where k_s is the secant stiffness in the strong direction, the knitted direction with the highest tension at rupture, and k_w in the weak direction.

Two statistical analyses were computed on uniaxial parameters in order to investigate the variability between the two perpendicular directions and differences among the different medical meshes grouped by density or among the urogynecologic devices. A t-test analysis was finalized to assess the intra material comparison, whereas a one-way ANOVA analysis with a Tukey-Kramer post hoc test was implemented for the inter material comparison.

C. Suture retention test protocol and parameters computation

The attachment and the test bench, showed in Figure 1c, were designed, adapting the setup used by [1] and rectangular specimens (70 x 55 mm) are clamped without preload at the upper grip. A Assusteel® monofilament wire with a diameter of 0.350-0.399 mm is then inserted 10 mm from the inferior edge of each specimen. The test is performed at a rate of 300 mm/min in displacement control while recording force and displacement data.

The suture retention strength (F_{max}) for the single specimen is computed from the raw data as prescribed by the ASTM D2261-13. Therefore, the method of computation depends on the number of peaks identifiable in the force vs displacement curves. Intra and inter material differences were examined performing the statistical analyses described above for uniaxial tensile test.

D. Test protocol verification

The suitability and replicability of the test protocol on surgical meshes was verify on fourteen polypropylene meshes, used for abdominal or inguinal hernia repair and three composite meshes used for abdominal hernia repair. The six urogynecologic devices were tested only in the uniaxial tensile test bench.

All the tests were performed using a universal testing machine, Instron E3000 (INSTRON®, Norwood, MA, USA). The optical system used for the acquisition of markers displacement during uniaxial tensile test was the VIC-3D system (Isi-sys GmbH, Kassel, Germany). Finally, the post-processing of the raw data was entirely performed in Matlab (version 9.10.0 (R2021a). Natick, Massachusetts: The MathWorks Inc.). The coefficient of variation (CV) was computed for all the extracted parameters in order to determine the dispersion level around the mean and to verify the test protocol repeatability.

III. Results

For each tested configuration five replicas were performed (335 specimens in total). A frequency analysis was conducted on the coefficients of variation (CVs) of the computed parameters in order to evaluate the repeatability of the test methods. Fig 2 shows the gaussian fits and the heat maps of frequency distributions obtained from the frequency analysis. In particular, the gaussian fits stand out the median values of CVs for the different tests are: 0.14 for the uniaxial tensile test, 0.05 for the ball burst test, and 0.08 for the suture retention test.

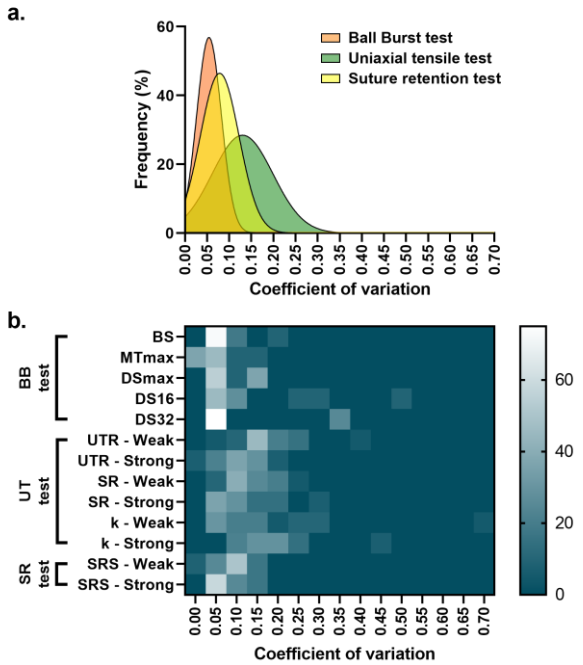


***Fig 2**: CVs frequency analysis among all the parameters for the selected test methods. a) Gaussian fits on the CVs frequency distributions for the three test methos; b) Heat map for the computed parameters where BB test: bursting ball test; BS: bursting strength; MTmax: maximum membrane tension; DSmax: maximum dilatational strain; DS16: dilatational strain at 16 N/cm; DS32: dilatational strain at 32 N/cm; UT test: uniaxial tensile test; UTR: uniaxial tension at rupture; SR: strain at rupture; k: secant stiffness; SR test: suture retention test; SRS: suture retention strength.*

Moreover, the heat map draws the attention on the CVs distribution of the different parameters in each setup. The lightest colours of the heat map highlight a concentration of CV values in a range between 0.05 and 0.20. Ultimately, both graphs highlight negligible differences between the range of CV values of the three test methods.

The range of values of the computed parameters are reported in TABLE I only as reference. From the statistical analysis of BB test results, a great heterogeneity is obtained among most of meshes grouped by density for all the computed parameters except DSmax. The t-test analyses, computed for UT test and SR test parameters, show significant differences between the two directions without regards to mesh density.

IV. Discussion

The variability of tests setups and methods for parameters computation could be reduced by the adoption of International Standards specifically drafted for surgical meshes. Therefore, the aim of this study is to design a test protocol useful to assess and compare mechanical characteristics of various surgical meshes. The chosen test methods turned out easily replicable, using small specimens and simple setups. Moreover, detailed computation of parameters is reported in order to ensure the comparisons between different studies and devices without neglecting the possibility of comparison with physiological conditions. The reduction of specimens dimension is paramount in order to test material collected by small patch such as preshaped devices. In this context, the suture retention test should be excluded if the insufficiency of material precludes the execution of all the test methods. The uniaxial tensile test and the ball burst test provide, in our opinion, the most significant results to assess and compare the mechanical properties of surgical meshes.

TABLE I: Parameters ranges

Ball Burst test

	BS [N]	MTmax [N/cm]	DSmax [%]	DS16 [%]	DS32 [%]
LW	181.07 - 258.37	49.87 - 71.72	34.79 - 45.09	15.02 - 25.18	-
SW	475.67 - 649.05	77.47 - 133.62	55.22 - 109.18	8.60 - 31.84	20.78 - 77.25
Comp	218.26 - 312.35	44.30 - 65.57	51.27 - 63.66	18.33 - 40.25	-

Uniaxial tensile test

	UTR [N/cm]		SR [%]		k [N/mm]		α
	Weak	Strong	Weak	Strong	Weak	Strong	
LW	3.28 - 26.26	13.48 - 36.61	52.03 - 107.59	44.75 - 94.06	0.36 - 2.21	1.45 - 2.21	0.03 - 1.27
SW	14.83 - 51.48	63.78 - 91.88	96.43 - 118.60	65.57 - 102.01	0.9 - 4.07	2.4 - 4.85	0.03 - 0.69
HW	17.38 - 36.75	84.50 - 136.07	58.61 - 155.86	41.72 - 72.22	1.63 - 4.24	16.56 - 22.25	0.59 - 1.07
UD	15.93 - 54.66		35.06 - 121.97		0.54 - 9.87		-

Suture retention test

	SRS [N]	
	Weak	Strong
LW	13.77 - 33.76	21.56 - 35.53
SW	53.01 - 81.95	45.66 - 63.82

The computed parameters are reported as ranges having grouped the meshes by density: light weight (LW), standard weight (SW) and high weight (HW) [22].

The use of dogbone specimens in uniaxial tensile test was essential in order to reduce the specimens dimension and concurrently achieving a failure in the central part of the specimen. This choice made mandatory the use of optical system to measure the local displacement. Although, no mention to local measurements is found in other studies that use dogbone specimens performing uniaxial tensile test on surgical meshes, a local strain measure is needed in order to obtain the correct displacement of the narrow section and therefore correctly estimate strains and tensions [1], [3], [7]. On the other hand, in our protocol all the parameters computed in uniaxial tensile test could be affected by the choice of a small width that results in a small amount of load-bearing threads, especially in lighter meshes [7].

In ball burst test to obtain easily comparable results a change in specimens dimensions must be followed by a comparable change in aperture diameter in order to maintain the ratio between the two dimension equal to 1.75 (as suggested by ASTM D6797-15 standard).

The suture retention strength is mostly affected by the specimen dimension and the distance of the Assusteel wire from the specimen dimension that determine indeed the number of mesh threads withstanding the tear propagation.

Moreover, we provide a detailed description of the extraction of the mechanical parameters which are of greatest interest, to encourage the adoption of easily comparable results. Furthermore, a collection of an extended and uniform set of data could support the determination of acceptability criteria and mechanical requirements for surgical meshes that are to date tough to establish [23]–[25]. Indeed, a crucial aspect of surgical meshes is the need to avoid alteration of the native tissue mobility. In this context, the implant stiffness and anisotropy are the key parameters. The significant differences found between the tested principal directions demonstrate that a mesh misalignment could heavily impact on the mechanical properties of the implant. In regards to patient comfort, the parameters evaluated in multiaxial test (e.g., ball burst test) are, in our opinion, the most suitable parameters for the evaluation of patient's comfort after the implantation [20], [26]. On the other hand, the stiffness computed in uniaxial tensile test is a convenient parameter to determine meshes anisotropy.

V. Conclusion

In this study we proposed a test protocol composed of three quasi-static test methods with the aim of promoting its adoption in other laboratories. The ease and the replicability of execution of the test protocol is verified on 23 surgical meshes with different intended uses and producers assessing an intra-subject variability characterized by a coefficient of variation with similar ranges. Its use within other laboratories could allow the determination of the inter-subject variability assessing its repeatability among users of alternative universal testing machines. Moreover, an extended evaluation of surgical meshes by the mean of the same test protocol could aid the determination of harmonized mechanical characteristic and thus, the definition of acceptability criteria and mechanical requirements for these implantable devices.

References

[1] C. R. Deeken, M. S. Abdo, M. M. Frisella, and B. D. Matthews, "Physicomechanical evaluation of polypropylene, polyester, and polytetrafluoroethylene meshes for inguinal hernia repair," *J. Am. Coll. Surg.*, vol. 212, no. 1, pp. 68–79, 2011.

[2] T. Wolloscheck, A. Gaumann, A. Terzic, A. Heintz, T. Junginger, *et al.*, "Inguinal hernia: Measurement of the biomechanics of the lower abdominal wall and the inguinal canal," *Hernia*, vol. 8, no. 3, pp. 233–241, 2004.

[3] X. Li, J. Kruger, J. Jor, P. Nielsen, M. Nash, *et al.*, "Characterizing the ex vivo mechanical properties of synthetic polypropylene surgical mesh," *J. Mech. Behav. Biomed. Mater.*, vol. 37, pp. 48–55, 2014.

[4] M. M. Maurer, B. Röhrnbauer, A. Feola, J. Deprest, and E. Mazza, "Mechanical biocompatibility of prosthetic meshes: A comprehensive protocol for mechanical characterization," *J. Mech. Behav. Biomed. Mater.*, vol. 40, pp. 42–58, 2014.

[5] C. R. Deeken, M. S. Abdo, M. M. Frisella, and B. D. Matthews, "Physicomechanical evaluation of absorbable and nonabsorbable barrier composite meshes for laparoscopic ventral hernia repair," *Surg. Endosc.*, vol. 25, no. 5, pp. 1541–1552, 2011.

[6] B. M. Soares, R. G. Guidoin, Y. Marois, L. Martin, M. W. King, *et al.*, "In vivo characterization of a fluoropassivated gelatin-impregnated polyester mesh for hernia repair," *J. Biomed. Mater. Res.*, vol. 32, no. 3, pp. 293–305, 1996.

[7] P. P. Pott, M. L. R. Schwarz, R. Gundling, K. Nowak, P. Hohenberger, *et al.*, "Mechanical Properties of Mesh Materials Used for Hernia Repair and Soft Tissue Augmentation," *PLoS One*, vol. 7, no. 10, pp. 1–10, 2012.

[8] J. P. Shepherd, A. J. Feola, S. D. Abramowitch, and P. A. Moalli, "Uniaxial biomechanical properties of seven different vaginally implanted meshes for pelvic organ prolapse," *Int. Urogynecol. J.*, vol. 23, no. 5, pp. 613–620, 2012.

[9] K. A. Jones, A. Feola, L. Meyn, S. D. Abramowitch, and P. A. Moalli, "Tensile properties of commonly used prolapse meshes," *Int. Urogynecol. J.*, vol. 20, no. 7, pp. 847–853, 2009.

[10] P. A. Moalli, N. Papas, S. Menefee, M. Albo, L. Meyn, *et al.*, "Tensile properties of five commonly used mid-urethral slings relative to the TVT™," *Int. Urogynecol. J.*, vol. 19, no. 5, pp. 655–663, 2008.

[11] S. Velayudhan, D. Martin, and J. Cooper-White, "Evaluation of dynamic creep properties of surgical mesh prostheses - Uniaxial fatigue," *J. Biomed. Mater. Res. - Part B Appl. Biomater.*, vol. 91, no. 1, pp. 287–296, 2009.

[12] E. R. Saberski, S. B. Orenstein, and Y. W. Novitsky, "Anisotropic evaluation of synthetic surgical meshes," *Hernia*, vol. 15, no. 1, pp. 47–52, 2011.

[13] C. R. Deeken and S. P. Lake, "Mechanical properties of the abdominal wall and biomaterials utilized for hernia repair," *J. Mech. Behav. Biomed. Mater.*, vol. 74, no. February, pp. 411–427, 2017.

[14] K. Junge, U. Klinge, A. Prescher, P. Giboni, M. Niewiera, *et al.*, "Elasticity of the anterior abdominal wall and impact for reparation of incisional hernias using mesh implants," *Hernia*, vol. 5, no. 3, pp. 113–118, 2001.

[15] H. P. Dietz, P. Vancaillie, M. Svehla, W. Walsh, A. B. Steensma, *et al.*, "Mechanical properties of urogynecologic implant materials," *Int. Urogynecol. J.*, vol. 14, no. 4, pp. 239–243, 2003.

[16] B. Klosterhalfen, K. Junge, and U. Klinge, "The lightweight and large porous mesh concept for hernia repair," *Expert Rev. Med. Devices*, vol. 2, no. 1, pp. 103–117, 2005.

[17] B. J. Eliason, M. M. Frisella, B. D. Matthews, and C. R. Deeken, "Effect of repetitive loading on the mechanical properties of synthetic hernia repair materials," *J. Am. Coll. Surg.*, vol. 213, no. 3, pp. 430–435, 2011.

[18] D. O. Freytes, A. E. Rundell, J. Vande Geest, D. A. Vorp, T. J. Webster, *et al.*, "Analytically derived material properties of multilaminated extracellular matrix devices using the ball-burst test," *Biomaterials*, vol. 26, no. 27, pp. 5518–5531, 2005.

[19] S. Sahoo, K. R. Delozier, A. Erdemir, and K. A. Derwin, "Clinically relevant mechanical testing of hernia graft constructs," *J. Mech. Behav. Biomed. Mater.*, vol. 41, pp. 177–188, 2015.

[20] Y. Bilsel and I. Abci, "The search for ideal hernia repair; mesh materials and types," *Int. J. Surg.*, vol. 10, no. 6, pp. 317–321, 2012.

[21] L.-M. Zhu, "Mesh implants: An overview of crucial mesh parameters," *World J. Gastrointest. Surg.*, vol. 7, no. 10, p. 226, 2015.

[22] A. Coda, R. Lamberti, and S. Martorana, "Classification of prosthetics used in hernia repair based on weight and biomaterial," *Hernia*, vol. 16, no. 1, pp. 9–20, 2012.

[23] W. S. Cobb, J. M. Burns, K. W. Kercher, B. D. Matthews, H. James Norton, *et al.*, "Normal intraabdominal pressure in healthy adults," *J. Surg. Res.*, vol. 129, no. 2, pp. 231–235, 2005.

[24] Y. Ozog, J. Deprest, K. Haest, F. Claus, D. De Ridder, *et al.*, "Calculation of membrane tension in selected sections of the pelvic floor," *Int. Urogynecol. J.*, vol. 25, no. 4, pp. 499–506, 2014.

[25] C. Song, A. Alijani, T. Frank, G. B. Hanna, and A. Cuschieri, "Mechanical properties of the human abdominal wall measured in vivo during insufflation for laparoscopic surgery," *Surg. Endosc. Other Interv. Tech.*, vol. 20, no. 6, pp. 987–990, 2006.

[26] A. Mangera, A. J. Bullock, C. R. Chapple, and S. MacNeil, "Are biomechanical properties predictive of the success of prostheses used in stress urinary incontinence and pelvic organ prolapse? A systematic review," *Neurourol. Urodyn.*, vol. 31, no. 1, pp. 13–21, Jan. 2012.

An Inverse Analysis for the Assessment of Material Properties of TAVI Patients

C. Catalano[1], S. Cannata[2], C. Gandolfo[2], and S. Pasta[1,3]
[1]*Dipartimento di Ingegneria, viale delle Scienze Ed.8, University of Palermo, Italy*
[2]*Interventional Cardiology Unit, IRCCS ISMETT via Tricomi, 5, Palermo, Italy*
[3]*Department of Research, IRCCS ISMETT via Tricomi, 5, Palermo, Italy*

***Abstract*— Patient-specific in-silico models of transcatheter aortic valve implantation (TAVI) have gained a high level of complexity and accuracy and may become a relevant tool for supporting clinical decision-making and device design. When focusing on patient-specific material properties, the advanced age and the lack of *ex-vivo* material characterizations makes particularly challenging the utilize of reliable material parameters for patient-specific computational simulations of TAVI. This study focuses on the calibration of patient-specific constitutive descriptors for both the aortic wall and calcific aortic valve using an inverse approach and imaging data. Once the optimal material parameters were obtained, numerical simulations of the pre-TAVI scenario were found in agreement with CT imaging, thereby leading to a robust non-invasive approach for *in-vivo* assessment of material properties.**

***Keywords*—TAVI, Material Calibration, Finite Element Modeling, Linear Regression.**

I. Introduction

GIVEN the increase in transcatheter aortic valve implantation (TAVI) over open-chest surgery, several simulation techniques including finite element analysis (FEA) and fluid–solid interaction (FSI) have been adopted to model this treatment [1-4]. Computational models have been adopted to virtually deploy the device in the patient-specific human host and then quantify structural and hemodynamic parameters related to the device–host interaction [5-7]. Computational models can therefore enhance the preprocedural planning, simulating different implantation scenarios, provide important insights in postprocedural care and metrics for the design of the next generation transcatheter heart valves.

However, simulations should be carried out at an increasingly challenging level related to the need for verification and validation of the model output. A useful and accurate *in-silico* tool should account for patient-specific material properties. Despite the findings reported by several research groups [6, 7], the actual material properties of anatomical parts of interest remain unknown and uncertain. This is due to the fact that patients undergoing TAVI are quite elderly (i.e., age of 82±6.4 yrs.) as suggested by Attinger-Toller et al. [8]. The older the patient is, the stiff the aortic root is. For this reason, recent studies have simple adopted a linear-elastic material model for the aortic root rather than sophisticated anisotropic material models [9, 10]. Moreover, the high surgical risk of TAVI patients does not allow us to collect tissue segments for *ex-vivo* mechanical characterization [11-13]. There are therefore not any realistic material properties for patients undergoing TAVI.

The aim of this work was to estimate patient-specific material parameters of aortic wall and calcified valve leaflets using an inverse analysis and electrocardiogram-gated computed tomography (ECG-gated CT) images. The inverse method is based on the simultaneous minimization of two cost functions which define the difference between model predictions and CT measurements of aortic wall strain and orifice area at systolic phase with respect to the diastolic phase (reference image set).

II. Materials and Methods

A. FE Model Development

Simulations were carried out for a group of n.20 patients underwent TAVI with the SAPIEN 3 Ultra transcatheter heart valve (Edwards Lifesciences, USA). ECG-gated CT imaging was carried out for each patient as part of the routine clinical care and not for the purpose of this study. Retrospective retro-reconstruction of the ECG-gated CT acquisition allowed to collect two sets of images representing the peak systole and early diastole [14]. Echocardiography and blood cuff pressure measurements were also collected for each patient. For each patient, aortic wall strain at systole were measured as the changes in aortic wall diameter between systole and diastole over the diastolic diameter. Additionally, the orifice area at peak systole was measured by an experienced radiologist. All patients were informed of the study purpose, and data were collected after signature of informed consent.

Starting from DICOM images collected at diastolic phase, the 3D medical image processing software (Mimics Innovation Suite v.22, Materialise, BE) was used to segment the LVOT geometry, calcific plaques, and aortic wall. Segmentation was initially performed by means of semi-automatic thresholding of grey images (Hounsfield Unit) and then finalized by manual editing of the coloured mask [5, 15-17]. Morphological operations and smoothing were performed to improve case-by-case the segmentation output. Since the very thin structure of the aortic valve leaflet cannot seen at CT imaging, a parametric design model based on anatomic measurement was used to develop the native valve leaflet geometry [18]. In brief, two 3rd-order NURBS curves interpolating commissures were delineated to model the free edge of valve leaflets, while the belly of each leaflet was considered using one control points. To model the leaflet-to-sinus attachments, a second set of 3rd-order NURBS curves were developed using Rhino software (v.7.1, McNeel & associates, USA). The NURBS curves were constrained to the aortic root surface by curve-to-surface projection, and then native valve leaflets were developed by a multi-patch network of NURBS surfaces [19].

Literature data were used for imposing the material thickness of the aortic wall (i.e., 2 mm) and valve leaflets (i.e., 0.5 mm) [20]. Prismatic elements (size of 0.5 mm) were adopted for the valve leaflets, triangular for the aortic wall (size of 0.6 mm), and tetrahedral elements (size of 0.4 mm) for calcifications as a result of convergence analyses. Given the stiffness of the highly calcified tissues that characterize our targeted patients, linear elastic behaviour was defined for the aortic wall and valve leaflets, with material parameters derived from the inverse approach. In a different way, the calcific plaques were modelled by a linear-elastic material with plasticity using data published by Bosi and collaborators [9, 10]. Patient-specific loading conditions were set for each patient [21]. Specifically, a physiological pressure waveform of 1 Hz obtained from literature data was scaled to match the heartbeat duration of a given patient. The systolic and diastolic peak of the reference pressure waveform were adjusted to match the cuff blood pressure measurement obtained for each patient. For the valve leaflets, the transmural pressure obtained by echocardiography was used as loading condition on the valve leaflet surface model. For boundary conditions, the distal and proximal ends of the aortic wall were constrained in the longitudinal directions. The native valve leaflets were tied to both the calcifications and aortic wall. All simulations were performed with Abaqus\Explicit solver (v.2021hf7, Dassault Systèmes, FR), enabling to account for a dynamic non-linear problem with large deformation and complex contact interactions, using a mass scaling of 1.0e-6.

B. Inverse Approach

The inverse approach adopts a quadratic regression model to link the input variables (i.e., the material properties) to the output variables (i.e., the aortic wall strain or the orifice area). The regression model consisted of an optimization algorithm to minimize the difference between predicted and CT-based measurements. Specifically, the variables of interest for the aortic wall and the calcified valve were the peak systolic strain of the aortic root and orifice valve area, respectively. Assuming linear elastic material behaviours for both the aortic wall and orifice area, the unknown material parameter is represented by only the Young's modulus. Poisson's coefficient was fixed to 0.475 to account of an incompressible material. The objective of inverse analysis is to predict the aortic wall strain or orifice area with respect to Young's modulus. Thus, the regression model can be written as:

$$f(E) = \beta_1 E + \beta_2 E^2 + \beta_3 \qquad \text{Eq.1}$$

For each patient, n.10 simulations of the cardiac beat were carried out varying each time randomly the material properties in their interval of definition [0.8-10 MPa]. For each simulation, the systolic strains (NE) were exported at different anatomic levels identified by several element set using a python script. To calculate the orifice valve area, a python script in the Rhinoceros CAD software was developed to automatically export the nodal coordinates of the valve leaflet free edges. Then, the coordinates were imported into the Grasshopper plug-in of Rhinoceros to automatically fit the point and calculate the orifice valve area (see Figure 1).

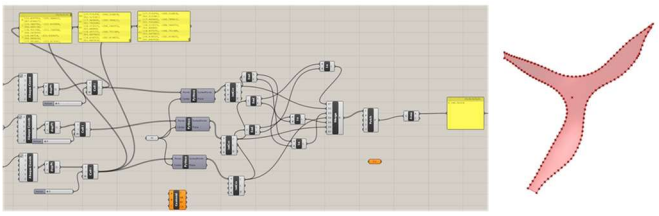


Fig. 1: Grasshopper algorithm to automatically quantify the orifice valve area from FE models

A matrix linking the input (i.e., material parameter for each random value of Young's modulus) and the output (systolic strain/orifice area) was generated in Matlab software. One cost function was therefore defined as:

$$F = f(E) - Strain_{STJ,Sinus,Annulus} \qquad \text{Eq.2}$$

This cost function should tend to zero so that the output variable given by the regression function for each patient tends to the value measured at CT scan. As the solution can lead to two different optimized material parameter sets, the selected set of material parameters was selected from the solution falling in the interval definition. If both values were contained in the range, these were averaged.

III. RESULTS

Figure 2 shows CT-based measurements of systolic strain (with respect to diastole) at different anatomic levels from the left ventricular outflow tract (LVOT) to the sino-tubular junction (STJ). Not any statistical difference was found on strain measurements at ANOVA, though strains at LVOT were slightly higher than those of Sinus of Valsalva.

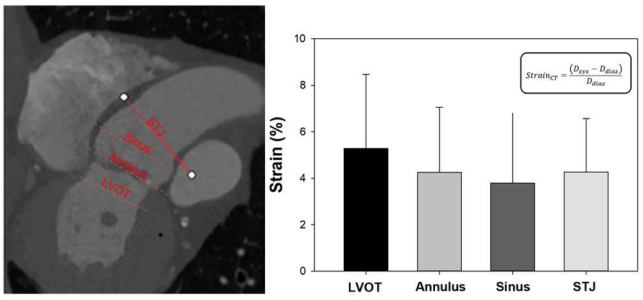


Fig. 2: Systolic strains at different anatomic levels derived from post-CT

Table 1 summarizes the material properties for both the aortic wall and orifice area as well as the good-of-fitness. Fitting results suggests a stiff behavior of the aorta as compared to literature data when the aortic wall is assumed as linear elastic [22]. The biomechanical behavior of the orifice area is very stiff, and this may be the results of the calcifications linked to the aortic valve leaflets or the severe stenotic condition.

	E (MPa)	SD	R	RMSE	p
Aorta	5.91	3.03	0.74-0.86	0.0068-0.0274	0.008-0.019
Valve	10.85	3.06	0.72-0.84	0.0041-0.0382	0.009-0.023

Once the optimal material parameters were achieved, a new analysis was carried out for each patient using the optimized material properties. For the aortic wall, the deformed shape was exported and compared to that from the CT images at

systole. The root mean square error (RMSE) representing the summatory of the Euclidean distance between corresponding point on the predicted surface and the correspondent point on the CT-based surface was used to quantify the difference between model predictions and CT images. The relative errors were in the range of 8.6% to 13.6 % for the n.20 patients with more marked differences in the distal LVOT than in the sinus and ascending aorta (see Figure 3).

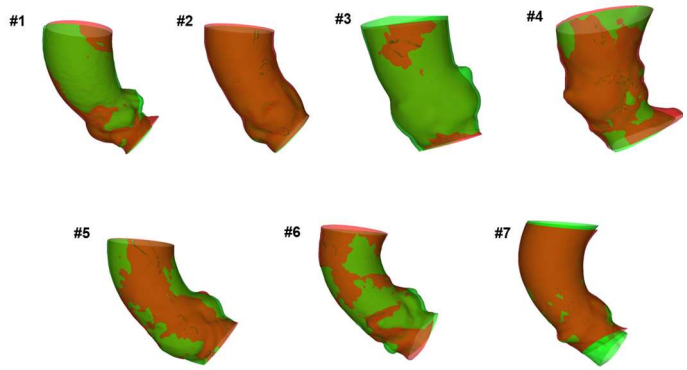


Fig. 3: Comparison between model predictions (red color) and CT-based shape (green color) of the aortic root at systole for several patients

Figure 4 shows the comparison of the CT-based measurement of orifice area versus the numerical predictions when the optimal material parameter values are used for the aortic valve. Not any statistical difference was observed between predictions and CT-based measurements (p=0.145). The relative errors between predictions and CT-based measurements were in the range of 0.08% to 11.86%. This suggests a realistic evaluation of the biomechanical response of the stenotic aortic valve.

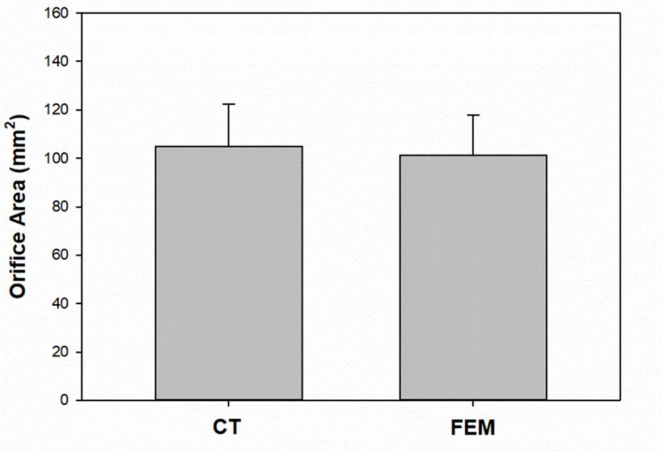


Fig. 4: Comparison between predicted and CT-based measurements of orifice area for all patients

Figure 5 shows the calcific valve leaflets at opened configuration using the optimal material parameter set. The stiff aortic valve behavior remarkably reduced the valve opening with diastolic orifice area of 92 mm^2 and systolic orifice area of 113 mm^2.

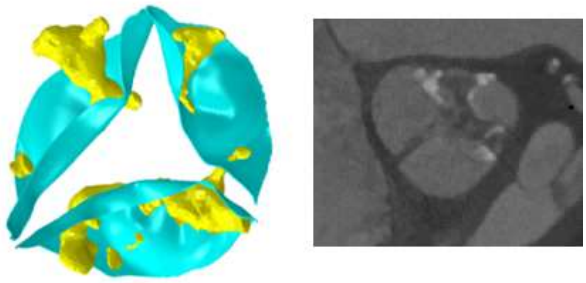


Fig. 5: Shape of calcific valve leaflets from simulation (left side) with the optimal elastic modulus and the CT-based image (right side)

IV. Discussion

The major novelty of this study is the development of a non-invasive inverse approach for the assessment of reliable material properties for the aortic root of patients with severe aortic valve stenosis. The approach used pre-TAVI ECG-gated CT images at two cardiac phase to optimize the material properties using a regression model for the minimization of the difference in the aortic wall strain and orifice area between predictions and CT-based measurements. These findings can be considered relevant as patients undergoing TAVI are very elderly so that the current *ex-vivo* material descriptors reported in literature are not suitable. Though a linear elastic material behavior was assumed, the present inverse analysis can be extended to the assessment of multiple materials descriptors and thus complex constitutive relationship. In this context, Trabelsi at al. [23] demonstrated that the potential of inverse analysis for determining the two-term Demiray's constitutive model. As compared to our approach, they adopted three cardiac phases (i.e., the systole, mid-cycle and diastole) to quantify the two-term material model using the aortic wall volume as the output parameter. Since ECG-gated CT imaging procedure is usually based on n.10 cardiac phases in the R-R interval, the present inverse approach can be extended to complex constitutive law using different parameters as aortic volume or strain at different cardiac phases or anatomic locations.

The fact that we adopted a simple linear elastic model to capture the biomechanical response of the aortic wall is based on recent findings using computational modeling and mechanical characterization [9, 10, 12]. In a large cohort of TAVI patients, a validated computational model demonstrated a good agreement between predictions and imaging measurements when the aorta is assumed linear elastic. The value of Young's modulus was 7.78 MPa as compared to our mean value of 5.91±3.03. Overall, these studies suggests a very stiff behavior for the aortic wall as compared to the physiological normal compliance of the ascending aorta reported in literature [22]. It should be also noted that a linear elastic model facilitates the springback seen once the transcatheter heart valve is numerically deployed. However, more complex constitutive models were used to model the aortic root. Several studies adopted fiber-reinforced constitutive models of the human aorta when simulating TAVI [1, 4]. Morganti et al. [7] considered the difference between the material properties of left-coronary sinus, non-coronary

sinus and right-coronary sinus using a six-term polynomial constitutive model. This model relies on biaxial testing data reported by Martin et al. [12] on eight human aortas from patients with 90.1±6.8 years underwent surgical valve replacement. Experimental data revealed the stiff material properties of the aortic root, with not any statistically significant difference among sinuses. Green strains were reported in the range of 4-6% as found in this study using ECG-gated image data.

There is a lack of information on the material properties of stenotic valve leaflets, and this is mainly caused by the impracticality of developing *ex-vivo* mechanical testing. It is clear the difference in the material properties between the healthy and calcific aortic valve. We found that the aortic valve leaflets had a stiff behavior with elastic modulus of 10.8±3.0 MPa, and this is likely caused by the constraining effect of embedded calcifications. Thus, the value of elastic modulus here found should be considered that of the combined effect (i.e., valve leaflets plus calcification) rather than the effect of valve leaflets only.

V. Conclusion

Using ECG-gated CT images of patients undergoing TAVI, we developed and applied an inverse analysis for the non-invasive identification of material properties of the aortic root and calcific aortic valve. Specifically, the inverse analysis minimized the difference in the aortic wall strain and orifice area between prediction and CT-images. Once the optimal material properties were obtained, simulations revealed a good agreement of numerical and CT-related aortic root shapes, with value < 13.6 % in all cases. The utilize of reliable estimations of material parameters could greatly enhance the prediction of numerical simulations of TAVI and thus improve the pre-operative planning.

Acknowledgement

This project has received funding from the European Union's Horizon 2020 research and innovation programme under grant agreement No 101017523.

References

[1] Luraghi G, *et al.* The impact of calcification patterns in transcatheter aortic valve performance: a fluid-structure interaction analysis. *Computer methods in biomechanics and biomedical engineering* 2020: 1-9.
[2] Pasta S, *et al.* Transcatheter Heart Valve Implantation in Bicuspid Patients with Self-Expanding Device. *Bioengineering* 2021; 8(7): 91.
[3] Pasta S, *et al.* Simulation study of transcatheter heart valve implantation in patients with stenotic bicuspid aortic valve. *Med Biol Eng Comput* 2020.
[4] Lavon K, *et al.* Biomechanical modeling of transcatheter aortic valve replacement in a stenotic bicuspid aortic valve: deployments and paravalvular leakage. *Med Biol Eng Comput* 2019; 57(10): 2129-43.
[5] Catalano C, *et al.* On the Modeling of Transcatheter Therapies for the Aortic and Mitral Valves: A Review. *Prosthesis* 2022; 4(1): 102-12.
[6] Finotello A, *et al.* Finite element analysis of transcatheter aortic valve implantation: Insights on the modelling of self-expandable devices. *Journal of the mechanical behavior of biomedical materials* 2021; 123: 104772.
[7] Morganti S, *et al.* Prediction of patient-specific post-operative outcomes of TAVI procedure: The impact of the positioning strategy on valve performance. *J Biomech* 2016; 49(12): 2513-9.
[8] Attinger-Toller A, *et al.* Age-Related Outcomes After Transcatheter Aortic Valve Replacement. *Jacc-Cardiovasc Inte* 2021; 14(9): 952-60.
[9] Bosi GM, *et al.* Population-specific material properties of the implantation site for transcatheter aortic valve replacement finite element simulations. *Journal of biomechanics* 2018; 71: 236-44.
[10] Bosi GM, *et al.* A validated computational framework to predict outcomes in TAVI. *Scientific reports* 2020; 10(1): 1-11.
[11] Di Giuseppe M, *et al.* Identification of circumferential regional heterogeneity of ascending thoracic aneurysmal aorta by biaxial mechanical testing. *J Mol Cell Cardiol* 2019; 130: 205-15.
[12] Martin C, *et al.* Significant differences in the material properties between aged human and porcine aortic tissues. *Eur J Cardiothorac Surg* 2011; 40(1): 28-34.
[13] Cosentino F, *et al.* On the role of material properties in ascending thoracic aortic aneurysms. *Computers in biology and medicine* 2019; 109: 70-78.
[14] Pasta S, *et al.* In Vivo Strain Analysis of Dilated Ascending Thoracic Aorta by ECG-Gated CT Angiographic Imaging. *Ann Biomed Eng* 2017; 45(12): 2911-20.
[15] Catalano C, *et al.* Atlas-Based Evaluation of Hemodynamic in Ascending Thoracic Aortic Aneurysms. *Appl Sci-Basel* 2022; 12(1).
[16] Catalano C, *et al.* 3D Printing and Computational Modeling for the Evaluation of LVOT obstruction in Transcatheter Mitral Valve Replacement. *Proc Cirp* 2022; 110: 273-78.
[17] Scardulla F, *et al.* Shear stress alterations in the celiac trunk of patients with a continuous-flow left ventricular assist device as shown by in-silico and in-vitro flow analyses. *J Heart Lung Transplant* 2017; 36(8): 906-13.
[18] Pasta S, *et al.* Three-dimensional parametric modeling of bicuspid aortopathy and comparison with computational flow predictions. *Artif Organs* 2017; 41(9): E92-E102.
[19] Pasta S, *et al.* Three-dimensional parametric modeling of bicuspid aortopathy and comparison with computational flow predictions. *Artif Organs* 2017.
[20] Pasta S, *et al.* Simulation study of transcatheter heart valve implantation in patients with stenotic bicuspid aortic valve. *Med Biol Eng Comput* 2020; 58(4): 815-29.
[21] Rinaudo A, *et al.* Regional variation of wall shear stress in ascending thoracic aortic aneurysms. *Proc Inst Mech Eng H* 2014; 228(6): 627-38.
[22] Beller CJ, *et al.* Role of aortic root motion in the pathogenesis of aortic dissection. *Circulation* 2004; 109(6): 763-9.
[23] Trabelsi O, *et al.* Predictive Models with Patient Specific Material Properties for the Biomechanical Behavior of Ascending Thoracic Aneurysms. *Ann Biomed Eng* 2016; 44(1): 84-98.

Mechanical characterization of hybrid membrane suitable for biomedical application

R. Gemelli[1], M. Todesco[2], E.L. Carniel[1], G. Gerosa[3] and A. Bagno[1]
[1] Department of Industrial Engineering, University of Padua, via Marzolo 9, 35131 Padua, Italy
[2] Department of Civil, Environmental and Architectural Engineering, University of Padua, Via Marzolo 9, 35131, Padova, Italy
[3] Department of Cardiac, Thoracic and Vascular Sciences, University of Padua, Padua, Via Giustiniani 2, 35128 Padua, Italy

***Abstract*— Current challenges in tissue engineering are aiming for the realization of materials that can be used for the replacement of damaged tissues/organs and that are able to integrate with the host organism. To this purpose, a hybrid membrane was made by coupling a decellularized tissue, e.g. porcine pericardium, with a commercially available polycarbonate urethane. The hybrid material was characterized from the biomechanical point of view and a constitutional model was formulated considering the hybrid material as the coupling of the two materials, pericardium and polymer. The model was then validated experimentally.**

***Keywords*—Hybrid membrane, tissue engineering, mechanical characterization.**

I. Introduction

TISSUE engineering is a field of research that proposes potential solutions to overcome the shortage of donor tissues/organs and aims at repairing or replacing damaged or diseased tissues/organs using a combination of cells, biomaterials, and growth factors [1].

The current challenge is to create a material that can perfectly integrate with the host body without evoking any adverse reaction: to this purpose, one of the most promising approaches is the use of hybrid materials.

Hybrid materials can be obtained by entanglement or interpenetration of at least two different types of materials, combining the advantages of both to create new and improved tissue constructs: they exhibit unique properties that are not found in either of the individual components [2], [3].

Hybrid materials can be divided into two main categories: those that combine organic and inorganic materials, and those that combine different types of organic materials. Examples of the first materials include scaffolds made of collagen or poly(lactic-co-glycolic acid) (PLGA) with hydroxyapatite for the substitution of natural bone tissue and cartilage [4], [5]. Examples of the second materials include hybrid hydrogels, e.g. collagen-poly(ethylene glycol) (PEG) hydrogels and polycaprolactone-collagen scaffolds [6], [7], which combine different types of synthetic polymers to create new materials with improved mechanical and biological properties.

The aim of the present work is the realization of a hybrid material, called hybrid membrane (HYME), involving the combination of a decellularized biological tissue, i.e., porcine pericardium, with an organic synthetic polymer, a commercially available polycarbonate urethane (Chronoflex ARLT). Synthetic materials provide mechanical support and other properties like impermeability and patency for the hybrid membrane; biological tissues give a natural extracellular matrix (ECM) able to support cell adhesion and proliferation, thus encouraging cell recruitment, attachment, growth, and differentiation, consequently guiding tissue regeneration *in vivo* [8], [9]. In the present study, HYME was assessed from a biomechanical point of view and a mechanical constitutive model was implemented.

II. Materials and methods

A. Pericardium decellularization

Fresh porcine pericardial tissues were collected from a local slaughterhouse, following EC regulation 1099/2009 protocols regarding animal health and protection, and treated within 3 hrs. The portion corresponding to the right anterior ventricle was isolated from the whole pericardium, and pre-pericardial fat was removed. The pericardium was decellularized using the Tricol method [10], which is based on the use of hypotonic and hypertonic solutions, a non-ionic detergent (Tergitol, code 15S9), and an ionic detergent (Sodium Cholate, code C1254). Removal of residual DNA was carried out with Benzonase® (cod. E1014). All reagents were supplied by Sigma Aldrich (Saint Louis, MO, USA).

B. Membrane production

Hybrid membranes were realized as described by Todesco et al. [11] by coupling decellularized porcine pericardium (DPP) with a polycarbonate urethane, Chronoflex AR-LT (AdvanSource Biomaterials Wilmington, MA, US).

DPP was laid into a custom-made aluminum frame and the polymer, supplied as 22% (w/v) solution in N,N-dimethylacetamide (DMAc), was gently poured onto the fibrous part. The membranes were dried for 24 hours at 38°C in a vacuum oven (Raypa, Barcelona, Spain). DPP and membranes made with only polymer were used as controls.

C. Mechanical tests

DPP, the hybrid membrane (DPP ARLT), and the membrane made with Chronoflex only, were cut into dog-bone-shaped specimens with a gauge length of 5 mm and 2 mm width using an in-house designed cutter [12], [13]. With regard to DPP and DPP ARLT, specimens were cut along the prevalent direction of the collagen fibres during visual inspection.

All samples (n = 9 for each material) were tested for stress–relaxation at room temperature using a customized apparatus (IRS, Padua, Italy) consisting of four linear actuators, each equipped with a 50 N load cell. During each test, samples were kept hydrated with saline solution. Before each type of test, samples were pre-loaded up to 0.1 N. Stress–relaxation tests were realized by elongating DPP and DPP ARLT samples until

10, 20, 30, 40, 50, 60, and 70% strain, whereas CFARLT samples until 10, 20, 30, 40, 50, 100, and 200 % strain, with an elongation rate of 1 mm/s, with 600 s holding time after each elongation. Force and elongation were measured during each test and stress curves over time were calculated as the ratio of the force to the cross-sectional area of the sample in gauge length. Thickness samples were measured with a digital calliper (Mitutoyo, ID-C112XB) and reported in Table I. Data analysis and graphs of the three materials were obtained with an in-house developed Matlab® script (Mathworks, Natick, MA, USA).

The stress–strain curves were obtained considering the different strain levels tested and the corresponding stress values at the end of the relaxation process, whereas the stress–relaxation graphs were obtained by normalizing the stress–relaxation curves of the materials.

TABLE I: THICKNESS OF TESTED SAMPLES OF DPP, DPP ARLT AND CF ARLT. DATA ARE REPORTED IN MEAN ± STANDARD DEVIATION.

Sample	*Thickness [mm]*
DPP	0.19 ± 0.09
DPP ARLT	1.18 ± 0.18
CF ARLT	0.80 ± 0.08

D. Mechanical constitutive model

A constitutive model is a mathematical tool that describes the general mechanical behaviour of a material; the mathematical formulation of the model includes constitutive parameters, which characterize the specific properties of a material.

Hence, a visco hyperelastic constitutive model of the membrane (DPP ARLT) has been formulated and validated. It was decided to consider the hybrid membrane as the coupling of the two materials separately (DPP and ChronoFlex ARLT), therefore the sets of hyperelastic and viscoelastic constitutive parameters were obtained for both materials: the polymer and the biological tissue. Finally, the constitutive parameters of the two materials were validated by developing a computational model of the hybrid membrane, simulating tensile tests, and comparing numerical results with experimental data.

Regarding the identification of the two materials' hyperelastic parameters, it was decided to use the one–parameter incompressible Ogden model, implemented in the simulation software *Abaqus/Standard* (Dassault Systèmes, Simulia Corp., Providence, RI). A specific tool of the software is provided for the parameter's identification by means of the inverse analysis of tensile tests, obtaining the hyperelastic parameters for the polymer and the tissue. The parameters obtained are μ_i and α_i, which are the material constants, and are reported in Table II.

A MatLab routine has been used to obtain the set of viscoelastic parameters (Table III) for both materials, by fitting the stress–relaxation experimental curves (showed in Fig. 1) with the Eq. (1), which illustrates the normalized stress depending on the relative stiffness and the relaxation time, and describe the viscoelastic phenomena:

$$\sigma_{norm} = (1 - \gamma_1 - \gamma_2) + \gamma_1 exp\left[-\frac{t}{\tau_1}\right] + \gamma_2 exp\left[-\frac{t}{\tau_2}\right] \quad (1)$$

The parameters obtained are γ_i and τ_i, which represent the relative stiffnesses and the relaxation times, respectively.

III. RESULTS

In Fig. 1 experimental stress–strain and stress–relaxation curves of each single material, i.e. DPP, CFARLT, and DPP ARLT, obtained from the mechanical tests, are reported. Figures A, C, and E represent the equilibrium stress–strain behaviour of DPP, CFARLT, and HYME. They were obtained considering results from stress relaxation tests at different strain conditions: for each strain value, the last point of relaxation curve defined the equilibrium stress. Mean data from experimentations on different samples were assumed.

Figures B, D and, F, which represent the stress relaxation behaviour, were obtained by normalizing the mean of each relaxation process (at the different strain rates) of each sample of the three investigated materials.

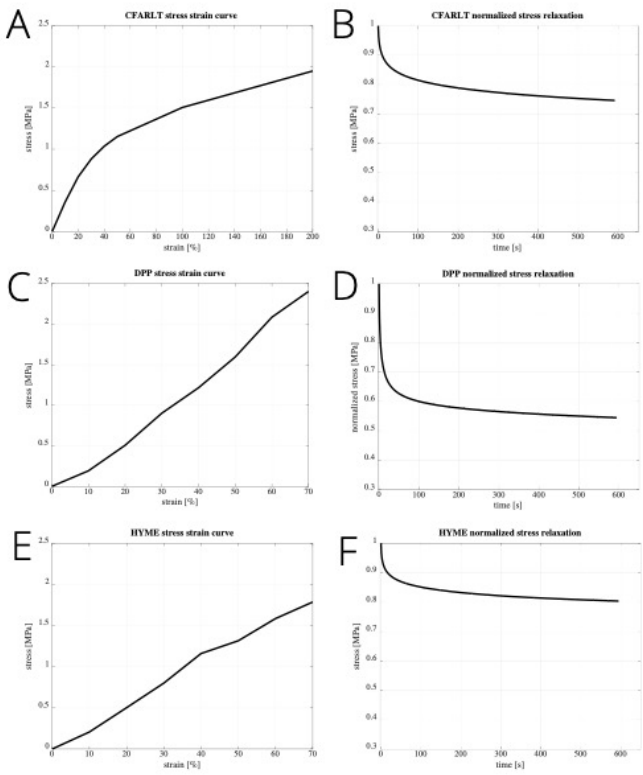


Fig. 1: Experimental DPP (A), CF ARLT (C) and DPP ARLT (E) stress–strain curve and DPP (B), CF ARLT (D) and DPP ARLT (F) stress–relaxation curves.

Table II shows the sets of hyperelastic parameters, whereas Table III shows the sets of viscoelastic parameters of the two materials.

TABLE II: HYPERELASTIC PARAMETERS

Samples	$\mu_i\ [MPa]$	α_i
Chronoflex ARLT	1.36	0.64
DPP	0.75	5.24

TABLE III: VISCOELASTIC PARAMETERS

Samples	γ_1	γ_2	$\tau_1\ [s]$	$\tau_2\ [s]$
Chronoflex ARLT	0.13	0.12	8.33	201.76
DPP	0.33	0.12	4.89	128.19

As mentioned above, the validation was carried out by comparing the experimental and computational data; the lasts were obtained by creating an Abaqus numerical simulation of the hybrid membrane sample, using the same experimental protocol and the constitutive parameters (for the two materials) presented above. The results demonstrated the reliability of the model, capable of correctly describing the mechanical behaviour of the hybrid membrane (Fig. 2).

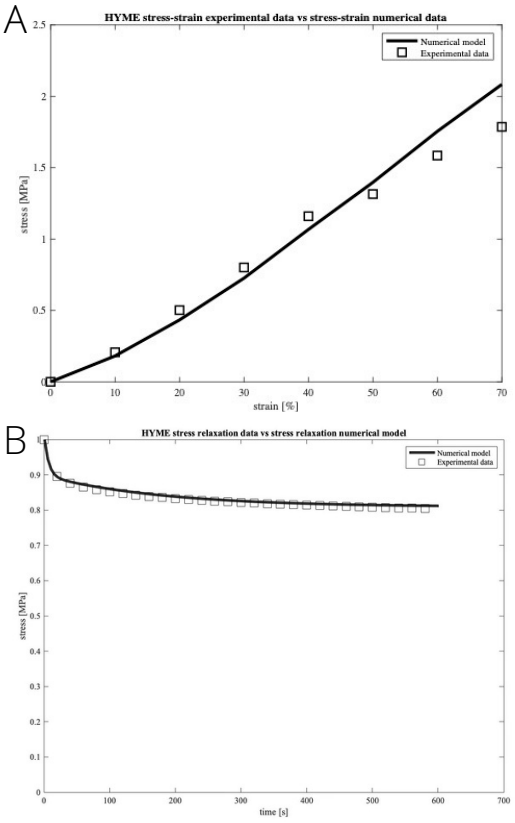


Fig. 2: Stress–strain (A) and stress–relaxation (B) validation curve of the membrane (DPP ARLT). Data obtained from the numerical model (continuous blue line) and experimental data (black squares) are overlapped.

IV. Conclusion

The development of new biomaterials that can integrate with the host body without causing adverse reactions is still very challenging. This work aimed at characterizing a hybrid membrane obtained by coupling a decellularized biological tissue and a synthetic polymer, able to provide blood compatibility and mechanical resistance. The membrane was mechanically characterized to formulate a constitutive model able to generally describe the material's behavior.

A visco hyperelastic model was then developed through stress–relaxation tests, and Abaqus and Matlab® software were used to obtain the sets of constitutive parameters of the two single materials composing the HYME. The validation was carried out with a numerical simulation of the hybrid membrane and comparing the simulation results with experimental data.

The proposed constitutive model shows to be reliable and able to describe the mechanical performances of the hybrid membrane.

The use of these hybrid membranes to replace damaged cardiac tissues, for vascular grafts, or as material to realize mechanical devices will be a big step towards the cure of cardiovascular diseases through regenerative medicine and tissue engineering.

References

[1] S. F. Badylak and R. M. Nerem, “Progress in tissue engineering and regenerative medicine,” *Proc. Natl. Acad. Sci. U.S.A.*, vol. 107, no. 8, pp. 3285–3286.

[2] H. Granel *et al.*, “Bioactive Glass/Polycaprolactone Hybrid with a Dual Cortical/Trabecular Structure for Bone Regeneration,” *ACS Appl. Bio Mater.*, vol. 2, no. 8, pp. 3473–3483, Aug. 2019.

[3] L. Zhou *et al.*, “Hybrid gelatin/oxidized chondroitin sulfate hydrogels incorporating bioactive glass nanoparticles with enhanced mechanical properties, mineralization, and osteogenic differentiation,” *Bioactive Materials*, vol. 6, no. 3, pp. 890–904, Mar. 2021.

[4] K. S. TenHuisen, R. I. Martin, M. Klimkiewicz, and P. W. Brown, “Formation and properties of a synthetic bone composite: Hydroxyapatite-collagen,” *J. Biomed. Mater. Res.*, vol. 29, no. 7, pp. 803–810, Jul. 1995.

[5] D. Zhao *et al.*, “Poly(lactic-co-glycolic acid)-based composite bone-substitute materials,” *Bioactive Materials*, vol. 6, no. 2, pp. 346–360, Feb. 2021.

[6] T. D. Sargeant, A. P. Desai, S. Banerjee, A. Agawu, and J. B. Stopek, “An in situ forming collagen–PEG hydrogel for tissue regeneration,” *Acta Biomaterialia*, vol. 8, no. 1, pp. 124–132, Jan. 2012.

[7] N. Munir and A. Callanan, “Novel phase separated polycaprolactone/collagen scaffolds for cartilage tissue engineering,” *Biomed. Mater.*, vol. 13, no. 5, p. 051001, Jun. 2018.

[8] K. Zheng, A. J. Salinas, and J. Lao, “Editorial: Hybrids Part A: Hybrids for Tissue Regeneration,” *Front. Bioeng. Biotechnol.*, vol. 9, p. 746641, Aug. 2021.

[9] P. M. Crapo, T. W. Gilbert, and S. F. Badylak, “An overview of tissue and whole organ decellularization processes,” *Biomaterials*, vol. 32, no. 12, pp. 3233–3243, Apr. 2011.

[10] M. Todesco *et al.*, “A New Detergent for the Effective Decellularization of Bovine and Porcine Pericardia,” *Biomimetics*, vol. 7, no. 3, p. 104, Aug. 2022.

[11] M. Todesco *et al.*, “Hybrid membranes for the production of blood contacting surfaces: physicochemical, structural and biomechanical characterization,” *Biomater Res*, vol. 25, no. 1.

[12] D20 Committee, “Test Method for Tensile Properties of Plastics by Use of Microtensile Specimens,” ASTM International.

[13] L. Wollmann *et al.*, “Characterization of Decellularized Human Pericardium for Tissue Engineering and Regenerative Medicine Applications,” *Arquivos Brasileiros de Cardiologia*, 2019.

Composite scaffolds based on polyvinyl alcohol and acellular cartilage matrix for hemophilic arthropathy treatment

M. Confalonieri[1,2], S. Barbon[2,3], E. Stocco[2,3], V. Macchi[2], R. De Caro[2,3], S. Todros[1], A. Porzionato[2,3,4] and P.G. Pavan[1,5]

[1] *Department of Industrial Engineering, University of Padova, Italy*
[2] *Department of Neurosciences, Section of Human Anatomy, University of Padova, Italy*
[3] *Fondazione per la Biologia e la Medicina della Rigenerazione, Tissue Engineering and Signalling - T.E.S. Onlus, Padova, Italy*
[4] *A.V.I.S. per Progresso Ematologico - A.P.E. Odv, Castelfranco Veneto, Treviso, Italy*
[5] *Fondazione Istituto di Ricerca Pediatrica Città della Speranza, Padova, Italy*

***Abstract*— Hemophilic arthropathy (HA) is a frequent complication of Hemophilia A and B, being caused by repeated episodes of joint bleeding which lead to the degeneration of the articular cartilage (AC). The current management of this side pathology can only slow down the osteo-chondral damage, with no effect on cartilage regeneration. Tissue Engineering (TE)-based approaches represent a valid and poorly investigated option to replace the cartilage in HA patients, restoring the continuity of the osteochondral interface. Thus, in this project we developed a composite scaffold combining synthetic polyvinyl alcohol (PVA), which assures for the mechanical support, with decellularized human AC matrix, which increments the bioactivity of the hydrogel. Composite scaffolds in PVA at two different concentrations (15 % and 20 %) were fabricated by cross-linking a thin layer of decellularized, homogenized and lyophilized cartilage on hydrogel disks. Scaffolds were mechanically investigated by indentation and consolidation tests to define their compressive mechanical behavior in relation to hydrogel concentration. Subsequently, PVA/AC scaffolds were tested for their ability in promoting HM1-SV40 mesenchymal stem cells adhesion and proliferation, showing an increment of cell interaction capacity in comparison with the hydrogel alone. In conclusion, our preliminary evidence showed some promising mechanical and biological properties of PVA/AC composites for cartilage restoration in hemophilic patients suffering from HA.**

***Keywords*— hemophilic arthropathy, cartilage regeneration, polyvinyl alcohol, acellular cartilage matrix**

I. Introduction

Hemophilic arthropathy (HA) is a complication of Hemophilia A and B, which occurs as a consequence of repeated episodes of joint bleeding (hemarthrosis) and resulting exposure of the cartilage to blood [1]. Specifically, the chondrocytic metabolism is disrupted and consequently the proteoglycan synthesis is inhibited, causing the deterioration of the cartilage matrix. Therefore, HA has long-term consequences for bone health, causing chronic pain and functional disability. Generally, replacement therapy (i.e., prophylaxis with the missing coagulation factor) and conservative orthopedic approach (e.g., physiotherapy, hyaluronic acid injections, joint arthroplasty, and osteotomy) are the treatments of choice. Nevertheless, these therapies can only slow down the osteo-chondral damage [1].

Thus, the identifications of new strategies based on Tissue Engineering (TE) could represent a valid therapeutic approach to promote tissue regeneration in patients suffering from HA. Revising the literature, it can be noted that the main target of TE osteochondral repair techniques are patients suffering from osteoarthritis due to trauma, obesity and aging. On the contrary, the application of advanced TE strategies for the focal repair of early cartilage damages in hemophilic patients has been poorly considered so far [2].

In TE strategies, scaffold design needs to take into consideration that it has to highly mimic the target-tissue, presenting similar bioactivity and mechanical properties. Hydrogels represents a promising class of material as cartilage substitutes. Among them, polyvinyl alcohol (PVA) stands out for its peculiar characteristics: high-water content, good viscoelastic and compressive mechanical properties, well-established atoxicity and high biocompatibility [3]. Remarkably, its suitability is confirmed also by the satisfactory outcomes given by PVA-based medical devices which are already used in the clinical practice (e.g., CARTIVA®, marked CE in 2002) [4]. Nevertheless, PVA is not capable to sustain cell adhesion and proliferation, likely due hydrophilic moieties (i.e., hydroxyl groups) present on the polymer backbone [5]. For this reason, different studies combined the hydrogel with specific biomolecular components of the cartilaginous extracellular matrix (ECM) and other natural biomaterials [6].

Based on the above considerations, this work investigated the fabrication and characterization of a bioactive composite scaffold, consisting of a hydrogel support made of PVA at different concentrations (15 % and 20 %), which was cross-linked to a superficial layer of acellular AC matrix of human origin (Figure 1). In this composite, the synthetic PVA component, placed towards the inner layers of hyaline cartilage, assures for the adequate structural and mechanical support, whereas the biological counterpart, facing the synovial fluid, guarantees for scaffold bioactivity. In particular, the AC matrix was obtained by decellularization, homogenization and lyophilization of the native cartilage, removing the immunogenic component of the tissue (i.e., cells, DNA), while preserving the plethora of ECM biomolecules, that can provide specific biological cues for tissue regeneration. On the other hand, the original structural features of the cartilaginous tissue was not maintained.

In this work, the mechanical properties of PVA hydrogels at different concentrations were investigated in order to find the material that could better mimic the cartilaginous tissue. In fact, different studies in the literature proved that the concentration of PVA into the hydrogel influences the

properties of the material [3]. Moreover, the ultrastructural features and cell-interaction abilities of the composite PVA/AC scaffolds were assessed to demonstrate their enhanced bioactivity in comparison with PVA alone.

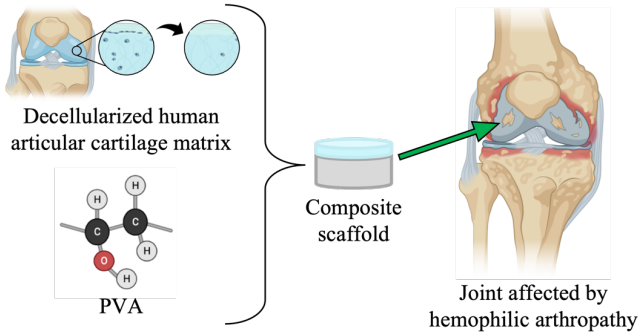


Fig. 1: Schematic representation of scaffold structure and application.

II. Materials and Methods

A. Scaffold manufacture

The composite scaffolds (PVA/AC) were fabricated using a PVA discoidal support as the bottom layer and combining it with a thin surface layer of decellularized cartilage matrix. Regarding PVA, two different polymer concentration were considered (i.e., 15 wt% and 20 wt%). Hence, the aqueous solutions of 15% and 20%PVA (Mw 146,000–186,000Da, 99+% hydrolysed) were obtained by heating the polymer suspension for 8 hours (h) at 90°C under stirring, until complete dissolution. The different PVA samples will be named as 15%PVA and 20%PVA, according to the polymer concentration they contain.

In parallel, for the AC matrix preparation, human cartilage samples (n = 3) were harvested from cadaver donors enrolled by the Body Donation Program of the Section of Human Anatomy, University of Padova [7], in compliance with European, Italian and regional guidelines [8].

Specifically, the tissue samples were rinsed several times in a 2% penicillin/streptomycin solution in PBS in order to remove any residual blood. After grinding the cartilage into small fragments, they were decellularized by a detergent-enzymatic method according to Stocco et al. [9].

The decellularized cartilage was soaked with a 10% acetic acid solution (2.5 M) in dH_2O and homogenized at 0°C in iced bath using Ultra-Turrax homogenizer (Janke & Kunkel GmbH, Staufen, Germany) 8 times/20 sec with intervals of 5 minutes (min). Thereafter, 400 μL of matrix solution were casted into each well of a 24-well cell culture plate, frozen at -20°C and finally lyophilized by a freeze-dry system (FreeZone, Labconco Corporation, Kansas City, USA).

For mechanical testing, 15%PVA and 20%PVA scaffolds were fabricated by pouring the hydrogel solutions into cylindrical molds (internal diameter 22 mm, height 7 mm) and performing physical cross-linking of the polymer through freeze-thawing (FT) cycles (24h at -20°C/24h at 4°C for three cycles). These samples were kept at -20°C until use.

Moreover, the two types of PVA/AC composite scaffolds were fabricated by pouring a layer of 15% or 20%PVA solution at 40°C into each well of a 24-well tissue culture plate. After that, a thin matrix layer of lyophilized AC matrix was carefully placed upon each hydrogel solution. The physical cross-linking of the hydrogel and the embedding of the matrix occurred through a FT treatment, as described before. The scaffolds were then stored at –20°C until use.

B. Mechanical tests

Indentation and consolidation tests were carried out on the PVA scaffolds only by Bose® ElectroForce Planar Biaxial TestBench (TA instruments, New Castle, USA), in accordance with the test protocol previously described by Todros et al. [10]. The samples were immersed in phosphate buffer saline (PBS), let unfrozen at RT for 1 h before the testing and maintained in submerged condition for the entire duration of the tests.

Samples were kept in the cylindrical molds they were fabricated in, which served also as sample holders. Indentation tests occurred using a rigid, spherical indenter with a diameter of 28 mm. The contact of the indenter with the hydrogel surface was assumed when measuring a compressive force equal to −0.05 N. According to the physiological range of maximum compressive strain for human cartilage, indentation tests were then carried out at a depth rate of 10 mm s^{-1}, up to −1.4 mm, corresponding to 20% of the overall sample height. Consolidation tests were performed by keeping constant compressive strain for 5400 s.

Each sample was used for a single test and five samples were tested for each material.

C. Ultrastructural characterization of composite scaffolds by Scanning Electron Microscopy

The ultrastructure of the composite scaffolds was assessed by SEM. Samples were fixed with 2.5% glutaraldehyde in 0.2M phosphate buffer (pH 7.2) for at least 24 h. Following dehydration through ascending graded ethanol series, critical point drying and gold sputtering, the samples were observed using a Scanning Electron Microscope (JSM-6490LA, JEOL, Eching b. München, Germany).

D. HM1-SV40 culture

For seeding experiments on the composite PVA/AC scaffolds, the immortalized human bone marrow cell line HM1-SV40 was used. This mesenchymal stem cell population was cultured at 37 °C, 95% relative humidity and 5% CO_2, using a proliferation medium containing Alfa-Modified Eagle Medium (α-MEM) Without Nucleosides (ThermoFisher Scientific), 16.5% fetal bovine serum (FBS) (ThermoFisher Scientific), 1% L-Glutamine 200 mM and 1% penicillin/streptomycin solution (100 mg/mL) (P/S; Life Technologies, Paisley, U). The medium was refreshed every 2-3 days.

E. Cell behavior on composite scaffolds

To test the bioactivity of the composite PVA/AC scaffolds, HM1-SV40 cells were seeded on the superficial cartilage layer of the supports. Briefly, 15%PVA/AC and 20%PVA/AC scaffolds were previously sterilized by soaking into 2% P/S solution in PBS under shaking for 72 h, then rinsing in PBS and finally leaving them for 1 h under UV light. To prepare the scaffolds for seeding, they were kept overnight into cell proliferation medium HM1-SV40 at 37 °C, 95% relative humidity and 5% CO_2. HM1SV40 cells were then detached by using trypsin/EDTA solution and counted with a TC20 Automated Cell Counter (Bio-Rad, Hercules, USA).

Finally, the scaffolds were seeded with 100,000 cells/support in 300 μL of proliferation medium and cultured for 7 and 14 days. In parallel, the same procedure was followed to seed 15% and 20%PVA scaffolds as controls. At the established end-points, cell viability and growth on the composite and synthetic scaffolds were evaluated by MTT assay. In brief, HM1-SV40 cells were treated with 3-(4,5-dimethylthiazol-2-yl)-2,5-dimethyltetrazolium bromide (MTT; 0.5 mg/ml) for 4 h and resulting formazan crystals were dissolved in 2-propanol acid (0.04 M HCl in 2-propanol) for 15 min under mild agitation. Finally, the optical density at 570 nm of samples was measured by using a microplate auto-reader EL 13 (Bio-Tek Instruments, Winooski, VT, USA). The results were expressed as number of viable cells detected on scaffolds by plotting the optical density values measured for each sample on the standard curve obtained by seeding defined cell numbers and evaluating them by MTT.

F. Statistical analysis

The statistical analysis was developed using the software Prism (v. 9.3.1, GraphPad Software, San Diego, USA). Mann-Whitney test was performed to evaluate differences among experimental groups, which were considered statistically significant with $p < 0.05$.

III. RESULTS

A. Indentation test

In order to design an effective scaffold for repairing osteo-chondral defects, the biomaterial should mimic the native cartilage tissue mechanical properties. It has to be able to withstand the joint loading environment, especially compressive forces, and it should have a stiffness comparable to the native cartilage, because it is known that this factor represent an important cue to regulate cell behavior during cartilage regeneration [11].

The compressive behavior of composite scaffold is expected to be mostly due to the PVA layer, due to its considerably higher thickness and stiffness. Thus, indentation tests were preliminary performed on 15%PVA and 20%PVA to assess which polymer concentration better resembles AC mechanical features. In Figure 2 a, the results of indentation tests are shown as values of indentation load as a function of indentation depth. To highlight possible significant differences among the hydrogels, a measure of the material stiffness was calculated by dividing the maximum absolute value of indentation load measured in each experimental test by the maximum indentation depth (1.4 mm) (Figure 2, b). From these results, it can be observed how the almost-instantaneous compressive behavior of PVA varies with the hydrogel concentration. At maximum penetration depth, the lower is the PVA concentration, the lower is the indentation load. Moreover, a statistically significant difference was calculated between PVA at 15 wt% and at 20 wt% (p-value = 0.0317). As expected, these results suggest an increment in material stiffness as polymer concentration increases. In perspective of in-vivo application, to choose the most suitable hydrogel, indentation tests in the same condition and setup should be performed on human AC and the results should be compared.

B. Consolidation test

Tissues at high water content like cartilage, subjected to compressive loads, undergo consolidation: the load causes the exudation of the fluid and the compaction of the solid phase. This effect, producing hydraulic lubricant, reduces friction and mitigates the impact of sudden loads [12], [13].

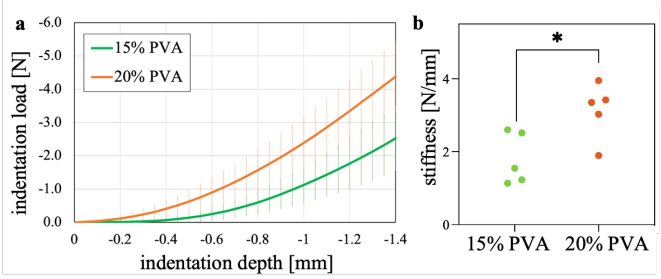


Fig. 2: Results of indentation tests on PVA hydrogels at different concentrations (15 wt% and 20 wt%): (a) Indentation load (mean and standard deviation) vs. indentation depth; (b) Values of stiffness for each concentration of hydrogel. Significant differences among hydrogels are indicated by (*) for p-values < 0.05.

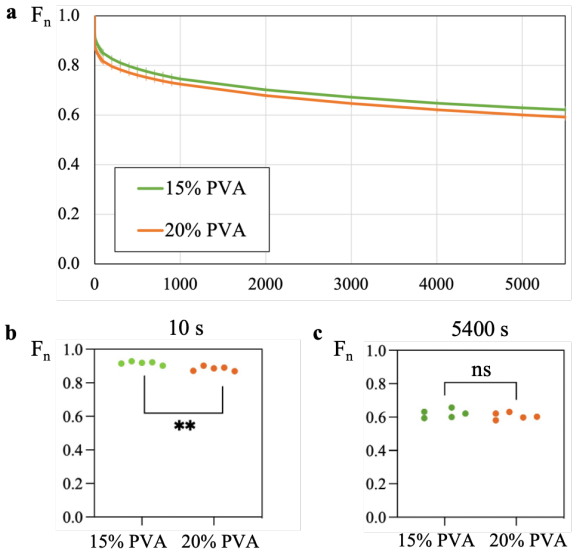


Fig. 3: Results of consolidation test on PVA hydrogel at different concentrations (15 wt% and 20 wt%). (**a**) Mean of normalized indentation force vs. time; values of F_n for each samples of hydrogel at a specific time points during consolidation tests: (**b**) at 5 s; (**c**) at 5400 s. Significant differences are indicated by (**) for p-values < 0.01.

Considering the end-use destination of these scaffolds, mechanical consolidation tests were performed to fully characterize the behavior of PVA hydrogels subjected to compressive loads. For each test, the normalized indentation force F_n was calculated dividing the force at the current time by the maximum force measured at the initial time of the consolidation process.

In Figure 3 a, the variation of F_n in time are represented for each sample at different concentration of hydrogel. It can be noticed that the 15% and 20%PVA curves are almost overlapping. To assess possible significant differences in the consolidation process, ascribable to the variation of hydrogel concentration, normalized force values for the five experimental tests conducted on each hydrogel were analyzed in the short time (i.e., 10 s) and at the end of the test (i.e., 5400 s). A significant difference was detected only at 10 s (p-value = 0.0079), highlighting a greater force reduction in 20%PVA.

C. *Gross appearance and ultrastructural morphology of PVA/AC scaffolds*

After FT, the AC matrix were firmly embedded into the hydrogel. This result confirmed F/T to be an adequate method for composite scaffold fabrication, as already proven in previous studies [2], [9].

Macroscopically, the AC matrix layer was well identifiable on each type of composite scaffold surface (Figure 4, a-d). The matrix appeared slightly darker and rougher than the hydrogel underneath. Considering the side view of the scaffolds (Figure 4, b and d), the reduced thickness of the acellular matrix layer comparing to the hydrogel can be appreciated. This data is consistent with the structural and mechanical function that the PVA layer of the scaffold has to exert.

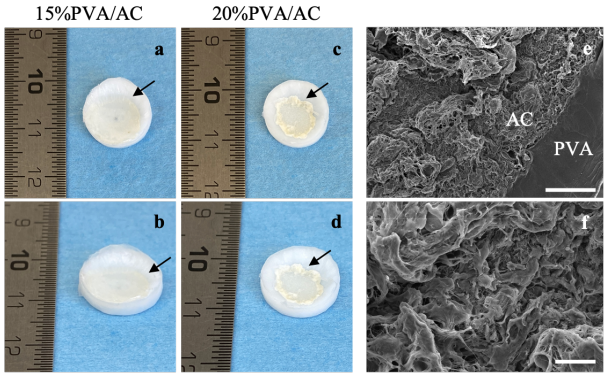


Fig. 4: (**a**-**d**) Structural appearance of composite scaffolds: (**a**, **b**) 15%PVA/AC and (**c**, **d**) 20%PVA/AC. (**a**, **c**) Top view; (**b**, **d**) Side view. In all figures the articular cartilage matrix superficial layer is indicated by a black arrow. (**e**, **f**) Representative scanning electron microscopy (SEM) micrographs of PVA/AC scaffolds: in (**e**) the interface between AC and PVA can be detected; in (**f**) the spongy appearance of AC based matrix can be observed. Scale bars: (**e**) 500 µm, (**f**) 100 µm.

The ultrastructural morphology of scaffold surface was well characterized by SEM, showing no relevant differences among the two types of composite supports, since the top layer of all scaffolds consisted of the same biomaterial. Thus, they all appeared irregular and spongy (Figure 4, e and f). The morphology was coherent with the one observed by Stocco et al. [1,3] on composite scaffolds consisting of AC derived matrices and both 16 wt% PVA and partially oxidized PVA (1%) hydrogels.

D. *Cell behavior on composite scaffolds*

Different studies in the literature proved that PVA hydrogels exhibit a low level of non-specific interaction with solutes and they do not sustain cell adhesion and proliferation [5]. Hence, the bioactivity of the PVA hydrogels was enhanced by the combination with the decellularized and homogenized AC matrix and assayed by culturing HM1-SV40 mesenchymal stem cells on the composite scaffolds for 7 and 14 days.

Comparing to synthetic PVA scaffolds, the composites acquired the capacity to effectively sustain HM1-SV40 cell adhesion and proliferation. As expected, no significant differences among the three type of composite scaffolds were calculated, because the surface that interacted with the cells consisted of the same biomaterial (i.e., AC derived matrix).

These results confirm that biological acellular matrices effectively increase the bioactivity of the PVA. Specifically, the acellular cartilage matrix can generate signaling cues that will guide the cells activity, directly binding cells to ECM components, and sequestering and regulating the access to soluble growth factors and cytokines [14]. Simultaneously, the matrix will not elicit any immune reaction due to the removal cellular component, allowing to fabricate non-immunogenic, biocompatible and bioactive scaffolds to improve cartilage tissue regeneration.

IV. Conclusion

Our in vitro model, consisting of a bilayer composite scaffold in PVA and acellular AC matrix, demonstrated to have the adequate mechanical and biological properties to support cartilage restoration in patient suffering from hemophilic arthropathy. Starting from these promising results, future studies may focus on alternative kinds of scaffolds, which could be prepared by combining the same components with different fabrication strategies (e.g., PVA/AC blend).

Acknowledgement

The authors would like to thank and A.P.E. (A.V.I.S. per il Progresso Ematologico) Association and T.E.S. (Fondazione per la Biologia e la Medicina della Rigenerazione, Tissue Engineering and Signalling) Onlus for supporting the present research.

References

[1] R. Gualtierotti, L. P. Solimeno, and F. Peyvandi, "Hemophilic arthropathy: Current knowledge and future perspectives," *Journal of Thrombosis and Haemostasis*, vol. 19, no. 9, pp. 2112–2121, Sep. 2021.

[2] E. Stocco *et al.*, "Autologous chondrocytes as a novel source for neo-chondrogenesis in haemophiliacs," *Cell Tissue Res*, vol. 366, no. 1, pp. 51–61, Oct. 2016.

[3] M. I. Baker, S. P. Walsh, Z. Schwartz, and B. D. Boyan, "A review of polyvinyl alcohol and its uses in cartilage and orthopedic applications," *J Biomed Mater Res B Appl Biomater*, vol. 100B, no. 5, pp. 1451–1457, Jul. 2012.

[4] F. v Sciarretta, "5 to 8 years follow-up of knee chondral defects treated by PVA-H hydrogel implants," *Eur Rev Med Pharmacol Sci.*, vol. 17, no. 22, pp. 3031–3038, Nov. 2013.

[5] M.-H. Alves, B. E. B. Jensen, A. A. A. Smith, and A. N. Zelikin, "Poly(Vinyl Alcohol) Physical Hydrogels: New Vista on a Long Serving Biomaterial," *Macromol Biosci*, vol. 11, no. 10, pp. 1293–1313, Oct. 2011.

[6] S. Barbon *et al.*, "Enhanced Biomechanical Properties of Polyvinyl Alcohol-Based Hybrid Scaffolds for Cartilage Tissue Engineering," *Processes*, vol. 9, no. 5, p. 730, Apr. 2021.

[7] R. de Caro, V. Macchi, and A. Porzionato, "Promotion of body donation and use of cadavers in anatomical education at the University of Padova," *Anat Sci Educ*, vol. 2, no. 2, pp. 91–92, Mar. 2009.

[8] R. Boscolo-Berto, A. Porzionato, C. Stecco, V. Macchi, and R. de Caro, "Body donation in Italy: Lights and shadows of law No. 10/2020," *Clinical Anatomy*, vol. 33, no. 6, pp. 950–959, Sep. 2020.

[9] E. Stocco *et al.*, "Tailored PVA/ECM Scaffolds for Cartilage Regeneration," *Biomed Res Int*, vol. 2014, pp. 1–12, 2014.

[10] S. Todros *et al.*, "Compressive Mechanical Behavior of Partially Oxidized Polyvinyl Alcohol Hydrogels for Cartilage Tissue Repair," *Bioengineering*, vol. 9, no. 12, p. 789, Dec. 2022.

[11] L.-S. Wang, C. Du, W. S. Toh, A. C. A. Wan, S. J. Gao, and M. Kurisawa, "Modulation of chondrocyte functions and stiffness-dependent cartilage repair using an injectable enzymatically crosslinked hydrogel with tunable mechanical properties," *Biomaterials*, vol. 35, no. 7, pp. 2207–2217, Feb. 2014.

[12] M. A. Biot, "General Theory of Three-Dimensional Consolidation," *J Appl Phys*, vol. 12, no. 2, pp. 155–164, Feb. 1941.

[13] N. D. Broom and A. Oloyede, "The importance of physicochemical swelling in cartilage illustrated with a model hydrogel system," *Biomaterials*, vol. 19, no. 13, pp. 1179–1188, Jun. 1998.

[14] B. N. Brown and S. F. Badylak, "Extracellular matrix as an inductive scaffold for functional tissue reconstruction," *Translational Research*, vol. 163, no. 4, pp. 268–285, Apr. 2014.

Micropatterned PDMS substrates for cellular mechanotransduction modelling

E, Bianchi[1], C. Crescioli[1], P. De Stefano[1], G. Dubini[1*] and A.F. Pellegata[1*]
[1] *Politecnico di Milano, Department of Chemistry, Materials and Chemical Engineering "Giulio Natta"*
[*] *These authors contributed equally*

***Abstract*— Extracellular matrix (ECM) is the principal source of mechanical stimuli for cells in their native tissue environment. Different tissues means different stiffness: mechanotransduction signalling aims at the maintenance of specific homeostasis and function of each organs. In order to mimic different kinds of cell-ECM interaction, micropatterned polydimethylsiloxanes (PDMS) substrates were designed to feature different stiffnesses for the cells cultured in vitro. These microstructures are fabricated by soft-lithography on SU-8 molds, obtained by an optimized protocol of maskless photolithography. The different stiffness values are achieved by different geometrical, mechanical and topological features of fabricated micropillars. Preliminary results showed the ability of cells to spread on the selected substrates. This proof-of-concept optimization of the photolithography/soft-lithography protocol will allow us to test and observe cells in a wider interval of mechanical stimuli, mimicking defined physio-pathological environments.**

***Keywords*—Mechanotransduction, cell substrate interaction, modelling, microfabrication.**

I. Introduction

Cells are continuously in contact with different topographies ranging from macroscale to nanoscale in their native environment. Macroscale topographies are reflected in tissue organization, microscale in the cellular level architecture and nanoscale ones in the subcellular architectures [1]. Cells are stimulated not only by biological and chemical signals but also by mechanical stimuli. These stimuli are exerted by physiological flow [2], e.g. inside blood vessels, but also by the surrounding extracellular matrix (ECM) [3] or from neighbouring cells, and they affect various biological functions such as activation of signalling pathways that in turn control cellular differentiation, migration and proliferation [4].

The ECM features different values of stiffness within the different organs, and each one suits the function of that specific organ. These specific values usually contribute to the maintenance of tissue homeostasis via mechanotransduction signalling to the cells. However, in pathological conditions, the ECM can stiffen or soften, thus affecting the cell-cell and cell-ECM interaction [5]. Over the last years, improvements in micro- and nanotechnology have enabled the manufacturing of micro- and nanoscale sized substrates with different geometrical and mechanical features that could be exploited to mimic the environment that surrounds the cells.

The present work aims at the development of micro-pillar based substrates that can mimic different stiffnesses via geometrical and topographical features to test the mechanostransduction response of endothelial cells. In particular, we aimed at the optimization of a standard photolithography and soft-lithography protocol for for 3D PDMS (Polydimethylsiloxane, Dow Sylgard 184) micropillars substrates. The use of such SU8 and PDMS techniques helps integrate fine microstructures in microwells and microchambers, normally used in biology, exploiting the potentiality of this approach to increase testing possibilities in microfluidic devices, too [6] .

II. Materials and Methods

A. Design of geometrical patterns

Micropillar substrates were designed to obtain a homogeneous distribution of circular micropillars, arranged in a hexagonal pattern fashion. We tested cellular adhesion and spreading of cells happened on a height range 2,7 ÷ 3,7 µm, with ∅3,3 µm and spatial density of 4 µm [7]. Since spatial density might affect cell extension [5], different pattern pitches were tested ranging from 4 to 5.5 µm. Furthermore, we introduced pillars featuring an oval section to model heterogeneity versus anisotropy of the substrate stiffness. The minor axis was fixed at 3.5 µm while the major axis ranged from 7 to 8 µm. (Fig.1)

B. Photolithography for molds microfabrication

To optimize the mold fabrication (Fig.2), we used the epoxy based negative SU-8 2005 photoresist, characterized by low viscosity and suitable to produce a thickness ranging between 2 and 5 µm (spin rate 1800 rpm / 900 rpm). SU8 was spun (Spin Coater–Sawatec SM-150) directly on silicon substrate.

Based on a standard SU8 photolithography protocol, a customized protocol was set up and adapted to obtain the described micropillars. A double layer fabrication was set: the first layer acts as crucial reinforce to the pattern of the second, to avoid undesired deformations or detachments. This second layer is characterized by cavities devoted to shape PDMS pillars: the thickness of the photoresist coating will establish the depth of micro-cavities and, consequently, the maximum height of PDMS micropillars.

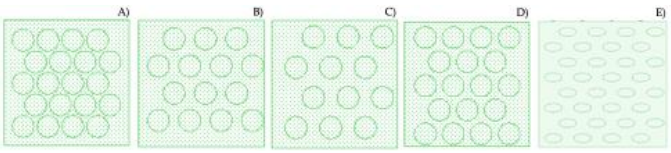


Fig. 1: Layout Editor designs of different geometrical patterns: 4 µm (A), 4.5 µm (B), 5 µm (C) and 5.5 µm (D) spacing with ∅3.5 µm and oval dimensions (E).

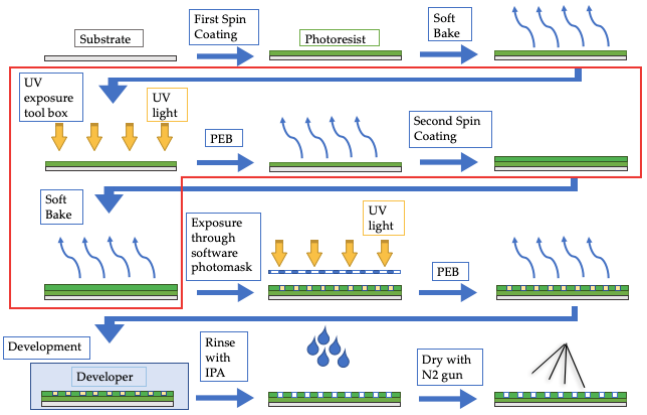


Fig. 2: Complete photolithographic protocol. The red contour includes the four steps added to improve the stability of the structures as mold for PDMS.

The design of the pattern was obtained by the selective exposure (maskless) of the coated film to a high-power LED light source (Direct Write Lithographer Heidelberg MLA100) to a pattern defined by software.

C. Optimization of microfabrication process and characterization

When the design is transferred to the coating, the critical settings of the exposure step are *dose* (exposure energy in terms of mJ/cm^2) and *defocus* (focus position of the write head for a fine tuning of the exposure focus). Starting from a series of exposure modes, different *dose*s (200 – 500, by 25 steps) and *defocus* values (-2 + 4 by 1 step) were combined and tested to achieve the best resolution and accuracy of the pattern during the exposure.

PDMS micropillars were obtained by molding DOW Sylgard 184 Silicone on the SU8 micropatterned substrates. Two ratios resin/curing agent have been tested, 9:1, 10:1 (weight ratio), targeting different mechanical properties.

Despite the affinity of PDMS to silanized mold surfaces (Chlorotrimethylsilane, Sigma–Aldrich), second degassing time with uncured polymer on the mold, in a vacuum chamber for 2 h, is necessary to allow PDMS to fill the cavities and reach the actual height of the final PDMS structures. Samples were then placed to cure in a furnace at 70 °C or 80 °C, for 15 h. Although the profilometer (3D Optical Profilm3D) seemed to read the interior shape of cavities of SU8 patterned substrates, the data was dominated by artefacts and did not reflect the actual ability to get PDMS pillars from the cavities of the molds.

The lack of information required an indirect measurement on the obtained PDMS replica to characterize the size of the related cavities. The micron scale size, the translucent aspect and the electrical insulating properties of both PDMS and SU8 needed a metallization of surface to improve the visualization and characterization of samples under interferometry profilometer and the observation via SEM. These measurements were necessary to perform a precise process control and to find the best working point for a successful photolithography. Characterization of the sample led to set out the best process settings as 275 mJ/cm^2 for the *dose* and *defocus* 3 and 4, for 900 and 1800 rpm, respectively.

TABLE: 1 PILLARS CHARACTERIZATION

	9:1	*10:1*
L = 2.7 µm	E_{eff} = 460 kPa	E_{eff} = 381 kPa
L = 3.7 µm	E_{eff} = 173 kPa	E_{eff} = 147 kPa

The evaluation of the effective elastic modulus of micropillar depending of PDMS ratio for 2,7 µm and 3,7 µm, with 3.3 µm diameter.

D. Mechanical modelling of the substrates

We used a simple Euler-Bernoulli beam theory approximation to assess the elastic moduli of micropillars (Tab.1). This approximation assumes a micropillar as an elastic spring whose constant bending k_{bend} is defined by Eq. (1) and the effective Young modulus can be assessed according to Eq. (2):

$$k_{bend} = \frac{3\pi E D^4}{64 L^3} \quad (1)$$

$$E_{eff} = \frac{9k_{bend}}{4\pi r} = \frac{18k_{bend}}{4\pi D} \quad (2)$$

where E is the elastic modulus of PDMS material [8], D the diameter and L the height of the micropillar.

Regarding the oval micropillars, the calculation of the elastic spring of the single oval post is given by Eq. (3), where *a* is the semi-major axis, *b* is semi-minor axis and α is the angle of the deflection with respect to the major semiaxis:

$$k(\alpha) = \frac{3}{4} * \pi E \frac{a*b}{L^3} * [a^2 * \cos^2(\alpha) + b^2 \sin^2(\alpha)] \quad (3)$$

III. RESULTS

A. Micropatterned substrate fabrication

A number of PDMS micropillar substrates, different in height, size, pitch and mechanical properties of the materials were realized. SEM analysis showed that the profilometer overestimated the heights of the structure by a not-negligible factor, as shown in Fig.3

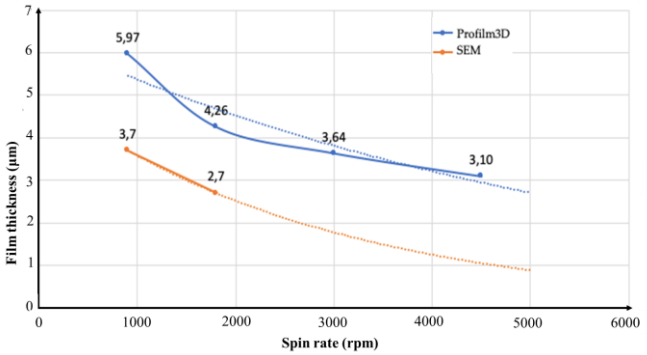


Fig.3: Plot of the relationship between film thickness and spin speed obtained from optical profiler analysis (Profilm3D in blue and SEM in orange) on the SU-8 master mold. The dotted lines indicate the exponential trend.

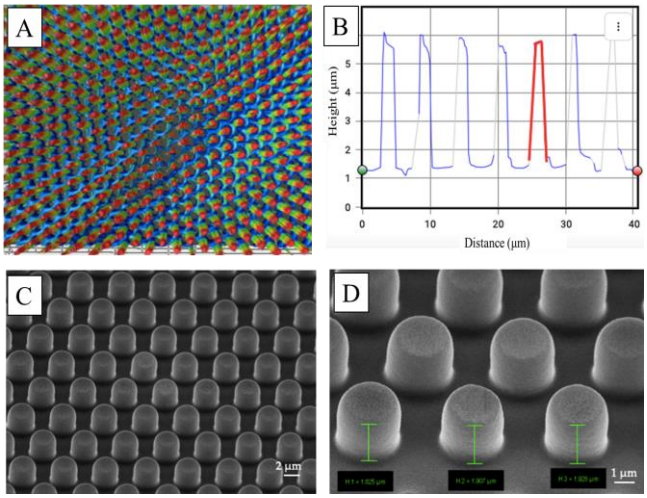


Fig. 4: Profilm3D images (A, B) and SEM images with InLens detector (C, D). Top view (A), step-height (B) of sample spin at 1800 rpm with spacing center-center 5.5 µm. SEM images tilted by 45° at scale bar 2 µm (C) and 1 µm (D) with measured tilted height in overlay.

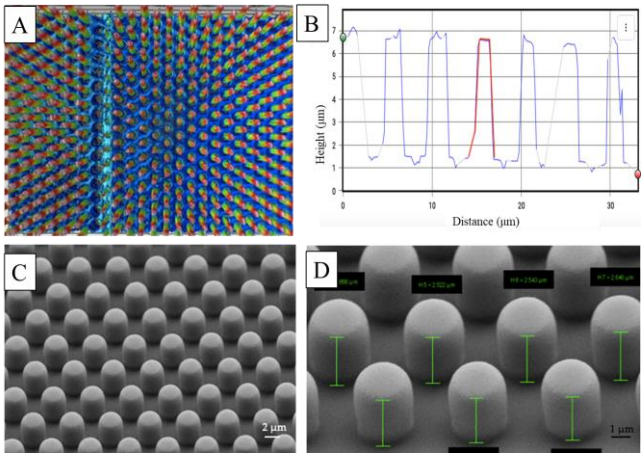


Fig. 5: Profilm3D images (A, B) and SEM images with InLens detector (C, D). Top view (A), step-height (B) of sample spin at 900 rpm with spacing center-center 5.5 µm. SEM images tilted by 45° at scale bar 2 µm (C) and 1 µm (D) with measured tilted height in overlay.

We selected sample characterized by 2.7±0.1 µm and 3.7±0.08 µm in heights (Fig.4, Fig.5).

Structures featuring a higher aspect ratio combined with tight pitches made the micropillars irreversibly stick to each other after demolding, thus generating a compact pattern of pillars that increases the overall stiffness of the substrate We identified a threshold of 4.5 µm as the limit to avoid this phenomenon (Fig. 6). Despite the fact that the mask was designed with a ∅3.5 µm, a difference in circumferential terms can be appreciated via SEM analysis (Fig.7), that shows a size of ∅3.3 µm for the horizontal section of pillars. ∅3,5 µm on the layout was been observed to be the minimum limit to obtain well-defined and empty cavities in SU8 substrates. This can be explained analyzing the functioning of the Direct Write Lithographer because high exposure dose is associated with higher polymerization, leading to a diametrical reduction of cavities.

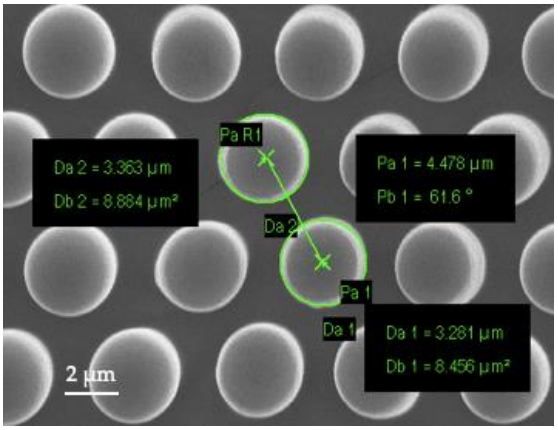


Fig. 6: SEM image with InLens detector of substrate sample with 4.5 µm spatial density (scale bar 2 µm).

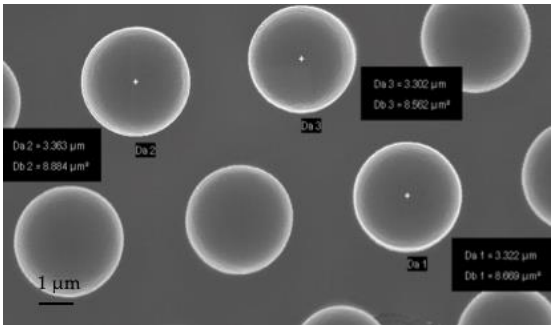


Fig. 7: Diameter measurements at SEM microscopy with InLens detector (scale bar 1 µm).

The different PDMS ratios (9:1 and 10:1), cured at temperature 70 °C and 80 °C impacted on the substrate stiffness. In addition, the spatial density among micropillars varied from 4-4.5 µm up to 5.5 µm.

B. Cell adhesion assay

We selected eleven conditions for biological testing. Each PDMS sample (11 conditions x 3 replicates) was punched with a ∅6 mm-biopsy puncher, sterilized and positioned in a standard multiplate for cell culture.

The preliminary cellular adhesion assay conducted revealed a preferential adhesion of endothelial cells on substrates featuring a stiffness in the range of 173 – 381 kPa and featuring a circular cross-section (Fig. 8).

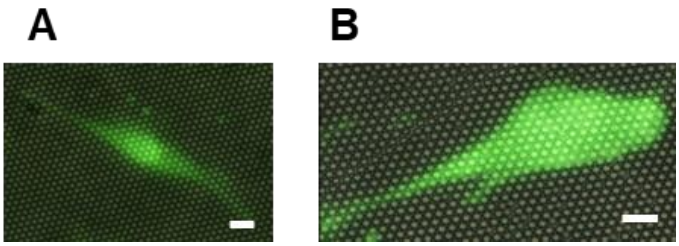


Fig. 8: Representative images of endothelial cells on 2,7 µm height pillars with 4 µm pitch made of 10:1 PDMS ratio (A) and 3,7 µm height pillars with 4.5 µm pitch made of 9:1 PDMS ratio (B) (10 µm scale bar).

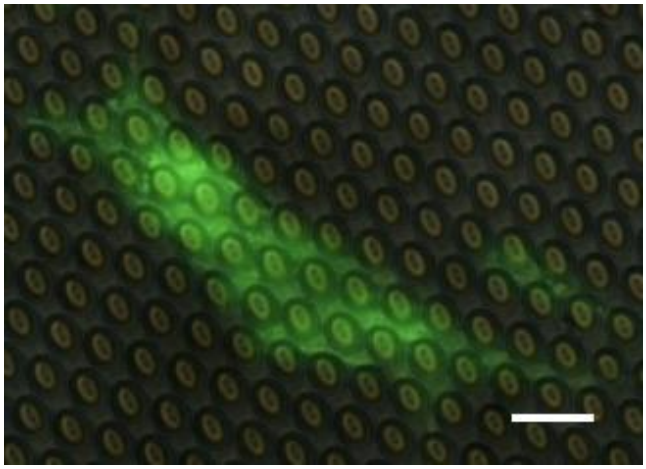


Fig. 9: Representative image of endothelial cells on oval pillars showing spreading along the major axis (scale bar 10 µm).

Interestingly, we observed that endothelial cells preferentially elongated in line with the major axis of pillars when oval-pillared substrates were used (Fig. 9).

CONCLUSIONS

Overall, this study optimized the microfabrication process of micropatterned substrates to model mechanotransduction response in endothelial cells. This proof-of-concept study allowed us to define the best size, height and pitch that promotes the adhesion of endothelial cells. Of note, we preliminary assessed how an asymmetric pillar pattern direct the elongation of endothelial cells. These results open up the possibility of study endothelial cells on substrates that features different stiffnesses and investigate their response. Further studies will be directed to investigate the cellular mechanism involved in these processes.

REFERENCES

[1] Y. Alapan, K. Icoz e U. Gurkan, «Micro and nano devices integrated with biomolecular probes,» *Biotechnology Advances*, vol. 33, pp. 1727-1743, 2015.

[2] E. Bianchi, R. Molteni, R. Pardi e G. Dubini, «Microfluidics for in vitro biomimetic shear stress-dependent leukocyte adhesion assays,» *Journal of Biomechanics*, n. 46, p. 276–283, 2013.

[3] M. Lorvellec, A.F. Pellegata, C. Turchetta, E. A. Mediavilla, S. Shibuya, B. Jones, F. Scottoni, D. Perocheau, A. Cozmescu, J. Delhove, D. Kysh, A. Gjinovci, J. Counsell, W. Heywood, K. Mills, T. McKay, P. D. Coppi e P. Gissen., «An In Vitro Whole-Organ Liver Engineering for Testing of Genetic Therapies iScience. n. 23(12):101808.,» *iScience*, vol. 23, n. 12.

[4] H. van Hoorn, R. Harkes, E. Spiesz, C. Storm, D. van Hoort, B. Ladoux e T. Schimdt, «The nanoscale architecture of force-bearing focal adhesions,» *Nano Letters*, vol. 14, pp. 4257-4262, 2014.

[5] L. E. Dickinson, D. Rand, J. Tsao, W. Eberle e S. Gerecht, «Endothelial cell responses to micropillar substrates of varying dimensions and stiffness,» *Journal of Biomedical Materials Research*, vol. 100, pp. 1457-1466, 2012.

[6] P. De Stefano, E. Bianchi e G. Dubini, «The impact of microfluidics in high-throughput drug-screening applications.,» *Biomicrofluidics*, vol. 16, n. Issue 31 May, 2022.

[7] O. Iendaltseva, V. Orlova, C. L. Mummery, E. Danen e T. Schmidt, «Fibronectin patches as anchoring points for force sensing and transmission in human induced pluripotent stem cell-derived pericytes,» *Stem Cell Reports*, vol. 14, pp. 1107-1122, 2020.

[8] M. L. Fitzgerald, S. Tsai, L. M. Bellan e Y. X. a. D. L. R. Sappington, «"The relationship between the Young's modulus and dry etching rate of polydimethylsiloxane (PDMS)",» *Biomedical Microdevices*, vol. 21, 2019.

ACKNOWLEDGEMENTS

This work is part of the Accelerator Award no. A26815 entitled: “Single-cell cancer evolution in the clinic”, funded through a partnership between Cancer Research UK, London, and Fondazione AIRC (no. 22790), Milan.

Microfabrication was carried out at PoliFab, Milan, Italy (https://www.polifab.polimi.it/).

Cell encapsulation into silk fibroin microgels

G. Perotto[1], F. Ponti[2,3], G. Saroglia[1,2], S. Marcuzzo[4], E. Giagnorio[4], G. Lauria[5,6], E. Rosini[7], L. De Nardo[2], A. Athanassiou[1], G. Candiani[2], N. Bono[2]

[1] *Smart Materials, Istituto Italiano di Tecnologia, Genova, Italy*

[2] *Dept. Chemistry, Materials and Chemical Engineering "G. Natta", Politecnico di Milano, Milan, Italy*

[3] *LBB, CRC- I, Dept. Min-Met-Mat Eng. and CHU de Quebec Research Center, Laval University, Quebec City, Canada*

[4] *Neurology IV-Neuroimmunology and Neuromuscular Diseases Unit, Istituto Neurologico "C. Besta", Milan, Italy*

[5] *Dept. of Clinical Neurosciences, Istituto Neurologico "C. Besta", Milan, Italy*

[6] *Dept. of Medical Biotechnology and Translational Medicine, University of Milan, Italy*

[7] *The Protein Factory 2.0, Dept. of Biotechnology and Life Sciences, University of Insubria, Varese, Italy*

***Abstract*— Cell microencapsulation has been utilized for years as a means for cell shielding from the external environment while facilitating the transport of gases, general metabolites, and secretory bioactive molecules at once. In this work, we developed and characterized a novel way to obtain silk fibroin (SF) microgels (μgels) as a versatile platform to encapsulate relevant cell types for therapeutic purposes.**

***Keywords*—cell encapsulation, silk fibroin, hydrogels, cell therapy.**

I. Introduction

Cell microencapsulation is a very promising technique whereby living cells are entrapped within a biocompatible permeable membrane[1]. Such a strategy enables cells to be nourished and to secrete catabolites and paracrine factors while preventing them to exit the encapsulating device and cells and proteins of the immune system to enter[2].

In the search for the most suitable material for prolonged cell microencapsulation, natural polymer-based hydrogels have been extensively explored due to their high-water content and physical features resembling those of the extracellular matrix (ECM)[3]. Despite alginates, keratin and collagen have been exploited as starting materials for the development of microencapsulation systems, their poor mechanical properties make these materials hard to handle and process[4,5,6].

As an alternative, silk fibroin (SF) extracted from the *Bombyx mori* (*B. mori*) silkworm cocoon possesses many interesting features, such that the ease of processing, excellent biocompatibility, remarkable mechanical properties, and tunable degradability. Of note, the highly repetitive Gly-Ser-Gly-Ala-Gly-Ala (GSGAGA) motifs found in its structure enable the protein to self-assemble from its water solution into different crystalline structures, making it appealing for a wide variety of applications[7,8].

Despite being used in different material formats, a proper methodology to obtain SF hydrogel-based microcapsules is still lacking. In this context, we herein propose a clever strategy based on water-in-oil (W/O) emulsion to fabricate SF μgels obtained under mild gelation conditions and in a relatively short time to encapsulate living cells[9]. Drawing inspiration from previous works[10,11], we exploited ultrasonication as a smart way to speed up the SF gelation process. The strategy allowed the efficient encapsulation of both immortalized cells and primary myoblast cells. Encapsulated cells showed excellent cell viability and proliferation overtime. Moreover, SF μgels allowed for the release of soluble factors with paracrine activity while inhibiting antibody entry.

II. Materials and Methods

A. Preparation of SF solutions

SF solutions with different molecular weights (M_W) were obtained as previously described[12]. Briefly, 5 g of *B. mori* silk cocoons (Cantiere della Provvidenza SPA Scs Onlus) were boiled for 30 min in 2L of 0.02 M Na_2CO_3. The resulting SF solution (i.e., 30 MB) was rinsed three times in deionized water (dH_2O), dried at room temperature (r.t.), dissolved in 9.3 M LiBr at 60 °C for 4 hrs, then dialyzed for 3 days against MilliQ water. 60 mg/mL SF solutions were centrifuged to remove impurities and stored at 4 °C until use.

B. Determination of SF gelation time

The gelation time of 30 MB SF solutions was assessed by preparing 5 mL of the SF solution at different concentrations (i.e., 10, 12, 15, and 20 mg/mL) in either MilliQ water, Phosphate Buffer Saline (PBS), or cell culture medium (Dulbecco's Modified Eagle's Medium, DMEM). SF solutions underwent ultrasonication at a frequency of 20 kHz and 30 % amplitude for 5, 10, 15, and 20 s using a Fisherbrand™ Model 505 Sonic Dismembrator (Fisher Scientific). After sonication, the SF solution were kept at 37 °C and the sol-gel transition was visually monitored.

C. Preparation of cell-free SF μgels

SF μgels were prepared as illustrated in **Figure 1**. Briefly, 5 mL of sonicated 30 MB SF solution was loaded in a 10 mL syringe with a 20 G needle connected to a Tygon tube ($\emptyset = 1$ mm). The syringe was mounted onto a Landgraf LA-100 syringe pump (Colaver). The SF solution was dripped at 250 μL/min onto a 2 % (v/v) Span80-in-oil emulsion. The emulsion was next stirred at 2,000 rpm for 1 hr at 37 °C, then washed three times in PBS to separate μgels from the oil phase. SF μgels were suspended in PBS for further analysis.

D. Morphological and physicochemical characterization of cell-free SF μgels

SF μgels were analyzed using a cold field emission Scanning Electron Microscope (SEM). Briefly, SF μgels were dehydrated in graded ethanol series, then transferred into a critical point dryer and rinsed 5 times with CO_2 under supercritical conditions. Samples were mounted on conductive

tape, gold-sputtered and examined using a 10 kV accelerating voltage. SF dimension was determined by ImageJ software.

To investigate the SF µgel chemical structure, Fourier Transformed Infrared Spectroscopy (FTIR) was used. Briefly, samples were analysed with a Vertex 70 v FTIR (Bruker), and spectra were measured in the range from 400 cm^{-1} and 4000 cm^{-1}. The β-sheet content was quantified by performing self-deconvolution of the Amide I region according to literature[13].

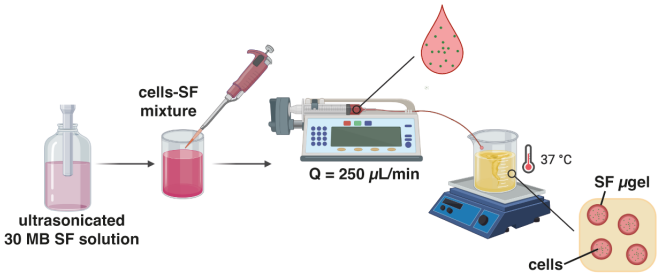


Figure 1. Schematic representation of the cell-laden SF µgels production through the water-in-oil emulsion procedure.

E. Mechanical characterization of cell-free SF µgels

SF gels fabricated as both µgels and macroscopic cylindrical samples (Ø = 10 mm, height = 16 mm) were mechanically characterized by indentation test using a Chiaro Nanoindenter (Optics11 Life) equipped with a 26 µm-SiO_2 bead tip and a cantilever with an elastic constant of 0.48 N/m. To compare the mechanical characteristics of µgels and macroscopic gels, microindentation tests (800 nm/s with an indentation depth of 2.5 µm) were performed both on the surface and in the core of the samples. The compressive modulus was determined by Hertzian best fit of the linear part of the indentation curve.

F. L929 cell encapsulation in SF µgels and biochemical characterization of cell-laden SF µgels

Mycoplasma-free L929 cells were routinely cultured in high glucose DMEM supplemented with 10 % (v/v) fetal bovine serum (FBS), 1 mM sodium pyruvate, 10 mM HEPES buffer, 100 U/mL penicillin, 0.1 mg/mL streptomycin, and 2 mM glutamine (hereafter referred to as complete DMEM, cDMEM) in a humidified atmosphere and 5 % (v/v) CO_2 at 37 °C (hereafter referred to as standard culture conditions).

L929 cells were detached with 1× trypsin-EDTA solution and resuspended in cDMEM. L929 cell suspension was next mixed 1:4 (v/v) with 30 MB SF solution to give 2.7 × 10^7 cells/mL and a SF concentration of 15 mg/mL. Next, 5 mL of the cell-SF mixture was loaded into a 10 mL syringe and µgels were obtained by batch emulsion as illustrated in Figure 1A. The resulting emulsions were resuspended in cDMEM and kept in standard culture conditions for 1, 4, and 7 days.

Cell viability was assessed at different time points by Live/Dead Cell Viability assay. Briefly, at given time points L929 cell-laden µgels were rinsed with PBS, incubated with 1 µM calcein AM and 2.5 µM propidium iodide (PI) to stain live and dead cells, respectively, and incubated for 15 min at 37 °C in dark. Samples were next washed with PBS, resuspended in cDMEM and analyzed using a fluorescence microscope.

Cell proliferation within µgels was evaluated by quantifying the DNA content. Briefly, at different time steps (i.e., 1, 4, and 7 days post encapsulation) cell-laden SF µgels were washed in PBS, resuspended in 200 µL of 0.01 % (v/v) Triton X-100 in 50 mM HEPES (homogenization buffer), and subjected to three freeze-thawing cycles. Next, samples were disrupted with a tissue homogenizer and centrifuged at 12,000 rpm at 4 °C for 5 min. Next, 20 µL of each supernatant were mixed with 10 µL of 200× SYBR Green I, incubated 15 min in dark, then the fluorescence was read with a Sinergy H1 Spectrophotometer (Biotek; λ_{ex} = 497 nm, λ_{em} = 520 nm). To determine the DNA content in the samples, a standard curve using salmon sperm DNA was used. The DNA content was normalized to the total protein content of each sample, as determined by the bicinchoninic acid (BCA) assay. Data were expressed as µg of DNA per mg of SF.

G. Primary myoblasts encapsulation in SF µgels and assessment of the release of paracrine factors

Transgenic SOD1-G93A (male) mice were purchased from Charles River, Inc and maintained and bred at the Fondazione ICCRS Istituto Neurologico "C. Besta" in compliance with institutional guidelines, international regulations (EEC Council Directive 86/609) and project approvals from the Italian Ministry of Health (ref. IMP183/2018-PR). At week 18, SOD1-G93A were euthanized with CO_2 and gastroctnemius muscles biopsies obtained[14]. Muscle fragments were seeded onto 60 mm dishes and cultured in DMEM supplemented with 20 % FBS, 100 U/mL penicillin, 0.1 mg/mL streptomycin, 2 mM glutamine, 10 µg/mL insulin, 2.5 mg/mL basic fibroblast growth factor (bFGF) and 10 ng/mL epidermal growth factor (EGF). After 10-15 days, confluent monolayers were detached and subcultured. Primary myoblasts were purified by means of pre-plating treatment.

Myoblasts-encapsulating SF µgels were prepared as described herein above and kept in standard culture conditions for different periods (i.e., 1, 4, and 7 days). At any time point, 1 mL of cDMEM containing SF µgels was collected, then µgels and supernatants were separated by gentle centrifugation.

TRIzol reagent (Thermo Fisher Scientific) was used to extract RNA from myoblasts-SF µgels. RNA quality was next assessed by means of a 2100 Nano Bioanalyzer (Agilent Technologies). The gene expression analysis was performed by means of quantitative Real-Time Polymerase Chain Reaction (qRT-PCR). Briefly, total RNA was then retro-transcribed using the SuperScript Vilo cDNA Synthesis kit (Thermo Fisher Scientific) in a thermocycler system, according to the following thermal protocol: 25 °C for 10 min, 42 °C for 60 min, 85 °C for 5 min. Next, 0.5 µL of cDNA (corresponding to 10 ng of RNA) were mixed with 5 µL of Fast Universal Master Mix, 3.5 µL of RNAse-free water, 0.5 µL of TaqMan® gene expression assay (specific for the following genes: Neural cell adhesion molecule 1 (Ncam1) for myoblast phenotype, Paired box 3 (Pax3) for myoblast proliferation, and apoptosis regulator (Bcl2)). The cDNA was amplified (in duplicate) at the following thermal protocol: 95 °C for 20 s (reverse transcriptase inactivation), 95 °C for 1 s, and 60 °C for 20 s (40 PCR cycles). The 18 S was used as the housekeeping gene. The mRNA expression levels were normalized against 18 S, and the relative mRNA expression levels were calculated using the formula $2^{-\Delta\Delta Ct}$.

To evaluate the release of paracrine factors from encapsulated myoblasts, we quantified the amount of vascular endothelial growth factor (VEGF) in undiluted supernatants. The amount of VEGF was assessed using a Bio-Plex ProTM Mouse Cytokine 9-plex immunoassay 96-well kit (Bio-Rad Laboratory). Supernatants were transferred into a 96-well plate, then the plata was read with a BioPlex 200 system (Bio-Rad), powered by Luminex xMAP technology. Data were expressed as pg of VEGF/mL.

H. Statistical analysis

Statistical analysis was carried out with GraphPad version 8 (GraphPad Software, La Jolla, CA, USA). Data were initially analyzed using the Shapiro-Wilk normality test. Comparisons between groups were performed with one-way analysis of variance (ANOVA) and multiple t-tests. Significance was retained when $p < 0.05$. Experiments were performed at least in triplicate.

III. Results and Discussion

In recent years, therapeutic strategies relying on cell encapsulation have been in the spotlight. However, open challenges related to limited cell survival and passive cell displacement have fueled much interest in the design of novel delivery vectors. In this scenario, hydrogels have emerged as a powerful solution to these quests.

A. SF µgels fabrication and characterization

In the present study, ultrasonication was used to trigger the sol-gel transition of the SF. Because the gelation time is a critical parameter for the production of hydrogels and the subsequent cell encapsulation, the kinetics of SF gelation was carefully characterized to develop a fabrication protocol for the production of µgels. We thus assessed the effect of different SF concentrations and sonication times on the ultimate gelation time. As shown in **Figure 2A**, the SF gelation time invariably decreased with increased sonication time, irrespective of the SF concentration used. We thus decided to sonicate a 30 MB SF solution at a concentration of 15 mg/mL for 15 s at 30 % amplitude for further experiments. Of note, this allows the gelation of SF solutions after 1 hr post-sonication, thus providing enough time to conveniently mix the sonicated solution with cells, while SF is in the sol state, and to create micro-sized droplets in the emulsion. The so-formed cell-free SF µgels were morphologically characterized. Optical images of the µgels confirmed the presence of spherical shaped µgels, with a diameter of ≈ 200 µm (**Figure 2B**), while SEM analysis allowed us to appreciate the peculiar microstructure of the µgels, which is characterized by the presence of a dense network of nanosized silk fibrils (Ø ≈ 20 nm, **Figure 2C**). Spectroscopic analysis using FTIR showed the presence of β-sheet content, that is typical of highly crystalline and water-soluble SF (data not shown).

The mechanical properties of SF µgels and macroscopic SF gels were assessed by using microindentation tests. As reported in **Figure 2D**, the SF µgels showed compressive moduli ranging between 15 kPa and 25 kPa, with little influence of SF concentration on the compressive modulus. Of note, when prepared at 12 and 15 mg/mL SF concentration, µgels displayed a compressive modulus 2-fold greater than the respective macroscopic counterparts (**Figure 2E**), thus suggesting a strong influence of the microstructure on the overall mechanical properties. These results suggest that the microstructure of SF in the µgels leads to a significant improvement in their overall mechanical performances, that is, one of the most critical issues when using natural polymer-derived hydrogels.

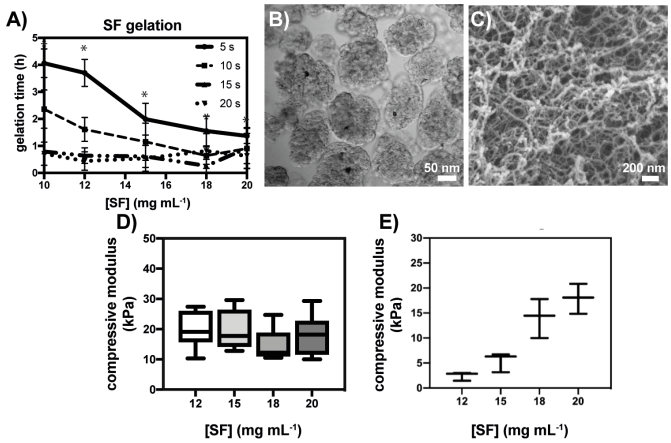


Figure 2. **A**) Gelation time of SF solutions prepared in DMEM at different SF concentrations as a function of the ultrasonication time. Data are presented as mean ± SD (n = 3), $p < 0.05$. **B**) Digital picture of the 30 MB SF µgels at 15 mg/mL SF concentration imaged through an optical microscope. Scale bar = 50 µm. **C**) SEM micrograph of the internal microstructure of SF µgels. Scale bar = 200 nm. **D-E**) Compressive elastic moduli of **D**) SF µgels and **E**) macroscopic SF gels calculated through microindentation tests. Data are presented with inter-quartile range box blots and whiskers indicating the min and max percentiles. The solid lines in the box represent the median value of each dataset.

B. Cells encapsulation and paracrine factors release

Hydrogels used for developing encapsulation systems must fulfil three main requirements, namely i) achieving high encapsulation efficiency, ii) maintaining high viability, iii) and optimizing the environment in which the cells are embedded. Therefore, all three of these aspects were tested for the SF µgels.

To evaluate the feasibility of the encapsulation process, the viability of encapsulated L929 was monitored overtime by means of the Live/Dead assay. As shown in **Figure 3A**, the number of viable cells embedded in the µgels steadily increased from ≈ 30% on day 1 to ≈ 70% on day 7, thus indicating an excellent biocompatibility of the SF µgels. Of note, a significant increase in the total cell DNA content was found in SF µgels after 4 and 7 days of culture with respect to day 1 (**Figure 3B**). Overall, these results demonstrated the reliability of our protocol to fabricate cell-encapsulating SF µgels and that SF µgels kept cells alive once encapsulated. Another extremely important aspect of cell-encapsulating hydrogels relies on their porosity, as it determines their ability to allow molecules diffusion in and out of the hydrogel while preventing the passage of cells.

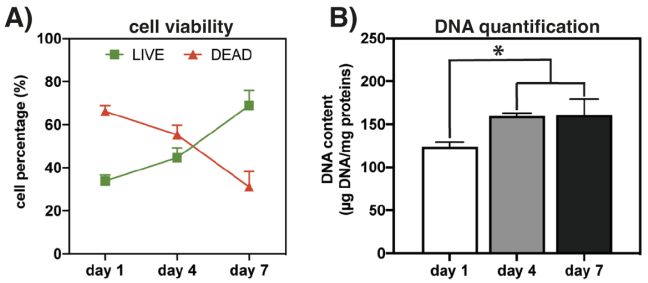


Figure 3. A) Quantification of cell viability of encapsulated L929 cells in SF µgels cultured for 1, 4, and 7 days post-cell encapsulation. **B)** Quantification of DNA content, expressed as µg of DNA per mg of protein in L929-encapsulating SF µgels cultured for 1, 4, and 7 days. Data are expressed as mean ± SD (n = 3), $p < 0.05$.

To this aim, we encapsulated extremely sensitive myoblasts into SF µgels, and investigated their proliferation and secretion of VEGF (40 kDa) outside the capsules. The expression of three regulatory messenger RNAs involved in myoblasts survival, namely Ncam1, Pax3, and anti-apoptotic regulation, namely Bcl2, was thus assessed by means of qRT-PCR. As shown in **Figure 4**, a significant increase in the expression levels of the three messengers was found after 7 days of culture, thus suggesting that the microenvironment inside SF µgels was suitable for the maintenance of myoblasts cell functions.

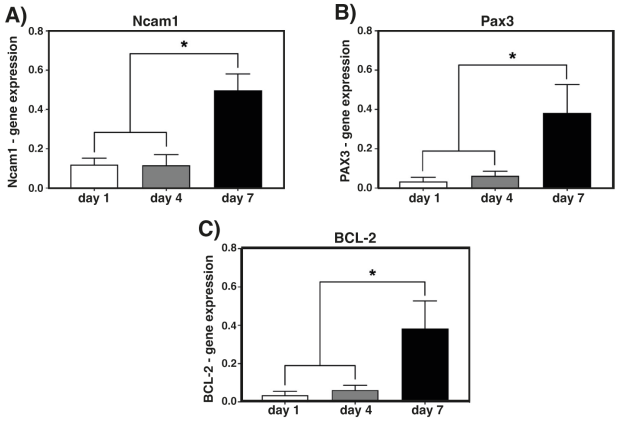


Figure 4. Gene expression levels of **A**) Ncam1, **B**) Pax3 and **C**) BCL-2 genes, as determined by qRT-PCR analysis, in total RNA extracted from myoblasts on days 1, 4, and 7 post-cell encapsulation. Relative expression data are shown as mean ± SD (n = 4) of $2^{-\Delta\Delta Ct}$ values normalized against endogenous control 18 S. *$p < 0.05$.

Moreover, we also assessed the presence of paracrine factors, such as VEGF, in the cell supernatants on 1-, 4-, and 7-days post-cell encapsulation. As shown in **Figure 5A**, the VEGF levels slightly increased from day 1 (4.5 pg/mL) to day 4 (9 pg/mL) and significantly rose further on day 7 (22 pg/mL). This implies that some signalling biomolecules and metabolites can freely diffuse out of the µgels. On the other hand, other macromolecules ($M_W \geq 150$ kDa), such as IgG antibodies, cannot enter the µgels, but stick on their surface (**Figure 5B**). Overall, such results suggest that the SF µgels possess a selective permeability to biomacromolecules, and thus represent a promising cell encapsulation system.

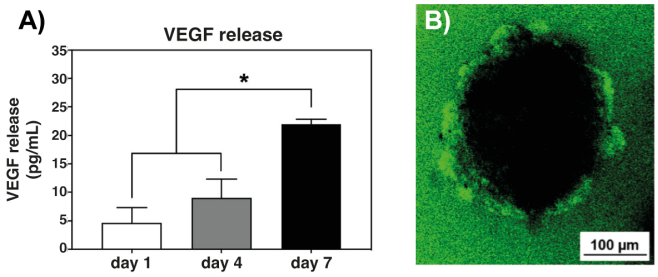


Figure 5. **A**) VEGF levels, expressed in pg/mL, quantified into the supernatant on days 1, 4, and 7 after cell encapsulation were measured by multiplex immunoassay. Data are expressed as mean ± SD (n =3), *$p < 0.05$. **B**) Assessment of the permeability of the SF µgels to FITC-donkey anti-mouse IgG imaged using fluorescence microscopy. Scale bar = 100 µm.

IV. Conclusion

In this study, we proposed a simple method for the fabrication of cell-encapsulating SF µgels. We optimized fabrication parameters to obtain µgels displaying a gelation time around 1 hr, thus allowing cell loading and cell viability overtime. The resulting cell-SF µgels were 200 µm in size and displayed a selective porosity that allowed the exchange of metabolites and gases to keep the encapsulated cells alive and proliferating, and the release of biomacromolecules such as VEGF (MW = 40 kDa) through the gel network, while restricting the entry of other molecules such as IgG. This work thus laid the ground for the development of advanced therapies.

References

[1] G. Orive *et al.* Application of cell encapsulation for controlled delivery of biological therapeutics. Adv. Drug Deliv. Rev. (2014) 3-14.
[2] G.J. Lim *et al.* Cell microencapsulation. Adv. Exp. Med. Biol. (2010), 670, 126-136.
[3] L. Kandilogiannakis *et al.* Addressing stem cells:hydrogels for encapsulation. Process (2021), 9(11).
[4] S.M. Kang *et al*. Alginate microencapsulation for three dimensional in vitro cell culture. ACS Biomater Sci Eng. (2021), 2864-2879.
[5] E. Jacques *et al.* Collagen-based microcapsules as therapeutic materials for stem cell therapy of the infarcted myocardium. ACS Biomater. Sci. Eng. (2020), 6:4614-4622.
[6] J.G. Rouse *et al.* A review of keratin-based biomaterials for biomedical applications. Materials (2008), 1113-1122.
[7] X. Hu *et al.* Determining beta-sheet crystallinity in fibrous proteins by thermal analysis and infrared spectroscopy. Macromolecules (2006), 39:6161-6170.
[8] E.M. Pritchard *et al*. Physical and chemical aspects of stabilization of compounds in silk. Biopolymers (2012), 479-498
[9] N. Bono *et al.* Silk fibroin microgels as a platform for cell microencapsulation. *J Mater Sci: Mater Med* (2023), 34, 3.
[10] X. Wang *et al*. Sonication-induced gelation of silk fibroin for cell encapsulation. Biomaterials (2008), 29: 1054-1064.
[11] T. Yucel *et al.* Silk-based biomaterials for sustained drug delivery. J. Control. Release (2014), 381-397.
[12] D.N. Rockwood *et al.* Materials fabrication from Bombyx mori silk fibroin. Nat. Protocol (2011), 99:89.101.
[13] X. Hu *et al.* Regulation of silk material structure by temperature-controlled water vapor annealing. Biomacromolecules (2011), 12:1686-1696.
[14] S. Marcuzzo *et al.* Hind limb muscle atrophy precedes cerebral neuronal degeneration in G93A-SOD1 mouse model of amyotrophic lateral sclerosis: a longitudinal MRI study. Exp. Neurol. (2011), 231:30-37.

Tuning the features of microphysiological systems for biomimetic intestinal *in vitro* models

A.M.A. Rando[1], L.P. Coppadoro[1], S. Nicolò[2], M. Lombardi[2], C. Foglieni[2], G.B. Fiore[1] and M. Soncini[1]
[1]*Department of Electronics, Information and Bioengineering, Politecnico di Milano, Milano, Italy*
[2]*Cardiovascular Research Area, IRCCS San Raffaele Scientific Institute, Milano, Italy*

***Abstract*—The intestinal epithelium, which consists mostly of an enterocytic monolayer, forms a physical barrier that is pivotal in the molecular absorption process. Despite the need for complex intestinal *in vitro* models to carry out predictive and reliable pharmacological investigations, cell cultures are mainly performed using standard culture systems in which cells are cultured on membranes in static conditions, thus failing in replicating the micro-physiological environment. We developed a modular bicompartmental versatile culture system, named True Tissue on Platform (TTOP) which allows to host tunable culture substrates, such as microporous membranes or scaffolds. After the biological validation with intestinal epithelial cells, we focused on the substrate's characteristics, by comparing different scaffolds and coatings, to obtain a biomimetic intestinal *in vitro* model. The results suggest that gelatin based substrates promote proliferation and better support colonization.**

***Keywords*—*in vitro* model, intestine, scaffold, microphysiological system.**

I. INTRODUCTION

In the bioengineering field, one of the current main challenges is to develop reliable and predictive *in vitro* models which could replicate the physiological microenvironment. Indeed, the need for recapitulating the complexity of the human cell/tissue microenvironment for physio-pathological studies and assessment of new drugs and treatments, has driven the development of Micro Physiological Systems (MPSs). MPSs better mimic the key structures and functions of the biological tissues, aiming at revolutionize the pharmaceutical industry, according to the reduce, refine, and replace animal models (3Rs) principles [1]. In this scenario, the proper selection of cell sources and culture substrates plays a fundamental role in bridging the gap between *in vivo* and *in vitro* models. Indeed, *in vivo*, the function of an organ emerges from the interaction between complex cellular structures, physiochemical factors within the extracellular matrix and secreted by various types of cells, and external electromechanical stimuli [2]. The recapitulation of the tissue microenvironment opens the way to the development of new *in vitro* platforms for the investigation of the mechanisms underpinning cell behavior and tissue/organ functionality as well as pathology onset and progression, the screening of newly developed therapeutic approaches, the assessment of toxicity and the development of personalized therapies. However, despite the need for complex *in vitro* model to carry out predictive and reliable pharmacological investigations, standard cell cultures are mainly performed using standard culture systems that lack of versatility and do not allow the choice of different culture substrates, although they are crucial to enhance the biomimicry of the model and its predictive potential.

Drugs orally delivered follow a precise path starting from the mouth, and terminating in the intestine. The latter represents the major absorptive site, which consists mostly of an enterocytic monolayer that forms a physical barrier that regulates the paracellular transport of ions, metabolites, and macromolecules. Paracellular transport and barrier integrity are pivotal in drug absorption, hence in pharmacokinetic and pharmacodynamic studies. Therefore, complex intestinal epithelium *in vitro* models are required for carrying out more predictive and reliable pharmacological investigations. Previous *in vitro* models based on monocultures of intestinal cell lines (e.g., Caco-2) were successfully used as frontline assays for intestinal drug absorption/permeability but were limited as a routine screen for intestinal toxicity [3]. Although these methods have facilitated the discovery of many basic biological processes, enabling high-throughput analysis, they often fail to provide an adequate representation of key physiological characteristics.

As stated by Horvath and colleagues [4], the main limitations of current *in vitro* models can be summarized as follows:

- Most cell-based assays are based on immortalized cells, that could have lost their epigenetic and physiological fingerprint [5]
- Conventional *in vitro* approaches usually are based on static systems, not able to provide continuous medium renewal and waste removal [6]
- Cells are often cultured on planar, stiff substrates (2D), instead of 3D ECM-like microenvironments, perturbing cellular functions and differentiation [7] [8] [9]

Therefore, we aim at developing an innovative *in vitro* intestinal model, based on a novel cell culture platform, by evaluating different culture substrates in order to better mimic the physiological microenvironment, and perspectively perform dynamic cultures with human-derived biological material, thus providing a useful tool to carry out predictive and reliable pharmacological investigations.

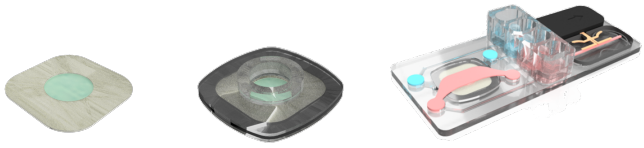
II. MATERIALS AND METHODS

These studies were performed by using a innovative platform, designed by our research group, named True Tissue

on Platform (TTOP). First, we carried out the biological validation of the TTOP system with intestinal epithelial cells. Then, thanks to the possibility to host different substrates in TTOP, we focused specifically on the substrate's features, by comparing different coatings and scaffolds, with respect to standard microporous membranes.

A. Platform

In order to realize a biomimetic intestinal *in vitro* model, a novel bi-compartmental versatile modular culture system has been employed. The TTOP allows real time imaging and direct evaluation of viability/growth of the biological sample without affecting the culture, but also permeability changes, molecule absorption or localization.
The innovative strategy of TTOP is the cartridge-based design, that enables the easy retrieval of the biological sample without any morphological damage, to perform post treatment analyses, and the possibility to reuse the biological material, enabling to design sequential treatments and conditioning on the same sample. Thanks to the aforementioned features, two different TTOP modules have been designed, in order to perform static and dynamic cell cultures respectively.
The TTOP static module is based on an "open-well" design, compatible with standard 12-well plates, enabling the preparation of an intestinal *in vitro* model on a microporous membrane. Once the cells grow until confluence in static conditions, the "open-well" static module can be placed in the "closed-well" perfusion module, enabling continuous recirculation of apical and basolateral culture media generated with embedded piezoelectric micropumps. Bubble traps are integrated to capture flowing microbubbles. Flow rates are programmed through an Arduino-based control unit. Cells can be monitored during the culture by bright field microscopy, thanks to the optical accessibility to both sides of the sample, while at the end it is possible to retrieve the cartridge with a simple procedure and perform fluorescence microscopy to verify the expression of membrane and junctional markers.



(a) **(b)** **(c)**

Fig. 1: Design of the cartridge (a), TTOP static preparation module (b) and TTOP advanced perfusion module (c)

B. Biological validation

For what concerns the biological validation of the gut model, a human colorectal adenocarcinoma epithelial cell line (Caco-2) has been used. Cells were cultured in low glucose Dulbecco's Modified Eagle's Medium (DMEM), containing 1% L-glutamine, 1% non-essential amino acids, 1% of Pennycilin-Streptomicin , supplemented with 10% heat-inactivated Fetal Bovine Serum (FBS). After the expansion of Caco-2 cells in T75 or T25 flasks, the growth rate and morphology in the TTOP static module has been monitored during long-term cell cultures. In detail, once at confluence, cells were passaged with 0.25% trypsin/1mM EDTA and seeded in TToP static preparation modules, on microporous membranes ($3x10^4$ cells/system) and cultured in static conditions in a 37°C, 5% CO2 standard incubator. In order to assess the barrier functionality of the cellular constructs, the Trans Epithelial Electric Resistance (TEER), using the EVOM3 & STX2-PLUS electrodes, was measured at different time points. At the same time, the TEER values were compared with the data obtained from the live staining of the samples, thus correlating the trans epithelial electric resistance with the confluency of the cells. Caco-2 growth was monitored every two days both with TEER measurements and Hoechst 33342 live imaging, by using a Olympus IX83 inverted microscope, until 25 days of culture, obtaining increasing TEER values over time. Immunofluorescence (IF) was performed for the presence of Villin (Rabbit/IgG anti-Human, Mouse, Rat Villin; 1:1000, Invitrogen, Eugene, OR) and ZO-1 (Mouse/IgG1 anti-Human ZO1-1A12; 1:400, Invitrogen, Eugene, OR). The antigens localization was revealed with AlexaFluor 594 Donkey anti-Rabbit IgG (H+L) and AlexaFluor 488 Donkey anti-Mouse-IgG (H+L) (1:500, 45min at RT, Molecular Probes - Invitrogen, Eugene, OR), respectively. Nuclei were stained with 4',6-diamidino-2-phenylindole (DAPI, 0.2nM, 10min at RT, Sigma Immunochemicals, St Louis, MO) and F-actin was stained with Phalloidin–Tetramethylrhodamine B isothiocyanate (50μg/ml, 45min at RT, Sigma Immunochemicals, St Louis, MO). Sections were examined under a Olympus fluoVIEW FV3000RS confocal microscope, free projection max images were obtained from singles channel acquired Z-series.

C. Substrate functionalization

To develop a three-dimensional cellular construct it is crucial to use an appropriate culture substrate which could promote a self 3D cellular organization and differentiation. To verify the dependency of cellular behavior on the culture substrate, we carried out a comparative study by using Caco-2 cell lines cultured on bare polycarbonate porous membranes, gelatin coated membranes and various types of scaffolds, such as gelatin based scaffolds and silk fibroin based scaffolds. Up to now, investigations on gelatin based scaffolds were performed and further characterizations are still ongoing. For what concerns the coatings, since it is known that the gelatin melts over time in the incubator, we monitored if, at a fixed concentration (5 μg/ml of gelatin in PBS), different volumes of gelatin coating (50 μl, 150 μl) behave differently. Caco-2 expansion and seeding in TTOP static preparation modules was carried out as described previously, as well as Caco-2 growth rate monitoring through Trans Epithelial Electric Resistance, Hoechst 33342 live imaging, and IF analyses. IF endpoint assays evaluated the differentiation by staining

tight junctions and specific membrane proteins and the three-dimensional architecture, thanks to Z-stack imaging.

III. Results

The long-term experiments carried out with Caco-2 cells in TTOP static modules demonstrated the suitability of the device to realize *in vitro* intestinal models. Indeed, as shown in fig. 2, which represents a representative curve of TEER values over 25 days, the trans-epithelial electrical resistance kept increasing over time, meaning that the cells grew until confluence and then differentiated according to their phenotype.
During the same experiments, Caco-2 growth rate was also monitored through Hoechst 33342 live staining. According to fig. 3, Caco-2 cells reached confluence and formed a monolayer after 14 days of culture on bare polycarbonate porous membranes, as it was previous shown in studies with standard polycarbonate cell inserts [10]. Afterwards, the cells started to differentiate, therefore TEER values increase rapidly from day 14 to day 25. IF endpoint analyses, by staining the nuclei, villin and the tight junctions (fig. 4), confirmed the cell differentiation in the TTOP static module.

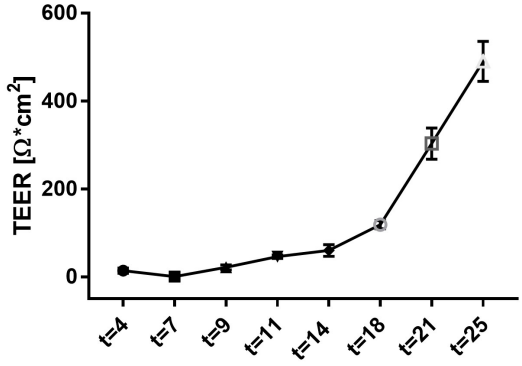
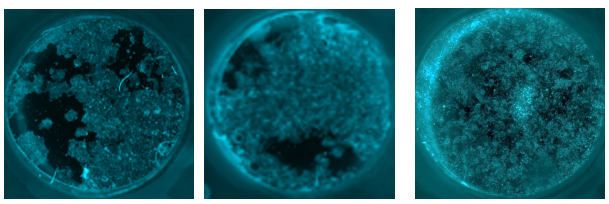
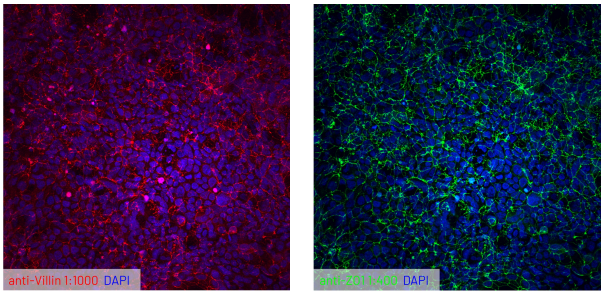


Fig. 2: Representative TEER curve for Caco-2 cells cultured in TTOP static module on a polycarbonate porous membrane



(a) **(b)** **(c)**

Fig. 3: Representative Hoechst 33342 live imaging of Caco-2 cells cultured in TTOP static module. (a) refers to Caco-2 cells cultured for 7 days; (b) 11 days; and (c) 14-25 days. In this case Caco-2 cells reached confluence and created a uniform monolayer



(a) Villin, DAPI **(b)** ZO-1, DAPI

Fig. 4: DAPI, Villin and ZO-1 staining on Caco-2 cells cultured in TTOP static module

For what concerns the culture substrates, the results showed that they played a fundamental role in the formation and tightness of the gut barrier. Indeed, with respect to the cells cultured on bare membranes, the gelatin coated samples and the scaffold-based cultures reached a monolayer earlier. This was confirmed also by TEER measures at different time points. Fig. 5 compares the trans-epithelial electrical resistance of Caco-2 cells cultured on polycarbonate porous membranes either untreated or with gelatin coatings. After 10 days of culture, the gelatin coated samples have much higher TEER values than the untreated ones. At the same time, no relevant differences have been observed among the samples coated with different volumes of gelatin.
Although there aren't standard TEER values for Caco-2 monolayers, previous studies have demonstrated that confluent and differentiated Caco-2 cells have TEER values ranging from 250 to 2000 Ωcm^2 [11] [12] [13]. Therefore, both data shown in Fig. 2, for Caco-2 cells cultured on bare polycarbonate membranes for 25 days, and data shown in Fig. 5, for the gelatin coated samples, are consistent with previous studies. On the other hand, Caco-2 cells cultured on untreated polycarbonate substrates after 10 days (fig. 5) have still low TEER, due to the fact the cells hadn't reached confluence yet, as shown in fig. 6.

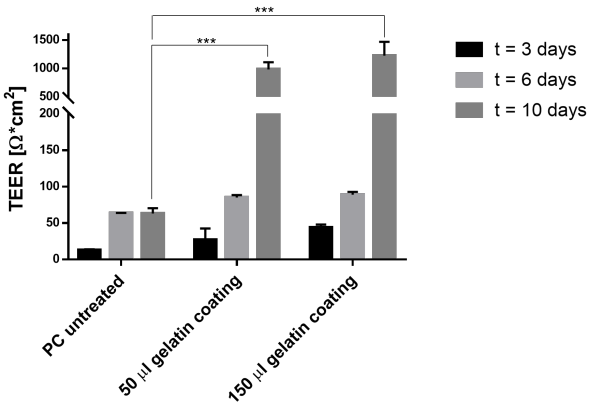
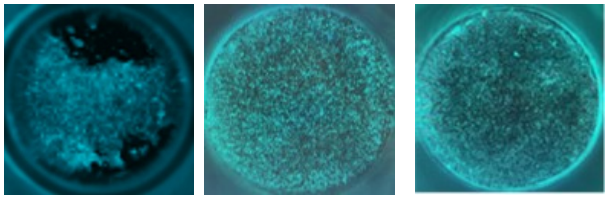


Fig. 5: Representative TEER for Caco-2 cells cultured in TTOP static module on polycarbonate porous membrane either untreated or with different gelatin coatings

Other than gelatin coatings, also gelatin-based scaffolds were tested as Caco-2 culture substrates. Fig. 6 shows Hoechst 33342 live staining images of Caco-2 cells cultured either on untreted (fig. 6a) or gelatin coated (fig. 6b) polycarbonate porous membranes or on gelatin-based scaffold (fig. 6c) after only 7 days of culture. It is evident that the presence of gelatin promote cellular proliferation, and that the cellular distribution is homogeneous within the culture surface. Indeed, with respect to the cell cultures on bare polycarbonate membranes, these results suggest that gelatin promotes an even distribution of the cells on the surface. Moreover, IF staining demonstrated that the substrate properties promote differentiation.



(a) **(b)** **(c)**

Fig. 6: Representative Hoechst 33342 live imaging of Caco-2 cells cultured in TTOP static module for 7 days. In fig. (a) cells are cultured on untreated polycarbonate porous membrane, (b) on a gelatin coated polycarbonate porous membrane, (c) on a gelatin scaffold.

IV. Conclusion

In conclusion, the TTOP can be considered a versatile system since it enables to host different culture substrates without altering other environmental conditions. Indeed, the use of the same support both for polycarbonate membranes and scaffolds makes it possible to really analyze the influence of the substrate on the culture. On the other hand, previous studies were carried out employing different devices to host different substrates, thus introducing a bias in the experimental conditions. Therefore, the unique characteristics of TTOP allow to carry out comparative studies with different culture substrates in order to tune the extracellular environments and develop a predictive intestinal barrier model.

The biological results demonstrated that the mechanical features of the gelatin based substrates promote differentiation, and suggest that the formation of three-dimensional cellular constructs is enhanced accordingly.

Up to now, the device's ease of use and tunability allowed to use different culture substrates in the same experiments. In addition, in perspective, TTOP could enable simple preparation in the static module and advanced dynamic conditions for intestinal barrier tissue in-vitro replication, by using the perfusion module. Therefore, further studies could investigate dynamic enterocytic cultures in the TTOP perfusion module. The optical access to both sides of the hosted sample also enables live imaging studies (absorption of drugs, circulating cells) under dynamic controlled conditions.

Acknowledgement

PhD fellowship to A.M.A. Rando sponsored by Istituto Nazionale di Previdenza Sociale (INPS). Research partially supported by Poli360 proof of concept grant.

References

[1] Ramadan, Q. & Zourob, M. Organ-on-a-chip engineering: Toward bridging the gap between lab and industry. Biomicrofluidics vol. 14 (2020).

[2] Bennett, M. et al. Molecular clutch drives cell response to surface viscosity. Proc. Natl. Acad. Sci. U. S. A. 115, 1192–1197 (2018).

[3] Peters, M. F. et al. Developing: *in vitro* assays to transform gastrointestinal safety assessment: Potential for microphysiological systems. Lab Chip 20, 1177–1190 (2020).

[4] Peter Horvath, Nathalie Aulner, Marc Bickle, Anthony M Davies, Elaine Del Nery, Daniel Ebner, Maria C Montoya, Päivi Östling, Vilja Pietiäinen, Leo S Price, Spencer L Shorte, Gerardo Turcatti, Carina von Schantz, and Neil O Carragher. Screening out irrelevant cell-based models of disease. Technical report, 2016

[5] John R Masters and Glyn N Stacey. Changing medium and passaging cell lines. Nature Protocols, 2(9):2276–2284, sep 2007.

[6] Neda Azizipour, Rahi Avazpour, Derek H. Rosenzweig, Mohamad Sawan, and Abdellah Ajji. Evolution of biochip technology: A review from lab-on-a-chip to organ-on-a-chip. Micromachines, 11(6):1–15, 2020.

[7] Marco Cantini, Hannah Donnelly, Matthew J. Dalby, and Manuel Salmeron-Sanchez. The Plot Thickens: The Emerging Role of Matrix Viscosity in Cell Mechanotransduction. Advanced Healthcare Materials, 9(8), 2020.

[8] Cristina González-García, Marco Cantini, José Ballester-Beltrán, George Altankov, and Manuel Salmerón-Sánchez. The strength of the protein-material interaction determines cell fate. Acta Biomaterialia, 77:74–84, 2018.

[9] Mark Bennett, Marco Cantini, Julien Reboud, Jonathan M. Cooper, Pere Roca-Cusachs, and Manuel Salmeron-Sanchez. Molecular clutch drives cell response to surface viscosity. Proceedings of the National Academy of Sciences of the United States of America, 115(6):1192–1197, 2018.

[10] Hubatsch, I., Ragnarsson, E. & Artursson, P. Determination of drug permeability and prediction of drug absorption in Caco-2 monolayers. Nat Protoc 2, 2111–2119 (2007)

[11] Arnaud Béduneau, Camille Tempesta, Stéphane Fimbel, Yann Pellequer, Vincent Jannin, Frédéric Demarne, Alf Lamprecht, A tunable Caco-2/HT29-MTX co-culture model mimicking variable permeabilities of the human intestine obtained by an original seeding procedure, European Journal of Pharmaceutics and Biopharmaceutics, 87(2):290-298, 2014.

[12] Simonetta Ferruzza, Carlotta Rossi, Yula Sambuy, and Maria Laura Scarino, Serum-Reduced and Serum-Free Media for Differentiation of Caco-2 Cells, ALTEX, 30(2):159–168, 2013

[13] onstanze Hilgendorf, Hildegard SpahnLangguth, Carl G. Regardh, Elke Lipka, Gordon L. Amidon, and Peter Langguth. Caco-2 versus Caco-2/HT29-MTX Co-cultured Cell Lines: Permeabilities Via Diffusion, Inside- and Outside-Directed Carrier-Mediated Transport. Journal of Pharmaceutical Sciences, 89(1):63–75, 2000.

Injectable gelatin-based photocurable fiber-reinforced hydrogel for the treatment of osteochondral defects

I. Niosi[1,2], D. Trucco[2,3], L. Vannozzi [1,2], S. Farè [4,5], L. Ricotti[1,2]
[1] *The Biorobotics Institute, Scuola Superiore Sant'Anna, Italy*
[2] *Department of Excellence in Robotics & AI, Scuola Superiore Sant'Anna, Italy*
[3] *IRCCS Istituto Ortopedico Rizzoli, SC Laboratorio di Immunoreumatologia e Rigenerazione Tissutale, Italy*
[4] *Department of Chemistry, Materials and Chemical Engineering "G. Natta", Politecnico di Milano, Italy*
[5] *INSTM, National Interuniversity Consortium of Materials Science and Technology, Local Unit Politecnico di Milano, Italy*

***Abstract*— Osteochondral defects are one of the most motor-disabling conditions worldwide. A limited intrinsic regenerative capability features cartilage and bone tissues involved in large osteochondral lesions and, to date, there is no clinical treatment capable of appropriately restoring them. We report an innovative injectable composite hydrogel based on gelatin methacryloyl (GelMA) loaded with dispersed fibers made of a blend polycaprolactone (PCL)/GelMA. The fibers were produced by electrospinning, and cut in stripes using a cryostat-based cutting approach. Their embodiment in the GelMA matrix improved the compressive mechanical properties of the pristine GelMA hydrogel. Specific conditions (needle size: 18G and 20G; temperature: 30 and 37°C) were found compatible with the injection of the composite hydrogel, before crosslinking, matching the criteria reported in EN ISO 7886 1:2018 standard. These preliminary results are promising in view of the optimization of injectable reinforced GelMA-based formulations to be used for the treatment of osteochondral injuries.**

***Keywords*—Osteochondral defects, injectable composite hydrogel, electrospinning, dispersed fibers.**

I. INTRODUCTION

The osteochondral (OC) unit consists of the multilayer cartilage tissue and the subchondral bone plate, characterizing the diarthrosis joints. Chondral and OC defects are lesions that result from osteoarthritis or traumatic events, leading toward an irreversible degenerative process of the joint structure. These injuries often hit elderly people in load-bearing joints, such as the knee [1]. The regenerative capacity of these tissues is limited, and the mechanisms of attempted healing and the pathophysiological mechanisms are still not completely understood [2].

Among possible clinical approaches, open surgery related to either cellular and acellular scaffolds usage for regenerative purposes, has high risks of infection and the need for hospitalization, matching site implantation issue, with related iatrogenic conditions and the high costs related to cell use and manipulation. Minimally invasive injectable materials might overcome these issues, guaranteeing the same clinical outcomes [4].

Among the approaches proposed for OC tissue applications, injectable natural hydrogels represent promising candidates given their cell-friendly properties, osteo- and chondrogenic potential, and capability to fill irregular defects. However, one of the main limitations of injectable hydrogel-based materials (especially natural ones) is the control of their mechanical properties, which is important for OC treatment. In fact, it has been shown that mechanical stimuli are crucial in maintaining a healthy OC tissue [5], as well as in promoting its regeneration (i.e., stiffness influences differentiation) [6][7].

Gelatin-based materials, particularly gelatin methacryloyl (GelMA) are attractive options in this field [8]-[10]. However, considering injectable formulations, no studies report the possibility to match the mechanical properties of OC biological tissues. To tune the properties of naturally-derived materials their combination with synthetic components (e.g., semi- or interpenetrated polymeric networks and copolymer systems) and with reinforcement fillers are under investigation [11]-[15]. Recently, fiber-based fillers have attracted interest due to their capability to provide additional features to hydrogel-based composite materials.

In this study, an injectable composite hydrogel made of GelMA as a matrix, reinforced with a fibrous filler made of a PCL/GelMA blend, is proposed, with the final aim to improve GelMA mechanical properties, in view of a future injectable solution for OC treatment, crosslinkable *in situ*. We report the optimization process for the production of the dispersed fibers (DFs) to be embedded in the GelMA solution, as well as the characterization of the composite in terms of mechanical properties and injectability.

II. MATERIALS AND METHODS

A. GelMA synthesis

Gelatin (Gel, type A, strength: 300, Sigma Aldrich, Merck) was dissolved in a pre-heated PBS at 50 °C to achieve a concentration of 10 % w/v. Methacrylic anhydride (MA, 0.6 g per Gel gram) was added and the solution was left reacting for 2 h. The solution was purified by dialyzing against deionized water (DIW) at 40 °C for 7 days. Finally, the solution was freeze-dried (FreeZone 2.5 Plus, Labconco) and stored at -80 °C.

B. Electrospun mesh and DFs fabrication

For the electrospinning solution, PCL (15 % w/v) and GelMA (5 % w/v) were dissolved separately in acetic acid and stirred at room temperature (RT) for 12 h and 1 h respectively in a sealed glass flask. Then, the GelMA and PCL solutions were mixed (ratio 1:1) to obtain PCL75:GelMA25 at 20 % w/v total polymer concentration and stirred for 1 h to achieve a homogeneous solution. The electrospinning parameters used for the fabrication of aligned fiber meshes are reported in Table I [16].

TABLE I: ELECTROSPINNING PARAMETERS

Parameter	*Value*
Rotating mandrel speed	2000 rpm/min
Electric field	16 kV
Distance (syringe-collector)	13 cm
Flow rate	0.5 mL/h
Electrospinning time	1 h

Then, the electrospun aligned meshes were cut (1x1 cm^2), rolled in a cylindrical shape, embedded in a cryomedium (PolyFreeze. Sigma Aldrich, Merk), and then perpendicularly cut using a cryostat (YD-1900, JINHUAYIDI), setting a cutting thickness of 20 µm. The frozen slices were washed in DIW and centrifugated at 4000 rpm/min for 5 min sequentially three times. The DFs were collected and then freeze-dried.

C. *Photocrosslinking of GelMA, GelMA+DFs*

Freeze-dried GelMA was dissolved in DIW to reach a 10 % w/v concentration. To obtain the DFs-loaded GelMA (GelMA+DFs) suspension, 0.5 % w/v DFs was added to the GelMA solution. Irgacure 2959 (Sigma Aldrich, Merk) was used as photoinitiator (0.5% w/v), and added to GelMA solution and GelMA+DFs suspension. They were poured into a cylindrical mold (diameter: 7 mm, height: 5 mm) for the photo-crosslinking by a UV light source (l = 365 nm, 3.5 $W/cm^{2,}$ Lightninningcure LC5 lamp, Hamamatsu) for 2 min.

D. *Morphological analysis*

Aligned electrospun mesh, DFs and lyophilized UV-crosslinked samples (GelMA+DFs) were observed by Scanning Electron Microscope (SEM, Phenom XL, Thermo Fisher Scientific) to evaluate the fiber size, orientation and directionality distribution (ImageJ), the surface morphology and the interaction of DFs with the GelMA matrix.

E. *Injectability*

Injectability tests (n = 3) were performed on solutions of DFs-free GelMA and GelMA+DFs using a custom-made set-up adapted to an MTS electro-mechanical machine (MTS, 1/MH), equipped with a thermostatic chamber and a 5 kN load cell. The test was carried out at different temperatures (20, 25, 30, and 37 °C) and needle diameters (18, 20, and 22G). The test speed was set at 1.6 mm/s, corresponding to a 0.2 mL/s flow rate [17]. All the parameters selected (needle types and injection velocity) were based on those used for intra-articular [18] and *in-vivo* injections [19], following the EN ISO 7886 1:2018 standard.

F. *Mechanical characterization*

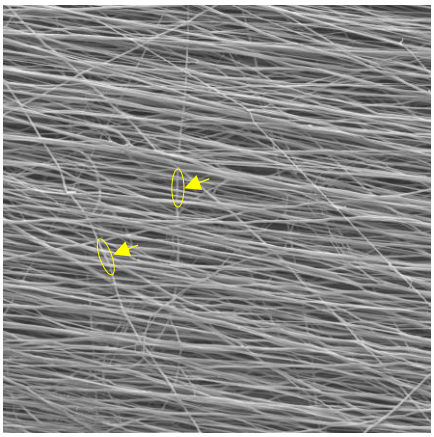
An Instron 5965 machine (1 kN load-cell) was used to perform compressive mechanical tests on photo-crosslinked GelMA and GelMA+DFs samples (n = 3). A 1 mm/min compression deformation rate was applied. The following mechanical parameters were considered: compressive modulus (slope of the curve in the strain range of 0-10 %), toughness (area under the curve), and maximum deformation and stress.

III. RESULTS AND DISCUSSION

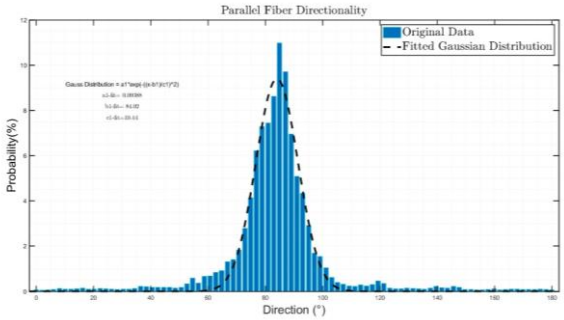
A. *Morphological analysis*

The electrospun GelMA/PCL meshes showed no aggregated beads and a diameter of 724.9 ± 159.4 nm (Fig. 1a), which is comparable with the diameter size of collagen fibril bundles in the native chondral tissue [20]. The fibers were highly oriented along a preferential direction (Fig.1b). Increasing the mandrel rotation speed can improve fiber orientation reducing the presence of transversal fibers. However, an optimal match between the percentage of oriented fibers and fiber diameters was set at 2000 rpm/min to maintain adequate mechanical properties.

As shown in Fig. 2a, cutting the electrospun matrix with a cryostat, the corresponding length of the obtained strips is 51.96 ± 18.6 µm, a value dimensionally comparable with those reported in [13]-[15]. The DFs, once embedded in the GelMA matrix, showed a 3D organization (Fig. 2b). For DFs, it was hypothesized that the interaction between the DFs and the GelMA matrix determined a reinforcing mechanism. Indeed, the presence of GelMA in both DFs and matrix could generate a surface chemical affinity, qualitatively evaluable (Fig. 2b, yellow arrows). The interaction between the filler of fibers and the matrix material was hypothesized in another study [20]. Future analyses will be performed to assess the chemical interaction between these components.

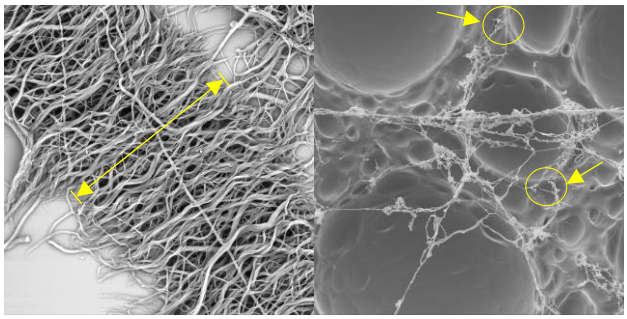


(a)



(b)

Fig. 1: (a) Aligned fiber mesh showed an anisotropic morphology. Yellow arrows show lateral connection fiber filaments. Scale bar= 30 µm. (b) Directionality distribution. A sharp and narrow histogram around 90 ° demonstrates the high percentage of electrospun-aligned fibers.



(a) (b)

Fig. 2: (a) DFs suspended in solution, dried, and observed by SEM on a slide. The yellow line indicates the measured microscale dimension. Scale bar= 20 μm. (b) DFs within the GelMA matrix act as web structures. Yellow arrows indicate the adhesion point between the matrix and DFs. Scale bar= 20 μ*m*.

B. Injectability

For 20 and 25 °C, the DF-free GelMA solution was not injectable with the selected needle sizes due to the proximity of the sol-gel transition temperature ($T_g \approx 20$ °C, data not shown). Therefore, the GelMA+DFs solution was not tested at 20 and 25 °C. At 30 and 37° C, both DFs-free GelMA and GelMA+DFs were injectable and the injection force profiles were lower than the upper limit value of 10 N [17] with smooth profiles and well-defined plateau regions for 18G and 20G needles (Fig. 3a-c). The plateau region indicated a homogeneous and continuous extrusion of the material. The lowest injection force value (F = 2.3 ± 0.4 N) was found at 37°C using an 18G needle for DFs-free GelMA solution (Fig. 3c, red line). The presence of DFs did not significantly affect the injectability at 30°C by using both the 18G and the 20G needles and at 37°C with the 18G needle (Fig. 3b). However, using a 20G needle at 37 °C, the maximum peak force was higher (F = 5.6 ± 0.4 N) compared to the bare GelMA (Fig. 3d).

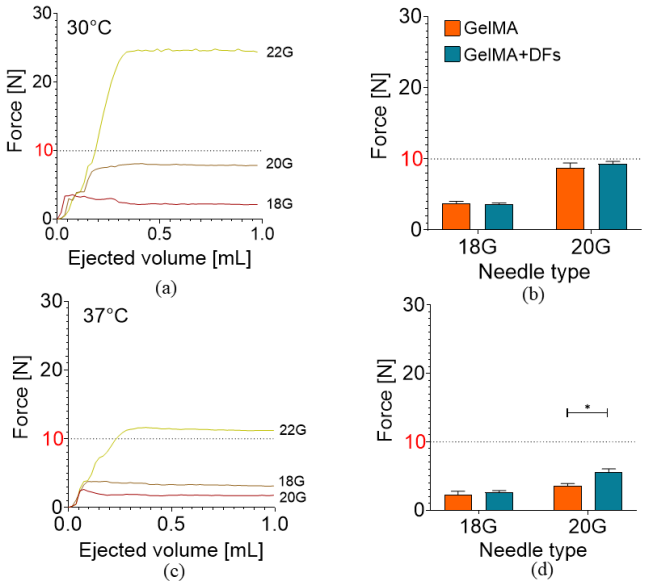


Fig. 3: (a) Representative force profiles showed by DFs-free GelMA and GelMA+DFs solutions at 30°C. (b) Maximum peak force of GelMA and GelMA+DFs for 18G and 20G at 30 °C. (c) Representative force profiles showed by DFs-free GelMA and GelMA+DFs solutions at 37 °C. (d) Maximum peak force of GelMA and GelMA+DFs for 18G and 20G at 37 °C. (*p< 0.05).

The results obtained at different test temperatures suggest that 30°C represents the minimum suitable temperature to inject both DFs-free GelMA and GelMA+DFs solutions homogeneously (reaching a well-defined plateau zone), while keeping the force needed below the threshold value (F<10N). A focus was placed on understanding the best temperature and parameters configuration to inject the formulation. For a GelMA solution concentration such as ours and equal to 10 % (w/v), to the best of our knowledge, a study for chondral and osteochondral applications has never been carried out to determine configuration in terms of parameters and temperatures of injectability.

C. Mechanical characterization

The mechanical characterization results (Table II) show that the composite GelMA+DFs achieved a higher maximum stress value and compressive modulus (150 and 75 kPa, respectively), increasing the values by 100% compared to DF-free GelMA. The composite formulation exhibited an increase in the maximum deformation (corresponding to the one at break) and toughness as well (Fig. 4a). The DFs acted within the GelMA matrix as reinforcing fillers. This feature can be related to the intrinsic characteristic of PCL in addition to the random distribution DFs, which might bear part of the load, guaranteeing a strengthening of the GelMA+DFs composite. Compared to one of the most similar casted GelMA scaffold (degree of functionalization ≈ 60%, 10 % w/v polymer concentration, photoinitiator concentration= 0,5 %, $D = 10$ mm, thickness = 1 mm, UV irradiation time= 60 s [10]), fabricated for bone tissue engineering, which was shown compressive modulus values around 10 kPa [10], the proposed GelMA+DFs composite showed higher compressive mechanical properties.

Compared to other works in which a dispersed PCL-based fiber filler was used for not bearing application [22]-[24], our work focused on exploiting the dispersed fibers to increase the mechanical properties of a GelMA+DFs injectable composite, with the aim to be used for load-bearing applications (e.g. OC).

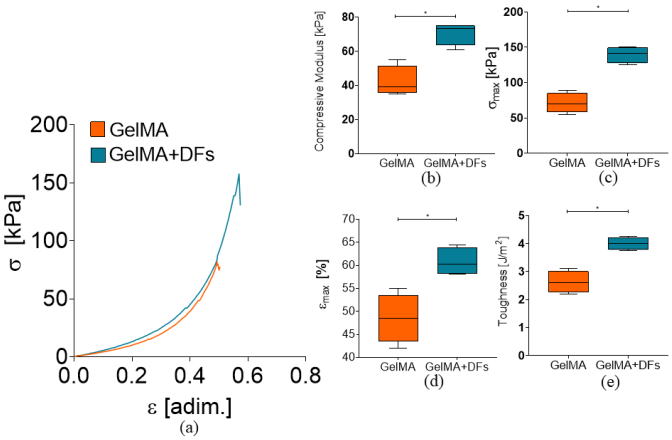


Fig. 4: Mechanical parameters. (a) Stress-strain curves. (b) Compressive modulus. (c) Maximum stress. (d) Maximum deformation. (e) Toughness. (*p<0.05).

TABLE II: MECHANICAL PARAMETERS

Parameter	*DFs-free GelMA*		*GelMA+DFs*	
Compressive Modulus	42 ± 8.9	kPa	70.8 ± 5.8	kPa
Maximum stress	71 ± 14	kPa	139.3 ± 10	kPa
Maximum deformation	48.5 ± 5.3	%	60.8 ± 2.6	%
Toughness	2.63 ± 0.39	J/m^2	4 ± 0.19	J/m^2

IV. CONCLUSIONS

In this study, we propose a composite formulation with enhanced mechanical properties, as injectable material cross-linkable *in situ*, for the potential treatment of OC injuries. A cryostat-based cutting technique was applied to obtain DFs from electrospun-aligned meshes. GelMA and GelMA+DFs were injectable using a force lower than 10 N at 30 and 37 °C, using 18 and 20G needles. The mechanical compression performance for the composite GelMA+DFs increased, supporting the hypothesis that a dispersed fiber-based filler can enhance the mechanical properties of the GelMA matrix.

A relevant aspect of our GelMA+DFs formulation lies in its possible usage with a minimally invasive approach, exploiting an *in-situ* cross-linkable natural-based GelMA material, which, compared to many other natural hydrogels proposed for this type of application, although not designed as injectables, has comparable if not superior mechanical properties.

In future work, a broader range of DFs concentrations will be investigated to find the concentration that guarantees optimal mechanical performance while still ensuring injectability below the imposed force limit. The use of such dispersed fibers might be further engineered to enable their controllable orientation once embedded. This strategy might lead to a biomimicking process in which the DFs would mimic the fibrous structures of collagen arranged in different ways in the layered natural tissue, giving different levels of anisotropy to the different composite layers.

ACKNOWLEDGMENT

This study received funding from the European Union's Horizon20 20 research and innovation program, grant agreement Nº 814413, project ADMAIORA (ADvanced nanocomposite MAterIals fOr in situ treatment and ultRAsound-mediated management of osteoarthritis).

REFERENCES

[1] Ali Mobasheri and Mark Batt, *"An update on the pathophysiology of osteoarthritis.Annals of Physical and Rehabilitation Medicine"*, 59, 2016.

[2] DI Chen, *"Osteoarthritis: toward a comprehensive understanding of pathologyical mechanism".* Bone research, 5, 2017.

[3] Matthew Howell, *"Surgical management of osteochondral defects of the knee: an educational review".* Current Reviews in Musculoskeletal Medicine, 14, 2021.

[4] Chengchong Ai, *"Osteochondral tissue engineering: Perspectives for clinical application and preclinical development".* Journal of Orthopaedic Translation, 2021.

[5] Salter, *"Differential responses of chondrocytes from normal and osteoarthritic human articular cartilage to mechanical stimulation."* Biorheology, 2002.

[6] Ravalli Silvia, *"New insights on mechanical stimulation of mesenchymal stem cells for cartilage regeneration."* Applied Sciences, 2020.

[7] Engler, *"Matrix elasticity directs stem cell lineage specification."* Cell, *2006.*

[8] Jingyi Liu, *"3D printing of biomimetic multi-layered GelMA/nHA scaffold for osteochondral defect repair".* Materials & Design, 2019.

[9] Yu, *"Implementation of Photosensitive, Injectable, Interpenetrating, and Kartogenin-Modified GELMA/PEDGA Biomimetic Scaffolds to Restore Cartilage Integrity in a Full-Thickness Osteochondral Defect Model."* ACS Biomaterials Science & Engineering, 2022.

[10] Celikkin, *"Gelatin methacrylate scaffold for bone tissue engineering: the influence of polymer concentration."* Journal of Biomedical Materials Research Part A106, 2018.

[11] Tzu-Hsiang Lin, *"A bilineage thermosensitive hydrogel system for stimulation of mesenchymal stem cell differentiation and enhancement of osteochondral regeneration".* Composites Part B: Engineering, 2022.

[12] Hairui Suo, *"Interpenetrating polymer network hydrogels composed of chitosan and photocrosslinkable gelatin with enhanced mechanical properties for tissue engineering"*. Materials Science and Engineering: C, 2018.

[13] Xiangbo Zhu, *"Biomimetic bacterial cellulose- enhanced double-network hydrogel with excellent mechanical properties applied for the osteochondral defect repair".* ACS Biomaterials Science & Engineering, 4,2018.

[14] Bin Wang, *"Affinity-bound growth factor within sulfated interpenetrating network bioinks for bioprinting cartilaginous tissues".* Acta Biomaterialia, 2021.

[15] Ziyuan Fang,*"Injectable and biodegradable double-network nanocomposite hydrogel with regulable sol-gel transition process and mechanical properties"*. Polymer Testing, 2022.

[16] MariaChiara Ullo, "*Master thesis in Biomedical Engineering"*, Politecnico di Milano, 2020-21.

[17] Mazzocchi, Tommaso, *"A Novel Approach for Multiple Material Extrusion in Arthroscopic Knee Surgery."* Annals of Biomedical Engineering, 2022.

[18] Testa, *"Intra-articular injections in knee osteoarthritis: A review of literature."* Journal of functional morphology and kinesiology 6, 2021.

[19] Ricotti Leonardo, *"Ultrasound stimulation of piezoelectric nanocomposite hydrogels boosts cartilage regeneration."* . 2022.

[20] Tschaikowsky, *"The articular cartilage surface is impaired by a loss of thick collagen fibers and formation of type I collagen in early osteoarthritis."* Acta Biomaterialia, 2022.

[21] Zhong, *"Surface Modification of Nanofibers by Physical Adsorption of Fiber-Homologous Amphiphilic Copolymers and Nanofiber-Reinforced Hydrogels with Excellent Tissue Adhesion.",* ACS Biomaterials Science & Engineering7., 2021.

[22] Paria Ghaderine, "*An injectable anisotropic alginate hydrogel containing oriented fibers for nerve tissue engineering"*. Chemical Engineering Journal, 2021.

[23] Abdolrahman Omidinia-Anarkoli,*"An injectable hybrid hydrogel with oriented short fibers induces unidirectional growth of functional nerve cells"*. Small, 13, 2017.

[24] Li, *"A nanofiber-hydrogel composite improves tissue repair in a rat model of Crohn's disease perianal fistulas." Science Advances* 9. 2023.

Green-Based Anti-Biofilm Nanoformulations Against Bacterial Contaminations In Nosocomial Environments

Giovanni Lo Bello[1], Roberto Raiteri[1], Elena Dellacasa[1], Maria Luisa Cristina[2] Orietta Monticelli[3], Pastorino Laura[1]

[1]*Department of Informatics, Bioengineering, Robotics, and System Engineering, University of Genova, via Opera Pia 13*
[2]*Department of Health Science, University of Genova, via Pastore 1*
[3] *Department of Chemistry and Industrial Chemistry, University of Genova, via Dodecaneso 31*

Abstract— Nosocomial infections or healthcare associated infections (HAIs) refer to a set of infectious diseases acquired in a health facility. These infections are mainly due to the spread of a pathogen agent into a vulnerable host and pose an important cause of mortality, morbidity, prolonged hospitalization, and increased treatments with antimicrobial agents. Among the pathogens involved in HAIs, it has been observed that bacteria can adhere to surfaces and aggregate, forming a complex structure, called biofilm, which makes them much less sensitive to external agents. This structure mainly consists in extracellular polymeric substances (EPS) composed of water, proteins, nucleic acids, and provides a fully secured and functional environment for the formation of microcolonies, their sustenance and recolonization of sessile cells after its dispersal. From this scenario, the urgent need to explore innovative strategies for the treatment of biofilm infections arises. The goal of this work is to develop a multitarget nano-platform capable of degrading bacterial biofilm and killing dispersed cells to reduce diverse types of infection, allowing safer treatment paths. More in details, modified PCL-based nanoparticles have been prepared and conjugated to bioactive molecules having antibiofilm activity and deeply characterized by Dynamic Light Scattering (DLS), Zeta potential (ZP), and Atomic Force Microscopy (AFM), showing a good stability over time with a mean diameter of 200 nm, that increases to 800 nm after enzyme conjugation. The effectiveness of this nano-formulation can be investigated by AFM, monitoring, at the nanoscale, the morphology, and the Young Modulus of *Staphylococcus aureus* biofilms before and after treatment.

Keywords— **Nosocomial infections, *Staphylococcus aureus*, Antimicrobial Resistance, Biofilm formation, Atomic Force Microscopy, Nanoformulation.**

I. Introduction

Nosocomial infections or HAIs are the most common adverse event in health care that affects patient safety. HAIs affect 3.2% of all hospitalized patients in the United States, 6.5% in the European Union/European Economic Area, and worldwide prevalence is likely much higher [1]. It has been shown that over the next 30 years, infections related to antimicrobial-resistant microorganisms could cost up to US$ 3.5 billion annually [2]. These infections can be caused by the presence of viruses, fungi, and bacteria on both biotic and abiotic surfaces. Although pathogen transfer from a colonized or infected patient to a susceptible patient most commonly occurs via the hands of healthcare personnel, contaminated hospital surfaces and medical equipment can be directly or indirectly involved in the transmission pathways [3]. As a relevant example, methicillin-resistant *Staphylococcus aureus* (MRSA) strains are one of the best known at the global level. *Staphylococcus aureus* is an opportunistic, gram-positive, nosocomial bacterium causing different infectious diseases. When considering *S. aureus*, drugs are increasingly becoming partially or fully inactive due to the presence of a biofilm surrounding the bacterial cells [4]. Such biofilm is impenetrable by the drug and therefore, the concentration of antibiotics needed to eradicate the bacteria in the biofilm is up to 1000-fold higher than the concentration needed to kill planktonic cells [5]. Nowadays, antibiofilm strategies are mainly of two types:

- Inhibition or prevention of new biofilm formation, using material and coatings that exhibit chemical or structural antibacterial properties [6], [7].
- Dispersal or eradication of existing biofilms, i.e. treatments such as heat, cleaning regimens, low-power laser, sonication, and chemical treatments, also through the use of vectors that allow the transport of bioactive molecules within the biofilm [8], [9].

Traditional approaches that aim to eradicate bacterial biofilms include antibiotics treatments and antifouling agents. However, the therapeutic effect of antibiotics strongly depends on their concentration. Moreover, antibiotics need to penetrate the bacterial membrane and accumulate until a sufficient therapeutic concentration is reached. This process can also be dependent on bacterial structure [10]. It has been shown that bacterial biofilms show more tolerance than bacteria in planktonic form to antibiotics treatments, because cells enter dormancy [11]. Nevertheless, recent studies show that biofilm-associated *S. aureus* cells can have different metabolic states: they can be growing aerobically, be fermentative, dormant, or dead [12]. Treatment of *S. aureus* biofilm infections is further complicated by the existence of different phenotypes of clinical MRSA and MSSA strains, resulting in mixed-strain biofilms. For these reasons, research has been focused on the use of nanoformulations, including polymeric and metallic nanoparticles, capable of hindering the formation of the biofilm, thus reducing bacterial activity, and improving the bioavailability and targeted delivery of antibiotics/drugs. Having a high surface-to-volume ratio, these nanoformulations can be loaded with a high amount of antimicrobials, increasing the stability and avoiding burst release associated problems. Moreover, it has been shown that the effectiveness of the antibacterial treatment depends on both

the shape and size of the NPs. As the size decreases, the penetration inside the bacterial membrane becomes easier, increasing the effectiveness of the treatment [13]. It has also been observed that the bare application of nanoparticles does not allow to obtain effective results, precisely due to the presence of the biofilm. For this reason, many studies aimed at the decoration of nanoparticles with bioactive molecules to confer them antibiofilm activity [14]. Numerous biodegradable polymers such as polycaprolactone (PCL), polylactic acid (PLA), polyglycolic acid (PGA), and polylactide-coglycolide (PLGA) are being used to formulate biocompatible nano/microparticles as carriers of bioactive molecules [15], [16]. From this scenario, it is evident that there is an urgent need to explore innovative strategies for the treatment of biofilm infections [11]. This work focuses on the limitation of the transmission of nosocomial infections by setting up efficient and totally green strategies for surfaces disinfection, to be safely used in different environment. PCL, chemically modified with the addition of carboxylic groups was used. Thanks to this modification, the polymer chain assumes a star shape, increasing the surface/volume ratio of the nanoparticles, and favoring the covalent coupling with the selected enzyme thank to the carboxylic groups' enrichment. Specifically, the selected bioactive component is the Alpha amylase enzyme, capable to hydrolyze α (1,4) glycosidic linkages of the polysaccharidic part of *S. aureus* extracellular matrix, exhibiting dispersal of mature biofilms and showing the capability to prevent and disrupt biofilm formation at nanomolar concentrations when added exogenously in solution [11]. The enzyme can be conjugated to biocompatible and biodegradable polymeric nanoparticles that confer increased stability and bioavailability [4].

II. METHODS

Nanoparticles were prepared by "nanoprecipitation method" [17]. Briefly, 2% Poly viny alcohol (PVA) was dissolved in pure water, stirred at 50°C for 2h, then 1h at room temperature and filtered. Then, 5 mg/mL of modified PCL solution in acetone was added dropwise, using a syringe pump, in an equal volume of PVA solution, and kept under stirring at 650 rpm for 2h. Finally, after organic solvent evaporation, pure water was poured into the so formed NPs dispersion, to restabilize the initial PCL concentration, and kept under stirring at 250 rpm overnight for their stabilization. The next day, the nanoparticle dispersion was first centrifuged at 1500 rpm at 4°C for 20 min to allow eventual micrometric aggregates to precipitates. Then, two final washings at 11000 rpm for 20 min were carried out to remove any solvent residues. After washings, nanoparticles were stored at 4°C for subsequent analysis.

An accurate morphological characterization of PCL NPs before and after enzyme conjugation was carried out. The size distributions of nanoparticles and the surface potential of plain and functionalized nanoparticles were measured by DLS and Zeta Potential with a Zetasizer Nano ZS (Malvern Instruments, Worcestershire, U.K). AFM topography images were obtained using a Nanowizard JPK Bio-AFM (Bruker) and a Zeiss optical microscope (Axio Zoom V16). MSCT-AUHW cantilevers, with a nominal spring constant K=0,159 N/m, was used for acquisitions.

III. RESULTS

AFM characterization on PCL NPs was carried out by letting them precipitate and adsorb on a functionalized mica surface. Single nanoparticles with diameters between 70 and 150 nm were found, along with large aggregates.

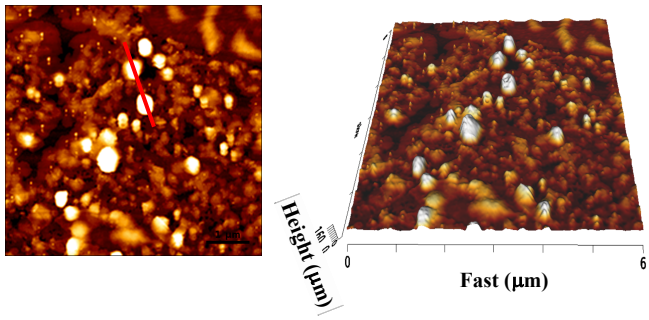


Figure 1: AFM images of PCL NPs and 3D overview. Samples from three different production batch processes were analyzed in Quantitative Imaging mode (QI) with a MSCT-AUGH tip (spring constant k = 0.159 N/m), set-point of 0.7 nN.

Fig. 1 shows the synthesized PCL NPs with spherical shape, and some material in the background. This could be due to PVA residues or non-reacted PCL.

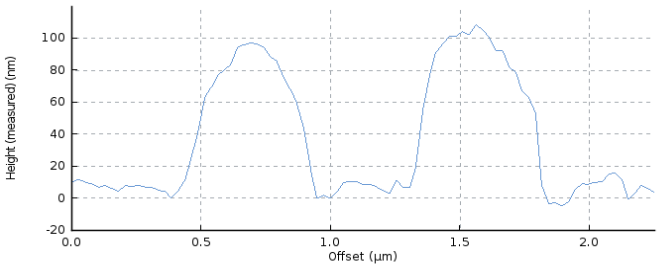


Figure 2: Cross-section of PCL NPs (red line in Fig.2).

In Fig. 2 a cross section of two NPs (corresponding to the red line in Fig.1) is represented. It is important to point out that topography obtained by AFM can affected by artifacts arising from the convolution of sample topography with the tip shape that limit the lateral resolution that can be achieved [18].

Table I reports the results obtained by DLS and ZP analyses. Plain PCL nanoparticles diameter was found to be around 230 nm, with a polydispersity index (PDI) of 0.16 which confirms the presence of a narrow distribution. The same analysis was repeated after 1 month of storage and no significant differences were found.

	DLS (nm) ± st. dev.	**ZP (mV) ± st. dev.**	**PDI**
PCL NPs	235.6 ± 76.71	-41.6 ± 7.67	0.16
PCL NPs + E	807.2 ± 137.7	-23.5 ± 4.55	0.25

Table I: DLS and ZP results.

The average of functionalized NPs diameter increased to a value of about 800 nm, with a PDI of 0.25. Trying to give an explanation to these results, ZP analysis was performed.

PCL NPs also showed differences in ZP values before and after the conjugation with the enzyme, with a mean of -41.6 ± 7.67 mV and -23.5 ± 4.55 mV respectively. This parameter shows the degree of repulsion between the charged particles in a suspension. A Zeta Potential value greater than −30 mV to +30 mV is considered to have enough repulsive force to attain better physical colloidal stability. On the other hand, a small zeta potential value can result in particle aggregation due to the van der Waals attractive forces. Overall, it can be assumed that the synthesized NPs are sufficiently charged to generate repulsive forces, and this explain the absence of aggregation phenomena. After the conjugation process, ZP value decreased, resulting in an increase in the mean particle size. Furthermore, it should be noticed that the differences in diameter obtained using DLS and AFM can be ascribed to the fact that AFM measures the physical height of the sample spread on a substrate, while DLS reports its hydrodynamic diameter.

For characterization of S. aureus biofilm, bacteria were cultured in a petri dish for 24h. Fig. 3 shows a high-resolution image of a community of bacterial cells, with the typical spherical shape and a mean diameter of about 0.8 µm. As can be seen from images, some of them have a smooth and clean surface, while others were embedded within the EPS, displaying the non-homogeneity of biofilm structures.

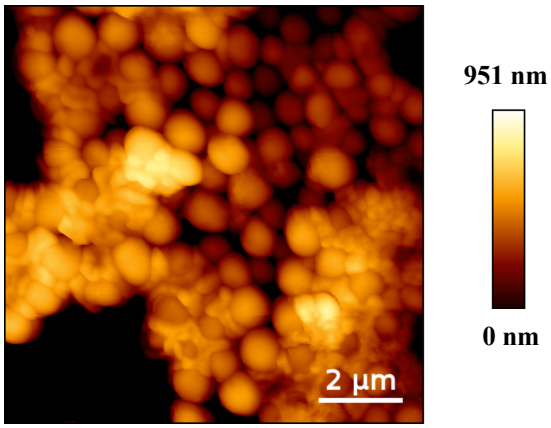


Figure 3: AFM image of *S. aureus* 24h biofilm.

The height of the biofilm was also evaluated and confirmed the observed heterogeneity, showing an irregular height ranging from few nm to 1-2 µm.

Finally, in Fig. 4 is shown an optical characterization of a 24h *S. aureus* biofilm before and after treatment with PCL NPs + E for 2.5h. After several washes it has been notice a huge reduction of the biomass.

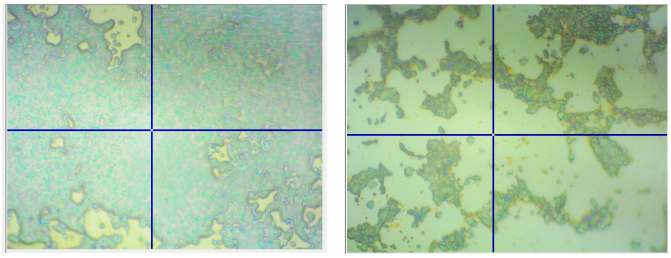


Figure 4: optical characterization of 24h *S. aureus* biofilm before (left) and after (right) treatments with PCL NPs for 2.5h.

This is only a preliminary result that shows the effectiveness of these treatments. It should be considered that the bacterial residues that has been removed are still virulent so they should be killed using some antimicrobial, to avoid the spread of these pathogens.

IV. Conclusion

We have shown the successful synthesis and characterization of a novel anti-biofilm formulation. This nano-platform has displayed a narrow size distribution and good stability over time, together with high retention of enzyme. AFM characterization on *S. aureus* biofilms was also performed. This technique has proven to be a powerful tool for investigating the antibacterial effects. AFM not only allows high-resolution images under ambient air or fluid conditions, but it can also probe the nanomechanical characteristics. The mechanical properties of bacterial cells play an important role in crucial bacterial processes such as cell growth, colonization, and biofilm formation. For these reasons, AFM will be used to calculate the Young Modulus of *S. aureus* biofilm before and after treatment with the nanoformulation observing, characterizing, and understanding the behavior of live bacterial cells as never before.

The main innovation of the proposed strategy, when compared to the state of the art, resides in the mutual action of biofilm-degrading enzymes with plant extracts having antibacterial activity. Once the biofilm has been dissolved, the use of antibacterial plant extracts together with the nanoparticles should allow the elimination of the exposed planktonic cells. The developed formulation is highly promising for removing bacterial biofilms in healthcare facilities, medical devices, and, ultimately, even for fighting infections in patients. The success of this project would pave the way for the search of new innovative strategies useful for reducing contamination and therefore nosocomial infections, making the treatment path safer and, above all, saving time, money, and, possibly, lives. Interestingly, this platform could be also in other scenarios where biofilms are associated with microbial fouling and corrosion, such as in terrestrial water-distribution systems and extended spaceflight missions [19].

References

[1] "Sikora A, Zahra F. Nosocomial Infections. [Updated 2022 Jul 4]. In: StatPearls [Internet]. Treasure Island (FL): StatPearls Publishing; 2022 Jan-. Available from: https://www.ncbi.nlm.nih.gov/books/NBK559312/?report=classic, " p. 559312, 2022.

[2] B. P. Singh, S. Ghosh, and A. Chauhan, "Development, dynamics and control of antimicrobial-resistant bacterial biofilms: a review," *Environmental Chemistry Letters*, vol. 19, no. 3. Springer Science and Business Media Deutschland GmbH, pp. 1983–1993, Jun. 01, 2021. doi: 10.1007/s10311-020-01169-5.

[3] D. J. Weber, D. Anderson, and W. A. Rutala, "The role of the surface environment in healthcare-associated infections," *Curr Opin Infect Dis*, vol. 26, no. 4, pp. 338–344, 2013, doi: 10.1097/QCO.0b013e3283630f04.

[4] R. Patel, "Biofilms and antimicrobial resistance," *Clin Orthop Relat Res*, vol. 437, no. 437, pp. 41–47, 2005, doi: 10.1097/01.blo.0000175714.68624.74.

[5] C. W. Hall and T. F. Mah, "Molecular mechanisms of biofilm-based antibiotic resistance and tolerance in pathogenic bacteria,"

FEMS Microbiol Rev, vol. 41, no. 3, pp. 276–301, 2017, doi: 10.1093/femsre/fux010.

[6] L. Cegelski *et al.*, "Small-molecule inhibitors target Escherichia coli amyloid biogenesis and biofilm formation," *Nat Chem Biol*, vol. 5, no. 12, pp. 913–919, 2009, doi: 10.1038/nchembio.242.

[7] R. P. Carlson, R. Taffs, W. M. Davison, and P. S. Stewart, "Anti-biofilm properties of chitosan-coated surfaces," *J Biomater Sci Polym Ed*, vol. 19, no. 8, pp. 1035–1046, 2008, doi: 10.1163/156856208784909372.

[8] A. Gupta *et al.*, "Engineered Polymer Nanoparticles with Unprecedented Antimicrobial Efficacy and Therapeutic Indices against Multidrug-Resistant Bacteria and Biofilms," *J Am Chem Soc*, vol. 140, no. 38, pp. 12137–12143, 2018, doi: 10.1021/jacs.8b06961.

[9] K. Rupel *et al.*, "Blue laser light inhibits biofilm formation in vitro and in vivo by inducing oxidative stress," *NPJ Biofilms Microbiomes*, vol. 5, no. 1, pp. 1–11, 2019, doi: 10.1038/s41522-019-0102-9.

[10] C. Han, N. Romero, S. Fischer, J. Dookran, A. Berger, and A. L. Doiron, "Recent developments in the use of nanoparticles for treatment of biofilms," *Nanotechnol Rev*, vol. 6, no. 5, pp. 383–404, 2017, doi: 10.1515/ntrev-2016-0054.

[11] Y. Hu *et al.*, "Biofilm microenvironment-responsive nanoparticles for the treatment of bacterial infection," *Nano Today*, vol. 46, p. 101602, 2022, doi: 10.1016/j.nantod.2022.101602.

[12] M. Idrees, S. Sawant, N. Karodia, and A. Rahman, "Staphylococcus aureus biofilm: Morphology, genetics, pathogenesis and treatment strategies," *Int J Environ Res Public Health*, vol. 18, no. 14, 2021, doi: 10.3390/ijerph18147602.

[13] C. N. Lok *et al.*, "Proteomic analysis of the mode of antibacterial action of silver nanoparticles," *J Proteome Res*, vol. 5, no. 4, pp. 916–924, 2006, doi: 10.1021/pr0504079.

[14] A. Taraszkiewicz, G. Fila, M. Grinholc, and J. Nakonieczna, "Innovative strategies to overcome biofilm resistance," *Biomed Res Int*, vol. 2013, 2013, doi: 10.1155/2013/150653.

[15] 2 Aleksandra Zieli ´nska 1 *et al.*, "Polymeric Nanoparticles: Production, Characterization, Toxicology and Ecotoxicology," *Molecules*, vol. 25, p. 3731, 2020.

[16] K. Divya, S. Vijayan, T. K. George, and M. S. Jisha, "Antimicrobial properties of chitosan nanoparticles: Mode of action and factors affecting activity," *Fibers and Polymers*, vol. 18, no. 2, pp. 221–230, Feb. 2017, doi: 10.1007/s12221-017-6690-1.

[17] H. Fessi, F. Puisieux, J. P. Devissaguet, N. Ammoury, and S. Benita, "Rapid Communication Nanocapsule formation by interfacial polymer deposition following solvent displacement," 1989.

[18] J. Canet-Ferrer, E. Coronado, A. Forment-Aliaga, and E. Pinilla-Cienfuegos, "Correction of the tip convolution effects in the imaging of nanostructures studied through scanning force microscopy," *Nanotechnology*, vol. 25, no. 39, Oct. 2014, doi: 10.1088/0957-4484/25/39/395703.

[19] L. Zea *et al.*, "Potential biofilm control strategies for extended spaceflight missions," *Biofilm*, vol. 2, no. January, 2020, doi: 10.1016/j.bioflm.2020.100026.

Near Field Electrospinning Process Using a Multi-Axis Robot

S. D'Alessandro[1,2], A. Pica[1], F. Marinozzi[1,2], F. Bini[1,2], and G. Cidonio[2]
[1] *Department of Mechanical and Aerospace Engineering (DIMA), University of Rome "La Sapienza", 00184 Rome, Italy*
[2] *3D Microfluidic Biofabrication laboratory, Center for Life Nano- & Neuro- Science – CLN2S, Italian Institute of Technology (IIT), 00161 Rome, Italy*

***Abstract*— Clinical treatments for osteochondral defects (OCD) are only palliative, therefore the development of novel tissue engineering (TE) approaches for the active repair of damaged cartilage-bone interfaces is of utmost importance. To date, the morphological and functional renewal of OCD remains an unsolved clinical challenge. Conventional 2D and 3D morphology of TE scaffolds is not yet able to reproduce the complex tissue architecture. Here, we aim to explore a novel surface technology tailored to the OCD patient, using a robotic 3D electrospinning platform (3DES) to design ad-hoc woven scaffolds that correspond to the diseased tissue surfaces.**

***Keywords*— electrospinning, cartilage, bone, resurfacing.**

I. Introduction

Skeletal pathological conditions such as cancer and osteoarthritis, directly drive the degeneration of the boundary interlayered cartilage and bone substrates leading to extensive and incurable osteochondral defects (OCD) [1]. Variations in the morphology of the joint are correlated with the localization of OCDs and develop a complex cascade of degenerative processes that lead to the impairment of the joint functionality [2, 3]. Due to the poor regenerative capacity of cartilage and subchondral bone, the current clinical treatments of OCD are only palliative effective, reducing pain and improving joint function, but failing to achieve complete repair of osteochondral (OC) lesions and reconstruction of the joint functions [4]. Thus, the development of novel tissue engineering (TE) approaches for the active resurfacing of damaged cartilage-bone interfaces is of pivotal clinical importance [5]. To date, the morphological and functional resurfacing of OCD remains an unsolved clinical challenge. The reproduction of the native anatomic morphology is mandatory to distribute and balance the load during joint movement, playing a vital role in the maintenance of cartilage function [6]. The conventional 2D and 3D structure of TE scaffolds is not yet able to reproduce the complex morphology of the tissue [7]. Here, we aim to investigate a novel OCD patient-specific resurfacing technology, harnessing a novel 3D near field electrospinning (3DES) platform robotic-guided platform, designing ad-hoc woven scaffolds to match diseased tissue surfaces. We replaced the cartesian printer configuration with a five-axis robotic arm using a non-planar surface as a fibre collector, as shown here by using a spherical collector. Additionally, we deposit the spun fibres on a spherical and irregular support, which is placed among the spinneret and the spherical collector. The combination of these techniques allows us to use the near field electrospinning (NFES) more broadly in tissue engineering where the geometric shapes of scaffold need to be expanded.

II. Materials and Methods

A custom-made robotic arm with five degrees of freedom (DOF) is used as a 3D guiding tool for the electrospinning (ES)process to fabricate woven scaffolds on complex surfaces. The ES spinneret is fixed on the appendices of the computer-aided arm and guided over a spherical collector to deposit polycaprolactone (PCL) polymeric solution, as shown in Figure 1. The trajectory is calculated with the Robotics System Toolbox of MATLAB code, while the arm movements are controlled with a custom-made LabView script. Specifically, we optimize the experimental setup and the arm trajectory with a fine negative feedback control, to increase the capacity of the system to reproduce the irregularities and to create scaffold with comparable compositional, structural, and functional characteristics of the extracellular matrix (ECM).



Figure 1. Schematic diagram of the new ES setup, where the ES spinneret is fixed on the robotic arm end-effector and the traditional planar collector is replaced with a fiber spherical collector.

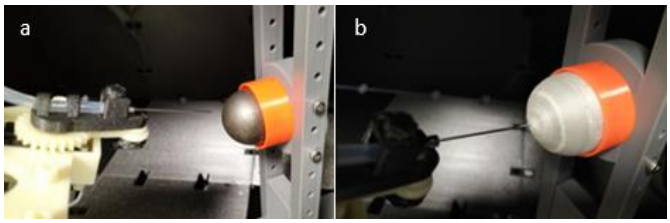


Figure 2. (a) Electrospinning setup; (b) Jet initiation phase with a spherical support fiber collector in PVA.

Figure 2a shows the ultimate setup where the collector distance of 5 mm was selected and maintained throughout. The PCL filaments were cut into short segments of ≃3 mm and solubilized in dichloromethane (DCM). The solution was used immediately after 4h of mixing. The experiments were performed at 20-40% relative humidity and at an ambient temperature of 18-19 °C. Figure 2b shows the electrospinning process of the above solution on the spherical support collector in polyvinyl alcohol (PVA). During this phase, the trajectory of the nozzle describes concentric circles while end-effector speed is kept constant during the toolpath. The PCL spun fibers were deposited on a shell support 3D printed with water-soluble polymer filament, PVA. After the deposition, the scaffold can be retrieved removing the soluble support in a

water batch. Then, spun solution was deposited on a PVA support to mimic the irregular surface of the native tissue morphology (Figure 3). The PVA supporting structure was fabricated starting from CT scan of anatomical districts (e.g., humerus epiphysis) precisely patterning PCL fibers onto a 3D collector.

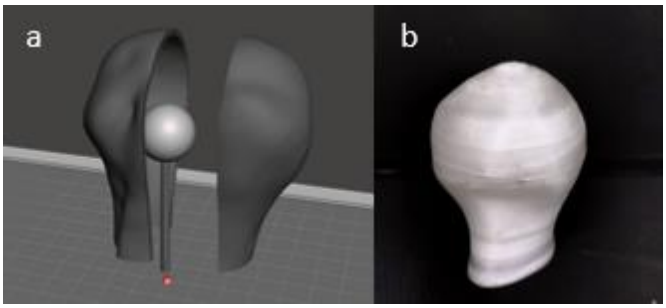


Figure 3. (a) Stl file of the shell support obtained from CT scan of humerus epiphysis; (b) Shell support 3D printed with PVA.

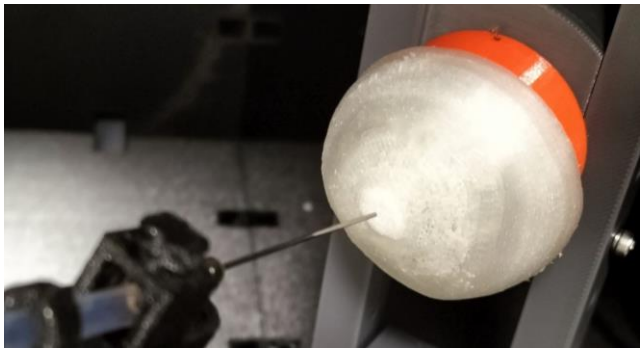


Figure 4. Jet initiation phase with an irregular support fiber collector in PVA reproducing the anatomic morphology

The PVA anatomical supporting structure was used to deposit the PCL fiber. The nozzle's trajectory follows the irregular shape of the support, and the end-effector's velocity is constant during the toolpath.

III. Results and discussion

PCL were dissolved in DMC and spun using a custom-made electrospinning apparatus. The robotically guided spinning was carried out using a custom Matlab-LabView code for precise positioning. A number of optical sensors were housed close to the spinneret to monitor the relative positioning and loop effective feedback information directly to the arm motors. The 3DES platform was optimised to reach high precision in spinning deposition. Firstly, the velocity of the nozzle along the tool path was adjusted and monitored. Particularly, the smaller portion of printed semi-sphere was found to be exposed to an over-deposition of the 3DES. This was accounted and accordingly adjusted to reach a seamless and even surface deposition in three dimensions.
Secondly, the velocity of the end-effector was found insufficient to stretch the fibers and deposit straight fibers to create aligned fibers. This issue was solved by up-scaling the hardware and software support, improving a greater ultimate higher accuracy.

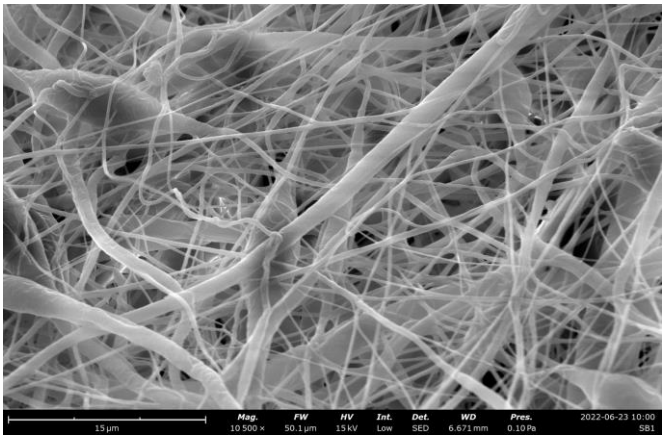


Figure 5. Scanning electron microscopy (SEM) of random fibres of 3D electrospun scaffold (scale bar 15 µm).

Figure 5 shows a scanning by SEM of random fibres deposited by 3DES, demonstrating therefore the ability of the 3D electrospinning to re-surface humerus and femur epiphysis, both of standard models and patient specific defects reconstructions. PVA water-soluble supports were found suitable to temporarily aid the fibres deposition.

IV. Conclusion

The resurfacing of OCDs is an attractive clinically relevant approach for the rapid functionalisation of skeletal defects. However, current clinical treatments are still ineffective, thus posing an urgent need for novel approaches for the resurfacing of OCD. We have reported the use of a novel custom-made robotic arm equipped with a 3D electrospinning apparatus, capable of functionalising patient-specific surfaces. In future, we will attempt to increase the efficiency and accuracy of our custom-made experimental setup to reach higher mechanical performance and improve the deposition accuracy and diameter control of the spun fibres. Then, we will validate the ability of PCL material and nanoclay-enhanced composites to retain growth factors (GFs) of interest at the site of injury, using different macromolecules to test this behaviour.

Acknowledgement

The authors have no conflicts of interest to declare. GC acknowledge funding from AIRC Aldi Fellowship under grant agreement No. 25412.

References

[1] S.-S. Seo, C.-W. Kim, and D.-W. Jung, "Management of Focal Chondral Lesion in the Knee Joint," *Knee Surg. Relat. Res.*, vol. 23, no. 4, pp. 185–196, 2011, doi: 10.5792/ksrr.2011.23.4.185.

[2] E. B. Hunziker, K. Lippuner, M. J. B. Keel, and N. Shintani, "An educational review of cartilage repair: Precepts & practice - myths & misconceptions - progress & prospects," *Osteoarthr. Cartil.*, vol. 23, no. 3, pp. 334–350, 2015, doi: 10.1016/j.joca.2014.12.011.

[3] F. Bini, A. Pica, A. Marinozzi, and F. Marinozzi, *Prediction of stress and strain patterns from load rearrangement in human osteoarthritic femur head: Finite element study with the integration of muscular forces and friction contact*, vol. 999. 2019. doi: 10.1007/978-3-030-23073-9_4.

[4] B. J. Erickson, P. N. Chalmers, A. B. Yanke, and B. J. Cole, "Surgical management of osteochondritis dissecans of the knee," *Curr. Rev. Musculoskelet. Med.*, vol. 6, no. 2, pp. 102–114, 2013, doi: 10.1007/s12178-013-9156-0.

[5] W. Wei and H. Dai, "Articular cartilage and osteochondral tissue engineering techniques: Recent advances and challenges,"

Bioactive Materials, vol. 6, no. 12. KeAi Communications Co., pp. 4830–4855, Dec. 01, 2021. doi: 10.1016/j.bioactmat.2021.05.011.

[6] L. Bartha, A. Vajda, Z. Duska, H. Rahmeh, and L. Hangody, "Autologous osteochondral mosaicplasty grafting," *J. Orthop. Sports Phys. Ther.*, vol. 36, no. 10, pp. 739–750, 2006, doi: 10.2519/jospt.2006.2182.

[7] A. P. Kishan and E. M. Cosgriff-Hernandez, "Recent advancements in electrospinning design for tissue engineering applications: A review," *J. Biomed. Mater. Res. - Part A*, vol. 105, no. 10, pp. 2892–2905, 2017, doi: 10.1002/jbm.a.36124.

Peptide-functionalized chitosan sponges for bone tissue regeneration

E. Zeni[1], P. Brun[2], L. Cassari[1], G. Iucci[3], A. Gloria[4], A. Zamuner[5] and M. Dettin[1]
[1] *Department of Industrial Engineering, University of Padova, 35122 Padova, Italy*
[2] *Department of Molecular Science, University of Padua, Via A. Gabelli 63, 35121 Padua, Italy*
[3] *Department of Science, Roma Tre University of Rome, Via della Vasca Navale 79, 00146 Rome, Italy*
[4] *Institute of Polymers, Composites and Biomaterials, National Research Council of Italy, 80125 Naples, Italy*
[5] *Department of Civil, Environmental, and Architectural Engineering, University of Padova, Padova, Italy*

Abstract— **This paper focuses on the development of functionalized spongy chitosan scaffolds for bone tissue regeneration. Chitosan is a natural polymer that is readily available, biocompatible, and antibacterial. In this work, chitosan was covalently functionalized with two different bioactive peptide sequences, HVP (FRHRNRKGY) to improve cell adhesion, and GBMP1a (PFPLADHLNSTNHAIVQTLVNSF) to increase osteoblast proliferation and differentiation. HVP is an adhesive peptide mapped on human vitronectin, whereas GBMP1a reproduces a sequence derived from BMP-2 protein. Six different scaffolds were obtained by various combinations of both functionalized chitosan, also functionalizing the chitosan simultaneously with the two considered peptides. These matrices were then evaluated in *in vitro* biological assays with human jaw derived osteoblasts to assess their ability to induce modification of gene expression of characteristics proteins for this cell phenotype. Characterization of the matrices was completed with biomechanical tests, analysis by scanning electron microscope (SEM), and x-ray photoelectron spectroscopy (XPS).**

***Keywords*—peptide, chitosan, covalent functionalization, bone regeneration.**

I. Introduction

BONE diseases are still a clinical challenge, causing half of all chronic diseases in people over the age of 50 [1].

Nowadays, autologous bone grafting is considered the *gold standard* for bone reconstruction. However, there are still several drawbacks, such as secondary damages or donor site morbidity [2], [3]. To overcame grafts limitations, bone tissue engineering (BTE) has proposed different scaffolding materials properly enriched with bioactive molecules and cells [4].

Chitosan is a natural polysaccharide produced by deacetylation of chitin. Since it is a biocompatible and biodegradable biomaterial it has been employed for various biomedical applications. Chitosan has two specific functional groups, an amine group NH_2 in C2 and various hydroxyl groups (OH) that simplify its functionalization with peptides for engineering purposes [5]. Moreover, it can be used to obtain different shapes, such as 3D sponges, hydrogels, films, or nanofiber matrices. In particular, the porosity gained by lyophilized chitosan scaffolds allow cell migration and exchange of nutrients and waste [6].

In this work, HVP and GBMP1a peptides were covalently bind to chitosan to improve its bioactive properties. HVP is an adhesive sequence derived from fragment (351-359) of human vitronectin, and it has shown to be effective in osteoblast adhesion and in promoting cellular migration [7], [8]. GBMP1a is a 22 amino acids sequence peptide derived from fragment (48-69) of BMP-2 protein, and it is able to increase osteogenic differentiation of mesenchymal stem cells [9].

Several methods have been used to bind covalently a bioactive sequence to chitosan, such as 1-ethyl-3-(3-dimethylaminopropyl)-carbodiimide (EDC) and N-hydroxy succinimide (NHS) [10], [11]. Here, a different functionalization chemistry is proposed. It consists of Schiff bases production, successively reduced, between chitosan amino groups and aldehyde groups appositely inserted in the peptide backbone during solid phase peptide synthesis [5], [12]. One of the advantages of this method is the specific anchoring of a bioactive sequence in a single-step reaction carried out in aqueous solution and mild conditions [13].

In this work, it is proposed a 3D-spongy chitosan scaffold for BTE, bioactivated with the covalently anchoring of two peptide sequences, also used in combination, to ensure faster bone healing improving osteoblast differentiation, adhesion, and proliferation.

II. Methods

A. Peptide synthesis, characterization, and purification

The S-x-HVP peptide (sequence H-Ser-x-Phe-Arg-His-Arg-Asn-Arg-Lys-Gly-Tyr-NH_2, where x represents 7-aminoheptanoic acid) and S-x-GBMP1a peptide (sequence H-Ser-x-Pro-Phe-Pro-Leu-Ala-Asp-His-Leu-Asn-Ser-Thr-Asn-His-Ala-Ile-Val-Gln-Thr-Leu-Val-Asn-Ser-NH_2) were synthesized, characterized and purified as described in [13].

B. S-x-HVP and S-x-GBMP1a N-terminal conversion in an alpha-oxo-aldehyde and purification

Both peptides were oxidized to provide the sequence with an alpha-oxo-aldehyde group at the N-terminal following the procedure described in [13].

C. Chitosan functionalization with S-x-HVP aldehyde and S-x-GBMP1a aldehyde

Seven conditions of functionalized chitosan scaffolds were prepared: pure chitosan 100% (chit); pure chitosan + S-x-HVP functionalized chitosan (50:50 w:w), (chit:chitHVP); pure chitosan + S-x-GBMP1a functionalized chitosan (50:50 w:w), (chit:chitBMP); S-x-HVP functionalized chitosan + S-x-GBMP1a functionalized chitosan (50:50 w:w), (chitHVP:chitBMP); pure chitosan + S-x-HVP functionalized chitosan + S-x-GBMP1a functionalized chitosan (50:25:25 w:w:w), (chit:chitHVP:chitBMP); pure chitosan + chitosan functionalized with both S-x-HVP and S-x-GBMP1a (50:50

w:w), (chit:chitHVP-BMP); 100% chitosan functionalized with both S-x-HVP and S-x-GBMP1a, (chitHVP-BMP).
The functionalization of chitosan with S-x-GBMP1a was carried out by dissolving 21.89 mg of chitosan in 1404 µL of 0.2 M acetic acid solution under magnetic stirring. Then, 815 µL of ethanol were added and the pH was adjusted to 5.1. 19.96 mg of peptide were dissolved in MilliQ water (1 mg/mL solution). The two solutions were then mixed, and 21.89 mg of $NaCNBH_3$ were added under magnetic stirring. The reaction was stopped after 24 h adding NaOH until the pH reached 7. The solution was then precipitated with cold ether, mixed under magnetic stirring for 10 min and then placed overnight into the fridge. The solution was subsequently filtered and dried in a vacuum chamber for 1 hour. The same procedure was followed to functionalize chitosan with S-x-HVP, (maintaining 7.734 µmol of peptide in 40 mg chitosan+peptide) and to functionalize chitosan with both S-x-HVP and S-x-GBMP1a (3.867 µmol of each peptide).

D. Set-Up of the chitosan-based sponges

The mentioned scaffolds were prepared by dissolving 1.68 mg of chitosan (enriched with peptides or not) in 252 µL of acetic acid solution 0.2 M under magnetic stirring. 200 mg of the solution were then poured in different wells of a 48-well plate, frozen with liquid nitrogen, and freeze-dried. After the lyophilization, washes were performed by filling each well three times with ethanol and later three times with sodium phosphate buffer PBS 10X. Then, the scaffolds were once again frozen with liquid nitrogen and freeze-dried. Subsequently, the matrices were soaked in 400 µL of MilliQ water and frozen overnight at -20°C. Finally, they were frozen once again with liquid nitrogen and freeze-dried.

E. Scaffolds characterization

X-ray photoelectron spectroscopy (XPS) analysis was performed using a homemade instrument, consisting of preparation and analysis UHV chambers separated by a gate valve. All spectra were energy referenced to the C1s signals of aliphatic carbons at BE = 285.0 eV. Curve fitting of the C1s, N1s, O1s and F1s spectra was performed using Gaussian profiles fitting functions. Atomic ratio values were calculated from peaks intensities. Scaffold morphology was investigated by scanning electron microscopy (SEM) using a Stereoscan-205 S (Cambridge Instruments, Pine Brook, NJ, USA). ImageJ (National Institutes of Health) was utilized to investigate the pores dimension of each scaffold. Biomechanical compression tests were performed on the cylindrical chitosan matrices, having a radius R0 = 5 mm and a height H0 = 0.3 mm. These specimens were soaked in physiological solution at 37°C and tested using a compression machine (INSTRON 5566) at a speed of 1mm/min to a deformation of 50%. Considering the measured force F, initial specimen area ($A0 = \pi R0^2$), change in specimen height (ΔH), and initial specimen height (H0), engineering stress (σ) and engineering strain (ε) were calculated as $\sigma = F/A0$ and $\varepsilon = \Delta H/H0$. Statistical analyses were performed using ANOVA and Turkey HSD test. p-value <0.05 were considered statistically significant.

F. Biological assays

Osteoblasts were seeded on chitosan scaffolds and incubated for 2 hours at 37°C to evaluate their adhesion potential. At the end of the incubation period, the cell culture was washed with PBS and a solution of 5mg/ml MTT in PBS was added. The samples were incubated again under the same conditions for 4 hours. Consequently, a 10% (w/v) solution of sodium dodecyl sulfate (SDS), acidified with 0.01N HCl was added. Finally, absorbance values were read with a microplate reader (Thermo scientific Varioskan Lux) at 620nm on 100 µL of solution. Osteoblasts proliferation on chitosan scaffolds was assessed at 4 days from seeding using carboxyfluorescein diacetate succinimidyl ester CFSE (Molecular Probe, Invitrogen), a cell-permeable fluorescent probe equally partitioned among daughter cells. Cells were first incubated for 10 min with CFSE 25 µM at 37 °C. The reaction was stopped by adding 5 volumes of ice-cold culture media. Cells were then washed, counted using Trypan blue, and seeded on chitosan scaffolds. At the end of incubation, cellular monolayers were washed in PBS and incubated for 5 min with trypsin-EDTA. Cell proliferation was assessed using BD FACS-Calibur flow cytometer by evaluating the percentage of CFSE-positive cells in 10,000 events. Specific mRNA transcript levels coding human runt-related transcription factor 2 (Runx2), vitronectin (VTN), and osteopontin (OPN) were quantified in osteoblast cells cultured for 24 h on chitosan scaffolds. At the end of incubation, the total RNA was extracted using the SV Total RNA Isolation System kit (Promega, Milan, Italy). Contaminating DNA was removed by DNase I digestion (Omega Bio-Tek, Norcross, GA, USA). cDNA synthesis and subsequent polymerization were performed in one step using the iTaq Universal SYBR Green One-Step Kit (Bio-Rad, Hercules, CA, USA). The reaction mixture contained 200 nM forward primer, 200 nM reverse primer, iTaq universal SyBR Green reaction mix, iScript reverse transcriptase, and 200 ng total RNA. Real-time PCR was performed using the ABI PRISM 7700 Sequence Detection System (Applied Biosystems, Milan, Italy). Data were quantified by the ΔΔCT method using human GAPDH as the reference gene. Target and reference genes were amplified with efficiencies near 100%. Biological data are reported as mean ± standard error. The statistical analysis was performed using the One-way ANOVA test followed by Bonferroni's multicomparison test, using Graph-Pad Prism 3.03. p-values < 0.05 were considered statistically significant.

III. RESULTS

A. XPS analysis

XPS measurements were performed to demonstrate the anchoring of the peptides to the chitosan scaffolds.

TABLE I: N/O RATIOS OF FUNCTIONALIZED SCAFFOLDS

Sample	N/O
Chit	0.05
Chit:chitHVP	0.1
Chit:chitBMP	0.09
Chit:chitHVP:chitBMP	0.1
ChitHVP:chitBMP	0.09
Chit:chitHVP-BMP	0.1
ChitHVP-BMP	0.2

The increase of the N/O ratios of functionalized scaffolds compared to the pure chitosan shown in Table I confirmed the anchoring of both peptides to chitosan, as the increment of

nitrogen is strictly related with the peptide presence. In particular, all data are similar to each other except for ChitHVP-BMP that induce a higher N/O ratio.

B. SEM analysis

A morphological characterization of functionalized chitosan scaffolds was carried out with SEM and reported in Fig 1.

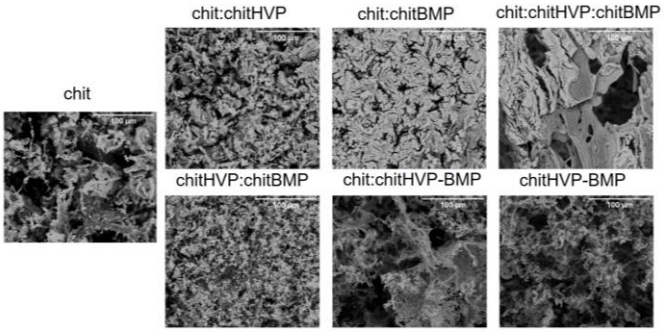


Fig. 1: Ultrastructural characteristics of the functionalized chitosan scaffolds investigated by scanning electron microscopy. Scale bar: 100µm; magnification 600x.

TABLE II: SCAFFOLDS PORES DIMENSION

Samples	Mean length [µm] ± std [µm]	Mean width [µm] ± std [µm]
Chit	22.18 ± 3.62	13.79 ± 3.58
Chit:chitHVP	16.71 ± 3.18	9.63 ± 2.79
Chit:chitBMP	14.53 ± 2.08	11.07 ± 2.89
Chit:chitHVP:chitBMP	20.46 ± 2.17	15.94 ± 2.96
ChitHVP:chitBMP	14.45 ± 3.76	10.14 ± 1.75
Chit:chitHVP-BMP	20.43 ± 5.73	12.76 ± 2.99
ChitHVP-BMP	19.52 ± 2.55	15.08 ± 3.17

Porous mean length and width reported as mean value ± standard deviation. the measures were obtained by ImageJ software.

The pure chitosan matrix shows the standard open-cell porous scaffold. Pores dimension was measured using ImageJ software, measuring both the length and the width of the pores, the results are shown in Table II. The pores dimension of pure chitosan matrices is 22.18 µm ± 3.62 µm; 13.79 µm ± 3.58 µm. Chit:chitHVP matrices are very similar structurally to the pure chitosan control; in fact, the HVP peptide is strongly basic and it is positively charged like chitosan itself. In this case the pore size is slightly smaller (16.71 µm ± 3.18 µm; 9.63 µm ± 2.79 µm). In contrast, chit:chitBMP matrix (14.53 µm ± 2.08 µm; 11.07 µm ± 2.89 µm) appears less spongy and porous, and this may be caused by a crushing effect due to the transfer of the matrix into the SEM plate. The chit:chitHVP:chitBMP matrix is morphologically very different from the control and filamentous (20.46 µm ± 2.17 µm; 15.94 ± 2.96 µm). The chitHVP:chitBMP matrix is similar to the structure of the control but with smaller pores (14.45 µm ± 3.76 µm; 10.14 µm ± 1.75 µm). Finally, the last two conditions, chit:chitHVP-BMP and chitHVP-BMP, are visually very similar to each other and to the control matrix (20.43 µm ± 5.73 µm; 12.76 µm ± 2.99 µm, and 19.52 µm ± 2.55 µm; 15.08 µm ± 3.17 µm, respectively).

C. Adhesion and proliferation assays

Biological assays were performed using osteoblasts derived from human jaw to evaluate functionalized chitosan scaffolds bioactivity. An MTT assay for cell adhesion and a CFSE assay for cell proliferation were carried out 2 hours and at 4 days from seeding, respectively (Fig 2).

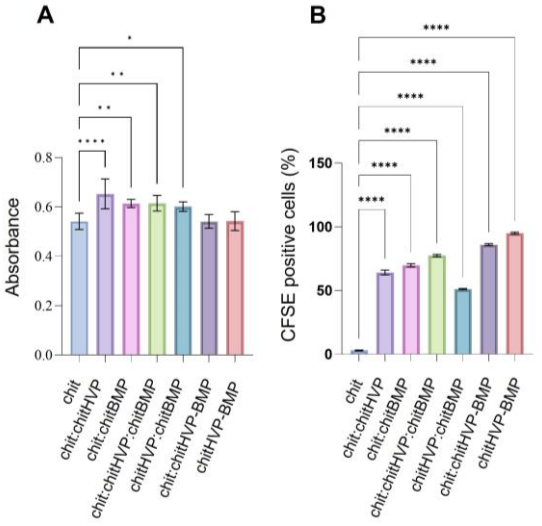


Fig 2: A) Human osteoblast cell adhesion on functionalized chitosan-based scaffolds, evaluated by MTT at 2 hours from the seeding; B) human osteoblast cell proliferation on functionalized chitosan-based scaffolds, evaluated by CFSE at 4 days from the seeding; * p <0.05, ** p <0.01, **** p <0.0001.

The results of the MTT assay are reported in Fig 2A. Chit:chitHVP is the scaffold that induces a higher osteoblastic adhesion compared to the others, with a statistical significance compared to chit ($p < 0.0001$). This is an expected result since the peptide HVP is an adhesive sequence. Other matrices with a statistically significant difference compared to chit are chit:chitBMP and chit:chitHVP:chitBMP ($p < 0.01$) and chitHVP:chitBMP ($p < 0.05$).

The results of the CFSE assay performed at 4 days from seeding are shown in Fig 2B. All functionalized scaffolds induce a higher proliferation compared to the control ($p < 0.0001$). Specifically, the highest values are obtained by chitHVP-BMP and chit:chitHVP:chitBMP, that induce a proliferation 32 and 28 times higher than the control, respectively.

D. Gene expression

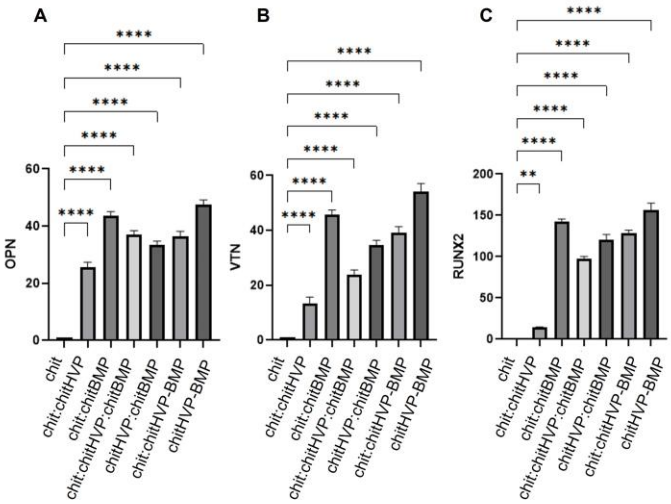


Fig 3: A) OPN expression in all chitosan scaffolds; B) VTN expression in all chitosan scaffolds; C) Runx2 expression in all chitosan scaffolds; * p <0.05, ** p <0.01, **** p <0.0001.

The results of the RNA extraction and amplification through quantitative polymerase chain reaction (qPCR) are reported in Fig 3. The expression of three genes, runt-related transcription factor 2 (Runx2), vitronectin (VTN) and osteopontin (OPN) was examined.
The most promising results are expressed by chit:chitBMP and chitHVP-BMP matrices. However, all functionalized matrices increment the expression of these genes compared to the control.

E. Biomechanical compression tests

A biomechanical compression test was carried out in all the 7 scaffolds. The Young's modulus (E) and the maximum stress (σ_{max}) with the corresponding standard deviations are reported in Table III. The general behavior is similar to that of a flexible foam.

TABLE III: MECHANICAL PROPERTIES OF SCAFFOLDS

Scaffold	E (kPa)	σ_{max} (kPa)
Chit	22.6 ± 2.0	8.9 ± 0.5
Chit:chitHVP	21.3 ± 2.1	7.3 ± 0.4
Chit:chitBMP	23.0 ± 2.3	7.1 ± 0.4
Chit:chitHVP:chitBMP	16.4 ± 1.4	5.6 ± 0.3
ChitHVP:chitBMP	10.1 ± 1.0	4.0 ± 0.3
Chit:chitHVP-BMP	22.7 ± 2.3	6.9 ± 0.5
ChitHVP-BMP	8.5 ± 0.8	4.1 ± 0.3

Mechanical properties of functionalized chitosan scaffolds: compressive modulus (E) and maximum stress (σ_{max}) reported as mean value ± standard deviation.

The maximum stress value was measured on chit (8.9 ± 0.5 kPa). However, the Young's modulus are similar among chit (22.6 ± 2.0), chit:chitHVP (21.3 ± 2.1 kPa), chit:chitBMP (23.0 ± 2.3 kPa), and chit:chitHVP-BMP (22.7 ± 2.3 kPa), and no significative statistical differences were found among these samples. Regarding the maximum stress, there were not statistical differences among chit:chitHVP (7.3 ± 0.4 kPa), chit:chitBMP (7.1 ± 0.4 kPa) and chit:chitHVP-BMP (6.9 ± 0.5 kPa). The compression modulus and maximum stress measured in chit:chitHVP-BMP (16.4 ± 1.4 kPa and 5.6 ± 0.3 kPa) were significantly higher compared to the ones of chitHVP:chitBMP (10.1 ± 1.0 kPa and 4.0 ± 0.3 kPa) and chitHVP-BMP (8.5 ± 0.8 kPa and 4.1 ± 0.3 kPa).

IV. CONCLUSION

In this work, the functionalization of a spongy chitosan scaffold with different percentage of two peptides, HVP and GBMP1a, was studied. XPS characterization of the matrices confirmed the successful anchoring of S-x-HVP and S-x-GBMP1a peptides on chitosan. The peptides' presence is proven by the increased N/O ratio in functionalized scaffolds with respect to unfunctionalized chitosan. SEM imaging showed the porous morphology of the 3D spongy matrices of chitosan and functionalized chitosan, which are necessary for BTE scaffolds, allowing cell migration and exchanging of nutrients and waste. Furthermore, the porous scaffold better mimic the extracellular matrix.
Biological assays showed an higher osteoblast adhesion in chit:chitHVP as expected by the nature of the vitronectin-derived peptide. In any case, all functionalized matrices stimulated cell adhesion. Moreover, the bioactive nature of the scaffolds is further evidenced in the four-day proliferation assays, where osteoblast proliferation is significantly higher for all matrices compared to the pure chitosan control. The powerful osteoblast differentiation factor GBMP1a is proved by the gene expression assay, where the chit:chitBMP scaffold reported the highest expression of all 3 genes. Finally, mechanical tests highlighted that chit:chitHVP, chit:chitBMP, and chit:chitHVP-BMP scaffolds showed similar compressive behavior to the pure chitosan matrix, while the remaining samples showed a reduction in mechanical properties, probably due to the more complex structure and steric hindrance due to the inclusion of both peptides in the same scaffold. These materials could be used to treat small bone defects or as a coating for implants, considering their mechanical properties that result lower than the natural bone ones.

ACKNOWLEDGEMENT

The authors would like to thank Alissa Di Giulian and Vittoria Facchin for their help in the peptide synthesis and scaffolds functionalization.

REFERENCES

[1] H. Qu, H. Fu, Z. Han, and Y. Sun, "Biomaterials for bone tissue engineering scaffolds: a review," RSC Adv., vol. 9, no. 45, pp. 26252–26262, 2019, doi: 10.1039/C9RA05214C.
[2] A. Oryan, S. Alidadi, A. Moshiri, and N. Maffulli, "Bone regenerative medicine: classic options, novel strategies, and future directions," J. Orthop. Surg., vol. 9, no. 1, p. 18, Mar. 2014, doi: 10.1186/1749-799X-9-18.
[3] J. F. Keating and M. M. McQueen, "SUBSTITUTES FOR AUTOLOGOUS BONE GRAFT IN ORTHOPAEDIC TRAUMA," J. BONE Jt. Surg., vol. 83, no. 1, 2001.
[4] A. R. Amini, C. T. Laurencin, and S. P. Nukavarapu, "Bone Tissue Engineering: Recent Advances and Challenges," Crit. Rev. Biomed. Eng., vol. 40, no. 5, 2012, doi: 10.1615/CritRevBiomedEng.v40.i5.10.
[5] P. Brun et al., "Bio-Functionalized Chitosan for Bone Tissue Engineering," Int. J. Mol. Sci., vol. 22, no. 11, Art. no. 11, Jan. 2021, doi: 10.3390/ijms22115916.
[6] A. Oryan and S. Sahvieh, "Effectiveness of chitosan scaffold in skin, bone and cartilage healing," Int. J. Biol. Macromol., vol. 104, pp. 1003–1011, Nov. 2017, doi: 10.1016/j.ijbiomac.2017.06.124.
[7] P. Brun et al., "Mechanisms underlying the attachment and spreading of human osteoblasts: From transient interactions to focal adhesions on vitronectin-grafted bioactive surfaces," Acta Biomater., vol. 9, no. 4, pp. 6105–6115, Apr. 2013, doi: 10.1016/j.actbio.2012.12.018.
[8] A. Zamuner et al., "Biofunctionalization of bioactive ceramic scaffolds to increase the cell response for bone regeneration," Biomed. Mater., vol. 16, no. 5, p. 055007, Jul. 2021, doi: 10.1088/1748-605X/ac1555.
[9] E. Rampazzo et al., "A synthetic BMP-2 mimicking peptide induces glioblastoma stem cell differentiation," Biochim. Biophys. Acta BBA - Gen. Subj., vol. 1861, no. 9, pp. 2282–2292, Sep. 2017, doi: 10.1016/j.bbagen.2017.07.001.
[10] M.-H. Ho et al., "Preparation and characterization of RGD-immobilized chitosan scaffolds," Biomaterials, vol. 26, no. 16, pp. 3197–3206, Jun. 2005, doi: 10.1016/j.biomaterials.2004.08.032.
[11] R. S. Tiğli and M. Gümüşderelioğlu, "Evaluation of RGD- or EGF-immobilized chitosan scaffolds for chondrogenic activity," Int. J. Biol. Macromol., vol. 43, no. 2, pp. 121–128, Aug. 2008, doi: 10.1016/j.ijbiomac.2008.04.003.
[12] V. Secchi et al., "Biofunctionalization of TiO2 Surfaces with Self-Assembling Layers of Oligopeptides Covalently Grafted to Chitosan," ACS Biomater. Sci. Eng., vol. 5, no. 5, pp. 2190–2199, May 2019, doi: 10.1021/acsbiomaterials.9b00430.
[13] P. Brun et al., "Chitosan Covalently Functionalized with Peptides Mapped on Vitronectin and BMP-2 for Bone Tissue Engineering," Nanomaterials, vol. 11, no. 11, Art. no. 11, Nov. 2021, doi: 10.3390/nano11112784.

Biological evaluation *in vitro* and *in vivo* of hybrid membrane to assess biomedical application

M. Todesco[1], R. Luisetto[2], M. Casarin[2], S.J. Imran[3], G. Gerosa[3], C.G. Fontanella[4], A. Bagno[4]
[1] *Department of Civil, Environmental and Architectural Engineering, University of Padua, Via Marzolo 9, 35131, Padova, Italy*
[2] *Department of Surgery, Oncology and Gastroenterology, University of Padua, Via Giustiniani 2, 35128 Padua, Italy*
[3] *Department of Cardiac, Thoracic and Vascular Sciences, University of Padua, Via Giustiniani 2, 35128 Padua, Italy*
[4] *Department of Industrial Engineering, University of Padua, Via Marzolo 9, 35131 Padua, Italy*

***Abstract*— Currently the main challenge of tissue engineering is the realization of materials that can replace tissues and organs and perfectly integrate with the host organism ensuring the proper functionality. Hybrid Membranes (HYMEs) were produced by coupling a decellularized tissue (porcine pericardium) with a polymeric material (polycarbonate urethane). HYMEs biocompatibility was assessed *in vitro* by direct contact cells seeding and *in vivo* by implantation in the rat model. *In vitro* no cytotoxicity was observed and cells growth was demonstrated until 7 days. *In vivo* HYMEs appeared better integrated with the host tissue than the polymer alone (control) after 4 weeks from implantation. Moreover, the polymer was not affected by degradation.**

***Keywords*—Hybrid membrane, biocompatibility, tissue engineering.**

I. Introduction

As reported by the World Health Organization, Cardiovascular diseases (CVDs) are the leading cause of death globally [1]. Among CVDs, atherosclerosis is one of the most frequent conditions: in the arterial intima, it is characterized by the formation of plaques containing cells, fragments of collagen and elastic fibers, proteoglycans and lipids. Atherosclerotic plaques generally evolve causing the reduction of the lumen and/or the damage of vascular tissues with the subsequent decrease of blood flow. This condition can cause thromboembolic events [2]-[4].

When a severe injury to cardiovascular structures occurs, the ideal therapy is the substitution of the damaged tissue with an autologous one to prevent the immune reaction. Indeed, this approach is limited by to the low availability of compatible healthy tissues due to patient's pathologies or harvesting procedures [5].

To bypass the lack of autologous cardiovascular substitutes, synthetic vascular grafts, e.g. polytetrafluoroethylene (PTFE) and polyethylene terephthalate (PET), and chemically treated biological tissues, e.g. glutaraldehyde treated pericardium, are currently used [6]. Unfortunately, these materials have shown insufficient reliability with increased risks of contamination and infections, thrombogenic reactivity and intimal hyperplasia formation [7]. Additionally, these grafts are non-viable materials and cannot be endothelialized *in vivo*, are not prone to remodeling and regeneration, hampering the process of integration with the recipient's organism [8].

Tissue engineering offers new strategies in order to minimize the drawbacks of current materials and improve patients' quality of life. The aim consists in obtaining higher biocompatibility using decellularization procedures, which allow removing cellular components, but preserving the original extracellular matrix (ECM) components, such as growth factors. Therefore, the acellular scaffold is prone to be repopulated by patient's cells and has the ability to optimally integrate with the host's body. However, mechanical performances, impermeability and patency of decellularized tissues are not completely satisfactory.

For these reasons, the present work aims at improving the mechanical features of decellularized pericardium by coupling it with a synthetic material (Chronoflex AR or Chronoflex ARLT). This novel material was named hybrid membrane (HYME). On the one side, the synthetic polymer provides mechanical resistance to the membrane, on the other side the decellularized tissue guaranties biocompatibility [9]. HYMEs cytotoxicity was assessed *in vitro* by direct contact tests and biocompatibility was investigated *in vivo* on the rat model by means of subdermal implantation.

II. MATERIALS AND METHOD

A. Pericardium procurement and decellularization

Fresh native porcine pericardia (NPP) were collected from a local slaughterhouse that followed EC regulation 1099/2009 protocols regarding animal health and protection. Tissues samples from the anterior right ventricular region were isolated and pre-pericardial fat was removed [10]. Tissue samples were decellularized in according to TergiCol methods [10], which was carried out using protease inhibitors, hypo- and hypertonic solutions, Tergitol (cod. 15S9) and Sodium Cholate (cod. C1254). Finally, samples were treated with an isopropanol based solution and endonuclease (Benzonase®, cod. E1014) was used to remove residual DNA fragments. All reagents were supplied by Sigma Aldrich (Saint Louis, MO, USA).

B. Membrane preparation and sterilization

HYMEs were made using the solution casting technique [11]. Pericardium was placed in a customized aluminium frame, and the polycarbonate urethane (ChronoFlex AR or ChronoFlex AR-LT, AdvanSource Biomaterials, Wilmington, MA, US) was poured over the fibrous face. Both polymers were supplied as 22% (w/v) solution in N,N-

dimethylacetamide (DMAc). The membranes were dried for 24 hours at 38°C in a vacuum oven (Raypa, Barcelona, Spain). Two types of membranes were made: DPP AR and DPP ARLT by coupling porcine pericardium with Chronoflex AR and Chronoflex ARLT, respectively. Two other polymeric membranes (CF AR and CF ARLT) were made and used as controls.

HYMEs were sterilized with a two-step treatment with a cocktail of antibiotics and antimycotics and peracetic acid [12]. In Fig. 1 two types of HYMEs are shown.

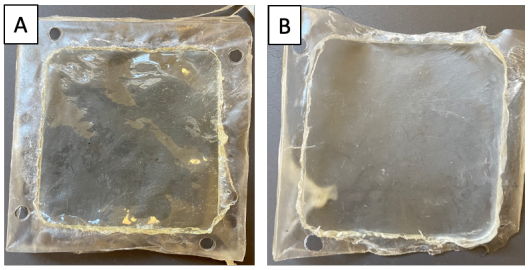


Fig. 1: HYMEs made by coupling DPP with CF AR (A) and CF ARLT (B).

C. In vitro cytocompatibility

HYMEs cytocompatibility was first assessed *in vitro* by direct contact tests, carried out by seeding HUVECs (cat. no. C12200, PromoCell, Heidelberg, Germany) on decellularized pericardium (control group 1), hybrid membranes on tissue side and polymers alone (control group 2), in accordance with ISO 10993 part 5 [13]. In order to perform direct cells seeding, DPP were cut into 2×2 cm^2 squares and mounted in aseptic conditions in inserts with a culture area of 0.5 cm^2, which were then placed in 24-well plates. Conversely, hybrid membranes and polymeric samples were cut into 8 mm diameter circular patches and directly placed into 48-well plate. All samples groups were equilibrated overnight in fresh culture medium (cat. no. C-22211, PromoCell, Heidelberg, Germany) containing SupplementPack (cat.no. C-39211) and 1% penicillin-streptomycin at 37°C in incubator. On the following day (day 0), samples were directly seeded with Huvec cells (30,000 cells/ cm^2), which were cultured for 1, 3 and 7 days. Cell viability was assessed using the Live and Dead assay (Thermo Fisher Scientific, Waltham, MA, USA), following the manufacturer's instructions: it allowed staining live cells with calcein (green) and dead cells with Ethidium homodimer-1 (red). Images of cultured tissues and hybrid membranes were acquired with an epifluorescence microscope Leica AF6000, connected to a Leica DC300 digital camera and equipped with LAS AF Software (Leica Micro-System, Wetzlar, Germany) while polymers images were acquired with an Olympus IX71 fluorescence microscope (Olympus, Tokyo, Japan). Pictures were then processed with an opensource software, Fiji.

Cells metabolic activity was measured on day 1 and 7 with WST-1 assay kit (Boster Biological Technology, Pleasanton, USA), by incubating samples with 2.5% (v/v) WST solution in culture medium at 37°C for 1.5 hrs in incubator. The amount of reduced WST-tetrazolium was calculated by absorption at 450 nm with a spark 10M TECAN microplate reader (Tecan, Männedorf, Switzerland).

Finally, samples were fixed in 4% v/v PFA for 5 min at room temperature, permeabilized with 0.1% v/v Triton X-100 for 15 min, followed by blocking in 1% w/v BSA solution for 30 min. Samples were then stained with phalloidin—Atto 647N (1:200) to counterstain filamentous actin, and with DAPI to stain nuclei. Pictures were taken with an epifluorescence microscope Leica AF6000 connected to a Leica DC300 digital camera and equipped with LAS AF Software (Leica Micro-Systems, Wetzlar, Germany). Post-imaging analysis was performed using Fiji software.

D. In vivo tests

Samples of polymers (CF AR and CF ARLT) and HYMEs (DPP AR and DPP ARLT) were subdermally implanted in rats to evaluate possible effects due to calcification and polymer degradation. Reaction of the host tissues in direct contact with the materials was also evaluated. Sixteen 21 days-old Sprague Dawley rats (Charles River, USA) with a mean body weight of 73.2 ± 11.04 g were anesthetized with inhalation of Sevoflurane in oxygen medical atmosphere (4%) and locally treated with bupivacaine. A subdermal dorsal pouch was created on each rat and a round specimen (8 mm diameter) was implanted. Each material was grafted into 4 rats and explanted after 4 weeks [14].

All experiments were carried out as stated in authorization of the Italian Ministry of Health No. 782/2021-PR (protocol number 965E9.41) and animal were treated in according to UNI EN ISO 10993-2 [15].

The weight of the animals was collected all along the observation period and considered as an indicator of animals' well-being [16].

Fourier Transform Infrared Spectroscopy Attenuated Total Reflection FTIR-ATR (Nicolet iS-50, Thermo Fisher Scientific, Waltham, Massachusetts, USA) analysis was performed on explanted materials to determine whether any chemical changes appeared on the surface of the polycarbonate urethane. Before FTIR-ATR analysis, all materials were equilibrated in deuterium oxide (Janssen, Beerse, Belgium) to reduce the contribution of interfering water.

The geometric characteristics of the explanted patches were evaluated to check possible degradation effects. A digital caliper (Mitutoyo, Kawasaki, Japan) was used to measure thickness, and area was calculated on images of the specimens processed with Fiji.

III. RESULTS

A. In vitro cytocompatibility

Live and Dead assay (Fig. 2A-E) allowed evaluating the presence of live (green) and dead (red) cells at 1, 3 and 7 days after seeding DPP, hybrid membranes and polymers alone with HUVECs. Some dead cells were detected only in DPP-ARLT on day 1 and in DPP on day 3, while in other groups very few dead cells were displayed at each timepoint. On the contrary, a significative increasing of live cells was evident both on day 3 and 7 in all groups, especially in the case of hybrid membranes, which were completely covered by live cells.

Metabolic assay using WST (Fig. 2F) performed after 1 and

7 days from seeding showed no significant difference in the case of seeded DPP; differences appeared over DPP AR and CF AR, where metabolic activity of seeded cells was found at day 7. Lastly, an increase of metabolic activity was detected at day 7 on DPP ARLT and CF ARLT, but it was not significant.

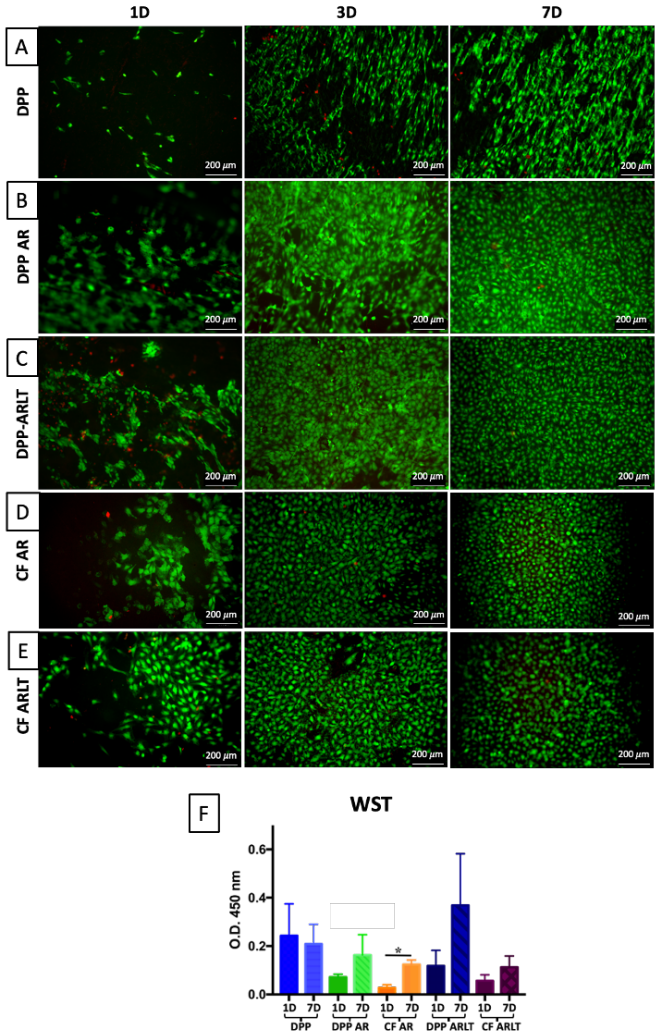


Fig. 2: Live and Dead assay of decellularized pericardium (A), DPP AR (B), DPP ARLT (C), CF AR (D) and CF ARLT (E) after 1, 3 and 7 days from seeding. Metabolic assay with WST (F) of decellularized tissue, hybrid membranes and polymers alone at 1 and 7 days after seeding.

DAPI (cyan) and phalloidin (magenta) staining highlighted the presence of nuclei and F-actin in DPP, hybrid membranes and polymers alone on day 1, 3 and 7 (Fig. 3). Evident cells proliferation was found in all groups, especially after 7 days. In the case of DPP alone, cells needed a longer time to cover the whole sample surface: on day 3 it was the only group for which cells were not completely spread, but after 7 days they completely covered the surface.

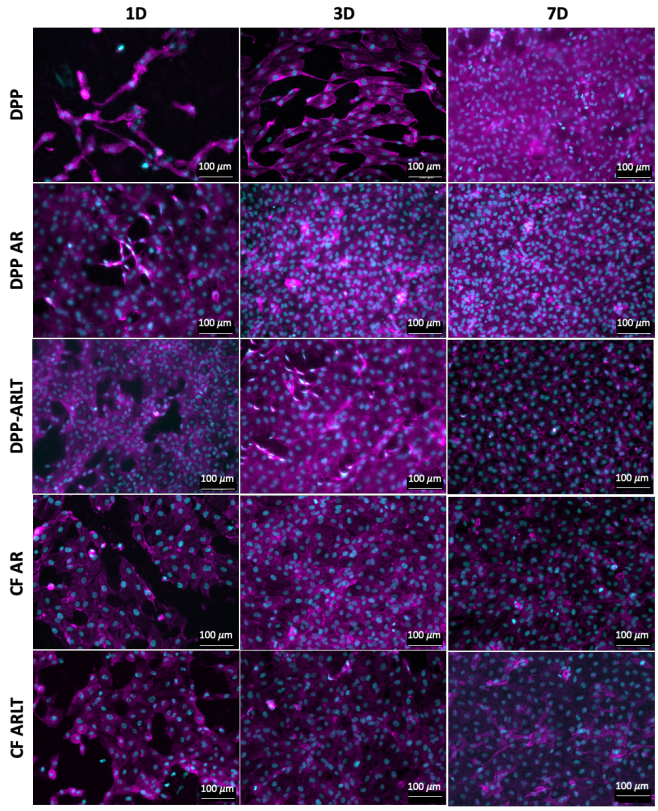


Fig. 3: DAPI (cyan) and phalloidin (magenta) staining of nuclei and F-actin, respectively of DPP, hybrid membranes and polymers alone.

B. In vivo test

All samples were explanted 4 weeks after implantation. As it is illustrated in Fig. 4A, the surgical wound has completely healed and the materials were well integrated with the surrounding tissues, which appeared vascularized: no signs of inflammation were evident.

Within 4 weeks, the rats increased in weight ~2.5 times, from 73.2 ± 11.04 g to 265.06 ± 49.54 g. Weight growth is in accordance with the characteristics of the animal reported by the supplier [17]. This aspect confirmed the good health of the animals and was considered as an index of successful biocompatibility. During surgery and subsequent clinical follow-up, any score of suffering or distress was monitored.

Analyzing the explanted materials, area and thickness of each sample were calculated and no significant difference was found before and after implantation for both polycarbonate urethane (CF AR and CF ARLT) and HYMEs (DPP AR and DPP ARLT).

FTIR-ATR spectra of CF AR and DPP AR explanted specimens, analyzed from polymer side, are reported in Fig. 4B. The spectra of the implanted materials coincided with the spectrum of the CF AR polymer used as ~~a~~ control. The characteristic peaks of the CF AR were present: peaks of urethane and carbonate groups were found at 1737 and 1251 cm^{-1}, while peaks around 1251, 956 and 791 cm^{-1} were due to carbonate groups in the soft segment. The presence of aromatic molecules in the hard segment was confirmed by the peak at 1598 cm^{-1}, while the peak at 1637 cm^{-1} was due to the presence of diamine [18].

The same results were found for CF ARLT and DPP ARLT (Fig. 4C). The composition of CF ARLT was the same of CF

AR, with the exception for the presence of micro-silica particles whose peaks were detected in the interval 1200- 900 cm^{-1}.

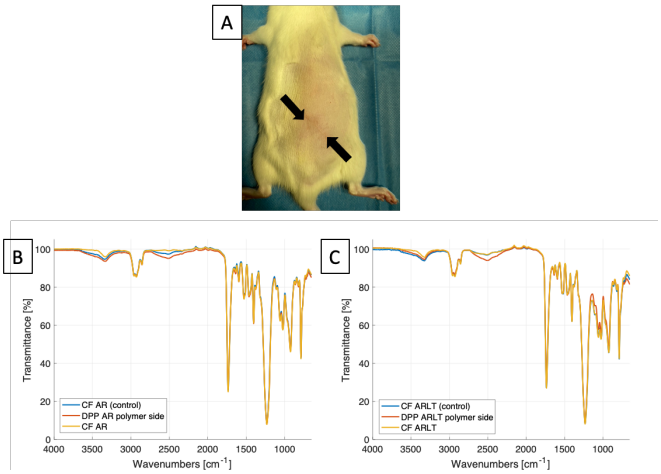


Fig. 4: View of the rat's back at 4 weeks after implantation: arrows indicate where the cutting had been made (A). FTIR-ATR spectra of CF AR and DPP AR (polymer side) (B) and CF ARLT and DPP ARLT (polymer side) (C).

IV. Conclusion

This preliminary *in vivo* and *in vitro* assessment of HYMEs confirmed their high biocompatibility. In vitro, the membranes did not show any cytotoxic effect and promoted cells proliferation 7 days after seeding. Preliminary *in vivo* results were promising as well: neither inflammation nor rejection occurred after implantation and the polymeric part did not degrade.

Further investigations are in progress to assess the ability of the hybrid membranes to integrate *in vivo* and to evaluate the effects of possible calcification. Additionally, an *in vivo* functional implantation in the long term has to be performed for a comprehensive characterization of the investigated materials in order to analyze their ability to properly interact with blood.

Acknowledgement

This work was supported by LifeLab Program of the 'Consorzio per la Ricerca Sanitaria (CORIS) of the Veneto Region, Italy (DGR1017, 17 July 2018).

Authors wish to thank Prof. Michele Modesti (Department of Industrial Engineering, University of Padova) and his research group for the valuable assistance during FTIR-ATR analysis of the membranes.

References

[1] "World Health Organization (WHO)". Available: https://www.who.int/health-topics/cardiovascular-diseases#tab=tab_1

[2] S.-G. Chen, F. Ugwu, W.-C Li, N.M. Caplice, E. Pectu, S. Ping, and C.-L Huang, "Vascular Tissue Engineering: Advanced Techniques and Gene Editing in Stem Cells for Graft Generation," *Tissue Eng. Part B Rev.*, vol. 27, no. 1, pp. 14–28, Feb. 2021.

[3] F. Schaftenaar, V. Frodermann, J. Kuiper, and E. Lutgens, "Atherosclerosis: the interplay between lipids and immune cells," *Curr. Opin. Lipidol.*, vol. 27, no. 3, pp. 209–215, Jun. 2016.

[4] V. Kumar, A. Sbbas, J. Aster, *Pathologic basis of disease.* Philadelphia, PA: Elsevier, 2021.

[5] S. Pashneh-Tala, S. MacNeil, and F. Claeyssens, "The Tissue-Engineered Vascular Graft—Past, Present, and Future," *Tissue Eng. Part B Rev.*, vol. 22, no. 1, pp. 68–100, Feb. 2016.

[6] J. S. Soares, S. K. Saunders, F. Potere, S. Toldo, and A. Abbate, "Engineered tissue vascular grafts: Are we there yet?," *Appl. Eng. Sci.*, vol. 12, p. 100114, Dec. 2022.

[7] R. Zizhou, X. Wang, and S. Houshyar, "Review of Polymeric Biomimetic Small-Diameter Vascular Grafts to Tackle Intimal Hyperplasia," *ACS Omega*, vol. 7, no. 26, pp. 22125–22148, Jul. 2022.

[8] J. M. Aamodt, and D. W. Grainger, "Extracellular matrix-based biomaterial scaffolds and the host response," *Biomaterials*, vol. 86, pp. 68–82, Apr. 2016.

[9] M. Todesco *et al.*, "HYBRID MEMBRANE AS INNOVATIVE MATERIALS FOR BIOMEDICAL APPLICATIONS".

[10] M. Todesco, *S.* J. Imran, T. Moderno Fortunato, D. Sandrin, G. Borile, F. Romanato, M. Casarin, G. Giuggioli, F. Conte, M. Marchesan, G. Gerosa, and A. Bagno, "A New Detergent for the Effective Decellularization of Bovine and Porcine Pericardia," *Biomimetics*, vol. 7, no. 3, p. 104, Aug. 2022.

[11] M. Todesco, C. Zardin, L. Iop, T. Palmosi, P. Capaldo, F. Romanato, G. Gerosa, and A. Bagno, "Hybrid membranes for the production of blood contacting surfaces: physicochemical, structural and biomechanical characterization," *Biomater. Res.*, vol. 25, no. 1, p. 26, Dec. 2021.

[12] C. Fidalgo, L. Iop, M. Harder, D. Mavrilas, S. Korossis, A. Bagno, G. Palù, P. Aguiari, and G. Gerosa, "A sterilization method for decellularized xenogeneic cardiovascular scaffolds," *Acta Biomater.*, vol. 67, pp. 282–294, Feb. 2018.

[13] "Biological evaluation of medical devices. Part 5, Tests for in vitro cytotoxicity (ISO 10993-5:2009)". London: BSI, 2009.

[14] M. Spina, F. Ortolani, A. El Messlemani, A. Gandaglia, J. Bujan, N. Garcia-Honduvilla, I. Vesley, G. Gerosa, D. Casarotto, L. Petrelli, and M. Marchini, "Isolation of intact aortic valve scaffolds for heart-valve bioprostheses: Extracellular matrix structure, prevention from calcification, and cell repopulation features," *J. Biomed. Mater. Res. A*, vol. 67A, no. 4, pp. 1338–1350, Dec. 2003.

[15] "Biological Evaluations of medical devices. Part 2: Animal welfare requirements (ISO 10993-2:2006)". London: BSI, 2006."

[16] A. Ghasemi, S. Jeddi, and K. Kashfi, "The laboratory rat: Age and body weight matter," *EXCLI J.*, vol. 20, pp. 1431–1445, 2021.

[17] "CD® (Sprague Dawley) IGS Rat - Growth Chart". Available: https://www.criver.com/products-services/find-model/cd-sd-igs-rat?region=27

[18] M. Yang, Z. Zhang, C. Hahn, G. Laroche, M. W. King, and R. Guidoin, "Totally implantable artificial hearts and left ventricular assist devices: Selecting impermeable polycarbonate urethane to manufacture ventricles," *J. Biomed. Mater. Res.*, vol. 48, no. 1, pp. 13–23, 1999.

Bio-fabrication of in vitro tissues possessing organ-specific endogenous extracellular matrices

Urciuolo. F[1,2,3], Imparato, G[3], V. De Gregorio[4], C. Casale[1], P.A. Netti[1,2,3]
1 CRIB University of Naples Federico II, P.le Tecchio 80, 80125 Naples, Italy
2 DICMAPI University of Naples Federico II, P.le Tecchio 80, 80125 Naples, Italy
3 CABHC@CRIB Istituto Italiano di Tecnologia, Largo Barsanti e Matteucci n. 53, 80125 Napoli, Italy
4 Department of Biology, University of Naples Federico II, via Cintia 4, Napoli, I-80126, Italy

***Abstract*—The extracellular matrix plays a crucial role in the regulation of tissues and organ functions under both physiologic and pathologic conditions. In our body, each organ is provided with a site-specific ECM presenting to the cells the instructive molecular signals triggering and guiding organ-specific biological processes. Here we report a bioengineering method to obtain scaffold-free organotypic tissues composed of an endogenous and site-specific connective microenvironment.**

***Keywords*—modular tissue engineering, endogenous ECM, stroma, morphogenesis.**

I. Introduction

Organotypic tissues (e.g. skin, lung, cervix, gut) are composed of a connective compartment supporting the growth and the differentiation of a highly specialized epithelium. The difference between such tissues is not only represented by the epithelial cells which display different functions. The connective compartment also plays a crucial role in of developing and maintaining the whole organ [1]. Depending upon body location and tissue origin, fibroblasts elaborate and assemble different ECMs in terms of composition, mechanical, transport properties, and architecture. Such properties are tissue-specific establishing specific signaling to the corresponding epithelia. For instance, hair follicle morphogenesis occurs via the talk cross-talk between specific signals deposited in the dermis and the epithelial cells [2]. However, the dynamic reciprocity between cells and their own ECM plays a crucial role in many biological processes such as cancer progression [3], alterations in the ECM during organ diseases [4]–[6], branching morphogenesis [7], and functional epithelial development in vitro [8], [9]. The in vitro fabrication of functional organotypic tissues results of key relevance to studying the effect of both aging and extrinsic factors (e.g. AGEs, pollutant, dietary regimes, chemicals, etc..) on organ functionalities. In most in vitro applications involving barrier organs, both on-chip, and off-chip, the epithelial part is considered the only functional one. Therefore, the in vitro replication of barrier tissues is often obtained by inducing epithelial cell polarization on porous membranes, the so-called 2.5D model. More complex full-thickness 3D models, make use of fibroblasts-populated exogenous biomaterials to mimic the connective compartment. In such approaches, the mostly used ECM analogs for the in vitro fabrication of connective tissues are collagen type I or type III, mixtures of collagen and glycosaminoglycans, Matrigel, or hydrogels of either synthetic or natural origin. Although such matrices provide a suitable environment to maintain fibroblasts viability and support the differentiation of the corresponding epithelia, hold different limitations. Their exogenous origin does not allow a correct replication of spatial-temporal signal presentation necessary for the maintenance of organ functions. Often, the same material is used as a feeder for different epithelia with a clear loss of tissue specificity. At last, exogenous matrices are not able to evolve (in terms of composition, architecture, and biophysical properties) according to a specific pathophysiological status. This represents a strong limitation if one wishes to replicate, for instance, inflammatory status involving the connective compartment also. Compared to exogenous matrices, connective tissue made of fibroblasts-synthesized ECMs has been proven to be more functional [8], [9] compared to exogenous matrix-based counterparts. We previously demonstrated that an engineered full-thickness human skin composed of an endogenous dermis was able to replicate crucial biological phenomena that are not observed in the traditional full-thickness tissues: inward differentiation of human keratinocytes with subsequent formation of hair-follicle structures; (ii) rete ridge profile of the dermal/epidermal interface; (iii) replication of the ECM remodeling after a damage [8]. Also, full-thickness intestinal models possessing an endogenous connective submucosa resulted a more functional tissue compared to the corresponding exogenous one [9]. To build utissue-specific connective microenvironment, in this work, we use a modular tissue engineering approach [10] to fabricate different endogenous ECMs starting from human fibroblasts coming from different body locations (skin, lung and cervix). Fibroblasts are firstly used to build up connective microtissues (μT) having a mean diameter of 200 μm. During the μT formation fibroblasts were induced in synthesizing their own ECM. Such microtissue are then used as building blocks to form macroscopic 3D tissues (3D-Dermis, 3D-Lung and 3D-Cervix respectively) as reported in Figure 1. We will demonstrate that each fibroblast synthesized and assembled a tissue specific ECM paving the way for the building up of completely endogenous, functional and histological competent full thickness barrier organs.

II. Material ad methods

A. Cells expansion

Human dermal fibroblasts (neonatal HDF 106-05n ECACC), Human lung fibroblasts (NHLF Lonza CC-2512), and extracted Human cervical fibroblast (HCF obtained by National Cancer Institute 'Fondazione Pascale' after informed consent, were sub-cultured onto 150 mm^2 Petri dishes in culture medium (Eagle's BSS Minimum Essential Medium containing 20% fetal bovine serum, 100 µg/mL L-glutamine, 100 U/mL penicillin/streptomycin, and 0.1 mM Non Essential Amino Acids). Cells were maintained at 37 °C in humidified atmosphere containing 5% CO2. Cells in a range of passages 4-7 were used [8], [11].

B. Microtissue fabrication

Gelatin microbeads having a diameter of 75-150 µm, stabilized by 4% of glyceraldehyde were fabricated by means of a modified double emulsion technique (O/W/O) as previously reported [10]. Briefly, gelatin (type B Sigma Aldrich Chemical Company, Bloom 225, Mw 176,654 Da) was dissolved into 10 ml of water containing TWEEN 85 (6% w/v) (Sigma Aldrich Chemical Company) at 60 °C. Toluene containing SPAN 85 (3% w/v) (Sigma Aldrich Chemical Company) was continuously added to the aqueous gelatin solution (8% w/v) to obtain primary oil in water emulsion. Microbeads of gelatin containing droplets of toluene were produced through the addition of excess toluene (30 ml). After cooling below 5 °C, 20 ml of ethanol were added to extract toluene and stabilize gelatin microbeads. The resulting microspheres were filtered and washed with acetone and then dried at room temperature. To make the Dermis–µT, Lung–µT and Cervix–µT, spinner flask bioreactor (250 ml, CELLSPIN, Integra Biosciences) was inoculated with a cell density of 105 cell/ml and a gelatin microbeads density of 2 mg/ml (corresponding to $5*10^3$ beads/mg), to obtain an initial ratio of 10 cells per microbead. The culture suspension was stirred intermittently at 30 rpm (5 min stirring and 30 min static incubation) for the first 6 h post-inoculation to allow cell adhesion, and then continuously at 30 rpm for up to 10 days. All cultures were maintained at 37 °C in a humidified 5% CO2 incubator. The culture medium was replenished on the first day and every 2 days until the end of the experiments. 50 µg/ml of ascorbic acid (l-ascorbic acid Sigma A-5960) was added at each medium change Figure 1 top right).

C. Connective macrotissues fabrication 3D-Dermis, 3D-Lung and 3D-Cervix

After 10 days of culture time the Dermis–µT, Lung–µT and Cervix–µT suspension were withdrawn from the spinner flask and transferred and cultured in an assembling chamber. The assembling chamber has a sandwich-like structure in the middle of which is a silicon mold with empty spaces (1 mm in thickness, 5 mm in diameter) where the Dermis–µT, Lung–µT and Cervix–µT assembly respectively takes place [8], [11]. The silicon mold is delimited on both the top and bottom sides by two stainless steel rigid grids; the grids are posed on both sides of the system and are fastened to each other using stainless steel screws to close the assembling chamber. The assembling chamber was then placed on the bottom of a spinner flask (Bellco biotechnology code 1967-00050) and surrounded by culture medium that was exchanged every 3 days (Figure 1 bottom right). The spinner was operated at 60 rpm allowing convective mass transport across the entire thickness of the assembling chamber in which the tissue maturation process takes place [10].

Macrotissue characterization

Histology. For histological analysis, 3D-Dermis, 3D-Lung, and 3D-Cervix were fixed in a solution of 10% neutral buffered formalin for 24 h, dehydratases in in an incremental series of ethanol, and embedded in paraffin. Cross sections 7 µm thick were obtained by using a microtome (MICROM HM355S Bioptica) and stained using hematoxylin/eosin (Sigma Aldrich) following standard procedure.

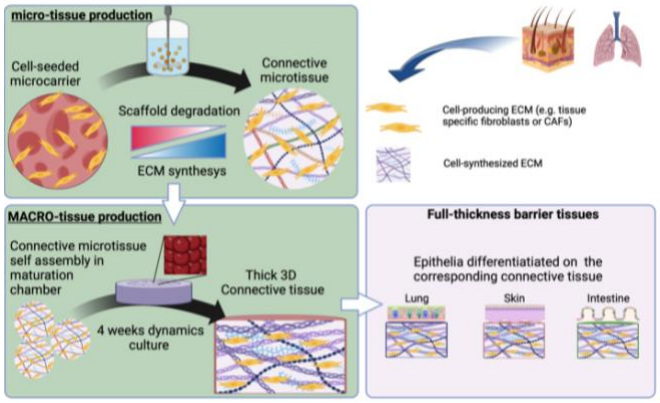


Fig. 1. Two-step bio fabrication method. Once obtained stromal cells from tissues, they were cultured in a spinner flask bioreactor in presence of porous microbeads (top left). During this step de novo synthesized ECM takes place and porous microbeads will degrade. The endogenous connective microtissues are then assembled in macroscopic structures (bottom left) to obtain 3D macroscopic tissue-specific connective tissue. In the final step o the process, each epithelial cell will be seeded on the corresponding connective to obtain full-thickness, tissue-specific and endogenous barrier tissues.

The sections were observed with a BX53 Olympus microscope and the images were acquired using an Olympus DP 21 camera.

Multiphoton imaging. The 3D-Dermis, 3D-Lung, and 3D-Cervix were fixed with 4% paraformaldehyde, and rinsed twice with PBS. The samples were imaged under multi-channeled Leica TCS SP5 II coupled with a Multiphoton Microscope where the NIR femtosecond laser beam was derived from tunable compact mode-locked titanium: sapphire laser (Chamaleon Compact OPO-Vis, Coherent). The samples were observed to induce second harmonic generation (SHG) (λex=840 nm, λem = 420±5) of unstained neo-synthesized collagen structures.

Scanning electron microscopy (SEM). The 3D-Dermis, 3D-Lung, and 3D-Cervix were dehydratases in an incremental series of ethanol (75%, 85%, 95%, and 100% twice, each step 30 min at RT. The samples place were placed on conductive stub stubs, metalized by Cressington 208HR High-Resolution Sputter Coater with 10nm of Au, and then examined by scanning electron microscopy (SEM) (Leica S400).

ECM composition. 3D-Dermis, 3D-Lung, and 3D-Cervix samples were fixed in paraformaldehyde 4% (20 min at room temperature), dehydratases in an incremental series of ethanol, and embedded in paraffin. Cross sections 7 µm were incubated for 3 h at room temperature with primary antibodies, followed by incubation with the appropriate secondary antibody for 2 h

at room temperature. The primary monoclonal antibodies used in this study included: anti-Elastin antibody (diluted 1:200; Abcam, Cambridge, UK); anti-Laminin antibody (diluted 1:50; Abcam), anti-Fibronectin antibody (diluted 1:400; Abcam) and anti-Hyaluronic acid antibody (diluted 1:100; Abcam). The secondary antibodies used were: AlexaFluor 488 goat anti-mouse (Life Techologies, Milan, Italy); AlexaFluor 568 goat anti-mouse (Life Techologies); all secondary antibodies were diluted 1:500 in PBS/BSA 3%. After rinsing with PBS, the tissue in the device was stained by 4',6-diamidin-2-fenilindolo (DAPI) 1:10000 and incubated for 10 min at room temperature. The simples were imaged with multichanneled Leica TCS SP5 II coupled with a Multiphoton Microscope where the NIR femtosecond laser beam was derived from a tunable compact mode-locked titanium: sapphire laser (Chamaleon Compact OPO-Vis, Coherent). The excitation/emission wavelengths were set as follows: λex= 500 nm, λem = 510-530 nm (single photon mode, for Elastin and Fibronectin) and λex= 580 nm, λem = 612-623 nm (single photon mode, for Laminin and Hyaluronic acid); λex = 720 nm, λem = 460 ± 10 nm (two photon mode, for DAPI). The fluorescence quantifications were obtained by dividing the green/red pixels number by the cells number. The number of pixels and the number of cells were obtained by using ImageJ software. The analysis was performed in three independent experiments.

III. RESULTS

A. *ECM architecture and composition*

ECM architecture. Fig. 2A-C shows the histological sections of 3D-Dermis, 3D-Lung and 3D-Cervix respectively. After the maturation time, no more microbeads were still detected, and compact tissues scaffold-free were obtained. In Fig. 2 D-F was showed the macroscopic collagen architecture for each proposed model; in particular, the collagen network appears to get organized in parallel fibers in the cases of 3D-Dermis and 3D-Cervix. Only in the 3D-Lung model, the fibroblasts organize the collagen network recreating the alveolar-like structures of about 50 μm. Although in this model, no pneumonocytes were added as epithelial alveolar cells, the fibroblasts still organize the ECM in order to accommodate such alveolar structures. By increasing the zoom factor in the ECM space (Fig. 2 G-I), once again the sponge-like micro/nano architecture of the lung tissue was detected. Indeed, collagen niches of 200 nm were recreated (Fig. 2M); on the contrary, for 3D-Dermis and 3D-Cervix an intricate network of collagen fiber is present (Fig. 2L, 2N).

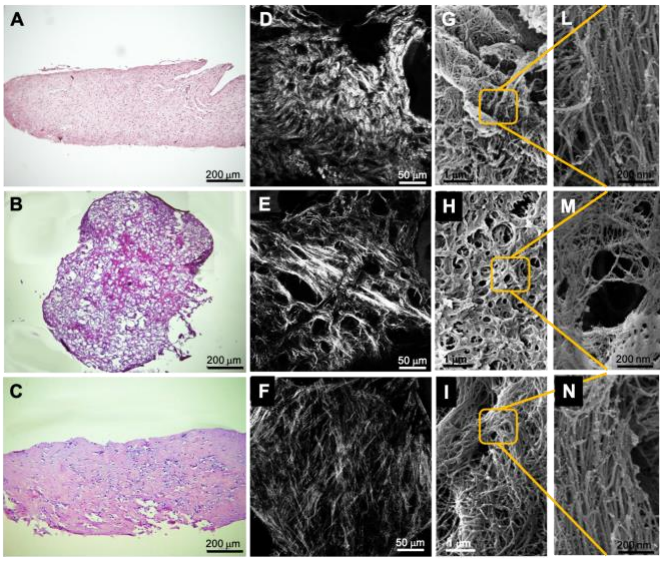


Figure 2. Architecture and organization of the 3D connective tissues. First row: histology of the 3D Dermis (A), SHG images (B), SEM images (G, L). Second row: histology of the 3D Lung (B), SHG images (E), SEM images (H, M). Histology of the 3D Cervix (C), SHG images (F), SEM images (I, N).

ECM composition. From a compositional point of view the endogenous ECMs were different in terms of HA elastin, and collagen fraction as reported in Figure 3. 3D-Cervix showed the highest amount of HA (Fig. 3, top) while 3D-Lung the lowest, the content of HA in the 3D-Dermis was in the between, with no statistical differences both with D-Cervix and 3D-Lung. The elastin fraction (Fig. 3, centre) resulted higher in 3D-Cervix if compared with the 3D-Dermis, while the 3D-Lung was in the middle, with no statistical differences with both 3D-Cervix and 3D-Dermis. The collagen fraction (Fig. 3 bottom) showed a lower collagen amount for 3D-Lung model. Indeed, both in the macroscopic and micro/nanoscopic scale, the circular shapes recreated in the ECM represented a non-collagen zone. On the contrary, in 3D-Dermis and 3D-Cervix models, higher values were reported with no statistical differences.

IV. CONCLUSIONS

Here we have reported a bioengineering method to build up scaffold-free, and tissue-specific thick endogenous ECMs. In particular, we fabricated connective tissue of the dermis, lung and cervix. We demonstrated that fibroblasts from different sites, when induced in producing their own ECM in vitro, elaborated different microenvironments resembling their native site-specific context (Fig. 2 and 3). As tissue functionalities, both in vivo and in vitro, are strictly related to the local microenvironment, we argue that this approach will have tremendous implications in the future fabrication of full thickness barrier tissue and in organotypic tissues. In fact, endogenous ECMs has been proved to be responsive and adaptive to different stimuli, by changing their composition and architecture in concert with cells' actual needs [12], [13]. This will make in vitro studies concerning aging and other pathologic conditions (e.g. cancer, inflammations, AGEs) more truthful.

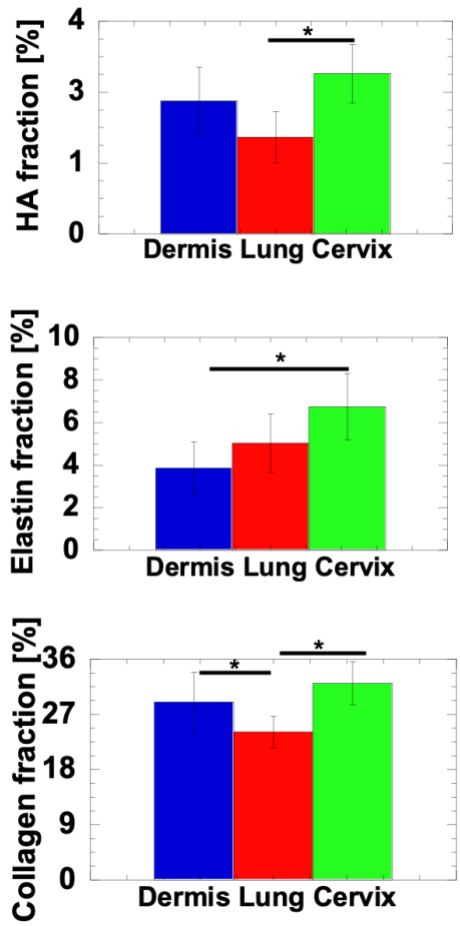


Figure 2. Composition of the three different engineered ECMs. Hyaluronic acid (HA), Elastin, and collagen fraction.

REFERENCES

[1] N. K. Karamanos *et al.*, "A guide to the composition and functions of the extracellular matrix," *FEBS J.*, vol. 288, no. 24, pp. 6850–6912, 2021.

[2] M. Q. Mao, J. Jing, Y. J. Miao, and Z. F. Lv, "Epithelial-Mesenchymal Interaction in Hair Regeneration and Skin Wound Healing," *Front. Med.*, vol. 9, no. April, pp. 1–11, 2022.

[3] M. Hu and K. Polyak, "Microenvironmental regulation of cancer development," *Curr. Opin. Genet. Dev.*, vol. 18, no. 1, pp. 27–34, 2008.

[4] O. Hallgren *et al.*, "Altered fibroblast proteoglycan production in COPD," *Respir. Res.*, vol. 11, pp. 1–11, 2010.

[5] T. Rozario and D. W. DeSimone, "The extracellular matrix in development and morphogenesis: A dynamic view," *Dev. Biol.*, vol. 341, no. 1, pp. 126–140, 2010.

[6] M. J. Merrilees, P. S. T. Ching, B. Beaumont, A. Hinek, T. N. Wight, and P. N. Black, "Changes in elastin, elastin binding protein and versican in alveoli in chronic obstructive pulmonary disease," *Respir. Res.*, vol. 9, pp. 1–9, 2008.

[7] J. E. Fata, Z. Werb, and M. J. Bissell, "Regulation of mammary gland branching morphogenesis by the extracellular matrix and its remodeling enzymes," *Breast Cancer Res.*, vol. 6, no. 1, pp. 1–11, 2004.

[8] C. Casale, G. Imparato, F. Urciuolo, and P. A. Netti, "Endogenous human skin equivalent promotes in vitro morphogenesis of follicle-like structures," *Biomaterials*, vol. 101, pp. 86–95, 2016.

[9] V. De Gregorio *et al.*, "Intestine-on-chip device increases ECM remodeling inducing faster epithelial cell differentiation," *Biotechnol. Bioeng.*, vol. 117, no. 2, pp. 556–566, 2020.

[10] G. Imparato, F. Urciuolo, C. Casale, and P. A. Netti, "The role of microscaffold properties in controlling the collagen assembly in 3D dermis equivalent using modular tissue engineering," *Biomaterials*, vol. 34, no. 32, pp. 7851–7861, 2013.

[11] V. De Gregorio *et al.*, "An Engineered Cell-Instructive Stroma for the Fabrication of a Novel Full Thickness Human Cervix Equivalent In Vitro," *Adv. Healthc. Mater.*, vol. 6, no. 11, 2017.

[12] F. Gioiella, F. Urciuolo, G. Imparato, V. Brancato, and P. A. Netti, "An Engineered Breast Cancer Model on a Chip to Replicate ECM-Activation In Vitro during Tumor Progression," *Adv. Healthc. Mater.*, vol. 5, no. 23, pp. 3074–3084, 2016.

[13] C. Casale *et al.*, "Engineering a human skin equivalent to study dermis remodelling and epidermis senescence in vitro after UVA exposure," *J. Tissue Eng. Regen. Med.*, vol. 12, no. 7, pp. 1658–1669, 2018.

Hydrogel-based photopolymers for 3D printing of scaffolds by bench-top stereolithography

C. Merli[1,2], C. Capitini[2,3], M. Calamai[2,3], G. Frediani[1], F. Carpi[1], and C. Credi[2,3]

[1] *Department of Industrial Engineering, University of Florence, Florence (Italy)*
[2] *European Laboratory for Non-Linear Spectroscopy, University of Florence, Sesto Fiorentino (Italy)*
[3] *National Institute of Optics – National Research Council, Sesto Fiorentino (Italy)*

***Abstract*—As an attempt to find alternatives to expensive microfabrication processes for polymer-based scaffolds for tissue engineering, in this work hydrogel-based photopolymers were engineered to be microstructured at high resolutions by low-cost stereolithography (SLA). To this end, both synthetic and natural/synthetic materials were blended with additives, directly affecting the SLA-printing resolution. Different formulations with tunable mechanical properties were selected for the rapid prototyping of biocompatible millimetric scaffolds with varied internal porosity, potentially exploitable for tissue engineering applications.**

***Keywords*— Stereolithography, hydrogel, tissue engineering, scaffold.**

I. Introduction

To date, 3D printing techniques are considered well-established methods in tissue engineering and regenerative medicine for the fabrication of 3D synthetic structures [1]. Among all, photopolymerization-based techniques, such as stereolithography (SLA) and two-photon polymerization (2PP), have been exploited to realize stable scaffolds with tailored geometry and porosity, which is crucial to guide cells response [2], [3]. Novel 3D photocurable materials have been developed to address specific requirements in terms of biocompatibility, biofunctionality, and stiffness [4]. Despite their rapid growth, research efforts are still needed to improve scaffolding materials. In this scenario, double network (DN) systems based on methacrylated hyaluronic acid (HAMA) and polyethylene glycole diacrylate (PEGDA) are of great interest, due to the synergic combination of natural/synthetic hydrogels whose ratio can be tuned to tailor the substrate stiffness while guaranteeing biocompatibility [5].

Here, a PEGDA-HAMA system was optimized for high-resolution 3D printing scaffolds exploiting low-cost bench-top SLA, instead of expensive and time consuming 2PP [6]. High printing speed and high printing resolution were successfully obtained by blending with additives, whose content was optimized in terms of key parameters used to quantify the SLA behaviour, namely critical energy E_c (required energy dose to cross-link the resin) and depth of penetration D_p (length of penetration of the laser within the resin, respectively) [7].

II. Materials and Methods

A. SLA-curable hydrogel double-networks

DN systems were developed by adding HAMA (20-50% substitution, molecular weight Mw 20,000-30,000) to PEGDA (average molecular weight Mn = 700), mixed with photoinitiator (PI) TPO-L (4 wt%) at varied PEGDA-HAMA ratios (Table I). In order to tune the number of photons absorbed by the PI and thus to control the laser penetration, the photons absorbing competitor Brilliant Yellow (BY) dye was added at varied concentrations to the hydrogel-based formulations (Table I). All materials were purchased from Merck. According to the procedure described in reference [7], a "wedgeplot" method adapted from the standard diagnostic WINDOWPANE technique was exploited to determine the depth of penetration D_p and the critical energy E_c of the developed formulations, when they were used with a bench top SLA printer (XFAB2500HD, Digital Wax Systems, Italy) equipped with a monochromatic actinic laser source (Solid State Bluedge BE-1500A/BE-1500AHR); the latter had an emitting output power of 30 mW at a wavelength of 405 nm and a beam diameter of 50 μm [8], [9]. Each composition was measured thrice. The SLA processing parameters were adjusted according to the D_p and E_c values obtained, so as to fabricate millimetric scaffold prototypes with pores sizes in the range 250-500 μm.

B. Characterization Techniques

Optical microscope (OM) images were taken to study the morphology of the 3D printed scaffolds in terms of pore size and geometry. A custom-made indenter equipped with a 5 N-load cell was exploited to evaluate the stiffness of the 3D-printed hydrogels at their swollen equilibrium. Swelling experiments were conducted to measure the extent of the hydrogels' mass swelling, which, according to the Flory-Rehner theory, was correlated to the mechanical strength of the crosslinked networks and to their density of crosslinking [10]. To this end, hydrogels samples were swollen at ambient temperature in phosphate buffer saline (PBS) solution. Indentation tests and swelling measurements were repeated twice.

C. Cell Cultures

In order to preliminarily assess their biocompatibility, the SLA-printed scaffolds were thoroughly washed with phosphate buffer solution (PBS), sterilized under UV-light for 25 min, seeded with primary dermal fibroblasts (FBs) extracted from human connective tissue and cultured for 1 week in a dedicated incubator. Then, the scaffolds were analysed by confocal microscopy following conventional staining protocols with wheat germ agglutinin (WGA)-594 and Hoechst 33342, for membrane and nuclei visualization, respectively.

III. Results and Discussion

The first objective of the present work was the formulation of laser-curable hydrogel-based photopolymers that could be processed with a bench-top SLA apparatus for the direct fabrication of millimetric scaffolds. To this end, starting from pure PEGDA, we investigated the effect of increasing amounts of BY on the resins' behaviour in terms of SLA processability. Table I presents D_p and E_c values experimentally determined for the developed formulations. As expected, by increasing the BY content, which competed in photons absorption with the PI (whose content was fixed at 4 wt%, following previous studies [11]), D_p progressively decreased, moving from 0.29 mm down to 0.11 mm, for a BY content increasing from 0 to 0.5 wt%. Conversely, no apparent trend was observed for the E_c values.

Blending PEGDA with natural-derived hydrogel HAMA was found to further decrease D_p values, down to around 0.08 mm (Table I), similarly to commercial high-performance SL resins taken as a benchmark (e.g. DL260 resin by Digital Wax Systems, Italy, with D_p = 0.079 mm and E_c = 9.5 mJ/cm^2). The higher E_c values obtained for these blends were likely due to the HAMA's higher molecular weight and lower methacrylates substitution with respect to PEGDA.

TABLE I: Hydrogel double-networks for SLA-processing and related values of depth of penetration and critical energy.

PEGDA:HAMA	Brilliant Yellow [wt%]	D_p [mm]	E_c [mJ/cm^2]
100:0	0	0.29 ± 0.004	1.4 ± 0.07
100:0	0.01	0.28 ± 0.005	1.7 ± 0.082
100:0	0.1	0.23 ± 0.003	1.8 ± 0.065
100:0	0.25	0.21 ± 0.001	2.9 ± 0.033
100:0	0.5	0.11 ± 0.001	1.1 ± 0.043
90:10	0.25	0.07 ± 0.001	11.4 ±1.4
70:30	0.25	0.09 ± 0.002	25.3 ± 1.3
65:35	0.25	0.08 ± 0.002	18.3 ± 1.25

The PEGDA pristine formulation with the lowest D_p value (PEGDA with 0.5 wt% BY) and the PEGDA:HAMA formulation with the average D_p value (65:35) were exploited for SLA-printing of millimetric scaffolds with micron-sized features. Circular and square scaffolds with varied micro-pore geometry in terms of size and shape (Figure 1) were successfully fabricated within 20 minutes. OM images revealed excellent physical integrity of the printed structures and confirmed that the pore shapes and sizes were consistent with the nominal values from CAD drawings. All pores were completely open throughout the millimetric scaffolds, which showed a fully interconnected pore networks and a well-defined and repetitive architecture.

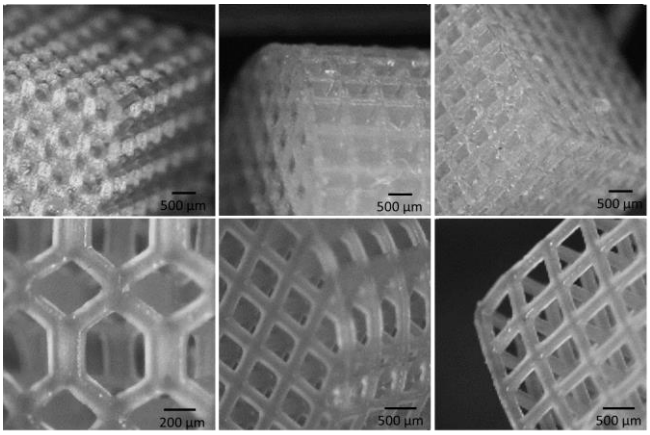


Fig. 1: OM images of SLA-printed hydrogel-based scaffolds with varied geometries.

The mechanical properties of the SLA-printed scaffolds based on the two selected formulations were characterized in terms of mechanical strength. Swelling measurements were used with the Flory-Rehner theory to calculate the crosslinking densities υ_{FR}. Data reported in Table II indicate that higher crosslinking densities were obtained for the pristine PEGDA formulation (2.4×10^{-4} mol/cm^3) relative to the PEGDA:HAMA blend (6.1×10^{-5} mol/cm^3). The decrease of mechanical strength upon blending with HAMA was confirmed by the indentation tests: the Young's modulus Y measured on the PEGDA-based scaffolds was ~688 kPa, whilst that of the PEGDA:HAMA blend was ~187 kPa (Table II).

TABLE II: Hydrogel double-networks for SLA-processing and related values of crosslinking density and Young's modulus.

PEGDA:HAMA	Brilliant Yellow [wt%]	Crosslink Density V_{FR} [mol/cm^3]	Y [kPa]
100:0	0.5	2.4×10^{-4} ± 0.1	688 ± 0.3
65:35	0.25	6.1×10^{-5} ± 5.7	187 ± 3.3

As for the E_c values, this result was probably due to the HAMA's higher molecular weight and lower methacrylates substitution with respect to PEGDA, resulting in a higher average molecular weight among crosslinks [5]. Interestingly, the Young's moduli of the 3D printed scaffolds obtained with the hydrogel formulations cover a broad range, which makes them potentially suitable to mimic a variety of physiological values typical of different soft biological tissues [12].

The biocompatibility of the scaffolds was investigated by performing preliminary cell cultures. After 1 week of incubation, cells were alive and randomly distributed within the micro-pore architecture. As visible in Figure 2, the cells showed flat and elongated spindle-like morphology, which is typical of optimal adhesion to the substrate.

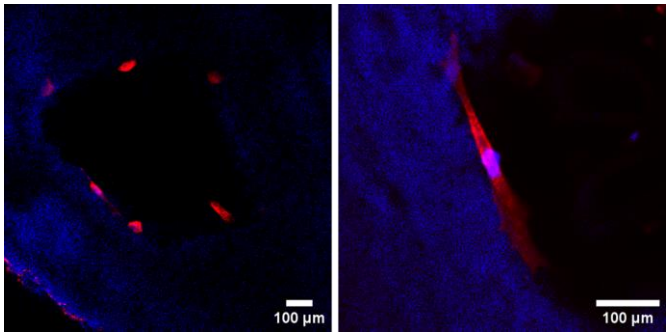


Fig. 2: FBs cultured onto the 3D scaffolds, showing typical elongated morphology.

IV. Conclusions

Synthetic and interpenetrating natural/synthetic photopolymers based on hydrogels were successfully optimized for high-resolution 3D printing of cell scaffolds, by means of a low-cost bench-top SLA apparatus. By optimizing the additive content, the SLA behaviour of the formulations was engineered for the rapid prototyping of millimetric scaffolds, with fully interconnected internal microarchitectures at high resolution, avoiding the use of expensive 2PP fabrication processes. Mechanical properties and preliminary evidence of biocompatibility of the SLA-printed scaffolds indicated their potential applicability for engineering biological tissues on substrates with physiologically-relevant elastic moduli in the 10^2 to 10^3 kPa range.

Future developments of this work will include a more systematic campaign of formulation and testing of such hydrogels network and an in-depth investigation on their possible adoption to obtain cell scaffolds actually useful for tissue engineering.

References

[1] A. Bagheri and J. Jin, "Photopolymerization in 3D printing", *ACS Applied Polymer Materials*, 1, 4, 593–611, 2019.

[2] M. Layani, X. Wang, S. Magdassi, "Novel materials for 3D printing by photopolymerization", *Advanced Materials*, 30, 1−7, 2018.

[3] M. M. Nava. et al., "Interactions between structural and chemical biomimetism in synthetic stem cell niches", *Biomedical Materials*, 10(1), 015012, 2015.

[4] O. Kufelt, A. El-Tamer, C. Sehring, S. Schlie-Wolter and B. N. Chichkov, "Hyaluronic Acid Based Materials for Scaffolding via Two-Photon Polymerization", *Biomacromolecules*, 15, 650−659, 2014.

[5] U. D'amora, "Bioactive composites based on double network approach with tailored mechanical, physico-chemical, and biological features", *Journal of Biomedical Research Part A*, 106(12), 3079-3089, 2018.

[6] B. N. L. Costa et al., "Cellular interaction of bone marrow mesenchymal stem cells with polymer and hydrogel 3D microscaffold templates", *ACS Applied Materials & Interfaces*, 14, 13013−13024, 2022.

[7] P. F. Jacobs, *Rapid Prototyping & Manufacturing: Fundamentals of Stereolithography*; Society of Manufacturing Engineers, 1992.

[8] I. Gibson, D. W. Rosen, B. Stucker, *Additive Manufacturing Technologies*; Springer, 2010.

[9] C. Credi et al., "3D Printing of cantilever-type microstructures by stereolithography of ferromagnetic photopolymers", *ACS Applied Materials & Interfaces*, 8, 26332−26342, 2016.

[10] C. Credi et al., "Fine tuning and measurement of mechanical properties of crosslinked hyaluronic acid hydrogels as biomimetic scaffold coating in regenerative medicine", *Journal of the Mechanical Behavior of Biomedical Materials*, 29, 309–316, 2014.

[11] C. Credi, M. Levi, G. Griffini, S. Turri, "biotinylated photopolymers for 3D-printed unibody lab-on-a-chip optical platforms", *Small*, 1702831, 2017.

[12] S. S. Sheiko, A. V. Dobrynin, "Architectural code for rubber elasticity: from supersoft to superfirm materials", *Macromolecules*, 52, 7531−7546, 2019.

Assessment of printability on autoclaved biomaterial inks for extrusion bioprinting

E. Spessot[1], A. Battistella[1], A. Motta[1] and D. Maniglio[1]
[1] *BIOtech Research Centre, Department of Industrial Engineering, University of Trento*

***Abstract*—3D bioprinting is a powerful method to produce layered cell-laden scaffolds with complex architecture. Natural polymers, such as gelatin and hyaluronic acid, are usually exploited for this purpose. An open challenge is the sterilization of the inks before printing, since it can impact their chemical/physical properties and mechanical stability. This paper investigates the suitability of autoclaving methacrylated gelatin (GelMA) and hyaluronic acid (HaMA) blends for their use as inks in extrusion-based bioprinting.**

***Keywords*—3D-Bioprinting, Biomaterial ink, Printability, Autoclave sterilization**

I. Introduction

In the field of tissue engineering and regenerative medicine, 3D-Bioprinting is an emerging technology that allows the fabrication of cell-laden scaffolds with customized chemical composition and morphology [1]. Extrusion-based bioprinting is one of the most widely adopted technique and allows the processing of a variety of ink formulations based on high-concentrated water-soluble polymers [2] or pre-crosslinked hydrogels [3]. To achieve an adequate shape fidelity and accurately reproduce the CAD model, the formulation of the inks should be careful designed to match specific rheological and physical properties [4]. Blends of gelatin and hyaluronic acid (HA) have been widely studied showing potential applications for different tissues by tuning the chemical and mechanical properties [5], [6]. They can be chemically modified with methacrylate groups to obtain a photocurable material (i.e., methacrylated gelatin -GelMA- and methacrylated hyaluronic acid -HaMA-). Bioink formulations based on GelMA/HaMA blends have been explored [7]–[10]. One big challenge in the design of the biomaterial blends is their sterilisation, since it has a strong impact on the materials inducing chemical degradation with significant impact on the mechanical properties or triggering secondary crosslinkings [11]. The main recognized treatments comprehend gamma ray- irradiation, filtration, autoclaving and exposure to ethylene oxide (EtO) gas [11], [12]. It was demonstrated the autoclave determines significative reduction in the GelMA and HaMA properties, so some authors suggest EtO treatment as the preferred method for the sterilization of the blend [12]. However, the access to EtO is less available, especially in research laboratories, and it requires specific location for installation and special operative procedures, due to extreme gas toxicity [13], making autoclave still a preferred option.

In the present work, we used GelMA and HaMA as base matrices for the ink development and we studied the suitability of the autoclave treatment on these blends, evaluating the printability and the physico-mechanical properties before and after printing.

II. Materials and Methods

A. Materials

Gelatin (from porcine skin, powder gel strength ~300 g Bloom; type A), methacrylic anhydride and hyaluronidase (hyaluronidase from bovine testes, Type I-S, lyophilized powder, 400-1000 units/mg solid) were purchased from Sigma Aldrich. Hyaluronic acid sodium salt (m.w. 1.0-1.5 MDa) was purchased by Glentham Life Sciences. Lithium phenyl-2,4,6-trimethyl-benzoylphosphinate (LAP, >98.0% (T)(HPLC)) was purchased by TCI Chemicals. All the reagents were used as received.

B. Methacrylation of the polymers, ink formulation and sterilization

Methacrylation of gelatin and hyaluronic acid (HA) was carried out following previously reported protocols [14], [15]. Then, freeze-dried GelMA was dissolved at 20% w/v in PBS at 50°C under magnetic stirring. Freeze-dried HaMA was dissolved in the GelMA solution at the desired concentrations: 2.4%, 3.4% or 4.4% (w/v), as reported in Table 1. LAP was added at a concentration of 5% with respect to the total polymer amount. GelMA/HaMA prepolymer solutions were autoclaved for 15 minutes at 121°C under vacuum, and with slow discharge process.

TABLE I: Biomaterial Ink formulations

Sample	*GelMA %(w/v)*	*HaMA %(w/v)*
GelMA	20	0
GelMAHaMA2	20	2.4
GelMAHaMA3	20	3.4
GelMAHaMA4	20	4.4

C. Rheological evaluation on the solutions before printing

The rheological evaluations were carried out on a Discovery Hybrid Rheometer DHR-2 (TA ® Instruments, New Castel, USA) equipped with a stainless-steel cone/plate system (50 mm diameter, 2° cone angle and 100 μm truncation gap distance) and a Peltier plate for the temperature control. All the GelMA/HaMA solutions were subjected to the following tests, performed in triplicates:

Oscillatory temperature sweep: Measurements were carried out to record the storage modulus (G'), the loss modulus (G''), and the loss tangent (tan δ) at different temperatures. Tests were performed from 15°C to 40°C, with

a thermal ramp of 2°C/min, at fixed frequency and shear strain of 1 Hz and 5%, respectively. From the analysis of the resultant curves, it was possible to extrapolate the crossover point between G' and G'', which corresponds to the sol-gel transition of the solution. The test was performed on the solutions before and post-autoclave to assess the change in the sol-gel transition temperature.

Rotational shear rate sweep: The test was carried out to investigate the flow behaviour properties of the inks [16]. Samples were equilibrated at 30°C and then subjected to a shear rate sweep from 0.1 to 300 s^-1. Viscosity curves were fitted with the power-law model (Eq.1)

$$\tau = k\,\dot{\gamma}^{n} \qquad (1)$$

where τ is the shear stress, $\dot{\gamma}$ is the shear strain rate, n is the power law index, and k is the flow consistency index.

D. Printability assessment

The printability of the different inks was evaluated by means of an extrusion-based bioprinter (BIOX, Cellink) equipped with standard pneumatic printheads. The printability experiments were carried out on a polystyrene Petri dish substrate under the same printing conditions of 30° C cartridge temperature, 5° C printing bed temperature, 5 mm/s printing speed, 27G conical needle.

The extrudability of the inks was evaluated slowly increasing the air pressure until a continuous filament was extruded. The mass flow rate was determined by weighting the amount of an extruded ink in 30 second and calculating the gravimetric flow. Five different extrusion pressures were tested for each formulation selected starting from the minimum extrusion pressure and incrementing it of 5 kPa.

The quality of the printed structures has been evaluated considering the uniformity ratio (U) and the spreading ratio (S) on 5 strings 3 cm long. The parameter U is defined as the ratio between the length of the extruded strand and the length of a theoretical extruded strand, while S is defined as the ratio among the width of the printed filament and the needle diameter. The parameters were analyzed by ImageJ and MATLAB® software.

E. Swelling and mechanical characterization of the hydrogels after crosslinking

Swelling and mechanical tests were carried out on cylindrical hydrogels (diameter 8 mm, thickness 5 mm). GelMA/HaMA prepolymer solutions were extruded in silicon molds and the crosslinking was performed by means of a 365 nm UV lamp SpotLED Curing Equipment for 30 seconds at 15 cm of distance.

The water absorbency of the crosslinked hydrogels was measured gravimetrically. The as-prepared hydrogels were weighted (W0) and immersed in PBS (pH 7.4) at 37 °C. The samples were weighted every 60 minutes for 8 hours and after 24h. The wet weight of swollen hydrogels was determined at each time point by gently removing the excess of liquid with a filter paper. For each composition three replicates were tested, and the swelling degree (SD, in percentage) was determined as reported in Eq.2:

$$SD(\%) = \frac{Wt - W0}{W0} * 100 \qquad (2)$$

The mechanical properties of the crosslinked hydrogels were evaluated in compression mode. Hydrogels were kept in PBS at 37 °C for 24 h and then subjected to unidirectional compression tests with a Bose ElectroForce 3200 equipped with a 200N load cell (full scale) at a crosshead speed of 1 mm/min until sample breakage. Young's modulus (E) was calculated from the slope of the stress-strain curve in the linear range.

III. RESULTS

A. Rheological results

Rheological analysis was carried out to understand the temperature dependance and the inks flow behavior, evaluating the properties variation before and after the autoclave process.

The determination of the temperature at which the investigated materials shifted from solution state to gel state revealed an effect of the sterilization process and a dependency on the blend formulation. As reported in Fig. 1, there were no significant variations in the crossover point between different formulations before the autoclave treatment. While after the sterilization, the sol-gel transition occurred at lower temperatures depending on the amount of HaMA.

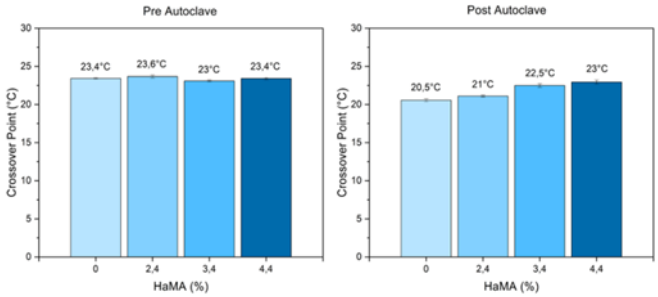


Fig. 1: Sol-gel transition of the inks pre and post autoclave

To examine the effect of different shear rate on the viscosity of the blends before and after autoclave, the properties were monitored at 30 °C, which was the temperature considered for the printing. As displayed in Table II, by increasing the amount of HA, the values of the power law index n are reduced indicating a higher degree of shear thinning, which is preferred to facilitate the extrusion. However, it is worth to notice that this effect is decreased in the autoclaved samples and the printability of these formulations was analyzed.

TABLE II: POWER LAW INDEX OF THE INKS PRE- AND POST- AUTOCLAVE

Sample	*n_pre AC*	*n_post AC*
GelMA	1.00 ± 0.01	1.01 ± 0.00
GelMAHaMA2	0.76 ± 0.03	0.97 ± 0.01
GelMAHaMA3	0.65 ± 0.07	0.82 ± 0.03
GelMAHaMA4	0.59 ± 0.05	0.71 ± 0.02

B. Printability assessment

In the design of biomaterial inks, rheological measurements are usually performed to study the flow properties of the inks and can give a preliminary information on the suitability of the

ink for extrusion 3D printing. However, they should be supported with an extended printability assessment to understand their extrudability and define the optimal printing parameters. Extrudability is the capability of the ink to produce uniform and continuous filaments when exiting the printing needle. In this work, the pressure was increased until a continuous filament was obtained and the calculated mass flow rate on different pressures is represented in Fig. 2.

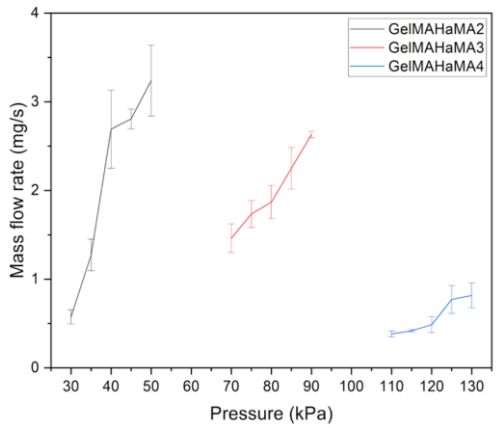


Fig. 2: Mass flow rate of the inks

Once defined the pressures, the uniformity and the width of the printed filaments was evaluated on printed straight lines, reported in Appendix. The results on the quantification of the uniformity ratio (U) are reported in Fig. 3. It is possible to observe that there are no trends correlating the printing parameter U and the increasing polymer concentration or the extrusion pressure. All ink formulations displayed a uniformity ratio that approached or slightly exceeded the unitary value. Therefore, printed strands were close to the perfect straight lines designed. This was expected since U is normally a parameter correlated to the degree of over or under crosslinking of a material. U values close to 1 indicate linear extrusion and are usually associated with polymer solutions having a fluid-like behavior [17], as in this case, since the printing temperature is higher than the sol-gel transition (Fig. 1).

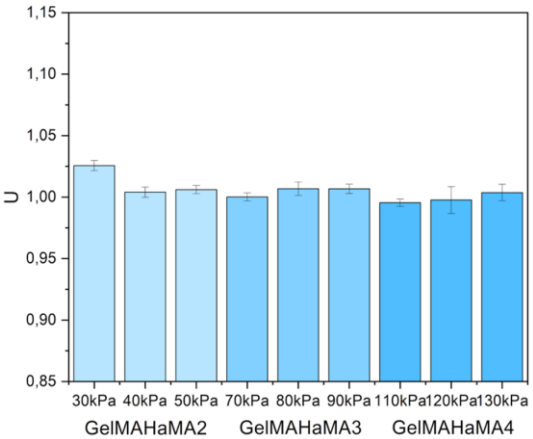


Fig. 3: Uniformity ratio (U) of the inks

The spreading ratio (S) is a useful parameter to measure the width of the printed filament considering its ability to maintain the cylindrical shape and against the spreading. As shown in Fig. 4, all ink formulations displayed S values greater than one varying from 3 to 7.5. Thus, all the tested blends largely deviated from the theoretical width due to a post-extrusion relaxation of polymer chains. Spreading ratio values higher than 2 were obtained also in other works [18], [19]. All the tested blends showed an increase of S with increasing extrusion pressure. For this reason, the selection of lower pressures must be preferred to obtain high precision printed constructs. However, even if GelMAHaMA4 was characterized by lower S compared to the other ink formulation, the printing was not completely uniform and there were problems related to needle clogging, maybe due to the high polymer concentration and the low mass flow rate.

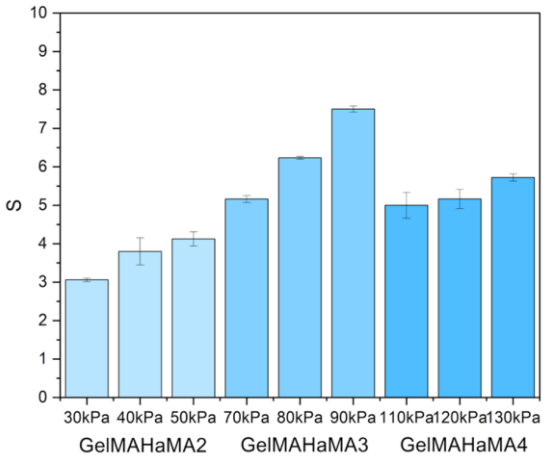


Fig. 4: Spreading ratio (S) of the inks

C. *Post-printing properties*

The swelling property of hydrogels is fundamental for cell adhesion, proliferation and nutrient exchange. The degree of swelling strongly depends on the polymer network, the interaction between the material and the solvent and the porosity. Fig. 5 demonstrates the change in the swelling degree of the hydrogels with the HaMA content. Among them, the equilibrium swelling degree of GelMAHaMA4 was the largest, as expected due to the highly hydrophilic nature of hyaluronic acid. For all the samples, the equilibrium swelling was reached within 24h after the immersion in PBS at 37°C.

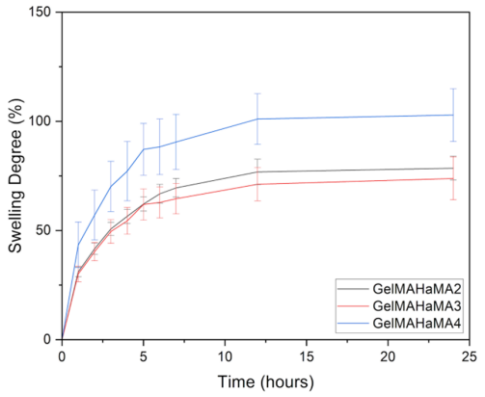


Fig. 5: Swelling degree (SD) of the inks as a function of time

The mechanical properties of hydrogels are fundamental for the stability of 3D printed structures. Compression tests were carried out to evaluate the mechanical properties of the final hydrogels after the autoclave treatment. The stress-strain curves and the compressive moduli of the different samples are

reported in Fig. 6. It can be observed that the increase of the HaMA content affects the stress-strain behaviour and can improve the compressive modulus of the hydrogel. The compressive moduli were determined to be 322±108 kPa, 361±121 kPa and 496±30 kPa for GelMAHaMA2, GelMAHaMA3, and GelMAHaMA4, respectively.

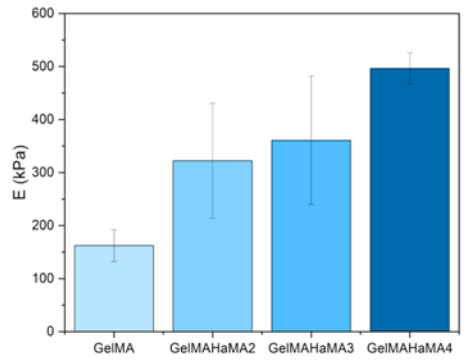


Fig. 6: Elastic moduli of the hydrogels after 24h in PBS at 37°C

IV. Conclusion

This work demonstrated the suitability of autoclave for the sterilization of a blend of GelMA and HaMA for the formulation of a sterile ink "ready to use". The autoclaved GelMA/HaMA blends displayed rheological properties suitable for extrusion bioprinting, a good geometrical accuracy on the printed structures, while maintaining good mechanical and physical properties after photocrosslinking.

Appendix

Printed straight lines for the evaluation of the parameters U and S.

Pressure (kPa)	GelMAHaMA2	GelMAHaMA3	GelMAHaMA4
30-70-110			
40-80-120			
50-90-130			

Acknowledgement

This project has received funding from the European Union's Horizon 2020 research and innovation programme under the Marie Skłodowska-Curie: grant agreement No. 101008041. This project was realized with the aid of the funding from Fondazione VRT.

References

[1] S. Agarwal, S. Saha, V. K. Balla, A. Pal, A. Barui, and S. Bodhak, 'Current Developments in 3D Bioprinting for Tissue and Organ Regeneration–A Review', Frontiers in Mechanical Engineering, vol. 6, 2020.

[2] S. Dani et al., 'Homogeneous and Reproducible Mixing of Highly Viscous Biomaterial Inks and Cell Suspensions to Create Bioinks', Gels, vol. 7, no. 4, 2021.

[3] C. Nelson, S. Tuladhar, L. Launen, and A. Habib, '3D Bio-Printability of Hybrid Pre-Crosslinked Hydrogels', International Journal of Molecular Sciences, vol. 22, no. 24, 2021.

[4] A. Schwab, R. Levato, M. D'Este, S. Piluso, D. Eglin, and J. Malda, 'Printability and Shape Fidelity of Bioinks in 3D Bioprinting', Chem. Rev., vol. 120, no. 19, pp. 11028–11055, 2020.

[5] P. C. Dromel et al., 'A bioinspired gelatin-hyaluronic acid-based hybrid interpenetrating network for the enhancement of retinal ganglion cells replacement therapy', npj Regen Med, vol. 6, no. 1, 2021.

[6] S. Poveda-Reyes, V. Moulisova, E. Sanmartín-Masiá, L. Quintanilla-Sierra, M. Salmerón-Sánchez, and G. G. Ferrer, 'Gelatin—Hyaluronic Acid Hydrogels with Tuned Stiffness to Counterbalance Cellular Forces and Promote Cell Differentiation', Macromolecular Bioscience, vol. 16, no. 9, pp. 1311–1324, 2016.

[7] M. Kuss et al., 'Effects of tunable, 3D-bioprinted hydrogels on human brown adipocyte behavior and metabolic function', Acta Biomaterialia, vol. 71, pp. 486–495, 2018.

[8] B. Duan, E. Kapetanovic, L. A. Hockaday, and J. T. Butcher, 'Three-dimensional printed trileaflet valve conduits using biological hydrogels and human valve interstitial cells', Acta Biomaterialia, vol. 10, no. 5, pp. 1836–1846, 2014.

[9] S. Posniak et al., 'Bioprinting of Chondrocyte Stem Cell Co-Cultures for Auricular Cartilage Regeneration', ACS Omega, vol. 7, no. 7, pp. 5908–5920, 2022.

[10] K. Martyniak, A. Lokshina, M. A. Cruz, M. Karimzadeh, R. Kemp, and T. J. Kean, 'Biomaterial composition and stiffness as decisive properties of 3D bioprinted constructs for type II collagen stimulation', Acta Biomaterialia, vol. 152, pp. 221–234, 2022.

[11] R. Galante, T. J. A. Pinto, R. Colaço, and A. P. Serro, 'Sterilization of hydrogels for biomedical applications: A review', Journal of Biomedical Materials Research Part B: Applied Biomaterials, vol. 106, no. 6, pp. 2472–2492, 2018.

[12] C. D. O'Connell et al., 'Evaluation of sterilisation methods for bio-ink components: gelatin, gelatin methacryloyl, hyaluronic acid and hyaluronic acid methacryloyl', Biofabrication, vol. 11, no. 3, p. 035003, 2019.

[13] G. C. C. Mendes, T. R. S. Brandão, and C. L. M. Silva, 'Ethylene oxide sterilization of medical devices: A review', American Journal of Infection Control, vol. 35, no. 9, pp. 574–581, 2007.

[14] J. W. Nichol, S. T. Koshy, H. Bae, C. M. Hwang, S. Yamanlar, and A. Khademhosseini, 'Cell-laden microengineered gelatin methacrylate hydrogels', Biomaterials, vol. 31, no. 21, pp. 5536–5544, 2010.

[15] C. Loebel, C. B. Rodell, M. H. Chen, and J. A. Burdick, 'Shear-thinning and self-healing hydrogels as injectable therapeutics and for 3D-printing', Nat Protoc, vol. 12, no. 8, 2017.

[16] S. Ansari, Md. A. I. Rashid, P. R. Waghmare, and D. S. Nobes, 'Measurement of the flow behavior index of Newtonian and shear-thinning fluids via analysis of the flow velocity characteristics in a mini-channel', SN Appl. Sci., vol. 2, no. 11, p. 1787, 2020.

[17] T. Gao et al., 'Optimization of gelatin–alginate composite bioink printability using rheological parameters: a systematic approach', Biofabrication, vol. 10, no. 3, p. 034106, 2018.

[18] A. C. Daly, S. E. Critchley, E. M. Rencsok, and D. J. Kelly, 'A comparison of different bioinks for 3D bioprinting of fibrocartilage and hyaline cartilage', Biofabrication, vol. 8, no. 4, p. 045002, 2016.

[19] F. E. Freeman and D. J. Kelly, 'Tuning Alginate Bioink Stiffness and Composition for Controlled Growth Factor Delivery and to Spatially Direct MSC Fate within Bioprinted Tissues', Sci Rep, vol. 7, no. 1, 2017.

Intestinal epithelium on chip for absorption studies

Alessandro Cordiale[1], Mattia Ballerini[2], Luigi Nezi[2], Paola Occhetta[1,3], Marco Rasponi[1]
[1] *Department of Electronics, Information and Bioengineering, Politecnico di Milano, Milan, Italy*
[2] *Department of Experimental Oncology, European Institute of Oncology- IRCCS, Milano, Italy*
[3] *BiomimX s.r.l. Milan, Italy*

***Abstract*— Absorption of orally administered therapeutics occurs at the gastrointestinal tract level and its efficiency is paramount for their success through the drug development pipeline.**

Current methods used to assess drugs absorption lack in recapitulating 3D physiological microenvironment of intestinal epithelium. Organs-on-chip (OoC) models have been lately proposed to overcome this limitation. We developed an *in-vitro* model of intestinal epithelial barrier in an OoC able to mimic peristaltic motion by providing a controlled mechanical stimulation. The created barrier functionality was assessed through immunofluorescence analyses and permeability tests.

***Keywords*— Gut on chip, OoC, ADME, Drug discovery.**

I. INTRODUCTION

DEVELOPMENT of new therapeutics is an expensive and risky process: success rate of candidate drugs is lower than 0.1% with severe waste of investments, in terms of money, time and human safety [1].

The main reason for such high failure can be ascribed to the poor efficacy and safety predictive power of preclinical studies. Animal models, despite their intrinsic ability of replicating systemic responses, often fail in faithfully recapitulating human biology due to interspecies mismatch. On the other hand, *in-vitro* human models such as standard 2D cultures, although based on human-derived material, often fail to properly mimic the *in-vivo* biological complexity [2], [3]
Development of accurate human *in-vitro* models is thus crucial to speed up translational processes and better predict the outcome of clinical trials [4].

In the last ten years increasing attention has been dedicated to the Organs-on-Chip technology (OoC). OoCs are miniaturized *in-vitro* culture systems able to mimic the *in-vivo* microenvironment by controlling cell-cell and cell-matrix interactions as well as biochemical and mechanical cues [5]. Despite their recent introduction, worldwide scientific community and regulatory agencies are collaborating to speed up the adoption of OoC. For instance, Food and Drug Administration (FDA) has recently signed memorandums of agreement with commercial companies to start adopting the OoC technology [6]

In this scenario, the study of absorption, distribution, metabolism and excretion (ADME) processes is crucial to assess the efficacy of drug candidates. The greatest share of newly developed compounds is orally administered, and their absorption mainly occurs at the gastrointestinal tract level, making the intestinal epithelium absorption of paramount relevance for drug candidates' success [7].

Current 2D methods used to assess gut absorption exploit monolayer structures made of gut epithelial immortalised cells (mainly Caco-2 line) cultured on porous membranes (transwell systems) that are used as a model of intestinal barrier. However, such model lacks in recapitulating the 3D and dynamic microenvironment of intestinal epithelium characterized by crypts and villi structures and peristaltic motion. OoC models have been lately proposed to overcome this limitation [8].
The purpose of this work was to develop an *in-vitro* model of intestinal epithelial barrier in an OoC capable of mechanically stimulate the cultured cells. In this regard, a stimulation with sinusoidal pattern was adopted in order to best replicate the phenomenon of peristalsis and induce the functional maturation of the tissue.

II. MATERIALS AND METHODS

In order to create a functional 3D intestinal epithelium on chip, the commercial device *uBeat® Stretch Platform* from BiomimX® was used to mimic the mechanical stimulation that the tissue undergoes during peristalsis.
The device is endowed with two microstructured layers separated by a thin membrane (**Fig. 1A**). The first layer is the one dedicated to the 3D cell culture, it has a chamber with two arrays of hanging pillars. Pillars were designed to divide the space of the chamber in three channels and confine a prepolymer hydrogel solution in the central channel one. The lateral channels, in the gut model, are intended to be perfused with medium or seeded with cell suspension. (**Fig. 1B**).
The second layer has a chamber that can be pressurized to deform the membrane and induce the controlled mechanical conditioning of the construct(**Fig. 1C**) [9].
The mechanical stimulation is finally tuned by the cross-section shape of the pillar and by their height that define the maximum displacement of the membrane.
Furthermore, an electronic control system (*uBox*) was designed to produce pneumatic stimulation patterns with complex waveforms resembling peristaltic movements.
The deformation obtained in the OoC was characterized as previously described [10]

After technical characterisation, the intestinal epithelial barrier was recapitulated by seeding Caco-2 and HT29 cells mixed in a 9:1 ratio ($8x10^6$ cells/mL) in one of the later channels and allowed them to adhere to a central fibrin

hydrogel matrix. 10% uniaxial strain stimulation at 0.2 Hz was exerted for 9 days to induce tissue maturation and epithelial monolayer formation.

The effects of an impulse-wave stimulation and a sine-wave stimulation were compared to the cells cultured in static conditions.

As readouts, brightfield and fluorescence microscopy analyses were performed in order to compare cell proliferation (Ki-67), epithelial integrity (ZO-1), and specific protein production (villin, mucin) among groups. Moreover, fluorescent dextran (4 kDa) diffusion studies from epithelial compartment to the empty channel were performed to assess the integrity of the epithelial barrier.

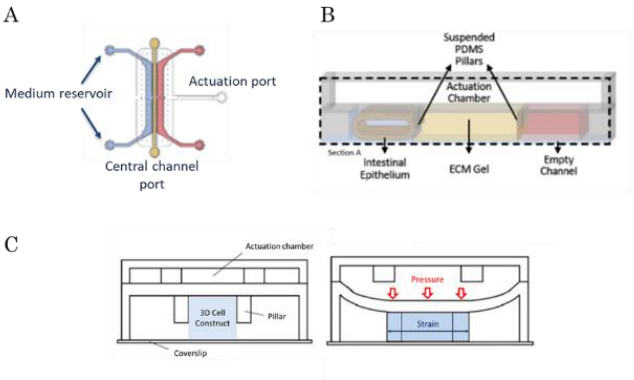


Fig. 1 *:* Gut on chip model. (A) Top view of the chip showing the ports for medium change and cell seeding, and for ECM (fibrin hydrogel) injection. (B) cross-section of the device showing the biological experiments configuration. (C) Stimulation on the gut on chip through the pressurisation of the pneumatic chamber located on top of the cell culture compartment

III. Results and Discussion

The mechanical stimulation pattern provided by the uBox electronic control system to the OoC platform was characterised before biological experiments. The stretching applied to a 3D-beads laden hydrogel seeded in the central channel of the culture layer was proved to faithfully follow complex waveform such as sinusoidal ones (**Fig. 2**). In fact, the deformation pattern reached a maximum of 11 ± 1.1% and was synchronous with the applied pressure wave frequency, therefore proving that the stimulation exerted on a 3D constructs can be finely modulated.

As a result, the characterization has proved that the device is able to reproduce complex physiological-like stimulation waves within microfluidic devices: deformation curves and strain magnitude are strictly dependant from the pressure value over time, proving that the setup is able to provide for mechanical stimulation of cell populations seeded in Organ-on-a-chip devices with any desired pattern.

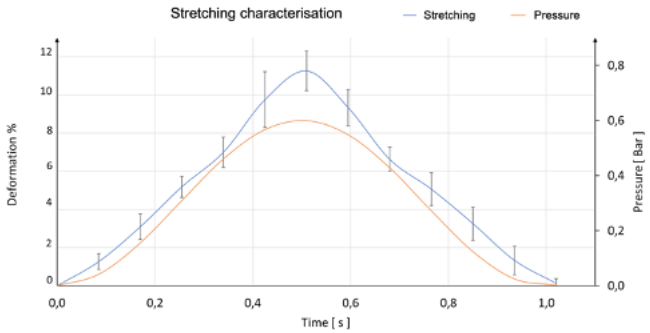


Fig. 2 :Deformation acquired in dynamic conditions (blue) and a sine pressure wave 0.6 bar, 1 Hz (orange).

Cells were seeded in the device and cultured with different mechanical conditioning (impulse-wave vs. sine-wave stimulation) for 9 days. At the experiment endpoint, brightfield microscopy images showed the presence of cells proliferating and forming a uniform epithelial barrier in both mechanically stimulated conditions. Cells self-assembled in 3D villi-like structures during culture period. Specifically, the amount of such structures was higher in both stimulated groups while the static control mainly showed a 2D cells monolayer (**Fig. 3**). This behaviour confirms the relevance of mechanical stimulation in the *in-vitro* recapitulation of functional gut morphology as already proved by literature [11].

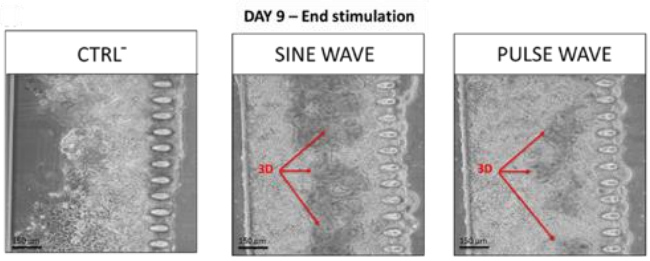


Fig. 3 *:* Comparison of the intestinal epithelium on chip after 9 days of culture. Cells subjected to two different patterns of stimulation were compared to unstimulated constructs showing that physiological mechanical cues are able to generate 3D villi-like structures (red arrows). Scalebar= 150 µm

At the end of the culture period, immunofluorescence analysis was performed to compare the stimulated groups and static control, by assessing specific markers production (ZO-1, Villin, Mucin), cells arrangement and proliferation (Ki-67).

After 9 days of culture, cells proliferated in all conditions as evidenced by the positivity for Ki67. Mechanically stimulated conditions exhibited an abundant expression of villin, a protein related to brush borders of epithelial cells, and mucin, involved in mucus secretion (**Fig. 4**). Positive expression of ZO-1 staining proved that cells formed a closed epithelium characterized by cell-cell tight junctions. Notably, expression of these proteins was enhanced within the 3D villi-like structures found mostly in stimulated constructs, as already displayed in bright field images.

The amount of the expressed proteins was also quantified to compare the experimental groups (**Fig. 5**): mechanically stimulated tissues feature a higher ZO-1 level as compared to static ones. Sine-wave stimulation was responsible for an increase in villin-positive zones and exhibited larger areas hosting 3D-structures, with a statistical difference with respect to both other experimental conditions.

Furthermore, the application of a stimulation characterized by impulse waves promoted the activity of mucus secreting cells, presenting higher levels of mucin expression than sinusoidal stimulations and static devices. This suggests that

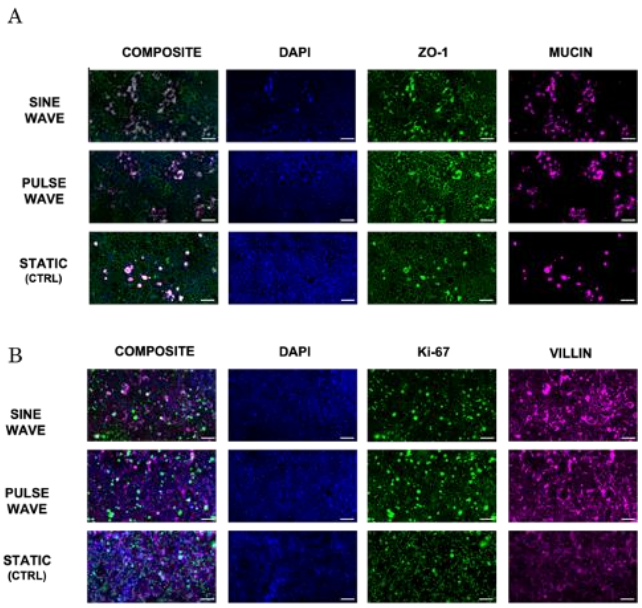


Fig. 4 : Immunofluorescence microscopy images of the epithelial barrier cultured on chip with sine stimulation, pulse stimulation and no stimulation (CTRL). A) Nuclei (blue), morphology of the tight junction between cells (ZO-1, green) and the amount of produced mucin (magenta) were stained to assess the physiological reliability of the model. B) Nuclei (blue) and Ki-67+ cells were counted to assess proliferation while villin (magenta) was stained to highlight villi-like structures.

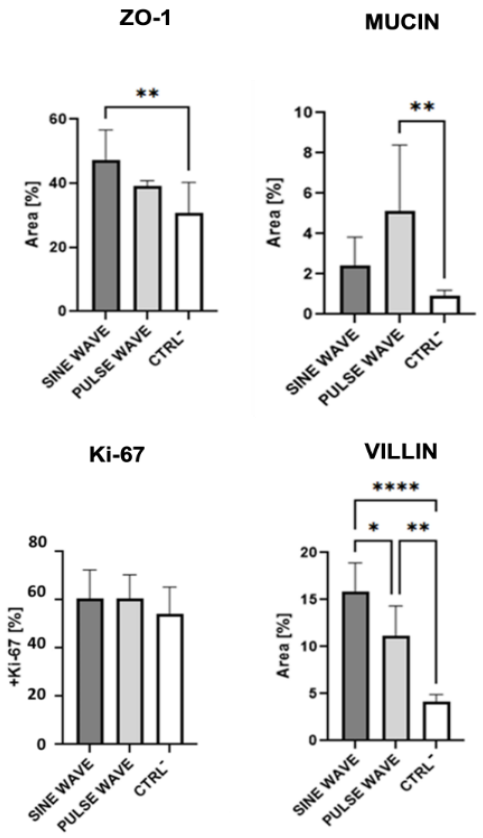


Fig. 5 : Quantitative analysis of ZO-1, mucin, Ki-67 and villin staining for sine wave (dark grey), pulse wave (light grey) and CTRL- (white) conditions. The expressions of villin, a protein related to the brush border of epithelial cells, mucin and ZO-1 were proved to be enhanced when stimulation was applied. The *, ** and **** indicate the statistic differences between conditions (P value < 0.05, P value < 0.01, and P value < 0.0001 respectively)

the two different stimulations have different effects on Caco-2/HT-29 coculture: sine wave stimulation directs cell differentiation towards villin production, while impulse wave stimulation seems to promote mucus secretion.

After biological characterisation of the developed epithelial barrier, functional permeability tests were carried out. 4 kDa Dextran was chosen as a candidate small molecule because it is not able to cross tight and functional barrier through active nor passive transport mechanisms.

The on-chip epithelial barrier developed with sine-wave stimulation was shown to be impermeable to Dextran even after 1 hour of incubation (**Fig. 6**), therefore proving the functionality of the *in-vitro* model.

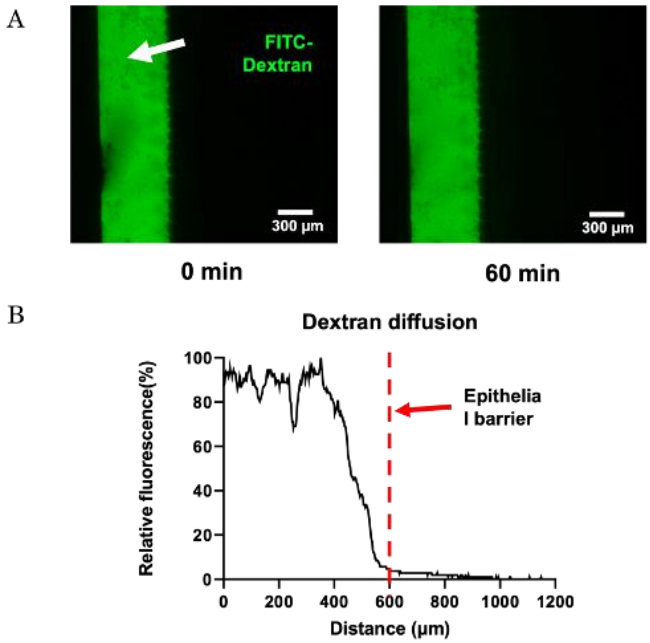


Fig. 6 : Barrier integrity analysis. (A) FITC-Dextran was inoculated in the compartment hosting the epithelial barrier and pictures were acquired over 60 minutes to assess its passage through the *in-vitro* epithelium. (B) Distribution curve of dextran across the OoC channels after 60 min: the barrier was shown to completely hinder the diffusion of dextran, proving the tightness of cell-cell junctions and the physiological relevance of the model.

IV. Conclusion

In this work, an electronic control system was designed to stimulate Organ-on-a-chip devices with pneumatic actuation, by creating customised pressure waves. In particular, we focused on sinusoidal stimulations to mimic peristaltic movements that can be exploited for the generation of an intestinal epithelial barrier model on chip.

Application of such native-like mechanical stimulation was demonstrated to be a fundamental cue to guide cell behaviour. Physiological-like stimulation led indeed to a massive generation of three-dimensional villi-like structures and improved the stability of the epithelium.

The developed gut-on-chip model represents a powerful tool for drug discovery that can provide for more accuracy and physiological relevance when it comes to ADME profiling.

References

[1] J. A. DiMasi, H. G. Grabowski, and R. W. Hansen, "Innovation in the pharmaceutical industry: New estimates of R&D costs," *J Health Econ*, vol. 47, pp. 20–33, 2016, doi: https://doi.org/10.1016/j.jhealeco.2016.01.012.

[2] M. J. Waring *et al.*, "An analysis of the attrition of drug candidates from four major pharmaceutical companies," *Nat Rev Drug Discov*, vol. 14, no. 7, pp. 475–486, Jul. 2015, doi: https://doi.org/10.1038/nrd4609.

[3] M. Hay, D. W. Thomas, J. L. Craighead, C. Economides, and J. Rosenthal, "Clinical development success rates for investigational drugs," *Nat Biotechnol*, vol. 32, no. 1, pp. 40–51, 2014, doi: 10.1038/nbt.2786.

[4] I. W. Mak, N. Evaniew, and M. Ghert, "Lost in translation: animal models and clinical trials in cancer treatment.," *Am J Transl Res*, vol. 6, no. 2, pp. 114–118, 2014.

[5] L. Wang, Z. Li, C. Xu, and J. Qin, "Bioinspired Engineering of Organ-on-Chip Devices," in *Biological and Bio-inspired Nanomaterials: Properties and Assembly Mechanisms*, S. Perrett, A. K. Buell, and T. P. J. Knowles, Eds. Singapore: Springer Singapore, 2019, pp. 401–440. doi: 10.1007/978-981-13-9791-2_13.

[6] L. A. Low, C. Mummery, B. R. Berridge, C. P. Austin, and D. A. Tagle, "Organs-on-chips: into the next decade," *Nat Rev Drug Discov*, vol. 20, no. 5, pp. 345–361, 2021, doi: 10.1038/s41573-020-0079-3.

[7] A. Fedi, C. Vitale, G. Ponschin, S. Ayehunie, M. Fato, and S. Scaglione, "In vitro models replicating the human intestinal epithelium for absorption and metabolism studies: A systematic review," *Journal of Controlled Release*, vol. 335, pp. 247–268, 2021, doi: https://doi.org/10.1016/j.jconrel.2021.05.028.

[8] A. Bein *et al.*, "Microfluidic Organ-on-a-Chip Models of Human Intestine," *Cell Mol Gastroenterol Hepatol*, vol. 5, no. 4, pp. 659–668, 2018, doi: https://doi.org/10.1016/j.jcmgh.2017.12.010.

[9] M. Rasponi, P. Occhetta, and A. Redaelli, "A microfluidic device for controlled generation and/or culture and/or maturation of three-dimensional cells and/or tissue constructs.," 2015

[10] A. Marsano *et al.*, "Beating heart on a chip: a novel microfluidic platform to generate functional 3D cardiac microtissues.," *Lab Chip*, vol. 16, no. 3, pp. 599–610, Dec. 2016, doi: 10.1039/c5lc01356a.

[11] H. J. Kim, D. Huh, G. Hamilton, and D. E. Ingber, "Human gut-on-a-chip inhabited by microbial flora that experiences intestinal peristalsis-like motions and flow," *Lab Chip*, vol. 12, no. 12, pp. 2165–2174, 2012, doi: 10.1039/C2LC40074J.

Effect of Chitosan coating on PLA electrospun scaffolds for pre-osteoblastic cells proliferation

F. Lopresti[1],V. La Carrubba[1], S. Campora[2], and G. Ghersi[2,3]
[1] *Department of Engineering, University of Palermo, RU INSTM, Viale delle Scienze, Ed. 6, Palermo, Italy*
[2] *Department STEBICEF University of Palermo, Viale delle Scienze, Ed. 16, 90128 Palermo, Italy*
[3] *Abiel s.r.l, c/o University of Palermo, Viale delle Scienze, Ed. 16, 90128 Palermo, Italy*

***Abstract*—Electrospun hybrid scaffolds composed of synthetic and natural polymers are gaining increasing interest for tissue engineering applications. In this work, scaffolds composed of polylactic acid (PLA) electrospun fibers were coated with high molecular weight chitosan at different thickness to create a core-shell microfibrous structure. The scaffolds were fully characterized from a physical point of view and their biocompatibility was investigated by seeding mouse pre-osteoblastic MC3T3-E1 cells**

***Keywords*— Electrospinning; Polylactic acid; Chitosan; Core-shell structure.**

I. Introduction

Aiming at fabricating biopolymeric porous structures for regenerative medicine purposes, hybrid scaffolds composed of synthetic and natural biopolymers can offer superior performances [1]. Electrospun fibers with core-shell architectures composed of synthetic and natural biopolymers potentially exhibit the advantages of both kinds of materials [2].

For bone regenerative purposes, polylactic acid (PLA) is considered one of the most adequate synthetic polymers due to its interesting properties [1]. However, several studies highlighted the poor hydrophilicity of PLA that might inhibit its biocompatibility in terms of amount of absorbed proteins and cell adhesion [2].

On the other hand, Chitosan (Chi) was widely explored as a natural biopolymer suitable for bone regeneration thanks to its biocompatibility [3], [4]. Chitosan is able to improves cell adhesion, proliferation and differentiation [5] and eases hydroxyapatite formation in an osteogenetic environment [6]–[8] However, chitosan-based constructs can often lack mechanical stability or offer insufficient elastic modulus and tensile strength to be used for direct implantation [9].

In this work, core-shell PLA/Chi microfibrous hybrid scaffold were produced by direct coating of Chi on PLA electrospun scaffolds. The Chi coating affected the fibers morphology, mechanical properties, and wettability. Finally, biocompatibility of each type of scaffold was investigated by seeding pre-osteoblastic MC3T3-E1 cells and evaluating the cell proliferation via scanning electron microscopy and colorimetric assays.

II. Materials and methods

A. Materials

PLA (2002D) was supplied by NatureWorks while Chitosan, Acetone (Ac), Chloroforms (TCM), and glacial acetic acid (AA) were purchased from Sigma Aldrich.

B. PLA electrospun mats fabrication

PLA electrospun mats followed a fabrication route similar to those described in a previous work [13]. In brief, the solvent system for PLA was TCM:Ac (2:1 vol/vol). PLA was added to obtain a concentration of 10 wt% with respect to the TCM:Ac mixture and dissolved at room temperature under continuous magnetic stirring overnight. A semi-industrial electrospinning equipment (NF-103, MECC CO., Ltd., Japan) was used to prepare PLA microfibrous scaffolds. A 5-mL syringe fitted with a 19-gauge stainless steel needle was filled with the polymeric solution. The electrospinning process was then carried out using the following constant parameters: flow rate, 1 mL/h; distance between the needle tip and the collector, 13 cm; supplied high voltage, 15 kV; temperature, 25 °C and relative humidity, 40%. The microfibers obtained were collected on a grounded rotary drum (diameter = 10 cm, speed = 10 rpm) wrapped in an aluminum foil for 120 min in order to obtain membranes approximately 70 μm thick. The collected electrospun membranes were subsequently dried for at least 2 days under fume hood to remove any residual solvents.

C. Morphological analysis

The morphology of the microfiber mats was evaluated by Scanning Electron Microscopy, (SEM-FEI QUANTA 200F.). The samples (3 mm diameter) were attached on an aluminum stub using an adhesive carbon tape. Therefore, they were sputter coated with gold (Sputtering Scancoat Six, Edwards) for 60 s under argon atmosphere before imaging to avoid electrostatic discharge during the test. Fiber diameter distribution of the electrospun mats was determined using a dedicated plugin for ImageJ (DiameterJ) that permits to analyze an image obtained by SEM to produce a histogram of the fiber diameter distribution.

D. Chitosan coating

The Chitosan coating onto electrospun PLA microfiber mat was conducted via direct immersion coating. The control of the Chitosan coating thickness was carried out by changing the concentration of Chitosan/water solutions added to the PLA electrospun mats according to the following theoretical approach.

It was assumed that the whole PLA electrospun mat was composed of a single fiber with diameter equal to the mean diameter estimated via image processing. According to this hypothesis and known the PLA density ρ_{PLA}, it was possible to estimate the PLA fiber length. Then, three Chitosan coating

thicknesses were arbitrarily chosen i.e., 85, 165, and 300 nm that corresponded to three Chitosan weight amounts. Therefore, three solution concentrations were prepared by solubilizing these amounts of Chitosan in a volume of water deduced from the water uptake of the PLA scaffolds. According to these theoretical evaluations, the weight percentage of Chitosan in water were the 0.5 wt%, 1.0 wt% and 2.0 wt% to theoretically reach the Chitosan coating thickness of 85, 165, and 300 nm, respectively. The solubilization of Chitosan was carried out in an aqueous AA solution (0.5 wt%) at 60 °C for 3 hours under magnetic stirring. 4 g of Chi/water solution was dropped in 0.1 g of electrospun PLA membranes until it was completely absorbed. Then the wet membranes were let to dry under fume hood overnight at room temperature in order to allow the water phase to evaporate.

The samples were coded as follow: PLA/Chi X% where X is 0.5, 1.0, or 2.0 on the basis of the Chitosan concentration in solution used for the coating.

E. FTIR-ATR analysis

FTIR/ATR analysis (FT-IR/NIR Spectrum 400 spectrophotometer from Perkin-Elmer Inc., Wellesley, MA, USA) was performed to investigate the sample chemical surface properties. For each sample, 4 accumulations scans with a resolution of 4 cm^{-1} were collected in the range 4000–400 cm^{-1}.

F. Mechanical properties

Tensile mechanical measurements were carried out by using a dynamometer (Instron model 3365) equipped with a 1 kN load cell. The tests were performed on rectangular-shaped specimens (10 × 90 mm) cut off from the membranes along the radial direction of the rotary drum collector. The measurements were performed by using a single crosshead speed at 1 mm/min for all the samples. The thickness of each sample was measured before test (~50 μm) whereas the gauge length was 20 mm for all the samples. The representative nominal stress-strain curves were reported for each material. The elastic modulus (E) was calculated from the slope of the initial part of the engineering stress-strain curves. Seven samples were tested for each material and the average values of the mechanical parameters were reported with their standard deviations.

G. In vitro cell cultures

The scaffolds were sterilized by UV light treatment for 2 h under the laminar fume hood and all of them were pre-conditioned overnight with complete culture medium. Mouse pre-osteoblastic MC3T3-E1 cell line (ECACC, European Collection of Cells Cultures) were grown in Dulbecco's modified Eagle's-high glucose medium (DMEM, Sigma Aldrich) supplemented with 10% (v/v) fetal bovine serum (FBS) (Euroclone, Celbar), 100 units per ml penicillin G, 100 μg/ml streptomycin (Euroclone, Celbar) and 2 mM L-glutamine (Euroclone, Celbar) at 37 °C, in a humidified atmosphere of 5% CO2.

5×10^3 cells were resuspended in 5 μl of complete medium, which corresponds to the volume of the scaffold seeded on each sample, and incubated in a humidified incubator (37°C; 5% CO2). After 30 minutes required for the cell adhesion, each scaffold was transferred to one well of 48-well plate supplemented with DMEM complete medium which was refreshed every three days.

H. Cell proliferation essay and cell morphology

At different times (1, 7, 14 and 21 days) from cell seeding, the viability and cell proliferation rate on each type of electrospinning device, were evaluated using Alamar-Blue colorimetric assay (Thermo Scientific, Foster City, CA, USA) according to the manufacturer's recommendations. Cells grown on each type of scaffold were incubated with Alamar-Blue reagent solution (10% in culture medium) in a complete medium for 2 h in a humidified incubator (37°C; 5% CO_2).

Fluorescence intensity (λ_{exc} 530/25 nm and λ_{emm} 590/35 nm), which changes according to the degree of cell viability, was evaluated through a microplate reader (Synergy HT, Biotek, Winooski, VT, USA). The fluorescence values of each type of scaffold were normalized against the same type of unseeded device, used as a blank. The assay was performed in quadruplicate for each scaffold formulation and repeated three times.

For SEM analysis, after appropriate washing in PBS, samples were fixed with 4% (v/v) glutaraldehyde at 4 °C for 2 h, rinsed with water and dehydrated with ethanol series (25%, 50%, 75% v/v and pure ethanol). Finally, samples were dried under prior vacuum gold-sputtering and analyzed by SEM at the same conditions described above.

III. Results and Discussion

A. Spectroscopical and morphological analysis

The presence of Chitosan molecules on the PLA electrospun microfibers was evaluated via FTIR-ATR spectroscopy (Fig. 1). According to the literature, the ATR-FTIR spectrum of PLA showed various absorption bands usually attributed to this polyester such as the carbonyl stretch at 1747 cm^{-1}, the C–O stretch at 1180 cm^{-1}, 1129 cm^{-1} and 1083 cm^{-1} and the OH bend at 1044 cm^{-1} [10]. The FTIR-ATR spectrum of neat chitosan powder reveals main absorption bands at 3352 cm^{-1} (stretching vibration of O–H group [11]), 3290 cm^{-1} (stretching vibration of N–H [11]), 1645 cm^{-1} (stretching vibration of the carbonyl group (C=O) in amide I [12], [13]), and 1039 cm^{-1} (stretch vibrations of C–O [14]).

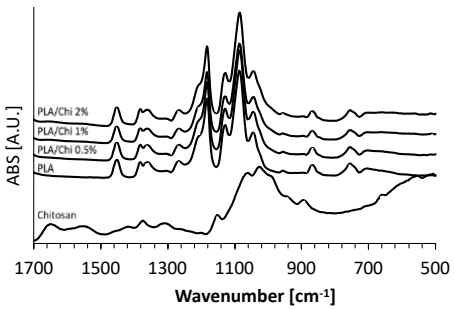


Fig. 1: FTIR-ATR spectra of PLA//Chi hybrid scaffolds as a function of the Chitosan concentration in the coating solutions.

The peaks related to PLA in the PLA/Chi hybrid scaffolds were found to be dominant although the characteristic peaks of Chitosan were visible and their intensity increased upon increasing the Chitosan concentration, thus corroborating the effective inclusion of the polysaccharide into the PLA mats (Fig. 1)

The microstructure of the scaffold was investigated via SEM analysis and the results are shown in Fig. 2. PLA fibers displayed smooth fibers morphology, randomly oriented and with a mean diameter around 1.2 µm. The addition of chitosan caused several modifications on the morphology PLA fibers. Firstly, in Figure 2 it can be qualitatively noticed an increase of the fiber diameter upon increasing the Chitosan content. This result was confirmed by mean fiber diameter quantitative evaluation via an image processing software. Interestingly, the mean fiber diameter of PLA/Chi 0.5% was very close to the expected one. Since the theoretical values of the fiber diameters were obtained by assuming that the whole volume of added chitosan increased the starting mean diameter of PLA fibers, this result corroborates the evidence that, at this concentration, Chitosan film effectively wrapped the individual PLA fibers during the water evaporation thus structuring them in a core-shell configuration.

The fiber diameters of PLA/Chi scaffolds treated with more concentrated Chitosan solutions were higher than that of PLA/Chi 0.5% but lower than the theoretical values, in particular for the PLA/Chi 2% hybrid scaffolds (Fig. 2). This result can be likely explained by observing the SEM images that reveal edges among the fibers of PLA/Chi 1% and 2% which can be presumably ascribed to an excess of Chitosan that is not able to wrap the PLA fibers during the solidification, thus being unable to increase the PLA fiber diameter up to the theoretical values. Furthermore, for those scaffolds, bundles composed of 2 to 4 fibers glued to each other were observed.

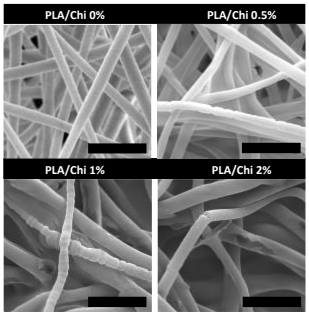


Fig. 2: SEM micrographs of PLA/Chi hybrid scaffolds as a function of the Chitosan concentration in the coating solutions. Scale bar is 5 µm

B. *Mechanical analysis*

Fig. 3 summarizes the E, TS and deformation at break (ε_b) evaluated by the nominal stress-strain curves. The elastic modulus of PLA/Chi scaffolds displayed a dramatic increase when coated with chitosan-based solutions and it increased upon raising the Chitosan concentration reaching values more than 10 times higher than PLA scaffolds.

Also TS of PLA/Chi scaffolds were higher than that of PLA, although the increase was visible up to PLA/Chi 0.5% system and then TS remained constant for PLA/Chi 1% and 2% hybrid scaffolds. As expected, the deformation at break was dramatically reduced by the addition of Chitosan to the PLA scaffolds.

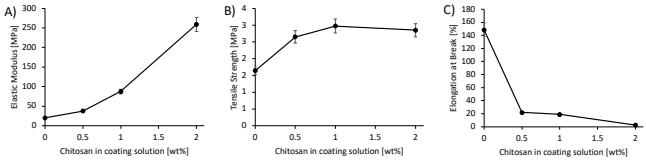


Fig. 3: A) Elastic modulus, B) Tensile Strength, and C) Elongation at break of PLA/Chi electrospun scaffolds as a function of the Chi content.

C. *Scaffolds biocompatibility*

The biocompatibility of the different types of PLA scaffolds was investigated by seeding mouse pre-osteoblastic MC3T3-E1 cells and analysing their viability and proliferation rate after different times (1, 7, 14 and 21 days). PLA/Chi hybrid scaffolds present good biocompatibility and the capability to be substrates for cells. After 7 and 14 days, there was no significant difference in proliferation rate on PLA/Chi scaffolds, which appeared more evident after 21 days in a chitosan-dependent way. According to literature that reported the chitosan effect on attachment and proliferation of many types of cells including osteoblast [15]–[17], the addition of chitosan increases the cell viability compared with PLA, and the PLA/Chi 0.5% sample presents the highest value.

These data were confirmed also by SEM investigation in which was evident an increase in cell density over time (Data not shown). After 14 days of culture, cells started to contact each other and to form a dense cell layer until the entire scaffolds were completely overgrown with cells after 3 weeks, Fig. 4. The identification of cells within it suggests a complete colonization of the scaffold.

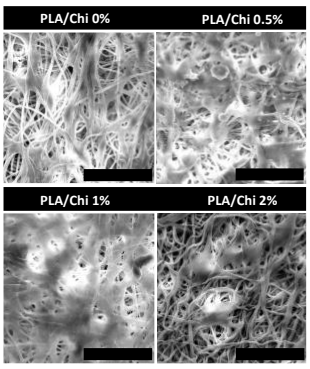


Fig. 4: SEM micrographs of MC3T3 E1 cells grown for 21 days on PLA/Chi hybrid scaffolds as a function of the Chitosan concentration in the coating solutions. Scale bar is 50 µm.

IV. CONCLUSION

In this work the physical and biological properties of hybrid PLA electrospun scaffolds coated with Chitosan were assessed. Spectroscopic and morphological investigations confirmed the effective formation of a thin Chitosan layer wrapped on the PLA fibers with controllable thickness up to 0.15 µm. From a mechanical point of view, the Chi coating on PLA fibers caused a strong increase of the elastic modulus, a slight increase of the TS and a steep decrease of the elongation

at break.

Alamar-Blue colorimetric assay and SEM analyses confirmed the biocompatibility of the scaffolds investigated by seeding mouse pre-osteoblastic MC3T3-E1 cells for different times (1, 7, 14 and 21 days).

REFERENCES

[1] Z. U. Arif, M. Y. Khalid, R. Noroozi, A. Sadeghianmaryan, M. Jalalvand, and M. Hossain, "Recent advances in 3D-printed polylactide and polycaprolactone-based biomaterials for tissue engineering applications," *Int. J. Biol. Macromol.*, vol. 218, pp. 930–968, 2022, doi: https://doi.org/10.1016/j.ijbiomac.2022.07.140.

[2] E. Capuana, F. Lopresti, M. Ceraulo, and V. La Carrubba, "Poly-l-Lactic Acid (PLLA)-Based Biomaterials for Regenerative Medicine: A Review on Processing and Applications," *Polymers (Basel).*, vol. 14, no. 6, 2022, doi: 10.3390/polym14061153.

[3] L. R. Yadav, S. V. Chandran, K. Lavanya, and N. Selvamurugan, "Chitosan-based 3D-printed scaffolds for bone tissue engineering," *Int. J. Biol. Macromol.*, vol. 183, pp. 1925–1938, 2021, doi: https://doi.org/10.1016/j.ijbiomac.2021.05.215.

[4] A. Baranwal *et al.*, "Chitosan: an undisputed bio-fabrication material for tissue engineering and bio-sensing applications," *Int. J. Biol. Macromol.*, vol. 110, pp. 110–123, 2018.

[5] S. Ahmed, A. Ali, J. Sheikh, and others, "A review on chitosan centred scaffolds and their applications in tissue engineering," *Int. J. Biol. Macromol.*, vol. 116, pp. 849–862, 2018.

[6] B. Li, Y. Wang, D. Jia, and Y. Zhou, "Gradient structural bone-like apatite induced by chitosan hydrogel via ion assembly," *J. Biomater. Sci. Polym. Ed.*, vol. 22, no. 4–6, pp. 505–517, 2011.

[7] J.-W. Hou, L. Qian, J.-M. Kou, C.-W. Zhang, X.-J. Jia, and W. Tian, "Effect of water-soluble chitosan on the osteoblast function in MC3T3-E1 cells," *Int. J. Biol. Macromol.*, vol. 72, pp. 1041–1043, 2015, doi: https://doi.org/10.1016/j.ijbiomac.2014.10.012.

[8] S. Mathews, P. K. Gupta, R. Bhonde, and S. Totey, "Chitosan enhances mineralization during osteoblast differentiation of human bone marrow-derived mesenchymal stem cells, by upregulating the associated genes," *Cell Prolif.*, vol. 44, no. 6, pp. 537–549, 2011.

[9] S. Singh, G. Singh, C. Prakash, S. Ramakrishna, L. Lamberti, and C. I. Pruncu, "3D printed biodegradable composites: An insight into mechanical properties of PLA/chitosan scaffold," *Polym. Test.*, vol. 89, p. 106722, 2020, doi: https://doi.org/10.1016/j.polymertesting.2020.106722.

[10] R. Scaffaro, F. Lopresti, and L. Botta, "Preparation, characterization and hydrolytic degradation of PLA/PCL co-mingled nanofibrous mats prepared via dual-jet electrospinning," *Eur. Polym. J.*, vol. 96, pp. 266–277, 2017, doi: 10.1016/j.eurpolymj.2017.09.016.

[11] M. Matet, M. C. Heuzey, E. Pollet, A. Ajji, and L. Avérous, "Innovative thermoplastic chitosan obtained by thermo-mechanical mixing with polyol plasticizers," *Carbohydr. Polym.*, vol. 95, no. 1, pp. 241–251, 2013, doi: 10.1016/j.carbpol.2013.02.052.

[12] G. Lawrie *et al.*, "Interactions between alginate and chitosan biopolymers characterized using FTIR and XPS," *Biomacromolecules*, vol. 8, no. 8, pp. 2533–2541, 2007.

[13] C. Zanca *et al.*, "Composite Coatings of Chitosan and Silver Nanoparticles Obtained by Galvanic Deposition for Orthopedic Implants," *Polymers (Basel).*, vol. 14, no. 18, p. 3915, 2022.

[14] W. Sui, L. Huang, J. Wang, and Q. Bo, "Preparation and properties of chitosan chondroitin sulfate complex microcapsules," *Colloids Surfaces B Biointerfaces*, vol. 65, no. 1, pp. 69–73, 2008, doi: 10.1016/j.colsurfb.2008.02.022.

[15] P. Brun *et al.*, "Bio-Functionalized Chitosan for Bone Tissue Engineering," *Int. J. Mol. Sci.*, vol. 22, no. 11, 2021, doi: 10.3390/ijms22115916.

[16] E. Martín-López, M. Nieto-Díaz, and M. Nieto-Sampedro, "Influence of Chitosan concentration on cell viability and proliferation in vitro by changing film topography," *J. Appl. Biomater. Funct. Mater.*, vol. 11, no. 3, pp. 151–158, 2013, doi: 10.5301/JABFM.2012.10449.

[17] C. Heinemann, S. Heinemann, A. Bernhardt, H. Worch, and T. Hanke, "Novel Textile Chitosan Scaffolds Promote Spreading, Proliferation, and Differentiation of Osteoblasts," *Biomacromolecules*, vol. 9, no. 10, pp. 2913–2920, Oct. 2008, doi: 10.1021/bm800693d.

Microgels as a Biosensing Platform

E. Battista[1], S. Napoletano[2], M.I. Maremonti[2,3], D. Dannhauser [2,3], P.A. Netti[2,3], and F. Causa [2,3]
[1] *Department of Innovative Technologies in Medicine &Dentistry, University "G. D'Annunzio" Chieti-Pescara,Chieti, Italy*
[2] *InterdisciplinaryResearch Centre on Biomaterials (CRIB), Università degli Studi di Napoli "Federico II", Naples*
[3] *Dipartimento di Ingegneria Chimica del Materiali e della Produzione Industriale (DICMAPI), University "Federico II", Naples*

***Abstract* — Microgels represent a versatile sub-class of hydrogels enabling new functions in biomolecule detection thanks to the highly tuneable chemistry. The microgels-based platform is composed of multifunctional particles which possess multiple components and properties to fulfil the requirements of the biodetection applications. Indeed, from the synthesis to the final read-out microgels prove advantageous and unique in overcoming issues in detection and quantification directly in biofluids. The chemical flexibility of hydrogel microparticles and microgels allows to embed several building blocks into their structure during the synthesis. Anchoring groups on particles are used to immobilize probes of diverse natures such as antibodies, enzymes, or oligonucleotide strands. In such a way particles active for the detection of a target or more than one biomarker can be obtained. Moreover, the high biocompatibility and antifouling properties of hydrogels make possible to use microgels in biosensing directly in biofluids overcoming washing and separation steps. As for the read-out steps, microgels can be easily manipulated in flow with simple microfluidics making the detection more efficient and sensitive in multiplex context.**

Here we are presenting a PEG-microgel platform for the detection of oligonucleotides and other biomarkers by using barcoded particles for multiplex analysis. In the final part of the presentation, we discuss on the use of easy microfluidics for the interrogation of microgels in-flow.

***Keywords*—Biosensing, Microgels, Detection of Biomarkers, Microfluidics.**

I. Introduction

MICROGELS are small, crosslinked polymer particles that can range in size from a few nanometers to a few micrometers. They have both liquid and solid properties due to their crosslinked structure, which allows them to swell and shrink in response to changes in their environment, such as temperature, pH, or the presence of certain chemicals. They can be synthesized using various methods and can be used in a wide range of biomedical applications, such as drug delivery, and bio-sensing [1]. In that context, microgels can be used as a chemical toolbox for the on-demand synthesis of polymer particles with different characteristics useful for the final application by using combinatory approaches and microfluidic devices.

Microgels for assays must respond to specific requirements that have been tested towards oligonucleotides and other biomarker [2,3]. The flexibility of such platform materials allowed to produce multifunctional particles that provide unique properties in the bulk and on the surface. Indeed, such kind of particles can be used in multiplex assays to detect and quantify multiple biomarkers in the same run and in the same vessel at once [4]. This feature is enabled uniquely by barcoded microgels that are univocally encoded in fluorescence and with a core/shell architecture in a limited space of sub-micrometer particles. With this kind of microgels the bulk properties are modulated differently by the surface chemical functionalities. The surface of microgel can be tailored with different number of functional groups to accommodate specific probes for the capture of targets [5]. The high surface hydration of PEG ensures antifouling properties so that particles can be used for assays directly in native biofluids reducing manipulations and addressing low LOD sensitivity [6,7]. The advantageous properties of soft and highly hydrated microgels enables the integration of the assay inside miniaturized devices so that increasing the possibilities to address high demanding assay in terms of sensitivity. Assays for small oligo sequences that are circulating in bodily fluids are represented by microRNAs (or miRNAs). Such small sequences are promising in the so-called liquid biopsies where circulating biomarker are the potency of diagnosis and prognosis in different diseases like cancer. In this context miRNAs can act in panels to allow the stratification of the disease [3,8].

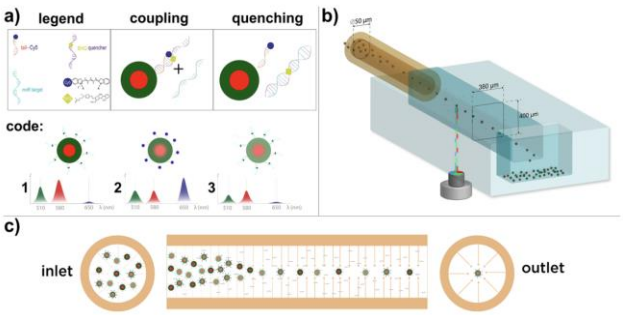


Fig 1 - The microgels platform for miRNAs sensing. In a) oligoprobes conjugated to encoded PEG-Microgels for miRNA sensing. b) and c) the straight channel with focusing microgels inside. (Reprinted from [9])

Here, we present a comprehensive platform based on PEG-microgels for the detection of circulating biomarkers with a quasi-real-time fluorescence detection of single microgels in microfluidic flows using non-Newtonian fluids at a low concentration level (Fig1) [9].

The advances made by our group will be reviewed widely highlighting the versatility of the material platform in terms of chemical functionalities, target detection and automatized read-out by using miniaturized devices for quasi-real-time acquisition and identification of signals [10-15].

II. Materials & Methods

Microgels Synthesis

Microgels were prepared by free-radical precipitation polymerization, using 1% (w/v) total monomer concentration. Polymerization was carried out in a three-neck, 100 mL round-

bottom flask to which a filtered, aqueous solution of all monomers and 1% (w/v) PVA and KPS (30mg) were added and bring to 65°C for the initiation. The monomer used was PEGDA (550Mn, Polyethylenglycoldiacrylate, SIGMA) with Acrylic Acid. The encoding was realized by the incorporation of Atto-532 dye (Atto-tec, Germany) derivatized as maleimide. The dye was added after 10 minutes of initiation and left to react for about 6 hrs. Afterward the reaction product was washed by centrifuge and left to dialyze for one week in deionized water. The characterization of microgels was performed by measuring the size and surface charge (Zeta-sizer, Malvern UK) and by fluorescence spectra and imaging. Potentiometric titration was used to assess the amount of carboxyl groups incorporated in the mircogels, while the viscometer titration (Hubbelode) for microgels concentration in the solution.

Probe design

The molecular Beacon (MB) probe was designed to specifically detect the miR-21 target. The thermodynamic parameters (melting temperature, stability, and folded fraction at the dosage conditions) were calculated using appropriate tools (OligoAnalyzer 3.1; IDT-Integrated, D.N.A. 2014 and UNAFold). Briefly, the length of the probes was carefully evaluated to allow stable hybridization between the probe strand and the target at physiological ionic strength, and the free energy (ΔG) of folded MB and opened MB hybridized to the target, were calculated.

MB conjugation to microgels.

Bioconjugation was optimized by coupling 0.1 nmol of MB with 1 mg of microgels; after 5 hrs of incubation in MES pH 6, the carboxylic groups on the microgel were activated using the coupling agent EDC, subsequently; MB solution was added to the microgels by incubating overnight at room temperature. MB microgels were washed 3 times to remove the unreacted MB and suspended in PBS buffer.

Microgels-assay

Microgels at a concentration of 0.5 ug/mL (corresponding to $1.45 \cdot 10^7$ microgels) conjugated with 0.1 nmol miR-21 MB probe were used for the microgel assay that was easily performed by mixing the microgels to the target sequences, without preliminary steps of amplification. The samples were analyzed by confocal microscopy. A calibration curve to evaluate microgels assay dynamic range was done using serial dilution of synthetic miR-21 in PBS. For each target concentration, 20 images were collected and analyzed. Images were processed and analyzed by ImageJ software.

III. RESULTS & DISCUSSIONS

After synthesis, microgels with monomodal distribution (667,1±6,407 (PDI=0,244)) were obtained with a net surface charge of -14 mV. A uniform fluorescence, due to the incorporation of Atto-532 dye, was observed. Moreover, the fluorescence behavior of microgels is compatible with that of the free dye in solution (Fig 2).

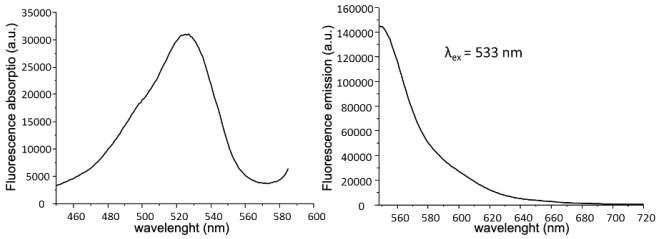


Fig 2 – Absorption (left)/Emission (right) spectra of microgels (50ug/mL) loaded with Atto-532.

As in Fig 3 A the uniform distribution of the dye molecules inside microgels enable the imaging by using fluorescence microscopy. To evaluate microgels assay performance (the working range and sensitivity), a calibration tube with tenfold serial dilution of miR-21 target concentrations was constructed tuning the number of microgels to reach the best sensitivity. We proved that the minimum amount of target distinguishable from the background noise had a concentration in the femtomolar with a limit of detection (LOD) of 17,9 fM and with dynamic range between fM and nM. Moreover, the proposed assay is easily performed with very small amount of sample (2 µL), in a volume as that of 20 µL at 25°C.

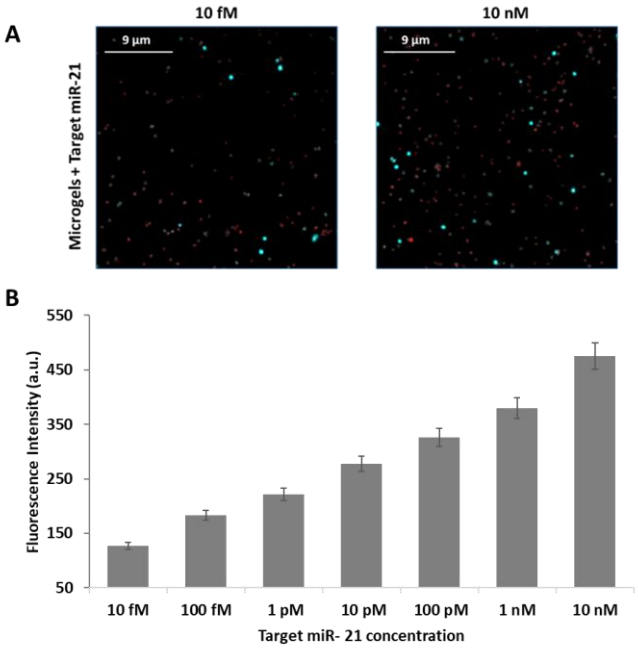


Fig 3 - Microgel assay performance. **A)** Images of microgels assay at lower (10 fM) and higher (10 nM) tested concentrations collected by CLSM. In red is rhodamine. In blue is Atto-647N. **B)** Dynamic range of 0,5 µg/mL microgels functionalized with 0,1 nmol of the molecular beacon (MB) and put in contact with the target miR-21 in a range of concentrations from fM to nM.

For an easier read-out microfluidics can be used to align microgels in the optical field-of-view of a fluorescent microscope [9, 10]. Different systems can be used for particle alignment in microfluidics generally requiring complex geometrical channel design for the focusing. Viscoelastically induced particle alignment—at low volume concentrations—permits the optical observation of target particles in a simple and cost-effective way as shown in Fig 4 [9].

In fact, particle alignment was accomplished by a viscoelastic medium (0.2wt% of Polyethylene-oxide 4MDa) and a pressure driven flow. Thanks to the resulting fluid properties, generated by viscoelastic fluid forces, particles are aligned to the centreline of the round shaped channel and subsequently remain aligned in the centreline of the microfluidic readout channel (see Fig 4). Next a routine calculated the relative fluorescence ratios (barcode *versus* target fluorescence) to detect microgel types down to the fM range. We obtained a signal to noise ratio above 20 dB for in-flow investigated microgel particles, which is comparable to quiescent miRNA investigations.

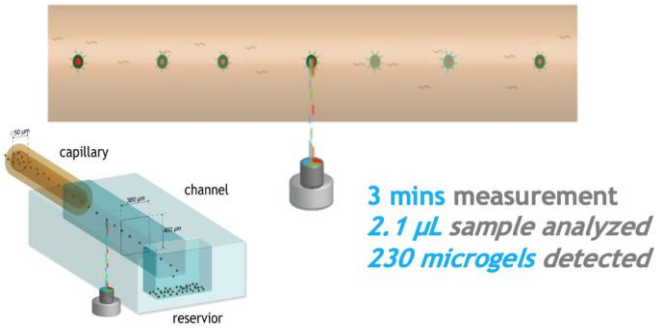


Fig 4 – Flow focusing realized by viscoelastic approach in a straight channel allows for high-throughput analysis of microgels.

IV. Conclusion

Circulating miRNAs recur at low amount (below fM) so that a sensitive method is needed for an easy detection that would overcome the enzymatic amplification and directly quantified in the biofluid. Microgels decorated by appropriate and specific oligo-probes (linear for displacement or molecular beacons) proved a wide working range down to fM in the detection of different miRNAs directly in serum without any enzymatic amplification. We tested our miRNA detection approach in microfluidic flow condition. Results show a fM detection limit, which enables the precise detection of circulating miRNA in low amounts. Next more complex samples of different miRNA subtypes will be investigated in microfluidic flow condition to highlight the therapeutic potential of this measurement approach.

V. AKNWOLEDEGEMENT

Work founded by AIRC IG2020 Title: miRNA lab-on-chip: a new tool to revolutionize miRNA biomarkers for liquid biopsy.

References

[1] Battista, E., Causa, F., & Netti, P. A. (2017). Bioengineering Microgels and Hydrogel Microparticles for Sensing Biomolecular Targets. *Gels*, *3*(2).

[2] Causa, F., Aliberti, A., Cusano, A. M., Battista, E., & Netti, P. A. (2015). Supramolecular spectrally encoded microgels with double strand probes for absolute and direct miRNA fluorescence detection at high sensitivity. *Journal of the American Chemical Society*, 137(5), 1758-1761.

[3] Aliberti, A., Cusano, A. M., Battista, E., Causa, F., & Netti, P. A. (2016). High sensitive and direct fluorescence detection of single viral DNA sequences by integration of double strand probes onto microgels particles. *The Analyst*, *141*(4), 1250-1256.

[4] Causa, F., Aliberti, A., Cusano, A., Battista, E., & Netti, P. (2015). Microgels for multiplex and direct fluorescence detection. In *Proc. of SPIE Vol* (Vol. 9529, pp. 952919-1).

[5] Battista, E., Mazzarotta, A., Causa, F., Cusano, A. M., & Netti, P. A. (2016). Core− shell microgels with controlled structural properties. *Polymer International*, *7*(65), 747-755.

[6] Caputo, T. M., Battista, E., Netti, P. A., & Causa, F. (2019). Supramolecular microgels with molecular beacons at the interface for ultrasensitive, amplification-free, and SNP-selective miRNA fluorescence detection. *ACS applied materials & interfaces*, *11*(19), 17147-17156.

[7] Battista, E., Causa, F., Cusano, A. M., Di Natale, C., Scognamiglio, P. L., Mazzarotta, A., Netti, P. A. (2017). Multifunctional microgels for direct, multiplexed and high sensitive detection. *Procedia technology*, *27*, 31-32.

[8] Caputo, T. M., Cummaro, A., Lettera, V., Mazzarotta, A., Battista, E., Netti, P. A., & Causa, F. (2019). One-step scalable fluorescent microgel bioassay for the ultrasensitive detection of endogenous viral miR-US4-5p. *Analyst*, *144*(4), 1369-1378.

[9] Dannhauser, D., Causa, F., Battista, E., Cusano, A. M., Rossi, D., & Netti, P. A. (2016). In-flow real-time detection of spectrally encoded microgels for miRNA absolute quantification. Biomicrofluidics, 10(6), 064114.

[10] Di Natale, C., Battista, E., Lettera, V., Reddy, N., Pitingolo, G., Vecchione, R., ... & Netti, P. A. (2021). Easy Surface Functionalization and Bioconjugation of Peptides as Capture Agents of a Microfluidic Biosensing Platform for Multiplex Assay in Serum. *Bioconjugate Chemistry*, *32*(8), 1593-1601.

[11] Mazzarotta, A., Caputo, T. M., Raiola, L., Battista, E., Netti, P. A., & Causa, F. (2021). Small Oligonucleotides Detection in Three-Dimensional Polymer Network of DNA-PEG Hydrogels. *Gels*, *7*(3), 90.

[12] Mazzarotta, A., Caputo, T. M., Battista, E., Netti, P. A., & Causa, F. (2021). Hydrogel Microparticles for Fluorescence Detection of miRNA in Mix-Read Bioassay. *Sensors*, *21*(22), 7671.

[13] De Masi, A., Scognamiglio, P. L., Battista, E., Netti, P. A., & Causa, F. (2022). PEG-based cleavable hydrogel microparticles with controlled porosity for permiselective trafficking of biomolecular complexes in biosensing applications. *Journal of Materials Chemistry B*, *10*(12), 1980-1990.

[14] Martone N., Battista E., Causa F., Netti P.A. Platform set-up by multifunctional PEG microgels for bead-based assay in immunoglobulin detection - 07 March 2022 by **MDPI** in The 2nd International Electronic Conference on Biosensors session Biosensors in POCT https://doi.org/10.3390/IECB2022-12343.

[15] Di Natale, C., Celetti, G., Scognamiglio, P. L., Cosenza, C., Battista, E., Causa, F., & Netti, P. A. (2018). Molecularly endowed hydrogel with an in silico-assisted screened peptide for highly sensitive small molecule harvesting. *Chemical Communications*, *54*(72), 10088-10091.

[16] Celetti, G., Di Natale, C., Causa, F., Battista, E., & Netti, P. A. (2016). Functionalized poly (ethylene glycol) diacrylate microgels by microfluidics: In situ peptide encapsulation for in serum selective protein detection. *Colloids and Surfaces B: Biointerfaces*, *145*, 21-29.

Experimental and computational pipeline for identifying oxygen metabolic rate parameters in 2D and 3D *in vitro* constructs

P. Mancini[1,2 *], E. Botte[1,2 *], C. Magliaro[1,2], A. Ahluwalia[1,2]
[1] *Department of Information Engineering, University of Pisa, Pisa, Italy*
[2] *Research Center "E. Piaggio", University of Pisa, Pisa, Italy*
** These authors contribute equally to the work*

***Abstract*—Oxygen consumption rates in 2D and 3D *in-vitro* cell cultures are difficult to measure accurately because of limitations in oxygen sensor technology and the challenge of identifying and maintaining initial and boundary conditions during measurement. Hence, the OCR or oxygen consumption rate of cells is usually considered as a constant. But given the importance of oxygen as the primary source of energy in living organisms and the problem of ensuring an adequate supply in non-vascularised constructs, it is necessary to develop more reliable methods for predicting the metabolic requirements of cells in culture. The aim of this study is thus to develop an experimental and computational pipeline for measuring metabolic parameters as a function of cell-density and structural complexity (i.e. dimensionality) in *in vitro* constructs.**

***Keywords*—Cell metabolic parameters, Michaelis Menten, monolayer, 3D cell-laden construct.**

I. Introduction

Oxygen utilization by cells has a pivotal role in the design of biomimetic models. In fact, oxygen is one of the key actors in cellular respiration and influences cell growth and fate, but its low solubility and diffusivity in aqueous media may result in an inadequate supply [1].
Mammalian cells adapt their aerobic metabolism to O_2 availability; traditionally, this adaptive oxygen consumption rate R $[\frac{mol}{m^3 s}]$ is described via the Michaelis-Menten's (MM) equation (Eq. 1):

$$R(x,y,z,t) = \rho_c OCR \frac{C(x,y,z,t)}{k_M + C(x,y,z,t)} \quad (1)$$

where C $[\frac{mol}{m^3}]$ is the oxygen concentration, ρ_c $[\frac{cell}{m^3}]$ is the volumetric cell density, OCR $[\frac{mol}{cell\ s}]$ is the maximum oxygen consumption rate per cell, and k_M $[\frac{mol}{m^3}]$ is the MM constant, a descriptor of O_2 cell uptake efficiency. In particular, the values of OCR and k_M, also known as the MM parameters, have generally been assumed as constants for a given cell phenotype [2].

Few reports have to date focused on O_2 metabolism *in vitro* considering the associated cell behavior as a function of construct dimensionality (i.e., 2D and 3D). Magliaro *et al.* [3] have recently shown that OCR and k_M depend on cell density, but their study is limited to 3D constructs. Hence, a systematic investigation on the effect of dimensionality as well as cell density is still lacking.
Here we established an integrated in vitro-in silico method for accurate estimation of the oxygen consumption parameters in aggregates with increasing cell density and dimensionality (2D and 3D). We focused on hepatocytes for their pivotal role of the liver in endogenous and exogenous metabolism [4].

II. Materials and Methods

A. Theoretical rationale

The volume of interest is the cell culture in its well with and its surrounding media, which is in contact with a gas phase on one boundary. The O2 concentration is governed by oxygen transport, which depends on its diffusion constant, D $[\frac{m^2}{s}]$ and its consumption (from Eq. 1):

$$\frac{\partial C}{\partial t} = D\nabla^2 - R \quad (2)$$

In the case of monolayers, assuming that cells are homogeneously distributed over a boundary and that their thickness is much smaller than the total height of the system (Fig. 1), O_2 consumption by cells can be considered as a unidirectional inward flux $(J_c(0,t))$. In this situation, oxygen dynamics can be assumed as dependent on the axial direction only (Eq. 3).

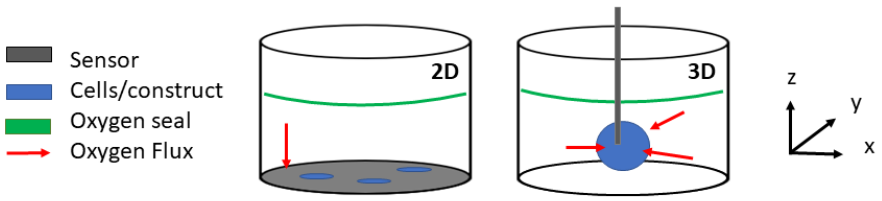


Figure 1 Schematics of 2 and 3D geometry and sensing configurations.

$$\begin{cases} \frac{\partial C(z,t)}{\partial t} = D\frac{\partial^2 C(z,t)}{\partial z^2} & (3) \\ J_c(0,t) = -\rho_c OCR\frac{C(0,t)}{km+C(0,t)} & (4) \end{cases}$$

In Eq. (3), ρ_c $[\frac{cell}{m^2}]$ is the surface cell density, and a single average O_2 concentration readout over time at the monolayer level is sufficient to characterize its consumption kinetics. Identifying the MM parameters through Eq. (2), and (3 - 4) requires performing a time dependent measurement of oxygen concentration in a fixed point in space. Furthermore, to accurately estimate km, $C << k_M$. As k_M is often much lower than ambient C, this requires that the system be brought to near-hypoxia.

B. *Experimental setup*

All measurements were conducted at 37C using a customised thermostatic chamber [3].

To establish fixed initial conditions and enable the system to attain hypoxia, it needs to be sealed to avoid O_2 infiltration from the air. We achieved this using a thick layer of silicone oil (Agilent Technologies) and, as an extra precaution an O_2-consuming chemical (AnaeroGen, Thermo Fisher Scientific) was placed in the chamber.

For the monolayer configuration, a contactless sensor spot (OXP5, Pyroscience GmbH) attached to the bottom of the well was used to monitor O_2 dynamics (Figure 1).

For cell-laden constructs we employed a needle probe microsensor (XR50, Pyroscience, GmbH, Figure 1 and 2). The needle was carefully inserted at the center of the construct using a micromanipulator and a frontal camera.

Both of the oxygen sensor systems chosen are based on quenching. The luminescence signal emitted by the spot in response to the concentration level is conveyed via an optical fiber to an oxygen-meter. Before each experiment, a two-point calibration was carried out by exposing the sensor to well-oxygenated culture medium (Dulbecco's Modified Eagle Medium), corresponding to a 100% oxygen saturation, and to a 1% w/v solution of sodium bisulphite, an oxygen scavenger guaranteeing hypoxia for the duration of the experiment. Between consecutive acquisitions, sensors were rinsed with a 70% v/v ethanol solution.

The oxygen concentrations over time obtained from the experiments were post-processed using Matlab (R2020b).

Generation of in vitro models

For monolayers, we first prepared a well of a 96 plate with sensor spots coated with a 1% w/v gelatin solution (Sigma-Aldrich) to promote cell adhesion. Human Hepatoma (HepG2) cells at different surface densities (Table I) were seeded onto the sensor spot and incubated overnight.

In the 3D experiments, hepatic spheroids were fabricated through the SpHyGa extrusion-based biofabrication platform, using a needle with internal diameter of 1.6 mm as extrusion nozzle [5]. In particular, cells were suspended at different volumetric densities (Table I) in DMEM containing 1% w/v alginic acid (Sigma-Aldrich) and 0.04% type I collagen (Life Technologies Corporation, New York, USA). Then, cell suspension drops were extruded in an electrolytic bath of calcium chloride ($CaCl_2$) 0.1 M and incubated (37 °C, 95% RH, 5% CO_2) during alginate cross-linking for 15 min. The cell-laden spheroids so-obtained were incubated overnight.

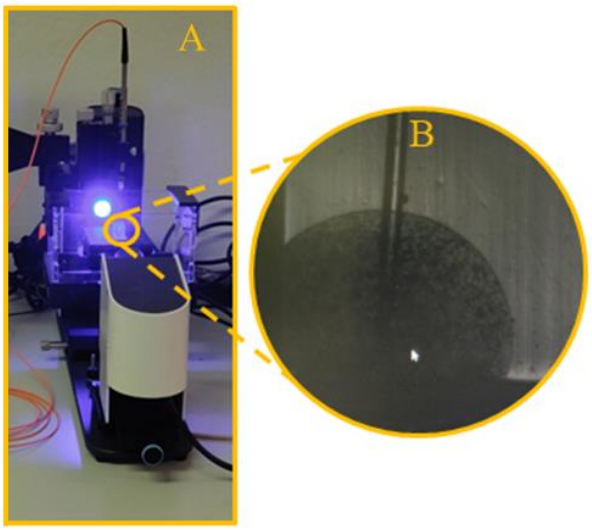


Figure 2 A) Spheroid experimental Set-up, B) Zoom showing oxygen needle sensor at the center of spheroid.

TABLE I: CELL DENSITIES IN 2D AND 3D

2D	*3D*
$\boldsymbol{\rho_{cell,s}}$ *(cell m^{-2})*	$\boldsymbol{\rho_{cell,v}}$ *(cell m^{-3})*
3.10×10^{8}	1×10^{12}
1.72×10^{9}	2.5×10^{12}
2.56×10^{9}	5×10^{12}
3.30×10^{9}	7.5×10^{12}

C. *Parameter identification*

Experimental time versus concentration data were post-processed to estimate the MM parameters characterizing cell consumption through the multiparameter identification pipeline shown in Figure 3. The model prediction is designed *ad-hoc* for each experiment exploiting the Partial Differential Equations (PDE) toolbox in Matlab (R2020b), which allows to solving a non-dimensional form of Eq. (2). Briefly, the parameters were identified by minimizing the root mean square error (MSE) between the experimental data and the model. Statistical analysis of the obtained parameters were carried out using Graph Pad Prism 7.

III. RESULTS

Figure 4 reports the results of parameter estimation for the 2 and 3D configurations as a function of cell density.

Regarding monolayers (Fig. 4 A and B), for both parameters, the Kruskal-Wallis test highlighted that medians are not constant across densities ($p < 0.0001$ and $p = 0.002$ for OCR and k_M, respectively), with significant correlations reported by means of a Spearman coefficient $r = -0.8$ for OCR and $r = 1$ for k_M. The dependency of OCR on the volumetric cell density of spheroids observable in Figure 4C could be interpreted in the same light. In fact, statistical differences (p

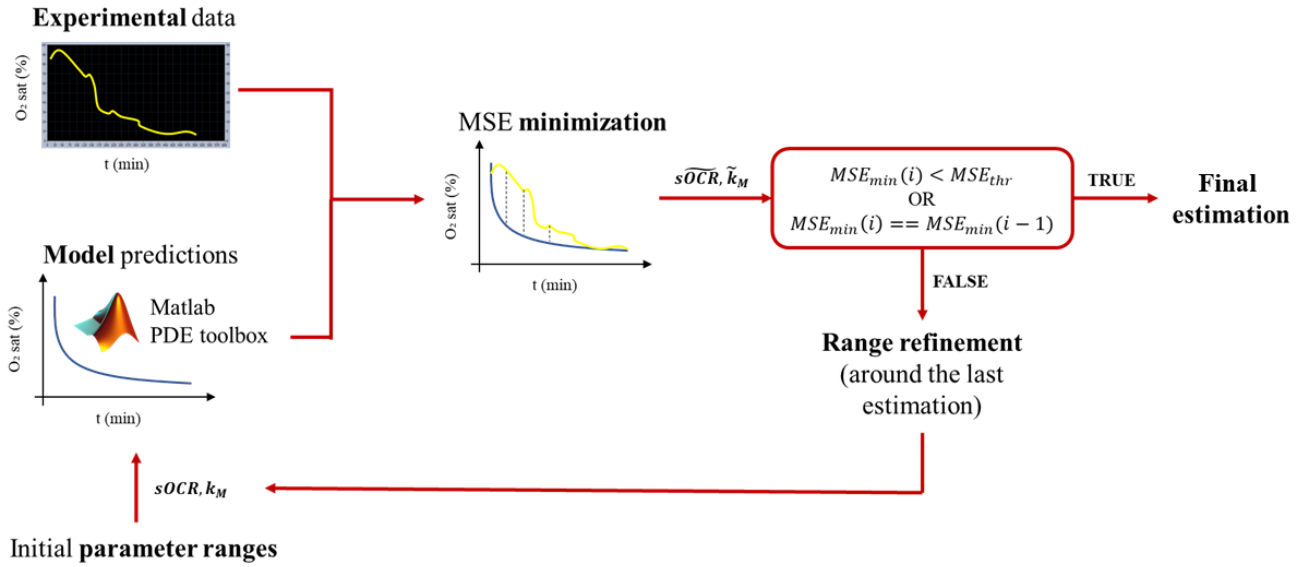


Figure 3 Pipeline of the multiparameter identification procedure for OCR and km.

< 0.0001) together with a Spearman coefficient r = -0.8 might indicate a cooperative behaviour in terms of O_2 metabolism of HepG2 cells embedded within spheroidal hydrogels, analogue to that noticed for monolayers. Neither significant differences among medians (p = 0.9030) nor correlations (r = -0.2) resulted instead for k_M in this configuration (Fig. 4D).

IV. Discussion and Conclusion

The results for 2D cultures show that OCR decreases with cell surface density (negative correlation, r = -0.8), while there is a positive correlation between k_M and ρ_c (r = 1). Our estimates for OCR are fairly close to those reported in the literature. Very few studies report k_M values – indeed oxygen consumption rates are usually considered to be constant for cells. Notably, our estimates are much higher than that reported by [6]. This could be because we took particular precautions to eliminate the passage of ambient oxygen into the medium during measurements to avoid errors due to oxygen infiltration. In the 3D case, OCR again decreases with volumetric cell density (r = -0.8). No significant differences in k_M with volumetric density were observed (r = -0.2, indicating very low correlation) and the values are similar to the few we found in the literature.

This study proposes a computational and experimental pipeline for identifying the kinetic parameters for both 2D and 3D cell constructs. The different correlation of OCR and k_M between cell density in *in vitro* constructs of different dimensionality may be evidence of a metabolic cooperation, manifested by the decrease of OCR, but also to the reduction of the O_2 uptake efficiency, explained by the increase of k_M. Future developments could include the investigation of how the kinetics parameters are dependent on the material used for both 2D and 3D cell cultures – e.g., the alginate -, as stated by Guaccio *et al.* [8]. Our current efforts are directed towards the identification of single cell consumption and the effects of fluctuations [9], coexistence and cooperation on cell metabolism.

Acknowledgement

This work has received funding from the Swiss National Science Foundation, through Project SINERGIA 2019 572 CRSII5_186422.

References

[1] G. Mattei, S. Giusti, and A. Ahluwalia, "Design Criteria for Generating Physiologically Relevant In Vitro Models in Bioreactors," *Processes*, vol. 2, no. 3, pp. 548–569, 2014.

[2] Foy, B.D., Rotem, A., Toner, M., Tompkins, R.G.; Yarmush, M.L. "A device to measure the oxygen uptake rate of attached cells: Importance in bioartificial organ design." *Cell Transplant*, vol 3, p. 515–527, 1994.

[3] C. Magliaro, G. Mattei, F. Iacoangeli, A. Corti, V. Piemonte, and A. Ahluwalia, "Oxygen Consumption Characteristics in 3D Constructs Depend on Cell Density," *Front. Bioeng. Biotechnol.*, vol. 7, p. 251, 2019.

[4] M. M. Adeva-Andany, N. Pérez-Felpete, C. Fernández-Fernández, C. Donapetry-García, and C. Pazos-García, "Liver glucose metabolism in humans," *Biosci. Rep.*, vol. 36, no. 6, p. 416, Dec. 2016.

[5] A. Tirella, C. Magliaro, M. Penta, M. Troncone, R. Pimentel, and A. Ahluwalia, "Sphyga: a multiparameter open source tool for fabricating smart and tunable hydrogel microbeads," *Biofabrication*, vol. 6, no. 2, p. 025009, Apr. 2014

[6] J. F. Patzer, "Oxygen Consumption in a Hollow Fiber Bioartificial Liver - Revisited," Artif. Organs, vol. 28, no. 1, pp. 83–98, Jan. 2004.

[7] B. A. Wagner, S. Venkataraman, and G. R. Buettner, "The rate of oxygen utilization by cells," *Free Radic. Biol. Med.*, vol. 51, no. 3, pp. 700–712, Aug. 2011.

[8] A. Guaccio, C. Borselli, O. Oliviero, P. A. Netti, "Oxygen consumption of chondrocytes in agarose and collagen gels: A comparative analysis", *Biomaterials*, vol 29, Issue 10, p. 1484-1493, 2008.

[9] E. Botte, F. Biagini, C. Magliaro, A. Rinaldo, A. Maritan and A. Ahluwalia; "Scaling of joint mass and metabolism fluctuations in *in silico* cell-laden spheroids", *PNAS, 118(38)*, (2021).

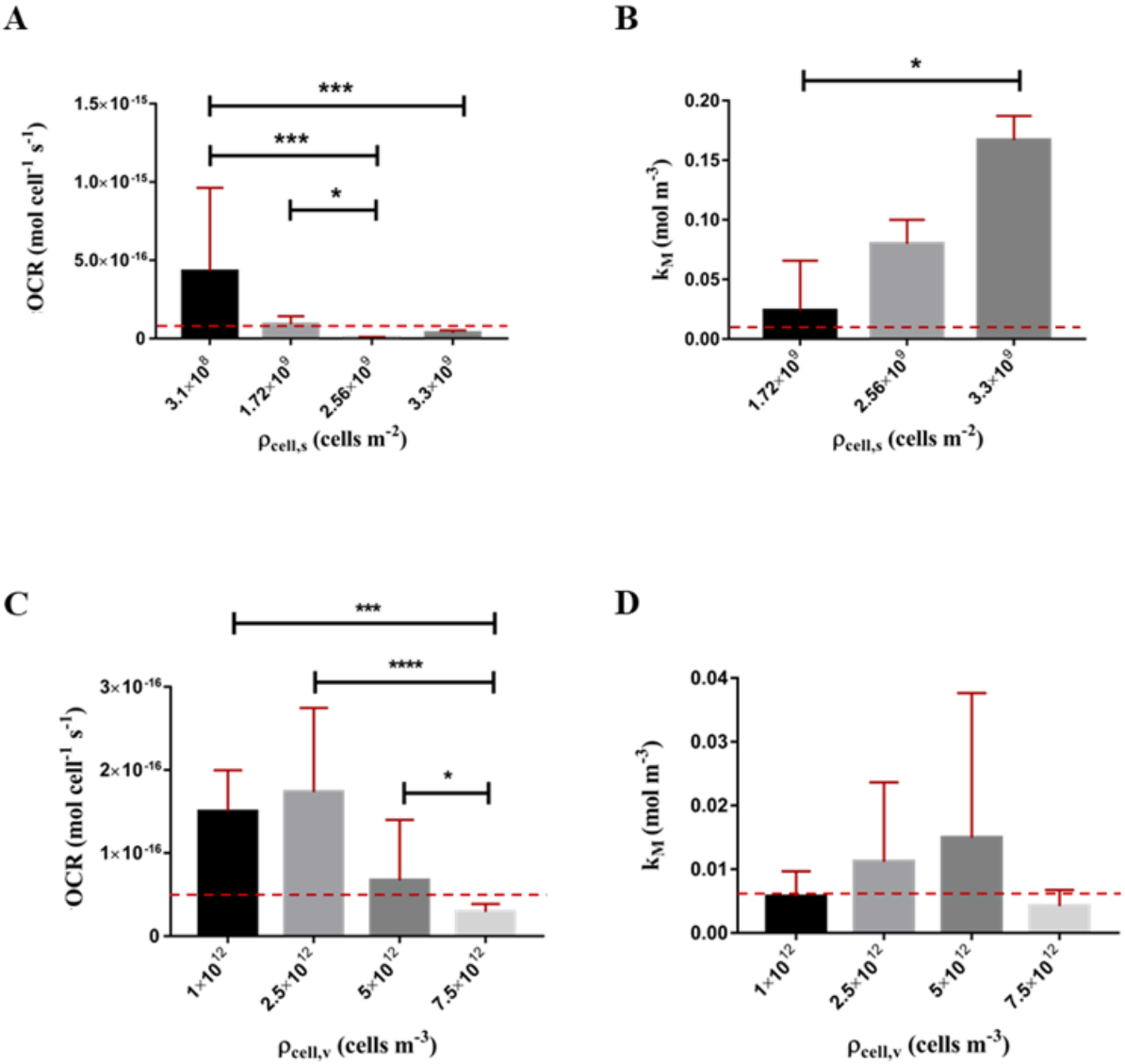


Figure 4 Outcome of the multiparameter identification procedure for parameters characterizing the MM kinetic model for HepG2 cells cultured in monolayer (A) and B)) or in spheroidal hydrogels (C) and D)). Red dashed lines depict OCR and k_M values from the literature [3], [7]. All data are expressed as median ± range.

GNB2023, June 21st-23rd 2023, Padova, Italy

Antibacterial activity of bacterial cellulose based wound care paste

S. Villani[1], S. Kunjalukkal Padmanabhan[1], M. Stoppa[1,2], R. Nisi[2], A. Licciulli[1,2], P. Alifano[3] and C. Demitri[1]

[1] *DII - University of Salento, Lecce, Italy*
[2] *Biofaber Srl, Brindisi, Italy*
[3] *DISTEBA - University of Salento, Lecce, Italy*

***Abstract*—In this work, we discuss the development and antibacterial activity of bacterial cellulose/neem–hypericum oil paste for wound healing. The paste is made by mixing BC pulp with neem-hypericum oil/water emulsion. Unlike pure BC, the paste showed promising biofilm detachment properties against *Pseudomonas aeruginosa* and *Staphylococcus aureus* biofilm, laying the foundation for the development of a new strategy for the treatment of chronic wound infections.**

***Keywords*—Bacterial cellulose, neem oil, wound healing, bacterial biofilm**

I. INTRODUCTION

Cellulose is the most widely available biopolymer in nature, and it is obtained by different methods such as extraction, biosynthesis, enzymatic synthesis, and chemosynthesis [1]. Plants and microorganisms are the two main sources of cellulose production. It is well-known that bacterial cellulose (BC) is the cellulose hydrogel derived from bacteria (e.g. *Acetobacter xylinum*) by the fermentation of sugar and can produce cellulose fiber with a high aspect ratio and diameter of less than 100 nm [2]. BC has high purity, good water-holding capacity, and biocompatibility compared to vegetable cellulose (VC) derived from wood or cotton. These advantages make them extensively used in various biomedical applications such as drug delivery, tissue engineering, and wound dressing. BC is a good choice for wound healing applications because it can control wound exudate and provide a moist environment for healing. However, using BC alone is not recommended for wound healing as it lacks antibacterial activity [3].

It has been estimated that about 8 million people around the world are affected by wounds [4]. The disruption of the skin integrity enables bacteria to rapidly colonize the burn injury or the surgical incision [5]. Both commensal and pathogen microorganisms can colonize the wound site: they are Gram-positive bacteria, such as *Staphylococcus aureus*, *Enterococcus* spp., and Gram-negative bacteria like *Pseudomonas aeruginosa*, *Acinetobacter* spp., and fungi like *Candida* spp [5]. Scientific evidence demonstrates that *S. aureus* usually colonizes the top layer of wounds, while *P. aeruginosa* is localized in the deepest region of the wound bed [6]. In chronic wounds, *S. aureus* and *P. aeruginosa* react by increasing the expression level of some virulence factors that lead to the development of severe infections and antibiotic resistance [7], [8]. Moreover, chronic infections are generally associated with the development of biofilm, a polymicrobial population that adheres to the skin surface and that is difficult to eradicate because of the antimicrobial tolerance profile of the microorganisms [4]. Because of the essential role of bacterial biofilm, a major challenge is the development of new strategies that can optimize biofilm eradication in the treatment of chronic wound infection.

There are many research works reported on the antibacterial activity of bacterial cellulose incorporated with antibiotics, metal nanoparticles, microbial agents, and natural oils for wound healing applications. In most of these works, they used BC hydrogel films [9]. As an alternative to traditional hydrogel-based strategies, we optimized a BC-based paste incorporating a mix of neem and hypericum oil. Neem oil is a plant-derived product with antioxidant and anti-inflammatory properties, that has been already used alone [10] and in combination with hypericum oil [11] to promote wound healing. In this work, we try to explore the antibacterial properties of the resulting BC/neem-hypericum oil paste as a biofilm detaching agent.

II. MATERIALS AND METHOD

A. Bacterial cellulose (BC) synthesis and BC-neem-hypericum oil paste

BC pellicles were obtained by the fermentation process of the sweetened black tea with *Gluconacetobacter xilinus* strains, as reported in our previous work [12]. Purified BC pellicles were shredded into small pieces and fibrillated using a mini mixer. Finally, for making the BC paste, the pulp is made by concentrating fibrillated BC fragments by centrifugation, and the aliquot was further concentrated by vacuum pump filtration using a Whatman 41 filter. The oil mix, neem-hypericum was kindly provided by ENEA (Brindisi, Italy).

The oil-water emulsion of the neem-hypericum was prepared using the ultrasonic homogenizer (Velp OV5). Pluronic F127 was used as the surfactant and 24-weight percentage oil in water emulsion was prepared. Finally, BC/ neem oil paste was made by mixing BC pulp and emulsion in a 2:1 ratio and mixed with a homogenizer.

B. Characterization of BC pulp and neem-hypericum oil/water emulsion

The particle size of BC pulp was analyzed by laser diffraction using a CILAS 1190 multi-laser particle size analyzer. The zeta potential of the emulsion was measured using a zeta sizer (Malvern). The morphology of the BC pulp was analyzed using a Zeiss (Sigma VP, Carl Zeiss, Jena, Germany) field-emission scanning electron microscope (FESEM).

C. *Biofilm detachment properties evaluation*

P. aeruginosa and *S. aureus* were grown in Luria-Bertani (LB) medium (per liter, 10 g of NaCl, 10 g of Tryptone, 5 g of Yeast Extract, and 15 g of Agar for LB solid medium), stirring at 120 rpm at 37 °C. Bacteria were incubated overnight (ON) at 37 °C and were resuspended in the medium reaching an Optical Density (O.D.) of 0,3-0,4 measured at 600 nm. Then, each of the 12-well plates containing 20-mm square cover glasses were inoculated with 1 ml of *P. aeruginosa* or *S. aureus* suspension and were incubated at 37 °C for 24 h.

Two solutions of 10% and 1% w/v of paste were prepared in NaCl 0,9%. After 24 h of biofilm growth, cover glasses were treated with 2 ml of 10% or 1% paste solution for 5 min. To better investigate BC detachment properties, a 10% and 1% solutions of vegetable cellulose (VC) have been prepared in NaCl 0,9%, to be used as a comparative agent. Some samples were treated for 5 min with 2 ml of 1% Sodium Dodecyl Sulfate (SDS) as a standard cleaning agent.

To determine the number of Colony Forming Unit (CFU/ml), the different types of cover glass samples were put in 2 ml of LB medium and vortexed for 2 min. Then, 10 µl of the liquid phase was diluted and spotted on solid LB Petri dishes and incubated at 37 °C until the next day.

Each cover glass sample was also fixed and subjected to crystal violet staining to carry out a microscopy analysis using Leica LB30S optical microscope (*Leica Microsystems Wetziar GmbH*).

III. RESULTS AND DISCUSSION

A. *Particle size and microstructure of BC pulp and zeta potential of emulsion*

The fibrillated cellulose in BC pulp showed an average diameter of 200 microns analyzed by master sizer. The microstructure observed by SEM shows even after fibrillation, cellulose retained the nanofibrous structure (Fig 1a). A high zeta potential value of -29 mV was obtained for neem-hypericum/water emulsion indicating the stability of the emulsion. After proper mixing with BC pulp and oil emulsion, an injectable paste has been obtained (Fig. 1b).

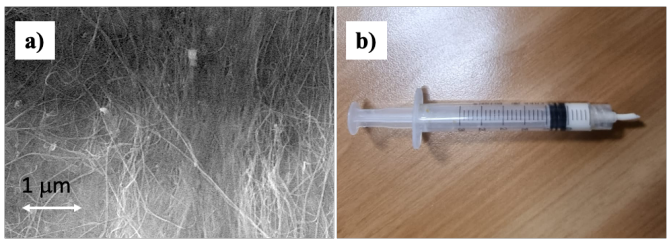


Fig. 1: Scanning electron microscopy image of fibrillated BC (a) and a photograph of injectable BC/neem-hypericum oil paste (b).

B. *Biofilm detachment properties evaluation*

In the present study, *P. aeruginosa* and *S. aureus* were chosen as common bacteria that often colonize the surface of chronic wounds. The protocol has been standardized for both species, leading to the formation of a 24 h bacterial biofilm that could be used for further investigations about biofilm detachment agents. To estimate the paste's capability to eradicate bacterial biofilms, the quantification of CFU/ml has been chosen, and these data have been confirmed through optical microscopy analysis. To conduct the biofilm detachment assay, a contact period of 5 min between the biofilm and the detachment agents was chosen as the probable application time for a cleanser agent to be used for skin lesions cleansing. Further investigations are needed to better investigate the time-response behavior of these biomaterials in the detachment of bacterial biofilms.

In this *in vitro* model, the BC/neem-hypericum oil paste shows promising biofilm eradication properties for both bacterial species that have been investigated. In particular, the application of 10% solution of BC/neem-hypericum oil paste reduced the number of CFU/ml in *P. aeruginosa* (Fig. 2A) and, more significantly, in *S. aureus* (Fig. 2B). In both cases, the use of 10% paste solution exhibits better biofilm detachment properties than SDS, which is considered a common cleaning agent capable of disrupting bacterial biofilm [13], [14]. Also, the application of 1% solution of BC/neem-hypericum oil paste exhibits biofilm detachment properties that are more evident for *S. aureus* (Fig. 2B). The use of 1% and 10% VC solutions exhibited stronger detachment capabilities against *S. aureus* biofilm than *P. aeruginosa* biofilm; however, VC detachment properties seems to be worse than that of BC/neem-hypericum oil paste for both bacterial species investigated. The greater effect of biofilm detachment that occurs with *S. aureus* compared to *P. aeruginosa* may be attributable to the different outer cell envelopes between Gram-positive and Gram-negative bacteria that can influence the strategies of surface colonization. Also, motility strategies can modulate surface colonization and biofilm formation: *P. aeruginosa* uses flagellar motility to colonize surfaces, while *S. aureus* does not possess flagella [15]. It is also necessary to consider the possible different affinity of the bacteria to the BC fibers of the formulation, which could justify the differences in the biofilm detachment capabilities of the paste. To confirm this, further investigations will be performed involving other Gram-positive and Gram-negative bacteria that commonly infect skin lesions.

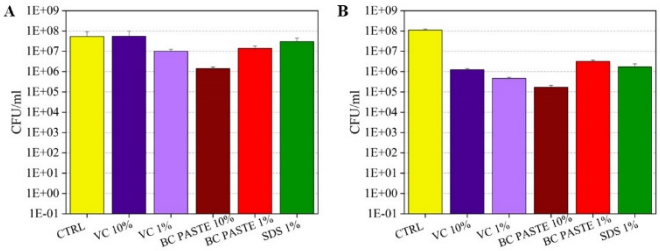


Fig. 2: Determination of the number of Colony Forming Unit (CFU/ml) for P. aeruginosa (A) and S. aureus (B) after 5 min treatment with 10% and 1% VC solution, 10% and 1% BC paste solution and 1% SDS as a standard cleaning agent.

This investigation continued by conducting an optical microscopy analysis to support the quantitative evaluation of the CFU/ml assay. The 5 min treatment with 10% solution of BC/neem-hypericum oil paste showed a significant reduction in the biofilm density for both *P. aeruginosa* (Fig. 3A) and *S. aureus* (Fig. 3B) if compared with the control. The performance obtained from the 10% solution is also higher than that of the VC solutions and of the 1% SDS (Fig. 3).

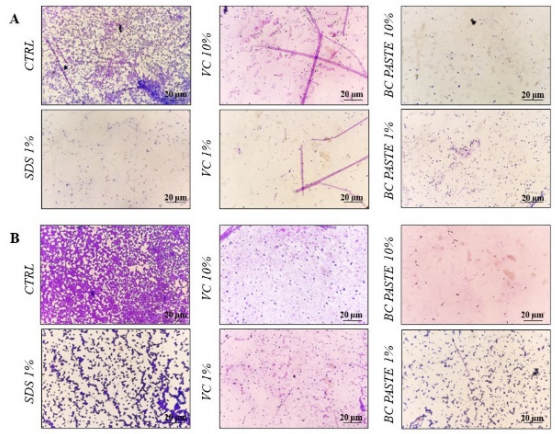


Fig. 3: Optical microscopy evaluation of the biofilm detachment properties of 10% and 1% BC/neem-hypericum oil paste solution, compared with the control, with 10% and 1% VC solutions and with 1% SDS treatments for P. aeruginosa (A) and S. aureus (B).

IV. Conclusion

In conclusion, this work highlighted the synergic effect of BC combined with a naturally derived antibacterial agent in creating a paste for wound healing application. The major result of this study is the significant reduction of biofilm formation when both *Pseudomonas aeruginosa* and *Staphylococcus aureus* bacteria are used. This feature can be further investigated in the future, especially in combination with the regenerative effect of BC.

Acknowledgement

This work is carried out as a part of the project funded by regional Puglia- REFIN—Research for Innovation project "Medicazioni innovative per rigenerazione tissutale a base di idrogeli funzionalizzati di cellulosa batterica", project no. 8AE55352, in the framework of POR PUGLIA FESR-FSE 2014/2020 projects.

This work was supported by the Italian Minister of Research with the Ministerial Decree n. 351/2022 – PNRR Mission 4, Component 1.

References

[1] Klemm, D.; Heublein, B.; Fink, H.-P.; Bohn, A. Cellulose: Fascinating Biopolymer and Sustainable Raw Material. Angew. Chem.Int. Ed. 2005, 44, 3358–3393.

[2] Klemm, D.; Schumann, D.; Udhardt, U.; Marsch, S. Bacterial synthesized cellulose—Artificial blood vessels for microsurgery.Prog. Polym. Sci. 2001, 26, 1561–1603

[3] Zhong, C. Industrial-Scale Production and Applications of Bacterial Cellulose. Front. Bioeng. Biotechnol. 2020, 8, 1425.

[4] Falcone, Marco et al. "Challenges in the management of chronic wound infections." Journal of global antimicrobial resistance vol. 26 (2021): 140-147. doi:10.1016/j.jgar.2021.05.010

[5] Sen, Chandan K. "Human Wounds and Its Burden: An Updated Compendium of Estimates." Advances in wound care vol. 8,2 (2019): 39-48. doi:10.1089/wound.2019.0946

[6] Serra, Raffaele et al. "Chronic wound infections: the role of Pseudomonas aeruginosa and Staphylococcus aureus." Expert review of anti-infective therapy vol. 13,5 (2015): 605-13. doi:10.1586/14787210.2015.1023291

[7] Coates, Rosanna et al. "Staphylococci: colonizers and pathogens of human skin." Future microbiology vol. 9,1 (2014): 75-91. doi:10.2217/fmb.13.145

[8] Vanderwoude J, Fleming D, Azimi S, Trivedi U, Rumbaugh KP, Diggle SP. The evolution of virulence in *Pseudomonas aeruginosa* during chronic wound infection. Proc Biol Sci. 2020 Oct 28;287(1937):20202272. doi: 10.1098/rspb.2020.2272. Epub 2020 Oct 21. PMID: 33081616; PMCID: PMC7661302.

[9] Lu Zheng, Shanshan Li , Jiwen Luo and Xiaoying Wang, Latest Advances on Bacterial Cellulose-Based Antibacterial Materials as Wound Dressings,Front. Bioeng. Biotechnol., 23 November 2020 Volume 8 -2020

[10] Manca ML, Manconi M, Meloni MC, Marongiu F, Allaw M, Usach I, Peris JE, Escribano-Ferrer E, Tuberoso CIG, Gutierrez G, Matos M, Ghavam M. Nanotechnology for Natural Medicine: Formulation of Neem Oil Loaded Phospholipid Vesicles Modified with Argan Oil as a Strategy to Protect the Skin from Oxidative Stress and Promote Wound Healing. Antioxidants (Basel). 2021 Apr 25;10(5):670. doi: 10.3390/antiox10050670. PMID: 33923127; PMCID: PMC8146128.

[11] Özdemir S, Bostanabad SY, Parmaksız A, Canatan HC. Combination of St. John's Wort Oil and Neem Oil in Pharmaceuticals: An Effective Treatment Option for Pressure Ulcers in Intensive Care Units. Medicina (Kaunas). 2023 Feb 27;59(3):467. doi: 10.3390/medicina59030467. PMID: 36984468; PMCID: PMC10054705.

[12] Sudipto Pal, Rossella Nisi, Mariangela Stoppa, and Antonio Licciulli, Silver-Functionalized Bacterial Cellulose as Antibacterial Membrane for Wound-Healing Applications, ACS omega, 2017, 2, 7, 3632–3639

[13] Díaz De Rienzo, M A et al. "Pseudomonas aeruginosa biofilm disruption using microbial surfactants." Journal of applied microbiology vol. 120,4 (2016): 868-76. doi:10.1111/jam.13049

[14] Gawande, P V et al. "Antibiofilm activity of sodium bicarbonate, sodium metaperiodate and SDS combination against dental unit waterline-associated bacteria and yeast." Journal of applied microbiology vol. 105,4 (2008): 986-92. doi:10.1111/j.1365-2672.2008.03823.x

[15] Ruhal R, Kataria R. Biofilm patterns in gram-positive and gram-negative bacteria. Microbiol Res. 2021 Oct;251:126829. doi: 10.1016/j.micres.2021.126829. Epub 2021 Jul 23. PMID: 34332222.

Microfluidic system for a label-free, real-time functional assessment of thrombotic risk

T. Mencarini[1], E. Puce[1], M. Calogiuri[2], M. Scavone[2], S. Bozzi[1] and A. Redaelli[1]
[1] *Department of Electronics, Information and Bioengineering, Politecnico di Milano, 20133 Milan*
[2] *Unità di Medicina 2, ASST Santi Paolo e Carlo, Dipartimento di Scienze della Salute, Università degli Studi di Milano, 20142 Milan*

***Abstract*—High incidence of thrombotic diseases worldwide, together with the variability of patients' response to antiplatelet drugs, makes the management of antithrombotic regimes of paramount importance. Platelet function testing is the most promising tool in addressing this clinical need. Here we present the first prototype of a microfluidic system for rapid, label-free, real-time functional assessment of the thrombotic risk of patients undergoing antiplatelet treatment. Our platform allows to monitor pressure drop variations on a collagen-coated microchannel under a range of blood flow conditions, and to relate these measurements to thrombus formation and ultimately to platelet functionality. The preliminary testing campaign presented in this work demonstrated the feasibility of our approach and allowed us to determine the most suitable working range of the current system.**

***Keywords*—Thrombotic risk, label-free, real-time monitoring, microfluidics.**

I. Introduction

ISCHEMIC cardio- and cerebrovascular events are the leading cause of morbidity and mortality in high-income countries, mainly caused by thrombotic or thromboembolic events. Platelets represent the main target for therapeutic treatments of thrombosis via antiplatelet medications. Yet, patients' responses to antiplatelet therapy significantly vary, with individuals showing high residual platelet activity, with higher susceptibility to thrombotic events [1]. To personalize thrombosis management and possibly predict pathological events, platelet function testing (PFT) has been suggested as a promising tool able to monitor the haemostatic impact of antiplatelet agents in real-time [2]. Most of the commercially available systems, though, are lab-based cumbersome instruments which hardly replicate physiological flow conditions [3]. Moreover, they usually allow a minimum degree of freedom, offering pre-set cuvettes and testing conditions.

To address this clinical need, we aim at developing a label-free microfluidic platform for identification of patients at risk of thrombosis. The platform performs experiments under flow conditions and can span a wide range of shear stresses. Unlike traditional immunoassays which require chemicals/antibodies, our label-free approach is low cost and more scalable for large scale patient screening, potentially becoming a point-of-care (POC) system. It also satisfies other critical requirements such as the use of a small blood volume, low-to-none blood handling and real-time analysis.

The present work presents the results obtained with the preliminary tests.

II. Materials and Methods

A. Blood sampling

The recruited healthy subjects (N=14) abstained from drugs known to affect platelet function for at least 10 days before enrolment. The study was carried out at ASST Santi Paolo e Carlo and approved by the institutional ethical committee; all subjects signed their informed consent. Blood samples were collected in the morning from an antecubital vein using a 21-gauge butterfly needle with minimal stasis. The first 3 mL of blood were collected into K-EDTA tubes (Becton Dickinson vacutainer, Australia) for a complete blood count; the following 10–15 mL were collected in 250 µg/mL INN-desirudin (Canyon Pharmaceuticals, United Kingdom), gently mixed, and allowed to rest at room temperature for 15 min before use. Platelets were marked with the green fluorescent dye DiOC6 (1 µM; ThermoFisher Scientific, Italy) for 15 min at room temperature.

B. Microfluidic device and experimental setup

Microfluidic devices featured six independent channels (1000 µm wide, 100 µm high and 3 cm long). The devices were fabricated in polydimethylsiloxane (PDMS, Sylgard™ 184, Dow Corning, USA) from silicon masters using standard soft lithography techniques (10:1 PDMS to curing agent ratio). Inlet and outlet fluidic ports were punched with a 1.5 mm diameter biopsy puncher. The PDMS layer was plasma-bonded to a glass coverslip (Figure 1, above).

Microfluidic channels were incubated at 4°C overnight with Horm fibrillar collagen type I (Mascia Brunelli, Italy) at two concentrations (10 and 100 ug/ml) [4], passivated with bovine serum albumin and finally rinsed with phosphate buffered saline (PBS).

The channels were connected to tubing for pumping system (Cellix, Ireland) and blood was perfused at two different shear rates, 950 and 1600 s^{-1}, simulating an arterial flow and a slightly pathological shear rate.

At this preliminary stage, we wanted to validate pressure measurements against the results obtained by image acquiring and processing using a platform from our previous works [3]. To this aim, all the experiments were performed under a fluorescence microscope (Axiovert A1 FL, Zeiss, Italy) equipped with a 16-bit camera (Crisel Instruments, Italy) (Figure 1, below). Images of the first portion of the collagen coating were acquired at 40x magnification every minute up to 4 min during blood perfusion through the microchannel. Mean and maximum fluorescence intensity (FI), together with

further parameters, were calculated, being FI an indicator of 3-dimensional thrombus growth in the channel lumen.

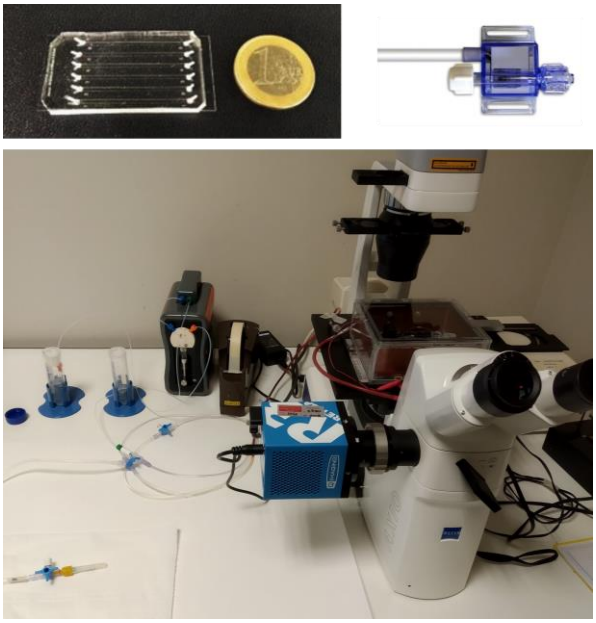


Fig. 1: Microfluidic chip and pressure transducer (above) and setup used for the preliminary testing campaign (below), comprising: an inverted fluorescence microscope equipped with a 16-bit camera, a micropump, a thermostatic chamber, the pressure transducer connected to a laptop and the microfluidic chip.

For pressure reading, an inline pressure transducer (PendoTech, USA) was placed along the circuit, to detect the pressure drop due to thrombi formation inside the channel. It was chosen for its working range, its affordability and washability. The transducer was connected to an amplifier and then to a laptop to record and visualise the pressure signal.

All the experiments were performed at 37°C thanks to a customised thermostatic chamber mounted on the microscope stage.

III. Results and Discussion

Figure 2 shows pressure drop measurements (n=14) in microchannels coated with two different collagen concentrations, 10 and 100 ug/ml, and at two shear rates, 950 and 1600 s^{-1}. A two-way ANOVA test found statistically significant differences between the pressure readings at 1600 s^{-1} with a 100 ug/ml collagen concentration and all the other conditions (****p<0.0001).

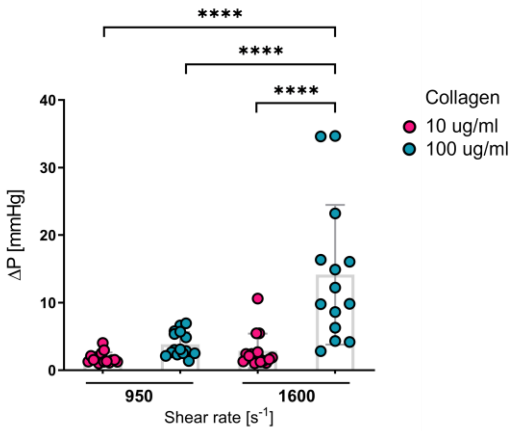


Fig. 2: Pressure drop due to thrombi formation inside the microchannel after 4 min experiments, classified for different shear rate and collagen concentration of the substrate. Bars represent mean ± standard deviation. N=14. Two-way ANOVA was applied. ****p<0.0001.

This indicates a transducer's sensitivity better working under more intense conditions. The higher collagen concentration appears to be a more suitable experimental condition, as indicated by the difference found between the data at the two different shear rates, conversely to what can be observed at 10 ug/ml. This is due to the bulkier thrombi forming on the 100 ug/ml substrate, as it works as a strong stimulus for platelets and exposes many bonding sites. The difference is more evident for increasing shear rate (Figure 3).

100 ug/ml is one of the most used concentrations in literature [5], [6], [7], while some groups employ even higher ones [8], [9].

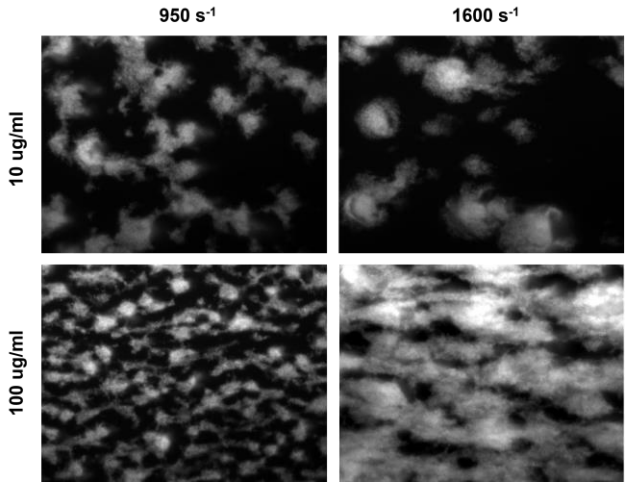


Fig. 3: Fluorescent images (magnification 40x) showing the typical thrombus formation over the two collagen substrates (10 and 100 ug/ml) at different shear rates (950 and 1600 s^{-1}).

The pressure drop results after 4 min of experiment, divided by collagen concentration, were compared with the mean and maximum fluorescence intensity computed via MATLAB from the corresponding images (Figure 4). The computed correlation demonstrated a fair agreement (R^2=0.81) between the two datasets, max FI and pressure variation, only at the higher collagen concentration, in accordance with our previous

observation. The encumbrance of the thrombi under this condition leads to partial occlusion of the channel, thus higher pressure drops.

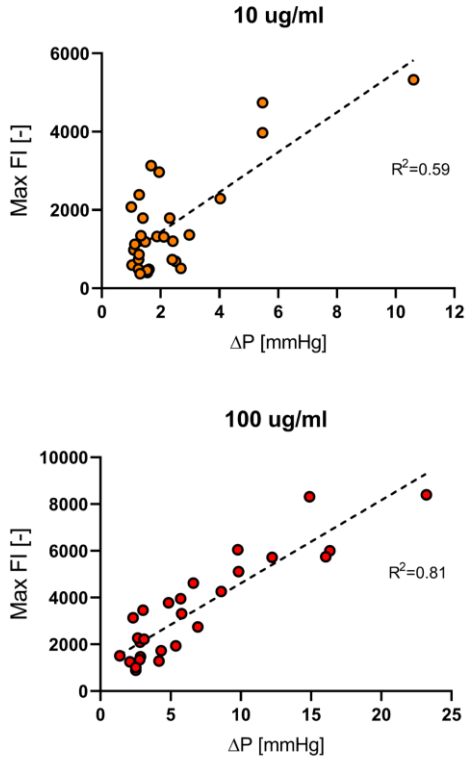


Fig. 4: Pressure drop after 4 min experiments plotted against the maximum fluorescence intensity for collagen concentration 10 and 100 ug/ml. Linear regression found R^2=0.59 and 0.81, respectively. N=14, n=28.

On the lower collagen concentration substrate, thrombi usually remain smaller and lower in height, and the employed transducer is not sensitive enough to detect low pressure variations.

Pressure kinetics was also analysed by monitoring pressure drop and fluorescence intensity throughout the experiments (4 min). Figure 5 shows a typical trend of the two parameters in an experiment carried out at 1600 s^{-1} on a 100 ug/ml collagen.

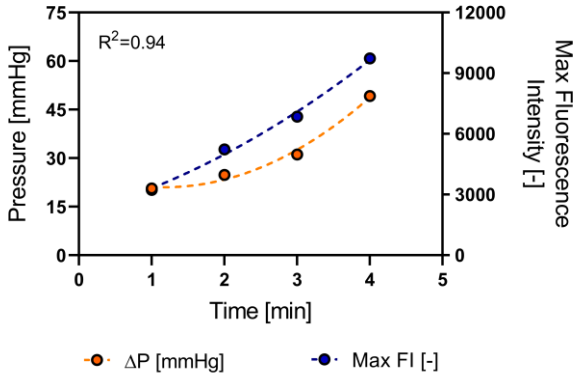


Fig. 5: Typical trend of pressure drop and max fluorescence intensity in time during an experiment conducted on collagen 100 ug/ml at 1600 s^{-1}. Dashed lines represent second order polynomial fitting. Pearson correlation coefficient R^2=0.94.

Under these conditions, platelets massively adhere to the collagen fibrils immediately after the start of the experiment and thrombi start to build up quickly. The pressure increases promptly in the first minute, then a parabolic trend can be noticed, while the channel lumen progresses towards occlusion (partial, within 4 min). A forming big thrombus is usually observed at the beginning of the coated area: it generates a hydraulic resistance which induces a concentrated pressure drop. This result shows how the pressure transducer is able to catch the kinetics of the process, especially after 2 min of experiment, displaying a trend similar to the one of the maximum FI (Pearson correlation coefficient R^2=0.94).

IV. Conclusion

Herein we presented the results of a preliminary testing campaign of a microfluidic platform for label-free, real-time functional assessment of the thrombotic risk, with the ultimate goal of a rapid monitoring of the therapeutic treatment. We demonstrated the feasibility of our approach by showing a good correlation between pressure drop and fluorescence images. These experiments allowed us to define the suitable working range of the current setup.

Future studies will investigate the correlation between pressure drop readings and occlusion rate of microchannels, obtained by confocal microscopy. Moreover, we will verify whether the pressure transducer is able to detect the detachment of thrombi from the substrate, to potentially study the patient population presenting aggregation defects.

A further improvement will be the addition of surface microelectrodes on the glass substrate, to detect platelet adhesion through electrical impedance variations.

This platform has the potential to become a POC PFT device, providing a useful tool for fast, real-time and label-free stratification of patients' thrombotic risk.

References

[1] M. Cattaneo, "Aspirin and clopidogrel: efficacy, safety, and the issue of drug resistance", *Arterioscler. Thromb. Vasc. Biol.*, vol. 24 (11), pp. 1980-1987, 2004.

[2] A. D. Michelson, A. L. Frelinger, M. I. Furman, "Current options in platelet function testing", *Am. J. Cardiol.*, vol. 98(10A), pp. 4N–10N, 2006.

[3] R. Paniccia, R. Priora, A. A. Liotta, R. Abbate, "Platelet function tests: a comparative review", *Vasc. Health Risk Manag.*, vol. 11, p. 133, 2015.

[4] M. Scavone, S. Bozzi, T. Mencarini, *et al.*, "Platelet adhesion and thrombus formation in microchannels: The effect of assay-dependent variables", *Int. J. Mol. Sci.*, vol. 21(3), p.750, 2020.

[5] K. B. Neeves, A. A. Onasoga, R. R. Hansen, *et al.*, "Sources of variability in platelet accumulation on type 1 fibrillar collagen in microfluidic flow assays", *PLoS ONE*, vol. 8(1), 2013.

[6] M. Moroi, S. M. Jung, K. Shinmyozu, *et al.*, "Analysis of platelet adhesion to a collagen-coated surface under flow conditions: The involvement of glycoprotein VI in the platelet adhesion", *Blood*, vol. 88, 1996.

[7] J. Berry, F. Peaudecerf, N. A. Masters *et al.*, "An "occlusive thrombosis-on-a-chip" microfluidic device for investigating the effect of anti-thrombotic drugs", *Lab Chip*, vol. 21(21), pp. 4104-4117, 2021.

[8] S. Rahman and V. Hlady, "Downstream platelet adhesion and activation under highly elevated upstream shear forces", *Acta Biomater.*, vol.91, 2019.

[9] E. Gutierrez, B. G. Petrich, S. J. Shattil, *et al.*, "Microfluidic devices for studies of shear-dependent platelet adhesion", *Lab Chip*, vol. 9, 2008.

Circulating tumour cells deformability measurement in microfluidics

M.I. Maremonti[1], D. Dannhauser[1], P.A. Netti[1] and F.Causa[1]
[1]*Interdisciplinary Research Centre on Biomaterials (CRIB), Università "Federico II", P.le Tecchio 80, 80125 Naples, Italy.*

***Abstract*— During the last years, the deformability characterization of non-adherent cells like circulating tumour cells (CTCs) and immune cells gained a lot of attention since mechanical forces regulate the deformation, organization, and translocation of cytoskeleton leading to changes in T-cell mobility, migration, and infiltration. However, deformability measurements on non-adherent cells is challenging since any kind of contact between a physical probe or substrate could induce alterations into the cell state and then deformability outcome. Thus, new strategies are needed to overcome such problems. In-flow viscoelastic compression represents a straightforward way to deform CTCs and immune cells in a controlled and contactless manner. Here, we present a study of cell deformability by application of such viscoelastic compression forces on CTCs and healthy lymphocytes, eliciting a higher deformability of cancer cells with respect to healthy lymphocytes. Thus, our approach opens up to the possibility to characterize and distinguish CTCs and healthy lymphocytes depending on the resulting deformability in a rapid and versatile way.**

***Keywords*—Circulating tumour cells, microfluidics, contactless compression, deformability.**

I. Introduction

As label-free biomarker for cell phenotyping, the analysis of single cell mechanical properties has emerged as an interesting complementary approach to the well-known classical molecular biology [1]. In particular, cell deformability turned out to provide useful information about the state of a cell [2]. In fact, in cancer research, one of the most promising ways of understanding condition and mechanism of tumour metastasis, is the study of circulating tumour cells (CTCs) distinguishing them from the other circulating cells like immune cells. However, separation, classification and deformability measurement of CTCs are technically challenging, so new strategies are needed [3]. This importance of the deformability measurements justifies the interest in developing simple procedures to measure mechanical properties of these cells with easy-to-use, versatile and highly tuneable methods [4]. The current techniques for the mechanical characterization of CTCs and immune cells use different methods to apply a force and measure the corresponding deformation. For example, the micropipette aspiration technique consists of aspirating the cell by a capillary of inner dimension smaller that the cell diameter itself and analysing the aspirated length corresponding to a given suction pressure. Instead, the atomic force microscopy is based on the cell indentation into a specific location point, and it can be used also for suspended cells when fixed on a substrate. In magnetic twisting rheology, the response of a cell-attached magnetic bead is probed in response to an external magnetic field [5]. However, all of the aforementioned techniques present some drawbacks such as low cell throughput, not highly versatility in force calibration, and a mechanical contact of the used probe -atomic force microscopy and magnetic twisting rheology- with the cell which could lead to possible adhesion and active cellular responses that are crucial for CTCs and immune cells functions [5], [6].

To overcome the aforementioned drawbacks, a variety of microfluidic systems enabled alignment, deformation and/or separation of cells at high-throughput rates with precise force calibration. In particular, the combination of microfluidic based approaches like deformability cytometry, microfluidic constrictions and hydrodynamic stretching techniques demonstrated to solve the throughput problem while still lacking in the solution of the force calibration [6]. To date, viscoelastic fluids have been employed for such a kind of purposes since their intrinsic viscous and elastic properties allow to better govern in-flow cell manipulation, as deformation and separation [7]-[10].

Recently, we presented a viscoelastic-based microfluidic approach used for the in-flow compression of cells in a contactless, controlled and precise manner [11], [12]. We analysed and precisely classified breast cell lines -healthy and pathological- by coupling the classical descriptors of morphological and shape alterations with in-flow orientation angles [11].

Here, we propose to use our viscoelastic in-flow compression to deform human blood lymphocytes and immortalized lymphoid leukaemia cells as CTCs (Jurkat T-cell line) characterizing them in terms of cell deformation (CD), aspect ratio (AR) and orientation angles (φ). We demonstrate that a difference in cell deformability is present among healthy and pathological cells. Distinguishing variable deformability properties is crucial for phenotyping circulating cells since stiffer cells could be responsible of vaso-occlusion phenomena which can lead to organ failure.

Thus, our approach elicits the possibility to precisely classify Jurkat cells with respect to healthy lymphocytes in a completely label-free manner.

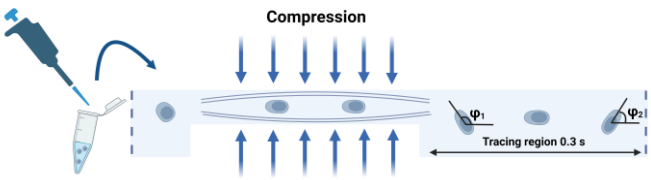


Fig. 1 Sketch representation of the microfluidic device. Cells pass through subsequent rectangular cross-sections where forces gradually change depending on the geometry. The sample arrives at the inlet capillary where it is loaded into a first section where they do not experience a deforming force. Instead, in the compression region, the deformation occurs, and it is then observed into an enlarged cross-section, conceived in order to detect in-flow deformation-dependent motion dynamics [11]. (Created with BioRender.com)

II. Material and Methods

A. Viscoelastic in-flow forces

To induce the compression of single cells under viscoelastic flow conditions, we used a highly biocompatible polyethylene-oxide (PEO - 4MDa, Sigma Aldrich). Fluid rheological

properties have been previously investigated and properly characterized [10]. We selected PEO 09 condition, which corresponds to polymer concentrations of 0.88 wt%. We calibrated the initial pressure and velocity conditions into the microfluidic device, as well as the channel geometry in order to align and deform cells in a contactless way [11].

B. Experimental setup for the in-flow measurement

The setup includes a pressure pump (P-pump, Dolomite Microfluidics), round shaped flexible fused silica capillary tubing (Molex), an ad hoc designed microfluidic chip, a fluid connector (N-333, IDEX) and an inverted microscope (X81, Olympus) with a CMOS camera (ORCA FLASH 4.0, Hamamatsu Photonics K.K.). Briefly, a pressure pump pushes the sample volume through the capillary in the microfluidic device inlet, while at the end of the chip a reservoir collects the cells. The chip is made of two separate parts made with polymethyl methacrylate, which are placed together by magnetic forces. The main part was machined using a standard CNC based micromilling technique (Minitech Machinery) to develop microfluidic duct sections. of different height, width, and length, while the cover part was simply used to close the chip. In particular, the compression section has the smallest height (W × H: 100 × 25 μm) implying that a well-defined viscoelastic compression over a certain time period on each passing cell is applied, enabling precise cell compression in-flow. Then, a subsequent enlarged section (W × H: 200 × 90 μm) is conceived for the observation and analysis of the compressed cells (Fig.1) [11].

C. Cell culture

Lymphocytes were obtained from healthy donor buffy coats obtained from the blood bank of the medical school of the Federico II University of Naples (Italy). At the time of blood donation, each donor signed an informed consent (model n. 5526 of Azienda Ospedaliera Universitaria "Federico II", Naples, Italy) in which is specified that waste parts of the blood, not useful for the medical-therapeutic purposes of blood donation, can be used for scientific research purposes. In more detail, a standard venepuncture procedure was performed using standard K 2 EDTA tubes (Vacutainer, BD) to prevent coagulation and standard density gradient centrifugation, with some adaptation to reduce a possible platelet contamination [13]. Briefly, the blood sample is gently layered on an equal volume of density gradient fluid (Ficoll) and centrifuged at 300 for 45 minutes (without brake). The peripheral blood mononuclear cell ring stratified at the interface between Ficoll and plasma is collected using a Pasteur pipette and washed twice with red blood cells lysis solution to eliminate possible erythrocyte contaminations. Next, lymphocytes are isolated by a negative selection procedure with specific Ab-coupled magnetic beads (Dynabeads Untouched kit, INVITROGEN) and suspended in phosphate buffered saline.

Jurkat human lymphoid leukaemia T cells were kindly donated by Siciliano's group (Center for Advanced Biomaterials for Healthcare@CRIB, Istituto Italiano di Tecnologia, Naples, Italy) and grown in RPMI 1640 medium supplemented with 10% FBS, 100 μg/ml l-glutamine and 100 U/ml penicillin/streptomycin.

D. Measurement procedure and data analysis

Before in-flow compression, cell diameters (d_{Static}) were measured with the inverted microscope. Then, the in-flow cell analysis was performed over the full cell tracing length(~0.3 s of measurement in the tracing region), after the compression region (Fig.1). We measured the dynamic in-flow cell parameters, such as the major axis (d_1), minor axis (d_2), circularity (c) and orientation angles (φ) in the range of [−90° to 90°], at each 0.03s. Out of such parameters, the cell deformation (*CD*), cell aspect ratio (*AR*) and angle variation (Δφ, at the beginning and the end of the tracing region) are calculated as follows (Fig. 1):

$$AR = \frac{d_1}{d_2} \quad (1)$$

$$CD = 1 - c \quad (2)$$

$$\Delta\varphi = |\varphi_1 - \varphi_2| \quad (3)$$

These parameters characterize the in-flow deformation-dependent dynamics analysis [10].

III. Results and Discussion

Firstly, we computed the compression as viscoelastic force applied on cells [11]. In order to do this, we measured the cell diameters in static conditions, before loading cells into the microfluidic device Table 1. The resulting force estimation gives 10^1 μN as order of magnitude for both the cell lines. Then, by the in-flow analysis, we collected the morphological and dynamic parameters describing the different deformability behaviour.

TABLE I: Major cell diameters before in-flow compression (N=30)

Cells	d_{Static} *(μm)*
Lymphocytes	7.1 ± 0.65
Jurkat	10.4 ± 0.75

In particular, we observed that Jurkat cells deform more than healthy lymphocytes (Fig. 2), confirming a higher deformability of lymphoid leukaemia cells with respect to the healthy counterpart [14]. As observed, both AR and CD are higher in Jurkat than Lymphocytes. In particular, looking at the ranges of CD, distinct in-flow deformation-dependent dynamics are distinguishable [11]. We observed that Jurkat cells cover Rolling (R with CD ~ (0:0.1)), Tumbling (T with CD ~ (0.10:0.21)) and Tank-Treading (TT with CD ~ (0.15:0.35)) motions, while the 81 % of Lymphocytes move as Rolling. Thus, our approach reveals a cell heterogeneity in deformability properties within the same line both for Lymphocytes and Jurkat, allowing a possible cell subclass identification. For lymphocytes such a kind of heterogeneity is associated to the two subpopulations of B and T lymphocytes that could be then identified by our deformability analysis. Our results are in well agreement with ones found with the same approach for breast cells, distinguished as healthy or pathological depending on the motion regime [15].

IV. Conclusion

The presented microfluidic approach is able to provide a deformability characterization of CTCs and healthy lymphocytes by using in-flow viscoelastic compression forces in a completely contactless manner. The absence of a physical contact avoids possible activation or cell function changes due to the interaction between a probe of mechanical properties with cells. Moreover, with the aim of promoting new rapid diagnostic approaches, our chip can be of significant interest for cell separation applications, developing an additional microfluidic stage with properly conceived channel sections to sort CTCs and healthy cells depending on their own distinct deformation induced cell trajectories or motion dynamics.

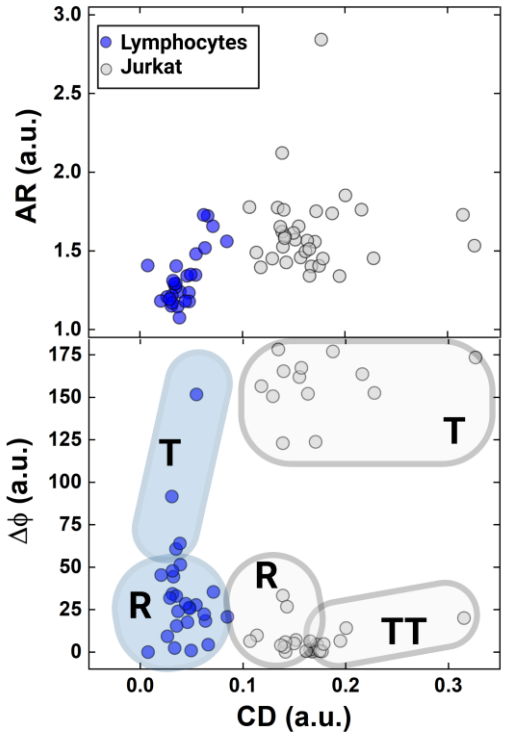


Fig. 2 Deformability measurements of healthy lymphocytes and Jurkat. AR and Δφ variation are shown with respect to CD values. We grouped the data depending on the detected motion dynamics with respect to the obtained range of CD (n_{Lymph}=27 and n_{Jurkat}=34).

References

[1] D. Di Carlo. A mechanical biomarker of cell state in medicine. Journal of laboratory automation, 17(1):32–42, 2012.

[2] J. Guck and E. R Chilvers. Mechanics meets medicine. Science translational medicine, 5(212):212fs41–212fs41, 2013.

[3] H. Chen, Z. Zhang, and B. Wang. Size- and deformability-based isolation of circulating tumor cells with microfluidic chips and their applications in clinical studies. AIP Advances, 8(12):120701, 2018.

[4] A. de la Zerda, M. J. Kratochvil, N. A. Suhar, and S. C. Heilshorn, Review: Bioengineering strategies to probe T cell mechanobiology, APL Bioeng. 2, 021501, 2018.

[5] G. Esteban-Manzanares, B. González-Bermúdez, J. Cruces, M. De la Fuente, Q. Li, G.V. Guinea, J. Pérez-Rigueiro, M. Elices, G.R. Plaza. Improved Measurement of Elastic Properties of Cells by Micropipette Aspiration and Its Application to Lymphocytes. Ann Biomed Eng. May;45(5):1375-1385, 2017.

[6] J.B. Dahl, J.M. Lin, S.J. Muller, S. Kumar, Microfluidic Strategies for Understanding the Mechanics of Cells and Cell-Mimetic Systems. Annu Rev Chem Biomol Eng.,6:293-317, 2015.

[7] Zhou, J., Papautsky, I. Viscoelastic microfluidics: progress and challenges. Microsyst Nanoeng 6, 113, 2020.

[8] D. Dannhauser, D. Rossi, M. Ripaldi,, P.A. Netti & F. Causa, Single-cell screening of multiple biophysical properties in leukemia diagnosis from peripheral blood by pure light scattering. Scientific reports, 7(1), 1-13, 2017.

[9] D. Dannhauser, D. Rossi, P. Memmolo, F. Causa, A. Finizio, P. Ferraro, & P.A. Netti, Label-free analysis of mononuclear human blood cells in microfluidic flow by coherent imaging tools. Journal of biophotonics, 10(5), 683-689,2017.

[10] D. Rossi, D. Dannhauser, B.M. Nastri *et al*., New Trends in Precision Medicine: A Pilot Study of Pure Light Scattering Analysis as a Useful Tool for Non-Small Cell Lung Cancer (NSCLC) Diagnosis. J Pers Med. 2021;11(10):1023. Published Oct 13, 2021.

[11] D. Dannhauser & M.I. Maremonti, V. Panzetta, D. Rossi, P.A. Netti & F. Causa, Mechanical phenotyping of breast cell lines by in-flow deformation-dependent dynamics under tuneable compressive forces Lab on a Chip, 20(24):4611–4622, 2020.

[12] M. I. Maremonti, V. Panzetta, D. Dannhauser, P. A. Netti and F. Causa, Wide range viscoelastic compression forces in microfluidics to probe cell-dependent nuclear structural and mechanobiological responses, J. R. Soc., Interface, 2022, 19, 20210880.

[13] T. B. Casale and M. A. Kaliner, Rapid method for isolation of human mononuclear cells free of significant platelet contamination, J. Immunol. Methods, 55, 347–353, 1982.

[14] M. J. Rosenbluth,A. Lam Wilbur and D. Fletcher, Force Microscopy of Nonadherent Cells: A Comparison of Leukemia Cell Deformability, Biophysical journal 90.8, 2994-3003, 2006.

[15] M.I. Maremonti, D. Dannhauser, V. Panzetta, P. A. Netti & F. Causa, Cell deformability heterogeneity recognition by unsupervised machine learning from in-flow motion parameters, Lab Chip, 22:4871-4881 (2022).

Mesenchymal Stem Cell Response to Micropatterns and Dynamic Topographies

C. Cimmino[1], P.A. Netti[1,2,3] and M. Ventre[1,2,3]
[1] *Dept. Chemical, Materials and Industrial Production, University of Naples Federico II, Naples Italy*
[2] *Interdisciplinary Research Centre on Biomaterials, University of Naples Federico II, Naples, Italy*
3 Center for Advanced Biomaterials for Heathcare@CRIB, Fondazione Istituto Italiano di Tecnologia, Naples, Italy

***Abstract*—The native extracellular matrix is a dynamic environment, but it is not clear how cells react to time changing signals. To investigate this, we exploited light responsive azobenzene based platforms, able to display spatiotemporal changes of topographic signals. Mesenchymal stem cells were cultivated on either rectangular or circular adhesive islets in order to promote either a high or low contractile phenotype. Submicron scale topography was switched on at selected time points to interfere with adhesion and cytoskeleton assembly. Cells responded to the dynamic changes by altering their mechanical properties, lamins expression and YAP nuclear import. Changes at receptor or cytoskeleton level are observed a relatively small timeframes, whereas Lamins and YAP nuclear accumulation required longer times. Our data could be useful to develop culturing systems able to challenge stem cells with specific programmes of mechanical/topographical signals thus understanding how cells integrate those in time.**

***Keywords*—dynamic substrates, adhesive patterns, topographic patterns, mechanotransduction**

I. INTRODUCTION

THE extracellular matrix (ECM) continuously changes its biochemical/biophysical features displaying different signals to cells in a spatio-temporal dependent manner [1]. Temporal variations of the ECM, including changes in the microarchitecture, play a crucial role in regulating different biological processes in vivo as gene transcription and morphogenesis and also the progression of pathologies [2], [3]. Recently, stimulus-responsive materials have been used as 'dynamic' substrates that replicate some spatio-temporal changes of the ECM, thus enabling understanding cell response to microenvironmental changes [4], [5]. Particular attention has been focused on light-sensitive materials, exploiting the peculiarity of light to be precisely localized over a substrate, programmed in time and space, and remotely addressable at an appropriate wavelength without compromising cell viability. Among the various light-sensitive materials, those containing azobenzene molecules have shown the ability to effectively display topographical features dynamically by providing remarkable surface mass transport under appropriate illumination conditions. Our objective was to investigate cellular response in terms of cell mechanics, nucleus deformation, YAP and lamins density in cells on surfaces on which nanotopography was varied dynamically.

II. EXPERIMENTAL SECTION

Dynamic Sample Preparation: Spin coating technique was used to produce thin films of poly-(Disperse Red 1 methacrylate) (pDR1m) on 10 mm diameter cover glasses. pDR1m was dissolved in chloroform at a 3% w/v concentration. 15 µl of solution was spun over the cover glass at 5000 rpm. Coatings of ~300 nm of thickness were achieved.
Micropatterning protocol: pDR1m substrates were activated by exposure to deep UV light for 15 min. Then the samples were incubated for 1 h with 0.1 mg ml^{-1} poly-L-lysine-g-poly(ethyleneglycol) at room temperature (40 µL for each sample). After washing with distilled water, the treated surface was illuminated with deep UV light through a photomask. The mask contained circles (C) and rectangles (R) having the same surface area (1300 μm^2). 2.5µL of millipore H_2O were added on the quartz mask and the PEGylated side of the sample was gently dropped onto the mask. Using the deep UV Printer, the mask was illuminated for 8 min. The activated side was than incubated 1h at room temperature with 50 µL of fibronectin (final concentration of 50 µg ml^{-1}) and was rinsed with PBS afterwards.
Cell culture: hTERT are cultured in Mesenchymal Stem Cell Basal Medium (ATCC PCS-500-030) with, Mesenchymal Stem Cell Growth Kit (ATCC PCS-500-040). 25000 cells were seeded per sample. Cells were cultured at 37 °C in a humidified atmosphere of 95% air and 5% CO_2.
Nanopatterning protocol: hTERT cells were cultured on pDR1m coated glass slides previously micropatterned (C, R) for 24 h. Afterwards, real-time linear nanopattern inscription on cell-populated samples was performed by using a Axio Observer Z1 microscope. The isomerization of the azopolymer and its consequent mass transport were induced with an Argon laser at 488 nm and 1.3 mW of intensity with a 10x objective lens. Nanopatterns were embossed on the pDR1m substrates by illuminating with the laser light for 60 s in specifically drawn regions-of-interest controlled by software with a high spatial resolution (nm order). The final nanopattern consisted of 7 rectangular relieves (ridges) in the case of the rectangular cell and 17 rectangular relieves in the case of the circular cell. In both cases the relives were oriented parallel to the scan direction. In the reminder we will refer to “flat” substrates as the substrates displaying circular or rectangular adhesive micropatterns without having embossed a topographic pattern. Conversely “patterned” substrates refers to substates displaying circular or rectangular adhesive micropatterns over which a topographic pattern was inscribed.
Cell Mechanics: Mechanical characterization of cells was performed with a JPK NanoWizard II AFM. With SiN cantilevers with a square pyramid tip (k=0.06 N/m). All indentations were performed over the central region of the cell in an area where the nucleus was visible. Typically, 64 force curves were measured over a cell area of 10 x 10 µm. Mechanical properties of cells, in terms of Young’s modulus (*E*) values were estimated by fitting the force-indentation curve with Hertzian model for linearly elastic materials. *E* of

the hTERT cells on each sample was quantified by calculating the median of the eight values with the greatest distance from the substrate (approximately corresponding to the nucleus).
YAP and Lamins immunostaining: Cells were fixed at different time-points: flat and 1 h, 4 h, 24 h, 48 h after pattern inscription. Cell fixation was performed by incubating cells in a 4% paraformaldehyde solution for 15 minutes. Then, cells were permeabilized with 0.1% Triton X-100 in PBS for 15 min. Samples were blocked in 3% bovine serum albumin in PBS for 1 h to avoid non-specific binding. Anti-YAP primary antibodies in BSA were added to the samples and incubated overnight at 4 °C. Subsequently, lamins were labelled by incubating samples with an anti-LMNA for 1 h at room temperature. Samples were then incubated at room temperature with secondary antibodies for 1 h at room temperature.

III. RESULTS AND DISCUSSION

A. *Embossing of topographic patterns*

hTERT cells were seeded on pDR1m flat substrates, which was previously micropatterned using a photomask to produce circular (C) and rectangular (R) adhesive islands with the same area (1300 μm^2). 24 hours after seeding, we embossed a linear topographic pattern on the initial flat surface using a 488 nm laser mounted in a confocal microscope. Patterns were embossed beneath cells adhering on the islets directly through the irradiation for 60 s with the laser (Fig. 1). Using topography analysis performed with AFM we verified the width of each ridge (0.70 ± 0.09 µm) the pitch between two ridges (1.40 ± 0.04 µm) and the height of the ridges (0.20 ± 0.02 µm).

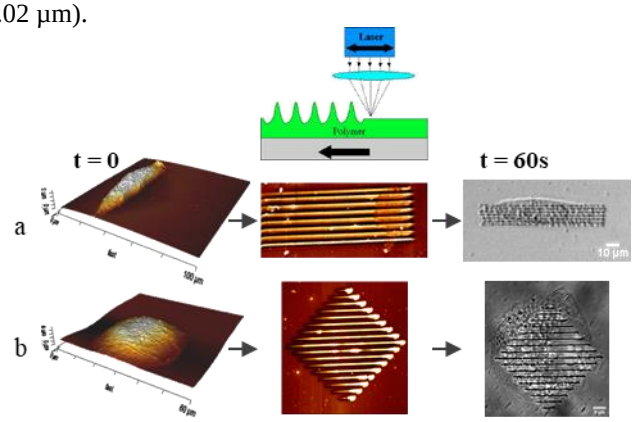


Fig. 1: Representation of the topographic pattern fabrication technique onto the micropatterned substrate. Rectangular pattern (a) and circular pattern (b). 3D reconstruction of the micropatterned cells on flat substrate (left), AFM images of the topographic reliefs (middle), brightfield images of hTERT cells cultivated onto the adhesive micropattern superimposed to the topography (right).

B. *Cell Mechanics on Dynamic Topogrphies*

Changes in the adhesive properties, here in terms of the surface topography, is expected to impact cytoskeleton structure, cell mechanics and nucleus shape. To characterize these changes, we first measured Young's moduli of cells on R in proximity to the nuclear region. Despite the change of surface topography, i.e. the transition from a flat to a grooved surface (Fig. 2a), the values of the cell modulus did not change over time, if compared with the modulus measured immediately before the pattern inscription, t = 0- (Fig. 2b). Also, the elastic moduli of cells cultivated on flat control surfaces (i.e., on which the topographic pattern was not embossed) fluctuated around a constant value (Fig. 2b). In particular, the variance of the measured moduli of the nuclear region of cells on control samples was higher with respect to the variance to the modulus measured on cells on patterned substrates. Therefore, although the superposition of a pattern does not significantly alter the stiffness of the nuclear region, the presence of a submicron scale topographic pattern exerts a stabilizing effect on the cytoskeletal structures, presumably by confining and aligning focal adhesions (FAs). Cell's modulus, at least of the nuclear region, is mostly affected by the macroscopic, rectangular shape, rather than by the presence of an underlying nanotopography.

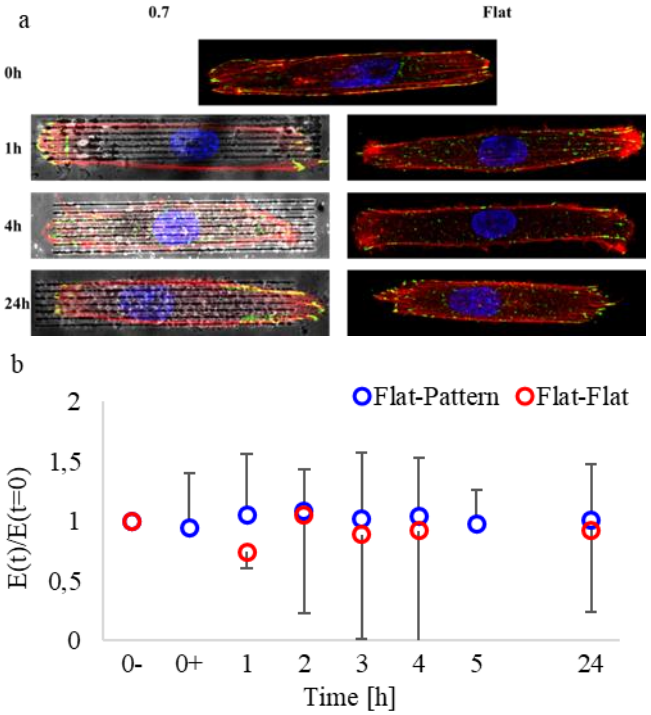


Fig. 2: (a) Confocal images of fixed rectangular hTERT on flat rectangular micropattern and 1, 4 and 24 hours after the linear pattern inscription (left). Cells on flat substrates on the right. Cell cytoskeleton is stained with Phalloidin (red), FAs are immunostained for vinculin (green), and nuclei are stained with DAPI (blue). (b) Plots of the Young's moduli measured up to 24 h after the nanopattern inscription (blue marks) and on flat substrates (red marks).

In contrast, cells confined in circular shapes, in the absence of topography, were characterised by randomly oriented actin fibres (Fig. 3 a). Their Young's moduli evaluated in the nuclear region was constant over time (Fig. 3 b red marks). As soon as the linear nanopattern was applied at t = 0+, there was first a rapid decrease in stiffness followed by a gradual increase up to a roughly constant value (Fig. 3 b blue marks). We associate this behaviour with the redistribution of FAs and the reassembly of the cytoskeleton. In fact, the presence of the topographic pattern induced a greater orientation of the basal fibres even in the case of cells with isotropic shapes compared to flat surfaces. For this reason, the stress fibres re-orientation following the surfacing of the topography, caused the values of the elastic moduli to increase in time. However, the plateaux value was lower than that corresponding to the flat case. This

is probably because when shape confinement affects the FA confinement, the mechanical stability of cells is disrupted by the presence of the topographic nanograting that reduces the space available for FA formation and growth.

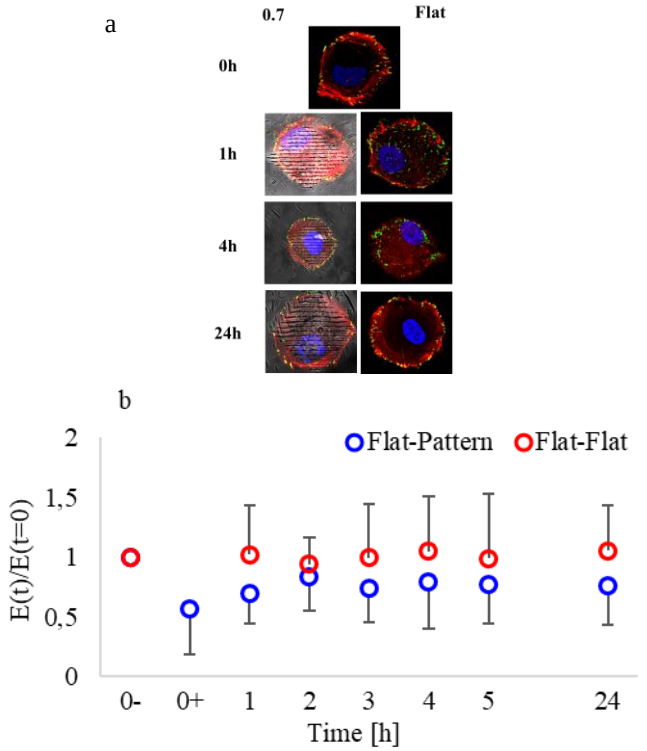


Fig. 3: (a) Confocal images of fixed hTERT on a flat circular micropattern and 1, 4 and 24 hours after the linear pattern inscription (left). Cells on flat substrates on the right. Cell cytoskeleton is stained with Phalloidin (red), FAs are immunostained for vinculin (green), and nuclei are stained with DAPI (blue). (b) Plots of the Young's moduli measured up to 24 h after the nanopattern inscription (blue marks) and on flat substrates (red marks).

C. Lamin and YAP expression and localization

The nucleus is a deformable organelle that adapts to external mechanical stimuli, not only by changing its morphology but also by rearranging its nucleoskeleton and inner composition. A-type lamins and YAP (Yes-associated protein) attracted interest as their mechanosensitive nuclear localization correlates with cell differentiation and other cellular functions [6]. The nuclear lamina performs different essential functions in the mechanotransduction pathway modulating the nuclear stiffness, governing the chromatin remodeling, and transmitting cytoskeletal forces to the nucleus [7]. YAP is a transcription factor widely studied owing to its sensitivity to mechanical (i.e., the ECM rigidity) and topographical signals (i.e., the micro- or nano-pattern) [8]. YAP shuttles between the cytoplasm and nucleus where it associates with diverse promoter-specific transcription factors. Being the expression and localization of Lamins and YAP two important readout of the actual mechanical state of the nucleus and the cell, we stained cell cultures (on flat or on grated surfaces), at different time points for Lamin and YAP. Regarding the nuclei of rectangular cells, we observed that after pattern inscription a slight decrease in Lamins intensity was observed up to 4 hours. Afterwards, Lamins intensity significantly increased and attained a high level of fluorescence intensity up to 48 hours. Conversely, cells on the control, flat substrates, expressed constant levels of Lamins, with some fluctuations at late time-points (Fig. 4). However, Lamins intensity on flat substrates was significantly lower, with respect to the nanopatterned samples at 24 h and 48 h time points.

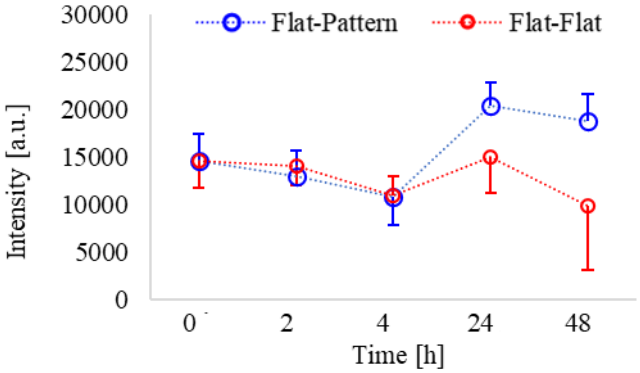


Fig. 4: Plots of the lamins A/C intensity variation over time in nuclei of cells on rectangular micropatterns cultured either on flat surfaces (red indicators) or in contact with nanotopographic pattern (blue indicators).

Concerning the nuclear import of YAP in our experimental setup, we wanted to observe whether the nuclear transport of YAP was sensitive to dynamic changes of the adhesive conditions. We found a higher fluorescence density of YAP in the nuclear region with respect to the cytoplasmic fluorescence density on flat substrates (t=0) (Fig. 5). After pattern inscription, we observed a gradual decrease in YAP fluorescence density in both cellular compartments (2h post patterning). However, at longer time intervals (above 24h), YAP was intensely localized in the nucleus, whereas it remained at low values of fluorescence density in the cytoplasm. Cells on the control substrates behaved in a similar manner at short times, with a gradual reduction of YAP fluorescence in either the cytoplasm or the nucleus (data not shown). Also, fluorescence tended to remain at low levels even at later time points.

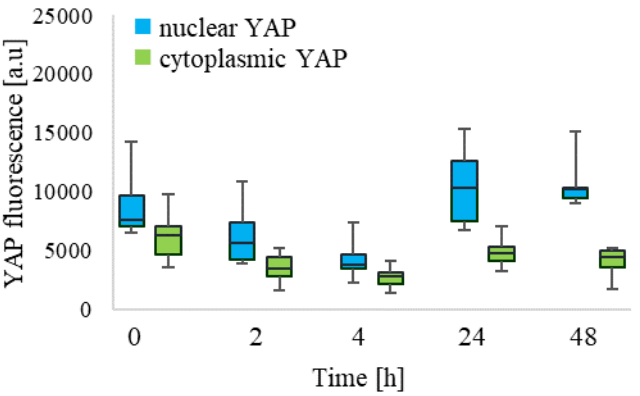


Fig. 5: Box and whiskers of the time evolution of fluorescence intensity of YAP. Cell cultivated on rectangular micropatterns for 48 h after the surfacing of the topographic nanopattern (72 h of culture in total).

Then, we analysed Lamins intensity on the isotropic circular micropattern, which produces a less contractile phenotype as opposed to the rectangular micropattern. Also in this case, we observed an increase in Lamins intensity after the nanopattern superposition, but at a later point (48h) (Fig. 6). Cells on control surfaces (absence of topographic relieves) expressed

constant values of Lamins in the time under consideration (24-72 h post seeding) (Fig. 6).

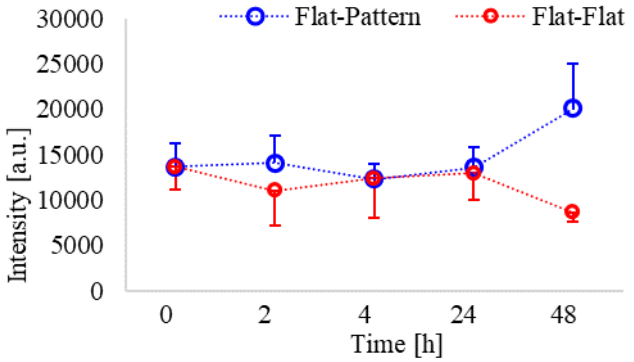


Fig. 6: Plots of the lamins A/C intensity variation over time in nuclei of cells on circular micropatterns cultured either on flat surfaces (red indicators) or in contact with nanotopographic pattern (blue indicators).

Finally, we analysed YAP fluorescence density and its localization in the cells on circular micropatterns. Similarly, to what observed in the case of rectangular micropatterns, we found higher levels of nuclear YAP with respect to cytoplasmic YAP (Fig. 7). The superposition of a topographic pattern did not affect the distribution significantly, for short time intervals (up to 4 h). However, at longer time intervals we observed a marked increase in nuclear YAP. In comparison, cells on control substrates (without nanopattern) exhibited relatively constant values of fluorescence density all over the time frame of the analysis (data not shown). Hence, despite the lower contractile phenotype of cells on a circular adhesive area, the superposition of a topography over the adhesive signal does affect Lamin expression and YAP transport at longer times.

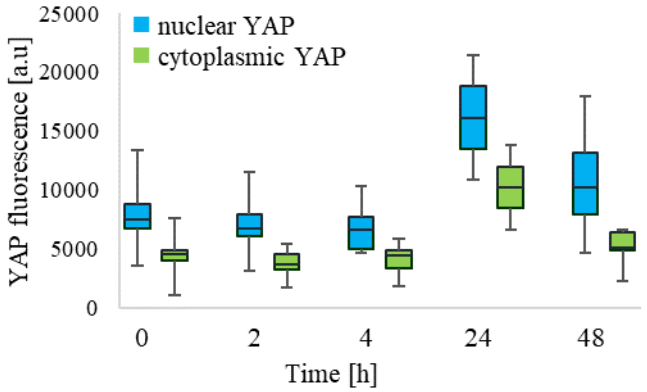


Fig. 7: Box and whiskers of the time evolution of fluorescence intensity of YAP. Cell cultivated on circular micropatterns for 48 h after the surfacing of the topographic nanopattern (72 h of culture in total)

Several works in the literature, including those carried out by Swift et al. [9] and Gonzalez-Cruz et al. [10], found a positive correlation between the expression of Laminin proteins and cell moduli. Here we observed that changes in lamins localization occur at longer time points after the superposition of topographic signal and prior to this no change in cell elasticity was evident. It is likely that cell modulus is affected by lamin localization and cytoskeleton assembly, both affected by the topographic signal. Similarly, a greater influx of YAP is observed 24 h after the inscription of the topographic pattern, suggesting that cells respond to changes to the adhesive microenvironment at long time intervals.

IV. CONCLUSION

Here we have shown how cells sense mechanical signals from their microenvironment and transfer these up to the nucleus affecting its mechanics and composition. In particular, we observed how cell geometric constraints and topographical patterns of submicron scale affect over time the cell mechanical properties and subsequently induce cytoskeleton-mediated alterations in the nuclear properties. Moreover, the changes in the physical properties of the nucleus have been observed to correlate with alterations in nuclear architecture and transcriptional factors expression and localization.

We showed that cell geometry controls these nuclear properties by regulating the local tensile stresses. In more details, we observed how the physical properties of the microenvironment, in particular nano topography, impact the properties of the cytoskeleton and nucleus by regulating the dynamic reciprocities between the tension-dependent formation of FAs, the polymerisation of actin filaments, the stiffening of the nuclear envelope lamina network and the nucleocytoplasmic displacement of transcription factors. These data might be of interest in the biomedical field, for the development of culturing platforms to develop chronoprogrammes to guide stem cells towards differentiation programmes in an efficient manner.

REFERENCES

[1] M. Wu, J. Fannin, K. M. Rice, B. Wang, and E. R. Blough, ‘Effect of aging on cellular mechanotransduction’, *Ageing Research Reviews*, vol. 10, no. 1, Art. no. 1, Jan. 2011, doi: 10.1016/j.arr.2009.11.002.

[2] A. M. Handorf, Y. Zhou, M. A. Halanski, and W.-J. Li, ‘Tissue Stiffness Dictates Development, Homeostasis, and Disease Progression’, *Organogenesis*, vol. 11, no. 1, pp. 1–15, Jan. 2015, doi: 10.1080/15476278.2015.1019687.

[3] P. Lu, K. Takai, V. M. Weaver, and Z. Werb, ‘Extracellular Matrix Degradation and Remodeling in Development and Disease’, *Cold Spring Harbor Perspectives in Biology*, vol. 3, no. 12, pp. a005058–a005058, Dec. 2011, doi: 10.1101/cshperspect.a005058.

[4] D. M. Le, K. Kulangara, A. F. Adler, K. W. Leong, and V. S. Ashby, ‘Dynamic Topographical Control of Mesenchymal Stem Cells by Culture on Responsive Poly(ϵ-caprolactone) Surfaces’, *Advanced Materials*, vol. 23, no. 29, pp. 3278–3283, Aug. 2011, doi: 10.1002/adma.201100821.

[5] C. C. A. Ng *et al.*, ‘Using an Electrical Potential to Reversibly Switch Surfaces between Two States for Dynamically Controlling Cell Adhesion’, *Angewandte Chemie International Edition*, vol. 51, no. 31, pp. 7706–7710, Jul. 2012, doi: 10.1002/anie.201202118.

[6] G. Halder, S. Dupont, and S. Piccolo, ‘Transduction of mechanical and cytoskeletal cues by YAP and TAZ’, *Nature Reviews Molecular Cell Biology*, vol. 13, no. 9, Art. no. 9, Aug. 2012, doi: 10.1038/nrm3416.

[7] F. Donnaloja, F. Carnevali, E. Jacchetti, and M. T. Raimondi, ‘Lamin A/C Mechanotransduction in Laminopathies’, *Cells*, vol. 9, no. 5, p. 1306, May 2020, doi: 10.3390/cells9051306.

[8] S. Dupont *et al.*, ‘Role of YAP/TAZ in mechanotransduction’, *Nature*, vol. 474, no. 7350, pp. 179–183, Jun. 2011, doi: 10.1038/nature10137.

[9] J. Swift *et al.*, ‘Nuclear Lamin-A Scales with Tissue Stiffness and Enhances Matrix-Directed Differentiation’, *Science*, vol. 341, no. 6149, Art. no. 6149, Aug. 2013, doi: 10.1126/science.1240104.

[10] R. D. González-Cruz, J. S. Sadick, V. C. Fonseca, and E. M. Darling, ‘Nuclear Lamin Protein C Is Linked to Lineage-Specific, Whole-Cell Mechanical Properties’, *Cel. Mol. Bioeng.*, vol. 11, no. 2, pp. 131–142, Apr. 2018, doi: 10.1007/s12195-018-0518-y.

Cell-aware optimization of the extrusion-based bioprinting process

Amedeo Franco Bonatti[1], Irene Chiesa[1], Gabriele Maria Fortunato[1], Aurora De Acutis[1], Giovanni Vozzi[1], Carmelo De Maria[1]

[1] *Research Center "E. Piaggio" and Department of Information Engineering, University of Pisa, Pisa, Italy*

***Abstract*—Extrusion-based bioprinting is currently one of the most used techniques to fabricate constructs for Tissue Engineering applications. When using bioinks (*i.e.*, inks containing cells), the embedded cells may be damaged during extrusion mainly due to high shear stresses and/or the high exposure times to those stresses, posing a severe risk for the correct functionality of the final bioprinted product. The entity of this damage is strictly connected to the printing set-up (*e.g.*, needle shape and internal diameter) and parameters chosen (*e.g.*, printing speed, flowrate, layer height), which should be carefully tuned considering the trade-off with the printability requirements. In this context, we propose a novel mathematical model to predict cell damage during extrusion which integrates with an already existing one for printability assessment. The combined model can help predict *a priori* the outcome of a print, both in terms of cell viability and printability, and to fine-tune the printing parameters according to both constraints. The model equations were implemented in a web-page application (available at https://www.prin-vision.it/resources/), which can be used by the bioprinting community to optimize the printing process and thus speed-up the printing parameters selection process.**

***Keywords*—Extrusion-based bioprinting, mathematical modelling, printability, cell damage.**

I. Introduction

Bioprinting has recently seen a surge of interest as a promising technology to fabricate constructs for Tissue Engineering applications [1]. Among the many available technologies, extrusion-based bioprinting (EBB) is currently the most used, thanks to its simple set-up and the ability to process a wide variety of materials in clinically sized constructs [2]. In the typical EBB set-up, an extruder tool-head is attached to a micro-positioner to deposit an ink (usually stored in a syringe) layer-by-layer on a printing plate. The ink may be made of one or more biomaterials (*i.e.*, a biomaterial ink) or one or more supporting biomaterials mixed with cells (*i.e.*, a bioink) [3].

During extrusion, the ink flows through a syringe needle under the application of a force. When extruding a bioink, cells are subjected to mechanical forces (*e.g.*, pneumatic pressure, extensional and shear stresses), which may damage them if these forces exceed certain thresholds or are applied beyond a certain period. This is a major concern as the number of viable cells is strictly correlated to the final functionality of the bioprinted construct [4]. Shear stress is thought to be the primary mechanism that influence cell damage during extrusion [5]-[7]. Several studies have proposed mathematical modelling as a key tool to predict *a priori* the entity of this damage. For example, Li *et al.* used a probability density function to model cell damage due to shear stress as a function of both the stress magnitude and exposure time. The parameters for this function were determined experimentally and were dependent on the tested cell type [8]. Interestingly, the needle geometry has a significant effect on cell damage. Billiet *et al.* developed a Finite Element model to investigate the shear stress distribution in conical vs. cylindrical needles. The authors found that conical needles induced less cell damage at lower extrusion pressures [9], but this advantage was not present at higher extrusion flowrates [10]. In the latter case, cell damage is correlated more with extensional stresses (*i.e.*, stresses generated due to the abrupt area contraction between the syringe main body and the needle) then shear ones, as recently studied by Ning *et al.* [11]. The authors developed a mixed model that considers the effect of both shear and extensional stresses. By extruding alginate-based bioinks with different pressures and needle diameters, the authors found that cell damage predicted only by shear stresses was not consistent with experimental data above a certain extrusion pressure whereas the addition of the extensional component yields a better fit in this region [11].

Even though the previous examples highlight the importance of mathematical modelling in bioink extrusion, to the best of our knowledge no model is described in literature that combines cell damage with printability evaluation (*i.e.*, a combination of several aspects of the EBB process, including material, scaffold geometry and printing apparatus, that determines *a priori* if the printing process will be successful or not [12]). Such a model would help an *a priori* assessment of the printing process considering both the shape fidelity of the final construct and the cell fate, thus minimizing the trial-and-error tuning of the parameters and the related material and time waste.

In this context, building on a printability prediction tool that we recently published [12], here we propose a 'plug-in' cell damage model that can help optimize the printing parameters considering also shear stress-related cell damage during extrusion. The 'plug-in' model equations were integrated with the printability ones and implemented in a web-page application (accessible at https://www.prin-vision.it/resources/) that can be readily used by the bioprinting researchers to optimize the printing process.

II. Model Rationale

A. Overview of the model

The general pipeline of the model, consisting of the printability and cell damage models, is described in Fig. 1. As can be seen from the figure, the model requires as input information related to: i) cells' properties, including the cell type and related shear stress-exposure time data, from relevant literature or from experiments, ii) the EBB set-up, including for example the needle geometry (internal diameter and length), iii) the material to be used (including its rheological

and mechanical properties), and iv) the printing settings, which may include constraints on the printing parameters like printing speed, flowrate, and layer height, as well as the overall scaffold dimension. The main model output includes a list of optimized printing parameters based on both the cell viability and printability constraints.

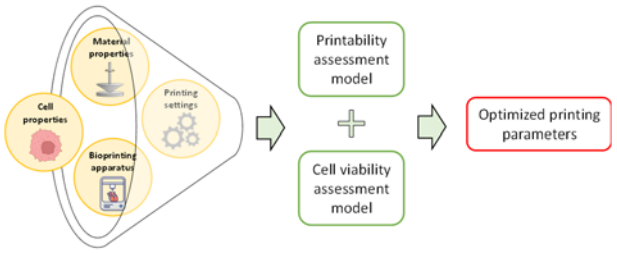


Fig. 1: Overview of the composite model to optimize the EBB process, considering constraints related to both the printability and cell viability.

B. *Printability assessment model*

The EBB printability assessment model for biomaterial inks has already been described elsewhere [12]. Briefly, the model can provide: i) the printability of a given biomaterial ink using a specific bioprinting apparatus, scaffold geometry, and printing parameters, and ii) if the biomaterial ink is found to be printable, provide a set of optimized printing parameters to maximize the shape fidelity. The model was developed by taking into consideration multiple aspects of EBB (referred to as 'stages' for brevity), as can be seen in Fig. 2: i) Stage 1, where the extrudability, *i.e.*, the easiness of extrusion of the given material from the syringe needle, is evaluated, ii) Stage 2, in which the line deposition process when printing the first layer is studied, and iii) Stage 3, where the wood-pile scaffold stabilization after printing is evaluated to assess the final shape fidelity.

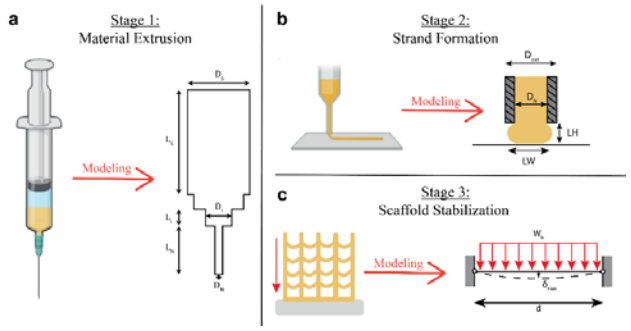


Fig. 2: Summary of the three stages of the printability assessment model. a) Stage 1 refers to the evaluation of the extrudability of the ink from the syringe; b) Stage 2 studies the line formation during extrusion of the first layer; c) Stage 3 evaluates the three-dimensional scaffold stabilization over time and its shape fidelity when compared to the digital design (image adapted with permission from [16]).

The analytical model was implemented in a web-based application (available at https://www.prin-vision.it/resources/) to help determine *a priori* the ink printability and optimize the printing parameters. Briefly, the web application is composed of two pages: a form page, in which the user can input the EBB set-up properties, scaffold overall size, and material properties. At the end of the form, the user can select different optimization constraints, including the layer height, printed line width dimensions, and flowrate to be used. After submitting the form, the results for each separate stage are presented in a new page alongside a brief description and possible ways to improve the printability.

C. *Cell damage assessment model*

A summary of the main symbols used in the cell damage assessment model is reported in Table I. The following paragraphs will detail the hypothesis underlying the model and its governing equations.

Table I: Summary of the parameters considered for the cell viability assessment model, alongside their unit of measure.

Group name	*Parameter*	*Description*	*Unit of measure*
EBB set-up	R	Needle internal radius	[m]
	L	Needle length	[m]
Material properties	K	Flow consistency index	[Pa*s^n]
	n	Flow behavior index	-
	τ_y	Critical yield stress	[Pa]

1) *Model hypothesis*

Fig. 3 shows the case of a bioink being extruded from a syringe needle. To simplify the problem, the bioink will be considered as an incompressible fluid (*i.e.*, with a constant density) under a steady, fully developed, and isothermal flow. Furthermore, we will suppose that cells are homogeneously distributed, and their presence does not alter the rheological properties when compared to an equivalent biomaterial ink, which is valid for cell densities lower than 100x10^6 cells/ml [13].

Regarding the constitutive equations, the bioink will be modelled as Herschel-Bulkley fluid, which is a common case for inks used in EBB [16] (Eq. 1):

$$\tau = \tau_y + K\dot{\gamma}^n \quad (1)$$

Here, K represents the consistency factor (in [Pa*s^n]) and n the consistency index (a-dimensional, and lower than 1 for shear-thinning materials). The Herschel-Bulkley model describes both shear-thinning (*i.e.*, apparent viscosity decreases with an increase of shear rate) and yield stress (*i.e.*, the stress at which the material starts to flow under an applied external force) behaviours, which determine the printability in EBB.

Finally, from a geometry point of view, the cell damage model will focus on the needle region (Stage 1 in the printability assessment model of Fig. 2) as it is the region where the cells are subjected to a high shear stress when compared to the syringe main body. The modelled needle geometry is a cylinder with a length L and an internal radius R, both measured in [m].

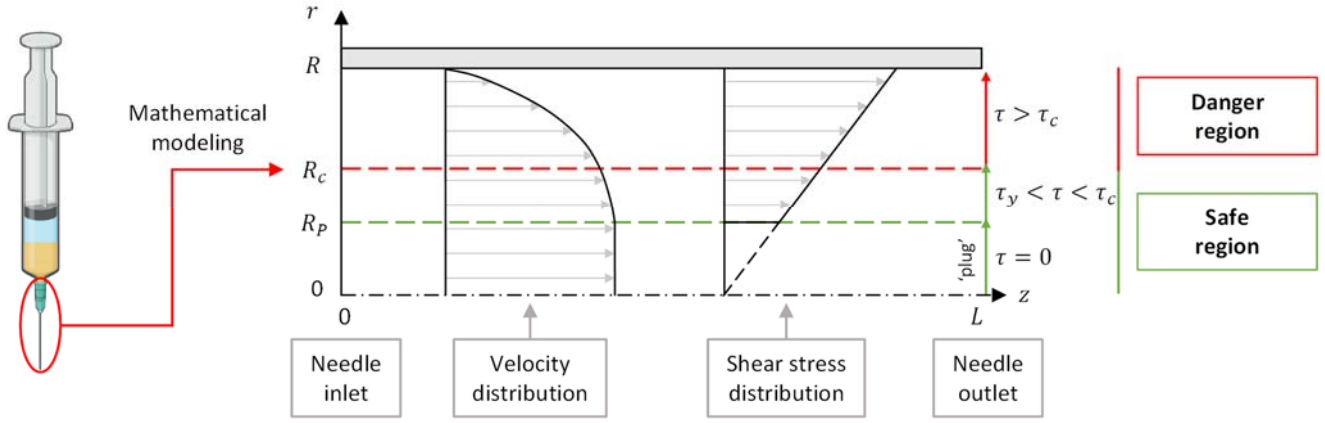


Fig. 3: Summary of the mathematical model set-up to evaluate the cell damage in a bioink during extrusion. The velocity (on the left) and shear stress distributions (on the right) inside the needle region for an Herschel-Bulkley bioink during flow are reported. In the figure, τ_y (in [Pa]) is the yield stress of the material, τ_c (in [Pa]) the stress above which cells embedded in the bioink may be damaged, R_P (in [m]) is the radius of the 'plug' region, R_C (in [m]) refers to the critical radius at which $\tau \geq \tau_C$.

1) Computing the percentage of damaged cells during EBB

The fluid velocity and shear stress distributions are reported in Fig. 3 [15]. As can be seen from the figure, we can divide the problem in two main regions: a 'danger' region, where cell damage may be present due to high shear stresses, and a 'safe' region, where the shear stress is lower and thus all the embedded cells may survive the extrusion process.

Due to the material showing a yield stress, the 'safe' region will include a central 'plug' area of radius R_P (in [m]). R_P represents the radial coordinate at which $\tau(r = R_P) = \tau_y$, while for $r < R_P$ the material behaviour will be solid-like. As a result, no shear stresses will be present inside this area and embedded cells will not be damaged.

Outside the 'plug' area, τ depends linearly on r as in Eq. 2:

$$\tau(r) = \frac{\tau_w}{R} \cdot r \tag{2}$$

where τ_w is the wall shear stress (in [Pa]). In this area, embedded cells may be damaged only if τ exceeds a critical value τ_c (which depend on the cell type). From Eq. 2, we can express the radial coordinate R_c at which $\tau > \tau_C$ as in Eq. 3:

$$R_c = \frac{\tau_w}{\tau_c} \cdot R \tag{3}$$

Thus, for $R_P < r < R_c$, cells will experience shear stresses which are not enough to permanently damage them. On the other hand, the radial coordinates $R_c < r < R$ identify the 'danger' region. Cells in this region will experience a mean shear stress $\bar{\tau}_{damaged}$ which can be found as the mean value between τ_w and τ_c (Eq. 4):

$$\bar{\tau}_{damaged} = \frac{\tau_w - \tau_c}{2} \tag{4}$$

Even though $\bar{\tau}_{damaged}$ may be high enough to damage cells, the mean exposure time $\bar{t}_{damaged}$ (*i.e.*, the time cells remain on average in this high-stress region during extrusion (in [s]) should also be computed. To do so, we consider that the velocity profile $v(r)$ (in [m/s]) outside the 'plug' area for a Herschel-Bulkley fluid is given by Eq. 5 [16]:

$$v(r) = \frac{n}{n+1} \cdot \left(\frac{R^n \tau_w}{K}\right)^{\frac{1}{n}} \cdot \left[\left(1 - \frac{Rp}{R}\right)^{\frac{n+1}{n}} - \left(\frac{r}{R} - \frac{Rp}{R}\right)^{\frac{n+1}{n}}\right] \tag{5}$$

where the 'plug' radius can be expressed from Eq. 2 knowing τ_w as $R_P = \frac{\tau_y}{\tau_w} \cdot R$. The mean speed $\bar{v}_{damaged}$ of the bioink contained inside the 'damaged' region can be found by integrating the velocity profile over r as follows (Eq. 6):

$$\bar{v}_{damaged} = \frac{1}{R - R_C} \int_{R_C}^{R} v(r)\, dr \tag{6}$$

By plugging Eq. 5 in Eq. 6 and solving the integral, we can finally compute $\bar{t}_{damaged}$ as in Eq. 7:

$$\bar{t}_{damaged} = \frac{L}{\bar{v}_{damaged}} \tag{7}$$

The combination of Eq. 4 and Eq. 7 can be used to measure the cell damage ϕ (*i.e.*, the percentage of cells that are not viable after applying a shear stress) by comparing the values with data for example found in literature for specific cell types, as reported in Table II.

Table II: Summary of data available in literature for shear stress-induced damage

Cell type	*Shear stress range [Pa]*	*Exposure time range [s]*	*ϕ range [%]*	*Ref*
Schwann cells	100-1000	10-120	2-31	[12]
Myoblasts	100-1000	10-120	2-26	[12]
Fibroblasts	100-1000	10-120	12-89	[8]

However, ϕ is usually computed by applying a prescribed shear stress using a rheometer and then measuring cell viability afterwards. In such a configuration, the whole bioink is sheared, and, as a result, to translate the ϕ values to the extrusion model, this percentage should be referred to only the 'damaged' region. We can thus find the overall percentage of damaged cells by first computing the volume ratio *VR* (expressed as a percentage) of the 'damaged' region compared to the overall needle as in Eq. 8:

$$VR = \frac{V_{damaged}}{V_{tot}} = \left(1 - \frac{R_c}{R}\right)^2 \tag{8}$$

and then multiplying by ϕ to find the overall cell damage *CD* (Eq. 9):

$$CD = \phi \cdot VR \tag{9}$$

D. 'Plug-in' integration with the printability model

The previously described cell damage assessment model was integrated with the Stage 1 of the printability assessment, described in Fig. 2. In particular, in Stage 1 the wall shear stress is computed for a given ink, syringe geometry, and

extrusion flowrate. For an Herschely-Bulkley fluid τ_w is found by inverting Eq. 5 and solving using iterative methods (bisection root finding method) knowing the flowrate during printing (input to the model) [13].

The computed value for τ_w can then be used to evaluate $\bar{\tau}_{damaged}$ in Eq. 4, as well as the integral $\bar{v}_{damaged}$ (Eq. 6). Finally, the mean cell residency time in the 'damaged' region $\bar{t}_{damaged}$ can be computed from Eq. 7 knowing the needle length (input to the model). The values found using Eq. 4 and Eq. 7 can be than compared to values found in literature (as reported in Table II) or through experimental data (*e.g.*, by measuring cell viability after a prescribed shear stress-exposure time combination at a rheometer) to find the estimated *CD* percent value (Eq. 9).

The two models, connected as above, were then integrated inside the already existing web application. In particular, after writing the required inputs in the form (including the cell type selection among the types listed in Table II), the user can check if they want the cell damage to be computed in the optimization section. If the checkbox is selected, in the Stage 1 results section the predicted cell damage will be computed using data for the cell type specified by the user. Besides the value, suggestions on how to reduce the damage will also be provided to the user, including increasing the needle diameter to decrease τ, or lowering the printing speed. In this way, the user can infer if the optimized set of printing parameters considering only the (bio-)ink printability is compatible with the cell viability requirement and, if not, modify the parameters accordingly.

III. Conclusion

In this work, we presented a novel analytical model to predict cell damage in extrusion bioprinting using a complex constitutive equation for the bioink (*i.e.*, Herschel-Bulkley model), which describes both shear-thinning and yielding behaviour commonly found in EBB inks. The cell damage model was integrated with an already developed printability assessment one, and the related equations were added to a web-page which is freely available at https://www.prin-vision.it/resources/. The improved application will represent a valid tool for the bioprinting researcher to predict *a priori* the printability and cell viability when printing a bioink, but also optimize the printing parameters considering both the shape fidelity of the final construct and the post-extrusion viability of the embedded cells.

Future works will be carried out to experimentally validate the cell damage model by assessing the cell viability post-extrusion using a combination of different printing parameters (including needle geometry and internal diameter, flowrate). Furthermore, at its current stage the model uses shear stress/exposure time data coming directly from the literature. These data are available only for a few selected cell types, so in the future experiments will be carried out to expand this library. Finally, as pointed out in relevant literature, extensional stresses play an important role in determining cell viability during extrusion. Taking into consideration results from the experimental validation, the model will be modified to include cell damage related to these stress components, but also damage in other steps of the printing process (*e.g.*, when depositing lines on the printing bed for the first layer), to obtain a more comprehensive and realistic damage evaluation.

Acknowledgements

All the authors acknowledge the support of the Crosslab Additive Manufacturing of the Department of Information Engineering of the University of Pisa. This research has received funding from: i) the European Union's Horizon 2020 research and innovation program under the project GIOTTO: "Giotto: Active ageing and osteoporosis: The next challenge for smart nanobiomaterials and 3D technologies"; grant agreement No 814410, ii) the Italian Ministry of University and Research (MUR) under the PRIN Project VISION "Development and promotion of the Levulinic acid and Carboxylate platforms by the formulation of novel and advanced PHA-based biomaterials and their exploitation for 3D printed green-electronics applications"; grant 2017FWC3WC , iii) the European Union by the Next Generation EU Project ECS00000017 'Ecosistema dell'Innovazione' Tuscany Health Ecosystem (THE, PNRR, Spoke 4: Nanotechnologies for diagnosis and therapy and Spoke 9: Robotics and Automation for Health).

References

[1] Santoni, S., Gugliandolo, S. G., Sponchioni, M., Moscatelli, D., & Colosimo, B. M. (2022). 3D bioprinting: current status and trends—a guide to the literature and industrial practice. *Bio-Design and Manufacturing*, *5*(1), 14-42.

[2] Bonatti, A. F., Fortunato, G. M., De Maria, C., & Vozzi, G. (2022). Bioprinting technologies: an overview. *Bioprinting*, 19-49.

[3] Groll, J., Burdick, J. A., Cho, D. W., Derby, B., Gelinsky, M., Heilshorn, S. C., ... & Woodfield, T. B. F. (2018). A definition of bioinks and their distinction from biomaterial inks. *Biofabrication, 11(1), 013001.*

[4] Lepowsky, E., Muradoglu, M., & Tasoglu, S. (2018). Towards preserving post-printing cell viability and improving the resolution: Past, present, and future of 3D bioprinting theory. *Bioprinting*, *11*, e00034.

[5] Boularaoui, S., Al Hussein, G., Khan, K. A., Christoforou, N., & Stefanini, C. (2020). An overview of extrusion-based bioprinting with a focus on induced shear stress and its effect on cell viability. *Bioprinting*, *20*, e00093.

[6] Blaeser, A., Duarte Campos, D. F., Puster, U., Richtering, W., Stevens, M. M., & Fischer, H. (2016). Controlling shear stress in 3D bioprinting is a key factor to balance printing resolution and stem cell integrity. *Advanced healthcare materials*, *5*(3), 326-333.

[7] Han, S., Kim, C. M., Jin, S., & Kim, T. Y. (2021). Study of the process-induced cell damage in forced extrusion bioprinting. *Biofabrication*, *13*(3), 035048.

[8] Li, M., Tian, X., Zhu, N., Schreyer, D. J., & Chen, X. (2010). Modeling process-induced cell damage in the biodispensing process. *Tissue Engineering Part C: Methods*, *16*(3), 533-542.

[9] Lemarié, L., Anandan, A., Petiot, E., Marquette, C., & Courtial, E. J. (2021). Rheology, simulation and data analysis toward bioprinting cell viability awareness. *Bioprinting*, *21*, e00119.

[10] Billiet, T., Gevaert, E., De Schryver, T., Cornelissen, M., & Dubruel, P. (2014). The 3D printing of gelatin methacrylamide cell-laden tissue-engineered constructs with high cell viability. *Biomaterials*, *35*(1), 49-62.

[11] Ning, L., Betancourt, N., Schreyer, D. J., & Chen, X. (2018). Characterization of cell damage and proliferative ability during and after bioprinting. *ACS Biomaterials Science & Engineering*, *4*(11), 3906-3918.

[12] Bonatti, A. F., Chiesa, I., Vozzi, G., & De Maria, C. (2021). Open-source CAD-CAM simulator of the extrusion-based bioprinting process. *Bioprinting*, *24*, e00172.

[13] Diamantides, N., Dugopolski, C., Blahut, E., Kennedy, S., & Bonassar, L. J. (2019). High density cell seeding affects the rheology and printability of collagen bioinks. *Biofabrication*, *11*(4), 045016.

[14] Swamee, P.K., Aggarwal, N. (2011). Explicit equations for laminar flow of herschel-bulkley fluids, *Can. J. Chem. Eng.,* 89 (6), 1426–1433, https://doi.org/10.1002/cjce.20484.

3D bioprinting as a tool for the early correction of leather defects in the tanning industry

C. Daddi[1,2], M. Baggiani[3], M. Nicoletta[1], S. Micalizzi[1,2], G.M. Fortunato[1,2], A. De Acutis[1,2], C. De Maria[1,2], M. Onorati[3] and G. Vozzi[1,2]

[1] *Department of Information Engineering, University of Pisa, Via G. Caruso 16, Pisa, Italy.*
[2] *Research Center "E. Piaggio", University of Pisa, Largo Lucio Lazzarino 1, Pisa, Italy.*
[3] *Department of Biology, University of Pisa, Via Luca Ghini 13, Pisa, Italy.*

***Abstract*— 3D bioprinting not only has paved the way for advances in life sciences and healthcare but it is also emerging as a key driver behind an ongoing paradigm shift in the production process of various industrial domains, ranging from food to fashion. The potential of such technology is underexplored and this work assesses 3D bioprinting as a valuable approach for developing novel and more effective solutions for leather defect correction during the animal-leather tanning process, with the aim at increasing the outlet market for tanneries.**

***Keywords*—bioprinting, leather defect correction, bioink, robotic biofabrication platform.**

I. Introduction

OVER the past decades, 3D bioprinting has gained a foothold as a high-impact technology in various fields, with major applications in life sciences, healthcare, food technology and cruelty-free fashion, and has led to huge advances in tissue engineering, regenerative medicine, organ printing, high-throughput screening, and drug printing [1], [2]. The potential of 3D bioprinting is enormous; therefore, evaluating and researching potential applications in other fields is essential. The tanning process transforms raw or semi-finished skins and hides, a by-product of the food industry, into a valuable product suitable for various market sectors, from fashion to furniture and automotive [3]. The presence of defects on the grain side deeply affects the product's quality and, thus, its market price. Currently, available defect correction methods are applied in the final stages of the tanning process, when the destination of the leather has already been established [3], which reduces the outlet market for tanneries. Therefore, the possibility to correct defects before the tanning and/or retanning processes would allow tanneries to place themselves in the raw or semi-processed leather segment, a much larger market segment. In this context, 3D bioprinting could be a valuable enabling technology. Gelatin methacryloyl (GelMA) is a widely-used, versatile photo-crosslinkable polymer with tunable properties [4] that has already proven to be an effective solution for a broad range of applications, including wound healing and skin regeneration [5]. This work describes the development of a novel approach for the early correction of leather defects by exploiting the 3D bioprinting technology and GelMA-based bioinks.

II. Materials and Methods

A. Materials

The bioink used in this study was composed of GelMA, as the photo-crosslinkable polymer, and lithium phenyl-2,4,6-trimethylbenzoylphosphinate (LAP) (Sigma-Aldrich, USA), as photoinitiator, embedding bovine fibroblasts, as living component. LAP was chosen over other commonly used photoinitiators (*e.g.*, Irgacure 2959) as it guarantees improved cell viability [6]. GelMA was synthesized according to the procedure described in [7]. Bovine fibroblasts were provided by the Department of Biology of the University of Pisa.

B. Photopolymerisation tests

Photopolymerisation tests were carried out to optimise the light-curing time of the GelMA/LAP solution. Literature evidence assessed the ability of solutions with 5% w/v GelMA concentration and 0.25% w/v LAP concentration to promote cell viability [8]; therefore, such solutions were initially used for this study. After the preparation of a GelMA (5% w/v) and LAP (0.25% w/v) solution, 300 µl aliquots were manually extruded into a 24-well plate and then exposed to 405 nm light using a 3W torch. Such volume (300 µl) ensures complete coverage of the well's bottom. The number and positioning of the filled wells were planned to minimise the amount of energy striking neighbour-filled wells during exposure. The torch was placed at a fixed distance of 17 mm, corresponding to the depth of a standard 24-well plate, since the torch's diameter is larger than the well's diameter. 5, 10, 15, 20, 25 and 30 s exposure times were evaluated.

C. Biological tests on manually extruded bioink

Following the optimisation of the photopolymerisation parameters, biological tests were carried out on the bioink after its manual extrusion into the wells of a 24-well plate and exposure to the 405 nm light. These tests aimed at assessing the viability and metabolic activity of bovine fibroblasts when embedded in 5% w/v GelMA and 0.25% w/v LAP hydrogels. Specifically, after dissociation with Trypsin/EDTA 0.25% (Thermo Fisher Scientific, USA) and cell count, a bovine fibroblasts suspension ($1.25 \cdot 10^6$ cells/ml) was combined in a 1:1 ratio with the GelMA/LAP solution, previously warmed to 37°C and sterilised through a 0.2 µm filter. 300 µl aliquots of the bioink were pipetted into the wells of a 24-well plate and light-cured through exposure to 405 nm light for 10 and 25 s. The plated wells were then filled with culture medium and left in the cell incubator for 24 h. After incubation, the cells were fixed with 4% formaldehyde for 12 min at room temperature. Immunofluorescence analysis was then performed to assess cell presence (DAPI dye), cytoskeletal morphology (alpha-tubulin, TUBA), and the potential presence of apoptotic dead cells (activated caspase 3, cCASP3).

D. *Surface activation of skin samples*

The treatment of the leather's surface with an activating solution was evaluated as a potential approach to increase the bioink's adhesion to the defect's surface on different leather samples. Particularly, one possible strategy involves N-ethyl-N'-(3-dimethylaminopropyl)carbodiimide (EDC) (Sigma-Aldrich, USA) and N-hydroxysuccinimide (NHS) (Sigma-Aldrich, USA) solution, commonly used to promote cell adhesion on glass surfaces. The activation procedure was applied to four 50 x 50 mm specimens of bovine leather samples from different tanning phases (Table I). Pickled and wet-blue-tanned leather samples were chosen since the collection of leather samples following the pickel and wet blue tanning steps is much easier compared to other phases in the tanning process, and this will facilitate the industrial translation of the optimized bioprinting protocol.

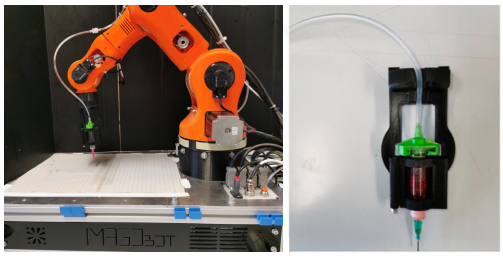
TABLE I: LEATHER SAMPLES USED IN SURFACE ACTIVATION TESTS

Specimen Name	*Description*
NT_pickled	Specimen of pickled leather not to be treated with the activating solution
T_pickled	Specimen of pickled leather to be treated with the activating solution
NT_wetblue	Specimen of wet-blue-tanned leather not to be treated with the activating solution
T_wetblue	Specimen of wet-blue-tanned leather to be treated with the activating solution

Some defects were carved on the specimens using a scalpel. A pH 6.4 buffered aqueous solution of NHS 0.002 M and EDC 0.005 M was then prepared. A quantity of EDC/NHS with the same weight as the T_pickled specimen was mixed with sodium chloride (NaCl) to obtain a final solution with 10% w/v NaCl concentration (quantities and concentrations were established in previous tests); the T_pickled specimen was then immersed in this solution for at least 60 min (NaCl prevents the acid swelling typical of pickled leather when in contact with aqueous solutions). The T_wetblue specimen was immersed in EDC/NHS solution for at least 60 min (NaCl is not necessary as wet-blue-tanned leather does not undergo acid swelling in aqueous solutions). After the 60 min immersion, which is essential for the activation of the leather and defects' surfaces, a 5% w/v GelMA and 0.25% w/v LAP solution preheated to 37°C was manually extruded on the defects of the specimens (NT_pickled, T_pickled, NT_wetblue, T_wetblue) and exposed to 405 nm light for 25 s. The T_wetblue and T_pickled specimens were then left for 60 min under ambient conditions to allow bond formation between the extruded material and the activated surface. The T_wetblue and NT_wetblue specimens were immersed in deionised water (dH_2O) and incubated in an oven at 37°C overnight, while T_pickled and NT_pickled specimens were immersed in dH_2O and NaCl solutions (an amount of dH_2O equal to the weight of the T_pickled and NT_pickled specimens was mixed with NaCl to obtain a 10% w/v NaCl concentration) and were incubated in an oven at 37°C overnight.

E. *Bioprinting tests*

The bioink was printed on 330 x 330 mm samples of pickled and wet-blue-tanned bovine leather. Leather samples of such dimensions are essential to allow the completion of the tanning process in a laboratory test drum after the defect correction phase. Therefore, a 5-axes robotic arm [9] (Figure 1A) equipped with a pneumatic syringe-pump extruder (controlled by the SMC ITV001 2BLQ pressure regulator) as an end-effector (Figure 1B) was used. Indeed, this bioprinting system ensured an adequate workspace (350 x 350 x 350 mm) to print on such wide leather samples.



A B

Fig. 1: 3D bioprinting system set-up. A) Robotic arm. B) Pneumatic extruder.

Optimisation experiments were carried out to define the optimal combination of printing parameters to allow smooth printing of the bioink and adequate defect correction on the leather samples. Specifically, a scalpel was used to obtain three 50 x 50 mm pickled leather specimens and three 50 x 50 mm wet-blue-tanned leather specimens and to manually create defects on their surface (Figure 2). Different GelMA/LAP solutions (Table II, III) were prepared and kept liquid at 37°C. The 5 ml pneumatic extruder's syringe was loaded with the evaluated GelMA/LAP solution and then mounted on the robotic arm's end effector. Finally, the ink was printed on the specimens' defects and then exposed to the 405 nm light for 25 s. LAP concentration was always equal to 0.25% w/v and conic nozzles were used to reduce the shear stress that would be exerted on the cells. In the experiments, different printing parameters were evaluated, such as GelMA concentration values within the ink, extrusion pressure, the time between the loading of the material into the syringe and printing, nozzle gauge values, and printhead's speed values in the XY plane.

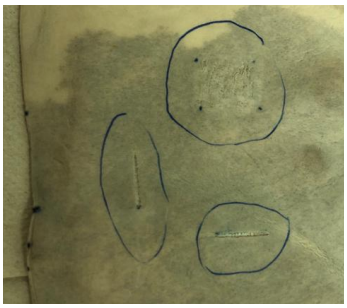


Fig. 2: Image of manually created defects on the pickled leather's surface.

III. RESULTS

A. *Photopolymerisation tests*

The photopolymerisation of the solution occurred for each of the evaluated exposure times. To validate this result, wells containing light-cured GelMA/LAP hydrogels were filled with dH_2O and the plate was subsequently incubated in an oven at

37°C overnight. The following day, the presence of the solidified material in all wells used for the test confirmed the success of the photopolymerisation process.

B. Biological tests on manually extruded bioink

Since the stiffness of the light-cured ink increases with exposure time [10], biological tests were carried out on hydrogels obtained with 10 s and 25 s exposure times, which represent the central values of the [5;15] s and [20;30] s exposure ranges. The results of the immunofluorescence analysis (Figure 3) show that the cells maintained physiological viability with no apoptosis following treatment and started gaining a rather elongated shape, similar to the typical fibroblasts' morphology, after a 24 h incubation. Therefore, the biological tests proved that the GelMA/LAP ink does not affect the viability of bovine fibroblasts. Given the positive outcomes, an exposure time of 25 s was chosen and used as a reference for any subsequent experiment.

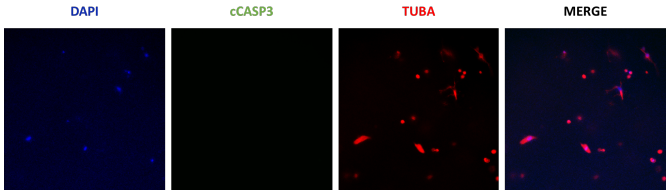


Fig. 3: Immunofluorescence on bovine fibroblasts after 24 h incubation of the GelMA/LAP/bovine fibroblasts hydrogels (25 s exposure to 405 nm light).

C. Surface activation tests of skin samples

The hydrogel on the NT_wetblue sample's defects underwent partial detachment and melting during the 37°C overnight incubation (Figure 4B), while the hydrogel on the NT_pickled sample's defects gained a silver colour (Figure 4A). This didn't happen to the T_pickled and T_wetblue specimens (Figures 4C and 4D). Consequently, the activation tests confirmed the adhesion of the GelMA/LAP hydrogel on leather surfaces previously treated with EDC/NHS solution.

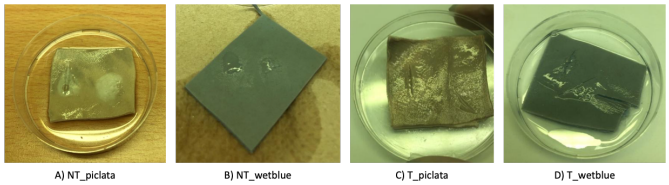


Fig. 4: Light-cured biomaterial ink conditions on the four different specimens after overnight incubation at 37°C.

D. Optimisation tests of the ink's 3D printing parameters

The optimisation experiments were performed over several days and at different times of the day. Since the bioink's rheology doesn't significantly differ from the ink's rheology for cell densities usually used for bioprinting [11], each optimisation experiment involved the loading of the pneumatic extruder's syringe with a cell-free GelMA/LAP solution, previously kept at 37°C. The principal combinations of the different parameters evaluated in this set of optimisation experiments are highlighted in Table II. Since no temperature control of the ink in the pneumatic extruder on the robotic arm was possible, the strong influence of the room temperature on the GelMA/LAP solution's viscosity emerged. Solutions with 5% w/v GelMA required too much time to reach sufficient viscosity levels to allow the printing of the material, whereas solutions with 10% w/v GelMA quickly reached excessive viscosity levels [12] (Table II).

TABLE II: FIRST SET OF OPTIMIZATION EXPERIMENTS

% [a] w/v	*T [b] [min]*	*v [c] [mm/min]*	*P [d] [bar]*	*Nozzle*	*Outcome*
10	4	180	0.7	Conic white 27 G	Failed: ink leakage with no pressure.
	9	60	0.6	Conic white 27 G	Failed: too viscous ink. Ink leakage with no pressure.
	15	180	1	Conic white 27 G	Failed: too liquid ink coming out in drops.
	26	60	1	Conic white 27 G	Failed: too viscous ink. Extrusion is not possible. Nozzle occlusion.
	40	60	1	Conic red 25 G	Failed: too viscous ink. Extrusion is not possible.
5	12	60	0.7	Conic white 27 G	Failed: too liquid ink coming out in drops.
	42	100	0.76	Conic white 27 G	Failed: too liquid ink coming out in drops.

[a] GelMA concentration. [b] Time between syringe loading and printing. [c] Printhead's speed. [d] Pressure regulator's outlet pressure.

Consequently, in a second set of optimization experiments (Table III), the ink-loaded syringe was kept at 4°C before printing in order to reduce the ink's temperature. This allowed to more accurately tune the ink's viscosity and to enable its pneumatic printing.

TABLE III: SECOND SET OF OPTIMIZATION EXPERIMENTS

% [a] w/v	*T_1 [b] [min]*	*v [c] [mm/min]*	*P [d] [bar]*	*Nozzle*	*Result*
7.5	4	180	0.4	Conic white 27 G	Failed: too liquid ink
	2	180	0.4	Conic blue 22 G	Failed: too viscous ink
5	4.5	180	0.4	Conic blue 22 G	Non optimal
	4.5	240	0.36	Conic blue 22 G	Non optimal
	4.5	180	0.4	Conic red 25 G	Good but non reproducible
	6	180	0.4	Conic white 27 G	Good and reproducible

[a] GelMA concentration. [b] Period of time during which the loaded syringe is kept at 4°C. [c] Printhead's speed. [d] Pressure regulator's outlet pressure.

Therefore, the printing parameters that were identified as optimal for this application are the following: a 5% w/v GelMA concentration, loaded syringe kept 6 min at 4°C, a

conic white 27 G nozzle, a 180 mm/min printhead's speed, and a 0.4 bar pressure regulator's outlet pressure.

E. Bioink 3D printing experiments with optimised parameters

Following the leather surface activation and bioink preparation protocols described in sections II C and II D, respectively, and using the experimental setup described in section II E and the optimised printing parameters defined in section III D, GelMA(5% w/v)/LAP(0.25% w/v)/bovine fibroblast bioink printing experiments were performed on 330 x 330 mm samples of pickled and wet-blue-tanned bovine leather. As described before, in order to facilitate the shape retention of the printed pattern, the bioink was pre-cooled at 4°C; moreover, the syringe loaded with the bioink and the nozzle were transferred to the robotic platform within ice, to facilitate the material's subsequent extrusion.

The optimised printing parameters outlined in section III D allowed a successful bioprinting of the bioink on leather defects, and the results of the printing process are shown in Figure 5.

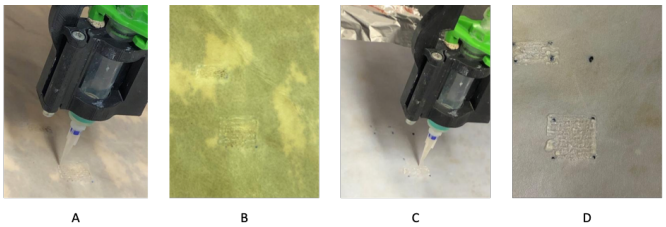


Fig. 5: Bioink printing on leather defects. A) Printing on pickled leather. B) Result of printing on pickled leather. C) Printing on wet-blue-tanned leather. D) Result of printing on wet-blue-tanned leather.

The bioprinted bioink was light-cured with a 25 s exposure to 405 nm light and the samples were then left for 60 min under ambient conditions to allow bond formation between the extruded material and the activated surface. The samples were stored at 4°C.

Five days after printing, dH_2O was poured over the corrected defects on the wet-blue-tanned leather sample. This rehydration procedure confirmed the presence of the hydrogel on the leather sample even five days after the experiment (Figure 6).



Fig. 6: Printed material's condition after rehydration.

IV. Conclusion

The experimental tests demonstrated the effectiveness of the proposed bioprinting approach outlined in section III D for the bioprinting of the GelMA(5% w/v)/LAP(0.25% w/v)/bovine fibroblast bioink on leather defects. Furthermore, the know-how acquired during the optimisation experiments guided the appropriate tuning of the printing parameters during the bioprinting process itself in order to achieve the desired result. Future experiments will investigate the collagen-producing ability of bovine fibroblasts inside the bioink, as it could be essential in the defect-repairing process.

These promising results open up numerous future perspectives, among which the development of a temperature-controlled bioprinting environment (*i.e.*, a heated printhead or a temperature-controlled printing chamber) and the integration of a defect-detection tool (*i.e.*, a vision system) compatible with the robotic arm are of utmost priority for the permanent integration of the technology into the industrial tanning process. Globally, this work sets the foundations for a significant and stable employment of this 3D bioprinting technology in the tanning industry, highlighting the potentialities of evaluating alternative applications and application fields for 3D bioprinting.

Acknowledgement

This work was partially supported by the LEATHERUP Project, co-financed from Tuscany POR FESR 2014-2020, action 1.1.5 Sub. A1 and by the Next Generation EU project I53C22000780001 "Ecosistema dell'Innovazione" Tuscany Health Ecosystem (THE, PNRR, spoke 9: Robotics and Automation for Health).

References

[1] A. Bejoy et al., "An insight on advances and applications of 3D bioprinting: A review.", *Bioprinting*, 24, e00176, 2021.
[2] I.T. Ozbolat, W. Peng, V. Ozbolat, "Application areas of 3D bioprinting", *Drug discovery today*, 21(8), 1257-1271, 2016.
[3] P. Maina, M. A. Ollengo, E. W. Nthiga, "Trends in leather processing: A Review", 2019.
[4] J.H. Wang et al., "An injectable, dual crosslinkable hybrid pectin methacrylate (PECMA)/gelatin methacryloyl (GelMA) hydrogel for skin hemostasis applications", *International Journal of Biological Macromolecules*, *185*, 441-450, 2021.
[5] D. Zhao et al., "GelMA combined with sustained release of HUVECs derived exosomes for promoting cutaneous wound healing and facilitating skin regeneration", *Journal of Molecular Histology*, *51*(3), 251-263, 2020.
[6] H. Xu, J. Casillas, S. Krishnamoorthy, C. Xu, "Effects of Irgacure 2959 and lithium phenyl-2, 4, 6-trimethylbenzoylphosphinate on cell viability, physical properties, and microstructure in 3D bioprinting of vascular-like constructs", *Biomedical Materials*, *15*(5), 055021, 2020.
[7] Y.C. Chen et al., "Functional human vascular network generated in photocrosslinkable gelatin methacrylate hydrogels", *Advanced functional materials, 22*(10), 2027-2039, 2012.
[8] C. Luo et al., "Low-temperature three-dimensional printing of tissue cartilage engineered with gelatin methacrylamide", *Tissue Engineering Part C: Methods*, *26*(6), 306-316, 2020.
[9] G.M. Fortunato et al., "Robotic platform and path planning algorithm for in situ bioprinting", *Bioprinting*, *22*, e00139, 2021.
[10] C.D. O'Connell et al., "Tailoring the mechanical properties of gelatin methacryloyl hydrogels through manipulation of the photocrosslinking conditions" *Soft matter*, *14*(11), 2142-2151, 2018.
[11] J. Emmermacher et al., "Engineering considerations on extrusion-based bioprinting: interactions of material behavior, mechanical forces and cells in the printing needle", *Biofabrication*, *12*(2), 025022, 2020.
[12] A.F. Bonatti, I. Chiesa, G. Vozzi, and C. De Maria, "Open-source CAD-CAM simulator of the extrusion-based bioprinting process", *Bioprinting*, *24*, e00172, 2021.

An engineered breast cancer model on chip for personalized and multiple drug therapy

G. Imparato[1], C. Mazio[1], F. Urciuolo[2], P.A. Netti[1,2]

[1] *Center for Advanced Biomaterials for Healthcare@CRIB, Istituto Italiano di Tecnologia, Naples*

[2]*Department of Chemical, Materials and Industrial Production Engineering, University of Naples Federico II,*

Abstract

Breast cancer is one of the most common tumors worldwide featured by heterogeneity. The expression of hormone receptors marks different breast cancer subtypes. Each type is pharmacologically treated by using molecules targeting hormone receptors, but this frequently drives chemoresistance. For this reason, the possibility to replicate this hostile human pathology *in vitro* represents an urgent need to understand the biological basis behind heterogeneity and chemoresistance and explore the efficiency of pharmacological treatments.

***Keywords*: engineered tumor, tumor microenvironment; tumoral micro-tissues.**

A. INTRODUCTION

Cancer development is a complex and dynamic process regulated by interactions between cancer cells and their microenvironment composed of activated stromal cells and soluble and insoluble components of the extracellular matrix (ECM). The dynamic reciprocity existing between cancer cells and their microenvironment is involved in cancer differentiation, proliferation, invasion, metastasis, and drug response. Understanding the molecular mechanisms underlying the cross-talking between cancer cells and their surrounding tissue (*i.e.,* tumor stroma) and how this interplay affects the disease progression, is fundamental to designing and validating a novel, more robust, and reliable therapeutic approaches. As an important regulator of tumor progression, tumoral ECM has been identified as a very promising target of anticancer treatment, revolutionizing the traditional therapeutic paradigm that sees neoplastic cells as the preferential objective to fight cancer[1]. To design and validate such target therapy, advanced 3D preclinical models are necessary to correctly mimic the complex, dynamic, and heterogenous tumor stroma. The possibility to couple 3D bioengineered tumor models with a microfluidic device, open the way to a new class of tumor-on-chip model able to replicate the pathological microenvironment, offering a reliable platform for developing novel anti-cancer approaches[2]. Here we showed the development of a breast cancer micro-tissue model able to present intra- and extra-tumor morphological heterogeneity in a dynamic and responsive endogenous ECM. The 3D tissue consists of MCF7(Adenocarcinoma cells), endothelial cells, and stromal fibroblasts. In this highly physiologically relevant environment, tumor cells show different cluster morphologies in the stroma recapitulating tumor spatiotemporal heterogeneity. We cultured the breast cancer micro-tissue on a customized microfluidic device, to replicate a physiological fluid dynamic environment and to online collect high-throughput data of live cell and ECM dynamics upon time-varying microenvironmental conditions.

B. MATERIAL AD METHODS

Cell Culture

Human mammary fibroblasts (HMFs) were extracted from healthy breast biopsies and cultured in enriched MEM: MEM with 20% of FBS, 2% of Non-Essential Aminoacids, 1% of L-Glutamine and 1% of penicillin/streptomycin, until passage 4/7. HUVECs (GIBCO C0035C) were cultured in enriched M200: M200 (GIBCO Invitrogen) supplemented with LSGS Kit until passage 3. Human breast adenocarcinoma cells (MCF7) were kindly donated by Daidone's group (IRCCS, Istituto Nazionale dei Tumori, Milano, Italy) and cultured in enriched RPMI: RPMI-1640 medium supplemented with 10% FBS, 1% L-glutamine, 1% penicillin/streptomycin. MCF7 cells weretransfected with pLVX-ZsGreen1-N1 (λex 493nm, λem 505 nm) viral vector purchased from Clontech, USA

MicroTissue Fabrication

As described in the reference[3], 3,5 10^6 P5/8 HMF were seeded on 64mg of engineered porous gelatin microspheres in spinner flask bioreactors After 7-9 days of suspension culture, de-novo synthesized ECM occupied inner porosity and covered

microbeads surface. At this time, 10^6 HUVECs were seeded on the HMF-ECM-microsphere system. After other 9 days of culture, 7 10^6 MCF7 were added to obtain the final Tumor micro-tissues (T-μT). By following the same approach we fabricated:

- MCF10-μT (by adding nonmalignant epithelial cells);
- Control-μT (tissue without endothelial and composed of fibroblasts and HUVECs).

Immunofluorescence on tissue samples

Sample were fixed in 4% Paraformaldehyde for 30 minutes at Room Temperature (RT) and washed in PBS1X. They were permeabilized using 0,1% Triton in PBS1X for 5 min at RT, washed in PBS1X and blocked in 3%BSA, 3%FBS, 0,01%Triton in PBS1X for 1 hour at RT. The tissues were stained with Rhodamine Ulex Europaeus Agglutinin I at a final concentration of 20 μg/ml in blocking solution to mark the endothelium. The nuclei were stained with 40,6-diamidino-2-phenylindole (DAPI) diluted 1:10.000 in PBS1X for 20 min at RT. Samples were investigated by Confocal Leica TCS SP5 II. Images were analyzed using Image J.

Quantitative Capillary-like structures (CLS) analysis

Whole samples were investigated by Confocal Leica TCS SP5 II performing z-stacks in different random points of different μTPs. Each stack was composed of 16 sequential images with a z-slice-space of 1,98 μm. Samples were observed using λex = 543 nm/ λem=550/560 nm to detect Rhodamine (UEA 1) and λex=700 nm (two photons)/ λem = 400/450 nm to detect DAPI. The stacks were acquired with a resolution of 12 bit, 512x512 pixels, by using a 25X water immersion objective (HCX IRAPO L 25.0X0.95 Water, n.a. 0.95). Image analysis was performed by Image J.

Imaging of newly formed collagen

Cell-assembled collagen was detected by Second Harmonic Generation (SHG). SHG is generated by collagen type I, without staining, when the sample is exited under two-photon light at λex = 820 nm and acquiring the signal at λem = 420 nm. Image analysis was performed by Image J.

Image analysis of hyaluronic acid quantity

Hyaluronic acid was detected by immunofluorescence on tissue sections after enzymatic with CaCl2 and Trypsin. Image analysis was performed by Image J.

Device fabrication and tissue dynamic culture

The microfluidic device was designed using computer-aided design software. The CAD file was converted into a computer-aided machine (CAM) file using DESKAM software and used to obtain a poly(methylmethacrylate) (PMMA) stamp by a micro milling machine. The microfluidic device was fabricated by replica molding technique by curing Polydimethylsiloxane (PDMS) on the PMMA master. The chip was composed of two chambers in series for microtissues and two channels, adjacent to the chambers and separated by pillars. The chip was connected to a syringe pump by tubes and connectors and operated at Q=1μl/min.

C. Results And Discussion

The T-μTs are composed of tumor epithelial cells, stromal cells, and endothelial cells embedded in their native environment. T-μTs present intra- and extra-tumor morphological heterogeneity in a dynamic and responsive endogenous ECM. In this highly physiologically relevant environment, tumor cells showed different cluster morphologies in the stroma recapitulating tumor spatiotemporal heterogeneity. In Fig. 1A and 1B, TME of the breast cancer micro-tissue is shown: cell-synthesized collagen network in grey, malignant cells clusters in green, and the vascular network in red. The initial porous gelatin microsphere had the unique role to induce fibroblasts in synthesizing new ECM components, as described in our previous works[4–7]. Graphics in Fig.1C, D, and E show the extension of capillary-like structure (CLS in Fig. 1C) as well as the amount of neo-formed collagen (Fig. 1D) and neo-formed hyaluronic acid (Fig. 1E) after 10 days of heterotypic culture. Figure 1 demonstrates that our model replicates some important features found in human TME. The presence of MCF7 induces an increase in CLS fraction according to the abnormal vascularization of tumoral tissues and also induces hyperproduction of collagen and hyaluronic acid. When cultured in a microfluidic device (Figure 2) the dynamic flow promotes the synthesis and assembly of endogenous ECM among multiple T-μTs as detected using Second harmonic generation imaging at multiphoton microscopy. In this condition, the T-μTs were able to sustain long-lasting culture (up to 27 days), maintaining high viability and a well-structured collagen network (Figure 3). The effect of specific drugs and their combination on collagen architecture, and cell

viability, will be assessed to establish the best therapy on the chip.

D. Conclusion

Here we have presented a tumor-on-chip model to replicate a functional tumor microenvironment. We were able to detect the variation of the collagen network, vascular network organization, and cell invasion mechanisms over tumor progression. The possibility to culture the 3D bioengineered tumor models in a microfluidic device, open the way a new class of tumor-on-chip model able to replicate the pathological microenvironment, offering a reliable platform for developing novel anti-cancer approaches.

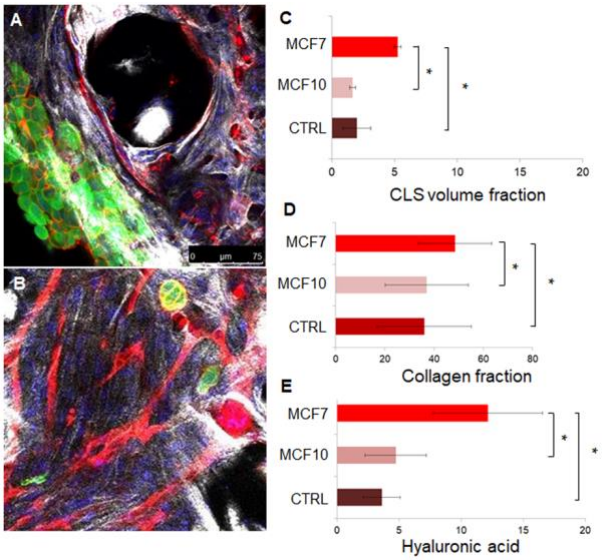


Figure 1. **TME remodeling**. A, B: Tumor microtissue (T-µT) presenting cell-synthesized collagen network (gray), cancer cells (green), endothelial cells (red). C, D, E: graphics indicating the behavior of CLS volume fraction (C), collagen fraction (D), and hyaluronic acid (E) in T-µT (whit MCF7), MCF10-µT, and Control-µT.

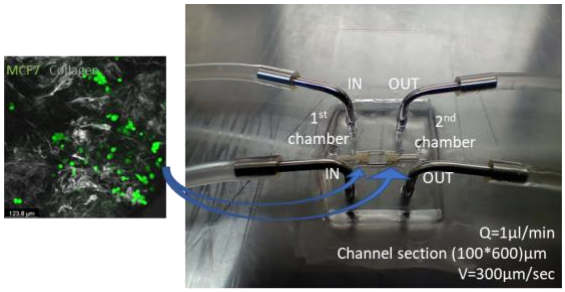


Figure 2. **T-µTs-on-chip**. Picture of the T-µTs-on-chip, the blue arrows highlight T-µTs charged in the chambers of the device. On the left, the collagen matrix is marked in gray and tumor cells are green, Tubes and connectors were used to establish a dynamic flow of the culture medium from the inlet (IN) to the outlet (OUT), by using a syringe pump.

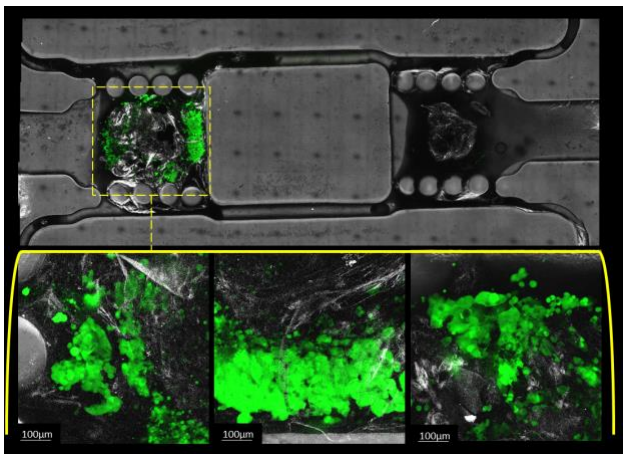


Figure 3. Long time culture of T-µTs-on-chip: Confocal al multiphoton analysis of T-µTs-on-chip after 27 days of dynamic culture, Tumor cells in green and collagen matrix in gray

Acknowledgements

The research leading to these results has received funding from AIRC under IG 2021 - ID. 26185 project – P.I. Paolo Antonio Netti.

References

(1) Roma-Rodrigues, C.; Mendes, R.; Baptista, P. V.; Fernandes, A. R. Targeting Tumor Microenvironment for Cancer Therapy. *Int. J. Mol. Sci.* **2019**, *20* (4). https://doi.org/10.3390/ijms20040840.

(2) Imparato, G.; Urciuolo, F.; Mazio, C.; Netti, P. A. Lab on a Chip Tumor Stroma for On-Chip Optimization of Microenvironmental Targeting Nanomedicine. *Lab Chip* **2022**. https://doi.org/10.1039/d2lc00611a.

(3) Mazio, C.; Casale, C.; Imparato, G.; Urciuolo, F.; Netti, P. A. Recapitulating Spatiotemporal Tumor Heterogeneity in Vitro through Engineered Breast Cancer Microtissues. *Acta Biomater.* **2018**, *73*, 236–249. https://doi.org/10.1016/j.actbio.2018.04.028.

(4) Imparato, G.; Urciuolo, F.; Casale, C.; Netti, P. a. The Role of Microscaffold Properties in Controlling the Collagen Assembly in 3D Dermis Equivalent Using Modular Tissue Engineering. *Biomaterials* **2013**, *34* (32), 7851–7861. https://doi.org/10.1016/j.biomaterials.2013.06.062.

(5) Chung, M.; Ahn, J.; Son, K.; Kim, S.; Jeon, N. L. Biomimetic Model of Tumor

Microenvironment on Microfluidic Platform. *Adv. Healthc. Mater.* **2017**, *1700196*, 1–7. https://doi.org/10.1002/ADHM.201700196.

(6) Brancato, V.; Comunanza, V.; Imparato, G.; Corà, D.; Urciuolo, F.; Noghero, A.; Bussolino, F.; Netti, P. A. Bioengineered Tumoral Microtissues Recapitulate Desmoplastic Reaction of Pancreatic Cancer. *Acta Biomater.* **2017**, *49*, 152–166. https://doi.org/10.1016/j.actbio.2016.11.072.

(7) Gioiella, F.; Urciuolo, F.; Imparato, G.; Brancato, V.; Netti, P. A. An Engineered Breast Cancer Model on a Chip to Replicate ECM-Activation In Vitro during Tumor Progression. *Adv. Healthc. Mater.* **2016**, *5* (23), 3074–3084. https://doi.org/10.1002/adhm.201600772.

RNA Sequencing analysis to study Duchenne dilated cardiomyopathy in patient-derived 3D organoid models

V. Marini[1], F. Marino[1], F. Aliberti[2,3], M. Sampaolesi[1,4] and Y. Chin Chai[1]

[1] Translational Cardiomyology Laboratory, Stem Cell Biology and Embryology, Department of Development and Regeneration, KU Leuven, Belgium

[2] Department of Public Health, Experimental and Forensic Medicine, Human Anatomy Unit, University of Pavia, Pavia, Italy

[3] Fondazione IRCCS Policlinico San Matteo, Center for Inherited Cardiovascular Diseases, Transplant Research Area

[4] Histology and Medical Embryology Unit, Department of Anatomy, Histology, Forensic Medicine and Orthopedics, Sapienza University of Rome, Rome, Italy

***Abstract*— Duchenne Muscular Dystrophy (DMD) is an X-linked neuromuscular disease which is, to date, incurable. The main cause of death, in the advanced stages of the disease, is due to the manifestation of dilated cardiomyopathy. However, the pathogenesis is still unclear since the existing cellular and animal models are not able to fully reproduce the human disease phenotype. In this study, cardiac organoids from patient-derived pluripotent stem cells (DMD-CO) and isogenic-corrected controls (DMD-Iso-CO) were generated to investigate if DMD-related cardiomyopathy and disease progression occur in the organoids upon long-term culture. RNA sequencing analysis were carried out supporting a distinct transcriptomic profile in DMD-CO. These were associated with functional enrichment in hypertrophy/dilated cardiomyopathy, adipogenesis and fibrosis pathways. Moreover, five miRNAs were identified to be crucial in this dysregulated gene network. In conclusion, a patient-derived cardiac organoid model was obtained. Specifically, it displayed DMD-related cardiomyopathy and disease progression phenotypes in long-term culture. Currently, we are focusing on developing a more complex, realistic, and reliable *in vitro* 3D human cardiac-model to study DMD-related cardiomyopathies, exploiting 3D bioprinting technology.**

***Keywords*—Duchenne Muscular Dystrophy, Cardiac Organoids, RNA sequencing, 3D models.**

I. Introduction

Muscular dystrophies (DM) are an heterogeneous complex of genetically determined diseases characterized by a chronic and progressive degeneration of skeletal and cardiac muscles. [1], [2]. One of the most widespread and common forms of the aforementioned group of pathologies is Duchenne Muscular Dystrophy (DMD), a neuromuscular disorder caused by mutations affecting the dystrophin gene (DYS), located on the short arm of the X chromosome, which results in the total expression absence of the homonymous protein (DYS) [3], [4]. The lack of the dystrophin protein expression, which essential function is to stabilize the fibers during contractions, results in symptoms manifestation including muscle weakness and atrophy, respiratory and cardiac insufficiency significantly aiding the probability of death before the age of 30 [5], [6].

The main cause of death, in the advanced stages of the dystrophic cardiac pathology, is to be attributed to the manifestation of Duchenne dilated cardiomyopathy (DDC); DDC can occur as a result of an initial cardiomyocyte degeneration – due to the activation of an inflammatory response - resulting in replacement of heart muscle with adipose and connective tissue, thus causing reduction in heart wall thickness [7], [8]. To date, no great research attention has been directed to DDC despite is being the main cause of death in patients with DMD. Indeed, the main reason is partly due to limited accessibility to human cardiac tissues, and the intrinsic limitation of two-dimensional (2D) cardiomyocyte cultures since it is not yet able to reproduce, *in vitro*, a biological model as similar as possible to the pathophysiological one *in vivo* [9].Thus, this project aimed to develop a three-dimensional (3D) in *vitro* model that allowed to reproduce, and therefore to study, the progression of DDC. The creation of 3D patient-derived cardiac organoids (COs) from induced pluripotent stem cells (hiPSCs), – generated by Sendai virus technology - enabled to fill this scientific gap. All experiments were carried out using in parallel isogenic control iPSCs, generated by CRISPR/Cas genomic modification system, originally discovered from the microorganism *Streptococcus pyogenes* [10], [11].

II. Material and Methods

Induce Pluripotent Stem Cell Culture

Experiment were performed using Duchenne Muscular Dystrophy iPSC (DMD-hiPSC) obtained from DMD fibroblast patients carrying a point mutation in exon 35 (c.4 996C>T; p.Arg1,666X) of the Dystrophin gene that leads to a premature stop codon [10]. Human DMD isogenic control (DMD-Iso iPSC) was obtained using CRISPR/Cas9 gene editing from the *S. pyogenes* system (5'-NGG PAM) as previously described [10], [12]. Both human iPSC lines were cultured feeder-free on Geltrex LDEV-Free hESC- and maintained in Essential 8 Flex Basal Medium supplemented with Essential 8 Flex Supplement and 0.1% penicillin–streptomycin, at 37 °C under normoxic conditions (21% O2 and 5% CO2). HiPSC colonies were routinely passaged non-enzymatically with 0.5 mM EDTA in Phosphate-Buffered Saline (PBS).

Human iPSC cardiac differentiation in monolayer culture

DMD-hiPSC and isogenic-corrected control were differentiated into functional cardiomyocytes (CMs) according to a monolayer-based cardiac differentiation protocol, as previously described by Burridge et al.,[13].

Cardiac organoids generation

DMD-hiPSC and isogenic-corrected control were detached as mentioned above and re-suspended in specific hiPSC medium,

were plated in agarose inserts and incubated at 37 °C under hypoxic conditions (5% O2 and 5% CO2) to promote embryoid bodies (EBs) formation. Cardiac differentiation of the EBs into cardiac organoids (COs) was initiated as previously described by Burridge et al.,[13]. Afterwards, the COs were transferred from the agarose moulds to an ultra-low attachment 6-well plate and dynamic culture was carried out using an orbital shaker. Contracting COs start to appear from day 8 of the differentiation protocol. The samples were collected at different time points for further analysis.

RNA isolation, RNA sequencing and bioinformatic analysis

For RNA sequencing assays, total RNA was isolated and treated according to manufacturer protocol (Purelink® RNA mini kit and Turbo DNA free kit). As quality control, the concentration of extracted RNA (>10 µg) was measured with Nanodrop and quality was checked with Bioanalyzer.

The Lexogen QuantSeq 3' mRNA-Seq library prep kit was used according to the manufacturer protocol, then the libraries were measured with Qubit and put on the Fragment analyser, hence the libraries were pooled equimolar. Thereafter, final pool (2 nM) was made for single-read sequencing on the HiSeq4000. Splice aware alignment was performed running HiSat2 against the human reference genome hg38 using the default parameters. Reads mapping to multiple loci in the reference genome were discarded. Resulting BAM alignment files were handled with Samtools v1.5 [14]. Reads quantification per gene was performed using HT-seq Count v2.7.14. Count-based differential expression analysis was carried out with R-based Bioconductor package DESeq2 (Love et al., 2014). Reported p-values were adjusted for multiple testing with the Benjamini-Hochberg procedure. Gene Ontology (GO) and Biological Kyoto Encyclopedia of Genes and Genomes (KEGG) pathway enrichment analyses were identified using g:Profiler [15]. The significant terms and pathways were selected with the threshold of adjusted p-value < 0.05.

Protein-protein interaction (PPI) network generation

The PPI network of differentially upregulated genes in DMD-CO was generated by using a list of gene symbols and their log2fold changes into the NetworkAnalyst platform (http://www.networkanalyst.ca/) using the IMEx interactome database. Afterwards, the gene-miRNA interactions for the selected KEGG pathways were made based on the miRTarBase (v8.0) database, and the network was reduced using the Steiner Forest Network (SFN) algorithm. The degree of each node was calculated based on its number of connections to other nodes. In the network, the colour represents the expression and the area of an individual node specify the degree. The identified top five miRNAs were mapped out in the KEGG pathways for showing their interactions with the genes of a specific pathway.

Statistical analysis

All data were statistically analysed using GraphPad Prism. Differences between groups were analysed for statistical significance using ANOVA test. Significance of the differences was shown as follows: *p <0.05, **p < 0.01, ***p < 0.001, and ****p<0.0001.

III. Results

Cardiomyocyte monolayer differentiation protocol was adapted to generate cardiac organoids (COs) by direct differentiation of embryoid bodies (EB). Self-aggregation of the DMD-hiPSCs and DMD-Iso-hiPSCs into EBs was stimulated by using the agarose microwell culture insert. The resulting DMD-CO and DMD-Iso-CO, after 5 days of differentiation protocol, were transferred to plates on orbital shaker for dynamic culture thus promoting self-organized cellular structures and contractile cardiomyocyte clusters. Immunofluorescence assays for studying Sarcomeric Actin proteins α(αACTN) and NKX2.5 expression were performed to evaluate the expression of the key genes of cardiac differentiation and the contractile proteins activation. Indeed, a transient expression of the gene marker NKX2.5 in both *DMD-CO and DMD-Iso-CO* and a progressive decrease of α-sarcoglycan (SCGA) protein expression in CO-DMDs, compared to isogenic controls was observed. Subsequently, the progressive worsening of the DMD-CO phenotype was demonstrated by carrying out histological analyses: indeed, fibrotic and adipocytic areas - pathological manifestations like those associated with cardiomyopathies - were observed. To confirm what previously observed, RNA sequencing analyses were performed. RNA transcriptomic data were displayed in Figure 1. Based on the enhanced volcano plot, out of 22371 gene variables, 1518 and 554 genes were differentially upregulated in DMD-CO and DMD-Iso-CO, respectively (Cut-off: $\log_2$ fold change = 1.5; $-\text{Log}_{10}$ p = 10^{-14}). Among the most differentially upregulated genes in DMD-CO, the expression of MGP, MYL1, COL1A2, HAPLN1 and OGN were the five most significant upregulated genes in DMD-CO (Fig.1). Hence, in order to identify the molecular pathways and biological information related to the aforementioned genes, a Gene Ontology analysis was performed on the set of isolated genes based on gProfiler analysis.

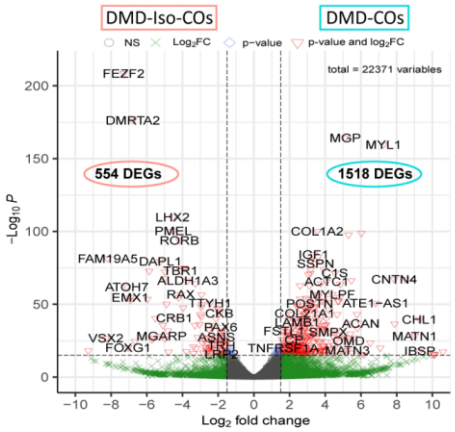


Fig. 1, *adapted from Fig.6B in* [8]: Enhanced volcano plot showing the differentially expressed genes (DEGs) in DMD-COs versus DMD-Iso-COs. Cut-off $\log_2$ fold change = 1.5; Cut-off $-\text{Log}_{10}$ p = 10^{16}.

Gene ontologies which were significantly enriched for molecular function in extracellular matrix regulation (*i.e.*, collagen and glycosaminoglycan; GO:MF), cardiac tissue structure formation (*i.e.*, external encapsulating structure such as sarcolemma; GO:CC), and cardiovascular development (GO: BP) were identified in DMD-CO (Fig. 2).

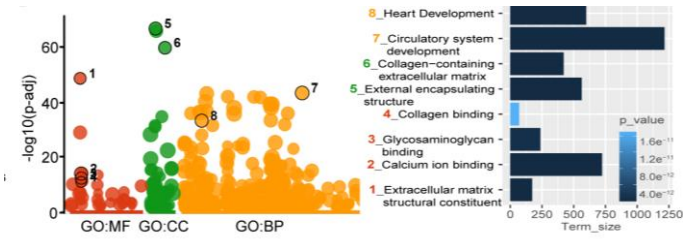


Fig. 2, *adapted from Fig.6D in* [8]: Functional enrichment analysis of the differentially upregulated genes in DMD-COs versus DMD-Iso-COs using gProfiler2 for Gene Ontology.

In addition, the gProfiler analysis also identified three top miRNA regulators for the differentially upregulated genes in DMD-CO, *i.e.*, hsa-mir-335-5p, hsa-mir-29a-3p and hsa-mir-29b-3p. Moreover, KEGG pathways associated with protein digestion and absorption, dilated and hypertrophic cardiomyopathy, ECM-receptor interaction, and cGMP-PKG signalling pathway were significantly enriched in DMD-CO. These findings were corroborated by the analysis on human phenotype ontology. Overall, the RNA sequencing data corroborated the histological observations (data not shown) on cardiomyocyte deterioration, adipogenesis and fibrosis at the transcriptomic level. Subsequently, a Protein-protein interaction (PPI) network analysis of differentially upregulated genes in DMD-CO was performed to identify the most significant genes in the complex network of gene interconnections. The identification of genes with the major regulatory potential of the entire network was carried out by node (gene) grade analysis, thus referring to the number of interlinked genes. Integration of miRNA-gene hybridization data from the mirTarBase v8.0 database identified two more miRNAs, hsa-mir-124-3p and hsa-mir-26b-5p, associated with HNF4A genes (rank = 257), UBC (degree = 108), UBD (degree = 66), APP (degree = 38), and EGR1 (degree = 31) (Fig.3).

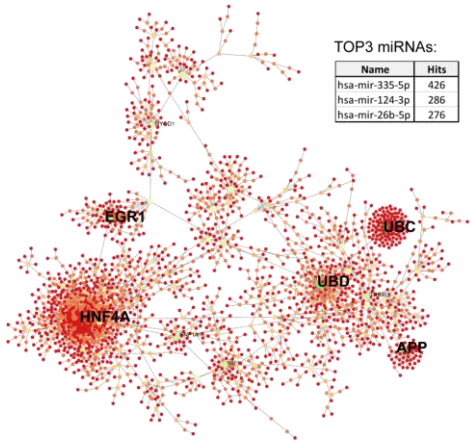


Fig. 3, *adapted from Fig.7A in* [8]: Protein-protein interaction network analysis based on differentially upregulated genes in DMD-COs using Network Analyst platform in DMD-COs showing the top five hub genes (HNF4A, UBC, UBD, APP and EGR1) based on the degree level.

To identify the association between the ontology result and the miRNAs identified were mapped among the gene-miRNA regulatory networks obtained for each KEGG pathway characterizing the DMD-CO condition, previously obtained through the analysis of the Biological Process ontology (BP): hypertrophic cardiomyopathy, dilated cardiomyopathy, arrhythmogenic right ventricular cardiomyopathy (ARVC), PPAR pathway for adipogenesis, PI3K-Akt pathway for cardiac fibrosis. The results showed that the hypertrophy and dilated cardiomyopathy networks shared the same gene set (50 nodes, 49 edges), miRNA interactions (Fig.4A), and similarity of 16 genes with the ARVC network (Fig.4B). Except for hsa-mir-124-3p, the other four major miRNAs mapped into these three networks, respectively.

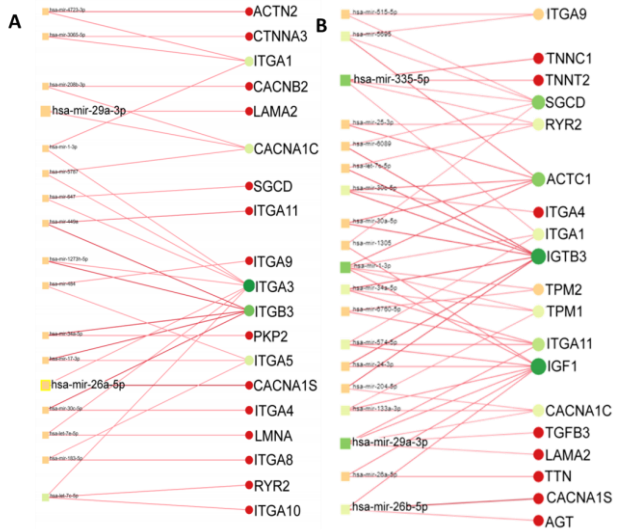


Fig. 4, *adapted from Fig. 7B and 7C in* [8]: The gene-miRNA networks for arrhythmogenic right ventricular cardiomyopathy (A), hypertrophy/dilated cardiomyopathy (B).

In addition, the PPAR signalling gene-miRNA network consisted of 33 nodes and 43 edges (Fig.5A) and has-mir-29b-3p, hsa-mir-26b-5p and hsa-mir-355-5p were the main miRNA regulators in the PI3K-Akt signalling (147 nodes, 146 edges), which interact with one of the two hub genes CCND2 (Fig. 5B).

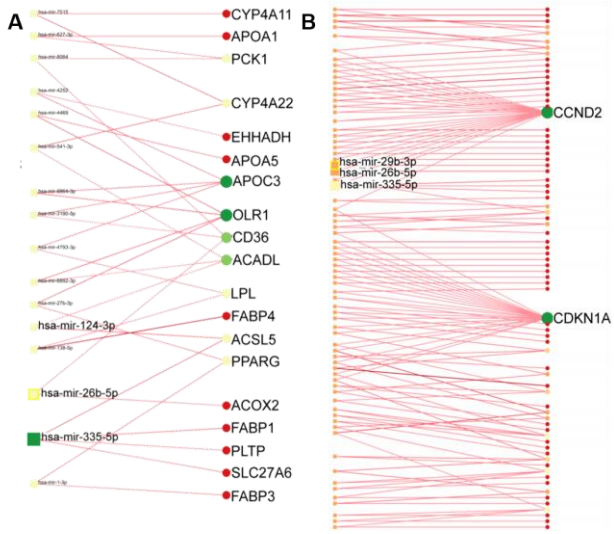


Fig. 5, *adapted from Fig. 7D and 7E. in* [8]: The gene-miRNA networks for PPARgamma (A) and PI3K-Akt (B) signaling pathways.

IV. Discussion

There is currently no cure for DMD patients, thus they are treated symptomatically via palliative therapies used in conjunction with cardio-respiratory supporting devices in case of cardio-pulmonary complications – a main lethal cause in DMD patients. DMD related cardiomyopathy often occurs as hypertrophic or dilated heart due to cardiomyocyte damage followed by fibrosis and adipose tissue formation. For these reasons, it should be necessary to develop a new therapeutic strategy to prevent the occurrence of these pathological events; therefore, it is crucial acquiring a thorough knowledge of the mechanism through which disease develops. However, to date due to limited accessibility to patient biopsy and the intrinsic limitation of 2D cardiomyocyte cultures, have precluded this scientific endeavour. Hence, in this study *in vitro* 3D human cardiac-mimics of DMD-relevance to bridge this scientific gap were developed. In this study, DMD-CO that functionally and transcriptionally modelled the cardiac evolution in DMD patients were generated. Particularly this model showed a lack in proliferative capacity, cell death and a progressive deterioration of cardiomyocytes in early culture stage (10, 14, 28 days) followed by adipose tissue and fibrous-like tissue formation at later culture stage. These results were corroborated through RNA sequencing analysis demonstrating that the DMD-CO generated on long term culture (93 days) were a 3D cellular models to gain insight into the disease mechanism of DMD-associated hypertrophic/dilated cardiomyopathy, as well as adipogenesis and fibrosis. Hence, we focused on mapping out the functionally enriched pathways based on the differentially upregulated genes in DMD-CO as compared to DMD-Iso-CO, as well as their main miRNA regulators. Among the top five hub genes identified in the protein-protein interaction network, only HNF4A ($log_2FC = 1.89$, $p<2.92e^{-5}$, UBD ($log_2FC = 2.69$, $p<7.37e^{-5}$) and EGR1 ($log_2FC = 1.47$, $p<5.31e^{-12}$) were significantly and differentially upregulated in DMD-CO. Afterwards, assays for identifying regulating miRNAs for genes overexpressed in pathological COs were performed, producing three potential sequences: hsa-mir-335-5p, hsa-mir-29a-3p, hsa-mir-29b-3p, hsa-mir-124-3p and hsa-mir-26b-5p. According to literature, the 5 identified miRNAs may be associated with different conditions: the miRNA hsa-mir-335-5p is responsible for controlling the regulation of cardiac differentiation since, potentially mediated by the activation of WNT and TGFβ pathways [16], is able to upregulate the commitment of cardiac progenitors; hsa-mir29a-3p and hsa-mir-29b3p are overexpressed in patients with congenital heart disease; hsa-mir-26a/b-5p is highly expressed in patients with cardiac hypertrophy [17] and is responsible for activating the cell death process caused by myocardial infarction [18]; finally, hsa-mir-124-3p promotes the activation and proliferation of cardiac fibroblasts [16] and its inhibition protects against acute myocardial infarction, by inhibiting the apoptosis process of cardiomyocytes [19]. Therefore, the use of the RNA sequencing technique and of the *in-silico* analysis allowed the identification of five miRNAs significantly expressed in the pathological COs that could be associated with the development of dilated cardiomyopathy and with the pathways of adipogenesis and fibrosis – confirming what was observed with the morphological tests.

References

[1] J. Camps, H. Grosemans, R. Gijsbers, C. Maes, and M. Sampaolesi, “Growth factor screening in dystrophic muscles reveals PDGFB/PDGFRB-mediated migration of interstitial stem cells,” *Int. J. Mol. Sci.*, vol. 20, no. 5, 2019.

[2] J. C. Carter, D. W. Sheehan, A. Prochoroff, and D. J. Birnkrant, “Muscular Dystrophies,” *Clin. Chest Med.*, vol. 39, no. 2, pp. 377–389, 2018.

[3] A. F. Muntoni, Silvia Torelli, “Dystrophin and mutations: one gene, several proteins, multiple phenotypes,” *Lan Neurol.*, vol. 2, 2001.

[4] K. M. Flanigan, “Duchenne and becker muscular dystrophies,” *Neurologic Clinics*. 2014.

[5] M. S. Falzarano, C. Scotton, C. Passarelli, and A. Ferlini, “Duchenne muscular dystrophy: From diagnosis to therapy,” *Molecules*, vol. 20, no. 10, pp. 18168–18184, 2015.

[6] Y. Ogura, M. M. Tajrishi, S. Sato, S. M. Hindi, and A. Kumar, “Therapeutic potential of matrix metalloproteinases in Duchenne muscular dystrophy,” *Front. Cell Dev. Biol.*, vol. 2, no. APR, pp. 1–11, 2014.

[7] R. Adorisio *et al.*, "Duchenne Dilated Cardiomyopathy: Cardiac Management from Prevention to Advanced Cardiovascular Therapies". *J Clin Med.* vol.9 (10): 3186.

[8] V Marini *et al.* ,"Long-term culture of patient-derived cardiac organoids recapitulated Duchenne muscular dystrophy cardiomyopathy and disease progression." *Front Cell Dev Biol.* vol. 10: 878311, 2022

[9] M. Quattrocelli *et al.*, “Mesodermal iPSC-derived progenitor cells functionally regenerate cardiac and skeletal muscle,” *J. Clin. Invest.*, vol. 125, no. 12, pp. 4463–4482, 2015.

[10] R. Duelen *et al.*, “Human iPSC model reveals a central role for NOX4 and oxidative stress in Duchenne cardiomyopathy,” *Stem Cell Reports*, vol. 17, no. 2, pp. 352–368, 2022.

[11] R. Aman, A. Mahas, H. Butt, Z. Ali, F. Aljedaani, and M. Mahfouz, “Engineering RNA virus interference via the CRISPR/Cas13 machinery in arabidopsis,” *Viruses*, vol. 10, no. 12, 2018.

[12] F. A. Ran, P. D. Hsu, J. Wright, V. Agarwala, D. A. Scott, and F. Zhang, “Genome engineering using the CRISPR-Cas9 system,” *Nat. Protoc.*, vol. 8, no. 11, pp. 2281–2308, 2013.

[13] P. W. Burridge *et al.*, “Chemically Defined and Small Molecule-Based Generation of Human Cardiomyocytes HHS Public Access,” *Nat Methods*, vol. 11, no. 8, pp. 855–860, 2014.Chemically.

[14] H. Li *et al.*, “The Sequence Alignment/Map format and SAMtools,” *Bioinformatics*, vol. 25, no. 16, pp. 2078–2079, 2009.

[15] U. Raudvere *et al.*, “G:Profiler: A web server for functional enrichment analysis and conversions of gene lists (2019 update),” *Nucleic Acids Res.*, vol. 47, no. W1, pp. W191–W198, 2019.

[16] M. Kay, B. M. Soltani, F. H. Aghdaei, H. Ansari, and H. Baharvand, “Hsa-miR-335 regulates cardiac mesoderm and progenitor cell differentiation,” *Stem Cell Res. Ther.*, vol. 10, no. 1, pp. 1–13, 2019.

[17] L. Tang, J. Xie, X. Yu, and Y. Zheng, “MiR-26a-5p inhibits GSK3β expression and promotes cardiac hypertrophy in vitro,” *PeerJ*, vol. 8, pp. 1–19, 2020.

[18] S. E. Jung *et al.*, “MicroRNA-26a/b-5p promotes myocardial infarction-induced cell death by downregulating cytochrome c oxidase 5a,” *Exp. Mol. Med.*, vol. 53, no. 9, pp. 1332–1343, 2021,.

[19] H. Hu, G., Ma, L., Dong, F., Hu, X., Liu, S., and H. Sun, “Inhibition of microRNA-124-3p protects against acute myocardial infarction by suppressing the apoptosis of cardiomyocytes,” *Mol Med Rep 20(4)*, 2019.

Innovation in neuronal cell culture: from adhesion to maturation, chitosan promotes developing nervous system

Donatella Di Lisa[1], Lorenzo Muzzi[1], Elena Dellacasa[1], Monica Frega[2], Sergio Martinoia[1], Laura Pastorino[1]

[1]*University of Genova, Dept. of Informatics, Bioengineering, Robotics and System Engineering, Via all'Opera Pia 13, 16145 Genova, Italy*
[2]*University of Twente, Dept. of Clinical Neurophysiology, University of Twente, Drienerlolaan 5, 7522, NB, Enschede, Netherlands*

***Abstract*—The extracellular matrix plays a pivotal role during nervous system development, offering adhesion points for neuronal growth and differentiation, as well as for nervous tissue formation. For that reason, neuronal functional and morphological *in vitro* studies have been performed functionalizing culture supports by extracellular matrix components or synthetic biopolymers. In this study, chitosan was validated as an alternative adhesion. Primary neurons and neurons differentiated from human induced pluripotent stem cells were plated onto chitosan and standard adhesion factors modified supports. The development of individual cells was followed at daily intervals until both axons and dendrites had been established; electrophysiological behavior was studied to validate the ability of chitosan to sustain long-term maturation.**

***Keywords* — Chitosan, Cell adhesion factors, Neuronal development, Electrophysiological characterization.**

I. Introduction

The main extracellular matrix components involved in the developing nervous system are the glycoproteins laminin and fibronectin, which are expressed at stages critical for neuronal differentiation and are functional in neurite outgrowth in vitro [1]. Usually, neuronal culture supports, such as plastic or glass surfaces for traditional 2D neuronal cultures, can be bioactivated either with molecules able to interact with the negatively charged cell membrane [2], or with receptors on the cell membrane [3], [4] to guide neuronal adhesion and growth. Poly-ornithine, laminin and poly-lysine are the most popular adhesion molecules. These macromolecules containing amino groups, have been frequently used as coating materials for *in vitro* neuronal substrates, as electrostatic interaction between the positive charges of the NR_3^+ groups on a culture substrate and the negatively charged neuronal membranes has been suggested as an indispensable factor for stable neuronal adhesion and proper development, [5]-[7].

In the last year, 3D tissue model gained a great popularity. As for 2D culture supports, biomaterials used for 3D cultures need surface functional groups to promote neuronal adhesion and development. Researchers have focused on functionalizing biomaterials surfaces with adhesion molecules [8].

Among the different tested biopolymers for nervous tissue engineering, chitosan has been investigated both in 2D and 3D neuronal cultures. Chitosan is a copolymer of glucosamine and N-acetyl-glucosamine, obtained by the deacetylation of chitin, which is the main component of crustacean and insect exoskeletons [9]. Chitosan is well known for its biocompatibility, biodegradability, muco-adhesiveness as well as its antibacterial activity. Moreover, in chemical structural terms, chitosan shows similarities to the extracellular glycoprotein carbohydrates. In this respect, recently studies showed the ability of chitosan to sustain the development of 3D functional neuronal networks, both for primary rat neurons and neurons differentiated from h-iPSCs without any pre-functionalization [10]-[12]. Based on these results, the starting hypothesis of this work is that chitosan can be used as an adhesion molecule in standard 2D cultures of rat and human neurons, promoting the formation of functional networks comparable with traditional commercial adhesion molecules and. Cell culture upports were bioactivated using chitosan (*Chito*) and poly-ornithine (*PolyO*) or poly-ornithine /laminin (*PolyO/Lam*) as controls. Primary hippocampal and cortical neurons and h-iPSCs differentiated in excitatory cortical neurons (iNeurons) were plated onto the functionalized supports. In order, to validate the ability of chitosan to support neuronal adhesion, networks development and the differentiation capacity, morphological and functional characterization were carried out. This model has been compared with the well-established model introduced by Dotti et al. for the polarization process on hippocampal neurons evaluating plating efficiency, neurite outgrowth at different stages after plating and found that, on poly-ornithine as control substrate, [13]. As relates to iNeurons, plating efficiency and polarization were evaluated and compared to those obtained by using *PolyO/Lam* coated supports, following the protocol by Frega et al. [14].

This work demonstrated that chitosan, besides all its well-known properties, displays bioactivity towards both rat neurons and iNeurons. Moreover, as already demonstrated in literature [10]-[12], *chito* can be easily shaped both in 2D and 3D without any modification of its chemical cues, representing an innovative bridge between different neuronal dimensional *in vitro* models.

II. Material and Methods

A. Culture supports functionalization

Chito solutions were prepared at concentrations of 0.1 and 1% w/v in 0.1M acetic acid. *PolyO* and *Lam* were used at a concentration of 0.15 µg/ml and 5 µg/ml in ${}_{dd}H_2O$ respectively. 0.1% *Chito* solutions were sterilized by

filtration, while 1% *Chito* solution was autoclaved at 120 °C. Culture supports were functionalized by solution casting following the standard protocol [15] and incubated overnight at 37°C. The excess of solutions was removed, supports were then washed twice with sterile $_{dd}H_2O$ and finally normalized in cell culture medium. For iNeurons, after *PolyO* functionalization, *Lam* solution was pipetted on the supports and incubated for 2 hours at 37 °C; later, the supports were washed with sterile $_{dd}H_2O$ and normalized in the proper cell culture medium.

B. *Cell plating*

Cells were plated at low cell density (28-30 cells/mm^2) in the presence of astrocyte conditioned medium, for the evaluation of neurite outgrowth. The synaptic count was carried out onto cultures with a cell density of 260-300 cells/mm^2. The electrophysiological characterization was performed with a cell density of 1200 cells/mm^2. Primary hippocampal and cortical cultures were prepared according to methods developed by Banker and Goslin, [15]. H-iPSCs were generated by lentiviral transduction from fibroblast taken from a healthy donor. Cells were kindly provided by Frega et al. Full protocol regarding generation and maintenance of the rtTa/NgN2 positive cell line have been described in Frega et al. [14]. The experimental protocol was approved by the European Animal Care Legislation (2010/63/EU), by the Italian Ministry of Health in accordance with the D.L. 116/1992 and by the guidelines of the University of Genova. All efforts were made to reduce the number of animals used for the project and to minimize their suffering.

C. *Characterization of coatings*

To determine the amount of free amino groups, ninhydrin (Sigma-Aldrich, NHN) assay [16] was carried out. *Chito*, *PolyO* and *PolyO/lam* films adsorbed were obtained following the same procedure exposed in "Culture supports functionalization" section. The amount of free amino groups was proportional to the optical absorbance of the solution at 570 nm.

D. *Morphometry evaluation*

Morphometry study was carried out to characterize neuronal development and polarization. The main neuronal development parameters were extracted: number of neurites per cell, total neurite length per cell, length of major neurites per cell, total length of all minor neurites per cell and polarity index.

E. *Morphological characterization*

To evaluate neuronal network development, microtubule-associated protein (MAP-2), glial fibrillary acidic protein (GFAP) and Dapi were used to show dendritic arborization, glial cells and nuclei, respectively. Moreover, neuronal cultures were co-immunostained for the excitatory pre-synaptic maker vesicular glutamate transporter and the excitatory post-synaptic density marker to carry out the synaptic count.

F. *Electrophysiological characterization*

Standard MEA-60 (MultiChannel System) were used to record the electrophysiological activity of neuronal network. Electrophysiological activity was recorded at different developmental stages.

III. RESULTS

A. *Characterization of coatings*

As it is reported in literature, free amino groups of polyaminoacid electrostatically interacts with the negative charges of the cell membrane, promoting cell adhesion. In this respect, NHN assay was carried out to evaluate the amount of free amino groups of all used adhesion factors [16]. The amount of free amino groups for 0.1 % and 1 % Chito was respectively three and six times higher compared to the one for *PolyO*, Fig.1.

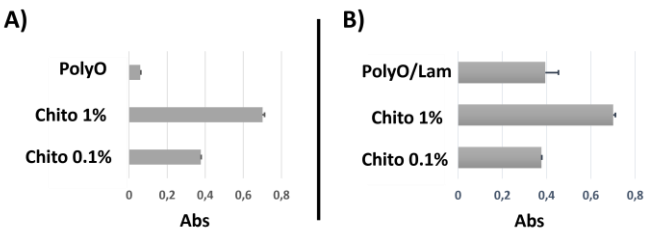


Fig. 1: Amount of free amino groups of Chito, *PolyO* and *PolyO/Lam*

B. *Morphometric evaluation*

The morphological differentiation (two distinct types of processes, namely, axons and dendrites) of rat and human neurons was investigated onto all coatings at 24h intervals between 0 and 72h *in vitro*. Fig.2 and Fig. 3 show the main parameters characterizing neuronal early-stages development: number of neurites, average length, average length of minor and major neurites. For both rat neurons and iNeurons, the number of neurites per cell increased during the whole culture period. In terms of the average neurites length, no significant differences between the coatings were observed for both neuronal populations. The mainly difference observed in rat neuronal development onto two different substrates, is that *Chito* showed a temporary decrease of total neurite length, favouring the growth of major neurites over the growth of the minor ones, and therefore promoting neuronal polarity at later stages of neuritogenesis Fig.2.

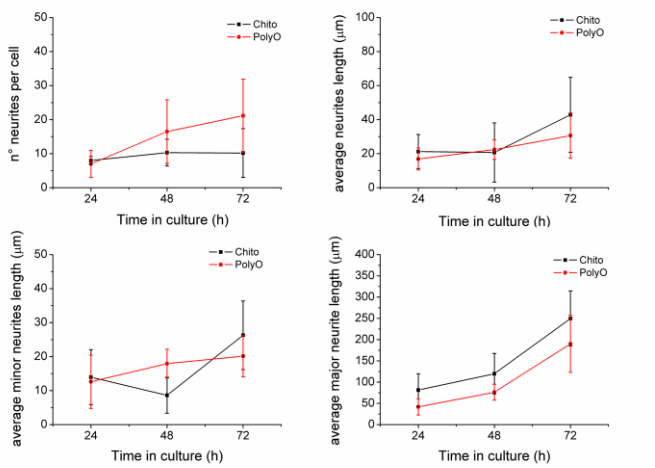


Fig. 2: Coatings influence on number of neurites, neurites lengths, minor neurite lengths, major neurites lengths of Rat neurons over time.

As relates to iNeurons, *Chito* favoured the growth of the minor neurites over the growth of the major one Fig. 3. These results suggest that iNeurons axonal growth is slower than the primary neuron one. This has been attributed to different maturation of primary rat neurons and iNeurons.

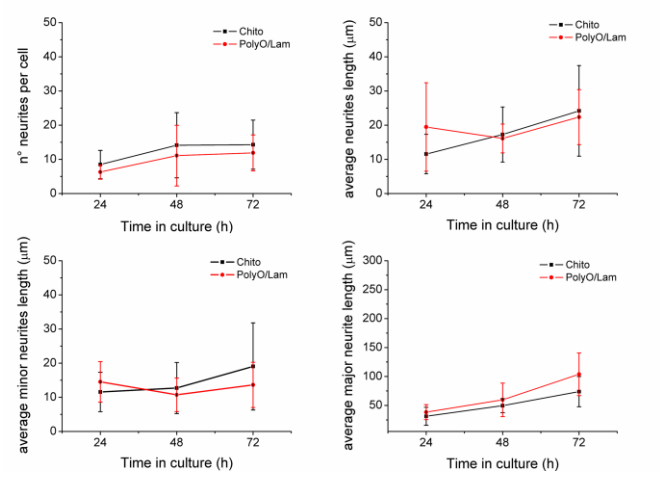
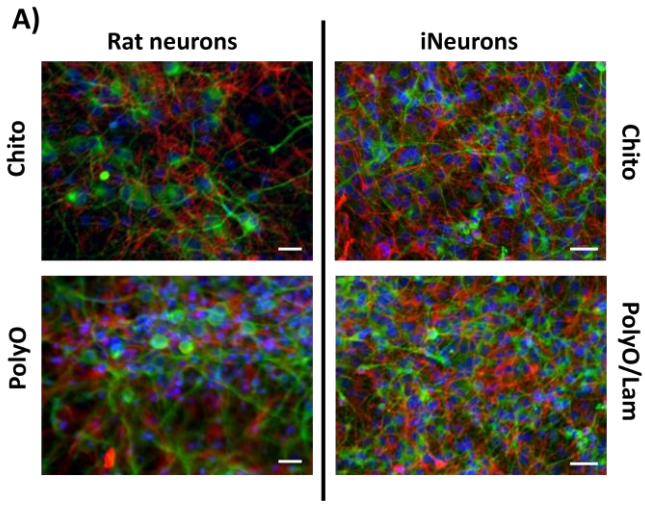


Fig. 3: Coatings influence on number of neurites, neurites lengths, minor neurite lengths, major neurites lengths of iNeurons over time.

C. *Morphological characterization*

The immunocytochemistry characterization allowed us to obtained information on the morphology of 2D neuronal networks after 21 days of culture and distinct features of the neurons and glial cells, Fig. 4A. For both rat neurons and iNeurons, the two cells' populations (neurons in green and glia in red) present a morphology similar onto all coatings showing a homogeneous distribution and the formation of a dense network.

A related to synaptogenesis, the expression of synaptic puncta increased with time in all experiments, for both neuronal populations onto all coatings, pointing out a progressive and adequate cell maturation, Fig. 4B. For both cell types, during the first week of culture, synapse development was almost absent. For rat neurons, after 14 days a robust synaptogenesis was observed on *Chito* as well as on *PolyO* coatings. For iNeurons, synaptogenesis wasn't observed, Fig.4B, since not all marker signals matched, confirming that iNeurons maturation is slower than the one of primary rat neurons.



B)

Rat neurons

DIV	Chito	PolyO
7	0.3 ± 0.05 µm	0.25 ± 0.08 µm
14	3 ± 0.07 µm	2.9 ± 0.09 µm

iNeurons

DIV	Chito	PolyO/Lam
7	0.05 ± 0.01 µm	0.1 ± 0.01 µm
14	0.45 ± 0.02 µm	0.5 ± 0.05 µm
21	0.98 ± 0.03 µm	1 ± 0.04 µm

Fig. 4: A) Immunochemistry staining images of Rat neurons and iNeurons onto *Chito*, *PolyO* and *Poly/Lam* at DIV21, labelled for MAP2 (green), GFAP (red) and DAPI (blue). Scale bar: 20 µm. **B)** Quantification of synaptic puncta in rat neurons at DIV 7 and 14 and in iNeurons at DIV 7, 14 and 21.

D. *Electrophysiological characterization*

The spontaneous activity of rat neuronal networks and iNeuronal networks developed onto all coatings was recorded. The electrophysiological analysis showed that both cultures on all coatings increased their activity towards mature network dynamics, indicating a stable interface between the coatings and adherent cells.

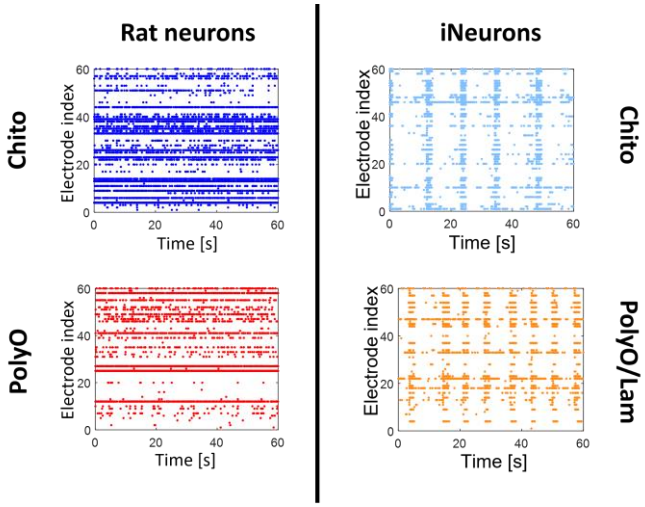


Fig. 5: Raster plots showing 60 s of spontaneous activity of 2D rat neuronal networks at DIV26 and 2D iNeuronal networks at DIV42.

IV. Conclusion

The results of this study show that *Chito* can be used as an alternative adhesion molecule to support neuronal culture, showing strong neuronal adhesion properties, and promoting neuritic growth in way comparable with the traditional adhesion molecules. In terms of functional development, *Chito* sustained a maturation of neuronal networks in long-term cultures. The validation was carried out for both rat neurons and human derived neurons. The advantage to have a material that can be used both in 2D and 3D cultures without any further bioactivation, represents a great advantage since 2D cultures are always considered the gold standard in neuroengineering, neurophysiological and neurodegenerative experimental studies, favouring thus the comparison of the results obtained for the two different configurations.

Acknowledgement

The authors thanks CNPH lab (University of Twente) for providing h.iPSCs rtTa/NgN2 positive line, Marloes R. Levers from CNPH group for teaching stem cell maintaining and differentiation, *Chitolytic* for kindly providing CHI2 and Maria Teresa Tedesco for support in rat neurons experiments.

References

[1] Lochter, A., and M. Schachner. "*Tenascin and extracellular matrix glycoproteins: from promotion to polarization of neurite growth in vitro.*" Journal of Neuroscience 13.9 (1993): 3986-4000.

[2] Milky, Bridget, et al. "*Long-term adherence of human brain cells in vitro is enhanced by charged amine-based plasma polymer coatings*." Stem cell reports 17.3 (2022): 489-506.

[3] Rao, S.S. and Winter, J., 2009. "*Adhesion molecule-modified biomaterials for neural tissue engineering*." Frontiers in neuroengineering, p.6.

[4] Rauti, R., Renous, N. and Maoz, B.M., 2020. "*Mimicking the brain extracellular matrix in vitro: a review of current methodologies and challenges*." Israel Journal of Chemistry, 60(12), pp.1141-1151.

[5] Banker, G.A. and Cowan, W.M., 1977. "*Rat hippocampal neurons in dispersed cell culture*." Brain research, 126(3), pp.397-425.

[6] Letourneau, P. C. "*Possible roles for cell-to-substratum adhesion in neuronal morphogenesis*." Developmental biology 44.1 (1975): 77-91. W. D. Doyle, "Magnetization reversal in films with biaxial anisotropy," in *1987 Proc. INTERMAG Conf.*, pp. 2.2-1–2.2-6.

[7] Yavin, E. and Yavin, Z., 1974. "*Attachment and culture of dissociated cells from rat embryo cerebral hemispheres on polylysine-coated surface.*" The Journal of cell biology, 62(2), p.540.

[8] Vallejo-Giraldo, C., Genta, M., Cauvi, O., Goding, J. and Green, R., 2020. "*Hydrogels for 3D neural tissue models: Understanding cell-material interactions at a molecular level.*" Frontiers in bioengineering and biotechnology, 8, p.601704.

[9] Younes, I. and Rinaudo, M., 2015. *"Chitin and chitosan preparation from marine sources. Structure, properties and applications."* Marine drugs, 13(3), pp.1133-1174.

[10] Arnaldi, Pietro, et al. *"A facile approach for the development of high mechanical strength 3D neuronal network scaffold based on chitosan and graphite nanoplatelets*." Carbohydrate Polymers 271 (2021): 118420.

[11] Muzzi, L., et al. "*Rapid generation of functional engineered 3D human neuronal assemblies: network dynamics evaluated by micro-electrodes arrays."* Journal of neural engineering 18.6 (2021): 066030.

[12] Tedesco, Maria Teresa, et al. *"Soft chitosan microbeads scaffold for 3D functional neuronal networks."* Biomaterials 156 (2018): 159-171.

[13] Dotti, C.G., Sullivan, C.A. and Banker, G.A., 1988. "*The establishment of polarity by hippocampal neurons in culture.*" Journal of Neuroscience, 8(4), pp.1454-1468.

[14] Frega, Monica, et al. *"Rapid neuronal differentiation of induced pluripotent stem cells for measuring network activity on micro-electrode arrays."* JoVE (Journal of Visualized Experiments) 119 (2017): e54900.

[15] Kaech, S., Banker, G. *"Culturing hippocampal neurons."* Nat Protoc 1, 2406–2415 (2006). https://doi.org/10.1038/nprot.2006.356.

[16] Mi, F.L., Tan, Y.C., Liang, H.C., Huang, R.N. and Sung, H.W., 2001. "*In vitro evaluation of a chitosan membrane cross-linked with genipin. "* Journal of Biomaterials Science, Polymer Edition, 12(8), pp.835-850.

Development of an analytical model to predict self-folding of 4D bioprinted scaffolds

Alessio Esposito[1], Irene Chiesa[1], Claudia Dell'Amico[2], Marco Onorati[2], Carmelo De Maria[1]

[1]*Department of Information Engineering and Research Center Enrico Piaggio, University of Pisa, Italy*
[2]*Unit of Cell and Developmental Biology, Department of Biology, University of Pisa, Italy*

***Abstract*—Four Dimensions (4D) printing is a fabrication approach which adds the fourth dimension "time" at the three spatial dimensions of Three-Dimensional (3D) printing. A 4D printed object can change its shape and function after receiving an appropriate stimulus. 4D printing finds application in tissue engineering and biofabrication. Indeed, the change in shape of a 4D printed object can mimic physiological movements, and promote cell growth and differentiation. In this work, we developed an analytical model to predict, in space, the movement of a scaffold that, from a planar geometry, turns into a tubular one. This specific shape change, referred to as "folding", has been chosen because it can mimic several anatomical structures, such as trachea, blood vessels and, in particular, the neural tube, which will be here modelled through human pluripotent stem cells.**

***Keywords*—4D printing, bioprinting, modelling, neural stem cells.**

I. Introduction

4D printing is a fabrication technique that increases capabilities and application of additive manufacturing (AM) adding time dependent shape changing. In general, a 4D printed structure is defined as a 3D printed structure that changes shape, function and properties because of a predefined external stimulus [1]. Active materials are at the base of 4D printing. They can change their properties in a predefined way after the application of an external stimulus (*e.g.*, variation of moisture, pH, temperature and electromagnetic field). Thus, by combining different materials in a specific spatial distribution it is possible to achieve the desired change of the structure's shape [2]. The control in the spatial arrangement of different materials is achieved with AM, that allows to deposit different materials in a specific pattern with limited constraints [3]. Biomedical related fields of application of 4D printing include: tissue engineering, drug delivery and medical devices. For example, Zareck *et al.* developed a personalized luminal stent using shape memory polymers. More in detail, the device was printed by stereolithography and was capable of increasing its diameter by unfolding once it reaches the site of interest (ideally the patient trachea). Therefore, the final shape of the device is equal to the anatomical site of interest [4]. Another example of 4D printed biomedical application is given by shape memory hydrogels, which have been used to control the target delivery and controlled release of a certain drug after receiving an appropriate stimulus [5]. In the tissue engineering field, 4D printing has been used to produce scaffolds that can influence cell differentiation and growth by shape changing. An example is the study of Hendrikson *et al.* in which they produced a scaffold based on memory shape polyurethane by extrusion based bioprinting, seeded it with human mesenchymal stem cells and demonstrated that scaffold stretching and contraction improved cell activity and adhesion [6]. All these applications are only possible with an appropriate modelling of the shape changing phenomenon. A model is needed to predict the final geometry once the initial shape, material properties and intensity of stimulus are known, due to the several variables that are entangled in the 4D printing process [7]. In this study, an analytical model is developed to predict the shape changing of planar bilayer structures that turn in tubular ones (*i.e.*, self-folding) after immersion in a water solution. More in detail, these structures are homogeneous films of gelatin (fabricated by solvent casting, using an applicator) at high concentration with parallel lines at lower concentration, that were 4D printed on top of the casted gelatin film. Dipping these structures in a water-based solution, the two layers absorb water differently, due to the different gelatin and crosslinker concentrations that determinate a difference of expansion coefficient. This leads to the folding of the structure (Fig.1). The selection of a tubular shape is linked to the evidence that several anatomical parts have a hollow-cylinder like geometry, as examples: blood vessels, nerves and trachea. Additionally, this particular movement is present in the neural tube formation during embryogenesis [8]. The developmental process of neurulation involves a series of coordinated morphological events during embryogenesis, which result in the conversion of the flat neural plate (generated from dorsal ectoderm) into the neural tube, the primordium of the entire central nervous system (CNS) (Fig.1). Failure during neurulation results in neural tube defects, main cause of sever neurodevelopmental pathologies in human [9]. Here, the 4D bioprinted self-folding structure was used to model the neural tube formation, to validate its usability in a biological environment.

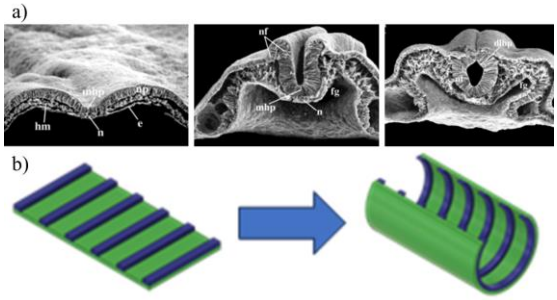


Fig. 1: a) Neurulation process [10] *. b) Folding of produced scaffold*

II. MATERIAL AND METHODS

A. Geometry definition and known models

The geometry to be modelled, can be schematized as a parallelepiped with a series of smaller parallelepipeds on its top (Fig.2).

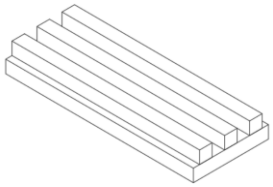


Fig.2: View of modelled geometry

In literature, the most used analysis to predict the bending of a bilayer structure is the Timoshenko's model [11]. In 1925 Timoshenko developed a model that can predict the radius of curvature of a bimetal beam once known the section dimension, mechanical and physical properties of the used materials and the temperature difference. The model is formulated only for beams and in consequence limited to one dimensional (1D) structure. In the next sections, the same steps of Timoshenko's analysis have been applied to the geometry of Fig.1b to obtain the radius of curvature as function of geometric parameters (*e.g.*, moment of inertia of section, thickness of layers, number and dimension of printed lines), material properties (*e.g.*, elastic modulus, expansion coefficient) stimulus intensity (*e.g*., temperature variation).

B. Hypothesis and simplification

Before starting with model derivation a few assumptions need to be done.

- Since shape morphing happens only where there are two different materials in the film, if parallel lines are thin enough, we can assume that the lines will bend like Timoshenko's beams.
- Zones with only one material will expand but do not contribute to structure folding.
- If the beam width is small enough, the bending angle in this direction can be considered negligible.

With these hypotheses we can assume that the printed lines create a preferential direction for shape change and this direction is the same of the printed ones. In other words, the main axes of the hollow-cylindrical shape will be perpendicular to the printed lines. Moreover, for an easier analysis, expansion coefficients incorporate stimulus intensity. Briefly, instead of expansion coefficient multiplied by the stimulus intensity, we consider directly the resulting strain. This is justified by the use of moisture as trigger, because moisture intensity is always the same in water solutions.

C. Model derivation

The following material and geometrical properties are known: Young's modules (E_1 and E_2), expansion coefficients along L direction ($\alpha_1$par, $\alpha_2$par), expansion coefficients along h direction ($\alpha_1$per, $\alpha_2$per), thickness of homogeneous film and printed lines (h_1, h_2), width of lines (D), width of homogeneous film (W) (Fig.3). Hypotheses are verified if D is negligible compared to W and to total length (L). Therefore, without external forces we can consider only internal forces (P) and torques (m) acting along the direction parallel to lines. All geometrical parameters and acting forces are shown in Fig.3.

Since no external forces are present, internal forces and torques are in equilibrium (Eq.1 and Eq.2):

$$P_1' + P_1'' = P_2 = P \quad (1)$$

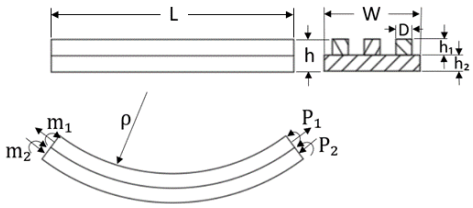


Fig.3: Geometrical parameter and acting force on the structure, before and after shape change.

$$P * \frac{h}{2} = m_1' + m_1'' + m_2 \quad (2)$$

In the Eq.1 and Eq.2 only two lines of material 1 are considered. More in general, since we have N printed lines, total force and momentum in the lines is the sum of forces and momentum in each line (Eq.3 and Eq.4):

$$\sum_1^N P_{1i} = P_2 = P \quad (3)$$

$$P * \frac{h}{2} = \sum_1^N m_{1i} + m_2 \quad (4)$$

If we consider that printed lines have all same size and are equally spaced, then also lines internal forces and torques are all equal ($P_1 i = P_1 \; and \; m_1 i = m_1$), and Eq.3 and Eq.4 become Eq.5 and Eq.6, respectively.

$$N * P_1 = P_2 = P \; (5)$$

$$P * \frac{h}{2} = N m_1 + m_2 \quad (6)$$

Defining ρ as radius of curvature of the structure, torques are obtained from Eq.7, where $I_1 = \frac{D * {h_1}^3}{12} \; and \; I_2 = \frac{W * {h_2}^3}{12}$.

$$m_1 = \frac{E_1 * I_1}{\rho} \qquad m2 = \frac{E_2 * I_2}{\rho} \; (7)$$

Substituting Eq.7 in Eq.6 we obtain Eq.8:

$$P * \frac{h}{2} = \frac{N * E_1 * I_1 + E_2 * I_2}{\rho} \quad (8)$$

The sheared surface between the two materials (parallel direction) the strains of the two materials must be equal (Eq.9):

$$\alpha_1 + \frac{P_1}{E_1 * h_1 * D * N} + \frac{h_1}{2 * \rho} = \alpha_2 - \frac{P_2}{E_2 * h_2 * W} - \frac{h_2}{2 * \rho} \; (9)$$

In Eq. 9 the first terms $\alpha 1$ and $\alpha 2$ are deformations caused by material expansion, second terms are strain calculated according to Hooke model and third terms describe the folding from Navier's Equation.
Substituting Eq.8 in Eq.9 we obtain Eq.10:

$$\frac{1}{\rho} = \frac{(\alpha_2 par - \alpha_1 par)}{\frac{h}{2} + \frac{2 * (N * E_1 * I_1 + E_2 * I_2)}{h} * \left(\frac{1}{E_1 * h_1 * N * D} + \frac{1}{E_2 * h_2 * W} \right)} \; (10)$$

Defining $m = h_1/h_2$, $n = E_1/E_2$ and $\beta = ND/W$, Eq.10 can be written as Eq.11:

$$\frac{1}{\rho} = \frac{6(\alpha_2 par - \alpha_1 par)(m+1)^2}{h\left(3(m+1)^2+(1+\beta mn)(m^2+1/\beta mn)\right)} \quad (11)$$

The radius of curvature results proportional to the total thickness and inversely proportional to the difference in elongation of the two materials. The other parameters m, n and β influence the value of ρ but in a not trivial way.

D. Model validation

To validate this analytical model we produced samples with the same geometry described in section IIA.

These structures were made by a homogeneous film produced by solvent casting using an applicator, thus guaranteeing a homogeneous thickness, composed by a 15% w/v type A gelatin from porcine skin in PBS solution 1X with the addition of 92µl of γ-glycidoxypropyltrimethoxysilane (GPTMS) for each gram of gelatin. On top of the film equidistant parallel lines were printed by extrusion-based bioprinting. Those lines consist of a 5% w/v type A gelatin from porcine skin in PBS solution 1X with 368µl of GPTMS for each gram of gelatin (Fig.4a).

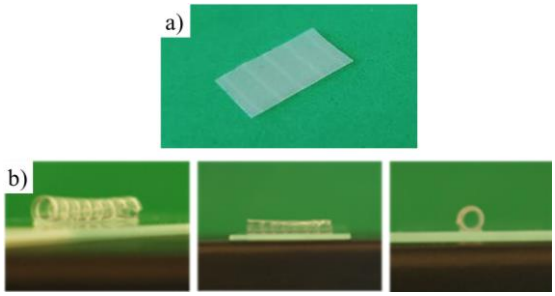


Fig. 4: Scaffold produced of dimension 10x5mm, a) before actuation, b) after folding

The material was chosen for its biocompatibility [12], and the solutions concentrations were chosen to maximise the difference of swelling ratio between the two materials (data not shown). Since the two layers are made by the same bulk materials a chemical bound occur between the two layers. This phenomenon eliminates the risk of delamination of the structure. Both materials have been physically and mechanically characterized to determinate elastic modulus (under wet and dry conditions) and expansion coefficients ($\alpha = \frac{final\ length - initial\ length}{initial\ length}$). The results of these characterization are shown in Table I.

TABLE I: MECHANICAL AND PHYSICAL PROPRIETIES

Material	E wet (MPa)	E dry (MPa)	αpar (%)	αper (%)
Gelatin 15%	3.81 ± 0.43	3170 ± 280	8.54±1.35	164.70±8.67
Gelatin 5%	63.13 ± 26.72	1820 ± 550	3.14± 1.89	38.67±16.52

Values are written as mean ± standard deviation, 4 samples are used to estimate E and 10 samples are used to estimate α

Validation of the model is based on comparing the model predicted radius of curvature (mean and standard deviation STD of the model derived from estimated variability of physical/mechanical properties) of the structure and the effective radius of curvature measured on the real samples, as function of one or more parameters. The thickness of the homogeneous film is the parameter that, from Timoshenko's model, gives larger variation of the radius of curvature. For this reason, the radius of curvature was measured for different h2 values and compared to the predicted ones.

Fabricated samples are 10x5mm on plane and have a total thickness varying from 50µm to 160µm. Layers thickness was measured with a micrometer (h_1, h_2 and h), while lengths on the plane was measured from hi-res figures using the software ImageJ (D and W). Results of measurement are shown in Table II. To trigger the shape changing of the structures the samples were dipped in PBS 1X and after 3 hours (time needed to reach the plateau of expansion, determined during the measure of the expansion coefficient, data not shown) the radius of curvature was measured from pictures using ImageJ.

TABLE II: GEOMETRICAL PARAMETERS

h2 (µm)	h1 (µm)	D (mm)	W (mm)
50-160±5	33.1 ± 14.1	1.0±0.1	10.2±0.4

Values are written as mean ± standard deviation, 30 samples are used to obtain h1, D and W measures

E. Biological application

Scaffolds used to validate the model have been also used to explore the effects of 4D bioprinting in cell differentiation and growth. More in detail, *in vitro* modelling of neural tube formation was explored. A customized holder was put on the scaffold while it was still flat in water-based solution to kept the scaffold flat. The operator just needed to remove the holder to actuate the folding movement. Holder was needed to give time to cell to attach on the scaffold, otherwise shape changing would start too early and the cells would not follow the scaffold movement.

Human induced pluripotent stem cells (hiPSCs) were seeded on 4D bioprinted scaffolds and on 2D static films. After 24 hours, 4D scaffolds were actuated and 3 days later, when the cells reached > 90% confluence, neural induction protocol [13] started. After 12 days of neural induction, cells were driven to differentiation for 4 days, by adding neural differentiation supplemented with the neurotrophin BDNF. Neural differentiation was evaluated through immunofluorescence assay. Confocal imaging of immunoassayed 4D scaffold revealed homogeneous positivity for Nestin [14] (intermediate filament protein of neural progenitors) and SOX2 [15] (transcription factor expressed in neural progenitors), thus confirming successful neural identity.

III. RESULTS

A. Predicted and measured radius comparison

Radius of curvature values are plotted as function of the total thickness as shown in Fig.5.

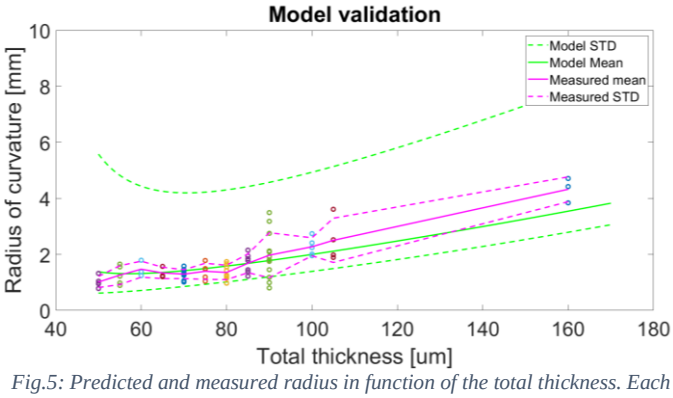


Fig.5: Predicted and measured radius in function of the total thickness. Each dot is a sample.

Mean values of the model (continuous green line) are calculated using mean value of measured material and geometrical parameters (*i.e.*, Young's modulus, expansion coefficients, film thickness, lines thickness and width) STD values of the model (dotted green lines) are calculated using upper and lower values of material and geometrical parameters. For each thickness and radius measure a dot is plotted, obtaining mean (continuous magenta line) and STD (dotted magenta lines). Predicted and experimental values fall in the same region, when the total thickness of the 4D printed structure is between 55 and 105µm.

B. Biological application

Cells attached to the scaffold within 24h after seeding (Fig.6a, top panels). After holder removal, cells still adhere to scaffold surface and within 48h colonize the whole scaffold surface (Fig.6a, bottom panels). Morphological changes occurring during neural induction phase suggest neural commitment (Fig.6b).

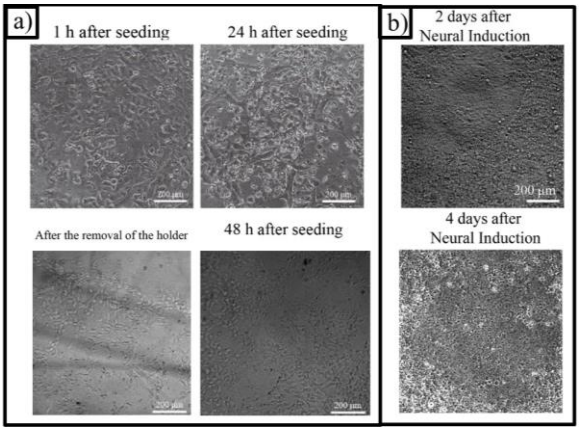


Fig. 6: a) Cells attachment after seeding b) Cells are homogeneously distributed on scaffold surface during neural induction showing morphological change due to neural commitment

After 12 days of neural induction, cells extensively express Nestin and SOX2 neural progenitor typical markers (Fig.7a) and organize into neural rosettes (Fig.7a, bottom panel). Moreover, after 4 days of differentiation, cells seem to be oriented along the thickness of the scaffold, showing a similar organization of neural progenitors in the native neural tube (Fig.7b).

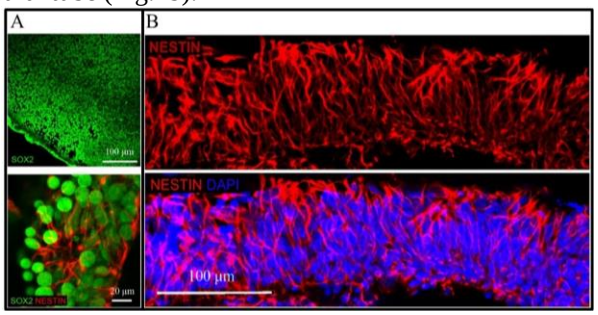


Fig.7: Representative confocal analysis showing A) neuroepithelial-like structure expressing Nestin and SOX2 (DIV12) B) maintenance of the apical-basal orientation of neural precursor at DIV16

IV. Conclusion

The developed model can be used to design self-folding scaffolds that can have multiple purposes in tissue engineering. The model allows to completely control bending orientation and predict the curvature radius of the scaffolds, and to achieve self-folding scaffolds with customizable length, diameter and degree of curvature as a result. Looking at the mathematical model itself, it needs to be improved by adding the time dependent behaviour. In this way, we can achieve a model capable to predict the change in shape through space and time.

The 4D printed scaffold was then used to develop a neural tube in vitro model. Indeed, the self-folding movement of the scaffold recapitulate the formation of neural tube in vitro. The scaffold resulted to be highly biocompatible. Moreover, shape change seems to sustain neural differentiation as showed by immunofluorescence assay with diagnostic markers. Neural tube experiment showed the differentiation from pluripotent cells (hiPSCs) to patterned neural progenitor cells, as highlighted by the expression of Nestin and SOX2. An exhaustive gene characterization in longer period of differentiation is ongoing, to evaluate if 4D printed scaffolds can support neural progenitor differentiation into mature neurons.

Acknowledgement

This study received funding from the European Union Next-Generation – National Recovery and Resilience Plan (NRRP) – MISSION 4 COMPONENT 2, INVESTMENT ECS00000017 - Tuscany Health Ecosystem, CUP N. 153C22000780001 (Spoke4: Nanotechnologies for diagnosis and therapy and Spoke8: Biotechnologies and imaging in neuroscience). This manuscript reflects only the authors' view and options, neither the European Union nor the European Commission can be considered responsible for them.

References

[1] J. Choi, O. C. Kwon, W. Jo, H. J. Lee, and M. W. Moon, "4D printing technology: A review," *3D Printing and Additive Manufacturing*, vol. 2, no. 4. Mary Ann Liebert Inc., pp. 159–167, Dec. 01, 2015

[2] Q. Ge, C. K. Dunn, H. J. Qi, and M. L. Dunn, "Active origami by 4D printing," *Smart Mater Struct*, vol. 23, no. 9, 2014

[3] A. Sydney Gladman, E. A. Matsumoto, R. G. Nuzzo, L. Mahadevan, and J. A. Lewis, "Biomimetic 4D printing," *Nat Mater*, vol. 15, no. 4, pp. 413–418, Apr. 2016

[4] M. Zarek, N. Mansour, S. Shapira, and D. Cohn, "4D Printing of Shape Memory-Based Personalized Endoluminal Medical Devices," *Macromol Rapid Commun*, vol. 38, no. 2, Jan. 2017

[5] Y. Wang *et al.*, "Three-dimensional printing of shape memory hydrogels with internal structure for drug delivery," *Materials Science and Engineering C*, vol. 84, pp. 44–51, Mar. 2018

[6] W. J. Hendrikson, J. Rouwkema, F. Clementi, C. A. van Blitterswijk, S. Farè, and L. Moroni, "Towards 4D printed scaffolds for tissue engineering: Exploiting 3D shape memory polymers to deliver time-controlled stimulus on cultured cells," *Biofabrication*, vol. 9, no. 3, Aug. 2017

[7] F. Momeni, S. M.Mehdi Hassani.N, X. Liu, and J. Ni, "A review of 4D printing," *Mater Des*, vol. 122, pp. 42–79, May 2017.

[8] N. D. E. Greene and A. J. Copp, "Development of the vertebrate central nervous system: Formation of the neural tube," *Prenatal Diagnosis*, vol. 29, no. 4. pp. 303–311, Apr. 2009

[9] C. Dell' Amico, A. Tata, E. Pellegrino, M. Onorati, and L. Conti, "Genome editing in stem cells for genetic neurodisorders," *Prog Mol Biol Transl Sci*, vol. 182, pp. 403–438, Jan. 2021

[10] J. Ois Colas and G. C. Schoenwolf, "Towards a Cellular and Molecular Understanding of Neurulation," 2001.

[11] S. Timoshenko, "Analysis of bi-metal thermostat," *Josa*, 11.3:233-255, Sept. 1925.

[12] A. Lapomarda *et al.*, "Pectin as rheology modifier of a gelatin-based biomaterial ink," *Materials*, vol. 14, no. 11, Jun. 2021

[13] L. Conti and E. Cattaneo, "Neural stem cell systems: Physiological players or in vitro entities?," *Nature Reviews Neuroscience*, vol. 11, no. 3. pp. 176–187, Mar. 2010.

[14] Gilyarov, A. V. "Nestin in central nervous system cells." *Neuroscience and behavioral physiology* 38.2: 165-169. 2008

[15] L. H. Pevny and S. K. Nicolis, "Sox2 roles in neural stem cells," *International Journal of Biochemistry and Cell Biology*, vol. 42, no. 3. pp. 421–424, Mar. 2010

Dose-controlled low-intensity pulsed ultrasound and pulsed electromagnetic fields stimulations modulate inflammation in human macrophages

F. Iacoponi[1,2], F. Orlando[1,2], S. Gasparini[1,2], T. Pratellesi[3], A. Cafarelli[1,2] and L. Ricotti[1,2]
[1] *The BioRobotics Institute, Scuola Superiore Sant'Anna, Piazza Martiri della Libertà 33, 56127 Pisa, Italy*
[2] *Department of Excellence in Robotics & AI, Scuola Superiore Sant'Anna, Piazza Martiri della Libertà 33, 56127 Pisa, Italy.*
[3] *BAC Technology s.r.l., 50063 Florence, Italy*

***Abstract*—In this work, we stimulated M0-like and M1-like macrophages (obtained from the THP-1 cell line) with low-intensity pulsed ultrasound (LIPUS) and pulsed electromagnetic fields (PEMF) to induce beneficial anti-inflammatory effects in terms of gene expression and cytokine release. The results show a significant reduction of some pro-inflammatory markers (IL-8, TNF-α after LIPUS stimulation and IL-1β, IL-8, TNF-α after PEMF stimulation) and a significant increase of anti-inflammatory markers (IL-10 after LIPUS and IL-10, CD206 after PEMF). These results show the potential of LIPUS and PEMF for possible future clinical translation, in clinical settings in which decreasing inflammation has a crucial role to enable therapy efficacy.**

***Keywords*—Biophysical stimulation, LIPUS, PEMF, macrophages.**

I. INTRODUCTION

Inflammation is a key factor in several diseases [1]. Pharmacological treatments to lower inflammation levels are often poorly effective and can cause side effects, dangerous for the organism [2]. Very promising results have been recently obtained by applying biophysical stimulation technologies, such as low-intensity pulsed ultrasound (LIPUS) [3], [4] and pulsed electromagnetic fields (PEMF) [5], [6]. Both these tools show interesting features such as safety, non-invasiveness and low cost. The Food and Drug Administration clinically approved LIPUS for fracture healing [7] and started analyzing several PEMF devices [8].

The efficacy of LIPUS and PEMF in regulating the inflammatory response has also been explored in the last years, with promising results [5], [9], [10]. However, the underlying mechanisms at the biological level have not been fully understood yet. Moreover, the set-ups used in the state of the art did not guarantee precise control of the dose, a factor that hampers finding a proper and reliable dose/effect correlation [11], [12].

When inflammation is active, macrophages produce a large variety of pro-inflammatory cytokines, such as IL-1β, IL-8 and TNF-α [13]. In this work, we investigated possible anti-inflammatory bioeffects induced by LIPUS and PEMF regimes in terms of possible decrement of pro-inflammatory cytokines and increment of pro-inflammatory cytokines, using two custom-made in vitro stimulation systems, which guaranteed high control of the dose released to the cells.

II. MATERIALS AND METHODS

A. THP-1 cell culture

THP-1 cells (ATCC) were seeded at a density of 10^6 cells/mL on a polystyrene thin film (Goodfellow) stretched and mounted within a CellCrown™ insert (Scaffdex). Cells were kept in growth medium (GM) composed of RPMI (Gibco), supplemented with 10% fetal bovine serum (FBS, Sigma-Aldrich), 100 IU/mL penicillin, 100 µg/mL streptomycin (Sigma-Aldrich) and 0.05 mM of 2-mercaptoethanol (Gibco). Cells were differentiated into an M0 phenotype by adding 100 ng/mL Phorbol 12-myristate 13-acetate (PMA, Sigma-Aldrich) to GM, for 24 hours. To further differentiate M0 into M1 or into M2 phenotypes, PMA was removed and 1 µg/mL Lipopolysaccharide (LPS, Sigma-Aldrich) for 24 hours or 50 ng/mL IL-4 (Sigma-Aldrich) for 24 hours was added to GM, respectively.

B. Study design

Five groups were defined, for both the LIPUS and PEMF experimental sessions: (i) group named "M0", in which macrophages were not treated neither with LPS nor with IL-4 and just cultured in GM for 3 days; (ii) group named "M1", in which macrophages were treated with LPS, then cultured in GM for 3 days; (iii) group named "M2", in which macrophages were treated with IL-4, then cultured in GM for 3 days; (iv) group named "M0+LIPUS" in which M0 macrophages were cultured in GM for 3 days and stimulated with LIPUS; (v) group named "M0+PEMF" in which M0 macrophages were cultured in GM for 3 days and stimulated with PEMF; (vi) group named "M1+LIPUS" in which M1 macrophages were cultured in GM for 3 days and stimulated with LIPUS; (vii) group named "M1+PEMF" in which M1 macrophages were cultured in GM for 3 days and stimulated with PEMF.

C. LIPUS and PEMF set-ups and stimulation protocols

In this work, a highly-controlled LIPUS setup was used [14]. The system guarantees high precision in delivering the ultrasound dose to the cells, in terms of applied parameters, i.e., frequency (F), intensity (I), Duty Cycle (DC), sonication time (T), and pulse repetition frequency (PRF). The LIPUS system is composed of a 5 MHz piezoceramic transducer (Precision Acoustic) and a wave generator (Image Guided Therapy). The PEMF system was provided by BAC Technology s.r.l (Florence, Italy) and consisted of a wave modulator, connected to a generator, able to generate a signal and a polycarbonate retaining system in which cells are placed during the stimulation. The parameters that could be varied were F, DC, T, and PRF. PEMF output I was fixed for the system generator and equal to 0.3 mT. The LIPUS and PEMF setups are depicted in Fig. *1*.

In light of safety considerations and previous studies, for the LIPUS stimulation protocol the parameters applied were: F = 5 MHz, I = 500 mW/cm^2, DC = 20 %, PRF = 1 kHz, and T = 5 min/day for 3 days. For the PEMF stimulation protocol, the parameters applied were F = 13.5 MHz, I = 0.3 mT, DC = 10%, PRF = 20 Hz, and T = 3 h/day for 3 days.

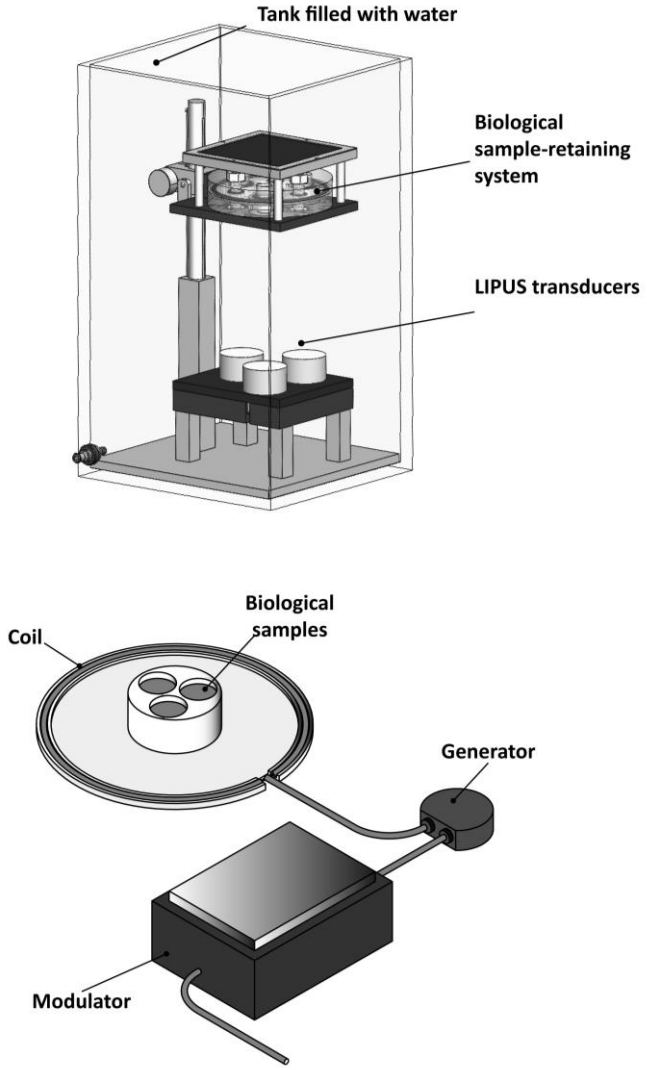


Fig. 1: LIPUS and PEMF set-ups.

D. Real-Time Quantitative Reverse Transcription Polymerase Chain Reaction (qRT-PCR) analysis

Twenty-four hours after the last stimulation, the total RNA was extracted with TRIzol® (Invitrogen) and purified with ReliaPrep™ RNA Miniprep System (Promega). Reverse transcription was performed using PrimeScript™ RT Master Mix (Takara Bio) and Real-Time qRT-PCR using PowerUp™ SYBR™ Green Master Mix (Thermo Fisher) in a Rotor-Gene Q (Qiagen). Relative gene expression of TNF-α, IL-1β, IL-6, IL-8, CD206 and IL-10 were normalized to 18SrRNA, analyzed with the ΔΔC(T) method [15] and expressed as Fold Change with respect to "M0" group for both the experiments.

E. Enzyme-Linked Immunosorbent Assay (ELISA)

Twenty-four hours after the last stimulation, the supernatant was collected and the concentration of TNF-α, IL-1β, IL-6, IL-8 and IL-10 was determined using Human ELISA kits (Invitrogen). The outcome was read in terms of absorbance at 450 nm with a Victor Nivo Multilabel plate reader (PerkinElmer).

III. RESULTS.

A. LIPUS stimulation

The results are represented in Fig. *2* (cytokine release) and Fig. *3* (gene expression). The gene expression of IL-8 decreased in the "M1+LIPUS" group, compared to the "M1" one. For IL-8, the same behavior was observed also at cytokine release level. An increase in IL-10 cytokine release was observed in the "M0+LIPUS" and "M1+LIPUS" groups, with respect to non-stimulated control.

B. PEMF stimulation

The results are shown in Fig. *2* (cytokine release) and Fig. *3* (gene expression). Both the gene expression and cytokine level of IL-1β and IL-8 decrease in the "M1+PEMF" group, compared to the "M1" group. Only for IL-8, a decrease was observed also comparing the "M0+PEMF" with the "M0" group. Moreover, a decrement of TNF-α was observed between the "M1+PEMF" group with respect to the "M1" group, both at gene and cytokine levels. An increase in IL-10 gene expression was observed in the "M0+PEMF" group, with respect to the "M0" group, whereas an increase in the CD206 marker was observed in the "M0+PEMF" group, compared to the "M0" group.

IV. DISCUSSION AND CONCLUSION

When inflammation occurs, ion channels are deeply involved in the activation of intracellular signal cascades and the corresponding production of cytokines. Mechanosensitive and calcium ion channels have been shown to be activated by ultrasound [16] and electromagnetic fields [17], respectively. This may be the reason for the beneficial results obtained, by applying LIPUS and PEMF stimulation protocols. The results of this work could constitute the ground for future studies, in which the underlying mechanisms of such a cell response could be investigated. Furthermore, LIPUS and PEMF treatments, thanks to their inherent safety, can be easily translated in vivo for the treatment of many diseases in which inflammation plays a key role.

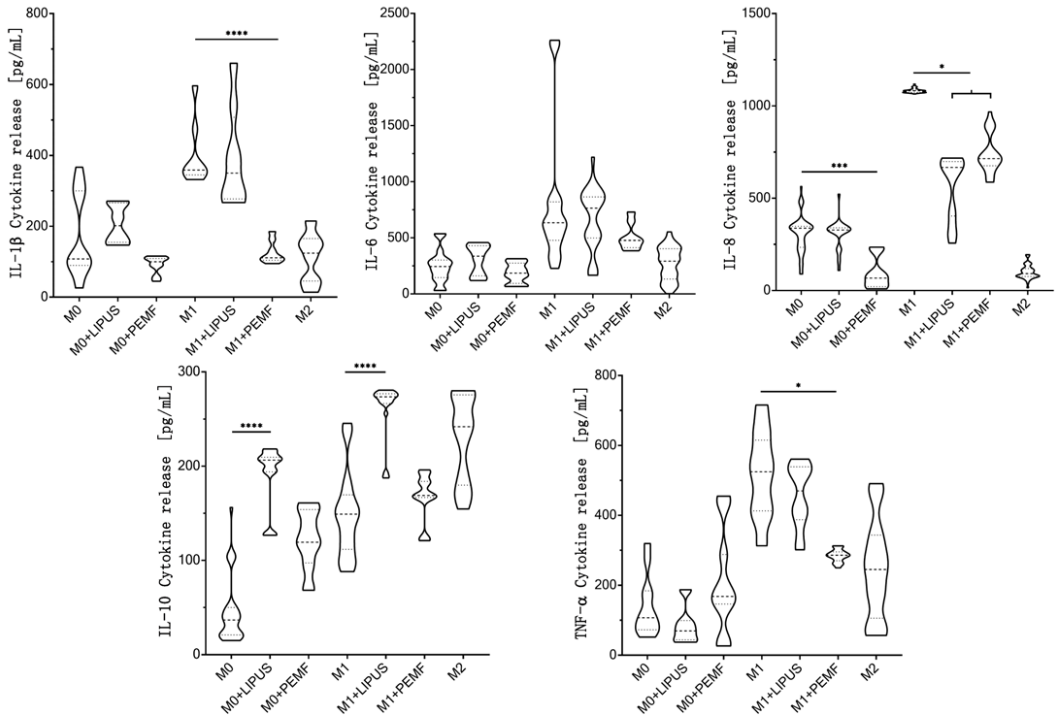


Fig. 2: Cytokine release of pro-inflammatory markers (IL-1β, IL-6, IL-8, TNF-α) and anti-inflammatory marker (IL-10), after LIPUS or PEMF stimulation. Only statistical differences between the "M0" groups and between the "M1" groups are reported. Kruskal-Wallis was applied, followed by Dunn's post-hoc test (GraphPad Prism 8); * = $p < 0.05$; ** = $p < 0.01$; *** = $p < 0.001$; **** = $p < 0.0001$. (N = 3)

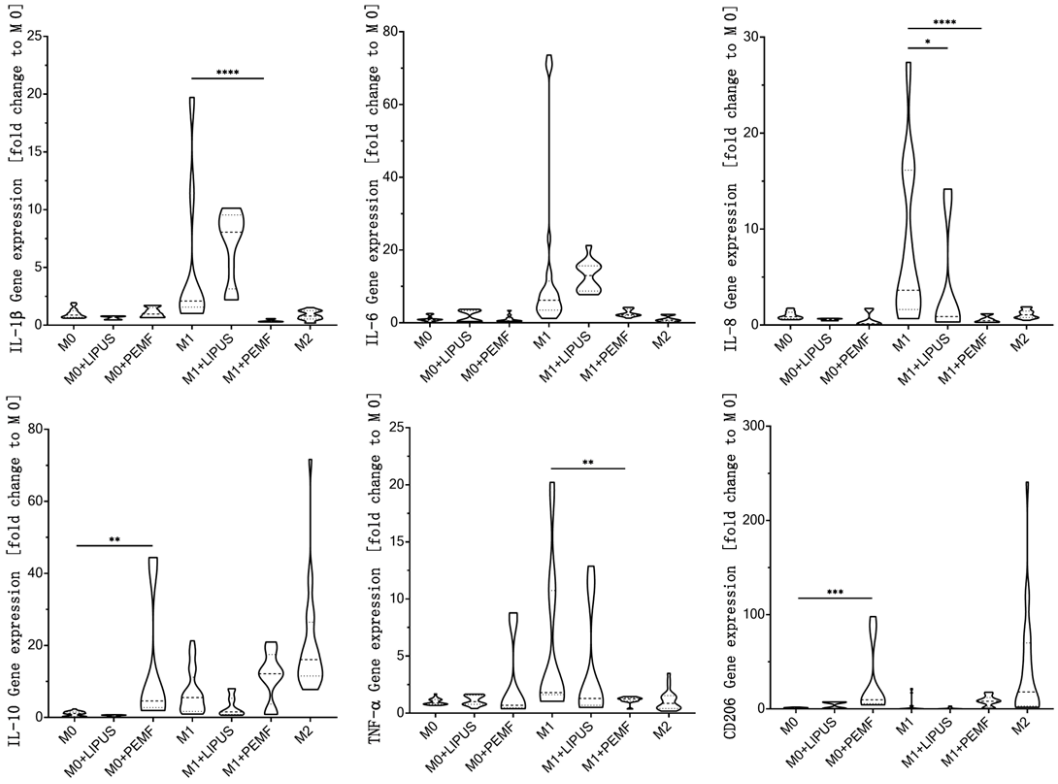


Fig. 3: Gene expression of pro-inflammatory markers (IL-1β, IL-6, IL-8, TNF-α) and anti-inflammatory markers (IL-10, CD206), after LIPUS or PEMF stimulation. Only statistical differences between the "M0" groups and between the "M1" groups are reported. Kruskal-Wallis was applied, followed by Dunn's post-hoc test (GraphPad Prism 8); * = $p < 0.05$; ** = $p < 0.01$; *** = $p < 0.001$; **** = $p < 0.0001$. (N = 3)

ACKNOWLEDGEMENT

This work received funding from the European Union's Horizon 2020 research and innovation program, grant agreement No 814413, project ADMAIORA (ADvanced nanocomposite MAterIals fOr in situ treatment and ultRAsound-mediated management of osteoarthritis). It also received support from the "UltraHeal" Project, in collaboration with BAC Technology s.r.l. (Florence, Italy).

REFERENCES

[1] D. Furman *et al.*, "Chronic inflammation in the etiology of disease across the life span," *Nat. Med.*, vol. 25, no. 12, 2019.

[2] T. J. Atkinson and J. Fudin, "Nonsteroidal Antiinflammatory Drugs for Acute and Chronic Pain," *Phys. Med. Rehabil. Clin. N. Am.*, vol. 31, no. 2, 2020.

[3] U. Farkash, O. Bain, A. Gam, M. Nyska, and P. Sagiv, "Low-intensity pulsed ultrasound for treating delayed union scaphoid fractures: Case series," *J. Orthop. Surg. Res.*, vol. 10, no. 1, pp. 1–7, 2015.

[4] A. Khanna, R. T. C. Nelmes, N. Gougoulias, N. Maffulli, and J. Gray, "The effects of LIPUS on soft-tissue healing: A review of literature," *Br. Med. Bull.*, vol. 89, no. 1, pp. 169–182, 2009.

[5] J. S. Gaynor, S. Hagberg, and B. T. Gurfein, "Veterinary applications of pulsed electromagnetic field therapy," *Res. Vet. Sci.*, vol. 119, pp. 1–8, 2018.

[6] R. Lekhraj, D. E. Cynamon, S. E. Deluca, E. S. Taub, A. A. Pilla, and D. Casper, "Pulsed electromagnetic fields potentiate neurite outgrowth in the dopaminergic MN9D cell line," *J. Neurosci. Res.*, vol. 92, no. 6, pp. 761–771, 2014.

[7] C. Rubin, M. Bolander, J. P. Ryaby, and M. Hadjiargyrou, "The use of low-intensity ultrasound to accelerate the healing of fractures," *J. Bone Jt. Surg. - Ser. A*, vol. 83, no. 2, pp. 259–270, 2001.

[8] M. S. Markov, "Expanding use of pulsed electromagnetic field therapies," *Electromagn. Biol. Med.*, vol. 26, no. 3, pp. 257–274, 2007.

[9] M. Xu *et al.*, "Review on experimental study and clinical application of low-intensity pulsed ultrasound in inflammation," *Quant. Imaging Med. Surg.*, vol. 11, no. 1, pp. 443–462, 2021.

[10] W. S. Su, C. H. Wu, S. F. Chen, and F. Y. Yang, "Low-intensity pulsed ultrasound improves behavioral and histological outcomes after experimental traumatic brain injury," *Sci. Rep.*, vol. 7, pp. 1–10, 2017.

[11] J. J. Leskinen and K. Hynynen, "Study of Factors Affecting the Magnitude and Nature of Ultrasound Exposure with In Vitro Set-Ups," *Ultrasound Med. Biol.*, vol. 38, no. 5, 2012.

[12] H. Hu *et al.*, "Promising application of Pulsed Electromagnetic Fields (PEMFs) in musculoskeletal disorders," *Biomed. Pharmacother.*, vol. 131, p. 110767, 2020.

[13] K. Y. Lee, "M1 and M2 polarization of macrophages: a mini-review," *Med. Biol. Sci. Eng.*, vol. 2, no. 1, pp. 1–5, 2019.

[14] F. Fontana *et al.*, "Development and Validation of Low-Intensity Pulsed Ultrasound Systems for Highly Controlled in vitro Cell Stimulation," *Ultrasonics*, vol. 15, no. 116, p. 106495, 2021.

[15] K. J. Livak and T. D. Schmittgen, "Analysis of relative gene expression data using real-time quantitative PCR and the 2-ΔΔCT method," *Methods*, vol. 25, no. 4, pp. 402–408, 2001.

[16] A. G. Solis *et al.*, "Mechanosensation of cyclical force by PIEZO1 is essential for innate immunity," *Nature*, vol. 573, no. 7772, pp. 69–74, 2019.

[17] L. Cristiano and T. Pratellesi, "Mechanisms of Action And Effects of Pulsed Electromagnetic Fields (PEMF) in Medicine," *J. Med. Res. Surg.*, vol. 1, no. 6, pp. 1–4, 2020.

Hydrogels scaffolds as 2D in vitro models to explore the impact of microenvironmental stiffness on lung adenocarcinoma cells

V. Panzetta[1,2,3], C. Frascogna[1,3], C. Mazio[2,3], F. Catuogno[1,3], G. Imparato[3], F. Urciuolo[1,2,3] and P.A. Netti[1,2,3]

[1] *Dipartimento di Ingegneria Chimica, dei Materiali e della Produzione Industriale, Università degli Studi di Napoli Federico II, 80125 Napoli, Italy*
[2] *Centro di Ricerca Interdipartimentale sui Biomateriali, Università degli Studi di Napoli Federico II, 80125 Napoli, Italy*
[3] *Centre for Advanced Biomaterial for Health Care, Istituto Italiano di Tecnologia, 80125 Napoli, Italy*

***Abstract*—Mechanobiology aims at disclosing the functions and mechanisms by which mechanical, and architectural signals of the tissue microenvironment, control cell behaviors and cell states. Alteration in cellular mechanoperception and responsiveness is now recognized at the roots of cancer, and this is particularly well-appreciated in the context of lung adenocarcinoma. Here, adopting cutting-edge techniques from materials science, the different mechanical properties of microenvironment were precisely tuned within 2D polyacrylamide platforms over a range of pathophysiological stiffness (0.2–20 kPa). A first biophysical characterization of the effects of these platforms on normal (BEAS-2B) and tumoral lung epithelial cells (NCI-H23 and NCI-H1573) was performed. It emerged that cell ability to respond to substrate stiffness by regulating their adhesion and mechanical properties was progressively reduced with increasing cell tumorigenic potentials from BEAS-2B to NCI-H23 and metastatic NCI-H1573. Surprisingly, cell migration was less affected by both substrate stiffnesses and cell tumorigenicity, when analyzed in terms of cell speed. However, cell directionality, a parameter that describes cell ability to migrate in a persistent way without changing direction and then, to reach distant sites, was significantly increased in metastatic lung cells. This preliminary work lays the foundation for exploiting the behavior of lung adenocarcinoma cells in relationship to their mechanical microenvironment and unveil its potentiality as a diagnostic and/or prognostic and /or therapeutic.**

***Keywords*—Mechanobiology, Lung Adenocarcinoma, ECM stiffness, Cell Mechanics.**

I. Introduction

In the context of cancer mechanobiology, a large body of knowledge is continuously growing providing comprehension of the mechanical role of the local microenvironment as a cooperator of tumor cells in tumor onset and progression [1,2]. It is now widely appreciated that, during tumor growth, morpho-physical features of both cells and their neighborhood extracellular matrix (ECM) are altered, and these alterations result into a departure from the homeostatic cell-ECM mechanical equilibrium towards a new status characterized by an increased stiffness of the cell microenvironment. The tissues affected by malignant tumors are, in fact, characterized by ECM accumulation, that leads to a severe fibrotic response, known as desmoplasia, and consequent tumor stiffening [3]. Furthermore, the stiffening process occurring at the ECM level promotes the invasive nature of different tumor cells through the activation of specific molecular pathways and the mechanical transformation of tumor cells [4]. The lung adenocarcinoma, which is the most common histologic subtype of lung cancer in men and women [5], recapitulates the typical physical and mechanical properties of solid tumors: tumor cells undergo a softening process although residing in a stiffer matrix [6]. In fact, an altered ECM cross-linking has been found within lung cancer, where high laminin-5 expression and Lysyl oxidase-mediated collagen crosslinking correlated with lung cancer invasiveness [7]. All these aspects enlighten the pivotal role of the mechanical microenvironment in mediating tumor cell transformation and call for a systematic analysis to disclose the collaborative and synergistic interaction between cells and ECM in lung adenocarcinoma.

This can be performed by evaluating what happens in terms of biophysical and mechanical cell transformation, when lung cells with different oncogenic and tumorigenic potentials interact with highly controlled mechanical microenvironments. For this purpose, tissue engineering offers very advanced technological strategies to develop in vitro microenvironments with precisely incorporated topographical, biochemical, and mechanical cues. Specifically, hydrogels are considered crucial biomaterials in the field of tissue engineering since their mechanical properties (or stiffness) can be accurately tuned to replicate a variety of different human tissues, both in physiological and pathological conditions [8]. Here, epithelial cells of normal human lung (BEAS-2B cell line), and two mutant cell lines, the first one derived from a primary lung adenocarcinoma (NCI-H23) and the second one from a soft tissue metastasis of a stage 4 lung adenocarcinoma (NCI-H1573) were plated in sparse culture condition on soft (~0.2 kPa) and stiff (~24 kPa) polyacrylamide substrates which corresponds to the stiffnesses of normal and tumor tissues, respectively [9], and characterized in terms of adhesion, migration capability and mechanical properties.

II. Materials and methods

A. Preparation of substrates for cell culture

Polyacrylamide substrates were prepared as previously described [10] by using two solutions of acrylamide and methylene-bis-acrylamide (2.5% acrylamide/0.15% methylene-bis-acrylamide and 10% acrylamide/0.1% methylene-bis-acrylamide corresponding to 0.2 and 24 kPa,

respectively). Briefly, glass-bottom culture dishes (WillCo Wells, HBST-3522) were treated with 3-aminopropyltriethoxysilane (Sigma-Aldrich, St. Louis, MO, USA) for 10 min and the activated with 0.5% glutaraldehyde for 10 min. Polymerization of acrylamide/methylene-bis-acrylamide solutions was initiated by adding 1/100 total volume of 10% ammonium persulfate and 1/1000 total volume N,N,N′,N′-tetramethylethylenediamide (TEMED, Sigma-Aldrich, T7024, St. Louis, MO, USA). Twenty-five microliters of acrylamide/methylene-bis-acrylamide solutions were pipetted on the functionalized dishes and covered with a 20-mm coverslip. After 20 min, the coverslip was removed and PBS was added to the dish. To allow for cell adhesion, substrates were functionalized with ECM proteins. Briefly, the polyacrylamide was activated by covering the substrates with 0.5 mg/ml sulfo-SANPAH (Sigma,22589) in double-distilled water and exposing to 365 nm UV light for 6 minutes. The process was repeated once with a fresh aliquot of sulfo-SANPAH before substrate washing with 1× phosphate buffer saline (PBS, Microgem L0615) to remove unreacted reagent. Then, the hydrogels were coated with 30 µg/ml collagen solution from bovine skin (Sigma, C4243), 10 µg/ml fibronectin (Sigma, F0895) and 10 µg/ml bovine serum albumin (BSA, Sigma, A3059) and incubated at 37 °C for 3 hours before cell culturing.

B. Cell culture

BEAS-2B were cultured in BEBM Bronchial Epithelial Cell Growth Basal Medium (Lonza, CC-3171) complemented with the related growth factors and supplements (Lonza, CC-4175). NCI-H23 and NCI-H1573 were cultured in HiGlutaXL (TM) RPMI-1640 (Microgem, AL028G) supplemented with 10% fetal bovine serum (FBS, Sigma F7524), 1000 U/L penicillin and 100 mg/l streptomycin (Sigma, P4333). They were cultured at 37 °C in 5% CO2 in a humidified incubator.

C. Cell adhesion analysis

Cells were fixed and immunostained to evaluate the spreading area at 24 h from seeding. They were washed in PBS, fixed in 4% paraformaldehyde (Sigma Aldrich, 158127) for 15 min, and then rinsed three times with PBS and permeabilized in 0.1% Triton X-100 (Sigma-Aldrich) for 15 min. Cells were washed twice in PBS and blocked for 1 h and 30 min in 3% BSA. After washing in PBS, cells were incubated with Alexa 488 phalloidin (Invitrogen, A12379) at a dilution of 1:200 in PBS for 1 h and 30 min. Then, to facilitate cell recognition, nuclei were stained with Hoechst 33342 (ThermoFisher, 62249), at a dilution of 1:1000 in PBS for 15 min.

Specimens were imaged using an inverted microscope system (Multiphoton microscope, Leica) equipped with a 20× objective. The images were imported into ImageJ software (NIH, USA) for postprocessing and analysis. Individual cells were manually outlined, and their spreading areas were determined. At least 50 cells were analysed for each condition.

D. Cell mechanical properties

The cell mechanical properties were probed with a commercial atomic force microscope (AFM, Nanowizard II, JPK Instruments, Germany) as previously described [10]. At least 5 square arrays of 8 × 8 indentations, covering (2 × 2) µm^2 areas of cells were performed to quantify cell stiffness (Young's modulus).

E. Cell motility

To explore cell dynamics, migration experiments were performed using time-lapse microscopy (STED Leica inverted microscope with 10× objective and integrated stage incubator). The images were acquired at 10-minute intervals for 24 hours. The trajectories of individual cells were analysed using the software Fiji (NIH, Bethesda, MD, USA). The average cell speed was calculated as the path length divided by time and the cell directionality as the straight-line length between the start point and the endpoint of the migration trajectory, divided by the length of the trajectory. At least 40 cells were analysed for each condition.

F. Statistical analysis

Statistical comparisons were performed with a Student's unpaired test when data exhibit a normal distribution. Otherwise, a nonparametric Kruskal–Wallis test followed by post-hoc Dunn's test was used and the *p*-value is indicated (*$p < 0.05$, **$p < 0.01$, ***$p < 0.001$).

III. Results and Discussion

A. Cell Adhesion

A large body of literature has accumulated showing the relationship between ECM mechanical properties and cell adhesion. To evaluate the ability of all three cell lines to mechano-sense the external microenvironment, their adhesion was analysed in terms of cell spreading area on soft and stiff substrates (Fig. 1).

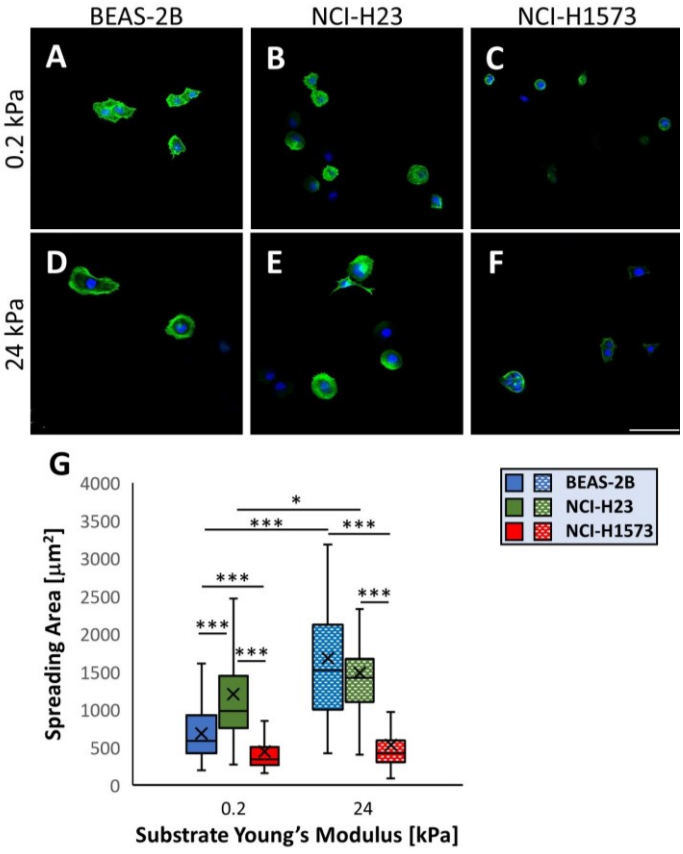


Fig. 1: Representative images of BEAS-2B (A, D), NCI-H23 (B, E) and

NCI-H1573 (C, F) cultured on soft, i.e., 0.2 kPa (A-C), and stiff, i.e., 24 kPa (D-F), are shown. Box plots (mean, median, and interquartile range) of spreading areas (G). Scale bar, 100 µm.

All three cell lines showed a cell spreading area positively correlated with substrates stiffnesses, except the metastatic cell line, i.e., NCI-H1573. Furthermore, NCI-H23 cells exhibited a higher spreading area than that of BEAS-2B on the soft substrate, whereas this behavior was reversed on the stiff one. A similar behavior has been observed in KRAS-mutated breast cancer cells (MDA-MB-231) characterized by greater and mature focal adhesion complexes when cultured in 1 kPa polyacrylamide substrates [10]. The most aggressive cell line (NCI-H1573) exhibited a significantly reduced adhesiveness on both soft and stiff substrates, indicating an impaired mechanosensory machinery.

B. Cell mechanics

A broad spectrum of works has demonstrated that the intimate association between substrate stiffness and cell morphology is mediated by adhesive structures formed in the plasma membrane, which connect the external ECM to the actin cytoskeleton. These structures can mature into larger structures called focal adhesions only when internally supported by the formation of contractile actin cables (stress fibers) which foster the cell spreading in a proportional way to their tensional state [11].

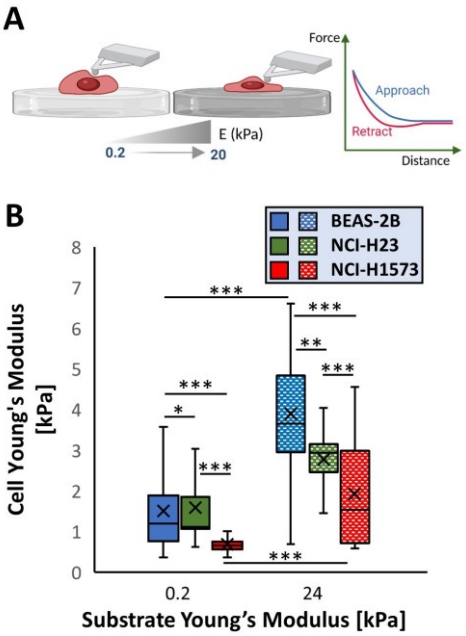


Fig. 2: Measuring the mechanical properties of cells cultured on substrates with different stiffnesses by AFM. Spherical AFM probe (6 µm-diameter) were used to squeeze the cortex filaments by applying 100 nm-indentation depths (A, left). Schematic diagrams of a force curve used to calculate cell mechanical properties (i.e., Young's modulus, A, right). Box plots (mean, median, and interquartile range) of cell Young's modulus (B).

Considering the differences in terms of cell adhesion among the three cell lines (Fig. 1), it is easy to figure that the actin cytoskeleton could be differently structured impacting on their mechanical properties. To validate this hypothesis, the AFM technique was used to investigate in which way changes in the oncogenic potential and substrate stiffness affected the elastic modulus of all cells (Fig. 2A). As expected, the cell Young's modulus positively correlates with the spreading area. Specifically, (1) a positive correlation between polyacrylamide stiffness and cell Young's modulus was found in all three cell lines, and, as reported for many other cell lines [6,10,12-14], (2) cell deformability directly correlates with the progression of a transformed phenotype form benign (BEAS-2B), tumor (NCI-H23) and metastatic cells (NCI-H1573, Fig. 2B).

C. Cell migration

The migration capability of BEAS-2B, NHI-H23, and NCI-H1573 cells in response to substrate stiffness was evaluated by computing two parameters: the average cell speed over a 24-h period and the cell directionality (Fig. 3).

As shown in Fig. 3A, NCI-H23 cells exhibited the lowest speed compared to the other two cell lines which resulted to move at similar average speed. Furthermore, all the three cell lines exhibited a cell speed which reduced with substrate stiffness, even if not in a significant way expect. This result can be explained by considering that substrate stiffness affects cell adhesion and mechanics and, probably, focal adhesion dynamics. Cell migration is, in fact, a process regulated by repeated cycles of adhesion to and de-adhesion from the ECM whose duration directly depends on focal adhesion dimensions: greater focal adhesions, generally associated to greater level of adhesion and stiffer cytoskeleton (as happens on stiff substrates), are characterized by longer life cycles which slow down the cell migration velocity [15].

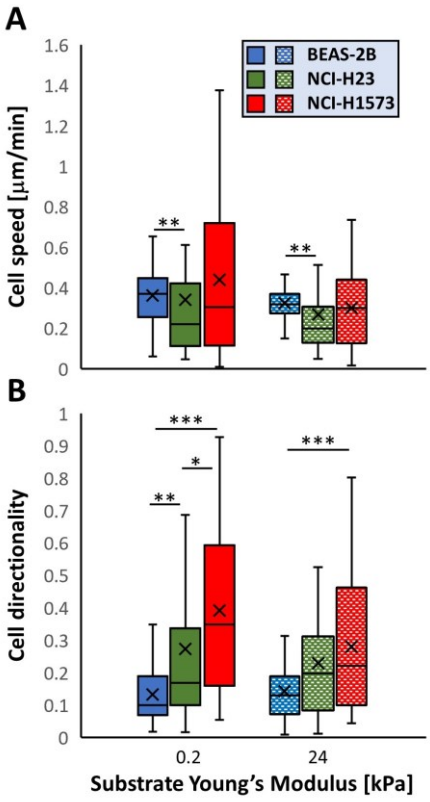


Fig. 3: Box plots (mean, median, and interquartile range) of cell speed (A) and cell directionality (B).

However, it is interesting to notice that the spread of cell speed in the data set of NCI-H1573 (see box plots in Fig. 3) is significantly larger compared to BEAS-2B and NCI-H23, because of a very inhomogeneous behavior with highly dynamic cells and other unable to move. On one side, the high cell dynamics can be explained by the increased level of focal adhesion kinase (FAK, a nonreceptor tyrosine kinase which regulates the disassembly process of focal adhesions) exhibited by some tumor cells [16]; on the other side, when the cell adhesion strength is very low (i.e., cell cytoskeleton is made by disorganized and not well-structured actin filament bundles), the contractile stress of the acto-myosin cytoskeleton is not sufficient to retract the trailing edge and to protrude forward the leading edge (i.e., cell migration is absent). Additional investigations will be performed to ascertain these hypotheses. It is important to underline that all the experiments on NCI-H23 and NCI-H1573, included migration, were performed in low-glucose conditions, even if ATCC recommends the use of high-glucose media. Further experiments will be conducted to evaluate the influence of the glucose concentration on cell functions and migration.

Another relevant parameter which describes the efficiency of cell migration is the directional persistence, here calculated as cell directionality. This parameter is the ratio between the start point-endpoint distance and the total length of cell trajectory. Values close to 0 indicate curved trajectories, whereas when the directionality approaches to 1, the trajectories are straight lines. What emerged from the experimental results was that cell directionality increased significantly with cell tumorigenic potential, whereas no substantial differences were found on soft and stiff substrates. This finding, in agreement with previous study performed on other tumor cells [10,17], indicates the natural propensity of metastatic tumor cells to move directionally.

IV. Conclusion

The stiffened tumor mechanical microenvironment of lung adenocarcinoma results to be involved in very important pathways associated with the cell malignant transformation. Notably, lung adenocarcinoma undergoes to an asymmetric mechanical modification of ECM and cell components: a lysyl oxidase-mediated collagen cross-linking engenders a stiffened ECM, whereas the mechanical properties of lung cancer cells result to be reduced in comparison with those of normal lung cells. It is worth considering that both modifications are correlated with stages of tumor development and seem to constitute conspicuous regulator factors of cancer invasiveness. Here, a first and preliminary analysis of the correlation between tumor ECM and oncogenic cell state has been proposed. Future investigations are needed to evaluate how the biophysical and mechanical properties of lung cells with different oncogenic and tumorigenic potentials and interacting with highly controlled mechanical microenvironments, are correlated with biomolecular pathways and, specifically with the activation of the epithelial-mesenchymal transition and the triggering of Hippo-YAP/TAZ signaling pathway.

Acknowledgement

This work was supported by a grant from “University of Naples Federico II” and “Fondazione Compagnia di San Paolo”: “Tumor Mechanoscore as a Tool for Novel Mechanodiagnostic and Mechanotherapy Approaches” (Project N. D 21-UNINA-EPIG-135).

References

[1] Joyce, Johanna A., and Jeffrey W. Pollard. "Microenvironmental regulation of metastasis." Nature reviews cancer 9.4: 239-252,2009.
[2] Swartz, Melody A., and Amanda W. Lund. "Lymphatic and interstitial flow in the tumour microenvironment: linking mechanobiology with immunity." Nature Reviews Cancer 12.3: 210-219, 2012.
[3] Travis, William D., et al. "International association for the study of lung cancer/american thoracic society/european respiratory society international multidisciplinary classification of lung adenocarcinoma." Journal of thoracic oncology 6.2: 244-285, 2011.
[4] Panciera, Tito, et al. "Reprogramming normal cells into tumour precursors requires ECM stiffness and oncogene-mediated changes of cell mechanical properties." Nature materials 19.7: 797- 806,2020.
[5] Travis, William D., et al. "International association for the study of lung cancer/american thoracic society/european respiratory society international multidisciplinary classification of lung adenocarcinoma." Journal of thoracic oncology 6.2: 244-285,2011.
[6] Panzetta, Valeria, et al. "Mechanical phenotyping of cells and extracellular matrix as grade and stage markers of lung tumor tissues." Acta biomaterialia 57: 334-341,2017.
[7] Wood, Steven L., et al. "The role of the tumor-microenvironment in lung cancer-metastasis and its relationship to potential therapeutic targets." Cancer treatment reviews 40.4: 558-566,2014.
[8] Vedadghavami, Armin, et al. "Manufacturing of hydrogel biomaterials with controlled mechanical properties for tissue engineering applications." Acta biomaterialia 62: 42-63, 2017.
[9] Liu F, Mih JD, Shea BS, Kho AT, Sharif AS, Tager AM, TschumperlinDJ. Feedback amplification of fibrosis through matrix stiffening andcox-2 suppression. J Cell Biol;190:693–706, 2010
[10] Panzetta, Valeria, et al. "Adhesion and migration response to radiation therapy of mammary epithelial and adenocarcinoma cells interacting with different stiffness substrates." Cancers 12.5: 1170, 2020.
[11] Chamaraux, F., et al. "Kinetics of cell spreading." Physical review letters 94.15: 158102., 2005.
[12] Li, Q. S., et al. "AFM indentation study of breast cancer cells." Biochemical and biophysical research communications 374.4: 609-613, 2008.
[13] Ketene, Alperen N., et al. "The effects of cancer progression on the viscoelasticity of ovarian cell cytoskeleton structures." Nanomedicine: Nanotechnology, Biology and Medicine 8: 93-102, 2012
[14] Panzetta, Valeria, et al. "ECM Mechanoregulation in Malignant Pleural Mesothelioma." Frontiers in Bioengineering and Biotechnology 10: 797900, 2022.
[15] Fusco, Sabato, Valeria Panzetta, and Paolo A. Netti. "Mechanosensing of substrate stiffness regulates focal adhesions dynamics in cell." Meccanica 52: 3389-3398, 2017.
[16] Provenzano, P.P.; Inman, D.R.; Eliceiri, K.W.; Keely, P.J. Matrix density-induced mechanoregulation of breast cell phenotype, signaling and gene expression through a FAK–ERK linkage. Oncogene, 28, 4326–4343, 2009.
[17] Levental, K.R.; Yu, H.; Kass, L.; Lakins, J.N.; Egeblad, M.; Erler, J.T.; Fong, S.F.; Csiszar, K.; Giaccia, A.; Weninger, W.; et al. Matrix crosslinking forces tumor progression by enhancing integrin signaling. Cell, 139, 891–906, 2009.

A microfluidic platform to unravel immune cells cross-talk in rheumatoid arthritis

C. Palma[1], B. Aterini[1], C. Catozzi[2], L. Nezi[2], Lopa S.[3], T. Manzo[2], M. Rasponi[1], P. Occhetta[1]
[1] *Department of Electronics, Information and Bioengineering, Politecnico di Milano, Milan, Italy*
[2] *Department of Experimental Oncology, European Institute of Oncology IRCCS, Milan, Italy*
[3] *IRCCS Istituto Ortopedico Galeazzi, Cell and Tissue Engineering Laboratory, Milan, Italy*

***Abstract*—Rheumatoid arthritis (RA) is a chronic, inflammatory autoimmune disease that can cause irreversible joint damage and significant disability. Joint inflammation in RA is closely related to infiltration of immune cells, among which circulating T-cells and synovial resident macrophages play a critical role. Thus, including immune system in in vitro models is of crucial importance to better understand RA pathogenesis. Here, we developed a novel 3D microfluidic platform aimed at evaluating the active role of immune cells involved in RA. In particular, the platform was used to study spontaneous migration of Th1 T-cells towards pro-inflammatory M1 macrophages, thanks to the insertion of specific valves mechanism, allowing the trapping of immune cells inside the device and the stimulation of different cell types separately.**

***Keywords*—rheumatoid arthritis, immune cells, organ-on-chip, microfluidic valves.**

I. Introduction

RHEUMATOID arthritis (RA) is a chronic autoimmune disease involving diarthrodial joints that seriously affects human health [1], whose hallmark is an uncontrolled systemic inflammatory response that first undermines the synovium and progressively leads to articular joint damage, with severe joint swelling and pain [2]. In detail, joint inflammation in RA is closely related to the disruption of signalling networks and to the involvement of multiple immune cell types, among which synovial resident macrophages and circulating T-cells are considered key players [3]. However, the exact mechanism of RA development is still unknown, and it is well established that none of the currently available animal models fully represents human onset and progression [4], [5]. In this scenario, organs-on-chip offers a valuable solution to evaluate *in vitro* the involvement and the interaction of different cell types in RA conditions, and to assess patient-specific differences. To this end, we developed a novel microfluidic platform allowing to study the active role of immune cells involved in RA, initially aiming at validating a known mechanism in RA, characterized by the migration of Th1 T-cells towards pro-inflammatory macrophages [6], [7].

II. Materials and Methods

The proposed microfluidic platform (Fig. 1a) is realized through replica molding procedure and is composed of three PDMS layers: a top layer hosting valves mechanisms, a culture chamber layer, and a bottom unpatterned membrane (Fig. 1b). In detail, the culture chamber layer comprises two separate culture areas, whose communication is controlled through normally closed curtain valves (Fig. 1c). The first compartment, named *3D chamber*, is intended to host cells seeded in a 3D matrix, e.g. synovial resident macrophages, and is made of a central gel channel separated by two rows of post from two lateral medium channels. The second compartment, named *sieving valve chamber*, is composed of a single channel and is designed to precisely locate and culture cells in suspension, e.g. T-cells.

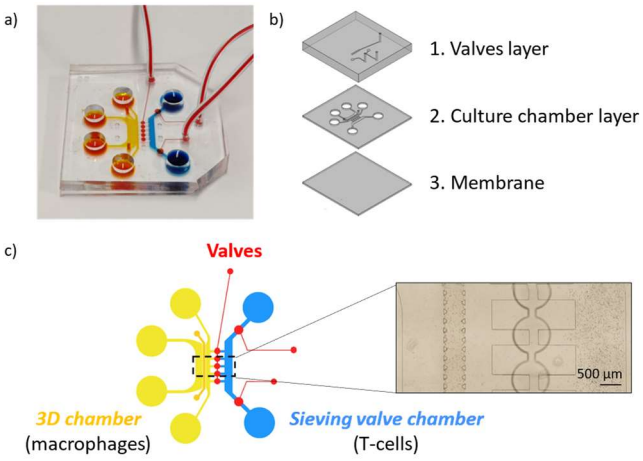


Fig. 1: a) Assembled microfluidic device; b) PDMS layers; c) Layout of the microfluidic device, with brightfield image of the two culture compartments.

The sieving valve chamber encompasses a novel technology, named *sieving valves*, which relies on normally closed curtain valves with underneath microgrooves that at rest allow the perfusion of fluids, but impair cell escaping, while once opened permit cell seeding and retrieval (Fig. 2).

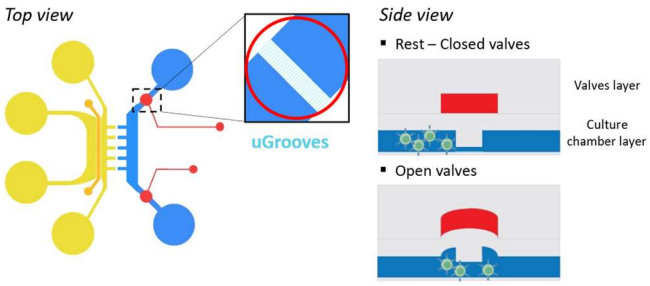


Fig. 2: Schematic of the *sieving valves* and their working mechanism.

After design and fabrication, the microfluidic platform was technically characterized. Firstly, sieving valves working mechanism was evaluated by using spherical polystyrene beads to mimic cell seeding in the *sieving valve chamber* with open sieving valves, as well as to assess proper cell trapping upon valves closure. Fluid perfusion over time through microgrooves with closed sieving valves was evaluated using color dyes. Moreover, this set-up was used to monitor beads behaviour upon central valves opening, in order to verify that

beads were not moving towards the *3D chamber* compartment due to convection given by the opening. Finally, FITC-dextran was used to assess proper communication between the two compartments with open communication valves, as well as the possibility to generate a concentration gradient from the *3D chamber* to the *sieving valve chamber*. In detail, the central channel of the *3D chamber* was filled with fibrin gel, and 4 kDa FITC-dextran was injected in the outermost medium channel. FITC-dextran diffusion towards the *sieving valve chamber* with open communication valves was then assessed through quantification of fluorescence intensity over time along the width of the culture chamber layer (Fig. 3).

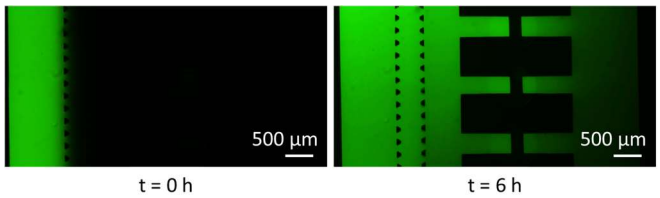


Fig. 3: Fluorescence microscope images showing FITC-dextran diffusion over time.

To carry out the biological experiments, after isolation by magnetic cell separation from human buffy coat, CD14+ monocytes were pre-cultured in flask for 5 days with MCSF (20 ng/ml), in order to let them differentiate into macrophages. Then, they were seeded into the *3D chamber* embedded in a fibrin gel (i.e., 10 mg/ml of fibrinogen and 2.5 U/ml of thrombin) at a final cell density of 12,5 x 10^6 cells/ml, and culture conditions were optimized to induce a pro-inflammatory M1 phenotype. Specifically, culture medium was supplemented with 100 ng/ml IFN-γ and 100 ng/ml TNF-α for three days, and proper macrophage polarization was assessed at day 3 and at day 4 through immunofluorescence analysis of M1 markers (e.g. CD80, CD86) and of CXCL16, i.e. a protein relevant in RA mechanisms [8].

A protocol was then optimized to induce T-cells differentiation towards Th1 phenotype. Naïve CD4+ T-cells isolated from human buffy coat were seeded in the *sieving valve chamber,* taking advantage of the novel technology, and stimulated for three days with 2 µg/ml anti-CD3, 2 ng/ml IL-12 and 5 µg/ml anti-IL-4. T-cells polarization was evaluated through flow cytometry analysis of intracellular cytokines (i.e. IFN-γ), as well as through immunofluorescence staining of transmembrane markers, e.g. CXCR6 [8].

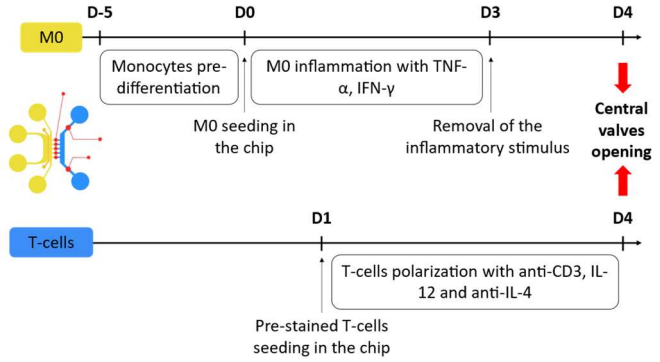


Fig. 4: Schematic of the experimental plan to assess Th1 T-cells migration towards M1 macrophages inside the microfluidic platform.

Finally, an experiment was carried out to study the interaction between pro-inflammatory macrophages and Th1 T-cells. Briefly, human monocytes-derived macrophages (M0) embedded in fibrin gel were seeded at day 0 in the *3D chamber* and stimulated with TNF-α, IFN-γ for 72 hours to induce polarization towards M1. At day 3, the inflammatory stimulus was removed. CD4+ T-cells were stained with CellTracker™ Green CMFDA (Invitrogen), seeded in the *sieving valve chamber* at day 1, and stimulated with anti-CD3, IL-12 and anti-IL-4 until day 4. On day 4, recruitment of Th1 T-cells operated by M1 macrophages upon central valve opening was evaluated. The experimental plan is summarized in Fig. 4.

III. RESULTS

Technical characterization with polystyrene beads proved the necessity to include sieving valves to trap cells in suspension inside the platform. After seeding beads in the *sieving valve chamber* with open sieving valves, a blue dye was inserted in the medium reservoirs. With open sieving valves, i.e. simulating the absence of sieving valves, all the beads were immediately flushed away. On the other hand, with closed sieving valves, beads remained confined in the *sieving valve chamber*, and a slow but sustained perfusion of dye through the microgrooves was detected over time (Fig. 5a). Moreover, specific tests confirmed that beads migration does not occur just upon central valves opening, while slow diffusion of the color dye could be observed.

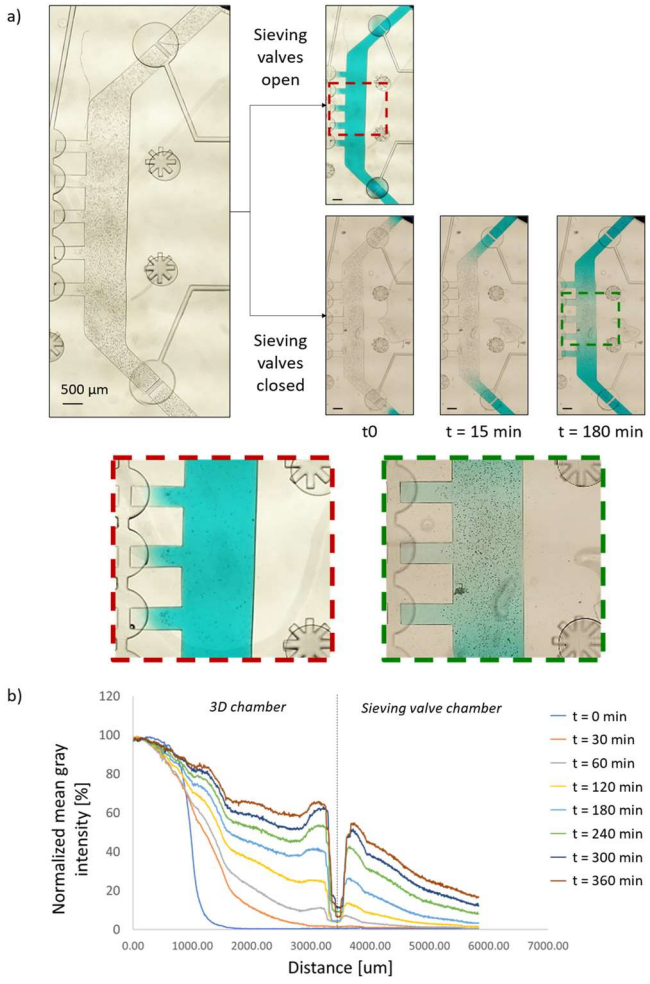


Fig. 5: Technical validation of the platform. a) Characterization of sieving valves working mechanism by using polystyrene beads and color dye. b) Quantification of dextran diffusion from the 3D chamber towards the sieving valve chamber at different time-points.

Results of the FITC-dextran diffusion tests demonstrated that the two culture compartments were in proper communication with open central valves, and that a FITC-dextran gradient was created from *3D chamber* to *sieving valve chamber* and was maintained up to 6 hours (Fig. 5b), confirming that this device can be used to recapitulate a concentration gradient to induce cells migration towards an appropriate chemotactic stimulus.
As proven by immunofluorescence staining (Fig. 6) of M1 marker CD80, macrophages polarized to a pro-inflammatory state after three days of inflammatory stimuli inside the platform. Moreover, an increase in the secretion of CXCL16 was detected. Importantly, these results were maintained also at day 4, i.e. one day after having removed the inflammatory stimulus. This indicates that the pro-inflammatory phenotype is stable, and in a complete experiment it gives the possibility to open the central valves at day 4, having removed from the culture medium cytokines (i.e. TNF-α, IFN-γ) that could mask the effect of proteins directly secreted from the macrophages.

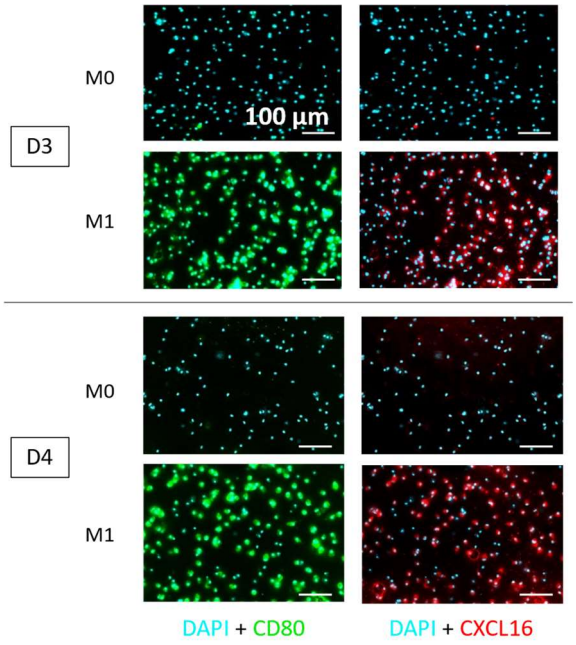


Fig. 6: Immunofluorescence staining of macrophages embedded in fibrin gel in the device, in control (M0) vs. inflammatory conditions (M1).

Consequently, as demonstrated through flow cytometry analysis of intracellular cytokines (i.e. IFN-γ), T-cells stimulation could induce polarization to Th1 phenotype after three days. Moreover, Th1 T-cells overexpressed CXCR6 with respect to controls (Fig. 7).

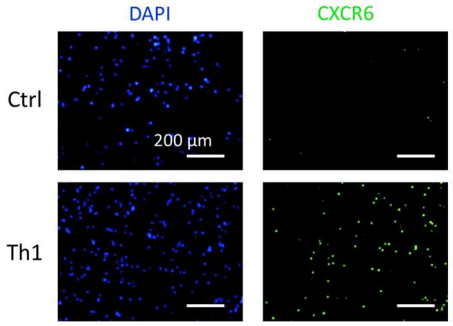


Fig. 7: Immunofluorescence staining of T-cells inside the platform in control (Ctrl) vs. inflammatory conditions (Th1).

Finally, after having validated the possibility to stimulate the two cell types independently thanks to the platform compartmentalization, a comprehensive biological validation was performed, assessing CXCR6-expressing T-cells migration from the *sieving valve chamber* towards the *3D chamber* in presence of M1 macrophages. After stimulation, migration of Th1 T-cells towards pro-inflammatory macrophages (M1) occurred spontaneously (Fig. 8), as compared to controls (M0), indicating the suitability of the platform to study immune cells cross-talk and migration due to chemoattraction.

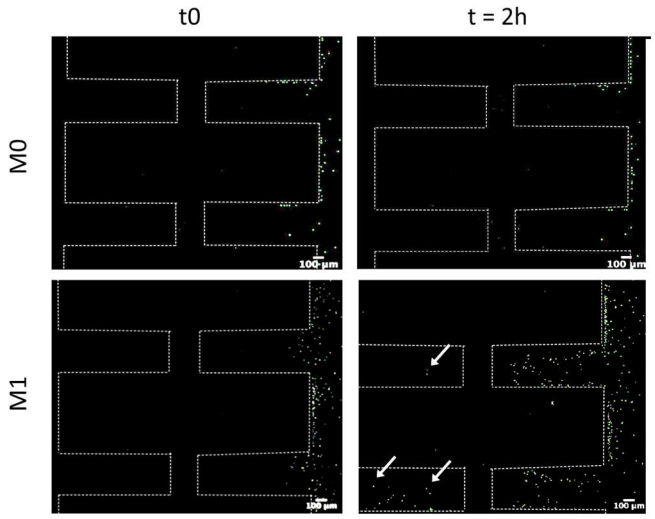


Fig. 8: Migration of pre-stained T-cells from the *sieving valve chambers* towards the *3D chamber*, comparing the effect of M1 macrophages with respect to control (M0 macrophages). White arrows indicate migrating T-cells.

IV. Conclusion

The proposed device offers an innovative solution to trap a limited number of immune cells inside microfluidic chips and to study the cross-talk between different cell types, having the possibility to stimulate them separately. The platform was proved to be a suitable tool to assess Th1 T-cells migration towards pro-inflammatory resident macrophages, replicating a known mechanism in RA. The use of the technology in combination with more complex synovial microscaled constructs is currently under evaluation, and will eventually increase the understanding about unknown mechanisms in RA progression. Moreover, the *sieving valves* technology is highly versatile and can be potentially applied to assess the interaction of immune system in manifold disease and more complex models.

Acknowledgement

This work was supported by Fondazione Cariplo-uKNEEque - Rif. 2018/0551 and OAonChip – Rif. 2021-1564 and has received funding from the European Union's Horizon 2020 research and innovation programme under the Marie Sklodowska-Curie grant agreement No 841975.

REFERENCES

[1] C. Y. Wu, H. Y. Yang, and J. H. Lai, 'Anti-Citrullinated Protein Antibodies in Patients with Rheumatoid Arthritis: Biological Effects and Mechanisms of Immunopathogenesis', *International Journal of Molecular Sciences 2020, Vol. 21, Page 4015*, vol. 21, no. 11, p. 4015, Jun. 2020, doi: 10.3390/IJMS21114015.

[2] D. M. Lee and M. E. Weinblatt, 'Rheumatoid arthritis', *Lancet*, vol. 358, no. 9285, pp. 903–911, Sep. 2001, doi: 10.1016/S0140-6736(01)06075-5.

[3] J. Tu, W. Huang, W. Zhang, J. Mei, and C. Zhu, 'A Tale of Two Immune Cells in Rheumatoid Arthritis: The Crosstalk Between Macrophages and T Cells in the Synovium', *Front Immunol*, vol. 12, p. 2359, Jun. 2021, doi: 10.3389/FIMMU.2021.655477/BIBTEX.

[4] J. S. Smolen *et al.*, 'Rheumatoid arthritis', *Nature Reviews Disease Primers 2018 4:1*, vol. 4, no. 1, pp. 1–23, Feb. 2018, doi: 10.1038/nrdp.2018.1.

[5] C. A. Paggi, L. M. Teixeira, S. le Gac, and M. Karperien, 'Joint-on-chip platforms: entering a new era of in vitro models for arthritis', *Nature Reviews Rheumatology 2022 18:4*, vol. 18, no. 4, pp. 217–231, Jan. 2022, doi: 10.1038/s41584-021-00736-6.

[6] M. Mellado, L. Martínez-Muñoz, G. Cascio, P. Lucas, J. L. Pablos, and J. M. Rodríguez-Frade, 'T cell migration in rheumatoid arthritis', *Frontiers in Immunology*, vol. 6, no. JUL. Frontiers Research Foundation, 2015. doi: 10.3389/fimmu.2015.00384.

[7] K. Liu, 'Immune, metabolism and therapeutic targets in RA (Rheumatoid Arthritis)', *BIO Web Conf*, vol. 55, p. 01016, Nov. 2022, doi: 10.1051/bioconf/20225501016.

[8] C. A. Roberts, A. K. Dickinson, and L. S. Taams, 'The interplay between monocytes/macrophages and CD4+ T cell subsets in rheumatoid arthritis', *Front Immunol*, vol. 6, no. NOV, 2015, doi: 10.3389/fimmu.2015.00571.

Valve-jet technology for robotic-based *in situ* bioprinting applications

E. Batoni[1,2], G.M. Fortunato[1,2], A. Guerra[1,2], G. Vozzi[1,2], C. De Maria[1,2]
[1] *Department of Information Engineering, University of Pisa, Pisa, Italy*
[2] *Research Centre "E. Piaggio", University of Pisa, Pisa, Italy*

***Abstract*— In recent years *in situ* bioprinting has gained more attention thanks to the possibility of automatically and precisely depositing biomaterials ink/bioinks directly on the patient's site, thus, overcoming the limitations of the current approaches. This study aimed at evaluating the possibility of using a valve-jet technology for *in situ* bioprinting. When combined with other bioprinting technologies, such as extrusion-based bioprinting, multimaterial and multiscale *in situ* bioprinting can be achieved to recapitulate the complex structure and architecture of native tissues.**

***Keywords—In situ* bioprinting, valve-jet technology, multimaterial/multiscale scaffolds.**

I. Introduction

Recently, *in situ* bioprinting has gained more attention since the possibility to print directly inside the patient's body, for instance, by using a robotic system, which resolves the limitations of conventional bioprinting approaches, e.g., scaffold manipulation and sterilization, incomplete tissue-scaffold integration, the need for bioreactors [1].

Different bioprinting techniques have been adapted *for in situ* bioprinting, such as extrusion-based bioprinting (EBB), laser-assisted bioprinting (LAB), and droplet-based bioprinting (DBB). While the first is usually applied for printing high viscous solutions, the others can process low viscous bioinks which, however, limit the fidelity of the fabricated structures [1]. This issue may be overcome by combing diverse bioprinting strategies as reported by Moncal et *al.,* who applied EBB to print a high viscous bone bioink and DBB for printing skin layers with less viscous bioinks [2].

Among the DBB technologies, valve-jet technology is a promising Drop-on-Demand deposition system with the capability of handling solutions with a wide range of viscosities (i.e., 0.05-500 Pa*s [3]) than conventional inkjet printing, as well as larger drop volumes (i.e., more than 1nL vs. 1-100 pL for thermal/piezoelectric inkjet [4]). It is possible to generate a greater force by adjusting the pneumatic pressure, as opposed to conventional inkjet where the driving force is heat or acoustic waves. In fact, an orifice-valve mechanism controls the droplet generation and the break-up through a piezoelectric or solenoid actuator [5]. The valve-jet mechanism is also useful for printing solutions containing drugs and/or biomolecules which may be susceptible to the processing conditions such as temperature and stress elements [4]. Furthermore, some studies demonstrated the feasibility of the valve-jet technology in the bioprinting of cells, such as human pluripotent stem cells (hPSC) and human embryonic stem cells (hESC) without interfering with their biological properties and vitality [6,7].

Taking into consideration the potential of valve-based systems, this study aimed at integrating valve-jet technology in a previously designed robotic platform for *in situ* bioprinting [8]. Compared to the pneumatic extrusion currently used in the robotic platform, this will give the possibility to print more viscous biomaterials, and deposit precise volumes. Firstly, hardware and software upgrades were made by developing ad-hoc electronics for controlling the valve-jet system. Secondly, the valve-based dispensing system was characterized in terms of the printability of solutions with Pluronic® F-127 since the well-known rheological properties [11]. Droplets were quantitatively (*i.e.*, diameter dimension) evaluated by changing the printing parameters (*i.e.*, applied pressure, valve signal period, and distance from the substrate) while keeping the same dispensing needle. Keeping the applied pressure and distance constant, the optimal valve signal period was chosen in order to have a good overlapping between droplets, enabling the formation of a continuous line. Lastly, as a proof-of-concept, *in situ* printing tests were executed on a 3D printed poly-L-lactic acid (PLA) complex substrate.

II. Materials and Methods

A. In situ bioprinting platform

The bioprinting platform consists of a 5 Degrees-of-Freedom (DoF) robotic arm – IMAGObot – featured with different tools for surface scanning and reconstruction, and EBB *in situ* bioprinting, also on moving substrates [8–10]. The platform is controlled through LinuxCNC, a software for Computer Numerical Control (CNC) machines control, while a previously designed MATLAB Graphical User Interface (GUI) is used for the generation and planning of the *in situ* bioprinting path.

B. Hardware and software upgrades

The valve-jet system used in this study is a needle valve (DA 400 EV, DAV tech, Italy) designed to dispense in a controlled, precise, and repeatable way, fluids with medium to high viscosity[11]. The valve is featured nozzles in various shapes and sizes. Since the solenoid valve is mounted directly on board, it allows a high-precision deposition making it ideal to be integrated into automated systems, such as robotic arms. The valve jet was connected to the robotic arm taking advantage of the previously designed semi-automatic tool change. Briefly, this consists of an electromagnet on the end-effector and a metallic disk placed on the tool, whose connection/disconnection is controlled by the user through the LinuxCNC GUI [9] (Fig. 1).

Ad-hoc electronics were designed to control the opening/closing of the solenoid valve through an Arduino UNO microcontroller. A pressure regulator (ITV0011-2BL-Q, SMC Pneumatics) was used to control the material extrusion via flexible tubing.

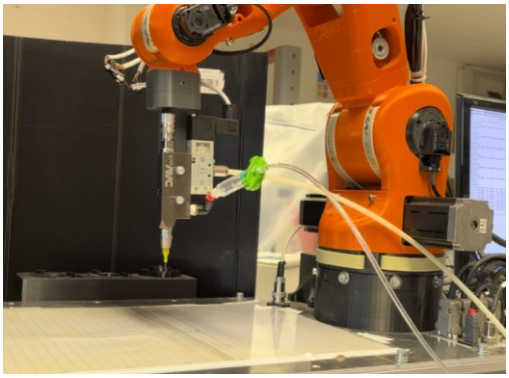


Fig. 1. *In situ* bioprinting robotic platform integrated with the valve-jet deposition system

A user-defined command was created, namely *M103*, to control the valve opening/closing through the G-code file uploaded in LinuxCNC. In detail, the opening and closing are controlled by the M command parameter *P* (*i.e.*, *M103 P1* and *M103 P0* to open and close the valve, respectively). A Python script was written to send, by serial communication, the value assigned to *P* to the Arduino digital pin which controls the valve status.

Two different modalities were created: (i) pausing the movements between droplets deposition; (ii) continuous deposition while moving. In the first case, the opening and closing time is defined by the G-code command *G4 PX*, which stops the program for *X* seconds, keeping the robot in a fixed position. Thus, the droplet is generated by alternating the opening command (*M101 P1*), the pause (*G4 PX*), the closing command *(M101 P0),* and another pause. In the second case, another parameter is added to the opening command *M101 P1*, namely *QX*, which defines the valve signal period in seconds (*i.e.*, *M101 P1 Q1* means that the valve is kept open and close for 0.5s each). The command is sent to Arduino at the beginning of the G-code, enabling droplet formation and deposition while the robot is moving.

The valve signal period, as well as the droplet generation modality, is defined by the user in the MATLAB GUI used for *in situ* printing path planning.

Similarly, the pressure applied to the reservoir is controlled through a specific M command, *M3* which allows the material extrusion to define the desired pressure in *bar*. The command is defined at the beginning of the G-code, or before the valve opening command if changed during the printing process (Fig. 2B). As for the opening valve time, the pressure is set by the user in the MATLAB GUI.

C. *Printing tests*

Preliminary printing tests were performed by using a solution of Pluronic® F-127 (Sigma-Aldrich, Italy) 20% (w/v) with a 0.66mm-inner diameter dispensing needle. Since its well-known rheological properties (*e.g.*, viscosity of 200 mPa*s at 25 °C 20% (w/v) [12,13]), this limits the printing parameters to investigate the reservoir pressure, the valve signal period, and the end-effector distance from the substrate. The generated droplets were quantitively and qualitatively characterized by analyzing their diameter and shape. In detail, arrays of 4 droplets (5mm equally spaced) were deposited on a glass slide along the X axis, keeping the nozzle diameter constant, and changing one of the parameters at a time, *i.e.*, the applied pressure (from 0.5 bar to 1bar), the valve signal period (from 0.02s to 1s) and the distance from the substrate (from 2.5 mm to 10 mm). For each test, the droplet diameter was measured in ImageJ software [14].

Once the optimal pressure and distance were selected, droplets were weighted with a precision balance (1µg), and the droplet volume was estimated given the solution density.

To perform a continuous deposition of droplets (i.e., second printing modality), it is necessary to define the optimal valve signal period in order to guarantee a good overlapping between consecutive droplets. Hence, different arrays of droplets were continuously deposited only varying the valve signal period and keeping the robot's linear speed at 1 mm/s.

Lastly, as a Proof-of-Concept, the valve-jet system was used for the *in situ* printing Pluronic® F-127 of a serpentine pattern onto a substrate 3D printed in PLA, using the optimal printing parameters (i.e., applied pressure, distance, and valve signal period) which ensured the formation of continuous lines.

III. Results and Discussions

The possibility of using the valve-based technology on the *in situ* printing platform was feasible thanks to the upgraded electronics and software. As expected, the diameter of the dispensed droplets increased with the applied pressure (Fig. 2A) and the valve signal period (Fig. 2B)

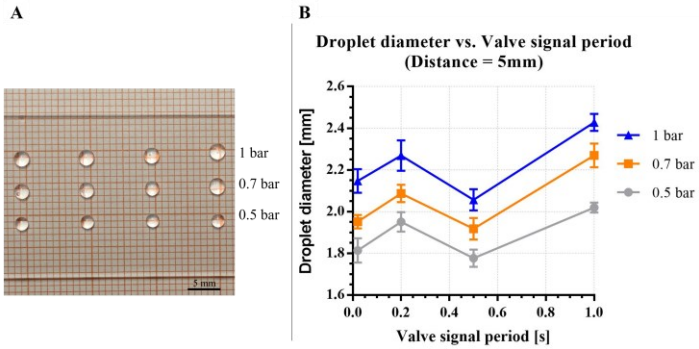


Fig. 2. (A) Array of droplets deposited varying the applied pressure (0.5-1 bar) and keeping the distance and valve signal period respectively at 5mm and 1s; (B) Droplet diameter vs. Valve signal period, varying the pressure from 0.5 bar to 1 bar, and keeping the distance at 5mm.

Since droplets formed and deposited only when varying the pressure between 0.5 and 1 bar, a pressure of 1 bar was selected in order to ensure the formation of the droplets. Considering the distance from the substrate, a 5 mm distance was selected, giving an average droplet diameter of 2.2 mm (Fig. 3).

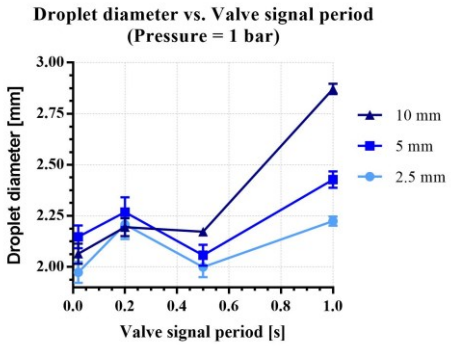


Fig. 3. Droplet diameter vs. Valve signal period, varying the distance from 2.5mm to 10mm, and keeping the pressure at 1 bar.

Keeping the pressure of 1 bar and the distance at 5mm, the droplet volume varied from 0.5 to 1 µL as the opening time (depending on the valve signal period) increased (Fig. 5).

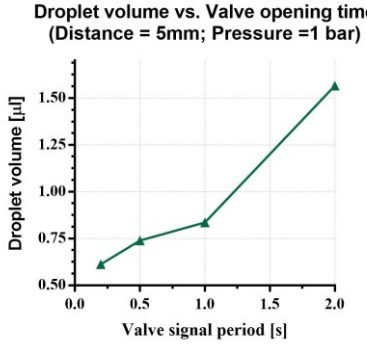


Fig. 4. Droplet volume vs. Valve signal period, keeping the pressure and distance at, respectively, 1 bar and 5mm.

Considering the valve signal period, the optimal that ensured a good overlapping was 1s, as depicted in Figure 6.

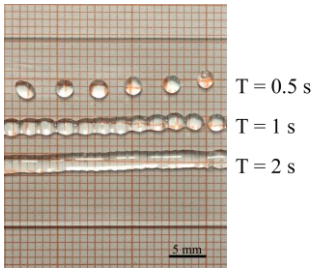


Fig. 5. Droplet deposition varying the valve signal period (0.5-2s) to form a continuous line while moving.

Thus, *in situ* printing tests were performed with Pluronic® F-127 keeping the pressure at 1 bar, a distance of 5mm from the substrate, and a valve signal period of 1 s, and keeping the robot linear speed at 1mm/s. *In situ* printing was successfully performed on a substrate 3D printed in PLA, featuring a complex curved surface. As expected, continuous lines were formed with the optimal parameters selected (Fig. 6).

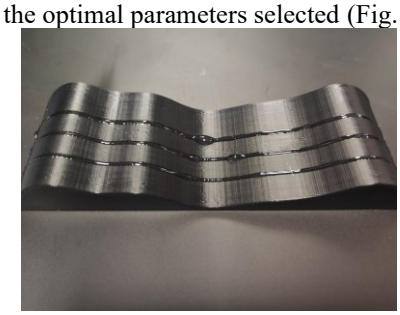


Fig. 6. Proof-of-Concept: *In situ* printing test on a curved surface substrate, with the optimized printing parameters to form a continuous line.

CONCLUSION

The present study demonstrated the possibility to use the valve-jet technology for *in situ* bioprinting applications with a robotic platform. The versatility of the valve-based techniques in handling various viscous solutions combined with the presented robotic platform enables the possibility to deposit droplets in a precise and automatic manner compared to the current pneumatic extruder used in the robotic platform. In addition, valve-jet technology can also be used in drug delivery, specifically, to print drug-loaded solutions, and thus create functional patches or scaffolds not printable with other AM technologies. Furthermore, by exploiting the semi-automatic change-tool system of the robotic platform, the valve-jet and extrusion bioprinting tools can be combined to print hydrogels with different viscosities and creating structures at different scales, which could be useful to recapitulate the complex multimaterial/multiscale structures of native tissues.

ACKNOWLEDGMENT

We acknowledge the support of the European Union by the Next Generation EU project ECS00000017 ‘Ecosistema dell’Innovazione’ Tuscany Health Ecosystem (THE, PNRR, Spoke 4: Nanotechnologies for diagnosis and therapy).

REFERENCES

1. Samandari, M.; Mostafavi, A.; Quint, J.; Memić, A.; Tamayol, A. In Situ Bioprinting: Intraoperative Implementation of Regenerative Medicine. *Trends Biotechnol* **2022**, *40*, 1229–1247, doi:10.1016/j.tibtech.2022.03.009.
2. Moncal, K.K.; Gudapati, H.; Godzik, K.P.; Heo, D.N.; Kang, Y.; Rizk, E.; Ravnic, D.J.; Wee, H.; Pepley, D.F.; Ozbolat, V.; et al. Intra-Operative Bioprinting of Hard, Soft, and Hard/Soft Composite Tissues for Craniomaxillofacial Reconstruction. *Adv Funct Mater* **2021**, *31*, 1–15, doi:10.1002/adfm.202010858.
3. Yang, H.; He, Y.; Tuck, C.; Wildman, R.; Ashcroft, I.; Dickens, P.; Hague, R. High Viscosity Jetting System for 3D Reactive Inkjet Printing. *24th Int SFF Symp - An Addit Manuf Conf SFF 2013* **2013**, 505–513.
4. Kollamaram, G.; Faucher, A.; Croker, D.M.; Walker, G.M. Valvejet Technology for the Production of a Personalised Fixed Dose Combination of Ramipril and Glimepiride: An Investigative Study on the Stability of Ramipril. *Pharm Res* **2018**, *35*, doi:10.1007/s11095-018-2465-7.
5. Vadodaria, S.S.; He, Y.; Mills, T.; Wildman, R. Fabrication of Surfactant-Polyelectrolyte Complex Using Valvejet 3D Printing-Aided Colloidal Self Assembly. *Colloids Surfaces A Physicochem Eng Asp* **2020**, *600*, 124914, doi:10.1016/j.colsurfa.2020.124914.
6. Faulkner-Jones, A.; Greenhough, S.; A King, J.; Gardner, J.; Courtney, A.; Shu, W. Development of a Valve-Based Cell Printer for the Formation of Human Embryonic Stem Cell Spheroid Aggregates. *Biofabrication* **2013**, *5*, doi:10.1088/1758-5082/5/1/015013.
7. Faulkner-Jones, A.; Fyfe, C.; Cornelissen, D.J.; Gardner, J.; King, J.; Courtney, A.; Shu, W. Bioprinting of Human Pluripotent Stem Cells and Their Directed Differentiation into Hepatocyte-like Cells for the Generation of Mini-Livers in 3D. *Biofabrication* **2015**, *7*, doi:10.1088/1758-5090/7/4/044102.
8. Fortunato, G.M.; Rossi, G.; Bonatti, A.F.; De Acutis, A.; Mendoza-Buenrostro, C.; Vozzi, G.; De Maria, C. Robotic Platform and Path Planning Algorithm for in Situ Bioprinting. *Bioprinting* **2021**, *22*, e00139, doi:10.1016/j.bprint.2021.e00139.
9. Fortunato, G.M.; Batoni, E.; Bonatti, A.F.; Vozzi, G.; De Maria, C. Surface Reconstruction and Tissue Recognition for Robotic-Based in Situ Bioprinting. *Bioprinting* **2022**, *26*, e00195, doi:10.1016/j.bprint.2022.e00195.
10. Fortunato, G.M.; Bonatti, A.F.; Batoni, E.; Macaluso, R.; Vozzi, G.; Maria, C. De Bioprinting Motion Compensation System for Robotic Based in Situ Bioprinting to Balance Patient Physiological Movements. *Bioprinting* **2022**, *28*, e00248, doi:10.1016/j.bprint.2022.e00248.
11. DAVtech Dispensing Needle Valve Da 400 Ev, Datasheet.
12. Lenaerts, V.; Triqueneaux, C.; Quartern, M.; Rieg-Falson, F.; Couvreur, P. Temperature-Dependent Rheological Behavior of Pluronic F-127 Aqueous Solutions. *Int J Pharm* **1987**, *39*, 121–127, doi:10.1016/0378-5173(87)90206-7.
13. Gioffredi, E.; Boffito, M.; Calzone, S.; Maria, S.; Rainer, A.; Trombetta, M.; Mozetic, P.; Chiono, V. Pluronic F127 Hydrogel Characterization and Biofabrication in Cellularized Constructs for Tissue Engineering Applications . *Procedia CIRP* **2016**, *49*, 125–132, doi:10.1016/j.procir.2015.11.001.
14. Rasband, W.S. ImageJ. *US Natl Institutes Heal Bethesda, Maryland, USA*.

Cryopreservation effects on biological tissues: histological and mechanical assessments

M. Casarin[1], M. Todesco[2], C.G. Fontanella[3], A. Morlacco[1], F. Dal Moro[1] and A. Bagno[3]
[1] *Department of Surgery, Oncology and Gastroenterology, University of Padua, Via Giustiniani 2, 35128, Padua, Italy*
[2] *Department of Civil, Environmental and Architectural Engineering, University of Padua, Via Marzolo 9, 35131, Padua, Italy*
[3] *Department of Industrial Engineering, University of Padua, Via Marzolo 9, 35131 Padua, Italy*

***Abstract*—Biological tissue substitutes need to be appropriately stored in order to provide ready-to-use solutions for patients with immediate necessity. In this preliminary study, different native porcine tissues (i.e., pericardium, ureter, descending aorta, and small intestinal submucosa) were subjected to cryopreservation at -80°C with a specific solution based on the use of 10% DMSO with the aim to evaluate the effects on ECM composition by means of histological analysis and biomechanical tests (i.e., tensile and stress-relaxation tests). Morphologically, all tissues appeared microscopically well preserved; from the biomechanical point of view, some tissue-dependent changes were detected.**

***Keywords*—Cryopreserved tissue, tissue engineering, regenerative medicine.**

I. Introduction

THE need for ready-to-use substitutes for surgical purposes is increasingly growing in order to repair or substitute non-functional or diseased organs and tissues. Next to synthetic materials, which have the advantage of suitable and predictable mechanical features and biodegradability, but with limited biocompatibility, biological materials derived from animal tissues are preferred for their biological characteristics that can favour tissue regeneration upon *in vivo* implantation, since they are rich in growth factors. However, one of the limitations in the use of biological tissues is due to the time needed to decellularize them and make them compatible by removing all the animal cells and DNA, while maintaining the integrity of the extracellular matrix (ECM) which has to work as a scaffold for the recipient's cells. Generally, decellularization procedures take some days; moreover, a sterilization step is also needed after decellularization and before seeding the tissue with the patient's cells, thus extending the duration of the procedure. For these reasons, the possibility to cryopreserve the decellularized tissue in order to have a ready-to-use scaffold with unaltered morphological and mechanical features is becoming more and more attractive. In this way, cryopreservation allows the immediate availability of implantable tissues and organs. Until now, several studies on cryopreservation have been reported especially for ovarian tissue [1]–[3] and for other materials [4]–[19], but only limited investigations concern decellularized tissues [20], [21].

In this preliminary study, we decided to focus on native tissues, which include porcine pericardium, small intestinal submucosa (SIS), ureter and descending aorta; future experiments will be performed on decellularized tissues in order to assess and optimize the cryopreservation protocol.

Native tissues were cryopreserved using a solution with 10% Dimethyl Sulfoxide (DMSO) and 10% FBS at -80°C and were compared with fresh ones in terms of mechanical behaviour and histology, in order to evaluate possible effects of cryopreservation on different types of native tissues.

II. Materials and Methods

A. Tissue collection and cryopreservation

Porcine pericardium, ureters, jejunum and descending aorta were obtained from a local slaughterhouse, whose protocols followed EC regulations 1099/2009, were supervised by the Italian government, and approved by Food and Consumer Product Safety Authority. Pericardium was isolated as illustrated by Aguiari et al. [22] and SIS as described by Casarin et al. [23]. In the case of ureter and descending aorta, external fibrous tissue was removed by surgical scissors.

Native tissue samples were split into 2 groups: the fresh group and the cryopreserved group. Once grossly dried, the native tissues underwent the cryopreservation protocol: it consisted in soaking the tissues in a solution composed by 10% FBS (Fetal Bovine Serum, Gibco, cod. 10270106) and 10% DMSO (Dimethyl Sulfoxide, Sigma, cod. 452301) in DMEM high glucose (Life technologies, cod. 41965-039) and immediately stored at -80°C. When needed for subsequent analyses (after 1.5 – 4.5 months), cryopreserved tissues were thawed at 37°C in a water bath and then statically washed at room temperature with saline solution, which was changed several times until samples remained completely transparent.

B. Histological Analysis

Fresh and cryopreserved native tissue samples were frozen in optimum cutting temperature (OCT) compound and then cryosectioned with 6 µm thickness. Hematoxylin and Eosin (BioOptica, cod. 04-061010) were performed following manufacturer's instructions in order to stain nuclei in blue and cytoplasm in pink.

C. Mechanical tests

Mechanical evaluations of fresh and cryopreserved native pericardium, SIS, ureter and descending aorta were assessed along the circumferential and/or longitudinal direction as specified in Table I.

TABLE I: DETAILS OF TESTS PERFORMED ON FRESH AND CRYOPRESERVED TISSUES

Tissue	*Test*	*Type*	*Test direction*	*# samples*
Pericardium	Rupture	Fresh	Circumf	9
		Cryo		13
	Stress relaxation	Fresh	Circumf	4
		Cryo		4
Ureter	Rupture	Fresh	Longitud	18
		Cryo		10
	Stress relaxation	Fresh	Longitud	9
		Cryo		7
SIS	Rupture	Fresh	Circumf	12
		Cryo		6
		Fresh	Longitud	12
		Cryo		6
	Stress relaxation	Fresh	Circumf	9
		Cryo		4
Descending aorta	Rupture	Fresh	Circumf	9
		Cryo		9
		Fresh	Longitud	9
		Cryo		9
	Stress relaxation	Fresh	Circumf	8
		Cryo		6

Cryo = cryopreserved native tissue; Circumf = circumferential direction; Longitud = longitudinal direction.

Conduits (i.e., SIS, descending aorta and ureter) were cut longitudinally, along the parallel direction of the conduit axis, and circumferentially, along the perpendicular direction. For pericardium, the chosen direction was the circumferential one, which corresponds to the circumferential direction of the heart.

Tissues were cut into dog-bone shaped specimens (gauge dimensions of 5mm × 2mm) [24] and their thickness was measured with a digital calliper (Mitutoyo, ID-C112XB). Samples were submitted to uniaxial rupture tests and stress-relaxation tests at room temperature using a custom-made apparatus (IRS, Padova, Italy); during the tests, samples were maintained hydrated with saline solution. Before each type of test, samples were pre-loaded up to 0.1 N and then subjected to a constant mechanical load with 0.2 mm/s elongation rate (L_0=5mm). Rupture tests were performed elongating the sample until failure; from the corresponding stress-strain curve, the Young's modulus (E) was calculated as the slope of the curve in the linear region, while the Ultimate Tensile Strength (UTS) and the Failure Strain (FS) were calculated as maximum resistance and elongation, respectively. Finally, stress-relaxation tests were realized by elongating samples (0.2 mm/s) until 10, 20, 30 40 and 50% of the initial length with 300 s holding time after each elongation. Stress decreasing (%) was evaluated as the difference between the maximum stress and the plateaux of the curve.

Graphs of mechanical tests were obtained with an in-house developed Matlab® script (Mathworks, Natick, MA, USA).

D. Statistical Analysis

All variables were expressed as mean ± standard deviation. Comparisons between native and cryopreserved tissues were conducted with t-test using GraphPad Prism (version 7.0 for MacOs) (GraphPad Software, San Diego, California, USA). Significance was set at $p<0.05$.

III. RESULTS

A. Histological evaluations

Microscopically, fresh and cryopreserved tissues were histologically evaluated using Hematoxylin and Eosin staining (Fig. 1), which demonstrated optimal ECM preservation in all investigated tissues.

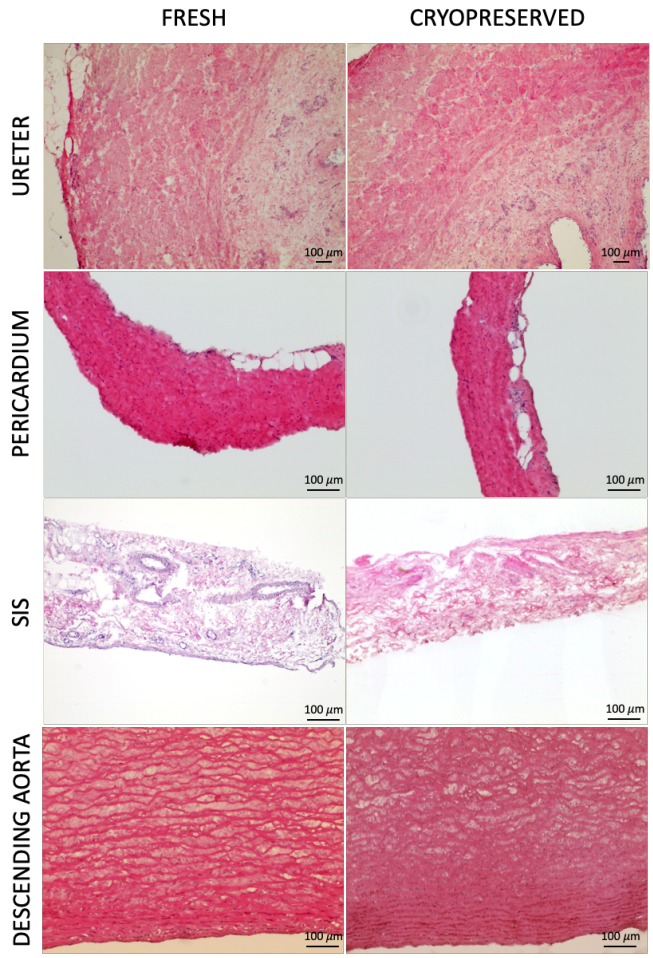


Fig. 1: Histological evaluation with Hematoxylin and Eosin staining of fresh and cryopreserved ureters, pericardia, SIS, and descending aortas.

B. Mechanical evaluations

Rupture tensile tests performed on fresh and cryopreserved pericardium demonstrated the absence of any significant difference between the two groups in thickness, FS, E and UTS, while in the case of ureters, significant differences were found in FS (it increased in cryopreserved tissue) and E (it decreased). Significative differences were observed also in SIS thickness ($p < 0.0001$), which increased in the case of cryopreserved samples, and Young's modulus both in circumferential and longitudinal directions: it decreased in cryopreserved tissues, but no statistical difference was found in FS and UTS values along both directions. Overall, tissue anisotropy was maintained after cryopreservation process. Finally, a significant increase of thickness ($p = 0.0443$) and UTS along the circumferential direction was detected in aorta samples; significant increases of FS along the longitudinal direction and of E along the circumferential one were found.

No significant difference was checked for FS along the circumferential direction and for E along the longitudinal one. The biomechanical parameters from the rupture tests are shown in Fig. 2 and thickness values are reported in Table II.

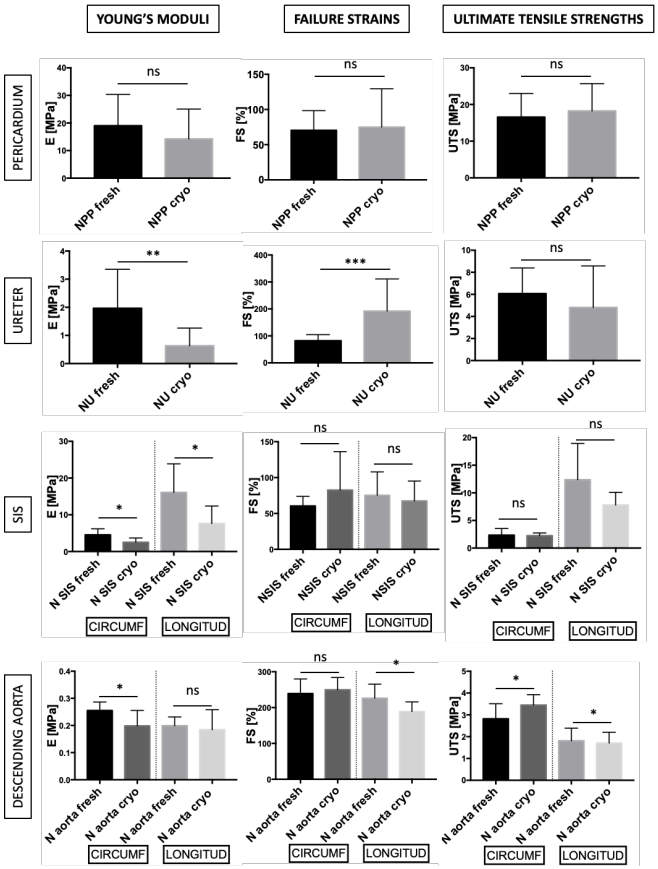


Fig. 2: Biomechanical parameters (E, UTS and FS) from rupture tests of fresh and cryopreserved pericardium (NPP), ureter (NU), small intestinal submucosa (SIS) and descending aorta. SIS and aorta were tested both along circumferential (circumf) and longitudinal (longitud) directions. Data on graphs are expressed as mean ± standard deviation; data were statistically analysed by t-test: ns=non-significant difference, *p<0.05, **p<0.01 and ***p<0.001.

TABLE II: THICKNESS OF FRESH AND CRYOPRESERVED SAMPLES (MEAN ± STANDARD DEVIATION).

Sample	*Thickness [mm]*
NPP fresh	0.14 ± 0.03
NPP cryopreserved	0.15 ± 0.04
Ureter fresh	0.78 ± 0.14
Ureter cryopreserved	0.86 ± 0.26
SIS fresh	0.08 ± 0.03
SIS cryopreserved	0.13 ± 0.02
Descending aorta fresh	1.28 ± 0.17
Descending aorta cryopreserved	1.41 ± 0.19

Results of the stress relaxation tests are reported in Fig. 3. Relaxation decreases over time for all tissues as reported in Table III. However, there is a significant difference between the relaxation reached after 300s by fresh and cryopreserved pericardium (p = 0.0002), and between native and cryopreserved SIS (p = 0.034). There is no significant difference between native and cryopreserved samples from ureter and descending aorta.

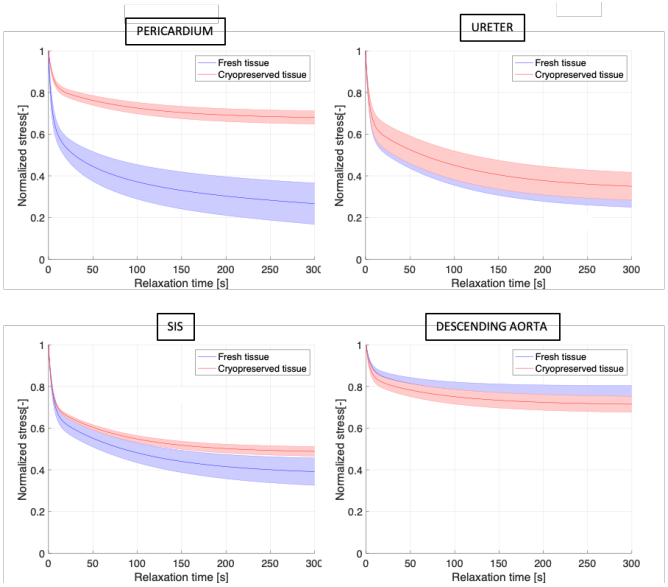


Fig. 3: Stress relaxation normalized curves of porcine pericardium, ureter, SIS and aorta. Each graph compares native tissue (red) with cryopreserved tissue (blue). Curves were normalized and then fitted by 3-term Prony series.

TABLE III: TISSUE RELAXATION (%) VALUES (MEAN ± STANDARD DEVIATION).

Sample	*Relaxation [%]*
NPP fresh	73.34 ± 9.8
NPP cryopreserved	31.97 ± 3.1
Ureter fresh	68.61 ± 6.4
Ureter cryopreserved	64.98 ± 6.6
SIS fresh	60.87 ± 6.5
SIS cryopreserved	51.16 ± 2.28
Descending aorta fresh	25.42 ± 5.8
Descending aorta cryopreserved	28.54 ± 3.8

IV. CONCLUSION

Cryopreservation procedure can provide ready-to-use biological tissues as graft materials for surgical purposes. Specific cryopreservation protocols have to be investigated for each particular tissue, in order to assess possible effects on ECM microarchitecture integrity and mechanical resistance. In this preliminary study, four different tissues were compared: they were studied in terms of ECM integrity and thickness, and from the histological and biomechanical points of view, before and after cryopreservation using 10% DMSO and 10% FBS in DMEM High Glucose solution. Histologically, the optimal maintenance of the ECM structure for all tissues (e.g., porcine pericardium, ureter, SIS and descending aorta) was demonstrated. From the mechanical point of view, uniaxial

rupture tests highlighted good preservation of pericardium behaviour, which did not show any significant difference between fresh and cryopreserved samples. However, stress-relaxation tests allowed checking a significant decrease in relaxation for cryopreserved samples in comparison with fresh ones. For the other tissues, some significant differences were found as to the values of E, UTS and FS during tensile tests to rupture; only in the case of SIS, a significant difference was found during stress-relaxation tests. This result suggests that the cryopreservation protocol can affect the mechanical behaviour of tissues, but the effect depends mainly on tissue composition and thickness.

This preliminary study represents the first effort to evaluate how and how much cryopreservation protocols can alter the characteristics of the treated tissues in terms of histological and mechanical properties. Further studies have to be performed to optimize the cryopreservation procedure with the aim to: i) increase the mechanical resistance of decellularized tissues; ii) quantify the residual presence of DMSO in cryopreserved tissues before proceeding with their clinical exploitation. Moreover, further analyses are in progress to assess possible effects due to cryopreservation on cues fundamental for proper cells-ECM interactions.

REFERENCES

[1] S. Klocke, N. Bündgen, F. Köster, U. Eichenlaub-Ritter, and G. Griesinger, "Slow-freezing versus vitrification for human ovarian tissue cryopreservation," *Arch. Gynecol. Obstet.*, vol. 291, fasc. 2, pp. 419–426, feb. 2015, doi: 10.1007/s00404-014-3390-6.

[2] Q. Shi, Y. Xie, Y. Wang, and S. Li, "Vitrification versus slow freezing for human ovarian tissue cryopreservation: a systematic review and meta-anlaysis," *Sci. Rep.*, vol. 7, fasc. 1, p. 8538, ago. 2017, doi: 10.1038/s41598-017-09005-7.

[3] S. Lee, K.-J. Ryu, B. Kim, D. Kang, Y. Y. Kim, and T. Kim, "Comparison between Slow Freezing and Vitrification for Human Ovarian Tissue Cryopreservation and Xenotransplantation," *Int. J. Mol. Sci.*, vol. 20, fasc. 13, p. 3346, lug. 2019, doi: 10.3390/ijms20133346.

[4] T. M. Farooque, Z. Chen, Z. Schwartz, T. M. Wick, B. D. Boyan, and K. G. M. Brockbank, "Protocol Development for Vitrification of Tissue-Engineered Cartilage," *Bioprocessing*, vol. 8, fasc. 4, pp. 29–36, 2009, doi: 10.12665/j84.brockbank.

[5] M. D. Kofron, N. C. Opsitnick, M. A. Attawia, and C. T. Laurencin, "Cryopreservation of tissue engineered constructs for bone," *J. Orthop. Res. Off. Publ. Orthop. Res. Soc.*, vol. 21, fasc. 6, pp. 1005–1010, nov. 2003, doi: 10.1016/S0736-0266(03)00103-7.

[6] H. Miyoshi, T. Ehashi, N. Ohshima, and A. Jagawa, "Cryopreservation of fibroblasts immobilized within a porous scaffold: effects of preculture and collagen coating of scaffold on performance of three-dimensional cryopreservation," *Artif. Organs*, vol. 34, fasc. 7, pp. 609–614, lug. 2010, doi: 10.1111/j.1525-1594.2009.00933.x.

[7] O. Batnyam, "Direct cryopreservation of adherent cells on an elastic nanofiber sheet featuring a low glass-transition temperature," *RSC Adv.*, 2017.

[8] A. Bissoyi, K. Pramanik, N. N. Panda, and S. K. Sarangi, "Cryopreservation of hMSCs seeded silk nanofibers based tissue engineered constructs," *Cryobiology*, vol. 68, fasc. 3, pp. 332–342, giu. 2014, doi: 10.1016/j.cryobiol.2014.04.008.

[9] Y. A. Petrenko, A. Y. Petrenko, I. Martin, and D. Wendt, "Perfusion bioreactor-based cryopreservation of 3D human mesenchymal stromal cell tissue grafts," *Cryobiology*, vol. 76, pp. 150–153, giu. 2017, doi: 10.1016/j.cryobiol.2017.04.001.

[10] P. F. Costa, A. F. Dias, R. L. Reis, and M. E. Gomes, "Cryopreservation of cell/scaffold tissue-engineered constructs," *Tissue Eng. Part C Methods*, vol. 18, fasc. 11, pp. 852–858, nov. 2012, doi: 10.1089/ten.TEC.2011.0649.

[11] H. Yin, L. Cui, G. Liu, L. Cen, and Y. Cao, "Vitreous cryopreservation of tissue engineered bone composed of bone marrow mesenchymal stem cells and partially demineralized bone matrix," *Cryobiology*, vol. 59, fasc. 2, pp. 180–187, ott. 2009, doi: 10.1016/j.cryobiol.2009.06.011.

[12] E. Lippens and M. Cornelissen, "Slow cooling cryopreservation of cell-microcarrier constructs," *Cells Tissues Organs*, vol. 192, fasc. 3, pp. 177–186, 2010, doi: 10.1159/000313419.

[13] K. Kubo and Y. Kuroyanagi, "The possibility of long-term cryopreservation of cultured dermal substitute," *Artif. Organs*, vol. 29, fasc. 10, pp. 800–805, ott. 2005, doi: 10.1111/j.1525-1594.2005.00132.x.

[14] G. Spoerl, R. Mai, E. Klingner, T. Gedrange, and G. Lauer, "Cryopreserved tissue engineered mucosa," *Folia Histochem. Cytobiol.*, vol. 46, fasc. 4, pp. 541–544, 2008, doi: 10.2478/v10042-008-0073-9.

[15] Y. Zheng, S. Ji, H. Wu, S. Tian X. Wang, "Acceleration of diabetic wound healing by a cryopreserved living dermal substitute created by micronized amnion seeded with fibroblasts," *Am. J. Transl. Res.*, vol. 7, fasc. 12, pp. 2683–2693, 2015.

[16] H. Gurruchaga, L. Saenz Del Burgo, A. Garate, D. Delgado, P. Sanchez, G. Orive, J. Ciriza, M. Sanchez, J.L. Pedraz, "Cryopreservation of Human Mesenchymal Stem Cells in an Allogeneic Bioscaffold based on Platelet Rich Plasma and Synovial Fluid," *Sci. Rep.*, vol. 7, fasc. 1, p. 15733, nov. 2017, doi: 10.1038/s41598-017-16134-6.

[17] F. Wen, R. Magalhaes, S.S. Gouk, G. Bhakta, K.H. Lee, D.W. Hutmacher, L.L. Kuleshova, "Vitreous cryopreservation of nanofibrous tissue-engineered constructs generated using mesenchymal stromal cells," *Tissue Eng. Part C Methods*, vol. 15, fasc. 1, pp. 105–114, mar. 2009, doi: 10.1089/ten.tec.2008.0237.

[18] F. Chen, W. Zhang, W. Wu, Y. Jin, L. Cen, "Cryopreservation of tissue-engineered epithelial sheets in trehalose," *Biomaterials*, vol. 32, fasc. 33, pp. 8426–8435, nov. 2011, doi: 10.1016/j.biomaterials.2011.07.008.

[19] Y. Wu, F. Wen, S. S. Gouk, E. H. Lee, and L. Kuleshova, "Cryopreservation Strategy For Tissue Engineering Constructs Consisting Of Human Mesenhymal Stem Cells And Hydrogel Biomaterials," *Cryo Letters*, vol. 36, fasc. 5, pp. 325–335, 2015.

[20] M. Gallo, A. Bonetti, H. Poser, F. Naso, T. Bottio, R. Bianco, A. Paolin, P. Franci, R. Busetto, A.C. Frigo, E. Buratto, M. Spina, M. Marchini, F. Ortolni, L. Iop, G. Gerosa, "Decellularized aortic conduits: could their cryopreservation affect post-implantation outcomes? A morpho-functional study on porcine homografts," *Heart Vessels*, vol. 31, fasc. 11, pp. 1862–1873, nov. 2016, doi: 10.1007/s00380-016-0839-5.

[21] E. Díaz-Moreno, D. Durand-Herrera, V. Carriel, M.A. Martìn-Piedra, M.d.C. Sanchez-Quevedo, I. Garzòn, A. Campos, R. Fernandez-Vadelez, M. Alaminos, "Evaluation of freeze-drying and cryopreservation protocols for long-term storage of biomaterials based on decellularized intestine: Evaluation Of Freeze-Drying And Cryopreservation," *J. Biomed. Mater. Res. B Appl. Biomater.*, vol. 106, fasc. 2, pp. 488–500, feb. 2018, doi: 10.1002/jbm.b.33861.

[22] P. Aguiari, L. Iop, F. Favaretto, C.M.L. Fidalgo, F. Naso, G. Milan, V. Vindigni, M. Spina, F. Bassetto, A. Bagno, R. Vettor, G. Gerosa, "*In vitro* comparative assessment of decellularized bovine pericardial patches and commercial bioprosthetic heart valves," *Biomed. Mater.*, vol. 12, fasc. 1, p. 015021, feb. 2017, doi: 10.1088/1748-605X/aa5644.

[23] M. Casarin, T.M. Fortunato, S. Imran, M. Todesco, D. Sandrin, G. Borile, I. Toniolo, M. Marchesan, G. Gerosa, A, Bagno, F. Romanato, E.L. Carniel, A. Morlacco, F. Dal Moro, "Porcine Small Intestinal Submucosa (SIS) as a Suitable Scaffold for the Creation of a Tissue-Engineered Urinary Conduit: Decellularization, Biomechanical and Biocompatibility Characterization Using New Approaches," *Int. J. Mol. Sci.*, vol. 23, fasc. 5, p. 2826, mar. 2022, doi: 10.3390/ijms23052826.

[24] L. Wollmann, P. Suss, J. Mendonca, C. Luzia, A. Schittini, G.W. Xavier da Rosa, F. Costa, F.F. Tuon, "Characterization of Decellularized Human Pericardium for Tissue Engineering and Regenerative Medicine Applications," *Arq. Bras. Cardiol.*, 2019, doi: 10.5935/abc.20190094.

Design and fabrication of a novel bioreactor for the engineering of tendon/ligament-to-bone interfaces

Ginevra Pegollo[1,2], Simone Micalizzi[1,2], Aurora De Acutis[2], Carmelo De Maria[1,2], Giovanni Vozzi[1,2]
[1]*Research Center 'E. Piaggio', University of Pisa, Pisa, Italy*
[2]*Department of Information Engineering, University of Pisa, Pisa, Italy.*

***Abstract*— In this work we present the design and development of a new bioreactor for supporting the regeneration of the enthesis, the area where the tendon or ligament insert into bone. Specifically, to optimize the proliferation, cell differentiation, and thereby the mechanical properties of a bioartificial construct, the bioreactor is designed to apply cyclic strains on a scaffold over a range of stress. The bioreactor was designed to meet several criteria. It allows applying precise control of the strain field on a scaffold. The hardware design guarantees real-time monitoring of the tensile stress applied to the scaffold and provides data to the user to perform mechanical characterization. It can be placed in standard incubators and provides a simple but effective scaffold clamping system. It ensures an airtight seal during the working phases to avoid contamination of the culture medium and provides a sterile environment during use. Finally, the developed software allows to select both pre-set or customizable stimulation cycles by setting traction frequency and test duration. All the critical specifications were met, so this work sets the stage for testing the proposed device with scaffolds developed in the framework of the TRITONE project, in order to support the biofabrication of autologous enthesis-like constructs.**

***Keywords*— Tissue engineering, enthesis, scaffold, bioreactor.**

I. INTRODUCTION

In the field of orthopedic surgery, tendon and ligament (T/L) injury is one of the most common soft tissue damage [1] Of the approximately 30 million musculoskeletal injuries reported each year, more than half are believed to involve tendons and ligaments [2]. Current surgical approaches to reconstruct the injury and/or defect fail to replicate the structural and functional organization and mechanical properties of these tissues. These limitations may compromise the regeneration process leading to poor bone integration and a high incidence of postoperative failure. Therefore, there is an urgent need to fabricate engineered tissues that are increasingly bioinspired and capable of replicating the spatial inhomogeneity and biomechanical properties of damaged tissue [3]. In tissue engineering, the key elements for engineering a tissue are cells, the vital component essential for obtaining an autologous tissue, scaffolds, three-dimensional structures capable of emulating the extracellular matrix of the target tissue, on which cells are seeded, and a system capable of implementing biochemical and physical conditioning on the cellular construct. Particular attention in the field of T/L engineering is given to the osteotendinous junction, also called the enthesis [4], through which T/Ls insert into the bone. There are two types of enthesis in the human body: i) fibrous and ii) fibrocartilaginous. The latter is characterized by gradients in physicochemical and morphological properties. The enthesis has the task of making soft tissue and bone cooperate by facilitating the transmission of forces during the movement of limbs and joints. Because of this function it is an area of high stress concentration and goes often prone to injury. It is evident from the literature that mesenchymal stem cells (MSCs) appear to be the most promising for this type of application [5]. In addition, the need to provide appropriate biochemical stimuli to promote cell proliferation and viability is coupled with the application of appropriate mechanical stimulation to ensure that differentiation into tenocytes by MSCs is promoted [5]. Tensile stimuli are imposed on the scaffolds in culture using bioreactors. These devices are intended to replicate the in-vivo environment and are characterized by basic components, such as: i) a culture chamber with a tensile system capable of providing mechanical stimulation; ii) a circulation system for the culture medium; ii) monitoring and control system [6]. Each bioreactor is sized according to the type of sample to be stimulated and the mode of stimulus application. The magnitude and regimes of applied forces can therefore vary considerably among configurations. This work focuses on the development of a novel bioreactor that can apply cyclic strains on a cellular construct to improve cell proliferation and differentiation and thereby the mechanical properties of cultured constructs. Specifically, the design choices are the result of an in-depth analysis of the pros and cons of devices present both in the literature and market [7-9].The result of this analysis is summarised in the following specific requirements for T/L and enthesis regeneration: i) capability of providing precise control of the applied strain field on a scaffold biofabricated scaffold; ii) capability of in-line monitoring the tensile stress applied to the scaffolds and providing data to perform any mechanical analysis; iii) possibility to be placed in commercially available incubators; iv) capability of providing an effective fixation system of the scaffolds without causing any damage to them; v) capability of ensuring an airtight seal during to avoid contamination and leakages of culture medium; vi) ensuring a sterile environment during use. The bioreactor was then specifically designed in terms of hardware and software to stimulate the scaffold, developed in the framework of the TRITONE project, with a cyclic frequency and strain required for tendon and ligament regeneration as highlighted in the literature [7-9]. Briefly, these scaffolds consist of an electrospun poly(lactic-co-glycolic acid) (PLGA) zone that interfaces with the tendon and one of polycaprolactone (PCL) obtained by fused deposition modeling (FDM) printing technology. The joining component

between the two parts, obtained by the overlapping of the two materials represents the enthesis. Thus, we are dealing with scaffolds bi-material with structures that have different mechanical and morphological properties [10,11]. However, it is easily scalable, to be used for the stimulation of scaffolds or mechanic excitable tissues.

II. Materials and Methods

A. Bioreactor design

The whole bioreactor is composed of a culture chamber and a cyclic tensile stimulation and monitoring system. All parts were designed using Fusion 360 software and checked for fit in an assembly file. The dimensions of the culture chamber were constrained by the standard-specific dimensions of a TRITONE scaffold (e.g., 30 x 5 x 0.4mm) and by the need to guarantee a low encumbrance inside a commercial incubator.

The design of the culture chamber is shown in Fig. 1. The culture chamber presents an upper cover that was designed to hermetically accommodate a 15 ml of culture medium to ensure the possibility of performing standard biochemical analysis on it.

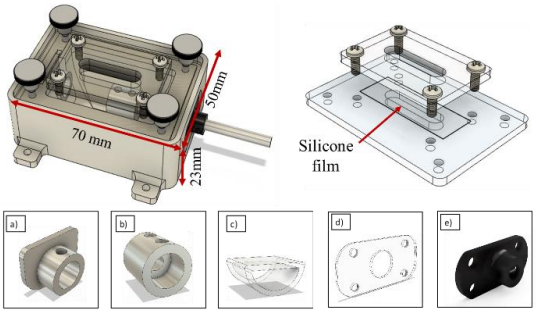


Fig. 1: Top left: CAD model assembly of the culture chamber with external dimensions. Top right: cover of the culture chamber with gas exchange system highlighted. Down: a) fixed coupling system, b) movable coupling system, c) silicone insert, d) silicone gasket, e) flange for compressing the gasket.

To ensure easy and effective sterilization of the culture chamber, all media contact bioreactor parts can be easily disassembled and are made of biocompatible and autoclavable materials (aluminum and Polyoxymethylene (POM)) by milling. Specifically, the culture chamber was made of POM, while the interlocking lid was made up of transparent Plexiglass to allow optical analyses on the cells without opening the chamber. Moreover, a biomedical silicone gasket was foreseen below the covering to isolate the internal environment of the chamber from the external one, and a hole was foreseen on the lid, covered with a 200 µm thick ELASTOSIL® [12] film, to keep the culture properly ventilated.

The cyclic stimulation system is composed of a scaffold anchoring system, a linear actuating system, and a load cell. The anchoring system (Fig. 2) was placed inside the culture and consists of a commercial aluminum-based shaft (4 mm in diameter and 60 mm in length), connected to a movable cylindrical clamp to constrain one end of the TRITONE scaffold, and of a fixed clamp to constrain the second end of the same scaffold. Both the cylindrical clamps consist of a hollow cylindrical element fabricated by milling process from aluminum. Each clamp was provided with a medical grade polydimethylsiloxane (PDMS) (Sylgard 184 with mixing ratio 10:1) insert whose compression via a commercial nylon screw constrained the scaffold without causing any damage (Fig.1 a, b, c).

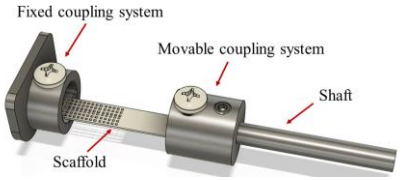


Fig. 2: CAD assembly of the scaffold anchoring system.

The linear actuating mechanism is made up of a stepper motor (Nema 17) and a screw-lead screw coupling (MTSFR8 T-type brass screw nut) to pull the scaffolds during the cyclical stimulation. To prevent the loss of culture medium at the point where the shaft is inserted into the chamber, a PDMS gasket was purposely fabricated (Fig.1(d)) by molding process using Sylgard 184 (10:1 mixing ratio). An aluminum flange was designed and milled to properly fix the gasket to culture chamber's wall (Fig.1(e)). A key component included in the cyclic stimulation system is the load cell (S-type 3kg, sensitivity 2.0 ± 0.05mV/V) that allows real-time mechanical analysis and control feedback based on scaffold changes over time. Finally, a purposely designed component (see Fig. 3) was designed and connects on one side to the cell load and to the other to the shaft, thereby allowing the chamber to be separated from the rest of the system. The whole cyclic stimulation system is solidly attached to a mechanical carriage to allow the anchoring system to move in the direction of stimulation of the sample (see Fig.3).

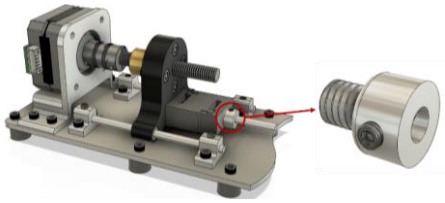


Fig. 3: On the left is the CAD assembly model of the pulling system. On the right the component for connecting the load cell is highlighted.

B. Bioreactor Electronics and Controller

System input and control were implemented in the Arduino development environment to: i) drive the stepper motor and pull the scaffold according to custom or pre-defined stimulation test programs; ii) monitor the tensile stress applied to the scaffold; iii) store data from each stimulation test thus giving the operator the possibility to perform a post-test mechanical analysis. To this aim, an Arduino Uno board (Arduino®) was used to control the stepper motor through a stepper driver (micro-stepping DM240) that translates high/low voltage digital inputs (generated by the Arduino) into appropriate settings (e.g., rotation direction or step resolution) and prescribed rotation steps. The load cell was powered through a JY-S60 board by a DC power supply (24V@5A) which also allows the amplification and transmission of the acquired data to the Arduino board, as an analog signal. To store data during a tensile mechanical stimulation test, a module for reading and writing to micro-SD memory cards was foreseen. The communication of this board with the

Arduino board took place via the Serial Periferal Interface (SPI) communication protocol. Finally, to allow the user to interface with the bioreactor electronics, a display, a rotary encoder, and buttons were provided to choose the type of stimulation protocol from the standard present ones or create a customised one by setting stimulation frequency strain and test time.

C. Leakage tests

Both static and dynamic (with the cyclic stimulation system activated) tests were conducted to assess the tightness of the culture chamber by filling it with 15 ml of deionized water. For tests in a static condition, the chamber was filled and checked after 24h and 48h for leaks. For tests in dynamic conditions, the culture chamber was checked for leaks after activating the cyclic stimulation system for 30 minutes twice a day for 3 days with standard stimulation protocols (e.g., 0.5 Hz 10% strain).

D. Stimulation test

The bioreactor was validated by performing TRITONE scaffold stimulation tests. Twice daily cyclic stimulation sessions were performed on 4 groups of TRITONE scaffolds stored in PBS (phosphate-buffered saline, pH 7.4) for 7, 14 and 21 days, plus a control group (samples in PBS overnight). Tests were conducted in triplicate. The ability of the load cell to monitor the tensile loading applied on samples was also evaluated. Therefore, tensile mechanical tests with a frequency of 0.5 Hz and 10% strain were carried out. Each sample was stimulated for 30 minutes twice at 7-hour intervals. For each group, a stimulation session without sample was carried out to acquire, from the load cell, the voltage values referring only to the effect of friction due to the seal. These values were then subtracted from those obtained from stimulation tests with samples to isolate the voltage values representing the tensile stress applied to the scaffold. Equation (1) was then used to convert these data into Force (Newton) data information for the scaffold under testing.

$$\text{Force} = \frac{\text{Output}_{\text{LoadCell}} \cdot \text{CellRange}}{\text{Sensitivity} \cdot \text{V}_{\text{LoadCell}}} \cdot \frac{\text{g}}{\text{A}} \qquad (1)$$

Where:

- $\text{Output}_{\text{LoadCell}}$ is the load cell output voltage [V];
- CellRange is the max value the load cell can read [kg]
- Sensitivity is the smallest force a load cell can reliably detect [mV/V];
- $\text{V}_{\text{LoadCell}}$ is the input voltage to load cell [V];
- g is gravitational acceleration [9.81 m/s2]
- A is the gain of signal conditioning electronics.

At this point, to obtain the stress-strain curve for the scaffold under stimulation, we convert the data from Eq. 1 into tensile stress (MPa) by knowing the cross-sectional area of the scaffold using the equation 2.

$$\text{Stress} = \frac{\text{Force}}{\text{Section}} \qquad (2)$$

Where:

- Force is calculated via Equation (1) [N];
- Section is the cross-sectional area of the scaffold measured prior to mechanical stimulation [mm^2].

The strain-strain curve was evaluated up to the strain set at the start of stimulation.

III. Result

A. Bioreactor design

Based on the mandatory requirements presented in section I, a bioreactor system was designed and prototyped. The whole bioreactor in its final layout is shown in Fig. 4. As shown in Fig. 4, a plexiglass case (290mm in width, 140mm in depth and 93mm in height) was also designed and fabricated to protect the bioreactor during travel and from dirtiness. All the design choices led to a completely modular bioreactor, where the culture chamber can be mechanically and environmentally isolated from the cyclical stimulation system. Isolating the culture chamber allows modularity in experimental design (e.g., a single the stimulation system several scaffolds can be stimulated in succession within their culture chambers) and enables simple part change-out in case repair is needed. As shown in in Fig. 4 (b), a second chamber was also built for static sample control experiments to verify the effectiveness of stimulation of the TRITONE scaffold.

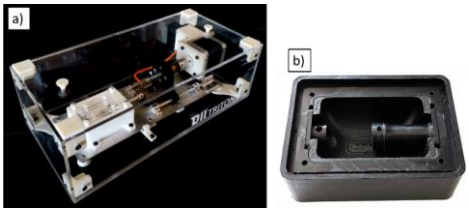


Fig. 4: (a) Bioreactor inside the case, (b) control culture chamber.

B. Bioreactor Electronics and Controller

The electronics and the control system of the bioreactor were designed to manage all the device's operations while ensuring the repeatability of the experimental tests. The electronic components were chosen to properly manage the stepper motor for the tensile stimulation of the scaffold; to select the stimulation program via buttons, rotary encoder, and display, to monitor via load cell the state of the samples during traction and to save the data on a microSD memory card for later analysis. All the electronic components were placed inside a case shown in Fig.5.

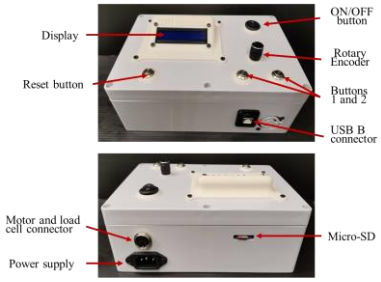


Fig. 5: Electronics case. The two images show the components that allow the user to interface with the electronic part of the bioreactor system.

To control the overall bioreactor system a software was developed with the aim of making the use of the device as simple as possible. Via the buttons on the right-hand side of

the box lid, it is possible to choose from two preinstalled programmes with stimulation frequencies of 1 and 0.5 Hz and the same strain set at 10%, which appear from the literature to be the most commonly used stimulation conditions [4]. It is also allowed the customization of the stimulation program, through the display and the rotary encoder, in terms of the frequency of stimulation, the strain to be applied and the test duration time. The operating workflow initially required the user to calibrate the system by setting a pre-strain of the sample. This is possible by rotating the rotary encoder, whose rotation corresponds to that of the motor. When the load cell reads a value in the set range, is communicated via the display that pre-strain has taken place. The software then waits for the user's choice in the type of stimulation to be performed. A timer then starts counting and when it expires, the system stops. At any time, the reset button can be pressed to stop the motor and restart the menu and a new stimulation test.

C. Leakage tests

Under both static and dynamic conditions, no leaks were detected as a demonstration of the effective functionality of both the chamber covering and the gasket inserted near the shaft. This ensures that the required amount of culture medium is maintained sterile during the mechanical stimulation tests and the possibility to perform any biochemical tests on the culture medium if needed.

D. Stimulation tests

To demonstrate that the bioreactor functions accurately stimulation tests with a frequency of 0.5Hz and 10% strain were carried out. Graphs of the data obtained from the load cell during and store in a memory card stimulation without and with sample are shown in Fig.6. From this data, the stress-strain curve of the stimulated scaffold was obtained as described in section II D. As can be seen in the figure below, the voltage recorded is positive and periodic, so we have demonstrated that the system can stimulate the scaffolds as specified in section 1.

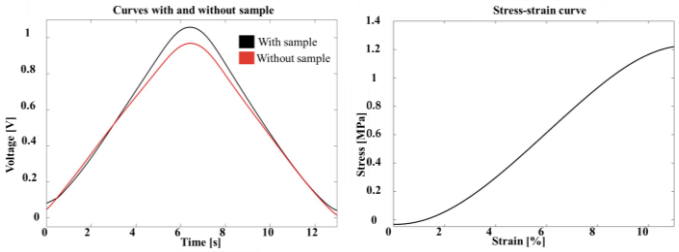


Fig. 6: On left: superposition of one period of the curves obtained from the load cell by performing a tensile mechanical test with and without the sample. In both cases, a filtering of the data by means of moving average filter was applied for smoothing the signal. On right: stress-strain graph curve relating to the tensile of the sample.

IV. Discussion and Conclusion

In this work, a novel bioreactor capable of cyclically stimulating a scaffold with a specific design developed for T/L and enthesis regeneration was presented. Tests carried out on the bioreactor show the capacity to apply constant cyclic traction to the scaffold over time without leakage of the culture medium; moreover, all the critical design specifications identified were meet. Globally, the results obtained demonstrated the potential of the device to stimulate and promote entheses regeneration. Cell culture tests are ongoing to validate the system. Possible future developments may include the modification the culture chamber with inlet/outlet ports to recirculate the culture medium, driven by a peristaltic pump, and thus facilitate long-term experiments.

Acknowledgement

This work was supported by the TRITONE project financed by the Region of Tuscany under the Bando Ricerca Salute 2018 and by the Next Generation EU project I53C22000780001 "Ecosistema dell'Innovazione" Tuscany Health Ecosystem (THE, PNRR, spoke 9: Robotics and Automation for Health).

References

[1] R. A. E. Clayton e C. M. Court-Brown, «The epidemiology of musculoskeletal tendinous and ligamentous injuries», *Injury*, vol. 39, fasc. 12, pp. 1338–1344, dic. 2008, doi: 10.1016/j.injury.2008.06.021.

[2] C. T. Thorpe, E. M. Spiesz, S. Chaudhry, H. R. C. Screen, e P. D. Clegg, «Science in brief: recent advances into understanding tendon function and injury risk», *Equine Vet. J.*, vol. 47, fasc. 2, pp. 137–140, mar. 2015, doi: 10.1111/evj.12346.

[3] J. E. Phillips, K. L. Burns, J. M. Le Doux, R. E. Guldberg, e A. J. García, «Engineering graded tissue interfaces», *Proc. Natl. Acad. Sci. U. S. A.*, vol. 105, fasc. 34, pp. 12170–12175, ago. 2008, doi: 10.1073/pnas.0801988105.

[4] M. Benjamin, B. Moriggl, E. Brenner, P. Emery, D. McGonagle, e S. Redman, «The ?enthesis organ? concept: Why enthesopathies may not present as focal insertional disorders», *Arthritis Rheum.*, vol. 50, fasc. 10, pp. 3306–3313, ott. 2004, doi: 10.1002/art.20566.

[5] I. Donderwinkel, R. S. Tuan, N. R. Cameron, e J. E. Frith, «Tendon tissue engineering: Current progress towards an optimized tenogenic differentiation protocol for human stem cells», *Acta Biomater.*, vol. 145, pp. 25–42, giu. 2022, doi: 10.1016/j.actbio.2022.04.028.

[6] T. Wang *et al.*, «Bioreactor Design for Tendon/Ligament Engineering», *Tissue Eng. Part B Rev.*, vol. 19, fasc. 2, pp. 133–146, apr. 2013, doi: 10.1089/ten.teb.2012.0295.

[7] G. Subramanian, A. Stasuk, M. Elsaadany, e E. Yildirim-Ayan, «Effect of Uniaxial Tensile Cyclic Loading Regimes on Matrix Organization and Tenogenic Differentiation of Adipose-Derived Stem Cells Encapsulated within 3D Collagen Scaffolds», *Stem Cells Int.*, vol. 2017, p. 6072406, 2017, doi: 10.1155/2017/6072406.

[8] «1508-ElectroForce-BioDynamic-5100-Brochure-Short.pdf».

[9] G. H. Altman *et al.*, «Advanced bioreactor with controlled application of multi-dimensional strain for tissue engineering», *J. Biomech. Eng.*, vol. 124, fasc. 6, pp. 742–749, dic. 2002, doi: 10.1115/1.1519280.

[10] Micalizzi et al., Multimaterial and multiscale scaffolds for tendon and ligament regeneration, TERMIS-EU 2022 Conference, Krakow, Poland, 28th June - 1st July, 2022

[11] Criscenti G, Longoni A, Di Luca A, De Maria C, van Blitterswijk CA, Vozzi G, Moroni L. Triphasic scaffolds for the regeneration of the bone-ligament interface. Biofabrication. 2016 Jan 29;8(1):015009. doi: 10.1088/1758-5090/8/1/015009. PMID: 26824799.

[12] «Innovative Silicone Films». https://www.wacker.com/cms/en-us/products/product-groups/silicone-rubber/siliconfilm.html. [online, verified on Jan 2023]

Biological validation of thiolated food grade secondary oil in water nanoemulsions with enhanced mucus-adhesion properties in *Intestine-on-a-chip* model

E. Lagreca[1,2], R. Vecchione[1*], R. Crispino[1,2,3] and P.A. Netti[1,2,3]
[1]*Center for Advanced Biomaterials for Health Care (CABHC), Istituto Italiano di Tecnologia, Napoli*
[2]*Department of Chemical Materials and Industrial Production (DICMaPI), University of Naples Federico II, Napol*[2]
[3]*Interdisciplinary Research Centre on Biomaterials (CRIB), University of Naples Federico II, P.le Tecchio 80, Napoli*

Abstract*— Recently, oral delivery systems have gained more and more attention and among them oil in water nano-emulsions (O/W NEs) are of particular interest for their capability of loading and delivering lipophilic compounds, improving their pharmacokinetic. Few years ago, our group developed a method to stabilize O/W NEs by adding a polymeric shell on the oil core, using pharma grade formulations. To effectively exploit this formulation as food supplement we tried to enhance muco-adhesion properties of the polymer shell, namely chitosan (Ct) towards the intestinal barrier. However, in the field of food supplements, food grade materials should be used, because of both their safety and cost effectiveness. Therefore, in this work, we first have replaced pharma grade (PG) materials with food grade (FG) ones for the preparation of the polymer coated O/W NEs, namely secondary O/W NEs, performing a comparative study between the two formulations. Then we have modified Ct by adding thiol groups via a simple non-covalent procedure based on N-acetylcysteine (NAC) salification, which is compliant with food supplement formulations. PG and FG formulations were prepared and physio-chemically characterized using different techniques, including DLS, ^{1}H-NMR, ITC, obtaining comparable results. We validated these systems in terms of physiological behaviour. Very importantly, we assessed mucus-adhesion properties of the two polymeric coatings (Ct and Ct-NAC) within a microfluidic device in the shape of an intestine-on-chip device capable of mimicking the *in-vivo* intestinal microenvironment, verifying a significant enhancement in the mucus-adhesive properties of Ct-NAC with respect to Ct due to the presence of thiol groups, as expected. Nonetheless, in-vivo assays are required as a final assessment for the proposed system to be commercialized.

Keywords: Oil in water Nanoemulsions, Intestine-on-a-chip, Mucus-adhesion.

I. Introduction

Food grade nano-formulations are becoming a promising option for the encapsulation of bio-active molecules with limited oral bioavailability, due to the protection they guarantee in the harsh conditions typical of the gastrointestinal tract (GIT) after their ingestion [1-3]. Oil in water nano-emulsions (O/W NEs) are an ideal oral delivery system, thanks to their physicochemical and functional properties, such as high encapsulation efficiency for lipophilic molecules, high bioavailability [4, 5] and time stability. In our group, we were able to implement a remarkable strategy to improve the stability of completely nature-based O/W NEs by optimizing process and composition [6]. In this work, we have proposed a completely food grade (FG) secondary O/W NE for oral delivery of lipophilic substances, comparing it to the pharmagrade (PG) counterpart by means of stability, size distribution and material interactions. Then, taking advantage of a simple yet effective microfluidic platform in the shape of a gut-on-chip device, we assessed mucus-adhesion properties of the nanocarrier. Each PG component of the nano-carrier was replaced step by step and compared with the FG analogous in terms of size distribution (DLS) and in terms of materials interaction, strictly connected to the final stability of the formulation (Isothermal titration calorimetry, ITC). Aiming to enhance Ct-NEs mucus-adhesiveness, we developed a Ct salification reaction with a food grade N-acetyl-cysteine (NAC) [7]. Since salification is not a covalent reaction and does not need activator agents, there is no need to remove secondary reaction products. Firstly, this derivative was employed for building SNEs with an improved mucus adhesive property in substitution of covalent derivatives [7]-[29]. Finally, to assess the improvement in terms of mucus-adhesion, we exploited an organ-on-chip, i.e. a microfluidic cell culture system, with controlled dynamic conditions able to replicate the assembly, function and physiology of a human organs *in vitro* [8]. We designed an Intestine-on-a-chip (InOA-chip) platform composed of a single PDMS microfluidic channel on which human intestinal epithelial cells were cultivated in a controlled environment [9, 10]. InOA-chip platform was produced by culturing human colorectal adenocarcinoma (Caco-2) cell line under dynamic fluid flow on PDMS. In these conditions Caco-2 cells form a polarized epithelial monolayer that can mimic adsorptive enterocytes. Thanks to it we were able to evaluate and compare mucus-adhesion properties of polymeric coated nanocarriers (Ct and Ct-NAC). In the end, confocal imaging was used to qualitatively estimate the transport and localization of Ct and Ct-NAC NEs. This is a key point because muco-adhesiveness is strictly related to the release of the encapsulated active molecule.

II. Results and Discussion

A. Materials characterization

We proposed a non-covalent functionalization of chitosan with NAC, adding thiol groups to it. Since this is a simple salification, we are able to avoid activator agents and, more importantly, elimination of secondary reaction products. For each Ct-NAC, we calculated % NAC, which is related to the

presence of thiol groups, whose concentration was measured by Ellman's test, i.e., a colorimetric assay able to quantify free thiol groups. Ellman's test results show very similar %NAC (average value ≈ 15.8 ± 1.1 %) regardless of FG or PG Ct. To corroborate Ellman's test results, the Ct salification was evaluated by ^{1}H-NMR[11]. Each spectrum shows a triplet signal at 3 ppm (H-2-2'), meaning that there are not any covalent bonds between Ct and NAC, which acts like Ct counter-ion by salification. The Deacetylation degree (%DD) and Acetylation degree (%DA) calculated by ^{1}H-NMR analysis were respectively in PG Ct NAC 81% and 47% and FG Ct NAC 68% and 55%.

B. Nanocarrier assembly and characterization

ITC experiments allowed to identify an exothermic binding event followed by an aggregation for both PG Ct and FG Ct due to electrostatic interaction between the negative O/W NEs and the positive charged Ct. The binding was characterized by unfavorable enthalpic contribution, but favorable entropic contribution to Gibbs energy change, as already found in a previous work [12], where the O/W NE was titrated with PG Ct in similar solution conditions. The ITC proved that the interaction between polymer and NE is not influenced by the grade (FG or PG) of Ct and that the thermodynamic parameters determined for both types of Ct are comparable (**Fig. 1**), corroborating that the typology of Ct did not influence the electrostatic interaction between polymer and NE.

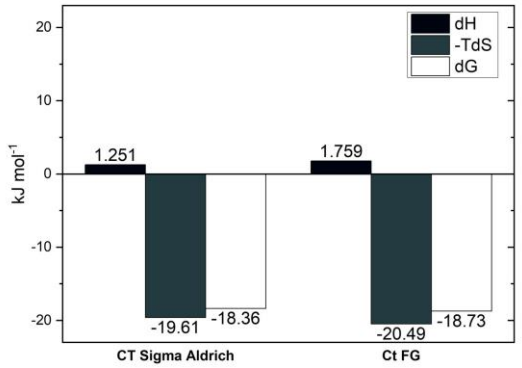


Fig. 1: Diagram of the thermodynamic parameters of electrostatic interaction of 0.7 w/v % PG Ct (**A**) and FG Ct (**B**) into O/W NE 1.1 wt% oil at 25 °C.

After having characterized Ct in all its configurations, we used it to coat primary NEs (**Fig. 2-A**). This coating produces a charge switching from a negative to a positive ζ-potential value. In all cases, we observed a little increase of the hydrodynamic diameter of NE droplets, although remaining monomodal, a symptom of the formation of a nanometer shell around the oil core. On the overall, we observed no difference, especially in terms of stability, between FG and PG formulations, confirming the possibility of exploiting entirely FG based O/W Ct NEs, enabling the nanocarrier for a possible entry in the food industry. Furthermore, FG Ct and Ct-NAC NEs (10 wt % oil and 0.1 w/v % polymer) loaded with curcumin (CUR) were also prepared and checked by DLS showing maintenance in values (**Fig. 2-B-E)** (Particle size distribution of 94.17 ± 0.30 nm; PDI value of 0.01 ± 0.02; ζ-potential value of 43.3 ± 0.6 mV for curcumin loaded Ct-NAC NEs; Particle size distribution of 87.16 ± 0.62 nm; PDI value of 0.07 ± 0.02; ζ-potential value of 43.3 ± 0.6 mV for curcumin loaded Ct NEs) with results which are comparable to FG empty formulations **(Data not shown)** (Particle size distribution of 98.58 ± 0.70 nm; PDI value of 0.099 ± 0.004; ζ-potential value of 39.5 ± 2.0 mV for empty Ct-NAC NEs; Particle size distribution of 93.03 ± 0.9 nm; PDI value of 0.088 ± 0.001; ζ-potential value of 35.0 ± 0.9 mV for empty Ct NEs). The DLS data were corroborated by Cryo electron transmission microscopy (CRYO-TEM) which showed a nanosized distribution for both Ct-NEs and Ct-NAC NEs CUR loaded formulations (**Fig 2 -C and D**).

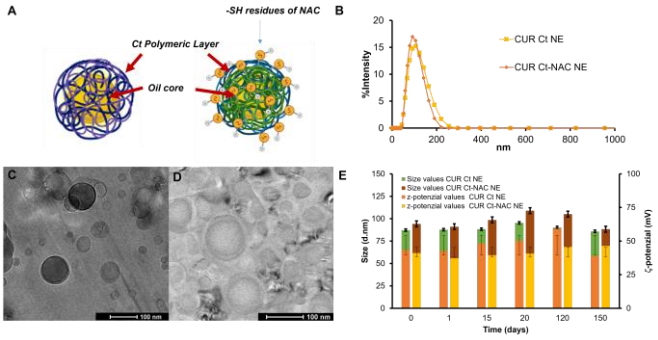


Fig. 2: A) Schematic representation of Ct NE (right) and Ct-NAC (left) **B**) Size value distributions of secondary NEs 10 wt% oil - 0.1 w/v % polymer: CURCt NE. **C**) Ct NEs CRYO TEM image and **D)** Ct-NAC NEs CRYO TEM image, **E**) CUR Ct NEs and CUR Ct NAC NEs stability in term of size and ζ-Potential value. Data are reported as mean (n = 3) (s.d.).

C. Mucus-adhesion properties in InOA-chip

Finally, we tested the muco-adhesive properties of Ct-NAC in comparison with simple Ct. This has been assessed through an InOA-chip device in which we culture Caco-2 cells that, given the dynamic fluid flow and shear stresses typical of the intestine, formed a monolayer. In literature it is possible to find many *in vitro* approaches to quantify mucus permeation [13], among them microfluidic systems able to reproduce the formation of the intestinal dynamic mucus architecture are of great interest [14]. Moreover, this gives the possibility of have human-like mucus without the effort of 3D Intestine *in vitro* models, which are more complex and obtained from biopsies of human intestinal tissues [15]. We used this functional microfluidic platform for the first time to monitor *in situ* real-time the intestinal microenvironment formation and to simulate Ct and Ct-NAC NEs interaction with intestine. For this purpose, we implemented confocal analysis to detect the FITC, with which we labelled the polymer coating of NEs as to monitor the cellular uptake and retention of nanoemulsions on the mucus layer [16]. The Caco-2 monolayers treated with FITC-Ct NEs and FITC-Ct-NAC NEs showed a tight junction-modulation, due to chitosan ability to open the intercellular tight junctions enhancing paracellular permeability [17] (**Fig. 3-A,B**), differently from the not treated Caco-2 monolayer (**Fig. 3-C**). In addition, we observed a spread signal of FITC in Caco-2 monolayers treated with Ct NEs (**Fig. 3-D**) compared with Ct-NAC NEs in which, together with the strong FITC signal, there were some fluorescent spots due to monolayer aggregates (**Fig. 3 -E**). We continued monitoring FITC signal for both formulations for over 140 min (**Fig. 3-F**).

They reached the same plateau after 1 h of treatment, probably due to a saturation in the signal of FITC that did not permit to detect any difference in fluorescence intensity during the treatment. Knowing this and aiming to assess muco-adhesion, we washed the channel to remove the excess of the two systems and re-analyzed the fluorescence intensity of FITC in Ct NEs and Ct-NAC NEs. The images show almost no FITC signal, representative of few Ct NEs linked to mucus produced by Caco-2 cells **(Fig. 3-G**), compared to the higher signal of Ct-NAC NEs (**Fig. 3-I**), shown also in the high magnification insets (**Fig. 3-H** and **J**), indicating much higher adhesion for this system. After washing, the intensity of Ct-NEs signal decreased whereas Ct-NAC showed a greater intensity due to a steady adhesion to the mucus layer (**Fig. 3-K)**.

We believe that the enhanced mucus-adhesions properties of Ct-NAC NEs are due to the formation of covalent S–S bonds by free thiol groups of Ct-NAC and cysteine from mucus domains, further enhanced by the electrostatic interactions between the positively charged Ct and the negatively charged mucosa layer, as it has been reported in literature for covalent bounded Ct-NAC nanocarriers [7], [17, 18],[7, 19].

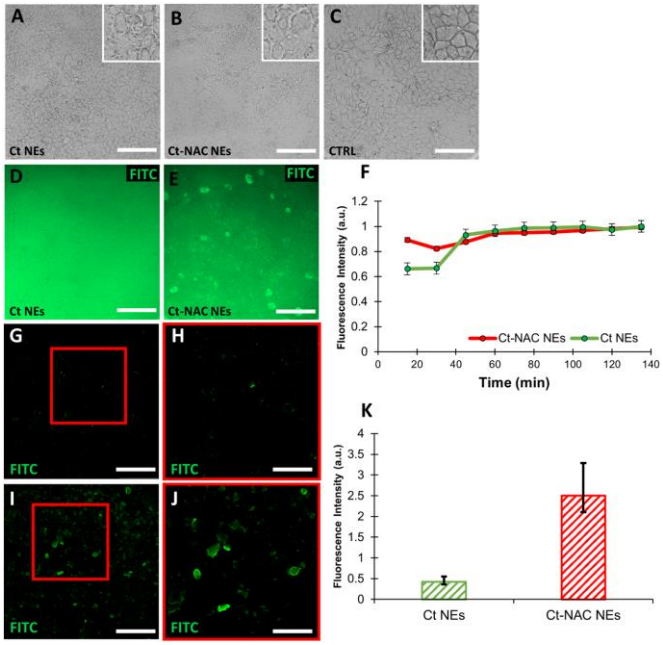


Fig. 3: Analyses of mucus adhesions properties of Ct-FITC NEs and Ct-NAC-FITC NEs. Bright-field images of **A**) Ct NEs, **B**) Ct-NAC NEs and **C**) CTRL with high magnification views of Caco-2 monolayers; FITC images of Caco-2 monolayer treated with **D**) Ct NEs and **E**) Ct-NAC NEs; scale bar 100 µm. **F**) Graph of fluorescence intensity of Ct-FITC NEs and Ct-NAC-FITC NEs time-dependent. FITC images of **G**) Ct NEs and **I**) Ct-NAC NEs after washing and fixing and high magnification views shown in red squares (**H**, **J**); scale bar 100 µm and 70 µm. **K**) Graph of fluorescence intensity of Ct-FITC NEs and Ct-NAC-FITC NEs after washing and fixing.

Recently, we have also started to work on the replacement of acetic acid with citric acid for a matter of taste improvement and thus patient compliance and at least in the first 20 days the size is perfectly stable (**Table I**). Size stability is under monitoring.

TABLE I: TIME STABILITY OF CT NES IN CITRIC ACID

Day	*Size (nm)*	*PdI*	*Z-potential(mV)*
0	106.7±0.2	0.074±0.2	16.2±3.27
2	107.1±0.5	0.081±0.3	22.9±3.24
10	98.6±7.6	0.108±0.4	26.2±3.73
20	108.8±0.2	0.1±0.4	28.1±3.37

III. CONCLUSION

To conclude, we presented for the first time, a full FG delivery system based on a secondary O/W NE coated with Ct-NAC obtained by non-covalent bound thiols that in turn enhance mucus-adhesion properties. FG and PG formulations have been morphologically, thermodynamically, and chemically compared. The are no differences between them from both size and stability perspectives. Last but not least, the Ct and Ct-NAC mucus adhesive properties were compared for the first time within an innovative and accessible intestine-on-chip platform, InOA-chip, proving that thiolated Ct NEs possess much better mucus adhesive properties, as a consequence of S-S bonds formation with the mucin produced by the Caco-2 monolayers. The proposed totally FG system opens a new route in nutraceutical field, being a novel emulsion-based formulation with enhanced mucus-adhesiveness thanks to the Ct salification with NAC. Nonetheless, the chosen non-covalent thiol functionalization of chitosan opens the door to an immediate use of such formulation with no need for safety clinical tests.

REFERENCES

1. Dasgupta, N. and S. Ranjan, *An introduction to food grade nanoemulsions*. Vol. 13. 2018: Springer.
2. McClements, D.J. and J. Rao, *Food-grade nanoemulsions: formulation, fabrication, properties, performance, biological fate, and potential toxicity.* Critical reviews in food science and nutrition, 2011. **51**(4): p. 285-330.
3. Tripathi, A.D., et al., *Nanoemulsions based edible coatings with potential food applications.* International Journal of Biobased Plastics, 2021. **3**(1): p. 112-125.
4. Marhamati, M., G. Ranjbar, and M. Rezaie, *Effects of emulsifiers on the physicochemical stability of Oil-in-water Nanoemulsions: A critical review.* Journal of Molecular Liquids, 2021. **340**: p. 117218.
5. Li, J., et al., *Effects of chitosan coating on curcumin loaded nano-emulsion: Study on stability and in vitro digestibility.* Food Hydrocolloids, 2016. **60**: p. 138-147.
6. Vecchione, R., et al., *Tunable stability of monodisperse secondary O/W nano-emulsions.* Nanoscale, 2014. **6**(15): p. 9300-9307.
7. Bravo-Osuna, I., et al., *Mucoadhesion mechanism of chitosan and thiolated chitosan-poly (isobutyl cyanoacrylate) core-shell nanoparticles.* Biomaterials, 2007. **28**(13): p. 2233-2243.
8. Xiang, Y., et al., *Gut-on-chip: Recreating human intestine in vitro.* Journal of Tissue Engineering, 2020. **11**: p. 2041731420965318.
9. De Gregorio, V., et al., *Intestine-on-chip device increases ECM remodeling inducing faster epithelial cell differentiation.* Biotechnology and Bioengineering, 2020. **117**(2): p. 556-566.
10. De Gregorio, V., et al., *Intestine-liver axis on-chip reveals the intestinal protective role on hepatic damage by emulating ethanol first-pass metabolism.* Frontiers in bioengineering and biotechnology, 2020. **8**: p. 163.
11. Boonsongrit, Y., B.W. Mueller, and A. Mitrevej, *Characterization of drug–chitosan interaction by 1H NMR, FTIR and isothermal titration calorimetry.* European Journal of Pharmaceutics and Biopharmaceutics, 2008. **69**(1): p. 388-395.

12. Fotticchia, I., et al., *Thermodynamic signature of secondary nano-emulsion formation by isothermal titration calorimetry.* Langmuir, 2014. **30**(48): p. 14427-14433.
13. Wright, L., et al., *Mimicking the Gastrointestinal Mucus Barrier: Laboratory-Based Approaches to Facilitate an Enhanced Understanding of Mucus Permeation.* ACS Biomaterials Science & Engineering, 2021.
14. Lindner, M., et al., *Physiological Shear Stress Enhances Differentiation, Mucus-Formation and Structural 3D Organization of Intestinal Epithelial Cells In Vitro.* Cells, 2021. **10**(8): p. 2062.
15. Shi, M., et al., *Phytochemicals, Nutrition, Metabolism, Bioavailability, and Health Benefits in Lettuce—A Comprehensive Review.* Antioxidants, 2022. **11**(6): p. 1158.
16. TM, M.W., W.M. Lau, and V.V. Khutoryanskiy, *Chitosan and Its Derivatives for Application in Mucoadhesive Drug Delivery Systems.* Polymers (Basel), 2018. **10**(3).
17. Vllasaliu, D., et al., *Tight junction modulation by chitosan nanoparticles: comparison with chitosan solution.* International journal of pharmaceutics, 2010. **400**(1-2): p. 183-193.
18. Kast, C.E. and A. Bernkop-Schnürch, *Thiolated polymers—thiomers: development and in vitro evaluation of chitosan–thioglycolic acid conjugates.* Biomaterials, 2001. **22**(17): p. 2345-2352.
19. Noi, I., et al., *Permeability of novel chitosan-g-poly (methyl methacrylate) amphiphilic nanoparticles in a model of small intestine in vitro.* Polymers, 2018. **10**(5): p. 478.

Design and fabrication of a micro-dialyser for the study of the gut microbiota-tissues cross-talk

A. De Acutis[1], C. Daddi[1,2], F. Biagini[1], E. Russello [2], M. Calvigioni[3], E. Ghelardi[3], C. De Maria[1,2] and G. Vozzi[1,2]

[1] *Department of Information Engineering, University of Pisa, Pisa, Italy.*
[2] *Research Center "E. Piaggio", University of Pisa, Pisa, Italy*
[3] *Department of Translational Research and New Technologies in Medicine and Surgery, University of Pisa, Pisa, Italy.*

***Abstract*—The co-culture of the human gut microbiota and eukaryotic cells is still a great challenge in biomedical research. Direct exposure to microbes could in fact cause cell infections or death, as microbial metabolites may have cytotoxic effects. Moreover, cells and microbes usually require different culture conditions. Accordingly, this work presents the design, development and performance of a novel micro-dialyser to allow the microfluidic co-culture of eukaryotic cells and microbes thereby assessing their crosstalk while preventing their direct contact.**

***Keywords*—Microfluidic device, dialysis, gut microbiota.**

I. Introduction

THE gastrointestinal tract houses an extremely variable microflora called "human gut microbiota" (HGM), which constantly impacts the state of health and disease of the host [1]-[3]. The symbiotic interaction between the HGM and the host has considerable effects both locally, due to the HGM's intimate contact with the intestinal cells, and systemically, as the alteration of the HGM's composition towards a pathologic profile (*i.e.*, dysbiosis) has been associated with numerous disorders and diseases, from allergies to neurodegenerative diseases and even cancer [2], [3]. To better understand dysbiosis-associated diseases and the related therapeutic strategies, it is essential to deepen our knowledge of the HGM, its symbiotic interaction with the host, and the role of intestinal dysbiosis in the disease's onset. Among the common HGM study approaches the analyses of human and animal faeces are not fully representative of the microbial composition in the different intestinal districts and results from in vivo animal models have limited translatability to human applications due to inter- and intra-species variability [3]-[5]. Additionally, the 3Rs European directive is increasingly encouraged [3], [5]. In vitro culture models represent powerful tools to recapitulate the specific anatomical, physiological and environmental conditions in which the HGM proliferates and to investigate its cross-talk with the host [1]-[5].

Bioengineering is currently aiming to develop novel in vitro culture devices, which can integrate microbial fermentation technologies with advanced systems for the in vitro co-culture of HGM and host cells [6]. In this perspective, a selective filtration system becomes crucial as some HGM's metabolites have beneficial effects on eukaryotic cells (*e.g.*, short-chain fatty acids [4], [7]) while others can be cytotoxic (*e.g.*, colibactin) [7].

Accordingly, this work presents the design and fabrication of a novel micro-dialysis system that can be used in a co-culture microfluid system for allowing the chemical crosstalk between eukaryotic cells and microbes and investigating host-HGM interactions without allowing their physical contact.

II. Materials and Methods

A. Design and fabrication of the micro-dialysis system

The micro-dialysis system consists of two symmetrical parts (upper and lower) (Figure 1b, Figure 2h) and a dialysing membrane between them. The upper part allows the flow of the HGM's culture medium, while the lower part allows the flow of the dialysed fluid. A schematic representation of the device and its coupling with the hydraulic circuit is presented in Figure 1.

Both the lower and upper parts were fabricated by casting, using Sylgard 184 (Dow Corning, USA), a biocompatible silicone [8]; a ratio of 10:1 w/w was used for the base agent and curing agent, respectively. Each batch of silicone was degassed before use for removing trapped air within the mixed materials. A 30% w/v Pluronic F-127 (Sigma-Aldrich, USA) hydrogel was prepared through the procedure described in [9] and used at room temperature as a sacrificial material to create microfluidic channels in the silicone part. The mould for the lower and upper part of the device was fabricated by firstly printing the microfluidic channels (200 μm height, 200 μm width) and tubing entry guides using the pluronic-based sacrificial ink into a petri dish (60 x 15 mm) using an INKREDIBLE 3D printer (CellInk, USA). Different printing models were designed using Solidworks CAD software and then converted into a G-Code file using Slic3r with 0.2 mm layer height,100% infill and 260 μm conic nozzle diameter. Thereafter, the degassed silicone mixture was poured into the mould up to the mid-height of the petri dish. After a 30 min curing process at 60°C, commercial silicone tubes were inserted into the previously-printed Pluronic-based guides and additional silicone was poured in until complete filling of the petri dish, which was then left at 60°C for 30 min. The mould was placed at 4°C to allow the Pluronic liquefaction and its subsequent removal. The entire procedure is summarised in Figure 2.

To guarantee the hydraulic sealing of the microfluidic device, once a 14 kDa dialysing membrane (Sigma-Aldrich, USA) is placed between the silicone parts, two different ABS sealing systems (Figure 3) were designed and fabricated using an FDM printer (Stratasys 250 MC, USA): a bolted closure system and a snap-fit closure system.

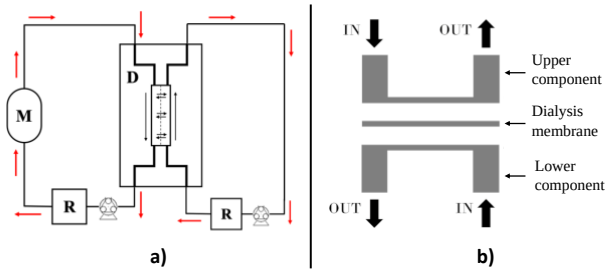


Fig. 1: Schematic representation of the micro-dialysis system. a) Coupling with the hydraulic circuit. M: human gut microbiota culture chamber, R: culture medium's reservoir, D: dialyser. b) Scheme of the device.

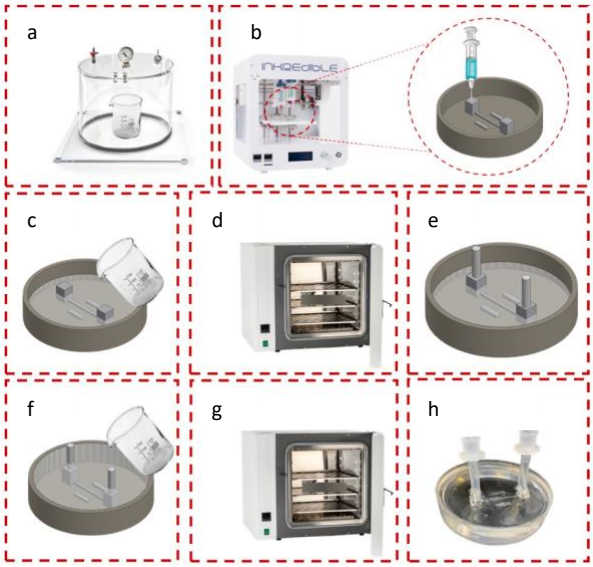


Fig. 2: Micro-dialyser fabrication. a) Silicone preparation and degassing procedure. b) Printing process. c) Poured silicone up to the mid-height of the petri dish. d) Curing phase. e) Insertion of the tubes into the guides. f) Final pouring of the silicone. g) Final curing phase. h) The fabricated upper or lower silicone parts.

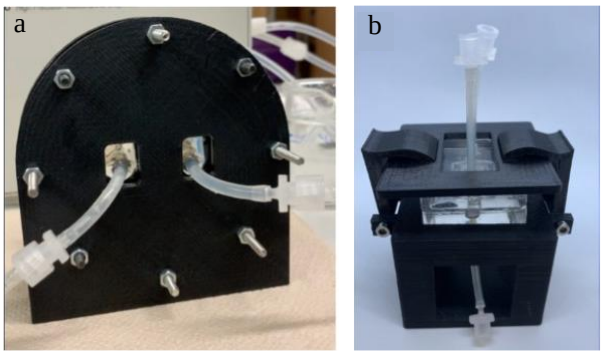


Fig. 3: Prototype of the closure systems. a) Bolted system. b) Snap-fit system.

B. Testing of different microfluidic circuit geometries

Different microfluidic circuit geometries (*i.e.*, with spiral, hexagonal, and serpentine paths) were designed and tested: a dye was dissolved in deionised water (dH_2O), which was then flowed through the microfluidic system using a peristaltic pump (Ismatec IPC, Fisher Scientific). The performance of the two sealing systems was evaluated, as well.

C. Finite element simulations

Finite element simulations were performed using COMSOL Multiphysics 5.5 software to highlight the most time-efficient combination of the different circuit geometries and dialysing configurations (*i.e.*, co-current and counter-current).

The adopted geometry is composed of three domains, modelling the upper compartment, the dialysing membrane and the lower compartment. The "Laminar Flow" and "Transport of Diluted Species in Porous Media" modules were used and coupled via the fluid velocity field. The liquid media and the dialysing membrane were modelled as water and a porous medium, respectively. A fluorescent marker (5(6)-Carboxyfluorescein, CF, Sigma-Aldrich, USA) solution's diffusion through the membrane was simulated with Yamashita's model [10]. A closed-loop circuit configuration was adopted, as recirculation increases fluid velocity and improves mass transfer [11], and was modelled with the periodic condition. A 5 ml/min flow was set and a time-dependent model was implemented over a 22 h (79200 s) period of time with an 1800 s time-step that simulates the periodic sampling of the dialysed fluid.

D. Micro-dialyser efficacy tests

To evaluate the dialysing ability of the microfluidic system, two dynamic experimental tests with fluorescent markers were carried out, using the dialysing membrane.

The first test involved a 2500 nM CF solution in PBS 1X, while the second test involved a 100 µg/ml albumin-fluorescein isothiocyanate (AFI) (Sigma-Aldrich, USA) solution in dH_2O. The CF is expected to diffuse across the dialysing membrane, while the AFI's diffusion is expected to be prevented, as their molecular weights are, respectively, lower and higher than the membrane's cut-off.

For each experiment, the calibration curve was first derived and then a 22-hour dynamic test was carried out with the hexagonal micro-dialyser in the counter-current configuration. For both dynamic tests, the setup (Figures 4 and 5) involved the peristaltic pump for setting a 5 ml/min flow, the printed microfluidic device (hexagonal shape) and two beakers, one containing 20 ml of the fluorescent marker solution and the other containing 20 ml of dH_20.

Samples with a 300 µl volume of the dialysed fluids were taken at 0, 30, 60, 90, 180, 240, 360, and 1320 min. Then, 100 µl aliquots of those samples were placed in a 96-well plate and scanned with a plate spectrofluorometer (SpectraMax Gemini™ XPS/EM Microplate Reader, Molecular Devices).

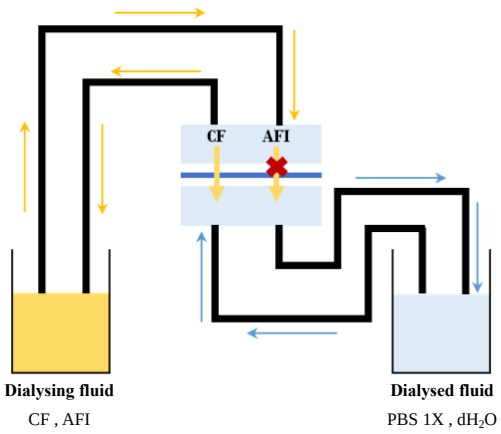


Fig. 4: Schematics of the experimental setup.



Fig. 5: Image of the dialysis setup.

III. Results

A. *Testing of different microfluidic circuit geometries*



Fig. 6: The fabricated micro-dialysis system.

The completely assembled micro-dialysis system is shown in Figure 6.

Both closure systems showed optimal hydraulic sealing for 24 h under a 5 ml/min fluid flow. Nevertheless, the snap-fit closure system was adopted since it simplified the assembly and disassembly procedures. Concerning the circuit geometry, in the hexagonal-shaped and serpentine-shaped circuits the liquid filled the channels completely and by following the path, while in the spiral-shaped channel, the liquid flowed from one channel to the other without following the default path (Figure 7). Thus, this latter configuration was discarded.

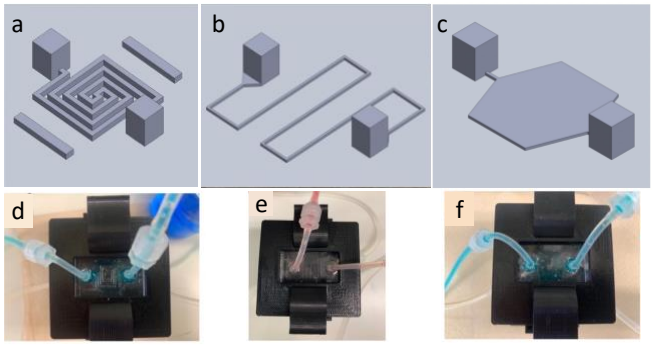


Fig. 7: Different circuit geometries CAD models. a) Spiral. b) Serpentine. c) Hexagonal. d, e, f) Results of the tests for the spiral, serpentine and hexagonal configurations.

B. *Finite element simulations*

The effectiveness of hexagonal and serpentine-shaped dialysers in both the co-current and counter-current configurations was compared. The steady-state achievement was evaluated as the ratio between the concentration at a specific time t and the equilibrium concentration.

The hexagonal-shaped dialyser in the counter-current configuration is the first to reach the steady state (Figure 8). In fact, the counter-current configuration contributes to a better maintenance of the concentration gradient between the two compartments [12], [13] and the greater exchange area between the two compartments of the hexagonal-shaped dialyser increases the device's clearance [14].

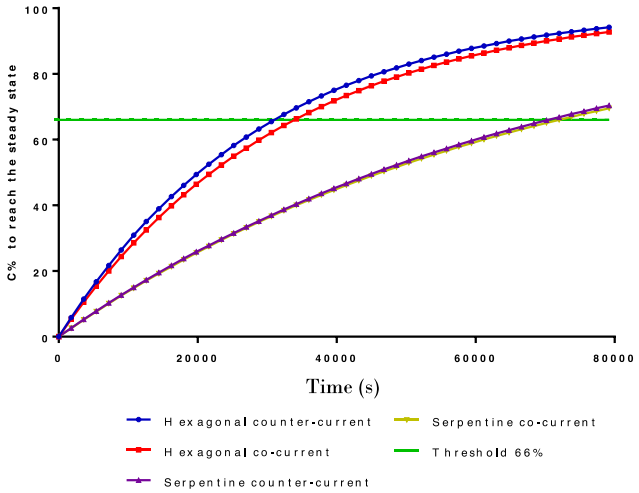


Fig. 8: Steady-state achievement comparison between the two circuit geometries (*e.g.*, hexagonal and serpentine) in the two different configurations (*e.g.*, co-current and counter-current).

C. *Micro-dialyser efficacy tests*

As expected, the tests resulted in the CF's diffusion through the membrane, as its concentration in the dialysed fluid rose (Figure 9a) and the AFI's retention, as its concentration in the dialysed fluid is always almost comparable to 0 (Figure 9b). Moreover, the experimental data on the CF's concentration over time showed no statistical differences with FE-computed CF's concentration over time (Figure 10), therefore validating the computational model described in section II C.

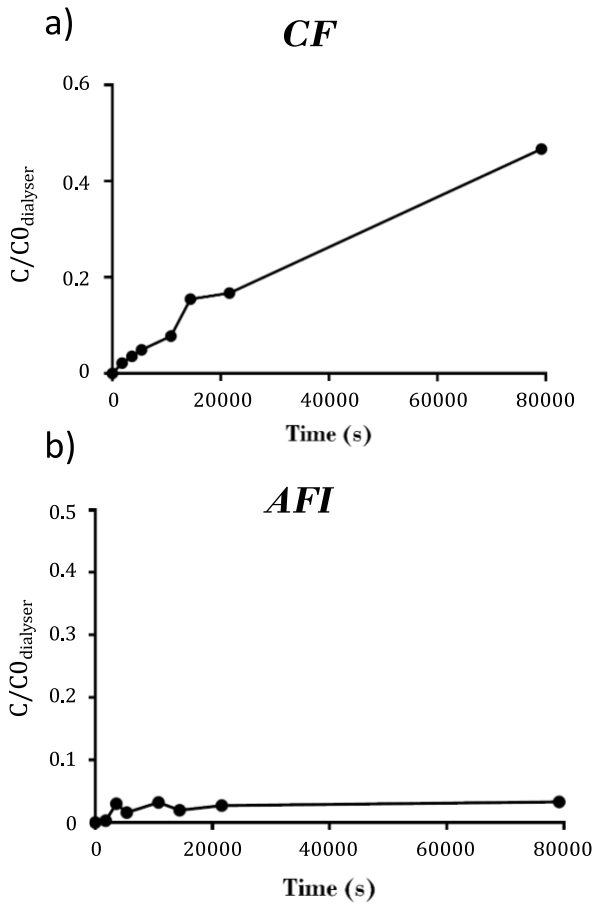


Fig. 9: Fluorescent markers' concentrations in the dialysed fluids over time. a) CF concentration over time. b) AFI concentration over time.

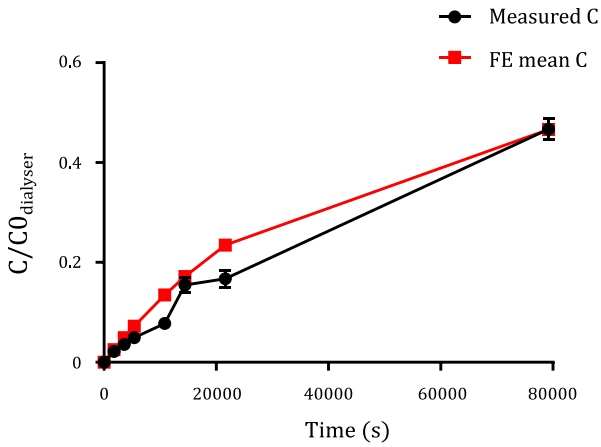


Fig. 10: Comparison between the experimentally and computationally obtained CF's concentration over time in the dialysed fluid.

IV. Conclusion

The fabricated novel micro-dialyser guaranteed the total absence of leaks in all tests and an optimal dialysing ability, as observed in the experimental dialysing tests described in sections II D and III C. Those experiments assessed also the better performance of the hexagonal-shaped microfluidic circuit in the counter-current configuration compared to the alternatives. This outcome is in line with the results obtained with numerical simulations, thereby validating the designed FE model.

Among the future perspectives, the micro-dialysis system represents a promising tool to evaluate the indirect effects of the HGM's metabolites on eukaryotic cells, by simply exposing them to the dialysed surnatants of the HGM in vitro culture. Additionally, other circuit geometries could be considered to further improve the device's dialysing ability and dialysis membranes with different cut-offs could be used to give deeper insights into the different HGM metabolites and how they impact eukaryotic cells' metabolism or viability. Future design optimizations of the device could include bubble-trap systems to limit cell membrane damage or even cell death due to air bubbles. Finally, a specifically designed culture chamber could be integrated into the system to perform the dynamic in vitro culture of the HGM and the dialysis process simultaneously. An external chamber could moreover enable the generation and maintenance of anaerobic environmental conditions and the connection of the microfluidic platform with external cell compartments and, consequently, the analysis of the HGM-tissues/organ interactions.

Acknowledgement

This work was supported by the Next Generation EU project I53C22000780001 "Ecosistema dell'Innovazione" Tuscany Health Ecosystem (THE, PNRR, spoke 9: Robotics and Automation for Health).

References

[1] R.M. Shah et al., "An integrated multi-disciplinary perspective for addressing challenges of the human gut microbiome", *Metabolites*, *10*(3), 94, 2020.
[2] L. Sardelli et al., "Technological tools and strategies for culturing human gut microbiota in engineered in vitro models", *Biotechnology and Bioengineering*, *118*(8), 2886-2905, 2021.
[3] L. Sardelli et al., "Towards bioinspired in vitro models of intestinal mucus", *RSC advances*, *9*(28), 15887-15899, 2019.
[4] F. Biagini et al., "A novel 3D in vitro model of the human gut microbiota", *Scientific reports*, *10*(1), 1-12, 2020.
[5] F. Biagini et al., "Designs and methodologies to recreate in vitro human gut microbiota models" *Bio-Design and Manufacturing*, 1-21, 2022
[6] F. Biagini et al., "Study of the Adhesion of the Human Gut Microbiota on Electrospun Structures", *Bioengineering*, 9.3, 96, 2022.
[7] P. Louis, G.L. Hold, and H.J. Flint, "The gut microbiota, bacterial metabolites and colorectal cancer", *Nature reviews microbiology*, *12*(10), 661-672, 2014.
[8] S.W. Allison, E.S. Baker, K.J. Lynch, and F. Sabri, "In vivo X-Ray excited optical luminescence from phosphor-doped aerogel and Sylgard 184 composites", *Radiation Physics and Chemistry*,*135*, 88-93, 2017.
[9] I.R. Schmolka, "Artificial skin I. Preparation and properties of pluronic F-127 gels for treatment of burns", *Journal of biomedical materials research*, 6(6), 571-582, 1972.
[10] A.C. Yamashita, and K. Sakurai, "Dialysis membranes–physico-chemical structures and features", *Updates in Hemodialysis*, 159-187, 2015
[11] H.M. Yeh, "Numerical analysis of mass transfer in double-pass parallel-plate dialyzers with external recycle", *Computers & Chemical Engineering*, *33*(4), 815-821, 2009.
[12] H.M. Yeh, and Y.H. Chang, "Mass transfer for dialysis through parallel-flow double-pass rectangular membrane modules", *Journal of membrane science*, *260*(1-2), 1-9, 2005.
[13] H.M. Yeh, "Numerical analysis of mass transfer in double-pass parallel-plate dialyzers with external recycle", *Computers & Chemical Engineering*, *33*(4), 815-821, 2009.
[14] N.A. Peppas, and R.E. Hannenman, "Biomedical engineering principles" David O. Cooney, Marcel Dekker, New York, 1976, xiv+ 458 pages, 1977.

Natural polymer-based bioinks exploiting internal gelation mechanism for cardiac tissue engineering

Giovanni Paolo Stola [1,2,3,†], Elena Marcello [1,2,3,†], Camilla Paoletti [1,2,3], Letizia Nicoletti [1,2,3] and Valeria Chiono [1,2,3]

[1] *Department of Mechanical and Aerospace Engineering, Politecnico di Torino, Torino, Italy*
[2] *Centro 3R, Interuniversity Center for the Promotion of the 3Rs Principles in Teaching and Research, Italy*
[3] *POLITO BioMedLab, Politecnico di Torino, Turin, Italy*
[†] *These authors share first authorship*

***Abstract* – 3D bioprinting techniques are rapidly increasing their relevance in the field of tissue engineering as potential tools for the fabrication of complex 3D structures that could find applications as therapeutic patches or *in vitro* models. In this work, we investigated the use of alginate and gelatin based bioink for cardiac tissue engineering. The hydrogels were developed through an internal gelation mechanism, allowing 3D printing of uniform self-supporting fibres without the need for post-crosslinking or the use of support materials. Varying gelatin content, bioinks with tuneable rheological properties were developed. Biological validation showed that the bioinks were biocompatible and promoted cell adhesion.**

Keywords - Alginate dialdehyde, gelatin, bioink, internal gelation

I. INTRODUCTION

Cardiovascular diseases (CVDs) represent a social and economic worldwide burden, causing about 18 million deaths per year [1]. New resolutive therapies are highly demanded as heart transplantation still remains the only effective therapeutic option in case of end stage heart failure.

3D bioprinting techniques are gaining tremendous attention in tissue engineering and regenerative medicine as the precise and controlled deposition of bioinks can be exploited for the fabrication of complex 3D structures [2]. In cardiac tissue engineering, bioinks can be employed to develop scalable and reproducible bioprinted constructs as therapeutic patches for cardiac regeneration or *in vitro* models for preclinical validation of new advanced approaches.

Alginate (Alg)-based bioinks have been widely investigated thanks to their tuneable properties and cost-effectiveness [3]. Alg-based materials are currently being investigated in clinical trials for cardiac regeneration. Algisyl-LVR™ is an Alg-based injectable hydrogel designed to confer mechanical support to the left ventricle to prevent or reverse the progression of heart failure [4].

Alg-based hydrogels are usually obtained through physical crosslinking of Alg chains with polyvalent cations (e.g., calcium ions, Ca^{2+}). The sol/gel transition of Alg occurs under physiological conditions and almost instantly [5].

Alg 3D bioprinting usually exploits an external gelation mechanism, by the extrusion of an Alg sol phase into Ca^{2+} enriched supporting bath [6]. The crosslinking is fast and non-homogeneous, localized at the interface between the printed filament and the coagulation bath [7]. A thermosensitive supporting bath containing calcium ions derived from dissociations of salts, such as calcium chloride ($CaCl_2$), has been proposed to achieve higher 3D spatial resolution and shape fidelity, in the so-called "FRESH" method [8], [9].

Recently, internal gelation of Alg chains has been investigated to develop 3D self-standing constructs without the use of a supporting bath [10]. In this case, a water-insoluble calcium salt (e.g., $CaCO_3$) is dispersed within the Alg sol phase, and Alg crosslinking is triggered by pH-induced progressive release of Ca^{2+} promoted by the addition of an acidifying compound (e.g., glucono-d-lactone - GDL). [7] Internal gelation results in homogeneous gel and allows the 3D printing of uniform self-supporting fibers without the need for post-crosslinking or the use of supporting materials or bath. 3D printing based on this crosslinking mechanism has been limited to Alg-based bioinks. Even though Alg is biocompatible, non-immunogenic and non-toxic, its applications are restricted due to the lack of cell-adhesive motives and poor *in vivo* degradation [4]. To overcome such limitations, herein we investigated the use of oxidized alginate or alginate dialdehyde (ADA) to improve materials degradability, and its combination with gelatin (Gel) to promote cell adhesion and enhance biological properties. In this work, novel Alg-ADA-Gel hydrogels based on internal gelation mechanism were optimized for applications as bioinks for prospective applications in *in vitro* cardiac tissue engineering.

II. MATERIALS AND METHODS

ADA was produced through partial oxidation of sodium alginate via sodium metaperiodate following the protocol by Sarker *et al.* [11]. The oxidation degree was calculated through a starch-iodine method, measuring the unconsumed sodium metaperiodate as described by *Sarker et al.* [11]. Attenuated total reflectance Fourier transform infrared spectroscopy (ATR-FTIR) and ^{13}C CPMAS (cross polarization/magic angle spinning) NMR of alginate powder and ADA lyophilized samples were carried out to investigate the successful formation of aldehyde groups in the alginate chains. Molecular weight of ADA and Alg were determined through viscometric analysis using an Ubbelohde viscometer.

Alg-ADA-Gel hydrogels were optimized maintaining constant ADA, $CaCO_3$ and GDL concentration and varying the polymer weight ratios of Alg:Gel (% w/w) from 100:0 to 50:50 keeping

the final content of Alg + Gel equal to 3% w/v. Rheological characterizations were performed at 37°C using MCR 302 rheometer (Anton Paar) equipped with a parallel plate geometry with a diameter of 25 mm.

In vitro water absorption and dissolution tests were carried out by immersing bulk hydrogels in phosphate buffered saline (PBS) at 37°C to investigate their stability as a function of time. At each time point, the weight of the samples was measured both in wet state and, then, in dry state after freeze-drying. Water absorption degree was calculated as the percentage of water absorbed by hydrogel samples *versus* time. Dissolution degree was calculated as the percentage of dry sample weight loss *versus* time.

Hydrogel printability was assessed using RegenHU - 3D Discovery^{TM} bioprinter by optimizing printing parameters. Model filaments and grid geometries were printed. To investigate changes in printability over time, grid structures were printed at selected time points (from 10 to 90 min). Images were collected with Nikon Eclipse Ti2 spinning disk and NIS-Elements software (Nikon) and the data were analysed using ImageJ software.

In vitro cytocompatibility studies on printed cells-laden Alg-ADA-Gel hydrogels were performed using adult human cardiac fibroblasts (AHCFs), according to ISO 10993-5. Cell viability of AHCFs embedded in printed hydrogel filaments was assessed by Live/Dead assay. Briefly, AHCFs were dispersed in PBS and incorporated in the bioinks with the dual syringe mixing method. 3D bioprinted grid structures were obtained on a 12-well plate, maintained in a humified incubator at 37 $^{\circ}$C, 5% CO_2 and images were collected using Nikon Eclipse Ti2 fluorescence microscope equipped with a spinning disk.

III. Results and Discussions

Alginate dialdehyde was successfully prepared through partial oxidation of alginate via sodium metaperiodate with an average production yield of 75% and an average oxidation degree of 25%. ATR-FTIR and ^{13}C CPMAS NMR spectra further confirmed aldehyde groups formation and successful ADA production. Furthermore, 93% decrease in the viscosity average molecular weight of ADA respect to Alg was measured. Aldehyde groups of ADA are expected to undergo Schiff base reaction with primary amino groups in Gel. On the other hand, ADA carboxyl groups may electrostatically interact with calcium ions.

Initially, the effect of the addition of ADA into Alg-based hydrogels was investigated. The relative amount of the polymers in Alg-ADA hydrogels was optimized to achieve a stiffness value similar to that of Algysil and close to that of cardiac tissue (i.e., G': 1-3 kPa) [12]. The presence of ADA in the selected Alg-ADA hydrogel compositions caused an increase in the hydrogel dissolution rate compared to initial Alg-hydrogels: after 21 days of incubation in PBS, a weight loss of 42% *vs* 25% was measured in bulk Alg-ADA vs. Alg hydrogels, respectively.

Then, Alg-ADA-Gel hydrogels were prepared by optimizing Gel amount to confer cell-adhesive properties to the samples. Alg-ADA-Gel hydrogels preserved cardiac tissue-like viscoelastic properties by properly tuning Gel concentration.

Rheological tests showed a decrease in storage modulus G' as a function of Gel content. Moreover, printability studies of Alg-ADA-Gel hydrogels, moreover, evidenced that all the compositions possessed time-dependent shear thinning properties suitable for 3D bioprinting and influenced by Gel content. Alg-ADA bioinks alone (without Gel) underwent a rapid crosslinking, forming self-standing scaffolds with a printability window of up to 30 min. For bioinks containing Gel, cross-linking time increased, hence the printability interval increased consistently as a function of the amount of Gel in the bioinks, reaching 90 min for samples with 50:50 of Alg:Gel ratio. Within the printability windows, optimal printability times were identified for each hydrogel composition, depending on crosslinking time. Exemplary images of printed grid structures are reported in Fig.1.

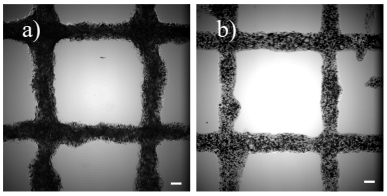


Fig. 1: Representative optical microscopy images of printed grid-shaped structures using: (a) Alg-ADA ink and (b) Alg-ADA-Gel ink with 50:50 Alg:Gel weight ratio. Structures were printed at the optimal printability times for each composition. The scale bar is equal to 250 um

Furthermore, *in vitro* tests showed that viability of AHCFs in contact with the analyzed samples was high (ISO-10993-5) and an increase in Gel content also improved cell adhesive properties of hydrogels.

Finally, the production of cell-laden constructs was investigated using a bioink with the highest content of Gel (1.5% w/v) tested in this work. As shown in Fig. 2, Live and Dead staining performed on a bioprinted cellularized hydrogel grid demonstrated the absence of death cells suggesting the biocompatibility of the bioinks and biofabrication conditions.

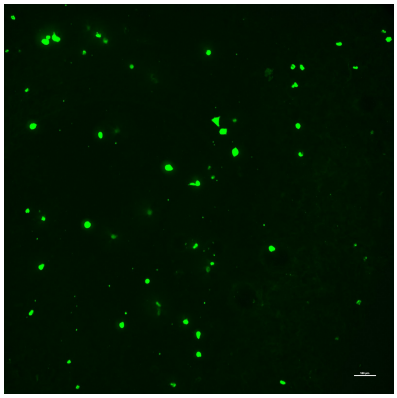


Fig. 2: Live/Dead stained AHCFs in 3D bioprinted constructs visualized after an incubation time of 1h Scale bar equal to 100 um.

IV. Conclusion

In this work, novel Alg-ADA-Gel inks based on internal gelation mechanism were developed to provide suitable properties for bioprinting in cardiac tissue engineering. Specifically, the incorporation of Gel through ADA was investigated to improve the biological features of Alg-based hydrogels and to study the influence of Gel on the cross-linking mechanism. Shear thinning inks with biomimetic viscoelastic properties, cell adhesion ability and tunable stability in physiological conditions were obtained by varying ADA and Gel contents. Printability studies showed that increasing Gel content delayed the cross-linking time of the hydrogels widening the printability window and increasing the optimal printing time. *In vitro* cell tests demonstrated the biocompatibility of Alg-ADA-Gel bioinks. Finally, 3D cell-laden constructs were printed using a selected Alg-ADA-Gel bioink containing AHCFs. In the future such bioink could be exploited to design *in vitro* models of cardiac fibrotic tissue. Alternatively, by changing the types of encapsulated cells, the bioink could be used for the biofabrication of patches for cardiac tissue regeneration.

Acknowledgement

BIORECAR project has received funding from the European Research Council (ERC) under the European Union's Horizon 2020 research and innovation program grant agreement No 772168.

References

[1] Roth, G. A., Mensah, G. A., Johnson, C. O., Addolorato, G., Ammirati, E. et al. GBD-NHLBI-JACC Global Burden of Cardiovascular Diseases Writing Group (2020). Global Burden of Cardiovascular Diseases and Risk Factors, 1990-2019: Update From the GBD 2019 Study. Journal of the American College of Cardiology, 76(25), 2982–3021. https://doi.org/10.1016/j.jacc.2020.11.010

[2] Samandari, M., Quint, J., Rodríguez-delaRosa, A., Sinha, I., Pourquié, O., & Tamayol, A. (2022). Bioinks and Bioprinting Strategies for Skeletal Muscle Tissue Engineering. Advanced materials (Deerfield Beach, Fla.), 34(12), e2105883. https://doi.org/10.1002/adma.202105883

[3] Axpe, E., & Oyen, M. L. (2016). Applications of Alginate-Based Bioinks in 3D Bioprinting. International journal of molecular sciences, 17(12), 1976. https://doi.org/10.3390/ijms17121976

[4] Lee, R. J., Hinson, A., Bauernschmitt, R., Matschke, K., Fang, Q., Mann, D. L., Dowling, R., Schiller, N., & Sabbah, H. N. (2015). The feasibility and safety of Algisyl-LVR™ as a method of left ventricular augmentation in patients with dilated cardiomyopathy: initial first in man clinical results. International journal of cardiology, 199, 18–24. https://doi.org/10.1016/j.ijcard.2015.06.111

[5] Cattelan, G., Guerrero Gerbolés, A., Foresti, R., Pramstaller, P. P., Rossini, A., Miragoli, M., & Caffarra Malvezzi, C. (2020). Alginate Formulations: Current Developments in the Race for Hydrogel-Based Cardiac Regeneration. Frontiers in bioengineering and biotechnology, 8, 414. https://doi.org/10.3389/fbioe.2020.00414

[6] Jin, Y., Compaan, A., Bhattacharjee, T., & Huang, Y. (2016). Granular gel support-enabled extrusion of three-dimensional alginate and cellular structures. Biofabrication, 8(2), 025016. https://doi.org/10.1088/1758-5090/8/2/025016

[7] Paques, J. P. (2015). Alginate Nanospheres Prepared by Internal or External Gelation with Nanoparticles. In L. M. C. Sagis (Ed.), *Microencapsulation and Microspheres for Food Applications* (pp. 39-55). Academic Press. https://doi.org/10.1016/B978-0-12-800350-3.00004-2

[8] Mirdamadi, E., Tashman, J. W., Shiwarski, D. J., Palchesko, R. N., & Feinberg, A. W. (2020). FRESH 3D Bioprinting a Full-Size Model of the Human Heart. ACS biomaterials science & engineering, 6(11), 6453–6459. https://doi.org/10.1021/acsbiomaterials.0c01133

[9] Afghah, F., Altunbek, M., Dikyol, C., & Koc, B. (2020). Preparation and characterization of nanoclay-hydrogel composite support-bath for bioprinting of complex structures. Scientific reports, 10(1), 5257. https://doi.org/10.1038/s41598-020-61606-x

[10] Sardelli, L., Tunesi, M., Briatico-Vangosa, F., & Petrini, P. (2021). 3D-Reactive printing of engineered alginate inks. Soft matter, 17(35), 8105–8117. https://doi.org/10.1039/d1sm00604e

[11] Sarker, B., , Papageorgiou, D. G., , Silva, R., , Zehnder, T., , Gul-E-Noor, F., , Bertmer, M., , Kaschta, J., , Chrissafis, K., , Detsch, R., , & Boccaccini, A. R., (2014). Fabrication of alginate-gelatin crosslinked hydrogel microcapsules and evaluation of the microstructure and physico-chemical properties. Journal of materials chemistry. B, 2(11), 1470–1482. https://doi.org/10.1039/c3tb21509a

[12] Choy, J. S., Leng, S., Acevedo-Bolton, G., Shaul, S., Fu, L., Guo, X., Zhong, L., Guccione, J. M., & Kassab, G. S. (2018). Efficacy of intramyocardial injection of Algisyl-LVR for the treatment of ischemic heart failure in swine. International journal of cardiology, 255, 129–135. https://doi.org/10.1016/j.ijcard.2017.09.179

Design and fabrication of an intestinal phantom to mimic intestinal tone and motility

P. Signorello[1,2], L. Cacopardo[1,2,3], N. Guazzelli[1,2,3], I. Nicolai [2], F.Viti[4], P. Gandullia[5], R.O. Heuckeroth[6], A. Ahluwalia[1,2,3]

[1] *Research Centre "E. Piaggio", University of Pisa, Italy*
[2] *Department of Information Engineering, University of Pisa, Italy*
[3] *Centro 3R, Italy*
[4] *Institute of Biophysics of the National Research Council, Genova, Italy*
[5] *IRCCS Istituto Giannina Gaslini, Genova, Italy*
[6] *Children's Hospital of Philadelphia and Perelman School of Medicine at the University of Pennsylvania, Philadelphia, Pennsylvania*

Abstract **Childhood visceral myopathy (VM) is one of the most severe and life-threatening pathologies affecting intestinal tone and motility. There is currently no cure. Novel engineering solutions are urgently required to provide longer life expectancy and quality to people with VM. In this context, replicating gut anatomy and mechanics is fundamental for pre-clinical studies. However, replicating complex gut anatomy and its combination with intestinal mucosa is still challenging. For this reason, we designed and fabricated a multiscale phantom-based model reproducing the bowel anatomy and mechanical properties of a 10-year-old child. PDMS was used as a material to mimic intestinal wall mechanics, while alginate with type II mucins was selected for the luminal lining. The luminal content was also replicated using pectin solution mimicking physiological viscosity ranges.**

Keywords **Phantom, peristalsis, lumen content, viscosity, pH.**

I. Introduction

THE bowel is a vital organ that acts as a barrier protecting the body from pathogens while digesting food, absorbing nutrients, and eliminating waste. These processes depend on coordinated intestinal muscle contraction and relaxation [1] along a long-twisted tube with variable diameter. The intestinal wall consists of five overlapping tissue layers: serosa, longitudinal and circular smooth muscle, submucosa, and mucosa, from external to inner, respectively. Longitudinal muscles shorten or lengthen bowel segments while circular muscles narrow or widen the bowel lumen. At functional level, these muscles are controlled by the enteric nervous system, enabling segmentation, peristalsis, and other complex movements. Segmentation is a series of directionless contractions and relaxations that mix intestinal contents, while peristalsis is a wave of unidirectional contractions that push the luminal contents along the bowel [2]. These physiological processes can be disrupted by various pathologies affecting gut function and motility. Among the most severe disease bowel motility disorders are visceral myopathies (VM), typically genetic diseases characterised by profound bowel, bladder, and uterine smooth muscle weakness [3], [4]. The most severe form is called megacystis microcolon intestinal hypoperistalsis syndrome. All VM causes marked bowel dilation, prolonged dependence on intravenous nutrition, and often causes death in childhood. Current therapy is purely supportive, inadequately relieves symptoms, and leaves children at risk for dangerous complications of prolonged intravenous nutrition (e.g., sepsis, vessel thrombosis).

Pre-clinical studies with intestinal phantoms are thus fundamental for the identification of strategies to support gut wall tone and motility. Table I summarises the intestinal phantoms in the literature according to the intestinal portion addressed, and the materials used to model gut wall, mucosa, and intestinal contents.

TABLE I: Current solutions to mimic the gut

Author	*Gut portion and shape*	*Material for intestine and luminal content models*	*Mucosa layer*
Suzuki et al [5]	Intestine, straight tube	Phantom: rubber latex and carbonium fibres Luminal content: water	No
Wrigth et al [6]	Duodenum, tube with un-physiological loops	Phantom: acrylic cylinder and dialysis membrane Luminal content: protein isolate and arabic gum [7]	Presence of mucins in the lumen content but without a real mucus layer
Ashigaki et al [8]	Small intestine, straight tube	Phantom: nitrile rubber Luminal content: polybutadiene with hydroxyl radicals	No
Tharakan et al [9]	Small intestine, straight tube	Phantom: cellulose ester membrane Luminal content: guar gum [10]	No
Minekus et al [11], Blanquet et al [12]	From stomach to colon, tube systems	Phantom: glass and silicone Luminal content: guar gum	No
Guerra et al [13]	Stomach and small intestine, straight tube	Phantom: polycarbonate Luminal content: diethylenetriamin epentaacetic acid in water [14]	No
Hribar et al [15]	Small intestine, straight tube	Phantom: silicone Luminal content: polyethylene oxide and water	No
Wang et al [16]	Stomach and duodenum, tube with un-physiological loops	Phantom: silicone Luminal content: beef stew and orange juice [17]	No

However, most of these studies do not accurately reproduce small intestine anatomy, the presence of an inner mucosa layer and/or mechanical properties in physiological or pathophysiologic conditions. Moreover, although different examples of artificial intestinal mucosa can be found in the literature [18], their integration with intestinal phantom is still missing.

The aim of this work is to address current limitations, engineering an advanced intestinal phantom or 'physical twin' for a 10 year-child preserving shape, complexity, size of the bowel and deformation capabilities.

II. Material and Methods

○ *Phantom*

The phantom was designed according to the following specifications, focusing on the small bowel:

- Anatomy: duodenum with physiological loops, as shown in fig 1. The size is based on a 10-year-old child (length 185 mm, diameter 21 mm and thickness 1.4 mm). These dimensional parameters were obtained by extrapolating adult data [1], [2] through scaling, keeping the ratio of tube diameter to thickness constant.
- Mechanical properties: elastic modulus of healthy tissue is approximately 2-3 MPa [19-20]. The value may be lower in people with VM due to loss of tone or higher due to fibrosis [3].

A realistic simplified version of the phantom was developed using CAD (Computer Aided Design) software (Fusion 360). Polydimethylsiloxane (PDMS) was selected to mimic gut mechanical properties. The properties of this material can be modulated according to monomer - crosslinking agent ratio to replicate the different properties of pathophysiological gut walls. In particular, the following ratios were selected: 4:1, 5:1 and 6:1 [21]. Solutions were then degassed for 15 minutes and, after casting in custom moulds (obtained thanks to fused deposition modelling in Acrylonitrile Butadiene Styrene - ABS), samples were cured at 60°C for 6h. Tensile tests were performed at a strain rate of 6 mm/s using a universal testing machine (*Zwick-Roell, Z005 ProLine)*. A 60% maximum deformation was selected corresponding to the limit beyond which the muscle, at a physiological level, remains in the elastic regime and therefore does not exceed the critical deformation that leads it to leave the elastic region [19-20]. PDMS was silanized with (3-Aminopropyl) tiethoxysilane (APTES) to increase surface wettability and coupling with the mucosa layer. PDMS samples were soaked for i) 5 minutes in a 1% of APTES v/v - 50% ethanol solution with, ii) 3 minutes in a 33% v/v acetic acid solution and iii) dried for 1 minute in a vacuum chamber. The wettability of silanized-PDMS and PDMS samples was tested with 1% alginate solution with a tensiometer (*Biolin scientific*), measuring the contact angle over time for 10 minutes.

○ *Luminal content modelling*

Replicating small bowel luminal content rheology at different pH values is also fundamental to testing the efficiency of the technology in assisting luminal content propulsion within the bowel. As food moves from the stomach into the duodenum, the pH changes from a range of 1.5-3.5 to 5-6 as the acidic gastric contents are neutralised by pancreatic secretions. pH increases to 8 at the end of the intestine [22]-[24]. The intestinal tract's viscosity also changes because of nutrient absorption. Numerous studies use animals and predictive models to estimate viscosity due to the difficulty in measuring it [25], [26]. In the intestine physiological shear rate (1-10 s^{-1}), the estimated viscosity values fall between 0.1 and 10 Pas [26]. Buffers were obtained by dissolving 0.681 % w/v potassium dihydrogen phosphate and 0.022, 0.1164, and 0.187 % w/v sodium hydroxide in distilled water, obtaining solutions at pH 6, 7 and 8, respectively, to reproduce the different portions of the small intestine. pH values were assessed with a pH meter (*Hanna, Edge series).*

Different materials were then dissolved in the buffer solutions (pluronic from 15 to 20% w/v, pectin from 0.5 to 5% w/v). Viscosity measurements were performed using a *Brookfield DV-II+PRO* Viscosimeter.

○ *Mucosa layer modelling*

0 to 0.7% Alginate was selected for its ability to adhere to the intestinal mucosa thanks to polymer chain length and the presence of ionisable groups. [27]. Type II Mucins, present in the physiological mucus, were added to alginate solutions at a concentration of 0.5, 1, and 1.5%. Solutions with different concentrations of alginate and mucins were tested in terms of viscosity. Viscosity was measured as described in the previous subsection.

III. Results

Fig. 1 shows the CAD design for the phantom, while Fig. 2 reports CAD designs of the moulds for two sections. The phantom is finally obtained by coupling the different PDMS sections.

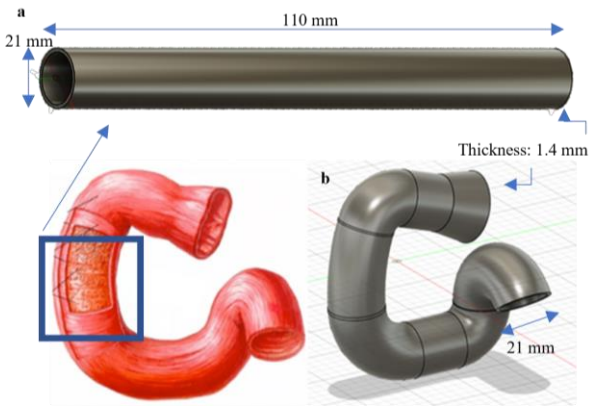


Fig. 1: Comparison between physiological duodenum and technical drawings of a) simplified mould, b) realistic mould.

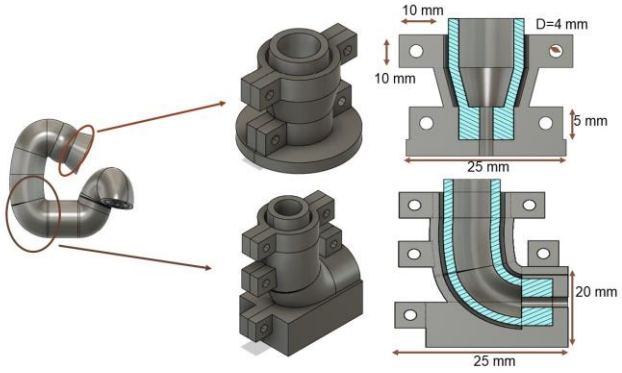


Fig. 2: Technical drawing of the moulds of two different parts of the duodenum.

Mechanical results are shown in Fig. 3. the 5:1 ratio apparent elastic modulus (2.09 ± 0.17 MPa) resulted close to the desired range (2-3 MPa [19-20]) and was selected for phantom fabrication. However, ratios and curing times can be further optimised to better match both diseased tissues.

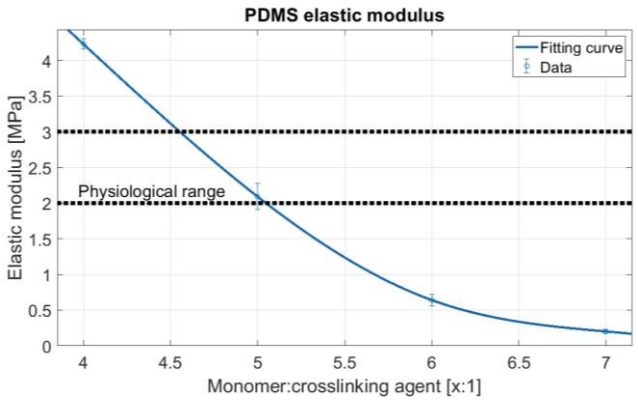


Fig. 3: PDMS elastic modulus with different ratios.

Moreover, the wettability results in Fig. 4 show that the contact angle on silanized PDMS is significantly decreased with respect to the untreated PDMS, confirming the improvement of the wettability of the substrate.

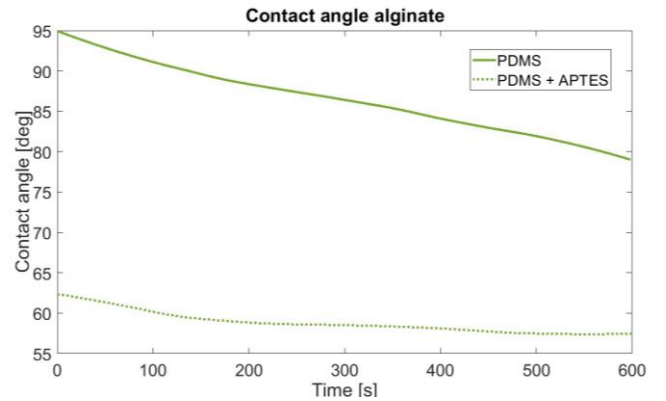


Fig. 4: Contact angle of 1% alginate on silanized PDMS and PDMS over time.

Table II shows that pluronic cannot be used to reproduce the luminal content because the viscosity values do not cover the entire physiological range at 37 °C (0.1-10 Pas [26]). Indeed, pluronic gelling temperature increases with increasing concentration. Thus, solution viscosity was not measurable at 18 and 20% w/v.

TABLE II: PLURONIC VISCOSITY AT PH6 AND 37°C

Concentration [% w/v]	*Viscosity [Pas]*
15	0.0657
17	0.37
18	Not measurable
20	Not measurable

Differently, pectin viscosities (Figure 5) fall within the desired physiological range at all pH. Moreover, it was also observed that viscosity decreases as the pH increases. This behaviour can be related to hydrogen bonding between protonated carboxylic acid groups on the pectin backbone [28].

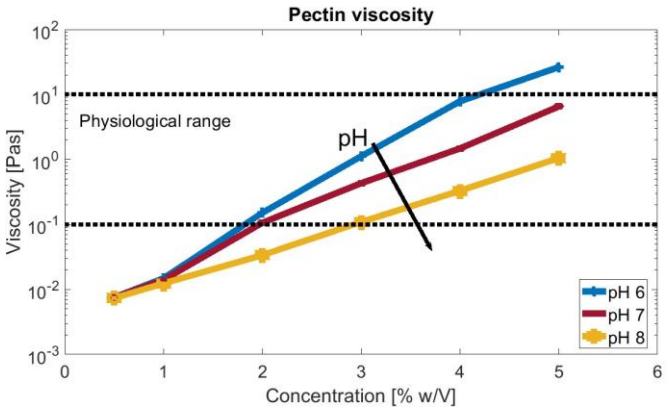


Fig. 5: Pectin viscosity in buffer solutions with different pH, plotted in logarithmic scale with respect to pectin concentration.

Finally, the viscosity of alginate as a function of polymer and mucin concentration is shown in Figure 6, demonstrating its compatibility with the physiological mucus range (3.8 and 25.8 mPas [29]).

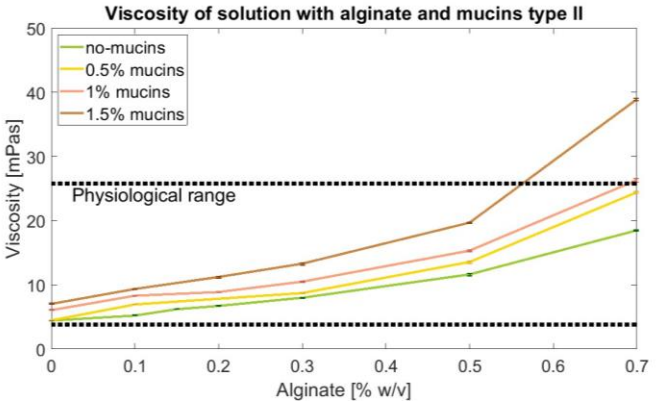


Fig. 6: Alginate with mucins viscosity in buffer solution at pH 7.

IV. CONCLUSION AND FUTURE DEVELOPMENTS

In this work, the first steps toward the design and fabrication of a physiologically relevant intestinal phantom were presented. PDMS was used to match healthy intestine mechanical features and functionalised to improve the coupling with an artificial mucus layer. The materials to reproduce the mucosa layer and luminal content were also characterised in terms of pH and viscosity properties.

We are currently investigating further conditions to replicate diseased conditions. Future studies will also involve the further development of digital twins by combining computational models with endoscopic images of bowel motion to inform the design of a magnetic actuation field. Developing non-animal phantoms, this work is also in line with 3R principles (Reduction, Refinement and Replacement of animal experiments as prescribed by EU directive 2010/63 and national legislation).

REFERENCES

[1] John T. Hansen, Bruce M. Koeppen, (2002), *Netters Atlas of Human Physiology*, Icon Learning Systems, University of Michigan, 223.

[2] Linda S. Costanzo, (2011), *Physiology*, Lippincott Williams & Wilkins, Two Commerce Square, 330.
[3] S. K. Hashmi, R. H. Ceron, R. O. Heuckeroth Visceral Myopathy: clinical syndromes, genetics, pathophysiology, and fall of the cytoskeleton. American Journal of Physiology-Gastrointestinal and Liver Physiology, 320(6): G919-G935 (2021).
[4] C.D. Guzé, P.E. Hyman, V.J. Payne. Family studies of infantile visceral myopathy: a congenital myopathic pseudo-obstruction syndrome. Am J Med Genet, 82(2):114-22 (1999).
[5] K. Suzuki and T. Nakamura. Development of a peristaltic pump based on bowel peristalsis using for artificial rubber muscle. IEEE/ RSJ International Conference on Intelligent Robots and Systems 3085-3090 (2010).
[6] N. D. Wright, F. Kong, B.S. Williams, L. Fortner. A human duodenum model (HDM) to study transport and digestion of intestinal contents. Journal of Food Engineering, 171, 129–136 (2016).
[7] F. P. Flores, R. K. Singh, W.L. Kerr, R.B. Pegg, F. Kong. Total phenolics content and antioxidant capacities of microencapsulated blueberry anthocyanins during in vitro digestion. Food Chemistry 153, 272–278 (2014).
[8] K. Ashigaki et al. Considering Mixing Process of Rocket Solid Propellant Using Mixing Transport Device Simulating Peristaltic Movement of Intestinal Tract. 7th IEEE International Conference on Biomedical Robotics and Biomechatronics (Biorob) 1291-1296 (2018).
[9] A. Tharakan, I.T. Norton, P.J. Fryer, S. Bakalis. Mass transfer and nutrient absorption in a simulated model of small intestine. Journal of Food Science, 75(6), E339–E346 (2010).
[10] P.R. Ellis, F.G. Roberts, A.G. Low, L.M. Morgan. The effect of high-molecular-weight guar gum on net apparent glucose absorption and net apparent insulin and gastric inhibitory polypeptide production in the growing pig: relationship to rheological changes in jejunal digesta. Br J Nutr 74(4):539-56 (1995).
[11] M. Minekus, P. Marteau, R. Havenaar, J.H.J.H. Veld. A Multicompartmental Dynamic Computer-controlled Model Simulating the Stomach and Small Intestine. Alternatives to Laboratory Animals 23(2):197-209 (1995).
[12] S. Blanquet, E. Zeijdner, E. Beyssac et al. A Dynamic Artificial Gastrointestinal System for Studying the Behavior of Orally Administered Drug Dosage Forms Under Various Physiological Conditions. Pharm Res 21, 585–591 (2004).
[13] A. Guerra, S. Denis, O. le Goff, V. Sicardi, O. François, A.F. Yao, G. Garrait, A.P. Manzi, E. Beyssac, M. Alric, S. Blanquet-Diot. Development and validation of a new dynamic computer-controlled model of the human stomach and small intestine. Biotechnology and Bioengineering, 113(6), 1325–1335 (2016).
[14] J.A. Siegel, J.L. Urbain, L.P. Adler, N.D. Charkes, A.H. Maurer, B. Krevsky, L.C. Knight, R.S. Fisher, L.S. Malmud. Biphasic nature of gastric emptying. Gut (1):85-9 (1988).
[15] M. Hribar, J. Trontelj, U. Klančar, B. Markun, T. Čeligoj Dujc, I. Legen. A Novel Intestine Model Apparatus for Drug Dissolution Capable of Simulating the Peristaltic Action. AAPS PharmSciTech. 18(5):1646-1656 (2016).
[16] J. Wang et al. An advanced near real dynamic in vitro human stomach system to study gastric digestion and emptying of beef stew and cooked rice. Food Funct. 10, 2914–2925 (2019).
[17] J.G. Moore, P.E. Christian, R.E. Coleman. Gastric emptying of varying meal weight and composition in man. Evaluation by dual liquid- and solid-phase isotopic method. Dig Dis Sc 26(1):16-22 (1981).
[18] L. Wright, P. Joyce, T. J. Barnes, & C. A. Prestidge. Mimicking the Gastrointestinal Mucus Barrier: Laboratory-Based Approaches to Facilitate an Enhanced Understanding of Mucus Permeation. In ACS Biomaterials Science and Engineering. American Chemical Society (2021).
[19] S. Bourgouin, T. Bège, C. Masson, P.J. Arnoux, J. Mancini, S. Garcia, C. Brunet, S. Berdah. Biomechanical characterisation of fresh and cadaverous human small intestine: Applications for abdominal trauma. Medical and Biological Engineering and Computing, 50(12), 1279-1288 (2012).
[20] B. Johnson, S. Campbell, & N. Campbell-Kyureghyan. Biomechanical properties of abdominal organs under tension with special reference to increasing strain rate. *Journal of Biomechanics*, *109*, 109914. (2020).
[21] C. Jin, C. Ma, Z. Yang, H. Lin. A Force Measurement Method Based on Flexible PDMS Grating. Applied Sciences 10, 2296 (2020).
[22] L. Ovesen et al. Intraluminal pH in the stomach, duodenum, and proximal jejunum in normal subjects and patients with exocrine pancreatic insufficiency. Gastroenterology 90, 958-962 (1986).
[23] D.F. Evans, G. Pye, R. Bramley, A.G. Clark, T.J. Dyson, J.D. Hardcastle. Measurement of gastrointestinal pH profiles in normal ambulant human subjects. Gut 29, 1035-1041 (1988).
[24] S. Fujimori. Gastric acid level of humans must decrease in the future. World Journal of Gastroenterology. 26, 6706-6709 (2020).
[25] R.G. Lentle & P.W.M. Janssen. Physical characteristics of digesta and their influence on flow and mixing in the mammalian intestine: a review. J Comp Physiol B 178, 673-690 (2008).
[26] A.K. Hardacre, R.G. Lentle, S.Y. Yap & J.A. Monro. Predicting the viscosity of digesta from the physical characteristics of particle suspensions using existing rheological models. Journal of The Royal Society Interface 15, 20180092 (2018).
[27] K.I. Draget, C. Taylor. Chemical, physical, and biological properties of alginates and their biomedical implications. Food Hydrocolloids 25, 251-256 (2011).
[28] O. Yuliarti, A.L. Hoon & S.Y. Chong. Influence of pH, pectin, and Ca concentration on gelation properties of low-methoxyl pectin extracted from Cyclea barbata Miers. Food Structure 11, 16-23 (2017).
[29] A. Macierzanka, A. R., Mackie, & L. Krupa. Permeability of the small intestinal mucus for physiologically relevant studies: Impact of mucus location and ex vivo treatment. *Scientific Reports*, *9*(1). (2019).

Nanostructured coatings with bacteria-triggered antimicrobial response for medical devices

M. A. Cassa[1,2], G. Ciardelli[1,2,3] , P.G. Gentile[4] and I. Carmagnola[1,2]
[1] *Politecnico di Torino, Department of Mechanical and Aerospace Engineering, Torino, 10129, Italy*
[2] *Politecnico di Torino, Polito BIOMed Lab, Torino 10129, Italy*
[3] *National Research Council, Institute for Chemical and Physical Processes (CNR-IPCF), Pisa, 56124, Italy*
[4] *School of Engineering, Newcastle University, Newcastle Upon Tyne, NE1 7RU, United Kingdom*

***Abstract*—Bacterial colonization and biofilm formation on medical devices is one of the most pressing current healthcare issues, posing serious threats to patients health other than having a great economic impact on national healthcare systems. Smart and tailored biomaterials for the fabrication of medical devices are needed to contrast this problem, in particular the development of surface modification strategies, preventing bacteria adhesion and proliferation into mature biofilm. Layer-by-layer (LbL) assembly technique allows for easy, reproducible and specially designed surface modifications, providing the material with the desired antibiofilm activity. More interestingly, LbL coatings can also display smart, stimuli-responsive features to favour a controlled, on-demand antibacterial response which is triggered only when bacteria are present (self-defensive coatings).**

***Keywords*— antibacterial coating, layer-by-layer technique, surface functionalization, responsive behaviour**

I. INTRODUCTION

One of the main criticalities associated with short and long-term use medical devices is bacterial colonization with subsequent formation of biofilm. Among the most problematic medical devices we find invasive ones, both implantable such as dental [1] and orthopaedic prostheses [2], cardiac valves and pacemakers [3]-[5], silicone prosthesis used in multiple surgical procedures [6]-[8], catheters used for several anatomical districts [9] [10], endotracheal tubes for pulmonary ventilators [11], suture threads [12], and also non-implantable ones like ophthalmological contact lenses [13]. The incidence of nosocomial and medical device-associated infections is still unacceptably high [14], given that biofilm formation on such devices and implants leads to severe functional and medical problems, not to mention aesthetical discomfort in some cases. These malfunctions, along with the infection itself, can seriously threaten patients health and well-being, apart from weighing on healthcare costs because of prolonged hospital stays, revisions of surgeries, new production of devices and frequent clinical visits [15]. It is impossible to completely eliminate all potential causes of contamination, spreading from surrounding environment, human skin, administered intravenous fluids, unsterile instruments, poorly aseptic medical procedures, difficulty of cleaning/treating complex or hidden anatomical regions. The increasing resistance of microorganisms to antibiotic drugs and the inadequacy to eradicate them when in the biofilm mode of growth [16] have boosted research to develop new smart and specifically designed antimicrobial biomaterials. An interesting solution is offered by surface treatments and coatings that do not affect bulk material properties, allowing to limit the antibacterial action only to the region actually colonized by biofilm formation. Such approaches should focus both on prevention of bacterial adhesion (antifouling action) and treatment of bacterial infections (antimicrobial action), preferably exerting their antimicrobial action in a smart and controlled way. In fact, current antibacterial strategies for biomaterials aim at preserving their antimicrobial potency until actual bacteria have adhered on the surface, thus avoiding premature loss of efficiency and potential side effects to surrounding living tissue. Among such useful surface modifications that allow bacteria-triggered antibacterial activity, layer-by-layer (LbL) surface deposition technique in particular stands out as a simple, versatile technique which is able to incorporate a plethora of antimicrobial agents like antibiotics, antimicrobial peptides (AMPs) or nanoparticles and be applied to a wide range of different substrate chemistries and geometries. This work has the aim of introducing the most interesting and innovative LbL antimicrobial strategies recently developed, focusing on coatings that exert their action in response to stimuli specifically linked to the bacterial colonization microenvironment present at the site of infection.

II. THE GENESIS OF BACTERIAL BIOFILM

Bacterial microorganisms do not only exist as planktonic, single floating entities. On the contrary, they tend to aggregate and organize themselves in colonies in order to improve their adhesion, nutritional support and resistance to environmental stresses. For medical device-associated biofilms such external threats could be host immune response, antibiotic therapy or antimicrobial agents in general. Once adhered on the device surface, the attachment can be considered a trigger for biofilm organization and thus the bacteria start to produce biopolymers like polysaccharides, DNA, proteins and lipids which constitute their extracellular matrix (ECM), becoming embedded in it [17] [18]. The ECM is the major component of the resulting biofilm, holding together the developing microcolonies. The process of biofilm formation is supported and controlled by constant communication within and between bacterial species (e.g. quorum sensing). It can be divided in four essential steps (Fig. 1) [19]:

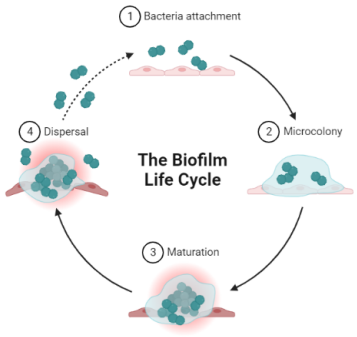


Fig. 1: the essential four steps in biofilm formation
Reprinted from "The Biofilm Life Cycle", by BioRender, November 2022, retrieved from https://app.biorender.com/t-636d1940a2064909c86a9b8c-the-biofilm-life-cycle
Copyright © 2023 by BioRender.

1) initial reversible attachment of bacteria through several mechanisms that guarantee a stable anchorage;
2) aggregation in microcolonies, mainly through bacterial replication and adhesion of new cells, leading to spatial expansion and irreversible attachment;
3) maturation of biofilm, tridimensional growth and proliferation secured by the ECM stability and protection;
4) dispersal of cellular aggregates from the biomass into the surrounding environment, probably because of increased cellular density within the biofilm.

Given the possibility of detachment and dispersal of bacteria after maturation, it is clear that medical device-associated biofilms constitute a health risk not only at the site and time of contamination but expose the patient to possible chronic infection and/or sepsis. This is one of the main reasons why strategies for prevention and treatment of biofilm are extensively investigated when dealing with medical devices. Such antibiofilm strategies could be grouped in four main categories on the basis of their action [17]:

1) prevention of microbial adhesion (antifouling surfaces);
2) inhibition of bacterial communication (quorum quenching);
3) killing of adhered microorganisms;
4) disruption of early stages biofilm formation.

All of these strategies could be pursued by means of surface modifications. In the first line of defence, antiadhesive surfaces are obtained both through physical parameters modification (changes in roughness, wettability) and also functionalization with antifouling moieties e.g. polyethylene glycol (PEG). Regarding the second, third and fourth approach, the design of surface coatings comprising specific active molecules (quorum sensing blockers e.g. furanones, antimicrobial peptides/nanoparticles/drugs, degradative enzymes e.g. dispersin B) represent the preferential line of action, either by immobilization of such molecules on the surface or through release systems.

III. Possible Solutions through Surface Functionalization

Since microorganisms proliferating inside mature biofilm are extremely difficult to extinguish because of the protective layer provided by the ECM, the best way to avoid bacterial colonization of medical devices is to prevent its formation. In order to do so, the device surfaces must exert an antibiofilm action. Surface functionalization of biomaterials could provide the necessary antifouling and antimicrobial activity, whether it be inhibition of bacteria adhesion, inhibition of their growth from the surface or direct bacteria suppression [17]. Self-defensive coatings stand out as an extremely interesting solution, being able to exert their antimicrobial action only when bacteria are actually colonizing the surface: thus, the antibacterial efficacy is preserved and readily available when needed. One of the key features of such innovative coatings is represented by their capacity of tuneable antibiotic release in response to specific triggers found in bacterial colonization microenvironment, mainly acidic pH and presence of degradative enzymes [20]. During bacteria metabolism, production of organic acids like, for example, lactic acid for *S. Aureus* or acetic acid for *E. Coli* leads to local acidification of pH. Moreover, bacteria release virulence factors that assist them in host colonization by evading/suppressing host immune response and allowing them efficient cellular adhesion and nutrition. Out of all these factors, degradative enzymes, e.g. hyaluronidase (HAS) and chymotrypsin (CMS), are frequently secreted. Among the plethora of surface modification techniques, LbL self-assembly stands out as a very versatile fabrication method, able to yield coatings that display antiadhesive properties and/or incorporate therapeutic agents while retaining their biological activity. Such LbL coatings could be easily rendered self-defensive: through incorporation of weak polyelectrolites, acidic pH would trigger an increase in permeability and/or direct disruption of the coating with subsequent release of antimicrobial agent [21] [22]; alternatively, if the LbL building blocks are sensitive to enzymatic degradation the presence of the afore-mentioned enzymes would lead to delamination of the coating with subsequent elimination of adhered bacteria and controlled release of integrated antibiotic drugs [20].

A. LbL surface functionalization

LbL self-assembly is one of the most popular bottom-up nanostructured surface modification techniques due to its reproducibility, efficiency, robustness and flexibility. The deposition results from spontaneous assembly of multivalent building blocks which are complementary thanks to the specific interaction between them (electrostatic attraction is very common, but also hydrogen bonds, covalent bonds, hydrophobic/charge-transfer/host-guest/biologically driven interactions) [23]. The process requires mild conditions, avoiding extreme temperature/pH or aggressive solvents, thus making it easy, cost-effective and suitable for a wide range of substrate chemistries and geometries. Its versatility also lies in the variety of molecules that can be incorporated as building blocks, allowing a targeted design of the coating features for the final application. The fabrication process, in the case of oppositely charged polyelectrolytes, is illustrated in Fig. 2: briefly, the substrate is alternatively exposed to the chosen polyanion and polycation solutions, a step of washing before each layer deposition is needed to eliminate residual unbound polyelectrolytes. Also, a preliminary step of substrate

processing could be necessary to allow suitable interaction with the first polyelectrolyte layer [24].

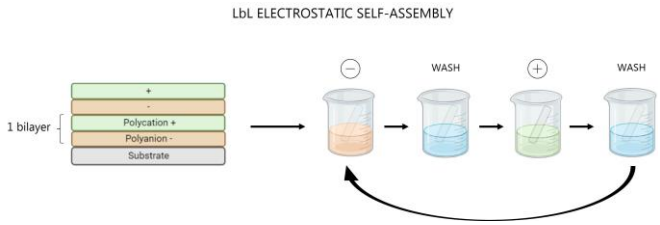


Fig. 2: LbL electrostatic self-assembly fabrication scheme

B. Bacteria-triggered antimicrobial response in LbL coatings

In the last decade, several self-defensive antibacterial LbL coatings have been developed exploiting acidification of pH or degradative enzymes as possible bacteria-related triggers. Wu et al. [25] incorporated two polycations such as 1,2-ethanediamine (EDA)-modified polyglycerol methacrylate (PGMA) and lysozyme, which provide multivalent interactions with bacterial membranes, in a LbL coating together with hyaluronic acid (HA) acting as a substrate for HAS and therefore, able to delaminate in its presence . Such coating was deposited on silica nanoparticles containing antibiotics, hence the delamination triggered the release of drug only in presence of bacteria. Another LbL coating that incorporates HA was developed by Wang et al. [26] and deposited on medical silicone substrates. The coating was composed of montmorillonite (MMT) and HA, both of which could electrostatically interact with gentamicin (GS) leading to successful high loading of antibiotic. The progressive degradation of HA by HAS leads to drug release but also film peeling, exerting a dual antimicrobial-antifouling action (Fig. 3).

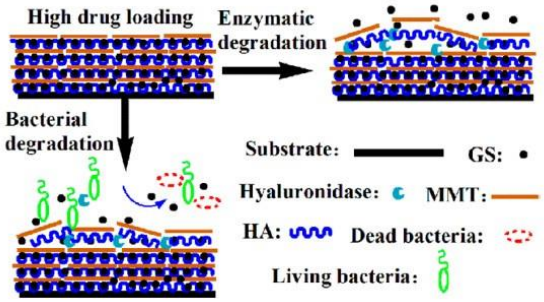


Fig. 3: enzyme- and bacteria-triggered drug release scheme of $(MMT/HA\text{-}GS)_n$ self-assembled multilayers.
Reprinted with permission from B. Wang et al., "Construction of high drug loading and enzymatic degradable multilayer films for self-defense drug release and long-term biofilm inhibition", *Biomacromolecules* 2018, 19, 1, 85–93.

Copyright © 2023 American Chemical Society

A very similar approach was proposed by Xu et al. [27] but using poly-L-lysine (PLL) in combination with MMT and gentamicin. In this case, the degradation and delamination of the coating with subsequent drug release was due to CMS acting on PLL. Moving on to pH triggers, there has been extensive investigation that unfolded several interesting solutions. Employing weak polyelectrolytes that become poorly ionized at acidic pH determines weak electrostatic interactions with incorporated antibiotics and thus, slow diffusion of drug from the coating. Such sensitive building blocks could be natural polymers such as polyphenols [28] and chitosan [29] [30], synthetic polycarboxylic acids [31] but also inorganic compounds such as polyphosphazenes [32]. A peculiar strategy is represented by LbL hydrogel coatings made of poly (2-alkylacrylic acids) which were used for electrostatic adsorption of antibiotic [33] or simply as tuneable hydrophobic coatings with intrinsic antibacterial properties [34]. Both works use polyacids and the LbL technique in order to achieve an open molecular structure of polymeric cross-linked hydrogel. In the first study, the coating permitted self-hydration, which hinders bacterial adhesion, and loading of cationic antibiotics that could be released upon acidification of pH thanks to weaker electrostatic interactions. In the second, hydrogels were constituted of poly(2-alkylacrilic) acids with increasing hydrophobicities and acidic pH triggers could yield charge and water content changes thus interfering with the membrane of adhered bacteria.

IV. Summary and Future Perspective

Medical device-associated biofilm and infections are currently one of the open challenges in biomedical research. Self-defensive coatings stand out as an innovative and smart solution which is able to activate its antibacterial action only in presence of initial bacterial colonization, thus preventing coating premature loss of efficiency, antibiotic resistance and potential damage to surrounding tissues/cells. A particularly beneficial surface functionalization method able to yield such coatings is LbL deposition, allowing for a wide range of building blocks and possible geometries/chemistries of substrates, not to mention the possibility of incorporating several antimicrobial features (e.g. bactericidal and antifouling properties) in one coating. A step further in this direction, worthy of future investigation, would be to synthesize customable polyelectrolytes specifically designed for the application of interest. Making them responsive to a trigger of choice and imparting them with biomimetic or bioactive features for better biocompatibility or tissue integration are just a few of the possible interesting strategies.

Acknowledgement

Maria Antonia Cassa acknowledges co-financing by the Horizon 2020 Programme for her Ph.D scholarship through the ALTERNATIVE [grant n. 101037090] and EVPRO [grant n. 814495] projects.

References

[1] S. Hahnel, *Biofilms and Implantable Medical Devices*. Regensburg: Woodhead Publishing, 2017, ch. 5 - Biofilms on dental implants
[2] S. J. McConoughey et al., "Biofilms in periprosthetic orthopedic infections", in *Future Microbiology*, vol. 9, no. 8, pp. 987-1007, Oct 2014
[3] K-i Okuda et al., "The Composition and Structure of Biofilms Developed by *Propionibacterium acnes* isolated from Cardiac Pacemaker Devices", in *Frontiers in Microbiology*, vol. 9, Feb 2018
[4] H. Elgharably MD, S. T. Hussain MD, N. K. Shrestha MD, E. H. Blackstone MD, and G. B. Pettersson MD, PhD, "Current hypothesis in

cardiac surgery: biofilm in infective endocarditis", in *Seminars in Thoracic and Cardiovascular Surgery*, vol. 28, no.1, pp. 56-59, Mar 2016

[5] N. Abdullah, O. S. Erdmann, and B. E. Borges, "The impact of biofilm formation on implantable cardiac devices", *in Research, Society and Development*, vol.10, no. 16, pp. 1-11, Dec 2021

[6] J. Spalek et al., "Biofilm growth causes damage to silicone voice prostheses in patients after surgical treatment of locally advanced laryngeal cancer", in *Pathogens*, vol. 9, no. 10: 793, Sep 2020

[7] G. Rezende-Pereira, MSc et al., "Biofilm formation on breast implant surfaces by major gram-positive bacterial pathogens", in *Aesthetic Surgery Journal*, vol. 41, no. 10, pp. 1141-1151, Oct 2021

[8] A. Kumar, M. K. Seenivasan, and A. Inbarajan, "A literature review on biofilm formation on silicone and polymethyl methacrylate used for maxillofacial prostheses", in *Cureus*, vol. 13, no. 11, Nov 2021

[9] N. Ielapi et al., "The role of biofilm in central venous catheter related bloodstream infections: evidence-based nursing and review of the literature", in *Reviews on Recent Clinical Trials*, vol. 15, no. 1, pp. 22-27, Jan 2020

[10] D. J. Stickler, "Clinical complications of urinary catheters caused by crystalline biofilms: something needs to be done", in *Journal of Internal Medicine*, vol. 276, no. 2, pp. 120-129, Mar 2014

[11] S. Baidya et al., "Biofilm formation by pathogens causing ventilator-associated pneumonia at intensive care units in a tertiary care hospital: an armor for refuge", in *BioMed Research International*, vol. 2021, May 2021

[12] E. Adler, D. Miller, O. Rock, O. Spierer, and R. Forster, "Microbiology and biofilm of corneal sutures", in *British Journal of Ophthalmology*, vol. 102, no. 11, pp. 1602-1606, Nov 2018

[13] S. Kackar, E. Suman, and M.S. Kotian, "Bacterial and fungal biofilm formation on contact lenses and their susceptibility to lens care solutions", in *Indian Journal of Medical Microbiology*, vol. 35, no. 1, pp. 80-84, Mar 2017

[14] M. H. Kollef, A. Torres, A. F. Shorr, I. Martin-Loeches, and S. T. Micek, "Nosocomial Infections", in *Critical Care Medicine*, vol. 49, no. 2, pp. 169-187, Feb 2021

[15] M. Càmara et al., "Economic significance of biofilms: a multidisciplinary and cross-sectoral challenge", in *npj Biofilms and Microbiomes*, vol. 8, no. 42, May 2022

[16] P. G. Bowler, "Antibiotic resistance and biofilm tolerance: a combined threat in the treatment of chronic infections", in *Journal of wound care*, vol. 27, no. 5, pp. 273-277, May 2018

[17] Y. Su et al, "Biofilms: formation, research models, potential targets and methods for prevention and treatment", in *Advanced Science*, vol. 9, no. 29: 2203291, Oct 2022

[18] Z. Kathoon, C. D. McTiernan, E. J. Suuronen, T-F Mah, and E. I. Alarcon, "Bacterial biofilm formation on implantable devices and approaches to its treatment and prevention", in *Heliyon*, vol. 4, no. 12: e01067, Jan 2019

[19] K.A. Floyd, A.R. Eberly, and M. Hadjifrangiskou, *Biofilms and Implantable Medical Devices.* Regensburg: Woodhead Publishing, 2017, ch. 3 – Adhesion of bacteria to surfaces and biofilm formation on medical devices

[20] D. Alkekhia, P.T. Hammond, and A. Shukla, "Layer-by-Layer biomaterials for drug delivery", in *Annual Review of Biomedical Engineering*, vol. 22, no. 1, pp. 1-24, Jun 2020

[21] K. Sato, K. Yoshida, S. Takahashi, and J-i Anzai, "pH- and sugar-sensitive layer-by-layer films and microcapsules for drug delivery", in *Advanced Drug Delivery Reviews*, vol. 63, no. 9, pp. 809-821, Aug 2011

[22] S. Park, U. Han, D. Choi, and J. Hong, "Layer-by-layer assembled polymeric thin films as prospective drug delivery carriers: design and applications", in *Biomaterials Research*, vol. 22, no. 29, Sep 2018

[23] J. Borges, and J.F. Mano, "Molecular interactions driving the layer-by-layer assembly of multilayers", in *Chemical Reviews*, vol. 114, no. 18, pp. 8883-8942, Aug 2014

[24] J. Campbell, and A.S. Vikulina, "Later-by-layer assemblies of biopolymers: build-up, mechanical stability and molecular dynamics", in *Polymers*, vol. 12, no. 9: 1949, Aug 2020

[25] Y. Wu et al, "Later-by-layer (LBL) self-assembled biohybrid nanomaterials for efficient antibacterial applications", in *ACS Applied Materials & Interfaces*, vol. 7, no. 31, pp. 17255-17263, Jul 2015

[26] B. Wang et al., "Construction of high drug loading and enzymatic degradable multilayer films for self-defense drug release and long-term biofilm inhibition", in *Biomacromolecules*, vol. 19, no. 1, pp. 85-93, Jan 2018

[27] Q. Xu et al., "Bacterial self-defense antibiotics release from organic-inorganic hybrid multilayer films for long-term anti-adhesion and biofilm inhibition properties", in *Nanoscale*, vol. 9, no. 48, pp. 19245-19254, Nov 2017

[28] I. Zhuk et al., "Self-defensive layer-by-layer films with bacteria-triggered antibiotic release", in *ACS Nano*, vol. 8, no. 8, pp. 7733-7745, Aug 2014

[29] F. Kazemi-Andalib, M. Mohammadikish, A. Divsalar, and U. Sahebi, "Hollow microcapsule with pH-sensitive chitosan/polymer shell for in vitro delivery of curcumin and gemcitabine", in *European Polymer Journal*, vol. 162: 110887, Jan 2022

[30] X. Hao et al., "pH responsive antifouling and antibacterial multilayer films with self-healing performance", in *Chemical Engineering Journal*, vol. 356, pp. 130-141, Jan 2019

[31] S. Pavlukhina et al., "Small-molecule-hosting nanocomposite films with multiple bacteria-triggered responses", in *NPG Asia Materials*, vol. 6: e121, Aug 2014

[32] V. Albright et al., "Polyphosphazenes enable durable, hemocompatible, highly efficient antibacterial coatings", in *Biomaterials*, vol. 268: 120586, Jan 2021

[33] V. Albright et al., "Self-defensive antibiotic-loaded layer-by-layer coatings: imaging of localized bacterial acidification and pH-triggering of antibiotic release", in *Acta Biomaterialia*, vol. 61, pp. 66-74, Oct 2017

[34] Y. Lu, Y. Wu, J. Liang, M.R. Libera, and S.A. Sukhishvili, "Self-defensive antibacterial layer-by-layer hydrogel coatings with pH-triggered hydrophobicity", in *Biomaterials*, vol. 45, pp. 64-71, Mar 2015

An advanced culture system to investigate electrospun graft biomechanisms for vascular tissue engineering

E. Pederzani[1], C. E. Campiglio[2], M. Ripamonti[3], M. Esposito[1], A. Rizzo[1], A. Caldiroli[4], S. A. Riboldi[4], A. Remuzzi[2], G. B. Fiore[1], M. Soncini[1]

[1] *Department of Electronics, Information and Bioengineering, Politecnico di Milano, via Giuseppe Ponzio 34, Milano, IT 20133*
[2] *Department of Management, Information and Production Engineering, University of Bergamo, via Pasubio 7, 24044 Dalmine, Italy*
[3] *Department of Biomedical Engineering, Istituto di Ricerche Farmacologiche Mario Negri-IRCCS, 24126 Bergamo, Italy*
[4] *Dialybrid S.r.l., R&D, via Vivaldi 32/A, Cantù, IT 22063*

***Abstract* — Vascular tissue engineering aims to regenerate vessels "at the target site" using cell-free synthetic scaffolds supporting endogenous regeneration. This approach aims to harness the natural wound healing process. This physiological response involves a complex series of events that could lead to detrimental outcomes, such as fibrosis and chronic inflammation. A critical aspect impairing the success of endogenous regeneration is the fine balance between functional neo-tissue formation, haemodynamic stimuli, and scaffold degradation.**

With the aim of investigating the biomechanisms at the basis of the interplay among these factors, we have developed an advanced *in vitro* culture system able to mimic *in vivo*-like physiological wall shear stress and pulsatile pressure. In the present work, we performed first biological tests to validate the device functionalities, in particular cell seeding and conditioning of a vascular graft.

This novel culture system will make possible to achieve fundamental insight concerning cell-graft interaction, synthetic scaffold colonization, and their response to haemodynamic cues.

***Keywords* — advanced culture system, *in vitro* model, hybrid fibroin/polyurethane vascular graft, vascular tissue engineering.**

I. Introduction

Recent developments in vascular tissue engineering strategies show a shift towards *in situ* vascular tissue engineering while using cell-free synthetic scaffolds promoting tissue regeneration inside the human body [1,2]. Ideally, the regenerated tissue is remodelled, guided by physiological hemodynamic loads, to resemble a vessel with native-like structural and functional properties, while the graft slowly degrades [3,4]. Despite encouraging *in vivo* proof-of-concept studies [5,6], intimal hyperplasia, early stenosis, and aneurysm formation remain prevalent complications in vascular graft implantation. These adverse events are often attributed to a mismatch between graft properties (e.g., microstructure, geometry, and mechanical properties) and haemodynamic induced mechanical loading, resulting in aberrant inflammation and pathological tissue deposition [7]. Nevertheless, the biomechanisms underlying tissue maladaptation remain elusive.

With the aim of investigating these phenomena, *in vitro* and *ex vivo* models are becoming increasingly more relevant as alternatives to *in vivo* animal tests, that up to now remain the standard [8]. The newly conceived *in vitro* models allow reproducing controllable hemodynamic, tuneability of single parameters - thereby avoiding neurohormonal effects-, none of which are possible *in vivo*. Controllability of the mechanical and chemical environment is also possible. Therefore, an advanced *in vitro* model could be a helpful tool for studying cell and tissue responses to graft implantation, applying mechano-chemical *in vivo*-like stimuli [9]. Moreover, the extensive use of such in vitro culture systems would significantly reduce costs in the preclinical and clinical phases, while not being subject to the ethical burden of animal experimentation and in accordance with the principles of the so-called three Rs principle: Replacement, Reduction and Refinement.

The aim of this project is indeed to develop a new device to fulfil the major requirements of an ideal system that allows simultaneous seeding, conditioning, and perfusion under *in vivo*-like stimuli for long-term experiments. So far, we succeeded in developing an advanced and versatile culture system able to host a cell-free vascular graft on which human endothelial cells can be seeded and grow properly in culture under perfusion conditions. Currently, experiments with different seeding and culture conditions and related biological analyses are ongoing to verify the suitability of the system to be used in a cell culture lab and its performances under different experimental protocols.

Its extensive use will enable the investigation of the mutual role of mechanical cues on cells-mediated neotissue formation.

II. Methods

A. Culture system design

The main design requirements are semi-automatic cell seeding, *in vivo*-like stimuli (fluid dynamic stresses and chemical factors), versatility of use, and compactness for being easily used within a standard incubator. Moreover, components that are in direct contact with cell media, cells, and/or tissues need to be suitable sterilizable.

The system main components are: a culture chamber, a rotating mixer for semi-automatic cell seeding, a pinch-valve to generate controlled pressure circumferential stress on the sample, and two fluid dynamic circuits – one for the luminal compartment and one for the extraluminal compartment – each one composed by a roller pump, a reservoir and an air chamber to dampen the pump's pulsatility (Figure 1A-D).

The culture chamber is adaptable to different vessel lengths (30 – 120 mm) and diameters (1.6 – 6.4 mm) and its geometry is optimized for nutrient and oxygen transport through fluid dynamics simulations thanks to the Comsol Multiphysics® software. All peripheral devices are managed by four microcontrollers which are set up through a custom wireless graphic user interface (GUI) developed in Labview® (Figure 1E); the communication between them is through TCP/IP protocol, allowing a stable and fast remote wireless control.

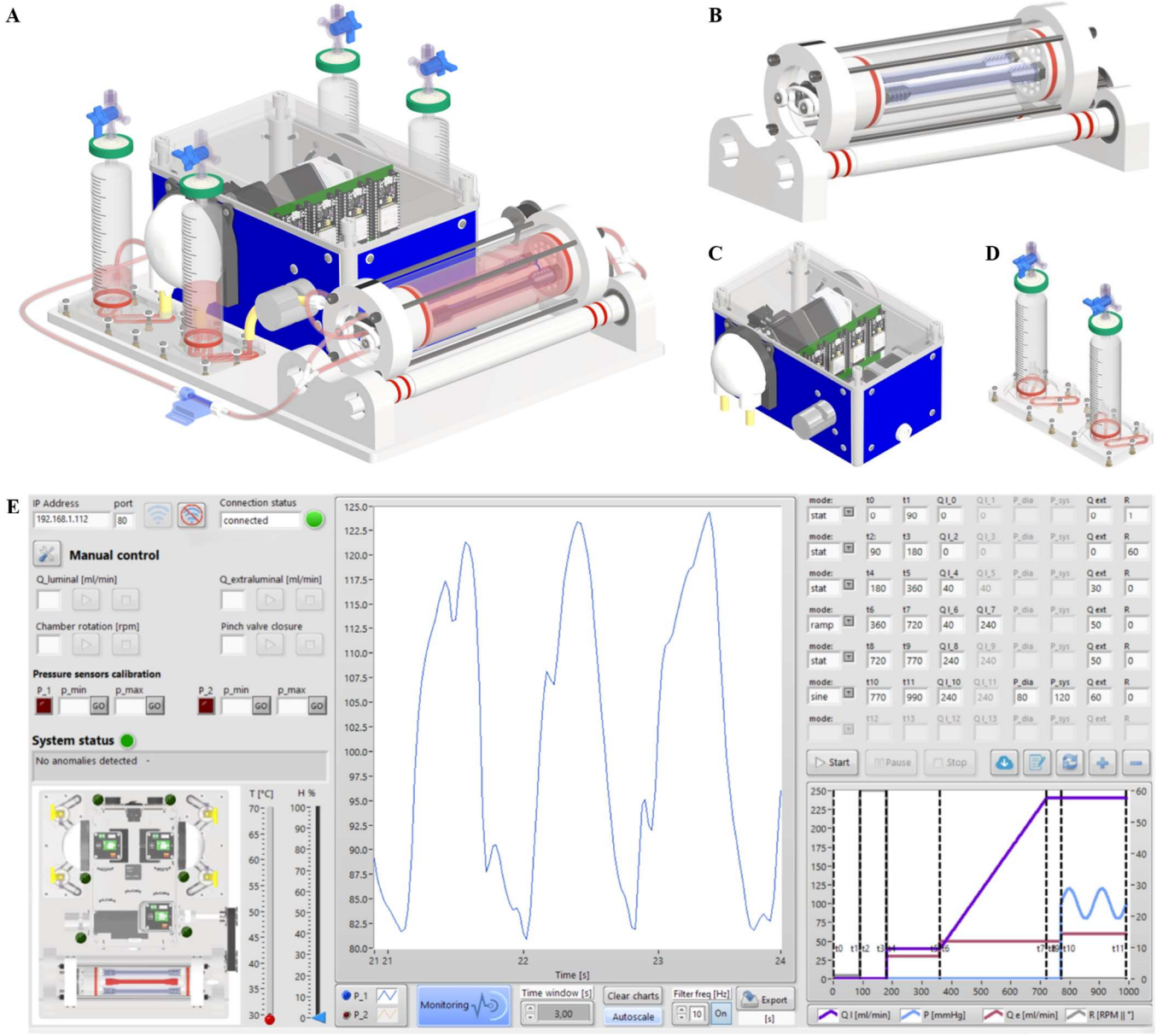


Fig. 1 (A) Culture system assembly CAD; (B) Culture chamber and rotating mixer; (C) Electronic control unit containing the peripheral devices (pinch-valve, roller pumps and stepper motor); (D) Syringe base with reservoir and air chamber; (E) Custom wireless graphic user interface developed in Labview®

Through the GUI it is possible to act on each peripheral device in manual control or to set an experiment by specifying the duration, the pumps' flow rate, the pressure regime, and the culture chamber's rotation speed for the seeding. The control unit constantly monitors the physical variables (pressure, bioreactor's rotation, temperature, and humidity inside the control unit case) and when unexpected events are detected (by pre-setting of parameters' thresholds), the execution of each peripheral device is interrupted, thus guaranteeing an elevated safety grade during system's use.

B. Cell-free hybrid graft

Three-layered electrospun grafts ($Ø_{in}$ = 6 mm, l = 60 mm), composed of a nanometric mesh of silk fibroin (SF) and polyurethane (PU) enclosed within SF layers, were manufactured and used for these tests [10].

C. Cell seeding and conditioning protocol

The first requirement to biologically validate our system is to obtain a homogenous cellular monolayer on the graft luminal side setting appropriate cell seeding and cell conditioning parameters. To reach this goal, the identification of an effective cell seeding protocol is crucial.

The cell culture experimental protocol consists of the human umbilical vein endothelial cells (HUVECs) seeding through an *ad hoc* semi-automated procedure. HUVECs were isolated from human umbilical cords and characterized, as previously described [11]. Cell seeding (10^6 cells/ml) was achieved using discrete rotations (4 angular position, each kept for 30 minutes). Concerning the conditioning protocol, initially we applied a steady WSS of 0.1Pa for 12h, we gradually increased WSS up to 0.4Pa during 24h, and we applied a steady WSS of 0.4Pa for 12h.

D. Morphological and functional analyses

To accurately verify the critical steps of cell seeding and graft colonization, small ring samples of the graft ($Ø_{in}$ = 6 mm, l = 5 mm) were taken at different time points: after seeding phase (1 ring sample), after conditioning phase (3 ring samples at different positions) (Figure 2A).

Cell morphology was investigated by immunostaining of graft pieces and subsequent imaging through a fluorescence wide-field Zeiss Axio Imager microscope, equipped with the Apotome module (structured illumination). As markers, we selected DAPI (nuclear staining), phalloidin (actin cytoskeleton), and cell adhesion molecules. The latter, including VE-Cadherin, pFAK, paxillin, and ZO-1, will allow an initial assessment on the functionality of the tissue. Afterwards, we will evaluate flow-induced changes on HUVECs morphology, function, and gene expression (e.g., KLF-2, vWF).

III. Results and Discussion

A. Culture system bench tests and validation

The system was successfully subjected to bench tests to verify the no cytotoxicity of all components that are in direct contact with the sample and cell medium, the compatibility with the assembly procedures under laminar flow hood, the hydraulic sealing (up to 400mmHg), and the maintenance of sterility inside an incubator up to 21 days.

We believe that the versatility and easiness of use are the features that most distinguishes the culture system here developed and presented from those commercially available or present in the state-of-the-art. Indeed, the system is robust and reliable in setting and exploit different seeding and stimuli protocols and allow to carry out cell colonization experiments in a precise and controlled way, allowing to perform a fine tuning of the experimental procedures both in terms of rotary seeding and fluid dynamic conditions.

B. Cell seeding and conditioning results

According to previously published data [11], initial cell seeding protocols revealed the high affinity of HUVECs for the chosen hybrid electrospun vascular graft. Cell adhesion occurred rapidly following injection of cell suspension within the graft. Although the luminal surface was not entirely populated, the first morphological analyses are highly promising. We observed that HUVECs almost completely covered the graft (*i.e.,* without leaving empty spaces between them) and establish a complex cell-graft and cell-cell interaction network (Figure 2B-C). Of note, the staining of cell nuclei show that a complex architecture generated by the cell-graft binomial and composed of a compact cellular monolayer. All these observations endorse the possibility to obtain a functional cell-populated graft to subject to physio-pathological environments of fluid flow.

Following cell seeding, we applied a venous-like wall shear stress (up to 0.4Pa). Compared to the sample taken after seeding, only few cells were observed 48 hours after starting perfusion. We hypothesize that this is mainly due to conditioning protocol itself: WSS maximum value of 0.4Pa attained after 36h and maintained for 12h could be too high or applied too quickly in combination with a not yet optimal adhesion of all cells to the graft after seeding phase. Furthermore, given the intrinsic permeability of the electrospun graft, we found extravasation which could affect the stress state of the cell layer.

Currently, we are carrying out a fine optimization of the conditioning protocol parameters, mainly acting on the WSS maximum value and application duration.

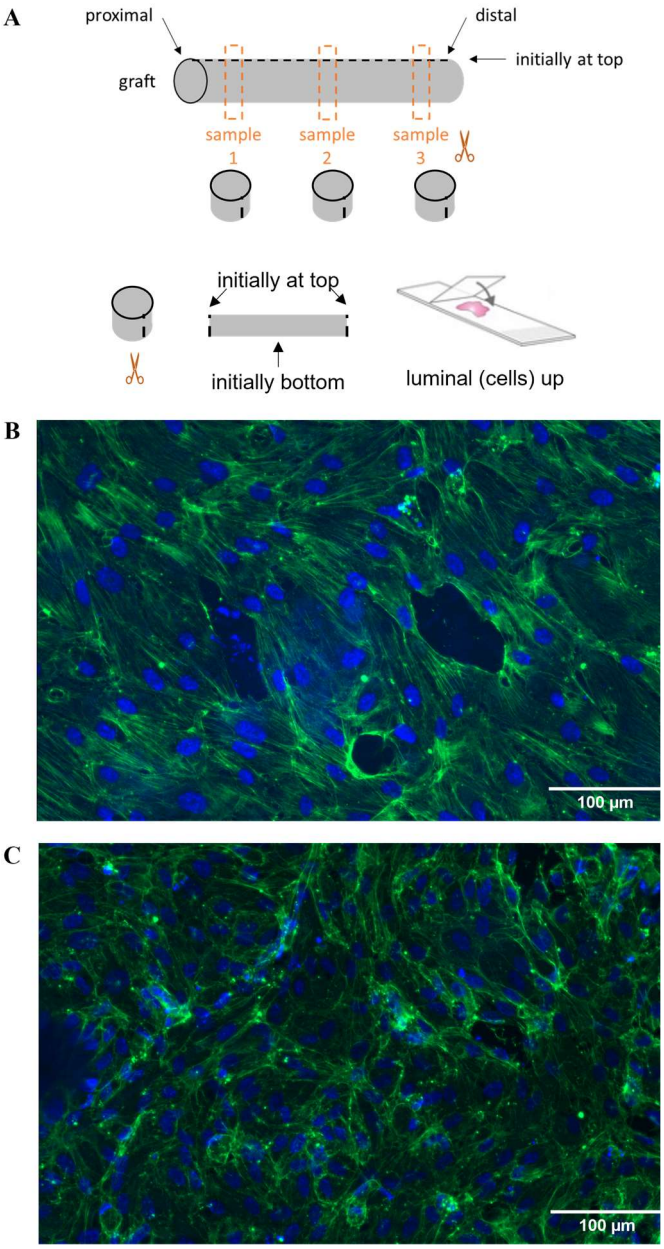


Fig. 2 (A) Representative scheme of sampling method for the cultured graft (proximal and distal respect to the cells injection site); (B)-(C) Immunostaining images (DAPI (blue), phalloidin (green)) at different sample position.

Once a completely circumferentially colonized graft will be achieved, it will be possible to fine tune the wall shear stress parameters to study the effects of haemodynamic conditions on vascular cells, as well as the process of inflammation *in vitro* (with the addition of other components into the cellular system, e.g. immune cells) and pathological tissue deposition or adaptation.

IV. Conclusion

In this study, we successfully developed an advanced culture system to investigate *in situ* biomechanisms of electrospun vascular prosthesis. We demonstrated its effectiveness in allowing semi-automatic seeding followed by finely controlled fluid dynamic stresses. The encouraging biological results that we obtained represent a preliminary, but crucial step. Indeed, obtaining a reproducible graft colonization is fundamental for

the exploitation of a custom-made culture system for blood vascular grafts. Now we are testing how a combination of circumferential deformation and WSS affect HUVECs cytoskeleton organization, as well as protein regulation and gene expression. In the future, the system shall be used to perfuse also native vessel harvested by slaughterhouses, under controlled arterial and venous haemodynamic conditions. In this way, it will be possible to investigate whether native vessel cell functions respond differently to physical stimuli, and their mechanobiology. In experiments with native vessels, as read out, we will consider matrix growth, tissue remodelling, and gene expression, and early pro-pathological markers.
In perspective, through the developed advanced culture system and the drafting of *ad hoc* protocols for both graft cellular colonization and native vessel experiments, it will be possible to establish an accurate *in vitro* model that allows to investigate the complex biological interactions that occur in vascular tissue engineering.

ACKNOWLEDGEMENT

PhD fellowship to Elia Pederzani sponsored by Istituto Nazionale di Previdenza Sociale (INPS).

REFERENCES

[1] Gaharwar, A.K., Singh, I. & Khademhosseini, A. Engineered biomaterials for in situ tissue regeneration. Nat Rev Mater 5, 686–705 (2020). https://doi.org/10.1038/s41578-020-0209-x

[2] Sengupta, D., Waldman, S.D. & Li, S. From In Vitro to In Situ Tissue Engineering. Ann Biomed Eng 42, 1537–1545 (2014). https://doi.org/10.1007/s10439-014-1022-8

[3] Wissing, T.B., Bonito, V., Bouten, C.V.C. et al. Biomaterial-driven in situ cardiovascular tissue engineering—a multi-disciplinary perspective. npj Regen Med 2, 18 (2017). https://doi.org/10.1038/s41536-017-0023

[4] van Haaften EE, Bouten CVC, Kurniawan NA. Vascular Mechanobiology: Towards Control of In Situ Regeneration. Cells. 2017 Jul 3;6(3):19. doi: 10.3390/cells6030019. PMID: 28671618; PMCID: PMC5617965.

[5] L. A. Bockeria, O. Svanidze, A. Kim, K. Shatalov, V. Makarenko, M. Cox, T. Carrel, Total cavopulmonary connection with a new bioabsorbable vascular graft: First clinical experience, J. Thorac. Cardiovasc. Surg.2017, 153, 1542.

[6] Hibino, N., Yi, T., Duncan, D.R., Rathore, A., Dean, E., Naito, Y., Dardik, A., Kyriakides, T., Madri, J., Pober, J.S., Shinoka, T. and Breuer, C.K. (2011), A critical role for macrophages in neovessel formation and the development of stenosis in tissue-engineered vascular grafts. The FASEB Journal, 25: 4253-4263. https://doi.org/10.1096/fj.11-186585F

[7] N. Hibino, E. McGillicuddy, G. Matsumura, Y. Ichihara, Y. Naito, C. Breuer, T. Shinoka, Late-term results of tissue-engineered vascular grafts in humans, J. Thorac. Cardiovasc. Surg.2010, 139, 431

[8] Salacinski HJ, Goldner S, Giudiceandrea A, et al. The Mechanical Behavior of Vascular Grafts: A Review. Journal of Biomaterials Applications. 2001;15(3):241-278. doi:10.1106/NA5T-J57A-JTDD-FD04

[9] Design Approaches to Myocardial and Vascular Tissue Engineering Olukemi O. Akintewe, Erin G. Roberts, Nae-Gyune Rim, Michael A.H. Ferguson, Joyce Y. Wong Annual Review of Biomedical Engineering 2017 19:1, 389-414

[10] van Uden, S., Catto, V., Perotto, G., Athanassiou, A., 2, 2, Greco, F. G., Riboldi, S. A. 2019. Electrospun fibroin/polyurethane hybrid meshes: Manufacturing, characterization, and potentialities as substrates for hemodialysis arteriovenous grafts. J Biomed Mater Res Part B 2019: 107B: 807– 817. https://doi.org/10.1002/jbmb.34177

[11] Franzoni M, Cattaneo I, Longaretti L, Figliuzzi M, Ene-Iordache B and Remuzzi A 2016 Endothelial cell activation by hemodynamic shear stress derived from arteriovenous fistula for hemodialysis access Am. J. Physiol. Circ. Physiol. 310 H49–59

[12] A. Caldiroli et al, Hybrid fibroin/polyurethane small-diameter vascular grafts: from fabrication to in vivo preliminary assessment, 2022 Biomed. Mater. 17 055015

3D printing of a nanomaterials-embedded gelatin/pectin hydrogel for the development of an *in vitro* drug testing platform

Lorenzo Guidi[1], Elisabetta Rosellini[1], Giovanni Vozzi[2], Carmelo De Maria[2], Gabriele Maria Fortunato[2], Anna Lapomarda[2,] Luigi Lazzeri[1], Maria Grazia Cascone[1]

[1]*Department of Civil and Industrial Engineering, University of Pisa*
[2]*Department of Information Engineering, University of Pisa*

***Abstract*—In this work we propose a novel nanocomposite hydrogel formulation, composed of food waste-sourced polymers (gelatin and pectin) and nanosytems (multiwall carbon nanotubes), and produced by extrusion-based 3D printing, to lay a foundation for nanostructured 3D printed drug testing platforms.**

***Keywords* — 3D printed hydrogels, carbon nanotubes, tissue engineering, drug testing**

I. Introduction

Natural polymer-based hydrogels, three-dimensional hydrated polymeric structures, are extensively used in tissue engineering studies for their extracellular matrix mimicking properties, biocompatibility, and biodegradability [1]. Drug investigation urgently requires advanced *in vitro* models to investigate and test new pharmacological options. In fact, current in silico or *in vitro* approaches and animal models can't replicate the morphology, functionality, and biochemistry of certain complex human tissues, such as the pulmonary blood/air barrier or the blood-retinal barrier [2].

Recent progress in tissue engineering has led to the development of advanced 3D hydrogel systems. The complexity of human tissues requires tissue engineering practices to ensure precise control over architectural cues and cell activity, viability, and stress [3], [4].

Nanosystems have caught the scientific community's interest for their capability of improving hydrogel structural stability, shape fidelity, cell-interaction, and viability, while maintaining scaffold biocompatibility. Moreover, they can allow a more efficient drug delivery, by enhancing cellular uptake and bioavailability while reducing adverse side effects [2], [5], [6]. Nanosystems exist in different structures (2D and 3D), organizations, and nature, such as carbon-based (nanotubes and graphene), polymeric (nanoparticles and micelles), silica oxides, metal oxides, nanocrystals, lipids (liposomes and solid lipids), and quantum dots [7].

Among nanomaterials, carbon nanotubes (CNTs) present appealing physicochemical properties, easily tuneable by surface functionalization. The functionalization of CNTs with various biomolecules has allowed interesting drug delivery applications [8]. CNTs have in fact been employed to trigger drug release in a hydrogel system thanks to their sensitivity to near infrared radiation (NIR) or UV light [6], [9]. However, the introduction of nanosystems could affect the matrix hydrogel's printability [10].

In the present study, an eco-friendly biodegradable biomaterial ink, printable by extrusion-based 3D printing (EBP), was designed for the development of a 3D tissue-engineered drug testing platform. The aim was to investigate the properties of the material and the effect of the addition of multi-wall carbon nanotubes (MWCNTs) on the printability and post-printing stability. The biomaterial ink was based on a blend of two natural polymers, namely gelatin and pectin. MWCNTs functionalized with -COOH groups (MWCNT-COOH) were added to the polymeric biomaterial ink solution. The 3D printed hydrogels were crosslinked using a genipin solution. Morphological analysis, mechanical characterization and degradation tests were carried out.

II. Materials and methods

A. Materials

Gelatin from porcine skin (type A, gel strength 300g bloom) was acquired from Sigma Aldrich (Saint Louis, MI, USA). Pectin from fruit waste (classic CU 701, DE 36%, MW 100-400 kDa) was acquired from Herbstreit&Fox (Neuenburg, Germany). Genipin (98% purity HPCL), was acquired from Challenge Bioproducts Co. LTD, CBC (Taiwan). Multi wall carbon nanotubes (93%wt purity) were acquired from CNT Co. LTD (South Korea) and functionalized with carboxylic groups (-COOH) in a nitric acid tank (68% HNO_3, Sigma Aldrich) for 50 hours at the Technology University of Warsaw, by Professor Leszek Stobinski. Dulbecco's phosphate buffered saline (DPBS) 1X (9.55 g/l in deionized water) was acquired from Biowest (Meda, Italy), and Tween 20 was acquired from Sigma Aldrich (Italy).

B. Preparation of the gelatin/pectin solutions

The polymeric solution GelPec (5% gelatin and 1% pectin w/v in DPBS) was prepared by mixing polymer powders in the solvent at 70°C under stirring at 700rpm for 60 minutes.

C. Preparation of the GelPec/MWCNT solutions

Tween 20 (100µl) was added to the MWCNT-COOH powder, which was then diluted in PBS (0.1%w/v) and sonicated in a cold environment for two hours at 59kHz and 2W power (Vibra Cell 130, Sonics&Materials Inc., Newton, MA, USA) to produce a dispersion. Three MWCNT-COOH/GelPec solutions were created (0.3%, 0.9%, 1.2% w/w, respectively) adding the gelatin and pectin powders to the MWCNT dispersion (beforehand stirred at 70°C, 700 rpm for 15 minutes), diluting accordingly in DPBS and stirring for 60 minutes at 700 rpm at 70°C.

D. 3D printing and crosslinking of the scaffolds

All solutions were left to cool at room temperature before printing. Disposable syringes were loaded with the gels and inserted in a NEMA17 motor driven 3D printing platform. Depending on the characterization method, different CAD designs were printed: woodpile (square based, 25% infill, six 3-by-3 crossed 250µm layers) and filled (65% infill, three 250µm layers, various base areas). The extruding nozzle diameter was 400µm. The speed of the extruder on the x-y plane was 8 mm/s. CAD designs were produced with Autodesk Fusion 360 and the G-code was generated with Repetier Host. Samples were printed on laboratory slides or acetate sheets depending on their dimensions. Figure 1 displays some printed woodpile and filled samples.

E. Crosslinking optimization

Samples were solvent casted in a multiwell plate (13mm well diameter) at 4°C, cut to 5mm heights and crosslinked in different solutions: genipin 0.5% w/v in ethanol or genipin 0.5, 0.25 and 0.2% w/v in DPBS. The samples were completely submerged in the solutions. The crosslinking took place in two phases: room temperature overnight and 40°C for 24h.

F. Scaffold characterization

1) Degradation test

Woodpile samples were printed, weighed, crosslinked, kept in water at 40°C (hydration phase) and weighed again at set timepoints during a 9-day test span. Genipin-crosslinked pure gelatin samples were included as a control. Average post-crosslinking weight and relative weight loss (printed vs crosslinked sample) were analysed by ANOVA.

2) Morphological characterization

Printed woodpile samples were analysed (Leica Microsystems srl, Varese, Italy) before and after the crosslinking and during the hydration phases. Dimensions were extracted from microscope photos with ImageJ at set timepoints (as printed, crosslinked, hydrated for 24h). ANOVA analysis was used to evaluate the effect of carbon nanotubes percentage and timepoints on line and pore features.

3) Mechanical characterization

Filled samples were printed, crosslinked, and tested on a uniaxial tensile texting machine (Zwick Roell ProLine Z005, Zwick Gmbh & Co, Germany). Young's modulus, breaking stress and strain were calculated. A pretension was set at 0.005N and testing speed was set at 2.6 mm/s. Average nominal length and surface of the samples were respectively 26.7mm and 5.4 mm^2.

III. Results

GelPec resulted in a printable and crosslinkable biomaterial ink exhibiting post-printing stability. The printability of GelPec biomaterial ink was not affected by the addition of carbon nanotubes. Genipin 0.2% in DPBS showed the best crosslinking results in terms of integrity and stability of the hydrogel (Figure 1 and Figure 2).

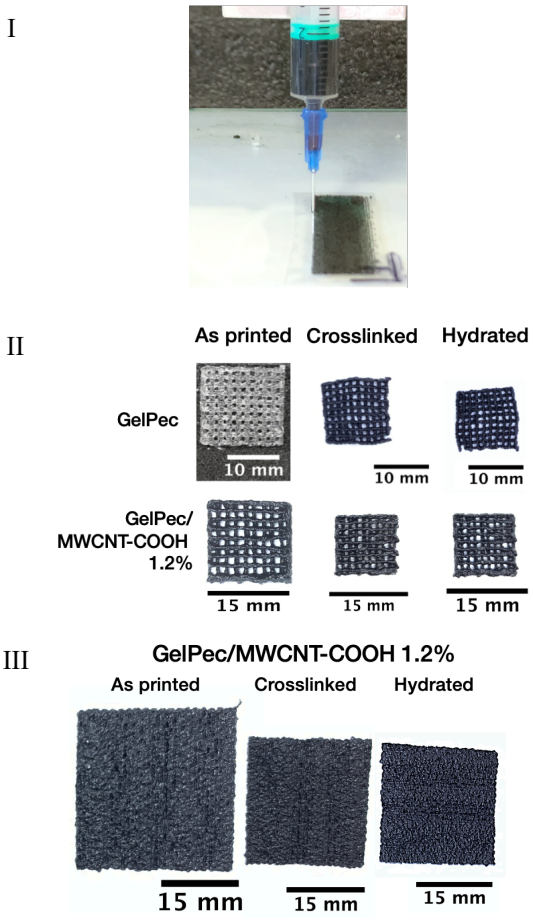


Fig. 1: The images display I) a photograph from a 3D printing process of a filled GelPec/MWCNT-COOH sample II) a woodpile 3D printed GelPec and GelPec/MWCNT-COOH sample right after being printed, crosslinked, and hydrated for 24h and below, III) a 3D printed filled GelPec/MWCNT-COOH sample during the three mentioned phases

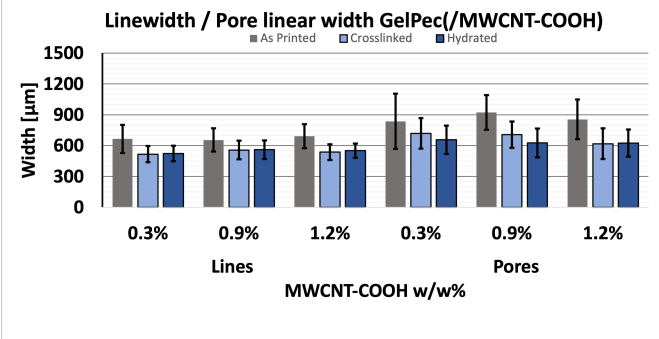
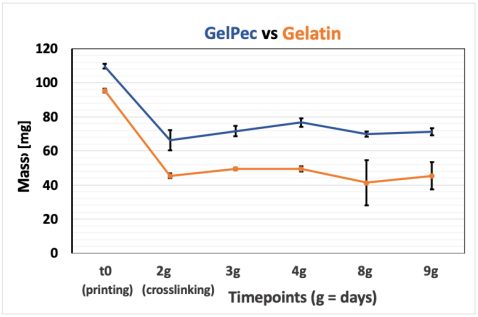


Fig. 2: The image displays the linewidth (left) and pore linear width (right) of 3D printed woodpile GelPec and GelPec/MWCNT-COOH samples over three timepoints (as printed, crosslinked, and hydrated for 24h)

As expected, the degradation test showed that control gelatin hydrogels were poorly stable while GelPec hydrogels were able to better maintain their shape. Therefore, pectin seems to act as a structural stabilizer of gelatin. GelPec samples added with MWCNT-COOH showed a significantly higher weight loss with respect to unloaded GelPec (Figure 2).

I



II

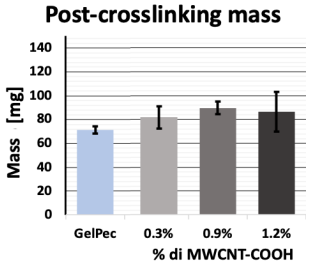


Fig. 3: The images display I) a graph of GelPec and gelatin samples' mass over time, II) GelPec and GelPec/MWCNT-COOH samples' mass following the crosslinking process

GelPec hydrogel had a Young's modulus of 400kPa, breaking strain of 20% and breaking stress of 80kPa. The elastic modulus of GelPec is agreement with data reported in literature for human choroidal tissue [11].

Mechanical properties of hydrogels loaded with MWCNT-COOH (1.2% w/w) did not show statistical difference with respect to those of unloaded hydrogels, while for hydrogels loaded with lower amounts of MWCNT-COOH (0.3% and 0.9% w/w) mechanical parameters, apart from breaking strain, decreased (Figure 4). This indicates the need for testing different embedded percentages of nanotubes, both greater and lower than 1.2%.

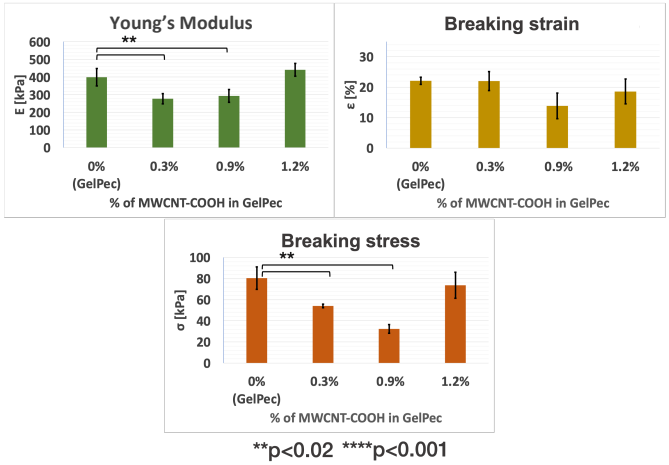


Fig. 4: The image displays histograms of the values of Young's modulus, breaking strain and breaking stress of 3D printed GelPec and GelPec/MWCNT-COOH samples.

IV. Conclusions

We successfully produced a gelatin/pectin biomaterial ink for potential application as 3D tissue-engineered drug testing platforms. The material resulted optimally extrudable and able to maintain the programmed architecture after genipin crosslinking. The loading of carbon nanotubes in the GelPec biomaterial ink does not affect the printability and post-printing stability of the material. Given the promising results obtained with the designed nanotubes incorporation protocol, a future development may include the use of different nano-fillers, in particular polymeric nanoparticles loaded with specific drugs, to evaluate the use of the GelPec hydrogel as a drug testing platform.

Acknowledgements

We acknowledge the support of the European Union by the Next Generation EU projectECS00000017 'Ecosistema dell'Innovazione' Tuscany Health Ecosystem (THE, PNRR, Spoke 4: Nanotechnologies for diagnosis and therapy)

We'd also like to thank Professor Leszek Stobinski from Warsaw University of Technology for kindly providing us with the multi-walled carbon nanotubes.

References

[1] J. L. Drury and D. J. Mooney, "Hydrogels for tissue engineering: Scaffold design variables and applications," *Biomaterials*, vol. 24, no. 24. Elsevier BV, pp. 4337–4351, 2003. doi: 10.1016/S0142-9612(03)00340-5.

[2] Z. Peng, L. Zhou, J. K. W. Wong, and Y. K. Chan, "Eye-on-a-chip (EOC) models and their role in the future of ophthalmic drug discovery," *Expert Review of Ophthalmology*. Taylor and Francis Ltd., pp. 259–261, 2020. doi: 10.1080/17469899.2020.1788388.

[3] A. Bhattacharyya, G. Janarthanan, and I. Noh, "Nano-biomaterials for designing functional bioinks towards complex tissue and organ regeneration in 3D bioprinting," *Additive Manufacturing*, vol. 37. Elsevier B.V., Jan. 01, 2021. doi: 10.1016/j.addma.2020.101639.

[4] A. Khademhosseini and G. Camci-Unal, "3D Bioprinting in Regenerative Engineering," 2018.

[5] J. Yeste, X. Illa, M. Alvarez, and R. Villa, "Engineering and monitoring cellular barrier models," *Journal of Biological Engineering*, vol. 12, no. 1. BioMed Central Ltd., Sep. 12, 2018. doi: 10.1186/s13036-018-0108-5.

[6] X. Dong, C. Wei, J. Liang, T. Liu, D. Kong, and F. Lv, "Thermosensitive hydrogel loaded with chitosan-carbon nanotubes for near infrared light triggered drug delivery," *Colloids Surf B Biointerfaces*, vol. 154, pp. 253–262, Jun. 2017, doi: 10.1016/j.colsurfb.2017.03.036.

[7] A. F. Moreira, "Nanomaterials in Drug Delivery Applications," *Nanomaterials*, vol. 12, no. 20. MDPI, Oct. 01, 2022. doi: 10.3390/nano12203565.

[8] M. Izadifar, D. Chapman, P. Babyn, X. Chen, and M. E. Kelly, "UV-Assisted 3D Bioprinting of Nanoreinforced Hybrid Cardiac Patch for Myocardial Tissue Engineering," *Tissue Eng Part C Methods*, vol. 24, no. 2, pp. 74–88, Feb. 2018, doi: 10.1089/ten.tec.2017.0346.

[9] F. Cardano, M. Frasconi, and S. Giordani, "Photo-responsive graphene and carbon nanotubes to control and tackle biological systems," *Frontiers in Chemistry*, vol. 6, no. APR. Frontiers Media S. A, Apr. 01, 2018. doi: 10.3389/fchem.2018.00102.

[10] Bonatti, A. F., Chiesa, I., Vozzi, G., & De Maria, C. (2021). Open-source CAD-CAM simulator of the extrusion-based bioprinting process. Bioprinting, 24, e00172.

[11] Ferrara, M., Lugano, G., Sandinha, M.T. et al. Biomechanical properties of retina and choroid: a comprehensive review of techniques and translational relevance. Eye 35, 1818–1832 (2021). https://doi.org/10.1038/s41433-021-01437-w

Optimization of advanced setups with integrated readouts for evaluation of cardiac toxicity in a heart on chip device

G. Cretti[1], R. Visone[2], U. Kraushaar[3], P. Occhetta[1,2], M. Rasponi[1]

[1] *Department of Electronics, Information and Bioengineering, Politecnico di Milano, 20133 Milano, Italy*

[2] *BiomimX Srl, Viale Decumano 41, 20157 Milano, Italy*

[3] *NMI Natural and Medical Sciences Institute at the University of Tübingen, 72770 Reutlingen, Germany*

***Abstract* — With the aim of studying the cardiotoxic effect of different compounds on cardiac tissue, in this work a microfluidic platform (uHeart) was exploited to generate 3D cardiac models from different cell sources (i.e., chick embryo CMs and human iPSC-CMs), developed by exploiting different stimulation set-ups (i.e, mechanical and/or electrical stimulation). uHeart enabled to analyze 3D cardiac microtissues through combined readouts (e.g. video acquisition and electric field recording). A comparison between uHeart and commercially available MEA systems, the gold standard for 2D cardiac electrophysiology, was then performed by evaluating functional parameters (e.g. spontaneous beating onset time, synchronicity, electrophysiological parameters). Finally, a drug screening was carried out to preliminarily assess the ability of uHeart to be used as a predictor of cardiotoxicity, such as MEA systems.**

***Keywords*—Heart on chip, cardiac toxicity, drug screening.**

I. INTRODUCTION

CARDIOTOXICITY still represents one of the most important side effects in the drug development pipeline. According to different studies drugs may disturb the delicate orchestration of cardiac ions fluxes [1]. To reduce incorrect termination of compound development and to prevent market withdrawal for unpredicted cardiotoxic effects in humans, regulatory agency recently developed new guidelines (International Committee on Harmonization, ICH S7B) to better determine TdP [2]. In such a context, pre-clinical in vitro cardiac models developed by combining human induced pluripotent stem cells derived cardiomyocytes (hiPSC-CMs) and Organs-on-Chip (OoC) technology have emerged as promising predictive and reliable tools [3]. hiPSC-CMs represent predictive and relatively easy-to-handle source of human cells, despite they have been often reported to lack the typical myocardial maturation in classical 2D culture systems. To overcome this limitation, OoC are advanced cell culture setups able not only to recapitulate in vitro the key aspects of the in vivo cardiac physiology with an unprecedented level of accuracy [4], thanks to a combination of biochemical and biophysical stimuli, but they can also integrate multifunctional readouts. Being inserted in the safety screening field, the aim of the present work was to develop and validate an experimental set-up (uHeart) able to predict functional cardiotoxicity of compounds by exploiting 3D engineered cardiac microtissues, benchmarked against state-of-the-art 2D Multi Electrodes Array (MEA) based models. uHeart was first developed from an animal source and then validated with iPSC-CMs, and integrated a combination of readouts (i.e., motion analysis, calcium imaging, viability assays and field potential recordings).

II. MATERIALS AND METHODS

A. Platforms

At first, a comparison between a commonly used 2D platform (MEA, Fig. 1a) and an advanced 3D culture system (uHeart, 1b) was performed.

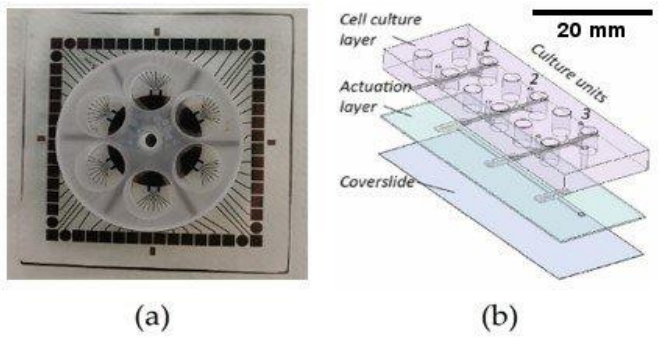


Fig. 1: (a) MEA and (b) uHeart platforms

MEAs (Multi Channel Systems MCS GmbH, Germany) have an arrangement of 60 surface electrodes which are meant for extracellular field potential (FP) recording, since the cells are cultivated in 2D directly on them. uHeart platforms consist in three layers: 1) an upper cell culture layer, where the cells are seeded embedded in a fibrin gel and are feed thanks to two lateral channels filled of medium by four wells per chamber, 2) an intermediate actuation layer which provides a means to mechanically stimulate (i.e., uniaxial strain of 10%, 1 Hz) the 3D microtissue through a pneumatic actuation system and 3) a bottom coverslip. uHeart platforms can additionally hosts electrodes to provide electrical stimulation, alone or in combination with the mechanical one, or to measure the electrical activities of the cells (Fig. 2). Specifically, the electrical stimulation was provided through the implementation of a pair of coaxial guides which allow the insertion of microelectrodes in correspondence of the lateral channels, while the electrical measurement through electrodes positioned in the central channels, in contact with the microtissues. uHeart platforms were produced by replica molding. Briefly, PDMS (Syligard 184 Sylicon Elastomer Kit), made by mixing in 1:10 ratio the curing agent and the pre-polymer, was poured on previously fabricated acrylic resin

molds (10 10 CFS, C-system) to obtain the culture layer. The same process was performed on a micropatterned wafer to obtain the actuation layer. In the case of uHeart platforms the two layers were then bonded through a plasma treatment (Harrick Plasma, PDC-002) and a glass coverslip was finally bonded to the actuation layer. For the electrical devices, the culture layer is directly bonded on a PDMS membrane, 800 µm thick.

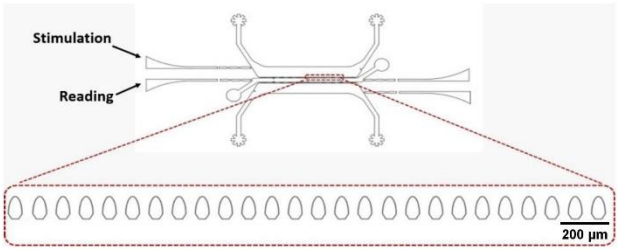


Fig. 2: electrical platform encompasses four electrode guides: two for stimulation and two for reading. The semihexagonal pillar shape was optimized to allow cell-laden gel confinement during injection.

B. Cell sources and models generation

For the first part of the work embryonic chicken cardiomyocytes were isolated from 13 days old embryonic chicken hearts, by enzymatic and mechanical digestion. The so obtained single cells were then seed on MEAs and uHeart by means of different protocols. In first case 4µl of cell suspension (density 20000 cells/µl in 3% FBS medium) was seeded onto the nitrocellulose-coated electrode surface. In second case CMs were seeded into the devices after embedment in a fibrin gel (i.e., 10 mg/ml of fibrinogen and 2.5 U/ml of thrombin) at a final density of 100 x 10^6 cells/ml. in uHeart, the mechanical actuation was started at Day 2 [5]. For the human models, hiPSC previously differentiated in CM were thawed (Day 9) and used after 2 days of pre-culture (Day 11). CM were mixed with human cardiac fibroblasts in a 3:1 ratio (i.e., 75% CM and 25% of hCF), embedded in different hydrogels (i.e., Geltrex or fibrin gel 10 mg/ml of fibrinogen and 2.5 U/ml of thrombin) at a final density of 100 x 10^6 cells/ml and inoculated into uHeart platforms.

C. Readout set-up development

The evolution of microtissues in terms of morphology, viability and functionality was assessed by means of different ad-hoc readouts, singularly exploited.

1) Cell viability

Calcein, AM (Thermo Fisher Scientific Inc., USA) and Propidium Iodide (Sigma; P-4170) were used to stain living and dead cells respectively. A solution of PBS containing propidium 3.3 µM was mixed with Calcein AM 1 µM and it was inoculated in the platforms after a cell wash with PBS and incubated for 1 hour before performing the imaging through a reverse microscope (Life Technologies EVOS® FL).

2) Contractility

Time series images were acquired at 25 fps through an inverted microscope and were analyzed with "MUSCLEMOTION" software [6], which assessed the development, the synchronicity and the beating properties of microtissues by measuring four standard parameters (i.e., beating period-BP; contraction duration–CD)

3) Electrophysiology

The electrical activity of samples cultured in MEAs was assessed by means of MEA2100-Systems. In uHeart platforms the signal recordings were performed thanks to a custom-made set-up. Briefly, working and reference electrodes were manually inserted in the platforms and connected to an extracellular amplifier (Ext-10C, Npi Electronic GmbH, Germany). Electrical signals were acquired at 2 kHz by means of an electronic board (Analog Discovery 2, Digilent, Washington, USA) connected to a personal computer through the "Scope" function included in the software of the instrument. The acquired signals were then elaborated through MATLAB to derive the relevant parameters, such as RR interval, and the Field Potential Duration (FPD).

D. Drug test

As for the chicken cardiac microtissues, the responsiveness of the cardiac samples to a commonly recognized IKr blocker drug (E4031) was assessed. An increasing ramp of concentration (i.e., 0 nM, 5 nM, 50 nM, 250 nM and 500 nM in medium) was administered to the samples and after 15 minutes of incubation, the specific readout (i.e., calcium transient, motion analysis or FP recording) was performed. Human 3D cardiac microtissues were administered with a non-selective β-adrenoreceptor agonist (Isoprenaline), usually used to treat bradycardia or heart block since it has positive inotropic and chronotropic effects. A cumulative dose administration was followed, testing different concentrations (i.e., 0.1 nM, 10 nM and 1 µM).

III. RESULTS

A. Chicken cardiac models

After the isolation of CMs from the primary tissue, the cells were cultured in the platforms. The 2D culture in MEAs (Fig. 3a) differs from 3D microtissues in uHeart (Fig. 3b) in terms of morphology. 2D cardiomyocytes well spread at the bottom of the wells, while in the 3D configuration more branched cells were evidenced. Spontaneous beating onset was detected at Day 4 for 2D samples cultured on MEA and at Day 2 for 3D samples in uHeart.

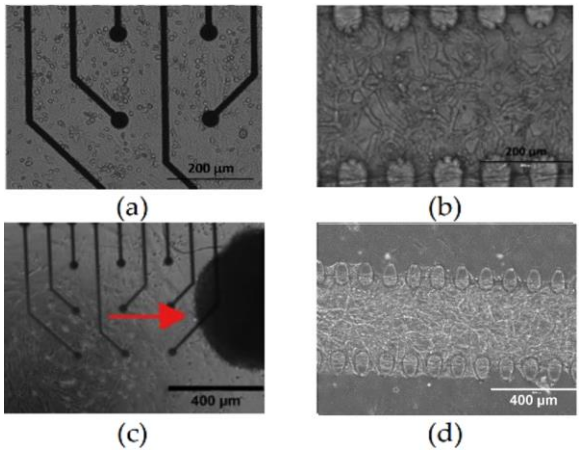


Fig. 3: comparison of morphology between 2D culture on MEA (a) and 3D in uHeart (b).

After a prolonged culture (i.e., ten days), 3D microtissues maintained their branched architecture (Fig. 3d), while 2D microtissue formed differently sized cluster of cells after the detachment from the substrate (red arrow Fig. 3c). Viability assays at Day 1 didn't evidence any difference between the samples in the different platforms, while a larger difference emerged at Day 10 (Fig. 4), with static and dynamic uHeart platform having higher viability (78.02 ± 4.62 % and 77,83 ± 3.72%, respectively) than MEA (60.7 ± 9.71%).

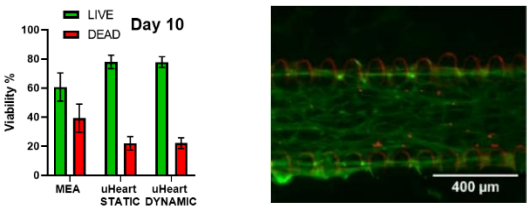


Fig. 4: viability results at day 10 (left) and an example of L/D assay on uHeart platforms.

Since in 2D the cells clustered together after a prolonged time in culture, functional readouts were performed at Day 4 to compare the conditions (2D and 3D). Motion analysis accomplished to determine the synchronicity of the beating throughout the microtissues (Fig. 5), calculated as correlation coefficient of the effective overlap of all the contraction peaks (Fig. 5a). The highest values were detected for actuated 3D microtissue (97%), followed by 2D culture (94.6%). The lowest score was obtained in static uHeart, showing a correlation coefficient of about 56.2%.

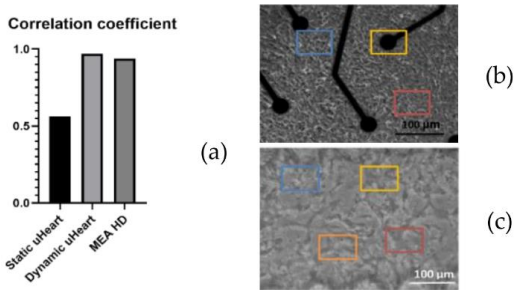


Fig. 5: (a) correlation coefficient computed by analyzing the trace of CA in different zones if the same microtissue in MEA (b) and uHeart (c).

The same trend was obtained by computing the correlation coefficient derived from the calcium transient analysis. Thanks to its well-established method of FP recordings, MEAs were used to assess the relation between electrical parameters and motional ones. In particular, the comparison between RR parameter and the corresponding BP carried out on the same day on the same samples (n=5) yield to a correlation coefficient of 0.996. Since the different readouts resulted consistent, they were exploited to assess the effect of E4031 on cardiac microtissue. In all the samples a concentration higher than 5 nM induced an increase in BP and CD with respect to controls without drug (red, Fig. 6), both if analyzed by means of video analysis (Fig. 6), or through calcium transient. The same results were obtained also with the computation of RR interval through FP recordings, while it wasn't possible to determine the FPD since the huge noise in the signal covered the repolarization wave. A further administration of 250 nM induced the arrest of the beat in all the samples, except in 33% of dynamic ones, which were subjected to a further increase in BP and CD. Another exception was found in one 2D sample, in which the highest dose yield to an arrhythmic event.

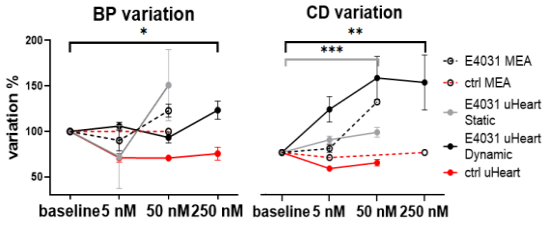


Fig. 6: variation of BP and CD, computed by means of motion analysis, induced by the dose escalation of E4031 in all differently cultured samples.

B. Human Cardiac Models

3D cardiac microtissue model were developed by seeding hiPSC-CM in uHeart and their development was monitored daily to assess the effect of mechanical and/or electrical stimulation compared to a static culture. Video analyses revealed a gradual decrease in BP from Day 3 (1245.68 ± 37.49 ms) until Day 11 (784.84 ± 42.94 ms), while from this time point a huge variability among samples occurred in all models. The mechanically actuated samples emerged as the most capable to keep a stable and constant pace of CM, while both mechanical and electrical stimulation allowed to induce a precise pace after 10 days of training. The implementation of the setup to achieve FP recordings allowed to combine it with video analysis. The incremental administration of isoprenaline yielded in a decrease of both BP/RR and CD/FPD computed through both MUSCLEMOTION and FP recordings.

IV. DISCUSSION

In the first part of the work a comparison between an innovative OoC platform and the platforms currently used as gold standard (i.e., MEA) for new studies of cardiotoxicity screening was carried out using chick embryo CMs as animal model to preliminary validate the setup. Since after the isolation from the native 3D myocardium, cell–cell contacts are disrupted and extracellular matrix is destroyed, causing cells to lose extra cellular network connections, it is fundamental to recapitulate these aspects in vitro, to recover physiological cellular functions. A combination of architectural (i.e. three dimensionality and cell density), biophysical (i.e. mechanical stimulation) and environmental (the substrate) cues was thus demonstrated to be fundamental and the combination of different developed readouts allowed to determine that 3D stimulated microtissues have higher capability to get faster a more mature and synchronous beating with respect to both 2D and 3D static samples. This was reflected on the highest correlation coefficient relative to the beating motion of different area of the same sample obtained by the stimulated 3D CM. The 3D environment resulted fundamental to elicit an early onset of spontaneous beating, that was detected after just 48h from the seeding in 3D

platforms and after 72/96h for 2D models. Calcium imaging corroborated the results obtained from motion analysis, with the highest score of correlation obtained by dynamic uHeart (0.962), followed by MEA HD (0.498) and static uHeart (0.398). On the other hand, this analysis yielded to discover a mild electrical activity in MEA LD, which was not detected in video analysis, confirming the advantages and importance to have the possibility to couple different readouts in the same platform. The FP recordings carried out at Day 4 on different 2D samples through MEA confirmed the presence of the synchronous beating, showing the presence of some BP variability between different samples. The different developed readouts resulted fundamental and were further preliminary validated to accomplish the drug test on all three types of platforms. FP recordings, calcium imaging and motion analysis were performed to screen the effect of an administration at incremental concentration of E4031. In both 2D and 3D models, all the readouts yielded a negative chronotropic effect, with an increase of BP for concentration > 5 nM. Moreover, the chicken cardiac models stopped beating within a range of concentration of [50-500 nM] in all the platforms. Interestingly, only in case of mechanically stimulated microtissues in uHeart, the stop of the beating occurred only with the highest concentration (i.e., 500 nM), while in static devices the threshold was lower (i.e., 50 or 250 nM). This may be due to the higher grade of maturation of the actuated cardiac microtissues, since younger CMs have an action potential more sensitive to the IKr blockade having less density of repolarizing currents [7]. A further confirmation was the onset of an arrhythmic event only in case of 2D microtissue, in which the blockade effect of E4031 is most prominent and could more easily induce early afterdepolarization events.

After having the preliminary validation, a new biological campaign was carried out on uHeart platforms equipped with electrical stimulation capabilities that could be used alone or in combination with the mechanical system. Human iPSC-CMs were co-cultured with supportive human cardiac fibroblasts. As for animal model, two days of stimulation (i.e., mechanical, electrical or combined) resulted sufficient to drive an interconnected and branched shape of cardiac microtissues, while a delay of few days was observed in the static control samples. The development of cardiac functionality was monitored for a longer interval and with more timepoints with respect to the previous experiments to observe the evolution of the hiPSC-CMs microtissues. The monitoring of functional parameters such as the BP and CD was achieved through motion analyses. The decrease in BP of actuated samples from Day 3 to Day 11 might be due to the actuation, acting not only as a training in their maturation but also as a pacing system. In fact, the devices mechanically actuated with a frequency of 1 Hz reached at Day 14 a beating period of 855.4 ± 92.3 ms, while electrically stimulated one passed from 1361.8 ± 81.3 ms of the Day 3 to a BP of 735.7 ± 231.2 ms at Day 14. Furthermore, as compared to Day 3 and Day 7, the later time points resulted in higher variability between samples, with a standard deviation substantially increased in Day 11 and 14. This behavior may be due to a different degree of maturation of the construct between samples [7]. The most variable samples were the hybrid ones, while the most stable during all the time of culture were the mechanically actuated, suggesting that a continuous mechanical pace at a constant frequency yield different effect respect to an increasing frequency stimulation (electrical and hybrid conditions).

To further validate the capability of this setup to assess chronotropic and inotropic effects induced on the CMs by drugs, isoprenaline was administered with increasing concentration. Both video and electrical recordings were used, by means of the optimization of a multi-parameter setup which allowed to record at the same time FP and video imaging. The trend highlighted through these combined readouts confirmed the results in literature as regards the chronotropic effects of the drug [1,4], with the BP/RR and CD/FPD decreasing by increasing the administered dose of isoprenaline. Conversely, it wasn't possible evaluate the inotropic effect, which can be revealed by means of motion analysis [5,8], since the values of CA achieved weren't consistent with each other, maybe due to the sensitivity on luminosity of the tracking software.

V. CONCLUSIONS

Intending to develop a system allowing for combined readouts to assess drug cardiotoxicity, this work exploited different platforms to culture cardiac microtissue models with different architectures (i.e., 2D and 3D), species origin (i.e., chicken embryo and human) and incorporating several analysis systems. The comparison between video, calcium transient analyses, and FP recordings on MEAs, showed a clear superimposition and consistency in their results obtained from animal models. The validity was proved through a drug test with a potent hERG channel blocker (E4031), which brought the expected results. The setup was further tested in human cells, after the implementation of an electrical readout. The experiments highlighted the capability of uHeart platforms to be not only a very useful and reliable system in achieving more advanced and highly functional cardiac microtissues from different cells sources (i.e., chick embryo CMs and hiPSC-CMs) but also in allowing a higher number of combined readouts, potentially evaluated at the same time, compared to other commercially available systems (i.e., MEA).

REFERENCES

[1] A. Mathur *et al*., "Human iPSC-based Cardiac Microphysiological," Sci. Rep., vol. 8883, p. 5, 2015.
[2] "cipaproject" 2019. [Online]. Available: https://cipaproject.org/.
[3] Leung, C.M., de Haan, P., Ronaldson-Bouchard, K. *et al*., "A guide to the organ-on-a-chip," Nat Rev Methods Primers, vol. 2, no. 33, 2022.
[4] R. Visone, "Micro-electrode channel guide (μECG) technology: an online method for continuous electrical recording in a human beating heart-on-chip," Biofabrication, vol. 13, no. 035026, 2021.
[5] A. Marsano, C. Conficconi, M. Lemme, P. Occhetta, E. Gaudiello, E. Votta, G. Cerino, A. Redaelli and M. Rasponi, "Beating Heart on a Chip: A Novel Microfluidic Platform to Generate Functional 3D Cardiac Microtissues.," Lab Chip, vol. 16, no. 3, pp. 599-610, 2016.
[6] L. Sala, *et al*., "Musclemotion: A Versatile Open Software Tool to Quantify Cardiomyocyte and Cardiac Muscle Conxtraction in Vitro and in Vivo," Circ. Res., vol. 122, no. 3, pp. e15-e16, 2018.
[7] H. Nouchi *et al*., Developmental Changes in Action Potential Prolongation by K+-Channel Blockers in Chick Myocardium. J Pharmacol Sci. 2011;115(2):235-238.
[8] R. Visone *et al*., "A microscale biomimetic platform for generation and electro-mechanical stimulation of 3D cardiac microtissues," APL Bioengineering, 2018.

Peptide anchoring methods for PEEK surfaces

L. Cassari[1], A. Zamuner[2], G.M.L. Messina[3], M. Marsotto[4], H.C. Chang[5], T. Coward[5], C. Battocchio[4], G. Iucci[4], G. Marletta[3], L. Di Silvio[5] and M. Dettin[1]

[1] *Department of Industrial Engineering, University of Padova;*
[2] *Department of Civil, Environmental, and Architectural Engineering, University of Padova;*
[3] *LAMSUN, Department of Chemical Sciences, University of Catania and CSGI;*
[4] *Department of Science, Roma Tre University;*
[5] *Faculty of Dentistry, Oral & Craniofacial Sciences King's College London.*

***Abstract*—Polyetheretherketone (PEEK) is a polymer that has been widely employed as bone implant thanks to its biocompatibility and mechanical properties. However, its bio-inertness does not induce bone integration once the material is implanted. In this work, the surfaces of 3D-printed PEEK disks were functionalized with the fragment (48-69) of BMP2 protein (GBMP1α) proved to significantly enhance calcium deposition and expression of genes involved in osteoblast differentiation. Different chemical methods were evaluated for covalently grafting the peptide onto PEEK surface: (a) anchor through specific covalent bond via oxime chemistry; (b) anchor through photoactivation of an azido group. All functionalized PEEK samples were characterized by water contact angle (WCA) measurements, atomic force microscopy (AFM), and X-ray photoelectron spectroscopy (XPS). The biological results showed that the peptide GBMP1α anchored through the two different methods is able to increase human osteoblast proliferation at 1 and 21 days with higher calcium deposition.**

Keyword – PEEK, surface functionalization, human osteoblasts, bone implant.

I. Introduction

THE clinical need for biomaterial therapies for bone is unrelenting. Polyetheretherketone (PEEK) is an ideal substitute material for bone tissue engineering. PEEK is a semi-crystalline polyaromatic linear polymer with (–C_6H_4–O–C_6H_4–O–C_6H_4–CO–)n chemical formula. It is finding popularity in bone replacement as it has been shown to have bio-mechanical properties close to human bones. It represents a promising polymeric alternative to metal implant components thanks to its excellent property combinations, of strength, stiffness, toughness, and environmental resistance. The Young's modulus of PEEK is much lower than any metallic material employed in common bone implant and is tunable through additive inclusion. It may increase up to 18 GPa, which is similar to the values of the cortical bone (18.4–20.7 GPa) [1], avoiding the effect of the stress shielding. PEEK is a thermoplastic polymer and in the range of its melting temperature, it can be processed using 3D-printing. The possibility to use PEEK polymer in the 3D-printing process has increased scientific interest and impact future development [2]. Furthermore, PEEK has interesting biological properties: it is highly resistant to thermal degradation, to the attack by organic and aqueous environments, and to biodegradation. Therefore, PEEK implants are biocompatible and biologically inert [3]. However, inertness has constrained PEEK potential applications. PEEK has a hydrophobic surface, which neither allows protein absorption nor promotes cell adhesion [4]. The aim of this research project is improving its biological properties. PEEK disk surface was functionalized with a bioactive peptide: the fragment (48-69) of BMP2 protein (GBMP1α) proved to drive a greater calcium deposition, to guide osteogenic differentiation of mesenchymal stem cells, and to promote human osteoblasts' (HOB) proliferation and expression of genes involved in osteoblast differentiation [5], [6]. Covalent bonds were realized through two different chemical strategy. The former occurred with a reaction between an aminooxy groups inserted in the peptide N-terminus and the ketone groups of the PEEK surface [7], the second one includes photoactivation of an azido group (also inserted in the peptide N-terminus) that can binds several sites of PEEK monomer [8].

II. Methods

A. Sample Preparation

Aoa-x-GBMP1α (sequence: H-Aoa-(7-aminoheptanoic acid)-Pro-Phe-Pro-Leu-Ala-Asp-His-Leu-Asn-Ser-Thr-Asn-His-Ala-Ile-Val-Gln-Thr-Leu-Val-Asn-Ser-NH_2) and N_3-x-GBMP1α (sequence H-Phe(p-N_3)-Gly-γAbu-Phe-Pro-Leu-Ala-Asp-His-Leu-Asn-Ser-Thr-Asn-His-Ala-Ile-Val-Gln-Thr-Leu-Val-Asn-Ser-NH_2) were synthesized using the solid phase peptide synthesis (SPPS). The peptide was purified by reverse phase-high performance liquid chromatography (RP-HPLC) (at least purity grade 95%) and characterized by analytical RP-HPLC and its identity was determined by mass spectrometry (SCIEX TOF-TOF 4800 instrument).

AutoDesk Fusion 360 (Autodesk, California, USA) computer-aided-design (CAD) software was used to design PEEK disks 10mm in diameter and 4mm in height and exported in a stl format into Simplify 3D software (Simplify3D- USA, OH, USA). The files were then sliced to generate printer ready G-code and printed using an Apium P155 PEEK filament printer (Apium Additive Technologies GmBh, Willy, Germany). The resulting 3D-printed PEEK disks possess a flat surface and a patterned one.

PEEK scaffolds were covalently functionalized with all the peptides. The linkages between the aminooxy group on the N-terminus of the peptide chain and ketonic groups in PEEK surface are realized by means of chemoselective ligation. Each peptide was dissolved in 40 mM monobasic sodium phosphate at 6 pH and left to react with PEEK samples for 24 hours at

room temperature. Peptide concentration used was 10^{-4}M. After that, the disks were rinsed three times with buffer and three times with MilliQ.

Functionalization through azido group occurred as in [8]. The peptide was dissolved in MilliQ with concentration equal to 1mg/ml.

B. Surface characterization

X-ray photoelectron spectroscopy (XPS) analysis was performed with a homemade instrument, consisting of preparation and analysis UHV chambers separated by a gate valve. The spectra were energy referenced to the C1s signal of aromatic and aliphatic C atoms having a binding energy BE = 284.7 eV. Curve-fitting analysis of the C1s, N1s, O1s, F1s spectra was performed using Gaussian profiles as fitting functions, after subtraction of a Shirley-type 219 background. Atomic ratio values were calculated from peak intensities.

Atomic force microscopy (AFM) analyses were carried out on different functionalized PEEK disks at room temperature in order to evaluate separately the effects of the peptides on the mechanical properties of interfaces. The Young's modulus was calculated from the collected force–distance curves measured with the NTEGRA AFM (NT-MDT, Moscow, Russia). Stiff single crystal silicon cantilevers with a symmetric tip shape were used (model Tap300Al-G, BudgetSensors, Bulgaria: nom. Frequency 300 kHz, nom. Spring constant 40 Nm−1, tip radius < 10 nm). For adhesion force measurements, Au-coated silicon nitride tips were used. AFM measurements were made in triplicate.

The surface wettability was traced by measuring the static water contact angle (WCA). An OCA30 instrument (Dataphysics) was used at 25 °C and 65% relative humidity. At least three measurements were made for each sample and then averaged.

Superficial characterization analyses were performed on flat PEEK surfaces.

C. Biological assays

All biological studies were performed on the patterned surface of the 3D-printed PEEK disks. Human osteoblasts (HOB) were used to evaluate the functionalized PEEK disks. Prior to seeding, PEEK specimens were sterilized in 70% ethanol for 24 hours and then washed with PBS. Cells were cultured in Dulbecco's Modified Eagle Medium (DMEM) containing, 10 ml of 1 M HEPES, 5 ml of 200 mM L-glutamine, 5 ml of 100x penicillin/streptomycin, 50 ml of Fetal Calf Serum (FCS), 5 ml of minimal essential medium and 0.075 g of solid ascorbate acid. HOB cells were microseeded onto the surfaces of the disks at a density of $1x10^5$ cells per disc. Seeded samples were incubated at 37°C and 5% CO2 for the time duration required or all tests performed. For gene expression evaluation, a density of $2x10^5$ HOB cells/per disc was used. Culture media was changed every three days for optimal growth conditions.

Cell viability was assessed using a LIVE/DEAD™ Viability/Cytotoxicity Kit (Thermo Fisher Scientific, Waltham, MA, USA) after 48 hours of cell culture. Images were captured with an Olympus IX51 fluorescent microscope. ImageJ software was used to display and process images of living cells (green fluorescence at 530 nm) and dead cells (red fluorescence at 600 nm).

Morphology of HOB cells after 48 hours from seed on the 3D printed PEEK structures were observed using SEM (Zeiss Gemini SEM 360) at a voltage of 10kV.

Calcium deposition was evaluated by Alizarin Red S staining on HOB cells. Alizarin Red S is an anthraquinone dye that reacts with calcium and forms an Alizarin Red S/calcium complex that is birefringent. HOB cells were cultured for 21 days. The results were achieved using a microplate reader (Opsys MRTM 96-well microplate reader, Dynex Technologies, VA, USA) at 570 nm.

The proliferation of osteoblasts cultured on functionalized and non-functionalized PEEK disks was assessed at 1, 4, 7, 14, or 21 days using AlamarBlue™ kit. For each sample three replicates were measured with the same microplate reader, which measured the fluorescence values at 570 nm test wavelength and 630 nm reference wavelength.

Specific mRNA transcript levels coding human SRY-Box transcription factor 9 (Sox9), Runt-related transcription factor 2 (Runx2), Alkaline Phosphatase (Alp), and Osteocalcin (Oct) were quantified in osteoblast cells cultured for 24 hours on functionalized and non-functionalized PEEK. Data were quantified by the ΔΔCT method using human Gapdh as the reference gene.

All assays were performed at least in triplicate and all values are reported as mean ± standard deviation. Data were analyzed and processed with Prism (GraphPad Software 9). Alizarin Red S results were compared by using one-way analysis of variance (ANOVA) test. Tukey's multiple comparisons test was carried out to confront every condition. AlamarBlue™ and gene expression results were compared with two-way ANOVA tests, followed by Tukey's post-hoc test. The significance level applied was 5%.

III. RESULTS

A. Surface characterization

XPS measurements were performed to confirm the presence of peptide on the surface of PEEK indicated by nitrogen increase. Table I shows the ratio nitrogen/carbonium (N/C) on the functionalized and non-functionalized PEEK. In non-functionalized PEEK, nitrogen was detected, while in functionalized PEEK it was. Also, Table I reports that peptide grafted through azido group was more available on the surface than through oxime chemistry.

TABLE I: XPS EVALUATION. QUANTIFICATION OF N/C RATIO FOR EACH FUNCTIONALIZED SCAFFOLDS AND NOT FUNCTIONALIZED SCAFFOLD.

Sample	*N/C*
PEEK-Control	/
PEEK+Aoa-x- GBMP1α	0.14
PEEK+N3-Phe-x-GBMP1α	0.17

AFM analyses achieved Young's modulus and adhesion force values on the surface of PEEK. As shown in Fig.1a, all functionalizing conditions induced an increased stiffness denoted by a higher value of the surface Young's modulus. The increase of surface rigidity with the functionalization of the PEEK substrate may be explained in terms of the expected stronger interchain. Fig.1b shows the adhesion forces measured on the bare and peptide-functionalized surfaces. All the functionalizing conditions show enhanced adhesion tip-sample forces, compared to non-functionalized PEEK, since the peptide at the interface promotes intermolecular interactions with the tip.

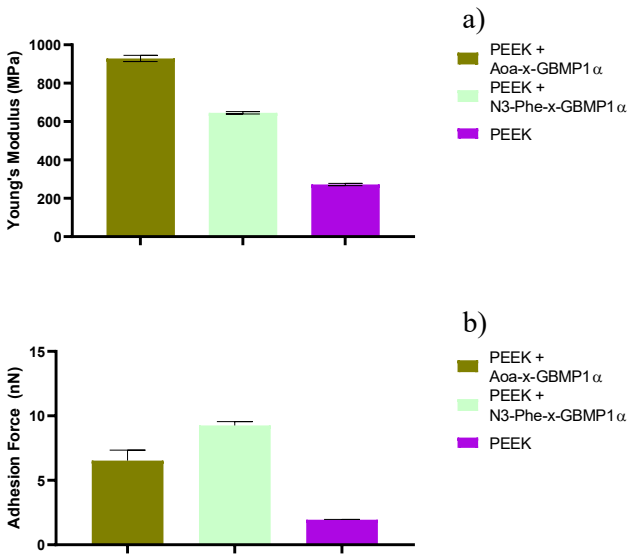


Fig. 1: AFM analysis of functionalized PEEK. (a) Surface Young's modulus and (b) adhesion forces for the bare and functionalized PEEK. Values are reported as mean ± SD.

WCA (Fig.2) showed how differently the functionalization through azido and aminooxy affected the superficial behavior of PEEK. PEEK functionalized with Aoa-x-GBMP1α slightly increases the hydrophobicity of the surface. While the samples functionalized through azido group increase the hydrophilic behavior of PEEK.

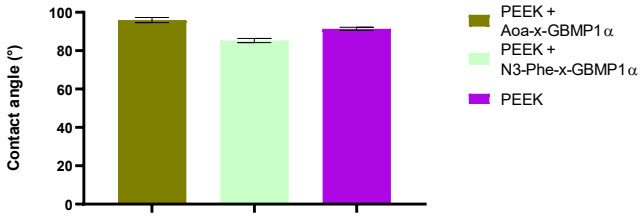


Fig. 2: WCA analysis on bare and functionalized PEEK. Values are reported as mean ± SD..

B. Biological assays

Cell viability tests (Fig.3) showed that HOB colonized all test samples. Generally, no cell death (red cells) was observed on test surfaces after 48 hours in culture, demonstrating that there was no cytotoxic effect, only non-functionalized PEEK showed a few dead cells.

The SEM analysis (Fig.4) at 48 hours from cell seed showed a homogeneous cell layer on the material surface. Focusing on PEEK functionalized with Aoa-x-GBMP1α (Fig.4b) overlapped cell multilayers are present.

As reported through Alizarin Red assay in Fig.5, all the conditions significantly increased the deposition of calcium ions after 21 days in culture. Also, functionalization through azido statistically improved the mineralization over the functionalization through aminooxy.

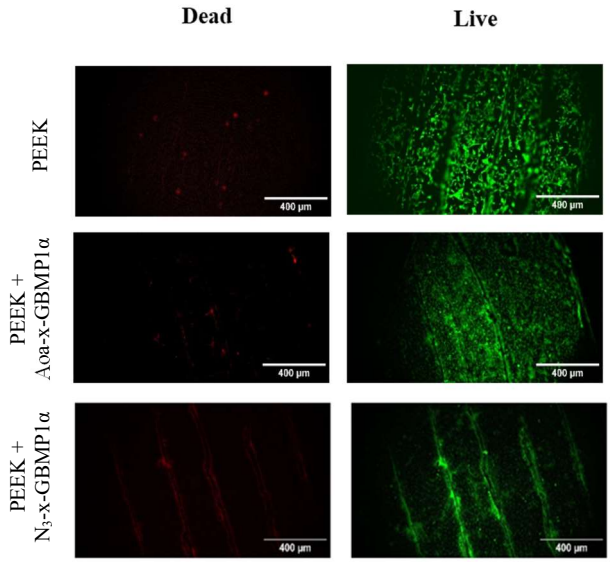


Fig. 3: Live and Dead staining of HOB cultured for 48 hours on non-functionalized and functionalized PEEK at 48 hours. Mag = 10x. Scale bar = 400 µm.

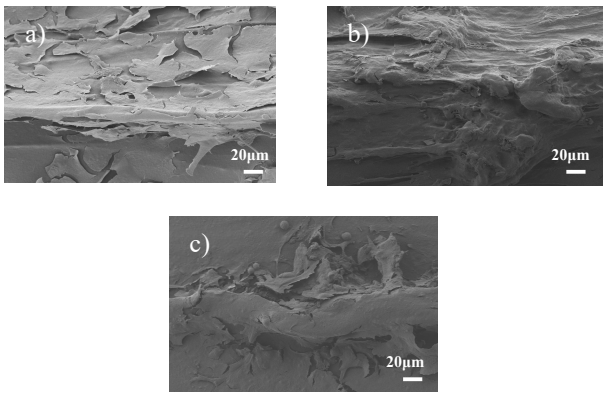


Fig. 4: PEEK sample (a) PEEK-Aoa-x-GBMP1α (b), and PEEK-N3-x-GBMP1α (c). Mag = 3.00 K X. Scale bars = 20 µm.

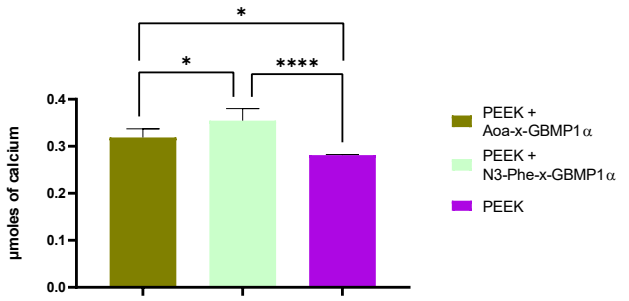


Fig. 5: Mineralization assay. Evaluation of calcium deposition on differently functionalized PEEK disks, at 21 days. *p-value < 0.05, **p-value < 0.01, ***p-value < 0.001, and ****p-value < 0.0001.

HOB proliferation on differently functionalized PEEK samples was evaluated at 1, 4, 7, 14, and 21 days from cell seeding using AlamarBlue™ kit (Fig.6). All the functionalizing conditions showed a significant increase over non-functionalized PEEK in cell proliferation at day 1 and 21.

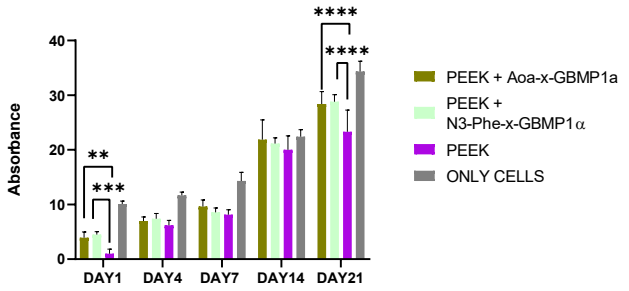


Fig. 6: HOB proliferation assay. Results were achieved at 1, 4, 7, 14, and 21 days from cell seeding. *p-value < 0.05, **p-value < 0.01, ***p-value < 0.001, and ****p-value < 0.0001.

From Gene expression assay (Fig.7), it is underlined that Sox9, and Alp gene was up-regulated with respect to the other conditions at day 1 by Aoa-x-GBMP1α. Functionalized samples had statistically significant increase over non-functionalized PEEK in Oct at day 14 and 21.

IV. Conclusion

We investigated the effect of functionalizing PEEK to determine whether performance could be enhanced. Our studies have shown that the biological properties of PEEK can be enhanced, and this combined with its other properties, makes PEEK a favourable material for applications in bone tissue engineering.

Functionalization of PEEK with GBMP1α showed that can allow a control of material surface behavior in wettability, Young's modulus, and force adhesion and can induce improvements in both calcium deposition and cell proliferation. Moreover, grafting peptide through azido group instead of via oxime have shown a higher N/C ratio (as index of peptide presence of PEEK surface), a higher hydrophilicity of the material, and a higher deposition of calcium on the scaffold.

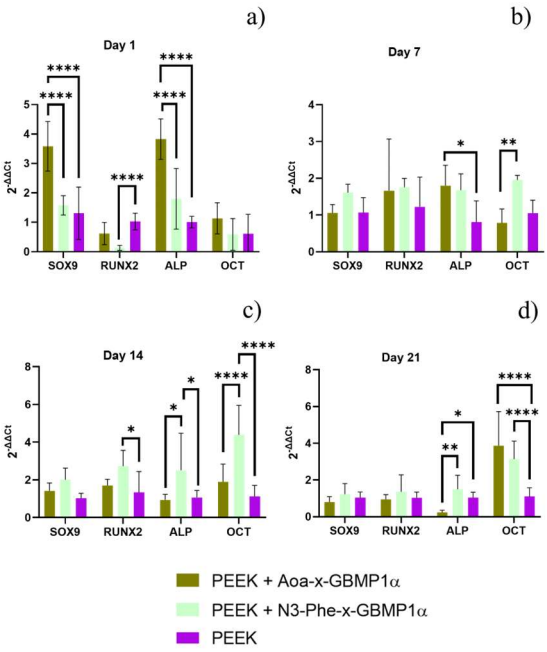


Fig. 7: qRT-PCR assay. Gene expression of Sox9, Runx2, Alp, and Oct, was evaluated on differently functionalized PEEK samples at 1 day (a), 7 days (b), 14 days (c), and 21 days (d) from HOB seeding. *p-value < 0.05, **p-value < 0.01, ***p-value < 0.001, and *** *p-value < 0.0001.

Acknowledgement

The authors thank Ilaria Vignato and Francesco Tolomei for their help in synthesizing the peptides and preparing the functionalized scaffolds.

References

[1] Williams D. F., McNamara A., Turner R.M. "Potential of polyetheretherketone (PEEK) and carbon-fibre-reinforced PEEK in medical applications". Journal of Materials Science Letters. 1987. pp. 188–190. doi:10.1007/bf01728981 W.-K. Chen, *Linear Networks and Systems* (Book style). Belmont, CA: Wadsworth, 1993, pp. 123–135.

[2] Oladapo B. I., Abolfazl Zahedi S., Chong S., Omigbodun F. T., Malachi I.O. "3D printing of surface characterisation and finite element analysis improvement of PEEK-HAP-GO in bone implant". The International Journal of Advanced Manufacturing Technology. 2020. pp. 829–841. doi:10.1007/s00170-019-04618-w

[3] Harting R., Barth M., Bührke T., Pfefferle R. S., Petersen S. "Functionalization of polyetheretherketone for application in dentistry and orthopedics". BioNanoMaterials. 2017. doi:10.1515/bnm-2017-0003

[4] Panayotov I. V., Orti V., Cuisinier F., Yachouh J. Polyetheretherketone "(PEEK) for medical applications". J Mater Sci Mater Med. 2016;27: 118. DOI:10.1007/s10856-016-5731-4

[5] Brun P., et al, "Chitosan Covalently Functionalized with Peptides Mapped on Vitronectin and BMP-2 for Bone Tissue Engineering". Nanomaterials(Basel), vol. 11, pp.. 2784, https://doi.org/10.3390/nano11112784.

[6] P. Brun et al., "Mechanisms underlying the attachment and spreading of human osteoblasts: From transient interactions to focal adhesions on vitronectin-grafted bioactive surfaces", Acta Biomater., vol. 9, no. 4, pp. 6105-6115, Apr. 2013, doi: 10.1016/j.actbio.2012.12.018.

[7] W.E. Truce, and W.R. Ray Jr, "Rearrangements of Aryl Sulfones. II. The Synthesis and Rearrangement of Several o-Methyldiaryl Sulfones to o-Benzylbenzenesulfinic Acids", J. Am. Chem. Soc., 1959, vol.81, no.2, pp. 481-484, https://doi.org/10.1021/ja01511a054

[8] M. Dettin et al., "Facile and selective covalent grafting of an RGD-peptide to electrospun scaffolds improves HUVEC adhesion". Journal of Peptide Science. 2015, pp. 786-795. https://doi.org/10.1002/psc.2808

Design and validation of a microfluidic cartridge to prepare non-viral gene delivery complexes

G. Protopapa,[1] N. Bono,[1] R. Visone,[2] F. D'Alessandro,[1] M. Rasponi,[2] and G. Candiani.[*1]
[1] *genT_LAB, Department of Chemistry, Materials and Chemical Engineering "G. Natta", Politecnico di Milano, Milan, Italy.*
[2] *Department of Electronics, Information and Bioengineering, Politecnico di Milano, Milan, Italy*

***Abstract*—Recent years have witnessed the use of microfluidics to shape different types of nanoparticles, such as gene delivery complexes. Herein, we developed a user-friendly microfluidic cartridge for the fast and repeatable preparation of non-viral gene delivery complexes at different N/Ps and their storage.**

***Keywords*—non-viral gene delivery, microfluidic device, polyplexes, reproducibility.**

I. Introduction

NON-VIRAL gene delivery (i.e., transfection), the process of introducing exogenous nucleic acids (NAs) into target cells, is the cornerstone of (nano)medicine, for the prevention[1] or treatment at a genetic level of several diseases,[2] and (nano)biotechnology, for the production of recombinant proteins.[3]

Cationic lipids and polymers, collectively called transfection reagents, are very popular because they are reasonably effective in transfecting cells. Indeed, they spontaneously assemble with anionic NAs in a vial to form lipoplexes and polyplexes, respectively, which are next dripped onto cell cultures to deliver their payload intracellularly.[4] Polyplexes are typically prepared in a vial, following one of these procedures: (i) dripping the solution containing one component into the other (i.e., bulk mixing of transfection reagent and NA solutions), eventually followed by (ii) vortexing the test tube, or (iii) manual mixing of the two solutions through pipetting.[5] However, intra- and inter-individual imprecision in pipetting is likely to be a source of poor data reproducibility to be seriously reckoned with in daily laboratory practice. Moreover, because of the clinical quest for an ever-larger quantity of nanocomplexes, the development of tools for scaling up and standardizing the production of gene delivery particles cannot be delayed further.[6]

As microfluidics allows the most accurate manipulation of small amounts of fluids by simply tuning the experimental parameters such as species concentrations and flow rates, this technology has thus been extensively used to produce optimally tailored gene delivery nanoassemblies.[7]

Nevertheless, to the best of our knowledge, none has addressed the most impellent quest for the simultaneous generation of multiple polymer-to-NA ratios (N/Ps). Specifically, N/P is the mole ratio of the amino groups (N) borne by the cationic polymer used to complex the phosphate groups (P) of a given amount of NA.[3] Driven by the need to fill this gap and motivated to address the lack of standardization in test procedures underpinning the low reproducibility of results,[8] we herein describe the development and validation of a polydimethylsiloxane (PDMS)-made microfluidic cartridge. This platform enables the fast and repeatable preparation of non-viral gene delivery complexes at different N/Ps, their recovery, and storage until use[9].

II. Materials and Methods

A. Architecture of the microfluidic device

The chip layout was designed using CAD software (AutoCAD, Autodesk Inc.). Briefly, the device encompasses four different units (Fig. 1): *i)* a serial dilution generator (SDG) for the increasing dilution of the polymer solution; *ii)* a NA divider to dispense the DNA solution to a downstream region; *iii)* a mixing area made up of seven mixing units in which the polymer and DNA, coming respectively from the SDG and the NA divider, are mixed to give polyplexes. These are collected within *iv)* a storage area consisting of seven different tanks, which are eventually punched to make the outlet ports (O_1–O_7) and recover the polyplex suspensions.

B. Fabrication of the microfluidic device

The master mold was patterned through standard photolithography and consisted of integrated two layers of SU8 negative photoresist (MicroChem, Westborough, MA, USA) composed of *a)* a 100 μm-thick layer for fluidic channels and tanks and *b)* a 36 μm-thick layer for herringbone grooves (HBGs), placed on the top of *i)*. Microfluidic devices were obtained by replica molding of PDMS on the master mold. Briefly, PDMS was cast on the mold (10:1 (w/w) of pre-polymer to curing agent). After degassing at room temperature (r.t) and curing at 65 °C for 3 h, the input (I_1–I_3) and output (O_1–O_7) ports were obtained using a biopsy puncher with a 1.5 mm-diameter tip (Harris Uni-Core™). PDMS was bonded to a glass slide (75 mm × 50 mm × 1 mm) through an air plasma treatment (Harrick Plasma), and next heated at 80 °C for 15 min.

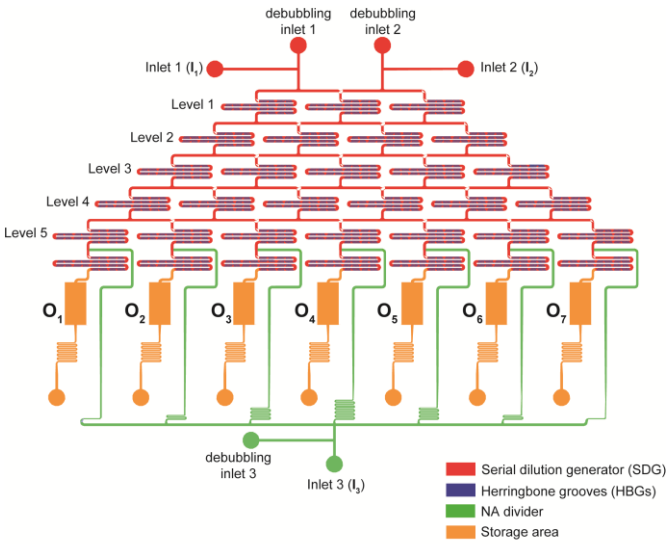


Figure 1. The microfluidic cartridge consists of *i)* an upstream 5-level serial dilution generator (SDG) integrated with herringbone grooves (HBGs), *ii)* a NA divider, *iii)* a mixing area, and *iv)* a storage area. The polymer solution and the water-based medium are injected into the two main inlets (inlets 1 and 2, I_1 and I_2) through the SDG and moved to the downstream area. An additional inlet (I_3) allows for the addition and distribution of the DNA solution to the seven mixing units, where the polymer and DNA are mixed to give rise to polyplexes. These are collected into the storage tanks.

C. Validation of the SDG and the NA divider

The proper mixing of a cationic polymer solution within the SDG was assessed using the commercial transfection reagent jetPEI-FluoF® (λ_{ex} = 490 nm, λ_{em} = 520 nm). Briefly, equal volumes of the polymer solution (prepared by adding 5 µL of jetPEI-FluoF® to 995 µL of 150 mM NaCl) and 150 mM NaCl were injected through I_1 and I_2 of the SDG, respectively, utilizing a two-channel syringe pump (World Precision Instrument, model AL 1000), each set at a flow rate of 25 µL min^{-1} and then the fluorescence intensities of the polymer solutions recovered from O_1–O_7 were measured. Data were expressed in terms of RFU and normalized to the fluorescence value of the jetPEI-FluoF® solution in the syringe, which was taken as 100%, as follows (eq (1)):

$$RFU\ (\%) = \frac{RFU_{sample}}{RFU_{jetPEI-FluoF}} \times 100 \quad (1)$$

Experiments were run with three different cartridges (n = 3).

The effectiveness of the NA divider to split the same volume in each mixing unit was assessed by fluorescence analysis. Briefly, a fluorescently labelled DNA solution was prepared by mixing 1 : 1 (v/v) salmon sperm DNA (ssDNA; 1 µg μL^{-1} in 0.1× TE buffer) with 200× SYBR Green I dye (λ_{ex} = 497 nm, λ_{em} = 520 nm), and pumped through I_3 into the NA divider utilizing a single-channel syringe pump set at a flow rate of 50 µL min^{-1}, while 10 mM HEPES buffer was injected through I_1 and I_2 using a two-channel syringe pump (flow rates = 25 µL min^{-1}). Next, 20 µL of the DNA solution were recovered from O_1–O_7 and analyzed. Data were expressed in terms of relative fluorescence units (RFU) and normalized to the fluorescence value of the DNA solution loaded into the syringe, which was taken as 100%, as follows (eq (2)):

$$RFU\ (\%) = \frac{RFU_{sample}}{RFU_{DNA}} \times 100 \quad (2)$$

Experiments were run with three different cartridges (n = 3).

D. Polyplex preparation with the microfluidic device

Equal volumes of a 25 kDa *l*PEI solution (prepared at a concentration of 0.017 µg μL^{-1} in 10 mM HEPES, corresponding to an amine concentration ([N]) of 0.4 mM) and 10 mM HEPES were first injected into the chip through I_1 and I_2 (flow rates of 25 µL min^{-1}), respectively, and then flowed through the SDG to obtain seven different polymer concentrations. Such polymer solutions and a fluorescent DNA solution, injected through I_3 (flow rate = 50 µL min^{-1}), were simultaneously mixed to give rise to polyplex suspensions at N/Ps from 0 to 6. Right after complexation, micrographs of the mixing units containing the polyplexes were taken by means of a fluorescence microscope and processed using ImageJ software. Next, 20 µL of polyplexes were recovered from O_1–O_7 and analyzed. Data were expressed in terms of relative fluorescence units (RFU) and normalized to the fluorescence value of the fluorescent DNA solution loaded into the syringe, which was taken as 100%, as follows (eq (3)):

$$complexed\ DNA\ (\%) = \left(1 - \left(\frac{RFU_{sample}}{RFU_{DNA}}\right)\right) \times 100 \quad (3)$$

Experiments were run with three different cartridges (n = 3).

E. In vitro transfection experiments

Mycoplasma-free L929 cells were routinely cultured in Dulbecco's Modified Eagle's Medium (DMEM) supplemented with 1 mM sodium pyruvate, 10 mM HEPES buffer, 100 U mL−1 penicillin, 0.1 mg mL−1 streptomycin, 2 mM glutamine and 10% (v/v) fetal bovine serum (FBS) (hereafter referred to as complete culture medium), at 37 °C, in a humidified atmosphere and under constant supply of 5% (v/v) CO_2 (hereafter referred to as standard culture conditions). L929 were seeded in 96 multi-well culture plates at a density of 2×10^4 cell/cm^2 and cultured under standard culture conditions for 24 h. For transfection assays, cells were challenged with polyplexes prepared as described above by complexing 320 ng pDNA per cm^2 with PEI solutions. Briefly, the microfluidic device was used to prepare polyplexes at seven different N/Ps (i.e., 0, 10, 20, 30, 40, 50, and 60) that were used right after collection. The final DNA concentration of every polyplex suspension was invariably 20 ng μL^{-1}.

Twenty-four hours after polyplex delivery, the cytotoxicity was evaluated by means of the AlamarBlue® assay. Briefly, the culture medium was replaced with 100 µL per well of 1× resazurin dye solution in complete culture medium. Next, plated cells were kept in the dark for 2 h under standard culture conditions, and then the fluorescence was read using a Synergy H1 reader (λ_{ex} = 540 nm; λ_{em} = 595 nm). The viability of non-transfected cells was assigned to 100% and the cytotoxicity was determined according to the following (eq (4)):

$$cytotoxicity\ [\%] = 100\% - viability\ [\%] \quad (4)$$

Transfection efficiency (TE) was evaluated by measuring luciferase activity in the culture media. Briefly, 20 µL of cell supernatant were mixed with 50 µL of the corresponding assay substrate and the luminescence signal (expressed as Relative Light Units, RLU) was measured using the Synergy H1 reader.

The transfection efficiencies of complexes prepared with the cartridge were compared to those of manually-prepared ones (n = 3 operators).

F. Statistical analysis

Statistical analysis was carried out with Minitab® 21.1.1 statistical software. All data were initially analyzed using the Kolmogorov–Smirnov normality test. As an indicator of reproducibility and repeatability of the results, comparisons among groups were performed with the test for two variances using Bonett's method to test whether variances of transfection efficiencies and cytotoxicities were homogeneous or not. Statistical significance was retained when the p-value < 0.05.

III. RESULTS AND DISCUSSION

A. Design of the microfluidic device

The cartridge encompasses four functionally distinct modules: *i)* a chaotic serial dilution generator (SDG); *ii)* a NA divider; *iii)* a mixing area; *iv)* a storage region (Fig. 1). The *i)* SDG features two input ports (inlets 1 and 2, I_1 and I_2) and is based on a resistive flow model consisting of a symmetric microfluidic network[10] arranged on 5 levels of 240 µm-wide and 100 µm-high channels. Their length was properly dimensioned to mix and split the stock solutions (i.e., an aqueous medium and a polymer solution) and give rise to seven linearly diluted solutions (from 100% stock to 0% in steps of 16.7%), independently addressed to the iii) downstream mixing area. Optimized staggered herringbones grooves (HBGs)[11] are integral to the ceiling of each channel, and each channel encompasses 12 serial HBG units. Besides, the *ii)* NA divider area was based on a one-input (I_3) resistive flow model of seven microfluidic channels, designed and properly sized to enable equal partition of the stock DNA solution into the mixing area. As for the SDG, the seven polymer–NA mixing units that make up the mixing area were dimensioned in length to mix the polymer solutions at different concentrations from the SDG with those from the NA divider. Each mixing unit is a 1.64 mm-long channel encompassing 12 serial HBG units. Furthermore, a *iv)* storage area comprising seven parallelepiped-shaped reservoirs was designed downstream to collect the polyplex suspensions.

B. Validation of the SDG and the NA divider

Since the SDG was designed to mix and split (poly)cations, the function of this area was assessed using a solution of the polymeric transfectant jetPEI-FluoF®. The linear decrease in fluorescence from O_1 to O_7 ($R^2 = 0.96$) (Fig. 2) meant that the polymer was linearly diluted while passing through the SDG.

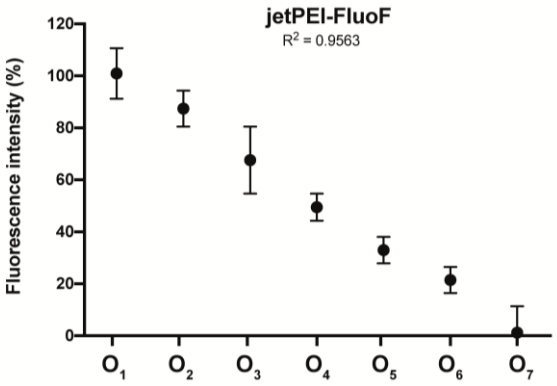


Figure 2. Fluorescence was recorded at each of the seven outlets (O_1–O_7) of the SDG after injecting the jetPEI-FluoF®. Fluorescence intensities were expressed as percentage fluorescence loss in comparison to the fluorescence of jetPEI stock solutions. Results are expressed as mean ± SD (n = 3).

These results highlight that the device was well suited to serially dilute the transfection reagents to be next used to prepare polyplexes at different N/Ps.

To assess the effectiveness of the NA divider to dispense a DNA stock solution to the seven polymer–DNA mixing units, the DNA was made detectable using the SYBR Green I fluorescent dye. Of note, we noticed no significant difference in fluorescence intensity between the DNA solutions harvested from O_1–O_7, meaning that the NA divider operated properly. In summary, we validated the function of the individual chip areas, which are operated by microsyringe pumps controlling the flow rate of the solutions injected into the cartridge.

C. Assessment of the polyplex preparation with the microfluidic device

We took advantage of the DNA complexation assay to assess the effectiveness of the microfluidic cartridge for the simultaneous production and recovery of polyplexes at different N/Ps. The polymer used in the present study is a gold standard transfection reagent known to fully complex the NAs at N/P ≥ 5. Under these conditions, the polymer completely displaces the fluorochrome while binding to the DNA, such that no fluorescence is detected once the samples are excited.[3] To spot any difference in DNA complexation between the mixing units, we imaged them using a fluorescence microscope (Fig. 3A), and the fluorescence signal of every polyplex suspension recovered from the cartridge was quantified with a spectrofluorometer (Fig. 3B). Of note, as *l*PEI and DNA were blended and the complexation took place while moving downwards through the mixing units, the fluorescence steadily decreased (by way of example, refer to N/P 2 in Fig. 3B). In good agreement with the literature,[12] N/Ps 6 and 5, which correspond to the mixing units O_1 and O_2, showed maximal DNA complexation due to the large excess of the cationic polymer. Of note, the extent of DNA complexation was also rather high at N/Ps 4 and 3, as the residual fluorescence was less than 10% of the pristine DNA shown in O_7 (N/P 0) (Fig. 3B). Afterward, the percentage of complexed DNA decreased as the N/P decreased, meaning that there was more and more uncomplexed DNA in O_5 and O_6. These results point to the potential of using the microfluidic cartridge described herein to obtain gene delivery complexes over a given range of N/Ps.

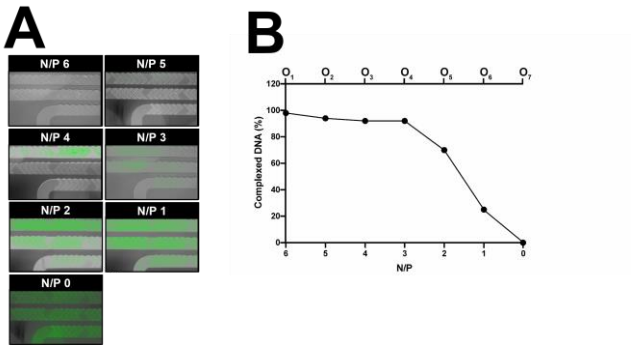
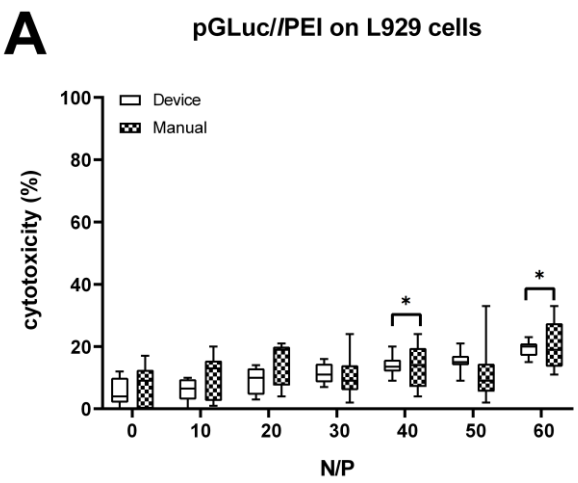


Figure 3. A) Acquisition of fluorescence images of the seven different mixing units. The fluorescence increases as the N/P decreases. Polyplexes at different N/Ps are next collected in the downstream storage tanks that may feature outlet ports (O_1–O_7). B) Complexed DNA (%) in each outlet port was evaluated by monitoring the fluorescence as a function of the N/P (n = 3).

D. Evaluation of polyplex efficacy in vitro

25 kDa *l*PEI and the pGLuc plasmid encoding the secreted luciferase enzyme were complexed through the device and manually using different polymer concentrations to yield a linear N/P scale spanning from 0 to 60 with N/P steps of 10 and dripped onto L929 cells (Fig. 4A and B). The cytotoxicities and transfection efficiencies given by polyplexes produced with the microfluidic cartridge were remarkably homogeneous. Indeed, it is apparent at a glance that each dataset shows very short whiskers and small box sizes, indicating data points consistently hovering around the center value. Besides, the results of microfluidic preparations were more repeatable than the manually-prepared counterparts.



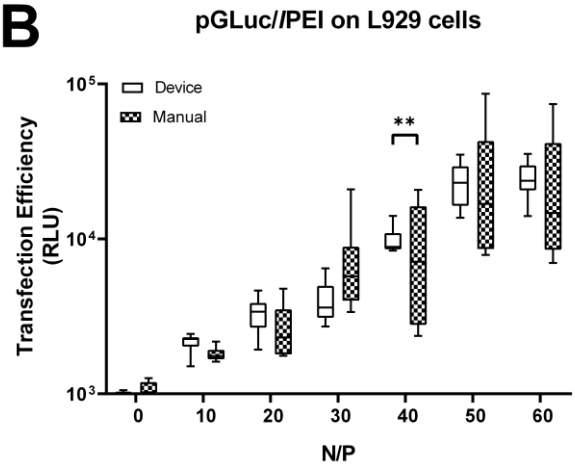


Figure 4. A) Cytotoxicity and B) transfection efficiency of polyplexes prepared with the microfluidic mixing (empty boxes) and by manual pipetting (checked boxes), mixing variable amounts of *l*PEI and a constant concentration of pGLuc in 10 mM HEPES buffer to give different N/Ps (0, 10, 20, 30, 40, 50, and 60). Results on L929 are displayed as box and whisker plots (n ≥ 3). *p < 0.05, **p < 0.01, and ***p < 0.001 between microfluidic and manual preparations (n = 3 operators) (in test for two variances).

IV. CONCLUSIONS

This work addresses the on-chip production of non-viral gene delivery assemblies across a range of N/Ps. Here above, we described the development and validation of a user-friendly, dual-mode microfluidic cartridge that enables the repeatable preparation, recovery and storage of non-viral gene delivery assemblies at desired N/Ps.

REFERENCES

[1] M. Lim, A.Z.M. Badruddoza, J. Firdous, M. Azad, A. Mannan, T.A. Al-Hilal, C.S. Cho, M.A. Islam, Engineered nanodelivery systems to improve dna vaccine technologies, Pharmaceutics. 12 (2020) 1–30.

[2] H. Zu, D. Gao, Non-viral Vectors in Gene Therapy: Recent Development, Challenges, and Prospects, AAPS J. 23 (2021).

[3] N. Bono, F. Ponti, D. Mantovani, G. Candiani, Non-viral in vitro gene delivery: It is now time to set the bar!, Pharmaceutics. 12 (2020) 1–23.

[4] D. Pezzoli, G. Candiani, Non-viral gene delivery strategies for gene therapy: A “ménage à trois” among nucleic acids, materials, and the biological environment: Stimuli-responsive gene delivery vectors, J. Nanoparticle Res. 15 (2013).

[5] Y. Yue, F. Jin, R. Deng, J. Cai, Y. Chen, M.C.M. Lin, H.F. Kung, C. Wu, Revisit complexation between DNA and polyethylenimine - Effect of uncomplexed chains free in the solution mixture on gene transfection, J. Control. Release. 155 (2011) 67–76.

[6] A. Tejeda-Mansir, A. García-Rendón, P. Guerrero-Germán, Plasmid-DNA lipid and polymeric nanovaccines: a new strategic in vaccines development, Biotechnol. Genet. Eng. Rev. 35 (2019) 46–68.

[7] W.J. Duncanson, T. Lin, A.R. Abate, S. Seiffert, R.K. Shah, D.A. Weitz, Microfluidic synthesis of advanced microparticles for encapsulation and controlled release, Lab Chip. 12 (2012) 2135–2145.

[8] A.L. Plant, R.J. Hanisch, Reproducibility and Replicability in Science , A Metrology Perspective, Harvard Data Sci. Rev. (2018) 1–21.

[9] G. Protopapa, N. Bono, R. Visone, F. D’Alessandro, M. Rasponi and G. Candiani, A new microfluidic platform for the highly reproducible preparation of non-viral gene delivery complexes, Lab Chip. 23 (2023) 136–145.

[10] N.L. Jeon, S.K.W. Dertinger, D.T. Chiu, I.S. Choi, A.D. Stroock, G.M. Whitesides, Generation of solution and surface gradients using microfluidic systems, Langmuir. 16 (2000) 8311–8316.

[11] P. Occhetta, N. Glass, E. Otte, M. Rasponi, J.J. Cooper-White, Stoichiometric control of live cell mixing to enable fluidically-encoded co-culture models in perfused microbioreactor arrays, Integr. Biol. (United Kingdom). 8 (2016) 194–204.

Biomimetic platform for investigating in vitro the cell biological response to mechanical stretching – periodontal ligament stem cell application

B. Masante[1,2,3], G. Putame[1,3], A.T. Lugas[1], M. Tosini[1], I. Roato[2], F. Mussano[2], M. Terzini[1,3], A. Audenino[1], D. Massai[1,3]
[1] *PolitoBIOMed Lab and Department of Mechanical and Aerospace Engineering, Politecnico di Torino, Italy*
[2] *Bone and Dental Bioengineering Lab, CIR-Dental School, Department of Surgical Sciences, University of Torino, Italy*
[3] *Interuniversity Center for the Promotion of the 3Rs Principles in Teaching and Research, Italy*

***Abstract*—*In vivo,* mechanical cues are fundamental in promoting cell and tissue development and in maintaining homeostasis. Thus, the use of advanced investigation platforms able to mimic and combine native-like physical stimuli is crucial for studying *in vitro* the cellular behaviour under defined mechanical stimuli. Here, we designed, characterized and tested a biomimetic platform, based on a flexible substrate and a previously developed stretch bioreactor, for exposing adherent cells to controlled uniaxial stretch culture protocols in view of mechanotransduction studies.**

***Keywords*—Flexible substrate, Stretch bioreactor, Mechanotransduction, Digital image correlation.**

I. Introduction

MECHANICAL forces play a crucial role *in vivo*, with consequences in cell differentiation, tissue renewal and homeostasis, as well as in pathogenesis [1, 2]. Although it is well known that most cells are able to sense mechanical stimuli and to respond by a set of biological responses that critically impact (patho)physiology, when it comes to laboratory experiments the mechanical stretching experienced *in vivo* by the cells is not often replicated, limiting the relevance of the experimental model results [3].

In this scenario, investigation platforms designed for mimicking *in vitro* the physical stimuli of the native environment have the potential to pave the way for advanced mechanotransduction studies [4-8], for ultimately unravelling the cellular biological responses to specific physical culture conditions. In this study, we developed, characterized, and tested an automated biomimetic investigation platform for culturing adherent cells under controlled uniaxial stretch. The platform is based on a customized flexible substrate to be used in combination with a tunable stretch bioreactor previously developed [9, 10]. As a preliminary biological application, we used the platform for culturing periodontal ligament-derived stem cells (PDLSCs) and adipose-derived stem cells (ASCs) under controlled uniaxial stretch. The final aim of the study was to investigate the role played by mechanical stretching on different cell types in view of exploiting the obtained advancement of knowledge for future tissue engineering applications.

II. Materials and Methods

The biomimetic investigation platform is composed of a stretch bioreactor, previously developed [8-10] and an appositely designed flexible substrate to be clamped in the bioreactor culture chamber. Briefly, the bioreactor is based on two opposite clamps which grasp the substrate and, since one clamp is connected to a stimulation unit motor, allows stretching the substrate and consequently stimulating the adherent cells.

The flexible substrate has been designed (Solidworks) with two parallel rectangular wells (Fig. 1A), for allowing experiment parallelization and optimization of the culture medium volume. Finite element (FE) analyses (Abaqus) were performed for defining the optimal substrate geometry suitable for guaranteeing planar and uniform uniaxial strain. In detail, the substrate was modelled with linear tetrahedral elements (size 0.1mm) and a uniaxial displacement of 3 mm (15% of strain), mimicking the bioreactor stretching, was imposed on one side of the substrate, while constraining the opposite one. Once the optimal design was identified, a corresponding mold was designed, 3D-printed, and used to cast the flexible substrate (Fig. 1B) in polydimethylsiloxane (PDMS, Sylgard 184), cured at 60°C for 6 h.

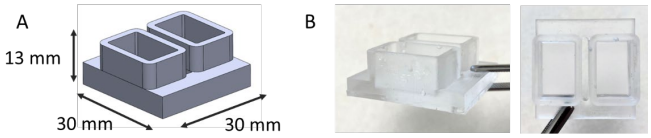


Fig. 1. Flexible substrate design. A) Substrate size. B) Substrate manufactured in PDMS.

The digital image correlation method (DIC, isi-sys GmbH) was adopted for characterizing experimentally the mechanical behavior of the substrate under uniaxial stretch.

For the preliminary biological tests, after autoclave sterilization, the flexible substrates (n=6 for each cell type) were functionalized with collagen I (Sigma Aldrich) and seeded with human primary PDLSCs harvested from healthy subjects, in accordance with ethical principles (protocol n. 0107683, 03/10/2022) or with ASCs cell line (ASC52-telo hTERT, ATCC), used as reference cell type. After 4 h of static culture, required for enabling cell adhesion, the cell-seeded substrates (n=3 for each cell type) were clamped in the bioreactor culture chamber (Fig. 2) and were exposed to cyclic uniaxial stretch (8% pre-strain combined with cycles of additional 7% strain for 90 s, at 1 Hz, every 6 h [3]) for 3 days. As control group, cell-seeded substrates (n=3 for each cell type) were cultured statically for 3 days. At the end of day 3, the expression of osteogenic markers, i.e., alkaline phosphatase (ALP), osteocalcin (OCN), and runt-related transcription factor 2 (RUNX2) was assessed through real-time PCR.

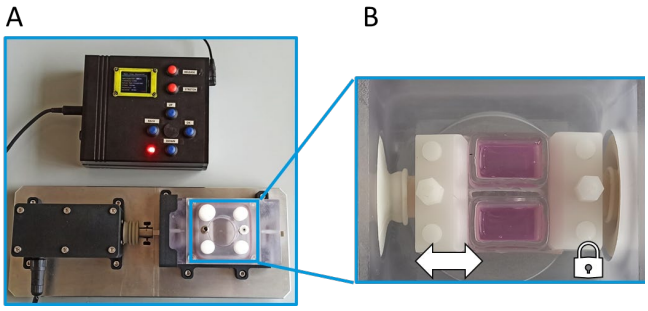


Fig. 2. Biomimetic investigation platform. A) Stretch bioreactor [10]. B) Flexible substrate clamped in the bioreactor culture chamber.

III. Results

FE analyses demonstrated that, when uniaxially stretched, the flexible substrate is characterized by an almost planar and uniform strain distribution at the well bottom (13.36 ± 0.25 %), in good agreement with the DIC results (14.33 ± 0.25%) (Fig. 3).

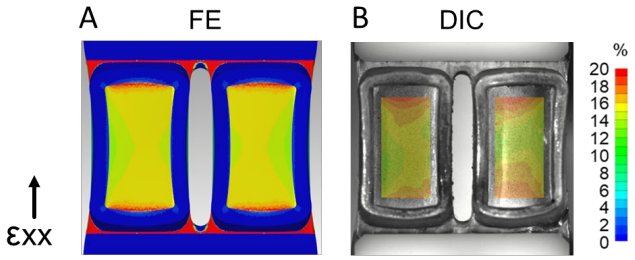


Fig. 3. Flexible substrate characterization. A) FE analysis. B) DIC analysis. Results are shown for the ϵ_{xx} strain.

Preliminary biological tests revealed that PDLSCs and ASCs respond differently to the applied uniaxial stretch culture protocol. In detail, stretched PDLSCs showed an increasing trend of ALP, OCN, and RUNX2 expression, with a significant double fold increase in OCN gene expression ($p<0.05$) in comparison to control, similarly to previously published works [12-14]. Contrarily, ASCs did not show significant differences in osteogenic marker expression between the stretched and the control groups ($p>0.05$) (Fig. 4).

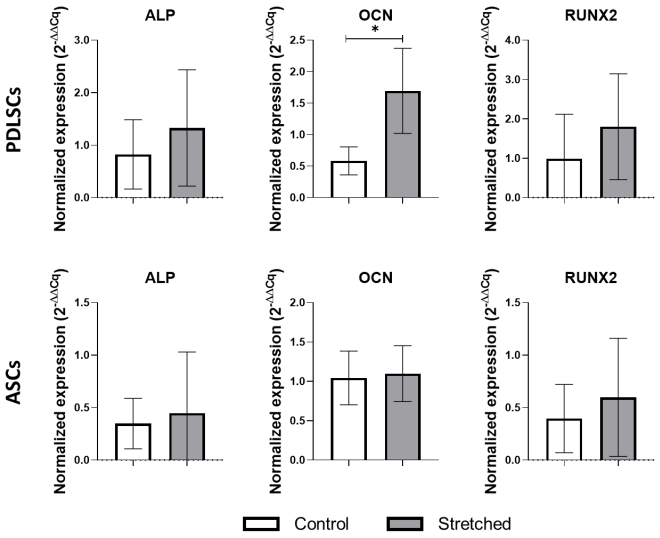


Fig. 4. Osteogenic markers expression of PDLSCs (top panel) and ASCs (bottom panel). Significative results for $p<0.05$.

IV. Conclusion

A biomimetic investigation platform for investigating the biological response of adherent cells to defined stretch protocols was developed and tested. In detail, the mechanical characterization of the flexible substrate through FE and DIC analyses allowed assessing that the platform exposes the adherent cells to highly controlled uniaxial stretch conditions, with uniform strain values over a wide area of each well bottom.

Preliminary biological tests, besides confirming the cytocompatibility of the flexible substrate, revealed that PDLSCs and ASCs respond differently to uniaxial stretch. In particular, cyclic stretching promoted osteogenic marker expression in PDLSCs, which seemed more responsive to the applied stretch stimulus than ASCs.

Combining the numerical and the experimental strain characterization with the cells biological response, this platform provides, for the first time, a powerful investigation tool for correlating the effective strain sensed by the cells and their response.

Further biological tests, imposing different stretch patterns for longer culture time and using different cell sources (healthy and pathological subjects), are ongoing with the final aim to understand in-depth the cause-effect relationships between mechanical stretch and specific cell behaviour. Moreover, such biomimetic platform, thanks to its versatility, will be used for investigating the effect of tensile and compressive stress on 3D constructs, in view of periodontal ligament engineering applications.

Such a biomimetic platform represents a powerful investigation tool for mechanotransduction studies on healthy and pathological cells and culture conditions and could lead to a significant advancement of knowledge for future tissue engineering applications.

References

[1] T. Mammoto, "Mechanobiology and developmental control," *Annual review of cell and developmental biology*, vol. 29, pp 27-61, 2013

[2] F. Martino, "Cellular Mechanotransduction: From Tension to Function". *Frontiers in physiology,* vol. 9 824. 5 Jul. 2018.

[3] I. Constantinou, “Cell-stretching devices: advances and challenges in biomedical research and live-cell imaging” *Trends in biotechnology,* S0167-7799(22)00332-8. 3 Jan. 2023.
[4] I. Martin, “The role of bioreactors in tissue engineering”. *Trends in biotechnology* vol. 22,2 (2004): 80-6, 2004.
[5] A.B. Yeatts, “Bioreactors to influence stem cell fate: augmentation of mesenchymal stem cell signaling pathways via dynamic culture systems”. *Biochimica et biophysica acta* vol. 1830,2 (2013): 2470-80, 2013.
[6] A. Ravichandran, “Review: bioreactor design towards generation of relevant engineered tissues: focus on clinical translation”. *Journal of tissue engineering and regenerative medicine* vol. 12,1 (2018): e7-e22, 2018.
[7] S. Gabetti, “An automated 3D-printed perfusion bioreactor combinable with pulsed electromagnetic field stimulators for bone tissue investigations”. S*cientific reports* vol. 12,1 13859. 16 Aug. 2022
[8] D. Massai, “Bioreactors as engineering support to treat cardiac muscle and vascular disease”. *Journal of healthcare engineering* vol. 4,3 (2013): 329-70, 2013.
[9] D. Massai, “Bioreactor Platform for Biomimetic Culture and *in situ* Monitoring of the Mechanical Response of *in vitro* Engineered Models of Cardiac Tissue”. *Frontiers in bioengineering and biotechnology* vol. 8 733. 14 Jul. 2020.
[10] G. Putame, “Compact and tunable stretch bioreactor advancing tissue engineering implementation. Application to engineered cardiac constructs,” *Medical Engineering and Physics, vol.* 84, pp. 1-9, 2020
[11] T. de Jong, “Adipose-Derived-Stem-Cell-Seeded Fibrin Matrices for Periodontal Ligament Engineering: The Need for Dynamic Strain,” *Journal of Biomaterials and Tissue Engineering,* vol. 7(12), pp 1303-1312, 2017.
[12] I. Roato, “Challenges of Periodontal Tissue Engineering: Increasing Biomimicry through 3D Printing and Controlled Dynamic Environment.” *Nanomaterials (Basel, Switzerland)* vol. 12,21 3878. 2 Nov. 2022
[13] T. Nemoto, “Differential induction of collagens by mechanical stress in human periodontal ligament cells.” *Archives of oral biology* vol. 55,12 (2010): 981-7, 2010.
[14] D.A.W, Oortgiesen, “A three-dimensional cell culture model to study the mechano-biological behavior in periodontal ligament regeneration.” *Tissue engineering. Part C, Methods* vol. 18,2 (2012): 81-9, 2012.

Evaluation of the optimal pore size for 3D printed bone scaffolds in a perfusion bioreactor

E. Batoni[1], C. De Maria[1], and G. Vozzi[1]
[1] *Research Centre "E. Piaggio" and Dpt. of Information Engineering, University of Pisa, Pisa, Italy*

***Abstract*— In the bone tissue engineering field, the scaffold design has a great influence on cell behaviour in terms of metabolism, differentiation, and morphogenesis. Additive Manufacturing technologies can be used to fabricate scaffolds with controlled internal pore sizes, shapes, and distribution. Among the bioreactors used for culturing, perfusion bioreactor is preferred since the capability of providing efficient nutrient supply and waste removal, as well as mechanical stress which, if within a specific range, stimulates and enhances bone formation. For that purpose, experiments and computational models are needed to select the optimal scaffold design and culture conditions (e.g., flow rate and type) in order to achieve specific biological cell responses. This study aims at implementing a computational model to evaluate the influence of the scaffold pore sizes and strand orientation on the oxygen uptake and mechanical stress applied to cells cultured in a direct perfusion bioreactor. The model results will help to find the optimal pore size which will provide good oxygenation and enhance the osteogenic differentiation in bone scaffolds cultured in a perfusion bioreactor.**

***Keywords*— Bone tissue engineering, 3D-printed scaffold, perfusion bioreactor, computational modelling**

I. Introduction

Bone tissue engineering (BTE) is a multidisciplinary field aiming at developing biological substitutes for the repair and regeneration of bone tissue. This is based on three fundamental components, *i.e.*, cells, three-dimensional (3D) scaffold, and bioreactors [1].

Considering the influence of the scaffold on the cell behavior (*e.g.*, cell metabolism, differentiation, and morphogenesis), Additive Manufacturing (AM) technologies, such as Fused Deposition Modelling (FDM), can be useful to provide higher control over the scaffold design, as well as to optimize its internal morphology (*i.e.*, pore size, shape, and distribution) with high reproducibility and accuracy.

Among the dynamic culture systems for 3D scaffolds, the perfusion-based bioreactor is considered the most efficient as the medium is forced to flow through the scaffold architecture, thus, providing a more uniform and not diffusion-limited nutrient supply to the cells. Furthermore, the fluid movement through the pores provides mechanical stress to the cells improving their growth and guiding their differentiation toward a specific lineage. Studies demonstrated that fluid shear stress, within a specific range of intensities, enhances the activity of osteoblasts in bone formation and stimulates the expression of genes specific to the bone tissue [1,2].

Since the influence of the scaffold architecture on the biological cell response cultured in a perfusion bioreactor, the identification of the scaffold design is critical for BTE applications. For that purpose, computational models can be used to predict fluid dynamics and thus select the optimal design to achieve specific target properties. For instance, several studies implemented computational tools to optimize the scaffold design in terms of the transport of nutrients, the mechanical loads, as well as the scaffold degradation [3–5]. In addition, these represent a helpful tool to investigate the spatial and temporal distribution of the cellular responses to the difficulty to obtain real-time measurements in perfused scaffolds [1]. However, to the best of our knowledge, there is no study focused on optimizing the pore size and orientations of 3D printed scaffolds with cells seeded on the surface in a perfusion bioreactor.

The objective of the study was to implement a Finite Element Method (FEM) model to evaluate the optimal pore size of 3D-printed poly-L-lactic acid (PLLA)-based scaffolds seeded with cells in a direct perfusion bioreactor. Three different studies were implemented: (i) cylindrical scaffolds with different pore sizes and without lateral pores; (ii) cylindrical scaffolds with different pore sizes and lateral pores; and (iii) cylindrical scaffolds with different pore sizes, lateral pores, and different strand orientations. The model results will help to select the optimal scaffold porous design which provides good oxygenation and enhances the osteogenic differentiation of cells cultured in a direct perfusion bioreactor.

II. Materials and Methods

Cylindrical scaffolds (8 mm in diameter, and 6 mm in height) were designed in Autodesk® Fusion 360™ implementing a parametric function on the pore length and the presence of lateral pores. Three different studies were performed:

i. in the first study, three scaffolds without lateral pores were created differing in pore size (l [mm]), namely, 0.4 – 0.9 – 1.3mm, within the typical macropores range for BTE scaffolds (i.e., 0.1 to 1.2mm) (Fig. 1A) [2];
ii. in the second study, lateral pores were also created in each scaffold (Fig. 1B);
iii. in the third study, the orientation of the strands was varied for each scaffold, namely, 90° - 45° - 20°, in the XY plane, and featured with lateral pores (Fig. 1C).

Scaffolds are assumed to be fabricated through FDM by using PLLA-based filaments, thus, the deformations due to the medium flow are neglected and the scaffolds are considered as rigid bodies, which is also applicable to a wide range of thermoplastic polymers.

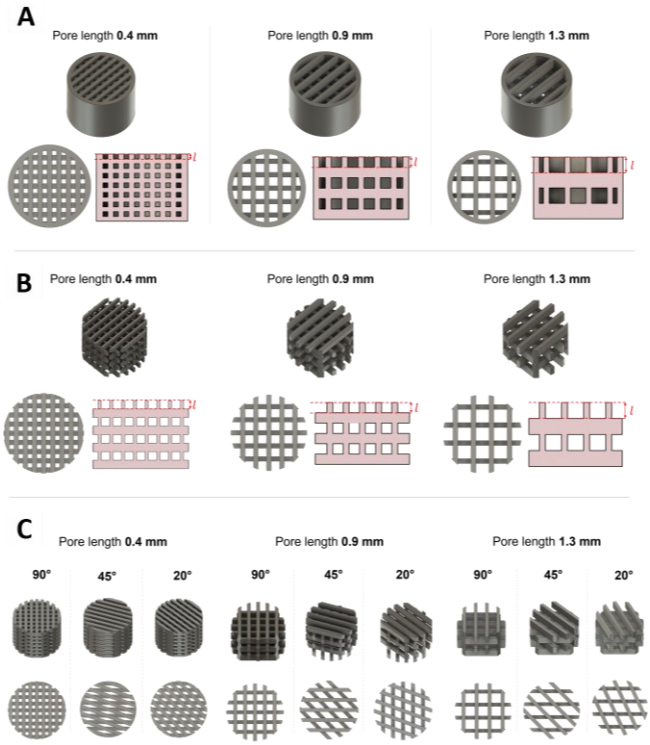


Fig. 1 Scaffold geometry. Scaffolds (A) without and with (B) lateral pores with different pore sizes (l [mm]), and (C) with lateral pores and strands oriented at different angles.

The FEM model was implemented in COMSOL Multiphysics® v6.0 using the "*Transport of Diluted Species*" and "*Laminar Flow*" modules. Like other studies [3-4], it was assumed that laminar flow conditions are verified for all porous scaffolds and flow rates. The geometry of the fluid domain, representing the culture medium, was obtained by the Boolean difference between the scaffold and the bioreactor geometry, taking as a model the perfusion-based bioreactor (8mm in diameter ($\varnothing_b$), and 24mm in length (L_b)) reported in the study of Coletti *et al.* [1] (Fig. 2). In detail, the culture medium is fed from the top channel of the bioreactor by a volumetric peristaltic pump, flows through the inlet section, perfuses through the scaffold pores, and then exits from the bottom channel through the outlet section. The channels dimensions are 2mm in diameter ($\varnothing_c$) and 3mm in length (L_c).

Regarding the boundary conditions of the "*Laminar Flow*" module, the flow rate was parametrically assigned to the inlet and a pressure of 0Pa was placed at the outlet. The medium fluid properties were assumed to be that of water.

In the "*Transport of Diluted Species*", an inflow concentration of 0.2 mol/m^3 was set on the inlet, whereas a surface reaction was placed on the scaffold surface where cells are seeded. A Michaelis-Menten kinetic was assumed for the oxygen consumption, given the following expression for the surface reaction (Eq. 1):

$$R = -\frac{OCR * \rho_s * c}{c + K_m} \quad (1)$$

where the oxygen consumption rate (OCR) was set equal to 2.75x10^{-17} mol/(s*cells), the superficial cellular density (ρ_s) to 3x10^9 cells, and the Michaelis-Menten constant (K_m) to 0.011 mol/m^3. The parameters were taken from the literature, considering the typical values for common scaffold and cell cultures given by experimental data [1].

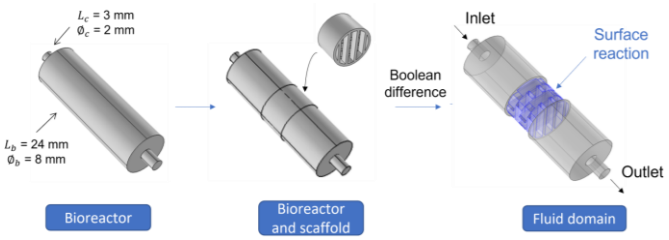


Fig. 2 FEM geometry and model setup. The geometry was obtained by the Boolean difference between the perfusion bioreactor (Coletti et *al.* [1]) and the scaffold, then, specific boundary conditions were placed on the inlet, outlet, and the seeded surface highlighted in blue.

A parametric sweep of the flow rate (0.01 – 0.2 – 0.5 ml/min) was also added in the first study (scaffolds without lateral pores) to evaluate the best condition in terms of oxygen supply and Wall Shear Stress (WSS) evaluated on the seeded surface. A stationary study was implemented to evaluate the cell viability and WSS effects after the transient.

III. Results and Discussions

For each study, the average and maximum WSS on the seeded surface were evaluated in all pore lengths and flow rates. According to the literature [6], the acceptable WSS range for osteogenic differentiation of cell lines in 3D perfusion bioreactors varies from 0.1 mPa to 15 mPa, whereas the critical oxygen concentration for cell vitality is equal to 0.04 mol/m^3. Thus, these values were taken as a threshold for finding the optimal scaffold pore size and flow rates. Considering the scaffolds without lateral pores, an inlet flow rate between 0.2 ml/min and 0.5 ml/min is preferred for all pore lengths both in terms of WSS and cell oxygenation (Fig. 3A/B).

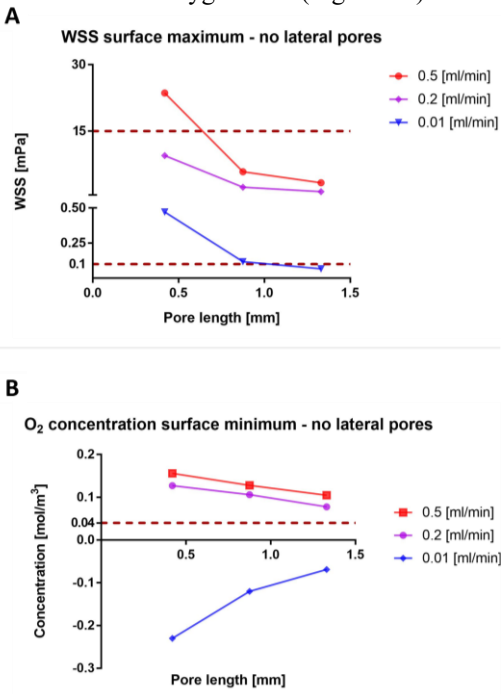


Fig. 3 (A) WSS and (B) oxygen concentration values in the scaffolds without lateral pores evaluated with three different flow rates, namely, 0.01 - 0.2 - 0.5 ml/min.

Comparing the WSS in the scaffold without and with lateral pores, no differences are shown for each of the flow rates (Fig. 4A/B). However, it results that a pore length greater than 0.4 mm (minimum size evaluated) is the optimal condition in

terms of WSS, being lower than the maximum acceptable value (i.e., 15 mPa) for osteogenic differentiation (Fig. 4A). On the other hand, cell oxygenation is improved in the lateral porous scaffolds (Fig. 4B).

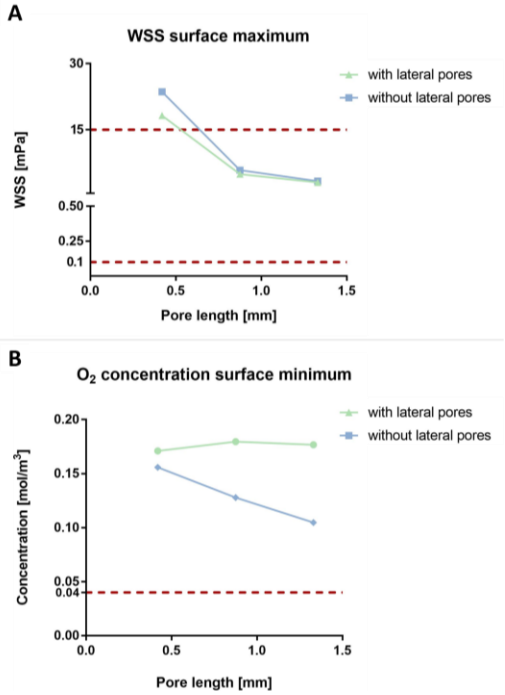


Fig. 4 (A) WSS and (B) oxygen concentration values in the scaffolds without and with lateral pores, with a flow rate of 0.5 ml/min.

Similarly, no differences were found in terms of WSS among the lateral porous scaffolds presenting different strand orientations (Fig. 5A). However, the 90°-oriented is the best condition to guarantee better oxygenation among the seeded cells (Fig. 5B).

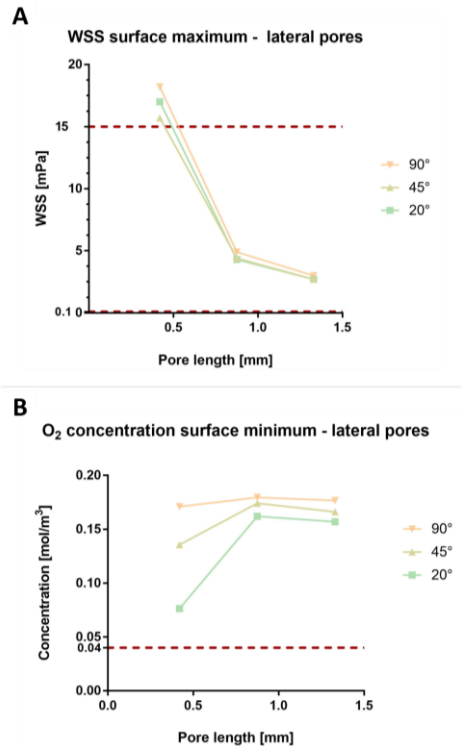


Fig. 5 (A) WSS and (B) oxygen concentration values in the scaffolds with lateral pores and different strands orientation evaluated with a flow rate of 0.5 ml/min.

It is important to highlight that model results are not applicable for scaffolds made in soft materials (e.g., hydrogels), which have low mechanical strength, and thus exhibit not negligible deformations even at low flow rates. In this case, the fluid flow and solid mechanics should be coupled to capture the fluid-solid interactions.

IV. Conclusion

For all pore sizes, the scaffold presenting lateral pores improved the oxygenation and showed acceptable WSS values for osteogenic differentiation. Although the strand orientation had little influence on the WSS, the 90° orientated scaffolds showed better oxygenation. Furthermore, among the scaffolds with lateral pores and 90° orientation, a pore length greater than 0.4 mm is recommended in terms of WSS acceptable values. Among the flow rates considered in this study, the 0.5 ml/min condition is preferable for oxygenation and WSS when pores are greater than 0.4 mm.

In the future, the selected optimal scaffold design will be used to evaluate the spatial-temporal variation with a transient study over the culture period (typically 7 days). In addition. the recirculation condition at the inlet and outlet of the bioreactor will be added to simulate a close system like a real experiment. Furthermore, the model will be integrated with different kinetic models to account for the cell growth and/or detachment/death, as well as the changes in the porosity due to the formation of extracellular matrix (ECM) and cellular activities, and scaffold degradation. Additionally, the model will be validated in vitro seeding cells on the PLLA-based scaffolds in a perfusion bioreactor.

Acknowledgment

This project has received funding from the European Union's Horizon 2020 research and innovation program under grant agreement No814410.

References

[1] Coletti, F.; Macchietto, S.; Nlvassore, N. Mathematical Modelling of Three-Dimensional Cell Cultures in Perfusion Bioreactors. Part II. *Comput Aided Chem Eng* **2006**, *21*, 1699–1704, doi:10.1016/S1570-7946(06)80292-0.

[2] Bouet, G.; Marchat, D.; Cruel, M.; Malaval, L.; Vico, L. In Vitro Three-Dimensional Bone Tissue Models: From Cells to Controlled and Dynamic Environment. *Tissue Eng - Part B Rev* **2015**, *21*, 133–156, doi:10.1089/ten.teb.2013.0682.

[3] McCoy, R.J.; O'Brien, F.J. Influence of Shear Stress in Perfusion Bioreactor Cultures for the Development of Three-Dimensional Bone Tissue Constructs: A Review. *Tissue Eng - Part B Rev* **2010**, *16*, 587–601, doi:10.1089/ten.teb.2010.0370.

[4] Magrofuoco, E.; Flaibani, M.; Giomo, M.; Elvassore, N. Cell Culture Distribution in a Three-Dimensional Porous Scaffold in Perfusion Bioreactor. *Biochem Eng J* **2019**, *146*, 10–19, doi:10.1016/j.bej.2019.02.023.

[5] Zhou, X.; Lee, S.; Nowicki, M.; Zhang, L.G. 3D Bioprinting Novel Graphene Oxide Scaffold for Improving Human Bone Marrow Mesenchymal Stem Cell Chondrogenic Differentiation. **2019**, 21003.

[6] Seddiqi, H.; Saatchi, A.; Amoabediny, G.; Helder, M.N.; Abbasi Ravasjani, S.; Safari Hajat Aghaei, M.; Jin, J.; Zandieh-Doulabi, B.; Klein-Nulend, J. Inlet Flow Rate of Perfusion Bioreactors Affects Fluid Flow Dynamics, but Not Oxygen Concentration in 3D-Printed Scaffolds for Bone Tissue Engineering: Computational Analysis and Experimental Validation. *Comput Biol Med* **2020**, *124*, 103826, doi:10.1016/j.compbiomed.2020.103826.

Extrusion control strategy for robotic-based *in situ* bioprinting

G. M. Fortunato[1,2], M. Molisani[2], G. Vozzi[1,2], C. De Maria[1,2]
[1] *Department of Information Engineering, University of Pisa, Pisa, Italy*
[2] *Research Centre "E. Piaggio", University of Pisa, Pisa, Italy*

***Abstract*—Robotic-based in situ bioprinting is a very promising technology to overcome the limitations of the traditional scaffold-based tissue engineering approach. One of the most used bioprinting technologies to deposit the biomaterial directly onto/into a damaged site of the patient is based on a pneumatic extrusion. During the printing phase, the robotic manipulator end-effector is subjected to continuous changes in speed and direction to follow complex anatomical surfaces. For this reason, in this work we describe the development of an extrusion control strategy to obtain a uniform biomaterial deposition during a robotic-based in situ bioprinting procedure. The proposed algorithm was tested onto IMAGObot, a 5-axes robotic platform optimized for in situ bioprinting applications.**

***Keywords*—robotic-based in situ bioprinting, pneumatic extrusion-based bioprinting, extrusion control strategy.**

I. Introduction

In recent years bioprinting technologies are attracting interest in the field of tissue engineering (TE) since they offer a promising solution to those diseases that damage a tissue/organ to such an extent that transplantation is necessary. These technologies allow precise placement of cells, biomaterials, and biomolecules in three-dimensional (3D) structures developed through a computer aided design (CAD) software [1-2].

Bioprinting approaches can be divided into two branches, *in vitro* and *in situ*, respectively. The first involves the development of a biocompatible scaffold (potentially built using cell-laden materials), colonized with cells, whose growth is promoted in a bioreactor. A surgical procedure can then be performed to transfer the scaffold into the patient's lesion. In contrast, *in situ* bioprinting consists of the direct deposition of the biomaterial on the intended anatomical location in the living body, using the body itself as a bioreactor. The *in situ* approach is promising because, given the direct printing into the defect, the risks of implant failure due to geometric mismatches is reduced, and the scaffold-tissue integration is promoted [1, 3].

Robotic-based *in situ* bioprinting is the most promising approach since it integrates the advantages of using a robotic manipulator for a precise biomaterial deposition. Once medical images are acquired, a digital model of the defect is obtained, and a printing trajectory is planned for the biomaterial printing onto the lesion. A list of commands, usually in a G-code format, is processed and provided to the robotic manipulator that executes the instructions and builds the desired structure. This approach provides multiple advantages such as: high printing accuracy, rapid biofabrication of complex multi-material scaffolds, minimization of human errors and compatibility with minimally invasive internal surgery tools [3].

One of the most common technologies for *in situ* bioprinting purposes is extrusion-based bioprinting [4-5]. Considering the robotic approach, a pneumatic actuation is preferred to reduce the load (*e.g.,* due to motor or other actuation systems) on the end-effector. Nevertheless, during the bioprinting step, an inhomogeneous biomaterial deposition can occur if a constant pressure is applied. Under/over extrusion problems arise when the extruder (used as end-effector of the robot kinematic chain) undergoes abrupt changes in velocity, when printing on uneven surfaces or during sudden changes in direction. Since most anatomical surfaces have such features, it is crucial to implement a strategy to improve the printing quality.

In this work, we present the implementation of a pressure control strategy to increase the accuracy of the bioink deposition with the robotic manipulator IMAGObot [6-8]. An algorithm was developed in Matlab to predict the end-effector speed and the optimal printing pressure and was integrated in the previously developed IMAGObot application.

II. Materials and Methods

A. IMAGObot robotic platform

IMAGObot (Fig. 1A) is a robotic biofabrication platform, developed from the 5 Degrees-of-Freedom (DoF) open source MOVEO robot from BCN3D [9], totally re-engineered both in hardware and software for *in situ* bioprinting applications [3]. The robotic manipulator has an electro-magnet as end-effector that enables quick and easy tool switching so that many instruments may be used for a single operation (e.g., touch probe, pneumatic extruder). In this work, the syringe-pump extrusion module based on a pneumatic actuation was used. IMAGObot is position-controlled using LinuxCNC, an open-source software that allows the interaction with the robot using a G-code, while the path planning is performed using the previously developed Matlab® R2020a application. The Linux CNC source code has also been released as open-source project on the GitHub platform [10] and is constantly updated.

B. Extrusion-control strategy

A preliminary analysis was conducted observing IMAGObot behaviour during simple trajectories, such as diagonal, vertical, and horizontal planar lines. The desired paths (Fig. 1B) were planned in Matlab and tested in the IMAGObot workspace at different z heights and with different points density. A Python code was written to collect end-effector speed and position (*i.e.*, joint angles for each point of the trajectory) data from LinuxCNC during printing

movements, every time that the robot reads a different G-code line. The collected data were then imported in Matlab, converting joint angles into Cartesian coordinates with a Direct Kinematic algorithm, and successively analysed to highlight any speed variation while traveling along horizontal and vertical lines according to the position in the robot workspace. From these data, two descriptive laws of motion along vertical and horizontal trajectories were derived. Combining all the data acquired from this analysis, a predictive algorithm was developed that, starting from the linear speed set by the user, and knowing the position and density of the trajectory in the IMAGObot workspace, computes multiplying coefficients to predict speed variations along the path. On the basis of the obtained speed data, the pressure value can be modulated for each portion of the trajectory to achieve a uniform biomaterial deposition.

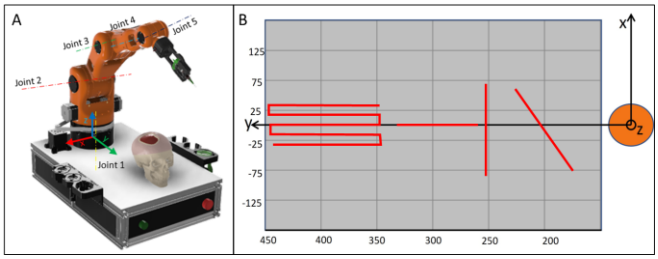


Fig. 1: A) Schematic of the IMAGObot platform: the robot workspace reference frame and the 5 joint axes are shown – B) Top view of the IMAGObot workspace. The robotic platform is here schematized with an orange circle, the reference axes are indicated with the black arrows, and the red lines indicate the trajectories tested for the preliminary analysis.

C. *Validation of the extrusion-control strategy*

The accuracy of the algorithm was tested by comparing the predicted (*i.e.*, obtained in Matlab) and real speed of the end-effector (*i.e.*, acquired from LinuxCNC), while executing both planar and non-planar serpentine trajectories.

Successively, to assess the printing quality provided by the algorithm, tests were performed depositing a 20% w/v Pluronic acid F127 (Sigma-Aldrich, Italy) biomaterial ink onto a planar surface: the same serpentine trajectory was printed without the pressure control algorithm (constant pressure value of 0.5 bar along all the pattern), and with the adaptive pressure values provided by the developed algorithm. The goal was to obtain a printed strand as uniform as possible, and a line width similar to the needle used for extrusion (0.82 mm internal diameter). The width value was obtained with the ImageJ® software averaging 28 values acquired on different cut lines along the trajectory (as shown in Fig. 7).

Finally, preliminary *in situ* bioprinting tests were performed by depositing the same biomaterial ink previously used onto two different non-planar surfaces.

III. Results and Discussion

A. *Extrusion-control strategy*

Preliminary tests were performed by executing simple trajectories to evaluate IMAGObot speed variations in its workspace and adjust pressure value accordingly. Results are shown in Fig. 2. Considering the diagonal paths (Fig. 2A), as can be seen from Fig. 2B the speed decreases if the end-effector is moving from the furthest to the closest point at the base of the robot while increases if travelled in the opposite way. The same behavior can be observed for vertical trajectories (Fig. 2C), where the speed decreases moving the end-effector towards the robot base but is not affected by x coordinate. Hence, moving away from the base of the robot, the contribution of joint 3 is added to that of joint 2 and consequently, the maximum speed attainable increases. Finally, considering horizontal paths, the speed decreases as y coordinate increases. In this case, this trend is due to the fact that joint 1 is the most involved in the movement and, given the robot configuration, would tend to perform a circumference (dotted line in Fig. 3, radius equal to the distance from the robot base).

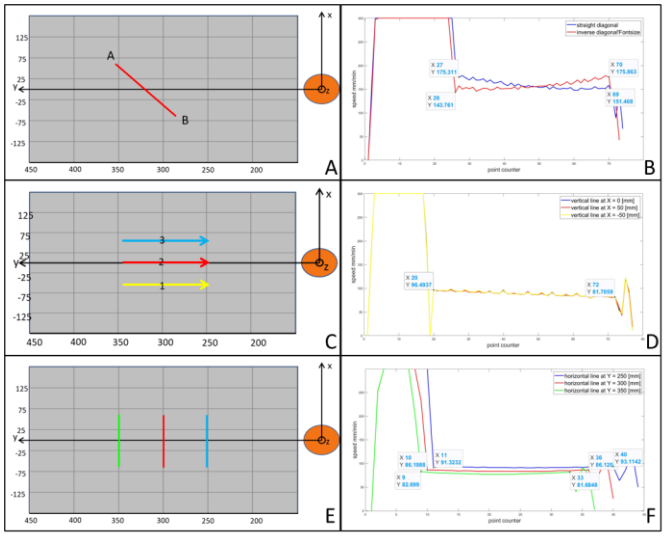


Fig. 2: A) Diagonal trajectory: two different tests were carried out moving the end-effector from A to B and *vice versa* – B) Speed trend for the two diagonal trajectories: going from A to B the speed decreases (blue plot), from B to A increases (red plot) – C) Vertical trajectories at different x coordinates – D) Speed trend along different vertical trajectories: varying the x coordinate the speed value does not change – E) Horizontal trajectories at different y coordinates – F) Speed trend along horizontal trajectories: the speed values increases as distance from the robot base (y coordinate).

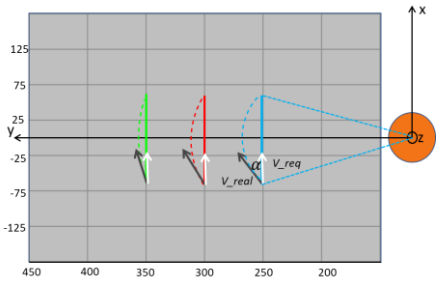


Fig. 3: Relationship between real and set speed for the end-effector movement along x axis is dependent on the distance from the robot base.

The contribution due to *z* height in the workspace can be neglected since it does not introduce a speed variation.

From the preliminary tests previously shown, two interpolation surfaces were obtained (Fig. 4) to relate all the considered parameters: distance between adjacent point s of the trajectory (x), set speed of the end-effector (y), distance from the robot base (z).

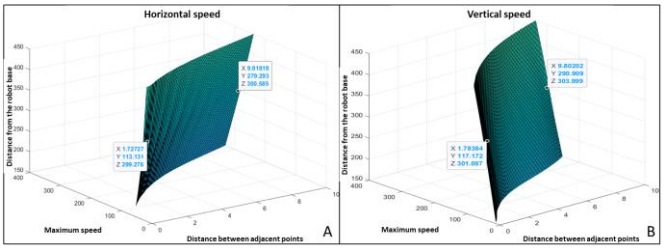


Fig. 4: Interpolation surface describing speed variation along x direction (A) and y direction (B).

The speed was thus found to be mainly influenced by two factors: the distance between the points of the trajectory, and the distance of these points from the robot base. Exploiting these data, the developed Matlab algorithm computes multiplying coefficients that starting from the set speed provides the predicted speed for each portion of the trajectory.

B. Validation of the extrusion-control strategy

Using the developed predictive algorithm, printing tests were performed on different substrates, both planar and non-planar (Fig. 5), and the predicted speed values for each point of the trajectory (Fig. 6A-C) were compared with the real speed acquired from LinuxCNC (Fig. 6B-D).

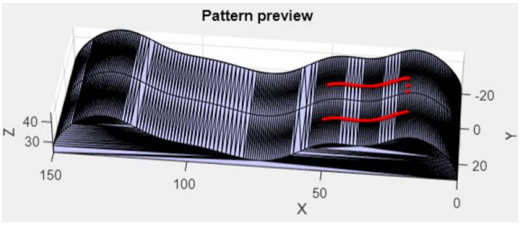


Fig. 5: Non-planar substrate tested for the validation of the extrusion-control strategy

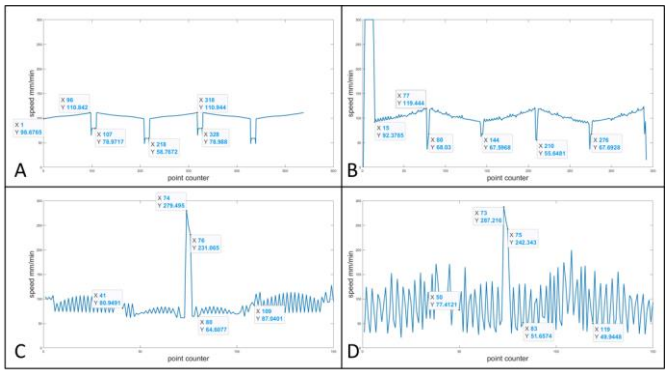


Fig. 6: Comparison between predicted (A-C) and measured (B-D) speed for a serpentine trajectory onto a planar (A-B) and non-planar (C-D) substrate.

Fig. 6A and 6B compare the speed of the end-effector during a planar serpentine trajectory. As shown in the outlined data, the computed speed value at the starting point is 7% higher than the real value, while in the ending point of the trajectory is 19% higher than the measured one. The change of direction is traveled at ~68 mm/min while the computed speed for this segment was ~78 mm/min (12% higher). The speed values were close enough to allow a notable improvement in the printing quality. Fig. 6C and 6D show the predicted vs measured speed of the end-effector while printing the non-planar serpentine trajectory. As can be seen, the speed profiles differ, but this is caused by the robotic arm vibration (due to low rigidity of the 3D printed manipulator), not predictable in the code. Nevertheless, the speed values match in most parts: the central spike was traveled at ~287mm/min, and the computed speed was ~279 mm/min, the following point is reached at a speed of ~242 mm/min when the computed speed was ~231 mm/min: also in this case the speed is thus predicted with an average accuracy >80%.

The improvement of printing quality was assessed by performing the same bioprinting test with and without the extrusion control strategy developed. The Fig. 7A shows the pattern printed with a constant pressure value of 0.5 bar along the entire pattern. The printed line width is not uniform, and several clots are visible when the pattern changes direction. The Fig. 7B shows the same trajectory being printed with adaptable pressure value (from 0.28 to 0.50 bar), according to the end-effector predicted speed.

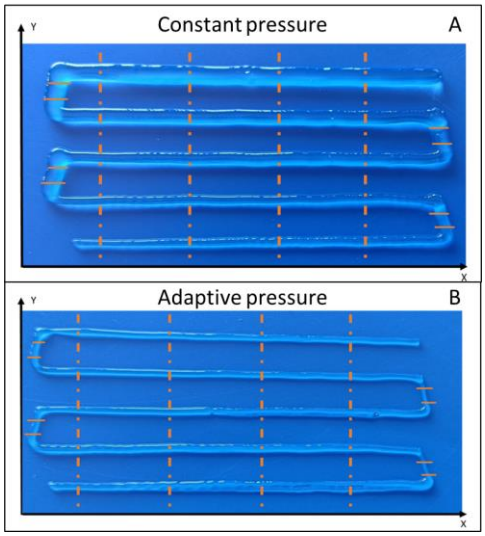


Fig. 7: Analysis of the printing quality: dashed orange lines represent the points where line width value was measured with the ImageJ® software. The obtained average value was compared between the printed pattern with a constant (A) and adaptive pressure (B).

A general improvement in printing quality is shown: the deposited filament is much uniform and there are no clots when the end-effector changes direction. The bar plot in Fig. 8 compares the average values of the printed line width highlighting how the obtained width with the extrusion control strategy is closest to the target needle internal diameter. The lower standard deviation also confirms a higher line width homogeneity.

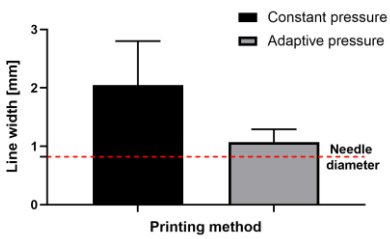


Fig. 8: Comparison between the line width obtained with and without the extrusion control strategy developed. Needle internal diameter was 0.82 mm.

Preliminary *in situ* bioprinting tests were then performed by printing a serpentine trajectory onto a non-planar surface using the developed algorithm (Fig. 9A-B). The printed line width is uniform and continuous. In the figure 9C the same trajectory was printed using a constant pressure value equal to the minimum computed by the algorithm (0.26 bar), while in the figure 9D the value is the maximum computed by the algorithm (0.5 bar). Both tests performed with constant pressure value showed printing inaccuracies, lack of material and biomaterial blobs, respectively.

A final printing test was conducted onto a surface with sudden changes in slope, with appreciable uniformity and continuity of the printed line width, as shown in Fig. 9E.

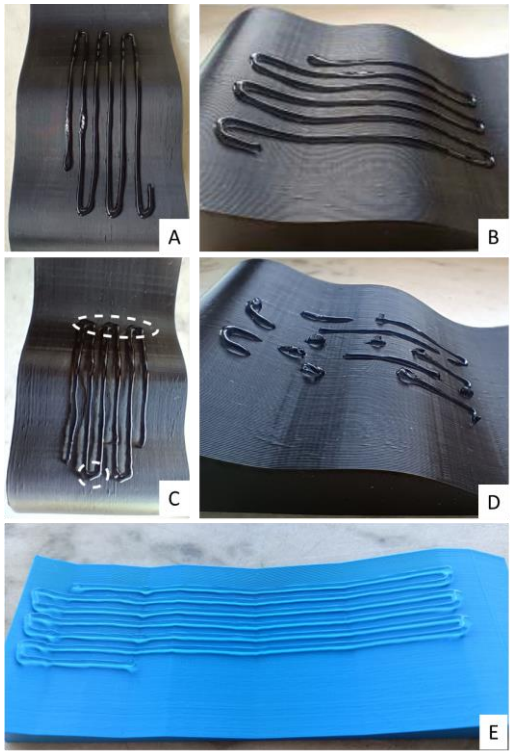


Fig. 9: Preliminary *in situ* bioprinting tests onto complex surfaces: A-B) Printed pattern with the adaptive pressure. - C-D) printing with a consatnt pressure equal to the maximum (C) and minimum D) pressure value obtained from the developed algorithm. Clots of material are visible in C, indicatd with white circles. In D a too low pressure causes a discontinous line.– E) Printing test onto a substrates with steep-slope changes using adaptive pressure

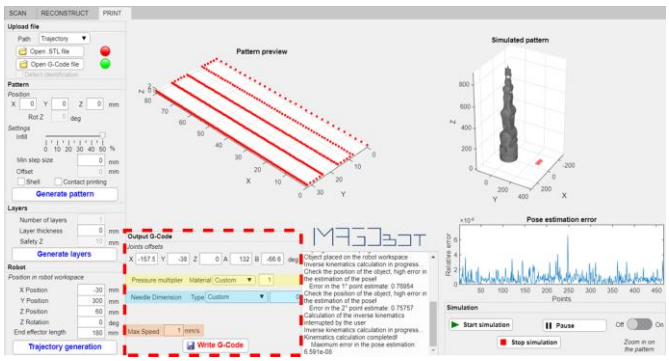


Fig. 10: IMAGObot Matlab application with the addition of the extrusion control strategy. The material and the needle diameter can be set from the user to adjust the obtained pressure value

The extrusion control algorithm was then implemented in the IMAGObot Matlab application using Matlab App Designer as shown in Fig. 10. Two dropdown menus were added to make the algorithm customizable based on the material and needle used.

IV. Conclusion

In this work we presented the development of an extrusion control strategy for pneumatic robotic-based *in situ* bioprinting. The implemented algorithm proved to be able to predict the printing speed for different trajectories according to the position in the robot workspace. Based on this outcome, the pressure value can be adjusted accordingly for each portion of the printed pattern. This approach was successfully tested onto different planar and non-planar substrates showing an improved printing quality when compared with a constant pressure along the entire path. The approach is very promising for robotic-based *in situ* bioprinting applications where complex surfaces are typical of anatomical defects. Furthermore, the pressure control algorithm was successfully integrated into the IMAGObot Matlab application allowing for higher customization as well as an easier interaction and usability by non-expert users. Future developments include refinement of the algorithm, with a finer control of the end-effector speed, as well as an expansion of the material library.

Acknowledgement

We acknowledge the support of the European Union by the Next Generation EU project ECS00000017 ‘Ecosistema dell’Innovazione’ Tuscany Health Ecosystem (THE, PNRR, Spoke 4: Nanotechnologies for diagnosis and therapy).

References

[1] Moroni, L., Boland, T., Burdick, J. A., De Maria, C., Derby, B., Forgacs, G., ... & Vozzi, G. (2018). Biofabrication: a guide to technology and terminology. Trends in biotechnology, 36(4), 384-402.

[2] Bonatti, A. F., Fortunato, G. M., De Maria, C., & Vozzi, G. (2022). Bioprinting technologies: an overview. Bioprinting, 19-49.

[3] Singh, S., Choudhury, D., Yu, F., Mironov, V., & Naing, M. W. (2020). In situ bioprinting–Bioprinting from benchside to bedside?. Acta biomaterialia, 101, 14-25.

[4] Manyi Wang, Jiankang He, Yaxiong Liu, Meng Li, Dichen Li, and Zhongmin Jin. “The trend towards *in vivo* bioprinting”. *International Journal of Bioprinting*, 1.1, (2015)

[5] Fortunato, G. M., Bonatti, A. F., Micalizzi, S., Chiesa, I., Batoni, E., De Acutis, A., De Maria, C., Vozzi, G. (2022): “In situ bioprinting - current applications and future challenge”, Additive Manufacturing in Biomedical Applications, Vol 23A, ASM Handbook, Edited By Roger J. Narayan, ASM International, p 225–236

[6] Fortunato, G. M., Rossi, G., Bonatti, A. F., De Acutis, A., Mendoza-Buenrostro, C., Vozzi, G., & De Maria, C. (2021). Robotic platform and path planning algorithm for in situ bioprinting. Bioprinting, 22, e00139.

[7] Fortunato, G. M., Batoni, E., Bonatti, A. F., Vozzi, G., & De Maria, C. (2022). Surface reconstruction and tissue recognition for robotic-based in situ bioprinting. Bioprinting, 26, e00195.

[8] Fortunato, G. M., Bonatti, A. F., Batoni, E., Macaluso, R., Vozzi, G., & De Maria, C. (2022). Motion compensation system for robotic based in situ bioprinting to balance patient physiological movements. Bioprinting, 28, e00248.

[9] BCN3D MOVEO-https://github.com/BCN3D/BCN3D-Moveo, Last accessed January 2023

[10] IMAGObot repository-https://github.com/CentroEPiaggio/IMAGObot, Last accessed January 2023

Effects of different degumming methods on the quality of sericin samples

Ivana Dragojlov[1], Simone Vesentini[2], and Elisa Fasoli[3]

[1] *Dep. of Electronics, Information and Bioengineering, Politecnico di Milano Piazza Leonardo da Vinci 32 - 20133 Milano, Italy*
[2] *Dep. of Electronics, Information and Bioengineering, Politecnico di Milano Piazza Leonardo da Vinci 32 - 20133 Milano, Italy*
[3] *Dep. of Chemistry, Materials and Engineering Chemistry "Giulio Natta" via Mancinelli 7, 20131, Milano, Italy*

***Abstract*— This study evaluates degumming methods to obtain the best purity of silk sericin (SS) and the most suitable physicochemical features without affecting the yarn quality and the extractable sericin quantity. However, SS extracted by various methods results in SS exhibiting different physical and biological properties. The molecular weight of SS, which ranges from 10 to 400 kDa, is determined by the extraction and purification process. Higher molecular weight sericin peptides enable their use for many applications, including medical biomaterials, functional bio-membranes, and others. Lower molecular weight sericin peptides are mostly employed in cosmetic products. This study evaluates the molecular weight distribution of SS samples via sodium dodecyl sulphate-polyacrylamide gel electrophoresis (SDS-PAGE) in addition with mass spectrometry. Also, the conformational properties of SS samples obtained by heat-under-pressure method were investigated by Fourier transform infrared (FTIR) and Circular dichroism (CD) spectroscopy.**

***Keywords*—silk sericin, degumming methods, physiochemical features, molecular weight.**

I. Introduction

Bombyx Mori sericin, a globular protein synthesized in the middle silk gland of B. Mori silkworm, has started to receive attention due to its unique properties desired in biomedical applications. A variety of discoveries on the structure, properties, biocompatibility, and processability have revealed the uniqueness of silk sericin (SS) and have opened new possibilities of applying SS as a major product in a wide variety of applications, including antibacterial, wound healing, antidiabetic, moisturizing, promotion of collagen synthesis, cryopreservation, replacement of serum for cell culture [1], [2].

SS has a larger content of hydrophilic amino acids than fibroin, another protein produced from silkworm that has undergone extensive research. Thus, it possesses more hydrophilicity and is more susceptible to chemical modification than fibroin. However, sericin's real biomedical value has not been completely investigated due to the difficulty in processing it into useable materials, unlike the already extensively studied silk fibroin [3]–[5].

Although SS has desirable composition, biocompatibility, and potential to be made into various biomaterials, the economic recovery of SS from the degumming process is still a challenge because the structure of SS varies depending on the ways through which it is obtained [6]. The dynamics of pH, temperature, chemicals and processing time will affect sericin's molecular and functional properties.

Different degumming methods can be used to extract SS. Using heat or heat under pressure has the advantage of producing no contaminants [1]. However, because the process takes too long, this approach is rarely used in the silk industry. Since they do not degrade fibroin and are very simple processes, soaps and detergents are currently used in practically all industrial removal techniques [7]. Since alkali, soaps, and detergents need to be removed prior to additional applications, these techniques make it very difficult to get high-quality SS for further investigations or applications.

This study aims to obtain SS from silk cocoons by degumming processes (heat-under-pressure method, alkali and acid-degradation and urea degradation) and evaluate them to get the best purity of SS and the most suitable physicochemical features. The molecular weight of recovered SS also affects its end-use; it has been reported that high molecular weight sericin (greater than 20 kDa) is suitable for making biomaterials and membranes, whereas low molecular weight sericin (less than 20 kDa) is suitable for cosmetics, skincare products and medications [1], [7].

The processability of the SS obtained is deeply related to its physio-chemical features; hence, SS extracts have to be evaluated in detail.

We started examining the molar mass distribution of SS obtained by different degumming methods by sodium dodecyl sulphate-polyacrylamide gel electrophoresis accompanied by mass spectrometry.

We did this to compare the molecular weight of SS products made using various degumming methods. This allows us to evaluate which degumming method suits the project's future objectives regarding the final target product.

SS secondary structure is characterized by FTIR (Fourier transform infrared) and CD (circular dichroism) spectroscopy.

II. Materials and Methods

A. Silkworm cocoons

Fresh B. Mori cocoons were kindly supplied by CREA (Council of Research in Agriculture and Analysis of Agricultural Economic, Padua, Italy), a germplasm bank responsible for the production of cocoons and collection by the

farmers who have been assisted with the traceability process by the CREA staff itself, together with cocoon sorting in different classes, cocoon cutting, pupae extraction, cocoon shell storage and preservation.

B. Extraction of silk sericin by heat-under-pressure (autoclaving) method

Applying a modified version of Aramwit et al.'s procedure [8], SS was extracted from the cocoons. 30 g of cocoons of B. Mori silkworms were placed in distilled water for autoclaving at 121°C, 15 lbs pressure for 20, 30 and 60 min (SS_{20MIN}, SS_{30MIN}, SS_{60MIN}), respectively. The aqueous solution obtained from autoclaving silk cocoons was centrifuged, followed by filtration to separate the silk fibroin and other solid residues. The filtrate was finally stored at −20 °C until further use.

C. Extraction of silk sericin by urea-degradation

SS from the cocoons was extracted using protocol reported by Aramwit et al. [9], cutting 6 g of freshly cocoon pieces, followed by soaking in 8 M urea (150 mL) and heating at 85 °C for 30 min. Afterwards, the SS solution was subjected to centrifugation (4000 rpm) and filtration to remove silk fibroin and other residues. The SS solution was then dialyzed (cellulose tube with MWCO of 6-8 kDa) for 48 h against distilled water with frequent changes. Dialyzed silk sericin solution was stored at −20 °C.

D. Extraction of silk sericin by acid and alkali-degradation

Acid and alkali-degraded SS was extracted from the cocoons using the modified protocol of Kurioka et al. [10]. Cocoons were cut into small pieces and soaked in 1.25% citric acid (for acid-degradation) or 0.5 M sodium carbonate (alkali-degradation) solution and boiled for 30 min. Post boiling, silk fibroin was removed, followed by filtration and centrifugation (4000 rpm). The obtained supernatant was dialyzed, and the pH of the final protein solution was measured to verify the removal of citric acid or sodium carbonate. Dialyzed protein solution was preserved at −20 °C.

E. Sample preparation and mass determination

SS solutions obtained using urea (200 and 400 µL), alkali (400 and 600 µL), and acid (400 and 600 µL) degumming methods were concentrated using a vacuum concentrator until 15 µL and used directly for further investigations.
SS solutions obtained using the heat-under-pressure method with different extraction times were processed using a spray drying machine (Shanghai Pilotech Instrument & Equipment Co., Ltd, YC-015) into SS powders.

To determine the molecular mass of SS, SDS-PAGE was performed.
Briefly, sample solutions obtained by urea, acid, and alkali degradation were prepared by adding an equal volume of Laemmli sample buffer to each protein solution. Each sample solution was then loaded on a gel.
Regarding the heat-under-pressure method, 2 mg of SS powder was solubilized in 1 mL of different buffers (Laemlli sample buffer 2X, Phosphate Buffer Saline (PBS) 2X, and IEF sample buffer) and loaded into a gel.
In each case, the gels obtained had smearing and lacked a distinct band pattern. The SS samples' precipitation through Chloroform Methanol Precipitation for 2D and AMICON ultrafiltration devices was performed to concentrate and purify them from contaminants, and the SDS-PAGE process was repeated. Nevertheless, the final SDS-PAGE results remained the same.
Therefore, having unsatisfactory results using a sericin powder, we switched to SS solution and presuming that insufficient protein concentration in our samples caused a predominantly smeared gels, a BCA protein kit was employed to detect the exact protein concentration in 30 µL of each of our samples obtained by 20, 30, and 60 min extraction time (SS_{20MIN}, SS_{30MIN}, SS_{60MIN}), respectively. After getting the exact protein concentrations in each sample Table 1, a protocol for further processing our sample was made to obtain more satisfactory results.

Sample	SS_{20MIN} (30 µL)	SS_{30MIN} (30 µL)	SS_{60MIN} (30 µL)
protein concentration	1.9 mg/mL	4 mg/mL	6 mg/mL

Table 1. Protein concentration in 30 µL of SS solutions obtained by 20, 30, and 60 min extraction time.

Subsequently, we mixed 50 mL sericin solution obtained with 60 min extraction time with a protease inhibitor tablet and prepared two aliquots containing 70 mg of protein.
The first aliquot was filtrated with filter paper, and the waste was recovered. Afterward, it was solubilized in Leammli-ß-mercaptoethanol at 99°C.
The filtrated solution was subjected to ProteoMiner™ technology using 200 µL of beads. Two obtained elutions (E11 and E12) were concentrated to 15 µL and mixed with 5 µL Leammli-ß-mercaptoethanol.
The second aliquot was subjected to ProteoMiner™ technology using 250 µL of beads. After 2 h of incubation, centrifugation at 4000 rpm for 10 min was done, and the supernatant was eliminated. The pellet was washed with water and centrifuged again, after which the elutions were performed. Both elutions (E21 and E22) obtained were concentrated until 15 µL and mixed with 5 µL Leammli-ß-mercaptoethanol.
The waste, elutions from the first aliquot, and elutions from the second one were loaded on a new gel, respectively.
Post-run, both gels were washed with distilled water and stained with Coomassie brilliant blue G-250.

Mass spectrometry analysis was done on solutions that contained all the denatured proteins extracted from SDS-PAGE gel, including urea samples (200 and 400 µl), elution 1 (E11) and elution 2 (E12) from the first aliquot and elution 1 (E21) and elution 2 (E22) from the second aliquot since those are the only ones with clear bands patterns in both gels.

A nano chromatography system (UltiMate 3000 RSLCnano System, Thermo Scientific) was coupled with a mass spectrometer (LTQ XL ion trap, Thermo Scientific). The MS data were analyzed by the Mascot search engine (Version 2.3.01), using the Proteome Discoverer software (v. 1.2.0 Thermo) and consulting specific UniProtKB/Swiss-Prot protein database.

F. Fourier transform infrared (FTIR) and Circular dichroism (CD) spectroscopy.

FTIR spectroscopy is used to analyse the maintenance of characteristic secondary structures. According to the literature, SS FTIR absorption spectra display the characteristic amide bands between wavenumbers 1700 cm^{-1} to 1600 cm^{-1} (Amide I), between wavenumbers 1600 cm^{-1} to 1520 cm^{-1} (Amide II) and between wavenumbers 1350 cm^{-1} to 1200 cm^{-1} (Amide III). Based on experimental FTIR studies on model peptides and proteins with known structure and theoretical analyses, it has been possible to correlate the peak position of the spectral components to a specific protein secondary structure [11], [12].
Assuming that the heat-under-pressure method is the most suitable procedure, we adopted it as the first one for this kind of analysis.
The SS powder was used for subsequent characterization.
Firstly, we preliminary tested the possibility of characterizing a small amount of SS sample by FTIR analysis, after which circular dichroism, a complementary spectroscopic approach, was employed to support the peak assignments to the protein secondary structures.

III. RESULTS AND DISCUSSION

A. SDS-PAGE

Fig. 1 shows the SDS-PAGE gel exhibiting the molecular weight distribution of SS after extracting from the cocoons using urea, acid and alkali degradation methods. SS extracted using urea-degradation exhibited a clear band pattern with molecular weight ranging from 15 to 160 kDa. Whereas SS extracted using alkali- and acid-degradation exhibited smear.

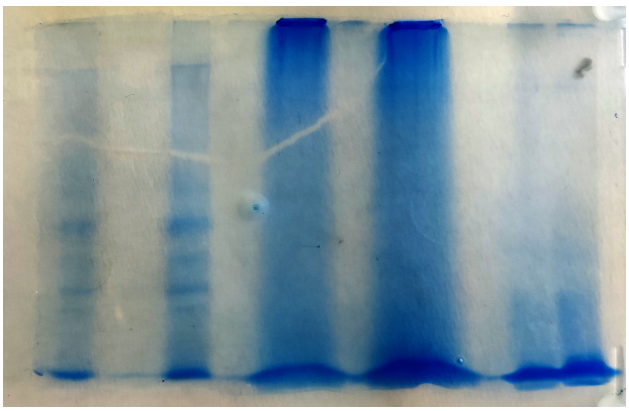


Fig. 1. The molecular weight distribution of SS solution extracted from cocoons using urea-degradation (200 and 400 µL), alkali-degradation (400 and 600 µL) and acid-degradation (400 and 600 µL) methods in SDS-PAGE.

SDS-PAGE of SS obtained by the heat-under-pressure degumming method, after which the sample solution was prepared using beads, is shown in Fig. 2. In the first row represented by the waste, we can see only the smear. In the two elutions obtained from the first aliquot, we can see some bands ranging from 15 to 100 kDa. Elutions obtained by the second aliquote show bands in the range of 30 to 50 kDa.

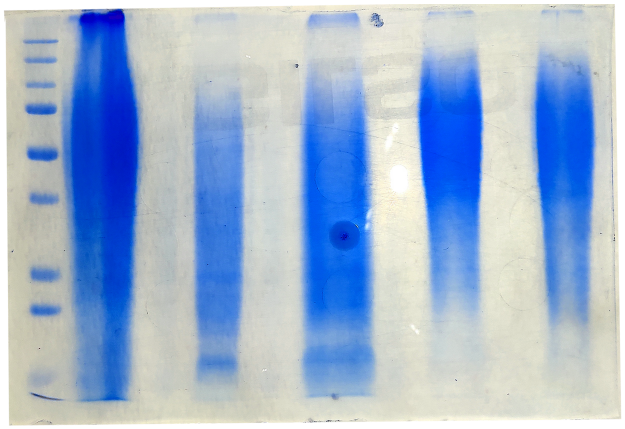


Fig. 2. The molecular weight distribution of SS solution extracted from cocoons using a heat-under-pressure method in SDS PAGE. SDS-PAGE gel showing bands of protein ladder, waste, elution 1 (E11) and elution 2 (E12) from the first aliquot, elution 1 (E21) and elution 2 (E22) from the second aliquot, respectively.

B. Mass spectrometry data

Mass spectrometry data with the highest MASCOT score of 14432 is represented in Fig. 3 and it is related to the second elution from the first aliquot (E12). The MASCOT score uses mass spectrometry data to identify proteins from peptide sequence databases. Furthermore, this number reflects the combined scores of all observed mass spectra that can be matched to amino acid sequences within the protein. Therefore, a higher score indicates a more confident match.

Prot. Number	Accession Number	Protein Name	Mascot Score	Mr	N° peptides	m/z	z	Peptide error	Pep. Score	Peptide sequence	Peptide Modification
1	P07856	Sericin 1 OS=Bombyx mo	14432	119702	34	491,7111	2	-0,0803	40,64	SKSDAFVQR	
						502,7479	2	-0,0486	23,79	TKDSISGGQAK	
						513,2629	2	-0,9817	32,32	NDNVFVYR	
						514,3589	2	0,1826	46,36	NVAHSSGSR	
						522,6641	2	0,8192	30,73	RSNAYYNR	
						648,311	2	0,0802	80,23	DSDKSESAGLSDR	
						680,2025	2	-0,2198	34,49	YTSGPEGVSYSGR	
						707,7397	2	0,823	34,5	DGTSAYSNEDSDK	
						717,1167	2	-0,4281	40,03	YNASSESSYLNK	
						733,9779	2	-0,7952	51,93	ASSTYADDDQR	
						744,0444	2	0,4159	38,78	ADKDGFSSTNTEK	
						748,852	2	0,0243	30,4	QSNTNYADQNSVR	
						512,026	3	0,407	25,32	TSGSSSTYDYSSSHR	
						525,3164	3	0,1742	20,39	SASSSKNDNVFVYR	
						526,7067	3	0,339	50,44	GYSDWNVAHSSGSR	
						557,5708	3	0,8614	32,2	NVAHSSGSRGSQNQK	
						559,009	3	0,2154	44,49	QANYYDEHTAASK	
						869,023	2	0,2089	71,86	QSSAQDSSGPEGTSYSSK	
						894,1722	2	-0,467	22,21	FSSNSVVETSQGASASR	
						907,2659	2	-0,232	90,95	SDAASSEDGFWWWNR	
						614,5895	3	0,9007	43,81	TSRQENTNYADQNSVR	
						616,6982	3	0,2283	27,43	NVHYVDSDEAVAASSDAR	
						637,2479	3	-0,1442	39,12	GHLGTVSSTGSTSTSNTDSSSI	
						657,6072	3	0,9494	32,44	SDAASSEDGFWWWNRR	
						1001,941	2	-0,0569	26,78	SEFSSSNSVVETSDGASASR	
						1004,528	2	0,0618	71,98	QSSAQDSSGPEGTSYSSKER	
						691,3631	3	0,7625	32,19	SSNSNVEDDKSNKQSSSSSI	
						721,8805	3	-0,2754	29,36	SNAYYNRDSDGSESAGLSD	
						1155,246	2	-0,5276	113,01	SAQQNAQAWWNADSSYC	
						787,7272	3	-0,8984	30,55	NVHYVSDGEAVAASSDARI	
						860,9918	3	0,9104	28,4	SSYDSGESDAYYNESPDSSYI	
						981,5692	3	0,3923	114,35	SAQQNAQAWWNADSSYC	
						1496,079	2	0,9168	64,88	SSSSSSASSSSSSNVSSSS	
						1546,488	2	5,638	56,83	SGASSSTQATTVSGADSSA	
2	P05790	Fibroin heavy chain OS=I	1660	391653	4	1461,538	1	-0,2049	72,82	DASGAVEEQITTK	
						796,319	2	-0,2074	57,44	DASGAVEEQITTKK	
						844,2485	2	0,722	97,4	GYSQSGASSGAASSVSSASSR	
						1229,649	2	0,1357	139,56	TPVITTDSGDNESVEEDVLI Oxidation (M)	
3	Q99050	Fibroin heavy chain (Fra	1328	18429	3	731,4637	2	-0,8471	27,69	DASGAVEEEITTK	
						796,0748	2	0,3202	43,34	DASGAVEEEITTKK	
						1229,649	2	0,1357	139,56	TPVITTDSGDNESVEEDVLI Oxidation (M)	
4	P81902	Trypsin inhibitor OS=Bor	155	6365	2	1077,378	1	-0,0592	64,94	YAYDSSDK	
						369,5169	3	-0,005	26,8	TDPCKDSYPR	

Fig. 3. Mass spectrometry data on elution 2 from the first aliquot (E12).

Since a mass spectrometry low-resolution instrument was used, we could not specify the amount of SS in our samples obtained by autoclaving. However, looking at the MS data in Fig. 3, we could conclude that our samples are enriched with SS protein having a high MASCOT score and many identified peptide sequences. Moreover, we detected fibroin-heavy chains in our samples in addition to the SS. However, when we compare their MASCOT scores in Table 2, we can notice a crucial difference, reaffirming that we have identified a significant portion of a SS protein's primary structure.

Silk sericin	14432
Fibroin heavy chain 1	1660
Fibroin heavy chain 2	1328

Table 2. MASCOT scores of SS and fibroin heavy chains.

Mass spectrometry data on urea samples will be provided in the nearest future due to technical problems we had with a mass spectrometer machine.

C. Fourier transform infrared (FTIR) and circular dichroism (CD) spectroscopy

In Fig. 4A, the IR spectrum is given. Absorption (blue line) and second derivative (green line) FTIR spectrum of SS powder was measured in attenuated total reflection (ATR). In particular, a small amount of the material was put directly in contact with the diamond ATR element and the spectrum was collected by a Varian 670-IR spectrometer [13]. The assignment of the main peaks is reported (Fig. 4A), which is in line with those reported in other IR analyses for SS [12].
The SS powder was resuspended in water and loaded in a custom-made sample cell. CD measurements were performed with the sample-cell close to the detector.
After averaging the spectra collected at different angles, the final spectrum was provided to avoid scattering and linear dichroism artefacts (Fig. 4B).
The hypothesis is that the envisioned extraction is suitable for an exhaustive study of SS.

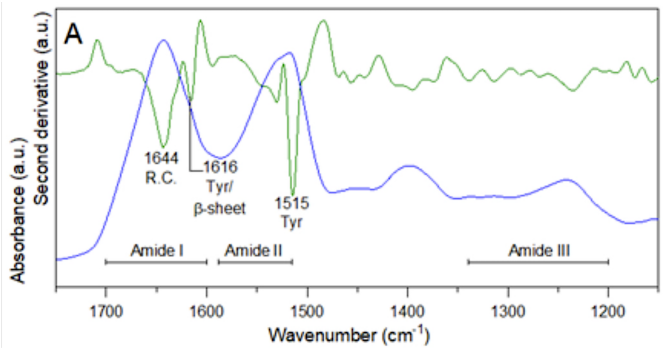


Fig. 4A. FTIR analyses on SS powder.

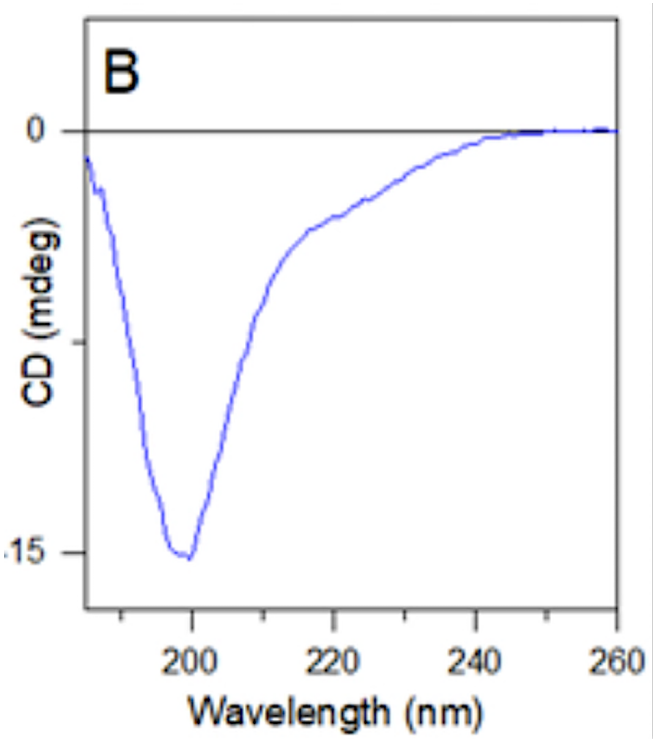


Fig. 4B. CD analyses on SS powder.

CONCLUSION

In the present study, the observed discrete clear bands and smear pattern in electrophoresis analysis (with each extraction procedure) demonstrated the breakage of SS into different-length peptides, which are of wide-ranging molecular weights.

The urea extraction method appears to be the most efficient way to obtain distinguishable bands with a broad range of molecular masses. This indicates that sericin degradation is less affected by the urea-based extraction method, allowing for sericin recovery with more precise molecular weights. However, this approach is time-consuming and expensive, and sericin extracted using urea is extremely hazardous to cells [8].

Given these drawbacks, heat-under-pressure is the most often utilized sericin extraction method. Sericin undergoes some deterioration with this procedure as well, particularly when high temperatures are utilized, or the solutions are administered for an extended period of time [14], but sericin still keeps its outstanding properties. However, the number of bands from the heat-under-pressure methods was less than those from SS extracted with urea, showing a lower range of molecular masses. Despite that, present findings propose using autoclave cocoon degumming on an industrial scale since the process is cost-effective and chemical-free, leaving no hazardous effect.

From the MS data regarding the autoclaving method samples, we could identify a high number of peptide sequences, which allowed us to recognize long sequences of the primary

structure of the entire protein. Moreover, SS FTIR results suggest that the chemical aspect of sericin was preserved during heat-under-pressure methods.

However, after obtaining MS data regarding urea samples, we would be able to proceed with a final comparison.

ACKNOWLEDGEMENT

This work was supported by SME (Leonardino Srl, www.leonardino.eu), which has the experience and full facilities in the degumming processes and electrospinning in Milan, Italy and CREA, in particular the moriculture and sericulture laboratory of the Agriculture and Environment Centre which is located in the Venetian Region, Padua, Italy.

REFERENCES

[1] P. Aramwit, T. Siritientong, and T. Srichana, "Potential applications of silk sericin, a natural protein from textile industry by-products," *Waste Manag Res*, vol. 30, no. 3, pp. 217–224, Mar. 2012, doi: 10.1177/0734242X11404733.

[2] R. I. Kunz, R. M. C. Brancalhão, L. de F. C. Ribeiro, and M. R. M. Natali, "Silkworm Sericin: Properties and Biomedical Applications," *BioMed Research International*, vol. 2016, pp. 1–19, 2016, doi: 10.1155/2016/8175701.

[3] S. Sofia, M. B. McCarthy, G. Gronowicz, and D. L. Kaplan, "Functionalized silk-based biomaterials for bone formation," *J. Biomed. Mater. Res.*, vol. 54, no. 1, pp. 139–148, Jan. 2001, doi: 10.1002/1097-4636(200101)54:1<139::AID-JBM17>3.0.CO;2-7.

[4] Y. Wang, H.-J. Kim, G. Vunjak-Novakovic, and D. L. Kaplan, "Stem cell-based tissue engineering with silk biomaterials," *Biomaterials*, vol. 27, no. 36, pp. 6064–6082, Dec. 2006, doi: 10.1016/j.biomaterials.2006.07.008.

[5] B. B. Mandal and S. C. Kundu, "Cell proliferation and migration in silk fibroin 3D scaffolds," *Biomaterials*, vol. 30, no. 15, pp. 2956–2965, May 2009, doi: 10.1016/j.biomaterials.2009.02.006.

[6] T.-T. Cao and Y.-Q. Zhang, "Processing and characterization of silk sericin from Bombyx mori and its application in biomaterials and biomedicines," *Materials Science and Engineering: C*, vol. 61, pp. 940–952, Apr. 2016, doi: 10.1016/j.msec.2015.12.082.

[7] R. Wang, Y. Zhu, Z. Shi, W. Jiang, X. Liu, and Q.-Q. Ni, "Degumming of raw silk via steam treatment," *Journal of Cleaner Production*, vol. 203, pp. 492–497, Dec. 2018, doi: 10.1016/j.jclepro.2018.08.286.

[8] P. Aramwit, S. Kanokpanont, T. Nakpheng, and T. Srichana, "The Effect of Sericin from Various Extraction Methods on Cell Viability and Collagen Production," *IJMS*, vol. 11, no. 5, pp. 2200–2211, May 2010, doi: 10.3390/ijms11052200.

[9] P. Aramwit, S. Damrongsakkul, S. Kanokpanont, and T. Srichana, "Properties and antityrosinase activity of sericin from various extraction methods," *Biotechnol. Appl. Biochem.*, vol. 55, no. 2, pp. 91–98, Feb. 2010, doi: 10.1042/BA20090186.

[10] A. Kurioka, F. Kurioka, and M. Yamazaki, "Characterization of Sericin Powder Prepared from Citric Acid-degraded Sericin Polypeptides of the Silkworm, *Bombyx Mori*," *Bioscience, Biotechnology, and Biochemistry*, vol. 68, no. 4, pp. 774–780, Jan. 2004, doi: 10.1271/bbb.68.774.

[11] A. Natalello and S. M. Doglia, "Insoluble Protein Assemblies Characterized by Fourier Transform Infrared Spectroscopy," in *Insoluble Proteins*, E. García-Fruitós, Ed., in Methods in Molecular Biology, vol. 1258. New York, NY: Springer New York, 2015, pp. 347–369. doi: 10.1007/978-1-4939-2205-5_20.

[12] L. K. H. Rocha *et al.*, "Sericin from Bombyx mori cocoons. Part I: Extraction and physicochemical-biological characterization for biopharmaceutical applications," *Process Biochemistry*, vol. 61, pp. 163–177, Oct. 2017, doi: 10.1016/j.procbio.2017.06.019.

[13] M. Maleki, A. Natalello, R. Pugliese, and F. Gelain, "Fabrication of nanofibrous electrospun scaffolds from a heterogeneous library of co- and self-assembling peptides," *Acta Biomaterialia*, vol. 51, pp. 268–278, Mar. 2017, doi: 10.1016/j.actbio.2017.01.038.

[14] T. V. Chirila, S. Suzuki, and N. C. McKirdy, "Further development of silk sericin as a biomaterial: comparative investigation of the procedures for its isolation from Bombyx mori silk cocoons," *Prog Biomater*, vol. 5, no. 2, pp. 135–145, Jul. 2016, doi: 10.1007/s40204-016-0052-8.

Engineering the tumor environment *in vitro* using peptide-enriched, hyaluronic acid-based hydrogels

A. Zamuner[1], L. Cassari[2], M. Dettin[2], M.T. Conconi[3] and E. Sieni[4]

[1] *Department of Civil, Environmental, and Architectural Engineering, University of Padova, Padova, Italy*
[2] *Department of Industrial Engineering, University of Padova, Padova, Italy*
[3] *Department of Pharmaceutical and Pharmacological Sciences, University of Padova, Padova, Italy*
[4] *Department of Theoretical and Applied sciences, University of Insubria, Varese, Italy*

***Abstract*— Electrochemotherapy (ECT) is a clinically used and effective treatment in the care of melanoma, and recently it was suggested as a promising tool for the treatment of other deep-seated solid tumors (*e.g.*, liver tumors).**

In general, ECT efficacy is evaluated *in vitro* on cell suspensions or in adhesion, and *in vivo* on animal models. Nevertheless, the first two mentioned approaches completely lack extracellular matrix (ECM) components, leading to unreliable results because they do not reflect the natural tissue architecture. To overcome this issue, several three-dimensional (3D) *in vitro* models, such as spheroids and hydrogel-based cultures, have been proposed to mimic the complex tumor microenvironment. In this frame, a new synthetic scaffold based on hyaluronic acid (HA) and self-assembling peptides (EAbuK) is proposed as an advantageous alternative.

HA-EAbuK scaffolds promote spheroids formation where cells experiment cell-cell interactions, but also improve cell-ECM interactions. Liver cancer (HepG2) cell lines were cultured on HA and HA-EAbuK scaffolds and preliminary bioassays were carried out to assess cell viability and spheroids formation. Then, cells were electroporated at different electric field amplitudes. 3D cultures on HA scaffolds and cells in adhesion (2D cultures), electroporated using culture medium or phosphate-based EP buffer, were taken as controls.

Our data showed that HepG2 cells cultured on HA-EAbuK scaffolds were already completely electroporated at 800 V/cm, whereas cells cultured on HA started to be electroporated at 1200 V/cm. In 2D cultures, HEPG2 cells were electroporated at 1000 V/cm and 1200 V/cm in EP buffer and in culture medium, respectively. Collectively, our preliminary results suggest that HepG2 cell cultures on HA-EAbuK hydrogels may represent a promising tool for *in vitro* evaluation of EP efficiency.

***Keywords*—Electroporation, hyaluronic acid, self-assembling peptide, liver tumor model**

I. Introduction

ELECTROCHEMOTHERAPY is a well-assessed therapy used for some skin-related tumors like melanoma or breast cancer recurrences after mastectomy [1]-[4]. In recent years it was evaluated in the treatment of some other types of tumors, such as liver, head and neck, colon carcinomas, and soft tissue sarcomas [5-6]. The electroporation (EP) efficiency of the cell membrane depends on cell size and density as well as on the conductivity and composition of the medium where cells are suspended during the EP. It is well known that in the tissue the cells experience cell-cell connection and are surrounded by the extra-cellular matrix (ECM) that is a component of the tumor microenvironment. Thus, several three-dimensional (3D) *in vitro* models have been used in EP experiments: the cell-cell interactions have been simulated using spheroids, whereas the cell-ECM interactions have been considered in cultures grown in hydrogels [7].

Herein, low molecular weight hyaluronic acid (HA) porous scaffolds were enriched with an ionic-complementary self-assembling peptide named EAbuK [9]-[12]. In aqueous solution, EAbuK forms β-sheet planes that pile up each other generating hydrogels [12]. Liver cancer (HepG2) cells were cultured on the above-mentioned scaffolds and were characterized by cell viability assessment and hematoxylin/eosin.

Eventually, cell cultures were electroporated varying the electric field amplitude in order to find the optimal EP condition. The use of these HA-EAbuK scaffolds can be considered as an optimization of *in vitro* EP tests, which would hopefully cause a drastic reduction in the need for animal tests, giving rise to a significant cut of the costs and time of pre-clinical studies, not to mention the great ethical impact of reducing the death of animals involved in cancer research.

II. Materials and Methods

A. Matrix preparation

The main stages of preparation of the matrices were: (i) Solid-phase peptide synthesis of self-assembling peptide EAbuK, followed by peptide purification by reverse phase high performance liquid chromatography (RP-HPLC), and characterization by MALDI-TOF mass spectrometry [9]; (ii) preparation of the hyaluronic acid:self-assembling peptide solution (95:5 % w/w) in H_2O Milli-Q (0.8% w/v of HA); (iii) freezing at -178 °C and freeze-drying; (iv) crosslinking with 60 mM EDC in 95% EtOH for 24 hours; (v) eventually matrices were washed 6 times with EtOH and 6 times with Milli-Q water, all washes were carried out sonicating for 2 min and without sonicating for an additional 1 min; (vi) freezing at -178 °C and freeze-drying [10].

B. Cell culture

The HepG2 cells were grown with DMEM containing 10% fetal bovine serum, 1% L-glutamine, and 1% antibiotic/antimycotic solution (Sigma-Aldrich) at 37°C in a humified atmosphere with 5% CO_2. Cells (1.8×10^5) were seeded on scaffolds previously put in different wells of a 24-well cell suspension culture plate. Cultures were daily observed with a phase contrast microscope (Nikon T-s). At 3 and 7 days from seeding, cell viability was assessed by using the PrestoBlue™ Cell Viability Reagent (Thermo Fisher

Scientific) according to the manufacturer's instruction, and culture morphology by hematoxylin/eosin staining.

C. *Electroporation of cell suspension – EP curve*

A suspension of 2.5×10^6 cells/mL (HepG2) was prepared. This HepG2 suspension was inserted in a chamber slide multi-well (245µL/well) and an EP sequence of 8 voltage pulses 100 µs long at 5 kHz, different amplitude, was applied. Eventually, cells were seeded in a 96-well plate to evaluate viability at 24 h after EP through Presto Blue assay. The experiments were repeated both in cell medium and in EP buffer (EPB,10 mM K_2HPO_4/KH_2PO_4, 1 mM $MgCl_2$, and 250 mM sucrose, pH 7.4) [13]-[15].

Cell suspension was put in a second chamber slide (245µL/well), and Propidium Iodide (PI) (15µL from 1mg/mL, Sigma Aldrich) was added, then EP sequence was applied and the PI fluorescence was recorded using a Victor plate reader (excitation 555 nm, emission 610 nm). The procedure was repeated for different voltage amplitudes.

D. *3D culture Electroporation procedure*

After 24h or 3 days of cell culture within the HA-EAbuK matrix, the culture medium was added with PI water solution (15µL from 1mg/mL, Sigma Aldrich). PI was added to mark EP cells since it penetrates the cell membrane when electroporated. EP sequence (8 voltage pulses 100 µs long at 5 kHz) at different voltage amplitude was applied to each sample. Then, Hoechst 33342 (5µL from 1mg/mL solution, Thermo Fisher Scientific) was added to mark all cell nuclei.

Image acquisition was assessed using a Fluorescence microscope (LEICA DMI4000) (Bright field, Hoechst 33342: exciting 360 nm, emission 470 nm, and PI: exciting 515-540 nm, emission 590 nm). Image analysis was performed using ImageJ software.

III. Results

A. *Cell viability*

At 3 days from the seeding, no significant differences in cell viability were detected between cultures grown in HA/EAbuK matrices and tissue culture-grade plastic (TCP), whereas at 5 days MFI was significantly lower in all HA-based cultures vs TCP (Fig. 1).

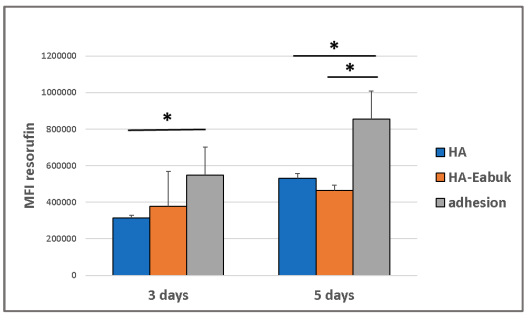


Fig. 1: Cell cultures on HA-based hydrogels. Cell viability at 3 and 5 days from seeding. MFI: mean fluorescence intensity. The control "adhesion" represents cells seeded on TCP. * p < 0.05, Student's t-test.

HepG2 cells organized themselves to form clusters inside both hydrogels and, at various degrees, spheroids were visible on their surface (Fig. 2)

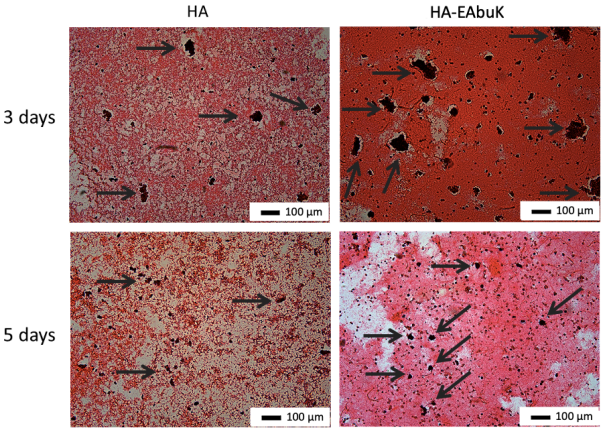


Fig. 2: Hematoxylin/eosin staining of cell cultures on HA-based Hydrogels. Arrows indicate the spheroids (scale bar=100 µm).

B. *Electroporation*

EP was carried out on cells in suspension, and cultures grown on TCP and HA-based hydrogels by applying increasing electric fields. Cell membrane permeabilization and cell viability were verified through PI staining immediately after EP and at 24 h from the treatment, respectively (fig. 3-4). In cell suspensions, PI uptake significantly increased starting from 1000 V/cm. Moreover, at 1200 V/cm it was higher in cultures where EP was carried out by using culture medium than that detected with EP buffer (Fig. 3).

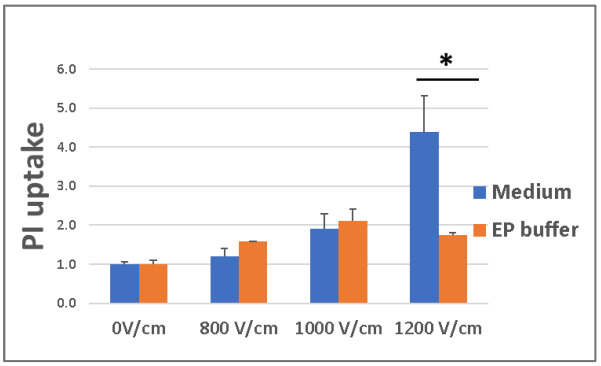


Fig. 3: Effects of EP on cell suspension. PI uptake immediately after EP. *=p<0.05, Student's t-test.

Significant decreases in cell viability were found only with culture medium at 1000 and 1200 V/cm (Fig. 4).

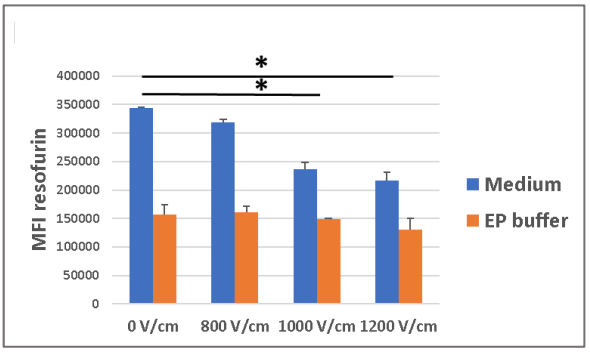


Fig. 4: Effects of EP on cell suspension. Cell viability at 24 h from EP. *=p<0.05, Student's t-test.

In HepG2 cultures grown on TCP, PI uptake was well visible starting from 1000 V/cm (Fig. 5). However, cell permeabilization was higher in cultures where EP was carried out by using EP buffer rather than culture medium.

No variations in cell viability were detected at all electric fields in medium cell suspension.

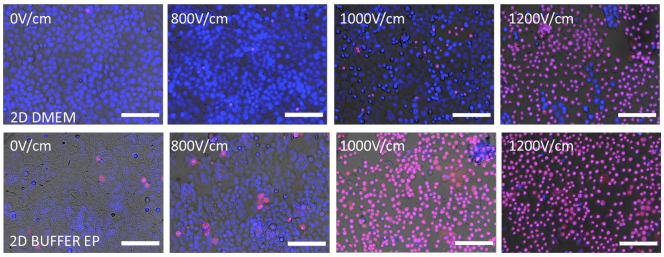


Fig. 5: Effects of EP on adherent cell cultures. Representative micrographs of cultures stained with PI (red) and Hoechst (blue) immediately after EP (bars: 100 µm).

HepG2 cultures on HA-based hydrogels appeared more sensitive to EP than those in suspension and adhesion (Fig. 6). Indeed, PI uptake was detected starting from 800 V/cm.

Moreover, cell permeabilization was higher in HA-EAbuK cultures than in HA ones.

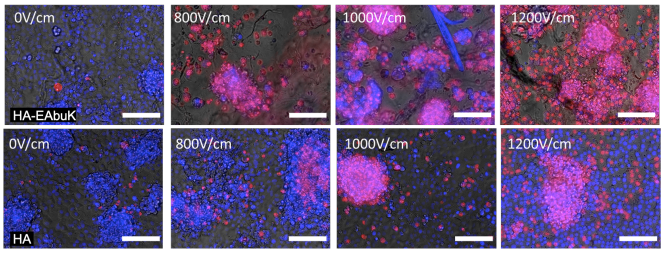


Fig. 6: Effects of EP on cultures grown on HA-based hydrogels. Representative micrographs of cultures stained with PI (red) and Hoechst (blue) immediately after EP (bars: 100 µm).

On the other hand, in HA and HA-EAbuK cultures cell viability significantly decreased starting from 800 V/cm and 1000 V/cm, respectively (Fig. 7).

Moreover, at all electric fields, MFI values were significantly lower in HA cultures than those detected in HA-EAbuK ones.

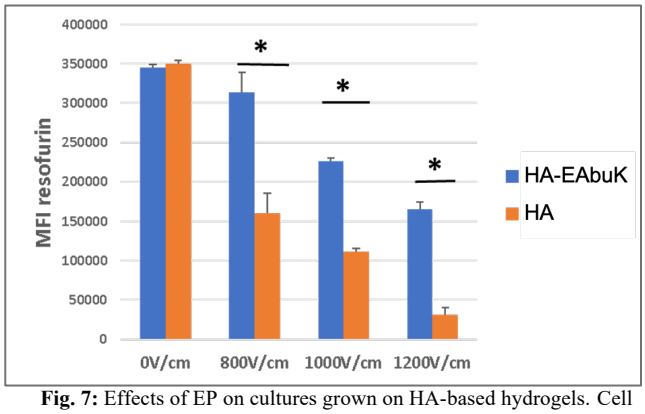


Fig. 7: Effects of EP on cultures grown on HA-based hydrogels. Cell viability at 24 h from EP, *=p<0.05, Student's t-test.

IV. Conclusion

HA-based hydrogels are widely used to obtain 3D cell cultures useful for anti-cancer studies, since HA, a major component of the extracellular matrix, allows migration, proliferation, and invasiveness of malignant cells [16]. In particular, hepatocytes, the main cell type of the liver, need extracellular matrix to maintain their morphology and biological functions. So far, several HA-based *in vitro* matrices have been developed to provide a cell friendly microenvironment and, ultimately, valuable liver models for drug screening and disease study [17]-[19]. Nevertheless, their application for EP studies has not been deeply investigated.

Herein, the effects of EP on HA-EAbuK-based hepatocyte cultures were evaluated, starting from our previous study [20] where HA-based hydrogels allowed ECM production by breast cancer cells.

Our data showed that HepG2 cells cultured on HA-EAbuK scaffolds were already completely electroporated at 800 V/cm, whereas cells cultured on HA started to be electroporated at 1200 V/cm. In 2D cultures, HEPG2 cells were electroporated at 1000 V/cm and 1200 V/cm in EP buffer and in culture medium, respectively. Collectively, our preliminary results suggest that HepG2 cell cultures on HA-EAbuK hydrogels may represent a promising tool for *in vitro* evaluation of EP efficiency. Further experiments will be performed to verify whether HepG2 cells could produce ECM molecules.

Acknowledgement

The authors are grateful to Igea S.p.A. (Carpi, Italy) for pulse generator and electrodes. The project was granted by CPDA138001 (Padua University) and partially by COST TD1104 action (www.electroporation.net).

References

[1] Wichtowski M, Murawa D. Contemp Oncol (Pozn). 2018;22(1):8-13. doi: 10.5114/wo.2018.74387. Epub 2018 Apr 3.
[2] Tasu JP, Tougeron D, Rols MP. Diagn Interv Imaging. 2022 Nov;103(11):499-509. Epub 2022 Oct 17. doi: 10.1016/j.diii.2022.09.009.
[3] M. Marty, *et al.* European Journal of Cancer Supplements. 4 (2006) 3–13. doi: 10.1016/j.ejcsup.2006.08.002.
[4] L.M. Mir, *et al*. EJC Supplements. 4 (2006) 14–25.
[5] Tsoneva I, *et al*. Biophys Chem. 2022 Jul; 286:106819. Epub 2022 Apr 15. doi: 10.1016/j.bpc.2022.106819.
[6] Cemazar M, Sersa G. Bioelectricity. 2019 Dec 1;1(4):204-213. Epub 2019 Dec 12. doi: 10.1089/bioe.2019.0028.
[7] Miklavčič D, *et al*. Med Biol Eng Comput. 2012 Dic; 50(12): 1213–25.
[8] Gibot L, *et al*. In: Jarm T, Kramar P, editors. 1st World Congress on Electroporation and Pulsed Electric Fields in Biology, Medicine and Food & Environmental Technologies [Internet]. Singapore: Springer Singapore; 2016 [cited 2017 Jul 25]. p. 200–3.
[9] Zhang S, *et al*. Proc Natl Acad Sci USA. 1993 Apr 15;90(8):3334–8.
[10] Dettin M. *et al*. Cells. 2019 Nov, 8, 1470. doi: 10.3390/cells8111470.
[11] Zhang S. Interface Focus. 2017 Dec 6;7(6):20170028. Epub 2017 Oct 20. doi: 10.1098/rsfs.2017.0028.
[12] Gambaretto R, *et al*. Biopolymers. 2008 Nov; 89(11):906-15. doi: 10.1002/bip.21030. PMID: 18521888.
[13] Pavlin, M., *et al*. Biophysical Journal. 88, 4378–4390 (2005). doi: 10.1529/biophysj.104.048975.
[14] Silve, A., *et al*. Sci Rep. 6, 19957 (2016). doi: 10.1038/srep19957.
[15] Dermol, J., *et al*. PLoS ONE. 11, e0159434 (2016). doi: 10.1371/journal.pone.0159434.
[16] L. David, *et al*. Acta Biomater. 4 (2008) 256–263, https://doi.org/10.1016/j. actbio.2007.08.012.

[17] Messelmani, T., *et al*. Bioengineering (Basel, Switzerland), 9(9), 443. (2022) doi: 10.3390/bioengineering9090443.
[18] Bucatariu, S. M., *et al*. International journal of biological macromolecules, 165 (Pt B), (2020) 2528–2540. doi:10.1016/j.ijbiomac.2020.10.095.
[19] Jiang, J., *et al*. Colloids and surfaces. B, Biointerfaces, 206, (2021) 111980. doi: 10.1016/j.colsurfb.2021.111980.
[20] Sieni, E., *et al*. Bioelectrochemistry, 136, (2020) art. no. 107626. doi: 10.1016/j.bioelechem.2020.107626

Multiscale computational models for predicting hydrogel viscoelastic properties

N. Guazzelli[1,2,3], L. Cacopardo[1,2,3], V. Inghirami[2] and A. Ahluwalia[1,2,3]
[1]*Department of Information Engineering, School of Engineering, University of Pisa*
[2]*Research Centre "E. Piaggio", University of Pisa*
[3]*Centro Interuniversitario per la Promozione dei Principi delle 3R nella Didattica e nella Ricerca, Centro 3R, University of Pisa*

***Abstract*—Modelling hydrogel mechanical behaviour is fundamental for supporting the design of physiologically relevant scaffolds capable of guiding and maintaining cell phenotype and behaviour. In the literature, several approaches to describe the mechanics of soft structures has been proposed; however, they exploit complex algorithms with high computational times or do not include any experimental validation. Here, we propose a multiscale computational model based on the coupling of molecular diffusion and material mechanics. The model describes the viscoelastic properties of a hydrogel as a function of the liquid phase composition. Specifically, we combine mass transport equations and mesh size to describe the time dependent mechanical behaviour of agarose hydrogels. The simulations are coherent with the experimental characterisation of the hydrogels, confirming the predictive power of the model and its versatility. Further studies will be implemented to adapt the model to different materials and to couple material properties with cell mechanotransduction. This multiscale computational tool will be essential for targeted material design for regenerative medicine application and for the definition of advanced in-vitro models.**

***Keywords* — in silico models, viscoelastic properties, engineered hydrogels, agarose.**

I. Introduction

Predicting hydrogel mechanical behaviour is essential for defining precise mechanical stimuli to control and guide cell behaviour [1]. Hydrogel viscoelastic behaviour is strongly related to the interaction of liquid molecules with the solid network. Although different mathematical models have been proposed to simulate chemical and transport phenomena in gels (e.g. reaction, diffusion, and hindered convection), most of them lack the correlation with gel viscoelastic properties (e.g., relaxation time, τ_{rel}) or do not provide experimental validation [2], [3].

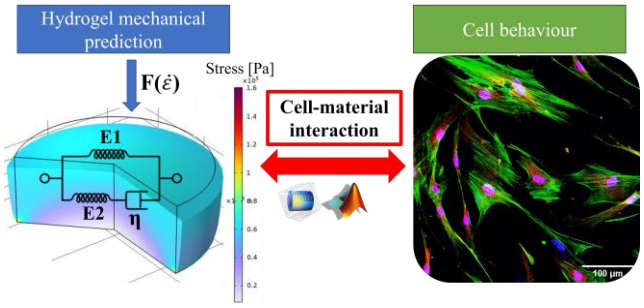


Fig. 1. Graphical description of the work ultimate goal.

For these reasons, we propose a versatile computational model to predict the viscoelastic behaviour of agarose hydrogels in the presence of tunable liquid phases. As reported in the literature, modulating the hydrogel liquid phase without altering the elastic network affects hydrogel mechanical behaviour. We investigated how the viscoelastic properties of agarose are affected by the presence of soluble polysaccharides in the liquid phase. In particular, we studied: dextran which is known to react mainly with water molecules thus augmenting the gel's liquid-like behaviour [4] and hyaluronic acid, which also binds to polymeric network, affecting both elastic and the viscous properties [5].

To correlate the hydrogel diffusive and mechanical properties, we considered the average gel mesh size ξ_{avg}, a fundamental structural parameter for the description of hydrogel architectures, which is related with the maximum size of molecules that can move through the polymeric network. This parameter is shown to be fundamental for the prediction of soft materials mechanical properties [6].

II. Materials and Methods

A. Modelling agarose hydrogel mechanics

Agarose hydrogels were modelled as a homogeneous porous system, while the viscous phase (i.e., dextran or hyaluronic acid (HA)) was considered as a spherical agglomerate linked to the water molecules. In the case of dextran, the hypothesis was that it can only bind water molecules in the liquid phase [4], while hyaluronic acid molecules can bind both water molecules and agarose fibres [5]. Therefore, the lumped parameter schematization considered for describing the mechanical behaviour of the agarose hydrogel in the presence of dextran was the Maxwell Standard Linear Solid model (SLS) (fig. 2A), while in presence of hyaluronic acid, the SLS model was adapted including a spring E_1 in parallel to E_0 (fig. 2B) to represent the hyaluronic acid effect on the elastic properties. In both the configurations, a dashpot η_2 in parallel with η_1 was included to represent the effect of dextran/hyaluronic acid on the viscous properties.

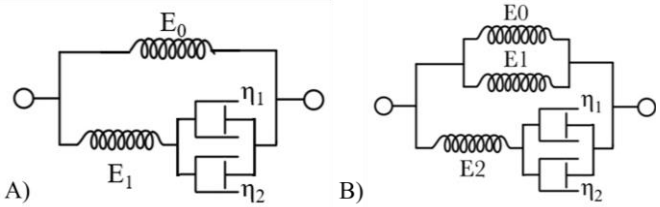


Fig. 2. A) SLS lumped parameter schematization in Maxwell configuration considered for the agarose-dextran hydrogel, and B) adapted SLS model in case of hyaluronic acid – agarose hydrogels.

The model, implemented on Matlab R2022a, consisted in solving the reaction-diffusion equation (eq. 1) that regulates the movement of the hydrogel liquid phase during a uniaxial compression test to derive the values of the lumped parameters, and thus the values of the viscoelastic descriptors,

i.e., the instantaneous (E_{inst}) and equilibrium (E_{eq}) elastic modulus, and the characteristic relaxation time (τ) (tab. I). E_{inst} refers to the initial elastic response, which is given by the sum of all the springs in the lumped model since the viscous components are shorted out and do not deform while sustaining the load. E_{eq} refers instead to the static response after the viscoelastic dynamics have occurred, as the viscous components are on open circuit, so they cannot sustain any load or stress. A lower relaxation time τ denotes a more viscous-like behaviour, i.e., when $\tau \to 0$ the material is ideally viscous and vice versa when $\tau \to \infty$ we have an ideally elastic material [1].

$$\frac{\partial c}{\partial t} = D_{app} \cdot \nabla^2 c - c \cdot \nabla v - v \cdot \nabla c - k_r c_{vm} \qquad (1)$$

TABLE I: LUMPED PARAMETERS COMBINATION FOR OBTAINING THE VISCOELASTIC DESCRIPTORS.

	Dextran - agarose hydrogel (Fig.3A)	*Hyaluronic acid - agarose hydrogel (Fig.3B)*
Equilibrium Elastic Modulus (E_{eq})	E0	E0+E1
Instantaneous Elastic Modulus (E_{inst})	E0+E1	E0+E1+E2
Characteristic Relaxation Time (τ)	η_1/E1	(η1+ η2)/E2

An apparent liquid phase diffusion coefficient D_{app} (eq. 2) was introduced using Brinkmann's theory of hindered diffusion in porous media, which adapts the Einstein-Stokes diffusion coefficient D_0 (eq. 3) through the coefficient β (eq. 4) that considers the obstacle imposed by the porous matrix using the permeability κ of the molecules. The latter was estimated through the Carman-Kozeny equation [3].
The coefficient δ (eq. 5) introduced the correlation between the diffusive and the mechanical properties of the agarose hydrogel, by considering the average mesh size (ξ_{avg}), i.e., the most important descriptor of the hydrogel porous structure defined as the distance between two adjacent cross-links (fig. 3). More specifically, Flory's theory of rubber elasticity and the Amsden obstructing-scaling model [6] were implemented to correlate ξ_{avg}, D_{app}, and the elastic modulus ($E(t)$) (eq. 5 - 6).

$$D_{app} = \beta \cdot \delta \cdot D_0 \qquad (2)$$

$$D_0 = \frac{k_b T}{6\pi\eta R_H} \qquad (3)$$

$$\beta = \left\{1 + \left(\frac{{R_H}^2}{\kappa}\right)^{\frac{1}{2}} + \frac{1}{3}\left(\frac{{R_H}^2}{\kappa}\right)\right\}^{-1} \qquad (4)$$

$$\delta = e^{-\frac{\pi}{4}\left(\frac{R_f + R_h}{R_f + 0.5\cdot\xi_{avg}(t)}\right)^2} \qquad (5)$$

$$\xi_{avg}(t) = \left(\frac{18 k_B T}{\pi E(t)}\right)^{\frac{1}{3}} \qquad (6)$$

The reaction between water and dextran or hyaluronic acid molecules was expressed using a first order equation as a function of the free polysaccharide concentration (c_{vm}); the binding rate k_r was estimated by a 0D Finite Element Model (FEM) implemented on Comsol Multiphysics 6, using the Chemical reaction module, and optimizing the simulation on the experimental viscosity data, acquired as described in section II.B.

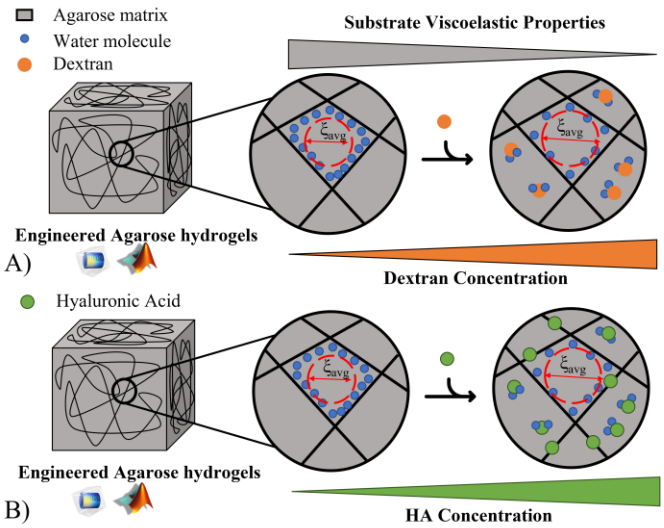


Fig. 3. Schematic picture representing the interaction of dextran (A) and hyaluronic acid (B) molecules with the polymer network and its effects on the hydrogel mesh size and therefore on its and diffusive and mechanical properties.

Finally, the hydrodynamic radius R_H of dextran and hyaluronic acid molecules (tab. II) was extrapolated from a 2D-axialsymmetric time-dependent FEM simulation of the molecule release from the agarose hydrogel, performed on Comsol Multiphysics 6. The physic module implemented was the Transport of Diluted species in porous media. The computational results were optimised on the experimental evaluation of Fluorescein isothiocyanate-Dextran-Conjugate (FITC-dextran, 500 kDa, Sigma-Aldrich, 1:100) and Fluorescein isothiocyanate-Hyaluronic acid-Conjugate (FITC-HA, 500 kDa, Sigma-Aldrich, 1:100) release from dextran/HA (50mg/mL) - agarose (5 mg/mL) hydrogels, after 1, 4 and 24 hours.

TABLE II: MODEL PARAMETERS

Parameter	*Symbol*	*Unit*	*Value*
Agarose hydrogel porosity	ε	-	0.57
Agarose fibre radius	R_f	m	$1.90\cdot10^{-9}$
Dextran diffusion coefficient (Stokes)	$D_{0\text{-}dex}$	m^2/s	$1.18\cdot10^{-12}$
Dextran hydrodynamic radius	Rh_{dex}	m	$2.20\cdot10^{-8}$
Hyaluronic acid diffusion coefficient (Stokes)	$D_{0\text{-}HA}$	m^2/s	$2.27\cdot10^{-12}$
Hyaluronic acid hydrodynamic radius	Rh_{HA}	m	$7.00\cdot10^{-8}$

B. Dextran/HA – agarose hydrogel fabrication and characterisation

Dextran and hyaluronic acid solutions were prepared dissolving the powders in different concentrations (tab. III) in deionised water on a magnetic stirrer. Agarose hydrogels were prepared by dissolving 5 mg/mL of agarose powder in the previous solutions on a magnetic stirrer, casted in a custom-made PDMS mold (cylindrical well dimensions: 13 mm diameter, 8 mm height) and crosslinked at 4°C for 30 minutes. The dynamic viscosity μ of the dextran/hyaluronic acid solutions was measured using a dynamic viscometer (DV-II+, Brookfield, Germany) as a function of the cooling

temperature; the LV1 spindle was chosen considering the range of viscosity values ($3 \cdot 10^0$ - $6 \cdot 10^5$ cP).

TABLE III: MATERIALS USED FOR HYDROGEL FABRICATION

Material	*Quantity [mg/mL]*
Agarose (A9539, Sigma Aldrich)	5
Dextran (D1037, Sigma Aldrich)	20, 30, 40
Hyaluronic acid (FH71634, Biosynth)	5, 7.5, 10

The hydrogel viscoelastic parameters were tested by means of the epsilon-dot method [7]. Briefly, unconfined bulk compression tests at different constant strain rates $\dot{\varepsilon}$ (0.0005, 0.001, 0.005, 0.01 s^{-1}) were performed using the Zwick/Roell ProLine Z005 uniaxial testing device (Germany). Each sample was tested partially submerged in the respective aqueous phases, to maintain the hydration. The time-force curves were collected and globally fitted to the Maxwell Standard Linear Solid model (SLS) (eq. 7, fig. 2A) in case of dextran and to the adapted SLS model (aSLS) (eq. 8, fig. 2B) in case of hyaluronic acid, to obtain the values of the lumped parameters, and thus E_{inst}, E_{eq} and τ.

$$\sigma_{SLS}(t) = \dot{\varepsilon}\left[E_0 \mathrm{t} + (\eta_1 + \eta_2)\left(1 - e^{-\frac{E_1}{\eta_1+\eta_2}t}\right)\right] \quad (7)$$

$$\sigma_{aSLS}(t) = \dot{\varepsilon}\left[(E_0 + E_1)\mathrm{t} + (\eta_1 + \eta_2)\left(1 - e^{-\frac{E_1}{\eta_1+\eta_2}t}\right)\right] \quad (8)$$

Moreover, the apparent elastic modulus (E_{app}) was estimated from the slope of the stress-strain curves in the linear viscoelastic region. 1-way ANOVA and t-tests were performed using OriginPro to determine respectively the significance of the results ($\alpha = 0.05$) and the fitting of the curve ($R^2 = 0.98$).

C. Numerical solving method and model validation

The reaction-diffusion equation was solved using Matlab 2022a by implementing discretization through the method of lines (MoL). Transport equations are commonly solved using MoL [8]. Briefly, the spatial domain was discretised and thus the partial differential equations (PDEs) were replaced with a vector system of ordinary differential equations (ODEs) and the solved using Matlab's ODE45. The conditions are reported in tab. IV.

TABLE IV: BOUNDARY CONDITIONS FOR SOLVING THE REACTION-DIFFUSION EQUATIONS ON MATLAB WITH MOL.

Parameter	*Symbol*	*Unit*	*Value*
Initial position	xi	m	0
Final position	xf	m	$1 \cdot 10^{-3}$
Geometric step	dx	m	$1 \cdot 10^{-5}$
Temporal step	dt	s	$1 \cdot 10^{-2}$
Upper concentration boundary	cU	mol/m^3	0
Lower concentration boundary	cL	mol/m^3	$C0_{dex} - C0_{HA}$

The mechanical compression test was simulated on Simulink (Matlab 2022a) proving a graphical tool for the prediction of the stress-time curves for both dextran (fig. 4a) and hyaluronic acid – agarose hydrogels (fig. 4b). The simulation results were compared to the experimental ones to optimise and validate the computational model, following the least squares method.

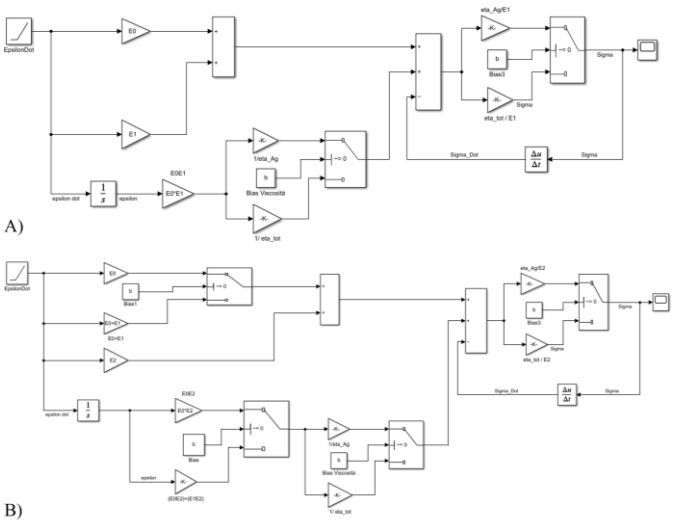


Fig. 4. Block diagram architecture of SLS (A) and adapted SLS Maxwell model (B) for simulating the mechanical behaviour, respectively, of dextran and HA-agarose hydrogel during a compression test according to the epsilon dot method.

III. RESULTS AND DISCUSSION

The simulation of dextran diffusion and the parameter optimisation on experimental results provided a hydrodynamic radius of $2.2 \cdot 10^{-8}$ m for dextran (fig. 5D) and of $7.0 \cdot 10^{-8}$ m for hyaluronic acid in water.

The liquid phase diffusion time (fig. 5A) predicted by the computational model showed that resistance to flow decreases as dextran concentration increases. This trend was also confirmed by the relaxation time. Moreover, the comparison with experimental data confirmed the capability of the model to predict the mechanical behaviour of agarose hydrogel in the presence of different molecule concentrations in the liquid phase (fig. 5B). It is reasonable to associate this behaviour to the modulation of the mesh size. Indeed, the dextran concentration increase results in a reduction of the amount of water molecules linked to the polymer, as demonstrated by the mesh size increase (fig. 5C), which promotes the liquid phase flow through hydrogel pores. In particular, the more the relaxation time decreases, the more the flow resistance decreases as the mesh size increases.

The mechanical characterization confirmed the capability of dextran to modulate the viscous properties of agarose hydrogels [4]. Indeed, as the dextran concentration increased, the instantaneous elastic modulus and the characteristic relaxation time decreased, as predicted by the computational model (fig. 6). Despite the increase in dextran concentration and hence liquid phase viscosity, τ_{rel} decrease (i.e., shifting toward a more liquid-like behaviour) is related to the reduction of liquid phase diffusion time and to the mesh size increase.

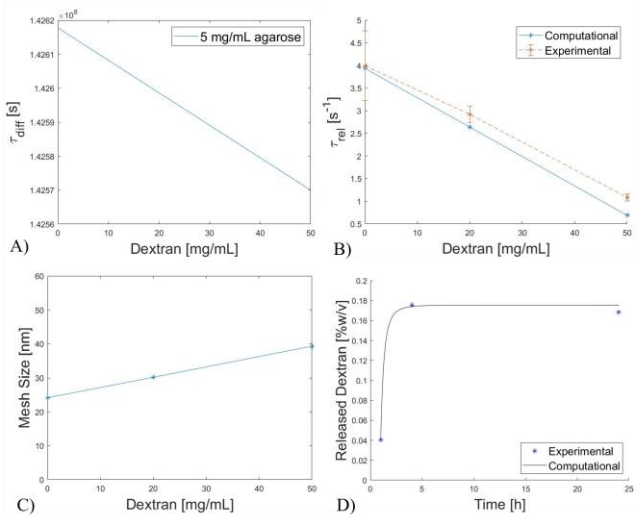


Fig. 5. A) Liquid phase diffusion time, B) relaxation time (p value > 0.05) and C) average mesh size of dextran-agarose hydrogel as a function of the dextran concentration. D) Dextran release profile compared to the experimental measures, in case of 50 mg/mL dextran - 5 mg/mL agarose hydrogels.

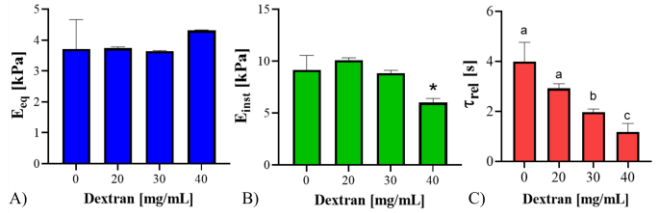


Fig. 6. A) Equilibrium (E_{eq}) and B) instantaneous (E_{inst}) elastic moduli and C) characteristic relaxation time (τ) as a function of different dextran concentrations for 5 mg/mL agarose hydrogels. Different letters indicate statistical significance (*= $p < 0.05$).

Mechanical analyses are ongoing to validate the model in the case of hyaluronic acid. However, preliminary tests on the apparent elastic modulus (E_{app}), suggested that the predicted values are comparable with the experimental ones. Moreover, the E_{app} increase with increasing HA concentration is coherent with previous results reported in the literature [5] (fig. 7).

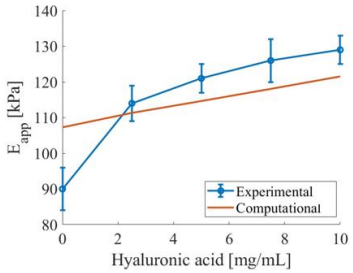


Fig. 7. Comparison between computational and experimental [5] trend of apparent elastic modulus of HA-agarose hydrogels as a function of HA concentration.

IV. Conclusion

The computational framework presented in this work resulted effective in predicting gel transport properties (mesh size and liquid phase diffusion time) and their effect on the resulting viscoelastic features. Indeed, the model can describe the interaction of molecules in the liquid phase with the solid network, and it can be used to predict bulk viscoelastic behaviour of hydrogels.

The model was validated on agarose gels with dextran in the liquid phases, showing its influence in weakening the bonds between water and agarose, with a consequent decrease of the steric hindrance and a faster flow. Therefore, although liquid phase viscosity increases with increasing dextran concentration, it contributes to reduce the resistance to flow preventing the formation of water-agarose bonds [4].

Preliminary simulations also suggested that the model can be used with different viscoelastic modulators, such as hyaluronic acid, which is a physiological component of extracellular matrix, thus its use will improve the physiological relevance of the hydrogels [5]. In this case, the model was adapted to consider its effect on both the elastic and viscous component. Comparison between experimental and computational data are ongoing to confirm the preliminary results; computational simulations on the Simulink workflow will be performed to determine the stress-time curves of agarose hydrogels for their mechanical characterization.

In the future, the model will be adapted to other material combinations by coupling it with in silico models well established in the literature for describing the effect of the crosslinking process. Moreover, it will be coupled with in silico descriptions of cell behaviour in response to the mechanical stimuli, e.g., the molecular clutch model [1], to provide a useful tool for the design of hydrogels with well-defined mechanical properties that mimic the physiological/pathological extracellular matrix. In conclusion, the presented computational framework will be essential for regenerative medicine applications and for the definition of advanced in-vitro models.

References

[1] L. Cacopardo, N. Guazzelli and A. Ahluwalia, " Characterizing and engineering biomimetic materials for viscoelastic mechanotransduction studies", *Tissue Engineering Part B: Reviews*, vol. 28, n. 4, 2022

[2] D. Caccavo, S. Cascone, G. Lamberti and A. A. Barba, "Hydrogels: experimental characterization and mathematical modelling of their mechanical and diffusive behaviour", *Chemical Society Reviews*, vol. 47, pp. 2357 -2373, 2018

[3] A. Pluen, P. A. Netti, R. K. Jain, D. A. Berk, " Diffusion of macromolecules in agarose gels: comparison of linear and globular configurations", *Biophysical Journal*, vol. 77, pp. 542 – 552, 1999

[4] L. Cacopardo, N. Guazzelli, R. Nossa, G. Mattei and A. Ahluwalia, "Engineering hydrogel viscoelasticity", *Journal of the Mechanical Behaviour of Biomedical Materials*, vol. 89, pp. 162-167, 2019

[5] J. H. Choi et al., "Evaluation of hyaluronic acid/agarose hydrogel for cartilage tissue engineering biomaterial", *Macromolecular Research*, vol. 28, pp. 979–985, 2020

[6] K. T. Campbell, K. Wysoczynski, D. J. Hadley, and E. A. Silva, "Computational-based design of hydrogels with predictable mesh properties", *ACS Biomaterial Science Engineering*, vol. 6, pp. 308 – 319, 2020

[7] A. Tirella, G. Mattei, and A. Ahluwalia, "Strain rate viscoelastic analysis of soft and highly hydrated biomaterials", *Journal of Biomedical Materials Part A*, vol. 102A, pp. 3352– 3360, 2014

[8] H. S. Lee, C..J. Matthews, R. D. Braddock, G. C. Sander, and F. Gandola, "A MATLAB method of lines template for transport equations", *Environmental Modelling and Software*, vol. 19, pp. 603-614, 2004

[9] A. Hajikhani, P. Wriggers, and M. Marino, "Chemo-mechanical modelling of swelling and crosslinking reaction kinetics in alginate hydrogels: A novel theory and its numerical implementation.", *Journal of the Mechanics and Physics of Solids*, vol. 153, 2021

Engineering of poly(urethane)-based porous constructs for cardiac tissue model design.

A. Alliaud[1,2], M. Boffito[1], R. Laurano[1], S. Sartori[1], and G. Ciardelli[1]
[1] *Politecnico di Torino, Department of Mechanical and Aerospace Engineering, Turin, Italy*
[2] *Università di Torino, Department of Surgical Sciences, Turin, Italy*

***Abstract*—Humans are continuously exposed to a wide variety of chemicals. Animal and bi-dimensional (2D) *in vitro* models currently represent the gold standard for chemical toxicity assessment, although they do not adequately reproduce the real human scenario, thus resulting in poorly predictive results. Conversely, three-dimensional (3D) bioengineered *in vitro* models hold the potential to closely represent the human physio-pathological milieu, enabling a more reliable evaluation of chemical toxicity. Among human tissues/organs, the myocardium is a target organ for chemical- and drug-induced toxicity. In this work, a custom-made poly(ester urethane) was synthesized and used as raw material to fabricate a platform of multi-layered structures with different geometrical features through melt extrusion additive manufacturing. The designed matrices were also surface functionalized with proteins to improve their biomimesis of the native cardiac extracellular matrix. The physico-chemical properties of the constructs proved their suitability for the development of *in vitro* bioengineered cardiac tissue models, enabling the investigation of physio-pathological processes and cardiotoxicity testing.**

***Keywords*—poly(urethane)s, *in vitro* cardiac tissue models, additive manufacturing, surface functionalization.**

I. INTRODUCTION

Drug development, chemical toxicity assessment, and disease modeling heavily rely on the use of animal models and two-dimensional *in vitro* models [1]. However, these models exhibit several drawbacks that make their outcomes poorly predictive of the real human scenario. Two-dimensional models are extremely simple and do not allow to replicate the complexity of human tissue structure [2]. Conversely, animal models present high management costs and ethical issues. Furthermore, due to interspecies differences, animal models are unlikely to faithfully replicate the human physio-pathological behavior. The concordance between toxicity levels evaluated in humans and laboratory animals is around 71% when both rodent (mice and rats) and non-rodent (dogs and monkeys) models are used. This concordance is reduced to 43% using only rodents as animal models [3].

The consequences of these issues are diverse and heterogeneous. The selection effectiveness of preclinical trials is reduced: only 11.8% of drugs entering clinical trials reaches approval. In addition, there are considerable cases of approved drugs showing undesirable toxic effects. For instance, during the last decade eight non-cardiovascular drugs have been reported to induce ventricular arrhythmia and sudden death, and thus they have been withdrawn from the market [4]. Furthermore, the proper and reliable assessment of the toxicity of chemicals and chemical mixtures is another key target to achieve, with important health, social and economic repercussions. Until 2008, only 5,000 chemicals out of 100,000 present on the western market had been subjected to an approved analysis process due to the limitations of two-dimensional and animal models [3].

In this complex scenario, the development of reliable 3D bioengineered *in vitro* models is of central importance since they can be very useful tools for overcoming the limitations of previously adopted approaches [5] [6]. In particular, the design of reliable 3D *in vitro* models of the cardiac tissue in gaining increasing interest in the research community. On the PubMed database the number of publications related to "cardiac tissue models" is exponentially increasing over time, with around 4000 publications in 2022. This trend can be correlated to the very high social and economic impact of heart diseases, that are responsible for around 17.5 million deaths worldwide each year [7]. Secondly, the high complexity of the cardiac tissue and the very limited possibility of modelling it with two-dimensional or animal models clearly prove the urgent need for reliable 3D bioengineered *in vitro* models of the cardiac tissue in different physio-pathological conditions and at different degrees of ageing [8].

Based on these premises, in this work, an *ad-hoc* synthesized poly(ester urethane) (PU) was microfabricated into 3D porous constructs by melt extrusion additive manufacturing and superficially modified with vacuum plasma treatment followed by immobilization of an extracellular matrix (ECM) protein (e.g., fibronectin, laminin) using the carbodiimide chemistry. Complete physico-chemical characterization of the developed constructs was performed, demonstrating the suitability of the designed matrices for the establishment of bioengineered cardiac tissue models.

II. MATERIALS AND METHODS

The PU used in this work to fabricate the 3D structures was synthesized using poly(ε-caprolactone) diol (2000 Da) as macrodiol, 1,4-butanediisocyanate as diisocyanate and L-lysine ethyl ester as chain extender [9]. The synthesis was performed under inert atmosphere through a two-step procedure according to an already optimized protocol [9]. The physico-chemical properties of the synthesized material were studied using infrared (IR) spectroscopy, size exclusion chromatography (SEC), and tensile tests. Rheological (dynamic temperature ramp tests, frequency sweep tests) characterization, differential scanning calorimetry (DSC) and thermogravimetric analysis (TGA) were also conducted to investigate the thermal and thermo-mechanical properties of the PU. A melt extrusion additive manufacturing (AM) system was employed to realize three-dimensional multi-layered structures with different patterns (e.g., square and rhomboid grid). A vacuum plasma treatment in the presence of acrylic acid vapor was then employed to superficially modify the

structures and expose carboxyl groups subsequently used to covalently decorate the surface of the scaffolds with ECM proteins (laminin, LN, fibronectin, FN) through the carbodiimide chemistry [13] [14]. Optical microscopy was employed to analyze the morphology of the structures. IR spectroscopy, X-ray photoelectron spectroscopy (XPS), contact angle measurements and colorimetric assays (e.g., toluidine blue assay, bicinchoninic acid assay) were used to characterize the surface chemistry of the scaffolds.

III. RESULTS

The synthesis procedure of the PU was successfully carried out. IR spectroscopy evidenced the appearance of the typical peaks of the newly formed urethane and urea bonds: at *ca.* 1630 cm^{-1} the stretching vibration of carbonyl groups, at 1535 cm^{-1} the concurrent C-N stretching and N-H bending vibrations, and at 3340 cm^{-1} N-H stretching vibration. SEC analyses revealed a number average molecular weight of around 70 kDa, with a polydispersity index of 1.4. The PU showed an elastic behavior (Young's Modulus around 10 MPa, strain at break of hundreds %) suitable for the engineering of *in vitro* models replicating the cardiac tissue. Rheological characterization coupled with DSC and TGA results demonstrated the suitability of the material for processing via melt extrusion additive manufacturing. Dynamic temperature ramp tests evidenced a transition from a rubbery towards a viscous behavior around 135 °C while DSC thermogram evidenced a complete melting of both soft and hard domains at *ca.* 140 °C. Frequency sweep tests evidenced a shear thinning behavior at these temperatures, which is useful for PU processing through melt extrusion AM. Furthermore, TGA highlighted that PU thermal degradation started at 230 °C, thus enabling polymer microfabrication within a wide range of temperature.

Multi-layered structures with different patterns were successfully fabricated (Fig. 1) with high resolution and good fidelity to the CAD models.



Fig. 1: Multi-layered structures with different patterns fabricated by melt extrusion additive manufacturing.

The scaffold fibers had a diameter of about 500 μm, Plasma surface modification and subsequent surface binding of LN or FN was validated with contact angle measurements (decrease in static contact angle from around 90° to 60°), spectroscopic analyses and colorimetric assays. The bicinchoninic acid assay confirmed the presence of a protein coating of 10-15 μg/scaffold. Tests with human induced pluripotent stem cell-derived cardiomyocytes are currently in progress. Preliminary data have showed good cell viability accompanied by cell adhesion to the polymeric structures.

IV. DISCUSSION

The search for adequate biomaterials and processing techniques is a fundamental step towards the development of three-dimensional cardiac models. Biomaterials not only perform a passive function of structural support for the cellular counterpart of the model, but directly influence cellular development with their chemical and mechanical properties [8]. Biomaterials can be of synthetic or natural origin. The main synthetic polymers studied in the cardiac tissue engineering field are poly(lactic acid), poly(glycolic acid), poly(lactic-co-glycolic acid) (PLGA), and poly(ε-caprolactone) (PCL). Particularly interesting polymers of natural origin are, for example, collagen, gelatin, fibronectin, alginate, fibrin, chitosan and hyaluronic acid [10]. Synthetic materials are cheap, easily processed and tunable in terms of mechanical and chemical properties, but they do not exhibit the biochemical features of the native ECM. Natural materials more faithfully reproduce the biochemical properties of the extracellular matrix, but they show high production costs, poor physico-chemical stability, inadequate mechanical properties, limited processability, and higher batch-to-batch variability. To integrate the characteristics and overcome the limits of both categories of materials, numerous bioartificial systems and functionalization procedures have been studied in the literature [11]. The manufacturing techniques of polymer scaffolds are numerous. The conventionally used techniques are difficult to control and do not allow to obtain structures with controlled properties. Examples of these techniques are induced phase separation, emulsion freeze-drying, particle leaching and solvent casting [10] [12]. In order to produce structures with more precise geometries, spinning and additive manufacturing techniques can be used. In particular, additive manufacturing allows the fabrication of complex three-dimensional structures with controlled geometry [7]. The main AM techniques are inkjet, laser and extrusion-assisted bioprinting and melt extrusion AM. These technologies present different advantages and disadvantages. Inkjet-based bioprinting allows to reach very high resolution (< 100 μm) and to combine different biomaterials. The main disadvantage is the low structural and mechanical stability of the constructs. Laser-assisted bioprinting is a nozzle-free technique enabling high cell viability. However, this system is very expensive and the size of the fabricated structures is small for clinical applications. Lastly, extrusion-assisted bioprinting is a versatile technology that could be used with a wide range of different biomaterials. It is also economic, but the resolution that can be achieved is quite low (> 100 μm) [7]. One of the

most important drawbacks of bioprinting relies in the limited mechanical properties of the printed structures, that should also exhibit proper features (e.g., gas/molecule exchange) allowing cell encapsulation within the filaments. Furthermore, the printing of large-size structures is very complicated [13].
The melt extrusion AM technique is based on the use of thermoplastic polymeric materials. These materials exhibit a wide variety of mechanical and chemical characteristics, which can be combined to control the characteristics of the printed structures. The printing process is extremely fast, economical and highly repeatable [14]. The main limitations are the impossibility of printing cells due to the high temperature and the thermoplastic nature of the printed materials, and low resolution. However, the thermoplastic polymeric structures could be used as support to realize large-size constructs and to overcome the stability deficiency of biomaterial inks and bioinks [15]. The cells can then be grown on the printed structures or inserted using bioinks placed inside the constructs [16] [15]. For instance, a elastomer composed of poly-[glycerol sebacate] and poly-[ε-caprolactone] was printed with melt extrusion AM technique to realize scaffolds for cardiac application. The scaffolds had Young's modulus very similar to native myocardium (≈1 MPa) and the size of the fibres was about 300 µm. *In vitro* tests with rat cardiomyocytes, H9c2, showed good cell viability after 72 h, while *in vivo* tests confirmed a positive impact of the scaffold on cardiac tissues [17]. In another study, a complex and large structure (62.4 mm × 62.4 mm × 21.3 mm) was realized using polyvinyl alcohol and a melt extrusion AM system. The structure was filled with a hydrogel containing rat cardiomyocytes, H9c2, and umbilical vein endothelial cells. The survival rate of the cells was about 90% after 14 d of cell culture.

Within this context and with the aim to further advance the current state of the art, in this work we designed 3D structures based on a custom-made PU as potential frameworks for 3D cardiac tissue model establishment. A polyurethane consisting of a thermoplastic polyester and an amino acid-derived chain extender was used to combine the processability characteristics of synthetic polymers with the bioactive features of natural materials. Furthermore, it presented suitable mechanical characteristics for the fabrication of porous constructs with Young's modulus matching the requirements for cardiac tissue engineering applications [10]. The melt extrusion AM technique was then used to fabricate PU-based porous structures, relying on its high reproducibility, simplicity and low costs. The fiber size was consistent with typical values of the melt extrusion AM technology. To improve the resolution of the fibers it is possible to modify the printing process parameters. Surface modification resulted in a functional protein coat for cellular tests. The study of the mechanical properties of the printed structures and tests with human induced pluripotent stem cell-derived cardiomyocytes are currently underway. The synthesized PU and the used AM process have manifested excellent characteristics for the realization of large sized cellularized constructs.

V. Conclusion

The customized polyurethane showed excellent mechanical characteristics, good processability through melt extrusion additive manufacturing technique and suitability for surface functionalization with proteins. The developed matrices could pave the way towards the design of *in vitro* bioengineered cardiac tissue replicas. Interestingly, the chemical and technological versatility of polyurethane biomaterials, additive manufacturing techniques and surface functionalization procedures could be exploited to finely tune the physico-chemical properties of the fabricated structs, enabling cardiac tissue modelling in different physio-pathological conditions and at different degrees of ageing. In the end, this would significantly advance our knowledge of the mechanisms underpinning ageing and pathology onset and progression, while providing reliable tools for cardiotoxicity testing.

Acknowledgement

This work was developed in the framework of the ALTERNATIVE project (https://alternative-project.eu/), which has received funding from the European Union's Horizon 2020 research and innovation programme under Grant Agreement No. 101037090. The content of this publication reflects only the author's view and the Commission is not responsible for any use that may be made of the information it contains.

References

[1] J. Wang, A. Khodabukus, L. Rao, K. Vandusen, N. Abutaleb, e N. Bursac, «Engineered skeletal muscles for disease modeling and drug discovery», *Biomaterials*, vol. 221, p. 119416, nov. 2019, doi: 10.1016/j.biomaterials.2019.119416.

[2] Y. Shao, J. Sang, e J. Fu, «On human pluripotent stem cell control: The rise of 3D bioengineering and mechanobiology», *Biomaterials*, vol. 52, pp. 26–43, giu. 2015, doi: 10.1016/j.biomaterials.2015.01.078.

[3] J. E. May, J. Xu, H. R. Morse, N. D. Avent, e C. Donaldson, «Toxicity testing: the search for an *in vitro* alternative to animal testing», *Br. J. Biomed. Sci.*, vol. 66, fasc. 3, pp. 160–165, gen. 2009, doi: 10.1080/09674845.2009.11730265.

[4] J. M. Miller *et al.*, «Biomimetic cardiac tissue culture model (CTCM) to emulate cardiac physiology and pathophysiology ex vivo», *Commun. Biol.*, vol. 5, fasc. 1, p. 934, set. 2022, doi: 10.1038/s42003-022-03919-3.

[5] K. Duval *et al.*, «Modeling Physiological Events in 2D vs. 3D Cell Culture», *Physiology*, vol. 32, fasc. 4, pp. 266–277, lug. 2017, doi: 10.1152/physiol.00036.2016.

[6] T. Eschenhagen, A. Eder, I. Vollert, e A. Hansen, «Physiological aspects of cardiac tissue engineering», *Am. J. Physiol.-Heart Circ. Physiol.*, vol. 303, fasc. 2, pp. H133–H143, lug. 2012, doi: 10.1152/ajpheart.00007.2012.

[7] T. Agarwal *et al.*, «Recent advances in bioprinting technologies for engineering cardiac tissue», *Mater. Sci. Eng. C*, vol. 124, p. 112057, mag. 2021, doi: 10.1016/j.msec.2021.112057.

[8] A. Mathur, Z. Ma, P. Loskill, S. Jeeawoody, e K. E. Healy, «In vitro cardiac tissue models: Current status and future prospects», *Adv. Drug Deliv. Rev.*, vol. 96, pp. 203–213, gen. 2016, doi: 10.1016/j.addr.2015.09.011.

[9] S. Sartori *et al.*, «Synthesis and structure–property relationship of polyester-urethanes and their evaluation for the regeneration of contractile tissues», *React. Funct. Polym.*, vol. 73, fasc. 10, pp. 1366–1376, ott. 2013, doi: 10.1016/j.reactfunctpolym.2013.01.006.

[10] C. V. C. Bouten, P. Y. W. Dankers, A. Driessen-Mol, S. Pedron, A. M. A. Brizard, e F. P. T. Baaijens, «Substrates for cardiovascular tissue engineering», *Adv. Drug Deliv. Rev.*, vol. 63, fasc. 4–5, pp. 221–241, apr. 2011, doi: 10.1016/j.addr.2011.01.007.

[11] A. Shapira, R. Feiner, e T. Dvir, «Composite biomaterial scaffolds for cardiac tissue engineering», *Int. Mater. Rev.*, vol. 61, fasc. 1, pp. 1–19, gen. 2016, doi: 10.1179/1743280415Y.0000000012.
[12] B. Zhang, Y. Xiao, A. Hsieh, N. Thavandiran, e M. Radisic, «Micro- and nanotechnology in cardiovascular tissue engineering», *Nanotechnology*, vol. 22, fasc. 49, p. 494003, dic. 2011, doi: 10.1088/0957-4484/22/49/494003.
[13] G. Gao, Y. Huang, A. F. Schilling, K. Hubbell, e X. Cui, «Organ Bioprinting: Are We There Yet?», *Adv. Healthc. Mater.*, vol. 7, fasc. 1, p. 1701018, gen. 2018, doi: 10.1002/adhm.201701018.
[14] F. Shalchy, C. Lovell, e A. Bhaskar, «Hierarchical porosity in additively manufactured bioengineering scaffolds: Fabrication & characterisation», *J. Mech. Behav. Biomed. Mater.*, vol. 110, p. 103968, ott. 2020, doi: 10.1016/j.jmbbm.2020.103968.
[15] Q. Zou *et al.*, «Biofabrication of valentine-shaped heart with a composite hydrogel and sacrificial material», *Mater. Sci. Eng. C*, vol. 108, p. 110205, mar. 2020, doi: 10.1016/j.msec.2019.110205.
[16] V. Chiono *et al.*, «Polyurethane-based scaffolds for myocardial tissue engineering», *Interface Focus*, vol. 4, fasc. 1, p. 20130045, feb. 2014, doi: 10.1098/rsfs.2013.0045.
[17] Y. Yang *et al.*, «Elastic 3D-Printed Hybrid Polymeric Scaffold Improves Cardiac Remodeling after Myocardial Infarction», *Adv. Healthc. Mater.*, vol. 8, fasc. 10, p. 1900065, mag. 2019, doi: 10.1002/adhm.201900065.

FRESH approach for the development of 3D channel network in 3D *in vitro* models

M. Pitton[1], C. Liguori[1], and S. Farè[2]
[1]*Department of Chemistry, Materials and Chemical Engineering, Politecnico di Milano, Milan, Italy*
[2]*National Interuniversity Consortium of Materials Science and Technology, Local Unit Politecnico di Milano, Milan, Italy*

***Abstract*—Freeform Reversible Embedding of Suspended Hydrogels (FRESH) printing technique is arising as a novel strategy to obtain a 3D channel network in 3D *in vitro* models, aiming to recapitulate human vascularization and tissues properties. In our work, we coupled a novel combination of Pluronic F127 (fugitive ink) and GelMA (supportive bath) to obtain and characterize vascularized hydrogel-based 3D models. By optimizing the FRESH printing of Pluronic into pre-crosslinked GelMA bath, we aimed to realize 3D *in vitro* models with an internal hollow channel which dimensions resulted comparable with human vasculature. Moreover, we obtained models whose physical, mechanical and biological features resembled properties of pathological breast cancer conditions.**

***Keywords*—FRESH printing, adipose tissue, vascularization, extracellular matrix.**

I. Introduction

HYDROGEL-BASED models recently gained attention to recapitulate *in vitro* physical, mechanical and biological properties of tissue extracellular matrix (ECM). Two-dimensional (2D) cell cultures were traditionally employed in drug discovery and validation process, and for investigating cell behaviour and tissue physiology. Anyway, 2D cell cultures cannot perfectly recapitulate *in vivo* conditions, exhibiting non physiological cell growth kinetics and attachment [1]. Hence, three-dimensional (3D) cell cultures arose as an ideal solution to better mimic cell-cell and cell-ECM interactions, offering cells a 3D space where they are able to adhere, grow, proliferate, and interact each other in a 3D microenvironment. Moreover, 3D-based models are under study to reproduce tumour microenvironment (TME) by mimicking hypoxic and nutrient deprivation conditions, which typically appear in cancer progression [1]. Pathological models claimed to better understand disease development and offered versatile platforms to test new drugs and treatments. 3D-based models are produced using hydrogels, bulk scaffolds, decellularized tissues, to realize an ideal 3D environment for cell cultures. Among all the possible biomaterials, natural hydrogels were largely investigated for 3D models, due to their high porosity, hydrated nature, excellent biocompatibility, biochemical and biophysical tunability [1].

Nevertheless, lack of vascularization in 3D models represents nowadays the main limitation in the obtainment of suitable constructs for tissues mimicking. Among all the applied strategies to overcome latter drawback, Freeform Reversible Embedding of Suspended Hydrogels (FRESH) printing technique is arising as a novel technique to directly print a vasculature network in a supportive bath [2]. For this purpose, the selected supportive material should exploit an ideal viscosity to allow nozzle movement and subsequent printing in the bath, ensuring the maintenance of the printed structure integrity at the same time. The supportive bath was traditionally realized in gelatin or Carbopol [2], both sacrificial materials which dissolved once the 3D structure has been printed into the hydrogel. Alternatively, a fugitive ink could be printed in a permanent supportive bath [3], as we performed in our work. Herein, we optimized a FRESH printing approach for the printing of a sacrificial material in a permanent supportive bath, aiming to obtain a hollow internal channel resembling human vasculature into the permanent hydrogel (i.e., scaffold). Indeed, FRESH approach has never been reported for 3D *in vitro* models vascularization, while a permanent supportive bath which exploited favourable rheological properties for FRESH printing and resembled human tissues features has never been described in literature. For this purpose, we selected Pluronic F127 as sacrificial material to print a channel network, while methacrylated gelatin (GelMA) acted as permanent bath mimicking adipose tissue (AT) properties. FRESH printing approach was optimized by investigating rheological properties of sacrificial ink and supportive bath, which was pre-crosslinked at different exposure times to increase its viscosity allowing accurate extrusion of Pluronic. Once the FRESH printing of the channel network was optimized, the 3D model was characterized in physical, mechanical and biological terms, by assessing preadipocytes growth, proliferation and differentiation into mature adipocytes in the model. Moreover, endothelial cells were perfused into the obtained channel network.

II. Materials and Methods

A. Supportive GelMA bath and Pluronic F127 fugitive ink

GelMA was synthetized by following a procedure described elsewhere [4]. Briefly, gelatin (Gel) type A was fully dissolved in Dulbecco's Phosphate Buffered Saline (DPBS) at 50 °C (10% w/V), and methacrylation was carried out by dropwise addition of methacrylic anhydride (MA). The polymeric mixture was then dialyzed and freeze-dried. Degree of methacrylation (DoF) was evaluated by H-NMR spectroscopy (Bruker ARX 400 Instrument). Obtained GelMA was employed as permanent supportive bath; hence, GelMA hydrogels were obtained by dissolution in DPBS (10% w/V), addition of 2-hydroxy-4'-(2-hydroxyethoxy)-2-methylpropiophenone, Irgacure 2959 (0.05% v/V), and subsequent pre-crosslinking with UV light (TissueStart UV light, $\lambda = 405$ nm) exposure for 60, 90, 120 and 150 s. Different exposure times were investigated to increase GelMA viscosity which should be comparable to the ink one. Pluronic F127 was

fully dissolved in distilled water at 4 °C (23% w//V), and fugitive ink was obtained.

B. Rheological characterization

Rheological properties of the selected materials were investigated by using a rotational rheometer (Anton Paar GmbH, Austria), equipped with parallel plates and cone-plate (25 mm) geometry, respectively for GelMA and Pluronic F127. Strain (0.01-100%), temperature (4-50 °C) and shear rate (0.1-1000 s^{-1}) sweep tests were performed on both materials, to assess their transition temperature and viscosity. Moreover, thixotropy tests were carried out on GelMA hydrogels (0.1 s^{-1} for 120 s, 100 s^{-1} for 100 s, 0.1 s^{-1} for 300 s). Rotational properties of GelMA were modelled Herschel-Bulkley model (Eq. (1)) [5]:

$$\sigma = \sigma_y + K\dot{\gamma}^n \quad (1)$$

where σ = total stress, σ_y = yield stress, $\dot{\gamma}$ = shear rate, K and n are fitting parameters.

C. Pluronic F127 printing parameters optimization

Channel network template was designed (SolidWorks 2020) and printed (TissueStart, TissueLab, CH) in planar platform. The template geometry was a serpentine model, characterized by 6 sides (L,l), where L = 8.50 mm, l = 1.70 mm, α (L,l) = 90°. Different printing parameters were investigated to assess printing accuracy: extrusion multiplier (EM) = 0.4-0.8, velocity = 8-12 mm s^{-1}, flow = 300%. Then, printing parameters were investigated in the GelMA supportive bath for embedded 3D printing optimization: EM = 1-6, velocity = 3-8 mm s^{-1}, flow = 300-800%. All the printing tests were performed at 25 °C.

D. 3D in vitro models characterization

Channel network template was printed in the supportive bath which was pre-crosslinked as previously described. Then, GelMA/Pluronic samples were photocrosslinked by UV rays exposure (OSRAM Ultra Vitalux, 150 s). Obtained structures were immersed in deionized water (24 h, 37 °C) allowing Pluronic leaching and obtaining an opened internal channel. GelMA structures with channels (GelMA_ch) were characterized and compared to bulk GelMA samples (GelMA).

Channel morphology was analyzed with an optical stereomicroscope (Leica) by acquiring images before and after manually perfusion of the samples (n = 3). Then, models stability in physiological-like environment (distilled water, 37 °C) was evaluated considering the percentage weight variation ($\Delta W\%$) up to 4 weeks (GelMA_ch vs GelMA), by applying formula reported in Eq. (2):

$$\Delta W\% = \frac{w_t - w_0}{w_0} * 100 \quad (2)$$

where w_t = weight at the scheduled time point, w_0 = weight prior to water immersion.

Compressive mechanical properties were evaluated by testing hydrated samples (n = 3) with a Dynamic Mechanical Analyzer (DMA Q800, TA Instruments) at 37 °C. Briefly, a load phase was carried out by applying a strain ramp down to -30% strain at 2.5% min^{-1} rate, followed by an unload phase at 5% min^{-1} rate up to 1% strain.

E. In vitro biological tests

Cytocompatibility tests were performed by encapsulating 3T3-L1 preadipocytes (1×10^6 cells mL^{-1}) in GelMA solution prior to UV pre-crosslinking and Pluronic FRESH printing. AlamarBlue assay was performed up to 14 days to evaluate cells metabolic activity in terms of Relative Fluorescence Unit (RFU) (n = 3), as in Eq. (3):

$$RFU = f_{sample} - f_{control} \quad (3)$$

where f_{sample} = cell-laden sample fluorescence, $f_{control}$ = control sample fluorescence.

Live/Dead staining (1 µM calcein-AM, 10 µM propidium iodide) was carried out to qualitatively observe cells distribution in the cell-laden hydrogel (GelMA_ch vs GelMA). Moreover, model suitability as a 3D *in vitro* model of AT was assessed by testing the encapsulated preadipocytes ability in differentiating into mature adipocytes. For this purpose, cell-laden samples (n = 3, GelMA_ch vs GelMA) were prepared and cultured for 24 h (37 °C, 5% CO_2) in complete growth medium (Dulbecco's Modified Eagle Medium, DMEM, added with 10% bovine foetal serum, 1% penicillin-streptomycin P/S, 1 mM sodium pyruvate PyR, 10 mM 4-(2-hydroxyethyl)-1-piperazine ethane sulfonic acid HEPES, 4 mM L-glutamine Glut). Then, growth medium was replaced by differentiating medium (growth medium added with 0.5 mM 3-isobutyl-1-methylxanthine IBMX, 1.0 µM dexamethasone, 2.0 µM rosiglitazone, 10 µg mL^{-1} insulin) and, after 48 h of incubation, the medium was substituted by maintenance medium (growth medium added with 10 µg mL^{-1} insulin). Metabolic functionality was qualitatively evaluated by NileRed staining (1 mg mL^{-1} NileRed stock solution), which stained intracellular lipidic droplets accumulated into mature adipocytes. Finally, preadipocytes and endothelial cells (EA.hy 926) were co-cultured up to 7 days, by embedding 3T3-L1 into GelMA and by injecting EA.hy 926 into the hollow channel. After 7 days of co-culture, cell growth of co-cultured cells was evaluated by Live/Dead staining.

III. Results and Discussion

A. GelMA and Pluronic F127 preparation

GelMA methacrylation was successfully verified by H NMR spectra acquisition. Briefly, samples of Gel and GelMA, dissolved in deuterium oxide (2% w/V), were analyzed by spectroscopy and obtained spectra were processed with Mestrenova software. DoF was calculated as the percentage of the amino groups (i.e., lysine, hydroxylysine) which resulted properly modified in synthetized GelMA macromers [6] and resulted approximately equal to 40.42%.

B. Rheological properties

Pluronic F127 exhibited a gel-like behaviour (G' > G'') at shear strain lower than 1%, while its gelation temperature was detected at 23 °C. For this finding, the printing temperature was set at 25 °C, above Pluronic 3D sol-gel transition. GelMA rheological behaviour was investigated towards thixotropy tests, as supportive bath should promote nozzle movement during the printing and restore its initial morphology after the printing process. This test claimed to establish the speed recovery of the supportive bath material after exposure to shear

rate [7]. As regard, GelMA should exploit an elastic behaviour in rest condition, and act as a liquid-like material when a sufficient shear rate (i.e., yield stress) is applied. GelMA recovered approximately 60% of its initial viscosity, exploiting a recovery time of 38.70 s. Although its recovery time resulted higher than values reported in literature for supportive bath in agarose (0.89 s) or Carbopol (1.42 s) [7], its ability in maintaining the morphology of the internal printed structure was enforced by post-printing photocrosslinking.

Additionally, we evaluated the viscosity kinetic of both materials once exposed to shear rate ramp (Fig. (1)). Both materials should contemporarily exhibit a comparable viscosity to accommodate nozzle movement and print a more precise internal 3D structure [8]. Different exposure times for GelMA pre-crosslinking were tested, and 120 s was selected as the most suitable exposure time to ensure a comparable viscosity between ink (i.e., during the printing) and bath (i.e., static conditions). Yield stress value of the supportive bath (σ_y = 0.29 Pa) perfectly fell in the range reported in literature for FRESH printing approach (0.16-8.80 Pa) [8].

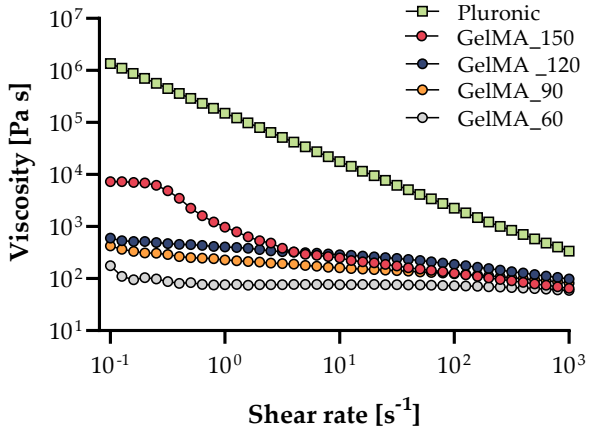


Fig. 1: viscosity curves of Pluronic F127 (square) and pre-crosslinked GelMA for 60 (gray), 90 (orange), 120 (blue), 150 (red) s. 120 s was chosen as the best exposure time since GelMA resulted in comparable viscosity in rest conditions to the one of Pluronic at high shear rates.

C. *FRESH printing parameters definition*

Optimal printing parameters for FRESH printing of Pluronic F127 were selected by starting from printing a serpentine geometry: v = 10 mm s^{-1}, EM = 0.6, flow = 300%. Printing of Pluronic F127 in the GelMA supportive bath required higher EM and flow, compared to Pluronic alone. Contrarily, printing speed should be decreased, to enhance printing process success. For this purpose, optimized parameters for FRESH printing were reported in Table I.

TABLE I: OPTIMIZED PARAMETERS FOR FRESH PRINTING OF PLURONIC

Printing parameters	*Value*	*Unit of measurement*
Printing speed	6	mm s^{-1}
Extrusion multiplier	4	-
Flow	400	%
Needle gauge	25	G
Extruder temperature	25	°C

D. *3D in vitro model properties*

Once Pluronic F127 was printed towards FRESH printing in GelMA supportive bath, images of the obtained internal channel were acquired by optical stereomicroscope. As regard, cross-section of the sample showed the successful obtainment of the channel, which diameter ranged (400-900 µm) in values reported in literature for vascular-like structures FRESH printed with Pluronic F127 [3]. Moreover, 3D printed channel diameter resulted comparable with human arteries diameters (0.1-10 mm). Latter finding enlightened the consistency of our work, aiming to mimic a microenvironment as close as possible with physiological one. Preliminary perfusion tests strengthened the feasibility of the model, as dye solution, which was manually injected, gradually flew towards the obtained channel (Fig. (2)).



Fig. 2: perfusion tests performed on vascularized 3D models by manually injecting colouring solution (scale bar: 5 mm)

Stability of 3D *in vitro* vascularized models was investigated by weight loss kinetic evaluation. GelMA_ch structures lost 45% of their initial weight due to the release of uncrosslinked gelatin chains and the dissolution of the Pluronic F127 ink.

Mechanical compressive tests were performed on 3D models to assess their suitability in fully recapitulate AT properties (Table II).

TABLE II: MECHANICAL COMPRESSIVE PARAMETERS (AVERAGE VALUE ± STANDARD DEVIATION)

Printing parameters	*GelMA_ch*	*GelMA*
Elastic modulus (kPa)	8.57 ± 2.01	10.45 ± 0.79
Stiffness (kPa)	33.94 ± 4.94	32.73 ± 8.95
Maximum stress (kPa)	6.31 ± 1.48	5.90 ± 1.71
Residual strain (%)	4.90 ± 0.20	5.50 ± 2.30
Hysteresis area (J dm^{-3})	0.13 ± 0.03	0.13 ± 0.02

Statistical differences between obtained values were not found ($p > 0.05$), enlightening how the FRESH printing process did not affect the mechanical features of the GelMA_ch. Moreover, 3D *in vitro* models exploited an elastic modulus comparable to the range reported in literature for AT in pathological conditions [9], depending on the progression state of the cancer disease. As regard, insurgence of benignant fibroadenoma express an elastic modulus equal to 6.41 kPa, while elastic modulus of low grade invasive ductal carcinoma (IDC) and ductal carcinoma *in situ* (DCS) resulted equal to 10.40 and 16.38 kPa, respectively, as reported in Fig. (3). Both latter conditions are referred to breast cancer, which determined an increase in AT stiffness [9]. This finding resulted highly interesting for our work, as the supportive bath should accommodate nozzle movement during the printing by restoring its initial conformation and should recapitulate

mechanical properties of physiological/pathological AT.

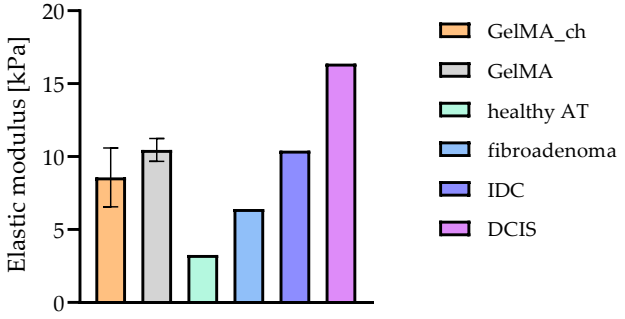


Fig. 3: Comparison between elastic modulus (kPa) of GelMA_ch and GelMA samples with healthy AT, fibroadenoma and early stages breast cancer conditions (i.e., IDC, DCIS) [9]

E. In vitro biological properties

Metabolic activity of encapsulated preadipocytes increased ($p < 0.05$) from day 1 up to day 14 of cell culture, enlightening how 3D *in vitro* models recreated a favourable microenvironment for cells proliferation. In particular, RFU values resulted higher ($p < 0.05$) for GelMA_ch than GelMA bulk samples at day 1 and 14, showing the effectiveness of the obtained internal hollow channel in promoting nutrients, oxygen and metabolites diffusion from the external to the internal environment of the sample. Live/Dead staining allowed to qualitatively evaluate the cells distribution into the samples, strengthening the importance of the internal hollow channel also in influencing cells proliferation. As regard, preadipocytes resulted highly active and closer to the internal hollow channel walls, where a possible higher exchange of gas and nutrients can be present (Fig. (4)). Contrarily, bulk GelMA samples resulted more homogeneously colonized in the whole scaffold volume than GelMA_ch hydrogels.

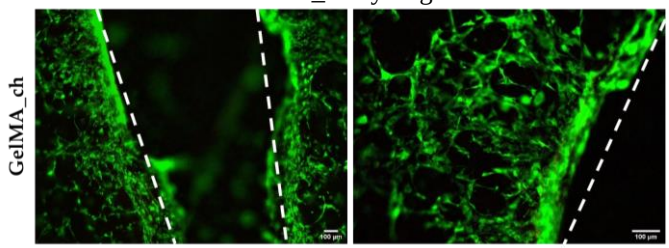


Fig. 4: Live/Dead staining of encapsulated 3T3-L1 in GelMA_ch samples (scale bar: 100 µm)

Moreover, suitability of GelMA_ch samples in recapitulating AT features was successfully verified by investigating the ability of encapsulated preadipocytes in differentiating into mature adipocytes. For this purpose, preadipocytes were cultured in proper conditions for the differentiation. After 14 days of culture, differentiated and undifferentiated samples were stained by NileRed staining, to qualitatively enlighten the accumulation of intracellular lipidic droplets into mature adipocytes. A higher amount of lipidic droplets qualitatively accumulated into cultured cells in GelMA_ch, and this finding claimed how developed vascularized 3D models worked as a versatile *in vitro* platform for preadipocytes which remained metabolically active in exploiting all their physiological functions.

Once GelMA supportive bath was investigated in preadipocytes proliferation and differentiation, a co-culture with EA.hy926 endothelial cells was tested. After 7 days of co-culture, Live/Dead staining qualitatively showed that endothelial cells resulted active and well attached to the walls of the internal hollow channel, showing a more elongated morphology ($p < 0.05$) during time. Cell morphology was analyzed by ImageJ software, comparing the endothelial cells diameter between day 1 and day 7 of co-culture, enlightening how endothelial cells assumed a typical flat morphology due to the attachment to RGD motifs of GelMA polymeric chains.

IV. Conclusion

3D *in vitro* models were realized aiming to recapitulate the AT ECM. For this purpose, we successfully optimized the FRESH printing technique by carefully characterizing in terms of rheological properties both the fugitive ink of Pluronic F127 and the supportive bath of GelMA. Findings from the characterization enlightened how the developed 3D models resulted suitable for mimicking AT ECM, as preadipocytes 3T3-L1 proliferated and differentiated once cultured in GelMA, while endothelial cells tended to colonize the internal walls of the hollow channel. Future perspectives could be directed in better investigating AT pathologies, since our model showed mechanical properties close to IDC and DCIS.

References

[1] K. Unnikrishnan, L. V. Thomas, e R. M. Ram Kumar, «Advancement of Scaffold-Based 3D Cellular Models in Cancer Tissue Engineering: An Update», *Front. Oncol.*, vol. 11, p. 733652, ott. 2021.

[2] D. J. Shiwarski, A. R. Hudson, J. W. Tashman, e A. W. Feinberg, «Emergence of FRESH 3D printing as a platform for advanced tissue biofabrication», *APL Bioeng.*, vol. 5, fasc. 1, p. 010904, mar. 2021.

[3] W. Wu, A. DeConinck, e J. A. Lewis, «Omnidirectional Printing of 3D Microvascular Networks», *Adv. Mater.*, vol. 23, fasc. 24, pp. H178–H183, giu. 2011.

[4] M. Sun, X. Sun, Z. Wang, S. Guo, G. Yu, e H. Yang, «Synthesis and Properties of Gelatin Methacryloyl (GelMA) Hydrogels and Their Recent Applications in Load-Bearing Tissue», *Polymers*, vol. 10, fasc. 11, p. 1290, nov. 2018.

[5] A. F. Bonatti, I. Chiesa, G. Vozzi, e C. De Maria, «Open-source CAD-CAM simulator of the extrusion-based bioprinting process», *Bioprinting*, vol. 24, p. e00172, dic. 2021.

[6] C. Claaßen *et al.*, «Quantification of Substitution of Gelatin Methacryloyl: Best Practice and Current Pitfalls», *Biomacromolecules*, vol. 19, fasc. 1, pp. 42–52, gen. 2018.

[7] M. E. Prendergast e J. A. Burdick, «Computational Modeling and Experimental Characterization of Extrusion Printing into Suspension Baths», *Adv. Healthc. Mater.*, vol. 11, fasc. 7, p. 2101679, apr. 2022.

[8] A. M. Compaan, K. Song, W. Chai, e Y. Huang, «Cross-Linkable Microgel Composite Matrix Bath for Embedded Bioprinting of Perfusable Tissue Constructs and Sculpting of Solid Objects», *ACS Appl. Mater. Interfaces*, vol. 12, fasc. 7, pp. 7855–7868, feb. 2020.

[9] A. Samani, J. Zubovits, e D. Plewes, «Elastic moduli of normal and pathological human breast tissues: an inversion-technique-based investigation of 169 samples», *Phys. Med. Biol.*, vol. 52, fasc. 6, pp. 1565–1576, mar. 2007.

Mathematical model of nutrients transport and cell growth in a bioprinted hydrogel

I. Parodi[1], S. Scaglione[2], M.M. Fato[1] and R. Repetto[3]
[1] *Department of Informatics, Bioengineering, Robotics, System Engineering (DIBRIS), University of Genoa, Genoa, Italy*
[2] *Institute of Electronics, Computer and Telecommunications (IEIIT), National Research Council of Italy, Genoa, Italy*
[3] *Department of Civil, Chemical and Environmental Engineering (DICCA), University of Genoa, Genoa, Italy*

***Abstract*—A proper oxygenation and nutrients substances supply such as glucose are crucial in 3D *in-vitro* models. In most cases, hydrogel-based scaffolds are employed as culture systems. 3D bioprinting allows uniform cell distribution and to create complex structures in high reproducible manner. However, the diffusion of molecules be difficult in the innermost areas of the scaffolds and the presence of gradients could impact on cell proliferation. Hence, the mathematical modelling of the transport of oxygen and other nutrients as well as their consumption by the expanding cell culture withing the scaffold, can be useful to optimize the tissue construct properties, for generating more predictive and robust outcomes.**

***Keywords*—Mathematical modelling, Homogenization, Tissue engineering, Hydrogels**

I. Introduction

Three-dimensional (3D) in-vitro models are fundamental tools in tissue engineering and drug discovery. Differently from two-dimensional (2D) systems, where cells grow in an unnatural spatial environment, characterized by a uniform exposure to culture medium and gas supply, in 3D cultures, cells have different access to nutrients, in a way strictly dependent on the size of the *in-vitro* model [1].

In general, cells close to the medium are exposed to high levels of oxygen, while those further away perceive lower levels. Additionally, their behavior is drastically affected by the chemical/topological/biomechanical conditioning provided by the artificial 3D extracellular matrix [2]. In particular, cancer cells exposure to hypoxic conditions activates, through the hypoxia-inducible factor (HIF-1α) expression, several target genes related to angiogenesis, extracellular matrix remodeling and metabolic adaptation (Warburg effect) and finally metastatic progression. All these internal variations make chemotherapeutic agents inefficient and fail on hypoxic cells [3], [4]. For these reasons, there is a growing need to develop research tools capable of reproducing the complexity of a tumor microenvironment (TME), including physiologically relevant oxygen conditions, to better understand drug resistance, ensuring an in-vivo like cell response, and eventually allowing one to test novel, more effective therapies.

To this purpose, 3D bioprinting is a particularly promising technique because it allows to produce hydrogels characterized by a high spatial control of the tissue model, also encapsulating different cell types, thus more accurately mimicking the complexity of the TME [5]. Furthermore, 3D bioprinting offers the possibility of tuning the physical and mechanical properties of biomaterials through a specific crosslinking method [6] or by modulating parameters such as printing speed, pressure and temperature during the printing process [7], [8].

As previously discussed, the diffusion of oxygen and nutrients such as glucose plays a key role in 3D culture. However, this can be difficult in the innermost parts of the hydrogel, due to various factors such as the large size of the structure. Therefore, it is of great importance to model at a mathematical level the diffusion of gases, nutrients and their consumption by proliferating cells inside the scaffold, with the fundamental aim of avoiding anoxic conditions. In case of healthy cells, it is fundamental to maintain the oxygen level above a critical value, the hypoxic threshold. For tumor cells, it is interesting to study cell behavior both in oxygenated and hypoxic conditions.

In this perspective a synergic approach based on computational modelling and experimental validation can be useful to optimize the tissue construct properties, for generating more predictive and robust outcomes. Several mathematical models have been developed using continuum and discrete approaches to capture the dynamics of cell proliferation. Considering the oxygen as the main nutrient, Obradovic *et al*. [9] showed the development of spatial tissue cell density heterogeneities in scaffolds, modelling oxygen consumption with Michaelis-Menten kinetics. The study conducted by Lewis *et al*. [10] about the interaction between oxygen and cell distributions in static cultures proved that the lack of perfusion produces high proliferative regions near the border of the construct, where the oxygen level is higher. Shakeel *et al*. [11] developed a continuous mathematical model of cell proliferation and nutrient transport in a perfused bioreactor, considering the time variation in scaffold porosity induced by cell culture evolution and the effect of shear stress on nutrient consumption and cell proliferation. This last model can be easily adapted for a static culture by excluding perfusion advection terms. Recently, Mendoza-Juez *et al*. [12] described the growth and phenotype switching of two populations of oxidative and glycolytic tumor cells. Despite the predictions of this mathematical model being in good agreement with different cancer cell lines, the spatial variability of nutrients has not been considered, limiting the validity of the study to two-dimensional culture systems.

The present study aims at investigating the spatial and temporal variability of oxygen and glucose within an alginate-based hydrogel, finding the critical thickness which guarantees an oxygen level above the hypoxic threshold for the entire height of the scaffold and for the entire duration of a cell culture. To this purpose an *in-silico* model was implemented in COMSOL Multiphysics. The most innovative part of our

study concerns a mathematical procedure called homogenization, allowing to macroscopically analyze the behavior of a hydrogel with a heterogeneous and porous microstructure. Therefore, firstly, homogenization theory [13] was applied to estimate the diffusion coefficient of the two nutrients within a porous and heterogeneous scaffold. Then, a time-dependent study was performed to predict oxygen transport/consumption and time evolution of cell density and the nutrients concentrations.

II. MATERIALS AND METHODS

A. Application of homogenization theory

Considering the extrusion bioprinting technique, a scaffold with a cross-fiber microstructure was chosen. The transport of nutrients within the construct takes place both inside the polymeric material and in the culture medium that not only surrounds the hydrogel but also fills the hydrogel pores.

To conduct simpler computational analysis, homogenization theory was applied, following the approach by Mei *et al.* [13], based on the use of multiples scale asymptotic expansions. This mathematical method allows one to replace a heterogeneous material with a homogeneous fictitious material whose overall characteristics are macroscopically equivalent to those of the original material. A representative volume element (RVE) Ω composed of two different materials is considered, where Ω_a e Ω_b are respectively the volumes occupied by the hydrogel and the culture medium. For generality, each component material is nonhomogeneous and anisotropic.

Solution of an appropriate set of PDEs on the RVE subject to periodic boundary conditions leads to the determination of the components of the diffusivity tensor $\boldsymbol{D}_{\alpha,}$ which described the diffusion properties of the homogenized material. This implies that with this approach it is possible to reproduce the transport properties of materials that are not isotropic, as they might contain fibers that have a preferential direction. It is important to note that the effective diffusivity is not simply the volume average of the diffusivities of the two materials.

In the case of interest, a bioprinted fibrous scaffold has been considered. For the application of the homogenization theory, the Weak Form PDE module in COMSOL Multiphysics was employed. The problem was solved on a parallelepipedal RVE, which represents the culture medium unit cell, including two crossed layered cylinders, which represent the hydrogel fibers.

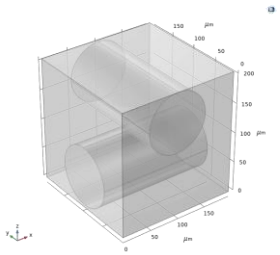


Fig. 1: Representative volume element (RVE) of the alginate fibrous scaffold with a porosity of 60%

The fibers diameter was set to 100 µm, in agreement with the minimum nozzle diameter of the available bioprinter, while it was chosen to vary the porosity in the range 30-90%. The height of the parallelepiped is slightly more than twice the diameter, while the base side is obtained through a simple calculation, as a function of the porosity.

Starting from literature data, the oxygen and the glucose homogenized diffusion coefficients through the alginate scaffold were obtained [14] – [17].

B. Nutrient transport and cell growth modelling

Subsequently, the evolution of a static cell culture inside the hydrogel previously described has been studied through development and implementation in COMSOL of a continuous mathematical model of transport/consumption of oxygen and glucose and cell proliferation. The whole static culture system consists in the culture medium domain Ω_m and the hydrogel one Ω_h. The scaffold, having a radius of 2.5 mm, is put in a 24 multi-well plate and covered by 250 µl of culture medium. An axisymmetric geometry allows to simplify the calculations. In the actual model, the following assumptions have been made:

- the deformation of the scaffold due to its biodegradation and due to the deposition of the extracellular matrix by the cells is neglected
- oxygen at the top surface of the medium is constant and it is the only element on which cell growth depends, since the efficiency of aerobic energy production is higher than the anaerobic glycolysis, despite the upregulated consumption of glucose [18]
- the nutrient consumption is linear in the nutrient concentration and cell density
- the doubling time of the cells is about of 5 days at least in the external and more oxygenated part of the construct

In static culture, nutrients surround the scaffold and don't flow. Therefore, in the culture medium domain nutrients are transported by diffusion, as described in Eq (2) and (3). D_{sm} and D_{gm} are the diffusive coefficient of oxygen and glucose in the culture medium.

$$\frac{ds}{dt} = -\nabla \cdot (-D_{sm}\nabla s) \qquad (2)$$

$$\frac{dg}{dt} = -\nabla \cdot (-D_{gm}\nabla g) \qquad (3)$$

In the hydrogel domain, also nutrients consumption and cell growth take place. D_{sh} and D_{gh} represent the homogenized diffusive coefficient previously obtained. α_s and α_g are multiplicative coefficients related to the single breast cancer cell oxygen consumption rate and glucose consumption rate [19], [20]. The dynamics of cancer cells density n [1/m^3] is given by a term which represented the effect of random movements and a logistic proliferation term, as shown in Eq. (6). The parameter β is related to the growth rate of the cell population, while D_n is the coefficient of diffusion of the cells [11].

$$\frac{ds}{dt} = -\nabla \cdot (-D_{sh}\nabla s) - \alpha_s sn \qquad (4)$$

$$\frac{dg}{dt} = -\nabla \cdot (-D_{gm}\nabla g) - \alpha_g g n \quad (5)$$

$$\frac{dn}{dt} = -\nabla \cdot (-D_n \nabla n) + \beta(s - s_{min})n\left(1 - \frac{n}{n_{max}}\right) \quad (6)$$

It has been hypothesized that the cells cannot migrate out of the hydrogel, thus a condition of zero-flux at the scaffold boundary has been fixed, while as regards the nutrients a continuity condition has been applied at the interface between the two domains.

In this first model, a normoxic cancer cell culture has been studied for 6 days. To this purpose, a hypoxic threshold s_{min} of 0.04 mM has been established, under which the cell culture exhibits a metabolic alteration. Moreover, the initial cell density was set to 10^{13} cell/m^3, while a maximum cell density of $2\text{x}10^{14}$ cell/m^3 has been estimated. The initial concentration of oxygen and glucose within the hydrogel and the medium were set to 0.2 mM and 25 mM. It is important to highlight the complete change of culture medium was simulated at day 3, refreshing the initial condition of glucose.

III. Results

A diffusivity matrix was obtained and the elements on the diagonal were considered (D_{11}, D_{22}, D_{33}), which respectively represent the diffusive coefficients in the *x*, *y* and *z* directions. The results achieved from the application of the homogenization theory show that, as porosity increases, the coefficient of the homogenized material assumes values close to that of the culture medium. On the contrary, by decreasing the porosity, the coefficient is reasonably more like that of hydrogel. Moreover, D_{11} and D_{22} are identical, owing to the symmetry of the microcell, while D_{33} is slightly lower, indicating a more limited diffusion along the vertical axis. In Fig. 2 oxygen diffusivity through the homogenized structure is shown.

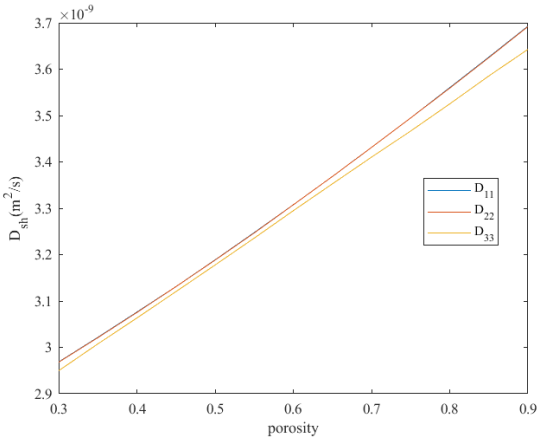


Fig. 2: Oxygen homogenized diffusive coefficient in alginate fibers vs hydrogel microstructure porosity

Results related to nutrients concentration and cell density during a 6 days *in-vitro* culture have been calculated using the values of the diffusion tensor computed with the homogenization approach. As shown in Fig. 3, within the hydrogel, an oxygen gradient is produced. According to the implemented *in-silico* model, the maximum height required to ensure a normoxic microenvironment for breast cancer cells is 350 µm. In particular, according to this model, the minimum level of oxygen above hypoxia is reached in the bottom core of the scaffold in a relatively short time, of the order of ten minutes (data not shown) and maintained for all the days of *in-vitro* culture (Fig. 4). It is also possible to note a great difference of oxygen tension between the outer zone of the hydrogel and the internal one. More specifically, in the bottom core, an oxygen reduction of the 80% is observed.

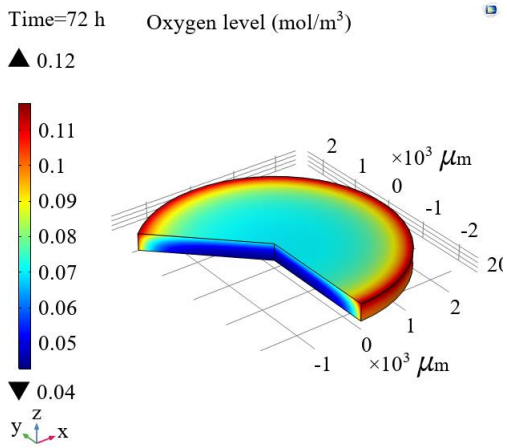


Fig. 3: Oxygen concentration in the homogenized scaffold at day 3

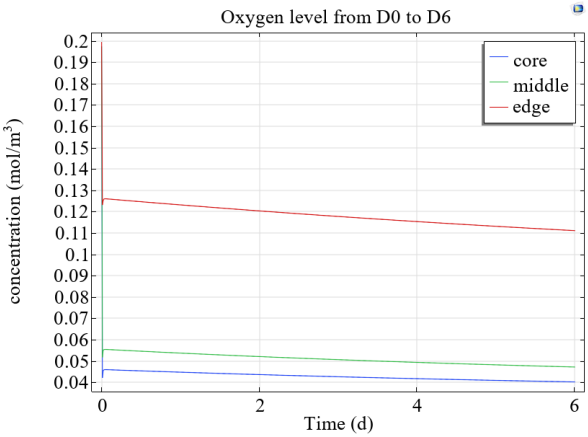


Fig.4: Oxygen profile during in vitro culture

This discrepancy is also observable in the cell growth profile, where there is a greater proliferation in the top outer edge of the hydrogel. This is because it has been hypothesized that cell growth depends only on oxygen, even though cells also consume glucose. As shown in Fig. 5, the cell density duplicates at day 5. Therefore, a more oxygenated zone leads to a more proliferative cell behavior.

In contrast, glucose does not exhibit a great gradient in the different zones of the scaffold. In fact, Figure 6 displays three almost overlapping trends. The refresh of culture medium is simulated at day 3, immediately after reaching a level of just over 80%, compared to the initial condition. Starting again from a concentration of 25 mM, at day 6 a lower glucose level is reached than at day 3, due to a greater number of cells present in the hydrogel.

However, the concentration of the different nutrients should

be experimentally monitored with sensors and/or chemical kits to validate the mathematical model.

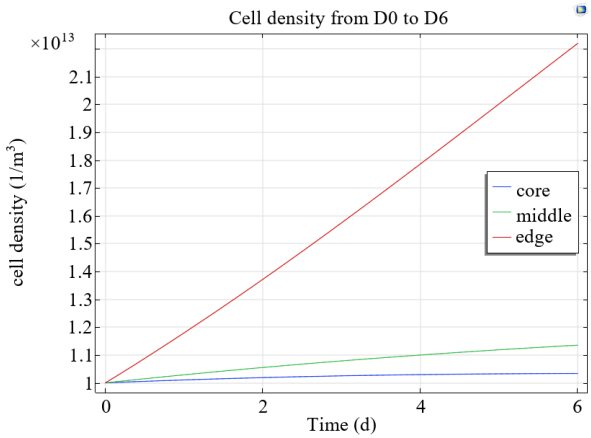


Fig. 5: Cell growth profile during in vitro culture

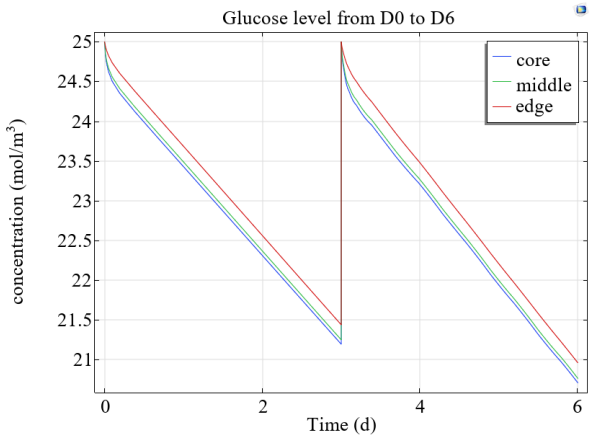


Fig. 6: Glucose profile during in vitro culture

IV. CONCLUSION AND PERSPECTIVE

In this study a mathematical model for nutrient transport and cell growth in a homogenized fibrous hydrogel was discussed. The homogenization represents a powerful tool to simplify heterogeneous structures such as bioprinted fibrous scaffolds. To study oxygen tension and glucose concentration within an alginate hydrogel a normoxic breast cancer cell culture was considered. From the mathematical model, that couples nutrients and cells, we established the maximum height of a porous hydrogel scaffold. This approach contributes to optimize a 3D printed hydrogel by providing information about how to ensure the correct amount of oxygen and glucose throughout the construct during a static culture. However, the model is subject to some limitations. In particular, the main challenges of future studies will have to concern the definition of a law that accurately describes the consumption of nutrients by cells, defining a relationship between oxygen and glucose, considering the Warburg and, thus, the incorporation of both normoxic (oxidative) and hypoxic (glycolytic) cancer cells. Moreover, deposition of extracellular matrix by cells or hydrogel degradation, which mechanically and chemically influences the microenvironment of the cells, could be considered.

REFERENCES

[1] Tse, H. M., Gardner, G., Dominguez-Bendala, J., & Fraker, C. A. (2021). The Importance of Proper Oxygenation in 3D Culture. In *Frontiers in Bioengineering and Biotechnology* (Vol. 9). Frontiers Media S.A. https://doi.org/10.3389/fbioe.2021.634403

[2] Urbanczyk, M., Layland, S. L., & Schenke-Layland, K. (2020). The role of extracellular matrix in biomechanics and its impact on bioengineering of cells and 3D tissues. In *Matrix Biology* (Vols. 85–86, pp. 1–14). Elsevier B.V. https://doi.org/10.1016/j.matbio.2019.11.005

[3] Giraldo, N. A., Sanchez-Salas, R., Peske, J. D., Vano, Y., Becht, E., Petitprez, F., Validire, P., Ingels, A., Cathelineau, X., Fridman, W. H., & Sautès-Fridman, C. (2019). The clinical role of the TME in solid cancer. In *British Journal of Cancer* (Vol. 120, Issue 1, pp. 45–53). Nature Publishing Group. https://doi.org/10.1038/s41416-018-0327-z

[4] Neophytou, C. M., Panagi, M., Stylianopoulos, T., & Papageorgis, P. (2021). *cancers The Role of Tumor Microenvironment in Cancer Metastasis: Molecular Mechanisms and Therapeutic Opportunities*. https://doi.org/10.3390/cancers

[5] Persaud, A., Maus, A., Strait, L., & Zhu, D. (2022). 3D Bioprinting with Live Cells. In *Engineered Regeneration* (Vol. 3, Issue 3, pp. 292–309). KeAi Communications Co. https://doi.org/10.1016/j.engreg.2022.07.002

[6] GhavamiNejad, A., Ashammakhi, N., Wu, X. Y., & Khademhosseini, A. (2020). Crosslinking Strategies for 3D Bioprinting of Polymeric Hydrogels. In *Small* (Vol. 16, Issue 35). Wiley-VCH Verlag. https://doi.org/10.1002/smll.202002931

[7] Fakhruddin, K., Hamzah, M. S. A., & Razak, S. I. A. (2018). Effects of extrusion pressure and printing speed of 3D bioprinted construct on the fibroblast cells viability. *IOP Conference Series: Materials Science and Engineering*, *440*(1). https://doi.org/10.1088/1757-899X/440/1/012042

[8] Moncal, K. K., Ozbolat, V., Datta, P., Heo, D. N., & Ozbolat, I. T. (2019). Thermally-controlled extrusion-based bioprinting of collagen. *Journal of Materials Science: Materials in Medicine*, *30*(5). https://doi.org/10.1007/s10856-019-6258-2

[9] Obradovic, B., Meldon, J. H., Freed, L. E., & Vunjak-Novakovic, G. (n.d.). *Glycosaminoglycan Deposition in Engineered Cartilage: Experiments and Mathematical Model*.

[10] Lewis, M. C., MacArthur, B. D., Malda, J., Pettet, G., & Please, C. P. (2005). Heterogeneous proliferation within engineered cartilaginous tissue: The role of oxygen tension. *Biotechnology and Bioengineering*, *91*(5), 607–615. https://doi.org/10.1002/bit.20508

[11] Shakeel, M., Matthews, P. C., Graham, R. S., & Waters, S. L. (2013). A continuum model of cell proliferation and nutrient transport in a perfusion bioreactor. *Mathematical Medicine and Biology*, *30*(1), 21–44. https://doi.org/10.1093/imammb/dqr022

[12] Mendoza-Juez, B., Martínez-González, A., Calvo, G. F., & Pérez-García, V. M. (2012). A Mathematical Model for the Glucose-Lactate Metabolism of in Vitro Cancer Cells. *Bulletin of Mathematical Biology*, *74*(5), 1125–1142. https://doi.org/10.1007/s11538-011-9711-z

[13] Mei, C. C. & Vernescu, B.2010-Homogenization methods for multiscale mechanics. World Scientific, Singapore.

[14] Androjna, C., Gatica, J. E., Belovich, J. M., & Derwin, K. A. (2008). Oxygen diffusion through natural extracellular matrices: Implications for estimating "critical thickness" values in tendon tissue engineering. *Tissue Engineering - Part A.*, *14*(4), 559–569. https://doi.org/10.1089/tea.2006.0361

[15] Mehmetoglu, U., Ate, S., & Berber, R. (1996). *Oxygen diffusivity in calcium alginate gel beads containing gluconobacter suboxydans* (Vol. 24, Issue 2).

[16] Bashkatov, A. N., Genina, E. A., Sinichkin, Y. P., Kochubey, V. I., Lakodina, N. A., & Tuchin, V. v. (2003). Glucose and Mannitol Diffusion in Human Dura Mater. *Biophysical Journal*, *85*(5), 3310–3318. https://doi.org/10.1016/S0006-3495(03)74750-X

[17] Itamunoala, G. F. (n.d.). *Effective Diffusion Coefficients in Calcium Alginate Gel*.

[18] Gatenby, R. A., & Gillies, R. J. (2004). Why do cancers have high aerobic glycolysis? In *Nature Reviews Cancer* (Vol. 4, Issue 11, pp. 891–899). https://doi.org/10.1038/nrc1478

[19] Wagner, B. A., Venkataraman, S., & Buettner, G. R. (2011). The rate of oxygen utilization by cells. *Free Radical Biology and Medicine*, *51*(3), 700–712. https://doi.org/10.1016/j.freeradbiomed.2011.05.024

[20] Schornack, P. A., & Gillies, R. J. (n.d.). *Contributions of Cell Metabolism and H + Diffusion to the Acidic pH of Tumors 1*. http://www.atcc.org

In vitro exposure of endothelial cells to mechanical vibrations

E. Carrara[1], S. Poloni[2], C.E. Campiglio[3], E. Riceputi[2], M. Bozzetto[1] and A. Remuzzi[3]
[1] *Department of Biomedical Engineering, Istituto di Ricerche Farmacologiche Mario Negri IRCCS, Bergamo, Italy*
[2] *Department of Engineering and Applied Sciences, University of Bergamo, Dalmine, Italy*
[3] *Department of Management, Information and Production Engineering, University of Bergamo, Dalmine, Italy*

***Abstract*—Mechanobiology of vascular cells plays an important role in vascular remodelling and stenosis formation. Mechanical stresses acting on vascular wall may derive from mechanical vibrations. This preliminary study aims to investigate the effects of vibrations on endothelial cells (ECs) exploiting an experimental setup capable of expose cells to mechanical vibrations obtained by a 50 Hz sound-generated pressure wave. To validate the efficacy of the system, a preliminary cell viability evaluation was performed on ECs exposed for 48 hours to vibrations. A mean displacement of 71 μm was measured and sound recording showed consistency between sound and culture dish vibrations during the time course. Phase-contrast analysis of the stimulated and unstimulated cell cultures showed that sound-induced vibrations caused changes in ECs typical cobblestone shape and determined their detachment from the substrate, with a number of death cells higher than the static control. Alamar Blue assay highlighted a significant reduction in the metabolic activity of live cells after the mechanical stimulation, as compared to the static culture.**

***Keywords*— endothelial cells, sound, vibration, frequency.**

I. Introduction

Despite huge research efforts, cardiovascular diseases remain the primary cause of mortality and morbidity worldwide [1]. The understanding of the fundamental processes responsible for vascular remodelling, crucial in vascular pathology such as stenotic vascular disease [2], is still limited. The main cause of stenosis is the development of neointimal hyperplasia (NH), a fibrotic-muscular thickening of the vascular wall due to the migration of smooth muscle tissue cells into the intimal layer of the vessel [3].

Beyond flow disturbance, the mechanobiology of the vessel plays a key role in vascular remodelling and stenosis formation [4]. Indeed, a large body of evidence [5]–[7] showed that turbulent hemodynamics largely influence endothelial cells (ECs) functions *in vitro*.

Cells are capable of sensing and adapting to their mechanical environment through dynamic processes involving multiple signalling pathways. This property is crucial because mechanical stimuli are critical regulators of homeostatic processes, physiological conditions and are involved in the development of diseases [8], [9].

The effect of mechanical stresses on vessels remodelling was recently investigated through numerical simulations, revealing that "turbulent-like" blood flows might induce vascular wall vibrations [10]. However, the biological effects of high frequency dynamic mechanical stresses on cellular functions remain still unclear.

Therefore, this preliminary study aims to investigate the effects of vibrations on ECs. To achieve this goal we developed an experimental setup capable of providing cells with mechanical vibrations and related mechanical stresses by means of a pressure wave generated by reproducing a sound at a known frequency. Thus, a preliminary cell viability evaluation was performed to investigate the effect of vibration on ECs.

II. Methods

A. Study design

An aluminium support structure was built and embedded with an instrument for sounds generation. Cell culture was mounted and positioned in order to make it receive vibrations. Human umbilical vein endothelial cells (HUVECs) were seeded and cultured in two 150 mm cell culture dishes, one of them subjected to low frequency vibration and the other used as static control for 48 hours, a time interval previously shown to induce changes in ECs by shear stress [7]. The sounds emitted by the speaker and the vibrations of the cells subjected to low frequencies were recorded at the start of the experiment, after 24 and 48 hours. At the end of the experiment a viability assay was performed both on the cells subjected to vibrations and on static control ones.

B. Experimental setup

To expose a cell culture dish to vibrations, a support structure was built with aluminium profiles and corner fittings. At 10 cm from the base, a perforated aluminium plate was fixed in which the speaker was soldered. At 4 cm from this, a second aluminium plate, with a hole of the same size as the cell culture dish, was placed. The use of screws allowed securing the cell dish making it integral with the speaker. In this way the lower part of the dish, where the cells were located, was affected only by the vibration from the sound wave. To generate the sound induced vibrations, the speaker was connected with a two-channel digital power amplifier (Kinter 500W MA-700) capable of receiving as input a sound recording in .wav file format. The frequency of the sound was 50 Hz, continuously applied for 48 hours. The choice of the sound frequency of 50 Hz was selected in order to simulate the vibrations of the wall of an arteriovenous fistula under turbulent-like flow conditions, that was estimated by a preliminary fluid-structure interaction simulation (FSI). During the 48-hour experiment, the structure was placed in a 37 °C, 5% CO_2 incubator, while the amplifier and electronic

components remained isolated from the humid environment.

On the other hand, the control cells weren't subjected to vibrations and were kept for the same duration of the experiment in an incubator, acoustically isolated from the other one, under the same conditions of the cells subjected to vibrations.

C. Cell culture

HUVECs were isolated from umbilical cords collected by a local hospital (Azienda Ospedaliera, Bergamo EST). Before tissue harvesting, informed consent by the donor was obtained. Cells were isolated by collagenase digestion, as described in our previous publication [7], cultured on gelatin-precoated culture dishes [7] and propagated in M199 medium supplemented with 10% newborn calf serum (Gibco™), 10% human serum (directly separated in our laboratory from human plasma), 1% (v/v) 200 mM L-glutamine (Gibco™), 1% antibiotics (100 U/mL Penicillin-Streptomycin, Gibco™), 1% amphotericin B solution (Sigma-Aldrich), 0.1% heparin (5000 U.I./mL, Teva Italia S.r.l.), and 25 µg/mL endothelial cell growth supplement (Sigma-Aldrich). HUVECs were maintained at the temperature of 37 °C and 5% CO_2 of humidified environment and used between passages 3 and 5. The medium was changed every 3-4 days. When the cells reached 80-90% confluency, they were plated on two gelatin-precoated 150 mm cell culture dishes at a density of 1 x 10^6 cells per dish and incubated for 4 days. At day 4, when the cells reached about 80% confluency, the experiment was started.

D. Sound and vibrations tests

Sound recordings were performed with an in-house device consisting of an Adafruit Pulse Density Modulation (PDM) microphone and an Arduino Nano 33 BLE board. Adafruit PDM Microphone Breakout is an audio sensor, mounting on board a Micro Electrical Mechanical System (MEMS) omnidirectional digital microphone (MP34DT01-M produced by ST electronics). The Arduino Nano 33 BLE board bias the microphone and allows data collection. The system is also equipped with an ad-hoc designed circuit to trigger the start and the end of sound recordings. Data were stored real time on a .txt file using Coolterm (version 1.9.1.964), a simple serial port terminal application that is customized to exchange data with hardware connected to serial ports. Sound recordings were analyzed in time and frequency using MATLAB R2022a (9.12.0).

The vibrations of cell culture dishes were detected using the accelerometer (LSM9DS1) mounted on the Arduino platform. Acceleration data were collected with Coolterm and analyzed in MATLAB. Specifically, acceleration data were evaluated in time and frequency domain: information of cell culture dish velocity and displacement during time were obtained by the integration, respectively one and two times, of the acceleration data following appropriate high-pass filtering steps to avoid the drift effect due to integration of the accelerometer offset [11].

Preliminary sound tests were performed before starting the experiment and the noise emitted by the incubator was also recorded to check the possible effect on cell vibration.

At the beginning of the experiment, after 24 and 48 hours the sound emitted by the speaker were recorded by the PDM Microphone. The sound was recorded just below the bottom of the cell dish to test what cells were receiving.

Similarly, the acceleration of the dish was recorded with the Arduino-based accelerometer at 0, 24 and 48 hours from the experiment start. Vibrations were detected on the bottom of the dish carefully securing the device to the cell culture dish so that its movements were joint to the accelerometer ones.

E. Cell morphology and viability evaluation

The morphology of vibrations-exposed and static control cells was investigated at the end of the experiment by taking phase-contrast microscopy images, ascertaining the homogeneity within the dishes as well. Then, cell counting was performed to evaluate the effect of vibrations on HUVECs, quantifying the number of detached cells in the two conditions.

To determine the viability of HUVECs, Alamar Blue assay was performed on the samples. After the experiment, 10% v/v Alamar Blue solution (Sigma-Aldrich) was added to the cells and was further incubated for 1.5 hours at 37 °C and 5% CO_2 environment. The solution containing the reduced form of the compound was then transferred into a 96-wells plate, and the fluorescence of each sample was measured with a microplate reader (Tecan Infinite 200 PRO) at the excitation and emission wavelength of 570 nm and 600 nm respectively. The percentage of cell viability was calculated by comparing the fluorescence of the culture subjected to sound-induced vibrations to the fluorescence of the static culture, considered as 100% of cells metabolic activity.

III. Results

A. Experimental setup

In Figure 1a shows the experimental setup, while the device used for sounds and vibrations recording was reported in Figure 1b.

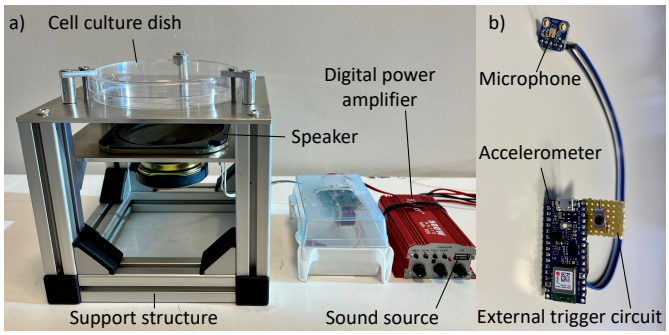


Figure 1: a) experimental setup. b) Arduino-based device for sound and vibration measures.

B. Sound and vibrations tests

Before the beginning of the experiment, the noise of the incubator was recorded. A main frequency of 90 Hz was detected, with a significantly lower amplitude (2 orders of magnitude) with respect to the sound imposed to generate the ECs vibration.

The sound emitted by the speaker and received by cell culture dish were acquired with the PDM Microphone. Figure 2 shows a representative example of the acoustic

recordings at the experiment beginning. In addition to the main frequency at 50 Hz there are also its odd harmonics of lower amplitude and other very low amplitude peaks spread over the entire frequency spectrum.

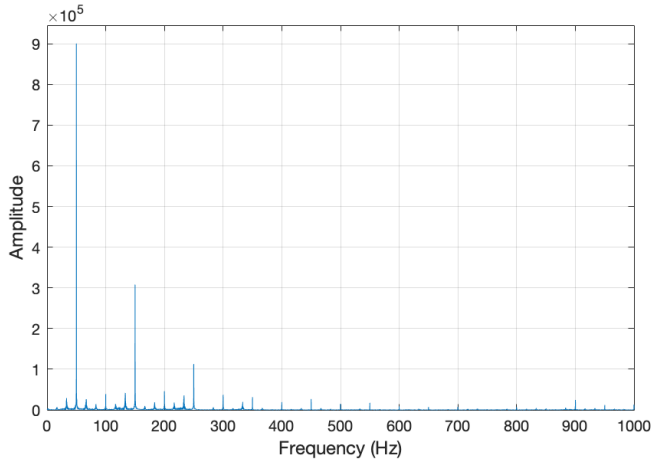


Figure 2: 50 Hz sound emitted by the speaker.

The acceleration was recorded with the Arduino-based accelerometer integral with the cell culture dish. Acceleration, velocity and displacement of the plates were relevant only in the direction perpendicular to the dish. Assumed a normal distribution of velocity and displacement, mean velocity obtained from acceleration data was 0.04 m/s (4σ) and the associated $2\sigma = 71$ μm indicates the amount of movement of the cell culture dish given by vibrations. The Fourier transform of the acceleration data showed a frequency consistent with that detected in sound. In Figure 3 is reported a representative example on the HUVECs displacement due to sound induced vibrations.

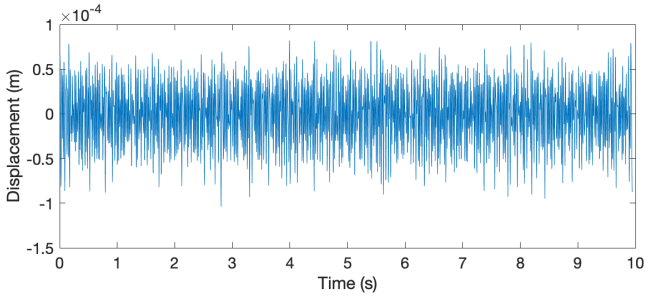


Figure 3: Vibration induced displacement of the cell culture dish.

C. Cell morphology and viability evaluation

As shown in Figure 4, HUVECs morphology was affected by vibrations exposure. Indeed, the cell culture stimulated for 48 hours by the sound-generated vibrations presents cells with irregular edges and some empty spaces between them, which were the result of HUVECs detachment (black arrows in Figure 4). On the contrary, the culture maintained in static condition during the time course consisted in a monolayer of cells with the typical randomly oriented cobblestone shape. Morphology of vibrations-exposed and control cells were homogenous within their cell culture dishes.

Cell counting confirmed the result of the morphologic analysis. The total cells number per dish, which was the same at the beginning of the experiment, was significantly lower in cells exposed to vibrations as compared to control cell (3.7 and 4.7 million cells, respectively). This indicates that the mechanical stimulation led to detachment of approximately 24% of total HUVECs which accumulated in culture medium, compared to about 4.5% detachment in control cells.

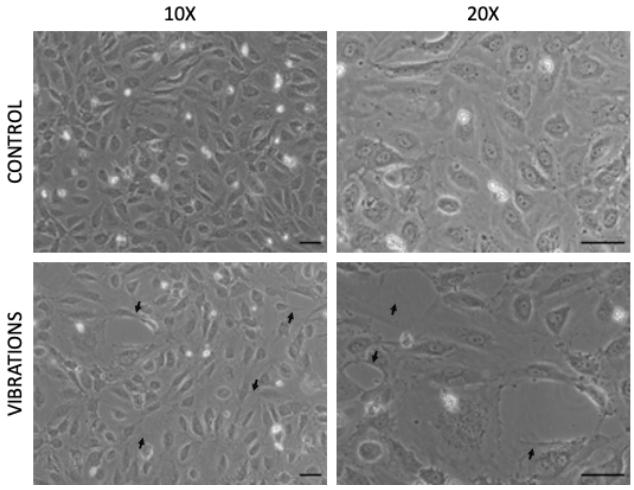


Figure 4: Effect of vibrations exposure on HUVECs morphology. Black arrows indicate the detachment-induced empty spaces in the cell monolayer. Left: magnification 10X and scale bars 50 μm; right: magnification 20X and scale bars 50 μm.

Alamar Blue assay was performed on HUVECs at the end of the 48 hours experiment both on stimulated and unstimulated cells. The results are reported in Figure 5, as metabolic activity normalized to the number of live cells. A decrease in cell viability was observed for HUVECs exposed to the mechanical stimulus compared to control ones. In details, the metabolic activity of stimulated cells resulted more than 50% lower than that measured in the static culture, suggesting that 48 hours exposure to mechanical vibrations importantly affected cell functions.

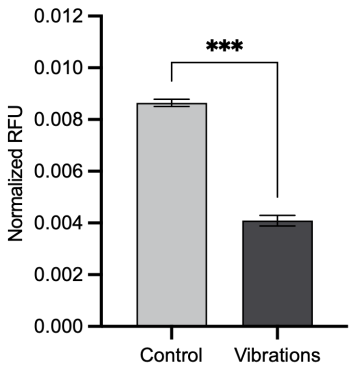


Figure 5: Alamar Blue assay to determine cell viability of HUVECs exposed to 48 hours vibrations and maintained in static conditions. Data are normalized to the number of live cells and are represented as mean ± SD (****p* < 0.001*, using student paired t test, n = 1).

IV. Discussion

In this preliminary study we developed and tested an experimental procedure to investigate the effects of mechanical vibrations on ECs in vitro. The development of an experimental setup capable of providing HUVECs with sound-induced mechanical vibrations is a results per se.

The choice to look at vibrations effects at 50 Hz is consistent with what reported by Bittle [12] about blood flow vortex frequencies in post-stenotic location. While Bittle examined

the effects of vibrations on vascular smooth muscle cells, we for the first time studied ECs, that play an important role in vascular remodelling and stenosis formation [6], [7].

The 90 Hz low amplitude noise of the incubator didn't importantly affect the cells since it was overpowered by the sound emitted by the speaker. The main frequency of the latter was at 50 Hz, and the presence of its odd harmonics suggests the imposition of a square wave, while the white noise spread along the entire spectrum is negligible compared to the amplitude of the main frequency. The multiple recordings in time of the 50 Hz sound and cell culture dish vibration demonstrate the consistency of the experiment during the entire duration of the experiment. Furthermore, the fact that the measurements were taken under the cell dish confirms that those data actually represent the vibration sensed by ECs adherent to the bottom of the culture dish and are not due to interference effects within the incubator. The Fourier transform of the data obtained with the accelerometer shows the same frequencies as the sound imposed on the cells, confirming that the recording device was integral with the structure. This is also shown by the fact that the vibrations occur only in the direction perpendicular to the cell dish, and that the imposition of a sound at a certain frequency causes a vibration consistent with it. From the acceleration data, an average displacement of the cell culture dish of about 70 μm was measured. This result is in line with the displacement values of vascular vibrations, based on preliminary data of a CFD simulation [10].

Phase-contrast analysis of the stimulated and unstimulated cell cultures shows that sound-induced vibrations affected HUVECs morphology, causing changes in their typical cobblestone shape and determining their detachment from the substrate, which led to the formation of empty spaces in cell monolayer. This evidence was confirmed by the number of death cells found in the culture medium of vibrations-exposed HUVECs, about 20% higher than the static control cell monolayer.

Preliminary viability evaluation by Alamar Blue assay strongly supported previously results, highlighting a significant reduction in the metabolic activity of the residual live cells after the mechanical stimulation, compared with that of the static culture.

A large body of evidence proofs that the dynamics of wall shear stress largely influence ECs functions *in vitro,* which play a crucial role in NH development [5]–[7]. Furthermore, recent FSI results revealed that turbulent-like blood flows cause the vessel-wall to vibrate, but no data about the effect of mechanical vibrations on ECs are available in literature. Thus, this is the first feasibility study exploring this linking. Overall, the results of our preliminary work confirm that mechanical vibrations affect ECs *in vitro*.

The current study is a preliminary investigation, and the experiment must be further investigated to ensure its reproducibility and statistical significance. As a future development, the effect of vibrations on ECs functions may be investigated by more specific cell function tests, such as LDH, ROS production and Caspase-3 activation assays. Furthermore, it would be interesting to identify a displacement threshold over which cells show detachment or reduced viability, and relate it to turbulent-like flow. Another future development may be the investigation of the effects of vibrations on ECs after different time of exposure.

V. Conclusion

Our study provides a simple but reliable system to explore the effects of vibrations on ECs function. The preliminary results underline a lowering of cell viability when cells are stimulated by a 50 Hz frequency for 48 hours. Our framework showed a great potential for the investigation of vascular remodelling and the related cell dysfunctions that are responsible for vascular diseases.

References

[1] G. A. Roth *et al.*, «Global Burden of Cardiovascular Diseases and Risk Factors, 1990–2019», *J. Am. Coll. Cardiol.*, vol. 76, fasc. 25, pp. 2982–3021, 2020.

[2] Y.-T. Shiu, J. I. Rotmans, W. J. Geelhoed, D. B. Pike, and T. Lee, «Arteriovenous conduits for hemodialysis: how to better modulate the pathophysiological vascular response to optimize vascular access durability», *Am. J. Physiol.-Ren. Physiol.*, vol. 316, fasc. 5, pp. F794–F806, 2019.

[3] T. Lee and S. Misra, «New Insights into Dialysis Vascular Access: Molecular Targets in Arteriovenous Fistula and Arteriovenous Graft Failure and Their Potential to Improve Vascular Access Outcomes», *Clin J Am Soc Nephrol*, p. 9, 2016.

[4] H. Koseki *et al.*, «Two Diverse Hemodynamic Forces, a Mechanical Stretch and a High Wall Shear Stress, Determine Intracranial Aneurysm Formation», *Transl. Stroke Res.*, vol. 11, fasc. 1, pp. 80–92, 2020.

[5] A. Brahmbhatt, A. Remuzzi, M. Franzoni, and S. Misra, «The molecular mechanisms of hemodialysis vascular access failure», *Kidney Int.*, vol. 89, fasc. 2, pp. 303–316, 2016.

[6] M. A. Gimbrone and G. García-Cardeña, «Endothelial Cell Dysfunction and the Pathobiology of Atherosclerosis», *Circ. Res.*, vol. 118, fasc. 4, pp. 620–636, 2016.

[7] M. Franzoni, I. Cattaneo, L. Longaretti, M. Figliuzzi, B. Ene-Iordache, and A. Remuzzi, «Endothelial cell activation by hemodynamic shear stress derived from arteriovenous fistula for hemodialysis access», *Am. J. Physiol.-Heart Circ. Physiol.*, vol. 310, fasc. 1, pp. H49–H59, 2016.

[8] J. D. Humphrey and M. A. Schwartz, «Vascular Mechanobiology: Homeostasis, Adaptation, and Disease», *Annu. Rev. Biomed. Eng.*, vol. 23, fasc. 1, pp. 1–27, 2021.

[9] V. Swaminathan and M. Gloerich, «Decoding mechanical cues by molecular mechanotransduction», *Curr. Opin. Cell Biol.*, vol. 72, pp. 72–80, 2021.

[10] A. Souche and K. Valen-Sendstad, «High-fidelity fluid structure interaction simulations of turbulent-like aneurysm flows reveals high-frequency narrowband wall vibrations: A stimulus of mechanobiological relevance?», *J. Biomech.*, vol. 145, p. 111369, 2022.

[11] J. G. T. Ribeiro, J. T. P. de Castro, and M. A. Meggiolaro, «An algorithm to minimize errors in displacement measurements via double integration of noisy acceleration signals», *J. Braz. Soc. Mech. Sci. Eng.*, vol. 43, fasc. 8, p. 385, 2021.

[12] B. B. Bittle, «An investigation into the role of arterial wall vibration in the pathogenesis of atherosclerosis», PhD thesis, Iowa State University, 1994.

Vibropolyfection: boosting polymer-mediated gene delivery by mechanical cell loading

N. Bono[1], F. Ponti[1,2], L. Russo[3], P. Bigini[3], D. Mantovani[2] and G. Candiani[1]

[1] *genT_LAB, Dept. of Chemistry, Materials and Chemical Engineering "G. Natta", Politecnico di Milano, Milan, Italy*
[2] *LBB, CRC- I, Dept. Min-Met-Mat Eng. and CHU de Quebec Research Center, Laval University, Quebec City, Canada*
[3] *Dept. of Molecular Biochemistry and Pharmacology, Istituto di Ricerche Farmacologiche Mario Negri, Milan, Italy*

***Abstract*—In recent years, non-viral vectors have gained some public acceptance and come to the forefront of advanced therapies. Unfortunately, the use of non-viral vectors is still plagued by low efficiency due to their scarce ability to overcome cellular barriers. Herein, we used mechanical cell stimulation as a tool to boost polymer-based nanoparticles effectiveness.**

***Keywords*—transfection, mechanical stimulation, non-viral gene delivery, polyethyleneimine.**

I. Introduction

The rise of nucleic acids (NAs)-based therapeutics has emerged as a breakthrough in molecular medicine and set the stage for the development of advanced therapeutics and preventatives[1,2]. Broadly speaking, the introduction of NAs into target cells is achieved by either physical means or vector-mediated delivery systems. Physical methods, such as electroporation, sonoporation, and optoporation, enable the delivery of the genetic cargo intracellularly through the use membrane-disruptive stimuli[3]. Despite being very effective in accomplishing the delivery task, such methods are often associated with extensive cell damage as a consequence of cell membrane disruptions[4]. On the other hand, vector-based delivery systems rely on the use of carriers able to pack the NA cargo into (nano)particles, making it easier to overcome the cell membrane barrier. Viral vectors, i.e., an engineered version of highly evolved viruses that naturally gain access to cells, currently dominate the clinical trial landscape[5]. Nevertheless, some issues in terms of safety and manufacturing have fuelled the development of non-viral alternatives. Non-viral gene delivery vectors are categorized as cationic lipids (such as the key components of COVID-19 Pfizer/BioNTech's and Moderna's mRNA vaccines)[6] and polymers[2,7]. These molecules spontaneously self-assemble with NAs into nano/micro-sized particles called lipoplexes and polyplexes, respectively, ultimately protecting the NA payload from the harsh extracellular environment[8]. Unfortunately, the efficiency of such delivery systems is greatly hampered by several extra- and intra-cellular barriers that stand in the way toward a successful intracellular delivery of genes. In this context, although a tremendous effort has been made to optimize the vector chemistry[9], there is still a long way to go. In this work, we focus on a way to enhance the transfection efficiency (TE) of commonly used non-viral vectors by triggering cell responses through mechanical stimuli. Of note, cells are constantly subjected to a combination of chemical and mechanical cues, which orchestrate any cell process, such as motion, proliferation, and phenotypic switching events[10]. In line with this, the interaction between the cell membrane and the underlying cytoskeleton regulates the endocytic and trafficking processes[12]. In this light, we herein propose an innovative *in vitro* cell transfection strategy relying on the combination of polymer-mediated transfection (hereafter referred to as polyfection) and a short-lived mechanical stimulation in terms of micro-to-nanovibrations applied to cells to temporarily control their behaviour[11]. Overall, this resulted in a boost of polyplexes TE.

II. Materials and Methods

A. Vibrational loading device

The vibrational loading device (**Figure 1a**) comprises i) a sine wave signal generator (Lascells, Market Drayton, UK), able to modulate the wave frequencies from 0.1 Hz to 10 kHz and characterized by a peak-to-peak wave amplitude from 0 to 24 V. This is connected to ii) a mechanical wave driver (Arbor Scientific, Ann Arbor, MI, USA), equipped with a motion arm consisting of iii) a driveshaft moving in vertical (z-axis) direction and iv) a built-in-home cell culture plate housing on the top of it. The shaft displacement along the z-axis was assessed as a function of the wave frequency (f_{in}) by using a *homemade* accelerometer sensor.

B. Evaluation of vibrational loading on cell viability and proliferation

Mycoplasma-free adherent L929 (murine fibroblasts from subcutaneous connective tissue, CCL-1; American Type Culture Collection (ATCC®), Manassas, VA, USA) cells were routinely cultured in Dulbecco's Modified Eagle's Medium (DMEM) supplemented with 10 % (v/v) fetal bovine serum (FBS), 1 mM sodium pyruvate, 10 mM HEPES, 100 U/mL penicillin, 0.1 mg/mL streptomycin and 2 mM glutamine (hereinafter referred to as complete DMEM, cDMEM) at 37°C in a humidified atmosphere under constant supply of 5% (v/v) CO_2 (hereafter referred to as standard culture conditions). L929 cells were seeded in 96-well plates at a density of 2×10^4 cell/cm^2 and maintained in standard culture conditions for 24 hrs. Afterward, cells were stimulated for 5 min at different vibration frequencies (f_{in} = 10 Hz, 50 Hz, 100 Hz, 500 Hz, and 1,000 Hz) and maintained in standard culture conditions. Twenty-four hrs after the discontinuation of the stimulation, cell viability was evaluated using AlamarBlue® assay according to the manufacturer's instructions. Briefly, the medium was removed from each well and replaced with 100 µL/well of 1× resazurin dye solution in cDMEM. Next, plates were incubated in standard culture conditions for 2 hrs, then the fluorescence was read with a Synergy H1 reader (BioTek, Winooski, VT, USA) (λ_{ex} = 540 nm; λ_{em} = 595 nm). The viability of unstimulated cells (CTRL) was assigned to 100 %

and the viability of stimulated ones was determined as follows:

$$\text{Viability [\%]} = \frac{F_{stimulated\ cells}}{F_{CTRL}} \times 100$$

where F is the recorded fluorescence.

To assess the effect of vibrational loading on cell proliferation, the viability assay was repeated 48 hrs from the discontinuation of the stimulation as described above, then the cell doubling time was calculated as follows:

$$\text{Doubling time [hrs]} = log_2(\frac{F_{t48}}{F_{t24}})$$

Where F is the recorded fluorescence 48 hrs (F_{T48}) and 24 hrs (F_{T24}) from the discontinuation of stimulation.

C. Evaluation of vibrational loading on cell morphology

The effect of vibrational loading on cell morphology was assessed by means of Scanning Electron Microscopy (SEM). Briefly, L929 cells were seeded at a density of 2×10^4 cell/cm^2 on sterile glass coverslips (Ø = 15 mm) inserted into separate wells of 24-well plates, and kept in standard culture conditions for 24 hrs. Twenty-four hrs post-seeding, cells were stimulated for 5 min at different vibration frequencies (f_{in} = 10 Hz, 50 Hz, 100 Hz, 500 Hz, and 1,000 Hz), next prepared for SEM analysis right after the stimulation was discontinued or at different time periods post-stimulation (i.e., 5 min, 30 min, and 60 min). Unstimulated cells were used as controls. For SEM analysis, cells were fixed in 2 % (v/v) glutaraldehyde solution for 20 min, dehydrated with graded ethanol series, then samples were gold-sputtered, mounted onto stubs, and examined using an accelerating voltage of 10 kV. SEM images were acquired at ×1,500 and ×7,000 magnification.

D. Evaluation of vibrational loading on transfection efficiency

For transfection assays, the *gold standard* transfectant 25 kDa linear polyethyleneimine (*l*PEI) was used to prepare polyplexes. Briefly, polyplexes were prepared at r.t. by adding an aqueous solution of pDNA encoding the secreted *Gaussia* luciferase (pGLuc, 160 ng/cm^2) to *l*PEI solutions at a stoichiometric ratio of 1:10 (v/v) to give a final DNA concentration of 20 ng/µL and N/P 30, where N/P is defined as the number of amines (N) of *l*PEI used to complex the phosphate groups (P) of a given amount of pDNA. *l*PEI/pDNA polyplexes were incubated for 20 min at r.t.. Transfection assays were carried out either in standard (i.e., static, polyfection) conditions, that served as internal transfection control, or upon vibrational loading (vibropolyfection conditions).

For polyfection, cells were challenged with 100 µL/well of polyplexes-containing culture medium, then incubated under standard culture conditions for 24 hrs. For vibropolyfection, cells were next stimulated for 5 min at different stimulation frequencies (f_{in} = 100 Hz, 500 Hz and 1,000 Hz), then cultured in standard conditions for 24 hrs. The cytotoxicity was evaluated 24 hrs from transfection using the AlamarBlue® viability assay as described hereinabove. The viability of unstimulated, non-transfected cells (CTRL) was assigned to 100 % and the cytotoxicity was determined as follows:

$$\text{Cytotoxicity [\%]} = \left(1 - \frac{F_{transfected\ cells}}{F_{CTRL}}\right) \times 100$$

To evaluate the overall luciferase activity, 20 µL of cell supernatant were mixed with 50 µL of luciferase assay substrate and the luminescence signal (expressed as Relative Light Units, RLU) was measured by means of a Synergy H1 reader.

E. Evaluation of vibrational loading on polyplexes internalization

Plasmid uptake was quantified in transfected L929 cells via real-time polymerase chain reaction (qRT-PCR). Briefly, 24 hrs after *l*PEI/pGLuc polyplexes delivery either via classical polyfection or vibropolyfection (f_{in} = 1,000 hz), cells were washed with sterile PBS and total DNA from whole cells was extracted with SingleShot Cell Lysis kit. RT-PCR reactions were carried out in a CFX Connect Real-Time PCR Detection System (Bio-Rad Laboratories) using the SsoAdvancedTM Universal SYBR® Green Supermix (BioRad Laboratories) (hereafter referred to as the master mix) as recommended by the manufacturer. Absolute quantification of pGLuc in transfected cells was achieved by comparing the C_T values of test samples to a standard curve generated by 10-fold serial dilution of the pGLuc template. Data were expressed as a fold-increase in pDNA uptake in vibropolyfected cells with respect to the polyfected counterparts. Confocal microscopy analyses were carried out as well to shed light on the role of mechanical stimulation on polyplex uptake. Briefly, seeded L929 cells were challenged with fluorescently labelled *l*PEI/pDNA polyplexes following either polyfection or vibropolyfection protocol at 1,000 Hz. Four hrs from polyplexes delivery, cells were fixed in 4% (v/v) paraformaldehyde, permeabilized with 0.1% (v/v) Triton X-100, next F-actin and nuclei were stained with TRITC-Rhodamine Phalloidin and Hoechst dyes, respectively, to better localize polyplexes. Stained samples were subsequently mounted on glass slides and digital images were taken with a Nikon A1 Confocal Microscope.

F. Evaluation of polyplex uptake by endocytosis inhibition and protein expression

Transfection assays in the presence of endocytosis inhibitors were carried out to investigate the contribution of each endocytic route on the polyplex uptake by cells undergoing polyfection and vibropolyfection. Briefly, L929 cells were seeded as described before. Twenty-four hrs post-seeding, cells were pre-treated with subtoxic concentrations of either chlorpromazine (10 µg/mL) or filipin (5 µg/mL) to inhibit clathrin-mediated endocytosis (CME) and caveolin-mediated endocytosis (CvME), respectively. The medium was replaced and the cells either underwent vibrational loading at 1,000 Hz for 5 min or were rested. Cells were next challenged with *l*PEI-based polyplexes for 3.5 hrs, the medium was replaced, and cells were cultured in standard conditions for 20 hrs before assessing the cytotoxicity and the transfection efficiency. Transfected cells in the absence of inhibitors served as positive controls. Immunostaining of clathrin and caveolae was performed as well. Briefly, L929 cells were seeded, transfected and fixed as described before, then mouse anti-clathrin heavy chain and mouse anti-caveolin 1 primary antibodies were used to stain clathrin and caveolin, respectively. Immunostained samples were mounted on glass slides and digital images were taken with Nikon A1 Confocal Microscope.

G. Statistical analysis

Statistical analyses were carried out using Prism version 8 (GraphPad software, La Jolla, CA). All data collected from at least three independent experiments were initially analyzed using the D'Agostino & Pearson omnibus normality test. Unpaired t-test and one-way ANOVA (multiple comparisons) with posthoc Tukey test were used to compare two or more experimental groups, respectively. Significance was retained when $p < 0.05$. Data are expressed as mean ± standard deviation (SD, $n \geq 3$).

III. Results and Discussion

A. Assessment of the vibrational loading device

A vibrational-loading device was conceived to apply sinusoidal micro-to-nanoscale displacements to adherent cells in culture. The displacements caused by the input frequencies (f_{in}) set on the sine wave generator were characterized using an accelerometer. As shown in **Figure 1b**, the higher the sinusoidal wave frequencies applied, the smaller the displacement of the culture plate. Specifically, the device allowed controlling the generation of vibrational cues ranging from the millimeter (f_{in} = 10 Hz) to the nanometer (f_{in} = 1,000 Hz) scale, such that they can be used to control cells' behavior.

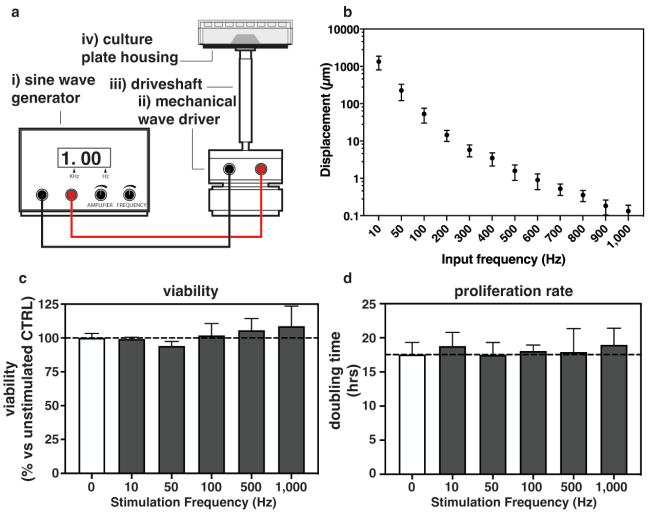


Figure 1. (**a**) Representation of the vibrational loading device. (**b**) Displacement values of the motion shaft as a function of the input frequency (f_{in}). (**c**) Viability and (**d**) doubling time of L929 cells that underwent vibrational loading for 5 min at different stimulation frequencies. Data are expressed as mean ± SD (n = 3).

B. Assessment of the cell response to vibrational loading

To assess the effects of the vibrational loading on the overall cell response, the viability and proliferation rate of adherent L929 cells were evaluated upon a 5 min-long vibrational loading. Interestingly, there were no changes in the cell viability as a function of the wave frequency applied (**Figure 1c**) nor alterations in the cell doubling time (**Figure 1d**).

To shed more light on the effect of vibrational loading on cell response, SEM analyses of stimulated cells were carried out. Because plasmalemma defines cell boundaries, it is the first barrier to the delivery of exogenous cargoes into the cell. In this case, a 5-min vibrational loading at $f_{in} \geq 100$ Hz did elicit gross cell morphological changes (**Figure 2a**). As opposed to unstimulated controls that appeared markedly smoother, stimulated cells at $f_{in} \geq 100$ Hz exhibited a rough surface, densely studded with membrane protrusions, which are blister-like outgrowths of the plasma membrane that may occur upon membrane detachment from the underlying cytoskeleton in diverse circumstances[12]. We also decided to monitor the cell membrane recovery after vibrational loading. As reported in **Figure 2b**, cells mostly reverted to normal morphology within about 1 hr, thus suggesting that mechano-induced membrane destabilization could be harnessed to enhance membrane trafficking and improve the delivery of NAs into cells.

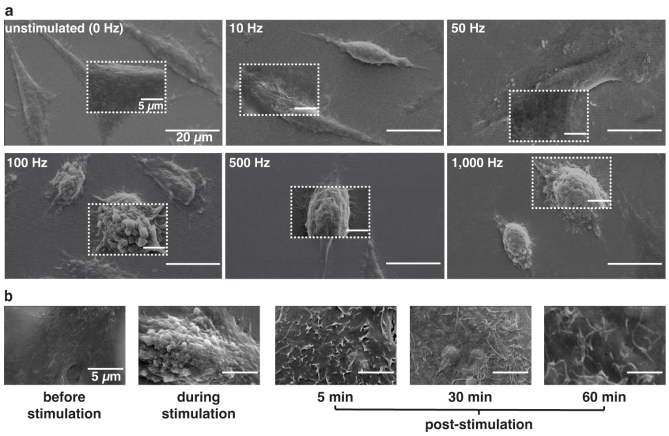


Figure 2. SEM images of L929 cells (**a**) undergoing vibrational loading at different input frequencies and (**b**) before, during and at 5, 30 and 60 min after discontinuation of the vibrational loading. Scale bar = 20 µm (a), 5 µm (insets in (a) and (b)).

C. Effectiveness of the vibropolyfection strategy

To explore whether the vibropolyfection strategy would improve transfection, we challenged vibrational loaded L929 cells with non-viral gene delivery particles consisting of the *gold standard* *l*PEI and pGLuc as described in the previous section. It is apparent from **Figure 3a** that the cytotoxicity induced by vibropolyfection was negligible, thus highlighting that the combination of vibrational loading and polyplexes delivery does not compromise cell viability.

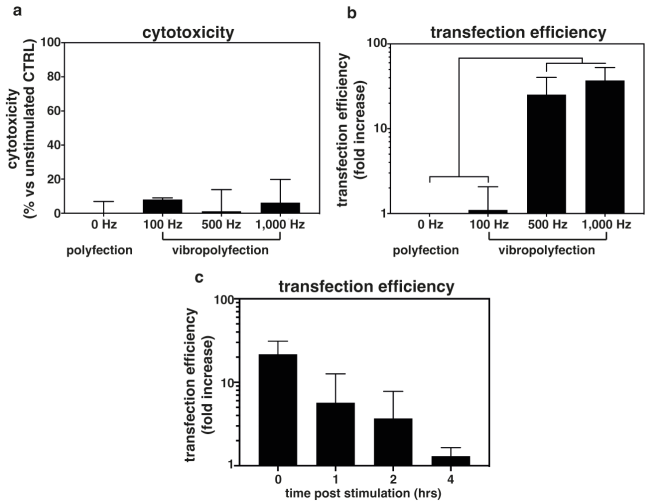


Figure 3. (**a**) Cytotoxicity and (**b**) TE, expressed in terms of fold increase with respect to polyfection, of /PEI/pDNA complexes delivered in the presence of 5-min vibration loading at different frequencies. (**c**) Fold increase in TE of /PEI/pDNA complexes on L929 cells transfected at different periods from stimulation. Data are expressed as mean ± SD (n≥3), *p<0.05.

Besides, the higher the f_{in} the higher the TE. Of note, cells stimulated at f_{in} = 1,000 Hz displayed a 37-fold increase in TE compared to polyfected cells (**Figure 3b**).

We observed that the positive effect of the vibrational loading on transfection steadily decreased over time, alongside membrane recovery, and was practically lost 4 hrs upon the discontinuation of the stimulation (**Figure 3c**). We can speculate that the cell membrane recovery that occurs in response to the mechano-induced plasmalemma blebbing and ruffling may favourably impact endocytosis[13], which ultimately improves transfection efficiency.

D. Vibrational loading positively affects polyplex uptake

To study the effect of vibrational loading on polyplex uptake, we quantified the amount of pDNA internalized during classical transfection *vs*. vibropolyfection by means of qRT-PCR. As depicted in **Figure 4a**, vibropolyfection induced a ≈ 8.5-fold increase in the amount of pDNA uptaken by cells. We thus assumed that the boost in TE found in vibropolyfected cells directly relates to an increase in polyplexes internalization, as also suggested by the greater amount of polyplexes (green dots) found in vibropolyfected cells assessed by confocal microscopy (**Figure 4b**).

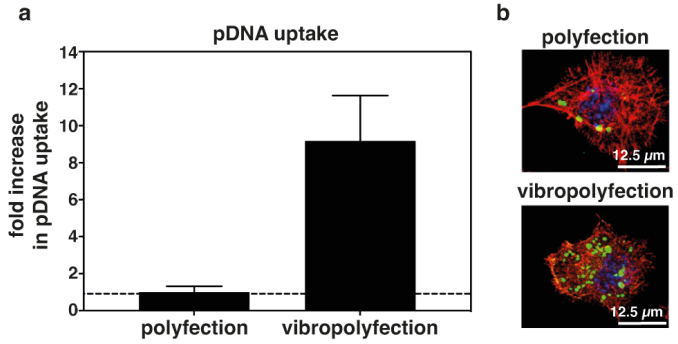


Figure 4. (**a**) Fold increase in pDNA uptake by polyfected *vs.* vibropolyfected cells as determined by qRT-PCR. Data are expressed as mean ± SD (n=3). (**b**) Confocal images of L929 transfected cells according to polyfection and vibropolyfection at 1,000 Hz. Cells were fixed 4 hrs from polyplex delivery. Polyplexes are in green, F-actin in red and nuclei in blue. Scale bar = 12.5 μm.

E. Vibrational loading triggers clathrin-mediated endocytosis

There is a general consensus that two distinct endocytic pathways (i.e., CME and CvME) may contribute to polyplex internalization[14]. To investigate the contribution of each endocytic pathway to the overall polyplex uptake in vibropolyfected cells, L929 cells were treated with either chlorpromazine or filipin, which are two inhibitors of CME and CvME, respectively, before undergoing polyfection and vibropolyfection. In polyfected, cells, TE was not affected by the inhibition of clathrin-mediated endocytosis (**Figure 5a**), whereas luciferase expression was dramatically reduced by caveolae inhibition, in accordance with literature data[15]. On the contrary, the separate inhibition of CME and CvME significantly impaired TE in vibropolyfected cells (**Figure 5a**), thus suggesting that vibrational loading triggers the activation of CME. Of note, CME was found to be upregulated in response to changes in cell membrane tension. To gain more insight into the role of CME and CvME on polyplex uptake, we also immunolabelled clathrin heavy chain and caveolin-1 proteins in polyfected and vibropolyfected cells. As shown in **Figure 5b**, vibropolyfected cells showed significantly higher clathrin levels than polyfected cells, in accordance with data reported in **Figure 5a**.

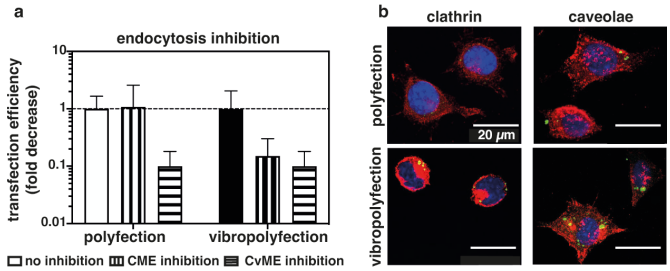


Figure 5. (**a**) Effect of CME and CvME inhibitors on polyfected and vibropolyfected cells. Data are expressed as fold decrease in TE in cells treated with inhibitors compared to cells transfected in the absence of inhibitors. Data are expressed as mean ± SD (n = 3), *p<0.05 vs cells transfected in the absence of inhibitor. (**b**) Confocal images of polyfected and vibropolyfected L929 cells. Clathrin heavy chain and caveolin-1 are stained in red, polyplexes in green and nuclei in blue. Scale bar = 20 μm.

IV. Conclusion

Herein, we developed a safe, user-friendly, and efficient *in vitro* transfection strategy based on the coupling of mechanical loading to commonly used polymeric particles. The study paves the way for using mechanical cell stimulation as a tool to improve the effectiveness of gene delivery vectors by modulating cell responses.

References

[1] J.K.L. Wong *et al.* Will nanotechnology bring new hope for gene delivery? Trends Biotechnol. 2017, 35:434-451

[2] N. Bono *et al*. Non-viral *in vitro* gene delivery: it is now time to set the bar! Pharmaceutics (2020) 12:183.

[3] A.J. Mellott *et al*. Physical non-viral gene delivery methods for tissue engineering. Ann. Biomed. Eng. (2013), 41:446-468.

[4] S. Mehier-Humbert and R.H. Guy. Physical methods for gene transfer: Improving the kinetics of gene delivery into cells. Adv. Drug Deliv. Res. (2005), 57:733-753.

[5] C.E. Thomas *et al*. Progress and problems with the use of viral vectors for gene therapy. Nat. Rev. Genet. (2003), 4:346-358.

[6] F. Ponti *et al*. Cationic lipids for gene delivery: many players, one goal. Chem. Phys. Lipids (2021), 235:105032.

[7] M.A. Mintzer and E.E. Simanek. Nonviral vectors for gene delivery. Chem Rev. (2009), 109(2):259-302.

[8] C. Tros de Ilarduya *et al*. Gene delivery by lipoplexes and polyplexes. Eur. J. Pharm. Sci. (2010), 40:159-170.

[9] T. Wang *et al*. Design of multifunctional non-viral gene vectors to overcome physiological barriers: dilemmas and strategies. Int. J. Pharm. (2012), 427:3-20.

[10] F. Martino *et al*. Cellular mechanotransduction: from tension to function. Front. Physiol. (2018); 9:824.

[11] F. Ponti *et al.* Vibropolyfection:coupling polymer-mediated gene delivery to mechanical stimulation to enhance transfection of adherent cells. J. Nanobiotech. (2022), 20:363.

[12] E. Paluch *et al.* Dynamic modes of the cortical actomyosin gel during cell locomotion and division. Trends Cell. Biol. (2006), 16:5-10.

[13] N.C. Gauthier *et al*. Mechanical feedback between membrane tension and dynamics. Trends Cell. Biol. (2012), 22:527-535.

[14] K. von Gersdorff *et al.* The internalization route resulting in successful gene expression depends on both cell line and polyethyleneimine polyplex type. Mol Ther. Cell Press (2006), 14:745-753.

[15] J. Rejman *et al.* Role of clathrin- and caveolae-mediated endocytosis in gene transfer mediated by lipo- and polyplexes. Mol. Ther. Cell Press (2005), 12:468-474.

Rapid prototyping of a microfluidic platform for nasal mucosa models

M. Testa[1], F. Lopresti[1], O. Manna[2], S. Burgio[2], G. Intilli[2], A. Fucarino[2], and V. La Carrubba[1]
[1] *Dipartimento di Ingegneria, Università di Palermo, Palermo, Italy*
[2] *Dipartimento di Biomedicina, Neuroscienze e Diagnostica avanzata, Università di Palermo, Palermo, Italy*

***Abstract*— In-vitro 3D models of human nasal mucosa cells can offer a deeper understanding of airway pathophysiology and drug discovery. In this work, a microfluidic chip was designed with an air-liquid interface (ALI) as a model to mimicry the *in vivo* environment of the respiratory mucosa. A biopolymeric scaffold was integrated to act as biocompatible ALI membrane. The platform was structured using a rapid prototyping technique. A computational fluid dynamic (CFD) analysis was conducted to evaluate the air-induced shear stress on the scaffold. CFD was employed to find the target flow rate to replicate desired mechanical characteristics within a specific region of the human nasal cavity. According to this data, peristaltic pumps for air and liquid flows, were programmed to replicate physiological flows and dynamic air-induced shear stresses shear stresses on the culture.**

***Keywords*— Air-Liquid-Interface; Organ-on-Chip; Laser ablation; Rapid prototyping; PLLA scaffold.**

I. Introduction

Long-term functional solutions for extensive airway diseases and damages a central focus of research in the fields of regenerative medicine and tissue engineering. Among the airway tissue of the human body, the nasal mucosa is the first site to be exposed to inhaled agents, such as pollutants, particles, allergen, or gases [1]. Three-dimensional (3D) cultures represent a significant advancement in the field of cellular biology and regenerative medicine, providing more realistic and physiologically relevant models for the study of cells and tissues. The 3D culture outgrowth model is based on the formation of self-organized three-dimensional structures derived from patient biopsy tissue, which grow and interact similarly to what is observed *in vivo*.

To create a nasal mucosa biological model, an air–liquid-interface (ALI) culture is needed so that the basal cells can differentiate in goblet and ciliated cells, allowing the movement of mucus and foreign particles that *in vivo* are pushed along the airways. The direct exposure of epithelial cells to air is the pivotal differentiation stimulus to obtain properly developed ciliated elements [2], [3]. Previous studies reported values from CFD simulations performed on computed tomography (CT)-based nasal cavity models investigating the velocities and shear forces applied to mucosal walls during quiescent breathing [4].

Organ-on-Chip (OoC) platforms play a key role in actively supporting the three-dimensional (3D) maturation of cells by replicating the proper biomechanical and biological conditions, such as providing adequate hydrodynamic stimuli and mass transport [5].

This study aimed to develop an air-liquid interface (ALI) microfluidic device for growth of human respiratory mucosa biopsies by means of a rapid prototyping fabrication technique. The device was manufactured by laser cutting and multilayer assembling of polymethylmethacrylate (PMMA) sheets. A biopolymeric scaffold made in Poly-L-Lactic Acid (PLLA) was also integrated into the platform and used as biocompatible ALI membrane [6].

In order to induce the physiological range of wall shear stresses on the outgrowth [4], fluid dynamic simulations were carried out to determine the appropriate air flow rate to be delivered. The flow delivery system of both the air and medium chambers was controlled by a microcontroller connected to peristaltic pumps. To investigate the effective dynamics of both air and medium flows in the OoC, the fluids of interest were characterized through the use of pressure sensors. The morphology of the scaffold was evaluated before and after their integration in the OoC platform.

Finally, preliminary cytocompatibility tests were performed on human nasal mucosa grown under dynamic conditions in the OoC.

II. Materials and Methods

A. Design and fabrication of the ALI microfluidic device

The ALI -OoC consisted of (1) channels for the transport of air and medium, and (2) a 0.32 cm^2 culture chamber.

The culture chamber was designed with two compartments separated by a biopolymeric membrane. The upper compartment was designed for the gaseous flow while the bottom compartment consisted of micro-channels for the medium flow.

The design of whole device was divided into 6 functional layers to be fabricated by means of laser cutting (Maitech, 40 W, Italy) of PMMA sheets (Clarex, Nitto Jushi Kogyo Co. Ltd., JP). The functional PMMA layers were then bonded together by means of multilayer assembling in hot press. Layers were aligned in a custom-made mold endowed with metallic pins. The PMMA layers and the scaffold were placed in the mold and was applied to their surfaces before bonding. The bonding was process was conducted at 70 °C and 100 bar for 3 min in a laboratory press [6].

B. Design and fabrication of the tubing connectors

The customized tubing connector was designed by means of a CAD software (Fusion 360©) and printed via stereolithographic 3D printer (FormLab, Form 2) by using a commercial resin (Clear V4, FormLab). The connector included pins for the easy alignment with the OoC platform and holes for the integration of commercial plastic ferrules and

PTFE tubing (OD 1/16", ID 1/32"). The sealing of the connector with the ALI-OoC was ensured via screws.

C. PLLA scaffold preparation

The biopolymeric scaffolds were prepared via Thermal induced phase separation TIPS technique. TIPS membranes were prepared by dissolving PLLA (4 wt%) in an 87/13 *w/w* dioxane-water mixture at 120 °C. The solution, kept above 60 °C to ensure homogeneity, was hot poured in a cylindrical high-density polyethylene (HDPE) mold. The mold filled with the polymer solution was first immersed for 10 min in a 0 °C bath and then moved to a –20 °C bath for 20 min in order to allow the complete freezing of the as-obtained structure. Successively, the foams were extracted from the mold and subjected to a washing step in distilled water. Finally, the foams were dried under vacuum for 24 h to ensure the complete removal of any solvent trace. The subsequently obtained membranes were then cut to obtain slices 0.5 mm thick. The scaffolds were furtherly cut via laser cutting and surface modified by means of air-plasma treatment before assembling in the OoC platform.

D. Morphological Analysis

The morphology of the PLLA scaffolds was evaluated by scanning electron microscopy, (SEM-FEI QUANTA 200F) before and after integration in the ALI platform. The samples were attached on an aluminium stub using adhesive carbon tape. Therefore, they were sputter coated with gold (Sputtering Scancoat Six, Edwards) for 60 s under argon atmosphere before imaging to avoid electrostatic discharge during the test.

E. Chip transparency

The transparency of the PMMA sheets 0.5 mm thick before and after bonding was tested by analysing the transmittance of the light through in the visible region using a UV-vis spectrophotometer (model UVPC 2401, Shimadzu Italia s.r.l., Milan, Italy).

F. Flow analysis

Fluid dynamic simulations were performed by using ANSYS Fluent © as software to determine the WSS in the culture chamber of the OoC platform. Those values were compared to previously reported data from CFD simulations performed on computed tomography (CT)-based nasal cavity models.

Culture chamber geometry was created in Fusion 360© and imported into ANSYS ICEM CFD© in which mesh geometry was generated with tetrahedral elements. The final culture chamber geometry mesh ranged from 300×10^3 to 400×10^3 hybrid finite elements.

The generated mesh was imported into ANSYS Fluent, and a steady state laminar flow was simulated at various inlet velocities whit a outlet pressure of 0 Pa. The fluid material properties was set as air, and the usual no-slip velocity condition was assumed.

The SIMPLEC algorithm was used to link pressure and velocity and convergence was obtained when the scaled residuals of continuity and momentum quantities were less than 10^{-5}. WSS values were obtained in the lower wall of the culture chamber that coincides to the upper surface of the scaffold.

LabSmith pressure sensor (LabSmith uPS-series pressure sensor, model: uPS1800-T116-10) was used to measure both medium and air pressure in the device as a function of time.

G. Outgrowths

Upon obtaining a respiratory mucosa biopsy sample (nasal mucosa from patients undergoing partial turbinectomy), the specimen is washed in PBS (supplemented with 100 µg/ml of streptomycin and 100 IU/ml of penicillin) to remove excess blood and mucus. The tissue is then transferred for the subsequent 24 hours to a Petri dish containing Dulbecco's Modified Eagle Medium with the addition of 10% fetal bovine serum and supplemented with 100 µg/ml of streptomycin and 100 IU/ml of penicillin. After 24 hours, necessary for assessing the presence of contaminants, the tissue was processed, creating fragments of approximately 0.5 mm^3. This tissue fragment includes the epithelial, the endothelial, and the connective cellular elements of the original tissue, as well as the progenitor cells required to ensure tissue turnover.

The OoC system was sterilized by flowing 70% ethanol for 5 minutes inside the channels and chambers, dried, washed with sterile Dulbecco's phosphate-buffered saline (DPBS) and irradiated with UV for 6 hours.

The biopsy was placed in the center of the upper surface of the scaffold and 13 µl of protein gel (Cultrex Basement Membrane Extract, BME) was added to the chamber and polymerized at 37 °C for ten minutes.

Both peristaltic pumps were connected to the microfluidic inlets of the device and to the reservoirs using 3D printed customized connectors. The entire platform was placed in a cell incubator and the pumps were turned on.

A constant flow of the culture medium (1.4 ml/s) was supplied for the replacement of the liquid medium. The dynamic flow rate of the aeriform medium was set according to the FANTASIA database of respiration belt data by means of a microcontroller. The outgrowth was maintained for up to 14 days and both microscopical evaluation and histological analysis (hematoxylin & eosin staining) were performed to visualize the tissue.

III. Results and Discussion

A. OoC Platform fabrication

The fabrication of the OoC for the nasal mucosa involved the laser ablation of six PMMA layers according to the design in Fig. 1A. The processing allowed obtaining patterns with maximum resolution of 200 µm. After assembling, the device appears transparent exception for the biopolymeric membrane, Fig. 1B. By flowing water containing a green dye, no leaking was observed thus convincing about the correct sealing of channels, chambers, and tubing connectors, Fig. 1C. The transparency of the device was measured by UV-Vis transmittance of 0.5 mm thick PMMA layers before and after bonding. Results (not shown) highlighted a transmittance greater than 91.7% for both samples in the entire visible

spectrum (400-700 nm). The transmittance of the bonded system is slightly lower than the single layer of PMMA, only for wavelengths lower than 400 nm. Therefore, this characterization allowed us to conclude that the transparency of the chosen materials is preserved even after the multilayer assembly process making them suitable for direct investigation of the culture by means of optical micrographs.

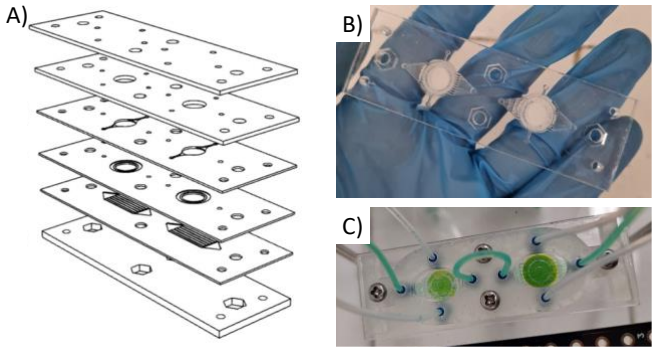


Fig. 1: A) Design of the six layers composing the whole OoC; B) Picture of the assembled OoC; C) Picture of the OoC filled with a green dye.

B. *Flow analysis*

In order to imitate the physiological breath, the air flow peristaltic pump has been programmed to manage a bidirectional flow following the trend of a single breath isolated from the Fantasia data.

According to the CFD analyses (Figure 2), the air flow at the peak of the inhalation was set at 0.2 ml/s to allow a gradient of the wall shear stresses (WSSs) in the range 0 - 0.3 Pa. This range of WSSs agree with the physiological values in healthy humans according to [4].

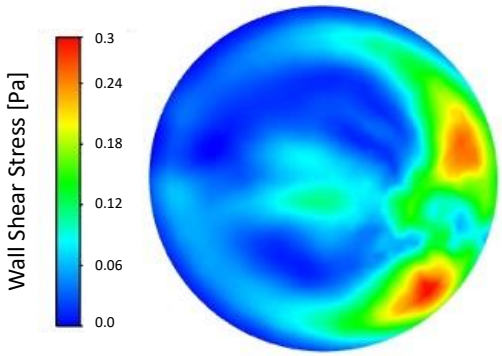


Fig. 2: Wall shear stress map evaluated on the top surface of the scaffold.

Figure 3 reports the pressure due to the air and medium flow inside the culture chambers measured at the inlets of the device. Interestingly, the air pressure curve is comparable to the physiological data obtained from the Fantasia database in terms of breath frequency and inhalation vs. exhalation amplitude ratio. These results convinced about the correct functioning of the programming code implemented in the microcontroller for the regulation of the flows. The pressure the fluid flow was evaluated at a constant flow rate equal to 1.4 ml/s, Fig. 2. It can be observed that the liquid pressure varies in a range of about -1 and -3 kPa, tanging an average value of -2 kPa. This result was desired since the liquid pump was plugged at the medium outlet in order to suck up the liquid phase thus avoiding the flooding of the upper culture chamber.

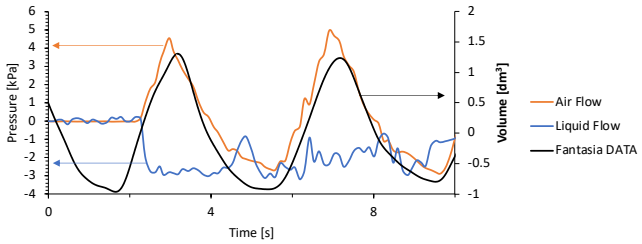


Fig. 3: Pressure of liquid and air flow in the OoC and breath volume obtained from FANTASIA belt data.

C. *Scaffold morphology*

Fig. 4 reports SEM images of the PLLA before (Fig. 4A) and after (Fig. 4B) their integration into the OoC platform. From the micrographs, it is possible to appreciate that the liquid-liquid phase separation process has correctly taken place since a porous structure with well-interconnected pores can be observed. The mean pore size is around 25 µm and the pore size distribution is quite homogenous. This pore size was chosen as adequate since allowed the diffusion of the liquid medium avoiding the permeation of the outgrowth cells inside the scaffold. The effect of thermal treatment needed for the integration of the scaffold in the OoC platform had no effect on the porous architecture of the scaffolds. This result convinced us about the efficacy of the chosen processing route for the integration of biopolymeric porous structures made in PLLA by means of TIPS.

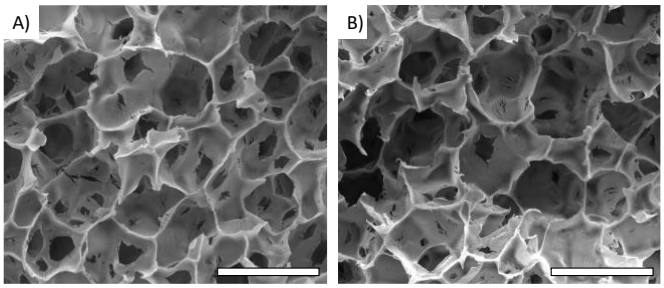


Fig. 4: SEM images of the PLLA scaffolds A) before and B) after integration in the OoC platform. Scale bars are 50 µm.

D. *Nasal mucosa viability*

The device allowed maintaining the air–liquid interface up to 2 weeks. After two weeks of culture, the cell populations start to outgrowth from the initial biopsy fragment to form a 3D structure. Histological results showed the presence of viable cells above the membrane, (Fig. 4). Furthermore, the outgrowth appears well-adherent on the PLLA membranes used as support for the culture.

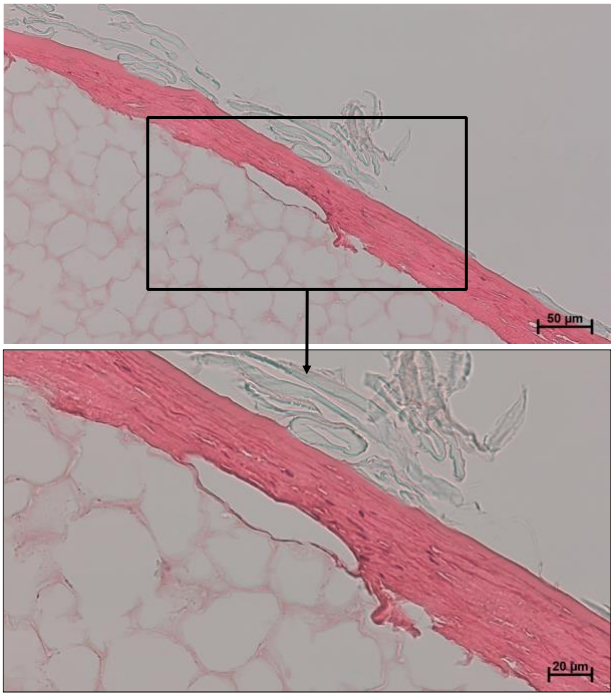


Fig. 5: Histological assay in hematoxylin and eosin of human nasal mucosa tissue after 14 days of culture in the OoC platform.

IV. Conclusion

This work demonstrated the feasibility of an ALI device for nasal mucosa outgrowth culture by means of a rapid prototyping technique. The processing route allowed integrating a biopolymeric scaffold to separate the air-liquid chambers and able to support the growth and differentiation of nasal mucosa cell population . The customized control of the air-pumps allowed for replicating physiological air flows and shear stresses on the culture. The device allowed maintaining the ALI condition for up to 2 weeks and to allow for the growth and differentiation of the outgrowth culture.

References

[1] L. Müller, L. E. Brighton, J. L. Carson, W. A. Fischer II, and I. Jaspers, “Culturing of human nasal epithelial cells at the air liquid interface,” *JoVE (Journal of Visualized Experiments)*, no. 80, p. e50646, 2013.

[2] J. P. Soleas, A. Paz, P. Marcus, A. McGuigan, and T. K. Waddell, “Engineering airway epithelium,” *Journal of Biomedicine and Biotechnology*, vol. 2012, 2012.

[3] E. Capuana *et al.*, “A dynamic air-liquid interface system for in vitro mimicking of the nasal mucosa,” *Biotechnology and Bioengineering*, 2022, doi: https://doi.org/10.1002/bit.28090.

[4] C. Li *et al.*, “Computational fluid dynamics and trigeminal sensory examinations of empty nose syndrome patients,” *The Laryngoscope*, vol. 127, no. 6, pp. E176--E184, 2017.

[5] I. Francis, J. Shrestha, K. R. Paudel, P. M. Hansbro, M. E. Warkiani, and S. C. Saha, “Recent advances in lung-on-a-chip models,” *Drug Discovery Today*, vol. 27, no. 9, pp. 2593–2602, 2022, doi: https://doi.org/10.1016/j.drudis.2022.06.004.

[6] F. Lopresti, I. Keraite, A. E. Ongaro, N. M. Howarth, V. La Carrubba, and M. Kersaudy-Kerhoas, “Engineered Membranes for Residual Cell Trapping on Microfluidic Blood Plasma Separation Systems: A Comparison between Porous and Nanofibrous Membranes,” *Membranes*, vol. 11, no. 9, 2021, doi: 10.3390/membranes11090680.

Associations between fatigue and functional connectivity of dopamine and noradrenaline circuits in Parkinson's disease

M. Moretto[1,2], I. Di Vico[3], A. Tamanti[3], G. Tomelleri[3], D. Martins[4], O. Dipasquale[4], M. Veronese[1,4], A. Bertoldo[1,5], S. Ottaviani[6], F. Pizzini[7], M. Tinazzi[3], M. Castellaro[1]

[1] *Department of Information Engineering, University of Padova, Italy*

[2] *Center for Mind/Brain Sciences, University of Trento, Italy*

[3] *Neurology Unit, Department of Neurosciences, Biomedicine and Movement Sciences, University of Verona, Italy*

[4] *Department of Neuroimaging, Institute of Psychiatry, Psychology and Neuroscience, King's College London, London, UK*

[5] *Padova Neuroscience Center, University of Padova, Italy*

[6] *Neurology Unit, Azienda Ospedaliera Universitaria Integrata, Verona, Italy*

[7] *Department of Diagnostics and Public Health, University of Verona, Italy*

***Abstract*— Patients with Parkinson's disease are often afflicted by non-motor symptoms including fatigue. Alterations of multiple neurotransmitter systems, including dopamine and noradrenaline, have been hypothesized to play a role in the pathogenesis of fatigue. However, whether and how dysfunction in their underlying neurocircuitries contribute to fatigue remains elusive. Here, we used resting-state functional MRI data of 29 patients with Parkinson's disease to investigate associations between clinical ratings of fatigue and functional connectivity within dopamine and noradrenaline transporter-defined functional networks by applying a recently developed multimodal framework "Receptor-Enriched Analysis of functional Connectivity by Targets". We found a negative linear relation between fatigue and noradrenaline-enriched functional connectivity in regions of the sensorimotor and salience networks, and a positive linear trend between fatigue and dopamine-enriched functional connectivity in regions of the default mode network. These findings provide empirical support to the hypothesised dysfunctions in the brain's monoaminergic circuits in Parkinson's patients with fatigue.**

***Keywords*— Parkinson's disease, fatigue, resting state functional connectivity, neurotransmitter.**

I. INTRODUCTION

Fatigue is a frequent symptom in patients with Parkinson's disease (PD) and it affects about half of PD patients, reducing the quality of life and limiting their physical and cognitive performances [1]. To date the precise neurobiological mechanisms underlying fatigue in PD remain elusive, posing limitations to the identification of targeted treatments.

PD is associated with abnormal degeneration of nigrostriatal dopamine (DA) neurons combined with alterations of multiple neurotransmitter systems [2]. Previous studies have examined the role of DA in fatigue, showing that a disruption in the pathways between the striatum and the prefrontal cortex, which is regulated by DA, is linked to fatigue [3]. Moreover, functional and structural neuroimaging studies of PD have shown abnormalities in the frontal and striatal regions that are heavily innervated by DA neurons [3].

In addition to DA, another neurotransmitter, noradrenaline (NE), has also been hypothesized to play a role in the pathogenesis of fatigue. However, the link between NE and fatigue in PD has been explored only in one single study [4] so far, which has reported no significant correlations between fatigue severity and degeneration of the locus coeruleus, where NE is mainly synthesized.

To date, the brain mechanisms underlying fatigue in PD have been investigated mostly using functional magnetic resonance imaging (fMRI). Employing resting-state fMRI (rs-fMRI), two studies [5], [6] have shown that fatigue is correlated with decreased functional connectivity (FC) within the sensorimotor network in the supplementary motor area and increased FC in the prefrontal and posterior cingulate cortices within the default mode network. However, since BOLD fMRI lacks specificity to dissect the contribution of specific neurotransmitters to the signal changes observed in patients, identifying which neurotransmitters might hold greater value as potential targeted treatments has been challenging.

Recently, a new framework of analysis named "Receptor-Enriched Analysis of functional Connectivity by Targets" (REACT) [7] has been developed to enhance rs-fMRI with Positron Emission Tomography imaging data derived from publicly available receptor templates to investigate FC changes within networks informed by the spatial distribution of the density of specific molecular targets. Applying this new framework to rs-fMRI data of multiple sclerosis patients, a recent study [8] has found a negative linear association between cognitive fatigue and noradrenaline transporter (NET)-related FC in frontal regions.

In this study we applied REACT to rs-fMRI data of PD patients to investigate how the functional networks associated to the dopamine transporter (DAT) and NET relate to interindividual differences in fatigue severity. Based on previous findings, we hypothesised that DAT- and NET-enriched FC would correlate with clinical ratings of fatigue in regions of the motor and cingulate cortices.

II. MATERIALS AND METHODS

The study involved 29 consecutive patients (17 men; mean age 64.9y, range [49-77y]) affected by PD, recruited at the Neurology Unit, Movement Disorders Division, University of Verona, Italy. Inclusion criteria were: age 30–80 years, diagnosis of idiopathic PD [9], mild-to-moderate PD (Modified Hoehn & Yahr stage I–III). Participants with pacemakers or ferromagnetic implants and patients with

dementia (Montreal Cognitive Assessment test score<21), or severe psychiatric disorders were excluded. Fatigue was assessed using the Fatigue Severity Scale (FSS), a nine-item easy to administer scale [10] recommended for screening and grading severity in PD [11]. To control for the main potential confounding factors of fatigue, scales for psychiatric disturbances (Hospital Anxiety and Depression Scale), apathy (Apathy Evaluation Scale), excessive daytime somnolence (Epworth Sleepiness Scale) and sleep disorders (Parkinson's disease sleep scale) were administered. Disease severity was assessed by means of UPDRS part III. All examinations were performed with patients ON their dopaminergic treatment. The total dose of dopaminergic drugs was converted to the common metric so-called levodopa equivalent daily dose (LEDD). All participants gave written informed consent to the research protocol, which was approved by the ethical committee of the University Hospital of Verona, conforming to the Helsinki declaration.

Patients' main clinical and demographical characteristics are reported in Table I.

TABLE I
DEMOGRAPHIC INFORMATION

	PD PATIENTS
Age	64.9±7.1y
Gender	17M / 12F
FSS score	3.9±1.6
LEDD	504.8±317.5

PD=Parkinson's disease; FSS=Fatigue Severity Scale; LEDD=levodopa equivalent daily dose

A. MRI acquisition protocol

Images were acquired at the University Hospital of Verona, on a 3T Philips Elition S scanner equipped with a 32-channels head coil. The MR brain imaging protocol included the following sequences: a structural T1-weighted Turbo Field Echo (TR/TE 8.2/3.7ms, 1x1x1mm^3 Acc. Factor Compressed SENSE 3); 10 minutes of rs-fMRI acquired with single shot Echo-Planar Imaging (TR/TE 1100/30ms, FA 64°, 2.4x2.4x2.4mm^3, Acc. factor: MultiBand 4, SENSE 1.9, anterior-posterior phase encoding direction, 500 volumes); two spin echo Echo-Planar Imaging sequences acquired for distortions correction purposes and geometrically matched with the rs-fMRI sequence (Acc. factor: SENSE 1.9, anterior-posterior and posterior-anterior phase encoding directions).

B. MRI data analysis

Pre-processing: Structural and functional images were processed using a combination of the following software: Advanced Normalization Tools software [12] and FMRIB Software Library (FSL) [13].

The T1-weighted image was bias field corrected with N4 [14], skull-stripped and registered to the FSL's MNI atlas, using a nonlinear diffeomorphic registration [12]. The T1-weighted image was also used to extract a subject-specific estimate of the total intracranial volume with FreeSurfer [15].

Rs-fMRI data were pre-processed in the native space following these steps: slice timing, readout distortion (FSL's TOPUP [16]) correction and affine realignment of volumes to the central image of the acquisition. The estimated motion parameters were exploited to compute the framewise displacement [17] for each patient. To remove possible sources of noise, we performed multiple regression of the six head motion parameters, their temporal derivatives, mean white matter and cerebrospinal fluid signals [18]. Rs-fMRI volumes were high-pass filtered (cut-off frequency = 1/128 Hz) and then non-linearly co-registered to the MNI space exploiting the subject-specific T1-weighted image (via FSL's boundary-based registration [19]). Finally, rs-fMRI data were smoothed with a Gaussian kernel of 5 mm^3.

REACT analysis: For the REACT analysis [7], we used publicly available molecular templates of the DAT [20] and NET [21] neuroreceptor systems. The DAT template derived from ^{123}I-Ioflupane Single-Photon Emission Computerized Tomography images from 30 healthy subjects without evidence of nigrostriatal degeneration. The NET template was obtained by averaging the [^{11}C]MRB Positron Emission Tomography brain parametric maps from a cohort of 10 healthy subjects. Both the templates were normalized by scaling the map values between 0 and 1. Then, the occipital areas, used as reference regions for quantification of the molecular data in the kinetic model, were masked out.

To investigate changes in functional connectivity related to the DAT and NET systems, the REACT pipeline employs a two-steps multiple regression analysis [22]. Specifically, in the first step, the two molecular templates are used as a set of spatial regressors to weigh the subject-specific rs-fMRI volumes and estimate the dominant BOLD fluctuation related to each molecular system. In the second step, the subject-specific time series obtained before are used as temporal regressors to estimate the subject-specific spatial maps associated to each molecular system. Thus, after running REACT, two spatial maps reflecting the specific transporter-enriched FC are obtained for each subject. The REACT analysis was conducted within the grey-matter mask.

Statistical analysis: The subject-specific target-enriched FC spatial maps were used as input to a non-parametric permutation-based statistical test using FSL's PALM to investigate the linear relationship between both DAT- and NET-enriched FC and FSS [23]. To speed up the permutation test we set the number of the permutations to 500 and we used the tail approximation approach [23]. FSS scores were used as predictors, while age, sex, LEDD and total intracranial volume as covariates of no-interest. The threshold-free cluster enhancement [24] was used to identify statistically significant clusters (p-value<0.05) of voxels while maintaining familywise-error control. Threshold-free cluster enhancement parameters were set respectively to H = 2, E = 2, C = 6. Next, we identified networks of the Schaefer's functional atlas [25] overlapping with clusters of voxels resulted statistically significant in the permutation test. Within these networks we conducted a partial correlation analysis to assess the relationship between FSS scores and averaged target-enriched FC values, considering age, sex, LEDD and total intracranial volume as covariates.

III. RESULTS

Figure 1 reports the spatial maps of the clusters that resulted statistically significant after permutation testing (p-values<0.05, threshold-free cluster enhancement and familywise-error corrected). For the NET-enriched FC (Figure 1, top panel), these clusters were located around the supplementary motor area, left postcentral gyrus, left precuneus and left middle-cingulate cortex and right rolandic operculum, regions belonging to sensorimotor and salience networks in the Schaefer's atlas. For the DAT-enriched FC (Figure 1, bottom panel), these clusters were located in the precuneus and posterior-cingulate cortex, regions belonging to the default mode network in the Schaefer's atlas.

In Figure 2, left panel, we provide for illustrative purposes the partial correlation results between FSS scores and NET-enriched FC within the sensorimotor and salience networks (left panel) and, in the right panel, between FSS and DAT-enriched FC within the default mode network.

FSS scores and NET-enriched FC were anticorrelated (Pearson's r=-0.48), while between FSS scores and DAT-enriched FC a positive correlation was found (Pearson's r=0.33).

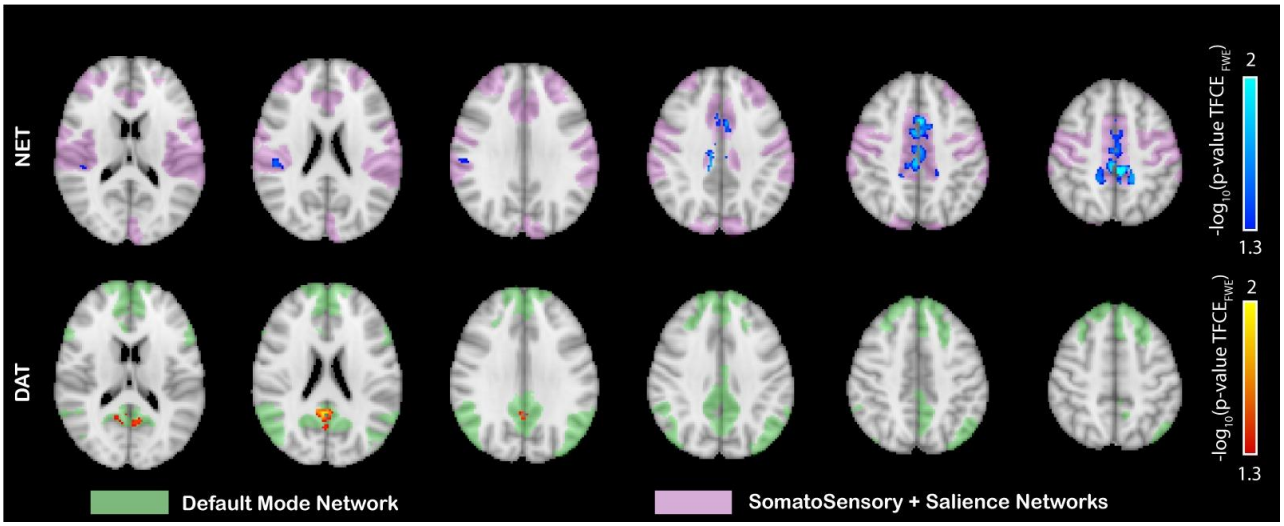


Fig. 1: Clusters of statistically significant NET-enriched FC (top row), overimposed to Schaefer's functional salience and sensorimotor networks in green. In the bottom row, clusters of statistically significant DAT-enriched FC are overimposed to Schaefer's functional default mode network in green. The color scales represent -log(p-value), after correction for multiple comparisons. The statistical maps are overlaid onto the MNI atlas. Abbreviations: NET=noradrenaline transporter; FC=functional connectivity; DAT= dopamine transporter; TFCE= threshold-free cluster enhancement; FWE=familywise-error.

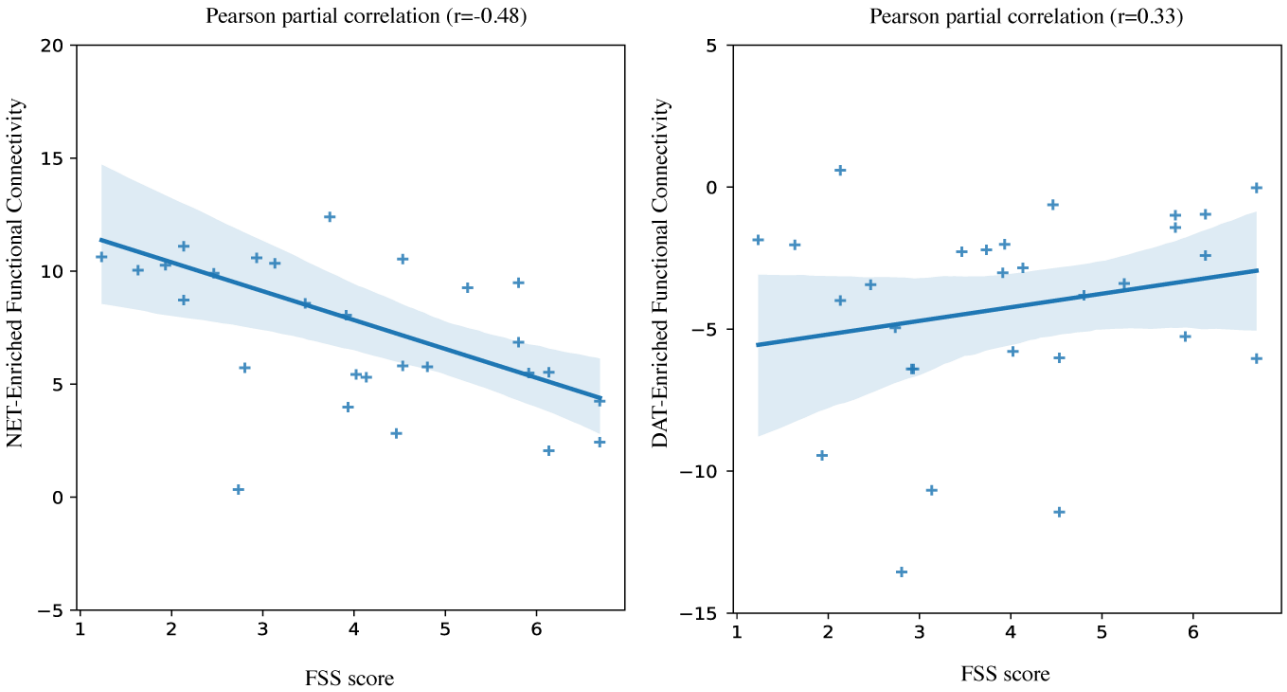


Fig. 2: The left panel reports the partial correlation results between FSS scores and NET-enriched FC within the sensorimotor and salience networks. In the right panel, the partial correlation results between FSS and DAT-enriched FC within the default mode network are shown. Abbreviations: NET=noradrenaline transporter; FC=functional connectivity; DAT= dopamine transporter; FSS=Fatigue Severity Scale.

IV. CONCLUSION

In this study we used a recently developed multimodal approach to investigate associations between clinical ratings of fatigue and FC measured at rest associated with the NET and DAT circuits in patients with PD. We found a negative linear relationship between NET-enriched FC and FSS in regions of the sensorimotor and salience networks and a positive linear relationship between DAT-enriched FC and FSS in regions of the default mode network. Since previous studies reported FC decreases within the sensorimotor network and FC increases within the default mode network in PD patients with fatigue [5], [6], we hypothesize that these FC alterations could be directly related to NET- and DAT- functional circuits.

In addition, our results on NET-enriched FC are in agreement with previously reported FC decreases in NET-related functional circuits in patients with multiple sclerosis and cognitive fatigue [8]. Although in a different clinical population with a different form of fatigue, the results highlight the potential role of NE in explaining the pathogenesis of fatigue.

Taken together, our findings provide preliminary empirical evidence supporting potential dysfunctions in the functional networks associated to the dopaminergic and noradrenergic systems in PD patients with fatigue.

Moreover, our work highlights the value of the multimodal integration of features derived from Positron Emission Tomography imaging and rs-fMRI through REACT as a way forward to advance our understanding of the neural mechanisms underlying fatigue in PD and test the effects of newly targeted treatments.

REFERENCES

[1] I. A. Di Vico *et al.*, “Fatigue in hypokinetic, hyperkinetic, and functional movement disorders”, *Parkinsonism Relat. Disord.*, vol. 86, pp. 114–123, 2021.

[2] G. M. Halliday, J. B. Leverenz, J. S. Schneider, and C. H. Adler, “The Neurobiological Basis of Cognitive Impairment in Parkinson’S Disease”, *Mov. Disord. Off. J. Mov. Disord. Soc.*, vol. 29, no. 5, pp. 634–650, 2014.

[3] E. Dobryakova, H. M. Genova, J. DeLuca, and G. R. Wylie, “The Dopamine Imbalance Hypothesis of Fatigue in Multiple Sclerosis and Other Neurological Disorders», *Front. Neurol.*, vol. 6, 2015.

[4] O. Solopchuk *et al.*, “Locus Coeruleus atrophy doesn’t relate to fatigue in Parkinson’s disease”, *Sci. Rep.*, vol. 8, no. 1, p. 12381, 2018.

[5] M. Siciliano *et al.*, “Supplementary motor area functional connectivity in “drug-naïve” Parkinson’s disease patients with fatigue”, *J. Neural Transm.*, vol. 127, no. 8, pp. 1133–1142, 2020.

[6] A. Tessitore *et al.*, “Functional connectivity underpinnings of fatigue in “Drug-Naïve” patients with Parkinson’s disease”, *Mov. Disord.*, vol. 31, no. 10, pp. 1497–1505, 2016.

[7] O. Dipasquale, P. Selvaggi, M. Veronese, A. S. Gabay, F. Turkheimer, and M. A. Mehta, “Receptor-Enriched Analysis of functional connectivity by targets (REACT): A novel, multimodal analytical approach informed by PET to study the pharmacodynamic response of the brain under MDMA”, *NeuroImage*, vol. 195, pp. 252–260, 2019.

[8] M. Cercignani *et al.*, “Cognitive fatigue in multiple sclerosis is associated with alterations in the functional connectivity of monoamine circuits”, *Brain Commun.*, vol. 3, no. 2, 2021.

[9] R. B. Postuma *et al.*, “MDS clinical diagnostic criteria for Parkinson’s disease”, *Mov. Disord. Off. J. Mov. Disord. Soc.*, vol. 30, no. 12, pp. 1591–1601, 2015.

[10] L. B. Krupp, “The Fatigue Severity Scale: Application to Patients With Multiple Sclerosis and Systemic Lupus Erythematosus”, *Arch. Neurol.*, vol. 46, no. 10, p. 1121, 1989.

[11] R. G. Brown, A. Dittner, L. Findley, and S. C. Wessely, “The Parkinson fatigue scale”, *Parkinsonism Relat. Disord.*, vol. 11, no. 1, pp. 49–55, 2005.

[12] B. B. Avants, N. J. Tustison, G. Song, P. A. Cook, A. Klein, and J. C. Gee, “A reproducible evaluation of ANTs similarity metric performance in brain image registration”, *NeuroImage*, vol. 54, no. 3, pp. 2033–2044, 2011.

[13] S. M. Smith *et al.*, “Advances in functional and structural MR image analysis and implementation as FSL”, *NeuroImage*, vol. 23 Suppl 1, pp. S208-219, 2004.

[14] N. J. Tustison *et al.*, “N4ITK: Improved N3 Bias Correction”, *IEEE Trans. Med. Imaging*, vol. 29, no. 6, pp. 1310–1320, 2010.

[15] R. L. Buckner *et al.*, “A unified approach for morphometric and functional data analysis in young, old, and demented adults using automated atlas-based head size normalization: reliability and validation against manual measurement of total intracranial volume”, *NeuroImage*, vol. 23, no. 2, pp. 724–738, 2004.

[16] J. L. R. Andersson and S. N. Sotiropoulos, “An integrated approach to correction for off-resonance effects and subject movement in diffusion MR imaging”, *NeuroImage*, vol. 125, pp. 1063–1078, 2016.

[17] J. D. Power, K. A. Barnes, A. Z. Snyder, B. L. Schlaggar, and S. E. Petersen, “Spurious but systematic correlations in functional connectivity MRI networks arise from subject motion”, *NeuroImage*, vol. 59, no. 3, pp. 2142–2154, 2012.

[18] H. J. Jo *et al.*, “Effective Preprocessing Procedures Virtually Eliminate Distance-Dependent Motion Artifacts in Resting State FMRI”, *J. Appl. Math.*, vol. 2013, 2013.

[19] D. N. Greve e B. Fischl, “Accurate and robust brain image alignment using boundary-based registration”, *NeuroImage*, vol. 48, no. 1, pp. 63–72, ott. 2009.

[20] F. J. García-Gómez *et al.*, “Elaboration of the SPM template for the standardization of SPECT images with 123I-Ioflupane”, *Rev. Esp. Med. Nucl. Imagen. Mol.*, vol. 32, no. 6, pp. 350–356, 2013.

[21] S. Hesse *et al.*, “Central noradrenaline transporter availability in highly obese, non-depressed individuals”, *Eur. J. Nucl. Med. Mol. Imaging*, vol. 44, no. 6, pp. 1056–1064, 2017.

[22] L. D. Nickerson, S. M. Smith, D. Öngür, and C. F. Beckmann, “Using Dual Regression to Investigate Network Shape and Amplitude in Functional Connectivity Analyses”, *Front. Neurosci.*, vol. 11, 2017.

[23] A. M. Winkler, G. R. Ridgway, M. A. Webster, S. M. Smith, and T. E. Nichols, “Permutation inference for the general linear model”, *NeuroImage*, vol. 92, no. 100, pp. 381–397, 2014.

[24] S. M. Smith and T. E. Nichols, “Threshold-free cluster enhancement: addressing problems of smoothing, threshold dependence and localisation in cluster inference”, *NeuroImage*, vol. 44, no. 1, pp. 83–98, 2009.

[25] A. Schaefer *et al.*, “Local-Global Parcellation of the Human Cerebral Cortex from Intrinsic Functional Connectivity MRI”, *Cereb. Cortex N. Y. NY*, vol. 28, no. 9, pp. 3095–3114, 2018.

Breast Cancer Detection via Two-dimensional Ultrasound Tomography

S. Franceschini[1], M. Ambrosanio[2], M.M. Autorino[1], V. Pascazio[1] and F. Baselice[1]
[1] *University of Naples Parthenope, Department of Engineering;*
[2] *University of Naples Parthenope, Department of Economics, Law, Cybersecurity and Sport Sciences;*

***Abstract*—In the framework of biomedical imaging, ultrasound tomography has recently proven to be an attractive solution for non-invasive, non-destructive diagnostic imaging. More in detail, this technique exploits mechanical waves which are safe for the patient and can be considered for frequent screening. The aim of this technique is to retrieve the mechanical information of breast inner tissue via the analysis of pressure waves acquired by sensors surrounding the region of interest. In this paper a stepped breast-cancer-imaging approach via ultrasound tomography is proposed. The tumour extension and localisation are retrieved via solving a set of linear inverse scattering problems in a step-by-step fashion. The proposed approach seems to be promising in terms of malignancy identification.**

***Keywords*—Ultrasound tomography, tomographic imaging, MIMO systems, inverse scattering, coherent imaging, biomedical imaging.**

I. Introduction

Breast tumour represents a type of cancer with the highest incidence among adult women (higher than 29% as reported in [1]). During the last decades several research groups focused on the development of new strategies for efficient early breast cancer diagnosis by means of either quantitative or qualitative imaging.

Numerous conventional techniques for breast cancer imaging (BCI) are based on the use of ionizing radiations such as X and γ rays (e.g., computed tomography, positron emission tomography, etc.). These former approaches share the same drawback of limited time exposition due to the use of ionising radiations [2]. A further conventional technique for breast cancer diagnosis is the magnetic resonance imaging (MRI), which exploits static magnetic fields and radio-frequency pulses to perform this investigation and thus it is safe from patient's perspective. Despite a good spatial resolution, MRI presents long acquisition time and high costs. Mechanical properties of the breast in terms of density, attenuation and propagation speed are substantially different between healthy and malignant tissues [3]. For this reason ultrasound waves can be exploited for breast cancer imaging. Conventional ultrasound (US) considers a hand-held probe that scans the region under investigation. Thus, this aspect is one of the main bottlenecks of conventional US imaging.

In this framework a recent solution is represented by ultrasound tomography (UST). This technique considers the analysis of pressure waves generated and measured by US sensors placed around a region of interest [4], [5]. Most recent UST prototypes exploit several US sensors and in some cases the UST is used in combination with other imaging techniques, e.g. microwave tomography [6], [7].

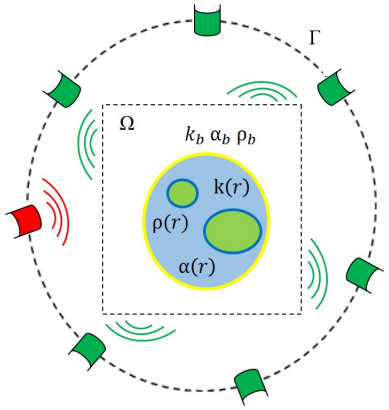


Fig. 1: Sketch of the 2D ultrasound tomography. Γ is the curve containing the ultrasound transducers. Ω is the region under investigation. The quantities κ, ρ and α are the acoustic compressibility, density and attenuation of the objects located inside the background medium with parameters κ_b, ρ_b and α_b.

The problem of retrieving the mechanical properties of breast inner tissues is non-linear and ill-posed [8], [9]. Therefore, most inversion algorithms exploit strong a-priori information and advanced regularisation strategies to obtain reliable recoveries [10], [11]. Among the most adopted linear approximations, it is worth to mention the well-known Born approximation (BA), which assumes that the presence of the target slightly perturbs the field [12].

In this paper some two-dimensional (2D) numerical simulations of an UST system for breast cancer imaging purposes are proposed. The forward solver is carried out via K-Wave, a Matlab toolbox designed for photo-acoustic simulation in time domain[13]. The considered scenarios include simplified phantoms mimicking breast inner tissues (fat and fibroglandular). Once acquired the US scattering data, a qualitative inversion to retrieve tumour extension is obtained via the Born approximation in a three-step procedure. The results show the possibility to retrieve information about position and size of the malignant tissue.

The remainder of the paper is the following: in Section II a brief mathematical recall of the problem at hand is provided, while in Section III the considered methodology and related imaging results are presented and discussed. Some conclusions

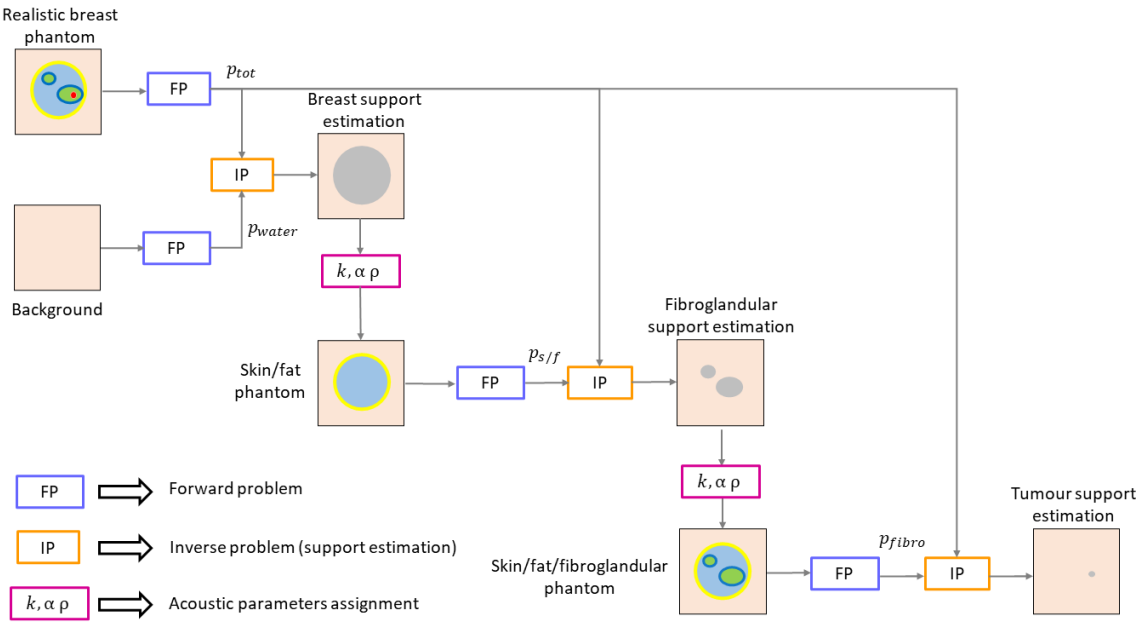


Fig. 2: Block diagram of the proposed tumor detection scheme. At each support estimation step, a new phantom is generated by assigning some average mechanical properties to the identified tissues.

end the paper in Section IV.

II. Mathematical Formulation

Let us assume a 2D simplified scenario as shown in Fig. 1. The integral equation governing the scattering phenomena is a function of the mechanical properties of both targets and background, i.e. density, compressibility and attenuation. Omitting the frequency dependence and considering an homogeneous background, the scattering field equation can be written as [14]:

$$p_{scat}(\mathbf{r}) = k_b^2 \iint_{\Omega} g(\mathbf{r},\mathbf{r}') \left[\chi_1(\mathbf{r}') - j\frac{2\delta\alpha(\mathbf{r}')}{k_b}\right] p_{tot}(\mathbf{r}')d\mathbf{r}' + \iint_{\Omega} g(\mathbf{r},\mathbf{r}')\nabla\cdot[\chi_2(\mathbf{r}')\nabla p_{tot}(\mathbf{r}')]\, d\mathbf{r}', \quad \mathbf{r}\in\Gamma, \quad (1)$$

where p_{scat} and p_{tot} are the scattered and the total pressure fields, respectively. The quantity $k_b = \frac{\omega}{c_b}$ is the lossless background wavenumber, ω is the angular frequency and c_b is the propagation speed in the background. The operator $g(\cdot,\cdot)$ refers to the background Green's function and Ω refers to the imaging domain. The two quantities $\chi_1(\mathbf{r})$ and $\chi_2(\mathbf{r})$ represent the contrast function for the compressibility and density defined as:

$$\chi_1(\mathbf{r}) = \frac{\kappa(\mathbf{r})-\kappa_b}{\kappa_b}, \qquad \chi_2(\mathbf{r}) = \frac{\rho^{-1}(\mathbf{r})-\rho_b^{-1}}{\rho_b^{-1}}, \quad (2)$$

where κ and ρ are the compressibility and density, and the subscript b refers to the same quantities related to the background. The quantity $\delta\alpha(\mathbf{r})$ is defined as the difference between the object and background attenuation ($\delta\alpha(\mathbf{r}) = \alpha(\mathbf{r}) - \alpha_b$).

The task of retrieving the quantities $\chi_1(\mathbf{r})$, $\chi_2(\mathbf{r})$ and $\delta\alpha(\mathbf{r})$ is a non-linear and ill-posed, and therefore, typically a-priori information are exploited in order to reduce the complexity of the inversion algorithm.

The aim of the proposed analysis is to retrieve a reliable estimate of the breast cancer location and extension. To this purpose, by adopting the BA and observing that the first integral in Eq. (1) has a stronger impact on the scattered pressure field, it is possible to write:

$$p_{scat}(\mathbf{r}) \approx k_b^2 \iint_{\Omega} g(\mathbf{r},\mathbf{r}')\mathcal{I}(\mathbf{r}')p_{tot}(\mathbf{r}')d\mathbf{r}' = \mathcal{L}\left[\mathcal{I}(\mathbf{r})\right], \quad (3)$$

with $\mathbf{r}\in\Gamma$ and:

$$\mathcal{I}_{norm}(\mathbf{r}) = \frac{|\,\mathcal{I}(\mathbf{r})\,|}{\mathcal{I}_{max}}, \quad (4)$$

in which $\mathcal{I}_{max} = \max[\,|\,\mathcal{I}(\mathbf{r})\,|\,]$.

$\mathcal{I}_{max}$ is a qualitative indicator providing information about the contrast of the profile under test. Although this reconstruction does not provide any physical quantity, due to different acoustic parameters exhibit by the healthy and malignant tissues, it is still possible to detect anomalies possibly related to breast cancer.

III. Proposed Method and Imaging Results

In the following, the breast is approximated by phantoms composed of different homogeneous tissues of circular shape. In particular, water is assumed as background and a 1.5-mm-thick layer is considered for the skin. Likewise, some circles and ellipses were used to simulate fat, fibroglandular and tumour tissues with homogeneous mechanical properties, as shown in Fig. 3(a,b). The parameters adopted in the following simulations were chosen based on [15] and the corresponding values are reported in Tab. I.

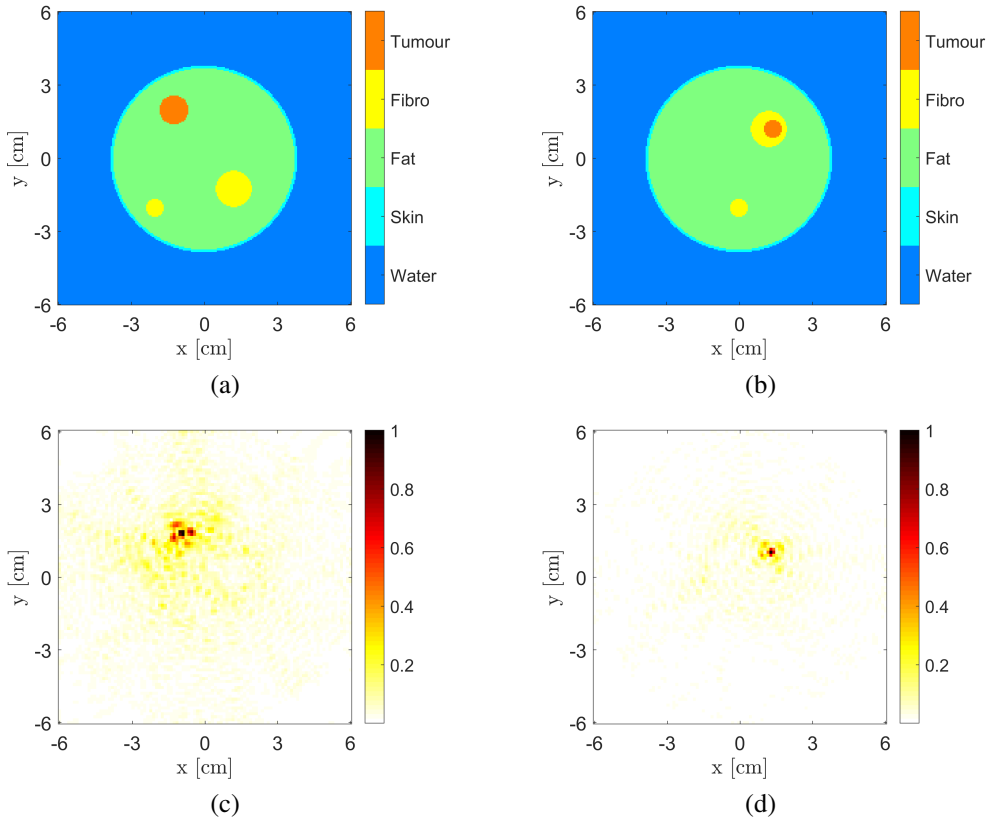


Fig. 3: Results of the proposed tumor detection strategy. (a,b) Numerical breast phantoms and (c,d) corresponding estimates of tumour support maps (indicator of Eq. (4)).

The whole breast is assumed to be a 10-cm-diameter circle. It is worth to note that the attenuation depends on the frequency according to the following relation:

$$\alpha(f) = \alpha_0 f^b, \tag{5}$$

where it was assumed $b = 1$.

The K-Wave forward simulation considers a monochromatic ultrasonic source at the operative frequency of 200 kHz. Regarding the US transducers, a total of 83 elements located on a circle of 6-cm radius surrounding the breast were considered in a multiview-multistatic configuration. Therefore, per each view, a total of 83 measures (including the monostatic contribution) was taken into account. It is worth to note that only the steady-state signals were considered.

The proposed solution for addressing the inverse problem consists of a three-step iterative procedure based on the BA. The workflow reporting the overall scheme is shown in Fig. 2. At the first step, a linear inversion via BA is carried out for the support estimation of the breast. To this aim, both the field in presence of the breast (p_{tot}) and the background one (p_{water}) are required. From this initial qualitative recovery and assuming the skin thickness as known, the estimated support is used to create a new phantom with both estimated skin and adipose tissues. Regarding the assigned mechanical properties (density, compressibility and attenuation coefficient), the values reported in Table I were adopted. Starting from this profile, a new forward simulation is performed and the related pressure field is obtained ($p_{s/f}$). At this step, a new linear inversion is carried out to retrieve information about the support of fibroglandular tissues, and the procedure goes on until tumour support estimation is reached.

TABLE I: Propagation speed ($c = \frac{1}{\sqrt{\kappa\rho}}$), density ($\rho$) and attenuation ($\alpha_0$) of breast inner tissues

Tissue	$c\ [\frac{m}{s}]$	$\rho\ [\frac{kg}{m^3}]$	$\alpha_0\ [\frac{dB}{cmMHz}]$
Skin	1735	1137	0.75
Fat	1430	951	0.5
Fibroglandular	1560	971	1.2
Tumor	1600	990	2.6

Fig. 3(c,d) show the spatial maps of the indicator defined in Eq. (4), which represent the estimates of the tumour support in the case of the two numerical phantoms of Fig. 3(a,b). It is worth to note that the proposed scheme manages to identify the malignancy with good accuracy both in case the tumour is surrounded by fibroglandular tissues or by adipose one.

IV. Conclusion

In this paper a three-step method based on the BA for breast cancer detection via ultrasound tomography was proposed. The approach considers a cascade of inversion blocks each adding progressively new information regarding the extension of the interior breast tissues. A preliminary numerical analysis was proposed by testing the method in two different scenarios including a malignancy either surrounded by fibroglandular tissue or by adipose one. In both cases, the proposed solution is able to retrieve tumor location correctly with good accuracy.

Future work includes testing the methodology in more realistic scenarios and considering its robustness against model error.

References

[1] Siegel, R., Miller, K. & Jemal, A. Cancer statistics, 2015.. *CA: A Cancer Journal For Clinicians*. 65, 5 (2015)

[2] Smith, N. & Webb, A. Introduction to Medical Imaging: Physics, Engineering and Clinical Applications. (Cambridge University Press,2010)

[3] Goncharsky, A., Romanov, S. & Seryozhnikov, S. Low-frequency ultrasonic tomography: mathematical methods and experimental results. *Moscow University Physics Bulletin*. 74, 43-51 (2019)

[4] Gemmeke, H. & Ruiter, N. 3D ultrasound computer tomography for medical imaging. *Nuclear Instruments And Methods In Physics Research Section A: Accelerators, Spectrometers, Detectors And Associated Equipment*. 580, 1057-1065 (2007)

[5] Franceschini, S., Ambrosanio, M., Baselice, F. & Pascazio, V. A Tomographic Multiview-Multistatic Ultrasound System for Biomedical Imaging Applications.. *BIODEVICES*. pp. 274-279 (2020)

[6] Qin, Y., Rodet, T., Lambert, M. & Lesselier, D. Joint Inversion of Electromagnetic and Acoustic Data With Edge-Preserving Regularization for Breast Imaging. *IEEE Transactions On Computational Imaging*. 7 pp. 349-360 (2021)

[7] Abdollahi, N., Kurrant, D., Mojabi, P., Omer, M., Fear, E. & LoVetri, J. Incorporation of ultrasonic prior information for improving quantitative microwave imaging of breast. *IEEE Journal On Multiscale And Multiphysics Computational Techniques*. 4 pp. 98-110 (2019)

[8] Hadamard, J. Lectures on Cauchy's problem in linear partial differential equations. (Courier Corporation,2014)

[9] Colton, D. & Kress, R. Inverse acoustic and electromagnetic scattering theory. (Springer Science & Business Media,2012)

[10] Bertero, M. & Boccacci, P. Introduction to inverse problems in imaging. (CRC press,1998)

[11] Ambrosanio, M., Franceschini, S., Autorino, M., Baselice, F. & Pascazio, V. An Experimental Ultrasound System for Qualitative Tomographic Imaging. *Sensors*. 22, 7802 (2022,10)

[12] Habashy, T., Groom, R. & Spies, B. Beyond the Born and Rytov approximations: A nonlinear approach to electromagnetic scattering. *Journal Of Geophysical Research: Solid Earth*. 98, 1759-1775 (1993)

[13] Treeby, B. & Cox, B. k-Wave: MATLAB toolbox for the simulation and reconstruction of photoacoustic wave fields. *Journal Of Biomedical Optics*. 15 pp. 021314 (2010,3)

[14] Mojabi, P. & LoVetri, J. Ultrasound tomography for simultaneous reconstruction of acoustic density, attenuation, and compressibility profiles. *The Journal Of The Acoustical Society Of America*. 134, 1813-1825 (2015)

[15] Mojabi, P. & LoVetri, J. Composite Tissue-Type and Probability Image for Ultrasound and Microwave Tomography. *IEEE Journal On Multiscale And Multiphysics Computational Techniques*. 1 pp. 26-35 (2016)

Computer Vision and Deep Learning for Human Motion Analysis

Matteo Moro[1,2], Vito Paolo Pastore[1,2], Giorgia Marchesi[3], Luca Garello[4], Chiara Tacchino[5], Paolo Moretti[5], Matilde Inglese[6,7], Francesca Odone[1,2] and Maura Casadio[1]
[1] *DIBRIS Department, University of Genova, Genova (GE), Italy*
[2] *Machine Learning Genoa (MaLGa) Center, Genova (GE), Italy*
[3] *Movendo Technology, Genova (GE), Italy*
[4] *Italian Institute of Technology (IIT), Genova (GE), Italy*
[5] *Istituto Giannina Gaslini, Genova (GE), Italy*
[6] *DINOGMI Department, University of Genova, Genova (GE), Italy*
[7] *Ospedale Policlinico San Martino-IRCCS, Genova (GE), Italy*

***Abstract*—State-of-the-art technologies usually adopted to characterize human motion rely on wearable sensors, motion capture systems and markers. These system provide useful and accurate quantitative kinematic measures. Unfortunately, marker-based systems require expensive laboratory settings with several infrared cameras, limiting their use in uncontrolled environments. This could modify the naturalness of subjects movements and induce discomfort. Also, markers are intrusive and their number and location must be determined a priori. Recent advances on pose estimation and semantic features detectors based on computer vision and deep neural networks are opening the possibility of adopting efficient video-based methods for extracting movement information from RGB video data. In this contest, in the last few years, we introduced and tested the effectiveness of a video-based markerless pipeline for the quantitative analysis of human motion in the rehabilitation domain. In this paper, we summarize the implemented pipeline, we highlight possible application fields where its use can be beneficial also providing examples of applications.**

***Keywords*—Markerless, Human motion analysis, Computer Vision, Deep Learning**

I. Introduction

Human motion understanding is a relevant task in many fields of science and medicine. Predicting and describing quantitative and qualitative human behavior while performing different actions is essential in neuroscience to understand the brain behaviour in both physiological and pathological conditions [6], [1]. Moreover, it is helpful for human-computer interaction applications [12], [23], for human-robot interaction [10] and for augmented reality applications for gaming and rehabilitation [27]. Lastly, human motion understanding is largely adopted to study and predict how people interact [14].

Nowadays, the gold standard techniques commonly adopted to accurately describe and study human motion rely on wearable sensors, motion capture systems and markers placed on the body skin [16]. However, markers are intrusive and they may limit natural movements [5], making the analysis of motion patterns challenging in some application fields such as infants motion analysis [18], sports biomechanics and musicians motion characterization.

For these reasons, recently, RGB video analysis has been considered to become a possible alternative to marker-based systems [7], [24]. This is due to the increasing progress of deep learning and computer vision algorithms [29]. In particular, recent advances on pose estimation algorithms and on semantic features detectors based on deep neural networks are opening the possibility of adopting efficient methods for tracking human pose and extracting motion information starting just from video data [25]. In this context, we studied, implemented and tested a markerless pipeline able to extract quantitative information related to human motion and we compared the measures obtained with our pipeline to those commonly obtained using gold standard marker-based systems. We used our pipeline to address different problems and we report here the results obtained in two cases: (i) the characterization of preterm infants motion patterns and (ii) gait analysis.

II. Proposed markerless pipeline

Our aim is to create a markerless system able to describe in a quantitative way human motion. We tested our pipeline in applications related to the medical and the rehabilitation domains with the aim to support physicians in their medical evaluations and to allow them to timely plan appropriate rehabilitation treatments. In this context, an important requirement to take into account is the need for interpretable methods: for this reason, we can not rely on end-to-end architectures and we need to build a multi-level system to better understand the results of each step. In this way it is also possible to use this system in different application scenarios with just small changes. Specifically, we divide the pipeline into the following steps.

1) *Landmark points detection*: we leverage Convolutional Neural Networks (CNN) and we detect the positions of meaningful landmark points in the image plane. This can be done thanks to the high number of pre-trained pose estimators [4], [2] and semantic features detectors [25], [17] developed in the last few years.

2) *From 2D to 3D*: if the acquisition setup includes multiple viewpoints, the information from the different views can be combined in order to reconstruct the 3D positions (X, Y, Z) of each landmark point. This is particularly useful because the standard marker-based approaches to study human motion provide 3D information. In this case we include the use of biomechanical modeling software such as Opensim [9] to describe the motion.
3) *Motion characterization*: depending on the problem addressed, it is necessary to define and extract the set of parameters helpful to describe the motor patterns.

A. Landmark points detection

We start from the same logic behind gold standard marker-based systems and we detect the position of meaningful landmark points in the videos of humans. To do that, it is first necessary to locate them in 2D image planes. Depending on the application, we start by relying on: (i) pose estimation algorithms [4], [2]; (ii) pre-trained semantic features detectors [17], [25] fine tuned on specific keypoints depending on the motion patterns to characterize.

Inputs to our procedure are frames extracted from RGB videos. Independently from the algorithm adopted, the outputs are the positions of the keypoints in the image plane. Specifically, for each image we have $\{(x, y, c)_l\}$, where $(x, y)_l$ is the position of the $l-$th keypoint in the image and c_l is a number in the interval $[0, 1]$ and represents the probability the $l-$th keypoint had been correctly detected. With c_l we are able to quantify the uncertainty behind the detection of each point in each image. In Figure 1 we show an example of keypoints detected in the image plane.

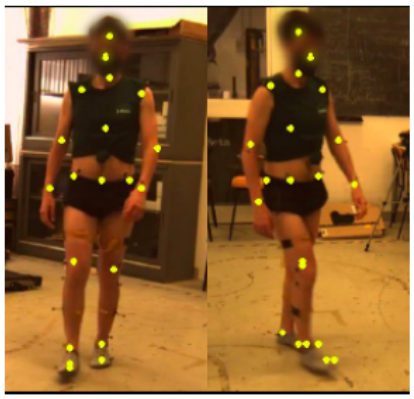


Fig. 1: Examples of keypoints extracted in the image plane.

B. From 2D to 3D

In the literature there are algorithms for 3D reconstruction specific for the human pose. There are methods relying on single images (*e.g.*, [28]); others that work under the hypothesis that calibration is not available, and generally require very large datasets (*e.g.*, [11], [3]). Other works approach the problem using a similar prior as calibrated reconstruction (multi-view calibrated inputs during training) but in a data-driven fashion (*e.g.*, [15]). Unfortunately, the previously mentioned approaches do not appear to be appropriate for our purpose. In fact, we need a method as precise and accurate as possible. For this reason we opt for a geometric approach relying on stereo vision [13]. The choice of a general purpose geometric approach is also motivated by its simplicity and high generalization potential. For these reasons, we include in our analysis the 3D reconstruction step only when a multi-view camera system (two or more cameras) is available. In particular, in [19] we studied the error made by adopting our implemented markerless pipeline in the localization of the 3D positions of the markers with respect to their actual positions tracked with a motion capture system (Optotrak 3020). The markers were placed on the violin and on the bow of violin players. We highlighted that the error done in the localization of the markers with our pipeline is in the order of a few millimeters (below 6 mm in at least 70% of the cases).

C. Motion characterization

Starting from the 2D or 3D signals that represent the evolution over time of the positions of each landmark point, it was possible to extract quantitative parameters that characterize the motion patterns. The relevant parameters to computer depend on the application domain as highlighted in Section III.

III. Applications

In this section, we report two examples of application of our markerless pipeline different but both related to assessment in the rehabilitation domain.

A. Infants motion analysis

Here we report the results of the application of our proposed markerless approach to study the motion of 142 preterm infants, 59 with a clinical diagnosis of neuromotor disorders. This work was carried out in collaboration with the Istituto Giannina Gaslini (Genova, Italy) and was presented in [22]. The analysis of preterm infants' spontaneous movements is essential for an early diagnosis of neuro-motor disorders. Inspired by the neuro-motor literature and following the General Movements theory [26], we computed quantitative motor parameters to describe infant's motion. We included generic parameters such as the mean, standard deviation, median, maximum and minimum speed, acceleration and jerk; the total covered distance and the Euclidean distance between the starting and the final position of each keypoint; the entropy, the peak magnitude, the sum of the spectrum and the spectral half point of the power spectral density of the total covered distance and of the speed of each keypoint. Furthermore, we computed specific parameters such as the skewness, the periodicity, the area out of moving average and the cross-correlation between the motion of hands and feet [22]. We used these parameters to train and test different binary classifiers (*e.g.*, Support Vector Machine, Random Forest and Long short-term memory) in order to identify infants likely to manifest neuro-motor disorders. In this way, we obtained a maximum

accuracy of 85.7% in the discrimination of infants with and without neuro-motor disorders.

B. Gait analysis

Here we report the results of the application of our proposed markerless approach for 2D and 3D gait analysis. In particular, we used our pipeline to characterize the gait of stroke survivors [21], unimpaired adults [20] and people with multiple sclerosis. Part of this work was founded by Fondazione Italiana Sclerosi Multipla (FISM – 2019/PR-single050) and carried out in collaboration with San Martino Hospital (Genova, Italy), Dipartimento di Neuroscienze, Riabilitazione, Oftalmologia, Genetica e Scienze Materno-Infantili (DINOGMI).

Our goal was to evaluate the appropriateness of our markerless pipeline as an alternative to classical marker-based systems. To do that, we performed gait analysis with gold standard systems and with our proposed markerless approach on the same dataset and we statistically compared the results obtained both in 2D and in 3D.

a) 2D analysis: Firstly, we focused on the 2D experimental assessment and we compared the quality of our estimated parameters with the ones obtained with a standard marker-based analysis and reported promising results: most of the 2D parameters may be computed by our markerless method at a comparable precision [21]. For this work, we adopted a subset of the dataset presented in [8], where RGB videos of the gait of 10 stroke survivors (mean age $\pm$ standard deviation: 62.75 $\pm$ 12.29 years old) were acquired with the aim of visual assessment and not for an organized computer-aided analysis.

We did not find statistically significant differences between the elevation angles computed with marker-based system and markerless one. Furthermore, we succeeded in highlighting the differences between the spatio-temporal parameters of the impaired leg and the unimpaired leg in hemiparetic stroke survivors, similarly to analysis carried out by conventional methods.

b) 3D analysis: We extended our analysis and we performed a comparison in 3D [20]. We acquired an *ad hoc* multimodal dataset of 16 unimpaired participants with a gold standard marker-based motion capture system and a multi-view RGB cameras system to be able to perform a geometric 3D reconstruction. We computed the spatio-temporal parameter and the joint angles relying on the biomechanical modeling open source software Opensim [9] with both marker and video data. Also in this case we did not observe relevant differences among the two approaches. For this reason, we adopted the pipeline to characterize and monitor kinematic patterns in Multiple Sclerosis people. In Figure 2 we show the knee, hip and foot angles in the sagittal plane of a person with Multiple Sclerosis with asymmetric gait. The right ankle has a reduced dorsi-plantar flexion and a decreased knee flexion in the swing phase.

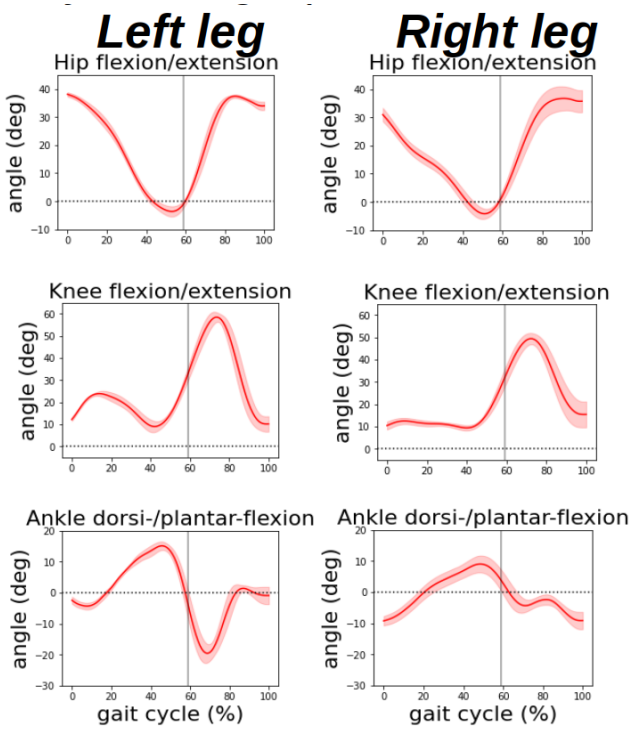


Fig. 2: Mean and standard deviation of hip, knee and foot angles in the sagittal plane for the left and right leg of a person with Multiple Sclerosis. We considered a total of 20 gait cycles.

IV. Strengths and Weaknesses of our Markerless Approach

Here we summarize the main advantages of markerless methods for human motion analysis.

- In general, the overall process to perform markerless analysis requires less preparation for the final users and it is not operator dependent. While the practitioner during marker-based data acquisition needs to place markers very carefully on the body skin in order to reduce as much as possible the bias, markerless systems are fully automatic, and are less operator dependent.
- The naturalness of movements is not affected by cumbersome markers placed all over the body skin. Thanks to the non-invasive nature of markerless systems, it is possible to adopt them to study human motion in application fields where the invasiveness of markers do not allow or reduce the possibilities to perform analysis (such as with infants, music players and athletes).
- It is less expensive. We estimated that the cost for markerless analysis is almost 20 times lower with respect to marker-based systems and it can be based on mobile phone or computer camera recordings.
- Markerless analysis has the potential to be performed in non-controlled, unconstrained environments, satisfying the need of a technique adoptable also at home. However, at this stage, we tested the pipeline only in controlled environments (*e.g.*, laboratories and hospitals) with one person involved in the scene.

On the other side, they present some limitations that should be further explored.

- If from one side there are few and well defined marker-based system for human motion analysis, on the other

side there are many different RGB cameras with different resolutions, sensors type and frame rates. For these reasons and for the variability of the application environment, it is difficult to create a standard reproducible system based on RGB cameras.
- Due to intrinsic physical limitation of camera sensors (spatial limitation related to pixel size), the level of detail achievable with this type of analysis is limited.
- A too low temporal resolution (frame rate) of the camera combined with fast movements may lead to motion blur and, consequently, to small errors in the detection of the keypoints in the image plane. One immediate way to reduce the motion blur is to adopt RGB cameras with a high temporal resolution (*i.e.*, high acquisition rate).

In conclusion, markerless analysis represent an interesting alternative not yet fully explored to marker-based techniques.

ACKNOWLEDGEMENT

This research was partially funded by: Fondazione Italiana Sclerosi Multipla (FISM – 2019/PR-single050) and RAISE, NextGeneration EU (PNRR Italy, innovation ecosystems program).

REFERENCES

[1] Melissa Bateson and Paul Martin. *Measuring behaviour: an introductory guide*. Cambridge University Press, 2021.

[2] Valentin Bazarevsky, Ivan Grishchenko, Karthik Raveendran, Tyler Zhu, Fan Zhang, and Matthias Grundmann. Blazepose: On-device real-time body pose tracking. *arXiv preprint arXiv:2006.10204*, 2020.

[3] Magnus Burenius, Josephine Sullivan, and Stefan Carlsson. 3d pictorial structures for multiple view articulated pose estimation. In *Proceedings of the IEEE conference on computer vision and pattern recognition*, pages 3618–3625, 2013.

[4] Zhe Cao, Tomas Simon, Shih-En Wei, and Yaser Sheikh. Realtime multi-person 2d pose estimation using part affinity fields. In *Proceedings of the IEEE conference on computer vision and pattern recognition*, pages 7291–7299, 2017.

[5] Bruce Carse, Barry Meadows, Roy Bowers, and Philip Rowe. Affordable clinical gait analysis: An assessment of the marker tracking accuracy of a new low-cost optical 3d motion analysis system. *Physiotherapy*, 99(4):347–351, 2013.

[6] Claire Chambers, Nidhi Seethapathi, Rachit Saluja, Helen Loeb, Samuel R Pierce, Daniel K Bogen, Laura Prosser, Michelle J Johnson, and Konrad P Kording. Computer vision to automatically assess infant neuromotor risk. *IEEE Transactions on Neural Systems and Rehabilitation Engineering*, 28(11):2431–2442, 2020.

[7] Steffi L Colyer, Murray Evans, Darren P Cosker, and Aki IT Salo. A review of the evolution of vision-based motion analysis and the integration of advanced computer vision methods towards developing a markerless system. *Sports medicine-open*, 4(1):24, 2018.

[8] Alice De Luca, Honoré Vernetti, Cristina Capra, Ivano Pisu, Cinzia Cassiano, Laura Barone, Federica Gaito, Federica Danese, Giovanni Antonio Checchia, Carmelo Lentino, et al. Recovery and compensation after robotic assisted gait training in chronic stroke survivors. *Disability and Rehabilitation: Assistive Technology*, pages 1–13, 2018.

[9] Scott L Delp, Frank C Anderson, Allison S Arnold, Peter Loan, Ayman Habib, Chand T John, Eran Guendelman, and Darryl G Thelen. Opensim: open-source software to create and analyze dynamic simulations of movement. *IEEE transactions on biomedical engineering*, 54(11):1940–1950, 2007.

[10] David Droeschel and Sven Behnke. 3d body pose estimation using an adaptive person model for articulated icp. In *International Conference on Intelligent Robotics and Applications*, pages 157–167. Springer, 2011.

[11] Ahmed Elhayek, Edilson de Aguiar, Arjun Jain, Jonathan Thompson, Leonid Pishchulin, Mykhaylo Andriluka, Christoph Bregler, Bernt Schiele, and Christian Theobalt. Marconi—convnet-based marker-less motion capture in outdoor and indoor scenes. *IEEE transactions on pattern analysis and machine intelligence*, 39(3):501–514, 2016.

[12] Yun Fu and Thomas S Huang. hmouse: Head tracking driven virtual computer mouse. In *2007 IEEE Workshop on Applications of Computer Vision (WACV'07)*, pages 30–30. IEEE, 2007.

[13] R. Hartley and A. Zisserman. *Multiple View Geometry in Computer Vision*. Cambridge University Press, ISBN: 0521540518, second edition, 2004.

[14] Hyungsook Kim, David O'Sullivan, Ksenia Kolykhalova, Antonio Camurri, and Yonghyun Park. Evaluation of a computer vision-based system to analyse behavioral changes in high school classrooms. *International Journal of Information and Communication Technology Education (IJICTE)*, 17(4):1–12, 2021.

[15] Muhammed Kocabas, Salih Karagoz, and Emre Akbas. Self-supervised learning of 3d human pose using multi-view geometry. In *Proceedings of the IEEE Conference on Computer Vision and Pattern Recognition*, pages 1077–1086, 2019.

[16] Irvin Hussein Lopez-Nava and Angélica Muñoz-Meléndez. Wearable inertial sensors for human motion analysis: A review. *IEEE Sensors Journal*, 16(22):7821–7834, 2016.

[17] Alexander Mathis, Pranav Mamidanna, Kevin M Cury, Taiga Abe, Venkatesh N Murthy, Mackenzie Weygandt Mathis, and Matthias Bethge. Deeplabcut: markerless pose estimation of user-defined body parts with deep learning. *Nature neuroscience*, 21(9):1281, 2018.

[18] L Meinecke, N Breitbach-Faller, C Bartz, R Damen, G Rau, and C Disselhorst-Klug. Movement analysis in the early detection of newborns at risk for developing spasticity due to infantile cerebral palsy. *Human movement science*, 25(2):125–144, 2006.

[19] Matteo Moro, Maura Casadio, Leigh Ann Mrotek, Rajiv Ranganathan, Robert Scheidt, and Francesca Odone. On the precision of markerless 3d semantic features: An experimental study on violin playing. In *2021 IEEE International Conference on Image Processing (ICIP)*, pages 2733–2737. IEEE, 2021.

[20] Matteo Moro, Giorgia Marchesi, Filip Hesse, Francesca Odone, and Maura Casadio. Markerless vs. marker-based gait analysis: A proof of concept study. *Sensors*, 22(5):2011, 2022.

[21] Matteo Moro, Giorgia Marchesi, Francesca Odone, and Maura Casadio. Markerless gait analysis in stroke survivors based on computer vision and deep learning: a pilot study. In *Proceedings of the 35th Annual ACM Symposium on Applied Computing*, pages 2097–2104, 2020.

[22] Matteo Moro, Vito Paolo Pastore, Chaira Tacchino, Paola Durand, Isabella Blanchi, Paolo Moretti, Francesca Odone, and Maura Casadio. A markerless pipeline to analyze spontaneous movements of preterm infants. *Computer Methods and Programs in Biomedicine*, 226:107119, 2022.

[23] Matteo Moro, Fabio Rizzoglio, Francesca Odone, and Maura Casadio. A video-based markerless body machine interface: A pilot study. In *International Conference on Pattern Recognition*, pages 233–240. Springer, 2021.

[24] Laurie Needham, Murray Evans, Darren P Cosker, Logan Wade, Polly M McGuigan, James L Bilzon, and Steffi L Colyer. The accuracy of several pose estimation methods for 3d joint centre localisation. *Scientific reports*, 11(1):1–11, 2021.

[25] Vito P. Pastore, Thomas G. Zimmerman, Sujoy K. Biswas, and Simone Bianco. Annotation-free learning of plankton for classification and anomaly detection. 10(1):12142.

[26] Heinz F Prechtl. Qualitative changes of spontaneous movements in fetus and preterm infant are a marker of neurological dysfunction. *Early human development*, 1990.

[27] Yale Song, David Demirdjian, and Randall Davis. Continuous body and hand gesture recognition for natural human-computer interaction. *ACM Transactions on Interactive Intelligent Systems (TiiS)*, 2(1):1–28, 2012.

[28] Denis Tome, Chris Russell, and Lourdes Agapito. Lifting from the deep: Convolutional 3d pose estimation from a single image. In *Proceedings of the IEEE Conference on Computer Vision and Pattern Recognition*, pages 2500–2509, 2017.

[29] Athanasios Voulodimos, Nikolaos Doulamis, Anastasios Doulamis, and Eftychios Protopapadakis. Deep learning for computer vision: A brief review. *Computational intelligence and neuroscience*, 2018, 2018.

fMRI characterization of intrinsic brain networks relevant for motor control with and without visual feedback by fractal dimension

C. Sala[1], A.P. Bagshaw[4], S.D. Mayhew[4] and C. Porcaro[2,3,4]
[1] Department of Information Engineering - Università Politecnica delle Marche, Ancona, Italy
[2] Department of Neuroscience and Padova Neuroscience Center (PNC), University of Padova, Padova, Italy
[3] Institute of Cognitive Sciences and Technologies (ISTC) — National Research Council (CNR), Rome, Italy
[4] Centre for Human Brain Health and School of Psychology University of Birmingham, Birmingham, UK

***Abstract*—The bilateral visuo-parietal-motor network is responsible for fine control of hand movements. However, the subregions devoted to maintaining contraction stability in the presence/absence of visual feedback remain unclear. It is widely recognized that continuous sensory feedback plays a crucial role in accurate motor control in everyday life. Feedback information is used to adapt force output and to correct errors. While the primary motor cortex contralateral to the movement (cM1) plays a dominant role in this control, converging evidence supports the idea that the ipsilateral primary motor cortex (iM1) also directly contributes to hand and finger movements. Similarly, when visual feedback is available, the primary visual cortex (V1) and the visuospatial network and their interactions with the motor network are essential for accurate motor performance. To clarify this problem and investigate the regions involved in a visuomotor task, we performed functional magnetic resonance imaging (fMRI) measurements during isometric compression of a compliant rubber bulb, at 10% of maximum voluntary contraction, both with (visuomotor task) and without visual feedback (motor task). Here, by using a multivariate approach focusing on intrinsic connectivity between voxels through group ICA of fMRI Toolbox (GIFT), we have answered the following two main questions:**

1) which are the networks involved during a motor task (i.e. without visual feedback) and a visuomotor task (i.e. with visual feedback)?

2) Is there any hemodynamic signal complexity difference between the visuomotor and the motor task?

Interestingly, we have found that during the visuomotor task, the involvement of the visuospatial network (FEF), the ipsilateral primary motor area (iM1), the contralateral primary motor area (cM1), the sensorimotor network (SMN) the Executive Control Network (ExCN), the Silence Network (SN), the Default Mode Network (DMN), the Basal Ganglia (BG), the Cerebellum (Cb) and Precuneus are essential for the fine motor control of the movement while maintaining the grip force level indicated by the visual feedback together with higher complexity estimated by Higuchi's Fractal Dimension.

The study shows that the brain networks show greater hemodynamic complexity in the presence of visual feedback, due to the processing of the visual stimulus and the maintenance of the required level of force.

***Keywords*—functional Magnetic Resonance Imaging (fMRI), Fractal Dimension (FD), Resting State Networks (RSN), Motor, Visuomotor**

I. Introduction

A key component of human interaction with our surrounding environment is the planning and execution of motor actions to coordinate movements of the body. Grasping and manipulation of objects in a controlled and precise manner is an essential action that depends upon smooth coordination and integration of diverse sensory components such as visual cues, tactile and cutaneous feedback, grip force control and internal representations. [1] The organization of the brain's activity during the coordination of precision or force gripping, using either dynamic or isometric contractions, has been investigated by numerous functional magnetic resonance imaging (fMRI) studies as a foundation for studying more complex motor tasks. This body of work has identified a bilateral fronto-parietal cerebellar network, primarily comprised of primary sensorimotor cortex (M1/S1), dorsal and ventral premotor cortices (PMd and PMv), supplementary and cingulate motor areas (SMA and CMA), prefrontal cortex, parietal association cortex and the cerebellum. However, during unimanual motor and somatosensory tasks, the activity of ipsilateral M1 (iM1) is neither quiescent nor idling but substantially perturbed by the task, typically in the form of a reduction in mu frequency (8– 13 Hz) M/EEG power or fMRI signal below baseline levels. Second, the visual feedback signal control emphasises this aspect, especially during fine movement control. [1]

From a metrological point of view, another key point is that all the studies using fMRI to study motor control and execution have used the mass-univariate voxel-based approach, which focuses on segregating and localizing processes, failing to account for the integration across functions within more extensive networks. In addition, the mass-univariate voxel-based analysis also relies on subtraction methods between conditions, emphasising more significant differences than similarities between processes. Functional connectivity analysis is an alternative multivariate method to assess the functional architecture of the central nervous system that integrates brain signals across multiple regions. This approach uses correlations between distant regions as the dependent variable. Independent component analysis (ICA) is often used to identify clusters of regions that show high correlations of signal change within a given time window. These clusters are assumed to reflect intrinsic connectivity networks. Consistent intrinsic networks have been repeatedly identified using ICA. These include networks that connect homologous regions processing visual, auditory, and sensory-motor output. But also, a higher cognitive function such as the default mode network (anterior and posterior midline and inferior parietal); the lateralized dorsal frontal-parietal network, putatively involved in attention; the saliency network, which comprises the insula and the anterior cingulum; the frontal network involving prefrontal, frontotemporal, and cingulate cortex, thought to reflect executive control; the left-lateralized ventral,

frontal, and parietal network, involved in language processing and the precuneus, basal ganglia, and a cerebellum network. Importantly, similar networks are detected when participants are engaged in a task (goal-driven behavior). In addition, differences between specific task conditions are modelled as a reconfiguration of connections within and between networks. It has been argued that the task-based spatial ICA data-driven approach is advantageous over conventional mass-univariate analysis of signal amplitude change. This is because it does not rely on assumptions regarding the time course, the temporal characteristics, and the shape of the hemodynamic response function. In this work, we analyzed fMRI data using a multivariate data-driven approach focusing on intrinsic connectivity between voxels through group ICA of fMRI Toolbox (GIFT), asking the following main questions:

1. which are the networks involved during a motor task (i.e. without visual feedback) and a visuomotor task (i.e. with visual feedback)?
2. Is there any hemodynamic signal complexity difference between the visuomotor and the motor task and in which brain networks?

II. MATERIALS AND METHODS

A. Partecipants

Sixteen right-handed volunteers (age = 26±4 years, 7 females) performed an isometric contraction of a pneumatic rubber bulb [2] opposing the thumb to the first two fingers of their right-hand.

B. Experimental Paradigm

Individual's maximal voluntary contraction (MVC) of this grip was measured prior to the experiment using a mechanical hand dynamometer (0–100 kgs, Lafayette 78010, Indiana) [2]. Three quick contraction were performed where subject's held maximum contraction for 5 s and the mean force value across trials was used as their MVC. Prior to the experiments, the pneumatic equipment was calibrated so that the conversion of applied force to current was known. The contraction force was continuously recorded throughout all experiments at 100 Hz sampling rate. During the experiment, subjects were instructed to maintain the isometric contraction for the 5-second trial duration 10% of MVC. Throughout the experiment subjects viewed a visual display, which was projected onto a screen situated behind them at the rear of the scanner bore, via a mirror mounted on the MRI headcoil. Subjects kept their eyes open at all times and maintained fixation upon a vertical, white force-gauge that was centrally displayed upon a grey background throughout.

Subjects were instructed to smoothly increase the contraction force and to then maintain this target force level as accurately as possible until the end of the trial, signaled by the disappearance of the two segments aside the gauge. At the trial offset, subjects were instructed to terminate the contraction and completely relax their hand for the duration of the inter-stimulus interval lasting either 5, 7 or 9 s. Isometric contractions at the force levels were executed in two experimental conditions:

1) Visuomotor condition (VM), where a horizontal, black force indicator bar appeared centrally in the force gauge upon trial onset. The vertical position of this horizontal indicator provided continuous visual feedback information to the subject about the exerted contraction force. The force indicator was removed from the visual display at trial offset.

2) Motor condition (M), where subjects were asked to perform the isometric contraction without the display of the horizontal force indicator.

Although matching the target force level was obviously more difficult in this M-task, subjects had been familiarized with the task during a single-run of each of the tasks conducted outside of the MRI scanner immediately before the fMRI experiment and were reasonably competent at performing the task at the required force levels. Experimental cues were visually presented to participants via a projector display and the visual display was controlled using the Psychophysical toolbox running in MATLAB (MathWorks). Immediately before fMRI scanning each subject performed a practice run. During fMRI, two experimental runs of each of the VM- and M-task conditions were acquired in an inter leaved order that was randomized across subjects. All experiments were conducted at the Birmingham University Imaging Centre using a 3T Philips Achieva MRI scanner. An eight channel phased-array head coil was used to acquire T1-weighted anatomical image (1 mm isotropic voxels) and four task-related whole-brain T2*-weighted, functional EPI data (365 volumes, 3x3×4 mm voxels, 32 slices, TR=2000 ms, TE=35 ms, SENSE factor=2, flip angle=80°). Cardiac and respiratory cycles were continuously recorded (pulse oximeter and respiratory belt).

C. fMRI Pre-processing and analysis

fMRI analysis by Statistical Parametric Mapping (SPM-Toolbox)

The fMRI data were analyzed using SPM12 (Wellcome Department of Imaging Neuroscience, London; https://www.fil.ion.ucl.ac.uk/spm/). Pre-processing of the data included slice time correction, spatial realignment to correct for movement artefacts and motion by distortions interactions and normalized to the MNI standard space. The data were re-sampled given a 2x2x2 voxel size and smoothed using 6 FWHM Gaussian Kernel to account for residual inter-subject differences and to accommodate assumptions of random field theory used for family wise error corrections. We first estimated the effect size for each participant on each of the four conditions (recall 2x2 design) using the general linear model. Each condition was modelled by a separate regressor; the onsets of each trial corresponded to the time when a correct response was given. All the regressors were convolved with three bases functions: the canonical HRF, its derivatives and dispersions. To correct for signal changes due to head movement, the 6 realignment parameters were included in the design matrix. An additional set of regressors was added for force contraction.

fMRI analysis by Group ICA of fMRI Toolbox (GIFT)

Data were decomposed into functional networks using a group-level spatial ICA as implemented in the GIFT toolbox (https://trendscenter.org/software/gift/). The individual datasets were temporally concatenated and reduced for computational feasibility through three stages of principal component analysis (PCA) in order to reach the final dataset, which was then decomposed by ICA with Infomax [3] algorithm into 100 (ICs=100) spatially independent components.

In GIFT, after each subject's functional data were reduced, the data were then concatenated into groups and put through another data reduction step. The number of subjects to put into

each group is called partitions with the number of datasets in a partition being equal to the one-fourth of the number of data-sets selected for. After reduction within each partition the data were stacked into one group and put through the final data reduction. At this stage, the number of components was estimated using the minimum description length criteria (MDL).

Task-related networks

In order to compute the degree of task-relatedness of component we regressed the corresponding time-courses against the design matrix, using the temporal multiple linear regression implemented in GIFT. We performed temporal sorting fourth times one for each conditions of interest: Visuomotor (VM), Motor (M), selecting in turn the regressors associated to each condition. Stats on beta weights option in Utility of GIFT toolbox after temporal sorting was used, it allows one to test the significance of the ICs obtained. The resulting beta weights (β) reflect the degree to which the task events of interest modulated a component. β for each task condition was tested against zero using one-way ANOVA (Regressor). Twenty-eight independent components (ICs) were selected for the final analysis; only the ICs with a p-value that survived to False Discovery Rate (FDR) correction were considered. ICs were named accordingly to the template (Functional ROIs- https://findlab.stanford.edu/functional_ROIs.html) they were spatially correlated with or based on visual inspection of the corresponding spatial map.

Higuchi's fractal dimension

Neurophysiological processes are generally non-stationary and non-linear in nature, therefore it is useful to use the Higuchi fractal dimension (FD) (Higuchi 1988) as it is a quantitative measure of signal dynamics. It is a non-linear measure of the complexity of the waveform in the time domain: in practice, the original curve or signal can be divided into smaller parts with or without overlap, called "windows". FD values are calculated for each window, with or without an overlay. Individual FD values can be averaged across all windows for the entire curve, and the average FD value can be used as a measure of curve complexity [4].

Higuchi's FD [5] has been used to characterize the complexity of fMRI BOLD activity in the time domain [6].

Statistical Analysis

Statistical analysis on beta weights as implemented in GIFT toolbox was performed to identify differences between conditions (M vs. VM). The resulting beta weights (β) reflect the degree to which a component was modulated by the events of interest, i.e. how well did the IC's time course correlate with the condition time-course. To test for FD differences in each ICs between M and VM task, paired t-tests was performed. FDR was used to correct for multiple comparisons [7].

III. RESULTS

One hundred ICs were identified. Of these, 28 were determined to be task-related after One-Way Anova (Regressor). In the Tab.1 the results, after One Way ANOVA (Regressor) implementation are reported. P-values and networks for all the components FDR corrected in each condition of interest are present. The components common to the tasks are highlighted.

In Fig.1 all the fifteen components task-related are shown. Tab.1 and Fig.1 allow to identify the components related to each network active during the two tasks (VM and M): the visual network is mainly active during the VM task (IC 2, 3, 70), but it shows the presence of this network also during the M task (IC 74), underlined in Tab.1 as a component common to the two tasks. The sensorimotor network instead has more components common to VM and M task (IC 40, 92), and only one (IC7) active exclusively during the VM task. The same applies to the Executive Control Network (IC 4, 54) and to the Cerebellum (IC 27, 45, 60). The Frontal Eye Fields is more active during the visuomotor task (IC 44, 46), with the IC 46 also active during the motor task. Finally, the activations are totally different between the two tasks regarding the Silence Network, the Basal Ganglia, the Precuneus and the Default Mode Network, the latter only of the four to have an active component between the two tasks, the IC 42, the ventral one.

The hemodynamic FD analysis highlighted sixteen ICs with statistical differences between M and VM tasks significance. Fig.3 shows the ICs, grouped by the network showing the grand average and standard error for the FD and the relative spatial map. At the univariate level, the FD values of the VM task differ from those of the M task. Higher FD values were observed for the VM than for the M task.

Significant components (Fig. 3) include the VN, both pVN and hVN, the SMN, both bilateral M1 and iM1, the FEF, the ExCN and Cb. The components belonging to the same networks were averaged between them and compared in the two task.

TABLE I: TASK-RELATED COMPONENTS.

Visuomotor			*Motor*		
ICs	*p_value FDR*	*Network*	*ICs*	*p_value FDR*	*Network*
Visual Network (VN)					
2	0.03	hVN			
3	0.01	pVN			
70	0.007	pVN			
74	**0.001**	**pVN**	**74**	**0.03**	**pVN**
Sensorimotor Network (SMN)					
7	<0.001	iM1			
40	**<0.001**	**cM1**	**40**	**0.001**	**cM1**
92	**0.03**	**SMN**	**92**	**0.03**	**SMN**
Frontal Eye Fields (FEF)					
44	<0.001	FEF			
46	**<0.001**	**FEF**	**46**	**0.02**	**FEF**
Silence Network (SN)					
32	0.003	aSN	64	0.007	aSN
69	<0.001	aSN	89	0.008	aSN
Executive Control Network (ExCN)					
4	**0.001**	**lExCN**	**4**	**0.001**	**lExCN**
54	**0.005**	**rExCN**	**54**	**0.005**	**rExCN**
78	0.02	rExCN			
Default Mode Network (DMN)					
34	0.03	dDMN			
42	**0.02**	**vDMN**	**42**	**0.002**	**vDMN**
68	0.01	dDMN			
83	0.005	dDMN			
Basal Ganglia (BG)					
87	0.02	BG	81	0.009	BG
Cerebellum (CB)					
27	**0.02**	**CB**	**27**	**<0.001**	**CB**
45	**0.04**	**CB**	**45**	**0.007**	**CB**
60	**0.001**	**CB**	**60**	**0.004**	**CB**
			77	0.007	CB
Precuneus					
57	0.005	Prec	49	0.007	Prec

All the FDR corrected value for each condition are reported. The components common to the tasks due are highlighted.



Fig 1. Spatial map (SMs) of the 28 ICs identified as task-related. They are displayed at the three most informative slices (Axial, Sagittal and Coronal views). They are divided into groups based on their anatomical and functional properties.

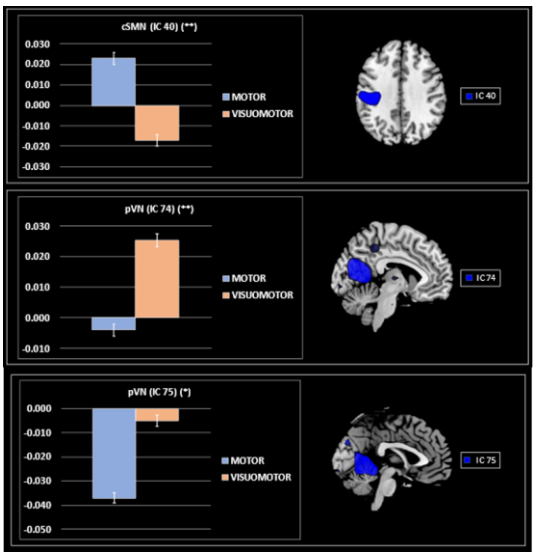


Fig 2. The plots represented effects size for the ICNs (y-axis beta efect size in arbitrary units). Labels: MOTOR: NoFeedback Task; VISUOMOTOR: Feedback task. ** indicates p<0.01 FDR corrected; * indicate p<0.05 FDR corrected

IV. Conclusion

This approach used in this study is more advantageous than conventional univariate analysis, as it does not rely on assumptions about temporal characteristics and the shape of the hemodynamic response function. In general, the study shows that the brain networks, active in both tasks, show greater hemodynamic complexity in the presence of visual feedback due to the processing of the visual stimulus and the maintenance of the required level of force. Understanding the mechanisms underlying fine motor movements is essential for rehabilitation strategies, helping elucidate neuronal mechanisms underlying neurodegenerative illnesses such as Parkinson's disease and other movement disorders and improving Brain-Computer Interface (BCI) application, among others.

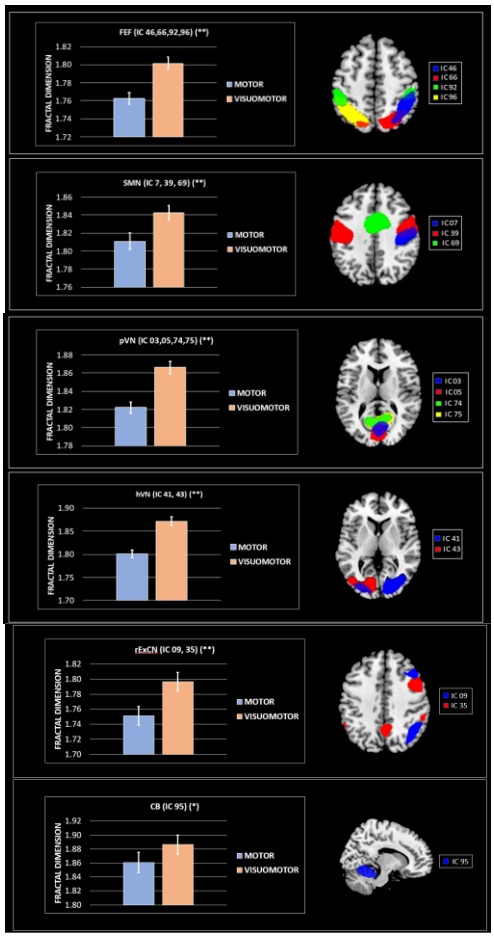


Fig 3. Hemodynamic activity characterization by Fractal Dimension. To the right grand average and standard error for the FD values (k = 7) are shown for groups M (light blue) and VM (light orange) and to the left spatial maps of the IC obtained by GIFT toolbox. * indicates p<0.05, ** indicate p<0.01

V. Referance

[1] C. Porcaro, S. D. Mayhew, and A. P. Bagshaw, "Role of the Ipsilateral Primary Motor Cortex in the Visuo-Motor Network during Fine Contractions and Accurate Performance," *Int. J. Neural Syst.*, vol. 31, no. 6, pp. 1–17, 2021, doi: 10.1142/S0129065721500118.

[2] B. C. M. Van Wijk, A. Daffertshofer, N. Roach, and P. Praamstra, "A role of beta oscillatory synchrony in biasing response competition?," *Cereb. Cortex*, vol. 19, no. 6, pp. 1294–1302, 2009, doi: 10.1093/cercor/bhn174.

[3] A. J. Bell and T. J. Sejnowski, "An Information-Maximization Approach to Blind Separation and Blind Deconvolution," *Neural Comput.*, vol. 7, no. 6, pp. 1129–1159, Nov. 1995, doi: 10.1162/neco.1995.7.6.1129.

[4] C. Porcaro, S. D. Mayhew, M. Marino, D. Mantini, and A. P. Bagshaw, "Characterisation of Haemodynamic Activity in Resting State Networks by Fractal Analysis," *Int. J. Neural Syst.*, vol. 30, no. 12, pp. 1–15, 2020, doi: 10.1142/S0129065720500616.

[5] T. Higuchi, "Approach to an irregular time series on the basis of the fractal theory," *Phys. D Nonlinear Phenom.*, vol. 31, no. 2, pp. 277–283, Jun. 1988, doi: 10.1016/0167-2789(88)90081-4.

[6] C. Porcaro, S. D. Mayhew, M. Marino, D. Mantini, and A. P. Bagshaw, "Characterisation of Haemodynamic Activity in Resting State Networks by Fractal Analysis," *Int. J. Neural Syst.*, vol. 30, no. 12, p. 2050061, Dec. 2020, doi: 10.1142/S0129065720500616.

[7] T. E. Nichols and A. P. Holmes, "Nonparametric permutation tests for functional neuroimaging: A primer with examples," *Hum. Brain Mapp.*, vol. 15, no. 1, pp. 1–25, Jan. 2002, doi: 10.1002/hbm.1058.

Radiofrequency Echographic Multi Spectrometry for Fragility Fracture prediction through Fragility Score

F.A. Lombardi[1], P. Pisani[1], A. Natale[2], E. Casciaro[1], F. R. Contaldo[3], R. Franchini[1], M. Muratore[4], F. Conversano[1], S. Casciaro[1]

[1] *National Research Council, Institute of Clinical Physiology, Lecce (Italy)*
[2] *R&D Department, Echolight SPA, Lecce (Italy)*
[3] *Department of Engineering for Innovation, University of Salento, Lecce, Italy*
[4] *Vito Fazzi Hospital, ASL-LE, O.U. of Rheumatology, Lecce (Italy)*

***Abstract*— Radiofrequency Echographic Multi Spectrometry (REMS) is non-ionizing technique to diagnose osteoporosis on lumbar spine and femoral neck. In this prospective study, a new REMS-based parameter, named Fragility Score (FS), was used to identify bone fragility from lumbar spine REMS scans. FS parameter is a direct indicator of the status of bone microarchitecture and estimates skeletal frailty.**

The aim of this study was to investigate the effectiveness of the FS to discriminate between fractured and non-fractured patients with respect to the T-score values measured by Dual-energy X-ray Absorptiometry (DXA) and REMS.

Collected data from 376 Caucasian women were analysed and the occurrence of the incident fragility fractures was recorded during the follow-up period up to 5 years. Subsequently, the ability of the FS to discriminate between two patients group (with and without incident fragility fracture) in comparison to that of the DXA- and REMS- T-score was evaluated through ROC analysis.

The obtained results showed that FS provided an higher AUC value (0.770) with respect DXA- and REMS- based T-scores, (AUC=0.656 and AUC=0.691, respectively).

In conclusion, FS has proven to be a useful tool for the identification of incident fragility fractures, and its integration into clinical practice would enable early detection and monitoring of frail patients as well as fracture prevention.

***Keywords*—incident fragility fracture, REMS, Fragility Score, lumbar spine acquisition.**

I. INTRODUCTION

Radiofrequency Echographic Multi Spectrometry (REMS) is a non-ionizing technology for bone health status assessment [1]-[2] and fracture prediction [3]. The operating principle of REMS is based on the examination of native raw, unprocessed radiofrequency (RF) ultrasound signals that are collected during a simple echographic scan of the reference anatomical sites (proximal femur and/or lumbar spine) [1]. The bone health status is evaluated by comparing the acquired signal spectra with previously developed reference spectral models for the considered pathological and healthy conditions [4]-[5]. The large amount of information that has been gathered from the internal bone structure includes both quantity- and quality-related data, thereby it is possible to estimate bone strength and predict fracture risk [6]. Therefore, this technology does not only provide a quantitative measurement of bone density, but it can also provide information about bone quality [3]. On the base of several scientific evidences that demonstrate the high REMS accuracy in the diagnosis of osteoporosis and fracture risk prediction [1]-[2]-[3]-[6]-[7]-[8]-[9], REMS technology was included in the National Health Ministry Guidelines on Fragility Fractures (FF) from the Italian Institute of Health [10] as appropriate diagnostic tool able to improve the management of frail subjects.

To improve the FFs management, a new parameter based on REMS technology has been developed, the Fragility Score (FS), that allows the assessment of the quality of bone microarchitecture. FS is a direct indicator of the status of bone microarchitecture and estimates skeletal frailty independent of BMD (bone mineral density) [11], [12]. It ranges from 0 to 100 depending on the degree of frailty.

The aim of this prospective study was to investigate the effectiveness of the FS to identify bone fragility from lumbar spine REMS scans. In particular, the ability of the REMS-based FS to discriminate between fractured and non-fractured women with respect to the DXA (Dual X-ray Absorptiometry)- and REMS-based T-score values has been estimated. In clinical practice, T-score represents a reference parameter for the assessment of the osteoporosis diagnosis. It is expressed in terms of standard deviations (SDs) and obtained by comparing the measured BMD value with the average BMD of a reference healthy population of young individuals (30 years). As established by theWorld Health Organization (WHO), the patients were classified as “healthy” (normal BMD) if their T-score $\geq$ -1, “osteopenic” if -2.5 < T-score < -1, “osteoporotic” if T-score $\leq$ -2.5 or “severely osteoporotic” if T-score $\leq$ -2.5 in the presence of one or more fragility fracture.

II. MATERIALS AND METHODS

A. Study design and enrolment

The clinical information was gathered from female patients who met the following inclusion criteria: Caucasian women with age below 65 years and a medical prescription for lumbar spine. The 376 enrolled patients underwent a lumbar spine scan both with DXA and REMS. Subsequently, the occurrence of incident fragility fractures was recorded during the follow-up period lasting up to 5 years.

B. DXA and REMS acquisitions

DXA scans were carried out in accordance with standard clinical practices: the spinal scan was performed with the hip and knee flexed at 90° by using the following device: Discovery W (Hologic, Waltham, MA, USA). For all lumbar spine acquisitions, arm and table controls were used to position the laser’s cross hair 2.5 to 5 cm below the iliac crest and to

centre at the patient's mid-line, in order to obtain the correct position of the lumbar spine (*i.e.*, with the ribs attached to T12 on the image). Each of all the DXA reports were made anonymous.

REMS scans of the lumbar spine, were carried out by placing the echographic transducer in a trans-abdominal position under the sternum, in order to visualize L1 lumbar vertebra and then moving it until L4 according to the on-screen and audible indications provided by the device software. REMS scans were performed employing the EchoStation device (Echolight S.p.a., Lecce, Italy), equipped with a convex transducer operating at the nominal frequency of 3.5 MHz and used as recommended by the manufacturer. Transducer depth and focus scan were adjusted for all lumbar spine acquisitions in order to place the target bone interface (*i.e.*, vertebral surface) in the focal zone of the ultrasound beam and at least 3 cm away from the bottom of the B-mode picture.

All the REMS reports, together with all the echographic data (images and RF signals), were anonymised before the subsequent analyses.

According to Di Paola et al. [1], before the analysis, all DXA and REMS medical reports were checked in a rigorous way in order to avoid any type of errors than could occur during DXA and REMS scans. Erroneous REMS reports were excluded, while inaccurate DXA reports were re-analysed, if possible, or excluded [1].

C. REMS-based FS operating principle

According to the main operating principle of REMS technology, the first step is represented by an echographic acquisition of the anatomical reference sites. Immediately after the scan, an automatic processing of the acquired echographic signals allows to identify and analyse the target bone structure and the internal region of interest. Subsequently, the native raw unfiltered echographic signals acquired during the echographic scan are analysed in order to retain the maximum information about the characteristics of the investigated tissues. In order to calculate the FS value, the same RF data acquired for bone mineral density evaluation at the femur and/or lumbar spine are used. After data acquisition, through dedicated spectral and statistical analyses on raw signals related to the region of interest (ROI), the spectral profiles of the patient are classified as "frail" or "non-frail" on the basis of the comparison with dedicated reference spectral models representative of fractured and non-fractured patients.

In particular, on each patient dataset, the data analysis involved the following steps:

1. Automatic vertebral identification, using the segmentation method described in Conversano *et al.* [4].
2. Automatic ROI identification for each vertebrae image (according to the method described in Conversano *et al.*) by using a specific RF signal portion for each scan line crossing the bone surface.
3. Classification of each RF signal portion as "frail" or "non-frail" based on the correlation between its frequency spectrum, as determined by a FFT computation, and each of the two age-matched models stored in a reference database that was previously acquired [12].
4. Calculation of the FS value for each vertebra (defined as the percentage of the analysed vertebra segments that were classified as "frail" in the previous step) [12].
5. Calculation of the FS value for the patient under examination as the average of the single vertebra values [12].

D. Statistical Analysis

Receiver Operating Characteristic (ROC) curves analysis allowed to evaluate and compare the ability of the:

- T-score values measured by DXA and REMS to discriminate between the patients with and without incident fragility fracture;
- FS values to discriminate between patients with and without incident FF.

To test the statistical significance of the difference between the areas under ROC curves De Long [13] test was used.

III. Results

A. Patients' characteristics

In the entire lumbar spine dataset (376 enrolled patients), 59 patients (18.6%) experienced an incident fragility fracture after a median follow-up of 3.5 years (range 2-5).

Table 1 lists of the means and standard deviations of the anthropometric characteristics for the overall dataset of fractured and non-fractured patients.

TABLE I: ANTHROPOMETRIC CHARACTERISTICS

Female Lumbar Spine (LS)	*Mean ± SD*		
	Overall dataset	*Fractured patients*	*Non-fractured patients*
Number of patients	376	59	317
Age (y)	55.6 ± 6.0	56.4 ± 6.8	55.4 ± 5.8
Height (cm)	152 ± 6.3	163 ± 5.7	161 ± 6.4
Weight (kg)	64 ± 9.6	63.9 ± 10.1	64 ± 9.6
BMI (kg/m^2)	24.7 ± 3.5	24.9 ± 3.9	24.6 ± 3.5

FS values showed to be significantly higher in the fractured group than in non-fractured counterpart, similar to DXA and REMS-measured T-score (as it is shown in **Table II**). *P-values* in table II refer to the comparison between patients with and without incident fragility fracture, evaluated using the t-test.

TABLE II: FS, DXA- AND REMS-T-SCORE

Female Lumbar Spine (LS)	*Mean ± SD*			
	Overall dataset	*Fractured patients*	*Non-fractured patients*	*p-value*
Number of patients	376	59	317	
DXA T-score	-1.7 ± 1.3	-2.3 ± 1.1	-1.6 ± 1.3	p<0.0001
REMS T-score	-1.7 ± 1.4	-2.5 ± 1.3	-1.6 ± 1.3	p<0.0001
FS	28.6 ± 8.2	37.9 ± 12.5	26.9 ± 5.7	p<0.0001

B. Performance of DXA- and REMS- T-score in the prediction of fragility fractures

The AUC obtained from DXA- and REMS T-score values in the discrimination between patients with and without an incident fragility fracture were equal to 0.656 and 0.691, respectively. The AUC obtained by REMS- T-score was significantly higher than that obtained using DXA (**p<0.005**).

Moreover, ROC curves analysis allowed to evaluate and compare the ability of the FS and DXA – and REMS based T-score values to discriminate between the two groups of patients. The results showed that the AUC by the FS, equal to 0.770, was superior than the AUCs obtained using the T-score values, equal to 0.656 for DXA and 0.691 for REMS. The FS AUC was significantly higher than that obtained using T-score values for both DXA and REMS technology (**p<0.005)**.

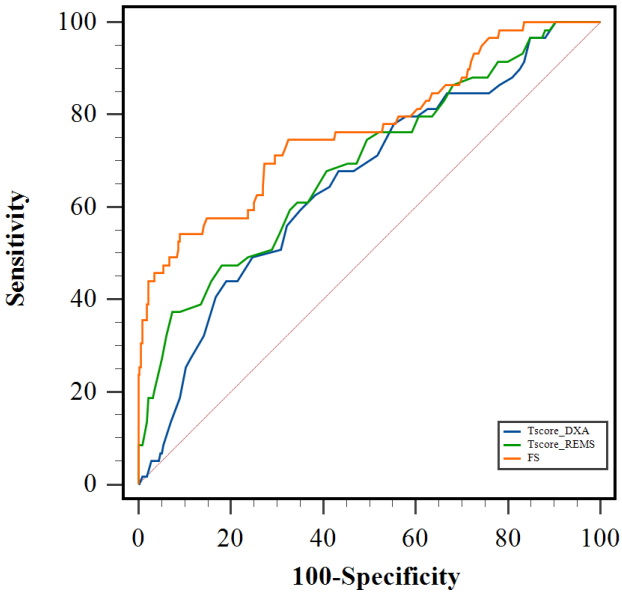


Fig. 2: shows a ROC analysis comparison between FS (orange line), and the DXA- (blue line) and REMS- (green line) T-score values in identifying patients who have or have not had incident fragility fractures.

IV. Discussion

The need to identify parameters and technologies that can predict the occurrence of fragility fractures is of great interest to the medical community, especially due of the enormous economic and social burden related to these fractures. In this study, the usefulness of the FS measured by REMS in identifying patients at risk for fragility fractures over a 5-years period was evaluated. Measurements were performed at the lumbar spine, one of the reference anatomical sites considered for the diagnosis of osteoporosis. The performance of the FS was evaluated and compared with respect to the DXA and REMS T-score value. T-score is considered the clinical parameter for the diagnosis of osteoporosis and primary clinical indicator to predict the fracture risk [6]. In this work the highest predictive capability of the FS, with respect to T-score measured both with DXA and REMS, to recognize patients with incident fragility fractures has been demonstrated. The fracture risk prediction capability of T-score DXA and REMS is similar to that assessed in previous studies [3].

V. Conclusion

Finding characteristics and technologies that could, in a clinically viable context, predict the occurrence of fragility fractures is currently of great interest [6]-[14]-[15]. This need is primarily motivated by the related reduced people quality of life and the high economic and social costs associated with fragility fractures, which are predicted to increase as people live longer [16]-[17].

In this context, the preliminary data obtained from this study demonstrated that the FS can be an effective parameter to identify incident fragility fractures. The integration of this tool into clinical routine would allow for early identification and monitoring of frail patients as well as for fracture prevention.

Indeed, this study has demonstrated the capacity of the FS to better discriminate than DXA- and REMS-based T-scores between fractured and non-fractured patients in a 5-year longitudinal study.

VI. Declarations

A. Statement of human and animal rights

Azienda Sanitaria Locale (ASL) Lecce's national Ethics Review Board granted the study approval (ID: 2258/2011). The 1964 Helsinki Declaration and its following revisions, as well as any other comparable ethical norms, were followed during every procedure.

B. Informed consent

All participants in the study have given their informed consent for inclusion and publication.

References

[1] M. Di Paola *et al.*, "Radiofrequency echographic multispectrometry compared with dual X-ray absorptiometry for osteoporosis diagnosis on lumbar spine and femoral neck," *Osteoporos. Int.*, vol. 30, no. 2, pp. 391–402, 2018, doi: 10.1007/s00198-018-4686-3.

[2] B. Cortet *et al.*, "Radiofrequency Echographic Multi Spectrometry (REMS) for the diagnosis of osteoporosis in a European multicenter clinical context," *Bone*, vol. 143, p. 115786, 2021, doi: 10.1016/j.bone.2020.115786.

[3] G. Adami *et al.*, "Radiofrequency echographic multi spectrometry for the prediction of incident fragility fractures: A 5-year follow-up study," *Bone*, vol. 134, no. February, p. 115297, 2020, doi: 10.1016/j.bone.2020.115297.

[4] F. Conversano *et al.*, "A Novel Ultrasound Methodology for Estimating Spine Mineral Density," *Ultrasound Med. Biol.*, vol. 41, no. 1, pp. 281–300, 2015, doi: 10.1016/j.ultrasmedbio.2014.08.017.

[5] S. Casciaro *et al.*, "An Advanced Quantitative Echosound Methodology for Femoral Neck Densitometry," *Ultrasound Med. Biol.*, vol. 42, no. 6, pp. 1337–1356, 2016, doi: 10.1016/j.ultrasmedbio.2016.01.024.

[6] A. Diez-Perez *et al.*, "Radiofrequency echographic multi - spectrometry for the in - vivo assessment of bone strength : state of the art — outcomes of an expert consensus meeting organized by the European Society for Clinical and Economic Aspects of Osteoporosis , Osteoarthritis," *Aging Clin. Exp. Res.*, vol. 31, no. 10, pp. 1375–1389, 2019, doi: 10.1007/s40520-019-01294-4.

[7] D. Valentina Anna *et al.*, "First assessment of bone mineral density in healthy pregnant women by means of Radiofrequency Echographic Multi Spectrometry (REMS) technology," *Eur. J. Obstet. Gynecol. Reprod. Biol.*, vol. 263, pp. 44–49, 2021, doi:

10.1016/j.ejogrb.2021.06.014.

[8] A. Fassio *et al.*, "Radiofrequency Echographic Multi-Spectrometry (REMS) technology and DXA for BMD assessment in kidney transplant recipients," *J. Clin. Densitom.*, vol. 25, no. 2, p. 277, Apr. 2022, doi: 10.1016/J.JOCD.2022.02.015.

[9] C. Caffarelli, M. D. Tomai Pitinca, A. Al Refaie, E. Ceccarelli, and S. Gonnelli, "Ability of radiofrequency echographic multispectrometry to identify osteoporosis status in elderly women with type 2 diabetes," *Aging Clin. Exp. Res.*, vol. 34, no. 1, pp. 121–127, 2021, doi: https://doi.org/10.1007/s40520-021-01889-w.

[10] S. Nazionale and L. Guida, "rischio e continuità assistenziale delle Fratture da Fragilità."

[11] P. Pisani *et al.*, "A quantitative ultrasound approach to estimate bone fragility: A first comparison with dual X-ray absorptiometry," *Measurement*, vol. 101, pp. 243–249, 2017, doi: 10.1016/j.measurement.2016.07.033.

[12] A. Greco *et al.*, "Ultrasound Fragility Score: An innovative approach for the assessment of bone fragility," *Measurement*, vol. 101, pp. 236–242, 2017, doi: 10.1016/j.measurement.2016.01.033.

[13] E. R. DeLong, D. M. DeLong, and D. L. Clarke-Pearson, "Comparing the areas under two or more correlated receiver operating characteristic curves: a nonparametric approach - PubMed," *Biometrics*, vol. 44, no. 3, pp. 837–845, 1988, Accessed: Apr. 19, 2023. [Online]. Available: https://pubmed.ncbi.nlm.nih.gov/3203132/.

[14] K. Raum, Q. Grimal, P. Varga, R. Barkmann, C. C. Glüer, and P. Laugier, "Ultrasound to Assess Bone Quality," *Curr. Osteoporos. Rep.*, vol. 12, pp. 154–162, 2014, doi: 10.1007/s11914-014-0205-4.

[15] U. Ferizi, S. Hoing, and G. Chang, "Artificial Intelligence, Osteoporosis and Fragility Fractures," *Curr Opin Rheumatol*, vol. 31, no. 4, pp. 368–375, 2020, doi: 10.1097/BOR.0000000000000607.Artificial.

[16] V. J. Sabesan, T. Valikodath, A. Childs, and V. K. Sharma, "Economic and social impact of upper extremity fragility fractures in elderly patients," *Aging Clin. Exp. Res. Exp Res*, vol. 27, pp. 539–546, 2015, doi: 10.1007/s40520-014-0295-y.

[17] M. Ruiz-Adame and M. Correa, "A systematic review of the indirect and social costs studies in fragility fractures," *Osteoporos. Int.*, vol. 31, pp. 1205–1216, 2020.

Development of a novel surface-based approach to quantify fNIRS-fMRI spatial correspondence

A. Bonilauri[1*], A. Pirastru[1,2*], Francesca Sangiuliano Intra[2,3], Sara Isernia[2], Marta Cazzoli[2], Valeria Blasi[2], Giuseppe Baselli[1], Francesca Baglio[2]

[1] *Department of Electronics, Information and Bioengineering, Politecnico di Milano, 20133 Milan, Italy*
[2] *IRCCS Fondazione Don Carlo Gnocchi ONLUS, CADITER, 20148 Milan, Italy*
[3] *Faculty of Education, Free University of Bolzano-Bozen, 39042 Brixen, Italy*
**Equal contribution*

***Abstract*—Functional Near-Infrared Spectroscopy (fNIRS) and functional Magnetic Resonance Imaging (fMRI) are employed as imaging techniques to non-invasively assess brain activity. Current fNIRS-fMRI integration studies have addressed the temporal correlation of these two modalities, but often miss a quantitative method to assess spatial correspondence. In this context, we propose a novel surface-based approach to quantify spatial correspondence of non-simultaneous fNIRS and fMRI measurements referred to a motor task, as well as the temporal correlation of averaged brain responses. This method proposes a robust definition of region-of-interests over the cortical surface based on statistical activation maps. Results indicate that there is a high reliability between fMRI and fNIRS data according to cortical surface representations, both considering spatial and temporal correspondence. Specifically, moderate-to-substantial spatial agreement (0.58-0.71 Dice Coefficient) and moderate-to-strong temporal correlation (0.69-0.82) were found at subject level. These results strengthen at group level. As prospective applications, we find the support of clinical longitudinal applications, such as the investigation of disease progression and treatment efficacy of rehabilitation procedures.**

***Keywords*—fNIRS, fMRI, multimodal imaging, spatial agreement.**

I. Introduction

Among non-invasive functional neuroimaging techniques, functional Magnetic Resonance Imaging (fMRI) is considered the gold standard [1] given its optimal spatial specificity and resolution and its in-depth penetration (volumetric measure). However, fMRI acquisitions cannot be performed over all clinical populations (i.e., participants with MRI incompatible devices/prosthesis, suffering from claustrophobia) and/or in ecological settings (i.e., in an open environment during the execution of a wide variety of tasks), hence giving rise to the adoption of alternative technologies such as optical imaging.

In this framework, functional Near-Infrared spectroscopy (fNIRS) has gained relevance allowing to quantitatively measure brain activity in an open environment, including people not eligible for MRI acquisition, and exploiting a higher temporal resolution. However, fNIRS is intrinsically limited to superficial measurements, and suffers from lower spatial resolution with respect to fMRI, being dependent on source-detector distances. For this reason, appropriate ex-post fNIRS data integration preliminarily to the comparison with both anatomical and functional MRI is warranted to determine fNIRS reliability.

Previous studies evaluated fNIRS-fMRI correspondence both performing simultaneous [2]–[6] or separated acquisitions [1], [7]–[10] during task execution. Despite the temporal correlation between fNIRS and fMRI being widely investigated, the spatial correspondence between the two techniques has been often overlooked or only qualitatively assessed according to fNIRS optodes localization and anatomical MRI [11]–[14].

In this context, the aim of our study was two-folded.

As a preliminary step, we propose a novel surface-based approach for ex-post data integration between non-simultaneous fNIRS fMRI acquisition.

Namely, instead of individually processing fNIRS and fMRI data in their native spaces (i.e., surface channels space for fNIRS and volumetric space for fMRI), we projected individual source maps of both fNIRS and fMRI onto MRI cortical surface.

This allowed us to perform the second aim of our work which focused on the reliability assessment of fNIRS data with respect to the fMRI. Specifically, we performed a vertex-wise quantitative spatial comparison, using cluster overlap methods. Besides the spatial correspondence, we finally assessed temporal comparison between fNIRS $\Delta[HbO_2]$ and $\Delta[HbR]$ and BOLD signals to confirm our methods results with respect to literature ones.

II. Materials and Methods

A. Participants

Eighteen healthy volunteers (age mean±SD 30.55±4.7, 7 males) were enrolled in this study. Written informed consent was signed by each participant. The study was approved by the IRCCS Fondazione Don Gnocchi Ethical Committee.

B. Motor Task Paradigm

We employed a block-design experimental paradigm using E-Prime 3.0 (https://pstnet.com/products/e-prime/). The motor paradigm consisted of AB-AC block-design alternating 2 conditions: active periods (B, C, 10 seconds), in which the subjects performed hand movements by squeezing a rubber ball and resting periods (A, 20 seconds), consisting of white-cross fixation. The B and C active conditions were pseudo-randomized in equal numbers of Left (L, condition B) and Right (R, condition C) hand movements.

C. Acquisition Protocols

Subjects underwent separate fMRI and fNIRS sessions and were randomized according to the order of acquisition.

The MRI protocol was acquired on a 3T Siemens Prisma scanner equipped with a 64-channel head-neck coil. The protocol included: 1) a 3D high-resolution T1-weighted MPRAGE sequence (TR = 2300 ms, TE = 3.1 ms, isotropic resolution = 0.8x0.8x0.8 mm^3) used as anatomical reference for both fMRI and fNIRS datasets; 2) a functional sequence with TR = 2000 ms, TE = 30 ms, resolution 3x3x3 mm^3, 310 measurements, BOLD sampling frequency = 0.5 Hz.

The fNIRS protocol was acquired using a continuous-wave system at 760 and 850 nm wavelengths with 1.95 Hz sampling rate (NIRScoutX 32x32, NIRx Medizintechnik, Berlin, Germany) which uses 32 LED sources and 32 avalanche photodiode detectors. The resulting configuration consisted of 102 measurement channels able to cover the entire subject's scalp surface.

D. fNIRS and fMRI Preprocessing and ex-post integration

The 3D MPRAGE images were skull stripped and corrected for bias field using FSL (FMRIB Software Library v6.0) and successively preprocessed using the FreeSurfer (http://surfer.nmr.mgh.harvard.edu/) recon-all pipeline.

The functional dataset was preprocessed using FreeSurfer FS-FAST (https://surfer.nmr.mgh.harvard.edu/fswiki/FsFast) and included motion correction, smoothing, and sampling on the subject's left and right hemisphere cortical surfaces, obtained from the processing of the anatomical dataset. Using Matlab (2017b, MathWorks) the data were saved as vectors containing BOLD time series per surface vertex and were successively imported in Brainstorm [15] using user-defined scripts to perform integration with fNIRS data.

The fNIRS dataset was preprocessed using standardized pipeline implemented in Nirstorm package of Brainstorm (https://github.com/Nirstorm/nirstorm) comprising removal of bad signal channels, conversion of raw intensity signal in optical density variations, motion correction, linear trend removal using the Temporal Derivative Distribution Repair Algorithm [16] and band-pass filtering [0.01-0.08]. Similarly, to fMRI preprocessing, anatomical 3D MPRAGE data were used in order to project fNIRS signals onto individual subjects' cortexes. Briefly, the optical properties from the work of Tak et al. [17] and Eggebrecht et al. [18] were used to implement a Monte Carlo (MC) simulation (5·107 photons) using a five-layered model, and volumetric fluences were interpolated onto the cortical surface using Voronoi-based method [19].

E. fNIRS fMRI measure reliability

fNIRS and fMRI integration and statistical activation maps were computed in the same environment constituted by the Brainstorm interface using user-defined Matlab scripts. Specifically, fNIRS and BOLD signals were separately analyzed through the Generalized Linear Model (GLM) to contrast L and R task conditions and generate the respective t_{value} cortical maps of significant activation. Group-level statistical maps were computed following normalization of subject-specific contrasts onto ICBM152 template [20]. fMRI and fNIRS ROIs were considered significant if the t_{value} map was associated to $p<0.05$, thus resulting in 2 different ROIs for HbO_2 and HbR. The functional ROIs were anatomically constrained (acfMRI and $acfNIRS_{HbO2}$ $acfNIRS_{HbR}$) to pre- and post-central parcels derived by the Desikan-Killany atlas [21] considering both contralateral and ipsilateral activation (Fig. 1).

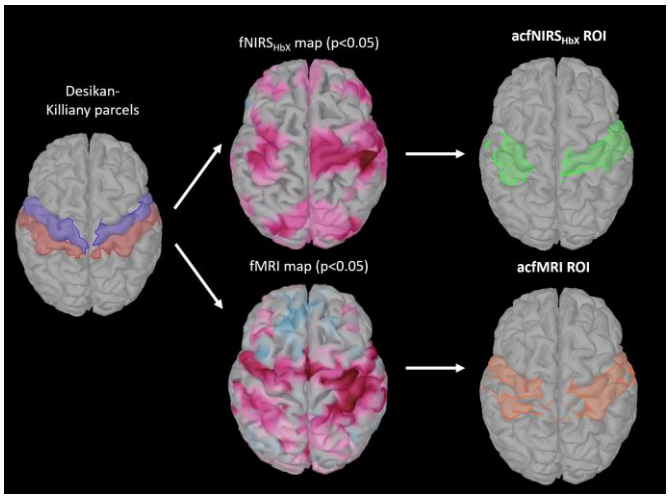


Fig. 1: Surface-based approach to define anatomically constrained functional ROI (acfROI) over t_{value}-maps of fNIRS ($acfNIRS_{HbX}$), fMRI (acfMRI) and their intersection ($acf_{\cap}$); t_{value} maps were associated to significant activation ($p < 0.05$).

The spatial extents of acfNIRS and acfMRI ROIs were compared using cluster overlap methods to assess global reliability of the measures [22]. Specifically, the Dice Coefficient (DC) was computed as follows:

$$DC(acfMRI, acfNIRS) = \frac{2 \cdot acf_{\cap}}{acfMRI + acfNIRS_{HbX}}$$

where $acf_{\cap} = acfMRI \cap acfNIRS_{HbX}$ represent the common regions between fMRI and fNIRS, and HbX being referred either to HbO_2 or HbR. A DC comprised between $0 \leq DC \leq 0.2$ was considered as slight agreement, fair between $0.21 \leq DC \leq 0.4$, moderate between $0.41 \leq DC \leq 0.6$, substantial between $0.61 \leq DC \leq 0.8$ and almost perfect between $0.81 \leq DC \leq 1$ [23].

Furthermore, the temporal Pearson's correlation between normalized BOLD and fNIRS $\Delta[HbO_2]$ or $\Delta[HbR]$ block average responses was performed over acfMRI and acfNIRSHbX respectively. Correlation values were considered weak between 0 and 0.3 (0 – -0.3), moderate between 0.3 and 0.7 (-0.3 – -0.7) and strong between 0.7 and 1 (-0.7 – -1).

Spatial and temporal comparisons were performed both at subjects' and group-level.

III. RESULTS

A. Spatial comparison – Dice Coefficient

The results derived from the spatial comparison between acfMRI and acfNIRS are reported in Table 1 at single-subject level and Table 2 for group level.

At subject level, moderate-to-substantial DC and moderate DC were found respectively for HbO2 and HbR relatively to the contralateral hemisphere with respect to the hand performing the movement. Fair-to-moderate DC and fair DC were instead respectively found for HbO2 and HbR regarding the ipsilateral activation maps.

At group level, we found a substantial DC for brain activation maps relative to the contralateral hemisphere for both HbO2 and HbR. Lower agreement, resulting in fair-to-

moderate DC for HbO2 and slight-to-fair DC for HbR was instead observed for ipsilateral hemisphere.

Table 1. Subject-level spatial agreement of fMRI BOLD vs. fNIRS HbO_2 and HbR maps across $acf_\cap$ ROIs. Results are reported as mean and standard deviation Dice Coefficient across subject-specific $acf_\cap$ ROIs. Legend: L=Left, R=Right, $acf_\cap$ = functional ROIs intersection; n.a.= either fNIRS/fMRI maps or their intersection is not available.

$acf_\cap$	$acfMRI \cap acfNIRS_{HbO2}$ *Mean±SD*		$acfMRI \cap acfNIRS_{HbR}$ *Mean±SD*	
	Left Hand	Right Hand	Left Hand	Right Hand
L precentral	0.47±0.22	0.61±0.23	0.37±0.26	0.52±0.26
R precentral	0.58±0.23	0.4±0.2	0.53±0.25	0.31±0.2
L postcentral	0.42±0.26	0.71±0.18	0.33±0.27	0.49±0.29
R postcentral	0.66±0.15	0.35±0.19	0.55±0.27	0.25±0.18

Table 2. Group-level spatial agreement of fMRI BOLD vs. fNIRS HbO_2 and HbR maps across $acf_\cap$ ROIs. Results are reported as Dice Coefficient between $acf_\cap$ ROIs over fMRI vs, fNIRS maps. Legend: L=Left, R=Right, $acf_\cap$ = functional ROIs intersection; n.a.= either fNIRS/fMRI maps or their intersection is not available.

$acf_\cap$	$acfMRI \cap acfNIRS_{HbO2}$		$acfMRI \cap acfNIRS_{HbR}$	
	Left Hand	Right Hand	Left Hand	Right Hand
L precentral	0.6	0.79	0.31	0.76
R precentral	0.7	0.41	0.61	0.15
L postcentral	0.45	0.8	0.19	0.62
R postcentral	0.81	0.38	0.62	n.a.

B. Temporal comparison – Correlation

The temporal correlation results between BOLD signal and either HbO or HbR signal computed over acfROIs are reported in Table 3 and Table 4 respectively for single-subject level and group level.

At subject level, moderate-to-strong correlation was found for contralateral activation between BOLD and HbO_2 signal, while moderate (inverse) correlation was found between BOLD and HbR.

Correlation between BOLD and HbO_2 was moderate-to-strong also for ipsilateral activation; however lower values were found between BOLD and HbR, ranging between weak-to-moderate correlation.

At group level, strong correlation was found both considering HbO2 and HbR signals for both contralateral and ipsilateral activation, except when comparing MRI BOLD and fNIRS HbR signals across the ipsilateral activation obtained during the right hand movement.

Table 3. Subject-level correlation results for fMRI BOLD vs. fNIRS HbO_2 and HbR signals across $acf_\cap$ ROIs. Results are reported as mean and standard deviation correlation values across subject-specific $acf_\cap$ ROIs. Legend: L=Left, R=Right, $acf_\cap$ = functional ROIs intersection; n.a.= either fNIRS/fMRI maps or their intersection is not available.

acfROI	$acfMRI \cap acfNIRS_{HbO2}$ *Mean±SD*		$acfMRI \cap acfNIRS_{HbR}$ *Mean±SD*	
	Left Hand	Right Hand	Left Hand	Right Hand
L precentral	0.75±0.13	0.82±0.12	-0.44±0.47	-0.67±0.51
R precentral	0.74±0.41	0.61±0.36	-0.63±0.53	-0.29±0.7
L postcentral	0.63±0.33	0.8±0.13	-0.47±0.51	-0.65±0.45
R postcentral	0.69±0.44	0.64±0.36	-0.65±0.49	-0.44±0.58

Table 4. Group-level correlation results for fMRI BOLD vs. fNIRS HbO_2 and HbR signals across $acf_\cap$ ROIs. Results are reported as correlation values between $acf_\cap$ ROIs over fMRI vs, fNIRS maps. Legend: L=Left, R=Right, $acf_\cap$ = functional ROIs intersection; n.a.= either fNIRS/fMRI maps or their intersection is not available.

acfROI	$acfMRI \cap acfNIRS_{HbO2}$		$acfMRI \cap acfNIRS_{HbR}$	
	Left Hand	Right Hand	Left Hand	Right Hand
L precentral	0.93	0.96	-0.82	-0.92
R precentral	0.94	0.80	-0.89	-0.47
L postcentral	0.89	0.95	-0.86	-0.91
R postcentral	0.97	0.89	-0.93	n.a.

IV. DISCUSSION AND CONCLUSION

In this work we proposed a novel surface-based approach to integrate and compare fMRI vs. fNIRS data projected onto cortical surfaces. The validity of our approach was tested on a motor task, since providing well localized and robust activations with both fNIRS [24] and fMRI [25]. Resulting analyses involved the assessment of fNIRS vs. fMRI spatial correspondence, which is often overlooked or not directly quantified in literature, as well as their temporal correlation.

Spatial correspondence was assessed through DC, yielding a moderate to substantial agreement for contralateral activation at subject-level, while fair to moderate for ipsilateral activation. This trend was accentuated at group-level, namely increasing for contralateral activation, while decreasing or remaining constant for ipsilateral activation.

In line with other fNIRS-fMRI integration studies [1]–[4], [7], [11], [12], [26], we found a high temporal correlation of block averaged BOLD responses with either HbO_2 or HbR. This result was evidenced both across task conditions and contralateral vs. ipsilateral hemisphere activation. The temporal correlation was moderate to strong at subject-level, while strong at group-level.

Taken together, results indicate that there is a high reliability between fMRI and fNIRS data according to cortical surface representations, especially when considering group-level analysis.

A quantitative assessment of the spatial correspondence between fNIRS and fMRI improves the evaluation of tasks reproducibility across modalities. Previous fNIRS-fMRI integration studies mostly assessed the temporal correspondence between BOLD and fNIRS signals, while confining the assessment of spatial agreement between the measured activation maps to fNIRS channels correspondence over significant fMRI maps [3], [9], [11]–[14]. Similarly, other approaches have considered the definition of statistically-driven ROIs around the most activated voxels in fMRI maps [1], [2], [26], or based on thresholding methods with respect to significant fMRI regions [7], [27].

Few studies have quantitatively assessed fNIRS-fMRI spatial correspondence. Among them, Cai et al. [8] validated the spatial accuracy of an fNIRS image reconstruction algorithm by employing thresholded fMRI z-maps over cortical surface to define activated/non-activated regions as

gold standard for the comparison with fNIRS maps. Conversely, Eggebrecht et al. [18] considered the voxel-wise spatial correspondence as localization error between fMRI maps and high-density diffuse optical tomography (HD-DOT).

Compared to other fNIRS-fMRI integration studies, our approach proposes a robust definition of cortical ROIs based on the computation of statistical activation maps. Employing cortical surface representations increases the flexibility of the proposed approach, since allowing the integration of other functional or structural cortical parcellations to compute acfROIs.

Moreover, the proposed ex-post analysis methods were applied to non-simultaneous fNIRS and fMRI acquisitions, but it can be directly extended also to simultaneous acquisitions. As well, the proposed approach can be extended to the comparison of fNIRS/fMRI data with other surface-based neuroimaging techniques, such as magnetoencephalography, electroencephalography and HD-DOT.

Establishing a direct fNIRS vs. fMRI spatial correspondence, together with assessing their temporal correlation, promotes the translation of well-established fMRI task into fNIRS routines.

Hence, the proposed approach can support clinical longitudinal applications, such as the investigation of disease progression and treatment efficacy of rehabilitation procedures. Indeed, fNIRS can provide multiple measurements of cerebral activity in those experimental setting where fMRI is not an available or feasible approach. For instance, fNIRS may represent a low-cost and ecological monitoring throughout rehabilitation steps, while confining fMRI acquisitions only at predefined time points, such as pre- and post-rehabilitation stages.

REFERENCES

[1] F. Klein, S. Debener, K. Witt, and C. Kranczioch, “fMRI-based validation of continuous-wave fNIRS of supplementary motor area activation during motor execution and motor imagery,” *Sci. Rep.*, vol. 12, no. 1, p. 3570, Dec. 2022.

[2] A. R. Anwar *et al.*, “Effective Connectivity of Cortical Sensorimotor Networks During Finger Movement Tasks: A Simultaneous fNIRS, fMRI, EEG Study,” *Brain Topogr.*, vol. 29, no. 5, pp. 645–660, Sep. 2016.

[3] V. Toronov *et al.*, “Investigation of human brain hemodynamics by simultaneous near-infrared spectroscopy and functional magnetic resonance imaging,” *Med. Phys.*, vol. 28, no. 4, pp. 521–527, Apr. 2001.

[4] T. Huppert, J. Barker, B. Schmidt, S. Walls, and A. Ghuman, “Comparison of group-level, source localized activity for simultaneous functional near-infrared spectroscopy-magnetoencephalography and simultaneous fNIRS-fMRI during parametric median nerve stimulation,” *Neurophotonics*, vol. 4, no. 1, p. 15001, 2017.

[5] S. Wijeakumar, T. J. Huppert, V. A. Magnotta, A. T. Buss, and J. P. Spencer, “Validating an image-based fNIRS approach with fMRI and a working memory task,” *Neuroimage*, vol. 147, pp. 204–218, Feb. 2017.

[6] H. Sato *et al.*, “A NIRS–fMRI investigation of prefrontal cortex activity during a working memory task,” *Neuroimage*, vol. 83, pp. 158–173, Dec. 2013.

[7] J. A. Noah *et al.*, “fMRI Validation of fNIRS Measurements During a Naturalistic Task,” *J. Vis. Exp.*, no. 100, Jun. 2015.

[8] Z. Cai *et al.*, “Evaluation of a personalized functional near <scp>infra-red</scp> optical tomography workflow using maximum entropy on the mean,” *Hum. Brain Mapp.*, vol. 42, no. 15, pp. 4823–4843, Oct. 2021.

[9] J. C. Wagner *et al.*, “Comparison of Whole-Head Functional Near-Infrared Spectroscopy With Functional Magnetic Resonance Imaging and Potential Application in Pediatric Neurology,” *Pediatr. Neurol.*, vol. 122, pp. 68–75, Sep. 2021.

[10] E. Maggioni *et al.*, “Investigation of negative BOLD responses in human brain through NIRS technique. A visual stimulation study,” *Neuroimage*, vol. 108, pp. 410–422, Mar. 2015.

[11] D. J. Mehagnoul-Schipper *et al.*, “Simultaneous measurements of cerebral oxygenation changes during brain activation by near-infrared spectroscopy and functional magnetic resonance imaging in healthy young and elderly subjects,” *Hum. Brain Mapp.*, vol. 16, no. 1, pp. 14–23, May 2002.

[12] G. Strangman, J. P. Culver, J. H. Thompson, and D. A. Boas, “A Quantitative Comparison of Simultaneous BOLD fMRI and NIRS Recordings during Functional Brain Activation,” *Neuroimage*, vol. 17, no. 2, pp. 719–731, Oct. 2002.

[13] A. Kleinschmidt *et al.*, “Simultaneous Recording of Cerebral Blood Oxygenation Changes during Human Brain Activation by Magnetic Resonance Imaging and Near-Infrared Spectroscopy,” *J. Cereb. Blood Flow Metab.*, vol. 16, no. 5, pp. 817–826, Sep. 1996.

[14] V. Toronov *et al.*, “The roles of changes in deoxyhemoglobin concentration and regional cerebral blood volume in the fMRI BOLD signal,” *Neuroimage*, vol. 19, no. 4, pp. 1521–1531, Aug. 2003.

[15] F. Tadel, S. Baillet, J. C. Mosher, D. Pantazis, and R. M. Leahy, “Brainstorm: A User-Friendly Application for MEG/EEG Analysis,” *Comput. Intell. Neurosci.*, vol. 2011, pp. 1–13, 2011.

[16] F. A. Fishburn, R. S. Ludlum, C. J. Vaidya, and A. V. Medvedev, “Temporal Derivative Distribution Repair (TDDR): A motion correction method for fNIRS,” *Neuroimage*, vol. 184, pp. 171–179, Jan. 2019.

[17] S. Tak, A. M. Kempny, K. J. Friston, A. P. Leff, and W. D. Penny, “Dynamic causal modelling for functional near-infrared spectroscopy,” *Neuroimage*, vol. 111, pp. 338–349, May 2015.

[18] A. T. Eggebrecht *et al.*, “A quantitative spatial comparison of high-density diffuse optical tomography and fMRI cortical mapping,” *Neuroimage*, vol. 61, no. 4, pp. 1120–1128, Jul. 2012.

[19] C. Grova, S. Makni, G. Flandin, P. Ciuciu, J. Gotman, and J. B. Poline, “Anatomically informed interpolation of fMRI data on the cortical surface,” *Neuroimage*, vol. 31, no. 4, pp. 1475–1486, Jul. 2006.

[20] V. Fonov, A. C. Evans, K. Botteron, C. R. Almli, R. C. McKinstry, and D. L. Collins, “Unbiased average age-appropriate atlases for pediatric studies,” *Neuroimage*, vol. 54, no. 1, pp. 313–327, Jan. 2011.

[21] R. S. Desikan *et al.*, “An automated labeling system for subdividing the human cerebral cortex on MRI scans into gyral based regions of interest,” *Neuroimage*, vol. 31, no. 3, pp. 968–980, Jul. 2006.

[22] J. H. Fröhner, V. Teckentrup, M. N. Smolka, and N. B. Kroemer, “Addressing the reliability fallacy in fMRI: Similar group effects may arise from unreliable individual effects,” *Neuroimage*, vol. 195, pp. 174–189, Jul. 2019.

[23] A. Pirastru *et al.*, “Consistent Cerebral Blood Flow Covariance Networks across Healthy Individuals and Their Similarity with Resting State Networks and Vascular Territories,” *Diagnostics*, vol. 10, no. 11, p. 963, Nov. 2020.

[24] N. H. Kashou, B. M. Giacherio, R. W. Nahhas, and S. R. Jadcherla, “Hand-grasping and finger tapping induced similar functional near-infrared spectroscopy cortical responses,” *Neurophotonics*, vol. 3, no. 2, p. 025006, Jun. 2016.

[25] V. S. Mattay and D. R. Weinberger, “Organization of the human motor system as studied by functional magnetic resonance imaging,” *Eur. J. Radiol.*, vol. 30, no. 2, pp. 105–114, May 1999.

[26] T. J. Huppert, R. D. Hoge, S. G. Diamond, M. A. Franceschini, and D. A. Boas, “A temporal comparison of BOLD, ASL, and NIRS hemodynamic responses to motor stimuli in adult humans,” *Neuroimage*, vol. 29, no. 2, pp. 368–382, Jan. 2006.

[27] X. Cui, S. Bray, D. M. Bryant, G. H. Glover, and A. L. Reiss, “A quantitative comparison of NIRS and fMRI across multiple cognitive tasks,” *Neuroimage*, vol. 54, no. 4, pp. 2808–2821, Feb. 2011.

Towards 3D Virtual Histology of melanoma tissue by means of lab-based X-ray Phase Contrast Computed Micro-Tomography

G. Saccomano[1,2], L. Brombal[3], D. Dreossi[2], M. Pinamonti[4], G. Tromba[2] and F. Brun[1]

[1] *Department of Engineering and Architecture, University of Trieste, Trieste*

[2] *Elettra-Sincrotrone Trieste S.C.p.A., Trieste*

[3] *Department of Physics, University of Trieste, Trieste*

[4] *Department of Pathology, Cattinara Hospital, Trieste*

***Abstract*—Melanoma is a serious form of skin cancer which originates from melanocytes. The diagnosis of melanoma occurs through histological examination, which is a destructive and labor-intensive technique where a "blind" sectioning without landmarks is performed.**

X-ray phase contrast computed micro-tomography (micro-CT) overcomes these limitations by providing virtual sections of the excised tissue along arbitrary planes without causing its destruction. However, up to date, synchrotron radiation (SR) micro-CT seems to be the only way to obtain high-resolution phase contrast 3D data. In sight of introducing x-ray virtual histology in the clinical practice, compact laboratory x-ray phase contrast micro-CT solutions are needed.

This study aims to move towards a new concept of 3D x-ray virtual histology in the clinical trial of melanoma diagnosis by showing preliminary results from a compact and cheap lab-based micro-CT setup based on the edge-illumination principle. A thorough comparison of SR micro-CT against laboratory micro-CT of the very same melanoma tissue is presented and discussed. Conventional histological images are also included.

Although the achieved spatial resolution and the scanning speed are not comparable to those obtained with SR, the proposed lab-based micro-CT solution still provides a comprehensive understanding of the morphological and functional aspects of the melanoma tissue in a non-destructive way, thus justifying further destructive exams such as conventional histology. This lays promising foundations for a wider clinical translation of the proposed approach.

***Keywords*— Melanoma, x-ray Virtual Histology, synchrotron radiation Computed micro-Tomography, lab-based Computed micro-Tomography.**

I. INTRODUCTION

DESPITE advances made over the past decades, melanoma remains the most aggressive type of skin cancer due to its aggressive nature of rapidly spreading to other organs and becoming metastatic. Even though it accounts for only 5% of all skin cancer, it is responsible for the majority of deaths in this category [1].

Melanoma develops when DNA damage from burning or tanning due to UV radiation changes and mutates in the melanocytes, which are the cells in the upper layer of the skin that produce a pigment known as melanin, resulting in uncontrolled cellular growth. The skin phenotype plays an important role with higher risk for fair-skinned persons: in 2006 American Caucasians accounted for 70% of melanoma cases [2], while black population had an increased mortality as a results of late detection and a different biology [3].

First melanoma signs are often associated with a change in an existing mole and the development of a new pigmented or unusual-looking growth on the skin. The detection of melanoma is based on the revised ABCDE rule of pigmented lesions (Asymmetry, irregular Border, change in Color, Diameter, Evolution): when one or more of the features listed above are identified in a mole, biopsy material is removed and analysed in laboratory. Although non-invasive in-vivo approaches such as e.g., optoacoustic and ultrasonography techniques [4] have been proposed, histological examination of bioptic material is still the standard for diagnosis of pathological tissues, mainly based on cancer cells recognition and diffusion in the excised tissue which can occur also at higher penetration depths. However, the histological staining process is based on a complex and time-consuming chemical preparation of the excised biopsy, followed by sectioning the pathological tissue into thin slices for viewing under the light microscope.

To overcome the lack of reproducibility and destructiveness of the histological technique, x-ray Virtual Histology (xVH) exploits x-ray Computed micro-Tomography (micro-CT) in the production of 3D high-contrast maps of the soft tissue specimen. By virtually sectioning the whole excised sample, xVH allows to investigate structures (e.g., lesions) and computing parameters (e.g., max infiltration depth) that could be lost or damaged during the histological sectioning process.

Synchrotron Radiation Computed micro-Tomography (SR micro-CT) is the optimum technique in term of high-resolution and high-contrast properties for xVH. However, it lacks the possibility of an easy integration in the clinical workflow due to its limited-access policy and high cost of maintenance.

This work aims to show the potentiality of a lab-based phase-contrast micro-CT technique to perform xVH on a soft tissue suspected-melanoma biopsy. As a preliminary result, we focus on enhancing the contrast-to-noise ratio by working on two aspects: a physical property (edge illumination principle) and a computational method (denoising with deep learning). SR micro-CT and histology images are considered in this study.

II. Material and Methods

A. Staining and embedding

One surgical excision of a human suspected melanoma tissue was embedded in paraffin (standard histology paraffin block of about 2.5x3.5x1.0 cm^3) and then sectioned using a microtome. The resultant skin tissue remains inside the paraffin block for micro-CT analysis.

B. Histological examination

Paraffin embedded melanoma sections were stained with haematoxylin & eosin (HE). Histological images were acquired using a D-Sight 2.0 digital microscope with a 200× magnification.

C. Lab-based Computed micro-Tomography

The paraffin block including the melanoma specimen was investigated by means of x-ray phase-contrast micro-CT at PEPILab [5] (Fig. 1). The acquisition was performed with a Hamamatsu microfocus x-ray source (tube voltage: 50kV, tube current: 120µA) and a Pixirad-1/Pixie-III detector [6]. The sample and the detector were placed respectively 355 mm and 635 mm far from the x-ray source. Two structured absorbing masks (M1: sample mask, M2: detector mask) were introduced in the micro-CT setup to exploit the edge illumination principle: the source-to-M1 distance and the sample-to-M2 distance were 315 mm and 255 mm. The mask aperture was 10 µm wide and the mask pitch was 61 µm. The pixel size obtained was 12 µm. Five points were sampled over the illumination curve and 6 dithering steps were considered. A total of 720 projections were acquired over a 360 degrees rotation of the sample with an exposure time of 3000 ms per projection.

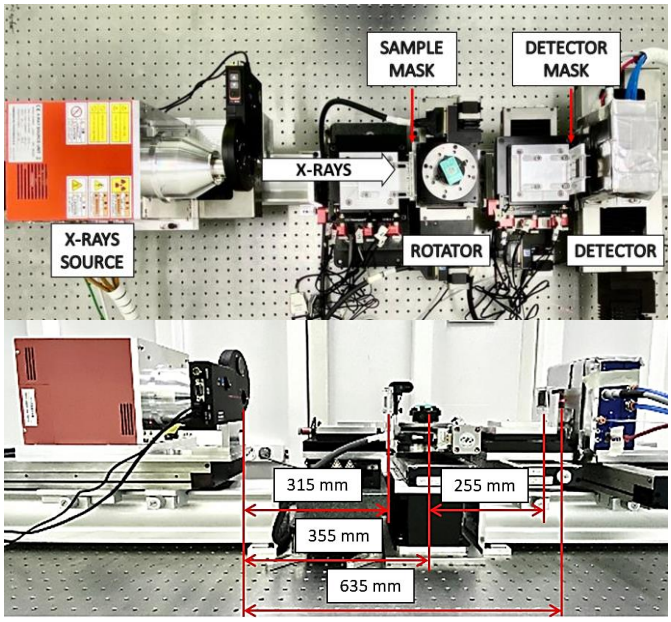


Fig. 1: Compact phase contrast micro-CT setup at PEPILab.

After being processed for phase retrieval, the stack of projections was split into 4 sets of projections and each set was reconstructed using TIGRE Toolbox [7]. Noise2Inverse denoising method [8] was applied by considering each set of reconstructed slices to get the final reconstructed volume. The Mixed-Scale Dense (MSD) convolutional neural network was used.

D. Synchrotron Radiation Computed micro-Tomography

The very same human melanoma excision was scanned at SYRMEP beamline [9] of Elettra synchrotron facility. The 2.4 GeV storage ring operating mode flux was filtered with a 1.0 mm Si filter to obtain an x-ray average energy spectrum of 23.6 keV. The pixel size was set to 1.6 µm and the sample-to-detector distance was set at 150 mm to improve the contrast-to-noise ratio by exploiting the propagation-based principle [10]. The paraffin block was placed orthogonally between the x-ray source and the detector (a Hamamatsu ORCA-FLASH 4.0 Digital CMOS camera coupled to a 17 µm GGG scintillator). 1800 projections over a 180 degrees sample rotation were collected with an exposure time of 100 ms per projection.

Projection digital images were filtered with a phase retrieval algorithm [11] and a δ/β ratio of 150. Tomographic axial slices were reconstructed using SYRMEP Tomo Project software [12] and, since two vertical scans were acquired to cover the whole mole, the two stacks were registered and stitched together with a Python script.

E. Quantitative image analysis

In order to compare the results obtained with two phase-contrast based micro-CT techniques, a quantitative evaluation was performed by computing the contrast-to-noise ratio (CNR). As shown with different colours in Fig. 2, several 20x20 pixels region-of-interests (ROIs) were considered to estimate the detectability of skin layers (epidermis, dermis, and subcutaneous fat) and pathological elements (lesion and ulceration), while confronted to the background (BKG). ROIs in Fig. 2 appear having different size due to different image pixel size (12 µm and 1.6 µm, respectively). CNR was computed as in Eq. (1):

$$CNR = \frac{|\mu_{ROI} - \mu_{BKG}|}{\sqrt{\frac{1}{2}(\sigma_{ROI}^2 + \sigma_{BKG}^2)}} \quad (1)$$

where μ is the mean and σ is the standard deviation of the gray levels within the ROI.

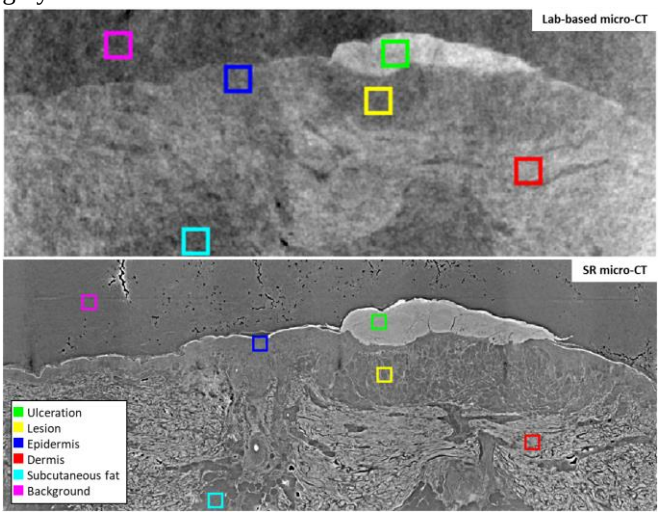


Fig. 2: Highlighted ROIs in micro-CT images used for quantitative analysis: each color marks a specific element of the skin tissue, while magenta is used as reference (background).

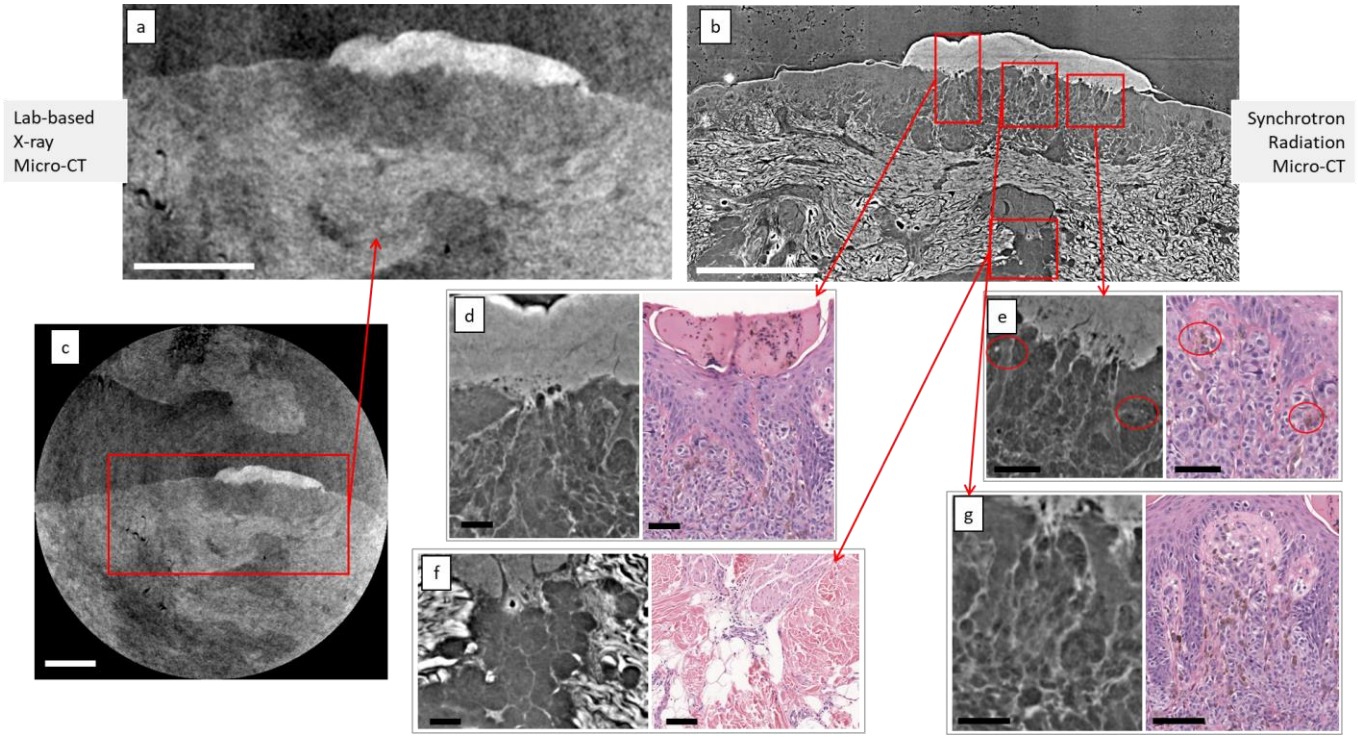


Fig. 3: The same lesion area of melanoma with (a) the lab-based and (b) the SR micro-CT techniques. (c) A lab-based micro-CT slice of the whole excision. Selected SR micro-CT and histology matches: (d) the full-thickness loss of the epidermis, (e) melanin pigment in malignant melanocytes nests, (f) dermis and subcutaneous fat and (g) the presence of malignant melanocytes in epidermis and dermis. White scale bar = 1mm, Black scale bar = 100µm.

III. Results And Discussion

From the whole 3D reconstructed datasets of micro-CT techniques¸ two slices were extracted and matched together via visual inspection. These slices are reported in Fig. 3.a and Fig. 3.b.

A. X-ray virtual histology with lab-based micro-CT

As visible for Fig. 3.c, the first aspect to consider is the challenging discrimination of the soft tissue from the paraffin due to the high density and internal artefacts introduced by the paraffin.

The application of the adopted phase retrieval to the edge-illumination technique revealed boundaries of the skin structure, thus allowing the identification of the top two layers, i.e. the epidermis and dermis (Fig. 3.a). The hypodermis, which is mainly composed by subcutaneous fat and blood vessels, is not properly observable due to its low density. Even the distinction between epidermis and dermis is not well defined with this technique, but it is an unnecessary information when finalizing the diagnosis.

On the contrary, the blood density ensures the high visibility of the ulceration above the epidermis. Considered that the ulceration is a result of the uncontrollable proliferation of neoplastic cells due to expansive activity of the tumor, this aspect is an important marker for tumor manifestation.

To support this thesis, a wide inflammatory process lays below the ulceration, causing even the destruction of the epidermis in some parts which are visible only in the SR image (Fig. 3.b). The thickness of melanoma lesion, which is one of the fundamental parameters for evaluation of staging, is easily assessable even at this level of magnification.

B. X-ray virtual histology with SR micro-CT

By exploiting the propagation-based characteristics of the synchrotron setup, the high-contrast SR micro-CT allows to enhance soft tissue properties making easier to detect morphological and pathological aspects on a microscopic scale. As shown in Fig. 3.b, the SR micro-CT image categorizes skin layers in different shades of gray: the epidermis is the outer layer in dark gray, while dermis is the fibrous part in light gray, and subcutaneous adipose tissue is of a dense dark gray.

In Fig. 3.f it can be noticed that histology fails to appreciate the subcutaneous fat, which appears as background. Due to its weak structure, it is easily damageable by undergoing the mechanical compression of sectioning causing tears and rips in the histological tissue.

By virtually sectioning the 3D micro-CT dataset, the chosen slice in Fig. 3.d testifies the absence of an intact epidermis and the association between consumption of epidermis and ulceration [13]. Failing to recognize this could decrease the degree of severity and thus lead to a less rigorous prognosis [14]. However, an experienced pathologist can predict and capture the full-thickness loss of epidermis overlying melanoma by evaluating the infiltration of the epidermis by malignant melanocytes in the histological section. This fundamental aspect for staging, diagnosis and prognosis cannot be solved by SR micro-CT image due to its spatial resolution.

A great inflammation under the ulceration as in Fig. 3.b is a clear symptom of cancerogenesis, but it is difficult to differentiate malignant melanocytes from lymphocytes.

However, xVH provides good contrast to enhance high dense material giving complementary morphological information to the histology technique which highlight cells' nuclei in purple.

For this purpose, Fig. 3.g shows the structure of stratum basale, which is a single layer of basal cells, visible as a purple bow in the histological image and as a light gray coloured bow in the micro-CT one. Then, clusters of melanoma cells are observable as purple and gray nests in histology, while they appear as dark gray regions bounded by a white membrane in the micro-CT image. Melanin pigment is also visible in both images and even in Fig. 3.e as brownish elements in the histology image, and as white dots in the micro-CT one.

However, these aspects cannot be investigated by lab-based micro-CT which cannot reach a similar spatial resolution. Further improvements are needed to increase the visibility of tissue components at the microscopic scale.

C. *X-ray virtual histology quantitative analysis*

Table I reports the quantitative results obtained for the two micro-CT techniques.

TABLE I: RESULTS OF THE QUANTITATIVE ANALYSIS

Tissue element	*CNR Lab-based micro-CT*	*CNR SR micro-CT*
Ulceration	7.28	8.92
Lesion	2.10	1.30
Epidermis	2.41	1.13
Dermis	5.40	2.02
Subcutaneous fat	0.30	1.86

All results from both techniques are above the unity with only one exception, thus meaning an overall good visibility of the tissue. For both techniques, ulceration and dermis tend to have the highest CNR due to their high densities, while the lesion does not have a high CNR value due to its non-uniform composition. Due to the noisy paraffin background used as reference, lab-based technique reveals higher CNR values than SR ones, but this does not imply higher image definition. Consequently, the lowest CNR measure for lab-based method comes for subcutaneous fat because of the similar noisy pattern as the reference background.

IV. CONCLUSION

A suspected melanoma excised tissue was examined by histology and measured with two different micro-CT setups. While the SR micro-CT technique reaches a very high-resolution comparable to that achievable via large magnification in conventional histology, the compact phase-contrast lab-based micro-CT technique shows promising results when considering its use to assess the correct malignancy of the suspected melanoma. In addition, the computed quantitative measurements support the need of phase-contrast while performing xVH in both scenarios (synchrotron and laboratory) instead of conventional absorption X-ray scanning.

The proposed phase-contrast laboratory micro-CT cannot reach the performances of the considered SR micro-CT setup, due to the limited spatial resolution and low scanning speed, but still provides a comprehensive understanding of morphological and functional aspects of the melanoma tissue in a non-destructive way. Once fully operating and optimized, the inclusion of a lab-based micro-CT setup in a clinical context would help to provide information about the pathological stage of the disease.

ACKNOWLEDGEMENT

Authors acknowledge Elettra-Sincrotrone Trieste S.C.p.A. for providing access to the synchrotron radiation facility and for using SYRMEP beamline. This work is carried out in the framework of the PEPI project, supported by Istituto Nazionale di Fisica Nucleare (National Scientific Commission 5 for Technological and Inter-disciplinary Research, No. 22260/2020).

REFERENCES

[1] N. H. Matthews, W.-Q. Li, A. A. Qureshi, M. A. Weinstock, and E. Cho, 'Epidemiology of Melanoma', in *Cutaneous Melanoma: Etiology and Therapy*, W. H. Ward and J. M. Farma, Eds., Brisbane (AU): Codon Publications, 2017. Accessed: Oct. 18, 2022. [Online]. Available: http://www.ncbi.nlm.nih.gov/books/NBK481862/

[2] M.-F. Demierre, 'Epidemiology and prevention of cutaneous melanoma', *Curr. Treat. Options Oncol.*, vol. 7, no. 3, pp. 181–186, May 2006, doi: 10.1007/s11864-006-0011-z.

[3] K. H. Kaidbey, P. P. Agin, R. M. Sayre, and A. M. Kligman, 'Photoprotection by melanin--a comparison of black and Caucasian skin', *J. Am. Acad. Dermatol.*, vol. 1, no. 3, pp. 249–260, Sep. 1979, doi: 10.1016/s0190-9622(79)70018-1.

[4] K. Kratkiewicz *et al.*, 'Photoacoustic/Ultrasound/Optical Coherence Tomography Evaluation of Melanoma Lesion and Healthy Skin in a Swine Model', *Sensors*, vol. 19, no. 12, p. 2815, Jun. 2019, doi: 10.3390/s19122815.

[5] L. Brombal, F. Arfelli, R. H. Menk, L. Rigon, and F. Brun, 'PEPI Lab: a flexible compact multi-modal setup for X-ray phase-contrast and spectral imaging', *Sci. Rep.*, vol. 13, no. 1, Art. no. 1, Mar. 2023, doi: 10.1038/s41598-023-30316-5.

[6] R. Bellazzini *et al.*, 'PIXIE III: a very large area photon-counting CMOS pixel ASIC for sharp X-ray spectral imaging', *J. Instrum.*, vol. 10, no. 01, p. C01032, Jan. 2015, doi: 10.1088/1748-0221/10/01/C01032.

[7] A. Biguri, M. Dosanjh, S. Hancock, and M. Soleimani, 'TIGRE: a MATLAB-GPU toolbox for CBCT image reconstruction', *Biomed. Phys. Eng. Express*, vol. 2, no. 5, p. 055010, Sep. 2016, doi: 10.1088/2057-1976/2/5/055010.

[8] A. A. Hendriksen, D. M. Pelt, and K. J. Batenburg, 'Noise2Inverse: Self-Supervised Deep Convolutional Denoising for Tomography', *IEEE Trans. Comput. Imaging*, vol. 6, pp. 1320–1335, 2020, doi: 10.1109/TCI.2020.3019647.

[9] G. Tromba *et al.*, 'The SYRMEP Beamline of Elettra: Clinical Mammography and Bio-medical Applications', *AIP Conf. Proc.*, vol. 1266, no. 1, pp. 18–23, Jul. 2010, doi: 10.1063/1.3478190.

[10] S. Donato *et al.*, 'Optimization of a customized simultaneous algebraic reconstruction technique algorithm for phase-contrast breast computed tomography', *Phys. Med. Biol.*, vol. 67, no. 9, p. 095012, Apr. 2022, doi: 10.1088/1361-6560/ac65d4.

[11] D. Paganin, S. C. Mayo, T. E. Gureyev, P. R. Miller, and S. W. Wilkins, 'Simultaneous phase and amplitude extraction from a single defocused image of a homogeneous object', *J. Microsc.*, vol. 206, no. 1, pp. 33–40, 2002, doi: 10.1046/j.1365-2818.2002.01010.x.

[12] F. Brun *et al.*, 'SYRMEP Tomo Project: a graphical user interface for customizing CT reconstruction workflows', *Adv. Struct. Chem. Imaging*, vol. 3, no. 1, p. 4, 2017, doi: 10.1186/s40679-016-0036-8.

[13] R. F. Walters *et al.*, 'Consumption of the epidermis: a criterion in the differential diagnosis of melanoma and dysplastic nevi that is associated with increasing breslow depth and ulceration', *Am. J. Dermatopathol.*, vol. 29, no. 6, pp. 527–533, Dec. 2007, doi: 10.1097/DAD.0b013e318156e0a7.

[14] M. L. Bønnelykke-Behrndtz and T. Steiniche, 'Ulcerated Melanoma: Aspects and Prognostic Impact', in *Cutaneous Melanoma: Etiology and Therapy*, W. H. Ward and J. M. Farma, Eds., Brisbane (AU): Codon Publications, 2017. Accessed: Dec. 20, 2022. [Online]. Available: http://www.ncbi.nlm.nih.gov/books/NBK481861/

Discriminatory power of Global Longitudinal Strain and Left Ventricular Ejection Fraction for Identification of Dilated Cardiomyopathy

K. Iscra[1], A. Miladinović[1,2], M. Ajčević [1], L. Munaretto[3], J. G. Rizzi[3], M. Merlo[3], A. Accardo[1]
[1] *Department of Engineering and Architecture, University of Trieste, Italy*
[2] *Institute for Maternal and Child Health "Burlo Garofolo", Trieste, Italy*
[3] *Cardiovascular Department, ASUGI and University of Trieste, Italy*

Abstract— **Dilated cardiomyopathy (DCM) is one of the leading causes of heart failure. Left ventricular ejection fraction (LVEF) is one of the most used features for assessing heart health and predicting outcomes in DCM patients. However, it does have numerous pitfalls. Recent studies suggest that global longitudinal strain (GLS) and heart rate variability (HRV) can be used to predict DCM. Furthermore, numerous studies have demonstrated how essential it is to deploy interpretable machine learning models to aid clinicians in the cases when the diagnosis is challenging. Therefore, we aimed to investigate discriminatory power of GLS and LVEF as a feature of logistic regression models for identification of DCM. The study encompassed 138 DCM and 138 healthy controls (HC). The models were produced by logistic regression algorithms considering the set of selected HRV features and GLS ($LogReg_{GLS}$) or LVEF ($LogReg_{LVEF}$). The results showed that the accuracy of produced $LogReg_{GLS}$ model was 86%, higher than the one observed in case of $LogReg_{LVEF}$ model (83%). The produced nomograms also supported the hypothesis of the relevance of the GLS and LVEF features, indicating that these two measurements are the most useful in identification of DCM. In conclusion, our findings highlight the value and efficacy of interpretable machine learning models and suggest that GLS may have more discriminatory power in differentiating between DCM and healthy participants than LVEF.**

***Keywords*—Interpretable Machine Learning, GLS, HRV, DCM**

I. Introduction

DILATED cardiomyopathy (DCM) is a progressive cardiac muscle disease. DCM is a significant cause of heart failure and the most common reason for heart transplantation worldwide [1].

The left ventricular ejection fraction (LVEF) is the most commonly used characteristic in DCM patients to assess heart function and predict outcomes [2]. However, it does have some inherent disadvantages, such us LVEF decrease that occurs only in advance fase of cardiac disease, low reliability in patients with left ventricular hypertrophy and volume reduction, extremely low inter- and intra-observer variability, and problematic endocardial boundary identification [2]. Therefore, there is still a need for the identification of reliable non-invasive biomarkers for early DCM differential diagnosis. Recent studies have reported left ventricular global longitudinal strain (GLS) and heart rate variability (HRV) as promising features for diagnosis and prediction of various heart diseases [3]–[12].

GLS is a myocardial deformation analysis parameter that could play an important role in the prediction of cardiovascular outcomes [13]. When compared to LVEF measurement alone, GLS has demonstrated superior efficacy in detecting the overall degeneration of the left ventricle [3].

As a result of the interaction between sympathetic and parasympathetic activity, the HRV measurement is instead utilized to quantify cardiac autonomic activity. Prognostic information, which might not be contained within GLS and LVEF, may be provided by the pathophysiologic changes linked to heart disorders and the accompanying changes in HRV [14].

The design of machine learning models for computer-aided diagnosis that take advantage of the collected HRV characteristics in conjunction with other available clinical data is gaining scientific attention [15]. However, clinicians are still dissatisfied with the limited interpretability of the produced models because they cannot be evaluated on the level of single input features. For this reason, interpretable models that not only provide output information about a specific disease but also aid in intrinsically evaluating the model's plausibility are more desirable in medicine [16]. Therefore, by using interpretable models end-users and healthcare professionals can examine the rationale behind prediction models before accepting or rejecting the output [15]. Because of their high degree of interpretability and ease of use in practice, approaches such as linear/logistic regression, classification trees, and naive Bayes models are used in several sectors of healthcare, including toxicology [16], [17], endocrinology [18], neurology [17], and cardiology [19]–[21].

Logistic regression is a statistical model that shows the relationship between input parameters and can be interpreted using nomograms to determine the likelihood of an event occurring. A nomogram is a graphical representation of numerical relationships and is a basic- and self-explanatory visualization that is both helpful and powerful in diagnosing a disease. The logistic regression nomogram not only enables prediction but also illustrates the model's structure and the relative contributions of the features on the class probability. This is especially important when investigating the GLS, HRV, and LVEF thresholds to introduce new aids for DCM diagnosis, especially when the research is still in its early stages.

Therefore, the aim of this study was to investigate discriminatory power of GLS and LVEF as a feature of logistic regression models for identification of DCM.

II. METHODS

A. Study population and protocol

The study encompassed 138 DCM (81M/57F, aged 61± 15 y) and 138 healthy controls (HC), (66M/72F, aged 59±19 y). The DCM patients were enrolled after clinical assessment. Coronary angiography was systematically performed in patients older than 35 and with cardiovascular risk factors and/or without a familial history of DCM. Patients with known trigger factors, such as toxic insults from alcohol or drug abuse, and tachyarrhythmias were excluded from the study. The LVEF has been obtained by the Simpson biplane method [22] and the GLS has been obtained by speckle tracking echocardiography. The measurement of GLS was performed offline using dedicated software (TomTec Arena v2.0, TomTec Imaging Systems, Unterschleißheim, Germany). The investigators visually assessed the detected endocardial border and, if necessary, manually adapted the tracing to ensure the correct tracing of the contours. The study was conducted according to the principles of the Declaration of Helsinki. All participants released their written informed consent.

B. Heart Rate Variability acquisition and processing

All subjects underwent a 24h Holter ECG recording using the ambulatory electrocardiographic recorder SpiderView (Sorin Group, Italy) with a sampling rate of 200Hz. The RR intervals were extracted and labeled by using SyneScope analysis software (Sorin Group, Italy). The RR interval records were cut into 5 min segments without overlap. Each RR 5-minutes segment was included in the analysis only if the longest ectopic beats subsequence (labeled with "ectopic" by the ECG Holter) or the longest artifact subsequence does not exceed 10s (so-called Hearth rate Total variability [4]). The segments were interpolated with cubic spline and resampled at 2 Hz. Subsequently, for each segment, linear and non-linear HRV features were extracted. In particular, the linear parameters MeanRR, SDNN, RMSSD, NN50 and pNN50 evaluating the RR variability were calculated directly from the RR sequence, whilst in the frequency domain, the absolute powers in Low (LF=0.04-0.15Hz) and High (HF=0.15-0.40Hz) frequency bands, related to the vagal and sympathetic nerve control on the heart rhythm, were estimated from the interpolated HRV signal. Moreover, the normalized low and high- frequency powers (LFn, HFn) and their ratio (LF/HF) were calculated from the latter parameters. The non-linear analysis was carried out by calculating Poincaré plot parameters (SD1, SD2) reflecting the short and long-term variability [23] and extracting Fractal Dimension (FD) and beta exponent (betaExp) [24] quantifying the complexity of the system generating the signal.

C. Feature selection and classification

For feature selection, we used Information Gain [25] method, which has been widely applied in machine learning tasks to improve classification performance. The cut-off of Information Gain's estimates of the informative attribute was set to 0.07. The models were produced by logistic regression algorithms considering the set of selected HRV features, age, and sex, one with GLS ($LogReg_{GLS}$) and the other with LVEF ($LogReg_{LVEF}$). The classification accuracy (CA), area under the curve (AUC), F1, precision, and recall of the dataset were estimated using 5-fold cross-validation, and average metric values were calculated. Finally, the nomograms have been created and used to interpret and validate the obtained models.

III. RESULTS

The results of features selection analysis showed that the most informative features for classification between DCM and HC listed from higher to lower Information Gain coefficients were GLS, SD1/SD2, RMSSD, betaExp, and LFn for $LogReg_{GLS}$ model and LVEF, SD1/SD2, RMSSD, betaExp and LFn for $LogReg_{LVEF}$. The selected features were used as the set of variables to produce LogReg models.

The classification performance of produced LogReg models based on HRV features and GLS in one case and based on HRV features and LVEF in the other are reported in Table 1. The CA, AUC, F1, precision, and recall were higher in the model based on HRV features and GLS ($LogReg_{GLS}$) compared to the logistic regression model constructed with the HRV features and LVEF ($LogReg_{LVEF}$).

TABLE I: CLASSIFICATION PERFORMANCE OF PRODUCED $LOGREG_{GLS}$ AND $LOGREG_{LVEF}$ MODELS

Model	*AC*	*AUC*	*F1*	*Precision*	*Recall*
$LogReg_{GLS}$	0.86	0.89	0.85	0.86	0.86
$LogReg_{LVEF}$	0.83	0.87	0.83	0.83	0.83

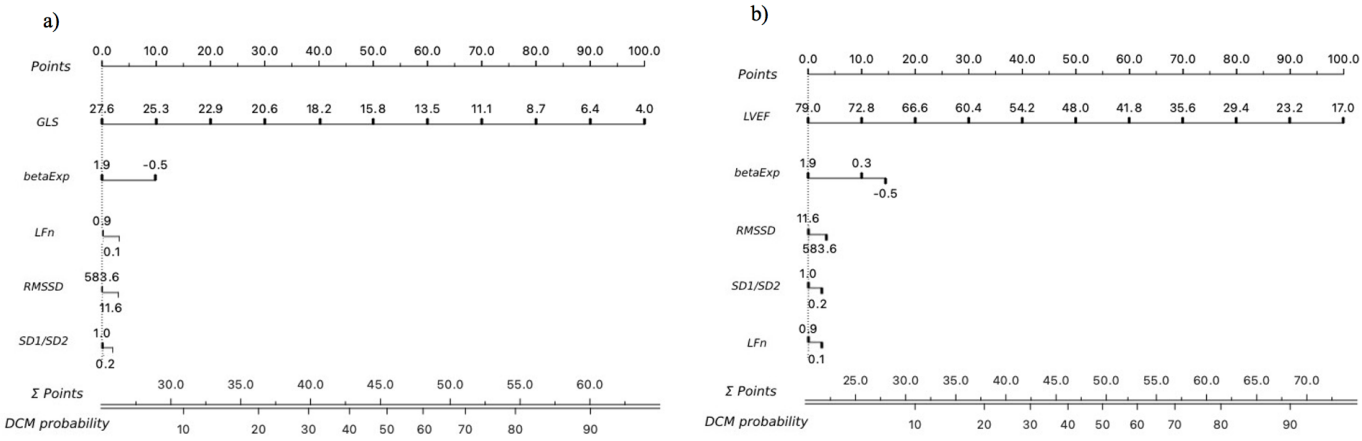


Fig. 1: Nomograms for DCM output class for (a)$LogReg_{GLS}$ and (b)$LogReg_{LVEF}$ models.

Confusion matrices obtained for $LogReg_{GLS}$ and $LogReg_{LVEF}$ are reported in Table 2. Confusion matrices show that DCM patients were correctly classified with 88.3% (Table 2A) and 86.3% (Table 2B) with $LogReg_{GLS}$ and $LogReg_{LVEF}$, respectively.

The produced nomograms for $LogReg_{GLS}$ and $LogReg_{LVEF}$ are reported in Figure 1 and the features are listed in order of importance. The produced nomograms can be interactively used to determine the likelihood of being in the DCM or HC group. In particular, for each of the features a score (point) corresponding to the specific features value is assigned. Subsequently the sum of the points of all considered features is converted into the probability that the subject belongs to the specific group. For example, in the Figure 1a, if the patient has a GLS value equal to 17.5 (43 points on the scale), betaExp equal to 0.9 (4 points), LFn equal to 0.5 (1 point), RMSSD equal to 87.5 (1.5 points) and SD1/SD2 equal to 0.4 (0.5 points), the total sum of points is equal to 50, which corresponds to probability of 65% that the specific subject is affected by DCM.

TABLE II: CONFUSION MATRICES OBTAINED BY (A) $LOGREG_{GLS}$ AND (B) $LOGREG_{LVEF}$ MODELS

A)		*Predicted*		
		DCM	*HC*	*Σ*
	DCM	88.3%	16.9%	138
Actual	*HC*	11.7%	83.1%	138
	Σ	128	148	276
B)		*Predicted*		
		DCM	*HC*	*Σ*
	DCM	86.3%	20.4%	138
Actual	*HC*	13.7%	79.6%	138
	Σ	124	152	276

IV. DISCUSSION

Dilated cardiomyopathy (DCM) is one of the leading causes of heart failure [1]. Left ventricular ejection fraction (LVEF) is the most often utilized feature for assessing heart health and forecasting outcomes in DCM patients. It does, however, have some inherent problems. On the other hand, there is growing scientific and clinical interest towards GLS parameter [10]–[12], [26] as a predictive feature in various heart diseases, including DCM. Additionally, several studies have shown how crucial it is to use interpretable machine learning models to support clinicians in the challenging diagnosis of different diseases [17]–[21]. Therefore, this study aimed to investigate discriminatory power of GLS and LVEF as a feature of logistic regression models for identification of DCM.

Our results showed that SD1/SD2, RMSSD, betaExp, LFn, and GLS in one case and LVEF in the other case are the most informative features for differential classification of DCM from HC. The $LogReg_{GLS}$ model accuracy was 86%, better than the accuracy of the $LogReg_{LVEF}$ model (83%). Therefore, we may conclude that the $LogReg_{GLS}$ model slightly outperformed the $LogReg_{LVEF}$ model, partially confirming that GLS could bring more information than LVEF in the diagnosis of DCM.

The importance of GLS, LVEF, and HRV features has been confirmed yet again by the nomograms. We can observe that the clinical parameter, GLS or LVEF, appears to be the most significant in the differential classification between DCM and HC in both nomograms, supporting the literature that suggest these two measures are the most helpful in the diagnosis of this condition [2], [10], [27]. Furthermore, the models empirically identified two thresholds, 50 for LVEF and 17 for GLS, for the diagnosis of DCM, which is in line with thresholds reported in recent studies [26], [27].

The nomograms also revealed the importance of the HRV features. In particular, betaExp measures the relationship between the frequency and power spectrum of the RR interval, providing an index of the HRV signal's long-term scaling properties [28], which may change in DCM. LFn is often associated with the joint action of the vagal and sympathetic system [29] that can alter in DCM patients. RMSSD is an indicator of the irregularities of the heart rhythms, also characteristic of DCM. Finally, SD1/SD2 describes diastolic blood pressure, which appears to be more variable in DCM patients than in healthy subjects [30].

Furthermore, the results support that nomograms can be an easy-to-use tool by the physicians to estimate the probability of presence of specific disease based on explainable classification process.

In conclusion, our findings highlight the value and efficacy of interpretable machine learning models and suggest that GLS may be more effective in differentiating between DCM and healthy participants than LVEF.

ACKNOWLEDGEMENT

Work partially supported by postgraduate Master in Clinical Engineering, University of Trieste.

REFERENCES

[1] B. J. Maron *et al.*, "Contemporary definitions and classification of the cardiomyopathies: an American Heart Association Scientific Statement from the Council on Clinical Cardiology, Heart Failure and Transplantation Committee; Quality of Care and Outcomes Research and Functional Genomics and Translational Biology Interdisciplinary Working Groups; and Council on Epidemiology and Prevention," *Circulation*, vol. 113, no. 14, pp. 1807–1816, Apr. 2006, doi: 10.1161/CIRCULATIONAHA.106.174287.

[2] I. H. Jung *et al.*, "Left Ventricular Global Longitudinal Strain as a Predictor for Left Ventricular Reverse Remodeling in Dilated Cardiomyopathy," *J Cardiovasc Imaging*, vol. 28, no. 2, pp. 137–149, Apr. 2020, doi: 10.4250/jcvi.2019.0111.

[3] F. Ferrari and W. R. Menegazzo, "Global Longitudinal Strain or Measurement of Ejection Fraction: Which Method is Better in Stratifying Patients with Heart Failure?," *Arq Bras Cardiol*, vol. 113, no. 2, pp. 195–196, Aug. 2019, doi: 10.5935/abc.20190151.

[4] A. Accardo *et al.*, "Toward a diagnostic CART model for Ischemic heart disease and idiopathic dilated cardiomyopathy based on heart rate total variability," *Med Biol Eng Comput*, vol. 60, no. 9, pp. 2655–2663, Sep. 2022, doi: 10.1007/s11517-022-02618-9.

[5] E. Agliari, A. Barra, O. A. Barra, A. Fachechi, L. Franceschi Vento, and L. Moretti, "Detecting cardiac pathologies via machine learning on heart-rate variability time series and related markers," *Sci Rep*, vol. 10, no. 1, Art. no. 1, Jun. 2020, doi: 10.1038/s41598-020-64083-4.

[6] L. Zhang, H. Wu, X. Zhang, X. Wei, F. Hou, and Y. Ma, "Sleep heart rate variability assists the automatic prediction of long-term cardiovascular outcomes," *Sleep Med*, vol. 67, pp. 217–224, Mar. 2020, doi: 10.1016/j.sleep.2019.11.1259.

[7] X. Yan, L. Zhang, J. Li, D. Du, and F. Hou, "Entropy-Based Measures of Hypnopompic Heart Rate Variability Contribute to the Automatic Prediction of Cardiovascular Events," *Entropy*, vol. 22, no. 2, Art. no. 2, Feb. 2020, doi: 10.3390/e22020241.

[8] A. Accardo, G. Silveri, M. Merlo, L. Restivo, M. Ajčević, and G. Sinagra, "Detection of subjects with ischemic heart disease by using machine learning technique based on heart rate total variability parameters," *Physiol Meas*, Oct. 2020, doi: 10.1088/1361-6579/abc321.

[9] G. Silveri, M. Merlo, L. Restivo, M. Ajčević, G. Sinagra, and A. Accardo, "A big - data classification tree for decision support system in the detection of dilated cardiomyopathy using heart rate variability," *Procedia Computer Science*, vol. 176, pp. 2940–2948, Jan. 2020, doi: 10.1016/j.procs.2020.09.209.

[10] J. Ma, L. Guan, L. Yang, A. Mahemuti, and Y. Mu, "Relationship Between Myocardial Perfusion and Myocardial Function in Dilated Cardiomyopathy by Shown Ultrasonography," *Int Heart J*, vol. 62, no. 4, pp. 792–800, Jul. 2021, doi: 10.1536/ihj.20-599.

[11] M. C. Pastore *et al.*, "Speckle Tracking Echocardiography: Early Predictor of Diagnosis and Prognosis in Coronary Artery Disease," *Biomed Res Int*, vol. 2021, p. 6685378, 2021, doi: 10.1155/2021/6685378.

[12] J. Schroeder *et al.*, "Myocardial deformation by strain echocardiography identifies patients with acute coronary syndrome and non-diagnostic ECG presenting in a chest pain unit: a prospective study of diagnostic accuracy," *Clin Res Cardiol*, vol. 105, no. 3, pp. 248–256, Mar. 2016, doi: 10.1007/s00392-015-0916-2.

[13] K. Ashish, M. Faisaluddin, D. Bandyopadhyay, A. Hajra, and E. Herzog, "Prognostic value of global longitudinal strain in heart failure subjects: A recent prototype," *Int J Cardiol Heart Vasc*, vol. 22, pp. 48–49, Dec. 2018, doi: 10.1016/j.ijcha.2018.11.009.

[14] R. E. Kleiger, J. P. Miller, J. T. Bigger, and A. J. Moss, "Decreased heart rate variability and its association with increased mortality after acute myocardial infarction," *Am J Cardiol*, vol. 59, no. 4, pp. 256–262, Feb. 1987, doi: 10.1016/0002-9149(87)90795-8.

[15] M. A. Ahmad, C. Eckert, and A. Teredesai, "Interpretable Machine Learning in Healthcare," in *Proceedings of the 2018 ACM International Conference on Bioinformatics, Computational Biology, and Health Informatics*, New York, NY, USA, Aug. 2018, pp. 559–560. doi: 10.1145/3233547.3233667.

[16] G. Stiglic, P. Kocbek, N. Fijacko, M. Zitnik, K. Verbert, and L. Cilar, "Interpretability of machine learning-based prediction models in healthcare," *WIREs Data Mining and Knowledge Discovery*, vol. 10, no. 5, p. e1379, 2020, doi: 10.1002/widm.1379.

[17] Y. Zhang and Y. Ma, "Application of supervised machine learning algorithms in the classification of sagittal gait patterns of cerebral palsy children with spastic diplegia," *Comput Biol Med*, vol. 106, pp. 33–39, Mar. 2019, doi: 10.1016/j.compbiomed.2019.01.009.

[18] S. Sossi Alaoui, B. Aksasse, and Y. Farhaoui, "Data Mining and Machine Learning Approaches and Technologies for Diagnosing Diabetes in Women," in *Big Data and Networks Technologies*, Cham, 2020, pp. 59–72. doi: 10.1007/978-3-030-23672-4_6.

[19] A. K. Feeny *et al.*, "Machine Learning Prediction of Response to Cardiac Resynchronization Therapy: Improvement Versus Current Guidelines," *Circ Arrhythm Electrophysiol*, vol. 12, no. 7, p. e007316, Jul. 2019, doi: 10.1161/CIRCEP.119.007316.

[20] I. Salman, "Heart attack mortality prediction: an application of machine learning methods," *Turk J Elec Eng & Comp Sci*, vol. 27, no. 6, pp. 4378–4389, Nov. 2019.

[21] P. Melillo, N. De Luca, M. Bracale, and L. Pecchia, "Classification tree for risk assessment in patients suffering from congestive heart failure via long-term heart rate variability," *IEEE J Biomed Health Inform*, vol. 17, no. 3, pp. 727–733, May 2013, doi: 10.1109/jbhi.2013.2244902.

[22] R. M. Lang *et al.*, "Recommendations for cardiac chamber quantification by echocardiography in adults: an update from the American Society of Echocardiography and the European Association of Cardiovascular Imaging," *J Am Soc Echocardiogr*, vol. 28, no. 1, pp. 1-39.e14, Jan. 2015, doi: 10.1016/j.echo.2014.10.003.

[23] M. A. Woo, W. G. Stevenson, D. K. Moser, R. B. Trelease, and R. M. Harper, "Patterns of beat-to-beat heart rate variability in advanced heart failure," *Am Heart J*, vol. 123, no. 3, pp. 704–710, Mar. 1992, doi: 10.1016/0002-8703(92)90510-3.

[24] T. Higuchi, "Approach to an irregular time series on the basis of the fractal theory," *Physica D. Nonlinear Phenomena*, Jun. 1988, doi: 10.1016/0167-2789(88)90081-4.

[25] S. Lei, "A Feature Selection Method Based on Information Gain and Genetic Algorithm," in *2012 International Conference on Computer Science and Electronics Engineering*, Mar. 2012, vol. 2, pp. 355–358. doi: 10.1109/ICCSEE.2012.97.

[26] W.-T. Chang *et al.*, "The predictive value of global longitudinal strain in patients with heart failure mid-range ejection fraction," *Journal of Cardiology*, vol. 77, no. 5, pp. 509–516, May 2021, doi: 10.1016/j.jjcc.2020.10.018.

[27] M. Jiménez-Blanco, D. Cordero, and J. L. Zamorano, "Left ventricular ejection fraction… What else?," *Cardiol J*, vol. 27, no. 1, pp. 6–7, Feb. 2020, doi: 10.5603/CJ.2020.0014.

[28] M. Cusenza, A. Accardo, G. D'Addio, and G. Corbi, "Relationship between fractal dimension and power-law exponent of heart rate variability in normal and heart failure subjects," in *2010 Computing in Cardiology*, Sep. 2010, pp. 935–938.

[29] M. Pagani *et al.*, "Power spectral density of heart rate variability as an index of sympatho-vagal interaction in normal and hypertensive subjects," *J Hypertens Suppl*, vol. 2, no. 3, pp. S383-385, Dec. 1984.

[30] A. Voss, R. Schroeder, S. Truebner, M. Goernig, H. R. Figulla, and A. Schirdewan, "Comparison of nonlinear methods symbolic dynamics, detrended fluctuation, and Poincare plot analysis in risk stratification in patients with dilated cardiomyopathy," *Chaos*, vol. 17, no. 1, p. 015120, Mar. 2007, doi: 10.1063/1.2404633.

Comparison of autonomic signals between healthy subjects and chronic low back pain patients at rest and during noxious stimulation

S. Moscato[1,2], W. Zhu[1], Y. Guo[1], S. Kamarthi[1], C. A. Colebaugh[3], K. L. Schreiber[3], R. R. Edwards[3], R. D. Urman[4], Y. Xiao[5], L. Chiari[2,6], and Y. Lin[1*]

[1]*Intelligent Human Machine Systems Lab, Mechanical and Industrial Engineering Department, Northeastern University, Boston, MA, USA*

[2]*Department of Electrical, Electronic, and Information Engineering "Guglielmo Marconi" (DEI) University of Bologna, Italy*

[3]*Department of Anaesthesiology, Perioperative and Pain Medicine, Brigham and Women's Hospital, Harvard University, Boston, MA, USA*

[4]*Department of Anaesthesiology, College of Medicine, The Ohio State University, OH, US*

[5]*College of Nursing and Health Innovation University of Texas at Arlington TX, Arlington, TX, US*

[6]*Health Sciences and Technologies - Interdepartmental Center for Industrial Research (CIRI-SDV), University of Bologna, Italy*

[*]*The Corresponding Author: yi.lin@northeastern.edu*

***Abstract*—Chronic pain is a major cause of disability worldwide. While acute pain may serve as a protective function, chronic pain and the associated changes in neural processing negatively impact function and quality of life. This neural plasticity may include changes to the autonomic nervous system (ANS) potentially detectable as changes in various physiological signals. Our aim is to evaluate differences in the physiological signals reflecting ANS changes, by comparing healthy subjects and patients with chronic low back pain during standardized pain stimuli. We extracted several features from photoplethysmography (PPG), electrodermal activity (EDA), and respiration, both at rest and during a repeated pinprick test. We found significant group differences in some PPG parameters at rest and in response to the repeated pinprick test. Chronic pain patients had consistently higher basal sympathetic activity, as well as a blunted autonomic response when subjected to nociceptive stimuli.**

***Keywords*—Pain assessment, physiological signals, autonomic nervous system.**

I. Introduction

Pain is an "unpleasant sensory and emotional experience associated with, or resembling that is associated with, actual or potential tissue damage" [1]. Different types of pain can be experienced. One of the main distinctions is between acute and chronic pain.

Acute pain is the pain arising from the activation of nociceptors when a thermal, mechanical, or chemical nociceptive stimulus affects the body. Noxious stimuli activate neural transduction at the peripheral, spinal, and brain level, collectively falling under the concept of "pain neuromatrix". Acute pain has a protective function to the body, acting as an alarm bell for a potential threat [2].

On the other hand, chronic pain is defined as persistent or recurrent pain that lasts for more than three months [3]. It is now well known that chronic pain leads to a significant neural plasticity [4], with substantial functional and anatomical changes to reach a new equilibrium different from that of healthy subjects [5]. Chronic pain does not serve a protective function, being maintained despite the absence of the inciting stimulus, and is associated with physiologic and psychosocial changes [6].

Manifestations of physiologic change may include activity of the Autonomic Nervous System (ANS). Pain and ANS are anatomically and functional linked, as pain influences the activity of ANS and vice versa [7]. In the case of chronic pain, previous studies have observed decreased ANS reactivity, potentially leading to a reduced ability of the body to promptly respond to internal and external stimuli [8].

ANS activity can be evaluated by monitoring some physiological signals, commonly called "autonomic" signals precisely because of the ANS' regulation of them. Examples of these signals are Photoplethysmography (PPG), representing the blood volume changes occurring at each heartbeat, Electrodermal Activity (EDA), referring to variations of the electrical properties of the skin due to sweat secretion, and Respiration (Resp).

Autonomic signals have been extensively used in "emotion recognition" studies so far, representing a new way to analyse emotions, and increasingly bridging the gap in human-computer interaction [9]. Gaining greater facility with measurement of fluctuations and variability of autonomic signals under the condition of pain transduction is twofold: from a clinical point of view, this may allow insight into the impact of nociceptive activation on physiology, both in the acute and chronic phase ; from a more technical point of view, it would allow to better tailor algorithms to more sensitively detect a wide variety of painful stimuli in different individuals, and to distinguish the extent of neural remodeling inherent in an individual with chronic disease.

The aim of this study is to explore differences in autonomic signals by comparing healthy control (HC) subjects and chronic Low Back Pain (cLBP) patients i) under rest conditions and ii) when stimulated with a noxious stimulus. This is a further work based on the Intelligent Human Machine System (IHMS) laboratory's exploration work in the past [10], [11].

II. Materials and Methods

A. Protocol

The study involves enrolment of both HC subjects and cLBP patients. The inclusion criteria in common for the two samples are the following:

- 18 years or older
- No evidence of neurological and/or cognitive impairment
- No history of myocardial infarction or other serious cardiovascular condition in the prior 12 months
- Ability to speak sufficient English to complete questionnaire measures.

In addition, HC subjects had to be free of any history or diagnosis of chronic pain. cLBP patients were required to have a history of cLBP for at least 3 months, with an average pain intensity higher than 3/10.

The study protocol was approved by the Institutional Review Board of Brigham and Women's Hospital, Boston, MA, USA, (protocol code2019P002781, 18/11/2019). The protocol included Quantitative Sensory Testing, where defined nociceptive stimuli are applied in a clinical lab setting to assess pain transduction across a variety of modalities.

For the purpose of this study, two experimental conditions have been evaluated:

- Rest: as a baseline, the participant is asked to remain quiet for 1 minute while the signals are recorded
- Repeated pinprick test (i.e., repeated, mildly to moderately painful, punctate mechanical stimuli): the participant is non-invasively stimulated with a weighted, fine metal probe on the right hand, 10 times in a row at 1 Hz frequency. The stimulus intensity is tailored to an individual's pain sensitivity, choosing a probe weight that induces mild pain upon single stimulation.

B. Autonomic signals

In the following, the recorded autonomic signals are presented, together with the pre-processing applied to each of them.

All signals used in this study have been recorded with the Flexcomp system, with a sampling frequency of 256 Hz.

PPG sensor is placed on the left hand's middle finger. The recorded signal has been subjected to a 5th order Butterworth band-pass filter, with [0.5 12] Hz as cut-off frequencies. The filtered PPG signal has been then segmented into PPG pulses by detecting systolic feet [12]. Each pulse was then normalized with a z-score procedure.

EDA has been recorded through electrodes placed on the left hand's ring and index finger. EDA signal has been subjected to a 5th order low-pass Butterworth filter, with 1 Hz as cut-off frequency. We applied a z-score normalization procedure on a subject basis and then we extracted the tonic and phasic component by using the *cvxEDA* algorithm [13].

Respiratory signal was recorded using a band placed around the low chest. The signal has been subjected to a 4th order Butterworth low-pass filter, with 0.1 Hz as cut-off frequency. We implemented the Advanced Counting Method to detect the respiration cycle [14].

C. Autonomic parameters extraction

For the baseline recording, features have been extracted by the whole recording (i.e., 1 minute).

For the repeated pinpricks test, the recording has been segmented into four phases:

- Pre-test: 5 seconds before the beginning of the test
- Between 1st and 5th repetition (5 seconds)
- Between 5th and 10th repetition (5 seconds)
- Post-test: 5 seconds after the end of the test

Twelve parameters have been extracted from the analysis of PPG pulses:

- Heart Rate Variability (HRV) analysis - we estimated the Interbeat Intervals (IBIs) as time differences between two consecutive systolic feet (i.e., the minimum point of a PPG pulse). The obtained IBIs time series has been then filtered by using the approach described in [15]. Extracted HRV parameters are mean value of IBIs (meanIBI), standard deviation of normal heartbeats (SDNN), root mean squared of successive differences (RMSSD), Poincaré plot standard deviation perpendicular (SD1) and along (SD2) the line of identity.
- Morphological analysis: by analysing the morphology of each PPG pulse, we estimated PPG pulse amplitude (PulseAmpl), area under the curve between systolic foot and successive systolic peak (A1), area under the curve between the systolic peak and the successive systolic foot (A2), area under the PPG pulse (A), time between systolic foot and the successive systolic peak (T1), time between systolic peak and the successive systolic foot (T2) [16].

For the EDA, we estimated a total of 8 parameters:

- Whole EDA signal: mean (meanEDA) and standard deviation (stdEDA), and the symbolic information entropy (SIE) [17]
- Tonic component: mean (meantonic) and standard deviation (stdtonic)
- Phasic component: relevant peaks have been retrieved as those peaks with a slope (by analysing the first derivative) higher than 0.01. From the relevant peaks, the mean (meanampEDR) and standard deviation (stdampEDR), together with the frequency (freqEDR) expressed as number of peaks per minute have been retrieved.

For the Resp signal, we retrieved the mean respiration rate (meanRR). Since we used the Advanced Counting Method as an automatic algorithm to detect the respiration cycle, we discarded those estimates exceeding 30 breaths/min.

D. Statistical analysis

To compare the parameters during the rest condition between HC subjects and cLBP patients, we used a Mann-Whitney U test. To assess any statistical differences in different phases during repeated pinprick test, we used a Wilcoxon signed-rank test for paired data by comparing rest and pain phases. We applied a Bonferroni correction for the multiple comparison for the repeated pinprick test, having 6 comparisons in total, thus resulting in a corrected significance level of 0.05/6 = 0.008.

III. RESULTS

A. Dataset

Twenty-three subjects were enrolled in this study, 15 HC subjects (age 27.20 ± 11.58, 4 M, 11 F) and 9 cLBP patients (age 43.67 ± 14.97, 4 M, 5 F). Recordings failed for one cLBP patient, who therefore was not included in the analysis.

B. Baseline recording

Results about the comparison between HC subjects and cLBP patients are presented in Table 1.

By analysing the baseline recordings, mean IBI, A2, A, and T2 were significantly different between HC subjects and cLBP patients, such that all these parameters are significantly lower for cLBP patients than for HC subjects.

C. Repeated pinpricks test

We compared the four different phases of the repeated pinpricks test separately for HC subjects and cLBP patients.

Below, and in Figure 1, are the significant changes in autonomic variables:

- Mean IBI for HC subjects: significantly higher values were detected during the 5th-10th rep phase, compared to pre- and post-test, and a significant decrease from 1st-5th rep to post-test.
- SDNN, RMSSD, and SD1 for cLBP patients: significant lower value from the pre-test to post-test.
- A for cLBP patients: significant decrease from the pre-test to 1st-5th rep and 5th-10th rep.
- T2 for HC subjects: significant increase by comparing 1st-5th rep with 5th-10th rep and post-test.
- meanEDA and meantonic for HC subjects: significant lower values in pre-test compared to all the other phases.
- stdEDA and stdtonic for HC subjects: significant decrease from 1st-5th rep to post-test.
- SIE for cLBP patients: significant decrease from 1st-5th rep to post-test.
- stdampEDR for HC subjects: significant decrease from 5th-10th rep to post-test.
- freqEDR for cLBP patients: significant decrease from pre-test to 1st-5th rep and 5th-10th rep, and a significant increase by comparing 1st-5th rep and 5th-10th rep with post-test.
- meanRR for HC subjects: significant decrease by comparing pre-test with post-test. For cLBP patients: significant increase from 1st-5th rep to the post-test phase.

Numerical values are reported in the Appendix.

Table 1 – Baseline recordings' results. HC = Healthy controls, cLBP = chronic low back pain patients

	HC	*cLBP*	*p-value*
	mean (std)	*mean (std)*	
meanIBI [ms]	865.51 (93.80)	720.20 (133.36)	**0.048**
SDNN [ms]	58.68 (12.99)	26.14 (27.99)	0.067
RMSSD [ms]	66.76 (29.69)	38.16 (34.16)	0.057
SD1 [ms]	47.19 (21.00)	26.96 (24.13)	0.057
SD2 [ms]	65.30 (12.20)	41.55 (31.94)	0.078
PulseAmpl [a.u.]	3.27 (0.15)	3.28 (0.26)	0.944
*A1 [a.u.*sample]*	69.01 (20.25)	61.93 (20.25)	0.159
*A2 [a.u.*sample]*	269.55 (42.91)	211.62 (62.26)	**0.014**
*A [a.u.*sample]*	338.56 (53.13	2743.55 (64.91)	**0.034**
T1 [ms]	156.78 (30.17)	146.72 (44.24)	0.290
T2 [ms]	710.48 (104.42)	575.70 (110.74)	**0.024**
meanEDA [n.u.]	-1.32 (0.55)	-0.91 (0.97)	0.438
stdEDA [n.u.]	0.11 (0.11)	0.16 (0.25)	0.944
SIE [ ]	0.78 (0.29)	0.74 (0.25)	0.833
meantonic [n.u.]	-1.33 (0.55)	-0.91 (0.97)	0.438
stdtonic [n.u.]	0.10 (0.10)	0.16 (0.25)	0.888
meanampEDR [n.u.]	0.04 (0.06)	0.01 (0.02)	0.488
stdampEDR [n.u.]	0.04 (0.08)	0.01 (0.02)	0.384
freqEDR [peaks/min]	3.14 (3.04)	1.80 (1.42)	0.438
meanRR [breaths/min]	16.17 (2.58)	17.40 (5.03)	0.672

IV. Discussion

We carried out a study to assess the different autonomic activity by comparing healthy control subjects and chronic low back patients both in a rest condition and when subjected to an acute noxious mechanical stimulus.

In the rest condition, only certain parameters extracted from the PPG were statistically different between HC subjects and cLBP patients. In particular, mean IBI was significantly lower in cLBP patients. This is in line with previous study findings on chronic pain patients [18]. Greater basal sympathetic nervous system outflow could potential lead to a higher basal heart rate (corresponding to a lower meanIBI) [19].

Some PPG morphological parameters, namely A2, A, and T2, were also found to be significantly lower in cLBP patients compared to HC subjects. Both A2 and A are related to T2, that is the time difference between the systolic peak and the successive systolic foot. This can be also the basis for the lowering of the meanIBI: chronic pain induces a change in the second part of the cardiac cycle, during the diastolic phase. Morphological parameters have been studied in relation to stress, finding similar results as the ones reported in this study [20].

Regarding the analysis of physiologic parameters during the repeated pinpricks test, HC subjects and cLBP patients showed a different autonomic reaction. Overall, cLBP patients appeared to exhibit a blunted degree of change, in agreement with some previous studies [21].

With regards to EDA, while HC subjects showed a dynamic change in several parameters, cLBP patients only demonstrated change in the SIE parameter, related to the complexity of the signal, and the frequency of EDA peaks (freqEDR). Specifically for freqEDR, since EDA is influenced only by the sympathetic branch of the ANS, it is supposed that a noxious stimulus should increase the number of EDA peaks [22]. Conversely, for cLBP patients the frequency of EDA peaks diminished during a noxious stimulus. This also suggests the possibility that a maladaptive functional neural rearrangement may have taken place over time in cLBP patients.

The study presents some limitations that can hamper the generalizability of the results. Firstly, our dataset consisted in an unbalanced number of subjects for the two populations (15 HC vs 8 cLBP). Some changes may have not been detected because of the small number of patients with cLBP. More subjects for both populations should be involved in this study. Another limitation is given by the short phases related to noxious stimuli test. A strategy to gain more robust results could be to repeat the same nociceptive stimulus or to making last longer. Finally, the different age distributions for the two groups can be a significant confounding factor for our analysis.

As future studies, we are planning to compare reactions in the two populations to different noxious stimuli and to develop automatic methods to assess pain.

V. Conclusion

We carried out a study to explore differences in the autonomic activity, as measured by a set of physiologic measures, between HC subjects and cLBP patients both at rest and during a noxious stimulation. Our findings suggest a higher basal sympathetic activation at rest for cLBP patients,

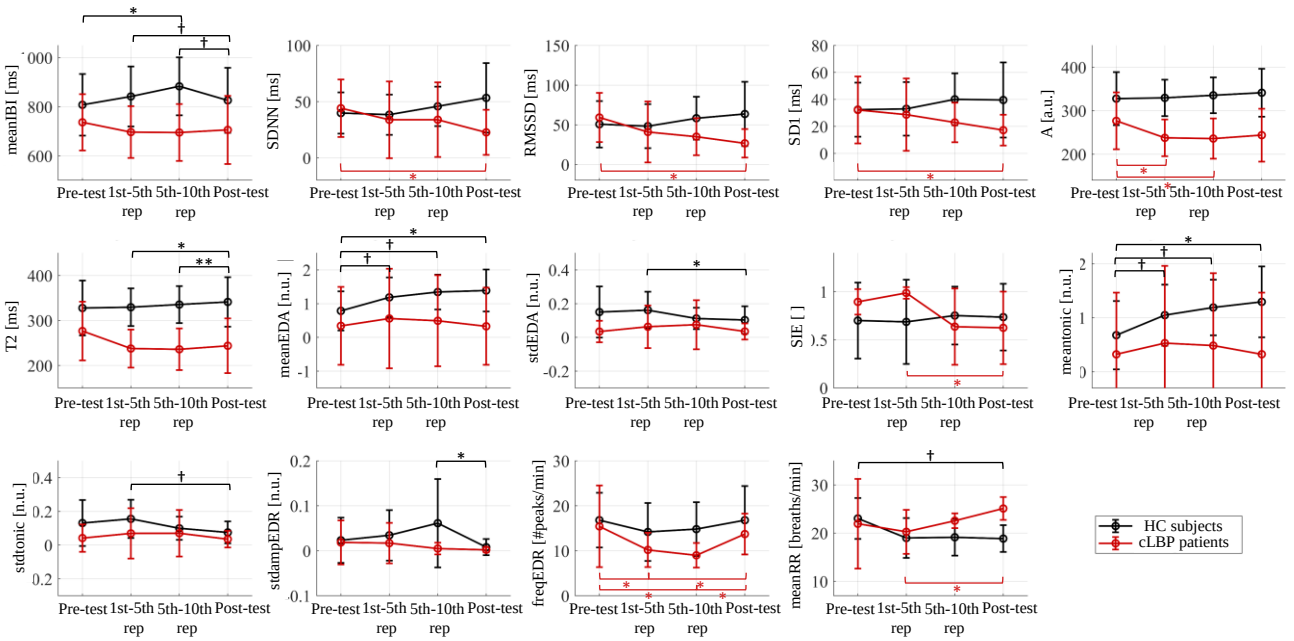


Figure 1 - Statistically significant changes during repeated pinpricks test in healthy controls and cLBP patients.
*** p-value < 0.05, **p-value < 0.01. †Bonferroni correction : p-value (=0.05/6) < 0.008**

but a less dynamic response when subjected to a noxious stimulus.

APPENDIX

Tables related to the results of the repeated pinprick tests are reported as Appendix.

ACKNOWLEDGEMENT

This research has been financially supported by US National Science Foundation (NSF) the Smart and Connected Health (SCH) program through awards #1838796, #1838650, and #1838621.

REFERENCES

[1] S. N. Raja *et al.*, "The revised International Association for the Study of Pain definition of pain: concepts, challenges, and compromises," *Pain*, vol. 161, no. 9, pp. 1976–1982, Sep. 2020, doi: 10.1097/j.pain.0000000000001939.

[2] E. St. John Smith, "Advances in understanding nociception and neuropathic pain," *J. Neurol.*, vol. 265, no. 2, pp. 231–238, Feb. 2018, doi: 10.1007/s00415-017-8641-6.

[3] R.-D. Treede *et al.*, "A classification of chronic pain for ICD-11," *Pain*, vol. 156, no. 6, pp. 1003–1007, Jun. 2015, doi: 10.1097/j.pain.0000000000000160.

[4] D. De Ridder, D. Adhia, and S. Vanneste, "The anatomy of pain and suffering in the brain and its clinical implications," *Neurosci. Biobehav. Rev.*, vol. 130, pp. 125–146, Nov. 2021, doi: 10.1016/j.neubiorev.2021.08.013.

[5] J. Barroso, P. Branco, and A. V. Apkarian, "Brain mechanisms of chronic pain: critical role of translational approach," *Transl. Res.*, vol. 238, no. 5, pp. 76–89, Dec. 2021, doi: 10.1016/j.trsl.2021.06.004.

[6] W. Raffaeli *et al.*, "Chronic Pain: What Does It Mean? A Review on the Use of the Term Chronic Pain in Clinical Practice," *J. Pain Res.*, vol. Volume 14, pp. 827–835, Mar. 2021, doi: 10.2147/JPR.S303186.

[7] D. J. Hohenschurz-Schmidt *et al.*, "Linking Pain Sensation to the Autonomic Nervous System: The Role of the Anterior Cingulate and Periaqueductal Gray Resting-State Networks," *Front. Neurosci.*, vol. 14, Feb. 2020, doi: 10.3389/fnins.2020.00147.

[8] D. Arslan, "Interactions Between The Painful Disorders and The Autonomic Nervous System," *Ağrı - J. Turkish Soc. Algol.*, 2022, doi: 10.14744/agri.2021.43078.

[9] H. Plácido da Silva, N. M. Garcia, and E. T. Solovey, "Editorial: Biomedical Signals for Human-Computer Interaction," *Front. Comput. Sci.*, vol. 3, Nov. 2021, doi: 10.3389/fcomp.2021.799952.

[10] Y. Lin *et al.*, "Experimental Exploration of Objective Human Pain Assessment Using Multimodal Sensing Signals," *Front. Neurosci.*, vol. 16, Feb. 2022, doi: 10.3389/fnins.2022.831627.

[11] L. Wang, Y. Guo, B. Dalip, Y. Xiao, R. D. Urman, and Y. Lin, "An experimental study of objective pain measurement using pupillary response based on genetic algorithm and artificial neural network," *Appl. Intell.*, vol. 52, no. 2, pp. 1145–1156, Jan. 2022, doi: 10.1007/s10489-021-02458-4.

[12] M. Elgendi, I. Norton, M. Brearley, D. Abbott, and D. Schuurmans, "Detection of a and b waves in the acceleration photoplethysmogram," *Biomed. Eng. Online*, vol. 13, no. 1, p. 139, 2014, doi: 10.1186/1475-925X-13-139.

[13] A. Greco, G. Valenza, A. Lanata, E. Scilingo, and L. Citi, "cvxEDA: a Convex Optimization Approach to Electrodermal Activity Processing," *IEEE Trans. Biomed. Eng.*, pp. 1–1, 2016, doi: 10.1109/TBME.2015.2474131.

[14] A. Schäfer and K. W. Kratky, "Estimation of breathing rate from respiratory sinus arrhythmia: Comparison of various methods," *Ann. Biomed. Eng.*, vol. 36, no. 3, pp. 476–485, 2008, doi: 10.1007/s10439-007-9428-1.

[15] A. Bánhalmi, J. Borbás, M. Fidrich, V. Bilicki, Z. Gingl, and L. Rudas, "Analysis of a Pulse Rate Variability Measurement Using a Smartphone Camera," *J. Healthc. Eng.*, vol. 2018, pp. 1–15, 2018, doi: 10.1155/2018/4038034.

[16] F. Li, L. Yang, H. Shi, and C. Liu, "Differences in photoplethysmography morphological features and feature time series between two opposite emotions: Happiness and sadness," *Artery Res.*, vol. 18, no. C, p. 7, 2017, doi: 10.1016/j.artres.2017.02.003.

[17] Z. Visnovcova, M. Mestanik, M. Gala, A. Mestanikova, and I. Tonhajzerova, "The complexity of electrodermal activity is altered in mental cognitive stressors," *Comput. Biol. Med.*, vol. 79, pp. 123–129, Dec. 2016, doi: 10.1016/j.compbiomed.2016.10.014.

[18] L. M. Tracy, L. Ioannou, K. S. Baker, S. J. Gibson, N. Georgiou-Karistianis, and M. J. Giummarra, "Meta-analytic evidence for decreased heart rate variability in chronic pain implicating parasympathetic nervous system dysregulation," *Pain*, vol. 157, no. 1, pp. 7–29, Jan. 2016, doi: 10.1097/j.pain.0000000000000360.

[19] Z. He, "The control mechanisms of heart rate dynamics in a new heart rate nonlinear time series model," *Sci. Rep.*, vol. 10, no. 1, p. 4814, Mar. 2020, doi: 10.1038/s41598-020-61562-6.

[20] M. Rinkevičius *et al.*, "Photoplethysmogram Signal Morphology-Based Stress Assessment," Dec. 2019. doi: 10.22489/CinC.2019.126.

[21] T. D. Yeater *et al.*, "Chronic Pain is Associated With Reduced Sympathetic Nervous System Reactivity During Simple and Complex Walking Tasks: Potential Cerebral Mechanisms," *Chronic Stress*, vol. 5, p. 247054702110302, Jan. 2021, doi: 10.1177/24705470211030273.

[22] D. S. Bari, H. Y. Y. Aldosky, C. Tronstad, H. Kalvøy, and Ø. G. Martinsen, "Electrodermal activity responses for quantitative assessment of felt pain," *J. Electr. Bioimpedance*, vol. 9, no. 1, pp. 52–58, Dec. 2018, doi: 10.2478/joeb-2018-0010.

Table A1 Results from Repeated pinpricks test - Healthy control subjects

	Pre	1st-5th rep	5th-10th rep	Post	p-value					
	mean (std)	mean (std)	mean (std)	mean (std)	Pre – 1st-5th rep	Pre - 5th-10th rep	Pre - Post	1st-5th rep - 5th-10th rep	1st-5th rep - Post	5th-10th rep - Post
meanIBI [ms]	807.89 (125.40)	841.93 (122.36)	883.35 (117.97)	826.21 (132.24)	0.208	0.018*	0.934	0.303	0.008†	0.001†
SDNN [ms]	39.85 (18.27)	38.40 (17.89)	45.83 (17.53)	53.34 (30.96)	0.890	0.599	0.135	0.151	0.135	0.639
RMSSD [ms]	50.68 (29.20)	48.30 (27.68)	58.30 (26.97)	63.61 (40.55)	0.934	0.277	0.389	0.169	0.083	0.720
SD1 [ms]	32.41 (20.05)	33.01 (19.82)	40.07 (19.19)	39.56 (27.85)	0.639	0.229	0.524	0.169	0.303	0.934
SD2 [ms]	30.39 (16.00)	33.88 (18.40)	40.09 (18.40)	40.61 (26.79)	0.720	0.135	0.151	0.252	0.489	0.847
PulseAmpl [a.u.]	3.10 (0.30)	3.12 (0.35)	3.21 (0.32)	3.20 (0.38)	0.762	0.489	0.208	0.524	0.252	0.847
A1 [a.u.*s]	71.75 (30.40)	67.70 (23.72)	64.56 (17.49)	81.98 (68.27)	0.229	0.679	1.000	0.978	0.720	0.720
A2 [a.u.*s]	256.08 (39.74)	261.83 (39.21)	270.90 (37.33)	259.31 (55.60)	0.421	0.252	0.303	0.121	0.599	0.389
A [a.u.*s]	327.82 (60.93)	329.52 (41.91)	225.45 (41.20)	341.29 (55.08)	0.561	0.489	0.489	0.639	0.599	0.599
T1 [ms]	158.31 (46.45)	151.87 (48.27)	145.04 (27.80)	168.57 (95.40)	0.498	0.296	0.715	0.498	1.000	0.679
T2 [ms]	667.04 (104.71)	686.57 (106.65)	706.39 (101.79)	646.90 (146.47)	0.720	0.135	0.815	0.421	0.035*	0.003
meanEDA [n.u.]	0.79 (0.58)	1.19 (0.59)	1.34 (0.52)	1.39 (0.62)	0.001†	0.008†	0.010*	0.303	0.489	0.599
stdEDA [n.u.]	0.15 (0.15)	0.16 (0.11)	0.11 (0.06)	0.10 (0.08)	0.762	0.679	0.277	0.135	0.015*	0.389
SIE [ ]	0.70 (0.39)	0.69 (0.44)	0.75 (0.30)	0.74 (0.35)	0.804	0.934	0.847	0.761	0.847	0.978
meantonic [n.u.]	0.68 (0.63)	1.05 (0.57)	1.19 (0.52)	1.30 (0.66)	0.002†	0.005†	0.010*	0.421	0.303	0.252
stdtonic [n.u.]	0.13 (0.14)	0.16 (0.11)	0.10 (0.07)	0.08 (0.07)	0.489	0.804	0.454	0.095	0.003†	0.073
meanampEDR [n.u.]	0.12 (0.25)	0.18 (0.23)	0.17 (0.29)	0.08 (0.14)	0.080	0.330	0.735	1.000	0.110	0.268
stdampEDR [n.u.]	0.02 (0.05)	0.03 (0.06)	0.06 (0.10)	0.01 (0.02)	0.492	0.123	0.461	0.232	0.160	0.014*
freqEDR [#peaks/min]	16.80 (6.09)	14.18 (6.45)	14.81 (5.98)	16.80 (7.59)	0.352	0.421	1.000	0.761	0.454	0.551
meanRR [breaths/min]	23.04 (4.25)	18.98 (4.13)	19.14 (3.80)	18.86 (2.77)	0.054	0.193	0.008†	0.787	1.000	1.000

* p-value < 0.05, **p-value < 0.01. †Bonferroni correction: p-value (=0.05/6) < 0.008

Table A2 Results from Repeated pinpricks test – Chronic low back pain patients

	Pre	1st-5th rep	5th-10th rep	Post	p-value					
	mean (std)	mean (std)	mean (std)	mean (std)	Pre – 1st-5th rep	Pre - 5th-10th rep	Pre - Post	1st-5th rep - 5th-10th rep	1st-5th rep - Post	5th-10th rep - Post
meanIBI [ms]	736.68 (114.50)	696.85 (105.38)	695.07 (116.07)	705.71 (139.08)	0.469	0.297	0.688	0.578	0.688	0.813
SDNN [ms]	44.14 (25.50)	33.84 (34.19)	33.94 (33.18)	22.70 (20.03)	0.375	0.375	0.031*	0.578	0.375	0.375
RMSSD [ms]	59.21 (31.07)	41.00 (38.36)	35.06 (23.40)	26.69 (18.04)	0.375	0.109	0.031*	0.688	0.219	0.297
SD1 [ms]	32.18 (24.82)	28.69 (26.85)	22.91 (14.67)	17.22 (11.41)	1.000	0.219	0.047*	0.688	0.219	0.297
SD2 [ms]	29.52 (27.68)	33.89 (38.79)	35.02 (40.05)	18.05 (22.20)	0.938	0.813	0.156	0.578	0.219	0.219
PulseAmpl [a.u.]	3.32 (0.20)	3.21 (0.33)	3.24 (0.29)	3.25 (0.26)	0.297	0.297	0.375	1.000	0.578	0.469
A1 [a.u.*s]	70.63 (25.96)	55.90 (9.53)	55.85 (5.61)	67.06 (23.94)	0.109	0.469	0.688	0.938	0.297	0.578
A2 [a.u.*s]	206.00 (63.57)	181.81 (41.17)	180.24 (43.95)	176.80 (61.10)	0.109	0.078	0.219	1.000	0.375	0.297
A [a.u.*s]	276.64 (65.19)	237.71 (42.30)	236.09 (46.28)	243.86 (60.79)	0.047*	0.031	0.219	1.000	0.813	0.813
T1 [ms]	180.40 (73.95)	137.99 (20.50)	149.14 (28.34)	171.05 (61.56)	0.109	0.688	0.813	0.156	0.297	0.813
T2 [ms]	567.84 (122.49)	560.06 (99.24)	545.67 (98.77)	548.06 (106.24)	0.938	0.219	0.469	0.219	0.219	0.813
meanEDA [n.u.]	0.34 (1.16)	0.56 (1.48)	0.49 (1.35)	0.33 (1.14)	1.000	1.000	0.688	0.688	0.375	0.219
stdEDA [n.u.]	0.03 (0.06)	0.06 (0.13)	0.08 (0.15)	0.04 (0.05)	0.297	0.156	0.688	0.375	0.578	0.469
SIE [ ]	0.89 (0.13)	0.99 (0.06)	0.64 (0.40)	0.62 (0.38)	0.156	0.219	0.297	0.078	0.016*	0.813
meantonic [n.u.]	0.32 (1.14)	0.53 (1.43)	0.49 (1.34)	0.33 (1.14)	1.000	0.938	0.813	0.688	0.375	0.219
stdtonic [n.u.]	0.04 (0.08)	0.07 (0.15)	0.07 (0.14)	0.04 (0.05)	0.578	0.156	0.688	0.938	0.688	0.469
meanampEDR [n.u.]	0.02 (0.06)	0.04 (0.08)	0.003 (0.01)	0.003 (0.0.01)	0.250	1.000	1.000	0.250	0.375	1.000
stdampEDR [n.u.]	0.02 (0.05)	0.02 (0.05)	0.001 (0.004)	0.005 (0.008)	1.000	1.000	1.000	1.000	1.000	1.000
freqEDR [#peaks/min]	15.43 (9.07)	10.20 (3.81)	8.99 (2.73)	13.71 (4.54)	0.016*	0.031*	1.000	0.203	0.016*	0.031
meanRR [breaths/min]	21.94 (9.32)	20.27 (4.56)	22.56 (1.53)	25.11 (2.37)	1.000	1.000	1.000	0.625	0.031	0.187

* p-value < 0.05, **p-value < 0.01. †Bonferroni correction: p-value (=0.05/6) < 0.008

XGBoost vs. TabPFN in Neuroimaging Machine Learning-based analysis

A. P. De Rosa[1], A. D'Ambrosio[1], C. Marzi[2], M. Cirillo[1], A. Bisecco[1], M. Altieri[1], S. Diciotti[3,4], M. A. Rocca[5,6,9], N. De Stefano[10], P. Pantano[11], M. Filippi[5,6,7,8,9], G. Tedeschi[1], A. Gallo[1], F. Esposito[1]

[1] *Department of Advanced Medical & Surgical Sciences (DAMSS), University of Campania "Luigi Vanvitelli", Naples, Italy*
[2] *Institute of Applied Physics "Nello Carrara" (IFAC), National Research Council (CNR), Sesto Fiorentino (FI), Italy*
[3] *Department of Electrical, Electronic, and Information Engineering "Guglielmo Marconi" - DEI, Alma Mater Studiorum - University of Bologna, Bologna, Italy*
[4] *Alma Mater Research Institute for Human-Centered Artificial Intelligence, University of Bologna, Bologna, Italy*
[5] *Neuroimaging Research Unit, Division of Neuroscience, IRCCS San Raffaele Scientific Institute, Via Olgettina 60, 20132 Milan, Italy*
[6] *Neurology Unit, IRCCS San Raffaele Scientific Institute, Via Olgettina 60, 20132 Milan, Italy*
[7] *Neurorehabilitation Unit, IRCCS San Raffaele Scientific Institute, Via Olgettina 60, 20132 Milan, Italy*
[8] *Neurophysiology Service, IRCCS San Raffaele Scientific Institute, Via Olgettina 60, 20132 Milan, Italy*
[9] *Vita-Salute San Raffaele University, Via Olgettina 58, 20132 Milan, Italy*
[10] *Department of Medicine, Surgery and Neuroscience, University of Siena, Siena, Italy*
[11] *Department of Human Neurosciences, Sapienza University of Rome, Viale Dell'Università, 30, 00185 Rome, Italy*

***Abstract*—Machine learning (ML) and deep learning (DL) applications have gained popularity in the field of neuroimaging in recent years. Here, we present a comparison between a state-of-the-art gradient boosting technique, the extreme gradient boosting (XGBoost), and a recently developed DL method, TabPFN, to assess the prediction of cognitive deficit in a large pathological population through structural and functional MRI markers. Overall, our results showed that conventional ML might still be the preferable choice for noisy tabular datasets (like neuroimaging data), also for their better explainability.**

***Keywords*—machine learning, classification, artificial intelligence, neuroimaging, MRI**

I. Introduction

SUPERVISED learning denotes the class of methods where input features of the data and the corresponding target labels are provided to a learning system, aiming to learn the mapping between input and label in order to make individual-level predictions on unseen data. Over the last decades, machine learning (ML) algorithms have been widely used in the field of neuroimaging. Many have argued that predictive methods are key for translating neurobiological findings to clinical practice [1], [2]. In neuroimaging research, the application of advanced ML techniques can help to disentangle the hidden complex patterns in high-dimensional data, in order to better understand how biological systems behave and to predict outcomes or future behaviour [3]. Recently, major methodological advances in the analysis of the neuroimages have been made thanks to the availability of large, shared, data repositories [4]. Magnetic resonance imaging (MRI) is essential to better understand the mechanisms underlying cognitive decline and deficits in many neurological conditions, including multiple sclerosis (MS) [5]–[7]. In MS - an inflammatory, demyelinating and neurodegenerative disease of the central nervous system - in particular, both anatomical and functional markers can provide invaluable information about patients' cognitive status: i) anatomical MRI volumes have proved to be good prediction markers of cognitive disability and progression [7], [8]; ii) functional markers - extracted from blood oxygen level dependent (BOLD) functional MRI (fMRI) time series - have also been recently used to study and predict cognitive changes [9]. Cognitive impairment is common (30-70% depending on disease duration and phenotype) in MS and has a strong impact on daily social activities and quality of life of these patients. Thus, there is an increasing attention in monitoring the cognitive status of MS patients [5]. In this regard, symbol digit modalities test (SDMT) has been recommended as a valid screening test, due to its brevity, reliability and sensitivity [5]. Among the many ML techniques, classification problems are dominated by gradient boosted decision trees (GBDT) [10] mainly due to their relatively short training time and robustness. Among these, the extreme gradient boosting (XGBoost) [11] has beenrecently applied to neuroimaging data with state-of-the-art performances [8]. On the other hand, deep learning (DL) methods, e.g. deep neural networks (DNN), despite excelling on many ML applications, do not have a significant advantage over conventional ML methods on tabular data. Nonetheless, efforts have been made to transfer the DL paradigm into tabular data classification [12]. Recently, a new DL method for tabular datasets, TabPFN, was proposed [13]. Here, we extracted anatomical and functional features from a large dataset of MRI scans of patients with MS. Aim of this study was to compare the performances in predicting cognitive impairment on the basis of SDMT between the state-of-the-art conventional ML method for tabular data, XGBoost, and the most recent advancement of DL targeting tabular data problems, TabPFN.

II. Methods

A. Dataset

MRI data from MS patients were retrieved from a large online database (https://database.inni-ms.org) based the availability of at least one anatomical 3D T1-weighted (3D-T1w) scan and one resting-state functional MRI (rs-fMRI) scan. As a result, MRI data from the exams of 489 MS patients were pooled together from four different acquisition sites. Details about the anatomical and functional data preprocessing (along with clinical and demographical data and acquisition parameters) can be found in [8] and [14], respectively. Patients

with excessive head motion on rs-fMRI time series (i.e. mean framewise displacement > 0.5 mm) were excluded from the dataset (i.e. 5 patients). Anatomical features comprised segmented brain volumes (i.e. cortical gray matter, white matter, thalamus, nucleus accumbens, putamen, nucleus caudate, globus pallidus, amygdala, hippocampus, cerebellum and lesion load); functional features comprised intra-network functional connectivity averaged across seven pre-defined large-scale functional networks [15] (i.e. visual, somatomotor, dorsal attention, ventral attention, limbic, frontoparietal and default mode). Cognitive status was assessed by means of SDMT, where the score is the number of correct answers (ranging from 0 to 110): thus, higher SDMT scores represent better performances. The scores were adjusted for demographical data (age, sex and years of education) using normative data based on a sample of 200 healthy Italian adults [16], and then Z-scores were calculated. For the classification task, MS patients were subdivided into cognitively impaired (CI) and cognitively preserved (CP) based on their SDMT Z-score. One standard deviation below the mean (i.e. SDMT Z-score $\leq$ -1.0) was selected as the cut-off for cognitive deficit [9]. Moreover, patients with a SDMT Z-score ranging in the interval [-1.1, -0.9] were excluded from the dataset due to uncertain assignment between the two classes. Thus, 240 MS patients were classified as CP and 215 as CI, and 29 patients were excluded.

B. XGBoost

XGBoost is a scalable and end-to-end tree boosting algorithm. The system is built with an ensemble of decision tree models and a gradient boosting framework, meaning that, starting from a single weak tree, the process additively generate weak models to improve performance [11]. XGBoost is widely used to achieve state-of-the-art performances on both classification and regression tasks. One of its major benefits regards the great interpretability due to its recursive tree-based decision system, which allows assessing the importance gain, i.e., the improvement in performance brought by each feature. The model provides a large number of hyperparameters that require adequate tuning.

C. TabPFN

TabPFN is a single trained transformer that has been pre-trained to approximate probabilistic inference for a novel prior in a single forward pass, and has thus learned to classify unseen tabular data with performances competitive with state-of-the-art classification methods [13]. TabPFN is built on prior-data fitted networks (PFNs). PFNs approximate bayesian inference given any prior and approximate the posterior predictive distribution directly (PPD). The priors are defined via parametric distributions and are based on bayesian neural networks and structural causal models to model complex feature dependencies and potential causal mechanisms underlying tabular data [17].

D. Train, validation and test

The models have been trained, validated and tested using the following stratified split approach: 80% of the entire dataset (i.e. 364 randomly chosen patients) was used as the training/validation set, and the remaining 20% (i.e. 91 patients) was used as the test set. On the training/validation set, a stratified nested 5-fold cross validation (CV) strategy was adopted to estimate the generalization performance of the models and to perform, at the same time, hyperparameter tuning [18]. In more detail, the inner loop was used to grid-search the best hyperparameter configuration of the model for each outer fold, and the outer loop to estimate the generalization performance on the validation test. This framework was repeated twice and separately for anatomical and functional features. The performances were quantified in terms of area under receiver operating system (AUROC). Moreover, since the outcomes may vary depending on how the training/validation set is randomly split in each fold of the nested CV, the latter has been repeated 10 times. Since both anatomical and functional features have large variability across MRI centers due to differences in scanner manufacturers and imaging protocols, both were (separately) harmonized with a state-of-the-art methodology (i.e. ComBat) in order to minimize site effects [19]. We included age, sex, and group as biological covariates in the harmonization process to preserve them from the removal of scanner-related effects in the presence of different age and sex distributions between sites. To avoid data leakage, the harmonization process was performed separately on the training/validation and test set. No additional preprocessing was applied on the feature set, since TabPFN model works best when the dataset has not been preprocessed [13].

Although XGBoost has an internal procedure to calculate feature importance, in order to standardize the methods and make the models more comparable, we used the permutation feature importance technique, which is defined as the decrease in the model score when a single feature is randomly shuffled. It is worth noting that permutation importance scores could assume also negative values when better scores result after feature shuffling; in this case, those features are likely to negatively impact the prediction. All the experiments were carried out with custom-made scripts in python (v3.7.13) and using xgboost (v1.6.2) and tabpfn (v0.1.8) packages on a linux workstation equipped with two 8-core Intel (R) Xeon (R) Bronze 3106 @1.70 GHz, for a total of 16 CPU threads and 128 GB RAM.

TABLE I: MODELS PERFORMANCE

Anatomical features	*XGBoost*	*TabPFN*
Training/validation score	0.64 (0.02)	0.64 (0.01)
Test score	0.63 (0.02)	0.61 (0.01)
Functional features	*XGBoost*	*TabPFN*
Training/validation score	0.55 (0.01)	0.55 (0.02)
Test score	0.55 (0.04)	0.51 (0.01)

Performance on the dataset using anatomical and functional features. Results are reported as mean AUROC (standard deviation).

III. RESULTS

Performances from XGBoost and TabPFN are summarized for both anatomical and functional features in Table 1. For the

prediction of the cognitive class (CP and CI) using only anatomical features, XGBoost reached a mean AUROC of 0.64 (0.02) on the training/validation set and 0.63 (0.02) on the unseen test set, whereas TabPFN reached a mean AUROC of 0.64 (0.01) on the training/validation set and 0.61 (0.01) on the unseen test set. Fig. 1 reports anatomical feature rankings for both models. Using functional features, XGBoost reached a mean AUROC of 0.55 (0.01) on the training/validation set and 0.55 (0.04) on the unseen test set, whereas TabPFN reached a mean AUROC of 0.55 (0.02) on the training/validation set and 0.51 (0.01) on the unseen test set. Fig. 2 reports functional feature rankings for both models. When we repeated the training of the TabPFN without those features with a negative estimated importance score (i.e. dorsal attention, frontoparietal and default network), the model showed an improved AUROC of 0.56 (0.01) on the training/validation set and of 0.53 ($4 \cdot 10^{-3}$) on the unseen test set.

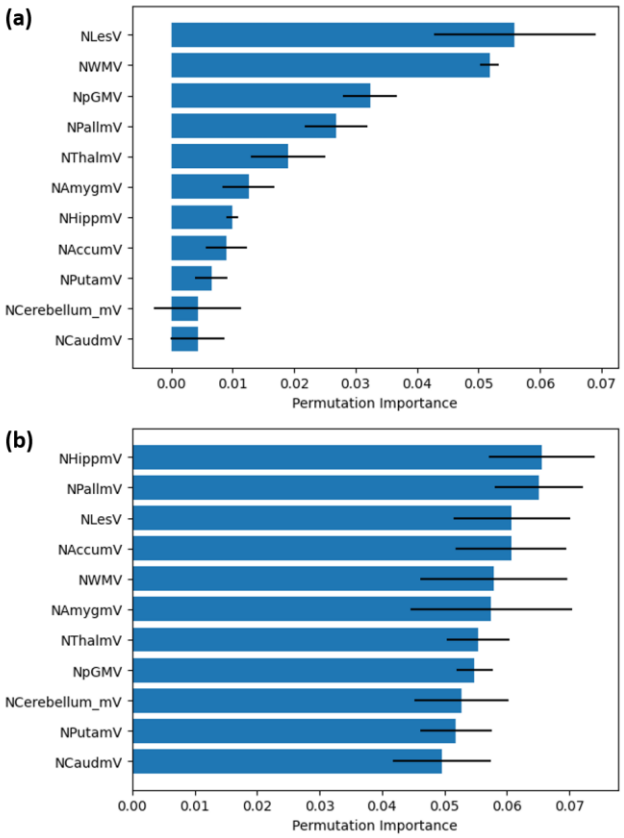


Fig. 1: Anatomical feature ranking from permutation feature importance for XGBoost (a) and TabPFN (b). Average values are reported (using 10 repetitions of 5-fold nested cross-validation inner loop on the training set and selecting the best model for each repetition). Abbreviations: NAccumV, normalized mean accumbens volume; NAmygmV, normalized mean amygdala volume; NCaudmV, normalized mean caudate volume; NCerebellm_mV, normalized mean cerebellum volume; NpGMV, normalized cortical grey matter volume; NHippmV, normalized mean hippocampus volume; NWMV, normalized white matter volume; NPallmV, normalized mean pallidus volume; NPutamV, normalized mean putament volume; NLesV, normalized lesion volume; NThalmV, normalized mean thalamus volume.

IV. Conclusion

ML tools are broadly applied to neuroimaging data nowadays. Although classification models for tabular datasets are still dominated by gradient-boosted decision trees, many progresses have been made to adapt advanced deep learning architectures (e.g. transformers) for predicting classes. In this work, we compared the XGBoost model, a state-of-the-art model for tabular datasets, with TabPFN, a novel transformer-based deep learning architecture specifically built and trained to solve tabular classification problems, to explore the

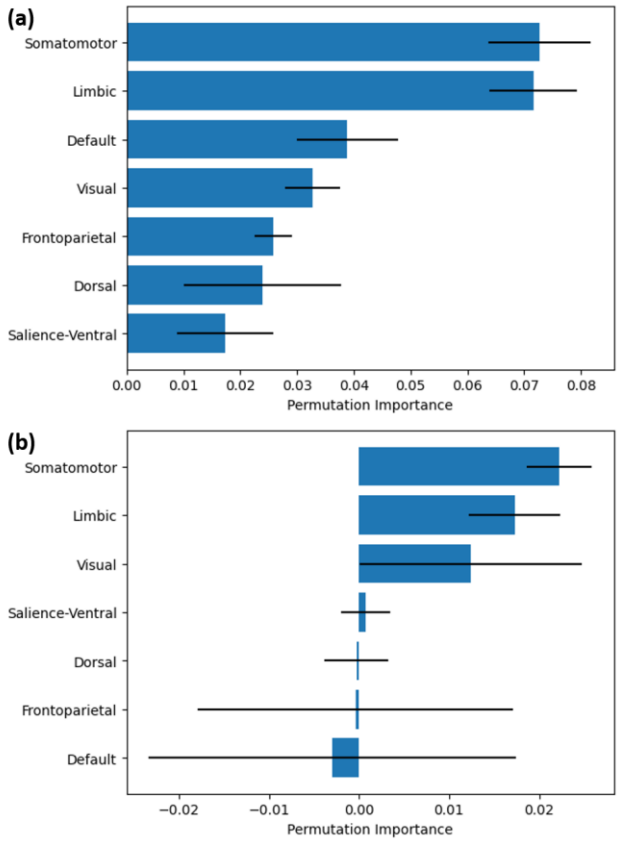


Fig. 2: Functional feature ranking from permutation feature importance for XGBoost (a) and TabPFN (b). Average values are reported (using 10 repetitions of 5-fold nested cross-validation inner loop on the training sett and selecting the best model for each repetition).

predictive abilities on two sets of typical MRI-derived anatomical and functional features, in order to predict the cognitive status of MS patients on an individual level. Both the models were trained, validated and tested using a combined CV/hold-out scheme (80% of the entire dataset for the training/validation set and 20% for the test set). Moreover, since performances may depend on how the training/validation set is split, the (nested) CV scheme was repeated 10 times using different random splits. Overall, our results showed that TabPFN classification performances are comparable to, but not better, than XGBoost. Indeed, for both anatomical and functional features, XGBoost provides equal results on the training/validation set (mean AUROC = 0.64 for the anatomical dataset and mean AUROC = 0.55 for the functional dataset), but better results on the unseen test set (mean AUROC = 0.63 vs 0.61 for the structural dataset and mean AUROC = 0.55 vs 0.51 for the functional dataset), even when we excluded from the feature set those features yielding a negative impact on the model (mean AUROC = 0.53). Beyond reporting which model would be showing the best performance, we were also interested in knowing if the two

models estimated similar importance scores for the features. Our findings showed that, for anatomical features, there is a discrepancy between the two models; in fact, while the XGBoost estimated high importance scores only for a few features (i.e., lesion volume, pallidus volume, cortical grey matter volume and white matter volume), the TabPFN model importance score estimates were more similar, i.e., there was no evidence for a subset of features clearly predominant with respect to the others. However, findings in the feature importance estimated with XGBoost were consistent with previous literature reporting cognitive dysfunction associated with volume abnormalities in lesion load [21], pallidus, gray and white matter volumes [8], [21]. On the other hand, the feature rankings for the functional dataset were more similar, with the somatomotor and limbic networks having the two highest importance scores for both datasets; indeed, these two functional networks have been previously showed to be related to clinical disability [22], [23]. Still, differences were present, e.g. the default network was ranked third in the XGBoost model, but, on average, negatively impacted the TabPFN prediction. Although the permutation importance technique is model-agnostic, i.e., it can be applied to any predictive model, these discrepancies between feature importance estimations could be partially explained by the intrinsic differences between the two models and how they treat the input features (besides the stochastic nature of both algorithms). In fact, XGBoost adds decision tree models sequentially to correct errors made by existing models while giving more importance to features useful to have better overall performances, whereas TabPFN, having a transformer-based architecture (i.e., a neural network), initializes random weights to input data and updates them given the data distribution and their prior probability [13]. In conclusion, our comparative study showed that gradient-boosted models, such as XGBoost, may still be the preferable choice for noisy tabular datasets, such as those derived from neuroimaging data. Moreover, neural network architectures like TabPFN, given their black box nature, pose issues about explainability, whereas XGBoost has a relatively straightforward method to automatically evaluate feature importance.

ETHICAL APPROVAL

Ethical approval was received from the local ethical standards committee of each participating center, and written informed consent was obtained from all participants at the time of data acquisition.

ACKNOWLEDGEMENT

REFERENCES

[1] D. Bzdok and A. Meyer-Lindenberg, “Machine Learning for Precision Psychiatry: Opportunities and Challenges,” *Biological Psychiatry: Cognitive Neuroscience and Neuroimaging*, vol. 3, no. 3, pp. 223–230, Mar. 2018, doi: 10.1016/j.bpsc.2017.11.007.

[2] T. Hahn, A. A. Nierenberg, and S. Whitfield-Gabrieli, “Predictive analytics in mental health: applications, guidelines, challenges and perspectives,” *Mol Psychiatry*, vol. 22, no. 1, Art. no. 1, Jan. 2017, doi: 10.1038/mp.2016.201.

[3] D. Bzdok, N. Altman, and M. Krzywinski, “Statistics versus machine learning,” *Nature Methods*, vol. 15, no. 4, Art. no. 4, Apr. 2018, doi: 10.1038/nmeth.4642.

[4] S. Eickhoff, T. E. Nichols, J. D. Van Horn, and J. A. Turner, “Sharing the wealth: Neuroimaging data repositories,” *NeuroImage*, vol. 124, pp. 1065–1068, Jan. 2016, doi: 10.1016/j.neuroimage.2015.10.079.

[5] R. H. B. Benedict, M. P. Amato, J. DeLuca, and J. J. G. Geurts, “Cognitive impairment in multiple sclerosis: clinical management, MRI, and therapeutic avenues,” *The Lancet Neurology*, vol. 19, no. 10, pp. 860–871, Oct. 2020, doi: 10.1016/S1474-4422(20)30277-5.

[6] J. M. Sheffield and D. M. Barch, “Cognition and resting-state functional connectivity in schizophrenia,” *Neuroscience & Biobehavioral Reviews*, vol. 61, pp. 108–120, Feb. 2016, doi: 10.1016/j.neubiorev.2015.12.007.

[7] F. C. Pérez-Miralles *et al.*, “Brain region volumes and their relationship with disability progression and cognitive function in primary progressive multiple sclerosis,” *Brain and Behavior*, vol. 11, no. 4, p. e02044, 2021, doi: 10.1002/brb3.2044.

[8] C. Marzi *et al.*, “Prediction of the information processing speed performance in multiple sclerosis using a machine learning approach in a large multicenter magnetic resonance imaging data set,” *Human Brain Mapping*, vol. n/a, no. n/a, doi: 10.1002/hbm.26106.

[9] K. Buyukturkoglu *et al.*, “Classifying multiple sclerosis patients on the basis of SDMT performance using machine learning,” *Mult Scler*, vol. 27, no. 1, pp. 107–116, Jan. 2021, doi: 10.1177/1352458520958362.

[10] J. H. Friedman, “Stochastic gradient boosting,” *Computational Statistics & Data Analysis*, vol. 38, no. 4, pp. 367–378, Feb. 2002, doi: 10.1016/S0167-9473(01)00065-2.

[11] T. Chen and C. Guestrin, “XGBoost: A Scalable Tree Boosting System,” in *Proceedings of the 22nd ACM SIGKDD International Conference on Knowledge Discovery and Data Mining*, Aug. 2016, pp. 785–794. doi: 10.1145/2939672.2939785.

[12] Y. Zhu *et al.*, “Converting tabular data into images for deep learning with convolutional neural networks,” *Sci Rep*, vol. 11, no. 1, Art. no. 1, May 2021, doi: 10.1038/s41598-021-90923-y.

[13] N. Hollmann, S. Müller, K. Eggensperger, and F. Hutter, “TabPFN: A Transformer That Solves Small Tabular Classification Problems in a Second.” arXiv, Nov. 29, 2022. doi: 10.48550/arXiv.2207.01848.

[14] A. P. De Rosa *et al.*, “Resting-state functional MRI in multicenter studies on multiple sclerosis: a report on raw data quality and functional connectivity features from the Italian Neuroimaging Network Initiative,” *J Neurol*, Nov. 2022, doi: 10.1007/s00415-022-11479-z.

[15] B. T. Thomas Yeo *et al.*, “The organization of the human cerebral cortex estimated by intrinsic functional connectivity,” *Journal of Neurophysiology*, vol. 106, no. 3, pp. 1125–1165, Sep. 2011, doi: 10.1152/jn.00338.2011.

[16] M. P. Amato *et al.*, “The Rao’s Brief Repeatable Battery and Stroop test: normative values with age, education and gender corrections in an Italian population,” *Mult Scler*, vol. 12, no. 6, pp. 787–793, Nov. 2006, doi: 10.1177/1352458506070933.

[17] S. Müller, N. Hollmann, S. P. Arango, J. Grabocka, and F. Hutter, “Transformers Can Do Bayesian Inference.” arXiv, Aug. 12, 2022. doi: 10.48550/arXiv.2112.10510.

[18] S. Varma and R. Simon, “Bias in error estimation when using cross-validation for model selection,” *BMC Bioinformatics*, vol. 7, no. 1, p. 91, Feb. 2006, doi: 10.1186/1471-2105-7-91.

[19] J.-P. Fortin *et al.*, “Harmonization of cortical thickness measurements across scanners and sites,” *NeuroImage*, vol. 167, pp. 104–120, Feb. 2018, doi: 10.1016/j.neuroimage.2017.11.024.

[20] S. Hechenberger *et al.*, “Information processing speed as a prognostic marker of physical impairment and progression in patients with multiple sclerosis,” *Mult Scler Relat Disord*, vol. 57, p. 103353, Jan. 2022, doi: 10.1016/j.msard.2021.103353.

[21] M. Grothe *et al.*, “Performance in information processing speed is associated with parietal white matter tract integrity in multiple sclerosis,” *Frontiers in Neurology*, vol. 13, 2022, Accessed: Apr. 18, 2023. [Online]. Available: https://www.frontiersin.org/articles/10.3389/fneur.2022.982964

[22] M. Strik *et al.*, “Increased functional sensorimotor network efficiency relates to disability in multiple sclerosis,” *Mult Scler*, vol. 27, no. 9, pp. 1364–1373, Aug. 2021, doi: 10.1177/1352458520966292.

[23] A. Bisecco *et al.*, “Resting-State Functional Correlates of Social Cognition in Multiple Sclerosis: An Explorative Study,” *Frontiers in Behavioral Neuroscience*, vol. 13, 2020, Accessed: Sep. 19, 2022. [Online]. Available: https://www.frontiersin.org/articles/10.3389/fnbeh.2019.00276

Effect of EDA-driven sympathetic responses on the central processing of faces cued by hedonic odors: a preliminary ERP study

G. Rho[1], A.L. Callara[1,2], C. Cecchetto[3], R. Garofalo[4], T. Lomonaco[5], E.P. Scilingo[1,2] and A. Greco[1,2]
[1] *Dipartimento di Ingegneria dell'Informazione, University of Pisa, Italy*
[2] *Research Center "E. Piaggio", University of Pisa, Italy*
[3] *Department of General Psychology, University of Padova, Italy*
[4] *Feel-ING S.r.l., spin-off of the University of Pisa, Italy*
[5] *Department of Chemistry and Industrial Chemistry, University of Pisa, Italy*

***Abstract*—Olfactory stimuli are powerful cues capable of modulating behavioral and physiological responses to other stimuli, such as visual stimuli. In this study, we investigated the integration of autonomic-driven information into the central nervous system dynamics during a contextual presentation of neutral faces and hedonic odors. To this aim, we simultaneously acquired the electrodermal activity (EDA) and EEG signals from a group of 20 healthy volunteers. We applied a novel methodological approach to identify event-related potentials (ERPs) with and without a concomitant EDA-related sympathetic response. Then, we investigated the effect of both sympathetic responses and contextual odors on ERP components involved in the processing of faces. Preliminary results showed a significant increase of the N170 amplitude in the left parieto-temporal region when a sympathetic response was present, compared to ERPs associated with no sympathetic responses, irrespective of odors' valence. This may suggest that sympathetic responses identified from EDA have an effect on the early central processing of faces with background odors, possibly reflecting enhanced arousal triggered by salient features of the stimuli.**

***Keywords*—Face processing, ERP, sympathetic responses, hedonic olfaction**

I. Introduction

Facial expressions are powerful non-verbal means through which the emotional state or the identity of a person can be efficiently decoded [1]. However, when expressions are ambiguous, their interpretation relies on the integration with other sensory modalities [2]. Previous research indicated contextual odors as powerful emotional triggers for the processing of faces, with odors' valence and arousal playing a key role as modulatory factors [3]–[5]. Moreover, their influence is not limited to subjective ratings but extends also to the physiological response as measured by EEG event-related-potentials (ERPs).

ERPs are EEG changes time locked to sensory, motor or cognitive events that provide a noninvasive approach to study psychophysiological correlates of mental processes. These waveforms are characterized by some key features, namely components, that can reflect early "sensory" or late "cognitive" responses [6]. Previous studies highlighted a contextual effect of emotional odors occurring at different stages of face processing, including the N1/P1 [7], N170 [8], VPP [9], and LPP [10] components.

Parallel to ERP analyses, other studies focused on the autonomic response elicited by contextual visual/odor stimulation [11], [12]. Particularly, enhanced peripheral sympathetic activations have been observed following the presentation of either visual or olfactory stimuli and that reflected the perceived level of arousal [11]–[13]. In this light, it would be of particular interest integrating the sympathetic responses with ERP measures for analyzing the multimodal integration of visual-odor processing.

Here, we investigate the effect of peripheral sympathetic responses on the central processing of neutral faces modulated by hedonic odors. We combine standard ERP analysis with the information provided by electrodermal activity (EDA). EDA is the most commonly used index to assess peripheral sympathetic activity, as the eccrine sweat glands generating it are mainly controlled by afferent sudomotor sympathetic fibers [13]. Accordingly, we apply a rigorous deconvolution procedure based on [14] to estimate the EDA underlying sudomotor nerve activity (SMNA), and identify the occurrence of significant sympathetic responses associated with the presentation of the stimuli. We exploit these events to compare ERPs with and without a sympathetic response [15]. Moreover, we evaluate the influence of contextual odors on both types of ERPs.

II. Material and methods

A. Subjects

The study was conducted according to the guidelines of the Declaration of Helsinki, and approved by the Bioethics Committee of the University of Pisa Review No. 14/2019, May 3rd, 2019. Twenty healthy volunteers (age 27 $\pm$ 3, 5 females) with similar olfactory threshold according to the double-blind forced-choice olfactory test [16] were enrolled in the study. Volunteers were not allowed to have any food or drink in the 30 minutes preceding the experiment.

B. Experimental setting

We selected three different odorants: i.e., banana (isoamyl acetate), isovaleric acid, and n-butanol, to convey positive, negative, and neutral valence, respectively [17]–[19]. We additionally used clean air as a control condition. For each subject, we prepared $1ml$ isointense solutions diluting pure odorant substances in distilled water according with the ratios of 1/20 (banana, n-butanol) and 1/10 (isovaleric acid) respectively. Odorants were delivered through an in-house built computer-controlled olfactometer at a constant flow rate of $60ml/min$. Before starting the experiment participants rated the odorants in terms of valence (from -2 to +2) and arousal (from 1 to 5) according to the Self-Assessment Manikin (SAM) test [20].

Moreover, we selected 128 different neutral face images from the Chicago Face Database [21]. Particularly, according to previous studies, we balanced the stimuli across gender, age, and ethnicity, to mitigate potential confounding effects related to the intrinsic characteristics of the actors [10]. The pictures were shown on a 15" laptop screen with a refresh rate of 60Hz and a resolution of 1920x1080. The pictures' size was 15cm in width and 10cm in height, and they were displayed at about 50cm from the eyes of the participants .

Each subject underwent an experimental protocol made of 128 trials of concurrent odor/image administration. A schematic representation of each trial is reported in Fig.1, which consisted of: (1) 3s of gray background; (2) 3s of fixation cross; (3) 1.5s of neutral face image presentation; (4) 6s of inter-trial rest during which subjects rated the facial expression in terms of valence and arousal according to the SAM test. Odorants were administered from phase (1) to (3), while during (4) clean air was used to washout the odor. Each odor condition comprised a total of 32 trials.

The experimental timeline for the olfactory/visual stimulation was controlled using the PsychoPy software [22]. The EDA signals were acquired at a sampling frequency of 50Hz with a Shimmer3 GSR+ unit (Shimmer, USA). The EEG signals were recorded at the sampling frequency of 500Hz using a high-density 128-channel geodesic EEG System 300 from Electrical Geodesic, Inc. (EGI). Electrodes were grounded through two additional channels placed between Cz and Pz and referenced through Cz. We always kept electrode impedances below $20k\Omega$ during the acquisitions.

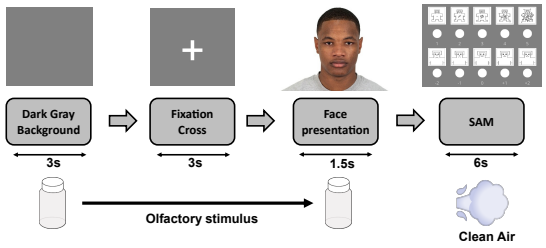


Fig. 1: Experimental protocol. For each trial a random odor among banana, n-butanol, isovaleric acid and clean air was delivered starting from *Dark Gray Background* to *Face presentation*. A wash-out with clean air was performed during *SAM*.

C. EDA processing and sympathetic activity estimation

EDA is comprised of a slow-varying tonic component overimposed to a fast-varying phasic component. In particular, the phasic component manifests as a series evoked-responses called skin conductance responses, whose elicitation is driven by sympathetic neural bursts (i.e., the sudomotor nerve activity - SMNA) [13].

We applied the cvxEDA algorithm to estimate the SMNA from each EDA signal (see [14]). According to the experimental protocol, we divided the SMNA signal into 128 different epochs of 5 seconds starting from the onset of each face presentation. Afterwards, we labeled and discriminated those epochs containing at least an SMNA burst (*symp-evoking*) from those not showing any neural sympathetic response (*symp-absent*).

D. EEG processing

We preprocessed the EEG signal using EEGLAB [23] with a pipeline comprising: (1) zero-phase antialiasing filter (filter cut-off = 30Hz) and downsampling to a sampling frequency of 100Hz, (2) a zero-phase high-pass filter (cut-off = 0.1Hz) to improve data stationarity, (3) bad channel removal with poor correlation with their neighboring channels (i.e., ρ <0.8) [24], (4) channel recovery through spherical spline interpolation, (5) re-referencing to average. Then, preprocessed EEG was epoched in the (-200,1000)ms range around the face-stimulus onset. For each epoch we removed a baseline estimated in the (-200,0)ms time-range. Epochs contaminated by irreducible artifacts were identified by visual inspection and removed. Finally, we decomposed EEG data through ICA [25], and we removed components resembling noise sources (e.g., EMG, eye blinks).
Once the preprocessing was completed, we selected the epochs with the same odor condition and averaged those with the presence of the SMNA bursts (*symp-evoking*) and those with the absence of SMNA bursts (*symp-absent*) (see Section II-C) estimating two stimulus-locked ERPs for each odor condition.

ERP components were then analyzed on specific regions of interest (ROIs) of the scalp with the guidance from previous literature [7]–[9], [26], [27]. More specifically, we extracted (1) the P1 component in the 120-160ms interval after stimulus onset in the occipital region around O1 and O2 (10 electrodes); (2) the N1 component at the same latency as P1, in the central region around Cz (15 electrodes); (3) the N170 component in the 160-200ms interval at both the left and the right parieto-temporal regions (7 electrodes near P7 and P8, respectively); (4) the Vertex Positive Potential (VPP) in the 160-200ms interval in the same ROI of the N1 component; (5) P2 component at 220-300ms in the same occipital region of P1; (6) the Late Positive Potential (LPP) in the 300-500ms range around Pz (9 electrodes). For each subject and for each component, we extracted the mean amplitude within the respective time interval and ROI.

E. Statistical analysis

Due to their nature, the subjective ratings of both odors and faces were not normally distributed. Therefore, we investigated possible differences in the perceived valence and arousal among the 4 different odorants (i.e., clean air; banana, n-butanol, and isovaleric acid) through non-parametric Wilcoxon sign-rank tests. The same procedure was applied to test for possible modulation of the valence and arousal ratings of faces by the 4 different odorants. P-values were adjusted for multiple comparisons with Bonferroni correction (6 comparisons).

Concerning the ERP analysis, after checking for data normality, we performed a two-way within-within ANOVA (first way: *symp-absent* vs *symp-evoking*; second way: odorant) to test the effect of sympathetic responses and odors on the amplitudes of each of the six ERP components described in section II-D. False positives were controlled with false-discovery rate (FDR) [28]. Post-hoc comparisons were conducted with a t-test (Bonferroni corrected; 3 comparisons).

III. Results

A. SAM statistical analysis results

1) Odor rating: Subjects rated isovaleric acid as significantly more unpleasant (mean $\pm$ standard error (SE); valence = -0.62 ± 0.18) and more arousing (arousal = 2.81 ± 0.22) with respect to banana and n-butanol. We did not find any significant difference between the valence and arousal ratings of banana (valence = 0.38 ± 0.20; arousal = 2.33 ± 0.21) and n-butanol (valence = 0.10 ± 0.18; arousal = 1.86 ± 0.17).

2) Face rating: We did not find any significant difference in the subjective ratings of faces among odors for both valence (clean air = -0.05 ± 0.05; banana = -0.14 ± 0.06; n-butanol = -0.03 ± 0.05; isovaleric acid = -0.09 ± 0.07) and arousal (clean air = 2.17 ± 0.16; banana = 2.23 ± 0.17; n-butanol = 2.18 ± 0.16; isovaleric acid = 2.15 ± 0.17).

B. ERP statistical analysis results

Since the banana odor did not elicit a SAM scoring significantly different than the n-butanol, we limited the ERP analysis to the study of clean air, n-butanol, and isovaleric acid effects. In addition, in this way, we increased the statistical power by reducing the number of comparisons.

We observed a significant difference between *symp-absent* and *symp-evoking* on the N170 amplitude at the ROI around P7 ($F_{1,19} = 4.62, p < 0.05$) (Fig.2). Particularly, the presence of a sympathetic response resulted in the increase of the N170 amplitude, irrespective of the valence of the odors. Moreover, we found a significant effect of the odor on the N1 ($F_{2,38} = 6.28, p < 0.05$) and VPP ($F_{2,38} = 7.19, p < 0.05$) components' amplitude at the ROI centered on Cz (Fig. 3). Post-hoc analysis highlighted a more negative N1 component during the administration of isovaleric acid, with respect to clean air. Moreover, the VPP amplitude during the administration of both isovaleric acid and n-butanol was significantly lower with respect to clean air. We did not find a significant interaction between the effect of odor and sympathetic responses for any of the ERP components investigated.

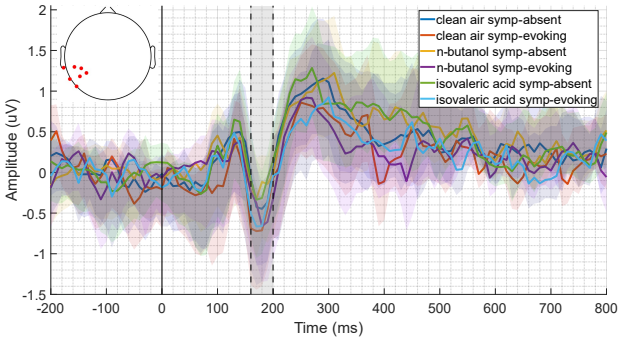


Fig. 2: ERP grand-averages for the clean air symp-absent (blue), clean air symp-evoking (red), n-butanol symp-absent (yellow), n-butanol symp-evoking (purple), isovaleric acid symp-absent (green), and isovaleric acid symp-evoking (light blue) conditions, averaged across 7 electrodes around P7 (scalp map on the left). The gray area highlights a higher N170 amplitude observed during *symp-evoking*, compared to *symp-absent*.

IV. Discussion

In this study, we provided a novel methodological approach based on the analysis of the EDA signal to integrate peripheral sympathetic activity information onto ERP analysis of key components associated with the processing of faces and contextual hedonic odors. Although preliminary, our results showed a significant difference between ERPs with and without a sympathetic response at the early stages of face processing.

We did not find any significant difference in the ratings of faces for both valence and arousal among odors. Yet, we observed an effect of olfactory stimulation on the N1 e VPP ERP components. Particularly, the amplitude of the VPP was lower during the administration of both isovaleric acid and n-butanol, with respect to clean air. This is in line with previous studies reporting an overall effect of olfactory stimuli, irrespective of their valence [9]. Considering N1, we observed a higher amplitude during the administration of isovaleric acid, with respect to clean air. Higher N1/P1 amplitudes have

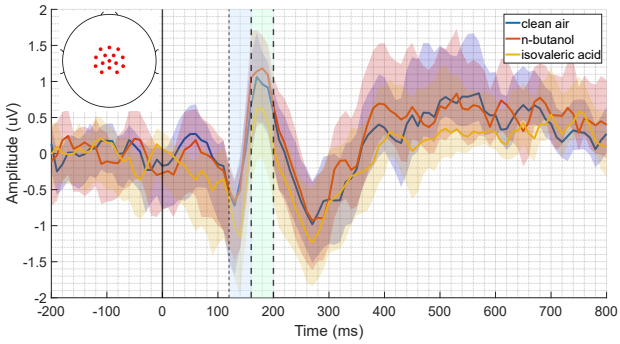


Fig. 3: ERP grand-averages for the clean air (blue), n-butanol (red), and isovaleric acid (yellow) conditions, averaged across 15 electrodes around Cz (scalp map on the left). The N1 amplitude was higher during isovaleric acid, compared to clean air (blue area). Conversely, the VPP amplitude was lower during both isovaleric acid and n-butanol, compared to clean air (green area)

been associated with the enhanced allocation of attention towards faces [7]. In this light, we may suggest that isovaleric acid had a greater arousing effect on the early processing of visual stimuli, compared to the other odorants. This is further corroborated by our findings on the SAM ratings of odors, showing isovaleric acid as being perceived as more arousing and unpleasant compared to banana and n-butanol.

The amplitude of the N170 increased for the P7 cluster in the presence of a sympathetic response. Previous studies have found a significant correlation between the N170 amplitude and the perceived level of arousal associated with faces, irrespective of their valence, such that arousing stimuli were associated with increased ERP responses [29]. Further, during the N170 window, it is hypothesized that multiple cortical processes underlie the fine-graining categorization of faces based on their main characteristics, such as expression, eye gaze, and identity [27]. Hence, we may suggest that the higher N170 amplitude observed during sympathetic responses reflects enhanced arousal associated with salient features of the stimuli.

Of note, banana was rated neutral rather than positive. In this light, we cannot exclude that such an effect may be related to the flow rate at which odors were delivered (i.e., $60ml/min$), which is lower than flow rates commonly used in the literature (e.g., 1-6l/min) [30]. In this light, future works could evaluate the influence of low flow rates on key features of perceived odors.

Although preliminary, our results suggest that integrating peripheral sympathetic information in the analysis of the central responses to the contextual presentation of visual and olfactory stimuli may be of interest for future studies investigating potential effects at the source level through the application of more sophisticated techniques.

ACKNOWLEDGMENT

Research partly founded by the EU Horizon 2020 project "POTION-Promoting Social Interaction through Emotional Body Odours" with the grant agreement number 824153 and by the Italian MIUR (i.e., Ministry of Education and Research) in the framework of the CrossLab project (Departments of Excellence). Research also partly funded by PNRR - M4C2 - Investimento 1.3, Partenariato Esteso PE00000013 - "FAIR - Future Artificial Intelligence Research" - Spoke 1 "Human-centered AI", funded by the European Commission under the NextGeneration EU programme. Research produced with the co-funding European Union - Next Generation EU, in the context of The National Recovery and Resilience Plan, Investment 1.5 Ecosystems of Innovation, Project Tuscany Health Ecosystem (THE), CUP: I53C22000780001.

REFERENCES

[1] E. Syrjänen et al., "A review of the effects of valenced odors on face perception and evaluation," *i-Perception*, vol. 12, no. 2, p. 20416695211009552, 2021.

[2] H. Aviezer et al., "The inherently contextualized nature of facial emotion perception," *Current opinion in psychology*, vol. 17, pp. 47–54, 2017.

[3] S. Cook et al., "Pleasant and unpleasant odors influence hedonic evaluations of human faces: An event-related potential study," *Frontiers in human neuroscience*, vol. 9, p. 661, 2015.

[4] S. Cook et al., "Pleasant and unpleasant odour-face combinations influence face and odour perception: An event-related potential study," *Behavioural Brain Research*, vol. 333, pp. 304–313, 2017.

[5] J. M. Leppänen and J. K. Hietanen, "Affect and face perception: odors modulate the recognition advantage of happy faces.," *Emotion*, vol. 3, no. 4, p. 315, 2003.

[6] S. Sur and V. K. Sinha, "Event-related potential: An overview," *Industrial psychiatry journal*, vol. 18, no. 1, p. 70, 2009.

[7] D. Adolph et al., "Context counts! social anxiety modulates the processing of fearful faces in the context of chemosensory anxiety signals," *Frontiers in human neuroscience*, vol. 7, p. 283, 2013.

[8] E. Syrjänen et al., "Background odors modulate n170 erp component and perception of emotional facial stimuli," *Frontiers in Psychology*, vol. 9, p. 1000, 2018.

[9] A. Leleu et al., "Contextual odors modulate the visual processing of emotional facial expressions: An erp study," *Neuropsychologia*, vol. 77, pp. 366–379, 2015.

[10] A. L. Callara et al., "Human body odors of happiness and fear modulate the late positive potential component during neutral face processing: a preliminary erp study on healthy subjects," in *2022 44th Annual International Conference of the IEEE Engineering in Medicine & Biology Society (EMBC)*, pp. 4093–4096, IEEE, 2022.

[11] P. Bonifacci et al., "Familiarity of faces: Sense or feeling? an exploratory investigation with eye movements and skin conductance.," *Journal of Psychophysiology*, vol. 29, no. 1, p. 20, 2015.

[12] P. Brauchli et al., "Electrocortical and autonomic alteration by administration of a pleasant and an unpleasant odor," *Chemical senses*, vol. 20, no. 5, pp. 505–515, 1995.

[13] W. Boucsein, *Electrodermal activity*. Springer Science & Business Media, 2012.

[14] A. Greco et al., "cvxeda: A convex optimization approach to electrodermal activity processing," *IEEE Transactions on Biomedical Engineering*, vol. 63, no. 4, pp. 797–804, 2015.

[15] H. Bahramali et al., "Evoked related potentials associated with and without an orienting reflex," *Neuroreport*, vol. 8, no. 12, pp. 2665–2669, 1997.

[16] J. C. Stevens et al., "Variability of olfactory thresholds," *Chemical Senses*, vol. 13, no. 4, pp. 643–653, 1988.

[17] M. Naudin et al., "State and trait olfactory markers of major depression," 2012.

[18] A. L. Callara et al., "Cortical network and connectivity underlying hedonic olfactory perception," *Journal of Neural Engineering*, vol. 18, no. 5, p. 056050, 2021.

[19] G. Rho et al., "Valence, arousal, and gender effect on olfactory cortical network connectivity: A study using dynamic causal modeling for eeg," *IEEE Access*, vol. 10, pp. 127313–127327, 2022.

[20] M. M. Bradley and P. J. Lang, "Measuring emotion: the self-assessment manikin and the semantic differential," *Journal of behavior therapy and experimental psychiatry*, vol. 25, no. 1, pp. 49–59, 1994.

[21] D. S. Ma et al., "The chicago face database: A free stimulus set of faces and norming data," *Behavior research methods*, vol. 47, no. 4, pp. 1122–1135, 2015.

[22] J. W. Peirce, "Psychopy—psychophysics software in python," *Journal of neuroscience methods*, vol. 162, no. 1-2, pp. 8–13, 2007.

[23] A. Delorme and S. Makeig, "Eeglab: an open source toolbox for analysis of single-trial eeg dynamics including independent component analysis," *Journal of neuroscience methods*, vol. 134, no. 1, pp. 9–21, 2004.

[24] T. R. Mullen et al., "Real-time neuroimaging and cognitive monitoring using wearable dry eeg," *IEEE Transactions on Biomedical Engineering*, vol. 62, no. 11, pp. 2553–2567, 2015.

[25] S. Makeig et al., "Independent component analysis of electroencephalographic data," *Advances in neural information processing systems*, vol. 8, 1995.

[26] S. A. Trautmann-Lengsfeld et al., "The perception of dynamic and static facial expressions of happiness and disgust investigated by erps and fmri constrained source analysis," *PLoS One*, vol. 8, no. 6, p. e66997, 2013.

[27] B. Rossion, "Understanding face perception by means of human electrophysiology," *Trends in cognitive sciences*, vol. 18, no. 6, pp. 310–318, 2014.

[28] Y. Benjamini and D. Yekutieli, "The control of the false discovery rate in multiple testing under dependency," *Annals of statistics*, pp. 1165–1188, 2001.

[29] P. R. Almeida et al., "Perceived arousal of facial expressions of emotion modulates the n170, regardless of emotional category: Time domain and time–frequency dynamics," *International Journal of Psychophysiology*, vol. 99, pp. 48–56, 2016.

[30] J. N. Lundström et al., "Methods for building an inexpensive computer-controlled olfactometer for temporally-precise experiments," *International Journal of Psychophysiology*, vol. 78, no. 2, pp. 179–189, 2010.

Comparative analysis of EMG-based classifiers for recognizing hand/wrist gestures and forces

R. Billardello[1], F. Cordella[1], F. Leone[1], F. Mereu[1], E. Gruppioni[2], L. Zollo[1]
[1] *Research Unit of Advanced Robotics and Human-centred Technologies, Università Campus Bio-Medico di Roma, Italy*
[2] *Centro Protesi Inail di Vigorso di Budrio, Italy*

***Abstract*—Hand gesture recognition through surface electromyographic (sEMG) signals represents a well-consolidated approach for a natural and intuitive prosthesis control. Several studies showed how the classification performance can differ between healthy subjects and amputees, due to the high complexity and variability of amputations. Nonetheless, the evaluation of the goodness of Machine Learning classifiers in terms of adaptability to the subjects has never been studied deeply, and only few studies involved a sufficient number of amputees in their analysis. In this paper, the performance of four state-of-the art classifiers in decoding both motor intention and forces were evaluated, using a hierarchical classification approach. Algorithms have been tested on 29 healthy subjects and 15 trans-radial amputees. Results showed high performance for both the Non Linear Regression Classifier and the Random Forest with bootstrap aggregation, for both the gestures and the forces classification problem. No significant differences were found between the two classifiers, suggesting that they may be used interchangeably.**

***Keywords*—EMG pattern recognition, prosthesis, Upper limb.**

I. Introduction

THE loss of a limb represents an event that can impact most everyday activities. The need to restore part of amputees' capabilities directly translates into the need of improved prosthesis control algorithms, capable of decoding the user intent and allowing a natural and intuitive control. In this context, sEMG pattern recognition has established itself as one of the most widespread technique to decode the user motor intention [1], [2]. Over the years, hand prostheses and their control strategies considerably evolved, allowing the amputees to move from purely cosmetic to single function devices capable of opening/closing the hand [3], up to robotic hands [4] and wrists [5] with multiple degrees of freedom [6]. Several pattern recognition approaches for gesture and force recognition have been proposed over the years. The most popular are Support Vector Machine (SVM) [7]–[9], Linear Discriminant Analysis (LDA) [7], [10]–[12], Non Linear Regression (NLR) [13]–[15], k-Nearest Neighbour [16], Random Forest (RF) [17], Neural Networks [18], [19]. However, despite their popularity, very few studies tested these classifiers on dataset with amputees [20]–[22], and only few compared their performance in gesture and forces recognition on the same dataset [13], [14], [20].

In order to identify the best performing classifier on both healthy subjects and amputees, in this paper we tested four state-of-the-art classifiers in a hierarchical architecture [13], [14] by decoding seven hand/wrist gestures and three levels of force simultaneously and compared their results between healthy subjects and amputees. The gesture set analyzed in this study included the *rest* condition, four hand gestures (*open hand, bidigital grasp, power grasp, pointing*) and two wrist gestures (*pronation, supination*), while for the two grasps (*bidigital* and *power*) three different levels of force were recorded.

II. Materials and Methods

A. Classification architecture

A hierarchical architecture strategy (Fig. 1) was used to decode gestures and force levels. The structure includes a high hierarchical level that involves a gesture classifier, and a low hierarchical level, which includes two forces classifiers specialized in recognizing three levels of forces from specific types of grasp (*power* or *bidigital* grasp). The force classifiers are activated only when the output of the gesture classifier indicates one of the two grasping classes.

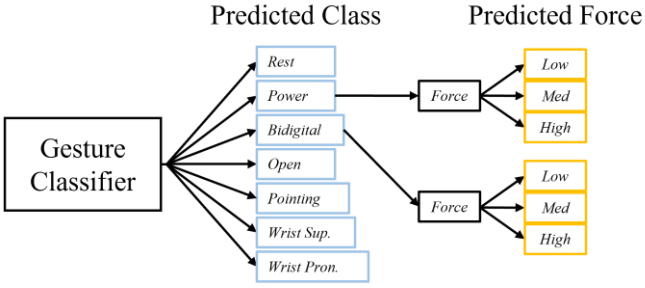


Fig. 1: Hierarchical architecture. The gesture classifier (black box on the left) predicts one of the seven classes (blue boxes). If Power or Bidigital class is predicted, the corresponding force classifiers (black box on the right) predict one of the three level of forces (yellow boxes).

B. Classifiers

The four most used state-of-the-art machine learning classifiers were tested [17]: LDA, SVM, RF with bootstrap aggregation and NLR [13], [14]. Moreover, in order to guarantee an intuitive and natural response of the classifiers with respect to physiological delays of muscle contraction, the signals were divided in time windows of 150 ms of length and 50 ms of overlap [23]. Five commonly used features in the time domain were extracted from the signal: Mean Absolute Value (MAV), Root Mean Square (RMS), Signal Slope Change (SSC), Window Length (WL), Variance (VAR) [24].

C. Experimental setup

Twenty-nine healthy subjects (age: 29.0 ± 7.3 years, 14 F) and fifteen amputees (age: 45.0 ± 13.4 years, 3 F) participated in the experiment. All the subjects signed informed consent for voluntary participation in the study. The studies involving human participants were reviewed and approved by Comitato Etico di Area Vasta Emilia Centro (protocol number: CP-

PPRAS1/1-01; date of approval: 04/10/2018). Muscular activity was acquired through six commercially available sEMG sensors (Ottobock 13E200 - range 0 − 5V, bandwidth 90 − 450Hz), that integrate a pre-processing module which provides a non-negative and enveloped signal as an output. Electrodes were placed equidistantly around the forearm of the participants, about 4 cm below the elbow, accordingly to the common placement in a prosthetic device [25].

For all the subjects (i.e. healthy and amputees), a hand dynamometer (Vernier HD BTA, 46x28x170 mm) was used to acquire exerted forces on the non-dominant/residual hand. EMG and force data were acquired simultaneously with a sampling frequency of 1 KHz, through a LabView interface for DAQ USB 6002 device, connected to a laptop (MSI 86 prestige 15, Intel (R) Core (TM) i7-1185G7 CPU @ 1.80 GHz 2.40 GHz) via USB port.

Prior to the acquisition, the subjects were asked to perform the grasp gestures with three different levels of perceived force (low, medium, high), using both limbs. Thus, EMG data was acquired on the dominant/amputated limb, and the forces with the dynamometers on the non-dominant/residual one. Three repetitions of three seconds were acquired for each force level. The average contraction levels were calculated from EMG signal for each force level, and the low, medium and high levels of force were defined for the two grasps as follows: the low level was set in the range of the average low contraction ± 10%, the medium was set in the range of the average medium contraction ± 10%, while the high level started from -10% of the average high contraction up to the maximum value.

Subsequently, all the subjects performed bi-manually six repetitions for each of the seven gestures, holding the position for 2 s. A rest period of at least 2 s was given after every repetition, and a longer recovery time (>30s) every six repetitions. Two repetitions for each of the three force levels were recorded for each grasp gesture, using the real-time force level and the recorded ranges as visual feedbacks for the users. Gestures were performed in a randomized order.

D. Data Processing and statistics

In order to analyze the steady part of the contraction, for each repetition we kept only the final 800 ms, discarding the rest state preceding the contraction and the subsequent transient state, without any further pre-processing other than the one obtained by the sensors. Thus, for each subject EMG data were organized in a 33600 × 6 matrix (6 repetitions × *7 gestures* × *800 samples* × *6 sensors*), with each column representing a sensor, and divided in time windows of 150 ms. For each subject, time windows were then separated into training and test sets with a 5-fold cross validation, using 30% of the windows for the test and 70% for the training. Features were extracted from each time window. In order to speed up the training process for NLR, a down sampling with a step=10 (keeping the first sample and discarding the following nine) was used on raw data from the time windows without any processing. Both features and raw data were then normalized with respect to their maximum per column (see Eq. (1)).

$$Sn = \frac{S - \min(S)}{Max(S) - \min(S)} \quad (1)$$

where *Sn* and *S* are respectively the normalized and the original signal.

All the classifiers were trained and tested using the same training and test validation sets, which contained a balanced number of observations per class. Since NLR gives one prediction per observation, the final classification output was calculated by using a majority voting (MV) among the prediction of the whole time window. The first-order iterative optimization algorithm "Gradient descent" was used to set the NLR classifier optimal internal hyper-parameters. One Vs. All approach [13] was used for NLR and SVM classifiers to adapt the algorithms to the multi-classification problem. In order to have a balance between classification accuracy and prediction time, RF number of trees was empirically set to 25. Confusion matrices, class accuracy and average accuracy were calculated for all the subjects. Wilcoxon signed rank test for paired samples was applied to the non-normal average accuracies to find significant differences between the classifiers, with a significance level set to $\alpha=0.05$ and applying Bonferroni correction ($\alpha=0.0083$). Wilcoxon rank sum test for independent samples was used to compare the non-normal results from healthy subjects and amputees. Lastly, the execution time for each classifier was calculated in an online test as the time spent from the receipt of 150 ms of signal to the prediction output. The online test simulated the receipt of ten time windows per class for the gesture classifier, and other ten time windows for *power* and *bidigital* grasp respectively. Execution time then averaged over the time windows. The analysis was entirely conducted on a laptop (Lenovo ThinkPad E570, Intel (R) Core (TM) i5 CPU @ 2.50 GHz) with MATLAB software.

III. RESULTS

A. Healthy subjects

The results of the gesture classifier are reported in Fig. *2*. In agreement with previous studies [13], [14], NLR achieved the highest median accuracy among subjects (97.9% ± 4.2), followed by RF (95.9% ± 3.0), LDA (93.9% ± 4.0), and SVM (92.9% ± 6.2). Significant differences were found between NLR and other classifiers, except with RF (p=0.08). All classes of NLR and RF achieved more than 90% of accuracy, while LDA only achieved 89% of accuracy for *bidigital* grasp, and SVM achieved 85% for *power* grasp (Fig. 3).

Force classifiers showed high accuracy for both the *power* grasps classifier (Accuracy NLR = 100% ± 0.0; Accuracy RF = 100% ± 3.0; Accuracy SVM = 100% ± 7.9; Accuracy LDA = 88.9 ± 12.5) and the *bidigital* grasp classifier (Accuracy NLR = 100% ± 6.2; Accuracy RF = 100% ± 6.4; Accuracy SVM = 88.9% ± 11.1; Accuracy LDA = 77.8% ± 14.4). Regarding the *power* grasp, significant differences were found between LDA and NLR ($p<10^{-4}$), LDA and RF ($p<10^{-4}$) and LDA and SVM (p=0.005), while for *bidigital* grasp significant differences between classifiers were found between all classifiers except for RF and NLR (p=0.77) (Fig. *4*).

B. *Amputees*

Similar results were found in amputees (Fig. 2), where NLR achieved the best median accuracy (99.0% ± 7.1), followed by RF (96.9% ± 4.9), SVM (90.8% ± 7.9), and LDA (89.8% ± 8.8). Significant differences were found between NLR and all the other classifiers, except for the RF ($p>0.65$). No significant difference was found between LDA and SVM. All classes of both NLR and RF achieved more than 90% of accuracy, in LDA *power* and *Bidigital* grasp achieved 76% and 78% of accuracy, and in SVM *power* grasp achieved 80% (Fig. 3).

Results from the force classifiers showed high accuracy for both the *power* grasps classifier (Accuracy NLR = 100% ± 4.0; Accuracy RF = 100% ± 9.5; Accuracy SVM = 100% ± 13.7; Accuracy LDA = 83.3 ± 9.5) and the *bidigital* grasp classifier (Accuracy NLR = 100% ± 9.5; Accuracy RF = 100% ± 12.5; Accuracy SVM = 88.9% ± 11.6; Accuracy LDA = 77.8% ± 12.9). A significant difference was found between LDA and NLR for *power* grasp ($p<9*10^{-4}$, while no significant differences between classifiers were found for the *bidigital* force classifier (Fig. 4).

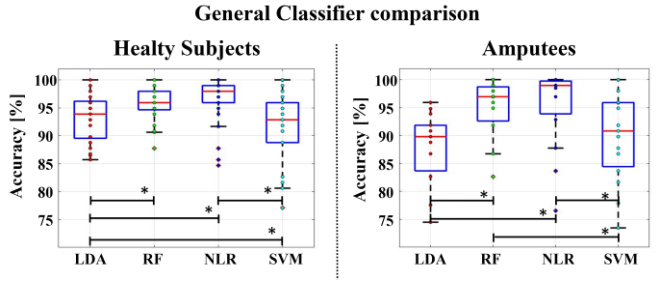


Fig. 2: Gesture classifier healthy subjects (left) and amputees (right). Significant differences are indicated with a star *.

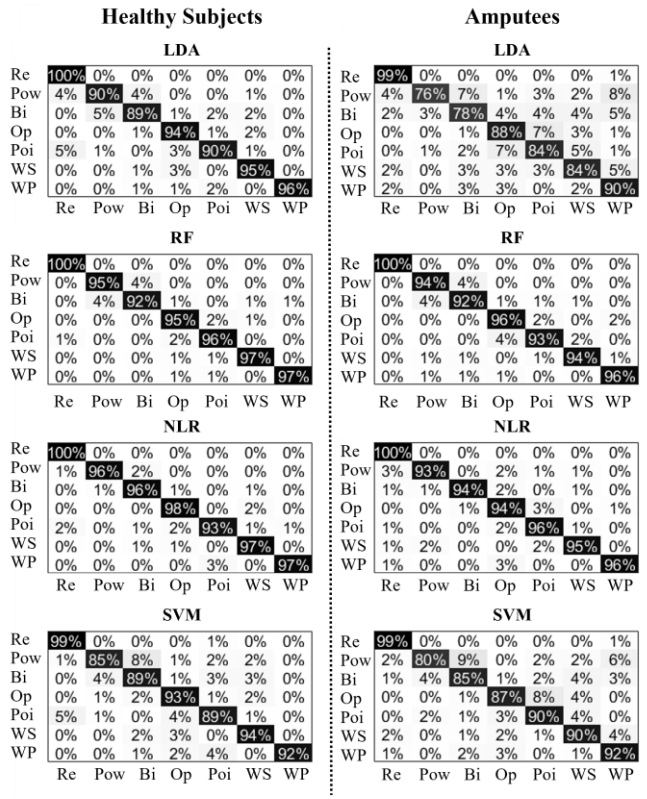


Fig. 3: Confusion matrices for all gesture classifiers and class accuracy for *rest* condition (Re), *Power grasp* (Pow), *Bidigital grasp* (Bi), *Open hand* (Op), *Pointing* (Poi), *Wrist Supination* (WS) and *Wrist Pronation* (WP).

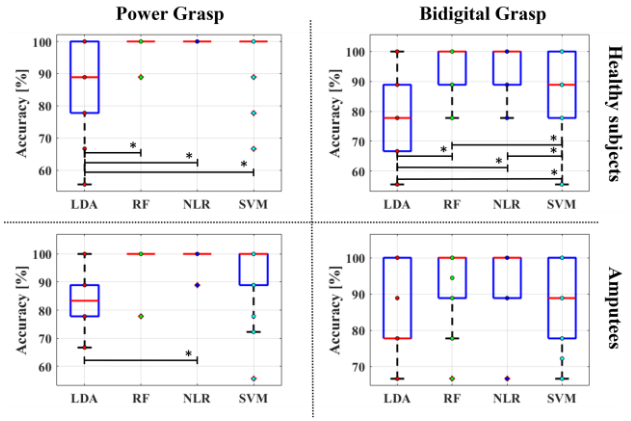


Fig. 4: Force classifier results for *power grasp* (left column) and *bidigital grasp* (right column) in healthy subjects (top row) and amputees (low row).

C. *Healthy subjects vs Amputees*

Despite some differences in the accuracy, Wilcoxon rank sum test showed no significant differences between healthy subjects and amputees, except for LDA classifier.

D. *Online test execution time*

All the classifiers need a time window of 150 ms of signal as an input, except for NLR, that can make a prediction for every new observation (i.e. one prediction per ms for a 1 KHz acquisition). In order to have comparable results, MV was applied to NLR predictions. Execution time reported in Table I shows that LDA has the fastest response in both the general and the force classifiers, followed by NLR, SVM, and RF.

TABLE I: CLASSIFIERS EXECUTION TIME

Classifier	*Gesture Classifier Execution Time*	*Force Classifier execution time – grasps averaged*
LDA	12.5 ± 3.8 ms	11.0 ± 4.7 ms
RF	73.0 ± 8.1 ms	69.3 ± 10.0 ms
NLR	15.9 ± 7.1 ms	13.8 ± 6.8 ms
SVM	34.8 ± 11.3 ms	24.9 ± 18.9 ms

Execution time for LDA, RF, NLR and SVM classifiers. Results were obtained as an average on ten time windows per class (150 ms length).

IV. CONCLUSION

In this paper, four state-of-the-art classifiers in a hierarchical architecture were tested to simultaneously decode seven commonly performed hand/wrist gestures and three levels of force. As expected, results showed high performance for NLR and RF classifiers, while no significant differences were found between the two. On the other hand, LDA and SVM achieved lower performance, suggesting that the nature of the problem of EMG signal decoding is not linearly separable, and thus linear classifiers might not be suitable for facing the problem. All classes of NLR and RF achieved more than 92% of accuracy in both healthy subjects and amputees, contrary to LDA and SVM, that achieved lower performance, in particular with *power* and *bidigital* grasps.

However, these classifiers showed high scalability from healthy subjects to amputees, with no significant differences between the two cases, except for LDA. This highlights the

fact that although amputees might present higher complexity due to their amputations and thus it is important to include them in future studies, high-performing classifiers can overcome this issue. Despite the absence of significant differences between NLR and RF, the online comparison on execution time showed a gap in the performance between the two classifiers, with the NLR being faster responding, and thus, more appropriate for the use in online applications. This is due to the classification algorithm of NLR, which only involves sums and multiplications, and the use of raw data, that eliminates the process of feature extraction. Therefore, results suggest that although NLR and RF may be used interchangeably in an offline scenario, further investigations must be conducted for RF in real time applications. Future studies will evaluate the effects of different features or time windows on classification accuracy or other metrics. Moreover, different under sampling steps and number of trees will be investigated for NLR and RF training, respectively.

ACKNOWLEDGEMENT

This study was supported partly by the European Union's Horizon 2020 Research and Innovation Program under Grant agreement no. 899822 (SOMA project) and partly by the Italian Institute for Labour Accidents (INAIL) prosthetic center with WiFi-MyoHand project (CUP: E59E19001460005).

REFERENCES

[1] C. Widehammar, I. Pettersson, G. Janeslätt, and L. Hermansson, "The influence of environment: Experiences of users of myoelectric arm prosthesis—a qualitative study," *Prosthet. Orthot. Int.*, vol. 42, no. 1, 2018, doi: 10.1177/0309364617704801.

[2] D. Farina and O. Aszmann, "Bionic limbs: Clinical reality and academic promises," *Science Translational Medicine*, vol. 6, no. 257. 2014, doi: 10.1126/scitranslmed.3010453.

[3] R. N. Scott and P. A. Parker, "Myoelectric prostheses: State of the art," *J. Med. Eng. Technol.*, vol. 12, no. 4, 1988, doi: 10.3109/03091908809030173.

[4] M. Owen, C. K. Au, and A. Fowke, "Development of a Dexterous Prosthetic Hand," *J. Comput. Inf. Sci. Eng.*, vol. 18, no. 1, 2018, doi: 10.1115/1.4038291.

[5] G. Kanitz, F. Montagnani, M. Controzzi, and C. Cipriani, "Compliant Prosthetic Wrists Entail More Natural Use Than Stiff Wrists during Reaching, Not (Necessarily) during Manipulation," *IEEE Trans. Neural Syst. Rehabil. Eng.*, vol. 26, no. 7, 2018, doi: 10.1109/TNSRE.2018.2847565.

[6] D. S. V. Bandara, R. A. R. C. Gopura, K. T. M. U. Hemapala, and K. Kiguchi, "Development of a multi-DoF transhumeral robotic arm prosthesis," *Med. Eng. Phys.*, vol. 48, 2017, doi: 10.1016/j.medengphy.2017.06.034.

[7] A. Stango, F. Negro, and D. Farina, "Spatial Correlation of High Density EMG Signals Provides Features Robust to Electrode Number and Shift in Pattern Recognition for Myocontrol," *IEEE Trans. Neural Syst. Rehabil. Eng.*, vol. 23, no. 2, 2015, doi: 10.1109/TNSRE.2014.2366752.

[8] D. Bai, S. Chen, and J. Yang, "Upper Arm Motion High-Density sEMG Recognition Optimization Based on Spatial and Time-Frequency Domain Features," *J. Healthc. Eng.*, vol. 2019, 2019, doi: 10.1155/2019/3958029.

[9] J. Lara, N. Paskaranandavadivel, and L. K. Cheng, "HD-EMG Electrode Count and Feature Selection Influence on Pattern-based Movement Classification Accuracy," in *Proceedings of the Annual International Conference of the IEEE Engineering in Medicine and Biology Society, EMBS*, 2020, vol. 2020-July, doi: 10.1109/EMBC44109.2020.9175210.

[10] D. Tkach, H. Huang, and T. A. Kuiken, "Study of stability of time-domain features for electromyographic pattern recognition," *J. Neuroeng. Rehabil.*, vol. 7, no. 1, 2010, doi: 10.1186/1743-0003-7-21.

[11] F. Nougarou, A. Campeau-Lecours, D. Massicotte, M. Boukadoum, C. Gosselin, and B. Gosselin, "Pattern recognition based on HD-sEMG spatial features extraction for an efficient proportional control of a robotic arm," *Biomed. Signal Process. Control*, vol. 53, 2019, doi: 10.1016/j.bspc.2019.04.027.

[12] A. Phinyomark, P. Phukpattaranont, and C. Limsakul, "Feature reduction and selection for EMG signal classification," *Expert Syst. Appl.*, vol. 39, no. 8, 2012, doi: 10.1016/j.eswa.2012.01.102.

[13] A. Dellacasa Bellingegni *et al.*, "NLR, MLP, SVM, and LDA: A comparative analysis on EMG data from people with trans-radial amputation," *J. Neuroeng. Rehabil.*, vol. 14, no. 1, 2017, doi: 10.1186/s12984-017-0290-6.

[14] F. Leone *et al.*, "Simultaneous sEMg classification of hand/wrist gestures and forces," *Front. Neurorobot.*, vol. 13, 2019, doi: 10.3389/fnbot.2019.00042.

[15] L. Zollo *et al.*, "Restoring tactile sensations via neural interfaces for real-time force-and-slippage closed-loop control of bionic hands," *Sci. Robot.*, vol. 4, no. 27, 2019, doi: 10.1126/scirobotics.aau9924.

[16] G. R. Kanitz, C. Antfolk, C. Cipriani, F. Sebelius, and M. C. Carrozza, "Decoding of individuated finger movements using surface EMG and input optimization applying a genetic algorithm," 2011, doi: 10.1109/IEMBS.2011.6090465.

[17] M. F. Wahid, R. Tafreshi, and R. Langari, "A Multi-Window Majority Voting Strategy to Improve Hand Gesture Recognition Accuracies Using Electromyography Signal," *IEEE Trans. Neural Syst. Rehabil. Eng.*, vol. 28, no. 2, 2020, doi: 10.1109/TNSRE.2019.2961706.

[18] C. Wu, H. Zeng, A. Song, and B. Xu, "Grip force and 3D push-pull force estimation based on sEMG and GRNN," *Front. Neurosci.*, vol. 11, no. JUN, 2017, doi: 10.3389/fnins.2017.00343.

[19] C. Li, J. Ren, H. Huang, B. Wang, Y. Zhu, and H. Hu, "PCA and deep learning based myoelectric grasping control of a prosthetic hand," *Biomed. Eng. Online*, vol. 17, no. 1, 2018, doi: 10.1186/s12938-018-0539-8.

[20] M. Atzori, M. Cognolato, and H. Müller, "Deep learning with convolutional neural networks applied to electromyography data: A resource for the classification of movements for prosthetic hands," *Front. Neurorobot.*, vol. 10, no. SEP, 2016, doi: 10.3389/fnbot.2016.00009.

[21] Y. A. Jarrah *et al.*, "High-density surface EMG signal quality enhancement via optimized filtering technique for amputees' motion intent characterization towards intuitive prostheses control," *Biomed. Signal Process. Control*, vol. 74, 2022, doi: 10.1016/j.bspc.2022.103497.

[22] A. Olsson, N. Malesevic, A. Bjorkman, and C. Antfolk, "Exploiting the Intertemporal Structure of the Upper-Limb sEMG: Comparisons between an LSTM Network and Cross-Sectional Myoelectric Pattern Recognition Methods," 2019, doi: 10.1109/EMBC.2019.8856648.

[23] L. H. Smith, L. J. Hargrove, B. A. Lock, and T. A. Kuiken, "Determining the optimal window length for pattern recognition-based myoelectric control: Balancing the competing effects of classification error and controller delay," *IEEE Trans. Neural Syst. Rehabil. Eng.*, vol. 19, no. 2, 2011, doi: 10.1109/TNSRE.2010.2100828.

[24] J. Too, A. R. Abdullah, N. M. Saad, and W. Tee, "EMG feature selection and classification using a Pbest-guide binary particle swarm optimization," *Computation*, vol. 7, no. 1, 2019, doi: 10.3390/computation7010012.

[25] F. Riillo *et al.*, "Optimization of EMG-based hand gesture recognition: Supervised vs. unsupervised data preprocessing on healthy subjects and transradial amputees," *Biomed. Signal Process. Control*, vol. 14, no. 1, 2014, doi: 10.1016/j.bspc.2014.07.007.

Osteoporosis Identification at Lumbar Vertebrae through a Neural Network Classifier

M. Maggio[1], T. De Marco[1], F. Conversano[2], G. Macchia[1], I. Primitivo[1], F. Lombardi[2], P. Pisani[2] and S. Casciaro[2]

[1]*R&D Department, Echolight S.p.A., Lecce,*

[2]*National Research Council, Institute of Clinical Physiology, Lecce, sergio.casciaro@cnr.it*

Abstract - The objective of this study is to design and implement a Neural Network-based model for classifying osteoporotic and non-osteoporotic patients. To accomplish this goal, an echographic scan was conducted on the first four lumbar vertebrae (L1-L4) of 375 patients previously evaluated using Dual Energy X-Ray Absorptiometry (DEXA), which is currently considered the goal standard in the field. The patients were divided into two groups based on their DEXA T-score: those with a T-score lower than or equal -2.5 were classified as Osteoporotic, and those with a T-score higher than -2.5 were classified as non-Osteoporotic. The model developed in this study demonstrates an accuracy value up to 74% as demonstration of the potential Neural Network-based models for the classification of Osteoporotic patients. However, these results are preliminary and require much larger datasets in order to be refined.

Keywords: Osteoporosis diagnosis - Lumbar spine - Neural Network - Ultrasound imaging - Automatic segmentation

I. Introduction

Osteoporosis is a widely prevalent bone disorder characterized by a decline in bone mineral density (BMD) and a degradation of the bone's inner microarchitecture, resulting in increased fragility and a higher risk of fracture [1]. With significant societal and medical costs, osteoporotic fractures are projected to affect nearly 7 million individuals in the European Union alone by 2040 [2]. Spinal and femoral fractures are the most common and debilitating types of osteoporotic fractures, often causing a significant reduction in the affected individuals' quality of life due to high rates of morbidity and mortality [3]; it is estimated that 200 million women worldwide suffer from osteoporosis [4],[5], with 40% of those cases occurring in Europe, United States, and Japan [6]. Unfortunately, many of these cases are undiagnosed due to the lack of accurate diagnostic tools [4]. With the projected increase in the prevalence of osteoporosis, it is imperative to develop more reliable and effective diagnostic and management methods for this disease. In this context, innovative tools for more reliable diagnosis of osteoporosis and more accurate identification of frail patients are needed, promoting public health measures and reducing the consequences of the disease in every aspect. The World Health Organization (WHO) defines osteoporosis as a decrease in BMD of 2.5 standard deviations or more at the lumbar spine or femoral neck compared to young adult reference populations [7]. Currently, dual energy X-ray absorptiometry (DEXA) is the reference method for BMD assessment and osteoporosis diagnosis [8]-[10]. Nonetheless, important intrinsic limitations have been identified for DEXA technology, which hinder its employment for screening purposes [11]. Quantitative ultrasound (QUS) method and others, such as Radiofrequency Echographic Multi Spectrometry (REMS), have been developed and clinically validated as a way to directly investigate the mechanical properties of bone tissue [12]-[18]. Ultrasound (US) waves are naturally suitable for the assessment of the mechanical properties of human tissues, and US devices are typically associated with several advantages such as: absence of ionizing radiation, low cost, small device size, wide accessibility not associated however to DEXA scan [19],[20]. The primary objective of the present research is to explore the correlation between ultrasound signal features and the bone mineral density (BMD) of the human lumbar vertebrae, as measured by Dual-energy X-ray absorptiometry (DEXA), with the aim of creating a Neural Network-based classifier for the diagnosis of osteoporosis. Neural Networks, specifically feed-forward neural networks (FFNNs), are a powerful subset of Artificial Intelligence that enable machines to emulate human cognitive functions. The aim of this study is to develop a diagnostic tool that can accurately classify patients as either osteoporotic or non-osteoporotic with a high degree of accuracy, sensitivity and specificity, investigating the relationships between ultrasound signal features and human lumbar vertebral BMD, as determined by DEXA, in order to implement a Neural Network-based classifier for the diagnosis of osteoporosis. Neural Networks, specifically feed-forward neural networks (FFNNs), are a branch of artificial intelligence that allows

machines to perform human-like cognitive functions. In this study, the FFNNs are implemented as the architecture where information flows in a single direction, from input to output, through layers of interconnected neurons.

The FFNN comprises an input layer one or more hidden layers, and an output layer. Each layer is made up of a set of interconnected "neurons" that process and transmit information to the next layer. In this architecture, the input is passed through the layer of the network and is transformed into the output through a series of linear and non-linear transformations. Through a process of supervised learning, FFNN can be trained to recognize patterns in data, making them a powerful tool for tasks such as classification and prediction. Some examples of machine learning techniques for osteoporosis diagnosis have been already reported in literature[22-23], but none of them has employed ultrasound data derived from vertebral scans. Therefore, the final goal is to develop a diagnostic tool that can accurately classify patients as either osteoporotic or non-osteoporotic with a high degree of accuracy, sensitivity and specificity.

II. Materials and methods

A cohort of 375 Caucasian female patients between the ages of 50 and 80 years (mean age of 60.5±3.0 years) with varying body mass index (BMI) levels (mean of 25.8±4.6 kg/m^2) underwent both DEXA and echographic scans. The acquired data were thoroughly reviewed for scan quality by Echolight Clinical Specialists, who are expert in acquisition control. Only high-quality data were used for the analysis.

In order to assess the osteoporosis status of lumbar spine, echographic scans were performed starting on the L1 vertebra and ending on the L4, with the ultrasound probe held as close and parallel as possible to the sagittal plane on the patient's abdomen. Due to variations in tissue characteristics among patients, the position of the vertebral interface could not be predicted without analyzing the specific ultrasound image.

The ultrasound device used in the study was an EchoStation system developed by Echolight Spa, a clinically-available device used for osteoporosis diagnosis at the axial sites that allows the simultaneous acquisition of both the conventional B-mode echographic images and the corresponding raw RF signals using a central working frequency of 3.5 MHz. The RF signals acquired are sampled with a rate of 40 MHz and a resolution of 16 bits. They are organized into RF frames, each consisting of 253 scan lines. Each scan on the lumbar site requires 80 seconds, corresponding to the acquisition of 100 RF frames (25 per vertebra). The raw data obtained from the scans are segmented using a proprietary algorithm [21], which extracts the Region of Interest (ROI) of the vertebral profile from each RF frame. For each frame, the RF signals are filtered using a band-pass Finite Impulse Response (FIR) filter with a cutoff frequency of 1.0 MHz and 2.5 MHz, respectively. The signal is then converted to its absolute value, filtered with a low-pass FIR with a cutoff frequency of 100 KHz, enveloped and offset to smooth out the top and bottom portions of the image. The image was then processed using luminosity masks, contrast optimization and a 2D Gaussian blurring filter before thresholding to obtain the vertebral profile. The ROI was extracted and represents an RF signal matrix with dimensions of NxM, where M is the number of scanning lines considered in the ROI and N is determined by the signal's information content.

A set of features, were extracted from the signal contained in the ROI. Specifically, the features, extracted from time domain and frequency domain, are computed for each scan lines. After that, in order to obtain a unique value, the mean value for the specific feature is evaluated. This process was repeated for each valid frame (where the vertebral profile is extracted) and the extracted features were previously selected using the "*relief*" method to focus on relevant features and minimize irrelevant and redundant ones [24].

The analysis of the acquired signal was conducted by analyzing one frame at a time, if it was segmentable. Each frame of each patient's scan was associated with a vertebra as follows: frame from 1 to 25 were associated to L1, frames 26-50 were associated to L2, frame 51- 75 were associated to L3 and the last 25 frame were associated to L4. The features that are extracted are considered both from the time domain and the frequency domain, depending on the vertebra under examinations. The group of features were used to train and test a Neural Network classifier for the diagnosis.

Feed-Forward back propagation Neural Networks, with a different number of hidden layers and different activation functions depending on the considered vertebra and based on gradient descent with momentum and adaptive learning rate were used to classify the Osteoporotic patients (labelled with "1") and the Healthy patients (labelled with "0"). Notably, the Neural Network used in the L1 and L3 vertebrae have four hidden layers with sigmoid activation functions. The Neural Network used for L2 has six hidden layers with sigmoid activation functions, and finally the Neural Network used for the last vertebra, L4, has three hidden layers with sigmoid and linear activation functions. The number of features used as input for the neural network varied depending on the vertebrae under examination. Specifically, for the first three lumbar vertebrae (L1, L2, and L3), a total of 20 features were utilized. For the last lumbar vertebra (L4), a total of 10 features were utilized as input for the neural network. To train the Neural Network, the data is partitioned into three groups: 40% for the training set, 30% for the validation set, and 30% for the test set. The amount of data used in each set also varied depending on the specific vertebra being studied. For the L1 vertebra, the neural network model was trained using 111 data, validated using 84 data, and tested using 83 data. For the L2 vertebra, the neural network model was trained using 150 data, validated using 113 data and tested using 112 data. For the L3 vertebra, the neural network model was trained using 145 data, validated using 109 data and tested using 109 data. Finally, for the L4 vertebra, the neural

network model was trained using 122 data, validated using 92 data and tested using 92 data. This distribution of data was implemented with the goal of achieving a balanced proportion of healthy and osteoporotic patients in the data sets for each vertebra, in order to prevent the neural network from becoming skewed towards one class. Moreover, for each patient, the class to which they belong is identified as the average by default of the classification of the individual vertebrae. Specifically, a patient is considered to be osteoporotic if the model classifies at least half of the segmented vertebrae as class "1". The entire workflow can be summarized as follows:

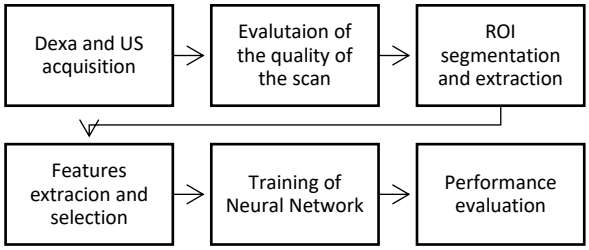


Figure I Flow-chart

In order to assess the efficiency of the implemented model, the following diagnostic parameters were considered:

- $\text{Accuracy} = \frac{TP+TN}{TP+TN+FP+FN}$;
- $\text{Sensitivity} = \frac{TP}{TP+FN}$;
- $\text{Specificity} = \frac{TN}{TN+FP}$;
- $\text{Positive Predictive Value} = \frac{TP}{TP+FP}$;
- $\text{Negative Predictive Value} = \frac{TN}{TN+FN}$;
- Area Under Curve.

In the above formulas: TP, TN, FP and FN indicate respectively the True Positive Class, the True Negative class, the False Positive Class and the False Negative Class.

III. Results and discussion

The study's key findings are summarized in Table I, which illustrates the performance of the classifier on the test set. On a test set of 83 patients, 41 of whom were osteoporotic, the classifier achieved a sensitivity of 62%, specificity of 77% and accuracy of 74%. These results demonstrate the classifier's ability to correctly identify positive and negative case.

Group	Patient	Sensitivity	Specificity	Accuracy
Test	83	62%	77%	74%

Table I Classification performance class accuracy

ROC curve (Figure II) has been plotted to further highlight the classifier's performance. The area under the curve (AUC) of the ROC is 0.70, which indicates the classifier's overall capability in distinguishing between the two classes.

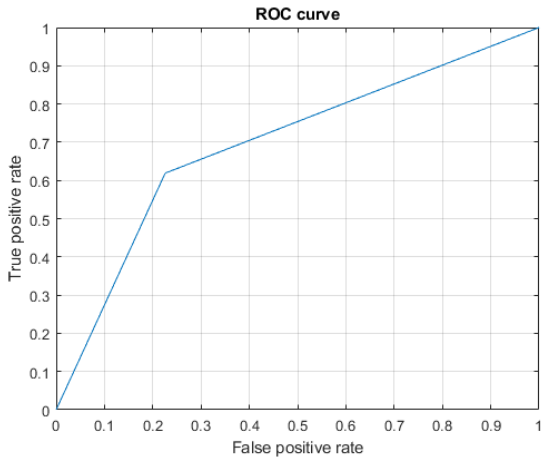


Figure II ROC curve

Finally, the Positive Predictive Value (PPV) and Negative Predictive Value (NPV) turned to be respectively 48% and 86%.

IV. Conclusion

This study utilizes a set of features extracted from in-vivo echographic scans of the lumbar spine to train a neural network-based classifier. The goal is to achieve a high level of accuracy in identifying osteoporotic patients. The trained classifier demonstrated an accuracy of 74% on the test set, with an AUC of 0.70, indicating a good performance of the classifier in distinguishing between osteoporotic and non-osteoporotic patients.

A potential next step for this study could be to expand the dataset with the aim of creating a classifier that has more robust performance. Furthermore, the extension of the dataset will make it possible to extend the age limits thus classifying more patients. Finally, it would be interesting to use other machine learning techniques in future studies.

V. References

[1] Bernabei, R., Martone, A. M., Ortolani, E., Landi, F., & Marzetti, E. (2014). Screening, diagnosis and treatment of osteoporosis: A brief review. Clinical Cases in Mineral and Bone Metabolism, 11, 201–207.

[2] Odén, A., McCloskey, E. V., Kanis, J. A., Harvey, N. C., & Johansson, H. (2015). Burden of high fracture probability worldwide: Secular increases 2010-2040. Osteoporosis International, 26(9), 2243–2248. https:/ /doi.org/10.1007/s00198-015-3154-6

[3] Albanese, C. V., De Terlizzi, F., & Passariello, R. (2011). Quantitative ultrasound of the phalanges and DXA of the lumbar spine and proximal femur in evaluating the risk of osteoporotic vertebral fracture in postmenopausal women. La Radiologia Medica, 116, 92– 101. https://doi.org/10.1007/s11547-010-0577-1

[4] Pisani, P., Renna, M. D., Conversano, F., Casciaro, E., Muratore, M., Quarta, E., et al. (2013). Screening and early diagnosis of osteoporosis through X-ray and ultrasound-based techniques. World Journal of Radiology, 5, 398– 410. https://doi.org/10.4329/wjr.v5.i11.398

[5] Kanis, J. A., & on behalf of the World Health Organisation Scientific Group. (2007). Assessment of osteoporosis at the primary health care level. WHO Collaborating Centre for Metabolic Bone Diseases, University of Sheffield. Kanis, J. A., Com

[6] World Health Organization. (1994). Assessment of fracture risk and its application to screening for postmenopausal osteoporosis. Report of a WHO Study Group. World Health Organization Technical Report Series, 843, 1–129.

[7] Genant, H. K., Cooper, C., Poor, G., Reid, I., Ehrlich, G., Kanis, J., et al. (1999). Interim report and recommendations of the World Health Organization task force for osteoporosis. Osteoporosis International, 10, 259–264. https://doi.org/10.1007/s001980050224

[8] Baim, S., & Leslie, W. D. (2012). Assessment of fracture risk. Current Osteoporosis Reports, 10, 28–41. https:// doi.org/10.1007/s11914-011-0093-9

[9] Link, T. M. (2012). Osteoporosis imaging: State of the art and advanced imaging. Radiology, 263, 3–17. https:// doi.org/10.1148/radiol.12110462

[10] Schnitzer, T. J., Wysocki, N., Barkema, D., Griffith, J., Lent, V., Romba, M., et al. (2012). Calcaneal quantitative ultrasound compared with hip and femoral neck dual-energy X-ray absorptiometry in people with a spinal cord injury. PM&R, 4, 748–755. https://doi.org/ 10.1016/j.pmrj.2012.05.011

[11] Casciaro, S., Conversano, F., Pisani, P., & Muratore, M. (2015). New perspectives in echographic diagnosis of osteoporosis on hip and spine. Clinical Cases in Mineral and Bone Metabolism, 12(2), 142–150. https:// doi.org/10.11138/ccmbm/2015.12.2.142

[12] Bréban, S., Padilla, F., Fujisawa, Y., Mano, I., Matsukawa, M., Benhamou, C. L., et al. (2010). Trabecular and cortical bone separately assessed at radius with a new ultrasound device in a young adult population with various physical activities. Bone, 46, 1620–1625. https:/ /doi.org/10.1016/j.bone.2010.03.005

[13] Nayak, S., Olkin, I., Liu, H., Grabe, M., Gould, M. K., Allen, I. E., et al. (2006). Meta-analysis: Accuracy of quantitative ultrasound for identifying patients with osteoporosis. Annals of Internal Medicine, 144, 832–841. https://doi.org/10.7326/0003-4819-144- 11-200606060-00009

[14] Paggiosi, M. A., Barkmann, R., Glüer, C. C., Roux, C., Reid, D. M., Felsenberg, D., et al. (2012). A European multicenter comparison of quantitative ultrasound measurements variables: The OPUS study. Osteoporosis International, 23, 2815–2828. https://doi.org/10.1007/ s00198-012-1912-2

[15] Pais, R., Campean, R., Simon, S. P., Bolosiu, C., Muntean, L., Bolosiu, H., et al. (2010). Accuracy of quantitative ultrasound parameters in the diagnosis of osteoporosis. Central European Journal of Medicine, 5, 478–485. https://doi.org/10.2478/s11536-009-0076-8

[16] Trimpou, P., Bosaeus, I., Bengtsson, B. A., & LandinWilhelmsen, K. (2010). High correlation between quantitative ultrasound and DXA during 7 y of follow-up. European Journal of Radiology, 73, 360–364. https:// doi.org/10.1016/j.ejrad.2008.11.024

[17] Conversano, F., Franchini, R., Greco, A., Soloperto, G., Chiriacò, F., Casciaro, E., et al. (2015). A novel ultrasound methodology for estimating spine mineral density. Ultrasound in Medicine & Biology, 41, 281–300. https://doi.org/10.1016/j.ultrasmedbio.2014.08.017

[18] Di Paola, M., Gatti, D., Viapiana, O., Cianferotti, L., Cavalli, L., Caffarelli, C., et al. (2019). Radiofrequency echographic multispectrometry compared with dual Xray absorptiometry for osteoporosis diagnosis on lumbar spine and femoral neck. Osteoporosis International, 30(2), 391–402. https://doi.org/10.1007/s00198- 018-4686-3

[19] Raum, K., Grimal, Q., Varga, P., Barkmann, R., Glüer, C. C., & Laugier, P. (2014). Ultrasound to assess bone quality. Current Osteoporosis Reports, 12, 154–162. https://doi.org/10.1007/s11914-014-0205-4

[20] Diez-Perez, A., Brandi, M. L., Al-Daghri, N., Branco, J. C., Bruyère, O., Cavalli, L., et al. (2019). Radiofrequency echographic multi-spectrometry for the in-vivo assessment of bone strength: State of the art-outcomes of an expert consensus meeting organized by the European Society for Clinical and Economic Aspects of Osteoporosis, Osteoarthritis and Musculoskeletal Diseases (ESCEO). Aging Clinical and Experimental Research, 31(10), 1375–1389. https://doi.org/10.1007/ s40520-019-01294-4

[21] M. Aventaggiato, F. Conversano, E. Casciaro, R. Franchini, A. Lay-Ekuakille, M. Muratore, and S. Casciaro (2014). Automatic segmentation of vertebral interfaces in echographic images. 3 rd Imeko TC13 Symposium on Measurements in Biology and Medicine “New Frontiers in Biomedical Measurements”

[22] Zhiwei Chen et al., Osteoprosisi Diagnosis Based On Ultrasound Radio Frequency Signal Via Multi-Channel Convolutional Neural Network (2021), doi: 10.1109/EMBC46164.2021.9629546

[23] Shilpi Ruchi Kerketta and Debalina Ghosh, Detection of Onset and Progression of Osteoporosis Using Machine Learning (2021), doi: https://doi.org/10.1002/9781119792611.ch9

[24] Urbanowicz, R.J., Meeker, M., Cava, W.L., Olson, R.S., Moore, J.H., Relief-Based Feature Selection: Introduction and Review, Journal of Biomedical Informatics (2018), doi: https://doi.org/10.1016/j.jbi. 2018.07.014

Cardiotocography in antenatal fetal monitoring of diabetes-complicated pregnancies

G. Steyde[1], E. Spairani[1,2], B. Daniele[1], G. Magenes[2], M. G. Signorini[1]
[1] *Department of Electronics, Information and Bioengineering (DEIB), Politecnico di Milano, Milan, Italy*
[2] *Department of Electrical, Computer and Biomedical Engineering, University of Pavia, Pavia, Italy*

***Abstract*— Reliable assessment of fetal health in pregnancies complicated by maternal diabetes is still challenging, but fundamental to reduce risks. Cardiotocography (CTG) is the most common tool in electronic fetal monitoring, but its utility in the management of diabetes-complicated pregnancies is still debated. Here we present some preliminary findings of a study aimed towards better defining the role of CTG in the management of pregnancies complicated by maternal diabetes by investigating the relation of CTG parameters with glycemic levels and pregnancy outcomes. A comprehensive set of standard and non-standard parameters was computed from the CTG traces collected at multiple gestational ages of 61 women with gestational diabetes, 25 with pregestational diabetes and 66 controls and related to pregnancy outcome and glucose levels. We identified an increase in the relative spectral power in the MF band and in the ternary Lempel Ziv Complexity in the diabetes-complicated pregnancies, as well as a week negative association between glucose level and signal variability. Associations with pregnancy outcomes are weak and call for further investigation.**

***Keywords*—Cardiotocography, Diabetes, Fetal Monitoring.**

I. INTRODUCTION

Diabetes Mellitus is one of the most common conditions in pregnancy and is known to increase risks for both the mother and fetus. It can be divided into Pregestational diabetes (PGDM) (i.e., diabetes of type 1 and type 2) and Gestational diabetes (GDM), a transient and generally milder form of diabetes that develops during pregnancy. The risks, which primarily depend on the level of glycemic control, include excessive fetal weight (LGA) and fetal hypoxia [1] [2].

To minimize the risk of adverse outcomes, various forms of antenatal fetal surveillance are usually recommended for pregnant women affected by PGDM and GDM with poor glycemic control [3][4]. The main goal is to reduce stillbirth, primarily by helping the clinicians identify as early as possible catastrophic events and informing for the optimal time of delivery. However, reliable assessment of the health of the fetus in diabetes-complicated pregnancies is still challenging. Ultrasonography is a useful tool but provides only anatomical information and cannot consistently diagnose macrosomia [3]; and doppler velocimetry does not appear to be a good predictor of adverse outcomes [5]. The most frequently used form of electronic fetal monitoring in diabetes-complicated pregnancies is Cardiotocography (CTG) [3], which consists of the simultaneous acquisition of the fetal heartbeats, uterine contractions, and fetal movements. In clinical practice, CTG tracings are classified as “reassuring” or “non-reassuring” based on signal characteristics such as the presence of accelerations and episodes of high variability [6], either by visual inspection or using computerized systems [7]. Despite its popularity, its utility is disputed [8]. One reason is that while reassuring CTG tracings can be reliably used to rule-out fetal compromise, especially when caused by hypoxia, the examination has low positive predictive value [3], [8]. In the work presented in [9], we used a large database of CTG recordings to investigate the impact of GDM on an extensive set of standard and non-standard parameters and we identified significant differences which we believe are indicative of variations in the autonomic control of the fetal heart rate (FHR) that are usually overlooked in standard analysis of CTG traces. However, we did not have information about the pregnancy outcome or the level of glycemic control. Here, we present preliminary results from a prospective observational study aimed at better defining the role of these non-standard CTG parameters in monitoring diabetes-complicated pregnancies. In particular, we investigated their variation in the diabetic population with respect to controls and their relation with glycemic levels and the pregnancy outcome.

II. METHODS

A total of 152 pregnant women were enrolled at Federico II University Hospital, Naples, Italy. 25 women had a diagnosis of diabetes that predated pregnancy and 61 were diagnosed with gestational diabetes following a 1-step glucose tolerance test. The remaining 66 women are healthy controls. All participants read and signed an informed consent for participation in the study.

Participants were subject to multiple CTG examinations at different stages of pregnancy. A total of 744 recordings distributed as depicted in Fig 1 was obtained. The recordings include: the FHR and a signal quality index, the uterine contraction signal, and the fetal movements series (FM), which is set to 1 when the mother presses a button to indicate a perceived movement and 0 when she does not. For each recording we consider here only the first 20 minutes, which is the minimum length available for all the recordings.

The fasting glucose levels were measured for all subjects during routine blood test performed at the third trimester.

We retrospectively divided the diabetic population into two groups on the basis of data at delivery. Group 1 includes pregnancies with good outcomes (i.e., no admission in neonatal intensive care units, Apgar scores at 1 and 5 minutes higher than 7, weight below the 90th percentile for gestational age) while Group 2 includes all pregnancies that did not respect at least one of the aforementioned criteria.

The purpose of the analysis is three-fold. Firstly, we tested for variations in CTG parameters between the three groups defined before the CTG examination (Controls, GDM and PGDM). Secondly, we tested for variations between two

groups retrospectively defined on the basis of data at delivery to assess the usability of CTG parameters as predictors of pregnancy outcomes. Lastly, we looked for relations between CTG parameters and glucose levels.

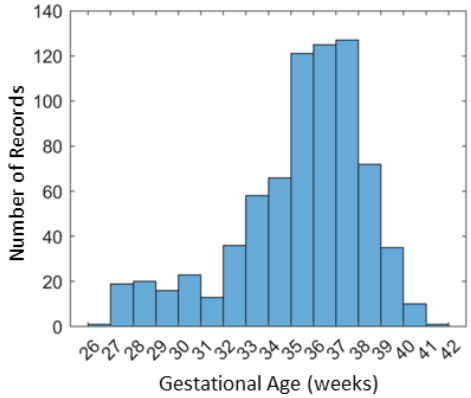


Fig 1. Distribution of CTG recordings by gestational age

A. *Feature computation*

For each recording, we identified the baseline, accelerations, and decelerations using the Mantel algorithm [10]. We then selected and computed a set of parameters belonging to different domains on the basis of the results obtained in [9]. The mean of the FHR baseline (MeanFHR), the number of accelerations per hour (#Acc) and the Short Term Variation (STV) [11] were chosen because they are widely used in clinical settings. We also included the Sample Entropy (SampEn), which was computed using x = 1, m = 0.1 and r = 1, and the ternary Lempel-Ziv complexity (LZ3), which was computed as explained in [12]. Both these features quantify the signal complexity. We then applied the Phase Rectified Signal Averaging (PRSA) technique [13] setting L=40, T=1 and s=2 and computed the Deceleration Reserve (DR) [14]. The continuous wavelet transform was applied at the centre of the signal obtained from the application of the PRSA and used to evaluate its power in Low Frequency (0.03-0.15Hz), Movement frequency (0.15–0.5Hz) and High Frequency (0.5-1Hz) ranges. We then normalized their values by the total power of the PRSA signal. More details on this procedure and its advantage over classical spectral analysis can be found in [13].

B. *Statistical analysis*

To address the dependency on the gestational age (G.A.) of the CTG parameters we divided the recordings into 3 groups: weeks 34 to 35, 36 to 37 and 38 to delivery. We excluded recordings from weeks prior to 34 due to the small sample size (in particular in the control group, that have no indication to undergo a CTG examination at this G.A.). Within each window, we employed the Mann-Whitney U-test to evaluate differences in median values of each feature among the considered populations. To ensure the independence of the samples inside each window, for the subjects who had multiple recordings we considered the median value of each feature.

When testing for differences between Group 1 and Group 2, we did not consider the group of weeks from 38 to delivery because caesarean sections before that G.A. were performed in several high-risk pregnancies.

To identify relations between CTG parameters and blood glucose levels we computed the Spearman's rank correlation between each CTG feature obtained at 36-37 weeks of gestation (one value per subject) and the blood glucose level.

Results are considered significant if p-value < 0.05.

III. RESULTS

The glucose levels in Controls, GDMs and PGDMs are reported in Fig 2. Unsurprisingly, the diabetic populations have higher blood glucose levels ($p<0.01$ for all comparisons). It is worth noticing however that, with the exception of a small number of cases in PGDMs, the values are good or excellent and there is a substantial overlap between Controls and GDMs, probably due to the success in diet control.

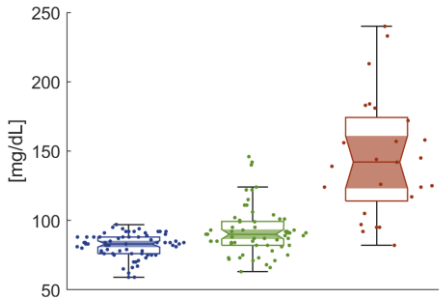


Fig 2: Blood glucose concentrations at the third trimester in Controls (blue), GDMs (green) and PGDMs (red).

The distribution of the features in the three populations discussed and significant variations are reported in Fig 3.

Regarding the comparison between physiological and GDM-complicated pregnancies, the results of this study largely align with the findings reported in [9].

Specifically, an increase in relative power in the MF band (even though here we considered the value obtained after the application of the PRSA and in [9] we employed classical spectral analysis) and an increase in ternary Lempel Ziv complexity. However, we were unable to replicate the results concerning the DR. Despite the difference in blood glucose levels reported in Fig 2 and the higher incidence of unfavourable outcomes in PGDMs (which is reported in Table I) we did not identify significant differences between GDM and PGDM in terms of CTG parameters.

TABLE I SIZE OF SELECTED GROUPS

	Group1	Group2
GDM	43	18
PGDM	12	13

Number of diabetic subjects divided per diagnosis and pregnancy outcomes as explained in Section II.

Fig 4 reports the comparisons between Group 1 and Group 2. The mean FHR, STV and the distribution of power in the PRSA spectrum varied significantly between pregnancies complicated by diabetes that had favourable and not favourable pregnancy outcomes. Concerning the last two features, the directions of the significances are the opposite of what we expected: diabetic pregnancies with unfavourable pregnancy outcomes had values more like those of the healthy controls.

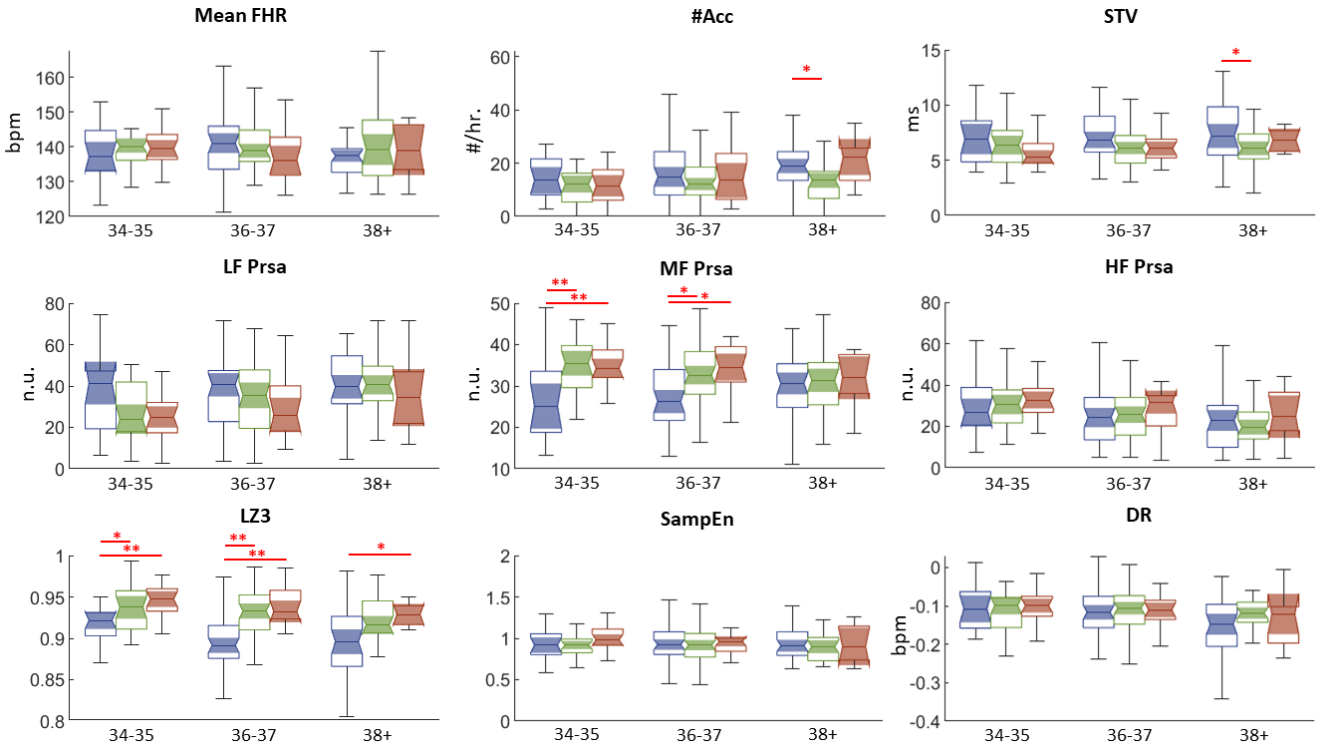


Fig 3: Boxplots are color coded: Controls in blue, GDM in green and Pregestational diabetes in red. Significances are represented with red lines. * indicates p<0.05 and ** p<0.01

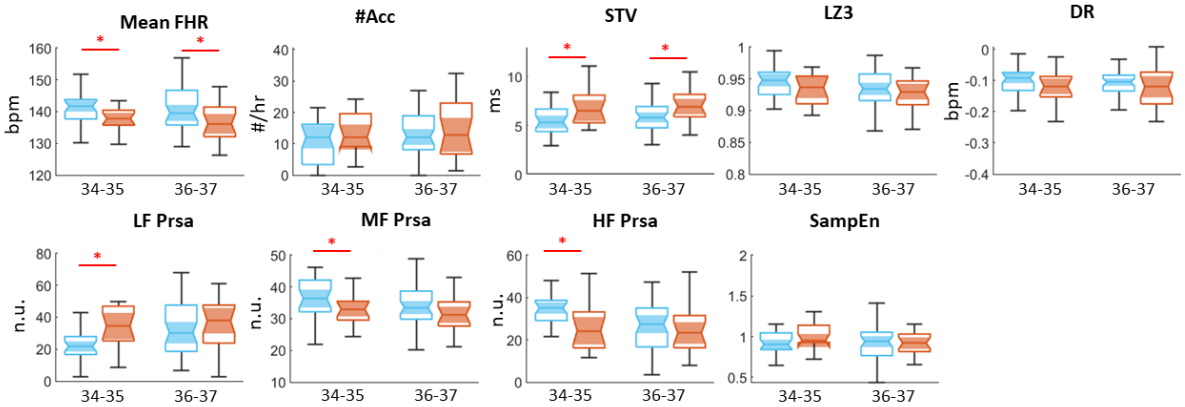


Fig 4: Group 1 (unfavourable pregnancy outcome) is in red and Group 2 is in blue.

TABLE 1I CORRELATIONS BETWEEN CTG PARAMETERS AND GLUCOSE

	r	p-value
MeanFHR	-0.09	0.316
#Acc	-0.20	0.032
STV	-0.26	0.005
SampEn	0.11	0.247
LZ3	0.27	0.003
DR	0.22	0.022
LF Prsa	-0.28	0.002
MF Prsa	0.19	0.039
HF Prsa	0.24	0.008

Spearman's rank correlations between fasting maternal blood glucose levels and CTG parameters

Regarding the relation with fasting glucose levels (measured during routine exam, and not at the time of the CTG examination) we found some significant results, even though the correlation coefficients are small or very small. Results are reported in Table II. Maternal glucose levels are associated with reduced variability of the FHR (lower STV and number of accelerations per hour) especially in the LF band, which is associated to a relative increase in the power in HF. These results are consistent with values found in adults [15], suggesting that maternal hyperglycemia is transferred to the fetus and has an impact on the FHR series at least to some extent comparable to the effect it has on adults.

IV. DISCUSSION

Research on CTG has been focused primarily on the identification of fetal hypoxemia and intra-uterine growth restriction, while its role in the management of pregnancies complicated by maternal diabetes, despite being very common in clinical practice, is still less clear. Traditional parameters appear to have little value in this application, while more interesting results have been obtained in the frequency domain and with non-linear analysis.

The results obtained in the comparison of CTG parameters between pregnancies with good and unfavourable pregnancy outcomes in the diabetic population are unexpected and require further research for proper interpretation. Specifically, a reduction in STV is usually considered a sign of fetal distress, but we observed higher values in pregnancies with unfavourable pregnancy outcomes. It should be noted, however, that most of the cases of bad outcomes were due to LGA and not hypoxemia, which is arguably the most common cause of fetal distress and is known to reduce STV [7]. We acknowledge as a limitation to the present study that we did not differentiate between pregestational diabetes of type 1 and type 2 and between subjects undergoing or not insulin therapy.

We believe it would be an interesting future development to add these distinctions, as well as dividing the causes of bad pregnancy outcomes. This is a goal for which, however, a larger population sample is necessary. The association between CTG parameters and maternal blood glucose levels also warrants further research, as we believe it could help towards a better understanding of fetal physiology in conditions of chronic hyperglycemia.

ACKNOWLEDGEMENT

The authors are grateful to Dr S. Tagliaferri from Federico II University, Naples, Italy for the collection of the data and his continuous support during the study. The work was carried out with the support of the MIUR PRIN Project Call 2017 “ICT4MOMs” 2017RR5EW3.

REFERENCES

[1] N. M. Ivers et al., “Diabetes and Pregnancy,” Canadian Family Physician, vol. 65, no. 1, pp. 255–282, 2019, doi: https://doi.org/10.1016/j.jcjd.2017.10.038.

[2] A. Caughey and M. Turrentine, “ACOG Practice Bulletin: Gestational Diabetes Mellitus,” Obstetrics and gynecology, vol. 130, no. 1, pp. e17–e31, 2017, doi: https://doi.org/10.1097/AOG.0000000000002501.

[3] C. R. Graves, “Antepartum Fetal Surveillance and Timing of Delivery in the Pregnancy Complicated by Diabetes Mellitus,” Clin Obstet Gynecol, vol. 50, no. 4, pp. 1007–1013, 2007, doi: 10.1097/GRF.0b013e31815a63cc.

[4] International Federation of Gynecology and Obstetric (FIGO), “Initiative on Gestational Diabetes Mellitus: A Pragmatic Guide for Diagnosis, Management, and Care,” 2015. doi: 10.1016/j.solidstatesciences.2005.08.010.

[5] S. F. Wong, F. Y. Chan, R. B. Cincotta, D. H. Mc Intyre, and M. Stone, “Use of umbilical artery Doppler velocimetry in the monitoring of pregnancy in women with pre-existing diabetes,” Australian and New Zealand Journal of Obstetrics and Gynaecology, vol. 43, pp. 302–306, 2003, doi: https://doi.org/10.1046/j.0004-8666.2003.00094.x.

[6] Fondazione Confalonieri Ragonese, “Raccomandazioni sulla cardiotocografia ante partum,” 2021.

[7] J. Pardey, M. Moulden, and C. W. G. Redman, “A computer system for the numerical analysis of nonstress tests,” Am J Obstet Gynecol, vol. 186, no. 5, pp. 1095–1103, 2002, doi: 10.1067/mob.2002.122447.

[8] R. M. Grivell, Z. Alfirevic, G. M. L. Gyte, and D. Devane, “Antenatal cardiotocography for fetal assessment,” Cochrane Database of Systematic Reviews, vol. 2015, no. 9, pp. 1–39, 2015, doi: 10.1002/14651858.CD007863.pub4.

[9] G. Steyde, B. Daniele, E. Spairani, G. Magenes, and M. G. Signorini, “Influence of Gestational Diabetes on Fetal Heart Rate in antepartum Cardiotocographic Recordings,” in Computing in Cardiology , 2022.

[10] R. Mantel, H. P. van Geijn, F. J. M. Caron, J. M. Swartjes, E. E. van Woerden, and H. W. Jongsma, “Computer Analysis of Antepartum fetal heart rate,” Int J Biomed Comput, vol. 25, no. 4, pp. 261–286, 1990, doi: 10.1016/0020-7101(90)90031-o.

[11] D. Arduini, G. Rizzo, and C. Romanini, “Computerized Analysis of Fetal Heart Rate,” J Perinat Med, vol. 22, no. Suppl.1, pp. 22–27, 1994, doi: 10.1515/jpme.1994.22.s1.22.

[12] M. Ferrario, S. Maria G, and G. Magenes, “Complexity analysis of the fetal heart rate variability: early identification of severe intrauterine growth-restricted fetuses,” Med Biol Eng Comput, vol. 47, pp. 911–919, 2009, doi: 10.1007/s11517-009-0502-8.

[13] A. Bauer et al., “Phase-rectified signal averaging detects quasi-periodicities in non-stationary data,” Physica A: Statistical Mechanics and its Applications, vol. 364, pp. 423–434, 2006, doi: 10.1016/j.physa.2005.08.080.

[14] M. W. Rivolta, T. Stampalija, M. G. Frasch, and R. Sassi, “Theoretical Value of Deceleration Capacity Points to Deceleration Reserve of Fetal Heart Rate,” IEEE Trans Biomed Eng, vol. 67, no. 4, pp. 1176–1185, 2020, doi: 10.1109/TBME.2019.2932808.

[15] J. P. Singh et al., “Association of Hyperglycemia With Reduced Heart Rate Variability (The Framingham Heart Study)”, doi: 10.1016/s0002-9149(00)00920-6.

Control Theory Measures for Dynamic Analyses of Human Functional Connectome Data

S. Papallo[1], E. Riccio[2], A.P. De Rosa[1], M. Cirillo[1], F. Amato[2], M. Sansone[2] and F. Esposito[1]
[1]Department of Advanced Medical and Surgical Sciences, University of Campania "Luigi Vanvitelli", Napoli, Italy
[2]Department of Electrical Engineering and Information Technology, University of Naples "Federico II", Napoli, Italy

Abstract — Control theory represents a new frontier in the study of the human connectome as it offers the possibility of introducing new explainable features with the potential of binding neural connectivity to its pathological alterations. Starting from resting-state functional MRI (rs-fMRI) data sets, we estimate the functional connectivity for a given brain parcellation, thus deriving the system matrix that can be studied with network control theory. We assess the energy efficiency of large-scale brain network dynamic reconfigurations occurring at rest as well as the extent to which the transitions between and across distinct dynamic states are not just random but preferentially follow energetically efficient trajectories. In addition, we derive novel dynamic features of system controllability, distinguishing between average and modal controllability. The application of these concepts is illustrated on real rs-fMRI data sets acquired in four adult subjects, highlighting the range of variability of these features, in relation to the analysis settings, and discussing their potentials for possible use in future studies.

Keywords—Neuroimaging, Human connectome, Functional MRI, Network Control Theory.

I. INTRODUCTION

In recent decades, non-invasive neuroimaging techniques have been growing and resting-state functional MRI (rs-fMRI) has emerged as one of the most widely used techniques for investigating the functional connectivity of the human brain (human connectome) [1]. Particularly, the complex neurophysiological dynamics underlying the large-scale brain reconfiguration mechanisms can be addressed with rs-fMRI, in both healthy and disease conditions. In this work, we focus on the calculation of specific dynamic features of the human connectome that can be obtained from the analysis of rs-fMRI time series using control theory [2] and have recently gained special attention for their possible benefit in the discrimination of health and disease conditions [3]. For illustration purposes, we apply these concepts to real rs-fMRI data sets acquired in four adult subjects and discuss the outcome of this approach. We resort to Schaefer's parcellation to pinpoint regions of the human cerebral cortex that can be nominally grouped into seven large-scale brain networks [4]. In this context, and with reference to [5], we present the concepts from control theory [6] that provide the mathematical framework for this type of human connectome analysis. We first introduce the interaction matrix, which describes how the whole brain evolves as a dynamic linear system from a given (current) state to another (future) state. Then, we characterize the dynamic reconfiguration mechanism of large-scale brain networks in terms of Energy Efficiency and Average and Modal Controllability. To derive control theory measures, we contrast the parameters derived from the static functional connectivity (sFC), i.e., by evaluating the average synchronization of fMRI time series between all pairs of regions over the entire interval of observation, to those derived from the dynamic functional connectivity (dFC), i.e., by evaluating the time-varying aspects of brain dynamics across several consecutive time windows and eventually using a sliding window approach.

II. METHODS AND MATH EQUATIONS

We model the brain state transitions through the classical linear dynamical system formulation:

$$\dot{x} = A(t) \cdot x(t) + B \cdot u(t) \quad (1)$$

Where **x**(t) is a N x 1 vector representing the brain states over time (t) and space (N regions). **A**(t) is the N x N interaction matrix, which we estimate from the static or dynamic functional connectivity analysis (or FC matrices). The static functional connectivity is calculated as the Pearson correlation between all pairs of regional fMRI time-courses and is kept constant over time in the model (1). Instead, the dynamic functional connectivity is estimated by dividing the signal into M windows and then calculating the Pearson correlation for each window. **B** is the control input matrix (N x m) obtained from the identity matrix, from which we select the m columns associated with the set of control nodes (regions) into which we wish to inject inputs, whereas **u**(t) is the input energy vector over time (m x 1). The interaction matrix is obtained via the following normalization with the weighted Laplacian matrix derived from the (dynamic or static) functional connectivity matrix:

$$L_{ij}(t) = \delta_{ij}\Sigma_k |FC_{ik}(t)| - FC_{ij}(t) \quad (2)$$

$$A(t) = \frac{-L(t)}{\lambda_{max}(L(t))} \quad (3)$$

In the control analysis with a static interaction matrix, for a given initial state $\boldsymbol{x_0}$ and a given target final state $\boldsymbol{x_f}$, the optimal control energy principle allows us to calculate the static energy as:

$$E_s(x_0, x_f) = \frac{1}{2} d^T W^{-1} d \quad (4)$$

Where:

$$d = x_f - e^{A\tau_s} x_0 \quad (5)$$

is the difference between the target final state and the hypothetical final state that the system can reach without control and **W** is the so-called controllability Gramian matrix. When selecting a single node *i* as control node (i.e., $B = B_i$) the controllability matrix is obtained via the Lyapunov equation as:

$$W_i = \int_0^{+\infty} e^{At} B_i B_i^T e^{A^T t}\, dt \quad (6)$$

From the trace of this matrix, it is possible to obtain a measure of Average controllability, i.e., the input energy that is to be applied to the selected control node to drive the state transition towards all possible target states:

(7) $\psi_i = Trace\ (W_i)$

We also calculate the Modal controllability that is the ability to control each evolutionary mode of the network:

(8) $\phi_i = \sum_{j=1}^{N}(1 - \lambda_j^2(A))v_{ij}^2$

According to the definition of temporal networks [6], for the dynamic analysis, we end up with having M time windows and for each one we define an interaction matrix:

(9) $A(t) = A_K$

Thus, under optimal control conditions, we define the dynamic energy as:

(10) $E_d(x_0, x_f) = \frac{1}{2} d^T W_{dyn}^{-1} d$

Where:

(11) $d = x_f - e^{A_M \tau_M} e^{A_{M-1}\tau_{M-1}} \dots e^{A_1 \tau_1} x_0$

And:

(12) $W_{dyn} = SWS^T$

is the dynamic controllability Gramian matrix, S given by:

(13) $S = (\prod_{i=M}^{2} e^{A_i \tau_i^d}, \dots, \prod_{i=M}^{m+1} e^{A_i \tau_i^d}, I)$

III. ENERGY ANALYSIS

We first estimate the energy cost for the series of transitions across brain states as driven by the interaction matrix (see section IV for mathematical details). We achieve this by selecting each group of brain regions assigned to a large-scale network as input (control) nodes. Assuming that the instantaneous brain state is represented by the (z-scored) rs-fMRI signal at each time point and that the control signal implements an optimal control strategy [7], we estimate the energy cost in case of a constant interaction matrix (i.e., derived from sFC values) as well as in the case of a time-varying interaction matrix (i.e., derived from dFC values). We hypothesize that the extent to which a dynamically updated interaction matrix reduces the energy cost, compared to a constant interaction matrix, can provide a useful measure of energy efficiency for the system.

A. Energy Efficiency

The choice of the interaction matrix to characterize the transition between states affects the efficiency of energy expenditure. We evaluate two hypothesis about the energy efficiency of the system. First, we explore how the control time interval τs is related to the estimated control energy and then calculate a measure for the energy cost. In fact, referring to [6], we expect that the control trajectory implied by the (time-varying) dFC should be energetically more efficient in driving the systems across states, compared to the (time-constant) sFC. We applied these concepts to a data set of 100 real rs-fMRI time-series (from 100 cortical regions) representing the evolution of the system across 600 brain states during an observation time of 10 minutes (sampling frequency = 1 Hz). In our Matlab analysis, using modified code from [6], we perform 50 computer simulations where the pair of initial and target states are randomly chosen from the first 25% of the time-series and the remaining interval, and set the Default Mode and Visual network regions as control nodes. We report the values of dynamic and static energy as a function of the control time τ_s resulting from all simulations. The control time defines the interval of decay of the input energy [6] and therefore the observed temporal window between the application of the input energy to the control regions and the reach of the final state from the initial state under optimal control conditions. In Fig 1, the energy cost is reported when using either dFC or sFC for the interaction matrix and we can easily observe a substantially reduction of energetic cost between dynamic and static conditions mainly at shorter control intervals, for $\tau_s < 50\ s$, while, e.g., for $\tau_s > 100\ s$ the difference between energy values is blurred. Hence, over shorter control times, a dynamic analysis seems to better emphasize the energetic advantage of the system in evolving between two states with a time-varying interaction matrix. Along this line, we evaluated the quantity $\log\frac{E_S}{E_D}$, i.e., the logarithm of the ratio between static and dynamic energy, as a heuristic measure of energy saving when the control time ranges between 10 s and 100 s. Referring to Table I, we show how the median of this quantity is significantly above zero (signed rank test, $p<0.05$) for the default-mode network in three (out of four) subjects and for the visual network in all four subjects. This underscores that the relationship between energy saving and control times might be peculiar in brain functioning and future studies on large samples of healthy control and pathological subjects might reveal whether this approach can yield a promising candidate marker for assessing the energetic (in)efficiency of brain large-scale networks evolving between two random states during rest.

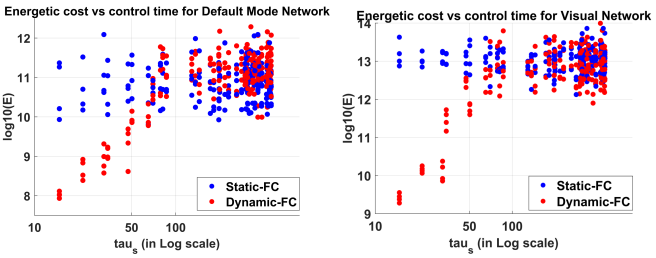


Fig. 1: Right Log of static (blue) and dynamic (red) energy estimates for all simulations (with random initial and final points) and subjects as a function of the log of the control time for default mode network as control nodes. Left: Log of static and dynamic energy estimates for all repetitions and subjects as a function of the log of the control time for visual network as control nodes.

TABLE I: EVALUATION OF THE MEDIAN OF THE LOGARITHM RATIO BETWEEN STATIC AND DYNAMIC ENERGY AT SHORTER CONTROL TIMES FOR EACH SUBJECTS IN DEFAULT MODE AND VISUAL NETS AND P VALUE WITH BONFERRONI'S CORRECTION

Subject	*Default Mode Network Median (p value)*	*Visual Net Median (p value)*
Subject 1	0.849 (2.88e-08)	0.577 (6.92e-07)
Subject 2	0.166 (2.25e-03)	0.724 (4.29e-07)
Subject 3	-0.060 (0.05)	0.486 (1.73e-06)
Subject 4	0.155 (2.40e-04)	0.451 (5.42e-06)

B. Energy Shuffle

In the previous analysis, the order of intermediate states is not taken into account. However, if we assume that a series of dynamic states is energetically more favorable, and if these transitions are effectively supported by a neurophysiologically meaningful dynamic evolution, the actual trajectory (i.e., the

exact sequence) should also be relevant. Thus, another analysis has been conducted to assess the relative energy cost corresponding to the observed order of dFC matrices compared to a randomly permuted order of dFC matrices. For this "shuffled state analysis", we perform additional 50 repetitions (with permuted orders) and evaluate the p-value of the comparison of the energy ratio $log\left(\frac{E_{shuffle}}{E_d}\right)$ against zero. Here we expected that, no matter which network (i.e., group of control regions) is set, the reconfiguration of connectivity matrices along the truly observed order of states should cost less energy to the system compared to the random reconfiguration across the same states if the brain network really followed physiologically driven state transitions, i.e., a non-random trajectory [2]. In contrast, if the median of the logarithm of the ratio between shuffled and dynamic energy results below zero, this would suggest that the brain might not have followed the most favorable trajectory of pattern reconfiguration. For example, in our analysis, we observed how a subject showed such a ratio significantly above zero for the default mode *(p=5.45e-19)* and for the visual network *(p=1.08e-29)*, but not for the limbic network *(p=0.99)*, suggesting that maybe for the limbic network energetic inefficiency exists in the dynamic transitions across brain states, at least within the selected range of control times. Thus, this parameter could yield another candidate marker of network energetic (in)efficiency that might deserve an extended investigation in future human connectome studies.

IV. CONTROLLABILITY

Controllability of the network refers to the possibility to manipulate the energy at certain nodes to drive the system along a pre-defined (desired) trajectory from an initial state to a target state. In this context, controllability could, e.g., usefully describe the mechanism of cognitive control where particular brain regions are forced (e.g., via neural stimulation) to act as drivers and facilitate the brain transitions to specific states or neural processing modes that would better support cognitive functions [7]. By again referring to control theory [6], we can distinguish between average and modal controllability, to respectively indicate an ability of the brain to reach more and less consolidated states (see section IV for mathematical details). A consolidated state would be one which is well-established from previous recurrent experiences (and therefore expected to occur very frequently during rest). In contrast, a non-consolidated state would be one which can be reached upon very specific conditions and task demands (and therefore expected to occur less frequently during rest). Thus, we first compare dFC vs. sFC derived controllability values across different time window sizes, to underscore the variable gain in terms of controllability from the dynamical observation of the fMRI time courses. Then, by using a sliding window approach, here we introduce a few novel measures from the analysis of the trends of dynamic vs. static controllability as a curve across time to better characterize the dynamic controllability of the system: the total time during which the dynamic controllability is above the static controllability, the area under this curve and the number of crossings. Finally, we report the variations of these measures in relation to the approach used for the dynamic analysis (i.e., overlapping vs. non-overlapping windows and fixed vs. variable window sizes).

A. Average Controllability

We evaluate the average controllability for a given network, i.e., the input energy needed to drive the system to a specific target state. This allows us to identify brain areas that steer the system towards easy-to-reach states, i.e., those that require shorter paths and less state transitions (e.g., to support internal thinking during resting conditions, see, e.g., [7]). For brevity, here we report the values obtained for the default-mode network as it is well known that this network connects areas that are more active when the brain goes through its baseline cognitive states (e.g., during the resting state), from which the brain transiently moves back and forth to/from a multitude of more task-oriented states [7]. As shown in Table II, dynamic average controllability is always higher than the static one for three out of four subjects. But this analysis also allows us to detect when and how the average controllability value changes, i.e., when the network is more (or less) dynamically controllable. We thus observe that reducing the window size increases the dynamic controllability and this is in line with the fact that reducing the control time has benefits in terms of energy cost, as we observed in the energy analysis. Indeed, in Table II, we can observe an increment of average controllability in all subjects at a window size of 30 s but not 60 s. A further analysis allows us to observe variations in the trends of controllability between non-overlapping and overlapping sliding window analysis (Fig 2). In the first case, each window is separated from another one, while in the second case a window slides continuously along the time course. The last option introduces more variability in the trends but also higher values of controllability. In this way, we could observe the evolution of the brain across many more controllability conditions and we could eventually be able to better control the network at specific times of high controllability.

TABLE II: COMPARISON BETWEEN VALUE OF STATIC AVERAGE CONTROLLABILITY AND DYNAMIC ONE WITH DIFFERENT WINDOW SIZE

Subject	*Static*	*Dynamic ws = 60 s*	*Dynamic ws = 30*
Subject 1	1.111	1.154	1.165
Subject 2	1.146	1.166	1.184
Subject 3	1.173	1.176	1.179
Subject 4	1.168	1.161	1.188

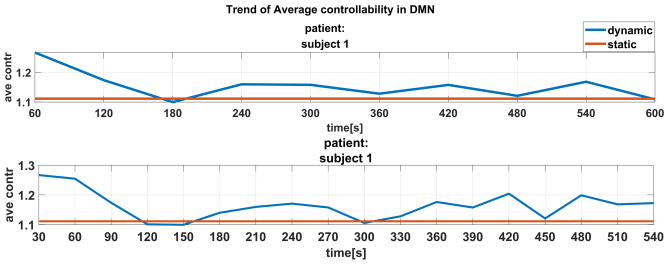


Fig. 2: On the top, dynamic average controllability trend against static average controllability value without overlapped analysis, while below we have the same trends but with overlapped analysis

Moreover, to underscore how window size affects the average controllability, we repeated the overlapping window analysis with two different window sizes (30 s and 60 s). In addition, we also evaluated the number of crossings of dynamic average controllability trends across the (constant) static value, the area under the curve and the time when the dynamic trend is above the static constant trend. As shown in Table III, the increment of controllability is strictly associated to the increment of these parameters. In particular, we can observe an increment of the number of crossings associated to more variability in the trend due to the reduction of the window size. The increment of area values can be another measure for the increment of average controllability while the increment of the time indicates that

longer time intervals would be available to control the network more efficiently. Therefore, alteration or reduction of these parameters could be yet more candidate markers of an altered mechanism of functional connectivity, e.g., due to a disease condition.

TABLE III: COMPARISON BETWEEN PARAMETERS FOR ONE SUBJECT IN CASE OF OVERLAPPED DYNAMIC AVERAGE CONTROLLABILITY IN DEFAULT MODE NETWORK BY VARYING WINDOW SIZE

Analysis	*No of Crossing*	*Area*	*Time*
Overlapping ws = 60 s	4	25.34	457 s
Overlapping ws = 30 s	11	44.33	513 s

B. Modal Controllability

Modal controllability identifies brain areas that can push the brain into states that require substantial input energy. From a cognitive perspective, it reflects the capacity of the brain to adapt to novel cognitive conditions but also to execute more complex cognitive functions, such as top-down regulation or control of mental operations in response to environmental changes or external stimuli [7], [9]. Indeed, modal controllability depends on the eigenvectors of the interaction matrix, which describes all possible dynamic modes of the system. The previous approach can be similarly applied to the modal controllability, but in this case, we report the results for the fronto-parietal network as it is known that this network functionally connect regions that are responsible for the execution of complex cognitive tasks [7], [9]. Comparing static and dynamic controllability values in Table IV, we again note, in three out of four subjects, the increase of modal controllability values in the dynamic vs. static configuration. This increment is also larger when reducing the window size. Thus, we could still suppose that the advantages of controlling specific dynamic modes of the system can be assessed using these measures.

TABLE IV: COMPARISON BETWEEN VALUE OF STATIC MODAL CONTROLLABILITY AND DYNAMIC ONE FOR FRONTO-PARIETAL NET WITH DIFFERENT WINDOW SIZE

Subject	*Static*	*Dynamic ws = 60 s*	*Dynamic ws = 30*
Subject 1	0.890	0.895	0.913
Subject 2	0.887	0.910	0.925
Subject 3	0,894	0,895	0,910
Subject 4	0,937	0,932	0,928

TABLE V: COMPARISON BETWEEN PARAMETERS FOR ONE SUBJECT IN CASE OF OVERLAPPED DYNAMIC AVERAGE CONTROLLABILITY IN FRONTO-PARIETAL NETWORK BY VARYING WINDOW SIZE

Analysis	*No of Crossing*	*Area*	*Time*
Overlapping ws = 60 s	8	-4.733	175 s
Overlapping ws = 30 s	18	4.250	364 s

Furthermore, as shown in Table V, for the overlapping window analysis, we can observe the same parameters and their increment by reducing the window size. In fact, we move from a negative area to a positive area and the time during which the dynamic behavior is favorable increases. This highlights the importance of the choice of the window size for the dynamic analysis because a negative area and a lower value of this time do not allow the possibility to control efficiently the brain regions and its dynamic modes. Overall, we have observed that modal controllability values are lower than average controllability ones, as expected, because it is easier to reach states across short paths associated with basal cognitive function rather than states across paths requiring more transitions. Anyway, higher controllability (either modal or average) indicates a better ability of the brain in reaching efficiently the target state.

V. CONCLUSION

Control Theory analysis is being presented as an innovative way to model the functional connectivity of the human brain, as it offers a new framework to investigate diseases and assess the consequence of lesions on behaviors and cognitive performances [10]. We highlighted some possible features that can become useful to describe the variability of the human functional connectome and possibly inspire new markers to address the alterations secondary to a disease, but also to open toward the design of novel paradigms of targeted external stimulation of the brain [10]. Starting from rs-fMRI data sets, we have obtained the interaction matrix in different ways in order to underscore the advantages in terms of energy and controllability when we model the brain as a temporal (dynamic) network. Through the energy analysis, we point out how the ratio of static and dynamic energetic cost could provide markers of energetic (in)efficiency of a specific brain region or network, albeit the control time appe ars to be a crucial parameter in the setting up of the control theory analysis. Then, with the analysis of average and modal controllability, we highlight some possible surrogate measures that can support an evaluation of the ability of the brain to respond to externally timed stimulations. In conclusion, we expect that further research into this kind of analysis can lead to introduce other features. Nonetheless, any of the illustrated features will require proper experimental validation to relate these candidate markers to the acquisition parameters settings. This will require the careful design of proper test-retest studies to assess the robustness of the features and proper cohort studies to address the relation with clinical features.

REFERENCES

[1] Biswal, B., Zerrin Yetkin, F., Haughton, V. M., Hyde, J. S. (1995). Functional connectivity in the motor cortex of resting human brain using echo-planar MRI. Magnetic resonance in medicine, 34(4), 537-541.

[2] Karrer, T. M., Kim, J. Z., Stiso, J., Kahn, A. E., Pasqualetti, F., Habel, U., Bassett, D. S. (2020). A practical guide to methodological considerations in the controllability of structural brain networks. Journal of neural engineering, 17(2)

[3] Xiaosong He,L. Caciagli,L. Parkes,J. Stiso,T. M. Karrer,J. Z. Kim,Zhixin Lu,T. Menara,F. Pasqualetti,et al.,Uncovering the biological basis of control energy: Structural and metabolic correlates of energy inefficiency in temporal lobe epilepsy, Science Advances, 8, 45,(2022).

[4] Schaefer A, Kong R, Gordon EM, Laumann TO, Zuo XN, Holmes AJ, Eickhoff SB, Yeo BTT. Local-Global Parcellation of the Human Cerebral Cortex from Intrinsic Functional Connectivity MRI. Cereb Cortex. 2018 Sep 1;28(9):3095-3114. doi: 10.1093/cercor/bhx179.

[5] S. Deng, J. Li, Thomas Yeo, B.T. et al. Control theory illustrates the energy efficiency in the dynamic reconfiguration of functional connectivity. Commun Biol 5, 295 (2022). doi.org/10.1038/s42003-022-03196-0. W.-K. Chen, Linear Networks and Systems (Book style). Belmont, CA: Wadsworth, 1993, pp. 123–135.

[6] Li, A., Cornelius, S. P., Liu, Y. Y., Wang, L., Barabási, A. L. (2017). The fundamental advantages of temporal networks. Science, 358(6366), 1042-1046. M. Young, The Techincal Writers Handbook. Mill Valley, CA: University Science, 1989.

[7] Gu S., Pasqualetti F., Cieslak M. et al. Controllability of structural brain networks. Nat Commun 6, 8414 (2015). doi.org/10.1038/ncomms9414

[8] Scheid, B. H., Ashourvan, A., Stiso, J., Davis, K. A., Mikhail, F., Pasqualetti, F., Bassett, D. S. (2021). Time-evolving controllability of effective connectivity networks during seizure progression. Proceedings of the National Academy of Sciences, 118(5)

[9] Barbey, A. K. (2018). Network neuroscience theory of human intelligence. Trends in cognitive sciences, 22(1), 8-20

[10] Lee MH, Smyser CD, Shimony JS. Resting-state fMRI: a review of methods and clinical applications. AJNR Am J Neuroradiol. 2013 Oct;34(10):1866-72. doi: 10.3174/ajnr.A3263.

EEG-based quantitative measures to support the clinical diagnosis of disorders of consciousness

I. Quattrociocchi[1,2], D. Mattia[2], A. Riccio[2], M. D'Ippolito[2], M. Aloisi[3], R. Formisano[3], J. Toppi[1,2]
[1] *Department of Computer, Control and Management Engineering, Sapienza University of Rome, Italy*
[2] *Neuroelectrical Imaging and Brain Computer Interface Laboratory, Fondazione Santa Lucia IRCCS, Rome, Italy*
[3] *Post-coma Unit, Fondazione Santa Lucia IRCCS, Rome, Italy*

***Abstract*—Severe acquired brain injury often leads to a disorder of consciousness (DoC) which can be classified as vegetative state (VS) or minimally consciousness state (MCS) according to its severity. The golden standard for DoC diagnosis is currently represented by the standardized Coma Recovery Scale Revised which, due to fluctuations in DoCs' vigilance, can lead up to 40% of misdiagnosis. EEG-based analyses have demonstrated promising results in DoC patients' assessment and quantitative EEG measures are candidates as a reliable instrument to support clinical diagnosis with high accuracy. Methodologies for spectral analysis and connectivity estimation were applied to EEG resting state data from 58 DoC patients clinically assessed as VS or MCS. Indices describing the global properties of the resting networks and the characteristics of power spectra resulted significantly different between the two groups of patients. The significant indices were used as features to train a classifier able to discriminate VS from MCS with performance metrics equal to 67% for accuracy and 85% for precision. These findings boost the promising role of EEG-based indices as valuable and reliable tool to support DoC clinical diagnosis.**

***Keywords*—Diagnosis, disorders of consciousness, connectivity analysis, spectral analysis.**

I. Introduction

PEOPLE who survive a severe brain injury, can suffer from disorders of consciousness (DoC), a clinical condition characterized by alteration in arousal (eye opening), and awareness (defined as the presence of nonreflexive behavior). Three main states can be included in DoC: coma, vegetative state (VS) and minimally conscious state (MCS). Coma is characterized by the total absence of both arousal and awareness, while VS patients show arousal, but they are unresponsive to external stimuli and only show reflexive behavior. MCS subjects, on the other side, demonstrate signs of awareness of themselves and the environment, but this condition is characterized by strong fluctuations [1]. The European Task Force has introduced the definition of "unresponsive wakefulness syndrome" (UWS) [2] to replace the term "vegetative state," although it has not been universally accepted [3]. For this reason, in this work we will use the double term VS/UWS for referring to that condition.

DoC classification is based on standardized neurobehavioral rating scales, among which Coma Recovery Scale Revised (CRS-R) is the most widely diffused and consists in 6 subscales evaluating auditory, visual, motor, oromotor, communication and arousal processes. Clinical scales represent the gold standard for DoC assessment. Although they represent a consistent and sensitive standard, clinical scales depend on behavioral responses, that can be affected by a multitude of factors, such as fluctuation of arousal, fatigue, pain, spasticity, to cite just few of them. Thus, the misdiagnosis rate is high and attested around 40% [4]. However, an accurate assessment is fundamental for DoC's diagnosis, prognosis and monitoring of treatment and rehabilitation effects [5].

The absence of quantitative measures for the diagnosis of DoC patients has motivated many researchers to find objective measures derived from brain signals as support for the clinical evaluation. Previous studies have performed EEG analyses of resting state acquisitions to investigate connectivity characteristics in DoC patients, but mainly using neuroimaging techniques (i.e., functional magnetic resonance imaging, fMRI). Results of this kind of studies demonstrated the correlation between the level of consciousness and the connections weight in the Default Mode Network (DMN), a circuit composed by specific brain areas active during rest condition and deactivated in attention-demanding tasks [6].

EEG shows invaluable advantages in comparison to other neuroimaging techniques, both at the theoretical and at the practical level: it allows to capture the dynamics of brain connectivity and its spectral distribution, by keeping it viable to handle severely disabled patients even with bedside testing, being therefore eligible for routine clinical application.

Previous studies have identified markers derived from a combination of connectivity estimators and graph theory able to classify MCS patients from VS/UWS and healthy subjects with an accuracy slightly above chance [7],[8].

Indeed, in this study a quantitative analysis of EEG recorded in resting condition was conducted to calculate spectral and connectivity indices that could be a reliable instrument to perform diagnosis in patients with disorders of consciousness.

II. Materials and Methods

A. Participants

The study involved 58 patients admitted at the Post-Coma Unit of Fondazione Santa Lucia of Rome and diagnosed with DoC (29 males/29 females, mean age 45±16 yr, CRS-R score: 11±5, etiology: 22 TBI, 6 anoxic, 27 vascular, 3 other). According to their CRS-R scores, 40 out of 58 patients were assessed as MCS (19 males, 21 females, mean age: 46.85±16.03 yr, CRS-R score: 14±3), while the remaining 18 were diagnosed with VS/UWS (10 males and 8 females, mean age: 39.67±15.38 yr, CRS-R score: 5±2). No significant differences were found between the two groups both in terms of age (unpaired t-test, p-value = 0.1157) and gender (χ-squared test, p-value = 0.5702). The present study protocol was approved by the local Ethics committee of Fondazione Santa Lucia (Prot. CE/PROG.603). Written informed consent

was obtained by the patients' legal surrogates.

B. EEG recordings

EEG signals were acquired by means of 19 bridge electrodes (Micromed) positioned over patients' scalp according to 10-20 International System (reference on Fpz, ground on Oz). EEG was acquired in resting state condition for approximately 5 minutes with a sampling frequency equal to 250 Hz.

C. Pre-processing

Raw signals were band-pass filtered (1-20 Hz) to select the frequency band of interest and to remove the contribution of muscular artefacts. Independent Component Analysis (ICA) was used to remove ocular artefacts when eye-blinks were recognizable on the traces. Subsequently signals were segmented in epochs of 1 second duration. A threshold approach for artefacts removal was then applied to exclude trials exceeding in absolute value the amplitude of 100 μV. A random sample of 100 trials was extracted for each subject to provide an equal amount of data for each patient to perform further analyses.

D. Spectral Analysis

Spectral analysis was executed on pre-processed data of the midline electrodes (Fz, Cz, Pz) computing Power Spectral Density (PSD) by means of Welch periodogram (Hann windows of 1 second duration with no overlap). Five out of 58 patients were excluded from spectral analysis due to residual muscular component. Relative Power (RP) was calculated to evaluate the contribution of the single frequency bands (delta: 1-3 Hz, theta: 4-7 Hz, alpha: 8-13 Hz) to the global power.

E. Connectivity Analysis

Connectivity analysis was conducted estimating functional resting state network using Partial Directed Coherence (PDC) [9], a multivariate spectral estimator providing weight and direction about functional links connecting different time-series in specific scalp positions. PDC values were averaged in delta (1-3 Hz), theta (4-7 Hz) and alpha (8-13 Hz) bands and asymptotic statistics validation method was applied to assess the significance of each connection against chance level [10]. Four out of 58 patients were excluded from connectivity analysis since estimated networks showed density values inferior to 10%.

To evaluate global properties of the estimated networks, the following indices were calculated: clustering coefficient, path length and small-worldness. Clustering coefficient is a segregation index that quantifies the presence of functionally specialized clusters in the estimated network and investigates the prevalence of clustered connectivity around individual nodes. Path length is a measure of integration of the network and reflects the distance between nodes. Small-worldness describes how well the properties of segregation and integration are combined to create a network that presents both segregated modules and intermodular (integrating) links [11].

F. Statistical Analysis and Classification

Basing on the exclusion criteria applied to spectral and connectivity analyses that were mentioned before, spectral indices were evaluated for 14 out of 18 UWS patients and 39 out of 40 MCS, while connectivity indices were calculated for 18 UWS and 36 out of 40 MCS. Afterwards the spectral and connectivity indices evaluated for the two groups were statistically compared using an unpaired t-test (alpha equal to 0.05).

Measures that resulted statistically different between the two groups were deployed as features to train a Supported Vector Machines (SVM) classifier with linear kernel able to discriminate MCS and UWS classes. Data augmentation was applied to numerically inferior class to compensate for unbalanced dataset. Leave-one-subject-out was used as validation approach and for each subject classification performance indices were calculated (i.e., accuracy, precision, specificity, sensitivity, area under curve).

III. Results

A. Comparing spectral and connectivity indices between VS/UWS and MCS

Relative powers in all the three bands considered (delta, theta and alpha) resulted significantly different between the two groups of patients on Pz channel. Moreover, relative power evaluated in delta and theta bands obtained a significant p-value (<0.05) also on Fz channel. As shown in Fig. 1, relative power in delta band on Pz channel is significantly higher in VS than in MCS patients. Conversely, relative power in theta and alpha bands showed the opposite trend, being lower in VS/UWS patients than in MCS. No significant differences were found in relative powers evaluated on Cz channel for all the three bands.

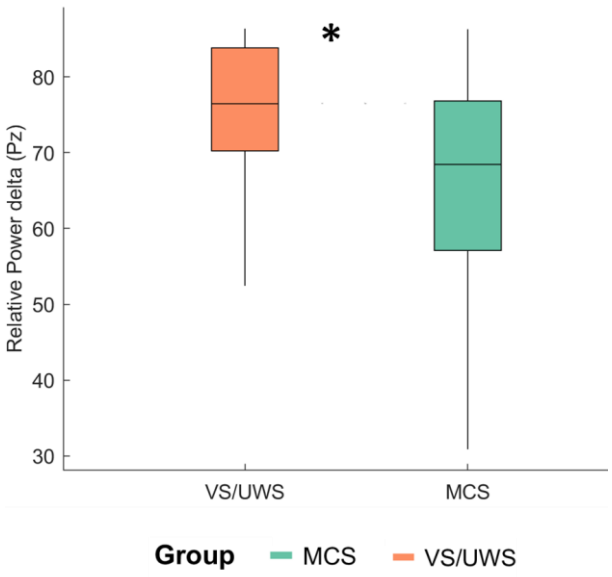


Fig. 1: Box plot representation of the statistical comparison of the relative power in delta band on Pz channel for VS/UWS group (in orange) and MCS group (in green). Statistically significant differences between the two groups are marked with the symbol *.

Statistical analysis applied to connectivity indices evidenced significant differences between the two groups for clustering coefficient and small-worldness, both in delta band.

As reported in Fig. 2, path length (Fig. 2, panel a) shows

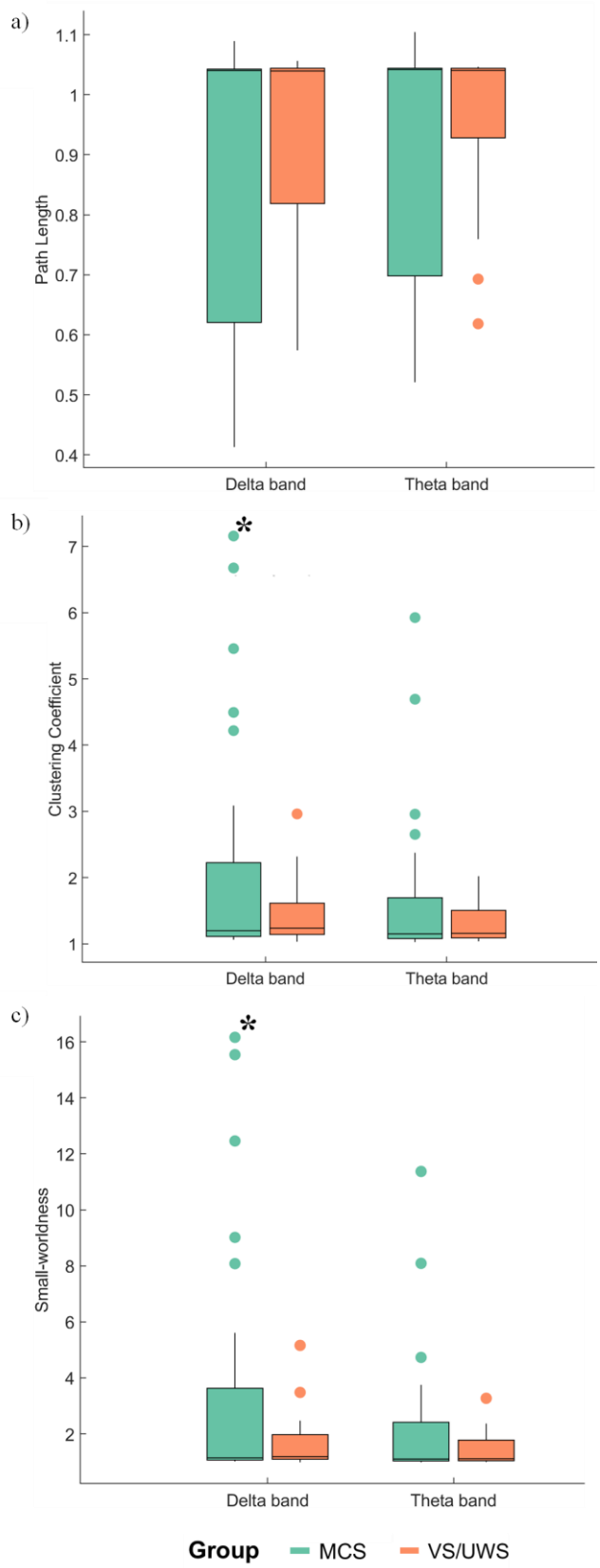


Fig. 2: Box plot representation of the statistical comparison of the connectivity indices distributions in delta and theta bands for VS/UWS group (in orange) and MCS group (in green): path length (panel a), clustering coefficient (panel b), small-worldness (panel c). Statistically significant differences between the two groups are marked with the symbol *.

significant differences between the two groups neither in delta nor in theta band, while both clustering coefficient (Fig. 2, panel b) and small-worldness (Fig. 2, panel c) evaluated in delta band are significantly lower in VS group. No significant p-values were obtained from statistical analysis of connectivity indices evaluated in theta and alpha bands.

B. EEG-based Classification of VS/UWS – MCS patients

Relative power on Pz channel, clustering coefficient and small-worldness, all evaluated in delta band and resulted as significant indices from statistical analysis, were used as features to train the SVM classifier. Figure 3 shows the values of the performance indices calculated for the classifier trained: the accuracy value obtained is equal to 67.35% with an AUC equal to 75%.

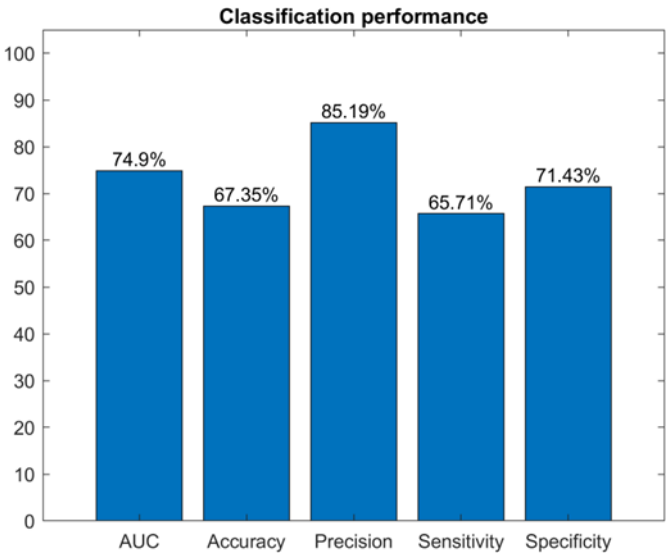


Fig. 3: Histogram reporting the performance of the SVM classifier with linear kernel trained using as features the following indices: relative power in delta band on Pz channel, clustering coefficient in delta band, small-worldness in delta band.

IV. Discussion

In this paper we aimed at providing quantitative and reliable indices, extracted from EEG resting state networks, to discriminate VS/UWS from MCS in order to corroborate the clinical/behavioral diagnosis of DoC patients.

Among the indices calculated small-worldness, clustering coefficient and relative spectral power on Pz channel, all evaluated in delta band, resulted as quantitative measures able to distinguish the two classes of patients. Indeed, these indices resulted significantly different between UWS/VS and MCS patients.

Previous EEG studies, based on graph theory indices extracted from connectivity networks at rest, have already pointed out the distinctive aspects of brain networks that characterize the DoC in comparison with healthy subjects and the correlations with their degree of behavioral responsiveness or hidden awareness [12].

According to the results obtained, clustering coefficient is significantly higher in MCS patients. This index quantifies the property of segregation of the estimated network. Segregation

measures describe the presence in the network of densely interconnected groups of brain regions that are specialized in fulfilling common functions. Higher values of clustering coefficient witness the presence of clusters in functional networks [11]. Therefore, the results obtained evidence that resting state networks in MCS were characterized by higher communication efficiency and higher tendency to organize their structure in clusters in comparison with UWS/VS. Previous studies already evidenced the correlation between the re-emergence of strong connectivity hubs in brain network and increasing levels of consciousness [13].

Integration measures are the other important category of indices that describe the global properties of the estimated network and that represent the ability of the brain to integrate the information deriving from distributed regions. Lower values of path length represent a major functional integration among different brain regions and an efficient propagation of information in the network [11]. Although MCS patients showed lower values of path length, the difference between the distribution of values was not significant between the two groups, so this measure was not considerate crucial to discriminate the two classes.

An optimal network needs to balance functional integration and segregation and this capacity is described by small-worldness. Small-world networks can simultaneously support segregation (high clustering coefficient) and integration (low path length) and are characterized by small-worldness index values superior to 1 [11]. The analyses conducted evidenced higher values of small-worldness in MCS group. The presence of highly inter-connected hubs in patients with increasing level of consciousness are believed to contribute to create a small-world functional network in the brain [14].

Several prior studies already stated the ability of spectral indices to distinguish between UWS and MCS patients. UWS/VS patients have shown increased delta power but decreased alpha power, compared to the values calculated in MCS [15]. Theta power is not so well studied, but it was found to be higher in UWS patients compared to healthy controls [16], moreover a study reported that UWS patients had lower theta power when compared to MCS patients [17]. These results are all consonant to the ones obtained in the current study.

Since connectivity indices showed significant differences only in delta band, the significant spectral index chosen to train the classifier was relative power in delta band. Albeit the accuracy of the classifier implemented has margins of improvement, it nevertheless exceeded the accuracy of clinical assessment methods. This finding further strengthens the potential and the relevance that such surrogate measure of the consciousness disorders might have to improve clinical diagnosis of DoC patients.

V. Conclusion

This study suggests how quantitative EEG measures could be a valid instrument to support clinical diagnosis in patients suffering from disorders of consciousness. The analyses conducted indicate how surrogate measures of consciousness disorders based on EEG might allow to improve the accuracy of the gold-standard clinical instruments for diagnosis. This can be achieved with just few minutes of EEG signal recording without requiring any voluntary contribution by the patient.

In order to better the classification performance obtained, this study can be considered as a preliminary one, with the purpose of investigating more specific indices describing resting state networks and to test alternative classification approaches.

Acknowledgement

This present work was supported by the Italian Ministry of Health (GR-2019-12369824), by European Union's Horizon 2020 Research and Innovation Program Under the Marie Skłodowska-Curie Grant Agreement No. 778234 - DoCMA Project, by Sapienza University of Rome - Progetti di Ateneo 2019 (RM11916B88C3E2DE), 2022 (RM1221816C8C757C), Progetto SEED PNR 2021, and Bit-Brain award 2020 (2962-B2B).

References

[1] B. Wutzl *et al.*, «Narrative Review: Quantitative EEG in Disorders of Consciousness», *Brain Sciences*, vol. 11, fasc. 6, Art. fasc. 6, giu. 2021, doi: 10.3390/brainsci11060697.

[2] S. Laureys *et al.*, «Unresponsive wakefulness syndrome: a new name for the vegetative state or apallic syndrome», *BMC Medicine*, vol. 8, fasc. 1, p. 68, nov. 2010, doi: 10.1186/1741-7015-8-68.

[3] R. Formisano, F. Pistoia, e M. Sarà, «Disorders of consciousness: A taxonomy to be changed?», *Brain Injury*, vol. 25, fasc. 6, pp. 638–639, giu. 2011, doi: 10.3109/02699052.2011.572948.

[4] D. T. Wade, «How often is the diagnosis of the permanent vegetative state incorrect? A review of the evidence», *European Journal of Neurology*, vol. 25, fasc. 4, pp. 619–625, 2018, doi: 10.1111/ene.13572.

[5] J. Xiao *et al.*, «An Auditory BCI System for Assisting CRS-R Behavioral Assessment in Patients with Disorders of Consciousness», *Sci Rep*, vol. 6, fasc. 1, Art. fasc. 1, set. 2016, doi: 10.1038/srep32917.

[6] A. Vanhaudenhuyse *et al.*, «Default network connectivity reflects the level of consciousness in non-communicative brain-damaged patients», *Brain*, vol. 133, fasc. 1, pp. 161–171, gen. 2010, doi: 10.1093/brain/awp313.

[7] Y. Höller *et al.*, «Connectivity biomarkers can differentiate patients with different levels of consciousness», *Clinical Neurophysiology*, vol. 125, fasc. 8, pp. 1545–1555, ago. 2014, doi: 10.1016/j.clinph.2013.12.095.

[8] L. Pollonini *et al.*, «Information Communication Networks in Severe Traumatic Brain Injury», *Brain Topogr*, vol. 23, fasc. 2, pp. 221–226, giu. 2010, doi: 10.1007/s10548-010-0139-9.

[9] L. A. Baccalá e K. Sameshima, «Partial directed coherence: a new concept in neural structure determination», *Biol Cybern*, vol. 84, fasc. 6, pp. 463–474, mag. 2001, doi: 10.1007/PL00007990.

[10] K. Sameshima, D. Y. Takahashi, e L. A. Baccalá, «On the Statistical Performance of Connectivity Estimators in the Frequency Domain», in *Brain Informatics and Health*, Cham, 2014, pp. 412–423. doi: 10.1007/978-3-319-09891-3_38.

[11] M. Rubinov e O. Sporns, «Complex network measures of brain connectivity: Uses and interpretations», *NeuroImage*, vol. 52, fasc. 3, pp. 1059–1069, set. 2010, doi: 10.1016/j.neuroimage.2009.10.003.

[12] S. Chennu *et al.*, «Spectral Signatures of Reorganised Brain Networks in Disorders of Consciousness», *PLOS Computational Biology*, vol. 10, fasc. 10, p. e1003887, ott. 2014, doi: 10.1371/journal.pcbi.1003887.

[13] S. Chennu *et al.*, «Brain networks predict metabolism, diagnosis and prognosis at the bedside in disorders of consciousness», *Brain*, vol. 140, fasc. 8, pp. 2120–2132, ago. 2017, doi: 10.1093/brain/awx163.

[14] D. J. Watts e S. H. Strogatz, «Collective dynamics of 'small-world' networks», *Nature*, vol. 393, fasc. 6684, Art. fasc. 6684, giu. 1998, doi: 10.1038/30918.

[15] Y. Bai, X. Xia, e X. Li, «A Review of Resting-State Electroencephalography Analysis in Disorders of Consciousness», *Frontiers in Neurology*, vol. 8, 2017, Consultato: 15 gennaio 2023. [Online]. Disponibile su: https://www.frontiersin.org/articles/10.3389/fneur.2017.00471

[16] J. Lechinger *et al.*, «CRS-R score in disorders of consciousness is strongly related to spectral EEG at rest», *J Neurol*, vol. 260, fasc. 9, pp. 2348–2356, set. 2013, doi: 10.1007/s00415-013-6982-3.

[17] A. Naro *et al.*, «Shedding new light on disorders of consciousness diagnosis: The dynamic functional connectivity», *Cortex*, vol. 103, pp. 316–328, giu. 2018, doi: 10.1016/j.cortex.2018.03.029.

A Novel Authentication System Based on Hand Gesture Ultrasound Signatures

S. Franceschini[1], M.M Autorino[1], M. Ambrosanio[2], V. Pascazio[1] and F. Baselice[1]
[1] *University of Naples Parthenope, Department of Engineering;*
[2] *University of Naples Parthenope, Department of Economics, Law, Cybersecurity and Sport Sciences;*

***Abstract*—In the framework of security, biometrics proved to be the new frontier for human identification/authentication. It is more and more easy to find system exploiting fingerprint, voice or face recognition in application ranging from forensic to smartphone unlocking. In this paper the possibility of considering hand gesture for authentication purposes is explored. Hand gesture Doppler signatures are extracted by means of an ultrasound prototype and a deep learning based detector is considered. The system is cheap, reliable and, based on the complexity of the gestures, allows different security level. The prototype performances have been evaluated in a one-vs-all authentication scenario with the help of a testing population of 25 subject. The feasibility of the system is confirmed by promising results.**

***Keywords*—Ultrasound, Hand Gestures, Person Authentication, Deep Learning**

I. Introduction

The importance of biometrics in security applications is exponentially growing in the last years. The idea of exploiting peculiarity in human morphology or habits for identify people is progressively replacing classic procedures like complex passwords or smart cards since biometrics do not involve in something related to knowledge and/or possess [1]. For example, in most of modern devices fingerprint, voice and face are exploited in order to unlock files or services [2] replacing passwords.

A biometric trait must satisfy constraints related to robustness, availability, universality, specificity and stability to be considered as a good candidate in identification purposes. Moreover, these types of system should be cheap and the related measures should be easy to be taken.

Based on literature studies, there are two major biometric families based on the nature of the trait: the former, morphological traits, is related to some physical feature of the user. Behavioural systems, conversely, exploit some peculiarity of the user while he/she does some tasks. This latter family present the advantage of being more robust to spoofing attacks compared to the morphological one [3] since, based on their nature, their are typically changeable in case of being compromise.

Many research groups focused their attention in finding appropriate behavioral traits and developing the related systems. For example, in [4] and [5] cardiac and brain electrical activity, respectively, are measured in order to identify person. Both systems present good results, but due to uncomfortable acquisition these systems are not feasible in most of the security applications. The possibility of exploiting gaits for identification task is explored in [6] where the gait Doppler spectrum is extracted by means of an FMCW radar. Main limitation of the system is related to the wide area required for the correct functioning.

A new frontier of behavioural biometrics is hand gesture. Gestures represent a trait easy to compute, change and reproduce and hand are already exploited by person in a normal conversation, as matter of the fact, studies have shown that, during a conversation, about 55% of information is provided by attitude and gestures [7]. Some examples of identification systems based on hand gestures are provided by [8] where smartphone accelerometers and gyroscopes are exploited to recognise people or by [9] where the touch screen of smartphones is considered for the same task. In [10], conversely, person are distinguished based on mouse gestures. All of these systems share the same requirement of contact whit some sensors limiting their usage in some context.

Contact-less gesture identification system have been, so, proposed in order to combine the advantage of exploiting gestures avoiding, at the same time, the limitation of the need of contact. For example, in [11] hand gesture are acquired by means of a Kinect system. A limitation, in this case, is represented by the sensibility the light changes and privacy issues may occur. Additionally, in [12], hand gesture are acquired due to a Wi-Fi system. In this case the criticism is related to low accuracy of the proposed solution.

In this paper an Ultrasound (US) prototype is proposed in order to extract hand gesture signatures for person authentication. The idea is to exploit the Doppler effect that affects the US reflected signal. Such incoming signal contains information related to several part of the hand movements.

Ultrasounds have been already exploited for both hand gesture detection [13] as well as in other biometric systems [14] but, based on the author's knowledge, this is the first approach to use ultrasound for sensing hand gesture in an identification/authentication scenario.

The basic idea of the proposed approach is that peculiarities in gesture execution should be reflected in some differences in the scattered signal extractable by a proper processing algorithm and discriminated by an ad-hoc deep learning based detector. In order to test the feasibility and evaluate the discrimination properties of the proposed system, a one-vs-all authentication scenario test with the help of 25 volunteers has been conducted obtaining promising results.

The remainder of the paper is the following: in Section II,

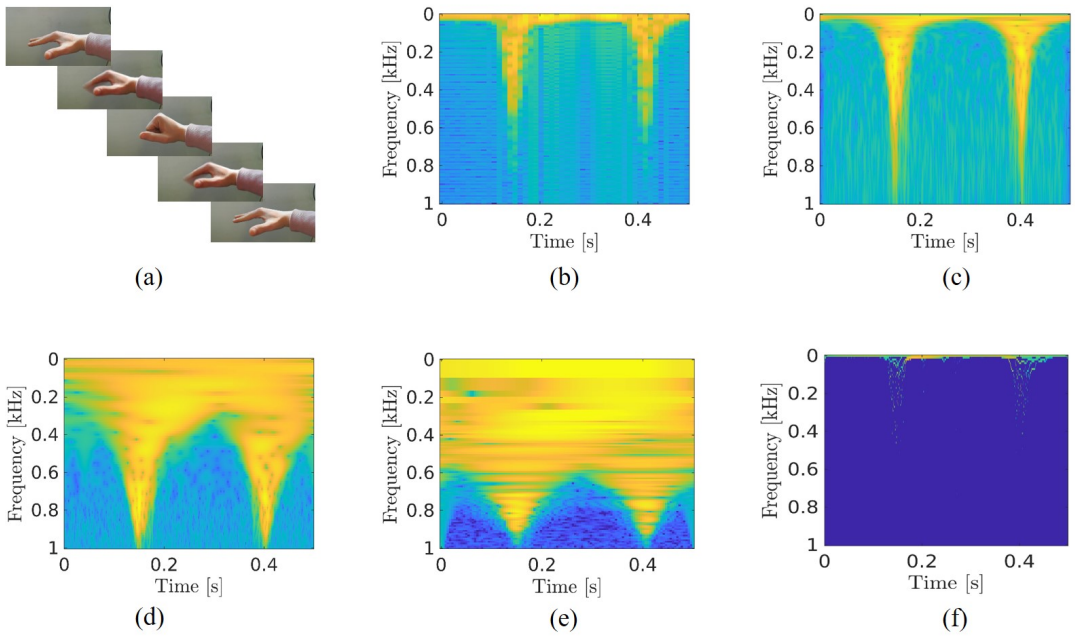


Fig. 1: Visual comparison of the considered time/frequency transforms. In (a) is shown the considered hand gesture, (b) shows STFT related to the its received signal, ST is shown in (c). (d) (e) and (f) show, respectively the WT, CQT and HHT of the gesture in (a).

the hand-gesture person authentication prototype is presented. Section III contains the description of the testing scenario and the related performances, finally, in Section IV, conclusions are drawn.

II. Proposed Method

Considering a principle similar to Sonar object speed detection, the proposed system exploit Doppler effected induced to the reflected US wave by the target motion impinged by the US transmitted wave. For this purpose, a prototype composed of an US transmitter, an US receiver, a waveform generator and an analog-to-digital acquisition board is proposed (a more rigorous prototype description can be found in [15]).

More in detail, considering a monochromatic source, the backscattered wave is the result of relationship among different contribution related to several parts of the target (e.g. human hand). By a multiplication between transmitted and received signals followed by a low pass filter (2 kHz of cut-off frequency for a 40 kHz sine wave source) it is possible to retrieve a beat signal manly related to the target motion.

Such signal is non-stationary and, therefore, a proper signal processing algorithm must be considered in order to preserve information in both time and frequency domains. In this framework 5 different time-frequency (t-f) have been considered [16], [17]: *Short-time Fourier Transform* (STFT), *Stokewell Transform* (ST), *Wavelet Transform* (WT), *Constant Q Transform* (CQT) and *Hilbert-Huang Transform* (HHT).

An example of the time-frequency matrix resulting from the considered algorithms is shown in Fig.1. All the figures refer to the same hand gesture (e.g. a closing-opening movement of the hand). From the images is possible to note evident differences among the approaches although they exhibit similar features clearly related to the considered gesture (two frequency spikes related to the time instant in which the hand is opened and successively closed).

The idea of the proposed system is that, even if two distinct user compute the same hand gesture, the resulting t-f matrix show differences due to peculiarities in the gesture execution. In order to detect and associate a t-f matrix the to corresponding user a deep learning based detector has been implemented. Such choice is motivated by the fact that such family of algorithms has been already successful exploited in many classification tasks.

Considering an authentication task, where the author of the gesture is known and system is asked to accept or deny a gesture sample, the proposed detector is shown in Fig. 2. The input is one of the considered t-f matrix. Such image is sent to a cascade of three convolutional layers (3×3 filters with 64 features) and, successively, to a fully connected layer with two nodes. The output of the network represent a similarity score between the feature extracted from gesture sample under test and those related to the user declared as genuine. Based on a threshold such sample is accepted or denied.

III. Results

In order to evaluate the performance of the proposed system, a one-vs-all authentication scenario is considered. For this purposes, a dataset of gestures have been acquired and exploited for training and testing the detector. More in detail, to a population of 25 volunteers have been asked to repeat 90 times 3 different gestures: *Closing and opening the hand*

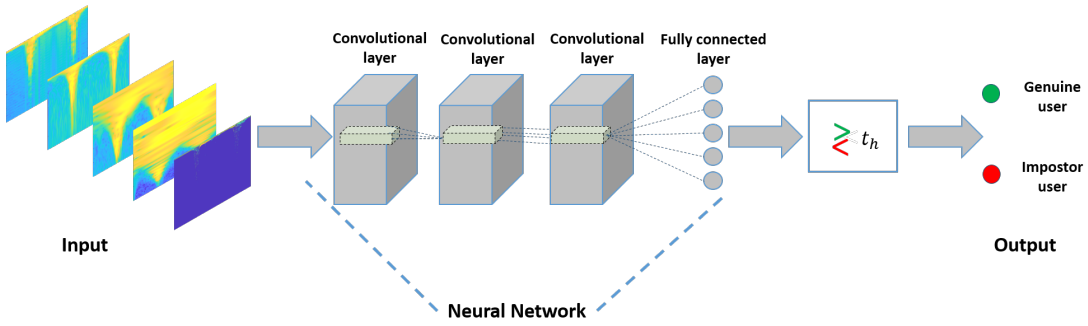


Fig. 2: Block diagram of the detector. The considered time/frequency transform is fed as input of a cascade of convolutional layers ended by a fully connected layer. The corresponding output (membership score) is compared with a threshold in order to accept or deny the gesture.

(Gesture 1), *shifting the hand from left to right* (Gesture 2) and *key-tapping* (Gesture 3).

For all the subjects and gestures the 90 repetitions have been divided into into two sets; 40 repetitions have been used for training the network and the remaining 50 for testing. In order to increase the number of training sample an augmentation strategy has been considering. Specifically, each gesture sample has been time shifted 4 times. In this way the detector has been trained to recognize the Doppler features independently from their time position in the time window of observation.

As mentioned in the previous section, a crucial parameter of the detection algorithm is the threshold t_h. If the similarity score provided by the network is greater of t_h such sample is considered as genuine if, conversely, is lower, such sample is rejected. By changing the value of t_h is possible to obtain different working point.

Under the assumption of defining the subject to be authenticate as *Genuine* and all the others as *Impostor*, for each working point the *True Positive Rate*, defined as the ratio between the correct *Genuine* assignment against all the *Genuine* testing samples and the *False Positive Rate*, that is the ratio between the incorrect *Genuine* assignment against all the *Impostor* gesture samples, are computed. Considering the true positive and false positive rates for different values of t_h it is possible to draw the Receiver Operative Curve (ROC) of the detector.

For each gesture and t-f algorithm it is possible to compute the corresponding ROC curve. In Fig. 3 for example, the ROC curves related to each one of the three considered gestures are shown (Gesture 1 is shown in Fig. 3(a), Gesture 2 in Fig. 3(b) and Gesture 3 in Fig. 3(c)). The curves in each graph represent the results of considering a different t-f algorithm as input of the detector. All the curves refer to the same subject to be authenticate.

By looking at the curves, it is possible to note that the behaviour of the system is related to the considered gestures and, in particular, Gesture 3 present worst performances compared to the other 2 gestures. This result can be motivated by the fact that Doppler spectral bandwidth related to gesture 3 is lower with respect to Gesture 1 and 2 and, so, the amount of "features" useful to the detector is lower. From Fig. 3 it is also possible to note that the system produce worst performances if the HHT is considered as t-f input matrix independently from the considered gesture.

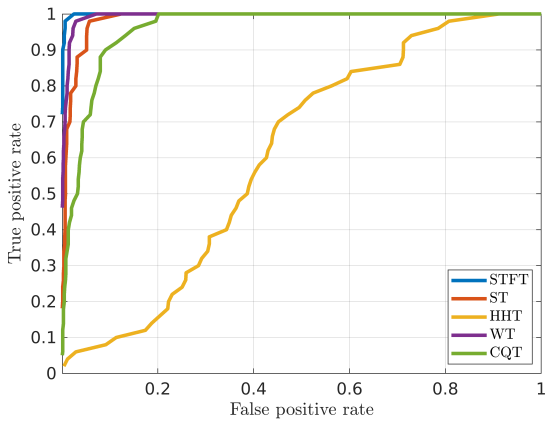
For generalizing the previous statements, the system have been also trained in order to authenticate each one of the 25 volunteers in a one-vs-all authentication scenario. From each obtained ROC curves two synthetic metrics have been extracted. In particular, the first, Area Under ROC (AUR), represents the overall performance of the receiver, the closer this value is to 1 the better the receiver has to be considered; the second, the Equal Error Rate (EER) is defined as the threshold which gives an FPR equal to 1-TPR. In this case, values closer to 0 represent better performance.

In Tab. I mean values of AUR and EER related to each t-f algorithm and gestures, averaged with respect to the 25 subjects, are shown. From the table it is possible to confirm what resulting from the Fig. 3 and, additionally, it is possible to observe promising performances specifically in case of Gesture 1 and STFT algorithm.

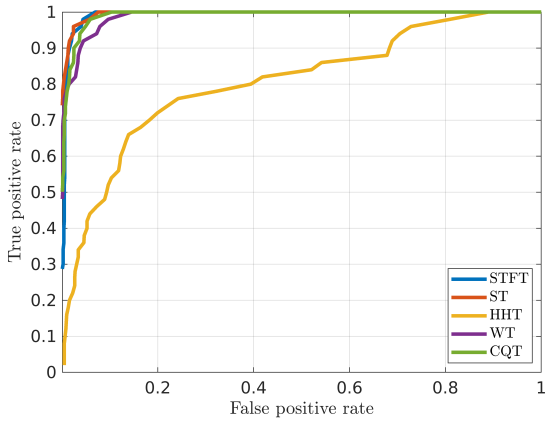
It is worth to note that all the proposed tests refer to the worst case scenario where the impostors know perfectly the correct gesture to compute.

IV. Conclusion

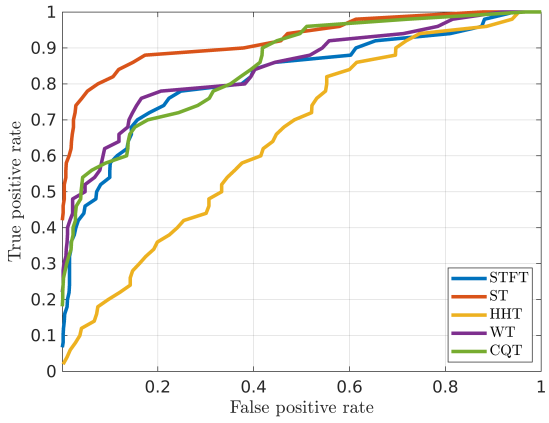
This paper presented a novel biometric approach in the framework of authentication. Ultrasound Doppler signatures are exploited for training a deep learning based detector. in this framework an ad-hoc prototype have been designed and tested and the Doppler spectrum information related to the hand gesture have been extracted by means of different time-frequency transform. The system have been tested in an one-vs-all authentication scenario showing promising result. The proposed solution is cheap, portable and robust to environmental noise. Additionally, is presents the advantage of changing the gesture if it is compromised. Moreover, in situation where an high degree of security is needed, more complex gestures can be considered. A further possibility is to consider such system also in multi-biometric configuration in combination with other biometric systems in order to increase the performance of the overall system.



(a)



(b)



(c)

Fig. 3: ROC curves of the results of an one-vs-all authentication test. (a) refers to Gesture 1 while (b) and (c) refer to Gesture 2 and 3, respectively.

TABLE I: Mean values of Area Under ROC (AUR) and Equal Error rate (EER) for all the considered gestures and time/frequency transform.

		Gesture 1	Gesture 2	Gesture 3
STFT	AUR	0.94	0.92	0.87
	EER	0.10	0.14	0.14
ST	AUR	0.92	0.93	0.87
	EER	0.13	0.13	0.19
WT	AUR	0.91	0.94	0.87
	EER	0.14	0.12	0.18
CQT	AUR	0.91	0.85	0.85
	EER	0.14	0.14	0.21
HHT	AUR	0.83	0.83	0.79
	EER	0.24	0.23	0.27

REFERENCES

[1] Jain, A.K.; Ross, A.; Prabhakar, S. An introduction to biometric recognition. *IEEE Trans. Circuits Syst. Video Technol.* 2004, *14*, 4–20.

[2] Kodituwakku, S.R. Biometric authentication: A review. *Int. J. Trend Res. Dev.* 2015, *2*, 2394–9333.

[3] Akhtar, Z.; Micheloni, C.; Foresti, G.L. Biometric liveness detection: Challenges and research opportunities. *IEEE Secur. Priv.* 2015, *13*, 63–72.

[4] Jaafar, H.; Ismail, N.S. Intelligent person recognition system based on ecg signal. *J. Telecommun. Electron. Comput. Eng. (JTEC)* 2018, *10*, 83–88.

[5] Johnson, B.; Maillart, T.; Chuang, J. My thoughts are not your thoughts. In Proceedings of the 2014 ACM International Joint Conference on Pervasive and Ubiquitous Computing: Adjunct Publication, Seattle, WA, USA, 13–17 September 2014; Association for Computing Machinery: New York, NY, USA, 2014, pp. 1329–1338.

[6] Vandersmissen, B.; Knudde, N.; Jalalvand, A.; Couckuyt, I.; Bourdoux, A.; Neve, W.; Dhaene, T. Indoor person identification using a low-power fmcw radar. *IEEE Trans. Geosci. Remote. Sens.* 2018, *56*, 3941–3952.

[7] Mehrabian, A.; Ferris, S.R. Inference of attitudes from nonverbal communication in two channels. *J. Consult. Psychol.*1967, *31*,248–252.

[8] Yang, L.; Guo, Y.; Ding, X.; han, J.; liu, Y.; Wang, C.; Hu, C. Unlocking Smart Phone through Handwaving Biometrics. *IEEE Trans. Mob. Comput.* **2015**, *38*, 1044–1055.

[9] Rzecki, K.; Pławiak, P.; Niedźwiecki, M.; Sośnicki, T.; Leśkow, J.; Ciesielski, M. Person recognition based on touch screen gestures using computational intelligence methods. *Inf. Sci.* 2017, *415–416*, 70–84.

[10] Sayed, B.; Traoré, I.; Woungang, I.; Obaidat, M.S.; Biometric authentication using mouse gesture dynamics. *IEEE Syst. J.* 2013, *7*, 262–274.

[11] Mendels, O.; Stern, H.; Berman, S. User identification for home entertainment based on free-air hand motion signatures. *IEEE Trans. Syst. Man, Cybern. Syst.* 2014, *44*, 1461–1473.

[12] Zheng, Z.Yu, N. Zhang, J. Dai, H. Wang, Q. Wang, Q. Wi-ID: WiFi-Based Identification System Using Rock-Paper-Scissors Hand Gestures. Wireless Personal Communications, 2022.

[13] Franceschini, S.; Ambrosanio, M.; Vitale, S.; Baselice, F.; Gifuni, A.; Grassini, G.; Pascazio, V. Hand Gesture Recognition via Radar Sensors and Convolutional Neural Networks. In Proceedings of the 2020 IEEE Radar Conference (RadarConf20), Florence, Italy, 21–25 September 2020; pp. 1-5.

[14] Iula, A. Ultrasound Systems for Biometric Recognition. *Sensors* 2019, *19*, 2317.

[15] Franceschini, S.; Ambrosanio, M.; Pascazio, V.; Baselice, F. Hand Gesture Signatures Acquisition and Processing by Means of a Novel Ultrasound System. *Bioengineering*, 2023, 10, 36.

[16] Sejdić, E.; Djurović, I.; Jiang, J. Time–frequency feature representation using energy concentration: An overview of recent advances. *Digit. Signal Process.* 2009, *19*, 153–183.

[17] Brown, J.C. Calculation of a constant Q spectral transform. *J. Acoust. Soc. Am.* 1991, *89*, 425–434.

A comparative study of Super-Resolution reconstruction methods in fetal MRI

Tommaso Ciceri[1,2], Letizia Squarcina[3], Adele Ferro[5a], Florian Montano[1], Alessandra Bertoldo[2,4], Nicola Persico[5b], Simona Boito[5b], Fabio Maria Triulzi[3,5c], Giorgio Conte[3,5c], Paolo Brambilla[3,5a], Denis Peruzzo[1]

[1]*NeuroImaging Lab, Scientific Institute IRCCS Eugenio Medea, Bosisio Parini, Italy*
[2]*University of Padua, Department of Information Engineering, Padua, Italy*
[3]*Department of Pathophysiology and Transplantation, University of Milan, Milan, Italy*
[4]*University of Padua, Padova Neuroscience Center, Padua, Italy*
[5]*Fondazione IRCCS Ca' Granda Ospedale Maggiore Policlinico, Milan, Italy* [a]*Department of Neurosciences and Mental Health;* [b]*Department of Woman, Child and Newborn;* [c]*Department of Services and Preventive Medicine*

***Abstract*— Fetal Magnetic Resonance Imaging (MRI) is a non-invasive method for neurodevelopment evaluation. In clinical settings, MRI of the fetal brain typically involves the acquisition of fast anatomical sequences such as T2-weighted Spin Echo or Gradient Echo, over different planes on which several biometric measurements are manually extracted. Recently, some automatic toolkits that use the acquired two-dimensional (2D) images to reconstruct a Super-Resolution (SR) isotropic volume have been developed, thus enabling three-dimensional analysis of the fetal central nervous system.**

In this study, we characterized the reliability of the Super-Resolution (SR) images reconstructed via NiftyMIC and MIALSRTK toolkits over a common clinical fetal MR dataset (20 - 21 weeks of gestation). We compared 15 biometric measures derived from the acquired 2D images with those extracted from the SR brain volumes. Furthermore, we examined two different acquisition sequences (TSE Vs. b-FFE) to evaluate which of them lead to more reliable measures and high-resolution reconstructions. Our findings strengthen the adoption of SR toolkits for fetal brain reconstructions to perform biometric evaluations, suggesting the acquisition of TSE sequences because of their robustness against intensity artifacts.

***Keywords*— Fetal brain, Magnetic Resonance Imaging, Super-Resolution Algorithm, Fetal biometry**

I. Introduction

FETAL MRI is a non-invasive exam used for diagnostic purposes via morphologic and biometric evaluations. In clinical practice, brain biometry relies on the comparison of measurements manually derived from MRI images to normative ranges and it is a good approach to assess fetal brain development [1,2].

Recently, new advanced image processing techniques based on Super-Resolution (SR) algorithms have been developed [3,4]. These techniques can handle multiple 2D fetal scans, even those corrupted by motion artifacts, and generate a high-resolution reconstruction of the fetal brain with isotropic voxel size. This enables the morphologic and biometric evaluation of the fetal brain, allowing for navigation of the reconstructed image in any plane, and to perform quantitative analysis of tissue volume development. Modern available tools for fully automatic brain reconstruction from fetal T2w-TSE MRI scans are NiftyMIC [3] and MIALSRTK [4].

In this study, we characterized qualitatively and quantitatively the reliability of the fetal brain images reconstructed by these tools. We collected a heterogeneous dataset of fetal MRI images and we compared the biometric measures derived from the 2D images to those obtained from the 3D reconstructions. Finally, we examined TSE and b-FFE sequences to determine which led to more reliable reconstructions.

II. Materials and Methods

A. Dataset

17 fetal brain MRI examinations of singleton pregnancies (20.24 ± 0.44 gestational weeks) were collected via a 3T Philips scanner at the IRCCS Fondazione Ca' Granda Ospedale Maggiore Policlinico. The protocol included T2w-TSE and/or b-FFE sequences, acquired with different set-ups due to the clinical context. The procedures were approved by the institutional ethical review boards of the hospital, and all women signed informed consent for the research use of data.

B. Super-Resolution Reconstruction

Fetal brains were reconstructed into SR volumes with an isotropic spatial resolution matching that of input sequences via NiftyMIC [3] (v0.8) and MIALSRTK [4] (v2.03). Acquired images were visually inspected to discard sequences with artifacts [5]. On average, 3 out of 6 sequences per subject were used for the reconstruction.

C. Qualitative evaluation of the SR brain volumes

The quality of the SR images was evaluated in a blinded protocol by two MR pediatric experts with a Likert scale [6] rate score between 1 and 4. A rating of 1 indicates a *bad* quality reconstruction that is not suitable for biometric purposes due to significant motion distortion and blurring effects. A rating of 2 indicates a *poor* quality reconstruction that may be useful for obtaining one reliable biometric measure, but the overall quality is still poor, with persistent motion distortion and blurring effects. A rating of 3 indicates an *acceptable* quality reconstruction that can be used for biometric purposes, despite some remaining blurring effects. A rating of 4 indicates an *excellent* quality reconstruction that is free of any blurring effects (Figure 1).



Figure 1: Example of fetal brain reconstructions obtained via NiftyMIC and MIALSRTK. The reconstructed brain quality was rated from bad to excellent.

D. Biometric measurements

The biometric measures were assessed manually via 3D Slicer [7] by one expert in pediatric image analysis, both on the 2D images and on the 3D reconstructions. In accordance with previous studies [1,8-10], we selected the biometric measures represented in Figure 2. Each measure was taken two times and then averaged on the subject.

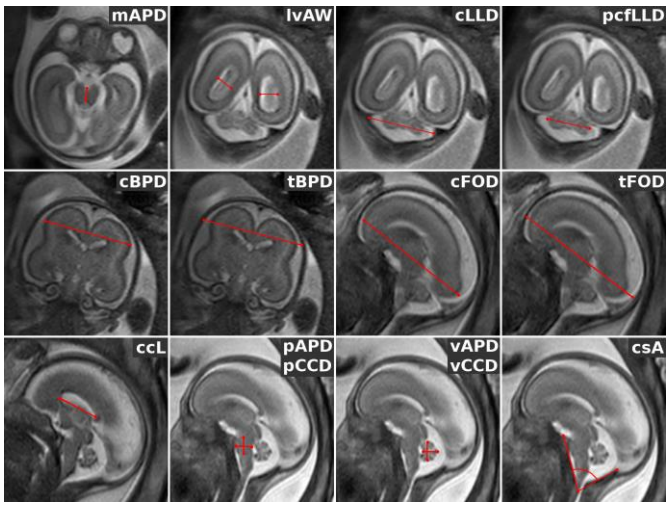


Figure 2: Biometric measurements (marked in red) representation in each orthogonal orientation. Axial orientation: the mesencephalic Antero-Posterior Diameter (mAPD). Coronal orientation: the lateral ventricles Atrial Width (lvAW), the cerebellar Latero-Lateral Diameter (cLLD), the posterior cranial fossa Latero-Lateral Diameter (pcfLLD), the cerebral BiParietal Diameter (cBPD), the thecal BiParietal Diameter (tBPD). Sagittal orientation the cerebral Fronto-Occipital Diameter (cFOD), the thecal Fronto-Occipital Diameter (tFOD), the corpus callosum Length (ccL), the pontine Antero-Posterior Diameter (pAPD), the pontine Cranio-Caudal Diameter (pCCD), the vermian Antero-Posterior Diameter (vAPD), the vermian Cranio-Caudal Diameter (vCCD), and the clivo-supraoccipital Angle (csA). For a more detailed description of how to perform the measurements please refer to [1].

E. Analyses

Three analyses were performed with R software v4.0.5:

- tools evaluation: we performed an agreement analysis between the biometric measures on each 2D acquisition and on the SR brain using Passing-Bablok regression with the Person's correlation coefficient [11], and Bland-Altman plot [12]. The reliability of the measurements obtained from the reconstructed volumes was evaluated by calculating the intraclass correlation coefficient (ICC) as a measure of correlation and agreement with those obtained from the 2D sequences. The criteria established by [13] was used to interpret the ICC magnitude. Finally, the mean values and the standard deviations of biometric measures were compared with the paired two-tailed t-test and F-test. The Shapiro-Wilk method [14] was used to test the normality of the biometric measures distribution.
- tools comparison: we performed a qualitative (Likert score) and quantitative (percentage error and Passing-Bablok regression) comparison between the fetal brain reconstructed images obtained via the tools investigated. The consistency of the quality assessment of brain volume reconstruction between raters was evaluated using Gwet's agreement coefficient (Gwet's AC1). To evaluate the magnitude of this coefficient, the Altman's benchmarking was adopted [15]. The slope coefficient and intercept of the Passing-Bablok regression line were compared using paired two-tailed t-test and F-test.
- sequences evaluation: we performed a qualitative and quantitative comparison, as introduced in previous steps, between TSE and b-FFE sequences to investigate differences in the SR images.

III. Results

A. Tools evaluation

Forty fetal brain volumes were reconstructed via NiftyMIC and MIALSRTK. Out of the reconstructions obtained via NiftyMIC and MIALSRTK, seven of them were found to be of bad quality and were therefore not considered in the subsequent analysis. Thus, 33 fetal brain images reconstructed via NiftyMIC and MIALSRTK were considered for the biometric analysis (Figure 3).

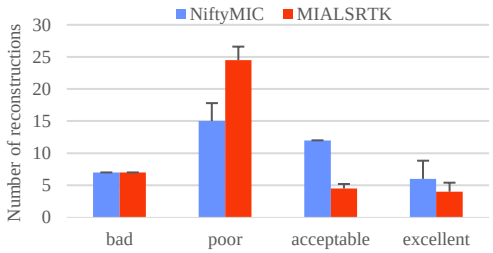


Figure 3: NiftyMIC and MIALSRTK comparison in terms of reconstruction quality. Each bar and whisker represent the average and standard deviation consensus among the two raters' assessment for each quality scale.

The statistical comparisons identified no significant differences between measures derived from reconstructed volumes and 2D images, with the only exception for the cLLD measures ($p = 0.01$ and $p < 0.001$ for NiftyMIC and MIALSRTK, respectively).

The Passing-Bablok test and the Bland-Altman plots confirm the significant agreement between the biometric measures derived from 2D images and reconstructed volumes ($r_{min} > 0.74$ and $r_{min} > 0.71$ with both $p < 0.003$, for each measure Pearson's correlation coefficient derived on NiftyMIC and MIALSRTK reconstruction, respectively).

The reconstruction reliability of both tools was assessed as Moderate to Good [13] (averaged ICC with 95% CI was 0.82 [0.62 - 0.92] for NiftyMIC, and 0.79 [0.57 - 0.90] for

MIALSRTK). The ICC results are reported for each biometric measurement in Table 1.

Table 1: Intraclass Correlation Coefficient (ICC) between biometric measurements derived from reconstructed fetal brain and 2D images. The ICC is reported for both toolkits, NiftyMIC and MIALSRTK.

Orthogonal Orientation	Biometric Measure	ICC	
		NiftyMIC	MIALSRTK
AX	mAPD	0.85	0.86
COR	r-lvAW	0.87	0.88
	l-lvAW	0.87	0.84
	cLLD	0.77	0.80
	pcfLLD	0.84	0.85
	cBPD	0.74	0.57
	tBPD	0.84	0.78
SAG	cFOD	0.75	0.70
	tFOD	0.73	0.74
	ccL	0.92	0.90
	pAPD	0.64	0.50
	pCCD	0.82	0.91
	vAPD	0.87	0.89
	vCCD	0.88	0.79
	csA	0.87	0.79

B. *Tools comparison*

The estimated agreement coefficient (GWet's AC1) between the two raters was 0.74 and 0.78 for NiftyMIC and MIALSRTK, respectively, based on the visual inspection and scoring of the reconstructed images. Using Altman's benchmarking scale, the magnitude of the estimated coefficient was considered to be *Good*, with a probability of 95.1% and 99.2% for NiftyMIC and MIALSRTK, respectively.

Results of the estimated biometric measurements percentage error (Table 2) showed an overall average error rate of -0.1% ± 4.9% and -0.7% ± 5.1% for NiftyMIC and MIALSRTK, respectively. Out of 15 measurements, NiftyMIC had a smaller magnitude of mean percentage error in 11 measures and a smaller standard deviation in 9 measures compared to MIALSRTK.

The two-tailed t-test showed no significant differences between the toolkits' Passing-Bablok regression slope and intercept values.

Table 2: Toolkits comparison in terms of biometric measurements percentage error. The error is calculated between the measurements derived from the reconstructed fetal brain and those derived from 2D images. The percentage values are discussed in terms of mean and standard deviation (SD).

Orthogonal Orientation	Biometric Measure	SR reconstruction	
		NiftyMIC	MIALSRTK
		Mean ± SD	Mean ± SD
AX	mAPD	0.53% ± 4.64%	0.12% ± 5.51%
COR	r-lvAW	-0.74% ± 7.51%	0.85% ± 4.76%
	l-lvAW	-0.9% ± 7.05%	1.36% ± 6.71%
	cLLD	-1.51% ± 2.86%	-3.31% ± 3.05%
	pcfLLD	-1.32% ± 4.08%	-1.53% ± 4.08%
	cBPD	0.4% ± 3.92%	-0.95% ± 3.92%
	tBPD	0.91% ± 3.45%	-0.01% ± 3.95%
SAG	cFOD	-1.12% ± 3.28%	-1.46% ± 4.38%
	tFOD	0.4% ± 3.22%	-0.08% ± 3.92%
	ccL	0.98% ± 5.45%	-2.46% ± 5.7%
	pAPD	0.5% ± 5.63%	-0.54% ± 6.36%
	pCCD	-0.95% ± 4.59%	-0.16% ± 4.45%
	vAPD	-0.36% ± 4.65%	0.66% ± 5.51%
	vCCD	1.18% ± 7.74%	-3.53% ± 7.66%
	csA	0.2% ± 5.62%	0.68% ± 6.88%

C. *Sequences evaluation*

The results of the visual quality assessment for SR images revealed that TSE sequences were rated lower than b-FFE sequences (Figure 4).

The agreement coefficient between the two raters for the visual quality assessment of the reconstructed images was estimated to be 0.89 and 0.64 for TSE and b-FFE reconstructions obtained via NiftyMIC, respectively, and 0.77 and 0.78 for TSE and b-FFE reconstructions obtained via MIALSRTK, respectively. The magnitude of the estimated coefficient was determined to be *Very Good* with a probability of 99.9% for TSE reconstructions via NiftyMIC, *Moderate* with a probability of 98.9% for b-FFE reconstructions via NiftyMIC, *Good* with a probability of 93.6% for TSE reconstructions via MIALSRTK, and *Good* with a probability of 93% for b-FFE reconstructions via MIALSRTK.

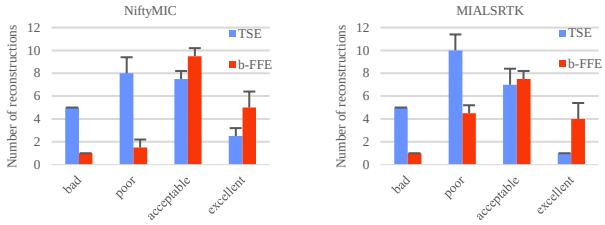


Figure 4: MRI sequences (T2w- TSE and b-FFE) quality comparison of the reconstructed fetal brain obtained via NiftyMIC and MIALSRTK. Each bar and whisker report the quality average and standard deviation consensus among the two raters' assessments for each quality scale.

Moreover, b-FFE sequences were usually characterized by the presence of intensity artifacts [16] affecting both the acquired 2D and reconstructed images, independently from the toolkit adopted (Figure 5).

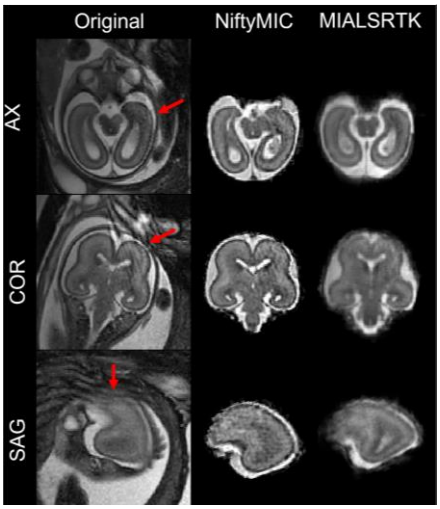


Figure 5: Examples of b-FFE acquisition artifacts. The artifact is reported on 2D images and reconstructions obtained via NiftyMIC and MIALSRTK. The artifact, pointed out by the red arrow, is shown in each orthogonal plane (axial, sagittal, and coronal).

The estimated biometric measurements percentage error showed an average error rate of 0.3% ± 4.9% and -0.4% ± 4.8% for NiftyMIC TSE and b-FFE reconstructions, respectively; -0.75% ± 5.37% and -0.61% ± 4.8% for MIALSRTK TSE and b-FFE reconstructions, respectively. The percentage error of different measurements was significantly different from 0 for ccL in b-FFE and vCCD in

TSE reconstructions via NiftyMIC; for cLLD in b-FFE and TSE, and vCCD in TSE reconstructions via MIALSRTK.

The Passing-Bablok regression slope coefficient of the MIALSRTK-TSE reconstructions showed significant ($p = 0.02$) differences with respect to a null distribution. The paired two-tailed t-test exhibited no significant differences between the two sequences' slope and intercept values. The F-test showed significant differences ($p = 0.03$) for the intercept values between NiftyMIC TSE and b-FFE reconstructions.

IV. Discussion

Automatic brain reconstruction methods from fetal MRI scans are crucial to perform quantitative volumetric studies of neurodevelopment. The publicly available modern toolkits which include a full pipeline for fetal brain MRI reconstruction are NiftyMIC and MIALSTRK. These toolkits were each proposed and validated on T2w spin echo sequence, but were not evaluated on a heterogeneous dataset (i.e., different acquisition set-ups and MRI sequences). In this study, we firstly validated the aforementioned methods, then we conducted a qualitative and quantitative comparison among them over a heterogeneous dataset including TSE and b-FFE sequences.

The results showed that the reconstructed volumes were geometrically reliable and, in 80% of the cases, clinically useful for biometric measurements. In detail, NiftyMIC reconstructions were qualitatively rated higher than MIALSRTK reconstructions since the latter were more blurred and less anatomically defined. Nevertheless, the measurements were very similar between the two methods, suggesting a good agreement between them.

Only the cLLD measure was found to be significantly different between measurements obtained from reconstructed volumes and 2D images. This may be due to the larger partial volume affecting the acquired 2D images.

The fetal brain reconstructions obtained from b-FFE sequences were rated higher than TSE ones. However, the presence of intensity bands on both the b-FFE images and derived volumes may be an important source of errors, suggesting that TSE sequences are more reliable for the 3D reconstruction and the possible subsequent volumetric measurements.

The main limitations of this method-comparison study are the reduced number of acquired subjects as well as the amount of sequences per orthogonal orientation adopted for the reconstructions, the narrow range of subjects' gestational age, and the use of the toolkits with default settings.

V. Conclusion

We compared two toolkits on a set of common clinical fetal MR scans acquired around the 21st gestational week. We found that NiftyMIC and MIALSRTK provide reliable reconstructed volumes, which can be used for biometric measurements. Moreover, the availability of SR images with an isotropic voxel size allows for conducting volumetric-based analyses, which may provide more faithful indices for assessing brain development. Finally, we disclosed that TSE sequences should be recommended for this aim as they are less affected by intensity artifacts.

Acknowledgement

This work was supported by Italian Ministry of Health, "Ricerca Corrente" funds and grant #RF-2019-12371349.

References

[1] G. Conte, S. Milani, G. Palumbo, G. Talenti, S. Boito, M. Rustico, F. Triulzi, A. Righini, G. Izzo, C. Doneda, A. Zolin and C. Parazzini, "Prenatal Brain MR Imaging: Reference Linear Biometric Centiles between 20 and 24 Gestational Weeks," *AJNR. American journal of neuroradiology*, vol. 39(5), pp. 963–967, 2018.

[2] V. Kyriakopoulou, D. Vatansever, A. Davidson, P. Patkee, S. Elkommos, A. Chew, M. Martinez-Biarge, B. Hagberg, M. Damodaram, J. Allsop, M. Fox, J. V. Hajnal and M. Rutherford, "Normative biometry of the fetal brain using magnetic resonance imaging," *Brain structure & function*, vol. 222(5), pp. 2295–2307, 2017.

[3] M. Ebner, G. Wang, W. Li, M. Aertsen, P. A. Patel, R. Aughwane, A. Melbourne, T. Doel, S. Dymarkowski, P. De Coppi, A. L. David, J. Deprest, S. Ourselin and T. Vercauteren, "An automated framework for localization, segmentation and super-resolution reconstruction of fetal brain MRI," *NeuroImage*, vol. 206, pp. 116324, 2020.

[4] S. Tourbier, P. De Dumast, H. Kebiri, P. Hagmann, M. Bach Cuadra, "Medical-Image-Analysis-Laboratory/mialsuperresolutiontoolkit: MIAL Super-Resolution Toolkit (Version v2.0.0)," Available: http://doi.org/10.5281/zenodo.4290209

[5] M. Khawam, P. de Dumast, P. Deman, H. Kebiri, T. Yu, S. Tourbier, H. Lajous, P. Hagmann, P. Maeder, J. P. Thiran, R. Meuli, V. Dunet, M. Bach Cuadra, and M. Koob, "Fetal Brain Biometric Measurements on 3D Super-Resolution Reconstructed T2-Weighted MRI: An Intra- and Inter-observer Agreement Study," *Frontiers in pediatrics*, vol. 9, pp. 639746, 2021.

[6] R. Likert, "A technique for the measurement of attitudes," *Archives of psychology*, 1932.

[7] A. Fedorov, R. Beichel, J. Kalpathy-Cramer, J. Finet, J. C. Fillion-Robin, S. Pujol, C. Bauer, D. Jennings, F. Fennessy, M. Sonka, J. Buatti, S. Aylward, J. V. Miller, S. Pieper and R. Kikinis, "3D Slicer as an image computing platform for the Quantitative Imaging Network." *Magnetic resonance imaging*, vol. 30(9), pp. 1323–1341, 2012.

[8] C. Garel, "Fetal cerebral biometry: normal parenchymal findings and ventricular size," *European radiology*, vol. 15(4), pp. 809–813.

[9] C. Parazzini, A. Righini, M. Rustico, D. Consonni, and F. Triulzi, "Prenatal magnetic resonance imaging: brain normal linear biometric values below 24 gestational weeks," *Neuroradiology*, vol. 50(10), pp. 877–883, 2008.

[10] R. Woitek, A. Dvorak, M. Weber, R. Seidl, D. Bettelheim, V. Schöpf, G. Amann, P. C. Brugger, J. Furtner, U. Asenbaum, D. Prayer and G. Kasprian, "MR-based morphometry of the posterior fossa in fetuses with neural tube defects of the spine," *PloS one*, vol. 9(11), pp. 112585, 2014.

[11] H. Passing and Bablok, "A new biometrical procedure for testing the equality of measurements from two different analytical methods. Application of linear regression procedures for method comparison studies in clinical chemistry," *Part I. Journal of clinical chemistry and clinical biochemistry*, vol. 21(11), pp. 709–720, 1983.

[12] J.M. Bland and D. G. Altman, "Measuring agreement in method comparison studies," *Statistical methods in medical research*, vol. 8(2), pp. 135–160, 1999.

[13] T. K. Koo, and M. Y. Li, "A Guideline of Selecting and Reporting Intraclass Correlation Coefficients for Reliability Research," *Journal of chiropractic medicine*, vol. 15(2), pp. 155–163, 2016.

[14] S. S. Shapiro and M. B. Wilk, "An analysis of variance test for normality (complete samples)," *Biometrika*, vol. 52(3/4), pp. 591-611, 1965.

[15] K. L. Gwet, "Handbook of inter-rater reliability: The definitive guide to measuring the extent of agreement among raters," *Advanced Analytics*, 2014

[16] A. Gholipour, J. Estroff, C. Barnewolt, R. Robertson, P. Grant, B. Gagoski, S. Warfield, O. Afacan, S. Connolly, J. Neil, A. Wolfberg and R. Mulkern, "Fetal MRI: A Technical Update with Educational Aspirations." *Concepts in magnetic resonance*, vol. 43 (6), pp. 237-266, 2014.

Brugada Syndrome: Characterization of QT Interval Components and Correction

A. Sbrollini[1], S. Romagnoli[1], E.T. Locati[2], M. Morettini[1] and L. Burattini[1,*]
[1]*Department of Information Engineering, Università Politecnica delle Marche, Ancona, Italy*
[2]*Arrhythmology Department, IRCCS Policlinico San Donato, San Donato Milanese, Milano, Italy*

***Abstract*— Brugada syndrome (BrS) is an inherited cardiac disorder at high risk of sudden death. There are two ECG patterns for BrS: Type 1 (coved-type), representing the only diagnostic pattern for BrS (BrS1), while type 2 (saddle-back type) is only suggestive of BrS (BrS2). The QT interval on surface ECG, known to be heart-rate (HR) dependent, characterizes ventricular activity and is associated with the risk of ventricular arrhythmias. Aim of this study is to investigate the role of QT-interval and QT-interval-segment correction in subjects with BrS1 and BrS2, compared to controls (CTR). Open-access "Brugada ECG Database" by Zenodo was considered, containing HR, QT interval and its segments (QJ, JT_p, and T_pT_e) of 60 subjects with BrS1, 27 subjects with BrS2 and 51 CTR. Time intervals and segments were corrected according to nine correction formulae. Feature distributions of BrS1, BrS2 and CTR were compared by unpaired Wilcoxon rank sum test. All BrS1 and BrS2 features were statistically different from CTR. QT interval and corrected QT interval were significantly longer in BrS1 and BrS2 than in CTR, mainly due to longer QJ and T_pT_e, while JT_p was significantly shorter in BrS1 and BrS2 than in CTR. No significant differences were observed in QJ and JT_p between BrS1 and BrS2, whereas five correction formulae revealed that BrS1 had significantly longer T_pT_e interval than BrS2, suggesting physiological differences between BrS1 and BrS2 in late repolarization phase. In conclusion, major differences exist between BrS patients and CRT in QT-interval duration, mainly due to longer QJ and shorter JT_p duration in BrS patients, while differences may exist between BrS1 and BrS2 patients in the late repolarization phase, highlighting the need of proper QT-HR correction to better characterize BrS patients.**

***Keywords*—QT Interval, Brugada Syndrome, QT Correction, Digital Cardiology.**

I. Introduction

BRUGADA syndrome is an inherited cardiac disease, defined also as sodium channelopathy [1,2], characterized by a prevalence of 1-5/10000 individuals; it is responsible for 4% of all sudden cardiac deaths [3-5]. Diagnosis of Brugada syndrome is also based on electrocardiogram (ECG) analysis. ECG is the measurement of cardiac electrical activity, that is composed of three wave patterns (Fig. 1): the P wave reflects the atrial depolarization; the QRS complex reflects the ventricular repolarization and covers the atrial repolarization and, finally, the T wave reflects the ventricular repolarization [6]. Considering the standard ECG pattern, diagnosis of Brugada Syndrome occurs if the precordial V1-V3 leads are characterized by ST-segment elevation of at least 0.2 mV. [1]. Brugada Syndrome is classified according with the topology of the T wave: if the T wave results to be negative, the Brugada Syndrome is of Type 1 (BrS1, Fig. 2a), while if the T wave results to be positive or biphasic (saddleback pattern), the Brugada Syndrome is of Type 2 (BrS2, Fig. 2b).

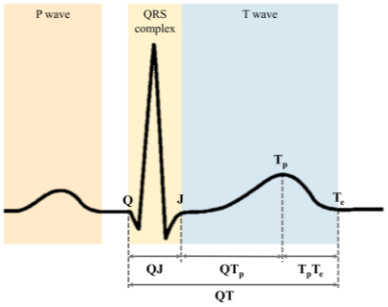


Fig. 1: Electrocardiogram (ECG) pattern, characterized by P wave, QRS complex and T wave. Measurement of QT and its fragmentation into QJ, QTp and TpTe segments is also depicted.

Subjects affected by BrS1 appear to have higher probability to suffer from malignant ventricular arrhythmias [7]. SCN5A gene mutations, occurring in about 25-30% of BrS cases, have been associated with a worse prognosis [8].

The most important ECG feature for the characterization on ventricular activity (depolarization and repolarization) is the QT interval (Fig. 1), defined as the time interval between the beginning of the QRS complex and the end of the T wave [6]. It can be also characterized by its composing segments (Fig. 1), that are the QJ segment (also called QRS duration), the JT_p segment and T_pT_e segment. QJ segment reflects the timing of ventricular depolarization, JT_p segment reflects the timing of early ventricular repolarization and T_pT_e segment reflects the timing of late ventricular repolarization.

It is widely known that QT interval is heart-rate (HR) dependent [9,10]. Specifically, an increase/decrease of the heart rate provokes a decrease/increase of the QT interval. Thus, the measurement of QT interval should be normalized according with HR. In the literature, nine QT-interval corrections have been proposed in order to adjust the QT-interval measure [9-19]. Despite the wide use of QT-interval correction, no studies investigated the role of correction in Brugada Syndrome and, specifically, in the correction of the different segments constituting the QT interval. Thus, aim of this study is to investigate the role of the correction of QT-interval segments in subjects affected by Type 1 and Type 2 Brugada Syndrome.

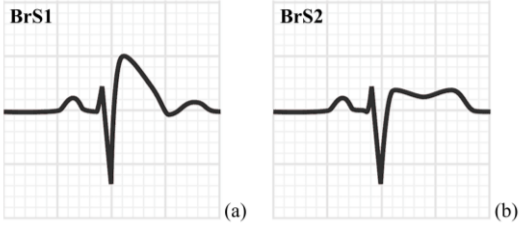


Fig. 2: Electrocardiographic pattern of Brugada Syndrome Type 1 (BrS1, panel a) and Brugada Syndrome Type 2 (BrS2, panel b).

II. Materials and Methods

A. Database

Open-access "Brugada ECG Database" by Zenodo was considered in this study [20-21]. The database contains ECG features of 60 subjects affected by Type 1 Brugada Syndrome (BrS1), 27 subjects affected by Type 2 Brugada Syndrome (BrS2) and 51 control subjects (CTR). Specifically, ECG features were extracted from 3 precordial leads, that are V1, V2 and V3. In this study, the heart rate (HR), the QT interval, the QJ segment, the JT_p segment and the T_pT_e segment of three leads were considered for each subject.

B. QT-Interval and QT-Interval-Segment Correction

QT interval and QT-interval segments (QJ, JT_p and T_pT_e) of three V1-V3 leads of BrS1, BrS2 and CTR were corrected according with the formulae [9,10] reported in Table I.

TABLE I: Formulae for QT-interval and QT-interval-segment correction.

Ref.	*Correction*	*Formulae*
[11]	Bazett	$\begin{cases} QTc=\frac{QT}{\sqrt{60/HR}} & JT_pc=\frac{JT_p}{\sqrt{60/HR}} \\ QJc=\frac{QJ}{\sqrt{60/HR}} & T_pT_ec=\frac{T_pT_e}{\sqrt{60/HR}} \end{cases}$
[12]	Fridericia	$\begin{cases} QTc=\frac{QT}{\sqrt[3]{60/HR}} & JT_pc=\frac{JT_p}{\sqrt[3]{60/HR}} \\ QJc=\frac{QJ}{\sqrt[3]{60/HR}} & T_pT_ec=\frac{T_pT_e}{\sqrt[3]{60/HR}} \end{cases}$
[13]	Dmitrienko	$\begin{cases} QTc=\frac{QT}{(60/HR)^{0.413}} & JT_pc=\frac{JT_p}{(60/HR)^{0.413}} \\ QJc=\frac{QJ}{(60/HR)^{0.413}} & T_pT_ec=\frac{T_pT_e}{(60/HR)^{0.413}} \end{cases}$
[14]	Ashman	$\begin{cases} QTc=\frac{QT}{\log_{10}\left[10\times\left(\frac{60}{HR}+0{,}07\right)\right]\times\log_{10}10.7} \\ QJc=\frac{QJ}{\log_{10}[10\times(60/HR+0{,}07)]\times\log_{10}10.7} \\ JT_pc=\frac{JT_p}{\log_{10}[10\times(60/HR+0{,}07)]\times\log_{10}10.7} \\ T_pT_ec=\frac{T_pT_e}{\log_{10}[10\times(60/HR+0{,}07)]\times\log_{10}10.7} \end{cases}$
[15]	Framingharm	$\begin{cases} QTc=QT+0.154\times(1-60/HR) \\ QJc=QJ+0.154\times(1-60/HR) \\ JT_pc=JT_p+0.154\times(1-60/HR) \\ T_pT_ec=T_pT_e+0.154\times(1-60/HR) \end{cases}$
[16]	Hodges	$\begin{cases} QTc=QT+0.00175\times(HR-60) \\ QJc=QJ+0.00175\times(HR-60) \\ JT_pc=JT_p+0.00175\times(HR-60) \\ T_pT_ec=T_pT_e+0.00175\times(HR-60) \end{cases}$
[17]	Schlamowitz	$\begin{cases} QTc=QT+0.205\times(1-60/HR) \\ QJc=QJ+0.205\times(1-60/HR) \\ JT_pc=JT_p+0.205\times(1-60/HR) \\ T_pT_ec=T_pT_e+0.205\times(1-60/HR) \end{cases}$
[18]	Rautaharju	$\begin{cases} QTc=QT+0.24251-0.434\times e^{-0.0097\times HR} \\ QJc=QJ+0.24251-0.434\times e^{-0.0097\times HR} \\ JT_pc=JT_p+0.24251-0.434\times e^{-0.0097\times HR} \\ T_pT_ec=T_pT_e+0.24251-0.434\times e^{-0.0097\times HR} \end{cases}$
[19]	Sarma	$\begin{cases} QTc=QT+0.04462-0.664\times e^{-2.7\times(60/HR)} \\ QJc=QJ+0.04462-0.664\times e^{-2.7\times(60/HR)} \\ JT_pc=JT_p+0.04462-0.664\times e^{-2.7\times(60/HR)} \\ JT_pc=JT_p+0.04462-0.664\times e^{-2.7\times(60/HR)} \end{cases}$

C. Statistics

Normality of HR, QT-interval, QT-interval-segment, corrected QT-interval and QT-interval-segment distributions was assessed by Lilliefors test. Not normal distributions of BrS1, BrS2 and CTR were reported as $50^{th}[25^{th};75^{th}]$ percentiles and compared using the unpaired Wilcoxon ranksum test for median values.

III. Results

HR distributions of BrS1, BrS2 and CTR were 73[66;81]bpm, 65[62;73]bpm, and 69[65;79]bpm, respectively; median HR of BrS1 and BrS2 were statistically different (p=0.04). QT-interval, QT-interval-segment, corrected QT-interval and QT-interval-segment distributions are reported in Table II. QT interval and corrected QT interval were statistically longer in BrS1 and BrS2 than in CTR, mainly due to longer QJ and T_pT_e durations, while JT_p was significantly shorter in BrS1 and BrS2 than in CTR. Regarding the comparison BrS1 and BrS2 (Fig. 3), BrS1 presents median value of JT_p in V3 lead statistically lower than BrS2 (BrS1:164 ms, BrS2:174 ms, p=0.04). Differently, BrS1 presents median value of JT_pc segment not statistically different than BrS2 in all corrections (Table II, p>0.05). Median value of T_pT_ec of BrS1 and BrS2 are statistically difference in V3 lead if considering correction by Framingharm, Hodges, Schlamowitz, Rautaharju and Sarma [15-19] and in V2 lead if considering correction by Rautaharju and Sarma [18,19].

IV. Discussion

This study aimed to investigate the role of the QT-interval and QT-interval-segment correction in subjects affected by BrS1 and BrS2. Evaluating the QT interval in BrS is essential because it may be a prevention tool against sudden death [7].

It is widely known that QT interval is HR dependent, *i.e.*, QT interval modulates according to the HR (lower HR associates to longer QT interval; higher HR associates to shorten QT interval). In the literature, several QT-interval corrections were proposed [9-19] to investigate HR-QT association and to normalize QT interval, avoiding misinterpretation. Despite the many studies, none of them evaluated the effect of HR on QT-interval segments, that are depolarization (QJ segment), early repolarization (JT_p segment) and late repolarization (T_pT_e segment).

According with our results, the effect of HR on QT-interval segments appears extremely important. Indeed, statistical difference of JT_p in V3 between BrS1 and BrS2 subjects might be misinterpreted, although it is the consequence induced by HR (same statistical significance). Thus, QT-interval and QT-interval-segment normalization is essential when discriminating Brugada Syndrome. Of note, five QT-interval corrections reveal that BrS1 and BrS2 presents statistically different T_pT_ec in leads V2 and V3. These results highlight a possible difference between BrS1 and BrS2 in the late repolarization phase, at a difference with what is shown by the uncorrected measurements, showing differences in the early repolarization phase. These results need to be confirmed by further clinical studies, possibly including patients with known genetic background.

TABLE II: QT-INTERVAL AND QT-INTERVAL-SEGMENT DISTRIBUTION OF SUBJECTS AFFECTED BY BRS1, BRS2 AND CTR.

			BrS1 (N=60)	*BrS2 (N=27)*	*CTR (N=51)*
NO CORRECTION	*V1*	*QT(ms)*	400* [364;437]	407* [373;453]	386 [353;406]
		QJ(ms)	115* [102;130]	116* [101;142]	100 [91;106]
		JT_p(ms)	189* [158;211]	186* [165;212]	206 [182;231]
		T_pT_e(ms)	86* [70;114]	86* [73;104]	72 [58;88]
	V2	*QT(ms)*	397* [363;426]	385* [373;418]	368 [347;389]
		QJ(ms)	115* [102;130]	116* [101;142]	97 [90;106]
		JT_p(ms)	164* [140;194]	164 [153;202]	181 [164;214]
		T_pT_e(ms)	107* [92;120]	102* [91;111]	86 [79;91]
	V3	*QT(ms)*	392* [367;409]	404* [363;416]	364 [346;386]
		QJ(ms)	116* [103;133]	114* [104;128]	97 [86;103]
		JT_p(ms)	164* [150;179]	176§[158;198]	189 [163;203]
		T_pT_e(ms)	104* [95;119]	104* [91;108]	86 [78;97]
BAZETT CORRECTION [10]	*V1*	*QTc(ms)*	438* [402;473]	437 [397;461]	411 [391;433]
		QJc(ms)	126* [113;146]	130* [110;146]	106 [98;116]
		JT_pc(ms)	213* [178;230]	198* [184;225]	225 [204;245]
		T_pT_ec(ms)	95* [76;127]	101* [76;111]	79 [69;93]
	V2	*QTc(ms)*	429* [401;474]	411* [398;438]	403 [384;413]
		QJc(ms)	126* [113;146]	130* [110;146]	105 [97;115]
		JT_pc(ms)	178* [152;217]	184* [166;204]	196 [186;213]
		T_pT_ec(ms)	117* [97;131]	105* [98;114]	93 [83;102]
	V3	*QTc(ms)*	427* [401;447]	419* [402;446]	399 [383;411]
		QJc(ms)	127* [114;144]	122* [106;141]	104 [93;116]
		JT_pc(ms)	179* [165;194]	185 [173;204]	199 [183;214]
		T_pT_ec(ms)	115* [101;131]	108* [97;114]	94 [83;103]
FRIDERICIA CORRECTION [11]	*V1*	*QTc(ms)*	427* [396;460]	423* [394;456]	398 [380;422]
		QJc(ms)	123* [111;140]	126* [108;143]	104 [95;112]
		JT_pc(ms)	205* [170;225]	195* [176;218]	219 [198;238]
		T_pT_ec(ms)	92* [75;123]	95* [74;109]	78 [65;89]
	V2	*QTc(ms)*	415* [393;458]	401* [392;427]	391 [374;402]
		QJc(ms)	123* [111;140]	126* [108;143]	103 [94;112]
		JT_pc(ms)	173* [148;207]	180* [163;200]	191 [179;213]
		T_pT_ec(ms)	112* [95;127]	104* [96;114]	91 [83;98]
	V3	*QTc(ms)*	415* [391;432]	413* [393;432]	387 [374;401]
		QJc(ms)	123* [110;140]	120* [106;136]	101 [91;112]
		JT_pc(ms)	171* [160;188]	182 [168;202]	196 [176;210]
		T_pT_ec(ms)	111* [99;128]	106* [93;115]	93 [81;101]
DMITRIENKO CORRECTION [12]	*V1*	*QTc(ms)*	429* [399;467]	427* [396;458]	406 [385;427]
		QJc(ms)	125* [112;143]	129* [110;145]	105 [97;114]
		JT_pc(ms)	209* [173;227]	196* [180;223]	221 [203;240]
		T_pT_ec(ms)	93* [75;125]	98* [75;110]	79 [67;91]
	V2	*QTc(ms)*	418* [397;465]	407* [395;430]	399 [379;406]
		QJc(ms)	125* [112;143]	129* [110;145]	104 [95;114]
		JT_pc(ms)	176* [150;212]	182* [165;202]	192 [184;213]
		T_pT_ec(ms)	114* [96;129]	104* [98;114]	92 [83;100]
	V3	*QTc(ms)*	419* [397;441]	416* [400;439]	392 [380;405]
		QJc(ms)	125* [112;142]	121* [106;138]	102 [92;114]
		JT_pc(ms)	175* [163;191]	183 [168;203]	198 [179;211]
		T_pT_ec(ms)	113* [100;130]	107* [95;114]	93 [82;101]
ASHMAN CORRECTION [13]	*V1*	*QTc(ms)*	406* [377;440]	407* [373;432]	385 [363;403]
		QJc(ms)	118* [106;135]	122* [104;136]	99 [91;108]
		JT_pc(ms)	197* [164;214]	185* [170;211]	208 [191;227]
		T_pT_ec(ms)	88* [71;118]	92* [71;104]	74 [63;86]
	V2	*QTc(ms)*	396* [375;439]	384* [372;406]	376 [357;384]
		QJc(ms)	118* [106;135]	122* [104;136]	98 [89;107]
		JT_pc(ms)	166* [142;200]	172* [156;190]	182 [174;201]
		T_pT_ec(ms)	108* [90;122]	98* [92;108]	87 [78;94]
	V3	*QTc(ms)*	395* [375;415]	392* [377;418]	369 [358;382]
		QJc(ms)	118* [105;134]	114* [100;130]	96 [87;107]
		JT_pc(ms)	166* [154;180]	173 [159;192]	186 [169;199]
		T_pT_ec(ms)	106* [94;123]	101* [90;108]	88 [77;95]

			BrS1 (N=60)	*BrS2 (N=27)*	*CTR (N=51)*
FRAMINGHARM CORRECTION [14]	*V1*	*QTc(ms)*	427* [398;458]	423* [395;456]	400 [382;422]
		QJc(ms)	149* [125;162]	138* [114;161]	118 [105;136]
		JT_pc(ms)	216* [191;235]	209* [189;231]	233 [212;248]
		T_pT_ec(ms)	115* [93;144]	112 [80;127]	100 [84;116]
	V2	*QTc(ms)*	415* [394;457]	403* [393;426]	393 [377;403]
		QJc(ms)	149* [125;162]	138* [114;161]	118 [105;138]
		JT_pc(ms)	189* [168;221]	187* [170;207]	205 [198;217]
		T_pT_ec(ms)	135* [111;149]	115 [102;127]	105 [96;124]
	V3	*QTc(ms)*	415* [394;432]	412* [395;432]	389 [376;402]
		QJc(ms)	142* [129;158]	130* [113;155]	115 [103;133]
		JT_pc(ms)	188* [176;204]	194* [182;208]	207 [194;222]
		T_pT_ec(ms)	129* [113;146]	114§[102;130]	109 [92;127]
HODGES CORRECTION [15]	*V1*	*QTc(ms)*	424* [394;457]	423* [394;456]	398 [379;420]
		QJc(ms)	147* [123;159]	137* [112;158]	114 [103;133]
		JT_pc(ms)	215* [188;233]	206* [187;230]	231 [208;246]
		T_pT_ec(ms)	113* [91;143]	109 [79;125]	96 [81;113]
	V2	*QTc(ms)*	415* [393;453]	400* [391;425]	390 [374;403]
		QJc(ms)	147* [123;159]	137* [112;158]	113 [101;134]
		JT_pc(ms)	186* [165;218]	186* [171;207]	203 [195;218]
		T_pT_ec(ms)	131* [108;147]	113* [100;124]	103 [92;121]
	V3	*QTc(ms)*	413* [393;428]	413* [392;429]	386 [376;401]
		QJc(ms)	141* [125;157]	127* [110;152]	111 [101;129]
		JT_pc(ms)	185* [173;201]	194* [180;205]	205 [198;220]
		T_pT_ec(ms)	130* [110;143]	112§[102;126]	106 [89;125]
SCHLAMOWITZ CORRECTION [16]	*V1*	*QTc(ms)*	431* [402;466]	428 [397;459]	411 [391;429]
		QJc(ms)	159* [132;174]	143 [115;169]	127 [108;147]
		JT_pc(ms)	224* [197;244]	216* [190;240]	242 [215;258]
		T_pT_ec(ms)	124* [99;154]	115 [83;139]	112 [84;130]
	V2	*QTc(ms)*	422* [400;466]	411* [398;433]	402 [384;409]
		QJc(ms)	159* [132;174]	143 [115;169]	124 [108;149]
		JT_pc(ms)	197* [172;229]	195* [172;219]	215 [205;229]
		T_pT_ec(ms)	143* [113;162]	120 [105;140]	110 [101;137]
	V3	*QTc(ms)*	422* [401;441]	417* [402;437]	395 [384;408]
		QJc(ms)	154* [138;171]	132 [117;167]	121 [108;143]
		JT_pc(ms)	198* [178;213]	206* [190;213]	216 [205;228]
		T_pT_ec(ms)	141* [114;156]	117§[103;140]	116 [98;139]
RAUTAHARJU CORRECTION [17]	*V1*	*QTc(ms)*	427* [399;461]	424* [395;457]	405 [384;424]
		QJc(ms)	155* [127;166]	138* [115;164]	121 [105;139]
		JT_pc(ms)	219* [193;239]	211* [189;234]	238 [212;252]
		T_pT_ec(ms)	118* [93;147]	111 [79;131]	104 [84;122]
	V2	*QTc(ms)*	417* [396;458]	407* [393;430]	398 [378;404]
		QJc(ms)	155* [127;166]	138* [115;164]	119 [105;141]
		JT_pc(ms)	191* [169;223]	190* [173;211]	210 [200;224]
		T_pT_ec(ms)	137* [113;155]	115§[101;132]	105 [95;128]
	V3	*QTc(ms)*	417* [397;435]	415* [399;437]	390 [379;404]
		QJc(ms)	146* [131;164]	130* [113;159]	115 [104;135]
		JT_pc(ms)	190* [178;209]	202* [185;209]	210 [201;223]
		T_pT_ec(ms)	133* [113;148]	114§[102;133]	108 [92;132]
SARMA CORRECTION [18]	*V1*	*QTc(ms)*	429* [398;460]	430* [394;456]	406 [384;424]
		QJc(ms)	155* [126;166]	136* [113;164]	120 [103;138]
		JT_pc(ms)	221* [192;238]	210* [188;239]	238 [212;254]
		T_pT_ec(ms)	117* [92;148]	110 [78;131]	105 [82;122]
	V2	*QTc(ms)*	418* [397;457]	407* [392;436]	397 [379;406]
		QJc(ms)	155* [126;166]	136* [113;164]	117 [104;140]
		JT_pc(ms)	193* [168;223]	192* [172;211]	211 [200;225]
		T_pT_ec(ms)	135* [112;158]	113§[101;132]	104 [94;129]
	V3	*QTc(ms)*	417* [400;434]	415* [399;443]	392 [382;406]
		QJc(ms)	146* [130;163]	128* [112;159]	114 [104;136]
		JT_pc(ms)	191* [177;210]	205* [184;210]	211 [201;223]
		T_pT_ec(ms)	135* [112;148]	113§[102;132]	107 [92;132]

*$p<0.05$ when comparing CTR vs. BrS1 and BrS2; §$p<0.05$ when comparing BrS1 vs. BrS2.

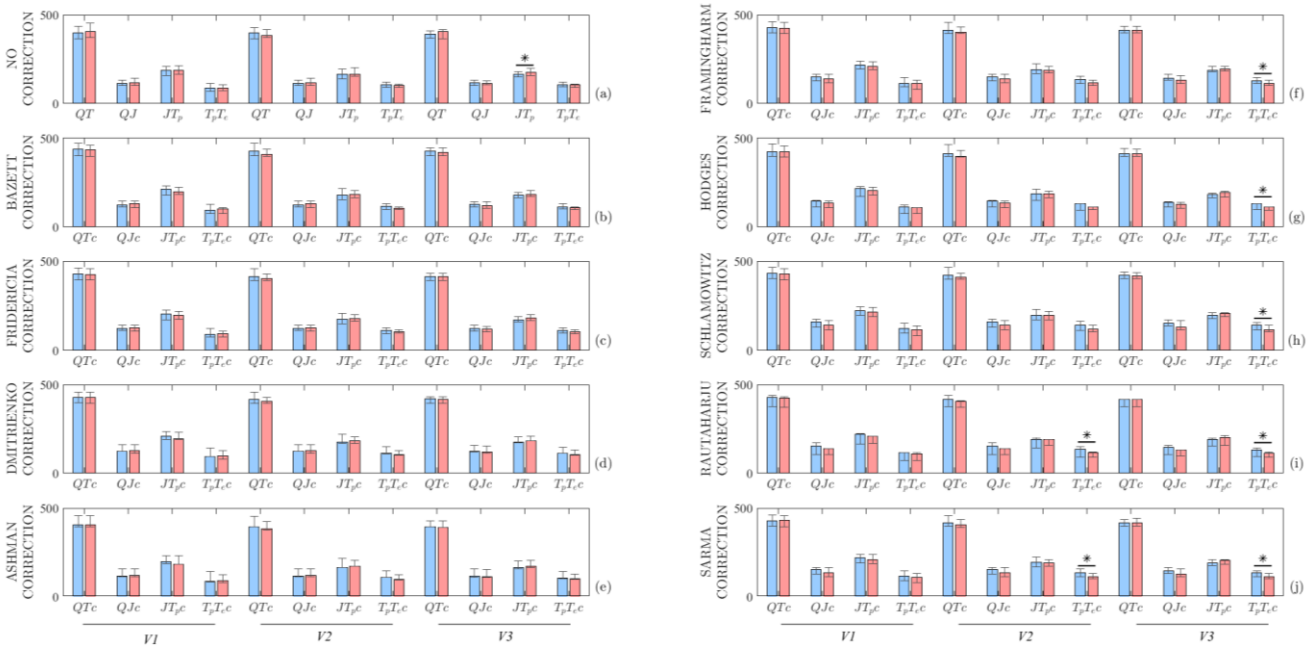


Fig. 3: QT-interval and QT-interval-segment distribution (in ms) of subjects affected by BrS1 (in blue) and BrS2 (in red). Different panels depict QT interval and QT-interval segments of (a) no correction, and corrections by (b) Bazett [10], (c) Fridericia [11], (d) Dmitrienko [12], (e) Ashman [13], (f) Framingharm [14], (g) Hodges [15], (h) Schlamowitz [16], (i) Rautaharju [17] and (j) Sarma [18].

V. Conclusion

QT-interval and QT-interval segment corrections are essential in Brugada syndrome. Future studies will investigate the difference in late depolarization between subjects affected by Type 1 and Type 2 Brugada Syndrome.

References

[1] D. C. Peritz and E. H. Chung. (2016, Mar-Apr). Criteria for evaluating rSr′ patterns due to high precordial ECG lead placement accurately confirm absence of a Brugada ECG pattern. *Journal of Electrocardiology*. *49(2)*, 182–186. Available: https://doi.org/10.1016/j.jelectrocard.2015.12.015

[2] B. Martini, A. Nava, G. Thiene, G. F. Buja, B. Canciani et al. (1989, Dec). Ventricular fibrillation without apparent heart disease: description of six cases. *American Heart Journal*. *118(6)*, 1203–1209. Available: https://doi.org/10.1016/0002-8703(89)90011-2

[3] V. L. Roger, A. S. Go, D. M. Lloyd-Jones, E. J. Benjamin, J. D. Berry et al. (2012, Jan) American Heart Association Statistics Committee and Stroke Statistics Subcommittee. Heart disease and stroke statistics--2012 update: a report from the American Heart Association. *Circulation*, *125(1)*, e2–e220. Available: https://doi.org/10.1161/CIR.0b013e31823ac046

[4] B. Benito, J. Brugada, R. Brugada, P. Brugada, P. (2009, Nov). Brugada syndrome. *Revista Espanola de Cardiologia*. *62(11)*, 1297–1315. Available: https://doi.org/10.1016/s1885-5857(09)73357-2

[5] C. Antzelevitch, P. Brugada, M. Borggrefe, J. Brugada, R. Brugada, et al. (2005, Apr). Brugada syndrome: report of the second consensus conference. *Heart Rhythm*. *2(4)*, 429–440. Available: https://doi.org/10.1016/j.hrthm.2005.01.005

[6] R.E. Klabunde, “Cardiovascular Physiology Concepts”, 2nd ed., Lippincott Williams & Wilkins, Ed., 2012.

[7] P. Delise, G. Allocca, E. Marras, C. Giustetto, F. Gaita, et al. (2011, Jan). Risk stratification in individuals with the Brugada type 1 ECG pattern without previous cardiac arrest: usefulness of a combined clinical and electrophysiologic approach. *European Heart Journal*, *32(2)*, 169–176. Available: https://doi.org/10.1093/eurheartj/ehq381

[8] G. Ciconte, M. M. Monasky, V. Santinelli, E. Micaglio, G. Vicedomini, L. Anastasia, et al. (2021, Mar). Brugada syndrome genetics is associated with phenotype severity. *European Heart Journal*, *42(11)*, 1082–1090. Available: https://doi.org/10.1093/eurheartj/ehaa942

[9] I. Andršová, K. Hnatkova, M. Šišáková, O. Toman, P. Smetana, et al. (2021, Jul). Influence of heart rate correction formulas on QTc interval stability. *Scientific Reports*. *11(1)*, 14269. Available: https://doi.org/10.1038/s41598-021-93774-9

[10] B. Vandenberk, E. Vandael, T. Robyns, J. Vandenberghe, C. Garweg et al. (2016, Jun). Which QT correction formulae to use for QT monitoring?. *Journal of the American Heart Association*. *5(6)*, e003264. Available: https://doi.org/10.1161/JAHA.116.003264

[11] J. C. Bazett. (1920) An analysis of time relations of electrocardiograms. *Heart*. *7*, 353–367.

[12] L. S. Fridericia. (1920) Die Systolendauer im Elekrokardiogramm bei normalen Menschen und bei Herzkranken. *Acta Medica Scandinavica*. *53*, 469–486. Available: https://doi.org/10.1111/j.0954-6820.1920.tb18266.x.

[13] A. A. Dmitrienko, G. D. Sides, K. J. Winters, R. J. Kovacs, D. M. Rebhun, J. C. Bloom et al. (2005, Oct). Electrocardiogram reference ranges derived from a standardized clinical trial population. *Therapeutic Innovation & Regulatory Science*. *39(4)*, 395–405. Available: https://doi.org/10.1177/009286150503900408

[14] R. Ashman. (1942) The normal duration of the Q-T interval. *American Heart Journal*. *23(4)*, 522–534. Available: https://doi.org/10.1016/S0002-8703(42)90297-7.

[15] A. Sagie, M. G. Larson, R. J. Goldberg, J. R. Bengtson, and D. Levy. (1992, Sep). An improved method for adjusting the QT interval for heart rate (the Framingham Heart Study). *The American Journal of Cardiology*. *70(7)*, 797–801. Available: https://doi.org/10.1016/0002-9149(92)90562-d

[16] M. Hodges, D. Salerno and D. Erlien. (1983). Bazett’s QT correction reviewed: Evidence that a linear QT correction for heart rate is better. *Journal of the American College of Cardiology*. *1*, 694.

[17] I. Schlamowitz. (1946, Mar). An analysis of the time relationships within the cardiac cycle in electrocardiograms of normal men. The duration of the Q-T interval and its relationship to the cycle length (R-R interval). *American Heart Journal*. *31*, 329–342. Available: https://doi.org/10.1016/0002-8703(46)90314-6

[18] P. M. Rautaharju, J. W. Warren, and H. P. Calhoun (1990). Estimation of QT prolongation. A persistent, avoidable error in computer electrocardiography. *Journal of Electrocardiology*. *23*, 111–117. https://doi.org/10.1016/0022-0736(90)90085-g

[19] J. S. Sarma, R. J. Sarma, M. Bilitch, D. Katz, and S.L. Song. (1984, Jul). An exponential formula for heart rate dependence of QT interval during exercise and cardiac pacing in humans: reevaluation of Bazett's formula. *The American Journal of Cardiology*. *54(1)*, 103–108. Available: https://doi.org/10.1016/0002-9149(84)90312-6

[20] Brugada ECG database. Available: https://doi.org/10.5281/zenodo.3266179

[21] G. Tse, S. Reddy, J. Chopra, S. Lee, T. Liu, T., et al. (2019, Jul-Aug). Electrocardiographic evidence of abnormal atrial phenotype in Brugada syndrome. *Journal of Electrocardiology*. *55*, 102–106. Available: https://doi.org/10.1016/j.jelectrocard.2019.05.005

Interhemispheric functional connectivity: an fMRI study in two split-brain patients

I. Marcantoni[1§], G. Piccolantonio[2§], E. Vitti[1], G. Polonara[3], M. Ghoushi[3], M. Valenti[3], L. Reversi[3], N. Foschi[4], S. Lattanzi[4], L. Burattini[1]*, M. Fabri[5]

[1]*Dipartimento di Ingegneria dell'Informazione, Università Politecnica delle Marche, Ancona*

[2]*Dipartimento di Informatica, Università di Verona, Verona*

[3]*Dipartimento di Scienze Cliniche Specialistiche e Odontostomatologiche, Università Politecnica delle Marche, Ancona*

[4]*Dipartimento di Medicina Sperimentale e Clinica, Università Politecnica delle Marche, Ancona, Italy*

[5]*Dipartimento di Scienze della Vita e dell'Ambiente, Università Politecnica delle Marche, Ancona, Italy*

[§]*Equally contributed to the article; *Corresponding Author*

***Abstract*— Resting state networks (RSNs) were most studied using functional magnetic resonance imaging (fMRI). Interhemispheric functional connectivity (FC) appears mostly supported by the corpus callosum (CC) and several studies have investigated this aspect, still not providing conclusive evidence. In this context, patients in whom the CC was resected for therapeutic reasons (split-brain patients) provide a unique opportunity of research. The purpose of this pilot study is to investigate, with resting state fMRI, the interhemispheric FC in two callosotomized patients operated in adult age, and in four healthy control subjects with intact brain. The analysis was performed with fMRI of the Brain (FMRIB) Software Library (FSL); the evaluation of interhemispheric FC and the recognition of the RSNs were performed by using the probabilistic independent component analysis (PICA). The multi-subject analysis on control subjects allowed the identification of three RSNs: medial visual, default mode, and sensory motor. Both patients showed a bilateral brain activation in the medial visual network, comparable with the controls; in the sensory motor and the default mode networks the activation was unilateral, at variance with controls. These results seem to suggest that the brain, during its maturation, builds new subcortical communication pathways, alternative to the CC, which might support interhemispheric FC in case of callosotomy. Further studies are needed to confirm the observations obtained and reported in this preliminary research.**

***Keywords* — callosotomy, interhemispheric connectivity, lateralization, resting-state functional connectivity.**

I. Introduction

THE resting state brain activity refers to spontaneous activity without deliberately given stimuli. Such activity shows relatively consistent distributed patterns and can be used to characterize network dynamics without needing an explicit task to drive brain activity [1]. Indeed, in resting conditions, left and right hemispheric regions are not silent but are active and show reciprocal high correlation suggesting ongoing information processing and functional connectivity (FC) between these regions during rest [2]. Although the relation between structural and FC has profound implications for our understanding of cerebral physiology and cognitive neuroscience, it remains incompletely understood.

The brain seems to be mainly driven by its intrinsic activity and possible external stimulations can modulate, rather than determine, its activity. The brain is always active, even in the absence of a specific task being performed or of a particular stimulus [2]. Moreover, one of the most striking features of resting state FC is symmetry about the midline. Resting state correlations tend to be particularly strong between corresponding loci in each hemisphere (homotopic FC) [3], [4]. Resting state networks (RSNs, *i.e.*, anatomically separated, but functionally linked, brain regions) show a high level of FC during rest. The most common RSNs were discovered and described by Beckmann and coworkers [5], and, more recently, by Smith and coworkers, who identified 10 networks of the state of rest studying 36 healthy patients during resting state [6].

The corpus callosum (CC) is the major commissure connecting the two hemispheres structurally and functionally. Accordingly, the CC is supposed to accounts for the prominent symmetry of FC. Patients in whom the CC was resected for therapeutic reasons (split-brain patients) provide a unique opportunity to study this question. However, data pertaining to this question are mixed and partially contradictory. Previous observations made in patients with intractable epilepsy, who have undergone therapeutic section of the CC, report conflicting results [7–9]. Specifically, a study on a 6-years-old boy before and after a complete callosotomy reports that FC was normal before surgery but largely lost afterward [7]. On the other hand, a partially intact interhemispheric FC was found four decades after total callosotomy [8]. A more recent study, carried out on young epileptic patients, followed up until 2 years after surgery, affirms that CC resection reduces interhemispheric FC [9].

The present study is a preliminary analysis considering two adult patients, operated in adult age to resect the CC. The aim is to evaluate their interhemispheric FC, analyzing functional magnetic resonance imaging (fMRI) data acquired in resting state condition. A healthy population, whose fMRI data were acquired in the same resting conditions, is used as control population.

II. Experimental Procedure

A. Participants

The data were obtained from two epileptic patients (42 and 52 years; males) who underwent complete callosal resection about 20 years before the study, and four healthy subjects (31-64 years; M/F=1/4), all right-handed. The fMRI data were acquired between June 2018 and September 2022. All participants gave their informed consent to the experimental

procedure, approved by the Ethical Committee of Università Politecnica delle Marche. Details of healthy subjects (controls) and callosotomized patients are reported in Table I.

TABLE I: DATA OF PARTICIPANTS

Participants	*G*	*AT*	*CR*	*Y2S*
		Controls		
S1	F	31	na	na
S2	M	56	na	na
S3	F	52	na	na
S4	F	64	na	na
		Callosotomized patients		
P1	M	42	Total	19
P2	M	52	Total	24

AT: age at testing; CR: callosal resection; G: gender; Y2S: years after second surgery.

B. Functional MRI data acquisition

Both controls and patients were instructed in advanced to lie down and remain still as much as possible during the fMRI acquisition, to keep their eyes open, to relax without falling asleep and without focusing on anything. Resting-state BOLD fMRI data and T1-weighted structural images were acquired using a 1.5 Signal HDxt GE Medical System MRI scanner.

Functional images were acquired with an echo planar image (EPI) gradient-echo sequence, with the following parameters: echo time (TE)=50 ms, repetition time (TR)=3000 ms, flip angle=90°, field of view (FOV) of 240×240 mm, matrix size of 64×64, number of volumes=300, number of axial slices=35, slice thickness=5 mm in controls and 4 mm in patients, with no gap between slice acquisition, voxel resolution 3×3×(slice thickness) mm. The duration of resting state fMRI was 15 min and 10 s. The T1-weighted structural images (3D; high-resolution whole-brain images, also called structural image) were acquired with a MPRAGE sequence with TE= 6.7 ms, TR=14.7 ms, FOV of 290×290 mm, matrix size of 288×288 mm, number of sagittal slices=158, slice thickness=1 mm with no gap between slice acquisition, voxel resolution 0.5664×0.5664×1 mm. The duration was 8 min and 8 s.

C. Data analysis

The structural and functional images were analyzed by means of the fMRI of the Brain (FMRIB) Software Library (FSL). [10]

A preprocessing procedure was performed on the raw data. The procedure includes several steps, as follows: (1) brain extraction, (2) motion correction, (3) slice time correction, (4) spatial smoothing, (5) temporal filtering and (6) registration. The step of brain extraction was performed using the brain extraction tool (BET) [11]. BET removes non-brain tissues (*e.g.*, skull and meninges) from the T1-weighted structural images according to the fractional intensity threshold parameter, which was set to 0.2. The remaining steps were performed within the Multivariate Exploratory Linear Optimized Decomposition into Independent Components (MELODIC), a FSL tool [5]. The slice time correction was performed on the functional images treating them as acquired sequentially in ascending order from bottom to top. The spatial smoothing was applied by setting the full width at half maximum at 5 mm. Finally, for temporal filtering, a high-pass filter was used, with a cutoff frequency of 0.01 Hz. The step of registration was performed using the FMRIB's Linear Image Registration Tool (FLIRT) [12]. By means of FLIRT, the co-registration of the T1-weighted structural image with the functional image was performed, as well as the normalization respect to a standard brain used as template to allow multi-subject analysis. The co-registration was different for controls and patients. In controls, it was performed with the 12 degree of freedom registration method; in patients, it was performed with the boundary-based registration method. For the normalization phase, the Montreal Neurological Institute (MNI) approach was used as template.

After pre-processing, independent component analysis (ICA) decomposition allowed to discriminate the data of functional images into non-Gaussian sources to improve the specificity and sensitivity of results derived from blood-oxygen-level-dependent (BOLD) signal evaluation. Specifically, with FSL the probabilistic ICA (PICA) model proposed by Beckmann and Smith was used [5]. At variance with the standard ICA, the PICA model quantifies the statistical significance for estimated spatial maps of brain activity and includes a noise/error term added to the source.

The spatial maps of brain activity estimated by PICA model show the active voxels, to which is associated a statistical significance. The activated voxels were not considered necessarily associated to a neural activity of interest, since the activation might also have been an artifact. In the implementation performed through MELODIC tool, the threshold defining the voxel activation was set to 0.5 and the number of independent components was automatically estimated by the tool. This analysis was performed on both patients through two single sessions and on all controls through a multi-session. This last procedure, by temporally concatenating the functional images of all controls in a data matrix, allows to identify common spatial maps of brain activity, which can be compared with the spatial maps obtained in both patients.

The information defined in the PICA decomposition is employed to discriminate noise independent components (characterized by noise/artifacts) and neural independent components (of interest), holding for the evaluation of brain activation patterns only the last ones. Specifically, these two classes of components were identified examining the respective differences in terms of spatial, temporal, and spectral characteristics. Because of the small number of controls, and because of the presence of patients with pathological characteristics, a visual inspection of the components was preferred, which represents, when possible, the gold standard technique [13]. Neural independent components are then classified according to the RSNs identified by Smith [6].

D. Results

The multi-subject analysis on controls allowed the identification of three activation networks attributable to Smith's RSNs: the medial visual network (MVN), the default mode network (DMN), and the sensory motor network (SMN). Both patients showed activation in these networks, although with different degree of bilaterality. Results from multi-subject analysis on controls and single subject analysis on patients are shown in figures 1-3, where panels in row A refer to the controls, in row B to P1, in row C to P2; the activations are shown, in sagittal, coronal, and axial planes, respectively. In particular, figure 1 shows activation reported in the MVN, figure 2 shows the DMN and figure 3 shows the SMN. The coordinates identifying the specific anatomical planes considered are indicated in the figures. In all panels, the lighter the color the more intense the activation. According to the radiological convention, the left hemisphere is on the right side of the figures. Both patients showed a bilateral cerebral activation in MVN, comparable with that of controls (Fig. 1). The activation in the DMN is bilateral in P1, although more pronounced in the right side (Fig. 2, B3) and only in the left hemisphere in P2 (Fig. 2, C3); the activation in the SMN is evident in the right hemisphere only in P1 (Fig. 3, B3), and in both sides in P2 (Fig. 3, C2 and C3).

III. Discussion and Conclusion

The aim of this study was to investigate the FC in the brain of patients undergone callosal resection to alleviate severe intractable epilepsy. These patients offer a unique opportunity for neuroscientists to examine the mechanisms of interhemispheric interactions, neuroplasticity, and compensatory reorganization [8]. The results are based on the analysis of resting-state fMRI data using the PICA method implemented in FSL.

Among the neural independent components identified on the multi-subject activation patterns of controls, only three networks of the Smith's resting state classification could be identified. This result could be due both to the small number of controls and to the individual variability of their brain activity in absence of intentional stimuli.

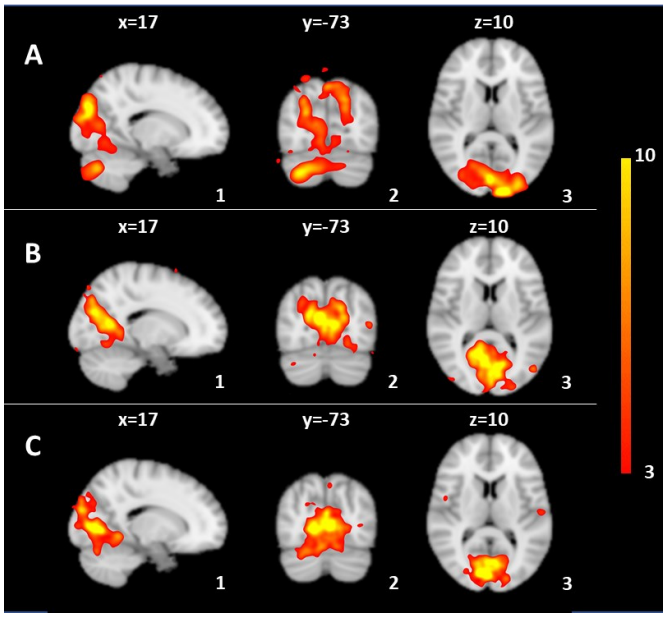


Fig. 1: Medial visual network (MVN) visualization on sagittal (1), coronal (2) and axial (3) planes. Panels show the results of multi-session analysis on controls (A), and single-session analysis on patients (P1 in B, P2 in C).

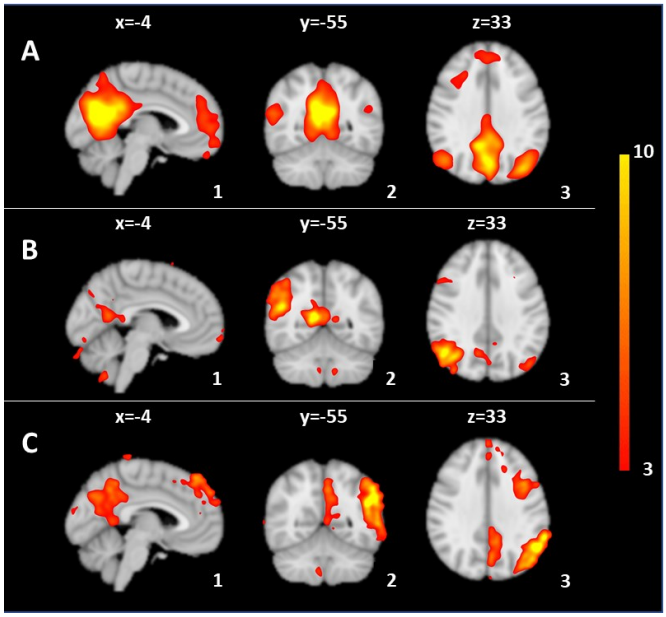


Fig. 2: Default mode network (DMN) visualization on sagittal (1), coronal (2) and axial (3) planes. Panels show the results of multi-session analysis on controls (A), and single-session analysis on patients (P1 in B, P2 in C).

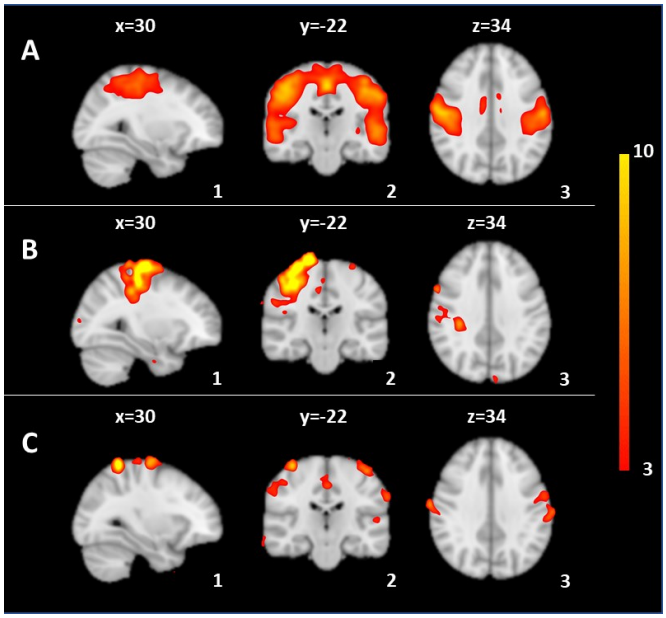


Fig. 3: Sensory motor network (SMN) visualization on sagittal (1), coronal (2) and axial (3) planes. Panels show the results of multi-session analysis on controls (A), and single-session analysis on patients (P1 in B, P2 in C).

Results from patients' analysis show a low degree of bilateral activation in most RSNs, probably due to callosotomy or pharmacological treatment of epilepsy. In both patients, the more unilateral networks were the DMN (figure 2), and the frontoparietal, both right and left, networks (not reported because they were not identified in controls' multi-subject analysis). Only the first could be compared with the population of controls considered in the present study. Thus, the FC of the networks resulted slightly altered. On the other hand, a high

degree of bilateral activation is shown in visual areas in both patients (figure 1).

Present results agree with those reported in a previous study, in which some bilateral activation was observed in occipital visual area and in fronto-parietal networks [8]. Both patients showed bilateral activation in the MVN network, patient P1 also in the DMN network, and patient P2, on the other hand, displayed bilateral activation in the SMN. In agreement with the results of Uddin and coworkers [8], it can be speculated that some degree of FC survives after callosotomy when this surgery is performed in adult age. This fact can be explained by considering that the brain, during its maturation over the years, usually builds other subcortical communication pathways, alternative to the CC, which were then reorganized and exploited once the callosotomy occurs. Through these alternative pathways the right hemisphere would be able to communicate with the left one, and thus maintain a possible interhemispheric communication even after callosotomy.

The brain reaches its maturity around 20 years of age and, once this maturity is reached, the communication routes between the two hemispheres, alternative to the CC, are fully developed. Thus, it is possible that, in callosotomized patients, alternative neural pathways to the CC for interhemispheric connections, prior to total callosotomy, have developed.

On the other hand, present results contrast with those reported in a more recent study in young patients [9]. In these patients, operated during the infancy or early adolescence, the FC was dramatically reduced after callosotomy. In this case, it can be suggested that the brain development was not completed yet at the time of callosotomy, and alternative routes, other than CC, did not have the time to be built. The comparison with intact brains suggests that in healthy subjects' brain a possible dual mechanism does exists, meaning that cortical and sub-cortical mechanisms work together to coordinate networks. The persistence of some bilateral networks in patients seem to suggest that the CC is not the only pathway involved in the connections between the two hemispheres. Further studies involving larger populations could help to confirm the results obtained in this preliminary study and the observations deduced.

A. Limitations of the study

The manual classification of components is certainly a limitation of the study, but also a necessity, given the peculiarity of the patients studied. Although the visual inspection implies a time consuming and non-automated analysis procedure, in conditions as those described in the present study, *i.e.*, when the data set analyzed comes from patients with altered neural activity and altered structural connectivity, this procedure becomes necessary. Moreover, the automatic classification may be more difficult when noise/artifacts are present, which can be incorrectly interpreted as signal of interest if not carefully visualized and classified. Thus, some components corresponding to valid RSNs, may not be recognized, and classified as noise.

Moreover, the registration phase of preprocessed controls' data may have been affected by the lower quality of functional images in controls than in patients. This issue may be the cause of activations of some voxels out of the brain template and/or interested area (indeed, it was more evident in results related to controls than in those related to patients). Nevertheless, derived errors can be considered neglectable. Future studies will consider an optimization of the registration procedure to manage low-resolution functional images.

The small number of controls (4) of the present analysis constitutes a limit in the identification of the different areas of activation. Considering a greater number of controls in the study would allow to recognize a greater number of components corresponding to Smith's RSNs.

Another limitation of the study is the small number of patients, which however is justified by the fact that the patients undergone callosotomy are rather few; this type of operation, being a solution carried out in the past to treat drug-resistant epilepsy, is at present performed very seldom.

ACKNOWLEDGEMENT

The Authors are especially grateful to Prof. Giorgio Innocenti, recently deceased, for initial stimulating suggestions, to the patients for participating in the study, to Gabriella Venanzi for scheduling the patients' exams, and to the radiology technicians Luigi Imperiale, Lucio Montesi and Alessio Canari for their invaluable help in collecting data during and soon after the volunteers' fMRI sessions.

REFERENCES

[1] L.Q. Uddin, "Complex relationships between structural and functional brain connectivity," *Trends in Cognitive Sciences*, vol. 17, pp. 600-602, Dec. 2013.

[2] M.P. van den Heuvel and H.E. Hulshoff Pol, "Exploring the brain network: a review on resting-state fMRI functional connectivity," *Eur. Neuropsychopharmacol.*, vol. 20, pp. 519-534, Aug. 2010.

[3] D.E. Stark, D.S. Margulies, Z.E. Shehzad, P. Reiss, A.M.C. Kelly, et al., "Regional variation in interhemispheric coordination of intrinsic hemodynamic fluctuations," *J. Neurosci.*, vol. 28, pp. 13754–13764, Dec. 2008.

[4] R. Salvador, J. Suckling, M.R. Coleman, J.D. Pickard, D.Menon, and E. Bullmore, "Neurophysiological architecture of functional magnetic resonance images of human brain," *Cereb. Cortex*, vol. 15, pp. 1332–1342, Sep. 2005.

[5] C.F. Beckmann and S.M. Smith, "Probabilistic independent component analysis for functional magnetic resonance imaging," *IEEE Trans. Med. Imaging*, vol. 23, pp. 137-152, Feb. 2004.

[6] S.M. Smith, P.T. Fox, K.L. Miller, D.C. Glahn, P.M. Fox, et al., "Correspondence of the brain's functional architecture during activation and rest," In *Proc. Natl. Acad. Sci. U. S. A.*, vol. 106, pp. 13040-13045, July 2009.

[7] J.M. Johnston, S.N. Vaishnavi, M.D. Smyth, D. Zhang, B.J. He, et al., "Loss of resting interhemispheric functional connectivity after complete section of the corpus callosum," *J. Neurosci*, vol. 28, pp. 6453–6458, June 2008.

[8] L.Q. Uddin, E. Mooshagian, E. Zaidel, A. Scheres, D.S. Margulies, et al., "Residual functional connectivity in the split-brain revealed with resting-state functional MRI," *Neuroreport.*, Vol. 19, pp. 703–709, May 2008.

[9] J.L. Roland, A.Z. Snyder, C.D. Hacker, A. Mitra, J.S. Shimony, et al., "On the role of the corpus callosum in interhemispheric functional connectivity in humans," In *Proc. Natl. Acad. Sci. U. S. A.*, vol. 114, pp. 13278-13283, Dec. 2017.

[10] M. Jenkinson, C.F. Beckmann, T.E.J. Behrens, M.W. Woolrich, and S.M. Smith, "FSL," *NeuroImage*, vol. 62, no. 2, pp. 782 – 790, Aug. 2012.

[11] S.M. Smith, "Fast robust automated brain extraction," *Hum. Brain Mapp.*, vol. 17, pp. 143-155, Nov. 2002.

[12] M. Jenkinson, P. Bannister, J.M. Brady, and S.M. Smith, "Improved optimisation for the robust and accurate linear registration and motion correction of brain images," NeuroImage, vol. 17, pp. 825-841, Oct. 2002.

[13] L. Griffanti, G. Douaud, J. Bijsterbosch, S. Evangelisti, F. Alfaro-Almagro, et al., "Hand classification of fMRI ICA noise components," Neuroimage, vol. 154, pp. 188-205, July 2017.

A convolutional neural network to identify osteoporosis from femoral echographic scans: a preliminary study

A. Colucci[1], G. Peluso[2], F.A. Lombardi[3], M. Bellone[1], F. Conversano[3], R. Franchini[3], P. Pisani[3], I. Epicoco[2], M. Cafaro[2] and S. Casciaro[3]
[1] *Echolight SPA, R&D Department, Lecce, Italy*
[2] *University of Salento, Department of Engineering for Innovation, Lecce, Italy*
[3] *National Research Council, Institute of Clinical Physiology, Lecce, Italy*

***Abstract*—This paper presents a preliminary study addressing the application of convolutional neural networks (CNN) for diagnosing of osteoporosis using a non-invasive ultrasound technology that can be used to predict bone fragility and fracture risk. Our method uses only raw RGB images, obtained from ultrasonic scans of 5,170 subjects on the femoral site as input to the CNN, and outputs a binary class in terms of healthy or osteoporotic. It is shown that semi-supervised learning performance reach 81% in terms of sensitivity and 76% of global accuracy, thus improving classification capacity with little effort in data annotation. These preliminary results highlight promising results that can be improved in future developments and by increasing the size of the dataset.**

***Keywords*—Osteoporosis, CNN, Semi-supervised learning**

I. INTRODUCTION

Recent research demonstrated that learning from data provides additional means to infer a diagnosis by automatically building accurate models of the specific phenomena described in the data. The statistical inference of a model strongly depends on two main factors: 1) the learning algorithm, and 2) the data used to build the model. While learning algorithms are well established in research, data collection, annotation and processing are still relevant for the resulting model. Clearly, the more the data, the better the result, but having big, well-annotated, dataset is not always achievable, particularly in the medical field in which data annotation is an extremely resource consuming task.

The idea of semi-supervised learning is to leverage knowledge capability using unlabelled data. Initially, the algorithm uses traditional supervision to update the model weights; then, it minimizes the difference in predictions between other similar unlabelled training examples. In our case, the pseudo-labels are data not annotated with *Dual Energy X-ray Absorptiometry* (DEXA) T-score (that is the gold standard for labels in osteoporosis), but with a fictitious label generated through the neural network.

The model used in this research is a convolutional neural network (CNN) [1] trained on RGB raw radiofrequency (RF) data to classify patients into two classes: healthy and osteoporotic. According to the clinical standard for femoral neck (extended also to entire femur and lumbar spine), a patient is considered as "osteoporotic" when the T-score is below the threshold of -2.5, as "osteopenic" when the T-score is between -2.5 and -1.0, and as "healthy" when the T-score is higher than -1.0. For simplicity, healthy and osteopenic are joint in the same class and labelled as "healthy".

The main purpose of this work is to introduce an innovative approach to osteoporosis diagnosis using a Deep Learning method applied to echographic scans, using pseudo-labels to enhance the performance of a statistical model, taking advantage of a semi-supervised approach.

II. RELATED WORK

From its development, quantitative ultrasound has been considering a potential technique for osteoporosis screening [2], [3] offering several advantages such as absence of ionizing radiation and portability when compared with DEXA scans [4], [5]. Traditional bone densitometry uses DEXA as the reference test for diagnosing osteoporosis, which is based on the well-known X-ray analysis. The exposition of subjects to X-rays over time constitutes a risk factor for humans as they produce ionizing radiations [6]. In contrast, the innovative *Radiofrequency Echographic Multi-Spectrometry* (REMS) is a non-invasive technology that uses ultrasonic imaging instead of X-ray to identify any changes in the human bone structure [7], [8].

The ultrasonic signals are widely used as a safe diagnosis tool; thus, the idea of this work is to define a learning system that, after being trained according to semi-supervised approach, is able to classify subjects characterized by a different degree of osteoporosis resembling DEXA [9], looking for obtaining the same performance in terms of sensibility, specificity and accuracy.

Several studies suggest that features in time and frequency domains are important to build a machine learning classifier to determine the class of a subject [9]. The first step in this procedure is the feature extraction from the RF signal. Feature extraction constitutes an extensive engineering work, and the choice of which features are relevant is an important problem to solve [10]. To overcome this limitation, deep learning methods based on CNN are built on the idea of automatic feature

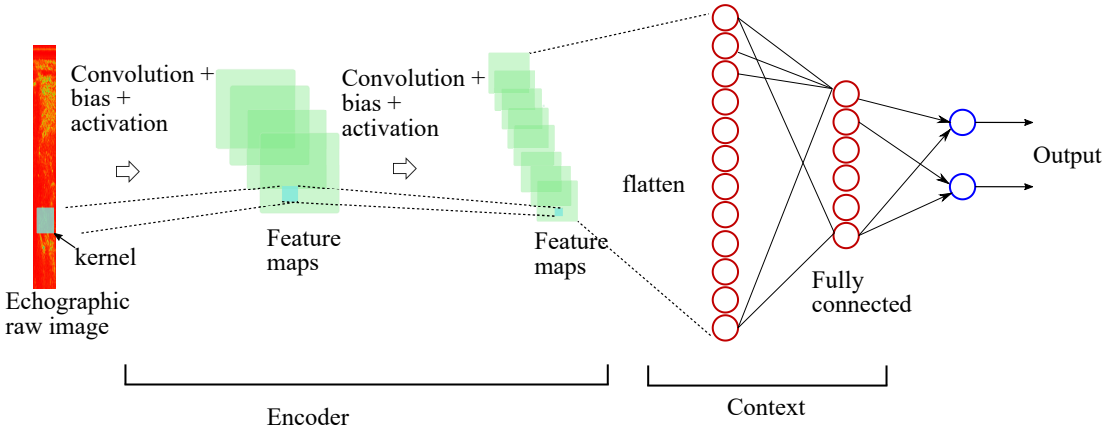


Fig. 1: Architecture of proposed CNN. The input is the raw RGB echographic image, the CNN is a multilayer convolutional network and each layer contains several convolutional kernels, bias and activation function. The flattened operator connects the convolutional network to the fully connected layer to classify the image. The output contains two neurons representing each class: healthy and osteoporotic.

identification [11]. According to the most recent literature, CNNs are considered an effective tool for pattern recognition, and widely used in many different clinical fields including ultrasound signals [12]. Several studies indicate that the use of CNNs with ultrasound signal as input data is a promising technique for the osteoporosis diagnosis, offering relevant scores about sensitivity, specificity and accuracy [13], although the size of the dataset constitutes the most relevant criticality to train the network and improve performance.

III. Materials and Methods

A. CNN architecture

The CNN structure used in this work is represented in Fig. 1, and it resembles the well-known AlexNet-type architecture [1] that was implemented using PyTorch and adapted to our use case. Each layer of the network contains several convolutional kernels (ranging between 2 and 128), bias and activation function. The activation function is the standard Rectified Linear Unit (ReLU). The final layers are built using a series of fully connected neurons, the output contains three neurons representing each class: healthy or osteoporotic. An additional softmax function to the output is used to represent the values in terms of the probability of each class.

The input is an ultrasonic frame containing raw radio frequency (RF) data. Such RF data, encoded as an RGB image, and used as input to the neural network, are acquired on the femoral site, the target used as annotation corresponds to the DEXA T-Score on the femoral neck. The RGB encoding reveals to be an effective and efficient way to integrate existing CNN implementations with our own dataset. This implies a massive amount of work of data gathering and analysis as each subject was scanned using both DEXA and REMS technology. Each ultrasonic acquisition on femoral site collects 50 frames, which are individually analyzed. The data is divided into subgroups: Training set, data used to train the network; Validation set, data used to validate the network; and Test set, data used to measure the abstraction capacity of the network.

B. Dataset construction

REMS scans of proximal femur were performed employing a dedicated echographic device (EchoStation, Echolight Spa, Lecce, Italy), equipped with a convex transducer operating at the nominal frequency of 3.5 MHz and used by clinical operator as recommended by the manufacturer [14]. The total of subjects is 5,170: of which 3,170 are paired with a DEXA measurement, the remaining 2,000 scans were not annotated with DEXA due to many technical reasons. The idea of using pseudo-labels was introduced in order to make use of these 2,000 subjects. Each subject is composed several images as one ultrasonic scan records up to 50 frames.

Information about the dataset is reported in Table I: the CNN used in this work was trained using roughly 2,300 annotated subjects, of which 450 are used for validation. Please note that the validation dataset is taken from the train set which is randomly split into five groups to carry out cross-validation. Due to the randomization in the selection of subjects in each group, the size of each set has roughly 1% variation along the cross-validation procedure. Furthermore, it is worth mentioning that all frames of each scan fall into the same group, either train, validation or test.

Furthermore, 870 patients are also randomly selected at the beginning of the operation and left aside. This group is used for testing only, thus not involved in the cross-validation procedure. The test corresponds roughly to 28% of all DEXA-annotated available patients. Lastly, additional 2,000 patients are annotated via pseudo-labels using the best performing model, and used to run an additional training cycle. It is worth mentioning that the learning flow relies only on the ultrasonic scan: in fact, no additional information about the subject (i.e., anthropometric data) is used in the learning algorithm, thus providing an agnostic approach.

All the patients used in this study are Caucasian women living in European countries, and signed an informed consent, though personal information are anonymized.

TABLE I: Number of subjects per dataset split. The dataset is divided in train, validation and test subsets, which constitute respectively the 72%, the 20% and the 28% of entire dataset. The data are shifted between data with T-score DEXA (annotated) and data with pseudo-labels. Please note that the validation set is a subset of the training set

Dataset split	# Subjects	% Subjects
Train	∼2300	∼72%
Validation	∼450	∼20%
Test	870	∼28%
TOT – DEXA annotated	3170	-
Pseudo-labels	2000	-

TABLE II: Number of subjects per each class (healthy and osteoporotic) and respective percentage. The classes are strongly unbalanced: the amount of osteopenic and healthy subjects is the majority of the dataset, while osteoporotic subjects are only about the 15% of dataset.

FSL	# Healthy	# Osteoporotic	# TOT
# Subjects	2700	470	3170
Percentage	∼85%	∼15%	-
# Test set	670	100	870
Percentage	∼89%	∼11%	-

C. Loss function

According to the trend in the general population, the classes are strongly unbalanced as only about 15% of the subjects in the dataset present a T-score lower than -2.5, and thus classified as osteoporotic. This underlines the difficulty in construction of an optimal dataset, due to a lack of availability of subjects with confirmed osteoporosis. What has been described so far is an additional complication for the problem as it is more important for the network to learn how to recognize the less-represented class in the data, that is "osteoporotic". This effect is also considered during the design of the loss function, weighed cross entropy for our case, through the definition of specific weights on the errors for each class.

The weights have been set to ensure class balancing, and optimize the knowledge abstraction capacity. The classical supervised learning technique uses a cycle of training and validation on well-annotated data, minimizing the loss function along the training.

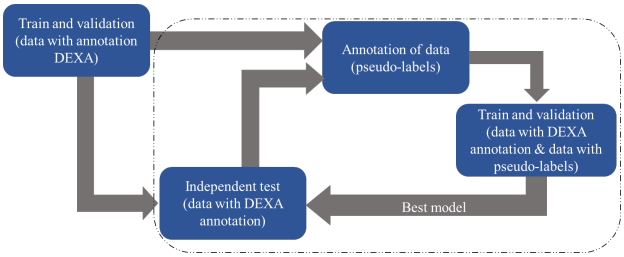


Fig. 2: Semi-supervised learning workflow. The procedure starts with supervised learning training cycle on subjects with DEXA annotations; then, synthetic annotations on unlabelled data are generated, using the minimum loss model. The training is repeated on all subjects (data with DEXA annotations and pseudo-labels). The performance of best model is evaluated on independent test.

D. Workflow

The entire workflow is shown in Fig. 2, and it implements the steps explained as follow:

- Step 1: Supervised learning on 2,300 data annotated with DEXA T-score;
- Step 2: Generate pseudo-labels (T-score diagnostic output) on 2,000 non-annotated data;
- Step 3: Re-training the neural network using all data (roughly 4300 subjects);
- Step 4: Evaluation of diagnostic performance on independent test data with DEXA annotation;

E. CNN setting

Training — An epoch of the training phase provides the random selection of all the subjects divided into subgroups: each frame of the single subject, also randomly selected, crosses the CNN correlated with its annotation as a function of the DEXA T-score.

Validation — During the validation phase, subjects are sequentially passed through the CNN (no randomization is applied), selecting only the first valid frame for each subject. The validation phase is designed in such a way to evaluate the effectiveness of the training while compromising between overfitting and underfitting, and to reduce the computational burden of analyzing all the frames for each patient. The validation is performed for each training session on one of the batches in the list, which is excluded from the training phase.

Test — The test phase can be carried out in two distinct ways: Frame test: only a single frame (the first in the list for each subject) is used for diagnosis inference. Patient test: all the frames of a single subject are analyzed, and the subject's diagnosis is obtained as the arithmetic average of the diagnosis on each single frame.

Model average — This probably represents the optimal method for combining learned models, exactly which have reached the best accuracy and the lowest value of loss function. The use of model averaging can improve the robustness of the system, stabilizing the imbalance of the classes that could occur in some models [15].

IV. Results and Discussion

The results were analyzed taking into account the models that obtained the best performance in terms of:

- Best global accuracy;
- Minimum loss value.

After each training session, both frame test and patient test were conducted, using the models that have reached the best accuracy, and the minimum value of the loss function.

A. Best accuracy Vs. Best loss

Comparing the results obtained using these different convergence criteria, one can see that: 1) the best accuracy case provides improved results on the class of interest, and the less represented in the dataset, due to data imbalance (performance on the osteoporotic class is of about 54%); 2)

TABLE III: Performance comparison of best accuracy Vs. best loss in terms of sensibility, specificity and global accuracy. The value are calculated using the average estimation over five models trained in a cross-validation setting.

	Sens	*Spec*	*Acc*
Best Acc	75%	54%	73%
Best Loss	81%	42%	76%

TABLE IV: Performance comparison between FSL and SSL in terms of sensibility, specificity and global accuracy.

	Sens	*Spec*	*Acc*
FSL	71%	66%	69%
SSL	73%	67%	71%
Gain (SSL-FSL)	2%	1%	2%

the best loss criterion provides higher global accuracy, that is 76% against 73% calculated as the weighed average for each class. However, the global accuracy value is biased by the high number of subjects in the osteopenic class, thus resulting in a low accuracy in the class of interest.

On one hand, the best accuracy model provides better performance on the osteoporotic class of about 54%, which represents the class of interest, and the less represented in the dataset due to data imbalance. On the other hand, the best loss model provides higher global accuracy, that is 76% against 73% calculated as the weighed average for each class. It is important to emphasize that the misclassification healthy to osteoporotic and vice-versa are very limited (6-7% for the best accuracy model and 9-6% for the best loss model). We conclude that the best accuracy critierion better fits the dataset used for the aim of this study.

B. FSL Vs. SSL

The results of the test patient for the fully supervised learning (FSL) case and semi-supervised learning (SSL) are reported in Table IV in terms of sensibility, specificity and global accuracy on the average estimation between five distinct models trained in a cross-validation setting thus using different data. Particularly in Table IV one can see that the SSL case consistently overperforms the FSL by a few percentage points. Clearly, this effect can be counted as an increase in the knowledge abstraction capacity gained using additional data points. The gain is consistent, 2% on sensibility, 1% on specificity and 2% on global accuracy. From this result it is possible to conclude that it is possible to leverage classification accuracy exploiting big quantities of unlabelled data.

V. Conclusion

In this study a CNN was trained as a classifier to infer the osteoporosis diagnosis for patients on a strongly unbalanced dataset. To enhance the classification performance, and make use of big unlabelled data, a semi-supervised learning technique was used, providing to algorithm annotated data and also pseudo-labels. It is shown that semi-supervised learning consistently increases global classification performance.

The major limitation and challenge to be addressed to further improve this method is data annotation, that is a labour-intensive process, but strongly required as CNN-based models learn from data and, though semi-supervised learning helps, most of the work is done in the fully-supervised setting, thus using DEXA annotated subjects. CNN systems are promising as they can provide high classification performance that could be reached through an increase of the dataset size. Further studies, and a bigger dataset, are required to support clinical application.

References

[1] Alex Krizhevsky, Ilya Sutskever, and Geoffrey E Hinton. Imagenet classification with deep convolutional neural networks. *Communications of the ACM*, 60(6):84–90, 2017.

[2] CM Langton, SB Palmer, and RW Porter. The measurement of broadband ultrasonic attenuation in cancellous bone. *Engineering in medicine*, 13(2):89–91, 1984.

[3] Sergio Casciaro, Marco Peccarisi, Paola Pisani, Roberto Franchini, Antonio Greco, Tommaso De Marco, Antonella Grimaldi, Laura Quarta, Eugenio Quarta, Maruizio Muratore, et al. An advanced quantitative echosound methodology for femoral neck densitometry. *Ultrasound in Medicine & Biology*, 42(6):1337–1356, 2016.

[4] Sergey N Makarov, Gregory M Noetscher, Seth Arum, Robert Rabiner, and Ara Nazarian. Concept of a radiofrequency device for osteopenia/osteoporosis screening. *Scientific reports*, 10(1):1–15, 2020.

[5] Paola Pisani, Maria Daniela Renna, Francesco Conversano, Ernesto Casciaro, Maurizio Muratore, Eugenio Quarta, Marco Di Paola, and Sergio Casciaro. Screening and early diagnosis of osteoporosis through x-ray and ultrasound based techniques. *World journal of radiology*, 5(11):398–410, 2013.

[6] Zeba Syed and Aliya Khan. Bone densitometry: applications and limitations. *Journal of Obstetrics and Gynaecology Canada*, 24(6):476–484, 2002.

[7] Francesco Conversano, Roberto Franchini, Antonio Greco, Giulia Soloperto, Fernanda Chiriacò, Ernesto Casciaro, Matteo Aventaggiato, Maria Daniela Renna, Paola Pisani, Marco Di Paola, et al. A novel ultrasound methodology for estimating spine mineral density. *Ultrasound in medicine & biology*, 41(1):281–300, 2015.

[8] Sergio Casciaro, Francesco Conversano, Paola Pisani, and Maurizio Muratore. New perspectives in echographic diagnosis of osteoporosis on hip and spine. *Clinical cases in mineral and bone metabolism*, 12(2):142, 2015.

[9] Laura J Brattain, Brian A Telfer, Manish Dhyani, Joseph R Grajo, and Anthony E Samir. Machine learning for medical ultrasound: status, methods, and future opportunities. *Abdominal radiology*, 43(4):786–799, 2018.

[10] Avrim L Blum and Pat Langley. Selection of relevant features and examples in machine learning. *Artificial intelligence*, 97(1-2):245–271, 1997.

[11] Hassan Ismail Fawaz, Germain Forestier, Jonathan Weber, Lhassane Idoumghar, and Pierre-Alain Muller. Deep learning for time series classification: a review. *Data mining and knowledge discovery*, 33(4):917–963, 2019.

[12] Chien-Liang Liu, Wen-Hoar Hsaio, and Yao-Chung Tu. Time series classification with multivariate convolutional neural network. *IEEE Transactions on Industrial Electronics*, 66(6):4788–4797, 2018.

[13] Wenqiang Luo, Zhiwei Chen, Qi Zhang, Baiying Lei, Zhong Chen, Yuan Fu, Peidong Guo, Changchuan Li, Teng Ma, Jiang Liu, et al. Osteoporosis diagnostic model using a multichannel convolutional neural network based on quantitative ultrasound radiofrequency signal. *Ultrasound in Medicine & Biology*, 2022.

[14] M Di Paola, D Gatti, O Viapiana, L Cianferotti, L Cavalli, C Caffarelli, F Conversano, E Quarta, P Pisani, G Girasole, et al. Radiofrequency echographic multispectrometry compared with dual x-ray absorptiometry for osteoporosis diagnosis on lumbar spine and femoral neck. *Osteoporosis International*, 30(2):391–402, 2019.

[15] Omer Sagi and Lior Rokach. Ensemble learning: A survey. *Wiley Interdisciplinary Reviews: Data Mining and Knowledge Discovery*, 8(4):e1249, 2018.

Comparison of Machine Learning Approaches for Physiological States Classification Using Heart Rate and Pulse Rate Variability Indices

Marta Iovino[1], Michal Javorka[2], Luca Faes[1], and Riccardo Pernice[1]
[1] *Department of Engineering, University of Palermo, Building 9, Viale delle Scienze, Palermo, Italy*
[2] *Department of Physiology, Jessenius Faculty of Medicine, Comenius University, Martin, Slovakia*

***Abstract*—In this work, we investigate the feasibility of classifying physiological states including conditions of postural and mental stress using heart rate variability (HRV) and pulse rate variability (PRV) time-, frequency- and information-domain indices. The performance of four different machine learning algorithms, i.e. Linear Discriminant Analysis (LDA), Support Vector Machines, Neural Networks (NN) and k-Nearest Neighbors, were compared, with and without prior applying the minimum Redundancy Maximum Relevance (mRMR) algorithm for feature selection. Analyses were conducted on 76 young healthy subjects under three different conditions (supine rest, orthostatic and mental stress). Results evidence higher accuracy for HRV indices if compared to PRV and better classification performance of orthostatic stress. The highest accuracy has been achieved by the NN algorithm on HRV time series, with a value of 90.9% after feature selection, while LDA is the best algorithm for PRV features (81.8%).**

***Keywords*—Heart Rate Variability (HRV), stress classification, feature selection, Machine Learning (ML).**

I. Introduction

In recent years, the application of machine learning (ML) techniques to medical data analysis has significantly increased in the research field and healthcare industry. ML has been especially exploited to help to classify various autonomic nervous system states related to different types of stress [1], their excess being considered one of the most important pathogenic factors of the modern life [2].

Usually, noninvasive stress assessment is carried out by studying Heart Rate Variability (HRV), i.e. the beat-to-beat variation of heart rate (HR), and its indices represent the most reliable markers of mental and physical stress [3]. HRV reflects the complexity of the cardiovascular regulation and, given the inhibition of parasympathetic accompanied by the activation of the sympathetic branch of the autonomous nervous system during stress conditions, can reflect the body's ability to respond to various (e.g. environmental and psychological) stimuli [3]. Short-term HRV is usually assessed by measuring the time interval between consecutive heartbeats (i.e. R-R intervals) from 5-minute recordings of electrocardiographic (ECG) signals (i.e. short-term HRV) and computing time-, frequency- and information-domain measures [3], [4]. Recently, there has been an increased interest in studying whether and to what extent HRV can also be studied from photoplethysmographic (PPG) or blood pressure recordings, providing the so-called Pulse Rate Variability (PRV). PPG is an optical technique able to detect changes in microvascular blood volume in tissues and is widely used in wearable devices, being simple, low-cost, safe and minimally invasive [5]. Even if the two techniques (PPG and ECG) are often considered interchangeable to measure HRV, several reasons suggest that the beat-to-beat variability recorded with the PPG is somewhat different from HRV [5], [4], [6]. PPG and blood pressure recordings can be affected by physiological factors related to the transmission of the pulse wave through the vascular system and measurement errors due to motion-induced signal corruption, lowering the peak detection accuracy and thus reducing the agreement between PRV and HRV.

Applying machine learning techniques to HRV and PRV features to classify the stress level thus represents nowadays an important challenge for researchers. In particular, various studies have focused on classifying physiological states using HRV [7], [8] or PRV [1] time- or frequency-domain indices. However, to the best of our knowledge, no works have carried out stress classification applying ML techniques to both HRV and PRV indices on the same data, using entropy measures and a feature selection phase as well.

The goal of this work was thus to compare the performances of four classic ML algorithms for classifying different physiological states in healthy young subjects. This study was aimed as well to investigate the reliability of using PPG in place of ECG signals and to evaluate the most suitable PRV features. Furthermore, a feature selection phase has been applied before classification to check whether this step improves the classification accuracy.

II. Materials and methods

A. Subjects and experimental protocol

The data used for this study belong to a historical dataset previously used to assess cardiovascular variability [4]. ECG and blood pressure signals were collected from 76 young, healthy, and normotensive subjects with normal body mass index (32 males; age: 18 ± 2.7 years; BMI = 21.3 ± 2.3 kg/m^2). All the procedures were approved by the Ethical Committee of the Jessenius Faculty of Medicine, Comenius University, Martin, Slovakia, and the participants signed a written informed

consent. The signals were acquired simultaneously (sampling rate: 1 kHz) using horizontal bipolar thoracic leads for ECG and the volume-clamp method for blood pressure. For this study, three different conditions of the experimental protocol fully described in [4] have been taken into account: (a) REST: subjects resting in the supine position on a motorized bed for a period of 15 minutes (baseline); (b) HUT: 8-minute-lasting head-up tilt state induced by tilting the bed to a 45° upright position to produce orthostatic stress; (c) MA: subjects lying in the supine position and undergoing a mental arithmetic test (consisting in performing of a 3-digit number and indicating whether the number obtained was even or odd) for 6 minutes to induce cognitive load (this phase was preceded by another resting state for a full recovery of parameters [4]).

B. Preprocessing and features extraction

Starting from the acquired signals, HRV and PRV indices were computed from time series of 300 consecutive heartbeats (~5 min) respectively extracted from ECG and PPG signals, i.e. R-R intervals (RRI) and pulse-pulse intervals (PPI). In a previous study [4], 12 HRV and PRV features belonging to three different domains were calculated and demonstrated to be useful for discriminating among different stress conditions. In the time domain, the mean (MEAN), the root mean square of the successive differences (RMSSD), and the standard deviation of the normal-to-normal intervals (SDNN) of RRI and PPI series were calculated. The frequency domain indices were the absolute power in the Low Frequency (LF, 0.04-0.15 Hz) and High Frequency (HF, 0.15-0.4 Hz) bands, the normalized powers (respectively LFn and HFn), the ratio traditionally used as the sympathovagal balance index (SVB, i.e. LF/HF ratio), and finally the frequency of the peak in HF band (f_{HF}, i.e. the respiratory peak). In the information domain, three entropy measures were computed: the entropy (H), the conditional entropy (CE), and the self-entropy (SE) of RRI and PPI time series. We refer the reader to [4] for further details on the computation of the above-mentioned features.

C. Classification algorithms

Four classic ML classifiers were selected to evaluate and compare their performance in discriminating between rest and orthostatic/mental stress, determining which one is most effective for the given task. The classifiers, hereinafter briefly introduced, were chosen given their widespread use for a variety of classification tasks, including those involving ECG signals [9]. By choosing common classifiers, it is easier to compare the obtained results with other findings in the literature, focusing on the performances of the proposed approach rather than on the characteristics of the classifier itself.

1) Linear Discriminant Analysis. The Linear Discriminant Analysis (LDA) is a supervised learning method that relies on classifying data into K classes based on K discrimination functions. Being a linear method, it assumes that the classes can be separated by a linear boundary. LDA has several advantages, such as its simplicity and computational efficiency, robustness to overfitting and good generalization performance, as well as the ability to provide a clear interpretation of the results. Nonetheless, it requires features normally distributed within the classes [9].

2) Support Vector Machines. The Support Vector Machines (SVMs) are a type of supervised learning algorithm that exploit either a linear or quadratic decision rule and work by finding the hyperplane in a high-dimensional feature space that maximally separates the classes [9]. SVMs have several advantages, including their ability to handle high-dimensional data. However, they are sensitive to the choice of kernel function and the values of the hyperparameters and may be computationally expensive to train on large datasets.

3) k-Nearest Neighbors. The *k*-Nearest Neighbors (kNN) is considered the most straightforward classification algorithm, classifying unknown data into a class closer to the data and having higher majority [9]. When using kNN, the user specifies the value of *k*, i.e. the number of nearest neighbours that the model uses to make a prediction. kNN has several advantages, i.e. simplicity, flexibility, and no *a priori* training, but it can be computationally expensive for large datasets and sensitive to the chosen distance metric and *k* value.

4) Neural Networks. A Neural Network (NN) is a machine-learning model consisting of multiple layers of interconnected nodes resembling the human “neurons” [9]. A NN is trained using a dataset and an optimization algorithm, which updates the weights and biases of the neuron interconnections to minimize the error between the predicted output and the true output. NNs are particularly useful for tasks involving complex patterns and connections, but as a drawback they could be computationally expensive to train, requiring a large amount of data to achieve good performance.

The analyses carried out in this work were aimed to compare the performances of the four above-mentioned algorithms to classify data into the three classes corresponding to different physiological states, i.e. REST (rest), HUT (orthostatic stress) and MA (mental stress), investigating as well whether the PRV features calculated from PPI time series can achieve results comparable to HRV indices computed from RRI series. The MATLAB Classification Learner app was used to train the various models. For each classifier and each set of features, the "Optimized version" has been chosen, allowing automatic parameter tuning. To carry out the training, validation, and testing of each classifier, a *k*-fold cross-validation (*k*=5) was used. This process was repeated *k* times, so each fold serves as the test set once. The model performance has then averaged across all *k* iterations. Each classifier was trained by giving as an input the HRV or PRV features described in section II.B, setting the same model parameters to allow for a comparison of the results. The performance of the classifiers was evaluated mainly through accuracy, but also calculating metrics by class, i.e. recall, specificity and precision [10].

D. Feature selection

Usually, using a feature selection approach for selecting a subset of features rather than all the available ones allows for improving classification accuracy and limiting the problem of

overfitting [11]. In this work, we have first used all the 12 extracted features, also considering them separately according to their domain; afterwards, the Minimum Redundancy Maximum Relevance (mRMR) [12] feature selection algorithm was used to rank the 12 features. The mRMR is a widely employed feature selection method in machine learning, being simple to implement and particularly useful when the goal is to identify the most important features for predicting the target variable. The mRMR algorithm uses mutual information (MI) to select the subset of features that exhibit the maximum correlation (denoted with D) with the target, alongside the minimum redundancy (denoted with R) between them. MI can be computed using the following equation [12]:

$$MI(X;Y) = \sum_{x\in X}\sum_{y\in Y} p(x,y)\log\frac{p(x,y)}{p(x)p(y)} \tag{1}$$

where X and Y are variables with joint probability density function $p(x,y)$ and marginal probability density functions $p(x)$ and $p(y)$, respectively. The mRMR features set is obtained by simultaneously optimizing the parameters D and R in terms of the Mutual Information Quotient (MIQ) criterion[12]:

$$\text{MIQ} = \max\left(\frac{D}{R}\right) = \max_{S\in\Omega}\left\{\frac{\sum_i MI\,(c;X_i)}{\left[\frac{1}{|S|}\sum_{i,j\in S} MI\,(X_i;X_j)\right]}\right\} \tag{2}$$

being X_i and X_j the features, Ω the feature set and c the classes (REST, HUT, MA) vector. The MATLAB implementation of the original mRMR algorithm by Peng was used, considering the HRV/PRV features as input structure which has been discretized with a 3-states quantization [12].

III. Results and Discussion

In this section we first investigate the performance of the four ML algorithms in classifying the different physiological states, using either RRI or PPI features, all together or grouped according to the domain of calculation of the feature (time, frequency or information). Subsequently, a feature selection phase through mRMR was performed, in order to assess how the classification accuracy varies by removing one by one feature according to the order established by the feature selection algorithm, once again comparing the use of either RRI or PPI indices.

1) Classification results without feature selection: Figure 1 shows the classification accuracy of the four ML algorithms (LDA, SVM, kNN, NN) in classifying the physiological state (rest, orthostatic or mental stress) when using all the 12 HRV or PRV features, or using only a group of features according to their domain (time, frequency and information). The accuracy values computed using PRV features extracted from PPG signals are overall slightly lower than those achieved obtained with HRV indices. This behaviour suggests that the difference between RRI and PPI affects the capability of discriminating among classes, even if it does not happen in all cases. Results also evidence that using only information-domain indices produces a lower accuracy for both RRI and PPI (almost always below 60%), and not allowing correct classification of

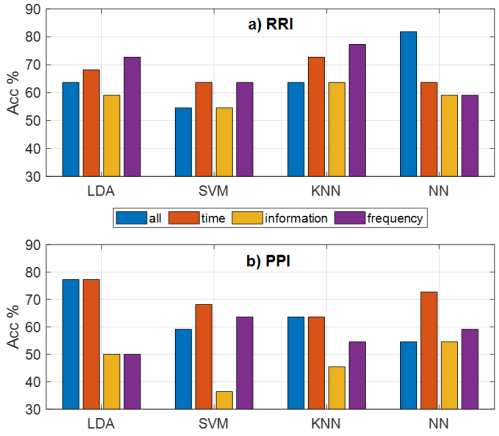


Fig. 1: Classification accuracy of the four ML algorithms for (a) RRI and (b) PPI indices, considering the features altogether (blue), or grouped according to their domain (orange: time; yellow: information; purple: frequency).

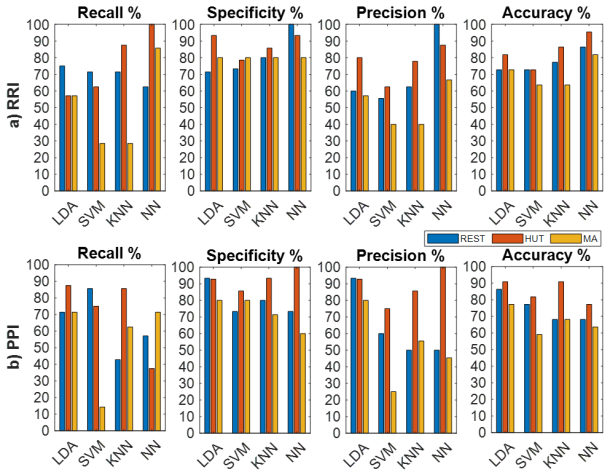


Fig. 2: Recall, specificity, precision and accuracy metrics by class (blue: REST; orange: HUT; yellow: MA) computed on (a) RRI and (b) PPI features

the three physiological stages. On the other hand, time- and frequency domain indices allow to achieve higher values of accuracy, the former performing always better in the case of PPI, the latter overall better in the case of RRI features (apart from NN). Considering all the HRV features together and comparing the ML classifiers, NN achieves the best results, performing however worse when considering only certain groups of features. This behaviour is expected, given that NN needs a larger amount of data and this need is not met when the features are considered separately by domains. The accuracy obtained by LDA classifier on PPI features was similar to that achieved by NN using RRI indices, thus supporting the use of PPG for identifying stress. Figure 2 depicts the results in terms of metrics by class, including recall, specificity, precision, and accuracy, to understand which stress state is best classified by each ML algorithm considering all the 12 features together. Overall, recall values are lower for PPI than RRI, with the maximum value obtained in the case of HUT class (100%). With regard to PPI indices, the highest recall value (87.5%) is obtained with LDA classifier again for HUT class. Analysing the other metrics, we highlight that higher values of specificity,

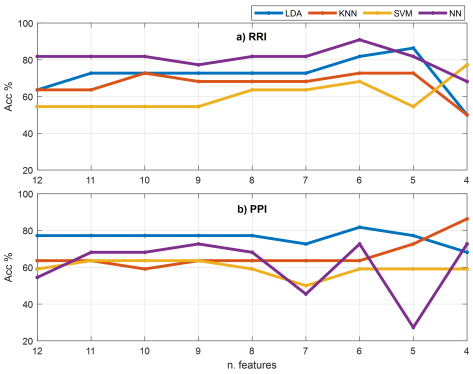
precision and accuracy are achieved with the NN classifier for RRI and with LDA for PPI. Nonetheless, the NN classifier is able to reach the maximum specificity and precision (100%) also for PPI with regard to HUT class. Summarising, the HUT class is classified by all the ML algorithms and for both RRI and PPI indices better than MA that in turn achieves lower values on average. This may be ascribed to the fact that orthostatic stress produces a stronger sympathetic activation and/or parasympathetic inhibition if compared to the mental one, in agreement with previous findings in the literature [4].

2) Classification results with mRMR feature selection: Figure 3 depicts the results in terms of accuracy obtained through the 4 ML classifiers performing first a feature selection phase using the mRMR algorithm. The table (Fig. 3c) lists the feature importance ranking according to mRMR (in descending order) for RRI and PPI indices, i.e. the order of minimally redundant and maximally relevant features. Fig.3(a) and (b) show the accuracy of each classifier, respectively for RRI and PPI indices, as the input features, starting from all 12, are gradually removed one by one, as in the table in inverse order (less important features are removed first). Also in this case, NN is the classifier with the best results for RRI (with a maximum accuracy of 90.9%), while LDA is the best for PPI (81.8%). For most classifiers and for both RRI and PPI indices, there is a slight increase in accuracy when reducing the features, with a peak around 6 or 5 features (apart from NN for PPI which presents an irregular trend). Overall, the maximum accuracy achieved with feature selection is higher than without (cf Fig. 1), with a more marked increase for RRI than PPI. For instance, for NN applied to RRI features the maximum accuracy increases from 81.8% to 90.9%, while for LDA applied to PPI the increase is from 77.2% to 81.8%. In [8] authors applied 3 out of 4 classifiers used in this work (kNN, LDA, SVM) and mRMR feature selection algorithm on RRI data in various conditions of stress corresponding to a range of everyday life conditions, obtaining accuracy values of 66.7% (kNN), 65.6% (LDA) and 73.6% (SVM) without pairwise transformation method. Even if the database and the stress conditions are not the same and the order of features selected by mRMR is different, our accuracy values are in line and sometimes higher.

IV. Conclusion

This work presented a comparison of the performances of various ML algorithms for classifying physiological states using either HRV or PRV features. Our results evidence that HRV features allow for achieving higher accuracy than PRV and that it is easier to discriminate postural than mental stress from rest. Moreover, the NN classifier outperforms the other ones, even if LDA works better on PPI data. Finally, a feature selection phase through the mRMR algorithm allows to increase accuracy.

Future activities may consider using different feature selection algorithms, other classifiers (e.g. Random Forest [8]), data augmentation techniques and shorter HRV/PRV recordings (i.e. ultra-short term HRV [3]).



c)

n	RRI	PPI
1	HF	HF
2	SE	SE
3	LF	LF
4	CE	MEAN
5	MEAN	RMSSD
6	HFn	HFn
7	RMSSD	CE
8	LFn	SDNN
9	SDNN	LFn
10	SVB	SVB
11	H	H
12	fHF	fHF

Fig. 3: Accuracy of the 4 ML classifiers at decreasing number of selected features for (a) RRI and (b) PPI data. (c) Feature importance ranking according to mRMR algorithm (in descending order)

Acknowledgement

The work was supported by "Sensoristica intelligente, infrastrutture e modelli gestionali per la sicurezza di soggetti fragili" (4FRAILTY) project, funded by Italian MIUR PON R&I 2014-20, grant no. ARS01_00345. R.P. is partially supported by European Social Fund (ESF) Complementary Operational Programme (POC) 2014/2020 of the Sicily Region.

References

[1] K. Awasthi, P. Nanda, and K. Suma, "Performance analysis of machine learning techniques for classification of stress levels using ppg signals," in *2020 IEEE International Conference on Electronics, Computing and Communication Technologies (CONECCT)*. IEEE, 2020, pp. 1–6.

[2] M. Umair, N. Chalabianloo, C. Sas, and C. Ersoy, "Hrv and stress: A mixed-methods approach for comparison of wearable heart rate sensors for biofeedback," *IEEE Access*, vol. 9, pp. 14 005–14 024, 2021.

[3] F. Shaffer and J. P. Ginsberg, "An overview of heart rate variability metrics and norms," *Frontiers in public health*, p. 258, 2017.

[4] R. Pernice, M. Javorka, J. Krohova, B. Czippelova, Z. Turianikova, A. Busacca, and L. Faes, "Comparison of short-term heart rate variability indexes evaluated through electrocardiographic and continuous blood pressure monitoring," *Medical & biological engineering & computing*, vol. 57, no. 6, pp. 1247–1263, 2019.

[5] E. Mejía-Mejía, J. M. May, R. Torres, and P. A. Kyriacou, "Pulse rate variability in cardiovascular health: A review on its applications and relationship with heart rate variability," *Physiological Measurement*, vol. 41, no. 7, p. 07TR01, 2020.

[6] S. Rinella, S. Massimino, P. Fallica, A. Giacobbe, N. Donato, M. Coco, G. Neri, R. Parenti, V. Perciavalle, and S. Conoci, "Emotion recognition: Photoplethysmography and electrocardiography in comparison," *Biosensors*, vol. 12, no. 10, 2022.

[7] K. M. Dalmeida and G. L. Masala, "Hrv features as viable physiological markers for stress detection using wearable devices," *Sensors*, vol. 21, no. 8, p. 2873, 2021.

[8] G. Giannakakis, K. Marias, and M. Tsiknakis, "A stress recognition system using hrv parameters and machine learning techniques," in *2019 8th International Conference on Affective Computing and Intelligent Interaction Workshops and Demos(ACIIW)*. IEEE, 2019, pp. 269–272.

[9] H. W. Lim, Y. W. Hau, C. W. Lim, and M. A. Othman, "Artificial intelligence classification methods of atrial fibrillation with implementation technology," *Computer Assisted Surgery*, vol. 21, pp. 154–161, 2016.

[10] S. A. Shah, A. Ren, D. Fan, Z. Zhang, N. Zhao, X. Yang, M. Luo, W. Wang, F. Hu, M. U. Rehman *et al.*, "Internet of things for sensing: A case study in the healthcare system," *Applied sciences*, vol. 8, no. 4, p. 508, 2018.

[11] X. Ying, "An overview of overfitting and its solutions," in *Journal of physics: Conference series*, vol. 1168, no. 2. IOP Publishing, 2019, p. 022022.

[12] C. Ding and H. Peng, "Minimum redundancy feature selection from microarray gene expression data," *Journal of bioinformatics and computational biology*, vol. 3, no. 02, pp. 185–205, 2005.

Bayesian Surprise from a Deep Learning Model of Italian Language to Model Neural Activity

A.G. Russo[1], A. Ciarlo[2], F. Di Salle[2], M. Sansone[3], G. Tedeschi[1], F. Esposito[1]
[1] *Department of Advanced Medical and Surgical Sciences, University of Campania "Luigi Vanvitelli", Naples, Italy*
[2] *Department of Medicine, Surgery and Dentistry, "Scuola Medica Salernitana", University of Salerno, Salerno, Italy*
[3] *Department of Electtical Engineering and Technology Information, University of Naples "Federico II", Naples, Italy*

***Abstract*—Deep learning (DL) language models are increasingly used to map the neural correlates of language processing.**

A DL language model for Italian was used to estimate the Bayes surprise that indexes the mismatch between our predictions about future inputs and the input itself. These values were applied to functional MRI data recorded during a narrative listening experiment.

The Bayes surprise significantly mapped the neural signals in temporal and frontal regions bilaterally. The results are in line with previous studies, strongly support the use of DL models in encoding neural signals and motivate several applications in different scenarios.

***Keywords*—fMRI, Deep Learning, Natural Language Processing, Bayes surprise.**

I. Introduction

Deep learning (DL) models have shown remarkable results when performing human tasks, such as text [1] and image [2] generation. Due to their ability to learn complex tasks from raw data rather than a set of given rules they represent an interesting framework to study the neural mechanisms of complex high-order functions [3].

Among the high-order functions, the ability to generate and comprehend language is one of the most suited to be investigated using DL models. Recent studies showed that large DL language models, such as the Generative Pretrained Transformer version 2 (GPT-2) [4], can provide useful metrics to encode both behavioural and neural signals related to language processing [5]. Due to its architecture based on the so-called "attention mechanism" and the fact that it uses only the information received to generate/predict the next word [4], GPT-2 is considered one of the most biologically plausible DL models and it outperformed other attention-based DL model in encoding neural signal [5]. In particular, it has been successfully used to model the linguistic prediction mechanism that is behind language comprehension [6–8] and a recent study suggested that GPT-2 shares some computational principles with the human brain [6]. For instance, Russo et al. (2022) reported that, for periods of at least 60 s, the GPT-2 and the brain have a similar strategy to evaluate the received words and assign a probability score to the next incoming word [8]. However, the potential of large DL models, in addressing some aspects of the complex neural mechanisms behind language comprehension is far from being fully exploited.

A consistent body of research suggested that human beings grasp the meaning of a narrative by parsing it into discrete small events [9,10] and that at each instant they maintain a working event model representing the current event features [9,11]. This model is actively stored in the working memory as the events unfold over time, and it is used to make reliable guesses about the incoming inputs [12]. When there is a mismatch between the model's predictions and the external stimulus received the model is updated accordingly. However, this update is not free of charge, and the higher the mismatch between the prediction and the received input the higher the amount of neural resources are needed to integrate the new information. Previous studies showed that this mechanism is shared across individuals listening to the same story, however when analysing its temporal dynamic some idiosyncrasies could be observed [13]. Among the possible measures that can index this phenomenon, there is the Bayesian surprise (BS) [14] that is given by the comparison of two probability distributions indicating respectively the *a priori* event model (prior distribution, before the arrival of the external stimulus) and the *a posteriori* event model (posterior distribution, after the arrival of the external stimulus). In a recent preliminary study, the BS has been shown to successfully encode the behaviourally marked event boundaries (e.g., the change of a scene) of a narrative that coincide with the highest shifts in the internal event model and, as a consequence, with the highest integration costs [9]. It is worth noting that the BS does not simply measure errors in the sentence or semantic shift in the text, but it models the gap between our internal model of the story and the received word.

The aim of this work is to add insights into the neural correlates of this model updating mechanism that supports language comprehension and, possibly, provide a novel metric/tool to help in the assessment of linguistic impairments. For this purpose, a previously published naturalistic functional magnetic resonance imaging (fMRI) data set [15], from a group of Italian participants listening to a story in both forward (FW) and backward (BW) conditions, was re-analysed. First, a GPT-2 model was used to estimate the BS associated with each word of the story. Second, the estimated BS values were used to encode the fMRI signal elicited by the group of listeners. In light of previous studies, significant positive activations are expected in brain areas known to track both low-level speech information, such as the superior and the middle temporal regions, and high-level speech information such as the inferior and the middle frontal gyri.

II. Materials and Methods

A. Participants

The experimental data used in this work, have been acquired and processed in previous studies about the neural correlates of linguistic prediction during spoken narrative listening. Full details can be found in the original paper [15].

All the volunteers enrolled in the experiment (6 males, 21 females, mean age 24.5 ± 4.5 years old) were Italian native speakers, right-handed, without known psychiatric or neurological problems, with normal or corrected-to-normal vision, and without hearing, developmental and language-related problems. The study was performed in accordance with the Declaration of Helsinki.

B. Stimuli and experimental procedure

Participants listened to a short story (12 minutes) in both the original and reversed version, while in the MRI scanner. The reversed audio waveform was selected as control condition as, while keeping the auditory characteristics of the non-reversed version, it omits meaning and linguistic components and does not generate the necessity of storing a mental model of the discourse and inferring the next incoming word.

C. Image acquisition and pre-processing

MRI acquisition was performed with a 3T scanner (Magnetom Skyra, Siemens Healthcare, Germany) equipped with a 20-channel parallel head coil. Full details on the sequence parameters can be found in [15]. MRI data were pre-processed using FSL (https://fsl.fmrib.ox.ac.uk/fsl/fslwiki) and the Data Processing Assistant for Resting-State fMRI toolkit (DPARSF 5.0 http://www.rfmri.org) that is implemented in MATLAB (The MathWorks, Inc., Natick, MA www.mathworks.com).

D. Definition of the Bayesian surprise

The notion of BS is defined as the Kullback-Leibler divergence between a prior and a posterior distribution [14] and can be estimated with the following formula:

$$Bayesian\ surprisal = -\sum_{v=1}^{V} p_v * \log(q_v) \quad (1)$$

where p_v and q_v are the probabilities belonging respectively to the prior and posterior distribution.

The BS can be interpreted as an index of how much our prior probability has been updated/changed according to the newly received information. Therefore, the larger its value the more our prior expectations have been violated and there is a need for an update. Compared to other measures tracking the violations of the expectations and successfully used in mapping both neural and behavioural signals, such as the surprisal [16,17], the BS has the advantage of considering the probability distribution in its entirety. For example, the BS can account for how much confident we are about our prior expectations as this is indexed by the width of the distribution, and it can track a complete change in our expectations [9].

E. Estimation of the Bayesian surprise

In this work, the BS was estimated using a version of the GPT-2 model for the Italian language, called GePpeTto [18]. GePpeTto includes 12 layers, 117M parameters, and a vocabulary of 30,000 tokens. It has been trained on a corpus of standard and less-standard Italian text for a total of 13 GB of data, and, for our purposes, was used without additional fine-tuning.

The narrative text, used as stimulus for the participants, was first tokenized (i.e., the narrative was split into smaller units) and then these tokens were used to estimate the BS. The narrative was sampled with a sliding window approach with a window size of 1024 tokens which is the maximum number of input tokens allowed. The tokens contained in the window were provided in input to the GPT-2 model and, for each step, the probabilities assigned to each word of the GPT-2's vocabulary was extracted. Therefore, the BS value was estimated as the difference between the distribution probability at word-point t-1 (i.e., prior distribution) and the distribution at word-point t (i.e., posterior distribution). A recent study showed that the BS estimated using this workflow is linked to prediction error, to the amount of information brought by the new word and to the shift from one part (e.g., a scene) to another of a narrative [9].

All these data were extracted using custom scripts written in python and mainly using PyTorch and NumPy package.

A graphical description of the experimental workflow and of the BS estimation is displayed in Fig.1.

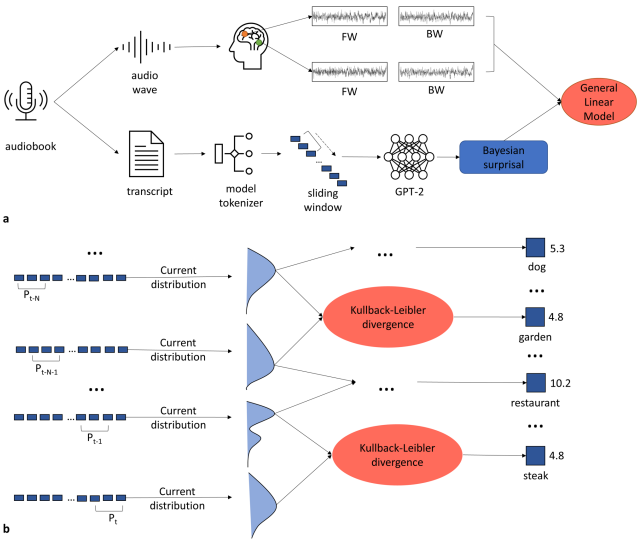


Fig. 1: Summary of the experimental framework (a) and of the workflow used to estimate the Bayesian surprise from the GPT-2 model (b).
Participants listened to a narrative twice, once in the forward (FW) and once in the backward (BW) condition while their brain signal was continuously measured using fMRI. Using a highly parcellated atlas, time series of fMRI signal were extracted for both narrative conditions for each region of the atlas itself. The transcript of the narrative was provided in input to the GPT-2 to extract the Bayesian surprise (a).
The transcript of the narrative was tokenized and sampled in a sliding window approach to be fed to the GPT-2 model. At each step of the sampling process, the distribution of probabilities over the vocabulary was first stored and then compared to the one extracted at the next step by using the Kullback-Leibler divergence. The resulting value was considered as the Bayesian surprise at that token-point and the process was repeated for each token in the narrative (b).

F. Functional MRI and statistical analysis

The estimated BS values were used as predictor of interest in a general linear model (GLM) where the dependent variable was the average neural signal of the 1000 region-of-interest (ROI) of the 7-networks Schaefer's parcellation [19] for both

speech conditions (i.e., FW and BW). For the GLM analyses only the time points characterized by the presence of the audio stimulus were retained, thus resulting in a set of functional data of 709 volumes, and the contrast between the FW and the BW conditions was evaluated. Besides the predictor of interest, other relevant linguistic features such as word duration (WD), lexical frequency (LF), and word sound (WS) were considered.

Before entering the mixed-effects GLM analysis, all the predictors were processed to account for the haemodynamic delay and the temporal resolution of the acquisition. In detail, the vector of surprisal values, LF, WD, and WS were convolved with a standard haemodynamic response function (HRF). The HRF represents the conventional approach for modelling the neural dynamics in the BOLD signals induced by a stimulus and it is derived from a Gamma distribution. As part of the convolution procedure, the resulting values are also downsampled to the fMRI temporal resolution (1 Hz), yielding a predictor matrix of size 709x4. A preliminary evaluation of the variance inflation factor (VIF) on the design matrix was performed to check possible collinearity and, due to their VIF being higher than 5, both WD and LF predictors were dropped from the final design matrix.

For each ROI the average fMRI signal was extracted for both speech conditions (i.e., FW and BW), concatenated along the time axis, and used as the dependent variable in a mixed-effects GLM analysis performed in MATLAB. As independent variables, the model included one categorical predictor encoding the speech direction (i.e., FW and BW), three fixed-effect predictors (i.e., BS, WS, and the interaction between surprisal and speech direction), and participants were considered as random-effect. To assess where the surprisal values significantly explained better the neural signal in the FW condition (i.e., comprehensible speech) compared to the BW condition (i.e., unintelligible speech), for each ROI the statistical value associated with the interaction between the speech direction and the BS was stored. The obtained statistical results were considered significant at $p < 0.05$ corrected with the Bonferroni criterion (considering $n = 1000$ comparisons), then were stored in a volumetric map (where they were assigned to the corresponding atlas' parcellation) that was eventually projected onto an inflated brain surface in the MNI space for visualization purposes using CAT12 (https://neuro-jena.github.io/cat/).

III. Results

The analysis of the head motion resulted in the exclusion of one participant due to excessive motion (translation/rotation higher than 3mm/3 degree) in one of the two fMRI runs. Therefore, the fMRI analysis was performed on a group of 26 participants (20 females).

The head motion was analysed also in terms of mean frame-wise displacement that resulted, for each participant, to be lower than the standard threshold of 0.5 mm.

The application of the BS predictor to encode the neural activity in the fMRI time series, observed in the contrast between the original and reversed version of the narrative (i.e., FW vs. BW) yielded a bilateral pattern encompassing temporal and frontal regions. In total, 102 out of 1000 ROIs were significantly activated ($p < 0.05$ Bonferroni corrected). The 102 significant ROIs were ranked in ascending order according to the elicited statistical value and the top 10 ROIs were reported in Table 1. The strongest effects for the BS were observed in ROIs located in the left superior and middle temporal gyrus (Table 1, Fig. 2). Activations were observed, in both hemispheres, also in frontal regions such as the middle and inferior frontal gyrus whose role in language processing is well established [20]. Finally, significantly positive activations were observed in the left, and to a lesser extent in the right, angular gyrus.

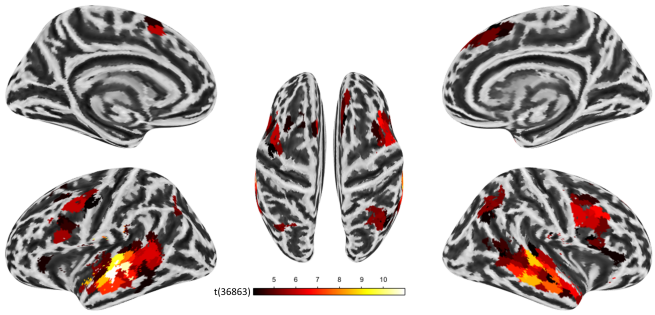


Fig. 2: Regional statistical map of the contrast FW versus BW projected on a surface in the standard MNI space (left and right hemisphere). Color-coded areas indicate the atlas' parcellations that yielded a significantly higher correlation with the BS predictor in the FW speech condition compared to the BW speech condition ($p < 0.05$, Bonferroni corrected). A bilateral regional pattern, encompassing regions mainly in the temporal and frontal areas was observed. The highest statistical values were observed in the areas located in the left superior/middle temporal gyrus.

Area	t(36863)	p-value	Coordnates (RAS space)		
7Networks_LH_Default_Temp_15	10.99	4.63E-28	-58	-14	-4
7Networks_LH_Default_Temp_18	10.53	6.57E-26	-58	-24	0
7Networks_LH_SomMot_8	9.50	2.06E-21	-52	-20	6
7Networks_LH_SomMot_3	9.407	5.36E-21	-62	-12	4
7Networks_RH_SomMot_12	8.78	1.69E-18	62	-24	2
7Networks_LH_Default_Temp_11	8.63	5.97E-18	-54	-4	-10
7Networks_RH_Default_Temp_12	8.52	1.56E-17	64	-22	-8
7Networks_LH_SomMot_9	7.79	6.55E-15	-60	-26	10
7Networks_LH_SomMot_4	7.72	1.11E-14	-66	-18	6
7Networks_RH_Default_Temp_6	7.62	2.43E-14	58	-4	-18

Table 1: The top 10 ROIs, ranked according to the statistical values elicited in the statistical analysis, are reported in the table. For each region, named

according to the naming convention of [19], the t-statistics, the p-value and the centroid in RAS space are displayed.

IV. Conclusion

Recent studies have demonstrated how DL language models represent powerful tools not only in performing or assisting human tasks but also in providing an independent model to investigate high-order cognitive functions. In this work, we provided further support to the latter idea and contributed novel findings about the neural correlates underpinning language comprehension.

The contribution of this study is two-fold: first our results show that, similarly to other metrics derived from the information theory (e.g., the surprisal [16,17]), the BS is able to capture the neural cost associated with the mismatch between the prediction about the next incoming input and the input received. Second, our findings illustrate that the BS is a reliable metric to encode the continuous update of the internal event model related to the unfolding of a series of events (e.g., events in a narrative) over time and the information carried with them. Therefore, the BS estimated from a DL language model for each word of a narrative can explain the impact of the newly received input and its information on our prior expectations, such as changes in the overall content of the narrative and the replacement of the current event model with a new one [9].

The observed bilateral activations are in line with previous studies supporting that language processing is not strictly confined to the left hemisphere [21]. The highest statistical values reported for the left middle/superior temporal gyrus are consistent with the putative role of these regions in tracking speech information and, in particular, in hosting a prediction mechanism [15,22]. In fact, activations in these areas have been reported in several previous studies that investigated language comprehension with both (simpler) stochastics [15,22] and DL-based language models [6–8,23]. The involvement of higher-order areas in frontal lobes is consistent with previous findings suggesting that these regions process speech information at paragraph level [20].

Our results highlight the versatility of the proposed experimental framework. In fact, the possibility of exposing to the same stimulus both a DL model and a group of human participants, with the purpose of generating predictors from the former and brain activations from the latter, can be applied to other scenarios that include different cognitive functions and biomedical signals [6,7]. Moreover, the possibility to generate informative predictors using parameters derived from DL models could have clinical applications. Indeed, this method could be highly suitable to investigate, and possibly assess, language dysfunctions in pathological coohorts such such as subjects affected by schizophrenia [24] or autism spectrum disorder [25].

References

[1] Brown T B, Mann B, Ryder N, Subbiah M, Kaplan J, Dhariwal P, Neelakantan A, Shyam P, Sastry G, Askell A, Agarwal S, Herbert-Voss A, Krueger G, Henighan T, Child R, Ramesh A, Ziegler D M, Wu J, Winter C, Hesse C, Chen M, Sigler E, Litwin M, Gray S, Chess B, Clark J, Berner C, McCandlish S, Radford A, Sutskever I and Amodei D 2020 Language Models are Few-Shot Learners

[2] Ramesh A, Dhariwal P, Nichol A, Chu C and Chen M 2022 Hierarchical Text-Conditional Image Generation with CLIP Latents

[3] Saxe A, Nelli S and Summerfield C 2021 If deep learning is the answer, what is the question? *Nat Rev Neurosci* **22** 55–67

[4] Radford A, Wu J, Child R, Luan D, Amodei D and Sutskever I 2019 Language Models are Unsupervised Multitask Learners *OpenAI, Blog* **1** 24

[5] Schrimpf M, Blank I A, Tuckute G, Kauf C, Hosseini E A, Kanwisher N, Tenenbaum J B and Fedorenko E 2021 The neural architecture of language: Integrative modeling converges on predictive processing *PNAS* **118**

[6] Goldstein A, Zada Z, Buchnik E, Schain M, Price A, Aubrey B, Nastase S A, Feder A, Emanuel D, Cohen A, Jansen A, Gazula H, Choe G, Rao A, Kim C, Casto C, Fanda L, Doyle W, Friedman D, Dugan P, Melloni L, Reichart R, Devore S, Flinker A, Hasenfratz L, Levy O, Hassidim A, Brenner M, Matias Y, Norman K A, Devinsky O and Hasson U 2022 Shared computational principles for language processing in humans and deep language models *Nat Neurosci* **25** 369–80

[7] Heilbron M, Armeni K, Schoffelen J-M, Hagoort P and de Lange F P 2022 A hierarchy of linguistic predictions during natural language comprehension *Proceedings of the National Academy of Sciences* **119** e2201968119

[8] Russo A G, Ciarlo A, Ponticorvo S, Di Salle F, Tedeschi G and Esposito F 2022 Explaining neural activity in human listeners with deep learning via natural language processing of narrative text *Sci Rep* **12** 17838

[9] Kumar M, Goldstein A, Michelmann S, Zacks J M, Hasson U and Norman K A 2022 Bayesian Surprise Predicts Human Event Segmentation in Story Listening

[10] Zacks J M, Speer N K and Reynolds J R 2009 Segmentation in Reading and Film Comprehension *J Exp Psychol Gen* **138** 307–27

[11] Kuperberg G R and Jaeger T F 2016 What do we mean by prediction in language comprehension? *Language, Cognition and Neuroscience* **31** 32–59

[12] Clark A 2013 Whatever next? Predictive brains, situated agents, and the future of cognitive science *Behavioral and Brain Sciences* **36** 181–204

[13] Russo A G, De Martino M, Elia A, Di Salle F and Esposito F 2022 Negative correlation between word-level surprisal and intersubject neural synchronization during narrative listening *Cortex* **155** 132–49

[14] Itti L and Baldi P 2009 Bayesian surprise attracts human attention *Vision Research* **49** 1295–306

[15] Russo A G, De Martino M, Mancuso A, Iaconetta G, Manara R, Elia A, Laudanna A, Di Salle F and Esposito F 2020 Semantics-weighted lexical surprisal modeling of naturalistic functional MRI time-series during spoken narrative listening *NeuroImage* **222** 117281

[16] Hale J 2016 Information-theoretical Complexity Metrics *Linguistics and Language Compass* **10** 397–412

[17] Levy R 2008 Expectation-based syntactic comprehension *Cognition* **106** 1126–77

[18] De Mattei L, Cafagna M, Dell'Orletta F, Nissim M and Guerini M 2020 GePpeTto Carves Italian into a Language Model *arXiv:2004.14253 [cs]*

[19] Schaefer A, Kong R, Gordon E M, Laumann T O, Zuo X-N, Holmes A J, Eickhoff S B and Yeo B T T 2018 Local-Global Parcellation of the Human Cerebral Cortex from Intrinsic Functional Connectivity MRI *Cerebral Cortex* **28** 3095–114

[20] Lerner Y, Honey C J, Silbert L J and Hasson U 2011 Topographic Mapping of a Hierarchy of Temporal Receptive Windows Using a Narrated Story *J Neurosci* **31** 2906–15

[21] Wilson S M, Molnar-Szakacs I and Iacoboni M 2008 Beyond Superior Temporal Cortex: Intersubject Correlations in Narrative Speech Comprehension *Cerebral Cortex* **18** 230–42

[22] Willems R M, Frank S L, Nijhof A D, Hagoort P and Van Den Bosch A 2016 Prediction during Natural Language Comprehension *Cerebral Cortex* **26** 2506–16

[23] Caucheteux C, Gramfort A and King J-R 2021 GPT-2's activations predict the degree of semantic comprehension in the human brain *bioRxiv* 2021.04.20.440622

[24] Meyer L, Lakatos P and He Y 2021 Language Dysfunction in Schizophrenia: Assessing Neural Tracking to Characterize the Underlying Disorder(s)? *Front. Neurosci.* **15** 640502

[25] Brennan J R, Lajiness-O'Neill R, Bowyer S, Kovelman I and Hale J T 2019 Predictive sentence comprehension during story-listening in autism spectrum disorder *Language, Cognition and Neuroscience* **34** 428–39

The role of hemodynamics in arteriovenous fistula remodelling and failure. A CFD longitudinal study

L. Soliveri[1], M. Bozzetto[1], P. Brambilla[2], A. Caroli[1] and A. Remuzzi[3]
[1] *Department of Biomedical Engineering - Istituto di Ricerche Farmacologiche Mario Negri IRCCS, Bergamo, Italy*
[2] *Diagnostic Radiology, Papa Giovanni XXIII Hospital, Bergamo, Italy - University of Milano-Bicocca, Milan, Italy*
[3] *Department of Management, Information and Production Engineering, University of Bergamo, Italy*

***Abstract*—The mechanism of vascular stenosis development in haemodialysis arteriovenous fistula is still mostly unknown. Almost all computational fluid dynamics (CFD) studies are performed at given time after surgery, but evolution of fistula remodelling and failure has not been studied so far. We then performed a longitudinal study on morphological and hemodynamic changes in an arteriovenous fistula that showed progressive stenosis and failure 1.5 years after surgery. The comparison of CFD and morphological changes showed that vascular wall remodelling acted as a protecting response, with progressive expansion of the stenosis in the venous outflow tract that induced regularization of velocity waveforms and decreased the disturbed flow metrics.**

***Keywords*—computational fluid dynamics, arteriovenous fistula, stenosis, hemodynamic**

I. INTRODUCTION

NATIVE arteriovenous fistula (AVF) is the preferred vascular access (VA) for haemodialysis (HD) patients, but it is still associated with a high rate of failure due to stenosis development. The main cause of stenosis is the formation of neointimal hyperplasia (NH) in the juxta-anastomotic vein (JAV) [1]–[3].

Already in 1999, Sivanesan [4] observed that vascular stenosis consistently develops in three specific areas of the JAV, suggesting that excessive neointimal growth might be related to local hemodynamic conditions. In recent years, a growing body of evidence has suggested that the damage provoked to the endothelium by AVF surgery and the altered local hemodynamics, resulting from the artificially created vessel shunt [5], stimulate both the initiation and progression of AVF stenosis [6]–[8].

Despite their clinical relevance, the process and the mechanisms of stenosis development and evolution in AVFs are still poorly understood. Over the last few decades, high-fidelity computational fluid dynamics (CFD) simulations have been exploited trying to shed more light on the quantification of the hemodynamic forces acting on the AVF lumen [9], [10].

Despite numerous studies on AVF hemodynamics, CFD longitudinal studies on AVFs are rare in literature. Sigovan et al. [11] and He et al. [12] were the first to demonstrate in their pilot studies that vascular remodelling in AVFs could be investigated using repeated magnetic resonance imaging (MRI) acquisitions. However, they could not distinguish a defined relationship between disturbed hemodynamics and vessel lumen changes. Recently, Colley et al. [13] coupled ultrasounds (US) and CFD to analyse the hemodynamics in 1 patient with successful AVF maturation over 15 weeks, finding that wall shear stress (WSS) immediately after AVF creation may be a useful indicator for proper maturation. Northrup et al. [14] followed 6 patients (3 with assisted and 3 with non-assisted maturation) with MRI at 1 day, 6 weeks and 6 months after surgery. They reported that larger venous velocity, WSS, and vorticity immediately after AVF surgery may be crucial for later lumen enlargement and VA maturation. Also, a recent massive work of the Haemodialysis Fistula Maturation (HFM) Study Group followed 120 patients for 6 months after the intervention [15]. CFD results highlighted that high WSS and low Oscillatory Shear Index (OSI) were associated with greater vein lumen expansion after AVF creation surgery. Despite these investigations, the causes and mechanisms underlying the development and progression of vascular stenosis in AVF remain largely unknown.

Our group has recently developed a non-contrast-enhanced MRI protocol that provides high-resolution black-blood images within few minutes, allowing non-invasive and accurate imaging of patient's AVFs at different timepoints. This MRI protocol, coupled with high-fidelity CFD simulations in a complete MRI-to-CFD pipeline, has shown to be a promising approach to characterize AVF morphologic and hemodynamic evolution over time [16], [17].

Thus, the current study aims at: *i)* to analyse the lumen remodelling trajectory over 1.5 year of a newly created AVF failed due to stenosis formation and *ii)* to investigate the impact of the altered hemodynamics on pathological vessel remodelling and VA failure.

II. METHODS

A. MRI acquisitions

Non-contrast-enhanced MRI acquisitions were performed in a 72-year male referred for primary radio-cephalic AVFs at the Unit of Nephrology and Dialysis of Papa Giovanni XXIII hospital (Bergamo, Italy). The patient had to sign a written informed consent before undergoing the acquisitions. Image sequences were acquired using a 1.5T scanner (GE, Optima 450w GEM) with a flexible 16-channel phased array medium coil and were cardiac gated using peripheral pulse gating. After a first three-plane scout sequence acquisition to correctly localize the anastomosis, 3D fast spin echo T1-weighted imaging was executed with variable flip angles using CUBE sequence, covering an arm region of approximately 5 cm above and 3 cm below the anastomosis. Further details on the MRI protocol are reported in our previous publication [16]. MRI examination was performed at 3 days after AVF creation and then repeated at 40 days, 6

months, 1 year and 1.5 year after surgery. On the same days, a complete Doppler US examination of the patient AVF was performed and the vessel diameters and blood flow volumes in the proximal artery (PA), distal artery (DA) and in the vein were collected.

B. 3D model reconstruction and mesh generation

Starting from MRI acquisitions, the AVFs were digitally segmented using ImageJ. Thus, the 3D AVF surface models were generated exploiting the Vascular Modeling Toolkit (VMTK) [18]. The primitive 3D surface model was smoothed and straight cylindrical extensions of five diameters in length were added at the extremities to achieve full development of flow conditions inside the computational domain. FoamyHexMesh of OpenFOAM suite was used to discretize the internal volume, obtaining meshes of ~ 1,000 k cells for all AVF models, with dominant-hexahedral core cells, low orthogonality and predominant alignment to the vessel surface. Two thin boundary layers were generated in order to catch the sharp velocity gradients close to the vessel wall. The mesh resolution was chosen based on the refinement study recently performed in our previous publication [17].

C. Computational fluid dynamic simulations

CFD simulations were solved using pimpleFoam, a transient OpenFOAM solver for incompressible flows based on the finite volume method, set with second-order spatial and time integration schemes. The time step was adjusted automatically by the solver, setting a maximum Courant–Friedrichs–Lewy (CFL) number equal to 1 and resulting in a mean timestep of 0.1 ms. Patient-specific boundary conditions at the inlets of the PA and DA were imposed using volumetric flow waveforms derived from Doppler US examinations, while for the vein outflow a traction-free condition was set. Three complete cardiac cycles were solved and only the third one was used for post-processing to avoid start-up transients. Blood was modelled as patient-specific, non-Newtonian fluid using the Bird-Carreau rheological model, assuming a blood density of 1.05 g/cm^3, patient's measured haematocrit and a total serum protein value equal to 7 g/dL. The no-slip condition was prescribed at the vessel walls, assumed as rigid.

D. Morphological and hemodynamic analysis

A rigid co-registration of the models at the different timepoints was performed using the iterative closest point registration algorithm of VMTK. Vascular lumen cross-sectional areas (CSAs) along the models' centreline were obtained at 0.1 mm intervals in each model to characterize lumen remodelling. Moreover, the angle between the PA and the vein was quantified using Paraview software. The velocity changes over time were characterized using the blood velocity waveforms extracted along the models' centreline.

The near-wall hemodynamic was categorized using the Oscillatory Shear Index (OSI), that quantifies the degree of deviation of the WSS (τ_ω) from its average direction, as

$$OSI = \frac{1}{2}\left(1 - \frac{\left|\int_0^T \tau_\omega \, dt\right|}{\int_0^T |\tau_\omega| dt}\right) \quad (1)$$

Also, the Spectral Power Index (SPI) of WSS, another flow instability index, was computed as

$$SPI = \frac{\sum_{n=n_c}^{+\infty} |Y[n\omega_0]|^2}{\sum_{n=1}^{+\infty} |Y[n\omega_0]|^2} \quad (2)$$

where $|Y[n\omega_0]|$ is the magnitude of the Fourier-transformed signal, ω_0 the fundamental angular frequency of the periodic signal, and n_c the harmonic corresponding to the cut-off frequency set to 25 Hz [19].

III. RESULTS

Patient-specific AVF geometrical models reconstructed for each follow-up visit and the corresponding mean blood flow rates in the PA and DA are reported in **Figure 1.a**. Qualitative local variations in vessel lumen develop with time; in particular blood vessel's lumen dilated at the anastomosis and along the vein, and stenosis developed at the curvature of the JAV starting from 1 year after surgery. Moreover, the angle between PA and JAV remained unchanged between 3 days and 3 weeks, while it significantly decreased at 6 months and then remained stable until the end of the follow-up period. The vascular lumen changes were accompanied by changes in VA blood flow rate, which showed a constant increase in the first 6 months after surgery and was followed by a rapid decrease until last visit at 1.5 year, when the flow became too low to perform HD treatment.

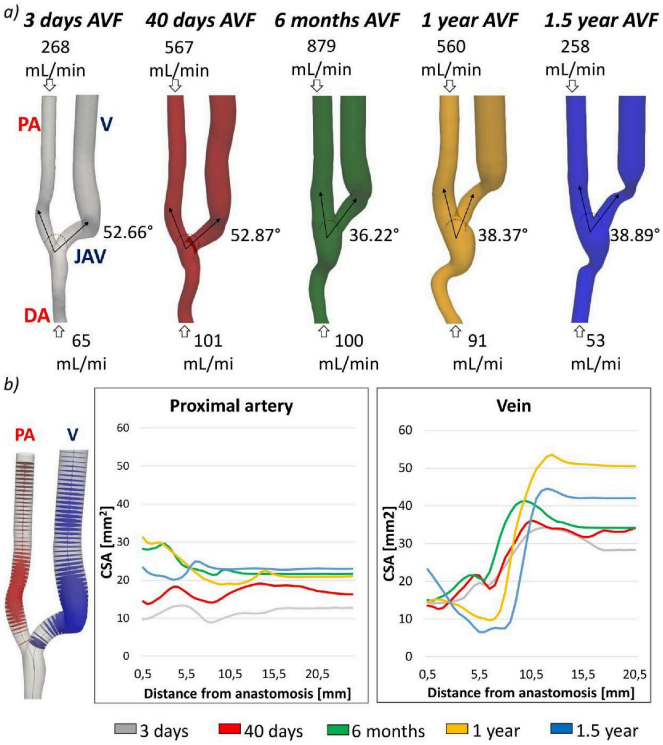


Fig. 1: a) 3D geometrical models and blood flow rates of the AVF at the five different timepoints. Notes: black arrows indicate the main direction of blood flow. b) Morphological changes occurring over time in the proximal artery (PA) and in the vein (V).

A quantitative analysis of the vascular lumen changes of PA and vein is shown in **Figure 1.b**. During VA maturation arterial dilatation was observed up to 6 months, with slight

regional-specific differences. The JAV segment also dilated after surgery and until 6 months, but at 1 year vessel stenosis developed, becoming very significant at 1.5 year.

Velocity–time traces at nine specific points sampled consistently along vessel centreline are shown in **Figure 2**. These points were similarly selected in all AVF models: points 1–3 are located in the PA, point 4 at the anastomosis, points 5–7 in the JAV, and 8 and 9 more distally in the vein.

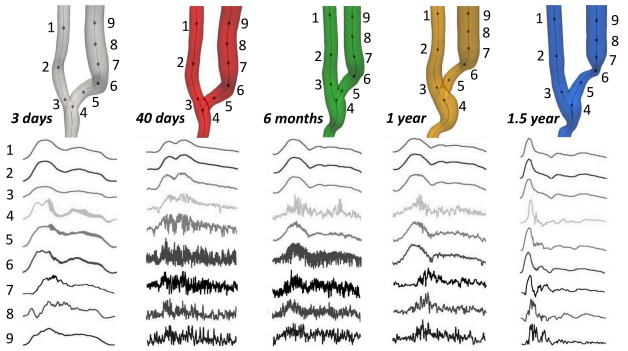


Fig. 2: Velocity-time traces, normalized by their respective cycle averages, at nine selected feature points along the centreline of the AVF model corresponding to the 5 different timepoints.

At all timepoints, velocity traces revealed stable laminar flow in the artery. Three days after surgery the velocity was stable also in the venous segment, while flow instabilities with high-frequency oscillations occurred starting from 40 days after surgery and at 6 months. After this time period, the vascular remodelling, mainly characterized by the enlargement at the anastomosis location and the stenosis formation at the curvature of the JAV, importantly reduced velocity fluctuations (1 year). The velocity traces then stabilized along the vein, specifically in the vessel segment where the stenosis developed, with an almost stable vein flow at 1.5 year.

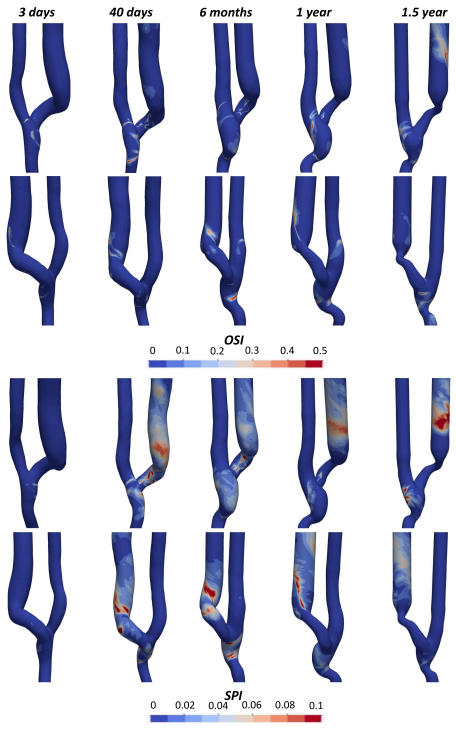


Fig. 3: Oscillatory Shear Index (OSI) and Spectral Power Index (SPI) maps at the five different timepoints.

Surface maps of OSI and SPI are reported in **Figure 3**. For all timepoints, OSI values are equal to zero in the PA, where the near-wall flow mostly maintains the main direction during the entire cardiac cycle. Areas of high OSI developed in the JAV starting from 40 days after surgery and were mostly located close to the inner curvature of the JAV. One year after surgery, lower OSI values were restored in the first segment of the JAV and in the stenotic area because of vessel remodelling, while areas of high OSI appeared in the distal segment of the vein. Same as OSI, SPI values are equal to zero in the PA. SPI values increase significantly during the first 40 days after surgery at the anastomosis and in the vein segment. Then, the vascular remodelling causes an important reduction of SPI values in the first segment of the JAV. Specifically, null SPI is progressively restored along the vein, following the stenosis progression. In the distal vein, on the other hand, flow instability still remains.

IV. DISCUSSION

In this study, morphological and hemodynamic AVF changes were investigated over a 1.5 year follow-up period after surgical creation. Interestingly, the patient under study developed a significant stenosis, allowing to investigate its progression until VA closure. Indeed, the patient's blood flow volume was sufficient to carry out HD until 1.5 years after surgery, when the AVF blood flow was not adequate to sustain the treatment. Patient-specific CFD simulations were performed at multiple timepoints to elucidate the possible impact of altered hemodynamics on pathological vessel remodelling and vessel stenosis.

The morphological analysis showed that the largest arterial dilatation occurred in the first postoperative 6 months and stabilized in the subsequent follow-up period. The vein also dilated until 6 months, but at 1 year a stenosis developed in the JAV, becoming very important at 1.5 year. These changes in the vessel lumen were accompanied by an increase in the blood flow rate during the first 6 months, followed by a progressive decrease starting from 1 year after surgery, resulting in the inadequacy to sustain HD treatment and the need of a new VA.

The hemodynamic analysis revealed the presence of laminar flow in the PA, but highly disturbed flow in the JAV after AVF maturation. These results are in line with previous findings by our [5] and other research groups [20]. Interestingly, the development of the venous stenosis was accompanied by the regularization of the blood flow pattern. The progressive expansion of the stenotic site along the distal vein occurred in parallel with velocity waveforms regularization along the centreline and a decrease of the disturbed flow indices, suggesting that vascular wall remodelling, and more specifically stenosis development, could be the result of a protective mechanism. Indeed, 1 year after surgery, flow parameters' disturbances in the stenotic site decreased, and the unsteady flow patterns shifted gradually along the distal vein. These results are in line with previous observations showing that the vessels remodel to restore the initial hemodynamic conditions [6], [21]. In this case vessel remodelling, like due to intimal hyperplasia, could be triggered by the presence of flow instabilities.

In literature there are just a few significant longitudinal studies on AVFs, and none of them have specifically

investigated the process of VA remodelling and closure and its relationship with local hemodynamic conditions. Despite He et al. [12] being the first ones to use a contrast-free MRI to CFD pipeline in the context of a longitudinal study, they only assessed vascular hemodynamics and remodelling in 1 patient with images taken at 4, 5, and 7 months after AVF creation. Probably due to the choice of those timepoints they just discussed the feasibility of the MRI-to-CFD pipeline. Sigovan et al. [11] studied 3 patients preoperatively and at 1 and 3 months after surgery, focusing again on the feasibility of the technique and not on the correlation between local hemodynamic conditions and vascular remodelling. More recently, Colley et al. [13] followed 1 patient with successful AVF maturation for 15 weeks, suggesting that baseline WSS at time of creation may be a useful indicator for successful maturation. Northrup et al. [14] studied 6 patients and reported that venous velocity, WSS, and vorticity may be used as indicators to diagnose poor AVF maturation earlier. The HFM Study Group followed 120 patients for 6 months, finding that high WSS and low OSI are associated with a positive AVF maturation [15]. All these studies show the potential of hemodynamic parameters as possible predictors for successful maturation, but do not investigate the dynamics of stenosis formation and evolution. Our work is the first longitudinal study that has followed an AVF over time until almost complete closure, allowing to investigate remodelling over time as well as the relation between local hemodynamics and vessel lumen stenosis formation and progression.

From a clinical perspective, this study raises the question of whether a close monitoring of hemodynamics may allow to identify AVFs which are developing stenosis.

The results suggest the presence of a biomechanical stimulus, that might act on the endothelium as well as on other vascular cells. This might explain the lack of a clear and specific correlation between AVF remodelling and conventional disturbed flow parameters and opens up to speculations on the role of the vascular wall itself. Fluid structure interaction might be used to better understand the biomechanical stimuli that might act in the AVF walls.

A limit of the present study is that it was performed on a single patient. Therefore, future clinical investigations with higher number of participants are required to extend current preliminary findings.

V. Conclusion

In this longitudinal study, performed on a AVF that developed stenosis after 1.5 year from surgery, we showed the presence of a focal remodelling process in the vein that was followed by progressive disturbed flow regularization. Our data suggest that local flow instabilities, mostly located in the JAV, may have induced progressive intimal hyperplasia during time with consequent narrowing of vessel lumen that was instrumental for blood flow stabilization.

Acknowledgement

The Authors would like to acknowledge V. Portalupi and S. Rota for their help with patient management, S. Poloni for fruitfull discussion, and Fondazione Dompè for funding.

References

[1] P. Roy-Chaudhury *et al.*, «Neointimal Hyperplasia in Early Arteriovenous Fistula Failure», *American Journal of Kidney Diseases*, vol. 50, fasc. 5, pp. 782–790, nov. 2007.

[2] T. Lee e S. Misra, «New Insights into Dialysis Vascular Access: Molecular Targets in Arteriovenous Fistula and Arteriovenous Graft Failure and Their Potential to Improve Vascular Access Outcomes», *CJASN*, vol. 11, fasc. 8, pp. 1504–1512, ago. 2016.

[3] A. Caroli *et al.*, «Validation of a patient-specific hemodynamic computational model for surgical planning of vascular access in hemodialysis patients», *Kidney International*, vol. 84, fasc. 6, pp. 1237–1245, dic. 2013.

[4] S. Sivanesan, «Sites of stenosis in AV fistulae for haemodialysis access», *Nephrology Dialysis Transplantation*, vol. 14, fasc. 1, pp. 118–120, gen. 1999.

[5] M. Bozzetto, B. Ene-Iordache, e A. Remuzzi, «Transitional Flow in the Venous Side of Patient-Specific Arteriovenous Fistulae for Hemodialysis», *ABME*, vol. 44, fasc. 8, pp. 2388–2401, ago. 2016.

[6] A. Remuzzi e B. Ene-Iordache, «Novel Paradigms for Dialysis Vascular Access: Upstream Hemodynamics and Vascular Remodeling in Dialysis Access Stenosis», *CJASN*, vol. 8, fasc. 12, pp. 2186–2193, dic. 2013.

[7] A. M. Malek, «Hemodynamic Shear Stress and Its Role in Atherosclerosis», *JAMA*, vol. 282, fasc. 21, p. 2035, dic. 1999.

[8] L. D. Browne, K. Bashar, P. Griffin, E. G. Kavanagh, S. R. Walsh, e M. T. Walsh, «The Role of Shear Stress in Arteriovenous Fistula Maturation and Failure: A Systematic Review», *PLoS ONE*, vol. 10, fasc. 12, p. e0145795, dic. 2015.

[9] B. Ene-Iordache e A. Remuzzi, «Disturbed flow in radial-cephalic arteriovenous fistulae for haemodialysis: low and oscillating shear stress locates the sites of stenosis», *Nephrology Dialysis Transplantation*, vol. 27, fasc. 1, pp. 358–368, gen. 2012.

[10] E. Colley, A. Simmons, R. Varcoe, S. Thomas, e T. Barber, «Arteriovenous fistula maturation and the influence of fluid dynamics», *Proc Inst Mech Eng H*, vol. 234, fasc. 11, pp. 1197–1208, nov. 2020.

[11] M. Sigovan, V. Rayz, W. Gasper, H. F. Alley, C. D. Owens, e D. Saloner, «Vascular Remodeling in Autogenous Arterio-Venous Fistulas by MRI and CFD», *Ann Biomed Eng*, vol. 41, fasc. 4, pp. 657–668, apr. 2013.

[12] Y. He, C. M. Terry, C. Nguyen, S. A. Berceli, Y.-T. E. Shiu, e A. K. Cheung, «Serial analysis of lumen geometry and hemodynamics in human arteriovenous fistula for hemodialysis using magnetic resonance imaging and computational fluid dynamics», *Journal of Biomechanics*, vol. 46, fasc. 1, pp. 165–169, gen. 2013.

[13] E. Colley, J. Carroll, S. Anne, T. Shannon, V. Ramon, e B. Tracie, «A longitudinal study of the arterio-venous fistula maturation of a single patient over 15 weeks», *Biomech Model Mechanobiol*, vol. 21, fasc. 4, pp. 1217–1232, ago. 2022.

[14] H. Northrup, Y. He, H. Le, S. A. Berceli, A. K. Cheung, e Y.-T. Shiu, «Differential hemodynamics between arteriovenous fistulas with or without intervention before successful use», *Front. Cardiovasc. Med.*, vol. 9, p. 1001267, nov. 2022.

[15] Y. He *et al.*, «Association of Shear Stress with Subsequent Lumen Remodeling in Hemodialysis Arteriovenous Fistulas», *CJASN*, p. CJN.04630422, nov. 2022.

[16] M. Bozzetto *et al.*, «Toward longitudinal studies of hemodynamically induced vessel wall remodeling», *Int J Artif Organs*, vol. 41, fasc. 11, pp. 714–722, nov. 2018.

[17] M. Bozzetto *et al.*, «Arteriovenous fistula creation with VasQ ™ device: A feasibility study to reveal hemodynamic implications», *J Vasc Access*, p. 112972982210871, apr. 2022.

[18] L. Antiga, M. Piccinelli, L. Botti, B. Ene-Iordache, A. Remuzzi, e D. A. Steinman, «An image-based modeling framework for patient-specific computational hemodynamics», *Med Biol Eng Comput*, vol. 46, fasc. 11, p. 1097, nov. 2008.

[19] M. O. Khan *et al.*, «On the quantification and visualization of transient periodic instabilities in pulsatile flows», *Journal of Biomechanics*, vol. 52, pp. 179–182, feb. 2017.

[20] L. D. Browne, M. T. Walsh, e P. Griffin, «Experimental and Numerical Analysis of the Bulk Flow Parameters Within an Arteriovenous Fistula», *Cardiovasc Eng Tech*, vol. 6, fasc. 4, pp. 450–462, dic. 2015.

[21] B. Ene-Iordache *et al.*, «Radial Artery Remodeling in Response to Shear Stress Increase Within Arteriovenous Fistula for Hemodialysis Access», *Endothelium*, vol. 10, fasc. 2, pp. 95–102, gen. 2003.

Abnormal Ventricular Potentials Identification Using a Siamese Neural Network

Andrea Pitzus[1], Giulia Baldazzi[1], Graziana Viola[2], Luigi Raffo[1] and Danilo Pani[1]
[1] *Department of Electrical and Electronic Engineering (DIEE), University of Cagliari, Cagliari, Italy*
[2] *Department of Cardiology, Santissima Annunziata Hospital, Sassari, Italy*

***Abstract*—Among the different treatments for ventricular tachycardia (VT), catheter ablation guided by the electroanatomic mapping is increasingly adopted. Ablation targets are currently identified by visual inspection from the cardiologist during the mapping procedures. To improve the outcome and consequently reduce the VT recurrences, in this study, an automatic approach exploiting the deep learning on intracardiac bipolar electrograms (EGMs) is proposed. A balanced dataset composed of 752 physiological and 752 abnormal ventricular potentials (AVPs) was collected from nine post-ischemic VT patients. By adopting the synchrosqueezed wavelet transform, for each EGM a time-frequency representation was obtained to be used for feeding a siamese neural network, known to be usable on small dataset. Our findings revealed accurate classification capabilities, thus encouraging the introduction of deep learning tools in the recognition of AVPs and paving the way for their use in supporting clinicians for targeting arrhythmogenic sites.**

***Keywords*—Cardiac electrophysiology, ventricular tachycardia, arrhythmogenic sites identification, abnormal ventricular potentials, deep learning.**

I. Introduction

VENTRICULAR tachycardia (VT) is one of the main causes of sudden cardiac death and unfortunately this is still one of the main cause of death in Europe [1], [2]. Different options for the treatment of this condition have been proposed, including drugs, implantable cardioverter defibrillators, and catheter ablation. The latter is increasingly adopted, because of the advantages with respect to the other two, such as the cost-efficacy ratio, the avoidance of following a long-term therapy and/or no need to implant any external device in the patient body. Although the advantages are interesting, it also presents some drawbacks; indeed, the electroanatomic mapping (EAM) procedure, which the catheter ablation relies on, is very time-consuming; furthermore, the interpretation of the intracardiac electrograms (EGMs) recorded locally on the ventricular endocardium depends obviously on the experience and on the attention of the cardiologist, as the identification of the arrhythmogenic sites to be ablated, to terminate the VT. Remarkably, a computer-aided analysis of the intracardiac recordings could increase the success ratio of the ablation procedure by fast and operator-independent interpretation of the EGMs, or at least support the electrophysiologist during the EAM. In this perspective, different solutions based on artificial intelligence have been introduced, both using machine learning [3], [4] and deep learning [5], trying to discriminate between physiological EGMs and abnormal ventricular potentials (AVPs). Recently, in [5], we adopted a deep learning approach by transfer learning, to overcome the limitation of our dataset size. The AlexNet convolutional neural network (CNN) [6], previously trained on the ImageNet dataset [7], was used along with the EGMs time-frequency representation computed via synchrosqueezed wavelet transform (SSWT) [8]. This choice was driven by previous findings [4] highlighting statistical differences in the spectral components among physiological EGMs and AVPs. Leveraging the spectrograms, AlexNet carried out the binary classification with an accuracy above 90%, underlining the efficacy of the SSWT in extracting the distinguishing features in time and frequency domains for both classes.

On the other hand, siamese neural networks (SNNs) [9] resulted effective in several applications exhibiting limited dataset size, also in cardiac electrophysiology applications. Specifically, in [10] a SNN has been used to recognize EGMs featuring highly distinguishable activations among a large set of signals in atrial fibrillation procedures, obtaining accuracy above 90% on a small dataset (N = 1006) and even outperforming of about 20% a traditional CNN with an equivalent number of parameters. As such, in order to deal with a limited dataset to train a CNN designed from scratch, in this work we investigated the adoption of a SNN for the identification of AVPs in real bipolar EGMs, with the final aim of improving the current CNN classification results and allowing for an effective computer-aided system to target arrhythmogenic sites in post-ischemic VT substrate mapping procedures.

II. Materials and Methods

The SNN architecture has been designed leveraging on a simple subnetwork to reduce the number of weights to be updated. Subnetworks are composed of an input layer, followed by a set of four stacks of 3 layers, i.e., a convolutional layer followed by a ReLu layer and then by a Max Pool layer, except for the fourth element of the stack where the last layer is replaced by a fully connected one. A detailed description of the subnetworks is reported in Figure 1 and in Table 1.

TABLE I: SUBNETWORKS ARCHITECTURE

Type	*Size (number)*	*Activation*
Image Input	*224x224x3 (1)*	*224x224x3*
Convolutional 1	*10x10x3 (64)*	*215x215x64*
ReLu 1		*215x215x64*
Max Pool 1	*2x2*	*107x107x64*
Convolutional 2	*7x7x64 (128)*	*101x101x128*
ReLu 2		*101x101x128*
Max Pool 2	*2x2*	*50x50x128*
Convolutional 3	*4x4x128*	*47x47x128*
ReLu 3		*47x47x128*
Max Pool 3	*2x2*	*23x23x128*
Convolutional 4	*5x5x128*	*19x19x256*
ReLu 4		*19x19x256*
Fully Connected 1	*4096*	*4096*

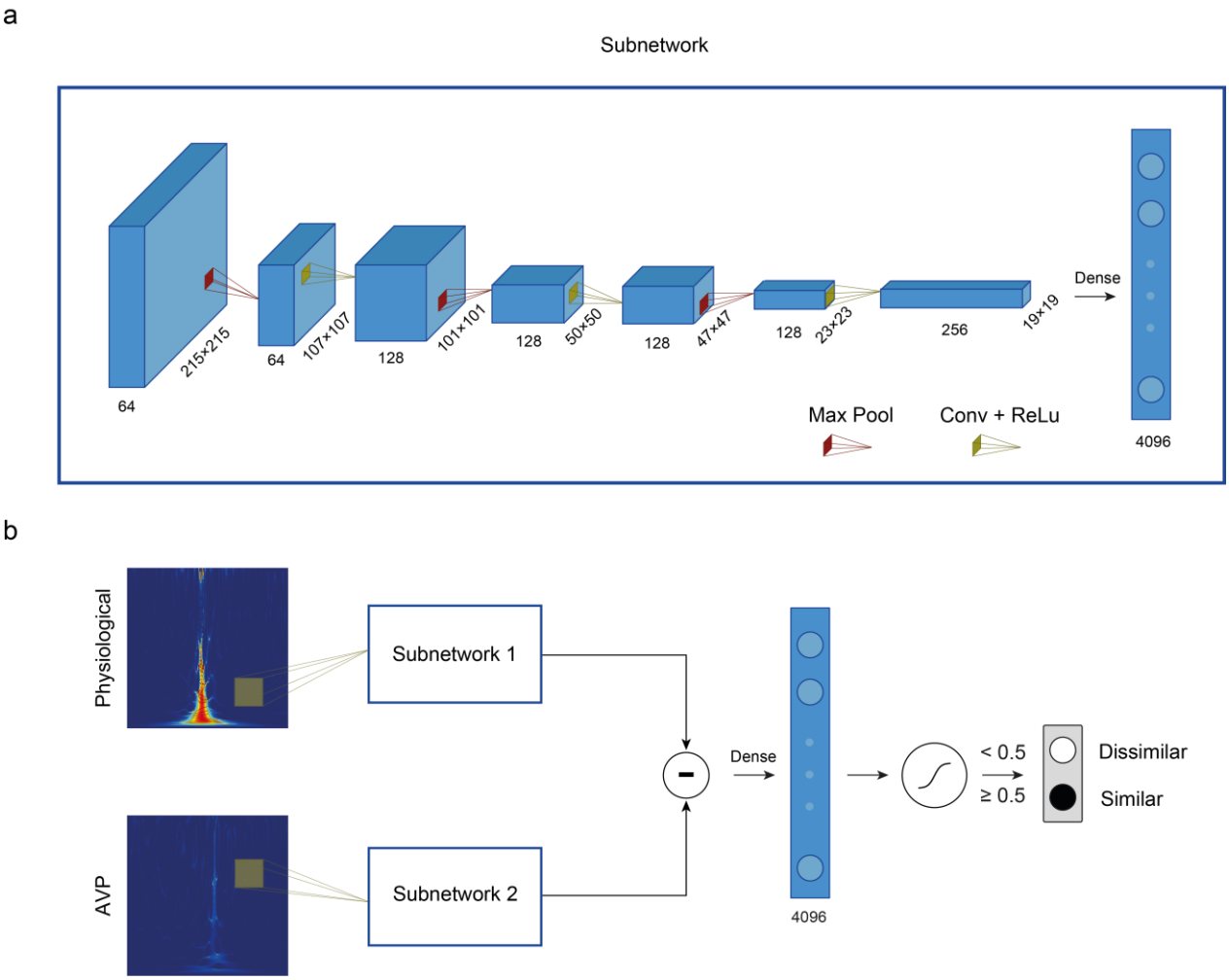


Fig. 1: In the top panel (a) the proposed subnetwork architecture of the siamese neural network; in the bottom panel (b) the overall classification algorithm architecture

The weights of the convolutional layers were initialized by random sampling from a normal distribution with zero mean and standard deviation of 0.01. Then, the difference between the subnetworks outcomes was used as input for the final fully connected layer.

As regards the training parameterizations and settings, different choices were made. Specifically, we performed a 10-fold cross validation by dividing the dataset in ten balanced and stratified folds: as such, eight folds were used for the training, while the remaining two were used for validation and testing, respectively. In this way, in each partitioning, 1204 samples (80%) were exploited for train, 150 samples (10%) for test, and 150 samples (10%) for validation. To update network weights, we used the stochastic gradient descent with momentum as training algorithm, and the binary cross-entropy as loss function to compute the gradient. We imposed a learning rate equal to 0.001, while the momentum was set to 0.9. Furthermore, a batch size of 30 instances per iteration was selected, to provide a stable and reliable training, which can improve generalization of the network predictions [11]. During the training phase, an early-stop condition was imposed to avoid overfitting, by evaluating the validation set every 50 training iterations, and halting the training after nine times in which the loss stopped decreasing. In this condition, the model with the minimum value of validation loss was kept for subsequent analyses. Once trained, the SNNs were tested by measuring the similarity between the test sample and a set of reference images for both classes, selecting as final class the one with the highest number of matches. The provided reference set corresponded to the validation one.

A. Dataset creation

The bipolar EGMs adopted in this study were recorded from nine patients with post-ischemic VT during left ventricle electroanatomic mapping procedures performed at San Francesco Hospital in Nuoro, Italy, by using the CARTO®3 mapping system (Biosense Webster, Inc., Diamond Bar, California). The intracardiac signals were acquired at a rate of 1000 Hz and band-pass filtered between 16 and 500 Hz. The EGMs were annotated by a cardiologist using a custom MATLAB graphical user interface. After this labelling procedure, a balanced dataset of 1504 signals, consisting of 752 physiological potentials and 752 AVPs, was extracted and adopted in this study.

The input images for the SNN were generated by computing the modulus of the SSWT of each 500-ms EGM, which provides information about AVPs and physiological EGM instantaneous spectral contents. Each image was stored as a .jpg file with a resolution of 224x224x3 pixels, which corresponds to the input layer size of the adopted architecture.

B. Performance evaluation

We computed various metrics to assess SNN performance:

$$Acc = (TP + TN)/(P + N) \quad (1)$$
$$TPR = TP/P \quad (2)$$
$$TNR = TN/N \quad (3)$$
$$PPV = TP/(TP + FP) \quad (4)$$
$$F1 = 2\,(TPR \times PPV)/(TPR + PPV) \quad (5)$$

where P represents the total number of samples of AVPs, N represents the total number of physiological EGMs, TP represents the number of EGMs that were correctly classified as AVPs, FP represents the number of EGMs that were incorrectly classified as AVPs, and TN represents the number of EGMs that were properly recognized as physiological signals. The exploited metrics are commonly indicated as accuracy (Acc), sensitivity (TPR), specificity (TNR), precision (PPV), and F1-score.

All computations have been carried out in MATLAB R2022a.

III. Results

Table 2 presents the mean and standard deviation of performance results from 10-fold cross-validation, along with the metrics obtained by AlexNet [5] for comparative purposes. The results show high discrimination performance, above 89% for Acc, TPR and F1 score, with a mean TNR and PPV above 86%. Though the performances of the SNN are generally worse than those obtained by transfer learning with AlexNet in previous studies, by looking at the TPR metrics, a slightly higher number of AVPs were correctly targeted by the SNN, which is a positive aspect in this application scenario. Despite the computation required for the SNN, the training time was fast, taking an average of 2143.6 ± 641.1 seconds on a 64-GB NVIDIA Tesla P100 GPU cluster, with a 1605 ± 480 number of training iterations. The best model was achieved after 1155 iterations on average.

TABLE II: Accuracy of the classification

Index	*CinC22*	*This work*
Acc (%)	*93 ± 3*	*90 ± 4*
TPR (%)	*92 ± 4*	*93 ± 3*
TNR (%)	*93 ± 3*	*86 ± 8*
PPV (%)	*93 ± 3*	*88 ± 6*
F1-score	*0.92 ± 0.03*	*0.90 ± 0.03*

IV. Conclusion

This study investigated on the use of SNN for the automatic identification of AVPs in VT electrophysiological procedures, representing potential arrhythmogenic sites to terminate VTs by catheter ablation.

The results reveal overall a good efficacy in the classification performance of the proposed method, slightly worse than previous studies adopting a CNN with the same dataset. However, the AVPs detection performance was better, which is in practice the most important metrics to avoid missing any ablation target. However, a fine-tuning of the SNN parameters can be performed to improve the performance, as commonly accepted values for the hyperparameters were used in this work.

Moreover, a deeper investigation involving a more complex SNN architecture and an hyperparameter optimization is being pursued.

Acknowledgement

The authors wish to thank Mr. Alberto Valdes Rey for his valuable contribution in the preliminary development of this study. The authors wish to thank the Division of Cardiology of San Francesco Hospital (Nuoro, Italy) for providing access to the clinical data used in this study. This work was carried out under the ARGO (Ablation Reinforcement by computer-aided Guidance and Optimization) project, approved by Azienda Tutela Salute Sardegna (ATS Sardegna).

References

[1] J.-T. Gräsner *et al.*, 'European Resuscitation Council Guidelines 2021: Epidemiology of cardiac arrest in Europe', *Resuscitation*, vol. 161, pp. 61–79, Apr. 2021, doi: 10.1016/j.resuscitation.2021.02.007.

[2] A. Timmis *et al.*, 'European Society of Cardiology: cardiovascular disease statistics 2021', *European Heart Journal*, vol. 43, no. 8, pp. 716–799, Feb. 2022, doi: 10.1093/eurheartj/ehab892.

[3] G. Baldazzi, M. Orrù, M. Matraxia, G. Viola, and D. Pani, 'Supervised Classification of Ventricular Abnormal Potentials in Intracardiac Electrograms', presented at the *2020 Computing in Cardiology Conference (CinC)*, Dec. 2020. doi: 10.22489/CinC.2020.397.

[4] G. Baldazzi, M. Orrù, M. Matraxia, G. Viola, and D. Pani, 'Efficacy of Spectral Signatures for The Automatic Classification of Abnormal Ventricular Potentials in Substrate-Guided Mapping Procedures', in *2022 Computing in Cardiology (CinC)*, Tampere, Finland, Sep. 2022.

[5] A. Pitzus *et al.*, 'Exploring Transfer Learning for Ventricular Tachycardia Electrophysiology Studies', in *2022 Computing in Cardiology (CinC)*, Tampere, Finland, Sep. 2022.

[6] C. Szegedy *et al.*, 'Going deeper with convolutions', in *2015 IEEE Conference on Computer Vision and Pattern Recognition (CVPR)*, Boston, MA, USA, Jun. 2015, pp. 1–9. doi: 10.1109/CVPR.2015.7298594.

[7] J. Deng, W. Dong, R. Socher, L.-J. Li, Kai Li, and Li Fei-Fei, 'ImageNet: A large-scale hierarchical image database', in *2009 IEEE Conference on Computer Vision and Pattern Recognition*, Miami, FL, Jun. 2009, pp. 248–255. doi: 10.1109/CVPR.2009.5206848.

[8] I. Daubechies, J. Lu, and H.-T. Wu, 'Synchrosqueezed wavelet transforms: An empirical mode decomposition-like tool', *Applied and Computational Harmonic Analysis*, vol. 30, no. 2, pp. 243–261, Mar. 2011, doi: 10.1016/j.acha.2010.08.002.

[9] H. Cartwright, Ed., *Artificial Neural Networks*, vol. 2190. New York, NY: Springer US, 2021. doi: 10.1007/978-1-0716-0826-5.

[10] B. Hunt, E. Kwan, D. Dosdall, R. S. MacLeod, and R. Ranjan, 'Siamese Neural Networks for Small Dataset Classification of Electrograms', in *2021 Computing in Cardiology (CinC)*, Brno, Czech Republic, Sep. 2021, pp. 1–4. doi: 10.23919/CinC53138.2021.9662707.

[11] D. Masters and C. Luschi, 'Revisiting Small Batch Training for Deep Neural Networks'. arXiv, Apr. 20, 2018. Accessed: May 31, 2022. [Online]. Available: http://arxiv.org/abs/1804.07612

Evaluation of breast density variability between right and left breasts

F. Angelone[1,†,*], A.M. Ponsiglione[1,†], M.P. Belfiore[2], G. Gatta[2], R. Grassi[2], F. Amato[1] and M. Sansone[1]
[1] *Dept. Electrical Engineering Information Technology, University of Naples, 'Federico II', Naples, Italy*
[2] *Dept. of Precision Medicine Division of Radiology, University of Campania 'Luigi Vanvitelli', Naples, Italy*

***Abstract*—Breast density is an established risk factor for developing breast cancer. In clinical routine it is qualitatively assessed by visual inspection of mammographies by radiologists on the basis of the American College of Radiology (ACR) Breast Imaging Reporting and Data System (BI-RADS) guidelines. This might lead to intra- and inter-observer variability.**

As a consequence, many Computer-Aided Diagnosis (CAD) systems, based on machine learning and artificial intelligence, have been developed in recent years to support radiologists in breast density evaluation. One difficulty arises when considering the evaluation of the performance of a CAD. It is well known that very large data sets must be used to obtain a reliable assessment of generalization ability. However, according to ACR guidelines, if the breasts appear not to be of equal density only the denser category should be reported; therefore it is not possible to access to densities of both breasts when analyzing retrospective data. This leads to difficulties in gathering large data sets of clinical mammographic images.

As a large number of clinical breast images data sets have been acquired using BI-RADS one can pose the question if it is possible to train an automatic system using one single label for both breasts potentially different.

In this study, we evaluated the what extent differences in density between breasts of the same patients occur in a real population. In particular we extracted multiple radiomics features from breast parenchyma using the Pyradiomics library and a preliminary clustering analysis has been conducted. Preliminary results showed different densities between right and left breast occur in 25-30% of cases.

***Keywords*—Breast density, Clustering, Digital mammography, Radiomic**

I. INTRODUCTION

Automatic assessment of risk factors is a major challenge for the early identification of breast lesions and increasing the survival rate. In fact, identifying risk factors in patients allows implementing personalized screening strategies by defining adequate exam scheduling, using appropriate radiological methods and prioritizing image analysis [1]. Full-Field Digital Mammography (FFDM) is considered the cornerstone in breast cancer (BC) diagnosis and also assumes a very important role in the identification of risk factors, specifically breast density (BD) [2]. In many previous studies, it has been established that women with dense breasts have an increased risk of developing BC [3], [4]. Moreover, breast density also affects the possibility to detect breast cancer, as mammography suffers from a loss of sensitivity [5], [6], despite the widespread effort to develop ever more effective methods for improving the quality of mammographic images [7], [8]. In clinical practice, BD is assessed only on a *qualitative* basis, through a visual evaluation, by the radiologists, based on the international guidelines BI-RADS (Breast Imaging - Reporting and Data System) by the American College of Radiology (ACR). According to these guidelines, four classes of breast density are defined on a qualitative basis [9]:

- Class A: Predominantly fibro-adipose;
- Class B: Scattered areas of fibroglandular tissue;
- Class C: Heterogeneously dense;
- Class D: Extremely dense.

This might lead to intra- and inter- observer variability, as well as the difficulties in creating automatic algorithms for supporting radiologists in critical decision for borderline breasts. Many Computer-Aided Diagnosis (CAD) systems which have been developed in recent years for breast density assessment have been typically based on quantitative approaches such as radiomics computation combined with Artificial Intelligence (AI) algorithms [10], [2], [11], [12], [13], [14], [15], [16], [17], [18], [19], [20], [21], [22], [23], [24]. The extraction of radiomic features from the breast parenchyma can offer quantitative parameters to evaluate the composition of fibroglandular tissue compared to adipose tissue, providing objective assessments of breast density. The analysis of this huge amount of data can be done only through the aid of AI algorithms, giving rise to automatic classification systems of breast density.

One of the most relevant and problematic aspects of automatic classification algorithms, especially in the medical field, is their performance evaluation. In fact, a correct classification is essential for the algorithm to be of support to the clinicians. While many AI algorithms are being developed in medical research, those actually being applied in clinical practice are not much numerous. To date, an emerging discipline is the Explainable AI (XAI) which seeks to understand what is happening inside the black box of the algorithm to give a more reliable explanation to the results [25], [26].

In this case, the evaluation of the performance of the classification algorithms is based on the agreement with the diagnosis made by the radiologists. According to the BI-RADS

[†]These authors (F.A. and A.M.P.) contributed equally
[*]Corresponding author: francesca.angelone@unina.it

guidelines used by radiologists, however, when the two breasts of a patient are of different density only the denser must be given in the clinical report. This leads to difficulties in gathering data-sets of clinical breast images with a reliable labelling for both breasts. It is apparent that when a single label is available for both breasts, disagreements between the results of the classifiers may appear because they analyze each image individually, capturing the differences in the features extracted between the two images of the right and left breast. This obviously affects the performance of the model.

As a large number of clinical breast images dataset have been acquired using BI-RADS one can pose the question if it is possible to train an automatic system using one single label for both breasts potentially different.

In this study, we evaluated the what extent differences in density between breasts of the same patients occur in a real population. In particular we extracted multiple radiomics features from breast parenchyma using the Pyradiomics library and a preliminary clustering analysis has been conducted.

II. Methods

A. Image acquisition and dataset

The reference dataset was acquired over a period of 5 months, from June 2020 to October 2020, for a total of 177 patients, all women, aged between 38 and 84 years. All women underwent bilateral, medio-lateral-oblique (MLO) full-field digital mammography (FFDM) under standard clinical protocol, using Giotto Class (IMS GIOTTO S.p.A., Sasso Marconi, Bologna, Italy). The mammography unit has been used with the aid of the Raffaello software in its version 4.11 which allows the visualization of the acquired images.

The subsequent processing has been carried out on the "FOR PROCESSING" images, i.e. original 16-bit DICOM images (of which 13-bit stored) without the processing step generally applied by proprietary mammography software to visually enhance the difference between tissues, because, being proportional to the attenuation of the X-rays on the breast tissue, they preserve the original information on the attenuation of the X-rays and therefore are more suitable for quantitative analysis [21]. In summary, two MLO images (right and left) for each patient were acquired, for a total of 354 images.

An expert radiologist reviewed each patient providing the breast density evaluation in the BI-RADS report. Moreover, he performed manual segmentation for removing background and pectoral muscle in order to subsequently compute radiomics features only on breast tissue. Fig. 1 shows a comparison among the visualization of the breast image before and after the manufacturer software processing with the relative manual segmentation from radiologists.

B. Features extraction

Radiomic features were extracted using PyRadiomics library (version 3.0.1) [27] in Python, following the guidelines of the Image Biomarker Standardisation Initiative (IBSI) [9].

The features extracted can be summarized:

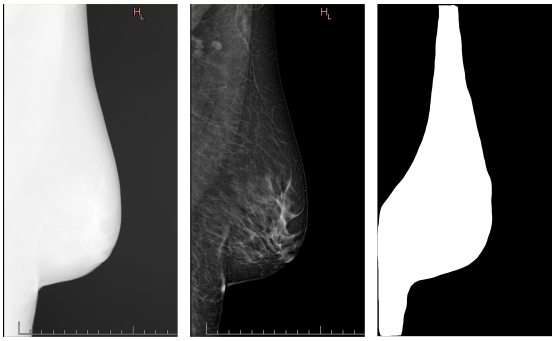


Fig. 1: Comparison among (a) "FOR PROCESSING" image (b) "FOR PRESENTATION" image (after manufacturer software processing) and (c) manual segmentation from radiologists.

- 18 first-order features (energy, total energy, entropy, kurtosis, maximum, minimum, mean, median, interquartile range (IQR), skewness, range, mean absolute deviation (MAD), robust mean absolute deviation (RMAD), root mean squared (RMS), variance, uniformity, 10th percentile and 90th percentile);
- 75 higher-order texture features (24 Gray level co-occurrence matrix (GLCM) features, 14 Gray level dependence matrix (GLDM) features, 16 Gray level run-length matrix (GLRLM) features, 16 Gray level size zone matrix (GLSZM) features, 5 neighboring gray tone difference matrix (NGTDM) features). For texture feature calculation, 128 levels of gray were considered in this study.

In particular, first-order statistics help describe how voxel intensities are distributed within the mask-defined region of the image (ROI) through common statistical metrics and commonly used metrics such as the maximum and minimum intensity within the ROI, entropy and energy. Higher-order texture features allow even more to evaluate the relationship between intensities of pixels within the ROI, through the calculation of some matrices, such as GLCM, a matrix that defines the distribution of grayscale values of pixels on an image by defining how often pairs of pixels with a specific value and position operator occur in the image, or GLSZM that quantifies the gray level zones in an image by calculating the number of connected voxels that share the same gray level intensity. All the listed features were used to perform the clustering analysis.

C. Cluster analysis

Breast tissues composition might be associated to textural features on mammographic images [28]. With this assumption in mind we performed a cluster analysis of our data-set: breasts of similar composition should have been assigned to the same cluster.

We used two distance-based clustering methods where a similarity quantification between objects is based on the distance. In particular, we used both a k-means algorithm [29] and a partitioning around medoids (PAM) algorithm [30]

which can overcome the problems of centroids initialization sensitivity and interpretability.

III. Results and Discussion

Preliminary results relating to the application of clustering algorithms to the dataset are shown in Fig. 2 and 3: for representation purposes data have been projected onto principal components. Breast images have been clustered in four groups corresponding to the four breast density BI-RADS categories. Each point in the figures corresponds to a single breast: the label indicates breast category, subject ID and laterality.

Looking at the results of the k-means algorithm, in Fig. 4 is shown the clustering vector and it is possible to note that for the same patient, the right and left breasts, which are two consecutive values in the clustering vector, are not always clustered in the same class. In particular, as shown in the Table I, out of a total of 177 patients, for 46 patients have right and left breasts not belonging to the same cluster, which corresponds to the 26.0%.

The clustering vector of the PAM algorithm, which overcomes the above mentioned limitations of the k-means algorithm, is shown in Fig. 4. In this case, as shown in the Table I, out of a total of 177 patients, 54 patients have right and left breasts not belonging to the same cluster, which corresponds to the 30.5%.

With both clustering algorithms we obtained a comparable number of patients presenting different BI-RADS densities between right and left breast. Nevertheless, since PAM algorithm is based on medoids, offers the most robust results to noise and outliers. The number of dissimilarities between right and left breasts is quite large compared to the total number of patients examined. From the results of this exploratory study, it is possible to note that the percentages of disagreement between the right and left breasts densities are not negligible confirming that this is an aspect to be taken into consideration when evaluating the agreement between the radiologist's diagnosis and the results of the classification algorithms, significantly affecting the performance of the classification models.

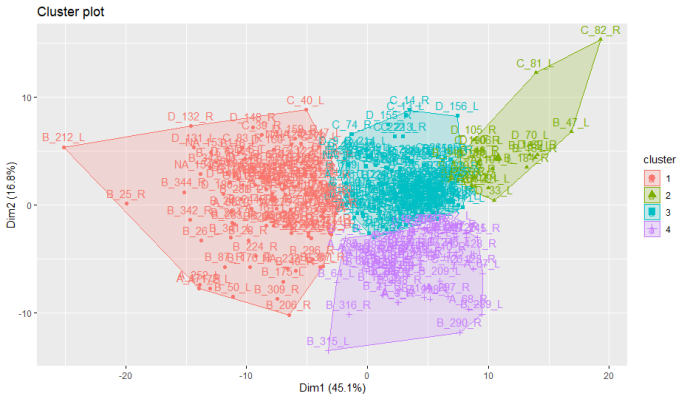


Fig. 2: Distribution of 354 breast images, corresponding to right and left breasts of each patient, grouped in four clusters using the k-means algorithm. Each image is labelled with the BI-RADS class, a patient identifier and right/left indication.

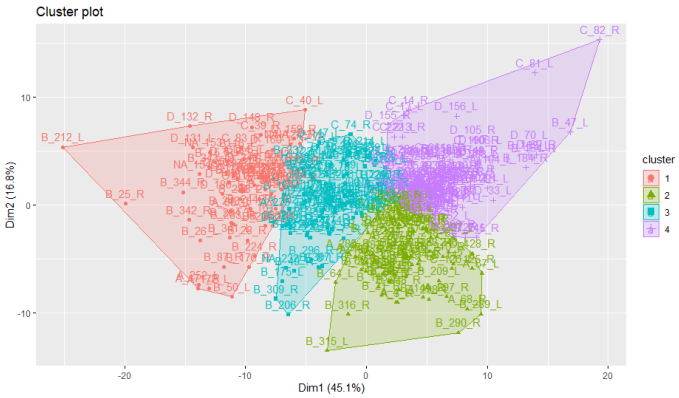


Fig. 3: Distribution of 354 breast images, corresponding to right and left breasts of each patient, grouped in four classes using the PAM algorithm. Each image is labelled with the BI-RADS class, a patient identifier and right/left indication.

```
Clustering vector:
  [1] 1 1 4 4 1 1 4 1 3 1 3 1 3 3 1 1 1 3 3 3 1 4 4 4 4 4 1 1 1 1 3 3 3 1 2 4 3 1 3 3 1 1 1 1
 [43] 3 3 3 3 2 2 1 1 4 4 4 4 1 1 1 1 1 1 2 3 4 4 3 3 4 4 2 2 3 3 1 3 3 3 1 3 4 4 2 2 1 1
 [85] 3 3 1 1 3 3 3 3 4 4 1 1 4 4 2 3 3 2 3 2 2 2 1 1 3 1 3 3 4 4 3 3 4 3 3 2 3 1 1 1 4 4
[127] 4 4 3 3 1 1 1 1 3 3 3 4 1 3 4 4 3 3 3 3 1 1 1 1 4 4 1 1 3 3 3 3 1 1 1 1 2 2 3 3 3 3
[169] 3 3 1 1 3 1 1 1 1 1 1 1 4 4 3 2 3 3 3 3 3 2 3 3 3 3 3 3 3 3 1 1 1 1 4 1 4 1 4 4
[211] 3 1 3 3 1 1 4 3 3 3 3 3 1 1 4 4 1 1 1 1 1 1 1 4 4 3 3 2 3 3 3 3 3 1 1 4 4 4 4 3 3 1 1
[253] 3 3 3 4 2 3 3 3 3 3 2 3 1 1 3 3 3 3 1 1 1 1 1 1 3 3 3 1 3 1 1 1 1 4 4 3 3 4 4 2 4 2 3
[295] 3 1 4 4 1 3 3 4 3 3 1 3 1 4 1 1 3 1 3 3 4 4 1 1 3 3 1 1 3 3 1 1 4 4 3 4 3 1 4 1 3 1
[337] 4 4 3 3 1 1 1 1 2 3 1 1 3 3 3 2 1 1
```

```
Clustering vector:
  [1] 1 1 2 2 1 1 3 3 3 3 4 3 4 4 1 1 4 4 3 3 2 2 2 2 1 1 3 1 3 4 3 3 4 2 3 3 4 4 1 1 1 1
 [43] 4 2 3 4 4 4 3 1 2 4 2 2 1 3 1 1 1 1 4 4 2 2 4 2 2 4 4 3 4 3 3 3 4 3 3 2 2 4 4 1 1
 [85] 2 4 1 3 2 2 2 2 2 1 1 2 2 4 4 4 4 2 4 4 4 1 1 3 3 4 4 2 2 2 2 2 4 4 4 3 3 3 1 1 2 2
[127] 4 2 2 2 1 1 3 3 3 4 2 2 3 3 3 2 3 3 3 4 3 1 1 1 2 2 1 1 4 4 4 4 1 1 1 3 4 4 4 4 3 3
[169] 4 4 1 1 4 3 3 1 1 3 1 1 2 2 4 4 4 4 4 3 4 4 4 4 4 2 2 4 4 4 4 4 4 3 3 3 1 2 3 2 3 2 2
[211] 4 1 4 3 3 3 2 4 3 4 4 4 3 1 2 2 3 3 3 3 3 3 2 2 4 4 4 4 3 3 4 4 1 1 4 2 4 2 2 3 3 1
[253] 4 4 4 2 4 4 4 4 4 4 3 3 3 2 3 4 4 3 3 3 3 3 3 4 4 1 3 1 3 1 1 2 2 4 4 2 2 4 2 4 4
[295] 4 3 2 2 3 3 4 2 4 4 3 4 3 2 3 1 2 1 2 4 2 2 1 1 4 4 3 3 3 4 1 1 2 4 3 2 3 3 2 3 3 3
[337] 2 2 3 3 1 1 1 1 4 4 1 1 2 2 4 4 1 1
```

Fig. 4: Clustering vectors in the application of the kmeans (upper part) and the PAM (lower part) algorithms where two nearby data points correspond to the right and left breast of the same patient and the clustering differences must be highlighted.

TABLE I: Number of patients having right and left breasts belonging to the same cluster (*Equal*) or not (*Not equal*).

Clustering algorithm	*Equal*	*Not equal*
K-means	131	46
PAM	123	54

IV. Conclusion

Breast density is an important risk factor, whose evaluation can help to early identify patients with a higher risk of developing breast cancer; these patients should be subjected to *ad hoc* screening programs to increase survival rate. Currently, breast density is qualitatively evaluated in the clinical environment, with inter- and intra-observer variability. Many efforts are being put into developing expert systems and artificial intelligence for objective assessment of BD.

One of the difficulties often encountered in developing such systems is the performance evaluation which should be done on the basis of adequately gathered large data set with proper labeling of both breasts. However, BI-RADS guidelines

indicate reporting only the denser breast in the case the patient has different breast densities. As a large number of clinical breast images dataset have been acquired using BI-RADS one can pose the question if it is possibile to train an automatic system using one single label for both breasts potentially different.

This study aimed to preliminary investigate to what extent this problem might affect automatic systems evaluation. Results from the present study, by applying a cluster analysis, suggest that in about 30% of cases the breasts of a single patient have different densities. As the percentage is not negligible further investigations might be required to address this problem.

Acknowledgements

This study has been conducted in the framework of a wider study ("Senologia per te") promoted by SIRM (Italian Society of Medical Radiology) approved by the Ethical Committee of University "Luigi Vanvitelli" (prot. N 469 of 23/07/2019). This study has been partially funded by IMS GIOTTO S.p.A. Sasso Marconi (BO), Italy.

References

[1] W. A Berg, E. A Rafferty, S. M Friedewald, C. B Hruska, and H. Rahbar. Screening algorithms in dense breasts: Ajr expert panel narrative review. *American Journal of Roentgenology*, 216(2):275–294, 2021.

[2] F. Angelone, C. Ricciardi, G. Gatta, M. Sansone, A.M. Ponsiglione, M.P. Belfiore, F. Amato, and R. Grassi. Breast density analysis on mammograms: Application of machine learning with textural features. In *2022 IEEE International Conference on Metrology for Extended Reality, Artificial Intelligence and Neural Engineering (MetroXRAINE)*, pages 295–300. IEEE, 2022.

[3] V. A. McCormack and I. dos Santos Silva. Breast density and parenchymal patterns as markers of breast cancer risk: a meta-analysis. *Cancer Epidemiology and Prevention Biomarkers*, 15(6):1159–1169, 2006.

[4] N. F. Boyd, L. J Martin, M. J Yaffe, and S. Minkin. Mammographic density and breast cancer risk: current understanding and future prospects. *Breast cancer research*, 13(6):1–12, 2011.

[5] K. Kerlikowske. The mammogram that cried wolfe, 2007.

[6] P. A Carney, D. L Miglioretti, B. C Yankaskas, K. Kerlikowske, R. Rosenberg, C. M Rutter, B. M Geller, L. A Abraham, S. H Taplin, M. Dignan, et al. Individual and combined effects of age, breast density, and hormone replacement therapy use on the accuracy of screening mammography. *Annals of internal medicine*, 138(3):168–175, 2003.

[7] Mario Sansone, Alfonso Maria Ponsiglione, Francesca Angelone, Francesco Amato, and Roberto Grassi. Effect of x-ray scatter correction on the estimation of attenuation coefficient in mammography: a simulation study. In *2022 IEEE International Conference on Metrology for Extended Reality, Artificial Intelligence and Neural Engineering (MetroXRAINE)*, pages 323–328. IEEE, 2022.

[8] JL Ducote and S Molloi. Scatter correction in digital mammography based on image deconvolution. *Physics in Medicine & Biology*, 55(5):1295, 2010.

[9] A. Zwanenburg, M. Vallières, M. A Abdalah, H. JWL Aerts, V. Andrearczyk, A. Apte, S. Ashrafinia, S. Bakas, R. J. Beukinga, R. Boellaard, et al. The image biomarker standardization initiative: standardized quantitative radiomics for high-throughput image-based phenotyping. *Radiology*, 295(2):328–338, 2020.

[10] J. E van Timmeren, D. Cester, S. Tanadini-Lang, H. Alkadhi, and B. Baessler. Radiomics in medical imaging—"how-to" guide and critical reflection. *Insights into imaging*, 11(1):1–16, 2020.

[11] C. Ricciardi, R. Cuocolo, F. Verde, G. Improta, A. Stanzione, V. Romeo, S. Maurea, M. D'Armiento, L. Sarno, M. Guida, et al. Resolution resampling of ultrasound images in placenta previa patients: Influence on radiomics data reliability and usefulness for machine learning. In *European Medical and Biological Engineering Conference*, pages 1011–1018. Springer, 2020.

[12] A.M. Ponsiglione, C. Ricciardi, A. Scala, A. Fiorillo, A. Sorrentino, M. Triassi, G. Dell'Aversana Orabona, and G. Improta. Application of dmaic cycle and modeling as tools for health technology assessment in a university hospital. *Journal of healthcare engineering*, 2021, 2021.

[13] A.M. Ponsiglione, G. Cesarelli, F. Amato, and M. Romano. Optimization of an artificial neural network to study accelerations of foetal heart rhythm. In *2021 IEEE 6th International Forum on Research and Technology for Society and Industry (RTSI)*, pages 159–164. IEEE, 2021.

[14] L. Donisi, G. Cesarelli, P. Balbi, V. Provitera, B. Lanzillo, A. Coccia, and G. D'Addio. Positive impact of short-term gait rehabilitation in parkinson patients: a combined approach based on statistics and machine learning. *Mathematical Biosciences and Engineering*, 18(5):6995–7009, 2021.

[15] A.M. Ponsiglione, F. Amato, and M. Romano. Multiparametric investigation of dynamics in fetal heart rate signals. *Bioengineering*, 9(1):8, 2021.

[16] A.M. Ponsiglione, C. Cosentino, G. Cesarelli, F. Amato, and M. Romano. A comprehensive review of techniques for processing and analyzing fetal heart rate signals. *Sensors*, 21(18):6136, 2021.

[17] S. Jang, J.Y. Chang, J.S. Lee, E. Lee, Y. Kim, J.H. Han, D. Chang, H.J. Cho, J. Cha, K.H. Yu, et al. Reliability and clinical utility of machine learning to predict stroke prognosis: comparison with logistic regression. *Journal of stroke*, 22(3):403, 2020.

[18] A.F. Leite, K. Vasconcelos, H. Willems, and R. Jacobs. Radiomics and machine learning in oral healthcare. *PROTEOMICS–Clinical Applications*, 14(3):1900040, 2020.

[19] M. Recenti, C. Ricciardi, K. Edmunds, M. K Gislason, and P. Gargiulo. Machine learning predictive system based upon radiodensitometric distributions from mid-thigh ct images. *European Journal of Translational Myology*, 30(1), 2020.

[20] D. Scrutinio, C. Ricciardi, L. Donisi, E. Losavio, P. Battista, P. Guida, M. Cesarelli, G. Pagano, and G. D'Addio. Machine learning to predict mortality after rehabilitation among patients with severe stroke. *Scientific reports*, 10(1):1–10, 2020.

[21] M. Sansone, R. Grassi, M.P. Belfiore, G. Gatta, F. Grassi, F. Pinto, G.V. La Casella, R. Fusco, S. Cappabianca, V. Granata, and R. Grassi. Radiomic features of breast parenchyma: assessing differences between for processing and for presentation digital mammography. *Insights Imaging*, 1(12):147, 2013.

[22] M. Sansone, S. Marrone, G. Di Salvio, M.P. Belfiore, G. Gatta, R. Fusco, L. Vanore, C. Zuiani, F. Grassi, M.T. Vietri, V. Granata, and R. Grassi. Comparison between two packages for pectoral muscle removal on mammographic images. *Radiol Med*, 8:848–856, 2022.

[23] M. Sansone, R. Fusco, F. Grassi, G. Gatta, M.P. Belfiore, F. Angelone, C. Ricciardi, A.M. Ponsiglione, F. Amato, R. Galdiero, et al. Machine learning approaches with textural features to calculate breast density on mammography. *Current Oncology*, 30(1):839–853, 2023.

[24] L. Donisi, G. Cesarelli, A. Castaldo, D. R. De Lucia, F. Nessuno, G. Spadarella, and C. Ricciardi. A combined radiomics and machine learning approach to distinguish clinically significant prostate lesions on a publicly available mri dataset. *Journal of Imaging*, 7(10):215, 2021.

[25] S. C. Wei, Y.H. Choo, A.K. Muda, and L.C. Sing. A survey of explainable artificial intelligence in bio-signals analysis. *Recent Advances in Computer Science and Communications (Formerly: Recent Patents on Computer Science)*, 16(3):70–79, 2023.

[26] L. Weber, S. Lapuschkin, A. Binder, and W. Samek. Beyond explaining: Opportunities and challenges of xai-based model improvement. *arXiv preprint arXiv:2203.08008*, 2022.

[27] J. JM Van Griethuysen, A. Fedorov, C. Parmar, A. Hosny, N. Aucoin, V. Narayan, R. GH Beets-Tan, J.C. Fillion-Robin, S. Pieper, and H. JWL Aerts. Computational radiomics system to decode the radiographic phenotype. *Cancer research*, 77(21):e104–e107, 2017.

[28] Y. Zheng, B. M Keller, S. Ray, Y. Wang, E. F Conant, J. C Gee, and D. Kontos. Parenchymal texture analysis in digital mammography: a fully automated pipeline for breast cancer risk assessment. *Medical physics*, 42(7):4149–4160, 2015.

[29] Mohiuddin Ahmed, Raihan Seraj, and Syed Mohammed Shamsul Islam. The k-means algorithm: A comprehensive survey and performance evaluation. *Electronics*, 9(8):1295, 2020.

[30] Leonard Kaufman. Partitioning around medoids (program pam). *Finding groups in data*, 344:68–125, 1990.

Estimating the degree of Non-Alcoholic Fatty Liver Disease (NAFLD) from ultrasound images: preliminary results

S. Kresevic[1], M. Ajcevic[1], M. Giuffrè[2], P. Pupa[3], C. Moretto[3], S. Pennini[3], L.S. Crocè [2] and A. Accardo[1]

[1] *Department of Engineering and Architecture, University of Trieste, Italy*

[2] *Department of Medicine, Surgery and Health Sciences, University of Trieste, Trieste, Italy*

[3] *Prodigys Technology s.r.l., Trieste, Italy*

***Abstract*—The early diagnosis of Non-Alcoholic Fatty Liver Disease (NAFLD) is crucial to prevent fibrosis progression or onset of advanced chronic liver disease. Among the non-invasive methods, ultrasound (US) B-mode imaging is recommended for population screening and follow-up. Hamaguchi's score was proposed to improve the objectivity in the evaluation of the fatty liver US imaging evaluation. In this study, we aimed to preliminary assess the possibility to estimate Hamaguchi's score by means of an advanced ultrasound image semi-automatic analysis.**

The study encompassed a dataset of 220 bariatric patients with NAFLD diagnosed by liver biopsy who underwent ultrasound assessment at the Liver Clinic at Trieste University Hospital. The classification models for the estimation of the three Hamaguchi's sub-scores were produced by semiautomatic US image analysis based on clustering and CNN with transfer learning techniques.

The results showed that the produced models were able to estimate the three sub-scores with high classification accuracy. The predictive models produced for the estimation of liver brightness hepatorenal echo contrast, the diaphragm deep attenuation, and the vessel blurring sub-scores presented a classification accuracy on the validation set of 90.5%, 83.3%, and 84.0%, respectively.

In conclusion, in this preliminary study, the results assessed the possibility to produce the NAFLD computer-aided diagnostic models based on analysis of US images.

***Keywords*—NAFLD, Hamaguchi's score, ultrasound images, Artificial Intelligence.**

I. Introduction

NAFLD represents a spectrum of diseases related to excessive fat deposition in the liver, ranging from simple steatosis (i.e., non-alcoholic fatty liver, NAFL) to non-alcoholic steatohepatitis (NASH), characterized by lobular inflammation and hepatocyte ballooning, which over time can increase liver fibrosis, thus promoting liver cirrhosis or hepatocellular carcinoma [1]. NAFLD is the most common chronic liver disease in the world (approximately 25% of the global population has been affected by NAFLD [2] and is projected to be 33.5 % by 2030 [3]). Current clinical guidelines recommend dietary treatment as the most efficient preventive intervention in addition to early evaluation and monitoring of liver functions to prevent advanced fibrosis or hepatocellular carcinoma [4], [5]. The gold standard for staging is liver biopsy, which is expensive and invasive, making it unsuitable for broad screening at the population level [6].

Among the noninvasive methods, ultrasound B-mode imaging has been recommended as the preferred first-line diagnostic procedure for imaging of NAFLD in adults by the clinical practice guidelines of the European Association for the Study of the Liver released together with the European Association for the Study of Diabetes and the European Association for the Study of Obesity [7].

But this method has the limitation that the evaluation of a US image is operator dependent: several studies conducted have reported significant intra- and inter-observer variability in the assessment of ultrasonographic findings of hepatic steatosis [8]-[10]. In particular, an agreement between pairs of experienced observers of only 47-59% on the first reading and 59-64% on the second reading was reported [9].

In daily practice, physicians evaluate hepatic steatosis on the US image by analyzing some of its features: the echogenicity of the liver parenchyma compared with the echogenicity of the kidney, the visibility of intrahepatic vessels and the diaphragm blurring [11]. These features allow physicians to assess the presence of hepatic steatosis because an excess fat component in the liver would make it shine brighter to a greater extent than in the kidney (normally isoecogenic) and would attenuate the ultrasound probe's beam making visualization of intrahepatic vascular structures and the diaphragm poor.

To improve objectivity, Hamaguchi et al. proposed a semi-quantitative US-based scoring method [12]. In particular, the proposed scoring system is based on the comparison of liver and kidney echogenicity, assessment of liver brightness (scored liver brightness from 0 to 3), of deep attenuation of diaphragmatic contours by the liver (scored from 0 to 2), and of liver vessel blurring (scored from 0 to 1). The sum of the aforementioned sub-scores yields Hamaguchi's score ranging from 0 (corresponding to a healthy liver) to 6 (corresponding to a fatty liver). Although Hamaguchi's score improved the standardization of the degree of hepatic lipid accumulation in the liver, it still suffers from the fact that the assessment is a subjective measure strongly influenced by the expertise of the physician evaluating the US image.

Over the past decade methods based on Artificial Intelligence (AI) are used for identifying and predicting patterns or connections within large datasets in various fields of medicine, demonstrating utility in the diagnostic process. A recent meta-analysis on the AI-based methods for liver diagnosis reported high-accuracy results of the application of these methods on diagnostic imaging for the diagnosis and staging of NAFLD [13]. However, despite the numerous

applications of AI in the diagnostic field of NAFLD, methods based on AI have never been applied to the analysis for Hamaguchi's score estimation. The aim of this study is to develop Machine Learning (ML) and Deep Learning (DL) algorithms for the advanced analysis of US images that can estimate the sub-scores of the various categories of Hamaguchi's score and thus propose a new approach for automatic analysis of the same.

II. Materials and Methods

A. Data acquisition and dataset definition

The study includes 220 bariatric patients with NAFLD diagnosed by liver biopsy who underwent US assessment at the Liver Clinic at Trieste University Hospital. The clinical and radiological data of included patients were analyzed to create the study dataset. The inclusion criteria were liver biopsy-based NAFLD diagnosis, and US assessment characterized by the visibility of liver and renal parenchyma, visibility of intrahepatic vessels, and visibility of the diaphragm.

To assign the sub-scores constituting the Hamaguchi score, three parameters must be evaluated on the US image, but not in all cases all three parameters are assessable on a single US scan as it depends on the bariatric patient's physical conformations: there are patients who have all three parameters of interest in one US image, patients who have liver and kidney in a single US image while diaphragm and intrahepatic vessels in another, as well as patients who have all three parameters in three different US images. So, with the support of physicians in the selection, three datasets were created: the Hepatorenal dataset, the Diaphragm dataset, and the Vessel dataset.

All three datasets contain 220 US images (one for each patient). For each of the three datasets, the images were appropriately evaluated by four physicians who independently assigned the respective sub-scores constituting the Hamaguchi score, and where ratings were not equal, the scores were reviewed and decided by consensus.

B. The proposed framework to evaluate automatically Hamaguchi's score

The proposed approach for automatic estimation of Hamaguchi's score is based on separate estimation of sub-scores by semiautomatic analysis of US images. Considering that the sub-score assessments are based on the identification of different features, three sub-score related algorithms were developed. For the evaluation of the liver brightness hepatorenal echo contrast score, a semi-automatic evaluation based on clustering was adopted, while for the evaluation of the diaphragm deep attenuation score and of the vessel blurring score a semi-automatic methodology based on the development of two CNNs with transfer learning techniques was implemented.

Considering the variability of the US images and moderate sample size, to produce performant classification algorithms, additional pre-processing was performed by manually delineating the ROIs to define Diaphragm dataset and Vessel dataset.

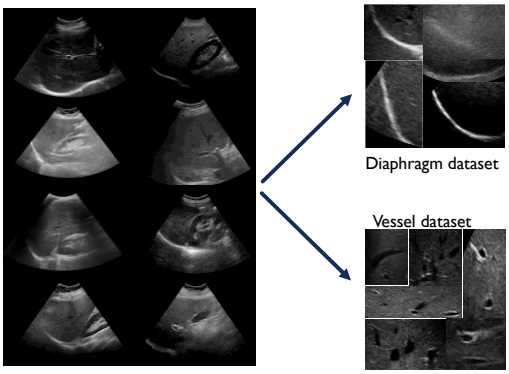


Fig. 1: The ROIs definition from raw US images for the Diaphragm and Vessel datasets.

C. Estimate of liver brightness hepatorenal echo contrast score

For the calculation of liver brightness hepatorenal echo contrast, two ROIs were manually identified by the medical team: one in the lighter region of the liver parenchyma, and the other in the darker area of the cortical area of the kidney. A script written in Python allows to select two ROIs (of size 5x5 pixel to ensure that the cortical region of the kidney is selected without including its interface with the liver) and process them to extract the feature of interest. In this way, features related to the echogenicity of the liver were obtained for each US image sample. All previously saved features are later analyzed with K-means by setting the number of four classes (liver brightness hepatorenal echo contrast score could be 0, 1, 2, and 3). In this way, four classes were distinguished.

Based on this clustering, a classification model was built to evaluate the feature extracted from an ultrasound image of the liver by assigning it a score ranging from 0 to 3.

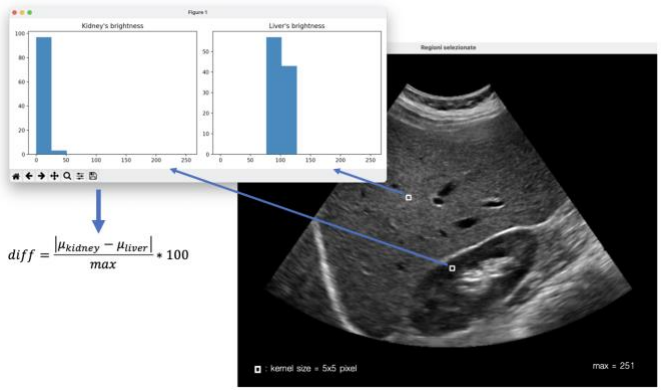


Fig. 2: The feature extraction for the liver brightness hepatorenal echo contrast sub-score. The two ROIs are manually selected by the physician from the raw image. One is in the lighter region of the liver parenchyma, and the other is in the darker region of the cortical zone of the kidney. When these two ROIs are selected, a feature is extracted by calculating the distance between the average intensity level of the area corresponding to the liver (μ_{liver}) and the average intensity level of the area corresponding to the kidney (μ_{kidney}). The difference is divided by the maximum intensity present in the US image.

D. Estimate of diaphragm deep attenuation score and liver vessel blurring score

The diaphragm deep attenuation score is evaluated according to how well the diaphragm is visible: the greater the presence of fat in the liver, the greater the absorption of ultrasound signal and thus the lower the visibility of the diaphragm. Similarly for liver vessel blurring score. So, we chose to evaluate these scores using CNNs and transfer learning for each kind of score.

Before implementing and training the CNNs, the image datasets of both the diaphragm's dataset and the vessel's dataset are divided into three sub-sets of images each: training set, validation set, and test set with a ratio of 75%, 15%, and 10% respectively. So, the sub-set consists of 165, 33, and 22 US images on the training set, validation set, and test set respectively. The test set is used only once the model has been fully trained. To give correct assessments, the test set must be well maintained and contain a variety of images covering the various classes of each sub-score.

Although the transfer learning technique is used to produce CNNs with high classification accuracy, many images are still required in the training set, and the sample case histories need to be balanced. So, the training set has been also augmented and balanced via data augmentation and the techniques which consisted of 10° right/left rotation, random in/out zooming ranging from 0.8 to 1.2, and horizontal flip operations in a random manner.

Ten CNNs were implemented with transfer learning techniques (TABLE I) to choose the most suitable and performing network for the diaphragm deep attenuation score and the vessel blurring score. The networks' development was implemented with Python scripts by importing the Tensorflow and Keras libraries. In particular, the pre-trained networks VGG-16 and VGG-19 from Keras are imported as the base model.

TABLE I: ARCHITECTURES OF THE TEN IMPLEMENTED CNNs

#	Base model	Additional convolutional block	Classification block
1	VGG-16	-	Flatten layer Dense layer (512 nodes) Dense layer (256 nodes) Output layer
2	VGG-16	Conv2D layer (512 nodes) Conv2D layer (512 nodes) MaxPooling2D layer	Flatten layer Dense layer (512 nodes) Dense layer (256 nodes) Output layer
3	VGG-16	Conv2D layer (512 nodes) Conv2D layer (256 nodes) MaxPooling2D layer	Flatten layer Dense layer (4096 nodes) Dense layer (512 nodes) Output layer
4	VGG-16	Conv2D layer (512 nodes) Conv2D layer (256 nodes) MaxPooling2D layer	Flatten layer Dense layer (4096 nodes) Dense layer (4096 nodes) Output layer
5	VGG-16	Conv2D layer (512 nodes) Conv2D layer (256 nodes) MaxPooling2D layer	Flatten layer Dense layer (512 nodes) Dense layer (256 nodes) Dense layer (128 nodes) Output layer
6	VGG-16	Conv2D layer (512 nodes) Conv2D layer (256 nodes) Conv2D layer (128 nodes) MaxPooling2D layer	Flatten layer Dense layer (1024 nodes) Dense layer (512 nodes) Dense layer (256 nodes) Output layer
7	VGG-16	Conv2D layer (512 nodes) Conv2D layer (256 nodes) Conv2D layer (128 nodes) MaxPooling2D layer	Flatten layer Dense layer (1024 nodes) Dense layer (512 nodes) Output layer
8	VGG-19	-	Flatten layer Dense layer (512 nodes) Dense layer (256 nodes) Output layer
9	VGG-19	Conv2D layer (512 nodes) Conv2D layer (256 nodes) MaxPooling2D layer	Flatten layer Dense layer (512 nodes) Dense layer (256 nodes) Output layer
10	VGG-19	Conv2D layer (512 nodes) Conv2D layer (256 nodes) Conv2D layer (128 nodes) MaxPooling2D layer	Flatten layer Dense layer (1024 nodes) Dense layer (512 nodes) Dense layer (256 nodes) Output layer

In output to VGG-Nets, a convolutional layers' block is added with trainable parameters to extrapolate additional features. After this block, there is a flatten layer that brings all the outputs of the previous layer onto a one-dimensional array to be given as input to the top layer. The top layer of the different implemented architectures shown in TABLE I change depending on the number of convolutional layers and the number of nodes per layer. All top layers share the fact that they have the same activation function (the Rectified Linear Unit - ReLU). Between the various dense layers of all models, there are dropout layers: these layers keep the overfitting of the model under control.

The output layer of the models differs between the two scores: the diaphragm deep attenuation score could be 0, 1, or 2, so should be able to predict three classes. Instead, the vessel blurring score should only involve two classes (0 or 1).

For the diaphragm deep attenuation score, which is a multi-class problem, then the network outputs an array containing the probability associated with each score value. The array index that will have obtained the highest probability will constitute the final output. The activation function is a softmax and the loss function is the categorical cross entropy. Instead the vessel blurring score is a binary problem and then the output layer has only one neuron. This neuron will report the value of the predicted parameter and the probability of the realized prediction. This is a binary classification problem, so the activation function is a sigmoid, and the loss function calculation is the binary cross entropy. The performances of models were evaluated by classification accuracy, loss, Area under the ROC curve (AUC), and precision.

III. RESULTS

The predictive model produced for the classification of liver brightness hepatorenal echo contrast score presented a classification accuracy of 90.5% considering the sub-scores labeled by physicians. In the misclassified cases the maximum error for this sub-score was one point. Regarding the model for estimation of the diaphragm deep attenuation and the vessel

blurring sub-scores, architecture #10 and architecture #2 (TABLE I) showed the best classification performance on the validation dataset, respectively. The classification accuracy, loss, AUC, and precision obtained for these models are reported in TABLE II.

TABLE II: THE PERFORMANCE PARAMETERS OF THE TWO SELECTED MODELS OF EACH SUBSCORES

	Accuracy	Loss	AUC	Precision
Diaphragm deep attenuation	83.25 %	0.48	0.93	83.0 %
Vessel blurring	84.05 %	0.44	0.89	89.0 %

The identified models were subsequently tested on the test dataset. The confusion matrixes for diaphragm deep attenuation and vessel blurring sub-score models are reported in TABLE III-A and III-B, respectively. The algorithm for the estimation of diaphragm deep attenuation showed an accuracy of 81.8%. The misclassified scores were under or over-estimated by one point. Reading the vessel blurring sub-score model the identified model presented a classification accuracy of 86.4% on the test dataset. In both cases, the models maintained the performance obtained during the training and validation process.

TABLE III: COMPARISON OF THE PREDICTED SUBSCORE AND THE SUBSCORE ASSIGNED BY THE PHYSICIANS ON THE TEST SET REPRESENTED BY A NORMALIZED CONFUSION MATRIX

A) DIAPHRAGM DEEP ATTENUATION SUBSCORE

True label	Score 0	0.875	0.125	0
	Score 1	0.125	0.75	0.125
	Score 2	0	0.125	0.875
		Score 0	Score 1	Score 2
		Predicted label		

B) VESSEL BLURRING SUBSCORE

True label	Score 0	0.73	0.27
	Score 1	0	1.00
		Score 0	Score 1
		Predicted label	

IV. DISCUSSION

The early diagnosis of NAFLD is important to prevent fibrosis progression, liver cirrhosis, or hepatocellular carcinoma [4], [5]. Among the noninvasive methods, US B-mode imaging is recommended for population screening and follow-up [7]. But this method has the limitation that the evaluation of a US image is operator dependent [8]-[10]. Hamaguchi's score improved the standardization of the degree of hepatic lipid accumulation in the liver [12], but this score suffers from the fact that the assessment is a subjective measure strongly influenced by the expertise of the physician evaluating the US image. In this study, we aimed to preliminary assess the possibility to estimate Hamaguchi's score by means of advanced image analysis.

The results of this study showed that methods based on AI can estimate the three sub-scores which determine Hamaguchi's score. Indeed, the produced models presented a high classification accuracy for all three sub-scores. The results obtained for all three sub-scores are clinically relevant and suggest that such decision support systems in the future may support the diagnosis of liver disease in a way that will reduce intra- and inter-operator assessment error.

The study presents the following limits: the possible reliance on manual segmentations, the use of images acquired from only one type of US scanner, the moderate sample size, and the retrospective nature of the study. The latter limited the possibility to build a dataset with balanced case histories.

These preliminary results should be confirmed and potentially improved on a larger sample size and more clinically balanced dataset. In addition, the presented approach could be additionally improved by developing an automatic tool for ROI selection.

In conclusion, in this preliminary study, the results assessed the possibility to produce the NAFLD computer-aided diagnostic models based on analysis of US images.

REFERENCES

[1] Brunt EM, Janney CG, Di Bisceglie AM, Neuschwander-Tetri BA, Bacon BR. Nonalcoholic steatohepatitis: A proposal for grading and staging the histological lesions. Am J Gastroenterol 1999;94:2467–74.

[2] Huang DQ, El-Serag HB, Loomba R. Global epidemiology of NAFLD-related HCC: trends, predictions, risk factors and prevention. Nat Rev Gastroenterol Hepatol. 2021;18(4):223-238. doi:10.1038/s41575-020-00381-6

[3] Estes C, Razavi H, Loomba R, Younossi Z, Sanyal AJ. Modeling the epidemic of nonalcoholic fatty liver disease demonstrates an exponential increase in burden of disease. Hepatology. 2018;67(1):123-133. doi:10.1002/hep.29466

[4] Styne DM, Arslanian SA, Connor EL, et al. Pediatric Obesity-Assessment, Treatment, and Prevention: An Endocrine Society Clinical Practice Guideline. J Clin Endocrinol Metab. 2017;102(3):709-757. doi:10.1210/jc.2016-2573

[5] Valerio G, Maffeis C, Saggese G, et al. Diagnosis, treatment and prevention of pediatric obesity: consensus position statement of the Italian Society for Pediatric Endocrinology and Diabetology and the Italian Society of Pediatrics. Ital J Pediatr. 2018;44(1):88. Published 2018 Jul 31. doi:10.1186/s13052-018-0525-6

[6] Ting Soon GS, Wee A. Liver biopsy in the quantitative assessment of liver fibrosis in nonalcoholic fatty liver disease. Indian J Pathol Microbiol. 2021;64(Supplement):S104-S111. doi:10.4103/IJPM.IJPM_947_20

[7] Ferraioli G, Soares Monteiro LB. Ultrasound-based techniques for the diagnosis of liver steatosis. World J Gastroenterol. 2019;25(40):6053-6062. doi:10.3748/wjg.v25.i40.6053

[8] Lee SS, Park SH. Radiologic evaluation of nonalcoholic fatty liver disease. World J Gastroenterol. 2014;20(23):7392-7402. doi:10.3748/wjg.v20.i23.7392

[9] Strauss S, Gavish E, Gottlieb P, Katsnelson L. Interobserver and intraobserver variability in the sonographic assessment of fatty liver. AJR Am J Roentgenol. 2007;189(6):W320-W323. doi:10.2214/AJR.07.2123

[10] Cengiz M, Sentürk S, Cetin B, Bayrak AH, Bilek SU. Sonographic assessment of fatty liver: intraobserver and interobserver variability. Int J Clin Exp Med. 2014;7(12):5453-5460. Published 2014 Dec 15.

[11] Targher G. What's Past Is Prologue: History of Nonalcoholic Fatty Liver Disease. Metabolites. 2020;10(10):397. Published 2020 Oct 8. doi:10.3390/metabo10100397

[12] Hamaguchi M, Kojima T, Itoh Y, et al. The severity of ultrasonographic findings in nonalcoholic fatty liver disease reflects the metabolic syndrome and visceral fat accumulation. Am J Gastroenterol. 2007;102(12):2708-2715. doi:10.1111/j.1572-0241.2007.01526.x

[13] Decharatanachart P, Chaiteerakij R, Tiyarattanachai T, Treeprasertsuk S. Application of artificial intelligence in chronic liver diseases: a systematic review and meta-analysis. BMC Gastroenterol. 2021;21(1):10. Published 2021 Jan 6. doi:10.1186/s12876-020-01585-5

Soft-tissue alterations identified with a CNN trained with simulated ultrasound images integrating expert knowledge

L. Antelmi[1], A. Colucci[1], F. A. Lombardi[2], A. Centonze[1], T. De Marco[1], F. Conversano[2], P. Pisani[2], S. Casciaro[2]
[1] *R&D Department, Echolight S.p.a., Lecce (Italy)*
[2] *National Research Council, Instute of Clinical Physiology, Lecce (Italy)*

***Abstract*—We present a novel approach for objectively measuring pathological changes in soft tissue, specifically those resulting from genetic disorders such as Osteogenesis Imperfecta (OI) and Pulmonary Arterial Hypertension (PAH), using Ultrasonography. The method employs high-frequency sound waves to generate images of internal soft tissue structures within the human body. Convolutional Neural Networks (CNNs) have been shown to be powerful techniques for evaluating the pathological status of soft tissue. However, the availability of high-quality echographic images for training machine learning models is often limited. We propose a technique that leverages expert knowledge to simulate pathological soft-tissue alterations of the desired degree in echographic images. Our results demonstrate that when a CNN is trained with such images, it is able to accurately separate images of healthy subjects from those with OI and PAH pathology, respectively with sensitivity of 0.93 and 0.97 and specificity of 0.91 and 0.81.**

***Keywords*—US Imaging, CNN, Disease Prediciton, Expert Knowledge.**

Ultrasonography is a widely used diagnostic technique that employs high-frequency sound waves to generate images of internal soft tissue structures within the human body. This modality can be used to detect pathological alterations in soft tissue, such as those resulting from disorders like Osteogenesis Imperfecta (OI) [3] and Pulmonary Arterial Hypertension (PAH) [13].

OI is a heterogeneous group of genetic disorders that affect the production of collagen type I in connective tissues and bones [19], [23]. For this reason it can affect various body parts, such as the skeletal system, the skin, and the teeth.

PAH is a lung disease that causes the narrowing of blood vessels in the lungs, leading to an increase in resistance to blood flow and strain on the right heart ventricle [8], [16]. People with PAH often experience fatigue and tiredness, which results in reduced movement and muscle performance [15].

Both OI and PAH have hence a significant impact on soft tissue, particularly noticeable in areas that humans normally use on a daily basis, such as the forearms for hand movement and the thighs for walking [5].

Convolutional Neural Networks (CNNs) have been shown to be powerful techniques for evaluating the pathology degree of biomedical imaging data [1], [17], [10], including echographic images of hard [14] and soft tissues [22], [20]. However, the availability of data for training machine learning models is often limited, which can negatively impact the performance of models trained on these images. To address this limitation, image generation methods such as deep generative models and generative adversarial networks have been proposed [6], [4].

Unfortunately, when data is scarce, these methods often fall short in accurately simulating pathological conditions [2]. In such cases, expert human knowledge is crucial in guiding the generation of high-quality [9] synthetic images that closely mimic real-world pathological scenarios [21]. The incorporation of expert knowledge in image generation is a promising strategy for improving the performance of machine/deep learning models in medical imaging.

This is where our approach comes in: we introduce a simple yet powerful technique that leverages expert knowledge to simulate pathological soft-tissue alterations of the desired degree in echographic images.

To do so, we take soft-tissue images of healthy subjects and we sample the Pathology Index (PI) from a uniform distribution. The healthy image is then corrupted with an adulteration level proportional to the random PI.

We demonstrate that when a CNN is trained with such images, it is able to accurately separate healthy subjects from those with pathology. This approach is particularly useful in situations where data is scarce and expert knowledge is required to generate pathological images. Our results suggest that the use of expert knowledge in image generation can be a valuable tool in improving the performance of machine learning models in the medical field.

By training the CNN model on a large dataset of synthetic images generated using expert knowledge, we aim to create a model that can accurately predict the degree of pathological changes in soft tissue. This will make the CNN model a valuable evaluation tool for the assessment of OI and PAH.

I. Methods

In this section, we will firstly describe the process of synthetic image generation for mimicking the effects of soft-tissue pathology in echographic images. We developed an algorithm utilizing a trial-and-error approach to capture and incorporate the expert knowledge of a specialist in the field.

By randomly sampling a Pathology Index from a uniform distribution, we are able to appropriately modify the original images and transform them into pathological ones. Secondly, we will describe the CNN architecture used in our work.

A. Synthetic Image Generation

In order to generate synthetic echographic images that accurately mimic the effects of soft-tissue pathology, we developed an algorithm utilizing a trial-and-error approach. Through this method, we were able to capture and incorporate the expert knowledge of a specialist in the field regarding the appearance of soft tissue disease on echographic images.

The training set consists of echographic images of the forearm and the thigh of subjects without known disease. For each image, the Pathology Index $\mathrm{PI} \sim \mathcal{U}(0, 100)$ is randomly sampled from a uniform distribution between 0 and 100. The PI value is then used to appropriately modify the original image and transform it into a pathological one.

The procedure is detailed in pseudo code in Algorithm 1. The core computation consists in the application of a *Shift* operator that horizontally translate the image by the desired number of pixels, followed by a pixel-wise *Max* operation between the original image and the shifted one. This computation is repeated as many times as the PI value to simulate the desired pathology level on the image. The *Shift* operator has a cyclic boundary symmetry such that column elements that are shifted beyond the last position are re-introduced at the first position. The final image serves as input for the CNN network, as well as the PI value serves as the target value for the network's regression model.

Algorithm 1 Creation of a random pathological image given an healthy one.

Require:
Dataset of US BMode 2D images of healthy subjects.
Max Pathology Index ($\mathrm{PI}_{\mathrm{max}}$) value.
Operator $\mathrm{Shift}(I, s)$, that given an image I and a shift value s return the original image shifted horizontally by s pixels.

Start processing

for $I \in$ Dataset **do**

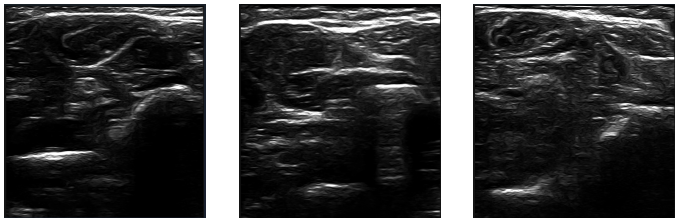
Sample $\mathrm{PI} \sim \mathcal{U}(0, \mathrm{PI}_{\mathrm{max}})$

for $i = 0 : \mathrm{PI}$ **do**
$I_i \leftarrow I + \mathrm{Shift}(I, i)$
$I \leftarrow \mathrm{Max}(I, I_i)$
end for

Save: (I, PI)

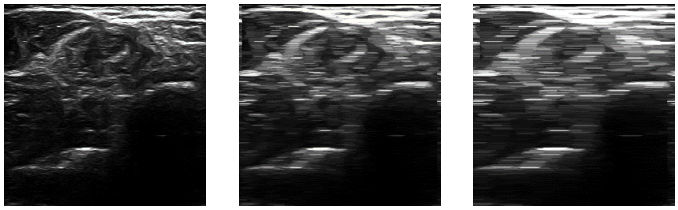
end for

End processing



(a) Healthy **(b)** OI **(c)** PAH

Fig. 1: Images acquired axially on the forearm of subjects: (a) Healthy, (b) with Osteogenesis Imperfecta, (c) with Pulmonary Arterial Hypertension.



(a) $\mathrm{PI} = 0$ **(b)** $\mathrm{PI} = 50$ **(c)** $\mathrm{PI} = 100$

Fig. 2: Simulated images with increasing Pathology Index (PI)

In Fig. 1 we show the real appearance of the OI and PAH disease on echographic images. In Fig. 2 we show the result of the application of Algorithm 1 to the BMode image of an healthy subject.

Along with the *Shift+Max* operators, we came up with other heuristics to simulate pathological images, such as addition of Gaussian blur and addition of white horizontal patches. These heuristics were poorly judged by the expert specialist, and hence discarded.

B. CNN architecture

AlexNet [12] is a classic convolutional neural network architecture. It consists of convolutions, max pooling and dense layers as the basic building blocks. Our network is a modified version of the AlexNet and consists of 6 Convolutional layers and 3 Linear layers. The activation used is the Rectified Linear Unit (ReLU). The structural details of each layer in the network can be found in the table I.

TABLE I: Network details, variation of the AlexNet [12].

Layer	in	out	post computation
Convolution	1	6	ReLu + MaxPool
Convolution	6	16	ReLu + MaxPool
Convolution	16	32	ReLu + MaxPool
Convolution	32	64	ReLu + MaxPool + Flatten
Linear	flattened	25	ReLu
Linear	25	1	-

II. Experiment

In this section, we will discuss the dataset used in our study and the process of fitting and evaluating the CNN regression model performance.

A. Dataset description

We recorded echographic Bmode images from 24 subjects: 22 healthy, 1 with Osteogenesis Imperfecta, and 1 with Pulmonary Arterial Hypertension. From each subject we acquired bilaterally images from: proximal third of the forearm and distal third of the thigh. Patient laying in supine position, palms down, and probe perpendicular to the table. Five axial sections were taken from the forearms, while for the thighs we took also five longitudinal sections. The acquisitions were performed with an *EchoStation* device (Echolight S.p.a., Italy) equipped with a linear probe of 40 mm and a graphical user interface specifically designed for this task. For more details please refer to [7], [18]. The total number of images available were 720 (24 subjects $\times$ 30 images per subject), from which we generated the training and testing set accordingly to the following procedure.

The train set is composed by all and only the 660 images (22 healthy subjects $\times$ 30 images per subject) coming from healthy subjects, preprocessed as follows. After a resize to 256×256 grayscale image space, we transformed the healthy images to pseudo-pathological ones according to the procedure described in §I-A, and lastly normalized them pixel-wise to have zero mean and unitary standard deviation.

The test set is composed by all the 60 images of non healthy sucjects, namely the ones with Osteogenesis Imperfecta and Pulmonary Arterial Hypertension, plus all the 660 images coming from healthy subjects, preprocessed as above, but this time not altered by the pathology mimicking preprocessing algorithm, leading, for this last reason, to a never-seen-before testing set. The numerosity of the total data used for the testing set amount hence to 720 images.

B. Model fitting and evaluation

We fitted the CNN model described in § I-B, with the training pseudo-pathological images as input of the network, and the associated Pathological Indexes as output. We trained the network for 30 epochs and batch-size 8 with the *Adam* optimization algorithm [11] and the *Mean Squared Error* cost function, until convergence of the latter was reached.

Performance on the test set was computed by fitting the predicted PI for the three classes Healthy, OI, and PAH with three Gaussian distributions $\mathcal{N}(\mu_c, \sigma_c^2)$, where c is the class label. Then we computed the sensitivity and specificity, along with the area under the Receiver Operating Characteristic curve, by using as threshold value the intersection point between the probability density functions.

III. Results

In Fig. 3 we show the histogram of PI predicted by the CNN regression model for the three classes Healthy, OI, and PAH images.

In Fig. 4 and Tab. II we present the results in terms of AUC, sensitivity and specificity when the class separation threshold is the one identified by intersection of the Gaussian probability density functions used to fit the PI values predicted by the CNN regression model. The latter is able to accurately separate images of healthy subjects from those with OI and PAH pathology, respectively with AUC of 0.98 and 0.96, sensitivity of 0.93 and 0.97, and specificity of 0.91 and 0.81.

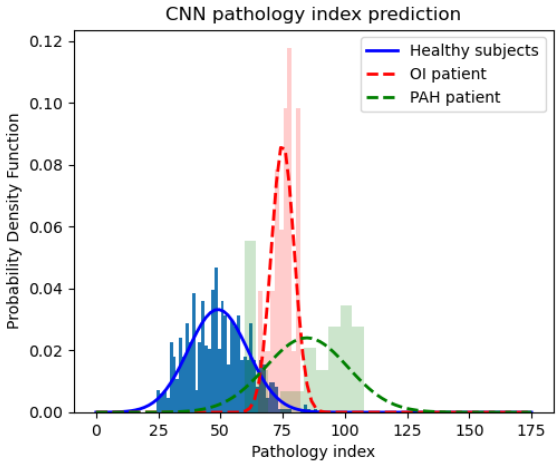


Fig. 3: Test set distribution of the CNN predicted Pathology Index for Healthy subjects, with Osteogenesis Imperfecta (OI), and with Pulmonary Arterial Hypertension (PAH)

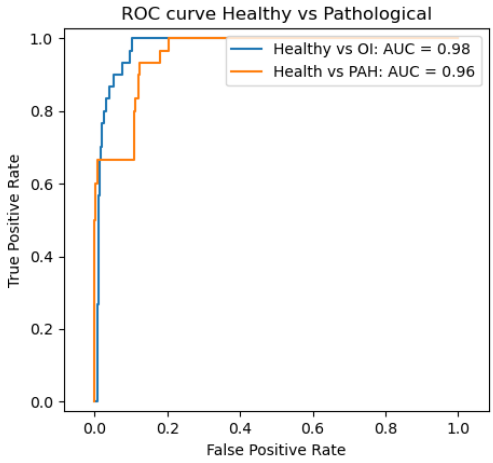


Fig. 4: Image classification performance based on distributions in Fig. 3 of Healthy subjects, with Osteogenesis Imperfecta (OI), and with Pulmonary Arterial Hypertension (PAH).

TABLE II: Image classification performance based on distributions in Fig. 3 of Healthy subjects, with Osteogenesis Imperfecta (OI), and with Pulmonary Arterial Hypertension (PAH).

Test	PI Threshold	Sensitivity	Specificity	AUC
Sano *vs* OI	66	0.93	0.91	0.98
Sano *vs* IPA	66	0.97	0.81	0.96

IV. Discussion

The study presents a valuable approach for objectively measuring pathological changes in echographic images of soft

tissue by using expert knowledge to simulate pathological changes in healthy images. It is intended as a promising preliminary investigation, which carries some initial limitations.

One limitation is that the sample size of pathological subjects may be too small to generalize the results to the entire population. However, we attempted to address this by collecting more images from different body regions and acquisition planes. It is nevertheless important to conduct more extensive studies with more variety in the pathological origin of the images to obtain more reliable and robust findings.

The simulated images are inherently different from real-world images, as they lack the noise, defects, and variability that are present in actual data. Nevertheless, by increasing the Pathology Index many more hyperechoic straight structures appear in the images as compared to the original healthy one. Such images seems then to provide enough variation in terms of size, location, of the artificial structures, to enable the algorithm to generalize to true pathological cases. Another strategy adopted to increase variation was to use in the learning phase images acquired on different anatomic sites and with different acquisition planes. With this strategy, the model is forced not to focus on specific anatomic details and not to take into account the unique characteristics of each body site or acquisition plane other than the ones needed for predicting the Pathology Index.

V. Conclusion

The results of this preliminary study show that a CNN trained on these pseudo-pathological images can effectively distinguish between healthy subjects and those with genetic disorders such as Osteogenesis Imperfecta and Pulmonary Arterial Hypertension, and that the simulation approach may be particularly useful in situations where data availability is limited.

References

[1] Aykat, S., Senan, S.: Deep learning in retinal diseases diagnosis: A review. Machine Learning and AI Techniques in Interactive Medical Image Analysis pp. 1–34 (2023)

[2] Bansal, M.A., Sharma, D.R., Kathuria, D.M.: A systematic review on data scarcity problem in deep learning: solution and applications. ACM Computing Surveys (CSUR) **54**(10s), 1–29 (2022)

[3] Cepollaro, C., Gonnelli, S., Pondrelli, C., Montagnani, A., Martini, S., Bruni, D., Gennari, C.: Osteogenesis imperfecta: bone turnover, bone density, and ultrasound parameters. Calcified tissue international **65**(2), 129–132 (1999)

[4] Chen, R.J., Lu, M.Y., Chen, T.Y., Williamson, D.F., Mahmood, F.: Synthetic data in machine learning for medicine and healthcare. Nature Biomedical Engineering **5**(6), 493–497 (2021)

[5] Coussens, M., Lapauw, B., Verroken, C., Goemaere, S., De Wandele, I., Malfait, F., Banica, T., Calders, P.: Bone mass, density, geometry, and stress–strain index in adults with osteogenesis imperfecta type i and their associations with physical activity and muscle function parameters. Journal of Bone and Mineral Research (2022)

[6] Cronin, N.J., Finni, T., Seynnes, O.: Using deep learning to generate synthetic b-mode musculoskeletal ultrasound images. Computer methods and programs in biomedicine **196**, 105583 (2020)

[7] De Giorgi, S., Ciardo, D., Aventaggiato, M., Lombardi, F., Pisani, P., Conversano, F., Casciaro, S.: Classification of rectus femoris muscle strength using a machine learning approach based on ultrasound scans: pilot study for application in sarcopenia diagnosis. In: OSTEOPOROSIS INTERNATIONAL. vol. 31, pp. S368–S369. SPRINGER LONDON LTD 236 GRAYS INN RD, 6TH FLOOR, LONDON WC1X 8HL, ENGLAND (2020)

[8] Farber, H.W., Loscalzo, J.: Pulmonary arterial hypertension. New England Journal of Medicine **351**(16), 1655–1665 (2004)

[9] Jain, A., Patel, H., Nagalapatti, L., Gupta, N., Mehta, S., Guttula, S., Mujumdar, S., Afzal, S., Sharma Mittal, R., Munigala, V.: Overview and importance of data quality for machine learning tasks. In: Proceedings of the 26th ACM SIGKDD International Conference on Knowledge Discovery & Data Mining. pp. 3561–3562 (2020)

[10] Kang, Z., Li, Y., Liu, J., Chen, C., Wu, W., Chen, C., Lv, X., Liang, F.: H-cnn combined with tissue raman spectroscopy for cervical cancer detection. Spectrochimica Acta Part A: Molecular and Biomolecular Spectroscopy p. 122339 (2023)

[11] Kingma, D.P., Ba, J.: Adam: A method for stochastic optimization. arXiv preprint arXiv:1412.6980 (2014)

[12] Krizhevsky, A., Sutskever, I., Hinton, G.E.: Imagenet classification with deep convolutional neural networks. Commun. ACM **60**(6), 84–90 (may 2017). https://doi.org/10.1145/3065386

[13] Lau, E.M., Iyer, N., Ilsar, R., Bailey, B.P., Adams, M.R., Celermajer, D.S.: Abnormal pulmonary artery stiffness in pulmonary arterial hypertension: in vivo study with intravascular ultrasound. PLoS One **7**(3), e33331 (2012)

[14] Luo, W., Chen, Z., Zhang, Q., Lei, B., Chen, Z., Fu, Y., Guo, P., Li, C., Ma, T., Liu, J., et al.: Osteoporosis diagnostic model using a multichannel convolutional neural network based on quantitative ultrasound radiofrequency signal. Ultrasound in Medicine & Biology (2022)

[15] Mainguy, V., Maltais, F., Saey, D., Gagnon, P., Martel, S., Simon, M., Provencher, S.: Peripheral muscle dysfunction in idiopathic pulmonary arterial hypertension. Thorax **65**(2), 113–117 (2010)

[16] McLaughlin, V.V., McGoon, M.D.: Pulmonary arterial hypertension. Circulation **114**(13), 1417–1431 (2006)

[17] Nasser, M., Yusof, U.K.: Deep learning based methods for breast cancer diagnosis: A systematic review and future direction. Diagnostics **13**(1), 161 (2023)

[18] Pisani, P., Natale, A., Lombardi, F.A., Muratore, M., De Marco, T., Antelmi, L., Centonze, A., Conversano, F., Casciaro, S.: Nuove prospettive per la valutazione delle patologie muscolo-scheletriche con radiofrequency echographic multi spectrometry (rems). In: ORTOMED, Firenze. Società Italiana di Ortopedia, Medicina e delle Malattie Rare dello Scheletro (2022)

[19] Rauch, F., Glorieux, F.H.: Osteogenesis imperfecta. The Lancet **363**(9418), 1377–1385 (2004)

[20] Remy-Jardin, M., Remy, J.: Artificial intelligence-based detection of pulmonary vascular disease. Artificial Intelligence in Cardiothoracic Imaging pp. 491–500 (2022)

[21] Roe, K.D., Jawa, V., Zhang, X., Chute, C.G., Epstein, J.A., Matelsky, J., Shpitser, I., Taylor, C.O.: Feature engineering with clinical expert knowledge: a case study assessment of machine learning model complexity and performance. PloS one **15**(4), e0231300 (2020)

[22] Shin, Y., Yang, J., Lee, Y.H., Kim, S.: Artificial intelligence in musculoskeletal ultrasound imaging. Ultrasonography **40**(1), 30 (2021)

[23] Van Dijk, F., Sillence, D.: Osteogenesis imperfecta: clinical diagnosis, nomenclature and severity assessment. American journal of medical genetics Part A **164**(6), 1470–1481 (2014)

Exploring the potential of MCVAE for patients stratification and skewed data compensation across the AD continuum

F. Cruciani[1], E. Cinquetti[1], L. Brusini[1], A. Aparo[2], C. Combi[2], I. Boscolo Galazzo[1], G. Menegaz[1]
[1]*Department of Engineering for Innovation Medicine, University of Verona, Verona, Italy*
[2]*Department of Computer Science, University of Verona, Verona, Italy*
federica.cruciani@univr.it (corresponding)

***Abstract*—Imaging Genetics (IG) focuses on integrative studies to assess the influence of genetic architecture on brain structure and function, which is particularly relevant to decrypt the underlying mechanisms of complex pathologies such as Alzheimer's Disease (AD). To this aim, in this work, we exploited a Multi-Channel Variational Autoencoder (MCVAE) for investigating the genetic underpinnings of Grey Matter (GM) and White Matter (WM) modulations in the AD continuum with the twofold goal of (i) capturing the associations among multimodal features in the latent space; (ii) assessing the generative potential of the model to be eventually exploited for data augmentation and mitigation of the data skewed problem. Three channels were considered, respectively representing morphometric, microstructural and genetic features. The resulting common latent space was well aligned across the different channels, highlighting a clustering of the latent components concordant with different stages of AD. Regarding the generative performance, reconstruction accuracy revealed that diffusion MRI led to the best performance, especially when decoded from structural MRI, while neither the microstructural nor the genetic channel allowed effective decoding of the others. This might most probably be due to the limited data numerosity and the inherent limitations of the MCVAE architecture. Our preliminary results provide evidence of the potential of multi-modal feature integration with MCAVE models for decoding subtle disease signatures and highlight some limitations of the model providing hints for further improvement.**

***Keywords*—MCVAE, Imaging Genetics, diffusion MRI, structural MRI, SKAT**

I. INTRODUCTION

Alzheimer's Disease (AD) is the most common cause of dementia, affecting 46.8 million people worldwide [1]. There is still much debate about the pathophysiology underpinning brain modulations in Alzheimer's Disease (AD). For example, while structural Magnetic Resonance Imaging (sMRI) derived phenotypes (IDPs) are well-established biomarkers for AD detection [2], it is not clear whether white matter (WM) alterations are related to, or independent from, gray matter (GM) degeneration in AD. For this reason, the role of microstructure is increasingly being considered in AD studies [3]. Moreover, there is consistent evidence of a strong genetic contribution to AD. Recent strategies to extract genotype traits linked with AD overran the classical Single Nucleotide Polymorphism (SNPs) approach and moved towards grouping multiple SNPs into the so-called SNP sets. A natural grouping technique consists in taking all SNPs that are found within a gene. Among such approaches, Wu and colleagues proposed the Sequence Kernel Association Test (SKAT) [4], a logistic kernel-machine regression model for testing the association between SNP sets and a given disease which has demonstrated promising results in different conditions, though its exploitation in AD is still limited. There is hence growing evidence that multimodality can aid in providing a more thorough understanding of mechanisms underlying complex and multifaceted diseases such as AD. The specific association between genetic measures and IDPs is, in particular, the target of Imaging Genetics (IG), which focuses on integrative studies to assess the influence of the genetic architecture on brain structure and function [5]. To this aim, mass-univariate methods or more advanced latent space based methods have been typically proposed [6]. However, because they are not generative, these approaches provide limited information regarding how this latent representation is reflected in the data as they do not provide a mean to sample observations when the distribution of latent variables (LVs) is known. To overcome this limitation, Kingma *et al.* [7], proposed a generative model for high-dimensional single-modality data, the Variational AutoEncoder (VAE). VAEs are models that couple a recognition function (encoder) to infer a lower dimensional representation of the data, with a generative function (decoder) which transforms the latent representation back to the original observation space. This approach was further expanded by Antelmi et al. [8] to ensure multimodal data could be enclosed in this framework without the need to concatenate multiple channels in a single input. In particular, a multichannel VAE (MCVAE) was proposed with each channel representing a different modality, requiring that their associated latent representation match a shared target distribution. This technique was successfully adopted in multiple scenarios, among which the very recent work of Diaz Pinto *et al.* where the authors predicted myocardial infarction through retinal scans and minimal personal information [9]. In relation to AD, an extension of MCVAE was recently exploited in [10] aiming at the modeling of the spatio-temporal dynamics of longitudinal imaging and clinical biomarkers along the history of the disease.

Along this line, the aim of this work is to assess the capabilities of multi-channel biomarkers for decrypting the underlying mechanism across AD continuum. We exploited

the MCVAE relying on two different imaging techniques describing both WM and GM IDPs, as well as gene-based variant scores as genetic determinants (GDs) aiming at assessing both the unsupervised latent space clustering and the decoding performance of one channel from another addressing skewed data compensation.

II. Materials and Methods

A. Study cohort and feature processing

IDPs and GDs were obtained from the ongoing Alzheimer's Disease Neuroimaging Initiative (ADNI) Phase 3 dataset. The cohort comprehended 297 subjects divided into 220 controls (CN) and 79 patients (PAT), 19 of which were AD while the remaining were mild cognitive impairment (MCI) subjects.

3D T1-weighted (T1-w) MRI and diffusion MRI (dMRI) volumes were used for IDPs extraction (3D T1-w: sagittal accelerated MPRAGE, $1mm$ isotropic voxel; single shell dMRI: $2mm$ isotropic voxel, b=$1000s/mm^2$). The T1-w volumes were preprocessed for bias-field correction with FSL (version 6.0). Subsequently, 84 anatomical Regions of Interest (ROIs) were extracted using FreeSurfer (version 7.0) including thicknesses and volumes for cortical and subcortical ROIs, respectively. The subcortical volumes were normalized by the estimated total intracranial volume of each subject. The ROIs were averaged over hemispheres resulting in 42 features. The dMRI volumes were preprocessed by applying brain extraction followed by Eddy currents correction (FSL, version 6.0). The data was then denoised using local principal component analysis (PCA) via empirical thresholds relying on Python *dipy* library. Subsequently, nonlinear registration to the MNI space was applied to correct for EPI-induced currents. The Diffusion Tensor Imaging (DTI) [11] model was fitted, and Fractional Anisotropy (FA) and Mean Diffusivity (MD) indices were extracted. The tract-based spatial statistics (TBSS) pipeline from FSL was then applied (FA threshold of 0.2). For all subjects, the average value of FA and MD was retained from 48 ROIs derived from the JHU-DTI atlas available in FSL and averaged over hemispheres, resulting in 27 features for each index. For the GDs, quality control (QC) procedures were conducted on genotype data (PLINK, Version 1.9). SNPs and subjects were filtered out based on missingness ($geno > 0.2$, $mind > 0.1$), minor allele frequency ($MAF > 0.05$) and deviations from Hardy–Weinberg equilibrium ($hwe > 1e{-}06$). QC kept 303.150 SNPs out of the 759.993 SNPs collected in ADNI3. No subjects were filtered out. SNP set analysis was applied using SKAT including the top ten principal components from PCA, age and gender as covariates. SNP sets were defined at the gene level, each one including only SNPs located in exon regions. Then, for each subject and for each significant gene resulting from SKAT, a gene-based variant score was extracted as a measure of the mutation rate of the SNP set located in each gene, resulting in 408 features for each subject. All the input features for each channel were standardized to reach zero mean and unitary variance. The influence of age was regressed out from imaging channels.

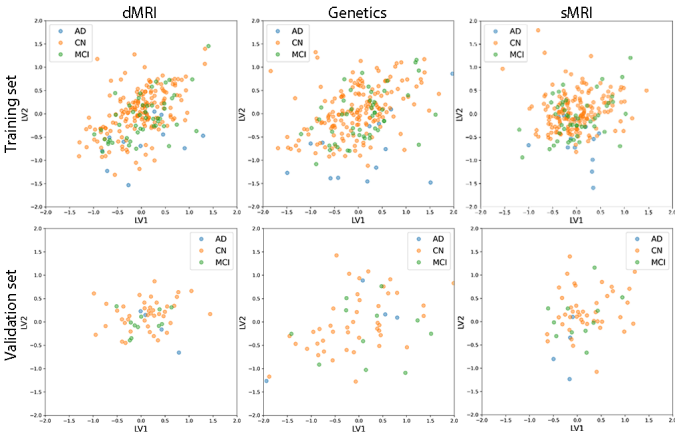


Fig. 1: Latent representation of the training and validation sets (rows) considering the two most significant LVs, separately for each input channel, namely dMRI, sMRI and genetics (columns, AD: blue, CN: orange, MCI: green)

B. Experimental Settings

A three channels MCVAE was employed. The 42 T1-w derived IDPs (cortical thickness/subcortical volumes) represented the sMRI channel, while the 54 tract-based average values for FA and MD were used for the dMRI channel. Finally, the 408 gene mutation scores were included in the genetic channel. A multivariate Gaussian distribution was assumed for the posterior, hence the encoder aimed at finding the parameters, representing the mean and variance for each channel. A single layer (linear) architecture for the encoder and the decoder was employed. This architecture resulted as the best performing in the experimental tests presented in [8]. Moreover, we performed several empirical tests by varying the number of layers and introducing nonlinearities, as well as dropout layers, without achieving a significant increase in performance. Three LVs were chosen for the latent space. Validation was performed following a 5-fold Cross Validation (CV) strategy. Decoding performance was assessed through the computation of Mean Squared Error (MSE) of each decoded feature for each channel, considering the best model derived from the 5-fold CV.

III. Results

A. Latent space

Fig. 1 shows the latent space generated by the first and the second LVs, separately for each input channel (columns) for both the training and the validation set (rows). The LVs were chosen based on the associated dropout probability, which reflects the related importance. In general, the latent spaces for each channel were well aligned, with the dMRI and the genetic components showing a more similar distribution compared with the sMRI one. Moreover, for the training set, a class clustering was present and was coherent among the input channels, with the AD subjects being located in the bottom-right part of the plot, and the MCI being located in the center

TABLE I: MSE reconstruction values for dMRI channel

dMRI feature reconstruction from Genetics		dMRI feature reconstruction from sMRI	
	MSE		MSE
PCT_MD	0.594	RLIC_MD	0.260
PLIC_MD	0.617	SCR_MD	0.296
CST_MD	0.643	SLF_MD	0.313
ALIC_MD	0.686	PLIC_MD	0.322
SCR_MD	0.741	SS_MD	0.344
EC_MD	0.752	FXST_MD	0.365
CST_FA	0.758	ALIC_MD	0.389
SLF_MD	0.784	PCT_MD	0.393
PCR_MD	0.817	EC_MD	0.395
CP_MD	0.841	SFO_MD	0.398

dMRI acronyms: Pontine crossing tract (PCT), Posterior limb of internal capsule (PLIC), Corticospinal tract (CST), Anterior limb of IC (ALIC), Superior corona radiata (SCR), External capsule (EC), Superior longitudinal fasciculus (SLF), Posterior CR (PCR), Cerebral peduncle (CP), Retrolenticular part of IC (RLIC), Sagittal stratum (SS), Fornix/Stria terminalis (FXST), Superior fronto-occipital fasciculus (SFO)

and overlapped with CN mostly located in the upper-left area. This clustering was not clearly present for the validation set.

B. Best-reconstructed features

Tab. I provides the reconstruction performance of the top ten best-reconstructed dMRI features for the validation set, decoding from genetics and sMRI. The ranges of the feature values for the standardized input feature were $[-5.355, 4.847]$ for sMRI, $[-5.611, 4.237]$ for dMRI, and $[-2.989, 4.658]$ for genetics, respectively, having zero mean and unitary variance after standardization. Fig. 2 shows the scatter plots of the top ten best-reconstructed features for the dMRI channel.

In general, a better reconstruction of dMRI features, compared with sMRI ones (not reported in table) was recorded. In particular, the best dMRI reconstructed features were the MD-derived either decoding from genetics or sMRI. SMRI led to the best reconstructions. The tracts part of the external and internal capsule were among the best-decoded ones with low MSE values (RLIC: 0.260; PLIC: 0.322; ALIC: 0.389; EC: 0.395). The SCR reached an MSE of 0.296, much lower compared to the 0.741 reached by decoding from genetics. The other well dMRI decoded features starting from sMRI were the SLF, SS and FXST with an MSE of 0.313, 0.344, 0.365 respectively. Considering the decoding performance of genetic features, they generally showed higher MSE, with the best-decoded dMRI metric being the PCT (MSE = 0.594). Moving to the reconstruction of sMRI features, better reconstruction was achieved decoding from dMRI compared to genetics. The decoding from dMRI saw the accumbens having the lowest MSE of 0.790 followed by the bankssts and the posterior cingulate gyrus (MSE = 0.826, 0.844). All the other top ten best-decoded features had an associated MSE higher than 0.9. Considering the genetic as decoding input, all the sMRI reconstructed features had an MSE greater than 0.9, with the AC being the best-decoded feature (MSE = 0.926). The other features were mainly part of the cingulus and the cuneus, each having an MSE value higher than 1.

IV. Discussion

In this work, we presented preliminary results for unraveling the underlying association between brain structural and microstructural modulations with gene-based variant scores in AD relying on an unsupervised MCVAE. A latent space consisting of 3 LVs was used along with three input channels, corresponding to the multi-modal features. In particular, ROI-based volumes and thicknesses represented the sMRI channel, tract-based FA and MD values the dMRI one, and gene-based variant scores the genetics. We analyzed both the resulting latent space, defined by the LVs having the lowest dropout probability, and the decoding performance of one channel from another. Our results showed that there is a good alignment between the latent spaces derived from each channel, as well as sufficient clustering between AD stages. Instead, the decoding performance was not competitive.

Our work is inspired to [9] where the MCVAE model proposed by [8] was applied for predicting myocardial infarction from retinal scans. The MCVAE and a deep regressor model were trained to estimate left ventricular mass and left ventricular end-diastolic volume and predicted the risk of myocardial infarction using only the retinal images and demographic data. Their results indicated that it is possible to identify patients at high risk of future myocardial infarction from retinal images that are available in every optician and eye clinic. Moreover, an extension of the MCVAE recently proposed by [8] was applied in relation to AD[10] to model the dynamics governing the joint evolution of longitudinal imaging and clinical biomarkers along disease progression. More in detail, the authors accomplished to simulate the effect of the intervention time and drug dosage on the biomarkers' progression in an ADNI study cohort, further verified on a separate independent AD cohort.

To the best of our knowledge, our work is the first attempt to jointly investigate genetics, sMRI and dMRI as inputs to a MCVAE model to highlight their association in the AD continuum, as well as their capability in differentiating AD stages in an unsupervised manner, and the pair-wise decoding capabilities of the considered modalities. With this work we firstly demonstrated that the obtained latent space for each channel resulted well aligned to the others, particularly for the training set and between dMRI and genetics channels. This confirms that a common representation between channels was effectively found by the MCVAE. Moreover, a gradient of the different classes considered, starting from CN and arriving at AD, passing through MCI, was also present, highlighting that despite the MCVAE being unsupervised, a latent space representative of the disease continuum could be captured. Moving to the reconstruction performance, the lower MSE was obtained when decoding dMRI from sMRI data. The genetic channel did not achieve sufficient reconstruction performance in either decoding from sMRI or dMRI IDPs. However, this possibly seeds in the MCVAE architecture. In fact, VAEs are trained to optimize a lower bound on the likelihood of the data which is a trade-off between the reconstruction error

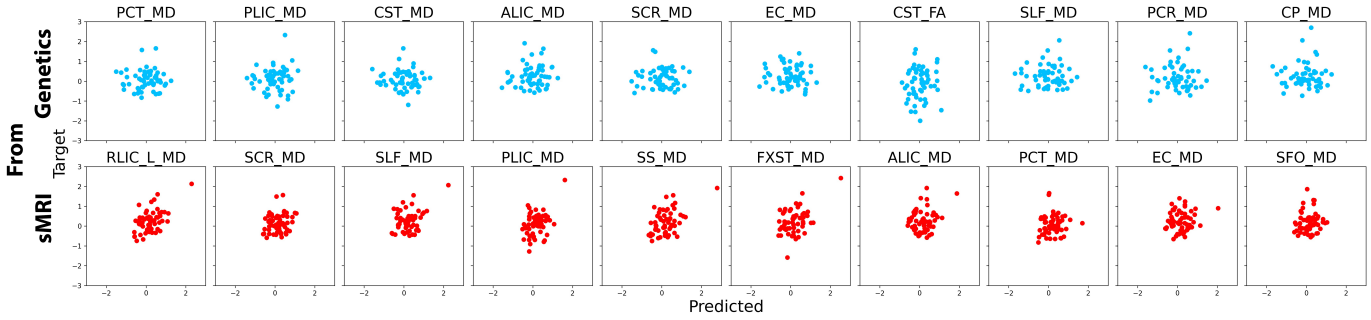


Fig. 2: Scatter plots of the best-reconstructed dMRI features decoded from the other two channels. The reconstructed features are plotted against the respective ground truth

and the divergence between the approximate posterior and the true posterior. This trade-off can result in the model prioritizing a low divergence over a high reconstruction accuracy, which leads to less precise reconstructions, while obtaining informative latent representations. Additionally, the posterior distribution estimated for the latent space of each channel is a multivariate Gaussian, which well fits the distribution of imaging data but not the genetic one which instead follows a categorical distribution. This represents the major limitation of this approach with the chosen input data. However, it is still interesting to analyze the best-decoded IDPs for clinical interpretation and validation. For dMRI, which achieved the best performance, the MD-derived IDPs were the best decoded, compared with FA. In particular, the best-decoded tracts were part of the internal capsule and the corona radiata which were also found with increased diffusivity in MCI compared to healthy controls in [12], demonstrating a relevant role in AD continuum. Decoding dMRI from sMRI can potentially impact clinical applications where important constraints related to image acquisition timing hold, particularly when dealing with AD patients. MRI image translation, is being hence studied since it would allow to exploit standard clinical acquisitions to derive advanced metrics such as microstructure IDPs [13]. In this respect, our results show the possibility to decode tract measures from sMRI images through MCVAE deserving further investigation. Future works will rely on a different prior latent space distribution from the Gaussian used in this study in order to better reflect the input feature distributions and thus potentially allowing to reach also better reconstruction performance. Finally, extending the study cohort would allow having an independent test set besides the validation sets of the 5-fold CV considered in this study in order to further evaluate the performance of the proposed MCVAE model.

V. Conclusions

This work is the first step towards the application of MCVAE with the twofold goal of finding a common latent space between input channels and decoding one channel from the other, demonstrating its potentialities to uncover the association between imaging (sMRI and dMRI) and genetics (gene-based variant scores) in the AD continuum.

Acknowledgment

This work was partly supported by Fondazione CariVerona (Bando Ricerca Scientifica di Eccellenza 2018, EDIPO project, num. 2018.0855.2019) and MIUR D.M. 737/2021 "AI4Health: empowering neurosciences with eXplainable AI methods".

References

[1] M. J. Prince, F. Wu, Y. Guo, L. M. G. Robledo, M. O'Donnell *et al.*, "The burden of disease in older people and implications for health policy and practice," *The Lancet*, vol. 385, no. 9967, pp. 549–562, 2015.

[2] G. B. Frisoni, N. C. Fox, C. R. Jack, P. Scheltens, and P. M. Thompson, "The clinical use of structural mri in alzheimer disease," *Nature Reviews Neurology*, vol. 6, no. 2, pp. 67–77, 2010.

[3] E. Horgusluoglu-Moloch, G. Xiao, M. Wang *et al.*, "Systems modeling of white matter microstructural abnormalities in alzheimer's disease," *NeuroImage: Clinical*, vol. 26, p. 102203, 2020.

[4] M. C. Wu, S. Lee, T. Cai, Y. Li, M. Boehnke *et al.*, "Rare-variant association testing for sequencing data with the sequence kernel association test," *The American Journal of Human Genetics*, vol. 89, no. 1, pp. 82–93, 2011.

[5] L. Shen and P. M. Thompson, "Brain imaging genomics: integrated analysis and machine learning," *Proceedings of the IEEE*, vol. 108, no. 1, pp. 125–162, 2019.

[6] F. S. Nathoo, L. Kong, H. Zhu, and A. D. N. Initiative, "A review of statistical methods in imaging genetics," *Canadian Journal of Statistics*, vol. 47, no. 1, pp. 108–131, 2019.

[7] D. P. Kingma and M. Welling, "Auto-encoding variational bayes," *arXiv preprint arXiv:1312.6114*, 2013.

[8] L. Antelmi, N. Ayache, P. Robert, and M. Lorenzi, "Sparse Multi-Channel Variational Autoencoder for the Joint Analysis of Heterogeneous Data," in *Proceedings of the 36th International Conference on Machine Learning*, K. Chaudhuri and R. Salakhutdinov, Eds. PMLR, 2019, pp. 302–311.

[9] A. Diaz-Pinto, N. Ravikumar, R. Attar, A. Suinesiaputra, Y. Zhao *et al.*, "Predicting myocardial infarction through retinal scans and minimal personal information," *Nature Machine Intelligence*, vol. 4, no. 1, pp. 55–61, 2022.

[10] C. Abi Nader, N. Ayache, G. B. Frisoni, P. Robert, M. Lorenzi *et al.*, "Simulating the outcome of amyloid treatments in alzheimer's disease from imaging and clinical data," *Brain communications*, vol. 3, no. 2, p. fcab091, 2021.

[11] P. J. Basser, J. Mattiello, and D. LeBihan, "Mr diffusion tensor spectroscopy and imaging," *Biophysical journal*, vol. 66, no. 1, pp. 259–267, 1994.

[12] X. Sun, D. Salat, K. Upchurch *et al.*, "Destruction of white matter integrity in patients with mild cognitive impairment and alzheimer disease," *Journal of investigative medicine*, vol. 62, no. 7, pp. 927–933, 2014.

[13] M. Ren, H. Kim, N. Dey, and G. Gerig, "Q-space conditioned translation networks for directional synthesis of diffusion weighted images from multi-modal structural mri," in *International Conference on Medical Image Computing and Computer-Assisted Intervention*. Springer, 2021, pp. 530–540.

A deep learning network from downsampled diffusion-weighted MRI k-space to image-space

M. Gaviraghi[1], B. Kanber[2,3], A. Ricciardi[2], F. Palesi[1], F. Grussu[2,4], C. Tur[2,5], A. Calvi[3], R. Samson[2] and C. A. M. Gandini Wheeler-Kingshott[1,2,6]

[1] *Department of Brain and Behavioural Sciences, University of Pavia, Pavia, Italy*
[2] *MR Research Unit, Department of Neuroinflammation, University College London, London, United Kingdom*
[3] *Department of Medical Physics and Biomedical Engineering, University College London, London, United Kingdom*
[4] *Radiomics Group, Vall d'Hebron Institute of Oncology, Vall d'Hebron Barcelona Hospital Campus, Barcelona, Spain*
[5] *Neurology-Neuroimmunology Department Multiple Sclerosis Centre of Catalonia, Barcelona, Spain*
[6] *Brain Connectivity Centre, IRCCS Mondino Foundation, Pavia, Italy*

***Abstract*— Advanced Magnetic Resonance Imaging (MRI) techniques, such as Diffusion Weighed Imaging, usually require long acquisition times and an open challenge is to reduce the acquisition time more and more in order to allow their use in the clinical routine. Downsampling k-space is a way to speed up MRI, but this can generate artefacts in the resulting images when reconstructing them with standard Fourier transform methods.**

Here, we used deep learning to perform the inverse Fourier transform from k-space to the Diffusion Weighted (DW) images. and used it to assess the quality of images obtained from significantly reduced k-space acquisition strategies. The hypothesis is that a deep learning algorithm would preserve data quality, learned from the fully sampled k-space association. We tested our deep learning algorithm by reducing the number of acquired k-space rows by 30%, which would correspond to a total acquisition time reduction. We considered different types of k-space downsampling. All the trained networks were able to map the relationship between k-space and DW images, reducing artefacts.

In conclusion, this work paves the way to designing acquisition strategies for fast diffusion imaging.

***Keywords*— k-space, deep learning, reduce time acquisition, diffusion magnetic resonance.**

I. INTRODUCTION

MAGNETIC resonance imagining (MRI) is a very powerful tool used in the clinical field to diagnose, to monitor and to study mechanisms behind human behaviour, function and dysfunction. The great power of MRI depends on the fact that this tool can be exploited to investigate several organ systems and that it can be made sensitive to specific properties of the tissues, such as the diffusion of water molecules to probe tissue microstructure. Diffusion Weighted Imaging (DWI) is sensitive to Brownian motion of water molecules in tissue and, hence, to the microstructure and its alterations in pathological conditions [1][2].

The use of MRI in the clinic is limited to qualitative assessments of brain lesions and morphology due to both high costs and long acquisition times for quantitative MRI.

Furthermore, it is to note that when an MRI acquisition is performed, the signal received with the coil is stored as an image containing the spatial frequency information of the object, called k-space. Importantly, each point of the k-space contains phase and frequency information about the signal coming from the entire sample. For this reason, applying the inverse Fourier transform (FT) to the k-space provides the image in physical space [3] [4].

Moreover, it is known that k-space is highly redundant [5]. It is indeed endowed with Hermitian symmetry [4]. Traditionally, the relationship between k-space data and image data is the Fourier transform (FT) [3].

Here we aimed to shorten the acquisition times of DWI of the brain reducing k-space coverage (i.e. the signal) and substituting the FT operation with a deep learning network, while maintaining image quality. In this way, one of the novelty of our method is that it was possible to downsample the k-space, in order to reduce the acquisition time, obtaining an image that is very similar to the one reconstructed from the entire k-space.

Previous work used a deep learning network to pass from the k-space to the DW physical image of the breast with the main goal of reducing DW-related artifacts [6]. However, in this work the network used as its input the entire acquired k-space, instead of a downsampled version like we did here.

We therefore optimised a network previously proposed [7] for reconstructing T1 and T2 weighted images from their k-space and adapted it to the specific case of DWI data [1]. One of the challenges is that DWI can produce very different contrasts depending on the applied diffusion weighting; mathematical or signal models can then be fitted to DWI data to obtain microstructure parameters maps. The automated transform by manifold approximation (AUTOMAP) [7] network was therefore adapted and optimised here to work with DWI k-space data, independently on the diffusion weighted applied. We gave it as input the k-spaces of the diffusion acquisitions and as output the corresponding magnitude images.

II. METHODS

A. Subjects

The database included images of 18 healthy controls (HC, 13 Females, 55.2±9.4 years), 8 primary progressive multiple sclerosis (PPMS, 3 Female, 56.3±9.9 years), 2 relapsing-remitting multiple sclerosis (RRMS; 1 Females, 64±3.6 years), and 31 secondary progressive multiple sclerosis (SPMS; 21 Females, 55.3±7.3 years). 18 subjects were acquired a second time, 18 months after baseline. The total number of datasets was 77.

B. MRI acquisition

A 3T Philips Ingenia CX scanner was used. The Diffusion Weighted (DW) imagining protocol included a spin-echo EPI with TR = 6287 ms, TE = 96 ms, 76 volumes with b = 1000/2000/2800 s/mm2 (20/20/36 DW per b-value) and 3 b0 volumes. The spatial resolution was 2x2x2 mm^3 and the matrix size was 112x112x72.

C. Network design

Each DW dataset was used as an independent sample, regardless of whether it belonged to a subject previously acquired. This choice depended by the fact that the problem to be solved was to associate each k-space with its magnitude image. Since the problem could be reduced to assess a regression between datasets, i.e. finding a relationship between input and output, instead of classifying them in different groups, we therefore used the entire dataset regardless the group (i.e., healthy subject or patient), gender (female or male), or any other demographic feature. The 77 acquisition samples were divided as follows: 53 acquisition samples were used for training, 12 for validation and 12 for test. In each set (training, validation and test) there were both healthy and MS subjects.

The magnitude image was calculated for each slide from real (Re(DW)) and imaginary images (Im(DW)):

$$magnitude\ image = \sqrt{Re(DW)^2 + Im(DW)^2} \quad (1)$$

Using the Fourier transform (FT), the k-space of the magnitude images was calculated:

$$k - space = FT(magnitude\ image) \quad (2)$$

Only DW volumes with a b-value of 0 or 1000 s/mm^2 were considered, so 23 volumes were used for each acquisition dataset. We limited the number of volumes by using the most commonly acquired b-value [8] in order to reduce the amount of data and thus the training time to cope with long calculation times and memory problems. Consequently, for training, the number of input data was 76337 (53 subjects, for each subject 23 volumes, and for each volume about 63 slices), for validation 18699, and for test 18446.

The k-space data had to be normalised before being passed as input: for each batch size, the real and imaginary part was divided by magnitude of the maximum of all values in the entire database.

The 2D k-space matrices in axial planes were then given as input to the network. The real and imaginary parts of the k-space were provided as 2 input channels.

The output target for the network was the magnitude image corresponding to the DW k-space data.

We adapted the AUTOMAP architecture [7]. The network was developed using TensorFlow (Keras) [9] and each network training was run using an NVIDIA Tesla T4 GPU.

We had a k-space of size m x n: the complex data of the k-space were separated into real and imaginary parts and were given to the network as input to two different channels (m x n x 2). The network architecture is pictured in Fig.1.

This architecture was made of two fully connect layers (FC) at the beginning, followed by three convolutional layers (Conv). Because of the fully connected layers, the number of network parameters increases noticeably and makes training very slow. For this reason, it was necessary to resize the k-space from a 112x112 matrix to a 64x64 one. The k-space and DW images were resampled using spline interpolation.

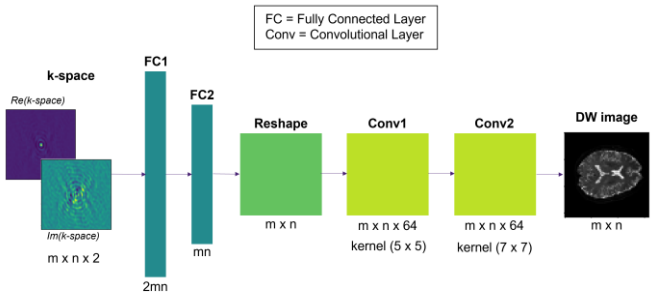


Fig. 1: Architecture of AUTOMAP.

D. Network training

The tuning of the hyperparameters was conducted by giving as input the k-space and as output the corresponding DW magnitude images, both of reduced size i.e. 64x64; we called this experiment *from 64 to 64*.

We searched manually for the best hyperparameter configuration by training the network several times and changing the loss function, activation functions and optimizer. The best hyperparameters were selected minimizing the Root Mean Square Error (RMSE) on the validation set.

In order to prevent the overfitting we applied data augmentation on the fly [10] using two different ways: images were randomly rotated anti-clockwise by 0, 90, 180 or 270° and images were scaled in intensity by a random value so that they became darker or brighter.

E. Network applications

Once the hyperparameters of the network were fixed, four experiments were considered to train the network accordingly:

- *from 64 to 112:* from a k-space of size 64x64 to a magnitude image of 112x112, increasing the resolution along each of the 2D dimensions of the image from 64 to 112. The DW magnitude image was therefore in the original space.
- *Zero fill*: from a k-space of size 64x64, with the last 19 rows filled with zeros, to a corresponding magnitude image of size 64x64.
- *Delete rows:* from a k-space of size 45x64, where the last 19 rows were deleted, to a corresponding magnitude image of size 64x64.
- *Mixed downsampling*: from a k-space of size 45x64, where the last 19 rows (top) or the first 19 rows (bottom) were deleted, to a corresponding magnitude image of size 64x64. This last network aims to test whether AUTOMAP can cope with different downsampling or needs retraining every time k-space

is sampled differently.

In the last three experiments we reduced the k-space acquisition of 30%, applying some downsampling by deleting k-space rows from different positions. Importantly, k-space was downsampled in ways that could be easily implemented from a pulse sequence design point of view, i.e., directly modifying sequences on an MRI scanner.

F. Quantitative evaluation

To compare the DW magnitude images obtained with the traditional FT of k-space and those obtained with the network, it was necessary to normalise the intensity of both images to eliminate simple scale factors. For each acquisition sample, both DW images (GT and network) were divided by the value of the maximum of the respective 4D volume (i.e. including all 23 DW volumes), limiting the calculation to voxels in the brain.

To quantitatively assess how much the two images (DWI GT and DWI network) differed, we calculated the difference image considering the case *from 64 to 64*.

For the experiment with mixed downsampling, we tested the network by giving as input once the first 45 rows (top) and once the last 45 rows (bottom) of k-space.

The Root Mean Square Error (RMSE), Mean Absolute Error (MAE) and Structural Similarity Index (SSIM) [11] calculated between the magnitude DW image and the network output within the brain were chosen as performance metrics.

III. RESULTS

The best hyperparameters were found to be: the sum of RMSE and SSIM as loss function, the hyperbolic tangent for the fully connected layers and the REctified Linear Unit (ReLU) for the convolutional layers using as activation function and the Root Mean Square Propagation (RMS Prop) as optimizer.

Fig. 2 shows the input, the k-space with real and imaginary part, the desired output (GT) and the output of the network of the performed experiments: from 64 to 64 (A), from 64 to 112 (B), zeros fill (C), delete rows (D), mixed downsampling (top) (E) and mixed downsampling (bottom) (F).

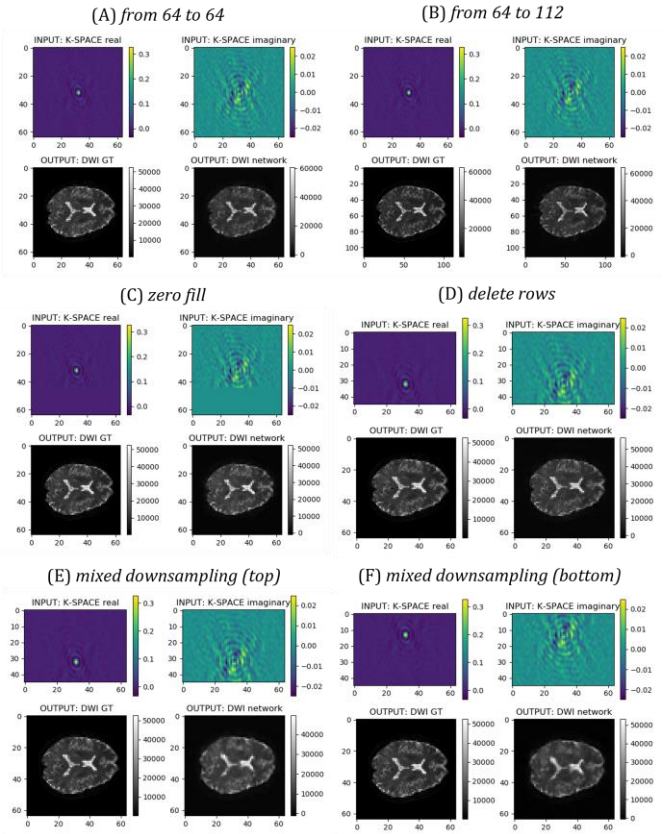


Fig. 2: Each different experiment is shown in each image from (A) to (F). The first row shows the input to the network: on the left the real part and on the right the imaginary part of the k-space. The second row shows the magnitude Diffusion Weighted (DW) image: on the left the ground truth (GT) (desired output) and on the right the output of the network.

Fig. 3 shows for a random test subject the DW images, i.e., DWI GT and DWI network, after the intensity normalization and their difference image in the case *from 64 to 64*.

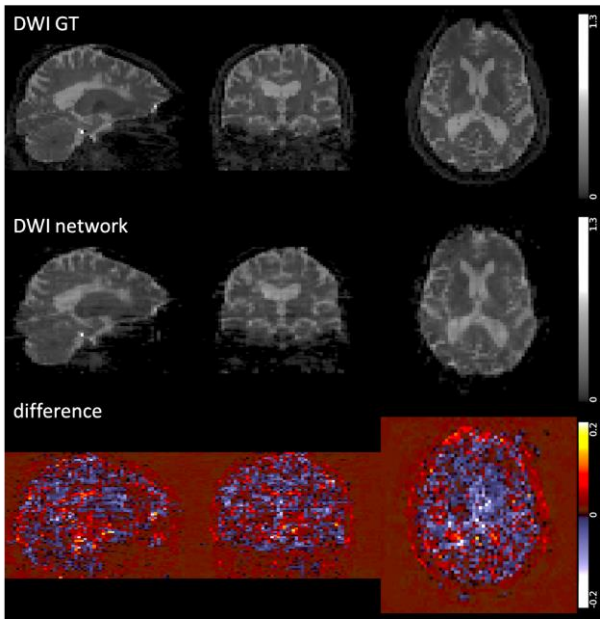


Fig. 3: The first row shows the DWI GT, the second row the DWI network and the third row the image of the difference between the first two rows for a random test subject.

Table I shows the performance metrics (mean and standard deviation) between the GT DW images and the network DW images, calculated on the 12 test subjects over voxels that belong to the brain mask.

TABLE I: PERFORMANCE METRICS ON THE TEST SUBJECTS FOR EACH NETWORK EXAMPLE.

	RMSE	**MAE**	**SSIM**
from 64 to 64	0.035 ±.0.004	0.022 ±.0.004	0.757 ±.0.057
from 64 to 112	0.020 ±.0.007	0.015 ±.0.006	0.734 ±.0.228
zeros fill	0.030 ± 0.012	0.020 ± 0.007	0.660 ± 0.208
delete rows	0.032 ± 0.01	0.021 ± 0.007	0.655 ± 0.206
mixed downsampling (top)	0.034 ± 0.011	0.021 ± 0.007	0.658 ± 0.207
mixed downsampling (bottom)	0.034 ± 0.011	0.022 ± 0.008	0.657 ± 0.207

IV. DISCUSSION AND CONCLUSION

We adapted the AUTOMAP network to obtain DW images starting from the relative k-space data.

The network was trained in five different types of experiment. In the simplest case, we started with a k-space of size 64x64 and obtained an image of 64x64. In this case, the best values of the performance metrics were obtained (RMSE = 0.035±0.004; MAE = 0.022±0.004; SSIM = 0.757±0.057).

Notably, the DW images reconstructed with the network showed no region-specific bias with respect to the original ones, as demonstrated with the difference image (Fig. 3).The next four experiments were performed to reconstruct the original DW images from a reduced k-space.

The network is able to capture the relationship between k-space and DW images, even in experiments performed to reconstruct the original DW images from a reduced k-space (Fig. 2; Table I).

In the mixed downsampling case, the network was trained by considering different downsampling of the k-space, i.e. removing rows from above or below the centre of the k-space. In this case, the output obtained on the 12 test subjects achieved similar performance by applying one of the two downsampling strategies.

Furthermore, it is to note that DW images obtained with the network appear to be less noisy. The intrinsic denoising function of the network may be due to the fact that the network learns the relationship between input and output only by structured associations and since noise is random, it is not learned.

To strengthen this work, further analysis will be performed: in the future, we will apply k-cross validation to better estimate the intrinsic power of the model and to assess it for potential overfitting. Furthermore, to evaluate the sensitivity of our DL reconstructions to the presence of pathology, we will calculate quantitative maps from DW images in both cases (i.e., GT and network) and perform group comparisons between healthy and neurological cohorts. We will therefore determine whether the images reconstructed with the network are able to maintain the details of the original images and are sensitive to pathology (e.g. in lesions of subjects with multiple sclerosis).

Furthermore, it would be useful to check whether it would be possible to further reduce the number of k-space rows without losing the quality of the DW image.

ACKNOWLEDGEMENT

Horizon2020 (Human Brain Project SGA3, Specific Grant Agreement No. 945539), BRC (#BRC704/CAP/CGW), MRC (#MR/S026088/1), Ataxia UK, MS Society (#77), Wings for Life (#169111). CGWK is a shareholder in Queen Square Analytics Ltd.

REFERENCES

[1] D. Le Bihan, R. Turner, P. Douek, and N. Patronas, “Diffusion MR Imaging: Clinical Applications,” *Am. J. Roentgenol.*, vol. 159, no. September, pp. 591–599, 1992.

[2] D. K. Jones, *Diffusion MRI: Theory, Methods, and Applications.* Oxford University Press, 2011.

[3] R. Mezrich, “A perspective on k-space,” *Radiology*, vol. 199, no. 3, pp. 874–875, 1995.

[4] R. Dale, B., Brown, M. and Semelka, *MRI basic principles and applications*. .

[5] R. W. Brown, Y.-C. N. Cheng, E. M. Haacke, M. R. Thompson, and R. Venkatesan, *Magnetic Resonance Imaging: Physical Principles and Sequence Design*, 2nd ed. Wiley Blackwell, 2014.

[6] E. J. Lee, Y. W. Chang, J. K. Sung, and B. Thomas, “Feasibility of deep learning k-space-to-image reconstruction for diffusion weighted imaging in patients with breast cancers: Focus on image quality and reduced scan time,” *Eur. J. Radiol.*, vol. 157, no. November, p. 110608, 2022.

[7] B. Zhu, J. Z. Liu, S. F. Cauley, B. R. Rosen, and M. S. Rosen, “Image reconstruction by domain-transform manifold learning,” *Nat. Publ. Gr.*, no. 3, 2018.

[8] K. M. Hasan, A. L. Alexander, and P. A. Narayana, “Does Fractional Anisotropy Have Better Noise Immunity Characteristics Than Relative Anisotropy in Diffusion Tensor MRI? An Analytical Approach,” *Magn. Reson. Med.*, vol. 51, no. 2, pp. 413–417, 2004.

[9] M. Abadi *et al.*, “TensorFlow: Large-Scale Machine Learning on Heterogeneous Distributed System,” *Netw. Comput. Neural Syst.*, vol. 16, no. 2–3, pp. 121–138, 2005.

[10] Z. Tang, Y. Gao, L. Karlinsky, P. Sattigeri, R. Feris, and D. Metaxas, “OnlineAugment: Online Data Augmentation with Less Domain Knowledge,” *Lect. Notes Comput. Sci. (including Subser. Lect. Notes Artif. Intell. Lect. Notes Bioinformatics)*, vol. 12352 LNCS, pp. 313–329, 2020.

[11] Z. Wang, A. C. Bovik, H. R. Sheikh, and E. P. Simoncelli, “Image quality assessment: From error visibility to structural similarity,” *IEEE Trans. Image Process.*, vol. 13, no. 4, pp. 600–612, 2004.

Distinguishing lymph nodes in head and neck cancer patients using MRI-based radiomics

J. Liu[1], A. Corti[2], G. Calareso[3], V. Corino[1], and L. Mainardi[1]
[1] *Department of Electronics, Information and Bioengineering, Politecnico di Milano, Milan, Italy*
[2] *Department of Chemistry, Materials and Chemical Engineering "Giulio Natta", Politecnico di Milano, Milan, Italy*
[3] *Radiology Department, Fondazione IRCCS Istituto Nazionale dei Tumori di Milano, Milan, Italy*

***Abstract*—The identification of the primary tumor location in patients with head and neck carcinoma of unknown primary involves an invasive and complex diagnostic protocol, thus fostering the development of non-invasive methods. Herein, a radiomic-based approach was proposed to distinguish between oropharynx and nasopharynx primary tumor location from the lymph nodes segmented in magnetic resonance images of head and neck cancer (HNC) patients. A total of 200 HNC patients (100 oropharynx and 100 nasopharynx) were considered. 10-fold cross-validation with class proportion was applied. Five different feature selection methods and five machine learning classification algorithms were tested. Overall, a high classification performance was achieved by all the combined feature selections/machine learning algorithms, with the best results obtained from the support vector machine and the neural networks algorithms with neighborhood component analysis (acc 100%).**

***Keywords*—Radiomics, machine learning, head and neck cancer.**

I. Introduction

Head and neck cancer (HNC) is the seventh most common type of cancer worldwide and affects around 660,000 people each year[1]. It is an aggressive and clinically and biologically heterogeneous disease, which makes patient stratification and treatment decisions challenging. Several different malignant tumors that grow in or around the throat, larynx, nose, sinuses, and mouth are referred to as HNC [2].

Up to 5% of all HNC are carcinomas of unknown primary, i.e., cancer that has spread to lymph nodes in the upper neck, but it is not known where it was first formed in the body[3]. The diagnostic protocol to identify the primary occult tumor is complex and extensive, but it is essential to guide the treatment. The protocol consists of initial clinical assessment (including fiberoptic laryngoscopy) followed by computed tomography and/or magnetic resonance imaging (MRI). When these examinations fail to identify the primary tumor, patients are requested to undergo a whole-body positron emission tomography imaging. Nevertheless, if the primary tumor is still occult, a panendoscopy with biopsy is performed at risk hidden tumor sites. As a result, developing methods to better and non-invasively identify the origin of the unknown primary tumor is a necessity [3], [4].

In recent years, radiomics has emerged to be a valuable tool in precision medicine. It is a novel type of omics that involves extracting high-throughput quantitative features from medical images and developing machine learning prediction models based on the extracted images features. It is capable of characterizing the overall tumor non-invasively while accounting for heterogeneity [5], [6]. Radiomics can also help to better diagnose and classify pathologies, guide treatment selection by forecasting illness evolution and even guide comprehensive postoperative care [7]–[9]. Moreover, radiomics provides a quick, low-cost, and repeatable method for longitudinal monitoring. Thus, it is a valuable tool to be used as clinical decision support [10], [11].

In previous studies, researchers have used radiomic and machine learning techniques in MRI images to build prognostic models in oral and oropharyngeal cancer [12], to predict the treatment response of metastatic cervical lymph nodes in nasopharyngeal carcinoma [13] and to grade and stratify risk in nasopharyngeal carcinoma [14], [15]. Ho et al.[16] aimed to distinguish malignant from benign and extranodal extension (ENE) from non-ENE lymph nodes in HNC patients. However, to the best of our knowledge, the differentiation of lymph nodes with respect to two primary tumor locations (oropharynx or nasopharynx) has never been addressed using radiomics and machine learning techniques. This study aims to fill this gap by developing and validating a novel MRI-based radiomic prognostic model for patients with HNC of unknown primary. The goal is to design the best machine learning model capable of assisting clinicians in predicting the primary tumor site of patients diagnosed with head and neck carcinoma of unknown primary.

II. Patients and Methods

A. Patient description

The dataset is composed by HNC patients collected within the European project BD2Decide (https://www.bd2decide.eu/), which consists in developing personalized prognostic tools for HNC patients with the goal to maximize the outcomes of the treatment while minimizing the effects. Details on the dataset can be found in [17]. In particular, a subgroup of the patients was considered: 100 having the primary tumor location found in oropharynx (OPh) and 100 in the nasopharynx (NPh) area. Table I summarizes the clinical characteristics of these patients. The region of interest (ROI) was defined as cervical lymph nodes manually segmented from T1-weighted (T1w) and T2-weighted (T2w) images acquired using turbo spin-echo pulse sequences. The protocols were approved by the Ethical Committee of the National Cancer Institute of Milan (Italy), and all patients signed an informed consent.

TABLE I: CLINICAL CHARACTERISTICS OF PATIENTS INCLUDED IN THE STUDY.

Patient characteristics	
Median follow-up (range)	48 [27 - 63] months
Gender	
F	123
M	77
Median age (range)	
Primary tumor site	
Oropharynx	100
Nasopharynx	100
AJCC 8th edition	
I	83
II	18
III	47
IV	52
Smoking	
Current/former	100
Never	100

B. Methods

The proposed radiomic workflow was based on a supervised learning approach and consisted in five steps: 1) feature extraction, 2) feature preprocessing, 3) dataset partition, 4) feature selection, 5) model development and validation. The software Matlab R2022b (MathWorks, USA) was adopted to accomplish these steps.

1) Feature extraction

Radiomic features were extracted using Pyradiomics software [18], including shape and size features, first order features, second order features as well as wavelet features [6]. A total of 1072 features were computed. Features stability was assessed using geometrical transformations (translations) of the ROIs as in [19] by applying different translation of the ROI in the positive and negative direction of the x and y, respectively. The entity of the translation was 10% of the length of the bounding box of the tumor in the corresponding direction (x or y). For each patient, the radiomic features were extracted from 5 different ROIs (the original cervical lymph node and the 4 translated versions). Intraclass correlation coefficient (ICC) was used to quantify the stability of each radiomic feature [20]. A feature was considered stable if ICC was higher than 0.75 [21]. The stability analysis was performed to first order, textural and wavelet features. A total of 265 stable radiomic features per patient was thus considered.

2) Feature preprocessing

In the feature preprocessing step, the redundant radiomic features were removed using pairwise correlation. In particular, when a pair of features had an absolute Spearman correlation coefficient above 0.85, the one with lower mean correlation with all the other *n-2* features was selected. After removing the highly correlated features, z-score standardization was performed to the remaining features.

3) Dataset partition

Dataset was partitioned by applying 10-fold cross validation method and considering the class proportion. As a result, a training set and test set composed of 180 and 20 patients were obtained, respectively.

4) Feature selection

To reduce the dimension of the feature set, feature selection was performed on the training set previously obtained. In particular, five feature selection methods were assessed, namely, sequential forward selection (SFS), sequential backward selection (SBS), sequential forward floating selection (SFFS), neighborhood component analysis (NCA) and minimum redundancy maximum relevance (MRMR). Both SFS and SBS feature selection techniques were applied in the study using Matlab function *sequentialfs*. The NCA and MRMR algorithm were assessed using Matlab function *fscnca* and *fscmrmr*, respectively. Concerning the SFFS method, the implemented algorithm consisted mainly in two parts: one that included features and the second that excluded. Every time a feature was included or excluded, an accuracy was obtained and compared with the previous maximum accuracy. When the current accuracy increased by adding (excluding) a feature, that feature was kept in (removed from) the feature set. In this way, the algorithm assessed the existent feature combinations extensively.

5) Model development and validation

After selecting the most relevant features according to each feature selection algorithm, various machine learning models were developed and validated with the test set. The five machine learning models assessed were neural network (NN), naïve Bayes (NB), support vector machine (SVM), decision tree (DT) and bagged trees (BT). Thus, for each feature set obtained from a feature selection method, the five models were trained and tested, resulting in a total of 25 radiomic-based models. To compare the performance of the models, accuracy and area under the ROC curve (AUC) were computed.

III. RESULTS

A systematic analysis was performed to study the influence of the feature selection methods (SFS, SBS, SFFS, NCA and MRMR) and machine learning algorithms (NN, NB, DT, BT and SVM).

Concerning feature selection methods, the summary of feature categories selected by each method is listed in Table II. The total number of features selected by each method was distinct, ranging from 3 features selected by MRMR algorithm and 26 selected by SBS. Overall, wavelet features were more often preferred by the feature selection methods compared to the original features. This might be attributed to the intrinsic characteristics of wavelet radiomic features compared to the original ones, such as: (i) the ability to highlight intricate details and allow for a more nuanced analysis of image texture and morphology at various scales, making them suitable for complex morphologies, and (ii) the increased robustness to noise [22].

TABLE II: LIST OF RADIOMIC FEATURE CATEGORIES SELECTED BY DIFFERENT METHODS

Feature selection	*Original*			*Wavelet*		*Total*
	SS	*FOF*	*SOF*	*FOF*	*S0F*	
SFS	1	1	1	3		6
SBS	2	3	2	6	13	26
SFFS	1		1	2		4
NCA	1	1	2	6	3	13
MRMR			1	2		3

SS: shape and size; FOF: first order feature; SOF: second order feature.

The influence of the feature selection methods and machine learning models were simultaneously compared plotting colormaps as represented in Figure 1, where each colormap refers to a performance metric (accuracy and AUC) obtained by the training set or the test set. The rows represent the feature selection methods (SFS, SBS, SFFS, NCA and MRMR), whereas the columns represent a machine learning model (NN, NB, SVM, DT, BT).

Comparing the colormaps obtained for each machine learning model, it is evident that NN and SVM (first and third columns in the figure) outperformed the other models. In particular, the accuracy ranged between 95% to 100% and the AUC was over 99% in the test set for NN. Similarly, SVM obtained an accuracy between 90% and 100% and an AUC over 92% in the test set. The performance of these models was not largely affected by the feature selection methods. However, there were differences in parsimonies of feature selection methods: MRMR, SFFS and SFS selected less than 10 features (3, 4 and 6, respectively), whereas the SBS and NCA methods selected a larger feature set (26 and 13, respectively).

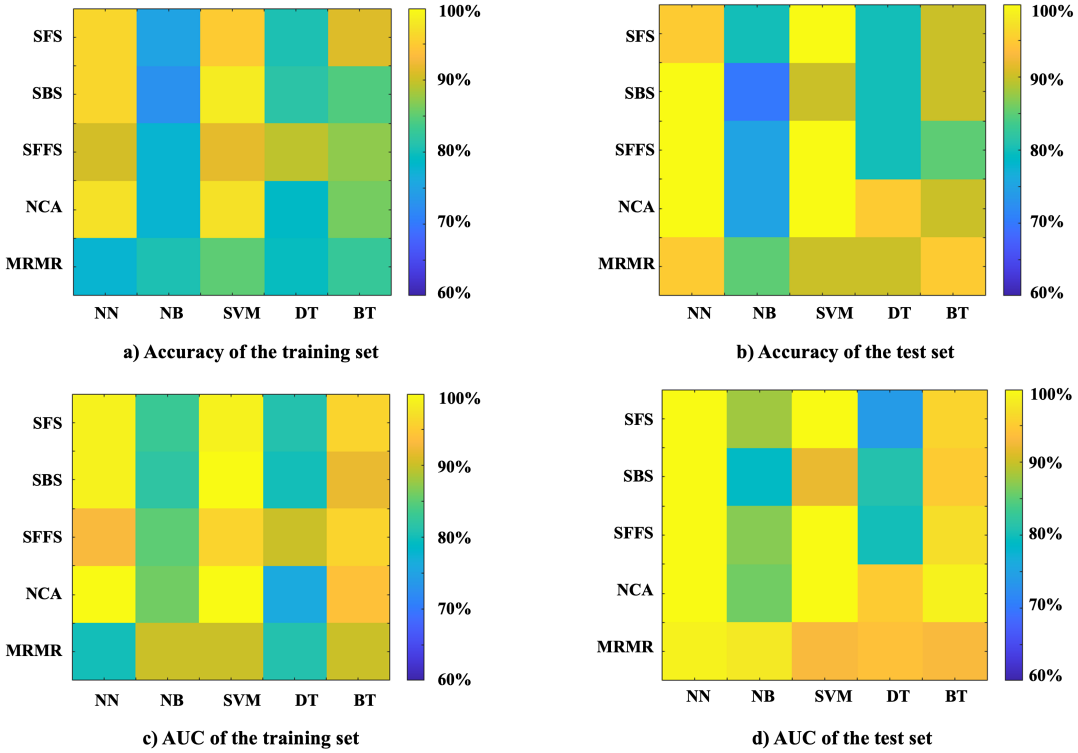


Figure 1: Influence of the feature selection methods in machine learning models

IV. DISCUSSION AND CONCLUSION

In the present study an MRI-based radiomic approach was proposed to develop machine learning models for the identification of the tumor primary location (OPh or NPh) from the lymph nodes segmented in MRI images of HNC patients. Different features selection methods as well as machine learning classification algorithms were tested.

As regards the machine learning models, NN and SVM outperformed NB, DT and BT, with the highest performance reached through the NCA feature selection methods obtaining an accuracy of 100% and an AUC of 100% in the test set. However, overall, the feature selection method did not marginally affect the performance of the models. Thus, the feature selection method resulting in fewer selected features should be preferred, favoring a more parsimonious model. In this case, the ideal trade-off between the number of features and the performance is reached by the six radiomic features selected by SFS together with SVM models. These features are:

- T1w_waveletLHL_firstorder_90Percentile,
- T1w_waveletLHL_firstorder_Median,
- T2w_waveletLLL_firstorder_InterquartileRange,
- T2w_original_shape_LeastAxisLength,
- T2w_original_firstorder_Entropy,
- T2w_original_glcm_Idm.

The first three features are wavelet-based first-order statistics that measure the distribution of pixel values in the wavelet sub-bands of T1w and T2w images. The fourth feature, “LeastAxisLength”, is a shape-based feature that measures the length of the shortest axis of the tumor in a T2w image. The fifth feature, “Entropy”, measures the randomness and complexity of the texture in a T2w image. The final feature,

"Idm", is a grey-level co-occurrence matrix feature that measures the local homogeneity of the texture in a T2w image.

In this study a simple binary classification problem was addressed, by considering only the two most prevalent primary tumor locations of HNC of the BD2Decide database patients (i.e., NPh and OPh). Thus, the excellent results that were achieved in this study, should be confirmed in future works by considering the more realistic and complex scenario characterized by the presence of other primary tumor locations such as larynx, oral cavity and hypopharynx.

In conclusion, the approach proposed herein demonstrated the potentiality of radiomics in the discrimination between OPh and NPh primary tumor locations from the lymph nodes in HNC patients. These findings suggest that radiomics can provide a remarkable contribution as preliminary assessment of the primary tumor location in head and neck carcinomas of unknown primary.

REFERENCES

[1] H. Sung *et al.*, "Global Cancer Statistics 2020: GLOBOCAN Estimates of Incidence and Mortality Worldwide for 36 Cancers in 185 Countries," *CA Cancer J Clin*, vol. 71, no. 3, pp. 209–249, May 2021, doi: 10.3322/caac.21660.

[2] L. Q. M. Chow, "Head and Neck Cancer," *New England Journal of Medicine*, vol. 382, no. 1, pp. 60–72, Jan. 2020, doi: 10.1056/NEJMra1715715.

[3] T. Kennel, R. Garrel, V. Costes, P. Boisselier, L. Crampette, and V. Favier, "Head and neck carcinoma of unknown primary," *Eur Ann Otorhinolaryngol Head Neck Dis*, vol. 136, no. 3, pp. 185–192, 2019.

[4] F. R. Miller, A. B. Karnad, T. Eng, D. H. Hussey, H. Stan McGuff, and R. A. Otto, "Management of the unknown primary carcinoma: Long-term follow-up on a negative PET scan and negative panendoscopy," *Head & Neck: Journal for the Sciences and Specialties of the Head and Neck*, vol. 30, no. 1, pp. 28–34, 2008.

[5] A. la Greca Saint-Esteven *et al.*, "Systematic Review on the Association of Radiomics with Tumor Biological Endpoints," *Cancers (Basel)*, vol. 13, no. 12, p. 3015, Jun. 2021, doi: 10.3390/cancers13123015.

[6] V. D. A. Corino *et al.*, "Radiomic analysis of soft tissues sarcomas can distinguish intermediate from high-grade lesions," *Journal of Magnetic Resonance Imaging*, vol. 47, no. 3, pp. 829–840, Mar. 2018, doi: 10.1002/jmri.25791.

[7] G. Kothari, "Role of radiomics in predicting immunotherapy response," *J Med Imaging Radiat Oncol*, vol. 66, no. 4, pp. 575–591, Jun. 2022, doi: 10.1111/1754-9485.13426.

[8] M. Bologna *et al.*, "Relevance of apparent diffusion coefficient features for a radiomics-based prediction of response to induction chemotherapy in sinonasal cancer," *NMR Biomed*, vol. 35, no. 4, Apr. 2022, doi: 10.1002/nbm.4265.

[9] B. Zhang *et al.*, "Advanced nasopharyngeal carcinoma: pre-treatment prediction of progression based on multi-parametric MRI radiomics," *Oncotarget*, vol. 8, no. 42, pp. 72457–72465, Sep. 2017, doi: 10.18632/oncotarget.19799.

[10] Z. Peng *et al.*, "Application of radiomics and machine learning in head and neck cancers," *Int J Biol Sci*, vol. 17, no. 2, p. 475, 2021.

[11] A. J. Wong, A. Kanwar, A. S. Mohamed, and C. D. Fuller, "Radiomics in head and neck cancer: from exploration to application," *Transl Cancer Res*, vol. 5, no. 4, p. 371, 2016.

[12] S. W. Mes *et al.*, "Outcome prediction of head and neck squamous cell carcinoma by MRI radiomic signatures," *Eur Radiol*, vol. 30, no. 11, pp. 6311–6321, Nov. 2020, doi: 10.1007/s00330-020-06962-y.

[13] H. Xu, J. Liu, Y. Huang, P. Zhou, and J. Ren, "MRI-based radiomics as response predictor to radiochemotherapy for metastatic cervical lymph node in nasopharyngeal carcinoma," *British Journal of Radiology*, vol. 94, no. 1122, Jun. 2021, doi: 10.1259/bjr.20201212.

[14] Q. Feng *et al.*, "Radiomics Analysis and Correlation With Metabolic Parameters in Nasopharyngeal Carcinoma Based on PET/MR Imaging," *Front Oncol*, vol. 10, p. 1619, Sep. 2020, doi: 10.3389/fonc.2020.01619.

[15] E. H. Zhuo *et al.*, "Radiomics on multi-modalities MR sequences can subtype patients with non-metastatic nasopharyngeal carcinoma (NPC) into distinct survival subgroups," *Eur Radiol*, vol. 29, no. 10, pp. 5590–5599, Oct. 2019, doi: 10.1007/S00330-019-06075-1.

[16] T. Y. Ho, C. H. Chao, S. C. Chin, S. H. Ng, C. J. Kang, and N. M. Tsang, "Classifying Neck Lymph Nodes of Head and Neck Squamous Cell Carcinoma in MRI Images with Radiomic Features," *J Digit Imaging*, vol. 33, no. 3, pp. 613–618, Jun. 2020, doi: 10.1007/s10278-019-00309-w.

[17] S. Cavalieri *et al.*, "Development of a multiomics database for personalized prognostic forecasting in head and neck cancer: The Big Data to Decide EU Project," *Head Neck*, vol. 43, no. 2, pp. 601–612, Feb. 2021, doi: 10.1002/hed.26515.

[18] J. J. M. van Griethuysen *et al.*, "Computational Radiomics System to Decode the Radiographic Phenotype," *Cancer Res*, vol. 77, no. 21, pp. e104–e107, Nov. 2017, doi: 10.1158/0008-5472.CAN-17-0339.

[19] M. Bologna *et al.*, "Assessment of Stability and Discrimination Capacity of Radiomic Features on Apparent Diffusion Coefficient Images," *J Digit Imaging*, vol. 31, no. 6, pp. 879–894, Dec. 2018, doi: 10.1007/s10278-018-0092-9.

[20] K. O. McGraw and S. P. Wong, "Forming inferences about some intraclass correlation coefficients.," *Psychol Methods*, vol. 1, no. 1, pp. 30–46, Mar. 1996, doi: 10.1037/1082-989X.1.1.30.

[21] T. K. Koo and M. Y. Li, "A Guideline of Selecting and Reporting Intraclass Correlation Coefficients for Reliability Research," *J Chiropr Med*, vol. 15, no. 2, pp. 155–163, Jun. 2016, doi: 10.1016/j.jcm.2016.02.012.

[22] S. Rizzo *et al.*, "Radiomics: the facts and the challenges of image analysis," *European Radiology Experimental*, vol. 2, no. 1. Springer, Dec. 01, 2018. doi: 10.1186/s41747-018-0068-z.

A deep learning approach for the analysis of voxel composition in magnetic resonance imaging

M. M. Autorino[1], S. Franceschini[1], M. Ambrosanio[2], V. Pascazio[1] and F. Baselice[1]
[1] *University of Naples Parthenope, Dipartimento di Ingegneria;*
[2] *University of Naples Parthenope, Dipartimento di Scienze Economiche, Giuridiche, Informatiche e Motorie;*

***Abstract*—This work proposes a machine learning algorithm for analyzing the composition of each voxel in Magnetic Resonance Imaging framework. Since the voxel defines the spatial resolution limit of the system, conventional imaging approaches are not able to distinguish an homogeneous voxel (composed by a single tissue) from an heterogeneous one (composed by several tissues). It causes loss of useful diagnostic information not allowing to detect tissues smaller than the voxel dimension. This paper proposes a neural network detection algorithm that, exploiting several acquisitions of the same voxel, is able to distinguish heterogeneous voxels from the homogeneous cases. A synthetic dataset was designed for the neural network training: homogeneous and heterogeneous voxels were simulated and several imaging sequences have been considered to acquire voxel signals. Results seem to be promising, in particular regarding on its application in a real clinical context: in order to analyse the voxel, the algorithm requires a reduced number of acquisitions (that means reduced time for the clinical examination) and its low computational complexity allows a quick analysis of all voxels of the examined body slice, as proved by the algorithm validation through a test on a real magnetic resonance data.**

***Keywords*—Magnetic resonance imaging, intra voxel analysis, machine learning, deep learning**

I. INTRODUCTION

Magnetic Resonance Imaging (MRI) is one of the most used method in diagnosis, staging and follow-up of disease for a variety of conditions. It is based on the non-invasive and non-ionising interaction between hydrogen protons and magnetic fields and the image acquisition occurs thanks to radio-frequency (RF) pulses applied to the interested area. In particular, RF pulses create a non-equilibrium state and after they have been switched off a relaxation phenomenon arises, characterised by two constants: *spin-lattice* relaxation time T_1 and *spin-spin* relaxation time T_2 [1]. Different tissues present different values of relaxation times and diseased tissues often have substantially altered relaxation time compared to healthy ones [2] - [4]. These differences form the basis for introducing contrast into the MR image. Depending on the application, the involved tissues and the acquisition sequence, images based on T_1 differences (named T_1-*weighted* images) or images based on T_2 differences (named T_2-*weighted* images) could be acquired and exploited for the diagnosis.

During an MRI acquisition, the investigated body area to scan results divided in voxels, whose number and size depend on to the system resolution. Per each voxel, the information about its tissues composition is brought with the respective pixel value in the MR image in term of T_1 or T_2. In case of homogeneous voxel (composed of a single tissue), pixel value describes exactly that single contribute. In case of an heterogeneous voxel (composed of two or more tissues), the respective pixel value describes it as the mean value of all the contributes, making it difficult to discriminate the quantity of the involved tissues and their nature. It involves that tissues smaller than the voxel dimension cannot be discriminated and detected in the MR image.

From a diagnostic point of view this represents an obstacle since in many pathologies the possibility of detecting the smaller diseased tissue could be very helpful in term of prevention and early diagnosis. In cancer lesions, for instance, it is well known that the sooner a diseased tissue is detected, the better is the prognosis [5]-[7].

In this framework, in order to avoid a further improvement of the spatial resolution of the system, a novel methodology was proposed in scientific literature, known as *Intra Voxel Analysis* (IVA) [8]. It works on T_2-*weighted* images and is able to analyse an heterogeneous voxel performing the detection of the number of contributions within it and the estimation of which tissues are involved, generating a T_2 distribution instead of a single value. This method was validated on a real brain MR image, providing to be promising and overcoming the standard non-negative least square fitting method [9] in term of noise-robustness and number of necessary acquisitions. Nevertheless the approach is not very suitable in clinical near real-time context, because of its computational complexity and time cost.

Also Yu Thomas at al. [10] proposed a methodology to recover the T_2 voxel distribution, in particular for the application on myelin water fraction mapping in brain tissues. Differently form [8], they exploit a machine learning algorithm that demonstrates to recover more accurate, robust and plausible T_2 distribution than standard methods. Although it overcomes the limit of the IVA approach in term of less computational complexity and time cost, it requires a huge number of acquisitions compromising the suitability of this approach in the real clinical context. High number of acquisitions means a strong increase in time for the medical examination.

This work aims to propose the a similar machine learning approach used in [10] exploiting its computational speed and reduced complexity, but in a simplified scenario: the proposed algorithm is able to detect pixels corresponding to heterogeneous voxels (distinguish them from the homogeneous case) but, differently form [8] and [10], it does not reconstruct

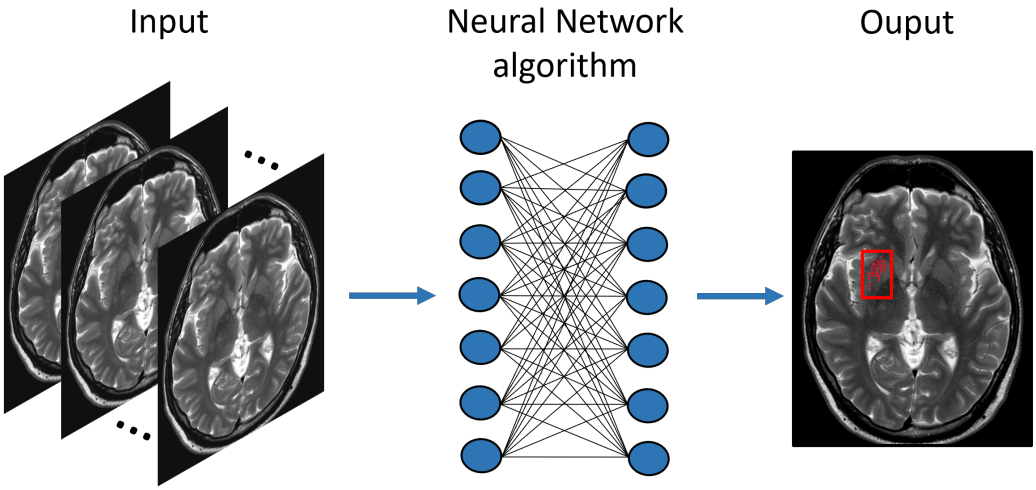


Fig. 1: Simplified sketch of the proposed machine learning algorithm. In order to detect pixels corresponding to heterogeneous voxels (highlighted in red in the output image), the neural network algorithm exploits L acquisitions of all the voxels of the body slice (the input images stack)

the respective T_2 distribution.

This simplification allows a quick analysis of the whole MR image and requires, at the same time, an acceptable number of acquisitions, making the method suitable in a clinical near real-time context and in the framework of prevention and staging of pathological patients, which need fast and frequent follow-up [11].

II. Mathematical model

Through several available sequences in the framework of MR image acquisition, the spin echo (SE) [1] is the one exploited in this paper.

According to SE and focusing on the particular case of T_2-*weighted* image acquisition [8], the signal amplitude of each voxel can be modeled as:

$$g(l) = ke^{-T_E(l)/T_2}, l = 1, ..., L \tag{1}$$

where k and T_2 depend on the tissues composing the voxel and T_E is an imaging parameter.

More in detail, k is a coefficient that takes in account proton density and *spin-lattice* relaxation time and T_2 is the *spin-spin* relaxation time.

The imaging parameter T_E is the vector of the *echo* times and allows to obtain several acquisitions of the same voxel, as many as its length L [12].

The hypothesis under the Eq. (1) is that the signal g comes form an homogeneous voxel since a single tissue relax back with its decay constant T_2. Actually, an heterogeneous scenario is possible [1], where more than one tissues compose the voxel. In this framework, considering the simplified case of a maximum of two tissues, the signal can be modeled as:

$$g(l) = k(1)e^{-T_E(l)/T_2(1)} + k(2)e^{-T_E(l)/T_2(2)}, l = 1, ..., L \tag{2}$$

where $\{k(1),\ T_2(1)\}$ and $\{k(2),\ T_2(2)\}$ describe, respectively, the two tissues merged in the voxel.

III. The proposed method

In this paper, a supervised machine learning [13] approach is exploited to analyse each voxel composition in the framework of magnetic resonance imaging. More in detail, a neural network (NN) algorithm is trained in order to detect heterogeneous voxels which present two tissues composing their volume.

As shown in Fig. 1, the algorithm takes as input several acquisitions of the examined body slice. Through the voxel-wise analysis done by NN inner layers, it returns the detection response per each voxel classifying it as homogeneous or heterogeneous. The output is a map in which pixels corresponding to the detected heterogeneous voxels are highlighted.

A. Neural Network Architecture

In the framework of neural network algorithms, a fully connected architecture was exploited: two fully connected layers and forty-five nodes per each layer. The activation function used was the ReLU one [14]. Batch normalization [15] was added to the first layer showing better learning and faster processing. Log SoftMax function after the last layer is the one expected by the negative log likelihood loss function used. Since the analysis is made voxel-wise, input layer of the neural network presents a number of nodes equal to L, as the number of acquisitions of the examined voxel, while the output layer presents two nodes assuming the voxel probability of belonging to homogeneous and heterogeneous case.

About the training, the optimization algorithm used was Adam [16] and the training parameters were: learning rate equal to 10^{-4}, batch size 64 and number of epoch equal to 30. The analysis have been made on a 24 GB NVIDA Quadro RTX 6000 gpu, through PyTorch framework, in Python.

B. Dataset

In order to train the proposed neural network architecture, a synthetic dataset has been generated for a total of one million {*input*, *target*} samples. Since the *input* part is the vector of the L acquisitions, first step was the design of synthetic voxels, second step their acquisition through the imaging sequence. One million voxels differing from their nature and composition was designed changing the two tissue characteristic parameters T_2 and k. Regarding T_2, two possible scenarios have been considered: homogeneous voxel composed by a single tissue and heterogeneous voxel composed by two tissues. Both cases present a contribute of an healthy tissue. In addition, the heterogeneous case presents a second contribute simulating a diseased tissue. Since this work is focused on brain imaging, their value must be coherently chosen. According to [17], T_2 values of healthy tissue are chosen randomly from uniformly distributed range [40, 150]ms, while values for tissue out of the healthy range are chosen randomly from uniformly distributed range [110, 250]ms. Moreover, in the heterogeneous case the volume percentage occupied by the two tissues varies per each sample. First contribute occupies a random value form 20% to 80% of the entire voxel volume, while the second contribute occupies the remaining part. About k, per each voxel it is chosen randomly from the uniformly distributed range [10^3, 10^5], according to [8] dataset and proportional to its image amplitude.

Once all synthetic voxels were generated, second step was their acquisition through the spin ehco sequence. According to it, the imaging parameter T_E was set in range [10, 350]ms, but several simulations have been done changing its length and spacing. Therefore, per each fixed T_E configuration, a new dataset made by one million samples was generated.

For a more realistic scenario, the whole datasets was corrupted by additive white Gaussian noise with mean SNR = 20dB.

Moreover, in order to obtain a good training of the designed neural network algorithm, balanced datasets were simulated splitting in half homogeneous and heterogeneous cases.

Since the proposed approach solve a detection problem, *target* values are labels representing the voxel class: homogeneous or heterogeneous.

IV. Analysis and Results

In this framework, an analysis was made to find the best spin echo acquisition scheme that lets the designed neural network better performs in the purpose. Once T_E range was selected ([10, 350]ms), seven cases were considered, in which T_E is linearly spaced in its range but differs in its length. The first case presents $L = 4$, the last $L = 10$.

In order to test the neural network algorithm considering all these configurations, seven datasets were generated, each one made of one million samples. Per each dataset, the 90% was used for the training and the last 10% for the validation.

Once the neural netoworks were trained, for the purpose of evaluating their performance, one testset per each dataset was simulated, each made by twenty-five thousand samples, splitted equally between homogeneous and heterogeneous cases.

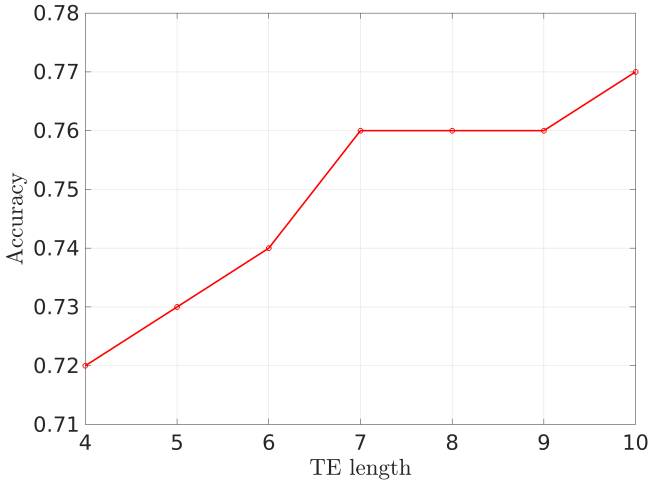


Fig. 2: Accuracy values achieved per each different acquisition scheme. Per each case T_E vector is linearly spaced in range [10, 350]ms, but several length were tested, from 4 to 10

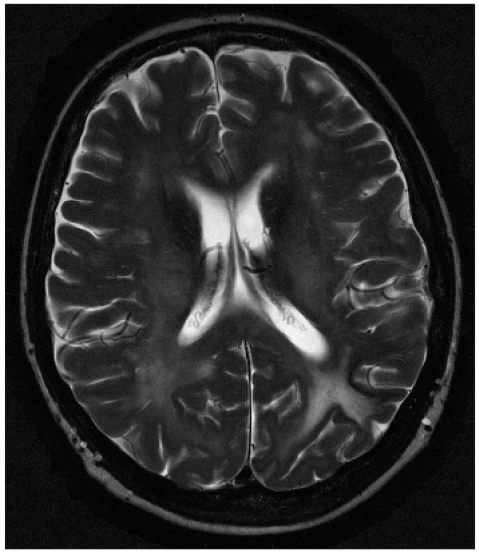
The analysis in Fig. 2 shows the comparison among the achieved results. It is possible to notice performance increasing with the increasing of the number of acquisitions L. Nevertheless, after $L = 7$ the improvement is not so sensitive. According to this scenario, T_E values are [10, 66.7 123.3 180 236.7 293.3, 350]ms and it represents a good compromise between the reached accuracy (76%) and length L, since the fewer are the acquisition the less is the time request by the clinical examination.

A real brain MR data was also available for the validation of the proposed method. It is an axial slice of the head, made of 351x426 pixels. It is composed by five spin echo images acquired with T_E = [82.45, 130, 180, 250, 350]ms. Despite it follows the same acquisition sequence considered in the simulation (i.e. spin echo sequence), this data does not fix exactly the best configuration found in the simulated scenario: T_E belongs to the range [10, 350]ms range, but differs for spacing (it is not linearly spaced) and length (five instead of seven). Consequently, in order to train the neural network in according to the real data acquisition parameters, a new synthetic dataset was generated assuming the right echo times.

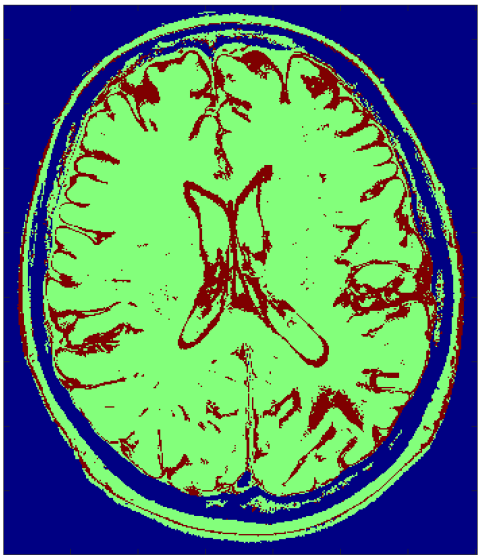
The testing result on the real data is the one shown in Fig. 3(b). According to [8], heterogeneous voxels are detected in the lesion region. The same results is obtained in boundary areas. Since they represent non-homogeneous transition areas between tissues, multiple contributes in a single voxel are expected.

V. Conclusions

This manuscript proposes a neural network algorithm to analyse voxels in MRI framework. In particular, it demonstrate to detect heterogeneous voxels distinguish them from the homogeneous cases achieving a good level of accuracy (more



(a)



(b)

Fig. 3: Validation of the proposed method in a real case study. In (a) a single slice of the available real MR brain data is shown, where an edema lesion is present in the occipital region (bottom right of the image). In (b) the result of the proposed detection algorithm. Blu is the background, green represents homogeneous voxels, red the heterogeneous ones.

than 70% considering a noisy scenario with mean SNR = 20 dB).

As proved by the validation of the method through the available real MR data, despite the approach works voxel-wise, it analyses all the brain image voxels in less than 2s. In addition, both in simulated and real data, a standard imaging sequence was used (i.e. the spin echo one), allowing the proposed detector to be used with any already existing MRI systems. Finally, the algorithm needs an acceptable number of acquisitions without involving an increase in time for the medical examination. All these features make the method exploitable in the clinical context and in near real-time applications.

Future work will focus on the extension of the approach to any other available imaging sequences as well as to other anatomical body areas.

A multi-step approach is also possible, combining the proposed neural network algorithm with an other technique able to add quantitative information on tissues composing the heterogeneous voxels, like [8],[9]. Since these algorithms are typically characterized by high computational time and complexity, the combination with the proposed detector, considered as pre-screening procedure, can be, potentially, a good candidate for almost real time analyses.

REFERENCES

[1] Barrie Smith, N. Webb, A. "Introduction to Medical Imaging: Physics, Engineering and Clinical Applications", *Cambridge University Press*. 2010

[2] Song, N., Wang, T., Zhang, D., Wang, Z., Zhang, S., Yu, J., Cai, L., Ma, A., Zhang, Q. & Chen, Z. The value of relaxation time quantitative technique from synthetic magnetic resonance imaging in the diagnosis and invasion assessment of prostate cancer. *Zhonghua Yi Xue Za Zhi*. **102**, 1093-1099 (2022)

[3] Larsson, H., Barker, G. & MacKay, A. Nuclear magnetic resonance relaxation in multiple sclerosis.. *Journal Of Neurology, Neurosurgery, And Psychiatry*. **64** pp. S70-6 (1998)

[4] McFarland, E., Mayo-Smith, W., Saini, S., Hahn, P., Goldberg, M. & Lee, M. Hepatic hemangiomas and malignant tumors: improved differentiation with heavily T2-weighted conventional spin-echo MR imaging.. *Radiology*. **193**, 43-47 (1994)

[5] Khalil, H., Patterson, S. & Panicek, D. Hepatic lesions deemed too small to characterize at CT: prevalence and importance in women with breast cancer. *Radiology*. **235**, 872-878 (2005)

[6] Koscielny, S. The rationale for early diagnosis of cancer: the example of breast cancer. *Acta Oncologica*. **38**, 295-303 (1999)

[7] Desai, S. Early diagnosis of spinal tuberculosis by MRI. *The Journal Of Bone And Joint Surgery. British Volume*. **76**, 863-869 (1994)

[8] Ambrosanio, M., Baselice, F., Ferraioli, G., Lenti, F. & Pascazio, V. Intra voxel analysis in magnetic resonance imaging. *Magnetic Resonance Imaging*. **37** pp. 70-80 (2017)

[9] Whittall, K. & MacKay, A. Quantitative interpretation of NMR relaxation data. *Journal Of Magnetic Resonance (1969)*. **84**, 134-152 (1989)

[10] Yu, Thomas, et al. "Model-informed machine learning for multi-component T2 relaxometry." Medical Image Analysis 69 (2021): 101940

[11] Eggen, A., Wind, T., Bosma, I., Kramer, M., Laar, P., Weide, H., Hospers, G. & Jalving, M. Value of screening and follow-up brain MRI scans in patients with metastatic melanoma. *Cancer Medicine*. **10**, 8395-8404 (2021)

[12] Liu, J., Nieminen, A. & Koenig, J. Calculation of T1, T2, and proton spin density images in nuclear magnetic resonance imaging. *Journal Of Magnetic Resonance (1969)*. **85**, 95-110 (1989)

[13] Mathew, A., Amudha, P. & Sivakumari, S. Deep learning techniques: an overview. *International Conference On Advanced Machine Learning Technologies And Applications*. pp. 599-608 (2021)

[14] Dubey, S., Singh, S. & Chaudhuri, B. Activation functions in deep learning: A comprehensive survey and benchmark. *Neurocomputing*. (2022)

[15] Ioffe, S. & Szegedy, C. Batch normalization: Accelerating deep network training by reducing internal covariate shift. *International Conference On Machine Learning*. pp. 448-456 (2015)

[16] Kingma, D.P.; Ba, J. ADAM: A method for stochastic optimization. *In Proceedings of the 3rd International Conference for Learning Representations—ICLR*, 2015, San Diego, CA, USA, 7–9 May 2015.

[17] Baselice, F., Ferraioli, G. & Pascazio, V. A Bayesian approach for relaxation times estimation in MRI. *Magnetic Resonance Imaging*. **34**, 312-325 (2016)

Association between inflammation and brain microstructure in First Episode Psychosis investigated with DTI

L. Squarcina[1], G. Delvecchio[2], M. Pavan[1], C. Perlini[3,4], M. Bellani[4,5], A. Lasalvia[4], A. Finardi[6], M. Ruggeri[4,5], R. Furlan[6], P. Brambilla[1,2]
[1]*Department of Pathophysiology and Transplantation, University of Milan, Milan, Italy*
[2]*Fondazione IRCCS Ca' Granda, Ospedale Maggiore Policlinico, Milan, Italy*
[3]*USD Clinical Psychology, Azienda Ospedaliera Universitaria Integrata (AOUI) of Verona, Verona, Italy*
[4]*Department of Neurosciences, Biomedicine and Movement Sciences, University of Verona, Verona, Italy*
[5]*UOC of Psychiatry, Azienda Ospedaliera Universitaria Integrata (AOUI) of Verona, Verona, Italy*
[6]*Clinical Neuroimmunology Unit, Institute of Experimental Neurology, IRCCS Ospedale San Raffaele, Milan, Italy*

***Abstract*—Diffusion tensor imaging (DTI) allows the non-invasive characterization of white matter integrity, thanks to a model fitting the diffusion profile of water inside the brain. It has been demonstrated that patients affected by psychosis show alterations in the white matter (WM), when investigated with DTI. At the same time, an involvement of immune system in psychosis has been shown, with pro-inflammatory changes. In this study, we combined the analysis of immunomarkers and white matter integrity, in a DTI-general linear model (GLM) framework, to identify possible interactions. We consider a sample of 100 subjects (DTI and peripheral blood immunomarkers, 29 first episode psychosis (FEP) patients, 26 chronic patients and 45 healthy controls), and applied a TBSS analysis with multiple aims: identifying differences in WM integrity between groups; identifying relationships between WM and immune system markers; identifying interactions between FA, immune system and group. We found, in aligmnent with the existing literature, that chronic patients show altered WM in respect both to controls and to FEP patients. Additionally, in FEP and chronic patients we found correlations between a pro-inflammatory status and WM alterations. Finally, we also demonstrated an interaction between group, WM integrity and immune system in the comparison between HC, FEP and chronic patients.**

***Keywords*—DTI, imaging, GLM, immunomarkers**

I. Introduction

Psychosis is a symptom common to several pathological conditions that involves alteration in the relationship with reality. The first episode of psychosis (FEP) is defined as the first occasion on which the subject manifests psychotic symptoms. It has been demonstrated that FEP patients show altered brain microstructure [1], measured with diffusion tensor imaging (DTI). DTI allows the quantification of diffusion indexes such as fractional anisotropy (FA), which measures how much one diffusion direction is prevailing on the others inside a particular voxel, or mean diffusivity (MD), related to the magnitude of the diffusion. In a 2013 meta-analysis [1] several white matter areas where significant FA changes can be observed in FEP were defined. In particular, a decrease in FA was identified in various regions, and the most significant changes were located in the corpus callosum, the uncinate fasciculus and the longitudinal fasciculus. With regard to the immune system, in FEP, a significant increase in blood levels of interleukin-1β (IL-1β), interleukin 12 (IL-12), interferon-γ (IFNγ), transforming growth factor α (TGFα) and especially tumor necrosis factor α (TNFα) has been ascertained [2], [3]. Since these are acute phase cytokines, they would probably indicate the presence of a proinflammatory state at a peripheral level. This state could have repercussions on the brain since these molecules are capable of altering the permeability of the blood-brain barrier. Regarding brain-derived neurotrophic factor (BDNF), a decrease in FEP was observed compared to healthy controls. This alteration tends to be accentuated when the psychosis becomes chronic [4]. In this work, we aim to investigate the complex interrelations between immune system and white matter in psychosis, at the early stages and in chronicity.

II. Materials and Methods

A. Subjects recruitment and data acquisition

100 subjects were involved in this study. Specifically, we included patients following a first psychotic episode (FEP; n = 29, 28.0 $\pm$ 10.1 years old (y.o.), 16 males), patients with chronic psychotic disorders (e.g., schizophrenia, bipolar disorder, and major depressive disorder) (CHR; n = 26, 35.0 $\pm$ 12.4 y.o., 18 males), and a group of healthy controls with no history of psychiatric disorders (HC; n = 45, 35.3 $\pm$ 12.4 y.o., 16 males). All the procedures were approved by the Biomedical Ethics Committee of the Azienda Ospedaliera di Verona and are in accordance with the Helsinki Declaration of 1975. All subjects signed a written informed consent to the protocol. MRI data were acquired on a 3T machine (Philips Achieva) with the following parameters: 35 diffusion directions, 1 non-diffusion weighted volume, b-value 1000 mm/s^2, TR = 5 s, TE = 0.12 s, flip angle = 90°, voxel size 1x1

mm^2, slice thickness 3 mm, matrix 256x256x50. Whole blood samples were collected in 2.5 ml PaxGene vials (Qiagen) and stored at -80 °C within 2–6 h of collection. RNA was extracted using the QIAsymphony PAXgene Blood RNA Kit. Real-Time qPCR for the analysis of Interleukin-10 (IL-10), Interleukin-12 alpha (IL-12α), Interleukin-6 (IL-6), Interleukin-1 beta (IL-1β), interferon gamma (IFNγ), Tumor necrosis factor alpha (TNFα) and Brain Derived Neurotrophic Factor (BDNF) was performed.

B. MRI data pre-processing

The acquired images were analysed using FSL (FMRIB Software Library) [5]. The images were skull-stripped using the brain extraction tool of FSL, and distortions due to eddy currents and small head motion were corrected aligning the diffusion-weighted images to the baseline using affine transformations (eddy currents correction tool from FSL). Subsequently, the data were fitted to the tensor model, as implemented in the function FDT in FSL, and FA values were obtained. TBSS [6] is a multiple steps procedure. Briefly, all FA images are non-linearly registered to a standard space and a mean FA image is created. Then, a skeleton consisting of the center of white matter tracts is obtained, which represents the center of the WM tracts common to all subjects.

C. Statistical Analysis

Data were then processed with voxel-wise cross-subject statistics, using FSL randomise function [7] ($p<0.05$). We corrected the results for multiple comparisons using threshold-free cluster enhancement (TFCE [8]), an approach similar to cluster-based thresholding. Age, gender and education were treated as nuisance variables. We used three distinct general linear model (GLM) approaches to investigate:

a) The differences in FA between groups
b) The influence of the immunological markers on FA in patients (FEP or CHR)
c) The interaction of immunological markers, FA and group (HC, FEP, CHR)

III. Results

A. Differences in microstructural integrity between groups

CHR and FEP showed statistically significant differences, after correcting for multiple comparisons, in corpus callosum, internal and external capsula, left longitudinal inferior fasciculus, and frontal and inferior gyri (Figure 1). The comparison between HC and CHR showed diffuse differences similar to those observed between CHR and FEP, located in the major white matter tracts (Figure 1). No significant differences were found between HC and FEP.

B. Regression between FA and immunomarkers

In the case of FEP patients, the only cytokine in which a statistically significant trend was observed was BDNF, which has an influence on FA of the left superior longitudinal fasciculus, as depicted in Figure 2. The linear regression between expression of BDNF and FA is depicted, as in all subsequent figures, for a representative voxel (the voxel with the lowest p-value was chosen among all the voxels with significant results). It is to be noted that the regression depicted in the figures has only representation purpose.

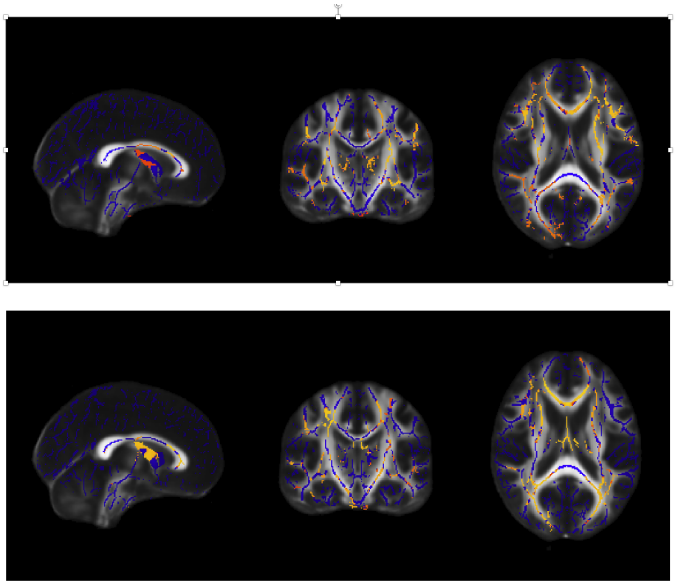


Fig. 1: (A) Results of TBSS comparison between FEP and CHR (B) Results of TBSS comparison between CHR and HC. Blue voxels: White matter skeleton; red-yellow voxels: significant voxels after multiple comparison correction.

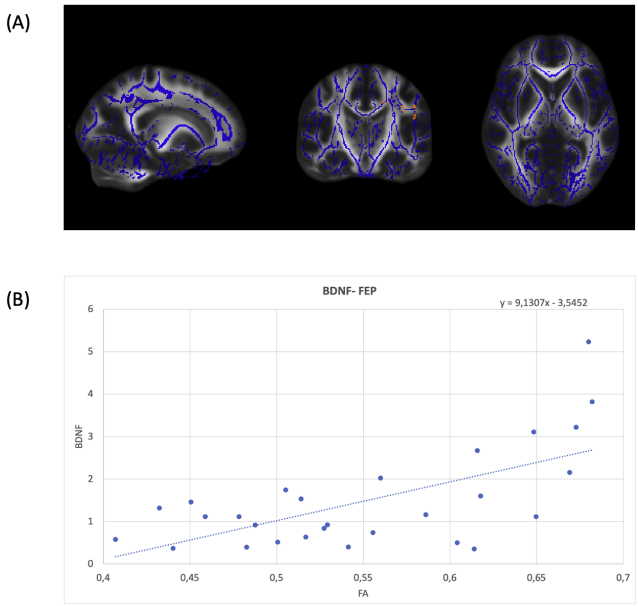


Fig. 2: (A) White matter tracts with significant correlation between FA and BDNF in FEP. The highlighted area is located in the left longitudinal superior fasciculus. Blue voxels: White matter skeleton; red-yellow voxels: significant voxels after multiple comparison correction. (B) Linear relationship between FA and BDNF for a representative voxel (p=0.02)

In CHR patients, a statistically significant trend was found

in the case of IFNγ. The white matter tracts in which the correlation is highlighted in these subjects can be viewed in Figure 3, and are located in particular in the splenium of corpus callosum and in the right internal capsule.

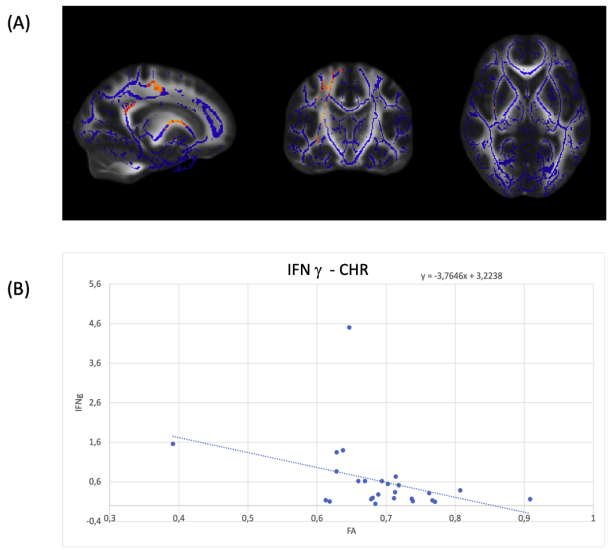


Fig. 3: (A) White matter tracts with significant correlation between FA and IFNγ in CHR. The highlighted area is located in the splenium of corpus callosum. Blue voxels: White matter skeleton; red-yellow voxels: significant voxels after multiple comparison correction. (B) Linear relationship between FA and INFγ for a representative voxel (p=0.03)

C. Interaction of FA, group and immunomarkers

This analysis showed the presence of differences regarding FEP compared to HC when assessing TNFα expression. In Figure 4 it is possible to observe that these differences occur at the level of the corpus callosum, in particular at the level of the genu. While in the controls a negative correlation was observed, in FEP subjects the correlation is positive. A significant interaction was found for TNFα also comparing FEP and CHR. In this case it mainly involves the left superior longitudinal fasciculus and the white matter of the left medial frontal gyrus (Figure 5). In this case, both in CHR and in FEP there is a negative correlation between expression of the pro-inflammatory cytokine and FA. However, this relationship is more evident in chronic patients. In fact, while in FEP patients the concentration of TNFα does not vary significantly depending on the FA values, in CHR patients the relationship is marked.

Finally, in the comparison between FEP and CHR a different relationship emerged also between FA and IFNγ expression. It appears to be more extensive than TNFα and is expressed in the occipital area, the frontal corpus callosum, the anterior cingulate and the white matter of the superior occipital gyrus (Figure 6).

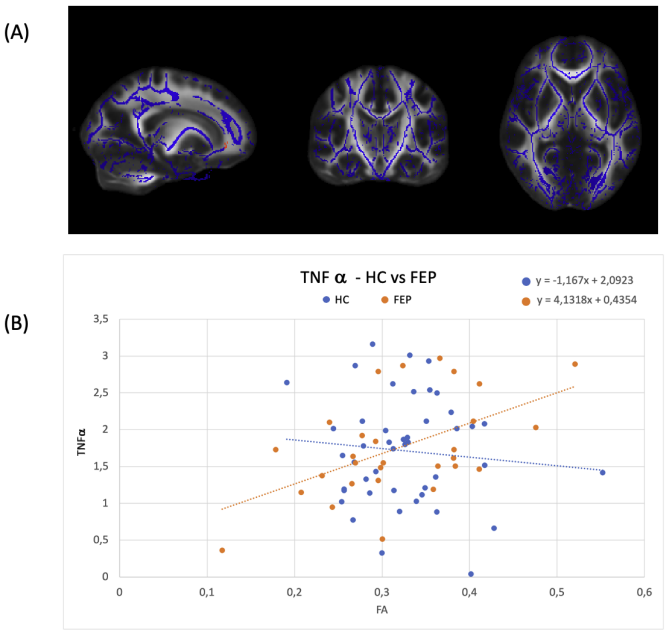


Fig. 4: (A) White matter tracts with different relationships between FA and TNFα in HC vs FEP. The highlighted area is located in the genu of corpus callosum. Blue voxels: White matter skeleton; red-yellow voxels: significant voxels after multiple comparison correction. (B) Relationships between FA and TNFα in a representative voxel (p=0.02)

IV. Discussion

Our TBSS results from the comparison of FA values between groups are in line with the literature, with decreased FA in CHR in respect to HC and FEP. A decrease in FA is due to the presence of alterations in the cerebral white matter, alterations which can be due to various causes such as anomalies concerning the integrity of the axons, their membrane, their orientation or their degree of myelination. In general, the presence of alterations in WM supports the "disconnection theory" underlying psychotic disorders such as schizophrenia. Our study highlighted the presence of alterations in the frontal white matter, especially involving the frontal gyrus. These structure is involved in attention, working memory, and the evaluation of linguistic and emotional information. The presence of these alterations seems to be related mainly to the presence of anomalies in executive functions, therefore in the planning, organization and regulation of behaviors [9]. Also the involvement of cingulate and corpus callosum in psychosis are confirmed by the literature [10], [11]. Regarding our results concerning the immune system, BDNF has a protective role in nervous system development and brain plasticity. Several studies have found a decrease in BDNF in various pathological conditions affecting the CNS, including schizophrenia [12], [13]. Several studies and meta-analyses [14] have found the presence of high levels of IFNγ in subjects with chronic psychosis. In addition, it was observed that these patients experienced a decrease in the concentration of this marker following drug therapy. It is likely that in subjects

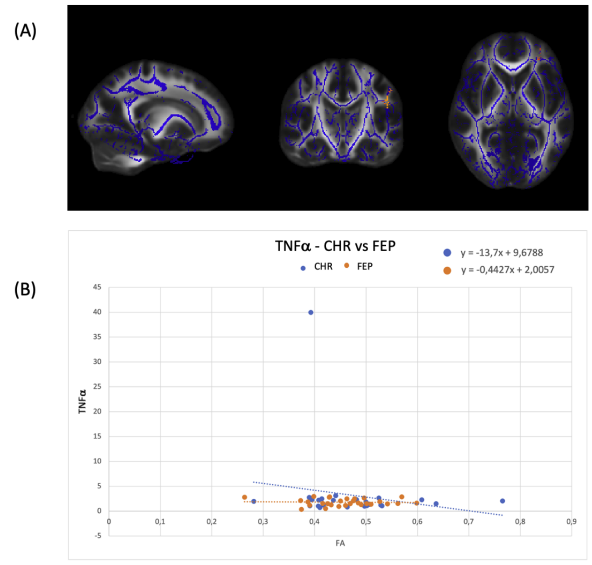


Fig. 5: (A) White matter tracts with different relationships between FA and TNFα in HC vs FEP. The highlighted area is located in the genu of corpus callosum. Blue voxels: White matter skeleton; red-yellow voxels: significant voxels after multiple comparison correction. (B) Relationships between FA and TNFαin a representative voxel (p=0.02)

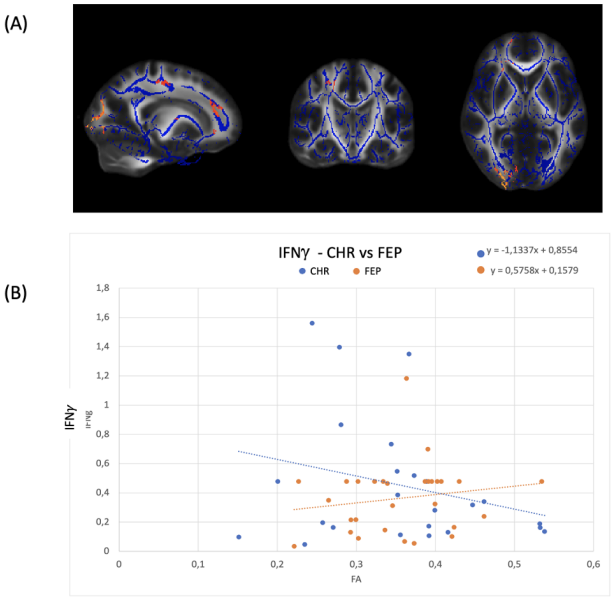


Fig. 6: (A) White matter tracts with different relationships between FA and IFNγ in CHR vs FEP. The highlighted areas are located in the corpus callosum, in the anterior cingulate and in the occipital area. (B) Relationships between FA and IFNγ in a representative voxel (p=0.01)

with chronic psychosis who have a higher concentration of IFNγ there is a greater degree of cerebral disconnection and therefore lower FA. Finally, the different interaction between immunological markers and FA in the different groups may explain a greater complexity in the interaction between the immune system and white matter integrity. In fact, although in FEP and in CHR there is an activation of the immune system in a pro-inflammatory sense which over time leads to progressive structural damage in the WM, it is possible that in the initial stages of the disorder there is a dys-regulation of the immune system which in limited brain areas it would determine a protective effect on WM. The association of DTI, TBSS, GLM and immune markers measurement allowed us to infer complex relationships between immune system and WM integrity.

V. Conclusion

Our study suggests the existence of a complex interaction between cerebral white matter and the immune system in psychotic patients and the need to further study these interactions. In this way, not only the additional elements involved in the pathogenesis of psychosis could be highlighted, but also which factors could slow down the onset and evolution of the structural alterations that characterize the disorder. This could have important repercussions from a prognostic and therapeutic point of view in psychotic subjects.

References

[1] L. Yao, S. Lui, Y. Liao, M.Y. Du, N. Hu, et al. White matter deficits in first episode schizophrenia: an activation likelihood estimation meta-analysis. Prog Neuropsychopharmacol Biol Psychiatry. 2013 Aug 1;45:100-6.

[2] B.J. Miller, P. Buckley, W. Seabolt, A. Mellor, B. Kirkpatrick. Meta-analysis of cytokine alterations in schizophrenia: clinical status and antipsychotic effects. Biol Psychiatry. 2011 Oct 1;70(7):663-71.

[3] T.A. Lesh, M. Careaga, D.R. Rose, A.K. McAllister, J. Van de Water J, et al. Cytokine alterations in first-episode schizophrenia and bipolar disorder: relationships to brain structure and symptoms. J Neuroinflammation. 2018 May 26;15(1):165.

[4] V. Mondelli, A. Cattaneo, M.B. Murri, M. Di Forti, R. Handley, et al. Stress and inflammation reduce brain-derived neurotrophic factor expression in first-episode psychosis: a pathway to smaller hippocampal volume. J Clin Psychiatry. 2011 Dec;72(12):1677-1684.

[5] M. Jenkinson, C.F. Beckmann, T.E. Behrens, M.W. Woolrich, S.M. Smith. FSL. Neuroimage. 2012 Aug 15;62(2):782-90.

[6] S.M. Smith, M. Jenkinson, H. Johansen-Berg,D. Rueckert,T.E. Nichols, et al. Tract-based spatial statistics: voxelwise analysis of multi-subject diffusion data. Neuroimage. 2006 Jul 15;31(4):1487-505.

[7] A.M. Winkler, G.R. Ridgway, M.A. Webster, S.M. Smith, T.E. Nichols. Permutation inference for the general linear model. Neuroimage. 2014 May 15;92(100):381-97.

[8] S.M. Smith, T.E. Nichols. Threshold-free cluster enhancement: addressing problems of smoothing, threshold dependence and localisation in cluster inference. Neuroimage. 2009 Jan 1;44(1):83-98.

[9] M. Quan, S.H. Lee, M. Kubicki, Z. Kikinis, Y. Rathi, et al. White matter tract abnormalities between rostral middle frontal gyrus, inferior frontal gyrus and striatum in first-episode schizophrenia. Schizophr Res. 2013 Apr;145(1-3):1-10.

[10] T.J. Whitford, M. Kubicki, J.S. Schneiderman, L.J. O'Donnell, R. King, et al. Corpus callosum abnormalities and their association with psychotic symptoms in patients with schizophrenia. Biol Psychiatry. 2010 Jul 1;68(1):70-7.

[11] R.A. Kanaan, J.S. Kim, W.E. Kaufmann, G.D. Pearlson, G.J. Barker, P.K. McGuire. Diffusion tensor imaging in schizophrenia. Biol Psychiatry. 2005 Dec 15;58(12):921-9.

[12] S. Bathina, U.N. Das. Brain-derived neurotrophic factor and its clinical implications. Arch Med Sci. 2015 Dec 10;11(6):1164-78.

[13] C.C. Lin, T.L. Huang. Brain-derived neurotrophic factor and mental disorders. Biomed J. 2020 Apr;43(2):134-142.

[14] S. Momtazmanesh, A. Zare-Shahabadi, N. Rezaei. Cytokine Alterations in Schizophrenia: An Updated Review. Front Psychiatry. 2019 Dec 6;10:892.

Autonomic response to virtual reality in oncological patients in real-world context

S. Moscato[1], S. Orlandi[1,2], A. Giannelli[3], R. Ostan[3], S.Varani[3], and L. Chiari[1,2]
[1] *Department of Electrical, Electronic, and Information Engineering "Guglielmo Marconi" (DEI) University of Bologna, Italy*
[2] *Health Sciences and Technologies - Interdepartmental Center for Industrial Research (CIRI-SDV), University of Bologna, Italy*
[3] *Fondazione ANT, Bologna, Italy*

***Abstract*—Virtual Reality (VR) can support traditional physiological treatments to help oncological patients who require positive stimuli and to be distracted from unpleasant thoughts, providing tools for relaxation and pain reduction. To date, VR is not implemented in clinical routine practice to support the mental states of oncological patients. Further research studies are needed to prove the correlations between VR and autonomic physiological signals. As such, we conducted a study to show the effects of VR on the autonomic signals of oncological patients. Photoplethysmography (PPG) and electrodermal activity (EDA) were recorded via a wearable device during VR sessions of 27 individuals. Linear Mixed-Effects Models (LMMs) were obtained using twenty-one parameters extracted from PPG and EDA. Our findings showed significant changes in some PPG variables comparing pre- and post- VR treatments due to the relaxation effects and in some EDA features due to the positive arousal and level of engagement experienced with the VR. Further studies are needed to better solidify the positive effects of VR as a complementary psychological intervention.**

***Keywords*—Virtual Reality, Autonomic Signals, Wearable device**

I. Introduction

Virtual Reality (VR) represents one of the most disruptive technologies developed in recent years, capable of creating a virtual environment and making feel the user completely immersed in it. VR technology is primarily enjoyed through portable head-mounted displays (HMDs), projecting the computer-generated virtual environment and occluding the view to the outside world [1].

Beyond the entertainment field, VR has proven to be a useful tool for many applications, not least in the health domain. Albeit limited to the research context, VR has been used as a complementary psychological therapy to treat various mental health conditions. Although it cannot substitute traditional psychological interventions, VR has been offering a new way of conveying positive stimuli, capturing the users' attention and distracting them from the current unpleasant situation, while simultaneously offering a feeling of relaxation [2].

The efficacy of VR interventions can be evaluated through either explicit or implicit methods. The former are based on an explicit evaluation by the user through interviews or questionnaires; the latter do not require an active involvement of the user, rather they are based on assessing the user's behaviour, for example by analysing the physiological reaction to VR stimuli [3].

Physiological reaction to VR can be assessed by properly processing the so-called autonomic signals, namely those physiological signals strongly influenced by the autonomic nervous system (ANS), which represents the neural system involuntarily reacting to external stimuli [4].

Examples of autonomic signals are photoplethysmography (PPG) and electrodermal activity (EDA). PPG represents the variations occurring in the blood flow at each heartbeat. The cardiovascular system is strongly influenced by both sympathetic and parasympathetic branches of the ANS, in particular by regulating the heart rate. These effects can be appreciated by conducting a Heart Rate Variability (HRV) analysis [5]. EDA provides information about the electrical conductance level of the skin, changed by the sweat secretion of eccrine sweat glands, in turn innervated by the ANS' sympathetic branch [6].

The aim of this study is to assess the physiological reaction to VR in oncological patients involved in a palliative care home program. Patients are provided with a VR-HMD and a wearable device to record autonomic signals.

II. Materials and Methods

A. Study design

The study is an interventional exploratory randomized controlled trial. Fifty-three patients have been recruited at Fondazione ANT and were then randomly divided into a VR group (27 patients) and a CTR one (26 patients). Tablets were provided to CTR participants and VR-HMD and wearable devices to monitor physiological signals to the VR ones. Only data from the VR group were analysed for the aims of this work. This study was approved by the Ethical Committee of Area Vasta Emilia Centro (Bologna, Italy; approval n° 542-2019-OSS-AUSLBO). All patients gave written informed consent.

B. VR headset and wearable device

Each VR participant was provided with a VR-HMD, a Lenovo Mirage Solo, to be freely used at home for four days. Patients were suggested to use the VR-HMD when experiencing moments of psychophysical discomfort, as growing anxiety and pain, but no minimum or maximum number of uses has been established. At the end of the four days, the log file of the VR sessions was downloaded by the investigator and later used to synchronize it with the physiological signals' recordings. VR-HMD was provided with both non-interactive and interactive contents: the former consisted in immersive 360° videos with different natural and relaxing scenarios, while the latter consisted in a basic skill game set in an underwater world specifically developed for ANT patients [7].

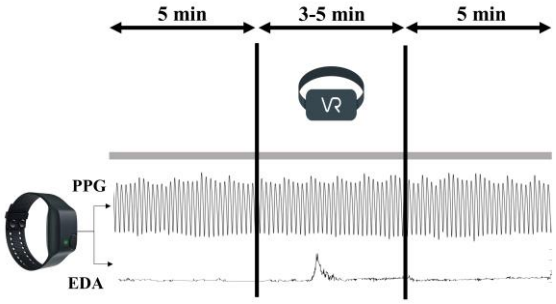


Figure 1 - Signal segmentation

The Empatica E4 wristband, a class IIa CE medical-grade wearable device, was used to monitor physiological signals. The following signals were recorded:

- Photoplethysmography (PPG), whose sensor is equipped with four light sources (two green, two red) and two photodetectors, and with a sampling frequency of 64 Hz.
- Electrodermal activity (EDA) is recorded by two dry electrodes placed on the ventral part of the wrist, with a sampling frequency of 4 Hz.
- Skin temperature (TEMP) is recorded through a thermopile with a sampling frequency of 4 Hz.
- Accelerometer (ACC) data is recorded through a tri-axial accelerometer with a sampling frequency of 32 Hz.

Before and after each use of the VR-HMD, the patient filled the digital version of the Edmonton Symptoms Assessment Scale (ESAS) [8], a simple and reliable multi-item instrument developed to rate the intensity of nine common symptoms experienced by cancer patients (pain, tiredness, nausea, depression, anxiety, drowsiness, appetite, well-being, and shortness of breath).

C. Synchronization

To assess the effect of VR through the analysis of physiological signals, we segmented the physiological signals' recordings into three phases:

- pre-VR phase: 5-minute window before the VR session
- VR phase: up to 5-minute window during the VR session
- post-VR phase: 5-minute window after the VR session

VR sessions were cut into 5-minute slots to extract features on a comparable time window compared to pre-VR and post-VR phases. For each VR session, the following rules were applied:

- If the VR session has been performed when the Empatica E4 wristband was not recording, that VR session was discarded
- If two VR sessions were closer than 5 minutes, the VR sessions have been merged and the pre-VR and post-VR phase have been selected as the pre-VR of the first merged session and the post-VR of the last merged session.

D. Signal processing

Only PPG and EDA were analysed for the aim of this work.

A 5th-order Butterworth band-pass filter [0.5 – 12] Hz was applied for each PPG recording. The algorithm by Elgendi et al. [9] was adapted to detect the systolic peak and systolic feet of each pulse. Each pulse was then z-scored and subjected to a signal quality check procedure [10], using information both from PPG and ACC data. It is worth noting that not all the available VR sessions will then be exploited for physiological parameters extraction because it can happen that a phase does not contain any reliable PPG pulse.

Once the interbeat intervals (IBIs) were estimated as time differences between two consecutive PPG pulses' systolic feet, we extracted 10 HRV parameters:

- 4 from time domain: mean heart rate (meanHR), standard deviation of normal heartbeats (SDNN), root mean square of successive differences between normal heartbeats (RMMSD), standard deviation of successive IBI differences (SDSD)
- 3 from the non-linear domain: Poincaré plot standard deviation perpendicular (SD1) and along (SD2) the line of identity, and Approximate Entropy (ApEn)
- 3 from the frequency domain: absolute power of the low frequency band (0.04 – 0.15 Hz) (LF), absolute power of the high frequency band (0.15 – 0.4 Hz) (HF), ratio between LF and HF (LF/HF).

EDA was filtered with a 4th-order Butterworth low-pass filter, with a cut-off frequency of 1 Hz and an automatic algorithm that uses EDA, TEMP, and ACC data was applied for quality check analysis [11]. Bad quality segments were replaced by a linear interpolation between the last and the following good quality segment. The normalized EDA signal, with a z-score procedure, was then used for further analysis.

A convex optimization algorithm [12] to divide EDA signal into its tonic and phasic components was also applied. From the phasic component, relevant peaks were identified as corresponding to a first derivative with a value higher than 0.01. Eleven features were extracted from the EDA:

- 5 from the whole EDA signal, namely maximum frequency (Fmax) [13], symbolic information entropy (SIE) [14], mean (meanEDA), standard deviation (stdEDA), and slope (slopeEDA)
- 3 from the tonic component, namely mean (meantonic), standard deviation (stdtonic), and slope (slopetonic)
- 3 from the relevant peaks of the phasic component, namely mean (meanampEDR), standard deviation (stdampEDR), and frequency (freqEDR)

E. Statistical analysis

To assess the effect of VR through the physiological parameters, we implemented Linear Mixed-Effects Models (LMMs). LMMs are used when data samples are non-independent, as this case in which a variable number of VR sessions can come from the same individual. We modelled each of the analysed physiological parameters as the outcome variable, obtaining 21 LMMs, the categorical variable identifying the pre-VR-post phase as the fixed effect, setting the pre-VR phase as the reference level, and as random effects, a number identifying the subject and a number identifying the session. A marginal F test was conducted to assess the significance of differences by comparing pre-VR,

VR, and post-VR phases. A p-value lower than 0.05 was considered a significance threshold.

For both signal processing and statistical analysis, we used Matlab 2022b.

III. Results

A. Study population

A total of 27 patients were enrolled in the VR group (14 M, 13 F, age 53.18 ± 12.41), using the VR-HMD for a total of 61 times. From the ESAS results, patients in the VR group showed significant improvement in tiredness, depression, anxiety, drowsiness, and well-being.

For HRV analysis, a total of 28 sessions from 18 individuals (10 M, 8 F, age 54.26 ± 13.17) were analysed, with 25 VR phases lasting 5 minutes and 3 lasting between 3 and 5 minutes. For EDA analysis, a total of 51 sessions coming from 21 individuals (12 M, 9 F, age 53.81 ± 12.70) were analysed, with 44 VR phases lasting 5 minutes and 7 lasting between 3 and 5 minutes.

The different number of sessions for HRV and EDA analysis is due to signal quality issues: it can happen that, as output from the PPG quality check, no pulses were available for further analysis. We built the LMMs for each parameter by maximizing the number of available sessions for the two autonomic signals.

B. Linear Mixed Effects Models

The results from the LMMs are shown in Table 1, while the parameters that significantly changed across different phases are depicted in Figure 2.

Among the HRV parameters, we found that LF/HF significantly decreased both during VR and post-VR phases (pre-VR vs VR p value = 0.0330, pre-VR vs post-VR p value = 0.0364), while the ApEn had a significant increase in the post-VR phase compared to the pre-VR phase (pre-VR vs post-VR p value = 0.0307).

Regarding EDA analysis, we obtained significant differences only by comparing pre-VR and VR phases, with a significant increase of meanEDA (pre-VR vs VR p value = 0.0008) and meanEDL (pre-VR vs VR p value = 0.0006), and a significant decrease of freqEDR during VR compared to the pre-VR phase (pre vs VR p value = 0.0443).

IV. Discussion

We conducted this study whose aim was to assess the physiological reaction to VR in an oncological population in a real-world context.

We found a significant decrease in the LF/HF parameter both during and after the VR use compared to the pre-VR phase. LF/HF represents the balance between sympathetic and parasympathetic systems. A decrease in its value can be seen as a greater activation of the parasympathetic branch than the sympathetic branch. This is in line with a more relaxed state of the participant while and after using the VR, representing a less stressful state [15].

We also observed a significant change in ApEn by comparing the post-VR phase with the pre-VR phase. ApEn is an indicator of the complexity of the heart rate time series. Higher ApEn values mean lower predictability of the time series, which can be seen as representing a system that can be more easily adapted to changes.

Some EDA features have also been found to significantly change. Specifically, variations in meanEDA and meanEDL have the same trend, with a significant increase during the VR phase compared to the pre-VR phase. EDA is influenced solely by the sympathetic branch of the ANS, and a higher value for meanEDA and meanEDL represents the activation of the sympathetic nervous system. This can reasonably be seen as a more aroused state of the subjects when using the VR-HMD [16]. On the other hand, freqEDR, representing the number of phasic component's peaks, resulted to be significantly lower during the VR session compared to the pre-VR phase. The concurrent presence of higher EDA tonic values and lower number of EDA phasic's peaks can be seen as a higher arousal and engagement of the individual [17] given by the VR experience, together with a less stressed state [18]. Finally, the significant changes in EDA features

Table 1 - Results from Linear Mixed-Effects Models

		Pre - Mean (S.E.)	VR - Mean (S.E.)	Pre - VR p value	Post - Mean (S.E.)	Pre-Post p value
28 VR sessions, 18 individuals	meanHR [bpm]	79.72 (2.43)	78.23 (2.14)	0.4885	78.30 (2.14)	0.5101
	SDNN [ms]	49.17 (4.91)	51.60 (3.51)	0.4889	48.62 (3.51)	0.8770
	RMSSD [ms]	59.26 (8.25)	67.66 (6.08)	0.1713	58.59 (6.08)	0.9124
	SDSD [ms]	61.21 (8.81)	71.09 (6.57)	0.1365	59.77 (6.57)	0.8260
	SD1 [ms]	61.51 (5.79)	47.51 (4.27)	0.1634	41.32 (4.27)	0.9453
	SD2 [ms]	49.99 (4.01)	47.52 (3.33)	0.4607	50.48 (3.33)	0.8826
	LF [ms^2]	1343.50 (1487.40)	3377.00 (2103.50)	0.3365	4249.70 (2103.5)	0.1709
	HF [ms^2]	107.62 (41.56)	151.32 (55.57)	0.4339	162.95 (55.57)	0.3224
	LF/HF [ ]	653.71 (191.00)	108.55 (251.33)	**0.0330**	119.01 (251.33)	**0.0364**
	ApEn [ ]	0.42 (0.10)	0.50 (0.08)	0.3341	0.60 (0.08)	**0.0307**
50 VR sessions, 21 individuals	Fmax [Hz]	0.03 (0.01)	0.02 (0.01)	0.3641	0.03 (0.01)	0.8985
	SIE [ ]	1.84 (0.07)	1.78 (0.07)	0.3679	1.74 (0.07)	0.1447
	meanEDA [a.u.]	0.21 (0.44)	1.56 (0.39)	**0.0008**	0.18 (0.39)	0.9339
	stdEDA [a.u.]	0.22 (0.08)	0.29 (0.08)	0.3648	0.20 (0.08)	0.8142
	slopeEDA [a.u.]/s	-7.95e-04 (6.44e-04)	9.14e-04 (9.10e-04)	0.0624	-1.02e-04 (9.10e-04)	0.4477
	meanEDL [a.u.]	0.11 (0.39)	1.39 (0.36)	**0.0006**	0.07 (0.36)	0.9073
	stdEDL [a.u.]	0.13 (0.04)	0.16 (0.06)	0.6780	0.11 (0.06)	0.6934
	slopeEDL [a.u.]	-5.42e-04 (5.43e-04)	7.16e-04 (7.22e-04)	0.0838	-2.26e-05 (7.22e-04)	0.4735
	meanampEDR [a.u.]	0.20 (0.08)	0.18 (0.06)	0.7719	0.19 (0.06)	0.8968
	stdampEDR	0.15 (0.06)	0.13 (0.07)	0.7512	0.17 (0.07)	0.8376
	freqEDR	5.07 (0.94)	3.00 (1.03)	**0.0443**	3.84 (1.03)	0.8376

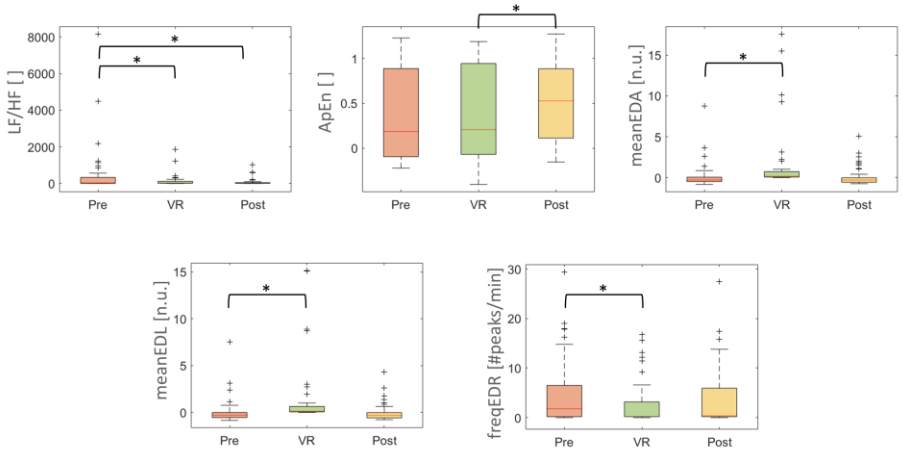


Figure 2 Physiological parameters significantly changed by comparing Pre-VR, VR, and Post-VR phases. * = p < 0.05, ** = p < 0.01

appear only during the VR-phase compared with the pre-VR phase, while they disappear during the post-VR phase. Further studies are needed to assess their behaviour on the long term after the use of VR.

Moreover, a more relaxed state is in line with the output from ESAS questionnaire, filled before and after each VR session. Indeed, it showed significant improvements in anxiety and well-being.

Several limitations need to be highlighted. The first is the limited dataset available for signal processing due to the bad quality of several recordings (45% of PPG recordings have been discarded due to poor quality). Secondly, the VR sessions were performed at different time of the day, so the analysed physiological signals could have been affected by circadian changes.

However, this study represents one of the few attempts in investigating the effects of VR on physiological signals in oncological patients in real-world context, making a step forward to a closer human-machine interaction and the use of VR systems to support therapeutic treatments. Further studies should be conducted on this topic, for example by exploiting physiological signals recordings to adapt the VR scenario to the emotions experienced by the user [19].

REFERENCES

[1] G. Riva, "Virtual Reality in Clinical Psychology," in *Comprehensive Clinical Psychology*, Elsevier, 2022, pp. 91–105. doi: 10.1016/B978-0-12-818697-8.00006-6.

[2] S. Bernaerts *et al.*, "Virtual Reality for Distraction and Relaxation in a Pediatric Hospital Setting: An Interventional Study With a Mixed-Methods Design," *Front. Digit. Heal.*, vol. 4, May 2022, doi: 10.3389/fdgth.2022.866119.

[3] A. Halbig and M. E. Latoschik, "A Systematic Review of Physiological Measurements, Factors, Methods, and Applications in Virtual Reality," *Front. Virtual Real.*, vol. 2, Jul. 2021, doi: 10.3389/frvir.2021.694567.

[4] J. A. Waxenbaum, V. Reddy, and M. Varacallo, *Anatomy, Autonomic Nervous System*. 2021. [Online]. Available: http://www.ncbi.nlm.nih.gov/pubmed/30969667

[5] B. Liu *et al.*, "The Assessment of Autonomic Nervous System Activity Based on Photoplethysmography in Healthy Young Men," *Front. Physiol.*, vol. 12, Sep. 2021, doi: 10.3389/fphys.2021.733264.

[6] W. Boucsein, *Electrodermal Activity*. Boston, MA: Springer US, 2012. doi: 10.1007/978-1-4614-1126-0.

[7] S. Moscato *et al.*, "Virtual Reality in Home Palliative Care: Brief Report on the Effect on Cancer-Related Symptomatology," *Front. Psychol.*, vol. In press, 2021, doi: 10.3389/fpsyg.2021.709154.

[8] D. Hui and E. Bruera, "The Edmonton Symptom Assessment System 25 Years Later: Past, Present, and Future Developments," *J. Pain Symptom Manage.*, vol. 53, no. 3, pp. 630–643, Mar. 2017, doi: 10.1016/j.jpainsymman.2016.10.370.

[9] M. Elgendi *et al.*, "Detection of a and b waves in the acceleration photoplethysmogram," *Biomed. Eng. Online*, vol. 13, no. 1, p. 139, 2014, doi: 10.1186/1475-925X-13-139.

[10] S. Moscato, S. Lo Giudice, G. Massaro, and L. Chiari, "Wrist Photoplethysmography quality assessment for reliable heart rate estimate and morphological analysis," *IEEE J. Biomed. Heal. Informatics*.

[11] S. Taylor *et al.*, "Automatic identification of artifacts in electrodermal activity data," in *2015 37th Annual International Conference of the IEEE Engineering in Medicine and Biology Society (EMBC)*, Aug. 2015, vol. 2015-Novem, pp. 1934–1937. doi: 10.1109/EMBC.2015.7318762.

[12] A. Greco, *et al.*, "cvxEDA: a Convex Optimization Approach to Electrodermal Activity Processing," *IEEE Trans. Biomed. Eng.*, pp. 1–1, 2016, doi: 10.1109/TBME.2015.2474131.

[13] H. F. Posada-Quintero *et al.*, "Time-varying analysis of electrodermal activity during exercise," *PLoS One*, vol. 13, no. 6, pp. 1–12, 2018, doi: 10.1371/journal.pone.0198328.

[14] Z. Visnovcova, M. Mestanik, M. Gala, A. Mestanikova, and I. Tonhajzerova, "The complexity of electrodermal activity is altered in mental cognitive stressors," *Comput. Biol. Med.*, vol. 79, pp. 123–129, Dec. 2016, doi: 10.1016/j.compbiomed.2016.10.014.

[15] B. Thielmann, J. Hartung, and I. Böckelmann, "Objective assessment of mental stress in individuals with different levels of effort reward imbalance or overcommitment using heart rate variability: a systematic review," *Syst. Rev.*, vol. 11, no. 1, p. 48, Dec. 2022, doi: 10.1186/s13643-022-01925-4.

[16] A. Bartolomé-Tomás *et al.*, "Arousal Detection in Elderly People from Electrodermal Activity Using Musical Stimuli," *Sensors*, vol. 20, no. 17, p. 4788, Aug. 2020, doi: 10.3390/s20174788.

[17] M. R. Amin and R. T. Faghih, "Tonic and Phasic Decomposition of Skin Conductance Data: A Generalized-Cross-Validation-Based Block Coordinate Descent Approach," in *2019 41st Annual International Conference of the IEEE Engineering in Medicine and Biology Society (EMBC)*, Jul. 2019, pp. 745–749. doi: 10.1109/EMBC.2019.8857074.

[18] M. E. Dawson, "The Electrodermal System," in *Handbook of Psychophysiology*, 2nd Ed., J. T. Cacioppo, L. G. Tassinary, and G. . Bernston, Eds. Cambridge: Cambridge Press, 2001, pp. 200–223.

[19] J. Kritikos, G. Alevizopoulos, and D. Koutsouris, "Personalized Virtual Reality Human-Computer Interaction for Psychiatric and Neurological Illnesses: A Dynamically Adaptive Virtual Reality Environment That Changes According to Real-Time Feedback From Electrophysiological Signal Responses," *Front. Hum. Neurosci.*, vol. 15, Feb. 2021, doi: 10.3389/fnhum.2021.596980.

Analysis of muscular activity of a cashier during different modalities of human robot collaboration

G. Corvini[1], S. Conforto[1], S. Ranaldi[1], M. Schmid[1] and D. Bibbo[1]
[1] *Department of Industrial, Electronic and Mechanical Engineering, Roma Tre University, Rome, Italy.*

***Abstract*— The effects of siding a collaborative robot (cobot) to a human operator on muscle activity during a scenario simulating a working task (i.e., a supermarket cashier moving cyclically packages) were investigated in this study, by considering different modalities of human-robot collaboration (HRC). Wearable sensors were used to collect kinematic and EMG data, and four different HRC interaction modalities were tested to determine their impact on the biomechanical risk associated with the examined working task. The range, amplitude, and smoothness values of accelerometer data coming from a sensor placed on the trunk, as well as coactivation indexes extracted from EMG data of different relevant muscles were calculated. Without cobot assistance, although a higher smoothness was found in the trunk movement, a high level of prolonged muscular activity was encountered usually associated to a potential increase in the biomechanical risk. In contrast, full assistance from the cobot resulted in the operator developing an intermittent motor control strategy, which reduces the muscular effort but losing smoothness in trunk movements. During two simulated tasks with a medium level of assistance, if the cobot imposed the cadence to complete the task, the required muscular effort remained constantly high, while if the operator was allowed to control the cadence, high smoothness combined with reduced muscular activity resulted. In conclusion, the use of cobots in repetitive tasks can influence the muscle strategy adopted by the operator during HRC. According to the analysis, the most effective approach is to reduce the workload of the operators while allowing them to maintain control over the speed at which tasks are completed.**

***Keywords*—Cobots, Biomechanical risk, Human-Robot Collaboration, surface EMG.**

I. INTRODUCTION

The adoption of cooperative and collaborative robotics in the industrial and commercial framework in recent years has represented and still represents one of the most significant aspects in terms of the renewal of production processes [1]. The interaction between humans and collaborative robots (cobots) produces advantages in the execution of those tasks that are associated with a significant level of biomechanical risk (such as repetitive motion, awkward postures, and lifting tasks) [2]. The HRC, in fact, has the double advantage of combining the potentials of the robotic systems, such as strength and accuracy in the execution of the task and its repetition, with those typical of humans, such as the physical dexterity and the adaptability to unexpected contexts. However, the presence of cobots in work environments leads to a revision of the biomechanical risk assessment paradigms associated with task execution. Biomechanical risk assessment methods known in the literature [3], such as the *level* (intensity of the force during an action), *repetitiveness (*the frequency of the task) and *duration* (the time in which the physical activity is performed) could be not completely adequate because the presence of the cobot could alter the outcome of these measures. Other indexes, such as the Risk index or the OCRA one [4], still do not consider that the cobot could completely remove the object's mass or constrain the task's frequency, yielding in unrealistic risk estimates. To address this problem, an instrument-based approach might play an important role, as it may help predict biomechanical risk values coming from standard methods applied directly to the human operator [5]. For this reason, particular attention has been placed on wearable sensors, such as Surface Electromyography (sEMG) which allows the acquisition of the physiological activity of muscles and Inertial Measurement Units (IMUs), which allow the recording of the kinematics of executed tasks: in fact, thanks to their portability and ease of use, in addition to their small size that does not affect the performed tasks, they might provide good quantitative indicators able to monitor and estimate the biomechanical risk associated to several working activities [6]. This study aims to verify the potentiality of this approach by analysing kinematic parameter and physiological one, extracting the time-varying multi-muscle coactivation index (CI), which can be interpreted as an indicator of the biomechanical risk [7], during the simulation of a specific working task using different modalities of human-robot collaboration. This work is framed in the "BRISK" project, a comprehensive project aimed at studying HRC in working activities through the development of an innovative wearable platform, with the ultimate objective of minimising the biomechanical risks. The data presented in this work are a subset of the whole dataset acquired within the project framework reported in the acknowledgement.

II. METHODS

In the following paragraphs, the experimental setup, the protocols, and the data processing are described.

A. Experimental setup

Tests were performed on a group of 12 male volunteers (right-handed, aged between 25 and 48 years). All volunteers were healthy and had no evident or stated mobility problems. The experiments have been approved by the local ethical committee of Roma Tre University. A specific working task (WT) (i.e., a cashier loading and scanning items for barcode detection) has been simulated considering a setup as reported in Figure 1: the cobot was positioned on the longer side of a 2x1m table with the operator facing it on the opposite side. A scanning area was defined in front of the operator at the center of the table. A set of 1 kg rectangular packages (14x12x5cm), each marked with a barcode on a different side, was used. In the tests, the WT was performed in four different cooperation modalities, in which the cobot cooperated partially, totally, or not at all. A single working cycle consisted of taking the item with the right hand from the departure station (DS), searching for the barcode and scanning it in the designed area, and laying it with the left hand in the arrival station (AS). In one of the four modalities (i.e., *full robot*), the AS is defined in a different

location, as shown in Figure 1. Each package was cyclically replaced in the DS during the task. Each subject was recommended to perform the tests as naturally as possible, without constraining on the gesture's speed (except for the cases in which the velocity constraint was given by the cobot).

B. Protocols

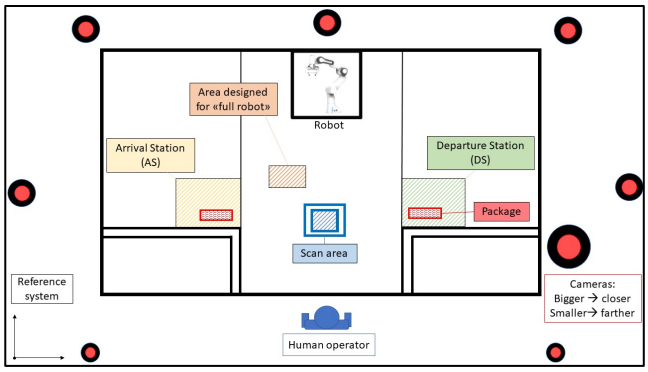


Figure 1: experimental setup for the loading activities simulation

Each test lasted about 5 minutes, in which subjects were asked to perform multiple times the same working cycle (picking, scanning and placing tasks) as naturally as possible, according to one of the following four different collaboration modalities:

a) ***No robot***: the operator picks up the item from the DS, examines it to detect the barcode, scans it in the appropriate area, and finally deposits it in the AS. The execution speed is dictated by the operator.
b) ***Full robot***: The cobot grabs the package and brings it in front of the operator, who takes it to scan the barcode. Then, the package is positioned in a specific area just in front of the operator, as shown in Figure 1, where the cobot picks the item up and moves it to the AS. The execution speed is constrained by the cobot performing all the operations. In this modality, the operator must wait for the execution time of the cobot to complete the working cycle.
c) ***Half robot***: the cobot picks up the item from the DS, brings it in front of the operator, goes back to the DS and picks a new package, without waiting for external output from the operator before starting a new working cycle. The execution speed is constrained by the velocity of the cobot in performing the carrying operation to the operator, return to the DS and grabbing a new item to start a new cycle.
d) ***Half robot touch***: the operator touches the cobot to give the start of the working cycle in the same test. As soon as it has been touched, the cobot picks up the item from the DS, brings it in front of the operator and goes back to the DS waiting for the next touch. At the same time, the operator detects the barcode, scans it and manually places the package in the AS. The execution speed of each cycle mainly depends on the operator touching the cobot, although the cobot, after releasing the package, must return to the DS to grab a new one.

The order of the packages was shuffled each time within the same test to randomize the position of the barcode. The sequential order of the four tests, each corresponding to one of the four different collaboration modalities, was randomized for each participant. This point is quite decisive for the speed of the gesture (constrained or not according to the modality). These collaboration modalities were chosen as they have been associated with different motor control schemes, based on a continuous or intermittent strategy that can lead to a variation in posture or muscular activations [8].

C. Data acquisition and processing

An Inertial Measurement Units (IMU, Shimmer Sensing) was used to acquire kinematic data (sampling frequency fs=102.4Hz) and it was positioned on the trunk.
An optoelectronic system (BTS SMART DX 6000 system with 8 cameras at 2 Mpixel, fs = 250 Hz) was used for the tracking of the body segments kinematics, with a reduced 9 marker set (2 wrists, 2 elbows, 2 shoulders, 2 posterior superior iliac spines and 1 on the neck). These data were mainly used as references for the IMU and for the data segmentation by identifying the beginning of each cycle during a single test. The reference system was fixed on the desk's lower corner at the left of the operator, with the mediolateral axis from left to right and the anteroposterior axis from back to front. The mediolateral coordinate of the left wrist was used to identify the end of each cycle, and thus the beginning of the subsequent one: the minima in the marker position were used to detect when the package was placed in the AS. Finally, physiological signals from muscles were acquired through a sixteen channels EMG system (BTS FREEEMG). Surface EMG signals were recorded using bipolar electrodes with fs=1000 Hz @16 bit. Four pairs of electrodes were placed according to the SENIAM recommendations [9] on the non-focal muscles of the lower and upper limbs. In this study, the following non-focal muscles were monitored: *i)* Upper Trapezius, *ii)* Erector Spinae, *iii)* Gluteus maximus and *iv)* Medial Gastrocnemius.

All data but the IMU were acquired using a common acquisition software environment (i.e., BTS SMART capture), running on a first workstation. For the IMU data, a custom software running on a second PC connected to the BTS workstation by means of a trigger system to synchronize data, was adopted. The different sampling frequencies were considered during the data processing, and data were resampled to a common domain in defining task cycles.

The cooperative activities were performed through interaction with the Franka Emika Panda Advanced Robotic System cobot, an industrial robotic arm with 7 degrees of freedom and a maximum payload of 3 kg. The cobot is equipped with torque sensors on all joints, has a working area of 360° with a maximum extension of 855 mm, and can reach a maximum movement speed of the end effector of 2 m/s.

During all the activities, the accelerometer placed on the trunk has been used to extract compact parameters of trunk kinematics, such as the dynamic range, root mean square value, and smoothness, quantified through the calculation of the log dimensionless jerk as described in equation 1, from the magnitude of the whole acceleration vector [10].

$$smoothness = -\ln\left(\frac{(t_2-t_1)}{v_{peak}^2}\int_{t_1}^{t_2}\left|\frac{da}{dt}\right|^2 dt\right) \quad (1$$

where t_1 and t_2 are the time instants of the window in which the acceleration a and the velocity v are considered. Note that higher values of the log dimensionless jerk correspond to higher value of smoothness.
EMG signals were filtered using a bandpass filter with cut-off frequencies (fc) at 20 and 400 Hz (3rd order of Butterworth). After filtering, envelopes were extracted (full wave rectification and low pass filtering with fc = 5Hz) and they

were segmented according to the length of each cycle (from the DS to the AS). Then, each envelope was normalized to the median value of the maximum peaks extracted from each cycle of the *no robot* trial. Since the length of each cycle was different, envelope signals were interpolated to 1000 points to normalize their length with respect to time. For the graphical representation, the temporal normalization is represented as a percentage of the completed working cycle from 0 to 100% [7]. Subsequently, the time-varying coactivation index, which represents the simultaneous activation of the muscles, was computed for each cycle, and finally, all cycles were averaged to obtain a global coactivation index representing the complete experiment for each subject. For the statistical analysis of the kinematic data, pairwise t-tests were conducted with "collaboration modality" as a grouping factor. To verify whether there is a significant difference in the kinematic parameters among the four modalities, a significance level of $\alpha = 0.05$ was set.

III. Results

The computed average number of packages handled by subjects in the 5-minute duration of the test was: a) n*o robot*: 76±9 packs (15±3 packs/minute); b) *full robot*: 23±1 packs (5±1 packs/minute); c) *half robot*: 66±3 packs (12±2 packs/minute) and d) *half robot touch*: 47±5 packs (9±2 packs/minute).

In Figure 2 the range, amplitude, and smoothness of the signals by the accelerometer on the trunk are displayed. For each collaboration modality, results were averaged among all subjects. The range average value of the n*o robot* trial is the highest among all. In addition, a high value of smoothness is highlighted, due to the absence of the cobot, which allows the subjects to complete the required task at their own velocity. The minimum range and amplitude in the acceleration of the trunk are produced in the *full robot* modality, where the cobot completes both the package loading and unloading phases. *Half robot* and *half robot touch* produce similar results in terms of trunk range and amplitude, but in the latter collaboration modality a greater smoothness is achieved. In the following table results on statistical analysis are reported, considering the paired tests: *no robot* (1) *full robot* (2) *half robot* (3) and *half robot touch* (4). Results show a significative differences for all the parameters in the four modalities, except for the range and RMS parameters between *half robot* and *half robot touch* distributions, and for the smoothness parameter between *no robot* and *half robot touch* distributions.

Table 1 Significance values for pairwise t-tests performed on the kinematic data

Parameter	1 vs. 2	1 vs. 3	1 vs. 4	2 vs. 3	2 vs. 4	3 vs. 4
Range	* ($p < 0.001$)	* ($p < 0.001$)	* ($p < 0.001$)	* ($p < 0.001$)	* ($p < 0.001$)	- **($p = 0.09$)**
RMS	* ($p < 0.001$)	* ($p < 0.001$)	* ($p < 0.001$)	* ($p < 0.001$)	* ($p < 0.001$)	- **($p = 0.58$)**
Smoothness	* ($p < 0.001$)	* ($p < 0.001$)	- **($p = 0.06$)**	* ($p = 0.03$)	* ($p < 0.001$)	* ($p < 0.001$)

In Figure 3 the coactivation indexes are shown. The coactivation index (averaged among cycles) of each subject is represented with a different color line, while the group mean pattern computed among all subjects together with its standard deviation are identified by the black line and the light grey areas, respectively. On the x-axis, the percentage of completion of the cycle is shown (i.e., zero indicates the initial action of the subject going towards the DS, while 100 indicates

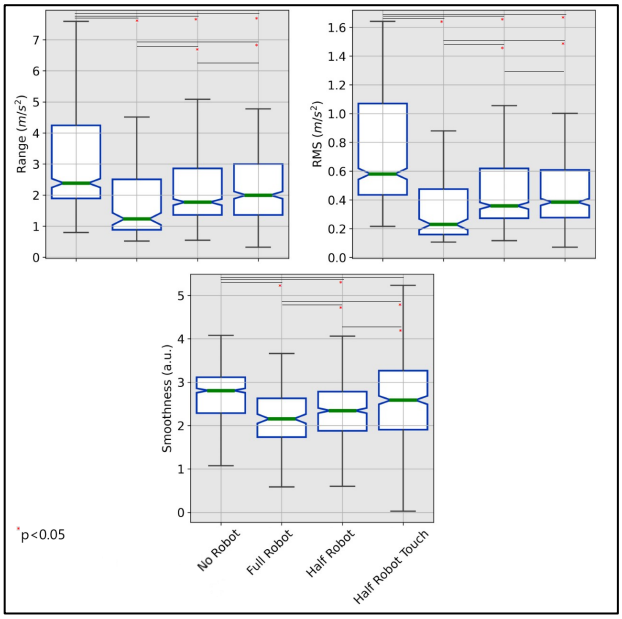


Figure 2 *The analysis of kinematic data extracted from the accelerometer placed on the trunk of the subjects. In descending order, the mean and standard deviations of the range, RMS amplitude, and smoothness are displayed.*

reaching the AS to place the package). The coactivation index of the *no robot* collaboration modality is constantly higher than all the other modalities. It can be noticed that *no robot* and *half robot* have a constant evolution over time indicating a continuous higher coactivation of muscle during the entire time of the trial. *No robot* modality has an increased CI up to 30% at the beginning and then a slow decrease up to 22-25% keeping almost constant values during the package's manipulation phase, and a a small increase to 25% at the end of the cycle. *Full robot* modality produces an great decrease of the CI up to 10% in the resting phase (i.e., when the cobot executes package loading and unloading), and a slower increase in the CI up to 20% during the package manipulation phase similar to those in the other modalities. H*alf robot* always has a constant value of CI around 20%, while *Half robot touch* presents a small peak of CI reaching 25% at the beginning, followed by a rest phase in which the CI reached 15%; from half of the cycle to the CI slowly increased up to 23%.

IV. Discussion and Conclusion

In this study, the working task of a cashier has been simulated with different collaboration modalities provided by a cobot. The objective was to investigate how in a HRC scenario the presence of the cobot induces changes in muscular activity, aiming at a biomechanical risk reduction. It is worth noting that the analysis of muscular activity refers to the involvement of the non-focal muscles characterized by low amplitude since they are mainly devoted to controlling and stabilizing the posture. High levels of trunk acceleration, in terms of amplitude and range, resulted, together with high values of smoothness, when there is no presence of the cobot. This agrees with the analyzed gesture because the working area is entirely covered by the operator and tasks are

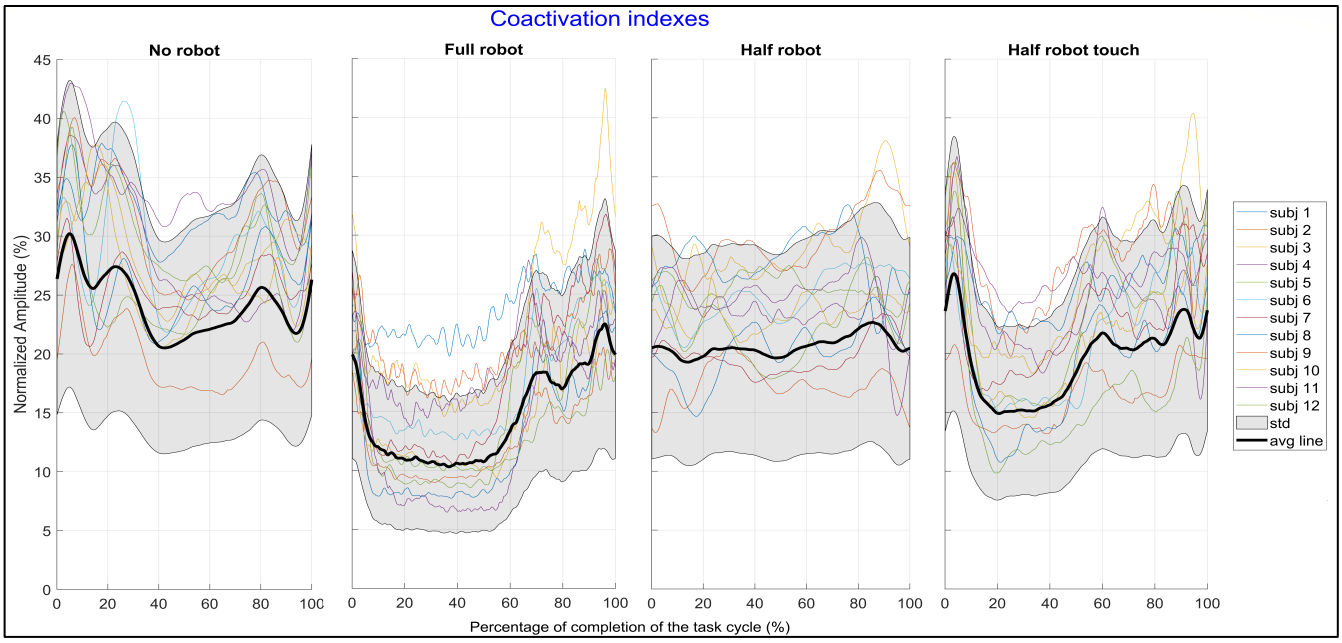


Figure 3 Time-varying Coactivation index computed on the four different trials. In each trial, the CI of each subject is displayed with a different coloured line, while the mean and standard deviations among all subjects are represented by the black line and the light grey area.

performed without any interruptions. In the *no robot* modality, from the analysis of the CI signals, we noticed a continuously high level of CI with increasing values at the beginning and at the end of the cycle, suggesting a continuous posture control to compensate for the packages' loading and unloading phases.

When the cobot cooperates to perform part of the task (i.e., taking the package and bringing it to the scanning station) with a specific cadence (i.e., *half robot* modality), the operator tends to lose control over its own velocity in completing the tasks, because of the inability to predict the timing of the next package to be processed. The result of this effect on the kinematic data is that the operator movement is less smooth, although the range and the amplitude of the acceleration are significantly reduced with respect to all other modalities ($p<0.05$). This modality effectively reduces the range and the amplitude of the movements, because removes the package weight from the loading phase, but the impact of the cobot assistance on the muscular activity is minimum. In fact, although a small decrease in the CI appears with respect to the *no robot* modality, there is still a continuous activation of the muscle throughout the entire duration of the task. This can be explained by a variation of the subject muscular strategy, due to the cobot intervention. Even if the package's loading phase is reduced, this does not help reduce the biomechanical risk, because a continuous muscular effort persists.

In the *full robot* modality, despite a relevant decrease of trunk acceleration, likely due to the higher level of cobot assistance, the operator is, from a theoretical perspective, still not able to predict when the next task will be executed. In practical terms, since the number of managed packages per minute is very low, due to the cobot performance limits, the operator easily and almost immediately seems to adapt their strategy to this specific condition. The smoothness levels are therefore not optimal, as the performed gesture is non-continuous, indicating the use of an intermittent strategy and control of the movement. Because of the increased support by the cobot, and the consequent decrease in the operator's effort, the muscular activity results modified with respect to the other modalities, showing lower average values of coactivation indexes during each cycle. Furthermore, the muscle activation switches from continuous to intermittent, showing different coactivation index values during the manipulation and the waiting phases, respectively.

Similar behavior in the coactivation index can be observed in the *half robot touch* modality, in which the trend oscillates between low values in the resting phase (waiting for the robot to bring the item) and high values in the manipulation one. Nevertheless, the possibility of deciding the beginning of each task (by touching the cobot) helps the operator control the timing of the successive task. This seems to elicit more natural movements, as seen by the significant increase in smoothness.

Therefore, by comparing the four proposed modalities, we could confirm that the introduction of a cobot could efficiently reduce the range and amplitude of the trunk movements of the operator, in addition to producing a lower level of muscle coactivation. Results showed that the collaboration modality can alter the muscle strategy employed by the operator, but it does not necessarily produce benefits, as observed in *half robot*, where the coactivation was maintained constant throughout the whole test. Moreover, it was shown that when the cobot imposes the working cadence on the operator, this produces an increase in the posture stiffness that could be associated with an increase in the biomechanical risk.

In conclusion, the best modality we have found in our analysis is the one where the cobot performs part of the package loading (or unloading) phase, but the operators remain the one that decides the rhythm of the working task.

ACKNOWLEDGMENT

This study is part of the Italian Project BRIC INAIL 2019-ID48 - BRISK: a multi-sensor wearable platform to assess Biomechanical Risk when Interacting with collaborative robotS in worK-related scenarios.

REFERENCES

[1] Ajoudani, A., Zanchettin, A.M., Ivaldi, S., Albu-Schäffer, A., Kosuge, K., & Khatib, O. (2018). Progress and prospects of the human–robot collaboration. Auton Robot 42, 957–975, https://doi.org/10.1007/s10514-017-9677-2

[2] Robla-Gomez, S., Becerra, V. M., Llata, J. R., Gonzalez-Sarabia, E., Torre-Ferrero, C., & Perez-Oria, J. (2017). Working Together: A Review on Safe Human-Robot Collaboration in Industrial Environments. IEEE

Access, 5, 26754–26773
https://doi.org/10.1109/ACCESS.2017.2773127

[3] David G. C. (2005). Ergonomic methods for assessing exposure to risk factors for work-related musculoskeletal disorders. Occupational medicine (Oxford, England), 55(3), 190–199, https://doi.org/10.1093/occmed/kqi082

[4] Cocca, P., Marciano, F., & Rossi, D. (2008). Assessment of biomechanical risk at work: practical approaches and tools. Acta of bioengineering and biomechanics, 10(3), 21–27.

[5] Ranavolo, A., Ajoudani, A., Cherubini, A., Bianchi, M., Fritzsche, L., Iavicoli, S., Sartori, M., Silvetti, A., Vanderborght, B., Varrecchia, T., & Draicchio, F. (2020). The Sensor-Based Biomechanical Risk Assessment at the Base of the Need for Revising of Standards for Human Ergonomics. Sensors, 20(20), 5750. https://doi.org/10.3390/s20205750

[6] Ranavolo, A., Draicchio, F., Varrecchia, T., Silvetti, A., & Iavicoli, S. (2018). Wearable Monitoring Devices for Biomechanical Risk Assessment at Work: Current Status and Future Challenges - A Systematic Review. International Journal of Environmental Research and Public Health, 15(9), 2001, http://dx.doi.org/10.3390/ijerph15092001

[7] Ranavolo, A., Mari, S., Conte, C., Serrao, M., Silvetti, A., Iavicoli, S., & Draicchio, F. (2015). A new muscle co-activation index for biomechanical load evaluation in work activities. Ergonomics, 58(6), 966–979. https://doi.org/10.1080/00140139.2014.991764

[8] D'Anna C, Schmid M, Bibbo D, Bertollo M, Comani S, et al. (2015) The Effect of Continuous and Discretized Presentations of Concurrent Augmented Visual Biofeedback on Postural Control in Quiet Stance. PLOS ONE 10(7): e0132711. https://doi.org/10.1371/journal.pone.0132711

[9] Hermens, H. J., Freriks, B., Disselhorst-Klug, C., & Rau, G. (2000). Development of recommendations for SEMG sensors and sensor placement procedures. Journal of Electromyography and Kinesiology, 10(5), 361–374. https://doi.org/10.1016/s1050-6411(00)00027-4

[10] Gulde, P., & Hermsdörfer, J. (2018). Smoothness Metrics in Complex Movement Tasks. Frontiers in Neurology, 9, 615. https://doi.org/10.3389/fneur.2018.00615

Machine learning-based classification of cortical response to visual stimuli recorded with an ECoG array in mice: a case study

D. De Luca[1], S. Moccia[1], R. Mazziotti[2,3], L. Lupori[2,4], T. Pizzorusso[2,4], and S. Micera[1,5]
[1] *The BioRobotics Institute and Dep. of Excellence in Robotics and AI, Scuola Superiore Sant'Anna, Pisa, Italy*
[2]*Institute of Neuroscience (IN-CNR), Pisa, Italy*
[3]*Department of Neuroscience, Psychology, Drug Research and Child Health, University of Florence, Florence, Italy*
[4]*BIO@SNS Lab, Scuola Normale Superiore, Pisa, Italy*
[5]*Bertarelli Foundation Chair in Translational Neuroengineering, EPFL, Geneva, Switzerland*

***Abstract*—Optic nerve has been proven to be a valid target for neuroprosthetic implants to restore vision in blind individuals. The optimization of stimulation parameters is crucial for the correct functioning of such implants. Closed-loop stimulation of the optic nerve exploiting the cortical activation pattern as feedback may be a valid optimization strategy. Animal experiments are needed to decode the visual cortex activity in response to simple visual stimuli with a view to testing, in vivo, closed-loop stimulation of the optic nerve. The design of such experiments must take into account the possibility of extending the study to blind human subjects. In this paper, we propose to use machine learning to classify the cortical activation of a mouse, recorded with an electrocorticography (ECoG) array, in response to visual stimuli. The mouse was anesthetized, and 10 different visual stimuli were displayed on a screen positioned 20 cm away from its right eye, while the ECoG array recorded the response of the mouse's left primary visual cortex. We tested 3 classifiers (Random Forest, support vector machine, and multilayer perceptron) and obtained above-chance classification accuracy (47% with 10 classes), showing interesting preliminary results of ECoG and machine learning in terms of visual cortex decoding.**

***Keywords*—ECoG, machine learning, visual cortex, decoding**

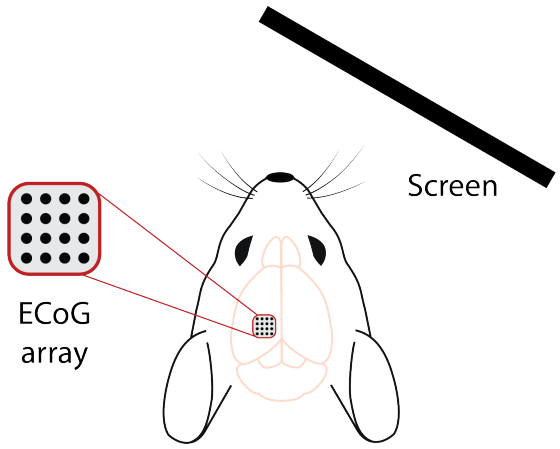


Fig. 1: Graphical representation of our experimental setting.

I. Introduction

Visual prostheses have been under investigation for years [1]. These devices are the last resort for patients suffering from blinding diseases for which no pharmaceutical cure exists and they usually consist of electrode arrays targeting the visual pathway not affected by the disease [1]. There is evidence that the optic nerve is a valid location for a visual prosthesis, which would exploit the ascending visual pathway and be less invasive than a cortical implant [2] [3] [4]. As with other types of neuroprostheses, it is important to optimize the stimulation protocols to elicit the desired visual perceptions [5]. A strategy may be to perform closed-loop electrical stimulation, where the feedback is the evoked cortical activation, that resembles the cortical activation naturally generated by visual stimuli [6]. It has been proven with animal models that optic nerve stimulation can selectively activate the visual cortex [4]. It is now necessary to test the possibility of discriminating simple visual stimuli through the evoked cortical response, a prerequisite for using such response as feedback.

Visual cortex decoding has been widely explored in animals, and research is mainly oriented toward neuronal level decoding [7]. Intracortical probes allow us to record signals with single-neuron resolution, but this information is confined in a limited portion of the primary visual cortex (V1) surface and, due to V1 retinotopic organization, corresponds to a limited portion of the visual field [8]. Moreover, it would be difficult to record single neurons in humans for both technical and ethical reasons [9]. On the other hand, electrocorticography (ECoG)-based visual cortex decoding of visual stimuli has been performed in humans [10] [11] [12], suggesting the possibility to translate these experiments from animal models to human subjects [9]. As another benefit of ECoG, large arrays allow us to record activity from the whole V1, and consequently relative to the whole visual field [8].

In this work, we propose machine learning-based classification of visually evoked potentials recorded with an ECoG array placed on a mouse V1. We delivered visual stimuli with

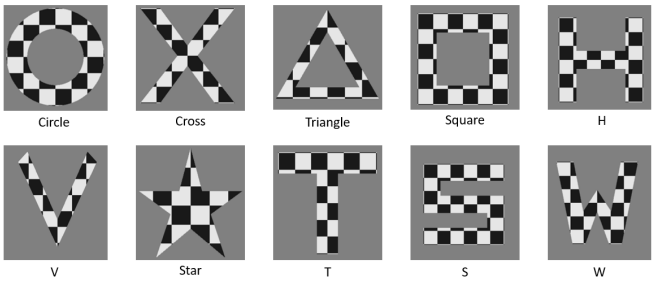


Fig. 2: Shapes displayed on the screen during the experimental session.

10 different shapes to the animal, recorded its V1 responses, and classified them into the corresponding 10 classes. This allowed us to explore the potential of ECoG arrays combined with machine learning techniques to perform visual cortex decoding, paving the way for *in vivo* testing of closed-loop stimulation of the optic nerve.

II. Materials and Methods

Section II-A describes the visual stimuli and the acquisition of ECoG signals. Data preprocessing and classification are described in Section II-B and Section II-C respectively.

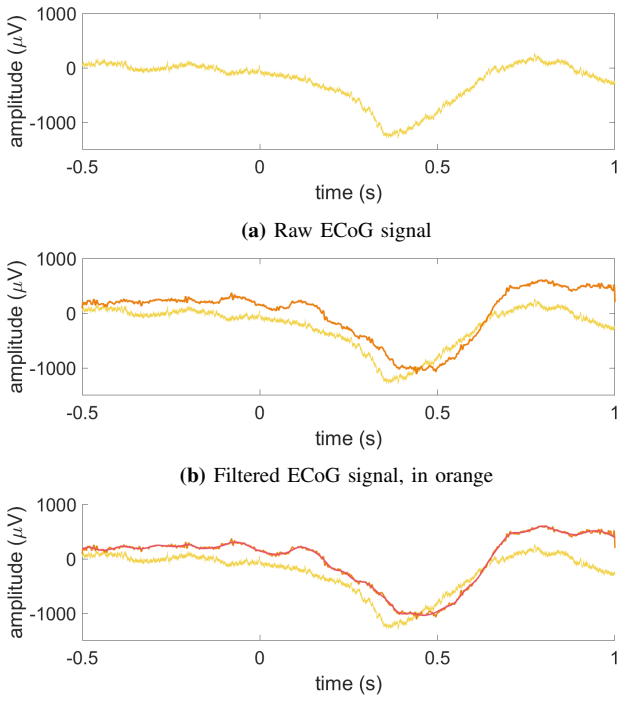
A. Experimental session

Our experiment involved one mouse, which was deeply anesthetized using isoflurane (concentration: 5% induction, 1.5% during surgery) and placed in a stereotactic frame. Craniotomy was performed to expose the left V1 and an ECoG array was placed 3.5mm lateral from lambda, as shown in Fig. 1. The ECoG array was composed of 16 (4x4) platinum sites, spaced of 500 μm (E16-500-5-200; NeuroNexus), and connected to the Neuralynx ERP-27 electrode reference panel.

During the recordings, the mouse was anesthetized using isoflurane (0.8-0.4%) and chlorprothixene 1.5 mg/kg intraperitoneally injected. The visual stimuli consisted of 100 repetitions of 10 different shapes displayed on a screen positioned 20 cm from the right eye of the animal, to elicit cortical responses corresponding to the monocular vision. The visual stimuli, shown in Fig. 2, have the outlines filled with a flickering checkerboard (temporal frequency of 5 Hz, spatial frequency of 0.08 cycles per degree). They were presented in random order after a 500 ms pre-stimulus gray background, lasted for 500 ms, and were followed by 1s of post-stimulus gray background.

B. Data preprocessing

Data preprocessing was performed using the FieldTrip toolbox [13]. The data were divided into segments of 1.5 s, from 0.5 s before to 1 s after the stimulus onset (Fig. 3a). The first step consisted in resampling the data, recorded at 30 kHz, to 1 kHz to improve processing time. A bandpass finite impulse response filter was applied to filter the signal between 0.1 and 200 Hz, and a notch infinite impulse response (IIR) filter was used to suppress the line noise (50 and 150 Hz) (Fig. 3b).



(a) Raw ECoG signal

(b) Filtered ECoG signal, in orange

(c) Wavelet-denoised ECoG signal, in red

Fig. 3: Sample results of signal preprocessing on one of the 16 channels of the ECoG array. The yellow signal in panel **a** is the raw ECoG signal, the orange in panel **b** is the filtered signal, and the red in panel **c** is the wavelet-denoised signal.

After visual inspection, faulty channels (9 and 16) were interpolated exploiting their neighbors. Finally, 5-level wavelet decomposition was performed using the Bior3.3 biorthogonal wavelet function. The level 5 approximation coefficient vectors were reconstructed (Fig. 3c), and a window of interest between 0 and 0.8 s was extracted for each channel and concatenated for each trial. The dataset used to train and test the classifiers comprised 1000 trials of 13104 time samples.

C. Classification

The same training procedure was used to test 3 classifiers, namely a Random Forest (RF) classifier, a support vector

TABLE I: Hyperparameters tested with grid search

Classifier	Parameter	Values
Random Forest	n_estimators	10, 100, 500
	max_features	32, 10, 20
	max_depth	10, 20, 30, 50
	min_samples_leaf	1, 2, 4
	min_samples_split	2,5,10
Support Vector Machine	kernel	linear, poly, rbf
	degree	2, 3
	gamma	scale, 0.01, 0.1, 1
	C	0.1, 1, 10
Multilayer Perceptron	hidden_layer_sizes	(8), (16), (32) (16,8), (32,8), (32,16)
	activation	identity, relu
	solver	sgd, adam
	learning_rate	adaptive

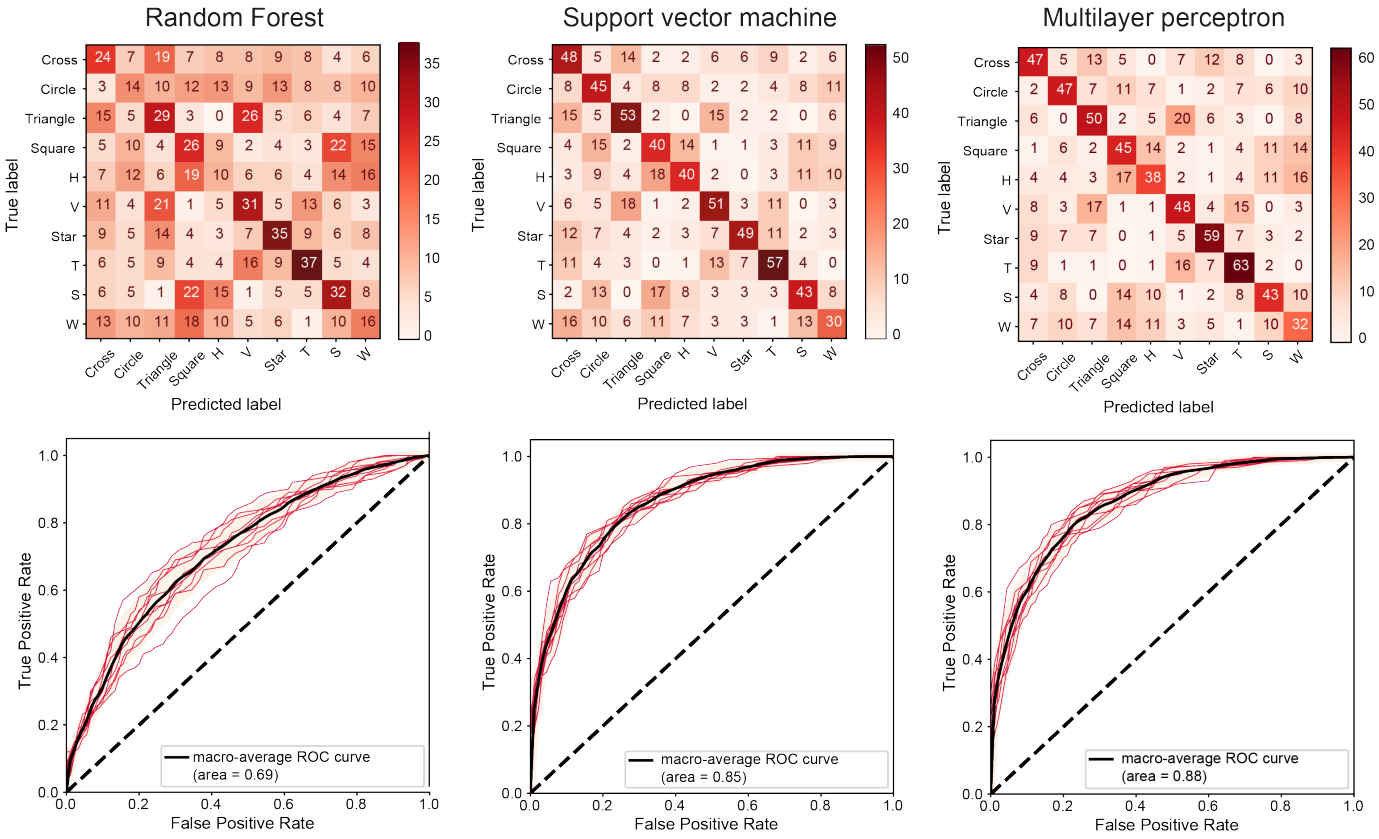


Fig. 4: Classification results. **A**, **B**, and **C** are the confusion matrices relative to the RF, SVM and MLP classifiers respectively. **D**, **E**, and **F** are the corresponding ROC curves and the macro-averages across the 10 folds.

machine (SVM), and a multilayer perceptron (MLP). Nested stratified cross-validation was performed for hyperparameter optimization. The dataset was divided into 10 folds in the outer loop and into 3 folds in the inner loop. The hyperparameters (Table I) were tuned by performing a grid search and selected according to the best classification accuracy on the validation set.

The metrics used to evaluate the models were the classification accuracy and the area under the receiver operating characteristic (ROC) curves, macro-averaged across the 10 folds. One-way ANOVA test was used to assess the statistical significance between the performance of the 3 classifiers.

All the experiments were performed on a Dell XPS 8940, Intel Core i7-10700 processor, 2.90GHz CPU, NVIDIA GeForce GTX 1660 Ti GPU, 16 GB RAM.

III. Results

The classification performance of the 3 tested classifiers are summarized in Fig. 4. RF classifier performed with an accuracy of 22.70±0.3% and an area under the ROC curve (AUC) of 0.66 (Fig. 4, **A** and **D**), slightly above the chance level despite the low classification accuracy. As shown in Fig. 5, classification performance with the SVM was significantly better ($p < 0.01$), and resulted in an accuracy of 44.20±0.05% and an AUC of 0.86 (Fig. 4, **B** and **E**). MLP outperformed in accuracy both the previous classifiers reaching an accuracy of 47.10±0.05%. The AUC was 0.84, lower than the SVM (Fig. 4, **C** and **F**).

Despite the different performances, there is consistency across the confusion matrices. With all the classifiers, Star and T are well identified, while V and Triangle are difficult to discriminate.

IV. Discussion and Future Work

The optic nerve is a possible target for a neural prosthesis aimed at vision restoration [2] [3] [4] and, as with all other neuroprostheses, a crucial aspect is the choice of the stimulation parameters and their optimization strategy. A viable idea is the closed-loop stimulation of the optic nerve, which exploits the cortical activation pattern as feedback [6]. According to this strategy, the cortical activation following the electrical stimulation of the optic nerve would be compared to and driven towards a certain target cortical activation, corresponding to visual perception. To achieve this, a target cortical activation must be identified in principle, therefore we need to classify the activity of the visual cortex based on the visual stimuli presented to the mouse.

The goal of this work was to investigate the feasibility of visual stimuli classification based on the cortical response recorded with an ECoG array. The stimuli set comprised 10 simple shapes, which were passively presented to the anesthetized animal, in random order. Machine learning was

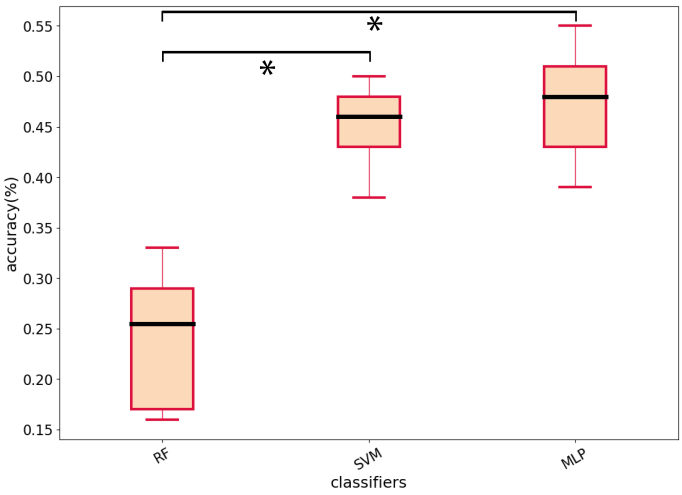


Fig. 5: Comparison of the classifiers' performance. The boxplots show the accuracy of the different classifiers on the test set.

exploited to perform the stimuli classification, and in particular, RF, SVM and MLP classifiers were tested. RF performance was not satisfactory, being above the chance level ($AUC > 0.5$) but not enough to be considered acceptable [14]. Conversely, SVM and MLP classifiers allow significantly better performance, as shown in Fig. 5. More than 40% accuracy has been reached on 10 classes, with AUCs of 0.86 and 0.84 respectively, which indicate good discrimination between classes and classification beyond the chance level.

One potential limitation of our study is that we only used data recorded from a single mouse, which may limit the generalizability of our findings. However, despite this limitation, our results suggest that it might be possible, to a certain extent, to associate a visual stimulus with the corresponding cortical response recorded with an ECoG array. It is important to note that ECoG has a low spatial resolution of recordings, which is likely why, to our knowledge, it has not been previously used for visual stimulus decoding in mice.

On the other hand, the advantages of this technique make it the most suitable for this study. It allows us to record evoked responses from large portions of V1 and consequently of the visual field [8], avoiding information loss. It is possible to record the electrically evoked potential in response to optic nerve stimulation [4], a crucial step for the implementation of closed-loop stimulation. ECoG-based decoding of visual stimuli in human subjects is feasible and has already been done in the literature [10] [11] [12], making it possible to move the study to humans. These advantages are of great importance for the future developments of the study, concerning the closed-loop electrical stimulation of the optic nerve on animal models first, and on humans in the future.

Short-term future steps involve data collection from several animals to investigate the possibility of generalization, the delivery of different visual stimuli to explore the performance of this technique when other areas of the visual field are involved, and the exploration of the closed-loop stimulation of the optic nerve on animal models.

Acknowledgements

This work was supported by #NEXTGENERATIONEU (NGEU) and funded by the association Sulle Ali Di Un Sogno ONLUS, by the Ministry of University and Research (MUR), National Recovery and Resilience Plan (NRRP), project MNESYS (PE0000006) – A Multiscale integrated approach to the study of the nervous system in health and disease (DN. 1553 11.10.2022), and by PRO3 2021-23 Ministry of University and Research (MUR), project NEMESI ("NErvous system at large-scale – MEaSurement and Intervention").

References

[1] E. Zrenner, "Fighting blindness with microelectronics," *Science Translational Medicine*, vol. 5, no. 210, pp. 210ps16–210ps16, 2013.

[2] C. Veraart, C. Raftopoulos, J. T. Mortimer, J. Delbeke, D. Pins, G. Michaux, A. Vanlierde, S. Parrini, and M.-C. Wanet-Defalque, "Visual sensations produced by optic nerve stimulation using an implanted self-sizing spiral cuff electrode," *Brain Research*, vol. 813, no. 1, pp. 181–186, 1998.

[3] M. E. Brelén, F. Duret, B. Gérard, J. Delbeke, and C. Veraart, "Creating a meaningful visual perception in blind volunteers by optic nerve stimulation," *Journal of Neural Engineering*, vol. 2, no. 1, p. S22, 2005.

[4] V. Gaillet, A. Cutrone, F. Artoni, P. Vagni, A. Mega Pratiwi, S. A. Romero, D. Lipucci Di Paola, S. Micera, and D. Ghezzi, "Spatially selective activation of the visual cortex via intraneural stimulation of the optic nerve," *Nature Biomedical Engineering*, vol. 4, no. 2, pp. 181–194, 2020.

[5] E. Losanno, M. Badi, S. Wurth, S. Borgognon, G. Courtine, M. Capogrosso, E. Rouiller, and S. Micera, "Bayesian optimization of peripheral intraneural stimulation protocols to evoke distal limb movements," *Journal of Neural Engineering*, vol. 18, no. 6, p. 066046, 2021.

[6] S. Romeni, D. Zoccolan, and S. Micera, "A machine learning framework to optimize optic nerve electrical stimulation for vision restoration," *Patterns*, p. 100286, 2021.

[7] Y.-J. Zhang, Z.-F. Yu, J. Liu, T.-J. Huang *et al.*, "Neural decoding of visual information across different neural recording modalities and approaches," *Machine Intelligence Research*, pp. 1–16, 2022.

[8] M. E. Garrett, I. Nauhaus, J. H. Marshel, and E. M. Callaway, "Topography and areal organization of mouse visual cortex," *Journal of Neuroscience*, vol. 34, no. 37, pp. 12 587–12 600, 2014.

[9] J. V. Cramer, B. Gesierich, S. Roth, M. Dichgans, M. Düring, and A. Liesz, "In vivo widefield calcium imaging of the mouse cortex for analysis of network connectivity in health and brain disease," *NeuroImage*, vol. 199, pp. 570–584, 2019.

[10] K. Majima, T. Matsuo, K. Kawasaki, K. Kawai, N. Saito, I. Hasegawa, and Y. Kamitani, "Decoding visual object categories from temporal correlations of ecog signals," *NeuroImage*, vol. 90, pp. 74–83, 2014.

[11] C. Kapeller, H. Ogawa, G. Schalk, N. Kunii, W. Coon, J. Scharinger, C. Guger, and K. Kamada, "Real-time detection and discrimination of visual perception using electrocorticographic signals," *Journal of Neural Engineering*, vol. 15, no. 3, p. 036001, 2018.

[12] B. Wittevrongel, E. Khachatryan, M. Fahimi Hnazaee, F. Camarrone, E. Carrette, L. De Taeye, A. Meurs, P. Boon, D. Van Roost, and M. M. Van Hulle, "Decoding steady-state visual evoked potentials from electrocorticography," *Frontiers in Neuroinformatics*, vol. 12, p. 65, 2018.

[13] R. Oostenveld, P. Fries, E. Maris, and J. Schoffelen, "Fieldtrip: Open source software for advanced analysis of meg, eeg, and invasive electrophysiological data (2011)," *Computational Intelligence and Neuroscience*, vol. 2011, p. 156869, 2010.

[14] D. W. Hosmer Jr, S. Lemeshow, and R. X. Sturdivant, *Applied Logistic Regression*. John Wiley & Sons, 2013, vol. 398.

Effects of State Representation on a Reinforcement Learning Based Decision Support System

C. Drudi[1], M. Mollura[1], and R. Barbieri[1]
[1] *Department of Electronic, Information and Bioengineering, Politecnico di Milano, Milano, Italy*

***Abstract*—Reinforcement Learning (RL) methods are increasingly seen as an effective paradigm for providing important solutions in healthcare applications. This is particularly true in critical care, where sequential decision making is closely related to the RL paradigm. However, there are still important issues to be addressed, including the crucial problem of defining an optimal Markov Decision Process (MDP) that best fits the real-world clinical scenario.**
Many proposed approaches to RL in the ICU have used k-means clustering to define the states of the MDP. The k-means algorithm is particularly vulnerable to high-dimensional data, which is needed to account for all possible confounders.
In this work, we use the k-medoids algorithm to define the Markov states. Since this method is more robust to noise and outliers, we investigate the effect of the clustering algorithm on the performance of the RL model.
Data from 20,496 ICU stays of septic patients were included in this study. Two different MDPs were built. The first had its states defined using the k-means algorithm, while the second had its states defined using the k-medoids algorithm. Both MDPs were then solved using an RL technique called policy iteration to obtain the optimal policy. The optimal policies were evaluated using the Weighted Importance Sampling (WIS) estimator.
The policy obtained using k-medoids converged to a 95% confidence lower bound (LB) of 88.67, performing better than the policy obtained using k-means (95% confidence LB of 86.01). This finding suggests that the use of k-medoids in the RL setting could be a key element within an AI-based clinical decision support system, potentially resulting in a lower mortality rate compared to current traditional treatment strategies.

***Keywords*—Reinforcement Learning, State Representation, Intensive Care Unit, Curse of Dimensionality**

I. INTRODUCTION

In recent years, healthcare research has seen a sharp increase in advanced statistical applications to develop new technologies aimed at assisting clinicians in the treatment of patients. These methodological advances have been fostered by the increasing amount of data available, the collection of which has been made possible thanks to technological advances in the collection, storage and processing of data [1], [2]. Critical care practice consists of a series of sequential decisions to be made, this makes the Intensive Care Unit (ICU) particularly compatible with the Reinforcement Learning (RL) paradigm. RL is able to infer which actions are statistically optimal from the pool of actions commonly selected by clinicians.
Many successful RL applications in the ICU context are available in the literature. Some relevant examples include [3], the authors applied RL to determine the optimal target glycemic level in critically ill patients and managed to reduce the mortality of the cohort from 31% to 24.7%. References [4], [5] managed to optimize the timing of mechanical ventilation (MV), reducing the incidence of reintubation and decreasing the total time under MV, while [6], [7], [8] optimized heparin dosages with RL.
One particular condition in critical care that has gained attention in healthcare is sepsis. Several studies [9], [10], [11], [12] have proposed RL applications to individualize and optimize the hemodynamic treatment of septic patients. Despite being a burdensome condition, there is no common consensus among clinicians regarding an optimal treatment strategy, with agreement on only a few treatment variables [13]. RL applications have shown great potential to fill the knowledge gap in sepsis management, allowing for personalized vasopressor (VP) and intravenous fluid (IV) treatment based on a patient's specific characteristics at any given time.
Despite its great potential, RL has some common limitations that need to be addressed [14], [15]. One of these shortcomings is the choice of state representation in the Markov Decision Process (MDP) definition. It is categorical that the state representation correctly and exhaustively summarizes the information contained in the data. One of the most popular methods to define the states is through partitioning clustering techniques, mainly using k-means algorithm. In general, RL applications require high-dimensional space data to ensure that all possible confounders have been included. High dimensionality is also shown to interfere with the k-means algorithm, which loses performance as the dimensionality of the data increases. Furthermore, [16] suggests that the k-medoids algorithm performs better for large datasets.
In this study, we compare the effect that the k-means and k-medoid algorithms have on the performance of RL agents.

II. METHODS

A. Data and preprocessing

This work considers the "Multi-parameter Intelligent Monitoring in Intensive Care (MIMIC-III) database, which contains data from 53,423 hospital admissions at the Beth Israel Deaconess Medical Center in Boston between 2001 and 2012 [17].

The study cohort consists of patients who meet the Sepsis-3 criteria [18] and excludes patients under 18 years of age, those with undocumented mortality or intravenous fluid administration, or those with treatment withdrawal, including those in palliative care or unrecoverable. Patient withdrawal is defined as death within 24 hours of the end of data collection and no receipt of vasopressor during the last 24 hours of data collection, but having received at least one previous administration. The final study population includes 20,496 unique ICU admissions.

Sepsis was identified using two criteria: the presence of a positive microbiological specimen prior to antibiotic administration or a positive microbiological specimen within 24 hours of prior antibiotic administration. In the first case, the onset of sepsis was defined only if the antibiotic was administered within 72 hours of the microbiological sample. The time of sepsis onset is determined as the time of the earliest event [18].

The data used in this study includes values collected from 24 hours before the estimated onset of sepsis to 48 hours after the estimated onset of sepsis. The data are organized in 4-hour time bins, and when multiple observations for the same variable were available in a given time bin, they were averaged or summed according to the type of variable. The study includes 48 variables such as vital signs, demographics, laboratory values, fluid balance, the Elixhauser comorbidity score, and the treatments of interest: intravenous fluids and vasopressors. The study assumes a baseline SOFA score of zero, consistent with previous work in the literature [19], and variables with heterogeneous units of measure were standardized and the numerical values of the variable are capped at plausible physiological values.

This study addresses data sparsity by using a zero order interpolation approach [20], which is commonly used when dealing with clinical time series and mimics the behavior of medical decision making [21]. Any remaining missing data is imputed using interpolation. The data are divided into a training set (80%) and a test set (20%).

In this study, an MDP is built on the dataset. Each patient is assigned to a state for each time step using a partitioning clustering algorithm. The total number of clusters is 750, and two additional absorbing states are added to represent either survival or death of the patient. A total of two models are built, one using k-means as the clustering algorithm and one using k-medoids as the clustering algorithm.

Five bins are created for each treatment type, with one bin reserved for the null dose and the remaining four bins being bounded by the 25th percentile, median, and 75th percentile. The total number of possible actions is 25. The rewards received by the agent are set to +100 if the MDP ends in the "survived" state and -100 if it ends in the "dead" state, this choice is to ensure that the RL agent tries to maximize the 90-day survival. The dynamic evolution of the MDP is determined by the transition matrix T (s',s,a), which defines the probability of each state-action-new-state (s-a-s') triplet. The transitions that occurred less than 5 times were excluded; this choice is made to force the RL agent to select only actions commonly chosen by clinicians, making the resulting policy safer.

B. Policy iteration and evaluation

The MDP underlying RL was solved using the policy iteration algorithm, which involves starting with a random policy, evaluating it, then updating the optimal action for each state, and repeating until convergence to the optimal policy [22].

The state-action value function $Q^{\pi}(s,a)$ represents the expected sum of discounted rewards from following policy π, given a particular state-action pair (*s,a*), and it indicates how beneficial it is to take action a when in state s.

The policy determined to be optimal by policy iteration is defined as:

$$\pi(s)^* \leftarrow \underset{a}{\operatorname{argmax}}\, Q^{\pi^*}(s,a) \forall s \tag{1}$$

Once the policy π to evaluate is known, the state-value of each state s when following policy π can be computed using the Bellman equation:

$$V^{\pi}(s) = \sum_{a} \pi(s,a) \sum_{s'} T(s',s,a)[R(s') + \gamma V^{\pi}(s')] \tag{2}$$

To determine the performance of the optimal AI policy, a technique called Weighted Importance Sampling (WIS) was used, where π_C represents the policy that generated the data and π_{AI} represents the policy of the AI.

The accumulated importance ratio at time step t is defined as:

$$\rho_{1:t} := \prod_{t'=1}^{t} \pi_{AI}(a_{t'} \| s_{t'}) / \pi_C(a_{t'} \| s_{t'}) \tag{3}$$

the average at time t of equation 3 is $w_t = \sum_{i=1}^{N} \rho_{1:t}(i)/N$, where N is the total number of trajectories.

The WIS estimator for a single trajectory can be defined as:

$$V_{WIS} = \frac{\rho_{1:T}}{w_T} \sum_{t=1}^{T} \gamma^{t-1} r_t \tag{4}$$

the overall WIS estimator is determined by averaging all V_{WIS} over each available trajectory.

III. RESULTS

To evaluate and compare the effects of the two different partitioning clustering methods on the RL agent, we visualized (Fig. 1) the evolution of the 95% confidence lower bound (LB) during the training process.

The performance of the RL agent obtained by performing policy iteration on the MDP with the state representation determined by k-means is shown with a solid orange line, while the solid blue line represents the performance of the RL agent obtained by performing policy iteration on the MDP with the state representation obtained by the k-medoids algorithm. Note that the RL agent obtained by k-means for model number

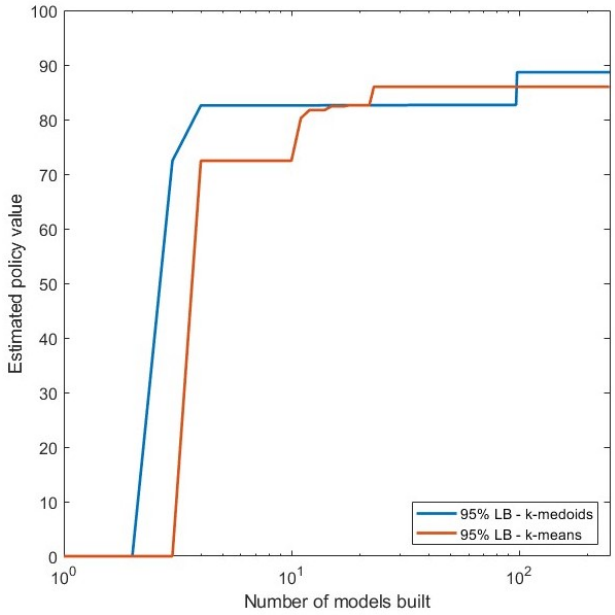


Fig. 1: Evolution of the 95% confidence LB of the *k-means* model and *k-medoids* model over the training of the RL policy

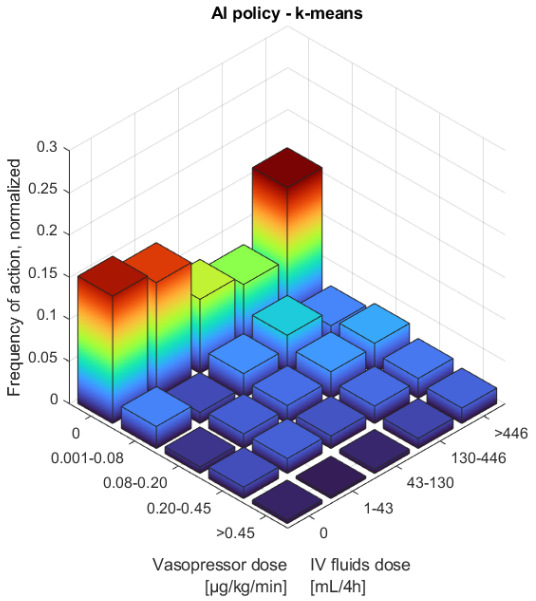


Fig. 2: Histogram of normalized frequencies of the action selected by the *k-means* policy

4 has a 95% LB of 72.45, 80.26 for model number 11, 81.73 for model number 12, 82.42 for model number 15, and 82.62 for model number 18. The improvement of the 95% LB stops at model number 23 and settles at 86.01.
For the RL agent obtained after k-medoids, we have a 95% LB of 72.43 for model number 3 and a 95% LB of 82.58 for model number 4. Two small improvements occur at models 14 and 33 with 95% LB of 82.62 and 82.67 respectively. The model then settles down to a value of 88.67 at model number 98, clearly outperforming its k-means counterpart.

The frequencies of the actions chosen by the k-means policy are visualized in Fig. 2, while the frequencies of the action chosen by the k-medoids policy are shown in Fig. 3.

The numerical results are shown in the tables 2 and 3. The *high* option corresponds to the highest bin (>446 mL/4h for IV and >0.45 μg/kg/min for VP). The k-medoids policy acts more frequently on our patient cohort than the k-means policy, thus less frequently resorting to extreme treatment options and preferring a more moderate treatment strategy.

	No VP	*Moderate VP*	*High VP*
No IV	0.1511	0.0474	0.0043
Moderate IV	0.3011	0.0974	0.0119
High IV	0.1611	0.0862	0.0183

TABLE I: Normalized frequencies of the action selected by the *k-means* policy

IV. DISCUSSION

The objective of this study was to analyze and compare the effect of different partitional clustering algorithms on the performance of the RL model. Two algorithms were compared: the k-means algorithm and the k-medoids algorithm.

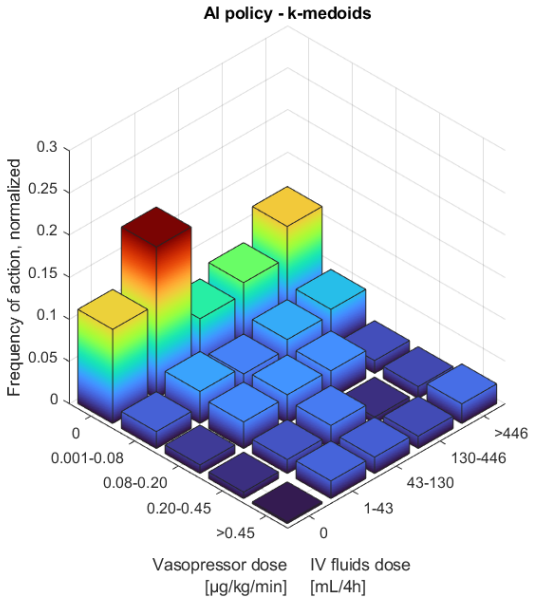


Fig. 3: Histogram of normalized frequencies of the action selected by the *k-medoids* policy

	No VP	*Moderate VP*	*High VP*
No IV	0.1117	0.0379	0.0021
Moderate IV	0.3226	0.080	0.0146
High IV	0.1149	0.0755	0.0233

TABLE II: Normalized frequencies of the action selected by the *k-medoids* policy

When the RL agent was computed using the k-medoids algorithm to define the states of the MDP, we observed a sharp improvement in model performance. This result may be

explained by the improved state representation obtained with the k-medoids algorithm.

This observation is consistent with other works in the literature that claim that k-medoids have some advantage over k-means [16], [23]. It has also been found from experimental results that k-means is advantageous for smaller datasets, while k-medoids tend to perform better for large datasets, a common characteristic of datasets used for RL. It is also shown that k-medoids is more robust to outliers and more resilient to noisy data, one of the common problems of high-dimensional feature spaces used in RL. In addition, the cluster quality is visually more convincing and with less class overlap when using k-medoids.

Finally, the k-medoids policy acts more often on the study cohort with respect to its k-means counterpart, and it is also less extreme. As a matter of fact, the k-medoids policy suggests extreme treatment options less frequently than the k-means policy.

This property might be preferable since extreme treatment dosages are usually used only as a last resort. Thus, the more moderate behaviour of the k-medoids policy may be the reason behind the performance boost of the RL policy and it also more closely reflects the behavior of clinicians who use extreme treatment options more sparingly.

V. CONCLUSION

In conclusion, we have shown that applying a k-medoids clustering algorithm to build the states for the MDP underlying RL leads to an improvement in the performance of the model. In particular, the RL agent obtained by k-medoids achieves a 95% LB equal to 88.67, while its k-means counterpart shows a 95% LB of 86.01. Given this result, it appears that using the k-medoids algorithm instead of the k-means algorithm to build the state representation could be beneficial, leading to a decision support system that minimizes mortality and improves sepsis treatment outcomes.

In addition, it is possible that the actions suggested by the k-medoids policy might be more welcome by clinicians, since they tend to be more moderate and realistic, incurring less often to high dosages.

REFERENCES

[1] L. Anthony Celi, R. G. Mark, D. J. Stone, and R. A. Montgomery, ""big data" in the intensive care unit. closing the data loop," *American Journal of Respiratory and Critical Care Medicine*, vol. 187, p. 1157–1160, Jun 2013.

[2] B. Gholami, W. M. Haddad, and J. M. Bailey, "Ai in the icu: In the intensive care unit, artificial intelligence can keep watch," *IEEE Spectrum*, vol. 55, no. 10, pp. 31–35, 2018.

[3] W.-H. Weng, M. Gao, Z. He, S. Yan, and P. Szolovits, "Representation and reinforcement learning for personalized glycemic control in septic patients," 2017.

[4] N. Prasad, L.-F. Cheng, C. Chivers, M. Draugelis, and B. E. Engelhardt, "A reinforcement learning approach to weaning of mechanical ventilation in intensive care units," *arXiv preprint arXiv:1704.06300*, 2017.

[5] C. Yu, J. Liu, and H. Zhao, "Inverse reinforcement learning for intelligent mechanical ventilation and sedative dosing in intensive care units," *BMC medical informatics and decision making*, vol. 19, no. 2, pp. 111–120, 2019.

[6] S. Nemati, M. M. Ghassemi, and G. D. Clifford, "Optimal medication dosing from suboptimal clinical examples: A deep reinforcement learning approach," in *2016 38th annual international conference of the IEEE engineering in medicine and biology society (EMBC)*, pp. 2978–2981, IEEE, 2016.

[7] R. Lin, M. D. Stanley, M. M. Ghassemi, and S. Nemati, "A deep deterministic policy gradient approach to medication dosing and surveillance in the icu," in *2018 40th Annual International Conference of the IEEE Engineering in Medicine and Biology Society (EMBC)*, pp. 4927–4931, IEEE, 2018.

[8] M. M. Ghassemi, T. Alhanai, M. B. Westover, R. G. Mark, and S. Nemati, "Personalized medication dosing using volatile data streams," in *Workshops at the Thirty-Second AAAI Conference on Artificial Intelligence*, 2018.

[9] A. Raghu, M. Komorowski, L. A. Celi, P. Szolovits, and M. Ghassemi, "Continuous state-space models for optimal sepsis treatment: a deep reinforcement learning approach," in *Proceedings of the 2nd Machine Learning for Healthcare Conference* (F. Doshi-Velez, J. Fackler, D. Kale, R. Ranganath, B. Wallace, and J. Wiens, eds.), vol. 68 of *Proceedings of Machine Learning Research*, pp. 147–163, PMLR, 18–19 Aug 2017.

[10] M. Komorowski, L. A. Celi, O. Badawi, A. C. Gordon, and A. A. Faisal, "The artificial intelligence clinician learns optimal treatment strategies for sepsis in intensive care," *Nature Medicine*, vol. 24, p. 1716–1720, Oct 2018.

[11] M. Mollura, C. Drudi, L.-W. Lehman, and R. Barbieri, "Optimal fluid and vasopressor interventions in septic icu patients through reinforcement learning model," in *2022 Computing in Cardiology (CinC)*, vol. 498, pp. 1–4, 2022.

[12] M. Mollura, C. Drudi, L.-W. Lehman, and R. Barbieri, "A reinforcement learning application for optimal fluid and vasopressor interventions in septic icu patients," in *2022 44th Annual International Conference of the IEEE Engineering in Medicine Biology Society (EMBC)*, pp. 321–324, 2022.

[13] J. E. Gotts and M. A. Matthay, "Sepsis: pathophysiology and clinical management," *BMJ*, p. i1585, May 2016.

[14] C. Yu, J. Liu, S. Nemati, and G. Yin, "Reinforcement learning in healthcare: A survey," Nov 2021.

[15] M. Mollura, C. Drudi, L.-W. Lehman, and R. Barbieri, "A reinforcement learning application for optimal fluid and vasopressor interventions in septic icu patients," in *2022 44th Annual International Conference of the IEEE Engineering in Medicine & Biology Society (EMBC)*, pp. 321–324, 2022.

[16] T. S. Madhulatha, "Comparison between k-means and k-medoids clustering algorithms," in *Advances in Computing and Information Technology* (D. C. Wyld, M. Wozniak, N. Chaki, N. Meghanathan, and D. Nagamalai, eds.), (Berlin, Heidelberg), pp. 472–481, Springer Berlin Heidelberg, 2011.

[17] A. E. Johnson, T. J. Pollard, L. Shen, L.-w. H. Lehman, M. Feng, M. Ghassemi, B. Moody, P. Szolovits, L. Anthony Celi, and R. G. Mark, "Mimic-iii, a freely accessible critical care database," May 2016.

[18] C. W. Seymour, V. X. Liu, T. J. Iwashyna, F. M. Brunkhorst, T. D. Rea, A. Scherag, G. Rubenfeld, J. M. Kahn, M. Shankar-Hari, M. Singer, C. S. Deutschman, G. J. Escobar, and D. C. Angus, "Assessment of Clinical Criteria for Sepsis: For the Third International Consensus Definitions for Sepsis and Septic Shock (Sepsis-3)," *JAMA*, vol. 315, pp. 762–774, 02 2016.

[19] E. P. Raith, A. A. Udy, M. Bailey, S. McGloughlin, C. MacIsaac, R. Bellomo, and D. V. Pilcher, "Prognostic accuracy of the sofa score, sirs criteria, and qsofa score for in-hospital mortality among adults with suspected infection admitted to the intensive care unit," *JAMA*, vol. 317, p. 290, Jan 2017.

[20] A. Lozano, J. Rosell, and R. Pallas-Areny, "On the zero- and first-order interpolation in synthesized sine waves for testing purposes," *IEEE Transactions on Instrumentation and Measurement*, vol. 41, no. 6, pp. 820–823, 1992.

[21] C. Hug, *Detecting hazardous intensive care patient episodes using real-time mortality models*. PhD thesis, Massachusetts Institute of Technology, Dept. of Electrical Engineering and Computer Science, 2009.

[22] R. S. Sutton and A. G. Barto, *Reinforcement learning: An introduction*. MIT press, 2018.

[23] K. Soni and A. Patel, "Comparative analysis of k-means and k-medoids algorithm on iris data," vol. 13, pp. 899–906, 01 2017.

Driver drowsiness detection relying on infrared thermal imaging: a machine learning approach

D. Cardone[1], D. Perpetuini[2], M. Tritto[3], S. Nocco[3], A. Tiberio[3] and A. Merla[1]
[1] *Dept. of Engineering and Geology, University of Chieti-Pescara, Italy;*
[2] *Dept. of Neuroscience, Imaging and Clinical Sciences, University of Chieti-Pescara, Italy;*
[3] *Next2U s.r.l., Pescara, Italy*

***Abstract*—One of the main factors contributing to road accidents all around the world is driver fatigue. For safety reasons, it is essential to identify drowsiness episodes as soon as possible. Numerous studies have shown that PERCLOS, i.e. the percentage of eyelid closure over the pupil across time, is one of the most accurate parameters for drowsiness state assessment. The evaluation of PERCLOS is, however, dependent on the lighting conditions because it is normally computed from the visible video of the subjects. The goal of this study is to get around these constraints by assessing sleepy states using inexpensive, high-resolution thermal infrared technologies. Twelve sleep-deprived participants were chosen for the study, which involved an hour-long driving activity on a driving simulator. Thermal camera Device Alab SmartIr640 was used to capture facial skin temperature throughout the trial, along with facial visible videos of the subjects. Relevant thermal features were estimated from facial regions of interest and extracted over a 30 second time span. A data-driven multivariate machine learning approach based on a three-level Decision Tree Classification of the drowsy state (AWAKE class: PERCLOS<0.15, FATIGUE class: 0.15<PERCLOS<0.23, and SLEEPY class: PERCLOS>0.23) was developed. The average classification accuracy was 0.72±0.05 (mean ± standard deviation). These preliminary results point to the possibility of determining drivers' drowsiness based on facial thermal traits, circumventing the limitations associated with lighting and eye detection that are typical of conventional approaches.**

***Keywords*—drowsiness detection; ADAS; thermal infrared imaging; machine learning;**

I. INTRODUCTION

ONE of the most frequent causes of fatal traffic accidents worldwide is driver fatigue.

The National Highway Traffic Safety Administration (NHTSA) estimates that around 100,000 accidents each year involve drowsy driving. More than 1,550 people die in these collisions, and 71,000 people are injured [1]. The scientific community has made various attempts over the past few decades to prevent accidents brought on by drowsy driving. The estimation of three different types of factors can be used to identify drowsiness:1) Vehicle based 2) Behavioural based 3) Physiological based [2]. Among all, one of the most effective methods to assess driver drowsiness is based on the estimation of a behavioural parameter related to the eye blink, i.e., PERCLOS (percentage of eyelid closure over the pupil across time).

PERCLOS is the cumulative eye closure duration excluding the time spent on normal eye blinks. PERCLOS has been shown to be a highly accurate measure for estimating the drowsy condition of the driver (accuracy of 91.6% stated in [3] and 94.58% in [4]). However, PERCLOS is normally calculated from the visible video of the subjects and its evaluation is highly dependent on the lighting conditions.

Given its independence from the ambient lighting conditions, thermal infrared (IR) imaging may provide a remedy for these shortcomings (i.e., applications also over night or in low-light situations). Additionally, it has the significant benefit of being able to assess autonomic parameters (such as respiratory, sudomotor, and cardiovascular functions) non-invasively and with no contact with the participants [5]. So, if compared to methodologies relying on visible imaging, IR imagery is very suitable for drowsiness detection solution especially in contexts of poor lighting/night conditions.

Given the benefits of using thermography for driver condition monitoring, there are a sizable number of scholarly publications in this area of study. The majority of these publications deal with monitoring driver fatigue and sleepiness. Driver drowsiness was examined by Ebrahimian-Hadikiashari et al. [6] by examining the respiratory function as measured by thermography. The authors saw a considerable reduction in the rate of driver breathing as they transitioned from extremely sleepy to awake states. Additionally, Knapik et al. [7] presented a method based on thermal imaging yawn detection for the evaluation of driver weariness. Recently, Cardone et al. [8] presented a preliminary study relying on a support vector classification able to evaluate the driver's drowsiness state. The present work represents an improvement of [8], employing a different classification model based on a decision tree approach.

In this study, supervised machine learning (ML) techniques and IR imaging were used to determine the driver's level of drowsiness. A three-level Decision Tree classification (DTC) of the drowsy state was carried out, relying on the physiological parameter PERCLOS, used as the gold standard, on the basis of key features of thermal signals extracted from peculiar regions of interest (ROIs), indicative of the psycho-physiological state. The PERCLOS relies on eyelid activity, which, as well as the temperature of the body, are both under the control of the autonomic nervous system. So we hypothesized a strict link between the gold standard used as output for the classification model and the input IR thermal features.

The three output classes have been defined using the work of Garcia et al. [9] and PERCLOS evaluation over time (i.e. AWAKE vs. FATIGUE vs. SLEEP). A leave-one-subject-out cross-validation was used to evaluate the model's

generalization capabilities.
The advanced driving-assistance systems (ADAS) technology and, generally, the degree of road security are both significantly improved by the contactless methodology described in this work for the identification of driver sleepy states.

II. MATERIALS AND METHODS

A. Participants

Twelve adults (6 males, age range 25–45 years, mean 32.7 years) were recruited for the experiment. Before each experimental session, participants were widely informed about the purpose and protocol of the study, and signed an informed consent form, explaining the methods and the purposes of the experimentation in accordance with the Declaration of Helsinki. All the participants were asked to sleep up to two hours the night before the experimental session. Additionally, they were instructed to abstain from consuming any stimulating drugs for the twelve hours prior to the experiment, such as tea, coffee, and cigarette smoke.

B. Procedure and data acquisition

Each individual spent 20 minutes in the experimental room prior to the test to allow the baseline skin temperature to stabilize. A thermostat was used to set the recording space's standard temperature (23 °C) and humidity level (50–60%).
The experiment was carried out using a static driver simulator. Three 27-inch monitors were used to show the scene. The stimulation's total video resolution was 5760 x 1080 pixels. The driver and the screen were separated by 1.5 meters. The horizontal view angle of the participant was 150 degrees.
The City Car Driving, Home Edition software (version 1.5) [10] was used to simulate driving. The experimental procedure involved running a driving simulation in an urban setting for 60 minutes. To guarantee monotonous driving circumstances and consistency of the study protocol for all subjects, the experimental conditions were predetermined (i.e., Traffic density: 0%; Traffic behavior: Low density of traffic; Fullness of traffic: 0%; Dangerous change of traffic: Never; Emergency braking of the car ahead: Never; Pedestrian crossing the road in a wrong place: Never; Accident on the road: Never; Dangerous entrance of the vehicle to the oncoming lane: Never).
Both visible and thermal IR videos were taken while the experimental technique was being carried out.
The depth visible camera Intel RealSense D415 (Full HD 1080p (1920 x 1080)) and the thermal IR camera Device Alab SmartIr640 (spatial resolution: 640x480 pixel, thermal sensitivity: < 50 mK) both recorded visible and thermal infrared (IR) videos.

C. Analysis of PERCLOS signals

The proportion of time that the eyelids are closed over the pupil is known as PERCLOS, and tracking facial landmark's position in relation to the eyes region is required for its evaluation. The technique proposed in [11] was applied to track the coordinates of 68 face landmarks over time.
The visible videos were used to extract PERCLOS signals, which were then computed over 30 second time intervals. The Eye Aspect Ratio (EAR) was first calculated with the procedure described in [12]. The ratio of the eye's height to width is known as the EAR. It is nearly constant and equal to one when the eye is open, and it is approximately zero while closing the eye.
When the EAR is lower than 0.8 for a period that is longer than 3 frames (i.e. 0.1 seconds since the acquisition frame rate was 30 Hz), PERCLOS is marked with 1, otherwise it is 0. Then, for each temporal window (i.e. 30 seconds), the occurrence of 1 is evaluated and a percentage value of this signal is evaluated (PERCLOS%). Referring to the classification thresholds defined in [9], three classes were identified as follows:
1. CLASS 0 - awake --> if $0 \leq PERCLOS\% < 15\%$
2. CLASS 1 - fatigue --> if $15\% \leq PERCLOS\% < 23\%$
3. CLASS 2 - drowsiness --> if $PERCLOS\% \geq 23\%$

A gold standard signal was thus produced for each individual and each interval of 30 seconds, serving as the reference (i.e. label output) for the classification model.

D. Analysis of visible and thermal imaging data

Visible and IR videos of the subjects' faces were simultaneously recorded during the driving experiment at an acquisition frame rate of 30 Hz.

Given the availability of computer vision algorithms for visible videos, visible imaging was used as reference for tracking facial landmark features. The visible facial landmark features were transferred to the thermal imagery, estimating the geometrical transformation between the two imaging optical devices. The tracking procedure described in [11] was used to identify the 68 facial landmark on the thermal images over time, relying on the co-registered visible video. Figure 1a shows an example of the 68 feature landmarks identified on a thermal image.

Two ROIs were considered and positioned on facial areas of physiological importance (nose tip and glabella). The ROIs' coordinates were automatically calculated from the location of the 68 landmarks. In this way, the initialization of the position of the ROIs was automatically determined (Figure 1a).
For each ROI, the average value of all the pixels belonging to the ROI was extracted over time (Figure 1b).

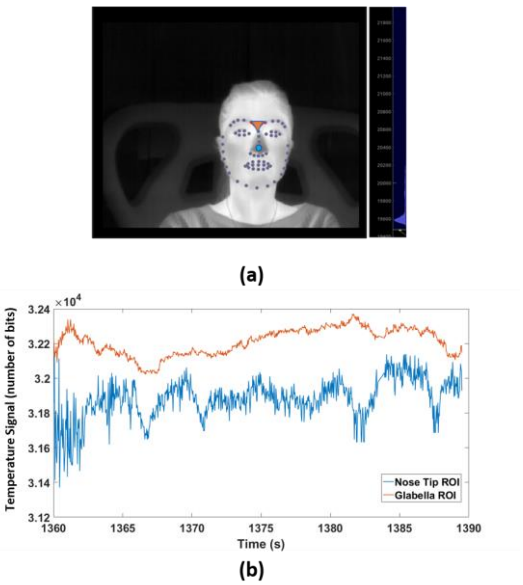


Fig. 1: Thermal signal extraction: (a) Facial landmark identification in the thermal image and ROI identification (nose tip and glabella

showed in orange and blue color respectively), (b) average thermal signals extracted from the ROIs in an exemplificative time window.

Eleven features were computed over successive 30-seconds temporal windows for each of the extracted signals:
1) average value of the raw thermal signals (M);
2) standard deviation of the raw thermal signals (STD);
3) kurtosis of the raw thermal signals (K);
4) skewness of the raw thermal signals (S);
5) absolute value of the difference between the average of the signal in the first 5 seconds and in the last 5 seconds (Δ);
6) 25th percentile of the raw thermal signals (25th P);
7) 50th percentile of the raw thermal signals (50th P);
8) 75th percentile of the raw thermal signals (75th P);
9) 90th percentile of the raw thermal signals (90th P);
10) slope of the raw signal, defined the angular coefficient of the line interpolating the signal (Sl);
11) sample entropy (SampEn).

Importantly, a feature selection based on wrapper approach was employed to consider only the minimal set of features that were relevant for the classification purpose. In this study, a number of 50 random combinations of features was chosen.

E. Application of supervised machine learning

A ML approach based on DTC was employed to classify the drowsy state of the subjects. The eleven thermal features described in Section *II.D* were used to perform a three-level classification of the driver's drowsy state (i.e. AWAKE - FATIGUE - SLEEP). The three classes were defined relying on the threshold defined from the PERCLOS evaluation (Section *II.C*). Cross-validation was employed to assess the generalization capabilities of the procedure. Specifically, a leave-one-subject-out cross-validation was executed.
Furthermore, given the different sample numerosity of the classes, a bootstrap procedure was implemented to test classification performance on balanced classes. The performances of the classification were evaluated by Receiver Operating Characteristic (ROC) analysis.

III. RESULTS

Since the three classes had a different number of samples (797 samples for AWAKE vs. 32 samples for FATIGUE vs. 42 samples for DROWSINESS conditions), a bootstrap procedure was implemented to provide a classification using balanced classes. The average Area Under Curve (AUC) was 0.72 and with standard deviation of 0.05. The distribution of the AUC obtained after the bootstrap is reported in Figure 2 whereas the confusion matrix is reported in Figure 3.

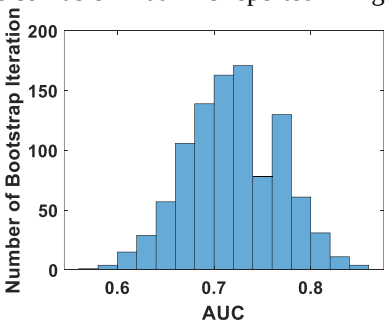


Fig. 2: Results after bootstrap procedure (n_iterations = 1000): distribution of the Area Under Curve (AUC) obtained after the bootstrap procedure.

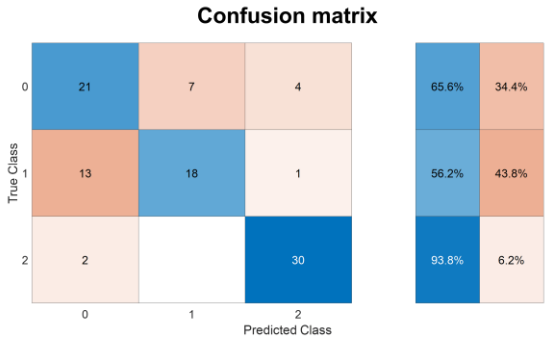


Fig. 3: Confusion matrix for the presented DTC model.

Relying on the confusion matrix, performance parameters, such as specificity and sensitivity were computed for each one of the classes considering the other ones as a unique class. The values of the parameters are reported in Table 1 for each class:

TABLE I: SENSITIVITY AND SPECIFICITY OF THE PRESENTED SVC CLASSIFIER

Standard parameter	***Sensitivity***	***Specificity***
Class 0	0.66	0.76
Class 1	0.56	0.88
Class 2	0.94	0.83
Average -global	**0.72**	**0.82**

Averaging the values reported in Table 1, a global sensitivity of 71.87% and a global specificity of 82.37% were obtained demonstrating a consistent improvement with respect to the authors' previous work [8], which reported a sensitivity of 72.52% and a specificity of 67.69%.

IV. DISCUSSION

This article describes a novel approach to measuring driver drowsiness based on thermal IR imaging and supervised ML. Thermal infrared images and visible videos were captured on twelve sleep deprived participants during an experiment on a driving simulator. In this study, PERCLOS was thus evaluated in consecutive 30-seconds time windows. In the same temporal window, eleven representative features from average thermal signals on two ROIs (i.e. nose tip and glabella) were extracted (Fig. 1). These specific ROIs are reported in literature as the most responsive regions to the autonomic responses and have been already employed to assess stress levels, cognitive workload on drivers. The two ROIs have been also used on drowsiness detection, especially the nose tip area [6],[7]. Using a multivariate ML method based on DTC, a three-level classification of the driver's drowsy state was carried out (i.e. AWAKE vs. FATIGUE vs. SLEEP). A bootstrap approach was used because of the three classes imbalance. The classifier performed well according to ROC analysis, with an average AUC of 0.72 (Fig. 2), a sensitivity of 71.87% and a specificity of 82.37% (Table 1), thus indicating promising performances of the developed model.
It is important to note that the cross-validation and bootstrap procedures tested the model's applicability to a large cohort of

drivers and offered the generalization performances of the model.

The developed method's main advantage over existing literature is its use of supervised machine learning, which is based only on thermal features and ignores any parameters related to the behavior of the driver or the vehicle [13]. This approach achieves performance levels that are comparable with those of more sophisticated methods. Additionally, because the model has already been tested and is ready for use, the established method paves the way for effective real-time implementation of monitoring drivers' sleepy states using simply thermal IR imaging.

However, additional research should be done to broaden the sample. The employed ML approach relied on supervised learning, which is inherently a data-driven analysis. Since data-driven analysis is greatly influenced by sample size, the model's performance could actually be improved by reducing a potential overfitting effect brought on by the small sample size. Another limitation of the study relies on the methodology used for IR features extraction. The IR tracking approach relied on visible imaging algorithms for facial landmark tracking. To benefit from the advantages of using the only thermal IR imaging (e.g. independence from poor/scarce lighting conditions), a completely IR imaging based tracking approach should be developed. The authors want to underline that the main aim of this study was to assess the possibility to develop a model for drowsiness detection based on the only IR thermal features. IR tracking algorithms development is still an open issue to be solved in the future. Finally, the data presented in this work are related to simulated driving scenarios, where factors like direct ventilation or sunlight that affect IR measurements were not taken into account. To broaden the technique's application, it would be necessary to apply the proposed methodology to real-world driving scenarios as well.

For future directions, since the PERCLOS thresholds clearly have an effect on the results, it would be interesting to investigate the ML performance with varying threshold levels and also to compare different typologies of ML classifiers.

V. CONCLUSION

The use of thermal IR imaging and ML algorithms to identify driver drowsiness is presented. The primary goal of the method was to identify the drowsy states of the drivers, overtaking the shortcomings associated with the use of visible cameras to identify indicators of fatigue. The drowsy condition of the individuals while driving in a simulated setting have been classified with a good level of accuracy using a machine learning approach based on thermal features. The presented research reveals that facial thermal traits could constitute a reliable sign of drowsiness in drivers.

ACKNOWLEDGMENT

This research was funded by the grants: PON FESR MIUR R&I 2014-2020-ADAS+, grant number ARS01_00459 and ECSEL Joint Undertaking (JU) European Union's Horizon 2020 Heliaus, grant number 826131.

REFERENCES

[1] 'Fatigued Driver - National Safety Council'. https://www.nsc.org/road-safety/safety-topics/fatigued-driving (accessed Jun. 30, 2021).

[2] V. Saini and R. Saini, 'Driver Drowsiness Detection System and Techniques: A Review', vol. 5, p. 5, 2014.

[3] L. Pauly and D. Sankar, 'Detection of drowsiness based on HOG features and SVM classifiers', in *2015 IEEE International Conference on Research in Computational Intelligence and Communication Networks (ICRCICN)*, Nov. 2015, pp. 181–186. doi: 10.1109/ICRCICN.2015.7434232.

[4] B. N. Manu, 'Facial features monitoring for real time drowsiness detection', in *2016 12th International Conference on Innovations in Information Technology (IIT)*, Nov. 2016, pp. 1–4. doi: 10.1109/INNOVATIONS.2016.7880030.

[5] D. Perpetuini, D. Cardone, C. Filippini, A. M. Chiarelli, and A. Merla, 'Modelling Impulse Response Function of Functional Infrared Imaging for General Linear Model Analysis of Autonomic Activity', *Sensors*, vol. 19, no. 4, Art. no. 4, Jan. 2019, doi: 10.3390/s19040849.

[6] S. Ebrahimian-Hadikiashari, A. Nahvi, A. Homayounfard, and H. Bakhoda, 'Monitoring the variation in driver respiration rate from wakefulness to drowsiness: a non-intrusive method for drowsiness detection using thermal imaging', *J Sleep Sci*, vol. 3, no. 1–2, pp. 1–9, 2018.

[7] M. Knapik and B. Cyganek, 'Driver's fatigue recognition based on yawn detection in thermal images', *Neurocomputing*, vol. 338, pp. 274–292, Apr. 2019, doi: 10.1016/j.neucom.2019.02.014.

[8] D. Cardone *et al.*, 'Driver drowsiness evaluation by means of thermal infrared imaging: preliminary results', in *Infrared Sensors, Devices, and Applications XI*, International Society for Optics and Photonics, 2021, p. 118310P.

[9] I. Garcia, S. Bronte, L. Bergasa, N. Hernández, B. delgado, and M. Sevillano, *Vision-based drowsiness detector for a realistic driving simulator*. 2010, p. 894. doi: 10.1109/ITSC.2010.5625097.

[10] 'City Car Driving 1.5 Description'. https://citycardriving.com/products/citycardriving (accessed Jun. 26, 2020).

[11] D. Cardone, E. Spadolini, D. Perpetuini, C. Filippini, A. M. Chiarelli, and A. Merla, 'Automated warping procedure for facial thermal imaging based on features identification in the visible domain', *Infrared Physics & Technology*, vol. 112, p. 103595, Jan. 2021, doi: 10.1016/j.infrared.2020.103595.

[12] T. Soukupová and J. Cech, 'Real-Time Eye Blink Detection using Facial Landmarks', 2016. https://www.semanticscholar.org/paper/Real-Time-Eye-Blink-Detection-using-Facial-Soukupov%C3%A1-Cech/4fa1ba3531219ca8c39d8749160faf1a877f2ced (accessed Jul. 05, 2021).

[13] J. Stemberger, R. S. Allison, and T. Schnell, 'Thermal imaging as a way to classify cognitive workload', in *2010 Canadian Conference on Computer and Robot Vision*, IEEE, 2010, pp. 231–238.

Supervised Learning-based Detection of Pressure-induced Failures in Continuous Glucose Sensors

E. Idi[1], E. Manzoni[1], A. Facchinetti[1], G. Sparacino[1] and S. Del Favero[1]
[1] *Department of Information Engineering, University of Padova*

***Abstract*—Continuous Glucose Monitors (CGMs) are minimally invasive sensors that are crucial for the management of Type 1 Diabetes (T1D). Pressure-induced sensor attenuations (PISAs) are common faults that occur in the every-day use of the devices. PISAs result in false low blood glucose readings that can impact the reliability in both real-time and retrospective use of the sensors. In this work, we investigate the detection of PISAs failures using supervised learning techniques. Specifically, 6 algorithms, namely Support Vector Machine, Logistic Regression, k-Nearest Neighbors, Decision Tree, Random Forest and Adaptive Boosting are tested and compared to recognize the failures on a dataset generated in-silico using a state-of-art T1D simulator. Encouraging performance are achieved by some of the algorithms tested. In particular, Random Forest recognized up to 90% of the failures with less than 1 false alarms every 10 days. The results obtained in the simulated scenario paves the way for further analysis on real-data and possible improving for detecting new types of fault of the sensors.**

***Keywords*—Continuous Glucose Monitors, Compression artifacts, Detection, Supervised learning.**

I. INTRODUCTION

Type 1 Diabetes (T1D) is a chronic metabolic disease characterized by the defecting or lacking production of insulin, a hormone that plays a key-role in the regulation of the concentration of glucose in the blood. The lack of endogenous insulin is due to the destruction of the pancreatic β-cells by the immune system, responsible of its secretion, and needs to be compensated with exogenous administration [1]. Even in presence of accurate therapy and management, T1D might lead to glycemic levels higher ($hyperglycemia$) and lower ($hypoglycemia$) than the normal range, possibly causing complications that could affect the vascular system, the central nervous system and organs, such as kidneys and eyes [2]. To avoid these scenarios and to maintain the blood glucose (BG) level inside safe limits, called *euglycemic range*, different strategies have been introduced to guarantee an appropriate glucose monitoring, allowing proper treatment decisions.

In the last two decades, minimally-invasive portable sensors, which can offer real-time "quasi-continuous" glucose concentration measurements at rates of 1–5 min for several days, have been developed and introduced in the market, showing a significantly improving of T1D daily treatment. These devices, that are usually referred to as continuous glucose monitoring systems, have revolutionized the management of diabetes, alleviating patients of the burden of the disease, and are proven to have a strong impact also in the clinical practice [3]. Indeed, CGMs can be used retrospectively by clinicians and caregivers to assess the quality of the treatments by extracting glycemic control metrics or analyzing glucose patterns, and by technicians to evaluate the efficacy of glucose control strategies [4], [5]. Faults in CGMs, even if temporary, can have an impact on the sensors' accuracy, leading to potential adverse effects on treatment decisions when used in real-time by patients and inaccurate analysis and evaluation when used retrospectively by clinicians [6].

A. Compression Artifacts

The sensing capability within minimally-invasive CGM systems relies on the glucose oxidase reaction taking place in an electrode deposited on a needle, that is commonly put on the abdomen or the upper arm skin of the patients. Unfortunately, the occasional mechanical compression of the device can alter the glucose diffusion process, reducing the blood glucose flow in the insertion site and causing an attenuation of the sensor sensitivity that results in an underestimation of the glucose concentration, as shown in Figure 1. This is one of the most common faults of the CGM sensors [7], and it is often referred to as Pressure-induced Sensitivity Attenuations (PISAs).

Thereby, to address the aforementioned issue related to the possible presence of false hypoglycemic events, it is important to develop fault detection techniques to identify these malfunctions and to increase the reliability and trustworthiness of CGM devices.

B. Aim of the study

In this study, we expand upon previous research by investigating the retrospective detection of PISAs in CGMs using supervised classification algorithms. We aim to develop a data-driven fault detection approach for the retrospective recognition of PISAs in order to improve the reliability of CGM sensors. Unlike model-based approaches, which rely heavily on the defined model that is difficult to identify due to inter-subject variability, the proposed algorithms rely solely on the availability of labeled historical data.

Moreover, we employ only the data collected with CGM sensors, excluding all the data that could be potentially useful for the purpose but require other devices (i.e. insulin pump) or the strong compliance of the users to be collected (i.e. meal intakes or physical activity).

II. DATASET

A dataset of 100 virtual subjects is generated using the Padova/UVa T1D simulator [8], an accurate physiology simulator that was approved by Food and Drug Administration

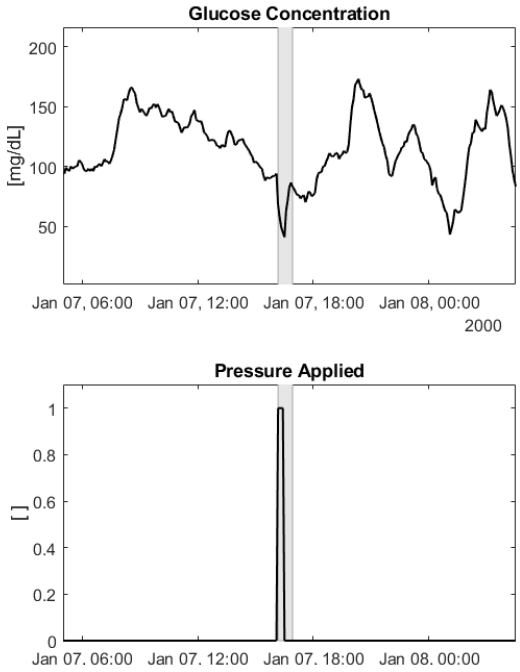


Fig. 1: The first panel shows an example of the compression artifact (highlighted with the gray band) while in the second panel is reported the value of the pressure that causes the fault.

(FDA) as a substitute of animal testing prior to clinical trials on humans. For each of the 100 subjects, a 10-days protocol is simulated with 3 meals per day (breakfast, lunch, and dinner) taking place with uniform probability at $[7.00-8.00]$, $[11.30-13.00]$, $[18.30-20.00]$ and carbohydrates assumption sampled according to the distribution introduced in [9] (namely 58.2 ± 22.5 g for breakfast, 77.7 ± 27.0 g for lunch, 83.9 ± 32.3 g for dinner). It is also considered the possible carbohydrates estimation errors performed by the patient as modeled in [9]. A proportional integral derivative (PID) controller is used as an hybrid closed-loop insulin delivery therapy. BG readings are corrupted with faults in perfectly known position: to simulate the PISAs we used the model described in [10] and validated on CGM time series collected in 72 T1D subjects by the Dexcom G4 Platinum sensor. Moreover, the number of faults in each trace is randomly sampled in accordance with [11]. Finally, the dataset is split in training and test set in a 80-20 proportion.

III. METHODS

The fault detection method's architecture is divided into two main steps. First, the feature extraction is performed by processing the CGM data and computing relevant variables designed to help discriminating normal and abnormal (or $faulty$) data.

Then, different supervised algorithms are applied to the set of features to complete the binary classification in terms of faulty/not-faulty. The performance of the methods tested are presented and discussed in Section IV.

A. Feature Extraction

The upper panel of Figure 1 shows a typical shape of a Pressure Induced Sensor Attenuation. PISAs are characterized by an initial quick dip in BG caused by the pressure applied to the sensor, followed by a subsequent rapid recovery.

Three features are used to highlight the typical pattern in CGM data. These features have already been presented in our previous work [12] and are briefly summarized in this section.

The first feature is defined as:

$$f_1(t) = \frac{1}{2w+1}\sum_{i=t-w}^{t+w} |d'CGM(i)| - \left|\frac{1}{2w+1}\sum_{i=t-w}^{t+w} d'CGM(i)\right|$$

where $d'CGM(t)$ is the first derivative of the CGM signal computed as

$$d'CGM(t) = \frac{1}{T}(CGM(t+1) - CGM(t))$$

with $T = 5$ min the sampling time of the CGM, and w the number of previous and subsequent samples consider (total window length: $2w+1$). The feature $f_1(t)$ is composed of two terms: the first is expected to be large in portions where the signal is rapidly varying, including during a fault, the second represents a correction to remove the possible presence of persistent increase (e.g. after a meal) or decrease, that are not compatible with the shape of the PISA events.

The second feature is obtained applying a moving mask to the CGM signal. This strategy for pattern recognition is frequently applied in biomedical signal analysis [13], e.g. to detect QRS complexes in an ECG trace. The mask looks for a rapid decrease and a subsequent rapid increase. Therefore, the mask focuses on the first derivative of the CGM, in particular its positive and negative components, computed respectively as:

$$|d'CGM(t)|_{>0} = \begin{cases} d'CGM(t) & \text{if} \quad d'CGM(t) \geq 0 \\ 0 & \text{if} \quad d'CGM(t) < 0, \end{cases}$$

$$|d'CGM(t)|_{<0} = \begin{cases} 0 & \text{if} \quad d'CGM(t) \geq 0 \\ -d'CGM(t) & \text{if} \quad d'CGM(t) < 0 \end{cases}$$

The feature $f_2(t)$ consists in the product of two terms $f_2(t) = s_1(t)s_2(t)$ with

$$s_1(t) = \frac{1}{L+1}\sum_{i=t}^{t+L} |d'CGM(i)|_{>0}$$

$$s_2(t) = \frac{1}{L+1}\sum_{i=t+d}^{t+d+L} |d'CGM(i)|_{<0}.$$

The feature f_2 is large if and only if $s_1(t)$ and $s_2(t)$ are simultaneously large at time t, and this happens only if there is a large decrease in the CGM signal followed by a large increase after d samples. The parameters L and d are fixed in accordance to the duration of the failures [10]: $L = d = 3$.

A third last feature $f_3(t)$ is based on the second derivative of the CGM signal $d''CGM(t)$ and is computed as:

$$f_3(t) = \frac{1}{2w+1} \sum_{i=t-w}^{t+w} |d''CGM(t)|. \quad (1)$$

This feature is large in presence of highly irregular data portions with frequent variations of the signal derivative.
An example of the features extracted is reported in Figure 2.

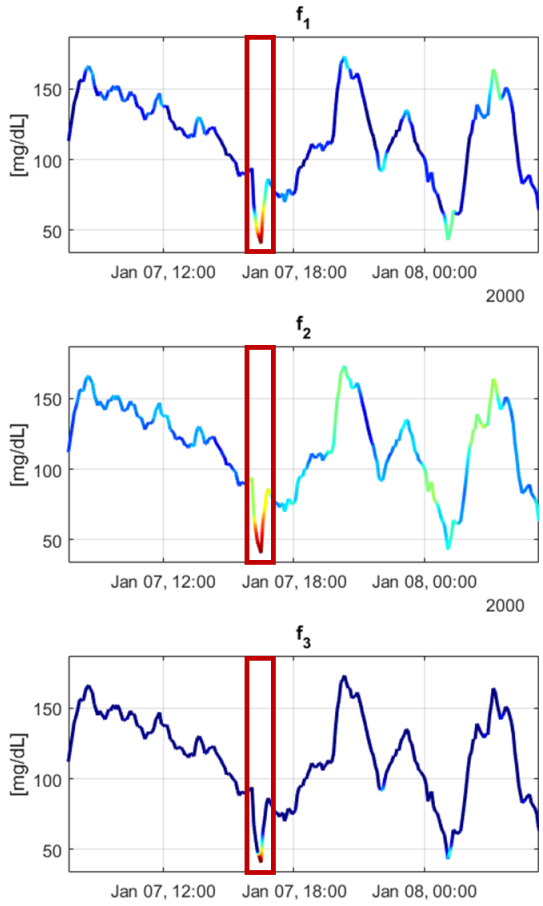


Fig. 2: The CGM trace is colored according to the value of the three features computed. All of them assume high values (corresponding to the red color) when a PISA occurs (highlighted with a red square). Instead, in normal conditions, the trace is colored in blue corresponding to low values of the features.

B. The chosen supervised algorithms

The detection of faulty events was traditionally investigated by employing model-based techniques [14], [15]. However, a significant hurdle of these approaches is the strong dependence on the quality of the model on which they leverage: to achieve accurate models of T1D physiology is a challenging task because of the physiological complexity and the significant inter- and intra-patient variability.

Thus, in this work, we develop a model-free fault detection strategy and we compared the PISA classification performance of several supervised machine learning algorithms: the list of algorithms (implemented in MATLAB2022b) and their parameters are provided in Table I.

TABLE I: ALGORITHMS TESTED

Algorithms	Settings
Logistic Regression	Distribution: $binomial$, probability threshold: 0.5
SVM	kernel: $gaussian$
Decision Tree	Split Criterion: Gini's diversity index
kNN	Distance: correlation, Number of Neighbors: 20
Random Forest	Number of trees: 100, minimum Leaf Size: 1
ADA-boost	Number of ensemble learning cycles: 100

C. Assessment of the algorithms

The performance of the supervised algorithms is evaluated and compared based on their ability to correctly classify instances of PISA faults. The accuracy of the algorithms is determined by comparing their classifications of faulty/non-faulty instances to the ground truth labels, which are known as the faulty events were deliberately added to the simulation in known positions.

In particular, we refer to an $alarm$ when the algorithm assigned a sample to the faulty class. When one or more alarms are raised during a pressure-induced failure, a true positive (TP) is assigned, otherwise the faulty portion is classified as a false negative (FN). Instead, if an alarm is wrongly raised, a false positive (FP) is considered. Moreover, the 25-minutes window after the generation of an alert is excluded by the evaluation, since the faults cause the system to remain in an anomalous state for some time.

To evaluate the algorithm performance and to deal with unbalanced dataset, the FP/day-Recall space [16] is considered. Specifically, we use as evaluation metrics, the number of false alarms per day (FP/day), and the Recall (also known as sensitivity), that represents the capability of the algorithm to effectively detect a fault and is computed as:

$$Recall = \frac{TP}{TP + FN}.$$

IV. RESULTS

The results of the supervised methods tested are summarized and reported in Table II.

In this highly unbalanced dataset, Support Vector Machine (SVM) and Logistic Regression show a limited discriminating power with the lowest number of false alarms generated but also the lowest number of faults recognized.

The best performance is achieved with Random Forest that shows similar results in terms of recall with Decision Tree, but with the half of false alarms generated, and an higher recall with respect to k-Nearest Neighbors, with the same false alarms generated.

An appealing trade-off between recall and FP/day is obtained with Adaptive-boosting algorithm (ADA-boost) that is able to recognize the 80% of the failures without generating false alarms.

TABLE II: TEST SET

	Recall	*FP/day*
SVM	0.29 [0.20-0.50]	0.00 [0.00-0.00]
Logistic Regression	0.50 [0.22-0.71]	0.00 [0.00-0.05]
k-NN	0.75 [0.45-1.00]	0.10 [0.00-0.20]
Decision Tree	1.00 [0.75-1.00]	0.20 [0.05-0.30]
Random Forest	0.90 [0.68-1.00]	0.10 [0.00-0.15]
ADA-boost	0.79 [0.60-1.00]	0.00 [0.00-0.00]

V. CONCLUSIONS

In this work, supervised algorithms were tested to detect compression artifacts (known as PISAs), which are temporary failures that affect the Continuous Glucose Monitors' accuracy by generating anomalous glycemic reading. The performance of the algorithm was evaluated basing on the recall and the number of false alarms generated per day.

Some of the proposed fault detection methods exhibit promising results, particularly Random Forest and ADA-boost which were able to detect the 90% and 80% of compression artifacts respectively, with less than 1 false alarm generated every 10 days.

Since this study is retrospective, one of its main limitation is the intrinsic inability of detecting the malfunctions in real time. This is only related to the features extracted, that benefit from knowing the future glucose concentration measurements in their definition.

Possible future research will expand this approach to real data affected by PISAs, to understand how much the training of the algorithm on simulated faults is affecting the accuracy of the method.

REFERENCES

[1] K. G. Alberti and P. Z. Zimmet, "Definition, diagnosis and classification of diabetes mellitus and its complications. part 1: Diagnosis and classification of diabetes mellitus. provisional report of a who consultation," *Diabetic medicine*, vol. 15, no. 7, pp. 539–553, 1998.

[2] A. D. Association *et al.*, "2. classification and diagnosis of diabetes," *Diabetes care*, vol. 39, no. Supplement 1, S13–S22, 2016.

[3] M. Vettoretti, G. Cappon, G. Acciaroli, A. Facchinetti, and G. Sparacino, "Continuous glucose monitoring: Current use in diabetes management and possible future applications," *Journal of diabetes science and technology*, vol. 12, no. 5, pp. 1064–1071, 2018.

[4] R. W. Beck, P. Calhoun, and C. Kollman, "Use of continuous glucose monitoring as an outcome measure in clinical trials," *Diabetes technology & therapeutics*, vol. 14, no. 10, pp. 877–882, 2012.

[5] E. I. Georga, V. C. Protopappas, and D. I. Fotiadis, "Glucose prediction in type 1 and type 2 diabetic patients using data driven techniques," *Knowledge-oriented applications in data mining*, pp. 277–296, 2011.

[6] D. M. Maahs et al., "A randomized trial of a home system to reduce nocturnal hypoglycemia in type 1 diabetes," *Diabetes care*, vol. 37, no. 7, pp. 1885–1891, 2014.

[7] K. L. Helton, B. D. Ratner, and N. A. Wisniewski, *Biomechanics of the sensor-tissue interface—effects of motion, pressure, and design on sensor performance and foreign body response—part ii: Examples and application*, 2011.

[8] R. Visentin et al, "The uva/padova type 1 diabetes simulator goes from single meal to single day," *Journal of diabetes science and technology*, vol. 12, pp. 273–281, 2 Mar. 2018.

[9] L. Meneghetti, A. Facchinetti, and S. Del Favero, "Model-based detection and classification of insulin pump faults and missed meal announcements in artificial pancreas systems for type 1 diabetes therapy," *IEEE Transactions on Biomedical Engineering*, 2020.

[10] A. Facchinetti, S. Del Favero, G. Sparacino, and C. Cobelli, "Modeling transient disconnections and compression artifacts of continuous glucose sensors," *Diabetes technology & therapeutics*, vol. 18, no. 4, pp. 264–272, 2016.

[11] N. Baysal et al, "A novel method to detect pressure-induced sensor attenuations (pisa) in an artificial pancreas," *Journal of diabetes science and technology*, vol. 8, no. 6, pp. 1091–1096, 2014.

[12] E. Idi, E. Manzoni, G. Sparacino, and S. Del Favero, "Data-driven supervised compression artifacts detection on continuous glucose sensors," in *2022 44th Annual International Conference of the IEEE Engineering in Medicine & Biology Society (EMBC)*, IEEE, 2022, pp. 1145–1148.

[13] J. Pan and W. J. Tompkins, "A real-time qrs detection algorithm," *IEEE Transactions on Biomedical Engineering*, vol. BME-32, no. 3, pp. 230–236, 1985.

[14] A. Facchinetti, G. Sparacino, and C. Cobelli, "Online denoising method to handle intraindividual variability of signal-to-noise ratio in continuous glucose monitoring," *IEEE Transactions on Biomedical Engineering*, vol. 58, no. 9, pp. 2664–2671, 2011.

[15] S. Del Favero et al., "Real-time detection of glucose sensor and insulin pump faults in an artificial pancreas.," *IFAC Proceedings Volumes*, vol. 47, no. 3, pp. 1941–1946, 2014.

[16] L. Meneghetti, G. A. Susto, and S. Del Favero, "Detection of insulin pump malfunctioning to improve safety in artificial pancreas using unsupervised algorithms," *Journal of diabetes science and technology*, vol. 13, no. 6, pp. 1065–1076, 2019.

Decoding Emotions through Music: A Physiological Analysis of Emotion Recognition

E.M. Polo[1], M. Mollura[2], A. Paglialonga[3] and R. Barbieri[2]
[1] *DIAG, Sapienza University of Rome, Italy*
[2] *Politecnico di Milano, Milano, Italy*
[2] *National Research Council of Italy (CNR), IEIIT, Milan, Italy*

***Abstract*—In this study, we have explored the field of emotion recognition, which has been gaining increasing interest for both the study of emotional control disorders and human-computer interaction. The majority of emotion recognition studies in the literature use visual or audio-visual stimuli, leaving the audio-only component often overlooked. In this study, we analyzed data from an experiment on emotion recognition induced by music. By processing signals from the electrocardiogram, respiration, and skin conductance, we identified features that were highly relevant for separating four emotions (i.e., joy, anger, sadness, pleasure). We then created a machine learning model to classify the four emotions using only three of the most relevant features selected based on a recent feature selection method utilizing a graphical visualization. The results showed an average accuracy of 85% in classifying the four emotions, and more than 90% of accuracy for classifying arousal and valence. This study highlights the potential of using only audio stimuli for emotion recognition and the effectiveness of music as a tool for studying emotional control.**

***Keywords*—Emotions, pshysiological signals, machine learning, music.**

I. INTRODUCTION

The emotional state of an individual plays a crucial part in their existence, acting as an essential aspect that has evolved over time to guarantee preservation and procreation through modifying behaviors in response to the surroundings [1]. Emotions hold a vital place in human conduct, as they regulate the movement of facial muscles and other regions of the body, leading to identifiable physical posture and expressions that mirror the current emotional state of the person.

Research on emotions is attracting a growing level of attention in our society due to its potential applications in a wide range of fields, including the emerging areas of Human-Computer and Human-Robot interaction [2].

The development of effective techniques for eliciting and identifying emotions can significantly aid in the evaluation and quantification of conditions that have a significant impact on human health and well-being.

Even if there is a growing interest in using music in more clinically oriented applications such as monitoring depression, anxiety, stress, chronic anger and mood disorders [3],[4], the emotional aspect of sounds has received comparatively less attention with respect to the extensive research on visual stimuli in the field of emotion recognition from physiological signals [5],[6].

Furthermore, we have recently discovered that sounds can evoke a stronger physiological response, both centrally and peripherally, compared to visual stimuli, and to the combination of auditory and visual stimuli [7],[8]. Building upon these results, we have conducted an analysis on an online dataset of emotion recognition through music, which has received relatively little attention in literature, especially in terms of the physiological changes induced by emotional music. In the field of emotion recognition, most studies tend to overlook the interpretation of features and instead focus on achieving high accuracy rates by using dimensionality reduction methods, calculating a high number of features without specifying which signals and features may be most relevant for creating a framework that can be applied in similar studies. Our aim is to create a simple framework for emotion recognition by investigating the meaning of features in relation to specific emotions and music.

II. MATERIALS AND METHODS

A. Data

The data employed in our study was obtained from the University of Augusta, Germany [9]. The research involved assessing a single individual over a period of 25 consecutive days. The participant was exposed to various musical selections, chosen on a daily basis, to gauge various emotional states: joy, anger, sadness, and pleasure. The aim of listening to these musical pieces was to guide the participant through a sequence of emotional states, starting with joy, moving to anger, sadness, and ending with pleasure. To elicit the intended emotional state, the participant was prompted to select songs that evoked personal memories.

During the listening of the musical pieces, the subject was monitored using biosensors to extract four physiological signals: skin conductance (SC), electrocardiogram (ECG), electromyogram (EMG), and respiration (RESP). After collecting the signals, the subject was given a break of varying duration to allow the parameters to return to their baseline, before proceeding with the next recording. In total, 25 recordings were obtained for each of the four emotions and for each of the signals. The recordings were made throughout the duration of the musical pieces, but were then standardized to 120 seconds from the start of each piece. The ECG was sampled at 256 Hz, while SC, EMG and RESP were at 32 Hz. In light of the advancements in wearable sensors currently available, we

have decided to discard the facial EMG sensor due to its increased invasiveness and lower level of integration. We will instead focus on analyzing only three signals for which there are already integrated sensors available on the market.

B. Data Processing and Feature Extraction

ECG: The ECG signal was first processed through a zero-phase, 4th order low-pass Butterworth filter. R peaks on the ECG signal were identified using a Pan-Tompkins based algorithm [10]. From these peaks, a total of 5 features were calculated. Given the relatevely short duration of songs (i.e., 120 seconds), only features related to the time domain were included. For each emotion five basic features were extracted from ECG: average and standard deviation of normal-to-normal intervals (*AVNN*, *SDNN*), first and second standard deviations and their ratio from the Poincare‘ analysis (*SD1*, *SD2*, *SD ratio*).

SC: The SC signal was first processed through a 2 Hz zero-phase, 4th order low-pass Butterworth filter, and then downsampled to a rate of 8 Hz to eliminate any redundant information. To identify the phasic component, a median filter was implemented by determining the median SC of the neighboring samples in a range of +/- 4 seconds centered on the current sample [11]. The raw signal was then adjusted by subtracting the median SC to obtain the phasic component. Once the peak onsets (amplitude > 0.005 μS) and offsets (0 μS < amplitude) were identified on the phasic signal, a SC peak was detected on the raw signal between each onset and offset occurrence. For each emotion eleven basic features were extracted from SC: the average and standard deviation SC values (*AVSC*, *SDSC*), the quantity of SC peaks (*SC n peaks*), the mean amplitude of the peaks (*AVSC n peaks*), the standard deviation of the peaks (*SDSC n peaks*), the average rise and recovery time of the pekas in seconds (*AVSC rise time*, *AVSC recovery time*) and the average of the integral of the phasic component's envelope (*AVenv*). Then, the SC signal filtered with a 2nd order Butterworth band-pass filter from 0.5 to 1 Hz is used to compute some metrics such as average, standard deviation and maximum of the SC derivative (*AVSC der*, *SDSC der*, *MAXSC der*).

RESP: The RESP signal was filtered by a Zero-phase digital band-pass filtering (1 Hz pass-band cutoff frequency and 1.5 Hz stop-band cut-off frequency)by using the Parks–McClellan algorithm [12]. The signal was then analyzed to identify its maximum and minimum values by applying a thresholding technique. For each emotion two basic features were extracted from RESP: the respiratory frequency (*f RESP*) and the average amplitude of breaths (*amp RESP*), computed as the difference between maximum and minimum of each breath.

C. Statistical analysis

The normality of the data was evaluated using the Shapiro-Wilk test. Since one or more emotions were characterized by a non-normal distribution for each feature, and in order to compare four distributions (one for each emotion) of the same subject on different days, the non-parametric Friedman's test with Bonferroni correction was applied.

D. Classification

A simple emotion recognition models was created using the k-nearest-neighbor classifier. In order to provide a simple and interpretable model, a feature selection method based on a graphical visualization that had already proven useful in this field was applied [13]. In this method, for each couple of statistically significant features, 2D boxplot are created where the center of the boxes is the average of the two features and the sides of the boxes are the 95% confidence intervals for the average estimation. Subsequently, the features that appear most frequently in the pairs where no intersection between the boxes is detected, are selected. Of these, the ones that are less correlated are then chosen.

Since the dataset consists of repeated measures of the same subject on different days, revised leave-one-out cross validations were applied to the entire dataset. In particular, to evaluate whether the influence of different days was negligible in the classification, a leave-5days-out cross validation was applied, where in each iteration, 5 entire days of measurements were left as the validation set. Then, in order to see if the performance persisted even with fewer observations, a leave-1day-out was applied, and finally, a leave-one-out, leaving only one observation in the validation set. The same analysis was repeated with the same three features for binary arousal and valence classification. Arousal represents the level of tension or relaxation associated with an emotion (i.e., high for joy/anger and low for sadness/pleasure) and valence represents the pleasantness or unpleasantness of an emotion (i.e., positive for joy/pleasure and low for sadness/anger) [16].

III. RESULTS

According to the statistical analysis, the majority of features have been found to be statistically significant in at least three out of six comparisons (i.e., joy-anger, joy-sadness, joy-pleasure, anger-sadness, anger-pleasure, sadness-pleasure). In particular, *AVNN*, *RESP f* and *RESP amp* have been the most effective features, obtaining five statistically significant differences out of six (i.e., all except anger-pleasure, joy-pleasure, and sadness-pleasure, respectively). Four statistically significant differences have also been found for *SDSC n peaks* and *MAXSC der* (i.e., all except anger-pleasure, sadness-pleasure). Median and interquartile range for each of the above mentioned relevant features are reported in Table I.

TABLE I: MEDIAN AND INTERQUARTILE RANGE OF THE FEATURES WHICH SHOW AT LEAST FOUR STATISTICALLY SIGNIFICANT DIFFERENCES AMONG THE FOUR EMOTIONS.

	JOY	*ANGER*	*SADNESS*	*PLEASURE*
AVNN [ms]	713 (57)	799 (56)	882 (50)	828 (90)
f RESP [n resp/min]	12.5 (2.6)	22 (3.7)	11 (0.62)	13 (1.75)
amp RESP [a.u.]	0.84 (0.38)	0.50 (0.28)	0.72 (0.35)	0.73 (0.28)
MAXSC der [nS]	7.1 (12.9)	2.8 (3.9)	0.94 (1.4)	1.1 (1.4)
SDSC n peaks	13 (8.5)	6 (4.25)	2 (5)	4 (4)

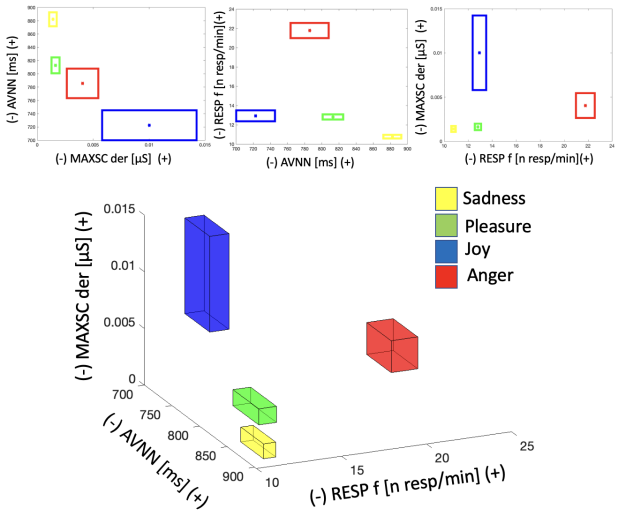


Fig. 1: 3D boxes are displayed, one for each emotion, where the center of each box (i.e., each emotion) is given by the mean of the three features and the length of the sides is given by the 95% confidence limits for the mean estimate. Specifically, the main figure shows the combination of the three most performing features in the space of the four emotions. Above, the projections of the 3D boxes in two dimensions are presented.

Form the feature selection step, *AVNN*, *MAXSC der*, *RESP f*, were the best features selected, able to separate the four emotions in the 2D plane and correlated minimally. A graphical representation is visible in Figure 1, which shows both the projections and a 3D representation of the four emotions in the plane of the most relevant features for the separation. Only these features were included in the following models.

The average validation accuracy in classifying the four emotions and both arousal and valence was calculated and reported in Table II.

TABLE II: KNN ACCURACY AS MEAN (S.D.) OBTAINED FOR FOUR EMOTIONS, AROUSAL AND VALENCE CLASSIFICATION.

	4 Emotions	*Arousal*	*Valence*
leave-5days-out	85 (0.07)	90 (0.03)	92 (0.09)
leave-1day-out	85 (0.17)	92 (0.11)	93 (0.13)
leave-one-out	85 (0.30)	92 (0.27)	93 (0.25)

IV. DISCUSSIONS

A. Feature characterization

Statistical analysis has revealed that SC, ECG, and RESP signals are able to distinguish among the four emotions (see Table I). The effectiveness of this protocol, indeed, lies in the fact that most people have a tendency to associate certain musical melodies with specific emotional states due to their frequent exposure to music throughout their daily lives.

The *AVNN* feature, which is related to the average of normal heartbeats, *RESP f*, and *RESP amp*, were found to be the best performing features, resulting in statistically significant differences in all comparisons among emotions except one.

In general, we can see from Table I and Figure 1 that the features related to the SC are able to separate the emotional dimension of arousal, that is, the emotions with the highest excitement (i.e., joy and anger) from those with the lowest excitement (i.e., pleasure and sadness). It can be noted that higher values are related to higher arousal, which is already widely accepted in literature [17],[14]. The interesting thing to notice is how at the level of excitement, the joy, positive-valence emotion, seems to win over anger. In fact, it seems that all the features related to SC have much higher values in joy than the other emotions, as can be easily seen from Figure 1, where the derivative of the SC stands out in height on the z-axis compared to the other three emotions.

At the cardiac level, we can see how *AVNN* has a very good performance and characterizes joy and sadness very well in an opposite way. These two emotions are, in fact, opposite to the circumflex model used to describe emotions in the dimensions of valence and arousal and, in fact, joy, with high arousal and positive valence, has the highest heart acceleration, while sadness, with low arousal and negative valence, has the highest deceleration.

Regarding the respiratory signal, it seems to be very relevant for the recognition of anger, which shows a much higher average rate than the other three emotions.

From a physiological point of view, summarizing the results, this study suggests that:

-Joy is characterized by a greater sympathetic activation, obtaining, in fact, much higher SC values than the other emotions, as well as a higher heart acceleration.

-Anger, on the other hand, seems to be described very well by respiratory frequency and breath amplitude, much higher and much narrower, respectively, than the other emotions.

-Sadness is the emotion characterized by the lowest responses in terms of respiratory frequency, heart acceleration, and sweating.

-Pleasure, very close to sadness at the physiological level, is characterized by values of all features located in the middle compared to the two emotions with high arousal and sadness.

B. Emotion classification

Regarding the classification part, the problem was addressed by trying to overcome the limitation given by the fact that the recordings are related to only one subject. In order to evaluate the dependence of the classification on time, that is, to see if on different days at the physiological level the emotional responses were different, it was decided to use a leave-one-out cross-validation, leaving in the first case five entire days, in the second case one entire day and in the third case only one observation in the validation set. This has avoided data leakage as for each iteration, the model was not trained on recordings belonging to days present in the validation set. From Table II, it can be seen that the KNN model performed very well. An average accuracy of 85% was obtained in discriminating the four emotions using only three features and very high average

accuracies were found for arousal (i.e., 90%/92%) and valence dimensions (i.e., 92%/93%). Looking at the results related to different leave-one-out models, we can see that time is not relevant in the classification, proving that musical stimuli used are able to evoke a similar physiological response even on different days. It is not the first time that the elicitation of emotions through music leads to very high results in terms of classification. It is indeed the case of Kim and Andre [15], who, by making measurements on three subjects over the course of three months using music as an emotional stimulus, were able to achieve an accuracy of 87% for each subject in discriminating the four emotions used in this study. Despite the fact that music and audio-only stimuli are not commonly used in literature for the study of emotions, it is clear that music can have a great potential in this field, also opening the possibility of extending auditory stimuli to other fields of psychophysiology.

Further studies are certainly necessary, particularly to overcome the limitation of subject-dependent classification. It is necessary to achieve good performance in a subject-independent setting in order to extend the models to real-world scenarios. It is also necessary to use not only music but also real-world sounds to understand if they can evoke emotions with similarly good performance.

V. Conclusion

In this study, we have presented an analysis of a dataset of emotions elicited by musical stimuli during the measurement of physiological signals. Specifically, we have focused on the study of the physiological differences induced by such emotions, with the aim of understanding how our body behaves depending on the emotion evoked. Through a simple machine learning model and using only three features, one for each signal analyzed, we were able to achieve high accuracy both in the four-class problem in separating the emotions, and in the binary problems for separating low/high arousal and positive/negative valence. The temporal variable, given by the fact that the same subject was tested on different days, did not seem to influence the results. Overall, this study suggests that music as a mode of stimulation appears to be effective, opening the door to its use in other fields beyond emotion recognition, such as the study of pathologies such as anxiety and mood disorders.

References

[1] Sorinas, J., Ferrández, J. M., & Fernandez, E. (2020). Brain and body emotional responses: Multimodal approximation for valence classification. Sensors, 20(1), 313.

[2] Cowie, R., Douglas-Cowie, E., Tsapatsoulis, N., Votsis, G., Kollias, S., Fellenz, W., & Taylor, J. G. (2001). Emotion recognition in human-computer interaction. IEEE Signal processing magazine, 18(1), 32-80.

[3] Cassileth, B. R., Vickers, A. J., & Magill, L. A. (2003). Music therapy for mood disturbance during hospitalization for autologous stem cell transplantation: a randomized controlled trial. Cancer, 98(12), 2723-2729.

[4] Koelsch, S., Offermanns, K., & Franzke, P. (2010). Music in the treatment of affective disorders: an exploratory investigation of a new method for music-therapeutic research. Music Perception, 27(4), 307-316.

[5] Li, L., & Chen, J. H. (2006, December). Emotion recognition using physiological signals from multiple subjects. In 2006 International Conference on Intelligent Information Hiding and Multimedia (pp. 355-358). IEEE.

[6] Valenza, G., Lanata, A., & Scilingo, E. P. (2011). The role of nonlinear dynamics in affective valence and arousal recognition. IEEE transactions on affective computing, 3(2), 237-249.

[7] Polo, E. M., Farabbi, A., Mollura, M., Barbieri, R., Paglialonga, A., & Mainardi, L. (2022, July). Analysis of the skin conductance and pupil signals for evaluation of emotional elicitation by images and sounds. In 2022 44th Annual International Conference of the IEEE Engineering in Medicine & Biology Society (EMBC) (pp. 1968-1971). IEEE.

[8] Farabbi, A., Polo, E. M., Barbieri, R., & Mainardi, L. (2022, July). Comparison of different emotion stimulation modalities: an EEG signal analysis. In 2022 44th Annual International Conference of the IEEE Engineering in Medicine & Biology Society (EMBC) (pp. 3710-3713). IEEE.

[9] Wagner, J. (2006). Augsburg biosignal toolbox (Aubt)–User Guide. University of Augsburg.

[10] Sedghamiz, H. (2014). Matlab implementation of Pan Tompkins ECG QRS detector. Code Available at the File Exchange Site of MathWorks.

[11] Bakker, J., Pechenizkiy, M., & Sidorova, N. (2011, December). What's your current stress level? Detection of stress patterns from GSR sensor data. In 2011 IEEE 11th international conference on data mining workshops (pp. 573-580). IEEE.

[12] Rabiner, L. R., & Gold, B. (1975). Theory and application of digital signal processing. Englewood Cliffs: Prentice-Hall.

[13] Polo, E. M., Mollura, M., Lenatti, M., Zanet, M., Paglialonga, A., & Barbieri, R. (2021, November). Emotion recognition from multimodal physiological measurements based on an interpretable feature selection method. In 2021 43rd Annual International Conference of the IEEE Engineering in Medicine & Biology Society (EMBC) (pp. 989-992). IEEE.

[14] Roth, W. T., Ehlers, A., Taylor, C. B., Margraf, J., & Agras, W. S. (1990). Skin conductance habituation in panic disorder patients. Biological psychiatry, 27(11), 1231-1243.

[15] Kim, J., & André, E. (2008). Emotion recognition based on physiological changes in music listening. IEEE transactions on pattern analysis and machine intelligence, 30(12), 2067-2083.

[16] Posner, J., Russell, J. A., & Peterson, B. S. (2005). The circumplex model of affect: An integrative approach to affective neuroscience, cognitive development, and psychopathology. Development and psychopathology, 17(3), 715-734.

[17] Grey, J. A., & McNaughton, N. (1982). The neuropsychology of anxiety. An enquiry into the functions of the septo-hippocampal system.

Quantitative validation of an automatic videoPPG technique during autonomic elicitations

A.C. Palmisciano[1], M. Mollura[1], R. Barbieri[1], and L. Mainardi[1]
[1]*Department of Electronics, Information and Bioengineering, Politecnico di Milano, Milano, Italy*

***Abstract*—The videophotoplethysmography (vPPG) is a technique that allows proxy measurements of blood volume variations in the peripheral microcirculation by detecting the periodical skin color variations during the phases of the cardiac cycle. Therefore, it is also possible to use vPPG signals to evaluate heart rate variability and autonomic modulation of the cardiovascular system. The main advantage of this technique is that it does not require physical contact. We developed and validated an automatic method for the extraction of the vPPG signal, with related HRV descriptors, focusing on different aspects of the vPPG workflow. First, we developed an automatic pixel classifier for the identification and tracking of the region of interest (ROI) and validated it by building a specific validation dataset, with the Dice similarity coefficient as the performance metric. We chose the hand palm as the ROI. Then, we devised an extraction and processing pipeline that can automatically obtain the vPPG signal from the video recording and remove the artifacts. The final step was the extraction of the pulse-to-pulse (PP) series and the pulse rate variability (PRV) parameters. For further validation with respect to contact PPG, we designed an autonomic elicitation protocol for the acquisition of the signals. The PP series and PRV features were evaluated. The strongest correlation ($r > 0.9$) was obtained for the average of the PP intervals (AVNN) while the lowest ($r < 0.75$) was for their standard deviation (SDNN) and the proportion of PP intervals differing by more than 50 ms (pNN50). The Bland-Altman analysis highlighted larger intervals of agreement during the handgrip phases. The sympatho-vagal balance (LF/HF) behaved as expected and its difference between experimental phases was found significant ($p < 0.01$) by a multiple comparison test with Bonferroni correction. Although improvements in the robustness of the algorithm are necessary, this study's results consistently demonstrate that vPPG is a viable technique for extracting blood volume variations and evaluating heart rate variability.**

***Keywords*—videoPPG, autonomic nervous system, HRV, skin detection**

I. INTRODUCTION

The monitoring of cardiovascular parameters is usually performed with recording techniques that require physical contact, such as electrocardiography (ECG) and photoplethysmography (PPG). Skin contact can be a major limitation in many circumstances: typical examples are recordings performed in neonatal intensive care units and vital signs measurements from subjects with damaged or sensitive skin or with autistic spectrum disorders. Videophotoplethysmography (vPPG) overcomes this limitation, as it measures variations in skin perfusion by detecting slight periodical skin color variations through a camera and yields a pulsatile signal similar to PPG. Telemedicine for monitoring chronically ill patients and elderly and non-clinical uses are other possible fields of application of this technique [1], taking advantage of the absence of physical obstructions and the relative simplicity of the required instrumentation. Since it was first proposed [2], many different vPPG techniques have been developed. However, the main stages of the vPPG general workflow [3] can be summarized as follows:

1) *Video recording* of a region of interest (ROI) with a camera. The most common ROIs are highly vascularised skin regions, like the face or the hand's palm.
2) *ROI detection and tracking*, a necessary phase to separate the skin, which is the area that contains the desired pulse signal, from other regions that do not contribute to the signal and may introduce noise.
3) *Signal extraction* is the stage in which a sample of a time series is obtained from each frame of the video.
4) *Signal processing* to obtain a useful pulse signal from the raw one previously extracted, which usually contains unwanted noise.

Heart rate variability (HRV) is an important indicator of health status. HRV descriptors, as listed in [4], are typically extracted from ECG signals. PPG can be employed to measure pulse rate variability (PRV) which can be used as a surrogate of HRV and to obtain the related parameters [5]. Obtaining the PRV parameters without contact would be an important step toward a more agile, continuative, and comfortable health assessment in a wide range of contexts.
In in this paper, we developed an automatic method for the extraction of the vPPG signal from a high frame rate RGB video. The final goal was to exploit vPPG to obtain PRV descriptors to assess the autonomic modulation of the cardiovascular system. We then proceeded to validate the pipeline and the resulting PRV parameters obtained during an experimental protocol devised to elicit specific autonomic nervous system responses. It must be stressed that the validation of the vPPG PRV descriptors against those obtained with contact PPG was a fundamental preparatory step performed before the evaluation of the autonomic modulation of the cardiovascular system.

II. METHODS

A. Experimental setup

Twenty-two (13 females, 9 males) healthy volunteers of different ages (25±2, range 20–31 years) were recruited for this study. Their skin phototypes were in the range II–IV of the Fitzpatrick scale. All subjects signed a written informed consent comprehensively describing the experimental procedure which was approved by the Politecnico di Milano ethical

committee. During the experimental sessions, the vPPG and finger PPG signals were recorded. The considered ROI is the hand palm's skin. The video was recorded with a The Imaging Source DFK-23UM021RGB camera at a resolution of 640×480 and 115 fps frame rate. The environmental conditions during the experiment were controlled in terms of illumination and background. A consumer-level ring light set to daylight color temperature (4500 K) was used as the only source of light. The employed background was dark and opaque. The subjects were asked to remain as still as possible. The finger PPG was recorded with the Thought Technology SA9308M sensor at a sampling frequency of 2048 Hz.

B. Automatic pixel classifier

ROI identification and tracking was performed with an automatic pixel classifier that does not require intervention by a human operator at any processing stage. The training of the classifier is patient-specific and therefore a new training set must be created for each new acquisition. The starting point for an automatic pixel classifier was the method described in [6]. It exploits the K-means clustering algorithm for the unsupervised labeling of the pixels of the first frame, which are assigned to "skin" or "non-skin" clusters. These labels are then used to train a Decision Tree (DT) classifier, which is used to segment each frame by classifying the pixels. In this work, we added a preprocessing stage before the K-means clustering. This stage consists of the conversion of the first frame from the RGB to the HSV color space and then the use of the PCA. The unsupervised labeling is then performed on the first two principal components. The "skin" cluster is identified as the one containing the central pixel of the frame. The DT is then trained on the first frame in the RGB color space using the obtained labels and the trained classifier is then used for the successive frames.

C. Pixel classifier validation

To validate the segmentation procedure, we created a dataset by asking four subjects of the experimental population to record a video of their hand in uncontrolled environmental conditions, specifically with free background and illumination. Then, we extracted four frames from each video and manually segmented them to create an annotated dataset. The manually segmented frames were used as ground truth. The performance of the proposed segmentation method was evaluated and compared to the algorithm described in [6] in controlled and uncontrolled environmental conditions. The chosen performance metric was the Dice similarity coefficient (DSC) [7] defined as in Equation 1, where $|X|$, $|Y|$, and $|X \cap Y|$ are respectively the cardinalities and the cardinality of the intersection of the sets X and Y.

$$DSC = \frac{2|X \cap Y|}{|X| + |Y|} \tag{1}$$

D. Signal extraction and processing

The signal was obtained from the green channel of the segmented video through spatial pooling. This signal may contain artifacts in the form of jumps and a non-linear trend. The latter is common in PPG signals as they are given by the combination of a slowly varying baseline and a pulsatile part [8]. Moreover, the acquired frames were unevenly spaced in time due to the lag of the video recording system. Hence, the signal produced by the spatial pooling was irregularly sampled. Taking these specific artifacts into account, we processed the signal in three different stages:

1) *Jumps correction and detrending*. The jumps were identified by computing the absolute value of the first derivative of the signal, finding its local maxima, and taking these points as breakpoints. Then the signal was dived into one-second-long windows and their extremes were added to the breakpoints vector. Finally, a linear interpolant was computed and subtracted from each interval between two breakpoints, eliminating both the jumps and the non-linear trend.
2) *Interpolation*. The corrected and detrended signal was linearly interpolated to obtain time series with evenly spaced samples.
3) *Filtering*. The signal was finally band-pass filtered with a Hamming filter with cut-off frequencies of 0.03 and 4 Hz obtaining the vPPG signal.

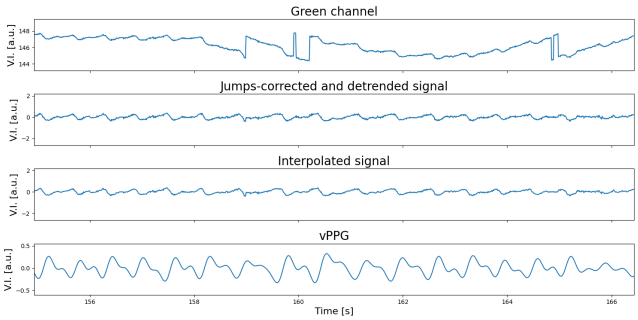


Fig. 1: Signal processing steps.

On the other hand, the contact PPG signal was resampled at 115 Hz and then bandpass filtered with a Hamming filter with cut-off frequencies of 0.03 and 4 Hz.

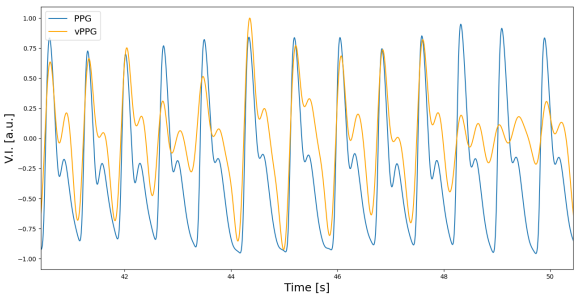


Fig. 2: Comparison of PPG (blue) and vPPG (orange).

E. PP series extraction and validation

Two of the twenty-two acquired signals had to be discarded due to issues in the video recording. Once the signals were obtained, we computed the PRV parameters from vPPG and PPG. The first step was the identification of the fiducial points. We chose the systolic peaks, identified with the Automatic Multiscale Peak Detection (AMPD) algorithm [9]. Then, the pulse-to-pulse (PP) series were computed. The PP series were validated by computing Spearman's correlation coefficient (r) between PP intervals from vPPG and PPG, with the latter taken as a reference. A specific threshold for a minimum correlation was set at 0.65. One more signal had to be discarded due to having $r < 0.65$, therefore the following analyses were conducted on 19 subjects.

F. Autonomic stimulation protocol

We designed the autonomic stimulation protocol as a series of simple tasks to elicit specific responses of the two branches of the autonomic nervous system. The protocol consisted of the following phases, interleaved by rest periods:

- *Baseline*. The subjects had to remain still and relax for 5 minutes.
- *Paced breathing*. The subjects were asked to breathe at the fixed frequency of 10 breaths per minute (6 seconds for each cycle) for 2 minutes.
- *Handgrip*. The subject was given a rubber ball and asked to alternatively squeeze and release it (1-second grip and 1-second release) with the hand not involved in the recording for 30 seconds. This phase was repeated twice.

The paced breathing and handgrip aimed at inducing vagal and sympathetic activation respectively. The instructions to perform the tasks were given to the subjects through animations displayed on an LCD monitor placed in front of them.

G. PRV parameters validation

The selected time domain parameters are the average of PP intervals (AVNN), the standard deviation of PP intervals (SDNN), and the percentage of PP intervals differing by more than 50 ms (pNN50). The chosen frequency domain parameters are the spectral power in the low-frequency range of 0.04-0.15 Hz (LF), the high-frequency range of 0.15-0.4 Hz (HF), and their ratio (LF/HF or sympatho-vagal balance). The vPPG parameters were validated in terms of correlation (with the Spearman's correlation coefficient) and agreement (with the Bland-Altman analysis) with the reference parameters obtained through PPG.

H. PRV parameters comparison among phases

To evaluate the effects of the different stimulations on the considered PRV descriptors, the Friedman test and the multiple comparison test with Bonferroni correction were adopted.

III. Results

A. Pixel classifier

The performance measured with the DSC of the proposed pixel classification algorithm (with preprocessing) and the algorithm in [6] (without preprocessing) are presented in Figure 3. The figure evidences that the proposed algorithm performs better in both conditions while achieving a reduced variability in segmentation capacity.

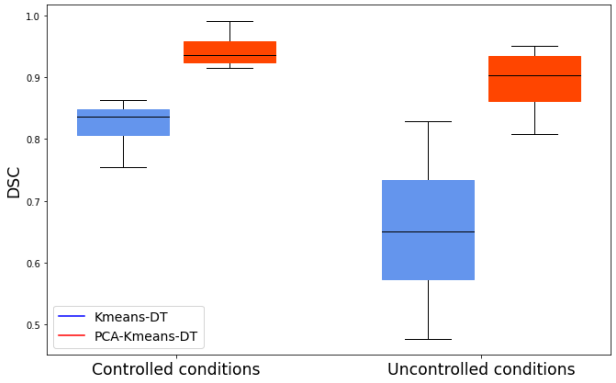


Fig. 3: Performance of the pixel classification algorithms in the tested conditions.

B. PRV parameters

The correlation results between the PRV parameters obtained with the two techniques are summarized in Table I. The highest correlation can be observed for the AVNN parameter ($r > 0.9$) while the lowest for SDNN and pNN50 ($r < 0.75$). The correlation remains high for the frequency domain parameters except for LF/HF during the first handgrip phase. Regarding the Bland-Altman analysis, it was observed that an almost null bias for AVNN during all phases, an underestimation of the LF/HF parameter, and an overestimation of the other parameters by the vPPG. Moreover, the limits of agreement (defined as $mean \pm 1.96SD$ of the difference of the PRV parameter obtained with vPPG and PPG) described a larger interval during the handgrip phases for all parameters, indicating a larger dispersion of errors. As an example, the scatterplots and Bland-Altman plots of PPG vs. vPPG for the sympatho-vagal balance LF/HF are reported in Figure 4 and 5.

TABLE I: PRV DESCRIPTORS CORRELATION

	Baseline	*Paced breathing*	*Handgrip 1*	*Handgrip 2*
AVNN	1.000	0.998	0.995	0.991
SDNN	0.614	0.740	0.707	0.739
pNN50	0.626	0.678	0.596	0.391*
LF	0.975	0.919	0.967	0.933
HF	0.932	0.893	0.840	0.895
LF/HF	0.886	0.804	0.402*	0.700

* indicates correlation coefficients with non-significant *p-value*.

The behavior of the sympatho-vagal balance during the four experimental phases is presented in Figure 6. We can notice the prevalence of HF components during the paced breathing phase while the LF components prevail during handgrip, coherently for vPPG and PPG.

The multiple comparison test revealed that the difference between LF/HF in paced breathing and handgrip phases is statistically significant ($p < 0.01$) in both vPPG and PPG.

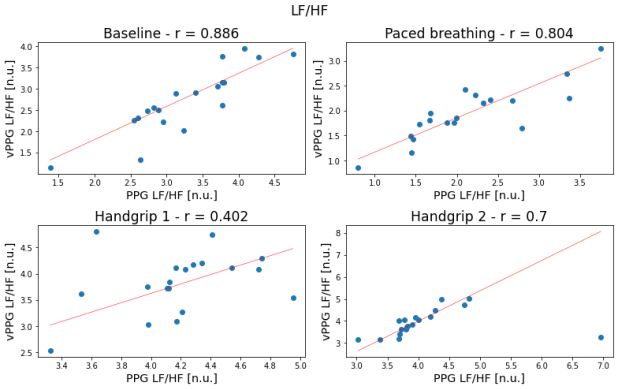


Fig. 4: Scatterplots of LF/HF during the experimetnal phases.

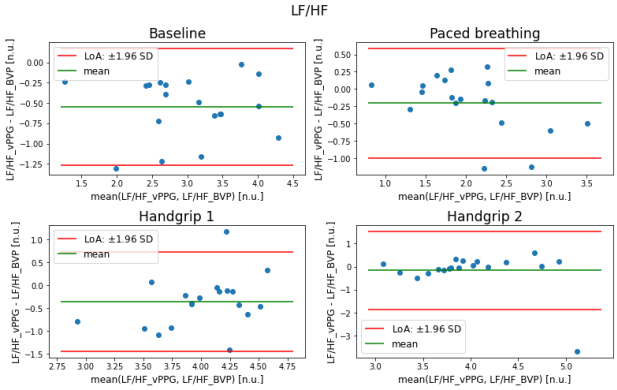


Fig. 5: Bland-Altman plots of LF/HF during the experimetnal phases.

IV. Conclusions

In this work, we developed and implemented an automatic method for extracting and processing the vPPG signal aiming at measuring pulse rate variability parameters. Then, we validated this method. The validation of the proposed automatic pixel classifier for the identification and tracking of the ROI showed improved performance in the considered environmental conditions, indicating the effectiveness of the preprocessing stage.

The correlation and agreement analyses highlighted that vPPG can provide satisfying estimations of the PRV parameters. However, a drop in correlation and larger intervals of agreement must be noticed for all parameters during the handgrip phases. This result is probably due to subjects' movements during this phase, since the vPPG is more prone to motion artifacts. A similar result was observed in a previous study, with weaker correlation and agreement during the stand phase of a rest-to-stand maneuver [10]. Regarding the comparison between experimental tasks, the sympatho-vagal balance presents the expected behavior in both vPPG and contact PPG, with vagal activation during paced breathing [11] and sympathetic activation during handgrip [12].

Further studies are required to improve the method's robustness to movements, and to validate it in conditions closer to those of real-world applications.

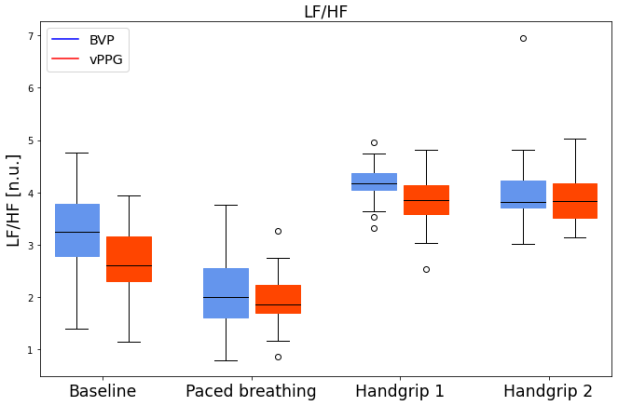


Fig. 6: LF/HF during the experimetnal phases for finger PPG (blue) and vPPG (red).

References

[1] A. Tohma, M. Nishikawa, T. Hashimoto, Y. Yamazaki, and G. Sun, Evaluation of remote photoplethysmography measurement conditions toward telemedicine Applications, Sensors 2021, Vol. 21, Page 8357, vol. 21, no. 24, p. 8357, Dec. 2021.

[2] W. Verkruysse, L. O. Svaasand, and J. S. Nelson, Remote plethysmographic imaging using ambient light, Opt. Express, vol. 16, no. 26, p. 21434, Dec. 2008.

[3] P. V. Rouast, M. T. P. Adam, R. Chiong, D. Cornforth, and E. Lux, Remote heart rate measurement using low-cost RGB face video: a technical literature review, Front. Comput. Sci. 2018 125, vol. 12, no. 5, pp. 858–872, Sep. 2018.

[4] Task Force of the European Society of Cardiology and the North American Society of Pacing Electrophysiology, Heart rate variability: standards of measurement, physiological interpretation, and clinical use, Circulation, vol. 93, no. 5, pp. 1043–1065, Mar. 1996.

[5] E. Gil, M. Orini, R. Bailón, J. M. Vergara, L. Mainardi, and P. Laguna, Photoplethysmography pulse rate variability as a surrogate measurement of heart rate variability during non-stationary conditions, Physiol. Meas., vol. 31, no. 9, pp. 1271–1290, 2010.

[6] R. Barbieri et al., Assessing an automatic procedure of extraction of physiological parameters from skin using video photoplethysmography, in Proc. Annu. Int. Conf. IEEE Eng. Med. Biol. Soc. EMBS, vol. 2020-July, pp. 4349–4352, Jul. 2020.

[7] L. R. Dice, Measures of the amount of ecologic association between species, Ecology, vol. 26, no. 3, pp. 297–302, Jul. 1945.

[8] J. Allen, Photoplethysmography and its application in clinical physiological measurement, Physiol. Meas., vol. 28, no. 3, pp. R1–R39, Mar. 2007.

[9] F. Scholkmann, J. Boss, and M. Wolf, An efficient algorithm for automatic peak detection in noisy periodic and quasi-periodic signals, Algorithms 2012, Vol. 5, Pages 588-603, vol. 5, no. 4, pp. 588–603, Nov. 2012.

[10] L. Iozzia, L. Cerina, and L. Mainardi, "Relationships between heart-rate variability and pulse-rate variability obtained from video-PPG signal using ZCA," Physiol. Meas., vol. 37, no. 11, pp. 1934–1944, Sep. 2016.

[11] C. Li, Q. Chang, J. Zhang, and W. Chai, "Effects of slow breathing rate on heart rate variability and arterial baroreflex sensitivity in essential hypertension," Medicine (Baltimore)., vol. 97, no. 18, May 2018.

[12] A. Zygmunt and J. Stanczyk, "Methods of evaluation of autonomic nervous system function," Arch. Med. Sci., vol. 6, no. 1, p. 11, 2010.

Assessment of cerebral autoregulation in patients undergoing anaesthesia with propofol: a comparison among spontaneous variability methods

Roberta Saputo[1], Laura Sparacino[1], Riccardo Pernice[1], Francesca Gelpi[2], Vlasta Bari[2,3], Alberto Porta[2,3], Luca Faes[1]

[1] *Department of Engineering, University of Palermo, Viale delle Scienze, Building 9, 90128 Palermo, Italy*
[2] *Department of Biomedical Sciences for Health, University of Milan, 20133 Milan, Italy*
[3] *Department of Cardiothoracic, Vascular Anesthesia and Intensive Care, IRCCS Policlinico San Donato, 20097 San Donato Milanese, Italy*

***Abstract*— Cerebral autoregulation (CA) is a fundamental homeostatic mechanism that maintains cerebral blood flow (CBF) within a constant range despite blood pressure variations. In this work, two different approaches for assessing CA are compared, i.e. the autoregulation index (ARI) and dynamic entropy measures. The arterial pressure and the CBF velocity were acquired on eighteen subjects undergoing coronary artery bypass graft surgery, before induction of general anaesthesia with propofol and during anaesthesia. The ARI-based method confirmed the known result that CA remains unchanged with propofol. Entropy measures led to complementary findings, suggesting an increased dependence of cerebral blood flow dynamics on systemic pressure, probably due to the effect of mechanical breathing during surgery.**

***Keywords*—Cerebrovascular autoregulation, autoregulation index, entropy, linear parametric autoregressive modelling.**

I. Introduction

Cerebrovascular autoregulation (CA) is a critical process in humans for maintaining adequate cerebral blood flow (CBF) values in response to external or internal system disturbances, such as changes in arterial blood pressure (AP) [1]. The assessment of CA can be carried out by measuring changes in CBF in response to slow (static method) [2] or rapid changes (dynamic method) [3] in AP. While the static method requires external invasive intervention to induce changes in AP, the use of the transcranial Doppler ultrasound technique (TCD) allow the non-invasive assessment of dynamic CA through the investigation of the beat-to-beat CBF changes in relation to AP changes occurring spontaneously [4], under the assumption that CBF velocity is approximately equal to CBF [3]. Indeed, the non-invasive characterization of CA is based on the study of the dynamic closed-loop interactions between the mean AP (MAP) and the mean CBF velocity (MCBFV) along the pressure-to-flow link of the closed-loop system, i.e. considering the interactions directed from MAP to MCBFV. CA is defined as the intrinsic control mechanism operating along this reflex and aiming to maintain a constant and stable MCBFV despite beat-to-beat variations of MAP, while preserving some degree of uncoupling between MCBFV and MAP over a range of values of MAP as wide as possible [4]–[6]. Dynamic CA has been evaluated exploiting different methods, such as the MAP-MCBFV closed-loop system transfer function [7], the autoregulation index (ARI) [4], [8], and linear parametric autoregressive models [9], [10]. In particular, the ARI index models the response of MCBFV to changes in MAP by a system of differential equations in which each estimated MCBFV curve, numbered from 0 to 9, represents a different level of CA [4]. The computation of ARI can be carried out by considering three different approaches, i.e. the time domain method (TDM) [11] , the non-parametric method (non-PM) [12] and the parametric method (PM) [9]. Recently, measures of dynamic entropy for bivariate systems [13] have been developed, which are derived from full and restricted autoregressive models and can be exploited to study the dynamic interactions along the pressure-to-flow link.

The present study focuses on the assessment of dynamic CA in patients scheduled for coronary artery bypass graft (CABG) surgery, before and during general anaesthesia with propofol [14]. Two different approaches are exploited to investigate CA mechanisms, i.e. the ARI and measures of dynamic entropy for bivariate systems [13]. Herein, we use the PM to assess CA, consistently with entropy measures which are also based on linear parametric modelling of time series under the hypothesis of Gaussian processes [13], [15]. The parametric ARI and entropy-based measures are compared evaluating their degree of correlation, with the aim to evidence whether the two investigated methods highlight similar or different aspects of cerebrovascular physiology, also allowing to better understand the role of confounding factors in the closed-loop interactions between CBF and AP.

II. Materials and Methods

A. Experimental protocol and series extraction

Eighteen patients (age: 63.8 ± 7.8 yrs, 1 female) scheduled for CABG surgery were enrolled at the Department of Cardiothoracic, Vascular Anaesthesia and Intensive Care of IRCCS Policlinico San Donato, San Donato Milanese, Milan, Italy [14]. Patients signed an informed consent before participating to the study and were examined ahead of surgery before induction of general anaesthesia (PRE) and after intubation of the trachea, during general anaesthesia, before opening the chest (POST). During the PRE session, subjects were breathing spontaneously, whereas during the POST session they were mechanically ventilated with a rate of 12-16 breaths/min. The PRE session was recorded after application of standard premedications including intramuscular administration of atropine (0.5 mg) and fentanyl (100 μg). Anaesthesia was induced by the intravenous bolus injection of propofol and remifentanil. The POST session was recorded when the target plasma concentration of propofol was expected to be around 3 μg/ml based the pharmacokinetic properties of the drug.

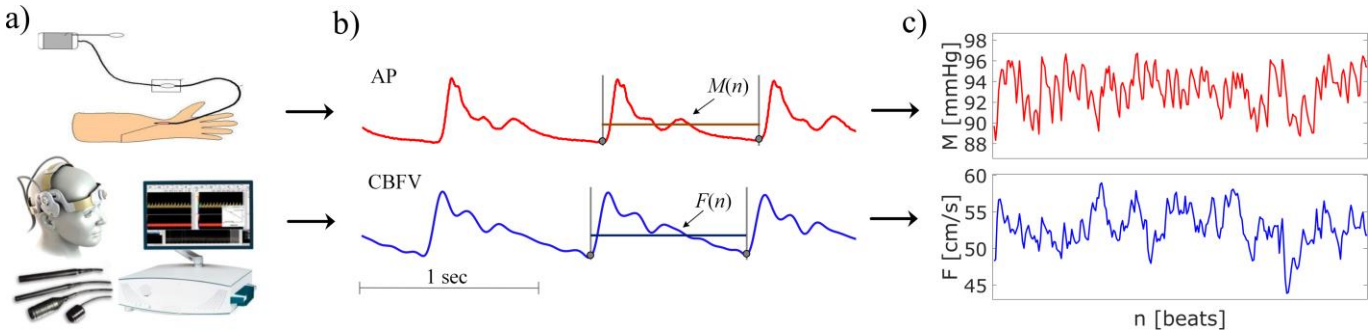


Fig. 1 (a) Schematic representation of the biomedical instrumentation used for data acquisition: (top) invasive measurement of AP by a catheter inserted into the radial artery; (bottom) transcranial Doppler ultrasound (TCD) device with ultrasound probes and adjustable helmet for CBFV acquisition from the middle cerebral artery (right or left). **(b)** exemplary traces of the acquired AP and CBFV signals for a representative subject; **(c)** the M and F time series are extracted respectively by integrating the AP signal within the diastolic pulse interval and the CBFV signal between its two minima within the cardiac period.

Electrocardiogram (ECG, lead II), invasive AP from the radial artery and CBF velocity (CBFV) from the middle cerebral arteries through a TCD device were simultaneously acquired. The acquisition phase in PRE and POST conditions lasted about 6 minutes. After signal acquisition, MAP and MCBFV stationary time series of 250 beats each were extracted by integrating respectively the AP and CBFV signals between two consecutive diastolic points and dividing by the time interval between them. In the following, we refer to MAP and MCBFV time series as M and F, respectively. Further details about the experimental protocol, signal acquisition and series extraction can be found in [14]. The schematic representation of the acquisition system, a representative example of the acquired signals and the extracted time series are shown in Fig. 1.

B. Autoregulation Index (ARI): parametric estimation

The autoregulation index (ARI) allows to assess CA by modelling F through a system of ten ordinary differential equations in agreement with the derivative filter model originally introduced by Tiecks et al. [4]. The Tiecks' model provides a set of ten step responses, in which each predicted F curve ranks the efficiency of CA from 0, i.e. absent CA, to 9, i.e. excellent CA, with ARI values lower than or equal to 4 indicating impaired CA [4]. The ten F curves derived from this model are compared with the F curve estimated from the parametric linear representation of the dynamic F-M relationship. More precisely, an auto and cross regressive model (ARX) is applied to describe the dynamical evolution of F due to beat-to-beat changes of both F and M [8]. After the application of a linear detrending to both series, the sample F_k, where k is the current time instant, is described as the linear combination of p past values of F weighted by the coefficients a_i, with $i = 1,\dots,p$, plus the linear combination of $p - \tau + 1$ past values of M weighted by the coefficients b_i, with $i = \tau,\dots,p$, plus a random unpredictable portion W_k being the sampling of a Gaussian white noise W with zero mean and variance λ^2:

$$F_k = \sum_{i=1}^{p} a_i F_{k-i} + \sum_{i=\tau}^{p} b_i M_{k-i} + W_k, \qquad (1)$$

where p is the model order and τ is the lag of the faster interactions from M to F. By representing the model coefficients in the Z domain as $A(z) = \sum_{i=1}^{p} a_i z^{-i}$ and $B(z) = \sum_{i=\tau}^{p} b_i z^{-i}$, the transfer function from M to F, which provides the coefficients of the impulse response, can be written as:

$$H_{F-M}(z) = \frac{B(z)}{1-A(z)}. \qquad (2)$$

The impulse response was truncated to 31 values taking the cardiac beats from 0 to 30. After integrating the impulse response to obtain the step response, the comparison between each of the ten step responses derived from the Tiecks' model and the data-driven step response was carried out via the normalized mean square prediction error (NMSPE), computed as the mean square value of the difference between the measured and the predicted F curves normalized by the mean square value of the measured F curve [8]. We selected the optimal ARI (i.e. from 0 to 9) as the value corresponding to the minimum value of NMSPE. Further details on the proposed method can be found in [8].

C. Dynamic information measures

Given the bivariate process S = {M, F}, where M is the driver and F is the target process, the framework of information theory allows the study of the dynamic interactions along the pressure-to-flow link by quantifying the information content of the target in terms of predictive information $P_{F|S}$ (i.e., information contained in the target that can be described by the past history of the entire process S). Using the chain rule, $P_{F|S}$ can be decomposed in two different ways [13]:

$$\text{(i)} P_{F|S} = S_F + T_{M\to F};\ \text{(ii)}\ P_{F|S} = C_{M\to F} + S_{F|M}, \qquad (3)$$

where S_F is the self-entropy (information carried by the present state of the target that can be predicted by its own past), $T_{M\to F}$ is the transfer entropy (information carried by the present of the target that can be predicted by the past of the driver above and beyond the part that is predicted by the past of the target), $C_{M\to F}$ is the cross-entropy (information carried by the present state of the target that can be predicted exclusively by the past of the driver), $S_{F|M}$ is the conditional self-entropy (information carried by the present state of the target that can be predicted by its past above and beyond the part that is predicted by the past of the driver) [13]. Under the assumption of joint gaussianity of the observed bivariate process [15], the dynamic information measures introduced above were evaluated using model-based estimators as:

$$S_F = \frac{1}{2} ln \frac{\sigma_F^2}{\sigma_{AR}^2};\ T_{M\to F} = \frac{1}{2} ln \frac{\sigma_{AR}^2}{\sigma_{ARX}^2} \qquad (4)$$

$$C_{M\to F} = \frac{1}{2} ln \frac{\sigma_F^2}{\sigma_X^2};\ S_{F|M} = \frac{1}{2} ln \frac{\sigma_X^2}{\sigma_{ARX}^2} \quad (5)$$

where σ_F^2 is the variance of the target process, σ_{AR}^2 is the prediction error variance of an auto-regressive (AR) model describing the present state of the target from its past values, σ_X^2 is the prediction error variance of a cross-regressive (X) model describing the present state of the target from the past values of the driver, σ_{ARX}^2 is the prediction error variance of an ARX model describing the present state of the target from the past values of the entire bivariate process. The computation of the dynamic information measures in (4) and (5) thus reduces to the estimation of the error variances of full (ARX) and restricted (AR, X) linear regression models, which was performed by solving the Yule-Walker equations [13].

D. Data pre-processing

The acquired M and F time series were first pre-processed to obtain zero-mean series. As regards the computation of the dynamic entropy measures, further pre-processing was performed using an AR high-pass filter for detrending (zero-phase filter, cut-off frequency of 0.0156 times the sampling frequency, the latter assumed to be the inverse of the mean HP for each subject); model identification was performed by setting the model order according to the Akaike Information Criterion (AIC) for each subject (with maximum scanned model order equal to 14). As regards the parametric ARI computation, the model order was set in accordance with [16].

E. Statistical and correlation analysis

The significance of the differences between experimental conditions (PRE vs. POST) was assessed using non-parametric tests, given the small sample size and that normality of the series assessed through Anderson-Darling test was rejected for most cases. Specifically, the paired Wilcoxon signed rank test was used with a significance level of 5%.

Moreover, the non-parametric Spearman correlation coefficient, corresponding to Pearson correlation coefficient computed from rank vectors [17] was used to assess the degree of correlation between the parametric ARI and the entropy-based linear measures. Indeed, given its non-parametric nature, the assumption of Gaussianity is not a necessary condition and thus it is used to compare discrete variables, such as the ARI, with continuous variables, such as the measures of dynamic entropy. In this study, the parametric ARI values were compared with each of the entropy measures (self-entropy, transfer entropy, cross entropy, and conditional self-entropy) for any given experimental condition.

III. RESULTS AND DISCUSSION

Figure 2 shows the distributions across subjects of ARI values obtained with the parametric method (Fig. 2a), transfer entropy and self-entropy (Fig. 2b, c), cross entropy and conditional self-entropy (Fig. 2d, e), evaluated in the PRE and POST experimental conditions. The ARI method evidenced that CA remained intact during the PRE-POST protocol (Fig. 2a), confirming that propofol general anaesthesia does not affect CA [16]. In fact, although propofol general anaesthesia is known to cause autonomic depression, which is a major determinant of CA [18], several studies exploiting the same experimental protocol have confirmed that CA does not vary with the anaesthetic pharmacokinetic properties of propofol [16].

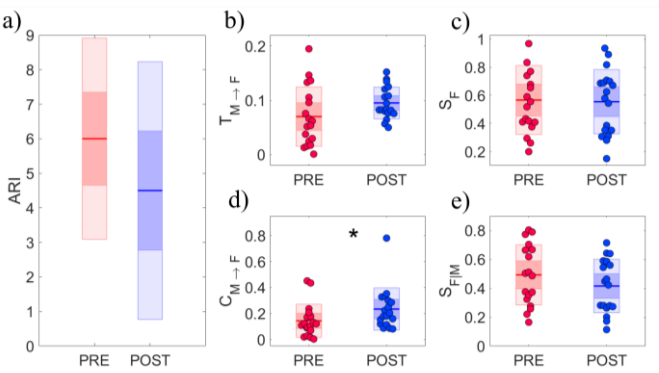


Fig. 2 Results of short-term cerebrovascular variability analysis. Boxplots depict the distributions of **(a)** ARI values computed with the parametric method, **(b)** transfer entropy $T_{M\to F}$, **(c)** self-entropy S_F, **(d)** cross entropy $C_{M\to F}$ and **(e)** conditional self-entropy $S_{F|M}$ in PRE (left boxplots, red dots) and POST (right boxplots, blue dots) conditions. Statistically significant differences (p<0.05): *****, PRE vs POST, Wilcoxon signed rank test for paired data.

Measures of dynamic entropy show different interpretations of how predictable dynamics in the target process are derived from its own past and the past of the driver process. The increased cross-entropy in POST (Fig. 2d, $p = 0.0386$) reflects a higher predictability of CBFV dynamics from AP values, documenting an increased cerebrovascular coupling that might be indicative of reduced cerebral autoregulation (CBFV changes are more dependent on AP variations). However, the finding that $T_{M\to F}$ and $S_{F|M}$ do not vary between conditions (Fig. 2b, c) leads us to suggest that the causal interactions from M to F and the internal dynamics of F may be unaffected by the investigated experimental protocol. Since variations in the cross-entropy can be induced by changes in the direct coupling along both directions of interaction (M→F and F→M in this case) [13], caution should be used in ascribing to a stronger coupling the increased cross-predictability of F given M. Moreover, the simultaneous effect induced by mechanical breathing on M and F during anaesthesia in POST, although not directly investigated, could have generated regular oscillations in both series at the frequency of mechanical ventilation. This would have caused an increased predictability of F from M, which appears when considering $C_{M\to F}$ but not $T_{M\to F}$, i.e. when conditioning also on the past dynamics of F apart from M [19].

Table 1 reports the correlation values between the ARI and each of the dynamic entropy measures, evaluated with the Spearman correlation index (ρ) in the PRE-POST protocol. The weak correlations, confirmed by p values higher than the significance threshold (level of significance of 5%), suggest that ARI and dynamic entropy measures provide different information on the short-term cerebrovascular control and on the functioning of CA in this group of patients.

IV. CONCLUSION

This work aimed to compare different methods for investigating the interaction link from arterial blood pressure to cerebral blood flow (i.e., the pressure-to-flow link), to investigate the physiological mechanisms related to cerebral

autoregulation. The ARI-based method showed that CA remained unchanged with the PRE-POST protocol in patients undergoing CABG surgery, confirming the known properties of propofol on CA maintenance. On the other hand, the statistically significant increase of cross-entropy after the induction of general anaesthesia showed that the dynamics of cerebral blood flow become more dependent on those of systemic pressure, suggesting a possible alteration of cerebral autoregulatory mechanisms. The weak correlation between the two methods confirms that they highlight different aspects of cerebrovascular physiology.

To corroborate the results of this work, future studies should be designed: (i) to investigate cerebrovascular interactions through a closed-loop analysis considering also the effects of cerebral flow variations on arterial pressure; and (ii) to quantify such interactions in the frequency domain separating respiration-related oscillations from effects within the very low frequency (0.02-0.07 Hz) and low frequency (0.07-0.2 Hz) bands during the PRE-POST protocol [6].

TABLE I
SPEARMAN CORRELATION: ARI VS. ENTROPY MEASURES

	PRE		*POST*	
	ρ	*p-value*	*ρ*	*p-value*
ARI vs $T_{M\to F}$	-0.012	0.961	0.447	0.063
ARI vs $C_{M\to F}$	-0.327	0.185	0.254	0.308
ARI vs S_F	-0.224	0.372	0.008	0.974
ARI vs $S_{F\|M}$	-0.012	0.423	-0.114	0.654

Comparison between parametric ARI and dynamic information measures (transfer entropy $T_{M\to F}$, self entropy S_F, cross entropy $C_{M\to F,}$ conditional self entropy $S_{F|M}$) using Spearman correlation index ρ during the PRE and POST experimental conditions. Rejection of the null hypothesis (*p*-value < 0.05) means that the two investigated metrics are significantly correlated.

ACKNOLEDGMENT

This work was supported by "Sensoristica intelligente, infrastrutture e modelli gestionali per la sicurezza di soggetti fragili" (4FRAILTY) project, funded by Italian MIUR (PON R&I 2014-20, grant no. ARS01_00345). R.P. is partially supported by European Social Fund (ESF) Complementary Operational Programme (POC) 2014/2020 of the Sicily Region.

REFERENCE

[1] N. A. Lassen, "Cerebral blood flow and oxygen consumption in man," *Physiol Rev*, vol. 39, no. 2, pp. 183–238, 1959.
[2] O. B. Paulson, S. Strandgaard, and L. Edvinsson, "Cerebral autoregulation.," *Cerebrovasc Brain Metab Rev*, vol. 2, no. 2, pp. 161–192, 1990.
[3] D. W. Newell, R. Aaslid, A. Lam, T. S. Mayberg, and H. R. Winn, "Comparison of flow and velocity during dynamic autoregulation testing in humans.," *Stroke*, vol. 25, no. 4, pp. 793–797, 1994.
[4] F. P. Tiecks, A. M. Lam, R. Aaslid, and D. W. Newell, "Comparison of static and dynamic cerebral autoregulation measurements," *Stroke*, vol. 26, no. 6, pp. 1014–1019, 1995.
[5] R. Aaslid, K.-F. Lindegaard, W. Sorteberg, and H. Nornes, "Cerebral autoregulation dynamics in humans.," *Stroke*, vol. 20, no. 1, pp. 45–52, 1989.
[6] J. A. H. R. Claassen, A. S. S. Meel-van den Abeelen, D. M. Simpson, R. B. Panerai, and I. C. A. R. N. (CARNet), "Transfer function analysis of dynamic cerebral autoregulation: A white paper from the International Cerebral Autoregulation Research Network," *Journal of Cerebral Blood Flow & Metabolism*, vol. 36, no. 4, pp. 665–680, 2016.
[7] R. Zhang, J. H. Zuckerman, C. A. Giller, B. D. Levine, J. H. Zuckerman, and C. A. Giller, "Transfer function analysis of dynamic cerebral autoregulation in humans," *American Journal of Physiology-Heart and Circulatory Physiology*, vol. 274, no. 1, pp. H233--H241, 1998.
[8] F. Gelpi *et al.*, "Dynamic cerebrovascular autoregulation in patients prone to postural syncope: comparison of techniques assessing the autoregulation index from spontaneous variability series," *Autonomic Neuroscience*, vol. 237, p. 102920, 2022.
[9] R. B. Panerai, S. L. Dawson, and J. F. Potter, "Linear and nonlinear analysis of human dynamic cerebral autoregulation," *American Journal of Physiology-Heart and Circulatory Physiology*, vol. 277, no. 3, pp. H1089–H1099, 1999.
[10] R. Pernice *et al.*, "Spectral decomposition of cerebrovascular and cardiovascular interactions in patients prone to postural syncope and healthy controls," *Autonomic Neuroscience*, vol. 242, p. 103021, Nov. 2022, doi: 10.1016/j.autneu.2022.103021.
[11] R. B. Panerai, P. J. Eames, and J. F. Potter, "Variability of time-domain indices of dynamic cerebral autoregulation," *Physiol Meas*, vol. 24, no. 2, p. 367, 2003.
[12] R. B. Panerai, R. P. White, H. S. Markus, and D. H. Evans, "Grading of cerebral dynamic autoregulation from spontaneous fluctuations in arterial blood pressure," *Stroke*, vol. 29, no. 11, pp. 2341–2346, 1998.
[13] L. Faes, A. Porta, and G. Nollo, "Information decomposition in bivariate systems: theory and application to cardiorespiratory dynamics," *Entropy*, vol. 17, no. 1, pp. 277–303, 2015.
[14] A. Porta, V. Bari, T. Bassani, A. Marchi, V. Pistuddi, and M. Ranucci, "Model-based causal closed-loop approach to the estimate of baroreflex sensitivity during propofol anesthesia in patients undergoing coronary artery bypass graft," *J Appl Physiol*, vol. 115, no. 7, pp. 1032–1042, 2013.
[15] L. Barnett, A. B. Barrett, and A. K. Seth, "Granger causality and transfer entropy are equivalent for Gaussian variables," *Phys Rev Lett*, vol. 103, no. 23, p. 238701, 2009.
[16] V. Bari *et al.*, "Exploring metrics for the characterization of the cerebral autoregulation during head-up tilt and propofol general anesthesia," *Autonomic Neuroscience*, p. 103011, 2022.
[17] S. Kim, M. Ouyang, and X. Zhang, "Compute spearman correlation coefficient with Matlab/CUDA," in *2012 IEEE international symposium on signal processing and information technology (ISSPIT)*, 2012, pp. 55–60.
[18] F. Boer, P. Ros, J. G. Bovill, P. van Brummelen, and J. van der Krogt, "Effect of propofol on peripheral vascular resistance during cardiopulmonary bypass," *Br J Anaesth*, vol. 65, no. 2, pp. 184–189, 1990.
[19] A. Porta *et al.*, "Categorizing the Role of Respiration in Cardiovascular and Cerebrovascular Variability Interactions," *IEEE Trans Biomed Eng*, vol. 69, no. 6, pp. 2065–2076, 2021.

Assessing Multisite PET Neuroimaging Harmonisation for Normative Modelling

A. Giacomel[1], D. Martins[1], G. Nordio[1], R. Easmine[1], O. Howes[2], S.C.R. Williams[1], F. Turkheimer[1], M. De Groot[3], O. Dipasquale[1], and M. Veronese[1,4]

[1]*Centre for Neuroimaging Sciences, IoPPN, King's College London, London, UK*
[2]*Department of Psychosis Studies, IoPPN, King's College London, London, UK*
[3] *Clinical Imaging, Clinical Pharmacology and Experimental Medicine, GSK R&D, Hertfordshire, UK*
[4] *Department of Information Engineering, University of Padova, Padova, IT*

***Abstract*—Although normative modelling has been recently widely adopted by the neuroimaging community to estimate deviation of cohorts or single subjects, from a reference population's trajectory, it has never been applied on molecular neuroimaging datasets. This is because the typical sample size of molecular imaging datasets of single studies is not adequate for a reliable estimation of population models. Here, we pooled scans from different datasets and compared the performance of common neuroimaging harmonisation techniques when used on molecular neuroimaging data, by measuring the effect of the harmonisation on the deviation scores of the normative model. As harmonisation methods we employed a 3D Gaussian filter and a Bayesian scale and shift estimation method (Combat). By statistically testing the parameters of the deviation-score distribution and inspecting the explained variance map of the model, we selected Combat, trading-off between the two parameters' performance, as the most suitable way to harmonise multi-site/multi-scanner molecular neuroimaging datasets.**

***Keywords*—Normative Modelling, Dopamine, PET Imaging, Multisite Data Pooling.**

I. Introduction

NORMATIVE modelling is a statistical framework increasingly adopted by the neuroimaging community to estimate the "*normal*" behaviour of a measure of interest (e.g., cortical thickness in a region or voxel) in relation with some covariates of interest (e.g., demographical, behavioural or clinical variables). The main characteristic of the methodology is the estimation of a model on a large sample size of a reference cohort (usually healthy controls – HCs), which can be then applied, after validation, to a patient cohort to assess potential deviation from normality at the individual or group level [1], [2]. This method has been applied on magnetic resonance imaging (MRI) data to analyse patterns of tissue loss in bipolar disorders [3], [4], schizophrenia [3]–[5], ADHD [6], and Parkinson's disease [7], but so far, it has never been used with molecular imaging data (i.e., Positron Emission Tomography – PET and Single Photon Emission Computed Tomography – SPECT).

Molecular neuroimaging can provide a unique *in-vivo* view of the biology of the healthy and diseased brain that no other neuroimaging method can provide. By selecting different molecular tracers we can visualize different targets in the brain, i.e., neuroreceptor distribution, synaptic transmission, brain metabolism, enzyme activities, protein synthesis, among others [8]. The application of normative modelling in molecular neuroimaging could prove beneficial in identifying patterns of deviation from normality in psychiatric patients and to develop individualised treatments based on the severity of these.

One of the main problems to apply normative modelling to molecular neuroimaging is the necessity to gather a large enough dataset to capture as much intrinsic variability of the system under investigation as possible. While in structural and functional MRI international collaborations (e.g., ENIGMA [9], UK BIOBANK [10]) are collecting datasets counting thousands of scans of healthy volunteers, in molecular neuroimaging the collection of such extensive datasets is unfeasible for various reasons. First, since molecular neuroimaging requires the injection of a radiotracer, the collection of datasets of HCs with the sole purpose of mapping the human brain could be considered harmful to the participants and therefore unethical. In addition, the acquisition of such datasets with PET would be far more costly than in MRI.

A possible solution to this issue is to gather data of HCs from existing studies. However, when pooling data from various acquisition sites, a harmonisation step is required to clear the data from batch and/or scanner effects before model estimation. Several studies address the issue of harmonisation of neuroimaging datasets [11]–[14], but the most widely used methods are: gaussian kernel smoothing, adjusted residual harmonisation methods (e.g., Combat [11], [12], [15]) and the incorporation of the site effect in the model (i.e., hierarchical models [13], [16], [17]).

In this work, we aim at addressing the issue of multisite harmonisation of molecular neuroimaging data by comparing two of the most widely adopted methods in the neuroimaging field, namely the Gaussian kernel smoothing and Combat harmonisation, evaluating their effects on normative modelling of PET HCs. We applied these methods to two datasets of [^{11}C]-(+)-PHNO and assessed their impact on the single-subject deviation scores of the normative model.

We then tested on an independent larger cohort of HCs acquired with [^{18}F]FDOPA if the method can be generalised to other tracers.

II. Materials and Methods

A. [^{11}C]-(+)-PHNO PET Dataset

We used PET baseline scans of 77 HCs from two existing datasets [18], [19] acquired in the same imaging centre (Invicro, London) using two different scanners (Siemens Hi-Rez Biograph 6, N=54, labelled as PET/CT; Siemens Biograph mMR, N=23, labelled as PET/MR) with [^{11}C]-(+)-PHNO, an

agonist tracer of the dopamine $D_{2/3}R$.

Experimental design, image acquisition, image processing and data analysis was consistent for the two studies and further details are reported in the original publications [18], [19]. Parametric images of dopamine receptor density, measured using non-displaceable binding (BP_{ND}) [20], were obtained using the same MATLAB-based pipeline for the two datasets, using a simplified reference tissue model with cerebellar grey matter as reference region. Final maps were all normalised to the MNI152 standard space prior to harmonisation and normative modelling.

B. *[18F]FDOPA PET Dataset*

6-[^{18}F]-fluoro-L-dopa (FDOPA) PET data of 142 healthy individuals from six different studies, acquired with five different scanners (Siemens Hi-Rez Biograph 6, Siemens Biograph 40 TruePoint, Siemens TruePoint 6, ECAT HR+ 962 and ECAT EXACT 3D) in three different imaging sites (South Korea, Imanet London and Invicro London), were used to check if the harmonisation method withheld the same performances with a different tracer. K_i^{cer} parameter (sometimes indicated as K_i, 1/min [20]) was used as main parameter of interest, quantified with Gjedde-Patlak graphical method using cerebellum as reference region. Acquisition protocol was consistent across sites; all data were quantified and normalised into standard MNI152 standard space with the same in-house developed pipeline (for more details refer to the paper [21]).

C. *Multisite data harmonisation*

To harmonise the data from the test dataset we employed Gaussian kernel smoothing and Combat harmonisation.

Gaussian kernel smoothing (hereafter referred only as smoothing) consists in the application of a 3D convolution filter defined by a gaussian kernel with a Full Width Half Maximum (FWHM) of:

$$FWHM = \sigma\sqrt{8\ln(2)} \cong 2.35\sigma$$

Where σ is the size of the kernel to be found by iteratively searching the best match between the data to be harmonised (PET/MR) and the target (PET/CT), in this case we used as target the PET/CT as it is the technology with the lower resolution between the two under investigation. To smooth the data, we used FSL maths (fslmaths -s flag) with the final kernel size of 3mm, as this provided, after some iterative search, the best visual resemblance between the target group (PET/CT) and the data on which smoothing was applied (PET/MR).

Combat is a Bayesian harmonisation method that estimates site-specific shift and scaling factors. This method, contrary to the Gaussian smoothing, allows to specify some covariates such as demographic variables whose contribution within the data variability is estimated and preserved. These covariates must be specified before the harmonisation, otherwise all variability not attributed to the specified covariates is assumed to be noise to remove during the harmonisation. For this type of harmonisation, we employed the function NeuroCombat from the NeuroCombat python library (version 0.2.10+) to estimate the scaling parameters. During the harmonisation we preserved the effect of the same covariates used in the modelling step, i.e., age, sex and body mass index (BMI) [11], [12], [15].

D. *Normative modelling*

We employed a Bayesian Linear Model (BLR) to estimate the model on HCs with [^{11}C]-(+)-PHNO and [^{18}F]FDOPA. The BLR is a Bayesian extension of the simple linear model where we assume that the response of interest is a linear function of the predictor, and that this relationship will vary normally at any point around the average prediction μ with a consistent standard deviation σ. We can briefly write the assumed data generating model as:

$$Y_{ji}|\beta_{0j}, \beta_{1j}, \sigma \sim N(\mu_j, \sigma_j^2) \text{ with } \mu_j = \beta_{0j} + \beta_{1j}X_i$$

Where β_{0j}, β_{1j} represent the effect parameters of the covariate for voxel j and X_i represents the subject-specific covariates. In our specific cases, we included as covariates only demographic variables (age and sex for both tracers and, additionally, BMI as additional covariate for the [^{11}C]-(+)-PHNO model). The selected covariates were selected from previous in-house analyses of the effects of these covariates on the tracers [21], [22], and from literature [23], [24].

The model is estimated using the PCNToolkit (version 1.20.0) Python library, using the default, weakly informative, prior distributions for the parameters and the Powell optimizer for faster convergence of the model fitting [1]. We estimated voxel-wise models on the 2mm isotropic quantified images, restricting the estimation to the voxels overlapping with a grey matter mask.

To evaluate the in-sample performance of the model, we estimated mean and standard deviation of the model response under k-fold cross validation (k=5). From these estimated metrics we calculated voxel-wise Z-score maps where each voxel is calculated as:

$$Z_j = \frac{Y_j - \hat{\mu}_j(\boldsymbol{X})}{\sqrt{\hat{\sigma}_j^2(\boldsymbol{X})}}$$

Where $\hat{\mu}_j(\boldsymbol{X_i})$ is the estimated mean response and $\hat{\sigma}_j^2(\boldsymbol{X_i})$ is the estimated variance of the response, for voxel j, given the specific set of covariates for subject i.

In addition to the single subject deviation map, we also obtained a voxel-wise map of the explained variance of the estimated model on HCs. This map was visually inspected to weigh the effect of the harmonisation methods had on it.

E. *Statistical analyses*

To assess the best harmonisation method, we first evaluated the effect of this step on the Z-scores by testing the differences of the median and the first four statistical moments of the distribution (mean, standard deviation, skewness, and kurtosis) using Welch two sample t-tests in R (version 4.2.1). In this step the working hypothesis is that, after harmonisation, the distribution of scores should be homogeneous, i.e., there should be no statistical differences between the datasets acquired using the two scanners, in addition the distribution parameters should be close to that of a normal distribution (i.e.,

skewness≈0 and kurtosis≈3).

For re-assessment on the second tracer, we repeated the analyses on the Z-scores by performing an ANOVA on the parameters of the distribution with the anova_test function of the rstatix package in R version 4.2.

III. RESULTS

A. *Muti-scanner [^{11}C]-(+)-PHNO image harmonisation*

From Fig. 1, it is possible to observe a clear scanner effect on the distribution of the Z-scores when no harmonisation is applied; such effect is no longer visible after the application of the harmonisation methods (Fig. 1).

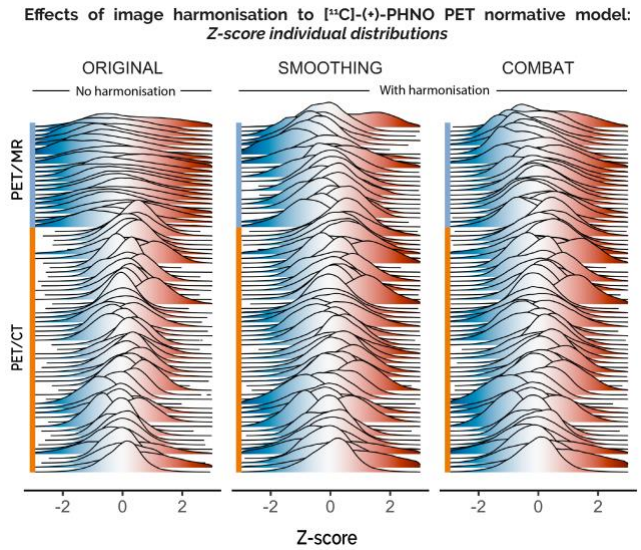


Fig. 1: Effects of harmonisation methods on the Z-scores of [^{11}C]-(+)-PHNO normative model. *The distributions within the ridgeline plots correspond to the Z-score distributions of each subject of the two datasets (PET/MR and PET/CT). While a scanner effect can be clearly seen in the plot representing the original data (on the left), this effect is reduced in both plots representing the scores after harmonisation.*

Quantitatively, the application of harmonisation is not able to remove all the statistical differences due to the scanner type. The difference of mean Z-score distribution between PET/CT and PET/MR is statistically significant for smoothed data (t=2.85, p<0.001), but not for Combat data (t=0.715, p=n.s.). The same trend is visible for the median (original: t=3.21, p<0.01; smoothed: t=3.13, p<0.01; Combat: t=1.53, p=n.s.). In terms of standard deviation, both harmonisation methods reduce the scanner effect, although the difference between methods remains statistically significant with Combat (original: t=-14.59, p<0.001; smoothed: t=-0.40, p=n.s.; Combat: t=-2.47, p<0.01). Considering the higher-order statistical parameters of the Z-score distributions, smoothing outperforms Combat both in terms of skewness (original: t=-4.79, p<0.001; smoothed: t=0.06, p=n.s.; Combat: t=-5.64, p<0.001) and kurtosis (original: t=0.24, p=n.s.; smoothed: t=0.24, p=n.s.; combat: t=3.32, p<0.01).

In addition to the deviation scores, we visually inspected the map of explained variance by the normative model. The model, both with harmonised and un-harmonised data, explains up to 30% of the variance of the data. However, in the map of the explained variance estimated with the original data and with the smoothed data, we can observe what appears to be a spill-over like artifact in the insula which is increased with smoothing and almost disappears with Combat (Fig. 2).

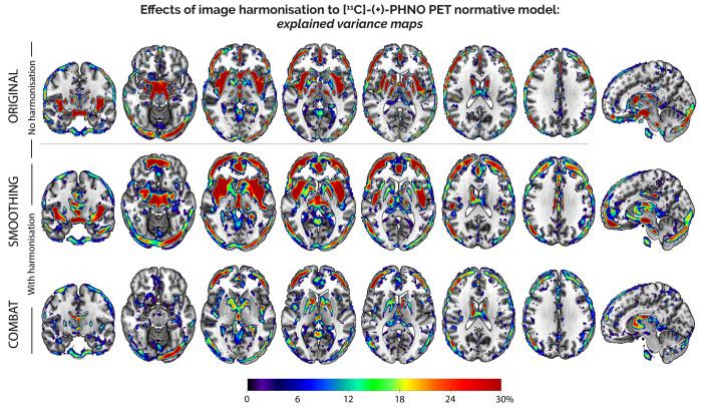


Fig. 2: Effects of harmonisation methods on explained variance of [^{11}C]-(+)-PHNO normative model. *Each row represents the explained variance by the BLR estimated with original, smoothed and Combat harmonised data. In the first two rows there is a visible spill-over like effect in the insula, which almost disappears in the last row.*

B. *Muti-scanner [^{18}F]FDOPA image harmonisation*

Based on the results from the [^{11}C]-(+)-PHNO model, we applied Combat harmonisation to a wider cohort of HCs acquired with 5 different scanners using [^{18}F]FDOPA to determine if the harmonisation yielded similar results with a different tracer.

One-way ANOVA on the first statistical moments to test the effect of different scanners on the Z-score distributions shows no statistical difference in the mean (F=0.12, p=0.98) and median (F=0.098, p=0.983) distribution. Furthermore, no statistical difference in the skewness was found (F=0.351, p=0.843), although there was a residual effect of scanner in the standard deviation (F=3.306, p<0.05) and kurtosis (F=11.01, p <0.001), consistently with the [^{11}C]-(+)-PHNO PET results. Post-hoc analyses highlighted that the differences in skewness are driven by the two scanners with the least number of scans (ECAT HR+ 962, N=12 and ECAT EXACT 3D, N=7).

IV. CONCLUSION

The aim of this work was to find the most suitable method for multi-site/ multi-scanner image harmonisation for normative modelling in the context of molecular imaging.

We applied two of the most used harmonisation methods to a dataset of [^{11}C]-(+)-PHNO PET data and found that Combat shows a reduction in the difference between datasets in term of mean, median and standard deviation, a visual harmonisation of the deviation scores and a reduction of spill-over like effects visible in the explained variance map, suggesting its better suitability for the harmonisation of this type of data.

The results given by Combat are upheld also in a wider cohort of controls, acquired with a different tracer, composed by 5 different datasets of [^{18}F]FDOPA PET, gathered with the same number of scanners. Some differences between groups

remain in standard deviation, skewness and kurtosis, possibly by non-linear contribution of some covariates, which are not fully removed with the linear harmonisation method (Combat) but are eliminated with smoothing. With Combat we can harmonise data in a more meaningful and robust way compared to simple smoothing, which would require an iterative search of the kernel size for any new scanner, even though the harmonisation is not perfect.

In future works additional methods for data harmonisation of multi-scanner PET data should be explored, like non-linear versions of Combat (e.g., Combat-GAM) or the incorporation of the scanner-effect directly in the normative model with the use of hierarchical models, which has been shown to be more robust than Combat, but it demands a higher computational power [16].

In this work we showed that Combat can be used not only to harmonise MRI data, but also for PET scans acquired in different centres/scanners to be used for normative modelling. This will allow the neuroimaging community to gather cohorts of HCs from past studies and different centres and estimate normative models of molecular systems.

ACKNOWLEDGEMENT

A.G. is supported by the KCL-funded CDT in Data-Driven Health; this represents independent research partly funded by the NIHR Maudsley's Biomedical Research Centre (BRC) at the South London and Maudsley NHS Foundation Trust and partly funded by GSK. D.M., O.D., F.T., and S.C.R.M. are supported by the NIHR Maudsley's Biomedical Research Centre at the South London and Maudsley NHS Trust. MV is supported by MIUR, Italian Ministry for Education, under the initiatives "Departments of Excellence" (Law 232/2016) and by the NIHR Biomedical Research Centre (BRC) at South London and Maudsley NHS Foundation Trust and King's College London. M.d.G. is an employee of GSK, GSK had no role in the design of this study. We thank all the members of the PET imaging working group for contributing to the data collection: I. Angelescu, M. Bloomfield, I. Bonoldi, F. Borgan, E. D'Ambrosio, T. Dahoun, A. Demjaha, A. Egerton, S. Jauhar, S. Kaar, E. Kim, S. Kim, J. Maccabe, R. Maria, J. Matthews, R. McCutcheon, P. McGuire, C. Nosarti, G. Rutigliano, P. Selvaggi, P.S Talbot, L. Vano.

REFERENCES

[1] A. F. Marquand, I. Rezek, J. Buitelaar, and C. F. Beckmann, 'Understanding Heterogeneity in Clinical Cohorts Using Normative Models: Beyond Case-Control Studies', *Biol. Psychiatry*, vol. 80, no. 7, pp. 552–561, Oct. 2016, doi: 10.1016/j.biopsych.2015.12.023.

[2] A. F. Marquand, S. M. Kia, M. Zabihi, T. Wolfers, J. K. Buitelaar, and C. F. Beckmann, 'Conceptualizing mental disorders as deviations from normative functioning', *Mol. Psychiatry*, vol. 24, no. 10, Art. no. 10, Oct. 2019, doi: 10.1038/s41380-019-0441-1.

[3] T. Wolfers *et al.*, 'Mapping the Heterogeneous Phenotype of Schizophrenia and Bipolar Disorder Using Normative Models', *JAMA Psychiatry*, vol. 75, no. 11, p. 1146, Nov. 2018, doi: 10.1001/jamapsychiatry.2018.2467.

[4] T. Wolfers *et al.*, 'Replicating extensive brain structural heterogeneity in individuals with schizophrenia and bipolar disorder', *Hum. Brain Mapp.*, vol. 42, no. 8, pp. 2546–2555, 2021, doi: 10.1002/hbm.25386.

[5] D. Elad *et al.*, 'Improving the predictive potential of diffusion MRI in schizophrenia using normative models—Towards subject-level classification', *Hum. Brain Mapp.*, vol. 42, no. 14, pp. 4658–4670, 2021, doi: 10.1002/hbm.25574.

[6] T. Wolfers, C. F. Beckmann, M. Hoogman, J. K. Buitelaar, B. Franke, and A. F. Marquand, 'Individual differences v. the average patient: mapping the heterogeneity in ADHD using normative models', *Psychol. Med.*, vol. 50, no. 2, pp. 314–323, Jan. 2020, doi: 10.1017/S0033291719000084.

[7] C.-L. Chen, M.-C. Kuo, W.-C. Wu, Y.-C. Hsu, R.-M. Wu, and W.-Y. I. Tseng, 'Advanced brain aging in multiple system atrophy compared to Parkinson's disease', *NeuroImage Clin.*, vol. 34, p. 102997, Jan. 2022, doi: 10.1016/j.nicl.2022.102997.

[8] M. Naganawa, J.-D. Gallezot, S. Rossano, and R. E. Carson, 'Quantitative PET Imaging in Drug Development: Estimation of Target Occupancy', *Bull. Math. Biol.*, vol. 81, no. 9, pp. 3508–3541, Sep. 2019, doi: 10.1007/s11538-017-0374-2.

[9] P. M. Thompson *et al.*, 'The ENIGMA Consortium: large-scale collaborative analyses of neuroimaging and genetic data', *Brain Imaging Behav.*, vol. 8, no. 2, pp. 153–182, Jun. 2014, doi: 10.1007/s11682-013-9269-5.

[10] C. Sudlow *et al.*, 'UK Biobank: An Open Access Resource for Identifying the Causes of a Wide Range of Complex Diseases of Middle and Old Age', *PLOS Med.*, vol. 12, no. 3, p. e1001779, Mar. 2015, doi: 10.1371/journal.pmed.1001779.

[11] J.-P. Fortin *et al.*, 'Harmonization of multi-site diffusion tensor imaging data', *NeuroImage*, vol. 161, pp. 149–170, Nov. 2017, doi: 10.1016/j.neuroimage.2017.08.047.

[12] J.-P. Fortin *et al.*, 'Harmonization of cortical thickness measurements across scanners and sites', *NeuroImage*, vol. 167, pp. 104–120, Feb. 2018, doi: 10.1016/j.neuroimage.2017.11.024.

[13] J. M. M. Bayer *et al.*, 'Accommodating site variation in neuroimaging data using normative and hierarchical Bayesian models'. bioRxiv, p. 2021.02.09.430363, May 30, 2021. doi: 10.1101/2021.02.09.430363.

[14] J. M. M. Bayer *et al.*, 'Site effects how-to & when: an overview of retrospective techniques to accommodate site effects in multi-site neuroimaging analyses'. PsyArXiv, Apr. 27, 2022. doi: 10.31234/osf.io/mpufv.

[15] 'Adjusting batch effects in microarray expression data using empirical Bayes methods | Biostatistics | Oxford Academic'. https://academic.oup.com/biostatistics/article/8/1/118/252073?login=false (accessed Dec. 20, 2022).

[16] S. M. Kia *et al.*, 'Hierarchical Bayesian Regression for Multi-Site Normative Modeling of Neuroimaging Data'. arXiv, May 25, 2020. doi: 10.48550/arXiv.2005.12055.

[17] S. M. Kia *et al.*, 'Federated Multi-Site Normative Modeling using Hierarchical Bayesian Regression'. bioRxiv, p. 2021.05.28.446120, May 30, 2021. doi: 10.1101/2021.05.28.446120.

[18] P. Selvaggi *et al.*, 'Increased cerebral blood flow after single dose of antipsychotics in healthy volunteers depends on dopamine D2 receptor density profiles', *NeuroImage*, vol. 188, pp. 774–784, Mar. 2019, doi: 10.1016/j.neuroimage.2018.12.028.

[19] T. Dahoun, M. M. Nour, R. A. McCutcheon, R. A. Adams, M. A. P. Bloomfield, and O. D. Howes, 'The relationship between childhood trauma, dopamine release and dexamphetamine-induced positive psychotic symptoms: a [11C]-(+)-PHNO PET study', *Transl. Psychiatry*, vol. 9, Nov. 2019, doi: 10.1038/s41398-019-0627-y.

[20] R. B. Innis *et al.*, 'Consensus Nomenclature for in vivo Imaging of Reversibly Binding Radioligands', *J. Cereb. Blood Flow Metab.*, vol. 27, no. 9, pp. 1533–1539, Sep. 2007, doi: 10.1038/sj.jcbfm.9600493.

[21] G. Nordio *et al.*, *Digital data repository and automatic analysis framework for FDOPA PET neuroimaging*. 2022. doi: 10.1101/2022.04.14.488129.

[22] 'NRM 2021 Abstract Booklet', *J. Cereb. Blood Flow Metab.*, vol. 41, no. 1_suppl, pp. 11–309, Nov. 2021, doi: 10.1177/0271678X211061050.

[23] D. Matuskey *et al.*, 'Age-related changes in binding of the D2/3 receptor radioligand [11C](+)PHNO in healthy volunteers', *NeuroImage*, vol. 130, pp. 241–247, Apr. 2016, doi: 10.1016/j.neuroimage.2016.02.002.

[24] 'Elevated Dopamine D2/3 Receptor Availability in Obese Individuals: A PET Imaging Study with [11C](+)PHNO | Neuropsychopharmacology'. https://www.nature.com/articles/npp2016115 (accessed Jan. 11, 2023).

A Multiparameter Statistical Approach for Cardiotocographic Signals Analysis

A.M. Ponsiglione[1,†], A. Tedesco[2,†], N. Pisani[3], L. Donisi[1,*], C. Ricciardi[1], M. Romano[1,‡] and F. Amato[1,‡]

[1] *Department of Information Technology and Electrical Engineering, University of Naples "Federico II", Naples, Italy*
[2] *Department of Engineering for Innovation, University of Salento, Lecce, Italy*
[3] *Department of Advanced Biomedical Sciences, University of Naples "Federico II", Naples, Italy*

† These authors contributed equally to this work; ‡ These authors also contributed equally to this work; * Corresponding author: leandro.donisi@unina.it

***Abstract*—Cardiotocography (CTG) is a widely way to assess foetal well-being status, both in antepartum and intrapartum period. Automatic computerized analysis was introduced to overcome limitations of visual analysis of CTG traces. The present study extended a software previously developed for the calculation of foetal heart rate signal (FHR), floatingline (FL) signal and uterine contractions signal introducing the extraction of five novel statistical parameters from signals mentioned. Dataset contained 580 signals acquired during daily routing foetal monitoring. A univariate statistical analysis was used to compare spontaneous deliveries from caesarean deliveries; an analysis of variance, and a post-hoc test was performed to distinguish the week of gestation (WG) in which the CTG trace was recorded. The results demonstrated that, whereas decelerations features were not able to classify CTG signals, accelerations features were. In particular, kurtosis of FHR accelerations (*p*-value=0.0029) was able to distinguish between CTG corresponding to caesarean and spontaneous delivery. Furthermore, by considering accelerations computed by the FL, their mean (*p*-value=0.034), standard deviation (*p*-value=0.032) and variance (*p*-value=0.011) were useful in discriminating among different WG classes. These are important and promising results because it is the first time that novel features are employed in CTG classification.**

***Keywords*—Cardiotocographic signals, foetal heart rate, uterine contractions, statistical analysis.**

I. Introduction

Cardiotocography (CTG) is a continuous electronic recording of foetal heart rate (FHR), uterine contractions (UC) activity obtained both in antepartum and intrapartum period [1] by means two probs placed on women's abdomen. Nowadays, it is well known that FHR monitoring is an important indicator of foetal health state, mainly about a correct blood oxygenation and a proper autonomous nervous system (ANS) work [2]. Some parameters which indicate a well-being foetal status are FHR variability; accelerations, which indicate ANS reactions to internal and/or external stimuli; the basal level of FHR signal, a running FHR average which, in absence of cardiac arrhythmia, is confined in some intervals dependent on week of gestation (WG) and, at the term of pregnancy, decelerations of FHR, which can be physiological or suspicious, mainly according to their shape and time-correlation with UC.

In clinical practice, visual analysis of CTG traces depends on clinician's experience, noting a variability both between observers and within the same observer. For this reason, visual analysis has been often substituted by computerized analysis of CTG traces [3], [4], which takes advantage of a reproducible and objective quantification of parameters not easily detected by the human eyes [5], [6]. Computerized CTG systems are not yet fully used in clinical fields, since results are not fully satisfying [6]. These techniques try to calculate the parameters usually detect by clinician's eye inspection for diagnosis such as, for example, presence of accelerations, decelerations, baseline trend, and then to add other characteristics, for example, morphological, or outcome of so-called nonlinear analyses, in order to provide physicians with a wider gamma of parameters on which rely their evaluation [7].

Due to their importance in foetal monitoring, this work focused on accelerations and decelerations events. Accelerations and decelerations were assessed both from FHR signals, for preserving the superimposed variability, and from floatingline (FL), for highlighting their shape. Moreover, for CTG traces recorded during the labour also UC were analysed.

In particular, the aim of the current study was to calculate statistical features in order to characterise in a novel way (for this research field) these events and verify if they might be able to distinguish the WG in which the CTG trace was recorded (expression of ANS maturation), and to discriminate CTG of spontaneous deliveries and CTG of caesarean sections.

Indeed, it is worth remembering that, in some countries, the CTG has recognised as a clinical report with legal value; so that the capability to understand if a caesarean section is necessary is still an important research topic.

II. Materials and Methods

A. Data set

CTG traces used in the present study are a subset of a database populated by signals acquired in medical contexts, during daily routine foetal monitoring consisting of 580 traces. All CTG signals last a minimum of 20 minutes from women being in a rest position. Sonicaid or HP-135x cardiotocographs were used to acquire CTG signals. In both cases, as it is known, FHR signals are recorded by an ultrasound Doppler probe while the UC signals by external pressure transducers.

B. Signal pre-processing and classical analysis

After the acquisition of CTG signals, it is useful/necessary to carry out a pre-processing phase whose main purpose is to select only FHR signals which can be considered of good quality. To be labelled of "good quality", signals included in the study matched the following requirements:

- a percentage of signal loss and outliers lower than 10%

and 5% respectively,
- acquired from singleton pregnancy,
- absence of complications during caesarean and spontaneous deliveries,
- correspondence with a healthy new-born, i.e., Apgar at least equal to 7 at the 1st minute,
- birth weight appropriate for gestational age.

Further, as detailed in previous works [8], [9], [10] the pre-processing software makes FHR and UC signals comparable and available for the analysis regardless to the acquisition device. The pre-processing software also provides a quality signal to identify "good" and "bad" quality signal tracts.

The estimation of the relevant clinical parameters in foetal monitoring was carried out with a software previously developed in MATLAB [11].

The software is able to give as outcome:
- baseline and FL, that is the median line of an FHR signal
- detected accelerations and decelerations, with their main features (e.g., time-duration and amplitude)
- detected uterine contractions
- some time and frequency characteristics (such as short-term variability, and power content of the different frequency ranges of FHR PSD)
- other more in-depth analyses (results of dynamic analysis, sample entropy, etc).

Clinical parameters calculation is based both on FIGO guidelines [12] and literature indications [13], [14], [15].

An example of FHR and UC signals are shown in Figure 1.

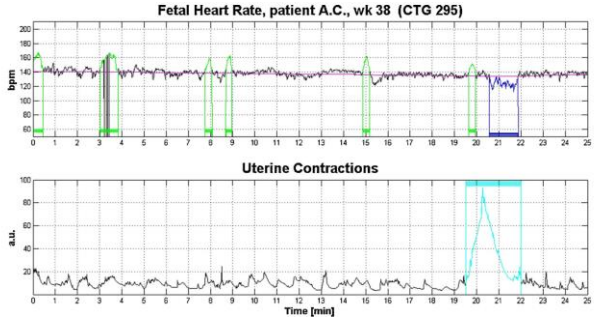


Fig. 1. Foetal heart rate and uterine contractions signals. By using different colours are identified accelerations (green), decelerations (blue) and uterine contractions (light blue).

C. Statistical features extraction

In the current study, the authors extended the above-mentioned software to add new information (listed below). MATLAB functions for statistical features extraction from detected CTG events (accelerations, decelerations, and contractions) were implemented. The functions need as input the following signals and parameters: asset (time axis expressed in s), FHR, FL, UC; plus, for each signal, number of events, time-start and time-end of the events. Of course, not all the signals are simultaneously necessary. The output returns a matrix with all the parameters calculated.

To have a synthetic indicator for each CTG trace, the values of statistical features, calculated for each event identified, were averaged over the number of events of the same type. The mean, min and max number of accelerations, decelerations and UC were respectively: 8.96, 0, 94 (accelerations); 0.12, 0, 7 (decelerations); 2.42, 0, 89 (UC).

Assessed statistical features are the most employed:
- mean
- standard deviation (sd)
- variance
- skewness
- kurtosis.

Statistical features were extracted from accelerations and decelerations of FHR signals, accelerations and decelerations of FL, and UC. The final matrix was 580 x 25 in which the rows represent CTG signals, and columns statistical features, above listed (5 related to: accelerations of FHR, accelerations computed on the FL, decelerations both on FHR and FL, UC).

For the post-processing, CTG were grouped based on the WG in which were recorded. Specifically, 27th-30th week that represents the antepartum period; 31st-35th week for considering preparatory contractions; and 36th-42nd week that represents the term period of a pregnancy.

D. Statistical analysis

Statistical analyses were performed using MATLAB software. The Anderson-Darling test was employed to evaluate the normality of statistical features previously calculated. For normally distributed data a *t*-test for independent sample was used, otherwise a Mann-Whitney test was performed. The univariate statistical analysis was conducted to try to classify CTG corresponding to spontaneous deliveries from CTG corresponding to caesarean ones.

An analysis of variance was also computed to try to distinguish the WG in which the CTG trace was recorded (27th – 30th week, 31st – 35th week or 36th – 42nd week). The same procedure as for the previous analysis was applied to assess the normality of statistical features. Specifically, one-way Anova test was employed for normally distributed data, while its corresponding non-parametric test, Kruskal-Wallis, for not normally distributed ones. Finally, when one-way Anova test or Kruskal-Wallis test was significant, a post-hoc analysis, Turkey test, was conducted to uncover differences between the three groups. The significance level for all statistical tests was fixed at $\alpha<0.05$.

III. Results

Statistical distributions, in terms of means ± sd, of 25 considered features are listed in the footnote[1].

A. Univariate statistical analysis

Univariate statistical analysis tried to classify CTG of spontaneous deliveries from CTG of caesarean sections based

[1] Mean of FHR acc. (146.03 ± 15.01); sd of FHR acc. (21738.81 ± 3721.87); variance of FHR acc. (539.12 ± 968.83); skewness of FHR acc. (-0.30 ± 0.39); kurtosis of FHR acc. (2.59 ±1.58); mean of FL acc (151.04 ± 8.17); sd of FL acc. (22895.60 ± 2491.10); variance of FL acc. (19.13 ± 11.38); skewness of FL acc. (-0.36 ± 0.23); kurtosis of FL acc. (2.15 ± 0.43); mean of FHR dec. (96.03 ± 32.14); sd of FHR dec. (10272.92 ± 5745.91); variance of FHR dec. (1713.16 ± 1604.19); skewness of FHR dec. (-0.86 ± 1.40); kustosis of FHR dec. (4.49 ± 5.35); mean of FL dec. (123.46 ± 10.45); sd of FL dec. (15349.23 ± 2646.55); variance of FL dec. (30.00 ± 22.30); skewness of FL dec. (0.21 ± 0.62); kustosis of FL dec. (2.65 ± 0.82); mean of UC (36.08 ± 14.79); sd of UC (1574.73 ± 1444.37); variance of UC (248.85 ± 352.17); skewness of UC (0.12 ± 0.69); kustosis of UC (2.55 ± 2.92).

on all 25 extracted statistical features. Before carrying out the classification, as above mentioned, a test for checking the normality of data was executed. According to the Anderson-Darling test, all the tested features resulted non normally distributed, except those one related to decelerations computed on the FL. About the separation between spontaneous deliveries and caesarean sections, the significance was reached by the variable kurtosis of accelerations of FHR signal with a *p*-value equal to 0.0029. This is in line with our expectations since grater accelerations generally represent a healthy foetus.

B. *Variance statistical analysis*

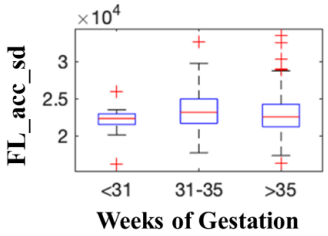
Analysis of variance is a way to compare CTG traces recorded in several WGs, among the 27th-30th week, 31st-35th week and 36th-42nd week considering the whole set of 25 extracted statistical features. The normality Anderson-Darling test showed that all variables were not normally distributed and consequently the Kruskal-Wallis test was applied for the whole analysis. Table I illustrates significant test variables.

TABLE I
KRUSKAL-WALLIS TEST RESULTS

Feature	*p-value (α<0.05)*
FL_acc_mean	0.034
FL_acc_sd	0.032
FL_acc_variance	0.011

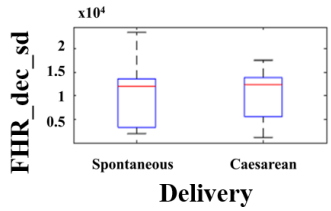
Abbreviations: FL=floatingline; acc=accelerations; sd=standard deviation

Mean, sd and variance of accelerations on FL signals were indicators of a difference among the three groups. This result is also relevant because accelerations increase in number and are better characterized as the progress of pregnancy. An example of the results is shown in Figure 2.



Abbreviations: FL=floatingline; acc=accelerations; sd=standard deviation
Fig. 2. Box plot of standard deviation of acceleration of floatingline signals.

It is worth highlighting, vice versa, that, a significant result on deceleration events of FHR signals would have been anomalous as they are absent in the first two WG groups, unless there are pathological situations or premature births; situations that were beyond the scope of this preliminary study. Figure 3 is an example of what mentioned above.



Abbreviations: FHR=foetal heart rate; dec=decelerations; sd=standard deviation
Fig. 3. Box plot of standard deviation of decelerations of FHR signals.

Based on Kruskal-Wallis test results, a post-hoc analysis was performed. The results are shown in Table II.

TABLE II
TURKEY TEST RESULTS

Group 1	*Group 2*	*p-value (α<0.05)*	*Feature*
31st-35th week	*36th-42nd week*	0.048	FL_acc_mean
31st-35th week	*36th-42nd week*	0.046	FL_acc_sd
27th-30th week	*31st-35th week*	0.032	FL_acc_variance
27th-30th week	*36th-42nd week*	0.029	FL_acc_variance

Abbreviations: FL=floatingline; acc=accelerations; sd=standard deviation

Specifically, mean and sd of accelerations of FL signals were significant comparing 31st-35th week and 36th-42nd week.

However, it is worth noting that the significance was not so good (*p*-value near to 0.05), this is due to the fact that the accelerations into the two groups, usually, have similar features; indeed, around the 30th week, the ANS is anatomically formed and, generally, a healthy foetus react to stimuli with accelerations of HR.

The variance of accelerations of FL signals were significant both for 27th-30th week and 31st-35th week and for 27th-30th week and 36th-42ndweek. In these cases, the *p*-value was lower, i.e., slightly more significant, according to a not yet complete maturation of the ANS in the WG from 27th to 30th [16].

It is worth highlighting that sd and variance give different results. In our opinion, this is due to the difference enhancement related to squaring.

IV. DISCUSSION AND CONCLUSIONS

CTG signals continue to be badly interpreted even though efforts are being made to overcome the problem using computerized systems for automatic analysis in diagnosis of foetal status. As it is well known, computerized CTG analysis has several benefits, one of which is the objectivity in FHR reading. Additionally, a proper pre-processing can enhance the quality of signals. Again, many computerized systems can evidence suspicious signals and provide a warning. Since computerized CTG is becoming increasingly important, different examples of software for automatic CTG analysis have been shown in literature.

For instance, let us cite the Dawes/Redman analytical criteria, the first ones proposed and which the Sonicaid Fetal Care system is rely on [17]. The SisPorto 2.0, the most recent iteration of a program for automatically analysing CTG traces developed at the University of Porto, which involves accurate analysis of the baseline [5], [18]. Finally, the 2CTG2 system that assesses other characteristics such as, for example, the sample entropy [19]. In this prospective, in previous works [8], [9], a software for CTG automatic analysis was developed.

This paper describes an extension of this software, calculating statistical parameters from events assessed on FHR, UC and FL signals. Statistical analyses were performed to classify different types of deliveries and to distinguish the WG in which the CTG were recorded.

Preliminary results obtained were quite interesting. The authors noticed the importance of kurtosis of acceleration events of FHR signals, which was a significant variable useful

for the classification of CTG related to spontaneous deliveries or caesarean deliveries as well as parameters extracted from the accelerations of FL tried to distinguish the WG. Furthermore, the post-hoc test emphasised among which WGs there is a statistically significant difference, as reported in Table II.

In summary, the obtained preliminary results represent an improvement in the study of CTG signals. On the one hand, although using a different methodology, the results confirmed known concepts; for example, that decelerations cannot be used as predictor events if CTG are recorded early during the pregnancy, or that accelerations change their features (not only the number) as the pregnancy as advances. These findings encourage us about the potential efficacy of the proposed methodology that can be usefully further developed. On the other hand, preliminary results and observations confirmed the importance of computerized CTG. Indeed, parameters here evaluated cannot be computed by naked eyes.

Once the proposed methodology is established, the preliminary results described above provide evidence that it could be useful to include a range of parameters (statistical and/or morphological) to improve the CTG classification; for example, by setting a threshold about mean, sd and variance of accelerations, calculated on FL signals, to assess if the CTG signal is proper for the WG or other diagnostic examinations are necessary. Furthermore, the same analysis techniques could be applied to variables extracted from pathological CTG signals to distinguish reassuring from non-reassuring traces. Finally, an additional development could be the introduction of machine learning algorithms, widely adopted for in different medicine fields for classification purposes [20], [21], [22], [23], [24], for the analysis of CTG traces [25], [26], [27].

REFERENCES

[1] T. Tongsong, A. Iamthongin, C. Wanapirak, W. Piyamongkol, S. Sirichotiyakul *et al.*, "Accuracy of fetal heart-rate variability interpretation by obstetricians using the criteria of the National Institute of Child Health and Human Development compared with computer-aided interpretation", *J. Obstet. Gynaecol. Res.*, vol. 31, no. 1, pp. 68–71, 2005.

[2] R. Czabanski, J. Jezewski, A. Matonia, and M. Jezewski, "Computerized analysis of fetal heart rate signals as the predictor of neonatal acidemia", *Expert Syst. Appl.*, vol. 39, no. 15, pp. 11846–11860, Nov. 2012.

[3] J. B. Trimbos and M. J. N. C. Keirse, "Observer variability in assessment of antepartum cardiotocograms", *BJOG Int. J. Obstet. Gynaecol.*, vol. 85, no. 12, pp. 900–906, 1978.

[4] J. Bernardes, A. Costa-Pereira, D. Ayres-de-Campos, H. P. van Geijn, and L. Pereira-Leite, "Evaluation of interobserver agreement of cardiotocograms", *Int. J. Gynecol. Obstet.*, vol. 57, no. 1, pp. 33–37, Apr. 1997.

[5] D. Ayres-de-campos, J. Bernardes, A. Garrido, J. Marques-de-sá, and L. Pereira-leite, "SisPorto 2.0: A Program for automated analysis of cardiotocograms", *J. Matern. Fetal Med.*, vol. 9, no. 5, pp. 311–318, Jan. 2000.

[6] D. Ayres-de-Campos, C. Costa-Santos, and J. Bernardes, "Prediction of neonatal state by computer analysis of fetal heart rate tracings: the antepartum arm of the SisPorto® multicentre validation study", *Eur. J. Obstet. Gynecol. Reprod. Biol.*, vol. 118, no. 1, pp. 52–60, Jan. 2005.

[7] D. Ayres-de-Campos and J. Bernardes, "Comparison of fetal heart rate baseline estimation by SisPorto® 2.01 and a consensus of clinicians", *Eur. J. Obstet. Gynecol. Reprod. Biol.*, vol. 117, no. 2, pp. 174–178, Dec. 2004.

[8] A.M. Ponsiglione, L. Donisi, S. Adamo, A. Tedesco, C. Ricciardi *et al.*, "A Sensitivity Analysis of Symbolic Dynamics indices for Fetal Heart Rate Monitoring", in *2022 E-Health and Bioengineering Conference (EHB)*, IEEE, pp. 01-04.

[9] A.M. Ponsiglione, F. Amato and M. Romano, "Multiparametric investigation of dynamics in fetal heart rate signals", *Bioengineering*, vol. 9, no. 1, pp. 8, Dec. 2021.

[10] C. Ricciardi, F. Amato, A. Tedesco, D. Dragone, C. Cosentino, A.M. Ponsiglione *et al.*, "Detection of Suspicious Cardiotocographic Recordings by Means of a Machine Learning Classifier", *Bioengineering*, vol. 10, no. 2, pp.252, Feb. 2023.

[11] M. Romano, P. Bifulco, M. Ruffo, G. Improta, F. Clemente *et al.*, "Software for computerised analysis of cardiotocographic traces", *Comput. Methods Programs Biomed.*, vol. 124, pp. 121–137, Feb. 2016.

[12] D. Ayres-de-Campos, S. Arulkumaran, and F. I. F. M. E. C. Panel, "FIGO consensus guidelines on intrapartum fetal monitoring: Introduction", *Int. J. Gynecol. Obstet.*, vol. 131, no. 1, pp. 3–4, 2015.

[13] R. Mantel, H. P. van Geijn, F. J. M. Caron, J. M. Swartjes, E. E. van Woerden *et al.*, "Computer analysis of antepartum fetal heart rate: 1. Baseline determination", *Int. J. Biomed. Comput.*, vol. 25, no. 4, pp. 261–272, May 1990.

[14] R. Mantel, H. P. van Geijn, F. J. M. Caron, J. M. Swartjes, E. E. van Woerden *et al.*, "Computer analysis of antepartum fetal heart rate: 2. Detection of accelerations and decelerations", *Int. J. Biomed. Comput.*, vol. 25, no. 4, pp. 273–286, May 1990.

[15] "Royal College of Obstetricians and Gynaecologists", *Br. Med. J.*, vol. 2, no. 5054, pp. 1170–1171, Nov. 1957.

[16] T. Ohta *et al.*, 'Alteration in the Low-Frequency Domain in Power Spectral Analysis of Fetal Heart Beat Fluctuations', *Fetal Diagn. Ther.*, vol. 14, no. 2, pp. 92–97, 1999, doi: 10.1159/000020896

[17] J. Pardey, "Sonicaid FetalCare: fetal heart rate analysis", *Br. J. Midwifery*, vol. 11, no. 10, pp. 620–624, Oct. 2003.

[18] D. Ayres-de-Campos, P. Sousa, A. Costa, and J. Bernardes, "Omniview-SisPorto® 3.5 – a central fetal monitoring station with online alerts based on computerized cardiotocogram+ST event analysis", *J. Perinat. Med.*, vol. 36, no. 3, pp. 260–264, May 2008.

[19] G. Magenes, M.G. Signorini, M. Ferrario and F. Lunghi, "2CTG2: A new system for the antepartum analysis of fetal heart rate", in *11th Mediterranean Conference on Medical and Biomedical Engineering and Computing 2007*, IFMBE Proceedings, vol. 16, pp. 781-784.

[20] L. Donisi, C. Ricciardi, G. Cesarelli, G. Pagano, F. Amitrano *et al.*, "Machine Learning applied on Poincaré Analyisis to discriminate different cardiac issues", in *2020 11th Conference of the European Study Group on Cardiovascular Oscillations (ESGCO)*, IEEE, pp. 1-2.

[21] C. Ricciardi, L. Donisi, G. Cesarelli, G. Pagano, A. Coccia *et al.*, *"*Feasibility of machine learning applied to poincaré plot analysis on patients with CHF", in *2020 11th Conference of the European Study Group on Cardiovascular Oscillations (ESGCO)*, IEEE, pp. 1-2.

[22] M. Sansone, R. Fusco, F. Grassi, G. Gatta, M.P. Belfiore *et al.*, *"*Machine Learning Approaches with Textural Features to Calculate Breast Density on Mammography", *Current Oncology*, vol. 30, no. 1, pp. 839-53, Jan. 2023.

[23] F. Angelone, C. Ricciardi, G. Gatta, M. Sansone, A.M. Ponsiglione *et al., "*Breast Density Analysis on Mammograms: Application of Machine Learning with Textural Features", in *2022 IEEE International Conference on Metrology for Extended Reality, Artificial Intelligence and Neural Engineering (MetroXRAINE)*, IEEE, pp. 295-300.

[24] C. Ricciardi, A.M. Ponsiglione, A. Scala, A. Borrelli, M. Misasi *et al.*, *"*Machine learning and regression analysis to model the length of hospital stay in patients with femur fracture", *Bioengineering*, vol. 14, no. 9, supp. 4, pp. 172, Apr. 2022.

[25] A.M. Ponsiglione, G. Cesarelli, F. Amato and M. Romano, "Optimization of an artificial neural network to study accelerations of foetal heart rhythm", in *2021 IEEE 6th International Forum on Research and Technology for Society and Industry (RTSI) 2021*, IEEE, pp. 159-164.

[26] A.M. Ponsiglione, C. Cosentino, G. Cesarelli, F. Amato and M. Romano, "A comprehensive review of techniques for processing and analyzing fetal heart rate signals", *Sensors*, vol. 21, no. 18, pp. 6136, Sep. 2021.

[27] P. Fergus, M. Selvaraj, C. Chalmers, "Machine learning ensemble modelling to classify caesarean section and vaginal delivery types using cardiotocography traces", in *Comput. Biol. Med.*, vol. 93, pp. 7–16, Feb. 2018.

Disclosing brain functional connections with multi-dimensional approaches

L. Marzetti[1,2], A. Basti[1], R. Guidotti[1], G. Nolte[3] and V. Pizzella[1,2]
[1] *Department of Neuroscience, Imaging and Clinical Sciences, University of Chieti-Pescara, Chieti, Italy*
[2] *Institute for Advanced Biomedical Technologies, University of Chieti-Pescara, Chieti, Italy*
[3] *University Medical Centre Hamburg-Eppendorf, Hamburg, Germany*

***Abstract*—In the last decades, it has become clear that functional interactions between brain regions are crucial for understanding brain's functioning. These interactions can be assessed through functional connectivity approaches that characterize statistical dependencies between time series obtained by time-resolved neuroimaging techniques. Nevertheless, these techniques provide information about brain activity at the scale of brain regions with an extent in the order of several millimetres that constitute a functional unit and are constituted by multiple voxels. To apply conventional bivariate connectivity metrics, the signal of voxels in a brain region (a multi-dimensional set) is usually reduced to a single signal per brain region with a potential loss of information. To overcome this limitation, we have developed a family of "multi-dimensional connectivity" methods that take direct advantage of the multi-dimensional nature of the data. Here, we present a collection of these methods and show, in simulations, that they outperform the approach based on dimensionality reduction and non multi-dimensional connectivity methods.**

***Keywords*—Electroencephalography, Magnetoencephalography, Functional connectivity, Multi-dimensional signals.**

I. INTRODUCTION

In the last decades, neuroimaging research has shown that the characterization of functional interactions between brain regions (i.e. functional connectivity) are crucial for understanding brain's functioning. Functional connectivity is inferred by assessing statistical dependencies between time series associated with regions of interest and obtained by time-resolved neuroimaging techniques (e.g. functional Magnetic Resonance Imaging -fMRI, Electroencephalography - EEG or Magnetoencephalography - MEG). Different bivariate methods for estimating this dependency have been developed (e.g. [1-7]). However, one aspect is often ignored: the fact ROIs are typically composed of multiple voxels, thus ROI signals are typically multi-dimensional and are usually reduced to a representative one-dimensional time series [8] before functional connectivity estimation, with a potential loss of information. To overcome this limitation, "multi-dimensional connectivity" methods have been recently developed to take advantage of the multi-dimensional nature of the data from various neuroimaging techniques: fMRI (e.g. [9,10]), EEG (e.g. [11]) and MEG (e.g. [8]). Here, we present a collection of frequency domain methods we developed to assess different properties of interactions between multi-dimensional signals as, for exampling, linear and non linear coupling as well as directed or undirected coupling.

II. METHODS

A. Multi-dimensional connectivity methods

All the multi-dimensional connectivity metrics we developed are based on assessing functional connectivity as phase coupling of neuronal oscillations exhibited by pairs of multi-dimensional ROIs. We focus on phase coupling metrics [12] given that phase coupling of neuronal oscillations is a putative mechanism for inter-areal communication, and that our methods are mainly intended to be used on MEG and EEG data which are ideally suited to extract neuronal oscillations from the measured signals.

The methods that we developed and tested are listed in Table I together with their properties in terms of the type of phase-coupling they can detect (i.e. coupling between oscillations at the same frequency or coupling between oscillations at different frequencies), as well as in terms of their ability to assess not only the coupling between two ROIs but also its directionality (i.e. directed or undirected).

TABLE I: MULTI-DIMENSIONAL CONNECTIVITY METHODS

Method name	*Coupling type*	*Directionality*
Multivariate Interaction Metric (MIM) [11]	Same frequency Linear	Undirected
Multivariate Phase Slope Index (MPSI) [8]	Same frequency Linear	Directed
Multivariate Antisymmetric Cross Bispectra (MACB)	Different frequencies Non linear	Undirected

In this paper, we will restrict ourselves to linear methods that allow to detect phase-coupling at the same frequency. Specifically, let $x_I(t) = (x_{i1}(t), \dots, x_{iN}(t))^T$ and $x_J(t) = (x_{j1}(t), \dots, x_{jM}(t))^T$ be the multivariate time series for the *N*-dimensional signals *I* and the *M*-dimensional signals *J*, where T denotes the transpose operator. Let also $X_I(f)$ and $X_J(f)$ be the corresponding vector Fourier transforms. The cross-spectral density matrix between $x_I(t)$ and $x_J(t)$ at a given frequency *f* is defined as

$$S_{IJ}(f) = \langle \mathrm{X_I(f)}\, X_J^H(f) \rangle = \begin{bmatrix} S_{II}(f) & S_{IJ}(f) \\ S_{JI}(f) & S_{JJ}(f) \end{bmatrix} \quad (1)$$

where $(\cdot)^H$ denotes the Hermitian conjugate of a matrix. The elements of $\mathrm{S_{IJ}(f)}$ are the cross-spectra between all the pairwise combinations of univariate time series of I and J.

Based on Eq. (1), the multi-dimensional connectivity methods are defined as:

1) Multivariate Interaction Metric- MIM

$$MIM_{IJ}(f) := Tr\left((S_{II}^{R}(f))^{-1}(S_{IJ}^{I}(f))(S_{JJ}^{R}(f))^{-1}(S_{IJ}^{I}(f))^{T}\right) \quad (2)$$

where the superscripts R and I denote the real and imaginary part of the complex-valued cross-spectral density matrices, $(\cdot)^{-1}$ and Tr $(\cdot)$ are the inverse and transpose operators, respectively. MIM does not lead to artefactual phase coupling detections due to artificial zero-lag correlations between the two ROIs. Furthermore, MIM is invariant under invertible and static linear transformation, such as rotations of the physical coordinate system [11].

2) Multivariate Phase Slope Index - MPSI

$$MPSI_{IJ}(f) := 4\sum_{f\in F} Tr\Big(\left(S_{II}^{R}(f+df) + S_{II}^{R}(f)\right)^{-1}\left(S_{IJ}^{I}(f+df)\right)\left(S_{JJ}^{R}(f+df) + S_{JJ}^{R}(f)\right)^{-1}\left(S_{JI}^{R}(f)\right) + \left(S_{II}^{R}(f+df) + S_{II}^{R}(f)\right)^{-1}\left(S_{IJ}^{R}(f+df)\right)\left(S_{II}^{R}(f+df) + S_{II}^{R}(f)\right)^{-1}\left(S_{JI}^{I}(f)\right)\Big) \quad (3)$$

where df and F denote an incremental step in the frequency domain and the frequency band of interest, respectively. MPSI detects the directionality of phase-lagged coupling; a positive value of MPSI indicates that the vector-signal I leads the vector-signal J, while a negative value indicates the opposite. Moreover, similarly to MIM, MPSI is invariant under invertible and static linear transformations, and thus it is independent on rotations of the physical coordinate system [8].

Simulations

We assessed the ability of these metrics to outperform non multi-dimensional metrics by simulating sets of multi-dimensional timeseries corresponding to the signals of two ROIs (*A* and *B*) in which the dimension of each ROI data space was set to N_A=N_B=3 and in which a directed multi-dimensional coupling was generated by introducing a time delay between the two multi-dimensional time courses.

Each set of multidimensional timeseries is written as follows:

$$X_A = \left(x_1, \ldots, x_{N_A}\right)$$
$$X_B = \left(x_{N_A+1}, \ldots, x_{N_B}\right) \quad (4)$$

with

$$x_i(t) = \sum_{i=1}^{N_A}\sum_{k=1}^{P} a_{ijk}\, x_j(t\text{-}\tau_k) + \xi_i(t), i = 1, \ldots, N_A$$
$$x_i(t) = \sum_{i=N_A+1}^{N_A+N_B}\sum_{k=1}^{P} b_{ijk}\, x_j(t\text{-}\tau_k) + \sum_{i=1}^{N_A}\sum_{k=1}^{P} c_{ijk}\, x_j(t\text{-}\tau_k) + \xi_i(t), \quad i = N_A + 1, \ldots, N_A + N_B \quad (5)$$

In addition, N_A+N_B= 6 noise sources were simulated with a temporal evolution given by:

$$y_i(t) = \sum_{k=1}^{P} d_{ik}\, y_i(t\text{-}\tau_k) + \varepsilon_i(t), i = 1, \ldots, N_A + N_B \quad (6)$$

In Eq. 5 and 6 a_{ijk}, b_{ijk}, c_{ijk}, d_{ik}, ξ_i and ε_i are realizations of independent Gaussian random variables of zero mean and a standard deviation equal to 1=10.

The final multidimensional signal is thus given by:

$$Z = (1\text{-}\gamma)\frac{X}{\|X\|_F} + \gamma\frac{Y}{\|Y\|_F} \quad (7)$$

where $X = [X_A\ X_B]'$ is the signal of interest and likewise for the noise , and γ is the noise weight as explained below.

In this model, each of the generated time courses has a length of T = 76200 data points, which, sampled at 254 Hz, corresponds to 5 min of continuous EEG/MEG data. The model order P is equal to 5. We used 20000 pairs of multi-dimensional time series obtained as the sum of a signal term and the noise term weighted by a factor γ in the range from 0 (i.e., no noise) to 0.9 (i.e., 10% signal and 90 % noise) with an incremental step of 0.1, thus leading to 2000 pairs for each γ value. Finally, to calculate the average and standard deviation of the performance indicators (number of right detections, of wrong detections, of not significant detections) of the methods, the generated signals were divided into 20 sets of 100 pairs for each γ.

In the following, we will present the results for the MPSI metric, defined in Eq. 3. Nevertheless, the results for the non-directed multi-dimensional simulated data and the MIM, as defined in Eq. 2, feature a similar behaviour when compared to the corresponding non multivariate version, i.e., the imaginary part of coherency [5] on the first principal component of the multivariate time series.

III. RESULTS

A. Results for the MPSI

In Figure 1, we shown the results obtained by the MPSI and compare it to the results obtained by first applying Canonical Correlation Analysis [13] to reduce the multi-dimensional signals to scalar timeseries, and then using the non multi-dimensional version of the Phase Slope Index [14]. The latter approach is referred to as CCAPSI in Figure 1.

It is evident (Figure 1, left panel) that the percentage of correct detections obtained by MPSI is always higher than the corresponding percentage obtained by CCAPSI for each proportion of signal and noise in the multi-dimensional data. Of course, for higher proportion of signal in the data, both approaches perform better than for the lower proportion of signal but the performance of CCAPSI are still low featuring only about 25% of correct detections for the best case. Conversely, MPSI features about 80% of correct detections for the best case.

Importantly, this effect is only marginally due to CCAPSI making less wrong detections as this percentage is very low and even lower for MPSI (Figure 1 middle panel). The main

reason for the lower number of correct detections featured by CCAPSI comes from its inability to statistically significantly assess if the simulated signals were coupled or not (Figure 1, right panel).

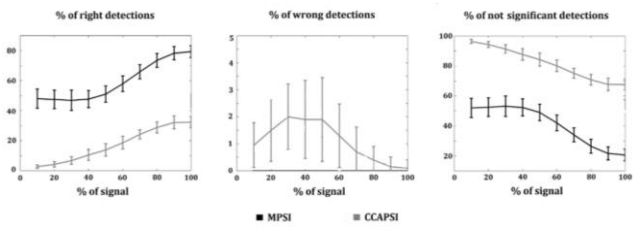


Fig. 1: In this figure the performance over the 2000 simulations for each percentage of signal in the multi-dimensional timeseries is shown. Left: Percentage of correct detections (average and standard deviation) for the MPSI (black) and percentage of correct detections for the CCAPSI (grey). Middle: Percentage of wrong detections for the MPSI (black) and percentage of wrong detections for the CCAPSI (grey). Right: Percentage of no responses (not significant detections) for the MPSI (black) and percentage of wrong detections for the CCAPSI (grey).

IV. Conclusion

In several neuroimaging applications, we do rely on information about brain activity at a meso- or even macro-scale (brain regions with an extent in the order of several millimetres). Usually, these activity is reduced to one signal per region to reduce the complexity. This is especially true when we aim at assessing functional connectivity, i.e. statistical dependencies between brain regions, where for N brain regions at least (N x N/2-1) connectivity values must be computed. Nevertheless, reducing multi-dimensional timeseries to a single one might results in an important loss of information about brain interactions since the regional brain signal is itself multi-dimensional. The development of multi-dimensional methods is thus crucial to avoid this information loss. Also, it must be noted that the difference between the multivariate methods and the corresponding bivariate approach increases for shorter the data length, or for higher the dimension of the single data space.

Here, we presented the definitions of the linear methods we developed in this framework, and the simulation results for the MPSI. In addition, it is important to notice that a similar approach can be applied to non-linear (i.e., cross-frequency interactions) methods, leading to the derivation of the multivariate antisymmetric cross bispectra (MACB). MACB performance can also be proven to be significantly higher than those obtained by antisymmetric cross bispectra after on the first principal component.

References

[1] J. F. Hipp, D. J. Hawellek, M. Corbetta, M. Siegel, and A. K. Engel, “Large-scale cortical correlation structure of spontaneous oscillatory activity”, *Nat. Neurosci.*, vol. 15, pp. 884–890, May 2012.

[2] S. L. Bressler, and A. K. Seth, "Wiener-Granger causality: a well established methodology", *NeuroImage*, vol. 58, pp. 323-329, Sep 2011.

[3] M. P. van den Heuvel, and H. E. Hulshoff Pol, "Exploring the brain network: a review on resting-state fMRI functional connectivity", *Eur. Neuropsychopharmacol.*, vol. 20, pp. 519-534, Aug 2010.

[4] C. J. Stam, G. Nolte, and A. Daffertshofer, “Phase lag index: assessment of functional connectivity from multichannel EEG and MEG with diminished bias from common sources”, *Hum. Brain Mapp.*, vol. 28, pp. 1178–1193, Nov 2007.

[5] G. Nolte, O. Bai, L. Wheaton, Z. Mari, S. Vorbach, and M. Hallett, “Identifying true brain interaction from EEG data using the imaginary part of coherency”, *Clin. Neurophysiol.*, vol. 115, pp. 2292–2307, Oct 2004.

[6] J.-P. Lachaux, E. Rodriguez, J. Martinerie, and F. J. Varela, (1999). “Measuring phase synchrony in brain signals”. *Hum. Brain Mapp.*, vol. 8, pp. 194–208, Nov 1999.

[7] B. Biswal, F. Z. Yetkin, V. M. Haughton, and J. S. Hyde, “Functional connectivity in the motor cortex of resting human brain using echo-planar MRI”, *Magn. Reson. Med.*, vol. 34, pp. 537-541, Oct 1995

[8] A. Basti, V. Pizzella, F. Chella, G. L. Romani, G. Nolte, and L. Marzetti, “Disclosing large-scale directed functional connections in MEG with the multivariate phase slope index”, *NeuroImage*, vol. 175, pp. 161–175, Jul 2018.

[9] S. Anzellotti, and M. N. Coutanche, “Beyond Functional Connectivity: Investigating Networks of Multivariate Representations”, *Trends. Cogn. Sci.*, vol. 22, pp. 258-269, Mar 2018

[10] L. Geerligs, and R. N. Henson, “Functional connectivity and structural covariance between regions of interest can be measured more accurately using multivariate distance correlation”, *NeuroImage*, vol. 135, pp. 16–31, Jul 2016

[11] A. Ewald, L. Marzetti, F. Zappasodi, F. C. Meinecke, and G. Nolte, “Estimating true brain connectivity from EEG/MEG data invariant to linear and static transformations in sensor space”, *NeuroImage*, vol. 60, pp. 476–488, Mar 2012

[12] L. Marzetti, A. Basti, F. Chella, A. D’Andrea, J. Syrjälä, and V. Pizzella, “Brain functional connectivity through phase coupling of neuronal oscillations: a perspective from magnetoencephalography”, *Front. Neurosci.*, vol. 13, pp. 964, Sep 2019

[13] H. Hotelling, “Relations between two sets of variates”, *Biometrika*, vol. 28, pp. 321–377, Dec 1936

[14] G. Nolte, A. Ziehe, V. V. Nikulin, A., Schlögl, N. Krämer, T. Brismar, and K.-R. Müller, “Robustly estimating the flow direction of information in complex physical systems”, *Phys. Rev. Lett.*, vol. 100, pp. 234101, Jun 2008

Enhancing Safety in Industry 4.0: The Use of Passive Brain Computer Interfaces for Vigilance Monitoring

E. Cinquetti[1], I. Siviero[1], G. Menegaz[1] and S.F. Storti[1]
[1]*Dept. of Engineering for Innovation Medicine, University of Verona*
silviafrancesca.storti@univr.it (corresponding)

***Abstract*—In the context of Industry 4.0 and human-robot interaction, ensuring the safety of operators by avoiding collisions and human errors is crucial. One important aspect of this is monitoring vigilance decrement in order to limit safety risks and improve productivity. While existing solutions for this problem rely on passive brain computer interface (BCI) based on electroencephalography (EEG) recordings, there has been limited exploration of their use in industrial environments. The presented study proposes a new experimental protocol for predicting vigilance degradation using EEG data. The dataset was acquired from five healthy volunteers observing a robotic arm performing three different movements for 23 minutes. The EEG power spectrum over time was computed using the continuous wavelet transform (CWT) and its increment was examined using a linear regression model. The results of the study show that there is an increasing α power band over the parietal brain area, while the vigilance of the operator is decreasing. The first order polynomial regressed to the time variant power spectrum had positive angular coefficients (values between 0 and 0.4) for all subjects. The findings suggest that monitoring vigilance degradation in Industry 4.0 is crucial to prevent accidents and reduced performance in repetitive human tasks.**

***Keywords*—Brain computer interface, electroencephalography, vigilance, industry 4.0.**

I. INTRODUCTION

The manufacturing industry is increasingly embracing heavy automation, with human workers playing a role in cooperating with and monitoring machinery such as robotic arms. While this has led to an increase in productivity, it also has the potential to negatively impact task performance and introduce safety risks and accidents. Performing repetitive tasks can result in a decrease in the operator's attention [1], with potential negative effects on both the operator's health and the quality of the final product.

A brain computer interface (BCI) is a system that acts as direct communication pathways between the brain and an external device exploiting the brain's electrical activity. Passive BCI is primarily used to track or assess brain activity employing signals involuntarily generated by a user to decode the cognitive state, attention, and intentions mainly using the electroencephalography (EEG) [2]. Current applications involve the clinical field, education, entertainment, driving, aviation, and also Industry 4.0 [3]. EEG is a cost-effective, non-invasive and portable way to monitor the operator's mental state, thanks to a headset connected to an amplifier which captures the electric potential differences produced by brain activity. EEG may be used to monitor vigilance, the ability to sustain attention over a long period of time under monotonous stimulus [2]; vigilance is critical in contexts such as plant surveillance, driving, and air traffic control [1], and its absence can lead to potential accidents [4], making it a crucial mental quality to track in Industry 4.0 workplaces. In EEG-based vigilance detection, power spectrum of different frequency bands and their ratios have been used extensively, with the most interesting being θ (4-8 Hz) [5] and α (8-12 Hz). Indeed, the α power spectrum can decrease or increase in response to a stimulus, with increased activity called event-related synchronization (ERS) and decreased activity called event-related desynchronization (ERD) [6]. ERD in the α band is associated with visual stimulation, and is related with activation of cortical areas related to information processing, selective attention and motor preparation. On the other hand, ERS is associated with inhibition of brain activity and may indicate a resting or idling cortical area in which no information is currently processed [7]. The α band activity is also influenced by increased mental fatigue [8]. Mental fatigue refers to a state that occurs when subjects are performing repetitive and monotonous tasks for a prolonged period of time, which is mirrored by loss of vigilance. Growing mental fatigue, and thus vigilance reduction, is characterised by an increase in power of α oscillations [2].

To evaluate the potential of EEG analysis within an industrial setting, we conducted an innovative experiment that aimed at gradually increasing subjects' mental fatigue over time. By closely monitoring EEG activity, we aimed at detecting patterns and trends in brain activity that could indicate changes in subjects' vigilance states as they performed repetitive supervisory tasks. This approach allowed to assess the feasibility of using EEG analysis to monitor vigilance within an industrial context and to identify potential markers of mental fatigue.

II. MATERIALS AND METHODS

A. Participants

The study involved five healthy subjects recruited on a voluntary basis (average age 26.6 $\pm$ 1.34 years, all males). Participants were asked to give informed consent before taking

part in the study. Data were collected according to protocols approved by the local ethics committee of the University of Verona (Comitato di approvazione della ricerca sulla persona [CARP]: protocol n. 2.R1/2022). The study design and data collection took place in the Industrial Computer Engineering (ICE) Laboratory, a research facility of the University of Verona (https://www.icelab.di.univr.it/) [9]. Participants completed a variation of the NASA task-load index questionnaire after the study [10], scoring on a subjective scale from 1 to 20 the perceived pace of the task (temporal demand), how much effort they had to put in the task (effort), and how frustrating it was to them (frustration).

B. Experimental Setup and Paradigm

The EEG was recorded using the portable BeMicro EEG amplifier (EBNeuro S.p.A, Firenze, Italy) and a cap providing 21 Ag/AgCl electrodes positioned according to a 10/20 system (impedance was kept below 10kΩ). The cap has the reference placed anteriorly to Fz, while the ground is posterior to Fz. EEG data were acquired at a sampling rate of 256 Hz and stored using the software Galileo (EBNeuro S.p.A, Firenze, Italy).
The experiment was conduced using a robotic arm KUKA LBR iiwa 14 R820, composed of 7 joints, a flange, and a GIMATIC electromechanical gripper at the end for grabbing small objects. All participants were seated in a comfortable armchair in front of a workbench, where they observed the movement of the robot. The protocol consisted of 3 different movements performed by the KUKA robot, as depicted in Fig. 1. The movement began with the robot picking an object of 2x4 cm from position 1 and moving it to position 2, then moving the object to position 3; the process was repeated 40 times. At each iteration, there were two different positions the object could be placed, marked as a tick or a cross in Fig. 1. The probability of success for the tick position was 80%, while it was 20% for the cross. The reaction times (RT) were measured using a keyboard, with a index finger press of the space-bar button (tick position) or the enter button (cross position), to minimize muscle EEG artifacts. Participants reacted the moment they assessed the position.

The visual vigilance task lasted 23 minutes and consisted of 40 trials. Each trial was a sequence of 3 movements of the KUKA robot, and lasted 33 s. Each sub-trial (individual robot movement) had a duration of at least 11 s, with a small time overhead caused by computation of the arm's trajectory. As shown in Fig. 1, at the start of the movement, the robot would be stationary in the middle of the workbench; after 1s, the robot would grasp the small object; at $t = 4s$, the small object would be moved to a different position. The RT were typically in the time interval around $t = 5s$. In addition to the task, two minutes of EEG with eyes open were recorded in a resting state before the task and a video was recorded to capture any failures or movements.

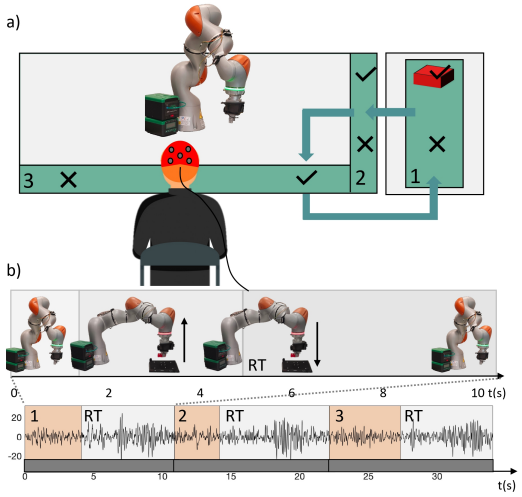


Fig. 1: Representation of the experimental procedure and signal acquisition. a) Robot workspace in which 3 different movements are continuously repeated (i.e., from position 1 to 2, from 2 to 3, from 3 to 1, etc.). b) Timing schedule of the robot movements and an example of processed EEG data acquired during an experimental trial. The RT are also reported.

C. EEG data analysis

EEG data were analyzed in Matlab (R2022a) using EEGLAB (https://sccn.ucsd.edu/eeglab/index.php). The EEG data were filtered by a 3-th order Butterworth band-pass filter with a pass-band frequency between 4 and 30 Hz. The raw EEG data were re-referenced to common average reference (CAR) and baseline corrected. Independent component analysis (ICA) was applied to remove residual artifacts.
We used a Continuous Wavelet Transform (CWT) to extract patterns from EEG signals [11], specifically using the Morlet wavelet, a commonly used method in EEG analysis. We estimated the power spectrum over time for both rest and task conditions from all EEG recordings on the θ and α frequency ranges.

The task is composed of 120 sub-trials. Data analysis was performed in two different ways: on each sub-trial (i.e. 11 s) and on the complete EEG signal (i.e. 23 min). In the first case, the analysis focused on time-variant power spectrum behavior along different phases of a sub-trial [Fig. 2]. Power signal trend following RT was obtained by a linear regression model. In the second case, we analyzed the time-variant power spectrum of each channel in the α frequency band in order to evaluate changes over the entire task recording. The obtained power spectrum was smoothed using an exponentially weighted moving average (EWMA) filter to reduce the variability inside the sub-trials, and then a linear regression model of the first order was used to evaluate increment or decrement over time.

III. Results

A. Sub-trial analysis

The sub-trial analysis for a representative subject (no. 1) is presented in Figs. 2 and 3. Fig. 2 illustrates the average of the power spectrum over sub-trial in the α frequency band

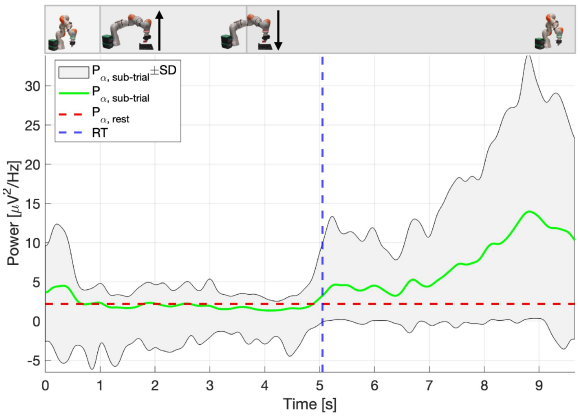


Fig. 2: *Sub-trial analysis*: Time-variant average power spectrum in the α frequency band across sub-trials of a parietal channel ($P3$) for subject 1 (average $P_{\alpha,sub-trial} \pm SD$ [light gray region], average $P_{\alpha,sub-trial}$ [green], average $P_{\alpha,rest}$ [red] and the average RT [blue]).

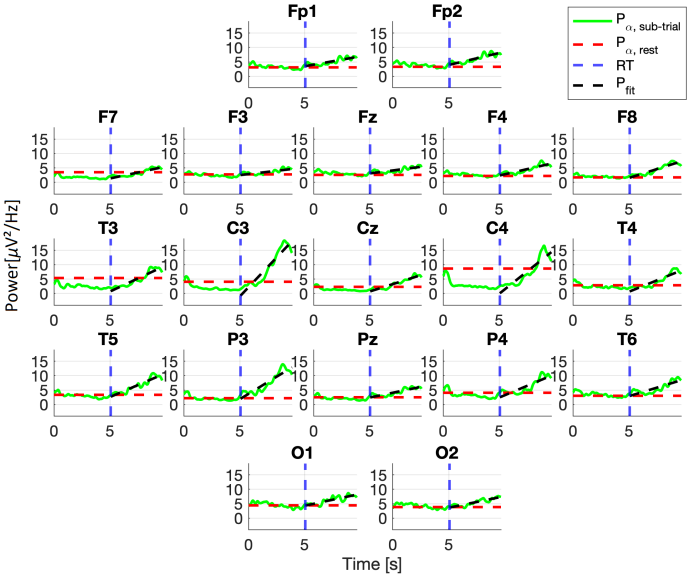


Fig. 3: *Sub-trial analysis*: Time-variant average power spectrum in the α frequency band across sub-trials of all channels for subject 1 (average $P_{\alpha,sub-trial}$ [green], average $P_{\alpha,rest}$ [red] and the average RT [blue]). Data fitted starting from RT (black).

for the channel P3, as well as the power calculated during a resting EEG and the average RT. The average power decreases when the robot grasps the small object, for at least 3 s, and then increases after the RT. Fig. 3 shows the power for each EEG channel and the fitted line, obtained with the linear regression model starting from RT. A positive trend is confirmed, coherent with the ERS behavior triggered by the subject's relaxation. The slope is higher for the channel C3, C4, P3, and P4. This trend has been observed in the other subjects as well. The slopes of the fitted lines for each sub-trial were averaged over each sub-trial and then over subjects, and the results are shown in Table I. The findings confirm that α power spectrum increments primary affect the centro-parietal brain areas.

TABLE I: *Sub-trial analysis*: The slopes of sub-trials computed following RT, averaged over subjects. The higher six values are reported. Despite high SD values, no single subject reports negative slopes. P-value of slope parameter is significant for all subjects ($p < 0.05$).

Ch	*Mean*	*SD*	R^2
C3	1.25	±1.46	0.63
P3	1.00	±0.77	0.66
T5	0.89	±0.59	0.61
C4	1.07	±1.05	0.62
P4	0.68	±1.09	0.60
PZ	0.60	±0.76	0.59

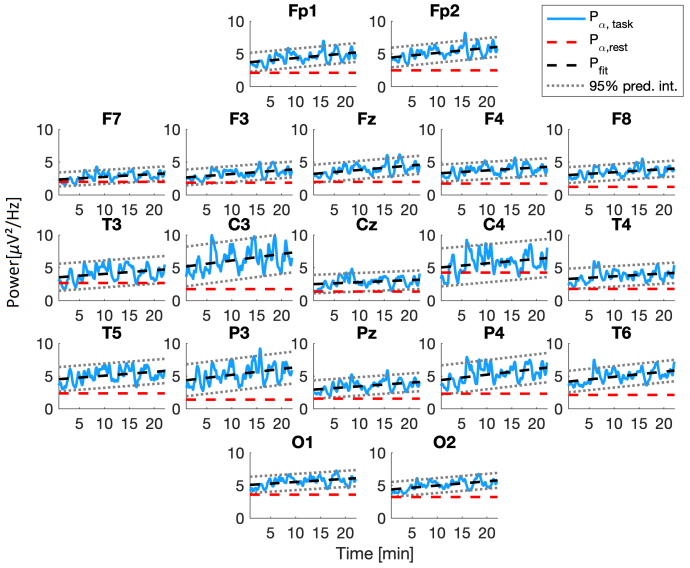


Fig. 4: *Overall EEG signal analysis*: Power spectrum in the α frequency bands over the entire acquisition for subject 1 (smoothed $P_{\alpha,task}$ [light blue], average $P_{\alpha,rest}$ [red], fitted line [black] and the 95% prediction interval [gray]).

B. Overall EEG signal analysis

The results of the experiment show that the mental fatigue increased in all subjects. Fig. 4 illustrates an example for the α frequency band, showing a growing trend in each channel linear regression, especially in centro-parietal areas. The 95% confidence interval is also reported, and a significant relationship between time and the increase of $P_{\alpha,task}$ was found (F-statistic: $p < 0.05$).

Additionally, Fig. 5 shows the slopes of the fitted line over $P_{\theta,task}$ and $P_{\alpha,task}$, both θ and α frequency bands for all the brain areas of interest, confirming a positive trend in α band and, in a reduced way, for θ band too. Subject 5, being the one with higher slope, is also the one having the higher combination of effort and frustration, as shown in Table II, hinting that the task was particularly tiresome to him. Conversely, subjects 1 and 4 reported the minimum degree of frustration possible, and their computed slopes are the lowest

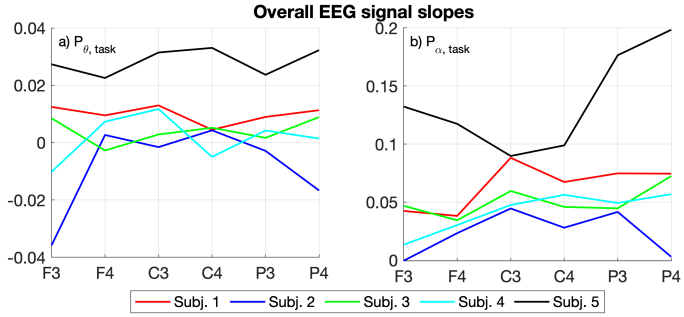


Fig. 5: *Overall EEG signal analysis*: Slopes of the fitted line over time-variant power, computed for each subject. Frontal and centro-parietal channels are reported for: a) θ band, b) α band.

two. Table II also reports the fact that subjects made errors only in the second half of the task, reinforcing the idea that they indeed became more tired over time.

TABLE II: Subjects' mistakes and self-evaluations.

Subject	*Mistaken Trials*	*Temporal Demand*	*Effort*	*Frustration*
1	no errors	2	15	1
2	85, 102	3	3	19
3	no errors	6	1	14
4	109	1	4	1
5	71, 105	3	15	14

IV. Discussion

In this study, a new experimental protocol was designed to assess the feasibility of using EEG-based passive BCI in an industrial context. The study aimed to capture the subjects' vigilance degradation while observing a robotic arm in a laboratory setting that mimicked an industrial production line. Results showed that the spectral power in the α frequency band increased with mental fatigue, making it a potential marker of the user's alertness state [7] during the execution of monotonous and automized tasks. The highest increment was found in the centro-parietial brain areas, as it is known from neurophysiological knowledge [1]. θ band was also characterized by increasing behaviour; this promising result calls for further analysis.

Despite the growing interest and research in EEG-based BCI, with recent methods including connectivity studies and machine learning applications [12, 13, 14], the focus on using BCI technology in Industry 4.0 is still limited, and is mostly confined to academic research labs. This experiment lays the foundation for potential monitoring applications that could greatly benefit operators by reducing risks and human errors, especially during long supervision tasks, without the need of any additional effort from the user. The limitations of this pilot study are the small sample size, which does not allow for significant aggregate data to be obtained, and the lack of a calibration phase. Additionally, the data can vary between individuals, and EEG frequencies should be analyzed carefully as similar spectral power patterns could be associated with different mental states. Despite these limitations, this study provides a proof of concept for using EEG-based passive BCI in industrial settings and highlights the need for further research in this area.

V. Conclusion

The use of EEG-based passive BCI technology in Industry 4.0 has the potential to enhance productivity, reduce safety risks, and improve decision making. This study proposes a new experimental protocol for capturing subjects' vigilance degradation while observing a robotic arm in a laboratory setting simulating an industrial production line. The results show that increased spectral power in the α frequency band is a potential marker of mental fatigue and thus lack of vigilance, which can lead to reduced performance and accidents in repetitive human tasks.

Acknowledgement

The work has been partially supported by the Italian Ministry of Education, University and Research (MIUR) with the grant "Dipartimenti di Eccellenza" 2018-2022 and by Fondazione Cariverona with the grant "Ricerca&Sviluppo".

References

[1] M. Sebastiani et al. Neurophysiological vigilance characterisation and assessment: Laboratory and realistic validations involving professional air traffic controllers. In: Brain sciences 10.1 (2020), p. 48.
[2] C. Maureen, B. Laurent, and L. Fabien. Brain-Computer Interfaces 1: Methods and Perspectives. Wiley, 2016, pp. 89–90.
[3] K. Douibi et al. Toward EEG-based BCI applications for industry 4.0: challenges and possible applications. In: Frontiers in Human Neuroscience (2021), p. 456.
[4] J. K. Hawley and A. L. Mares. Developing effective human supervisory control for air and missile defense systems. Tech. rep. ARMY RESEARCH LAB FORT BLISS TX, 2006.
[5] E. Wascher et al. Frontal theta activity reflects distinct aspects of mental fatigue. In: Biological psychology 96 (2014), pp. 57–65.
[6] W. Klimesch. Memory processes, brain oscillations and EEG synchronization. In: International journal of psychophysiology 24.1-2 (1996), pp. 61–100.
[7] G. Pfurtscheller, A. Stancak Jr, and C. Neuper. Event-related synchronization (ERS) in the alpha band—an electrophysiological correlate of cortical idling: a review. In: International journal of psychophysiology 24.1-2 (1996), pp. 39–46.
[8] A. Craig et al. Regional brain wave activity changes associated with fatigue. In: Psychophysiology 49.4 (2012), pp. 574–582.
[9] L. Geretti et al. Process-driven collision prediction in human-robot work environments. In: 2022 IEEE 27th International Conference on Emerging Technologies and Factory Automation (ETFA). IEEE. 2022, pp. 1–8.
[10] G. Borghini et al. Avionic technology testing by using a cognitive neurometric index: a study with professional helicopter pilots. In: 2015 37th Annual International Conference of the IEEE Engineering in Medicine and Biology Society (EMBC). IEEE. 2015, pp. 6182–6185.
[11] M. Akin. Comparison of wavelet transform and FFT methods in the analysis of EEG signals. In: Journal of medical systems 26.3 (2002), pp. 241–247.
[12] L. Brusini et al. A Systematic Review on Motor-Imagery Brain-Connectivity-Based Computer Interfaces. In: IEEE Transactions on Human-Machine Systems (2021).
[13] F. Stival et al. Connectivity Modeling meets Machine Learning: The next generation of EEG-based Brain Computer Interfaces. In: 2021 10th International IEEE/EMBS Conference on Neural Engineering (NER). IEEE. 2021, pp. 706–709.
[14] I. Siviero et al. Motor-imagery EEG signal decoding using multichannel-empirical wavelet transform for brain computer interfaces. In: 2022 IEEE-EMBS International Conference on Biomedical and Health Informatics (BHI). IEEE. 2022, pp. 1–4.

Optimization of a cardiac tissue segmentation pipeline in murine whole-heart reconstructions

F. Giardini*[1,2], E. Barcali*[2,3], M. De Santis[2], B. Olmi[2], E. Lazzeri[1], C. Nardi[3] and L. Bocchi[2]
[1]*European Laboratory for Non-Linear Spectroscopy (L.E.N.S.), Sesto Fiorentino, Italy*
[2]*Dept. of Information Engineering, University of Florence, v. Santa Marta, 3 - Florence, Italy*
[3]*Dept. of Biomedical Experimental and Clinical Sciences "Mario Serio", University of Florence, Florence, Italy*

***Abstract*—Image segmentation is an important branch of modern image processing, especially in biomedical or microscopy image analysis. Novel optical imaging techniques such as Light-Sheet Fluorescent Microscopy (LSFM) allow the reconstruction of massive biological samples with micron-scale spatial resolution. In this context, image segmentation is challenging due to the high variability of LSFM images. This article describes the optimization of an automatic segmentation pipeline to identify the cardiac tissue in LSFM-based high-resolution 3D reconstructions of five murine hearts, previously cleared and stained with Wheat Germ Agglutinin (WGA). We address the challenge using Trainable WEKA (Waikato Environment for Knowledge Analysis) Segmentation, a plug-in of Fiji software. Three different training sets were generated by means of a manual ground truth combined with two additional feature selection algorithms included in WEKA: CorrelationAttributeEvaluator and InfoGainAttributeEvaluator. To speed up the computational time, we also defined a reduced training dataset selecting only common features between the two sets: median diffusion, mean, anisotropy, and entropy. We trained four different classifiers for each of the three training sets in order to identify myocardium tissue from the background: RandomForest, J48, NaiveBayes, and MultilayerPerceptron. The performance of the classifiers was evaluated for each training set and we found that the RandomForest is the more accurate and stable model over different datasets with a Dice similarity coefficient of 0.895, 0.895, and 0.892, respectively. Results highlight the reliability of RandomForest to address high-resolution image segmentation, allowing the generation of 3D whole-heart reconstruction useful to investigate, in the future, structural features in pathological mouse models.**

***Keywords*—Trainable Weka Segmentation, Fiji, light-sheet fluorescence microscopy, cardiac tissue**

I. Introduction

The World Health Organization (WHO) estimates that 17.9 million people worldwide die of cardiovascular disease (CVD) every year [1]. Research in recent years has made many advances in this field to improve diagnosis, treat these diseases better, and reduce CVD mortality [2].

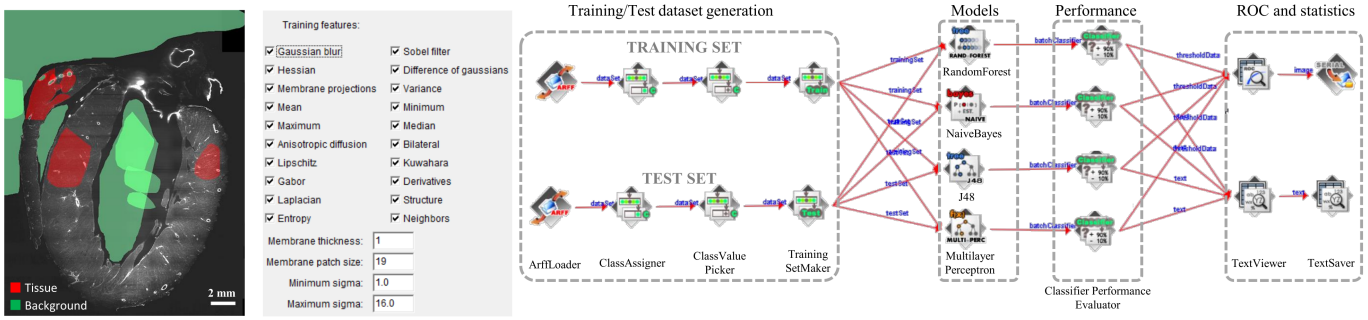
Several imaging modalities can be applied to studying the heart, including echography, CT, coronary angiography, PET, and MRI [3], [4]. All of these techniques are characterized by insufficient spatial resolution and the inability to detect fluorescence-marked particles usually used in biomedical research [5], [6], [7]. On the other hand, due to the intrinsic opacity of the cardiac tissue, conventional microscopy techniques have the disadvantage of requiring the use of small working distances, or a mechanical slicing of the sample, thus introducing the consequent risks of modifying sample dimensions, preventing a reliable three-dimensional (3D) reconstruction. Light Sheet Fluorescence Microscopy (LSFM), combined with novel advanced tissue-clearing techniques, overcomes these limitations [8], [9].

LSFM consists in illuminating the transparent sample with a single thin sheet of light orthogonally oriented to the detection path so that only the excited optical plane of the tissue is detected. The sample is then moved in an axial direction to perform a tomographic scan, imaging the volume section-by-section, and thus creating a 3D model after a post-processing step [10], [11], improving image contrast and allowing high speed and precise monitoring of cells or tissues combined with fluorescent multi-labeling within a complex and dynamic environment such as the cardiovascular one [12], [13]. LSFM image segmentation lacks fully automated techniques because of the inherent variability of images obtained with this imaging technique. New deep-learning techniques are emerging and showing good results, but currently manual segmentation remains the gold standard in terms of reliability. Naturally, automatic classification overcomes the problems associated with manual segmentation, which is time-consuming and sensitive to high inter- and intra-operator variability [3].

In this study, we optimized a system capable of automatically segmenting cardiac tissue in LSFM reconstructions of cleared adult murine hearts. To this aim, we adopted a plug-in from Fiji, Trainable Weka Segmentation (TWS), to perform a two-step optimization: first, we identified the most significant features to discriminate the tissue from the background with two different algorithms; then, we trained four models on the different training datasets to perform a real segmentation, finally comparing their performance. The ultimate goal of our project is to generate a 3D model of the heart anatomy, thus correlating, in the future, structural features between heart remodeling and electrical heart dysfunctions in pathological murine models.

II. Material And Methods

The present investigation is applied to five three-dimensional reconstructions of cleared hearts of control mice of 6 months (C57BL/6J). The experimental protocol was approved by the Italian Ministry of Health (protocol number 647/2015-106 PR). All the animals were provided by ENVIGO, Italy. Samples reconstructions were obtained by



(a) (b) (c)

Fig. 1: a) Representative longitudinal view of a cleared mouse heart reconstruction generated with light-sheet microscopy by staining cellular membranes (pixel size: 20.8 µm). A manual classification of *tissue* (red) and *background* (green) is superimposed on the image as an example of ground truth. b) Features selected to generate the training test using the Trainable Weka Segmentation (TWS) plugin. c) Scheme of the training/test workflow implemented using the tool *KnowledgeFlow* included in TWS. The main parts are highlighted with dashed gray lines.

performing a three-step imaging protocol: tissue clarification with CLARITY method optimized for the cardiac tissue [14], [15]; staining of cellular membranes with Wheat Germ Agglutinin (WGA) conjugated with Alexa Fluor 633; imaging by tiles with a custom-made light-sheet microscope [16] with an original voxel size of $0.65\,\mu m \times 0.65\,\mu m \times 2\,\mu m$ in x, y and z axis respectively. Final reconstruction was obtained by stitching tiles with custom-made software [17]. In this paper, three-dimensional (3D) images are downsampled to an isotropic pixel size of $20.8\,\mu m$.

Cardiac tissue segmentation is performed frame-by-frame in two-dimension (2D) using the plugin TWS, included in the image analysis software Fiji [18], [19], evaluating different classification models on three different sets of features.

A. Preliminary dataset and ground-truth

The preliminary dataset used to identify key features for prediction consists of ten images at different depths from the reconstruction of a single control mouse heart. By starting the TWS plugin, the two classes of interest "Tissue" and "Background" were defined. Ground truth was generated by manually classifying different regions of interest (ROIs) (Figure 1a) in all 10 frames. In the "Settings" tab, all features offered by the WEKA software were selected (Figure 1b) to generate as many features as possible from the images. Next, dimensionality reduction was performed using two different selection algorithms.

B. Feature extraction

Dimensionality reduction was performed using the "Select Attributes" tool in Weka Explorer. This is based on the joint action of an attribute evaluation algorithm (Attribute Evaluator) and a search algorithm (Search Method). The first evaluates each attribute in the data set in relation to the desired classification; the latter determines the most meaningful combination of attributes for the classification. Among the algorithms for attribute selection supported by Weka, we selected:

- CorrelationAttributeEvaluator: calculates the correlation between each attribute and the output variable: attributes are the more significant the closer the correlation values are to 1.
- InfoGainAttributeEvaluator: calculates the entropy of each attribute in relation to the output variable: attributes are the more significant the closer the entropy values are to 1.

In the present study, both evaluation algorithms described above were used, generating two different sets of features (defined as *Correlation set* and *InfoGain set* for simplicity). A set of the common attributes between the previous two sets was also considered and defined as *reduced set*.

C. Classifiers

The tool *KnowledgeFlow* presents a "data-flow"-inspired interface for Weka. Users can select Weka components from a toolbar, place them on a layout canvas, and link them together to form a "knowledge flow" for data processing and analysis. Here, the following classifiers were tested:

- RandomForest: this is the default algorithm when implementing a classifier in Weka;
- J48: characterized by a fast learning process;
- NaiveBayes: the Bayesian classifier is generally reliable and compact;
- MultilayerPerceptron: a classifier widely used in imaging, based on a supervised learning technique called *back-propagation*.

To compare these classifiers, we generate the KnowledgeFlow shown in Figure 1c.

D. Training set and test set

The training and the test datasets were generated by first selecting randomly 40 and 30 images from the five different reconstructions, respectively, and then manually labeling tissue and background on these images. Then we extracted from labeled images the three different sets of features derived through Weka Explorer: Correlation set, InfoGain set, and reduced set, thus generating three versions of training and test datasets. Exploiting the workflow shown in Figure 1c, the four

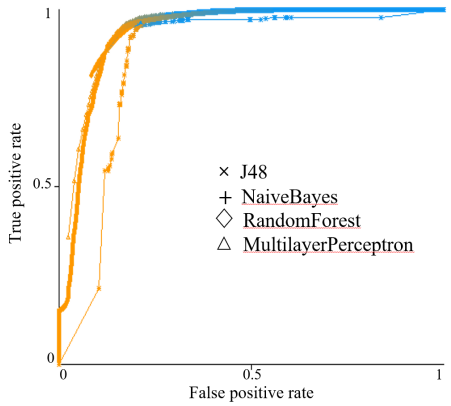


Fig. 2: ROC curve of the four models tested on the *reduced set* of features.

TABLE I: Dice similarity coefficient

Classifier	Correlation set	InfoGain set	Reduced set
J48	0.869	0.889	0.879
NaiveBayes	0.881	0.880	0.888
RandomForest	0.895	0.895	0.892
MultilayerPerceptron	0.872	0.893	0.865

different models were trained on the same training set and then used to classify the test set. Finally, the performance of each model was assessed by the "ClassifierPerformanceEvaluator" module, generating numerical statistics and plotting the Receiver operating characteristic (ROC) curve.

III. Results

Feature selection was performed using two different algorithms: the CorrelationAttributeEvaluator and the InfoGainAttributeEvaluator. In both cases, we defined the selection threshold as the correlation value obtained using the original image as a feature, without extracting any statistical index or morphological operator. In the first case, the correlation of the original image was 0.474554. The following features, having a correlation value larger than 0.474554, were selected: median, mean, anisotropic diffusion, entropy, membrane projection, Gaussian blur, and minimum. These were defined as *Correlation set*. With the second approach, the correlation of the original image was 0.53931, and the algorithm then identifies as fundamental those features with a correlation value larger than 0.53931, namely: median, mean, anisotropic diffusion, entropy, variance, and maximum, that were defined as *InfoGain set*. We defined also a *reduced set* of features, composed of the subset of features in common with the previous two sets: median, mean, anisotropic diffusion, and entropy.

The four models were trained and tested using these three different sets of features. The Dice similarity coefficient values for the 4 models and for the three different feature sets (Correlation, InfoGain, and reduced sets respectively) are shown in Table I.

The model with the best performance is the RandomForest for all the feature sets, and the error of this model is less variable than the other models over the different feature sets. Using the reduced set of features, the ROC curve of the four models is generated and shown in Figure 2, and the main metrics of the selected model (RandomForest) are reported in Table II.

TABLE II: RandomForest Performance

Class	TP Rate	FP Rate	Precision	Recall	F-Measure	ROC Area
Tissue	0.975	0.211	0.837	0.975	0.901	0.940
Background	0.789	0.025	0.966	0.789	0.869	0.940
Weighted Avg.	0.887	0.123	0.898	0.887	0.886	0.940

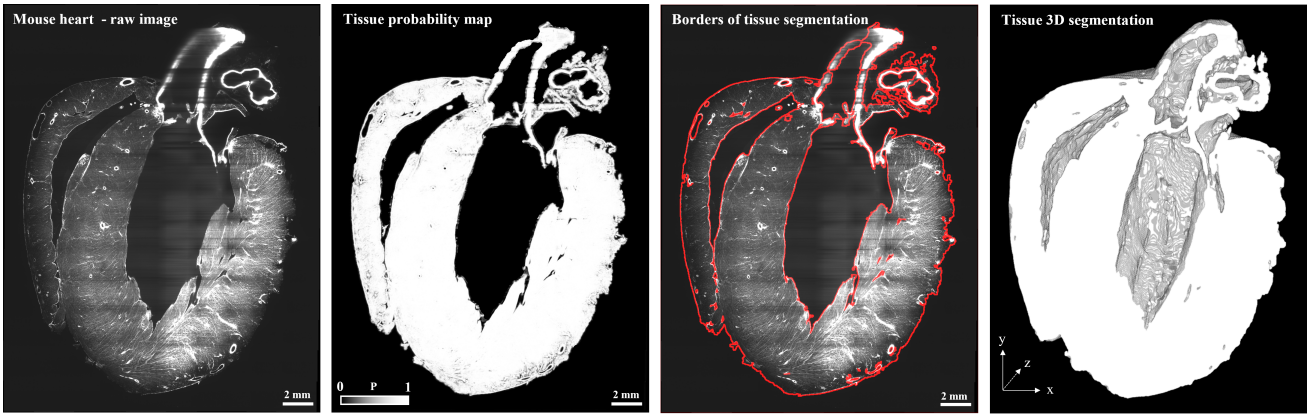
Finally, a tissue segmentation was performed on an entire mouse heart reconstruction (Figure 3a shows a representative frame of the sample classified). The 3D image was segmented frame-by-frame using the RandomForest trained with the reduced set of features. This model assigns to each pixel a probability $\mathbf{p} \in [0, 1]$ of belonging to the "tissue" class (Figure 3b). The final binary segmentation can be obtained by applying an arbitrary threshold on that probability map (here, the threshold is set $p = 0.5$, Figure 3c). A 3D segmentation is shown in Figure 3d. The model was able to correctly segment the myocardial tissue also in the regions affected by a low fluorescence signal intensity, without being affected by the variability of the background brightness.

IV. Discussion and Conclusion

This work aimed to optimize a software pipeline for cardiac tissue segmentation in LSFM reconstructions of cleared whole murine hearts. This aspect is important for the investigation of cardiac functioning [20], allowing in the future to correlate structural cardiac tissue remodeling with electrical dysfunctions of the heart detected by novel optical mapping techniques in murine hearts [21], [22]. The work was articulated in three phases: first, we manually segmented the cardiac tissue from the background frame-by-frame in 2D with a plugin of Fiji, TWS, then we extrapolated the most significant attributes exploiting two different feature selection algorithms included in WEKA and finally, we tested different models to evaluate their accuracy on two different ROIs: tissue and background. The optimized pipeline applied to the 3D reconstruction of the hearts showed a good functioning of our system providing a good approach for automatic segmentation of LSFM images. It could be interesting to perform the same test with more powerful processors, using a larger dataset. The main limit was connected to the resolution of the images and the reduced dataset. An improvement of the work could be to use a larger data set and involve images with a higher spatial resolution. The proposed method, applied to reconstructions of hearts of control and pathological models, will allow the extraction of anatomical features, enabling the quantification of the structural remodeling occurring in pathological hearts.

References

[1] World Health Organization, Cardiovascular diseases (CVDs), 2021, June 1, retrieved from https://www.who.int/en/news-room/fact-sheets/detail/cardiovascular-diseases-(cvds)



(a) (b) (c) (d)

Fig. 3: a) Representative frame of a cleared murine heart stained with WGA and reconstructed with light-sheet microscopy. b) Classification of the image in (a) obtained with the RandomForest trained on the *reduced* features set. The intensity of each pixel (from 0 to 255) is proportional to the probability (from 0, *background*, to 1, *tissue*) of falling into the "tissue" class. c) The borders (red lines) of the binary segmentation obtained by thresholding the probability map shown in (b) with a value of $p = 0\,5$ are superimposed on the original frame shown in (a). d) Longitudinal view of the three-dimensional reconstruction of the heart anatomy obtained by rendering 2D tissue segmentation at different depths.

[2] C. Chen, C. Qin, H. Qiu, G. Tarroni, J. Duan, W. Bai, D. Rueckert, Deep Learning for Cardiac Image Segmentation: A Review, Frontiers in cardiovascular medicine, vol. 7, no. 25, 2020, https://doi.org/10.3389/fcvm.2020.00025.

[3] C. Petitjean, J.N. Dacher, Dacher, J.: A review of segmentation methods in short axis cardiac MR images, Medical Image Analysis, vol. 15, pp. 169-184, 2011, 10.1016/j.media.2010.12.004.

[4] Y. Ding, J. Lee, J.J. Hsu, C.C. Chang, K.I. Baek, S. Ranjbarvaziri, R. Ardehali, R.R.S. Packard, T.K. Hsiai, Light-Sheet Imaging to Elucidate Cardiovascular Injury and Repair, Curr. Cardiol. Rep., vol. 20, no. 5, pp.35, 2018, doi: 10.1007/s11886-018-0979-6.

[5] A.J. Kim, R. Francis, X. Liu, W.A. Devine, R. Ramirez, S.J. Anderton, L.Y. Wong, F. Faruque, G.C. Gabriel, W.Chung, L. Leatherbury, K. Tobita, C.W. Lo, Microcomputed tomography provides high accuracy congenital heart disease diagnosis in neonatal and fetal mice, Circ Cardiovasc Imaging, vol.6, no. 4. pp. 551-9, 2013, doi: 10.1161/CIRCIMAGING.113.000279. Epub 2013 Jun 12. Erratum in: Circ Cardiovasc Imaging. 2013 Sep;6(5):e30. Chung, Wendy [added]. PMID: 23759365; PMCID: PMC3908688.

[6] C. Baltes, N. Radzwill, S. Bosshard, D. Marek, M. Rudin, Micro MRI of the mouse brain using a novel 400 MHz cryogenic quadrature RF probe, NMR Biomed. vol. 22, no. 8, pp. 834-42, 2009 Oct, doi: 10.1002/nbm.1396.

[7] C. Olianti, I. Costantini, F. Giardini, E. Lazzeri, C. Crocini, C. Ferrantini, F.S. Pavone, P.G. Camici, L. Sacconi, 3D imaging and morphometry of the heart capillary system in spontaneously hypertensive rats and normotensive controls, Sci Rep. vol. 10, no. 1, pp. 14276, 2020, https://doi.org/10.1038/s41598-020-71174-9

[8] Y. Ding, J. Lee, J. Ma, K. Sung, T. Yokota, N. Singh et al., Light-sheet fluorescence imaging to localize cardiac lineage and protein distribution, Sci Rep, vol. 7, no. 42209, 2017, https://doi.org/10.1038/srep42209

[9] C. Olianti, F. Giardini, E. Lazzeri, I. Costantini, L. Silvestri, R. Coppini, E. Cerbai, F. S. Pavone, L. Sacconi, et al., Optical clearing in cardiac imaging: A comparative study, Prog. Biophys. Mol., vol. 168, pp. 10-17, 2022, https://doi.org/10.1016/j.pbiomolbio.2021.07.012.

[10] Y. Ding, Z. Bailey, V. Messerschmidt, J. Nie, R. Bryant, S. Rugonyi, P. Fei, J. Lee, T.K. Hsiai, Light-sheet Fluorescence Microscopy for the Study of the Murine Heart, J Vis Exp, vol. 15; no. 139, pp. 57769, https://doi.org/10.3791/57769

[11] P.A. Santi, Light sheet fluorescence microscopy: a review, J Histochem Cytochem, vol. 59, no.2, pp.129-38, 2011, doi: 10.1369/0022155410394857.

[12] P. Fei, J. Lee, R. Packard, K.-I. Sereti, H. Xu, et al. Cardiac Light-Sheet Fluorescent Microscopy for Multi-Scale and Rapid Imaging of Architecture and Function. Sci Rep, vol. 6, no. 22489, 2016, https://doi.org/10.1038/srep22489

[13] Z. Wang, Y. Ding,S. Satta, M. Roustaei, P. Fei et al. A hybrid of light-field and light-sheet imaging to study myocardial function and intracardiac blood flow during zebrafish development, PLOS Computational Biology, vol. 17, no. 7, pp. e1009175, 2021. https://doi.org/10.1371/journal.pcbi.1009175

[14] K.Chung, J. Wallace, S.Y. Kim, S. Kalyanasundaram, A. S. Andalman ET AL. Structural and molecular interrogation of intact biological systems. Nature, vol. 497, pp. 332–337 2013. https://doi.org/10.1038/n.

[15] F. Giardini, E. Lazzeri, C. Olianti, G. Beconi, I. Costantini, L. Silvestri, E. Cerbai, F.S. Pavone, L. Sacconi, Mesoscopic Optical Imaging of Whole Mouse Heart. J. Vis. Exp. vol. 176, pp. e62795, 2021, doi:10.3791/62795

[16] L. Silvestri, M.C. Müllenbroich, I. Costantini, A. P. Di Giovanna, G. Mazzamuto, A. Franceschini, Universal autofocus for quantitative volumetric microscopy of whole mouse brains. Nat Methods vol. 18, pp. 953–958, 2021, https://doi.org/10.1038/s41592-021-01208-1.

[17] G. Mazzamuto, "ZetaStitcher: a software tool for high-resolution volumetric stitching,", https://github.com/lens-biophotonics/ZetaStitcher.

[18] J. Schindelin, I. Arganda-Carreras, E. Frise, V. Kaynig, M. Longair et al. Fiji: an open-source platform for biological-image analysis. Nature Methods, vol. 9, no. 7, pp. 676–682, 2012, doi:10.1038/nmeth.2019

[19] I.H. Witten, E. Frank . Data Mining: Practical Machine Learning Tools and Techniques, 2nd edition. Morgan Kaufmann, San Francisco, 2005.

[20] T. Seidel, T. Draebing, G. Seemann, F.B. Sachse . A Semi-automatic Approach for Segmentation of Three-Dimensional Microscopic Image Stacks of Cardiac Tissue. Lecture Notes in Computer Science, vol 7945. Springer, Berlin, Heidelberg., 2013 https://doi.org/10.1007/978-3-642-38899-6_36

[21] F. Giardini, V. Biasci, M. Scardigli, F.S. Pavone, G. Bub, and L. Sacconi, A Software Architecture to Mimic a Ventricular Tachycardia in Intact Murine Hearts by Means of an All-Optical Platform. Methods Protoc. 2019, 2, 7. https://doi.org/10.3390/mps2010007

[22] Biasci, V., Santini, L., Marchal, G.A. et al. Optogenetic manipulation of cardiac electrical dynamics using sub-threshold illumination: dissecting the role of cardiac alternans in terminating rapid rhythms. Basic Res Cardiol 117, 25 (2022). https://doi.org/10.1007/s00395-022-00933-8

Combining high-density electromyography and ultrafast ultrasound to assess individual motor unit properties *in vivo*

M. Carbonaro[1,2], R. Rohlén[3,4], S. Seoni[2,5], K. M. Meiburger[2,5], T. Vieira[1,2], C. Grönlund[3], A. Botter[1,2]
[1] *LISiN, Department of Electronics and Telecommunication, Politecnico di Torino, Turin, Italy*
[2] *PoliToBIOMed Lab, Politecnico di Torino, Turin, Italy*
[3] *Department of Biomedical Engineering, Lund University, Lund, Sweden*
[4] *Department of Radiation Sciences, Radiation Physics, Biomedical Engineering, Umeå University, Umeå, Sweden*
[5] *Biolab, Department of Electronics and Telecommunications, Politecnico di Torino, Turin, Italy.*

***Abstract*— This study aims to compare two methods for the identification of anatomical and mechanical motor unit (MU) properties through the integration of high-density surface electromyography (HDsEMG) and ultrafast ultrasound (UUS). The two approaches rely on a combined analysis of the firing pattern of active MUs, identified from HDsEMG, and tissue velocity sequences of the muscle cross-section, obtained from UUS. The first method is the spike-triggered averaging (STA) of the tissue velocity sequence based on the occurrences of MU firings. The second is a method based on spatio-temporal independent component analysis (STICA) enhanced with the information of single MU firings. We compared the capability of these two approaches to identify the regions where single MU fibers are located within the muscle cross-section (MU displacement area) *in vivo*. HDsEMG signals and UUS images were detected simultaneously from biceps brachii in ten participants (6 males and 4 females) during low-level isometric elbow flexions. Experimental signals were processed by implementing both STA and STICA approaches. The medio-lateral distance between the estimated MU displacement areas and the centroid of the MU action potential distributions was used to compare the two methods. We found that STICA and STA are able to detect MU displacement areas. However, STICA provides more precise estimations to the detriment of higher computational complexity.**

***Keywords*— high-density surface emg, ultrafast ultrasound, motor unit, averaging, independent component analysis**

I. Introduction

HIGH density surface electromyography (HDsEMG) and ultrafast ultrasound (UUS) provide complementary information about electrical and mechanical muscle properties. Both techniques have been proven successful in characterising single motor unit (MU) properties, opening exciting fronts in studying the neural control of muscle contraction from different perspectives. While HDsEMG decomposition enables identifying the firing pattern of individual MUs and assessing the characteristic MU action potentials (MUAP, electrophysiological information) [1], [2], the analysis of cross-sectional tissue velocity sequences extracted from UUS [3] can provide anatomical and mechanical characteristics of MU fibers [4]–[6].

Recently, these two techniques have been combined to exploit their complementarity and provide a comprehensive description of the neuromechanical MU properties [7]–[10]. This integration uses single MU firing instants, identified from HDsEMG decomposition, to isolate the corresponding muscle tissue mechanical response from UUS tissue velocity sequences (Fig. 1). In this way, it is possible to assess movements in the physiological cross-sectional area of the muscle associated with the excitation of single MU (hereafter referred to as *MU displacement area*) and their twitch characteristics. In this regard, two possible approaches can be implemented. The first one is the spike-triggered averaging (STA) of the tissue velocity sequence based on the occurrences of individual MU firings, as proposed for single MU analysis of mechanomyograms [11]. The second one, recently proposed by our group, is to decompose the tissue velocity sequences with spatio-temporal independent components analysis (STICA) [12] and use the firing information from HDsEMG to select, among the identified components, those associated with MU activity [7].

Previously, we used an electromechanical computer model to test the capability of the two methods to correctly identify single MU displacement areas in simulated contractions with different degrees of neural excitation (i.e., the number of active MUs) and different levels of MU synchronisation (i.e., degree of dependency between firing instants of different MUs) [13]. These variables and the duration of both EMG and ultrasound time series are potentially critical factors impacting both methods. Indeed, we showed that the performance of both approaches was negatively affected by the number of active MUs and synchronisation levels. However, STICA provided a more robust estimation of the MU displacement areas under all the tested conditions.

This study aimed to test whether these *in-silico* results extent to experimental conditions during isometric elbow flexions. Since the location of the MU fibers within the muscle cross-section is unknown in experimental data, we quantified the agreement between the HDsEMG amplitude distribution of the MUAP and the location of the corresponding MU displacement area identified by applying STA and STICA to UUS image sequences.

II. Methods

Ten participants (mean ± SD, 29.2 ± 4.6 years, 6 males and 4 females) with no history of neurological or musculoskeletal impairments or disease were enrolled. The study was conducted in accordance with the Declaration of Helsinki and the procedure approved by the Regional Ethics Committee. Informed consent was obtained from all participants after receiving a detailed explanation of the study procedure.

A. Experimental acquisitions

HDsEMG signals and UUS images were detected simultaneously from the biceps brachii for 8 seconds of low-

level (5% of maximum voluntary contraction) isometric elbow flexions (Fig. 1A). The details of the experimental protocol are reported in [7].

A 64-electrode matrix (8 rows by 8 columns with 10 mm inter-electrode distance) designed to allow the simultaneous acquisition of HDsEMG and ultrasound from the same muscle region [14] was placed over the muscle belly. Monopolar EMG signals were detected, conditioned (Bandwidth 10-500 Hz, gain 46 dB), and sampled at 2048 Hz with 16-bit resolution using a wireless HDsEMG acquisition system (MEACS, LISiN, Politecnico di Torino, Turin, Italy) [15].

Radiofrequency (RF) data were acquired using Verasonics Vantage 128 (Verasonics, Inc., Kirkland, WA, USA). Plane-wave data were obtained at a frame rate of 2500 Hz. The L11-5v probe (7.8125 MHz center frequency) was placed over the muscle to obtain cross-sectional scanning between the fourth and fifth rows and was cantered with respect to the columns of the EMG matrix (Fig. 1A).

A rectangular pulse provided by an external generator (StimTrig; LISiN, Politecnico di Torino, Italy) was used to start the ultrasound acquisition and was concurrently acquired by the HDsEMG system to synchronize EMG-ultrasound acquisitions [16].

B. Data analysis

Experimental signals were processed by implementing both STA and STICA approaches. The two approaches rely on a combined analysis of the firing pattern of active MUs and the tissue velocity sequence estimated from HDsEMG and ultrafast ultrasound imaging, respectively (Fig. 1). Spike trains of individual MU were decomposed from HDsEMG data using a validated method based on convolution kernel compensation (Fig. 1B) [17]. Displacement velocity images were estimated from the RF data using 2D autocorrelation velocity tracking, as in [18], to obtain a sequence of tissue velocities (Fig. 1C). After cropping the images at a depth of ~ 20 mm (outside the maximum EMG range), the sequence resulted in 19976 frames of 70 × 128 pixels.

1) Spike-triggered averaging (STA) approach

The STA of the tissue velocity sequence was performed using the discharge times of the MU identified from HDsEMG decomposition. For each MU, windows of 125 ms centered on each firing instant were averaged to obtain a short sequence in which the contribution of the considered MU might be emphasized over the others. A single image was extracted from this averaged sequence as follows: (i) the time sample at which the maximum velocity occurred was identified, and (ii) the sequence was averaged across ± 10 frames around the maximum time sample (20 frames in total). A global thresholding at 70% of the maximum was applied to the obtained image, providing the single MU displacement area.

2) Spatiotemporal independent component analysis (STICA) approach

STICA was applied to regions of interest (ROI) of the tissue velocity sequence of 35 × 35 pixels spanning the whole field of view with a shift of 5 pixels in both directions. The details of the method are reported in [7]. Here, a synthetic description is provided. Briefly, the algorithm extracted 50 components for each ROI, optimizing the independence over space and time. The components comprised a temporal signal and a spatial map. For each MU decomposed in HDsEMG, the convolution between its firing discharges and a synthetic waveform, representing the velocity of contracting fibers in the superficial-deep axis, was computed. This convolution produces what we refer to as the train of MU velocity twitches. The cross-correlations between these trains and the temporal signals of all UUS components were computed. For each ROI, the component with the maximum correlation within a ± 20 ms time lag was selected. This procedure provided a set of correlation coefficients for all considered ROIs for each decomposed MU. A group of adjacent ROIs with correlation values > 50% of the maximum of all ROIs was retained. The

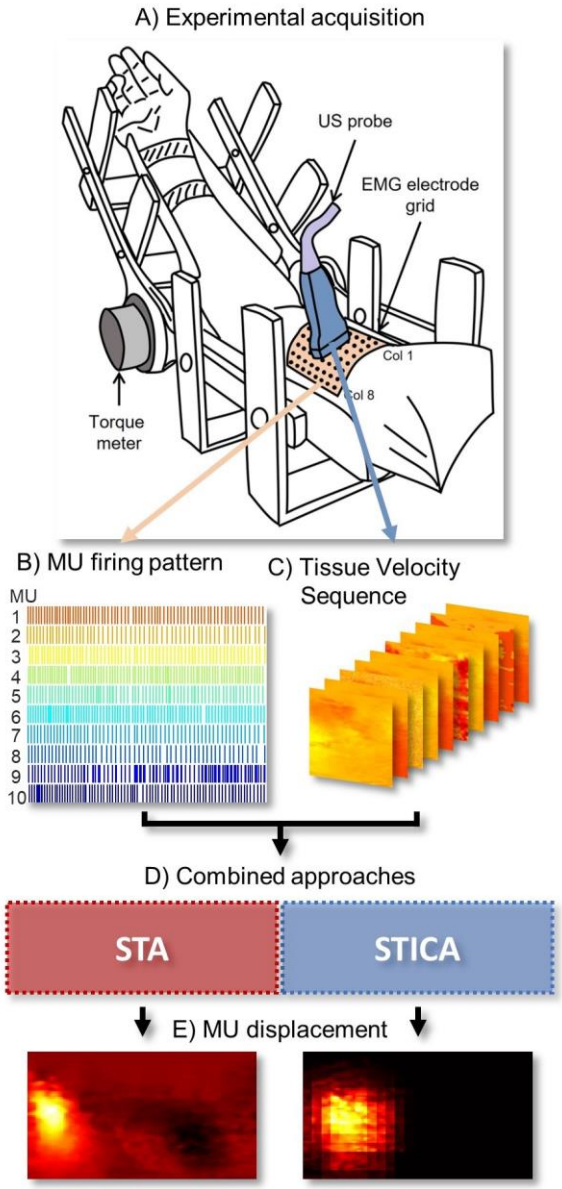


Fig. 1: Overview of data detection and analysis. A) Simultaneous acquisition of HDsEMG and ultrafast ultrasound data during isometric contractions. B) Example of a firing pattern of active MUs decomposed from HDsEMG signals. C) Estimated image sequence of the displacement velocities of the muscle tissue. D) Combined analysis of the MU firing pattern and tissue velocity sequence with two approaches, one based on the spike triggered averaging (STA) and one based on spatio-temporal independent component analysis (STICA). E) Output of the algorithms: images of muscle tissue displacement areas related to a single MU activation.

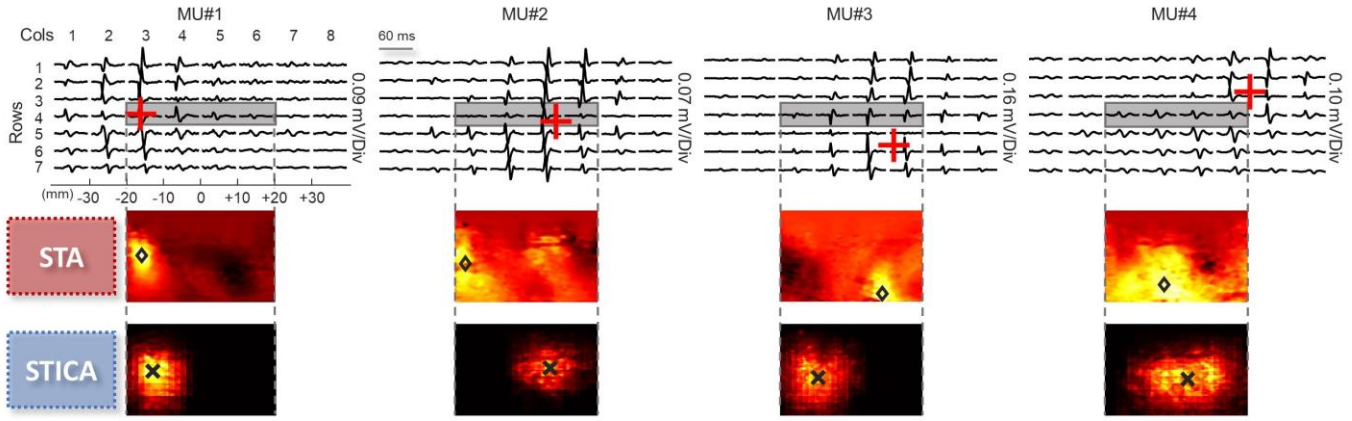


Fig. 2: Four examples of MUs (column wise) decomposed from HDsEMG and the corresponding identified region of displacement. First row: template of the motor unit action potential (MUAP) in single differential derivation along the rows of HDsEMG grid. Red + represents the centroid of the MUAP template distribution as calculated in [7]. The grey rectangle shows the region where the ultrasound probe was placed to scan the muscle cross-sectionally. Second row: images obtained with the spike triggered averaging (STA) approach representing the region of displacement of the corresponding MU. ◊ indicates the centroid of the tissue velocity image. Third row: final images of the approach based on the spatio-temporal independent component analysis (STICA) representing the region of displacement of the corresponding MU. × represents the centroid of the tissue velocity image. The figure shows from left to right: a well-detected MU (low centroid-to-centroid distance between EMG and ultrasound) for both approaches; a MU displacement area correctly identified only by STICA; a MU displacement area correctly identified only by the STA approach; a wrong MU displacement area identification for both STA and STICA.

spatial maps of the ROIs corresponding to the identified group were summed to obtain a single image. A global thresholding at 70% of the maximum was applied to the obtained image, providing the single MU displacement area.

C. Comparison of STICA and STA approaches

The centroids of the MU displacement areas obtained from STA and STICA were computed and compared with the centroids of the amplitude distribution of the MUAP of the corresponding MU (i.e., the MU whose firings were used as input to STA and STICA algorithms). The comparison was performed by computing the centroid-to-centroid (EMG-ultrasound) distance in the medio-lateral direction.

The two algorithms were processed considering the entire 8 s of acquisition and only the first 2 s of acquisition to evaluate the effect of the signal duration on their performance.

D. Statistical analysis

The effect of the factors “method” (STA and STICA) and “duration” (2 s and 8 s) were tested with a 2-way ANOVA on the centroid-to-centroid distance. Post-hoc assessments were conducted using the Bonferroni test whenever a main effect was verified. The significance level was set to $p < 0.05$.

III. Results and Discussion

The HDsEMG decomposition provided 180 MUs (mean ± SD, 18 ± 8 MUs per participant).

Fig. 2 shows the identification of the MU displacement areas of four representative MUs using the combined analysis of HDsEMG data and UUS images. The figure depicts, in the upper panel, the spatial distribution of single differential MUAPs computed longitudinally (i.e., along the fibers’ direction), the regions of displacement in the ultrasound identified with STA (middle panel) and with STICA (bottom panel), respectively. The examples reported in Fig. 2 show four different outcomes of the two algorithms in terms of spatial agreement between the MU displacement area in UUS and the EMG amplitude distribution. Specifically, MU#1 showed a good spatial match for both STA and STICA (as shown by the horizontal distance between the symbols ‘+’ in EMG, ‘◊’ for STA and ‘×’ for STICA). MU#2 and MU#3 showed a good match only with STICA and STA, respectively, while the MU displacement area identification seemed to fail for both STA and STICA in MU#4.

Fig. 3 shows the boxplots of distances between EMG and ultrasound centroid for all the considered MUs for both STA (red) and STICA (blue) when 8 seconds and 2 seconds of signal duration are considered. STICA approach provided lower distances for all the tested durations, as demonstrated by statistically significant differences with respect to STA ($p < 0.001$). Although not significant ($p = 0.054$), a trend associated with signal duration can be appreciated in both STA and STICA and to a larger extent for STA.

The distances obtained for STA and STICA were in the range [0–53 mm] and [0–37 mm], respectively and confirmed the results obtained in simulated conditions, with STICA providing lower distances. As expected, these values are larger than those obtained in simulated conditions where distances always lower than 20 mm were obtained by both methods and for contractions up to 20% MVC. Thus, although we considered lower contraction levels (5% MVC), the performance of both methods degraded in experimental conditions considerably. Besides the obvious differences between experimental and simulated conditions (e.g., the effect of connective tissue affecting the transversal force transmission between fascicles), this result can be explained by the fact that the in the experimental analysis, our reference for the “true” medio-lateral location of MU displacement area was the centroid of the MUAP distribution, that can be identified with a relatively low spatial resolution (inter-electrode distance), thus affecting the estimation error.

Concerning the effect of signal length, both approaches were expected to be affected by the duration of the EMG and ultrasound time series. However, our results suggest that STICA may provide better estimations of MU displacement

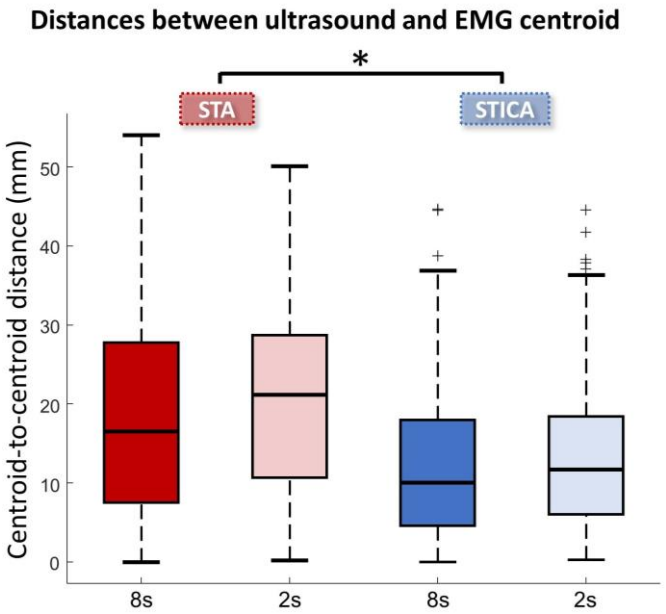


Fig. 3: Boxplots of distances between EMG and ultrasound centroid for all the considered MUs for both STA (red) and STICA (blue) when considering 8 seconds (dark color) and 2 seconds (light color) duration of the acquisition. *p<0.001

areas when short duration acquisitions are performed (light color boxes in Fig. 3). This can be an important advantage considering the large amount of data associated with the detection of sequences of high frame rate ultrasound images. Moreover, the capability to obtain good displacement area estimations for small signal epochs could allow the implementation of STICA-based algorithms exploiting the temporal segmentation of the detected signal to improve the estimation, e.g., by providing a repeatability index of the identified area across the contraction. On the other hand, the low computational complexity of STA may be preferable for applications where the computational time is relevant.

IV. Conclusion

This study compared two approaches (STA and STICA) to identify individual MU properties by combining HDsEMG and UUS. We showed that both STICA and STA can be used to detect regions of muscle tissue displacement whose location is associated with the representation of the MU electrophysiological activity (i.e., MUAP distribution). Although wrong estimations occurred for both methods, STICA provides more precise estimation of the MU displacement region location, to the detriment of higher computational complexity. The higher reliability in the assessment of the MU territory provided by STICA may be explained as a result of the decomposition of the sources' location and temporal information, while STA uses the global interfering signal. Our results expand those of our previous simulation study, providing new qualitative evidence on the suitability of the two proposed approaches for anatomical identification of individual MU using the combination of HDsEMG and UUS analysis. By providing electrophysiological, anatomical and mechanical information on active MUs, these multi-modal approaches are relevant to improve our understanding of the underlying mechanism of muscle contraction, from the neural command to the force production, with applications ranging from basic research to motor rehabilitation.

References

[1] A. Holobar and D. Zazula, "Multichannel blind source separation using convolution Kernel compensation," *IEEE Trans. Signal Process.*, vol. 55, no. 9, pp. 4487–4496, 2007.

[2] R. Merletti, *et al.*, "Advances in surface EMG: recent progress in detection and processing techniques," *Crit. Rev. Biomed. Eng.*, vol. 38, no. 4, pp. 305–45, 2010.

[3] T. Deffieux, J. L. Gennisson, M. Tanter, M. Fink, and A. Nordez, "Ultrafast imaging of in vivo muscle contraction using ultrasound," *Appl. Phys. Lett.*, vol. 89, no. 18, pp. 2006–2008, 2006.

[4] R. Rohlen, E. Stalberg, K. H. Stoverud, J. Yu, and C. Gronlund, "A method for identification of mechanical response of motor units in skeletal muscle voluntary contractions using ultrafast ultrasound imaging - simulations and experimental Tests," *IEEE Access*, vol. 8, pp. 50299–50311, 2020.

[5] R. Rohlen, E. Stalberg, K. H. Stoverud, J. Yu, and C. Gronlund, "A method for identification of mechanical response of motor units in skeletal muscle voluntary contractions using ultrafast ultrasound imaging - Simulations and Experimental Tests," *IEEE Access*, vol. 8, pp. 50299–50311, 2020.

[6] R. Rohlén, E. Stålberg, and C. Grönlund, "Identification of single motor units in skeletal muscle under low force isometric voluntary contractions using ultrafast ultrasound," *Sci. Rep.*, vol. 10, no. 1, pp. 1–11, 2020.

[7] M. Carbonaro, *et al.*, "Physical and electrophysiological motor unit characteristics are revealed with simultaneous high-density electromyography and ultrafast ultrasound imaging," *Sci. Rep.*, vol. 12, no. 1, p. 8855, 2022.

[8] A. Botter, T. Vieira, M. Carbonaro, G. L. Cerone, and E. F. Hodson-Tole, "Electrodes' Configuration influences the agreement between surface EMG and B-Mode ultrasound detection of motor unit Fasciculation," *IEEE Access*, vol. 9, pp. 98110–98120, 2021.

[9] R. Waasdorp *et al.*, "Combining Ultrafast Ultrasound and High-Density EMG to Assess Local Electromechanical Muscle Dynamics: A Feasibility Study," *IEEE Access*, vol. 9, pp. 45277–45288, 2021.

[10] E. Lubel, B. Grandi Sgambato, D. Y. Barsakcioglu, J. Ibáñez, M. X. Tang, and D. Farina, "Kinematics of individual muscle units in natural contractions measured in vivo using ultrafast ultrasound," *J. Neural Eng.*, vol. 19, no. 5, 2022.

[11] C Cescon, I. M. Gazzoni, I. M. Gobbo, C. Orizio, and D. Farina, "Non-invasive assessment of single motor unit mechanomyographic response and twitch force by spike-triggered averaging." *Med. Biol. Eng. Comput.*, vol. 42, p. 496-501, 2004.

[12] J. V. Stone, J. Porrill, N. R. Porter, and I. D. Wilkinson, "Spatiotemporal independent component analysis of event-related fMRI data using skewed probability density functions," *Neuroimage*, vol. 15, no. 2, pp. 407–421, 2002.

[13] M. Carbonaro, S. Zaccardi, S. Seoni, K. M. Meiburger, and A. Botter, "Detecting anatomical characteristics of single motor units by combining high density electromyography and ultrafast ultrasound: a simulation study," *Annu. Int. Conf. IEEE Eng. Med. Biol. Soc. IEEE Eng. Med. Biol. Soc. Annu. Int. Conf.*, vol. 2022, pp. 748–751, 2022.

[14] A. Botter, T. M. Vieira, I. D. Loram, R. Merletti, and E. F. Hodson-Tole, "A novel system of electrodes transparent to ultrasound for simultaneous detection of myoelectric activity and B-mode ultrasound images of skeletal muscles," *J. Appl. Physiol.*, vol. 115, no. 8, pp. 1203–1214, 2013.

[15] G. L. Cerone, A. Botter, and M. Gazzoni, "A modular, smart, and wearable system for high density sEMG detection," *IEEE Trans. Biomed. Eng.*, 2019.

[16] G. L. Cerone, *et al.*, "Design and validation of a wireless body sensor network for integrated EEG and HD-sEMG acquisitions," *IEEE Trans. Neural Syst. Rehabil. Eng.*, 2022.

[17] A. Holobar, M. A. Minetto, A. Botter, F. Negro, and D. Farina, "Experimental analysis of accuracy in the identification of motor unit spike trains from high-density surface EMG," *IEEE Trans. Neural Syst. Rehabil. Eng.*, vol. 18, no. 3, pp. 221–229, 2010.

[18] T. Loupas, R. W. Gill, and J. T. Powers, "An axial velocity estimator for ultrasound blood flow imaging, based on a full evaluation of the doppler equation by means of a two-dimensional autocorrelation approach," *IEEE Trans. Ultrason. Ferroelectr. Freq. Control*, vol. 42, no. 4, pp. 672–688, 1995.

Tensor-based morphometry of T1 weighted brain images reveals subtle volume enlargement of temporalis muscles

A. Ciarlo[1], A.G. Russo[2], A. Viggiano [1], C. Secondulfo[3], F. Di Salle [1,3], F. Esposito[2] and A. Canna[4]

[1]*Department of Medicine, Surgery and Dentistry, "Scuola Medica Salernitana", University of Salerno, Baronissi (SA), Italy*
[2]*Department of Advanced Medical and Surgical Sciences School of Medicine and Surgery University of Campania "Luigi Vanvitelli", Napoli, Italy*
[3]*University Hospital "San Giovanni di Dio e Ruggi D'Aragona", Salerno, Italy*
[4] *Center for Magnetic Resonance Research, Department of Radiology, University of Minnesota, Minneapolis, United States*

***Abstract*— Tensor-based morphometry (TBM) is a powerful analysis method to detect subtle morphological alterations in the brain from the statistical analysis of deformation field derived metrics. In this study, we used TBM to characterize longitudinal volumetric changes of non-brain soft tissues (especially muscles), exploiting an accurate registration procedure of different tissues across individuals. With the proposed approach, TBM could be a candidate prognostic tool for certain diseases, such as glioblastoma or sarcopenia, related to head muscles morphological alterations.**

***Keywords*— tensor-based analysis, morphometry, masticatory muscles, MRI**

I. Introduction

Brain morphometry (or computational neuroanatomy) based on MRI aims at statistically identifying and characterizing neuroanatomical differences due to development, aging or disease among populations [1]. Many approaches to detect differences in shape and tissue density across brains have emerged, and all of them require linear and/or non-linear transformations of the brain images to match structures of individual subjects with similar intensity patterns to a population-specific template (this procedure in known as normalization). One way to classify these approaches is to broadly divide them into those that deal with differences in the local composition of brain tissues, after discounting macroscopic shape differences, and those that deal with differences in brain shape (e.g., volume, length, area, or location). The former, known as voxel-based morphometry (VBM) techniques, use deformation fields for group-specific spatial normalization and compare images on a voxel basis to identify regional differences in the density of a particular tissue (e.g., grey or white matter [2], [3], [4]). The latter, so called deformation-based morphometry (DBM) approaches, use the above deformation fields to map any individual brain onto a standard brain template to identify regional displacements in the neuroanatomy [5]. Deformation fields encode the relative positions of different brain structures, but local shapes (such as volumes, lengths, and areas) are encoded in their gradients (Jacobian matrices) and various functions of these tensor fields can be used to characterize shape differences. These techniques are more properly referred to as tensor-based morphometry (TBM) [6]. For example, the Jacobian determinant of the deformation field represents the volume of a warped unit-cube and therefore is useful in studies posing specific questions about whether volume growth or loss has occurred. Particularly, in longitudinal studies, it could be possible to detect local relative volume changes over time: since the Jacobian measures the volume of the deformed unit-cube after time t, the rate of variation of the Jacobian (i.e., its temporal derivative) is the rate of the local volume change [6].

Longitudinal analyses are of particular interest in morphometrics, e.g., to monitor the progression of a disease [7], abnormal development [8], or to characterize brain features associated with pathological conditions, compared to a healthy population [9]. The analysis of longitudinal data requires a customized processing, that considers the characteristics of intra-subject analysis. While cross-sectional data images can be processed independently for each subject, longitudinal data require an additional registration to a baseline image (or mean image) for each subject. Furthermore, the deformation field for spatial normalization is estimated only for the baseline image and then applied to all images. Indeed, any coregistration technique that is not symmetric with respect to the multiple time points might potentially introduce false positive differences [10], [11], [12].

A seminal study [10] showed how the combination of symmetric diffeomorphic modelling of MRI structural images, used to optimize longitudinal data coregistration, with TBM, was able to reveal a pattern of atrophy, typically occurring in aging and dementia, in a subject with mild cognitive impairment. Furthermore, outside the brain, age-related skin thickness decrease has been observed [13], suggesting that this method could potentially be used to characterize anatomical changes of non-brain tissues.

In this work, TBM was used to analyse the effects of intensive mastication exercise, under controlled chewing rate, on volumetric properties of both brain and non-brain soft tissues, taking advantage of an optimized longitudinal registration procedure as well as a group specific spatial normalization approach [14]. Of course, we did not expect any alteration in brain tissues and the corresponding analysis were used as a control condition for our procedure. To the best of our knowledge, no previous study applied TBM to characterize morphological alterations of non-brain soft tissues (e.g., muscles) which could be useful in many clinical scenarios where they represent a prognostic biomarker [15], [16], [17], [18].

II. METHODS

A. Participants

Data from sixty healthy volunteers (18 female) aged 22.83 ± 2.70 (mean ± standard deviation), partly included in a previous study [19], were used in this work. All participants gave their written informed consent to participate in the study in line with the European general data protection regulation (GDPR). The study was approved by the local ethic committee and conducted according to the principle of the Declaration of Helsinki.

B. MRI Acquisition

Brain images were acquired using a 3T MRI scanner (Siemens MAGNETOM Skyra, Siemens Healthcare, Erlangen, Germany), equipped with a head and neck 20 channel radio-frequency coil. Participants underwent two identical acquisition sessions on the same day interleaved by ~1-hour mastication task outside the scanner (see Section II.C and reference [19] for additional details). Both scanning sessions included a 3D Pulsed Arterial Spin Labeling sequence (not used in this work) and a 3D T1-weighted Magnetization Prepared Rapid Gradient Echo (MPRAGE) sequence for anatomical acquisition. The MPRAGE sequence was acquired with the following parameters: repetition time (TR) = 2,400 ms, echo-time (TE) = 2.25 ms, resolution = 1 × 1 × 1 mm^3, matrix size = 256 × 256, number of slices = 192, anterior-posterior phase encoding direction, generalized auto-calibrating partially parallel acquisitions (GRAPPA) factor of 2 in phase-encoding direction, and total acquisition time of 5.25 min.

C. Experimental design

After the first scanning session, half of the participants (mastication group, MAS group) were asked to chew a gum on one side of the mouth for 1 h maintaining a rate of at least 1 bite per second. The mastication side was chosen pseudo-randomly, distributing homogenously subjects masticating on the preferred side and subjects masticating on the opposite side (see reference [19] for further details). Within the MAS group, 14 subjects were assigned to the right-side chewing task, whereas the remaining 16 subjects to the left-side chewing task. Furthermore, contact electrodes were placed on the skin to record the electromyography (EMG) signal from the masseter muscles (left and right) with a sampling rate of 1024 Hz. The EMG electrodes were connected to a computerized 2-channel electromyograph (I-330-C2+, J&J Engineering, Poulsbo, WA, United States) and custom software written with LabView (National Instruments, Austin, TX, United States) provided an acoustic alert if no bites were sensed for more than 1 s. This ensured that all participants maintained the approximate rate of (at least) 1 bite/s for the entire exercise. The other half of the participants rested without chewing (no mastication group, noMAS group). The mastication or the resting period was followed by a second MR scanning session.

D. MRI morphometric analysis

The analysis of the structural data was performed using SPM12 toolbox (Wellcome Trust Centre for Neuroimaging, London, UK; http://www.fil.ion.ucl.ac.uk/spm) and Matlab 2020b (The MathWorks, Inc., Natick, Massachusetts, United States, www.mathworks.com). Both anatomical scans of each subject were first segmented using SPM to obtain separate tissue class volumes for grey matter (c1), white matter (c2), cerebrospinal fluid (CSF, c3), bones (c4), non-brain soft tissues (c5), and image background (c6). Then, deformation fields to warp native images in the Montreal Neurological Institute (MNI) standard space [20] were obtained using SPM longitudinal coregistration pipeline, which is based on pairwise inverse-consistent alignment between the first and second scan of each subject, and incorporates a bias field correction step [10]. This procedure resulted in a single image for each subject, named mid-point image, which was used as input for the subsequent non-linear normalization step, performed using the Diffeomorphic Anatomical Registration using Exponentiated Lie Algebra (DARTEL) approach [21]. DARTEL normalization typically begins by creating a mean volume from the mid-point images of each subject, which is used as an initial group template. Deformations from this template to each of the individual mid-point images are computed, and the template is then re-generated by applying the inverses of the same deformations to the images and then averaging. This procedure was iterated 6 times and the last originated template was used to compute the diffeomorphic transformation of each individual image to the standard MNI space. All tissue class images were used to create the DARTEL group template to ensure good correspondence of all tissue compartments across subjects after the normalization.

Two different approaches were followed for the subsequent analyses. First, a standard VBM was used to test the difference in grey matter, white matter, and non-brain soft tissues between MAS and noMAS groups, as well as longitudinal volume changes and group-time interaction, to ensure the absence of any alteration in tissue compositions in our experimental groups that could have biased the interpretation of the subsequent analysis. For this analysis, images c1, c2 and c5 of both time points were normalized to MNI space using the DARTEL procedure with intensity modulation (i.e., the intensity of the initial image was rescaled based on the amount of the applied warping to preserve the original tissue density) and smoothed with a 6 mm full width at half maximum (FWHM) Gaussian kernel. The SPM flexible factorial model was applied to the data for the statistical analysis, including group and time as predictors, whereas age, sex and intra-cranial volume (ICV), the latter computed using SPM, were added as confounds.

Second, a TBM approach was used to investigate possible subtle morphometric changes between MAS and noMAS groups. The divergence of the velocity field that parametrizes the diffeomorphic transformation was here employed as a measure of volumetric variation, as it encodes the volumetric expansion rate required to achieve alignment of the images, according to the diffeomorphic registration model, similarly to the Jacobian determinant. The divergence is computed by summing up the diagonal elements of the Jacobian matrix of the velocity field. One advantage of working with the divergence operator, rather than the Jacobian determinants, is that these are linear functions of the velocity fields and can be better treated numerically [6], [5], [22]. Using the longitudinal

coregistration pipeline, the divergence rate maps describing the rate of volumetric expansion/shrinkage over time at each voxel were obtained by computing the difference between the divergence of the velocity field of the diffeomorphic transformation between both scans and the mid-point average image, divided by the interscan time. Divergence rate maps of each subject were normalized using DARTEL transformations with no intensity modulation and smoothed with a 6 mm FWHM Gaussian kernel. Then, a flexible factorial model was built in SPM to evaluate group effect, including age, sex, and ICV as confound predictors. For statistical comparisons, family-wise error (FWE) correction with an alpha level of 0.05 was applied to all analyses, together with a cluster extent threshold of 50 contiguous voxels [23].

E. EMG analysis

The absolute EMG signal from both channels was integrated and down sampled to 16 Hz. The mean signal value from both chewing sides and a heuristic estimate of the number of bites were derived from the signal integral and used for post-hoc analysis. For the latter, a peak detection algorithm using MATLAB function '*findpeaks*' was run on the chewing-side signal integral: the mean value on the signal integral was used as initial threshold for the peak detection, and the minimum allowed distance between two peaks was empirically set to 4 or 6 samples (i.e., 4/2.7 bites/s) to best fit the subject's average chewing speed. The results of the peak detection were visually inspected to correct for false detections and remove bad signal periods (e.g., due to amplifier saturation or bad contact of the electrodes).

III. RESULTS

A. MRI morphometric analysis

No significant volume differences were found between MAS and noMAS groups and no significant group-time interactions in the VBM analysis of the white matter, grey matter, and non-brain soft tissues.

In the TBM analysis, a cluster of significant difference was found after FWE correction ($p<0.05$) considering the group contrast MAS vs. noMAS (height threshold: $t(55) = 4.81$; cluster-level: $p_{FWE-corr} = 0.003$; peak-level: $p_{FWE-corr} = 0.004$, $t(55) = 5.62$) located in the left temporalis muscle area (Fig. 1).

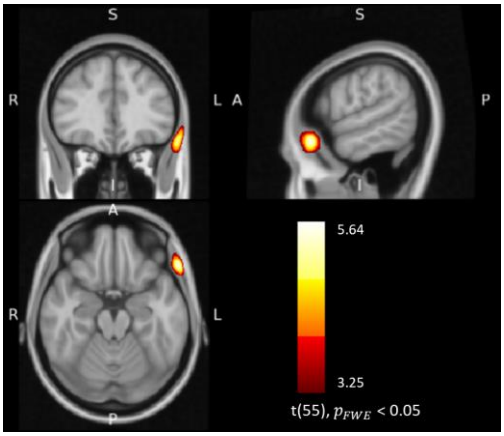


Fig. 1: TBM analysis results. Contrast t-map MAS vs. noMAS group after FWE correction ($p<0.05$).

Clusters of significant differences appeared bilaterally in the same anatomical area when lowering the statistical threshold to $p=0.001$ uncorrected (height threshold $t(55) = 3.25$; left cluster: cluster-level $p_{FWE-corr} = 0.035$, peak-level $p_{FWE-corr} = 0.004$, $t(55) = 5.62$, right cluster: cluster-level $p_{FWE-corr} = 0.251$, peak-level $p_{FWE-corr} = 0.35$, $t(55) = 4.07$) .

Indeed, the mean divergence rate maps of the two groups revealed an opposite pattern in that region, with the MAS group having positive divergence rate values, indicating an expansion trend over time (Fig.2).

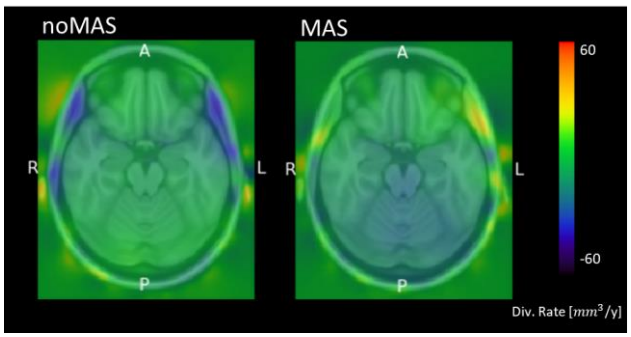


Fig. 2: Mean divergence rate maps for MAS and noMAS group (axial view in MNI space, z = -20).

Fig. 3 describes the distribution of the probability values at each voxel within the left FWE-corrected significant cluster for the membership to each tissue class as originally obtained in the image segmentation step (considering the average tissue probability maps after MNI normalization).

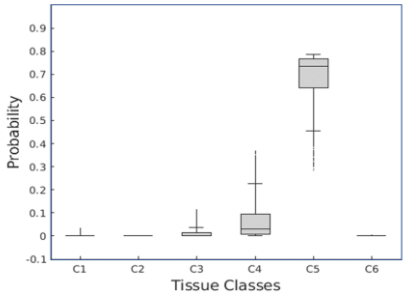


Fig. 3: Tissue probability distribution of the FWE significant voxels. C1 = grey matter, C2 = white matter, C3 = CSF, C4 = bones, C5 = non-brain soft tissues, C6 = image background.

All voxels of the FWE significant cluster were reliably labelled as non-brain soft tissues ($p<0.001$, Wilcoxon signed rank one-tailed paired test performed between C5 probability values and the probability values all other tissue classes).

However, the post-hoc analysis of the MAS group on the EMG-derived metrics revealed no significant correlation between the estimated number of bites, the mean EMG peak amplitude measured on the assigned chewing side, the mean EMG signal values from both channels, and the mean divergence rate value computed within the cluster located in the left side.

IV. CONCLUSION

TBM allows the localization of regions where local volume expansion or shrinkage occurs by measuring the rate of local

volume changes, improving the power to detect volumetric alterations within the limits of the accuracy of the registration algorithm. An advantage of this technique over the classical MRI-based volumetry (e.g., techniques that need the segmentation of the structure of interest at different time points) is that it does not require a priori knowledge of the region of interest to perform the morphological analysis, therefore it is suitable for explorative analysis where no hypothesis about the location of the possible volumetric change is available.

In this work, the combination of an accurate approach for longitudinal coregistration and normalization (that avoids asymmetry biases [24]) and TBM based on divergence rate maps allowed the detection of subtle volume enlargement in the temporalis muscles after 1-hour of intensive mastication exercise. Our results are in line with previous studies showing temporalis muscle hypertrophy due to bruxism, dental malocclusion or excessive chewing gum and trauma [25], and, more in general, increased workload of the masticatory muscles [26]. Temporalis muscle volume (in particular, temporalis muscle thickness, TMT) alterations have been found in migraine patients [27] with respect to healthy control. TMT has been previously proven to have a prognostic role in different diseases: for example it showed a high correlation with overall survival in patients with brain metastasis from melanoma, breast, and lung cancer, as well as in patients with progressive glioblastoma and sarcopenia [15], [16], [17], [18]. TMT is usually manually delineated from MR images or other imaging techniques (e.g., computer tomography or ultrasounds) [28], whereas the use of TBM for an automatic detection of temporalis muscle morphometric alterations could be in principle a more sensible and robust prognostic tool.

REFERENCES

[1] D. Mietchen and C. Gaser, 'Computational morphometry for detecting changes in brain structure due to development, aging, learning, disease and evolution', *Front. Neuroinformatics*, vol. 3, 2009. Available: https://www.frontiersin.org/articles/10.3389/neuro.11.025.2009

[2] J. Ashburner and K. J. Friston, 'Voxel-Based Morphometry—The Methods', *NeuroImage*, vol. 11, no. 6, pp. 805–821, Jun. 2000, doi: 10.1006/nimg.2000.0582.

[3] R. Manara *et al.*, 'White matter volume changes in adult beta-thalassemia: Negligible and unrelated to anemia and cognitive performances', *Am. J. Hematol.*, vol. 95, no. 6, pp. E142–E144, 2020, doi: 10.1002/ajh.25790.

[4] S. Seyedi *et al.*, 'Comparing VBM and ROI analyses for detection of gray matter abnormalities in patients with bipolar disorder using MRI', *Middle East Curr. Psychiatry*, vol. 27, no. 1, p. 69, Dec. 2020, doi: 10.1186/s43045-020-00076-3.

[5] M. K. Chung *et al.*, 'A Unified Statistical Approach to Deformation-Based Morphometry', *NeuroImage*, vol. 14, no. 3, pp. 595–606, Sep. 2001, doi: 10.1006/nimg.2001.0862.

[6] J. Ashburner and G. R. Ridgway, 'Tensor-Based Morphometry', in *Brain Mapping*, A. W. Toga, Ed. Waltham: Academic Press, 2015, pp. 383–394. doi: 10.1016/B978-0-12-397025-1.00309-2.

[7] M. Südmeyer *et al.*, 'Longitudinal Deformation-Based Morphometry Reveals Spatio-Temporal Dynamics of Brain Volume Changes in Patients with Corticobasal Syndrome', *PLOS ONE*, vol. 7, no. 7, p. e41873, Jul. 2012, doi: 10.1371/journal.pone.0041873.

[8] D. K. Thompson *et al.*, 'Tracking regional brain growth up to age 13 in children born term and very preterm', *Nat. Commun.*, vol. 11, no. 1, Art. no. 1, Feb. 2020, doi: 10.1038/s41467-020-14334-9.

[9] I. Driscoll *et al.*, 'Longitudinal pattern of regional brain volume change differentiates normal aging from MCI', *Neurology*, vol. 72, no. 22, pp. 1906–1913, Jun. 2009, doi: 10.1212/WNL.0b013e3181a82634.

[10] J. Ashburner and G. Ridgway, 'Symmetric Diffeomorphic Modeling of Longitudinal Structural MRI', *Front. Neurosci.*, vol. 6, p. 197, 2013, doi: 10.3389/fnins.2012.00197.

[11] W. K. Thompson and D. Holland, 'Bias in tensor based morphometry Stat-ROI measures may result in unrealistic power estimates', *NeuroImage*, vol. 57, no. 1, pp. 1–4, Jul. 2011, doi: 10.1016/j.neuroimage.2010.11.092.

[12] N. C. Fox, G. R. Ridgway, and J. M. Schott, 'Algorithms, atrophy and Alzheimer's disease: cautionary tales for clinical trials', *NeuroImage*, vol. 57, no. 1, pp. 15–18, Jul. 2011, doi: 10.1016/j.neuroimage.2011.01.077.

[13] S. Shuster, M. M. Black, and E. McVITIE, 'The influence of age and sex on skin thickness, skin collagen and density', *Br. J. Dermatol.*, vol. 93, no. 6, pp. 639–643, 1975, doi: 10.1111/j.1365-2133.1975.tb05113.x.

[14] J. Ashburner, 'A fast diffeomorphic image registration algorithm', *NeuroImage*, vol. 38, no. 1, pp. 95–113, Oct. 2007, doi: 10.1016/j.neuroimage.2007.07.007.

[15] J. Furtner *et al.*, 'Survival prediction using temporal muscle thickness measurements on cranial magnetic resonance images in patients with newly diagnosed brain metastases', *Eur. Radiol.*, vol. 27, no. 8, pp. 3167–3173, Aug. 2017, doi: 10.1007/s00330-016-4707-6.

[16] J. Furtner *et al.*, 'Temporal muscle thickness is an independent prognostic marker in melanoma patients with newly diagnosed brain metastases', *J. Neurooncol.*, vol. 140, no. 1, pp. 173–178, 2018, doi: 10.1007/s11060-018-2948-8.

[17] J. Furtner *et al.*, 'Temporal muscle thickness is an independent prognostic marker in patients with progressive glioblastoma: translational imaging analysis of the EORTC 26101 trial', *Neuro-Oncol.*, vol. 21, no. 12, pp. 1587–1594, Dec. 2019, doi: 10.1093/neuonc/noz131.

[18] A. Steindl *et al.*, 'Sarcopenia in Neurological Patients: Standard Values for Temporal Muscle Thickness and Muscle Strength Evaluation.', *J. Clin. Med.*, vol. 9, no. 5, p. E1272, Apr. 2020, doi: 10.3390/jcm9051272.

[19] A. Viggiano *et al.*, 'Vitamin C Acutely Affects Brain Perfusion and Mastication-Induced Perfusion Asymmetry in the Principal Trigeminal Nucleus', *Front. Syst. Neurosci.*, vol. 15, p. 14, 2021, doi: 10.3389/fnsys.2021.641121.

[20] A. C. Evans, D. L. Collins, S. R. Mills, E. D. Brown, R. L. Kelly, and T. M. Peters, '3D statistical neuroanatomical models from 305 MRI volumes', in *1993 IEEE Conference Record Nuclear Science Symposium and Medical Imaging Conference*, Oct. 1993, pp. 1813–1817 vol.3. doi: 10.1109/NSSMIC.1993.373602.

[21] J. Ashburner, 'A fast diffeomorphic image registration algorithm', *NeuroImage*, vol. 38, no. 1, pp. 95–113, Oct. 2007, doi: 10.1016/j.neuroimage.2007.07.007.

[22] J.-P. Thirion and G. Calmon, 'Deformation analysis to detect and quantify active lesions in three-dimensional medical image sequences', *IEEE Trans. Med. Imaging*, vol. 18, no. 5, pp. 429–441, May 1999, doi: 10.1109/42.774170.

[23] P. Liu *et al.*, 'The prognosis and changes of regional brain gray matter volume in MDD with gastrointestinal symptoms', *Neuropsychiatr. Dis. Treat.*, vol. 15, pp. 1181–1191, May 2019, doi: 10.2147/NDT.S197351.

[24] M. Hadj-Hamou, M. Lorenzi, N. Ayache, and X. Pennec, 'Longitudinal Analysis of Image Time Series with Diffeomorphic Deformations: A Computational Framework Based on Stationary Velocity Fields', *Front. Neurosci.*, vol. 10, 2016. Available: https://www.frontiersin.org/articles/10.3389/fnins.2016.00236

[25] J. S. Gomez and H. Cuellar, 'Temporalis muscle hypertrophy: Imaging and clinical implications', vol. 6, no. 12.

[26] C. Olchowy, K. Grzech-Leśniak, J. Hadzik, A. Olchowy, and M. Łasecki, 'Monitoring of Changes in Masticatory Muscle Stiffness after Gum Chewing Using Shear Wave Elastography', *J. Clin. Med.*, vol. 10, no. 11, Art. no. 11, Jan. 2021, doi: 10.3390/jcm10112480.

[27] A. Singh, J. Singhvi, A. Prasad, A. S. Sidhu, H. S. Mann, and S. S. Sidhu, 'Temporalis muscle thickness as surrogate marker of activation of motor component of trigeminovascular system in Migraine patients (4153)', *Neurology*, vol. 94, no. 15 Supplement, Apr. 2020. Available: https://n.neurology.org/content/94/15_Supplement/4153

[28] A. Maskos *et al.*, 'Diagnostic Utility of Temporal Muscle Thickness as a Monitoring Tool for Muscle Wasting in Neurocritical Care', *Nutrients*, vol. 14, no. 21, p. 4498, Oct. 2022, doi: 10.3390/nu14214498.

Pseudo resting-state investigation from task-evoked functional MRI signals

A. Giubergia[1, 2], S. Mascheretti[3], V. Lampis[4], T. Ciceri[1, 2], F. Maccarone[1], M. Villa[5, 6, 7], C. Andreola[8], F. Arrigoni[9], A. Bertoldo[2], and D. Peruzzo[1]

[1] *Neuroimaging Unit, Scientific Institute IRCCS Eugenio Medea, Lecco, Italy*
[2] *Department of Information Engineering, University of Padova, Padova, Italy*
[3] *Department of Brain and Behavioral Sciences, University of Pavia, Pavia, Italy*
[4] *Child Psychopathology Unit, Scientific Institute IRCCS Eugenio Medea, Lecco, Italy*
[5] *Department of Psychological Sciences, University of Connecticut, CT, USA*
[6] *Institute for the Brain and Cognitive Sciences (IBACS), University of Connecticut, CT, USA*
[7] *Haskins Laboratories, CT, USA*
[8] *Université Paris Cité, Laboratoire de Psychologie de Développement et de l'Éducation de l'Enfant, Paris, France*
[9] *Paediatric Radiology and Neuroradiology Department, V. Buzzi Children's Hospital, Milano, Italy*

***Abstract*— Functional connectomics studies the way different regions of the brain are *functionally* connected by means of time-series correlation of functional magnetic resonance imaging data (fMRI) based on Blood Oxygen Level-Dependent (BOLD) contrast. Typically, it is based on resting-state fMRI, which is meant to measure the effect of the spontaneous neural firing in absence of external stimuli. In this scenario, there is an effort in the scientific community to retrieve a "pseudo-resting" state from task-based fMRI and a need of a methodological consensus among task-state connectivity studies.**

This work takes place within this context and investigates whether a task-free "resting-state" connectivity can be inferred from task-fMRI and examine its impact upon behavioural traits on a clinical context, namely in the comparison of Typical Readers and children with Developmental Dyslexia.

Connectomes are derived with several processing options from the two administered tasks, namely the Sinusoidal Gratings and Coherent Motion detection, and analysed by means of classification experiments. The "pseudo-resting" state connectomes, derived from the regression of the task design information, were able to discriminate between the two tasks. Both "task" and "pseudo-resting" state connectomes successfully allows the discrimination between children with Developmental Dyslexia and Typical Readers (accuracy > 70%). Group discrimination seems to be driven by task-related features, independently from the processing pipeline.

Taken together, our results suggest that regression of task-fMRI signals does not lead to a reliable "pseudo-resting" state connectivity. Task based connectomics can still be used to highlight alterations in connectivity underpinning the different behavioral traits.

***Keywords*—fMRI, task-fMRI, functional connectivity, data processing.**

I. Introduction

Functional connectomics has gained attention in the neuroscientific community in the investigation of cognitive behaviours of the brain. Connectivity from fMRI time-series retrieves functional associations among brain regions, represented by nodes, as synchronization maps of their correlation with each other, represented by an edge. Functional Connectivity (FC) from healthy subjects (i.e., controls) and subjects with some neuropsychiatric disorders could be compared in sight of the detection of some functional biomarkers. Typically, FC is based on resting-state fMRI data [1] and measures connections due to spontaneous neuronal firing [2]. Yet, long scan durations are required to obtain reproducible quantitative connections free from spurious fluctuations of non-neural activity. Thus, many studies do not collect enough resting-state data [3] and seek to infer a "pseudo-resting" state by task-modulated data [4], [5]. "Pseudo-resting" state fMRI is meant to analyse the task-evoked fMRI signal in a resting-state processing approach accounting for the activation due to the task [4], [5].

A recent work shows that cognitive tasks related to the skill of interest amplify the trait-relevant individual differences in functional connectivity patterns [6], thus the removal of the task-related content from fMRI signal in the computation of FC might uncover the neuropsychological context. However, little is discussed about the processing of task-evoked functional data to inspect differences in brain functional organization to human behaviours and cognition.

The aim of this work is two-fold: (i) to perform an evaluation of the "pseudo-resting" condition inferred from task-fMRI examining the feasibility of removing the task information from the signal, and (ii) to explore the optimal processing of task-fMRI connectivity in view of subsequent analysis of differences in behavioural traits.

II. Materials and Methods

This work focuses on the fMRI data pre-processing and group level analysis required to investigate the functional connectivity. Accordingly, fMRI data and pre-processing approaches are presented.

A. Participants

Seventy-seven subjects (age range: 9-18 years, M/F: 49/28), 39 Typical Readers – TR and 38 subjects with Developmental Dyslexia – DD) volunteered in the study and were recruited from a project about the genetic basis of DD [7]. The two groups show significant differences in terms of age, gender distribution, QI and DSM-IV-Inattention (DSM-IV-I) trait as Table I reports.

B. Experimental procedure and fMRI task design

MRI data were collected on a 3T Philips Achieva dStream scanner with a 32-channel head coil. Visual stimuli were

delivered through a VisuaStim digital device for fMRI (Resonance Technology Inc., Northridge, CA, USA). The MRI protocol included the use of an anatomical T1-weighted (T1W) 3D Turbo Field Echo sequence as a subject morphological reference of MRI data, and the fMRI data acquired with T2*-weighted Gradient Echo planar sequences. Children were administered with two visual tasks, i.e., Sinusoidal Gratings (SG) and Coherent Motion (CM), with the aim of eliciting the dorsal stream pathway (both SG and CM) and the attention network (CM) [8].

TABLE I: DATASET STATISTICS

	Children with DD (n=39)	*Typical Readers (n=38)*	χ^2	*df*	*p*
Gender (Female/Male)	19/20	9/29	4.19	1	0.041
	Mean (SD)	*Mean (SD)*	*t-Test*	*df*	*p*
Age	12.69 (1.64)	14.29 (1.67)	-4.23	75	$<10^{-4}$
IQ, Block Design†	13.18 (3.28)	11.82 (2.25)	2.12	75	0.037
DSM-IV-I‡	48.21 (7.6)	60.47 (11.4)	-5.57	75	$<10^{-4}$

†Block design subtests of the WISC-II [12]. ‡The DSM-IV-Inattention

C. MRI data common pre-processing

The fMRI data were preprocessed using FreeSurfer (https://surfer.nmr.mgh.harvard.edu/) and the FsFast toolkit. Briefly, functional images were motion corrected, slice-timing corrected, resampled on the "fsaverage" template, a standard space representation implemented in the FreeSurfer software package, using the subject T1W image as an intermediate step, smoothed with a 3 mm FWHM Gaussian kernel and intensity normalized. The HCP-MMP1 atlas was used to divide each hemisphere into 180 cortical regions, which can be grouped into 22 macro-regions. Moreover, we considered 18 regions of the deep grey matter.

D. Subject level general linear models

We analysed the fMRI data with two approaches based on General Linear Models (GLMs), the first one preserves the task-related information, so we named it as "Task condition", and the other one seeks to remove the task-related component from the data, so we named it as "Pseudo-resting condition".

Task condition: GLM analysis conducted without removing task induced signal changes. Thus, regressors of the subject level GLM of task-fMRI BOLD time-series included six motion parameters estimated during realignment, first five principal components of cerebrospinal fluid (CSF), first five principal components of white matter (WM) and the global signal mean. This way, residual fMRI signals preserve the contribution due to the neural activity linked to the visual stimuli.

Pseudo-resting condition: GLM analysis performed with task predictors. The subject level GLM of task-fMRI BOLD time-series included task predictors as additional regressors to create a "pseudo-resting" condition by regressing out the BOLD signal associated with task execution and saving the unwhitened residuals of the signal. Boxcar functions of tasks were convolved with canonical Haemodynamic Response Function (HRF) implemented in SPM and regressed out from data. Multiple task-regression models were used in this analysis differing in terms of the number of derivatives used in the GLM's HRF by which time series were convolved to get the neural response.

E. Functional Connectivity estimation

Connectomes were portrayed by means of ROI-wise Pearson correlation of the entire signal time-series of the experiment (i.e., across all conditions of the experiment), resulting in a 378x378 symmetric FC matrix for each subject. Since BOLD signals are influenced by a number of non-neural processes, the disposal of spurious connections is a crucial step in neuroimaging connectivity analysis, and thresholding is a popular procedure to sparse the connectivity matrices [9] even though there is no gold standard algorithm to select the optimal threshold [10]. Therefore, experiments were conducted with several sparsification thresholds *th*. Specifically, for each thresholding level top N ($N=th*N_{tot}$) connections were preserved in each subject's connectome, zeroing all the others. Moreover, connections equal to zero in more than half of the subjects were removed to avoid the impact of multiple removed connections from the group level analysis.

F. Evaluation of "pseudo-resting" condition

Multiple classification experiments were performed on the GLM-processed data (HRF derivatives in the GLM and sparsification) with the aim to predict the original administered task (i.e., SG or CM) from the derived connectomes.

Classifiers were tested with their default settings (i.e., SVM, Logistic Regression, Decision Tree, Random Forest, K-NN, Gaussian Naive Bayes, simple Multi-Layer Perceptron) with a repeated Cross-Validation (CV) to evaluate the removal of task-related information in the "pseudo-resting" connectomes.

G. Impact of GLM-processing of connectomes in a clinical context

We fixed the sparsity level to 50% and the number of derivatives to zero for task regression, and performed a classification experiment with the aim of investigating the impact of task regression in the characterization of DD and TR. Group classification was performed for all conditions, i.e., in both SG and CM task and in both "task" and "pseudo-resting" conditions, using a SVM classifier (C=1, linear kernel) with a 6-folding CV approach. Significance of classification was tested with a 1000-permutations test and pair-wise differences in the performances of the 4 classification experiments were tested with a two-tailed homoscedastic t-test.

In each fold of each experiment, the relevant connections to be used as features in the classification were selected by a Mann-Whitney test ($p<0.001$). Accuracy, AUC (Area Under the Curve) and relevant connections were saved to dig in the discriminative process. Connections selected in at least 5 folds out of 6 were identified as stable and discriminative, and compared between the 4 SVM experiments (i.e., task SG, task CM, "pseudo-resting" SG and "pseudo-resting" CM). All connections were grouped by the belonging macro-ROIs as defined in the HCP-MMP1 atlas to get an overview of the areas devoted to the discrimination of DD and TR.

III. RESULTS

A. Evaluation of "pseudo-resting" condition

In fig. 1 are summarized the results of the task classification experiments. Each boxplot reports the distribution of the classification AUCs of the classification experiments for each condition. It illustrates how task regression reduces the task-related content from the fMRI signal, even though the stimulus can still be inferred from the derived connectomes independently of pre-processing (i.e., "task" or "pseudo-resting").

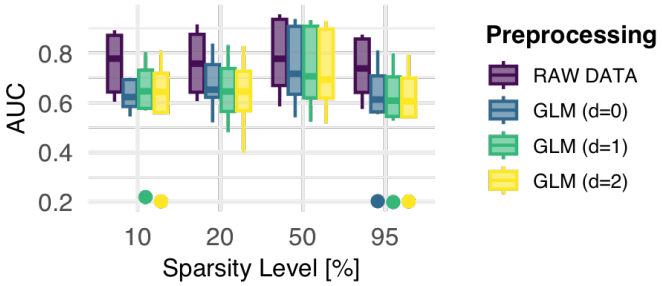


Fig. 1: Task discrimination (SG Vs CM) performances from connectome matrices among the different pre-processing techniques: applying different GLM derivatives (i.e., no derivatives – RAW DATA, 0 derivative – GLM (d=0), 1 derivative – GLM (d=1), or 2 derivatives – GLM (d=2)) and levels of graphs' sparsity (i.e., 10%, 20%, 50%, 95%).

B. Impact of GLM-processing of connectomes in a clinical context

Table II reports the Cross-Validated metrics of the 4 SVM experiments and suggests that classification of connectomes between DD and TR is significantly successful in both "task" and "pseudo-resting" conditions ($p<0.001$ in all experiments).

TABLE II: BEHAVIOURAL TRAIT CLASSIFICATION PERFORMANCES

Condition	*Accuracy mean (%)*	*AUC mean (%)*
Task Gratings	77 ± 11	82 ± 17
Pseudo Gratings	77 ± 13	83 ± 7
Task Coherent	72 ± 8	83 ± 5
Pseudo Coherent	79 ± 11	87 ± 11

Behavioral trait (DD Vs TR) classification performances from connectome matrices. Experiments were performed using both "task" and "pseudo-resting" (d=0) derived connectomes with a 50% sparsity level.

The performances of classification showed no significant differences when pair-wise tested with a two-tailed t-test (Table III reports pairwise *p*-values of accuracy and AUC in the upper and lower triangle, respectively).

TABLE III: TWO-TAILED T-TEST OF CLASSIFICATION PERFORMANCES

ACC / *AUC*	*Task gratings*	*Pseudo gratings*	*Task coherent*	*Pseudo coherent*
Task gratings	x	1	0.37	0.69
Pseudo gratings	0.92	x	0.43	0.71
Task coherent	0.37	0.43	x	0.18
Pseudo coherent	0.57	0.47	0.44	x

We investigated the impact of GLM-processing ("task" Vs "pseudo-resting") and the type of task (SG Vs CM) in the discriminative process. We quantified the overlap in the relevant connections selected by the classification experiments and reported the results in terms of overlap percentages in fig. 2. Very few connections are commonly selected by the classifiers working on SG and CM, either in "task" and "pseudo-resting" (*intra-processing* and *inter-task*), while >60% of the connections are commonly selected when comparing "task" and "pseudo-resting" conditions in both SG and CM (*intra-task* and *inter-processing*).

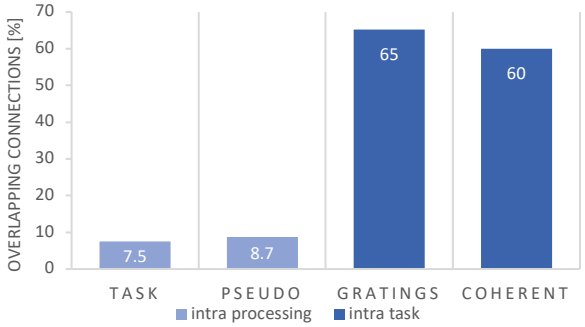


Fig. 2: Analysis of the ration of the overlap among connections chosen by the classifier in the group classification experiments (i.e., DD Vs TR). *Intra-processing* analysis explores the overlap between SG and CM with the same GLM-processing, while *intra-task* analysis highlights the overlap between the different GLM-processing on the same task.

From a macro-ROI point of view, Table IV shows the percentages of the most involved macro-ROIs defined by the HCP-MMP1 template in the 4 experiments. Results are more similar when comparing intra-task analyses than when comparing similar pipelines applied on different task, suggesting that a task related content is present in the derived connectomes independently of the processing pipeline.

IV. DISCUSSION AND CONCLUSIONS

In this work, processing of task fMRI data was analyzed to explore the contribution of the task information in connectomics.

The first aim of this study is the evaluation of the "pseudo-resting" condition got by regression of the BOLD signal in the fMRI data, i.e., to test whether "pseudo-resting" state connectivity can be inferred and investigated from task-fMRI data. The successful discrimination of the task in "pseudo-resting" conditions for all the tested conditions (fig. 1) indicates that connectomes preserve task information even after GLM regression, suggesting that a task-free "pseudo-resting" state cannot be inferred from task fMRI data, even if it can be inspected to study the context associated with DD not explicitly linked to the task-driven stimuli.

The second goal of this work explores the way GLM-processing in generating "pseudo-resting" condition affects subsequent analysis upon behavioral traits, seeking the optimal way to process fMRI data in the exploration of the clinical context. From fig. 2 we can deduce that discriminative connections mainly depend on the type of task, which drives the way the classifier discriminates between DD and TR, as

SG and CM share only few connections in both task and "pseudo" conditions. On the other hand, the greater intra-task and inter-processing coherence (i.e., a higher number of shared connections) shown in both SG and CM suggest that signal GLM-processing does not significantly influence the way the classification rules are inferred in the training, leading to similar evaluation of significant features. To verify this, we examined the macro-ROI analysis of table IV looking for DD-related networks highlighted by the classification of this behavioural trait. Overall, the most engaged macro-ROIs in the discrimination are known to be involved in DD, whereas differences between SG and CM are linked to the networks the two tasks are meant to elicit – dorsal and ventral visual paths in both SG and CM and attention network in CM. Yet, there is still a great deal of confusion and controversy regarding the processing of task-based connectivity in fMRI analyses. In some cases, this has led researchers to report two versions of their results, one version with task regression and another without task regression [11].

TABLE IV: MACRO-ROIS ANALYSIS OF RELEVANT CONNECTIONS

REGION NAME	*Task gratings*	*Pseudo gratings*	*Task coherent*	*Pseudo coherent*
Primary Visual Cortex	0	0	0	0
Early Visual Cortex	0	0	1.7	1.6
Dorsal Stream Visual Cortex	1.3	2.2	0.8	0
Ventral Stream Visual Cortex	5.0	8.7	3.3	0
MT+ Complex and Neighboring Visual Area	6.3	4.3	11.7	10.5
Somatosensory and Motor Cortex	2.5	2.2	2.5	2.4
Paracentral Lobular and Mid Cingulate Cortex	2.5	0	1.7	0
Premotor Cortex	3.8	2.2	6.7	4.8
Posterior Opercular Cortex	2.5	0	0.8	3.2
Early Auditory Cortex	2.5	2.2	0	0.8
Auditory Association Cortex	6.3	4.3	9.2	12.1
Insular and Frontal Opercular Cortex	3.8	2.2	4.2	6.5
Medial Temporal Cortex	6.3	8.7	3.3	6.5
Lateral temporal Cortex	2.5	4.3	11.7	9.7
Temporo-Parietal-Occipiatl Junction	2.5	0	0.8	1.6
Superior Parietal Cortex	2.5	4.3	2.5	3.2
Inferior Parietal Cortex	10.0	13.0	8.3	3.2
Posterior Cingulate Cortex	12.5	4.3	1.7	4.0
Anterior Cingulate and Medial Prefrontal Cortex	5.0	13.0	5.8	5.6
Orbital and Polar Frontal Cortex	7.5	10.9	9.2	10.5
Inferior Frontal Cortex	0	0	3.3	4.8
DorsoLateral Prefrontal Cortex	15.0	13.0	7.5	4.0
Cerebellum-Cortex	0	0	3.3	4.0
Thalamus	0	0	0	0
Basal ganglia	0	0	0	0.8

Analysis of the macro-ROI linked by the connections involved in the classification. For each classification experiment we report the ration of the selected connections linking the given macro-ROI. *TG*: Task Gratings, *PG*: Pseudo Gratings, *TC*: Task Coherent, *PC*: Pseudo Coherent.

REFERENCES

[1] B. B. Biswal *et al.*, "Toward discovery science of human brain function," *Proc Natl Acad Sci U S A*, vol. 107, no. 10, pp. 4734–4739, Mar. 2010, doi: 10.1073/pnas.0911855107.

[2] R. M. Birn *et al.*, "The effect of scan length on the reliability of resting-state fMRI connectivity estimates," *Neuroimage*, vol. 83, pp. 550–558, Dec. 2013, doi: 10.1016/J.NEUROIMAGE.2013.05.099.

[3] M. L. Elliott *et al.*, "General functional connectivity: Shared features of resting-state and task fMRI drive reliable and heritable individual differences in functional brain networks," *Neuroimage*, vol. 189, pp. 516–532, Apr. 2019, doi: 10.1016/j.neuroimage.2019.01.068.

[4] R. J. Harris *et al.*, "Altered functional connectivity of the default mode network in diffuse gliomas measured with pseudo-resting state fMRI," *J Neurooncol*, vol. 116, no. 2, pp. 373–379, Jan. 2014, doi: 10.1007/s11060-013-1304-2.

[5] R. Bhandari *et al.*, "Does higher sampling rate (multiband + SENSE) improve group statistics - An example from social neuroscience block design at 3T," *Neuroimage*, vol. 213, Jun. 2020, doi: 10.1016/j.neuroimage.2020.116731.

[6] X. Di and B. B. Biswal, "Toward Task Connectomics: Examining Whole-Brain Task Modulated Connectivity in Different Task Domains," *Cerebral Cortex*, vol. 29, no. 4, pp. 1572–1583, Apr. 2019, doi: 10.1093/cercor/bhy055.

[7] V. Riva *et al.*, "The influence of DCDC2 risk genetic variants on reading: Testing main and haplotypic effects," *Neuropsychologia*, vol. 130, pp. 52–58, Jul. 2019, doi: 10.1016/J.NEUROPSYCHOLOGIA.2018.05.021.

[8] S. Mascheretti *et al.*, "Selecting the most relevant brain regions to classify children with developmental dyslexia and typical readers by using complex magnocellular stimuli and multiple kernel learning," *Brain Sci*, vol. 11, no. 6, 2021, doi: 10.3390/brainsci11060722.

[9] Y. He and A. Evans, "Graph theoretical modeling of brain connectivity," *Current Opinion in Neurology*, vol. 23, no. 4. pp. 341–350, Aug. 2010. doi: 10.1097/WCO.0b013e32833aa567.

[10] H. Ahmadi, E. Fatemizadeh, and A. Motie-Nasrabadi, "Deep sparse graph functional connectivity analysis in AD patients using fMRI data," *Comput Methods Programs Biomed*, vol. 201, p. 105954, Apr. 2021, doi: 10.1016/J.CMPB.2021.105954.

[11] M. W. Cole, D. S. Bassett, J. D. Power, T. S. Braver, and S. E. Petersen, "Intrinsic and task-evoked network architectures of the human brain," *Neuron*, vol. 83, no. 1, pp. 238–251, Jul. 2014, doi: 10.1016/j.neuron.2014.05.014.

[12] C. Cornoldi, *Nuove Prove di Lettura MT per la Scuola Media Inferiore*. Organizzazioni Speciali: Firenze, Italy, 1995.

[13] Conners C. K. Nobile M. Alberti B.Zuddas A., *CRS-R. Conners' Rating Scales-Revised*. Organizzazioni Speciali: Firenze, Italy, 2007.

[14] C. K. Conners, G. Sitarenios, J. D. A. Parker, and J. N. Epstein1, "The Revised Conners' Parent Rating Scale (CPRS-R): Factor Structure, Reliability, and Criterion Validity," 1998.

[15] A. E. Cunningham and K. E. Stanovich, "Early reading acquisition and its relation to reading experience and ability 10 years later.," *Dev Psychol*, vol. 33, no. 6, pp. 934–945, 1997, doi: 10.1037/0012-1649.33.6.934.

Phase synchronization between breathing and PPG signals in sleep events recordings of adult subjects

A. Morelli[1], J. Kraemer[2], P. Francia[1], M. Glos[2], L. Bocchi[1], T. Penzel[2]
[1] *Department of Information Engineering, University of Florence, Florence, Italy*
[2] *Charité - Universitätsmedizin Berlin, Berlin, Germany*

***Abstract*—Sleep-disordered breathing (SDB) are recognised as significant risk factors for the development of major diseases and, even in their mildest forms, have a strong impact on a person's quality of life and general well-being. The prevalence of SDB is much greater than one is generally led to believe; there are many people who suffer from them without ever having received a diagnosis, because the symptoms, although debilitating, are often difficult to attribute, especially in cases where they present in a milder form. This, coupled with the fact that polysomnographies are complex examinations to perform, makes it even more difficult to directly identify the sufferer.**

It is therefore of interest the development of techniques for studying the acquired signals. Among those, we focused on the relation between breath and peripheral pulse. The frequencies in the breathing range were extracted from photoplethysmographic (PPG) signals using Empirical Mode decomposition, and the temporal relation between the two parameters is described by means of their relative phase shift, normalized with respect to the breathing period. Preliminary results indicate that some of the analyzed pairs exhibit a stabilization of the relative time-shift at deeper sleep stages.

***Keywords*—PPG, Sleep analysis, phase synchronization**

I. Introduction

SDB is considered a relatively common condition, reported to be 2% in the female population and 4% in the male population, whose main manifestation is Sleep Apnea Syndrome (SAS). From a clinical point of view, in adults, SAS is defined as frequent stops of respiratory activity lasting at least 10 seconds during sleep and it can be divided into three categories: Obstructive Sleep Apnea (OSA) is the most common and is due to partial or complete obstruction of the upper airway, Central Sleep Apnea (CSA) which has a lower incidence and is due to lack of respiratory effort despite the presence of an open airway, and finally, mixed sleep apnea (MSA) which is the combination of the previous two [1]. Sleep studies are difficult, costly, and troublesome for those who undergo them; for a successful outcome of the examination, in the most comprehensive cases of polysomnography, subjects must spend a night wearing a wide range of sensors and monitoring systems that may hinder peaceful sleep. This leads to severe limitations in the clinical application of such studies and in the interpretation of the results, due to the lack of certainty that the recorded sleep disturbances are actually physiological and not induced by the measuring devices that the subject needs to wear; therefore, a less invasive and simple, but equally effective, examination could allow for a wider spread of such studies, possibly conducted completely autonomously by the subject himself through a wearable device and, consequently, a more widespread identification of people affected by these disorders. For this reason, many recent studies have focused on attempting to develop new, minimally invasive but highly effective polysomnographic procedures [2], [3]; most of these have focused on using the raw PPG signal because of the ease with which it can be implemented in a wearable and compact sensing system. In this study we sought to identify possible relationships between the raw PPG signals, acquired with red and infrared light, and a number of other respiratory signals acquired during polysomnographic examinations of subjects with sleep apnea, looking for a possible correlation between sleep state-induced changes in the respiratory component of peripheral pulsations and the other signals.

A. Effects of breathing on circulation

It is known that respiration has a definite influence on circulation; although the reasons why this happens are not always clear or confirmed, the underlying mechanisms are. In particular, breathing influences circulation in two ways. First, it has a direct effect on heart rate variability through a nervous mechanism known as respiratory sinus arrhythmia (RSA), whereby, as a result of receptor extension in the lungs, inhibitory signals sent to cardiac vagal neurons (CVNs) exert inhibitory control over heart rate: so that during inspiration the heart rate increases and vice versa; second, it influences left ventricular output with a series of opposing effects. On the one hand, breathing increases venous return due to the expansion of the chest, which generates radial traction on the organs within it causing a reduction in pressure in the right atrium by a few mmHg and increasing flow from the periphery; in addition, lowering the diaphragm compresses the intra-abdominal veins slightly increasing venous return. In contrast to this, the radial traction exerted by the thorax during expansion also distends the vessels outside the lungs, increasing their capacity, with the effect of generating an accumulation of blood in the extra-alveolar vessels within the thorax; conversely, the alveolar vessels are compressed when the alveoli expand and fill with air, thus increasing the resistance downstream of the

right atrium and reducing the blood supply to the left side of the heart. Furthermore, as a consequence of right ventricular expansion, a shift in the intraventricular septum causes a reduction in left ventricular compliance and, consequently, a reduction in stroke volume [4]. The overall effect of these opposing mechanisms is a reduction in systolic blood pressure during inspiration (approximately 5 mmHg in healthy adults). Since the induced changes in stroke volume during inspiration are reflected both in central [5] and in peripheral perfusion [6], they can be recorded with a photoplethysmograph and later extracted from the overall signal.

II. Materials and Methods

The study used retrospective data collected from 11 male and female subjects who underwent an overnight polysomnographic examination from which the analyzed signals were recorded, according with the planned therapeutic procedure. All participants were informed on the purpose of the study and its experimental procedures before obtaining their written informed consent and the enrolment in the study. All the data were collected and processed anonymously in accordance with privacy regulations and the guidelines of the Declaration of Helsinki of the World Medical Association.

A. Data collection

Polysomnographies were conducted in a controlled clinical environment for the duration of one full night (approximately 8 hours) during which the following signals were recorded:

- Photoplethysmogram, obtained by means of a self-made device using a light in the red zone (Red) with a wavelength of $640\,\mathrm{nm}$ and one in the infrared band (Ir) with a wavelength of 9 $40\,\mathrm{nm}$; both signals were sampled at a frequency of $300\,\mathrm{Hz}$. The combination of these signals provides also the saturation curve.
- Abdomen (Abd) and thorax (Thx) respiratory movements recorded by means of two different plethysmogram belts placed around the abdomen and around the chest respectively.
- Nasal flow (Flw) obtained with a nasal cannula connected to a pressure transducer (range $\pm 5\,\mathrm{mbar}$). This is a qualitative signal whose shape follows respiration: during inspiration the pressure in the cannula decreases, during exhalation the pressure in the cannula increases. We observed a strong non linearity of the relation between pressure and flow. In order to improve the linearity of the relationship between pressure changes and flow changes, we empirically processed the measured signal by square root transformation.
- Data representing the sleep events obtained as a result of the polysomnographic examination were used: each 30-second block of the examination was associated with a sleep stage following the general criterion that divides sleep stages into five main classes: wake (W), REM (R), non-REM light sleep 1 (N1), non-REM light sleep 2 (N2) and non-REM deep sleep (N3).

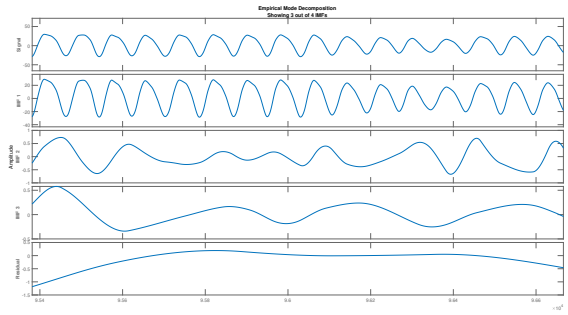


Fig. 1: Empirical mode decomposition of the infrared signal; the undecomposed signal is the one shown at the top, then the first 3 intrinsic mode functions are presented in order; the last section is the decomposition residuals.

The polysomnographic session also records several other signals, in addition to the ones listed above. For the sake of brevity, we will not list them here as they are unnecessary for the purposes of this study.

B. Data analysis

Given the small number of subjects, we tuned our system by using data corresponding to a single subject. The remaining 10 subject constitutes the test set for validating the outcome of the system.

In a preliminary step, all data tracks were synchronized, as their start and stop times were not perfectly aligned. The procedure identifies the latest starting time (t_s) and the earliest ending time (t_e); then each signal was clipped to the interval $[t_s, t_e]$. Also, all signal where resampled at a sampling rate of $300\,\mathrm{Hz}$. Next, a 7th-order IIR low-pass filter with a stop-band frequency of $f = 10$ Hz was applied to each signal to eliminate all higher-frequency noise, then down-sampling to 30 Hz to work with fewer samples. Finally, a 6th-order band-pass filter between 0.15 and 1.5 Hz isolates the respiratory frequencies, that vary approximately from 1 to 6 seconds per breath, and the heartbeat (Fig 1, top row).

Once the signals had been cleaned of noise, it was necessary to extract only the breathing-related components from Red and Ir signals. A recent approach proposed in 2011 by Madhav et al. [7] for extracting the breathing signal from PPG is Empirical Mode Decomposition (EMD), a time-frequency data analysis that has proven effective in extracting signals from data generated by non-linear, non-stationary noisy processes such as breathing and heartbeat.

Briefly, the Empirical Mode Decomposition is obtained by an iterative algorithm that decomposes the signal $s_0(t)$ into a finite number of components called Intrinsic Mode Functions (IMF); during each iteration i, first the local maxima and minima of the signal $s_{i-1}(t)$ are identified, then the respective interpolated signals are estimated obtaining the upper $U_i(t)$ and lower $L_i(t)$ envelopes, then the IMF $e_i(t)$ is calculated as the mean envelope:

$$e_i(t) = \frac{U_i(t) + L_(t)}{2}$$

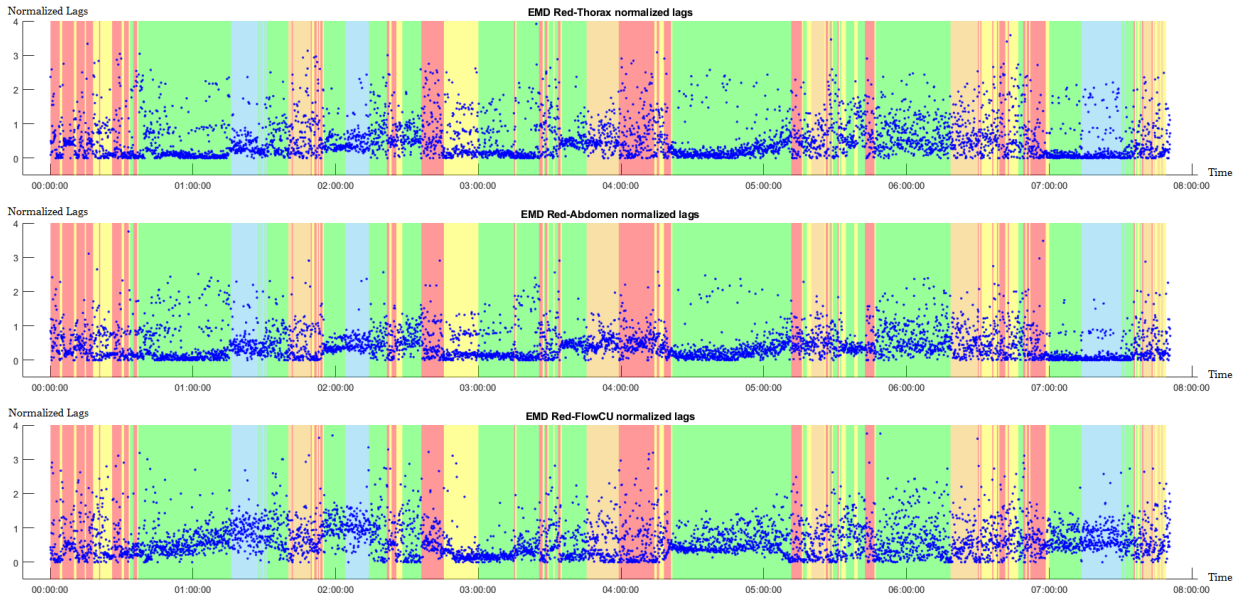


Fig. 2: Red normalized lags; Color indicate the sleep phase: red, W phase; orange, REM phase, yellow, N1; green, N2, and blue, N3

Finally, the residual signal $s_i(t)$ is obtained as the difference between $s_{i-1}(t)$ and $e_i(t)$, and a new iteration is performed. The algorithm can be stopped after an arbitrary number of iterations, in which case it provides an equal number of IMF, or it stops when the original signal remains nearly unaltered. An example of an EMD result is shown in Fig. 1.

In this study, respiration-related IMFs were identified by means of a power spectrum analysis, i.e. those whose main frequency components fell within the typical respiration range (0.2-0.6 Hz), which, typically, are those obtained from the second iteration ($e_2(t)$).

A cross-correlation analysis was conducted from the obtained IMFs. The cross-correlation is the measure of similarity of the periodicity of two signals which is expressed as a number between -1 e 1 (1 being the same periodicity and the same phase, - 1 the same periodicity and a 180° shift; in addition, the cross-correlation function allows the identification of the number of samples, referred to as lags, of which one signal must be shifted relative to the other in order to have the maximum periodicity similarity: it is, therefore, an index of the phase shift between the two signals. However, for cross-correlation to yield meaningful results, the analysed signals must be stationary, and neither the peripheral pulsation nor the respiratory signals are. For this reason, we considered only intervals of approximately two breaths, where both the PPG and respiratory signals could be considered reasonably stationary. Thus, we split both signals in 5-second signal windows (150 samples), and analyzed the cross-correlation in each window. Moreover, to increase resolution and accuracy, we introduced an overlap of ± 15 samples (± 0.5 seconds in the timeline) between adjacent windows.

In this procedure, each window is associated with the correlation values and the time lags between each of the respiratory IMFs extracted from both PPG signals (Red, Ir) and all respiratory signals (Abd, Thx, Flw), in the corresponding sleep phase (W, R, N1, N2 or N3). That is, for a set of possible combinations of feature pairs, Lags and correlation values were extracted; these pairs are: Red-Thx, Ir-Thx, Red-Abd, Ir-Abd, Red-Flw, Ir-Flw, Thx-Abd, Thx-Flw, Abd-Flw, Red-Ir. In order to compare the lags of the different windows into which the signals were divided, lags normalized to the period of the individual window were calculated: for each window, the positions of the peaks were identified and the period of the signal was evaluated as the difference of the position of two adjacent peaks, then the lag corresponding to the window was normalized divided by the period of the same window. Thus, we obtained a set of normalized lag, representing the phase shift in each 5-second time window for each considered signal pair. Those lags were finally grouped accordingly with the corresponding sleep phase, and their distribution was analyzed.

III. Results

Normalized lags results were collected in graphs that indicated with a blue dot each lag associated with a 5-second window within the whole-night sleep recording; sleep stages were highlighted with a color system that associated W phase with red, REM phase with orange, N1 with yellow, N2 with green, and N3 with blue. Graphs of normalized lags between the Red signal and the Thx, Abd, and Flw signals, respectively, were shown in Fig. 2.

A visual inspection of the lag histogram indicates the distribution is highly skewed, with most samples grouped together, but with a relatively large population of outliers, probably related to issues in the estimation procedure, in presence of signal artefacts (mainly, movement of the subject). For this reason, resorted to perform a preliminary analysis based on median and interquartile range. Visual inspection suggests also that the dispersion of the values tends to decrease

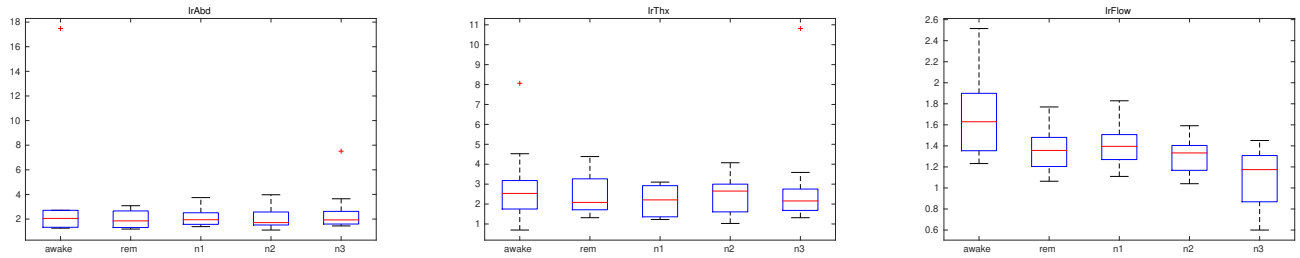


Fig. 3: Infrared interquartile and median ratios for sleep stage

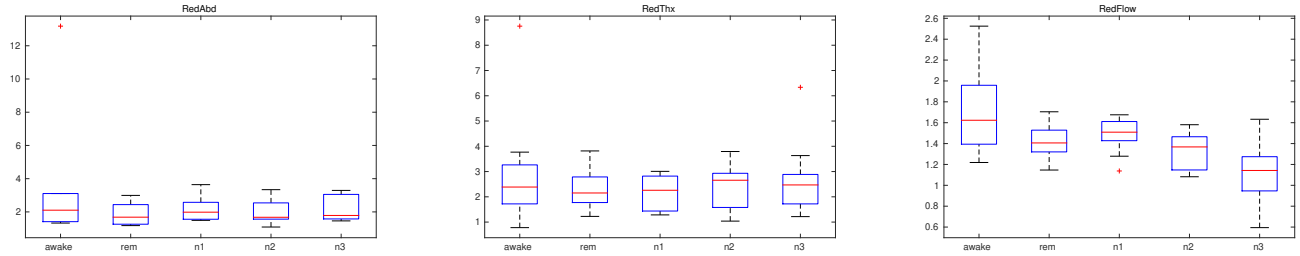


Fig. 4: Red interquartile and median ratios for sleep stage

with the increase of depth of sleep; therefore we decided to study this aspect by evaluating the ratio between interquartile range and median, for each parameter pair and for each sleep stage; the results have been reported in the form of box plots in Fig. 3 and Fig. 4 for both Red and Ir signal with Thx, Abd and Flw signal respectively.

IV. Discussion

Preliminary results do not seem to show a strong relation between PPG signals and the other signals. This could depend on many factors for which a multiparametric analysis seems necessary; for instance, we already observed a variability of the perfusion depending on the measurement site [8], as well as the feasibility of using a signal modelling technique for extracting a more robust representation of the PPG signal [9], [10].

However, an interesting aspect emerges from the box-plot analysis: it can be seen that while the ratio of interquartile to median normalized lags of both the Red signal with Abd and Thx and the Ir signal with Abd and Thx tends to remain constant for all sleep stages, that with the Flw signal tends to vary; in particular, the mean and dispersion decreases for deeper stages of sleep, suggesting an increased synchronization between those signal pairs. One interpretation of this phenomenon is that these are the effects of obstructive apnea, whereby during the obstructive event there are still chest and abdominal respiratory efforts that affect peripheral perfusion, but airflow in the nose is delayed or blocked, and this pattern is amplified in parallel with the transition from deep sleep stages toward awakening. The final result is, therefore, that perfusion signals remain synchronized with chest and abdominal movement signals throughout the awakening process whereas the same behavior does not occur with flow. One possible verification of this interpretation is to assess whether the same pattern arises in a healthy subject.

References

[1] Necmettin Sezgin, Gokhan Kirbas, and Mehmet Akin. The correlation analysis between airflow and oxygen saturation in obstructive sleep apnea events using correlation function. pages 1–5, 2007.

[2] Kevin Kotzen, Peter H. Charlton, Sharon Salabi, Lea Amar, Amir Landesberg, and Joachim A. Behar. Sleepppg-net: A deep learning algorithm for robust sleep staging from continuous photoplethysmography. *IEEE Journal of Biomedical and Health Informatics*, pages 1–8, 2022.

[3] H. Korkalainen, J. Aakko, B. Duce, S. Kainulainen, A. Leino, S. Nikkonen, I. O. Afara, S. Myllymaa, J. Töyräs, and T. Leppänen. Deep learning enables sleep staging from photoplethysmogram for patients with suspected sleep apnea. *Sleep*, 43(11), 2020.

[4] D. J. Meredith, D. Clifton, P. Charlton, J. Brooks, C. W. Pugh, and L. Tarassenko. Photoplethysmographic derivation of respiratory rate: a review of relevant physiology. *Journal of Medical Engineering & Technology*, 36(1):1–7, 2012. PMID: 22185462.

[5] S. Orlandi, L. Bocchi, G. Donzelli, and C. Manfredi. Central blood oxygen saturation vs crying in preterm newborns. *Biomedical Signal Processing and Control*, 7(1):88–92, 2012.

[6] A. Perrella, M. Sorelli, F. Giardini, L. Frassineti, P. Francia, and L. Bocchi. Wavelet phase coherence between the microvascular pulse contour and the respiratory activity. In *IFMBE Proceedings*, volume 68, pages 311–314, 2018.

[7] K. Venu Madhav, M. Raghu Ram, E. Hari Krishna, Nagarjuna Reddy Komalla, and K. Ashoka Reddy. Estimation of respiration rate from ecg, bp and ppg signals using empirical mode decomposition. In *2011 IEEE International Instrumentation and Measurement Technology Conference*, pages 1–4, 2011.

[8] M. Sorelli, Z. Stoyneva, I. Mizeva, and L. Bocchi. Spatial heterogeneity in the time and frequency properties of skin perfusion. *Physiological Measurement*, 38(5):860–876, 2017.

[9] V. Fleischhauer, N. Ruprecht, M. Sorelli, L. Bocchi, and S. Zaunseder. Pulse decomposition analysis in photoplethysmography imaging. *Physiological Measurement*, 41(9), 2020.

[10] C. Aliani, E. Rossi, P. Francia, and L. Bocchi. Vascular ageing and peripheral pulse: an improved model for assessing their relationship. *Physiological Measurement*, 42(12), 2021.

Impact of diffusion connectivity metrics on white matter abnormalities in glioma

Maria Colpo[1,2], Erica Silvestri[1], Umberto Villani[1,2], Mariagiulia Anglani[3], Diego Cecchin[2,5], Maurizio Corbetta[2,4] and Alessandra Bertoldo[1,2]

[1] *Department of Information Engineering, University of Padova, Padova, Italy,*
[2] *Padova Neuroscience Center, University of Padova, Padova, Italy,*
[3] *Neuroradiology Unit, University Hospital of Padova, Padova, Italy,*
[4] *Department of Neuroscience, University of Padova, Padova, Italy,*
[5] *Department of Medicine, Unit of Nuclear Medicine, University of Padova, Padova, Italy.*

***Abstract*—Structural connectivity (SC) matrix of brain tumours is usually quantified by number of streamlines (NOS) of tracts connecting regions of interest. Several are the limitations linked to this weight. This study aims to investigate the impact of different connectome metrics by evaluating the white matter abnormalities. We found that diffusion microstructure parameters provide higher and spatially different alterations with respect to NOS. With this fact, we can enrich the NOS-based connectivity integrating diffusion microstructure properties.**

***Keywords*—glioma; structural connectivity; number of streamlines; diffusion microstructure.**

I. Introduction

Diffusion magnetic resonance imaging (dMRI) is one of the best in vivo technique able to non-invasively investigate white matter (WM) axonal fibers. Specifically, dMRI tractography, also called fiber-tracking, indicates the use of algorithms applied to delineate WM pathways in the brain [1].

The dMRI results can be used to calculate the structural connectivity (SC), defined as the quantification of the white matter tracts physically interconnecting the different brain regions [2]. Specifically, SC can be quantified as number of streamlines (NOS) connecting each pair of regions, like a proportional estimate to the total cross-sectional area of WM bundles connecting those areas [3]. Even if it is not without any problems [4], this is the commonly used metric. SC matrix can be also represented as the mean of some diffusion microstructure measures. For instance, SC can be obtained, for each connected regions pair, by averaging the Fractional Anisotropy (FA) microstructural values measured along their axonal fibers. Eventually, the two just described modalities can be joint, weighting the SC matrix characterized by NOS with diffusion microstructure metrics.

It is worth mentioning that SC [5] has become an useful tool to non-invasively infer abnormalities of brain structural connectivity in pathology [6]. As a matter of fact, SC has been applied to assess the tumours' impact on patient's whole brain structural network [7].

Therefore, the aim of this research was to investigate the impact of SC metrics derived from microstructure diffusion parameters with respect to NOS, in a multimodal assessment of the connectome abnormalities in gliomas.

II. Material and Methods

A. Dataset

Forty-six patients (60.2±14.3 years, 20 F) affected by de novo glioma at different positions (lesion hemisphere: 23 left hemisphere, 15 right hemisphere, 8 bilateral) and grades (I-IV) were included in the research between July 2017 and February 2021 at the Neurologic Clinic in Padua University Hospital. All procedures were in accordance with the ethical standards of the institutional research committee and with the 1964 Helsinki declaration plus later amendments. All participants provided written and informed consent in accordance with the local University Hospital Institutional Review Board (No. 2771P prot:0065859/12).

An expert neuroradiologist, with more than five years of experience, supplied the lesion mask delineating the entire lesion area and distinguishing two lesion tissue types: tumour and oedema. Lesion masks were used for pre-processing steps and advanced analyses.

Positron emission tomography (PET) and magnetic resonance imaging (MRI) images were acquired with a 3T Siemens Biograph mMR-PET/MR scanner, equipped with a 16-channels head-neck coil. Specifically, diffusion data analyzed for this study were collected according to the optimized Neurite Orientation Dispersion and Density Imaging (NODDI) diffusion protocol [8] (TR/TE 5355ms/104ms; 2x2x2mm): 100 diffusion images with 10 images at b=0 s/mm^2, 30 images at b-value=710 s/mm^2 and 60 at b-value=2855 s/mm^2. Each diffusion direction was acquired in two reversed phase encoding directions, i.e., anterior-posterior and posterior-anterior.

B. Diffusion processing and Tractogram generation

Diffusion data standard pre-processing was performed with FSL [9] and MRtrix3 [10] software. Co-registration steps were conducted with Advanced Normalization Tools (ANTs [11] v. 2.0.1) software. Tractography generation and SC computation were implemented with MRtrix3 [10] software. Further statistical analyses were examined with in-house MATLAB scripts (MATLAB 2022b, The MathWorks, Inc., Natick, MA, USA).

For each patient, WM tractogram was reconstructed applying the iFOD2 tracking algorithm [12], fixing the gray/white matter interface as seeding area, setting a default cut-off of 0.1 and generating 100 million of streamlines. The Anatomically Constrained Tractography [13] framework was applied during tracking: lesion area was excluded from the application of anatomical priors. Eventually, the final number of tractography streamlines was filtered to 10 million, by pruning off unreliable streamlines via the spherical-deconvolution informed filtering of tractogram (SIFT) [14] framework. Furthermore, Neurite Orientation Dispersion and Density Imaging (NODDI) [8], Diffusion Tensor Imaging (DTI) [15] and Diffusion Kurtosis Imaging (DKI) [16] models

were fitted on dMRI pre-processed data to estimate microstructure maps of the next eight microstructure parameters: intracellular volume fraction, isotropic volume fraction, orientation distribution fraction (NODDI model), FA, mean diffusivity (MD) and mean kurtosis (DKI model), FA and MD (DTI model). NODDI and DKI models were fitted on the dataset applying off-the-shelf toolboxes publicly available ([17] NODDI and [18] DKI). DTI models were fitted with *dtifit* command of FSL software [9]. All microstructure maps were checked for outliers: if voxels' values were outside the respective known literature range, voxels' outlier values were substituted by their new values, obtained from the application of a spatial median filter on the selected microstructure map.

C. SC matrices creation

For each patient, Schaefer [19] functional atlas (200 parcels, 17 Networks), joint with subcortical parcels of Automated anatomical (AAL3) atlas (Thalamus, Caudate, Putamen, Pallidum, Hippocampus) [20], were overlayed to the whole brain tractogram to then define the SC matrix (each parcel corresponds to a node). Each entry of the matrix represented the strength of the connection between each pair of nodes. Connectome matrices were quantified according to two different metrics of connectivity: *Number of Streamlines* (SC_{NOS}) and *Mean Microstructure* Parameter (SC_{MICRO}). A functional atlas was chosen given that this study is part of a project aiming to integrate functional, structural and PET connectivity for brain network analysis.

D. SC abnormalities definition

Structurally altered links were generally identified applying a non-parametrical statistic.

Concerning SC_{NOS}, for each subject, a $SC_{NOS\text{-}cleaned}$ was created. Specifically, the pseudo-healthy entries of the matrix were preserved if two conditions hold: 1) for each link, the parcels regions at the endpoints of the tract needed to feature an overlapping with the lesion for less than 5% of the total volume of the parcel, and 2) streamlines connecting such endpoints were required to not cross the lesion. Moreover, one-streamline entries of SC matrix were discarded from the analyses. Thus, a draft pseudo-healthy matrix was obtained computing the median among the patients. Then, the pseudo-healthy $SC_{NOS\text{-}MED}$ was obtained sparsifying the intra and inter hemispheres links with respectively 80% and 85% thresholds, by considering their different range of reconstructed track density. Eventually, an additional mask was overlayed to analyze only those tracts set as unaffected for more than five patients.

About SC_{MICRO}, for each patient, the SC_{MICRO} was masked by its $SC_{NOS\text{-}cleaned}$, to then compute the median among the patients and to obtain a draft pseudo-healthy SC_{MICRO}. At last, the pseudo-healthy $SC_{MICRO\text{-}MED}$ was derived masking the draft pseudo-healthy SC_{MICRO} with the pseudo-healthy $SC_{NOS\text{-}MED}$.

Thus, for a generic SC_{NOSi}, a link (j,k) was generally labelled as altered comparing the SC_{NOS} of each subject with its $SC_{NOS\text{-}MED}$ reference by the median absolute deviation $SC_{NOS\text{-}MAD}$, according to the following condition:

$$SC_i(j,k) < SC_{MED}(j,k) - 3 \cdot SC_{MAD}(j,k) \quad (1)$$

This constraint was imposed since a glioma can cause a displacement, infiltration, or disruption of the white matter fibers, thus potentially causing a decrease in the NOS of the potentially affected links [21].

Besides, a SC_{MICROi} link (j,k) was generally labelled as altered comparing the SC_{MICRO} of each subject with its $SC_{MICRO\text{-}MED}$ reference by the median absolute deviation $SC_{MICRO\text{-}MAD}$, according to the next conditions:

$$SC_i(j,k) < SC_{MED}(j,k) - 4 \cdot SC_{MAD}(j,k) \quad (2)$$
$$SC_i(j,k) > SC_{MED}(j,k) + 4 \cdot SC_{MAD}(j,k) \quad (3)$$

The threshold, equal to 4, was set to be more conservative on the links alterations definition. The double condition was applied because a white matter tract can present a deviation from the healthy behavior in both directions.

E. Degree of disconnections

Once the individual SC alteration matrix was defined, a measure of alteration was defined for each Cortical Schaefer and Subcortical AAL3 parcel (matrix nodes). At first, for each node, the normalized number of affected connections was computed dividing the number of affected links starting from that node by the reliable number of tracts seeding from the same node and derived by the pseudo-healthy SC_{MED}. Thus, given N nodes, the degree of disconnections, computed summing the number of altered links connecting each node with the other N-1, was derived to assess the impact of the metric of connectivity on the definition of the altered links. The Network degree of disconnections was derived summing the degree of disconnections of each node within a network with respect to other networks. Furthermore, the Global degree of disconnections was quantified summing the total amount of affected links for a patient.

III. Results

Collinearity of the eight types of SC_{MICRO}, derived from the inclusion of different signal models, was reduced based on the high correlation values, computed among the patients, between SC_{MICRO} of FA (1 +/- 0.002) and MD (0.99 +/- 0.004) of DTI and DKI models. For each patient, the links with an overlap of minimum 4 SC_{MICRO} affections were detected and labelled in the SC_{4MICRO} alteration matrix. Figure 1a) and 1b) show the Mean and Standard Deviation (SD) Correlations values among the different SCs types.

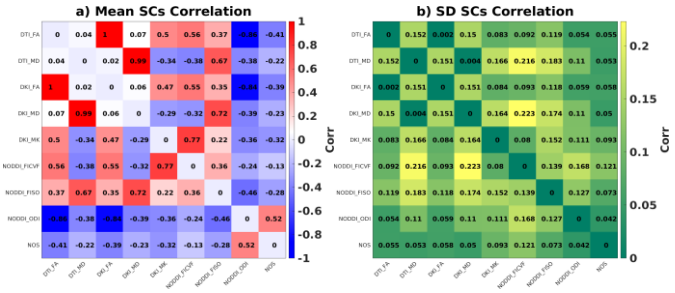


Fig. 1: On the left, fig. a) displays mean correlation values of different types of SCs among the patients. On the right, fig. b) displays SD values of different types of SCs among the patients.

A. Degree of disconnections

Figure 2a represents the Network degree of disconnections of SC_{NOS}, derived for each patient. Observing the figure, patients are characterized by a higher SC_{NOS} Network degree of disconnections derived for intra-hemisphere Cortical-

Cortical links homolateral to the lesion. Indeed, Network degree of disconnections derived for inter-hemisphere Cortical-Cortical links is sparser. A similar but less evident behavior can be observed for SC_{NOS} Network degree of disconnections of intra and inter hemisphere Cortical-Subcortical links. Looking at fourth row of Figure 2a, patients with a bilateral lesion show a behavior like patients with a right lesion.

Figure 2b refers to SC_{4MICRO} Network degree of disconnections. It is worth noting that intra-hemisphere Cortical-Cortical links homolateral to the lesion feature a high Network degree of disconnections. On the contrary, intra-hemisphere Cortical-Cortical links contralateral to the lesion rarely present an overlap of abnormalities detected from more than 4 SC_{MICRO} matrices. Indeed, SC_{4MICRO} distinguishes a low

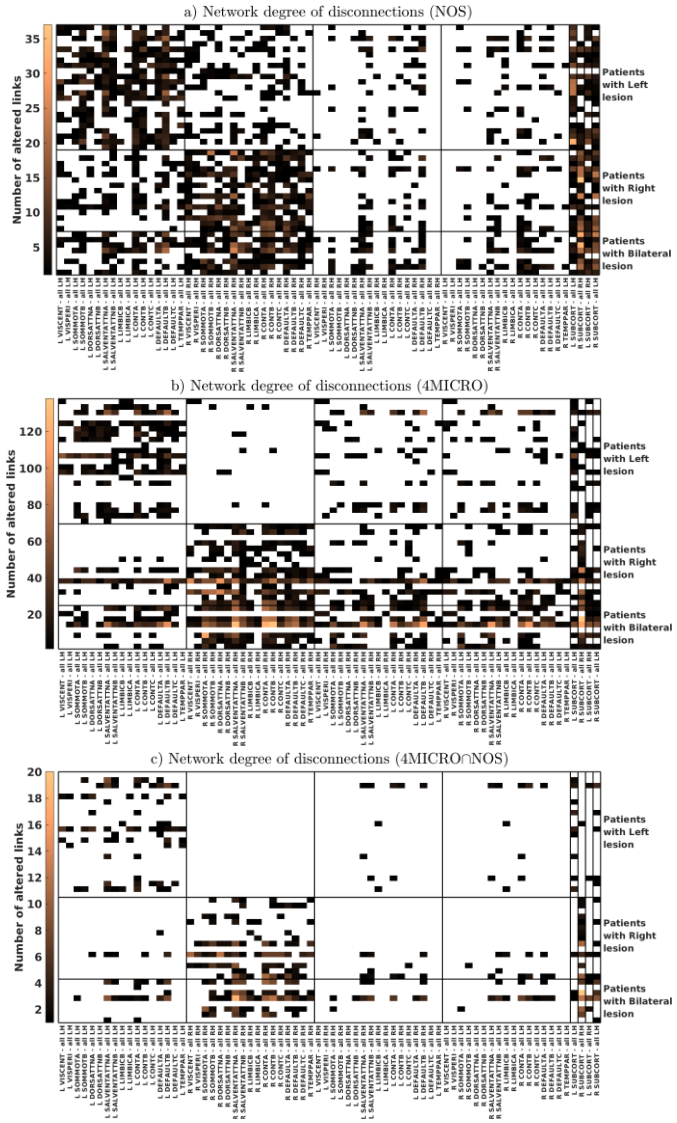


Fig. 2: Each subfigure refers to the Network degree of disconnections derived from SC_{NOS}, SC_{4MICRO} and $SC_{4MICRO} \cap SC_{NOS}$. For each subfigure, from the left: altered intra left hemisphere Cortical-Cortical links, altered intra right hemisphere Cortical-Cortical links, altered inter left-right hemisphere Cortical-Cortical links, altered inter right-left hemisphere Cortical-Cortical links, altered intra left hemisphere Subcortical-Cortical links, altered intra right hemisphere Subcortical-Cortical links, altered inter left-right hemisphere Subcortical-Cortical links, altered inter right-left hemisphere Subcortical-Cortical links. Patients are grouped across the rows by the lesion hemisphere position (from the top, lesion on the left or right hemisphere, bilateral lesion).

Network degree of disconnections for the inter-hemisphere cortical-cortical links. Considering Cortical-Subcortical Network degree of disconnections, both SC_{4MICRO} intra and inter connections present abnormalities. Again, looking at the bottom row of Figure 2b, patients with a bilateral lesion show a behavior like patients with a right lesion.

In Figure 2c the overlap of $SC_{4MICRO} \cap SC_{NOS}$ altered links is reported. It can be noted that intra-hemisphere cortical-cortical and cortical-subcortical connections of the hemisphere homolateral to the lesion, present a low overlap of disconnections. This overlap is almost null for intra-hemisphere cortical-cortical and cortical-subcortical connections contralateral to the tumor. Finally, affected inter-hemisphere Cortical-Cortical links are low and quite symmetric.

Figure 3 represents the above-described behavior for a representative patient with a lesion in the right hemisphere: most of the affected links are intra-right hemisphere. The WM abnormalities quantified by SC_{NOS} and SC_{4MICRO} are spatially distributed in different way. A low overlap of altered connections can be appreciated.

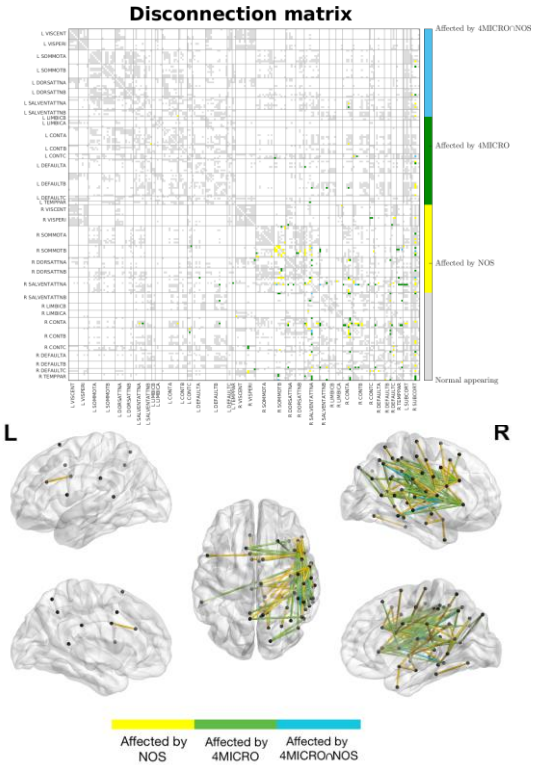


Fig. 3: On the top: Disconnection matrix for a representative patient with a right lesion. Links are grouped according to the Schaefer Cortical 17 Networks Parcellations joint with the AAL3 Subcortical parcels (Thalamus, Caudate, Putamen, Pallidum, Hippocampus), Left and Right hemispheres. Gray/white links represent reliable/unreliable connections according to the pseudo-healthy reference matrix. In yellow there are links affected by SC_{NOS}, in green there are links affected by SC_{4MICRO}, in light blue there are links affected by the intersection $SC_{4MICRO} \cap SC_{NOS}$. On the bottom: Ball and Stick representation of the disconnection matrix (only Schaefer Cortical Parcels). In black there are parcels that present altered connections. According to the matrix color bar, in yellow there are links affected by SC_{NOS}, in green there are links affected by SC_{4MICRO}, in light blue there are links affected by the intersection $SC_{4MICRO} \cap SC_{NOS}$.

Finally, the interest was about the number of WM abnormalities within the different lesion tissue types. Specifically, for each link alteration, it is possible to label it as crossing tumor, oedema, or normal appearing tissue. These distinctions highlight the impact of different brain tissues on the structural connectivity alterations. The distribution of the normalized number of affected links for the different SC types

is reported in Figure 4, grouping the patients according to the lesion position. Looking at the figure, it is evident that, for each type of SC metric and lesion position, the higher number of alterations is within the tumoral area. Concerning SC_{NOS}, the following lower normalized number of affected connections is within the normal appearing tissue. Finally, the lowest number of alterations is within the edematous area. Regarding SC_{4MICRO}, a low number of alterations is within the edematous area, while the least is within the healthy tissue. This could indicate a major impact of oedema on diffusion microstructure with respect to NOS.

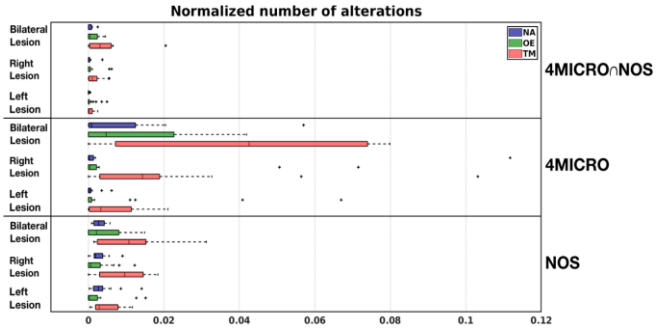


Fig. 4: Boxplots of distribution of normalized number of alterations within the different tissue types. For each lesion position hemisphere, each boxplot refers to the tissue type crossed by the altered links. Like in legend, in blue there is normalized number of altered links crossing normal appearing tissue, in green there is normalized number of altered links crossing edematous tissue, in red there is normalized number of altered links crossing tumoral tissue. Boxplots are also grouped according to the SC matrix type. From the top, for each block, there are boxplots derived for $SC_{4MICRO} \cap SC_{NOS}$, SC_{4MICRO} and SC_{NOS}. For visualization reason, an outlier value of 0.26 was cut by the image (SC_{4MICRO}, Bilateral Lesion, normalized number of altered links crossing tumoral tissue).

Eventually, comparing the distribution of normalized number of alterations between the different SC matrix type, SC_{4MICRO} generally shows a higher normalized number of alterations with respect to SC_{NOS}, thus indicating that microstructure alterations are more frequent than NOS alterations. Regarding the $SC_{4MICRO} \cap SC_{NOS}$, Figure 4 shows that the overlap is low, as already seen in Figures 2 and 3.

The last result concerns the Pearson correlation, among the patients, between the Global degree of disconnections and the tumoral/lesion volume. Considering SC_{NOS}, r values are equal to 0.65/0.81 (pval<0.05), while looking at SC_{4MICRO}, these values are equal to 0.33/0.38 (pval<0.05). The different r values suggest that, while SC_{NOS} seems to capture more the disrupted (by the glioma) structural fiber pathways, SC_{MICRO} depicts the overall neural fiber integrity related to the heterogeneity of tumor-infiltrating immune cells. It is worth observing that for both metrics, oedema plays a role in WM abnormalities.

IV. Conclusion

In this study we showed that the two different weight matrices of connectivity, SC_{NOS} and SC_{MICRO}, present a significant different spatial impact on the detection of the white matter alterations. These differences have the potential to provide complementary information of connections abnormalities. Furthermore, also given the impact of oedema on SC_{4MICRO} alterations, we can enrich the NOS-based connectivity integrating diffusion microstructure proprieties. This enrichment, when performing SC studies on glioma pathology, allows to empower our ability in the measures of alteration of glioma brain organization. Future studies could focus on the relationship between SC_{NOS} matrices enriched by the microstructure and other imaging modalities, given the multimodal acquisitions.

Acknowledgement

The authors report no competing interests.

References

[1] S. Mori and P. C. M. Van Zijl, “Fiber tracking: principles and strategies - a technical review,” *NMR Biomed*, vol. 15, no. 7–8, pp. 468–480, Nov. 2002.

[2] P. Hagmann *et al.*, “MR connectomics: Principles and challenges,” *J Neurosci Methods*, vol. 194, no. 1, pp. 34–45, Dec. 2010.

[3] R. E. Smith, J. D. Tournier, F. Calamante, and A. Connelly, “The effects of SIFT on the reproducibility and biological accuracy of the structural connectome,” *Neuroimage*, vol. 104, pp. 253–265, Jan. 2015.

[4] F. Calamante, “The Seven Deadly Sins of Measuring Brain Structural Connectivity Using Diffusion MRI Streamlines Fibre-Tracking,” *Diagnostics*, vol. 9, no. 15, 2019.

[5] C. H. Yeh, D. K. Jones, X. Liang, M. Descoteaux, and A. Connelly, “Mapping Structural Connectivity Using Diffusion MRI: Challenges and Opportunities,” *Journal of Magnetic Resonance Imaging*, vol. 53, no. 6, pp. 1666–1682, Jun. 2021.

[6] O. Sporns, G. Tononi, and R. Kötter, “The human connectome: A structural description of the human brain,” *PLoS Comput Biol*, vol. 1, no. 4, pp. 0245–0251, 2005.

[7] S. D’Souza, L. Hirt, D. R. Ormond, and J. A. Thompson, “Retrospective analysis of hemispheric structural network change as a function of location and size of glioma,” *Brain Commun*, vol. 3, no. 1, 2020.

[8] H. Zhang, T. Schneider, C. A. Wheeler-Kingshott, and D. C. Alexander, “NODDI: Practical in vivo neurite orientation dispersion and density imaging of the human brain,” *Neuroimage*, vol. 61, no. 4, pp. 1000–1016, Jul. 2012.

[9] M. Jenkinson, C. F. Beckmann, T. E. J. Behrens, M. W. Woolrich, and S. M. Smith, “FSL,” *Neuroimage*, vol. 62, no. 2, pp. 782–790, Aug. 2012.

[10] J. D. Tournier *et al.*, “MRtrix3: A fast, flexible and open software framework for medical image processing and visualisation,” *Neuroimage*, vol. 202, Nov. 2019.

[11] B. B. Avants, N. J. Tustison, G. Song, P. A. Cook, A. Klein, and J. C. Gee, “A reproducible evaluation of ANTs similarity metric performance in brain image registration,” *Neuroimage*, vol. 54, no. 3, pp. 2033–2044, Feb. 2011.

[12] J.-D. Tournier and and a. C. , F. Calamante, “Improved probabilistic streamlines tractography by 2 nd order integration over fibre orientation distributions,” *Ismrm*, vol. 88, no. 2003, p. 2010, 2010.

[13] R. E. Smith, J. D. Tournier, F. Calamante, and A. Connelly, “Anatomically-constrained tractography: Improved diffusion MRI streamlines tractography through effective use of anatomical information,” *Neuroimage*, vol. 62, no. 3, pp. 1924–1938, 2012.

[14] R. E. Smith, J. D. Tournier, F. Calamante, and A. Connelly, “SIFT: Spherical-deconvolution informed filtering of tractograms,” *Neuroimage*, vol. 67, pp. 298–312, 2013.

[15] P. J. Basser, J. Mattiello, and D. LeBihan, “MR diffusion tensor spectroscopy and imaging,” *Biophys J*, vol. 66, no. 1, pp. 259–267, Jan. 1994.

[16] A. J. Steven, J. Zhuo, and E. R. Melhem, “Diffusion Kurtosis Imaging: An Emerging Technique for Evaluating the Microstructural Environment of the Brain,” *American Journal of Roentgenology*, vol. 202, no. 1, Dec. 2013.

[17] http://mig.cs.ucl.ac.uk/index.php?n=Tutorial.NODDImatlab

[18] https://cai2r.net/resources/diffusion-kurtosis-imaging-matlab-toolbox/

[19] A. Schaefer *et al.*, “Local-Global Parcellation of the Human Cerebral Cortex from Intrinsic Functional Connectivity MRI,” *Cerebral Cortex*, vol. 28, no. 9, pp. 3095–3114, 2018.

[20] E. T. Rolls, C. C. Huang, C. P. Lin, J. Feng, and M. Joliot, “Automated anatomical labelling atlas 3,” *Neuroimage*, vol. 206, Feb. 2020.

[21] B. J. Jellison *et al.*, “Diffusion Tensor Imaging of Cerebral White Matter: A Pictorial Review of Physics, Fiber Tract Anatomy, and Tumor Imaging Patterns,” *AJNR American Journal of Neuroradiology*, vol. 25, no 3, pp. 356–369, March 2004.

Millimeter-Waves Imaging for Breast Cancer Detection: Development of Analytical Models for Scattering Matrices Computation

S. Di Meo[1], G. Bertuzzi[1], G. Matrone[1], G. Magenes[1] and M. Pasian[1]
[1] *Department of Electrical, Computer and Biomedical Engineering, University of Pavia, Pavia, Italy*

***Abstract*—This contribution is divided in two parts. In the first part, we present the work done at the Microwave Laboratory and the Laboratory of Bioengineering of the University of Pavia on the design of a millimeter-wave imaging system for breast cancer detection. In the second part, we present the analytical model we have developed for the numerical simulation of multi-static radar configurations against both simple scenarios, in which one or more targets share the same medium as the antenna array, and more complex configurations, in which the targets lie in a medium other than the antennas and skin is present at the interface. Normalized radar images, reconstructed with the Delay-And-Sum (DAS) algorithm, show the robustness of the model in all scenarios considered. The models proposed in this work, although based on illustrative assumptions, make it possible to overcome the bottleneck provided by the enormous computational and temporal demands of full-wave simulations, thus offering the possibility of generating in real time the desired number of configurations on which to test, for example, skin removal algorithms and/or train the neural networks for artificial intelligence purposes (aimed, as an example, to classify suspicious regions).**

***Keywords*—Breast cancer detection, millimeter-wave imaging, numerical models, scattering matrix.**

I. Introduction

BREAST cancer is one of the most diagnosed type of cancer among women in industrialized countries. Fundamental in the fight against the disease is early detection. There are many imaging techniques currently available for the diagnosis of breast cancer. The most widely used are mammography (also used in screening programs), ultrasound, and breast MRI. However, the limitations associated with each of these techniques, such as the use of ionizing radiation in mammography, the strong dependence of the outcome of the ultrasound examination on the physician's skill, as well as the high cost of MRI, are pushing toward the study of complementary or supplementary imaging techniques for this purpose.

Among the most studied imaging techniques are microwave imaging systems, which represent a safe and low-cost option. Such systems are based on the significant dielectric contrast, i.e., the different response to exposure to electromagnetic fields, between healthy and neoplastic tissues, which becomes particularly pronounced when neoplasms are located in healthy tissues with a high percentage of adipose content [1].

In recent years, several microwave imaging systems have been proposed by different research groups around the world, some of them even reached the pre-clinical stage, either using the radar (for detection of the dielectric anomaly in the domain of investigation only) or tomographic (for reconstruction of the dielectric profile) approach [2]-[4].

However, approximately all of these imaging systems make use of relatively low frequencies and relatively narrow bandwidths, on the order of a few GHz, and for this reason, although they are capable of reaching targets several centimeters below the skin and can offer reasonable resolutions in dense breasts, they tend to lose resolution in presence of particularly fatty tissues. The high values of complex dielectric permittivity characterizing high-density healthy tissues (hence little adipose), compensate for the wavelengths in the medium, thus offering an effective wavelength of a few millimeters while using frequencies in the lower microwave region. Conversely, in presence of particularly adipose tissues, which are characterized by low values of dielectric permittivity, this compensation is lacking, so that the wavelength in the medium is approximately similar to that in air and therefore cannot detect sub-centimeter lesions.

To address this problem, at the University of Pavia, we have been working on an imaging system in the millimeter (mm)-wave regime for the early detection of breast cancer in particularly fat breasts (which are currently the target of X-ray mammography).

We have worked on several design steps over these years, from dielectric characterization of *ex-vivo* breast tissues, both healthy and neoplastic, up to 50 GHz [5]-[7], to the numerical feasibility study [8], to the realization of tissue-mimicking breast phantoms [9], to the experimental proof-of-concept of the imaging system [10]. These steps are presented in the following section.

In addition, in the direction of making our phantoms more and more realistic and our imaging tests more and more robust, we are currently working on the production of skin phantoms, as well as on the development of algorithms for the removal of the artifact associated with it. However, in order to test artifact removal algorithms on perfectly controlled scenarios and given the enormous computational demands of full-wave simulators (which sometimes limits simulations to unrealistic scenarios), we have developed an analytical-numerical model for reconstructing scattering matrices related to single- and multi-layer configurations. In particular, starting from the radar equation [11], we analyzed both the case where both antennas and one or more targets lie in the same medium, and the case where antennas are in the air and targets are in a different medium, including also the interface representing the skin. This last topic is the focus of the present paper.

The article is divided in this way. In Section II, the main

design steps of the mm-wave imaging system are presented. In Section III, the analytical models implemented for computing synthetic scattering matrices, with punctiform targets and not, in both single- and multi-layer cases are presented and discussed. Finally, some conclusions are derived.

II. State-of-the-Art of mm-Wave Imaging System for Breast Cancer Detection

A. STEP 1: Dielectric characterization of human breast ex-vivo tissues

Exact knowledge of tissues dielectric properties across the bandwidth of interest is a cornerstone for the design of all biomedical microwave and millimeter-wave applications. For this reason, in 2014 and 2016, we performed two experimental campaigns to characterize the dielectric properties of *ex-vivo* breast tissues, healthy and neoplastic, in collaboration with the European Institute of Oncology in Milan, Italy. In this way, we characterized in the 0.5-50 GHz frequency range the dielectric properties of more than 300 *ex-vivo* healthy and cancerous breast samples from about 100 women aged 14-89 years.

The results of these two experimental campaigns showed a significant dielectric contrast in the whole investigated bandwidth between healthy and malignant tissues [5]-[7].

B. STEP 2: Feasibility study of mm-wave imaging system

Based on the significant dielectric contrast between healthy and neoplastic tissues, we performed a numerical and simulative feasibility study of the mm-wave imaging system both in a linear and conformal configuration. In particular, through link-budget evaluation in different scenarios (i.e., different breast types), we evaluated aspects such as the optimal number of antennas in the array maximizing the signal-to-noise ratio, the maximum detectable depth of the lesion, as well as the achievable resolution for this type of system [8].

C. STEP 3: Tissue-mimicking breast phantoms

The realization of tissue-mimicking phantoms is an important step in the experimental testing, in a controlled but realistic environment, of any system for biomedical applications. For this reason, in [9], we developed recipes capable of mimicking the dielectric properties of all breast tissues, both healthy and neoplastic. Compared with previously published works [12]-[13], our recipes make use of only low-cost, safe and easily handled components. Furthermore, as with *ex-vivo* breast tissues, for the first time, we have characterized their properties up to 50 GHz.

In addition, we have produced two types of complete phantoms, conformal and planar, with a dielectric inclusion mimicking the dielectric properties of tumor tissues embedded in a phantom mimicking the dielectric properties of healthy adipose tissues. For reasons of space, please refer to the reference articles for more details and figures.

D. STEP 4: Experimental test of the mm-wave imaging system against breast phantoms

Testing of the millimeter-wave imaging prototype was carried out at the Microwave Laboratory of the University of Pavia [10]. The setup used for the imaging tests includes: two double-ridge waveguides (PNR180) with mono-modal frequency bandwidth [18-40] GHz, mounted on four linear actuators (Zaber technology) to enable a synthetic array and connected to a PNA Network Analyzer (Keysight E8361C) for signal acquisition. Both the actuators and the network analyzer are connected to a computer for both the movement of the antennas in the desired positions and the scattering parameters acquisition through proper Matlab routines. All measurements were done in air, without a coupling medium.

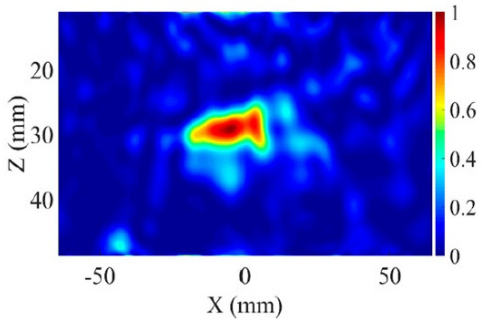


Fig. 1 Radar imaging result against experimental scenario, picture modified from [10].

The complete matrix including all combinations of transmitting and receiving antennas was created in post-processing and calibrated before using as input into the Delay-And-Sum algorithm, used for radar image reconstruction. An experimental image on phantom is shown in Figure 1 [10], showing a target 3 cm within the phantom.

III. Analytical Model for Scattering Matrix Calculation in Scenarios With/Without Interface

A. Work motivation

In the numerical study of the system presented in Section II.B, we first used Matlab for the implementation of the link-budget equations and system parameters, and then we used Ansys HFSS software for evaluation in the full-wave environment of a selected number of the scenarios.

Full-wave simulations are a very useful tool in the study of a new microwave system or device, since it describes the behavior of the propagating wave, as well as, in a noise-free environment, all the interactions between the different structures encountered by the electromagnetic wave in propagation. However, simulation times and computational demands tend to increase exponentially in the presence of biological tissues (due to their dielectric characteristics), to the point of making it practically impossible to model an anatomically realistic scenario for many practical cases.

To overcome this limitation, and to have a tool capable of providing in real-time scattering matrices corresponding to complex scenarios we implemented a numerical model starting from the radar equation [11]. In these models, one or more targets can be in a uniform medium, or in scenarios in which the antenna array is in air (or in a coupling medium) and one or more targets are embedded in a medium with dielectric properties similar to different types of healthy tissue, under a skin layer. The model was developed in Matlab (R2015a).

As an example of the model capabilities, a synthetized system based on a multi-static radar architecture, consisting of 28 elements, placed in the xz plane in linear configuration,

with symmetry with respect to the z axis and distance d between phase centers equal to λ/2 in the antenna medium at 30 GHz, was analysed. The frequency range investigated is 26.5–40 GHz, which is the mono-modal frequency bandwidth of the WR28, used in our full-wave simulations.

B. Case 1: Antenna array, punctiform target – same medium

In the first modeled configuration, the antennas and the target (one or more) lie in the same medium.

The scattering parameters corresponding to this configuration were derived starting from the radar equation, which is valid in far-field (in our case is an exemplifying assumption). In particular, to switch from powers to fields and to take into account that the scattering parameters are complex numbers, we arbitrarily added the phase terms. Therefore, the implemented equation is:

$$\sqrt{\frac{P_r}{P_t}} = \sqrt{\frac{GA_{eff}\sigma}{(4\pi)^2(R_t)^2(R_r)^2 e^{\alpha R_t} e^{\alpha R_r}}}\, e^{-j\beta R_t} e^{-j\beta R_r} \quad (1)$$

where P_r is the received power, P_t is the transmitted power, G is the gain and A_{eff} is the effective area of the antenna, σ is the radar cross section of the target, α is the attenuation constant, β is the phase constant, R_t is the path from the transmitting antenna to the target and R_r is the path from the target to the receiving antenna.

A sketch of the analysed configuration in this case is shown in Figure 2. The scattering matrix thus calculated was used as input into the image reconstruction algorithm, Delay-And-Sum, and Figure 3 shows the result. In this case, as an example, the target and antennas are both in air. Taking into account the many approximations that were necessary in modeling the scenarios, all images are normalized.

C. Case 2: Antenna array and punctiform target in different media

In the second modeled scenario, the antennas are in the air,

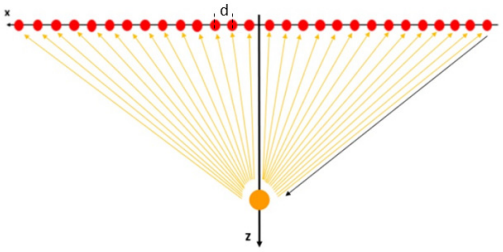


Fig. 2: Sketch of the analysed configuration in Case 1, where the red dots indicate the position of the antennas, separated by a distance d, the yellow dot the position of the target, and the yellow and black lines exemplify the propagation paths.

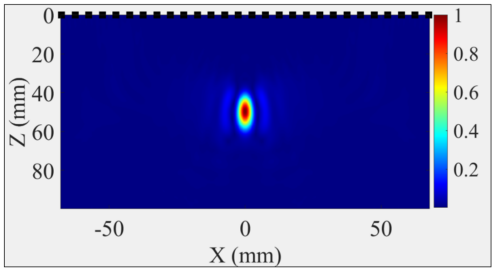


Fig. 3: Normalized DAS image for Case 1, in which both the target and the antenna array are in air. Black dots indicate the position of the antennas.

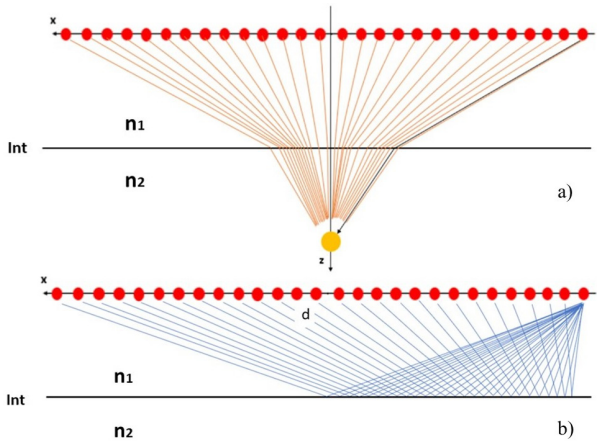


Fig. 4 Sketch of the analysed configuration in Case 2 showing the different contributions to the scattering matrix; a) target; b) skin. the red dots indicate the position of the antennas, separated by a distance d, the yellow dot the position of the target, and the yellow, black, and blue lines exemplify the propagation paths. The refractive index of the upper and lower medium is n_1 and n_2, respectively, while Int indicates the position of the interface.

while the target (one or more) is immersed in a second medium, separated by an interface representing the skin.

In this configuration, the signal received by the antennas is a function not only of the backscatter from the target, but also of the separation interface between the two media (Figure 4). In the real case, there are also the multiple reflections between the air-skin interface and the target, as well as between multiple targets and interfaces; however, in our modeling this contribution was not added for simplicity, without losing the validity (exemplifying assumption).

In this configuration, unlike the previous case, the path of the wave undergoes the presence of the second medium, so the calculation of the outward and return paths to and from the target needs to include Snell's law. Specifically, the paths are calculated by considering the following set of equations, with the nomenclature as per Figure 5:

$$\begin{cases} L1 = \sqrt{(x_{antenna\#} - x)^2 + d_{ant_{int}}{}^2} \\ L2 = \sqrt{(x - x_{target})^2 + d_{int_{tar}}{}^2} \\ \theta_1 = \cos^{-1}\left(d_{ant_{int}}/L1\right) \\ \theta_2 = \sin^{-1}\left((n_1/n_2)\sin(\theta_1)\right) \\ L2 = d_{int_{tar}}/\cos(\theta_2) \end{cases} \quad (2)$$

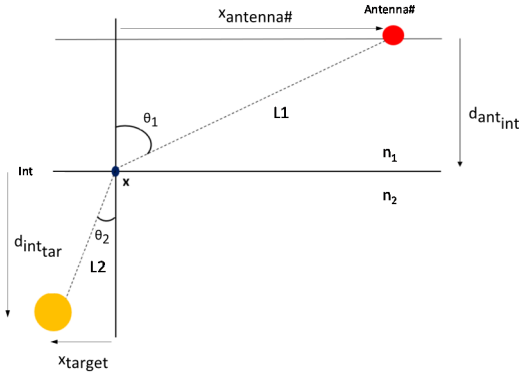


Fig. 5 Schematic drawing for path computation corresponding to one antenna by means of Snell's law.

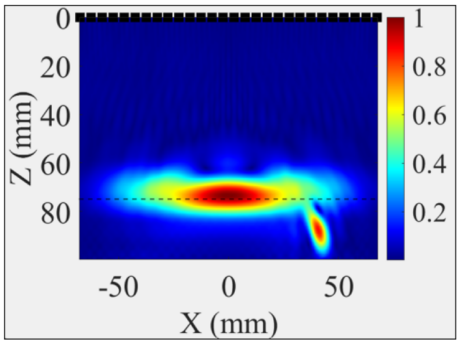


Fig. 6: Normalized DAS image for Case 2, in which the antenna array is in air, while the target in an adipose layer. Black dots indicate the position of the antennas, the black dashed line indicate the interface between air (from z=0 to z= 75 mm) and the adipose layer (from z=75 mm to z= 100 mm).

Downstream of the calculation of the round-trip path to and from the target, equation (1) was used to calculate the scattering matrix corresponding to the target.

The interface, on the other hand, was modeled as a delay matrix with an amplitude dependent on the dielectric characteristics of the skin, using the following equation:

$$S = \Gamma(\lambda^4) e^{-j2\pi f\tau} / {R_t}^2 {R_r}^2 \qquad (3)$$

Where Γ is the reflection coefficient used to model the reflection from the skin, λ is the wavelength, f is the frequency, R_t is the path from the transmitting antenna to the target, R_r is the path from the target to the receiving antenna, and τ is the corresponding round-trip time.

Then, this was added to the target contribution to create the complete matrix (exemplifying assumption). The full scattering matrix was used as input into the Delay-And-Sum beamforming algorithm. The propagation speed used in the image reconstruction in this second scenario was calculated as a weighted average over the two paths through the two media. In the configuration corresponding to Figure 6, the antennas are in air, while the target is immersed in a non-dispersive layer of fat with dielectric properties equal to ε' = 3 and ε " = 0.3 [6]. In this image, both the interface and the target are clearly seen.

D. Case 3: Non-punctiform targets in single and multiple layers

Finally, we tried to reconstruct the scattering matrix related to non-punctiform targets, both in absence and in presence of the interface. Specifically, multiple targets were modeled as a succession of punctiform targets, and the corresponding scattering matrices were summed. Again, for simplicity, we did not model the mutual interaction between targets (exemplifying assumption). To test the robustness of our models against targets at arbitrary positions in the domain of investigation, we modeled the logo of the Microwave Laboratory of the University of Pavia, which in some ways represents a relatively complex target. In Figure 7, its radar image in air is shown.

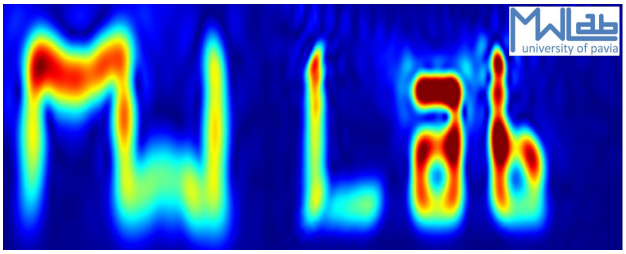


Fig. 7: DAS image of the modeled logo of the Microwave Laboratory of the University of Pavia in air.

IV. Conclusion

In this paper, some of the main results obtained in recent years by the Microwave Laboratory and the Bioengineering Laboratory of the University of Pavia about the study of a new mm-wave imaging system for breast cancer detection have been presented. In addition, we presented for the first time the numerical models we developed to overcome the limitations of full-wave simulations. In this way, even if with some tolerable exemplifying assumptions, it is possible to compute very quickly the scattering matrix corresponding to somehow complex synthetic scenarios, possibly useful not only for the tuning of skin-reflection removal algorithms, but also for the training of artificial neural networks to be used for artificial intelligence purposes, in which it becomes carrier to have a huge amount of data, albeit approximated.

Ultimately, the results obtained show the robustness of the models. This is the starting point for implementing also the mutual interaction between different structures.

References

[1] M. Lazebnik *et al.*, A large-scale study of the ultrawideband microwave dielectric properties of normal, benign and malignant breast tissues obtained from cancer surgeries, *Phys. Med. Biol.*, vol. 52, no. 20, pp. 6093–6115, 2007.

[2] M. Klemm, et al, Radar-based breast cancer detection using a hemispherical antenna array—Experimental results, *IEEE Trans. Antennas Propag.*, vol. 57, no. 6, pp. 1692–1704, Jun. 2009.

[3] T. M. Grzegorczyk, et al, Fast 3-D tomographic microwave imaging for breast cancer detection, *IEEE Trans. Med. Imag.*, vol. 31, no. 8, pp. 1584–1592, Aug. 2012.

[4] E. C. Fear, et al, Microwave breast imaging with a monostatic radar-based system: A study of application to patients, *IEEE Trans. Microw. Theory Techn.*, vol. 61, no. 5, pp. 2119–2128, May 2013.

[5] A. Martellosio, et al, Dielectric properties characterization from 0.5 to 50 GHz of breast cancer tissues, *IEEE Trans. Microw. Theory Techn.*,, Vol. 65, No. 3, pp. 998-1011, March 2017.

[6] S. Di Meo, et al, Dielectric properties of breast tissues: Experimental results up to 50 GHz, 12th European Conference on Antennas and Propagation (EuCAP 2018), London, UK, April 9-13, 2018.

[7] S. Di Meo, et al, Correlation between dielectric properties and women age for breast cancer detection at 30 GHz, 2018 IEEE International Microwave Biomedical Conference (IMBioC), Philadelphia, PA, USA, June 14-15, 2018.

[8] S. Di Meo, et al, On the feasibility of breast cancer imaging systems at millimeter-waves frequencies, *IEEE Trans. Microw. Theory Techn.*, Vol. 65, No. 5, pp. 1795-1806, May 2017.

[9] S. Di Meo, et al, Tissue-mimicking materials for breast phantoms up to 50 GHz, *Phys. Med. Biol.*, Vol. 64, 055006, Feb. 2019.

[10] S. Di Meo, G. Matrone, M. Pasian, Experimental validation on tissue-mimicking phantoms of millimeter-wave imaging for breast cancer detection, Applied Sciences, Vol. 11, No. 1, pp. 432, Jan. 2021.

[11] M. A. Richards, J. A. Scheer, and W. A. Holm, *Principles of Modern Radar: Basic Principles*. Rijeka, Croatia: SciTech, 2010.

[12] M. Lazebnik, E. L. Madsen, G. R. Frank, S. C. Hagness, Tissue-mimicking phantom materials for narrowband and ultrawideband microwave applications, *Phys. Med. Biol.* 50 (2005) 4245-4258. Doi:10.1088/0031-9155/50/18/001.

[13] S. Alshehri, et al., A UWB imaging system to detect early breast cancer in heterogeneous breast phantom, *Int. Conf. Electrical, Control and Computer Engineering*, Pahang, Malaysia, June 21-22, 2011.

mmWave Radars Data Processing for Gait Parameters Extraction

A. Nocera[1], F. Verdini[1], S. Fioretti[1], G. Ciattaglia[1], M. Raimondi[1], L. Burattini[1], L. Senigagliesi[1] and E. Gambi[1]
[1] *Marche Polytechnic University, Dept. of Information Engineering, Ancona, ITALY*

***Abstract*—A person's mobility can be examined to learn vital details about their health.Non-contact technology can be used for this investigation with the aim of ensuring freedom of movement of the subject and realistic analysis of movement. Automotive mmWaves radars, while made for different uses, are a powerful low-cost technology for detecting human movement without physical contact, which can introduce fascinating implications as an aid to health monitoring at home or at work. This paper shows how to process the data recorded by commercial radars to extract simple spatio-temporal parameters of people's walking. The processing algorithms provides the cadence, step length and step duration with a good approximation of the true gait parameters.**

***Keywords*—e-health, human gait, mmWave radar.**

I. INTRODUCTION

Under the broad umbrella of *e-health* [1], contactless monitoring of vital parameters aims at becoming a viable substitute for traditional methods, which often employ cumbersome and inconvenient sensors on the human body. On the other hand the advantage of non-contact methods is precisely to provide an unobtrusive measurement of different subjects' conditions.

The human gait provides useful information about a person's health status and its applications are numerous, such as clinical gait characterization for pathological disorders, automated person detection for security purposes, and even biometric identification [2]. Among the different contactless technologies, radars have attracted the attention of the scientific community thanks to their precision and versatility applied to the medical field. Examples include the remote monitoring of heart rate and respiratory frequency [3], the measurement of people's velocity and gait style [4] and the identification of different parts of the human body [5]. Furthermore, Continuous Wave (CW) radar are applied to acquire general gait parameters, as the speed of the torso, the step duration and the step asymmetry [6], or even more precisely the linear velocity of the single joint by making the subject walk on a treadmill and thus removing the main Doppler component given by the torso velocity [7]. In this paper we employ an automotive frequency Modulated Continuous Wave (FMCW) radar with the aim of extracting cadence, step length and step duration from the normal gait of one subject. We exploit radar bi-dimensional maps, which are related to range (distance) or Doppler signal (velocity) across time. Different algorithms are compared for the extraction of micro-Doppler signature envelopes which are related to the movement of limbs. The results are compared to the same parameters extracted from a motion capture system representing the gold standard. By adding the range information, our approach allows to directly compute the step lengths, differently from the CW radars used in the literature [6], [7], which allow only Doppler-time information to be extracted and thus to calculate the step length indirectly, using the estimated average velocity and step duration.

II. EXPERIMENTAL SETUP

The radar here employed is the Texas Instruments AWR 1642 [8] shown in Figure 1. It works in the frequency range between 77 and 81 GHz in FMCW mode, transmitting a chirp signal with a frequency that is linearly modulated in time. The chirps are sampled at a sampling frequency of 10 MHz for a total of 512 samples per chirps and the total time occupied by a single chirp is set to 0.16 ms. The chirps are grouped into 128 to form a frame lasting a 'periodicity' of 25 ms. Thus, the total chirp time is 81.92% of the periodicity to give the device time for the processing of the the chirp signals. 400 frames are collected, with a total acquisition time of 10 s. The slope is set up to 60.012e12 Hz/s, leading to a bandwidth of 3.6 GHz. The choice of the mentioned radar parameters is the same of [4], where the same radar was comprehensively tested for gait pattern analysis and classification.

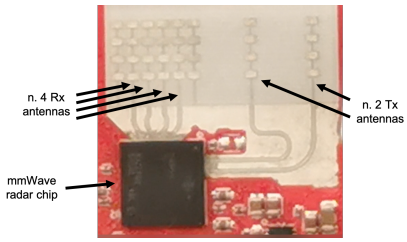


Fig. 1: mmWave radar component with antennas.

During the experimental tests, one subject was asked to walk on a straight path in a radial direction with respect to the radar for three trials, including both a motion towards the radar and a motion away from the radar. The reason we choose a radial walking direction is because the radial velocity components are the ones that produces the best frequency response. A diagonal or even perpendicular walk with respect to the radial direction of the radar will produce a decreased Doppler signal, because a smaller portion of the velocity of the limbs and torso is in the radial direction to the radar [9]. The three trials correspond to three slightly different experimental setups:

1) in trial 1 (T1) the subject starts at about 5 meters from the radar and walks towards the radar and then back;
2) in trial 2 (T2), the subject starts near to the radar, walks away for about 4 meters and came back;
3) in trial 3 (T3), the subject repeats the instructions given in trial 2 but with the hands in the pockets.

The rationale behind the choice of the first two experimental setup is given by the greater attenuation of the signal received by the radar as the subject is far away from the radar, therefore in the first trial we are going to see the subject and its steps with increased clarity as it proceed towards the radar, whereas the opposite is true for the second trial. In the third trial, we decided to remove the movement of the upper limbs, which contribute to the micro-Doppler signature extracted from the radar to understand if this is a way to increase the accuracy of the parameters extraction. The background environment in absence of subjects is also analysed in the same way with both range-time and Doppler-time maps. As a ground truth, two retro-reflective markers are placed on both feet at the position of the prominence of the calcaneus and the first metatarsal head (toe). The BTS Bioengineering motion capture system, composed of eight optoelectrical motion cameras, is employed to extract the position of both the markers at a frequency of 250 Hz. The markers define a three-dimensional position in x being the medio-lateral direction, y being the vertical direction and z being the anterior-posterior direction, corresponding to the radial direction to the radar. The vertical trajectory of the calcaneus is used to extract the heel strike event, corresponding to the start of a normal gait. Once the heel strike time points are defined it is possible to derive the steps duration, steps length and cadence of the subject exploiting the anterior-posterior trajectory of the marker positions (see Fig. 2). We examined a total of 13 steps for the first, 11 steps for the second and 12 steps for the third trial. We computed the cadence for each trial as the number of steps divided by the considered time period.

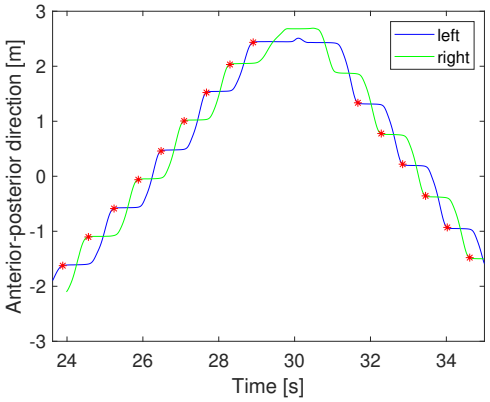


Fig. 2: Movement of both calcanei along the anterior-posterior direction (radial direction to the radar) extracted with the BTS; the red asteriks represent the heel strike time points events. The zero value corresponds to the center of the system of reference considered by the BTS.

III. Radar Data Signal Processing

A. Range-time map and Doppler-time map extraction

The data coming from four receiving antennas are summed together to improve the signal-to-noise ratio. The obtained signal is than reshaped into a three-dimensional configuration following in order the 512 samples, which represents the fast time, then the 128 chirps, representing the slow time, and the 400 frames. For each time frame, a raw matrix of dimension 512x128 is obtained, on which a two-dimensional Fast-Fourier Transform (FFT) is applied to extract the range-Doppler information. The result is a cube of data representing range, Doppler and time information. This cube is then compressed summing the values along the Doppler dimension to obtain a bi-dimensional range-time map (see Fig. 3). In addition, a Doppler-time map is extracted exploiting repeated spectrograms. The original mono-dimensional data extracted from the radar is reshaped into a 512 x 51200 bi-dimensional map. We first apply a FFT along the columns to extract range information and then along the rows a Short Time Fourier Transform, applied to Hamming windows of 128 samples with no overlap between them. The dimension of the obtained spectrograms is 128x400. The resulting 512 spectrograms, one for each range value, are summed to form a bi-dimensional description of Doppler-time evolution of dimension 128x400.

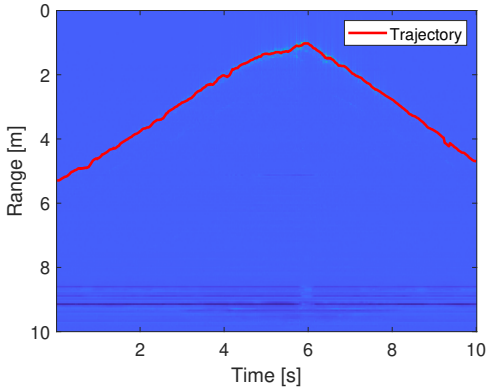


Fig. 3: Range-time map extracted from the first acquisition with the radar.

B. Extraction of torso Doppler envelope

The Doppler-time map is used to extract the torso Doppler envelope and the micro-Doppler envelope, dependent on the torso movement and on the limb movement, respectively. The torso Doppler envelope is extracted by computing the maximum Doppler intensity for each time frame. Then, we convert the torso Doppler values to velocity and the obtained torso velocity envelope was cleaned by removing from the signal derivative spikes values higher than 2g and maintaining the values below, which describe 99.21% of the possible accelerations values at the tested speed, always below 2 m/s [10]. The removed values from the torso velocity were then linearly interpolated using the remaining ones.

Given the torso velocity envelope, we extract the cadence, measured as number of steps per minute, with:

- The application of the FFT on the envelope to extract the higher harmonic, interpreted as the number of steps per seconds, then multiplied by 60 to obtain the cadence.
- The application of a second order butterworth bandpass filter with cutoff frequencies at 0.5 Hz and 2 Hz and the evaluation of the local minima of the torso Doppler envelope, from which the time points of individual steps were extracted. In this case the cadence is calculated as number of steps divided by total step duration.

In addition, the maximum intensity values are extracted from the range-time map to form a range profile curve. The time points corresponding to each step are then transferred to the range-time curve where the corresponding range are computed to extract the step length. We compute the median values and interquartile ranges of the absolute difference of step duration and length with respect to the ground truth. The choice of the median values is justified by the small number of steps analysed and to exclude possible outliers.

C. Extraction of micro-Doppler envelope

The extraction of the micro-Doppler Envelope (microDE) starts with a the application of a threshold to produce a binary map in the Doppler-time. The threshold is chosen according to five different methods:

- The mean Doppler intensity for each time point.
- The 1/100 of the maximum Doppler intensity for each time point [6].
- A two-dimensional Cell-Averaging Constant False Alarm Rate adaptive thresholding technique. A training size of 50 cells and a guard cells size of 10 was used to compute the adaptive threshold.
- A threshold based on the first deviation of the power histogram of the Doppler-time corresponding to the subject with respect to the background.

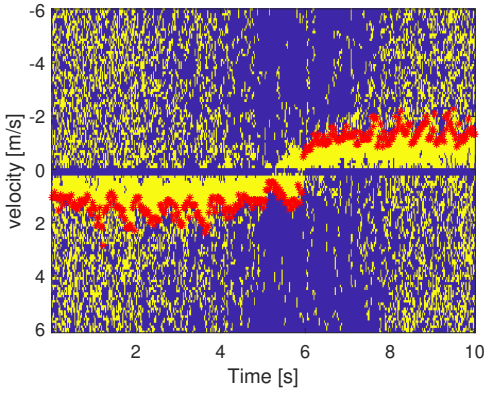


Fig. 4: Example of binary map extracted with a threshold equal to one hundredth of the max intensity of each row. The red asterisks represent the chosen envelope points.

The application of the mentioned threshold enables to create a noisy binary map which is first cleaned by removing the groups of less than two contiguous pixels with value 1 surrounded with background values equal to 0. The MicroDE

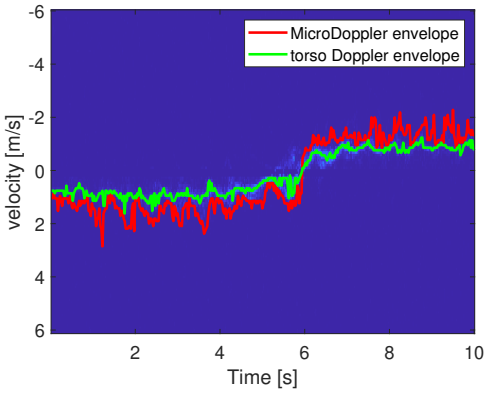


Fig. 5: Velocity-time map with the extracted torso doppler and micro Doppler envelope using the binary map in Figure 4.

is extracted by taking the first variation from 1 to 0 after the torso Doppler value in the positive direction for positive velocity and in the negative direction for negative velocities in each time point of the binary map as can be seen from figure 4 and 5. We apply the same processing on the microDE as explained for the torso Doppler envelope to extract cadence, step duration and length and compare the results with the ground truth.

IV. RESULTS

We now report the results obtained for the different gait parameters considering all the methods discussed in Section III. In the rest of this section, we consider the following notation to indicate the type of extraction process: GT = ground truth from markers; A = torso Doppler envelope; B = microDE from mean Doppler; C = microDE from fraction of the max Doppler; D = microDE from 2D-CFAR; E = microDE from power threshold. The computed cadence for the three trials is 97.9, 105.2 and 110.6, respectively. The results obtained for step length and step duration are compared to the ground truth extracted in a movement lab reporting median absolute error and interquartile ranges in Tables II, III and IV. The results about cadence are reported in Table I, where the numbers in the first column indicate the cadence extraction from one of the two local maxima (1) or first harmonic (2). Each row of the table show the difference (bias) of the cadence extracted from the respective method when compared to the ground truth. Considering all trials, the median absolute error of step length always remains in the centimeter range for method D and E, which is comparable to state-of-art methods for estimating the step length under indoor walking conditions using wearable sensors [11]–[13]. Method A has a median absolute error in the decimeter range for trials 1 and 2 while method B and C have the same magnitude of error for the step length estimation in trial 2. All methods perform well for the step duration estimation, but method B and C are affected by trial configuration 2. Compared with the other methods, D and E seem to be more robust against changes in experimental settings, probably because the thresholds are set according to the noise level of the background environment. Trials 2 and

3 produce the largest difference in cadence from the ground truth, as can be seen in Table I. The major cadence biases for trials 2 and 3 may be caused by the subject's choice of path, as explained in Section II. The reason why the robustness of methods D and E toward the test configuration is not valid for cadence estimation could be due to the observation time limited to 10s. Future approaches should increase the number of steps observed and the time window to report cadence with an higher reliability. A limitation of the proposed method can also be noticed in the last column of Tables II, III, IV, where the number of measured steps is always less than the actual number of steps performed by the subject with the exception of method B and E of Table III. This is probably due to the increasing attenuation of the received signal when the subject is far away from the radar, leading to a loss in the total measured steps.

TABLE I: Bias of each method when comparing the cadence (steps/min) to the BTS.

Method	*cadence T1*	*cadence T2*	*cadence T3*
A1	0.9	-4.0	-7.2
A2	-0.3	9.1	-7.4
B1	-1.1	-2.1	-11.6
B2	-0.1	-5.0	7.0
C1	-0.7	-11.8	-3.0
C2	-0.1	-5.0	-4.4
D1	-1.1	-3.5	-1.5
D2	-0.1	0.4	-7.4
E1	-6.3	-1.7	-1.0
E2	-0.1	-0.2	-7.4

TABLE II: Median Absolute Error (MedAE) with the respective Interquartile ranges of step duration and length for the first trial.

-	*MedAE length (m)*	*MedAE duration(s)*	*N° steps*
A	0.120 (0.029-0.166)	0.040 (0.017-0.062)	10
B	0.052 (0.035-0.088)	0.019 (0.010-0.041)	10
C	0.063 (0.014-0.091)	0.039 (0.017-0.055)	10
D	0.064 (0.049-0.113)	0.048 (0.013-0.089)	10
E	0.053 (0.030-0.110)	0.055 (0.020-0.064)	10

TABLE III: Median Absolute Error (MedAE) with the respective Interquartile ranges of step duration and length for the second trial.

-	*MedAE length (m)*	*MedAE duration(s)*	*N° steps*
A	0.110 (0.025-0.219)	0.090 (0.032-0.115)	10
B	0.143 (0.066-0.201)	0.118 (0.045-0.152)	11
C	0.116 (0.012-0.187)	0.110 (0.033-0.184)	10
D	0.029 (0.008-0.092)	0.027 (0.017-0.052)	10
E	0.044 (0.027-0.122)	0.053 (0.019-0.100)	11

TABLE IV: Median Absolute Error (MedAE) with the respective Interquartile ranges of step duration and length for the third trial.

-	*MedAE length(m)*	*MedAE duration(s)*	*N° steps*
A	0.019 (0.005-0.071)	0.054 (0.06-0.129)	10
B	0.071 (0.026-0.154)	0.072 (0.038-0.097)	9
C	0.059 (0.017-0.079)	0.086 (0.044-0.126)	10
D	0.056 (0.014-0.125)	0.053 (0.021-0.081)	10
E	0.061 (0.050-0.155)	0.046 (0.019-0.081)	10

V. CONCLUSION

In this paper, we studied the contactless extraction of typical parameters from the normal gait of a subject using a commercially available radar sensor. After extracting Doppler-time and range-time maps from raw radar data, the torso Doppler envelope and the micro-Doppler envelopes were derived to obtain the cadence, the step duration and the step length. The proposed methods have proven their effectiveness against the chosen ground truth, with low median absolute errors for step length and step duration and low biases for the cadence. We then demonstrated the feasibility of this contactless structure for the extraction of simple spatio-temporal gait parameters. Future works will include the application of this technique to larger groups of individuals to better validate the results and developing methods to better discriminate the motion of individual joints in order to extract their velocity curve.

ACKNOWLEDGEMENT

The research activity presented in this paper was supported by the financial program DM MiSE 5 Marzo 2018 project "*ChAALenge*" - F/180016/01-05/X43.

REFERENCES

[1] G. Eysenbach *et al.*, "What is e-health?" *Journal of medical Internet research*, vol. 3, no. 2, p. e833, 2001.

[2] J. Geisheimer, W. Marshall, and E. Greneker, "A continuous-wave (CW) radar for gait analysis," in *Conference Record of Thirty-Fifth Asilomar Conference on Signals, Systems and Computers (Cat.No.01CH37256)*, vol. 1, 2001, pp. 834–838 vol.1.

[3] G. Ciattaglia, L. Senigagliesi, A. De Santis, and M. Ricciuti, "Contactless measurement of physiological parameters," in *2019 IEEE 9th International Conference on Consumer Electronics (ICCE-Berlin)*, Sep. 2019, pp. 22–26.

[4] L. Senigagliesi, G. Ciattaglia, A. De Santis, and E. Gambi, "People walking classification using automotive radar," *Electronics*, vol. 9, no. 4, 2020. [Online]. Available: https://www.mdpi.com/2079-9292/9/4/588

[5] P. Held, D. Steinhauser, A. Kamann, T. Holdgrün, I. Doric, A. Koch, and T. Brandmeier, "Radar-based analysis of pedestrian micro-doppler signatures using motion capture sensors," in *2018 IEEE Intelligent Vehicles Symposium (IV)*, June 2018, pp. 787–793.

[6] J. Zhang, "Basic gait analysis based on continuous wave radar," *Gait & Posture*, vol. 36, no. 4, pp. 667–671, 2012.

[7] A.-K. Seifert, M. Grimmer, and A. M. Zoubir, "Doppler radar for the extraction of biomechanical parameters in gait analysis," *IEEE Journal of Biomedical and Health Informatics*, vol. 25, no. 2, pp. 547–558, 2020.

[8] "AWR1642 single-chip 77- and 79-Ghz FMCW radar sensor," (Date last accessed 05-May-2020. [Online]. Available: http://www.ti.com/lit/ds/swrs203a/swrs203a.pdf?\&ts=1588924138717

[9] Z. A. Cammenga, G. E. Smith, and C. J. Baker, "High range resolution micro-doppler analysis," in *Radar Sensor Technology XIX; and Active and Passive Signatures VI*, vol. 9461. SPIE, 2015, pp. 467–477.

[10] M. M. Morrow, W. J. Hurd, E. Fortune, V. Lugade, and K. R. Kaufman, "Accelerations of the waist and lower extremities over a range of gait velocities to aid in activity monitor selection for field-based studies," *Journal of applied biomechanics*, vol. 30, no. 4, pp. 581–585, 2014.

[11] E. Allseits, V. Agrawal, J. Lučarević, R. Gailey, I. Gaunaurd, and C. Bennett, "A practical step length algorithm using lower limb angular velocities," *Journal of biomechanics*, vol. 66, pp. 137–144, 2018.

[12] Z. Yang, L. C. Tran, F. Safaei, A. T. Le, and A. Taparugssanagorn, "Real-time step length estimation in indoor and outdoor scenarios," *Sensors*, vol. 22, no. 21, p. 8472, 2022.

[13] Z. Yang, L. C. Tran, and F. Safaei, "Step length estimation using the rssi method in walking and jogging scenarios," *Sensors*, vol. 22, no. 4, p. 1640, 2022.

Synthesis of ultrasound images from semantic labels with controllable texture features

Francesco Marzola[1], Nens van Alfen[2], Massimo Salvi[1], Jonne Doorduin[2], Kristen M. Meiburger[1]
[1] *Biolab, PolitoBIOMedLab, Department of Electronics and Telecommunications, Politecnico di Torino, Turin, Italy*
[2] *Department of Neurology, Donders Institute for Brain, Cognition and Behaviour, Radboud UMC, Nijmegen, Netherlands*

***Abstract*— Ultrasound imaging is the most accessible technique to study morphology and assess the condition of the neuromuscular system. Deep learning systems have already been developed and successfully applied in several tasks related to ultrasounds. Despite that, all automatic algorithms struggle in dealing with scarcity of data or underrepresented classes in bigger datasets. This study has the purpose of describing a complete pipeline from dataset creation to model validation to reliably generate B-mode ultrasound images. This pipeline is described presenting an application for the semantic guided generation of images of the gastrocnemius medialis muscle. To achieve this goal SPADE (SPatially-Adaptive (DE)normalization) algorithm [1] was applied. 480 images (400 train, 80 test) with a wide range of echogenicity levels in the cross-sectional area of the muscle were used to train and test this approach. On the test set, a PSNR (mean ± st.dev.) of 20.16 ± 0.67 dB and an SSIM of 0.38 ± 0.02 were achieved when giving to the model the original style-label pair as the one in the real dataset. The generated images from the test set were also used as input to a pretrained segmentation model. The resulting output showed a Dice score of 0.862 ± 0.147, closely matching the results using the real images that was 0.867 ± 0.154. In this work, a generic pipeline for applying a semantic guided method for image generation is presented. The developed framework could benefit both automated algorithms for augmenting the datasets and filling the gap in underrepresented classes, as well as clinicians to have a tool for assessing how a certain structure could look with a different texture representation or as a customizable teaching system.**

***Keywords*— GAN, image synthesis, ultrasound, SPADE.**

I. Introduction

Medical imaging has an important role in the assessment of subject conditions. Ultrasound (US) is the most easily accessible method when investigating several body districts such as the neuromuscular system, inner organs, breasts, and many others. In B-mode acquisitions, the echogenicity level is a clear indicator of the condition of the scanned organ. Some examples might be the echogenicity of the Cross-Sectional Area (CSA) of the muscle [2], nodule echogenicity in Thyroid assessment [3], or breast lesion echogenicity [4].

Organs that present an echogenicity or other image features that are correlated with a pathological condition, are a minority in the spectrum of clinical acquisitions and present a challenge for automatic algorithms due to their lower numerosity and reduced contrast with surrounding structures [5]. Having a way to produce synthetic images with controllable texture features could aid the training of down-stream deep learning systems for segmentation and classification by oversampling and better representing the minority classes. The intuition behind the possibility to oversample the minority class without adding redundancy to the dataset derives from the manifold hypothesis for generative models [6][7]. If the model learns a manifold in the solution space where the minority class is represented, we can traverse that manifold to generate realistic looking and semantically correct new samples.

Moreover, generating an image tuning only the texture features maintaining a fixed semantic content, can provide an image of how the same organ would look with a different texture. This possibility can help the physician to envision the possible evolution of the subject condition in time or can support the classification decision providing examples of the same structure at different pathology levels.

In the last years, generative models such as Generative Adversarial Networks (GAN) and more recently Diffusion models have gained importance in the medical field, being applied in several tasks such as super-resolution, conditional generation, image inpainting, and many others [8][9]. One particular model is the SPatially-Adaptive (DE)normalization (SPADE) model [10], a GAN that uses a conditional normalization block to preserve semantic information during the upsampling phase of the generation process. This model was one of the first solutions for semantic guided image synthesis. Other modes that perform the same task adopting similar solutions have been described in [11]-[14]. In medical imaging, this model was already applied in [15] and other examples of semantic guided image synthesis can be found in [16]-[18].

In this work, a generic pipeline for applying a semantic guided method for image generation is presented, and the main contribution is to test the SPADE model in a specific setting, proposing a validation method based on the comparison of the distribution of image features to have a quantitative assessment of model performance on domain specific indicators and performing a task-based validation centered on the automatic segmentation of the CSA.

To test the proposed pipeline, the SPADE model was applied to generate transverse B-mode ultrasound images of the gastrocnemius medialis muscle with controllable echogenicity level in the CSA, and the quality of the generated image was validated using texture features distributions and task-based methods. The final motivation of this work is to develop a tool which could be useful for developing teaching instruments for training physicians and systems to support clinical decisions.

II. Materials and Methods

A. Dataset

The dataset that was used in this work is a subset of the data presented in [1]. The images were acquired since 2003 at the

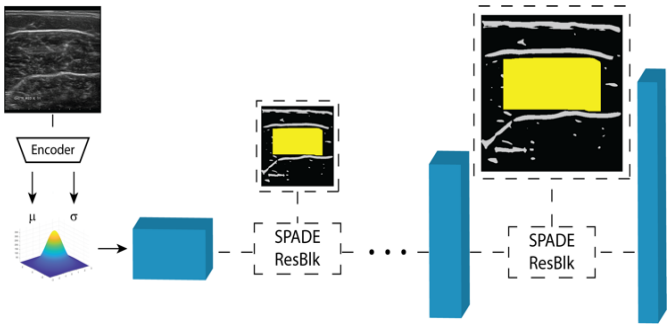


Fig. 1 Architecture of the SPADE generator.

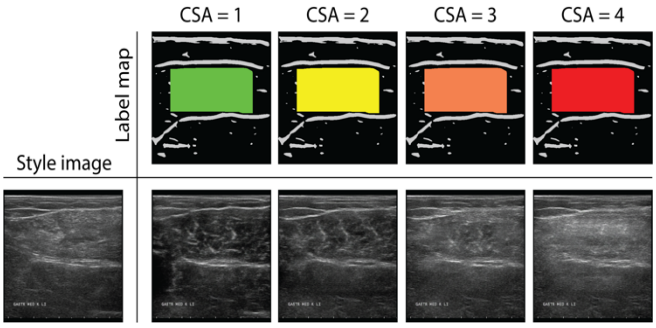


Fig. 2 Model output giving as input the same style image and changing the echogenicity level encoded in the CSA. In the label: background in black, CSA color coded, Frangi mask in light gray.

Radboud University Medical center with a fixed protocol and a convenience sample of 2.5 years of clinical results was taken. Acquisitions and annotations were performed by neurodiagnostic technicians with 5 to 10+ years of experience adopting an Esaote® MyLab Twice (Esaote SpA, Genoa, Italy) device. The probe was a 3–13 MHz linear broadband transducer, acquisition settings were the following: gain 50%, fixed depth of 40 or 60 mm depending on the muscle type, general mid-frequency setting, depth of focus at 40mm, image enhancers off. Data were anonymized so no further approval was requested from the regulatory board.

The semantic map that was fed to SPADE has 6 different labels: 0 for background, 1 to 4 to encode the gray level (i.e., the echogenicity) in the manually defined CSA, and 5 to label highly echogenic structures and especially the aponeuroses when visible. For the latter, these areas were automatically detected by applying the Frangi filter and thresholding its output at 0.4 (range 0-1) after increasing the contrast of the image. For the Frangi filter, the following parameters were used: Scale Range 6 to 9 pixels, Scale Ratio = 0.5, Beta1 = 2, Beta2 = 20. To encode the gray level of the CSA, label 1 was assigned to muscles with a mean gray level below 0.2 (range 0-1), label 2 from 0.2 up to 0.3, label 3 from 0.3 up to 0.4, and label 4 above 0.4. Image labeling can be visualized in Figure 2. We encoded the CSA to have control of its echogenicity level during inference while maintaining the same semantic structure of the image.

The dataset in [1] was sampled to have only images from the GM muscle. 100 images were randomly chosen for each CSA class in the Training set, and 20 images for each class in the Test set, for a total of 480 images. The choice not to use all the available GM images was made to have a balanced dataset, so the overall numerosity was limited by the number of images in the lowest represented class.

B. SPADE model

The official implementation of the SPADE model is available at https://github.com/NVlabs/SPADE under a CC BY-NC-SA 4.0 license. This model has the same Generator-Discriminator architecture usually seen in GANs. It takes two different inputs to decouple the style and the semantic information that it is fed to the generator. The latter takes as input a random vector of length 256 that is then passed through 5 residual SPADE blocks (SPADE ResBlks) up to a resolution of 512x512 pixels. Each ResBlks is a Resnet block, with nearest neighbor upsampling. At each block, the semantic information is input to the network via the SPADE block at the corresponding feature map resolution. This block modulates the activations of the previous layer at a pixel level depending on the label map. The Discriminator is similar to the one in the Pix2PixHD architecture and terminates with a Conv layer as in the Patch-GAN [19].

The Auto-Encoder version of the SPADE model was implemented for this study, hence using an image encoder to produce the noise input to the generator. A visualization of the SPADE generator is available in Fig. 1. More information about the architecture is available in the original paper [10].

The model was trained for 100 epochs, using a batch size of 3 and the Adam optimizer (beta1 = 0.0, beta2=0.9). The learning rate was set to constant to 0.0002 for the first 80 epochs and it decreased linearly to 0 up to epoch 100. Hinge loss and feature matching loss were used as loss functions. Training time was about 8h using a workstation with an RTX 3090 with 24Gb of VRAM.

C. Validation method

Metrics calculation for the validation of the results was performed using Matlab r2020b. To evaluate the quality of the synthetic images, all the images in the training set and the test set were generated every 5 epochs, giving as input the style image and the associated label map. As image quality metrics the 5th percentile for both the subsets for the *Peak Signal to Noise Ratio* (PSNR) and the *Structural Similarity Index Measure* (SSIM) [20] was calculated for each image. Moreover, the Frechet Inception Distance (FID) [21] of the generated training and test set were also calculated.

To validate if the network was able to reproduce a similar texture pattern as in the real dataset, all the first-order images features and four second-order Haralick features (*Contrast, Correlation, Energy, Homogeneity,* averaged for four angles 0°, 45°, 90°, 135°) were calculated. A paired T-test between each feature distribution calculated on the real and the synthetic image was made. Finally, the *Jansen-Shannon divergence* (JS) [22] was computed between the distribution of each feature in the real images and the one in the generated images to have a quantitative assessment of the distance between the real and the generated images.

The Unet model trained in [1] was applied to the Test set images both for the real images, as well for the generated ones. The original label-image pair, so with the CSA label describing the actual echogenicity of the CSA in the real image, was used generate the synthetic images. The results were compared in terms of *Dice* score between the manually defined annotations with the Unet output, using as input both the real images and the generated ones.

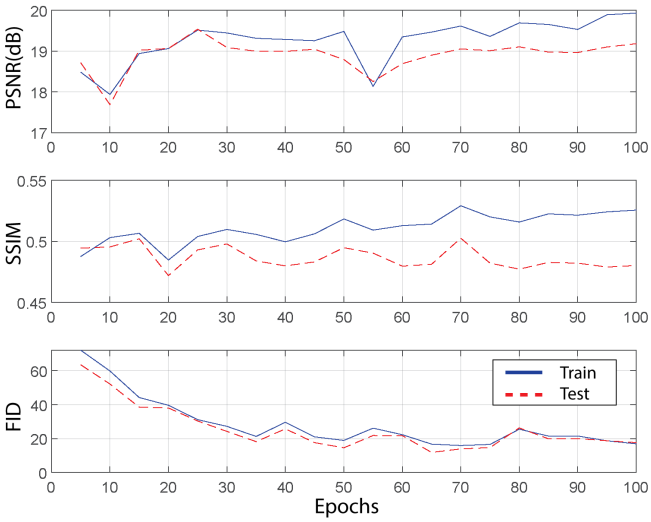


Fig. 3 Image quality indexes of generated images calculated on train (solid blue line) e test (dashed red line) set every 5 epochs. PSNR and SSIM are represented at the 5th percentile.

Finally, to qualitatively test the ability of the network to decouple the *Style* and the *Semantic* information, the ultrasound images were generated fixing the *Style* image and changing the CSA label to encode different echogenicity levels other than the one present in the *Style* image. The generated images with the corresponding inputs are presented in Fig. 2.

III. Results

Image quality assessment results are available in Fig. 3. The graph shows the progress of the 5th percentile of the metrics during training to promote the epochs. Epoch 100 presented the best mean PSNR and SSIM values, and the fourth-best FID, hence it was chosen for the following analysis.

PSNR and SSIM (mean ± st.dev.) on the test set were respectively equal to 20.16 ± 0.67 dB and 0.38 ± 0.02. Comparing FID scores across epochs on the test set shows a pattern like the one on the training set going from a value of 63.49 at epoch 5, to a value of 17.59 at epoch 100.

Table 1 summarizes the results of the JS calculation on the selected epoch (#100) of the train and test sets, along with the mean and standard deviation of every feature both in the real and in the synthesized set of images. Features with no statistical differences in the T-test are displayed in bold.

In the segmentation task, the pretrained Unet was able to adequately segment 100% of the images of the test set. Comparing network output to manual segmentations, the network achieved a Dice of 0.867 ± 0.154 on the real images. Using as input the synthesized images the Dice was 0.862 ± 0.147. To test statistical differences in segmentation performance using the two datasets, we performed a Wilcoxon paired test between the Dice metrics. P-value was 0.11 showing no statistical difference in segmentation performance using real or synthetic images.

IV. Discussion

In this work, a state-of-the-art model for image generation guided by semantic information was applied to muscle ultrasound images. The real images showed a large variability in terms of echogenicity in the CSA and the SPADE model was able to reproduce this reliably considering the whole distribution. Despite that, the difference between the same feature calculated on the real and the synthetic image is still significant for most of the features.

The comparison of feature distribution gives us the information that the SPADE model can reproduce more easily the mean value of a feature but lacks some variability of the real dataset.

Texture features analysis should be one aspect of real to simulated image comparison. The integration of human feedback and comparison of deep-learning generated feature spaces like outputs from a VGG net can give a more complete understanding of the quality and realism of simulated images.

The limitations can be addressed in future work in two main ways. The first is to add a Loss term that penalizes a narrow distribution of image features during training. The second is working on the training data both augmenting the input images or adding some noise in the label definition.
An important result can be visualized in Fig. 2. By changing the label map, the SPADE model can produce images with the same semantic content but with different levels of echogenicity while maintaining image quality across different setups. The semantic segmentation task was successful using the generated images. This result is promising especially when considering SPADE as a tool to improve existing datasets in their overall numerosity where data is scarce, and especially in the underrepresented classes that are often the ones with the worst performance indicators.

There are some limitations to this study. First of all, the choice of the best epoch during training needs to be improved. Our results in Fig.3 show a clear stabilization of the training process in the last epochs, that gives us positive feedback towards the stabilization of the GAN's training process, but there is a clear overfitting of the network. Moreover, we need to validate quantitatively the decoupling of Style and Semantic information and the reproduction of the different echogenicity levels in the CSA and more generally of the texture feature that is discriminant for the subject condition we want to simulate.

V. Conclusion

In this study, we showed a framework to implement and validate a semantic guided image generation method. We tested this pipeline using SPADE algorithm for synthesizing transverse B-mode ultrasound images of Gastrocnemius medialis. We proposed a validation method to quantify the performances of the generative model that incorporates standard image quality metrics used for natural images with domain specific metrics for medical imaging.

As future work, this framework will be tested with more modern models and different datasets comprising different organs and image modalities to investigate the performance in a wider set of tasks. It will also be necessary to improve the quality and variability of generated images and have more control over the objects in the image and their characteristics.

The final goal is to apply the described framework to develop teaching instruments for training physicians and systems to support clinical decisions. The first would be achievable generating new images from scratch, using those as a mean to evaluate the skill of the operator. The latter would be implemented as a smart tool to provide the operator with a spectrum of labelled images given the morphology of the

		Train			Test		
		Real	Synthetic	JS	Real	Synthetic	JS
First order	Mean	0.27 ± 0.05	0.27 ± 0.04	0.024	**0.27 ± 0.04**	**0.27 ± 0.04**	0.023
	St. dev.	0.12 ± 0.01	0.13 ± 0.01	0.024	0.13 ± 0.01	0.12 ± 0.01	0.030
	Entropy	0.31 ± 0.10	0.30 ± 0.10	0.035	0.30 ± 0.09	0.28 ± 0.08	0.045
	Skewness	1.51 ± 0.39	1.35 ± 0.40	0.051	1.58 ± 0.44	1.35 ± 0.41	0.076
	Kurtosis	6.69 ± 1.76	6.53 ± 1.63	0.045	7.12 ± 2.12	6.71 ± 1.65	0.073
Second order	Contrast	**186 ± 20.1**	**186 ± 16.6**	0.032	**182 ± 20.4**	**183 ± 17.5**	0.030
	Correlation	0.94 ± 0.01	0.93 ± 0.01	0.002	**0.93 ± 0.01**	**0.93 ± 0.01**	0.003
	Energy	0.008 ± 0.01	0.004 ± 0.00	0.192	0.007 ± 0.002	0.005 ± 0.00	0.070
	Homogeneity	0.30 ± 0.02	0.29 ± 0.01	0.018	0.31 ± 0.02	0.29 ± 0.01	0.015

Table 1. Comparison of distributions of first and second order features between real and synthetic images. The first two columns mean ± st.dev., third column Jensen-Shannon divergence (0-1 range, lower is better). In bold, comparison between real and synthetic feature distribution with no statistical differences (P > 0.05).

examined subject, hence enabling a similarity-based classification.

ACKNOWLEDGEMENT

No funding was received for conducting this study. The authors have no relevant financial or non-financial interests to disclose.

REFERENCES

[1] Marzola, Francesco; van Alfen, Nens; Doorduin, Jonne; Meiburger, Kristen (2021), "DATASET for "Deep learning segmentation of transverse musculoskeletal ultrasound images for neuromuscular disease assessment"", Mendeley Data, V1, doi: 10.17632/3jykz7wz8d.1

[2] van Alfen, Nens; Gijsbertse, Kajb; de Korte, Chris L.c,d How useful is muscle ultrasound in the diagnostic workup of neuromuscular diseases? Current Opinion in Neurology: October 2018 - Volume 31 - Issue 5 - p 568-574, DOI: 10.1097/WCO.0000000000000589

[3] Chi, J., Walia, E., Babyn, P. et al. Thyroid Nodule Classification in Ultrasound Images by Fine-Tuning Deep Convolutional Neural Network. J Digit Imaging 30, 477–486 (2017). https://doi.org/10.1007/s10278-017-9997-y

[4] Han S, Kang HK, Jeong JY, Park MH, Kim W, Bang WC, Seong YK. A deep learning framework for supporting the classification of breast lesions in ultrasound images. Phys Med Biol. 2017 Sep 15;62(19):7714-7728. doi: 10.1088/1361-6560/aa82ec. PMID: 28753132.

[5] Marzola, F., van Alfen, N., Doorduin, J., & Meiburger, K. M. 2021. Deep learning segmentation of transverse musculoskeletal ultrasound images for neuromuscular disease assessment. Computers in Biology and Medicine, 135(February), 104623. https://doi.org/10.1016/j.compbiomed.2021.104623

[6] Fefferman, Charles, Sanjoy Mitter, and Hariharan Narayanan. "Testing the manifold hypothesis." Journal of the American Mathematical Society 29.4 (2016): 983-1049., http://dx.doi.org/10.1090/jams/852

[7] Na Lei, Dongsheng An, Yang Guo, Kehua Su, Shixia Liu, Zhongxuan Luo, Shing-Tung Yau, Xianfeng Gu, A Geometric Understanding of Deep Learning, Engineering, Volume 6, Issue 3, 2020, Pages 361-374, ISSN 2095-8099, https://doi.org/10.1016/j.eng.2019.09.010.

[8] Singh, N. K., & Raza, K. (2021). Medical image generation using generative adversarial networks: A review. Health informatics: A computational perspective in healthcare, 77-96. doi.org/10.48550/arXiv.2005.10687

[9] Croitoru, Florinel, Hondru, Vlad, Ionescu, Radu T., and Mubarak Shah. "Diffusion Models in Vision: A Survey." ArXiv, (2022). Accessed April 24, 2023. https://doi.org/10.1109/TPAMI.2023.3261988.

[10] Park, T., et al. (2019). Semantic image synthesis with spatially-adaptive normalization. Proceedings of the IEEE Computer Society Conference on Computer Vision and Pattern Recognition, 2019-June, 2332–2341. https://doi.org/10.1109/CVPR.2019.00244

[11] Tan Z, Chen D, Chu Q, Chai M, Liao J, He M, Yuan L, Hua G, Yu N. Efficient Semantic Image Synthesis via Class-Adaptive Normalization. IEEE Trans Pattern Anal Mach Intell. 2022 Sep;44(9):4852-4866. doi: 10.1109/TPAMI.2021.3076487. Epub 2022 Aug 4. PMID: 33914680.

[12] Tan, Zhentao, Chai, Menglei, Chen, Dongdong, Liao, Jing, Chu, Qi, Liu, Bin, Hua, Gang, and Nenghai Yu. "Diverse Semantic Image Synthesis via Probability Distribution Modeling." ArXiv, (2021). doi.org/10.48550/arXiv.2103.06878

[13] Jiang, S., Liu, H., Wu, Y., & Fu, Y. (2019). Spatially constrained generative adversarial networks for conditional image generation. arXiv preprint arXiv:1905.02320. doi.org/10.48550/arXiv.1905.02320

[14] Wang, W., Bao, J., Zhou, W., Chen, D., Chen, D., Yuan, L., & Li, H. (2022). Semantic image synthesis via diffusion models. arXiv preprint arXiv:2207.00050. doi.org/10.48550/arXiv.2207.00050

[15] Abbasi-Sureshjani, S., Amirrajab, S., Lorenz, C., Weese, J., Pluim, J., & Breeuwer, M. (2020). 4D semantic cardiac magnetic resonance image synthesis on XCAT anatomical model. In T. Arbel, I. Ben Ayed, M. de Bruijne, M. Descoteaux, H. Lombaert, & C. Pal (Eds.), Proceedings of the Third Conference on Medical Imaging with Deep Learning (pp. 6-18). (Proceedings of Machine Learning Research; No. 121). PMLR. https://arxiv.org/abs/2002.07089

[16] Tomar, D., Zhang, L., Portenier, T., & Goksel, O. (2021). Content-Preserving Unpaired Translation from Simulated to Realistic Ultrasound Images. In M. de Bruijne, P. C. Cattin, S. Cotin, N. Padoy, S. Speidel, Y. Zheng, & C. Essert (Eds.), Medical Image Computing and Computer Assisted Intervention -- MICCAI 2021 (pp. 659–669). Springer International Publishing. doi.org/10.48550/arXiv.2103.05745

[17] Yu, Z., Xiang, Q., Meng, J., Kou, C., Ren, Q., & Lu, Y. (2019). Retinal image synthesis from multiple-landmarks input with generative adversarial networks. BioMedical Engineering Online, 18(1), 1–15. https://doi.org/10.1186/s12938-019-0682-x

[18] Liang, J., Yang, X., Huang, Y., Li, H., He, S., Hu, X., ... & Ni, D. (2022). Sketch guided and progressive growing GAN for realistic and editable ultrasound image synthesis. Medical Image Analysis, 79, 102461. doi.org/10.48550/arXiv.2204.06929

[19] Wang, T. C.,et al.,(2018). High-Resolution Image Synthesis and Semantic Manipulation with Conditional GANs. Proceedings of the IEEE Computer Society Conference on Computer Vision and Pattern Recognition, https://doi.org/10.1109/CVPR.2018.00917

[20] Z. Wang, A. C. Bovik, H. R. Sheikh, and E. P. Simoncelli, "Image quality assessment: from error visibility to structural similarity," IEEE transactions on image processing, vol. 13, no. 4, pp. 600–612, 2004. 10.1109/tip.2003.819861

[21] D. C. Dowson and B. V. Landau. The Fréchet distance between multivariate normal distributions. Journal of Multivariate Analysis, 12:450–455, 1982. https://doi.org/10.1016/0047-259X(82)90077-X

[22] Lin, J. (1991). Divergence Measures Based on the Shannon Entropy. IEEE Transactions on Information Theory, 37(1), 145–151. https://doi.org/10.1109/18.61115

Myelin quantification in Magnetic Resonance Imaging

E. Lupi[1], M. Gaviraghi[1], S. Rancati[2], F. Palesi[1], F. Grussu[3,4], M. Battiston[3], C. Tur[3,5], A. Calvi[3], S. Collorone[3], A. Ricciardi[3], F. Prados[3,6,7], B. Kanber[3,6], E. D'Angelo[1,8], R. S. Samson[3], and C. AM Gandini Wheeler-Kingshott[1,3,8]

[1]*Department of Brain and Behavioural Sciences, University of Pavia, Pavia, Italy*
[2]*Department of Electrical, Computer and Biomedical Engineering, University of Pavia, Pavia, Italy*
[3] *MR Research Unit, Department of Neuroinflammation, University College London, London, United Kingdom*
[4] *Radiomics Group, Vall d'Hebron Institute of Oncology, Vall d'Hebron Barcelona Hospital Campus, Barcelona, Spain*
[5] *Neurology-Neuroimmunology Department Multiple Sclerosis Centre of Catalonia, Barcelona, Spain*
[6] *Department of Medical Physics and Biomedical Engineering, University College London, London, United Kingdom*
[7] *E-Health Center, Universitat Oberta de Catalunya, Barcelona, Spain,*
[8] *Brain Connectivity Centre, IRCCS Mondino Foundation, Pavia, Italy*

***Abstract*— We can monitor the progression of demyelination by quantifying parameters sensitive to myelin *in vivo* using magnetic resonance imaging (MRI). g-ratio is an index used to monitor the myelin damage; here we developed a method to calculate g-ratio maps from different myelin-sensitive imaging techniques, i.e., quantitative magnetization transfer (qMT), considered as gold standard, and the T1W/T2W ratio. We compared the clinical sensitivity of the two methods, in a cohort of multiple sclerosis (MS) patients. Both approaches showed a similar trend of myelin damage in pathological subjects.**

***Keywords*—myelin, g-ratio, multiple sclerosis.**

I. Introduction

MYELIN is a lamellar structure wrapped around the axons of neurons. Since the presence of myelin significantly increases the conduction speed of the signal along the axon, myelin in essential for the transmission of the neuronal signals [1].

Multiple magnetic resonance imaging (MRI) techniques sensitive to the distribution of myelin and its quantity have been developed over time to analyze myelin *in vivo*. Among these techniques, myelin water imaging (MWI) [2] and magnetization transfer (MT) imaging [3] can be considered the most popular approaches, showing also a high correlation with myelin histological measures [4]. In this study, quantitative magnetization transfer (qMT) [5] and the T1W/T2W ratio [6] were used. Indeed, qMT estimates the magnetization transfer properties of liquid and semisolid components of tissues while T1W/T2W are semi-quantitative myelin-enhanced contrast maps.

g-ratio is an index used to quantify the state of myelin and the signal conduction speed. g-ratio estimates the thickness of the myelin for a certain axon diameter and it is calculated as the ratio between the internal and the external diameter of the myelin sheath.

Myelin thickness is influenced by demyelination and remyelination processes, which impact on the g-ratio values too. In demyelinating diseases such as multiple sclerosis (MS), g-ratio could be used to monitor the evolution of the disease.

In this study we developed an algorithm to obtain g-ratio maps from different imaging techniques and we compared their sensitivity to pathological changes in a cohort of MS patients.

II. Methods

A. MRI acquisition

Data were acquired using a Philips Ingenia 3T scanner. The protocol included: a diffusion weighted (DW) scan using an EPI spin-echo sequence (TR/TE = 6287/96 ms, resolution 2x2x2 mm^3, 3/20/20/36 DW images with b-value = 0/1000/2000/2800 s/mm^2), a high-resolution anatomical T1W 3D scan (TR/TE/TI = 6.9/3.1/810 ms, resolution 1x1x1 mm^3, flip angle = 8°) and a qMT sequence (TR/TE = 7626/59 ms, resolution 2x2x2 mm^3, 10 MT weighted and 2 reference images).

B. Subjects

59 subjects were analyzed, of which 17 healthy controls (HC; 13 females, 57±8 years), 3 relapsing-remitting MS (RRMS; 1 female, 64±3 years), 7 primary progressive MS (PPMS; 2 females, 61±4 years) and 32 secondary progressive MS (SPMS; 21 females, 56±6 years).

C. Images processing

To compute g-ratio maps both magnetization transfer and microstructural data were combined, therefore two different models were applied to different MRI images.

We pre-processed the acquired images to reduce noise and remove artefacts. Then, we processed qMT images using a two-compartment model of white matter (WM), where the hydrogen nuclei can be modeled as bounded to macromolecules or as free water protons. We obtained from these images the bound pool fraction (BPF) maps calculated as the fraction of hydrogen nuclei bounded to macromolecules [7].

Further to achieve microstructural features, the Neurite Orientation Dispersion and Density Imaging (NODDI) model was applied to obtain the isotropic volume fraction (v_{iso}) and intra-cellular volume fraction (v_{ic}) maps (Dmipy, https://nbviewer.jupyter.org/github/AthenaEPI/dmipy/) [8]. The NODDI model is a three-compartment model where each compartment (i.e., intracellular, extracellular and CSF) is associated with a different diffusion model and it is used to

estimate *in vivo* the microstructure of neurons [9].

D. g-ratio calculation from qMT

MRI-derived metrics, such as the Myelin Volume Fraction (MVF) and the Fiber Volume Fraction (FVF) [10], can be used to calculate the g-ratio *in vivo*.

$$\text{g-ratio} = \sqrt{1 - \frac{MVF}{FVF}} \qquad (1)$$

where $FVF = MVF + (1 - MVF)(1 - v_{iso})v_{ic}$ [11].

The MVF was calculated from the BPF maps and we assumed the g-ratio maps calculated from qMT as the gold standard.

$$MVF = k\,BPF \qquad (2)$$

The constant of proportionality k was estimated from the specific dataset by setting the mean g-ratio value in the forceps major to be equal to 0.7 [12] for 5 HC. The obtained k value was applied to all subjects to calculate g-ratio maps from qMT, called gratio_qMT (Figure 1).

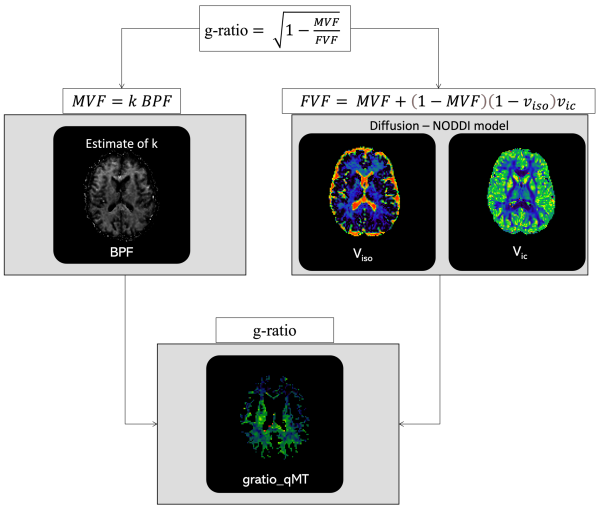


Fig. 1: pipeline for the g-ratio calculation from quantitative magnetization transfer (qMT). To calculate the Myelin Volume Fraction (MVF), the constant k for the Bound Pool Fraction (BPF) is estimated. The Fiber Volume Fraction (FVF) is calculated from v_{iso} and v_{ic} of the Neurite Orientation Dispersion and Density Imaging (NODDI) model. g-ratio maps are then obtained from MVF and FVF.

E. g-ratio calculation from T1W/T2W

We developed an innovative way to calculate the MVF, and consequently the g-ratio, from the T1W/T2W ratio. The Ganzetti method (MRtool, [6][13]) was used to obtain the T1W/T2W maps. The DW volume with b-value=0 was used as T2W input.

The existence of a significant relationship between the T1W/T2W ratio and BPF was examined in all the voxel belonging to the corpus callosum (CC). After checking for the presence of a linear relationship between T1W/T2W and BPF, parameters α and β were obtained from a linear regression model. MVF was calculated from the Eq. (3) (Figure 2).

$$MVF = \alpha \frac{T1W}{T2W} - \beta \qquad (3)$$

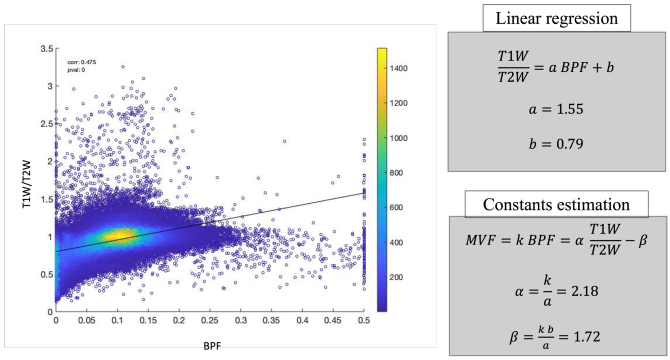


Fig. 2: on the left the linear regression line plotted on all BPF and T1W/T2W data in the corpus callosum. On the right the steps to obtain the constants α and β and the formula to calculate the Myelin Volume Fraction (MVF).

It was thus possible to calculate the map of the g-ratio, called gratio_t1wt2w (Figure 3).

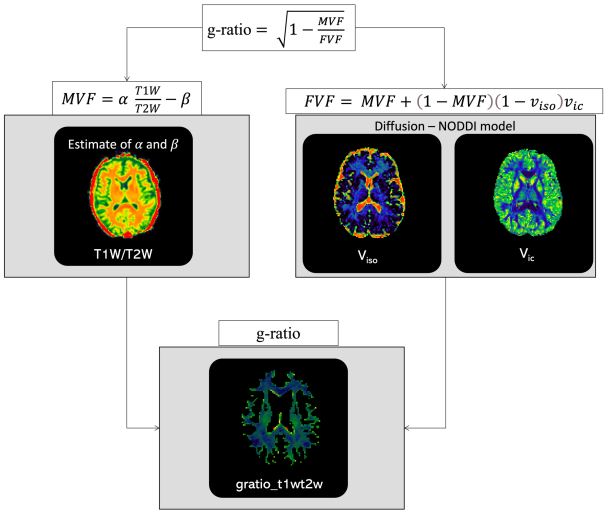


Fig. 3: pipeline for the g-ratio calculation from T1W/T2W ratio. To calculate the Myelin Volume Fraction (MVF), the constants α and β for the T1W/T2W are estimated. The Fiber Volume Fraction (FVF) is calculated from v_{iso} and v_{ic} of the Neurite Orientation Dispersion and Density Imaging (NODDI) model. g-ratio maps are then obtained from MVF and FVF.

F. Statistics

The g-ratio maps obtained with the two different approaches were compared within-subject for each of the 59 subjects. Since the non-normality of the data was verified, a Mann-Whitney U-test was performed to compare the g-ratio values of all voxels belonging to the CC.

The clinical sensitivity of the two g-ratio maps was evaluated performing a Mann-Whitney U-test between groups (i.e. HC, PPMS and SPMS). Due to the small sample size, the RRMS patients were not taken into consideration. The statistical evaluation was performed using mean values of the g-ratio in the following regions: WM, CC, and left and right optic radiations (OR_L, OR_R).

Since the small size of the groups, all of these test were performed without corrections for multiple comparisons.

III. Results

The mean value of k resulted 3.39, while α and β were respectively 2.18 and 1.72.

Figure 4 shows voxel-wise maps of the mean g-ratio in white matter obtained with the two methods across all HC subjects.

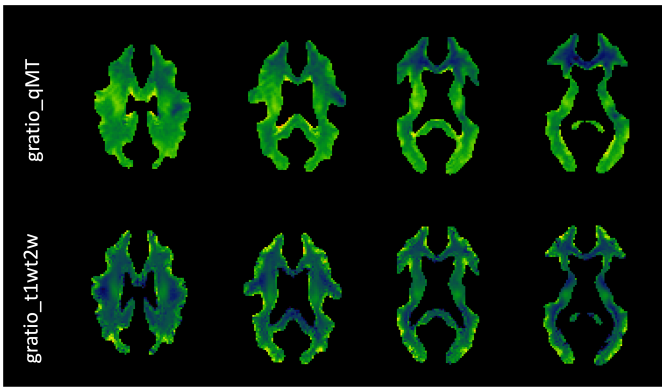


Fig. 4: Multiple axial slices (from head-to-feet) of the mean g-ratio in white matter across all HC subjects. The first row shows the g-ratio obtained from quantitative magnetization transfer (qMT), the second from T1W/T2W ratio.

From figure 4 gratio_qMT and gratio_t1wt2w maps seem to be different. According to this qualitative evaluation, Mann-Whitney U-test demonstrated that gratio_qMT and gratio_t1wt2w were statistically different ($p<0.05$).

Only the gratio_qMT showed significant differences ($p<0.05$) between groups in all the regions of interest (Figure 5).

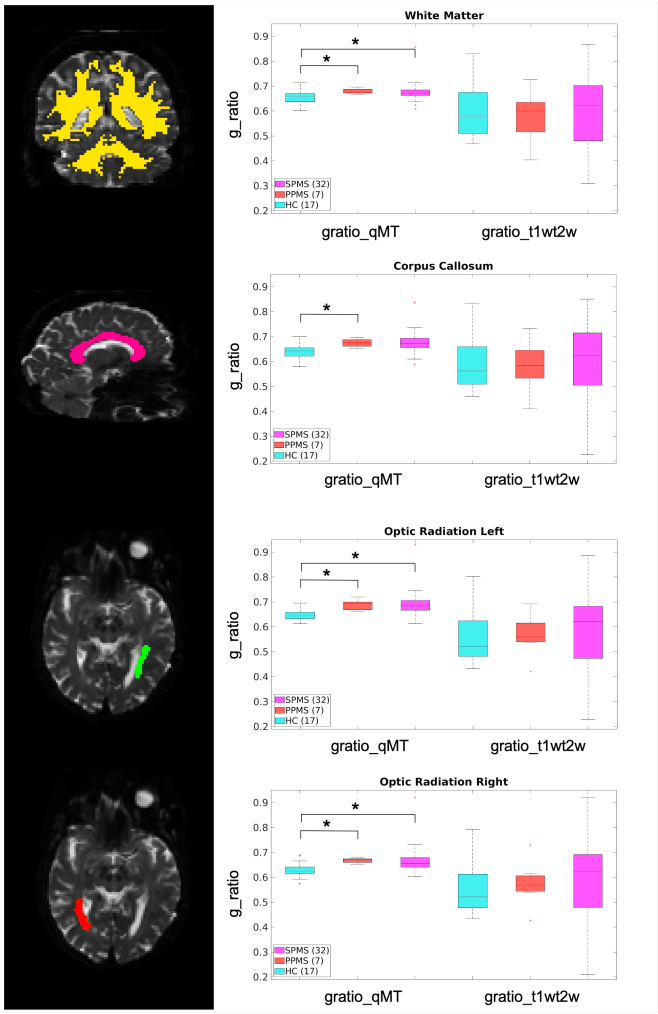


Fig. 5: boxplot of the mean g-ratio for the three groups investigated; the groups and the number of subjects per group are indicated in the legend (Healthy Controls: HC, Primary Progressive Multiple Sclerosis: PPMS, Secondary Progressive Multiple Sclerosis: SPMS). For each group, the mean value of the g-ratio is calculated in the following regions: white matter, corpus callosum, left and right optic radiations. The segmented regions are represented on the left. The asterisk indicates significant differences.

IV. Discussion and Conclusion

According to our findings, there was a difference between the values of gratio_qMT and gratio_t1wt2w. The main cause could be intrinsic to the nature of T1W/T2W images: indeed, T1W/T2W are semi-quantitative maps that are sensitive not only to the state of myelin but also to other pathological conditions, like edema and inflammation. The use of sub-optimal T2W images is another limitation of the gratio_t1wt2w maps.

Moreover, the gratio_qMT maps showed significant differences between HC and MS subjects, which were not replicated by gratio_t1wt2w - the gratio_t1wt2w maintained a similar trend of medians between groups but with a very large standard deviation of values that compromised statistical power (Figure 5). Overall, calculating a g-ratio map with the best available method could help detecting myelin damage in pathological subjects, highlighting progressive demyelination in patients with advancing MS. Therefore, g-ratio mapping might provide an additional tool to investigate the progression of demyelinating diseases and to evaluate pharmacological approaches to promote remyelination.

In this study we estimated the constant of proportionality k to obtain g-ratio maps from qMT; furthermore we developed a method to calculate g-ratio maps from T1W/T2W, starting from clinical images such as T1W and T2W. Future works can investigate the improvement of this method by using optimal T1W and T2W maps (<1 mm) in particular to see whether the large standard deviation is attributed to the sub-optimal T2W images used here. Finally, gratio_qMT displays a visible difference between the g-ratio of the frontal lobe and the occipital lobe, not seen in gratio_t1wt2w (Figure 4). Given recent publications on the whole brain connectivity, it remains to be determined whether this is biologically plausible and related to a different fiber density in different hemispheres.

Acknowledgement

Data were collected as part of a study funded by the MS Society grant #77 awarded to CWK and RS. RS has received research funding from the UK MS Society (grant #77), CureDRPLA and Ataxia UK & we thank the UCL-UCLH Biomedical Research Centre for ongoing support. CGWK receives funding from Horizon2020 (Human Brain Project SGA3, Specific Grant Agreement No. 945539), BRC (#BRC704/CAP/CGW), MRC (#MR/S026088/1), Ataxia UK, MS Society (#77), Wings for Life (#169111). CGWK is a shareholder in Queen Square Analytics Ltd. C. Tur is currently being funded by a Junior Leader La Caixa Fellowship (fellowship code is LCF/BQ/PI20/11760008), awarded by “la Caixa” Foundation (ID 100010434). She has also received the 2021 Merck’s Award for the Investigation in MS, awarded by

Fundación Merck Salud (Spain) and a grant awarded by the Instituto de Salud Carlos III (ISCIII), Ministerio de Ciencia e Innovación de España (PI21/01860). In 2015, she received an ECTRIMS Post-doctoral Research Fellowship and has received funding from the UK MS Society. She is a member of the Editorial Board of Neurology. She has also received honoraria from Roche and Novartis and is a steering committee member of the O'HAND trial and of the Consensus group on Follow-on DMTs. ED and FP receive funding from H2020 Research and Innovation Action Grants Human Brain Project (#785907, SGA2 and #945539, SGA3). ED receives funding from the MNL Project "Local Neuronal Microcircuits" of the Centro Fermi (Rome, Italy). FP and AR receive funding from Horizon2020 (#634541). FG receives the support of a fellowship from "la Caixa" Foundation (ID 100010434). The fellowship code is "LCF/BQ/PR22/11920010". AC is supported by the ECTRIMS post-doc fellowship (2022), previously received a UK MS Society PhD studentship (2020), a Guarantors of Brain "Entry" clinical fellowship (2019), and an ECTRIMS-MAGNIMS fellowship (2018). Eleonora Lupi is a PhD student enrolled in the National PhD in Artificial Intelligence, XXXVIII cycle, course on Health and life sciences, organized by Università Campus Bio-Medico di Roma.

REFERENCES

[1] J. Lee, «So You Want to Image Myelin Using MRI: An Overview and Practical Guide for Myelin Water Imaging,» *Journal of Magnetic Resonance Imaging,* pp. 360-373, 2021.

[2] Mackay, A., Whittall, K., Adler, J., Li, D., Paty, D. and Graeb, D. «*In vivo* visualization of myelin water in brain by magnetic resonance.» *Magn. Reson. Med.,* vol. 31, pp. 673-677, 1994.

[3] Wolff, S.D. and Balaban, R.S., «Magnetization transfer contrast (MTC) and tissue water proton relaxation *in vivo*. » *Magn. Reson. Med.,* vol. 10, pp. 135-144, 1989

[4] M. Mancini, A. Karakuzu, J. Cohen-Adad, M. Cercignani, T. E. Nichols e N. Stikov, «An interactive meta-analysis of MRI biomarkers of myelin,» *eLife,* 2020.

[5] D. F. Gochberg e J. C. Gore, «Quantitative Magnetization Transfer Imaging via Selective Inversion Recovery With Short Repetition Times,» *Magnetic Resonance in Medicine,* vol. 57, p. 437–441, 2007.

[6] M. Ganzetti, N. Wenderoth e D. Mantini, «Mapping pathological changes in brain structure by combining T1- and T2-weighted MR imaging data,» *Neuroradiology,* vol. 57, p. 917–928, 2015.

[7] M. Battiston, T. Schneider, F. Grussu, M. C. Yiannakas, F. Prados, C. A. M. G. Wheeler-Kingshott, F. D. Angelis e R. S. Samson, «Fast bound pool fraction mapping via steady-state magnetization transfer saturation using single-shot EPI,» *Magnetic Resonance in Medicine,* vol. 82, n. 3, pp. 1025- 1040, 2019.

[8] L. H. Fick Rutger, W. Demian e D. Rachid, «The Dmipy Toolbox: Diffusion MRI Multi-Compartment Modeling and Microstructure Recovery Made Easy,» *Frontiers in Neuroinformatics,* vol. 13, 2019.

[9] H. Zhang, T. Schneider, C. A. Wheeler-Kingshott e D. C. Alexander, «NODDI: Practical in vivo neurite orientation dispersion and density imaging of the human brain,» *NeuroImage,* vol. 61, n. 4, pp. 1000-1016, 2012.

[10] N. Stikov, J. S. Campbell, T. Stroh, M. Lavelée, S. Frey, J. Novek, S. Nuara, M.-K. Ho, B. J. Bedell, R. F. Dougherty, I. R. Leppert, M. Boudreau e S. Narayanan, «In vivo histology of the myelin g-ratio with magnetic resonance imaging,» *NeuroImage,* vol. 118, p. 397–405, 2015.

[11] A. Stecco e A. Ragozzino, L'essenziale nell'imaging RM di diffusione, 2011.

[12] M. Cercignani, G. Giulietti, N. G. Dowell, M. Gabel, R. Broad, P. N. Leigh, N. A. Harrison e M. Bozzali, «Characterizing axonal myelination within the healthy population: a tract-by-tract mapping of effects of age and gender on the fiber g-ratio,» *Neurobiology of Aging,* vol. 49, pp. 109-118, 2017.

[13] S. Nerland, K. N. Jørgensen, W. Nordhøy, I. I. Maximov, R. A. Bugge, L. T. Westlye, O. A. Andreassen, O. M. Geier e I. Agartz, «Multisite reproducibility and test-retest reliability of the T1w/T2w-ratio: A comparison of processing methods,» *Neuroimage,* vol. 245, 2021.

Automated quantification of FDOPA PET using XNAT

G. Nordio[1], R. Easmin[1], A. Giacomel[1], O. Dipasquale[1], D. Martins[1], A. Schiulaz[4], S. Williams[1], F. Turkheimer[1], O. Howes[2,3] and M. Veronese[1,4]

[1] *Department of Neuroimaging, Institute of Psychiatry, Psychology & Neuroscience, King's College London, London, United Kingdom*

[2] *Department of Psychosis Studies, Institute of Psychiatry, Psychology & Neuroscience, King's College London, London, United Kingdom*

[3] *MRC London Institute of Medical Sciences, Hammersmith Hospital, London*

[4] *Department of Information Engineering, University of Padua, Italy*

***Abstract*— In this study we evaluate the performance of a fully automated analytical framework for FDOPA PET neuroimaging data, and its sensitivity to demographic and experimental variables.**

An instance of XNAT imaging platform was used to store the King's College London institutional brain FDOPA PET imaging archive, alongside individual demographics and clinical information. By re-engineering the historical Matlab-based scripts for FDOPA PET analysis, a fully automated analysis pipeline for imaging processing and data quantification was implemented in Python and integrated in XNAT.

We found good reproducibility of the data analysis by the automated pipeline (for the controls ICC=0.71, for the psychotic patients ICC=0.88). From the demographic and experimental variables assessed, gender was found to most influence striatal dopamine synthesis capacity ($F=10.7$, $p<0.001$), with women showing greater dopamine synthesis capacity than men.

Our automated analysis pipeline represents a valid recourse for standardized and robust quantification of dopamine synthesis capacity using FDOPA PET data. Combining information from different neuroimaging studies has allowed us to test it comprehensively and to validate its replicability and reproducibility performances on a large sample size.

***Keywords* — FDOPA PET, data analysis pipeline, neuroimaging biomarker, big data repository.**

I. Introduction

POSITRON emission tomography (PET), in combination with the 6-[18F]fluoro-L-dopa (FDOPA) radiolabelled tracer, has been extensively used to image the dopamine system in vivo in living human brain [1].

The tracer was introduced in 1983 [2] to quantify the integrity of the nigrostriatal dopamine and it found immediate application in subclinical models of dopamine neuronal damage and in Parkinson's Disease (PD) studies [3], [4]. Besides PD and dopaminergic neurodegeneration, FDOPA PET has proved to be valuable in other medical specialties. In psychiatry, FDOPA PET has been extensively used to quantify the dopamine system in the pathophysiology of psychotic and other symptoms across conditions, including schizophrenia [5], [6]. Several lines of evidence have linked FDOPA PET to treatment response in psychosis [7]–[10] suggesting that it might be used as a neurochemical basis to discriminate between patients likely to respond and those unlikely to respond to first-line antipsychotic drugs [11].

However, to reach clinical translation, FDOPA PET would require further validation on larger clinical datasets, aiming to support future individualized treatment and patient stratification across the different brain diseases, together with a suitable data infrastructure and robust analytical protocols to ensure high quality of the data, accurate quantification, and replicable results.

This study aims to present and validate a new infrastructure for automated analysis of FDOPA PET neuroimaging, designed with the aspiration to provide a robust benchmark for the analysis of PET data acquired with this radiotracer, facilitating FDOPA PET imaging implementation across sites and research institutions. The project takes advantage of a large FDOPA PET data repository available at the Institute of Psychiatry Psychology and Neuroscience (IoPPN) at King's College London that has been exploited to test analysis pipeline replicability and reproducibility, as well as its sensitivity to experimental and demographic covariates.

II. Methods

A. FDOPA PET data acquisition

All FDOPA PET imaging sessions in the database were acquired with a continuous dynamic acquisition (no blood sampling), with scanning beginning with the tracer injection and lasting for 90-95 minutes. All participants received carbidopa (150 mg) and entacapone (400 mg) orally ~1 hour before imaging. The FDOPA tracer (injected dose ranging from 86.4 to 414.4 MBq) was administered by intravenous bolus injection after the acquisition of a brain CT or MRI for attenuation correction, depending on the scanner availability at each imaging site. PET data reconstruction varied across imaging sites and scanner types, but all included correction for random noise, scatter, and tissue attenuation.

All the research protocols for data acquisitions were approved by local ethics committees and institutional revision boards. Informed written consent was obtained for all the participants and the studies were conducted following the Declaration of Helsinki and Good Clinical Practice.

B. Data management infrastructure

A bespoken installation of XNAT imaging technology platform [12] was deployed using the Neuroimaging Analysis Network at the Centre for Neuroimaging Sciences (King's College London) to store for each subject's demographic,

clinical information and FDOPA PET imaging data. Representational State Transfer (REST) Application-Program Interface (API) was used to upload data. Prior to storage in XNAT, the data were anonymized, harmonized in neurological convention, and corrected for radioisotope decay to ensure consistency across the data.
Analytical pipelines were integrated in XNAT, allowing their automatic execution directly on the stored data and the storage of the outcomes at scan level.

C. Automated analysis pipeline

The analysis pipeline was developed to align with our previous FDOPA imaging studies published by the Psychiatric Imaging Group (King's College London) over the last two decades [13]–[19]. The analysis of FDOPA PET imaging data was performed in MATLAB (Mathworks) and it can be described as follows. First, dynamically non-attenuated and attenuated FDOPA PET images are inputted into the pipeline. The non-attenuated dynamic images are motion corrected frame-to-frame to a single reference frame with a linear transformation using Statistical Parametric Mapping (SPM) realign function [20]. The motion information is then used to realign the attenuated dynamic images, which are then summed together to create a motion-corrected individual static PET image. A tracer-specific template and atlas defining the striatum and cerebellum are co-registered to each individual motion-correct static PET image, using SPM 12 (https://www.fil.ion.ucl.ac.uk/spm/). The Gjedde-Patlak Graphical approach [21], [22], with the cerebellum as reference region, is applied region-wise and voxel-wise to quantify Ki^{cer} (unit 1/min), a kinetic parameter used as a proxy of dopamine synthesis capacity [23]. The parametric image for each scan is finally normalised into MNI standard coordinates using the participant's PET summation image to calculate the image transformation field (non-linear transformation). The Standardized Uptake Value Ratio (SUVr) is also calculated as ratio of the tracer activity to that in the reference region. The interval 60-75 min after the injection of the radiotracer is used for this analysis, since in this time window the Gjedde-Patlak plot is linear and used to derive Ki^{cer} [11], [23].

Starting from the available MATLAB code, a fully automated version of this analysis pipeline was written in Python and integrated in XNAT.

D. Validation of the automated data analysis pipeline for FDOPA PET quantification

All the historical FDOPA scans were automatically re-analyzed using the XNAT-based pipeline. A total sample of 521 scans was used to evaluate agreement between XNAT-based and the already available MATLAB-based results, using the same analysis settings.

Data from two independent different datasets were used to test XNAT-based pipeline reproducibility. The first dataset comprised FDOPA PET test-retest imaging data from 7 healthy controls, dynamically acquired using an ECAT/EXACT3D: Siemens/CTI (Knoxville, Tennessee) PET tomograph. Full details of the research protocol and subject inclusion criteria are reported in the original reference [17].

The second dataset comprised FDOPA PET imaging data from 7 patients with psychosis before and after placebo, dynamically acquired using a Siemens Hi-Rez Biograph 6 PET scanner (Siemens, Erlangen, Germany) in 3D mode.

E. Identification of experimental and demographical covariates for FDOPA PET imaging

To investigate the presence of potential confounding factors to account in statistical analysis of FDOPA PET imaging data, the baseline scans (no pre-scan intervention) of healthy controls were selected from the database together with their experimental and demographic information. The final sample included 115 scans acquired from 3 different PET tomographs (Siemens Biograph 6 Hi-Rez, Siemens Biograph 6TruePoint, ECAT/EXACT3D) with an injected radioactivity below 200 MBq and acquisition time of 95 minutes. The experimental variables included tomograph type and radiochemistry measures (i.e. injected radioactivity, injected cold mass, specific activity) and the demographic variables included participant gender, age and weight at the time of scanning. A similar analysis was then repeated on a subsample (N=103 scans), where the data were acquired using the Biograph PET tomographs (Siemens Biograph 6 Hi-Rez, Siemens Biograph 6 TruePoint) only.

F. Statistical methods

For statistical analysis, GraphPad Prism v9 for Mac (GraphPad Software, La Jolla, CA) and SPSS (Version 27) were used. The Ki^{cer} estimates obtained from the XNAT and MATLAB analysis pipelines were compared using the Bland-Altman plot with 95% limits of agreement [24]. Correlation and mean absolute percentage difference between the two pipelines were also calculated for the following six regions of interest (ROIs): whole striatum, right striatum, left striatum, whole sensorimotor subdivision, whole limbic subdivision, and whole associative subdivision. These ROIs are commonly the primary areas of analysis in PET imaging dopamine studies [25], [26]. For both XNAT and MATLAB pipelines, test-retest reliability was estimated with the Intraclass Correlation coefficient (ICC) using a 2-way mixed-model in SPSS (version 27, IBM®), while the within-subject variation was calculated as the absolute percentage test-retest difference [17]. A p-value < 0.05 was considered statistically significant.

To investigate the effect of demographic and experimental variables on dopamine measures, a multi-linear regression model analysis was run with the K_i^{cer} and SUVr of the whole striatum as dependent variable and both experimental and demographic variables as covariates.

III. RESULTS

A. Database

The infrastructure included 892 FDOPA PET scans from 23 different studies. After removing commercials studies for which we did not have permission for data reuse, the infrastructure consisted of 792 FDOPA PET scans from 666

individuals (female 33.9%, healthy controls 29.1%) collected from four different imaging sites between 2004-2021.

The Ki^{cer} distributions across the brain are presented in Figure 1. Among the ROIs, the highest estimates were reported in the whole striatum *(Ki^{cer} mean±SD: 0.0137±0.0015 min^{-1}; min-max: 0.0102-0.0246 min^{-1} // SUVr mean±SD: 2.30±0.22; min-max: 1.71-4.11)*. Outside the basal ganglia, the substantia nigra showed the highest signal *(Ki^{cer} mean±SD: 0.0072±0.0012 min^{-1}; min-max: -0.0019-0.0122 min^{-1} // SUVr mean±SD: 1.53±0.15; min-max: 0.82-2.49)* followed by the pallidum, the amygdala, the thalamus and the prefrontal cortex. The occipital lobe, which is sometimes used as reference region for FDOPA PET quantification instead of the cerebellum [27], showed the lowest estimates in ratio to the cerebellum *(Ki^{cer} mean±SD: 0.0005±0.0004 min^{-1}; min-max: -0.0009-0.0041 min^{-1} // SUVr mean±SD: 0.97±0.06; min-max: 0.79-1.72)*.

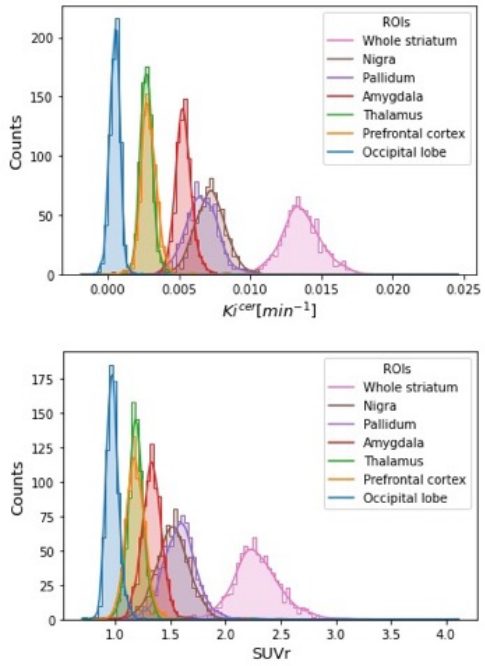


Fig. 1: Distribution of Ki^{cer} (top) and SUVr (bottom) of the main regions of interest.

B. *Validation of the automated data analysis pipeline for FDOPA PET quantification*

There was consistency between the XNAT and MATLAB pipeline, with a Ki^{cer} mean relative difference of 3.0±5.5% and a Pearson's correlation of 0.86. About 71% of the scans reported Ki^{cer} relative differences less than 5%.

In the test-retest datasets, the Bland-Altman plot confirmed good agreement between the XNAT and MATLAB pipelines for all the parameters, levels of analysis, datasets, and regions of interest. In the whole striatum, both XNAT-based Ki^{cer} and SUVr estimates are higher than the corresponding MATLAB ones within 5% mean relative difference (Figure 2). Consistently with the Bland-Altman analysis, XNAT-MATLAB Pearson's correlation ranges from 0.64 to 0.99 for Ki^{cer}, and from 0.79 to 1.00 for SUVr, with the lowest values for the limbic subdivision and the highest for the whole striatum/associative subdivision.

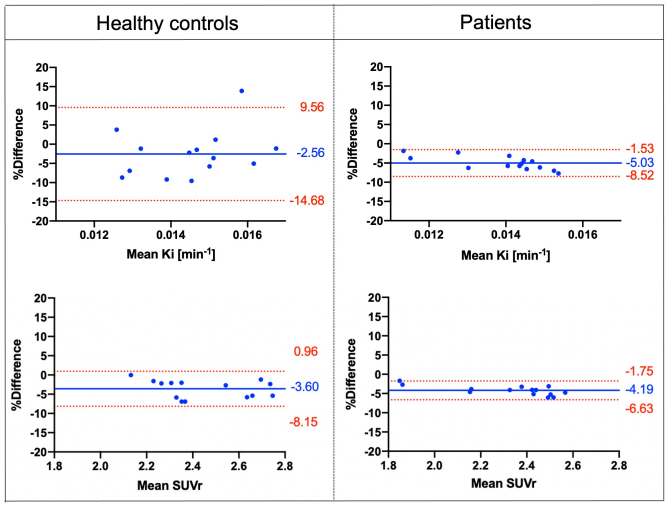


Fig. 2: Bland-Altman plots comparing Ki^{cer} and SUVr estimates of the whole striatum with XNAT-based and Python-based pipelines, both for healthy controls and patients.

In terms of test-retest reliability and within-subject variation, the automated pipeline provided reproducibility and reliability of FDOPA PET in the striatum and its subdivisions comparable to the ones previously described [17]. Averaging the results from healthy controls and patients, the ICC for the Ki^{cer} estimates ranged from 0.421 for the limbic subdivision to 0.810 for the associative subdivision. The %VAR for the Ki^{cer} estimates ranged from 6.1 for the right striatum to 12.3 for the limbic subdivision. For the SUVr, the ICC ranged from 0.865 for the limbic subdivision to 0.965 for the right striatum, while %VAR ranged from 3.0 for the right striatum to 5.1 for the whole limbic subdivision.

C. *Identification of demographical and experimental covariates for FDOPA PET imaging*

There was a significant relationship between gender and striatal Ki^{cer} estimates *($F(1,109)=10.7$, $p<0.001$)*, with dopamine synthesis capacity being higher in women than men (marginal means, women Ki^{cer}: 0.01353±0.00147 min^{-1}, men Ki^{cer}: 0.01270±0.00131 min^{-1}, effect size = 2.056E-5). Age, weight, injected radioactivity, injected cold mass, specific activity and tomograph were not significantly associated with striatal Ki^{cer}. A similar association between FDOPA PET and gender was also found when considering the subsample of scans (N=103) acquired only using the Siemens Biograph tomograph only *($F(1,98)=10$, $p=0.002$,* women Ki^{cer}: 0.01354±0.00145 min^{-1}, men Ki^{cer}: 0.01268±0.00130 min^{-1}). In contrast, none of the experimental and demographic variables were significantly associated with SUVr.

IV. Conclusion

In this study we characterized a standardized infrastructure for FDOPA PET neuroimaging to quantify brain dopamine function in living human brains. The platform was built from a harmonized FDOPA repository, integrating clinical and demographic information, together with FDOPA PET data. To our knowledge, this is the largest dataset of this type to date, including hundreds of scans with a very comparable acquisition protocol. The automated analysis framework for

FDOPA PET quantification, directly embedded in the platform, ensured full control on the analytical process and replicable results on the stored data, confirming the good replicability and reproducibility of the FDOPA PET measures in the striatum and its subdivisions. The proposed robust analytical framework aims to facilitate FDOPA PET imaging implementation across sites and research institutions and to boost the use of FDOPA PET as a clinical biomarker in psychosis and other mental disorders.

ACKNOWLEDGEMENT

This study was funded by Wellcome Trust Digital Award (no. 215747/Z/19/Z) and supported by the National Institute for Health Research Biomedical Research Centre at South London and Maudsley National Health Service Foundation Trust and King's College London. We thank all the members of the FDOPA PET imaging working group for contributing to the data collection: Sameer Jauhar, Rogdaki Maria, Robert McCutcheon, Stephen Kaar, Luke Vano, Grazia Rutigliano, Ilinca Angelescu, Faith Borgan, Enrico D'Ambrosio, Tarik Dahoun, Euitae Kim, Seoyoung Kim, Micheal Bloomfield, Alice Egerton, Arsime Demjaha, Ilaria Bonoldi, Chiara Nosarti, James Maccabe, Philip McGuire, Julian Matthews, Peter S Talbot.

REFERENCES

[1] M. B. H. Youdim, D. Edmondson, and K. F. Tipton, "The therapeutic potential of monoamine oxidase inhibitors.," *Nat. Rev. Neurosci.*, vol. 7, no. 4, pp. 295–309, Apr. 2006, doi: 10.1038/nrn1883.

[2] E. S. Garnett, G. Firnau, and C. Nahmias, "Dopamine visualized in the basal ganglia of living man.," *Nature*, vol. 305, no. 5930, pp. 137–138, Sep. 1983, doi: 10.1038/305137a0.

[3] D. B. Calne *et al.*, "Positron emission tomography after MPTP: observations relating to the cause of Parkinson's disease.," *Nature*, vol. 317, no. 6034, pp. 246–248, Sep. 1985, doi: 10.1038/317246a0.

[4] C. Nahmias, E. S. Garnett, G. Firnau, and A. Lang, "Striatal dopamine distribution in parkinsonian patients during life.," *J. Neurol. Sci.*, vol. 69, no. 3, pp. 223–230, Jul. 1985, doi: 10.1016/0022-510x(85)90135-2.

[5] K. L. Davis, R. S. Kahn, G. Ko, and M. Davidson, "Dopamine in schizophrenia: a review and reconceptualization.," *Am. J. Psychiatry*, vol. 148, no. 11, pp. 1474–1486, Nov. 1991, doi: 10.1176/ajp.148.11.1474.

[6] O. D. Howes and S. Kapur, "The dopamine hypothesis of schizophrenia: version III--the final common pathway.," *Schizophr. Bull.*, vol. 35, no. 3, pp. 549–562, May 2009, doi: 10.1093/schbul/sbp006.

[7] O. D. Howes *et al.*, "The nature of dopamine dysfunction in schizophrenia and what this means for treatment.," *Arch. Gen. Psychiatry*, vol. 69, no. 8, pp. 776–786, Aug. 2012, doi: 10.1001/archgenpsychiatry.2012.169.

[8] M. Avram *et al.*, "Reduced striatal dopamine synthesis capacity in patients with schizophrenia during remission of positive symptoms.," *Brain*, vol. 142, no. 6, pp. 1813–1826, Jun. 2019, doi: 10.1093/brain/awz093.

[9] S. Jauhar *et al.*, "Determinants of treatment response in first-episode psychosis: an 18F-DOPA PET study," *Mol. Psychiatry*, vol. 24, no. 10, pp. 1502–1512, 2019, doi: 10.1038/s41380-018-0042-4.

[10] E. Kim *et al.*, "Presynaptic Dopamine Capacity in Patients with Treatment-Resistant Schizophrenia Taking Clozapine: An [(18)F]DOPA PET Study.," *Neuropsychopharmacol. Off. Publ. Am. Coll. Neuropsychopharmacol.*, vol. 42, no. 4, pp. 941–950, Mar. 2017, doi: 10.1038/npp.2016.258.

[11] M. Veronese *et al.*, "A potential biomarker for treatment stratification in psychosis: evaluation of an [(18)F] FDOPA PET imaging approach.," *Neuropsychopharmacol. Off. Publ. Am. Coll. Neuropsychopharmacol.*, vol. 46, no. 6, pp. 1122–1132, May 2021, doi: 10.1038/s41386-020-00866-7.

[12] D. S. Marcus, T. R. Olsen, M. Ramaratnam, and R. L. Buckner, "The extensible neuroimaging archive toolkit," *Neuroinformatics*, vol. 5, no. 1, pp. 11–33, 2007, doi: 10.1385/NI:5:1:11.

[13] O. D. Howes *et al.*, "Dopamine synthesis capacity before onset of psychosis: a prospective [18F]-DOPA PET imaging study.," *Am. J. Psychiatry*, vol. 168, no. 12, pp. 1311–1317, Dec. 2011, doi: 10.1176/appi.ajp.2011.11010160.

[14] O. D. Howes *et al.*, "Elevated striatal dopamine function linked to prodromal signs of schizophrenia.," *Arch. Gen. Psychiatry*, vol. 66, no. 1, pp. 13–20, Jan. 2009, doi: 10.1001/archgenpsychiatry.2008.514.

[15] S. Jauhar *et al.*, "The Effects of Antipsychotic Treatment on Presynaptic Dopamine Synthesis Capacity in First-Episode Psychosis: A Positron Emission Tomography Study.," *Biol. Psychiatry*, vol. 85, no. 1, pp. 79–87, Jan. 2019, doi: 10.1016/j.biopsych.2018.07.003.

[16] O. D. Howes *et al.*, "Dopaminergic function in the psychosis spectrum: an [18F]-DOPA imaging study in healthy individuals with auditory hallucinations.," *Schizophr. Bull.*, vol. 39, no. 4, pp. 807–814, Jul. 2013, doi: 10.1093/schbul/sbr195.

[17] A. Egerton, A. Demjaha, P. McGuire, M. A. Mehta, and O. D. Howes, "The test-retest reliability of 18F-DOPA PET in assessing striatal and extrastriatal presynaptic dopaminergic function.," *Neuroimage*, vol. 50, no. 2, pp. 524–531, Apr. 2010, doi: 10.1016/j.neuroimage.2009.12.058.

[18] A. Egerton *et al.*, "Dopamine and Glutamate in Antipsychotic-Responsive Compared With Antipsychotic-Nonresponsive Psychosis: A Multicenter Positron Emission Tomography and Magnetic Resonance Spectroscopy Study (STRATA).," *Schizophr. Bull.*, vol. 47, no. 2, pp. 505–516, Mar. 2021, doi: 10.1093/schbul/sbaa128.

[19] A. Egerton *et al.*, "Presynaptic striatal dopamine dysfunction in people at ultra-high risk for psychosis: findings in a second cohort.," *Biol. Psychiatry*, vol. 74, no. 2, pp. 106–112, Jul. 2013, doi: 10.1016/j.biopsych.2012.11.017.

[20] K. Friston, "A short history of SPM," in *Statistical Parametric Mapping: The Analysis of Functional Brain Images*, 2007, pp. 3–9. doi: 10.1016/B978-012372560-8/50001-2.

[21] C. S. Patlak, R. G. Blasberg, and J. D. Fenstermacher, "Graphical evaluation of blood-to-brain transfer constants from multiple-time uptake data.," *J. Cereb. blood flow Metab. Off. J. Int. Soc. Cereb. Blood Flow Metab.*, vol. 3, no. 1, pp. 1–7, Mar. 1983, doi: 10.1038/jcbfm.1983.1.

[22] C. S. Patlak and R. G. Blasberg, "Graphical evaluation of blood-to-brain transfer constants from multiple-time uptake data. Generalizations.," *J. Cereb. blood flow Metab. Off. J. Int. Soc. Cereb. Blood Flow Metab.*, vol. 5, no. 4, pp. 584–590, Dec. 1985, doi: 10.1038/jcbfm.1985.87.

[23] Y. Kumakura and P. Cumming, "PET studies of cerebral levodopa metabolism: a review of clinical findings and modeling approaches.," *Neurosci. a Rev. J. bringing Neurobiol. Neurol. psychiatry*, vol. 15, no. 6, pp. 635–650, Dec. 2009, doi: 10.1177/1073858409338217.

[24] J. M. Bland and D. G. Altman, "Measuring agreement in method comparison studies.," *Stat. Methods Med. Res.*, vol. 8, no. 2, pp. 135–160, Jun. 1999, doi: 10.1177/096228029900800204.

[25] D. Martinez *et al.*, "Imaging human mesolimbic dopamine transmission with positron emission tomography. Part II: amphetamine-induced dopamine release in the functional subdivisions of the striatum.," *J. Cereb. blood flow Metab. Off. J. Int. Soc. Cereb. Blood Flow Metab.*, vol. 23, no. 3, pp. 285–300, Mar. 2003, doi: 10.1097/01.WCB.0000048520.34839.1A.

[26] A. C. Tziortzi *et al.*, "Connectivity-Based Functional Analysis of Dopamine Release in the Striatum Using Diffusion-Weighted MRI and Positron Emission Tomography," *Cereb. Cortex*, vol. 24, no. 5, pp. 1165–1177, May 2014, doi: 10.1093/cercor/bhs397.

[27] V. Dhawan *et al.*, "Comparative analysis of striatal FDOPA uptake in Parkinson's disease: ratio method versus graphical approach.," *J. Nucl. Med.*, vol. 43, no. 10, pp. 1324–1330, Oct. 2002.

Experimental Microwave Imaging of Human Forearm

M. Ambrosanio[1], M.T. Bevacqua[2], T. Isernia[2], J. Lo Vetri[3] and V. Pascazio[4]
[1] *DiSEGIM, Department of Economics, Law, Cybersecurity, and Sports Sciences, University of Naples Parthenope, Via Guglielmo Pepe (Rione Gescal), 80035, Nola, Italy.*
[2] *DIIES, Department of Information Engineering, Infrastructures and Sustainable Energy, Università Mediterranea di Reggio Calabria, 89124, Reggio di Calabria, Italy.*
[3] *Department of Electrical and Computer Engineering, University of Manitoba, Winnipeg, MB R3T 2N2, Canada.*
[4] *Department of Engineering, Unversity of Naples Parthenope, Centro Direzionale di Napoli, 80143, Italy.*

***Abstract*—Quantitative microwave imaging represents an interesting complementary/alternative non-invasive diagnostic modality in the medical imaging framework. This approach provides *quantitative* images of the electric properties of target tissues located in the region of interest. In the framework of quantitative medical imaging, this work proposes a multi-step microwave imaging approach for the quantitative retrieval of human-forearm-tissue permittivity and conductivity maps. The proposed method was tested on experimental data collected at the Electromagnetic Imaging Laboratory of the University of Manitoba.**

***Keywords*—Quantitative microwave imaging, biomedical imaging, multistatic systems, experimental medical imaging.**

I. INTRODUCTION

In the framework of medical imaging, the three most common modalities are ultrasound, X-rays and magnetic resonance imaging (MRI). Ultrasound is cheap and safe since it exploits mechanical waves to perform the imaging, allowing continuous screening but with scarce resolution and difficulties in distinguishing among soft tissues. X-ray-based medical imaging generates good-resolution images with good soft-tissue contrast but at the expense of using ionising radiation which are harmful for patient health. Conversely, MRI is safe since uses static magnetic field and radio frequencies, offers excellent soft tissue contrast but still is very expensive and bulky.

Microwave imaging (MWI) represents an interesting non-invasive diagnostic modality in alternative to other conventional techniques. By virtue of its frequency spectrum (300 MHz - 300 GHz), it allows a safer and cheaper imaging which is suitable especially in the biomedical field [1]. This technique presents several advantages compared to other more established imaging modalities, such as X-ray, ultrasound, or magnetic resonance imaging (MRI) [2]. Some of the main advantages include the relatively low cost, the use of non-ionising radiation and the capability to deliver *quantitative* imaging by providing an estimate of the dielectric permittivity and conductivity maps of the investigated area without the use of contrast agents [3].

Microwave imaging has been adopted for the noninvasive exploration of several body areas, especially for breast cancer [4], [5], but also other body districts such as extremities (arm and leg) [6], brain [7], neck [8] and bones [9]. Despite its advantages, MWI is characterised by a worse resolution if compared with conventional X-ray and/or MRI, but its synergy with other imaging modalities, such as MRI or ultrasound imaging [10], further to its complementary information regarding the investigated region, can strongly impact on the medical diagnostic performance in a positive fashion.

Due to its interesting capabilities and complementarity with regard to other imaging modalities, MWI technology has good chances to become a viable modality for medical examinations. Several studies have been proposed in the last years by the scientific community involving up to hundreds of volunteers, but still this solution has not been used yet in clinical practise outside research laboratories [1]. To support this process, further initial testing requires imaging experiments of live tissues and not only phantom-based or ex-vivo situations. Certainly, this last case is more challenging compared to the laboratory-controlled ones due to movement artifacts, variations in size and the presence of more complex tissues.

Furthermore, quantitative evaluation of the electromagnetic properties (EPs) of biological tissues is paramount for various biomedical applications [11]. Several databases exist in the scientific literature which collect the EPs of biological tissues, but most of this work is related to measurements performed on ex-vivo tissue samples [12]. Nevertheless, according to some studies there is a considerable difference in values between ex-vivo and in-vivo EPs [13], which can reach the 25-30%. Thus, the estimation of in-vivo EPs in a non-invasive way is paramount for proper diagnostics.

In this work the Authors propose a quantitative MWI procedure for the estimation of the EPs of human forearm. To this aim, the approach exploits a-priori information derived from qualitative processing, which provides fundamental information to carry out the quantitative inversion. The proposed approach was tested by adopting the experimental

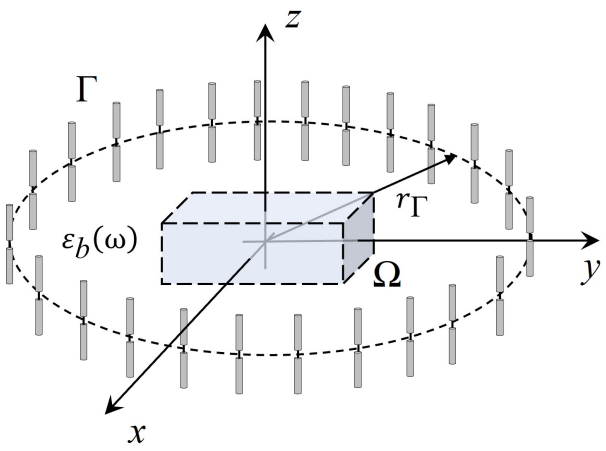


Fig. 1: Simplified sketch of the imaging system. The dipole antennas are aligned along the vertical z axis and located on a measurement circle Γ at a radius r_Γ. The imaging domain Ω is a parallelepiped and is immersed in a matching medium whose electric features are described by $\varepsilon_b(\omega)$.

data collected by the microwave tomography system developed at University of Manitoba [14]. Further details regarding the experimental imaging setup adopted for the data collection are reported in [15].

The remainder of the paper is as follows: Section II provides a brief overview of the mathematics related to the imaging problem at hand, while Section III illustrated the proposed methodology in terms of experimental data set and inversion procedure. Then, some experimental results and conclusions are reported in Sections IV and V, respectively.

II. Problem statement

A sketch of the considered geometry is shown in Fig. 1. The scenario under test Ω is assumed to include nonmagnetic, isotropic targets whose electric characteristics are described by the complex permittivity:

$$\varepsilon_x(\boldsymbol{r},\omega) = \varepsilon'_x(\boldsymbol{r}) - j\frac{\sigma_x(\boldsymbol{r})}{\omega\varepsilon_0}, \quad \boldsymbol{r}\in\Omega, \tag{1}$$

in which $\omega = 2\pi f$, f is the frequency [Hz], $\varepsilon_0 = 8.854\cdot 10^{-12}$ [F/m], and $\varepsilon'_x(\boldsymbol{r}), \sigma_x(\boldsymbol{r})$ are the relative permittivity and electrical conductivity maps of the investigated area Ω, respectively.

By assuming known (and everywhere constant) the complex permittivity of the background (matching) medium $\varepsilon_b(\omega) = \varepsilon'_b - j\frac{\sigma_b}{\omega\varepsilon_0}$, the contrast function which encodes targets properties can be defined as:

$$\chi(\boldsymbol{r},\omega) = \frac{\varepsilon_x(\boldsymbol{r},\omega) - \varepsilon_b(\omega)}{\varepsilon_b(\omega)}, \quad \boldsymbol{r}\in\Omega. \tag{2}$$

In this framework, the aim of the proposed analysis consists in retrieving the unknown contrast function, and thus the relative permittivity and conductivity maps of the targets located in the imaging domain Ω. For a fixed frequency and assuming known the "incident field", i.e. the electric field inside the imaging domain when there is no target, the scattering phenomena can be properly described by the following equations (after discretization):

$$\boldsymbol{e}_t = \boldsymbol{e}_i + \boldsymbol{\mathcal{A}}_i(\boldsymbol{x}\odot\boldsymbol{e}_t), \tag{3}$$

$$\boldsymbol{e}_s = \boldsymbol{\mathcal{A}}_e(\boldsymbol{x}\odot\boldsymbol{e}_t), \tag{4}$$

in which $\boldsymbol{x}$ is the discrete version of the unknown contrast function $\chi(\boldsymbol{r},\omega)$; $\boldsymbol{e}_t, \boldsymbol{e}_i$ are the discrete total and incident electric fields evaluated in the imaging domain Ω, $\boldsymbol{e}_s$ is the scattered electric field measured at receivers locations Γ per each illumination. The operators $\boldsymbol{\mathcal{A}}_i$ and $\boldsymbol{\mathcal{A}}_e$ are the discrete versions of the internal and external scattering operators, respectively. The symbol $\odot$ refers to the point-by-point product (i.e., Hadamard product).

At each time instant, only one transmitter is active and the remaining antennas are adopted as receivers. This scheme is repeated until all the antennas have illuminated the imaging area Ω, performing the data acquisition via a multiview-multistatic configuration.

Unfortunately, finding a reliable solution to the problem described by equations (3)-(4) is not trivial since it is nonlinear and ill-posed, and thus requires regularization strategies to reach a more stable solution. In this framework, the proposed approach strongly exploit the a-priori information derived from qualitative inversions to perform quantitative recoveries of the electric characteristics of human forearm biological tissues.

III. Methodology

A. Experimental data set

The experimental data set consists in the acquisition of five adults' forearms at microwave frequencies (0.4-2 GHz with a step of 100 MHz). The acquisitions were carried out at the Electromagnetic Imaging Laboratory at the University of Manitoba by means of an in-house microwave prototype [14]. The adopted MWI system is composed of 24 dipole antennas with a quarter-wavelength balun surrounding the investigation area Ω. The antennas are equally spaced on a circle of radius $r_\Gamma = 9.4$ cm and located at a mid-height of the hosting metallic cylinder.

Each acquisition consists of 23×24 single-frequency data points (S-parameter measurements) without considering the monostatic contribution. Due to direct coupling issues, the number of data points that can be used in practise for imaging purposes is further reduced to 19×24. The measurement procedure is repeated twice: with and without the human forearm in the imaging domain. Finally, a third measure with a 3.5-inch-diameter metallic cylinder is performed for the calibration.

B. Inversion procedure

Overall, the inversion approach consists of three steps. The first one exploits qualitative inversion methods to extract as much a-priori information as possible, while the second step consists in an enumeration analysis for the estimation of a suitable initial guess in order to ease the final quantitative

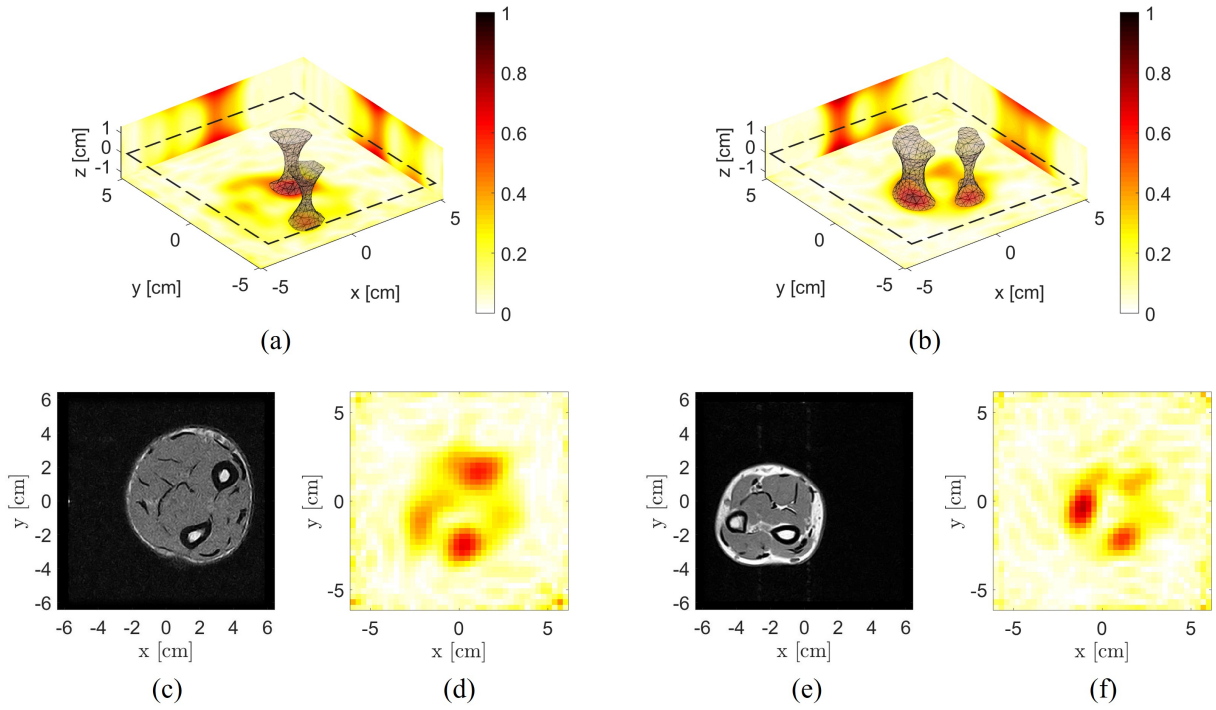


Fig. 2: (a)-(b): Qualitative three-dimensional (3D) recoveries obtained via BA for two volunteers of the Manitoba data set. (c)-(f): slices comparison between the retrieved support information obtained via 3D-BA (d, f) and corresponding MRI slices (c, e). It is worth noting that the two imaging modalities are not coregistered, even though they share the same axes.

recovery procedure (final step). More in detail, no hypothesis is assumed regarding the target location in the imaging domain and its size, which are estimated by the qualitative recoveries.

1) Step I - qualitative inversion: Among qualitative methods, the Linear Sampling Method (LSM) and the Born/distorted Born approximation (BA/dBA) are probably some of the most popular. For instance, the former one achieves the support information in a simple and effective way by solving, for a fixed frequency and point of the imaging grid, the well-known far-field equation. This method provides a map for the target support estimation (i.e., LSM indicator) which allows the generation of suitable initial guesses for successive quantitative inversions. Furthermore, the BA/dBA belong to the approximated methods and solve the inverse scattering problem by means of a convenient linearization of the discretized data equation (4). Also in these cases, the problem is still ill-posed and requires the use of proper regularization strategies.

2) Step II - enumeration analysis for suitable initial guess definition: Starting from the normalised LSM map, a pair of variable thresholds is adopted to generate a first raw approximation of the human forearm, i.e. one threshold is adopted for the forearm size definition and another one for the subcutaneous adipose tissue characterisation. More in detail, per each combination of the two thresholds, a raw estimate (i.e., without bones) of the human forearm is produced. Then, per each generated raw profile, the dBA is adopted to retrieve some spatial information regarding the bones location (a further third threshold is used to this aim). Finally, an estimate of the whole forearm morphology is derived.

Then, this estimate is assigned realistic electric tissues properties generating two quantitative maps (permittivity and conductivity). This estimated information is used to run a forward solver to calculate the electric scattered field at the receivers on Γ to be compared with the experimental data described in Subsection III-A. Lastly, the profile associated to the minimum mean square error among the simulated and experimentally-measured data is chosen as initial guess for the quantitative retrieval of the human forearm under consideration.

3) Step III - quantitative EPs refinement: The choice of the proper initial guess considered in the previous steps can be exploited for local minimization strategies to obtain reliable estimates of the dielectric in-vivo features of biological tissues. As a matter of fact, these properties are paramount for diagnostic and/or therapeutic treatments. To this aim, a multi-frequency distorted Born iterative method was adopted to perform the quantitative EPs estimation of human forearm tissues.

More details regarding the proposed approach will be provided at the conference.

IV. Results

Figure 2 reports some preliminary qualitative recoveries obtained via BA for the retrieval of some a-priori information (e.g., bones support) for two volunteers of the Manitoba data

set. More in detail, the operative frequency band adopted in the inversion procedure is $[0.8, 1.2]$ GHz with a frequency step of 100 MHz. With regard to the corresponding quantitative recoveries, they are not shown here due to space limitations and will be presented at the conference.

To provide a baseline as reference for the anatomy of the considered volunteers, the related MRI images are shown in Fig. 2(c, e) obtained with a 0.2 T Esaote E-scan XQ (T1 gradien echo protocol). Fig. 2(a, b) reports some qualitative three-dimensional (3D) inversions via BA of two volunteers of the Manitoba data set, while Fig. 2(d, f) illustrates the 2D slices at mid height with corresponding MRI reference slices in Fig. 2(c, e).

It is worth noting that the MRI and MWI images are not coregistered, even though the axes are the same. The accuracy of the coregistration is limited since the volunteer's arm and body positions were different in the MRI and MWI systems. In the former, the volunteer was supine and arm held horizontally, while in the latter the arm was held vertically with the hand clenched in a fist resting on a pad at the bottom of the chamber.

V. Conclusion

In this paper a multi-step quantitative MWI approach for the EPs retrieval of biological tissues was proposed. The methodology exploits a-priori information derived from qualitative inversion steps with the aim of providing a suitable initial guess for quantitative imaging via local minimisation procedures. As case study, the Authors considered the microwave data of human forearms collected by the group of the Electromagnetic Imaging Laboratory at the University of Manitoba.

Future work includes the testing of the proposed approach with other volunteers and the improvement of the refinement strategy with better performing quantitative inversions.

References

[1] Chandra, R., Zhou, H., Balasingham, I. & Narayanan, R. On the opportunities and challenges in microwave medical sensing and imaging. *IEEE Transactions On Biomedical Engineering*. **62**, 1667-1682 (2015)

[2] Chandra, R., Balasingham, I., Zhou, H. & Narayanan, R. Medical microwave imaging and analysis. *Medical Image Analysis And Informatics: Computer-Aided Diagnosis And Therapy*. pp. 451-466 (2017)

[3] Ambrosanio, M., Franceschini, S., Pascazio, V. & Baselice, F. An End-to-End Deep Learning Approach for Quantitative Microwave Breast Imaging in Real-Time Applications. *Bioengineering*. **9**, 651 (2022)

[4] Ambrosanio, M., Kosmasy, P. & Pascazio, V. An adaptive multi-threshold iterative shrinkage algorithm for microwave imaging applications. *2016 10th European Conference On Antennas And Propagation (EuCAP)*. pp. 1-3 (2016)

[5] Bevacqua, M., Di Meo, S., Crocco, L., Isernia, T. & Pasian, M. Millimeter-waves breast cancer imaging via inverse scattering techniques. *IEEE Journal Of Electromagnetics, RF And Microwaves In Medicine And Biology*. **5**, 246-253 (2021)

[6] Salvador, S., Fear, E., Okoniewski, M. & Matyas, J. Exploring joint tissues with microwave imaging. *IEEE Transactions On Microwave Theory And Techniques*. **58**, 2307-2313 (2010)

[7] Scapaticci, R., Di Donato, L., Catapano, I. & Crocco, L. A feasibility study on microwave imaging for brain stroke monitoring. *Progress In Electromagnetics Research B*. **40** pp. 305-324 (2012)

[8] Dachena, C., Fedeli, A., Fanti, A., Lodi, M., Pastorino, M. & Randazzo, A. Microwave imaging for the diagnosis of cervical diseases: A feasibility analysis. *IEEE Journal Of Electromagnetics, RF And Microwaves In Medicine And Biology*. **5**, 277-285 (2020)

[9] Golnabi, A., Meaney, P., Geimer, S., Zhou, T. & Paulsen, K. Microwave tomography for bone imaging. *2011 IEEE International Symposium On Biomedical Imaging: From Nano To Macro*. pp. 956-959 (2011)

[10] Qin, Y., Rodet, T., Lambert, M. & Lesselier, D. Joint inversion of electromagnetic and acoustic data with edge-preserving regularization for breast imaging. *IEEE Transactions On Computational Imaging*. **7** pp. 349-360 (2021)

[11] Wilson, A., Kosmas, P. & Thanou, M. Ex-vivo Dielectric Properties of Tissues in Athymic Nude Mice. *2022 3rd URSI Atlantic And Asia Pacific Radio Science Meeting (AT-AP-RASC)*. pp. 1-4 (2022)

[12] Hasgall, P., Neufeld, E., Gosselin, M., Kingenböck, A. & Kuster, N. IT'IS Database for Thermal and Electromagnetic Parameters of Biological Tissues. 2012.

[13] Zhang, X., Liu, J. & He, B. Magnetic-resonance-based electrical properties tomography: a review. *IEEE Reviews In Biomedical Engineering*. **7** pp. 87-96 (2014)

[14] Gilmore, C., Zakaria, A., Pistorius, S. & LoVetri, J. Microwave imaging of human forearms: Pilot study and image enhancement. *International Journal Of Biomedical Imaging*. **2013** (2013)

[15] Gilmore, C., Mojabi, P., Zakaria, A., Ostadrahimi, M., Kaye, C., Noghanian, S., Shafai, L., Pistorius, S. & LoVetri, J. A wideband microwave tomography system with a novel frequency selection procedure. *IEEE Transactions On Biomedical Engineering*. **57**, 894-904 (2009)

Early stages of cognitive decline are characterized by different EEG microstates dynamics

M. Lassi[1,2], C. Fabbiani[3], S. Mazzeo[3,4], R. Burali[3], A.A. Vergani[1,2], G. Giacomucci[4], V. Moschini[4], F. Emiliani[4], M. Scarpino[3], S. Bagnoli[4], A. Ingannato[4], B. Nacmias[3,4], S. Padiglioni[5], S. Micera[1,2,6], S. Sorbi[3,4], A. Grippo[3], V. Bessi[4] and A. Mazzoni[1,2]

[1]*The Biorobotics Institute, Sant'Anna School of Advanced Studies, Pisa, Italy*

[2]*Department of Excellence in Robotics and AI, Sant'Anna School of Advanced Studies, Pisa, Italy*

[3]*IRCCS Fondazione Don Carlo Gnocchi, Florence, Italy*

[4]*Department of Neuroscience, Psychology, Drug Research and Child Health, University of Florence, Florence, Italy*

[5]*Regional Referral Centre for Relational Criticalities, Tuscany Region, Florence, Italy*

[6]*Translational Neural Engineering Lab, École Polytechnique Fèdèrale de Lausanne, Lausanne, Switzerland*

***Abstract*—Neural changes due to Alzheimer's Disease (AD) appear much earlier than objective cognitive decline symptoms. Subjective cognitive decline (SCD) is the first pre-clinical stage at which future development of the disease may be intercepted, possibly followed by mild cognitive impairment (MCI), the first step of clinical cognitive decline. Recent studies suggest that resting EEG analysis tools describing whole-brain activity, such as microstates and brain areas functional connectivity, might support a characterization of SCD and MCI conditions, but notwithstanding their clinical relevance, the cortical underpinnings of these AD prodromic states are far from being untangled. Here we verify whether the EEG activity modeled as a sequence of microstates is a better marker than simple spectral analyses in discriminating between SCD (n = 57), MCI (n = 45) and healthy controls (n = 17). While no significant differences were found in the spectral activity of our cohort, we identified effective markers of the prodromic changes of the disease in the reconstructed microstates dynamics. Specifically, cognitive decline alters the average duration, the coverage and the transition probabilities of several microstates, with the most prominent differences found for the canonical microstate C. Overall, this work advances the search for non-invasive EEG biomarkers charaterizing pre-symptomatic stages of AD, that may be used to automatically diagnose the future development of the disease.**

***Keywords*—Subjective cognitive decline, Mild Cognitive Impairment, EEG, microstates**

I. INTRODUCTION

Alzheimer's Disease (AD) is currently seen as a continuum, with changes in the structure and function of the brain occurring even decades earlier than the first symptoms' appearance, but going unnoticed. Thus, it is fundamental to identify novel, non-invasive markers that are able to predict in advance patients who are most likely to develop the disease. This would allow to improve early intervention and coordinated care plans and to limit the later burden of the dementia[1]. In this context, subjective cognitive decline (SCD) patients have gained attention as possible optimal target population for early AD detection. SCD is the self-concerned experience of reduced cognitive function, not mirrored by an objective abnormal score in standardized clinical tests[2]. SCD is a heterogeneous condition: patients belonging to it may progress to objective forms of dementias or may remain stable during their lifetime. However, this population has an overall higher chance of developing the dementia compared to the healthy population[2]. For this reason, it may be the ideal target for disease-modifying therapies to preserve cognitive function. Conversely, the first clinical sign of possible AD is mild cognitive impairment (MCI), defined as a state of objective cognitive decline that is not impairing the activities of daily living[2]. Since SCD and MCI conditions represent the two nearest points in the AD continuum, separating clinical cognitive decline from pre-clinical decline, it is imperative to find inexpensive and non-invasive markers that can distinguish between these two stages. This would allow to scale the early diagnosis of AD to larger cohorts and make it clinically feasible.

EEG may be an optimal tool in this context, as it provides a relatively cheap, quick to setup and widely available tool to functionally image the brain. A large number of studies proposed EEG biomarkers to diagnose the AD and MCI populations[3]. In the spectral domain, most of the studies identified a slowing in the resting EEG oscillations towards the delta and theta bands. A lower degree of functional connectivity patterns was also identified, related to the decrease in the small-world properties of the whole-brain network. Moreover, EEG displays a reduced signal complexity in AD and MCI when compared to the healthy population. However, only few studies explored the use of resting-state EEG activity to characterize the SCD population[4][5][6]. Thus, in the present work, we aimed at further exploring the pool of EEG markers in the SCD condition, by comparing both spectral and microstate markers on the same cohort of patients. Moreover, we explored whether microstate transition probabilities is a

hallmark of the cognitive decline.

II. METHODS

A. Participants

Patients self-referring to the Careggi University Hospital in Florence where recruited in the study, after a comprehensive neuro-psychological assessment. Patients were included in the study if they satisfied the following inclusion criteria: complaint of cognitive decline with a duration of > 6 months; Mini Mental State Examination (MMSE) score greater than 24. Exclusion criteria were: comorbidities and diagnosis of other pathologies that may affect their EEG and their cognitive status (e.g. depression). A total of 103 subjects met the inclusion criteria. They were classified as 58 SCD, according to Subjective Cognitive Decline Initiative (SCD-I) Working Group criteria[2], and 45 MCI based on NIA-AA criteria[7]. Additionally, 17 healthy control subjects (H), aged 55 to 75 years, were recruited to compare their resting-state EEG. All subjects were recruited in accordance with the Declaration of Helsinki and the study was approved by the local Institutional Review Board. All participants in this study signed an informed consent.

Resting-state EEG data was collected from patients meeting inclusion criteria at the IRCCS Don Gnocchi (Florence, Italy). EEG was collected from patients resting on a chair in a comfortable position, using the 64-channels Galileo-NT system (E.B. Neuro S.p.a.), using the extended 10/20 channels location, and a sampling rate of 512 Hz. Approximately 15 minutes of eyes-closed EEG recording were collected from each participant (Fig. 1A). EEG data was offline pre-processed to remove physiological and non-physiological artifacts. A semi-automatic pipeline was developed to this aim, combining the use of the PREP pipeline and ICA artifact removal[8](Fig. 1B).

B. Spectral markers

The power spectral density of each EEG signal was computed by means of the Welch's method (5 s non-overlapping windows). The spectrum was divided in four canonical frequency bands: delta (1-4 Hz), theta (4-8Hz), alpha (8-13 Hz) and beta (13-30 Hz)[9]. The relative power in each band was obtained by normalizing it with respect to the total power in the bandwidth 1-48 Hz. From each channel relative power, an average scalp power is computed by averaging all channels activities. Moreover a region of interest (ROI) power is obtained by averaging over channels belonging to six different areas of the scalp as in [10]: frontal right, frontal left, central right, central left, occipital right and occipital left.

C. Microstates extraction

EEG microstates are quasi-stable topographies in the EEG time domain, lasting approximately 80 to 120 ms[11]. As reported in previous studies, the typical number of microstates appearing at rest is four and they have stereotypical topographies. Hence, to obtain a microstate representation of the input EEG signals, we applied the modified k-means clustering algorithm separately for each subject, setting the number of clusters to four[11]. The input to the modified k-means were the $30 * 10^4$ topographies having the highest global field power (GFP) on the entire EEG signal. To avoid obtaining sub-optimal clusters due to local minima, the algorithm was restarted 50 times for each EEG signal, and the solution minimizing intra-cluster distance was selected. Once four single-subject microstate topographies (the clusters' centroids) were obtained, we performed a second pass on the k-means clustering, now having as inputs the entire set of average single-subject topographies. We imposed that each topography coming from the same subject should belong to a different grand-average map. These grand-average maps were matched by visual similarity with the canonical maps observed in previous works and named A, B, C and D. Single-subjects maps were matched with the canonical grand-average maps. Group-level maps were also obtained as the centroids of the maps belonging to each diagnostic group. The temporal sequence of EEG microstates was then reconstructed by back-fitting the grand-average maps to each subject's signal with a winner-takes-all procedure: only the microstate topography with the lowest Euclidean distance from the topography at each time-point was considered active at that time-point. Segments with microstate duration less than 30 ms were rejected and reassigned to the subsequent most similar map.

Microstates were both tested for topographical and temporal differences among groups. We used TANOVA (topographical analysis of variance) to check for differences among SCD, MCI and H subjects in their average microstate maps. Regarding microstate dynamics, from the back-fitted microstate signals, we obtained a discrete sequence of microstates by only retaining transitions among different canonical microstates. We then computed the average microstate duration for each subject and we extracted each microstate's coverage, i.e. the percentage of time a given microstate remains active over the total recording time. We finally computed microstate transition probabilities. Transition probabilities p_{ij} were defined as the probability of passing to microstate j at time $t + 1$, given the current state at time t is microstate i.

For both domains of variables (spectral and microstates), we first assessed the normality of the sample by Shapiro-Wilk test. When the domain displayed normal behavior in most variables, we used one-way ANOVA to compare the three groups, followed by t-test post-hoc tests for pairwise comparisons. Otherwise, we used the Kruskal-Wallis test to compare the three groups, followed by Wilcoxon rank sum post-hoc tests. All post-hoc comparisons were corrected with the Bonferroni method.

III. RESULTS

First, we addressed the spectral differences among groups. Delta and alpha relative power displayed only a trend toward difference due to the large inter-subject variability (delta band: ANOVA F-statistic = 2.19, p = 0.065, η^2 =0.046; alpha band: ANOVA F-statistic = 1.92, p = 0.151, η^2 = 0.032). The highest effect size was found in the occipital areas for the delta band

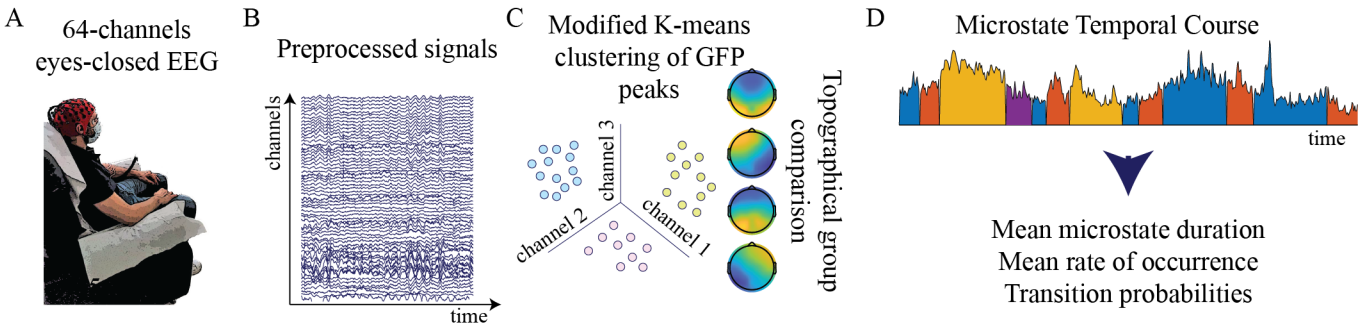


Fig. 1: Microstates extraction. (A) EEG is recroded in the eyes closed condition. (B) The signal is preprocessed to remove artifacts. (C) The clean signals is fed into the modified K-means algorithm and the single-subjects topographies are obtained. Mean topographies among groups are compared using TANOVA. (D) The gran-mean topographies are back-fitted into single-subject EEG signals and temporal metrics are computed it.

(left: ANOVA F-statistic = 2.95, p = 0.056, η^2 = 0.048; right: ANOVA F-statistic = 2.66, p = 0.074, η^2 = 0.043). In alpha, the left frontal area was the one with largest differences among groups (ANOVA F-statistic = 2.67, p = 0.073, η^2 = 0.043)

Regarding microstate topographies, the TANOVA test did not highlight any difference among groups (multi-group TANOVA average dissimilarity: microstate A d = 0.316, p = 0.79; microstate B d = 0.583, p = 0.32; microstate C d = 0.353, p = 0.71; microstate D d = 0.459, p = 0.40).

Conversely, several significant differences resulted in the microstates temporal sequence. Regarding duration (Fig. 2A) and coverage (Fig. 2B) of each microstate, we found significant differences in both measures for microstate C (duration: Kruskal-Wallis H-statistic = 9.68, p = 0.008; coverage: Kruskal-Wallis H-statistic = 7.92, p = 0.019). Additionally, the coverage of microstate B was altered in MCI subjects when compared to H controls (Kruskal-Wallis H-statistic = 9.68, p = 0.008). Also microstates transitions were altered (Fig. 2C), coherently with changes in the duration of each state. Prominently, transitions to the canonical microstate C were less likely in MCI, both compared to SCD and H. Transitions from microstate D to microstate B were more likely in MCI conditon compared to the SCD condition.

IV. DISCUSSION

In this work we concurrently analyzed possible spectral and microstate markers of prodromal stages of AD (SCD and MCI) and healthy controls, hence allowing for direct comparison on the power of these markers in detecting the progression of cognitive decline. We found that microstate dynamics markers, rather than their topographical representation, are able to discriminate between SCD and MCI, and are a better and more robust marker than the spectral ones.

While we did not find any significant difference in the spectral domain, we observed trends that were similar to the ones described in previous literature, both for AD and SCD[3][5]. Specifically, our results are consistent with the ones describing a slowing in the oscillations as the cognitive decline progresses, as depicted by an increase in delta band activity and reduced alpha peak power. However, as described in [4] microstates are relevant in characterizing cognitive decline. While we did not find any topographical difference among microstates related to the progression of cognitive decline, we additionally introduced the transition probability and identified it as a valid marker distinguishing SCD and MCI subjects. We can conclude that microstate temporal dynamics retain information regarding the progress of cognitive decline in the considered cohort. Such information is also related to functional networks in the brain[12], and hence could give insights on the pathogenesis of AD from very early pre-symptomatic stages of the disease.

There are, however, some limitations in this study that we will address in the future. First, our sample is relatively small when compared to the one previously used to study microstates in SCD[4]. We did not recruit any patient with AD, hence not having a reference on the other end of the Alzheimer's disease continuum. In future studies, we will also explore more advanced metrics of the temporal microstate dynamics, such as microstate complexity, as it has been shown to be a predictor of AD[13]. Finally, we will combine the identified resting-state EEG markers, along with other neuro-psychological, genetic and demographic factors, to better address the heterogeneity of the SCD population. We will use these features to build a machine learning classifier able to optimally discriminate between different levels of cognitive decline, with the ultimate goal of testing it in a longitudinal study.

ACKNOWLEDGEMENT

This project was funded by Tuscany Region - PRedicting the EVolution of SubjectIvE Cognitive Decline to Alzheimer's Disease With machine learning - PREVIEW - CUP. D18D20001300002

REFERENCES

[1] B. Dubois, A. Padovani, P. Scheltens, A. Rossi, and G. Dell'Agnello, "Timely Diagnosis for Alzheimer's Disease: A Literature Review on Benefits and Challenges," *Journal of Alzheimer's disease: JAD*, vol. 49, no. 3, pp. 617–631, 2016.

[2] F. Jessen, R. E. Amariglio, R. F. Buckley, W. M. van der Flier, Y. Han, J. L. Molinuevo, L. Rabin, D. M. Rentz, O. Rodriguez-Gomez, A. J. Saykin, S. A. M. Sikkes, C. M. Smart, S. Wolfsgruber, and M. Wagner, "The characterisation of subjective cognitive decline," *The Lancet. Neurology*, vol. 19, no. 3, pp. 271–278, Mar. 2020.

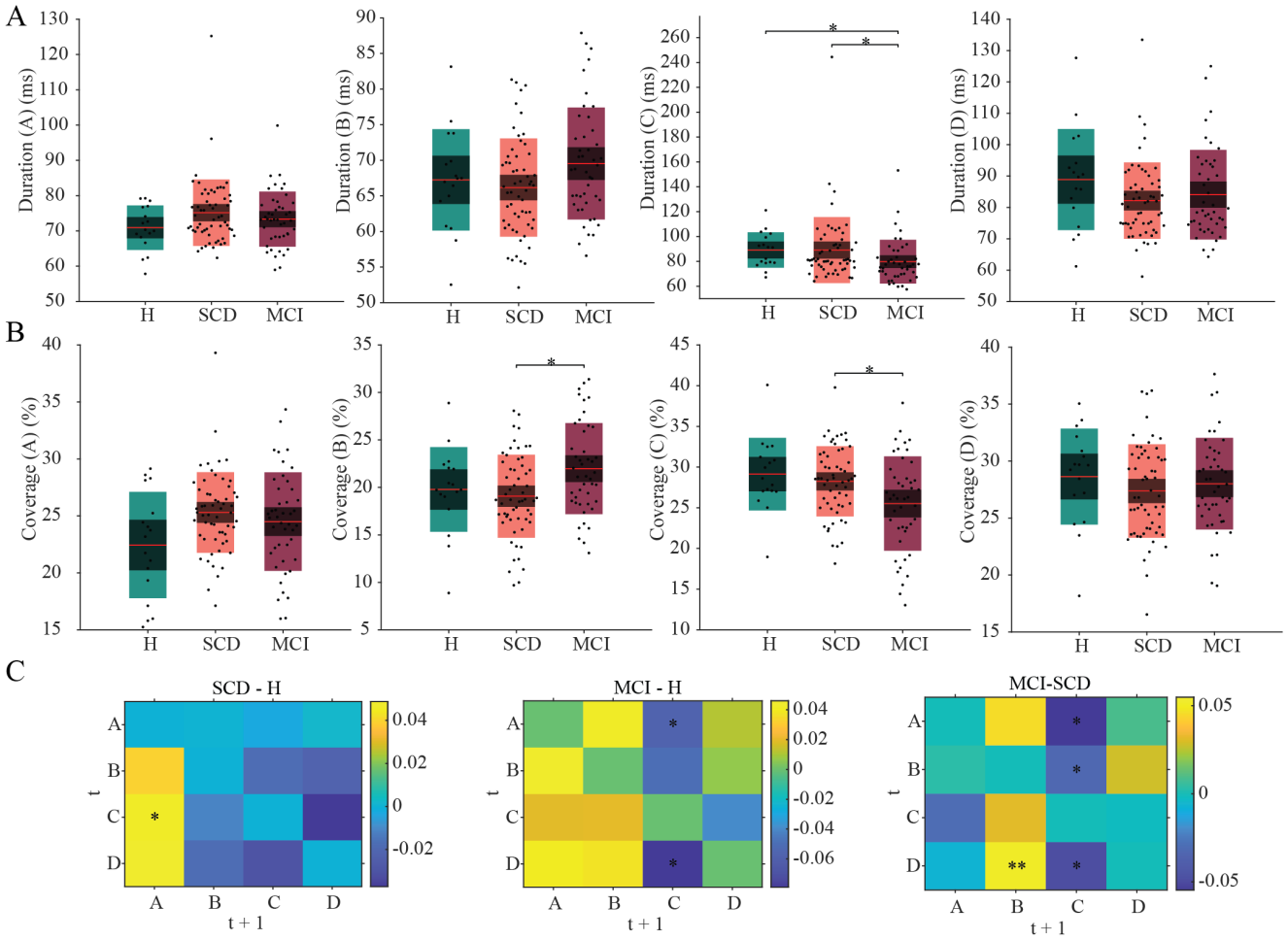


Fig. 2: Microstate metrics extracted from their temporal dynamics. (A) Mean duration of each canonical microstate. (B) Mean coverage (overall time covered by the microstate) of each canonical microstate. (C) Difference between transition probabilities between pairs of groups. In panels A and B, the red line indicates the mean value, the dark shaded area indicates the 95% confidence interval of the mean and the light shaded area represents the interquartile range. In each plot, statistical significance is defined as follows: *: $0.01 < p < 0.05$, **: $p < 0.001$

[3] P. M. Rossini, R. Di Iorio, F. Vecchio, M. Anfossi, C. Babiloni, M. Bozzali, A. C. Bruni, S. F. Cappa, J. Escudero, F. J. Fraga, P. Giannakopoulos, B. Guntekin, G. Logroscino, C. Marra, F. Miraglia, F. Panza, F. Tecchio, A. Pascual-Leone, and B. Dubois, "Early diagnosis of Alzheimer's disease: the role of biomarkers including advanced EEG signal analysis. Report from the IFCN-sponsored panel of experts," *Clinical Neurophysiology*, vol. 131, no. 6, pp. 1287–1310, Jun. 2020.

[4] U. Smailovic, T. Koenig, E. J. Laukka, G. Kalpouzos, T. Andersson, B. Winblad, and V. Jelic, "EEG time signature in Alzheimer´s disease: Functional brain networks falling apart," *NeuroImage: Clinical*, vol. 24, p. 102046, Jan. 2019.

[5] U. Smailovic, T. Koenig, I. Kåreholt, T. Andersson, M. G. Kramberger, B. Winblad, and V. Jelic, "Quantitative EEG power and synchronization correlate with Alzheimer's disease CSF biomarkers," *Neurobiology of Aging*, vol. 63, pp. 88–95, Mar. 2018.

[6] C. Babiloni, P. J. Visser, G. Frisoni, P. P. De Deyn, L. Bresciani, V. Jelic, G. Nagels, G. Rodriguez, P. M. Rossini, F. Vecchio, D. Colombo, F. Verhey, L.-O. Wahlund, and F. Nobili, "Cortical sources of resting EEG rhythms in mild cognitive impairment and subjective memory complaint," *Neurobiology of Aging*, vol. 31, no. 10, pp. 1787–1798, Oct. 2010.

[7] R. C. Petersen, P. Aisen, B. F. Boeve, Y. E. Geda, R. J. Ivnik, D. S. Knopman, M. Mielke, V. S. Pankratz, R. Roberts, W. A. Rocca, S. Weigand, M. Weiner, H. Wiste, and C. R. Jack, "Criteria for Mild Cognitive Impairment Due to Alzheimer's Disease in the Community," *Annals of neurology*, vol. 74, no. 2, pp. 199–208, Aug. 2013.

[8] A. Delorme and S. Makeig, "EEGLAB: an open source toolbox for analysis of single-trial EEG dynamics including independent component analysis," *Journal of Neuroscience Methods*, vol. 134, no. 1, pp. 9–21, Mar. 2004.

[9] C. Fanciullacci, A. Panarese, V. Spina, M. Lassi, A. Mazzoni, F. Artoni, S. Micera, and C. Chisari, "Connectivity Measures Differentiate Cortical and Subcortical Sub-Acute Ischemic Stroke Patients," *Frontiers in Human Neuroscience*, vol. 0, 2021, publisher: Frontiers.

[10] C. Fanciullacci, F. Bertolucci, G. Lamola, A. Panarese, F. Artoni, S. Micera, B. Rossi, and C. Chisari, "Delta Power Is Higher and More Symmetrical in Ischemic Stroke Patients with Cortical Involvement," *Frontiers in Human Neuroscience*, vol. 0, p. 385, 2017.

[11] C. M. Michel and T. Koenig, "EEG microstates as a tool for studying the temporal dynamics of whole-brain neuronal networks: A review," *NeuroImage*, vol. 180, pp. 577–593, Oct. 2018.

[12] P. Milz, P. L. Faber, D. Lehmann, T. Koenig, K. Kochi, and R. D. Pascual-Marqui, "The functional significance of EEG microstates—Associations with modalities of thinking," *NeuroImage*, vol. 125, pp. 643–656, Jan. 2016.

[13] L. Tait, F. Tamagnini, G. Stothart, E. Barvas, C. Monaldini, R. Frusciante, M. Volpini, S. Guttmann, E. Coulthard, J. T. Brown, N. Kazanina, and M. Goodfellow, "EEG microstate complexity for aiding early diagnosis of Alzheimer's disease," *Scientific Reports*, vol. 10, no. 1, 2020.

K-medoid clustering of premotor firing patterns supports fine decoding of macaque reach-and-grasp

E. H. Rondoni[1,2*], M. Pizzinga[1,2*], F. Lanzarini[3,4], M. Maranesi[3], D. Albertini[3], L. Bonini[3], and A. Mazzoni[1,2]

[1] *The BioRobotics Institute, Scuola Superiore Sant'Anna, Viale Rinaldo Piaggio 34, 56025, Pontedera, Pisa, Italy*
[2] *Dept. of Excellence in Robotics and AI, Scuola Superiore Sant'Anna, Piazza Martiri della Libertà, 33, 56127, Pisa, Italy*
[3] *Department of Medicine and Surgery, University of Parma, Via Volturno 39/E, 43125, Parma, Italy*
[4] *Ernst Strüngmann Institute (ESI) for Neuroscience in Cooperation with Max Planck Society*

***Abstract*— Cortical control of reach-and-grasp movements is one of the key challenges of brain machine interfaces (BMI). Recent advancements enabled tetraplegic subjects to control robotic arms through this approach. However, the fine control of such movements is usually automatic rather than controlled by the patient, and this might not be the optimal solution in real life environments. Here we show that fine properties of reach-and-grasp movement can be decoded thanks to K-medoid clustering. We recorded the activity of 71 neurons from the premotor cortex of a macaque performing different reach-and-grasp movements depending on the shape and the position of the object presented. The K-medoid algorithm selected in an unsupervised way four firing patterns associated with specific clusters of neurons' activity. Describing the cortical activity during each movement through the distances from these four medoids and feeding the resulting vector into a support vector machine (SVM) algorithm enabled the identification of the specific movement performed. This decoding approach could in future support a finer control of robotic arms - or other devices – through cortical BMI.**

***Keywords*—Reach-and-grasp, K-medoid, Victor-Purpura, Support Vector Machine.**

I. Introduction

DECODING motor intentions from neural activity is a key step for the development of neuroprostheses [1]. Neuroprostheses based on cortical recordings aim at restoring the ability of tetraplegic patients to communicate and act with the outside world. Motor intentions, indeed, can be decoded from patient's motor imagery, as demonstrated by different BMIs applications (e.g., from EEG data: [2]). Hand trajectories can be decoded from recorded motor cortical areas, as it is done in [3], [4]. However, the intention/planning of a movement can be decoded also from premotor cortex [5] to predict goals and expected targets, leaving the specific kinematic to be defined at the low level by the actuator.

Here, we focus on decoding what we reckon are three important features for defining any reach-and-grasp movement: extension, laterality, and type of grasp.

First, we compared two different behavioural tasks, in which the monkey is asked to grasp with any hand either some food or a carabiner. This choice of objects grants two different grasping techniques: pinch and palmar, respectively.

Second, we focused on pinch grasp only, since, according to the experimental protocol, the food could be presented in both reachable and non-reachable areas.

For both analyses, we computed pairwise distances among raw spike-trains, rather than work on a pre-processed representation of the neuronal response.

II. Methods

A. Implant and Data Acquisition

Electrode arrays were chronically implanted in the ventral premotor cortex of a monkey (*Macaca mulatta*). The implant site was defined choosing as landmarks the inferior and superior arcuate sulci, and the central sulcus.

The neuronal activity was then recorded by means of customized 32-channels floating microelectrode arrays (FMAs, Microprobes for Life Science, Gaithersburg, MD, USA). These arrays are relatively small and can be easily implanted in separate locations, thus allowing the simultaneous coverage of different areas of the cortex. Moreover, the electrodes can be designed to reach different depths intracortically.

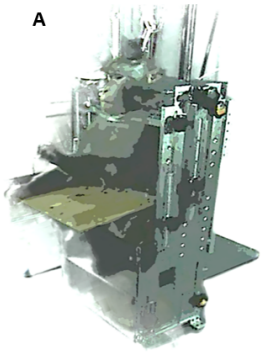
Four FMAs with alternating depths (2.5 mm and 4 mm) were implanted, for a total of 128 recording channels.

The collected data was wirelessly logged using a system (Deuteron technologies, RatLog-128) that allows to band-pass filter (2-7000 Hz) at a conversion rate of 32000 Hz. Thus, both local field potentials' and single/multi units' activity were available for analysis.

B. Experimental Protocol

The monkey was trained to sit on a primate chair and to respond to specific stimuli. Specifically, the behavioral tasks involved different reaching-grasping and mouth actions. In this study, the monkey was asked to grasp either food (*Pinch Grasp*) or a carabiner (*Palmar Grasp*). In both cases, the monkey was free to choose the hand for performing the task (*Right* or *Left Hand*). Furthermore, in case of pinch grasping, the food could be presented either in reachable or non-reachable areas (*Near* and *Far Presentation*).

A



PALMAR vs PINCH Grasps		
CLASS	# successful trials	
Palmar Right	15	Palmar: 25
Palmar Left	10	
Pinch Right	20	Pinch: 42
Pinch Left	22	
TOT	67	Right: 35 Left: 32

PINCH GRASP for FOOD		
CLASS	# successful trials	
Far Right	9	Far: 18
Far Left	9	
Near Right	11	Near: 22
Near Left	11	
TOT	40	Right: 20 Left: 20

B

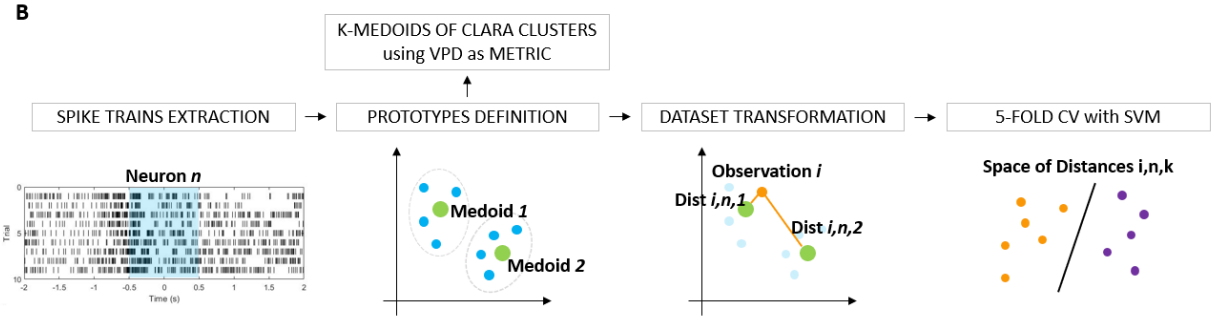


Fig. 1: Schematic of methods. A) Left: Monkey performing reach-grasp from a primate chair. Right: Tables with number of successful trials for each type of behavioral task. B) Flowchart of implemented pipeline. First, all the spike trains from the behavioral tasks under analysis are extracted. Then, the CLARA algorithm looks for the K medoids of the K clusters that best separate the training dataset. Each instance is then re-represented using its VPD with respect to all the medoids. Finally, a 5-fold CV with SVM and feature selection is performed to decode specific aspects of the movement from the transformed neuronal data.

The monkey was filmed while performing the behavioral tasks with an 8-high resolution camera system, and ethological scoring of the videos was performed to obtain the timestamps of the events. The list of successful trials for each type of grasp is reported in Fig.1A.

C. Data Processing for Classification

The neuronal recordings were first processed using a fully automated spike sorting algorithm (MountainSort4.0 [6]) and 71 single units were extracted. The features selected for the decoding process were the pairwise spike-train distances. Thus, based on the type of classification performed, specific windows of spike-trains were extracted from each sorted unit.

To reduce the number of spike-trains to be stored and the number of pairwise spike-train distances to be computed for training and testing the classifier, we defined representatives that best divided the training dataset. If the spiking pattern of a neuron is repeatable over different trials of the same task, and there is a high inter-task distance, then the dataset is likely to have well-defined clusters.

We used these clusters' centres to redefine the whole dataset: each spiking pattern of a neuron was represented by the Victor-Purpura distance (VPD) [7], [8] from the all the K representative spiking-patterns of the same neuron. The VPD is computed as the cost to transform one spike-train into another via spike removal/addition and spike shifting. The VPD depends on the parameter q_cost, which attributes different importance to temporal scales/jittering. In fact, it is good practice to test different values of this parameter to identify the one that gives the best discriminative performances. For our analysis, the q_cost search was performed on a logarithmic grid ($[1, 3, 5, 7]$ x $[1, 0.1, 0.01, 0.001]\ ms^{-1}$).

D. Clusters' Centres Definition

In order to keep the temporal structure of the activity without using a vector-space embedding [9], the *centre* of a cluster can be generated using random spiking patterns. However, a wiser choice is to select *medoids*, representative objects belonging to the same dataset.

For this purpose, we used *K-medoid*, a clustering algorithm that selects K medoids, so that the sum of distances between each medoid and any other instance belonging to the same cluster is minimized. In other words, the medoids are the most centrally located objects in the clusters. Indeed, K-medoid is generally considered more robust to outliers than K-means [10], which can select as *centre* elements placed outside the cloud of points.

We employed the CLARA (Clustering LARge Applications) algorithm [11] for performing the search of medoids. As K-means, this method requires the user to specify the number of clusters. We selected preliminarily K = 4. Moreover, we used VPD as metric for computing the clusters' dissimilarities. The CLARA algorithm was then repeated for each single unit.

E. Grasp Type and Laterality Decoding

In the first analysis we performed, we kept both food and carabiner grasping trials. Each repetition of the tasks was labeled as a combination of *{Pinch, Palmar} x {Right, Left}* features.

For each observation, the neurons' spike trains were extracted in a 500 ms window before the grasping event. For this type of classification, we considered only 38 out of 71 single units, basing our choice on neurons showing a discriminative distance matrix for *{Pinch, Palmar} x {Right, Left}* classes. The number of features amounted to 152 ($\#\ medoids * \#\ neurons$).

A 5-fold Cross-Validation (CV) was performed to train and evaluate the performances of a Support Vector Machine (SVM) in three different classification problems:

- *{Pinch, Palmar} x {Right, Left}*;
- *{Pinch, Palmar}*;
- *{Right, Left}*.

We refer to the first case as *multiclass* classification problem, whereas the last two are defined *binary* classification problems.

Optionally, inside the CV loop, a feature selection step can be performed. Only the training set is fed to the feature selection algorithm, in order to prevent data leakage and positively biased performances [12]. We chose the minimum-Redundancy-Maximum-Relevance (mRMR, MATLAB-fscmrmr [13]) feature selection algorithm, which is mainly based on mutual information between features and classes. Given the ratio between observations and predictors, we tested two different thresholds for feature selection to avoid overfitting: 4 and 16.

F. Presentation Proximity and Grasp Laterality Decoding

In a second set of analysis, we considered only the food grasping trials, as they added another level of classification. Even though, the reach-and-grasp movements were performed similarly across trials, the food could be presented either in reachable or non-reachable areas. In both situations, the monkey was trained to wait for the food to get closer to initiate the reaching movement.

Thus, each repetition of the food grasping task was labeled as a combination of *{Far, Near} x {Right, Left}* features.

Contrary to what done before, where only one timepoint was relevant for the study (*G*, grasping), here we explored the evolution of the spiking activity across all the different phases of food grasping. Thus, we identified three timestamps (*F*, food presentation; *G*, grasping; *M*, food touching the mouth) and we extracted the spike trains of the following windows: $(F, F + 500\ ms)$; $(G - 500\ ms, G)$; $(G, G + 500\ ms)$; $(M - 500\ ms, M)$. Each phase was treated as an independent dataset to be fed to the decoding algorithm.

Also in this case, we considered only the neurons showing, qualitatively, a discriminative distance matrix for *{Far, Near} x {Right, Left}*. Hence, 26 out of 71 single units were selected, creating a vector of 104 features.

In a similar fashion, a 5-fold CV was performed to train and test an SVM in three different classification problems:

- *{Far, Near} x {Right, Left}*;
- *{Far, Near}*;
- *{Right, Left}*.

Optionally, inside the CV loop, a feature selection step could be performed with thresholds 4 and 16.

III. RESULTS

A. {Pinch, Palmar} x {Right, Left}

First, we compared two different behavioural tasks, namely food and carabiner grasping. The aim was to capture and amplify the differences in neuronal response during the planning phase for two types of objects handling. We used a CV loop to train and test an SVM for the prediction of type of grasp (*{Pinch, Palmar}*) and hand chosen (*{Right, Left}*). We tested the predictions for both *multiclass* and *binary* classification problems. The performances (reported in Table I) were assessed in terms of mean accuracy over the 5 folds of the validation loop.

As Table I shows, the SVM classifier with no feature selection implemented (total of 152 features) reached 82.1% when trying to predict simultaneously both the type of grasp and the lateralization. For this *multiclass* problem, other two SVM models with 4 and 16 features were tested as well. The respective decoding performances were 62.6% and 77%.

As one would expect, the performances further improved in the two *binary* classification problems. For the prediction of type of grasp only (*{Pinch, Palmar}*), the classifier reached 88%, 94%, 95.5% with 4, 16, 152 features respectively. On the other hand, for laterality decoding, the classifier got 86.6%, 89.6%, 88% with 4, 16, 152 features respectively.

Table I also reports the values of q_cost for which the best performances were achieved. For the *multiclass* problem the values were generally lower than those used in the binary problems. The more the cost increases, the more the VPD is transformed from a rate distance to a temporal distance.

TABLE I: MEAN ACCURACY [%] (q_cost_VPD [$1/ms$])

	SVM_4	*SVM_16*	*SVM_152*
{Pinch, Palmar} x {Right, Left}	62.6 (0)	77 (0)	82.1 (7e-3)
{Pinch, Palmar}	88 (0.7)	94 (7e-3)	95.5 (0.3)
{Right, Left}	86.6 (0.03)	89.6 (0)	88 (0.5)

Mean accuracies over 5-fold CV. In brackets, the q_cost for which the accuracy associated was achieved.

B. {Far, Near} x {Right, Left} for each Phase

For the second analysis, we limited the study to food grasps only. Here, we wanted to observe the neuronal evolution through different phases of planning a food grasping movement. For this purpose, we independently trained and tested the four previously defined phases of grasping.

For each phase, we decoded the proximity of food presentation (*{Far, Near}*) and, again, the laterality (*{Right, Left}*). We tested for both *multiclass* and *binary* classification problems. The performances (reported in Table II) were assessed in terms of mean accuracy over the 5 folds of the validation loop.

Similarly to what done before, we created SVM models with different numbers of features (i.e., 4, 16, and 104), and we trained and tested them for all the possible combinations.

As Table II shows, the classifier for the *multiclass* problem reaches higher accuracies over the moment when the hand touches the food (72.5% with 16 feat). Whereas, for *{Far, Near}* higher performances can be found at the very beginning, when the food has just been presented (87.5% with 16 feat). Finally, for *{Right, Left}*, the best performances were again achieved over the actual grasp (95%-97.5% with 16 feat).

Table II also reports the values of q_cost for which the best performances were achieved.

TABLE II: MEAN ACCURACY [%] (q_cost_VPD [$1/ms$])

	Phase	*SVM_4*	*SVM_16*	*SVM_104*
{Far, Near} x {Right, Left}	1	50 (0.7)	60 (1e-3)	52.5 (0.3)
	2	70 (0.3)	72.5 (0.3)	67.5 (7e-3)
	3	52.5 (0.03)	72.5 (3e-3)	57.5 (0.3)
	4	52.5 (0.03)	52.5 (7e-3)	65 (0.01)
{Far, Near}	1	90 (0.1)	87.5 (0.01)	80 (0.1)
	2	65 (0.1)	65 (0.1)	77.5 (0.3)
	3	67.5 (0.7)	70 (3e-3)	65 (0.3)
	4	62.5 (0)	60 (0.07)	70 (0.3)
{Right, Left}	1	77.5 (3e-3)	87.5 (0.3)	62.5 (0.3)
	2	97.5 (0.01)	95 (0.05)	100 (0.3)
	3	92.5 (0.7)	97.5 (1e-3)	100 (0.1)
	4	80 (0.7)	87.5 (0.05)	95 (3e-3)

Mean accuracies over 5-fold CV. In brackets, the q_cost for which the accuracy associated was achieved.

IV. DISCUSSION

We explored the possibility of decoding three key features of grasp from clustering analysis of intracortical recordings in the ventral premotor cortex. We developed a cross-validated machine learning algorithm that can successfully predict the desired type of grasp and laterality, and that can decode the proximity of the food presented.

In both analyses, the algorithm reaches good accuracies in the *multiclass* problems, but its performances can be further improved in the *binary* classification problems. This suggests the possibility of using hierarchical decoding techniques for elevating the accuracies in case of simultaneous decoding of different features of grasping.

Moreover, in the second analysis, we observed an interesting response to food presentation. Even though the distinction between far and near is not reflected in a reaching movement, we are still able to differentiate between them. Since the electrodes are positioned in the premotor cortex, and, thus, the response cannot be vision-based, we speculate that a planning phase takes place even though the monkey does not perform a far or near grasp. Similarly to *motor imagery*, we are thus decoding an action possibility [14]. Then, as soon as the food gets closer, the planning is remodulated, and the option of choosing either right or left hand arises.

The processing pipeline that we suggest implementing is the one with 16 features selected. Indeed, the number of total features decreases by almost one order of magnitude (*e.g.*, 16 instead of 152) and, hence, there are less pairwise VPDs to be computed and less representative spike-trains (i.e., medoids) to be stored. This allows for virtually online computations without losing significantly in terms of performances.

This study is currently limited to a small set of grasp characteristics, but we intend to include other types of objects for defining a complete set of hand pre-shaping in the premotor cortex, and we also want to include the execution of different extensions of the arm during reaching phase. We also believe that an approach based on multi-units' activity, rather than single-units', might prove useful for online implementation of the algorithm, without losing sensitively in accuracy.

Finally, we want to complete the second analysis performed with a *phases-mix*. This means that we want to implement a classifier trained and tested simultaneously on all phases, in order to observe its ability of capturing the grasp phase as well.

ACKNOWLEDGEMENT

The work was supported by #NEXTGENERATIONEU (NGEU) and funded by the Ministry of University and Research (MUR), National Recovery and Resilience Plan (NRRP), project MNESYS (PE0000006) – A Multiscale integrated approach to the study of the nervous system in health and disease (DN. 1553 11.10.2022). It was also supported by #NEXTGENERATIONEU (NGEU) and funded by the Ministry of University and Research (MUR), National Recovery and Resilience Plan (NRRP), project BRIEF (IR0000036) - Biorobotics Research and Innovation Engineering Facilities (DN. 103 17.06.2022).

REFERENCES

[1] S. Shokur, A. Mazzoni, G. Schiavone, D. J. Weber, and S. Micera, 'A modular strategy for next-generation upper-limb sensory-motor neuroprostheses', *Med (N Y)*, vol. 2, no. 8, pp. 912–937, Aug. 2021, doi: 10.1016/j.medj.2021.05.002.

[2] G. Onose *et al.*, 'On the feasibility of using motor imagery EEG-based brain-computer interface in chronic tetraplegics for assistive robotic arm control: a clinical test and long-term post-trial follow-up', *Spinal Cord*, vol. 50, no. 8, pp. 599–608, Aug. 2012, doi: 10.1038/sc.2012.14.

[3] J. F. Kalaska, R. Caminiti, and A. P. Georgopoulos, 'Cortical mechanisms related to the direction of two-dimensional arm movements: relations in parietal area 5 and comparison with motor cortex', *Exp Brain Res*, vol. 51, no. 2, pp. 247–260, Jul. 1983, doi: 10.1007/BF00237200.

[4] C. Kemere *et al.*, 'Detecting neural-state transitions using hidden Markov models for motor cortical prostheses', *J Neurophysiol*, vol. 100, no. 4, pp. 2441–2452, Oct. 2008, doi: 10.1152/jn.00924.2007.

[5] R. A. Andersen, E. J. Hwang, and G. H. Mulliken, 'Cognitive neural prosthetics', *Annu Rev Psychol*, vol. 61, pp. 169–190, C1-3, 2010, doi: 10.1146/annurev.psych.093008.100503.

[6] J. E. Chung *et al.*, 'A Fully Automated Approach to Spike Sorting', *Neuron*, vol. 95, no. 6, pp. 1381-1394.e6, Sep. 2017, doi: 10.1016/j.neuron.2017.08.030.

[7] J. D. Victor and K. P. Purpura, 'Nature and precision of temporal coding in visual cortex: a metric-space analysis', *J Neurophysiol*, vol. 76, no. 2, pp. 1310–1326, Aug. 1996, doi: 10.1152/jn.1996.76.2.1310.

[8] T. Kreuz, 'Measures of spike train synchrony', *Scholarpedia*, vol. 6, no. 10, p. 11934, Oct. 2011, doi: 10.4249/scholarpedia.11934.

[9] W. Wu and A. Srivastava, 'Estimating summary statistics in the spike-train space', *J. Comput. Neurosci.*, vol. 34, no. 3, pp. 391–410, Jun. 2013, doi: 10.1007/s10827-012-0427-3.

[10] J. Han, M. Kamber, and J. Pei, '10 - Cluster Analysis: Basic Concepts and Methods', in *Data Mining (Third Edition)*, J. Han, M. Kamber, and J. Pei, Eds. Boston: Morgan Kaufmann, 2012, pp. 443–495. doi: 10.1016/B978-0-12-381479-1.00010-1.

[11] E. Schubert and P. J. Rousseeuw, 'Faster k-Medoids Clustering: Improving the PAM, CLARA, and CLARANS Algorithms', in *Similarity Search and Applications*, Cham, 2019, pp. 171–187. doi: 10.1007/978-3-030-32047-8_16.

[12] R. Hornung, C. Bernau, C. Truntzer, R. Wilson, T. Stadler, and A.-L. Boulesteix, 'A measure of the impact of CV incompleteness on prediction error estimation with application to PCA and normalization', *BMC Medical Research Methodology*, vol. 15, no. 1, p. 95, Nov. 2015, doi: 10.1186/s12874-015-0088-9.

[13] C. Ding and H. Peng, 'Minimum redundancy feature selection from microarray gene expression data', *J Bioinform Comput Biol*, vol. 3, no. 2, pp. 185–205, Apr. 2005, doi: 10.1142/s0219720005001004.

[14] L. Bonini, M. Maranesi, A. Livi, L. Fogassi, and G. Rizzolatti, 'Space-Dependent Representation of Objects and Other's Action in Monkey Ventral Premotor Grasping Neurons', *J. Neurosci.*, vol. 34, no. 11, pp. 4108–4119, Mar. 2014, doi: 10.1523/JNEUROSCI.4187-13.2014.

Impact of model selection procedure on Deep Neural Networks ensemble for the Choroid Plexus segmentation in Multiple Sclerosis

V. Visani[1], V. Natale[2], A. Colombi[3], A. Tamanti[3], A. Bertoldo[1], C. Marjin[3], G.K. Ricciardi[4], F.B. Pizzini[2], M. Calabrese[3] and M. Castellaro[1]

[1] *Department of Information Engineering, University of Padova, Padova, Italy*
[2] *Department of Diagnostic and Public Health, University of Verona, Verona, Italy*
[3] *Department of Neurosciences, Biomedicine and Movement Sciences, University of Verona, Verona, Italy*
[4] *Neuroradiology Section, Diagnostic Pathology Department, University of Verona, Verona, Italy*

***Abstract*— The Choroid Plexus (ChP) is a brain vascular tissue involved in regulatory processes. ChP Volume (ChPV) modifications are related to neurodegenerative disorders. Therefore, ChPV, that can be obtained from manual segmentation of brain MRI, is an imaging biomarker candidate to monitor disease evolution. This work proposes a method for the automatic segmentation of ChP based on hyperparameters optimization of Deep Neural Networks (DNNs). Twenty-Seven hyperparameters and architectures combinations were trained on T1-w MRI with two different selection strategies: select the best models using the routinely used Dice Coefficient and combining it to the Absolute Percentage Volume Difference. The selection of the ten best models was made on bias and variance of Absolute Percentage Volume Difference and best DNNs were ensembled by majority voting for both selection strategies. The proposed ensemble models outperform single DNNs (Dice Coefficient for both ensembles: 0.81±0.07; Percentage Volume Difference - ensemble Dice: 0.41±10.75%; ensemble Dice&Volume: -0.05±10.49%). Ensemble segmentations obtained using the combination of Dice and Absolute Percentage Volume Difference are preferable since the variance obtained in the testing phase is slightly lower than the commonly used Dice metric. Therefore, the proposed ensemble of DNNs, selected exploiting both Dice and Absolute Percentage Volume Difference, is a promising tool to obtain automatic quantification of the ChPV.**

***Keywords*—Choroid Plexus, Deep Neural Networks, Semantic Segmentation, Multiple Sclerosis.**

I. Introduction

The Choroid Plexus (ChP) is a vascular tissue located inside the brain ventricles. The ChP is present in all four ventricles, and it is part of the Blood-CSF-Barrier (BCSFB) [1]. The main role of the ChP is the production of relevant portion of the CSF, therefore it can be considered part of the glymphatic system [2]. Moreover, the ChP is involved in further features: active and passive transport of substances between BCSFB and Blood-Brain-Barrier (BBB); intercellular communication through gap junctions; maintenance of brain homeostasis; clearance pathways in the brain for drugs, proteins, and waste products; immunological function implicated in inflammatory processes [1], [3], [4]. Recent studies [5], [6] have shown the relation between functional and anatomical modifications of the ChP and several neurological and neurodegenerative disorders or worse symptoms in psychosis, like schizophrenia or depression. The ChP volume (ChPV) has been observed to be altered in presence of inflammatory states in Multiple Sclerosis and Alzheimer's disease [7], [8]. Therefore, the ChPV is a promising candidate to become a biomarker to improve the understanding and monitoring of neurological disorders [9]. Consequently, the need to robustly delineate ChP to obtain ChPV is gaining interest. The gold-standard technique to depict this anatomical region is the manual segmentation on T1-w MR images (here considered as ground-truth (GT)). However, this method is time-consuming, and it is affected by inter- and intra-operator variability due to the size, tortuosity, and low contrast between the ChP and the ventricles [10]. It has just been demonstrated the lack of accuracy of the freely available methods (FreeSurfer, Gaussian Mixture Model) to automatically segment the ChP [11].

The aim of this work is to propose a method for the automatic segmentation of the ChP based on Deep Neural Networks (DNNs). Dice Coefficient [12] is the metric broadly used in semantic segmentation task with DNNs to select the best model configuration during the validation phase. However, the final goal is having both a good ChP delineation and robust ChPV estimates. Our purpose is to firstly compare the performances of selected configurations using the Dice Coefficient or combining it to the Absolute Percentage Volume Difference. Secondly, we investigate whether the ensemble of the best ten DNNs obtained with both approaches improves the ChP segmentation in terms of ChPV estimate. The DNN performance will be compared to the GT performed by trained neuroradiologists with ITK-SNAP [13].

II. Materials and methods

A. Materials

The dataset was provided by the Multiple Sclerosis Centre of the University Hospital of Verona. The dataset is composed by 128 subjects (age 36.7±10.1 years): 24 healthy controls (HC) and 104 Relapsing-Remitting Multiple Sclerosis (RRMS). Images were acquired with two different Philips 3T MRI scanners: 67 subjects on a Philips Achieva TX with 8-channels head coil (Software version R3.2.3.2) (Scanne r1) and 61 subjects on a Philips Elition S with 32-channels head coil (Software version R5.7.2.1) (Scanner 2). Parameters of 3D T1-w MPRAGE sequences for Scanner 1 were: resolution 1x1x1 mm; SENSE acceleration factor: 2.5; TE/TR: 3.7/8.4 ms; FA: 9°; total acquisition time: 4min 50s. MPRAGE

sequence parameters for Scanner 2: 1x1x1 mm; compressed SENSE acceleration factor: 4; TE/TR: 3.7/8.4 ms; FA: 8°; total acquisition time: 3min 20s. On each T1-w MRI, the ChP in the two lateral ventricles were segmented by consensus of two neuroradiologists. We randomly divided the population into a training set (64 subjects: 12 HC/20 RRMS Scanner 1, 32 RRMS Scanner 2), a validation set (28 subjects: 5 HC/9 RRMS Scanner 1, 14 RRMS Scanner 2) and a testing set (36 subjects: 7 HC/14 RRMS Scanner 1, 15 RRMS Scanner 2).

B. Methods: DNNs training and performance

The first step of this work was the training of the DNNs using the Dice Coefficient or the combination of Dice Coefficient and Absolute Percentage Volume Difference to select the best model parameters. We tested twice twenty-seven combinations of architectures and hyperparameters. DNNs were implemented in MONAI version 0.8 [14]. We had selected three DNNs architectures: 3D U-Net [15]; DynUNET, MONAI implementation of nnU-Net [16]; UNETR [17]. We had considered as DNNs hyperparameters: the patch size (64x64x64, 96x96x96, 128x128x128), the loss function (Dice, CrossEntropy (CE), combination of Dice and CE (DiceCE)). We trained all the configurations with the application of data augmentation transforms (rotations, translations, small rotations, intensity shifts) to the training set.

We used the Adam-Weighted optimizer [18] with parameters: learning rate (1e-04), weight decay (1e-05), max iterations (4e04), batch size (1).

Goodness of each combination was assessed on the testing set. The analysed performance indices were: Dice Coefficient, Absolute Volume, Percentage Volume Difference (ΔVol%) and Absolute Percentage Volume Difference (|ΔVol%|) (Eq. (1)).

$$|\Delta Vol\%| = 100 * \frac{|Volume_{GT} - Volume_{Prediction}|}{Volume_{GT}} \ [\%] \quad (1)$$

To establish a minimum requirement in ChPV quantification, a threshold of 21.4% for |ΔVol%| was used to guarantee the ability of the DNNs in detecting Multiple Sclerosis (MS) pathological alterations based on recent findings [19]. A t-test (α=0.05%) was performed on Dice Coefficient between the two ensembles obtained and on Absolute Volume between the GT and the single ensembles. The influence of the model variance on the ChPV estimate was analysed also with Bland Altman plot.

C. Methods: DNNs selection criterion for the ensemble

We performed the ensemble for both the selection strategies employing the same selection criterion, aiming to refine the segmentation. DNNs were scored on mean |ΔVol%| and the ten best DNNs capable of keeping the bias under the pathological alteration detection threshold (21.4%) were selected. The ensemble procedure took together the results of the best networks possibly producing a more robust and more flexible output than a single network. We modified the standard ensemble method in MONAI to include the selected DNNs. Our module created the ensemble using a majority voting procedure considering the single-model predictions, averaging the ten best candidate prediction maps. A probability threshold of 50% was then used to produce the final ensembled segmentation.

III. RESULTS

For both selection strategies, all tested configurations return an estimate of ChPV that is adequately precise in detecting differences between MS and controls (|ΔVol%| < 21.4%). To be more restrictive, the ten best configurations selected for the ensemble are below this threshold considering not only the bias but also the variance (1.96SD).

Tables I and II show the most relevant performance metrics for the top ten models and for the ensembles for both selection strategies. Most of the selected configurations are equal for the two strategies.

TABLE I: PERFORMANCE METRICS – DICE ENSEMBLE

Configurations	*Dice Coefficient [0-1]*	*Absolute Volume [mm³]*	*Percentage Volume Difference [%]*
GT	n.a.	2515±834	n.a.
Ensemble	0.81±0.07	2465±654	0.41±10.75
DynUNET96CE	0.81±0.07	2395±661	-2.66±10.11
DynUNET128CE	0.81±0.07	2350±725	-5.66±8.66
UNET128DiceCE	0.77±0.07	2489±705	1.06±11.56
UNETR128Dice	0.80±0.07	2445±660	-0.20±12.92
UNET96Dice	0.77±0.06	2472±651	1.10±12.65
UNETR128DiceCE	0.80±0.07	2586±706	5.23±12.12
DynUNET128Dice	0.80±0.07	2374±605	-2.67±13.30
UNETR128CE	0.80±0.07	2358±612	-3.50±12.74
UNET128Dice	0.78±0.06	2603±736	5.50±12.04
UNET96DiceCE	0.77±0.07	2413±574	-0.42±14.7

Performance metrics of the selected models and the ensemble of them for the Dice Coefficient selection strategy. The configurations are presented in form Architecture-PatchSize-LossFunction. The results are reported in the form (mean±SD). Dice Coefficient and Percentage Volume Difference metrics are calculated using GT T1-w manual segmentation as reference.

TABLE II: PERFORMANCE METRICS – DICE&VOLUME ENSEMBLE

Configurations	*Dice Coefficient [0-1]*	*Absolute Volume [mm³]*	*Percentage Volume Difference [%]*
GT	n.a.	2515±834	n.a.
Ensemble	0.81±0.07	2451±638	-0.05±10.49
DynUNET96CE	0.81±0.07	2413±693	-2.34±9.72
DynUNET128CE	0.81±0.07	2350±725	-5.66±8.66
UNETR96CE	0.80±0.07	2349±602	-3.86±11.94
UNET128DiceCE	0.77±0.05	2465±666	0.48±12.12
UNET96Dice	0.77±0.07	2472±651	1.06±12.65
UNETR128DiceCE	0.80±0.07	2613±697	6.51±11.89
DynUNET128Dice	0.80±0.07	2374±605	-2.67±13.30
UNETR128CE	0.80±0.07	2358±612	-3.50±12.74
UNET128Dice	0.78±0.06	2603±736	5.49±12.04
UNETR96DiceCE	0.79±0.07	2387±548	-1.23±13.93

Performance metrics of the selected models and the ensemble of them for the Dice Coefficient and Absolute Percentage Volume Difference selection strategy. The configurations are presented in form Architecture-PatchSize-LossFunction. The results are reported in the form (mean±SD). Dice Coefficient and Percentage Volume Difference metrics are calculated using GT T1-w manual segmentation as reference.

Dice Coefficient for the selected models is in range [0.77-0.81] for both selection strategy. Considering ΔVol%, the range of value for the Dice selection strategy considering |1.96SD| is (min-max) [12.77-17.54%], while that of the Dice&Volume is [12.06-18.4%].

The ensemble results of the best configurations for the two selection strategies underly equal performance in terms of

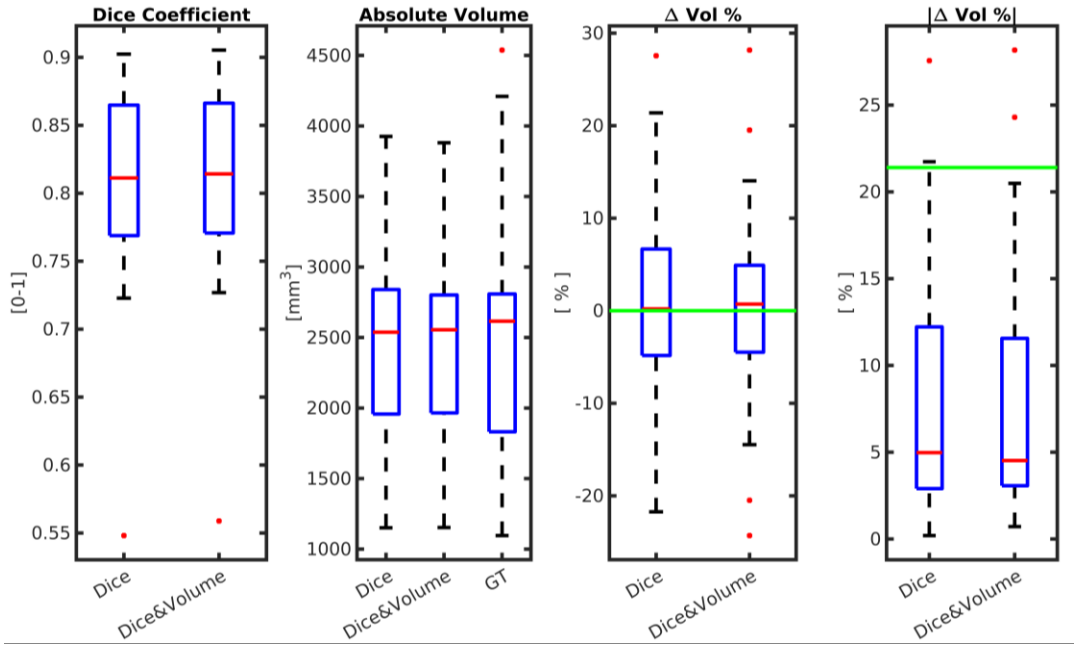


Fig. 1: Comparison between the ensemble of the ten best configurations selected considering as saving metric the Dice Coefficient (Dice) and the ensemble of the ten best configurations selected considering as saving metrics both Dice Coefficient and Absolute Percentage Volume Difference (Dice&Volume). From left to right, boxplot of: Dice Coefficient, Absolute Volume, Percentage Volume Difference (ΔVol%) and Absolute Percentage Volume Difference (|ΔVol%|) with highlighted in green the pathological alteration detection threshold for Multiple Sclerosis (21.4%). Reference: GT T1-w manual segmentation.

Dice Coefficient (0.81±0.07), while in terms of ΔVol% the ensemble Dice&Volume shows both a lower bias (-0.05%) than the other ensemble (0.41%), and slightly lower variance (SD ensemble Dice&Volume: 10.49%; SD ensemble Dice: 10.75%).

Fig. 1 shows the boxplot for the performance metrics calculated between the compared ensemble segmentations and the GT. As commented before, the Dice Coefficient is the same for both the ensemble predictions: the t-test accepts the null hypothesis. Concerning the volume metrics, by visual inspection the Absolute Volume, ΔVol% and |ΔVol%| are comparable. The t-test reveals that there are no statistically significant differences either between the two ensembles or between the single ensemble and the GT. However, the Inter Quartile Range between the 75th and the 25th percentiles for the ΔVol% metric are 9.39 for the ensemble Dice&Volume and 11.50 for the ensemble Dice, highlighting less variance when the selection method includes the |ΔVol%|.

In Fig. 2 it is shown a representative subject 3D T1-w MRI in coronal view with superimposed the ensemble segmentations and the GT manual segmentation. By visual inspection the two ensemble segmentations are comparable with GT.

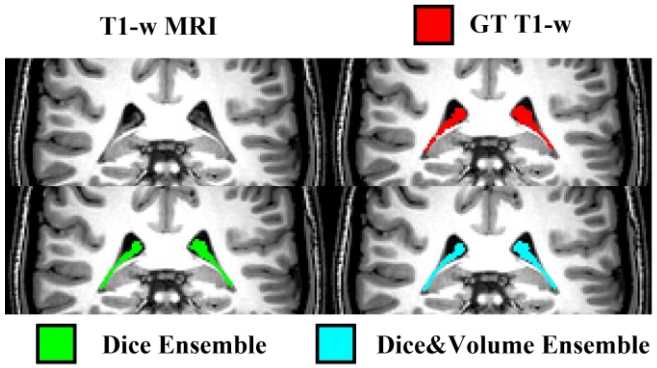


Fig. 2: Predicted segmentation results for a representative subject. 3D T1-w MRI (coronal view) with overlayed the ChP segmentations. From top left to bottom right: 3DT1-w MRI, 3D T1-w MRI with overlayed GT T1-w manual segmentation, the ensemble of the ten best configurations selected considering as saving metric the Dice Coefficient (Dice Ensemble), ensemble of the ten best configurations selected considering as saving metrics the Dice Coefficient and the Absolute Percentage Volume Difference (Dice&Volume Ensemble).

Fig. 3 shows the Bland Altman plot of the Dice Coefficient

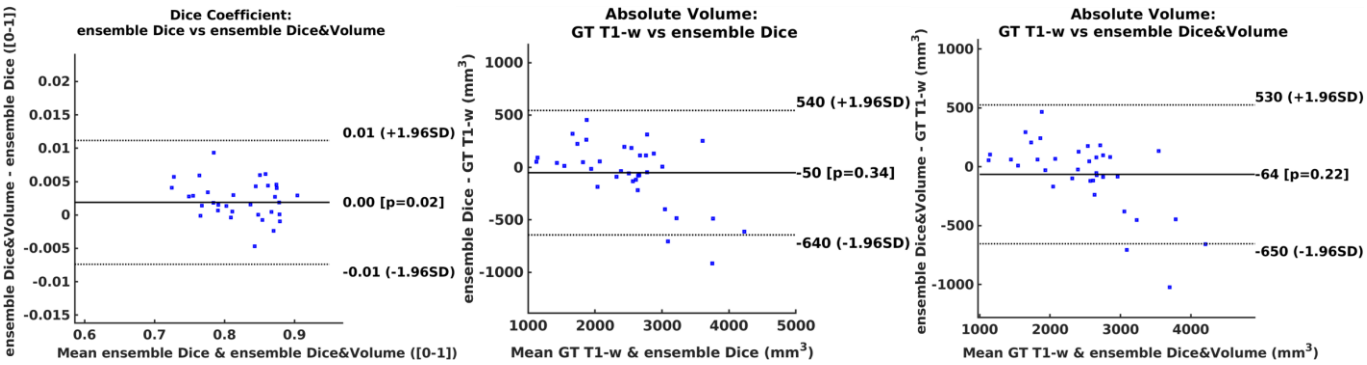


Fig. 3: Bland Altman plot for (left-right): Dice Coefficient of the two compared ensemble segmentations (Dice, Dice&Volume), Absolute Volume of GT T1-w manual segmentation and ensemble Dice and ensemble Dice&Volume.

of the two compared ensemble segmentations, Absolute Volume of GT T1-w manual segmentation and ensemble Dice and ensemble Dice&Volume. Regarding the Absolute Volume, the two ensembles behave similarly.

Taking into consideration the whole results, the addition of the volume information during the validation step gives better results in terms of less variability of ChPV.

IV. Discussion

Among the selected configurations, it is difficult to find a set of parameters that maximize the predicted segmentation performance in terms of accuracy, robustness and good ChPV estimate for both the selection strategies. The more selected loss functions are CE and DiceCE, suggesting that CE lowers the bias in ChPV estimates. The most selected patch size is 96x96x96, advising it as a good trade-off between the ChP size and the available image resolution preserving GPU memory occupancy. The more selected DNNs architectures are DynUNET and UNETR, suggesting that the use of self-configuring nets or transformers improves the results for this segmentation task. The goals of this work are to investigate if the addition of a volumetric score in the model selection during validation phase can improve the segmentation result and if the ensemble of a restricted pull of configurations exceeds the performance of a configuration taken individually.

Comparing the ensemble segmentations obtained with different selection strategies, on one hand it could be said that predictions don't differ in terms of Dice Coefficient and this result is confirmed by the visual inspection of the segmentations compared to the GT (Fig. 2), the t-test and the Bland Altman plot (Fig. 3). On the other hand, the t-test result reports they are not statistically different in terms of volume metrics. The ensemble predictions obtained with Dice selection strategy provide a higher variability in the estimates. Fig. 1 shows in the ΔVol% boxplot a lower variability in the ensemble segmentation obtained from the selection strategy that uses both Dice Coefficient and |ΔVol%| to save the models, suggesting this is the winning strategy to have the best trade-off between bias and variance in the ChPV estimate, improving the performance of the single selected DNNs.

The main limitation of this study is the small dataset, even if the studies published in this field have comparable number of samples with the GT obtained manually [20]. It should be tested the consistency of these results in a huge number of subjects varying the type of patients (e.g., Alzheimer's Disease, depression).

V. Conclusion

The ensemble of the selected DNNs provides reliable estimate of ChPV combining DNNs such as DynUNET and UNETR. In the validation phase, the use of both Dice Coefficient and Absolute Percentage Volume Difference metrics to save the best model parameters instead of just Dice Coefficient lowers the variability of the ChPV estimate, increasing the reproducibility and the robustness of the ChP segmentation.

These findings suggest that DNNs ensembles could be further used to automatically estimate ChPV in large cohort of patients; furthermore, the addition of a volume metric to select the models on which to perform the ensemble improves the performance of the segmentation task.

References

[1] H. H. Damkier, P. D. Brown, and J. Praetorius, "Cerebrospinal fluid secretion by the choroid plexus," Physiol Rev, vol. 93, no. 4, pp. 1847–1892, Oct. 2013.

[2] N. A. Jessen, A. S. F. Munk, I. Lundgaard, and M. Nedergaard, "The Glymphatic System: A Beginner's Guide," Neurochem Res, vol. 40, no. 12, pp. 2583–2599, Dec. 2015.

[3] H. Lassmann, "Pathogenic mechanisms associated with different clinical courses of multiple sclerosis," Front Immunol, vol. 9, no. 3116, 2019.

[4] R. Spector, R. F. Keep, S. Robert Snodgrass, Q. R. Smith, and C. E. Johanson, "A balanced view of choroid plexus structure and function: Focus on adult humans," Exp Neurol, vol. 267, pp. 78–86, May 2015.

[5] N. Althubaity et al., "Choroid plexus enlargement is associated with neuroinflammation and reduction of blood brain barrier permeability in depression," Neuroimage Clin, vol. 33, Jan. 2022.

[6] P. Lizano et al., "Association of Choroid Plexus Enlargement With Cognitive, Inflammatory, and Structural Phenotypes Across the Psychosis Spectrum," American Journal of Psychiatry, vol. 176, no. 7, pp. 564–572, Jul. 2019.

[7] V. A. G. Ricigliano et al., "Choroid Plexus Enlargement in Inflammatory Multiple Sclerosis: 3.0-T MRI and Translocator Protein PET Evaluation," Radiology, vol. 301, no. 1, pp. 166–177, Oct. 2021.

[8] E. Tadayon, A. Pascual-Leone, D. Press, and E. Santarnecchi, "Choroid plexus volume is associated with levels of CSF proteins: relevance for Alzheimer's and Parkinson's disease," Neurobiol Aging, vol. 89, pp. 108–117, May 2020.

[9] V. Fleischer et al., "Translational value of choroid plexus imaging for tracking neuroinflammation in mice and humans," Proc Natl Acad Sci U S A, vol. 118, no. 36, Sep. 2021.

[10] E. Tadayon, B. Moret, G. Sprugnoli, L. Monti, A. Pascual-Leone, and E. Santarnecchi, "Improving Choroid Plexus Segmentation in the Healthy and Diseased Brain: Relevance for Tau-PET Imaging in Dementia," Journal of Alzheimer's Disease, vol. 74, no. 4, pp. 1057–1068, Apr. 2020.

[11] V. Visani et al., "Hyperparameter and architecture optimization of Deep Neural Network to estimate the Choroid Plexus Volume in Multiple Sclerosis", ISMRM Workshop on "Neurofluids: Anatomy, Physiology & Imaging", Sapienza University of Rome, Rome, Italy, 21st-24th September 2022. [Online]. Available: https://www.ismrm.org/workshops/2022/Neurofluids

[12] J. Bertels et al., "Optimizing the Dice Score and Jaccard Index for Medical Image Segmentation: Theory & Practice," Nov. 2019.

[13] P. A. Yushkevich et al., "User-guided 3D active contour segmentation of anatomical structures: Significantly improved efficiency and reliability", NeuroImage, vol. 31, no. 3, pp. 1116–1128, Jul. 2006. Available: www.itksnap.org

[14] MONAI Consortium, "MONAI: Medical Open Network for AI (0.8.0)," Zenodo, 2021. [Online]. Available: https://doi.org/10.5281/zenodo.5728262

[15] O. Ronneberger, P. Fischer, and T. Brox, "U-Net: Convolutional Networks for Biomedical Image Segmentation," May 2015. [Online]. Available: https://arxiv.org/abs/1505.04597

[16] F. Isensee, P. F. Jaeger, S. A. A. Kohl, J. Petersen, and K. H. Maier-Hein, "nnU-Net: a self-configuring method for deep learning-based biomedical image segmentation," Nat Methods, vol. 18, no. 2, pp. 203–211, Feb. 2021.

[17] A. Hatamizadeh et al., "UNETR: Transformers for 3D Medical Image Segmentation," Mar. 2021. [Online]. Available: https://arxiv.org/abs/2103.10504

[18] D. P. Kingma and J. Ba, "Adam: A Method for Stochastic Optimization," in ICLR, Dec. 2015. [Online]. Available: http://arxiv.org/abs/1412.6980

[19] J. Müller et al., "Choroid Plexus Volume in Multiple Sclerosis vs Neuromyelitis Optica Spectrum Disorder," Neurology - Neuroimmunology Neuroinflammation, vol. 9, no. 3, p. e1147, May 2022.

[20] M. Schmidt-Mengin et al., "Axial multi-layer perceptron architecture for automatic segmentation of choroid plexus in multiple sclerosis," Sep. 2021. [Online]. Available: https://arxiv.org/abs/2109.03778

3D moles mapping and analysis for automatic melanoma detection

G. Nanto[1,2], A. Berto[1], L. Dall'Olmo[3,4], C. Ciolfi[5], F. Scolaro[5], M. Alaibac[5], S. Mocellin[3,4], A. Galgaro[2] and F. Scarpa[1]

[1] *Department of Information Engineering, University of Padova, Italy*
[2] *Department of Geoscience, University of Padova, Italy*
[3] *Department of Surgical Oncological and Gastroenterological Sciences, University of Padova, Italy*
[4] *Veneto Institute of Oncology IOV – IRCCS, Padova, Italy*
[5] *Department of Medicine, University of Padova, Italy*

***Abstract*— Melanoma is the most aggressive skin cancer and its detection in the early stage is crucial for a successful medical treatment. Many algorithms have been developed to provide an objective examination, but none proved effective in clinical practice. We propose an innovative and automatic method that derives a 3D model of the patient's body from multiple macroscopic images through photogrammetry, identifies all nevi and computes diagnostic indices related to asymmetry, border, colour, dimension, and volume for each detected nevus. Good preliminary results were obtained from 15 subjects, who underwent a cutaneous biopsy for a melanoma suspicious nevus. The proposed method provides an analysis of a large portion of the body, potentially the total body, identifying the nevi with a precise location in the skin surface, and calculating useful clinical indices. The derived 3D model allows computing novel volumetric information of nevi, which can provide new insight for melanoma diagnosis. In addition, the precise localization of each nevus in the patient's body can facilitate monitoring its evolution over time. For these reasons, the proposed method could be a major advance in melanoma screening and diagnosis.**

***Keywords*— melanoma, photogrammetry, 3D reconstruction, moles mapping.**

I. Introduction

Melanoma arises from melanocytic cells and it can occur anywhere these cells reside [1]. The most frequent type of melanoma is melanoma cutaneous, which is the most aggressive skin cancer. Melanoma affects over 300,000 [2] people worldwide every year.

Important risk factors for melanoma are skin phototype (type 1 and 2 according to Fitzpatrick scale), high-dose and intermittent UV light exposure, genetics, and the presence of a great number of moles on the skin surface.

Delayed diagnosis leads to worse outcomes, thus making early diagnosis a fundamental step to improve patient survival [3]. Through secondary prevention (screening of moles), early diagnosis could provide improved outcomes, a better quality of life, and reduced economic burden for the healthcare system.

Melanoma diagnosis is based on clinical examination of pigmented skin lesions, followed by epiluminesce microcopy. In particular, to identify a suspicious mole, the ABCDE (i.e., Asymmetry, Border irregularity, Colour variation, Dimension, Evolution over time) rule was developed, which considers the shape, structure, colour, dimension of the mole, and evolution of the mole over time. The ABCDE rule assumes that asymmetrical moles, with irregular contours, multiple colours or peculiar colours such as blue or white, and a diameter larger than 6mm are significant risk factors for melanoma [4]. The most relevant and prognostic factor for melanoma is tumour thickness, linked to the proliferation of malignant melanocytes toward the subcutaneous tissue [5].

Currently, melanoma diagnosis is dependent on the dermatologist's experience and consists in the identification of all suspected moles in the body, followed by the manual acquisition of the image of a single mole, the framing of the mole with a dermatoscope and the placement of a camera in the lens; this procedure is exposed to individual judgment and reasoning. Dermatologic examination application during everyday clinical practice is crucial but it is also time and resource-consuming. Furthermore, this procedure is affected by individual reasoning and judgment.

A dermatologic examination can identify melanoma-suspicious moles, but only a biopsy and the subsequent histological examination can lead to the final diagnosis of cancer [6]. It is thus useful to find new technologies and methods able to assist clinicians in identifying suspicious moles that need a more accurate evaluation, especially when dealing with patients with hundreds of moles.

In the last two decades, many algorithms have been developed to provide an objective examination, mainly providing an image-level classification, or estimating clinical indices from an image depicting a single mole. Recent research works indicate that Machine Learning [7][8][9][10] and Deep Learning [11][12][13][14] techniques can improve diagnostic procedures for skin melanoma detection. Currently, these methods analyze an image depicting a single mole usually acquired through a dermatoscope. Most of the Literature algorithms provide an image-level classification suggesting whether the image depicts a melanoma. Instead, some recent Literature algorithms [15][16][17] provide a pixel-wise segmentation that detects the region corresponding to the mole and can be used to extract quantitative clinical indexes that can be directly provided to clinicians or used to suggest an automatic melanoma classification. Despite the significant progress made over the last few years, the Literature shows a subjective assessment and limited clinical relevance of the proposed methodologies.

The most common instrument for skin lesions examination is the dermatoscope, also known as polarized dermatoscope or epiluminescence microscope. Various models are produced and marketed by different companies. It is a hand-held visual

aid device a clinician can use to examine and diagnose each single skin lesion. This tool does not allow automatic mapping of patient moles and is rarely integrated with automatic single mole analysis software. Systems that were recently proposed for total-body mapping are based on the analysis of a single macroscopic image depicting a large portion of the patient's skin, thus not providing a 3D moles mapping. In addition, further analysis of each single skin lesion is manually performed, thus reducing the benefit of an automated system.

The device that is proposed in this Project allows a 3D mapping of the patient body, potentially the total body, combined with the automated identification and analysis of every single mole in the skin surface. Thus, it could be a major advance in melanoma screening and diagnosis.

II. Methods

Fifteen adult patients referred to the Veneto Institute if Oncology (IOV) of Padova for a cutaneous excisional biopsy of an atypical mole were included in this study. To take part in the study, after being properly informed about the aim, methods, and implications of the study, all patients must sign the informed consensus, approved by the local Ethical Committee.

12 images of the whole patient's back and suspicious lesions to be biopsied had been taken at each session. The images were acquired for each patient using a system prototype which consists of a vertical structure with a horizontal movable arm containing 12 cameras and 4 polarized led lights. All 12 cameras shoot simultaneously so that the movements of the patient did not influence the acquisition of images. This structure was developed and made based on the Italian patent n° IT 102016000132357 [18]. Fig.1 shows a sketch of the medical device which is currently in use at University of Padova.

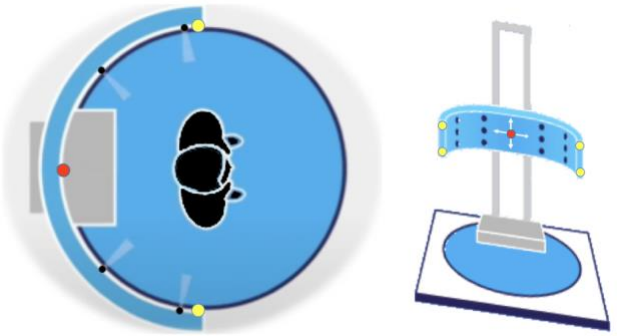


Fig. 1: Sketch of the medical device. Black dots correspond to cameras, yellow dots correspond to polarized led lights.

With the medical device, 12 pictures acquired from multiple viewpoints of the region of interest are taken a few days before the biopsy is performed.

A few weeks after the surgical biopsy, an histological exam of the excised lesion is available. This pathological report represents the gold standard for the diagnosis of cutaneous melanoma.

Photogrammetry technology may allow increasing the accuracy of clinical criteria. Moreover, depicting a large portion of the body allows for identifying the moles that differ from the others, which is one of the main clinical features indicating melanoma (the so-called ugly duckling sign) [19].

A 3D model is then reconstructed using the Structure from Motion (SfM) Photogrammetry technique. The procedure finds common key points between images, aligns the photos, creates a mesh, and then textures it. For the various parts of the obtained model, images corresponding to the best orientations for the specific part under analysis are extracted and called 2.5D images. The obtained 3D model is useful to evaluate the thickness of each mole and it could be an efficient tool for dermatologists to detect moles that are changed over time (part of the E criterion of the ABCDE rule).

A specific algorithm has been developed for the analysis of the obtained 3D model, to automatically identify and analyze every single mole.

For each 2.5D image, the HSV (Hue, Saturation, Value) colour space is considered and the positions of the moles in the skin area are identified by analyzing the intensity of channel S (Fig2.b). Channel S is indeed a relevant channel for drawing attention to the moles, which are lighter than the rest of the skin and therefore identified as local maxima. After the localization of every mole on the S channel as a local maximum of the region of interest, a cropped image of 120x120 pixels for every mole is produced from the original image. The crop is created so that each mole corresponds to an image in which approximately 30% of pixels belong to the mole. By creating the image this way, mole segmentation can easily and accurately be performed.

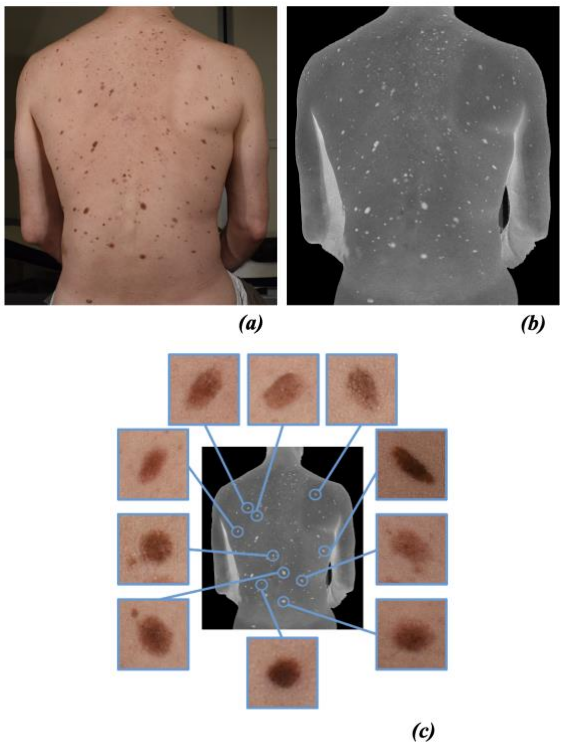


Fig. 2: (a) One of the 12 images of the back of a patient. (b) Representation with channel S. (c) Cropped images of some moles obtained by channel S representation.

Fig.2 shows one of the 12 pictures of the back of a patient (Fig2.a); its representation with channel S once the background was removed, which emphasizes the moles

(Fig2.b); an example of some cropped images with one mole on the centre, which are easily obtained thanks to the representation in channel S, that identifies all the moles as local maxima (Fig2.c).

The RGB (Red, Green, Blue) colour space of the cropped image is then considered, in particular channel blue, which is the one that allows the best identification of the border of the mole. The border is then segmented through local thresholding; active contours are then applied to refine the contour.

ABCDE characteristics are then derived. The asymmetry of the segmented area is estimated by using principal axes and calculated with the rotation matrix; the variance of the distances between the centroid and each border point is used to estimate a border index; the number of peaks in H is used to estimate information about the color; major and minor principal axes are used to compute the dimension of the mole (Fig3.a). In addition, the thickness (Fig3.b) of each individual mole is calculated on the corresponding region of the 3D model. Fig.3 shows a portion of the patient's back, focusing on one mole from which minor and major principal axes and their length are derived; moreover, Fig3.b shows the thickness of the mole which is derived from the 3D model. Fig.4 shows the histogram of the H channel of the mole in the previous figure and the histogram obtained by a mole with colour variation. The latter histogram (Fig.4b) denotes the presence of multiple distributions and peaks.

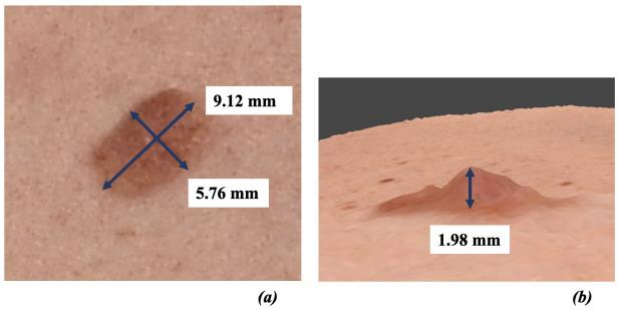


Fig. 3: (a) 2.5D crop image of nevus detected with automatic segmentation border and lengths of diameters. (b) Mole thickness was taken from the 3D model.

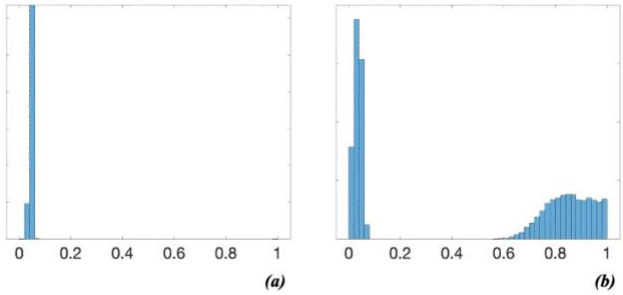


Fig. 4: (a) histogram of H channel of the mole in the previous figure. (b) histogram of H channel of a mole with variation in colour.

III. Results

Images from 15 subjects were considered. For each subject, 12 back skin images were simultaneously acquired using 12 digital cameras equipped with polarizing filters (Nikon D3500). Each subject had one mole considered suspicious by an expert dermatologist and was referred for a cutaneous excisional biopsy.

The proposed algorithm correctly identified all the main nevi in the patient's back and all suspicious moles were considered among the moles automatically identified.

For evaluating the segmentation, 30 moles were considered and analyzed both manually and automatically: for each subject, it was considered the suspicious mole, which was about to be biopsied, and another randomly selected mole. The IoU (Intersection over Union) index was therefore calculated in the 30 moles by comparing the automatic segmentation and the manual segmentation. All the segmented moles showed an IoU index of about 0.9: being this very close to 1, the result denotes a good correspondence between automatic and manual segmentation.

The automatically estimated clinical indices were used to distinguish normal moles from those with suspected melanoma. Although a global index has not yet been developed, in the considered limited dataset the suspicious moles differ in anomalous values of color variations (4 moles), asymmetry and dimension (3 moles), border irregularity (2 moles), or high values in all the derived clinical indexes (6 moles). The thickness proved to be useful for classifying as normal two moles which otherwise would have been misclassified as suspicious.

These preliminary results encourage the further development of the proposed method and the evaluation of a large number of subjects. An exhaustive investigate about accuracy, specificity and sensitivity of the proposed method for melanoma detection is also required.

IV. Conclusion

This Project aims to develop a system that can be beneficial for melanoma detection and for mole monitoring in a population screening program. Indeed, the current methodology is exposed to clinicians' experience, and subjective judgment, time consuming and attention demanding.

The medical device proposed in this Project consists of 12 cameras and 4 polarized led lights, which allow the simultaneous acquisition of 12 high resolution images of the patient cutaneous surface from different viewpoints. These images are used to build a 3D model of the patient skin surface, through photogrammetry. An algorithm has been developed to analyze the obtained 3D model, providing clinicians with a mole mapping and with visual and quantitative information automatically derived for each mole, providing a reliable map of the suspicious moles.

The proposed hardware and software system has been tested on 15 patients referring to IOV for a suspicious mole that needs to be excised. The acquired images allow obtaining a 3D model of the skin surface of each subject. The algorithm specifically developed in this Study was able to correctly identify all the main nevi depicted in the images. Consistency between manual and automatic segmentation was also obtained. Finally, the automatically derived clinical indexes (ABCD: asymmetry, border irregularity, colour variation, dimension), combined with the measurement of volume

(thickness) obtained by the 3D model, allow the correct identification of the suspicious moles among the others.

The results of the biopsies will be used to improve the specificity of the algorithm. In addition, once data will be collected from a large number of patients, images and verified labels will be used for the training of an algorithm based on Machine\Deep Learning techniques which can lead to the accurate and generalizable classification of suspicious moles.

Further developments of the proposed algorithm will include the identification of the ugly duckling sign, i.e., the mole which is different from the others because of its shape or colour. Indeed, the acquired macroscopic images depict a large portion of the skin surface in which many moles are present, and the one that looks different from the others can be easily detected and then highlighted for evaluation by clinicians.

In addition, a specific procedure for the computation of evolution over time from images acquired from the same patient at different times will be developed. Indeed, patients involved in this study took part in the follow-up session 5/6 months after the first one. The comparison and quantitative measure of the same mole imaged at different times might provide fundamental information about the evolution over time of pigmented lesions, a well-known criterion of suspicion presence of melanoma.

Although the two images of the same patients taken few months apart already show some small differences in nevi through image registration, more follow-up sessions need to be done to see relevant changes of each nevus.

REFERENCES

[1] K. Wolff, R. Johnson, and McGraw Hill Professional, *Fitzpatrick's Color Atlas and Synopsis of Clinical Dermatology*. 2009, p. 1104.

[2] M. Gracia-Hernandez, Z. Munoz, and A. Villagra, 'Enhancing Therapeutic Approaches for Melanoma Patients Targeting Epigenetic Modifiers', *Cancers*, vol. 13, no. 24, p. 6180, Dec. 2021, doi: 10.3390/cancers13246180.

[3] D. D. Xiong, P. Barriera-Silvestrini, and T. J. Knackstedt, 'Delays in the surgical treatment of melanoma are associated with worsened overall and melanoma-specific mortality: A population-based analysis.', *J. Am. Acad. Dermatol.*, vol. 87, no. 4, pp. 807–814, Oct. 2022, doi: 10.1016/j.jaad.2022.06.1190.

[4] E. M. Senan and M. E. Jadhav, 'Analysis of dermoscopy images by using ABCD rule for early detection of skin cancer', *1st Int. Conf. Adv. Inf. Comput. Trends Data Eng. AICDE - 2020*, vol. 2, no. 1, pp. 1–7, Jun. 2021, doi: 10.1016/j.gltp.2021.01.001.

[5] H. R. Ghasemi Basir, P. Alirezaei, S. Ahovan, and A. Moradi, 'The relationship between mitotic rate and depth of invasion in biopsies of malignant melanoma', *Clin. Cosmet. Investig. Dermatol.*, vol. Volume 11, pp. 125–130, Mar. 2018, doi: 10.2147/CCID.S158043.

[6] C. Garbe *et al.*, 'European consensus-based interdisciplinary guideline for melanoma. Part 2: Treatment - Update 2022', *Eur. J. Cancer*, vol. 170, pp. 256–284, Jul. 2022, doi: 10.1016/j.ejca.2022.04.018.

[7] V. Rajinikanth, S. C. Satapathy, N. Dey, S. L. Fernandes, and K. S. Manic, 'Skin Melanoma Assessment Using Kapur's Entropy and Level Set—A Study with Bat Algorithm', in *Smart Intelligent Computing and Applications*, vol. 104, S. C. Satapathy, V. Bhateja, and S. Das, Eds. Singapore: Springer Singapore, 2019, pp. 193–202. doi: 10.1007/978-981-13-1921-1_19.

[8] N. S. Zghal and N. Derbel, 'Melanoma Skin Cancer Detection based on Image Processing', *Curr. Med. Imaging Former. Curr. Med. Imaging Rev.*, vol. 16, no. 1, pp. 50–58, Jan. 2020, doi: 10.2174/1573405614666180911120546.

[9] A. Zakeri and A. Hokmabadi, 'Improvement in the diagnosis of melanoma and dysplastic lesions by introducing ABCD-PDT features and a hybrid classifier', *Biocybern. Biomed. Eng.*, vol. 38, no. 3, pp. 456–466, Jan. 2018, doi: 10.1016/j.bbe.2018.03.005.

[10] M. Masood *et al.*, 'Multi-Class Skin Cancer Detection and Classification Using Hybrid Features Extraction Techniques', *J. Med. Imaging Health Inform.*, vol. 10, no. 10, pp. 2466–2472, Oct. 2020, doi: 10.1166/jmihi.2020.3176.

[11] M. A. Albahar, 'Skin Lesion Classification Using Convolutional Neural Network With Novel Regularizer', *IEEE Access*, vol. 7, pp. 38306–38313, 2019, doi: 10.1109/ACCESS.2019.2906241.

[12] A. Adegun and S. Viriri, 'Deep learning techniques for skin lesion analysis and melanoma cancer detection: a survey of state-of-the-art', *Artif. Intell. Rev.*, vol. 54, no. 2, pp. 811–841, Feb. 2021, doi: 10.1007/s10462-020-09865-y.

[13] Y. Li and L. Shen, 'Skin Lesion Analysis towards Melanoma Detection Using Deep Learning Network', *Sensors*, vol. 18, no. 2, p. 556, Feb. 2018, doi: 10.3390/s18020556.

[14] K. H. Cheong *et al.*, 'An automated skin melanoma detection system with melanoma-index based on entropy features', *Biocybern. Biomed. Eng.*, vol. 41, no. 3, pp. 997–1012, Jul. 2021, doi: 10.1016/j.bbe.2021.05.010.

[15] R. Kaur, H. GholamHosseini, R. Sinha, and M. Lindén, 'Automatic lesion segmentation using atrous convolutional deep neural networks in dermoscopic skin cancer images', *BMC Med. Imaging*, vol. 22, no. 1, p. 103, Dec. 2022, doi: 10.1186/s12880-022-00829-y.

[16] S. Oukil, R. Kasmi, K. Mokrani, and B. García-Zapirain, 'Automatic segmentation and melanoma detection based on color and texture features in dermoscopic images', *Skin Res. Technol.*, vol. 28, no. 2, pp. 203–211, Mar. 2022, doi: 10.1111/srt.13111.

[17] H. Ashraf, A. Waris, M. F. Ghafoor, S. O. Gilani, and I. K. Niazi, 'Melanoma segmentation using deep learning with test-time augmentations and conditional random fields', *Sci. Rep.*, vol. 12, no. 1, p. 3948, Mar. 2022, doi: 10.1038/s41598-022-07885-y.

[18] A. Galgaro and G. Teza, 'Three Dimensional Mapping for Melanoma Diagnosis'. Italian Patent 102016000132357, 2018.

[19] C. Gaudy-Marqueste *et al.*, 'Ugly Duckling Sign as a Major Factor of Efficiency in Melanoma Detection', *JAMA Dermatol.*, vol. 153, no. 4, p. 279, Apr. 2017, doi: 10.1001/jamadermatol.2016.5500.

Error perception in different environments: Monitor vs Augmented Reality

A. Farabbi[1], L. Pizzulli[2], E. Sala[1], L. Santini[1], and L. Mainardi[1]
[1] *Dipartimento di Elettronica, Informazione e Bioingegneria, Politecnico di Milano,*
[2] *Dipartimento di Ingegneria dell'Informazione, Università di Pisa*

***Abstract*—Detection of errors results in a typical brain response, identified in the Electroencephalographic (EEG) signal called Error Potential (ErrP). The ErrP is widely used for correcting the output of external devices (e.g. autonomous driving, Brain-Computer Interfaces) and, therefore, its identification and its correct stimulation are crucial.**
In this paper, we present the analysis conducted on the EEG signal recorded from 17 subjects that underwent a protocol of error stimulation in two environments: through at a Monitor and in a Virtual Theatre. Each session consisted of three consecutive acquisitions.
The comparison of the two environments in terms of temporal characteristics of the ErrP (Grand Average and Single Trial analysis) resulted in a significantly more pronounced and faster response of the brain during the Monitor acquisition (Mann-Whitney test, with a p-value threshold of 0.05).
Moreover, it has been noticed that the amplitude of the characteristic peaks followed a decreasing trend along sessions, due to the repetitiveness of the experiments and therefore boredom of the participants.
In conclusion we were able to assess a more robust stimulation of the ErrP in the Monitor environment, reflected in a stereotypical waveform of the Evoked Potential. This may be due to the subjects not having the habit of using Augmented Reality or Virtual Reality.

***Keywords*—Signal processing, Electroencephalography, Evoked Potential, Augmented Reality.**

I. INTRODUCTION

The perception of errors by subjects is reflected in their brain activity and can be detected in the electroencephalographic signal (EEG). In particular, it results in a characteristic Evoked Potential (EP) named Error Potential (ErrP) [1]. The anterior cingulate cortex, a region located in the medial-frontal areas of the brain, is the primary location for the error-related activity [2]. Depending on the task, various types of ErrPs can be identified, one of which is elicited when there is an error in the interaction between a user and a machine. This type of ErrP exhibits a characteristic pattern, consisting of a negative peak at 250 ms post-error, a positive peak at 320 ms, and a final negative peak at 450 ms [3]. The ErrP finds major application in Brain-Computer Interfaces(BCI), systems that permit to use an external device using the interpretation of brain activity. In this field, the ErrP is mainly used to correct the erroneous output of the BCI system (i.e. the one not expected by the subject) [5].
Moreover, the detection of errors in real-time can be employed also in other sectors such as autonomous driving [6] or psychiatry. Concerning the latter case, literature has highlighted that the performance in detecting errors by subjects is strictly linked to their attention level [7].
The detection of errors during ErrPs stimulation experiments can be highly variable and dependent on the cognitive state and the engagement level of the subject during the trials. This variability can greatly impact the ability to accurately identify the presence of ErrPs in the EEG recordings. Therefore, it is essential to carefully design an engaging and effective protocol for catching user attention, as well as to use an appropriate experimental setup for stimulation, in order to obtain reliable and robust results [8].
Virtual Reality (VR) and Augmented Reality (AR) technologies have become increasingly popular in brain stimulation experiments due to their ability to enhance user engagement and involvement. However, research has shown that the performance of these technologies can be affected by the subject's level of familiarity and comfort when using them [9].
In this paper, we present a study that investigates the analysis of the ErrP signal when stimulated by video-games in two different environments: a standard monitor and a Virtual Theatre using Augmented Reality (AR) technology. The study aims to compare the ErrP signal in these two environments and to understand how the use of VR/AR technology affects the realization of the ErrP signal. The results will provide valuable information on the potential benefits and limitations of using VR/AR technology in brain stimulation experiments.

II. METHODS

A. Protocol

The analysis has been conducted on 7 females and 10 males participants (age: 21.8 $\pm$ 0.77 years). The protocol for stimulating the ErrP was created using Unity [10], and it involves a car moving along a road with randomly appearing checkpoints (represented as rings) on the left or right side of the street. The car has a 50% chance of approaching the checkpoint or going in the opposite direction. If the car misses the checkpoint, an ErrP is expected to be elicited. Each subject is presented with a total of 20 checkpoints per acquisition. The protocol is run twice for each subject, on different days at the same time. One session was taking place in a lab with the subject viewing the protocol directly on a monitor, while the other was in a Virtual Theatre, which is a room equipped with Augmented Reality technology. It consisted of a 360° round with a diameter of 7 meters and featured a projection on a curved surface of 360°. This advanced technology allowed

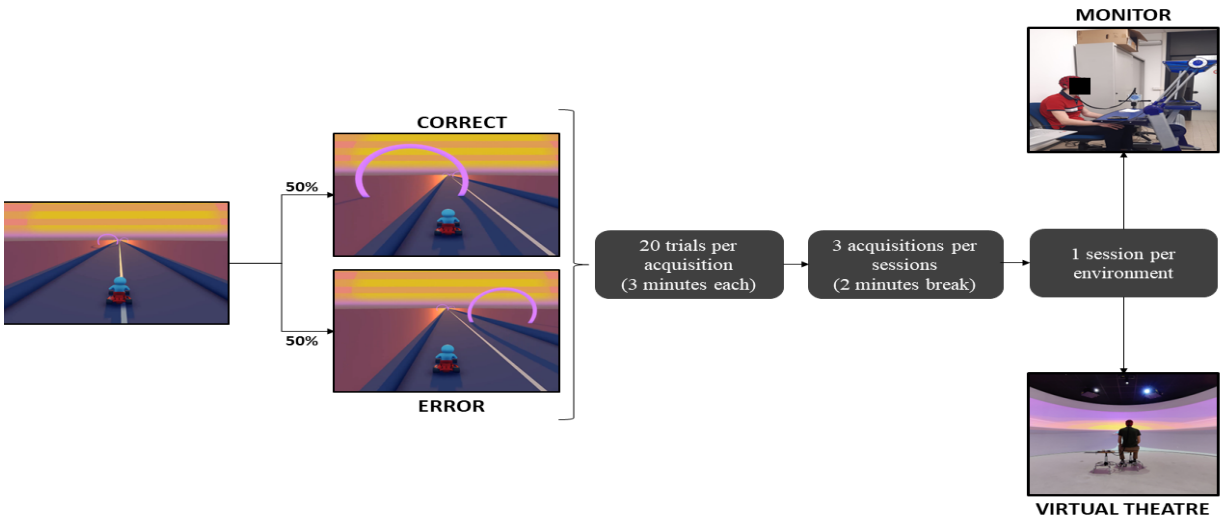


Fig. 1: Experimental protocol.

for a more immersive and interactive experience for the subjects during the feedback sessions. During each session, the participants were acquired three consecutive times with a break of 2 minutes between each acquisition. The environment of the first session was randomly chosen for each subject. The schematic of the complete protocol is reported in Fig. 1.
During the acquisition, the EEG signal was recorded with the EBNeuro BE Plust LTM amplifier with 64 electrodes placed on the scalp and with gel applied(EBNEURO, Florence, Italy). The synchronization of the EEG signal and the trigger of the event was made through software using the Lab Streaming Layer protocol.

B. EEG signal processing

The recorded EEG signal was first filtered between $1-30Hz$ to remove noise components at high frequencies. After having removed low amplitude channels (e.g. channels with flat recordings), Common Average Re-referencing was applied to attenuate the noise common to all channels. Thus, ErrP epochs of 1 second after the onset of the stimuli were extracted.
Artifacts related to eye movement (blinking and horizontal movement) were removed using Independent Component Analysis.
For each subject and for each acquisition, the Grand Average of the ErrP trials was computed together with the Single Trials estimates obtained by the subspace regularization method [11]. The subspace regularization is based on the regularized least squares scheme and needs an estimate of the background EEG to highlight the single ErrP response from the EEG.. In our work, we used the recorded EEG one second before the onset of each erroneous stimulus as an estimate of the background EEG of the corresponding Single Trial.

C. Extracted Features

We extracted the main characteristics of the ErrP both from the Single Trials and the Grand Averages. The main features extracted were: the latency and amplitudes of the positive peak between 200 and 500 ms; the latency and amplitude of the negative peak between 400 and 700 ms. The latency of the negative peak was computed with respect to the latency of the positive peak in order to avoid delay propagation.
These features were computed for the electrodes FCz and Cz since the ErrP realization is mainly localized in the fronto-cental area of the cortex.

D. Statistical analysis

The features extracted from the EEG recorded in the Monitor and Virtual Theatre environment were compared to assess any significant differences in the ErrP realization in the two different environments. In particular, we used the Mann-Whitney non-parametric test for each feature comparison and a p-value lower than 0.05 was used to assess significant differences.

III. RESULTS

In Fig.2 are reported the Grand Averages in Monitor(left) and Virtual Theatre(right) for the same subject as an example. We notice that the EP realization is closer to the characteristic waveform of the ErrP during Monitor acquisitions than during Virtual Theatre trials. In this latter case, no negative peaks are observable after the positive peaks, which also occurs with higher latency. These observations are confirmed by the distribution of the computed features reported in Tab.I. In the table are reported the medians, the 25th and the 75th quantiles of the distribution of each feature for each acquisition in Monitor and Virtual Theatre for electrodes FCz and Cz. The highlighted cells (in bold) show significant differences between the two environments ($p<0.05$; Mann Whitney test). It is worth noticing that, especially for the FCz electrode, the ErrP stimulated in the Monitor environment has more pronounced peaks (both negative and positive) and significantly lower latency for almost all acquisitions. It is also observable that

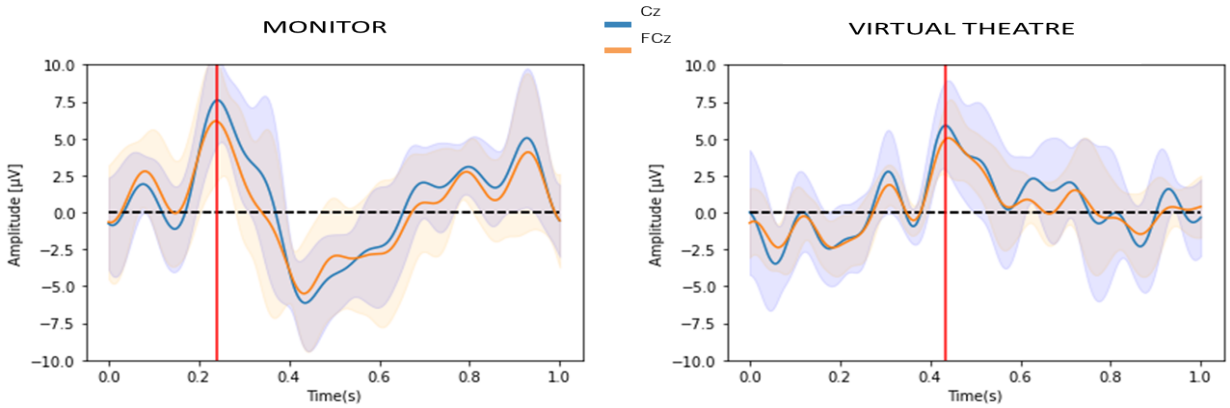


Fig. 2: Grand Average of the ErrP epochs in electrodes Cz(blue) and FCz(orange) in the investigated environments: Monitor (left) and Virtual Theatre(right). Shaded is reported as the confidence interval of the averaged epochs.

the amplitude of the peaks in absolute values tends to decrease along acquisition in both electrodes and environments. The Single Trial analysis confirms these findings. The distribution of the values of the computed features (after estimation of the single sweep with the subspace regularization method) are reported in Tab.II. Also in this type of analysis, the Monitor stimulation resulted in significantly higher amplitudes of the peaks and lower latencies, especially for electrode FCz. The amplitude of the peaks confirms the decreasing trend along the three acquisitions found in the Grand Average analysis. These differences along acquisitions have been tested with the Kruskall-Wallis non-parametric test, but no significant difference could be assessed both in the Grand Average and in the Single Trial analyses.

IV. Discussion

The presented results suggest that, in our data, the Monitor environment can better engage subjects during ErrP stimulation experiments. This is reflected in a faster and more pronounced response of the brain in the frontocentral area in presence of ErrP. Even if the characteristic waveform of the ErrP was obtained also when stimulated in the Virtual Theatre environment, the response was significantly slower and the amplitude of the peaks significantly lower. This issue can find

TABLE I: Distribution of the temporal features computed for the Grand Averages of the ErrP epochs. The values are reported with the following format: median(25th quantile,75th quantile). The latency of the negative peak was computed with respect to the latency of the positive peak. In bold are reported the values that resulted in a p-value less than 0.05 in the Mann-Whitney test.

	FCz			*Cz*		
Acquisition	1	2	3	1	2	3
Max Peak Amp[μV] (Monitor vs Virtual Theatre)	**4.35(2.79,4.98) vs 2.93(1.63,3.92)**	3.93(1.70,4.53) vs 2.093(1.51,3.96)	2.70(1.90,4.45) vs 2.31(1.38,3.14)	**6.63(5.31, 7.81) vs 3.42(1.85,5.77))**	4.83(3.63,7.17) vs 3.29(1.75,4.94)	**5.19(3.39,7.35) vs 2.78(1.45,5.21))**
Max Peak Lat[ms] (Monitor vs Virtual Theatre)	**246.09(226.56,277.83) vs 343.75(273.93,398.93)**	**251.95(225.10,275.88) vs 367.19(283.69,384.28)**	**240.23(220.70,261.23) vs 369.14(251.95,400.39)**	**244.14(226.56,280.27) vs 345.70(273.93,400.39)**	**251.95(229.98,308.11) vs 371.09(262.21,400.39)**	**257.81(239.75,268.07) vs 384.77(293.95,395.99)**
Min Peak Amp[μV] (Monitor vs Virtual Theatre)	-1.98(-2.97,-0.24) vs -0.45(-1.99,1.01)	**-2.78(-2.97,-1.23) vs -1.22(-1.65,-0.17)**	**-2.75(-3.92,-1.67) vs -1.75(-2.01,-0.38)**	-0.45(-3.82,0.11) vs -0.45(-2.12,-0.06)	-2.41(-2.78,-0.98) vs -0.96(-2.40,-0.32)	-2.31(-2.60,-0.35) vs -2.28(-2.75,-0.21)
Min Peak Lat[ms] (Monitor vs Virtual Theatre)	**87.12(82.13,91.44) vs 121.37(95.17,130.47)**	**98.32(84.44,106.75) vs 109.63(100.11,117.32)**	**94.77(81.33,102.08) vs 110.31(107.96,123.44)**	**86.39(82.76,90.98) vs 119.38(99.54, 127.66)**	102.06(89.98,108.62) vs 107.01(101.87,115.43)	99.65(85.32,107.00) vs 104.81(102.22,112.28)

TABLE II: Distribution of the temporal features computed for the ErrP Single Trials. The values are reported with the following format: median(25th quantile,75th quantile). The latency of the negative peak was computed with respect to the latency of the positive peak. In bold are reported the values that resulted in a p-value less than 0.05 in the Mann-Whitney test.

	FCz			*Cz*		
Acquisition	1	2	3	1	2	3
Max Peak Amp[μV] (Monitor vs Virtual Theatre)	**6.22(4.82,6.78) vs 3.61(1.98,4.41)**	**5.24(3.73,5.59) vs 3.27(1.89,4.77)**	**4.70(2.88,5.75) vs 2.76(1.49,3.21)**	**6.43(4.22, 7.12) vs 4.42(2.11,4.99))**	5.43(2.64,6.29) vs 4.27(3.71,5.33)	**5.11(3.41,6.21) vs 3.61(2.42,5.07))**
Max Peak Lat[ms] (Monitor vs Virtual Theatre)	**260.27(238.60,318.11) vs 317.81(263.13,374.43)**	**262.45(235.21,322.89) vs 321.64(253.29,376.17)**	**251.67(227.81,281.29) vs 307.94(248.08,386.20)**	**258.41(238.21,318.71) vs 309.61(251.44,381.21)**	**265.08(237.27,323.11) vs 331.12(255.01,376.88)**	**252.23(232.14,311.22) vs 315.91(250.45,372.06)**
Min Peak Amp[μV] (Monitor vs Virtual Theatre)	**-3.22(-6.83,-1.24) vs -1.11(-2.09,0.89)**	**-3.14(-3.81,-1.76) vs -1.32(-1.98,-0.11)**	**-2.75(-3.08,-1.73) vs -1.09(-1.81,-0.43)**	-3.11(-3.41,-2.22) vs -2.88(-3.98,-1.22)	-2.65(-3.13,-1.24) vs -1.99(-2.94,-1.45)	**-2.23(-2.85,-1.21) vs -2.41(-2.83,-1.67)**
Min Peak Lat[ms] (Monitor vs Virtual Theatre)	**78.24(58.98,95.21) vs 101.41(96.21,121.33)**	**65.02(54.45,98.05) vs 99.44(91.01,106.27)**	**82.71(75.77,87.10) vs 100.82(97.11,109.12)**	**80.75(62.90,93.41) vs 104.58(98.11, 117.62)**	**68.12(61.25,98.42) vs 98.60(93.22,106.07)**	**87.01(81.12,92.71) vs 102.31(99.23,107.91)**

answer in the feedback that the participants gave at the end of both sessions. Concerning the Virtual Theatre, they found the environment very distracting, not because of external factors, but due to the novelty of the environment itself. Indeed, none of the participants was used to work or play with AR or even VR.

The decreasing trend of amplitude peaks from the first to the third session may be a result of the repetition of the experiment. Additionally, a high rate of ErrP trials during acquisition may have removed the element of surprise, leading to weaker stimulation of the EP troughout the sessions.

V. Conclusions

In this paper, we presented a study on the differences in terms of temporal characteristics in stimulating brain response after an erroneous event looking at a Monitor and with AR. The Monitor provided a more robust stimulation of the ErrP mainly due to subjects being more used in interfacing with this type of technology. However, the repetition of acquisitions and the lack of interaction of subjects with the system led to the boredom of the participant. Lowering the probability of appearance of an erroneous event, integrating the presented protocol with an ErrP classifier and giving real-time correction of the position of the car, may engage more subjects' attention, resulting in a complete BCI system controlled by ErrP.

References

[1] W. Ferrez and J. del R. Millan. "Error-related EEG potentials generated during simulated brain-computer interaction. IEEE transactions on biomedical engineering". In: IEEE transactions on bio-medical engineering 55.3 (2008), pp. 923–929.

[2] Holroyd and M. Coles. "The neural basis of human error processing: Reinforcement learning, dopamine and the error-related negativity". In: Psychological Review 109.4 (2002), pp. 679–709. DOI:https://doi.org/10.1109/TBME.2007.908083.

[3] M. Falkenstein et al. "ERP components on reaction errors and their functional significance: a tutorial". In: Biological Psychology 51.2-3 (2000), pp. 87–107.

[4] M. E.Maier, N. Yeung, M. Steinhauser, "Error related brain activity and adjustments of selective attention following errors". In: Neuroimage 2011.56, pp.2339-2347, 2011.

[5] B. Dal Seno, M. Matteucci and L. Mainardi."Online detection of P300 and error potentials in a BCI speller". In: Computational intelligence and neuroscience, 2010.

[6] Z.Cao. "A review of artificial intelligence for EEG based brain computer interfaces and applications". In:Brain Science Advances, 2020. volume: 6(3). pp=162-170.

[7] Daffner KR, Scinto LF, Weitzman AM, Faust R, Rentz DM, Budson AE, Holcomb PJ. Frontal and parietal components of a cerebral network mediating voluntary attention to novel events. J Cogn Neurosci. 2003 Feb 15;15(2):294-313. doi: 10.1162/089892903321208213. PMID: 12683359.

[8] Fabien Lotte. "On the need for alternative feedback training approaches for BCI". Berlin Brain-Computer Interface Workshop, Sep 2012, Berlin, Germany. ⟨hal-00834391⟩

[9] R. Cassani, G. S. Novak, T. H. Falk and A. A. Oliveira. "Virtual reality and non-invasive brain stimulation for rehabilitation applications: a systematic review". In: Journal of NeuroEngineering and Rehabilation, 2020. Volume:17. pp=147. doi: https://doi.org/10.1186/s12984-020-00780-5.

[10] J.K. Haas. "A history of the unity game engine". 2014.

[11] P. Karjalainen, J. Kaipio, A. Holm, and M. Vauhkonen. "Subspace regularization method for the single-trial estimation of evoked potentials". In: IEEE transactions on bio-medical engineering, 1999.Vol: 46. pp:849-60. doi:10.1109/10.771195.

Time-frequency analysis of brain response to 3D slant texture and stereo cues

F. Peveri[1], G. Arnulfo[1], S. P. Sabatini[1] and A. Canessa[1]
[1] *University of Genoa, Department of Informatics, Bioengineering, Robotics and Systems Engineering*

***Abstract*— Visual system estimate surface slant from different visual cues, but on how and where these cues are integrated there is still much to be understood. The aim of this study is to fill the gap we identified regarding brain activity elicited by complex visual stimulation defined by different cue to slant. We used electroencephalography (EEG) and time – frequency analysis to characterize the cortical responses to monocular and binocular cues. We design slanted surfaces defined only by texture and binocular disparity, and surfaces defined by the two cues combined in a conflictual and non - conflictual configuration. The processing of these visual stimuli enhanced the same pattern of spectral modulation in all investigated ROIs but with different latencies and different patterns depending on the available visual cue.**

***Keywords*— EEG, visual cues, slant perception, texture, binocular disparity, conflictual cues**

I. Introduction

The primary aim of visual perception is to build an accurate representation of the outside world from the collection of signals impinging on the retina. One of the most difficult tasks is to estimate three-dimensional (3D) surface shape. The visual system makes use of different sources of information (cues) to accomplish it including binocular disparity, shading and lighting, and perspective / motion parallax [1]. The optimal estimation of 3D orientation of surfaces and shape recognition supports a range of behaviours, from placing and grasping objects to navigation in the environment. The 3D shape of an object at any point on a smooth surface can be closely approximated over a small neighbourhood by a plane and the most fundamental measure is local surface orientation [2]. Human adults can integrate different sensory estimations to reduce the uncertainty of the final percept (e.g., integrating stereo and texture information to judge surface slant). The optimal reduction in uncertainty is obtained by a weighted averaging of these estimates, in which each one is weighted in proportion to its relative reliability [3, 4]. We are then also able to integrate different visual cues when these are in *conflict* with each other, which means that each cue signals a different slant. Recent studies have investigated the neural mechanisms involved in processing individual visual cues [5, 6, 7] but the investigation of where and how cue combination occurs in the brain has not received the same interest, especially using electroencephalography (EEG) techniques. Two of the most prominent cues for estimating slant orientation are surface texture, that provide monocular information about the 3D structure and the binocular disparity, which results from the subtle differences between the two views of the eyes and provides a powerful cue to depth. In this work we focused on this two visual information to characterize the cortical responses to stimuli depicting slanted surfaces defined by texture and stereo cues in isolation, and the two cues combine in a conflictual and non-conflictual configuration.

II. Related work

Visual cues to slant have received a great deal of attention in the psychophysical, computational and neuroscience literature. Single cues combination is demanding for the brain, cortical activation measured with fMRI for different depth configurations are more discriminable when the other cues to depth (e.g., texture gradient) agree with disparity cues, suggesting [8, 9] a form of cooperative combination. Welchman et al [10] measured fMRI responses while observers judged the 3D slant of surface defined by binocular disparity and perspective. They compared behavioural and fMRI responses evoked by changes in one or both depth cues founding that the fMRI responses in extrastriate areas (hMT+/V5 and lateral occipital complex), rather than responses in early retinotopic areas, reflect differences in perceived 3D shape, suggesting that the cue-combination processes occur in higher visual areas. Other studies investigated the dynamic of visual processes [11] with EEG, which allows separating visual and later decisional processes in time. They combined EEG with a model-based analyses to determine at what latencies and electrode locations visual evoked potentials (VEPs) parametrically reflect visual cue reliability. Their stimuli were defined by contour and surfaces cues and the analyses shown that cue reliability effects are not systematically time-locked to response initiation or execution processes, but they observed effects at longer latencies, well after the typical latencies of visual processing mechanisms. They speculated that contour and surface cues are combined and the variations in their reliability are resolved at a relatively late stage of processing. Again, Murphy and Welchman [3] suggested that area V3B/KO is intricately involved in the integration of qualitatively dissimilar depth cues. In another recent work, Pegna et al. [12] used event-related potentials (ERPs) to study perceptual sensitivity to stereo versus mono input in a perceptual matching task. The task consisted of comparing the shape of two novel 3D objects under conditions of stereo and mono viewing. The results showed an early perceptual sensitivity to the mode of input shown by a negative amplitude modulation between 160 and 220 ms post-stimulus onset. Results also showed later modulation of ERP amplitude during an N2 component between 240 and 370 ms for stereo and mono input that was linked to the perceptual matching of shape. Moving to the time-frequency domain, some studies [13, 14, 15] have investigated, using desynchronization/synchronization (ERD, ERS) analysis, how different frequencies are modulated during visual cognitive tasks. They observed both alpha-band and beta-band ERD modulations during processing of visual cues. Gallotto at al. [20] probed alpha power modulations during directional cue

visualization, observing different modulations dependent on the type and direction of the presented stimulus.

III. Materials and Methods

Observers. Eight healthy participants with normal or corrected to normal vision from the University of Genoa. The mean age was 24 years.

Stimuli and set-up. Stimuli were grayscale stereograms of slanted textured surfaces, with slant (rotation about a central horizontal axis) defined separately by texture and binocular disparity. We generated the textures by Voronoi tessellation of a regular grid of points jittered in two dimensions [3]. We chose this type of texture in order to avoid the introduction of another cue-to-slant, the perspective. We presented the surfaces inside a circular aperture with a radius of 31.3° of visual angle and a blurred profile. We set the background color to a mid-grey. We design visual stimuli defined only by texture, only by binocular disparity and both cues combined in conflictual and non-conflictual manner.

We created stimuli and task using a 3D graphic engine, Unity3D, and exploiting Shaders, short powerful programs that render graphics data. Building incongruent visual cues to slant requires a virtual camera that renders the texture of a slanted plane and a projector, whose shader projects that texture on a plane with a different slant which is observed by two stereo cameras, see *Figure 1*. For stimuli defined only by disparity cue to slant we used random dots generated with Psychophysics Toolbox for MATLAB (PTB) [17], from there we obtained the two images for the right eye and left eye.

The set-up consists of 3D monitor (LG, 1920x1080, 42”, 100 Hz) connected to an Alienware with NVIDIA GeForce RTX 3090 Graphics card. To be able to stereoscopically see the stimulation with this apparatus, it was necessary to create the rendered visual stimulus by placing the two images (for left and right eye) side by side, halving the horizontal resolution. A photodiode was placed in the lower right corner of the monitor connected to an Arduino. This served to send trigger signals to the EEG amplifier though a Triggerbox, whenever the stimulus was displayed. For this reason, a white patch was lit for 0.1 s, on the lower right corner concurrently to the visual stimulus onset.

Procedure. We instructed subjects to wear 3D polarized glasses and sit at a viewing distance of 50 cm with the head stabilized by a chin rest. For each condition (only texture cue (condition *T*), only disparity cue (condition *D*), both cues (condition *TD*) and both cues conflictual (condition *TDc*), the task consisted of 360 total trials. As depicted in *Figure 2*, we presented the stimuli for 1.5 sec interspersed with a blank screen for 1 sec, for a total duration of each block of approximately 15 minutes. A 10-minute rest was provided between the four blocks. The slant value of the stimuli for the *T, D* and *TD* conditions were a random value in a range of 9 possible slants, from -40° to 40° with step 10°. Slant values for the *TDc* condition were chosen based on the perceptual metamers constructed by the subject. Before characterization task with EEG recording, subjects performed a perceptual matching task in order to produce a set of stimuli that were perceived to have the same slants but composed with a different combination of stereo and texture information. This was done by adjusting, with a handle-tracked board, the disparity cue of a stimulus (where the texture cue remains fixed to a random value between 15° to 45°, with a step of 5°) to match a cue-consistent reference stimulus with a slant of 30°. These 3D perceptual matches are sometimes called slant metamers: objects perceived to have the same slant but with different combinations of the available cues, the same thing that happens with the psychophysical phenomenon of color metamerism, where different spectral distributions can elicit the same perceived color [18].

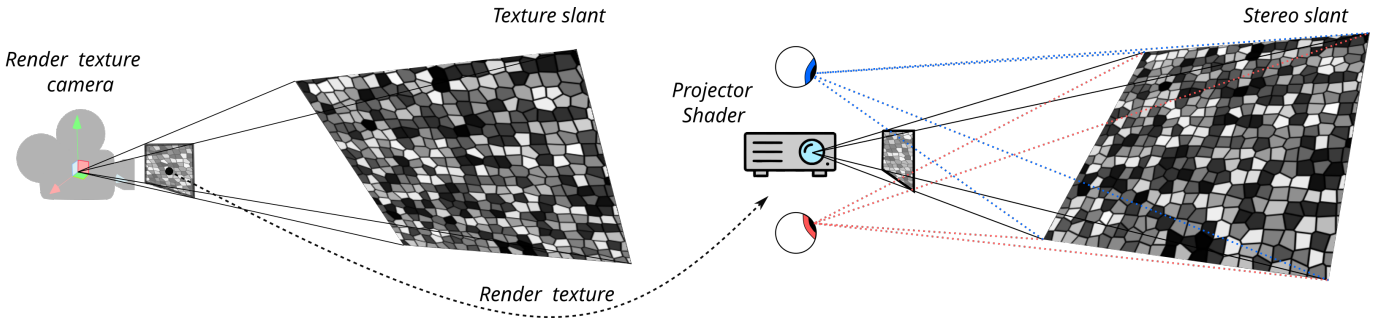


Figure 1: **Generation of cue - conflict stimuli with Unity3D.** How incongruent stimuli are generated. A textured plane object is viewed by a camera that creates a rendering texture that is passed to a projector that projects the "slanted texture" on a plane that physically has a different slant. This plane, viewed by two stereo cameras, yield the pair of images that define the final incongruent stimulus.

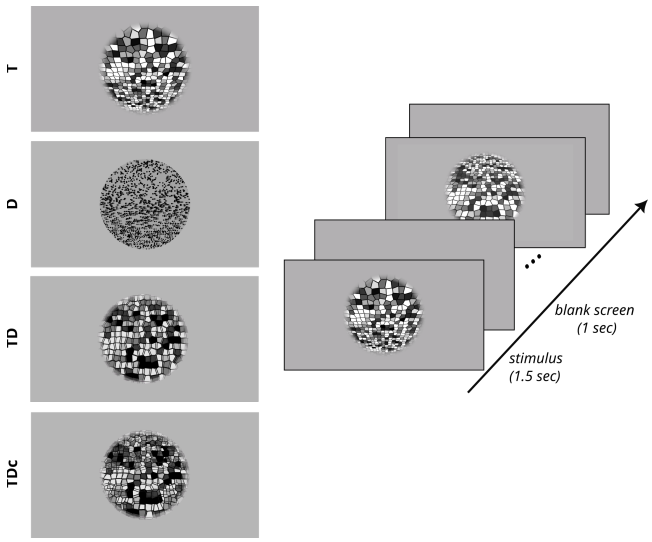


Figure 2: **Visual stimulation**. On the left, examples of displayed stimuli for all conditions. On the right, a block sequence of presentation. The task begins with a fixation cross, then the stimulus is presented for 1.5 sec follow by a blank screen for 1 sec.

EEG recordings and analysis. We recorded EEG activity using *BrainVisionRecorer* from *BrainProduct*. We used a 64-channel Ag/AgCl scalp electrodes that were referenced to the FCz. We adjusted individual electrodes until impedances were below 15 kΩ before starting and we continuously recorded EEGs at a sampling frequency of 500 Hz. Raw data underwent an off-line pre-processing artifact rejection and noisy electrodes removal. For this purpose, we used a dedicated pipeline to clean raw data. We firstly linearly detrend the data, in order to remove slow cortical activity, and applied a spectral and spatial filtering - *Zapline* filter [19] - to remove power line noise (50 Hz). Next, we removed ocular artifacts (e.g., blinks, horizontal eye movements). We decomposed the signal into physiological and artefactual components (muscle artifacts) by the use of independent component analysis (ICA method).
We carried out data processing with Brainstorm ®, an open-source software written almost entirely in MATLAB scripts that allows in-depth brain signals analysis [20] and custom scripts. Then, in order to study the behaviour of different ROI in the brain, electrodes were divided into four ROIs, based on their scalp position, representing frontal, central, parietal and occipital ROIs, summarized in table 1. ROIs signals were subsequently constructed averaging all electrodes data belonging to that group.

Time-frequency analysis and event related spectral perturbation. Time-frequency domain analysis was performed, in order to compute the event related spectral perturbation (ERSP), in each participant, for each ROI and for each condition. In order to obtain the ERSP we transformed data by means of a time-frequency decomposition using 80 Morlet wavelets in the [1;80]Hz range (central frequency = 1Hz, Full Width Half Maximum = 3s) [21]. To avoid border effect we applied the wavelet decomposition to the continuous data and then epoched the time-frequency representation around the stimulus onset with a window of 0.5 s pre-stimulus and 2.5 s post-stimulus.
To compute ERSP, firstly we performed a single trial division dividing the wavelet transform for each single trial by the power spectrum computed over the full trial interval [22]. After that, ERSPs trials data were averaged and log-transformed to better evaluate the intensity changes. Then, the magnitude of the spectrum was baseline-corrected by subtracting the mean log power spectrum computed within the pre-stimulus interval (−0.5 to 0 s).
Using ERSPs allowed us to evaluate possible synchronization and desynchronization latencies, for different stimulus conditions in the various considered ROIs. To better characterize amplitude and latencies of synchronizations and desynchronizations we computed also the Event related synchronization and desynchronization (ERD/ERS) integrating the ERSP in three specific frequency bands (theta [4-7] Hz, alpha [8-12] Hz and beta [13-30] Hz).

IV. Results

In *Figure 3* we reported the ERSP plot of each ROIs - from left to right - frontal, central, parietal and occipital, and for each stimulus condition, *T, D, TD* and *TDc* - top to bottom. Darker colour indicates stronger differences in spectral power compared to the baseline, red signals a power increment,

Table 1: ROIs electrodes table

Frontal	'Fp1','Fp2','F3','F1','Fz','F2','F4'
Central	'FC3','FC1','FC2','FC4','C3','C1','Cz','C2','C4'
Parietal	'CP3','CP1','CPZ','CP2','CP4','P3','P1','Pz','P2','P4'
Occipital	'PO7','PO3','POz','PO4','PO8','O1','Oz','O2'

which mean a synchronization, while blue signals a power decrement, which means a desynchronization. It is possible to see by eyes that there are synchronizations in theta and alpha bands and a desynchronization in beta band. More precisely it can be noted that, starting from the stimulus onset, there is a synchronization in the theta and alpha, while later these are followed by a greater desynchronization in the beta one. Regarding the duration and amplitude of these modulations, it is seen that synchronization has a higher amplitude but a shorter duration than desynchronization, which is more persistent, until the end of the stimulus presentation. Among the various ROIs, no major differences are identified, while what stands out is a difference in synchronization especially between condition *D* and the others and between *D* and *T* compared with the case in which both visual cues were presented (*TD* and *TDc*). *Figure 4* shows mean ERD/ERS values for the 4–7 Hz frequency band (first row), 8–12 Hz (second row) and 13–30 Hz (third row) as a function of time.

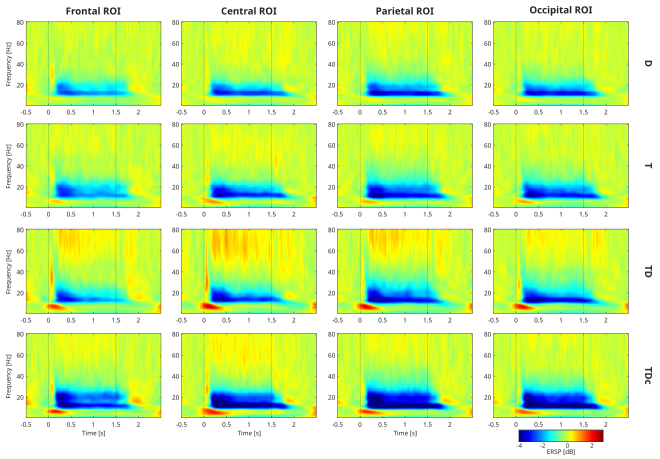


Figure 3: **ERSPs**. Mean time frequency maps representation across subjects for the four different ROIs. Each column represents a different ROIs, while each row is a different stimulus condition.

V. Conclusion

The aim of this work has been to investigate the cortical dynamics during a visual task to evaluate and highlight differences in how the brain process texture and stereo cues. We conducted EEG recordings on eight healthy participant and performed ERS/ERD analysis. We observed that slanted surfaces stimuli elicit synchronization in alpha and theta bands and a longer desynchronization in beta band. Further analysis is needed to investigate deeper the cortical activity. We did not perform a statistical analysis in this preliminary study because the number of subjects was relatively small. The next step will be to acquire a larger number of subjects in order to go looking for significant differences in cortical activity elicited by visual stimulation defined by monocular and binocular cues and defined by a conflicting combination of these.

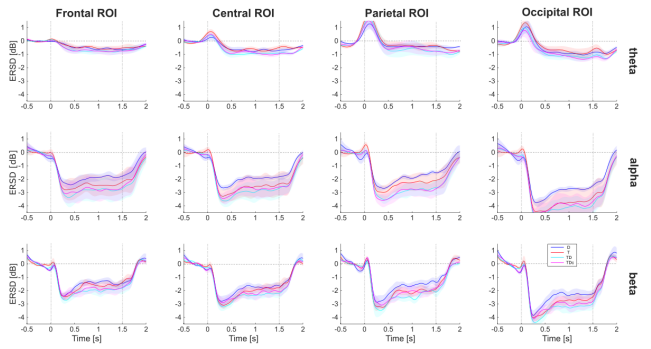


Figure 4: **Time course of ERSDs.** Mean ERSD (solid line) and SEM (shaded area, estimated using *jackknife* method) for the four different ROIs in theta, alpha and beta frequency bands, across subjects. The four colored lines in the plots represent the different conditions of the visual stimulus (*D, T, TD, TDc*).

REFERENCES

[1] Burge J, McCann BC, Geisler WS. Estimating 3D tilt from local image cues in natural scenes. J Vis. 2016 Oct 1;16(13):2. doi: 10.1167/16.13.2. PMID: 27738702; PMCID: PMC5066913.

[2] Oluk C, Bonnen K, Burge J, Cormack LK, Geisler WS. Stereo Slant Discrimination of Planar 3D Surfaces: Standard vs. Planar Cross-Correlation. bioRxiv; 2021. DOI: 10.1101/2021.03.11.434881.

[3] Nardini M, Bedford R, Mareschal D. Fusion of visual cues is not mandatory in children. Proc Natl Acad Sci U S A. 2010 Sep 28;107(39):17041-6. doi: 10.1073/pnas.1001699107. Epub 2010 Sep 13. PMID: 20837526; PMCID: PMC2947870.

[4] James M. Hillis, Simon J. Watt, Michael S. Landy, Martin S. Banks; Slant from texture and disparity cues: Optimal cue combination. *Journal of Vision* 2004;4(12):1. doi: https://doi.org/10.1167/4.12.1.

[5] Nguyenkim JD, DeAngelis GC. Disparity-based coding of three-dimensional surface orientation by macaque middle temporal neurons. J Neurosci. 2003 Aug 6;23(18):7117-28. doi: 10.1523/JNEUROSCI.23-18-07117.2003. PMID: 12904472; PMCID: PMC6740667.

[6] Tsutsui K, Sakata H, Naganuma T, Taira M. Neural correlates for perception of 3D surface orientation from texture gradient. Science. 2002 Oct 11;298(5592):409-12. doi: 10.1126/science.1074128. PMID: 12376700.

[7] Liu Y, Vogels R, Orban GA. Convergence of depth from texture and depth from disparity in macaque inferior temporal cortex. J Neurosci. 2004 Apr 14;24(15):3795-800. doi: 10.1523/JNEUROSCI.0150-04.2004. PMID: 15084660; PMCID: PMC6729342.

[8] Dövencioğlu D, Ban H, Schofield AJ, Welchman AE. Perceptual integration for qualitatively different 3-D cues in the human brain. J Cogn Neurosci. 2013 Sep;25(9):1527-41. doi: 10.1162/jocn_a_00417. Epub 2013 May 6. PMID: 23647559; PMCID: PMC3785137.

[9] Welchman AE, Deubelius A, Conrad V, Bülthoff HH, Kourtzi Z. 3D shape perception from combined depth cues in human visual cortex. Nat Neurosci. 2005 Jun;8(6):820-7. doi: 10.1038/nn1461. Epub 2005 May 1. PMID: 15864303.

[10] Mancuso G, Plomp G. Neural dynamics of cue reliability in perceptual decisions. J Vis. 2020 Aug 3;20(8):23. doi: 10.1167/jov.20.8.23. PMID: 32841319; PMCID: PMC7453047.

[11] Murphy AP, Ban H, Welchman AE. Integration of texture and Neurophysiol. 2013 Jul;110(1):190-203. doi: 10.1152/jn.01055.2012. Epub 2013 Apr 10. PMID: 23576705; PMCID: PMC3727040.

[12] Pegna AJ, Darque A, Roberts MV, Leek EC. Effects of stereoscopic disparity on early ERP components during classification of three-dimensional objects. Q J Exp Psychol (Hove). 2018 Jun;71(6):1419-1430. doi: 10.1080/17470218.2017.1333129. Epub 2018 Jan 1. PMID: 28524772.

[13] Alex I Wiesman, Boman R Groff, Tony W Wilson, Frontoparietal Networks Mediate the Behavioral Impact of Alpha Inhibition in Visual Cortex, *Cerebral Cortex*, Volume 29, Issue 8, August 2019, Pages 3505–3513, https://doi.org/10.1093/cercor/bhy220

[14] Klimesch W, Pfurtscheller G, Mohl W, Schimke H. Event-related desynchronization, ERD-mapping and hemispheric differences for words and numbers. Int J Psychophysiol. 1990 Apr;8(3):297-308. doi: 10.1016/0167-8760(90)90020-e. PMID: 2338409.

[15] Vecchio F, Nucci L, Pappalettera C, Miraglia F, Iacoviello D, Rossini PM. Time-frequency analysis of brain activity in response to directional and non-directional visual stimuli: an event related spectral perturbations (ERSP) study. J Neural Eng. 2022 Nov 9;19(6). doi: 10.1088/1741-2552/ac9c96. PMID: 36270505.

[16] Gallotto S, Duecker F, Oever ST, Schuhmann T, de Graaf TA, Sack AT. Relating alpha power modulations to competing visuospatial attention theories. Neuroimage. 2020 Feb 15;207:116429. doi: 10.1016/j.neuroimage.2019.116429. Epub 2019 Dec 2. PMID: 31805381.

[17] Brainard DH. The Psychophysics Toolbox. Spat Vis. 1997;10(4):433-6. PMID: 9176952.

[18] Cesanek E, Taylor JA, Domini F. Sensorimotor adaptation and cue reweighting compensate for distorted 3D shape information, accounting for paradoxical perception-action dissociations. J Neurophysiol. 2020 Apr 1;123(4):1407-1419. doi: 10.1152/jn.00718.2019. Epub 2020 Feb 26. PMID: 32101506.

[19] Klug M, Kloosterman NA. Zapline-plus: A Zapline extension for automatic and adaptive removal of frequency-specific noise artifacts in M/EEG. Hum Brain Mapp. 2022 Jun 15;43(9):2743-2758.

[20] Tadel F, Baillet S, Mosher JC, Pantazis D, Leahy RM. Brainstorm: a user-friendly application for MEG/EEG analysis. Comput Intell Neurosci. 2011;2011:879716. doi: 10.1155/2011/879716. Epub 2011 Apr 13. PMID: 21584256; PMCID: PMC3090754.

[21] Torrence C, Compo GP, Torrence C, Compo GP. A Practical Guide to Wavelet Analysis. Bull Am Meteorol Soc. 1998;79: 61–78.

[22] Grandchamp R and Delorme A 2011 Single-trial normalization for event-related spectral decomposition reduces sensitivity to noisy trials Front. Psychol. 2 236

Breast Cancer Imaging at Microwave Frequencies via Neural Networks

M. Ambrosanio[1], S. Franceschini[2], M.M. Autorino[2], F. Baselice[2] and V. Pascazio[2]
[1] *DiSEGIM, Department of Economics, Law, Cybersecurity, and Sports Sciences, University of Naples Parthenope, Via Guglielmo Pepe (Rione Gescal), 80035, Nola, Italy.*
[2] *Department of Engineering, Unversity of Naples Parthenope, Centro Direzionale di Napoli, 80143, Italy.*

***Abstract*—Several biomedical imaging modalities are available in the scientific literature for breast cancer diagnosis, each with its own advantages and limitations. In this framework, microwave tomography has gained a certain interest in the last years due to its capability to provide quantitative maps of tissues electric properties in a safe, non-invasive fashion. Furthermore, this imaging modality proved to be cheaper than traditional medical exams. By virtue of the great advantages that artificial intelligence, and more specifically deep learning, has delivered especially in the medical area, this paper proposes a novel procedure for breast cancer imaging by means of microwave radiation. The two-dimensional numerical results reported in this work seem promising and allow to identify and image potential malignancies in the breast.**

***Keywords*—Microwave tomography, breast cancer imaging, deep learning, multistatic systems.**

I. INTRODUCTION

Breast cancer represents one of the commonest types of cancer among women [1]. It is currently the second leading cause of death in the United States, and is expected to surpass heart diseases as the leading cause of death in the next few years. Its early detection is paramount for planning successful treatment and allowing a proper recovery for the patient.

Among the commonest medical imaging modalities adopted for its diagnosis it is worth mentioning X-ray mammography, which nowadays still represents the gold standard, the magnetic resonance imaging (MRI), ultrasound imaging and nuclear medicine [2]. Each of the previously-mentioned medical imaging technologies has its own advantages and limitations. X-ray and MRI are characterised by excellent spatial resolution, but on the other hand X-ray is harmful for patient's health due to the adoption of ionising radiations and due to breast compression, while MRI is very expensive and sometimes uncomfortable for claustrophobic patients. Furthermore, both imaging modalities are not portable, and more in detail in the MRI case, the acquisition process is slow and unsuitable for patients with metallic implanted devices.

Breast ultrasound imaging does not suffer from the X-ray and MRI limitations since it exploits mechanical waves for non-invasive diagnostics. It is used as a follow-up test for abnormalities found by mammogram and provides some guidelines for biopsy inspections. Its main limitation are related to the operator-dependent nature of this medical exam, to its poor resolution and low contrast of the image. Furthermore, complementary information regarding the molecular properties of the observed tissues can be inferred from nuclear medicine, which operates by injection of radioactive substances. This imaging modality is very expensive, uses ionising radiation and has limited resolution [3].

Due to the previously-mentioned limitations and drawbacks of the actual medical imaging technologies for breast cancer diagnosis, there has been a vivid interest from the scientific research community to explore frontier technologies and imaging approaches to perform early, reliable and less expensive diagnostics. In this framework, the use of microwave frequencies for breast cancer imaging has received significant attention in the last decades, since these radiations are safe for patient's health and can allow a better sensitivity [4], [5]. In this framework, microwave tomography (MWT) can offer several advantages over classical methods since it is inexpensive, non-ionising, and comfortable from patient's point of view [6]. By virtue of the differences in the electrical properties between normal and malignant tissues in the microwave frequency range, this technique might represents a good ally/alternative for safe, cheap, and early breast cancer diagnosis. Furthermore, it is able to provide *quantitative* information by retrieving tissues permittivity and conductivity maps [4].

In particular, MWT can provide complementary information on the investigated regions which can be merged with the one deriving from traditional exams to support medical decisions. Nevertheless, there are still some technical challenges and open topics to be solved, which involve both hardware and software [7]. Among the main drawbacks to obtain reliable quantitative images via MWT it is worth mentioning the well-known non-linearity and ill-posedness issues and their consequences affecting the mathematics of the considered inverse problem, such as the presence of local minima [8]. In this framework, fast and reliable nonlinear approaches are desirable for addressing the breast cancer imaging problem and, more in general, whatever diagnostic biomedical imaging problem. Among the most recent approaches, deep neural networks (DNNs) can represent a useful and flexible tool for quantitative imaging and, thus, for early breast cancer detection.

In this regard, the considered paper proposes a deep learning (DL) approach for breast cancer detection and imaging via MWT. The considered methodology consists of two steps: the

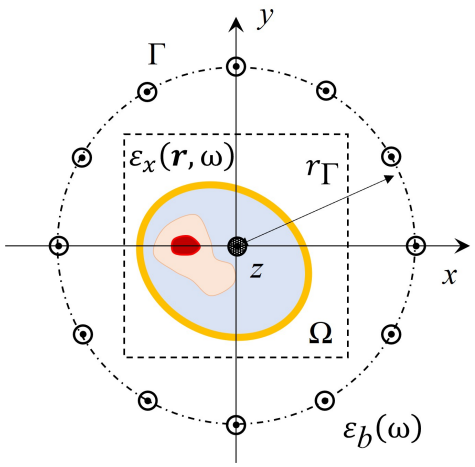


Fig. 1: Simplified 2D sketch of the imaging system. The antennas (dipoles) are located on a measurement circle Γ at a radius r_Γ, aligned along the vertical z axis. The imaging domain Ω includes the target of interest and is filled with a matching medium whose electric feature is $\epsilon_b(\omega)$.

former one adopts DL to firstly identify suspicious breasts which might be affected by malignancy, while the latter step consists of a fully-connected neural network performing the quantitative imaging for the localisation of the potential cancerous areas.

The remainder of the paper is as follows. Section II recaps the main equations ruling the scattering phenomena and describes the geometry of interest, while Section III illustrates the proposed methodology. Some results are reported in Section IV and some conclusions in Section V end the paper.

II. Problem Statement

In the following, a simplified two-dimensional (2D) geometry will be considered as shown in Fig. 1. The hosting medium is assumed to be homogeneous and non-magnetic, with complex permittivity $\epsilon_b(\omega) = \epsilon_b' - j\frac{\sigma_b}{\omega\epsilon_0}$, i.e. ϵ_b' and σ_b (S/m) being the relative permittivity and conductivity of the background medium, ω being the angular frequency and $\epsilon_0 = 8.854 \cdot 10^{-12}$ F/m.

The considered imaging system consists of a circular array of antennas located on a measurement circle Γ in a multiview-multistatic configuration, i.e. all the antennas can act as transmitter as well as receiver, but only one transmitter per time is active while all the remaining antennas work as receivers. The measurement circle Γ surrounds the imaging domain Ω in which the target breast is located immersed in the hosting medium. The targets located inside Ω are illuminated via transverse-magnetic electric field generated by z-oriented current wires located on Γ and adopted as antennas.

The scattering phenomena related to the interaction between the electric field generated by the antennas (known as *incident field*) and the target tissues depend on the contrast between the electric properties of the background medium and those of the target. By virtue of these differences, and measuring the scattered field on the measurement line Γ, it is possible to retrieve the breast tissues properties maps by solving an electromagnetic inverse scattering (EIS) problem. Thus, the electromagnetic scattering equations ruling these phenomena can be written as [8]:

$$E_s = \mathcal{A}_e(\epsilon', \sigma, E_t) + n\,, \tag{1}$$

$$E_t = E_i + \mathcal{A}_i(\epsilon', \sigma, E_t)\,, \tag{2}$$

in which the dependence on the spatial coordinates, operating frequency and background electric features has been implied. The quantities E_i and E_t represent the incident and total electric fields inside the imaging domain Ω, respectively, while E_s is the scattered field collected at receivers locations on Γ. The operators $\mathcal{A}_i$ and $\mathcal{A}_e$ are the internal and external radiating operators and n is the measurement noise which affects the data, here assumed to be additive, white and Gaussian (AWGN).

Concerning the imaging applications, the considered framework can be dealt with as an EIS problem whose aim consists in the retrieval of quantitative estimates of unknown electric permittivity ϵ' and conductivity σ functions inside Ω starting from the scattered field samples measured on Γ. As mentioned in Section I, this is here achieved by means of properly trained neural networks, allowing real-time applications with accurate, reliable reconstructions.

III. Methodology

The workflow of the proposed methodology consists of two steps: the former one which aims at identifying potentially-suspicious breasts by means of convolutional neural networks, and the latter one performing the quantitative imaging with the aim of retrieving the permittivity and conductivity maps of the tissues under consideration to identify the malignant areas through a fully-connected neural network.

To this purpose, an in-house 2D numerical realistic breast phantom repository has been considered for the training of the neural networks. More in detail, the Authors adopted the realistic breast repository described and proposed in [9], which consists of 120,000 numerically-generated 2D healthy breast phantoms organised into four classes according to their percentage of fibroglandular tissue. This data set has been further enriched with 30,000 malignant breast phantoms numerically generated by considering different shape, size, extension and location of the malignancies inside the tissues. Each breast profile, together with the corresponding "scattering matrix", represents the database for the neural networks training.

With regard to the first step, i.e. the classification of the considered breast phantom as *suspicious* or *healthy*, a ten-layer convolutional neural network (CNN) is adopted. In this case, the input of the network is the scattering matrix, i.e. the scattered field measured on Γ, while the output is a label which classifies the profile as healthy or not. Complementary to this first step, the second one adopts a different topology that is based on a three-layer fully-connected neural network. More specifically, this step is applied in those cases in which the CNN of the previous analysis has identified a suspicious

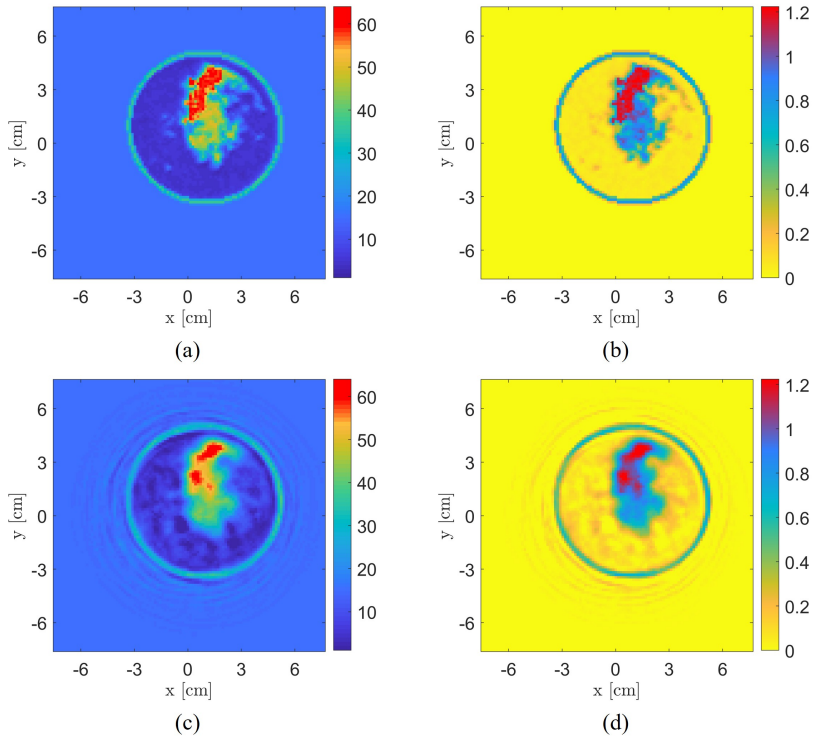


Fig. 2: Retrieved permittivity and conductivity profiles in the case of malignant tissues (light red areas). Reference permittivity (a) and conductivity (b), and corresponding recoveries (c)-(d).

breast phantom, and thus requires further investigation for the tumour spatial localisation. In this latter case, the input of the network is still the scattering matrix, while the output consists of the estimated permittivity and conductivity maps. Further details regarding this latter network architecture and training for the imaging are reported in Section 3.2 of [9]. Table I summarises all the training details and settings relatively to the adopted neural networks proposed in this paper.

IV. Results

Concerning the generation of the scattering matrix from the breast profile, a forward solver based on the method of moments (MoM) was adopted. The considered imaging system consists of 30 antennas equally-spaced in angle on a measurement circle of radius 12 cm arranged in a multiview-multistatic configuration. The transmitted signal is a line source at the fixed frequency of 1 GHz and the imaging domain has size equal to 15×15 cm^2 discretized according to Richmond's rule. In all the following simulations, the data have been corrupted by AWGN with SNR = 30 dB.

Table II shows the confusion matrix related to the classification step of the proposed approach. The reached accuracy is 99.46%. Relatively to the imaging step, it is worth noting that this analysis was performed by starting from the network trained on the healthy population (i.e., 120,000 breast profiles), as reported in Section III, and then by applying a fine-tuning strategy to re-train the network with the 30,000 malignant profiles (80% for the training and 15% for the validation with respect to the whole malignant database). As a result from the proposed approach, Fig. 2 reports the retrieved *quantitative* permittivity and conductivity maps with corresponding references (more results will be shown at the conference). It is easy to observe that the proposed imaging approach results quite accurate in retrieving the malignant areas, which are represented in light red in the figure.

Complementary to the information reported in Fig. 2, Fig. 3 illustrates the statistical 2D distribution (pdf) of the electromagnetic parameters for both healthy (subfigures (a) and (c)) and cancerous (subfigures (b) and (d)) tissues for the breast phantom reported in Fig. 2. It is worth to note that the limited overlapping of the distributions ensures good accuracy in the cancer detection task, making the tomographic microwave imaging suitable for diagnostic purposes.

V. Conclusion

In this paper, a two-step DL-based approach for breast cancer imaging via MWT has been proposed. The first step adopts a CNN to identify suspicious breasts which could be affected by cancer, while the second step exploits a fully-connected neural network to perform the imaging and identify the potentially malignant areas.

As supported by the results reported in Section IV, the proposed approach seems quite promising and able to provide accurate quantitative recoveries of the investigated regions. Furthermore, its generalisation to the more realistic three-

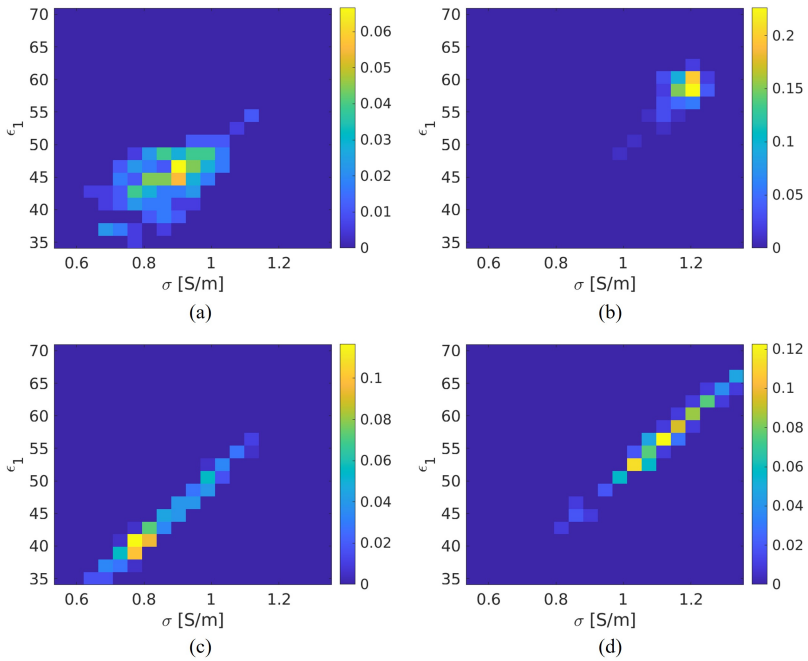


Fig. 3: Statistical distribution (bi-dimensional pdf) of the permittivity and conductivity values of the healthy (a, c) and malignant (b, d) tissues for both reference phantoms (a)-(b) and retrieved (c)-(d) profiles.

TABLE I: Details on the adopted neural networks architectures and training.

	Step I: Convolutional Neural Network	**Step II: Fully-connected Neural Network**
Input	Scattering matrix	Scattering matrix
Output	binary (healthy/malignant)	quantitative maps (ϵ, σ)
Optimization method	Adam, initial learning rate: $5 \cdot 10^{-5}$	Adam, initial learning rate: $5 \cdot 10^{-5}$
Training	From the ground up (50 epochs)	Fine tuning (30 epochs)
Mini-batch size	100	64
Architecture	10 convolutional layers, 32 features, 3x3 kernel size	3 fully-connected layers, 2,000 nodes each
Population	160,000 (80,000 healthy + 80,000 malignant) training: 85%, validation: 15%, testing: 5%	30,000 malignant training: 80%, validation: 15%, testing: 5%

TABLE II: Confusion matrix for the classification step of the proposed approach (step I).

		Prediction	
		Healthy	Malignant
Truth	Healthy	99.98%	0.02%
	Malignant	1.1%	98.9%

dimensional (3D) scenario is straightforward, even though at the expense of a higher computational burden.

Future work will focus on its application to the 3D case, to the performance improvement by adopting different NNs topologies and architectures, as well as on the study of the impact of model error and high noise on the recovery performance.

REFERENCES

[1] Fitzmaurice, C. et Al., The global burden of cancer 2013. *JAMA Oncology*. 1, 505-527 (2015)

[2] Jaglan, P., Dass, R. & Duhan, M. Breast cancer detection techniques: issues and challenges. *Journal Of The Institution Of Engineers (India): Series B*. 100, 379-386 (2019)

[3] James, A. & Dasarathy, B. Medical image fusion: A survey of the state of the art. *Information Fusion*. 19 pp. 4-19 (2014)

[4] Aldhaeebi, M. et Al., Review of microwaves techniques for breast cancer detection. *Sensors*. 20, 2390 (2020)

[5] Ambrosanio, M., Kosmasy, P. & Pascazio, V. An adaptive multi-threshold iterative shrinkage algorithm for microwave imaging applications. *2016 10th European Conference On Antennas And Propagation (EuCAP)*. pp. 1-3 (2016)

[6] O'Loughlin, D. et Al., Microwave breast imaging: Clinical advances and remaining challenges. *IEEE Transactions On Biomedical Engineering*. 65, 2580-2590 (2018)

[7] Chandra, R., Zhou, H., Balasingham, I. & Narayanan, R. On the opportunities and challenges in microwave medical sensing and imaging. *IEEE Transactions On Biomedical Engineering*. 62, 1667-1682 (2015)

[8] Colton, D., Kress, R. & Kress, R. Inverse acoustic and electromagnetic scattering theory. (Springer,1998)

[9] Ambrosanio, M., Franceschini, S., Pascazio, V. & Baselice, F. An End-to-End Deep Learning Approach for Quantitative Microwave Breast Imaging in Real-Time Applications. *Bioengineering*. 9, 651 (2022)

Hessian-based neck tracing of dendritic spines: a preliminary study on confocal images

E. Bruno[1], S. Cauzzo[2], A. L. Callara[1,2], A. Ahluwalia[1,2], C. Magliaro[2] and N. Vanello[1,2]
[1] *Dipartimento di Ingegneria dell'Informazione, University of Pisa, Pisa, Italy*
[2] *Research Center "E. Piaggio", University of Pisa, Pisa, Italy*

***Abstract*— Alterations in dendritic spines morphology and topology are known to be implied in several neurodegenerative diseases. However, visualizing and reconstructing the exact morphology of spine necks using conventional confocal imaging is still a challenge. In the light of this, we propose the extension of Hessian matrix eigenvalue analysis for the detection of tubular structures to the problem of 3D neck tracing. In this work we stress the relevance of the tracing procedure initialization, for the novel application of this standard approach to the specific scenario. Preliminary results on confocal microscopy images from ex-vivo human samples allowed to obtain almost 80% of necks keeping an average distance of less than one voxel from the reference segmentation and half of them fully overlapping with it. The preliminary results are promising, since they pave the way towards the development of this model-free solution to accurately trace spine neck.**

***Keywords*—Confocal microscopy, pyramidal cells, dendritic spines, tracing, neuronal reconstruction.**

I. Introduction

Dendritic spines are neuronal protrusions implied in synaptic function, supporting learning, memory and motivation [1]–[6]. Changes in spine density, size, shape and distribution have been detected in neurodegenerative diseases such as Alzheimer's, autism spectrum disorders and many others [7]–[9]. To this end, quantitatively characterizing such features would be of particular interest. However, obtaining faithful information on dendritic spine morphology is not an easy task. Indeed, spines necks have a thin and small structure which is hard to discriminate with conventional microscopy, since its size is close to the optical resolution limit of the imaging techniques [10]. On the other hand, the high density of spines makes the manual or a semi-automatic segmentation tedious and time-consuming, increasing the necessary introduction of automatic procedures.

Several approaches have been proposed for reconstructing spine necks. Some of them require a large database of images to create a library of deformable models [11] or train convolutional neural networks [12]. Models based on global approaches to segmentation might fail in detecting spine necks given the different signal-to-noise ratio (SNR) properties of small structures [13], [14]. Thus, approaches based on local intensity or morphological local characteristics were proposed [14]–[18]. One of the most adopted tools, NeuronStudio [16] exploits local geometrical models. However, this approach is optimized for head spine detection and is suboptimal for neck spine shape characterization. In [17], a curve based on Legendre functions is fitted between dendrite shafts and detached spine head in 2D microscopy images, to adapt to different possible neck geometries. Geometrical features, as those based on tubular structures exploited in [19] for vascular tree, was evaluated in [18]. Specifically, eigenvalue analysis of the Hessian matrix has been introduced to define vesselness measures in biomedical images [19]. In fact, within tubular structures, the smallest-magnitude eigenvalue of Hessian is associated with the eigenvector directed along the minimum intensity variation, i.e., the longitudinal axis of the tubular structure. In [18] the information from local Hessian matrix was used to design an adaptive filter for dendrite tracing and spine head detection. The approach proved to achieve a good performance on stimulated depletion image but was not applied to image stacks.

In this work, we present a novel neck-tracing approach that exploits the eigenvalue analysis of the Hessian matrix. Specifically, the proposed method will be applied to images where both dendrites and spine heads have already been segmented. The aim is to correctly identify and trace the spine necks. We will point out the relevance of the tracing algorithm initialization and we will propose and evaluate different strategies. We test our method on 3D stacks of confocal images of a human pyramidal cell dendrite. We validate our approach against ground truth assisted segmentation of spines performed by expert-users.

II. Material and Methods

A. Experimental data

We processed a confocal image stack of an intracellular injected layer III pyramidal neuron from the human brain cingulate cortex (freely available for the scientific community and presented in [20]). Sections were imaged with a Leica TCS 4D confocal scanning laser equipped with to a Leitz DMIRB fluorescence microscope. All the data was also provided with a reference segmentation of the dendritic branch and spines reconstructed manually using Imaris 6.4.0 (Bitplane AG, Zurich, Switzerland).

B. Neck tracing procedure

Tracing a neck consists in connecting two disconnected clusters of segmented voxels, one linked to the spine head, and one linked to the dendrite. Therefore, to test our approach, we firstly performed a binary segmentation of the intensity image leaving some spines disconnected. We created such segmentation employing Otsu's method in the Icy software [21] which defines the optimal threshold based on the observed intensity distribution of pixel values. We refer to this segmentation as Otsu segmentation, OS [22]. The proper neck tracing approach is run on the unsegmented portions of the intensity image, and it is composed of an initialization phase

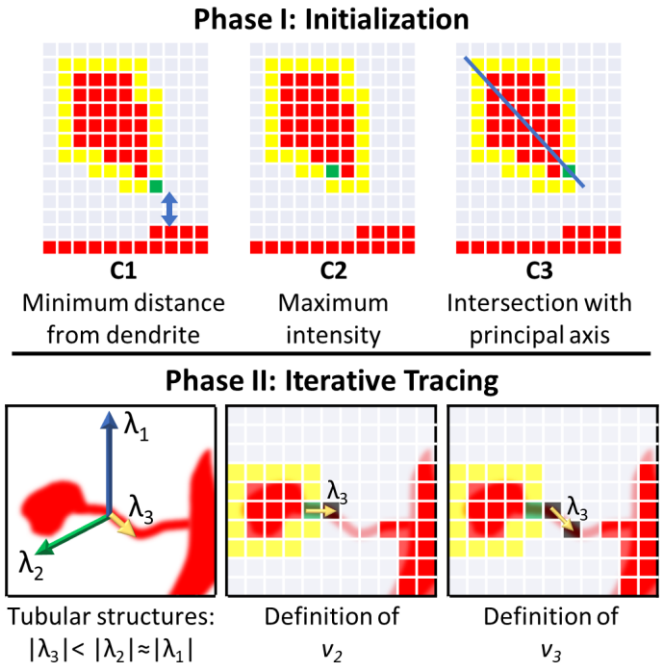


Fig. 1 *Schematization of the neck tracing approach. OS is marked in red, OB in yellow. Phase I) selection of the first voxel in the trace among those in OB, with the three tested criteria. Phase II) thanks to the properties of the Hessian matrix eigenvalues within tubular structures, the neck can be traced by 1) performing the eigenvalue analysis at voxel v_i; 2) defining v_{i+1} as the neighboring voxel intersected by the smallest eigenvector.*

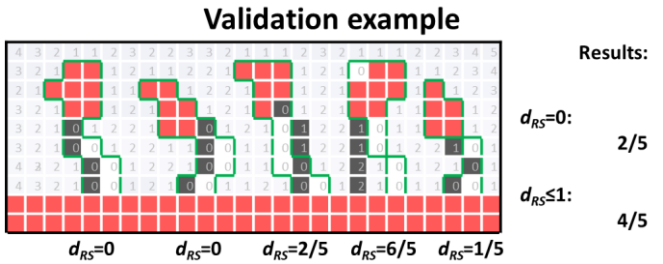


Fig. 2 *Validation example simplified in a 2D case: necks (black) connecting disconnected clusters of OS (red) are compared against RS (white with green borders) in terms of average Euclidian distances. Distance values in cells are rounded to the highest integer.*

(phase I) aiming at selecting the starting seed of the path-finding phase (phase II). The approach is sketched in Fig. 1.

Phase I defines the first voxel of the trace among those composing the outer border (OB) of the disconnected spine. We tested 3 different criteria: C1) the voxel in OB that is closest to the dendrite in terms of Euclidean distance; C2) the maximum intensity voxel within OB; C3) the voxel in OB intersected by the principal axis of the spine, placed on the side of OB that is closest to the dendrite.

Instead, phase II consists of a one-voxel step procedure starting from the first voxel and iteratively repeated to define the trace of the neck. For each voxel v_i in the trace, the Hessian matrix is defined computing the second order derivatives D_{xx}, D_{yy}, D_{zz}, D_{xy}, D_{xz}, D_{yz}. Eigenvectors and eigenvalues of the Hessian matrix are then extracted. Eigenvalues encode the information on second-order intensity variability along the axis defined by the eigenvector. Within a tubular structure, the direction parallel to the main axis is the one meeting no structure boundaries, i.e., the one along which the smallest intensity variations occur. This situation, schematized in the lower-left panel of Fig. 1, can be summarized by the formula $|\lambda_3| < |\lambda_2| \approx |\lambda_1|$. Therefore, starting from v_1 as defined in Phase I (shown in green in Fig. 1), v_2 is chosen within the 26-neighborhood of v_2 as the voxel being intersected by the eigenvector of the Hessian matrix associated to the smallest absolute eigenvalue λ_3, visualized with a golden arrow in Fig. 1. The procedure is repeated starting from v_2 to define v_3 (lower-right panel in Fig. 1), and then iterated on each v_i, to define v_{i+1}, until the trace meets the dendrite, or a given number of steps, Max_Steps, is reached. Max_Steps is identified to avoid the algorithm getting lost in a non-tubular structure or failing to reach the dendrite.

C. *Validation*

We preliminary validated our method on 350 spines included in one image stack. A gold-standard semi-automatic segmentation of these spines was published in [20] and is here labelled as Reference Segmentation, RS. This ground-truth was obtained with the software Imaris by combining spine-by-spine segmentations defining multiple ad hoc binary thresholds. Among the total number of spines, we focused only on those disconnected (26-neighbors) from the dendrite in the OS.

The tracings obtained using the three initialization strategies were evaluated, using a distance measure d_{RS} of each traced neck from the RS. Such measure is 0 when all the voxels in the neck overlap with the reference segmentation, and non-zero otherwise. The validation measure d_{RS} was estimated as it follows:

- For each voxel of the traced neck
  - we assign 0 if the voxel belongs to the RS
  - we estimate the Euclidean distance d_{RS} from the edge of the RS
- We average the obtained value across the voxels of the considered neck, to obtain the average d_{RS}

Using this approach, we can provide a quality assessment also for necks that do not fully overlap with RS.

III. Results

A. *Quantitative analysis*

Out of the 350 spines marked in RS, OS results in 88 spines disconnected from the structure core. We observed that segmented spines are separated on average by less than 10 voxels from the segmented dendrite, so we empirically set Max_Steps to 20. In Fig. 3, we report the quantitative evaluation of the three initialization criteria implemented for phase I, in terms of percentage of necks that fully overlap with RS, i.e., that show $d_{RS} = 0$, and percentage of necks showing $d_{RS} \leq 1$. C2 is the criterion providing the best results, with $d_{RS} = 0$ for the 47.7% of the 88 necks and $d_{RS} \leq 1$ for the 77.3% of them.

B. *Neck reconstructions*

In Fig. 4, we report four examples of traced necks, visualized with 3D reconstructions and overlayed on OS and RS. We observe that, with a good approximation, the majority

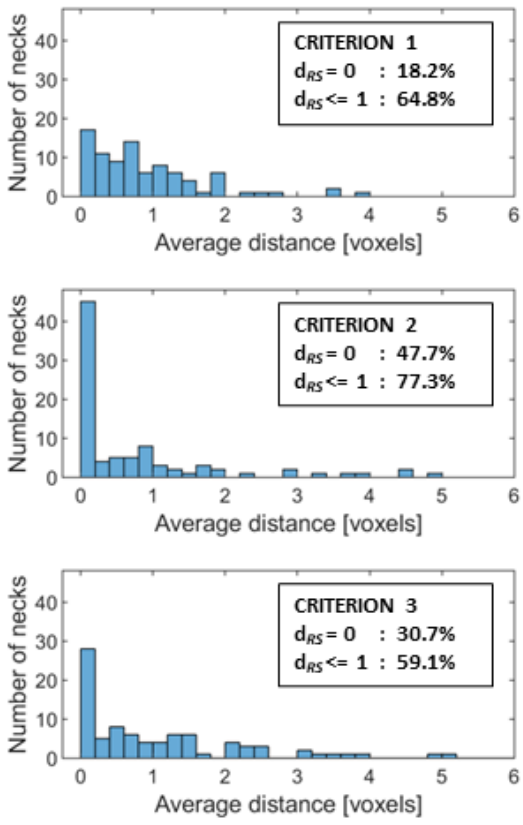


Fig. 3 Evaluation of the three initialization approaches of phase I in terms of average distance from RS for the 88 disconnected spines.

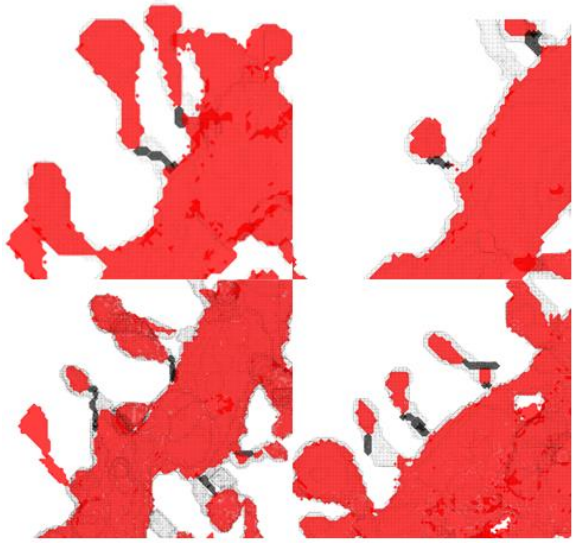


Fig. 4 Four examples of necks reconstructed by the algorithm (in black) overlaying OS (red) RS (gray).

spines have been successfully connected with the proper section of the dendrite.

IV. Discussions

In this work, we present a novel approach for spine neck reconstruction using the local information of the Hessian matrix. The geometrical information achievable by such analysis was already exploited for spatial filter design in [19] for spine head and neuron tracing. To our knowledge, the implementation for spine neck sequential tracing presented here is novel. Moreover, by testing three initialization criteria, we highlighted the relevance of this phase and assessed the maximum intensity voxel within the outer border of the spine as best starting point. With this criterion, we obtain a good percentage of tracings being in line with a published reference segmentation produced with a deep learning-based approach.

For the image used in this work, a reference segmentation RS capable of keeping spines connected to the corresponding dendrite was already available, since spine and neck identification was obtained using a manual 3D reconstruction of the same image sample performed with the software Imaris. Future tests will be required on samples on which a segmentation able to keep spines connected has not yet been achieved. This could be the case of confocal standard- or super-resolution STED images from clarified tissue. These tests will require a validation based on manual segmentation and a comparison against other available methods.

Due to the image type, which describes injected cells, and due to the bimodality of the intensity histogram, Otsu's method, that exploits a global intensity threshold, was selected as one of the simple strategies to segment this type of dataset. However, other methods employing different segmentation strategies can be used [23] and their results merged with the proposed approach when spine neck segmentation is failing.

To validate our results, we designed a strategy that estimates an average distance of the reconstructed neck from the RS. Since RS can be as thin as a single voxel, this strategy better characterizes the results with respect to a binary decision on a complete overlap between the reconstruction and the RS. We provide histograms of the average Euclidean distances between necks and RS, and we report the percentage of necks showing $d_{RS} \leq 1$, considered as satisfying reconstructions. In this work, this validation measure is also used to compare the three initialization criteria, highlighting a far better performance by C2 with respect to both C1 and C3 (Fig.3). Performance of the minimum distance criterion (C1) is impaired by the neck curvatures, which are often bent with respect to the direction normal to the dendrite surface. The performance of spine principal axis criterion (C3) is impaired by the multiple shapes that can be assumed by spine heads [24], which can present very wide caps and thus a principal axis that is aligned to the dendrite. Choosing the highest-intensity sub-threshold voxel resulted to be the best initialization criterion. In addition, on segmentations that do not rely on the sole magnitude (e.g., segmentation algorithms based on deep learning [11], [25], [26] structure enhancement filters [27], [28] or statistical modelling [29]), the use of C3 might not be optimal and should be further tested.

We have to stress that the generalizability of C2 criterion to images with lower SNR, with respect to the one here analysed, should be further tested. In fact, this solutionis likely to be sensitive to noise since it selects the maximum intensity voxel. As a result, a different criterion could better perform on a different image type.

We observed that definitions of the starting point on the wrong side of the spine produce erroneous tracings that could hardly be recovered. In this light, further research on the proper initialization of neck tracing algorithms is crucial. Future developments should focus on providing a less local definition of maximum intensity, e.g., adopting smoothing

filters in phase I prior to applying C2, or employing measures based on percentiles within a neighbourhood. Similarly, in phase II the eigenvalue analysis could be conducted with an approach that is still local, but less punctual, to be more robust to noise. A more noise-robust local eigenvalue analysis should impact the performance as well in Phase II: this could be achieved in the computation of the Hessian by weighing the contribution of a neighbourhood of voxels, e.g. using convolutions with derivatives of gaussians instead of punctual differentiation, as in [19], [30].

As our algorithm does not perform spine assignment, the presence of spines belonging to different dendrites within the same stack could lead it to the tracing of non-existing necks. To target this issue, in an interesting future development a crucial preliminary spine assignment step based on a 3D watershed transform could be integrated in the algorithm.

An application of our approach on super-resolution techniques (e.g., STED, STORM), which allow to resolve spine morphology even in clarified thick slices (500 μm), will be also explored in the future.

V. Conclusion

We present an algorithm to detect neck spines using an approach based on the Hessian matrix eigenvalue analysis applied to confocal microscopy. The centrality of initialization is addressed, assessing important changes in algorithm performance when different initialization criteria are employed. Our results suggest that a precise tracking of spine necks could be obtained using a model-free solution. An accurate reconstruction of spine necks will help to define the morphology of the synaptic transmission centre implied in neurodegenerative diseases.

Acknowledgement

The authors deeply thank the group of Professor Javier De Felipe at the Universidad Politécnica de Madrid for sharing data. This work was supported by the FLAG-ERA JTC 2019 project SENSEI (Partnering Project of the Human Brain Project, CUP: I54I19002660006). Research partly funded by the European Union - Next Generation EU, in the context of The National Recovery and Resilience Plan, Investment 1.5 Ecosystems of Innovation, Project Tuscany Health Ecosystem (THE), Spoke 3 "Advanced technologies, methods, materials and heath analytics " CUP: I53C22000780001.

References

[1] R. Yuste, A. Majewska, and K. Holthoff, “From form to function: calcium compartmentalization in dendritic spines,” *Nat. Neurosci.*, vol. 3, no. 7, pp. 653–659, 2000

[2] K. M. Harris and S. B. Kater, “Dendritic Spines: Cellular Specializations Imparting Both Stability and Flexibility to Synaptic Function,” *Annu. Rev. Neurosci.*, vol. 17, no. 1, pp. 341–371, 1994

[3] J. Bourne and K. M. Harris, “Do thin spines learn to be mushroom spines that remember?,” *Curr. Opin. Neurobiol.*, vol. 17, no. 3, pp. 381–386, 2007

[4] N. Spruston, “Pyramidal neurons: dendritic structure and synaptic integration,” *Nat. Rev. Neurosci.*, vol. 9, no. 3, pp. 206–221, 2008

[5] E. R. Kandel, Y. Dudai, and M. R. Mayford, “The Molecular and Systems Biology of Memory,” *Cell*, vol. 157, no. 1, pp. 163–186, 2014

[6] R. Yuste, *Dendritic spines*. Cambridge, MA: MIT Press, 2010.

[7] J. C. Fiala, J. Spacek, and K. M. Harris, “Dendritic Spine Pathology: Cause or Consequence of Neurological Disorders?,” *Brain Res. Rev.*, vol. 39, no. 1, pp. 29–54, 2002

[8] W. Yu and B. Lu, “Synapses and Dendritic Spines as Pathogenic Targets in Alzheimer’s Disease,” *Neural Plast.*, vol. 2012, pp. 1–8, 2012

[9] P. Merino-Serrais *et al.*, “The influence of phospho-tau on dendritic spines of cortical pyramidal neurons in patients with Alzheimer’s disease,” *Brain*, vol. 136, no. 6, pp. 1913–1928, 2013

[10] J. Son et al., “Morphological change tracking of dendritic spines based on structural features,” *J. Microsc.*, vol. 241, no. 3, pp. 261–272, 2011

[11] E. Erdil et al., “Combining Nonparametric Spatial Context Priors With Nonparametric Shape Priors for Dendritic Spine Segmentation in 2-Photon Microscopy Images,” in *2019 IEEE 16th International Symposium on Biomedical Imaging (ISBI 2019)*, 2019, pp. 204–207.

[12] I. Vidaurre-Gallart *et al.*, “A Deep Learning-Based Workflow for Dendritic Spine Segmentation,” *Front. Neuroanat.*, vol. 16, 2022

[13] I. Y. Y. Koh et al., “An Image Analysis Algorithm for Dendritic Spines,” *Neural Comput.*, vol. 14, no. 6, pp. 1283–1310, 2002

[14] C. M. Weaver, P. R. Hof, S. L. Wearne, and W. B. Lindquist, “Automated Algorithms for Multiscale Morphometry of Neuronal Dendrites,” *Neural Comput.*, vol. 16, no. 7, pp. 1353–1383, 2004

[15] J. Cheng *et al.*, “A novel computational approach for automatic dendrite spines detection in two-photon laser scan microscopy,” *J. Neurosci. Methods*, vol. 165, no. 1, pp. 122–134, 2007

[16] A. Rodriguez, D. B. Ehlenberger, D. L. Dickstein, P. R. Hof, and S. L. Wearne, “Automated Three-Dimensional Detection and Shape Classification of Dendritic Spines from Fluorescence Microscopy Images,” *PLoS One*, vol. 3, no. 4, p. e1997, 2008

[17] S. Jain, S. Mukherjee, L. Danglot, and J.-C. Olivo-Marin, “Morphological Reconstruction of Detached Dendritic Spines via Geodesic Path Prediction,” in *2021 IEEE 18th International Symposium on Biomedical Imaging (ISBI)*, 2021, pp. 944–947.

[18] R. Su, C. Sun, C. Zhang, and T. D. Pham, “A novel method for dendritic spines detection based on directional morphological filter and shortest path,” *Comput. Med. Imaging Graph.*, vol. 38, no. 8, pp. 793–802, 2014

[19] A. F. Frangi, W. J. Niessen, K. L. Vincken, and M. A. Viergever, “Multiscale vessel enhancement filtering,” 1998, pp. 130–137.

[20] R. Benavides-Piccione et al., “Age-Based Comparison of Human Dendritic Spine Structure Using Complete Three-Dimensional Reconstructions,” *Cereb. Cortex*, vol. 23, no. 8, pp. 1798–1810, 2013

[21] F. de Chaumont *et al.*, “Icy: an open bioimage informatics platform for extended reproducible research,” *Nat. Methods*, vol. 9, no. 7, pp. 690–696, 2012

[22] N. Otsu, “A Threshold Selection Method from Gray-Level Histograms,” *IEEE Trans. Syst. Man. Cybern.*, vol. 9, no. 1, pp. 62–66, 1979

[23] C. Magliaro, A. L. Callara, N. Vanello, and A. Ahluwalia, “Gotta Trace ‘em All: A Mini-Review on Tools and Procedures for Segmenting Single Neurons Toward Deciphering the Structural Connectome,” *Front. Bioeng. Biotechnol.*, vol. 7, 2019

[24] E. Pchitskaya and I. Bezprozvanny, “Dendritic Spines Shape Analysis—Classification or Clusterization? Perspective,” *Front. Synaptic Neurosci.*, vol. 12, 2020

[25] F. Nourbakhsh *et al.*, “Neural Cell Segmentation in Large-Scale 3D Color Fluorescence Microscopy Images for Developemental Neuroscience,” in *2018 25th IEEE International Conference on Image Processing (ICIP)*, 2018, pp. 3828–3832.

[26] G. Mazzamuto et al., “Automatic Segmentation of Neurons in 3D Samples of Human Brain Cortex,” 2018, pp. 78–85.

[27] S. Basu, B. Condron, A. Aksel, and S. T. Acton, “Segmentation and Tracing of Single Neurons from 3D Confocal Microscope Images,” *IEEE J. Biomed. Heal. Informatics*, vol. 17, no. 2, pp. 319–335, 2013

[28] S. Mukherjee, B. Condron, and S. T. Acton, “Tubularity Flow Field—A Technique for Automatic Neuron Segmentation,” *IEEE Trans. Image Process.*, vol. 24, no. 1, pp. 374–389, 2015

[29] A. L. Callara, C. Magliaro, A. Ahluwalia, and N. Vanello, “A Smart Region-Growing Algorithm for Single-Neuron Segmentation From Confocal and 2-Photon Datasets,” *Front. Neuroinform.*, vol. 14, 2020

[30] T. Lindeberg, “Edge detection and ridge detection with automatic scale selection,” in *Proceedings CVPR IEEE Computer Society Conference on Computer Vision and Pattern Recognition*, 1996, pp. 465–470.

On the use of PARAFAC algorithm in group network analysis: a simulation study

A. Ranieri[1,2], F. Pichiorri[2], E. Colamarino[1,2], V. de Seta[1,2], D. Mattia[2], J. Toppi[1,2]
[1] *Dept. Of Computer, Control and Management Engineering, Sapienza University of Rome, Rome, Italy*
[2] *Neuroelectrical Imaging and Brain Computer Interface Lab, IRCCS Fondazione Santa Lucia, Rome, Italy*

***Abstract*— Group level characterization of brain networks still represents an open issue in modern neuroscience. Investigating the functional mechanisms underlying the complexity of the human brain requires an analytical way to efficiently integrate information from multiple subjects, while properly handling the intrinsic inter-subject variability. Here we investigated the potentiality of the PARAllel FACtorization (PARAFAC) algorithm for the extraction of grand average brain connectivity matrices from simulated EEG datasets. Synthetic data were parametrized according to different levels of three parameters: network dimension (NODES), number of observations (SAMP-SIZE) and noise (SWAP-CON) in order to investigate the way they affect the reconstruction of grand average networks. Robustness to noise as well as the proper modulation of informative content have here been proved empirically, revealing that the best performances in terms of FPR, FNR and AUC were achieved for great number of observations and low noise level.**

***Keywords*— EEG, PARAFAC, group analysis, connectivity estimation.**

I. Introduction

The representation of the central nervous system as a complex network made its own way in modern biomedicine, being validated at both structural and functional levels by anatomical studies and noninvasive neuroimaging techniques[1]. In modern neuroscience, group level characterization of such a complex network can be either used to investigate pathological conditions or determine the existence of a common connectivity pattern elicited by the same experimental paradigm in different subjects (i.e. the grand average). Such a challenging issue implicitly requires an effective way to integrate information from multiple subjects, as well as handling the intrinsic inter-subject variability. Many different approaches have been proposed over the years, but there is currently no consensus on a univocal analysis pipeline for the extraction of the grand average connectivity pattern.

Especially in the last decades, PARAllel FACtoriation (PARAFAC) algorithm has made its own way as a useful tool for the analysis of multidimensional biomedical data. Pester et al. proposed the use of PARAFAC algorithm to extract grand average from fMRI derived networks in a group of subjects [2]. Under the hypotheses of linearity, this kind of approach allows to split the original data matrix into a sum of rank-one tensors (i.e. factors), revealing the presence of different connectivity patterns "hidden" in the original one. Miwakeichi and colleagues decomposed a multichannel time-varying EEG spectrum into a series of distinct components, by means of a PARAFAC decomposition in space, frequency and time domain [3]. Furthermore, combining PARAFAC algorithm together with hierarchical clustering, Belyaeva et al. proposed a tensor-based approach for the extraction of developmental signatures from multi-subject MEG data [4]. In particular, they were able to extract early and late latency event-related field components, allowing to discriminate between high and low performance groups.

Here we investigated the potentiality of a PARAFAC-based approach to estimate the grand average from a synthetic dataset mimicking brain connectivity matrices of different subjects exposed to the same experimental condition.

II. Materials and Methods

A. Tensor decomposition by means of PARAFAC algorithm

PARAFAC is a decomposition technique that factorizes an N^{th} order tensor into a sum of R rank one tensors, where R is the rank of the original tensor [5]. An N^{th} order tensor is rank one if it can be rewritten as the outer product of N vectors:

$$X = a^{(1)} \otimes a^{(2)} \otimes \dots \otimes a^{(N)} \tag{1}$$

where the symbol "$\otimes$" represents the vector outer product. The PARAFAC decomposition of a rank R third order tensor $X \in R^{I \times J \times D}$ can thus be rewritten as:

$$X = \sum_{r=1}^{R} X_r + E = \sum_{r=1}^{R} a^{(r)} \otimes b^{(r)} \otimes c^{(r)} + E \tag{2}$$

Where $a \in R^I, b \in R^J, c \in R^D$ and $E \in R^{I \times J \times D}$ is a residual error term. Elementwise, Eq. (2) can be rewritten as

$$x_{ijk} = \sum_{r=1}^{R} a_i{}^{(r)} b_j{}^{(r)} c_d{}^{(r)} + e_{ijd} \tag{3}$$

Each term $a_i{}^{(r)}$, $b_j{}^{(r)}$ and $c_d{}^{(r)}$ in Eq. (3) acts as a weight expressing the contribution of the r^{th} component of a, b and c on x_{ijd}. By setting the number of required rank-one tensors to any $1 \leq f \leq R$, the original informative content of X can be split into an arbitrary (but bounded) number of factors.

By switching the error term to the left side of Eq. (2), PARAFAC algorithm finds out the best approximation $\hat{X} = X - E$ for the original tensor X. The PARAFAC decomposition of X can thus be obtained by solving the optimization problem:

$$|| X - \hat{X} || \text{ with } \hat{X} = \textstyle\sum_{r=1}^{f} a^{(r)} \otimes b^{(r)} \otimes c^{(r)} \tag{4}$$

The solution to the problem in Eq. (4) can be found by means

of the alternating least squares (ALS) method [6].

B. PARAFAC to extract the Grand Average connectivity matrix

A generic brain connectivity dataset X obtained from a population of individuals is composed by s different $K \times K$ connectivity matrices, where s is the number of individuals and K is the number of nodes of the connectivity matrix.

By properly rearranging each subject's connectivity pattern as a first order tensor $\pi^{(s)} \in R^{K^2}$ with $s = 1, 2 \dots S$, PARAFAC algorithm can then be applied to the second order tensor $X \in R^{K^2 \times S}$ obtained by stacking each $\pi^{(s)}$ side by side.

$$X = \left[\pi^{(1)}\pi^{(2)} \dots \pi^{(S)}\right] \tag{5}$$

The PARAFAC decomposition of the bidimensional data tensor X can thus be written as:

$$X = \sum_{r=1}^{f} a^{(r)} \otimes b^{(r)} + E \tag{6}$$

or, elementwise

$$x_{ij} = \sum_{r=1}^{f} a_i{}^{(r)} b_j{}^{(r)} + e_{ij} \tag{7}$$

The terms $a_i{}^{(r)}$ (respectively $b_j{}^{(r)}$) indicate the way the i^{th} element of the vector $a^{(r)}$ (respectively the j^{th} element of $b^{(r)}$) modulates x_{ij}. In this kind of scenario a_i represents the strength of a specific functional connection, while b_j are the subject-wise loadings indicating how relevant is the pattern in $a^{(r)}$ for the reconstruction of X [7].

C. Synthetic data generation

For each virtual subject, a synthetic connectivity matrix was generated as a randomly modified version of a predefined ground-truth matrix, which emulates the behavior of an EEG-derived brain connectivity matrix. Since simulated network's density was fixed to 0.1, modifications of the original ground-truth consisted in connection swaps between different positions within the original synthetic connectivity matrix.

To investigate both validity and robustness of the reconstructed patterns, synthetic data analysis has been parametrized with respect to:

- dataset sample size (SAMP-SIZE, $s \in \{10, 20, 30, 50, 100\}$), defined as the number of participants included in the simulated cohort of subjects;
- dataset dimension, defined as the number of nodes of the simulated EEG connectivity matrices (NODES, $k \in \{20, 30, 50\}$);
- percentage of swapped connections with respect to the original ground-truth network (SWAP-CON, $m \in \{0.10, 0.30, 0.50\}$), representing different levels of inter-subject variability of the connectivity matrices (noise level).

D. Testing PARAFAC algorithm on synthetic data

PARAFAC algorithm was tested on different synthetic datasets representing a set of connectivity matrices obtained from a group of participants undergoing the same experimental condition. The simulation study repeats the following steps for $T = 100$ iterations:

1. Generation of synthetic datasets composed by different connectivity matrices (one per subject).
2. Application of PARAFAC algorithm in order to factorize the data matrix X as a sum of f rank-one tensors. Here we set $f = 2$, assuming that the first rank-one tensor represents the common mode, while the second one embodies a random pattern due to inter-subject variability.
3. Selection of the rank-one tensor that better represents the grand average connectivity pattern within the whole dataset. In particular, we looked for the pattern $\tilde{a}^{(r)}$ paired with the subject-dependent loadings in $\tilde{b}^{(r)}$ with minimum variance. In fact, since $\tilde{a}^{(r)}$ is supposed to be a recurrent connectivity pattern in X it is expected to be equally expressed in a large number of individuals: this means that the corresponding subject-wise loadings in $\tilde{b}^{(r)}$ are expected to be very similar each other.
4. Evaluation of the performances by comparing the rank-one tensor chosen at the previous point with the current ground-truth. In particular, we used False Positive Rate (FPR), False Negative Rate (FNR) and the Area Under the ROC (AUC) to evaluate how far the reconstructed pattern is with respect to the ground-truth.

Three separate two-way repeated measures Analyses of Variance (ANOVA) were carried out across the 100 iterations considering SAMP-SIZE ($s \in \{10, 20, 30, 50, 100\}$) and SWAP-CON, ($m \in \{0.10, 0.30, 0.50\}$) as main within factors. FPR, FNR and AUC were separately considered as dependent variables. The same ANOVAs were then repeated for each number of nodes considered in the study (NODES, $k \in \{20, 30, 50\}$). The statistical significance level for all tests was set to 0.05 and the Tukey's post-hoc test was performed to assess differences among the levels of the within factors.

III. RESULTS

A. Performances of PARAFAC algorithm on synthetic data - FPR

ANOVA results in Table I point out that either single or combined factors have a significant effect on the FPR distribution. In Fig.1 we reported FPR distributions obtained by applying PARAFAC algorithm to synthetic $k \times k$ connectivity matrices with $k = 20$, characterized by different sample sizes (SAMP-SIZE) and different levels of noise (SWAP-CON).

As reported in Fig.1, FPR values are close to zero when the sample size is greater or at least equal to 20 subjects, regardless for the percentages of swapped connections; on the other hand, when $s < 20$ FPR is still <5%. The number of involved subjects has a mitigating effect reducing FPR values as the cohort of recruited patients increases for all the percentages of noise corruption. Similar results were found for all NODES levels ($K = 30, 50$).

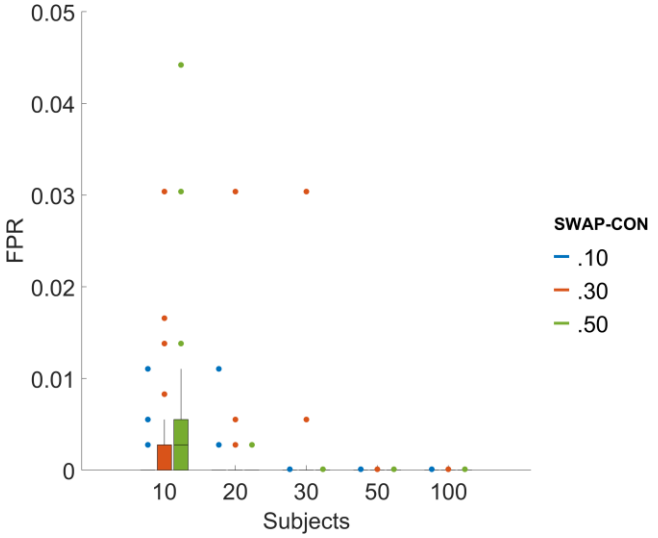


Fig.1. Boxplot diagrams reporting FPR distributions obtained applying PARAFAC algorithm on synthetic data generated using five different levels of SAMP-SIZE (along x-axis) and different levels of SWAP-CON (different colors of the bars). Results refer to synthetic datasets of dimension equal to 20 nodes.

TABLE I

Effect	DOF	F values - FPR		
		20 nodes	30 nodes	50 nodes
SWAP-CON	(2, 198)	$\mathbf{8,26}^{(*)}$	$\mathbf{8,04}^{(*)}$	$\mathbf{5,42}^{(*)}$
SAMP-SIZE	(4, 396)	$\mathbf{49,04}^{(*)}$	$\mathbf{44,20}^{(*)}$	$\mathbf{44,36}^{(*)}$
SWAP-CON* SAMP-SIZE	(8, 792)	$\mathbf{6,25}^{(*)}$	$\mathbf{7,20}^{(*)}$	$\mathbf{4,94}^{(*)}$

Results of three-way repeated measures ANOVA computed considering FPR as dependent variable, SWAP-CON and SAMP-SIZE as within main factors. The analysis was repeated for three different number of nodes (20, 30, 50). Acronym DOF is for degrees of freedom. The symbol (*) indicates significant effect of the factor ($p<0.01$).

B. Performances of PARAFAC algorithm on synthetic data - FNR

Results of the 2-way repeated measures ANOVA on FNR are summarized in Table II. As for FPR, either single or combined ANOVA factors significantly affect the FNR distribution. Boxplot in Fig.2 illustrates how the FNR distribution changes according to different levels of the generating variables (SWAP-CON and SAMP-SIZE).

TABLE II

Effect	DOF	F values - FNR		
		20 nodes	30 nodes	50 nodes
SWAP-CON	(2, 198)	$\mathbf{1208,60}^{(*)}$	$\mathbf{2554,72}^{(*)}$	$\mathbf{5548,21}^{(*)}$
SAMP-SIZE	(4, 396)	$\mathbf{118,01}^{(*)}$	$\mathbf{401,08}^{(*)}$	$\mathbf{748,47}^{(*)}$
SWAP-CON* SAMP-SIZE	(8, 792)	$\mathbf{85,36}^{(*)}$	$\mathbf{247,68}^{(*)}$	$\mathbf{480,37}^{(*)}$

Results of three-way repeated measures ANOVA computed considering FPR as dependent variable, SWAP-CON and SAMP-SIZE as within main factors. The analysis was repeated for three different number of nodes (20, 30, 50). Acronym DOF is for degrees of freedom. The symbol (*) indicates significant effect of the factor ($p<0.01$).

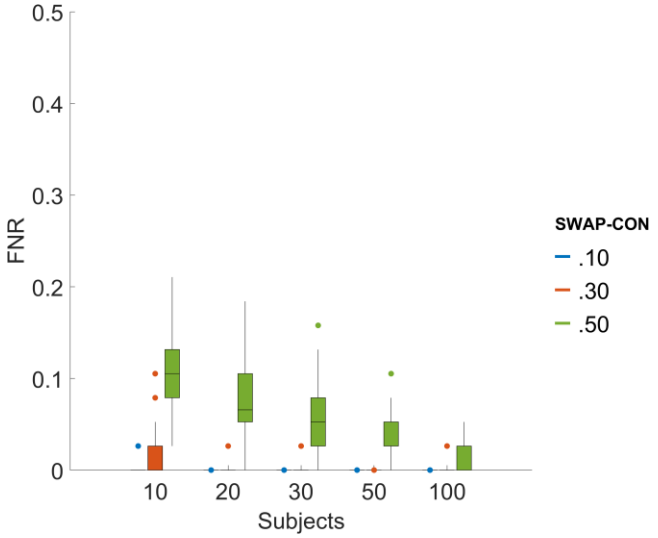


Fig.2. Boxplot diagrams reporting FNR distributions obtained applying PARAFAC algorithm on synthetic data generated using five different levels of SAMP-SIZE (along x-axis) and different levels of SWAP-CON (different colors of the bars). Results refer to synthetic datasets of dimension equal to 20 nodes.

Diagrams allow to appreciate that FNR values decrease in response to an increase in SAMP-SIZE or a decrease in SWAP-CON, as confirmed by Tukey's post-hoc test. Similar considerations were found for all NODES levels ($K = 30, 50$).

C. Performances of PARAFAC algorithm on synthetic data - AUC

Table III reported results of the 2-way repeated measures ANOVA on AUC values for different numbers of nodes. Either single or combined factors have a significant effect on AUC distribution, as confirmed by F and p values in Table III. According to boxplot representation in Fig.3, AUC values are close to 1 (i.e. optimal classification of null and non-null connections) for $s > 20$ without regarding of SWAP-CON level.

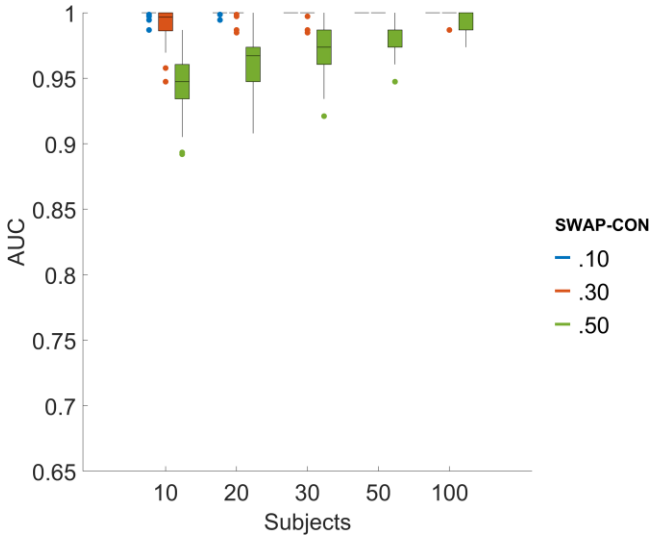


Fig.3. Boxplot diagrams reporting AUC distributions obtained applying PARAFAC algorithm on synthetic data generated using five different levels of SAMP-SIZE (along x-axis) and different levels of SWAP-CON (different colors of the bars). Results refer to synthetic datasets of dimension equal to 20 nodes.

TABLE III

Effect	DOF	F values - AUC		
		20 nodes	30 nodes	50 nodes
SWAP-CON	(2, 198)	**1160**(*)	**2428**(*)	**5053**(*)
SAMP-SIZE	(4, 396)	**137**(*)	**468**(*)	**797**(*)
SWAP-CON* SAMP-SIZE	(8, 792)	**87**(*)	**241**(*)	**466**(*)

Results of three-way repeated measures ANOVA computed considering AUC as dependent variable, SWAP-CON and SAMP-SIZE as within main factors. The analysis was repeated for three different number of nodes (20, 30, 50). Acronym DOF is for degrees of freedom. The symbol (*) indicates significant effect of the factor ($p<0.01$).

On the other hand, for $s \leq 20$ AUC values decrease when SWAP-CON level increases. As for FNR and FPR, AUC distributions confirmed that SWAP-CON and SAMP-SIZE have opposite effects on the overall result. Similar results were found for all NODES levels ($K = 30, 50$).

IV. Discussion

In this work we investigated the potentiality of a PARAFAC-based approach to extract the grand average pattern from a synthetic connectivity dataset.

As expected, noise corruption and sample size have opposite effects: low levels of noise allowed better estimation of the grand average pattern, while the opposite occurs for the sample size. Considering the noise corruption as the effect of the inter-subject variability and the number of subjects as the number of realizations of a noisy stochastic process, the research for the grand average pattern can be interpreted as the calculation of the "expected" pattern within the population. Since noise is assumed to be uncorrelated from the signal of interest (white process), under linearity assumptions the expected value for the sum between signal and noise is nothing but the summation of the expected value for the signal and the expected value for the noise. The expected value for a white noise process approaches 0 as the number of realizations of such a process approaches the infinitive, thus justifying results about the effects of sample size on the estimated common pattern.

Since we are interested in the identification of an average behavior across subjects, the best way to proceed is to set the lowest number of required rank-one tensors in order to identify the pattern in common to all the subjects included in the analysis. It has been empirically proved that when the number of required factors draw close to the rank of the original data matrix, each rank-one tensor approximates the specific pattern of each subject [2]. In the limit case for $f = rank(X) = S$, each factor (together with a residual error term) is expected to reflect the PDC pattern of each subject within the dataset, thus diverging from our purpose to look for the common mode.

V. Conclusion

In this work we investigated the potentiality of a PARAFAC-based approach for the extraction of the grand average connectivity pattern from a set of synthetic data.

Although it has been widely used for data fitting and tensor decomposition problems, our results encourage the use of PARAFAC as a useful tool for grand average estimation when dealing with group analysis. Robustness to noise as well as the proper modulation of informative content have here been proved empirically. As further analyses, we suggest to investigate the way the number of required rank-one tensors affects the grand average estimation. Moreover, an application on real EEG dataset would also be relevant to practical example of PARAFAC application in neuroscience.

Acknowledgement

This work was partially supported by the Italian Ministry of Health (GR-2018-12365874, RF-2018-12365210, RF-2019-12369396 and GR2019-12369207), Sapienza University of Rome - Progetti di Ateneo 2019 (RM11916B88C3E2DE), 2020 (RM120172B8899B8C), 2022 (RM1221816C8C757C), Progetto SEED PNR 2021, and Bit-Brain award 2020 (2962-B2B).

References

[1] O. Sporns, «Structure and function of complex brain networks», *Dialogues in Clinical Neuroscience*, vol. 15, fasc. 3, pp. 247–262, set. 2013, doi: 10.31887/DCNS.2013.15.3/osporns.

[2] B. Pester, F. de la Cruz, K.-J. Bar, H. Witte, e L. Leistritz, «Detecting spatially highly resolved network modules: A multi subject approach», in *2016 38th Annual International Conference of the IEEE Engineering in Medicine and Biology Society (EMBC)*, Orlando, FL, USA, ago. 2016, pp. 5481–5484. doi: 10.1109/EMBC.2016.7591967.

[3] F. Miwakeichi, E. Martínez-Montes, P. A. Valdés-Sosa, N. Nishiyama, H. Mizuhara, e Y. Yamaguchi, «Decomposing EEG data into space–time–frequency components using Parallel Factor Analysis», *NeuroImage*, vol. 22, fasc. 3, pp. 1035–1045, lug. 2004, doi: 10.1016/j.neuroimage.2004.03.039.

[4] I. Belyaeva *et al.*, «Multi-Subject Analysis for Brain Developmental Patterns Discovery via Tensor Decomposition of MEG Data», *Neuroinform*, ago. 2022, doi: 10.1007/s12021-022-09599-y.

[5] T. G. Kolda e B. W. Bader, «Tensor Decompositions and Applications», *SIAM Rev.*, vol. 51, fasc. 3, pp. 455–500, ago. 2009, doi: 10.1137/07070111X.

[6] S. Rabanser, O. Shchur, e S. Günnemann, «Introduction to Tensor Decompositions and their Applications in Machine Learning», 2017, doi: 10.48550/ARXIV.1711.10781.

[7] F. Cong, Q.-H. Lin, L.-D. Kuang, X.-F. Gong, P. Astikainen, e T. Ristaniemi, «Tensor decomposition of EEG signals: A brief review», *Journal of Neuroscience Methods*, vol. 248, pp. 59–69, giu. 2015, doi: 10.1016/j.jneumeth.2015.03.018.

Hidden Markov Models for the identification of fetal phases in CTG recordings

E. Spairani[1,2], G. Steyde[2], B. Daniele[2], M.G. Signorini[2] and G. Magenes[1]
[1] *Department of Electrical, Computer and Biomedical Engineering, University of Pavia, Pavia, Italy*
[2] *Department of Electronics, Information and Bioengineering (DEIB), Politecnico di Milano, Milano, Italy*

***Abstract*— Cardiotocography (CTG) is the most widely used diagnostic examination to check the status of the fetus during pregnancy. The complex nature of CTG signals strongly affects the interpretation of the latter, causing a large intra and inter-observer variability in the analysis. A very challenging task in this context is the automatic identification of fetal activity and quiet periods within the tracings. The importance of distinguishing these periods resides in the fact that different neural mechanism are involved in the regulation of fetal heart, depending on quiet or activity fetal stages. This would also allow the evaluation of any differences present in diverse fetal stages between signals from healthy and pathological fetuses, increasing the diagnostic capability of CTG analysis. With the present work we address the problem of fetal state clustering in a totally unsupervised manner, resorting to the use of Hidden Markov Models. The obtained results have been brought to the attention of an experienced clinician, who expressed a 93% level of agreement between his interpretation and the fetal state clustering obtained with the model.**

***Keywords*—Hidden Markov Models, signal segmentation, activity recognition, time series clustering.**

I. Introduction

CARDIOTOCOGRAPHY (CTG) is the most widely spread diagnostic examination to ascertain the status of the fetus during pregnancy. CTG consists of simultaneously recording the fetal heartbeat signal (FHR) and the uterine contractions (TOCO), to check the proper development of the fetus during pregnancy [1]. Despite its wide diffusion, the reliability of a CTG exam still suffers of misleading interpretations, due to large intra and inter-observer variability in the analysis, generally resulting from eye inspection of the tracings by an expert Ob-Gyn specialist. This derives from the complex nature of FHR signals, which are strongly non-deterministic and non-stationary. Over the last few decades, research has focused on the development of systems capable of carrying out an automatic interpretation of CTG recordings, starting from the computation of indices related with the neural control mechanisms of fetal heart, either in time, frequency and nonlinear domains. The use of Information Technology support in the analysis of CTG recordings has the potential to stem these limitations, conferring objectivity and reproducibility to the method [2].

A very challenging task is this context is the identification of fetal states. This means being able to identify, within a FHR tracing, the time periods when the fetus is in a condition of activity and those when it is in a quiet phase. Knowledge of the current fetal stage is of fundamental clinical relevance. In fact, from the duration of the different phases, important information about the state of fetal well-being is derived.

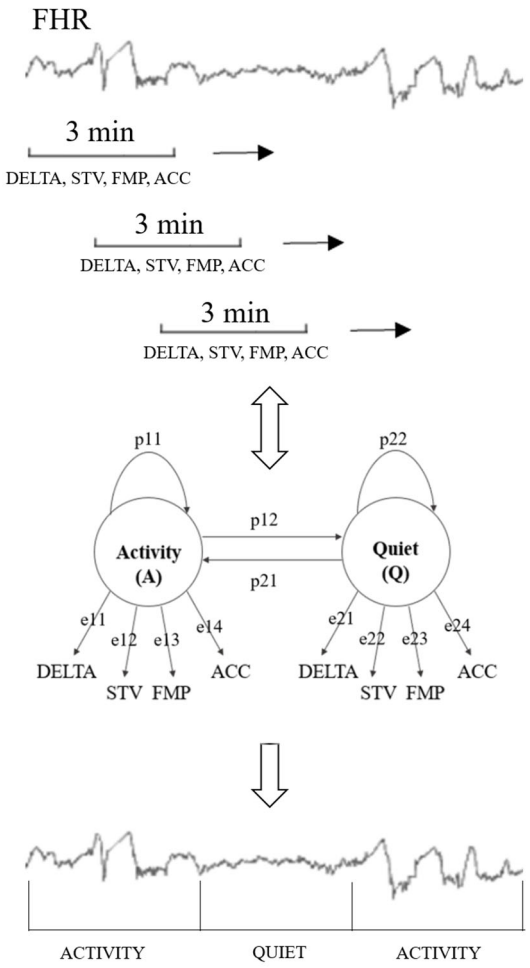


Fig.1*:* Scheme of the proposed fetal state detection method. A set of features is computed on windows of 3 minutes sliding on the FHR signal. The latter is seen as the set of emissions of a HMM consisting of two possible states, i.e., Activity (A) and Quiet (B). The pij and eij represented on each arrow of the HMM respectively stand for the transition and emission probability associated to that specific branch. After the training, the HMM is able to provide an automatic clustering of the points in the FHR signal, identifying quiet and activity phases.

Indeed, it has been observed that prolonged phases of inactivity are important indicators of pathological conditions [3]. The signal trend within the different phases (especially its variability) can also allow useful information to be derived for the purpose of interpreting the tracings.

The medical literature reports 4 possible behavioral states of the fetus. The quiet state includes two distinct phases, 1F of quiet sleep and 2F of active sleep. The activity state also

includes two possible stages, the 3F of quiet wakefulness and the 4F of active wakefulness [4].

The identification of different fetal phases within CTG tracings is, to date, still left to the clinician's experience and can consequently lead to discordance in interpretations.

With the aim of pursuing the goal of automatic identification of fetal phases within the collected CTG recordings, in the present work, we present a method for the unsupervised FHR signals clustering, based on Hidden Markov Models (HMM) [5].

The choice of such an approach is motivated in part by the need to implement a fully data-driven approach and in part by the urge to adopt a method that allows for interpretable results. As a first attempt, we decide to simplify the problem by modeling the system with an HMM consisting of only two possible states, i.e., activity and quiet. The idea behind this approach is to shift a fixed length sliding window on the FHR tracing, and to extract, at each slide, a set of features describing the portion of signal contained within the window; the latter is viewed as the set of emissions of the HMM. After learning the parameters of the model, during the training phase, the latter should be able to automatically cluster each point of the FHR signal, hence being able to identify periods of fetal activity and quiet. An illustration of the procedure is shown in Fig.1.

II. Methods

A. Data description

In the present work, we used the database described in [6]. The latter contains FHR tracings sampled at a frequency of 2Hz and lasting at least 20 minutes (i.e., 2400 points). From this dataset, we selected a subgroup of n = 150 signals related to fetuses with developmental ages between 35 and 40 weeks, that were used to train our unsupervised model. Since, for different reasons, the latter are corrupted by artefacts and signal losses, a denoising pre-processing step is needed; it includes the linear interpolation of signal losses lasting less than 15 s and the removal of portions where signal is lost for a longer duration.

B. Parameters computation

According to the study design, we decided to perform the computation of a set of parameters on 3-minute moving windows, corresponding to 360 points of the FHR tracing. At each step, the window is shifted along the signal with a 5-second stride (i.e., 10 signal points), and the calculation of the set of selected features is performed onto it (Fig.1).

The parameters we decided to compute at each shift comprehend two linear features relative to the time domain, i.e., DELTA and Short-Term Variability (STV) [7]. The latter are important indicators of fetal homeostasis, and in clinical practice, abnormal values of these indices reflect acute changes in fetal condition and are associated with an increased risk of motor and neurodevelopmental delay and damage in specific areas of the brain [8].

Besides these indices of cardiac variability, perceived fetal movements (FMP) and accelerations (ACC) are considered. The FMP signal is derived at each CTG examination and is the result of the pregnant woman pressing a button at the very moment she perceives fetal movements. From a technical point of view, the FMP is a signal of the same length as the FHR trace, with values of 1 at the perceived movement points and 0 at the remaining ones. FMP, as such, may be representative of actual fetal activity but may also indicate sporadic movements that may be present even in a quiet phase or may simply be the result of a mother's misperception.

As for the accelerations, following the definition provided in [9], the latter stand for periods lasting longer than 15 seconds in which the FHR signal remains above 15 bpm as respect to the baseline (large accelerations) or between 10 and 15 bpm above baseline (small accelerations). Accelerations of the FHR are an important sign of fetal healthy (accelerations indicate the fetus is moving), but their absence in labour is not unusual [10].

For the sake of terminological clarity, we will henceforth denote by FMP the percentage of perceived fetal movements within the 3-minute window and by ACC the number of accelerations in the window.

The choice of the parameters described above integrates a group of features derived from the FHR signal itself (DELTA, STV, ACC) with a signal-independent information (FMP), allowing objective and subjective information to contribute to the process of identifying fetal states within the signals.

Parameters computation has been performed through the software MATLAB R2022b (The Math Works, Inc.).

C. HMM and their application for fetal states assessment

The intent of the present work is to demonstrate how HMMs can be used as a tool capable of enabling the identification of fetal states within a FHR signal, starting from a set of information not exclusively derived from the FHR signal itself (e.g., FMP).

Markov models are random processes in which the transition probability that determines the transition from one state of the system to another one only depends on the immediately preceding state and not on how one got to that one. In classical Markov models, the states of the system are typically observable. In HHMs, on the other hand, the states are not directly observable, but are noticeable through a set of random variables that are probabilistically related to the unobservable states [11].

An HMM is defined through:

- A set S of N possible states $\{S_1, ..., S_N\}$.
- A set A of M possible emissions $\{a_1, ..., a_M\}$.
- A $N \times N$ transition matrix called P such that $P(i, j) = pij = p(S_j|S_i)$.
- A $N \times M$ emission matrix called E such that $E(i, j) = eij = p(a_j|S_i)$.
- A $1 \times N$ vector $\pi 0$ of prior probabilities.

As a first attempt to the problem of identifying fetal states within the FHR signals, we consider a simplified case. In particular, we make the modelling assumption that the system can be described by an HMM with two possible states (N= 2), i.e., activity (A) and quiet (Q). The evolutional dynamics of this system are governed by its emission and transition probabilities, which are learnt through the training phase, as will be stated in section E.

A representation of the developed HMM is depicted in Figure 2.

The HMM was implemented in Python, version 3.7.

D. *Observation set of the HMM and their codification*

As previously anticipated, the idea behind this approach is to interpret the set of parameters extracted at each sliding of the moving window (i.e., DELTA, STV, FMP, ACC) as the set of observable random variables emitted by the actual state of the HMM. These observations are probabilistically related to the state through the emission matrix E, that is estimated during the training.

Since each of the observed variables is continuous, as a first attempt, we decide to put ourselves in a simplified situation by making a categorization of the variables. Specifically, about DELTA, STV and FMP, these are categorized in high, middle and low according to their respective 33rd and 66th percentile values. ACC, on the other hand, was categorized with respect to the presence or absence of accelerations within the 3-minute window.

In this way, a 3-minute excerpt of FHR signal is converted into a vector of 11 symbols, where the first 3 groups of 3 digits respectively indicate low, middle and high values of DELTA, STV and FMP, and the last group of 2 symbols stand for the presence or absence of accelerations. For example, assuming we consider a 3-minutes chunk of FHR signal, characterized by a high DELTA, a medium STV, a low FMP and no accelerations, this will be coded as "0 0 1 0 1 0 1 0 0 1"

The emission set A is hence composed of 11 possible emissions: A= {DELTA low, DELTA middle, DELTA high, STV low, STV middle, STV high, FMP low, FMP middle, FMP high, ACC YES, ACC NO}.

This modelling choice hence makes the matrix E of size N x M, where N=2 and M=11.

E. *HMM parameters estimation*

After defining the structure of the model and coding the 3-minutes chunks of FHR, as explained in Sections C and D we proceed to the estimation of matrices E and P.

This is achieved through the Baum-Welch algorithm. The latter is a special case of the expectation-maximization algorithm (EM) used to learn the unknown parameters of HMMs [12]. The algorithm requires to provide an initial estimate of $\pi 0$, E and P, which are then updated to the current values during the training. To avoid any kind of bias due to particular a priori modelling choices, we chose the equiprobability condition for the initialization of $\pi 0$, E and P.

The proportion of data for training and testing was respectively set to 70:30.

F. *Estimation of the most likely path of the states of the system*

Once an estimate of matrices E and P has been obtained through the Baum-Welch algorithm, the model can be exploited to make predictions. Specifically, given a particular sequence of observations, the model will use the learnt knowledge to predict the trajectory of states most likely to have given rise to the observed sequence.

This task is addressed through the Viterbi algorithm [13][14].

III. RESULTS

Table I and II respectively illustrate matrices P and E. The high values on the diagonal of P indicate the tendency of the system to remain in the actual state for a long period rather than rapidly shifting to the other one. This is consistent

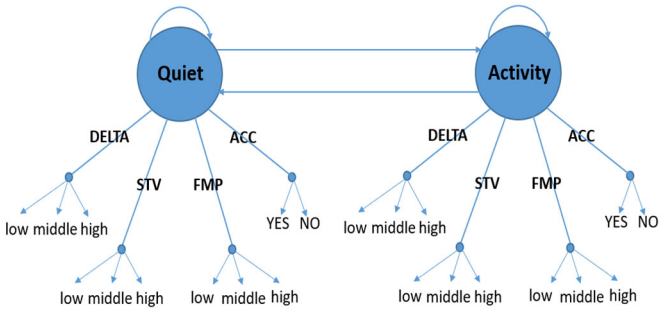


Fig.2: Scheme of the proposed HMM for the fetal state identification. The model presents two possible states, i.e., Quiet and Activity. According to its transition probabilities (P), once in a certain state, the system can continue to remain in the same state or change to the other one. The arrows branching off from the states and heading toward the bottom of the figure, on the other hand, represent the possible observable variables. These are probabilistically linked to the states its emission probabilities (E).

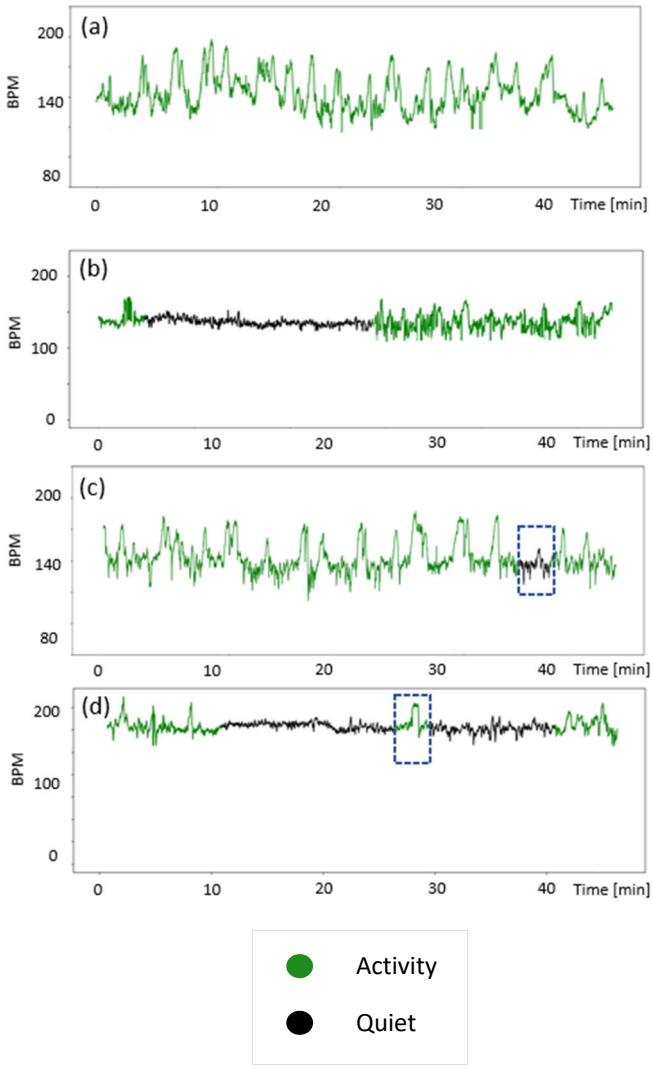


Fig.3: A set of FHR signals, together with fetal states, is shown, according to the predictions of the trained HMM. Green colour indicates the portions relating to fetal activity while black is relating to fetal quiet. The blue dashed rectangles in (c) and (d) point out that portions in which the HMM predictions are discordant with the interpretation of the clinic who analysed these signals.

with what is generally observed in clinics, since both active and quiet states are known to have a duration in the order of tens of minutes [15].

Matrix *E* shows, instead, the probability of emitting a particular variable given a certain state. By analysing *E,* we ascertain how high probabilities associated to low values of DELTA, STV and FMP are more likely to reflect a stage of fetal quiet. On the other hand, high probabilities associated to the presence of accelerations, together with high values of DELTA, STV and FMP are more probable to indicate a stage of fetal activity.

Figure 3 illustrates a set of 4 different FHR signals on which the periods related to the fetal stages predicted by the HMM were indicated. Already from an initial observation, it is evident that the portions of fetal quiet (black) exhibit lower variability and a lower tendency to accelerate, compared with the activity phases (green).

To validate the predictions provided by the model, we enlisted the help of an experienced clinician. He proceeded to analyse and annotate quiet and activity stages on a set of 10 FHR tracings provided to him from the database we have used. Comparatively, analysing the model's predictions with the clinician's annotations, we observe a 93% degree of agreement.

Discordant portions refer to short duration stretches, predicted as belonging to a certain state, that intersperse long portions of signal classified as belonging to the opposite state (see the dashed blue rectangles in Figure 3 (c) and (d)).

TABLE I: TRANSITION MATRIX *P*

State	***Quiet*** *(transition probabilities)*	***Activity*** *(transition probabilities)*
Quiet	**0.995**	0.005
Activity	0.005	**0.995**

TABLE II: EMISSION MATRIX *E*

Emission	***Quiet*** *(emission probabilities)*	***Activity*** *(emission probabilities)*
DELTA low	**0.136**	0.011
DELTA middle	**0.113**	0.018
DELTA high	0	**0.220**
STV low	**0.250**	0.027
STV middle	0	**0.106**
STV high	0	**0.116**
FMP low	**0.246**	0
FMP middle	0.003	0.009
FMP high	0	**0.24**
ACC YES	0.155	**0.238**
ACC NO	0.092	0.011

IV. CONCLUSIONS AND FUTURE DEVELOPMENTS

In this work we present a method for the unsupervised signals clustering, based on Hidden Markov Models (HMM), with the challenging aim of identifying fetal behavioral stages within FHR signals.

The obtained results seem to suggest that the developed model can identify fetal states of quiet and activity with a certain degree of reliability. In fact, the predictions of the model have shown a degree of agreement of 93% with the interpretations of an expert clinician.

The analysis of discordances could suggest an intrinsic limitation of HMM, i.e., the lack of memory. However, since fetal stages are known to have a duration of the order of the ten of minutes, the introduction of a threshold on the minimum acceptable duration of a fetal phase might be sufficient to curb the limitation.

Further developments for the current work include the introduction of new possible states in the HMM and the testing of the effects of a new set of observations, including parameters grasping different aspects of the FHR signals, not only related to time domain.

V. ACKNOWLEDGEMENTS

The authors are grateful to Dr. S. Tagliaferri, Dept. of Obstetrical– Gynaecological and Urological Science and Reproductive Medicine, Federico II University, Naples, Italy, for his help in inspecting and identifying fetal states in the FHR traces provided to him.

REFERENCES

[1] K. Hammacher et al., “Über die auswertung und dokumentation von ctg-ergebnissen”, *Gynecol. Obstet. Invest.*, 1968, 410-423.

[2] G. Dawes et al. “The advantages of computerized fetal heart rate Analysis”, *Journal of Perinatal Medicine*, 1991, 19:93-45.

[3] J.Lai et al., “Fetal movements as a predictor of health”, *Acta Obstetricia et Gynecologica Scandinavica*, 2016, 968-975.

[4] J. G.Nijhuis et al. “Are there behavioural states in the human fetus?” *Early Hum. Dev*., 1982, 177-195.

[5] B.Schuster-Bockler et al. “An Introduction to Hidden Markov Models”, *Protocols in Bioinformatics*, 2007.

[6] E. Spairani et al. “A Novel Large Structured Cardiotocographic Database”, *44th Annual International Conference of the IEEE Engineering in Medicine & Biology Society (EMBC)*, 2022,1375-1378.

[7] D. Arduini et al. “Computerized analysis of fetal heart rate”, *Journal of Perinatal Medicine*, 1991, 22–27.

[8] M. L. Annunziata et al., “Fetal vibroacoustic stimulation in computerized cardiotocographic analysis: The role of short-term variability and approximate entropy”, *Journal of Pregnancy*, 2012,7-9.

[9] D.Arduini et al., “Elementi di cardiotocografia clinica”, *Computers in cardiography, 2007.*

[10] M. Pettker et al. “Antepartum Fetal Assessment”, *10th edition of Avery’s Diseases of the Newborn*, 2018, 18-21.

[11] L. R. Rabiner et al. “An Introduction to Hidden Markov Models”, *IEEE ASSP Magazine*, 1986, 4–16.

[12] L.Rabiner. "First Hand: The Hidden Markov Model". *IEEE Global History Network*., 2013.

[13] J.Feldman et al. "A Fast Maximum-Likelihood Decoder for Convolutional Codes", *Proceedings IEEE 56th Vehicular Technology Conference*, 2002, 371–375.

[14] A. Viterbi, "Error bounds for convolutional codes and an asymptotically optimum decoding algorithm," *IEEE Transactions on Information* Theory, 1967, 260-269.

[15] B. Arabin et al., “An attempt to quantify characteristics of behavioral states”, American journal of perinatology, 1992, 9,2.

P300 event-related potential in patients with cognitive decline correlates with task performance

A. A. Vergani[1,2], C. Fabbiani[3,4], S. Mazzeo[3,4], R Burali[3], M. Lassi[1,2], G. Giacomucci[4], V. Moschini[4], F. Emiliani[4], M. Scarpino[3], S. Bagnoli[4], A. Ingannato[4], B. Nacmias[3,4], S. Padiglioni[5], S. Sorbi[3,4], A. Grippo[3], V. Bessi[4], A. Mazzoni[1,2]

[1]*The BioRobotics Institute, Sant'Anna School of Advanced Studies, Pisa, Italy*
[2]*Department of Excellence in Robotics and AI, Sant'Anna School of Advanced Studies, Pisa, Italy*
[3]*IRCSS Fondazione Don Carlo Gnocchi, Florence, Italy*
[4]*Department of Neuroscience, Psychology, Drug Research and Child Health, Careggi University Hospital, Florence, Italy*
[5]*Regional Referral Centre for Relational Criticalities – Tuscany Region, Florence, Italy*

***Abstract*—The conditions of subjective cognitive decline (SCD) and mild cognitive impairment (MCI) are two ordered stages in cognitive decline. The transition between the SCD stage and MCI is a phenomenon that largely depends on the individual's neurological characteristics. Monitoring these characteristics through non-invasive and portable methods such as electroencephalography (EEG) allows for extracting information that can be associated with the patient's clinical condition. Here, we investigated the differences between SCD and MCI in the P300 event-related potential obtained during a visual attention task. By looking central EEG channels (FC1, FCz, FC2, C1, Cz, C2), we compared the signals along the interval 300 [ms] - 500 [ms] between the two conditions, further stratifying for the task performance. We found that the P300 amplitude was larger in patient with a better performance, and that this effect was significantly more pronounced in MCI subjects. These results suggest that P300 during a simple task can be a useful neural marker to discriminate between the two conditions. In future longitudinal studies, this marker could support identify risk or protection profiles for conversion in the SCD and MCI continuum.**

***Keywords*—P300, EEG, Subjective Cognitive Decline (SCD), Mild Cognitive Impairment (MCI)**

I. Introduction

Cognitive decline is a physiological condition due to senescence. In some cases, however, this condition can become disabling for the everyday life of those affected. There is a range of cognitive decline that progresses through subjective and objective stages [1]. Subjective Cognitive Decline (SCD) is a self-reported change in memory, reasoning, and problem solving, but is not yet classified as pathological by neuropsychological tests. Mild Cognitive Impairment (MCI) is when neuropsychological tests reveal objective cognitive symptoms. SCD patient are considered a risk condition for more severe forms of cognitive decline, such as MCI and Alzheimer's disease.

A low-cost and portable methodology for studying the condition of a person's cognitive decline is the electroencephalogram (EEG). Numerous studies have focused on identifying markers that determine electrophysiological alterations in relation to the gradient of cognitive symptoms [2]. Recordings of the EEG trace in conjunction with the performance of a cognitive task are particularly suitable for this purpose. One possible marker that has been found in correspondence with altered cognitive status is the P300 potential. This voltage potential can be recorded by EEG electrodes in concomitance with decision-making during the performance of a task. The dynamics observed in the literature of this potential recognised a modulation of the P300 in relation to the quality of the decision-making process.

In this study, based on PREVIEW clinical protocol [3], we investigated the role of P300 as a neural electrophysiological correlate in patients with SCD and MCI, during a visual-attention task. The observation included the stratification of patients based on their different behavioural performances and computing a quantitative characterization of the dynamics of that event-related potential biomarker.

II. Methods

A. Patients and experimental task

The patients recruited in this study are 126, divided in 85 SCD (mean age 67.02, std 9.78) and 41 MCI (mean age 75.25, std 8.02). The cognitive task is a visual vigilance task consisting of the recognition of a target shape (triangle pointing upwards) against two confusion stimuli, i.e., 3 Choice Vigilance Test (3CVT) [4]. The patients' task performance is computed by using the F-Measure, which considers both reaction time and accuracy measures. The patients, ordered from the lowest to the highest F-Measure score, were divided into three categories sorted by low, medium, and high performance, where the cut-off between low and medium score is the 50th percentile of F-Measure, and between medium and high the 90th percentile.

B. EEG processing and statistical analysis

During the task, EEG recording was performed with a 65-channel headset (Galileo-NT system of E.B. Neuro S.p.a.) at sampling rate of 512 [KHz]. After pre-processing including band-pass filtering (1 [Hz] - 45 [Hz]) [5] , detection of noisy channels, average rereferencing and exclusion of artefactual components via ICA (Independent Component Analysis), epoching was performed for each channel, using a window of -300 to 1000ms, with onset stimulus centred on 0ms. Each trial of the experiment lasted 1000ms, with the first 200ms for stimulus presentation and the next 800ms for patients to respond. In this time window, the latent cognitive processes of decision making were studied specifically with EEG central

channels [FC1, FCz, FC2, C1, Cz, C2]. Statistical analyses were conducted to compare the EEG signals between groups by using Kruskal-Wallis H-test statistics and post-hoc and pair variables analysis were performed with Mann-Whitney U rank test, and both results were corrected using the Bonferroni technique (i.e., significative p-value if p< 7.5e-05).

C. Computation of the defined integral of voltage potential

The definite integral of EEG potential relates with the total amplitude of the P300 waveform over a specific time interval (300 [ms] - 500[ms]) and is used as a measure of the neural activity associated with performance. This integral is performed a sum of the voltage values comprised in the P300 temporal window, i.e., $\sum_{t=300\,[ms]}^{t=500\,[ms]} p_t$, where p_t is the voltage potential associated with specific time instant *t*.

III. RESULTS

A. Behavioural performances are overlapping SCD and MCI conditions

The behavioural study of the patients who performed the visual attention task showed that low, medium, and high F-Measure scores were common between the two diagnostic categories (Fig.1). Moreover, Pearson correlation between reaction time and accuracy reveals negative association for SCD (CC=-0.16, p-value=0.15) and positive association for MCI (CC=0.47, p-value=0.02). This outcome justifies the investigation into the neural mechanisms that are associated with performance.

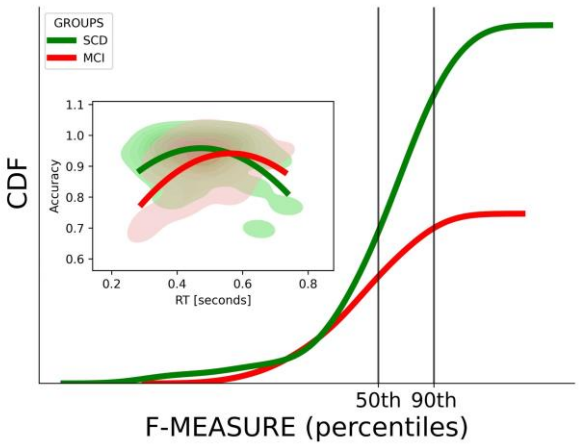


Fig. 1: Behavioural performances. Cumulative Density Function of F-Measure in SCD (in green) and MCI (in red). The 50th percentile of F-Measure defines the cut-off between low and medium performance, while the 90th percentile of F-Measure defines the cut-off between medium and high performance patients. The small scatter-density plot relates reaction time and accuracy in SCD and MCI subjects.

B. Performances are associated with specific ERP dynamic pattern shared in SCD and MCI patients

The temporal analysis of the ERP waveform, observed in central channels along the decision making process, showed that the different performance have a physiological correlate in patients (Fig2 panels A-B). In both SCD and MCI groups, the comparison of low, medium, and high performance waveforms was significant (see instant p-value above panels A-B). Post-hoc analyses, for both diagnostic categories, showed that differences were attributable to discrepancies between ERP patterns associated with low and high performance for SCD (average U statistic=9001.0, average instant p-value=0.008), and for MCI differences were related to ERP comparison between low and high performances (average U statistic=1754.0, average instant p-value=0.052) and between medium and high performances (average U statistic=964.0, average instant p-value=0.0003). Moreover, these significant differences observed when comparing the ERP waveforms with respect to performance show prolonged periods of significance (p-value blocks > 100ms). Therefore, statistical result indicates the robustness in time of the EEG dynamics associated with decision-making.

The ERP dynamics modulated with performances has changes in the prototypical P300 voltage pattern. The amplitudes of the that waveform are greater in the case of high performance, compared to medium and low performance, for both SCD and MCI conditions. The comparison between conditions also reveals that the P300 associated with high performance in MCI patients has a peak value almost double that of SCD patients (qualitative inspection in Fig2 panels A-B). This first-level observation has motivated a more rigorous treatment by extracting the integral of the P300 voltage potential defined in the 300 [ms] – 500 [ms] time interval, for both the neurological conditions and across performances.

C. The definite integral over the P300 temporal window depends on both condition and performance.

Measuring the integral of the voltage defined in the 300 [ms]-500 [ms] interval shows a positive Pearson correlation with the F-Measure in SCD (CC=0.38, p-value=0.0006) and MCI (CC=0.38, p-value=0.021)). This trend indicates a positive monotonic relationship between the amplitude of the P300 waveform and the level of performance shared between the conditions. The integral along the P300 returns a higher value as the F-Measure varies in MCI compared to SCD patients (Fig. 2 panel C).

An analysis of the integral values along the P300 was also conducted among the three performance categories (Fig. 2 panel C). The comparison between SCD patients revealed significant differences between the low and high performance categories (U statistic=173.0, p-value=0.01), while the comparison between MCI patients showed significant differences between low and medium performance categories (U statistic=17.0, p-value=0.015), as well as between the medium and high performance categories (U statistic=109.0, p-value=0.025). The comparison between the two patient groups also showed that the P300 integral levels in low performance SCD were significantly different from the values in high performance MCI (U statistic=20.0, p-value=0.0009), as were the differences between medium performance SCD and high performance MCI (U statistic=48.0, p-value=0.02).

A summary of the results can be seen in Table 1, which shows the association between diagnostic and performance category, in relation to age and measure of the voltage integral along the P300 time window. The patients who had the lowest behavioural scores during the 3CVT task were the oldest for each diagnostic category, while the patients who had the highest scores were the youngest, respect to their diagnostic category.

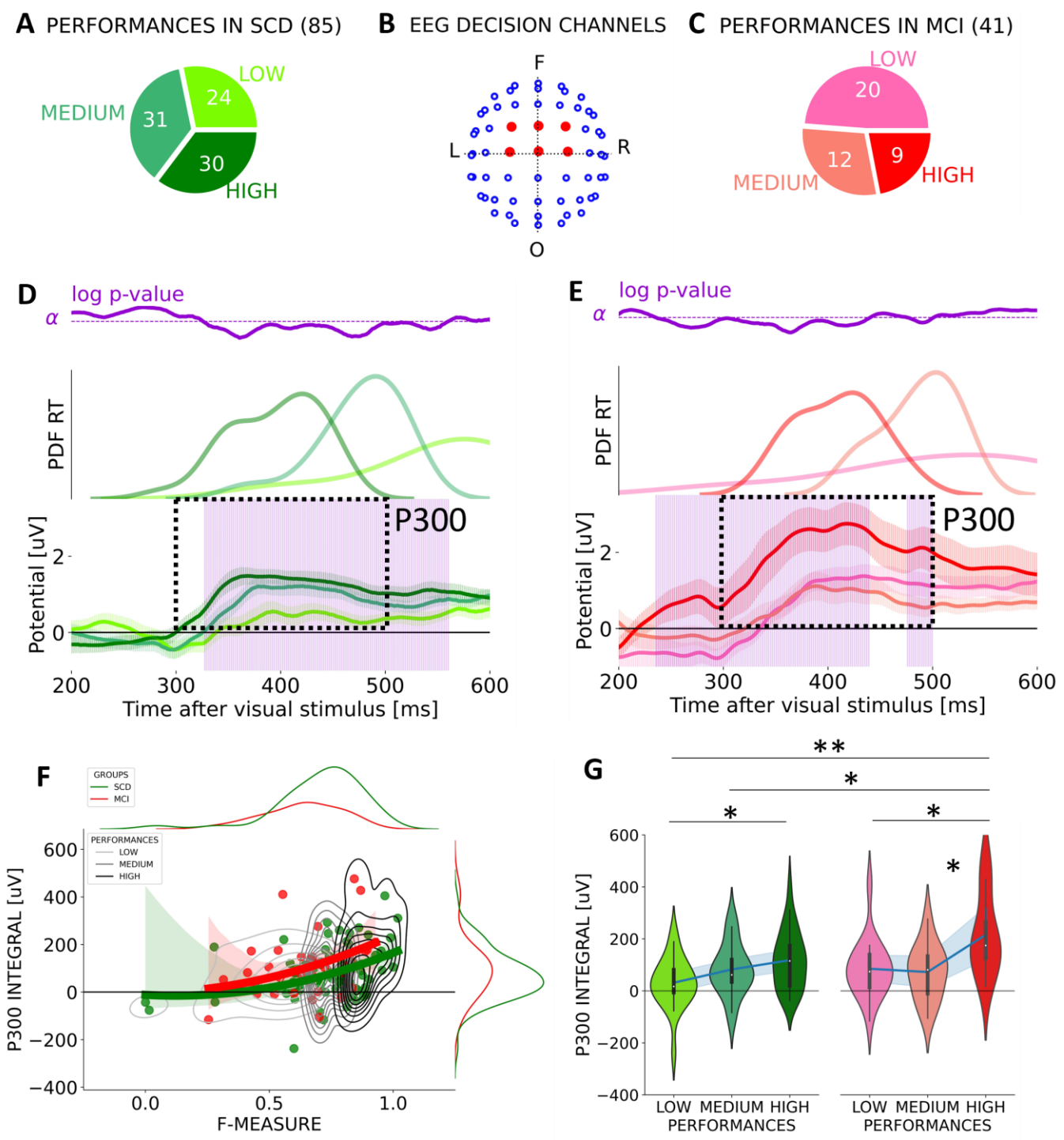


Fig 2. P300 dynamics are being investigated on EEG central channels in patients with SCD and MCI. Panel A and C are pie charts representing the number of total SCD and MCI patients and their performances, respectively, each associated with a specific colour. Panels A and C also serve as legends for all subsequent panels. Panel B indicates the EEG channels selected for the investigation of the decisional correlate, which are (FC1, FCz, FC2, C1, Cz, C2). Panel D represents the P300 dynamics in SCD patients in relation to their performances. At the bottom, the ERP correlate is displayed in the post-stimulus range. In the middle of the panel, the PSD of reaction time is presented as a function of performance. At the top, in purple, the instantaneous p-value logarithm calculated using the Kruskal-Wallis H-test, applied to the three performance categories. The term alpha indicates the Bonferroni threshold at which the p-value is significant ($p<7.5e-05$). The purple bands in the P300 graph indicate the portions of the signal for which the p-value is significant. Panel E is like Panel D but relates to MCI patients. Panel F indicates the integral of the P300 potential within the temporal range of 300 [ms] - 600 [ms] as a function of the F-Measure, with the PSDs of the dependent and independent variables at the margins. Panel G shows violin plots that identify differences in SCD and MCI conditions, stratified by performances (* if p-value < 0.05, ** if p-value < 0.01).

Diagnosis/Performance	*Age*	*P300 integral [μV]*
SCD/LOW (24#)	**71 (std 7)**	**35.52 (std 6.93)**
SCD/MEDIUM (31#)	69 (std 9)	89.10 (std 96.31)
SCD/HIGH (30#)	61 (std 9)	120.64 (std 108.62)
MCI/LOW (20#)	**79 (std 5)**	**82.15 (std 125.91)**
MCI/MEDIUM (12#)	72 (std 8)	73.94 (std 97.89)
MCI/HIGH (9#)	67 (std 8)	196.15 (std 149.28)

TABLE I: PATIENTS' NUMERICAL PROFILING

Comparing the high performance subjects with respect to the integral along the P300 potential, it can be observed that MCI patients more than double the value of SCD patients (82.15 versus 196.15), and the same applies to the values of the P300 integral with respect to low performance (35.52 versus 82.15).

IV. DISCUSSION

EEG signals of SCD and MCI patients were compared during a visual attention task. The analysis of task-related event potentials revealed specific correlates for subject performance, specifically, a modulated dynamics of P300, a marker of decision-making quality, was observed.

The voltage integral in the P300 temporal window was higher for patients with better performance and lower for those with worse performance in both SCD and MCI groups. The quantitative profiling with integral measure showed a positive correlation with performance, however, with higher values in MCI than in SCD. Conditions of high performance, as shown by a higher P300 amplitude, may indicate a level of protection from the progression of pathological conditions such as SCD to MCI. By opposition, patient with lower P300 amplitude may be at a higher risk of progression. The hypothesis of P300 dynamics as an evaluation of conversion risk is coherent with studies associating, in people affected with different stages of cognitive decline, the efficiency of P300 with high cognitive reserve[6], [7], that is a capacity of brain resilience governed by phenomena of neural plasticity [8]. By the way, this hypothesis needs more experimental support through the longitudinal observation of the same patients.

The dimensionality reduction of the ERP signal to a single value can be useful for training machine learning algorithms for the identification of risk (or protection) configurations for the onset of severe cognitive symptoms. Other studies have used measures such as negative and positive peaks [9], [10], but they lose the temporal information related to the duration of the potential of interest. Instead, the defined integral measure allows to identify in one measure both the information related to the potential (of maximum or minimum peak) and its dynamics, that is its time evolution in a defined observation window.

Potential limitations of this study include: i) the absence of control and Alzheimer's Disease (AD) subjects, which represent the low and high boundaries, respectively, along the dementia continuum for SCD and MCI conditions; ii) the use of CSF+/- biomarkers, which may have helped in discriminating actual neural degeneration in patients; iii) the lack of a machine learning decoder to validate the P300 integral as a classification feature for pathologies and performance.

V. ACKNOWLEDGEMENT

This project was funded by Tuscany Region - PRedicting the EVolution of SubjectIvE Cognitive Decline to Alzheimer's Disease With machine learning - PREVIEW - CUP. D18D20001300002

REFERENCES

[1] R. A. Sperling *et al.*, "Toward defining the preclinical stages of Alzheimer's disease: Recommendations from the National Institute on Aging-Alzheimer's Association workgroups on diagnostic guidelines for Alzheimer's disease," *Alzheimers Dement.*, vol. 7, no. 3, pp. 280–292, 2011, doi: 10.1016/j.jalz.2011.03.003.

[2] C. Micanovic and S. Pal, "The diagnostic utility of EEG in early-onset dementia: a systematic review of the literature with narrative analysis," *J. Neural Transm.*, vol. 121, no. 1, pp. 59–69, Jan. 2014, doi: 10.1007/s00702-013-1070-5.

[3] S. Mazzeo *et al.*, "PRedicting the EVolution of SubjectIvE Cognitive Decline to Alzheimer's Disease With machine learning: the PREVIEW study protocol." medRxiv, p. 2023.04.15.23288619, Apr. 19, 2023. doi: 10.1101/2023.04.15.23288619.

[4] S. Waninger *et al.*, "Event-related potentials during sustained attention and memory tasks: Utility as biomarkers for mild cognitive impairment," *Alzheimers Dement. Diagn. Assess. Dis. Monit.*, vol. 10, pp. 452–460, Jan. 2018, doi: 10.1016/j.dadm.2018.05.007.

[5] M. Klug and K. Gramann, "Identifying key factors for improving ICA-based decomposition of EEG data in mobile and stationary experiments," *Eur. J. Neurosci.*, vol. 54, no. 12, pp. 8406–8420, 2021, doi: 10.1111/ejn.14992.

[6] L. Gu *et al.*, "Cognitive reserve modulates attention processes in healthy elderly and amnestic mild cognitive impairment: An event-related potential study," *Clin. Neurophysiol.*, vol. 129, no. 1, pp. 198–207, Jan. 2018, doi: 10.1016/j.clinph.2017.10.030.

[7] E. Khachatryan, B. Wittevrongel, M. Perovnik, J. Tournoy, B. Schoenmakers, and M. M. Van Hulle, "Electrophysiological Proxy of Cognitive Reserve Index," *Front. Hum. Neurosci.*, vol. 15, 2021, Accessed: Jan. 16, 2023. [Online]. Available: https://www.frontiersin.org/articles/10.3389/fnhum.2021.690856

[8] Y. Stern, "Cognitive reserve," *Neuropsychologia*, vol. 47, no. 10, pp. 2015–2028, Aug. 2009, doi: 10.1016/j.neuropsychologia.2009.03.004.

[9] D. Yerlikaya *et al.*, "The reliability of P300 and the influence of age, gender and education variables in a 50 years and older normative sample," *Int. J. Psychophysiol.*, vol. 181, pp. 1–13, Nov. 2022, doi: 10.1016/j.ijpsycho.2022.08.002.

[10] J. Polich, "Meta-analysis of P300 normative aging studies," *Psychophysiology*, vol. 33, no. 4, pp. 334–353, 1996, doi: 10.1111/j.1469-8986.1996.tb01058.x.

Cortical correlates in upright static balance in adolescent idiopathic scoliosis

M. Rubega[1], M. Paramento[1], S. Masiero[1,2] and E. Formaggio[1]
[1] *Department of Neurosciences, Section of Rehabilitation, University of Padova, Padova, Italy;*
[2] *Ospedale Riabilitativo di Alta Specializzazione di Motta di Livenza, Motta di Livenza, Treviso, Italy*

***Abstract*—Adolescent idiopathic scoliosis (AIS) is the most common form of scoliosis, i.e., a three-dimensional morphological spinal deformity. So far, abnormalities in electroencephalography (EEG) power spectral density during simple motor tasks have been measured in the literature. This preliminary work investigates if nonlinear analysis is as sensitive as EEG signal spectral power changes. For such aim, we exploited a database obtained from 12 adolescent girls with AIS (8 with right main curve and 4 with left main curve) and 14 age-matched controls during a simple upright static balance task. First, we analyzed EEG data using the Higuchi's Fractal Dimension (HFD) as measure of signal irregularity. Second, we fit a linear model to HFD values using as predictors the values of theta and alpha rhythms. HFD revealed a statistically increase in EEG irregularity/complexity in adolescent girls with AIS compared to controls in line with an increase in the theta power in the central regions of the brain and a decrease of alpha power in the parietal regions of the brain. These results suggest a higher information processing load due to increased postural demands caused by the scoliosis.**

***Keywords*—Electroencephalography, Higuchi fractal dimension, nonlinear analysis, spine**

I. INTRODUCTION

Adolescent Idiopathic Scoliosis (AIS) is a three-dimensional morphological spinal deformity, characterized by the deviation of the spine in the frontal plane (> 10 Cobb degrees) and the concurrent rotation of the affected vertebral bodies [1], with a prevalence of about 1-3% in adolescents aged between 10 and 16 years with girls more severely affected. The cause and the pathophysiology of AIS is not yet completely understood, but multi-factorial hypotheses, including central nervous system abnormalities, have been proposed.

Neuroimaging studies revealed: asymmetries in brainstem corticospinal bundles [2], volumetric differences in brain regions functionally related to motor control and coordination [3], abnormal patterns in the motor network during movement execution [4]. Electroencephalography (EEG) studies reported paroxysmal activity at rest [5] i.e., bilaterally synchronous activity spread over large areas of both hemispheres. An increase of the amplitude of the peak in alpha rhythm was found at central, frontal, parietal and occipital brain regions suggesting the need for increased cortical processing to maintain balance control in normal upright standing in adolescents with AIS compared to healthy controls [6]. The increase in theta frequency power and the suppression of alpha, beta and gamma powers were also observed when proprioception was altered [7]. Results from our previous study revealed a significant increase of theta activity over central regions and a lateralized alpha activity over sensorimotor regions during four different standing positions [8].

Up to now, EEG modifications in AIS have been studied with linear analysis methods, such as spectral analysis or EEG topography. Spectral analysis reduced the EEG power spectral quantification to specific frequency range of interest to establish a priori. Nonlinear methods can increase the robustness of results obtained by linear analysis. Nonlinear analysis does not require a priori conditions as restricted as linear analysis ones. For instance, spectral analysis reduces the EEG power spectral quantification to a specific frequency range of interest to establish a priori and relies on the stationary properties of the input signal. Electrical potentials recorded at the scalp level are the coalescence of overlapping brain cell action potentials in time and space. EEG can exhibit complex behavior with nonlinear dynamic properties. Thus, nonlinear methods, such as Higuchi's measure of Fractal Dimension (FD) [9], may complement the description of cerebral electrical activity. Other indices, such as sample entropy (SampEn), empirical permutation entropy and empirical conditional entropy, can be used to detect signal complexity. The best results, obtained by training and testing a neural network on EEG data in a previous study [10], were however obtained by FD indices. Moreover, FD indices, besides having no need for storage memory, are classified as linear time algorithms (i.e., they have a time complex O(N)), whereas multi-scale entropy methods (e.g., SampEn) are classified as quadratic time algorithms (i.e., they have a complex $O(N^2)$) [11]. The Higuchi FD (HFD) identifies nonlinear dynamic properties of the brain based on the quantitative EEG data and provides complementary information to power spectral analysis. HFD tends to increase as the EEG signal irregularity/complexity increases [10], [12].

In this work, we aim to deepen the analysis of the EEG activity during a simple standing task in adolescent girls with AIS vs controls by means of HFD and the computation of power spectra in theta and alpha bands – i.e., EEG frequency bands involved in postural stability control [13]. Characterizing abnormal EEG patterns may help in describing the complex physiopathology of AIS and in promoting new multi-domain treatment approaches to improve patients' care quality.

II. MATERIALS AND METHODS

A. Experimental protocol

Twelve adolescent girls with a confirmed diagnosis of AIS (age range 13–17 years; Cobb angle: 20°–55°; Risser sign:

0–4; no spine surgery; 8 with right (right AIS) main curve and 4 with left (left AIS) main curve) and fourteen adolescent girls without AIS (age range 11–16 years; no spinal pathology or any known neurological or musculoskeletal disorders; no clinically relevant back hump), i.e., controls (CTRL), were asked to stand upright with eyes closed and with their arms raised laterally to 90° for 1 min (Fig. 1a). EEG signals (32-channels system; BrainAmp 32MRplus, BrainProducts GmbH, Munich, Germany) were acquired during the upright static balance task using an analog anti-aliasing band pass-filter at 0.1–1000 Hz and converted from analog to digital using a sampling rate of 500 Hz. The reference was between Fz/Cz and ground anterior to Fz (Fig. 1b).

For further details on the database and the experimental protocol, we refer the reader to [8].

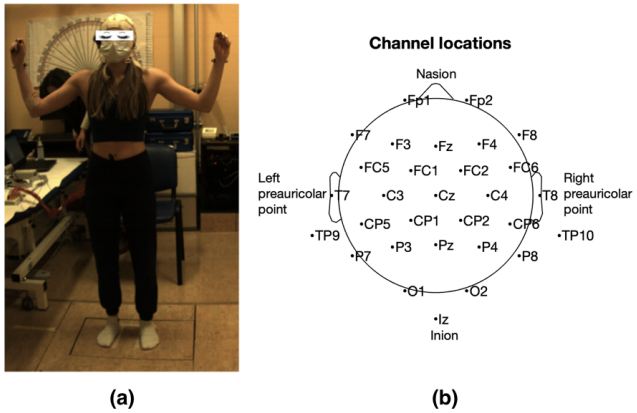


Fig. 1: **(a)** Participant standing upright with eyes closed and with arms raised laterally to 90° whilst wearing the EEG cap. **(b)** 30-channel locations according to the 10-10 system.

B. EEG data pre-processing

The data were band-pass filtered from 1 to 30 Hz considering that power spectral density shows a decrease in power with increasing frequency (1/f) and the presence of the power supply noise at 50 Hz (the optimal Chebyshev finite impulse response filters were designed using Parks–McClellan algorithm, the order was customized to minimize the error in the pass bands). Noisy channels – identified by visual inspection – were interpolated using the nearest-neighbour spline method. Cardiac activity was removed using independent component analysis (FastICA algorithm implemented in EEGLAB) based on the waveform, topography and time course of the component. Data were re-referenced to the average reference. Individual epochs containing non-stereotyped artifacts were identified by visual inspection and removed.

C. Higuchi Fractal Dimension

The FD provides a complexity index that describes how the measure of the length of a curve L(k) changes depending on the scale k used as a unit of measurement. Different approaches can be used to estimate FD [9]. The Higuchi FD standard approach calculates the FD of a time series in the time domain and is based on the log[**L**(k)] versus log(k) curve computed as follows.

(i) For each sample i of the EEG epoch **s** = **s**(1), **s**(2), …, **s**(N) of length N, the absolute differences between values s(i) and s(i-k) - i.e., the samples at distance k - are computed, considering $k = 1, \ldots, k_{max}$.

(ii) Then, each absolute difference is multiplied by a normalization coefficient that takes into account the different numbers of samples available for each value of k. The computation of this coefficient is based on the starting point m = 1, …, k and on the total number N of samples of an epoch.

(iii) $\mathbf{L}_m(k)$is computed as

$$\mathbf{L}_m(k) = \frac{1}{k} \cdot \left[\sum_{i=1}^{q} |\mathbf{s}(m + i \cdot k) - \mathbf{s}(m + (i-1) \cdot k)| \right] \cdot \frac{N-1}{q \cdot k} \tag{1}$$

where $q = int[(N-m)/k]$ and $\mathbf{L}(k)$ is computed by summing the obtained values and dividing by k:

$$\mathbf{L}(k) = \frac{1}{k} \cdot \sum_{m=1}^{k} \mathbf{L}_m(k) \tag{2}$$

(iv) From Eq. 2, the log[**L**(k)] versus log(k) curve can be derived. By definition, if $\mathbf{L}(k)$ is proportional to k^{-D} for $k = 1, 2, ..., k_{lin}$ where k_{lin} defines the upper range of the linear region of the log[**L**(k)] versus log(k) curve, then the curve is fractal with dimension D.

In this work, the linear region was defined by imposing k_{lin} equal to 5, according to [14], whilst k_{max} was set as equal to 100, $k_{max} \geq 3k_{lin}$ according to [12]. For each EEG channel, we computed the HFD of each non-overlapping 2-s EEG epoch (i.e., 1000 samples). Then, we averaged these values across epochs to obtain a single value of HFD for each EEG channel.

D. Relative power spectra

The fast Fourier transform was applied to non–overlapping epochs (Hanning-windowed to control for spectral leakage) of 2 s and then averaged across epochs. Relative power spectra (%) were calculated by dividing the power spectrum in theta band, i.e., [4.5–7.5] Hz, and alpha band, i.e., [8–12] Hz, with the total power of [1–30] Hz.

E. Multiple Linear Regression

In order to interpret and relate HFD and power spectra changes, for each group of subjects – i.e., CTRL ($N = 14$), right AIS ($N = 8$) and left AIS ($N = 4$) – a multiple linear regression model was used to predict HFD values based on the power spectral values of theta and alpha rhythms:

$$\mathbf{y} = \mathbf{X}\mathbf{a}; \tag{3}$$

where

$$\mathbf{y} = \begin{bmatrix} y_1 \\ y_2 \\ \vdots \\ y_N \end{bmatrix}; \mathbf{X} = \begin{bmatrix} 1 & x_{1\theta} & x_{1\alpha} \\ 1 & x_{2\theta} & x_{2\alpha} \\ \vdots & \vdots & \vdots \\ 1 & x_{N\theta} & x_{N\alpha} \end{bmatrix}; \mathbf{a} = \begin{bmatrix} 0 \\ a_{theta} \\ a_{alpha} \end{bmatrix} \tag{4}$$

are, respectively, a column vector containing the HFD of the N subjects; a matrix containing the values of the power spectra in theta (second column) and alpha (third column) bands of the N subjects; a column vector containing the coefficients to be estimated using the least square estimator:

$$\hat{\mathbf{a}} = (\mathbf{X^T X})^{-1}\mathbf{X^T y} \tag{5}$$

F. Statistics

First, we compared the EEG features (i.e., theta and alpha power spectra, HFD) among the three groups through Kruskal Wallis Test. We chose a nonparametric test since: (i) the EEG features were not normally distributed in all the EEG channels, (ii) the limited number of subjects. Second, for each channel, between-group differences in each EEG feature were investigated via an unpaired two-sided Wilcoxon rank sum test ($p_{value} < 0.05$) to highlight significant statistical differences between adolescent girls with AIS and controls.

III. RESULTS

Results are reported as EEG topographies in Fig. 2, 3, 4, 5. The EEG electrodes are placed onto the head, following a geometrical array of even-spaced points. Nasion and left and right pre-auricular points are depicted as anatomical landmarks (Fig. 1b). The values to represent are plotted by coding the amplitude in several tones of color (blue and green depicts lower amplitudes, while yellow and red depicts larger amplitudes). The spatial points lying between electrodes are calculated by interpolation.

The Kruskal Wallis Test indicated that the samples did not originate from the same distribution for both HFD and theta and alpha power spectra.

A. Higuchi Fractal Dimension

HFD was statistically significantly higher ($p_{value} < 0.03$) in adolescent girls with AIS with left main curve than in controls in the left frontal, central and parietal brain areas, i.e., in F3, FZ, FC1, C3, CP1, CP2 and PZ (Fig. 2a-c, Fig. 3b). Significant differences were also found in the HFD between left AIS and right AIS: left AIS showed higher HFD in the right central-parietal brain regions, and in the frontal brain areas, i.e., in F7, FC5, FC1, F4, PZ ($p_{value} < 0.01$), F3, C3, FZ, FC2, FC6, CP1, CP2, CP6, P4, and P8 ($p_{value} < 0.03$) (Fig. 2b-c, Fig. 3c).

B. Relative power spectra

Power spectra in theta band (Fig. 2d-e-f) were statistically significantly higher in:

- C4, TP9 ($p_{value} < 0.03$) in right AIS compared to CTRL (Fig. 4a).
- C4, FC2 ($p_{value} < 0.05$) in left AIS compared to CTRL (Fig. 4b).
- FP1 ($p_{value} < 0.03$) in left AIS compared to right AIS (Fig. 4c).

Power spectra in alpha band (Fig. 2g-h-i) were statistically significantly lower in:

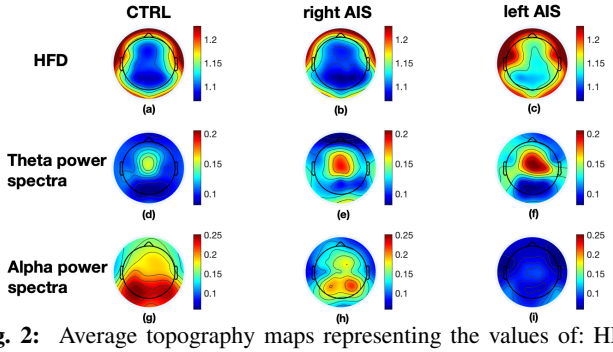


Fig. 2: Average topography maps representing the values of: HFD (first row), theta power spectra (second row) and alpha power spectra (third row) for **(a-d-g)** controls, adolescent girls with AIS with **(b-e-h)** right curve and with **(c-f-i)** left curve.

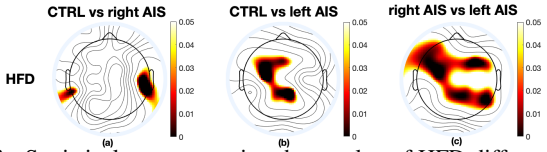


Fig. 3: Statistical maps reporting the p-value of HFD differences between: **(a)** controls vs adolescent girls with AIS with right curve; **(b)** controls vs adolescent girls with AIS with left curve; **(c)** adolescent girls with AIS with right curve vs adolescent girls with AIS with left curve.

- C3 ($p_{value} < 0.05$) in right AIS compared to CTRL (Fig. 4d).
- FZ, C3, CP5, CP6, P3 ($p_{value} < 0.02$), F3, F4, C4, P4, O1, F8, T8, P7, IZ, FC6 ($p_{value} < 0.05$) in left AIS compared to CTRL (Fig. 4e).
- P4 ($p_{value} < 0.05$) in left AIS compared to right AIS (Fig. 4f).

These results are also supported by our previous work [8].

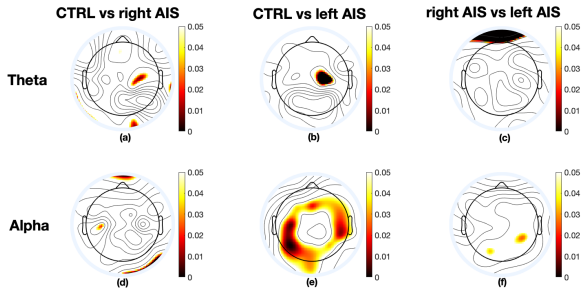


Fig. 4: Statistical maps reporting the p-value of the difference of theta (first row) and alpha (second row) power spectral between: **(a-d)** controls vs adolescent girls with AIS with right curve; **(b-e)** controls vs adolescent girls with AIS with left curve; **(c-f)** adolescent girls with AIS with right curve vs adolescent girls with AIS with left curve.

C. Multiple Linear Regression

The values of the coefficients weighting the power in theta band (i.e., a_{theta}) were distributed in a narrower range in

CTRL, i.e., [0.0469 0.0977], compared to right AIS, i.e., [0.0348 0.1163] and left AIS, i.e., [-0.0213 0.1249] (Fig. 5a-c-e).

The values of the coefficients weighting the power in alpha band (i.e., a_{alpha}) had values near to zero for CTRL and right AIS whilst had higher values in the occipital, parietal and temporal lobes in left AIS (Fig. 5f).

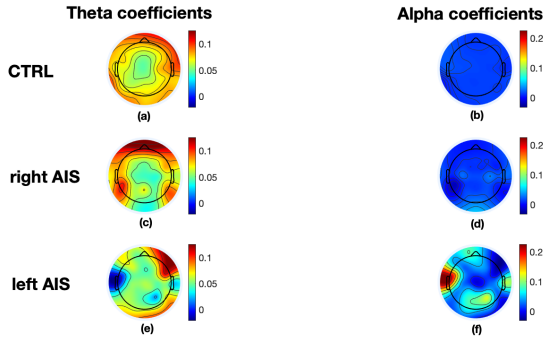


Fig. 5: Topography maps representing the coefficients of the linear regression model between the HFD values (dependent variable) and values of power in theta and alpha frequency bands (regressors) for **(a-b)** controls, adolescent girls with AIS with **(c-d)** right curve and **(e-f)** left curve. The first column reports theta coefficients and the second column alpha coefficients.

IV. DISCUSSION

Our preliminary results evidenced: (i) an increased of theta power in central clusters, (ii) a decrease of alpha power in parietal clusters parallel to (iii) an increase in Higuchi FD in girls with AIS (mainly with left curve) compared to CTRL. Interestingly, there is evidence that changes in the EEG power spectrum due to postural instability occur predominantly in the theta and alpha frequency bands [13]. In healthy adolescents, an increase in theta band power in frontal and central brain areas and a decrease in alpha power in central and parietal brain areas were evidenced with increasing balance task difficulty [13]. Similar EEG power spectral changes were found in our AIS participants compared to controls supporting the hypothesis that a simple symmetric static balance task requires an increased attentional processes and/or error monitoring as well as increased sensory information processing due to increasing postural demands in girls with AIS compared to controls.

In parallel, Higuchi FD revealed an increase in signal complexity mainly in brain regions in the brain hemisphere ipsilateral to the main curve (Fig. 3b). This suggests that girls with AIS seem to recruit the muscles contralateral to their main curve, thus activating the ipsilateral brain hemisphere, in order to maintain a symmetric static balance position.

V. CONCLUSION

In this preliminary study, Higuchi Fractal Dimension proved to be suitable to capture region-specific neural changes during static balance in girls with adolescent idiopathic scoliosis. The increase in theta rhythm in the central brain regions and the decrease of alpha rhythms in the parietal brain areas in girls with AIS compared to controls were paralleled by an increase of EEG complexity as evidenced by an increase of HFD.

Although further investigations are worth performing, adolescents with AIS show a different EEG activity compared to controls, probably related to their musculoskeletal dysfunction. Both a larger database and a longitudinal study are still needed to verify these EEG findings which may represent a valuable biomarker of scoliosis progression.

ACKNOWLEDGEMENT

This work was supported by the "Department of excellence 2018-2022" initiative of MIUR awarded to DNS - University of Padova, by Fondo di Beneficienza di Intesa Sanpaolo (B/2022/0205) and by REACT EU - PON "Ricerca e Innovazione" 2014-2020", DM 1062/2021 (MR).

REFERENCES

[1] S. Negrini, S. Donzelli, A. G. Aulisa, D. Czaprowski, S. Schreiber, *et al.*, "2016 SOSORT guidelines: Orthopaedic and rehabilitation treatment of idiopathic scoliosis during growth," *Scoliosis Spinal Disord.*, vol. 13(1), pp. 1–48, January 2018.

[2] A. E. Geissele, M. J. Kransdorf, C. Geyer, J. S. Jelinek, and B. E. Van Dam, "Magnetic resonance imaging of the brain stem in adolescent idiopathic scoliosis," *Spine*, vol. 16, pp. 761-763, July 1991.

[3] T. Liu, W. C. Chu, G. Young, K. Li, B. H. Yeung, *et al.*, "MR analysis of regional brain volume in adolescent idiopathic scoliosis: neurological manifestation of a systemic disease", *J. Magn. Reson. Imaging* , vol. 27, pp. 32–736, April 2008.

[4] J. Domenech, G. Garcıa-Marti, L. Marti-Bonmati, C. Barrios, J. M. Tormos, *et al.*, "Abnormal activation of the motor cortical network in idiopathic scoliosis demonstrated by functional MRI", *Eur. Spine J.*, vol. 20, pp. 1069-1078, July 2011.

[5] I. Petersen, T. Sahlstrand, and U. Sellden, "Electroencephalographic investigation of patients with adolescent idiopathic scoliosis", *Acta Orthop. Scand.* , vol. 50(3), pp. 283–293, June 1979.

[6] J. Lanthier, M. Simoneau, I. S. Knoth, S. Lippé, C. Bluteau, *et al.*, "Increased EEG alpha peak frequency in adolescents with idiopathic scoliosis during balance control in normal upright standing", *Neurosci. Lett.*, vol. 722, pp. 134836, February 2020.

[7] C. Fortin, J. P. Pialasse, I. S. Knoth, S. Lippé, C. Duclos, *et al.*, "Cortical dynamics of sensorimotor information processing associated with balance control in adolescents with and without idiopathic scoliosis", *Clin Neurophysiol*, vol. 130, pp. 1752–1761, July 2019.

[8] E. Formaggio, M. Bertuccelli, M. Rubega, R. Di Marco, F. Cantele, *et al.*, "Brain oscillatory activity in adolescent idiopathic scoliosis," *Sci. Rep.*, vol. 12(1), pp. 17266, October 2022.

[9] T. Higuchi, "Approach to an irregular time series on the basis of the fractal theory," *Phys. D: Nonlinear Phenom.*, vol. 31(2), pp. 277-283, June 1988.

[10] F. Scarpa, M. Rubega, M. Zanon, F. Finotello, A. S. Sejling, *et al.*, "Hypoglycemia-induced EEG complexity changes in Type 1 diabetes assessed by fractal analysis algorithm," *Biomed. Signal Process. Control*, vol. 38, pp. 168-173, September 2017.

[11] M. Rubega, F. Scarpa, D. Teodori, A. S. Sejling, C. S. Frandsen, *et al.*, "Detection of hypoglycemia using measures of EEG complexity in type 1 diabetes patients," *Entropy*, vol. 22(1), pp. 81, January 2020.

[12] F. Finotello, F. Scarpa, and M. Zanon, "EEG signal features extraction based on fractal dimension," *37th Annual International Conference of the IEEE Engineering in Medicine and Biology Society (EMBC), Milano, Italy* , pp. 4154-4157, August 2015.

[13] A. Gebel, T. Lehmann, and U. Granacher, "Balance task difficulty affects postural sway and cortical activity in healthy adolescents," *Exp Brain Res.*, vol. 238(5), pp. 1323-1333, May 2020.

[14] A. Accardo, M. Affinito, M. Carrozzi, and F. Bouquet, "Use of the fractal dimension for the analysis of electroencephalographic time series," *Biol. Cybern.*, vol. 77(5), pp. 339–350, November 1997.

Decoding the interplay between brain structural and functional connectivity in Alzheimer's disease

V. Filippi[1], E. Paolini[2], F. Cruciani[1], L. Brusini[1], F. Dal Santo[1], G. Menegaz[1], I. Boscolo Galazzo[1], and S.F. Storti[1]

[1] *Dept. of Engineering for Innovation Medicine, University of Verona*

[2] *Dept. of Computer Science, University of Verona*

silviafrancesca.storti@univr.it (corresponding)

***Abstract*—The relationship between brain structural (SC) and functional (FC) connectivity changes in Alzheimer's disease (AD) is crucial for understanding the progression and impact of the disease at different stages. In this study a multivariate statistical technique called Partial Least Squares (PLS) was used to capture the variations in SC and FC between control (CN) and pathological (PAT) subjects. The focus is on the ongoing AD Neuroimaging Initiative (ADNI)-3 cohort, relying on data from diffusion (dMRI) for SC and resting-state functional magnetic resonance imaging (rs-fMRI) for FC. Once standard data preprocessing and PLS were applied, the model weights were visualized based on the functional atlas used. This visualization allowed for a clearer representation of the relationships that were identified. Statistical tests on the original SC and FC data revealed significant differences between the two populations in SC, but not in FC, demonstrating a non-clear correspondence one-to-one between them. However, the PLS model showed unique patterns of SC and FC connections that optimally covary in 13 significant components. Interestingly, anticorrelation among the top weights was found between SC and FC in several components, suggesting an opposite behaviour between these two connectivities in the same links. These findings suggest that PLS can provide a more in-depth understanding of the relationship between SC and FC in AD and highlight the importance of their coupling in determining the pathophysiological pathways of the disease.**

***Keywords*—Alzheimer's disease, resting-state functional MRI, functional connectivity, structural connectivity, PLS.**

I. Introduction

Alzheimer's Disease (AD) is the most common type of dementia characterized by a progressive neurodegeneration that affects neurological, physical and cognitive domains that eventually interfere with daily life activities. The incidence of AD appears to double every five years after the age of 65 [1], and it is estimated that the number of individuals living with AD will continue to rise, especially in non-western countries [2]. Subjects affected by AD present a degeneration of brain tissues with loss of nerve cells, formation of β-amyloid plaques, and the development of neurofibrillary tangles [3] which can be captured with imaging techniques as magnetic resonance imaging (MRI). Despite the recent technical advancements, there is currently no effective treatment or prevention for AD [4]. Therefore more in-depth studies considering the multifaceted aspects of the AD continuum are necessary to provide novel insights on the biological contributors to AD.

Understanding the relationship between functional and structural changes occurring in AD, in terms of structural and functional brain connectivity (SC/FC), is one of the hottest challenges at the state-of-the-art, and such a link is far from being straightforward even in healthy conditions [5]. While the presence of a direct connection between two nodes determines the SC strength, FC is determined by the temporal coincidence of neural activity between spatially distant regions of the brain [6]. Previous research has suggested a positive correlation between SC and FC, meaning that structural degenerations are related to functional alterations encompassing the same areas, while a few cases have demonstrated an opposite behaviour [7]. Previous studies have used different methods to relate SC and FC data, such as graph-based measures, or specific analysis on a few networks, precluding a direct generalisability of the results. Despite the heterogeneous and sometimes controversial literature findings, possibly related to the different methodologies, the sample size and the included subjects, previous studies have suggested that structural changes may precede the functional ones in AD, as structurally impaired but functionally unaffected connections have been often disclosed [8]. In this framework, important information can be derived from more comprehensive analysis based on data-driven multivariate statistical approaches, such as Partial Least Squares (PLS) and Canonical Correlation Analysis (CCA), which are able to simultaneously model multiple variables and handle possible collinearity issues [5]. The goal of this study was to exploit PLS for identifying both structural and functional patterns that highly covary with each other and investigating their relationship in the context of AD.

II. Materials and methods

A. Study cohort

Data used in this study were obtained from the Alzheimer's Disease Neuroimaging Initiative 3 (ADNI3) database (adni.loni.usc.edu). Participants were selected based

on the availability of diffusion (dMRI) and resting-state functional magnetic resonance imaging (rs-fMRI) data, leading to a cohort of 587 subjects with 288 patients across the AD continuum (PAT) and 299 healthy controls (CN).

B. Acquisition protocol and data preprocessing

Single-shell dMRI and rs-fMRI acquisitions were acquired using 3T scanners, following the protocols and parameters outlined in the ADNI-3 database. After brain extraction, dMRI data were corrected for eddy currents-induced distortion, denoised by using local principal components analysis via empirical thresholds, and non-linearly registered to the 2-mm MNI space to remove EPI deformation. Standard preprocessing was applied to rs-fMRI data, followed by nuisance regression (6 motion parameters, white matter/CSF), pass-band filtering (0.01-0.08Hz), scrubbing and non-linear spatial normalization to the 2-mm MNI space [9].

C. Structural and functional connectomes

This study used a functional atlas to derive SC/FC connectomes instead of an anatomical atlas, as usually performed in the current literature. We hypothesised that using a functional atlas can more easily establish functional relationships with anatomical counterparts and avoid subdivided functional networks for better interpretability. To this aim, the Schaefer functional atlas with 100 parcels and 7 resting-state networks (RSNs) (visual [VIS], somatomotor [SMN], dorsal attention [DAN], ventral attention [VAN], limbic [LIM], frontoparietal control [CON], and default mode network [DMN]) [10] was chosen. Concerning SC, MRtrix3 (https://www.mrtrix.org/) was employed to derive an anatomically constrained probabilistic tractography (2 million streamlines, step = 0.3 mm, maximum length = 300 mm, and backtracking) filtered with SIFT2 [11]. The individual SC was then built by counting the number of streamlines connecting all pairs of regions from the functional atlas, ignoring self-connections. Conversely, the full Pearson correlation coefficient (*r-value*) between pairs of nodes was calculated to derive FC.

D. Partial Least Squares analysis

SC and FC were related through PLS [12]. Both the independent (X) and dependent (Y) variables were matrices of dimensions M$\times$N, with M = 587 (number of subjects) and N = 4950 (number of entries of the strictly upper triangular matrix from the 100$\times$100 symmetric SC/FC matrices). The N values of X were taken from the SC matrices, while the N entries of Y were taken from the FC ones. A Z-score normalization was applied to X, Y, and the confounding variables (age and gender), followed by deconfounding via linear regression. PLS was subsequently performed choosing 55 latent components as trade-off between the performance and the computational time, using the Nonlinear Iterative Partial Least Squares (NIPALS) algorithm [13]. PLS weights of structural and functional data, reflecting feature relevance in the generation of each latent component, were hence obtained. A permutation test (1000 permutations) was used to determine the statistical significance of the model. PLS projections scores were calculated for each component and their statistical difference between PAT and CN was evaluated through a group-wise Mann Whitney non-parametric U-rank test, separately for SC and FC derived scores. The latent components were further selected based on the significance ($p < 0.05$) obtained from the statistical test.

E. Visualization approaches of results

For each component, the projection scores for SC and FC were reported as scatterplots to visualise their relationship in the latent space, and as boxplots to compare their distributions in CN and PAT. The SC and FC PLS weights for each component were summarized as symmetric "14x14 matrices". In details, for each modality, the 4950 weights were averaged according to the original organization of the connectomes and keeping separately the two hemispheres, leading to a summary weight for each of the 7 RSNs and for each between-network pair (91 inter-network combinations). The original SC and FC matrices were similarly grouped in symmetric 14x14 matrices for each subject and statistically compared between PAT and CN groups (two-sample Mann Whitney non-parametric U-rank test, $p < 0.05$ with false discovery rate multiple comparison correction). This allows to preliminary test whether significant changes are identifiable in the original matrices and to further guide the interpretation of the SC-FC component weights. The component-specific weights were also thresholded at the 85^{th} percentile to identify the connections having the highest weights, being thus the most relevant in driving the SC-FC association. These were assigned to either one of the 7 RSNs or one of the 21 inter-network combinations (considering left/right hemispheres together) and the resulting percentage was then calculated, separately for positive and negative weights. Such percentages were reported as symmetric "7x7 matrices", and the similarity across positive/negative matrices of the two modalities was quantified using a spatial correlation coefficient.

III. Results

The PLS analysis was conducted using 55 components, explaining 35% of the data variability. Among them, 13 (components 2, 6, 7, 8, 11, 13, 19, 21, 24, 32, 33, 50, and 55) had significantly different projection scores in the PAT vs CN statistical analysis for either FC or SC. The significance of our model was confirmed by a permutation test, resulting in a p-value of 0.0. We focused on the top 9 significant components, with the corresponding p-values and explained data variability reported in Table I. Component 2 explained the highest data variability, but did not show a clear separation between PAT and CN in its latent space (Fig.1a). However, significantly different projection scores for both SC and FC were depicted (Fig.1b).

The 14x14 matrices of the significant PLS components reveal a pattern of strong either correlation or anticorrelation between the FC and SC PLS weights. For instance, component 2 exhibited an anti-correlated behaviour between the two matrices, with SC having negative weights in most of intra/inter-

TABLE I: Results of the statistical tests for the top 9 significant components. The table displays the p-values for each component, with those below the significance threshold ($p < 0.05$) highlighted, and the percentage of explained data variability.

Comp	*p - SC*	*p - FC*	*%*
2	$\mathbf{4.2204 \cdot 10^{-6}}$	$\mathbf{2.4323 \cdot 10^{-5}}$	1.8755
6	0.0895	**0.0103**	1.0139
7	**0.0339**	0.2280	0.9525
8	$\mathbf{1.2262 \cdot 10^{-5}}$	**0.0001**	0.9129
11	**0.0153**	0.4333	0.7974
13	0.1120	**0.0417**	0.6879
19	**0.0452**	0.0729	0.6159
21	**0.0043**	**0.0006**	0.5836
24	0.0583	**0.0012**	0.5486

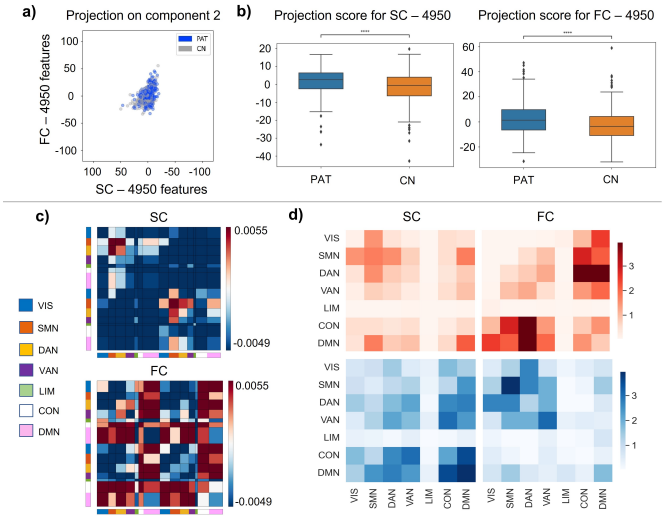


Fig. 1: Example of PLS results for component 2. **a)** Projection scores in the PLS-derived latent space, with subjects grouped as PAT (blue dots) and CN (grey dots). **b)** Boxplots representing the variability of the PAT (blue) and CN (orange) corresponding projections scores in the PLS-derived latent space for SC and FC, separately. **c)** 14×14 matrices showing the average PLS weights within/between RSNs (top: SC, bottom: FC). **d)** 7x7 matrices displaying the percentage of connections with PLS weights above the 85^{th} percentile separately for SC (left) and FC (right), further divided into positive (top) and negative (bottom) weights.

network connections while positive weights were associated with the same links in FC (Fig.1c).

When considering the most relevant weights for each component (85^{th} percentile) and the corresponding 7×7 percentage matrices, positive spatial correlations were found across the four negative/positive intermodality combinations (except for two cases), with correlation coefficients greater than 0.48 for the highest ones (Table II). Most of the components had a strong positive correlation for those matrices related to the concordant weights (i.e., positive SC [PS] - positive FC [PF] for components 6, 8, 21, and 24, or negative SC [NS] - negative FC [NF] for components 11 and 19). Interestingly, three components (2, 7 and 13) showed high spatial correlation between opposite percentage matrices, suggesting an anti-correlation between their corresponding top weights. Indeed, component 2 showed a generic covariation between PF and NS, while the highest percentages for the connections located within/between SMN and within DMN were observed for PS-NF (Fig.1d). A similar behaviour was found for component 13, in this case with a clear involvement of the within/between VIS connections for PS-NF and within DMN for PF-NS (Fig.2). Lastly, the statistical results on the original data (summarized in Fig.3) showed significant alterations between CN and PAT in both FC and SC. The differences in SC were primarily located in interhemispheric connections, whereas fewer differences were identified in FC, suggesting that there is no clear one-to-one correspondence between SC and FC.

TABLE II: Spatial correlation coefficients between the different 7×7 percentage matrices for the top 9 significant components.

	PS-PF	*NS-NF*	*PS-NF*	*PF-NS*
2	0.2244	0.0362	0.5699	**0.6251**
6	**0.5056**	0.1685	0.0106	0.1842
7	-0.0654	0.3102	**0.4865**	0.4790
8	**0.7732**	0.1976	0.0026	0.2980
11	0.0402	**0.5163**	0.4626	0.3605
13	0.3337	-0.2713	0.5063	**0.6559**
19	0.2374	**0.5587**	0.5484	0.1410
21	**0.8544**	0.4337	0.3380	0.3874
24	**0.5804**	0.4803	0.2799	0.4588

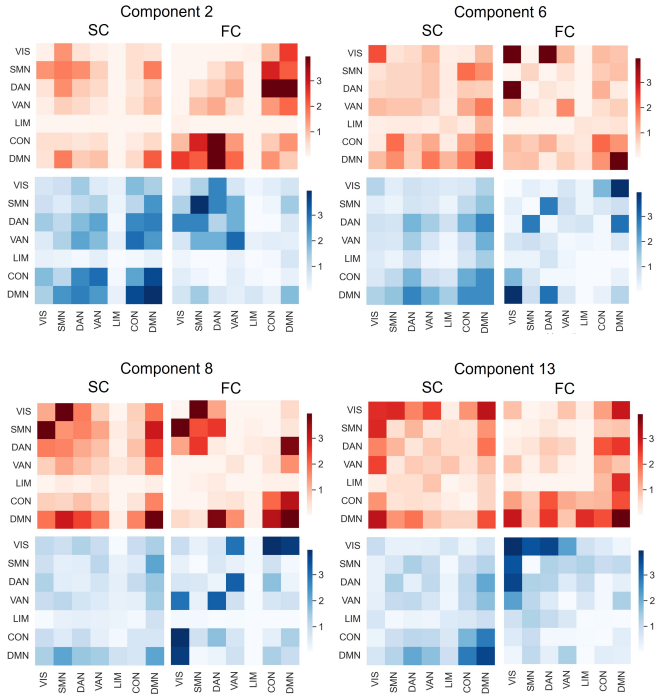


Fig. 2: Results obtained for components 2, 6, 8, and 13. The 7×7 percentage matrices related to the structural positive (PS) (top left), functional positive (PF) (top right), structural negative (NS) (bottom left) and functional negative (NF) (bottom right) top weights are represented for each component.

IV. Discussion

The main focus of this study was to investigate the relationship between SC and FC in individuals affected by AD

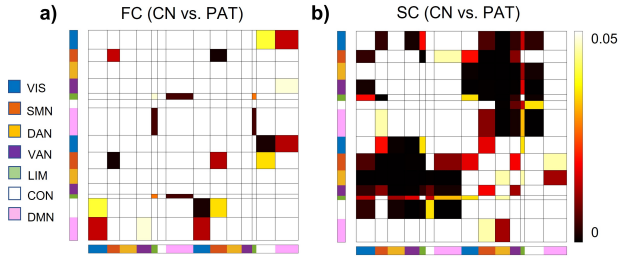


Fig. 3: Weighted matrices showing the significant differences between the CN and PAT in FC (a) and SC (b). The values shown are those that survive correction for multiple comparisons using the FDR-corrected Mann Whitney U-rank test ($q < 0.05$).

compared to controls using PLS. The results suggest that exploiting this model, though simple, can help elucidating this question. The statistical test comparing functional and structural features between CN and PAT populations shows partly divergent patterns of alteration among RSNs between the two imaging methods. On the other side, PLS analysis reveals 13 significant components that represent a unique pattern of SC and FC connections that optimally covary with each other, indicating a particular correlation or anti-correlation between the strongest weights of FC and SC. Therefore, traditional statistical analysis fails to demonstrate a clear one-to-one correspondence between network communities in FC and communities in underlying SC. In contrast, the PLS method shows what covaries between them. To the best of our knowledge, this is the first study that uses PLS to examine the coupling between SC and FC in the two populations under study, making the interpretation of the observed results challenging. Previous research in this field has mostly employed graph analysis methods to integrate information after extracting global and local network indices. Using the graph theory changes were observed in common network characteristics such as path length and global efficiency in AD [14]. Analysis of FC-SC coupling using graph theory is also a current research focus, with the DMN being a particularly important area of study. This network has been found to be highly correlated with neural activity, and changes in the DMN have been observed in both healthy aging and AD [15]. While graph network analysis has been a widely used method for investigating the two types of brain connectivity [16], PLS analysis has not been frequently used to study their coupling. A PLS model to explore the relationship between structure and function at the network level has been presented on controls by Mišić et al. [5]. They demonstrated systematic and statistically significant relationships, with a key finding being that FC patterns often diverge from SC patterns, likely due to complex network-wide interactions. Moreover, they showed that the presence of an individual structural connection can predict the magnitude of the corresponding functional connection, but the reverse is not necessarily true. However, interpreting the significance of the correlations and anti-correlations within the PLS components can be challenging as it does not directly reflect the association between values in the original domains. For example, it is difficult to interpret the relationship between the number of streamlines connecting a pair of regions and the Pearson correlation existing among them solely based on the PLS results. Despite this limitation, the PLS model remains a valuable tool for uncovering patterns in data.

In conclusion, this finding implies the potential of functional–structural network coupling as a promising biomarker for monitoring disease progression of AD.

Acknowledgement

This work was partly supported by Fondazione CariVerona (Bando Ricerca Scientifica di Eccellenza 2018, EDIPO project, 2018.0855.2019) and MIUR D.M. 737/2021 - AI4Health: empowering neurosciences with eXplainable AI methods.

References

[1] C. Qiu, M. Kivipelto, and E. Von Strauss, "Epidemiology of alzheimer's disease: occurrence, determinants, and strategies toward intervention," *Dialogues in clinical neuroscience*, 2022.

[2] S. Gao, H. N. Burney, C. M. Callahan, C. E. Purnell, and H. C. Hendrie, "Incidence of dementia and alzheimer disease over time: A meta-analysis," *Journal of the American Geriatrics Society*, vol. 67, no. 7, pp. 1361–1369, 2019.

[3] Alzheimer's Association, "2019 alzheimer's disease facts and figures," *Alzheimer's & dementia*, vol. 15, no. 3, pp. 321–387, 2019.

[4] J. Kim, M. Jeong, W. R. Stiles, and H. S. Choi, "Neuroimaging Modalities in Alzheimer's Disease: Diagnosis and Clinical Features," *Int J Mol Sci*, vol. 23, no. 11, 2022.

[5] B. Mišić *et al.*, "Network-level structure-function relationships in human neocortex," *Cerebral Cortex*, vol. 26, no. 7, pp. 3285–3296, 2016.

[6] E. Bullmore and O. Sporns, "Complex brain networks: graph theoretical analysis of structural and functional systems," *Nat Rev Neurosci*, vol. 10, no. 3, pp. 186–198, 2009.

[7] J. H. Ford and E. A. Kensinger, "The relation between structural and functional connectivity depends on age and on task goals," *Frontiers in human neuroscience*, vol. 8, 2014.

[8] M. Filippi *et al.*, "Changes in functional and structural brain connectome along the alzheimer's disease continuum," *Molecular psychiatry*, vol. 25, no. 1, pp. 230–239, 2020.

[9] B. De Blasi *et al.*, "Noise removal in resting-state and task fMRI: functional connectivity and activation maps," *J Neural Eng*, vol. 17, no. 4, 2020.

[10] A. Schaefer *et al.*, "Local-global parcellation of the human cerebral cortex from intrinsic functional connectivity mri," *Cerebral cortex*, vol. 28, no. 9, pp. 3095–3114, 2018.

[11] R. E. Smith, J.-D. Tournier, F. Calamante, and A. Connelly, "Sift2: Enabling dense quantitative assessment of brain white matter connectivity using streamlines tractography," *Neuroimage*, vol. 119, pp. 338–351, 2015.

[12] A. Mihalik *et al.*, "Canonical correlation analysis and partial least squares for identifying brain-behaviour associations: a tutorial and a comparative study," *Biological Psychiatry: Cognitive Neuroscience and Neuroimaging*, vol. 7, no. 11, pp. 1055–1067, 2022.

[13] H. Wold, "Nonlinear iterative partial least squares (nipals) modelling: some current developments," in *Multivariate analysis–III*. Elsevier, 1973, pp. 383–407.

[14] F. U. Fischer, D. Wolf, A. Scheurich, and A. Fellgiebel, "Altered whole-brain white matter networks in preclinical Alzheimer's disease," *Neuroimage Clin*, vol. 8, pp. 660–666, 2015.

[15] K. Mevel, G. Telat, F. Eustache, and B. Desgranges, "The default mode network in healthy aging and Alzheimer's disease," *Int J Alzheimers Dis*, vol. 2011, 2011.

[16] M. Guye, F. Bartolomei, and J.-P. Ranjeva, "Imaging structural and functional connectivity: towards a unified definition of human brain organization?" *Current opinion in neurology*, vol. 21, no. 4, pp. 393–403, 2008.

Closing the loop between neurostimulation and control theory

R. Guidotti[1], A. Basti[1], G. Pieramico[1], A. D'Andrea[1], G. L. Romani[2], V. Pizzella[1,2] and L. Marzetti[1,2]
[1] *Department of Neuroscience, Imaging and Clinical Sciences, University "G. D'Annunzio" Chieti-Pescara*
[2] *Institute for Advanced Biomedical Technologies (ITAB), University "G. D'Annunzio" Chieti-Pescara*

***Abstract*—Neurostimulation is a technique that allows to study the human brain using an external signal which modifies its current activity. The stimulation is usually performed with fixed parameters, in a classical open-loop control paradigm. This strategy does not consider the current status of the brain to adaptively modify the stimulation parameters such as location, intensity and timing. In control theory, the latter strategy is called closed-loop control and it is becoming popular in neuroscience community since it allows to study the causal relationship between brain and behaviour, and it paves the way to personalize treatments in clinics. Here, we reviewed this new branch of study, by introducing control theory and presenting the neurostimulation techniques that are implementing closed-loop neuromodulation.**

***Keywords*—closed-loop control, neurostimulation, TMS, EEG.**

I. Introduction

In the last decades neuroscientists have started to inspect the brain using several techniques that allowed to study its mechanisms at different scales: spatial, temporal, and functional. A fundamental tool that has been developed to help neuroscientists is the set of neurostimulation techniques. Neurostimulation techniques are used to excite or inhibit (a set of) neurons and provoke specific patterns of neuronal activity that are supposed to elicit a proper behavioural or neurophysiological response. Characterizing how the brain reacts to stimulation is crucial, to use targeted endogenous or exogenous stimulation techniques that may help to recover or improve the brain functions and related behavioural traits.

Currently, neurostimulation techniques are mainly used with fixed parameters (i.e. they remain unchanged throughout the whole session) on the basis of the subset of brain regions and mechanisms under investigation. In control theory, this general approach is called open-loop control, since the stimulation does not depend on the previously elicited effects. On the contrary, in closed-loop control the stimulation is constantly updated based on feedback information which is dependent on the difference between the current and the expected system response. The union of closed-loop approach and neurostimulation is not a completely novel approach, since several studies have used this paradigm to automatically target stimulation in several contests and with different strategies. The ultimate goal is to build an automatic and adaptive system that allows a sort of brain control by using the signals of the brain and targeting stimulations.

Here, we will review the most used approaches to control the brain, using exogenous stimulation techniques. Our goal is to illustrate the key concepts of the brain control paradigm and explore the challenges that still need to be addressed to fully adopt these techniques which may dramatically impact clinical and therapeutic applications.

II. Control theory

A. System definition and properties

Control theory is an interdisciplinary branch of engineering and mathematics that studies how to design a set of strategies to drive a dynamical system towards a desired state, and, possibly, following an optimal trajectory [1]. In general, the equation for dynamical systems, under the assumption of time invariance and linearity (LTI), can be written as:

$$\begin{aligned}\dot{\mathbf{x}}(t) &= \mathbf{A}\mathbf{x}(t) + \mathbf{B}\mathbf{u}(t)\\ \mathbf{y}(t) &= \mathbf{C}\mathbf{x}(t) + \mathbf{D}\mathbf{u}(t)\end{aligned} \tag{1}$$

where $\mathbf{x}(t) \in \mathbb{R}^N$ is the internal state of the system at time t, $\mathbf{u}(t) \in \mathbb{R}^M$ represents the input signal, $\mathbf{y}(t) \in \mathbb{R}^S$ the set of measured variables and N, M and S are the dimensions of variables. In addition, $\mathbf{A} \in \mathbb{R}^{N\times N}$ represents how the different variables of the state vector are interacting and is termed as the dynamics matrix, while $\mathbf{B} \in \mathbb{R}^{N\times M}$, the control matrix, indicates the impact of input on the system. The sensor matrix $\mathbf{C} \in \mathbb{R}^{S\times N}$ and the direct term $\mathbf{D} \in \mathbb{R}^{S\times M}$ represent how much the output is influenced by the state and the input, respectively. A system is defined as controllable in N steps, if the matrix $\mathbf{W} = [\mathbf{B}, \mathbf{AB}, ..., \mathbf{A}^{N-1}\mathbf{B}]$ has rank N.

This criterion is valid only if we have a precise knowledge of the dynamics and control matrices, while in complex systems it is often difficult to estimate correctly all the entries of the matrix $\mathbf{A}$ and thus to establish whether the system is controllable or not.

Another important characteristic of a system is its observability. In other words, the ability to precisely identify the system position in the state space to correctly apply an input and bring it to the desired state. For a LTI system, we can state that the system is observable if and only if the dual system composed by $(\mathbf{A}^T, \mathbf{C}^T, \mathbf{B}^T)$, in place of $(\mathbf{A}, \mathbf{B}, \mathbf{C})$, is controllable, where T indicates the transpose of the matrix. Using this property, the observability criterion state that the system is observable if and only if the rank of the matrix $\mathbf{O} = [\mathbf{C}, \mathbf{CA}, ..., \mathbf{CA}^{N-1}]^T$ is equal to N.

In many applications, such as brain control, the system is not fully observable, but we can have access to a few state

variables that are sufficient to infer the state of the system. The brain, albeit it is a nonlinear system, at certain scales [2], can be viewed as a LTI system. System observability is then necessary to identify the model and the parameters of the system. The characterization of the system model is crucial in control theory and is defined as *system identification* [3]. The goal of system identification is to characterize the mathematical formulation of the dynamical system of interest, given the output of the system. The system models are often defined using a gray-scale naming, for example when the physical equations of the system are perfectly known we have a *white-box* model, while with a *black-box* model, we have no information about the equations of the system.

B. Control strategies

In *open-loop* control, the controller sends a stimulus to a system, which modifies its state or trajectory, but no feedback signal is provided back and because of this, the control stimulus should be designed in advance. In *closed-loop*, the controller stimulates the system and tries to adjust the stimulation to reach a final state based on the error between the desired and the current output and optionally by minimizing the costs (e.g., energy, time). The simplest form of closed-loop control is the (scalar) *on-off* control, which is formulated as:

$$u(t) = \begin{cases} u_{max}, & if \;\; e(t) > 0 \\ u_{min}, & if \;\; e(t) \leq 0 \end{cases} \tag{2}$$

The term $e(t)$ indicates the error between the current and the expected state, while u_{min} and u_{max} are arbitrary parameters of the controller. The *proportional-integral-derivative* (PID) controller is an improvement of the on-off controller, in which the input $u(t)$ is:

$$u(t) = k_p e(t) + k_i \int_0^t e(\tau) d(\tau) + k_d \dot{e}(t) \tag{3}$$

where k_p, k_i and k_d are parameters of the controller.

These strategies are used with good performance in industrial settings and do not necessitate a model of the system, but the control process is not optimal.

Optimal control can be used only when the model is known and the state is perfectly accessible. This strategy is used to reach the target state and minimize a designed cost function, at the same time [4].

Unfortunately, in real cases, optimal control assumptions are not always met. In these cases, a relaxation of these hypotheses can be beneficial to control complex systems. Control techniques that relax these assumptions are named *suboptimal control* and *adaptive control* [5]. Suboptimal control strategies approximate the cost function with one which has less complexity or a limited horizon. In adaptive control the parameters of the controller are updated continuously as the system evolves to cope with the expected system behaviour.

Learning-based control encompasses all the strategies that leverage on statistical learning to determine the system model and the control strategy. Two approaches are mainly used: *Bayesian control* and *Reinforcement Learning*. The first is based on the use of Gaussian Processes to maximize a given cost function and learn the model under Gaussian assumptions. The latter uses a trial-and-error paradigm to learn control rules while the model is assumed to be a Markov Decision Process.

III. Brain control

In the last years, the neuroscience community increased the interest in brain control paradigm thanks to the advances in reliable stimulation techniques and readout devices, as well as in algorithms to study brain signals [6].

These advances added evidence to the fact that stimulating the human brain makes possible to bring it to some safe or expected states, and thus to be controlled [2].

The vast majority of stimulation techniques encompasses all the approaches that perturb the current state of the human brain using electrical, optical or pharmacological stimuli [7]. The perturbation is caused by an external stimulus that operates directly on the brain. These techniques can be further classified based on the stimulus type (electric, magnetic, optic or pharmacologic), the spatial scale (cells, neurons or brain areas), the temporal scale (from minutes to microseconds), or on the invasiveness of the stimulation. Among these, Deep and Transcranial Brain Stimulation play a central role in closed-loop neuromodulation.

A. System identification for brain control

System identification is crucial in brain control to correctly recognize biomarkers which should be causally related to the trait we want to modulate. In many cases, assessing the brain-behavior relationship directly and causally is difficult, since it needs an accurate understanding of all the brain mechanisms involved and proper instruments to readout the biomarker.

The use of brain decoding techniques has shown great potential to investigate brain-behaviour relationship and shed light on the fine-grained differences in brain signals that are not detected using univariate analyses [8]. Decoding techniques use supervised (or unsupervised) machine learning models to automatically select the patterns of brain activity related to an experimental manipulation. This can be used to understand how the stimulation is related to the readout signal and how the brain states can influence the stimulation response.

B. Control properties of the brain

The brain is a network of communicating neurons that are organized to be efficient functionally and energetically. In this scenario, network control can be used to study the properties of brain system Specifically, at macroscale level, the brain can be hypothesized to be a LTI system (Eq. 1) [2] and thus, we can investigate its controllability properties to then target particular brain areas that allows to optimal control it.

The pioneering work made by Gu et al. [9] found the controllability properties of the brain, by modeling it as a LTI using brain fibers to define the matrix $\mathbf{A}$. They found that, the brain is controllable from a single node, but controlling

it is difficult due to the energetic cost to bring the brain in a desired state.

The controllability profile of epileptic patients has been studied by Scheid et al. [10]. They found that the temporal profile of optimal control energy to bring the brain in a safe state was minimal at the onset of the seizure. In addition, they found specific nodes that require less energy to suppress the seizure and drive the system into a safe state.

Studying brain properties with optimal control theory has great potential, but needs further studies for the application it in real scenario, given that some limitations have been recently debated [11].

C. Brain control using Deep Brain Stimulation

Deep Brain Stimulation (DBS) is a technique that uses the implanted lead-mounted electrodes into deeper brain structures to perturb the flow of information at ionic, cellular, protein and network level [12]. The same set of electrodes is used to identify the brain state.

Ferleger et al. [13] used closed-loop DBS to reduce the tremor in patient with tremor. Here, they used a linear discriminant classifier to identify the brain state and to trigger the stimulation accordingly. The classifier was trained using the bandpower of DBS and ECoG signals and detects when the subjects are in the rest state or in the tremor state.

Similarly, Scangos et al. [14] used a penalized logistic regression algorithm with feature selection to identify major depressive disorder traits and stimulate the ventral striatum. They used, after a system identification step, the gamma band amygdala activity to target the stimulation with an *on-off* controller.

D. Brain control using Transcranial Stimulation

Non-invasive brain stimulation techniques elicit a change in the brain functions by a perturbation performed outside the skull. The two most popular techniques are the transcranial electrical (tES) and magnetic stimulation (TMS). TMS uses a magnetic field to induce an electric current in the brain tissues, while tES devices produce an electric current flowing between two electrodes that can depolarize the neurons beneath the stimulated area. Here, several techniques can be used to read out the status of the system and trigger the stimulation such as EEG, MEG and EMG.

A real-time EEG-TMS experiment by Zrenner et al. [15] found a relationship between the phase of the mu-rhythm and the amplitude of the motor evoked potential. In particular, they used the negative peak of the C3-Hjorth signal to stimulate the motor area and elicit a higher motor evoked potential amplitude and vice versa. Then an on-off controller was implemented in a closed-loop experiment to demonstrate the long-term plasticity effect of the cortico-spinal excitability.

Tervo et al. [16] carried out a EEG-TMS experiment to optimize the orientation of the TMS stimulus. They found that the difference between P20 and N40 components was influenced by the orientation. Then, they used a Bayesian controller to optimize in real-time the coil orientation and maximize the P20-N40 amplitude in a short amount of stimulations.

E. Brain models for control

Another crucial step for brain control is testing and building brain models. A fundamental tool to model and control brain signals is machine learning, specifically though deep learning and reinforcement learning approaches. These techniques can be used to test cutting-edge control techniques before applying them in-vivo given their similarity with brain functioning.

Tafazoli et al. [17] used a convolutional neural network to simulate the model of the visual cortex and properly stimulated to elicit specific patterns. They also tested this approach, in four mice, finding that the proposed algorithm correctly provoked the targeted response.

In Krylov et al. [18] an approach based on Reinforcement Learning was used to suppress the oscillatory activity of a population of oscillators coupled using the Bonhoeffer-van der Pol and the Bursting Hindmarsh-Rose models. The reward was designed separately for each model and allowed to effectively suppress the activity of these oscillators, which can be applied in DBS scenarios.

Reinforcement Learning may be fundamental for brain control but there is the need to develop and study sophisticated brain models to unveil possible problems and to effectively target personalized stimulations.

IV. Future directions and limitations

A. Open brain control

Open science principles are fundamental to implement more sophisticated control strategies and to model the functioning of the human brain.

Sharing data of experiments is fundamental to effectively map the causal relationship between the stimulation and its effects to then predict the expected stimulation responses. The community has expressed their concerns on the reproducibility crisis and the need of sharing data, but very few datasets have been released so far [19].

In parallel, open-source platforms that deliver stimuli with precise time constraints are crucial. Several open-source platforms have been developed for these purposes, with a focus on closed-loop applications and timing constraints [20]. In this scenario, sharing open-source software increases the number of software developers that maintain and test these platforms.

B. Advances in neurostimulation techniques

The development of multi-coil TMS (mTMS) [21] can be revolutionary, since, currently, the TMS has several limitation: the brain cannot be stimulated in different locations in a short amount of time and the coil is fixed manually. The mTMS overcome these issues by adjusting the currents flowing in a set of properly arranged coils, in order to stimulate electronically different areas in a short amount of time. This technique can be disruptive in the brain control field given these possibilities and to probe the brain with innovative stimulation protocols.

The development of advanced closed-loop techniques with the possibility to stimulate the brain in multiple locations may be determinant to study the brain mechanisms at different temporal and spatial scales.

C. Limitations

A proper model of the brain is necessary for designing optimal control strategies and this process varies depending on the brain process to be modeled and the neurostimulation techniques used for this purpose.

Modeling techniques should consider the different temporal and spatial scales of brain functioning, but this is a limit from a technological point of view since recording and stimulation instruments are built for specific scales and this does not help scientists to build an effective model that can be used by control systems.

V. Conclusions

We introduced the mathematical aspects and algorithms of control theory applied to brain stimulation.

Control theory has developed a set of algorithms and techniques to solve specific industrial problems, and the increasing use of neurostimulation techniques has provided a fundamental tool to investigate the human brain. The combination of control theory and neurostimulation paved the way for the automatic control of the human brain.

The brain control approaches presented here use basic, but effective, control algorithms that rely on a solid identification of stimulus-response relationship. The combination of different techniques to stimulate and read brain signals may help to investigate the brain from different perspectives and at different temporal and spatial scales. Support for studying both control algorithms and the brain can come from simulation studies and models that helped to understand crucial properties as controllability under linear approximation.

Brain control theory will bolster neuroscience research by using cutting-edge techniques to stimulate the brain and provide a reliable causal relationship between intervention and effect, but also to reduce the burden of choices made by experimenters.

Acknowledgement

This research was funded by European Research Council (ERC Synergy) under the European Union's Horizon 2020 research and innovation programme (ConnectToBrain; grant agreement No. 810377).

References

[1] Yang Yu Liu and Albert László Barabási. "Control principles of complex systems". In: *Reviews of Modern Physics* 88.3 (Sept. 2016), p. 035006.

[2] Evelyn Tang and Danielle S. Bassett. "Colloquium: Control of dynamics in brain networks". In: *Reviews of Modern Physics* 90.3 (2018), p. 31003.

[3] Lennart Ljung. "Perspectives on system identification". In: *Annual Reviews in Control* 34.1 (Apr. 2010), pp. 1–12.

[4] Dimitri Bertsekas. *Dynamic programming and optimal control: Volume I*. Vol. 2. Athena Scientific, 2012.

[5] Karl J Åström and Björn Wittenmark. *Adaptive control*. Courier Corporation, 2013.

[6] Steven J Schiff. *Neural control engineering: the emerging intersection between control theory and neuroscience*. MIT Press, 2011.

[7] Philip M. Lewis et al. "Brain Neuromodulation Techniques: A Review". In: 22.4 (Aug. 2016), pp. 406–421.

[8] James V Haxby. "Multivariate pattern analysis of fMRI: The early beginnings". In: *NeuroImage* 62.2 (Mar. 2012), pp. 852–855.

[9] Shi Gu et al. "Controllability of structural brain networks". In: *Nature Communications* 6 (2015).

[10] Brittany H. Scheid et al. "Time-evolving controllability of effective connectivity networks during seizure progression". In: *Proceedings of the National Academy of Sciences of the United States of America* 118.5 (2021), pp. 1–8.

[11] S. Suweis et al. "Brain controllability: Not a slam dunk yet". In: *NeuroImage* 200 (Oct. 2019), pp. 552–555.

[12] Andres M. Lozano et al. "Deep brain stimulation: current challenges and future directions". In: *Nature Reviews Neurology* 15.3 (Mar. 2019), pp. 148–160.

[13] B. I. Ferleger et al. "Fully implanted adaptive deep brain stimulation in freely moving essential tremor patients". In: *Journal of Neural Engineering* 17.5 (2020).

[14] Katherine W. Scangos et al. "Closed-loop neuromodulation in an individual with treatment-resistant depression". In: *Nature Medicine* 27.10 (2021), pp. 1696–1700.

[15] Christoph Zrenner et al. "Closed-loop neuroscience and non-invasive brain stimulation: A tale of two loops". In: *Frontiers in Cellular Neuroscience* 10.APR (2016), pp. 1–7.

[16] Aino E. Tervo et al. "Closed-loop optimization of transcranial magnetic stimulation with electroencephalography feedback". In: *Brain Stimulation* 15.2 (Mar. 2022), pp. 523–531.

[17] Sina Tafazoli et al. "Learning to control the brain through adaptive closed-loop patterned stimulation". In: *Journal of Neural Engineering* 17.5 (Oct. 2020).

[18] Dmitrii Krylov et al. "Reinforcement learning framework for deep brain stimulation study". In: *IJCAI International Joint Conference on Artificial Intelligence* 2021-Janua (2020), pp. 2847–2854.

[19] Paolo Belardinelli et al. *Reproducibility in TMS–EEG studies: A call for data sharing, standard procedures and effective experimental control*. May 2019.

[20] Olli-Pekka Kahilakoski et al. "Software architecture for closed-loop multi-locus transcranial magnetic stimulation". In: *Brain Stimulation* 14.6 (Nov. 2021), pp. 1647–1648.

[21] Jaakko O. Nieminen et al. "Multi-locus transcranial magnetic stimulation system for electronically targeted brain stimulation". In: *Brain Stimulation*. Vol. 15. 1. Elsevier Inc., Jan. 2022, pp. 116–124.

A machine learning approach for stride speed estimation based on a head-mounted IMU

P. Tasca[1], F. Salis[2], S. Rosati[1], G. Balestra[1] and A. Cereatti[1]
[1] *Politecnico di Torino*
[2] *Università degli Studi di Sassari*

***Abstract*—Walking speed in real-life conditions is typically estimated through wearable inertial sensors mounted on waist, lower limbs, or wrists. Very recently, head-mounted inertial sensors are emerging for gait assessment. The present study explores the feasibility of measuring the stride speed with a head-mounted inertial sensor in both laboratory and real-world settings. The developed algorithm exploits a Temporal Convolutional Network for the detection of the gait events and a Gaussian Process Regression for the stride speed estimation. The experimental evaluation was carried out on healthy young participants during both standardised indoor and real-world walking trials. For indoor trials, errors were smaller than previous studies (0.05 m/s). As expected, errors increased at lower speed regimes due to a reduced signals amplitude. During 2.5-hours real-world evaluation, errors were slightly larger but acceptable (0.1 m/s). Reported results are encouraging and show the feasibility of estimating gait speed with a single head-worn inertial sensor.**

***Keywords*— machine learning, gait analysis, head IMU, gaussian process regression**

I. Introduction

GAIT is the main form of locomotion for human beings, and it is strictly related to the individual's quality of life [1]. For this reason, gait-related spatio-temporal parameters have been widely explored in both healthy and pathological cohorts [2]. Walking speed is particularly relevant in the assessment of mobility and it is an indicator of one's health status [3]. In the last decades, accelerometers and gyroscopes housed within a single Inertial Measurement Unit (IMU) have emerged as the election technology for the tracking of gait in the real-world, thanks to their wearability and affordability [1]. Multiple body-worn IMUs configurations for estimating walking speed have been extensively explored in literature [4]. Although multi-sensor configurations provide more accurate results, they are less likely to gain acceptance in customer-oriented solutions, as they are less easy to use and comfortable for the subject [5]. Therefore, research groups have started to focus on single-sensor configurations [5]. The most exploited body sites for the positioning of single sensors include wrist [6], foot [7], and waist [8]. However, current IMU-based solutions typically lack in aesthetics and ease of use, resulting in low user engagement [9]. Recently, the use of head-worn devices with IMUs started to spread due to the unique characteristics of this location [10] and its potential integration in smart-glasses for daily life use [9]. Some head- worn devices with inertial sensors have already been translated into commercial solutions and validated for walking speed estimation, such as the Recon Jet [11] smart glasses. Not surprisingly, the use of head-mounted IMUs (H-IMUs), and head-worn devices in general, is expected to grow in the healthcare sector [12]. Traditionally, IMU-based walking speed estimation methods include biomechanical models of gait, direct integration methods and machine learning techniques [2]. Human gait models and direct integration methods respectively suffer from lack of customisation and drift errors [2]; moreover, walking speed is derived indirectly by estimating time and distance. Instead, machine learning allows to directly infer the stride speed through a mapping between stride-specific features and the walking speed [11]. The purpose of the present study is the estimation of the stride speed from signals recorded by a single H-IMU. Foot-to-ground initial contacts (ICs) are estimated through a Temporal Convolutional Network (TCN) and used to segment the strides. Then, time and frequency-domain features are extracted from the stride acceleration norm and fed to a GPR model that outputs the stride speed. The models are trained using data recorded in indoor standardised conditions and tested on data not used for training recorded in both standardised and real-world conditions.

II. Materials and methods

A. Experimental setup

Each subject was equipped with the INertial module with DIstance sensors and Pressure insoles (INDIP) system [14] with the configuration shown in Fig. 1. For the purpose of this study, it included an H-IMU positioned on the left side of the head, in addition to the standard INDIP setup used as wearable reference system (three IMUs on right foot, left foot and lower back, two pressure insoles and two distance sensors). Each INDIP IMU contains a 3-D gyroscope (±2000 dps), a 3-D accelerometer (±16 g) and a 3-D magnetometer (±50 G, not used in this study).

B. Experimental protocol

The experimental protocol included: i) a standardised indoor session comprising two motor tasks (12m-straight walk and double-ring walk, Fig. 2), each performed at different speeds (slow, comfortable, and fast) and repeated thrice, for a total of 12 trials; ii) a 2.5-hour unsupervised real-world acquisition in which the participants were asked to follow their daily life routine. All the INDIP sensors, sampling at 100 Hz, were synchronised before each acquisition by setting the timestamp of each unit. Data acquired during the standardised indoor session and the 2.5-hour real-world acquisitions will be referred to as the "standardised" and the "real-world" datasets, respectively.

C. Participants

Data were collected on fourteen young healthy adults (YHA) (6 females, age: 25 ± 3 years, height: 1.73 ± 0.08 m,

weight: 65 ± 10 kg). All participants provided written informed consent before taking part to the study. Of the 14 participants recruited, 11 participated to the standardised indoor session, while the remaining 3 performed the 2.5-hour real-world acquisition.

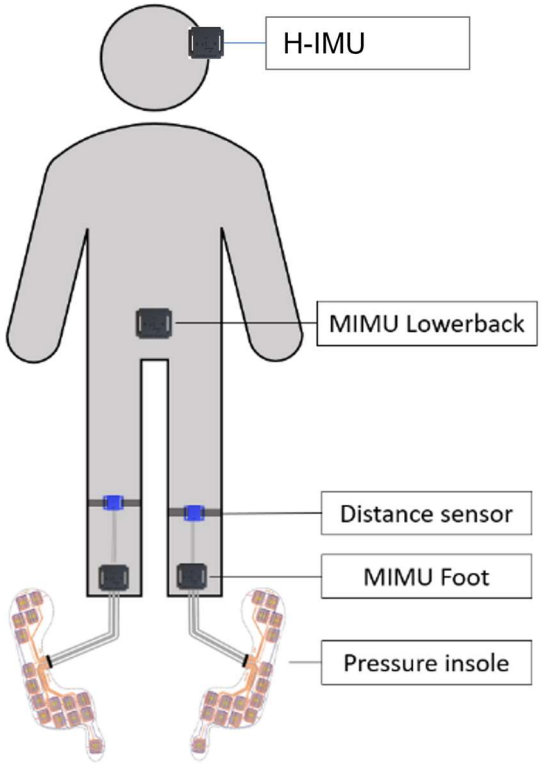


Fig. 1: The INDIP setup. IMUs and distance sensors are firmly attached to the body through Velcro bands to prevent any slippery o motion artifact.

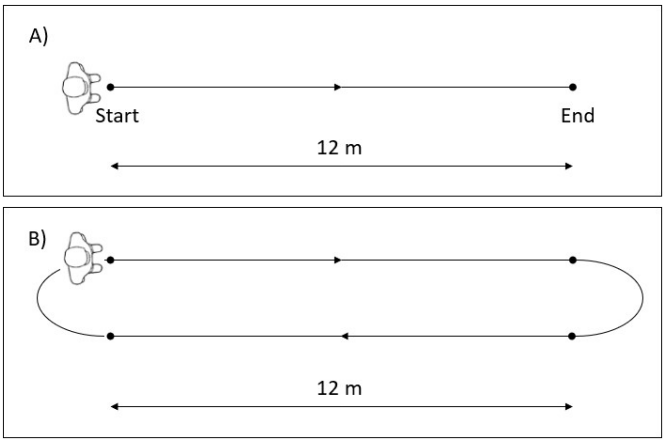


Fig. 2: Walking paths for the standardized acquisitions. A) Straight walk; B) "Double-ring" walk.

D. H-IMU algorithm

The estimation of the stride speed requires the previous segmentation of the stride. Therefore, the work was outlined as a two-tasks process:

i. Gait events detection
ii. Speed estimation

The gait events detection task was thought as a sequence classification task and was performed through a TCN [15], while the speed estimation task was organised as a regression task and was performed through a GPR model [11].

1) Pre-processing: H-IMU signals were virtually aligned to the direction of gravity, so that the x, y and z components of 3-D acceleration and angular rate were considered as parallel to the anteroposterior (AP), vertical (V) and mediolateral (ML) directions, respectively (Fig. 3).

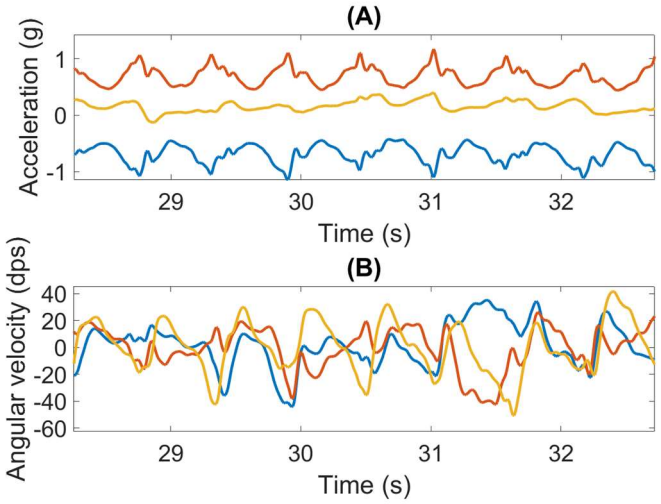


Fig. 3: A) Acceleration and B) angular velocity over four strides during a trial of standardized straight walking at comfortable speed. Acceleration is rotated with respect to gravity. Red: V component; Yellow: ML component; Blue: AP component.

2) *Gait events detection*: Norms of 3-D acceleration and angular rate were computed (Eq. 1).

$$a_n = \sqrt{{a_v}^2 + {a_{ml}}^2 + {a_{ap}}^2} \quad \omega_n = \sqrt{{\omega_v}^2 + {\omega_{ml}}^2 + {\omega_{ap}}^2} \qquad (1)$$

The six acceleration and angular rate components plus their norms were smoothed with a 5-points moving average filter and passed as predictors to a TCN. The network response was a binary signal of 0s and 1s with the same number of samples of the input sequence, with 0 denoting the double support phase (DS: both feet in contact with the ground, ~ 60% of the gait cycle) and 1 denoting the single support phase (SS: only right or left foot in contact with the ground, ~ 40% of the gait cycle). Portions of non-walking signals were ignored.

3) *Stride segmentation*: The ICs were detected at the falling edges of the network binary output i.e. at the end of the SS phases. Strides were determined as the time intervals between two ICs of the same foot. Since the TCN did not make a distinction between right and left SS phases, left and right ICs were not distinguished; however, the succession was preserved by picking adjacent ICs with a step of two.

4) *Stride speed estimation*: The raw acceleration norm of the segmented stride was filtered with a 4th-order Butterworth low pass filter with cut-off frequency of 5 Hz. A set of 134 features in the time and frequency domains were derived from the filtered norm and passed - together with height and weight of the subject - as input predictors to a GPR model (Table I). The decision regarding the number and typology of the input features was performed according to previous similar studies [11].

TABLE I: FEATURES FOR STRIDE SPEED PREDICTION

Domain	*Parameter*	*Definition*
Time (6)	Median	[g]
	Mode	[g]
	Signal Magnitude Area (SMA)	$\sum_{i=1}^{N}\lvert a_i\rvert$ [g]
	Energy	$\sum_{i=1}^{N}(a_i)^2$ [g^2]
	Zero-crossing rate	-
	Mean Absolute Value (MAV)	$\frac{1}{N}\sum_{i=1}^{N}\lvert a_i\rvert$ [g]
Frequency (128)	FFT coefficients	$\left\lvert\sum_{i=1}^{N} a_i e^{\frac{2\pi i}{N}(i-1)(k-1)}\right\rvert$ [g]
Anthro (2)	Weight	[kg]
	Height	[cm]

Features used by the GPR model to predict the stride speed. *Frequency (128)*: magnitudes of the 128 coefficients of the Fast Fourier transform (FFT). *g*: norm of gravity acceleration (9.81 m/s^2); *a*: samples of the acceleration norm for the current stride; *N*: number of samples of a; *Anthro*: anthropometric.

E. Training and testing

Both the TCN and the GPR models were trained with data of the standardised dataset (11 out of 14 participants). Data from participants 1-10 (construction set) were aggregated and used to train the models, while data from participant 11 (standardised test set) were used only for testing the trained architecture at the end of training. The TCN architecture included four residual blocks, a dilation base of 2, 64 filters of size 5 and a drop-out factor of 0.005. The TCN layer was followed by a fully connected layer, a SoftMax layer and a classification layer. The TCN was trained with a hold-out cross-validation scheme. The construction set was randomly split into a training set (TRS) of 7 subjects (for network training) and a validation set (VS) of 3 subjects (to evaluate the network performance and prevent overfitting) for five times. The network was trained for each of the five TRS-VS combinations for 60 epochs with the ADAM learning rule. Eventually, the network with the best performance overall was selected. At training stage, a label "0" was associated to samples in the DS phase, while a label "1" was associated to samples in the SS phase. To determine the beginning and the end of the DS and SS phases at training stage, gait events estimated by the INDIP reference system were exploited. The performance of the best TCN was evaluated on data of subjects not used for training, *i.e.* participant 11 of the standardised dataset and on the real-world dataset (3 out of 14 participants). The GPR model was trained according to a 5-fold cross-validation scheme on the construction set. At training stage, the GPR model was fed with 136 stride-derived features (predictors) and the reference value of the stride speed (target response) estimated by the INDIP system. At training stage, subjects' anthropometric features were used as constant predictors for their respective strides. An exponential kernel was selected for the GPR model basing on previous studies [11]. Performance of the best GPR model was evaluated on the standardised test set and on the real-world dataset.

F. Data analysis

Stride speed values predicted by the H-IMU algorithm were compared to the ones estimated by the INDIP reference system, that leverages validated algorithms [13] to predict gait parameters and events from data recorded by the pressure insoles and the IMUs (except the H-IMU). The adopted metrics for the method evaluation included mean absolute error (MAE), mean squared error (MSE), root mean squared error (RMSE), coefficient of adjusted determination (adR2) and Pearson index of correlation (ρ). Predicted and target response values were divided into three groups according to speed regime with two thresholds at 1 m/s and 1.5 m/s. Absolute percentage error was computed for each observation; then, errors out of the range [25th-percentile - 1.5 IQR; 75th-percentile + 1.5 IQR] were classified as outliers and discarded. A Shapiro-Wilk test was used to test the normality of the distribution. Then, as the distribution resulted to be non-normal, Wilcoxon ranked sum test was performed against the alternative hypothesis that the population mean of the slow-speed regime error distribution is greater than the population mean of the medium-and-fast-speed regimes error distribution. The significance level of the statistical test was set to 0.05.

III. RESULTS

Gait events, used to segment the strides, were detected by the TCN with a MAE of 0.05 ± 0.04 s on the test set and 0.02 ± 0.02 s on the training set.

Table II shows the results obtained from the comparison of the H-IMU algorithm with the reference system on the standardised dataset. Fig. 4 and 5 show the distributions of the absolute percentage errors for three speed regimes in the standardized construction set and test set, respectively. In both cases, the alternative hypothesis (Section II-F) was accepted at the specified significance level (p-value < 0.001). Table III shows the results obtained by the algorithm on the real-world dataset.

TABLE II: RESULTS ON STANDARDIZED DATASET

Set	*Number of strides*	*MAE (m/s)*	*RMSE (m/s)*	*MSE (m^2/s^2)*	ρ	*adR^2*
CS	3668	0.05 (4.6 %)	0.07	0.00	0.97	0.89
TS	354	0.07 (5.8 %)	0.08	0.01	0.97	0.70
CS+TS	4022	0.05 (4.7 %)	0.07	0.00	0.97	0.88

CS: Construction set; *TS*: Test set.

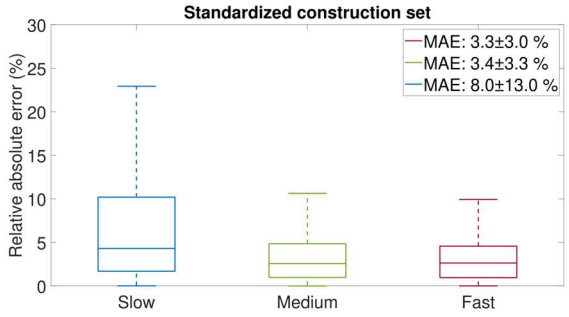


Fig. 4: Boxplot representation of the absolute percentage error distribution in the standardized construction set.

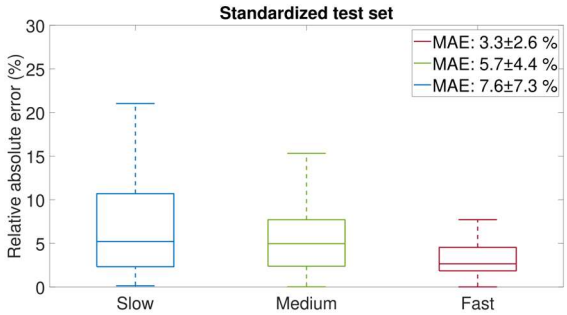


Fig. 5: Boxplot representation of the absolute percentage error distribution in the standardised test set.

TABLE III: RESULTS ON REAL-WORLD DATASET

Set	*Number of strides*	*MAE (m/s)*	*RMSE (m/s)*	*MSE (m^2/s^2)*	ρ	*adR^2*
RW	26498	0.1 (9.2 %)	0.12	0.13	0.80	0.37

RW: Real-world dataset.

IV. DISCUSSION

As shown in Table. II, a strong correlation exists between the predicted and the actual stride speed values for the standardised walking trials (ρ = 0.97). The fact that adR^2 is significantly lower than ρ suggests that some features have small contribution to the prediction output; therefore, dimensionality reduction methods shall be employed. The TCN-GPR-based algorithm has obtained a MAE of 0.05 m/s (4.7 %) on the standardised walking trials. Previous studies based on a single H-IMU for the estimation of the stride speed [11] have obtained higher errors in standardised conditions (6.5 %). As expected, significantly greater errors (p-value < 0.001) were found at lower speed regimes (MAE = 3.3±3.0% for medium and fast speed regime, MAE = 8.0±13.0% for slow speed regimes) due to smaller signals amplitude. This also suggests that the slow speed walking patterns of the participants are remarkably different than the medium and fast walking patterns. In real-world conditions, gait features show greater variability. As a result, correlation indices decrease, as shown in Table III (ρ = 0.80). The reported error (RMSE = 0.1 m/s) was equal to the one obtained by [6] through a single wrist-IMU (RMSE = 0.1 m/s). In the present study, the impact of gait events detection errors on the estimation of the stride speed was not investigated. However, MAE values obtained by the TCN were considerably low and in line with what achieved in other studies [15].

V. CONCLUSION

In this study, feasibility of walking speed estimation based on a head-mounted IMU using a TCN-GPR-based algorithm is investigated. TCN and GPR models were trained with the data acquired from 10 young healthy adults during standardised walking trials. Performance of the model was evaluated for both standardised and real-world walking trials. Results showed that the algorithm can estimate the stride speed in standardised conditions with lower errors with respect to other IMU-based methods. Nevertheless, accuracy of the method decreases at lower speed regimes. The algorithm also showed good generalisation skill on data acquired in real-world conditions. However, training of the algorithm with data acquired in real-world settings is suggested to increase accuracy. An approach based on a single H-IMU may be successful for many applications of fitness and health monitoring; however, it also comes with some limitations, as the upper the sensor location, the harder the extraction of gait features [16]. In the future, further aspects related to the implementation of models for the estimation of the stride speed should be addressed, such as dimensionality reduction, hyperparameters tuning, dataset completeness and eventually validation on pathological patients, where a machine learning-based approach may be effective for seizing the underlying features of abnormal walking patterns.

REFERENCES

[1] A. Cereatti, D. Trojaniello, U. Della Croce, Accurately measuring human movement using magneto-inertial sensors: techniques and challenges, *International Symposium on Inertial Sensors and Systems (ISISS),* 2015.

[2] S. Yang and Q. Li, Inertial sensor-based methods in walking speed estimation: a systematic review, *Sensors*, 2012.

[3] S. Fritz, White Paper: "walking Speed: the sixth vital sign", *J Geriatr Phys Ther,* 2009.

[4] W. Yeoh, I. Pek, Y. Yong, X. Chen, A.B. Waluyo, Ambulatory monitoring of human posture and walking speed using wearable accelerometer sensors, *Conference Proceedings: Annual International Conference of the IEEE Engineering in Medicine and Biology Society*, 2008.

[5] R. J. Mobbs, J. Perring, S. M. Raj, M. Maharaj, N. K. M. Yoong, et al., Gait metrics analysis utilizing single-point inertial measurement units: a systematic review, *mHealth*, 2022.

[6] A. Soltani, H. Dejnabadi, M. Savary and K. Aminian, Real-world gait speed estimation using wrist sensor: a personalized approach, *IEEE Journal of Biomedical and Health Informatics*, 2020.

[7] B. Mariani, C. Hoskovec, S. Rochat, C. Bula, J. Penders, et al., 3D gait assessment in young and elderly subjects using foot-worn inertial sensors, *Journal of Biomechanics*, 2010.

[8] S. Byun, H.J. Lee, J.W. Han, J.S. Kim, E. Choi, et al., Walking-speed estimation using a single inertial measurement unit for the older adults, *PLoS One*, 2019.

[9] A. Cristiano, A. Sanna and D. Trojaniello, Validity of a smart-glasses-based step-count measure during simulated free-living conditions, *Information*, 2020.

[10] C. Buckley, B. Galna, L. Rochester, C. Mazza, Attenuation of upper body accelerations during gait: piloting an innovative assessment tool for Parkinson's disease, *Biomed Res Int*, 2015.

[11] S. Zihajehzadeh and E. J. Park, A Gaussian process regression model for walking speed estimation using a head-worn IMU, *39th Annual International Conference of the IEEE Engineering in Medicine and Biology Society (EMBC),* 2017.

[12] N. Hunn, The market for hearable devices 2016–2020, *Technical report November, WiFore Consulting, London*, UK, 2016.

[13] F. Salis, S. Bertuletti, K. Scott, M. Caruso, T. Bonci, et al., A wearable multi-sensor system for real world gait analysis, *Annu Int Conf IEEE Eng Med Biol Soc.* 2021, 2021.

[14] F. Salis, T. Bonci, S. Bertuletti, M. Caruso, K. Scott, et al., Performance of a multi-sensor wearable system for validating gait assessment: preliminary results on patients and healthy, *Gait & Posture*, 2022.

[15] R. Romijnders, E. Warmerdam, C. Hansen, G. Schmidt and W. Maetzler, A deep learning approach for gait event detection from a single shankworn IMU: validation in healthy and neurological cohorts, *Sensors*, 2022.

[16] J. J. Kavanagh, S. Morrison, R. S. Barrett, Coordination of head and trunk accelerations during walking, *Eur J Appl Physiol*, 2005.

Differences in cortical reorganization during visuo-motor tasks executed with the dominant and non-dominant hands

A. Calcagno[1], S. Coelli[1], F. Temporiti[1,2,3], M. Galli[1], R. Gatti[2,3], and A.M. Bianchi[1]
[1] *Department of Electronics, Information and Bioengineering (DEIB), Politecnico di Milano, Milan*
[2] *Physiotherapy Unit, Humanitas Clinical and Research Center – IRCCS, Rozzano Milan*
3 Humanitas University, Department of Biomedical Sciences, Pieve Emanuele, Milan

***Abstract*— In the present study, we analysed EEG signals acquired during the execution of a visuomotor task with the right and the left hands in a group of young right-handed volunteers. The main aim was to assess differences in brain network organizations supporting movements with the dominant and non-dominant arms with respect to the resting period.**

Specifically, variations in the power content and network topology were explored in the subjective mu band with respect to a baseline condition. Our results showed that, although similar variations are observed in the power content during the movement with both hands, the motor tasks executed with the dominant hand are associated to an enhanced network reorganization with respect to the baseline condition. Conversely, the movement with the non-dominant arm was not associated to significant network reorganization. These findings are a further step towards the quantification of cortical effects related to motor training or motor rehabilitation techniques.

***Keywords*—Visuomotor task, EEG, brain, connectivity, handedness**

I. Introduction

It has been largely demonstrated in the literature that motor execution is a cognitive function that involves distributed brain areas [1]. Several studies demonstrated that, for example, besides the sensorimotor areas, also frontoparietal networks are involved in visuo-motor tasks to accomplish functions related to visual information processing and motor planning [2].

The main idea is that such a cognitive function is supported by the dynamical reorganization of brain networks consisting of the inhibition of unnecessary networks and maintenance of important ones [3], [4].These mechanisms are associated to the ability of the brain in optimizing its functioning, limiting the adopted resources. For this reason, different studies in the recent years aimed to describe these changes in distributed brain networks functioning by studying the effective and functional connectivity, mainly based on EEG and fMRI brain imaging techniques [4]. Literature evidence also showed how, the operation of brain functional networks during motor tasks could change in relation to health conditions, type of task executed and task difficulty[5], [6].

It is reasonable to speculate that even the execution of movements with the dominant and the non-dominant parts of the body could be supported by different network organization. Movement dominance consists, indeed, of the discrepancy in motor abilities performed with the two sides of the body, which depends on genetics and experience. We can reasonably hypothesize this difference in motor ability could be also accompanied to a difference in the efficiency of brain networks reorganization.

What is known from literature is that the execution of a movement with one side of the body is generally associated to a stronger activation of the contralateral sensorimotor areas. From an electrophysiological point of view, it has been shown that an event-related desynchronization (ERD) in the mu band occurs, and it is particularly enhanced in the contralateral sensorimotor cortex [7]. This reduction in power could therefore be associated to the activation and deactivation of more or less useful brain networks, respectively. Nevertheless, spectral analysis is not sufficient to describe such network reorganization and discriminate brain functional optimization processes occurring in different conditions.

Understanding the brain circuits related to such differences in motor abilities could lead to methods for the optimization of motor training and rehabilitation approaches. For example, the identification of brain functional changes induced by experience and motor training, both in healthy conditions and in neurorehabilitation frameworks could improve our knowledge in this context.

Even if some studies suggested that a different functional reorganization occurs for movements with the dominant and the non-dominant hands [8], the underlying mechanisms are still not completely understood.

In the present study, therefore, changes in brain rhythms and connectivity that occur passing from a resting condition (eyes open) to the execution of a visuo-integration motor task with the right and the left hands are explored. To the best of our knowledge, it is the first time that such a study is performed on continuous EEG data and on a comparable numerosity of the sample size.

II. Materials and methods

A. Experimental protocol and setup

EEG traces were recorded with the SD LTM 64 express recording system by Micromed (Mogliano Veneto, Italy) and sampled at 1024 Hz. Specifically, an EEG cap equipped with 61 channels placed according the international 10-20 system was, and with reference electrode placed between Pz and Cpz, was adopted.

The experimental protocol foresaw the acquisition during one minute at rest with eyes closed, one minute at rest with eyes open, two trials with the right hand and two trials with the left hand of the Nine Hole Peg Test (NHPT) [9].

For the analysis, the EEG signals acquired during the fastest execution were considered, for both the right and the left hands. Moreover, the eyes open phase was selected as baseline, given its higher similarity to the task execution.

B. Subjects

Data was acquired on a group of 44 healthy right-handed subjects (23 males, 21 females, mean age 23.3, std 2.48). All volunteers signed an informed consent, and their personal data was anonymized.
The protocol was approved by the Internal Ethical Committee of Humanitas Hospital.

C. EEG signal pre-processing

As a first step, a zero-phase pass band filter in the 1-45 Hz frequency range was applied on the raw EEG signals, and a consecutive downsampling to 256 Hz was performed.
Artefactual sources (e.g., eye blinks and muscular noise) were detected and removed by means of Independent Component Analysis (ICA).
Clean EEG signals were finally re-referenced to the common average.

D. Spectral analysis

The power variation induced by the execution of the NHPT hand with respect to the resting phase with eyes open was computed for both the dominant and non-dominant hands as follows (1):

$$P_{var} = \frac{P_{mt} - P_{rest}}{P_{rest}} \quad (1)$$

Where P_{mt} is the power content in a specific frequency band during the motor task, while P_{rest} is the power content in the same frequency band observed during the central 20 seconds of the baseline phase with eyes open.
For the present study, P_{var} was computed in the subjective mu frequency band, since this rhythm is involved in sensorimotor cortical processes.
Individual mu frequency was extracted starting from the EEG traces acquired during the baseline with eyes open on C3 and C4 electrodes, which are placed on the motor cortex. Specifically, the central mu frequency (muC) was identified as the mean between the two frequency values at which a peak in the power spectrum of C3 and C4 occurred in the frequency range 7-13 Hz. Afterwards, the individual mu (iMu) band was identified as the frequency range (muC-1Hz - muC+1Hz).

E. Connectivity analysis

Pairwise effective connectivity (EC) was studied by means of the Phase Slope Index (PSI) [10]. This index was chosen for its straightforward interpretability and for its robustness against volume conduction.

Specifically, the PSI is derived from the imaginary part I(·) of the complex coherence between two EEG channels i and j (C_{ij}) in a specific frequency band F according to equation (2).

$$\tilde{\psi}_{ij} = I(\sum_{f \in F} C_{ij}^{*}(f) C_{ij}(f + \delta f)) \quad (2)$$

C_{ij} was computed on non-overlapping windows of 1 second, resulting in a frequency resolution δf of 1 Hz.
As a result, an antisymmetric PSI matrix is extracted. If the directionality of information goes from rows to columns (i.e., from i to j) the PSI will be positive, while it will assume negative values otherwise.
The connectivity analysis was focused iMu frequency band.

F. Graph analysis

Graph analysis was performed by treating each EEG channel as a node in the graph, and the connectivity measure as the links between the nodes. This was done after a preliminary transformation process of the obtained PSI matrices: firstly, the non-significant connections were detected by means of a surrogation test [11] and set to zero; then, negative values were removed from the significant connectivity matrix in order to ignore redundant information and, finally, a matrix binarization was performed.
The Brain Connectivity toolbox (BCT) was used to compute the clustering coefficient (CC), the global efficiency (GE) and the Degree (D) on the transformed connectivity matrices [12]. Where, CC is a measure of network segregation and it is computed for each node, while GE is a measure of integration of the network as a whole. D count, instead, the total number of connections for each node of the network.

G. Statistical analysis

In order to assess differences of P_{var} between the righ-hand movement and the left-hand movement conditions, a Wilcoxon signed rank test was performed for each brain area listed in TABLE I. Differences in the graph measures among the three conditions of baseline, right-hand movement and left-hand movement, a Friedman's test with post-hoc Bonferroni correction was performed for each extracted metric. Specifically, CC and D measures were averaged within the four main brain areas listed in **TABLE I**. A separate test was performed for each area.
Concerning GE, a single statistical Friedman test was performed, since it provides a unique measure for the whole network.
Differences are considered statistically significant if associated to $p<0.05$.

TABLE I: BRAIN REGIONS OF INTEREST AND THE ASSOCIATED EEG CHANNELS

Brain area	*Electrodes*
Frontal	Fp1, Fp2, Fpz, AF7, AF3, AFz, AF4, AF8, F7, F5, F3, F1, Fz, F2, F4, F6, F8
Central	FC3, FC1, FCz, FC2, FC4, C5, C3, C1, Cz, C2, C4, C6, CP3, CP1, CPz, CP4, CP6
Parietal	P5, P3, P1, Pz, P2, P4, P6, PO7, PO8
Occipital	POz, O1, Oz, O2

III. RESULTS AND DISCUSSION

A. Spectral analysis

Fig. 1 shows the median topographical maps of P_{var} in the iMu band, both for the right and left-hand movements. As we expected, a power reduction, particularly enhanced on central areas, occurs for both conditions. Indeed, the execution of motor tasks triggers an event related desynchronization (i.e., a power reduction) in the mu band on cortical areas associated to the sensorimotor cortex [13]. The presence of both an ipsilateral and contralateral power reduction is justified by the length of the motor task.
Indeed, volunteers required on average about 20 seconds to execute the NHPT, therefore both the early desynchronization

of the contralateral cortex and the delayed desynchronization of the ipsilateral one were detected [13]. The Wilcoxon signed rank test revealed that no significant differences occur in iMu desynchronization between the movement executed with the dominant and the non-dominant hand, whatever the brain region considered. Given the simplicity of the motor task executed, a similar desynchronization in both conditions could be expected. Such a result suggests that spectral analysis could be not sufficient to discriminate possible differences in network functioning for the movement with the dominant and non-dominant hand.

B. Graph analysis

Results of the statistical analysis are reported in TABLE II. As can be observed in Fig. 2, a significantly lower GE was measured in the iMu during the right-hand movement with respect to both the baseline phase and the left-hand movement. Statistical analysis also revealed that the CC was always significantly lower during the dominant hand movement with respect to the resting condition in all brain areas, but in the occipital one. The left-hand movement, instead, differed significantly from the baseline condition only in the frontal and occipital area (Fig. 3).

D always showed a significant decrease with respect to the baseline condition during the right-hand movement. Interestingly, in the central area, associated to the motor cortex, a significant difference is also detected between the right and the left-hand movement Fig. 4.

Since the mu rhythm is associated to an idling state of the brain, it is reasonable to speculate that a motor task, beside a reduction of its power contribution, could also elicit a reduction in the number of connections (i.e., lower D), in the brain organization in functional subnetworks (i.e., lower CC) and in the ability to connect remote brain areas (i.e., lower GE). The significant decrease of CC and D observed in the frontal region during the left-hand movement could be associated to a comparable involvement of the attentional brain area during both the movement with the dominant and the non-dominant arm. Moreover, occipital CC decreases significantly only during the left-hand task: this result could be explained with a higher need to process visual input information to accomplish a motor task with the less able part of the body. These results could suggest that, in healthy conditions, a different strategy of brain networks reorganization in the iMu band is adopted for the dominant hand and non-dominant hand movement execution. Specifically, we can hypothesize that the movement of the left-hand is accompanied with a stronger involvement of the attentive and visual areas, in order to compensate a less pronounced activation of central and parietal regions, generally associated to the sensorimotor and motor planning brain areas.

IV. Conclusion

The present work had the purpose of evaluating if some differences in the brain mechanisms supporting motor tasks executed with the dominant and non-dominant hands exist in healthy conditions.

Spectral analysis showed that, during the NHPT, comparable event related desynchronizations are observed in the subjective mu band for the two conditions. This result suggests that power analysis of EEG signals is not sufficient to highlight differences in brain mechanisms associated to arm dominance, especially considering healthy volunteers and a simple motor task, such as the NHPT.

Connectivity and graph analysis, instead, revealed that dominant and non-dominant motor tasks are associated to different network reorganization processes in the iMu band. Specifically, despite the left-hand movement shows similar connectivity trends, only the right-hand movement showed a significant reduction in network integration, segregation and degree with respect to the baseline condition in almost all the brain areas considered.

A possible explanation could be associated to a different strategy for the allocation of brain resources depending on task demands, consisting of the activation of important brain networks for the execution of the motor task. These first results could lead to the identification of metrics for the quantification of the effects of motor training in healthy conditions and for rehabilitative purposes.

As a future step, we foresee to extend the analysis also to other relevant EEG rhythms. Moreover, the effect of a motor training period on the brain network reorganization will be analysed for the dominant and the non-dominant hands movements in the same group of healthy volunteers.

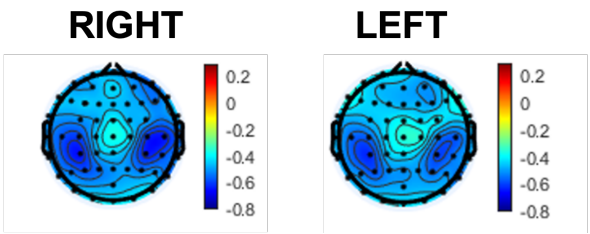


Fig. 1: Median topographical maps of Pvar in the iMu band for the right and the left hand. Blue color identifies a power reduction with respect to the baseline, red color is associated to a power increase.

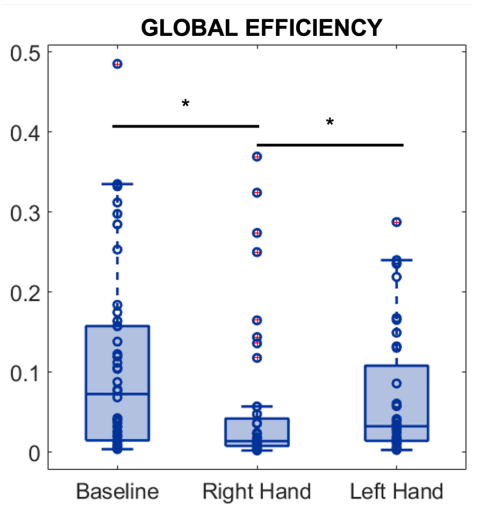


Fig. 2: Global Efficiency (GE) distribution during the baseline condition, the right-hand movement and the left-hand movement. *p<0.05

TABLE II: RESULTS OF THE STATISTICAL ANALYSIS PERFORMED ON GRAPH INDICES (ONLY SIGNIFICANT P ARE REPORTED)

Graph measure	*Friedman test*	*Brain area*	*Multiple comparison*		
			Baseline-Right Hand	Baseline-Left Hand	Right Hand-Left Hand
GE	$\chi^2 = 16.41$ p<.001	-	p<.001↓	-	p<.05↓
CC	$\chi^2 = 18$ p<.001	Frontal	p<.001↓	p<.05↓	-
	$\chi^2 = 6.32$ p<.05	Central	p<.05↓	-	-
	$\chi^2 = 9.32$ p<.01	Parietal	p<.05↓	-	-
	$\chi^2 = 7.4$ p<.05	Occipital	-	p<.05↓	-
D	$\chi^2 = 19.76$ p<.001	Frontal	p<.001↓	p<.05↓	-
	$\chi^2 = 16.23$ p<.001	Central	p<.001↓	-	p<.05↓
	$\chi^2 = 13.67$ p<.05	Parietal	p<.001↓	-	-
	$\chi^2 = 9.32$ p<.05	Occipital	p<.05↓	-	-

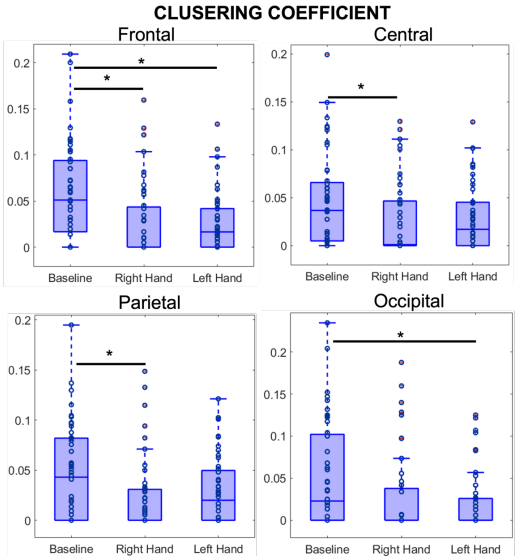


Fig. 3: Clustering coefficient (CC) distribution over the four brain areas of interest during the baseline condition, the right-hand movement and the left-hand movement. *p<0.05

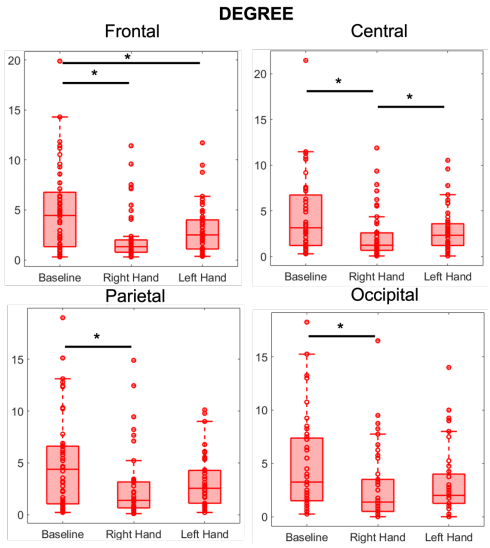


Fig. 4: Degree (D) distribution over the four brain areas of interest during the baseline condition, the right-hand movement and the left-hand movement. *p<0.05

REFERENCES

[1] G. Rizzolatti and G. Luppino, "The Cortical Motor System," *Neuron*, vol. 31, no. 6, pp. 889–901, 2001, doi: 10.1080/1059924X.2010.512854.

[2] F. Hamzei *et al.*, "Visuomotor control within a distributed parieto-frontal network," *Exp Brain Res*, vol. 146, no. 3, pp. 273–281, 2002, doi: 10.1007/s00221-002-1139-0.

[3] A. Brovelli, J. M. Badier, F. Bonini, F. Bartolomei, O. Coulon, and G. Auzias, "Dynamic reconfiguration of visuomotor-related functional connectivity networks," *Journal of Neuroscience*, vol. 37, no. 4, pp. 839–853, 2017, doi: 10.1523/JNEUROSCI.1672-16.2016.

[4] C. F. Lu *et al.*, "Reorganization of functional connectivity during the motor task using EEG time-frequency cross mutual information analysis," *Clinical Neurophysiology*, vol. 122, no. 8, pp. 1569–1579, 2011, doi: 10.1016/j.clinph.2011.01.050.

[5] A. R. Anwar *et al.*, "Effective Connectivity of Cortical Sensorimotor Networks During Finger Movement Tasks: A Simultaneous fNIRS, fMRI, EEG Study," *Brain Topogr*, vol. 29, no. 5, pp. 645–660, 2016, doi: 10.1007/s10548-016-0507-1.

[6] D. M. Herz *et al.*, "Task-specific modulation of effective connectivity during two simple unimanual motor tasks: A 122-channel EEG study," *Neuroimage*, vol. 59, no. 4, pp. 3187–3193, 2012, doi: 10.1016/j.neuroimage.2011.11.042.

[7] G. Pfurtscheller, C. Brunner, A. Schlögl, and F. H. Lopes da Silva, "Mu rhythm (de)synchronization and EEG single-trial classification of different motor imagery tasks," *Neuroimage*, vol. 31, no. 1, pp. 153–159, May 2006, doi: 10.1016/j.neuroimage.2005.12.003.

[8] P. Caliandro *et al.*, "Connectivity modulations induced by reach&grasp movements: a multidimensional approach," *Sci Rep*, vol. 11, no. 1, pp. 1–11, 2021, doi: 10.1038/s41598-021-02458-x.

[9] F. Temporiti *et al.*, "Kinematic evaluation and reliability assessment of the Nine Hole Peg Test for manual dexterity," *Journal of Hand Therapy*, pp. 4–6, 2022, doi: 10.1016/j.jht.2022.01.007.

[10] G. Nolte *et al.*, "Robustly estimating the flow direction of information in complex physical systems," *Phys Rev Lett*, vol. 100, no. 23, pp. 1–4, 2008, doi: 10.1103/PhysRevLett.100.234101.

[11] L. Faes, G. D. Pinna, A. Porta, R. Maestri, and G. Nollo, "Surrogate data analysis for assessing the significance of the coherence function," *IEEE Trans Biomed Eng*, vol. 51, no. 7, pp. 1156–1166, 2004, doi: 10.1109/TBME.2004.827271.

[12] M. Rubinov and O. Sporns, "Complex network measures of brain connectivity: Uses and interpretations," *Neuroimage*, vol. 52, no. 3, pp. 1059–1069, 2010, doi: 10.1016/j.neuroimage.2009.10.003.

[13] G. Pfurtscheller and A. Berghold, "Patterns of cortical activation during planning of voluntary movement," *Electroencephalogr Clin Neurophysiol*, vol. 72, no. 3, pp. 250–258, 1989.

Alteration of muscle recruitment in Parkinson's disease assessed by EMG-based occurrence frequency

M. Romanato[1], F. Di Nardo[2], F. Spolaor[1], D. Volpe[3], S. Fioretti[2], Z. Sawacha[1]

[1] *Department of Information Engineering, Università degli Studi di Padova, Padova, Italy*
[2] *Department of Information Engineering, Università Politecnica delle Marche, Ancona, Italy*
[3] *Fresco Parkinson Center, Villa Margherita, S. Stefano, Vicenza, Italy*

***Abstract*—Gait analysis has been widely adopted to describe Parkinson's disease (PD) dysfunctions. Nevertheless, only few efforts were made to investigate the role of muscle activity by surface-electromyography (sEMG). The current study aims to provide a quantification of muscle recruitment during walking in people with PD through the assessment of the sEMG-based occurrence frequency (OF). To this aim, sEMG signals from Tibialis Anterior (TA), Gastrocnemius Lateralis (GL), Rectus Femoris (RF), and Biceps Femoris (BF) of 20 people with PD and 10 age-matched healthy controls (HC) were acquired during walking. sEMG signals were processed to assess muscle-activation intervals and then the associate OF, i.e., the percentage of strides of each specific muscle activation occurrence. This OF-based analysis allowed to detect in people with PD an over-recruitment of proximal-leg muscles in the first half of stance. An impairment in muscle recruitment of proximal leg in the preparation of the transition between stance and of distal leg throughout the swing phase is also observed. The current approach provides a compact and synthetic representation of muscle recruitment alteration in PD which could turn out to be particularly suitable for application in clinics and rehabilitation.**

***Keywords*—surface electromyography, continuous wavelet transform, Parkinson's disease, clinical gait analysis.**

I. Introduction

THE number of people affected by Parkinson's disease (PD) across the world is expected to reach 17 million by the year 2040 as a consequence of the changes in aging, longevity, smoking rates, and industrialization [1]. PD is a neurodegenerative disorder associated with a deficiency of both the dopaminergic neurons located in the substantia nigra of the brain and the cells located in other regions of the neural network [2] which contributes to the arousal of motor signs affecting people with PD quality of life (e.g., bradykinesia, resting tremor, rigidity, and postural instability) [3]. Clinical gait and postural analysis have been frequently adopted to quantitatively assess the motor disorders associated with this pathology [4]. Among the motor manifestations, an altered motor control has been revealed in PD individuals in comparison with healthy age-matched controls [5].

In the last decades, an extensive involvement of surface electromyography (sEMG) to investigate the locomotion strategies in PD has been exploited [6]. Some studies highlighted a lower sEMG activity in the distal muscles of people with PD when compared with healthy peers. Meanwhile a greater muscle activity was detected in correspondence of the proximal muscles during the swing phase [7]. Further studies used sEMG signals analysis to assess the mean regions of muscle activation during PD walking in time-frequency domain [8].

In addition, sEMG analysis allows to assess the occurrence frequency (OF), a parameter recently introduced to characterize the frequency of muscular recruitment during cyclic tasks [9]. This parameter has been successfully adopted to provide a novel point of view in the characterization of muscular recruitment in healthy adults [11,12] and children [13] and in the quantification of motor control alterations in neurological patients [14,15]. Preliminary attempts of computing OF in PD have been also reported [16]. However, this analysis was performed only on Tibialis Anterior and Gastrocnemius Medialis, and without validation versus control subjects. To the best of our knowledge, an OF-based characterization of PD muscle recruitment strategy is still lacking.

The present study aims to provide a quantification of muscle recruitment during walking in PD through the assessment of the sEMG-based occurrence frequency (OF). Specifically, OF is computed as a single parameter useful to monitor the occurrence of muscle recruitment of the lower-limb muscles in people with PD. To quantify the variations with respect to healthy controls in a single compact representation, ΔOF is computed as the point-by-point difference in OF values between the two populations in every percentage of gait cycle (GC). The main hypothesis of the study is that the two populations (PD vs. HC) would portray sensitive differences in their muscle ΔOF within the gait cycle with respect to the assessed muscles. For this purpose, sEMG signals of four lower-limb bilateral muscles of 20 people with PD and 10 control subjects have been analyzed and compared.

II. Material and Methods

A. Participants and signal acquisition

Twenty people with PD (age = 64.6 ± 10.5 years, height = 1.69 ± 0.17 m, mass = 78.3 ± 16.1 Kg) and 10 age and BMI matched healthy peers (HC, age = 62.3 ± 6.4 years, height = 1.69 ± 0.12 m, mass = 76.2 ± 15.7 Kg) were considered for the study after Local Ethic Committee approval (CE/PROG 61/16–19/11/2015) at Casa di Cura "Villa Margherita" (Arcugnano (VI), Italy). Participant were considered eligible for the study if the inclusion\exclusion criteria reported in [17] were respected. Data from a stereophotogrammetric system (6 cameras, 60 Hz, SMART-E, BTS Bioengineering s.r.l., Italy), two force plates (960Hz, Bertec Corporation, USA) and an 8-channels EMG system (1000 Hz, BTS Free 1000, BTS Bioengineering s.r.l., Italy) that collected the electrical activity of Rectus Femoris (RF), Biceps Femoris (BF), Gastrocnemius Lateralis (GL), Tibialis Anterior (TA) bilaterally were

acquired synchronously at the BioMovLab (Department of Information Engineering, Università degli Studi di Padova) during self-selected speed overground gait. Spherical retroreflective markers placed on the posterior calcaneus were used to identify contralateral heel strikes. Data were collected until at least three complete GC were collected bilaterally. Steps were considered valid for the processing when the right/left foot naturally landed on the force plate.

B. Signal processing

Raw sEMG signals were segmented into separated GCs: heel strike instant was considered as the first frame at which the modulus of ground reaction force detected by the force plate was greater than 5N; toe off was considered as the first frame at which the modulus of ground reaction force was less than 5N; the consequent heel strike was considered as the minimum of the vertical component of the marker trajectory placed on the ipsilateral calcaneus [18]. sEMG signals were filtered with a band-pass Butterworth filter (20-450 Hz, cut-off frequency). Muscle activation was computed by implementing the methodology based on Continuous Wavelet Transform introduced in [19].

Muscular activation was characterized at each percentage point of the GC by the occurrence frequency (OF), a recently introduced parameter [9,10] defined as

$$OF = \frac{N_{A_{GC}}}{N_{GC}} \times 100 \qquad (1)$$

where $N_{A_{GC}}$ is the number of GCs with activation and N_{GC} is the total number of GCs. Then a point-by-point difference were computed over the two population (HC or PD) for the assessed muscles, and defined as

$$\Delta OF = OF_{PD} - OF_{HC} \qquad (2)$$

where OF_{PD} is the OF presented in the specific percentage of the GC by the PD population and OF_{HC} is the OF presented in the specific percentage of the GC by the HC.

III. Results and Discussion

The present study is fulfilled analysing 109 strides for PD group and 47 strides for HC. The comparison between the different strategies of muscle recruitment identified in PD vs HC is achieved by considering the point-by-point difference in OF values between the two populations (ΔOF), computed in every percentage of gait cycle (GC%).

A. Proximal muscles

The comparative analysis of muscle recruitment in terms of ΔOF in RF muscle is depicted in the following Fig. 1. The positive values (ΔOF > 0) of green area, detected from 0% to 35% of GC, indicate a more frequent recruitment of RF muscle in PD compared to HC, in the first half of stance phase. On the contrary, negative values (ΔOF < 0) of green area are detected from 36% to the end of GC, suggesting a reduced frequency of RF muscle recruitment in people with PD compared to HC, in the second half of stance phase and all over the swing phase.

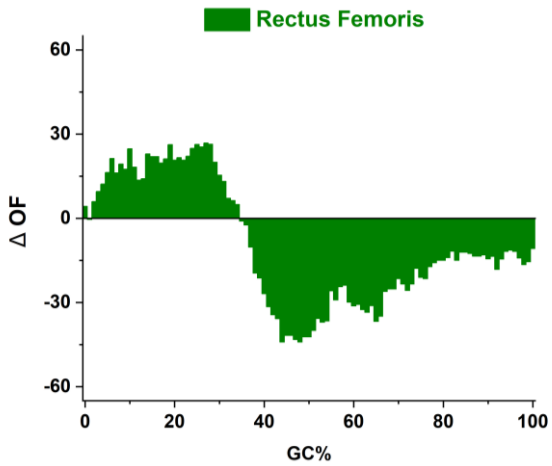


Fig. 1: Difference in occurrence frequency (ΔOF) of RF muscle recruitment during gait in PD population vs. HC population. Positive values of the green area indicate higher OF values in PD population compared to HC group. Negative values indicate lower OF values in PD population compared to HC group.

Fig. 2 shows as positive ΔOF values are detected from the beginning up to 15% of GC and from 91% to the end of GC (positive green area in Fig. 2). Otherwise, negative ΔOF values are detected in the central phases of GC, starting from 16% up to 90% of GC (negative green area in Fig. 2), except for some negligible positive values, mainly around the 80% of GC. This seems to suggest that people with PD are used to recruiting BF muscle more frequently than HC in the gait phase around the heel strike event.

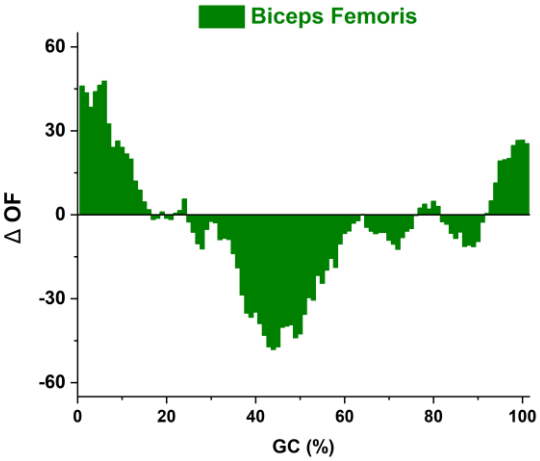


Fig. 2: Difference in occurrence frequency (ΔOF) of BF muscle recruitment detected during gait in PD population vs. Control population. Positive values of the green area indicate higher OF values in PD population compared to Control group.

Although the analysis of ΔOF for each single muscle reported in figures 1 and 2 is informative, the current study is designed to assess a further parameter useful to provide a compact description of the proximal-leg muscle recruitment in PD, i.e., the global ΔOF. This parameter represents the sum of the ΔOF computed for the RF and BF muscles. Results in function of the GC are displayed in light green in Fig. 3.

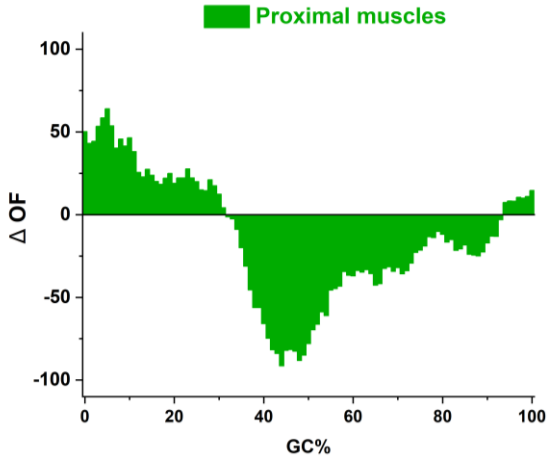


Fig. 3: Global difference in occurrence frequency (ΔOF) of proximal-leg muscle recruitment detected during gait in PD population vs. Control population. Positive values of the light green area indicate higher OF values in PD population compared to Control group.

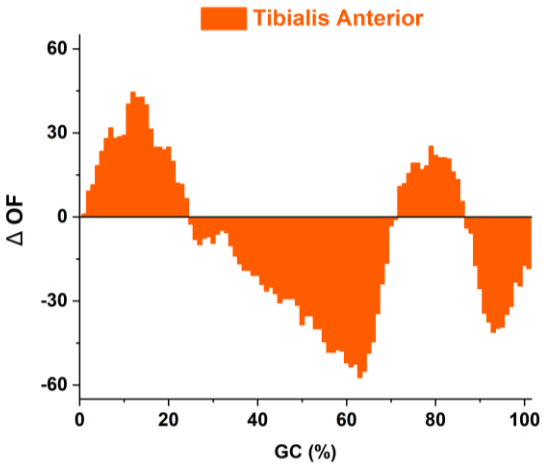


Fig. 4: Difference in occurrence frequency (ΔOF) of TA muscle recruitment detected during gait in PD population vs. Control population. Positive values of the orange area indicate higher OF values in PD population compared to Control group.

Positive values of the light green area are observed from the beginning up to 31% of GC and from 94% to the end of GC. Negative values are located in the central phases of GC, specifically from 32% to 93% of GC. Furthermore, a relevant negative peak of ΔOF is detected around the 40-60% of GC. Despite the agonist-antagonist nature of the two muscles, the concomitant evaluation of ΔOF in both proximal-leg muscles offered by Fig. 3 appears to be very appropriate to describe their recruitment in PD. Indeed, this single compact parameter allows to highlight an overall tendency of people with PD of over-recruiting the proximal-leg muscles from heel strike to loading response (≈ 0-30% of GC), compared to HC. This observation might be linked with both the loss of proprioception in the distal segments [20] and the typical camptocormic posture characterizing PD. Indeed, the bending of the trunk in a forward direction could have led towards the adoption of a hip strategy when walking [4]. Moreover, this compact representation permits also to notice as the employment of these muscles is impaired in people with PD in the preparation of the transition between stance and swing phases (≈ 40-60% of GC), which might be related with the lessen ability in shifting from double to single support [21]. The reduced range of motion on the sagittal plane of the hip joint displayed in people with PD [4] is highlighted by negative values of ΔOF in RF during the whole swing, where the muscle is not operating in its physiological range.

B. Distal muscles

The difference between PD and HC in the frequency of TA recruitment is quantified in Fig. 4 in terms of ΔOF. An alternance between two positive and two negative areas is clearly shown; specifically, a positive area from 0% to 23% of GC followed by a longer negative area from 24% to 70% of GC, covering all the stance phase. A further positive area from 71% to 85% of GC and a negative area from 86% to the end of GC cover the remaining of the swing phase. This positive-negative alternance of ΔOF impedes from identifying a clear trend in the recruitment of this muscle in people with PD.

Fig. 5 displays the trend of ΔOF between PD and HC in GL muscle. The positive area covers from 8% to 56% of GC, highlighting the adoption by people with PD of a more frequent recruitment of GL than HC during most of the stance phase. Otherwise, the negative area extends over all the swing phase up to the beginning of the following GC (from 57% of GC to the 8% of the successive GC), revealing a reduced frequency of GL muscle recruitment in people with PD compared to HC.

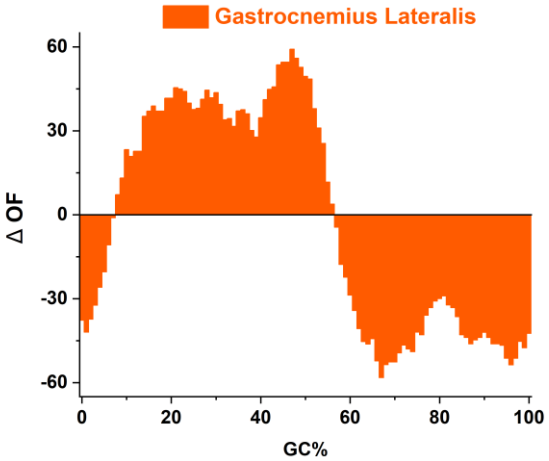


Fig. 5: Difference in occurrence frequency (ΔOF) of GL muscle recruitment detected during gait in PD population vs. Control population. Positive values of the orange area indicate higher OF values in PD population compared to Control group.

Since the approach adopting the global ΔOF turned out to be very suitable for the analysis of proximal-leg muscles, an attempt of characterizing muscle recruitment in PD by means of the same compact parameter has been made also for the distal-leg muscles (TA + GL). Results in function of the GC are displayed in Fig. 6. ΔOF assumes negative values all through the swing phase, characterized by two significant peaks around 65% and 95% of GC. Moreover, positive values of light orange area cover the most of stance from 5% up to 51% of GC. These results seem to suggest a reduced frequency

of distal-leg muscle recruitment during swing in PD people.

Compared with the promising results achieved for proximal-leg muscles, the only global ΔOF seems to be not as useful for the description of distal-leg muscle, because it tends to hide the behaviour of the single muscles highlighted by figures 4 and 5. Therefore, it has to be always interpreted together with the ΔOF analysis in the single muscle. In this case, it could really be supportive to the physiological interpretation, as for the analysis of Fig. 6 (together with figures 4 and 5) where the impaired employment during swing of distal-leg muscles detected in people with PD is mainly due to the GL muscle. This is probably associated with the altered motor control recurrent in people with PD [5]. The role of TA in this phenomenon needs to be further deepened.

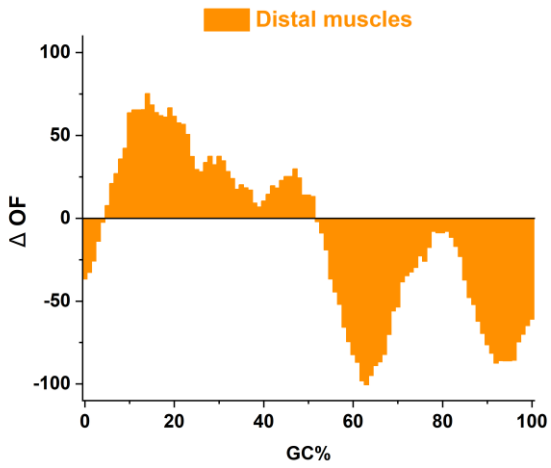


Fig. 6: Global difference in occurrence frequency (ΔOF) of distal-leg muscle recruitment detected during gait in PD population vs. Control population. Positive values of the light orange area indicate higher OF values in PD population compared to Control group.

IV. Conclusion

The main contribution of the study is to propose a novel approach for assessing the muscle-recruitment alteration in people with PD, based on the evaluation in PD of muscle occurrence frequency, OF, and its difference with a control population, ΔOF. Specifically, the point-by-point computation of ΔOF allowed to identify a PD-related tendency of over-recruiting the proximal-leg muscles in the first half of stance. ΔOF analysis highlighted also a PD-related impairment in recruiting proximal-leg muscles in the preparation of the transition between stance and of distal-leg muscles throughout the swing phase. The capability of providing a compact and synthetic representation of muscle recruitment alteration in PD makes this ΔOF-based approach particularly suitable for application in clinics and rehabilitation. Future developments will focus on comparison of present results with different classes of subjects and state of disease to further evaluate suitability and reliability of the proposed methodology.

Acknowledgement

The authors acknowledge: Fondazione Fresco Parkinson Institute Italia Onlus for the financial contribution to Marco Romanato's PhD scholarship; Fresco Clinical Research Grant 2019, Marlene and Paolo Fresco Institute for Parkinson's and Movement Disorders at NYU Langone Health (FI-NYU) for the financial contribution to Fabiola Spolaor research grant.

References

[1] E.R. Dorsey, T. Sherer, M.S. Okun, B.R. Bloem, "The Emerging Evidence of the Parkinson Pandemic, J Parkinsons Dis" 2018, 8, S3–S8.
[2] R.A. Barker, "Parkinson's disease as a preventable pandemic", The Lancet Neurology. 19 (2020) 813.
[3] B.R. de Miranda, J.T. Greenamyre, "CHAPTER 1: Etiology and Pathogenesis of Parkinson's Disease", in: Oxidative Stress and Redox Signalling in Parkinson's Disease, 2017: pp. 1–26.
[4] M.E. Morris, F. Huxham, J. McGinley, K. Dodd, R. Iansek, "The biomechanics and motor control of gait in Parkinson disease", Clinical Biomechanics. 16 (2001) 459–470.
[5] P. Mazzoni, B. Shabbott, J.C. Cortes, "Motor Control Abnormalities in Parkinson's Disease", Cold Spring Harbor Perspectives in Medicine. 2 (2012) a009282–a009282.
[6] A. Islam, L. Alcock, K. Nazarpour, L. Rochester, A. Pantall, "Effect of Parkinson's disease and two therapeutic interventions on muscle activity during walking: a systematic review", Npj Parkinsons Dis. 6 (2020) 22.
[7] O. Sofuwa, A. Nieuwboer, K. Desloovere, A.-M. Willems, F. Chavret, et al., "Quantitative Gait Analysis in Parkinson's Disease: Comparison With a Healthy Control Group", Archives of Physical Medicine and Rehabilitation. 86 (2005) 1007–1013.
[8] M. Romanato, A. Strazza, W.J. Piatkowska, F. Spolaor, S. Fioretti, D., et al., "Characterization of EMG time-frequency content during Parkinson walking: a pilot study", in: 2021 IEEE International Symposium on Medical Measurements and Applications (MeMeA), IEEE, Lausanne, Switzerland, 2021: pp. 1–6.
[9] F. Di Nardo, A. Mengarelli, A. Strazza, V. Agostini, M. Knaflitz, L. et al., "A new parameter for quantifying the variability of surface electromyographic signals during gait: The occurrence frequency", J Electromyogr Kinesiol. 36 (2017) 25–33.
[10] F. Di Nardo, V. Agostini, M. Knaflitz, A. Mengarelli, E, Maranesi et al. "The occurrence frequency: A suitable parameter for the evaluation of the myoelectric activity during walking", in: 37th Annual International Conference of the IEEE Engineering in Medicine and Biology Society, EMBC 2015, Milan, Italy, 2015: pp. 6070 – 6073,
[11] M.G. Benedetti, V. Agostini, M. Knaflitz, P. Bonato, "Muscle Activation Patterns During Level Walking and Stair Ambulation", Applications of EMG in Clinical and Sports Medicine. (n.d.) 16.
[12] F. Di Nardo, G. Laureati, A. Strazza, A. Mengarelli, L. Burattini, V. et al., "Is child walking conditioned by gender? Surface EMG patterns in female and male children", Gait & Posture. 53 (2017) 254–259.
[13] V. Agostini, A. Nascimbeni, A. Gaffuri, P. Imazio, M.G. Benedetti, et al., "Normative EMG activation patterns of school-age children during gait", Gait & Posture. 32 (2010) 285–289.
[14] M. Benedetti, V. Agostini, M. Knaflitz, V. Gasparroni, M. Boschi, et al., "Self-reported gait unsteadiness in mildly impaired neurological patients: an objective assessment through statistical gait analysis", J NeuroEngineering Rehabil. 9 (2012) 64.
[15] F. Di Nardo, A. Strazza, A. Mengarelli, S. Cardarelli, A. Tigrini, F. et al., "EMG-Based Characterization of Walking Asymmetry in Children with Mild Hemiplegic Cerebral Palsy", Biosensors. 9 (2019) 82.
[16] G. Pacini Panebianco, D. Ferrazzoli, G. Frazzitta, M. Fonsato, M.C. Bisi, et al., "A Statistical Approach for the Assessment of Muscle Activation Patterns during Gait in Parkinson's Disease", Electronics. 9 (2020) 1641.
[17] M. Romanato, W. Piatkowska, F. Spolaor, D.-K. To, D. Volpe, et al., "Different perspectives in understanding muscle functions in Parkinson's disease through surface electromyography: Exploring multiple activation patterns", Journal of Electromyography and Kinesiology. 64 (2022) 102658.
[18] M. Romanato, A. Guiotto, F. Spolaor, L. Bakdounes, G. Baldassarre, A. et al., "Changes of biomechanics induced by Equistasi® in Parkinson's disease: coupling between balance and lower limb joints kinematics", Med Biol Eng Comput. 59 (2021) 1403–1415.
[19] F. Di Nardo, T. Basili, S. Meletani, D. Scaradozzi, "Wavelet-Based Assessment of the Muscle-Activation Frequency Range by EMG Analysis", IEEE Access. 10 (2022) 9793–9805.
[20] S.M. Keloth, S.P. Arjunan, S. Raghav, D.K. Kumar, "Muscle activation strategies of people with early-stage Parkinson's during walking", Journal of NeuroEngineering and Rehabilitation. 18 (2021) 133.
[21] O. Sitek, M. Kalichová, P. Hedbávný, T. Boušek, M. Baláž, Kinematic "Relations during Double Support Phase in Parkinsonian Gait", Applied Sciences. 12 (2022) 949. https://doi.org/10.3390/app12030949

Quality enhancement of dermatological images using GANs: a proof of concept

F. Branciforti[1], K.M. Meiburger[1], E. Zavattaro[2], F. Veronese[3], V. Tarantino[2], P. Savoia[2] and M. Salvi[1]
[1] *Biolab, PoliTo^{BIO}Med Lab, Department of Electronics and Telecommunications, Politecnico di Torino, Turin, Italy*
[2] *Department of Health Science, University of Eastern Piedmont, Via Solaroli 17, 28100 Novara, Italy*
[3] *AOU Maggiore della Carità, C.so Mazzoni 18, 28100 Novara, Italy (F. Veronese)*

***Abstract*—High quality dermoscopic images are a fundamental requirement for proper clinical evaluation and implementation of artificial intelligence (AI) methods. However, due to several factors that are challenging to control (e.g., the acquisition device, image compression, etc.), it is difficult to have images with a high quality standard available all the time. Therefore, a tool capable of enhancing image quality is required to make remote clinical assessment more reliable and to develop even better performing AI tools for classification and segmentation.**

In this work, we present a customized Generative Adversarial Network for super resolution that can successfully enhance the quality of dermoscopic images and double their resolution.

The enhanced images by the proposed method achieve an average PIQE (Perception based Image Quality Evaluator) score of 19.71, a 35.76% improvement over the low-resolution source images. Our method was also validated through a visual assessment performed by an AI expert and an experienced dermatologist. The enhanced images proved to be suitable for both AI applications and clinical evaluation.

***Keywords*— Dermatology, AI, Deep Networks, Generative Adversarial Networks, Skin Lesions, Image Quality, Super Resolution.**

I. Introduction

DIGITAL dermatological skin lesions are acquired through a high-resolution dermoscope under epiluminescence conditions and then digitalized. Acquisition and digitalization process is decisive to ensuring high-quality images. Image quality is an essential requirement both for clinical evaluations [1]-[4] (e.g., Teledermatology), and for the development of reliable and high-performance artificial intelligence (AI) based tools for classification and segmentation [5]-[8].

In remote dermatological services, it is essential that the images transmitted from the patient to the physician are of sufficiently high quality to make a truthful evaluation. However, image quality depends on several factors including device used by the patient, exposure conditions, and transmission protocols, some of which are difficult to control. At the same time, developing AI-based tools that can assist the dermatologist requires large amounts of high-quality data. Today several open access databases of dermoscopic images used for AI challenges contain a wide range of images from several centres, acquired and digitized with different devices and techniques. As a result, not all of them have the same quality/resolution and therefor do not meet the required quality standards.

In recent years, GANs have proven to be powerful tools that can improve image quality and resolution in healthcare and other fields [9]-[19].

In this study we successfully adapted a super-resolution GAN called RealESR-GAN [10] to enhance and double the resolution of dermoscopic images. Processed images obtained significant scores on full reference metrics and higher scores when comparing with low-resolution images.

Finally, an AI specialist (M.S.) and a dermatologist (P.S.) were involved in this study to evaluate the suitability of the images produced by our method for artificial intelligence and clinical applications, respectively.

II. Materials and methods

A. Dataset

Starting from a pool of 70000 dermoscopic images from ISIC Archive [20]-[21], we selected 18000 high-resolution images characterized by high sharpness, resolution higher than 1024x1024 and absence of invasive artifacts.

To reduce GAN overfitting and increase the heterogeneity of the dataset, a data augmentation pipeline was carried out to increase the number of training samples. This step was performed using *Albumentation library* [22]. The following transformations were applied with a 50% probability for each image: flipping, scaling, changes in contrast, brightness and gamma, grid distortion and elastic transformation. This results in 30000 high-resolution images of size 1024x1024 pixels.

The RealESR-GAN requires during training a paired dataset, consisting of high-resolution images and the corresponding low-resolution images. To obtain the low-resolution images, a two-grade degradation pipeline was implemented to simulate real-world degradations such as camera blur, sensor noise, low resolution and JPEG compression [24]. To create the synthetic low-resolution images, the high-resolution images have been sequentially subjected to:

- *Blurring*, by using a generalized Gaussian blur kernels that approximate real camera blur.
- *Noising*, adding Gaussian and Poisson noise. In particular, the Poisson one simulates the noise introduced by camera sensor.
- *Downsampling*, by using combinations of different interpolation algorithms (nearest-neighbour, bilinear, bicubic) in order to recreate a wider variety of artifacts.
- *JPEG compression*, with different compression factor.

Each step is controlled by hyper-parameters that change for each image with a given probability, so that deteriorations are always different. The entire degradation pipeline is repeated twice for each image. At the end we obtain 30000 low-resolution images of size 512x512 pixels, coupled with the corresponding high-resolution images.

Finally, about 10000 images from the starting pool that did

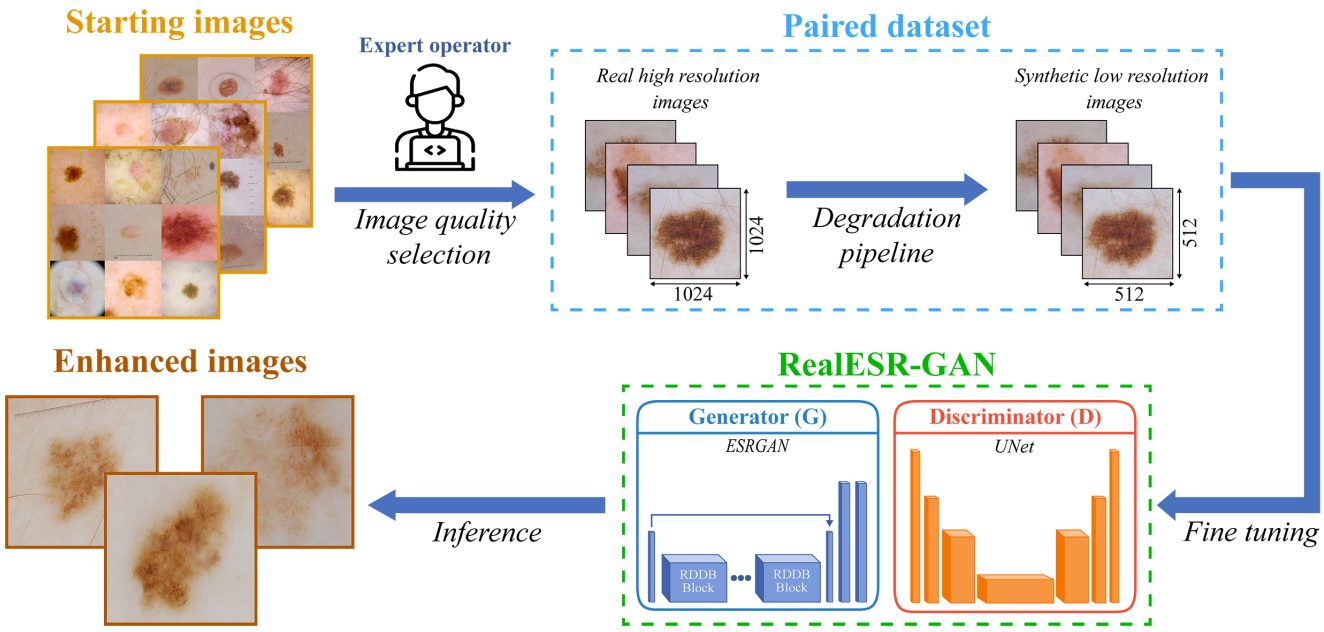


Fig. 1: Overview of the proposed pipeline.

not meet the quality requirements were used as a test set to evaluate the performance of the proposed method.

B. *Network architecture: Real-ESRGAN*

RealESR-GAN [10] is one of the most effective restoration model for real world images available today. For this reason, we chose this architecture to implement our quality enhancement task. The key features of this model are:

- A deep network generator with 23 residual-in-residual dense blocks (*RRDB*) capable of performing super resolution with a scaling factor of x2. In addition, there are no batch normalization layers, in order to reduce the generation of artifacts and increase the generalization capability of the entire network.
- A *U-Net* discriminator with skip connections and spectral normalization, able to soften oversharping artifacts introduced by GAN.
- A generator loss determined by the combination of perceptual loss, L1 loss and GAN loss, as in Eq. (1).

$$L_G = L_{percep} + \lambda L_{GAN} + \eta L_1 \qquad (1)$$

To adapt RealESR-GAN [10] to dermoscopic images, fine tuning was performed on a pre-trained model capable of super resolution with a factor of x2. The training phase was performed on a NVIDIA RTX 3090 24 GB using Pytorch framework.

Best model was chosen according to loss values. During inference, the trained model outputs an image with twice the resolution of that received as input. A complete overview of the entire pipeline (data preparation and model training) is provided in Figure 1.

C. *Evaluation metrics*

To assess the behaviour and effectiveness of the proposed method, a quantitative evaluation and a qualitative evaluate based on a visual assessment were carried out.

Performance metrics were calculated on the entire test set processed by our method. To evaluate the preservation of structural content, the following full-reference metrics were calculated between the source image and the image reconstructed by the model:

- *PSNR*, Peak Signal-to-Noise Ratio.
- *SSIM,* Structural Similarity Index Measure
- *FSIM,* Feature Similarity Index Measure.

In order to validate how well the model succeeds in enhancing image quality, the following non-reference metric was implemented:

- *PIQE*, Perception based Image Quality Evaluator, an opinion-unaware and unsupervised algorithm that provides a detailed analysis at a local level in addition to a global quality score [24]. A lower PIQE value indicates higher image quality.

All metrics are reported as mean ± standard deviation.

Qualitative visual assessment was carried out to understand how enhanced images are perceived by a human operator and to verify whether they were suitable for both AI-based methods development and clinical evaluation. For this purpose, 60 images with different quality levels (20 high-resolution images from the training set, 20 low-resolution images from the test set and 20 enhanced images generated from the test set) were submitted to an AI specialist skilled in dermatoscopic image analysis and a high experienced dermatologist.

III. Results

A. *Quantitative metrics*

Table I shows the full reference metrics calculated on the test set images processed by the proposed method. The processed images achieve an average PSNR value of 38.62 and SSIM and FSSIM values close to 1, indicating how the enhancement process preserved structures and patterns, without adding noise to the source images.

Table II shows a comparison between the original low-resolution images from the test set and the enhanced images. It is possible to see a percentage decrease in the PIQE value of 35.76%, indicating that the reconstructed images have higher quality than the originals.

TABLE I: FULL-REFERENCE METRIC

Metric	*Value*
PSNR	38.62 ± 2.27
SSIM	0.98 ± 0.01
FSSIM	0.98 ± 0.01

TABLE II: NO-REFERENCE METRIC

Metric	*Original images*	*Enhanced images*
PIQE	30.68 ± 8.02	19.71 ± 4.15

B. *Suitability assessment*

Figure 2 shows the results for the suitability assessment of images processed with our method.

Panel a. shows the scores assigned by the AI specialist. It is possible to observe that 85% of the enhanced low-resolution images are considered suitable for AI application, versus 5% for low-resolution images. The usability distribution of the enhanced images far exceeds that of low-resolution images, coming very close to that of high-resolution.

Figure 2b shows the assessment made by the expert dermatologist. Surprisingly, the enhanced images are considered more suitable for clinical evaluation than the original high-resolution images, 95% vs 45%, respectively.

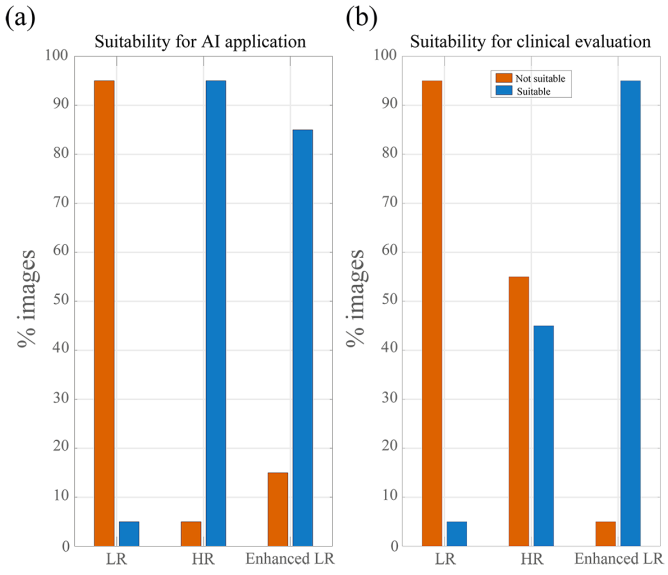


Fig. 2: Suitability assessment. Panel (a) reports the scores assigned by the AI expert, and Panel (b) those assigned by the dermatologist. LR indicates low-resolution images, HR high-resolution images, Enhanced LR the low-resolution images enhanced with our method.

IV. DISCUSSION AND CONCLUSIONS

In this paper, we propose a study on the application of one of the most powerful restoration models for quality enhancement of medical images. Specially, we implemented and customized the RealESR-GAN to increase the quality and the resolution of dermatoscopic images. The proposed strategy consists of three main steps:

- High-quality, sharped and artifact-free dermoscopic images selection from ISIC Archive [20]-[21].
- Degradation of high-resolution images to generate synthetic low-resolution versions that simulate realist artifacts, such as camera noise, blurring and JPEG compression.
- Fine tuning of RealESR-GAN [10] in order to realize a model that can double the resolution and enhance quality of input dermoscopic images.

To validate the proposed method, performance metrics were calculated on a test set of low-resolution images. It was observed that processed low-resolution images achieved an average PSNR value of 38.62, demonstrating how image reconstruction does not introduce noise to the original images. The enhancement process also preserved structures and patterns of the source images, as witnessed by SSIM and FSSIM mean values close to 1 (0.98 and 0.98, respectively). In addition, PIQE, a non-reference quality metric that mimics human visual perception [24], was calculated to quantify images quality for both low resolution and enhanced images. Reconstructed images obtained 35.76% lower PIQE mean value than the original images (19.71 vs 30.68, respectively), demonstrating how the proposed method succeeds in increasing image quality.

The behaviour of performance metrics, however, does not always reflect human perception. Sixty images of different quality and resolution were evaluated by an AI expert and an experienced dermatologist to test the suitability of enhanced images in AI and clinical evaluation.

From the perspective of the AI expert, 85% of the enhanced images would be suitable for AI application. The proposed method succeeds in increasing the number of suitable images by 80% compared to only 5% of low-resolution images. On the other hand, the experienced dermatologist perceived 95% of the enhanced images as suitable for clinical evaluation, with a 50% increase over high-resolution images and 90% over low-resolution images. This perception is probably explained by the fact that typical skin lesions patterns appear sharper and more defined, thus therefore easier to interpret. A comparison between low-resolution images and images enhanced by the proposed method is shown in Figure 3. It can be seen that out our method succeeds in greatly improving the definition of lesion textures definition and the overall sharpness of the image.

This study demonstrates how it is possible to successfully perform dermoscopic image enhancement by adapting an enhancing framework designed for non-healthcare applications. The produced images proved to be quantitatively better than the starting low-resolution images. Qualitatively, the proposed method can produce images that meet quality standard for both AI suitability and clinical assessment, with scores comparable with original high-resolution images.

Future development will focus on:

- Extension of the testing phase of the proposed method on different datasets.

- Further optimization and customization of the RealESR-GAN architecture.
- Implementation of the enhancement task through different models and architectures.
- Investigating the use of the enhancement tool as pre-processing step for classification and segmentation frameworks.

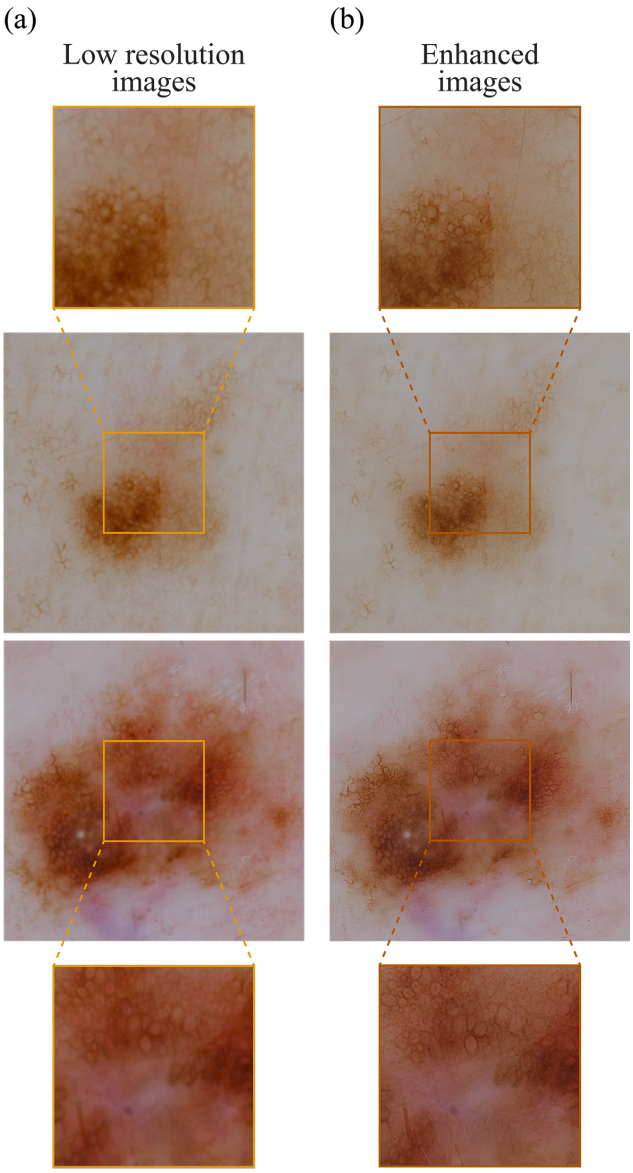


Fig. 3: Comparison between low resolution (a) and enhanced images (b). It can bee see that the proposed method succeeds in realistically enhancing low-resolution images, in detail it makes the lesion textures more sharped, preserving the macro structures.

REFERENCES

[1] S. J. Coates, J. Kvedar, and R. D. Granstein, "Teledermatology: From historical perspective to emerging techniques of the modern era: Part I: History, rationale, and current practice," *J. Am. Acad. Dermatol.*, vol. 72, no. 4, pp. 563–574, 2015, doi: 10.1016/j.jaad.2014.07.061.

[2] F. Veronese *et al.*, "The Role in Teledermoscopy of an Inexpensive and Easy-to-Use Smartphone Device for the Classification of Three Types of Skin Lesions Using Convolutional Neural Networks," *Diagnostics*, vol. 11, no. 3, p. 451, 2021, doi: 10.3390/diagnostics11030451.

[3] P. Pala, B. S. Bergler-Czop, and J. M. Gwiżdż, "Teledermatology: idea, benefits and risks of modern age – a systematic review based on melanoma," *Postep. Dermatologii i Alergol.*, vol. 37, no. 2, pp. 159–167, 2020, doi: 10.5114/ada.2020.94834.

[4] F. Veronese *et al.*, "Teledermoscopy in the Diagnosis of Melanocytic and Non-Melanocytic Skin Lesions: Nurugo^{TM} Derma Smartphone Microscope as a Possible New Tool in Daily Clinical Practice," *Diagnostics*, vol. 12, no. 6, pp. 1–11, 2022, doi: 10.3390/diagnostics12061371.

[5] A. Rezvantalab, H. Safigholi, and S. Karimijeshni, "Dermatologist Level Dermoscopy Skin Cancer Classification Using Different Deep Learning Convolutional Neural Networks Algorithms," *arXiv Prepr. arXiv*, Oct. 2018, doi: 10.48550/arxiv.1810.10348.

[6] S. K. Datta, M. A. Shaikh, S. N. Srihari, and M. Gao, "Soft Attention Improves Skin Cancer Classification Performance," *Lect. Notes Comput. Sci. (including Subser. Lect. Notes Artif. Intell. Lect. Notes Bioinformatics)*, vol. 12929 LNCS, pp. 13–23, 2021, doi: 10.1007/978-3-030-87444-5_2/FIGURES/2.

[7] E. Goceri, "Automated Skin Cancer Detection: Where We Are and the Way to the Future," *2021 44th Int. Conf. Telecommun. Signal Process. TSP 2021*, pp. 48–51, 2021, doi: 10.1109/TSP52935.2021.9522605.

[8] M. Salvi *et al.*, "DermoCC-GAN: A new approach for standardizing dermatological images using generative adversarial networks," *Comput. Methods Programs Biomed.*, vol. 225, p. 107040, 2022, doi: 10.1016/j.cmpb.2022.107040.

[9] Tian C, Zhang X, Lin JCW, Zuo W, Zhang Y, Lin CW. "Generative Adversarial Networks for Image Super-Resolution: A Survey". Published online April 28, 2022. doi:10.48550/arxiv.2204.13620

[10] Wang X, Xie L, Dong C, Shan Y. "Real-ESRGAN: Training Real-World Blind Super-Resolution with Pure Synthetic Data". Published online July 22, 2021. http://arxiv.org/abs/2107.10833

[11] Anran Liu, Yihao Liu, Jinjin Gu, Yu Qiaoand, and Chao Dong. "Blind image super-resolution: A survey and beyond". arXiv:2107.03055, 2021

[12] Ke Yu, Xintao Wang, Chao Dong, Xiaoou Tang, and Chen Change Loy. "Path-restore: Learning network path selection for image restoration". arXiv:1904.10343, 2019.

[13] Xintao Wang, Yu Li, Honglun Zhang, and Ying Shan. "Towards real-world blind face restoration with generative facial prior". In CVPR, 2021.

[14] Kelvin C.K. Chan, Xintao Wang, Xiangyu Xu, Jinwei Gu, and Chen Change Loy. "Glean: Generative latent bank for large-factor image super-resolution". In CVPR, 2021

[15] Xintao Wang, Ke Yu, Shixiang Wu, Jinjin Gu, Yihao Liu, Chao Dong, Yu Qiao, and Chen Change Loy. "Esrgan: Enhanced super-resolution generative adversarial networks". In ECCVW, 2018

[16] Jinjin Gu, Hannan Lu, Wangmeng Zuo, and Chao Dong. "Blind super-resolution with iterative kernel correction". In CVPR, 2019

[17] Pengxu Wei, Ziwei Xie, Hannan Lu, ZongYuan Zhan, Qixiang Ye amd Wangmeng Zuo, and Liang Lin. "Component divide-and-conquer for real-world image super-resolution". In ECCV, 2020.

[18] Xiaozhong Ji, Yun Cao, Ying Tai, Chengjie Wang, Jilin Li, and Feiyue Huang. "Real-world super-resolution via kernel estimation and noise injection". In CVPRW, 2020.

[19] Kai Zhang, Jingyun Liang, Luc Van Gool, and Radu Timofte. "Designing a practical degradation model for deep blind image super-resolution". arXiv preprint arXiv:2103.14006, 2021.

[20] Tschandl P, Rosendahl C, Kittler H. "Data descriptor: The HAM10000 dataset, a large collection of multi-source dermatoscopic images of common pigmented skin lesions". *Sci Data*. 2018;5:1-9. doi:10.1038/sdata.2018.161

[21] Combalia M, Codella NCF, Rotemberg V, et al. "BCN20000: Dermoscopic Lesions in the Wild". Published online August 6, 2019. doi:10.48550/arxiv.1908.02288

[22] Buslaev A, Iglovikov VI, Khvedchenya E, Parinov A, Druzhinin M, Kalinin AA. "Albumentations: Fast and Flexible Image Augmentations". doi:10.3390/info11020125

[23] Richard Shin and Dawn Song. "Jpeg-resistant adversarial images". In NeurIPS Workshop on Machine Learning and Computer Security, 2017.

[24] Venkatanath N, Praneeth D, Maruthi Chandrasekhar Bh, S. S. Channappayya and S. S. Medasani, "Blind image quality evaluation using perception based features," 2015 Twenty First National Conference on Communications (NCC), Mumbai, India, 2015, pp. 1-6, doi: 10.1109/NCC.2015.7084843.

Altered EEG amplitude coupling correlates to cognitive dysfunction in idiopathic rapid-eye-movement sleep behavior disorder patients

M. Roascio[1], R. Trò[1], D. Arnaldi[2,3], F. Famà[2,3], P. Mattioli[2,3], K. Jung[4,5,6], and G. Arnulfo[1,7,8]
[1] *Department of Informatics, Bioengineering, Robotics and System engineering, University of Genoa, Genoa, Italy.*
[2] *DINOGMI, University of Genoa, Genoa, Italy*
[3] *IRCCS Ospedale Policlinico San Martino, Genoa, Italy*
[4] *Department of Neurology, Seoul National University Hospital, Seoul, South Korea*
[5] *Program in Neuroscience, Seoul National University College of Medicine, Seoul, South Korea*
[6] *Neuroscience Research Institute, Seoul National University College of Medicine, Seoul, South Korea*
[7] *Neuroscience Center, Helsinki Institute of Life Science (HiLife), University of Helsinki, Helsinki, Finland*
[8] *RAISE Ecosystem, Genova, Italy*

***Abstract*— Prodromal stages of Neurodegenerative disorders represent an important phase of disease progression where novel therapeutic options might still be effective. Rapid-eye-movement sleep behaviour disorder (RBD is considered one of the principal prodromal conditions of synucleinopathies such as Parkinson's disease. In this longitudinal study, we aimed at quantifying the alterations of electroencephalographic (EEG) network-like metrics due to disease progression. Amplitude correlation and phase synchronization has been quantified using narrow-band high-density EEG recordings in 33 people with idiopathic RBD at distinct visits. We showed that phase synchrony and amplitude correlations are stronger in idiopathic RBD compared to age-matched healthy controls. A weaker amplitude correlation is linked to worst cognitive functions. Finally, our results show a significant (uncorrected) reduction of amplitude correlation but not phase synchronization over time with disease progression. Altogether these results represent additional evidence on the effects of disease progression in idiopathic RBD population.**

***Keywords*—cognitive impairment, rapid eye-movement sleep behavior disorder, large-scale network coupling.**

I. Introduction

RAPID eye-movement sleep behavior disorder (RBD) is a parasomnia associated with increased muscular tone as well as abnormal and potentially harmful movements occurring as dream enactments during REM sleep [1].
RBD can be categorized in idiopathic (iRBD) or symptomatic, that is in combination with other neurological disorders [2], and people with iRBD have a >70% chance of developing Parkinson's disease (PD), dementia with Lewy bodies (DLB), and multiple systemic atrophy [3], [4]. Clinical RBD symptoms include cognitive decline [3], impaired olfaction and color discrimination [5], abnormal metabolic network activity [6], and reduced striatal dopamine transporter (DaT) uptake [4]. Recently, numerous studies have focused on exploring the predictive value of iRBD diagnosis for α-synucleinopathies. Compared to healthy subjects, iRBD patients show a slowing of the power spectrum of the electroencephalographic (EEG) signal towards the lower frequencies [7]. However, the power spectrum is a frequency-wise measure of the amplitude distribution of individual cortical populations and lacks information about large-scale network interactions. Neurodegenerative disorders are recently considered as network pathologies, where the connectivity between different brain areas could provide a better understanding of the disorder and its progression. To investigate how RBD affects the large-scale network coupling, previous studies investigate phase synchronization, which quantifies the synchrony of the relative phase between two simultaneous signals, and amplitude correlation, which measures the correlation of the envelopes of two simultaneous oscillatory signals [8], [9]. These studies report an increment of the phase synchronization in alpha band in iRBD patients over time, and a reduction of the amplitude correlation [9]. Moreover, a weaker phase synchronization in the delta band is characteristic of iRBD compared to healthy subjects [8].
Anomalies in large-scale network coupling are reported also in a prodromal stage of Alzheimer's disease, where an increase of phase synchronization in the theta band are associated with a worsening of the cognitive functions [10]. Thus, we hypothesized that anomalies in phase synchronization and amplitude correlation could be common features in the prodromal stages of several neurodegenerative diseases. However, it remains unclear how such electrophysiological biomarkers evolve over time in prodromal synucleinopathies.
Here, we enrolled a longitudinal cohort of 33 iRBD patients to investigate disease progression-related evolution in large-scale brain network couplings through high-density electroencephalography. In addition, we correlated our findings with longitudinal clinical scores to observe whether altered large-scale network coupling are linked to a worsening of the motor and cognitive function in patients with iRBD.

II. Methods

A. Data Acquisition

A total of 33 people with iRBD (12 female; mean age 68,21 ± 7,21 years at the first clinical evaluation) were investigated at baseline and at 1st follow-up (after 17,78 ± 8,58 months), including clinical and EEG assessments. Out of these patients, a 11-subject subset also underwent a 2nd follow-up session (after 37,60 ± 11,36 months from baseline). The diagnosis of iRBD was made according to international criteria (ICSD 3) and was confirmed by overnight video-polysomnography. As a control dataset, we recruited 17 healthy people (8 female; mean age 68,48 ± 3,80 years). In accordance with the Declaration of Helsinki, all participants gave informed consent

before entering the study, which was approved by the local ethics committee.

Clinical assessment. Patients underwent general and neurological examinations to rule out other neurological and psychiatric disorders. Baseline clinical evaluations included (1) the Mini-Mental State Examination (MMSE) as a global measure of cognitive impairment; (2) the Movement Disorder Society-sponsored revision of the Unified Parkinson's Disease Rating Scale, motor section (MDS-UPDRS-III) to evaluate the presence of parkinsonian signs.

Electrophysiological signal recording. All people with iRBD underwent HD-EEG evaluation (sampling frequency = 400 Hz, electrode number = 60, cap = Grass Telefactor system, Grass Technologies, Quincy, MA) during relaxed wakefulness, late in the morning to minimize drowsiness. For each session, the acquisition protocol consisted of approximately 5 minutes of resting-state characterized by the alternance of 30 seconds with eyes-open and 30 seconds with eyes closed. Electrodes were placed according to the 10–10 International System. An EEG technician monitored the recording session to maintain a constant level of vigilance over the patient, prevent sleep and preserve a high signal quality. For each patient and for both visits, we selected the eyes closed condition for further analyses.

B. Data Preprocessing

We carried out data preprocessing and analysis in MATLAB, R2021a, using Brainstorm [11] and custom scripts. As a first step, we preprocessed the EEG data applying a zero-phase infinite impulse response notch filter (order 2) to remove the power line noise (50 Hz). Later, we excluded all channels and time windows showing artifactual activity using a combination of visual inspection and independent component analysis (ICA)-based rejection.

We thus removed an average of 0.15 ± 0.66 channels from each subject (range: minimum 0, maximum 4), and we interpolated those bad channels using spline method (kernel size: 4 cm). We used a bandpass finite impulse response filter (1–80 Hz, Kaiser window, order 1858) to suppress the low- and high-frequency artifacts.

For all cleaned datasets, we transformed the referenced EEG to scalp current densities (SCDs) [12], [13] for all clean sensors with the spline method (lambda 0.00001, order 4, degree 14).

C. Phase and amplitude correlation analyses

We computed phase synchronization and amplitude correlations across a range of frequencies for all channel pairs and for all sessions in both groups of subjects. We analyzed the broadband SCD time series by means of a time-frequency decomposition using 30 narrowband Morlet wavelets in the 2 - 70 Hz range (number of cycles = 5) [14].

To minimize the detrimental effect of volume conduction, signal mixing, and source leakage significantly on phase synchronization analyses of sensor EEG data [15], [16], we adopted the weighted phase-lag index [15] (wPLI), given its insensitivity to volume conduction and higher statistical power [15], [16] than other phase synchronization metrics. Similarly, as a volume conduction-insensitive measure, we adopted the orthogonalized Correlation Coefficient (oCC), which is defined as the Pearson correlation coefficient between two orthogonalized time series [17]. Both wPLI and oCC are limited in the [0, 1] range, where 1 represents the maximum of phase synchronization or amplitude correlation.

D. Statistical Analysis

First, we aimed to investigate whether EEG features showed significant changes between healthy controls and iRBD patients at baseline. To this end, we used the nonparametric Wilcoxon test. Later, we explored the difference in the wPLI and the oCC of subjects with iRBD to assess putative disease progression effects on large-scale brain networks. We wanted to observe whether the mean difference in the observed wPLI/oCC data was statistically significant. To assess any potential discrepancy between baseline and 1st follow-up, we resorted once again to Wilcoxon test. Conversely, we used Kruskal-Wallis as non-parametric test to inspect differences in EEG metrics between baseline, 1st, and 2nd follow-up.

As a last statistical analysis, we investigated whether there was a correlation between the altered phase synchronization and amplitude correlation with clinical data in subjects with RBD. Hence, we applied Kendall's coefficient of rank correlation tau-sub-b to these data. We FDR-adjusted all resulting p values with the Benjamini–Hochberg (BH) method.

III. Results

A. Global phase synchronization and amplitude correlation change with disease progression

We first investigated how phase synchronization and amplitude correlation changed between healthy controls and iRBD patients at baseline. We observed an increase in the strength of both populations averaged wPLI and oCC for subjects with iRBD compared to controls in theta (5-7 Hz) band (Figure 1). Nonetheless, these significant differences did not survive with BH correction ($p < 0.05$ before correction).

We then inspected how phase synchronization and amplitude correlation changed between baseline and subsequent follow-ups as for iRBD patients. In detail, we found no differences either in wPLI or in oCC between baseline and 1st follow-up (Figure 1b and 1e). Conversely, oCC in delta-theta (2-7 Hz) band exhibited a significant decrease (once again only before BH correction) over time, among recording sessions (Figure 1f). Altogether, these findings bring out the global functional modifications associated with disease progression in subjects affected by iRBD.

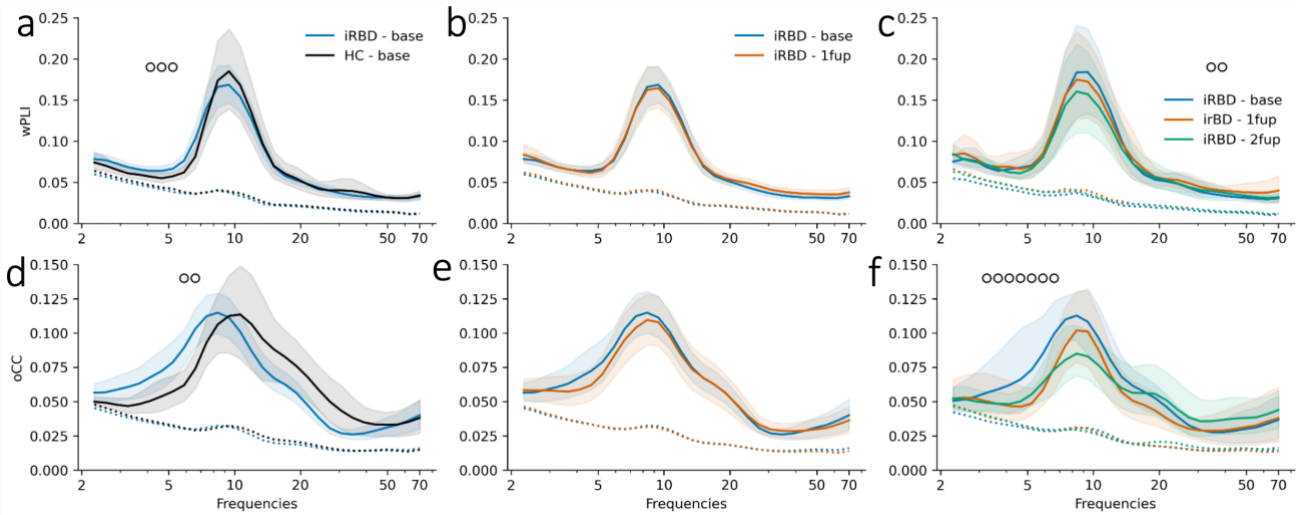


Figure 1: **Global phase synchronization and amplitude correlation change with the disease progression**. Strength of population averaged wPLI (a-c) and oCC (d-f) in iRBD patients at baseline (blue), at 1st follow-up (red), and at 2nd follow-up (red), and in HC subjects (black). Shaded areas represent confidence intervals around population mean (bootstrap, N = 1,000). Dashed lines represent surrogate averages. Empty black circles represent the significant frequency points with *(a,b,d,e)* Wilcoxon rank sums test *or (c,d) Kruskal-Wallis test*. Filled black circles represent the significant frequency points after Benjamini-Hochberg correction.

B. Amplitude correlation values correlate with clinical scores

Finally, we asked whether phase synchronization and amplitude correlation values correlate with the clinical scores. We thus computed the age-adjusted Kendall's coefficient of rank correlation tau-sub-b of clinical scores with wPLI and oCC in delta-theta, alpha-beta, and gamma bands (Figure 2), pooling subjects and visits. We observed a direct significant correlation between oCC values in alpha-beta band and MMSE score (p = .006; BH corrected).

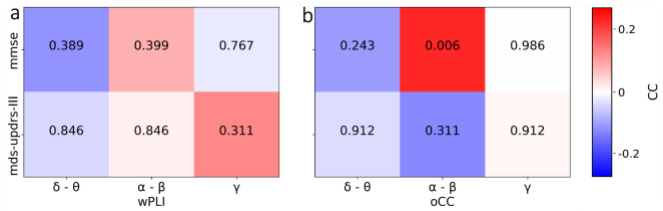


Figure 2: **Phase synchronization and amplitude correlation values correlate with clinical scores.** Age-adjusted Kendall's coefficient (CC) of rank correlation tau-sub-b with Benjamini–Hochberg correction of wPLI and oCC in delta-theta, alpha-beta, and gamma band with clinical scores. The color represents the correlation values and the number in each box represents the false discovery rate (FDR) corrected p values.

IV. Discussion

In this study, we investigated advanced electrophysiological markers in a longitudinal study of iRBD patients. They were examined at the time of iRBD diagnosis and in two following follow-ups.

Compared to other works about this topic [8], [9], the great advancement of the current study consists in increasing the number of subjects as well as of time-points under analysis, thus helping to clarify the clinical trajectories of iRBD patients with disease progression.

First, the significant increase in phase synchronization and amplitude correlation in the theta band found in iRBD patients compared to healthy subjects (Figure 1a,d) is in agreement with previous literature [9].

Moreover, we observed a significant decrease of amplitude correlation in the theta band at subsequent visits compared with the baseline (Figure 1e,f).

Conversely, the significant increase of phase synchronization in alpha band over time observed in [9] and reflecting disease progression [10], [18], [19] is not replicated here.

A potential motivation for this discrepancy may lie in the difference in (i) the kind of recording protocol, (ii) the recording duration, and (iii) the time interval of follow-ups between these two longitudinal studies.

On the other hand, significant positive correlation between oCC in the alpha-beta and MMSE score proposes that amplitude correlation is linked to cognitive function (Figure 2b). Observing that oCC decreases in the alpha band with disease progression (Figure 1e,f), we might speculate that a decrease of amplitude correlation in the alpha band reflects a worsening of the cognitive functions in iRBD patients.

V. Conclusion

In this work we inspected the modifications in phase synchronization and amplitude correlation in iRBD patients at three distinct time points using high-density EEG and correlating the data with longitudinal cognitive scores. Figuring out the coherent time-based evolution of joint clinical and EEG biomarkers in iRBD could deepen our knowledge about prodromal stages of synucleinopathy, possibly supporting in identification of those patients who are more likely candidates for neuroprotective treatment. Our results suggest that a reduction of amplitude correlation in the alpha band might reflect an electrophysiological correlation of the cognitive decline, highlighting the onset of pathological mechanisms due to the neurodegeneration.

REFERENCES

[1] C. H. Schenck, S. R. Bundlie, M. G. Ettinger, and M. W. Mahowald, "Chronic behavioral disorders of human REM sleep: A new category of parasomnia," *Sleep*, vol. 9, no. 2, pp. 293–308, 1986, doi: 10.1093/sleep/9.2.293.

[2] E. K. St Louis, A. R. Boeve, and B. F. Boeve, "REM Sleep Behavior Disorder in Parkinson's Disease and Other Synucleinopathies," *Mov. Disord.*, vol. 32, no. 5, pp. 645–658, 2017, doi: 10.1002/mds.27018.

[3] R. B. Postuma *et al.*, "Risk and predictors of dementia and parkinsonism in idiopathic REM sleep behaviour disorder: A multicentre study," *Brain*, vol. 142, no. 3, pp. 744–759, 2019, doi: 10.1093/brain/awz030.

[4] D. Arnaldi *et al.*, "Dopaminergic imaging and clinical predictors for phenoconversion of REM sleep behaviour disorder," *Brain*, vol. 144, no. 1, pp. 278–287, 2020, doi: 10.1093/brain/awaa365.

[5] R. B. Postuma, J. F. Gagnon, M. Vendette, C. Desjardins, and J. Y. Montplaisir, "Olfaction and color vision identify impending neurodegeneration in rapid eye movement sleep behavior disorder," *Ann. Neurol.*, vol. 69, no. 5, pp. 811–818, 2011, doi: 10.1002/ana.22282.

[6] S. K. Meles *et al.*, "The Metabolic Pattern of Idiopathic REM Sleep Behavior Disorder Reflects Early-Stage Parkinson Disease," *J. Nucl. Med.*, vol. 59, no. 9, pp. 1437–1444, 2018, doi: 10.2967/jnumed.117.202242.

[7] M. L. Fantini *et al.*, "Slowing of electroencephalogram in rapid eye movement sleep behavior disorder," *Ann. Neurol.*, vol. 53, no. 6, pp. 774–780, 2003, doi: 10.1002/ana.10547.

[8] J. S. Sunwoo *et al.*, "Altered functional connectivity in idiopathic rapid eye movement sleep behavior disorder: A resting-state EEG study," *Sleep*, vol. 40, no. 6, 2017, doi: 10.1093/sleep/zsx058.

[9] M. Roascio *et al.*, "Phase and amplitude electroencephalography correlations change with disease progression in people with idiopathic rapid eye-movement sleep behavior disorder," *Sleep*, 2022, doi: 10.1093/sleep/zsab232.

[10] S. Pusil, M. E. López, P. Cuesta, R. Bruña, E. Pereda, and F. Maestú, "Hypersynchronization in mild cognitive impairment: The 'X' model," *Brain*, vol. 142, no. 12, pp. 3936–3950, 2019, doi: 10.1093/brain/awz320.

[11] F. Tadel, S. Baillet, J. C. Mosher, D. Pantazis, and R. M. Leahy, "Brainstorm: A user-friendly application for MEG/EEG analysis," *Comput. Intell. Neurosci.*, 2011, doi: 10.1155/2011/879716.

[12] F. Perrin, J. Pernier, O. Bertrand, and J. F. Echallier, "Spherical splines for scalp potential and current density mapping," *Electroencephalogr. Clin. Neurophysiol.*, vol. 72, no. 2, pp. 184–7, 1989, doi: 10.1016/0013-4694(89)90180-6.

[13] F. Perrin, J. Pernier, O. Bertrand, and J. F. Echallier, "Erratum: Spherical splines for scalp potential and current density mapping (Electroenceph. Clin. Neurophysiol. 1989, 72: 184-187)," *Electroencephalography and Clinical Neurophysiology*. 1990.

[14] C. Torrence and G. P. Compo, "A Practical Guide to Wavelet Analysis," *Bull. Am. Meteorol. Soc.*, vol. 79, no. 1, pp. 61–78, 1998, doi: 10.1175/1520-0477(1998)079<0061:APGTWA>2.0.CO;2.

[15] M. Vinck, R. Oostenveld, M. Van Wingerden, F. Battaglia, and C. M. A. Pennartz, "An improved index of phase-synchronization for electrophysiological data in the presence of volume-conduction, noise and sample-size bias," *Neuroimage*, vol. 55, no. 4, pp. 1548–1565, 2011, doi: 10.1016/j.neuroimage.2011.01.055.

[16] J. M. Palva *et al.*, "Ghost interactions in MEG/EEG source space: A note of caution on inter-areal coupling measures," *Neuroimage*, vol. 173, pp. 632–643, 2018, doi: 10.1016/j.neuroimage.2018.02.032.

[17] J. F. Hipp, D. J. Hawellek, M. Corbetta, M. Siegel, and A. K. Engel, "Large-scale cortical correlation structure of spontaneous oscillatory activity," *Nat. Neurosci.*, vol. 15, no. 6, pp. 884–90, 2012, doi: 10.1038/nn.3101.

[18] R. Bajo *et al.*, "Differential Patterns of Connectivity in Progressive Mild Cognitive Impairment," *Brain Connect.*, vol. 2, no. 1, pp. 21–24, 2012, doi: 10.1089/brain.2011.0069.

[19] M. E. López *et al.*, "Alpha-band hypersynchronization in progressive mild cognitive impairment: A magnetoencephalography study," *J. Neurosci.*, vol. 34, no. 44, pp. 14551–14559, 2014, doi: 10.1523/JNEUROSCI.0964-14.2014.

Validating biomedical and clinical data via an annotations based framework: experiences within the PON VQA project.

B. Puccio[1], U. Lomoio[1], R. Giancotti[1], M. Cannistrà[1], S. Flesca[2],
F. Scala[2], G. Tradigo [3], P.H. Guzzi[1], P. Veltri[2], P. Vizza[1]
[1] *Dept. of Surgical and Medical Sciences, Magna Graecia University*
[2] *Dept. of Computer Engineering, Modeling, Electronics, and Systems Engineering, University of Calabria*
[3] *Dept. of Computer Science, eCampus University, Novedrate*

***Abstract*—Machine learning (ML) empowered software tools play a key role in assisting and supporting physicians in clinical procedures, diagnosis and follow-up. These tools analyze data extracted by the biomedical instruments to study diseases or effects of drugs on a large population of patients enabling precision and personalized medicine. In this paper, we present the definition and the implementation of a system based on machine learning algorithms to perform semi-automatic features annotation, question answering and data enrichment. The software prototype will is currently tested in a real clinical scenario in the University Hospital.**

***Keywords*—Artificial intelligence, machine learning, features annotation, question answering.**

I. Introduction

Currently, the introduction of novel technologies for the analysis of patients is producing a large amount of data. These data are heterogeneous both in format (from images to time series) and in dimension (from few kilobytes to gigabytes). These data represents a big challenge for the machine learning domain, in order to develop efficient models of analysis for producing medical relevant knowledge.

Consequently there is the need to integrate and annotate data to create high-quality training sets for machine learning models applied in different clinical domains [1]. In bioimages or biosignals analysis, tools for annotation and semi-automatic enrichment of datasets are useful to implement a continuous cycle of metaparameters exploration, supervised by a domain expert [2], [3]. In this way, it is possible to generate large number of high-quality datasets allowing to train machine learning models to make contributions in the research. A typical application example in the bioimages is the research of areas of neighboring voxels having similar features, e.g. from a statistical point of view. Another application context concerns the biomedical signals deriving from electrophysiological tests, in which a number of derivations are generated by measuring the electrical intensity of the cardio-circulatory system [4], [5] The development of new advanced semi-automatic methods and tools for tagging and annotating features of interest in the healthcare domain has the potential to improve the effectiveness of diagnostic tools based on artificial intelligence, operating on two different aspects: (i) the quality improvement of datasets obtained by introducing an intervention by the human expert, assisted by the tools and aimed at refining the tagging of the features which can lead to an increase in the quality of the data and (ii) the semi-automatic generation of large datasets (Big Data) obtained through automatic feature extraction tools.

We present the design and the implementation of a system for semi-automatic features annotation, question answering and data enrichment. Six modules have been proposed in the system to collect and analyze clinical data from different sources. The aim is to implement dataset enrichment and refinement functions allowing the execution of expert-assisted experiments in specific case studies. This system is based on machine learning algorithms and it represents the prototype result of the VQA - Validated Question Answering project (Horizon 2020 – PON 2014-2020 FESR).The system acquires main information sources in the health domain and the extracted data are examined and used on the study and the definition of models for extracting information from data sources of health interest, supporting physician in their clinical activity and research.

II. Prototype architecture

The architecture of the proposed system is shown in Figure 1. System has three layers: Connection Layer, ML Service Layer and Domain Specific Layer.

Connection Layer includes Audit Connector and Data Importers modules, to external audit and data import from external sources, respectively.

ML Service Layer includes Active Learning (AL), Sequence Analysis, Bio-images Analysis and ad-hoc Analysis cores, to tag, annotate and extract relevant information. These cores have been designed to a specific type of information and data.

Domain Specific Layer includes vertical modules to offer services in different application domains. Currently we included following modules: (i) Dismetabolic data annotation, (ii) Bioimage Annotation, (iii) Maxillo-Facial Images Annotation, (iv) ElectroCardiograms Anomaly Detector, (v) Protein Annotation, and (vi) Active Learning.

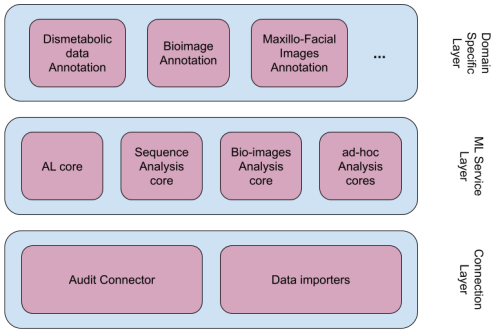


Fig. 1: Integrated system architecture for the annotation and information extraction.

Dismetabolic Data Annotation module integrates tagging techniques to extract relevant data from dismetabolic signal analysis [6] This module is useful in the evaluation of diabetes that represents one the leading cause of death with an exponential growth in recent years. In this context, the integration of heart rate data and glycemic data has been used to predict and/or follow hypo- or hyper-glycemic events.

Bioimage Annotation module performs annotations on different data sources enriching the overall information. The framework is easily usable and it offers a tool for interactive visualization, annotation and data exploration to support physicians in their daily clinical practice [7],[8].

Maxillo-Facial Images Annotation module performs graphic and textual annotations on maxillo-facial images (e.g. Magnetic Resonance or Computer Tomography Images) 2. Starting from the annotations, many tasks can be executed as meta-data extraction, image manipulation, query execution, and output visualization [9].

Electrocardiograms Anomaly Detector module uses semi-supervised learning techniques to identify points of interest within a 12-leads ECG signal synchronized with a 3-channels photoplethysmography (PPG) signal. This approach is based on the use of an Autoencoder architecture. It is used to reconstruct signal window, and to calculate its relative error due to signal reconstruction, needed to identify any possible anomaly.

Protein Annotation module allows to study and analyze protein structure by using the protein contact network (PCN) [10]. It helps to identify putative allosteric pathways and regions in protein structures. It allow the user to hypothesize the functional effect of the mutations, and (iii) recognize functional domains (communities or clusters) in proteins [11].

Active Learning module allows “learning-active-learning” algorithm execution. Initially, this technique trains a neural network with the available labeled examples. Then an initial set of samples is selected from the set of unlabeled examples using random sampling, and submitted to the clinical expert to be labeled, thus obtaining a new set of labeled examples. The neural network is trained with the labeled data, a classifier is trained using neural network gradients in order to identify the most representative examples and it is used to select the "best" examples [12].

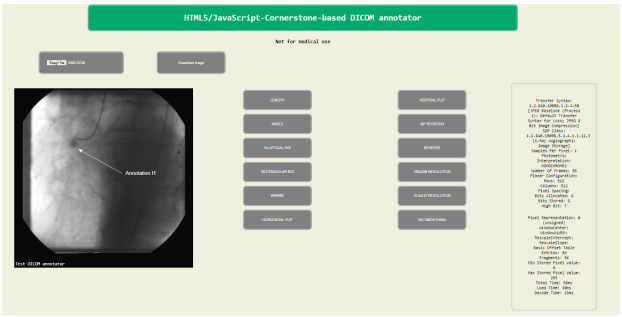


Fig. 2: Graphical user interface for Oral surgery Annotation module, with an imported DICOM image.

III. Case Studies

Experimental tests have been performed on the system to verify and validate the proposed solutions, also thank to the collaboration between biomedical and bioinformatics engineers with medical-clinical specialistis. Each module has been tested and it is currently in use at University Hospital of Catanzaro for research purposes by using anonymized data.

Dismetabolic Data Annotation module has been tested on patients with type 1 diabetes on data from a continuous blood glucose monitoring (CGM) system manufactured by DEXCOM. Results demonstrated that the module is a useful tool to identify interesting patterns from glucose daily measured values.

Testing of *Maxillo-Facial Images Annotation* module was conducted on carotid district images, for the identification of parotid tumors. The dataset consisted of a set of Magnetic Resonance images belonging to patients with neoplastic disease of the parotid gland compared with a set of control subjects. The tool allows to import and view the DICOM P10 images of interest, apply one or more annotations or transformation functions, and obtain information regarding the metadata present in the DICOM file.

All the changes made to the image can be saved in a special database to be available later. Also, the user can convert and save images in jpeg format. Furthermore, the tool allows to query datasets and this function could be very useful to the expert to study clinical cases and compare them with each other or with control subjects .

Electrocardiograms anomaly Detector have been tested by using ECG + PPG signals at 500 Hz and 15 channels (12 ECG channels and 3 PPG channels). To evaluate the module, synthetic ECG + PPG signals have been generated by the SIMARR3 arrhythmia simulator [13]. This simulator is capable of simulating normal ECG + PPG signals or containing atrial fibrillation, tachycardia and bradycardia events and at a specific sampling frequency.The results demonstrate that the autorencoder is able to perform a fairly precise identification of anomalies due to (1) atrial fibrillation events without noise,

to (2) a low-frequency noise component (breathing noise) or to (3) a component of noise deriving from muscle activity (EMG).

Protein annotation module implents Protein Contact Network Miner tool (PCN-Miner) [10], [11]. Its testing was directed towards three different case studies, relating to the study of the Spike protein of the SARS-CoV-2 virus [14], using the Protein contact network paradigm. The dataset used for test phase consists of the SARS-CoV-2 genomic sequences present in the GISAID database [16] and of the structures of main variants of the Spike protein of the virus in the RCSB Protein Data Bank [17].

Active Learning module was tested in the clinical setting on a dataset for the identification of melanoma in moles. The dataset was generated by the International Skin Imaging Collaboration (ISIC) [15] and the images come from the following sources: Hospital Clínic de Barcelona, Medical University of Vienna, Memorial Sloan Kettering Cancer Center, Melanoma Institute Australia , The University of Queensland and University of Athens Faculty of Medicine. The model obtained from training with this dataset will be able to predict a binary target for each image. In training data, 0 indicates the benign lesion and 1 indicates the malignant one.

IV. Conclusion

In this work we present a system based on machine learning algorithms aiming to perform semi-automatic features annotation, question answering and data enrichment. It consists of three layers: the Connection Layer, containing various modules dedicated to connectivity with services external to the system, the ML Service Layer, containing the basic services for labeling and extracting information based both on machine learning techniques and explicitly dedicated to a particular type of information, and the Domain Specific Layer containing, services specific to a particular application domain. Our aim is to provide a powerful tool, useful in healthcare domain for clinical decision support.

Acknowledgement

This work was supported by Validated Question Answering - VQA Project (Horizon 2020 – PON 2014-2020 FESR), and partially supported by PON “Ricerca e Innovazione” 2014-2020 (PON R&I)

References

[1] A. Astorino, A. Fuduli, P. Veltri, E. Vocaturo, On a recent algorithm for multiple instance learning. Preliminary applications in image classification, 2017 IEEE International Conference on Bioinformatics and Biomedicine (BIBM), 2017.

[2] J. Kumar Das, G. Tradigo, P. Veltri, P. H Guzzi, S. Roy, Data science in unveiling COVID-19 pathogenesis and diagnosis: evolutionary origin to drug repurposing, Briefings in Bioinformatics, 2021.

[3] Tradigo, G., De Rosa, S., Vizza, P., Fragomeni, G., Guzzi, P. H., Indolfi, C., Veltri, P., Calculation of intracoronary pressure-based indexes with jlabchart. Applied Sciences, 12(7), 3448, 2022.

[4] P. Vizza, A. Curcio, G. Tradigo, C. Indolfi, P. Veltri, A framework for the atrial fibrillation prediction in electrophysiological studies, Computer methods and programs in biomedicine, 2015.

[5] Palumbo, A., Calabrese, B., Cocorullo, G., Lanuzza, M., Veltri, P., Vizza, P., Gambardella, A., Sturniolo, M., A novel ICA-based hardware system for reconfigurable and portable BCI. International Workshop on Medical Measurements and Applications, 95-98, IEEE, 2009.

[6] P. Vizza, G. Tradigo, R. Giancotti, F. Scala, P.H. Guzzi, C. Ierace, S. Flesca, P. Veltri, On the identification of PoIs in glucosimeter data, 2022 IEEE 10th International Conference on Healthcare Informatics (ICHI), 2022.

[7] R. Giancotti, U. Lomoio, P. Veltri, P.H. Guzzi, P. Vizza, A machine-learning based tool for bioimages managing and annotation, 2022 IEEE International Conference on Bioinformatics and Biomedicine (BIBM), 2022.

[8] P. Vizza, M. Cannistra, G. Tradigo, G.L. Cascini, P.H. Guzzi, P. Veltri, DeLaBE: A Deep Learning architecture for Bio-images enhancing, 2022 IEEE 10th International Conference on Healthcare Informatics (ICHI), 2022.

[9] P. Vizza, G. Tradigo, I. Brunelli, P. Veltri, A Tool for clinical data annotation of parotid neoplasia, 2021 IEEE International Conference on Bioinformatics and Biomedicine (BIBM), 2021.

[10] P.H. Guzzi, L. Di Paola, A. Giuliani, P. Veltri, PCN-Miner: An open-source extensible tool for the Analysis of Protein Contact Networks. Bioinformatics, 2021

[11] J.C. Galicia, P.H. Guzzi, F.M. Giorgi, A.A. Khan, Predicting the response of the dental pulp to SARS-CoV2 infection: a transcriptome-wide effect cross-analysis. Genes and Immunity, 2020.

[12] S. Flesca, D. Mandaglio, F. Scala, A. Tagarelli Learning to Active Learn by Gradient Variation Based on Instance Importance. 26th International Conference on Pattern Recognition (ICPR), 2022.

[13] A. Solosenko, A. Petrėnas, B. Paliakaitė, L. Sornmo, V. Marozas, Model for Simulating ECG and PPG Signals with Arrhythmia Episodes, 2021.

[14] Y. Shu, J. McCauley, GISAID: Global initiative on sharing all influenza data - from vision to reality, Euro Surveill, 2017.

[15] N. C. F. Codella, D. Gutman, M. Emre Celebi,B. Helba, M, A. Marchetti, S. W. Dusza, A. Kalloo, K. Liopyris, N. Mishra, H. Kittler, A. Halpern, Skin lesion analysis toward melanoma detection: A challenge at the 2017 International symposium on biomedical imaging (ISBI), hosted by the international skin imaging collaboration (ISIC), 2018 IEEE 15th International Symposium on Biomedical Imaging (ISBI 2018), 2018.

[16] P. Bogner, I. Capua, D. J. Limpan, N. J. Cox, others, A global initiative on sharing avian flu data, Nature, 2006.

[17] H. M. Berman, J. Westbrook, Z. Feng, G. Gilliland, T. N. Bhat, H. Weissig, I. N. Shindyalov, P. E. Bourne, The Protein Data Bank, Nucleic Acids Research, 2000.

Drivers' mental workload assessment based on machine learning applied to multimodal physiological data

D. Perpetuini[1], D. Cardone[2], M. Tritto[3], S. Nocco[3], A. Tiberio[3], A. Merla[2]
[1] *Department of Neurosciences, Imaging and Clinical Sciences, University "G. d'Annunzio" of Chieti-Pescara, Chieti, Italy*
[2] *Department of Engineering and Geology, University "G. d'Annunzio" of Chieti-Pescara, Pescara, Italy*
[3] *Next2U srl, Pescara, Italy*

***Abstract*— Mental workload (MW) refers to the level of mental effort required to accomplish multiple concurrent tasks. Due to its correlation with the risk of traffic accidents, the assessment of MW is crucial for Advanced Driver-Assistance Systems. In this study, participants were given two cognitive tests (the Digit Span Test, DST, and the Ray Auditory Verbal Learning Test, RAVLT) while driving in a simulated environment. The tests were chosen to elicit different levels of MW from the drivers based on the task's difficulty. Electroencephalography (EEG), functional near-infrared spectroscopy (fNIRS), and heart rate variability (HRV) were used to assess features indicative of the psychophysiological states of the participants in order to feed a Support Vector Machine (SVM) classifier. Multimodal EEG + fNIRS + HRV feature-based classifiers performed better with respect to SVM fed by unimodal features (DST: 69.4% accuracy, RAVLT: 85.5% accuracy). These results showed the possibility of assessing the MW levels of drivers with high accuracy through multimodal physiological acquisitions, which could be easily implemented in ADAS applications, driving competitions, and automotive cockpit neuroergonomics.**

***Keywords*—Electroencephalography (EEG), functional near infrared spectroscopy (fNIRS), Heart Rate Variability (HRV), ADAS systems.**

I. Introduction

The underestimation of a driver's mental workload (MW) is a common cause of traffic accidents, which are a leading cause of death and injury [1]. Consequently, advanced driver assistance systems (ADAS) aim to predict excessive MW to prevent traffic accidents. According to the National Highway Traffic Safety Administration (NHTSA), the relationship between the driver's psychophysiological state and driving performance is direct. In this light, monitoring the driver's mental state is essential for enhancing road safety.

The psychophysiological state of a driver could be assessed by evaluating the driving errors made while doing the task or using questionnaires pertaining to the perception of the gravity of the task completed (e.g., NASA-TLX or the SWAT questionnaires) [2]. Moreover, the monitoring of the driver's central and autonomous neural systems, whose activity is indicative of the MW, can be performed by using neurophysiological methods during driving tasks.

Consequently, a number of machine learning (ML) and artificial intelligence (AI) frameworks have been developed to classify the psychophysiological condition of drivers based on behavioural characteristics (such as blinking frequency, percentage of eye closure, and yawning) and physiological signals (e.g., electrocardiography, ECG [3], photoplethysmography, PPG [4], electroencephalography, EEG [5], functional near infrared spectroscopy [6], infrared thermography [7,8]).

In detail, the fNIRS is a technique able to infer the functional modulations of the oxyhaemoglobin (HbO) and deoxyhaemoglobin (HbR) cortical concentrations [9]. Concerning the EEG, it is a scalp-located technique able to measure electrical brain activity. Frequency-domain approaches are often employed for EEG data analysis since the power spectral density (PSD) of different EEG frequency bands modulates according to the MW [5]. Regarding the ECG, it is possible to extract the temporal distance of successive R-peaks from the ECG signal, hence providing information about the Heart Rate Variability (HRV), which modulates secondary to the MW level [3].

Regarding MW classifications, it has been shown that multimodal approaches can enhance the performance of ML-based classifications [10]. Particularly, it has been demonstrated that combined EEG-fNIRS recordings are highly indicative of the drivers' MW [11].

To ensure driver comfort and avoid interference, contact sensors to collect physiological signals are typically avoided in common ADAS applications. However, these sensors are appropriate for racing applications, and cockpit design.

In this study, machine learning (ML) models based on multimodal measurements (EEG, fNIRS, and HRV) were developed to classify drivers' MW during the administration of two distinct cognitive tasks.

II. Material and Methods

A. Participants

Thirteen healthy adults (8 males, age range 19–42, mean 29.49, standard deviation 5.98) in possession of a valid driver's license participated in the experiment. Prior to the experimental sessions, the participants were properly instructed on the objective and procedure of the study, and they signed a Declaration of Helsinki-compliant informed consent form.

B. Experimental design

During the experimental sessions, a static driver simulator was utilized (Figure 1). The scenario was displayed on three 27-inch monitors with a total video resolution of 5760 ×1080 pixels. There was a 1.5-meter gap between the driver and the monitors. The drivers' horizontal view angle was 150 degrees.

The driving simulation software used was City Car Driving,

Home Edition, version 1.5.



Fig. 1: Driver simulator and City Car Driving, Home Edition software

The experimental protocol involved a 45-minute driving simulation in an urban setting. The experimental conditions were predetermined to ensure hazardous driving conditions and to deliver a reproducible experimental protocol to all study participants (i.e., Traffic density: 60%; Traffic behavior: Intense traffic; Pedestrian crossing the road in the wrong place: Frequently; Dangerous change of traffic: Frequently; Emergency braking of the car ahead: Frequently).

After fifteen minutes of baseline driving, two cognitive tests were administered to drivers in order to manipulate their MW relative to their baseline driving.

Specifically, the Digit Span Test (DST) is a cognitive test comprised of two distinct tasks that can evaluate short-term memory and working memory [12]. The participant was required to repeat sequences of digits presented verbally at a rate of one digit per second. The test began with a two-digit sequence, and a new set was presented each time the sequence was repeated correctly. If a participant could not recall a series, another of equal length was suggested. The test ended if the participant was unable to repeat two sequences of the same length. For the purposes of this study, the DST was administered both in the forward (repetition of digits in the same order as their presentation) and backward (repetition of digits in the reverse order of their presentation) versions.

The Rey Auditory Verbal Learning Test (RAVLT) is a cognitive task that can assess verbal learning and long-term memory [13]. It was administered by reading a list of 15 words to the participant at the rate of one word per second. At the conclusion of the reading, the participant was instructed to repeat as many words as possible, in any order. This procedure was repeated five times with the same word list, each time recording different elements. This phase of the examination is called Immediate Recall (ImmR). After a 15-minute interval during which the subject continued to drive, he/she was asked to recall as many words from the list as possible without the examiner restating the list. This second section of the RAVLT consisted of the Delayed Recall (DelR). Subsequently, the final portion of the test consisted of the Recognition (Rec) of the 15 words from the original list from a new list of 46 items. Then, the participant completed the test by driving for 10 minutes without further testing.

C. Data collection and analysis

The ADInstruments Powerlab system was used to record the ECG signals using the Standard Limb Leads configuration (i.e., electrodes placed on the right arm (RA), left arm (LA), and left leg (LL)). The ECG signals were acquired at a frequency rate of 1 kHz and band-pass filtered in the frequency band of [0.05–150] Hz. In addition, a notch filter (fnotch = 50 Hz) was used to eliminate the artifact caused by the mains power supply. Six features of HRV were computed from the ECG signal throughout the experimental phases: mean value (RRmean), Standard Deviation Normal to Normal (SDNN), root mean square of successive differences (RMSSD), mean value of the PSD evaluated in the low-frequency band (LF = [0.04–0.15] Hz), mean value of the PSD evaluated in the high-frequency band (HF = [0.15–0.4] Hz), and their ratio (LF/HF).

The ADInstruments Powerlab system was also employed to measure a 1 channel EEG, with a sample frequency of 1 kHz. Saturated or corrupted EEG data epochs were assessed by visual inspection and eliminated from the analysis. In addition, physiological artifacts were corrected using an Independent Component Analysis-based method. Data were band-pass filtered with a 2nd order, zero-lag, Butterworth digital filter (cut-off frequencies of 0.1 and 80 Hz). To estimate the MW of the drivers, the PSD of different EEG frequency bands (i.e., δ-band, 1.5-3.5 Hz, θ-band, 3.5-7.5 Hz, α-band, 7.5-12.5 Hz, β1-band, 12.5-25.2 Hz, β2-band, 25.2-35.2 Hz) were computed using Welch's method (2 s intervals, frequency resolution of 0.5 Hz). The following features were extracted from each EEG power frequency bands signal: mean value (Mean), standard deviation (SD), sample entropy (SampEn, embedded dimension=3; similarity factor:0.2*std).

The portable fNIRS Cortivision Photon cap device was used to measure the functional cortical hemodynamic (the device was provided by Cortivsion Pathfinder Program grant number CPP-2021/10/3). It is comprised of 16 LEDs emitting at 760 nm and 850 nm wavelengths and 10 detectors. The montage consisted of 34 channels that covered the frontal and prefrontal cortices, with optodes arranged according to the 10–20 system. Additionally, four short channels have been provided to reduce physiological contamination from fNIRS signals. [14]. The signals were filtered with a 2nd order, zero-lag, Butterworth digital filter (cut-off frequencies of 0.01 and 0.5 Hz) and the motion artifacts were corrected applying a Wavelet based procedure [15]. The following features were extracted from both the HbO and HbR signals and averaged across the channels: Mean, SD, and SampEn (embedded dimension=3; similarity factor:0.2*std).

In this study, a Support Vector Machines (SVM) with a radial basis function kernel was employed to classify the MW. Specifically, both unimodal (fNIRS, EEG, HRV) and multimodal (fNIRS+EEG+HRV) models were trained and tested to discriminate three MW levels for DST (i.e., baseline, forward DST, and backward DST), and four MW classes for RAVLT (baseline, immR, DelR, Rec). The input metrics were normalized (z-score) and a leave-one-subject-out cross validation was used to protect against overfitting. The feature selection was performed using F-tests, used to compare the null hypothesis that response values grouped by predictor variables are from populations with the same mean. The McNemar–Bowker was used to compare the classifiers.

III. Results

In Table 1, the features for the unimodal and multimodal frameworks are listed in the order determined by the F-tests. The first five features selected for each classifier were used for the classification.

TABLE I: Features ranking obtained through the features selection procedure

Cognitive task	*Physiological signals*	*Features selected*
DST	fNIRS	SD HbO, SD HbR, Mean HbO, SampEn HbO, SampEn HbR, Mean HbR
	EEG	Mean δ. SampEn θ, SampEn β2, Mean θ, SD δ, SD β1, SampEn δ, SampEn β1, Mean β2, Mean α, SD θ, SampEn α, SD β2, Mean β1, SD α
	HRV	LF/HF, meanRR, HF, SDNN, RMSSD, LF
	Multimodal	LF/HF, SD HbO, Mean δ, RRmean, HF, SampEn θ, SDNN, RMSSD, LF, SD HbR, SampEn β2, SampEn HbR, Mean θ, SD δ, SD β1, SampEn HbO, Mean HbR, SampEn δ, SampEn β1, Mean HbO, Mean β2, Mean α, SD θ, SampEn α, SD β2, Mean β1, SD α.
RAVLT	fNIRS	Mean HbO, Mean HbR, SampEn HbO, SD HbR, SD HbO, SampEn HbR
	EEG	SampEn θ, SD β1, Mean δ, Mean α, SampEn β1, SampEn α, SampEn δ, Mean β2, SD β2, Mean θ, Mean β1, SD δ, SD θ, SD α, SampEn β2
	HRV	LF/HF, LF, SDNN, RMSSD, MeanRR, HF
	Multimodal	LF/HF, LF, SDNN, RMSSD, RRmean, HF, SampEn θ, SD β1, Mean δ, Mean HbO, Mean HbR, Mean α, SD HbO, SampEn β1, SampEn α, SampEn δ, SD HbR, SampEn HbO, Mean β2, SD β2, SampEn HbR, Mean θ, Mean β1, SD δ, SD θ, SD α, SampEn β2

Table 2 reports the cross-validated classification performances obtained for the two cognitive tasks considered for the different physiological signals acquired.

TABLE II: Accuracies of the several models developed

Cognitive task	*Physiological signals*	*Accuracy (%)*
DST	fNIRS	66.7
	EEG	64.1
	HRV	64.1
	fNIRS+EEG+HRV	69.4
RAVLT	fNIRS	59.6
	EEG	70.8
	HRV	76.9
	fNIRS+EEG+HRV	85.4

Figure 2 shows the confusion matrix obtained for the cross-validated classification of three MW levels from DST based on the multimodal approach.

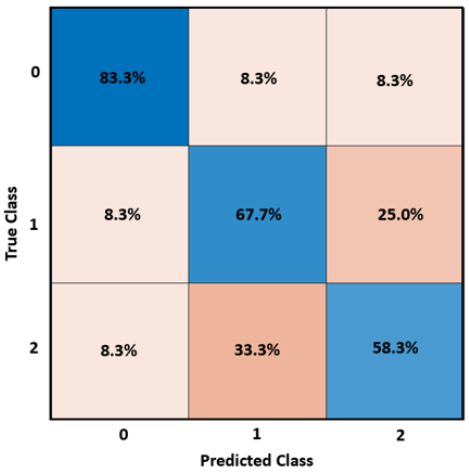


Fig. 2: Confusion matrix associated to the classification obtained to discriminate three MW levels from DST based on the multimodal approach.

Figure 3 describes the confusion matrix associated to the cross-validated classification of four MW levels from RAVLT based on the multimodal approach.

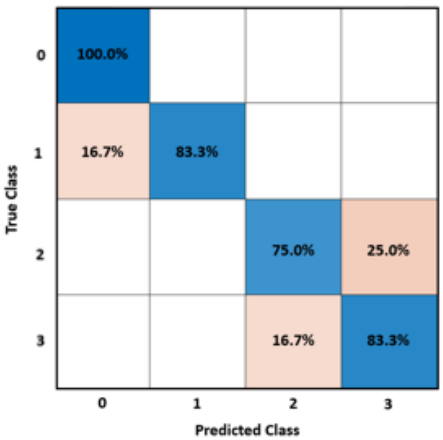


Fig. 3: Confusion matrix associated to the classification of four MW levels from RAVLT based on the multimodal approach.

The McNemar–Bowker test did not report any significant difference between the accuracies of the different models.

IV. Discussion

Monitoring the MW while driving is of the utmost importance due to its close correlation with the risk of car accidents. The primary objective of the present study was to develop models capable of classifying drivers' MW based on their psychophysiological characteristics.

DST and RAVLT were chosen to investigate different levels of MW, since it has been reported that the Backward DST and the DelR-RAVLT are more demanding with respect to forward DST and the other phases of RAVLT, respectively [16].

In the present study, the possibility of recognizing different levels of MW through non-invasive techniques and an SVM-based model was investigated. During the experimental

phases, fNIRS, EEG, and HRV characteristics were extracted.

Concerning the fNIRS signals, the feature selection analysis demonstrated that the SD and mean values of the HbO and HbR are relevant to discriminate the MW (Table I). In fact, it is known that cortical activations require increased oxygen consumption, producing functional hyperaemia, which is visible with an increase in the mean value of the HbO, a decrease in the mean value of the HbR, and an increase in the SD of the two signals [9].

Concerning the EEG, variations of the power in θ and δ bands seem to be relevant for the detection of MW (Table I). These results agree with previous findings demonstrating that increased EEG power in θ band occurred in high MW, and that increased EEG power in θ, δ and α bands characterize the transition between MW and mental fatigue [17].

Regarding the HRV, the LF/HF metric is the most crucial to estimate the MW (Table I), in line with previous findings [18].

Although an improvement in classification performance is present when comparing the multimodal approach with the different unimodal procedures (Table II), it is worth noticing that the McNemar–Bowker test did not highlight any significant difference between the accuracies of the different models. This result could be related to the poor sample numerosity. In fact, as the number of participants in the study sample has a significant impact on the supervised learning performances, further research is required to expand the sample size. In addition, the risk of overfitting may be decreased by increasing the number of participants. Notably, even if the findings are cross-validated and the generalization abilities of the model are thus examined, increasing the sample size might still lead to better classification results. In addition, because the participants' ages ranged from 19 to 42, the study only included young and middle-aged adults. Expanding the age range in future studies should be essential to creating models that are appropriate for older people as well. The MW examined in this study is primarily related to non-driving tasks rather than a complex driving condition, which is an important point to emphasize. Therefore, more research tracking the MW's variation in relation to driving-only tasks needs to be done. To broaden the model's scope of use, it is important to evaluate it in real-world driving scenarios as well, mainly focusing on contactless, lightweight and not-bulky sensors.

V. Conclusion

This study illustrated the benefits of using multimodal physiological acquisitions to measure the MW in drivers. Specifically, using an SVM classifier based on multimodal physiological features, MW was identified with an accuracy of 69.4% during the administration of the DST and 85.4% during the RAVLT. To lessen traffic accidents and enhance driver ergonomics, this technique could be successfully used in ADAS applications, racing competitions, and cockpit neuroergonomics.

Acknowledgement

This research was supported by the grants: PON FESR MIUR R&I 2014-2020-ADAS+ (No. ARS01_00459) and ECSEL Joint Undertaking (JU) European Union's Horizon 2020 Heliaus (No. 826131).

References

1. Kajiwara, S. Evaluation of Driver's Mental Workload by Facial Temperature and Electrodermal Activity under Simulated Driving Conditions. *International journal of Automotive technology* **2014**, *15*, 65–70.
2. Rubio, S.; Díaz, E.; Martín, J.; Puente, J.M. Evaluation of Subjective Mental Workload: A Comparison of SWAT, NASA-TLX, and Workload Profile Methods. *Applied Psychology* **2004**, *53*, 61–86, doi:10.1111/j.1464-0597.2004.00161.x.
3. Minhad, K.N.; Ali, S.H.M.; Reaz, M.B.I. Happy-Anger Emotions Classifications from Electrocardiogram Signal for Automobile Driving Safety and Awareness. *Journal of Transport & Health* **2017**, *7*, 75–89.
4. Lee, B.G.; Chong, T.W.; Lee, B.L.; Park, H.J.; Kim, Y.N.; Kim, B. Wearable Mobile-Based Emotional Response-Monitoring System for Drivers. *IEEE Transactions on Human-Machine Systems* **2017**, *47*, 636–649.
5. Zeng, H.; Yang, C.; Dai, G.; Qin, F.; Zhang, J.; Kong, W. Classification of Driver Mental States by Deep Learning Cogn. *Neurodyn* **2018**, *12*, 597–606.
6. Balters, S.; Baker, J.M.; Geeseman, J.W.; Reiss, A.L. A Methodological Review of FNIRS in Driving Research: Relevance to the Future of Autonomous Vehicles. *Frontiers in human neuroscience* **2021**, *15*, 637589.
7. Perpetuini, D.; Filippini, C.; Nocco, S.; Tritto, M.; Cardone, D.; Merla, A. A Machine Learning Approach to Classify Driver Mental Workload as Assessed by Electroencephalography through Infrared Thermal Imaging. In Proceedings of the 2022 E-Health and Bioengineering Conference (EHB); November 2022; pp. 1–4.
8. Perpetuini, D.; Cardone, D.; Filippini, C.; Spadolini, E.; Mancini, L.; Chiarelli, A.M.; Merla, A. Can Functional Infrared Thermal Imaging Estimate Mental Workload in Drivers as Evaluated by Sample Entropy of the FNIRS Signal?; 2021; Vol. 80, pp. 223–232.
9. Quaresima, V.; Ferrari, M. A Mini-Review on Functional near-Infrared Spectroscopy (FNIRS): Where Do We Stand, and Where Should We Go? In Proceedings of the Photonics; Multidisciplinary Digital Publishing Institute, 2019; Vol. 6, p. 87.
10. Hogervorst, M.A.; Brouwer, A.-M.; van Erp, J.B.F. Combining and Comparing EEG, Peripheral Physiology and Eye-Related Measures for the Assessment of Mental Workload. *Frontiers in Neuroscience* **2014**, *8*.
11. Chu, H.; Cao, Y.; Jiang, J.; Yang, J.; Huang, M.; Li, Q.; Jiang, C.; Jiao, X. Optimized EEG–FNIRS Based Mental Workload Detection Method for Practical Applications. **2021**.
12. Carlesimo, G.A.; Caltagirone, C.; Gainotti, G.; Fadda, L.; Gallassi, R.; Lorusso, S.; Marfia, G.; Marra, C.; Nocentini, U.; Parnetti, L. The Mental Deterioration Battery: Normative Data, Diagnostic Reliability and Qualitative Analyses of Cognitive Impairment. *European neurology* **1996**, *36*, 378–384.
13. Rey, A. L'examen Psychologique Dans Les Cas d'encéphalopathie Traumatique.(Les Problems.). *Archives de psychologie* **1941**.
14. Brigadoi, S.; Cooper, R.J. How Short Is Short? Optimum Source–Detector Distance for Short-Separation Channels in Functional near-Infrared Spectroscopy. *Neurophotonics* **2015**, *2*, 025005.
15. Perpetuini, D.; Cardone, D.; Filippini, C.; Chiarelli, A.M.; Merla, A. A Motion Artifact Correction Procedure for FNIRS Signals Based on Wavelet Transform and Infrared Thermography Video Tracking. *Sensors* **2021**, *21*, 5117.
16. Louie, J.F.; Mouloua, M. Predicting Distracted Driving: The Role of Individual Differences in Working Memory. *Applied ergonomics* **2019**, *74*, 154–161.
17. Borghini, G.; Astolfi, L.; Vecchiato, G.; Mattia, D.; Babiloni, F. Measuring Neurophysiological Signals in Aircraft Pilots and Car Drivers for the Assessment of Mental Workload, Fatigue and Drowsiness. *Neuroscience & Biobehavioral Reviews* **2014**, *44*, 58–75, doi:10.1016/j.neubiorev.2012.10.003.
18. Cardone, D.; Perpetuini, D.; Filippini, C.; Mancini, L.; Nocco, S.; Tritto, M.; Rinella, S.; Giacobbe, A.; Fallica, G.; Ricci, F.; et al. Classification of Drivers' Mental Workload Levels: Comparison of Machine Learning Methods Based on ECG and Infrared Thermal Signals. *Sensors* **2022**, *22*, 7300, doi:10.3390/s22197300.

Algorithm based on the "dynamic risk" concept allows ahead-of-time suggestion of corrective insulin boluses in type 1 diabetes therapies employing continuous glucose monitors

E. Pellizzari[1], F. Prendin[1], G. Cappon[1], G. Sparacino[1] and A. Facchinetti[1]
[1] *Department of Information Engineering, University of Padova, Padova, Italy.*

***Abstract*—Due to the lack of insulin secretion from the pancreas, individuals diagnosed with type 1 diabetes (T1D) must lower their blood glucose (BG) levels through exogenous insulin injection in order to avoid hyperglycemic episodes (BG $\geq$ 180 mg/dL). Unfortunately, excessive exogenous insulin dosing could lead patients to experience hypoglycemic episodes (BG $\leq$ 70 mg/dL). T1D management can be improved by utilizing continuous glucose monitoring (CGM) and decision support systems (DSSs), specific software tools that can assist patients during the daily decision-making process, recommending therapeutic actions such as carbohydrates intake and insulin injections. This study presents a novel algorithm, usable in a DSS, that utilizes physiological patient-specific information and a "dynamic risk" measure obtained from CGM to suggest the dose of anticipated corrective insulin boluses (CIBs), with the goal of reducing the duration of hyperglycemia. The approach has been retrospectively evaluated on a dataset of 30 T1D patients recorded in free-living conditions and compared with state-of-art approach. Results indicate that the proposed algorithm improves many indicators conventionally used in assessing the effectiveness of T1D therapies and the quality of glycemia, e.g., percentage of time spent in euglycemia ($+4.86\%$) and in hyperglycemia (-4.58%), hyperglycemia duration (-33.75 min) and glycemic control.**

***Keywords*—corrective insulin boluses, dynamic risk, preventive, type 1 diabetes.**

I. INTRODUCTION

Type 1 diabetes (T1D) is a chronic autoimmune disease characterized by the lack of pancreatic insulin secretion. Blood glucose (BG) levels in people affected by diabetes frequently exceed the safe range of [70 $-$ 180] mg/dL: hyperglycemia, i.e., BG $\geq$ 180 mg/dL can lead to serious long-term consequences as retinopathy and cardiovascular disease, whereas hypoglycemia, i.e., BG $\leq$ 70 mg/dL, can be dangerous in the short term since can cause coma or even death. Individuals with T1D must manage a lifelong therapy in order to maintain as much as possible the blood glucose concentration within the euglycemic range. The standard therapy for T1D includes frequent measurements of BG levels, estimation of carbohydrate intake at each meal, periodic administration of exogenous insulin to compensate for fluctuations in BG levels above the hyperglycemic threshold and rapid ingestion of carbohydrates when BG falls below the hypoglycemic threshold. These actions are commonly repeated throughout the day, leading to increased burden and negatively impacting patients' quality of life.

In recent years, the use of continuous glucose monitoring (CGM) devices has helped to ease the burden of standard therapy [1], [2]. CGM devices are minimally invasive sensors that provide BG measurement every 1-5 minutes for several days. Since their approval for nonadjunctive use [3], [4], patients can make treatment decisions based on the values provided by CGM. Additionally, CGM devices can provide patients with information on the glucose rate of change (ROC) and alarms when BG is outside safe range. Finally, use of CGM devices in combination with portable pumps for continuous subcutaneous insulin infusion (CSII), smart insulin pens, and dedicated mobile applications have stimulated the development of decision support systems (DSSs) [5]. These software tools can automatically record and analyze data from CGM sensors and CSII pumps to create personalized recommendations to improve BG control. For example, DSS can suggest the appropriate amount of prandial insulin or the ingestion of fast-acting hypotreatment to prevent/mitigate impending hypoglycemic events, and suggest corrective insulin boluses (CIBs) to reduce the duration of hyperglycemia. DSSs commonly incorporate multiple modules, such as insulin bolus calculators and BG ahead-of-time prediction algorithms capable of producing smart alarms targeting both hypoglycemia and hyperglycemia, thus providing the recommendations to the patients through a mobile interface.

In the literature, several CGM-based algorithms have already been published to improve the insulin bolus computation [6], [7], [8], [9] and suggest hypoglycemia treatments [10], [11], but a very few have coped with the possibility of exploiting CGM data to enhance the generation of CIBs [12], [13]. According to current guidelines, CIB is computed using the standard formula [14]:

$$CIB = \frac{BG - BG_T}{C_F} - IOB \tag{1}$$

where BG (mg/dL) is the actual BG value, BG_T (mg/dL) is the patient target BG value (e.g., 120 mg/dL), C_F (mg/dL/U) is the correction factor, i.e., how much 1 U of insulin lowers BG, and IOB (U) is the insulin-on-board, i.e., an estimate of the amount insulin still present in the blood from previous administrations. In Aleppo et al. [7], authors proposed a heuristic-based strategy for CIBs administration, modifying

the standard formula Eq. (1) by accounting for both current glucose level and its ROC provided by CGM devices. The approach proposed by Aleppo et al. achieved encouraging results, but it does not consider: i) the large variability among T1D individuals and ii) the risk associated to the upcoming hyperglycemia.

To fill this gap, this work proposes a CGM-based algorithm which, by exploiting physiological patient-specific information and a recently proposed risk measure, is able to trigger CIBs ahead-of-time and, hence, to reduce the duration of hyperglycemic events.

II. METHODS

A. The proposed approach for ahead-of-time CIB suggestion

A key input of the new algorithm for suggesting ahead-of-time CIBs is the dynamic risk (DR), a measure recently proposed by Guerra et al. [16] to improve, by leveraging the information made available by CGM sensors, the static risk (SR) measure previously proposed in [15]. Briefly, SR is a nonlinear transformation of BG designed to assign similar weighting to variations in both hypoglycemia and hyperglycemia, to obtain a symmetric distribution of glycemic ranges. SR quantifies the risk associated to a given BG level. Through a suitable modulation of SR based on the use of the ROC information, DR amplifies SR when BG is rapidly increasing or decreasing. In this way, DR measures how critical the actual BG level and trend can be for the patient, in terms of possible long- and short-term consequences. The fact that DR is sensitive to the trend allows its use for CIBs' preventive suggestion. Specifically, the novel algorithm, schematized in Fig. 1 and hereinafter referred as drCIB, is based on real-time calculation of DR and works as follows:

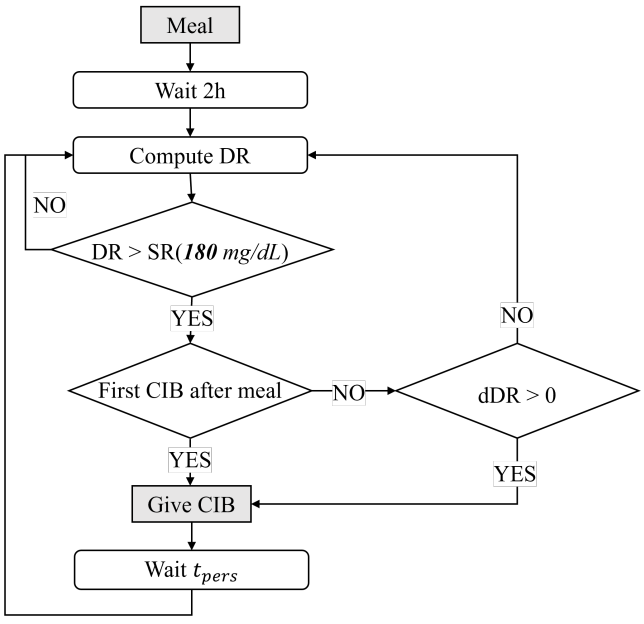


Fig. 1: drCIB flowchart. Abbreviations: dynamic risk (DR), static risk (SR), corrective insulin bolus (CIB).

1) waits two hours after meal ingestion;
2) for every new CGM sample available, computes DR;
3) if DR is greater than SR corresponding to the hyperglycemic threshold value, i.e., 180 mg/dL, and this is the first insulin bolus generated after a meal, triggers a CIB according to Eq. (1), then wait for at least a patient-specific time (t_{pers}) before delivering, if required, another CIB;
4) if DR is greater than SR corresponding to the hyperglycemic threshold value, i.e., 180 mg/dL, but a CIB has already been administered after the meal, computes the derivative of DR. If positive, triggers a CIB according to Eq. (1) and waits for at least a patient-specific time (t_{pers}) before delivering, if required, an additional CIB; otherwise, return to 2).

The patient-specific time between two insulin bolus suggestions is forced to be greater than 60 min and lower than 120 min (interquartile range [60, 91.5, 120] min) and it is retrieved from patient's personal glucose-insulin dynamics. In particular, we identified a white-box model of glucose-insulin dynamics based on the maximal physiological model of the UVa/Padova T1D Simulator [17]. Therefore, by considering the subcutaneous insulin absorption subsystem parameters, we calculated the 150% of the delay of insulin action for each patient.

B. State-of-the-art approach for CIB suggestion

As comparator, we implemented the empiric algorithm published by Aleppo et al. (AL) [7].

We precisely choose AL's approach because includes also specific post-prandial recommendation retrieved from the clinical trial REPLACE-BG [19], which fits to our purpose of managing post-prandial hyperglycemia. In particular, AL suggests to:

1) avoid correction of hyperglycemia for the first 2 hours following a meal, in order to prevent insulin stacking;
2) follow REPLACE-BG guidelines between 2 hours and 4 hours from meal, which include a CIB trigger based on BG and ROC values and the CIB entity calculated from Eq. (1);
3) follow specific guidelines for CIB correction after 4 hours from meal, which add or subtract a fixed amount of insulin to standard CIB calculated with Eq. (1) depending on ROC and patient's C_F, to be injected if BG ≥ 180 mg/dL.

C. Methodology assessment

The aforementioned methodologies were assessed through ReplayBG, an open source [18] tool that retrospectively assesses the outcome of alternative therapies on real-world T1D data. Briefly, it works in two steps: first, identifies a physiological nonlinear model of glucose-insulin dynamics from patient's data (CGM glucose, insulin, carbohydrates); second, uses the so identified model to infer the glucose concentration that would have been obtained, in the same individual and time window, by using an alternative insulin

therapy. In our case, the alternative insulin therapy is given by the delivery of CIBs suggested by the algorithms.

D. Dataset

The two approaches have been retrospectively assessed via ReplayBG on a dataset of 30 subjects acquired in free-living conditions and extracted from a larger study: the Control To Range 3 (CTR3) [20]. For each individual, CGM data, meals timing and amount, insulin boluses, basal insulin, and some personal patient information (carbohydrates-to-insulin ratio, C_F) are available. We partitioned the dataset into daily traces according to the following criteria: i) at least 3 meals per day (breakfast, lunch, and dinner) and ii) a three-hour average hyperglycemia duration. The identification procedure provided a total of 49 daily traces. For the second step (i.e., simulation phase) of ReplayBG we cleared the CIBs injected by the patient in order to test our new strategy. From now on, these data will be referred as baseline.

E. Evaluation metrics

For each individual, we computed time in range (TIR, i.e., 70<BG<180), time above range (TAR), and time below range (TBR); the number of suggested CIBs (CIB) and total daily insulin (INS) injected through them. We also calculated the number of hyperglycemic events per day (Hyper) and the duration of hyperglycemic events (HyperD). The efficacy in glycemic control is measured through the glycemia risk index (GRI) [21], which is an overall risk metric that accounts for very low-glucose and low-glucose hypoglycemia, very high-glucose and high-glucose hyperglycemia, time in range, mean glucose and coefficient of variation. The statistical significance was evaluated by using t-test when normality distribution assumption was not rejected, and through Wilcoxon signed-rank test otherwise, with a significance level of 5%. In particular, we assess both the statistical significance between drCIB and AL in comparison to the baseline and the statistical significance between the two methods.

III. RESULTS

Fig. 2 shows the simulation results of AL and drCIB algorithms via ReplayBG on a representative subject. In particular, it reports the glycemic traces obtained with no CIB (baseline, dotted line), CIBs generated with AL (green line) and CIBs generated with drCIB (red line).

As can be observed from the graphical representation, the dotted line, which serves as the baseline, displays a higher percentage of time spent above the hyperglycemic threshold (38.4%) as a result of the absence of any CIB being administered. AL algorithm generated two boluses (green dots) of 2.66 U and 2.86 U at time 10:25 and 15:55, reducing TAR to 35.0%. Similarly, drCIB algorithm administered two boluses (red dots) of 3.92 U and 3.61 U at time 8:25 and 13:55, just after the two hours waiting window (grey areas). As shown in Fig. 2, drCIB acts ahead in time with respect to AL and it lowers BG more rapidly, further reducing TAR to 22.3%, and HyperD by 31.4% when compared to AL. Notably, by considering the different risk levels, drCIB allows to avoid unnecessary CIBs, especially when glycemia is close to the normoglycemic region.

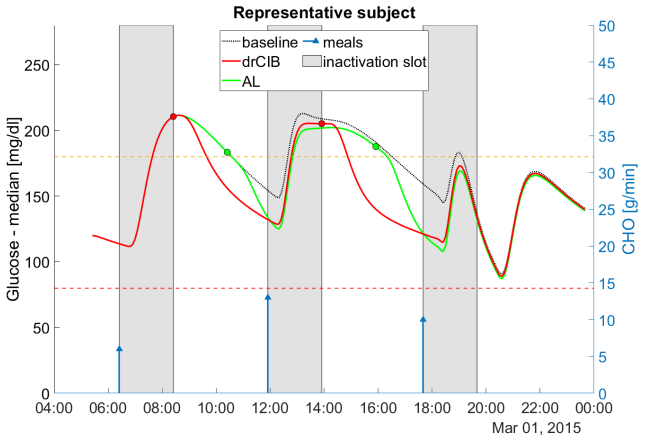


Fig. 2: Application of AL and drCIB algorithms via ReplayBG on a representative subject. The dotted line is the glycemic traces obtained with no CIBs (baseline); the green line is the glycemic trace resulting from AL guidelines and the red line is the glycemic trace resulting from drCIB algorithm. Meals are shown with the blue arrows in the bottom of the plot. The common inactivation slot after the meal of the aforementioned methodologies are highlighted.

Table I reports the main results on the 49 traces in terms of median and [25th-75th] ranges.

TABLE I: Comparison between baseline, AL and drCIB approach Metrics are reported as median [25th-75th].

Metrics	baseline	AL	drCIB
TIR (%)	52.28 [39.55, 62.61]	57.59 [47.81, 68.46]	62.45 * [49.52, 72.70]
TAR (%)	46.89 [37.39, 60.45]	39.76 [25.39, 48.15]	35.18 * [25.74, 41.53]
TBR (%)	0 [0, 0]	0 [0, 0]	0 [0, 2.63]
GRI (unit)	52.64 [35.46, 67.99]	42.14 [28.79, 62.69]	40.44 [27.87, 61.23]
Hyper (unit)	2 [1, 2]	2 [1, 2]	2 [1.75, 2]
HyperD (min)	258.75 [217.5, 325]	223.75 [180, 252.5]	190 * [141.88, 220]
CIB (unit)	-	2 [1, 2]	2 * [2, 3]
INS (U)	-	5.09 [3.15, 7.82]	6.27 * [4.76, 8.31]

* indicates a statistically significant variation of drCIB compared to AL

With respect to baseline, in which no CIBs are delivered, both AL and drCIB improve the overall glycemic control. As a matter of fact, both strategies significantly increase the time spent in the safe range reducing TAR, HyperD and GRI with statistical significance. Comparing drCIB and AL instead, drCIB significantly reduces both TAR (from 39.76% to 35.18%) and HyperD (from 223.75 min to 190 min), achieving the goal in mitigating post-prandial hyperglycemia. drCIB also significantly increases TIR (from 57.59% to 62.45%) without affecting median TBR, and reduces the overall risk index GRI (from 42.14 to 40.44), resulting in a safer approach compared

to AL. It is worth noting that the two approaches deliver a similar number of insulin boluses but the amount suggested by the drCIB is larger than the one provided by AL.

IV. DISCUSSION AND CONCLUSION

In this paper, a novel strategy for post-prandial CIB administration based on DR and a personalized time for CIB injection has been proposed. The new strategy is characterized by a trigger method based on actual DR value, which is easily computed in real-time from CGM values, and a personalized timing for CIB injection, directly estimated from easily accessible patient data e.g., during a medical examination. Preliminary results show that the use of DR to trigger CIBs suggestions proved to be effective in proactively manage hyperglycemia. Indeed, drCIB leads to an improve of TIR and TAR without affecting median TBR and increasing also patient safety in terms of GRI, compared to one of the most recent literature recommendation. For the assessment of the methodologies, data from the CTR3 closed-loop dataset have been used. Since our goal is to develop an open-loop algorithm, we replaced the time-varying basal insulin of the data with the mean across the entire data traces for each subject before the physiological model identification step via ReplayBG. This allowed us to simulate the effect of a long-acting insulin bolus in patients undergoing to multiple daily injections (MDI) therapy, typically administered in the morning. Thereby, we were able to determine the best open-loop therapy that replicates the original data and align the dataset with our aim of developing a therapy for MDI diabetic patients. We acknowledge this as limitation of the study and we will address it in future works when larger datasets, recorded in free-living conditions and in an open-loop set-ups, will be available.

In conclusion, drCIB, which is based on DR measure and a personalized time for CIB delivery, is a valuable alternative to the state-of-art heuristic based strategy for CIB suggestions. It is also suitable to be implemented in the insulin bolus calculators module of a DSS, particularly targeting CIBs.

It is worth underlying that we focused only on trigger and timing condition of CIBs while the amount is defined by Eq. (1). For this reason, future works will examine how changing the glycemic value for the threshold affects the performances, in order to optimize the risk threshold, and optimize the amount of injected insulin based on real-time DR.

ACKNOWLEDGEMENT

This work was partially supported also by MIUR under the initiative “PRIN: Programmi di Ricerca Scientifica di Rilevante Interesse Nazionale (2020),” project ID: 2020X7XX2P, project title: “A noninvasive tattoo-based continuous GLUCOse Monitoring electronic system FOR Type-1 diabetes individuals (GLUCOMFORT).”

REFERENCES

[1] Mian, Z., Hermayer, K. L., & Jenkins, A. (2019). Continuous glucose monitoring: review of an innovation in diabetes management. The American journal of the medical sciences, 358(5), 332-339.

[2] Cappon, G., Acciaroli, G., Vettoretti, M., Facchinetti, A., & Sparacino, G. (2017). Wearable continuous glucose monitoring sensors: a revolution in diabetes treatment. Electronics, 6(3), 65.

[3] Castle, J. R., & Jacobs, P. G. (2016). Nonadjunctive use of continuous glucose monitoring for diabetes treatment decisions. Journal of diabetes science and technology, 10(5), 1169-1173.

[4] Edelman, S. V. (2017). Regulation catches up to reality: nonadjunctive use of continuous glucose monitoring data. Journal of diabetes science and technology, 11(1), 160-164.

[5] Cappon, G., Noaro, G., Camerlingo, N., Cossu, L., Sparacino, G., & Facchinetti, A. (2021, November). A New Decision Support System for Type 1 Diabetes Management. In 2021 43rd Annual International Conference of the IEEE Engineering in Medicine & Biology Society (EMBC) (pp. 1993-1996). IEEE.

[6] Pettus, J., & Edelman, S. V. (2017). Recommendations for using real-time continuous glucose monitoring (rtCGM) data for insulin adjustments in type 1 diabetes. Journal of diabetes science and technology, 11(1), 138-147.

[7] Aleppo, G., Laffel, L. M., Ahmann, A. J., Hirsch, I. B., Kruger et al. (2017). A practical approach to using trend arrows on the Dexcom G5 CGM system for the management of adults with diabetes. Journal of the Endocrine Society, 1(12), 1445-1460.

[8] Bruttomesso, D., Boscari, F., Lepore, G., Noaro, G., Cappon, et al. (2021). A “slide rule” to adjust insulin dose using trend arrows in adults with type 1 diabetes: test in silico and in real life. Diabetes Therapy, 12(5), 1313-1324.

[9] Ziegler, R., von Sengbusch, S., Kröger, J., Schubert, O., Werkmeister, P., et al. (2019). Therapy adjustments based on trend arrows using continuous glucose monitoring systems. Journal of Diabetes Science and Technology, 13(4), 763-773.

[10] Camerlingo, N., Vettoretti, M., Del Favero, S., Cappon, G., Sparacino, G., & Facchinetti, A. (2019). A real-time continuous glucose Monitoring–Based algorithm to trigger hypotreatments to Prevent/Mitigate hypoglycemic events. Diabetes technology & therapeutics, 21(11), 644-655.

[11] Faccioli, S., Prendin, F., Facchinetti, A., Sparacino, G., & Del Favero, S. (2022). Combined Use of Glucose-Specific Model Identification and Alarm Strategy Based on Prediction-Funnel to Improve Online Forecasting of Hypoglycemic Events. Journal of Diabetes Science and Technology, 19322968221093665.

[12] Noaro, G., Cappon, G., Vettoretti, M., Sparacino, G., Del Favero, S., & Facchinetti, A. (2020). Machine-learning based model to improve insulin bolus calculation in type 1 diabetes therapy. IEEE Transactions on Biomedical Engineering, 68(1), 247-255.

[13] Zhu, T., Li, K., Kuang, L., Herrero, P., & Georgiou, P. (2020). An insulin bolus advisor for type 1 diabetes using deep reinforcement learning. Sensors, 20(18), 5058.

[14] Schmidt, S., & Nørgaard, K. (2014). Bolus calculators. Journal of diabetes science and technology, 8(5), 1035-1041.

[15] Kovatchev, B. P., Cox, D. J., Gonder-Frederick, L. A., & Clarke, W. (1997). Symmetrization of the blood glucose measurement scale and its applications. Diabetes care, 20(11), 1655-1658.

[16] Guerra, S., Sparacino, G., Facchinetti, A., Schiavon, M., Man, C. D., & Cobelli, C. (2011). A dynamic risk measure from continuous glucose monitoring data. Diabetes technology & therapeutics, 13(8), 843-852.

[17] Visentin, R., Campos-Náñez, E., Schiavon, M., Lv, D., Vettoretti, M. et al. (2018). The UVA/Padova type 1 diabetes simulator goes from single meal to single day. Journal of diabetes science and technology, 12(2), 273-281.

[18] Cappon, G. https://github.com/gcappon/replay-bg

[19] Aleppo, G., Ruedy, K. J., Riddlesworth, T. D., Kruger, D. F., Peters, A. L. et al. (2017). REPLACE-BG: a randomized trial comparing continuous glucose monitoring with and without routine blood glucose monitoring in adults with well-controlled type 1 diabetes. Diabetes care, 40(4), 538-545.

[20] Kovatchev, B., Cheng, P., Anderson, S. M., Pinsker, J. E., Boscari et al. (2017). Feasibility of long-term closed-loop control: a multicenter 6-month trial of 24/7 automated insulin delivery. Diabetes technology & therapeutics, 19(1), 18-24.

[21] Klonoff, D. C., Wang, J., Rodbard, D., Kohn, M. A., Li, C. et al. (2022). A Glycemia Risk Index (GRI) of Hypoglycemia and Hyperglycemia for Continuous Glucose Monitoring Validated by Clinician Ratings. Journal of diabetes science and technology, 19322968221085273.

Assessing the impact of brain gliomas on effective connectivity gradients

Pagnin G.[1], Baron G.[1], Silvestri E.[1], Chiuso A.[1], Cecchin D.[2], Corbetta M.[2,3], Bertoldo A. [1,2]
[1] *Department of Information Engineering, University of Padova, Padova, Italy*
[2] *Padova Neuroscience Center, Padova, Italy*
[3] *Department of Neuroscience, University of Padova, Padova, Italy*

***Abstract*— Spatial macroscale gradients have proved useful for understanding the relationship between specific cortical regions and function, by mapping brain connectivity matrices on a low-dimensional representational hierarchy that encodes increasingly abstract levels of cognition. While this approach is well-established with functional connectivity, it has never been applied to whole-brain effective connectivity, which accounts for the direction of propagating information. In addition, the study of EC has rarely been applied in brain pathology.**
In this work, we identified the so-called "gradients" of brain organization from effective connectivity matrices. In neuroscience "gradients of brain organization" is referring to the use of the Laplacian matrix to study spatial modularity and transitions of brain network structure. The aim was to assess the impact of glioma with respect to healthy controls on whole-brain effective connectivity gradients by accounting for the signaling directionality of the information flow. The results showed more differences between controls and tumour subjects in left-hemisphere networks, and in incoming links with respect to outgoing ones. These findings suggest that glioma has a different impact depending on the directionality of connections.

***Keywords*— resting state effective connectivity, brain gliomas, Laplacian eigenmaps, directionality**

I. Introduction

Gliomas are the most frequent malignant primary brain tumours, whose treatment requires neurosurgical resection combined with radio and/or chemotherapy[1], [2], In this view, the presurgical cognitive status has been demonstrated to be strictly linked to the patient's survival[3], [4], suggesting the importance of analyzing brain functional organization in resting-state conditions[5]–[7]. Previous studies dealing with brain connectivity in gliomas[8]–[10] have mostly focused on symmetric, undirected characterizations of the connectome. Those works have been developed through structural or functional connectivity, which respectively gives information about the anatomical and correlation links between regions, without considering any form of directionality in the information flow. On the other hand, the inference of effective connectivity (EC) allows the measure of directed interactions and, as a result, of causality between brain regions. EC has shown to be a more sensitive biomarker outperforming functional connectivity (FC) for other brain pathologies[11], motivating its study in the case of brain tumours. Moreover, previous work has shown that localized brain tumours cause widespread brain connectivity alterations[6], demonstrating that the disruption of a single region extends beyond the affected network and leads to global functional modifications of brain networks.

In this work, we employed a sparse Dynamic Causal Modelling framework[12] to infer whole-brain directional effective connectivity at rest from patients with brain gliomas. Specifically, we aimed to capture the alterations induced in EC through hierarchical processing gradients[13] (i.e. the spectral partitioning of the EC-based Laplacian matrix), which can provide a low-dimensional space to describe the brain macroscale hierarchy. Differently from other graph descriptions that usually discretize functional networks, connectivity gradients allow uncovering transitions in connectivity patterns along a continuous space[14], providing a novel framework for investigating gradual whole-brain perturbations induced by the lesion on brain functional organization[6], [9]. Given the broad need to better understand the mechanisms underlying spatiotemporal brain dynamics, this framework has been widely applied to functional and structural connectomes to both characterize brain regions in terms of the similarity between their connectivity profiles (i.e., spectral clustering[13]) and to provide a set of basis functions for the spectral decomposition of the graph signal (i.e., graph signal processing[15]).

To the best of our knowledge, this represents the first attempt at applying such a low-dimensional transformation to EC in patients with brain gliomas, while very few applications of undirected connectivity gradients to brain pathology can be found in the literature[16]. We analyzed the distribution of gradient values in each brain region and compare it with estimates extracted from a healthy cohort to assess possible alterations induced not only in areas overlapping with the lesion but also in pseudonormal nodes. We performed the analysis by discriminating between incoming and outgoing connectivity profiles to capture the different alterations induced by the pathology on the basis of the directionality of the information flow.

II. Materials and Methods

Pre-surgical data of 47 patients from 25 to 83 years old with de novo brain tumours collected at the University Hospital of Padova were enrolled for this study. All participants have regularly taken anticonvulsants for the control of epilepsy and corticosteroids. The protocol had been approved by the local Ethics Committee of the University Hospital of Padova and carried out in accordance with the 1964 Helsinki declaration and its later amendments. Informed consent was signed by all patients[6]. The cohort is composed of left- and right- tumour individuals affected by both high- and low- grade gliomas.

Data were acquired on a 3T Siemens Biograph mMR scanner equipped with a 16-channel head–neck coil. Anatomical imaging included T1-weighted (T1w) 3D magnetization-prepared rapid acquisition gradient-echo (TR = 2400 ms, TE = 3.24 ms, TI = 1000 ms, FA = 8°, FOV = 256 × 256 mm, voxel size = 1 mm × 1 mm × 1 mm) images acquired both before and after contrast agent injection, a 3D T2-weighted image (TR = 3200 ms, TE = 535 ms, FOV = 256 ×

256 mm, voxel size = 1 mm × 1 mm × 1 mm), a 3D fluid attenuation inversion recovery (TR = 5000 ms, TE = 284 ms, TI = 1800 ms, FOV = 256 × 256 mm, voxel size = 1 mm × 1 mm × 1 mm) image. In addition, functional imaging comprised rs-fMRI EPI scans (TR = 1260 ms, TE = 30 ms, FA = 68°, FOV = 204 × 204 mm, voxel size = 3 mm × 3 mm × 3 mm, volumes = 750, MBAccFactor = 2, iPAT = 0, phase encoding direction antero-posterior) and two spin echo-EPI acquisitions with reverse phase encoding (TR = 4200 ms, TE = 70 ms, FOV = 204 × 204 mm, voxel size = 3 mm × 3 mm × 3 mm, MBAccFactor = 1) for EPI distortion correction purposes[6].

Concerning the control cohort, resting-state fMRI scans (TR=1.400 ms, TE=39.4 ms, flip angle=69°, FOV=202x202 mm, voxel size=2.3x2.3x.2.3 mm, volumes=657, MBAccFactor=4) of 76 healthy subjects (age- and gender-balanced) were retrieved from the publicly available MPI-Leipzig Mind-Brain-Body dataset[17].

A. Tumour segmentation

For the MRI perspective, the regions affected by the tumour can be distinguished into four distinct subareas: the necrosis; the core of the tumour divided into the highly active region and the moderately active region, and the cerebral edema. Globally, this set of areas is called lesion areas, whereas the tumour consists in the first three subareas[6].

In order to exclude areas that are directly affected by the tumour (e.g., interested by necrosis), a lesion mask was manually delineated [6] and employed to disregard grey-matter voxels overlapping with the affected areas in the following rs-fMRI analysis.

B. Data preprocessing

Firstly, the canonical pre-processing of rs-fMRI data was performed as described in [6]. In addition, voxel-wise high pass filtering was applied, followed by the regression of spurious variance related to scanner artifacts by means of an ICA-based approach[6]. Moreover, the first 5 principal components related to cerebro-spinal fluid and white matter signal were regressed out from rs-fMRI timeseries, as well as head-motion parameters and the associated derivatives.

Then, fMRI signals were projected onto a 100-area cortical parcellation provided by Schaefer et al.[18]. Parcels were organized in 7 cortical large-scale Resting State Networks (RSNs). Volume despiking was then applied in order to reduce the contribution of large spikes signals that could deteriorate the accuracy of volume registration and performances of sparse DCM. After the despiking step, the timeseries were temporally filtered at ROI level with a band-pass Butterworth filter, keeping frequencies in the band 0.0078-0.2 Hz to retain the range of frequencies that is usually supported by the canonical HRF in the DCM framework[19], [20].

C. Definition of the atlas

Applying the sparse DCM algorithm is computationally demanding, thus the total number of nodes considered as inputs were reduced through a consensus clustering approach[21]. Of note, the clustering regarded only parcels that were functionally homogeneous (i.e. belonging to the same RSN) and spatially contiguous in order to preserve the spatial consistency of the hemodynamic properties. As a result, data were projected to a reduced space consisting of 62 cortical regions (henceforth referred as Schaefer62).

D. Sparse DCM

Sparse DCM allows estimating whole-brain effective connectivity from resting-state fMRI data through discretization of the original non-linear continuous-time model and statistical linearization of the hemodynamic response function, which generates a Gaussian prior on the HRF that can be later exploited for model inversion. This allows us to better exploit the low temporal resolution of fMRI scanners and decrease the computational burden without losing statistical performance. Moreover, following the Sparse Bayesian learning approach, this method is based on a sparsity-inducing prior formulated on the matrix describing the effective connectivity network, allowing the automatic pruning of irrelevant EC connections without requiring any post-hoc model selection[12]. Details of the inference method can be found in [12]. The application of sparse DCM yields a weighted sparse matrix of EC connections (including both positive and negative entries) and parcel-wise linear estimate of the hemodynamic response function for each subject.

E. Gradient analysis

Fig. 1 shows the workflow of the analyses. Sparse DCM has been first applied to the pre-processed rs-fMRI signal to obtain the EC matrices for each subject.

Analysis by gradients is performed to summarize the behavior of the network. Given the asymmetric nature of the EC matrix, both the effect that the link has on the node (incoming) and on the network (outgoing) were considered. Consequently, the method is applied separately in order to obtain, from the EC matrices, two separate affinity matrices A_{ij} (for incoming and outgoing) through a gaussian kernel.

The procedure of graph embedding through connectivity gradients requires as first step the computation of the graph Laplacian(1):

$$L_{ij} = k_i \delta_{ij} - A_{ij} \quad (1)$$

By summing a row of the affinity matrix A_{ij}, we obtain the degree of the corresponding node (k_{ij}) and by entering these values in a diagonal matrix it is possible to obtain the graph Laplacian.

From the L matrix, the eigenvectors (i.e., gradients) and corresponding eigenvalues can be obtained. Gradients computed separately for two or more individual datasets may not be directly comparable[14], thus Procrustes alignment was computed to improve comparability and correspondence across subjects.

More specifically, the computation of EC gradients was done using BrainSpace v0.2.1 Matlab toolbox, which implements various approaches to build macroscale gradients from neuroimaging and connectome data[14].

Specifically, two metrics were considered to evaluate the distributions of subjects in the space spanned by the first 3 gradients[22] proved to be those underlying the organization of intrinsic functional connectivity within the human cerebral cortex. The silhouette coefficient (SC) was evaluated for each 3D point (which represents respectively the first, second and third gradient) by considering each parcel across subjects as a cluster, both for controls and patients. This metric gives information about how a specific parcel is similar to the other parcels within that parcel/cluster (cohesion), compared to the parcels composing the other parcels/clusters (separation).

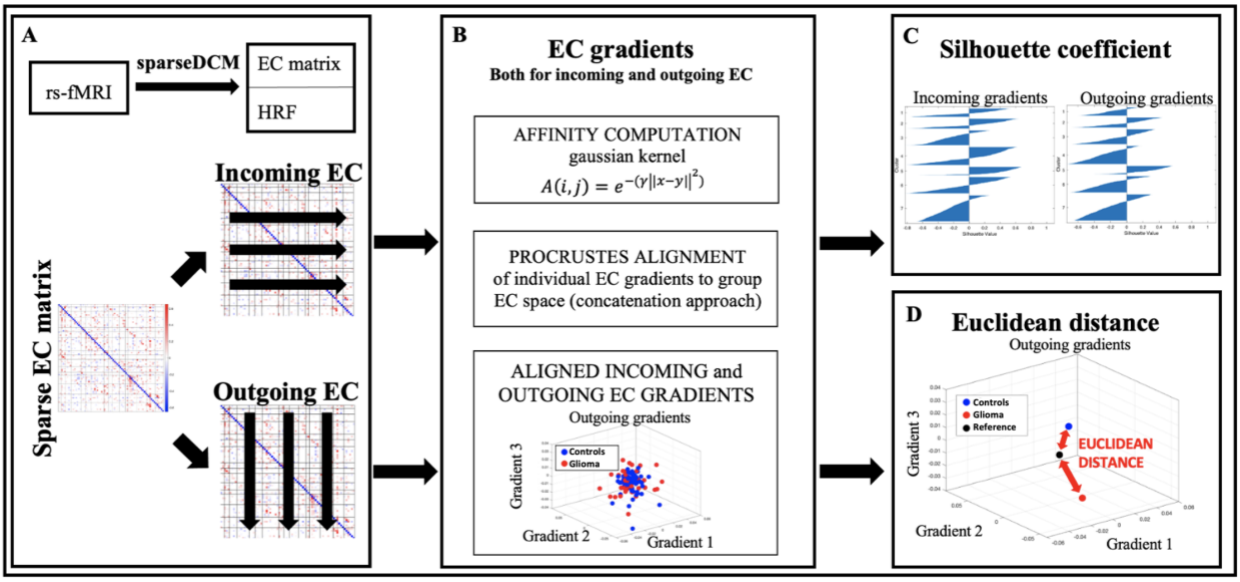


Fig. 1: Workflow of the key processing steps. Resting-state fMRI signal was provided as input to sparse DCM, which allows inferring the hemodynamic response function (HRF) and the effective connectivity (EC) matrix for each individual (panel A). By employing the Brainspace toolbox[14], Laplacian eigenmaps were inferred from each incoming/outgoing affinity matrix computed through a gaussian kernel. Procrustes alignment[14] was employed to align individual gradients to a common reference space identified by the concatenated EC gradients of the 76 healthy subjects[17]. Thus, incoming and outgoing aligned gradients are obtained for each control and glioma subject, reported in panel B for the outgoing gradients of the Vis1 parcel of the 76 controls and 47 pathological patients. Then, the silhouette coefficient was evaluated for each individual point (region in a 3D space), by considering each region across subjects as a distinct cluster (panel C). The final step regarded the computation of the Euclidean distance of each region between each subject and the corresponding reference point (panel D).

A subsequent analysis regarded the computation of the Euclidean distance for each parcel, which was carried out: 1st) by computing the pairwise distance between each individual gradient value and the reference point (i.e., the gradients of 76 controls' concatenated EC matrices); 2nd) by then comparing the distributions across control and oncological patients. For both metrics, differences between the two groups in each parcel have been assessed through t-test (significance level 5%, Holm-Bonferroni correction for multiple comparisons).

III. Results

The matrices in Fig. 2 show the percentage of directed links for control and oncological subjects for each entry. It is worth noticing that the intra-hemisphere profile of connections and inter-hemispheric diagonals are preserved, although the values for pathological subjects turn out to be scaled in terms of percentage magnitude. Therefore, the global structure of connections is preserved despite the presence of the lesion (Pearson's correlation of upper triangles: 0.928, lower triangles: 0.927), and allows the comparison of patients with healthy controls at a more specific single-parcel level.

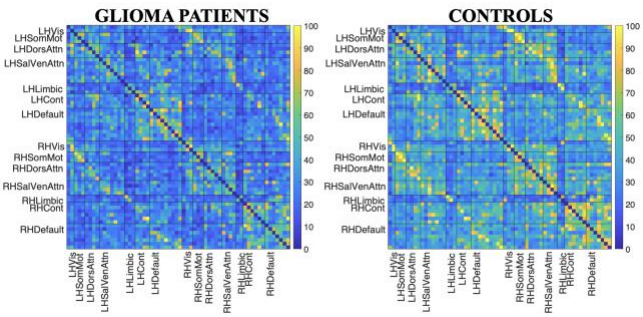


Fig. 2: Effective connectivity matrices reporting the percentage of directed links in oncological and control subjects.

The upper part of Fig. 3 shows the parcels revealing statistically significant differences in both silhouette coefficient and Euclidean distance gradients values between the two datasets.

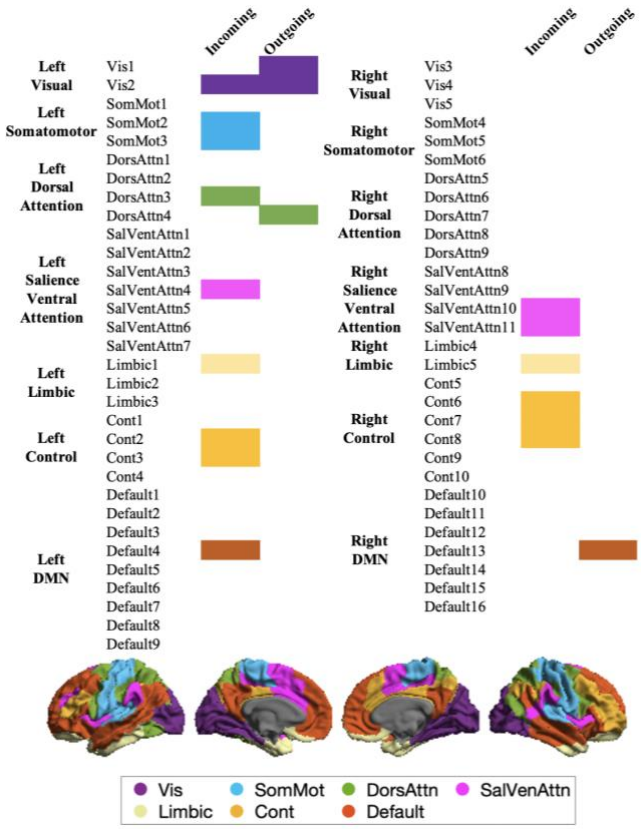


Fig. 3: Statistically significant parcels divided according to left/right network between control and oncological subjects and spatial distribution of the 7 Resting-State Networks (RSNs). Vis, visual network; SomMot, somatomotor network; DorsAttn, dorsal attention network; SalVenAttn, salience ventral attention network; Cont, control network; DMN, default mode network.

For incoming gradients, significant differences were found in parcels of all the 7 left networks, while in the right-hand side, differences are found only in the Salience Ventral Attention, Limbic and Control network.
For outgoing gradients, differences were found in all the left visual parcels, left Dorsal Attention and right DMN.
Specifically, DorsAttn3, SalVentAttn10, Cont6, Cont7 and Cont8 parcels, which result as the regions with the highest tumour overlap across subjects, revealed altered connectivity profiles only on incoming links. Nevertheless, there are also regions with a high tumour overlap that do not show any obvious alteration from such analyses, and whose role within the network needs to be further in deep investigated in future studies.

IV. Conclusions

The introduction of the notion of directionality as incoming and outgoing connections allowed us to interpret the altered nature of the communication flow associated with each RSN and region, and to unveil the altered topographic organization of large-scale brain organization in presence of brain gliomas[13]. For incoming gradients, differences between patients and controls resulted in visual, salience and control networks confirming the impact of the lesion as highlighted in [6]. Consequently, the information obtained from the incoming EC is similar to that of the FC, since the altered parcels belong to networks that appear to be impaired in both analyses.

At the parcel level we observed a hemispheric unbalance in the localization of regions that are statistically significant on the basis of the analysis computed, which may be due to the spatial heterogeneity of the tumour across subjects (24 left, 15 right and 8 bilateral lesion), and due to the fact that in healthy subjects the left hemisphere is more modular, thus presents groups of parcels with strong internal cohesion, and high separation between them[23]. This difference between the two hemispheres means that the effect of the tumour could be more evident in the left hemisphere's parcels, translating into an alteration of this cerebral organization that provides more heterogeneity between subjects (silhouette coefficient analysis), and in the distance from the reference (euclidean distance analysis).

Concerning outgoing gradients, only a few regions in visual, dorsal attention and default networks revealed statistical differences. These results also provide new insights into the key role of outgoing links in both Dorsal Attention (frequently activated in relation to other active brain networks) and Default Mode Network (DMN). Interestingly, both incoming and outgoing DMN links are compromised, which reveals a loss of connectivity investigated introducing links' directionality due to disruption of the connections, confirming the dual nature of that network[24].

In addition to regions with a non null intersection with the tumour mask that we expected to have an altered behavior due to the direct effect of the tumour, even parcels with no overlap with the lesion are altered, which can be explained by the widespread effect of the tumour even on regions that should have a potentially healthy profile.

References

[1] R. Stupp, M. Brada, M. J. van den Bent, J.-C. Tonn, and & G. Pentheroudakis, 'High-grade glioma: ESMO Clinical Practice Guidelines for diagnosis, treatment and follow-up † on behalf of the ESMO Guidelines Working Group * incidence and epidemiology', 2014.

[2] D. C. Ghinda, J. S. Wu, N. W. Duncan, and G. Northoff, 'How much is enough-Can resting state fMRI provide a demarcation for neurosurgical resection in glioma?', *Neurosci Biobehav Rev*, vol. 84, pp. 245–261, Jan. 2018.

[3] E. van Kessel *et al.*, 'Cognitive impairments are independently associated with shorter survival in diffuse glioma patients', *J Neurol*, vol. 268, no. 4, p. 1434, Apr. 2021.

[4] C. A. Meyers, K. R. Hess, W. K. A. Yung, and V. A. Levin, 'Cognitive function as a predictor of survival in patients with recurrent malignant glioma', *Journal of Clinical Oncology*, vol. 18, no. 3, pp. 646–650, Sep. 2000.

[5] C. D. Hacker, J. L. Roland, A. H. Kim, J. S. Shimony, and E. C. Leuthardt, 'Resting-state network mapping in neurosurgical practice: a review', *Neurosurg Focus*, vol. 47, no. 6, p. E15, Dec. 2019.

[6] E. Silvestri *et al.*, 'Widespread cortical functional disconnection in gliomas: an individual network mapping approach', *Brain Commun*, vol. 4, no. 2, Mar. 2022.

[7] R. J. Harris *et al.*, 'Altered functional connectivity of the default mode network in diffuse gliomas measured with pseudo-resting state fMRI', *J Neurooncol*, vol. 116, no. 2, pp. 373–379, Jan. 2014.

[8] V. M. Stoecklein *et al.*, 'Resting-state fMRI detects alterations in whole brain connectivity related to tumor biology in glioma patients', *Neuro Oncol*, vol. 22, no. 9, pp. 1388–1398, Sep. 2020.

[9] L. Pasquini, M. Jenabi, O. Yildirim, P. Silveira, K. K. Peck, and A. I. Holodny, 'Brain Functional Connectivity in Low- and High-Grade Gliomas: Differences in Network Dynamics Associated with Tumor Grade and Location', *Cancers (Basel)*, vol. 14, no. 14, p. 3327, Jul. 2022.

[10] E. Silvestri *et al.*, 'An ICA-based approach to study altered resting state functional networks in brain tumours', 2021, Accessed: Jan. 24, 2023.

[11] M. H. Adhikari *et al.*, 'Effective connectivity extracts clinically relevant prognostic information from resting state activity in stroke', *Brain Commun*, vol. 3, no. 4, Oct. 2021.

[12] G. Prando, M. Zorzi, A. Bertoldo, M. Corbetta, M. Zorzi, and A. Chiuso, 'Sparse DCM for whole-brain effective connectivity from resting-state fMRI data', *Neuroimage*, vol. 208, p. 116367, Mar. 2020.

[13] D. S. Margulies *et al.*, 'Situating the default-mode network along a principal gradient of macroscale cortical organization', *Proc Natl Acad Sci U S A*, vol. 113, no. 44, pp. 12574–12579, Nov. 2016.

[14] R. Vos de Wael *et al.*, 'BrainSpace: a toolbox for the analysis of macroscale gradients in neuroimaging and connectomics datasets', *Communications Biology 2020 3:1*, vol. 3, no. 1, pp. 1–10, Mar. 2020.

[15] M. G. Preti and D. van de Ville, 'Decoupling of brain function from structure reveals regional behavioral specialization in humans', *Nature Communications 2019 10:1*, vol. 10, no. 1, pp. 1–7, Oct. 2019.

[16] Ş. Bayrak *et al.*, 'The impact of ischemic stroke on connectivity gradients', *Neuroimage Clin*, vol. 24, Jan. 2019.

[17] A. Babayan *et al.*, 'A mind-brain-body dataset of MRI, EEG, cognition, emotion, and peripheral physiology in young and old adults', *Scientific Data 2019 6:1*, vol. 6, no. 1, pp. 1–21, Feb. 2019.

[18] A. Schaefer *et al.*, 'Local-Global Parcellation of the Human Cerebral Cortex from Intrinsic Functional Connectivity MRI', *Cerebral Cortex*, vol. 28, no. 9, pp. 3095–3114, Sep. 2018.

[19] J. E. Chen and G. H. Glover, 'BOLD fractional contribution to resting-state functional connectivity above 0.1 Hz', *Neuroimage*, vol. 107, pp. 207–218, Feb. 2015.

[20] R. Henson and K. Friston, 'Convolution Models for fMRI', *Statistical Parametric Mapping: The Analysis of Functional Brain Images*, pp. 178–192, Jan. 2007.

[21] S. Ryali, T. Chen, A. Padmanabhan, W. Cai, and V. Menon, 'Development and validation of consensus clustering-based framework for brain segmentation using resting fMRI', *J Neurosci Methods*, vol. 240, pp. 128–140, Jan. 2015.

[22] J. Zhang, O. Abiose, Y. Katsumi, A. Touroutoglou, B. C. Dickerson, and L. F. Barrett, 'Intrinsic Functional Connectivity is Organized as Three Interdependent Gradients', *Scientific Reports 2019 9:1*, vol. 9, no. 1, pp. 1–14, Nov. 2019.

[23] L. Jajcay, D. Tomeček, J. Horáček, F. Španiel, and J. Hlinka, 'Brain Functional Connectivity Asymmetry: Left Hemisphere Is More Modular', *Symmetry 2022, Vol. 14, Page 833*, vol. 14, no. 4, p. 833, Apr. 2022.

[24] M. G. Sharaev, V. v. Zavyalova, V. L. Ushakov, S. I. Kartashov, and B. M. Velichkovsky, 'Effective connectivity within the default mode network: Dynamic causal modeling of resting-state fMRI data', *Front Hum Neurosci*, vol. 10, no. FEB2016, p. 14, Feb. 2016.

Assessment of the effects of parcellation and frequency band on the definition of functional hubs in rsfMRI

Giulia Vallini[1], Erica Silvestri[1], Alessandro Panciera[1], Marco Aiello[2], Alessandra Bertoldo[1,3]
[1] *Department of Information Engineering, University of Padova, 35131 Padova, Italy*
[2] *IRCCS SDN, Istituto di Ricerca Diagnostica e Nucleare, 80143 Naples, Italy*
[3] *Padova Neuroscience Center, University of Padova, 35131 Padova, Italy*

***Abstract*— Functional hubs, defined from BOLD studies as brain regions with a large number of connections, have a crucial role in the integration and flow of information within the brain network. Furthermore, the functional configuration of hubs is correlated with individual cognitive performance and shows alterations in many neuropsychiatric disorders. However, how the spatial distribution of hubs depend on different choices in the analysis of the BOLD signal has not been extensively explored. Here we studied the influence of two major factors: the brain parcellation pattern and the spectral filtering strategy. Our findings suggest that they both affect the results. In addition, the organisation of brain network is strongly compromised when the BOLD signal does not contain the 0.01-0.05 Hz frequency range.**

***Keywords*— rsfMRI, hubs, brain parcellations, frequency bands.**

I. INTRODUCTION

Resting-state functional magnetic resonance imaging (rsfMRI) acquisitions are widely used in studies of brain functional connectivity (FC), defined as the zero-lag correlation between the BOLD (Blood Oxygenation Level Dependent) signal of spatially distant brain parcels [1]. For this purpose, volume parcellation by applying neural atlases is used [2]. Furthermore, before the FC estimation, the measured signal, BOLD signal, is filtered while generally keeping 0.01-0.1 Hz or 0.01-0.2 Hz frequency bands. This because BOLD needs to be cleaned by the contribution of the dominant noise source, and assuming that the frequency content due to the neural activity is below 0.15/0.2 Hz, while, the systemic components related to heartbeat and respiration, which represent background noise, have a frequency below 0.01 Hz [3].

In connectomics studies, the graph theory is a frequently used approach to investigate the brain network starting from FC maps, allowing functional hubs to be identified. These are regions that play crucial roles in the transmission and integration of information throughout the brain. Several studies have investigated how the spatial configuration of the hubs is linked to individual cognitive performance and that an alteration is found in many brain disorders [4].

To the best of our knowledge, little is known about the impact on hubs distribution of applying different atlases for brain parcellation [5] and filtering the temporal signal in different frequency bands [6]. Indeed, reliable network metrics are essential for inferring convincing conclusions from clinical studies and a precise identification of hubs patterns could provide rich insights into the mechanisms underlying cognition and brain disorders.

Therefore, the aim of this work is to simultaneously investigate the influence of the atlas choice and filtering of the temporal signal in different frequency bands in characterizing the spatial distribution of hubs. At the same time, an analysis of the brain networks modularity is carried out to assess which frequency bands most influence the brain organization.

II. MATERIALS AND METHODS

A. Materials

The dataset consists of 28 healthy subjects undergoing rsfMRI acquisition (Siemens 3T Biograph mMR scanner, equipped with standard head-neck coil) from two studies, *dataset A* [7] and *dataset B* [8], merged as no statistically significant difference was found [9]. During the scans, participants were instructed to remain lying down, with their eyes open and without doing any kind of activity.

Dataset A includes 11 subjects (3 F., age 52.2 ± 10.4), for each of them the rsfMRI data comprises 300 volumes acquired with gradient-echo planar imaging (GE-EPI) T2* (TR/TE=2000/30 ms and voxel-size=3x3x3.6 mm^3).

Dataset B includes 17 subjects (11 F., age 64.7 ± 7.9) with a rsfMRI data that comprises 240 GE-EPI T2* volumes (TR/TE=1920/32 ms and voxel-size=4x4x4 mm^3).

For each participant a magnetization prepared rapid acquisition gradient (MPRAGE) T1w structural image was acquired (voxel-size=1x1x1 mm^3).

B. Methods

The subjects' T1w images were bias field corrected using ANTs [10] and segmented into gray (GM) and white (WM) matter and cerebrospinal fluid (CSF) using SPM12 tool (https://www.fil.ion.ucl.ac.uk/spm/). Binarized probability maps (threshold=0.95) were linearly registered to the individual EPI space using ANTs. For each participant, the functional data were pre-processed with an FSL-based [11] in-house pipeline which included slice timing, geometric distortions, and motion corrections. In addition, further sources of noise such as white matter (WM) and cerebrospinal fluid (CSF) signals were regressed out.

To evaluate the effect of the parcellation, two atlases (3 different parcellation schemes) are tested: the AAL2 [12] and the Schaefer 7 Network at 100 and 200 parcels [13] integrated with subcortical regions from AAL2 and cerebellar functional regions from Buckner atlas [14], since the Schaefer only maps cortical area. These atlases differ in the principle used to outline their regions. In fact, the AAL2 atlas is anatomical, whereas the Schaefer and Buckner atlases are functional. The Fig. 1 shows few axial slices of the atlases used. For each parcel, the mean BOLD signal is extracted by averaging the rsfMRI data of all included voxels belonging to GM. In order

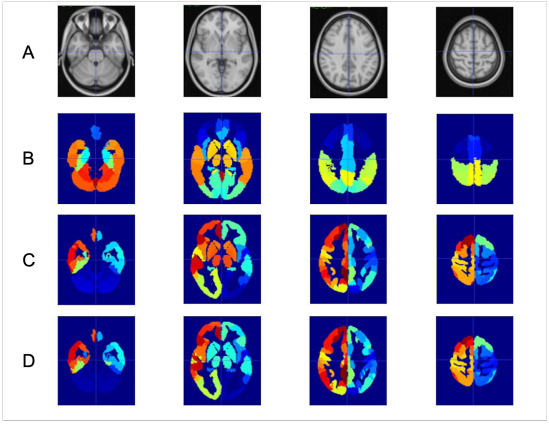


Fig. 1: (A) Structural image; (B) AAL2 atlas; (C) Schaefer 100 atlas, plus AAL2 for subcortical and Buckner for cerebellum; (D) Schaefer 200 atlas, plus AAL2 for subcortical and Buckner for cerebellum. Axial view from bottom to top.

to assess the effect on the hub regions distribution due to the frequency bands analyzed, mean BOLD signals are filtered as in [6] exploiting: 1) "canonical" bands, generally studied in literature to extract neural activity, and 2) "sub-bands" defined by dividing the entire spectrum into regular intervals of 0.05 Hz. In particular, the filter chosen is the Chebyschev type 2, with a pass-band ripple of 95%, a stop-band ripple of 5%, while transition region of 8%.

Namely, "canonical" bands are: 0.01-0.1 Hz (F1), 0.01-0.2 Hz (F2), 0.01 Hz (F3, high pass only); "sub-bands": 0.01-0.05 Hz (F4), 0.05-0.1 Hz (F5), 0.1-0.15 Hz (F6), 0.15-0.2 Hz (F7), 0.2-0.24 Hz (F8).

Next, for each subject the FC matrix is obtained by applying Pearson's correlation between the time courses of parcel pairs and z-Fischer transform. The procedure is done for each of the atlases considered and at each of the frequency bands.

In order to simplify the comparison and improve the signal-to-noise ratio, the average group matrices are calculated across subjects, therefore subsequent analyses are performed on these matrices. A binarization is applied to each matrix by defining a threshold at the 80th percentile to maintain only the most relevant interregional (positive) links in terms of functional connectivity. The node degree is calculated for each region as the total number of its connections after the application of the threshold and hubs as the 10% of nodes with the highest degree [4].

To assess the effect of the frequency, the Pearson's correlation between hub spatial distribution obtained in different bands within the same atlas is calculated. In addition, the modularity of each full FC matrix, which refers to the set of subnetworks or distinct communities that exist within the network, is investigated. Here we used the Louvain [15] implementation available in the Brain Connectivity Toolbox (http://www.brain-connectivity-toolbox.net). Finally, to evaluate the effect of parcellation, the dice coefficient between hubs spatial maps of atlas pairs within the same frequency is computed.

III. RESULTS

Fig. 2 shows the hubs distribution for each frequency band and parcellation scheme and the matrix of correlation coefficients between these distributions at different bands, within the same atlas.

The hubs pattern is similar (Fig. 2, panel A) when comparing the "canonical" bands F1 (0.01-0.1 Hz), F2 (0.01-0.2 Hz) and F3 (> 0.01 Hz, High-Pass only), but also the first "sub-band" F4 (0.01-0.05 Hz). Confirming the similarities, the correlation coefficients are significantly high (Fig. 2, panel B). Considering these bands, in AAL2 the hubs are located predominantly in the Cingulate Medial and Temporal Area,

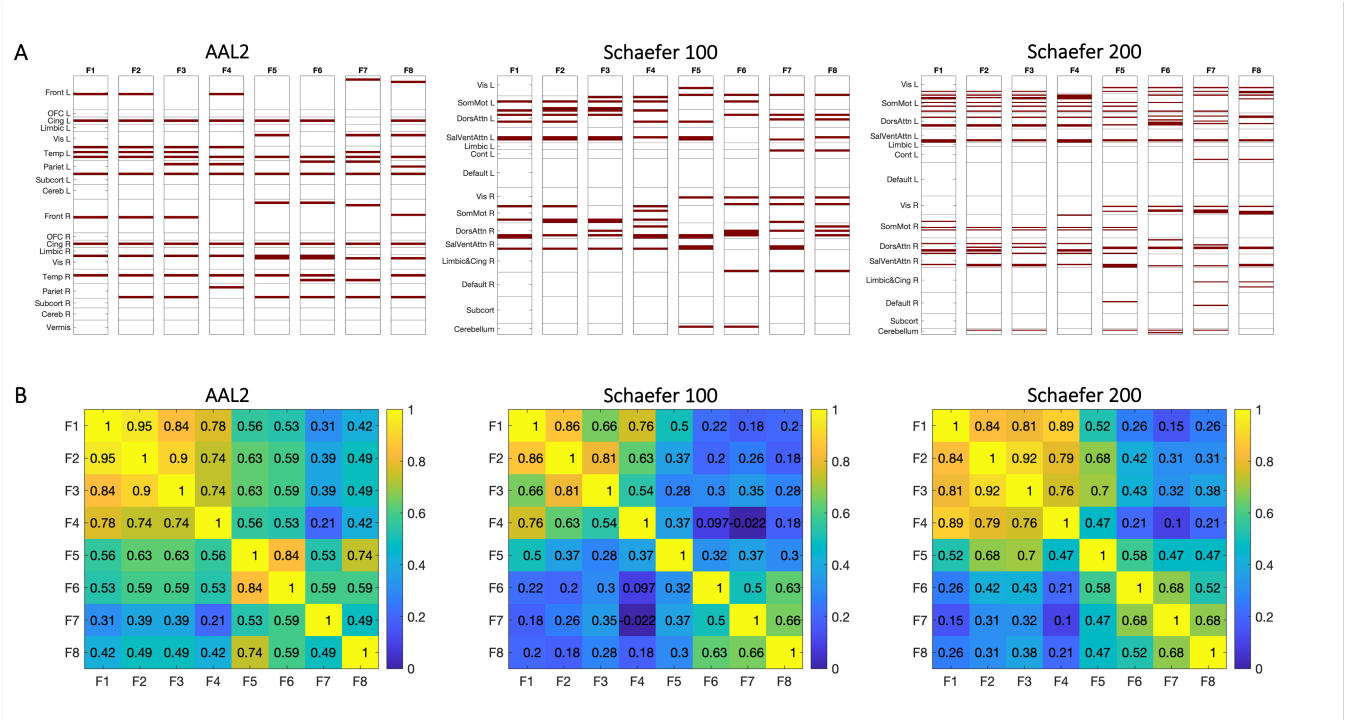


Fig. 2: (A) Distribution of hub regions in the three parcellation schemes and for each band; (B) Pearson's correlation coefficient matrices between the hubs' spatial distributions of pairs of bands. F1, F2, F3 and F4 show extremely high correlation values of hub distributions ($p < 0.05$).

whereas in both Schaefer 100 and 200 the hubs are located mainly in the in the Somato-motor Area and Dorsal Attention.

As the higher frequency bands are analyzed, the distribution of the hubs varies. F5 (0.05-0.1 Hz) and F6 (0.1-0.15 Hz), especially in AAL2 and Schaefer 200, have a similar distribution to each other, and show only partial variation in hub regions compared to the "canonical" bands and F4. The analyses of correlation coefficients confirm this finding, revealing a moderate correlation values. Then, analyzing the distribution of hub regions in the higher frequency bands F7 (0.15-0.2 Hz) and F8 (0.2-0.24 Hz), it is evident that only a few regions are preserved as hubs compared to the "canonical" bands. Pearson's coefficients confirm these results revealing the absence of correlation.

From the full FC matrices (Fig. 3 shows functional connectivity matrices only for the F1, F5 and F8 bands), the *Louvain modularity* values are derived for each parcellation pattern and frequency band (Table I).

TABLE I: LOUVAIN MODULARITY VALUES FOR EACH FC MATRIX

	F1	*F2*	*F3*	*F4*	*F5*	*F6*	*F7*	*F8*
AAL2	0.16	0.15	0.14	0.17	0.14	0.12	0.11	0.09
Sch100	0.17	0.16	0.15	0.18	0.14	0.12	0.10	0.09
Sch200	0.17	0.16	0.16	0.19	0.14	0.12	0.10	0.09

Louvain modularity of each FC matrix obtained for each parcellation and in each frequency band.

The matrix with the highest modularity is that obtained in F4, closely followed by "canonical" bands. Instead, considering higher frequency bands, from F5 the modularity progressively decreases, until it reaches its lowest value at F8. These results are consistent across the three parcellations.

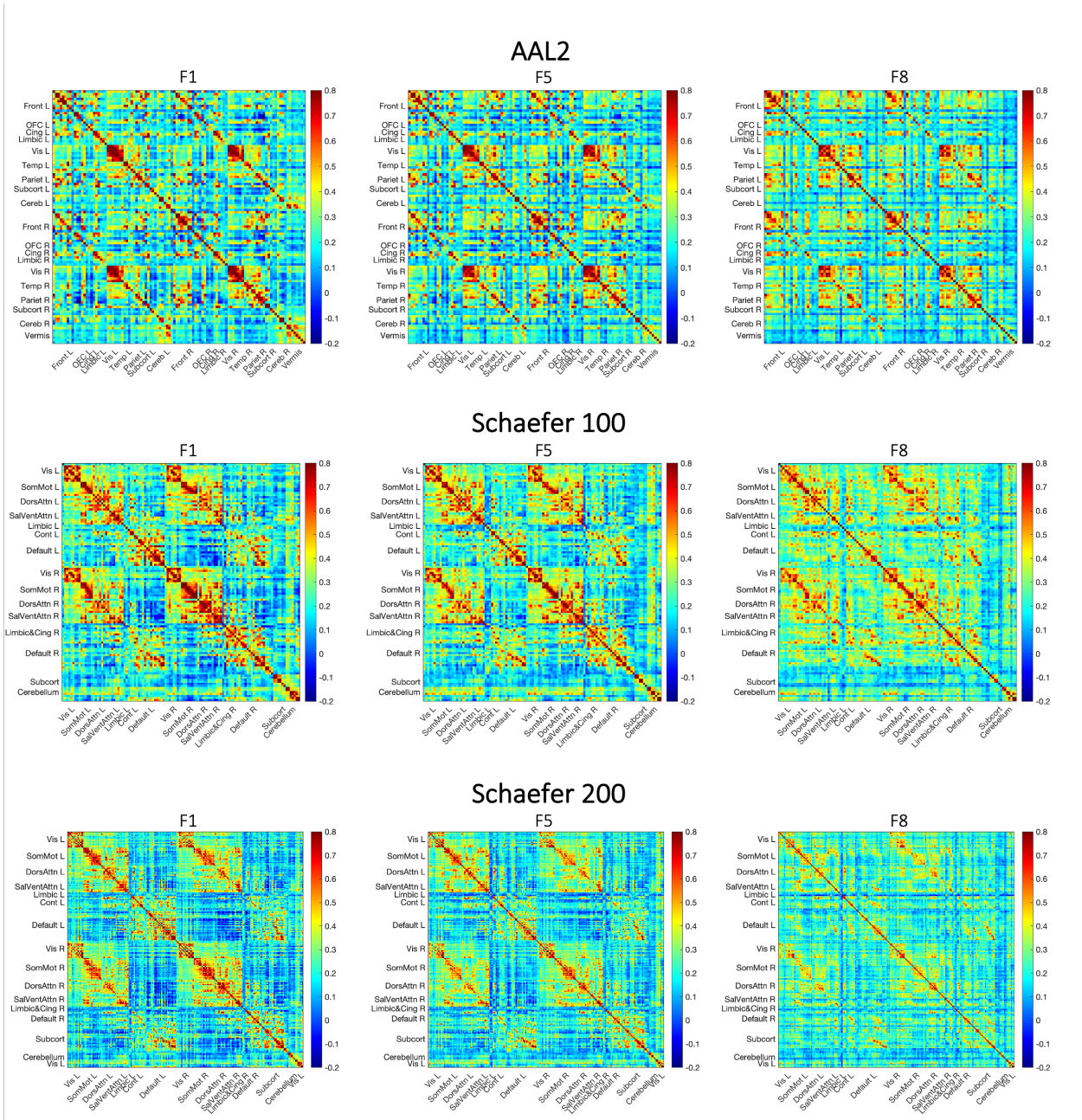


Fig. 3: FC matrices for the three parcellations schemes (AAL2, Schaefer 100 and Schaefer 200) and F1 (0.01-0.1 Hz), F5 (0.05-0.1 Hz) and F8 (0.2-0.24 Hz) bands.

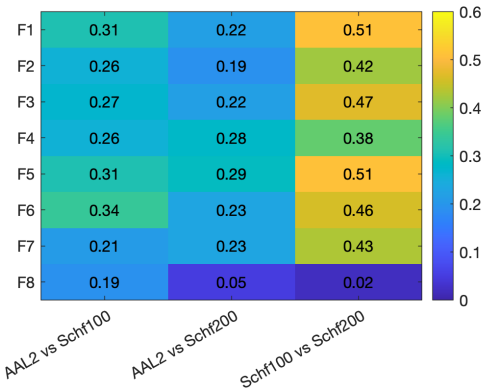


Fig.4: Values of dice coefficient between the hubs spatial maps of pairs of atlases while keeping the frequency band fixed.

To evaluate the effect of the parcellation, Fig. 4 shows the matrix of dice coefficients between the hubs' spatial maps of pairs of atlases, at a fixed frequency. Low similarities emerge, particularly when comparing AAL2 and Schaefer.

IV. DISCUSSION

Assessing the effect of the analyzed frequency bands, from the results obtained it is evident that in terms of both the spatial distribution of the hubs and the modularity, the bands containing the 0.01-0.05 Hz range (i.e., F1, F2, F3 and F4) have similar behavior. Considering the bands from F5 to F8, the spatial distribution of the hubs differs, and the modularity values progressively decrease. These discrepancies suggest that a large part of the contribution due to the description of the neuronal activity organization is already in the 0.01-0.05 Hz (i.e., in F4) and in the frequency bands containing this range.

When evaluating the effect of the parcellation scheme, the low similarity results are probably due to the different way of defining regions in the atlases: AAL2 was designed on the basis of the anatomical characteristics of each region, whereas the Schaefer atlas is functional and therefore regions were obtained by grouping voxels on the basis of appropriate functional homogeneity criteria.

V. CONCLUSION

The aim of this work is to assess whether the atlas used for the parcellation and the frequencies at which the rsfMRI signal is analyzed affect the distribution of brain regions with a central role in the brain network, i.e., functional hubs. From the results obtained, it is clear that both the parcellation using two different atlases and the extraction of the BOLD signal at different frequencies cause a variation in the functional connectivity detected and, consequently, in the spatial distribution of the hubs. In a connectivity study, therefore, the choice of atlas cannot be made exclusively based on those that are most widely used in the literature (e.g., AAL2), as this has a strong influence on the final results. In particular, due consideration must be given to the choice of an anatomical or functional atlas according to the final purpose. Concerning the effect of frequency, papers in literature that have investigated the impact of BOLD signal analysis in different frequency bands, e.g. [6], suggests that even at high frequency bands (not containing 0.01-0.05 Hz) there are significant functional hubs and network organization. However, we introduced an analysis of the modularity of brain networks to assess which frequency bands most influence brain organization. In contrast to previous findings, our results support that considering frequency bands that do not include 0.01-0.05 Hz leads to brain network disruption. Thus, the greatest contribution related to neuronal activity emerges in 0.01-0.05 Hz and in the bands containing this range (F1-F4) which reflect good spatial agreement in the pattern of hubs and similar modularity values. The disaggregation that instead emerges in the remaining bands is probably because this part of the signal starts to be strongly influenced by the presence of slow hemodynamic function information, thus driven by a purely vascular component.

ACKNOWLEDGEMENT

The authors would like to thank Dr. Valentin Riedl for making *dataset A* available.

REFERENCES

[1] K. J. Friston, C. D. Frith, P. F. Liddle, and R. S. J. Frackowiak, "Functional connectivity: The principal-component analysis of large (PET) data sets," *J. Cereb. Blood Flow Metab.*, vol. 13, no. 1, pp. 5–14, 1993.

[2] R. A. Poldrack, "Region of interest analysis for fMRI," *Soc. Cogn. Affect. Neurosci.*, vol. 2, no. 1, pp. 67–70, 2007.

[3] M. D. Fox and M. E. Raichle, "Spontaneous fluctuations in brain activity observed with functional magnetic resonance imaging," *Nat. Rev. Neurosci.*, vol. 8, no. 9, pp. 700–711, 2007.

[4] R. L. Buckner *et al.*, "Cortical hubs revealed by intrinsic functional connectivity: Mapping, assessment of stability, and relation to Alzheimer's disease," *J. Neurosci.*, vol. 29, no. 6, pp. 1860–1873, 2009.

[5] J. W. M. Domhof, K. Jung, S. B. Eickhoff, and O. V. Popovych, "Parcellation-induced variation of empirical and simulated brain connectomes at group and subject levels," *Netw. Neurosci.*, vol. 5, no. 3, pp. 798–830, 2021.

[6] L. Wang, X. Chen, Y. Xu, M. Cao, X. Liao, and Y. He, "Frequency-Resolved Connectome Hubs and Their Test-Retest Reliability in the Resting Human Brain," *Neurosci. Bull.*, vol. 38, no. 5, pp. 519–532, 2022.

[7] V. Riedl *et al.*, "Local activity determines functional connectivity in the resting human brain: A simultaneous FDG-PET/fMRI study," *J. Neurosci.*, vol. 34, no. 18, pp. 6260–6266, 2014.

[8] M. Aiello *et al.*, "Relationship between simultaneously acquired resting-state regional cerebral glucose metabolism and functional MRI: A PET/MR hybrid scanner study," *Neuroimage*, vol. 113, pp. 111–121, 2015.

[9] A. Palombit *et al.*, "Variability of regional glucose metabolism and the topology of functional networks in the human brain," *Neuroimage*, vol. 257, no. January, p. 119280, 2022.

[10] B. B. Avants, N. J. Tustison, G. Song, P. A. Cook, A. Klein, and J. C. Gee, "A reproducible evaluation of ANTs similarity metric performance in brain image registration," *Neuroimage*, vol. 54, no. 3, pp. 2033–2044, 2011.

[11] M. Jenkinson, C. F. Beckmann, T. E. J. Behrens, M. W. Woolrich, and S. M. Smith, "NeuroImage," vol. 62, pp. 782–790, 2012.

[12] E. T. Rolls, M. Joliot, and N. Tzourio-Mazoyer, "Implementation of a new parcellation of the orbitofrontal cortex in the automated anatomical labeling atlas," *Neuroimage*, vol. 122, pp. 1–5, 2015.

[13] A. Schaefer *et al.*, "Local-Global Parcellation of the Human Cerebral Cortex from Intrinsic Functional Connectivity MRI," *Cereb. Cortex*, vol. 28, no. 9, pp. 3095–3114, 2018.

[14] R. L. Buckner, F. M. Krienen, A. Castellanos, J. C. Diaz, and B. T. Thomas Yeo, "The organization of the human cerebellum estimated by intrinsic functional connectivity," *J. Neurophysiol.*, vol. 106, no. 5, pp. 2322–2345, 2011.

[15] V. D. Blondel, J. L. Guillaume, R. Lambiotte, and E. Lefebvre, "Fast unfolding of communities in large networks," *J. Stat. Mech. Theory Exp.*, vol. 2008, no. 10, 2008.

Radiomic analysis of Epicardial Adipose Tissue in cardiac MRI for hospitalization risk assessment

F. Lo Iacono[1], M. Minotti[1], M. Guglielmo[3], M. Penso[2], M.L. Carerj[2], G. Pontone[2,4] and V.D.A. Corino[1,2]
[1] *Department of Electronics, Information and Bioengineering, Politecnico di Milano, Italy*
[2] *Department of perioperative Cardiology and Cardiovascular Imaging, Centro Cardiologico Monzino IRCCS, Milan, Italy*
[3] *Department of Cardiology, Division of Heart and Lungs, University Medical Center Utrecht, Utrecht, The Netherlands.*
[4] *Department of Biomedical, Surgical and Dental Sciences, University of Milan, Milan, Italy*

***Abstract*— Epicardial Adipose Tissue (EAT) is a visceral fat depot whose local effects on cardiac function are incorporated into the complex pathomechanism of coronary artery disease, atrial fibrillation, and heart failure. The aim of this study is to create a radiomic signature to assess the hospitalization risk of 261 patients, from EAT cardiac magnetic resonance-based radiomics. 107 radiomic features were extracted from EAT segmented images and their robustness was assessed by means of ROI translations and intraclass correlation coefficient computation. Robust features were subjected to further selection steps comprising a statistical test and a univariate Cox regression model. Selected features were used to create the radiomic signature, testing three survival models: Cox Proportional Hazard (CPH) regression, random survival forest (RSF), and deep survival analysis (DeepSurv). Leave-one-out cross-validation was performed to build Kaplan-Meier curves and evaluate models' performances. Ten clinical variables were then added to the analysis to test that radiomic signature maintained its significative prognostic value. 56 radiomic features were identified as robust and two textural features, Gray Level Non-Uniformity Normalized and Cluster Shade, were kept to create the radiomic signature. CPH and DeepSurv significantly identified patients with a high risk of hospitalization. Fitting the CPH model with radiomic and clinical features, radiomic signature coefficients remained significant (p=0.04). In conclusion, results achieved in this study have shown that EAT-based radiomics could be a promising tool in assessing patient hospitalization risk.**

***Keywords*—Epicardial Adipose Tissue, radiomics, Survival models**

I. Introduction

Epicardial Adipose tissue (EAT) refers to the fat depot that exists between the surface of the myocardium and visceral layer of pericardium. Due to its biological activity, EAT has been suggested to have a role in the progression and development of leading causes of morbidity and mortality such as coronary artery disease (CAD), atrial fibrillation and heart failure [1]. Mancio et al. [2] provided a systematic review and meta-analysis reporting a significantly higher EAT level in subjects who experienced coronary stenosis, coronary calcification, myocardial ischemia or MACE (major adverse cardiac events. Also, EAT thickness and volume have been found to be a potential substrate for the pathogenesis of atrial fibrillation [1].

Radiomics is a rapidly developing field which allows the extraction and analysis of quantitative data from medical images. Radiomics have been widely employed in oncology, but it has gained increasing interest for the diagnosis and prognosis of cardiovascular disease.

Actually, literature reports only a few studies employing radiomic features extracted from EAT, but all of them have shown promising results in classifying and predicting atrial fibrillation [3]-[4]-[5]-[6]. In [3], a machine learning model using EAT radiomic features can distinguish patients with atrial fibrillation from those with normal sinus rhythm reaching high diagnostic performance: an AUC of 0.92 and 0.85 were achieved in the test cohorts of contrast-enhanced and non-enhanced scans, respectively. The study conducted in [4] built a radiomic model, using CT-based radiomic features extracted from EAT, whose performance achieved an area under the curve of 0.80 for discrimination between patients with post-operative atrial fibrillation and sinus rhythm. Yang et al. [5] has shown the power of left atrium EAT radiomic signature in differentiating atrial fibrillation subtype by developing a predictive model which integrates radiomic features and volume information to differentiate AF subtype. This model has provided an AUC of 0.853 in the validation cohort. In [4], textural features have been found to be a stronger predictor of lone AF recurrence compared with other established risk factors and EAT volume and attenuation.

This work aims at developing a radiomic signature to improve hospitalization risk assessment for cardiac reasons, using CMR (cardiac magnetic resonance) based radiomic features extracted from EAT.

II. Materials and methods

A. Study population

This study includes 261 consecutive patients, referred to perform clinically indicated dipyridamole stress CMR (Cardiovascular Magnetic Resonance) for suspected or known CAD between January 2011 and December 2014 at Centro Cardiologico Monzino (Milan, Italy). Clinical characteristics are shown in Table I.

B. Image acquisition

CMR has been performed with a 1.5-T unit (Discovery MR 450; GE Healthcare, Milwaukee, Wisconsin, USA). Breath-hold, steady-state free-precession cine imaging have been performed in vertical and horizontal long-axes and in short-axis orientations. A stack of short-axis slices encompassing both ventricles from base-to-apex has been used for biventricular volumes, mass, and systolic function assessment.

A contrast-enhanced breathhold segmented T1-weighted inversion- recovery gradient-echo sequence has been used for myocardial fibrosis using the late gadolinium enhancement

(LGE) imaging technique. LGE imaging has been performed 10–20 min after an intravenous bolus of 0.1 mmol/kg Gadobutrol (Gadovist; Bayer Schering Pharma AG, Berlin-Wedding, Germany). Inversion time has been individually adapted to null the signal of remote myocardium (usual range 220–30).

TABLE I: CLINICAL VARIABLES (MEAN ± STANDARD DEVIATION OR NUMBER OF PATIENTS/TOTAL NUMBER OF PATIENTS)

Features	*Hospitalized*	*Non-Hospitalized*	*Total*
Age	64.67 ± 9.63	63.08 ± 10.42	63.79 ± 10.07
Body Mass Index	25.81 ± 3.70	27.08 ± 3.54	26.49 ± 3.66
CMR Left Ventricular Ejection Fraction (%)	55.83 ± 13.11	56.45 ± 11.44	56.16 ± 12.23
Sex (F/M)	15/107	23/116	38/223
Familiar History (y/n)	30/83	30/96	60/179
Smoking (y/n)	45/68	45/81	90/149
Hypertension (y/n)	79/35	76/50	155/85
Hyperlipemia (y/n)	79/35	82/44	161/79
Diabetes (y/n)	32/83	20/106	52/189
Perioperative myocardial ischemia	84/37	70/66	154/103

TABLE II: PERCENTAGE OF MISSING VALUES

Features	*Missing values (%)*
Age	0
Body Mass Index	9.6
CMR Left Ventricular Ejection Fraction (%)	1.1
Sex (F/M)	0
Familiar History	8.4
Smoking	8.4
Hypertension	8
Hyperlipemia	8
Diabetes	7,7
Perioperative myocardial ischemia	1.4

C. Image Processing

EAT was manually segmented by expert radiologists.

Image pre-processing was performed to denoise images using a 3D Gaussian filter with a 3x3x3 voxel kernel and σ=0.5. Intensity-non uniformities were corrected using the N4ITK algorithm and intensity standardization was performed with z-score. Finally, B-spline interpolation was employed to resample the voxel size to a 2 mm isotropic resolution. MATLAB R2017a (MathWorks, Natick, MA, USA) was used to perform all the previous steps.

D. Radiomic Features Extraction

107 radiomic features were extracted from patients EAT, using Pyradiomics 3.0 [7]. Features pertain to three main classes: Shape and Size (14 Features), First Order Statistics (18 Features), and Textural features including GLCM (24 features), GLRLM (16 features), GLSZM (16 features), NGTDM (5 features) and GLDM (14 features). The full list of radiomic features is available in the Pyradiomics Python package documentation [7], [8]. A fixed-bin width histogram discretization (32 bins) was used prior to features extraction.

Since features were extracted with Pyradiomics, they were compatible with the Image Biomarker Standardization Initiative (IBSI).

E. Features Selection

A three step features selection was applied to radiomic features previously scaled with z-score normalization.

Geometrical translation method described in [9] were performed to assess features robustness. A minimal entity translation, corresponding to 0.5% of the length of the bounding box surrounding the ROI, was chosen to test features stability, while a maximal entity translation of 30% of the length of the bounding box surrounding the ROI, was considered to evaluate features discrimination capacity. Robust features were then selected by computing the Intraclass Correlation Coefficient (ICC) between the original and the translated ROI. According to the general guidelines reported in [10] two ICC threshold were set: 0.75 for ICC related to minimal entity translation (ICC_{min}) and 0.5 for ICC related to maximal entity translation (ICC_{max}). Features having an ICC_{min} higher than 0.75 and an ICC_{max} lower than 0.5 were considered robust, i.e., stable, and discriminative. Only first order statistic and textural features were subjected to robustness analysis since shape and size features of each ROI are kept constant throughout the geometrical transformations.

After this step, **Mann-Whitney U test** was applied to each feature, to identify features significantly different between the hospitalized and non-hospitalized patients.

Finally, a **univariate Cox regression model** was fitted for each of the selected feature, and p-value and Harrel's concordance index (C-index) were provided for each test. Features with coefficients not significantly different from 0 ($p>0.05$) were excluded from the analysis.

All the steps described in this paragraph were carried out using Python 3.7 [11].

F. Survival analysis models

In this work, three different survival models were tested: Cox Proportional Hazard (CPH) regression model [12], random survival forest (RSF) [13], and deep survival analysis (DeepSurv) [14].

CPH is a semi-parametric model that estimates the impact of observed variables on the risk of an event (e.g., hospitalization) occurring. The model assumes that covariate effects are additive and linear on the log risk scale: this assumption may often be an oversimplification for proper prognosis prediction.

RSF and DeepSurv models represent nonlinear alternatives to CPH.

RSF is an ensemble tree method for survival analysis which automatically assesses the complex effects and interactions among all variables.

DeepSurv is a nonlinear extension of the Cox proportional hazards model, based on a deep learning-based-survival prediction algorithm that uses a multi-layer feed-forward

network. It can model high-level interaction terms beyond the linear Cox model.

A Leave One Out Cross Validation (LOOCV) approach was used to estimate the performance of the three models. As a result, for each iteration, the test set contained only one observation, while the others were used as training.

The final feature set was used to train the three models for the risk of hospitalization. The features and regression coefficients of the optimal model were used to compute the radiomic signature, which for example for the CPH model was the linear combination of the selected features and the corresponding regression coefficients. At each LOOCV iteration the median signature in the training set was used as threshold to classify the test set subject into high and low risk groups (above and below the median, respectively). Finally, classified test set patients were gathered, and log-rank test was used to compare Kaplan-Meier curves of the two groups.

Last, ten clinical variables, reported in literature as relevant cardiovascular risk factors [15]-[16], were combined to the radiomic signature to train a CPH model. This step was performed to verify that clinical features integration did not affect the significance of radiomic signature prognostic value. Clinical variables included in the analysis are reported in Table I. Clinical data presented missing data, in a variable percentage, as shown in Table II. Missing data imputation was performed using the mode.

III. Results

A. Features selection

56 radiomic features were identified stable and discriminative after robustness analysis: 9 first-order statistic and 47 textural features. As a results, a total of 70 radiomic features, i.e., the 56 robust ones and the 14 shape-based features, were included in the further analysis.

Among the 70 selected features, four resulted statistically significant after Mann-Whitney U test: Gray Level Non-Uniformity Normalized (GLNUN), Cluster Shade, Gray Level Variance, Inverse Variance. All of them belong to the class of textual features.

Fitting the univariate Cox regression model, two of these features, Gray Level Non-Uniformity Normalized, Cluster Shade, were selected as their coefficient were significantly different from 0. P-values and C-index obtained from univariate Cox regression model are shown in Table III.

B. Survival models evaluation

The radiomic signature was obtained from the multivariate Cox model using the two features previously selected. The Kaplan-Meier curves for the final test set (obtained from LOOCV test patients merging) are shown in Fig.1. Both the Cox Proportional Hazard model and Deep Survival analysis model signature had a significant prognostic ability.

TABLE III: Univariate Cox model results

Feature	*P-value*	*C-Index*
Gray Level Non-Uniformity Normalized	0.049	0.553
Cluster Shade	0.040	0.558
Gray Level Variance	0.065	0.540
Inverse Variance	0.101	0.522

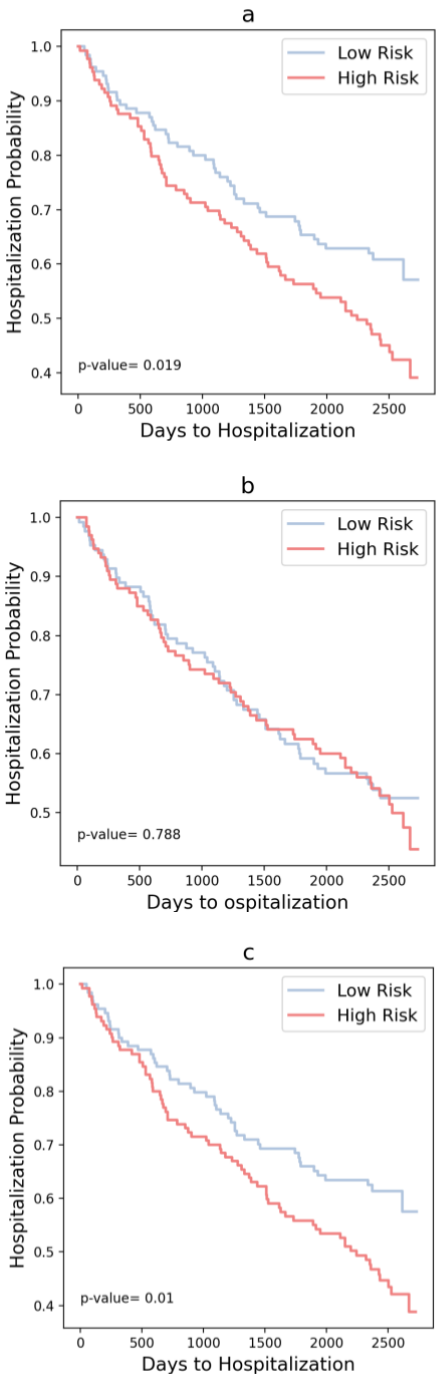


Fig. 1: Kaplan-Meier curves for the high and low risk groups obtained from (a) Cox Proportional Hazard, (b) Random Survival Forest and (c) Deep Survival analysis model signature.

Performing the log-rank test to compare the Kaplan-Meier curves obtained from CPH, RSF and DeepSurv, obtained p-values were 0.019, 0.788 and 0.01, respectively.

Finally, the results obtained fitting the CPH model with a combination of radiomic and clinical features confirmed the prognostic value of the signature (with a p-value of 0.04).

IV. Conclusion

In this work, a set of CMR based-radiomic features were extracted from EAT to investigate its association with hospitalization. The main finding of our study is that a radiomic signature can be created to divide a population into two groups according to the risk of hospitalization for cardiac reasons. Literature reports only a few studies employing CT-based radiomics features extracted from EAT [3]-[4]-[5]-[6] to investigate atrial fibrillation occurrence. To the best of our knowledge, this is the first study that developed a survival analysis model to study the relationship between EAT characteristics and hospitalization risk for cardiac reasons. Moreover, no previous studies on EAT have been performed their analysis using CMR-based radiomic features.

Also, a crucial point in the radiomic workflow is features robustness assessment as only stable and discriminative features should be used in prognostication or prediction models to improve their generalizability. Studies employing EAT radiomics models [4]-[5]-[6] have evaluated radiomic features by using repeated segmentation of the ROIs performed by multiple radiologists. Differently, in our study, features robustness has been assessed using the approach described in [9] based on ROIs geometrical translations. This method is less time-consuming than performing repeated segmentation and does not require many radiologists. In addition, small entity translations allow to evaluate features stability while large translations provide features discrimination capacity assessment.

Once identified, robust radiomic features have been selected according to their relevance with respect to the clinical question of interest. Differences in textural features, i.e., characteristics reflecting EAT graininess, uniformity, regularity, and roughness have been found to be more discriminative in dividing patients hospitalized and not hospitalized.

Thus, the radiomic signature was created for each patient testing three different survival models. DeepSurv and CPH models outperformed RSF showing a significative p-value in comparing the Kaplan Meier curves with a log-rank test. The radiomic signature remained predictive also when clinical covariates were added in the model.

The radiomic signature created in the study have included Gray Level Non-Uniformity Normalized and Cluster Shade: these texture characteristics can be signs of molecular peculiarities of adipose tissue, showing EAT dysfunction. In particular, in [6] changes of Gray Level Non-Uniformity Normalized have been suggested to be associated with morphological heterogeneity of the EAT caused by hypertrophy and hyperplasia of adipocytes, as well as by fibrotic changes.

However, one of the limits of this study is given by the lack of data on histological characteristics of EAT able to support radiomic analysis results.

Furthermore, the workflow developed in this study should be tested on different and larger dataset in order to validate the results achieved.

Despite these limitations, the results of this work were promising, indicating that the use of radiomics may be useful in investigating EAT characteristics to assess patient hospitalization risk.

References

[1] G. Iacobellis, “Epicardial adipose tissue in contemporary cardiology,” *Nat Rev Cardiol*, vol. 19, issue. 9, pp.593-606, March. 2022.

[2] J. Mancio *et al.*, “Epicardial adipose tissue volume assessed by computed tomography and coronary artery disease: a systematic review and meta-analysis,” *European Heart Journal - Cardiovascular Imaging*, vol. 19, issue. 5, pp. 490–497, Dec. 2017.

[3] L. Zhang *et al.*, “Machine-learning-based radiomics identifies atrial fibrillation on the epicardial fat in contrast-enhanced and non-enhanced chest CT,” *BJR*, vol. 95, issue. 1135, p. 20211274, July 2022.

[4] J. Mancio *et al.*, “Decoding the radiomic and proteomic phenotype of epicardial adipose tissue associated with adverse left atrial remodelling and post-operative atrial fibrillation in aortic stenosis,” *European Heart Journal - Cardiovascular*, vol. 23, issue. 9, pp.1248-1259, May 2022.

[5] M. Yang *et al.*, “Development and Validation of a Machine Learning-Based Radiomics Model on Cardiac Computed Tomography of Epicardial Adipose Tissue in Predicting Characteristics and Recurrence of Atrial Fibrillation,” *Frontiers in Cardiovascular Medicine*, vol. 9, March 2022.

[6] J. Ilyushenkova *et al.*, “Radiomic phenotype of epicardial adipose tissue in the prognosis of atrial fibrillation recurrence after catheter ablation in patients with lone atrial fibrillation,” *Journal of Arrhythmia*, 2022.

[7] Radiomic Features — pyradiomics 2.1.0 documentation https://pyradiomics.readthedocs.io/en/2.1.0/features.html.

[8] J. J. M. van Griethuysen *et al.*, “Computational Radiomics System to Decode the Radiographic Phenotype,” *Cancer Res*, vol. 77, issue. 21, pp. 104–107, Nov. 2017.

[9] M. Bologna *et al.*, “Assessment of Stability and Discrimination Capacity of Radiomic Features on Apparent Diffusion Coefficient Images,” *J Digit Imaging*, vol. 31, issue. 6, pp. 879–894, Dec. 2018.

[10] T. K. Koo e M. Y. Li, “A Guideline of Selecting and Reporting Intraclass Correlation Coefficients for Reliability Research,” *Journal of Chiropractic Medicine*, vol. 15, issue. 2, pp. 155–163, June 2016.

[11] scikit-learn: machine learning in Python — scikit-learn 1.1.1 documentation. https://scikit-learn.org/stable/.

[12] D. R. Cox, “Regression Models and Life-Tables,” *Journal of the Royal Statistical Society: Series B (Methodological)*, vol. 34, issue. 2, pp. 187–202, 1972.

[13] H. Ishwaran, U. B. Kogalur, E. H. Blackstone, e M. S. Lauer, “Random survival forests,” *Ann. Appl. Stat.*, vol. 2, issue. 3, pp. 851-860, Sept. 2008.

[14] C. Nagpal, X. R. Li, e A. Dubrawski, “Deep Survival Machines: Fully Parametric Survival Regression and Representation Learning for Censored Data with Competing Risks,” *IEEE Journal of Biomedical and Health Informatics*, vol. 25, Jan. 2021.

[15] C. Lu, H. Jia, e Z. Wang, “Association between epicardial adipose tissue and adverse outcomes in coronary heart disease patients with percutaneous coronary intervention,” *Biosci Rep*, vol. 39, issue. 5, p. 20182278, May 2019.

[16] N. Nerlekar *et al.*, “Association of Epicardial Adipose Tissue and High-Risk Plaque Characteristics: A Systematic Review and Meta-Analysis,” *Journal of the American Heart Association*, vol. 6, issue. 8, p. 6379, Aug. 2017.

Augmented Reality to Evaluate Temporo-Mandibular Joint Alterations in Orthognathic Patients

N. Emiliani[1], F. Babini[1], C. Gulotta[2], G. Badiali[2,3], E. Marcelli[1] and L. Cercenelli[1]
[1]*Laboratory of Bioengineering – eDIMES Lab, Department of Medical and Surgical Sciences (DIMEC), University of Bologna, Bologna, Italy*
[2]*Department of Biomedical and Neuromotor Sciences, University of Bologna, Bologna, Italy*
[3]*IRCCS Azienda Ospedaliero Universitaria di Bologna, Oral and Maxillofacial Surgery Unit, Bologna, Italy*

***Abstract*—Augmented Reality (AR) is a technology that offers the possibility to overlap virtual objects on the real scene. In recent years, AR has been proposed and applied also in the medical field. In this study, we aimed to develop an AR application for Microsoft HoloLens 2 to be used for the evaluation of temporo-mandibular joint (TMJ) alterations in orthognathic patients. The actual procedures to diagnose TMJ alterations consist of direct palpation of the joint and/or execution of kinesiographic exam which allows to record the jaw movements. The developed AR application provides the projection of the reconstructed virtual underlying bony structures directly on the visible patient's head, thus facilitating the diagnostic evaluation of the surgeon.**

The AR application was tested on a volunteer during TMJ tasks of opening and closing of the mouth. During the tasks, video recordings were taken from the HoloLens cameras, and then they were processed by Matlab to derive the kinematic curves and values describing the jaw movements. The AR-derived TMJ trajectories were then compared with standard kinesiographic acquisitions.

The results demonstrated a good match between the AR-derived kinematics and kinesiographic curves. Future improvements are needed for the tracking modalities to allow more accurate quantification of the TMJ kinematics in the frontal view.

***Keywords*—Augmented Reality, 3D printing, image processing, orthognathic surgery, kinesiography, Microsoft HoloLens2.**

I. Introduction

Augmented Reality (AR) offers the possibility to overlap virtual contains on the real world, thus allowing the user to view hidden underlying structures and/or to have additional digital information useful for guiding a procedural task.

AR in medicine is a technology that expands on image-guided surgery, allowing intraoperative guidance and navigation. This technique integrates imaging information with the real-world surgical field to give the surgeon a sort of "x-ray vision" [1]. In recent years, AR technology has been proposed and applied in several medical fields, including neurosurgery [2,3], urology [4–7], orthopedics [8,9] and craniomaxillofacial surgery [10-15].

Several technologies have been proposed and used to perceive the augmented surgical field. Specifically, commercial optical see-through Head Mounted Displays (HMDs), such as Microsoft HoloLens (Microsoft, Redmond, WA), Google Glass (Google Inc., Mountain View, California, USA) and Magic Leap (Magic Leap, Plantation, Florida, USA) have been always more used to explore their applications in surgery.

In craniomaxillofacial surgery, the AR technology can be considered a promising tool in aiding complex surgical procedures but could represent an effective tool also for preoperative planning and diagnosis phase [16-19]. Particularly, some procedures performed routinely by surgeons to evaluate possible surgical options could be improved using the AR technology.

Temporo-mandibular joint (TMJ) articulates the mandible to the temporal bone glenoid fossa, through the mandibular condyles. TMJ is fundamental for the movements of the mandible, including chewing and speaking. The conventional diagnostic procedure for possible alterations of the TMJ kinematics involves both the clinical observation of the interincisive line during the opening and closing of the mouth and the direct palpation of the joint. However, during this clinical examination, the surgeon cannot directly see the underlying bony structures involved in the mandibular movements.

Another method to assess the TMJ kinematics is the kinesiographic exam, consisting of an electronic system designed to trace and record the mandibular movement in three dimensions [20]. Advantages over kinesiography can be provided by AR, since the surgeon has the possibility to directly see-through the anatomy of the patient, having a direct visualization of the joint superimposed on the patient's face.

The aim of this work was to develop and test an AR application for Microsoft HoloLens2 HMD, which allows the surgeon to directly see on the patient's face the digital reconstruction of the mandibular condyles and temporal bone glenoid fossa, involved in the execution of TMJ movements.

The trajectories of the mandibular movement were reconstructed from the video recordings taken with HoloLens cameras during the AR view, and then they were compared to the trajectories obtained from the kinesiographic exam.

II. Materials and Methods

In the following sections the development steps and the experimental phase are reported.

Image segmentation

Starting from the Computed Tomography (CT) scan of a volunteer, the skull, the mandible, and the head skin were segmented using D2P™ software (3D Systems Inc., Rock Hill, USA). Three-dimensional meshes were then generated from all the segmented masks and saved in Standard Tessellation Language (STL) format.

Virtual content preparation and 3D printing

The STL files were imported in Autodesk Meshmixer software (Autodesk Inc., CA, USA): the skull was cut to have only the temporal bone glenoid fossa. The developed AR application consisted of both the frontal and the lateral view of TMJ movements; for this reason, the STL file of the mandible was duplicated and cut symmetrically to have only the right branch for the lateral view. Some virtual spherical markers were added both on the mandible and the glenoid fossa, to have some landmarks in the video recordings for the further reconstruction of TMJ trajectories from AR view.

Moreover, the reconstructed mandible was used to design a patient-specific dental splint fitting the lower arch teeth of the subject. The splint was jointly connected to a QR-code, which was used for the real-time tracking of the mandible during TMJ movements (Figure 1.C).

The virtual splint was then produced with stereolitography 3D printer (Form3B, FormLabs, Somerville, MA, USA) using a biocompatible resin (Surgical guide, FormLabs, Somerville, MA, USA).

Development of the AR application

All virtual models (i.e. the glenoid fossa, the mandible, the head skin and the dental splint) were imported into Unity 3D software (Unity Technologies, San Francisco, CA, USA) extended with the Vuforia Engine Package (PTC Inc., Boston, MA, USA).

For the purposes of the study, the AR application had to recognize and track the movement of two different objects involved in the TMJ, i.e., the glenoid fossa and the mandible.

For this, two different tracking methods were implemented. For tracking the glenoid fossa, we used the "Model Target" tracking modality of Vuforia Engine, which allows a marker-less tracking of the object by recognizing its shape. In this case, the head skin model was used as Model Target for virtual-to-real scene registration of the glenoid fossa (Figure 2.A). For tracking the mandible, we chose the "Image Target" tracking modality of Vuforia Engine which is based on the recognition and tracking of a pre-defined image, in this case, the QR-code anchored to the dental splint (Figure 2.B). Working with these two tracking modalities, the movement of the mandible can be tracked continuously, and its position is displayed to the user wearing the HoloLens 2 HMD in relation to the fixed glenoid fossa (Figure 3).

Two different AR applications running on HoloLens 2 were created: one for the lateral view and one for the frontal view (Figure 3). Moreover, interactable user interface toggles (check boxes) were added to turn on/off the rendering of each virtual anatomical structure during the AR view.

Experimental Phase and processing of AR video recordings

First, the standard kinesiographic exam (Myotronics Kynesiograph K7, Harari MS, Milan, Italy) was executed on the volunteer. For the exam, the volunteer has to wear a mask, composed of sensors, which lay on the ears and nose, and a tiny magnet which is attached to the lower incisal gingiva with adhesive material (Figure 1).

Following the indications of the specialist, the volunteer performed the opening and closing jaw movements (i.e. TMJ task) five consecutive times. The mask registered in real-time the variations of the magnetic field during the movement of the magnet in the three space directions, and with these coordinates, graphic recordings of the TMJ opening/ closing paths were provided.

The AR application was then tested on the volunteer: both lateral and frontal views were tested to three-dimensionally evaluate the trajectory of the TMJ during the opening and closing of the mouth (TMJ tasks). The volunteer was asked to follow the same procedure of the kinesiographic exam, with the opening and closing of the mouth five consecutive times.

During each TMJ task, the video recordings of the AR view displayed to the user wearing the glasses were taken using the HoloLens 2 cameras. Then, the video frames were extracted and imported in Matlab App-Designer (R2019b, MathWorks, Natick, MA, USA). A Matlab script was created to recognize the mandible marker (see the pink sphere in Figure 3) in each video frame, and to plot the mandible trajectory during the TMJ tasks.



Fig. 1: Frontal view of the volunteer with the mask used during the kinesiographic exam.

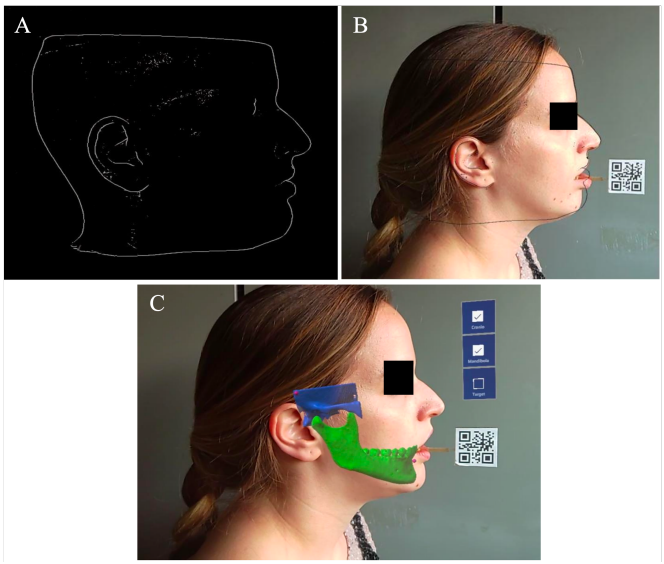


Fig. 2: A) Guide view of the Model Target tracking modality used for displaying the glenoid fossa, B) Image Target (QR-code) tracking modality used for tracking the moving mandible, C) Lateral AR view displayed from

the HoloLens 2 glasses: the fixed glenoid fossa (in blue) and the moving mandible (in green).

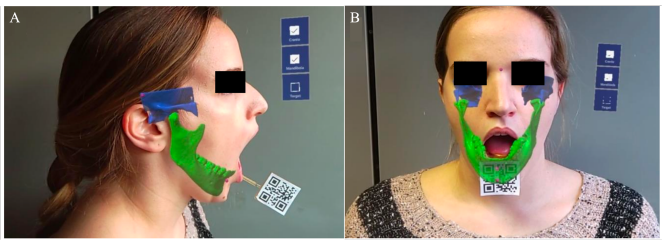


Fig. 3: Examples of AR views during the execution of TMJ tasks**:** A) Lateral view of the opening, B) Frontal view of the opening.

III. Results

The developed AR application demonstrated to work in a correct way, being able to track and display the anatomical structures of interest for evaluating the TMJ kinematics.

For the lateral view, the AR-derived trajectories of the opening and closing of the mouth showed a good match with the kinesiographic signals, both qualitatively and quantitively. Particularly considering the opening phase, we obtained a deviation of only 0.2 mm in the maximum vertical movement, and a deviation of 0.7 mm for the maximum horizontal movement, i.e. the posterior extension (Figure 4, black curve).

Regarding the frontal view, the AR application reproduced qualitatively the kinesiographic trajectory, while a considerable deviation was obtained for both the maximum vertical movement (6.5 mm) and the horizontal movement (2.1 mm), when considering the opening phase (Figure 5, black curve).

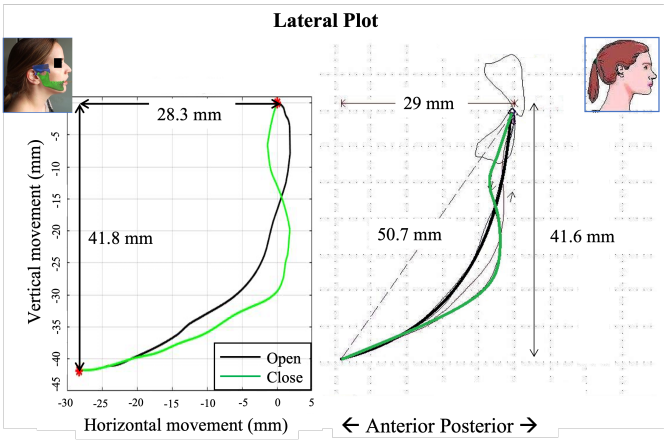


Fig. 4: Lateral plot of the opening and closing trajectories obtained from the AR video recordings (on the left) and from the kinesiographic exam (on the right).

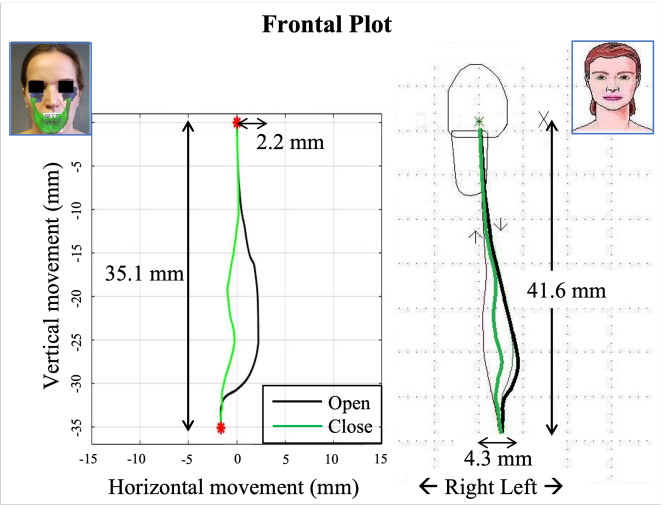


Fig. 5: Frontal plot of the opening and closing trajectories obtained from the AR video recordings (on the left) and from the kinesiographic exam (on the right).

IV. Discussion

This study aims to investigate the feasibility of an AR application for Microsoft HoloLens 2 as an additional tool to evaluate and diagnose any TMJ alterations. The developed AR application offers the advantage, over the currently used methods, to show the surgeon the underlying bony structures involved in the TMJ. Indeed, using the AR view, the surgeon may have a direct visualization of the joint superimposed on the patient's face.

Surely, as previously reported, critical points for this kind of application remain the depth perception [21] and the achievable accuracy of the virtual-to-real content registration [1, 22].

The experimental phase has shown the capability of the AR application to correctly visualize the virtual anatomical structures directly on the patient during the execution of the TMJ tasks. Particularly, the AR application was successful in tracking the moving mandible from an occlusion position to a maximum opening position and vice versa.

The trajectories obtained from the AR video recordings were qualitatively similar to the ones obtained from the kinesiographic exam. Particularly, these trajectories highlighted a non-completely symmetrical behavior between opening and closing (i.e., no overlapping of the trajectory during the opening and closing of the mouth), this suggesting a sub-optimal kinematics of the left TMJ.

Regarding the frontal view, the considerable deviation we obtained is probably due to the QR-code inclination during the mandibular movement. In fact, at the position of the maximum opening of the mouth, the QR-code no longer appears in a frontal position with respect to the observer, but is inclined; this results in a distortion of the perceived QR-code image target by the HMD cameras, which causes to lose tracking, therefore to detect a reduced vertical displacement.

Another limitation of the developed AR application regarded the speed of the performed movements: too fast opening or closing of the mouth may cause a loss of tracking, i.e., the misalignment between the virtual anatomical structures and the real scene, with consequent unreliable AR-derived

movements.
Future developments will investigate the use and accuracy of other tracking modalities that may provide more robust tracking of the moving mandible, to record the complete TMJ trajectory also in the frontal AR view. Indeed, it is extremely important to achieve the best alignment between the patient and the virtual structures, in order to avoid any effect of the rotations on the estimated kinematics.
Furthermore, it would be interesting to test the match between the AR and the reference kinematics on movements executed at different speeds. .
Finally, it could also be useful to implement a real-time quantification of the performed movement during the AR view. In this way, the surgeon could quantitatively assess in real-time the movement of interest, avoiding post-processing from videos recorded with the application.

V. Conclusion

In this study, we presented the development and preliminary testing of an AR application for Microsoft HoloLens 2, intended for the assessment of possible alterations in the TMJ. The system was tested on a volunteer during the opening and closing of the mouth: the TMJ trajectory derived from the AR application was compared to the one obtained from the kinesiographic exam. For the lateral view, the trajectories were highly comparable both qualitatively and quantitatively while for the frontal view, major deviations were found, probably due to a sub-optimal tracking modality of the moving mandible via the image target modality.
The tool seems to be promising and may represent an interesting alternative to kinesiographic exam.

References

[1] Cercenelli L, Babini F, Badiali G, Battaglia S, Tarsitano A, Marchetti C and Marcelli E (2022) Augmented Reality to Assist Skin Paddle Harvesting in Osteomyocutaneous Fibular Flap Reconstructive Surgery: A Pilot Evaluation on a 3D-Printed Leg Phantom. Front Oncol. 11:804748. doi: 10.3389/fonc.2021.804748

[2] Chidambaram S, Stifano V, Demetres M, Teyssandier M, Palumbo MC, Redaelli A, et al. Applications of Augmented Reality in the Neurosurgical Operating Room: A Systematic Review of the Literature. *J Clin Neurosci* (2021) 91:43–61. doi: 10.1016/j.jocn.2021.06.032

[3] Hersh A, Mahapatra S, Weber-Levine C, Awosika T, Theodore JN, Zakaria HM, et al. Augmented Reality in Spine Surgery: A Narrative Review. *HSS J* (2021) 17(3):351–8. doi: 10.1177/15563316211028595

[4] Reis G, Yilmaz M, Rambach J, Pagani A, Suarez-Ibarrola R, Miernik A, et al. Mixed Reality Applications in Urology: Requirements and Future Potential. *Ann Med Surg* (2021) 66:102394. doi: 10.1016/j.amsu.2021.102394

[5] Schiavina R, Bianchi L, Lodi S, Cercenelli L, Chessa F, Bortolani B, et al. Real-Time Augmented Reality Three-Dimensional Guided Robotic Radical Prostatectomy: Preliminary Experience and Evaluation of the Impact on Surgical Planning. *Eur Urol Focus* (2021) 7(6):1260–7. doi: 10.1016/j.euf. 2020.08.004

[6] Schiavina R, Bianchi L, Chessa F, Barbaresi U, Cercenelli L, Lodi S, et al. Augmented Reality to Guide Selective Clamping and Tumor Dissection During Robot-Assisted Partial Nephrectomy: A Preliminary Experience. *Clin Genitourin Cancer* (2021) 19(3):e149–55. doi: 10.1016/j.clgc.2020. 09.005

[7] Bianchi L, Chessa F, Angiolini A, Cercenelli L, Lodi S, Bortolani B, et al. The Use of Augmented Reality to Guide the Intraoperative Frozen Section During Robot-assisted Radical Prostatectomy, European Urology, Volume 80, Issue 4, 2021, Pages 480-488, ISSN 0302-2838, https://doi.org/10.1016/j.eururo.2021.06.020.

[8] Verhey JT, Haglin JM, Verhey EM, Hartigan DE. Virtual, Augmented, and Mixed Reality Applications in Orthopedic Surgery. *Int J Med Robot* (2020) 16 (2):1–9. doi: 10.1002/rcs.2067

[9] Matthews JH, Shields JS. The Clinical Application of Augmented Reality in Orthopaedics: Where Do We Stand? *Curr Rev Musculoskelet Med* (2021) 14 (5):316–9. doi: 10.1007/s12178-021-09713-8

[10] Badiali G, Cercenelli L, Battaglia S, Marcelli E, Marchetti C, Ferrari V, et al. Review on Augmented Reality in Oral and Cranio-Maxillofacial Surgery: Toward "Surgery-Specific" Head-Up Displays. *IEEE Access* (2020) 8:59015– 28. doi: 10.1109/ACCESS.2020.2973298

[11] Ceccariglia, F., Cercenelli, L., Badiali, G., Marcelli, E., Tarsitano A. Application of Augmented Reality to Maxillary Resections: A Three-Dimensional Approach to Maxillofacial Oncologic Surgery. Journal of Personalized Medicine, 2022, 12(12), 2047

[12] Cercenelli, L., Carbone, M., Condino, S., ...Ferrari, V., Badiali, G. The wearable VOSTARS system for augmented reality-guided surgery: Preclinical phantom evaluation for high-precision maxillofacial tasks. Journal of Clinical Medicine, 2020, 9(11), pp. 1–13, 3562

[13] Battaglia, S., Ratti, S., Manzoli, L., ...Tarsitano, A., Ruggeri, A. Augmented reality-assisted periosteum pedicled flap harvesting for head and neck reconstruction: An anatomical and clinical viability study of a galeo-pericranial flap. Journal of Clinical Medicine, 2020, 9(7), pp. 1–12, 2211

[14] Carbone, M., Cutolo, F., Condino, S., ...Badiali, G., Ferrari, V. Architecture of a Hybrid Video/Optical See-through Head-Mounted Display-Based Augmented Reality Surgical Navigation Platform. Information (Switzerland), 2022, 13(2), 81

[15] Benmahdjoub M, van Walsum T, van Twisk P, Wolvius EB. Augmented Reality in Craniomaxillofacial Surgery: Added Value and Proposed Recommendations Through a Systematic Review of the Literature. *Int J Oral Maxillofac Surg* (2021) 50(7):969–78. doi: 10.1016/j.ijom.2020.11.015

[16] Scherl, C., Stratemeier, J., Karle, C. et al. Augmented reality with HoloLens in parotid surgery: how to assess and to improve accuracy. *Eur Arch Otorhinolaryngol* 278, 2473–2483 (2021).

[17] Fatih Incekara, Marion Smits, Clemens Dirven, Arnaud Vincent, Clinical Feasibility of a Wearable Mixed-Reality Device in Neurosurgery, World Neurosurgery, Volume 118, 2018, Pages e422-e427, ISSN 1878-8750

[18] Rose AS, Kim H, Fuchs H, Frahm JM. Development of augmented-reality applications in otolaryngology-head and neck surgery. Laryngoscope. 2019 Oct; 129 Suppl 3:S1-S11. doi:10.1002/lary.28098. Epub 2019 Jul 1. PMID: 31260127.

[19] Jiang T, Yu D, Wang Y, Zan T, Wang S, Li Q. HoloLens-Based Vascular Localization System: Precision Evaluation Study With a Three-Dimensional Printed Model. *J Med Internet* Res. 2020;22(4):e16852. Published 2020 Apr 17. doi:10.2196/16852

[20] B Jankelson, C W Swain, P F Crane, J C Radke. Kinesiometric instrumentation: a new technology. J Am Dent Assoc. 1975 Apr;90(4):834-40.doi: 10.14219/jada.archive.1975.0164.

[21] Bremers AWD, Yöntem AÖ, Li K, Chu D, Meijering V, Janssen CP. Perception of Perspective in Augmented Reality Head-Up Displays. Int J Hum-Comput Stud (2021) 155:102693. doi: 10.1016/j.ijhcs.2021.102693

[22] Tokunaga DM, Corrêa CG, Bernardo FM, Bernardes J, Ranzini E, Nunes FLS, et al. Registration System Errors Perception in Augmented Reality Based on RGB-D Cameras. In: R Shumaker, S Lackey, editors. Virtual, Augmented and Mixed Reality. Cham: Springer International Publishing (2015). p. 119–29. Lecture Notes in Computer Science.

Transfer learning approaches to classify foetal occiput positions on transperineal ultrasound images

Morello R[1], Di Trani MG[2], Dall'Asta A[3], Conversano F[1], Pisani P[1], Di Paola M[1], Ghi T[3], Casciaro S[1]
[1] *National Research Council, Institute of Clinical Physiology, Lecce, Italy*
[2] *Research and Development Department, Amolab srl, Lecce, Italy*
[3] *Department of Medicine and Surgery, Obstetrics and Gynaecology Unit, University of Parma, Parma, Italy*

***Abstract*— This study aimed at comparing the effectiveness of different Transfer Learning (TL) approaches to automatically classify intrapartum ultrasound (US) images of direct and transverse foetal occiput position.**

We prospectively evaluated women in the second stage of labour from 14 clinical centres and a total of 612 transperineal ultrasound (TPU) images of the foetal head in the sagittal plane were selected. All the images were classified as direct or transverse occiput position, by an expert gynaecologist, acting as a gold standard.

The approach of TL with ResNet-18 convolutional neural network (CNN) was used to address the scarcity of data. Cross-domain and cross-modal TL approaches were compared. To perform cross-modal TL, the ResNet-18 was pre-trained on a public large dataset of foetal ultrasound, and subsequently was re-trained on our dataset.

The cross-modal approach provided the best performances, with highest accuracy, Cohen's k and F1-score. Our approach could effectively compensate for the issue of data scarcity in medical imaging diagnostic. The developed model could be employed as medical diagnostic tool to facilitate the individuation of the foetal position and the decision-making in labour management.

***Keywords*—Deep learning, transfer learning, foetal ultrasound, medical imaging, automatic.**

I. Introduction

THE interest in employing convolutional neural network (CNN) models in the medical imaging and, in particular, in foetal ultrasound has strongly increased in the past decade.

The potentialities of Machine Learning in image classification, segmentation and identification of diseases in multiple medical field have been largely demonstrated in several biomedical applications [1]–[3]. However, the main limitation of Deep Learning (DL) application is represented by the huge amount of data required to properly train a neural network, an issue particularly relevant in medical imaging, where data availability is limited and collecting data is a long and laborious process. In this work we opted for using and comparing different approaches of Transfer Learning (TL) to overcome the lack of data. This technique consists of using a model pre-trained on a very large dataset (millions of images) to perform one task and re-training the model for the desired similar task. Depending on whether the target and source data belong or not to the same domain, TL can be performed cross-modal (es. source: medical images – target: medical images), or cross-domain (es. source: images of objects – target: medical images) [4]–[6]. Models trained on object images poorly perform on medical images, as they typically have low contrast and rich textures.

In this work, cross-domain and cross-modal TL approaches were compared to classify trans-perineal ultrasound (US) images of foetal occiput positions.

Foetal occiput position is one of the main determinants for choosing the most adequate mode of delivery, a critical issue in obstetrics, particularly important in cases of poor progression and prior to start an instrumental vaginal delivery.

This crucial parameter is traditionally assessed at digital vaginal examination (DVE). However, recent evidence showed DVE can be subjective and uncomfortable for women, and it is associate with an error rate ranging from 20% to 70% [7], [8].

Despite international guidelines [9] recommendations on the use of intrapartum US to ascertain the position of the foetal occiput, most obstetricians are not familiar with this practice.

While transabdominal (TA) ultrasound is the preferred method to determine accurately foetal occiput position during labour, the use of transperineal (TP) acquisition allows the simultaneous evaluation of foetal head station, rotation and position in a single sonographic step [10]–[12]. However, transperineal ultrasound (TPU) has the disadvantage to be technically challenging for inexperienced operators [13].

Therefore, the second aim of this research is to develop an algorithm to enable the automatic and rapid assessment of the foetal occiput position from TPU acquisitions, providing an automatic and accurate classification of direct and transverse occiput positions.

II. Methods

A. Data collection

The data collection was conducted within the framework of the 'AI Occiput' International Multicentre Clinical Study, organized by the University of Parma, in collaboration with 14 maternity hospitals worldwide. In this prospective work, a total of 612 US images were collected from women in single, full-term and uncomplicated pregnancy (> 37 gestation weeks), placing the probe transperineally in transverse orientation.

Ultrasound examinations were performed using the following settings: convex probe with 65 mm radius of curvature, field of view 60°, nominal central frequency 3MHz (band from 2 to 5 MHz), scan depth 180 mm, multi-focused image with at least 2 focuses (30-50 mm and 100-150 mm) and linear Time Gain Control. The image acquisition was accomplished as a standard B-Mode image (PNG or BITMAP format with at least 512 x 512 pixels).

All the acquisitions were performed using either a generic ultrasound machine manually set in accordance with the above-mentioned parameters or the SensUS Touch system (Amolab Srl, Lecce, Italy), a tablet-like portable ultrasound system equipped with a software module specifically dedicated to this study.

An expert gynaecologist selected only images presenting foetal occiput in transverse position and classified each image as direct or transverse occiput position. The image with the best visualization of the anatomical landmarks was selected from 100 frames acquired during each US examination.

B. Data preparation

Three different databases were created to the scope of this work:

1. The images collected for this study were pre-processed to be anonymized and labelled. Patient and acquisition data, and information about the sonographer were eliminated from each image with a binary mask. This dataset will be called "AI Occiput-database". The final database counted 612 images.
2. From the large public dataset [14], a sub-set of images was selected including images of foetal abdomen, brain, femur and thorax; images of maternal cervix and other US

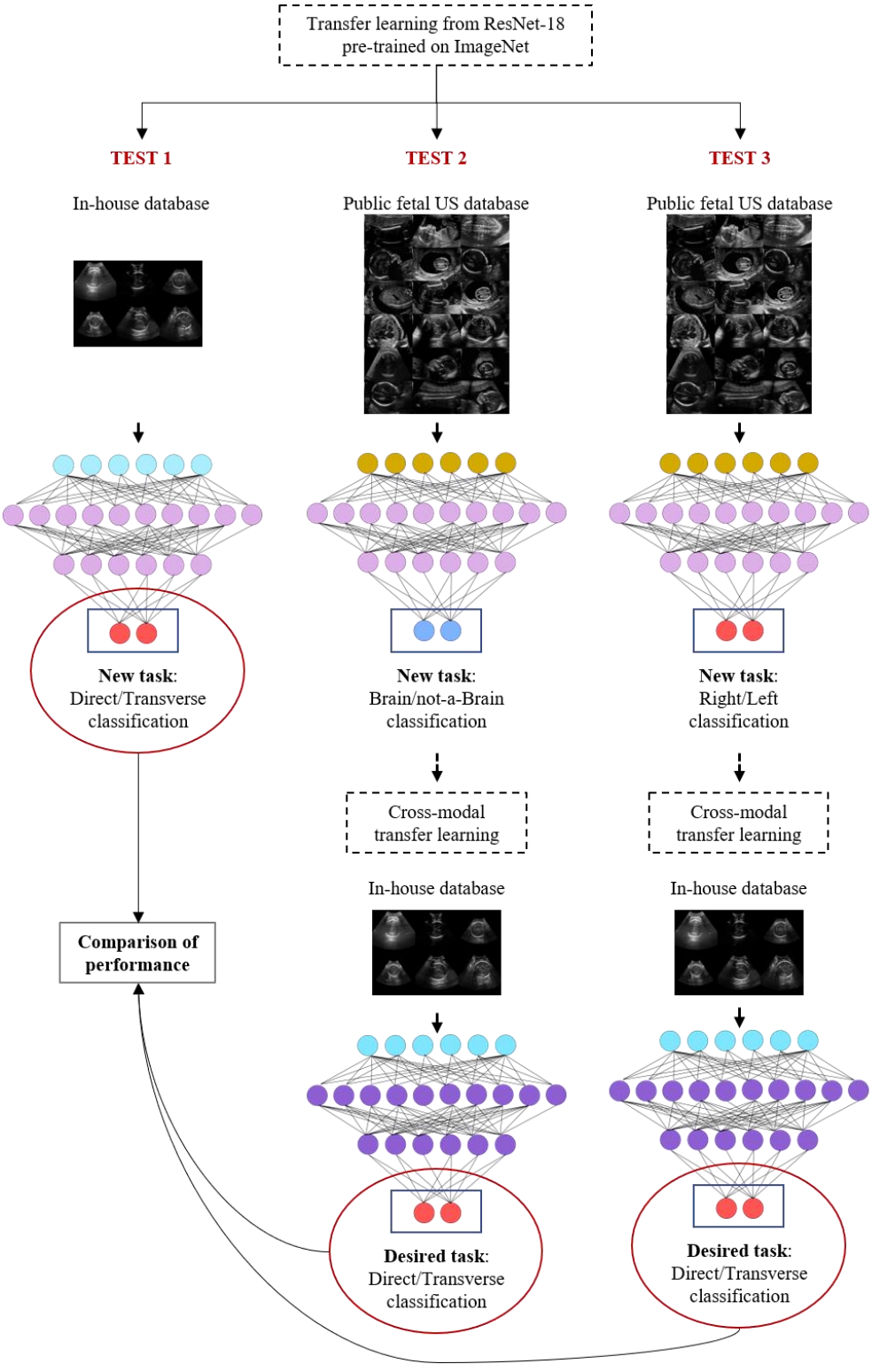


Fig. 1 – Graphical workflow of the used TL approaches.

images were excluded. Images were labelled to classify brain vs. not-a-brain task. The final database counted 8187 images. This dataset will be called "BnB-database".

3. From the large public dataset, another sub-set of images was selected, including only images of foetal brain in transversal position from TA ultrasound acquisition. Images were labelled to classify right vs. left occiput position. The final database counted 1386 images. This dataset will be called "RL-database".

Images were partitioned into train-, validation- and test-set with a ratio of 0.75/0.15/0.15 per category.

C. *Pre-training*

In this work, the approach of TL was used to address the lack of huge amount of data. We used the ResNet-18 convolutional neural network as classifier and we re-trained the network on a public large dataset of maternal-foetal screening ultrasound images [14] to perform cross-modal TL. Three different TL training processes were performed and compared (Figure 1):

1. ResNet-18 pre-trained on ImageNet [15] was re-trained on AI-Occiput database to classify direct and transverse occiput position (cross-domain transfer learning) – called Test 1;
2. ResNet-18 pre-trained on BnB-database to classify "brain, not-brain" was re-trained on AI Occiput-database to classify direct and transverse occiput position (cross-modal transfer learning) – called Test 2;
3. ResNet-18 pre-trained on RL-database to classify "right and left occiput position" was re-trained on AI Occiput-database to classify direct and transverse occiput position (cross-modal transfer learning) – called Test 3.

In summary, cross-domain TL was performed in Test 1, and two approaches of cross-modal-TL were performed in Test 2 and Test 3. The goal was to define the best TL method to train our small-sized database to classify direct and transverse occiput positions.

It is necessary to underline that the RL- and AI Occiput-database consisted of images acquired with different procedures: transabdominal and transperineal, respectively. Consequently, RL-database included higher-quality images than AI Occiput-database, since brain structures, such as choroid plexus, ventricles or cerebellum, showed low image contrast.

D. *Data augmentation*

Data augmentation was used to increase the training dataset and to enhance the model's performance. Our data augmentation strategy was based on geometric transformations (translation and shearing), noise injection (Gaussian and speckle) and contrast distortion. Each image in the original dataset thus underwent five transformations, whose parameters were chosen randomly from a continuous uniform distribution within the following intervals:

- Horizontal and vertical translation $\in [-20,20]$ $pixels$;
- Horizontal and vertical shearing $\in [-10°, 10°]$;
- Gaussian noise SD $\in [0, 1.1]$;
- Speckle noise density $\in [0.01, 0.05]$;
- Contrast distortion min $\in [0, 0.3]$, max $\in [0.7, 1]$.

E. *Statistical Analysis*

The model performances were evaluated through the confusion matrix by calculating accuracy, sensitivity, specificity and F1-score. The Cohen's kappa was also calculated to evaluate the degree of agreement between the CNN and the gold standard.

III. Results and Discussions

On the basis of sonographic findings, the AI Occiput-database images were classified as direct (n = 293) and transverse (n = 319) by the expert gynaecologist. The BnB-database included 3092 brain and 5095 not-a-brain images. Lastly, the RL-database consisted of 759 left transverse and 627 right transverse occiput position images.

The comparison of the performances resulted from the three TL approaches are shown in Figure 2.

In summary, the three classifiers tested on the in-house small database identified direct and transverse occiput position with 73.9%, 85.9% and 89.1% accuracy, respectively for Test 1, Test 2 and Test 3. The sensitivity was 71.4%, 87.0% and 92.7% and the specificity was 76.7%, 84.8% and 86.3% for Test 1, Test 2 and Test 3, respectively.

It is noticeable that between Test 1 and Test 3 there is a difference in accuracy that exceeds 15% and in sensitivity that is almost 20%. The Cohen's kappa was 0.48, 0.61 and 0.78, and the F1-score was 0.74, 0.83 and 0.88 respectively for Test 1, Test 2 and Test 3.

The results of this study indicate that our model pre-trained

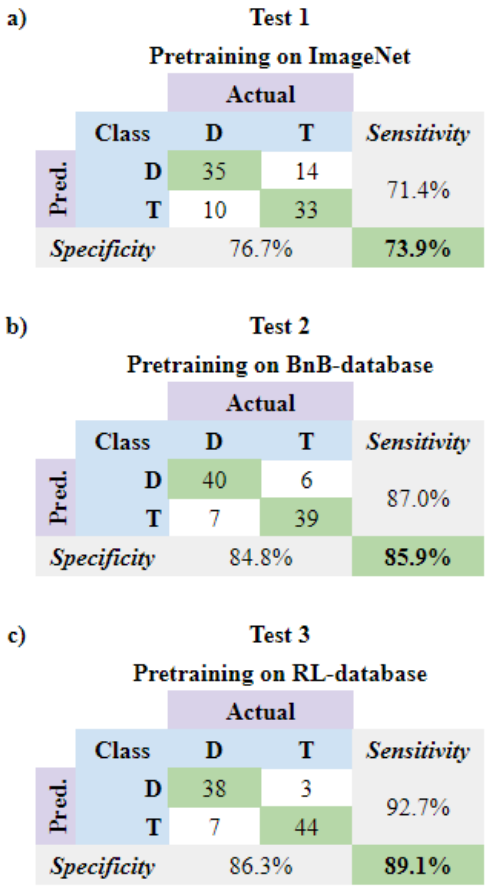


Fig. 2 - Confusion matrices of the performances resulted by: a) cross-domain TL (Test 1), b-c) cross-modal TL (Test 2 and Test 3).

on the RL-database outperformed the model pre-trained on the BnB-database in terms of accuracy (Test 3 accuracy = 89.1%; Test 2 accuracy = 85.9%). This is likely due to the similarity of the tasks and databases between Test 3 and the AI-Occiput database, which both feature foetal head with occiput in different positions. On the other hand, the BnB-database contained US images of foetal head, but also of different parts of the foetal and maternal body, making it less similar to the tested database. Therefore, the performance in Test 3 was enhanced by the representation of relevant features learned from a database more closely related to the tested database, resulting in higher accuracy and better generalizability.

The results of the cross-domain TL (Test 1), while effective, resulted in less accurate classifications of ultrasound images than the cross-modal TL (Test 2 and Test 3) tests. This is mainly due to the differences between the characteristics of ImageNet and medical images; such as contrast, shape and texture. Conversely, in cross-modal TL the weights from the pre-trained model are transferred to a model on the same domain, allowing the model to leverage the pre-trained model's general knowledge of the domain and thus recognize patterns more effectively in medical images.

Theoretically, TL could enable us to reduce the dependency on large datasets often required for automatic recognition tasks, while still providing optimal performance. While TL does require significantly fewer labelled data to be trained, the quality of the dataset remains the most important part of the re-training process. Without a well-structured and diverse dataset, the model will not be able to accurately represent the problem and generalize its solution to multiple contexts. Poor datasets will inevitably lead to poor predictions.

IV. Conclusions

In this work, three different approaches of transfer learning were compared to classify direct and transverse occiput position on TPU images.

Our research has indicated that the use of cross-modal transfer learning (TL) can result in an improved classifier performance when compared to cross-domain TL.

This study suggested that cross-modal TL could be an effective solution for medical imaging application to overcome the limitation of data scarcity and improve performance when images are affected by low contrast. Moreover, the developed model could provide a valid support to obstetricians in the delicate process of labour management, aiding the untrivial task of image interpretation, strongly dependent on the operator training experience, thus minimizing the intra-operator variability.

The future prospective of this work will be to expand the classification of additional occiput position directions and develop a model to predict the most successful delivery mode.

Acknowledgement

We would like to thank all the participants to the AI Occiput project, including midwives, obstetricians and gynaecologists, whose unceasing contribution and dedication to data collection was essential to perform this study.

References

[1] T. Ghi *et al.*, “Novel artificial intelligence approach for automatic differentiation of fetal occiput anterior and non-occiput anterior positions during labor,” *Ultrasound in Obstetrics & Gynecology*, vol. 59, no. 1, pp. 93–99, 2022.

[2] Y. Sun, H. Yang, J. Zhou, and Y. Wang, “ISSMF: Integrated semantic and spatial information of multi-level features for automatic segmentation in prenatal ultrasound images,” *Artif Intell Med*, vol. 125, p. 102254, 2022.

[3] D. Selvathi and R. Chandralekha, “Fetal biometric based abnormality detection during prenatal development using deep learning techniques,” *Multidimens Syst Signal Process*, vol. 33, no. 1, pp. 1–15, 2022.

[4] J. Schmidt, M. R. G. Marques, S. Botti, and M. A. L. Marques, “Recent advances and applications of machine learning in solid-state materials science,” *NPJ Comput Mater*, vol. 5, no. 1, pp. 1–36, 2019.

[5] R. N. D’souza, P.-Y. Huang, and F.-C. Yeh, “Structural analysis and optimization of convolutional neural networks with a small sample size,” *Sci Rep*, vol. 10, no. 1, pp. 1–13, 2020.

[6] D. Nguyen *et al.*, “Meta transfer learning for facial emotion recognition,” in *2018 24th International Conference on Pattern Recognition (ICPR)*, 2018, pp. 3543–3548.

[7] M. Ramphul *et al.*, “Instrumental delivery and ultrasound: a multicentre randomised controlled trial of ultrasound assessment of the fetal head position versus standard care as an approach to prevent morbidity at instrumental delivery,” *BJOG*, vol. 121, no. 8, pp. 1029–1038, 2014.

[8] E. A. Torkildsen *et al.*, “Prediction of delivery mode with transperineal ultrasound in women with prolonged first stage of labor,” *Ultrasound in obstetrics & gynecology*, vol. 37, no. 6, pp. 702–708, 2011.

[9] T. Ghi *et al.*, “ISUOG Practice Guidelines: intrapartum ultrasound,” *Ultrasound in Obstetrics & Gynecology*, vol. 52, no. 1, pp. 128–139, 2018.

[10] T. Ghi *et al.*, “Diagnosis of station and rotation of the fetal head in the second stage of labor with intrapartum translabial ultrasound,” *Ultrasound in Obstetrics and Gynecology*, vol. 33, no. 3, pp. 331–336, 2009.

[11]S. Casciaro *et al.*, “Automatic evaluation of progression angle and fetal head station through intrapartum echographic monitoring,” *Comput Math Methods Med*, vol. 2013, 2013.

[12]F. Conversano *et al.*, “A Non-invasive and Automatic Ultrasound Technique for Progression Angle Measurements during Childbirth Labor,” 2017.

[13]T. Ghi *et al.*, “Sonographic assessment of fetal occiput position during the second stage of labor: how reliable is the transperineal approach?,” *The Journal of Maternal-Fetal & Neonatal Medicine*, vol. 28, no. 16, pp. 1985–1988, 2015.

[14]X. P. Burgos-Artizzu *et al.*, “FETAL_PLANES_DB: Common Maternal-Fetal Ultrasound Images,” in *Nature Scientific Reports*, vol. 19, Zenodo, 2020, p. 10200.

[15]J. Deng, W. Dong, R. Socher, L.-J. Li, K. Li, and L. Fei-Fei, “Imagenet: A large-scale hierarchical image database,” in *2009 IEEE conference on computer vision and pattern recognition*, 2009, pp. 248–255.

The hidden structural complexity of the human cerebral cortex

F. Giorgini[1], S. Diciotti[1,*], and C. Marzi[2,*]

[1] *Dept. of Electrical, Electronic, and Information Engineering "Guglielmo Marconi", University of Bologna, Italy*

[2] *Dept. of Statistics, Computer Science, Applications "Giuseppe Parenti", University of Florence, Italy*

[*] *These authors supervised equally*

***Abstract*— The cerebral cortex exhibits an intrinsic structural complexity of folding. Fractal geometry may be used to describe the structural complexity of objects (such as the cerebral cortex) that show self-similarity throughout a proper range of spatial scales. The potential value of fractal dimension, estimated from T1-weighted MRI images, has already been widely demonstrated in previous literature, but how it is related to the cyto- and myeloarchitecture of the cerebral cortex is still unknown. In this study, we computed the fractal dimension of the six cortical layers, which present various cellular compositions and distributions, developmental trajectories, connections, physiology, and functional roles. The procedure for determining fractal dimension indices was applied to segmentations obtained from the public BigBrain dataset that consists of an ultrahigh-resolution three-dimensional (3D) model of a human brain based on histologically processed post-mortem brain reconstruction. Results denote an increasing trend in fractal dimension values from the outermost (layer I) to the innermost layers (the infragranular layers V and VI) of the cortex in both hemispheres. Layers V and VI are composed of sparse, low-density pyramidal neurons and fusiform cells. Differently from the supragranular layers (i.e., layers I, II, and III), the infragranular layers are characterized by a high content of myelin belonging to the projection fibers. Consequently, the structural complexity of the cerebral cortex seems to be coupled with the projection fibers network, rather than with neuronal density, and the presence of associative and commissural fibers.**

***Keywords*—BigBrain project, cerebral cortex, cortical layers, fractal dimension, projection fibers, structural complexity.**

I. Introduction

THE human brain is a complex system. Its hierarchical organization can be studied on multiple scales, from neurons and microcircuits to macro-network. From a structural point of view, the intrinsic folding of the cerebral cortex can be described through fractal geometry. Its popular index, the fractal dimension (FD) measures the structural complexity of objects, which show, in a proper range of spatial scales, the self-similarity property (i.e., a geometrical property of objects composed of subunits and sub-subunits that resemble the whole object [1], [2]).

In recent years, fractal analysis has been successfully applied to analyze brain morphology [3]-[5]. In particular, by exploiting T1-weighted magnetic resonance imaging (MRI), the fractal properties of the cerebral cortex [6], as well as the white matter (WM) [7],[8] have been shown. Indeed, FD is considered a compact measure of the structural complexity of the brain [9]. Specifically, the FD of the cerebral cortex condenses cortical thickness, sulcal depth, and folding area into a unique numeric value [10].

Although FD is an index capable of measuring mild structural changes induced by healthy aging [11]-[17], and the onset of neurological diseases [9], [18]-[25] the link between FD and the cyto- and myeloarchitecture of the brain is still unknown. In addition, the human brain's FD is generally estimated from the cerebral cortex and WM segmentations obtained from T1-weighted MR images, which rarely have a spatial resolution of less than one millimeter.

In the present study, we performed a step toward interpreting FD in neuroimaging by directly studying the individual layers that make up the cerebral cortex, which exhibit different cellular composition and distributions, developmental trajectories, connectivity, physiology, and functional roles [26]. This processing was made possible by the BigBrain dataset, a 3D reconstruction of an individual human brain stained for cell bodies at ultra-high, nearly cellular, spatial resolution that provides considerable neuroanatomical insight into the human brain [27].

II. Materials and Methods

A. Data

In this study, we employed the BigBrain dataset created by the Forschungszentrum Jülich center in Germany and McGill University in Montréal with the supercomputer Juropa [27]. BigBrain is freely available at https://bigbrainproject.org/index.html and contains a model of the brain of a 65-year-old subject with no neurological or psychiatric diseases in the medical records at the time of death [27]. They obtained the brain model using a large-scale microtome to cut the paraffin-embedded brain coronally. Then, they acquired 7400 sections at 20-µm thickness. Histological sections were subsequently digitized, resulting in images of maximally 13,000 x 11,000 pixels. In order to generate a dataset with isotropic resolution, they scaled down all images to a resolution of 20 microns. Histological processing has inevitably introduced artifacts. Before the 3D reconstruction of the whole brain as a contiguous volume, manual and automatic repairs were performed. The repaired sections were registered to the MRI, which served as an undistorted frame of reference and further aligned section-to- section with the use of nonlinear registration [27]. The final dataset contains the 3D histological volumes at different isotropic resolutions (100,

200, 300, and 400 microns), in MNI and histological space, the 3D classified volumes, and the MR volume in the histological space. Moreover, it includes the WM-cortex interface and pial surfaces along with the cortex layers surfaces [28]. Similarly to the work of Wagstyl and colleagues [28], in the current study, we used the 3D surfaces of the cortical layers outlined on the histological sections with a spatial resolution of 400 microns.

B. *Methods*

We rasterized each 3D surface corresponding to a single cortical layer using the 3D histological volume at the resolution of 400 microns as the reference volume. Thus, we obtained twelve (six for each hemisphere) non-overlapping 3D volumes representing the cortical layers (Fig. 1). Then, we computed the FD for each layer. In particular, the fractal analysis was performed through the box-counting algorithm [29] optimized with the automatically selected fractal scaling window [13]. Briefly, the box counting algorithm consists in superimposing a grid containing 3D cubes of side s on $I(x, y, z)$ (the 3D mask of the brain portion of interest) and counting the number of not null intersections between the grid and $I(x, y, z)$. This procedure was repeated for different s values. As suggested by Goñi et al. [30], for each s value, 20 uniformly distributed random offsets were applied on the grid origin in order to reduce the bias introduced by the selection of a fixed grid origin, and all the box counts (one for each offset) were averaged to obtain a single $N(s)$ value for each s. Plotting $N(s)$ against s in a bi-logarithm plane (Fig. 2), we build a linear regression model where the absolute value of the negative slope is the FD. In the natural scale, this linear relationship in the log-log plane corresponds to a power law $N(s) = k\, s^{-FD}$, where FD is the exponent (with a negative sign), and k is the prefactor [2]. In particular, the range of spatial scales where $I(x, y, z)$ manifests its fractal properties is unknown a priori, so we used an automated selection of this spatial interval, i.e., the fractal scaling window, by maximization of the coefficient of determination (adjusted for the number of data points) R^2_{adj} of the linear regression model [13].

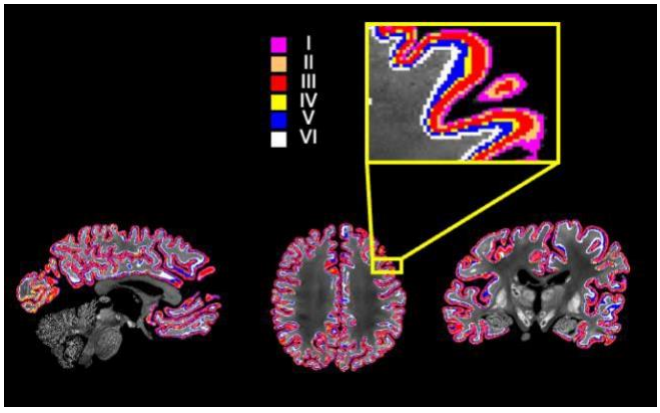


Fig. 1: 3D cortical layers. Six cortical layers segmented on the 3D volume in the three orthogonal planes, i.e., sagittal (left), axial (middle), and coronal (right). The box outlined in yellow contains an enlargement of a part of the cortex in the axial plane.

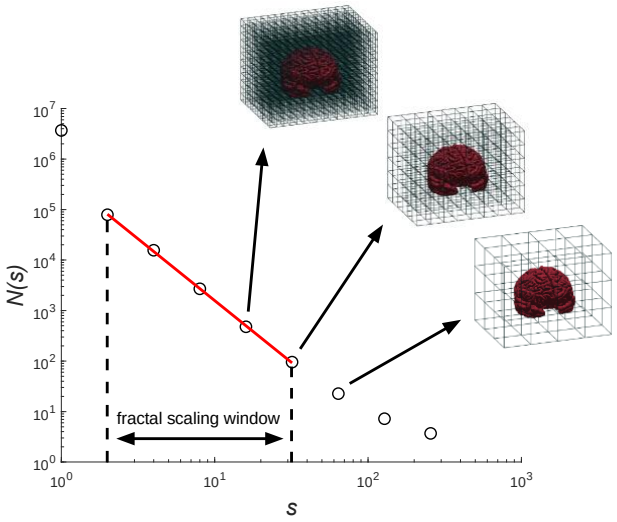


Fig. 2: 3D box-counting for computation of the FD. An example of the 3D box-counting algorithm that uses an automated selection of the fractal scaling window through the *fractalbrain* toolkit [13]. $N(s)$ is the average number of 3D cubes of side s needed to fully enclose the brain structure computed using 20 uniformly distributed random offsets to the grid origin. The regression line within the optimal fractal scaling window, whose slope (sign changed) is the FD, is depicted in red.

C. *Experimental Tests*

We performed the 3D surface voxelization using different tools. Firstly, we transformed our data into the FreeSurfer structure [31] to exploit FreeSurfer's extension for 3D Slicer (v. 5.0.3) to load, visualize, and rasterize the 3D surface meshes into 3D filled volumes with a spatial resolution of 400 microns. The final volumes of the surfaces were obtained using the mathematical manipulation tools of the FMRIB Software Library (FSL) (v. 6.0.3) [32]. Finally, for the estimation of the FD of each layer, we used the *fractalbrain* toolkit (v. 1.0) (https://github.com/chiaramarzi/fractalbrain-toolkit) [13].

III. Results and Discussion

Table I shows the FD measurements of the six layers of the cerebral cortex collected with a spatial resolution of 400 microns.

TABLE I: FD VALUES OF THE SIX LAYERS OF THE CEREBRAL CORTEX

Layer	*FD (left hemisphere)*	*FD (right hemisphere)*
I	2.2847	2.2885
II	2.3041	2.3084
III	2.3371	2.3381
IV	2.3422	2.3422
V	2.3728	2.3758
VI	2.3439	2.3466

Comparing the FD values obtained for the left and right hemispheres, a slightly higher FD is observed for the latter. This result might be explained by considering that healthy cerebral hemispheres appear perfectly symmetric only

macroscopically. A detailed examination reveals two subtle differences: 1) the right cerebral hemisphere has a larger size, and 2) it is slightly in a forward position than the left one [33]. Given the existence of a positive correlation between measures of volume and FD estimated from T_1-weighted MR images, the larger size of the right hemisphere may account for its slightly higher FD, as previously found in [15], [34], [35].

FD values tend to increase moving deeper into the cerebral cortex, highlighting that layers V and VI have higher structural complexity in both hemispheres. Given that the cerebral cortex has a cyto- and myeloarchitectonic structure that varies depending on the cortical area, each layer, with various cellular compositions and distributions, developmental trajectories, connections, physiology, and functional roles, represents a different cyto- and myeloarchitectural variety. Specifically, layers V and VI were named internal pyramidal layer and multiform layer, respectively. The internal pyramidal layer consists of large but relatively sparse pyramidal neurons, while the multiform layer has mostly fusiform cells with less dominant pyramidal cells and interneurons. Both of them are highly rich in myelin due to the high amount of projection fibers. Layer V is the source of the output of corticofugal fibers, which synapse with different subcortical motor centers. The axons of the fusiform and pyramidal cells of the VI layer, instead, distribute corticocortical commissural fibers and corticothalamic projection fibers that end in the thalamus [36]. Consequently, the structural complexity of the cerebral cortex seems to be coupled with the projection fibers network. A decrease in FD values of the cerebral cortex due to a neurological disease might therefore indicate a reorganization of the projection tracts, rather than a neuronal density decrease.

Moreover, in T1-weighted MR images, layers V and VI have an intensity similar to that of white matter. Indeed, the high presence of myelin in these cortical layers often leads to their classification as white matter [28]. Conventionally, in MRI processing, the white matter surface is placed at the maximum intensity gradient between gray and white matter, causing an outward shift in the location of the white matter surface (Fig. 3). By contrast, thanks to the high spatial resolution, the cortical layer boundaries have been manually located according to the presence of cortical neurons [28]. This has caused an inward shift in the location of the exact white matter surface.

These considerations are in line with previous literature studying structural complexity, measured by the FD, of the white matter. Notably, the FD of the white matter has generally higher FD values than the cerebral cortex [14],[20]. This could be partially explained by the fact that the most structurally complex regions of the brain are those with high intracortical connectivity, i.e., layers V and VI, which are generally included in the segmentation of white matter.



Fig. 3: Portion of the brain (in the axial plane) in which the six cortical layers and segmentation of white matter are visible. While there is no overlap between cortical layer segmentations, the white matter (green), defined by exploiting the maximum intensity gradient, partially overlaps with the VI (white) and V (blue) layers. The overlap is identified by the area where the colors combine.

III. CONCLUSION

Our findings enable a step forward in interpreting the FD as a measure of the structural complexity of the cerebral cortex. We figured out the coupling between the cyto- and myeloarchitectural composition of the cerebral cortex and its structural complexity, candidating the projection fibers network of layers V and VI as the main contributor to structural complexity of the cerebral cortex.

REFERENCES

[1] B. B. Mandelbrot. “How long is the coast of Britain? Statistical self-similarity and fractional dimension,” *Science*, vol. 156, pp. 636-638, May 1967. Available: https://doi.org/10.1126/science.156.3775.636

[2] B. B. Mandelbrot. “The Fractal Geometry of Nature,” *W. H. Freeman and Company ed*, January 1983.

[3] A. Di Ieva, F. Grizzi, H. Jelinek, A. J. Pellionisz and G. A. Losa “Fractals in the neurosciences, Part I: General principles and basic neurosciences,” *Neuroscientist*, vol. 20, pp. 403–417, December 2014. Available: https://doi.org/10.1177/1073858413513927

[4] A. Di Ieva, F. J. Esteban, F. Grizzi, W. Klonowski and M. Martin-Landrove, “Fractals in the neurosciences, Part II: Clinical applications and future perspectives,” *Neuroscientist*, vol. 21, pp. 30–43, February 2015. Available: https://doi.org/10.1177/1073858413513928

[5] A. Di Ieva, “The Fractal Geometry of the Brain,” *Springer*, New York, October 2016. Available: https://doi.org/10.1007/978-1-4939-3995-4

[6] V. G. Kiselev, K. R. Hahn and D. P. Auer. “Is the brain cortex a fractal?,” *NeuroImage*, vol. 20, pp. 1765–1774, November 2003. Available: https://doi.org/10.1016/s1053-8119(03)00380-x

[7] S.L. Free, S. M. Sisodiya, M. J. Cook, D. R. Fish and S.D. Shorvon, “Three-dimensional fractal analysis of the white matter surface from magnetic resonance images of the human brain,” *Cereb. Cortex*, vol. 6, pp. 830–836, November 1996. Available: https://doi.org/10.1093/cercor/6.6.830

[8] L. Zhang, J. Z. Liu, D. Dean, V. Sahgal and G. H. Yue. “A three-dimensional fractal analysis method for quantifying white matter structure in human brain,” *Journal of Neuroscience Methods*, vol. 150, pp. 242-253, January 2006. Available: https://doi.org/10.1016/j.jneumeth.2005.06.021

[9] R. D. King, A. T. George, T. Jeon, L. S. Hynan, T. S. Youn *et al.*, “Characterization of atrophic changes in the cerebral cortex using fractal dimension analysis,” *Brain Imaging Behav.*, vol. 3, pp. 154-166, June 2009. Available: https://doi.org/10.1007/s11682-008-9057-9

[10] K. Im, J. Lee, U. Yoon, Y.Shin, S. Hong *et al.*, “Fractal dimension in human cortical surface: multiple regression analysis with cortical thickness, sulcal depth, and folding area,” *Human Brain Mapping*, vol. 27, pp. 994-1003, December 2006. Available: https://doi.org/10.1002/hbm.20238

[11] C. R. Madan and E. A. Kensinger “Cortical complexity as a measure of age-related brain atrophy,” *Neuroimage*, vol. 134, pp. 617–629, 2016. Available: https://doi.org/10.1016/j.neuroimage.2016.04.029

[12] C. R. Madan and E. A. Kensinger "Predicting age from cortical structure across the lifespan," *Eur. J. Neurosci*., vol. 47, pp. 399–416, March 2018. Available: https://doi.org/10.1111/ejn.13835

[13] C. Marzi, M. Giannelli, C. Tessa, M. Mascalchi, and S. Diciotti "Toward a more reliable characterization of fractal properties of the cerebral cortex of healthy subjects during the lifespan," *Sci Rep.* vol. 10, October 2020. Available: https://doi.org/10.1038/s41598-020-73961-w

[14] J. Pani, C. Marzi, D. Stensvold, U. Wisløff, A. K. Håberg, *et al.*, "Longitudinal study of the effect of a 5-year exercise intervention on structural brain complexity in older adults. A Generation 100 substudy," *Neuroimage*, vol. 256, August 2022. Available: https://doi.org/10.1016/j.neuroimage.2022.119226

[15] N. Nazlee, G. D. Waiter and A. L. Sandu "Age-associated sex and asymmetry differentiation in hemispheric and lobar cortical ribbon complexity across adulthood: A UK Biobank imaging study," *Hum Brain Mapp*., September 2022. Available: https://doi.org/10.1002/hbm.26076

[16] C. Marzi, M. Giannelli, C. Tessa, M. Mascalchi and S. Diciotti, "Fractal analysis of MRI data at 7 T: how much complex is the cerebral cortex?," *IEEE Access*, vol. 9, pp. 69226-69234, May 2021. Available: https://doi.org/10.1109/ACCESS.2021.3077370

[17] C. Marzi, M. Giannelli, A. Barucci, C. Tessa, M. Mascalchi and S. Diciotti,(2022). "Efficacy of MRI data harmonization in the age of machine learning. A multicenter study across 36 datasets," *arXiv:2211.04125*, November 2022. Available: https://doi.org/10.48550/arXiv.2211.04125

[18] R. D. King, B. Brown, M. Hwang, T. Jeon and A. T. George "Fractal dimension analysis of the cortical ribbon in mild Alzheimer's disease," Neuroimage, vol. 53, pp. 471–479, November 2010 Available: https://doi.org/10.1016/j.neuroimage.2010.06.050

[19] C. Marzi, S. Ciulli, M. Giannelli, A. Ginestroni, C. Tessa et al., "Structural complexity of the cerebellum and cerebral cortex is reduced in spinocerebellar ataxia type 2," J. Neuroimaging, vol. 28, pp. 688– 693, November 2018. Available: https://doi.org/10.1111/jon.12534

[20] L. Pantoni, C. Marzi, A. Poggesi, A. Giorgio, N. de Stefano et al., "Fractal dimension of cerebral white matter: A consistent feature for prediction of the cognitive performance in patients with small vessel disease and mild cognitive impairment," NeuroImage Clin., vol. 24, August 2019. Available: https://doi.org/10.1016/j.nicl.2019.101990

[21] F. J. Esteban. J. Sepulcre, J. Navas, and J. R. de Miras "Fractal dimension analysis of grey matter in multiple sclerosis," J. Neurol. Sci. vol. 282, pp. 67–71, January 2009. Available: https://doi.org/10.1016/j.jns.2008.12.023

[22] T. H. Ha, U. Yoon, K. J. Lee, Y. W. Shin, J.M. Lee, et al., "Fractal dimension of cerebral cortical surface in schizophrenia and obsessive-compulsive disorder," Neurosci. Lett. vol. 384, pp. 172–176, August 2005. Available: https://doi.org/10.1016/j.neulet.2005.04.078

[23] I. Nenadic, R. A. Yotter, H. Sauer, and C. Gaser, "Cortical surface comlexity in frontal and temporal areas varies across subgroups of schizophrenia," Hum. Brain Mapp. vol. 35, pp. 1691–1699, April 2014. Available: https://doi.org/10.1002/hbm.22283

[24] A. L. Sandu, I. Rasmussen Jr, A. Lundervold, F. Kreuder, G. Neckelmann, et al., "Fractal dimension analysis of MR images reveals grey matter structure irregularities in schizophrenia," Comput. Med. Imaging Graph, vol. 32, pp. 150–158, March 2008. Available: https://doi.org/10.1016/j.compmedimag.2007.10.005

[25] R. Sheelakumari, V. Rajagopalan, A. Chandran, T. Varghese, L. Zhang et al., "Quantitative analysis of grey matter degeneration in FTD patients using fractal dimension analysis," Brain Imaging Behav, vol. 12, pp. 1221-1228, October 2018. Available: https://doi.org/10.1007/s11682-017-9784-x

[26] K. Wagstyl, C. Lepage, S. Bludau, K. Zilles, P. C. Fletcher et al,. "Mapping cortical laminar structure in the 3D BigBrain," Cerebral Cortex, vol. 28, No. 7, pp. 2551-2562, July 2018. Available: https://doi.org/10.1093/cercor/bhy074

[27] K. Amunts, C. Lepage, L. Borgeat, H. Mohlberg, T. Dickscheid et al., "BigBrain: an ultrahigh-resolution 3D human brain model," Science, vol. 340, pp. 1472-1475, June 2013. Available: https://doi.org/10.1126/science.1235381

[28] K. Wagstyl, S. Larocque, G. Cucurull, C. Lepage, J. P. Cohen et al., "BigBrain 3D atlas of cortical layers: cortical and laminar thickness gradients diverge in sensory and motor cortices," PLoS Biol, vol. 18, pp. e3000678, April 2020. Available: https://doi.org/10.1371/journal.pbio.3000678

[29] D. A. Russell, J. D. Hanson and E. Ott, "Dimension of strange attractors," Phys. Rev. Lett. 45, 1175–1178, October 1980. Available: https://doi.org/10.1103/PhysRevLett.45.1175

[30] J. Goñi, O. Sporns, H. Cheng, M. Aznárez-Sanado, Y. Wang et al., "Robust estimation of fractal measures for characterizing the structural complexity of the human brain: optimization and reproducibility," Neuroimage, vol. 83, pp. 646-657, December 2013. Available: https://doi.org/10.1016/j.neuroimage.2013.06.072

[31] B. Fischl, "FreeSurfer," Neuroimage, vol. 62, pp. 774–781, August 2012. Available: https://doi.org/10.1016/j.neuroimage.2012.01.021

[32] M. Jenkinson, C.F. Beckmann, T.E. Behrens, M.W. Woolrich and S.M. Smith. "FSL," NeuroImage, 62:782-90, August 2012. Available: https://doi.org/10.1016/j.neuroimage.2011.09.015

[33] S. Ocklenburg S and O.Güntürkün, "Hemispheric asymmetries: the comparative view," Front. Psychology, January 2012. Available: https://doi.org/10.3389/fpsyg.2012.00005

[34] J. M. Lee, U. Yoon, J. J. Kim, I. Y. Kim, D. S. Lee, et al., "Analysis of the hemispheric asymmetry using fractal dimension of a skeletonized cerebral surface," IEEE Trans Biomed Eng, vol. 51(8), pp. 1494-8, August 2004. Available: https://doi.org/10.1109/tbme.2004.831543

[35] H. Liu, T. Liu, J. Jiang, J. Cheng, Y. Liu et al., "Differential longitudinal changes in structural complexity and volumetric measures in community-dwelling older individuals," Neurobiol Aging, vol. 91, pp. 26-35, July 2020. Available: https://doi.org/10.1016/j.neurobiolaging.2020.02.023

[36] W. A. Grow, "Fundamental Neuroscience for Basic and Clinical Applications," Elsevier, ch. 32, pp.468-479.e1, August 2018. Available: https://doi.org/10.1016/C2014-0-03718-5

Prediction of injectables' stability leveraging inline analysis and machine learning

S. Fiorenza[1], P. A. Netti[2,3], E. Torino[2,3]
[1] *Department of Information Technology and Electrical Engineering, University of Naples Federico II, 80125 Naples, Italy*
[2] *Department of Chemical, Materials and Production Engineering, University of Naples Federico II, 80125 Naples,*
[3] *Interdisciplinary Research Center on Biomaterials, CRIB, University of Naples Federico II, 80125 Naples, Italy*

***Abstract*—Aggregation and modification of the structure of biologics (*i.e.*, proteins, mAbs, etc.) can significantly affect the quality of the final biopharmaceutical product, especially because of the increased risk of immunogenicity and the decreased specificity. The excipients in the final formulation are intended to mitigate destabilizing effects (*e.g.*, aggregation, structural/conformational modifications, etc.). Here, we describe a novel high-throughput screening approach based on a microfluidic inline analytical platform and machine learning methods, to select the best formula composition in terms of type and concentration of excipients needed to reduce the aforementioned destabilizing effects. We show how to collect stability-related information in a fast and reliable way, with minimum material amount (*i.e.*, few hundreds of microliters), and how to properly structure the dataset for subsequent machine learning-based processing. This approach is taught to dramatically reduce the number of experiments needed for later fine characterization of injectables' stability.**

***Keywords*—High-throughput screening, inline analysis, thermodynamic stability prediction, biotherapeutics.**

I. Introduction

In the industrial and academic fields, there is a lack of fast and reliable screening platforms for biologically active compounds. More than 90% of the API (Active Pharmaceutical Ingredient) compositions are not stable enough to enter the successive fine-tuning steps, resulting in an increased cost of drug development [1] and a decreasing number of marketed drugs.

Compared to small pharmaceutics, proteins are larger entities with superior physical and chemical complexities. Protein degradation, which is of major concern when dealing with pharmaceutical products, can be due to many different factors, either chemical and/or physical [2]. Chemical degradation accounts for the destruction and/or formation of covalent bonds, including processes such as oxidation and hydrolysis [2]; physical degradation accounts for precipitation, aggregation and/or disaggregation, unfolding, adsorption, and denaturation processes [2].

Depending on the destabilizing factor(s) to be characterized (*e.g.*, aggregation/disaggregation, denaturation, structural/conformational changes, etc.), different analytical techniques have been developed during the years [2], [3], [4]. Those techniques can be classified in multiple ways, based on different characteristics such as the detection method (*i.e.*, microscopic, light absorption/blockage, light scattering, separation, spectroscopic), properties of particle suspension (*e.g.*, size, particle concentration, polydispersity/polymodality, turbidity, refractive index, etc.), API's attribute (*e.g.*, aggregation status, chemical modifications, structural/conformational changes, etc.), and the operational mode (*e.g.*, single particle, ensemble, separation-based) [4].

Standard off-line analytical techniques are usually not allowing for fast and real-time measurements. Moreover, they require multiple sample pre-processing steps (*i.e.*, dilution, separation, buffer exchange) that may alter the native context of the API, impacting the stability and thus leading to misleading information. Plus, there is a lack of automation because different qualified operators perform different steps at different times. For example, one of the established and vastly employed techniques for the characterization of the monomer/oligomers/aggregates is the SE-HPLC (Size Exclusion – High-Performance Liquid Chromatography) [5]. However, SE-HPLC can provide misleading results because of (1) adsorption of protein aggregates to the column matrix, (2) dissociation or formation of protein aggregates during the sample preparation and measurement, (3) incapability to resolve larger aggregates that may coelute, (4) inability of large aggregates (*i.e.*, subvisible particles) to elute, and (5) underestimation of aggregate species and levels if only UV-absorbance detector is used [5] [6]. In addition, the analytical measurement is operator-, time-, and reagents-consuming.

Nowadays, pharmaceutical formulation development relies on classical trial-and-error approaches that are laborious, time-consuming and expensive [7]; it is almost impossible to reach the optimal formulation composition, in terms of type and concentration of excipients (*e.g.*, salts, buffer agents, sugars, amino acids, surfactants, etc), with the aforementioned approaches.

Over the years, several machine learning methods and algorithms have been introduced to deal with the problem of the stability prediction of injectable biologics, to fill the gap in the traditional approaches leveraging data-driven predictions [8], [9], [10]. Obrezanova et al. [11] developed a high-throughput screening algorithm able to classify antibody molecules based on their aggregation propensity, using their aminoacidic sequence as input; protein aggregation was assessed using standard SE-HPLC method and the Oligomer Detection assay (ODA) [12] to classify the antibodies according to low and high aggregation risk. Gentiluomo et al. [13] proposed the use of interpretable artificial neuronal networks (ANNs) to predict important biophysical properties of therapeutic monoclonal antibodies such as melting temperature T_m, aggregation onset temperature T_{agg}, and the interaction parameter k_D as a function of pH and salt concentration from the aminoacidic composition. Authors exploited the ANN to find relationships between these

biophysical properties and some specific residues [13]. Yang et al. [7] applied deep learning (DL) to predict successful pharmaceutical formulations by building regression models on the disintegration time (*i.e.*, output parameter), comparing two types of dosage forms with different formulations; moreover, they evaluated the predictive performance of six machine learning algorithms. Narayanan et al. [14] demonstrated the power of the Bayesian optimization algorithm in identifying the formulation that optimizes the thermal stability (in terms of T_m) of a target protein in 25 experiments, by considering eight factors (*i.e.*, pH, sodium chloride, l-arginine, l-lysine, l-proline, trehalose, mannitol, and Tween20) as independent variables for the algorithm; notably, the number of required experiments is much lower compared with the number of experiments required by a classical trial-and-error approach.

However, the totality of the aforementioned research works complies with the lack of sufficient amount of high-quality data referred to the stability characterization of pharmaceutical formulations. This lack is mainly due to the high cost and time required for the data generation. Furthermore, injectable biologics are usually formulated at high concentration (> 100 mg/ml) to reduce the amount of drug product to be administered to patients, while maximizing the deliverable dose [15]. Dealing with stability studies of injectable biologics at such high concentrations takes with it many challenges: (1) difficulties to process highly viscous solutions, (2) dilution should be avoided, since it may add unwanted destabilizing and/or stabilizing effect on the product, (3) heterogeneity of the solutions (*e.g.*, API, excipients) may represent an obstacle for some analytical techniques.

With this work, we aim to develop a fully automated microfluidic inline analytical platform for a fast screening of the stability of injectable biologics. Plus, stability data are processed through machine learning approaches to build an in-silico predictive model. The aim of the work is schematized in Figure 1 below.

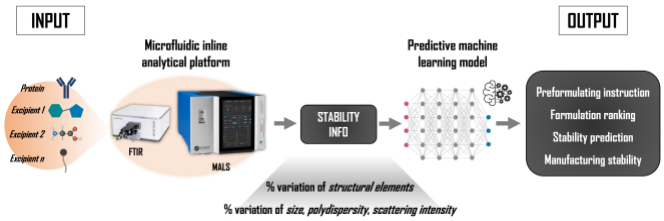


Fig. 1: Aim of the work

II. Inline Analysis – Stability Data

For our purpose, we selected two inline analytics based on different principles: a spectroscopic-based one that is ATR-FTIR (Attenuated Total Reflectance - Fourier Transformed InfraRed) spectroscopy, and a light scattering-based one that is MALS (Multi Angle Light Scattering). These two analytics were chosen considering a series of parameters: (1) the attribute measured (*e.g.*, hydrodynamic radius, gyration radius, turbidity, molecular spectra, etc.), (2) sample volume required, (3) measurement time, (4) flow rate and concentration range, (5) detection limits, and (6) availability of the technology.

Both the analytics require small amount of sample (100 microliters each) and measurement time (few seconds to few minutes, depending on the target quality), allowing for fast analysis and minimum sample consumption; plus, since they are non-destructive, the analyzed samples can be recovered and reused for further characterizations.

ATR-FTIR spectroscopy [16] allows to acquire information about the secondary structure of the protein inside the formulation, without requiring any dilution or separation. This information, extracted from the molecular spectrum, can be used to quantify the percentage change in structural elements (*i.e.*, α-helices, β-sheets, random coils, etc.) by evaluating specific region of the second derivative of the absorbance spectrum [17], [18]. For instance, intermolecular antiparallel β-sheets formation can be observed at the absorption band around 1620 cm^{-1} and this is a common feature of protein aggregation [19], [20].

MALS allows to acquire multiple information about average-weighted molecular weight (MW) and gyration radius (r_G) of the analyte in the formulation, leveraging the angular dependence of the scattered light intensity [3], [21]. The combination with QELS (Quasi Elastic Light Scattering) provides quantification of the hydrodynamic radius (r_H) of the molecule. This information can be used to quantify the percentage change of size (MW, r_G, and r_H), polydispersity, and scattering intensity that are related to aggregation and disaggregation dynamics due to components' interactions.

Inline ATR-FTIR spectroscopy and MALS are meant to be used together, given the different nature of the information they provide. Structural modifications (*e.g.*, conformational changes, loss in structural elements, etc.) are captured by the former, while components' interactions (*e.g.*, aggregation, disaggregation, API-excipient interactions, etc.) are captured by the latter. The combination of the two allows not to miss some destabilizing phenomena for every type of molecule in formulation: a change in the secondary structure does not necessarily imply an increased aggregation, and vice-versa.

The validity of inline ATR-FTIR as analytical technique for injectable biologics (*i.e.*, API plus excipients) without sample pre-processing, has been demonstrated through some preliminary studies. A drug product (DP), denoted as DP3, has been used; it is a solution in Tris 10mM (pH 7.5) containing a nanobody (at 150 mg/ml), trehalose, and Poloxamer-188 at specific concentrations. ATR-FTIR spectra were acquired by a ReactIR 702L (Mettler Toledo) with a microflow cell (Di-comp) equipped with a diamond crystal. A syringe pump (Harvard Apparatus) was used to flow the sample, at a fixed flow rate of 0.3 ml/min, inside the microflow cell. Three different spectra were acquired with a fixed number of scans per each sample of 100 and a resolution of 4 cm^{-1}: (1) untreated DP3, (2) thermally treated DP3 at 50°C for 3 minutes, and (3) thermally treated DP3 at 55°C for 3 minutes. The 2nd derivatives of the absorbance spectra were computed from the iC IR software (Mettler Toledo) with standard configuration. Results of ATR-FTIR spectroscopy are reported in Figure 2.

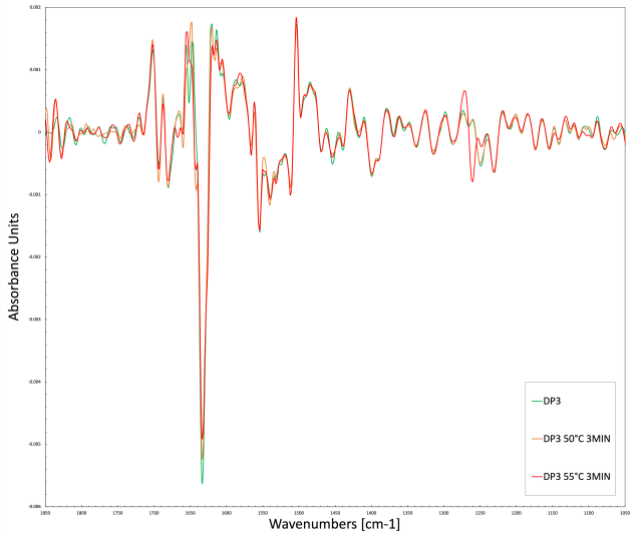


Fig. 2: 2nd derivative ATR-FTIR spectra of an injectable drug product (DP3). Untreated DP3 (in green), thermally treated DP3 at 50°C for 3 min (in yellow), and thermally treated DP3 at 55°C for 3 min (in red).

Figure 2 shows a progressive loss in the β-sheets content of the nanobody around 1630 cm^{-1} wavenumber with the increase of the thermal degree of the treatment. This technique appeared to be promising in classifying different formulations having different excipients (both type and concentration) depending on the extent of their secondary structure modifications. A greater extent (*i.e.*, a greater percentage change) of structural modifications is associated with a lower stability of the API.

III. Dataset Building

Dataset building and structuring is a crucial step, to have data properly organized to be processed through machine and/or deep learning methods. Depending on the kind of available data (*e.g.*, categorical, continuous, data range, missing values, etc.), different algorithms and pre-processing strategies may be chosen to maximize the accuracy of the in-silico model generated.

Given the analytics selected and the obtainable information, a possible way of dataset structuring is reported in Table I below.

TABLE I: Example Dataset

API	*Concentration (mg/ml)*	*pH*	*Trehalose (g/ml)*	*Arginine (mg/ml)*	*Poloxamer (mg/ml)*	*β-sheet loss (%)*	*Size change (%)*
1	*150*	*7*	*0.1*	*0*	*0.2*	*10*	*25*
1	*150*	*7*	*0.5*	*2*	*0*	*8*	*10*
1	*150*	*7*	*0.1*	*4*	*0.2*	*4*	*12*
1	*60*	*7*	*0.1*	*0*	*0.2*	*5*	*17*
1	*60*	*7*	*0.5*	*2*	*0*	*3*	*8*
1	*60*	*7*	*0.1*	*4*	*0.2*	*3*	*7*

A possible way of structuring a dataset for regression purposes. First six columns are input variables (independent variables), last two are output variables (dependent variables) evaluated through inline ATR-FTIR spectroscopy and MALS, respectively. For instance, further independent and dependent variables can be added to the dataset depending on the achievable information.

This example dataset is focusing on one API, at two concentrations, to exploit the excipients effect on the destabilization upon thermal treatment. Such dataset is well suitable for regression purposes, since the output variables (*i.e.*, β-sheet loss (%), and size change (%)) are continuous and not categorical. For classification, the output column must contain a categorical variable; therefore, a "stability-related label" (*e.g.*, stable, mildly stable, instable) should be defined. However, no uniquely defined stability thresholds are available in literature, since they strictly depend on the molecule under investigation.

For this kind of datasets (Table I), machine learning algorithms that are mostly used for regression are: (1) Multiple Linear Regression, (2) Polynomial Regression, (3) Logistic Regression, (4) Robust Regression, (5) Support Vector Regression, (6) k-Nearest Neighbors regression, (7) Decision Tree regression, (8) Random Forest regression, and (9) Gaussian process regression. Each of the previous has advantages and drawbacks, and algorithms' selection is a crucial step because their performances may vary a lot depending on the number of experimental datapoints available; the dataset splitting strategy (*e.g.*, K-Fold, stratified K-Fold, repeated K-Fold, Leave One Out, etc.) between training set and test set must be chosen accordingly. Moreover, if the number of the independent variables change, then also the algorithm's output is dramatically affected.

IV. Future Perspectives

This work paves the way for future machine- and deep-learning applications to build in-silico models capable of predicting thermodynamic stability behaviours of injectable biologics. Moreover, high amount of data can be leveraged to exploit the role of each one of the excipients in the thermodynamic stability of the API to build knowledge.

These machine learning-based computational tools can be beneficial to formulation design, since an early evaluation of the most promising formulations, in terms of type and concentration of excipients, dramatically reduces the formulation design-related costs and speeds up the overall process. In addition, an in-silico approach leveraging microfluidic inline analysis, allows to further enlarge the plethora of possible excipient(s)-API combination with less effort compared to classical trial-and-error approach [7] and minimum sample volume required (*i.e.*, few hundreds of microliters).

Further improvements may be introduced by encoding the amino-acidic sequence of the API as additional input parameter(s) to the model. Accounting for the quantity of each residue present in the primary sequence of a biologics could be a possible choice.

We envisage that this approach, characterizing the stability without pre-process the sample (*e.g.*, without separation) and getting advantage from machine learning tools, has a strong impact both in enhancing formulation development, and on a quality-by-design framework.

REFERENCES

[1] W. Wang, S. Ohtake, Science and art of protein formulation development, 568 (2019) 118505.
[2] V. Filipe, A. Hawe, J.F. Carpenter, W. Jiskoot, Analytical approaches to assess the degradation of therapeutic proteins, 49 (2013) 118-125.
[3] J. Gross-Rother, M. Blech, E. Preis, U. Bakowsky, P. Garidel, Particle Detection and Characterization for Biopharmaceutical Applications: Current Principles of Established and Alternative Techniques, Pharmaceutics 12(11) (2020).
[4] S. Zölls, R. Tantipolphan, M. Wiggenhorn, G. Winter, W. Jiskoot, W. Friess, A. Hawe, Particles in therapeutic protein formulations, Part 1: overview of analytical methods, J Pharm Sci 101(3) (2012) 914-35.
[5] J. den Engelsman, P. Garidel, R. Smulders, H. Koll, B. Smith, S. Bassarab, A. Seidl, O. Hainzl, W. Jiskoot, Strategies for the assessment of protein aggregates in pharmaceutical biotech product development, Pharm Res 28(4) (2011) 920-33.
[6] J.F. Carpenter, T.W. Randolph, W. Jiskoot, D.J. Crommelin, C.R. Middaugh, G. Winter, Potential inaccurate quantitation and sizing of protein aggregates by size exclusion chromatography: essential need to use orthogonal methods to assure the quality of therapeutic protein products, J Pharm Sci 99(5) (2010) 2200-8.
[7] Y. Yang, Z. Ye, Y. Su, Q. Zhao, X. Li, D. Ouyang, Deep learning for in vitro prediction of pharmaceutical formulations, SI: Enhancement of dissolution and oral bioavailability of poorly water-soluble drugs 9(1) (2019) 177-185.
[8] J. Vamathevan, D. Clark, P. Czodrowski, I. Dunham, E. Ferran, G. Lee, B. Li, A. Madabhushi, P. Shah, M. Spitzer, S. Zhao, Applications of machine learning in drug discovery and development, 18(6) (2019) 463-477.
[9] H. Narayanan, F. Dingfelder, A. Butté, N. Lorenzen, M. Sokolov, P. Arosio, Machine Learning for Biologics: Opportunities for Protein Engineering, Developability, and Formulation, Trends in Pharmacological Sciences 42(3) (2021) 151-165.
[10] S. Wang, J. Di, D. Wang, X. Dai, Y. Hua, X. Gao, A. Zheng, J. Gao, State-of-the-Art Review of Artificial Neural Networks to Predict, Characterize and Optimize Pharmaceutical Formulation, Pharmaceutics 14(1) (2022).
[11] O. Obrezanova, A. Arnell, R.G. de la Cuesta, M.E. Berthelot, T.R.A. Gallagher, J. Zurdo, Y. Stallwood, Aggregation risk prediction for antibodies and its application to biotherapeutic development, mAbs 7(2) (2015) 352-363.
[12] T. Aastrup, J. Zurdo, R. Michael, Y. Stallwood, K. Hedman, Improving the Developability of Biopharmaceuticals, 37 (2011) 35-40.
[13] L. Gentiluomo, D. Roessner, D. Augustijn, H. Svilenov, A. Kulakova, S. Mahapatra, G. Winter, W. Streicher, Å. Rinnan, G.H.J. Peters, P. Harris, W. Frieß, Application of interpretable artificial neural networks to early monoclonal antibodies development, 141 (2019) 81-89.
[14] H. Narayanan, F. Dingfelder, I. Condado Morales, B. Patel, K.E. Heding, J.R. Bjelke, T. Egebjerg, A. Butté, M. Sokolov, N. Lorenzen, P. Arosio, Design of Biopharmaceutical Formulations Accelerated by Machine Learning, Molecular Pharmaceutics 18(10) (2021) 3843-3853.
[15] P.-K. Lai, A. Gallegos, N. Mody, H.A. Sathish, B.L. Trout, Machine learning prediction of antibody aggregation and viscosity for high concentration formulation development of protein therapeutics, mAbs 14(1) (2022) 2026208.
[16] H. Tiernan, B. Byrne, S.G. Kazarian, ATR-FTIR spectroscopy and spectroscopic imaging for the analysis of biopharmaceuticals, 241 (2020) 118636.
[17] J. Kong, S. Yu, Fourier Transform Infrared Spectroscopic Analysis of Protein Secondary Structures, Acta Biochimica et Biophysica Sinica 39(8) (2007) 549-559.
[18] B. Shivu, S. Seshadri, J. Li, K.A. Oberg, V.N. Uversky, A.L. Fink, Distinct β-Sheet Structure in Protein Aggregates Determined by ATR–FTIR Spectroscopy, Biochemistry 52(31) (2013) 5176-5183.
[19] A. Dong, S.J. Prestrelski, S.D. Allison, J.F. Carpenter, Infrared spectroscopic studies of lyophilization- and temperature-induced protein aggregation, J Pharm Sci 84(4) (1995) 415-24.
[20] S.H. Jeong, Analytical methods and formulation factors to enhance protein stability in solution, 35(11) (2012) 1871-1886.
[21] M.A. Al-Ghobashy, M.M. Mostafa, H.S. Abed, F.A. Fathalla, M.Y. Salem, Correlation between Dynamic Light Scattering and Size Exclusion High Performance Liquid Chromatography for Monitoring the Effect of pH on Stability of Biopharmaceuticals, 1060 (2017) 1-9.

A testbed for mechanical and thermal stimulation in studies of somatosensory functions

M. Sperduti[1], N. L. Tagliamonte[1,2], C. Casale[3], P. A. Netti[3,4], L. Zollo[1]
[1]*Research Unit of Advanced Robotics and Human-Centered Technologies, Università Campus Bio-Medico di Roma*
[2]*Laboratory of Robotic Neurorehabilitation, Fondazione Santa Lucia*
[3]*Interdisciplinary Research Centre on Biomaterials, University of Naples Federico II*
[4]*Department of Chemical Materials and Industrial Production, University of Naples Federico II*

***Abstract*—To conduct studies on the somatosensory system, different physical stimuli, typically mechanical and thermal, are applied to *in-vivo* or *ex-vivo* samples. This paper presents a testbed able to produce both mechanical and localized hot/cold thermal stimuli in versatile conditions for studies on somatosensory functions. The paper describes the components of the testbed, which mainly includes a 3-axis positioning system, with a resolution of 0.5 μm and a total workspace of $150 \times 150 \times 150$ mm^3, a force- or position-controlled mechanical stimulator, that can deliver up to 5 N with a minimum resolution of 0.3 mN, and a thermal stimulator that can reach desired temperatures from 5 up to 60 °C. The testbed has been used for preliminary tests on a skin substitute, demonstrating the capability to mechanically and thermally stimulate the sample accurately.**

***Keywords*—Testbed, thermal and mechanical stimulation, somatosensory studies.**

I. INTRODUCTION

The somatosensory system and its underlying transduction principles have been the focus of multiple investigations. To conduct these studies, different physical stimuli, typically mechanical and thermal, have been applied on *in-vivo* (humans and animals, typically rodents), or on *ex-vivo* samples; the electrical response or the psychophysical one is then recorded and analyzed. Among the multiple purposes of the studies conducted so far (*e.g.* the characterization and classification of mechanoreceptors responding to given inputs, the analysis of inflammatory and neuropathic pain, the identification of mechanical and thermal thresholds), different methods have been employed to deliver physical stimuli of interest to a test sample. The Von Frey filaments represent the primary tools used in the literature to deliver mechanical stimuli and detect the touch threshold in humans and animals [1]–[3]. Moreover, custom solutions, mainly consisting of an automated indenter, are extensively used for generating mechanical sensations, in terms of touch and pain, on *ex-vivo* samples [4], humans and hand prostheses [5]. Thermal stimulation can be based on contact and contactless methods [3]. The use of Peltier cells represents a gold standard among the contact solutions. These devices can produce both hot and cold sensations and, due to their versatility and ease of use, they are widely employed on both humans and animal models [1], [6].

Solutions available on the market are mainly intended to deliver mechanical and (sometimes) thermal stimuli in *ex-vivo* models. The Mechanical Tester PB1000 by Nanovea is an automated indenter vertically controlled, integrated with a planar sample holder moving in two perpendicular directions. Even if it has been designed for materials mechanical characterization, it has also been used to test biological samples. The Piuma nanoindenter by Optics11 also provides accurate measurements of the micro-mechanical properties of soft samples, both in-air or liquids. These and other commercial systems are not employed for studies on somatosensory functions because: *i)* they typically do not integrate into a single platform a mechanical and thermal stimulator; *ii)* in case they include temperature-controlled stages to set pre-defined environmental conditions, they can not produce localized thermal stimuli and often only heating is included; *ii)* they are often not suitable to investigate touch and pain sensations *in-vivo*.

In this paper a testbed able to produce both mechanical and localized hot/cold thermal stimuli in *in-vivo* and *in-vitro* models is presented. This device was developed to perform a comparative analysis between an *in-vitro* skin model of human somatosensory system and an *in-vivo* animal counterpart when the same stimulation is provided. This skin model is being used as a testing sample for the validation of ultrasound-based interfaces for robotic hand prostheses developed within the SOMA European project.

II. TESTBED CHARACTERISTICS AND COMPONENTS

The functional characteristics of the developed testbed and its components will be presented in this section. As reported in Fig. 1, the testbed includes a sample holder, a positioning system, a mechanical and a thermal stimulator (not mounted simultaneously). A data acquisition system, and a custom interface with the user have also been added.

The technical specifications for the testbed design were identified based on a review of the scientific literature on the techniques used to thermally and mechanically stimulate *in-vivo* and *ex-vivo* models and on the ranges of somatosensory sensations to be elicited. For the mechanical stimulator, the dimensions of the tip have been selected to be suitable for tests on humans, small animals (rodents), and *in-vitro* skin models.

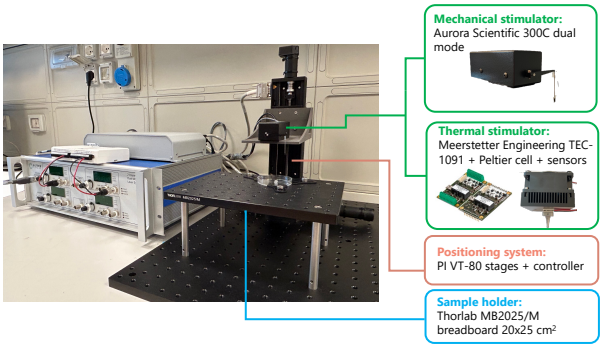


Fig. 1: Testbed main components.

For this reason, an interchangeable round tip with different sizes has been chosen in the range 0.5–3 mm in diameter. With this tip, the mechanical stimulator was required to deliver a force from 0.1 mN, corresponding to threshold recognizable as mechanical stimulation, to 1 N, to elicit pain sensation in humans and animals. Moreover, the thermal stimulator was required to include a round tip with diameter in the range 2–3 mm and generate a temperature stimulation in the range 5–60 °C, to induce a hot/cold sensation up to pain.

A. Sample holder

As a base frame, the Thorlab optical table MB6060/M (600×600 mm^2) has been selected to include all the testbed components. The sample holder was made of a second Thorlab optical table MB2025/M (200×250 mm^2) placed on 4 mounting posts (height: 100 mm).

B. Positioning system

To accurately stimulate the sample, a motorized 3-axis Cartesian positioning system is used. It includes three linear stages (PI VT-80), with DC motors controlled by one multi-axis driver (PI C-884.4DC), whose main features are reported in Table I.

TABLE I: Positioning system main characteristics.

	Linear stage PI VT-8
Stroke [mm]	150
Resolution [μm]	0.5
Maximum speed [mm/s]	20
Load capacity [N]	50

C. Mechanical stimulation

The mechanical stimulator is based on the 300C Dual Mode system device by Aurora Scientific, that has been already largely used in literature [6]. It is composed of a motor head whose indenter ends with an interchangeable tip (diameter from 0.5 to 3 mm) and it can be force- or position- controlled by means of an external analog signal. A picture is reported in Fig. 2. Two different motor heads can be mounted: one is able to deliver up to 1 N of indentation force with a resolution of 0.3 mN and the other is able to deliver up to 5 N with a resolution of 1 mN. This dual option increases versatility

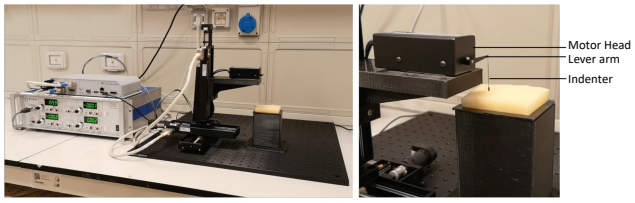


Fig. 2: 300C Dual Mode indenter by Aurora Scientific.

in the experiments since it allows to have alternatively high-range/low-resolution and low-range/high-resolution solutions. The main characteristics of the system are reported in Tab. II.

TABLE II: Mechanical stimulator main characteristics.

	Aurora Scientific 300C Dual Mode	
Maximum force [N]	1	5
Resolution [mN]	0.3	1.0
Stimulation diameter [mm]	0.5 – 3	

D. Thermal stimulation

A custom thermal stimulator was developed and is reported in Fig. 3. A Peltier cell has been employed, which is the most effective solution to generate both hot and cold stimuli. It is connected on one face to a heatsink to dissipate the heat produced when operating in cooling mode, and on the other face to a custom-made interchangeable aluminum tip. The tips have been designed in a shape that allows the highest contact with the Peltier cell on one side and a punctuate ending on the other one, to precisely stimulate the sample. They have been fabricated in two different dimensions (diameter: 2 or 3 mm). Moreover, an aluminum adapter has been fixed to the Peltier cell and consents to interchange the two tips easily. Both the tips and the adapter have been 3D-printed in aluminum. The Peltier cell was selected from Adaptiv with a surface of 15×15 mm^2, a cooling power of 8.6 W, and a 74 °C maximum temperature difference between the two faces. This device is also connected to two NTC thermal sensors: one is used as a feedback sensor to control the temperature of the tip, whereas the other one is used to monitor the temperature of the heatsink to avoid exceeding the maximum value allowed by the Peltier cell. The temperature regulation is performed by means of a ThermoElectric Cooling (TEC) controller by Meerstetter Engineering (TEC-1091). The main characteristics of the thermal stimulator are reported in Table III.

TABLE III: Thermal stimulator main characteristics.

	Thermal stimulator
Temperature range [°C]	5 - 60
Stimulation tip diameter [mm]	2, 3

E. Data acquisition system

To send analogue signals commanding desired position/force values to the mechanical stimulator, and also to acquire the analogue actual position and/or delivered force, a DAQ from National Instruments (USB-6212) was used.

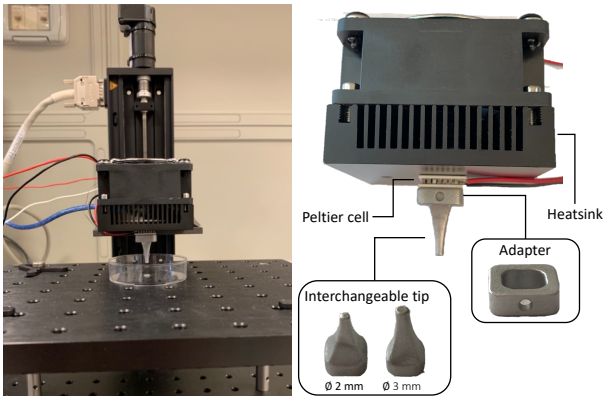


Fig. 3: Thermal stimulator main components.



Fig. 4: Mechanical stimulator custom user interface.

F. User interface

1) Positioning system: The multistage positioning system from PI came with the dedicated software PIMikroMove. It enables the experimenter to perform movements of the single stages by imposing the stroke and the desired velocity, to synchronize the movement of the three stages or to perform a pre-defined stimulation pattern by implementing a macro.

2) Thermal stimulator: For controlling the Peltier cell the software that came with the TEC-1091 controller by Meerstetter Engineering has been used. After setting the main characteristics of the Peltier cell (maximum input current, maximum difference of temperature between faces, and the direction of the current for cooling) and of the NTC thermal sensor, it is possible to set the desired temperature.

3) Mechanical stimulator: To control the mechanical stimulator, a custom interface has been developed by using NI Labview, as shown in Fig. 4. It allows the experimenter to set different stimulation profiles, also choosing between a force or position control of the indenter. Moreover, the temperature control tab has been added to control both the mechanical and thermal stimulation from a single interface. Once the temperature control tab is activated it is possible to set the desired temperature and monitor the actual temperature, the heatsink temperature, the actual current and voltage.

III. Testbed Preliminary Use

A. Experimental tests

Some preliminary *in-vitro* experiments to assess the performance of the testbed have been carried out on an artificial Skin Substitute (SS), with a diameter of 6 mm and thickness of 1 mm. The SS has been fixed with formalin 4% for 20 min and washed in PBS 3 times.

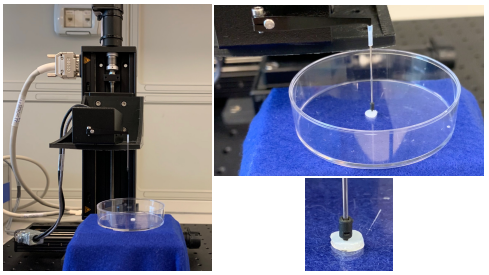


Fig. 5: *In-vitro* mechanical stimulation of the SS sample.

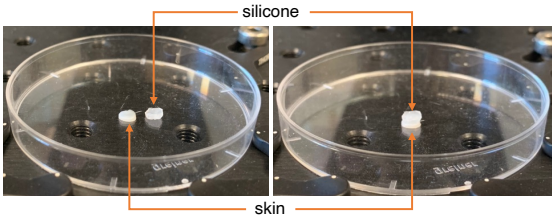


Fig. 6: *In-vitro* mechanical stimulation of the SS sample covered with a silicon layer.

1) Mechanical stimulation: In Fig. 5 the used setup is shown with a detail of the tip (diameter: 0.5 mm) in contact with the SS. The sample has been stimulated by using a triangular profile for a total (loading-unloading) duration of 20 s. After reaching the contact of the tip with the SS, by means of the positioning system, two different stimulations were performed. First, a position-based stimulation has been pursued, by applying a displacement from 0.1 to 0.7 mm with a step of 0.1 mm. Then, a force-based stimulation has been performed. In this case, a symmetric trapezoidal waveform, with a total duration of 6 s and steady-state stimulation of 2 s, has been applied with a force of 0.01, 0.02, 0.05, 0.1, 0.2, 0.5 N. However, this stimulation was not successful since the tip slept over the SS sample due to its high compliance. The issue was overcome by repeating the tests, considering the same range of forces, after adding over the SS sample a silicon layer with comparable shape and dimensions, as shown in Fig. 6.

2) Thermal stimulation: The tip (diameter: 3 mm) was brought to a predefined temperature and then placed for 10 s in contact with the sample (Fig. 5) by using the positioning system. Five randomly selected temperature values were tested in the range 5–50 °C. The temperature of the tip was continuously monitored.

B. Results

1) Mechanical stimulation: The actual displacement and delivered force when the SS was stimulated in position control mode have been recorded and are shown in Fig. 8. Desired and actual position profiles in all the conditions, *i.e.* with step displacement of 0.1 mm, are substantially superimposed thus demonstrating that it is possible to easily achieve a mechanical stimulation by using a position control mode. Fig. 8 also

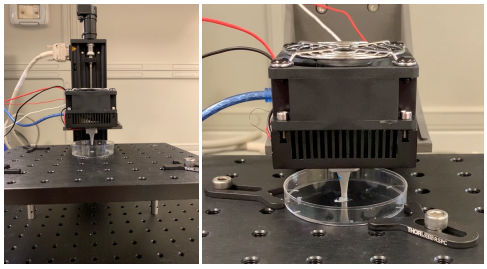


Fig. 7: Setup of the *in-vitro* thermal stimulation of SS sample.

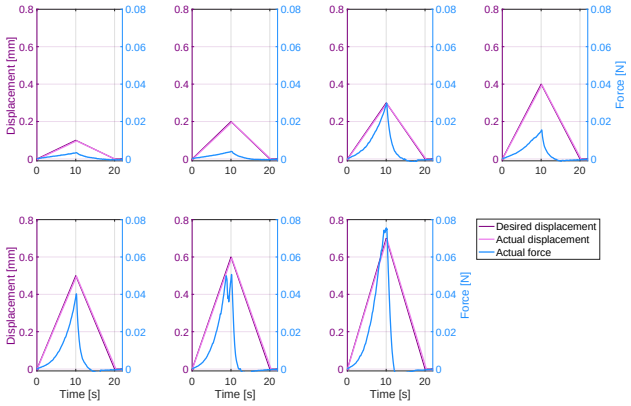


Fig. 8: Force and position data from the position-based mechanical stimulation tests.

indicates clear non-linear force-position characteristics and also a viscoelastic behavior (visible in asymmetric loading and unloading responses), more pronounced with increased displacement.

The results of the force-based stimulation applied on the compound SS-silicone sample are reported in Fig. 9. The tests were successfully performed thus demonstrating that a surface stiffer than the SS sample alone is needed to properly achieve force-based stimulation. Indeed, in this case, the actual force accurately replicates the desired one.

2) Thermal stimulation: The results of the thermal stimulation tests are shown in Fig. 10, where the desired and actual temperature measured at the contact point between the thermal tip and the SS sample are reported. It can be seen that the temperature is maintained almost constant during the stimulation period of 10 s and it is not influenced by

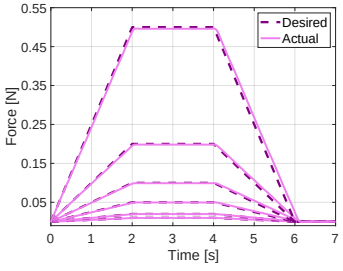


Fig. 9: Desired and actual force data from the force-based mechanical stimulation tests on the SS sample covered with the silicon layer.

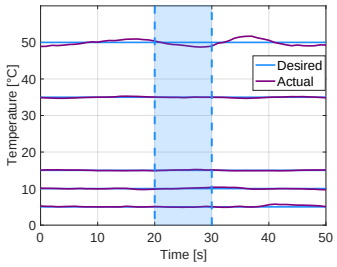


Fig. 10: Desired and actual temperature during thermal stimulation tests.

the contact with the sample, with the only exception of the test at 50 °C, which is likely influenced by the non-constant environmental conditions.

IV. Discussion and Conclusion

A new testbed for studies on somatosensory functions has been developed. It integrates a positioning system, a mechanical stimulator with interchangeable tips to be used in position- and force- controlled modes, and a thermal stimulator, able to deliver hot/cold localized stimuli on tips with two sizes. The testbed has been used in preliminary tests on a fixed SS to demonstrate the capability to produce the desired performance. Thermal and position-based stimulations were successfully obtained. Force-based stimulation suffered from the high difference between tip and sample stiffness. This limitation will be solved by including in the testbed a compliant stimulation tip. This solution will be also useful to potentially perform shear (brushing like) stimulations. Finally, in future works, the testbed will be used in *in-vitro* tests on an innervated skin model and its electrical somatosensory response will be recorded and compared with the one obtained in tests on an *in-vivo* animal model.

Acknowledgement

This work was partially supported by the EU Commission under the project SOMA (H2020-FETOPEN-2019-899822): Ultrasound peripheral interface and in-vitro model of human somatosensory system and muscles for motor decoding and restoration of somatic sensations in amputees.

References

[1] M. Szczot, J. Liljencrantz, N. Ghitani, A. Barik, R. Lam, *et al.*, "PIEZO2 mediates injury-induced tactile pain in mice and humans," *Science translational medicine*, vol. 10, no. 462, pp.eaat9892, 2018.

[2] S. R. Garrison, A. Dietrich, and C.L. Stucky, "Trpc1 contributes to light-touch sensation and mechanical responses in low-threshold cutaneous sensory neurons," *J neurophys*, vol. 107, no. 3, pp. 913–922, 2012.

[3] J. R. Deuis, L. S. Dvorakova, and I. Vetter, "Methods used to evaluate pain behaviors in rodents," *Front molec neuroscience*, p. 284, 2017.

[4] S. A. Wellnitz, D.R. Lesniak, G.J. Gerling, and E.g, and E.A Lumpkin, "The regularity of sustained firing reveals two populations of slowly adapting touch receptors in mouse hairy skin," *J neurophys*, vol. 103, no. 6, pp. 3378–3388, 2010.

[5] C. M. Oddo, L. Beccai, N. Vitiello, H. B. Wasling, J. Wessberg, *et al.*, "A mechatronic platform for human touch studies," *Mechatronics*, vol. 21, no. 3, pp. 604–613, 2011.

[6] N. Milenkovic, W.-J. Zhao, J. Walcher, T. Albert, J Siemens, *et al.*, "A somatosensory circuit for cooling perception in mice," *Nature neuroscience*, vol. 17, no. 11, pp. 1560–1566, 2014.

Engineering of biological entities through dynamic perturbations of lipidic membranes.

S.Silvestri[1], E.Romano[1], P.A.Netti[2], and E.Torino[2]

[1] *Department of Chemical, Materials and Production Engineering (DICMaPI), University of Naples Federico II, P.le Tecchio 80, 80125 Naples, Italy; Interdisciplinary Research Center on Biomaterials CRIB, - Italy*

[2] *Department of Chemical, Materials and Production Engineering, DICMaPI, Naples; Interdisciplinary Research Center on Biomaterials, CRIB, Naples; Istituto Italiano di Tecnologia, IIT, Naples – Italy*

***Abstract*— Synthetic and Natural Lipid Bilayer (LB) systems are attracting particular interest due to their distinctive pharmacokinetic profiles and physico-chemical properties. The elastic adaptability owing to the fluidity of lipidic membranes opens exciting possibilities to engineering these structures by properly stimulating them.**

However, a lack of knowledge of the mechanical responses and the high sensitivity to small perturbations are still hindering the accurate manipulation of these complex surfaces. Microfluidic approaches seem to be a good choice to finely manipulate local environmental conditions, in such a way to precisely alter biomembranes and control the final deformative outcomes. However, to the best of our knowledge, microfluidic approaches are mostly geared at stimulating single vesicles, rather than concentrated suspensions.

In a recent work, our group patented an innovative method for the encapsulation of U87-derived exosomes with various molecules, based on the application of high hydrodynamic pressures. It seemed that the pool of forces generated from this stimulation temporarily modified lipidic membranes, allowing the transit of molecules inside exosomes, with the resulting rise of their encapsulation efficiency.

Inspired from these results, we propose the application of controlled stresses on population of lipid-based systems as a way of handling, identifying, and manipulating membrane's mechanics and dynamics, in order to improve and widen their industrial applicability.

***Keywords*—Lipid Based Systems, Microfluidics, Permeabilization, Thermodynamics.**

I. Introduction

LIPID Bilayers (LBs) are complex systems that spontaneously form due to enthalpic and entropic forces established when lipidic molecules are exposed to aqueous environments. This is a result of their amphipathic nature that induce the formation of macromolecular assemblies aimed at reducing the exposure of hydrophobic lipidic fractions to water. [1]

The combination of various lipidic-related factors drives the formation of different architectures [2]. As elegantly described by Antonietti et al. [3] the self-assembly is a two-step process in which amphiphiles first form a bilayer, then rearrange to minimize the system free energy.

However, the structures formed are far from being static and permanent assemblies.

Indeed, the fluidic nature of membranes that may mostly be related to the presence of various lipids in different amounts, has been observed to confer a dynamic structural behaviour [4, 5] .

Accordingly, shapes and compositional arrangements are continuously modified depending on thermodynamic needs and external conditions.

Fluidity of lipid bilayers can be seen as the property filling the gap between the compositional variability and the structure dynamicity, since it allows the activation of remodelling pathways, supporting the lateral diffusion of molecules along the plane of the membrane, the inter-leaflet flip-flop movements as well as bending or thickness fluctuations. Consequently, alterations of membrane properties can be detected in terms of asymmetric molecule assemblies, deformations and rafts formations [6], to name a few.

These alterations may finally be related to variable mechanical properties and physical states, that in turn impact on several biological outcomes.

However, the complex biological remodelling machinery works adaptively [7] and complies with the variations in the external conditions.

It has already been reported [8] that cells are highly regulated by forces, which they are able to transmit from the exterior to the interior and vice versa, or to neighbour cells. Consequently, sensing molecular modulators [9, 10] are activated, showing how elastic features are responsible for activities like vesicle fusion and fission [11], cellular signalling [12], compositional membrane remodelling [7], shape modifications [13].

The distinctive fluidity of the lipidic counterpart has paved the way to the exciting possibility of exposing membrane-formed structures to multiple forces, in such a way to deform their architecture temporarily or permanently, in a controlled manner.

Spanning from cells to both natural and synthetic lipid-based systems, we are investigating how these deformations can be used to temporary permeabilize biomembranes in such a way to encapsulate different types of molecules, or to trigger and modify biological remodelling pathways. We believe that the application of controlled stresses on lipidic membranes may be useful for engineering different LB systems in order to increase their delivery abilities, by directly impacting on their encapsulation, diffusion, Nano-bio-interactions, cell targeting and uptake mechanisms.

II. THEORETICAL BACKGROUND

A. Pioneering descriptions of Lipid Bilayer membranes

The detection of Lipid Bilayers emerged in the first instance from pioneering studies of cells [14-19] and laid the ground to theorizations, debates, and release of various compositional and mathematical models.
The most complete and accepted description is currently considered the Fluid Mosaic model [20], released in 1972 by Sir Singer and Nicolson.
This model highlighted the heterogeneity of bilayers made of lipidic and protein molecules and the fluidic nature of these assemblies, that are able to rearrange according to thermodynamic demands.
Starting from these pillars, further studies were devoted to melting the bundle of the biomembrane dynamics complexity, at various level of interpretation.
The peculiar mechanical properties of lipidic bilayers have been studied for years to discuss the dynamic re-shaping that could be triggered by external or internal stresses.
Mathematical investigations were firstly introduced by Helfrich [21] in 1973.

B. Helfrich-Canham 2D Model

Through a continuum-mechanical approach Helfrich discussed the dynamism as the resulting deformations established after the application of external loads.
Accordingly, the ability to withstand these loads can be related to elastic abilities of storing energy of deformations until a limit, before being discharged under bending.
It can be showed that amphipathic fluid elements are characterized by a spontaneous curvature resulting from the repulsion between hydrophobic moieties and the water environment.
To minimize the contact area, spherical configurations are realized, driven by entropic forces.
A way to identify the spontaneous curvature is through two main radii of curvatures, that can be simplified as the total curvature J and the Gaussian curvature K of the surface.
Through the representation of membranes as bidimensional elastic interfaces [22] , Helfrich applied the principles of Gibbs theory of elastic interfaces [23] to derive a mathematical description that is only based on material properties.
By introducing the main radii of curvatures, as the total curvature J and the Gaussian curvature K, the excess of internal energy U^{exc}, entropy S^{exc}, and masses of components N_i^{exc}, on a diving surface at the lipid – water interface, can be described as:

$$dU^{exc} = TdS^{exc} + \sum \mu_i dN_i{}^{exc} + \gamma dA + A\tau dJ + A\bar{k}dK \quad (1)$$

From mathematical insights described elsewhere [22], by assuming to be in a small elastic deformation regime it is possible to define elastic moduli only dependent on the monolayer internal structure. They are the stretching modulus Γ, the bending modulus k, the mixed modulus E_{AJ}

$$\Gamma = A \cdot \frac{\partial \gamma}{\partial A} \quad (2)$$

$$k = \frac{\partial \tau}{\partial J} \quad (3)$$

$$E_{AJ} = \frac{\partial \gamma}{\partial J} = \tau + A \cdot \frac{\partial \tau}{\partial A} \quad (4)$$

These material parameters can be used along with the assumptions of constant entropy (i.e. ΔS=0), constant amount of lipid molecules (ΔN_i=0) and a flat monolayer (ΔJ=J). Moreover, the dividing surface can be chosen at the neutral surface, where the overall contribution coming from the mixing modulus is equal to zero. In this way, a more compact expression for Eq. (1) can be derived:

$$dU^{exc} = \gamma dA + A\tau dJ + A\bar{k}dK + \frac{1}{2}\Gamma\frac{(\Delta A)^2}{A} + \frac{1}{2}Ak(J)^2 \quad (5)$$

This is the most general expression for the description of the elastic bending forces in bidimensional fluid systems, according to the Helfrich-Canham 2D model [24]. By integrating this expression, it is possible to obtain the deformation energy that drives the shape remodeling:

$$f = \gamma dA + \frac{1}{2}\Gamma\frac{(\Delta A)^2}{A} + \tau \cdot J + \bar{k} \cdot K + \frac{1}{2}k(J)^2 \quad (6)$$

C. 3D Mathematical description of Biomembranes

While for a bidimensional depiction it is possible to neglect some contributions, trans-monolayer stresses become extremely relevant in the 3D case. Indeed, Lipid Bilayers are characterized by lateral stress profiles [6] rising along transverse structures.
Seifert and Langer developed a continuum model [25] explicitly accounting for the bilayer architecture and capturing the major energetic driving forces and dissipative drag forces involved in the dynamics of lipid membranes.
However, a good mathematical description for this class of soft materials must consider a solid–fluid duality, from a mathematical viewpoint.
Indeed, lipid monolayers have been demonstrated to exhibit a lateral liquid-like nature and transverse solid-like. Thus, the stored energy in the transverse direction causes tilt deformations that need to be included in the thermodynamic description through the integration of both a tilt modulus and mixed moduli.
By taking into account all these facts, a tridimensional expression for the excess internal energy of biomembranes can be derived:

$$dU^{exc} = \gamma dA + A\tau dJ + A\bar{k}dK + \frac{1}{2}\Gamma\frac{(\Delta A)^2}{A} + \frac{1}{2}Ak(\Delta J)^2 + E_{AJ}\Delta A\Delta J + Am_t d\theta_t \quad (7)$$

From this formula a complex expression for the total free energy of deformation can be obtained, in terms of the 4th order elastic moduli tensor.
While relying on multiple assumptions, this model provided the first mathematical description of biomembranes, by also including a simple estimation of their dynamic behaviour.

III. ENGINEERING FLUID LIPIDIC MEMBRANES

The mechanical profile of LB systems has emerged as a unique characteristic deriving from the synergic combination of both fluidity and viscoelasticity.

It dictates the ability to respond to applied forces, in light of the material thermodynamical state, architecture and composition.
The deformed states acquired under the application of external stresses and the elastic tendency of restoring initial configurations, are the most relevant contributions that are responsible for the activation of the remodelling machinery in biomembranes.
Deeper knowledge of their functionality could be useful to engineer structures in order to reach desired outcomes.
In particular, the temporary permeabilization of membranes could be an effective approach to increase the encapsulation efficiency of different molecules in various LB systems, by overcoming issues related to the highly impermeability.
Accordingly, the use of microfluidic forces may be an effective approach to establish locally controlled conditions in such a way to predict and manage the forces exerted on single and multiple cell populations.
On the other side, optimal deformations may be designed in such a way to stimulate biological pathways and modify vesicles properties. In this way, there would be a direct implication for both the delivery and the diffusive properties in various biological environments, as well as an improved interaction at different nano-bio-interfaces.
According to the specific aspect to be investigated, LB mechanics can be translated in different aims, moving from mechanical phenotyping or biological investigations to the engineering of drug delivery vesicles.
However, it is only recently that microfluidic approaches are emerging as tools for questioning and investigating mechanical properties of various LBs.
As the primary application, examples of cellular stimulations under hydrodynamic microfluidic forces are reported in the following sections. To the best of our knowledge, different types of stimulations on cells or various LB systems have only been used at single-cell level. Thus, section B is aimed at discussing the applicability of dynamic perturbations on concentrated suspensions, by reporting our innovative approach as a case study.

A. Microfluidic hydrodynamic permeabilization of single cells.

Chung et al. [26] developed a microfluidic platform to inertially focus cells at the centre of the channel and guide them to collide at a T-junction. This hydroporator is able to apply controlled compression and shear forces on single cells, in order to generate transient membrane discontinuities on their membranes and facilitate passive diffusion of various molecules into their cytoplasm, while preserving cell viability. However, despite the high delivery performances also with large nanoparticles, they obtained non-optimized cell deformation patterns that have hampered the applicability of the platform to gene delivery and primary cells.
Two years later, another inertially-based microfluidic platform ending with a cavity on the T-junction [27] was designed.
Adding the cavity instead of the tip, they were able to exploit hydrodynamics to elongate cells and let them collide with the fluidic wall instead of the PDMS.
In this way, the combination of compressive, shear, elongational and collision forces allowed the achievement of a homogeneous deformation field.
Another interesting application of microfluidic hydrodynamics is the investigation of mechanical phenotyping [28] and properties of both adherent and suspended cells [29]. However, to the best of our knowledge all the microfluidic devices already developed that are aimed at stimulating cells are only geared to work at a single-cell level.

B. Hydrodynamic permeabilization of LBs populations.

Differently, our group recently patented an innovative approach to manipulate lipidic membranes at a large scale [30]. We used complex deformative fields deriving from the application of high hydrodynamic pressures in a Microfluidizer (Model M-110P Microfluidizer^{TM} Materials Processor, Microfluidics, Westwood, MA, USA) to stimulate a suspension of U87-derived exosomes. By including recycling cycles, the same fluidic forces were applied to a large number of vesicles, thus realizing a uniform deformative field. The purpose was to temporarily modify external lipidic membranes of multiple vesicles in order to underpin the passive encapsulation of different molecules.
Encouraging results in terms of the highly encapsulation efficiencies of multiple molecules compared to literature, while preserving structure integrity and purity, demonstrated the potential role of high dynamic hydrostatic pressure in temporarily modifying lipidic membranes.

IV. Conclusion

This work is aimed at raising concerns about the necessity of expanding the field of investigation about the mechanical properties of Lipid Bilayer (LB) systems. By quickly introducing theoretical and biological backgrounds that are useful for a deeper understanding of mechanical aspects of these structures, the realization of controlled deformative frameworks is proposed as an engineering approach to modify physico-chemical properties. For this purpose, the optimally designed microfluidic devices seem to be optimal tools to locally control the extent of the forces applied, in such a way to finely modify the deformative outcomes. While microfluidics has been demonstrated to be largely used for mechanical phenotyping or cell manipulation at a single level, there is still a lack of techniques used for LBs manipulation at a large-scale. A high throughput approach based on the use of high hydrostatic pressures on exosomes populations has been recently developed by our group and it is reported here as a model for encouraging next microfluid translations.

References

[1] G.a.K.N.a.N.M.P.a.K.J. Pabst, Liposomes, Lipid Bilayers and Model Membranes: From Basic Research to Application, 2014.
[2] P.S.a.S.M. Phapal, Rapid Spontaneous Assembly of Single Component Liposomes, arXiv: Soft Condensed Matter (2015).
[3] M.a.F.S. Antonietti, Vesicles and Liposomes: A Self-Assembly Principle Beyond Lipids, Advanced Materials 15(16) (2003) 1323-1333.
[4] S. Gupta, R. Ashkar, The dynamic face of lipid membranes, 17(29) (2021) 6910-6928.
[5] L. Lamparter, M. Galic, Cellular membranes, a versatile adaptive composite material, 8 (2020) 684.
[6] L. Bagatolli, O. Mouritsen, Is the fluid mosaic (and the accompanying raft hypothesis) a suitable model to describe fundamental features of biological membranes? What may be missing?, 4 (2013).

[7] M.K. Dymond, Mammalian phospholipid homeostasis: evidence that membrane curvature elastic stress drives homeoviscous adaptation in vivo, Journal of The Royal Society Interface 13(121) (2016) 20160228.
[8] P.A. Janmey, C.A. McCulloch, Cell mechanics: integrating cell responses to mechanical stimuli, (1523-9829 (Print)).
[9] S. Ballweg, E. Sezgin, M. Doktorova, R. Covino, J. Reinhard, D. Wunnicke, I. Hänelt, I. Levental, G. Hummer, R. Ernst, Regulation of lipid saturation without sensing membrane fluidity, 11(1) (2020) 756.
[10] D.A. Los, N. Murata, Membrane fluidity and its roles in the perception of environmental signals, (0006-3002 (Print)).
[11] J. Eid, H. Greige-Gerges, L. Monticelli, A. Jraij, Elastic moduli of lipid membranes: Reproducibility of AFM measures, 234 (2021) 105011.
[12] A.S. Kashani, M. Packirisamy, Cellular deformation characterization of human breast cancer cells under hydrodynamic forces, 4(3) (2017) 400-414.
[13] R. Lipowsky, Remodeling of membrane compartments: some consequences of membrane fluidity, 395(3) (2014) 253-274.
[14] R. Hooke, K.o.G.B.f.o.U. George Iii, K.o.G.B.d.U. George Iv, Micrographia, or some physiological descriptions of minute bodies made by magnifying glasses, with observations and inquiries thereupon. By R. Hooke, Printed by Jo. Martyn, London.
[15] N.C.H.G. Grew, The anatomy of plants. https://archive.org/details/b3032435x_0001).
[16] M. Malpighi, Anatome plantarum. Cui subjungjungitur appendix, iteratas & auctas ejusdem authoris de ovo incubato observationes continens. Regiae societati, Londini ad scientan naturalem promovendam institutae, dicata, J. Martyn, Londini, 1675.
[17] J.S. Simon, B.S. Brodie, W.W.S. Gull, R.B. Todd, L. King's College, S. Physical, L. St. Thomas's Hospital. Medical School, A physiological essay on the thymus gland, Henry Renshaw, London :, 1845.
[18] F. Leydig, Lehrbuch der Histologie des Menschen und der Thiere, Meidinger, Frankfurt a.M., 1857.
[19] W. Hewson, XXXIII. On the figure and composition of the red particles of the blood, commonly called the red globules., Philosophical Transactions of the Royal Society of London 63 (1773) 303-323.
[20] S.J.S.a.G.L. Nicolson, The Fluid Mosaic Model of the Structure of Cell Membranes, Science 175(4023) (1972) 720-731.
[21] W. Helfrich, Elastic Properties of Lipid Bilayers: Theory and Possible Experiments, Zeitschrift für Naturforschung C 28(11-12) (1973) 693--703.
[22] F. Campelo, C. Arnarez, S.J. Marrink, M.M. Kozlov, Helfrich model of membrane bending: From Gibbs theory of liquid interfaces to membranes as thick anisotropic elastic layers, Special issue in honour of Wolfgang Helfrich 208 (2014) 25-33.
[23] J.W. Gibbs, On the equilibrium of heterogeneous substances, (1879).
[24] P.B. Canham, The minimum energy of bending as a possible explanation of the biconcave shape of the human red blood cell, 26(1) (1970) 61-81.
[25] U. Seifert, S.A. Langer, Viscous Modes of Fluid Bilayer Membranes, Europhysics Letters (EPL) 23(1) (1993) 71-76.
[26] Y. Deng, M. Kizer, M. Rada, J. Sage, X. Wang, D.-J. Cheon, A.J. Chung, Intracellular Delivery of Nanomaterials via an Inertial Microfluidic Cell Hydroporator, Nano Letters 18(4) (2018) 2705-2710.
[27] J. Hur, I. Park, K.M. Lim, J. Doh, S.-G. Cho, A.J. Chung, Microfluidic Cell Stretching for Highly Effective Gene Delivery into Hard-to-Transfect Primary Cells, ACS Nano 14(11) (2020) 15094-15106.
[28] D. Dannhauser, M.I. Maremonti, V. Panzetta, D. Rossi, P.A. Netti, F. Causa, Mechanical phenotyping of breast cell lines by in-flow deformation-dependent dynamics under tuneable compressive forces, Lab on a Chip 20(24) (2020) 4611-4622.
[29] D. Huber, A. Oskooei, X. Casadevall i Solvas, A. deMello, G.V. Kaigala, Hydrodynamics in Cell Studies, Chemical Reviews 118(4) (2018) 2042-2079.
[30] E. Romano, P.A. Netti, E. Torino, A High Throughput Approach Based on Dynamic High Pressure for the Encapsulation of Active Compounds in Exosomes for Precision Medicine, International Journal of Molecular Sciences 22(18) (2021).

Mechanical validation of an innovative intrafascicular neural interface to restore urinary bladder dysfunctions

E. Aprea[1*], A. Giannotti[1*], O. Akouissi[2], and S. Micera[1,2]
[1] *The Biorobotics Institute, Scuola Superiore Sant'Anna, Pisa, Italy*
[2] *Neuro-X Institute, École Polytechnique Fédérale de Lausanne, Geneva, Switzerland*
[*] *Equally contributed authors*

***Abstract*—Pudendal nerve stimulation has a proven efficacy in reducing overactive bladder symptoms in patients with, for example, spinal cord injury. Clinical neurostimulation devices provide electrical pulses to the whole nerve with tined lined electrodes. However, the low selectivity of such electrodes does not allow the specific targeting of nerve fascicles. Existing intrafascicular solutions showed higher selectivity but they can induce high nerve trauma or have an unsatisfying conductive site distribution within the cross-section of the nerve.**

Here, an existing tool is exploited for the modeling of mechanical stresses induced by the implant's micromotion, to validate the design of an innovative intrafascicular interface that selectively targets the pudendal nerve. The mechanical stresses induced by the latter are compared to currently used intrafascicular solutions. Our results indicate that the proposed innovative geometry enables the redistribution of micromotion-associated loads to less delicate parts of the interface.

***Keywords*—Pudendal neuromodulation, Bladder dysfunctions, Intra-fascicular implants, Finite elements modeling**

I. Introduction

Lower urinary tract (LUT) symptoms, including incontinence or urinary retention, affected 2.3 billion people in 2018 with negative consequences on their quality of life [1]. Since storage and elimination of urine are controlled by multiple nervous pathways, neurodegenerative diseases such as multiple sclerosis, Parkinson's disease or spinal cord injuries can affect bladder control. [2].

FDA approved sacral nerve stimulation (SNS) for the treatment of urinary urge incontinence, urgency, frequency, and refractory retention. SNS requires the placement of an implantable tined lead electrode to stimulate the sacral nerves [3]. The same technology has been proven to have higher efficacy when implanted within the pudendal nerve for pelvic pain, urgency, frequency, and bowel function [4]. However, the low selectivity of tined lead electrodes in fascicle recruitment can result in side effects, such as dorsiflexion of the toe or pelvic pain [5].

Alternative electrodes available for peripheral nerve stimulation can be classified as extra-neural and intrafascicular. The first ones are typically cuffs revolving around the nerve in a non-invasive way. Their customizable length and diameter give the possibility to target also small nerves. Hokanson studied pudendal nerve stimulation in rats with cuff diameters ranging from 200 µm to 400 µm [6]. Intrafascicular electrodes penetrate the nerve reaching nerve fascicles with higher selectivity [7]. Mathews proved selective recording of felines' pudendal nerve activity evoked by a variety of genitourinary stimuli with high-density Utah slanted electrode arrays (HD-USEA); however, the high degree of nerve damage may have been the cause of loss in neuronal signals over time [8]. Transversal intraneural multichannel electrodes (TIME) proved the higher biocompatibility in long-term applications and the ability to restore sensory feedback in upper-limb amputees [9, 10]. The limitation of TIME electrodes is the distribution of all the active sites along a cutline within the target nerve, which may result in the loss of the contribution of externally distributed fascicles within the nerve cross-section.

In this context, finite elements models (FEMs) are becoming increasingly useful as a guiding tool for the design of new electrodes prior to *in vivo* testing on animals. Akouissi proved the importance of simulating the mechanical effects of the implant's micromotions originating from connecting wires and muscle contractions on the target nerve to optimize electrode geometry and reduce foreign body reaction, which is responsible for the long-term performance of the implant [11].

Here, we used mechanical simulation to evaluate pig pudendal nerve micromotion-associated loads when implanted with an innovative peripheral nerve electrode (iPNE) geometry. The iPNE proposed is able to intersect the specificity of intrafascicular electrodes in selectively considering the fascicles and the non-invasiveness of extra-neural cuff electrodes with active sites distributed within the cross-sectional area of the nerve. The study also compares the mechanical behavior of iPNE with the already existing TIME, which proved their long-term safety in terms of mechanical interaction with nerves.

II. Materials and Methods

All experimental animal procedures were approved by the Italian Ministry of Health and were in accordance with the Italian law (D.lgs. 26/2014).

The behavior of two intrafascicular electrodes (iPNE and TIME) in the porcine pudendal nerve was simulated since LUT's gross anatomy of this animal model is comparable to the human one. The analysis followed the guidelines proposed

by Akouissi to design peripheral nerve implants, adapting the framework from a rodent's sciatic nerve to the porcine pudendal nerve [11]. The nerve simplified geometry and the two electrodes were implemented in the COMSOL 5.6 environment, with the Solid mechanics module. The FEM study was performed using a desktop PC (Windows 7 Professional, Intel Core i7-6700 CPU @ 3.4 GHz, 32 GB RAM) running the previously mentioned software.

A. 3D model of the porcine pudendal nerve

The histological evaluation of the porcine pudendal nerve was performed. The nerve sample was explanted at the ischioanal fossa level by using the transgluteal approach previously described by our group [13]. Histological image acquired with a digital optical microscope (Hirox, Japan) was then segmented using MATLAB (MathWorks, US). The exact shape of each fascicle was obtained from the segmented image. The epineurium surface was simplified into a circle with a radius of 500 µm, estimated as the mean value around the nerve. The simplified 2D geometry of the pudendal nerve was extruded in COMSOL to create a reliable three-dimensional (3D) nerve model. The extrusion length was set to 2 mm according to the boundary condition in section C.

The epineurium, internal epineurium and endoneurium are characterized by mechanical properties taken from literature and listed in Table I [13]. The pudendal nerve was considered composed of linear elastic components. The assumption of operating within the small (< 5%) strain regime allowed neglecting the viscoelastic and non-linear behaviors due to the complex interaction between cells, extracellular matrix and blood vessels.

The mesh was set as free tetrahedral, with a volume distribution increasing distally from the interface with the implants. The maximum growth rate was 1.5, while the minimum element size is 5 µm and the maximum element size was set at 400 µm. Edges and vertices have been smoothed to avoid singularities and further complexity.

TABLE I: Mechanical properties of nerve components

Element	*Poisson's ratio*	*Density [kg/m^3]*	*Young modulus [Pa]*
Epineurium	0.49	1043	100
Internal epineurium	0.49	1014	60
Endoneurium	0.49	1030	90

B. 3D model of iPNE and TIME electrodes

The iPNE implant was modeled as a cuff electrode revolving around the nerve and 5 equally spaced high-aspect ratio spines penetrating the nerve partially embedded within the cuff. The cuff was modeled as 500 µm thick and 1.6 mm long. A connector tip was modeled as a cylinder with 300 µm length and 100 µm radius and embedded in the cuff structure. The fibers were overall 550 µm long, with 350 µm inserted in the cuff and 200 µm inserted in the nerve.

The mechanical properties of the electrode's components are listed in Table II. For this preliminary study, the material chosen for the cuff and the connector tip was Polydimethylsiloxane (PDMS), such as most of the currently used extraneural interfaces [11]. Spines are supposed to be realized with 7 µm carbon fibers, thanks to the small dimension and their high tensile and compressive modulus.

The nerve-cuff and the nerve-fibers interfaces were provided with a triangular mesh with a maximum element size of 60 µm, minimum element size of 1 µm, and maximum element growth rate of 1.5. The cuff and the connector were provided with a tetrahedral mesh with a maximum element size of 300 µm, minimum element size of 5 µm, and maximum element growth rate of 1.5. The fibers were provided with a tetrahedral mesh with a maximum element size of 50 µm, minimum element size of 1 µm, and maximum element growth rate of 1.1.

The TIME implant has been modeled as a rectangular bar crossing the whole nerve, as it is shown in Figure 2 B. The dimensions of the bar are 18 µm in thickness and 545 µm in length, while the extrusion is long 1.6 mm. To reduce the effect of singularities, the edges of the TIME implant have been filleted with a radius of 9 µm. The material chosen for the TIME was Polyimide (PI), as reported in literature [11]. Other metallic elements have been neglected as they do not represent a major part of the electrode, thus they are not significant in the mechanical modeling [12].

The nerve-TIME surface perpendicular to the nerve was described with a triangular mesh having a maximum element size of 20 µm, minimum element size of 1 µm, and maximum element growth rate of 1.5. The nerve-TIME surface parallel to the nerve length was described with a triangular mesh having a maximum element size of 60 µm, minimum element size of 1 µm, and maximum element growth rate of 1.1.

TABLE II: Mechanical properties of electrode components

Element	*Poisson's ratio*	*Density [kg/m^3]*	*Young modulus [Pa]*
Cuff	0.49	965	10^6
Spines	0.3	1800 *10^3	234 *10^9
TIME	0.49	1300 *10^3	2.5 *10^9

C. Boundary conditions and solver

Three boundary conditions were imposed on the 3D models to reproduce the micromotions experienced by the nerve due to the movement of the cables linked to the implant.

Spring foundation boundary condition with elastic properties of the nerve applied to the XY surface at the two extremities of the nerve allowed to virtually extend the short simulated nerve with 6 mm on each side. This allowed to obtain results equivalent to a 14 mm nerve by modeling a shorter 2 mm long nerve with the same mechanical properties and reducing the computational complexity.

An *identity mapping pair* boundary condition linked the surface of the implants with the one of the nerve. This condition represented the worst-case scenario with the TIME and the iPNE electrodes having a complete adhesion to the

nerve. Thus, the condition pictures the stresses and the strains as fully transmitted to the nerve [12].

Prescribed displacement boundary condition simulated the micro-movements the nerve has to withstand when implanted with the two electrodes due to the presence of connecting cables. A displacement of 20 µm (under a small strain regime hypothesis) was applied to the TIME tip and to the iPNE connector tip, perpendicularly to their length.

Results were achieved in a standard stationary study performed at equilibrium. The linear direct solver was used, together with a constant Newton non-linear method with an initial damping factor of 1. The termination criterion was the residual and the procedure is tolerance based. The solution time took approximately 50 minutes.

D. Stress and displacement evaluation

The von Mises stress, called just 'stress' from now on, and the displacement generated on the nerve were evaluated as a consequence of the prescribed displacement of cables for both the iPNE and TIME electrodes implanted.

The maximum stress was evaluated at the interface nerve-implant. To compare results obtained from the two electrodes the maximum stress values were evaluated along cutlines. For the TIME electrode, the stress was evaluated at 5 µm from an in parallel to the rounded part of the implant. For the iPNE, maximum stress was evaluated by averaging the maximum stresses obtained over 5 cutlines, each of them considered at 5 µm from and in parallel to each of the spines.

Sharp changes in the geometries and material properties of the models may cause singularities, thus the evaluation of maximum stress and displacement may bring to unrealistic information. Bearing that in mind, the average stress at the interface nerve-implant was evaluated far from the entry point, where the effect of that uncertainty is not significant anymore. This distance was set to 100 µm as it is the minimum distance sufficient to avoid the effect of singularities [12]. The average stress was calculated by averaging the total stress retrieved on an XY cut plane at 100 µm from the implanted part of the electrode and dividing the obtained value by the total area of the implants. All the average stress results were normalized with respect to the maximum stress obtained in the simulations in the cut planes built at 100 µm from the implants, which is the one retrieved in the TIME model. For the TIME electrode, the average stress retrieved at 100 µm from the implantation site was normalized by dividing the TIME area. For the iPNE electrode, three different normalization areas were considered for the evaluation of the average stress retrieved at 100 µm: the array of spine constituting the iPNE electrode, the spine array together with the internal portion of the cuff, and the whole iPNE electrode surface in contact with the nerve. The internal portion of the cuff considered was limited to 200 µm since this area is supposed to withstand mostly the effect of friction. Displacement quantification followed a similar path, as the trend of the maximum displacement applied on the nerve was evaluated at intervals of 100 µm starting from the center of the implants.

III. Results

A. 3D model of the porcine pudendal nerve

Figure 1A shows the histological image of the explanted pudendal nerve. Figure 1B shows the simplified 2D geometry of the pudendal nerve implemented in COMSOL. The final 3D design of the nerve includes 19 fascicles (endoneurium) embedded in the internal epineurium, which is wrapped by the epineurium (100 µm thickness).

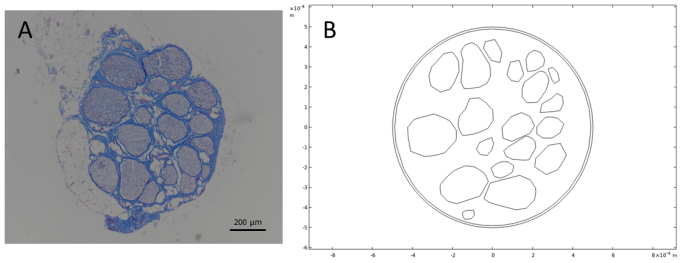


Fig. 1: A) Histological image of the pudendal nerve stained with Mallory's trichrome. B) Simplified 2D geometry of the pudendal nerve implemented in COMSOL.

B. 3D model of iPNE and TIME electrodes

The 3D model of the iPNE electrode inserted in the pudendal porcine nerve is shown in Figure 2A, while the one of the TIME is shown in Figure 2B. Both of them are pictured in their three-dimensional versions.

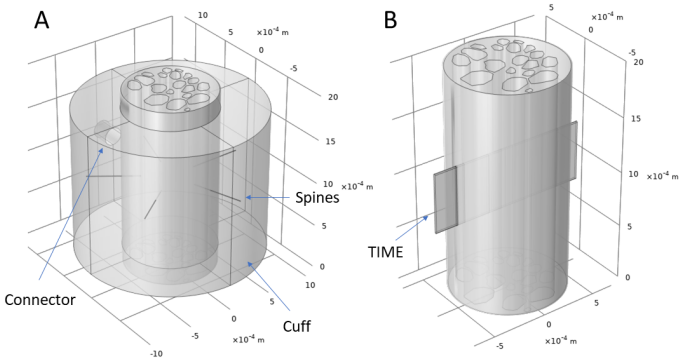


Fig. 2: A) 3D model of the iPNE and B) 3D model of the TIME with the 3D model of the pudendal nerve.

C. Stress and displacement evaluation

Figure 3A shows the maximum von Mises stress for both the TIME and iPNE electrode at the interface nerve-implant. The trend is descending in both cases. However, the stress produced from the TIME on the nerve is considerably higher (from 3 to 4 orders of magnitude) than the one resulting from the iPNE.

Figure 3B shows the stress retrieved at 100 µm from the implantation site, averaged by dividing it for the area of the

TIME, the array of spine constituting the iPNE electrode, the spine array together with the internal portion of the cuff and the whole iPNE electrode surface in contact with the nerve.

Finally, the results regarding the displacement are shown in Figure 3C. Consistently with the previous ones, even in this case, the displacement applied by the iPNE on the nerve is not only lower than the one applied by the TIME but also more consistent throughout the whole nerve length.

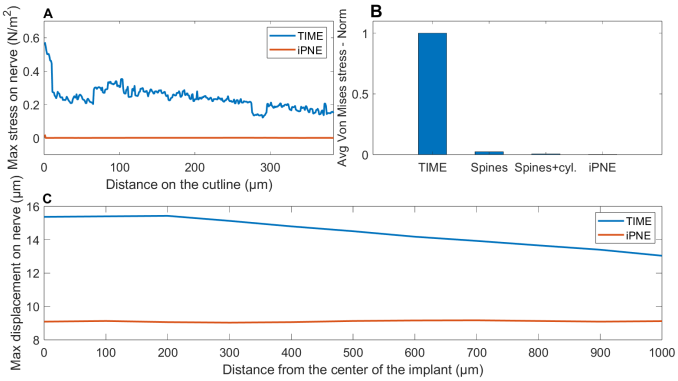


Fig. 3: A) Maximum von Mises stress on the nerve with varying distance on the cutline. B) Bar graph showing the average normalized von Mises stress at 100 µm from the implant. C) Displacement trend on the nerve with increasing distance from the center of the implant.

IV. Discussion & Conclusions

The results obtained with the FEM studies have shown promising results justifying the development of the iPNE interface as an alternative to currently used intrafascicular interfaces like the TIME.

The von Mises stress studies demonstrated that the maximum stress not only generally has a decreasing trend increasing the distance from the insertion point, coherently with the implantation of the electrodes (higher stresses will be closer to the insertion point), but it is also remarkably lower in the case of the iPNE. Moreover, the results obtained from the averaged stress study proved that even considering only the spines, which means averaging over a very small surface area, the averaged stress produced by the iPNE is orders of magnitudes lower than the one of the TIME interface.

Finally, the results regarding the displacement are in line with the previous reasoning. The displacement applied on the nerve by the iPNE is consistently lower than the one of the TIME. On top of that, the displacement enforced on the nerve is also more stable. This is a crucial point because it implies that the displacement does not twist the nerve in the case of the iPNE, rather it remains constant, shifting the twisting effect on the cuff itself.

Limitations of this work are the absence of an analysis of the different materials that could be used to construct the interface and the lack of an evaluation of the electrical selectivity performance of the iPNE. Although the properties of the design have been confirmed, new materials could be exploited to create an electrode that is more adherent to the nerve and more stable in terms of mechanical properties. Regarding selectivity, the distribution of active sites within the cross-sectional area of the nerve within the iPNE is expected to improve selectivity performance compared with placement along a straight line as in TIME, but future studies will evaluate these aspects. However, the model appears to be a reliable tool.

Acknowledgement

The authors would like to thank the INAIL Prosthesis Center for funding the BioSUP Project (PR19-CR-P2).

References

[1] Zhang AY, Xu X. Prevalence, Burden, and Treatment of Lower Urinary Tract Symptoms in Men Aged 50 and Older: A Systematic Review of the Literature. SAGE Open Nursing. 2018;4. doi:10.1177/2377960818811773

[2] de Groat WC, Griffiths D, Yoshimura N. Neural control of the lower urinary tract. Compr Physiol. 2015 Jan;5(1):327-96. doi: 10.1002/cphy.c130056. PMID: 25589273; PMCID: PMC4480926.

[3] Janssen DA, Martens FM, de Wall LL, van Breda HM, Heesakkers JP. Clinical utility of neurostimulation devices in the treatment of overactive bladder: current perspectives. Med Devices (Auckl). 2017 Jun 1;10:109-122. doi: 10.2147/MDER.S115678. PMID: 28615976; PMCID: PMC5460621.

[4] Spinelli, M., Malaguti, S., Giardiello, G., Lazzeri, M., Tarantola, J. and Hombergh, U.V.D. (2005), A new minimally invasive procedure for pudendal nerve stimulation to treat neurogenic bladder: Description of the method and preliminary data. Neurourol. Urodyn., 24: 305-309. https://doi.org/10.1002/nau.20118

[5] Yaiesh, S. M. , Al-Terki, A. E. , Al-Shaiji, T. F. (2020). Neuromodulation in Urology: Current Trends and Future Applications. In D. Larrivee, S. M. Rayegani (Eds.), Neurostimulation and Neuromodulation in Contemporary Therapeutic Practice. IntechOpen. https://doi.org/10.5772/intechopen.92287

[6] Hokanson, J.A., Langdale, C.L., Sridhar, A. et al. State-dependent bioelectronic interface to control bladder function. Sci Rep 11, 314 (2021). https://doi.org/10.1038/s41598-020-79493-7

[7] Navarro X, Krueger TB, Lago N, Micera S, Stieglitz T, Dario P. A critical review of interfaces with the peripheral nervous system for the control of neuroprostheses and hybrid bionic systems. J Peripher Nerv Syst. 2005 Sep;10(3):229-58. doi: 10.1111/j.1085-9489.2005.10303.x. PMID: 16221284.

[8] Kiran S. *et al.* Acute Monitoring of Genitourinary Function Using Intrafascicular Electrodes: Selective Pudendal Nerve Activity Corresponding to Bladder Filling, Bladder Fullness, and Genital Stimulation, Urology, Volume 84, Issue 3, 2014, Pages 722-729, ISSN 0090-4295, https://doi.org/10.1016/j.urology.2014.05.021.

[9] Wurth S. *et al.* Long-term usability and bio-integration of polyimide-based intra-neural stimulating electrodes, Biomaterials, Volume 122, 2017, Pages 114-129, ISSN 0142-9612, https://doi.org/10.1016/j.biomaterials.2017.01.014.

[10] Petrini FM *et al.* Six-Month Assessment of a Hand Prosthesis with Intraneural Tactile Feedback. Ann Neurol. 2019 Jan;85(1):137-154. doi: 10.1002/ana.25384. Epub 2018 Dec 24. PMID: 30474259.

[11] Christopher E. Larson, Ellis Meng, A review for the peripheral nerve interface designer, Journal of Neuroscience Methods, Volume 332, 2020, 108523, ISSN 0165-0270, https://doi.org/10.1016/j.jneumeth.2019.108523.

[12] Akouissi O., Lacour S.P., Micera S., DeSimone A. A finite element model of the mechanical interactions between peripheral nerves and intrafascicular implants. J of Neural Eng. 19 (4), 046017, 2022 July, doi: 10.1088/1741-2552/ac7d0e.

[13] Giannotti A.; Strauss I.; Bernini F; Recchia F. A.; Micera S., Surgical Access and Stimulation of the Pig Pudendal Nerve to Restore Bladder Dysfunctions, 2021, https://dx.doi.org/10.1002/nau.24751.

Development of excitatory neuronal networks derived from human induced pluripotent stem cells

G. Parodi[1], M. Chiappalone[1], and S. Martinoia[1]
[1]*Department of Informatics, Bioengineering, Robotics, and Systems Engineering (DIBRIS), University of Genova, Genova, Italy*

***Abstract*— The combination of neuronal networks derived from human induced pluripotent stem cells (h-iPSCs) with micro-electrode arrays (MEAs) opened new perspectives in the neuroscience and neuroengineering fields. In this paper, we present the electrophysiological characterization of excitatory h-iPSCs-derived neuronal networks obtained from healthy subjects. We recorded the neural activity from 35 up to 91 days *in vitro*, and we extrapolated the main features describing both firing and bursting patterns. With this work, we provide a solid baseline for future exploitation of *in vitro* human-derived experimental models in the field of personalized medicine.**

***Keywords*— *in vitro*, micro-electrode arrays, electrophysiology, spike, burst**

I. Introduction

The human brain is the most intricate system of the human body, composed by about 85 billion of neuronal cells that communicate with each other through electrical signals [1]. Over the years, understanding the processes and behaviour of the neural circuitry became of fundamental importance, as it can favorably impact the biomedical field. However, due to the complexity of such organized system, this is one of the major challenges in neuroscience, regardless of substantial advancement in *in vivo* electrophysiology investigation [2].

Thus, the intricacy of the human brain leads to the research of simplified *in vitro* models, replicating the *in vivo* neural activity and communication. Through the years, several *in vitro* models have been proposed to characterize the neuronal activity, mainly of animal origin [3], [4], [5]. However, to obtain *in vitro* systems that closely resemble the *in vivo* condition, human induced pluripotent stem cells (h-iPSCs) have been recently gaining popularity. One of the great strengths in the use of h-iPSCs is the possibility of deriving the cultures from human donor somatic cells [6], [7], this opening up new opportunities in the field of personalized medicine. Indeed, by using h-iPSCs, it is possible to create *in vitro* patient-specific systems that well mimic the activities and processes of the human brain, allowing to overcome limitations and ethical issues due to the use of animal species [8], [9]. To characterize these cultures, one of the most powerful technologies able to collect electrophysiological signals from *in vitro* networks is the micro-electrode array (MEA). MEAs can be coupled with electrogenic cells without affecting their viability and/or functionality [10], since they perform extracellular measurements. Hence, the combination of MEAs technology with neuronal networks derived from h-iPSCs can provide a reliable *in vivo*-like experimental model [11].

Despite the promising premises, these cultures have not been widely characterized from the electrophysiological point of view [12], [13], as most studies in the literature are focused on models of animal origin.

In this work, we perform a study centred on the development of *in vitro* h-iPSCs-derived neurons over a long time period, to understand the stability of our experimental model and its evolution over the time. In particular, we present the characterization of cortical excitatory h-iPSCs-derived neuronal networks obtained from healthy subjects by means of MEAs. The cultures of h-iPSCs were derived from somatic cells and gave rise to neuronal networks thanks to the overexpression of Neurogenin-2 (Ngn2). We recorded the electrophysiological activity during the spontaneous development, and we extrapolated the main features that describe the firing and bursting activity, typical of the *in vitro* populations. Our study provides a first, solid baseline in the characterization of h-iPSCs-derived neurons, necessary to identify the best experimental conditions which resemble the human *in vivo* development for applications in the personalized medicine field.

II. Materials and Methods

A. H-iPSCs cultures

The h-iPSCs cultures were maintained in E8Flex medium (Thermo Fisher Scientific) with the following supplements: E8F supplements (2%, Thermo Fisher Scientific), pen/streptomycin (1%, Sigma-Aldrich), G418 (50 µg/ml, Sigma-Aldrich), and puromycin (0.5 µg/ml, Sigma-Aldrich).

The medium was refreshed every two days. After stressful steps (e.g., thawing or splitting), to the aforementioned medium was added RevitaCell (1%, Thermo Fisher Scientific) to facilitate the recovery of the cells.

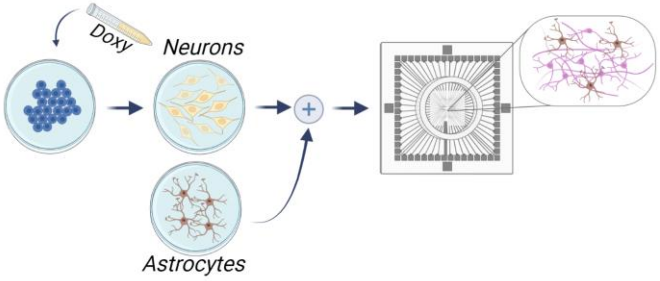


Fig. 1: Schematic representation of neuronal culture protocol. From left to right: h-iPSCs culture are induced to differentiate into neurons with doxycycline administration. Then, the early-stage neurons are co-plated with rat astrocytes on MEAs active area.

Neuronal cultures were obtained with the overexpression of Neurogenin-2 (Ngn2) [11]. The cells were induced to differentiate into excitatory cortical neurons with doxycycline (4 µg/ml, Sigma-Aldrich) treatment added to the medium (Fig. 1). The h-iPSCs cultures could be considered as early-stage neuronal cells after 3 days of doxycycline administration. The cultures were maintained at 37°C/5.5% CO_2 in incubator in stable condition.

B. Neuronal cultures

To obtain the neuronal cultures, early-stage neurons were detached with Accutase (Sigma-Aldrich). MEAs devices were previously cleaned, sterilized, and treated overnight with the following adhesion factors: poly-L-Ornithine (50 µg/ml, Sigma-Aldrich) and human laminin (20 µg/ml, BioLamina). After the detachment, excitatory neurons were co-plated on MEAs with rat astrocytes (30%) to promote neuronal development and maturation (Fig.1) [14]. The co-cultures were plated at a final density of 1200 cells/mm^2 and were maintained into Neurobasal medium with the following supplements: B27 supplements (2%, Thermo Fisher Scientific), penicillin/streptomycin (1%, Sigma-Aldrich), L-Glutamine (1%, GlutaMAX 100X, Thermo Fisher Scientific), human Brain-Derived Neurotrophic Factor (BDNF, 10 ng/ml, Sigma-Aldrich), human Neurotrophin-3 (NT-3, 10 ng/ml, Sigma-Aldrich), doxycycline (4 µg/ml, Sigma-Aldrich). After 7 days *in vitro* (DIV), Fetal Bovine Serum (FBS) was added to the abovementioned supplemented medium. After 14 DIV, doxycycline was removed from the culture medium. The medium was refreshed every two days at the 50%. The cultures on MEAs were stably maintained in the incubator (same conditions specified above) till up to 91 DIV.

C. MEA set up and data recordings

We used commercial MEAs for our study (i.e., 60 TiN electrodes on glass substrate, arranged in an 8x8 grid layout, Multi Channel Systems - MCS, Reutlingen, Germany). The electrodes were equally spaced with a 200 µm of distance and 30 µm in diameter. Electrophysiological data was acquired with the MEA2100 system (MCS, Reutlingen, Germany). The recordings were performed on 6 cultures at three different time points: DIV 42, DIV 70, and DIV 91. During each experimental session, after 10 minutes of rest out of the incubator, the electrophysiological spontaneous activity was recorded at a 10 kHz-sampling for 15 minutes (37 ℃, 5% CO_2).

D. Data analysis

Data analysis was performed using SpyCode [15] and custom-made codes developed in MATLAB (The Mathworks, Natick, MA, USA). We pre-processed the data adapting the pipeline presented in [4]. Briefly, to perform spike detection we used the precision time spike detection [16]. The threshold of noise for spike detection was set to 10 times the standard deviations, while the peak lifetime period and the refractory period were both set at 2 ms. The mean firing rate - MFR (i.e., number of spikes in the unit time) for each network was computed as the average among the firing rates of all the active channels. Channels with firing rate greater than 0.1 spikes/second were considered as active [11]. Bursts were detected using the logarithmic binning of the neuronal inter-spike interval (ISI) [17]. An event was defined bursts if the intra-burst frequency was higher than 50 spikes/second and if it was composed by at least 10 spikes. For two consecutive bursts, if the inter-burst interval (IBI) was lower than 50 ms, we merged the two bursts. Active channels with a bursting rate greater than 0.4 bursts/minute were considered as bursting channels [11]. The mean bursting rate (MBR) for each network was calculated by averaging the bursting rate of all the bursting channels. To characterize the neuronal activity, we extrapolated the IBI, defined as the time that elapses between the end of a burst and the beginning of the next one, and mean frequency intra burst (MFIB), defined as the number of spikes detected over the burst duration. We realized the raster plots by representing the spikes detected for each channel with a black dot. We computed the cumulative spike trains by merging the activity detected over all the electrodes. Subsequently, the cumulative spike trains were binned (bin = 10 ms) and all the spikes detected over all the electrodes in each bin were counted. In this way, we obtained the cumulative histogram, representing the network behavior.

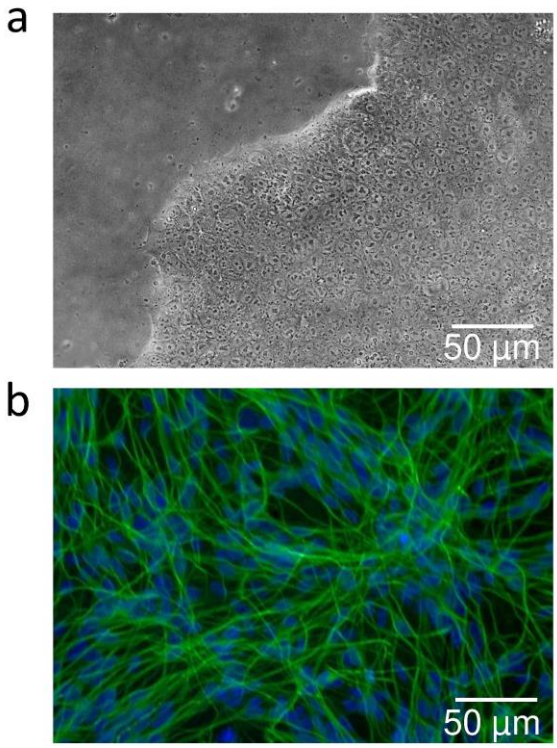


Fig.2: a) Representative h-iPSCs culture. **b)** Neuronal network image of excitatory neurons culture three days after the doxycycline administration (green: MAP2 and blue: DAPI).

E. Immunocytochemistry

The immunocytochemistry was performed on h-iPSCs-derived cultures after 3 days from the administration of doxycycline (early-stage neuronal cultures). Cells were fixed with 4% paraformaldehyde (PFA) in phosphate buffer solution (PBS) for 10 minutes at room temperature (RT) and permeabilized with 0.2% of Triton-X100 in PBS for 10 minutes at RT. We blocked unspecific binding sites with

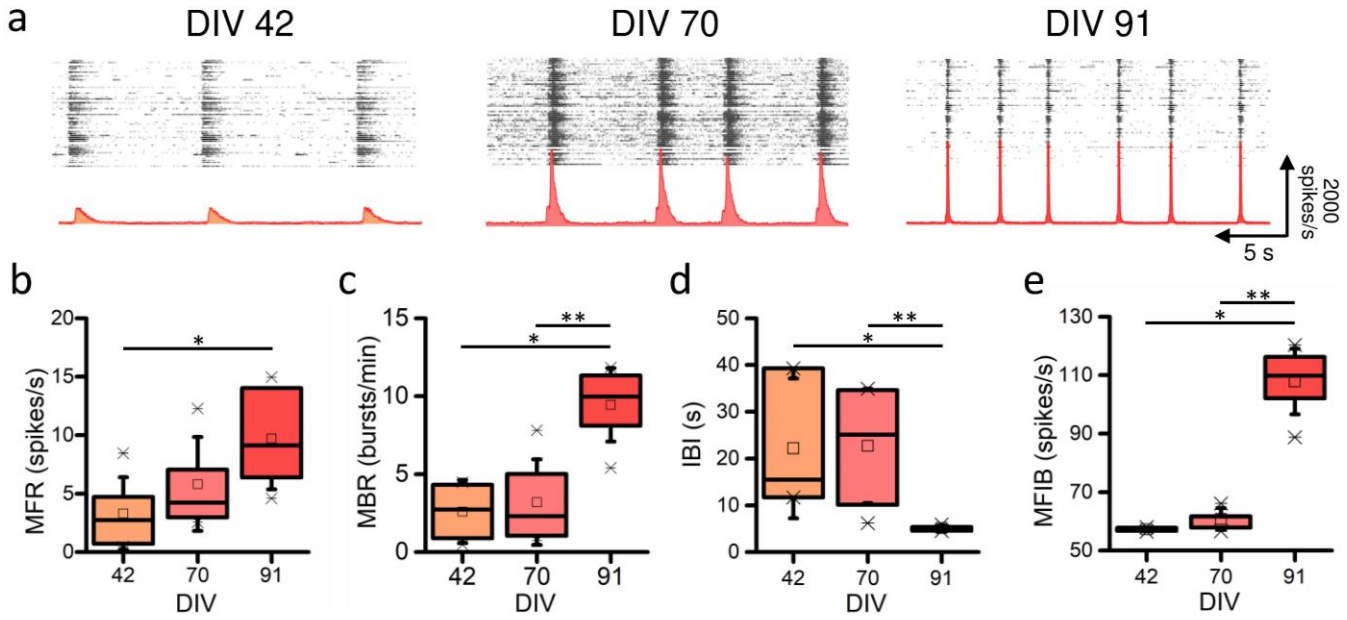


Fig. 3: Characterization during the development of excitatory neuronal networks derived from h-iPSCs. **a)** Representative electrophysiological spontaneous activity at DIV 42, 70, and 91 (from left to right). In particular, raster plots (on top), in which a black dot and a dense black band represent a detected spike and a network event, respectively, and the corresponding cumulative histograms (on bottom). **b-e)**: Box plots of the extrapolated features characteristic of the firing and bursting activity: **b)** mean firing rate (MFR); **c)** mean burst rate (MBR); **d)** inter burst interval (IBI); **e)** mean frequency intra burst (MFIB). In the box plots, the data are represented with the percentile 25-75 (box), the standard deviation (whiskers), the mean (square), the median (line), and the minimum and maximum (crosses) values.

blocking buffer solution (BBS) composed of 0.2% Triton-X100, 5% FBS in PBS for 1 hour at RT. We diluted in BBS the MAP2 primary antibody (rabbit polyclonal 1:500, Synaptic System) to label the microtubes' proteins of the neurons' cytoskeleton. Primary antibody solution was incubated overnight at 4°C. We diluted the following secondary antibodies in BBS: Alexa Fluor 488 (goat-anti rabbit, 1:700, Invitrogen) to label MAP2 primary antibody and DAPI (1:10000, Sigma Aldrich) to mark the cells' nuclei. Secondary antibodies solution was incubated for one hour at room temperature.

F. Statistical analysis

Statistical analyses were performed using MATLAB (The Mathworks, Natick, MA, USA). We exploited Kolmogorov-Smirnov normality test to assess the normal distribution of the data. As data were not normally distributed, we performed a non-parametric Kruskal-Wallis test. Statistical significance levels were set at $p < 0.05$. Asterisks over the plots show statistically significant differences. All values in the text are reported with mean ± standard deviation, unless otherwise indicated.

III. Results

The electrophysiological activity of h-iPSCs-derived neurons were monitored during their spontaneous development.

The acquired images of the cells indicated that the obtained cultures were characterized by compacted colonies with well-defined edges. Uniform and circular cellular morphologies among colonies and low levels of differentiated cells in the cultures were qualitatively observed (Fig. 2a). After the induction of the overexpression of Ngn2 with doxycycline administration, we performed immuno-cytochemistry to monitor the cell differentiation into neurons. In Fig. 2b, a neuronal network image is reported in which the excitatory neurons (green, MAP2) and the cells' nuclei (blue, DAPI) were labelled. The cultures qualitatively showed a high differentiation yield after 3 days from the administration of doxycycline.

We then recorded the electrophysiological activity of our cultures at DIV 42, 70, and 91. In Fig. 3a, we report the raster plots (top panels) and the respective cumulative histograms (bottom panels) of one representative culture at the different time points. Qualitatively, we can observe an increase of the activity along the development (Fig. 2a, top), during which more evident bursts are displayed. The increase in the number of network events and in the amplitude of the same was paralleled by a reduction of their duration (Fig. 2a, bottom). This implies that the neuronal cultures were characterized by a more packed and organized activity at DIV 91 with respect to the previous temporal steps. To quantify these differences, we computed a set of firing and bursting-related features (i.e., MFR, MBR, IBI, and MFIB).

The firing pattern showed an increasing MFR (Fig. 2b) with significantly statistical differences between DIV 42 and DIV 91 ($MFR_{DIV42} = 3.3 \pm 3.1$; $MFR_{DIV70} = 5.82 \pm 4.01$; $MFR_{DIV91} = 9.70 \pm 4.32$; 42 vs 91: $p = 0.025$). Subsequently, we investigated how the bursting activity evolved during the weeks. We observed a similar result: MBR demonstrated a relevant increase during the weeks (Fig. 2c, $MBR_{DIV42} = 2.60 \pm 2.02$; $MBR_{DIV70} = 3.20 \pm 2.75$; $MBR_{DIV91} = 9.43 \pm 2.36$; 42

vs 91: p = 0.01; 70 vs 91: p = 0.006). With the increasing MBR, a parallel and reasonable decrease of the IBI (Fig. 2d) was found (IBI_{DIV42} = 22.16 ± 14.94; IBI_{DIV70} = 22.67 ± 12.22; IBI_{DIV91} = 5.10 ± 0.57; 42 vs 91: p = 0.025; 70 vs 91: p = 0.006). Finally, since the aforementioned parameters were related only to the occurrence of the events, we were interested in understanding whether also the organization of the spikes intra burst was affected by variation during the development. Thus, we considered the MFIB, and we determined the range values of the feature to describe the neuronal network phenotype (Fig. 2e). MFIB showed significantly statistical differences between the DIV 91 with respect to both DIV 42 and DIV 70, supporting what observed in the raster plots and the cumulative histograms ($MFIB_{DIV42}$ = 57.25 ± 0.68; $MFIB_{DIV70}$ = 60.80 ± 3.76; $MFIB_{DIV91}$ = 107.84 ± 11.26; 42 vs 91: p = 0.01; 70 vs 91: p = 0.006). To conclude, multiple features describing both firing and bursting patterns suggested an increasing and more organized activity during the weeks *in vitro*.

IV. Conclusion

In the present work, we performed the electrophysiological characterization of h-iPSCs-derived excitatory neuronal networks over a long-period of time (until DIV 91) to quantify both firing and bursting patterns. During the first monitored weeks (from DIV 42 to DIV 70), the cultures maintained stable firing and bursting parameters. Later in the development, at DIV 91, the MFR, MBR, IBI, and MFIB exhibited a significant variation, according to the maturation stage of the networks. Thus, the presented results showed that neuronal networks derived from h-iPSCs self-organize into functional neuronal networks, modifying both firing and bursting patterns. Our findings, even if preliminary, provides an indication that the developmental profile of h-iPSCs-derived neurons is consistent with what observed in animal models [18]. Additionally, our experimental model presents a not negligible strength: being of human origin, it resembles more faithfully the *in vivo* condition, overcoming the problems due to the translation of species and ethical issues due to the use of animal models. Nevertheless, further studies are necessary to confirm the developmental profile, by for example performing more frequent recordings. Moreover, a substantial improvement might consist in the introduction of different neuronal types (e.g., inhibitory neurons) leading to a more physiological model which better resembles the *in vivo* conditions.

To conclude, we provided the characterization of excitatory neuronal networks that can be exploited as a reference to analyze the behavior of Ngn2-induced cultures. As a future perspective, our study can be relevant in the field of personalized medicine, to compare healthy phenotypes with patient-specific models and to facilitate the performance of targeted pharmacological tests.

Acknowledgement

The authors wish to thank University of Twente, in particular Dr. Monica Frega, to kindly supply the h-iPSCs cultures and Dr. Mariateresa Tedesco for gently providing rat astrocytes.

References

[1] Vogels, T. P., Rajan, K., & Abbott, L. F. (2005). Neural network dynamics. *Annual review of neuroscience*, *28*, 357.

[2] Brofiga, M., & Massobrio, P. (2022). Brain-on-a-Chip: Dream or Reality?. *Frontiers in Neuroscience*, *16*.

[3] Martens, M. B., Frega, M., Classen, J., Epping, L., Bijvank, E., Benevento, M., ... & Nadif Kasri, N. (2016). Euchromatin histone methyltransferase 1 regulates cortical neuronal network development. *Scientific reports*, *6*(1), 1-11.

[4] Brofiga, M., Pisano, M., Callegari, F., & Massobrio, P. (2021). Exploring the contribution of thalamic and hippocampal input on cortical dynamics in a brain-on-a-chip model. *IEEE Transactions on Medical Robotics and Bionics*, *3*(2), 315-327.

[5] Balemans, M. C., Ansar, M., Oudakker, A. R., van Caam, A. P., Bakker, B., Vitters, E. L., ... & van Bokhoven, H. (2014). Reduced Euchromatin histone methyltransferase 1 causes developmental delay, hypotonia, and cranial abnormalities associated with increased bone gene expression in Kleefstra syndrome mice. *Developmental biology*, *386*(2), 395-407.

[6] Zhang, Y., Pak, C., Han, Y., Ahlenius, H., Zhang, Z., Chanda, S., ... & Südhof, T. C. (2013). Rapid single-step induction of functional neurons from human pluripotent stem cells. *Neuron*, *78*(5), 785-798.

[7] Frega, M., Van Gestel, S. H., Linda, K., Van Der Raadt, J., Keller, J., Van Rhijn, J. R., ... & Kasri, N. N. (2017). Rapid neuronal differentiation of induced pluripotent stem cells for measuring network activity on micro-electrode arrays. *JoVE (Journal of Visualized Experiments)*, (119), e54900.

[8] Sasaki, T., Suzuki, I., Yokoi, R., Sato, K., & Ikegaya, Y. (2019). Synchronous spike patterns in differently mixed cultures of human iPSC-derived glutamatergic and GABAergic neurons. *Biochemical and biophysical research communications*, *513*(2), 300-305.

[9] Fukushima, K., Miura, Y., Sawada, K., Yamazaki, K., & Ito, M. (2016). Establishment of a human neuronal network assessment system by using a human neuron/astrocyte co-culture derived from fetal neural stem/progenitor cells. *Journal of biomolecular screening*, *21*(1), 54-64.

[10] Spira, M. E., & Hai, A. (2013). Multi-electrode array technologies for neuroscience and cardiology. *Nature nanotechnology*, *8*(2), 83-94.

[11] Mossink, B., Verboven, A. H., van Hugte, E. J., Gunnewiek, T. M. K., Parodi, G., Linda, K., ... & Frega, M. (2021). Human neuronal networks on micro-electrode arrays are a highly robust tool to study disease-specific genotype-phenotype correlations in vitro. *Stem cell reports*, *16*(9), 2182-2196.

[12] Mossink, B., Van Rhijn, J. R., Wang, S., Linda, K., Vitale, M. R., Zöller, J. E., ... & Nadif Kasri, N. (2022). Cadherin-13 is a critical regulator of GABAergic modulation in human stem-cell-derived neuronal networks. *Molecular Psychiatry*, *27*(1), 1-18.

[13] Hyvärinen, T., Hyysalo, A., Kapucu, F. E., Aarnos, L., Vinogradov, A., Eglen, S. J., ... & Narkilahti, S. (2019). Functional characterization of human pluripotent stem cell-derived cortical networks differentiated on laminin-521 substrate: comparison to rat cortical cultures. *Scientific Reports*, *9*(1), 17125.

[14] Banker, G. A. (1980). Trophic interactions between astroglial cells and hippocampal neurons in culture. *Science*, *209*(4458), 809-810.

[15] Bologna, L. L., Pasquale, V., Garofalo, M., Gandolfo, M., Baljon, P. L., Maccione, A., ... & Chiappalone, M. (2010). Investigating neuronal activity by SPYCODE multi-channel data analyzer. *Neural Networks*, *23*(6), 685-697.

[16] Maccione, A., Gandolfo, M., Massobrio, P., Novellino, A., Martinoia, S., & Chiappalone, M. (2009). A novel algorithm for precise identification of spikes in extracellularly recorded neuronal signals. *Journal of neuroscience methods*, *177*(1), 241-249.

[17] Pasquale, V., Martinoia, S., & Chiappalone, M. (2010). A self-adapting approach for the detection of bursts and network bursts in neuronal cultures. *Journal of computational neuroscience*, *29*, 213-229.

[18] Van Pelt, J., Wolters, P. S., Corner, M. A., Rutten, W. L., & Ramakers, G. J. (2004). Long-term characterization of firing dynamics of spontaneous bursts in cultured neural networks. *IEEE Transactions on Biomedical Engineering*, *51*(11), 2051-2062.

A novel microfluidic-based approach to study protein stability behavior in highly concentrated and viscous (HCV) systems

O. Bortone[1,2], P. A. Netti[1,2] and E. Torino[1,2]

[1] *Department of Chemical, Materials and Production Engineering (DICMaPI), University of Naples Federico II, 80125 Naples, Italy*

[2] *Interdisciplinary Research Center on Biomaterials (CRIB), University of Naples Federico II, 80125 Naples, Italy*

***Abstract* — The protein stability in protein-based therapeutic injectables (typically highly concentrated and viscous (HCV) solutions) is essential, as its lack determines mild to severe immune response in patients. Commonly, protein stabilization is attempted by adding stabilizers to the biomolecule solutions that are consequently studied by being exposed to physico-chemical solicitations to induce protein destabilization. Standard protocols to study protein HCV solutions rely on batch approaches, that exhibit poor controllability and are time- and reagent-consuming. Because of this and due to the rheological complexity of these fluids, there is still poor scientific knowledge about the correlation between protein stability in HCV systems and destabilization factors. Also, just a little is known about the role and the interaction of stabilizing agents with biomolecule in solution. Here a novel miniaturized approach based on microfluidics to study protein behavior in HCV systems is proposed. While requiring minimum solution volumes to be processed, the automated microfluidic platform can stimulate HCV protein solutions, offering fine controllability of stimulating environment in a wide viscosity range and in a broad spectrum of thermal and mechanical stimuli. As proof of concept, some results from light scattering-based analysis comparing stimulated and unstimulated HCV BSA solutions are presented.**

***Keywords* — Protein stability, process control, miniaturization, microfluidics**

I. Introduction

The study of biomolecules (lipids, carbohydrates, nucleic acids, oligonucleotides, proteins, peptides) covers a focal role and aims to broaden their potential utilizations in many fields, ranging from the industrial, to biological and biomedical sector. Protein-based therapeutics have been shown to be encouraging for the treatment of many diseases, performing much better than synthetic small-molecule drugs thanks to their high specificity and physicochemical properties [1]. Despite their potentials, protein-based injectables manifest some drawbacks mainly related to immunogenicity, determining either drug inefficacy or, in worse cases, harmful side effects in candidate patients. The phenomenon has been shown to lie in biomolecule instabilities occurring in the injectable solutions that cause the proteins to degrade or aggregate [2]-[5]. In fact, protein stability (both conformational and colloidal) is threatened by several factors, including *solution conditions* (ionic strength, pH), *temperature, mechanical stress, light* and *exposure to chemicals*, that are surely encountered throughout the biomolecule lifecycle, from the manufacturing to the transportation and patient injection [6]-[11]. With the aim to shield it against the overmentioned factors, the protein is typically solubilized with additives (sugars, amino acids, surfactants etc.), yielding to highly concentrated and viscous (HCV) systems, properly named *formulations*. These solutions are typically studied by subjecting them to physico-chemical stimulations (thermal, mechanical, photonic and chemical stress) and then analyzed through several spectroscopic, spectrometric, optical or chromatographic techniques to assess their impact on protein physical state (aggregation, fragmentation, degradation etc.) [12]-[17]. Studies on biomolecule stability in formulations are mainly conducted through time- and reagent-consuming batchwise protocols, that provide poor controllability of process parameters, low-throughput exploration of stress conditions and inadequate versatility in terms of stress combination. In addition, the use of *offline analysis techniques* includes long preparative phases (*e.g.,* high dilution), causing the stressed formulation to be analyzed in a context by far different from the original stimulated solution.

Because of the limitations posed by current approaches along with the challenging chemical and rheological features of the fluids in question, there exist a prominent lack of scientific knowledge about the correlation between physico-chemical stimulating factors and protein behavior. Also, a considerable gap is still present in the comprehension of the physical and chemical interactions among stabilizers and proteins in HCV formulation.

Here the *proof of concept* of the application of a novel microfluidic-based approach to study protein stability in HCV systems is presented. The automated microfluidic platform applies physico-chemical stimulations to HCV protein solutions in broad thermal and mechanical solicitation ranges. It manages an *ample fluid viscosity interval* offering *superb controllability* of the stimulating environment in terms of *intensity*, *stimulus duration* and *reproducibility*.

II. Materials and methods

A. Materials

Harvard syringe pumps, model 11 Elite, were employed to inject the formulations into the microfluidic platform. Automated valves, a Peltier cell, an aluminum heat sink, thermocouples and dedicated controllers were obtained from LabSmith microfluidics. The two-position three-port automated valves (part number AV201-T116) serve either as simple on/off or as switchers to create preferential pathways for the processed fluids. The 2x2 cm Peltier cell (part number uTE02-132020; max T 130°C; ΔT between faces 67°C; 13 W) was used as heating source. The heat sink (part number HS-2020) is placed on top of the cold side of the Peltier cell for fine temperature control as it provides the contribution to a

proper thermal module mass. Thermocouples (part number uTS01-STD-20) are used for real-time temperature control. The mentioned parts and the controllers are connected by flexible cable to enable electric signal transmission for their control. A miniaturized peristaltic pump (part number 3200243) was purchased from Dolomite microfluidics to realize the fluid recirculation. Nominally, it guarantees a non-tunable stable 0,45 ml/min flow rate with a 3V supply. For sake of completeness, the actual experienced miniaturized peristaltic pump flow rate was about 800 µl/min. Polymethyl methacrylate (PMMA) was processed through a Minitech CNC mini-mill/GX to build up the customized microfluidic chip. All the microfluidic parts, were interconnected through FEP tubing (0.8 mm ID, 1.6 mm OD).
Bovine Serum Albumin (BSA) was bought by Merck (product code A2153) and solubilized in phosphate buffered saline (PBS) 10 mM pH 7,4 (Sigma-Aldrich, product code P4417).
MilliQ water was used to prepare the buffer solution and to wash the microfluidic platform.

B. Methods

1) Microfluidic platform development

Considering the high concentration and viscosity of fluids being processed through the microfluidic plant, the sizing of the latter (microfluidic chip shape and dimension, inlet/outlet bore of valves, tubing diameter and length) was properly conducted through precise calculations and numerical simulations aiming to minimize the pressure drops.
For the thermal line setup, some microfluidic parts (automated two-position three-port valves, Peltier cell, heat sink, miniaturized peristaltic pump, 0.8 mm ID - 1.6 mm OD FEP tubing) were carefully selected from the market, verifying their geometrical and operational features to suit the purposes of the present work. Plus, the microfluidic chip was designed, optimized through numerical simulations and fabricated through a Minitech CNC mini-mill/GX machine. A feasibility study was conducted to define the process parameters and their impact on the temperature control. The explored variables were: *target temperature*, *heating voltage ramp* and *tolerance*. All other variables (*fluid flow rate* and *Peltier Cell operating voltage window*) were kept constant throughout this study (800 µl/min and ± 3.5 V, respectively).
Also, numerical simulations were carried out to characterize the and heat transfer kinetics into the microfluidic chip.
The same approach was used to build the mechanical stress microfluidic line. Automated programmable elements (valves, miniaturized pumping device) and tubing were properly chosen to promote versatility and ability to manage HCV fluids. In addition, A PMMA customized microfluidic chip was appropriately designed, optimized through numerical simulations and fabricated to have a controlled and defined shear rate.
The ability of the platform to manage HCV fluids was assessed by processing different protein solutions with variable viscosity: *low* [1; 4] mPa*s, *moderate* [4; 7] mPa*s and *high* [7; 15] mPa*s. According to literature study and data collected from pharma industries, the overmentioned fluid property thresholds are exhaustively representative of typical viscosity of injectable biologics.

2) Preparation of HCV protein solutions

The protein solutions having different viscosity values were prepared combining BSA and sucrose. For low viscosity (1-4 mPa*s) formulations, [0; 100] mg/ml of BSA and sucrose were dissolved in PBS. To obtain moderately viscous (4-7 mPa*s) solutions, [125; 175] mg/ml of the same components were solubilized in PBS. In addition, [200; 300] mg/ml of BSA and sucrose were solubilized in PBS in order to prepare the high viscosity (7-15 mPa*s) fluids. The system subjected to thermal and mechanical stress was a HCV BSA solution (≥300 mg/ml in PBS).
The overmentioned solutions were all filtered with a 0,22 µm syringe filter to remove any impurity and stored at 5 ± 3 °C.

3) Thermal stimulation of protein solution

The microfluidic platform was programmed to offer a 60°C stable environment and stimulate the HCV BSA solution for 5 min.

4) Mechanical stimulation of protein solution

The platform was programmed to recirculate the HCV BSA solution for 15 min while undergoing 8000 s^{-1} max shear rate intensity.

5) Protein stability analysis in HCV solutions

Nanoparticle tracking analysis (NTA) were performed to compare untreated and treated protein solutions. Both stimulated and unstimulated HCV BSA fluid systems were diluted 1000 times in PBS before being analyzed. The particle (aggregation body) concentration was identified for the thermally and mechanically treated and untreated fluids.

III. RESULTS

A. Microfluidic platform setup and rheological window

The microfluidic platform is composed of a syringe pump connected to the thermal and mechanical stress modules.
In particular, the thermal line presents some automated and programmable two-position three-port valves to create preferential pathways for the processed fluids (forward or backward directions). Moreover, a Peltier cell is in touch with a heat sink on the cold side and a customized PMMA microfluidic chip on the hot one. In addition, a miniaturized peristaltic pump enables the recirculation of the fluid to control the duration of the stimulation. The microfluidic parts of the thermal stress line are all linked through 0.8 mm ID, 1.6 OD FEP tubes. The overall volume of this module is around 300 µl.
The microfluidic mechanical stress line exhibits the same valve configuration of the thermal stress. Similarly to the latter, the automated valves are linked to a customized PMMA microfluidic chip. Furthermore, a miniaturized peristaltic pump is connected to achieve the fluid recirculation throughout the chip. As for the thermal stress, the recirculation enables a fine control on the extent of the stimulation. The components of the mechanical stress module are all connected through 0.8 mm ID, 1.6 mm OD FEP tubes and the overall volume of the mechanical module is slightly less than 300 µl.
The microfluidic platform was properly designed and developed to manage HCV fluids, precisely in viscosity ranges typical of injectable protein-based therapeutics. As matter of fact, the microfluidic plant can be used to process fluids whose *initial viscosity* ranges from 1 to 15 mPa*s. It must be said that this upper value is not a categorical limit of the platform. Indeed, while being stimulated, the rheological properties of

the HCV protein formulation can deeply change: typically, the fluids experience a considerable increase in the viscosity, reaching values far higher than 15 mPa*s. This behavior was also detected during the thermal stimulation of the HCV BSA solution and the platform did not show any tendency to clogging.

1) Thermal stress operational range and temperature control

Preliminary experiments conducted in a feasibility study clarified the influence of the process parameters, *i.e.* target temperature, heating voltage ramp and tolerance. Concisely, the following conclusions can be drawn:

1. the higher the target temperature, the longer the stabilization time (for a fluctuation-free thermal environment);
2. at the same target temperature, the higher the heating voltage ramp, the wider the temperature oscillations of the system;
3. at the same target temperature, the smaller the tolerance, the broader the system oscillations.

Based on the knowledge acquired in preliminary experiments, a combination of process parameters for an excellent temperature control in the range [50; 80] °C was defined (TABLE I).

TABLE I: COMBINATION OF PROCESS PARAMETERS FOR FINE TEMPERATURE CONTROL IN [50;80] °C

Process parameters	Value
Fluid flow rate	800 µl/min
Peltier Cell operating voltage window	± 3.5 V
Heating voltage ramp	0.001 V/s
Tolerance	± 1.5 °C

A typical stimulation temperature trend can be divided into three phases: the first is intended to reach the target temperature. This phase is characterized by the same process parameters reported in the TABLE I, except for the heating voltage ramp, that is set to 0.005 V/s to minimize the time needed for the thermal module to reach the target temperature. The second phase is needed to stabilize the temperature around the target; the third is the actual thermal stimulation. The second and third phases present the same parameter configuration reported in TABLE I.

TABLE II reports the equilibration time (extent of the second phases) at different target temperatures. In general, the higher the latter, the longer the stabilization time. The only dissonant voice is observed for 70°C that requires the largest equilibration time. In spite of this, the reported values seem to be reproducible.

TABLE II: THERMAL STRESS LINE EQUILIBRATION TIME AT DIFFERENT TARGET TEMPERATURE

Target Temperature (°C)	Equilibration time (s)
50	140
60	180
70	320
80	190

Once equilibrated, the thermal line is ready to dive into the third phase for a stable stimulation. In TABLE III the average temperature and standard deviation at different targets are reported over 2, 5 and 10 min of stimulation.

TABLE III: Average temperature and standard deviation for different targets

Target Temperature (°C)	2 min	5 min	10 min
50	49.0 ± 2.2	48.6 ± 1.6	48.5 ± 1.6
60	61.2 ± 0.1	61.4 ± 0.2	60.6 ± 0.9
70	70.4 ± 1.1	70.5 ± 1.2	70.6 ± 1.3
80	79.5 ± 0.9	78.2 ± 0.9	80.2 ± 1.9

2) Mechanical stress operational range and control

For the mechanical stress implementation, the fluid-solid interface offered by the microfluidic channel walls can be readily exploited to apply shear stress to the HCV protein solutions. Considering the candidate fluids spanning a broad viscosity range, the convenient parameter to design and develop the mechanical stress module is the *shear rate* (s^{-1}). In fact, unlike the shear stress, the shear rate is by definition insensitive to the fluid rheological properties (*e.g.*, viscosity). In particular, for a Newtonian fluid flow in a pipe, the shear stress is the multiplication between the shear rate and the liquid dynamic viscosity. Thus, with the same shear rate, solutions with different viscosity experience different shear stress. Guaranteeing a constant flow rate assures the processed fluids being subjected to the same shear rate regardless of their viscosity.

While keeping a fixed flow rate, diverse chip geometries (specifically, different cross sections) can be employed to control the shear rate range the fluid undergoes. According to this strategy, different squared cross-section straight channels were designed and fabricated to reach up to 20000 s^{-1} at 800 µl/min flow rate.

B. *Protein instability induced by the microfluidic platform*

The ability of the platform to induce a destabilization on a model HCV fluid was preliminarily proved by subjecting a BSA solution (≥300 mg/ml) to thermal and mechanical stress according to the protocols described in *Methods* (paragraphs 3 and 4). The treated solutions were compared to untreated ones through NTA. In *figure 1* and *2* the thermal and mechanical NTA analysis are respectively reported. Evidently, the stimulated solutions (orange curves) present an important increase in aggregation concentration with respect to unstimulated fluids (red curves), thus assessing the effectiveness of the microfluidic platform solicitations.

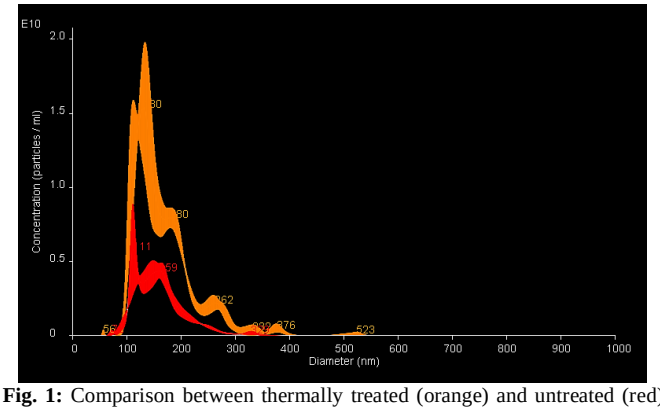


Fig. 1: Comparison between thermally treated (orange) and untreated (red) HCV BSA solution. The solution underwent 60°C thermal stimulation for 5

min. The concentration of aggregations is noticeably higher in the stimulated solution (orange).

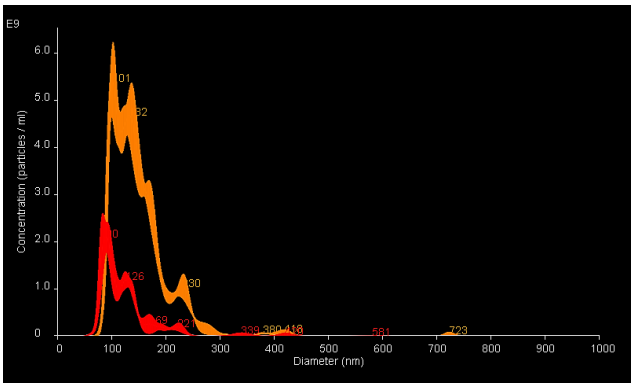


Fig. 2: Comparison between mechanically treated (orange) and untreated (red) HCV BSA solution. The HCV solution underwent 8000^{s-1} for 15 min. The concentration of aggregations is remarkably higher in the solicited solution (orange).

IV. Conclusion

In this work a novel miniaturized and automated approach based on microfluidics to study protein stability in challenging liquid systems is presented. The platform is properly design and sized to manage HCV fluids, with minimized pressure drop and absent tendency to clogging. Whilst it may seem trivial, such a step represents a noticeable achievement, as, at small scales, the control of pressure drops becomes tedious. The capability to manage high viscosity guarantees the process continuity, avoiding setbacks. This achievement resulted from matching data acquired from the pharma industry repertoire (chemical, physical and rheological properties of typical solutions), sound scientific knowledge and advanced engineering solutions.

To the current status, the proposed miniaturized approach is already a good option to address the expensiveness limitation posed by conventional technological approaches, with equal or superior versatility. In fact, minuscule solution volumes are required, thus providing a strong cost reduction compared to classical batch protocols. In addition, the automation of the process can facilitate the conduction of the stimulation, ensuring its reproducibility, reliability and easy exploration of a broad solicitation range while paying minimum effort.

The typical features of the microfluidics (*e.g.*, small volume and high predictability of transport phenomena), along with the automation of the platform and the potential integration of other technologies, such as sophisticated programmable pumping systems and real time inline analysis techniques, pave the way to a paradigm shift in the study of complex HCV protein systems. In fact, the vast screening of different environment conditions and composition of protein solutions through the microfluidic platform may help address the scientific gap of knowledge, clarifying the relation between physico-chemical environments and protein behavior in HCV solutions. Moreover, the microfluidic plant is intended to point out the influence of stabilizing agents on biomolecule stability. In other words, the platform may have a role in industrial contexts, promoting a *quality by design approach* in the setting of large scale processes (*e.g.*, development of protein-based therapeutics).

References

[1] Leader, Benjamin, Quentin J. Baca, and David E. Golan. "Protein therapeutics: a summary and pharmacological classification." *Nature reviews Drug discovery* 7.1 (2008): 21-39.

[2] Jiskoot, Wim, et al. "Protein instability and immunogenicity: roadblocks to clinical application of injectable protein delivery systems for sustained release." *Journal of pharmaceutical sciences* 101.3 (2012): 946-954.

[3] Laptoš, Tomislav, and Jasna Omersel. "The importance of handling high-value biologicals: Physico-chemical instability and immunogenicity of monoclonal antibodies." *Experimental and Therapeutic Medicine* 15.4 (2018): 3161-3168.

[4] Dingman, Robert, and Sathy V. Balu-Iyer. "Immunogenicity of protein pharmaceuticals." *Journal of pharmaceutical sciences* 108.5 (2019): 1637-1654.

[5] Pham, Ngoc B., and Wilson S. Meng. "Protein aggregation and immunogenicity of biotherapeutics." *International journal of pharmaceutics* 585 (2020): 119523.

[6] Roberts, Christopher J. "Protein aggregation and its impact on product quality." *Current opinion in biotechnology* 30 (2014): 211-217.

[7] Wang, Wei, Sandeep Nema, and Dirk Teagarden. "Protein aggregation—pathways and influencing factors." *International journal of pharmaceutics* 390.2 (2010): 89-99.

[8] Roberts, Christopher J. "Therapeutic protein aggregation: mechanisms, design, and control." *Trends in biotechnology* 32.7 (2014): 372-380.

[9] Wang, Wei, and Christopher J. Roberts. "Protein aggregation–mechanisms, detection, and control." *International journal of pharmaceutics* 550.1-2 (2018): 251-268.

[10] Zapadka, Karolina L., et al. "Factors affecting the physical stability (aggregation) of peptide therapeutics." *Interface focus* 7.6 (2017): 20170030.

[11] Li, Jinjiang, et al. "Interfacial stress in the development of biologics: fundamental understanding, current practice, and future perspective." *The AAPS journal* 21.3 (2019): 1-17.

[12] Wang, Wei, and Satoshi Ohtake. "Science and art of protein formulation development." *International journal of pharmaceutics* 568 (2019): 118505.

[13] Hawe, Andrea, et al. "Forced degradation of therapeutic proteins." *Journal of pharmaceutical sciences* 101.3 (2012): 895-913.

[14] Nowak, Christine, et al. "Forced degradation of recombinant monoclonal antibodies: A practical guide." *MAbs*. Vol. 9. No. 8. Taylor & Francis, 2017.

[15] Philo, John S. "A critical review of methods for size characterization of non-particulate protein aggregates." *Current pharmaceutical biotechnology* 10.4 (2009): 359-372.

[16] Zölls, Sarah, et al. "Particles in therapeutic protein formulations, Part 1: overview of analytical methods." *Journal of pharmaceutical sciences* 101.3 (2012): 914-935.

[17] Filipe, Vasco, et al. "Analytical approaches to assess the degradation of therapeutic proteins." *TrAC Trends in Analytical Chemistry* 49 (2013): 118-125.

Towards personalized electroceutical therapy: electrophysiological investigations in a pre-clinical model of ischemic lesion

M. Carè[1,2], F. Barban[1,2], M. Di Florio[1,2], R. Greco[3], C. Tassorelli[3] and M. Chiappalone[1,2]
[1] *Rehab Technologies IIT-INAIL Lab, Istituto Italiano di Tecnologia, 16163 Genova, Italy*
[2] *Department of Informatics, Bioengineering, Robotics System Engineering (DIBRIS), University of Genova, 16145 Genoa, Italy*
[3] *Headache Science & Neurorehabilitation Center, IRCCS Mondino Foundation, Pavia, Italy*

***Abstract*— Stroke is one of the main causes of long-term disability worldwide. Recently, an activity-dependent intracortical microstimulation technique demonstrated the capability of closed loop approaches to better entrain network activity with respect to standard random stimulation. This was demonstrated at the pre-clinical level, in rodent models following an ischemic lesion in the primary motor cortex. At the clinical level, stimulation-based therapy still relies on standardized protocols with not so convincing results. A possible explanation for these inconsistencies is the lack of tailored, personalized stimulation protocols. In this study, we aimed at investigating the changes in the electrophysiological activity occurring in a pre-clinical model of focal lesion and the subsequent effect of a personalized, open-loop stimulation therapy. We adopted anesthetized Long-Evans rats undergoing a focal ischemic injury in the caudal forelimb area (i.e., CFA). Microelectrode arrays were inserted in the ipsilesional rostral forelimb area (i.e., RFA) to record spike activity and in the somatosensory cortex (i.e., S1) also to deliver intracortical microstimulation. We found that the ischemic injury in CFA led to an overall decrease of the spiking activity both in RFA and S1. A neurostimulation treatment with tailored open loop microstimulation tended to increase the firing activity in both RFA and S1. Further studies will be necessary to confirm these preliminary findings, which can lead to design novel electroceutical therapies for stroke rehabilitation.**

***Keywords*—In vivo, rat, electrophysiology, lesion.**

I. INTRODUCTION

NOWADAYS non-communicable diseases represent the 80% of the top ten causes of death worldwide. Among these disorders, stroke is the second leading cause of death and disability [1]. Current assistive technology is limited and only a minority of survivors are able to achieve functional independence in simple activities of daily living. Thus, understanding the impact of a lesion on the brain networks and promoting functional and behavioural recovery has become a global priority in healthcare.

The standard-of-care for post-stroke rehabilitation is physical therapy, but its effects are often limited or incomplete [2]. To this end, research is exploring innovative approaches, such as ‘electroceutical’. Electroceutical provides an ‘electrical’ rather than ‘pharmacological’ treatment based on stimulation of the target organ/tissue. Electrical-based therapies have sparked interest among researchers, industries and funding agents since a while [3], [4], been successfully employed for treating neurological diseases, such as depression and epilepsy [5].

Recent studies have shown how brain stimulation could enhance functions after stroke in both animals and patients [6]. These studies have used electrical stimulation patterns that are ‘adapted’ (i.e., personalized) to the intrinsic dynamics of the networks under examination, primarily through two different modalities, i.e., open loop and closed loop. By using personalized stimulation is possible to: (i) promote both plasticity and motor recovery, as in the case of stroke or traumatic brain injury –TBI [7]; (ii) block the pathological activity and promote the physiological one within the damaged tissue, as in the case of Parkinson's disease [8] or epilepsy [9]; (iii) ‘entrain’ the network under examination and facilitate motor responses [10], [11]. Currently, at the clinical level, stimulation-based therapy relies on standardized protocols with not always convincing results [12]-[14]. A possible explanation for these inconsistent outcomes is the lack of a stimulation protocol ‘tailored’ on the intrinsic dynamics of the target system.

In this study, we aimed at investigating possible changes in electrophysiological activity induced by a focal lesion and the subsequent effect of a personalized, open loop stimulation protocol, with the idea to be further translated to clinics.

We capitalized on the work of Guggenmos [7] and our own works for the experimental design [15]-[18]. Briefly, we used anesthetized Long Evans rats implanted in the Rostral Forelimb Area (i.e., RFA, equivalent of the pre-motor cortex in the rat) and in the Somatosensory cortex (i.e., S1). A lesion was performed in the equivalent of motor cortex (i.e., CFA) by means of a local injection of endothelin-1 [19]. Differently from our previous studies, here we evaluated the effect of the lesion on a large dataset and we designed a novel personalised stimulation protocol by following an open-loop paradigm, inspired by the literature [20]. Specifically, we implemented a ‘repeated stimulation’, where trains of extracellular voltage-pulses were delivered, reproducing exactly the pattern and timing of spikes detected at one selected electrode during the ‘pre-lesion’ spontaneous activity. We found that the lesion had a clear-cut effect on decreasing the spontaneous activity at the two monitored locations. Moreover, the open-loop (i.e., repeated stimulation) protocol showed a tendency to increase the level of spiking activity.

II. Material and Methods

A. Animals

The Italian Ministry of Health and Animal Care (Italy: authorization n. 509/2020-PR) approved all experiments. Twenty-seven adult, male Long-Evans rats (weight: 300-400g; age: 4-5 months; Charles River Laboratories, Calco, LC, Italy), divided into two main categories, i.e. No lesion (Naive; n=14) and Lesion (n=13), were used in this study. To preliminary test the effects of a personalized stimulation treatment, we randomly assigned four animals of the lesion group to a third group (Lesion-Open Loop; n=4).

B. Surgical Procedure

Prior to surgery, the rats were anesthetized with gaseous isoflurane within a sealed vaporizer chamber. The anesthetization was followed by injections of ketamine (80-100 mg/kg IP) and xylazine (5-10 mg/kg). Anesthesia was maintained throughout the entire procedure with repeated bolus injections of ketamine (10-100 mg/kg/hr IP or IM) as needed. The rat was secured in the stereotaxic frame and placed on a homeostatically controlled heating blanket to maintain temperature. A midline skin incision was made spanning rostro-caudally between ~6 mm rostral to bregma and ~5 mm distal to the atlanto-occipital junction exposing the skull surface. The muscles of the neck overlying the cisterna magna or between the upper vertebrae were reflected, and a small puncture was made in the spinal dura to allow cerebrospinal fluid drainage and to control brain edema after craniotomy. In the lesion group (i.e., Lesion), six 0.7-mm diameter holes were drilled into the skull over the dominant hemisphere (contralateral to the preferred forelimb) as follows: +2.5, +1.5, +0.5 AP +2.5, +3.5 ML from bregma, corresponding to the CFA of the motor cortex (Fig. 1A). Burr holes (3 mm diameter) exposing RFA and S1 were made at +3.5, +2.5 and –1.25, +4.25 AP, ML [21]. Ischemic injury was induced through Endothelin-1 injection (ET-1; 0.3 µg ET-1 dissolved in 1 µl saline or 1 mg ET-1 dissolved in 3.33 ml saline; Merk Life Science S.r.l., Italy), ~ 1.5 mm below the pial surface at each of the 6 holes over CFA [19]. The spread of ET-1 with this procedure is confined to an area of 0.5 mm diameter; injections were placed to produce a continuous CFA infarct while leaving RFA and S1 intact [22].

C. Experimental protocol

For this study, we made use of three experimental groups: (i) Control (i.e., Naïve, animals who did not receive any lesion), (ii) Lesion (i.e., animals who did receive the lesion) and (iii) Lesion-Open Loop (i.e., a subset of the Lesion group which underwent a session of intracortical therapeutic stimulation), as schematically reported in Fig. 1B. In the Control group, the experimental timeline consisted of 2 phases of 20-min of spontaneous recordings before (i.e., PreL, light blue) and after (i.e., PoL, aqua green) the 'no lesion' period, which lasted approximately 1 hour. In the Lesion group, the experimental timeline consisted of the same 2 phases of 20-min of spontaneous recordings before (i.e., PreL, light blue) and after (i.e., PoL, aqua green) the 'lesion' period. Additionally, four animals of the Lesion group (i.e., Lesion-Open Loop) received 1 hour of stimulation (i.e., Stim, yellow) and were recorded for 20-min of spontaneous activity after the stimulation (i.e., PoS, blue).

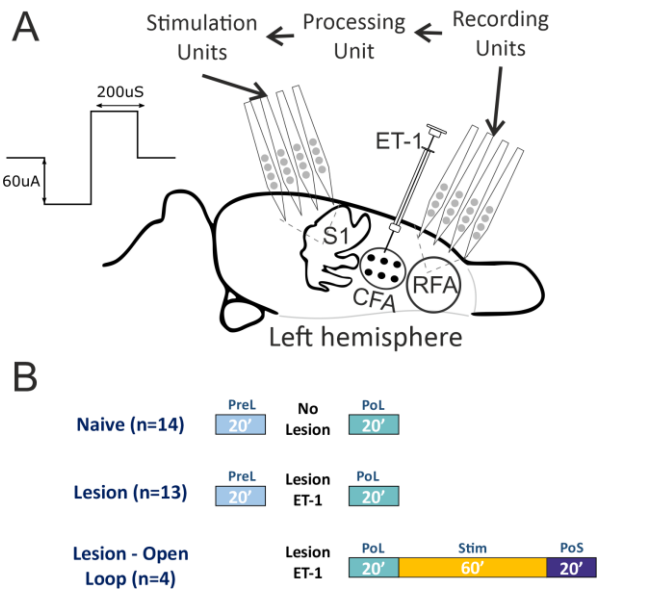


Fig. 1: Experimental protocol. A) Neural activity was recorded by means of Multi-Electrode Arrays-MEAs (four-shank, sixteen-contact site electrode, NeuroNexus) using a commercial data acquisition system (Intan Technologies). The electrophysiological activity was recorded simultaneously at two locations: the Rostral Forelimb Area (RFA) and the Somatosensory cortex (S1). For the stimulation session, the pulse was always designed to be a single squared 60 µA biphasic, cathodal-leading pulse (200 µs positive, 200 µs negative). The lesion was performed by means of a focal injection of endothelin-1 in the Caudal Forelimb Area (see Methods). B) Experimental timeline for the three groups (for details, see Methods).

D. Recording/Stimulation paradigms

As detailed in Fig. 1A, the cell activity was recorded in RFA using a four-shank, sixteen-contact site electrode, placed at a depth of 1500 µm (1-1.5 MΩ impedance, A4x4-3mm-100-125-703-A16, NeuroNexus). The stimulation was applied through a single contact on a four-shank, sixteen-contact electrode with an impedance of ~ 200 kΩ (A4x4-3mm-100-125-177-A16, NeuroNexus). In all the experiments, the stimulation pulse was designed to be a single squared 60 µA biphasic, cathodal-leading pulse (200 µs positive, 200 µs negative). The personalized Open Loop stimulation was created following a 'replay' and 'repeat' strategy. The stimulation pattern exactly reproduced the first 10-min of the healthy spontaneous activity recorded before the lesion (i.e., PreL1) on a selected channel in RFA (replay), and was delivered, using the INTAN RHS Stim/Recording System (http://www.intantech.com), by looping it six times over the course of an hour (repeat) [20].

E. Data Processing

All the analysis were performed in Matlab (The MathWorks, Natick, MA, USA). First, data were filtered using a 4th order elliptic bandpass filter in the range of 300-3000 Hz to remove low frequency components within the signal. A spike discrimination approach was used to detect spikes from the filtered data. This consisted of a power based spike detection

algorithm, named Stationary Wavelet based Teager Energy Operator (SWTTEO) [23]. The SWTTEO includes two levels of Stationary Wavelet Transform (SWT) followed by the use of the Teager Energy Operator (TEO). The TEO outputs are then smoothed and summed, and their combination is thresholded. No sorting method was applied to the detected spikes. Spikes were then analysed in terms of mean firing rate (MFR), i.e. we computed the average number of spikes within the unit time (s) in each recorded phase. We discarded those electrodes whose firing rate was less than 0.01 spikes/s [15].

For better efficiency in the data processing step, data were organized in blocks of 10-min recordings each. In total, for the experimental groups, we have six blocks: PreL1, PreL2, PoL1, PoL2, PoS1 and PoS2.

F. Statistical analysis

Statistical analysis was performed in Matlab (The MathWorks, Natick, MA, USA). First, we tested the normality of the data with the Kolmogorov-Smirnov test. Since data failed the test, we applied a non-parametric test, the Friedman test, to identify significant differences among firing rates at different experimental phases. P-values <0.05 were considered as significant and corrected for multiple comparisons when relevant.

III. Results

A. The ischemic lesion decreased the level of firing

We investigated how a focal ischemic lesion affected the firing activity at two distal areas (i.e., RFA and S1). Fig. 2A1-B1 shows some raster plots of a representative animal in the Lesion group. Here, the baseline activity (i.e., Pre Lesion, PreL) is characterized by a random and slight synchronous spiking in both RFA and S1. Immediately after the lesion (i.e., PoL), a significant decrease in the activity in both RFA and S1 is observed (Fig. 2A2-B2). The quantitative analysis of the inter-phase MFR confirmed these qualitative results. Both RFA (Fig. 2C) and S1 (Fig. 2D) are characterized by an overall significant decrease in the MFR from the PreL (PreL1 and PreL2) to the PoL (PoL1 and PoL2) phase. Interestingly, this is not true for the Naïve group, where the MFR remained constant over time (Fig. 2E-F).

B. Open loop stimulation increased the level of firing

We evaluated the effects of the repeated stimulation on the level of firing of both RFA and S1 in the Lesion-Open Loop group. The baseline activity in the pre stimulation phase (i.e., PoL) was characterized by a random spiking with sparse synchronous events (Fig. 3A1-B1). As shown in the representative raster plot (Fig. 3A2-B2), after the stimulation, in the PoS period, we observed an overall increase of spiking activity in both RFA and S1. Even if the statistical analysis did not show any significant change, in Fig. 3C-D, we can observe that the MFR values and their median are tended to increase after the stimulation phase in both RFA (Fig. 3C) and S1 (Fig. 3D). Moreover, in both areas we observed a change in the data distribution, tending from a unimodal (Fig. 3C, PoL1-PoL2) to a bimodal shape in RFA (Fig. 3C, PoS1-PoS2) and to a more pronounced bimodal distribution in S1 (Fig. 3D, PoS1-PoS2 vs. PoL1-PoL2). This suggests that the Open Loop repeated stimulation was able to elicit a change in the firing rate in the two considered areas, with a tendency to increase it.

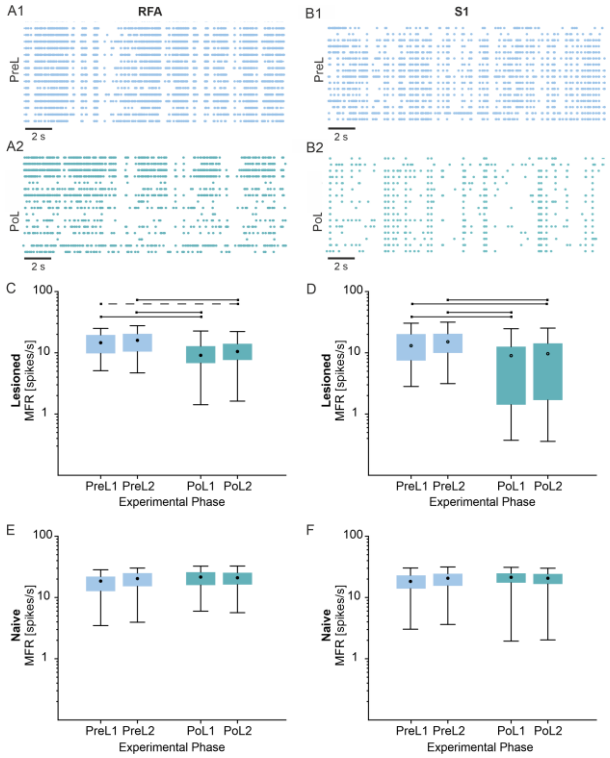


Fig. 2: Firing rate analysis of the lesion effects. (A,C,E) Activity in RFA. (B,D,F) Activity in S1. (A, B) Spike rasters (dotted graphs, one row per single channel during 10 s period before (i.e., PreL, top) and after (i.e., PoL, bottom) the lesion, in a single representative animal of the lesion group (i.e., Lesion). (C, D) Distribution of the Mean Firing Rate (MFR, spikes/s) for the Lesion group. (E, F) Distribution of the Mean Firing Rate (MFR, spikes/s) for the Naïve group. In both groups, each phase was split in 10 min windows (i.e., PreL1, PreL2, PoL1 and PoL2). Data is summarized in box plots, where the central black dot indicates the median; the box limits indicate the 25th and 75th percentiles. Whiskers represent the 5th and the 95th percentiles. Dashed line: p<5·10-3; solid line: p<5·10-5, Friedman nonparametric test.

IV. Conclusion

This study describes the impact of a lesion in the motor area and the effect of the subsequent personalized stimulation on the spiking activity of two cortical areas (RFA and S1) in the brain of anesthetized rats. We found that an ischemic lesion in the motor cortex induces a significant decrease of the firing level in both RFA and S1. These findings support and make stronger our previous outcomes [15]-[18], obtained for a smaller and less consistent dataset, where we observed a change in the spiking activity. Moreover, we showed that a personalized open-loop protocol tends to increase firing activity. These preliminary results are in line with the effects induced by a different type of personalized stimulation [15], i.e. the closed-loop one (ADS). We can conclude that non-periodic, tailored stimulation might be the key to restore the firing pattern in the damaged brain [9], in line with recent findings in healthy humans [10], [11]. Additional experiments are now necessary to confirm this preliminary finding, which can open up the possibility of translating the personalized electroceutical therapy to the clinical level.

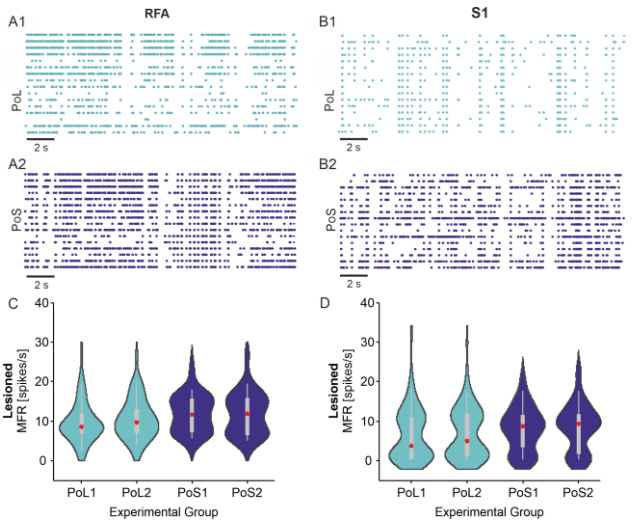


Fig. 3: Firing rate before and after stimulation. (A, C) activity in RFA. (B, D) activity in S1. (A, B) Spike rasters (dotted graphs, one row per channel during 10 s period before (i.e., PoL, top) and after (i.e., PoS, bottom) the stimulation in a single representative animal of the Lesion-OL group. (C, D) Distribution of the Mean Firing Rate (MFR, spikes/s) for each phase split into 10 min window (i.e., PoL1, PoL2, PoS1 and PoS2). Data is represented as violin plots, where the outlines illustrate probability density, i.e. the width of the shaded area represents the proportion of the data located there. Inside, we reported the box plots (grey) where the box represents the 25th and the 75th percentile values, the red dot the median value and the whiskers denote the 5th and the 95th percentile values.

Acknowledgement

The materials for the experimental campaigns have received funding from the Italian Ministry of Health [2021-2022] to IRCCS Mondino Foundation, Pavia, Italy. M. Carè and F. Barban are currently supported by #NEXTGENERATIONEU (NGEU) and funded by the Ministry of University and Research (MUR), National Recovery and Resilience Plan (NRRP), project MNESYS (PE0000006) – A Multiscale integrated approach to the study of the nervous system in health and disease (DN. 1553 11.10.2022).

References

[1] The top 10 causes of death. World Health Organization, 2020.

[2] Chiappalone, M., & Semprini, M. (2022). Using robots to advance clinical translation in neurorehabilitation. Science robotics, 7(64), eabo1966. https://doi.org/10.1126/scirobotics.abo1966

[3] Famm, K., Litt, B., Tracey, K. J., Boyden, E. S., & Slaoui, M. (2013). Drug discovery: a jump-start for electroceuticals. Nature, 496(7444), 159–161. https://doi.org/10.1038/496159a

[4] Reardon, S. Electroceuticals spark interest. Nature 511, 18 (2014). https://doi.org/10.1038/511018a

[5] Chiappalone, M., Cota, V. R., Carè, M., Di Florio, M., Beaubois, R., Buccelli, S., Barban, F., Brofiga, M., Averna, A., Bonacini, F., Guggenmos, D. J., Bornat, Y., Massobrio, P., Bonifazi, P., & Levi, T. (2022). Neuromorphic-Based Neuroprostheses for Brain Rewiring: State-of-the-Art and Perspectives in Neuroengineering. Brain Sciences, 12(11), 1578. https://doi.org/10.3390/brainsci12111578

[6] Boonzaier J, van Tilborg GAF, Neggers SFW, Dijkhuizen RM. Noninvasive Brain Stimulation to Enhance Functional Recovery After Stroke: Studies in Animal Models. Neurorehabilitation and Neural Repair. 2018;32(11):927-940. doi:10.1177/1545968318804425

[7] Guggenmos, D. J., Azin, M., Barbay, S., Mahnken, J. D., Dunham, C., Mohseni, P., & Nudo, R. J. (2013). Restoration of function after brain damage using a neural prosthesis. Proceedings of the National Academy of Sciences of the United States of America, 110(52), 21177–21182. https://doi.org/10.1073/pnas.1316885110

[8] Rosin, B., Slovik, M., Mitelman, R., Rivlin-Etzion, M., Haber, S.N., Israel, Z., Vaadia, E., & Bergman, H. (2011). Closed-Loop Deep Brain Stimulation Is Superior in Ameliorating Parkinsonism. Neuron.

[9] Cota VR, de Oliveira JC, Damázio LCM, Moraes MFD. Nonperiodic stimulation for the treatment of refractory epilepsy: Applications, mechanisms, and novel insights. Epilepsy & Behavior : E&B. 2021 Aug;121(Pt B):106609. DOI: 10.1016/j.yebeh.2019.106609.

[10] Cottone, C., Cancelli, A., Pasqualetti, P., Porcaro, C., Salustri, C., & Tecchio, F. (2017). A New, High-Efficacy, Noninvasive Transcranial Electric Stimulation Tuned to Local Neurodynamics. The Journal of Neuroscience, 38, 586 - 594.

[11] Tecchio, F., Cancelli, A., Pizzichino, A., L'Abbate, T., Gianni, E., Bertoli, M., Paulon, L., Zannino, S., Giordani, A., Lupoi, D., Pasqualetti, P., Mirabella, M., & Filippi, M. M. (2022). Home treatment against fatigue in multiple sclerosis by a personalized, bilateral whole-body somatosensory cortex stimulation. Multiple sclerosis and related disorders, 63, 103813. https://doi.org/10.1016/j.msard.2022.103813

[12] Gal A, Marom S. Entrainment of the intrinsic dynamics of single isolated neurons by natural-like input. J Neurosci. 2013;33(18):7912-7918. doi:10.1523/JNEUROSCI.3763-12.2013

[13] Milighetti, S., Sterzi, S., Fregni, F., Hanlon, C. A., Hayley, P., Murphy, M. D., Bundy, D. T., Nudo, R. J., & Guggenmos, D. J. (2020). Effects of tDCS on spontaneous spike activity in a healthy ambulatory rat model. Brain stimulation, 13(6), 1566–1576. https://doi.org/10.1016/j.brs.2020.08.016

[14] Marquez J, van Vliet P, McElduff P, Lagopoulos J, Parsons M. Transcranial Direct Current Stimulation (tDCS): Does it Have Merit in Stroke Rehabilitation? A Systematic Review. International Journal of Stroke. 2015;10(3):306-316. doi:10.1111/ijs.12169

[15] Averna, A., Pasquale, V., Murphy, M. D., Rogantin, M. P., Van Acker, G. M., Nudo, R. J., Chiappalone, M., & Guggenmos, D. J. (2020). Differential Effects of Open- and Closed-Loop Intracortical Microstimulation on Firing Patterns of Neurons in Distant Cortical Areas. Cerebral cortex (New York, N.Y. : 1991), 30(5), 2879–2896. https://doi.org/10.1093/cercor/bhz281

[16] Averna, A., Hayley, P., Murphy, M. D., Barban, F., Nguyen, J., Buccelli, S., Nudo, R. J., Chiappalone, M., & Guggenmos, D. J. (2021). Entrainment of Network Activity by Closed-Loop Microstimulation in Healthy Ambulatory Rats. Cerebral cortex (New York, N.Y. : 1991), 31(11), 5042–5055. https://doi.org/10.1093/cercor/bhab140

[17] Averna, A., Barban, F., Care, M., Murphy, M. D., Iandolo, R., De Michieli, L., Nudo, R. J., Guggenmos, D. J., & Chiappalone, M. (2022). LFP Analysis of Brain Injured Anesthetized Animals Undergoing Closed-Loop Intracortical Stimulation. IEEE transactions on neural systems and rehabilitation engineering : a publication of the IEEE Engineering in Medicine and Biology Society, 30, 1441–1451. https://doi.org/10.1109/TNSRE.2022.3177254

[18] Carè, M., Averna, A., Barban, F. et al. The impact of closed-loop intracortical stimulation on neural activity in brain-injured, anesthetized animals. Bioelectron Med 8, 4 (2022). https://doi.org/10.1186/s42234-022-00086-y

[19] Gilmour, G., Iversen, S. D., O'Neill, M. F., O'Neill, M. J., Ward, M. A., & Bannerman, D. M. (2005). Amphetamine promotes task-dependent recovery following focal cortical ischaemic lesions in the rat. Behavioural brain research, 165(1), 98–109. https://doi.org/10.1016/j.bbr.2005.06.027

[20] Zullo, L., Chiappalone, M., Martinoia, S., & Benfenati, F. (2012). A "spike-based" grammar underlies directional modification in network connectivity: effect on bursting activity and implications for bio-hybrids systems. PloS one, 7(11), e49299. https://doi.org/10.1371/journal.pone.0049299

[21] Kleim, J. A., Bruneau, R., VandenBerg, P., MacDonald, E., Mulrooney, R., & Pocock, D. (2003). Motor cortex stimulation enhances motor recovery and reduces peri-infarct dysfunction following ischemic insult. Neurological research, 25(8), 789–793. https://doi.org/10.1179/016164103771953862

[22] Fang, P. C., Barbay, S., Plautz, E. J., Hoover, E., Strittmatter, S. M., & Nudo, R. J. (2010). Combination of NEP 1-40 treatment and motor training enhances behavioral recovery after a focal cortical infarct in rats. Stroke, 41(3), 544–549. https://doi.org/10.1161/STROKEAHA.109.572073

[23] Lieb, F., Stark, H. G., & Thielemann, C. (2017). A stationary wavelet transform and a time-frequency based spike detection algorithm for extracellular recorded data. Journal of neural engineering, 14(3), 036013. https://doi.org/10.1088/1741-2552/aa654b

Boosted transport of Theranostic Angiopep-2 engineered crosslinked Hyaluronic Acid NanoParticles (Thera-ANG-cHANPs) in glioblastoma cells

Angela Costagliola di Polidoro[1,2], Joost Haeck[3], Laura Mezzanotte[3,4], Martine Lamfers[5], Enza Torino[1,2,6]
[1] *Interdisciplinary Research Center on Biomaterials, CRIB, University of Naples Federico II, 80125, Naples, Italy*
[2] *University of Naples Federico II, Department of Chemical, Materials and Production Engineering (DICMaPI), 80125, Naples, Italy*
[3] *Erasmus Medical Center, Molecular Genetics, 3015 CN Rotterdam, The Netherlands*
[4] *Medres medical research GmBH, 50931, Cologne, Germany*
[5] *Department of Neurosurgery, Brain Tumor Center, Erasmus Medical Center, 3015 CN, Rotterdam, the 14 Netherlands*
[6] *Fondazione Istituto Italiano di Tecnologia, IIT, 80125, Naples, Italy*

***Abstract*—Angiopep-2 is a 19 amino acid synthetic peptide that demonstrated the ability to shuttle active agents across the BBB in clinics by the interaction with LRP-1 receptors. The combination of such peptide with properly designed drug delivery systems can strongly improve the outcome of patients with brain tumours, a pathology in which the standard of care is scarcely effective because of poor transport and resistance. In this work, we engineered theranostic crosslinked hyaluronic acid nanoparticles (Thera-cHANPs), co-encapsulating Gd-DTPA with boosted relaxivity and the chemotherapeutic drug Irinotecan (CPT-11), with Angiopep-2, to produce Thera-ANG-cHANPs. Thera-ANG-cHANPs demonstrated stability in the biological environment, boosted uptake by patient derived Glioblastoma cells and, as consequence of improved transport, a boosted therapeutic effect exerted with a lower dose of drug in a reduced time window.**

***Keywords*—Angiopep-2; Glioblastoma (GBM); Nanoparticles; Hydrodenticity.**

I. INTRODUCTION

Angiopeps (ANGs) are a family of synthetic peptides that selectively target Low-density Lipoprotein Receptor Related Protein 1 (LRP-1). [1, 2]. Those receptors are relevant for the targeted transport across the Blood Brain Barrier (BBB) since they are highly overexpressed at the endothelial layer of the Neurovascular Unit, being also present in a greater extent with respect to other receptors (e.g. Transferrin and Insulin receptors) [3]. Demeule et al., demonstrated that one specific ANG peptide, Angiopep-2 (TFFYGGSRGKRNNFKTEEY) bears 10-folds higher transcytosis capacities at the BBB in vivo with respect to the endogenous substrates of LRP1 receptors, such as aprotinin [4]. Moreover, Angiopep-2 confirmed its shuttling ability into the Central Nervous System (CNS) in clinical settings, determining successful brain tumour accumulation of the drug paclitaxel, when formulated as a drug-peptide conjugate (ANG1005) in patients with recurrent gliomas [5]. Indeed, further evidence proved that LRP1 receptors are also overexpressed at glioma cell membrane, and thus that Angiopep-2 bears dual targeting ability, probably because of the marked proliferating phenotype characterizing cells of higher grade tumours, such as Glioblastomas (GBMs) [6] [7, 8].

GBM is the most aggressive and incurable CNS malignancy, with very poor patient prognosis[9]. Clinical protocols for diagnosis and therapy are constantly revised and updated based on the developing knowledge around tumour genotyping and stratification. The latest guidelines have been released in 2017 by the European Association of Neuroncology (EANO) [10]. They identify the tumour burden by T1-enhanced regions in MRI and confirm the Stupp protocol, based on chemo-radio-combinatorial therapy, as standard of care. However, Gadolinium (Gd)-based contrast agents are not able to cross the BBB and can accumulate only in the regions of the tumour where it is disrupted. Moreover, the only approved chemotherapeutic drug, Temozolomide (TMZ) has been proved to be ineffective in more than 50% of patients, in details those affected by the methylation of the O [6]-methylguanine-DNA methyltransferase (MGMT) promoter [11]. For all the aforementioned reasons, the use of Angioepep-2 engineered formulations constitutes a huge opportunity to improve GBM standard of care and expand it both for diagnosis and therapy, repurposing strongly effective active agents that are currently excluded because of poor CNS accumulation.

Hyaluronic Acid (HA) demonstrated the ability of boosting the relaxivity of Gd-based CAs through the properties of Hydrodenticity[12, 13]. In particular, when encapsulated in properly crosslinked HA nanoparticles, it is packed in gado-meshes, domains of packed water that is determining the boosting Gd-DTPA relaxivity up to 12-fold as a consequence of the improved hydration degree of the metal chelate [12-14]. Secondly, the camptothecin prodrug Irinotecan (CPT-11), approved for the treatment of colorectal cancer since 1996, has been recently proposed for the treatment of Glioblastoma as valuable alternative to the poorly effective TMZ. Despite some encouraging results, its poor serum stability and CNS penetration are still posing limitations to its approval for GBM treatment. Based on these observations, we designed Angiopep-2 engineered theranostic crosslinked HA NPs (Thera-ANG-cHANPs) encapsulating both Gd-DTPA with boosted relaxometric properties and the camptothecin drug Irinotecan for an earlier diagnosis and more effective therapy of GBM [14]. In this regard, the present study aims at highlighting the improved interaction of Thera-ANG-cHANPs with a relevant model of patient derived glioblastoma cells and its potential implication on GBM theranostics.

II. RESULTS

Table 1 reports the main methodologies applied for the production and in-vitro testing of Thera-ANG-cHANPs. The use of patient tumour material for cell culture establishment was approved by the 600 institutional review board of the ErasmusMC and obtained with patient's informed consent. Ethical Commette: MEC-2013-090.

Table 1. Main methodologies applied for Thera-ANG-cHANPs production and testing

	TECHNIQUE	*METHODOLOGY*
NP Production	Microfluidic Hydrodynamic Flow Focusing (HFF)	Nanoprecipitation in a quartz X-junction chip. Solvent phase: HA 0.05% w/V; Gd-DTPA 0.1% w/V: CPT-11: 0.025% w/V + EtOH 10% V/V. Non-solvent phase: Acetone; Divinyl sulfone 4% V/V. Process parameters: Middle Flow rate 30 µL/min Side Flow rate 110 µL/min
Angiopep-2 Conjugation	NH_2-COOH chemical crosslinking	EDC (0.02M) and NHS (0.006M) activation and 50 µg Angiopep-2 per mL of NPs. BCA assay kit for peptide quantification
NP physicochemical properties	Morphology: TEM Average Size: DLS	TEM observation of 5 µL of sample on copper grids; DLS measurement of 1 mL sample by Zetasizer Nano (Malvern)
NP relaxivity	1T MRI	Spin-echo sequence (repetition times 550, 880, 1400, 2000 ms, echo time 80 ms) and T1 signals calculated using MLE method to fit saturation recovery curves (a*exp(-TR/T1)+c). FOV 80-mm, a 96 × 96 matrix, and 2 mm slice thickness
Active Agents Encapsulation	ICP-MS Uv-VIS	Gd-DTPA: ICP-MS CPT-11: Abs 368 nm
Cell uptake	Flow cytometry (FACS)	Cell culture: U87 MG: Dulbecco's modified Eagle's medium (DMEM), 10% FBS, 1% penicillin/streptomycin, 1% L-glutamine; PDX: (DMEM)–537 F12 with 1% penicillin/streptomycin, B27, human epidermal growth factor (EGF; 5 538 µg/mL), human basic fibroblast growth factor (FGF; 5 µg/mL), and heparin (5 539 mg/mL). Seeding density: 50000 cells/well .

The theranostic design of Thera-ANG-cHANPs is schematically presented in Figure 1a.

The following sections present the rational for particle testing and the achieved results.

A. Impact of Angiopep-2 conjugation on LRP1 targeting ability

The targeting ability of Thera-ANG-cHANPs entirely depends on Angiopep-2 interaction with the receptor LRP1. For this reason, as a first step, a molecular docking simulation between the peptide and the LRP-1 portion responsible for the ligand binding (the double complement type repeats CR56) is performed. It allows to characterize the peptide/receptor binding in terms of energy, binding modes and, most importantly, know about both peptide and receptor amino acids involved, to assess the impact of peptide conjugation to NPs on its interaction with the LRP1, if any. As presented in Figure 1b, the binding is characterized by a quite high binding energy, -5.67 kcal/mol. Moreover, it appears that a specific region of the CR56 is involved. The analysis of the amino acids reveals that this LRP1 region comprises the Asp959, reported as the residue involved in the Receptor Associated Protein (RAP) binding, directly connected to the recycling of the receptors from the endosomes to the cell surface, thus to its transcytosis capacity [15, 16]. Moreover, all the residues of Angiopep-2 result to be involved in the binding with equal probability, allowing to conclude that a chemical crosslinking of the peptide on NP surface, preventing some amino acids from the binding with LRP1, should not negatively impact on its overall targeting ability.

B. ANG-cHANPs: production and characterization

Microfluidic production of crosslinked Hyaluronic Acid Nanoparticles (cHANPs) encapsulating multiple agents is a consolidated process[14, 17-19]. Briefly, by implementing a nanoprecipitation process in an X-junction chip through a hydrodynamic flow focusing regime, a highly uniform population of nanoparticles with tightly controlled features is produced. For the theranostic design, a co-solvation strategy is implemented allowing to maximize encapsulation of the poorly soluble CPT-11 without perturbing HA precipitation and crosslinking, and Gd-DTPA encapsulation. In optimal process conditions, a uniform population of spherical particles with mean size of 106.5 ± 46 nm is achieved. Encapsulation efficiencies (EE%) of Thera-cHANPs are 30% (80µM) and 18% (151µM) for Gd-DTPA and CPT-11, respectively.

After production, Angiopep-2 is conjugated to -COOH groups of HA exposed onto NP surface to produce engineered Thera-ANG-cHANPs. Briefly, after -COOH activation by EDC/NHS, Angiopep-2 is put in contact with Thera-cHANPs (50 µg per mL of NPs). After 4h, excess peptide is purified and particle size, morphology, and relaxometric properties are characterized. Dynamic Light Scattering (DLS) reveals a particle population of increased mean size (368 ± 61 nm). Neverthless, as showed by Transmission Electron Microscopy (TEM) observation in Figure 1c, particle morphology is preserved, and Angiopep-2 is successfully and uniformly conjugated to the polymer, as further confirmed by the BCA assay, measuring 32 µg/mL of Angiopep-2 in the purified sample. The increase in NP size might be due to polymer chain sliding consequent to interaction with the peptide causing water imbibition and hydrogel swelling.

Relaxometric properties of NPs are evaluated under a preclinical 1T MRI. Figure 1d present the T1 maps as measured for increasing concentration of Gd-DTPA encapsulated in NPs showing, as expected, T1 shortening as Gd-DTPA concentration increases. Figure 1e reports fitting of mean T1 values for longitudinal relaxivity evaluation. This analysis reveals a $r_1 = 13.08\, mM^{-1}s^{-1}$ for Thera-ANG-cHANPs that is 3.45 times higher than free Gd-DTPA ($r_1 = 4\, mM^{-1}s^{-1}$). This result suggests that the Hydrodenticity

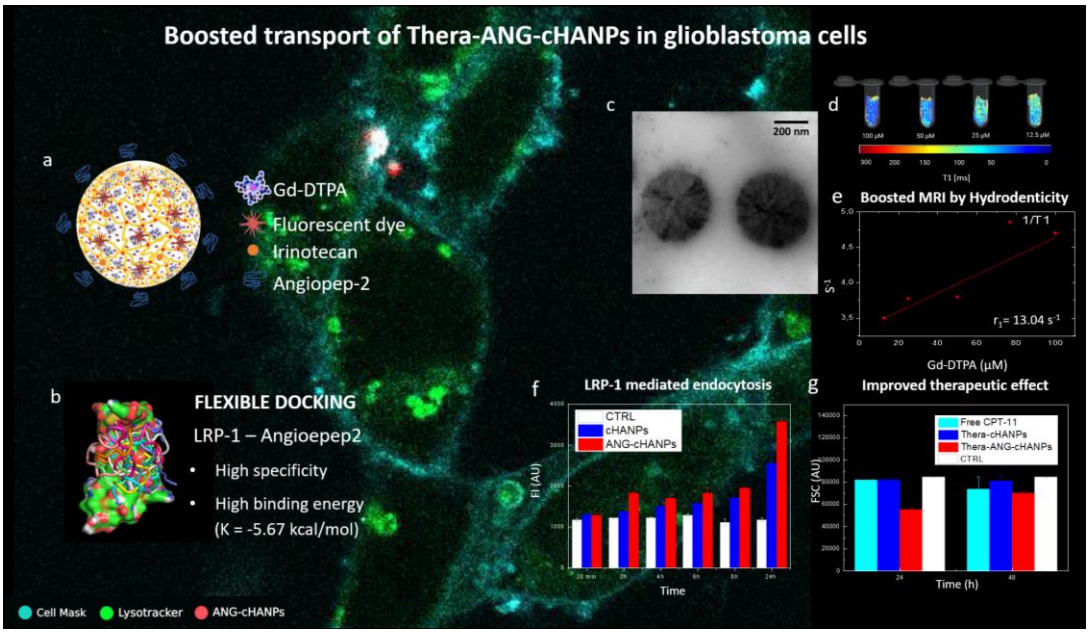


Fig. 1: Thera-ANG-cHANPs for boosted theranostics of Glioblastoma cells; a) Schematic representation of Thera-ANG-cHANPs architecture; b) Flexible Molecular Docking between Angiopep-2 and LRP-1 receptor; c) Transmission Electron Microscopy (TEM) of ANG-cHANPs; d) T1-map of NPs at 1T MRI; e) Longitudinal relaxivity estimation by T1 measurement; f) Uptake of ANG-cHANPs vs cHANPs by Flow Cytometry (FACS); g) Cytotoxicity of Thera-ANG-cHANPs vs free-CPT-11 and bare Thera-cHANPs by Forward Scattering Measurement in FACS.

boosting is preserved, as consequence of preserved hydrogel network.

C. 2.3 Boosted ANG-cHANPs transport into glioma cells

The interaction of Thera-ANG-cHANPs with glioma cells is evaluated by Flow Cytometry measurements, a single cell analysis technique that additionally allows to interrogate a statistically relevant cell population. NIR emitting cHANPs and ANG-cHANPs are produced by encapsulating the standard dye ATTO 633 ($\lambda_{ex/em}$ = 633/652 nm) to reduce the signal overlapping with cell autofluorescence, mostly present in the Vis spectrum. NP uptake is evaluated in a patient derived (PDX) cell population, as relevant model of human glioblastoma.

To quantify NP uptake, cells are seeded in 48-well plates at a density of 50000 cells/well and let adhere for 24h. Afterwards, cells are exposed to bare or engineered NPs (50 μg/mL). At selected time points, cells are washed three times with PBS for removal of non-internalized particles, detached by trypsinization and uptake is measured by flow cytometry. The analysis of the fluorescence at 650 nm is presented in Figure 1f comparing the uptake of bare cHANPs with engineered ANG-cHANPs over time. At the analysis of cHANPs internalization profile a linear increase in fluorescence over time can be observed. Differently, ANG-cHANPs show higher value of fluorescence, as indication of higher amount of internalized particles and also a sharper, exponential increase of signal after 24h of contact. As widely reported in literature, this behaviour is proper of energy dependent mechanisms which are not saturated over time as the gradient of concentration of the moving specie is vanishing across the cell membrane[20-22]. For this reason, it is possible to conclude that Angiopep-2 is mediating the boosted uptake of NPs by human derived glioma cells. Similar results are achieved in the standard U87-MG cell line (data not shown).

To investigate the possible implications of such improved transport properties, Thera-ANG-cHANPs are tested on U87-MG cells for their therapeutic potential. The cytotoxicity induced by encapsulated CPT-11 is compared to cell death caused by free CPT-11 at the same concentration (10 μM), both evaluated through the Forward Scattering Signal (FSC) measured by Flow cytometry that is widely recognized as indication of cell viability[22]. Results are presented in figure 1g. Cytotoxicity is measured at 24h and 48h since CPT-11 is a topoisomerase II inhibitor, and for this reason, is exerting its therapeutic effect at cell replication. At the analysis of the results, it is clear that free CPT-11 is producing slight or no effect on U87 cells, even after 48h of contact, as bare cHANPs. This result is not surprising if considering that the tested dose of 10 μM is 10-folds lower than the measured ED50 for CPT-11 in many cell lines. Differently, Thera-ANG-cHANPs are producing a strong reduction in cell viability already after 24h of contact, consolidating this result at 48h. In light of these results, it is possible to conclude that as a consequence of the boosted particle accumulation in U87 cells, a lower dose of CPT-11 resulted highly effective in a reduced time window.

III. CONCLUSION

GBM is characterized by several biological barriers that are very different in nature (physical, chemical, biological and mechanical) and highly dynamic among tumoral stages. They strongly limit the effectiveness of the standard of care and

vanish most of the efforts that literature is posing to design alternative but complex diagnostic and therapeutic approaches. To significantly impact on GBM diagnosis and therapy a deeper understanding of the cross-talk of active agents with disease-specific biological barrier is needed. In this sense, Thera-ANG-cHANPs are designed starting from approved materials and active agents, that already proved their effectiveness in clinics. The effort in this case is devoted to the understanding of the impact of their combination and the evaluation of nano-bio-interactions that arise at the cellular level between Thera-ANG-cHANPs and a relevant human model of Glioma.

IV. References

1. Demeule, M., A. Regina, C. Che, J. Poirier, T. Nguyen, R. Gabathuler, J. P. Castaigne and R. Beliveau. "Identification and design of peptides as a new drug delivery system for the brain." *Journal of Pharmacology and Experimental Therapeutics* 324 (2008): 1064-72. 10.1124/jpet.107.131318. <Go to ISI>://WOS:000253445200021.
2. Bertrand, Y., J. C. Currie, M. Demeule, A. Regina, C. Che, A. Abulrob, D. Fatehi, H. Sartelet, R. Gabathuler, J. P. Castaigne, *et al.* "Transport characteristics of a novel peptide platform for cns therapeutics." *Journal of Cellular and Molecular Medicine* 14 (2010): 2827-39. 10.1111/j.1582-4934.2009.00930.x. <Go to ISI>://WOS:000285064500012.
3. www.proteinatlas.org.
4. Regina, A., M. Demeule, C. Che, I. Lavallee, J. Poirier, R. Gabathuler, R. Beliveau and J. P. Castaigne. "Antitumour activity of ang1005, a conjugate between paclitaxel and the new brain delivery vector angiopep-2." *British Journal of Pharmacology* 155 (2008): 185-97. 10.1038/bjp.2008.260. <Go to ISI>://WOS:000258985100004.
5. Castaigne, J. P., K. M. Elian, D. Bouchard, A. Neale, S. Rosenfeld, J. Drappatz, M. Groves, P. Wen, P. Bento and B. Lawrence. "Ang1005: Preliminary clinical safety and tolerability in patients with recurrent malignant glioma." *Ejc Supplements* 6 (2008): 133-34. 10.1016/s1359-6349(08)72359-0. <Go to ISI>://WOS:000261221200424.
6. Maletinska, L., E. A. Blakely, K. A. Bjornstad, D. F. Deen, L. J. Knoff and T. M. Forte. "Human glioblastoma cell lines: Levels of low-density lipoprotein receptor and low-density lipoprotein receptor-related protein." *Cancer Research* 60 (2000): 2300-03. <Go to ISI>://WOS:000086696500039.
7. Xin, H. L., X. Y. Sha, X. Y. Jiang, W. Zhang, L. C. Chen and X. L. Fang. "Anti-glioblastoma efficacy and safety of paclitaxel-loading angiopep-conjugated dual targeting peg-pcl nanoparticles." *Biomaterials* 33 (2012): 8167-76. 10.1016/j.biomaterials.2012.07.046. <Go to ISI>://WOS:000309306800027.
8. Xin, H. L., X. Y. Sha, X. Y. Jiang, L. C. Chen, K. Law, J. J. Gu, Y. Z. Chen, X. Wang and X. L. Fang. "The brain targeting mechanism of angiopep-conjugated poly(ethylene glycol)-co-poly(epsilon-caprolactone) nanoparticles." *Biomaterials* 33 (2012): 1673-81. 10.1016/j.biomaterials.2011.11.018. <Go to ISI>://WOS:000300474000046.
9. Tamimi, A. F. and M. Juweid. "Epidemiology and outcome of glioblastoma." *Glioblastoma* (2017): 143-53. 10.15586/codon.glioblastoma.2017.ch8. <Go to ISI>://WOS:000424829000010.
10. Weller, M., M. van den Bent and J. C. Tonn. "European association for neuro-oncology (eano) guideline on the diagnosis and treatment of adult astrocytic and oligodendroglial gliomas (vol 18, e315, 2017)." *Lancet Oncology* 18 (2017): E642-E42. <Go to ISI>://WOS:000414134100021.
11. Lee, S. Y. "Temozolomide resistance in glioblastoma multiforme." *Genes & Diseases* 3 (2016): 198-210. 10.1016/j.gendis.2016.04.007. <Go to ISI>://WOS:000384979000007.
12. Russo, M., A. M. Ponsiglione, E. Forte, P. A. Netti and E. Torino. "Hydrodenticity to enhance relaxivity of gadolinium-dtpa within crosslinked hyaluronic acid nanoparticles." *Nanomedicine* 12 (2017): 2199-210. 10.2217/nnm-2017-0098. <Go to ISI>://WOS:000409049300005.
13. De Sarno, F., A. M. Ponsiglione, M. Russo, A. M. Grimaldi, E. Forte, P. A. Netti and E. Torino. "Water-mediated nanostructures for enhanced mri: Impact of water dynamics on relaxometric properties of gd-dtpa." *Theranostics* 9 (2019): 1809-24. 10.7150/thno.27313. <Go to ISI>://WOS:000460134200020.
14. Costagliola di Polidoro, A., G. Zambito, J. Haeck, L. Mezzanotte, M. Lamfers, P. A. Netti and E. Torino. "Theranostic design of angiopep-2 conjugated hyaluronic acid nanoparticles (thera-ang-chanps) for dual targeting and boosted imaging of glioma cells." *Cancers* 13 (2021): 10.3390/cancers13030503. <Go to ISI>://WOS:000615009800001.
15. Jensen, G. A., O. M. Andersen, A. M. J. J. Bonvin, I. Bjerrum-Bohr, M. Etzerodt, H. C. Thogersen, C. O'Shea, F. M. Poulsen and B. B. Kragelund. "Binding site structure of one lrp-rap complex implications for a common ligand-receptor binding motif." *Biological Magnetic Resonance Data Bank* (2010): 10.13018/bmr17055. <Go to ISI>://DRCI:DATA2020242020580251.
16. Jensen, G. A., O. M. Andersen, A. M. J. J. Bonvin, I. Bjerrum-Bohr, M. Etzerodt, H. C. Thøgersen, C. O'Shea, F. M. Poulsen and B. B. Kragelund. "Binding site structure of one lrp–rap complex:Implications for a common ligand–receptor binding motif." *Journal of Molecular Biology* 362 (2006): 700-16. https://doi.org/10.1016/j.jmb.2006.07.013. https://www.sciencedirect.com/science/article/pii/S0022283606008692.
17. Russo, M., P. Bevilacqua, P. A. Netti and E. Torino. "A microfluidic platform to design crosslinked hyaluronic acid nanoparticles (chanps) for enhanced mri." *Scientific Reports* 6 (2016): 10.1038/srep37906. <Go to ISI>://WOS:000388806000001.
18. Russo, M., A. M. Grimaldi, P. Bevilacqua, O. Tammaro, P. A. Netti and E. Torino. "Pegylated crosslinked hyaluronic acid nanoparticles designed through a microfluidic platform for nanomedicine." *Nanomedicine* 12 (2017): 2211-22. 10.2217/nnm-2017-0103. <Go to ISI>://WOS:000409049300006.
19. Tammaro, O., A. C. di Polidoro, E. Romano, P. A. Netti and E. Torino. "A microfluidic platform to design multimodal peg - crosslinked hyaluronic acid nanoparticles (peg-chanps) for diagnostic applications." *Scientific Reports* 10 (2020): 10.1038/s41598-020-63234-x. <Go to ISI>://WOS:000549142200028.
20. Salvati, A., C. Aberg, T. dos Santos, J. Varela, P. Pinto, I. Lynch and K. A. Dawson. "Experimental and theoretical comparison of intracellular import of polymeric nanoparticles and small molecules: Toward models of uptake kinetics." *Nanomedicine-Nanotechnology Biology and Medicine* 7 (2011): 818-26. 10.1016/j.nano.2011.03.005. <Go to ISI>://WOS:000297699900017.
21. Salvati, A., I. Nelissen, A. Haase, C. Aberg, S. Moya, A. Jacobs, F. Alnasser, T. Bewersdorff, S. Deville, A. Luch, *et al.* "Quantitative measurement of nanoparticle uptake by flow cytometry illustrated by an interlaboratory comparison of the uptake of labelled polystyrene nanoparticles." *Nanoimpact* 9 (2018): 42-50. 10.1016/j.impact.2017.10.004. <Go to ISI>://WOS:000428127400004.
22. Jochums, A., E. Friehs, F. Sambale, A. Lavrentieva, D. Bahnemann and T. Scheper. "Revelation of different nanoparticle-uptake behavior in two standard cell lines nih/3t3 and a549 by flow cytometry and time-lapse imaging." *Toxics* 5 (2017): 10.3390/toxics5030015. <Go to ISI>://WOS:000412074100002.

coupled Hydrodynamic Flow Focusing to design Lipid-Polymer NPs (LiPoNs) for theranostics

Felicia Roffo[1,2], Alfonso Maria Ponsiglione [1], Paolo Antonio Netti[1,2,3] and Enza Torino[1,2,3]
[1] *University of Naples Federico II, Department of Chemical, Materials and Production Engineering (DICMaPI), Naples,Italy;*
[2] *Interdisciplinary Research Center on Biomaterials, CRIB, University of Naples Federico II, Naples, Italy*
[3]*Center for Advanced Biomaterials for Health Care, CABHC, Istituto Italiano di Tecnologia, IIT@CRIBCABHC, Naples, Italy*

***Abstract*— Nanoparticles offered unique properties respect to their bulk counterpart that make them promising vehicles for diagnosis and therapy in cancer. However, only the 0.7 % of administered NPs effectively reach the tumour site. This limited efficacy is mainly due to filtration exerted on NPs by the biological barriers, encountered in their *in vivo* journey. To improve these nano-bio interactions, we present an optima design of hybrid nanovector, Lipid-Polymer NPs, through an innovative microfluidic process defined as coupled Hydrodynamic Flow Focusing (cHFF). We co-entrapped in the NPs, Gd-DTPA and Atto 633 for MRI and optical imaging, while the Gd-DTPA and Irinotecan for theranostics.**

***Keywords*—Microfluidics, LNPs, lipid-polymer, theranostics**

I. INTRODUCTION

Nanoparticles are promising vehicles for the delivery of therapeutic and diagnostic probes to the disease site[1].

Despite the huge effort made in manipulating the NPs properties to reach the tumour site, the majority of them still accumulate in off-target sites, with only 0.7 % of administered dose in tumour tissue[2, 3]. Indeed, the administered NPs during their journey to tumour site encountered several barriers, that filtered them out[4]. These unsuccessful data reported for current NPs, stand out the need for the development of optimal design carriers. Recently, hybrid NPs emerged as next generation vehicles offering unique properties from the integration of materials that improves the carrier stability upon the nano-bio interactions[5, 6]. Among these hybrid vectors, lipid-polymer NPs, made up of a polymer core enveloped by the lipid component, offered multifaced properties such as boosted structural stability, high cargo loading, improved deformability, prolonged blood circulation and enhanced cell/tissue interaction[3, 5-9]. The conventional manufacturing techniques for the production of lipid-polymer NPs rely on the addition of pre-formed polymer nanoparticles during the liposome formation or to pre-formed liposomes, requiring post-processing steps to improve the size and homogeneity of the formulation[10]. Due to the impact exerted by the physiochemical properties of NPs[3, 4], such as size, shape, charge and elasticity, on their in vivo fate, microfluidic processes have been designed for their production[11, 12]. Indeed, the microfluidics ability of controlling the fluids in the microscale range allows the fine tuning of the properties of the end-carrier. The complexity of guiding two mechanisms of NPs formation in microfluidics has led to the development of several strategies for the synthesis of hybrid NPs. First, the on-chip production of liposomes was combined to off-chip polymerization of the interiors of NPs to obtain hydrogel core[13]. Then, the hydrodynamic flow focusing in combination with passive mixing structures[14] and controlled microvortices[15] were exploited for the production of lipid-polymer NPs. Sun et al.[16] developed two-stage microfluidic chip for the synthesis of mono-disperse lipid-poly (lactic-co-glycolic acid) NPs.

In this framework, we present an innovative one-step microfluidic process, coupled Hydrodynamic flow focusing for the production of Lipid-Polymer NPs (LiPoNs)[17]. The engineered process allows to manipulate the diffusion of species and manage both the mechanisms of nanoparticle formation, nanoprecipitation and self-assembly, to obtain hybrid nanovectors. In particular, the LiPoNs are made up of a chitosan core covered by a lipid bilayer, to integrate the structural stability and cargo loading offered by the chitosan matrix with the biomimetic properties of lipid component. These multifaced nanostructures were exploited for multimodal imaging and theranostics applications. Even though the MRI is the most clinically applied modality, the Gadolinium-free contrast agents CAs suffer from transmetalation, nephrotoxic effects and abnormal brain deposition[18, 19]. Therefore, we selected the Gd-DTPA as Gadolinium-based Contrast agents (CAs) for MRI imaging and we combined an optical probe to increase sensitivity of MRI imaging [20]. We proved the ability of LiPoNs to co-entrap a model drug with the Irinotecan HCl, a chemotherapy already approved for several cancers[21].

II. MATERIALS AND METHODS

L-α-Phosphatidylcholine from soybean (SPC) and cholesterol (Chol); Chitosan (CH, 50-190 kDa); Diethylenetriaminepentaacetic acid gadolinium (III) dihydrogen salt hydrate (Gd-DTPA); Atto 633 (ex/em = 633/657 nm) have been purchased from Sigma-Aldrich (St. Louis, MO, USA). Irinotecan HCl Trihydrate (IRI) was purchased by Selleckchem Chemicals (Huston, TX, USA). As solvents, we used Acetic acid glacial (AcOH, ROMIL pure chemistry,Cambridge, UK), Ethanol (etOH, puriss. p.a., absolute, Carlo Erba Reagents, Italy) and filtered MilliQ water (Milli-Q Plus, Q-POD®, Merck KGaA, Darmstadt, Germany) and the phosphate-buffered saline (PBS, tablet, Sigma-Aldrich). The human glioblastoma cell line U87 MG (ATCC, Manassas, VA, USA) were cultured in Dulbecco Modified Eagle medium-high glucose (DMEM), 10 % v/v fetal bovine serum (FBS, Sigma Aldrich, St. Louis, MO, USA), 2 mM L-glutamine and 1 % v/v Antibiotic Solution liquid (Thermo Fisher Scientific, Waltham, USA). The methods used for the production, purification, characterization of LiPoNs are reported in table I.

TABLE I: METHODS

Methods	*Description*
Microfluidic set-up	A quartz microfluidic device (22.5 mm long;15 mm wide; 4 mm thick) with 5 parallel inputs (45 °) and one output purchased from Dolomite Centre Ltd. The chip is compatible with the H interface 7-way for FEP tubing connections (1/16 x 0.25 mm- 0.8 x 0.25 mm). All the channels have a cross section of 160µmx150µm.
coupled HFF production	The side phases are composed of etOH/Water solution (65/35% v/v) containing 0.0072% w/v of Lipids (mass ratio 8:1-SPC:Chol). The middle phase is made of an aqueous solution of 0.01% w/v of CH and 1% v/v of AcOH. The Gd-DTPA, Atto633 and Irinotecan HCl are added at 0.4 % w/v, 24 µg/ml and 145 µg/ml to the middle solution. A flow rate ratio of 0.073 (the Volume Flow Rate of the middle channel-3 µL/min and the Volume Flow Rate of the side channel-41 µL/min), was used. The process was carried out 40 min (its multiples), collected in 3.5 ml (its multiples) of water and stirred 40 min.
Purification and concentration	Mild solvent gradient dialysis (Dialysis Membrane Pre-wetted RC Tubing, MWCO = 25-50 kDa) is performed with the external phase of PBS diluted in water (1:1) for 1 h. The Rotary Evaporator (BUCHI Italia s.r.l, Cornaredo, Italy) at a vacuum pressure of 20 mbar at 25 °C was used to concentrate the sample.
Characterization	8 µL of the sample (osmium tetroxide smoke 1% v/v overnight) was observed at Transmission Electron Microscope after dried (TEM, FEI,Hillsboro, OR, USA). Dynamic light scattering (DLS) was used to determine nanoparticle size (Zetasizer). The zeta potential of NPs were determined with a Zetasizer Nano ZS (Malvern Panalytical, UK). Changes in the relaxation time (T1) were evaluated at 1.5 Tesla and 37°C by Minispec Bench Top Relaxometer (Bruker Corporation). The Multiplate Reader Photometer Enspire Perkin- Elmer Inc. (Waltham, MA, USA) was used to quantify the encapsulation efficiency (EE %) of compounds loading.
Cellular uptake	5x 10^4 U87 MG cells/well are seeded in 48-well plate and incubated for 24 h. Atto633-Gd-DTPA LiPoNs (lipid conc.60 µg/mL) were added to the cells at different time points. The cells were washed with PBS, trypsinized and analyzed by flow cytometry using a BD FACSCelesta Cell Analyzer (BD Biosciences, Franklin Lakes, NJ, USA). A total of 10,000 events were recorded for each sample, the cells were gated using Forward Scattering Area (FSC) and Side Scattering Area (SSC). For the FI distribution, the cells were excited at 561 nm and the fluorescence emitted by Atto 633 (PE_Cy5_A, Filter 688/33) was collected. Live cells were imaged with a Leica Microsystems TCS SP5 Laser Scanning Confocal Microscope (Wetzlar, Germany) with a 60xOil objective (HeNe 633 nm laser).

III. RESULTS AND DISCUSSION

Generally, in the hydrodynamic flow focusing process, the nanoparticles are produced by injecting the lipid or polymer material in the main stream dissolved in a solvent phase that is focused by a non-solvent phase flowing through side streams[22-24]. Here an innovative hydrodynamic flow focusing approach is presented for the production of hybrid Lipid-Polymer NPs (LiPoNs). The coupled hydrodynamic flow focusing (cHFF) is implemented by injecting the chitosan dissolved in acid solution in the middle stream while the lipids, dissolved in an ethanol/water solution, are injected from the side streams (Fig.1). The cHFF features govern the competition of two solvent extractions and consequently coordinate the relative kinetics of nuclei and the growth of two phenomena, self-assembly and nanoprecipitation[17]. In this way, each material is not only involved in its own thermodynamic process but mutually influences the other one.

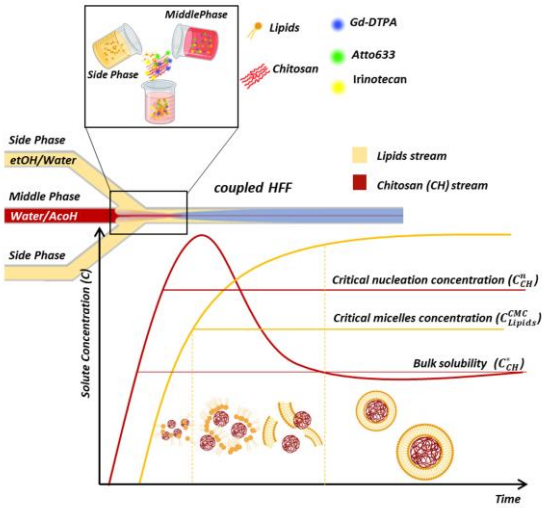


Fig. 1: Sketch of nanoprecipitation and self-assembly processes implemented in the coupled Hydrodynamic flow focusing. Some graphic elements were created with BioRender.com.

As schematized in Fig.1, in the focusing region there is the rapid extraction of acetic acid that leads to the formation of chitosan nuclei. Simultaneously, the increase in the microenvironmental polarity, due to the ethanol extraction, induces the formation of lipid bilayer fragments. Then, these bilayer fragments cover the polymer precipitate stabilizing the whole LiPoNs complex. We investigated this coupled phenomenon to obtain stable LiPoNs, by varying the process parameters, such as the solvent non-solvent ratio, the solute concentration and the flow rates. Following this study, the value of FR^2 equal to 0.073, (obtained at a middle flow rate of 3 µL/min, a side flow rate of 41 µL/min), a chitosan concentration of 0.01% w/v (dissolved in acetic solution 1% v/v-middle phase) and a Lipid concentration of 0.0072% w/v (dissolved in etOH/Water-65/35% v/v-side phase), were selected as optimal process conditions. A monodisperse population of nanoparticles is obtained as shown in Fig.2a,b. They displayed an average size around 80 nm (Fig. 2b,c).

This multimaterial nanostructure was exploited for the loading of different active agents for both multimodal imaging (Gd-DTPA- Atto633) and theranostics purposes (Gd-DTPA-Irinotecan).

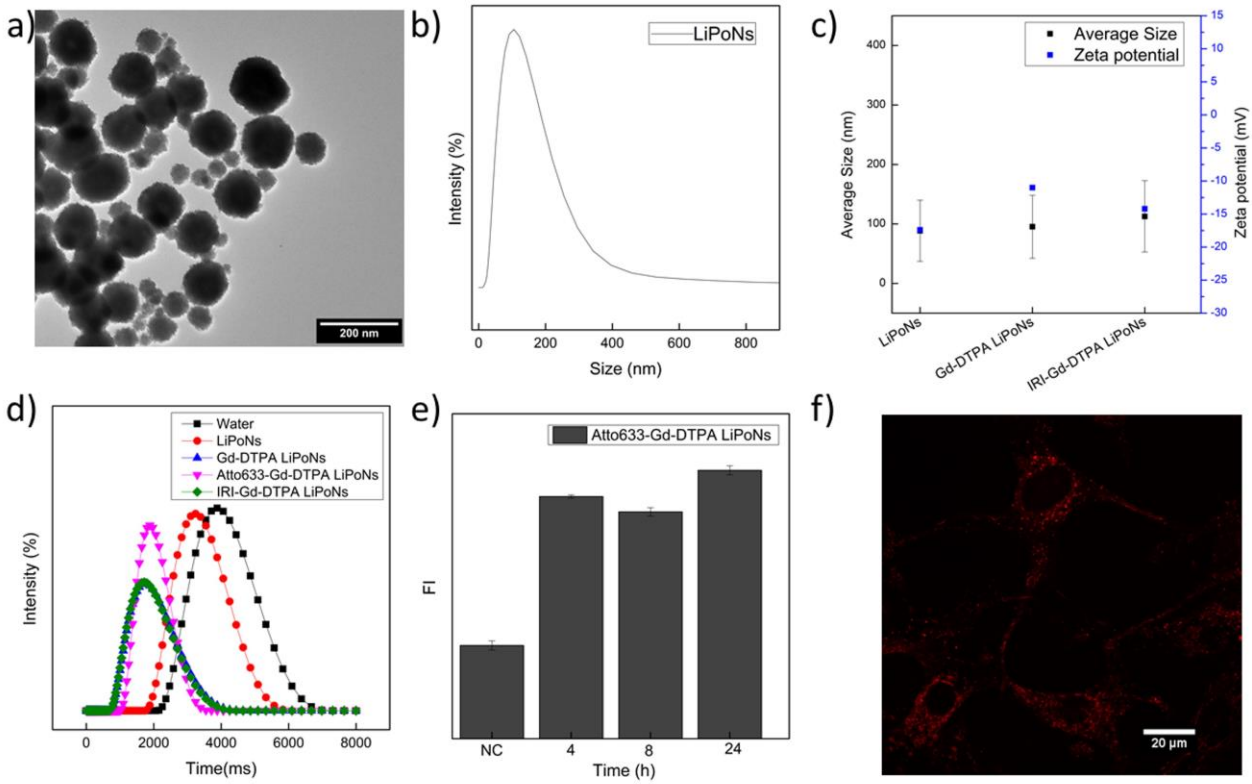


Fig. 2: Morphological characterization, size distribution, multimodal properties and cellular uptake of Lipid-Polymer NPs. **a**) TEM image (stained with osmium smoke), **b**) particle size distribution of LiPoNs, **c**) size and zeta potential of different LiPoNs formulations, **d**) in vitro MRI. Comparison of longitudinal relaxation time of LiPoNs formulations, **e**) Fluorescent intensity (FI) of U87 MG cells exposed to multimodal imaging LiPoNs (lipid conc. 60 µg/mL) and **f**) Confocal image of U87 MG cells upon 24 h of incubation with LiPoNs.

The cargos were dissolved in the chitosan solution and injected in the middle stream, forcing their loading in the chitosan matrix. We evaluated the effect of compound loading on nanoparticles size by DLS analysis (Fig.2c).

A slightly increase in the LiPoNs size is reported for the co-loading of Irinotecan and Gd-DTPA up to 113 nm (Fig.2c). Moreover, the lipid bilayer coverage conferred to the formulations a negative zeta potential ranging from -17 mV to -11 mV, according to the formulations (Fig.2c).

The slightly negative charge of LiPoNs combined with an average size around 100 nm strongly improve the nano-biointeractions that these carriers will encounter during their transport across multiple barriers *in vivo*. Yamamoto et al.[25] reported a long circulation time and lower accumulation in spleen and liver for neutral and anionic NPs, mainly due to lower absorption of serum proteins. Regarding the size, spherical nanoparticles with a size around 100 nm have the higher delivery efficacy in tumour due to their long half-live and reduced off-target accumulation[4, 11].

The optical and diagnostic properties of LiPoNs formulations were tested. The in vitro longitudinal relaxation time T1 was measured at 37 °C and 1.5 T in a the Minispec Bench Top Relaxometer (Bruker Corporation). The Gd-DTPA LiPoNs displayed a T1 of 1680 ms confirming the loading of the CA. All the formulations displayed diagnostic properties as reported in Fig. 2d.

The encapsulation efficacy (EE %) of Gd-DTPA was above 60 %, while the co-entrapment efficacy was in the range of 55-36 % for the Atto633 and Irinotecan.

To assess the delivery capability of LiPoNs, we studied their cellular uptake kinetics by fluorescence-activated cell sorting (FACs) and confocal microscope imaging. We interrogated U87 MG cells, upon incubation with Atto633-Gd-DTPA LiPoNs (lipid conc.: 60 µg/ml) at 4,8, and 24 h. No cytotoxic effects on cells were detected due to the high biocompatibility of materials that made up the LiPoNs[26-28]. The fluorescence intensity (FI) of the cells rapidly increased at 4 h and remained almost unchanged until 24 h, with a little increase in the last point of acquisition. Live cell imaging of U87 MG cells at 24 h upon the addition of LiPoNs confirmed their presence within the cells. We hypnotized that the LiPoNs uptake mainly occurred in the first 4 hours. These findings are in agreement with previous studies on the cellular internalization of lipid-based formulations, to which an energy-dependent mechanism has been associated[29-31]. Recently, Guo et al. [8]reported the impact exerted by the elasticity of NPs in mediated different cellular uptakes. By crosslinking the polymer core of the nanolipogels and consequently increasing their stiffness, they observed a shit from fusion to endocytosis in their cell internalisation pathway. Therefore, our un-crosslinked core in LiPoNs could confer a moderate elasticity to nanoparticles that could mediate the cellular uptake of both fusion and endocytosis pathways. However, this hypothesis requires further investigations because any differences in nanoparticle formulation (head group of lipids, cholesterol addition, protein corona absorption) and the physiochemical properties (size, shape, charge and elasticity) affect the NPs-cells

interaction[32].

IV. Conclusion

We proposed a one-step microfluidic process for the production of Lipid-Polymer NPs with an average size of 100 nm and a slightly negative charge. Their material configuration, where a chitosan core is covered by a lipid bilayer, can potentially stabilize the compound loading during the nano-bio interactions making them promising vehicles for cancer treatment. The chitosan matrix in the nanostructure acts as a reservoir, for the entrapment of active cargos, while the lipid material enables the cell-tissue interactions. The LiPoNs showed a higher cell internalization in first 4 hours. This ability of LiPoNs of presenting and delivery stable cargo could be connected to the fluidity or elasticity that characterized these hybrid vectors. These results support the concept that the microfluidics by controlling the material conformation and their extent, the component concentrations, solvent displacement, the amount of water entrapped between the polymer and lipid shell, provides hybrid NPs with well-defined properties to fill the lack of knowledge between synthetic identities and their nano-bio interactions.

Acknowledgement

This work has been supported by the project "NANOPARTICLES BASED ON A THERANOSTIC APPROACH FOR THE DELIVERY OF A MICRORNA SET TO BE USED FOR BREAST AND THYROID CANCERS RESISTANT TO DRUGS" funded by the MIUR "Progetti di Ricerca di Rilevante Interesse Nazionale (PRIN) Bando 2017"—grant 2017MHJJ55.

References

[1] G.Y. Chen, I. Roy, C.H. Yang, P.N. Prasad, Nanochemistry and Nanomedicine for Nanoparticle-based Diagnostics and Therapy, Chemical Reviews 116(5) (2016) 2826-2885.
[2] S. Wilhelm, A.J. Tavares, Q. Dai, S. Ohta, J. Audet, H.F. Dvorak, W.C.W. Chan, Analysis of nanoparticle delivery to tumours, Nature Reviews Materials 1(5) (2016).
[3] W. Poon, B.R. Kingston, B. Ouyang, W. Ngo, W.C.W. Chan, A framework for designing delivery systems, Nature Nanotechnology 15(10) (2020) 819-829.
[4] E. Blanco, H. Shen, M. Ferrari, Principles of nanoparticle design for overcoming biological barriers to drug delivery, Nature Biotechnology 33(9) (2015) 941-951.
[5] K. Hadinoto, A. Sundaresan, W.S. Cheow, Lipid-polymer hybrid nanoparticles as a new generation therapeutic delivery platform: A review, European Journal of Pharmaceutics and Biopharmaceutics 85(3) (2013) 427-443.
[6] Y. Hui, X. Yi, F. Hou, D. Wibowo, F. Zhang, D.Y. Zhao, H.J. Gao, C.X. Zhao, Role of Nanoparticle Mechanical Properties in Cancer Drug Delivery, Acs Nano 13(7) (2019) 7410-7424.
[7] B. Mandal, H. Bhattacharjee, N. Mittal, H. Sah, P. Balabathula, L.A. Thoma, G.C. Wood, Core-shell-type lipid-polymer hybrid nanoparticles as a drug delivery platform, Nanomedicine-Nanotechnology Biology and Medicine 9(4) (2013) 474-491.
[8] P. Guo, D.X. Liu, K. Subramanyam, B.R. Wang, J. Yang, J. Huang, D.T. Auguste, M.A. Moses, Nanoparticle elasticity directs tumor uptake, Nature Communications 9 (2018).
[9] J. Cao, D. Huang, N.A. Peppas, Advanced engineered nanoparticulate platforms to address key biological barriers for delivering chemotherapeutic agents to target sites, Advanced Drug Delivery Reviews 167 (2020) 170-188.
[10] A. Mukherjee, A.K. Waters, P. Kalyan, A.S. Achrol, S. Kesari, V.M. Yenugonda, Lipid-polymer hybrid nanoparticles as a next-generation drug delivery platform: state of the art, emerging technologies, and perspectives, International Journal of Nanomedicine 14 (2019) 1937-1952.
[11] R. Ferrari, M. Sponchioni, M. Morbidelli, D. Moscatelli, Polymer nanoparticles for the intravenous delivery of anticancer drugs: the checkpoints on the road from the synthesis to clinical translation, Nanoscale 10(48) (2018) 22701-22719.
[12] L. Zhang, Q.H. Chen, Y. Ma, J.S. Sun, Microfluidic Methods for Fabrication and Engineering of Nanoparticle Drug Delivery Systems, Acs Applied Bio Materials 3(1) (2020) 107-120.
[13] J.S. Hong, S.M. Stavis, S.H.D. Lacerda, L.E. Locascio, S.R. Raghavan, M. Gaitan, Microfluidic Directed Self-Assembly of Liposome-Hydrogel Hybrid Nanoparticles, Langmuir 26(13) (2010) 11581-11588.
[14] P.M. Valencia, P.A. Basto, L.F. Zhang, M. Rhee, R. Langer, O.C. Farokhzad, R. Karnik, Single-Step Assembly of Homogenous Lipid - Polymeric and Lipid - Quantum Dot Nanoparticles Enabled by Microfluidic Rapid Mixing, Acs Nano 4(3) (2010) 1671-1679.
[15] Y.T. Kim, B.L. Chung, M.M. Ma, W.J.M. Mulder, Z.A. Fayad, O.C. Farokhzad, R. Langer, Mass Production and Size Control of Lipid-Polymer Hybrid Nanoparticles through Controlled Microvortices, Nano Letters 12(7) (2012) 3587-3591.
[16] J.S. Sun, L. Zhang, J.L. Wang, Q. Feng, D.B. Liu, Q.F. Yin, D.Y. Xu, Y.J. Wei, B.Q. Ding, X.H. Shi, X.Y. Jiang, Tunable Rigidity of (Polymeric Core)-(Lipid Shell) Nanoparticles for Regulated Cellular Uptake, Advanced Materials 27(8) (2015) 1402-+.
[17] F. Roffo, A.M. Ponsiglione, P.A. Netti, E. Torino, coupled Hydrodynamic Flow Focusing (cHFF) to Engineer Lipid–Polymer Nanoparticles (LiPoNs) for Multimodal Imaging and Theranostic Applications %M doi:10.3390/biomedicines10020438 %U https://www.mdpi.com/2227-9059/10/2/438, Biomedicines %@ 2227-9059 10(2) (2022) 438.
[18] M. Rogosnitzky, S. Branch, Gadolinium-based contrast agent toxicity: a review of known and proposed mechanisms, Biometals 29(3) (2016) 365-376.
[19] A. Smeraldo, P.A. Netti, E. Torino, New Strategies in the Design of Paramagnetic CAs, Contrast Media & Molecular Imaging 2020 (2020).
[20] L.J. Cruz, I. Que, M. Aswendt, A. Chan, M. Hoehn, C. Lowik, Targeted nanoparticles for the non-invasive detection of traumatic brain injury by optical imaging and fluorine magnetic resonance imaging, Nano Research 9(5) (2016) 1276-1289.
[21] FDA approves irinotecan as first-line therapy for colorectal cancer, Oncology-New York 14(5) (2000) 652-+.
[22] M. Russo, P. Bevilacqua, P.A. Netti, E. Torino, A Microfluidic Platform to design crosslinked Hyaluronic Acid Nanoparticles (cHANPs) for enhanced MRI, Scientific Reports 6 (2016).
[23] A. Jahn, W.N. Vreeland, D.L. DeVoe, L.E. Locascio, M. Gaitan, Microfluidic directed formation of liposomes of controlled size, Langmuir 23(11) (2007) 6289-6293.
[24] R. Karnik, F. Gu, P. Basto, C. Cannizzaro, L. Dean, W. Kyei-Manu, R. Langer, O.C. Farokhzad, Microfluidic platform for controlled synthesis of polymeric nanoparticles, Nano Letters 8(9) (2008) 2906-2912.
[25] Y. Yamamoto, Y. Nagasaki, Y. Kato, Y. Sugiyama, K. Kataoka, Long-circulating poly(ethylene glycol)-poly(D,L-lactide) block copolymer micelles with modulated surface charge, Journal of Controlled Release 77(1-2) (2001) 27-38.
[26] M.J. Parnham, H. Wetzig, Toxicity screening of liposomes, Chemistry and Physics of Lipids 64(1) (1993) 263-274.
[27] T.L. Nguyen, T.H. Nguyen, D.H. Nguyen, Development and In Vitro Evaluation of Liposomes Using Soy Lecithin to Encapsulate Paclitaxel, International Journal of Biomaterials 2017 (2017).
[28] M. Huang, E. Khor, L.Y. Lim, Uptake and cytotoxicity of chitosan molecules and nanoparticles: Effects of molecular weight and degree of deacetylation, Pharmaceutical Research 21(2) (2004) 344-353.
[29] D. Montizaan, K.N. Yang, C. Reker-Smit, A. Salvati, Comparison of the uptake mechanisms of zwitterionic and negatively charged liposomes by HeLa cells', Nanomedicine-Nanotechnology Biology and Medicine 30 (2020).
[30] A. Salvati, C. Aberg, T. dos Santos, J. Varela, P. Pinto, I. Lynch, K.A. Dawson, Experimental and theoretical comparison of intracellular import of polymeric nanoparticles and small molecules: toward models of uptake kinetics, Nanomedicine-Nanotechnology Biology and Medicine 7(6) (2011) 818-826.
[31] E. Ducat, B. Evrard, O. Peulen, G. Piel, Cellular uptake of liposomes monitored by confocal microscopy and flow cytometry, Journal of Drug Delivery Science and Technology 21(6) (2011) 469-477.
[32] D. Manzanares, V. Cena, Endocytosis: The Nanoparticle and Submicron Nanocompounds Gateway into the Cell, Pharmaceutics 12(4) (2020).

Development of a microfluidic system for impedance-based cell sorting

C. Brandi[1], S. Spanò[1,2], G.C. Cardarilli[2], E. Verona[3], L. Businaro[3], P. Bisegna[1], A. De Ninno[3,*], and F. Caselli[1,*]

[1] *Department of Civil Engineering and Computer Science, University of Rome Tor Vergata*
[2] *Department of Electronic Engineering, University of Rome Tor Vergata*
[3] *Institute for Photonics and Nanotechnologies, Italian National Research Council*
E-mails: adele.deninno@cnr.it (A. De Ninno), caselli@ing.uniroma2.it (F. Caselli)

***Abstract*— Single-cell analysis and manipulation is recognized as a central task for developing novel precision medicine approaches. Label-free technologies are especially attractive due to their potential for reduced costs and suitability to cell-therapy applications. Here, we present the development of a label-free microfluidic system for single-cell sorting based on cell electrical phenotype.**

***Keywords*—Microfluidics, Impedance cytometry, Single-cell analysis, Cell sorting.**

I. Introduction

THE cell is the fundamental unit of life. Accordingly, understanding cell function in health and disease is critical to diagnosis and treatment. The heterogeneity displayed by cellular systems motivates the need for robust approaches for single-cell analysis and separation [1]–[4], to enable disease diagnostics based on cellular markers and to control cellular compositions for cell therapy applications [5]. Among other technologies, label-free approaches are especially attractive [6], since they reduce the costs associated with sample preparation and their non-invasiveness allows cell reuse after analysis.

Electric fields offer tremendous opportunities for label-free analysis and manipulation of biological cells, by means of versatile, effective, and yet simple sensing and actuation features. Microfluidic impedance cytometry [7] is increasingly used for the high-throughput label-free electrical characterization of single-cells flowing through microchannels with integrated electrodes. Electrical fingerprints obtained via impedance cytometry can provide information on cell size, morphology [8], deformability [9], viability [10], [11], and phenotype [12]. Adding a single-cell sorting functionality to impedance cytometry systems represents an attractive opportunity [13], [14]. This requires the development of tailored approaches for the online processing of impedance signals, coupled with a suitable microfluidic cell sorter.

In this work, we propose an electrical microfluidic system for impedance-based single-cell sorting. The conceptual design of the system is shown in **Fig.1**. A suspension of cells flows through a microfluidic channel (sample flow). Sheath flows are used to laterally focus the sample flow along the channel axis. The electrical phenotype of individual flowing cells is characterized by means of a sensing region comprising three coplanar electrodes: a multifrequency AC voltage is applied to the central electrode and the differential current from the lateral electrodes is measured ($I_{\mathrm{diff}} = I_2 - I_1$). That current is processed online as follows: (i) first, lock-in

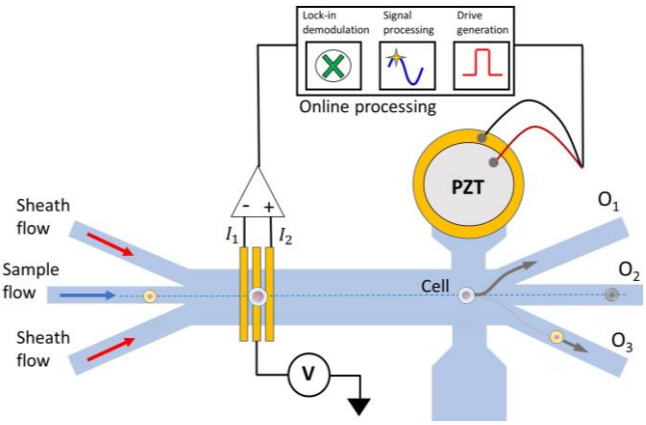


Fig. 1: Schematic representation of the label-free microfluidic system for impedance-based single-cell sorting.

demodulation provides the current traces at each applied frequency; (ii) then, those traces are processed (event detection and feature extraction) and the electrical phenotype of each detected cell is characterized; (iii) according to the cell electrical phenotype, a sorting decision is possibly made (i.e., sort to outlet O_1 or O_3), and a suited electrical signal is generated to drive a piezoelectric (PZT) actuator [15], [16]. Upon activation, the fluid displacement induced by the PZT actuator deflects the cells towards the desired outlet, whereas unsorted cells are collected at the central outlet (O_2).

The electrical sensing feature of the system has been extensively described in previous works (cf. e.g., [17]–[19]). The present work focuses on the development of the actuation feature and of the associated signal processing.

II. Materials and Methods

A. Microfluidic chip

As shown in **Fig. 2(a)**, the main channel of the microfluidic device is 150 μm wide, while the width of the three collection channels is 50 μm. Channels height is 40 μm. Two lateral regions are designed on the sides of the sorting region. The corresponding nozzles are 100 μm in width, with a distance from the diverging junction of about 50 μm. One of the lateral regions houses the actuator, that consists of a cylindrical chamber of 13 mm in diameter and 5 mm in height above which a circular ceramic transducer (lead zirconate titanate) is bonded. The PZT element has a diameter of 15 mm and a thickness of 110 μm, while its metal substrate (stainless-steel or brass) is 20 mm in diameter and 100 μm thick.

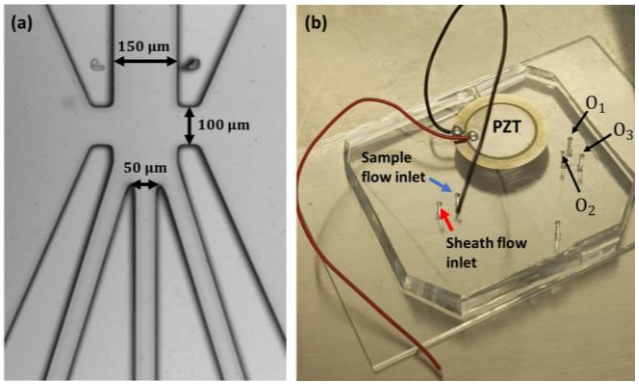


Fig. 2: (a) Microscopy image of the sorting region of the device, with indication of relevant dimensions. (b) Device photograph.

Fig. 2(b) shows a photograph of the device, with indication of the sample inlet, the common inlet of the two sheath flows, and the collection outlets. The fluidic layout is realized in a polydimethylsiloxane (PDMS, Dow Corning) block, fabricated by soft-lithography methods, and sealed to a 56 mm x 75 mm glass slide. The PZT disc is coated by a MPTS (3 mercaptopropyl trimethoxy silane) solution and then oxygen plasma-activated together with the assembled chip.

B. Numerical modelling of fluid flow and particle tracking

To analyse the fluid flow and the particles displacement induced by the PZT actuation, a 3D virtual microfluidic device is realized. The geometric model consists of the main channel, the sorting region, and the three collection channels. The overall length of the computational domain is 800 µm.

The fluid flow is modelled using the incompressible Navier-Stokes equations:

$$\rho\frac{\partial \boldsymbol{u}}{\partial t}+\rho(\boldsymbol{u}\cdot\nabla)\boldsymbol{u}=-\nabla p+\mu\nabla^2\boldsymbol{u}, \qquad (1)$$

where ρ is the fluid density, $\boldsymbol{u}$ the fluid velocity, p the fluid pressure, and μ the fluid dynamic viscosity. Boundary conditions are as follows: a laminar inflow condition at the inlet of the computational domain (average velocity $u_{av} =$ 3 cm/s), a pressure condition at the outlets ($p = 0$ Pa), and a no-slip condition on the device walls.

The movement of the particles is modelled using the Khan and Richardson's model [20]:

$$\boldsymbol{F}=\frac{\pi}{4}d^2\rho|\boldsymbol{u_r}|\boldsymbol{u_r}\left(1.84{Re_p}^{-0.31}+0.293{Re_p}^{0.06}\right)^{3.45}, \qquad (2)$$

where $\boldsymbol{F}$ is the particle drag force, d is the particle diameter, $\boldsymbol{u_r}$ is the relative velocity of the fluid with respect to the particle, and Re_p is the particle Reynold's number ($Re_p = |\boldsymbol{u_r}|d\rho/\mu$).

To mimic the PZT actuation, an inlet flow condition with applied pressure (p_{PZT}) is imposed in the sorting region, on the lateral aperture of the main channel [15]. Sinusoidal or pulse pressure conditions are considered. In the sinusoidal case, the following expression is used [15]: $p_{PZT} = p_A \sin(2\pi f t) + p_0$, where p_A is the amplitude, f is the frequency, and p_0 is the hydrodynamic pressure established by the flow. Typical values are: $p_A = 1500$ Pa, $f = 250$ Hz, and $P_0 = 630$ Pa. In the pulse actuation case, typical parameters are as follows: pulse duration $t_{OFF} - t_{ON}$ =5 ms, pulse amplitude $p_{ON} - p_{OFF} =$ 1500 Pa.

The model is implemented in COMSOL Multiphysics (Laminar Flow physics interface). The finite element mesh consists of fine unstructured triangular elements at the inlets, and coarse unstructured tetrahedral elements in the remaining geometry. Both are calibrated for fluid dynamics. The number of elements and the number of degrees of freedom typically considered are about 30000 and 26000, respectively. PARDISO solver is employed.

C. Online signal processing

As reported previously [17], [18], the lock-in demodulation is performed using the HF2IS impedance spectroscope (Zurich Instruments), which also generates the stimulation voltage applied to the centrale electrode of the sensing region. The demodulated signals (real and imaginary components at each frequency) are sent in real-time to a workstation, where they are processed with a custom Matlab script. The latter script implements the event detection using the routine findpeaks.m and extracts the corresponding event features (i.e., the particle velocity, and the electrical diameter and phase at each frequency, computed from the peak amplitudes [7]). According to the event features, a sorting decision is possibly made. In this case, instructions are sent to the HF2IS that accordingly generates the PZT drive signal at an auxiliary output connected to the PZT actuator. While the present implementation of the online signal processing is versatile and straightforward, its throughput is limited by the communication delay between the HF2IS and the workstation (~20 ms). Faster implementations are presently under development based on Field Programmable Gate Arrays (FPGAs).

III. Results and Discussion

A. Numerical characterization of piezoelectric actuation

Numerical simulations were carried out to investigate the effect of the PZT-actuation features (i.e., sinusoidal pressure amplitude and frequency; pressure pulse amplitude and duration). Water was used as the suspension fluid ($\rho = 1000$ kg/m^3, $\mu = 1.002 \cdot 10^{-3}$ Pa·s) and polystyrene beads as the particles (density $\rho_p = 1050$ kg/m^3). Different particle sizes and particle entrance positions were considered.

As an example, **Fig. 3** shows the effect of particle off-centring along the x axis (transverse direction to the main channel), which may arise due to imperfections of the sheath-flow focusing system. In the figure, different particle trajectories are shown, relevant to variable entrance position x_0 of a 5 µm bead. As the off-centring increases, the probability that the particle is deflected in the collection channel opposite to the boundary where the PZT actuation is applied decreases. The figure also shows a reduction in the length of the particle path (for fixed simulation time). In fact, as the off-centring increases the particle velocity decreases, due to the laminar flow velocity profile [21].

B. Experimental characterization of the PZT actuation

Fig. 4(a)-(b) show an experimental example of particle deflection (5 µm polystyrene bead) obtained with a sinusoidal voltage stimulation applied to the PZT transducer (10 V, 100 Hz). **Fig. 4(c)** shows an example of the time behaviour of the rotation angle (θ) of the sample stream, upon a 5 V sinusoidal

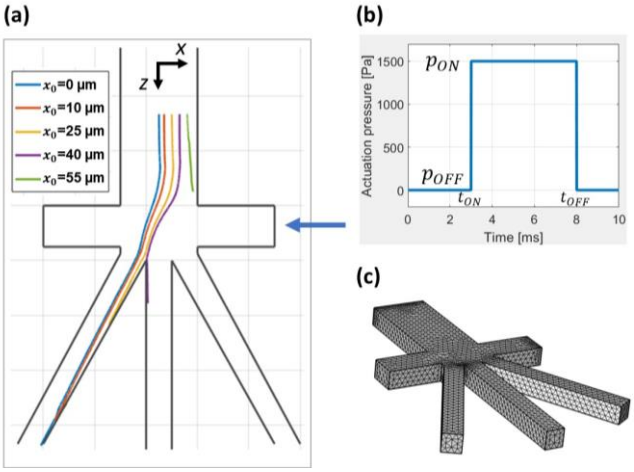


Fig. 3: Cell sorting parametric analysis with different particle's initial positions (a) under pulse pressure applied to the sorting region (b). (c) Typical computational mesh.

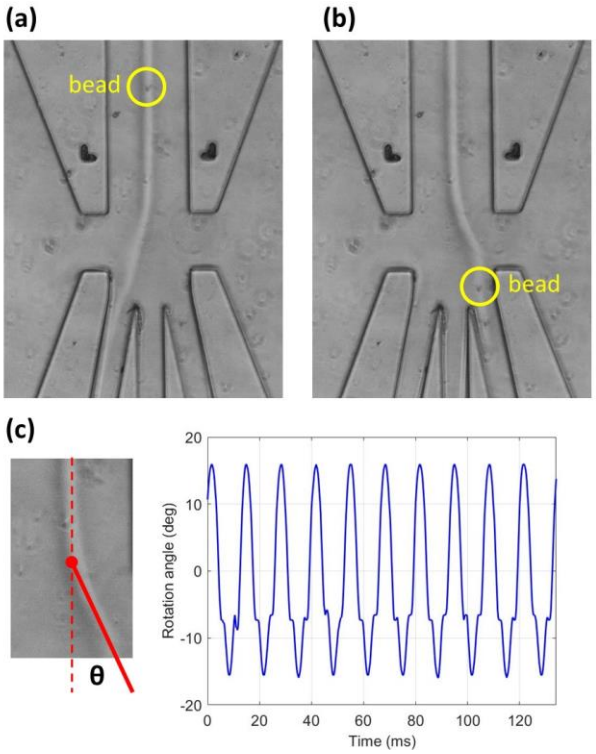


Fig. 4: (a)-(b) Microscopy snapshots showing an example of particle deviation (5 µm bead, sinusoidal PZT actuation, 10 V at 100 Hz). In panel (a) the bead (inside the yellow circle) is approaching the sorting region; in panel (b) the bead is entering the right outlet channel, due to sample flow displacement induced by the PZT actuation. (c) Rotation angle (θ) of the sample flow upon sinusoidal actuation (5 V, 75 Hz).

stimulation at 75 Hz. The angle θ was extracted from high-speed video recordings using a custom Matlab script. Oscillations with amplitude of about 16 degrees at a frequency of 75 Hz were found.

C. Online particle detection and generation of drive signal

Fig. 5(a) shows an example of online processing of the differential current I_{diff}. Two event signals are detected in the demodulated signal, corresponding to particle passages in the electrical sensing region. Particle velocity is computed from the signal peak-to-peak time. The time it takes for the particle to move from the sensing region to the actuation region (t_{SA})

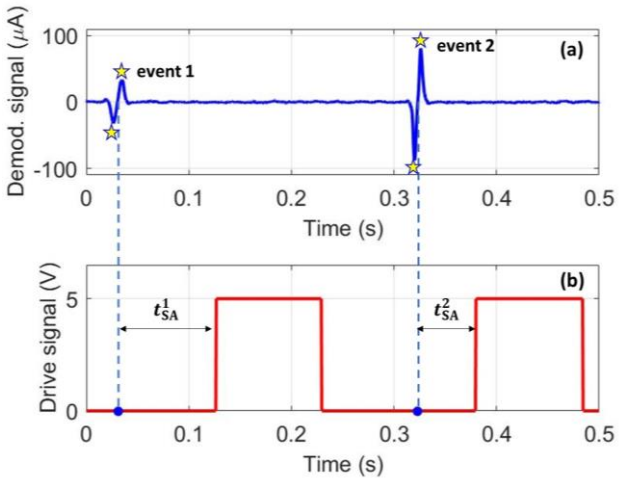


Fig. 5: (a) Example of event detection in the demodulated signal (0.5 MHz frequency channel, in phase component). (b) Corresponding drive signal.

is accordingly estimated and used to define the drive signal for the PZT actuator (**Fig. 5(b)**). It can be noticed that, due to different particle velocities, event 1 is slower than event 2 (i.e., particle 2 is closer to the channel axis - where the maximum velocity is achieved - than particle 1). Accordingly, t_{SA}^1 is larger than t_{SA}^2.

IV. Conclusion

We presented preliminary results toward the development of a label-free impedance-based microfluidic system for single-cell sorting. Specifically, we presented a numerical and experimental characterization of the PZT actuation system as well as a simple approach to online signal processing. Future activities will be dedicated to the testing and optimization of the overall system in relevant application scenarios. As a perspective, machine learning approaches tailored to impedance cytometry signals will be implemented [11], [22], [23], aiming at online cell characterization and sorting of complex samples (e.g., heterogeneous cell populations).

Acknowledgement

This work was supported by Regione Lazio under grant E85F21002390002 (MicroSystemQ project, Research Groups 2020 Programme, POR FESR Lazio 2014-2020).

References

[1] K. Klepárník and F. Foret, "Recent advances in the development of single cell analysis-A review," *Anal. Chim. Acta*, vol. 800, pp. 12–21, 2013, doi: 10.1016/j.aca.2013.09.004.

[2] "Biology of single cells shines a light on collaboration," *Nature*, vol. 547, no. 7661, p. 5, 2017, doi: 10.1038/547005a.

[3] M. Sivaramakrishnan, R. Kothandan, D. K. Govindarajan, Y. Meganathan, and K. Kandaswamy, "Active microfluidic systems for cell sorting and separation," *Current Opinion in Biomedical Engineering*, vol. 13. 2020, doi: 10.1016/j.cobme.2019.09.014.

[4] M. A. Witek, I. M. Freed, and S. A. Soper, "Cell Separations and Sorting," *Analytical Chemistry*, vol. 92, no. 1. 2020, doi: 10.1021/acs.analchem.9b05357.

[5] A. Salahi, C. Honrado, A. Rane, F. Caselli, and N. S. Swami, "Modified Red Blood Cells as Multimodal Standards for Benchmarking Single-Cell Cytometry and Separation Based on Electrical Physiology," *Anal. Chem.*, vol. 94, no. 6, pp. 2865–2872, Feb. 2022, doi: 10.1021/acs.analchem.1c04739.

[6] K. C. M. Lee, J. Guck, K. Goda, and K. K. Tsia, "Toward deep

biophysical cytometry: prospects and challenges," *Trends Biotechnol.*, 2021, doi: 10.1016/j.tibtech.2021.03.006.

[7] C. Honrado, P. Bisegna, N. S. Swami, and F. Caselli, "Single-cell microfluidic impedance cytometry: from raw signals to cell phenotypes using data analytics," *Lab Chip*, vol. 21, no. 1, pp. 22–54, 2021, doi: 10.1039/D0LC00840K.

[8] F. Caselli, M. Shaker, L. Colella, P. Renaud, and P. Bisegna, "Modeling, Simulation and Performance Evaluation of a Novel Microfluidic Impedance Cytometer for Morphology-Based Cell Discrimination," *J. Microelectromech. Syst.*, vol. 23, no. 4, pp. 785–794, 2014, doi: 10.1109/JMEMS.2014.2325979.

[9] R. Reale, A. De Ninno, T. Nepi, P. Bisegna, and F. Caselli, "Extensional-Flow Impedance Cytometer for Contactless and Optics-Free Erythrocyte Deformability Analysis," *IEEE Trans. Biomed. Eng.*, pp. 1–9, 2022, doi: 10.1109/TBME.2022.3197214.

[10] A. De Ninno *et al.*, "High-throughput label-free characterization of viable, necrotic and apoptotic human lymphoma cells in a coplanar-electrode microfluidic impedance chip," *Biosens. Bioelectron.*, vol. 150, p. 111887, 2020, doi: 10.1016/j.bios.2019.111887.

[11] C. Honrado, A. Salahi, S. J. Adair, J. H. Moore, T. W. Bauer, and N. S. Swami, "Automated biophysical classification of apoptotic pancreatic cancer cell subpopulations by using machine learning approaches with impedance cytometry," *Lab Chip*, p., 2022, doi: 10.1039/D2LC00304J.

[12] A. Salahi *et al.*, "Single-cell assessment of the modulation of macrophage activation by ex vivo intervertebral discs using impedance cytometry," *Biosens. Bioelectron.*, vol. 210, p. 114346, 2022, doi: https://doi.org/10.1016/j.bios.2022.114346.

[13] B. de Wagenaar *et al.*, "Towards microfluidic sperm refinement: impedance-based analysis and sorting of sperm cells," *Lab Chip*, vol. 16, no. 8, pp. 1514–1522, 2016, doi: 10.1039/C6LC00256K.

[14] Y. Ai and P. Li, "Label-free multivariate biophysical phenotyping-activated acoustic sorting at the single-cell level," *Anal. Chem.*, vol. 93, no. 8, 2021, doi: 10.1021/acs.analchem.0c05352.

[15] C. H. Chen, S. H. Cho, F. Tsai, A. Erten, and Y. H. Lo, "Microfluidic cell sorter with integrated piezoelectric actuator," *Biomed. Microdevices*, vol. 11, no. 6, 2009, doi: 10.1007/s10544-009-9341-5.

[16] Z. Cheng, X. Wu, J. Cheng, and P. Liu, "Microfluidic fluorescence-activated cell sorting (μFACS) chip with integrated piezoelectric actuators for low-cost mammalian cell enrichment," *Microfluid. Nanofluidics*, vol. 21, no. 1, 2017, doi: 10.1007/s10404-017-1847-1.

[17] V. Errico, A. De Ninno, F. R. Bertani, L. Businaro, P. Bisegna, and F. Caselli, "Mitigating positional dependence in coplanar electrode Coulter-type microfluidic devices," *Sens. Actuator B-Chem.*, vol. 247, pp. 580–586, 2017, doi: 10.1016/j.snb.2017.03.035.

[18] F. Caselli, A. De Ninno, R. Reale, L. Businaro, and P. Bisegna, "A Bayesian Approach for Coincidence Resolution in Microfluidic Impedance Cytometry," *IEEE Trans Biomed Eng*, vol. 68, no. 1, pp. 340–349, 2020, doi: 10.1109/TBME.2020.2995364.

[19] F. Caselli and P. Bisegna, "Simulation and performance analysis of a novel high-accuracy sheathless microfluidic impedance cytometer with coplanar electrode layout," *Med. Eng. Phys.*, vol. 48, pp. 81–89, 2017, doi: 10.1016/j.medengphy.2017.04.005.

[20] J. F. Richardson, J. H. Harker, and J. R. Backhurst, *Chemical Engineering: Particle Technology and Separation Processes: Fifth Edition*, vol. 2. 2013.

[21] M. Spiga and G. L. Morini, "A symmetric solution for velocity profile in laminar flow through rectangular ducts," *Int Commun Heat Mass*, vol. 21, no. 4, pp. 469–475, 1994, doi: 10.1016/0735-1933(94)90046-9.

[22] F. Caselli, R. Reale, A. De Ninno, D. Spencer, H. Morgan, and P. Bisegna, "Deciphering impedance cytometry signals with neural networks," *Lab Chip*, vol. 22, no. 9, 2022, doi: 10.1039/d2lc00028h.

[23] M. D'Orazio *et al.*, "Electro-optical classification of pollen grains via microfluidics and machine learning," *IEEE Trans. Biomed. Eng.*, vol. 69, no. 2, pp. 921–931, Feb. 2021, doi: 10.1109/TBME.2021.3109384.

Magnetoelectric nanoparticles as promising tools for motor nerve stimulation

V. Galletta[1,2], E. Chiaramello[2], S. Fiocchi[2], A. Marrella[2], G. Suarato[2], M. Bonato[2], M. Parazzini[2], and P. Ravazzani[2]

[1] *Politecnico di Milano, 20133, Milan, Italy*

[2] *CNR, Istituto di Elettronica e di Ingegneria dell'Informazione e delle Telecomunicazioni IEIIT, 20133, Milan, Italy*

***Abstract*—This study focuses on the assessment of the feasibility of using magnetoelectric nanoparticles for the stimulation of peripheral nerves. The analysis was performed by computational techniques, paring electromagnetic simulation and neuronal dynamic simulation. Results suggest the feasibility of the proposed technique, highlighting the high spatial resolution achievable by such nanomaterials.**

***Keywords*—Magnetoelectric nanoparticles, electrical nerve stimulation, numerical techniques.**

I. Introduction

Motor nerve stimulation is the application of safe levels of electric current for medical purpose. The electrical stimulation elicits muscle contraction using electric pulses over the peripheral sensory-motor system, contributing to recovery functions, strengthening atrophied muscles and relieve pain [1]–[3]. In the last decades, a fast evolution in motor nerve stimulation has been possible thanks to the increasing interest in new stimulation techniques. This technology had a rapid development in prosthetic technologies to achieve sensory feedback control with desirable high spatial and temporal resolution. Particularly, the technological rapid expansion is leading to less invasive but with higher selectivity stimulating approaches. Stimulating electrodes could be surface, percutaneous or implantable (cuff or epimysial ones) [2], [3].

Recently, magnetoelectric (ME) materials could represent an innovative tool to penetrate this field, overcoming actual stimulation approaches drawbacks. Among different ME devices, ME nanoparticles (MENPs) are particularly promising. They comprise a ferromagnetic core and a piezoelectric shell. When subjected to variation of the applied magnetic field ΔH, at the interface between the two ferroic phases there is the transmission of magnetostrictive stresses generated in the magnetic phase to the piezoelectric one, which in turn changes polarization ΔP and associated electric field ΔE [4]. This behavior is quantified by magnetoelectric coefficient $\alpha = \Delta P / \Delta H$ [5]. The progress in nanoengineering of ME materials opened the path to the development of less invasive devices without any wire connections, enabling cells to react at micro and nano scales. So far, few studies have explored the possibility of using the ME nanoparticles to such purposes, however there are some experimental and theoretical evidence that underly its efficacy for nervous system stimulation [6]–[11].

For example, some studies evidence the activation of neural pathways following the brain stimulation thought the ME effect [6], [12]. A low-intensity field generates AC signals at the same frequency as the activity of a healthy nerve charge, and the vibration of a ME nanoparticle leads to the activation of neurons around it with the same frequency, that is, to their stimulation non-invasively. In this scenario, computational approaches offer a unique tool for the evaluation of electric quantities within human tissues and allow to deep investigate physical phenomena behind the stimulation effect, thus representing an essential method for the advancement towards clinical application [13] .

In this work, we aim to prove the feasibility of using MENPs as tools for electric stimulation of peripheral nerves throughout computational approaches. We report the simulation settings of our computational approach, and we discuss the presented results.

II. Material and Methods

The methodology used to assess the feasibility of using MENPs for the stimulation of peripheral nerves consists of two simulation approaches. The first one involves the estimation of the electric field (**E**) distributions elicited by the MENPs localized in biological tissue, while the second one consists of the assessment, by dynamic model of nerve behaviour, of the electric response of a peripheral nerve model localized near the MENPs to such distribution. All the simulation steps have been implemented using Sim4life platform (by ZMT Zurich Med Tech AG, Zurich, Switzerland, www.zurichmedtech.com) as reported in the followings.

A. MENPs Model and electromagnetic stimulation settings

Due to their core and shell chemical compositions, MENPs are characterized by strong coupling between magnetic and electric fields, the so-called magneto-electric (ME) effect. The electric potential on each MENP surface was found to exhibit a dipole distribution aligned along the direction of the low-amplitude magnetic field used for stimulating the ME effect. A wide range of dimension of the MENPs is reporting in literature, with size varying between 30 and 600 nm [5], [6], [9], [14], depending on the synthetization method used. The potential generated by the MENP, and so its magnetoelectric coefficient, is influenced by both the MENP dimension, the material composition and on the frequency of the magnetic fields used to elicit the magneto-electric effect [5], [15].

In this study, we hypothesized that the MENPs could be approximated by dipoles with dimension equal to 80 nm. The geometric structure of the MENP is shown in Fig. 1 and consists of two conductive surfaces separated by an insulating layer, with the dielectric properties of the techotane material. A potential of +/- 0.5 V has been assigned over the two surfaces by using Dirichlet boundary conditions, with a total

charge of 1 V, as for typical implanted electrodes [16]. The biological material surrounding the MENP was fat. The dielectric properties of all the materials were assigned according to literature data [17] at the MENP stimulating frequency.

Focusing on the stimulus shape delivered by the MENP, a sinusoidal pulse of amplitude equal to 1 V has been chosen, at the frequency of 100 Hz which is in the frequency range for neural stimulation, as reported in literature [18].

The electrostatic approximation was used to solve Maxwell equations to estimate the electric field distribution, which is the input of the following neural simulation. Dirichlet boundary conditions in which V = 0 defined the potential on the borders of the computational domain.

MENPs were placed at different distances from the line representing the nerve, equal to 5 um, 10 um, 20 um and 30 um.

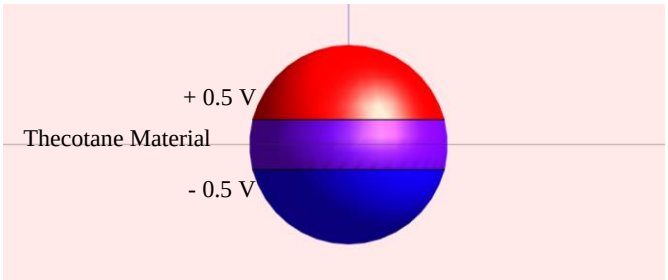


Fig. 1: MENP model in Sim4Life

B. Nerve Model

A neuronal fiber of 1000 um length and diameter equal to 5.7 um has been defined as simplified model of the peripheral nerve within NEURON environment implemented in Sim4Life.

In Sim4Life, NEURON is available as a solver library developed to simulate the effect of electromagnetic fields on neuronal dynamics and for studying interaction mechanisms. Moreover, the platform offers the possibility to directly couple the results of EM simulations with the neuronal dynamics solver. [19]. NEURON provides a powerful and flexible environment for implementing biologically realistic models of electrical and chemical signalling in neurons and networks of neurons. It has two main aims: testing the hypothesis about the mechanisms that governs electrical and chemical signals (to calculate the ionic concentrations) and efficiently simulating the mechanisms, so how nervous system functions develop from these mechanisms (by the computation of the extracellular potential next to the nerve membrane). [20]

In NEURON it is possible to define the time-response of a neuronal membrane, so basically there are different models of transmembrane dynamics. Among all, the one chosen for the simulation has been the MOTOR MRG model, thanks to its great physiological accuracy which designs it as the most realistic to represent human axons [21].

The MOTOR model allows to gain insights into the biophysical mechanisms of the fluctuation of the axonal excitability, by modelling the recovery cycle of the axon.

MOTOR models are computer-based double cable models of mammalian nerve fibers with an explicit representation of the nodes of Ranvier, paranodal, and internodal sections of the axon, and a finite impedance myelin sheath. Linear and nonlinear membrane dynamics represent the electrical behavior of the axon. Parameters associated with the kinetics of the channels were selected to enable the models to reproduce a wide range of experimental data. In the model, the nodes consist of parallel combination of nonlinear fast Na, persistent Na, slow K conductances, linear leakage conductance and membrane capacitance. Whereas the paranodal and internodal compartments comprise two layers, each including a linear conductance in parallel with the membrane capacitance. [22]

The titration mechanism implemented in the software was used to estimate the minimum pulse amplitude able to elicit and action potential. Titration consists of stimulating the axon with a series of increasing amplitude stimuli, to identify the threshold above which an action potential is generated. The equation used to find the final threshold current is: $IT(t) = I * T * a(t)$, where I is the current from the EM field, a(t) is the modulating pulse and T is the titration factor, which is varied until a response is detected [16].

The time pulse used to stimulate the nerve was simulated as a sinusoid with amplitude equal to the one obtained by the electromagnetic simulation, frequency equal to 100 Hz, and duration and time step equal to 200 ms and 0.0025 ms, respectively.

III. RESULTS

The analysis of results will be presented by considering separately the resulting electric field distribution on the nerve, the titration factor as estimation of the amplitude of the stimulus needed to elicit the action potential, and the neuron response for the different considered distances between the MENP and the nerve fiber.

The distribution of the **E** field has been studied everywhere around the MENP. We focused on a slice view over the YZ plane, which comprises the nerve along its full length. Between all the possible YZ planes, we chose to study the overall field distribution on the plane which holds the maximum RMS of **E** amplitude (V/m), as reported in Fig 2, for the case of 5 um distance. The colormap in Fig. 2 ranges between 0 and 10 V/m.

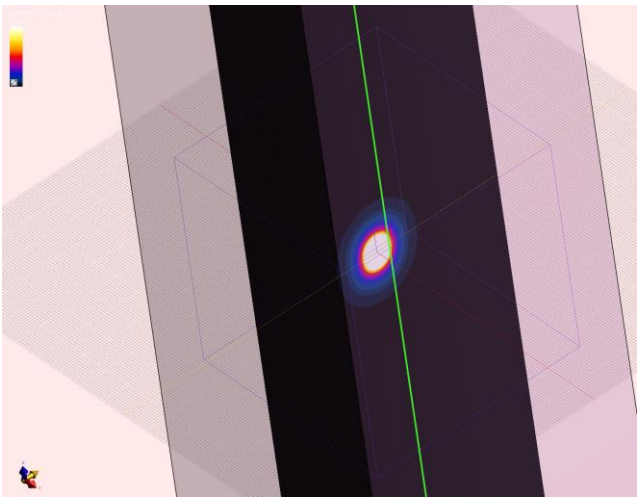


Fig. 2: View of the RMS of E amplitude. Visualization on the YZ plane, particularly the plan with maximum RMS E amplitude. The green line corresponds to the position of the neuron, and it's the line along with the E field is analysed. The MENP is placed at the centre of the white oval. This is the case with 5 um of MENP – neuron distance.

In Fig. 3, the overall field of the RMS of **E** along the neuron length is reported for all the MENP – neuron distances. In all the four different simulations, a similar bell shape of the distribution over the neuron length has been shown. What changed was the width of the bell and its maximum amplitude. In fact, it was noticed that increasing the MENP – neuron distance, the bell shape was wider. Conversely, by increasing the MENP – neuron distance, the maximum amplitude of the E field substantially decreased. The bell width was quantified at the 10% of the bell's maximum amplitude. The maximum values of the bell shape distributions were 10.35 V/m, 1.18 V/m, 0.14 V/m and 0.056 V/m and the bell width were 22 um, 52 um, 82 um and 104 um for the distances 5 um, 10 um, 20 um and 30 um, respectively.

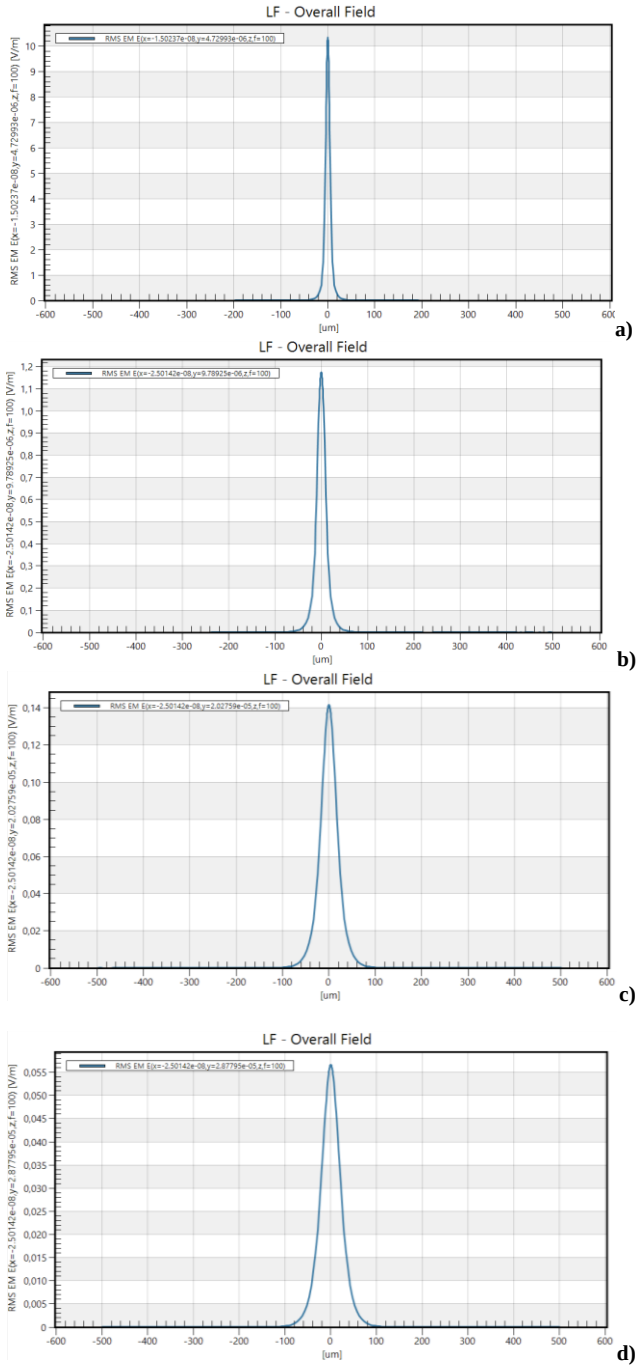


Fig. 3: Overall field of the RMS of E analysed along the neuron, for the different of MENP – neuron distances: a) 5 um, b) 10 um, c) 20 um and d) 30 um. For the sake of readability, we kept different scales in the plots.

TABLE I: TITRATION FACTOR

Distance [um]	*Time of first spike [ms]*	*Titration factor*
5	4.685	936
10	4.9275	3744
20	4.855	6240
30	4.2375	6784

The titration factor was set to define the stimulus amplitude of the MENP that causes the response of the neuron.

In Table I, the time of the first spike in ms and the relative titration factor are reported, differentiated by the corresponding MENP – neuron distance. As well expected, increasing the distance, the titration factor increases, so a bigger stimulus amplitude is necessary to stimulate the neuron.

The response of the neuron in terms of transmembrane potential, has the characteristic shape of an action potential, as shown in Fig. 4 for the distance of 5 um. When considering different distances between MENP and the nerve, negligible in the shape of the action potential were observed.

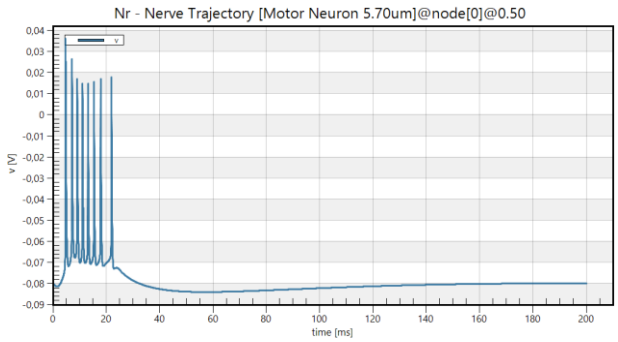


Fig. 4: Nerve response, in terms of transmembrane potential (V) during the stimulation, in the case of 5 um of MENP – neuron distance.

IV. Discussion and Conclusion

In summary, the computational approaches have proven the feasibility of using MENPs as tools for electric stimulation of peripheral nerves and have demonstrated how the MENP – axon distance influences over the EM field distribution and the axon response. In fact, the results showed that the distance between the MENP and the axon impacts the amplitude of the peak of the EM field distribution but not the shape of the distribution itself. Moreover, the overall field analysed along the neuron has shown how a punctual stimulation is feasible with MENP, allowing a very high spatial resolution. Particularly, increasing the MENP – neuron distance, the bell width of the RMS of E at the 10% of the maximum amplitude increases as well. So, the spatial resolution decreases by increasing the distance. We have confirmed the MENP capability to induce an action potential to the nerve and we have characterized the response of the nerve itself, considering the different distances. Finally, the titration factor gives information about the amplitude needed for the stimulus of the MENP. As expected, results confirmed how the titration factor increases by increasing the MENP – axon distance. The values are such to suggest that a single MENP is not able to stimulate the nerve itself, but previous experimental evidences and computational studies [10] in which MENPs have been

modelled as agglomerates [10], [11] have shown the plausibility of MENPs stimulation. Future work is needed to address the summation effects of MENPs distributions.

In conclusion, MENPs are a powerful tool for the stimulation of peripheral nerve, but a lot is still to be understood about their functioning.

ACKNOWLEDGEMENT

The authors wish to thank ZMT Zurich MedTech AG (www.zmt.swiss) for providing SIM4Life software.

This work was supported by the "Piano Nazionale per gli investimenti complementari al PNRR" under the project Fit4MedRob - Fit for Medical Robotics.

REFERENCES

[1] K. Chakravarthy, A. Nava, P. J. Christo, e K. Williams, «Review of Recent Advances in Peripheral Nerve Stimulation (PNS)», *Curr. Pain Headache Rep.*, vol. 20, fasc. 11, p. 60, nov. 2016, doi: 10.1007/s11916-016-0590-8.

[2] Y. Cho, J. Park, C. Lee, e S. Lee, «Recent progress on peripheral neural interface technology towards bioelectronic medicine», *Bioelectron. Med.*, vol. 6, fasc. 1, p. 23, dic. 2020, doi: 10.1186/s42234-020-00059-z.

[3] C. Russell, A. D. Roche, e S. Chakrabarty, «Peripheral nerve bionic interface: a review of electrodes», *Int. J. Intell. Robot. Appl.*, vol. 3, fasc. 1, pp. 11–18, mar. 2019, doi: 10.1007/s41315-019-00086-3.

[4] M. Fiebig, «Revival of the magnetoelectric effect», *J. Phys. Appl. Phys.*, vol. 38, fasc. 8, pp. R123–R152, apr. 2005, doi: 10.1088/0022-3727/38/8/R01.

[5] A. Kargol, L. Malkinski, e G. Caruntu, «Biomedical Applications of Multiferroic Nanoparticles», in *Advanced Magnetic Materials*, L. Malkinski, A c. di InTech, 2012. doi: 10.5772/39100.

[6] K. L. Kozielski *et al.*, «Nonresonant powering of injectable nanoelectrodes enables wireless deep brain stimulation in freely moving mice», *Sci. Adv.*, vol. 7, fasc. 3, p. eabc4189, gen. 2021, doi: 10.1126/sciadv.abc4189.

[7] T. Nguyen *et al.*, «In Vivo Wireless Brain Stimulation via Non-invasive and Targeted Delivery of Magnetoelectric Nanoparticles», *Neurotherapeutics*, vol. 18, fasc. 3, pp. 2091–2106, lug. 2021, doi: 10.1007/s13311-021-01071-0.

[8] R. Guduru *et al.*, «Magnetoelectric 'spin' on stimulating the brain», *Nanomed.*, vol. 10, fasc. 13, pp. 2051–2061, lug. 2015, doi: 10.2217/nnm.15.52.

[9] S. Fiocchi *et al.*, «Modeling of core-shell magneto-electric nanoparticles for biomedical applications: Effect of composition, dimension, and magnetic field features on magnetoelectric response», *PLOS ONE*, vol. 17, fasc. 9, p. e0274676, set. 2022, doi: 10.1371/journal.pone.0274676.

[10] S. Fiocchi, E. Chiaramello, A. Marrella, M. Bonato, M. Parazzini, e P. Ravazzani, «Modelling of magnetoelectric nanoparticles for non-invasive brain stimulation: a computational study», *J. Neural Eng.*, vol. 19, fasc. 5, p. 056020, set. 2022, doi: 10.1088/1741-2552/ac9085.

[11] E. Chiaramello *et al.*, «Magnetoelectric Nanoparticles: Evaluating Stimulation Feasibility of the Possible Next Generation Approach for Deep Brain Stimulation», *IEEE Access*, vol. 10, pp. 124884–124893, 2022, doi: 10.1109/ACCESS.2022.3225098.

[12] S. Kopyl, R. Surmenev, M. Surmeneva, Y. Fetisov, e A. Kholkin, «Magnetoelectric effect: principles and applications in biology and medicine– a review», *Mater. Today Bio*, vol. 12, p. 100149, set. 2021, doi: 10.1016/j.mtbio.2021.100149.

[13] S. Romeni, G. Valle, A. Mazzoni, e S. Micera, «Tutorial: a computational framework for the design and optimization of peripheral neural interfaces», *Nat. Protoc.*, vol. 15, fasc. 10, pp. 3129–3153, ott. 2020, doi: 10.1038/s41596-020-0377-6.

[14] S. Betal *et al.*, «Magneto-elasto-electroporation (MEEP): In-vitro visualization and numerical characteristics», *Sci. Rep.*, vol. 6, fasc. 1, p. 32019, ago. 2016, doi: 10.1038/srep32019.

[15] S. Kopyl, R. Surmenev, M. Surmeneva, Y. Fetisov, e A. Kholkin, «Magnetoelectric effect: principles and applications in biology and medicine– a review», *Mater. Today Bio*, vol. 12, p. 100149, set. 2021, doi: 10.1016/j.mtbio.2021.100149.

[16] A. M. Samoudi *et al.*, «Numerical modeling of percutaneous auricular vagus nerve stimulation: a realistic 3D model to evaluate sensitivity of neural activation to electrode position», *Med. Biol. Eng. Comput.*, vol. 55, fasc. 10, pp. 1763–1772, ott. 2017, doi: 10.1007/s11517-017-1629-7.

[17] «IT'IS Foundation, 2018. Tissue Properties Database V4.0. https://doi.org/10.13099/VIP21000-04-»,

[18] M. Pardo e S. Khizroev, «Where do we stand now regarding treatment of psychiatric and neurodegenerative disorders? Considerations in using magnetoelectric nanoparticles as an innovative approach», *WIREs Nanomedicine Nanobiotechnology*, vol. 14, fasc. 3, mag. 2022, doi: 10.1002/wnan.1781.

[19] «Sim4Lif Manual», in *2.12 Neuronal Dynamics Solver*,

[20] M. L. Hines e N. T. Carnevale, «The NEURON Simulation Environment», *Neural Comput.*, vol. 9, fasc. 6, pp. 1179–1209, ago. 1997, doi: 10.1162/neco.1997.9.6.1179.

[21] A. G. Richardson, C. C. McIntyre, e W. M. Grill, «Modelling the effects of electric fields on nerve fibres: Influence of the myelin sheath», *Med. Biol. Eng. Comput.*, vol. 38, fasc. 4, pp. 438–446, lug. 2000, doi: 10.1007/BF02345014.

[22] C. C. McIntyre, A. G. Richardson, e W. M. Grill, «Modeling the Excitability of Mammalian Nerve Fibers: Influence of Afterpotentials on the Recovery Cycle», *J. Neurophysiol.*, vol. 87, fasc. 2, pp. 995–1006, feb. 2002, doi: 10.1152/jn.00353.2001.

Integrated sensors for real-time monitoring of biological barriers in engineered cell culture dynamic *in vitro* models

S. Perottoni[1], A. Bonacina[1], R. Dell'Oro[1], F. Donnaloja[1], L. Boeri[1], L. Magagnin[1], D. Albani[2], C. Giordano[1]

1. *Department of Chemistry, Materials and Chemical Engineering "Giulio Natta", Politecnico di Milano, Milan, Italy*
2. *Istituto di Ricerche Farmacologiche Mario Negri IRCCS, Department of Neuroscience, Milan, Italy*

***Abstract* — Biological barriers in our body, like the intestinal epithelium or the blood-brain-barrier, are devoted to the selective transport of molecules across different organs. There is growing evidence that altered permeability of such barriers play a pathogenic role in disease.**

Transwell®-like inserts based tools are the gold standard for culturing and modelling the biological barriers *in vitro*. They allow reproducing the transport mechanisms of specific molecules across semi-permeable supports in bi-compartmental wells but do not allow a dynamic culture of the cells. Trans Endothelial/epithelial Electrical Resistance (TEER) measurement is a label-free assay that is conventionally used to asses barrier integrity by measuring ionic current exchanges across the cellular layer. Conventional TEER electrodes are dependent on operator handling and usually do not allow continuous real-time monitoring. In the present work, we have developed and tested an Integrated TEER Electrode (ITE) inside an innovative millifluidic device for dynamic culture of Transwell®-like inserts based biological barrier models, able to perform suitable TEER measurements and guarantee real-time monitoring of barrier functions over time.

***Keywords*— TEER, biosensor, bioreactor, biological barriers, in vitro.**

I. INTRODUCTION

BIOLOGICAL barriers serve the natural protective function inside the body. From skin, to intestinal barrier, to blood brain barrier, they are involved in controlling the passage of exogenous molecules, cells and microorganisms as well as the absorption of important solutes for the homeostasis of specific organs [1].

The impairment of their function due to microbial action or inflammatory process is demonstrating to be involved in the onset of pathological conditions [2]. Therefore, studying the biological barriers is important to understand their physiopathology and to assess molecules toxicities and drug efficacy. Conventional *in vitro* models consist in bi-compartmental wells, such as Transwell®-like inserts based systems, that generate an apical and a basal chamber separated by a semi-permeable membrane that can host cells and form a biological barrier [3]. In particular, epithelial and endothelial cells, that form the barrier cellular monolayers, express adhesion protein forming Tight Junctions (TJs) that contribute to the overall barrier permeability [4].

Trans-Endothelial/epithelial Electrical Resistance (TEER) measurement is one of the widely used assays to characterize barrier integrity depending on the physiological status of the TJs. TEER measurement returns indirect information on TJs expression and barrier tightness by measuring the resistance of cells to the flow of ionic currents through the cell monolayer. The most widely used TEER measuring systems exploit chopstick electrodes in the four-points measurement configuration to avoid charging of the cell layer and the electrodes [5] (**Fig. 1**). This consists in a couple of current injecting electrodes and a couple of voltage measuring electrodes. The recorded resistance include the contribution of the cellular layer, the porous membrane, the culture medium and the medium/electrode interface [6].

Recently, advanced cell culture tools have been developed to improve the reliability of barriers in *in vitro* models against pathophysiological conditions in the human body. Indeed, flow perfusion and 3D environment demonstrated to dictate barrier morphology and transport properties. Examples are miniaturised bioreactors based on the use of semi-permeable porous membranes or cell culture inserts [7], and the so-called micro-physiological systems exploiting microfluidics and microfabrication [8]. In all these cases, measuring TEER inside the device in non-invasive, reproducible and reliable manner is a strong requirement when modelling biological barriers.

The existing advanced cell culture fluid dynamic systems are based on the use of commercial permeable supports, with limited possibility of monitoring TEER without the need of interrupting the experiment or accessing the system from the outside [9] [10]. On the other hand, minimally invasive electrodes are often difficult to integrate inside bioreactors while maintaining easy assembling procedures and handling [6]. Moreover, popular micro-fluidic organ-on-a-chip devices have small volumes to host planar and uniform electrodes and require complex clean-room procedures to be suitably manufactured [11].

To overcome these limitations, we coupled conventional technology for patterning thin conductive films, to on-bench low-cost 3D printing. We propose the integration of planar electrodes within an innovative 3D printed millifluidic bioreactor, named MINERVA 2.0, which can host Transwell®-like inserts for advanced *in vitro* modelling of biological barriers [12].

We applied Physical Vapor Deposition (PVD), which is generally used to sputter films on flat substrates, to the complex 3D geometry of the bioreactor by exploiting 3D printed masks to generate conductive lanes on the walls of the device. In this way, electrodes do not interfere with flow direction or cell culture procedures, and allow the electric signal to travel outside the device without the need of inserting wires across the bioreactor.

Our integrated TEER electrodes (ITEs)-device represents a useful tool to detect barriers functionality, possibly altered by drug toxicity and absorption process. In this work, we present the design and the fabrication strategy of our innovative ITE-MINERVA 2.0 device and its assessment in recording real-time TEER on a cell-based gut epithelium barrier *in vitro* model.

II. Materials and Methods

ITEs design and manufacturing

3D models of the electrodes were designed in Solidworks (Dassault Systèmes SolidWorks Corporation, Waltham, MA, USA) in order to be hosted on both sides of our MINERVA 2.0 device, that consists of two 3D-printed components fitting a commercially available Transwell®-like insert, creating two hemi-chambers (apical and basal) interfaced through the Transwell®-like insert membrane. Silicon tubings connected to the system allow for flow perfusion. A transparent glass slide is hosted on the basal chamber to allow cell culture monitoring by optical or confocal microscopy.

The conductive films were sputtered both on the glass coverslip (basal component), and the apical component of the bioreactor. The sputtering process was performed by PVD (Leybold-Heraeus LH Z400). 50 nm thick Au electrodes with 100 nm Ti as adhesion layer were sputtered on both sides of a glass coverslip while 100 nm thick Au electrodes were sputtered directly on the apical component of the ITE-device.

Numerical analysis

The electrodes were designed in Solidworks and then imported into COMSOL Multiphysics (COMSOL Inc., Burlington, MA, USA). Finally, a discrete triangle elements mesh was built by exploiting the 'physics controlled' method with an average side dimension of 0,2 mm in the region of interest. The "electric current" physics was used to simulate electrical current distribution through the system. The sensitivity was then calculated at each point of the cellular layer as in Eq. (1),

$$S = \frac{J_1 \cdot J_2}{I^2} \cdot A^2 \quad (1)$$

where I is the magnitude of the applied current, J_1 and J_2 are the current densities across the cellular layer for the two pairs of electrodes, A is the area of the cellular layer. Boundary conditions included i) a ground domain at one of the 'current' electrodes; ii) 10 μA current injection at the other 'current' electrode; iii) and zero electric potential [V] as initial condition.

TEER measurement

All the resistance measurements were performed by using EVOM3 (WPI). To perform the measurements in Transwell®-like tissue culture inserts, we used the STX2 chopstick electrode set (WPI). Measurements with the ITEs were performed by connecting the sensorized bioreactor with EVOM3 by mean of an electrode adapter.

ITEs functional characterization

To confirm that the system was able to discriminate between different resistances, we assembled three different sensorized devices, each one hosting a Transwell®-like insert (Greiner Bio-One ThinCert™ tissue culture insert) with porosity 0.0025, using Dulbecco's Modified Eagle's Medium (DMEM) with 20% Fetal Bovine Serum (FBS) at room temperature, and we made nine measurements for each device. Then we disassembled the three devices and we made the same process with the culture inserts with porosity 0.015 and 0.125. As control, we performed the measurements on the same membranes by using conventional STX2 electrodes (WPI).

CaCo2 cell culture

CaCo2 gut epithelial cells (ATCC) were cultured until reaching the confluence at P31. CaCo2 were then seeded at a cell density of 50.000 cells/cm^2 on the Transwell®-like insert (Greiner Bio-One ThinCert™), and incubated at 37 °C with 5% CO_2.

ITEs biological assessment

CaCo2 were seeded on the cell culture inserts, assembled into the sensorized devices after being maintained in multiwell plate for 2 weeks. After 90 min, a 5 mM EDTA solution was injected inside the devices that were kept at 37 °C and 5% CO_2. TEER values were recorded every 30 min.

Statistical analysis

Results are presented as mean ± SD. Statistical test one-way ANOVA (GraphPad Prism 8) was used to assess the significance of the results (p value < 0.05).

III. Results

ITEs design and manufacturing

We have designed integrated electrodes to be hosted on both chambers of our MINERVA 2.0 millifluidic bioreactor (**Fig. 2**). The ITE-MINERVA 2.0 device is composed of "plug and play" components that fit the conventional Transwell®-like inserts generating a bi-compartimental bioreactor consisting in an apical chamber hosting the cellular barrier model, and an optically accessible basal chamber. In order to perform four points TEER measurement, we designed the ITEs so that each chamber can host a couple of electrodes (one for current injection and one for voltage measurement).

The design of the electrodes was chosen according to the results of the numerical simulations (**Fig. 3**).

Both the qualitative diagrams of the sensitivity and the numerical parameter highlighted the low uniformity of the

current density using the conventional STX2, while the symmetrical-ITEs (and the concentric-ITEs, not reported in the figure) have shown much more homogeneity and sensitivity next to the ideal value 1.

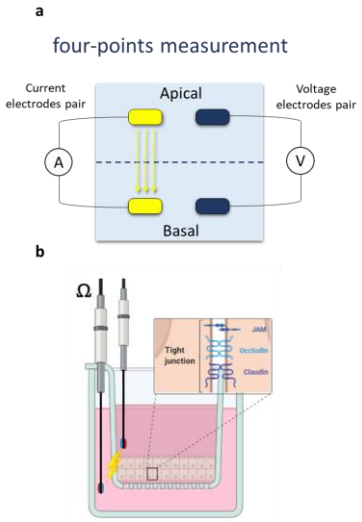


Fig. 1: Schematic representation of conventional approaches for TEER measurement. **a)** four-points TEER measurement **b)** conventional chopstick TEER electrodes.

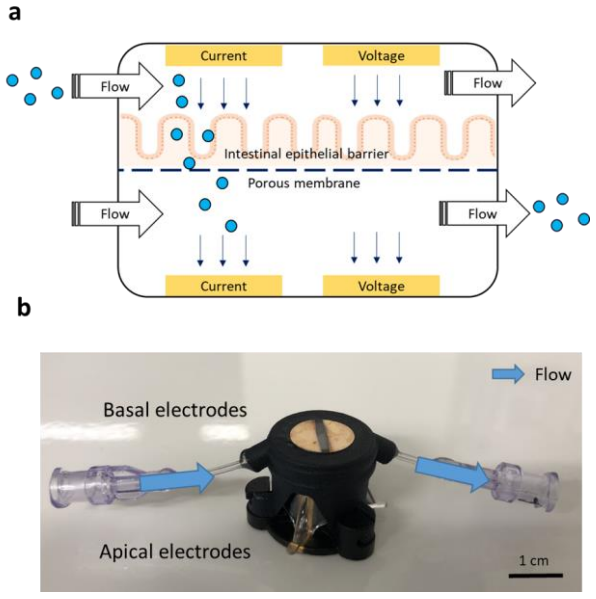


Fig. 2: ITE-MINERVA 2.0 device set-up. **a)** Schematic representation of the bi-compartmental flow chamber of the bioreactor hosting the electrodes in the four-points measurements configuration. **b)** The sensorized device.

ITEs discriminate membrane permeability with higher reproducibility than conventional electrodes.

We assessed the capability of ITEs to measure the resistance of the Transwell®-like insert membranes. The average value recorded by three devices was 25,6 ohm (SD ± 1,47). The values recorded by each device had a SD below 1,97 if compared to those measured by the STX2: 236,7 ohm (SD ± 20,87). The absolute resistance values recorded by our system differ of one order of magnitude if compared to conventional STX2. This might be due to different intrinsic characteristics of the two systems. The ITE-MINERVA 2.0 device was able to continuously detect the same resistance value over a long period proving to be suitable for real-time TEER monitoring. Finally, in order to functionally assess the sensorized bioreactor, we ensured that it was able to discriminate different resistance values of porous membranes with different porosity and permeability.

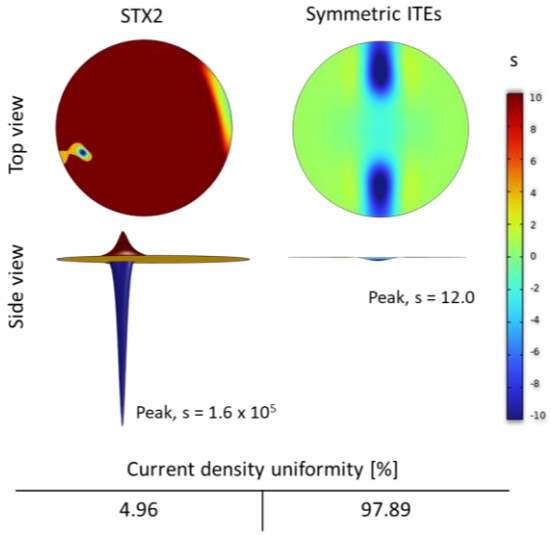


Fig. 3: Numerical simulation of current density uniformity inside the ITE-MINERVA 2.0 device. Colour map of the predicted sensitivity [s] distribution at the level of the cell culture membrane (top view and side view) comparing simulated resistance measurements by conventional STX2 with the ITEs.

ITEs detected real-time changes of CaCo2 barrier permeability

To demonstrate that the ITE-MINERVA 2.0 device is suitable to monitor barrier functionality, we measured changes in CaCo2 layer permeability due to exposure to EDTA, which is known to influence barrier integrity [13]. We recorded TEER every 30 min in each device hosting CaCo2 layers.
We injected EDTA solution (5 mM) inside the fluidic device at time point 100 min. We detected a sudden 35,6% (SD ± 3,6) average decrease of TEER value at time point 130 min.
The signal then stabilized with a slight decrease in the next three time points reaching a final drop of 62.1% (SD ± 1,1) at 210 min with respect to the initial values.
Thanks to the optical accessibility of the device we were able to assess gut epithelium cell response in concomitance with the TEER measurements by optical microscopy observations which revealed a change in cell morphology due to EDTA exposure: CaCo2 appeared rounded and separated if compared to control, where cells still displayed cuboidal shape and formed a tight layer. Future assessment should include immunostaining analysis to assess the expression of membranes protein involved in the tight junctions formation.

IV. Conclusion

In the present work we described the development of integrated electrodes for TEER monitoring inside an innovative millifluidic device for advanced cell culture *in vitro* models [14]. Our ITE-MINERVA 2.0 device showed to be potentially applicable to Transwell®-like inserts based models of biological barriers for advanced toxicity and drug screening experiments. Furthermore, our developed ITEs showed to be suitable to measure TEER in real-time and non-invasively representing a useful tool to be applied to biological barriers investigation, such as blood-brain barrier and gut epithelium.

Acknowledgement

This work was funded by the European Research Council under the European Union's Horizon 2020 research and innovation program (Grant agreement No. 724734-ERC CoG "MINERVA") to C.G. The results reflect only the authors' views and the Agency is not responsible for any use that may be made of the information contained.

References

[1] H. Choudhury, B. Gorain and P. Kesharwani, "Physiology of the biological barriers", *Theory and Application of Nonparenteral Nanomedicines*, pp 79-95, 2021.

[2] B. Hussain, C. Fang and J. Chang, "Blood-Brain Barrier breakdown: an emerging biomarker of cognitive impairment in normal aging and dementia", *Frontiers in Neuroscience*, vol. 15, pp 688090, Aug. 2021.

[3] N. L. Stone, T. J. England and E. O'Sullivan, "A novel transwell blood brain barrier model using primary human cells", *Frontiers in Cellular Neuroscience*, vol. 13, pp 230, Jun. 2019.

[4] K. Felix, S. Tobias, H. Jan, S. Nicolas and M. Michael, "Measurements of transepithelial electrical resistance (TEER) are affected by junctional length in immature epithelial monolayers", Histochemistry and Cell Biology, vol. 156, pp 609-616, Dec. 2021.

[5] B. Srinivasan et al., "TEER measurement techniques for in vitro barrier model systems", *Journal of Laboratory Automation*, vol. 20(2), pp 107-126, Apr. 2015.

[6] L. Cacopardo et al., "Real-time cellular impedance monitoring and imaging of biological barriers in a dual-flow membrane bioreactor" *Biosensors and Bioelectronics*, vol. 140, pp 111340, Sep. 2019.

[7] I. Harding et al., "Developing a transwell millifluidic device for studying blood-brain barrier endothelium", *Lab on a Chip*, vol. 22(23), pp 4603-4620, Nov. 2022.

[8] E. V. Koch, V. Ledwig, S. Bendas, S. Reichl and A. Dietzel, "Tissue barrier-on-chip: a technology for reproducible practice in drug testing", *pharmaceutics*, vol. 14, pp 1407-1451, Jul. 2022.

[9] S. Giusti et al., "A novel dual-flow bioreactor simulates increased fluorescein permeability in epithelial tissue barriers", *Biotechnology Journal*, vol. 9, pp 1175-1184, Sep. 2014.

[10] S. Chang, P. Ko, W. Liao, C. Peng, Y, Tung, "Transwell insert-embedded microfluidic devices for time-lapse monitoring of alveolar epithelium barrier function under various stimulations" *Micromachines*, vol. 12(4), pp 406, Apr. 2021.

[11] O. Y. Henry et al., "Organs-on-chips with integrated electrodes for trans-epithelial electrical resistance (TEER) measurements of human epithelial barrier function" *Lab on a Chip*, vol. 17, pp 2264-2271, May. 2017.

[12] M. Tunesi, L. Izzo, I. Raimondi, D. Albani and C. Giordano, "A miniaturized hydrogel-based in vitro model for dynamic culturing of human cells overexpressing beta-amyloid precursor protein", *Journal of Tissue Engineering*, vol. 11, pp 1-17, Jul. 2020.

[13] A. Fedi et al., "In vitro models replicating the human intestinal epithelium for absorption and metabolism studies: A systematic review", *J Control Release*, vol. 335, pp 247-268, Jul. 2021.

[14] M. Raimondi, D. Albani and C. Giordano, "An organ-on-a-chip engineered platform to study the microbiota–gut–brain axis in neurodegeneration", *Trends in Molecular Medicine*, vol. 25(9), pp 737-740, Sep. 2019.

PEDOT:PSS ink-jet printed microelectrodes on paper: towards low-cost and green MEA devices

F. Terranova[1], A. Spanu[2], S. Martinoia[1] and A. Bonfiglio[2,3]
[1] *University of Genova, Via All'Opera Pia, 13, 16145 Genova, Italy*
[2] *Scuola Universitaria Superiore IUSS, Palazzo del Broletto, Piazza della Vittoria 15, 27100 Pavia, Italy*
[3] *University of Cagliari, Via Marengo, 3, 09123 Cagliari, Italy*

***Abstract*—Microelectrode arrays (MEAs) represent one of the most important technologies for the study of electrogenic cells such as neurons and cardiomyocytes. The current standard commercial devices are expensive tools that researchers reuse extensively, with the downside of degrading the quality of recordings over time. Therefore, a low-cost fabrication process is needed to produce disposable and, possibly, biodegradable MEAs. Here we present a preliminary feasibility study of the fabrication of Poly(3,4-ethylenedioxythiophene):polystyrene sulfonate (PEDOT:PSS) microelectrodes on extremely low-cost, parchment paper, through ink-jet printing. To this aim, alkyd resin (AR) was used to improve the superficial proprieties of pristine cellulose paper. The rheological behaviour of ink formulations and the optimal printing parameters have been investigated, and preliminary tests showed resistivity values below those of current commercial gold MEA, in agreement with previous studies on PEDOT:PSS printed electrodes. Our results suggest that AR-treated cellulose paper could be employed to produce low-cost, flexible, and low-environmental impact devices, thus representing an interesting alternative in the field of cellular electrophysiology.**

***Keywords*—MEA, inkjet, PEDOT:PSS, paper.**

I. Introduction

MICROELECTRODE arrays (MEAs) are typically used to record the activity of electrogenic cells (e.g., neurons and cardiac cells) and their use ranges from the implantation in living organisms for *in vivo* studies, to the coupling with cells and tissues *in vitro*, allowing a large variety of applications, from the study of cell mechanisms to the study of pharmacological toxicity [1].

The structure of these devices consists of a two-dimensional spatial array of metal electrodes, with sizes in the range of 10 to 100 µm, that are fabricated relying on expensive materials (e.g., noble metals for electrodes), on the use of chemical compounds that may be harmful to the environment, and on high maintenance facilities and instrumentation (such as microfabrication setups in clean rooms). *In vitro* MEAs, for example, typically have a (rigid) glass substrate over which is built an integrated array of photoetched microelectrodes, each one insulated from the other, and composed of (or coated with) conductive materials such as indium-tin oxide, palladium, platinum, or gold. Thus, MEA systems represent costly pieces of equipment for a lab and, in the effort of reducing the expense of employing such technology, researchers typically reuse the devices as much as possible, which results in their inevitable wear and in the degradation of the quality of the recordings, especially in biological applications [2]. Nonetheless, this approach can also increase the risk of cross-contamination between samples, when there is no guarantee of full sterilization of the devices after their use. A solution could be to use disposable MEAs, which should be low-cost, and, possibly biodegradable. This approach would have the additional social benefit of making this technology more accessible.

Adopting flexible substrates instead of standard rigid ones is a widely studied option to stabilize contact impedance, which is affected by the mechanical mismatch between the device and cells [3, 4], and in literature many examples of soft electronics devices make use of plastics such as polyimide (PI) [2, 5] and polyethylene naphthalate (PEN) [6-8]. Biodegradable materials, which are attractive for their capacity to dissolve in a controlled manner when in contact with living organisms (e.g., bacteria and fungi) [9], can also be employed for this task: silk fibroin (SF), chitosan, and cellulose (like commercial cellulose fiber paper or the more sophisticated cellulose nanofiber paper [10]), are some examples. Indeed, although paper has already been used as a substrate for printed electronic devices [11], its use in the bioelectronics field is limited. Using a buffer layer on top of paper is usually required to smoothen its surface and, consequentially, render it suitable for the deposition of adequately conductive structures. For example, alkyd resin (AR), which is a biodegradable transparent resin, commonly employed as a binder in paints and coatings, can be used to impregnate cellulose paper to make its surface smoother and increase its optical transmittance [12], which could favour the use of inverted microscopy setups for optical cell analysis.

Biodegradable and biocompatible conductive polymers, such as PEDOT:PSS, which is a mixture of poly(3,4-ethylenedioxythiophene) (PEDOT) and polystyrene sulfonate (PSS), can be patterned on flexible substrates to build high-conductivity microelectrodes via ink-jet printing, a versatile, noncontact, mask-free, and low-cost technology, characterized by a reduced waste of materials and scaling potential benefits [13]. Furthermore, the addition of ethylene glycol (EG) increases the conductivity of PEDOT:PSS layers, by means of electron-phonon decoupling [14], and reduces the occurrence of nozzle clogging, thanks to its high boiling point (197 °C) and to the reduction of solid content in the final solution. Moreover, ink-jet printing allows high-resolution pattering and has shown to be suitable as a fabrication method for MEAs [2].

Here we present a preliminary feasibility study of the fabrication of MEAs on cellulose paper by means of ink-jet printing. We developed and optimized a substrate preparation process, evaluated the effect of ethylene glycol (EG) addition to waterborne PEDOT:PSS dispersions on their rheological

and conductive characteristics, and optimized the ink-jet printing process.

II. Materials and Methods

All printing substrates were obtained from flexible, biodegradable, and compostable sheets of commercial parchment paper, whose thickness was estimated to be around 100 µm. To improve the characteristics of the paper substrates (i.e., wettability, roughness, and optical transmittance), two different methods have been explored: application of a fast-drying, low viscous, long oil AR (Kremer Pigmente); coating of the paper with a layer of Parylene C through chemical vapor deposition (CVD) with a Labcoater 2 SCS PDS 2010 (Specialty Coating Systems).

To increase the surface free energy of the substrates and, therefore, optimize the printing process, two different methods have been explored: oxygen plasma (Colibrì, Gambetti) and UV ozone treatments.

The conductive structures were deposited using a drop-on-demand ink-jet printer (DMP 2850, Fujifilm) under ambient conditions (Fig. 1).

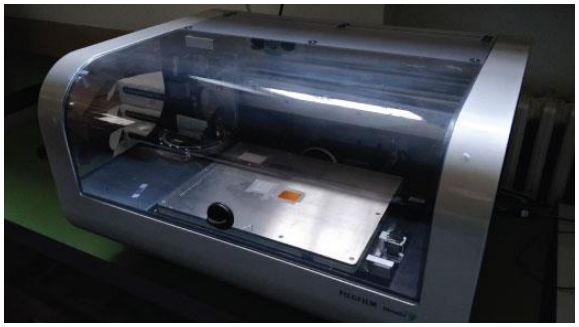


Fig. 1: The DMP 2850 ink-jet printer setup. Samples are loaded onto the printer plate that can be heated up to 60°C.

Starting from a commercial waterborne dispersion of PEDOT:PSS (Heraeus Clevios™ P Jet HC V2), various dilutions with ethylene glycol (EG) have been tested to find a formulation of rheological characteristics compatible with those of the ink-jet printer cartridge (Samba, 2.4 pL drop volume). The solutions were stirred for 30 minutes and filtered (0.20 µm average pore size, Sartorius GmbH) prior to their injection into the cartridge liquid reservoir for printing. The viscosity and shear stress of the inks has been measured using the MCR301 rheometer. The optimal printing parameters (printing height, waveform, drop spacing, and hot plate temperature) have been found after numerous trials and tuning by inspecting the printed test structures with both an upright microscope (Olympus BX-51) equipped with 4x and 10x objectives and the printer camera (for dimensional quantification), and by measuring their resistance with a multimeter.

III. Results

A. *Substrate preparation process*

The cellulose paper substrates where prepared following two different methods: bathing and spin coating. In the first method, the substrates were dipped in an alkyd resin (AR) solution (with varying solid content, by addition of acetone) for 30 minutes and air-dried under a fume hood for two days, resulting in smoother, mechanically resistant, and more transparent samples (Fig. 2). Higher solid content solutions gave thicker and smoother substrates, probably due to their slower drying times. For this reason, the pristine 65% solid content solution has been chosen.

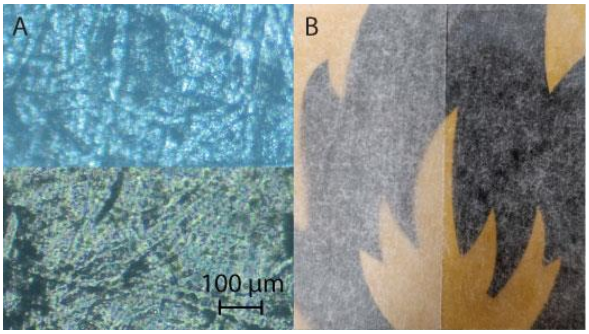


Fig. 2: Pristine vs. AR-treated cellulose paper. A) Optical microscope image of the untreated (top) and AR-treated (bottom) cellulose paper. B) Side-by-side picture of pristine (left) and AR-treated (right) substrates: the application of AR increases the optical transmittance of paper as can be qualitatively assessed by visual inspection.

Instead, the optimal spin coating parameters for 6x6 cm^2 sheets, have been evaluated by optical inspection and are 300 rpm for 60 seconds spinning after the deposition by pipette of 2 mL AR solution. Although this method requires a two-step drying process to coat both sides of the substrates, it gives thinner and more uniform layers in the macroscale.

B. *Rheological study of ink conductive formulations*

The optimal conductive ink formulation has been selected after the rheological characterization of various PEDOT:PSS and EG solutions. The viscosity and shear stress of the inks have been measured up to 2000 1/s shear rate both at 23°C and 50°C, which are the bounds of the range of operation of the printer cartridge. Adding EG to the pristine PEDOT:PSS dispersion, obtaining a 0.33 wt% EG solution (1/3 EG), gives a fluid compatible with the requirement of being in the 4 to 8 mPa·s range of viscosities (Fig. 3).

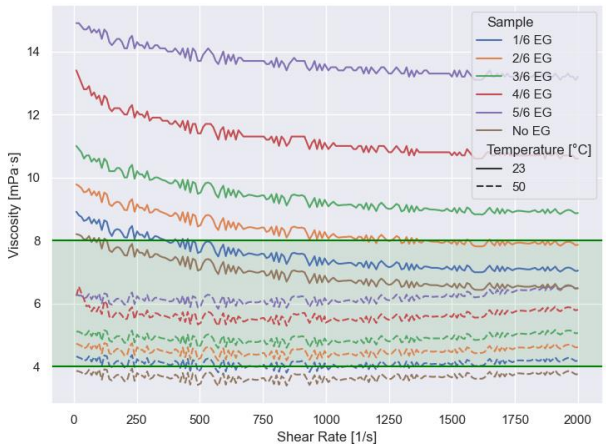


Fig. 3: Rheological behaviour of the pristine PEDOT:PSS dispersion and of different ink formulations, from 1/6 to 5/6 of EG content in weight.

C. *Optimization of the ink-jet printing process*

Being ARs highly hydrophobic, it was necessary to increase the surface free energy of the treated substrates, and, therefore, optimize the printing process. The effect of these methods has been assessed by inspecting the printed patterns with the microscope.

The use of Plasma O_2 on AR substrates at 100 W for 1-minute gives appropriate printing resolutions (around 50 µm) and continuity of structures (Fig. 4).

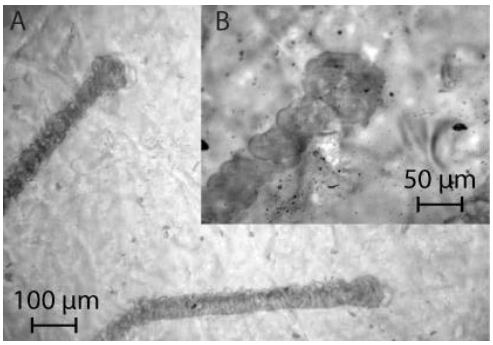


Fig. 4: Optical microscope images of PEDOT:PSS electrodes printed on cellulose paper treated with AR after oxygen plasma activation. A) Two microelectrodes. B) Zoom-in picture of one microelectrode.

A set of printing parameters (drop-spacing, printing height, plate temperature, and waveform) has been selected from previous studies and after numerous tests, by measure of achieved resolution, uniformity of layers, fidelity with the designed geometries, and conductivity of printed structures.

The resistance of printed test structures (20 µm drop-spacing) on paper treated with AR have shown values comparable with those reported in literature for PEDOT:PSS ink-jet printed electrodes, namely an average of 50.45 kΩ (7 printed layers, N = 4) for a 1.6 cm conductor line of 100 µm to 50 µm of width (Fig. 5), which is below the value observed on commercial gold-electrodes MEAs (160 kΩ) [2].

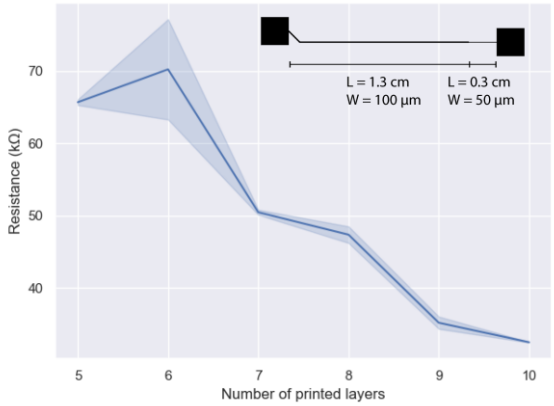


Fig. 5: Measured resistance of PEDOT:PSS lines vs. number of printed layers on AR-treated paper with the 1/3 EG ink. On the upper right the printed design geometry, which mimics the microelectrode dimensional features of MEAs.

IV. Conclusions

In this work we demonstrate the feasibility of fabricating PEDOT:PSS microelectrodes on paper-based substrates, as a starting point for the development of low-cost, disposable, and biodegradable MEAs for electrophysiological applications.

PEDOT:PSS has been selected as the only conductive element for its greater mechanical flexibility and optical transmittance, in comparison with metallic conductors, which are more brittle, and show larger mechanical mismatch with biological matter [4].

Although the effect of AR on the optical and mechanical proprieties of cellulose paper has already been demonstrated in literature [12], quantitative studies must be carried out to prove its effect on thicker sheets (as those used in this work).

Moreover, a passivation layer is required to electrically insulate the electrodes in the final device. A biodegradable option we are considering is chitosan, which has been demonstrated to be a good alternative for green dielectric films and is ink-jet printable [15, 16]. A non-biodegradable alterative is SU-8, which has already been shown to be suitable for MEA fabrication [2].

Although each individual component of the design is reported as biocompatible in literature [17, 18], work is in progress to confirm the compatibility of these multi-layered biodegradable structures with cell growth.

References

[1] Obien, Marie Engelene J., et al. "Revealing neuronal function through microelectrode array recordings." Frontiers in neuroscience 8 (2015): 423.

[2] Garma, Leonardo D., et al. "Inkjet-printed PEDOT: PSS multi-electrode arrays for low-cost in vitro electrophysiology." Lab on a Chip 19.22 (2019): 3776-3786.

[3] Discher, Dennis E., Paul Janmey, and Yu-li Wang. "Tissue cells feel and respond to the stiffness of their substrate." Science 310.5751 (2005): 1139-1143..

[4] Mehrali, Mehdi, et al. "Blending electronics with the human body: a pathway toward a cybernetic future." Advanced science 5.10 (2018): 1700931..

[5] Mariani, Federica, et al. "PEDOT: dye-based, flexible organic electrochemical transistor for highly sensitive pH monitoring." ACS applied materials & interfaces 10.26 (2018): 22474-22484.

[6] Kuzum, Duygu, et al. "Transparent and flexible low noise graphene electrodes for simultaneous electrophysiology and neuroimaging." Nature communications 5.1 (2014): 1-10.

[7] Sekitani, Tsuyoshi, et al. "Organic nonvolatile memory transistors for flexible sensor arrays." Science 326.5959 (2009): 1516-1519.

[8] Ji, Yongsung, et al. "Flexible and twistable non-volatile memory cell array with all-organic one diode–one resistor architecture." Nature communications 4.1 (2013): 1-7.

[9] Li, Rongfeng, et al. "Recent progress on biodegradable materials and transient electronics." Bioactive materials 3.3 (2018): 322-333.

[10] Nagashima, Kazuki, et al. "Cellulose nanofiber paper as an ultra flexible nonvolatile memory." Scientific reports 4.1 (2014): 1-7.

[11] Qian, Chuan, et al. "Flexible organic field-effect transistors on biodegradable cellulose paper with efficient reusable ion gel dielectrics." Rsc Advances 5.19 (2015): 14567-14574.

[12] Li, Guodong, et al. "Facile fabrication of transparent paper with tunable wettability for use in biodegradable substrate." ACS Sustainable Chemistry & Engineering 8.5 (2020): 2176-2185.

[13] Calvert, Paul. "Inkjet printing for materials and devices." Chemistry of materials 13.10 (2001): 3299-3305..

[14] Lin, Yow-Jon, Wei-Shih Ni, and Jhe-You Lee. "Effect of incorporation of ethylene glycol into PEDOT: PSS on electron phonon coupling and conductivity." Journal of Applied Physics 117.21 (2015): 215501.

[15] Nainggolan, I., et al. "Study on chitosan film properties as a green dielectric." IOP Conference Series: Materials Science and Engineering. Vol. 309. No. 1. IOP Publishing, 2018.

[16] Andolfi, Andrea, et al. "Ink-jet printed chitosan precise patterning for engineered 2D neuronal networks." Biomedical Science and Engineering 4.s1 (2021).

[17] Střiteský, Stanislav, et al. "Printing inks of electroactive polymer PEDOT: PSS: The study of biocompatibility, stability, and electrical

properties." Journal of Biomedical Materials Research Part A 106.4 (2018): 1121-1128..

[18] Teo, Siew Yong, et al. "Synthesis and characterization of novel biocompatible palm oil-based alkyds." European Journal of Lipid Science and Technology 118.8 (2016): 1193-1201.

Photosensitive pattern to control geometry and activity of a neural network

Andrea Andolfi[a], Pietro Arnaldi[a], Donatella Di Lisa[a], Monica Frega[b], Sergio Martinoia[a], Laura Pastorino[a]

[a]*Department of Informatics, Bioengineering, Robotics and Systems Engineering (DIBRIS), University of Genoa, Genoa, Italy*

[b]*Department of Clinical Neurophysiology, University of Twente, Enschede, The Netherlands*

***Abstract*— A key challenge in neuroscience is understanding how a neural network's structure affects its activity. A simple and controllable environment like the in vitro neural network remains a powerful tool for studying physiological and pathological behaviors. Thanks to innovative printing techniques, the control of the biopolymer deposition are improved. Inkjet printing has gained much attention among patterning techniques because of its high resolution and direct-write approach, which enables the production of patterned substrates. Controlled deposition of an adhesion factor on the surface of the microelectrode array (MEA) makes it possible to guide the development of a neuronal network on a substrate that can record its activity, allowing the geometry of the network to be related to its activity. However, the inks commonly used can guide only the structure of a neural network, neglecting the functionality part. In this work, we synthesize a photosensitive ink that can be printed with a commercial inkjet printer, where thanks to its photothermal properties, we can modulate the neural activity. The photosensitive pattern printed on the MEA substrate allows a device to control the neural network geometry, record and modulate its activity. This work aims to provide an easy, versatile, fast and low-cost tool for studying the recurring relationship between the structure and function of neuronal networks.**

***Keywords*— neural network micropattering, inkjet printing, chitosan, gold nanorods.**

I. Introduction

In the past few decades, MEAs have been effectively used to investigate the correlation between the functional activity of neural networks and their structural organization thanks to their versatility and large recording area [1,2]. Different fabrication methods are possible to obtain engineered networks, involving physical and/or chemical approaches to guide cell adhesion and growth [3,4]. Among all the technological developments, inkjet printing has gained much attention thanks to its low cost, scalability, non-invasiveness, and versatility properties, which allow the localized deposition of ink micro-droplets without contacting the printing substrate [5]. We recently demonstrated that the cationic polysaccharide chitosan could efficiently promote cell adhesion and neural network maturation [6,7]. Furthermore, we have demonstrated how it is possible to control its deposition to direct the geometry of a neural network [8]. However, to better understand the relationship between structure and function of a neural network, the control of the neural activity and the control of the neural network geometry are both important [9–11]. MEAs can stimulate the neuronal network, but the electrical stimulation leads to membrane depolarization and, thus, excitation of activity. At the same time, it has been shown how neuronal activity can be inhibited using the thermoplasmonic effect of gold nanorods (GNRs) [12–15]. In this work, we combined the plasmonic properties of GNRs with the bioactive and rheological of the chitosan to realize a photosensitive ink that can be printed using a commercial inkjet printer to realized a photosensitive pattern. The patterned substrate helps control both the structure and the activity of a neural network giving a useful tools to study the recurrent relationship between its structure and function.

II. Methods

A. Photosensitive ink synthesis and characterization

We synthesized GNRs using a seed-mediated method [16]. Briefly, we prepare the seed solution by mixing 3 mL of 0.2 M Cetyltrimethylammonium bromide (CTAB, Sigma), 3 mL of 5 mL of 0.5 mM HAuCl4 (Sigma), and 300 µL of 0.01 M NaBH4 (Sigma) in an ultrasonic bath, which was let aged for 2h. To grow into a rod shape, 12 uL of seed were mixed with 5 mL of 0.2 M CTAB, 5 mL of 1 mM HAuCl4, 250 µL of 4 mM AgNO3, and 70 µL of 78.84 mM ascorbic acid. The GNRs were centrifuged to obtain the pellet and resuspended in ultrapure water. After dissolving chitosan powder into a 1 M acetic acid solution, we uniformly resuspend GNRs inside. We evaluated the ink optical properties performing a UV-vis analysis.

B. Micropattern printing and characterization

Printing was carried out using a drop-on-demand (DOD) piezoelectric printer (Dimatix Materials Printer 2800 - DMP 2800m,Fujifilm, Santa Clara, CA), equipped with a 16 nozzle and 10 pL cartridge (DMCLCP-11610). The grid pattern, designed using the printer software, was printed on the MEA active area, and the photosensitive substrate obtained was characterized to evaluate its plasmonic properties. A fiber-optic laser (785 nm, 450 mW, B&W Tek, USA) was used to stimulate the patterned MEA, and the laser beam created an illumination area 5 mm in diameter on the MEA chip. An infrared thermographic camera (TG165-X, FLIR, USA) was used to measure the temperature change during near-infrared (NIR) irradiation (3 minutes at a time), and the samples were cooled to room temperature (RT) before the next measurement.

C. *Immunostaining*

On the top of the patterned device we seeded neuronal cells obtained differentiating human-derived induced pluripotent stem cells (h-iPSCs). After labelling the neuronal dendrites with Microtubule Associated Protein 2 (MAP-2) and the nuclei with 4′,6-diamidino-2-phenylindole (DAPI), we acquired the image using a fluorescent microscope.

D. *Neural activity recording, stimulation and analysis*

The neural activity was recorded at 35 days *in vitro* (DIV) using a standard MEA1060 system (MEA 1060-Inv-Standard amplifier, Multichannel Systems, Germany). Collected data inkjetwere processed using MATLAB (Mathworks) and the Spycode toolset [51]. A fiber-optic laser (785 nm, 450 mW, B&W Tek) was used as the light source for the photothermal stimulation, and the laser beam from the bottom generated an illumination area on the MEA chip that was 5 mm in diameter. The stimulation protocol consists of 20 cycles, with each cycle having the laser on for 10 seconds before switching off for 20 seconds. Recording channels whose mean firing rate (MFR) was higher than 0.1 spikes/sec were selected as active channels and used for neural activity analysis. We define MFR(ON) as the average firing rate when the laser is on, while MFR(OFF) corresponds to the average firing rate calculated 10 seconds before the laser stimulation. The following formula was used to calculate the inhibition percentage (IP):

$$IP\ [\%] = [1 - MFR(ON) / MFR(OFF)] * 100 \qquad (1)$$

III. Results

Figure 1a shows the spectrum of the photosensitive ink, where the two peaks characteristic of gold nanorods can be seen, concluding that the nanoparticles are uniformly dispersed and not aggregated. The synthesized ink was printed with grid geometry on an MEA, as shown in Figure 1b. The thickness of the lines is about 50 um, which is comparable to the size of microelectrodes, resulting in excellent control over the geometry concerning the resolution possible for activity recording.

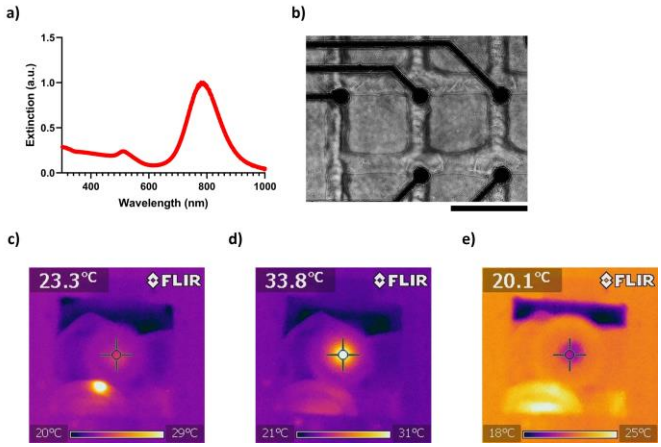


Figure 1: Photosensitive ink synthesis and characterization. a) Spectrum of the photosensitive ink. b) Contrast phase image of the grid pattern printed on the MEA substrate (scalebar: 200 µm). c) Thermal image of the patterned substrate realized using the control ink acquired during a laser stimulation with 450 mW. d) Thermal image of the patterned substrate realized using the test ink acquired during a laser stimulation with 450 mW. e) Thermal image of the patterned substrate realized using the test ink acquired during a laser stimulation with 0 mW.

To evaluate the photothermal properties of the patterned substrate, we stimulated it with a NIR infrared light and measured the temperature change on the surface of 1 mL of medium using a thermal imaging camera. In fact, thanks to the plasmonic properties conferred by GNRs, the ink can convert NIR light into heat, through which neuronal activity can be modulated [12,13,15]. Figure 1c shows the temperature change measured in a control sample (ink without GNRs) stimulated for 3 minutes with a power of 450 mW, while Figure 1d shows the test sample (ink with GNRs) stimulated under the same conditions. In the test sample, it can be seen that NIR stimulation leads to a temperature increase of about 10 degrees compared to the control sample (figure 1c), which remains close to the sample not stimulated (figure 1e). An increase in temperature close to 10 degrees is thought to be sufficient to inhibit the activity of an in vitro neural network [12,15]. After demonstrating the properties of the patterned substrate, we seeded neurons obtained by differentiating human stem cells on top of it. Figure 2a shows how the neuronal culture grows following the geometry indicated by the patterned substrate. In addition, Figure 2b shows the average waveform recorded by a microelectrode, demonstrating that the activity recording is not precluded by the pattern printed on the microelectrode array.

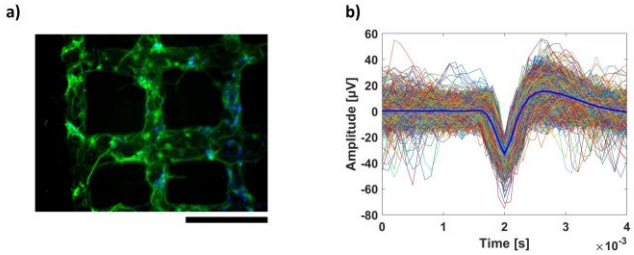


Figure 2: Neural network structure and activity recording. a) fluorescence image of a neuronal network growing onto a grid micropattern (green: MAP2, blue: DAPI, scalebar: 200 µm). b) set of waveforms with the average one (blue) recorded in an MEA's microelectrode.

Finally, we have shown that we can modulate the activity of a neuronal network by photothermal effect. Figure 3a shows the raw data where the stimulation protocol was performed with 0 mW power, from which we can conclude that the activity does not change its frequency when the sample is stimulated with zero power. In contrast, the activity is inhibited with a power of 450 mW. However, as shown in the figure, the inhibition is perfect within the 10 seconds of the stimulation, providing high temporal control over the activity modulation. Currently, the spatial resolution of stimulation is potentially that of the drop (diameter of 50 µm). In addition, the intensity of the inhibitory phenomenon can be controlled by changing the power of the laser used to stimulate the sample (figure 3c).

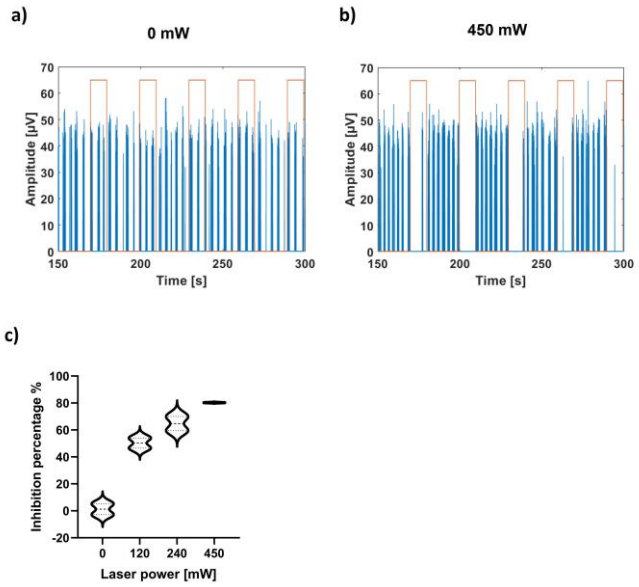


Figure 3: Photothermal modulation of the micropatterned neural network activity. a) raw neural network data grew on a photosensitive micropattern during laser stimulation with 0 mW (laser stimulation time: 10 s on and 20 s off, orange plot). b) raw neural network data grew on a photosensitive micropattern during laser stimulation with 450 mW (laser stimulation time: 10 s on and 20 s off, orange plot). c) inhibition percentage average at different laser power.

IV. DISCUSSION

The ink can be printed with a resolution comparable to the size of a microelectrode of MEA to obtain specific patterns and has both bioadhesive properties given by chitosan, which are necessary for cell anchoring and guided development of the neuronal network in the desired geometry, both those plasmonic given by GNRs, for the modulation of neuronal activity. Furthermore, it is also possible to independently stimulate different areas of the network, depositing the ink with GNRs in some areas and the ink without GNRs in others, which can be stimulated electrically using the MEA electrodes. This technology, therefore, provides a simplified system for studying a complex topic, such as the study of the recurrent relationship between the structure and function of a neuronal network. However, although a two-dimensional cell culture provides a simplified environment for studying such a complex subject, this is also a limitation of the system, which can hardly imitate the environment in vivo. For this reason, the next step would be to develop this system in three-dimensional cell cultures.

V. CONCLUSION

In this work, we have synthesized a photosensitive ink useful to realize patterns with a resolution comparable to an MEA's microelectrode. Due to its bioactive and plasmonic properties, it is possible to control a neuronal network's geometry and activity. By printing the pattern on the active area of a microelectrode array, it is possible to obtain a completed device that can control the geometry of a neuronal network, record its activity, and modulate it by thermoplasmonic effect. The photosensitive, patterned substrate MEA is helpful for the in vitro study of the recurrent relationship between structure and function of a neuronal network, providing a tool for studying neural communication and associated disorders.

REFERENCES

[1] *B.C. Wheeler, G.J. Brewer, Designing Neural Networks in Culture, Proceedings of the IEEE. 98 (2010) 398–406. https://doi.org/10.1109/JPROC.2009.2039029.*

[2] *E. Tibau, Ch. Bendiksen, S. Teller, N. Amigó, J. Soriano, Interplay activity-connectivity: Dynamics in patterned neuronal cultures, in: 2013: pp. 54–63. https://doi.org/10.1063/1.4776501.*

[3] *N. Hong, Y. Nam, Thermoplasmonic neural chip platform for in situ manipulation of neuronal connections in vitro, Nat Commun. 11 (2020). https://doi.org/10.1038/s41467-020-20060-z.*

[4] *H. Dermutz, G. Thompson-Steckel, C. Forró, V. de Lange, L. Dorwling-Carter, J. Vörös, L. Demkó, Paper-based patterned 3D neural cultures as a tool to study network activity on multielectrode arrays, RSC Adv. 7 (2017) 39359–39371. https://doi.org/10.1039/C7RA00971B.*

[5] *B.-J. de Gans, P.C. Duineveld, U.S. Schubert, Inkjet Printing of Polymers: State of the Art and Future Developments, Advanced Materials. 16 (2004) 203–213. https://doi.org/10.1002/adma.200300385.*

[6] *D. di Lisa, M. Tedesco, E. Dellacasa, M. Pesce, T. Catelani, P. Massobrio, R. Raiteri, S. Martinoia, L. Pastorino, Chitosan biopolymer: Alternative adhesion factor and scaffold matrix for 2D and 3D neuronal cultures, Biomedical Science and Engineering. 3 (2020). https://doi.org/10.4081/bse.2019.107.*

[7] *P. Arnaldi, D. di Lisa, L. Maddalena, F. Carosio, A. Fina, L. Pastorino, O. Monticelli, A facile approach for the development of high mechanical strength 3D neuronal network scaffold based on chitosan and graphite nanoplatelets, Carbohydr Polym. 271 (2021) 118420. https://doi.org/10.1016/j.carbpol.2021.118420.*

[8] *A. Andolfi, P. Arnaldi, D. di Lisa, S. Martinoia, L. Pastorino, Ink-jet printed chitosan precise patterning for engineered 2D neuronal networks, Biomedical Science and Engineering. 4 (2021). https://doi.org/10.4081/bse.2021.148.*

[9] *A.T. Sack, Transcranial magnetic stimulation, causal structure–function mapping and networks of functional relevance, Curr Opin Neurobiol. 16 (2006) 593–599. https://doi.org/10.1016/j.conb.2006.06.016.*

[10] *T. Sankar, M.M. Chakravarty, A. Bescos, M. Lara, T. Obuchi, A.W. Laxton, M.P. McAndrews, D.F. Tang-Wai, C.I. Workman, G.S. Smith, A.M. Lozano, Deep Brain Stimulation Influences Brain Structure in Alzheimer's Disease, Brain Stimul. 8 (2015) 645–654. https://doi.org/10.1016/j.brs.2014.11.020.*

[11] *S.F. Muldoon, F. Pasqualetti, S. Gu, M. Cieslak, S.T. Grafton, J.M. Vettel, D.S. Bassett, Stimulation-Based Control of Dynamic Brain Networks, PLoS Comput Biol. 12 (2016) e1005076. https://doi.org/10.1371/journal.pcbi.1005076.*

[12] *S. Yoo, S. Hong, Y. Choi, J.-H. Park, Y. Nam, Photothermal Inhibition of Neural Activity with Near-Infrared-Sensitive Nanotransducers, ACS Nano. 8 (2014). https://doi.org/10.1021/nn5020775.*

[13] *S. Yoo, R. Kim, J.-H. Park, Y. Nam, Electro-optical Neural Platform Integrated with Nanoplasmonic Inhibition Interface, ACS Nano. 10 (2016) 4274–4281. https://doi.org/10.1021/acsnano.5b07747.*

[14] *H. Jung, H. Kang, Y. Nam, Digital micromirror based near-infrared illumination system for plasmonic photothermal neuromodulation, Biomed Opt Express. 8 (2017) 2866. https://doi.org/10.1364/boe.8.002866.*

[15] *A. Andolfi, H. Jang, S. Martinoia, Y. Nam, Thermoplasmonic Scaffold Design for the Modulation of Neural Activity in Three-Dimensional Neuronal Cultures, Biochip J. (2022). https://doi.org/10.1007/s13206-022-00082-z.*

[16] *B. Nikoobakht, M.A. El-Sayed, Preparation and Growth Mechanism of Gold Nanorods (NRs) Using Seed-Mediated Growth Method, Chemistry of Materials. 15 (2003) 1957–1962. https://doi.org/10.1021/cm020732l.*

Exposure Assessment of Young People to Wearable Antennas at 5G frequencies

S. Gallucci[1,2], M. Benini[1,2], M. Bonato[1], E. Chiaramello[1], S. Fiocchi[1], G. Tognola[1], M. Parazzini[1]
[1] *Institute of Electronics, Information Engineering and Telecommunication (IEIIT), National Council of Research (CNR)*
[2] *Department of Electronics, Information and Bioengineering, DEIB, Politecnico di Milano, Milan, Italy*

***Abstract*—The present work aims to assess the exposure of young people due to two 5G wearable devices. The two antennas are posed on the trunk of the male and female teenager virtual models, in order to simulate typical scenarios in which the wearable devices are used. For the exposure assessment, the extracted parameters have been the Specific Absorption Rate averaged over 10 grams of tissue and the Absorbed Power Density averaged over a square of 4-cm^2 over the skin, depending on the frequency of the EMF emitted by the antenna, with an input power of 100 mW. The results showed no overcome of limit values set by international regulation in any of the cases when the input power is set as realistic values. Moreover, evident differences between the male and female model were observed in both studied cases.**

***Keywords*— RF human exposure assessment, wearable antennas, 5G, young people.**

I. Introduction

In recent years, we are witnessing the spread of new radiofrequency technologies, not only in terms of the common smartphone, but also involving new devices: the wearable devices. Examples of wearable devices commonly adopted are the smartwatches, the cameras mounted on the head and so on. The diffusion of the wearable technologies is evidentially growing and the age category purchasing and using more of them is the young people, for instance, in Germany in 2022 the 46% of the teenagers (12-19 years) has at least one wearable device at home [1].

It's important to discern "mobile" devices from "wearable" devices; the substantial difference is the fact that the mobile devices are designed for having many functionalities and not for being comfortable; conversely, in the word "wearable" there are many characteristics, such as the comfort, the integration in the garment and the continuous monitoring of the user's activities [2].

Furthermore, the characteristic that led to such a widespread diffusion of this technology is the versatility; indeed, the wearable device finds application in many fields: wireless communication, military environment, and medical monitoring [3, 4].

From the purely technologic point of view, a wearable device is the primary block of a larger network called Body-Area-Network (BAN), in which there are many sensors, each one able to detect a specific parameter (e.g., heart rate, respiration rate) and to transmit these data to the principal node of the network that has the aim to exchange information with an external device (e.g., smartphone) [5]. The IEEE 802.15.6 standard [6] gives a detailed characterization of the Wireless-BAN, a subgroup of the BANs, where the communication protocol is precisely defined. The typical bandwidth used so far for the wearable communication is called Industrial-Scientific-Medical (ISM) band where the central frequency is 2.45 GHz [7]. Nowadays, the requested functionalities for these devices are more and more and the amount of data requested to exchange is growing. In this perspective, the 5G technology is the option that may answer to this issue, therefore there are many studies regarding the design of 5G wearable antennas, involving their first two bands: the sub-6GHz band and the mm-wave band (>24GHz) [8].

Since by definition each wearable device must be worn by the user, the distance between the human tissues and the electromagnetic field (EMF) source is minimal. Therefore, the question about the quantitative assessment of the power absorption due to the wearable devices by biological tissues becomes crucial [9].

Thus, this work aims to address the question about the exposure assessment due to wearable devices, in particular wearable antennas working the 5G emerging frequencies considering the diffusion of the Internet-of-Things. More in detail, the simulated exposure regarded the use of two different antennas, each one tuned in a 5G typical band. Moreover, the assessment has been performed considering virtual models of young human, to assess the EMF exposure in a scenario as realistic as possible, also according to the statistics.

II. Materials and Methods

In order to study the exposure in realistic situations, two main scenarios have been simulated: in both of them the patch antennas have been posed on the trunk of the human model, at the height of the center of the model's heart, 2 mm apart from the trunk' skin. More in detail, for the study the young female and male models of the Virtual Population [10] have been deployed, Billie (age = 11 yo., height = 1.49 m, weight = 34 kg, BMI = 15.3 kg/m^2) and Louis (age = 14 yo., height = 1.68 m, weight = 49.7 kg, BMI = 17.6 kg/m^2) respectively.

From the point of view of the source, the antennas have been designed as simplified as possible in order to simulate an overall situation. They are wearable patch antennas, designed for off-body communication. More in detail, they are single-patch structure with a three-layered body: the patch layer and the ground plane are made of copper ($\sigma = 5.813\text{x}10^7$ S/m, $\varepsilon_r = 1$) and the substrate layer is made of polyester ($\sigma = 4.6785\text{x}10^{-8}$ S/m, $\varepsilon_r = 2.2$), a common material used for this application.

The first antenna is tuned in the lowest 5G band, the sub-6GHz band, with a central frequency of 3.5 GHz. The geometrical characteristics and the radiation performances are

reported in Fig.1.

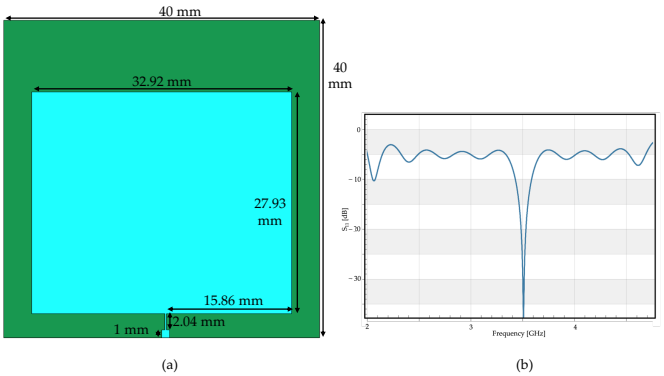


Fig. 1: First wearable patch antenna simulated, tuned to f = 3.5 GHz: (a) geometry of the antenna, front view; (b) performances of the antenna in terms of the reflection coefficient (S11).

In the second wearable antenna (Fig.2) the materials and the widths of each layer are the same for the first antenna; the main difference is the size of the patch, whose dimensions change the radiation pattern and the central frequency of the tuning. Indeed, the second antenna is tuned in the >24GHz-band, at frequency set as 26.5 GHz.

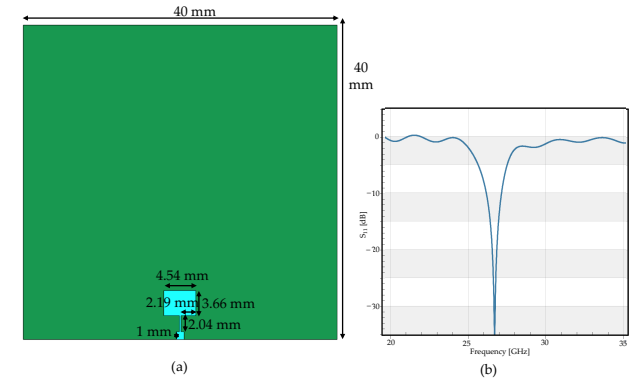


Fig. 2: Second wearable patch antenna simulated, tuned to f = 26.5 GHz: (a) geometry of the antenna, front view; (b) performances of the antenna in terms of the reflection coefficient (S11).

The computational exposure assessment has been carried out solving the Maxwell's equations by the Finite-Difference Time-Domain (FDTD) method implemented in the commercial simulation software Sim4Life v.6.2 (ZMT Zurich Med Tech AG, Zurich, Switzerland, www.zurichmedtech.com, accessed on 15 January 2023). More in detail, the boundary conditions have been set as Perfect Matched Layer (PML) and the mesh size ranges from 0.005 mm up to 1 mm. Finally, the dielectric properties of each human tissue have been chosen according to the literature [11-13] and the frequency of the antenna.

Finally, the parameters of interest extracted for the assessment have been the Specific Absorption Rate averaged over 10 grams of tissue (SAR_{10g}) and the Absorbed Power Density (S_{ab}) averaged over a square 4 cm^2 surface over the skin. According to the International ICNIRP Guidelines [14], the SAR_{10g} is the parameter to assess the exposure for the antenna tuned in 3.5 GHz because it is below the threshold of 6 GHz, whereas the S_{ab} is the parameter devoted to the exposure assessment due to frequencies greater than 6 GHz up to 300 GHz. Moreover, all the values have been extracted from a box with size of 250 x 250 x 250 mm; the study focused on the peak values of the parameters and the percentages of the values that are greater than the 70% of the peak value in order to better know the distributions of the data around the peak. Finally, the peak values have been compared with the ICNIRP Guidelines limits for the general public; the values here reported have been obtained with an input power to the antenna of 100 mW, a realistic power for the common use of the wearable devices.

III. Results and Discussion

In this section the results obtained in the study will be presented and discussed. More in detail, Table I shows the peak values of the SAR_{10g} obtained in the first simulated scenarios i.e., where the antenna emitting at 3.5 GHz is posed on the chest of Louis and Billie.

TABLE I: Peak SAR10g and percentages of S_{AB} values greater than 70% of the peak SAR10g for each configuration

Human Model	*Peak SAR_{10g} [W/m^2]*	*Values greater than 70% of the peak SAR_{10g} [%]*
Louis	0.12	0.78
Billie	0.16	0.72

The comparison between the obtained results and the general public limit in the ICNIRP Guidelines i.e., 2 W/kg, did not show the overcome of it and the values of the reported percentages mean that most of the data are not concentrated around the peak SAR_{10g} so most of the data are lower than the showed peaks, in both scenarios.

Furthermore, emphasizing the anatomical gender comparison, it is clear that the variation between the male and female model implies noticeable differences, considering that the peak SAR_{10g} in Louis is 76.4% of the Billie's peak SAR_{10g}.

Then, Table II shows the extracted results of S_{ab} in scenarios with the wearable antenna tuned to 26.5 GHz.

TABLE II: Peak S_{AB} and percentages of S_{AB} values greater than 70% of the peak S_{AB} for each configuration

Human Model	*Peak S_{ab} [W/m^2]*	*Values greater than 70% of the peak S_{ab} [%]*
Louis	6.67	0.27
Billie	3.35	0.18

Comparing the obtained peak values of S_{ab} with the respective ICNIRP Guidelines limit i.e., 20 W/m^2, it is noteworthy that both results do not exceed the international limit. Moreover, it must be considered that the values here reported have been obtained with a realistic input power, so these results correspond to an actual use of the wearable device.

Additionally, in these second scenarios, the difference depending on the anatomical gender is more evident than the first scenarios; indeed, here the peak S_{ab} of Billie is 50.2% of the peak S_{ab} in Louis. A possible explanation is the fact that the male model has a thinner layer of the skin instead of the female model and the S_{ab}, by definition, is averaged over the skin.

IV. Conclusions

The presented study is an attempt to assess the exposure due to 5G wearable antennas that are now spreading in the everyday life, also in the teenagers. Here, two different teenager human models have been simulated with two different antennas placed on the same position with respect to the model. Comparing the obtained results by gender, the most evident difference is in the case with the antenna tuned to 26.5 GHz; nevertheless, it is important to state that in the scenarios with the antenna at the lowest frequency the SAR_{10g} detected in the female male is higher than the one from the male model.

Overall, all the obtained values have been compared with the ICNIRP Guidelines and, when the peakx values are calculated according to a realistic value of input power, there is no overcome in any of the cases studied.

Acknowledgement

The authors wish to thank ZMT Zurich MedTech AG (www.zmt.swiss accessed on 16 January 2023) for providing the simulation software Sim4Life. The authors wish to thank the European Defence Agency (EDA) for their support in this work in the context of project no. B 0987 IAP2 GP "Biological Effects of Radiofrequency Electromagnetic Fields (RFBIO)" funded by the Italian MoD.

References

[1] Which electronic devices do you have at home? [Graph], mpfs, November 25, 2022. [Online]. Available: https://www.statista.com/statistics/457562/electronic-devices-in-households-with-teens-germany/ .

[2] R. Gravina, and G. Fortino, "Wearable Body Sensor Networks: State-of-the-Art and Research Directions," *IEEE Sensors Journal*, vol. 21, pp. 12511-12522, 2021.

[3] K. N. Paracha, S. K. A. Rahim, P. J. Soh, and M. Khalily, "Wearable Antennas: A Review of Materials, Structures, and Innovative Features for Autonomous Communication and Sensing," *IEEE Access*, vol. 7, pp- 56694, 56712, 2019.

[4] N. Chahat, M. Zhadobov, L. Le Coq, S. I. Alekseev, and R. Sauleau, "Characterization of the Interactions Between a 60-GHz Antenna and the Human Body in an Off-Body Scenario," *IEEE Transactions on Antennas and Propagation*, vol. 60, pp- 5958-5965, 2012.

[5] M. Chen, S. Gonzalez, A. Vasilakos, H. Cao, V. C. M. Leung, "Body Area Network: A Survey," *Mobile networks and applications*, vol. 16, pp. 171-193, 2011.

[6] *802.15.6-2012*; IEEE Standard for Local and Metropolitan Area Networks part 15.6: Wireless Body Area Networks. IEEE: New York, NY, USA, 2012.

[7] S. N. Mahmood, A. J. Ishak, A. Ismail, A. C. Soh, Z. Zakaria, and S. Alani, "ON-OFF Body Ultra-Wideband (UWB) Antenna for Wireless Body Area Networks (WBAN): A Review," *IEEE Access*, vol.8, pp. 150844-150863, 2020.

[8] S. Gallucci, M. Bonato, M. Benini, E. Chiaramello, S. Fiocchi, G. Tognola, and M. Parazzini, "Assessment of EMF Human Exposure Levels Due to Wearable Antennas at 5G Frequency Band," *Sensors*, vo. 23, 2023.

[9] A. Yadav, V. K. Singh, P. Yadav, A. K. Beliya, A. K. Bhoi, and P. Barsocchi, "Design of Circularly Polarized Triple-Band Wearable Textile Antenna with Safe Low SAR for Human Health," *Electronics*, vol. 9, 2020.

[10] M. C. Gosselin, E. Neufeld, H. Moseri, E. Huber, S. Farcito, L. Gerber, and N. Kuster, "Development of a New Generation of High-Resolution Anatomical Models for Medical Device Evaluation: The Virtual Population 3.0," *Phys. Med. Biol.*, vol. 41, pp. 5287-5303, 2014.

[11] C. Gabriel, S. Gabriel, and Y. E. Corthout, "Dielectric Properties of Biological Tissues: I. Literature Survey," *Phys. Med. Biol.*, vol. 41, pp.2231, 1996.

[12] S. Gabriel, R.W. Lau, and C. Gabriel, "The Dielectric Properties of Biological Tissues: II. Measurements in the Frequency Range 10 Hz to 20 GHz," *Phys. Med. Biol,* vol. 41, pp. 2251, 1996.

[13] S. Gabriel, R. W. Lau, and C. Gabriel, "The Dielectric Properties of Biological Tissues: III. Parametric Models for the Dielectric Spectrum of Tissues," *Phys. Med. Biol,* vol. 41, pp. 2271, 1996.

[14] International Commission on Non-Ionizing Radiation and Protection. "ICNIRP Guideline for Limiting Exposure to Time-Varying Electric, Magnetic and Electromagnetic Fields (up to 300 GHz)," *Health Phys.*, vol. 74, pp. 494-522, 2020.

Interconnected brain regions-on-a-chip: role of connectivity and heterogeneity in the electrophysiological activity

M. Brofiga[1,2], F. Callegari[1], F. Poggio[1], I. Donati della Lunga[1], L. Cerutti[1], M. Tedesco[3], and P. Massobrio[1,4]

[1] *Dep. of Informatics, Bioengineering, Robotics and System Engineering* (*DIBRIS*), *University of Genova, Genova Italy*
[2] *ScreenNeuroPharm srl, Sanremo, Italy*
[3] *3Brain Gmbh, Wadenswil, Switzerland*
[4] *National Institute for Nuclear Physics* (*INFN*), *Genova, Italy*

***Abstract*—The development of reliable *in vitro* models is particularly important to understand the basic physiology of the neuronal system, to study the insurgence of diseases and to test potential therapies. One of the main challenges is to develop a model that allows extracting realistic and easy-to-interpret information without forsaking some key aspects (e.g., modularity, heterogeneity, three-dimensionality, mechanical properties) of the complex organization of *in vivo* tissues. In the present work, we present the results we obtained by progressively integrating these essential features into *in vitro* models. We studied how information propagates in different neuronal types with particular topologies. Then, we investigated how modularity and heterogeneity interact in a cortico-hippocampal model, finding that micro-circuits emerge in this condition. This level of complexity of *in vitro* models already carries a different sensitivity to drugs with respect to the standard testbeds, as we demonstrated with bicuculline (BIC). Moving yet another step forward, we introduced the third dimension, finding a redistribution of the spiking and bursting activity. Then, we studied how to integrate the mechanical properties of the extracellular matrix by creating neurospheroids. Overall, these results demonstrate the improvements that could be achieved with modern *in vitro* models and aim at partly filling the ever-lasting need new more affordable, efficient, and cross-disciplinary *in vitro* models, therefore moving towards more ethical research.**

***Keywords*— *in vitro* brain models, micro-electrode arrays, modularity, heterogeneity, three-dimensionality.**

I. Introduction

THE human brain is composed of about 86 billion neurons which originate rich and intricate networks. Moreover, neurons are organized in well-defined spatial locations that define clusters of neurons or modules. From a morphological and physiological point of view, each module is composed of specific neurons that differ in shape and function. Examples of large-scale modules are the cortical or hippocampal regions. Each cognitive and motor function is possible thanks to the correct interaction between the different modules. The disruption, loss, or alteration of these connections can produce pathological conditions. To understand how the information is transmitted and computed, we need to investigate the communication among the different modules. Another essential feature to comprehend how the electrophysiological signals are transmitted is the three-dimensional (3D) spatial organization of such modules [1]. The 3D microenvironment is fundamental for the correct expression of the neuronal cell phenotypes and for the modulation of the electrophysiological activity patterns [2]. There are different approaches to investigating the transmission of the information: many studies use an *in vivo* approach but, in this case, it is very difficult to study a specific circuit. If the focus is understanding the effect of a specific module (e.g., of the hippocampal one on the activity of the cortical one), we are unable to isolate this specific system *in vivo* as we cannot severe the connections of the cortex with other brain districts. Thus, the cortical activity we observe is always influenced by all its inputs. In this perspective, *in vitro* engineered models could be a powerful tool. They reduce the complexity of the system, but at the same time they keep the key features of the *in vivo* environment of the brain, thus ensuring consistent results.

In the present work, we exploited polymeric masks coupled to Micro-Electrode Arrays (MEAs) to investigate the role of the key features of the human brain (modularity, heterogeneity and three-dimensionality) in the electrophysiological activity of *in vitro* neuronal networks. Studying the cortical-hippocampal circuit, we observed a more scattered signal propagation when the hippocampal population was present. We explained such behaviour by investigating the functional connectivity: in the cortical-hippocampal configuration, a higher segregation was observed. Moreover, the inhibitory hippocampal connections strongly modulated the cortical activity. The differences observed in the heterogenous networks arose a new question: how does the complexity of the *in vitro* models influence the effects of drugs? We investigated the effects induced by bicuculline (BIC) and our results suggested that oversimplified *in vitro* models could lead to under- or overestimate its effects. Finally, we introduced the third feature, three-dimensionality, recreating a wider pattern of activity with respect bidimensional networks. In perspective, we moved one more step towards recreating the mechanical properties of the extracellular matrix by building cortical and hippocampal spheroids, which are able to better reproduce the intrinsic characteristics of the native tissues, and which can be combined to create different interacting neuronal modules (building blocks). This new model can be exploited as platform for precision medicine.

II. Materials and Methods

A. Cell preparation and PDMS mask

We used two polymeric devices to recreate modular heterogeneous cultures [3], [4]. The dimensions of the device are reported in Table I. To recreate a biocompatible scaffold where neuronal networks can grow in a 3D fashion, we used pre-sterilized and pre-coated glass microbeads (Ø = 40 µm). About 4-6 layers were stacked, reaching a height of about 220 µm. The entire procedure is reported in [4].

TABLE I: Polymeric masks

	2-compartment mask	*3-compartment mask*
Compartments dimensions	4 mm x 2 mm	6.5 mm x 4.3 mm 3.4 mm x 3.4 mm
Microchannels dimensions (w x l x h)	10 µm x 250 µm x 5 µm	
Microchannels spacing	50 µm	

B. Electrophysiological characterization

We investigated both the homogenous (only cortical or hippocampal neurons were plated in each compartment) and heterogenous (cortical-hippocampal) cultures at 18 days *in vitro* (DIV). We detected the occurrence of spike events employing the Precision Spike Detection (PTSD) algorithm [5]. From the spike train, the burst identification was performed by applying the string method devised in [6]. The identification of the choral activity (network burst) was performed by means of the self-adaptive algorithm devised in [7]. Spiking and bursting activity were evaluated in terms of Mean Firing Rate (MFR) and Mean Bursting Rate (MBR). To derive the neuronal recruitment mechanisms of the network, we computed the average Spike Time Histogram (STH), and we extracted the slope of the rising and decaying phases [8], [9]. To investigate the signal propagation among the compartments, we delivered electrical biphasic stimuli (positive phase first) with a duration of 400 µs, 50% duty cycle, 0.2 Hz and an amplitude of 1.5 V peak-to-peak. We extracted information about the stimulus-evoked activity by computing the Post-Stimulus Time Histogram (PSTH) and investigating the early and late responses [10]. To discern the excitatory and inhibitory functional connectivity, we adopted the Total Spiking Probability Edges (TSPE) algorithm [11]. Then, we discarded the noisy connections applying a hard threshold [3] and a spatial-temporal filter that guarantees a physiological propagation speed [12].We evaluated the effects of increasing concentration of bicuculline (BIC) on the spontaneous activity in terms of IC_{50} value. It was computed for each condition by fitting normalized MFR values (with respect the basal value) with the Hill Function [13].

III. Results

A. Spontaneous and evoked activity of modular homogeneous cultures

Firstly, we evaluated the spontaneous electrophysiological activity of modular networks made up of two different neuronal populations, namely a cortical and a hippocampal one, to characterize their intrinsic parameters and highlight their differences. The homogeneous cortical (Cx) and hippocampal (Hp) modular cultures were created by means of the polymeric mask described in Sect. II.A. Qualitatively, both cortical and hippocampal dynamics displayed both a random spiking activity and highly packed bursts (Fig. 1A, *first row*). Generally, the cortical populations displayed higher spiking activity with respect to the one of hippocampal networks, which on the other hand had very little variability. Moving on to the characterization of the bursting dynamics of the two populations, we observed that the increase in the firing did not induce a difference in the bursting rate. However, the different cell types of the two networks brought a change in the shape of the bursts, as they were significantly longer in the Cx case.

Then, we investigated the low-frequency response (0.2 Hz stimulation) of these two populations to investigate how the signal propagates within modular cortical and hippocampal populations. We compared the stimuli-evoked response of the cortical and hippocampal populations as a function of the location of the stimulation sites (i.e., stimulated assembly) by means of the PSTH (Fig. 1A, *second row*). This analysis was carried out by considering the different synaptic responses of the network, namely, the early phase-mediated AMPA receptors, lasting no more than 35 ms; and the late NMDA mediated, lasting hundreds of milliseconds. The two considered neuronal types display a very different response. The cortical assemblies are generally more reactive than the hippocampal ones to the delivery of low-frequency stimulation protocols, as we can qualitatively deduce from the PSTH areas (Fig. 1A, *second row*). Moreover, although both the cortical and hippocampal cultures exhibited a fast (< 35 ms) response, this did not propagate uniformly in the hippocampal networks. In addition, only cortical assemblies displayed a significant late (35–500 ms) response (second peak in the PSTH).

B. Spontaneous activity of modular heterogeneous cultures

The difference in the signal propagation in cortical and hippocampal cultures suggests a different organization of the two networks, which facilitates synaptic integration in the case of cortical ensembles. However, these intrinsically different populations are densely connected and therefore constantly in communication in the brain. Therefore, we investigated how the two different circuitries influence each other. This was achieved by creating a heterogeneous configuration (CxHp) by means of the same polymeric mask, which allowed the separation of the cell bodies but the communication between the two neuronal types by means of bundles of neurites. The simultaneous presence of two different neuronal modules shaped the functional connections (excitation vs. inhibition), orchestrating the emerging patterns of electrophysiological activity. Our main findings demonstrated that hippocampal neurons project strong inhibitory connections toward the cortical counterpart from both a functional and a structural point of view (Fig. 1B). The strong inhibitory afferences modulated the typical “population event” signature of dissociated neuronal cultures, i.e., the network bursts, by acting on their temporal scale. In contrast, cortical neurons established a larger amount of intrapopulation connections, suggesting the emergence of micro-circuits. Moreover, we

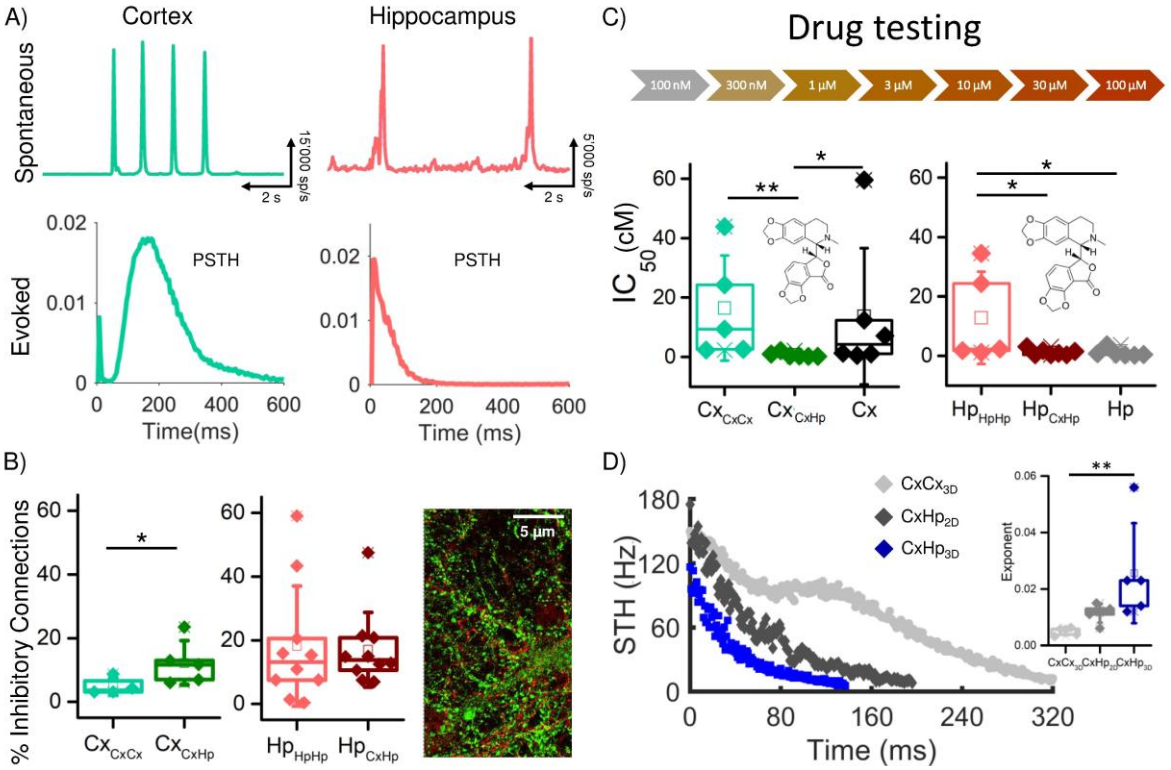


Fig. 1: Effect of an increasingly complex *in vitro* model on cortical and hippocampal populations. (**A**) Spontaneous and evoked activity of cortical and hippocampal modular populations. (**B**) Percentage of incoming inhibitory functional connections in modular homogeneous and modular heterogenous networks both in the cortical and hippocampal case. Representative stained glutamatergic (VGlut1, green) and GABAergic (VGAT, red) synaptic receptors used to quantify the morphological connections. (**C**) Drug administration protocol and relative IC_{50} value in modular homogeneous, modular heterogenous, and non-modular homogeneous networks both in the cortical and hippocampal case. (**D**) Modulation of the population events in 2D heterogeneous, 3D homogeneous and 3D heterogeneous networks evaluated by means of the Spike Time Histogram (STH) and decaying exponent, * refers to $0.01 < p < 0.05$ and ** to $0.001 < p < 0.01$, Kruskal-Wallis, non-parametric test.

proved topological properties such as small-worldness, degree distribution, and modularity of neuronal assemblies were favoured by the physical environment of this configuration [3].

C. Chemical modulation of the activity of modular heterogeneous cultures

We investigated whether the introduction of modularity and heterogeneity would determine different results (with respect to the conventional homogeneous models) when applying a chemical stimulation. In particular, we evaluated the effects of bicuculline (BIC), a competitive antagonist of $GABA_A$ receptors, on the firing activity of modular heterogeneous, modular homogeneous, and non-modular homogeneous networks. We computed a dose-response curve for each configuration, and then we extracted their IC_{50}value (Fig. 1C). IC_{50} values of the heterogeneous configuration were statistically lower than the ones of homogenous modular networks, both in the case of cortical and hippocampal assemblies. A statistical difference in terms of cortical IC_{50} emerged also among homogeneous non-modular and heterogeneous cortical configurations (which had the lowest values, indicating an anticipation of the effect). Instead, in the hippocampal case, another difference was highlighted by the addition of the modularity: modular IC_{50} resulted to be significantly higher than non-modular controls. These results showed clear differences between modular, homogeneous and heterogeneous cultures, suggesting that ignoring modularity and heterogeneity could lead to underestimate or overestimate the effect of a drug and therefore they should always be included in *in vitro* neuronal model adopted to perform pharmacological studies.

D. Increasing the realism of the in vitro model: 3D modular heterogeneous cultures

However more accurate a model that includes modularity and heterogeneity may be (cf., Sect. III.A and III.B), a key aspect of the *in vivo* microenvironment is still missing: three-dimensionality. By exploiting the same polymeric mask used in the previous sections, we created a simple 3D heterogeneous culture with glass microbeads as scaffold where neurons can organize their connectivity in 3D. Despite the differences in mechanical properties (porosity, Young' modulus, etc.) of this type of scaffold with respect to the *in vivo* extracellular matrix, the recreated 3D connectivity is nonetheless able to modulate the duration and the organization of the bursting activity of the entire network. The mere presence of three-dimensionality defined a redistribution of the spiking activity, less packed, and modulated the duration and the organization of the bursting activity, as suggested by the exemplary STH in Fig. 1D . On the other hand, the hippocampal inputs modulated the duration of the network bursts independently of the spatial organization of the cultures. When combined, these two features mainly act on the network bursting features: the activity rate is higher than the solely 3D control, but lower with respect to the 2D heterogeneous one, the coexistence of three-dimensionality and heterogeneity seems to drive the dynamics to an intermediate state.

E. 3D modular and heterogeneous cultures with realistic biomechanical properties

The previous 3D model, however, has a great limitation as it does not recreate the *in vivo*-like biomechanical properties of the extracellular matrix. To overcome this limit, we developed neurospheroids, i.e., neuronal 3D cultures obtained from primary cortical (Cx) and hippocampal (Hp) cells without any scaffold. Spheroids were realized by plating neurons in an ultra-low attachment 96-microwells (Life Technologies). The shape and the low adhesion properties of the wells induced the creation of a single neuronal spheroid per well of about 8'000 cells each (Fig. 2A). We evaluated the morphology of the Cx and Hp spheroids as a function of their maturation degree. During the development, Hp spheroids presented a faster volume growth than the Cx ones (Fig 2B). Indeed, Cx and Hp spheroids displayed a different growth curve from the DIV 1 (Fig. 2B), indicating a slower cellular aggregation in the cortical case. These results suggest a greater proliferation of hippocampal cells possibly supported by their phase, as they could still be in their mitotic state. Indeed, neurogenesis of hippocampal tissue is delayed during the development of neuronal system [14]. Overall, this 3D model is very powerful, and it could also be exploited to integrate modularity and heterogeneity by coupling spheroids of different neuronal types defining complex neuronal assembloids.

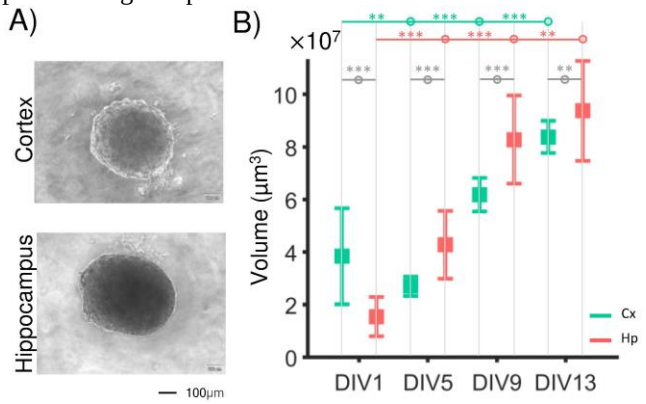


Fig. 2: Neurospheroids. (**A**) DIC microscopy image of a representative cortical and hippocampal spheroid. (**B**) Volume development of the cortical and hippocampal spheroids.

IV. Conclusion

In the present work, we showed that the engineering of *in vitro* neuronal networks allows the modulation of the spontaneous (Sect. III.A, B, and D) as well as the evoked electrophysiological activity (Sect. III.A, C). In particular, we proved the role of the three ingredients (modularity, three-dimensionality and heterogeneity) considering the case-study of cortical-hippocampal ensembles. Our results pointed out the relevance of the simultaneous presence of these features to achieve more realistic *in vivo*-like models of the brain. Considering these findings and exploiting the recent advances in the field of neuroengineering, in light of transferring stimulation protocols to *in vivo* applications, it becomes fundamental to design more and more realistic *in vitro* brain-on-a-chip models to investigate the dynamical properties of complex neuronal circuits. Neurospheroids are a step forward, as they combine many *in vivo* properties such as a realistic 3D connectivity and could be combined in a heterogeneous structure. As for future applications, they may be useful for therapeutics and diagnosis [15], to test and understand the different effects of nanoparticles and nanomedicines on the cells. The combination of these technologies will allow not only to perform a variety of tasks, such as drug delivery in a prolonged or targeted way, but also to identify the cells at the origin of a particular disease (such as cancer) to modulate their activity.

References

[1] F. Callegari, M. Brofiga, and P. Massobrio, "Modeling the three-dimensional connectivity of in vitro cortical ensembles coupled to Micro-Electrodde Arrays," *PLoS Comput Biol*, 2023.

[2] M. Brofiga, M. Pisano, R. Raiteri, and P. Massobrio, "On the road to the brain-on-a-chip: A review on strategies, methods, and applications," *J. Neural Eng.*, vol. 18, no. 4, Aug. 2021.

[3] M. Brofiga, M. Pisano, M. Tedesco, A. Boccaccio, and P. Massobrio, "Functional Inhibitory Connections Modulate the Electrophysiological Activity Patterns of Cortical-Hippocampal Ensembles," *Cereb. Cortex*, vol. 32, no. 9, pp. 1866–1881, Apr. 2022.

[4] M. Brofiga, M. Pisano, M. Tedesco, R. Raiteri, and P. Massobrio, "Three-dimensionality shapes the dynamics of cortical interconnected to hippocampal networks," *J. Neural Eng*, vol. 17, p. 56044, 2020.

[5] A. Maccione, M. Gandolfo, P. Massobrio, A. Novellino, S. Martinoia, and M. Chiappalone, "A novel algorithm for precise identification of spikes in extracellularly recorded neuronal signals," *J. Neurosci. Methods*, vol. 177, no. 1, pp. 241–249, Feb. 2009.

[6] M. Chiappalone, A. Novellino, I. Vajda, A. Vato, S. Martinoia, and J. van Pelt, "Burst detection algorithms for the analysis of spatio-temporal patterns in cortical networks of neurons," *Neurocomputing*, vol. 65–66, no. SPEC. ISS., pp. 653–662, Jun. 2005.

[7] V. Pasquale, S. Martinoia, and M. Chiappalone, "A self-adapting approach for the detection of bursts and network bursts in neuronal cultures," *J. Comput. Neurosci.*, vol. 29, no. 1–2, pp. 213–229, Aug. 2010.

[8] S. Van De Vijver *et al.*, "The effect of pharmacological inhibition of serine proteases on neuronal networks in vitro," *PeerJ*, vol. 2019, no. 4, 2019.

[9] D. Eytan and S. Marom, "Dynamics and effective topology underlying synchronization in networks of cortical neurons," *J. Neurosci.*, vol. 26, no. 33, pp. 8465–8476, Aug. 2006.

[10] F. Callegari, M. Brofiga, F. Poggio, and P. Massobrio, "Stimulus-Evoked Activity Modulation of In Vitro Engineered Cortical and Hippocampal Networks," *Micromachines*, vol. 13, no. 8, p. 1212, Jul. 2022.

[11] S. De Blasi, M. Ciba, A. Bahmer, and C. Thielemann, "Total spiking probability edges: A cross-correlation based method for effective connectivity estimation of cortical spiking neurons," *J. Neurosci. Methods*, vol. 312, pp. 169–181, Jan. 2019.

[12] S. Jacobi and E. Moses, "Variability and Corresponding Amplitude–Velocity Relation of Activity Propagating in One-Dimensional Neural Cultures," *J. Neurophysiol.*, vol. 97, no. 5, pp. 3597–3606, May 2007.

[13] J. G. Wagner, "Kinetics of pharmacologic response I. Proposed relationships between response and drug concentration in the intact animal and man," *J. Theor. Biol.*, vol. 20, no. 2, pp. 173–201, Aug. 1968.

[14] J. Altman and G. D. Das, "Autoradiographic and histological evidence of postnatal hippocampal neurogenesis in rats," *J. Comp. Neurol.*, vol. 124, no. 3, pp. 319–335, Jun. 1965.

[15] L. Yin and Z. Zhong, "Nanoparticles," *Biomater. Sci.*, pp. 453–483, Jan. 2020.

Comparison of RF exposure levels in 5G-V2X and ITS-5.9 GHz vehicular connectivity

M. Benini[1,2], M. Bonato[1], S. Gallucci[1,2], S.Fiocchi[1], E.Chiaramello[1], M.Parazzini[1] and G.Tognola[1]
[1] *Institute of Electronics, Computer and Telecommunication Engineering (IEIIT), CNR, 20133 Milano, Italy.*
[2] *Department of Electronics, Information and Bioengineering (DEIB), Politecnico di Milano, 20133, Milano, Italy*

***Abstract*— In the present study a comparison of radiofrequency (RF) exposure levels on a pedestrian in the nearby of the vehicle specifically generated by two different vehicle-to-everything (V2X) communication technologies, i.e., the well-validated ITS-5.9 GHz and the more innovative 5G-V2X was performed. EMF exposure was calculated using a numerical dosimetry approach. Two different kinds of vehicular connectivity antennas have been considered, i.e., two quarter-wave monopoles (for ITS-5.9 GHz) and two 4x2 patch array antennas (for 5G-V2X) that were mounted on a 3D CAD model of a city car. Numerical dosimetry simulations have been performed using the software Sim4Life exploiting the FDTD method. The human model was positioned near the vehicle in different configurations and orientations. The comparison of exposure assessment generated by the two different technologies was performed by comparing the Specific Absorption Rate (SAR) values over 10 g of human tissues. The results show generally higher exposure levels when the ITS-5.9 GHz technology is applied, rather than the 5G-V2X.**

***Keywords*— RF human exposure assessment, C-V2X, 5G, ITS-5.9 GHz.**

I. Introduction

The automotive field is nowadays increasingly pushing toward the development of new wireless technologies and remote sensing in vehicular connectivity to prevent the safety of people on road. This leads to the new concept called "Intelligent Transport System" (ITS) [1][2]. In particular, the ITS is a multifaced concept that embedded many services, among which there is the possibility to connect vehicles with other entities, generating the so-called vehicle-to-everything communication (V2X), such as (i) other vehicles (vehicle-to-vehicle communication, V2V), (ii) pedestrians (vehicle-to-pedestrian communication, V2P), (iii) infrastructures (vehicle-to-infrastructure communication, V2I), and (iv) networks (vehicle-to-network communication, V2N) [3][4]. The V2X communication technology mainly relies on two wireless technologies: (i) the WiFi mobility based on the well-consolidated IEEE 802.11p protocol (or ITS-G5 in the European version) that works at the ITS-5.9 GHz band [5] and the recent technology of the Cellular-V2X (C-V2X) based on the 3G/4G and LTE band [6][7][8]. The C-V2X is also widening to the 5G New-radio (NR) wireless communication, in which the vehicular communication technologies will be open on the 5G world, generating the 5G-V2X technologies. The 5G-V2X technology will enable a very reliable and efficient low-latency communication and high data rate transmission, thanks to the use of two additional larger RF frequency ranges, namely frequency range 1 (FR1), from 410 kHz to 7.125 GHz, and frequency range 2 (FR2), from 24.25 to 52.6 GHz, in the millimeter waves spectrum [9][10].

Many of these vehicular innovations will be widespread in the next years and will strongly change the radio frequency electromagnetic fields (RF-EMF) exposure of people in a car and in the vicinity of a car, causing possible concerns among the road-users [11]. To the best of our knowledge, few articles exist on the investigation of the dose absorbed by the human body generated by these vehicular technologies [12]. To that purpose, Tognola et al. [13] investigated the in-vehicle dose absorbed by a passenger generated by V2V communication operating at 5.9 GHz and Benini et al., [14] and Bonato et al., [15] investigated the exposure of a pedestrian nearby a vehicle equipped with V2V communication at ITS-5.9 GHz and 5G-V2X operating at 3.5 GHz, respectively. All the dose absorbed values obtained [13][14][15] were well below the limits imposed by the basic restriction of the ICNIRP [16] and IEEE guidelines [17]. However, it would be interesting to investigate the differences in the exposure levels of a pedestrian nearby the vehicle generated specifically by the well-known ITS-5.9 GHz and the innovative 5G-V2X technologies. Thus, the aim of this paper is to compare the exposure levels of a pedestrian generated by the consolidated ITS-5.9 GHz and the new 5G-V2X. In the next section the exposure scenario investigated will be presented.

II. Materials and Methods

The exposure levels were assessed by exploiting the simulator software Sim4Life (ZMT Zurich Med Tech AG, Zurich, Switzerland, www.zurichmedtech.com) though the use of the FDTD method. To provide the V2V communication based on the IEEE 802.11p protocol from literature two quarter-wave monopoles are used, operating at the 5.9 GHz [13][18], while the one based on the 5G-V2X communication are 4x2 patch elements array antennas operating at the 3.5 GHz, in the FR1 frequency range [19]. All the elements of the array had a phase shift of 0° to obtain a central frontal beamforming perpendicular to the plane of the array antenna. Figure 1 illustrates the two antennas used for performing the two different vehicular technologies which their respective geometrical dimensions; below each antenna are reported also the corresponding radiation patterns. For each technology investigated the corresponding antennas were positioned on a 3D CAD model of a city car, one in the front of the car, i.e., on the 36° tilted windscreen, and the other one on the back roof of the car to replicate the real montage setting [20]. Figure 2 showed the montage positions of the antennas highlighted by the red dot points.

An adult female phantom (Ella, 26-yo girl) was positioned in 5 configurations near the vehicle in two different orientations, i.e., frontal and orthogonal, for a total of 10 different simulations for each V2V technologies investigated. Figure 2

shows the human model in the 5 different configurations near the car: one configuration in the front of the car (CONF 1), one in the back of the car (CONF 5), and three on the lateral side of the car (CONF 2, CONF 3, CONF 4), in the frontal (Fig. 2A) and lateral orientation (Fig. 2B). The dielectric properties of the human model were chosen according to the literature [21][22][23]. The maximum step of the mesh in the simulations was made to correctly discretized all the human model tissues. For the absorbing boundary conditions was set the Perfectly matched layer (PML).

For assessing the exposure levels, as indicated by the ICNIRP guidelines [16], the peak of the Specific Absorption Rate (SAR [W/kg]) over 10 g of tissue ($pSAR_{10g}$) has been investigated, specifically for the skin of the whole body and the eyes tissues (composed of the vitreous humor, sclera, lens, and cornea) which are the most superficial tissue and organs, respectively.

The peak SAR values were calculated considering an input power of 1 W for each antenna.

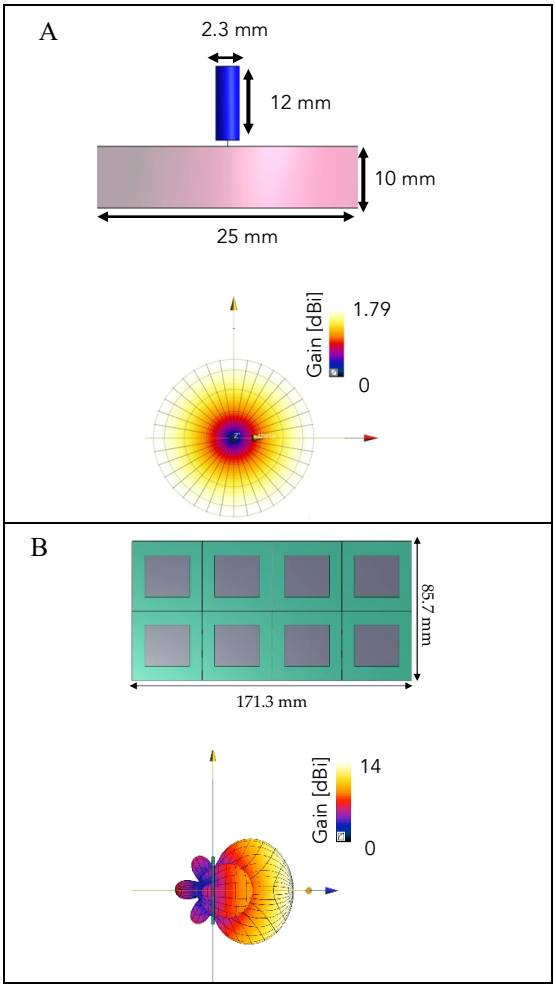


Fig. 1: The two different antennas used to operate the two V2V technologies: (A) the quarter-wave monopole used in the ITS-5.9 GHz and (B) the 4x2 patch elements array antenna operating at 3.5 GHz used for the 5G-V2X. Below each antenna are illustrated the corresponding radiation patterns.

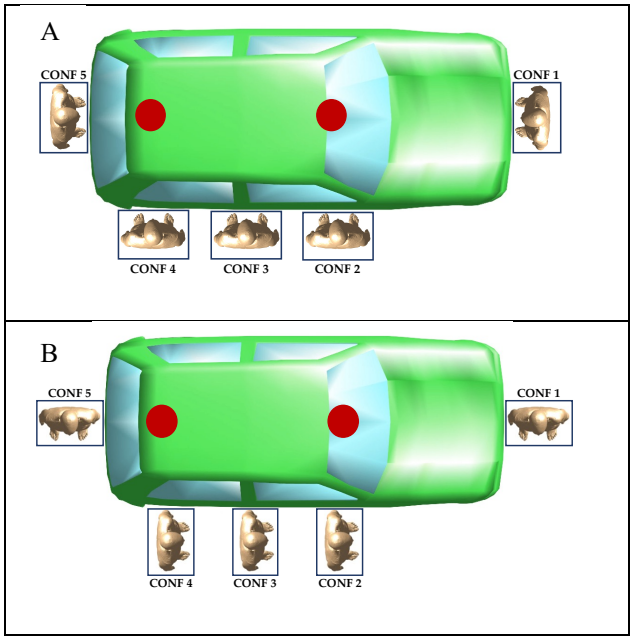


Fig. 2: Frontal view of the 5 different configurations (CONF 1, CONF 2, CONF 3, CONF 4, CONF 5) of the human model near the vehicle in the two different orientations: (A) frontal and (B) orthogonal orientation. The red dots represent the position of the two antennas.

III. Results

In this section we reported some results obtained from the comparison of the exposure levels on a pedestrian nearby the vehicle generated specifically by the ITS-5.9 GHz and 5G-V2X at 3.5 GHz. Figure 3 reported the $pSAR_{10g}$ values of the whole-body skin and eyes tissues as a function of the 5 configurations near the vehicle for each of the two technologies investigated, i.e., ITS-5.9 GHz and 5G-V2X, in the frontal (fig. 3A) and orthogonal (fig. 3B) orientation. Generally, from figure 3, for each technology, the $pSAR_{10g}$ values obtained in the frontal orientation (Fig. 3A) were always higher than that obtained in the orthogonal one (Fig. 3B). Furthermore, comparing the two technologies, for each tissue region investigated, the $pSAR_{10g}$ values generated by the ITS-5.9 GHz were always higher than that obtained with the 5G-V2X at 3.5 GHz except for the CONF 1 in the orthogonal orientation (Fig. 3B) in which the maximum $pSAR_{10g}$ values is when the 5G-V2X is applied. In both two technologies, the maximum $pSAR_{10g}$ was always located in the skin, more precisely in the upper body region, rather than in the eye's tissues. In particular, the maximum peak with the ITS-5.9 GHz, i.e., 34.67 mW/kg, was when the human model was located in the back of the car (CONF 5) in the frontal orientation (Fig. 3A), while with the 5G-V2X the maximum $pSAR_{10g}$, i.e, 6.8 mW/kg was presented when the human model was located in the front of the car (CONF 1) in the orthogonal orientation (Fig. 3B). These relevant differences lie on the different kind of antennas used during the simulations, i.e., the quarter-wave monopole antenna for the ITS-5.9 GHz and the array antenna for the 5G-V2X (previously mentioned in the *Materials and methods* section), which generated different radiation patterns which differently affected the human body region near the vehicle. The former is an omnidirectional antenna that spreads radiation equally on the azimuth plane; the latter is a directional antenna with 0° phase

shift that generates a beamforming perpendicular to the plane of the array antenna (as shown in figure 1).

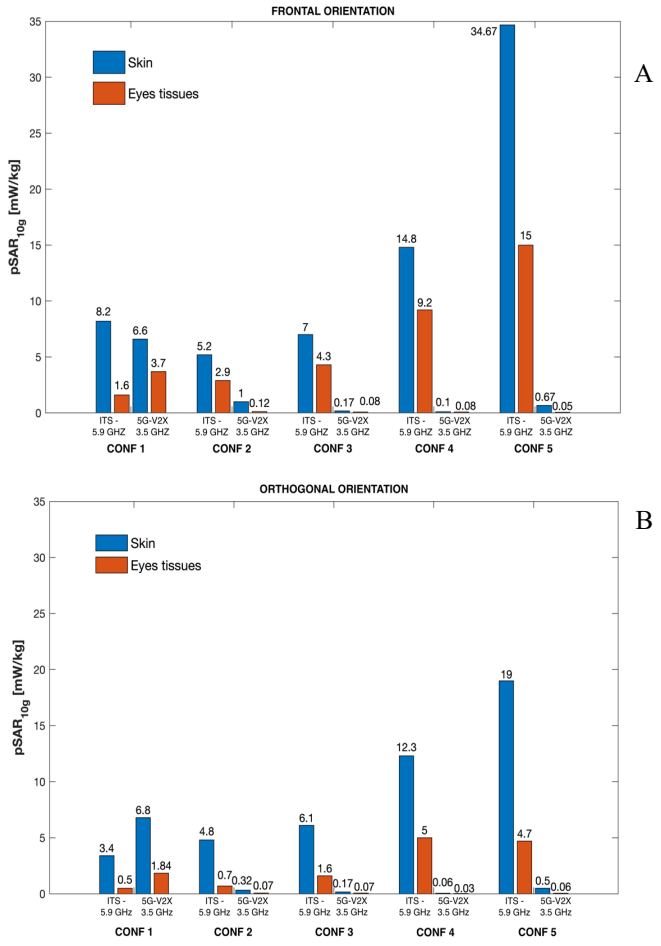


Fig. 3: $pSAR_{10g}$ values in the skin (blue bar) and eyes tissues (red bar) of the human phantom as a function of the five different configurations near the car in the frontal (A) and orthogonal (B) orientation generated by the ITS-5.9 GHz (data collected from [14]) and 5G-V2X at 3.5 GHz (data collected from [15]) technologies

IV. Conclusion

This is a preliminary study aimed to compare the exposure levels of a pedestrian nearby a vehicle equipped with the consolidated ITS-5.9 GHz and the innovative 5G-V2X vehicular technologies which will be widespread in the forthcoming years.

The main differences in the exposure levels generated by the two vehicular technologies are due to the different radiation patterns of the different antennas used to operate the two vehicular technologies. As a general remark, the human model was more exposed to the radiation in the ITS-5.9 GHz condition that the 5G-V2X condition. However, the exposure levels in both vehicular technologies were well below the safety limits imposed by the ICNRP [16] and IEEE guidelines [17]. Further investigations on different tissues (e.g., the head skin and in the skin of the genitals area) will complete the investigation of the comparison of the exposure assessment generated by the two technologies.

Funding

This work was financed by Project "EXPOAUTO - Cumulative real smart car exposure to radiofrequency electromagnetic fields in people of different ages from new technologies in automotive services and connected objects" [PNREST Anses, 2020/2 RF/05].

Acknowledgement

The authors wish to thank ZMT Zurich MedTech AG (www.zmt.swiss) for having provided the simulation software SEMCAD X/SIM4Life.

References

[1] Rebbeck T, Stewart J, Lacour HA, Lillen A, McClure D, Dunoyer A, "Socio-economic benefits of cellular V2X". Final Report for 5GAA (accessed on 31 August 2019) 2017 Dec.

[2] Bazzi A, Cecchini G, Menarini M, Masini BM, Zanella A, "Survey and perspectives of vehicular Wi-Fi versus sidelink cellular-V2X in the 5G era. Future Internet." 2019 Jun;11(6):122.

[3] 3GPP Technical Specification Group Radio Access Network, Study on New Radio Access Technology: Physical Layer Aspects (Release 14) TR 38.802 V14.2.0. 2017.

[4] 3GPP Technical Specification Group Radio Access Network, Study on Scenarios and Requirements for Next Generation Access Technologies (Release 16) TR 38.913 V16.0.0. 2020.

[5] IEEE Standard for Information technology, Local and metropolitan area networks. Specific requirements, Part 11: Wireless LAN Medium Access Control (MAC) and Physical Layer (PHY) Specifications Amendment 6: Wireless Access in Vehicular Environments, IEEE Standard 802.11p-2010, 2010.

[6] Intelligent Transport Systems (ITS); LTE-V2X Access layer specification for Intelligent Transport Systems operating in the 5 GHz frequency band, ETSI EN 303 613 V1.1.1, 2020.

[7] 3rd Generation Partnership Project; Technical Specification Group Radio Access Network; Study on LTE-based V2X services; (Release 14), 3GPP TR 36.885 V14.0.0, 2016.

[8] LTE; Evolved Universal Terrestrial Radio Access (E-UTRA); User Equipment (UE) radio transmission and reception (3GPP TS 36.101 version 14.20.0 Release 14), ETSI TS 136 101 V14.20.0, 2021.

[9] 3GPP TR 38.886 V16.3.0; Technical Specification Group Radio Access Network; V2X Services Based on NR; User Equipment (UE) Radio Transmission and Reception, Release 16. 3GPP Support Office: Valbonne, France, 2021.

[10] 3GPP TR 38.785 V0.3.0; Technical Specification Group Radio Access Network; NR Sidelink Enhancement; User Equipment (UE) Radio Transmission and Reception, Release 17. 3GPP Support Office: Valbonne, France, 2021.

[11] Bushberg JT, Chou CK, Foster KR, Kavet R, Maxson DP, Tell RA, Ziskin MC, "IEEE Committee on Man and Radiation—COMAR Technical Information Statement: Health and safety issues concerning exposure of the general public to electromagnetic energy from 5G wireless communications networks". Health Physics. 2020 Aug;119(2):236.

[12] Tognola, G.; Bonato, M.; Benini, M.; Aerts, S.; Gallucci, S.; Chiaramello, E.; Fiocchi, S.; Parazzini, M.; Masini, B.; Joseph, J.; et al. "Exposure to RF Electromagnetic Fields in the Connected Vehicle: Survey of Existing and Forthcoming Scenarios". IEEE Access 2022, 10, 47764–47781.

[13] Tognola, G.; Masini, B.; Gallucci, S.; Bonato, M.; Fiocchi, S.; Chiaramello, E.; Parazzini, M.; Ravazzani, P. "Numerical Assessment of RF Human Exposure in Smart Mobility Communications". IEEE J. Electromagn. RF Microw. Med. Biol. 2021, 5, 100–107.

[14] Benini, M., Parazzini, M., Bonato, M., Gallucci, S., Chiaramello, E., Fiocchi, S., & Tognola, G., "Road user exposure from ITS-5.9 GHz vehicular connectivity. *Sensors*, 2022, *22*(18), 6986.

[15] Bonato, M., Tognola, G., Benini, M., Gallucci, S., Chiaramello, E., Fiocchi, S., & Parazzini, M., "Assessment of SAR in road-users from 5G-V2X vehicular connectivity based on computational simulations". *Sensors*, 2022, *22*(17), 6564.

[16] International Commission on Non-Ionizing Radiation Protection. Guidelines for limiting exposure to electromagnetic fields (100 kHz to 300 GHz). Health physics. 2020 May 1;118(5):483-524.

[17] IEEE Standard for Information Technology, "Local and metropolitan area networks– Specific requirements, Part 11: Wireless LAN medium access control (MAC) and physical layer (PHY) specifications amendment 6: Wireless access in vehicular environments," IEEE Standard 802.11p, pp. 1–51, 2010.

[18] Gallo, M.; Bruni, S.; Pannozzo, M.; Zamberlan, D., "Performance evaluation of C2C antennas on car body". In Proceedings of the 7th European Conference on Antennas and Propagation (EuCAP2013), Gothenburg, Sweden, 8–12 April 2013; pp. 3136–3139.

[19] 5GCAR project, Deliverable D3.1: Intermediate 5G V2X Radio. 2018. Available at: https://5gcar.eu/wp-content/uploads/2019/05/5GCAR_D3.1_v1.0.pdf

[20] TE connectivity, White paper: V2X – _An important building block in cooperative intelligent transport systems (C-ITS). 2019. Available at: https://www.te.com/content/dam/te-com/documents/automotive/global/automotive-next-gen-mobility-v2x-09-2019-en.pdf

[21] Gosselin MC, Neufeld E, Moser H, Huber E, Farcito S, Gerber L, Jedensjö M, Hilber I, Di Gennaro F, Lloyd B, Cherubini E., "Development of a new generation of high-resolution anatomical models for medical device evaluation: the Virtual Population 3.0." Physics in Medicine & Biology. 2014 Aug 21;59(18):5287.

[22] C. Gabriel, S. Gabriel and Y.E. Corthout, "The dielectric properties of biological tissues: I. Literature survey," Physics in Medicine &Biology, 1996, 41(11), 2231.

[23] S. Gabriel, RW. Lau, and C. Gabriel, "The dielectric properties of biological tissues: II. Measurements in the frequency range 10 Hz to 20 GHz", *Phys Med Biol*, vol. 41, pp. 2251-2269, 1996.

Profiling of phase-amplitude couplings across sleep for personalized neuroengineering systems

V.R. Cota[1], G. Federici[2], G. Arnulfo[2], and M. Chiappalone[1,2]
[1] *Rehab Technologies Lab, Istituto Italiano di Tecnologia, Genoa, Italy*
[2] *Dept. Informatics, Bioengineering, Robotics and Biosystems Engineering, Università degli Studi di Genova, Genoa, Italy*

***Abstract*—In this work, we computed sleep-wake cycle (SWC) stage-specific cross-frequency couplings in order to identify patterns of neural synchronization with neurobiological relevance. This may be used for the control of neuroengineering systems capable of delivering personalized therapeutic electrical stimulation according to relevant sleep events.**

***Keywords*—Cross frequency coupling, neural plasticity, neuromodulation, sleep stages.**

I. Introduction

THE sleep-wake cycle (SWC) is a circadian neurobiological rhythm of major importance across several animal species, humans included [1]. It is characterized by a recurrent alternation of brain states (or stages) with distinct behavioural and electrophysiological features [2]. In a simplified fashion, states can be classified in three: 1) wakefulness (WK) with desynchronized low-amplitude local field potentials (LFP) and active movement; 2) slow wave sleep (SWS) with synchronized high-amplitude LFP in lower frequencies (delta range) and absence of movement, and; 3) rapid eye movement sleep (REM) with low-amplitude LFP or synchronization in the theta range with deeply reduced muscular tonus and absence of behaviour.

Differently from the lay notion of a brain "shut down", SWC is in fact a result of complex interactions of neurobiological phenomena serving multiples purposes indispensable for homeostasis and life in general [3]. These molecular and cellular processes result in the production of stereotypical electrophysiological oscillations, the synchronization of which is highly descriptive of the effectiveness of the interaction between areas. Among others, these interactions underlie cognitive processing during both wakefulness and sleep. Particularly, a triple coordination between oscillations of different frequencies (synchronization between cortical slow waves, corticothalamic spindles, and hippocampal ripples) during SWS is a key biomarker for the consolidation of memory traces and the migration of information from hippocampal to cortical areas [4], [5], [6].

Considering the importance of sleep in the support of core neural functions (such as those related to brain plasticity), taking SWC into account may be beneficial to the development of personalized solutions in neuroengineering. In this sense, algorithms for event detection (spindles and ripples), SWC staging and, particularly, measurements of synchronization are of great value. Among these, cross-frequency couplings described above, obtained by measurements of phase-amplitude coupling (PAC) such as comodulograms and modulation index and [7], seems well fit for the purpose. In line with this rationale, we hypothesize that, if PAC is in fact important for information transfer across areas of the brain – and thus memory consolidation – and also if such is carried out during SWC, then brain stages can be described on the basis of such synchronization pattern.

In this first work, we benefited from well-established SWC staging algorithms, as well as spindle detection tools, in order to assess the distinct PAC profiles of each major stage (WK, SWS, and REM) and during these specific events. The findings will be used for future developments of algorithms for real time assessment of sleep electrophysiology, including detection of signature waves (e.g. spindles and/or ripples), measurement of synchronization levels, novel PAC-dependent strategies of stage detection, and others.

II. Methods

A. Electrophysiological recordings

LFP recordings used for the SWC staging, creation of hypnograms, and PAC calculation were obtained from an open source database resulting from the study of Barger and colleagues [8] and can be found online at https://osf.io/py5eb/. They were recorded from C57BL/6 mice (N = 10) using surgical screws positioned in the parietal cortex and comprehended five daily sessions of at least 4 hours duration (bandpass filtered 1-500 Hz; sampling rate of 512 Hz).

B. Sleep-wake cycle staging

For the detection of SWC stages and construction of hypnograms (sequence of stages across time), we adopted two approaches. We first used AccuSleep [8]. This software package uses a machine learning approach to classify images composed by the z-scores of both mice LFP and their electromyography. For training the network, the model uses the dataset composed of all animals in the first day of recording which has been previously labelled (staged) by an experienced investigator. Sequentially, the network is applied to automatically label the other four days (five in total) of data. Results presented here correspond to non-labelled days.

The second staging algorithm is taken from the work of Gervasoni and colleagues [9]. Termed here 'State Space', the algorithm consists of describing the SWC as a dynamical system in which the trajectory is computed from LFP spectral content – particularly ratios of power in specific frequency ranges (ratio 1: 0.5–20/0.5–55 Hz; ratio 2: 0.5– 4.5/0.5–9 Hz) – further processed by dimensionality reduction (Principal Component Analysis) and smoothing. Such neurodynamical representation results in clear cluster of points which can be automatically (or manually) detected and which were empirically demonstrated to correspond to each one of the

major sleep stages. Differently from AccuSleep, it does not depend on EMG (although the signal can be used), nor does it need the input from manual labelling.

The purpose of applying both approaches and comparing them is twofold. First, although the State Space algorithm has been used in different studies (e.g. [10], [11]), it has never been compared with other approaches for additional validation. Second, the algorithm can run online [9], paving the way for hardware implementations.

C. *Spindle detection*

We used two filtering algorithms from [12] and [13] for the detection of spindles. They both consist essentially in filtering the LFP recording in the spindle range (e.g. 7 – 15 Hz) and later detecting the envelope of the filtered tracing for the detection of the "waxing and waning" format which characterizes the wave. Both detections are constrained in amplitude and time features for improved performance: minimum duration of spindles, minimum separation between events, minimum amplitude (detection threshold), and maximum amplitude to exclude artefacts. The goal of using more than one tool is similar to that of the SWC staging: comparison and further validation.

D. *Phase-amplitude coupling*

Cross-frequency coupling was measured here as the driving force between the phase of a low-frequency oscillation and the amplitude of a high-frequency oscillation, a type of synchronization called Phase-Amplitude Coupling or PAC, as mentioned before. To do this, we computed the coupling for several pairs of frequencies (phase frequencies: 1 – 30 Hz; amplitude frequencies: 10 – 210 Hz) using a well-established metric termed modulation index or MI [7]. Briefly, the LFP is first filtered in the frequency bands of interest (for which one wants to compute the coupling). In the filtering process, the phase of the slow oscillation is obtained. Then, the envelope of the high-frequency oscillation is computed using the Hilbert Transform to obtain its amplitude. After the Amplitude–Phase (0 to 720°) histogram is obtained, the presence and magnitude of peaks in this distribution (evidence of coupling) is computed by the Kulbach-Leibler distance, which yields the MI. By their turn, comodulograms are obtained when the MI values of a set of frequency pairs varying in a certain range are depicted as color-coded 3D plots (such as those in Figure 1). Comodulograms were obtained from 30 s excerpts of the LFP extracted from the middle of the periods in each of the stages.

E. *Profiling the coupling pattern*

After the comodulograms were built, we picked specific points (pairs of frequency) for statistical comparison. They were chosen for both their neurobiological relevance and also for the qualitative differences that could be observed by the visual inspection of the plots. Table I summarizes pairs of frequency (centre values) assessed in this study.

TABLE I: PAIRS OF FREQUENCIES ASSESSED BY PAC

Identifies	*Frequency used for phase (low)*	*Frequency used for amplitude (high)*
A	Theta (7.5 Hz)	High gamma (140 Hz) / ripples
B	Theta (7.5 Hz)	Low gamma (70 Hz)
C	Slow wave (1 Hz)	Theta (11 Hz) / spindles
D	Slow wave (1 Hz)	High gamma (150 Hz) / ripples
E	Theta (11 Hz) / spindles	Low gamma (70 Hz)
F	Delta (2.5 Hz)	Theta (11 Hz) / spindles
G	Slow wave (1 Hz)	Higher gamma (200 Hz) / ripples

III. RESULTS AND DISCUSSION

A. *SWC stages modulate couplings*

The algorithms for SWC staging and spindle detection displayed strong agreement between results (data not shown), specially after fine adjustment of filtering parameters in the second case. Hypnograms showed a healthy polyphasic alternation of WK, SWS, and REM, with REM always following SWS. Moreover, spindles were detected almost exclusively during SWS and virtually never (< 1% of times) during WK, as expected.

Stage-specific (obtained from AccuSleep) comodulograms of a representative animal (left: WK; center: SWS; right: REM) are displayed on Figure 1, which shows some regions that are strongly modulated across sleep, such as coupling between theta and gamma (low and high).

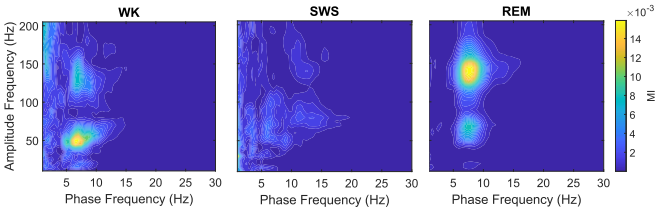


Fig. 1: Comodulogram plots of Mouse 1 during WK (left), SWS (center), and REM stages (right) show strong stage-specific modulation of PAC. Colour scale in the right represents MI values.

Group measures of specific frequency pairs can be found in the curves of Figure 2 (comparisons between WK and SWS), Figure 3 (WK and REM), and Figure 4 (SWS and REM). Each panel (A to G) corresponds to a specific frequency pair (as described in Table I) and shows all animals (light gray lines) and the mean with SEM (bold red lines). As it can be seen, the average MI for several frequency pairs displayed differences with statistical significance when comparing distinct stages (***p < 0.001; **p < 0.01; *p < 0.05; paired t-test).

From start, it is clearly apparent that the PAC between the phase of theta range and the amplitude of the gamma range (both high and low; Figures 3 and 4, panels A and B, respectively) are strongly increased during REM sleep in comparison to both WK and SWS. These same couplings also show to be slightly increased in WK when compared to SWS (Figure 2, panels A and B).

Interpretation of such results is straightforward and can be related to the acquisition of memory traces by active exploration during WK and posterior consolidation during sleep, both processes in which theta and gamma oscillations play important roles [14]. Particularly, theta is a very

stereotypical electrophysiological signature of REM and can be clearly noticed in raw tracings. Such observation is in line with other studies on theta-gamma coupling dynamics [15] and is reviewed in [16] on the context of High Frequency Oscillations. Although theta is a rhythm generated within hippocampal circuitry, its influence in cortical areas (such as the prefrontal region) can be captured by cortical electrodes such as those used in the acquisition of the recordings.

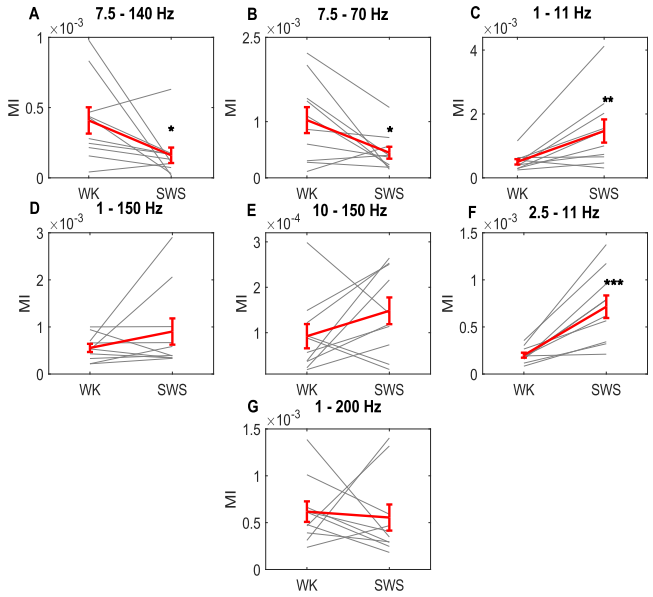


Fig. 2: Group measure of PAC for all different pairs of frequencies considered, comparing WK to SWS (***p < 0.001; **p < 0.01; *p < 0.05; paired t-test). Grey lines: individual animals; red lines: average and SEM.

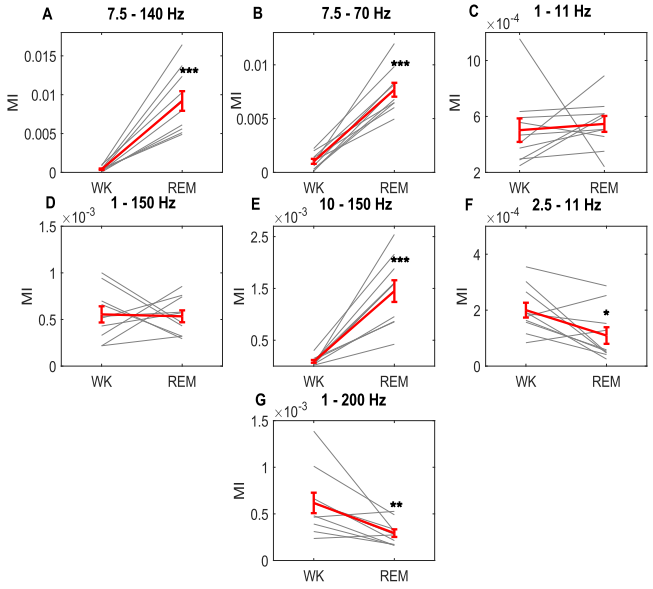


Fig. 3: Group measure of PAC for all different pairs of frequencies considered, comparing WK to REM (***p < 0.001; **p < 0.01; *p < 0.05; paired t-test). Grey lines: individual animals; red lines: average and SEM.

Additionally, PAC values between slow oscillations and theta or between delta and theta are clearly increased during SWS when compared to both WK (Figure 2, panels C and F) and REM (Figure 4, panels C and F). In fact, slow oscillations and delta waves are the predominant rhythms observed during this stage. On the other hand, theta rhythm during SWS is usually suppressed in comparison to the other stages, impairing a straightforward interpretation of this particular coupling result. One possible, even plausible, explanation relies on the known strong coupling between slow oscillations and spindles, which partially occupy the theta band.

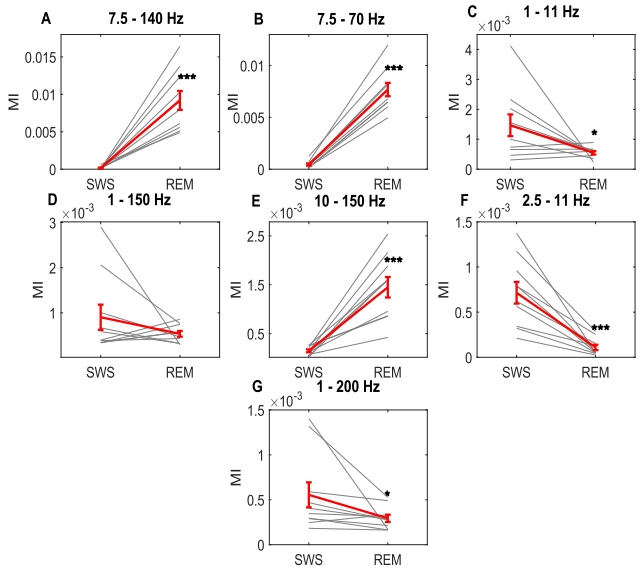


Fig. 4: Group measure of PAC for all different pairs of frequencies considered, comparing SWS to REM (***p < 0.001; **p < 0.01; *p < 0.05; paired t-test). Grey lines: individual animals; red lines: average and SEM.

B. Coupling strength during spindle events is uncertain

In line with this reasoning, it is intriguing that there is no increase in PAC values between theta and gamma during SWS (Figures 2 and 4, panels B and E), which could represent spindle-ripple coupling known to occur during this stage. For this purpose, we also assessed MI values in 30 s excerpts of LFP centered in every occurrence of detected spindles (see sections II.B and II.C). Figure 5 shows a representative animal to illustrate the results of this analysis. Here, hypnograms are depicted as a temporal sequence of color-coded SWC stages (WK: green; SWS: red; REM: blue) and spindles are indicated as dots in the uppermost portion of the hypnogram. In the bottom of hypnograms, black tracings depict the MI values computed across time each 30 s. Top hypnogram is superimposed with slow-oscillation and spindle PAC and bottom hypnogram with spindle and ripple PAC. It is important to register that, in this case, we did no use single comodulogram points, but actually computed the MI onto frequency ranges to better represent the oscillations of interest: 0 – 2 Hz for slow oscillations, 7 – 15 Hz for spindles, and 140 – 200 Hz for ripples.

Some clear features are immediately distinguishable from these plots. First, as mentioned before, hypnograms show clear stereotypical polyphasic alternation of stages with REM always preceded by SWS and spindles occurring mostly during SWS (spindles in WK are probably detection artifacts). Furthermore, REM seems to exert a strong stage-modulation between the frequency ranges of both slow oscillations to

spindle coupling (decreasing) and the spindle to ripple modulation (increasing). Notice, from the bottom hypnogram, that the MI curve peaks during REM periods in blues and flattes during SWS (red). On the other hand, when MI is computed only during occurrence of spindles (30 s windows), no statistically significant statistics can be found.

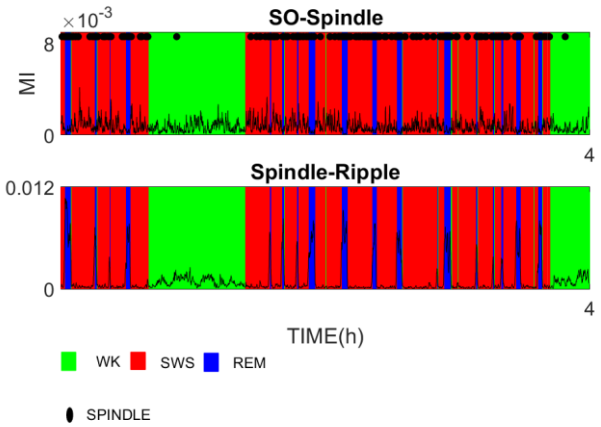


Fig. 5: Hypnograms superimposed with spindle events (dots) and MI values for slow oscillation-spindles (top) and spindle-ripples (bottom) pairs illustrate the fact that REM stage strongly modulate the latter (peaks on blue and flats on red periods of bottom panel), while the former (top panel) does not seem to be affected by states.

Although current results are not enough to explain the reason behind this, we hypothesize that the lack of difference may be due to the fact that spindles, and even more so ripples, are too short events to contribute enough to MI values computed over reasonably long-time windows of 30 s. Although this effect has not been directly measured here, we understand that this is one simple explanation that is in harmony with all results found here. In time, such long window has been adopted given the known errors induced on the measure if smaller windows are used [7].

IV. Conclusion

Although PAC (and measurements such as MI) may not be suitable for objectively quantifying the important coordination between slow oscillations, spindles, and ripples, its modulation across the SWC may be instrumental for stage detection methods based on neurobiological-plausible rationale such as cross-frequency synchronization. Table II summarizes the pattern of modulation found in this study, which may serve as basis for future staging algorithms. Here, arrows indicate significant increases or decreases during SWS or REM in comparison to WK.

TABLE II: SIGNIFICANT PAC ALTERATIONS REFERENCED TO WK

Pair	*SWS*	*REM*
A	↓	↑
B	↓	↑
C	↑	-
D	-	-
E	-	↑
F	↑	↓
G	-	↓

In any case, the possibility of being able to assess the SWC and detect its stages by solely the CFC pattern is of major neurobiological importance, particularly considering, as previously mentioned, the relationship of such synchronization mechanism with the function of sleep.

Acknowledgement

This work was supported by the Marie Skłodowska-Curie Individual Fellowship MoRPHEUS granted to V.R.C., Grant Agreement no. 101032054, funded by the European Union under the framework programme H2020-EU.1.3.-Excellent Science.

References

[1] Siegel JM. Phylogeny and the function of REM sleep. Behav Brain Res. 1995 Jul-Aug;69(1-2):29-34.
[2] Kandel, E. R., Schwartz, J. H., & Jessell, T.M. eds., 2000. “Sleep and Dream”. Principles of Neuroscience, 5th edn. New York: McGraw-hill.
[3] Rechtschaffen A. Current perspectives on the function of sleep. Perspect Biol Med. 1998 Spring;41(3):359-90.
[4] Ribeiro S, Gervasoni D, Soares ES, Zhou Y, Lin SC, Pantoja J, Lavine M, Nicolelis MA. Long-lasting novelty-induced neuronal reverberation during slow-wave sleep in multiple forebrain areas. PLoS Biol. 2004 Jan;2(1):E24.
[5] Born J, Wilhelm I. System consolidation of memory during sleep. Psychol Res. 2012 Mar;76(2):192-203.
[6] Blanco W, Pereira CM, Cota VR, Souza AC, Rennó-Costa C, Santos S, Dias G, Guerreiro AM, Tort AB, Neto AD, Ribeiro S. Synaptic Homeostasis and Restructuring across the Sleep-Wake Cycle. PLoS Comput Biol. 2015 May 28;11(5):e1004241.
[7] Tort AB, Komorowski R, Eichenbaum H, Kopell N. Measuring phase-amplitude coupling between neuronal oscillations of different frequencies. J Neurophysiol. 2010 Aug;104(2):1195-210.
[8] Barger Z, Frye CG, Liu D, Dan Y, Bouchard KE. Robust, automated sleep scoring by a compact neural network with distributional shift correction. PLoS One. 2019 Dec 13;14(12): e0224642.
[9] Gervasoni D, Lin SC, Ribeiro S, Soares ES, Pantoja J, Nicolelis MA. Global forebrain dynamics predict rat behavioral states and their transitions. J Neurosci. 2004 Dec 8;24(49):11137-47.
[10] Dzirasa K, Ribeiro S, Costa R, Santos LM, Lin SC, Grosmark A, Sotnikova TD, Gainetdinov RR, Caron MG, Nicolelis MA. Dopaminergic control of sleep-wake states. J Neurosci. 2006 Oct 11;26(41):10577-89.
[11] Réboli LA, Maciel RM, de Oliveira JC, Moraes MFD, Tilelli CQ, Cota VR. Persistence of neural function in animals submitted to seizure-suppressing scale-free nonperiodic electrical stimulation applied to the amygdala. Behav Brain Res. 2022 May 24;426:113843.
[12] Kim J, Guo L, Hishinuma A, Lemke S, Ramanathan DS, Won SJ, Ganguly K. Recovery of consolidation after sleep following stroke-interaction of slow waves, spindles, and GABA. Cell Rep. 2022 Mar 1;38(9):110426.
[13] Uygun DS, Katsuki F, Bolortuya Y, Aguilar DD, McKenna JT, Thankachan S, McCarley RW, Basheer R, Brown RE, Strecker RE, McNally JM. Validation of an automated sleep spindle detection method for mouse electroencephalography. Sleep. 2019 Feb 1;42(2):218.
[14] Aguilera M, Douchamps V, Battaglia D, Goutagny R. How Many Gammas? Redefining Hippocampal Theta-Gamma Dynamic During Spatial Learning. Front Behav Neurosci. 2022 Feb 1;16:811278.
[15] Bandarabadi M, Boyce R, Gutierrez Herrera C, Bassetti CL, Williams S, Schindler K, Adamantidis A. Dynamic modulation of theta-gamma coupling during rapid eye movement sleep. Sleep. 2019 Dec 24;42(12):182.
[16] Tort AB, Scheffer-Teixeira R, Souza BC, Draguhn A, Brankačk J. Theta-associated high-frequency oscillations (110-160Hz) in the hippocampus and neocortex. Prog Neurobiol. 2013 Jan;100:1-14.

Brain-Computer Interface assisted Motor Imagery training in post-stroke rehabilitation: longitudinal study of the EEG sensorimotor rhythms

E. Mongiardini[1,2], E. Colamarino[1,2], F. Pichiorri[2], A. Ranieri[1,2], J. Toppi[1,2], D. Mattia[2], F. Cincotti[1,2]
[1] *Department of Computer, Control, and Management Engineering, Sapienza University of Rome, Italy*
[2] *IRCCS Fondazione Santa Lucia, Rome, Italy*

***Abstract*— Brain-Computer Interfaces based on Motor Imagery (MI-BCI) have been validated as promising systems to support rehabilitative protocols for the post-stroke motor recovery of the upper limb. To date, the long-term effects of MI-BCI training in post-stroke patients need to be clarified. In order to fill this gap, we analysed electroencephalographic (EEG) data collected during the neurophysiological assessment sessions (longitudinal study) in a context of a two-arm Randomized Controlled Trial. Seventeen subacute stroke patients were enrolled and randomly assigned to the interventions: MI training supported by BCI (BCI group) and MI training without feedback (CTRL group). The aim of this work is to investigate for each intervention group the long-term effects of the MI training on the EEG sensorimotor responsiveness. Therefore, for each group we analysed the alpha and beta frequency band activity for the motor imagery task of grasping and finger extension, performed both with the affected and the healthy side separately collected, before and after the rehabilitation treatment and 1, 3 and 6 months later. Results obtained in this preliminary study show that in the BCI group the activity in alpha and beta band are located over the sensorimotor areas and that such pattern is maintained over time while the amplitude decreases. In the CTRL group the alpha activity is evident on the sensorimotor channels, the amplitude decreases with time till T4 when the pattern turns to be again widespread over the scalp and in the beta band no temporal modifications are reported. Our findings suggest that the MI-BCI induces a sensorimotor EEG reactivity rebalance in hemispheres.**

***Keywords*— Stroke, upper limb rehabilitation, Brain-Computer Interfaces, Motor Imagery.**

I. Introduction

Stroke survivors in 75% of cases face permanent disability mostly of the upper limb [1], [2]. This adversely impacts their quality of life and their integration into society. Hence the need to proposing and validating new rehabilitation treatments that can promote the recovery of the motor function.

Over the last decade Brain-Computer interfaces (BCIs) based on Motor Imagery (MI) have been validated as effective tool for supporting post-stroke motor rehabilitation [3], [4]. In the rehabilitation setting BCI paradigms are predominantly based on the electroencephalographic (EEG) technique to detect the modulation of neuroelectric signals like, in most cases, the sensorimotor rhythms (SMRs), EEG oscillations that occur in the alpha (8-13 Hz) and beta (13-30 Hz) bands over the sensorimotor areas. The amplitude of SMRs decreases during movement or movement imagination, indeed the MI elicits the same activation patterns as motor execution [5]. Hence the MI-BCI system based on SMRs tracks their amplitude changes and translates them in control signals for external devices that provide feedback to the patient about the specific processes occurring in his brain.

At IRCCS Fondazione Santa Lucia (Rome, Italy) the multidisciplinary team (neuroscientists, bioengineers, and clinical rehabilitation experts) of the Neuroelectrical Imaging and BCI Lab conceptualized and developed a BCI prototype to support hand MI training in stroke patients. The device, called Promotœr [6], is currently employed as add-on to standard therapy in one of the rehabilitation wards.

Briefly, during rehabilitation sessions with the Promotœr, patients perform affected hand MI tasks while their EEG activity is recorded and translated into movements of a virtual hand (feedback) shown on a screen placed in front of the patient.

To the best of our knowledge, however, the long-term effects of the MI-BCI training are still unclear and debated [7].

To address this question, we analysed in a longitudinal study the EEG activity recorded from a sample of subacute post-stroke patients that follow a rehabilitation MI training supported by the BCI system (BCI group) and from a sample of patients that perform the MI training without BCI feedback (control group). EEG data were recorded during 5 assessment sessions: before and after the rehabilitation treatment and at 1, 3 and 6 months apart.

The purpose of this study is to investigate the long-term effects of the MI-BCI training and the MI training without closed-loop feedback in the EEG bands related with MI tasks, i.e., alpha and beta bands.

II. Methods and Materials

A. Data Collection

The EEG dataset analyzed in the present study was collected in the context of the Randomized Controlled Trial described in [6]. The dataset includes 17 subacute stroke patients (48 ± 15 years mean ± standard deviation, 10 M / 7 F), who underwent a 12 – session rehabilitation treatments. Clinical and neurophysiological assessments were performed at different time points: before (T0) and after (T1) the rehabilitation intervention and 1 (T2), 3 (T3) and 6 (T4) months after the intervention. In every assessment EEG data were recorded from 61 channels, with a cap mounted according to an extension of the International 10/20 System. Simultaneously the electromyographic (EMG) activity of the Extensor Digitorum and Flexor Digitorum muscles were collected from both upper limbs. EEG and EMG data were sampled at 256 Hz. At each time point, participants were instructed to perform

the MI of grasping and finger extension tasks with both the healthy and affected hand, separately. For each experimental condition, 20±1 task trials and 20±1 rest trials were acquired, and the total trial duration was of 7 s; the first 3 s were of rest and the next 4 s of performance of the task (MI)/rest. The Fugl-Meyer Assessment (FMA) outcome measure was collected.
Patients were divided into two groups that receive a different rehabilitation treatment: the BCI group (N=8) performed the MI training in a close-loop condition receiving a feedback that was ecological and congruent with the MI task, i.e. a virtual representation of the affected hand that moves according to the modulation of SMRs, and the CTRL group (N = 9) performed the MI training in the same setting of the BCI group but in an open-loop condition, i.e. they did not see any movement of the virtual representation of the affected hand. The two groups were balanced in terms of age (45 ± 14 / 51 ± 16 years, BCI / CTRL mean ± standard deviation) and gender (4M/4F BCI, 6M/3F CTRL). All participants received the intervention as add-on to the standard therapy.

B. Data pre-processing

Both EEG and EMG of the assessment's recordings data were pre-processed in the Brain Products Analyzer (BrainVision Analyzer, Version 1.05.0005, Brain Products GmbH, Gilching, Germany) environment and following analysis were performed on MATLAB (R2020b; MathWorks, Natick, MA).
The continuous EEG data were 1-45 Hz bandpass filtered (Butterworth Zero Phase Filter, slope 48 dB/oct) and the Independent Component Analysis (ICA) was performed to remove ocular artifacts. Data were segmented in 4 s - trials considering the last 4 s of the total trial duration. Trials were further segmented into 1 s - windows, and an amplitude threshold (±100 μV) was applied on each window to detect artifacts; if the number of channels detected in each 1 s-segment was less than or equal to 5, the artefactual channels were replaced by spherical interpolation of neighboring channels, otherwise the entire segment was eliminated. EEG data were re-referenced to the Common Average Reference.
To verify the compliance with the motor imagery tasks, EMG data were pre-processed and visually inspected to identify any attempted movement. EMG data were high pass filtered at 10Hz (Butterworth Zero Phase Filter, slope 48 dB/oct), segmented in 7 s trials, considering all trial duration, and visually inspected. Trials in which EMG activity coherent with the experimental task (finger extension or grasping) was detected on the target muscle, i.e. flexor digitorum muscle for grasping and extensor digitorum muscle for the finger extension, were eliminated from the analysis.

C. Spectral Analysis and Focal Index

The power spectral density (PSD) was computed for each EEG channel on concatenated windows pooling the motor imagery tasks performed with the same side, due to the similarity between the spatial and frequency patterns elicited by finger extension and grasping MI task [3]. Welch's method was used to compute the PSD with 1-s Hamming window plus zero-padding to obtain 0.3 Hz resolution.
In patients with left-sided lesions, PSDs were flipped based on channel scalp positions along the midsagittal plane [8], [9] so that eventually all patients share the right hemisphere as the affected.
PSDs were averaged separately across the band ranges alpha (8-13 Hz) and beta (13-30 Hz) to extract a representative value for each band. PSD values, calculated for task and rest trials (PSD Task, PSD Rest), were used to obtain the statistical maps (see *D. Statistical Analysis*).
We introduced a biomarker accounting for desynchronization distributions on scalp maps, in particular, we considered a Focal Index, that quantifies the activity spread on scalp maps based on Event-Related Desynchronization (ERD). For each participant, we calculated the ERD according to G. Pfurtscheller [10] for each channel separately as PSD Task minus PSD Rest, divided by PSD Rest. From the ERD scalp distribution, we computed the Focal Index as an esteem of the variance over the scalp as in Eq. (1):

$$Focal\ Index_b = Var(ERD)_b \qquad (1)$$

where *b* stands for the frequency band.
This index was computed for the experimental task performed with the affected side, at each timepoint, separately in alpha and beta bands and compared between BCI and CTRL groups.

D. Statistical Analysis

Statistical PSD maps were generated for each group, i.e. BCI and CTRL, timepoint, i.e. T0, T1, T2, T3, T4, and task, i.e. MI of the affected hand and healthy hand as follows.
Having tested and verified the distributions normality, with the Kolmogorov-Smirnov test, the 2 tailed paired t-test was performed between MI and rest PSD values (patients were considered as observations of the t-test) and computed for each EEG channel and frequency band. The tests returned negative t values in the case that desynchronization occurred (i.e., a decrease in power) and a positive t value in the case of synchronization (an increase in power).
The Focal Index was compared (2 tailed independent t-test) between the BCI group and the CTRL group at each timepoint and for both bands, i.e. alpha and beta bands.
The FMA values collected at T0 on BCI and CTRL participants, were tested (2-tailed Wilcoxon rank sum test) in order to check the impairment level homogeneity between the two groups.
For all tests we set the significance level to 0.05.

III. RESULTS

At T0 no significant differences were found between the BCI and CTRL group in term of level of motor impairment ($p = 0.44$): FMA(T0) = 14.8±5.9 / 19.4±4.7 (average ± standard error) BCI / CTRL. The FMA measures at T1 reveal that both groups improved after the treatment (FMA(T1) = 27.4 ± 6.9 / 32.5 ± 7.8 BCI / CTRL, mean ± standard error) and at T4 participants reached an averaged (± standard error) FMA value of 48.3 ± 5.8 in the BCI group and 39.6 ± 8.9 in the CTRL group.
In Figure 1 are shown the topographical distributions of t values obtained from the comparisons between task and rest trials performed at all timepoints (T0, T1, T2, T3, T4). In the panels (a)-(b) the results obtained for the BCI group for the MI task executed with the affected hand, panel (a), and with the healthy hand, panel(b), are reported, both for alpha and beta bands on the first and second raw, respectively, of each panel. The t-value distributions obtained from the task/rest

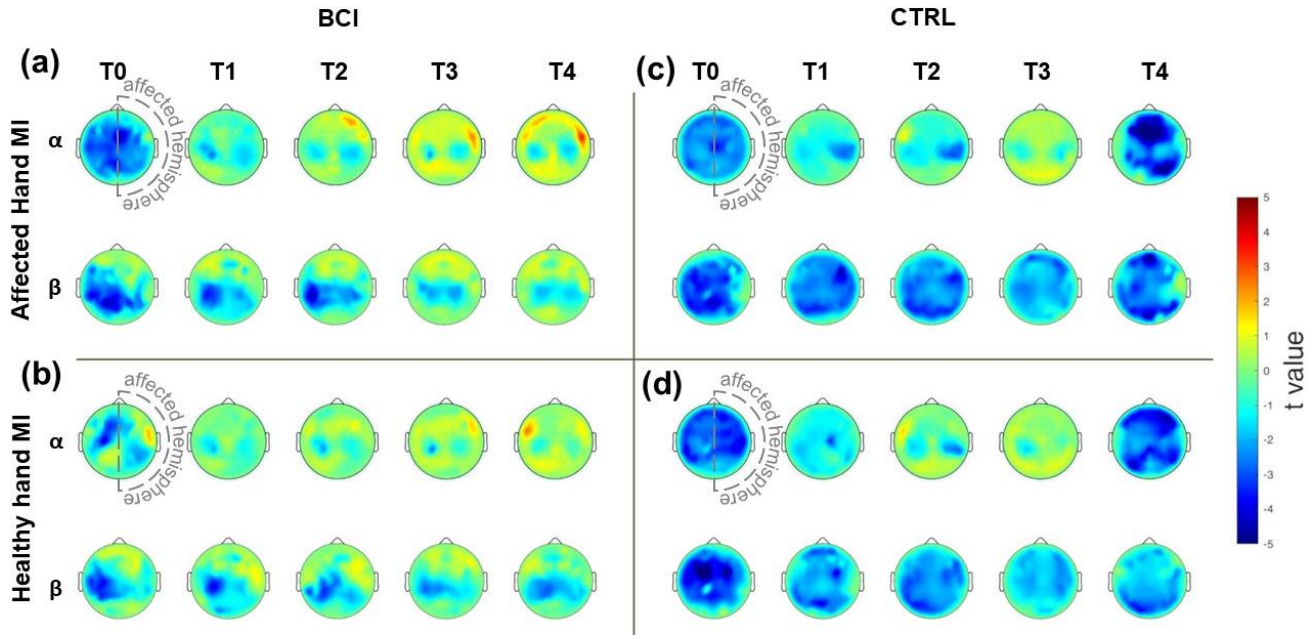


Figure 1. Scalp topographic distribution of the t-value obtained from the power spectral density (PSD) comparison (paired t-test, alpha=0.05) between task (MI) and rest conditions at timepoints T0 (baseline), T1 (after MI training), T2 (one month after training), T3 (three months after training), T4 (six months after training) for the BCI group, in the panel (a) for the task performed with the affected hand and panel (b) for the task performed with healthy hand, and for the CTRL group in the panels (c) and (d) respectively. The affected hemisphere is the right one for all participants; the task performed with the left hand refers to the affected side and vice versa. In each panel are reported the t values obtained from the comparisons both in the alpha band (first raw) and for the beta band (second raw).

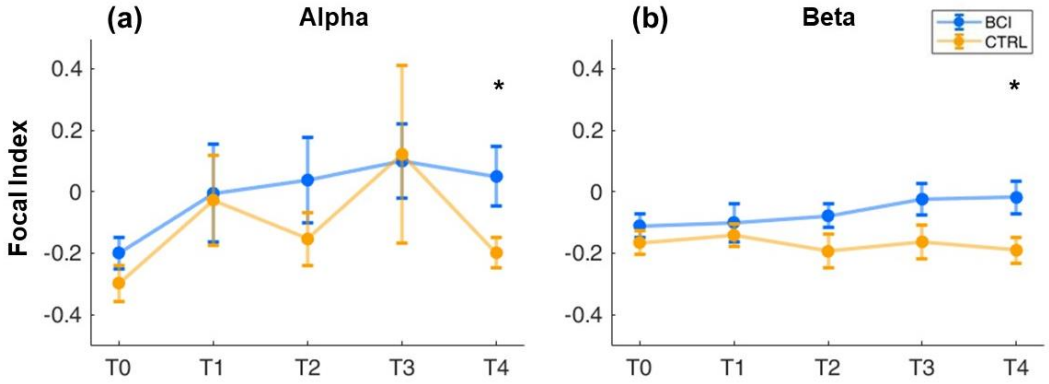


Figure 2. Focal index, computed as variance of event-related desynchronization across the EEG electrodes, presented as average ± standard error across 8 and 9 stroke patients for the BCI (blue) and CTRL (yellow) group at timepoints T0, T1, T2, T3, T4. The ERD variance is reported for the task performed with the affected hand, in alpha (panel (a)) and beta (panel(b)) bands. Significant differences (independent t-test) between the BCI and CTRL group are marked (*) for each timepoint.

comparisons in the CTRL group are shown in the panels (c)-(d), organized similarly to the BCI group panels. The results obtained for the task performed with the affected side in the BCI group in panel (a) show a desynchronization over the sensorimotor areas of both hemispheres, in the two bands, after MI-BCI-based rehabilitation training. This pattern is maintained up to 6 months after treatment while the t value amplitude decreases over time. When the MI task is performed with the healthy hand in the BCI group in panel (b), there is, likewise on the affected side, the activity in both bands is mainly over the sensorimotor areas contralateral to the involved hand in the task and it is maintained over time. The t-value maps obtained for the CTRL group, for both the affected, panel (c), and healthy hand, panel (d), show that the beta band activity is spread over the scalp and this pattern does not change over time. Results obtained in the CTRL group for the task performed with both the affected and healthy side, reveal a desynchronization in the alpha band over the sensorimotor areas of both hemispheres at time T1. This pattern is maintained for the next 3 months and then the amplitude decreases at T3 and returns to a widespread activation after 6 months (T4).

The results obtained from the comparison of the Focal Index between the two groups for the MI task performed with the affected hand are shown in Figure 2 at all timepoints for alpha and beta bands in panels (a)-(b). In both bands, the variance value of ERD turns out to be mainly lower in the CTRL group than in the BCI group. This difference is significant in both bands when the task is performed with the affected side at T4 ($p = 0.032$ in alpha, $p = 0.023$ in beta). Despite the graphical evidence, at 3 months from the treatment the difference of

ERD variance between the two groups in beta band, isn't significant ($p = 0.083$).

IV. Discussion

In this study, EEG data from two experimental groups were analysed, one that underwent MI-BCI-based training and the second that practiced only MI. As demonstrated by the clinical results both groups of patients improved their upper limb motor functions following treatment as expected since the patients were going through the subacute phase of the disease and also received the standard rehabilitation.

In the BCI group in alpha and beta bands, there is a bilateral desynchronization over sensorimotor areas for the task performed with the affected hand. This result is in line with the study [3] in which F. Pichiorri et al. investigated the effects of MI-BCI training but in the present work we observed a greater involvement of the healthy hemisphere after the training. Scalp maps of alpha-beta desynchronizations obtained for the healthy hand task in the BCI group after the treatment reflects a more contralateral activation. In the present work we discovered that such rebalance of activity in the two hemispheres, in the bands of interest, is maintained in the subsequent time instants up to 6 months from treatment highlighting the Motor Imagery activity learning via the closed-loop training and suggesting brain plasticity effects of such treatment.

Following the treatment, in the control group desynchronizations occurred over the sensorimotor regions only in the alpha band for the task performed with the affected and healthy hands, but after 6 months the responsiveness of SMRs seems to return to the initial condition. In beta band no temporal changes are evident in the CTRL group. Together the CTRL group findings suggest that there is an initial reorganization due to the Motor Imagery training, but it is not preserved over time.

Testing the significance of comparisons, between task and rest conditions, is part of the future purposes of this study, currently not yet implemented, which could be carried out using a cluster-based analysis approach.

The Focal Index confirms the results evidenced by the spectral maps, suggesting that the activations in the CTRL group are similar i.e. no differences resulted among EEG channels and therefore the ERD Variance is lower in the CTRL group rather than in the BCI group and such difference is significative at T4 in alpha and beta frequency bands. Further investigations including a larger sample of stroke patients will deepen effects on brain plasticity of the BCI-assisted MI training.

V. Conclusion

This preliminary study reveals long-term effects of MI-BCI, respect to the MI training opened-loop, on sensorimotor EEG reactivity. The Focal Index computed in alpha and beta frequency bands seems to be a good candidate to describe changes over time of the EEG patterns.

Acknowledgement

This work was partially supported by the Italian Ministry of Health (GR-2018-12365874, RF-2018-12365210, RF-2019-12369396) and by Sapienza University of Rome–Progetto di Ateneo 2019 (RM11916B88C3E2DE), 2020 (RM120172B8899B8C), 2022 (RM1221816C8C757C).

References

[1] E. Parkkonen *et al.*, "Strength of ~20-Hz Rebound and Motor Recovery after Stroke," *Neurorehabil. Neural Repair*, vol. 31, no. 5, pp. 475–486, 2017, doi: 10.1177/1545968316688795.

[2] F. Coupar, A. Pollock, P. Rowe, C. Weir, and P. Langhorne, "Predictors of upper limb recovery after stroke: A systematic review and meta-analysis," *Clin. Rehabil.*, vol. 26, no. 4, pp. 291–313, 2012, doi: 10.1177/0269215511420305.

[3] F. Pichiorri *et al.*, "Brain-computer interface boosts motor imagery practice during stroke recovery," *Ann. Neurol.*, vol. 77, no. 5, pp. 851–865, 2015, doi: 10.1002/ana.24390.

[4] M. A. Cervera *et al.*, "Brain-computer interfaces for post-stroke motor rehabilitation: a meta-analysis," *Ann. Clin. Transl. Neurol.*, vol. 5, no. 5, pp. 651–663, 2018, doi: 10.1002/acn3.544.

[5] C. Neuper, R. Scherer, M. Reiner, and G. Pfurtscheller, "Imagery of motor actions: Differential effects of kinesthetic and visual-motor mode of imagery in single-trial EEG," *Cogn. Brain Res.*, vol. 25, no. 3, pp. 668–677, 2005, doi: 10.1016/j.cogbrainres.2005.08.014.

[6] D. Mattia *et al.*, "The Promotoer, a brain-computer interface-assisted intervention to promote upper limb functional motor recovery after stroke: A study protocol for a randomized controlled trial to test early and long-term efficacy and to identify determinants of response," *BMC Neurol.*, vol. 20, no. 1, pp. 1–13, 2020, doi: 10.1186/s12883-020-01826-w.

[7] Z. Bai, K. N. K. Fong, J. J. Zhang, J. Chan, and K. H. Ting, "Immediate and long-term effects of BCI-based rehabilitation of the upper extremity after stroke: A systematic review and meta-analysis," *J. Neuroeng. Rehabil.*, vol. 17, no. 1, pp. 1–20, 2020, doi: 10.1186/s12984-020-00686-2.

[8] F. De Vico Fallani *et al.*, "Multiscale topological properties of functional brain networks during motor imagery after stroke," *Neuroimage*, vol. 83, pp. 438–449, 2013, doi: 10.1016/j.neuroimage.2013.06.039.

[9] L. Chen *et al.*, "EEG-controlled functional electrical stimulation rehabilitation for chronic stroke: system design and clinical application," *Front. Med.*, vol. 15, no. 5, pp. 740–749, 2021, doi: 10.1007/s11684-020-0794-5.

[10] G. Pfurtscheller, "Functional brain imaging based on ERD/ERS," *Vision Res.*, vol. 41, no. 10–11, pp. 1257–1260, 2001, doi: 10.1016/S0042-6989(00)00235-2.

[11] M. Sivan, R. J. O'Connor, S. Makower, M. Levesley, and B. Bhakta, "Systematic review of outcome measures used in the evaluation of robot-assisted upper limb exercise in stroke," *J. Rehabil. Med.*, vol. 43, no. 3, pp. 181–189, 2011, doi: 10.2340/16501977-0674.

A multimodal wearable system for Human Activity Recognition during daily activities

P. Benvenuti[1], E. Rovini[1], L. Fiorini[1,2], and F. Cavallo[1,2]
[1] *Department of Industrial Engineering, University of Florence, Via Santa Marta 3, Firenze, 50139, Italy*
[2] *The BioRobotics Institute, Scuola Superiore Sant'Anna, Viale Rinaldo Piaggio 34, Pontedera (Pisa), 56025, Italy*

***Abstract*—This study proposes a wearable system consisting of inertial and electromyography (EMG) sensors for the recognition of activities of daily living in the context of neurodegenerative diseases. The value of Human Activity Recognition (HAR) rests in its ability to test motor cognitive abilities objectively and precisely at home and to keep track of activities performed, for instance when it's necessary to follow the impact of pharmacological therapy. Current technologies for HAR primarily rely on two types of systems: camera-based systems and wearable sensor systems. In this study, a wearable multimodal system based on the fusion of EMG and inertial sensors was designed and developed. Data have been collected from 21 young subjects performing 5 gestures and, after a data pre-processing, a multi-modal dataset has been created. Then, classification has been performed using two machine learning techniques, i.e. a multiclass Support Vector Machine (SVM) and a Random Forest (RF). The best combination of sensors is analyzed, considering both classifiers' accuracy and wearability. Following the proposed approach, levels of accuracy of 79% are reached using EMG and the inertial sensor on the dominant index finger and wrist, whereas, using EMGs and only the hand's wrist sensor achieves an accuracy of 78%, showing that an excellent yet non-invasive activity recognition system can be obtained with just a few sensors. Finally, this system can be a reliable solution to be used both in clinics and home care.**

***Keywords*—Multimodal Wearable Sensor, Gesture Recognition, EMG sensors, inertial sensors, Neurodegenerative Disease.**

I. Introduction

ITALY in 2015 had the greatest portion of older people in the labour force in the European Union. By 2050, this statistic is expected to nearly double, prompting concems about caring, according to Eurostat predictions [10]. Human Activity Recognition (HAR) is one of this scenario's most promising assistive technologies. Indeed, recognition of activities of daily living can be of paramount importance in a monitoring context: people with dementia have difficulties performing daily activities and caring for themselves and are almost dependent on caregivers.

Smartphones, smartwatches, smart clothing, and other specialized devices are currently the most common wearable technology utilized in HAR [1,2,3]. In general, HAR can work better and be more robust by adding different types of sensors in different parts of the body [4,5].

In this context, this study aimed at designing and developing a multimodal wearable system composed of inertial devices and electromyography (EMG) sensors for upper limbs, for the recognition of activities of daily living (ADL) that can be useful for the non-invasive monitoring of frail people at home. Signals acquired by the sensors during a well-defined experimental protocol were processed to extract features characterizing the performed activities. Then, two machine learning classifiers (i.e., Support Vector Machine, Random Forest) were applied to identify the performed activities and their performance was evaluated. Finally, the authors figured out the best combination of sensors in terms of accuracy in activity recognition and wearability.

II. Materials and Methods

A. System Architecture

A multimodal wearable system was designed and developed including both inertial and electromyographic sensor devices (Fig. *1*). Then, a user interface was developed to collect data from both devices.



Fig. 1: The full wearable system with Myo & SensHand

- *Electromyographic sensor device: Myo Armband*

The Myo Armband (Thalmic Labs) consists of 8 EMG electrodes with a bipolar configuration that acquires muscle activity, and a low-energy Bluetooth (BLE) transmission module for transferring the acquired data to a docking station for post-processing data analysis. The sampling rate of this device is 200 Hz.

- *Inertial sensor device: SensHand*

The SensHand is a wearable device developed by the Assistive BioRobotics Joint Lab (Scuola Superiore Sant'Anna and University of Florence, Italy) composed of four inertial modules positioned in correspondence to the wrist and the first three fingers (thumb, index, middle finger). Each module is composed of a complete 9-axis inertial sensor (6-axis geomagnetic module LSM303DLHC and 3-axis digital gyroscope L3G4200D, STMicroelectronics, Italy) and includes a microcontroller (ARM®-based 32-bit STM32F10RE MCU, STMicroelectronics, Italy) which can acquire, filter and store data at a frequency of 100 Hz [6]. It collects and transmits data towards a generic control station through a wireless communication based on the SPBT2632C1A V3.0 (STMicroelectronics, Italy) Bluetooth serial device. The placement of the sensors has been

determined according to the state of the art, examining the gestures that need to be recognized [7].

- *The Wearable System Interface*

A user interface was developed using Python to integrate the two sensor devices (i.e., SensHand and Myo armband). The implementation of the interface guarantees the simultaneous gathering of data from all the sensors. Two Python executables have been developed: one to initiate data transfer and acquisition and the other one to connect SensHand and Myo to the Personal Computer (PC). As for SensHand, the transmission of data is based on Python's pySerial library, which reads directly from a serial port, whereas a Python module, "Pygatt", was used to connect Myo to the PC, to read and write to GATT descriptors on the BLE device. Then, a web interface, based on HTML code, has been developed for this work to manage the connection and data stream of the system's sensors. It is a navigable user interface that takes the form of a Web page and can be accessed with a common web browser.

B. Experimental Setup

Twenty-one people participated in the trial, including 13 males and 8 females, right-handed, who were asked to wear the SensHand and the Myo on their dominant arm. These people were then asked to perform 5 different activities (Fig. 2):

- Eat with the Fork (EF): take the fork from the table and simulate bringing food to the mouth ten times and then resting the fork.
- Grasp to Drink (GD): take a water bottle from the table and simulate drinking for 3 seconds and then resting the glass.
- Brushing Teeth (BT): take the toothbrush, simulate the brush teeth ten times, and put it back.
- Using Laptop (UL): type on the keyboard with both hands.
- Talking on the Phone (TP): to take the phone, talk on for 3 seconds, and put it back.



Fig. 2: Set of activities performed by the participants

These activities were chosen by comparing two of the most widely used public datasets in the field of HAR, i.e., the Comel Activity Dataset [8] and the MSR Daily Activity Dataset [9]. People performed the activities while seated, and 3 seconds before and after the execution of each gesture were also recorded, with people in a position of complete rest to have a baseline for each trial. While performing the movements, participants are always seated.

C. Data Analysis

Acquired signals from both devices were processed and analyzed to extract features able to characterize and differentiate the performed activities. Then, after the feature reduction, two supervised machine learning classifiers were applied to evaluate which configuration of sensors resulted in the best accuracy for recognizing the performed activities.

- *EMG Preprocessing*

A "full wave rectification" was done for the EMG signals and then they were filtered with a 4th-order Butterworth low pass filter with a cutoff frequency of 10 Hz. After that, signals have been normalized and segmented. Each signal was normalized according to the subject's baseline, calculated in the first two seconds of rest. Windows of 1 s length (two hundred samples), with 0.5 s overlap (i.e., 50%), were used to segment the signal. For the region of muscle activity to be detected automatically, the waveform length (WL) feature was used as in Eq.1.

$$WL = \sum_{n=1}^{N} |x_{n+1} - x_n| \qquad (1)$$

Where x_n is the EMG data and N is the number of samples in each time window. The maximum value in the waveform length values in the first 2 seconds of the resting signal was calculated. Then, the threshold value was determined by multiplying this value by $\sqrt{5}$. A second threshold was fixed $\sqrt{3}$ times the first threshold to determine the end of the gesture [11]. After extracting each channel's start and end index, we took the minimum and maximum of the previously found indexes as the start and end indexes. Thus, we established common indices to have the same samples on all channels. The method was evaluated one by one on all EMG signals in the dataset, and the correct region was detected.

- *Inertial Preprocessing*

A Fourier analysis of the signal was carried out. The signal's primary frequencies are between 0 and 3, hence a 4^{th}-order digital low-pass Butterworth filter was utilized with a 5 Hz cutoff frequency. Once the muscle activation window on EMG signals was found, we identified the precise instant the user began the action in the EMG signals, and then we looked for the correlated inertial sample closest to that EMG sample based on the system's time stamps. The same procedure was applied for the end movement detection. The signal has then been divided into segments by moving windows with a 3-second size and 50% overlap according to the typical length of each gesture.

- *Feature Extraction*

Twenty-seven parameters were extracted for each window. In particular, the following 17 features were from the EMG signals:

1. Root Mean Square
2. Mean Value
3. Mean Absolute Value
4. Standard Deviation
5. Variance
6. Waveform Length
7. Number of Peaks
8. Mean Peak Value
9. Mean Firing Velocity
10. Slope Sign Changes
11. Difference Absolute Mean Value
12. Willison Amplitude
13. Mean Absolute Value Slope
14. Integrated Absolute Value

15. Hjorth Mobility Parameter
16. Difference Absolute Standard Deviation Value
17. Maximum Fractal Length.

Moreover, 10 features were extracted from the inertial signals as follows:

1. Root Mean Square
2. Mean Value
3. Mean Absolute Value
4. Standard Deviation
5. Variance
6. Skewness
7. Kurtosis
8. Integrated Absolute Value
9. Root Mean Square Jerk
10. Mean Jerk.

Each instance was then assigned to the corresponding performed activity (Table I).

TABLE I: PERCENTAGES OF ACTIVITIES AND THE DISTRIBUTION OF THE NUMBER OF INSTANCES WITHIN THE DATASET

Label	*Activity*	*Percentage %*
0	Eat with the Fork (EF)	30
1	Grasp to Drink (GD)	18
2	Brush Teeth (BT)	19
3	Use Laptop (UL)	13
4	Talk on the Phone (TP)	20

- *Feature Reduction and Classification*

Seven different configurations of sensors were analyzed, including stand-alone systems (e.g., inertial data from wrist unit only) and different combinations of the sensors. Then, a Principal Component Analysis (PCA) was done to reduce the number of features in the dataset for each configuration. Once the new datasets were obtained, they were used to train and test two supervised classifiers: a Support Vector Machine (SVM) with a Radial Basis Function (RBF) kernel, and a Random Forest (RF). The datasets were split with percentages of 70% for training and 30% for testing, and a k-fold cross-validation with k=5 was performed. To evaluate classification performance, the following metrics were used: accuracy (2), precision (3), recall (4), and F-score (5):

$$Accuracy = \frac{TP+TN}{TP+TN+FP+FN} \quad (2)$$

$$Precision = \frac{TP}{TP+FP} \quad (3)$$

$$Recall = \frac{TP}{TP+FN} \quad (4)$$

$$Fscore = 2 \cdot \frac{Precision \cdot Recall}{Precision+Recall} \quad (5)$$

Where:

- TP: True Positive
- TN: True Negative
- FP: False Positive
- FN: False Negative

III. RESULTS

Overall, by evaluating the seven sensor combinations, SVM performed better than RF. The best combinations are given by the wrist inertial data combined with Myo data (W+M) and by the index and wrist inertial data jointed with Myo signals (I+W+M) (Fig. *3*), reaching an overall accuracy among all the activities for SVM equal to 0.78 and 0.79, respectively.

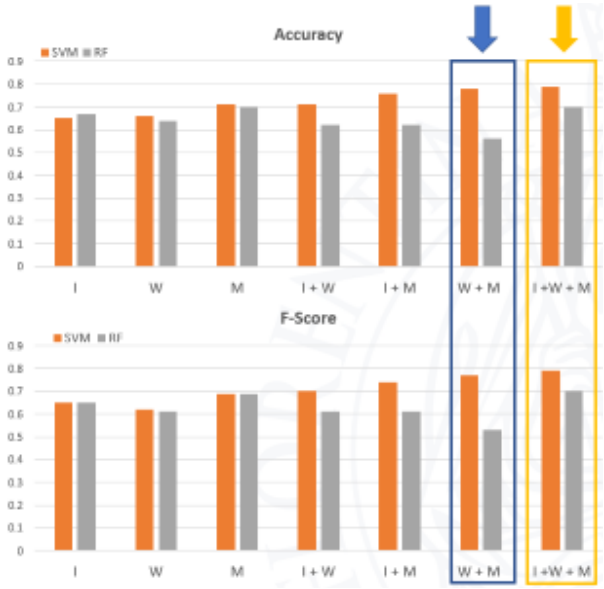


Fig. 3: Accuracy and F-score of the seven sensor combinations for RF and SVM. I = inertial data from the index finger unit; W = inertial data from the wrist unit; M = EMG data from Myo

The two best-performing configurations (i.e., W+M, and I+W+M), have similar classification performance (Fig. *4*):

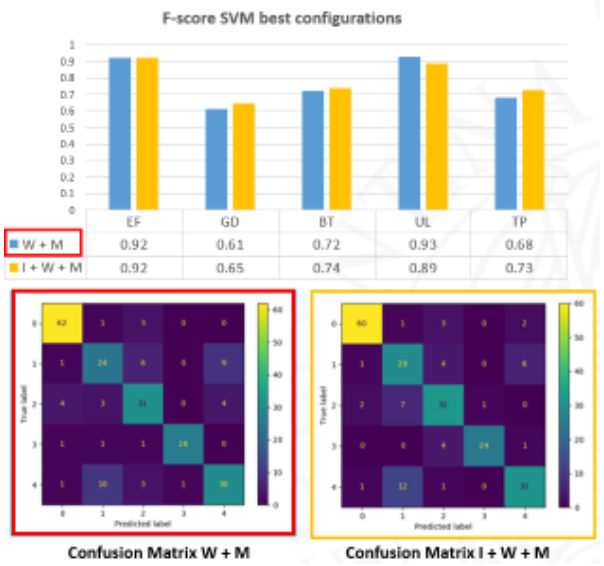


Fig. 4: F-score and Confusion Matrices for the two best configurations using the SVM classifier

However, there are some differences among the following activities:

- "Eat with the Fork" (EF) and the "Use the Laptop" (UL) activities, are those best predicted in the two configurations.
- "Grasp to Drink" (GD) and "Talk on the Phone" (TP)

activities are generally the most confusing among them.
- "Grasp to Drink" (GD) is the worst predicted activity.

In contrast, between the two best configurations there are also differences, indeed, adding the index inertial sensor:

- Increase discrimination between "Grasp to Drink" (GD) and "Talk on the Phone" (TP).
- Decrease "Using the Laptop" (UL) performances.
- "Eating with the Fork" (EF) and "Brushing Teeth" (BT) have similar performances in the two configurations.

IV. Discussion and Conclusion

A multimodal wearable sensor system, composed of EMG and inertial sensors, was designed and developed to support HAR during activities of daily living. With our system, we were able to obtain reliable gesture recognition for such activities. The wrist is the ideal site for wearables due to its low intrusiveness, and due to its capacity to capture hand orientations and hand movements [12], however, the results showed that this sensor alone is insufficient to distinguish between some gestures with finger movements. In our study, EMG sensors placed on the forearm improved the recognition of hand shapes and finger movements confirming the results from Wu, Sun and Jafari [12]. Finally, the combination of multiple sensors gives better results than standalone solutions. In particular, as for choosing the best configuration of the sensor system among the seven studied configurations, a trade-off between performance and wearability was applied. Best results were obtained by using wrist inertial sensor data combined with the EMG data and by using both wrist and index inertial sensor data combined with the EMG data. Given the similar performance, we can choose the one with the least number of sensors as the best configuration to maximize wearability without decreasing accuracy. Choosing the fewest number of devices could be a suitable solution that would allow the usage of such a system also in a home setting, where frail people can be monitored during the performance of their ADL. Therefore, in this study, the best combination of sensors in terms of a trade-off between accuracy and wearability encompasses the Myo wristband combined with the wrist inertial sensor, which achieves an overall accuracy of 78% among the five performed activities, exceeding 90% for eating activity. However, a modular solution that allows easy including or excluding some sensor units could be the best option to provide a multimodal system that can be adapted to different activities. Indeed, in this study, only the wrist and index finger from SensHand were included, but also information from the thumb unit could be important for activities encompassing the grasp or require a fine assessment of finger motion.

The main limitation of this study is the sample size. Indeed, a small sample of users was involved in the experimental tests and the dataset resulted unbalanced among the different activities. Moreover, the use of armband EMG sensors limits electrode placement and increases the likelihood of electrodes being placed in different positions from subject to subject due to natural muscle differences. In future works, the authors are planning to enlarge both the number of gestures and participants enrolled, including older people and people with motor-cognitive disabilities. Also, the authors are interested in introducing new types of sensors (e.g., other types of physiological signals) to investigate not only the motion and muscle activity during the ADL but also the physiological response of the users while performing such activities.

Concluding, this system is a promising solution for realizing an evaluation of physiological and kinetic parameters during the performance of specific activities. Finally, the system could be applied to people who may have physical disabilities, such as people with neurodegenerative diseases. In this context, a trial has already been started at the "Don Primo Mazzolari" hospital in Bozzolo (MN). Seventeen people with Parkinson's disease are participating in this trial, where the system designed and developed in this study is used to assess the patient's motor performance during the execution of standard motor exercise within the neurological examination to evaluate the effect of the assigned rehabilitation program.

Acknowledgement

This publication was produced with the co-funding European Union - Next Generation EU, in the context of The National Recovery and Resilience Plan, PE8 Consequences and challenges of ageing, Project: "A novel public-private alliance to generate socioeconomic, biomedical and technological solutions for an inclusive Italian ageing society" (Age-IT), CUP: B83C22004800006.

References

[1] R. Adaskevicius, "Method for recognition of the physical activity of human beings using a wearable accelerometer", *Elektronika ir Elektrotechnika*, 2014, 20.5: 127-131.

[2] A. Filippoupolitis, W. Oliff, B. Takand, G. Louka, "Location - enhanced activity recognition in indoor environments using off the shelf smart watch technology and ble beacons", *Sensors*, 2017, 17.6: 1230.

[3] M.M. Hassan, M. Z. Uddin, A. Mohamed, A. Almogren, "A robust human activity recognition system using smartphone sensors and deep learning", *Future Generation Computer System*, 2018, 81: 307-313.

[4] W. Huo, P. Angeles, Y. F. Tai, N. Pavese, S. Wilson, M. T. Hu, R. Vaidyanathan, "A Heterogeneous Sensing Suite for Multisymptom Quantification of Parkinson's Disease", *IEEE Transactions on Neural Systems and Rehabilitation Engineering*, 2020, 28.6: 1397-1406.

[5] L. Fiorini, F. G.Cornacchia Loizzo, A. Sorrentino, J. Kim, E. Rovini, A. Di Nuovo, F. Cavallo, "Daily gesture recognition during human-robot interaction combining vision and wearable systems". *IEEE Sensors Journal*, 2021, 21.20: 23568-23577.

[6] E. Rovini, C. Maremmani, and F. Cavallo, "A Wearable System to Objectify Assessment of Motor Tasks for Supporting Parkinson's Disease Diagnosis" *Sensors*, 2020, 20.9:2630.

[7] A. Moschetti, L. Fiorini, D. Esposito, P. Dario, F. Cavallo. "Recognition of daily gestures with wearable inertial rings and bracelets". *Sensors*, 2016, 16.8: 1341.

[8] Cornell Activity Datasets: CAD-60 & CAD-120; editing status 2021-12-07; re3data.org - Registry of Research Data Repositories. http://doi.org/10.17616/R3DD2D last accessed: 2023-04-28.

[9] A. Ben Tamou, L. Ballihi, D. Aboutajdine. "Automatic learning of articulated skeletons based on mean of 3D joints for efficient action recognition". *International Journal of Pattern Recognition and Artificial Intelligence*, 2017, 31.04: 1750008.

[10] Eurostat: https://ec.europa.eu/eurostat/cache/infographs/elderly/index.html

[11] T. Cengiz, M. C. Demir, "Detection and Classification of Muscle Activation in EMG Data Acquired by Myo Armband". *Avrupa Bilim ve Teknoloji Dergisi*, 2020, 178-183.

[12] J. Wu, L.Sun, and R. Jafari. "A Wearable System for Recognizing American Sign Language in Real-Time Using IMU and Surface EMG Sensors". *IEEE journal of biomedical and health informatics*. 2016 vol.20(5), pp.1281-1290.

Effectiveness of a home-based tele-rehabilitation program for post-Covid patients: preliminary results

Serena Cerfoglio[1,2], Paolo Capodaglio[2,3], Paolo Rossi[4], Federica Verme[2], Gabriele Boldini[2], Viktoria Cvetkova[4], Manuela Galli[1]and Veronica Cimolin[1,2]

[1] *Department of Electronics, Information and Bioengineering, Politecnico di Milano, Milano (IT)*
[2] *Orthopaedic Rehabilitation Unit, Istituto Auxologico Italiano, IRCCS, San Giuseppe Hospital, Piancavallo (IT)*
[3] *Department of Surgical Sciences, Physical Medicine and Rehabilitation, University of Turin (IT)*
[4] *Clinica Hildebrand, Centro di Riabilitazione Brissago (CH)*

***Abstract*— The aim of this study was to quantify the effectiveness of a tele-rehabilitation program for post-Covid-19 patients who reported disabling motor and respiratory symptoms after the infection. Nine post-covid patients were assessed in three session: at hospital admittance time (T0), at discharge time (T1) and at the end of the tele-rehabilitation program (T2) via instrumental (i.e. instrumented six-minute walking test and handgrip) and clinical (i.e. spirometry) tests. So far, just the data coming from the instrumented tests of three patients who completed the program were considered, showing an increasing trend in terms of both motor and strength parameters between the considered time points. The preliminary results suggested that the proposed tele-rehabilitation approach could have positive effects on motor function in post-covid patients.**

***Keywords*— Covid-19, tele-rehabilitation, 6-min walking test, handgrip.**

I. INTRODUCTION

THE Covid-19 pandemic significantly affected our daily life and brought new challenges to the global healthcare systems. Worldwide, even months beyond the discharge from acute care, many Covid-19 survivors reported incomplete healing [1]–[4], negatively impacting on daily activities and on the quality of life [5].

In fact, patients recovering from severe COVID-19 infection often report motor (e.g. muscle and joint pain, decreased exercise capacity) and respiratory symptoms (e.g. dyspnoea, impairment of pulmonary function) together with a wide range of other issues, such as chest pain, cognitive impairment, anxiety and sleep alterations [6]–[11].

In order to manage the disabling motor and respiratory post-Covid-19 symptoms and effects, an adequate rehabilitation is required in all stages of the disease, from the acute to the post-acute phase.

However, the suspension of the majority of outpatient services on the national territory and travel restrictions made the access to rehabilitation services more and more challenging, especially in those areas, such as the cross-borders, which were already poorly served by health facilities.

In this context, tele-rehabilitation represents a new solution to support health-care structures in the management of the rehabilitation demand for Covid-19 survivors.

Tele-rehabilitation programs mainly apply to physiotherapy and neural rehabilitation [12]–[14] and, according to the literature, they allow for the treatment of various phases of diseases by substituting the traditional face-to-face approach in the patient-rehabilitator interaction [15], [16] thus representing a solution to reconcile the quality of life and the sustainability of the health services. Additionally, such applications are useful to cover situations in which it is complicated for the patients to reach the traditional rehabilitation infrastructures [16].

The aim of this study is to evaluate the effectiveness of a home-based motor and respiratory rehabilitation program for post-Covid hospitalized patients.

II. METHODS

A. Participants

The study was approved by the Ethics Research Committees of Istituto Auxologico Italiano (Ospedale San Giuseppe, Piancavallo, VB) and Clinica Hildebrand – Centro riabilitazione Brissago (Brissago, CH).

A group of post-covid inpatients was recruited. The principal selection criteria were the follows:

1) Adults of both sexes, aged between 35 and 75 years, admitted to the functional recovery units due to disabling motor and/or respiratory SARS-CoV2 outcomes.
2) Subjects living in cross-border regions with low density of rehabilitation facilities.

Conversely, the exclusion criteria were:

1) Presence of psychiatric pathologies or cognitive deficits that did not allow for a correct use of the devices for the tele-rehabilitation

Considering these criteria, 9 post-covid individuals were enrolled (age: 54.5 ± 7.23 years, M: 2, F: 7) so far.

The recruited subjects were evaluated at the beginning of their hospital-based rehabilitation program (T0), at discharge time (T1) and the end of their three-week home-based rehabilitation program (T2) via instrumental (e.g. 6-minute walking tests) and clinical tests (e.g. spirometry).

B. Experimental set-up

Following their discharge from the hospital, the post-Covid patients continued their rehabilitation process at home, using a proper easy-to-use equipment. The technology provided to each patient consisted on a respiratory muscle training device

(SpiroTiger, MVM Italia, Lainate, MI) and a motor rehabilitation device (Euleria Home, Euleria, Rovereto, TN) respectively.

With regards to respiratory rehabilitation, the SpiroTiger system is a device designed for the specific training of the respiratory muscles without overloading the cardiovascular and the musculoskeletal system as it allows for the execution of deep and fast breathing acts were performed without incurring the consequences of hyperventilation (e.g. hypocapnia).

The device **(Fig. 1)** consists on a portable grip equipped with a bag for air recycling and a valve that controls the isocapnia state and provides via its software the information on how to perform the correct breathing in terms of depth and frequency.



Fig. 1: Visual representation of the device used for respiratory rehabilitation (SpiroTiger, MVM Italia, Lainate, MI)

With respect to motor rehabilitation, Euleria Home is a CE class 1/m medical device that allows clinicians to remotely configure and monitor exercise-therapy paths for their patients. The device **(Fig. 2)** consists on a wearable inertial sensor and a dedicated application, installed on a tablet, which guides the patient through a personalized rehabilitation program directly from home. Such technology, in addition to the guidance provided in the correct execution of the exercises, uses the biofeedback technology (i.e. audio and visual feedback) and integration with the sensor to simplify the execution of the exercises and the completion of the session, motivating the patient with an effective gamification mechanism based on scores, badges and prizes.



Fig. 2: Visual representation of the device used for motor rehabilitation (Euleria Home, Euleria Health, Rovereto, TN)

Using a cloud-based web-management system, the clinicians updated and personalised the exercise-therapy programmes to the patients, remotely monitoring their results, progress and compliance with the rehabilitation program on a weekly basis.

The exercise protocol for home-based rehabilitation was sorted by clinicians according to patients' health status and performance during their hospital stay. Regarding respiratory rehabilitation, each patient performed a set of breathing exercises personalized in terms of depth and frequency up to five times per week. With respect to motor rehabilitation, it was decided to keep the protocol as simple as possible, including only easy free body exercises up to five times per week. After a short warm-up, the patients performed a set of exercises for trunk (e.g. lateral bending and anterior flexion), upper and lower limbs (e.g. shoulder abduction and knee flexion). At the end of each training session, a report containing information about articular angles, repetitions and score was generated and checked out by the clinicians, in order to monitor patient's performance and eventually tune the program.

C. Instrumental and Clinical Tests

All the patients underwent instrumental and clinical test at the three time points in order to evaluate the effectiveness of their rehabilitation process. In particular, the performed instrumental evaluations were the maximum handgrip isometric force, assessed with a dynamometer, and the instrumented Six-Minutes Walking Test (i6MWT) [17]–[21].

The i6MWT was recorded via a miniaturized (70 mm x 40 mm x 18 mm) inertial sensor (G-Sensor®, BTSBioengineering, Milan, Italy), integrating different triaxial sensors (i.e. accelerometer, gyroscope and magnetometer), and performed indoor, along a 30-m hospital corridor with marked turnaround points, instructing the patients to walk as fast as they could [17], [22].

A report for each i6MWT trial was automatically generated via BTS G-Studio and the following parameters were considered for further analysis:

- Walked distance (m).
- Walking speed (m/s).
- Stride length (m).

Concerning the clinical evaluations, a complete spirometry with DLCO (Diffusing capacity of the Lungs for Carbon Monoxide), MIP (Maximal Inspiratory Pressure) and MEP (Maximal Expiratory Pressure) was performed. Additionally, oxygen saturation and dyspnoea perception after the i6MWT were tracked.

III. RESULTS

Out of the current sample of 9 subjects, 3 women have completed the tele-rehabilitation program so far. Due to the small sample for the data analysis, it was chosen not to perform a full statistical analysis and to report the results in term of percentage change to highlight changes between the considered time points. According to the preliminary data coming from the instrumental tests, an improvement of patient's performance could be noted between the considered

time points.

Concerning the i6MWT, the results shows an improving trend in terms of walked distance (T1-T0: + 16.4 %, T2-T0: 29.7 %) **(Fig. 3)**, walking speed (T1-T0: 15.3 %, T2-T0: 30.1 %) and stride length (T1-T0: +8.3 %, T2-T0: 19.5 %).

The same improving trend can be seen also for the maximum handgrip isometric force for the dominant limb between the baseline and the end of the tele-rehabilitation program (T2-T0: +13.8 %).

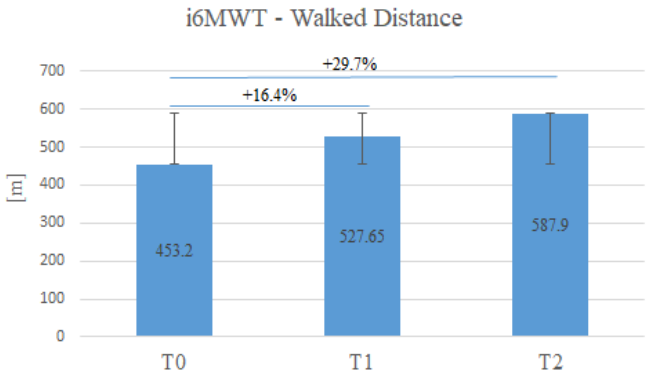


Fig. 3: Mean and standard deviation of walked distance during the i6MWT for the patients who have completed the program so far. Difference between T1-T0 and T2-T0 is reported in terms of percentage change.

IV. DISCUSSION

The purpose of this study was to evaluate and quantify the effectiveness of a motor and respiratory home-based tele-rehabilitation program for post-Covid patients. The preliminary results concerning the instrumental tests performed by the patients who complete the program showed encouraging data about the effectiveness of the proposed telerehabilitation approach. In fact, with respect to i6MWT, the considered parameters allow for the observation of a trend towards an increase that could be due to a general improvement of health conditions.

The same considerations could be done for the handgrip, with the difference that the increasing trend was noticeable between T0 and T2, probably because it normally takes more time to see visible changes in strength while following a targeted training [23].

So far, just the preliminary outcome of the instrumented tests was explored and the small number of participants who completed the program limited the actual strength of the statistical findings. The complete data analysis, including also the clinical tests and the respiratory aspects, will be performed on the full sample of participants to the tele-rehabilitation program.

ACKNOWLEDGEMENT

The research was conducted in the field of TRIALS Project “La teleriabilitazione nel paziente post-covid: l’esperienza Italia-Svizzera”, project co-funded by the European Union (FESR), Italy, Swiss Confederation and Swiss Cantons – Interreg V-A Italy-Switzerland".

The authors would like to acknowledge Eng. Federica Camuncoli, Eng. Serena Mandaresu and Eng. Cristina Ferrario for their valuable contribution to the project.

REFERENCES

[1] M. J. Estebanez-Pérez, J. M. Pastora-Bernal, and R. Martín-Valero, “The Effectiveness of a Four-Week Digital Physiotherapy Intervention to Improve Functional Capacity and Adherence to Intervention in Patients with Long COVID-19,” Int. J. Environ. Res. Public Health, vol. 19, no. 15, 2022, doi: 10.3390/ijerph19159566.

[2] J. Agergaard et al., “Myopathic changes in patients with long-term fatigue after COVID-19,” Clin. Neurophysiol., vol. 132, no. 8, pp. 1974–1981, 2021, doi: 10.1016/j.clinph.2021.04.009.

[3] J. Li et al., “A telerehabilitation programme in post-discharge COVID-19 patients (TERECO): A randomised controlled trial,” Thorax, vol. 77, no. 7, pp. 697–706, 2022, doi: 10.1136/thoraxjnl-2021-217382.

[4] M. Bures et al., “A Sensor Network Utilizing Consumer Wearables for Telerehabilitation of Post-acute COVID-19 Patients,” IEEE Internet Things J., vol. PP, no. 8, p. 1, 2022, doi: 10.1109/JIOT.2022.3188914.

[5] B. Raman, D. A. Bluemke, T. F. Lüscher, and S. Neubauer, “Long COVID: Post-Acute sequelae of COVID-19 with a cardiovascular focus,” Eur. Heart J., vol. 43, no. 11, pp. 1157–1172, 2022, doi: 10.1093/eurheartj/ehac031.

[6] W. Guan et al., “Clinical Characteristics of Coronavirus Disease 2019 in China,” N. Engl. J. Med., vol. 382, no. 18, pp. 1708–1720, 2020, doi: 10.1056/nejmoa2002032.

[7] C. Sohrabi et al., “World Health Organization declares global emergency: A review of the 2019 novel coronavirus (COVID-19),” Int. J. Surg., vol. 76, no. February, pp. 71–76, 2020, doi: 10.1016/j.ijsu.2020.02.034.

[8] C. Huang et al., “6-month consequences of COVID-19 in patients discharged from hospital: a cohort study,” Lancet, vol. 397, no. 10270, pp. 220–232, 2021, doi: 10.1016/S0140-6736(20)32656-8.

[9] M. Paneroni et al., “Muscle Strength and Physical Performance in Patients Without Previous Disabilities Recovering From COVID-19 Pneumonia.,” Am. J. Phys. Med. Rehabil., vol. 100, no. 2, pp. 105–109, Feb. 2021, doi: 10.1097/PHM.0000000000001641.

[10] S. Belli et al., “Low physical functioning and impaired performance of activities of daily life in COVID-19 patients who survived hospitalisation.,” The European respiratory journal, vol. 56, no. 4. England, Oct-2020, doi: 10.1183/13993003.02096-2020.

[11] C. Fernández-de-Las-Peñas, D. Palacios-Ceña, V. Gómez-Mayordomo, M. L. Cuadrado, and L. L. Florencio, “Defining Post-COVID Symptoms (Post-Acute COVID, Long COVID, Persistent Post-COVID): An Integrative Classification.,” Int. J. Environ. Res. Public Health, vol. 18, no. 5, Mar. 2021, doi: 10.3390/ijerph18052621.

[12] S. Mani, S. Sharma, B. Omar, A. Paungmali, and L. Joseph, “Validity and reliability of Internet-based physiotherapy assessment for musculoskeletal disorders: a systematic review,” J. Telemed. Telecare, vol. 23, no. 3, pp. 379–391, Mar. 2016, doi: 10.1177/1357633X16642369.

[13] N. Gal, D. Andrei, D. I. Nemeş, E. Nădăşan, and V. Stoicu-Tivadar, “A Kinect based intelligent e-rehabilitation system in physical therapy.,” Stud. Health Technol. Inform., vol. 210, pp. 489–493, 2015.

[14] H. Jagos et al., “A Framework for (Tele-) Monitoring of the Rehabilitation Progress in Stroke Patients: eHealth 2015 Special Issue.,” Appl. Clin. Inform., vol. 6, no. 4, pp. 757–768, 2015, doi: 10.4338/ACI-2015-03-RA-0034.

[15] J. R. Carey et al., “Comparison of Finger Tracking Versus Simple Movement Training via Telerehabilitation to Alter Hand Function and Cortical Reorganization After Stroke,” Neurorehabil. Neural Repair, vol. 21, no. 3, pp. 216–232, Mar. 2007, doi: 10.1177/1545968306292381.

[16] A. Peretti, F. Amenta, S. K. Tayebati, G. Nittari, and S. S. Mahdi, “Telerehabilitation: Review of the state-of-the-art and areas of application,” JMIR Rehabil. Assist. Technol., vol. 4, no. 2, pp. 1–9, 2017, doi: 10.2196/rehab.7511.

[17] V. Cimolin et al., “A Comparative Analysis of Shoes Designed for Subjects with Obesity Using a Single Inertial Sensor: Preliminary Results,” Sensors, vol. 22, no. 3, pp. 1–10, 2022, doi: 10.3390/s22030782.

[18] M. Pau et al., “Clinical assessment of gait in individuals with multiple sclerosis using wearable inertial sensors: Comparison with patient-based measure.,” Mult. Scler. Relat. Disord., vol. 10, pp. 187–191, Nov. 2016, doi: 10.1016/j.msard.2016.10.007.

[19] M. Zago et al., “Gait evaluation using inertial measurement units in subjects with Parkinson’s disease.,” J. Electromyogr. Kinesiol. Off. J.

Int. Soc. Electrophysiol. Kinesiol., vol. 42, pp. 44–48, Oct. 2018, doi: 10.1016/j.jelekin.2018.06.009.

[20] V. Cimolin et al., “Symmetry of Gait in Underweight, Normal and Overweight Children and Adolescents.,” Sensors (Basel)., vol. 19, no. 9, May 2019, doi: 10.3390/s19092054.

[21] M. Pau et al., “Smoothness of Gait in Healthy and Cognitively Impaired Individuals: A Study on Italian Elderly Using Wearable Inertial Sensor.,” Sensors (Basel)., vol. 20, no. 12, Jun. 2020, doi: 10.3390/s20123577.

[22] “ATS statement: guidelines for the six-minute walk test.,” Am. J. Respir. Crit. Care Med., vol. 166, no. 1, pp. 111–117, Jul. 2002, doi: 10.1164/ajrccm.166.1.at1102.

[23] T. Abe, D. V DeHoyos, M. L. Pollock, and L. Garzarella, “Time course for strength and muscle thickness changes following upper and lower body resistance training in men and women.,” Eur. J. Appl. Physiol., vol. 81, no. 3, pp. 174–180, Feb. 2000, doi: 10.1007/s004210050027.

Virtual prototyping of a robotic chess player for play therapy

M. Pesenti[1], R. Schinelli[1], A. Antonietti[1], M. Gandolla[1,2], and A. Pedrocchi[1]
[1] *Nearlab, Department of Electronic, Information and Bioengineering, Politecnico di Milano, Milano, Italy*
[2] *WE-COBOT, Department of Mechanical Engineering, Politecnico di Milano, Milano, Italy*

***Abstract*—We designed a robot capable of challenging an opponent on a board game for rehabilitation purposes, with the aim to keep the patient busy during rehabilitation hours while allowing them to learn or improve mobility and strategic skills using a recreational game. To maximize the effectiveness of the therapy, the user experience must be as close as possible to a real game (e.g., chess or draughts) with a physical opponent. For this reason, the robot has to move real pieces on a real board, mimicking the other player's role. In this preliminary study, the concept and design of the robot were performed in a simulated environment. The simulated robot is of the parallel type, having the end effector directly connected to the base through rigid structures that work in coordination. Robot Operating System (ROS) was used to develop and design the robot controller. We describe the assembly of the designed structure of the robot and the controllers for movement along the Cartesian axes. Finally, game intelligence was introduced to enable the robot to play a chess game against the user autonomously. As a result, the implemented simulated robot can conduct a game of chess: recognizing and moving the pieces within the board perimeter, while the user can interact using a graphical interface. In conclusion, we have implemented the simulated version of an autonomous robotic board game that could be translated into a physical system able to engage the user for rehabilitation purposes.**

***Keywords*—Robotics, Rehabilitation, Chess, Gazebo**

I. Introduction

After a traumatic or acute event, such as a stroke, the human brain suffers from a shock that may result in motor, cognitive, or language deficits. Regarding motor functions, in an attempt to regain lost abilities, patients undergo motor rehabilitation. Robotic devices deal with robotic technology that provides physically disabled people with tools to assist the rehabilitative exercise and to improve their quality of life. Key elements of an effective rehabilitation approach include high repetitions and patient involvement [1]. In this view, it is possible to design serious games or to take advantage of traditional games to assist in physical rehabilitation. In developing such an approach, particular attention must be paid to users' requirements, as they are part of the process. Possible target patients for this work are those who can move their upper limbs and are in Grade 1 of the NIH Stroke Scale [2]. Patients who have suffered from a stroke, spinal cord injury, or muscular dystrophy are ideal targets for the project [3], [4].

The rehabilitation therapy should include both sensorimotor and cognitive aspects, all fundamental during the execution of complex tasks and activities of daily life. Robot-assisted rehabilitation has proved to be similar and at least non-inferior to standard sessions with a physical therapist. It has also been proved that active participation from the patient is needed to maximize the therapeutic effects in people who suffered from stroke [5]. In this view, playing board games, particularly chess or draughts, might be an important asset since i) it foresees multiple repetitions of precise pinch movements in the space, ii) it foresees the full cognitive involvement of the subject, iii) it can be played anytime, even outside the standard therapy hours. While commercial solutions enable patients with impaired upper-limb functions to play board games such as chess or draughts, most of these solutions foresee only a virtual board displayed on a screen, making the game entertaining for the patient but without a rehabilitation outcome. Other solutions foresee the automatic movement of physical pieces on the board, moved using magnetic actuators hidden under the board plane, making the experience better but still far from an actual match between two human players. It was reported that people who played against a physically embodied agent had higher enjoyment experiences than those who had played with a virtual agent [6]. For these reasons, we designed and virtually prototyped a physical robot able to play a board game, like chess, in the most human-like way (i.e., reaching for physical pieces on the virtual board, picking and moving them around according to the strategies defined by its game intelligence system). In this way, the robotic chessboard can be used for rehabilitation purposes, keeping the patient engaged and entertained while he/she is recovering motor functions. The goal is to allow patients suffering from motor impairments to perform tasks that can be muscularly feasible and within their reach, such as lifting and moving a simple object. The robot is not designed to assist the user or help them in the movement; rather, it is proposed as an opponent to be able to lead a game of chess.

II. Materials and methods

The choice of the robot fell on a parallel robot for ease of use and simulation, as a device that can move on a Cartesian plane and lift the pieces in order to lead the game is sufficient. Parallel robots are also preferable on this occasion because, despite their rigidity, they are reliable and precise when working on limited areas, such as the edge of a chessboard. They are also simple to adapt to physical devices such as a 3D printer, with easy-to-find hardware and inexpensive additional parts.

In order to simulate the structure of the robot and the movements, ROS (Robot Operating System) Melodic and Gazebo were used [7]. ROS is an open-source system for robot programming. It provides the services expected from an operating system, like hardware abstraction, device control, implementation of functionality, message-passing among processes, and package management. It has therefore proved to be the ideal solution to simulate a robot that, although simple, must be able to move in space and needs specific libraries to meet our objectives. In addition, we used Gazebo, an open-source 3D robotics simulator, to simulate the physical world and to visualize the robot. It offers a robust physics engine, high-quality graphics, and a convenient programmatic that includes an advanced graphical interface. It also offers useful functionalities for knowing the behavior of the robot and what is around it.

A. *The robotic chessboard*

A parallel robot is a structure composed of mechanical arms that converge in a platform or end effector. In this case, the robot is composed of a base that supports the whole object, four rigid poles on which there are links for movement along the z axis, and an upper structure on which there are spools and a platform for movement in y and x axes (Fig. 1). The pieces on the board are taken by the robot end-effector from above.

The robot can either play against a human player by moving only its pieces or the pieces of black and white, as happens in the simulation. The former is the rehabilitation scenario, where the human player is the patient performing the rehabilitation session. In principle, the opponent can either be the robot itself, controlled by its game intelligence, or remotely controlled by another human opponent via an internet connection. From a control point of view, in this work, we have implemented a simple game intelligence so that the rehabilitation session can happen without any external intervention.

The 32 pieces are the soul of the game and each one moves distinctly. Pieces can be generally distinguished from others by their shape, but this difference represents a problem for the robot, as it lacks a sophisticated grasping end-effector. For this reason, simplified geometries were used. They had to be defined as static robots to enable a proper interaction between the pieces and the robot. The main robot is described by its Unified Robot Description Format (URDF) and it is composed of dynamic parts that interact with each other and move, while the pieces are other static robots defined with simple URDFs. Therefore, every piece has its own name, allowing the robot to correctly identify each piece and its position throughout the game. There are also other important parameters that must be set to make sure that each piece remains in its initial position and does not move: the initial position (within the limits of the board range, from -0.6125 to 0.6125 m), a visual tag (each piece is a square base box with a side of 0.15 m and a height of 0.3 m), and inertia (0.00833 $kg \cdot m^2$).

All the pieces are thus arranged in their initial positions and ready to be moved by the robot. We have added a Graphical User Interface (GUI) to show the top view positions of the pieces and to let the human player select their move with a drag-and-drop movement via mouse or trackpad (Fig. 2).

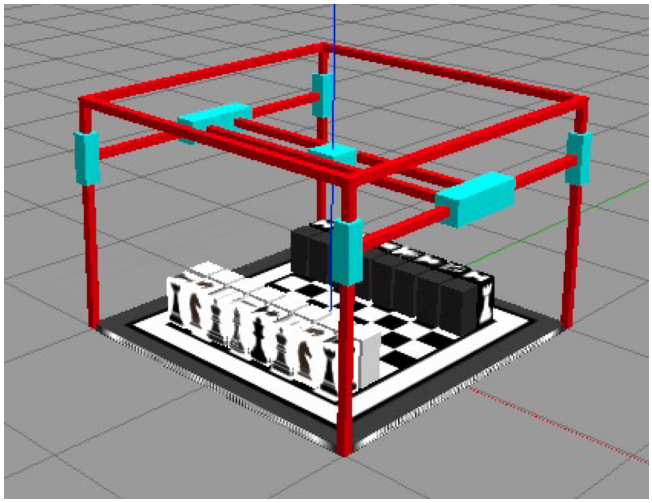


Fig. 1: The full structure of the robot (links in red and moving joints in light blue) and the chessboard on which it operates. 16 pieces per team, black and white, are instantiated on the board and initially positioned on their starting squares.

B. *Robot controller*

We have designed the controller for the robot arm to move the pieces on the board. Each square on the board is mapped to x and y axes coordinates, and the vertical position (z) has only two states: low, 0.3 m above the board level, therefore touching the underlying piece, and up, 0.9 m. Controllers receive the position and modulate the velocity of the joints to move the robot. The *ROS control* package takes as input the joint state data from the robot actuators' encoders and a target set point [8]. It uses a generic control loop feedback mechanism, which is a simple proportional controller (P = 2 s^{-1}), to set the linear velocity of the actuators, moving the end-effector horizontally and vertically and the side fuses that allow the lowering. Each

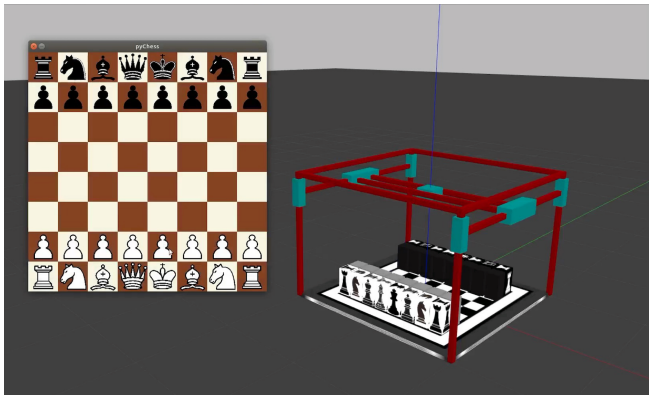


Fig. 2: The game setup with the integration of the GUI shows the top view of the chessboard and the current position of the pieces. The GUI is used by the human player to select the next move.

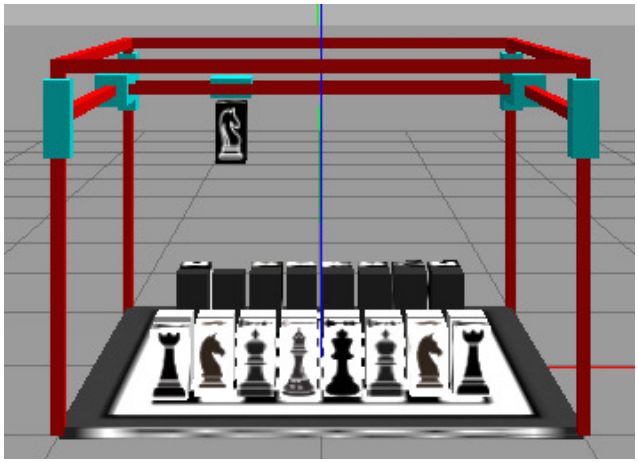


Fig. 3: Frontal view (from the human player side, playing with whites) of the board while the robot is moving one of its knights. In particular, this is the situation at the end of step 3).

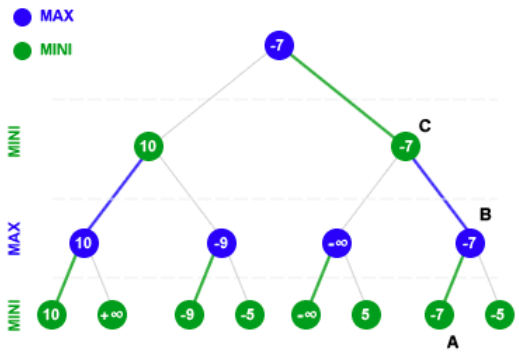


Fig. 4: Simple example of the decision tree generated by the *Minimax* algorithm. Lowest level: at the terminal nodes, it is the turn of the MINI player. It finds the minimum values at the terminal nodes and assigns them to the parent node. Middle level: here, it is MAX player's turn. It chooses the nodes with the highest values and assigns them to the parent node. Upper level: again, it is MINI player's turn; between the nodes 10 and -7 it chooses the latter one, and it reports it at the root node of the tree (current position). Once the tree is reconstructed, the *Minimax* algorithm chooses the sequence with the best strategic choices for the MINI player from its current position, which is the path C→B→A.

move is composed of at least six steps: 1) move the end-effector to the desired x, y position, where the piece to be moved is located; 2) lower the end-effector and attach the piece; 3) raise up the end-effector (e.g., as depicted in Fig. 3); 4) move the end-effector to the final x, y position, where the piece needs to be moved; 5) lower the end effector and detach the piece; 6) raise up the end-effector. In case of special moves, e.g., *castling*, promotion of a pawn, or capturing an opponent piece, the 6-step sequence has to be repeated two times. For instance, if a piece is captured, it has to be moved outside of the board perimeter first, and then the capturing piece is moved to the position previously occupied by the removed one.

C. Game intelligence

We used a decision system (i.e., game intelligence) to let the robot decide the moves of its pieces. We adopted a machine learning system based on convolutional neural networks, leveraging the *MiniMax* algorithm, which is often used in 2-players games [9], [10]. The game intelligence system is connected to the GUI to both read the status of the game and to show the user the situation of the board in a comfortable way. It is also connected to the robot controllers in order to execute the planned moves.

The *MiniMax* algorithm is a recursive algorithm for finding the best move in a zero-sum game (as chess) that takes place between two players. It is a decision rule that minimizes the maximum possible loss of a worst-case scenario for the player. The *MiniMax* algorithm is able to minimize potential loss by using positional evaluations to predict the opponent's next move. Algorithms of this type have to find ways of reducing computational cost in games where it would otherwise be impossible to find a good move with a certain depth of search, as the computational load increases considerably going down the branches. Since the tree of combinations can become very large, it is requested some kind of mechanism to cut down the number of built sub-trees, ideally eliminating (pruning) moves that do not look promising and concentrating on those which are likely to lead to a positive outcome. For this purpose, it is introduced the idea of a cost function that assigns a number to a game position representing how likely that position is to lead to a win. This score can be calculated for each playable position. The *MiniMax* algorithm allows to identify the best choices of the two players (one called MINI and one MAX) during the game, analyzing backward the game tree starting from the terminal nodes, i.e., from possible situations in which the game can end and progressively ascending to the current position of the players. For example, in the game tree reported in Fig. 4, a sequential game between two players is represented. The first player (MAX) must maximize the value of the game, while the second player (MINI) must minimize the output. In addition, a pruning mechanism called the *Alpha-Beta* algorithm had been added to reduce the number of branches and nodes in the research tree to analyze [11]. We have adapted the code that can be found at https://github.com/luweizhang/chess-ai.

III. Results and Discussion

A. Physical simulation and control

The physical simulation is simple and intuitive for the user: it is enough to open the command GUI and execute the selected move, waiting for the artificial intelligence response. The robot's decision is not instantaneous but takes a few seconds to execute. This improves the game's realism and, at the same time, allows the human player some time to think about future moves. Furthermore, one can expect that the robot can perform similar moves in the opening and deviate from them only at a certain point in the game. This is due to the intrinsic architecture of intelligence, which selects the

best move from a set of choices. Initially, when the choices are limited and the pieces are in the same position, the robot responds in a similar way. As the game progresses, the intelligence deviates from the main path. In the simulation, the control of the pieces takes place directly on the GUI. Here the player can make their move by dragging the piece to the desired position.

As shown previously, it is possible to play a match against the robot. For convenience, white has been chosen as the color for the human player and the robot will use black. The game intelligence chosen is not particularly strong, but it is still able to establish a certain advantage if the opponent makes unusual moves. In case of capture of other pieces, they are moved outside the game perimeter. This is very similar to what would happen in a real chess game, and it is more realistic than virtual games, where the captured pieces just disappear from the screen.

B. Potential rehabilitation use

Although the result of this work is only a virtual prototype, we can foresee the potential rehabilitation effectiveness for patients suffering from upper limb disabilities. In the case of patients who have suffered from spinal cord injury, the device can be useful for people with a non-disabling degree of disease. If the injury is too severe or at a too advanced stage, e.g., for neurodegenerative diseases, it is impossible for the patient to move the pieces on the board. Even in the case of particularly disabling strokes in which there is a low level of consciousness (important to play a game with a significant cognitive load), or the motor skills are so limited that they prevent movement against gravity, a patient's ability to engage in this game is out of the question. In the case of muscular dystrophy, on the other hand, there is an impoverishment of motor skills over time. A limitation can be represented by age: Duchenne Muscular Dystrophy affects patients who are generally very young and may find it difficult and little fun to try a complex game such as chess. In the case of Becker Muscular Dystrophy, loss of ambulation generally appears later. It is, therefore, more natural for these patients to become interested in a board game.

The robotic chess game itself has two types of advantages as regards the rehabilitation aspect: i) it allows patients to grasp and move their pieces, exercising different muscles and motor strategies; ii) it requires intellectual effort and, for this reason, can be stimulating and can entice the patient to play multiple games in a single session.

C. Future implementations

We foresee implementing a real physical model based on the simulations presented to fulfill the rehabilitation purposes. The robot can be adapted to a system that reproduces the geometry and structure of a parallel robot, such as a 3D printer. In this case, the nozzle (which will become the grasper) can move on the Cartesian space similarly to the virtual prototype. With a physical system, the patient could move the piece by themselves. However, it may happen that they suffer from a degree of impairment that prevents them from moving the piece without support or help. In this case, it is possible to use a motion adapter (e.g., a joystick). Other robot structures can be used (e.g., an anthropomorphic robot arm, potentially a solution that integrates a vision system already), with the advantage of having a robotic opponent more closely resembling a human player, with the potential of using the same robot for different tasks and not only for playing. The higher versatility yields an increased cost for the platform. Regardless of the choice of the robot, solutions for active and passive safety need to be included to avoid possible harm in human-robot interactions. Finally, the game intelligence can be modulated according to the skill of the human player, and sophisticated controllers can be employed to generate a more realistic game experience, especially for advanced players.

IV. Conclusion

The implemented simulated robot is able to conduct a game of chess: recognizing and moving the pieces. While the use of robotic games is not still present in clinical practice, one can expect that patients can benefit from this type of technology. The main limitation of the project is that the robot was developed in a virtual environment. In case of future implementations, we expect that patients will be interested in playing with a physical system. It is also important to highlight the greatest value of the robotic approach in rehabilitation: while physical therapists can devote a limited time to each patient, the robotic system can engage the user for several sessions, prolonging the therapy and its effectiveness.

References

[1] F. Scotto di Luzio, F. Cordella, M. Bravi, F. Santacaterina, F. Bressi, S. Sterzi, and L. Zollo, "Modification of hand muscular synergies in stroke patients after robot-aided rehabilitation," *Applied Sciences*, vol. 12, no. 6, p. 3146, 2022.

[2] L. K. Kwah and J. Diong, "National institutes of health stroke scale (nihss)," *J Physiother*, 2013.

[3] V. Longatelli, A. Antonietti, E. Biffi, E. Diella, M. G. D'Angelo, M. Rossini, F. Molteni, M. Bocciolone, A. Pedrocchi, and M. Gandolla, "User-centred assistive system for arm functions in neuromuscular subjects (useful): a randomized controlled study," *Journal of NeuroEngineering and Rehabilitation*, vol. 18, no. 1, 2021.

[4] M. Gandolla, A. Antonietti, V. Longatelli, and A. Pedrocchi, "The effectiveness of wearable upper limb assistive devices in degenerative neuromuscular diseases: A systematic review and meta-analysis," *Frontiers in Bioengineering and Biotechnology*, vol. 7, 2020.

[5] R. Ranzani, O. Lambercy, and J. Metzger, "Neurocognitive robot-assisted rehabilitation of hand function: a randomized control trial on motor recovery in subacute stroke.," *J Neuroeng Rehabil.*, 24 Aug 2020.

[6] A. Pereira, C. Martinho, I. Leite, and A. Paiva, "Icat, the chess player: The influence of embodiment in the enjoyment of a game," vol. 3, p. 1229 – 1232, 2008.

[7] N. Koenig and A. Howard, "Design and use paradigms for gazebo, an open-source multi-robot simulator," vol. 3, p. 2149 – 2154, 2004. Cited by: 1961.

[8] S. Chitta, E. Marder-Eppstein, W. Meeussen, V. Pradeep, A. Rodríguez Tsouroukdissian, J. Bohren, D. Coleman, B. Magyar, G. Raiola, M. Lüdtke, and E. Fernández Perdomo, "ros_control: A generic and simple control framework for ros," *The Journal of Open Source Software*, 2017.

[9] K. O'Shea and R. Nash, "An introduction to convolutional neural networks," 2015.

[10] G. Strong, "The minimax algorithm," *Glenn strong cs*, 10 Feb 2011.

[11] S. Fuller, G. Gaschnig, and J. Gillogly, "Analysis of the alpha-beta pruning algorithm," *Carnegie-Mellon University*, July 1973.

A hydraulic implantable artificial detrusor for controlled bladder voiding

Simone Onorati[#1], Federica Semproni[#1], Linda Paternò[#1], Giada Casagrande[1], Veronica Iacovacci[1,2] *, and Arianna Menciassi[1]

[1] *The BioRobotics Institute, Scuola Superiore Sant'Anna, Pontedera (Pisa), Italy*
[2] *Department of Mechanical and Automation Engineering, The Chinese University of Hong Kong, Hong Kong, China*
*# These authors contributed equally to the work. * Corresponding author: veronica.iacovacci@santannapisa.it*

***Abstract* — Severe spinal cord injuries or detrusor muscle degeneration due to aging can cause the loss of contractility of the urinary bladder. To date, long-term clinical solutions to restore contraction control include neurostimulators with unpleasant long-term side effects. Thus, implantable artificial detrusors turn out to be an urgent promising solution in this field.**

In this paper, an origami-based fluidic system is proposed as a robotic prosthesis for human bladder voiding. Both on-the-bench and *ex vivo* tests highlighted promising results with a bladder voiding efficiency range of 75-90%.

***Keywords* — spinal cord injury, bladder, soft robotics, implantable prostheses**

I. Introduction

Millions of people in the world are affected by the inability to contract the detrusor muscle, which is essential for the voiding of the urinary bladder. Underactive or inactive bladder is usually the consequence of severe spinal cord injuries below the thoracic segment (T12 vertebra), which are approximately 30% of the total cases [1], [2]. In Europe, severe spinal cord injuries have an estimated incidence of 10,000 new cases per year [3]. Impairments in the control of bladder voiding are also associated with body aging due to detrusor muscle degeneration and spinal neural tissue alterations [4].

In this field, medical treatments are often based on intermittent or indwelling catheterization, which turn out uncomfortable and induce several complications [5]. Sacral neural stimulators are the only available permanent option but feature severe long-term side effects [6]. Therefore, a different kind of permanent solution is extremely urgent.

To date, no commercial implantable artificial detrusor is available. Researchers have recently proposed prototypes based on thermo-responsive hydrogels [7], or on shape memory alloy (SMA) elements [8] embracing the bladder. Nevertheless, these devices have been designed for small animal bladders, and several challenges have to be faced in order to upscale these designs to achieve effective solutions for humans.

In this paper, we propose a new kind of implantable artificial detrusor based on a fluidic actuation strategy, with the aim of exploring an intrinsically safe approach for controlled bladder voiding. Indeed, fluidic systems have already been demonstrated to be a successful solution in many different applications, such as direct cardiac compression (*i.e.*, artificial myocardium) [9] or valve systems in the widespread commercial artificial sphincter AMS 800™ [10].

The proposed solution is composed of two identical, hull-shaped actuators embracing the natural bladder. Each one consists of a water-filled chamber made of soft silicone skin enclosing a flexible acetate origami skeleton with a '*waterbomb*' pattern [11]. This kind of origami has proven a volumetric contraction of up to 90% at a depression of –60 kPa in a shape-morphing actuator [11]. It has been exploited for self-expanding stents [12] but not yet for implantable artificial prostheses.

In our device, the significant shape change of the waterbomb origami guides that of the whole artificial detrusor. From a domed shape at rest, the two actuators become almost flat when they are depressurized, subtracting space from the inside bladder and thus assisting its voiding.

For operating the system, a liquid was selected instead of gas for safety reasons. Indeed, an implantable gas reservoir would require storing the gas at moderate to high pressures for all of the device life, with a high risk of bursts [13]. On the contrary, a liquid medium can be stored at the same abdominal pressure, thanks to a higher force-to-volume ratio [14]. Water was used in the current design, but it might be easily replaced by an isotonic saline solution.

Two different sizes of the *waterbomb* origami were compared in terms of produced bladder voiding efficiency. The design, manufacturing, and used experimental setup are presented in Section II. The results of the voiding performances are reported in Section III. Finally, in Section IV, the added value of the proposed work in the field of implantable urinary prostheses is discussed.

II. Materials and Methods

A. Design overview

The proposed artificial detrusor muscle relies on two identical fluidic actuators, which are bound together by a surgical thread and can totally embrace the human bladder (Fig. 1a). The two-module design allows for a convenient surgical procedure for the prosthesis implant, in which no temporary resection of the urinary ducts (ureters and urethra) is needed.

Each actuator is featured by a semi-rigid sheet shaped as a *waterbomb* origami and enclosed between two ellipsoidal, soft but inextensible skins (Fig. 2c). These two skins delimitate the actuation chamber, which is filled with the service fluid by means of a rigid tube, connected to a miniaturized fluidic circuit. When the fluid is drawn out of the chamber, the generated depression promotes a shape switch of the origami skeleton from a domed configuration to a contracted and flat one. Indeed, the soft chamber pulls the adjacent sheet crests of the origami one towards the other during depressurization, since the skins cannot extend. The shape transition of the actuators produces a uniform contraction force over the natural bladder, promoting its voiding.

To evaluate the effect of different origami cell square sizes (SQ in Fig. 1b) on the contraction capabilities of the bladder, two different detrusor models are proposed.

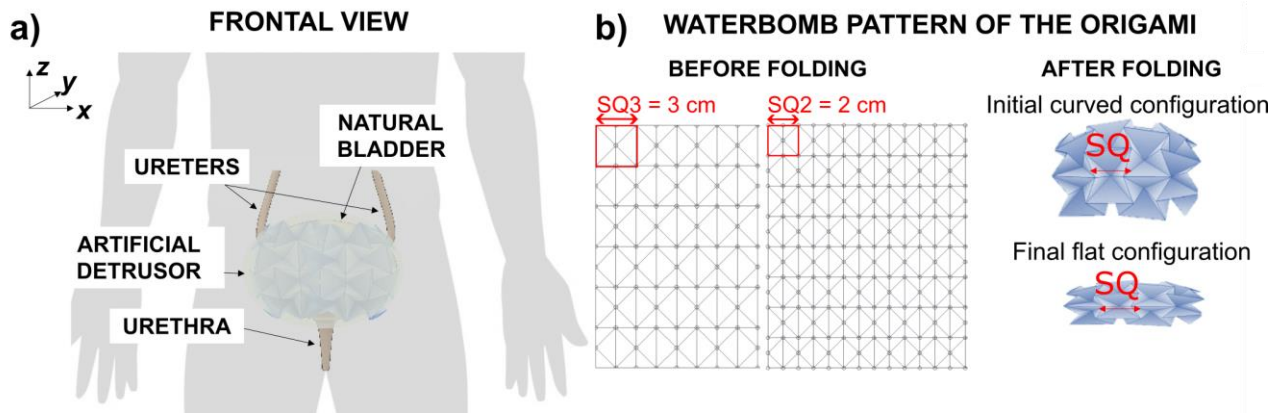


Fig. 1: (a) Drawing of the fluidic artificial detrusor in situ, installed around the urinary bladder (one of the two actuators is visible). (b) Structure and operating principle of the *waterbomb* origami. SQ = squared cell size.

The 'SQ3' model origami skeleton consists of 6 x 4 square cells with a side of 3 cm and 1 mm-thick silicone skin; while the 'SQ2' model origami skeleton consists of 8 x 6½ cells with a side of 2 cm and 0.5 mm-thick skin.

B. Fabrication method

The artificial detrusor was fabricated following four phases (Fig. 2). Firstly, two origami skeletons (one for each actuator) were realized by engraving through a laser cutting machine the *waterbomb* pattern on a semirigid sheet, composed by the stacking of 0.16 mm-thick acetate (EVA), 0.07 mm-thick polyethylene (LDPE), and thin double-sided tape (in between) (Fig. 2a). The pattern was folded manually.

Secondly, the two skins composing the fluidic chamber of each actuator were fabricated by molding a soft silicone (Ecoflex™ 00-30, Smooth-On, Inc., USA) in which a medical gauze was embedded prior to curing (Fig. 2b). The gauze gives the skin inextensible yet flexible properties. The used mold was designed in the SolidWorks CAD software, and 3D-printed.

Subsequently, the single actuator was assembled by sewing with a thin thread the origami skeleton to one of the skins, which in turn was sewed to the second one (Fig. 2c). Then, the chamber was hermetically closed by pouring some fresh silicone all over the seams and a polyurethane tube was fastened to the outer wall with silicone glue (Sil-Poxy™, Smooth-On, Inc.).

Finally, the hydraulic artificial detrusor is obtained by tightly sewing the two actuators around the natural bladder upon implantation (Fig. 2d).

C. Characterization of the detrusor voiding performances

For the evaluation of the effectiveness of the proposed solution, the prosthesis was tested on *ex vivo* adult swine bladders, whose sizes are similar to the human bladder.

The electro-hydraulic circuit drawn in Fig. 3 was exploited for this purpose. It included two operative lines:

- *Line 1*, connecting a syringe pump (NE-1000, New Era Pump Systems, Inc., USA) to the two actuators around the bladder and to a reservoir. A differential pressure sensor (MPX5100DP, Freescale Semiconductor, Inc., USA, interfaced to an Arduino™ Mega 2560 connected to MATLAB™ R2021b) was placed just upstream of the detrusor actuators to monitor the inlet pressure.
- *Line 2*, connecting the *ex vivo* bladder to a collection reservoir placed onto an electronic scale (WLC 2/A2, Radwag, Poland). This allowed recording the ejected simulated urine weight for deriving the ejected volume over time, $V_{out}(t)$. In addition, a second MPX5100DP sensor was placed just downstream of the bladder to monitor the intravesical pressure. The micturition was allowed via a two-way manual valve emulating the natural sphincter.

A micturition test was conducted by: (*i*) filling the actuators with water by exploiting Line 1; (*ii*) filling the bladder with water by a manual syringe, at a volume (V_u) corresponding to an intravesical pressure of 3.0 kPa – this value was chosen from the literature, being below the average threshold of self-urination reflex triggering (*i.e.*, 4.3 kPa) [15]; (*iii*) opening the artificial sphincter contemporarily to the actuation start by triggering the syringe pump.

During the assisted micturition, time and ejected volume on the scale (V_{out}) were recorded. All tests were conducted with the bladder oriented horizontally to simulate the worst condition for voiding (*i.e.*, bed-ridden patient). The micturition was allowed until the V_{out} increment was lower than 0.03 g in the last 50 samples, corresponding to ~8 s with the used laptop.

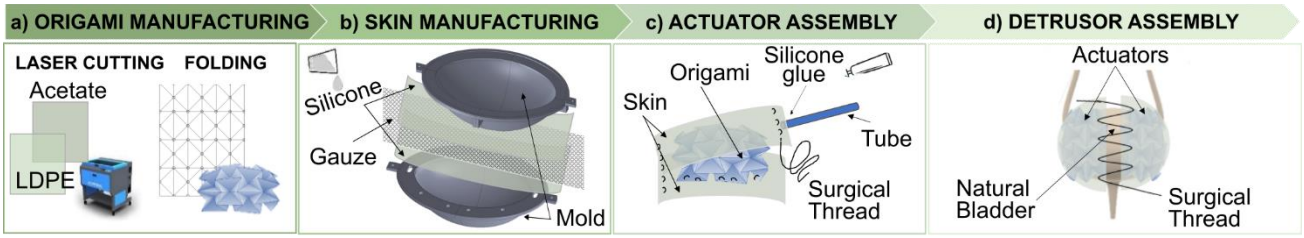


Fig. 2: Manufacturing procedure of the fluidic artificial detrusor.

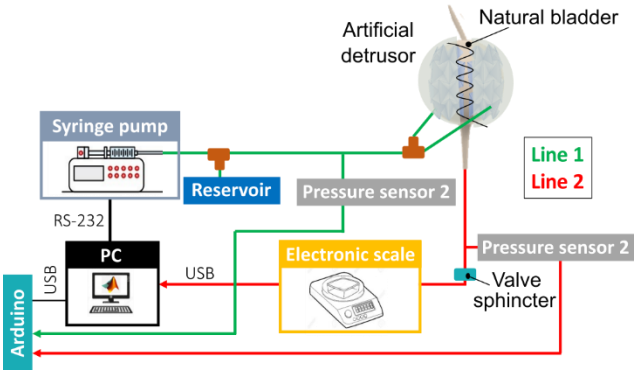


Fig. 3: Experimental setup for the ex vivo characterization of the fluidic artificial detrusor. Line 1 connects the syringe pump to the detrusor, Line 2 connects the natural bladder to a collection pool on an electronic scale.

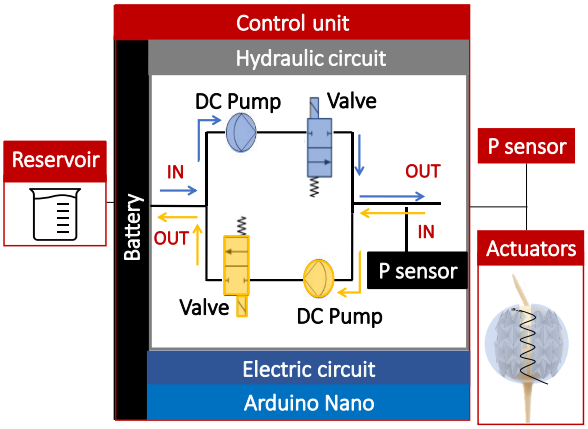


Fig. 4: Schematic representation of the compact micropumps-based control unit for the prosthesis actuation.

For each detrusor model (SQ2 and SQ3), two parameters of the micturition were considered as performance indicators of the prosthesis: (*i*) the Voiding Efficiency (VE [%]), *i.e.* the ratio of V_{out} and V_u (target VE value 90%); and (*ii*) the Post-Voiding Residual volume (PVR [mL]), *i.e.*, the urine in the bladder when the micturition was ended (target PVR value below 50 ml [16]). Each parameter was tested on bladders surrounded by the artificial detrusor, oriented horizontally, in the 'active' and 'passive' states (namely, with detrusor units activated and not activated), and for both the SQ3 and SQ2 designs. Moreover, each configuration was tested 4 times on 3 different *ex vivo* bladders, to include also the role of biological variability.

D. Driving circuit design

A first prototype of a compact electro-hydraulic circuit was developed to manage the activation of the artificial detrusor. As shown in Fig. 4, the circuit comprises two opposite hydraulic lines to drive water from the actuators to a reservoir during the contraction phase (actuator ON, in yellow), and from the reservoir to the actuators for restoring the initial state (actuator OFF, in blue).

A micropump for liquids (SP 270 EC-L, Schwarzer Precision, Germany) and an electromagnetic 2-way valve (Series 3, Parker Hannifin, USA) are integrated into each line. The output of an MPX5100DP differential pressure sensor is used to stop the water flow and close the electro-valves at the pre-defined *P* pressure thresholds for each state. The logic of the system is managed by an Arduino™ Nano 3 microcontroller connected to MATLAB R2021b on a Windows PC.

A powering circuit provides 5 V to the pumps and to the Arduino, while 12 V to the electro-valves. The source is a 7.4 V battery.

The designed control unit was tested with the artificial detrusor positioned on an *ex vivo* swine bladder, placed inside a human manikin (Fig. 5). Surrounding organs were simulated by placing other swine *ex vivo* tissues around the prosthesis. Only the SQ3 model, featuring higher performances on bench, was tested also in the simulated environment.

III. Results

A. Voiding performances in ex vivo setup

The results of VE and PVR obtained from the *ex vivo* tests are reported in Fig. 6.

The tests performed with active micturition yield significantly better results compared to the passive one, especially for the SQ3 model (VE increases by ~ 1.5 times and PVR decreases by ~ 4 times). Indeed, a VE of 91% and an average PVR < 10 mL is reached with the actuation of the SQ3 model, while VE of 75% and PVR < 30 mL are obtained with the SQ2 model.

The performances of the SQ3 model are particularly good compared to the SQ2, since the origami with a lower fold density (SQ3) is found to contract more at the same depression grade. Considering the results obtained for assisted urination, the use of the actuation system allows for a more effective urination.

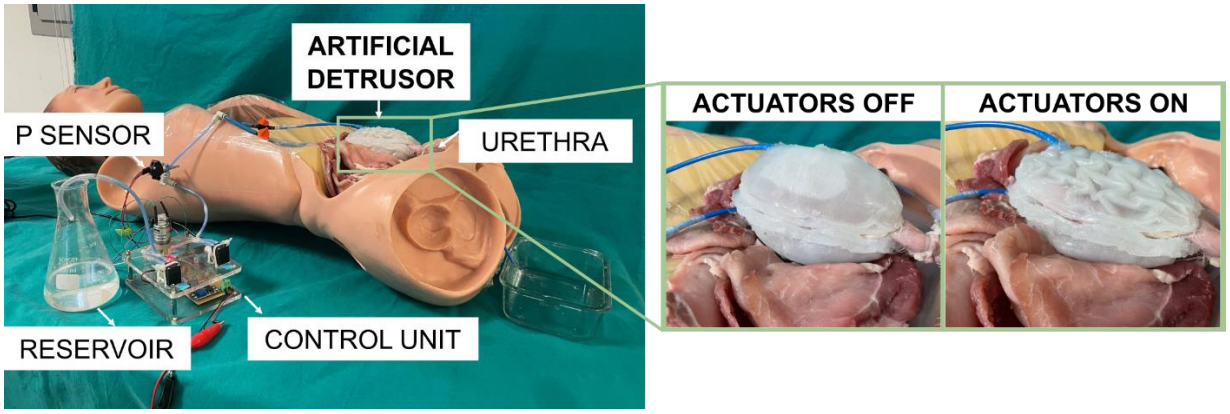


Fig. 5: Photo of the fluidic artificial detrusor in a simulated anatomical environment, connected to the first prototype of the control unit. *Ex vivo* tissues placed above the prostheses during the tests are here removed for visualization purposes. The prototype is mounted around an *ex vivo* swine bladder.

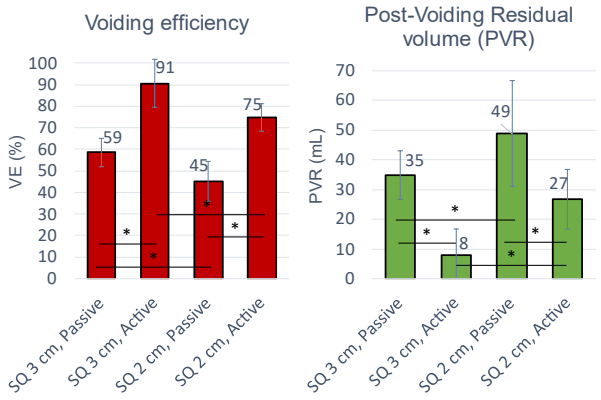


Fig. 6: Experimental results of the micturition quality evaluated by: voiding efficiency (VE [%]) and post-voiding residual volume (PVR [mL]). * denotes *p-value* < 0.05 in two-population *t*-test with the specified groups (*a* = active, *p* = passive urination).

B. Voiding performances in the anatomical simulated environment

When located among the simulated surrounding organs (Fig. 5), the fluidic soft robotic detrusor demonstrated an active VE of 84.8% ± 7.4%, which is similar to the results observed during bench tests.

IV. Discussion and Conclusion

In this work, we proved the feasibility of using a hydraulic, origami-based soft actuator as an artificial detrusor for controlled micturition. It is the first time that such strategy is applied to urinary system – while fluidic devices for direct cardiac compression are present in the literature [9], [17].

The advantage of using the *waterbomb* origami as a core element for the actuation is the large contraction stroke achieved on the bladder. The shape of the proposed artificial detrusor was found essential to produce acceptable voiding degrees on a thin and hollow organ such as the bladder. Indeed, we were able to obtain VE around 90% and PVR below the clinical warning threshold of 50 mL, both on the bench and in a simulated environment.

Some research-stage prototypes of implantable artificial detrusors have been proposed in the last five years (*e.g.*, based on thermo-responsive hydrogels [7], shape-memory alloy wires [8], and magnetic solutions [18]). All these devices share with our fluidic detrusor the easiness of implantation, and comparable voiding performances (respectively of ~75% in [8] and 90-100% in [18]). However, the proposed artificial detrusor is featured by an inherent safety (no heating of elements in direct contact with organs, nor high current/ voltages needed), the uniformity of the compressive action on the bladder, and the use of low-cost electro-mechanic components.

Compared to the temperature-based and magnetic coupling-based approaches, our prosthesis suffers from higher encumbrance and weight, due to the presence of the service fluid. Based on the above considerations, future developments on fluid-based detrusors will include a redesign of the origami-based actuators to reduce the hull thickness and the actuating water volume. Furthermore, to allow full system implantability, the stand-alone control circuit – here successfully tested – will be miniaturized, powered by a single rechargeable battery, and endowed with autonomous firmware for wireless operation.

In conclusion, this work represents a valuable contribution to the field of implantable and totally artificial biorobotic organs, specifically for coping with the challenge of assisted voiding of the inactive bladder.

Acknowledgement

This work was supported by INAIL, the Italian National Institute for Insurance against Work-related Injuries (non-commercial entity), within the PR19-CR-P2 BioSUP (BIOnic Solutions for Urinary impaired People) project framework.

References

[1] A. Ruffion *et al.*, 'Systematic Review of the Epidemiology of Urinary Incontinence and Detrusor Overactivity among Patients with Neurogenic Overactive Bladder', *NED*, vol. 41, no. 3–4, pp. 146–155, 2013, doi: 10.1159/000353274.

[2] L. H. S. Sekhon and M. G. Fehlings, 'Epidemiology, Demographics, and Pathophysiology of Acute Spinal Cord Injury', *Spine*, vol. 26, no. 24S, p. S2, Dec. 2001.

[3] Nogo Inhibition in Spinal Cord Injury, 'NISCI: NISCI's scientific background'. https://nisci-2020.eu/nisci-s-scientific-background.html (accessed Jan. 12, 2023).

[4] P. P. Smith, 'Aging and the underactive detrusor: A failure of activity or activation?', *Neurourology and Urodynamics*, vol. 29, no. 3, pp. 408–412, 2010, doi: 10.1002/nau.20765.

[5] Heersink School of Medicine and Spinal Cord Injury Model System, 'SCI Fact sheets - Bladder Management Options Following Spinal Cord Injury', 2015. https://www.uab.edu/medicine/sci/uab-scims-information/sci-infosheets (accessed Jan. 12, 2023).

[6] S. M. Yaiesh, A. Al-Terki, and T. F. Al-Shaiji, 'Neuromodulation in Urology: Current Trends and Future Applications', 2020. doi: 10.5772/intechopen.92287.

[7] X. Yang *et al.*, 'Soft Artificial Bladder Detrusor', *Advanced Healthcare Materials*, vol. 7, no. 6, p. 1701014, 2018, doi: 10.1002/adhm.201701014.

[8] F. Arab Hassani, H. Jin, T. Yokota, T. Someya, and N. V. Thakor, 'Soft sensors for a sensing-actuation system with high bladder voiding efficiency', *Sci Adv*, vol. 6, no. 18, p. eaba0412, May 2020, doi: 10.1126/sciadv.aba0412.

[9] E. T. Roche *et al.*, 'Soft robotic sleeve supports heart function', *Sci. Transl. Med.*, vol. 9, no. 373, p. eaaf3925, Jan. 2017, doi: 10.1126/scitranslmed.aaf3925.

[10] 'AMS 800™ Artificial Urinary Sphincter', *www.bostonscientific.com*. https://www.bostonscientific.com/en-US/products/artificial-urinary-sphincter/ams-800-artificial-urinary-sphincter.html (accessed Sep. 08, 2022).

[11] S. Li, D. M. Vogt, D. Rus, and R. J. Wood, 'Fluid-driven origami-inspired artificial muscles', *Proc. Natl. Acad. Sci. U.S.A.*, vol. 114, no. 50, pp. 13132–13137, Dec. 2017, doi: 10.1073/pnas.1713450114.

[12] W. Zhao, N. Li, L. Liu, J. Leng, and Y. Liu, 'Origami derived self-assembly stents fabricated via 4D printing', *Composite Structures*, vol. 293, p. 115669, Aug. 2022, doi: 10.1016/j.compstruct.2022.115669.

[13] L. Paternò, G. Tortora, and A. Menciassi, 'Hybrid Soft–Rigid Actuators for Minimally Invasive Surgery', *Soft Robotics*, vol. 5, no. 6, pp. 783–799, Dec. 2018, doi: 10.1089/soro.2017.0140.

[14] M. De Volder and D. Reynaerts, 'Pneumatic and hydraulic microactuators: a review', *J. Micromech. Microeng.*, vol. 20, no. 4, p. 043001, Apr. 2010, doi: 10.1088/0960-1317/20/4/043001.

[15] R. T. Kershen, K. M. Azadzoi, and M. B. Siroky, 'Blood flow, pressure and compliance in the male human bladder', *J Urol*, vol. 168, no. 1, pp. 121–125, Jul. 2002.

[16] M. H. Ho and N. N. Bhatia, 'CHAPTER 51 - Lower Urinary Tract Disorders in Postmenopausal Women', in *Treatment of the Postmenopausal Woman (Third Edition)*, R. A. Lobo, Ed. St. Louis: Academic Press, 2007, pp. 693–737. doi: 10.1016/B978-012369443-0/50063-6.

[17] J. Bonnemain, P. J. del Nido, and E. T. Roche, 'Direct Cardiac Compression Devices to Augment Heart Biomechanics and Function', *Annual Review of Biomedical Engineering*, vol. 24, no. 1, pp. 137–156, 2022, doi: 10.1146/annurev-bioeng-110220-025309.

[18] Y. Yang *et al.*, 'Magnetic soft robotic bladder for assisted urination', *Sci. Adv.*, vol. 8, no. 34, p. eabq1456, Aug. 2022, doi: 10.1126/sciadv.abq1456.

Brain signals in semi-immersive and immersive VR environments: a feasibility study

V. A. Arcobelli[1], K. Marcaccini[1], P. G. Hassaballah[1], L. Tonin[2, 3], S. Tortora[2, 3], and S. Orlandi[1,4]
[1]*Department of Electrical, Electronic and Information Engineering, "Guglielmo Marconi" (DEI) University of Bologna, Italy*
[2]*Intelligent Autonomous Systems Laboratory, Department of Information Engineering, University of Padova, Padua, Italy*
[3]*Padova Neuroscience Center, University of Padova, Padua, Italy*
[4]*Health Sciences and Technologies - Interdepartmental Center for Industrial Research (CIRI-SDV), University of Bologna, Italy*

***Abstract*— In recent years, the integration of virtual reality (VR) technology is seeing a significant increase and has the potential to greatly impact the future of healthcare. The use of VR systems in conjunction with electroencephalography (EEG) offers new possibilities in rehabilitation scenarios. This study focuses on comparing the feasibility of using a head-mounted display (HMD) while acquiring EEG data in both semi-immersive and fully immersive environments. The impact of an Oculus Quest 2 on the frequency domain of 64-channel EEG measurements recorded on healthy subjects was investigated by performing six different tasks, including a 3D video game.**

Results showed statistically significant differences in beta and gamma frequency bands with and without the use of the HMD. Also, significant differences were found in the occipital brain region while playing the 3D video game with the HMD vs desktop mode due to the introduction of the immersive visual feedback.

Based on our preliminary findings, future studies will test the feasibility of combining HMDs and EEG headsets before running EEG brain-computer interface studies.

***Keywords*—virtual reality (VR), electroencephalogram (EEG), rehabilitation, human-computer interaction (HCI).**

I. Introduction

VIRTUAL reality (VR) is a next-generation technology and VR applications have the potential to revolutionize healthcare and rehabilitation treatments [1]. VR technologies emulate a virtual environment that immerses the user to experience the concept of "being there", such as a realistic representation of themselves in the VR setting.

There are three types of VR: i) non-immersive virtual experience; ii) semi-immersive VR; iii) immersive VR. Non-immersive VR uses a computer or a video game console with an embedded computer-generated environment and keyboard or other controllers, allowing the user to keep control of their physical environment. Semi-immersive VR provides users with a partially virtual environment, including 3D graphics game applications to improve a more immersive feeling, high-resolution displays, and computers. Lastly, fully immersive VR gives users the most realistic simulation experience. In this case, the user needs VR glasses, or head-mounted displays (HMDs) and 3D game applications installed on the HMD or on a laptop connected to the HMD [2].

The use of VR is rapidly increasing in healthcare and research applications, and it is often combined with other wearable sensors and technology. Virtual environments offered via VR technology make it possible for individuals with disabilities who undergo rehabilitation therapies (e.g., individuals with cerebral palsy, amyotrophic lateral sclerosis, ALS, multiple sclerosis, etc. [3-4] to perform physical tasks in a fun way in more naturalistic settings like those encountered in real life, instead of, for example, watching a video of someone showing the exercises [5]. There is an increasing need to investigate how VR can be used in combination with other wearable devices, especially in research protocols that include hardware and electrodes positioned close to the HMD systems. Existing VR simulators rely on joysticks or hand trackers, which are unusable for individuals with severe upper limb (UL) motor impairments. Eye-tracking and voice recognition may be alternative solutions, but they are not always suitable for people with visual, speech, and motor impairments. In this context, brain-computer interfaces (BCIs) would constitute an innovative control interface for most individuals with UL motor impairments [6]. Related to this context, in recent years, there has been an increase in studies that employed both VR and electroencephalography (EEG) headsets focused on cognitive and neuromotor rehabilitation. For instance, BCIs have already been integrated into VR systems for neurorehabilitation and game entertainment [7]. A few studies tried to control a virtual wheelchair via BCI achieving high performance using motor imagery EEG-BCI [8], EEG event-related desynchronization BCI, and tactile P300 BCI [9].

A few studies compared brain activity in virtual and non-virtual environments [10-13]. Also, there is an urgent need for frameworks and guidelines to combine VR and EEG headsets and headcaps. In fact, current HMDs may affect the EEG signal quality due to the sensor positions. Differences in the frontal midline theta rhythm may be due to the effect of being in a virtual setting, as shown in cognitive visuospatial tasks by comparing HMDs and computer displays [10] during VR-EEG data collections. However, it has been proved that HMDs may introduce artifacts in frequencies beyond 50Hz during eyes-open and eyes-closed tasks [12]. Considering the recent advances in EEG and VR technologies [14-15], we should carefully consider previous findings due to the differences in the hardware and sensor montages of the systems available in the market and deeper research should be conducted. Previous studies [11-13] conducted data collection via Oculus Rift (Facebook Technologies LLC, 2018) or HTC Vive Pro devices (HTC Corporation, 2018), and a 64-channel wet-gel electrode EEG cap (WaveGuard ANT Neuro) [12], or an 8-channel wet-gel electrode cap (g.LADYBIRD, Guger Technologies) [11], or Oculus Quest 2 (Facebook Technologies LLC, 2021) combined with the NextMind (NextMind, 2021), a commercially available sensor for entertainment with 8 dry electrodes, placed on the back of the head [13].

In this study, we aimed to compare for the first time, EEG

data collected using a 64-channel wet-gel electrode EEG cap eego™sport (ANT Neuro, Hengelo, Netherlands) with and without the VR HMD Oculus Quest 2 through 6 different tasks, including one using a three-dimensional (3D) game developed to simulate wheelchair driving tasks, by using semi-immersive and fully-immersive VR. Through this feasibility study, we want to explore the possibility of controlling a 3D game application for HMD through an EEG-BCI, exploring the possibility of combining EEG and VR technologies.

II. Material and Method

A. Experimental setup and procedure

To compare the EEG signal quality during standard EEG data collection (i.e., no-VR condition) and VR-EEG one (i.e., VR condition), we prepared a protocol to be repeated once wearing only the EEG cap and once while participants also wore the HMD. Participants were then asked to perform six tasks during the two conditions, as follows:

1. Eyes-closed task: keeping head still and eyes closed.
2. Eyes-open task: keeping head still and eyes open.
3. Teeth grinding task: forcefully clenching and unclenching the jaw while maintaining a still head position.
4. Head rotation task: rotating the head repeatedly to the right and left.
5. Head elevation task: repeatedly head up and down tilting.
6. 3D game task: playing a video game to move forward a wheelchair on a basketball court following a specific path.

Participants executed the tasks first without and then with the HMD. For each condition, the first 5 tasks lasted 30 seconds each. All tasks were repeated five times consecutively. During the no-VR condition, participants were asked to look in front of them and listen to the researcher's instructions. During the VR condition, participants were instructed to navigate in the HMD menu environment during 1-5 tasks and listen to the researcher's instructions. As such, participants were placed in a 3D menu environment without being asked to perform any additional VR tasks that required cognitive efforts. These tasks aimed to evaluate how the coupling of the HMD with the EEG headset affected the reliability of the signals, while task 6 was used to investigate the effect of fully immersive VR on the quality of the EEG signals. Participants were asked to play a 3D game where they had to control a wheelchair avatar, navigating from a starting point to an endpoint. This task was conducted in two modalities, semi-immersive (Desktop mode) and then fully immersive (HMD mode). Both modes were played wearing the EEG cap as follows:

- Desktop mode: participants played the game on a computer desktop using a keyboard to control the wheelchair and a mouse to control the avatar's visual field. To avoid EEG artifacts, participants were asked to only move their fingers on the keyboard/mouse.
- HMD mode: participants played the same video game immersed in 3D VR using the HMD and two VR controllers positioned in their hands.

B. Electroencephalography acquisition

EEG signals were acquired via the eego™sports amplifier (ANT Neuro, Hengelo, Netherlands) and a 24-bit resolution and 64-channel wet-gel electrode EEG cap (WaveGuard, ANT Neuro, Hengelo, Netherlands). The 64 scalp positions were positioned according to the 10-20 system [16]. Ag/AgCl electrodes were filled with conductive gel and the superficial layers of the skin were abraded using a blunt needle. The reference electrode was placed at Cz and the signal was sampled at 512 Hz.

C. Head-mounted display (HMD)

An Oculus Quest 2 HMD (Facebook Technologies LLC, 2021) and two Oculus Touch Controllers were used in this study.

D. 3D video game

The 3D video game was developed to enhance the driving skills of individuals with neuromotor disabilities who require powered wheelchairs. The game was designed to be suitable for both laptops and HMD devices. It was developed using the Unity Game engine and C# programming language. The game includes several driving levels but for the aim of this work only the moving forward level was played. The levels of difficulty can be adjusted through the 1-5 speed levels. In our protocol, speed level was set to 3. Figure 2 (a) shows the scenario and the path (from the green square to the red one) that each participant was asked to follow. Figure 2 (b) shows the avatar wheelchair. To start the level, participants had to press the X button on the left controller, and then move the joystick on the right one to control the wheelchair avatar.

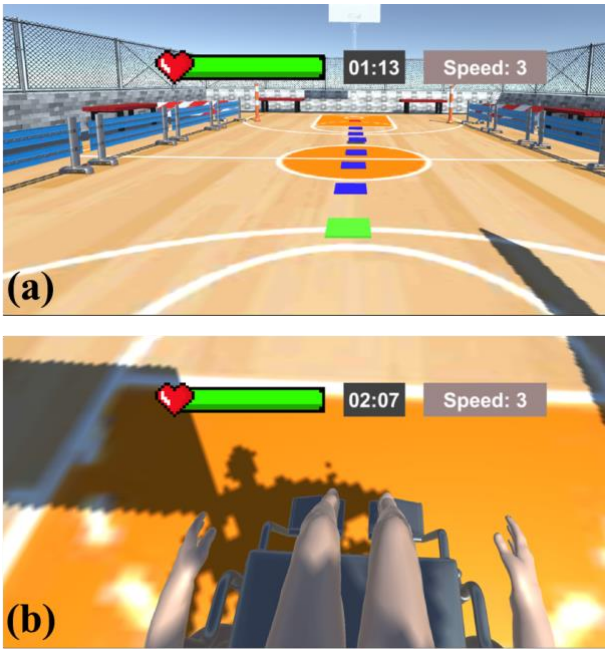


Fig. 2: 3D video game: (**a**) frontal view and (**b**) lower view.

E. Data processing

EEG signals were processed using both Python and MATLAB™ R2022a.

Figure 3 illustrates an overview of the signal processing pipeline applied to compare EEG (no-VR condition) vs VR-EEG (VR condition) scenarios.

All signals were collected during both conditions and the same pipeline was applied to all recordings.

Pre-processing consists of normalizing the signals with respect to the maximum absolute value. Signals were then filtered with a 0.1 Hz High-Pass and a 40 Hz Low-Pass Butterworth Filter (3rd order) [17], both of which were applied in a forward and backward direction using the *filtfilt* function from the SciPy library.

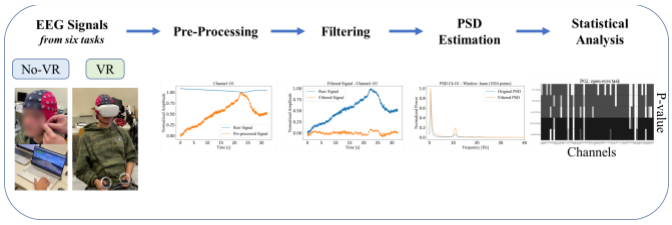


Fig. 3: System overview. EEG signals are processed through a pipeline that includes a pre-processing stage composed of LP and HP filters, in order to obtain an accurate PSD estimation for statistical analysis. Plots refer to participant P02 and channel O1 during the Eyes-open task.

Lastly, Power Spectral Density (PSD) was calculated using the Welch method [18], built into the SciPy library [19].

EEG signals were windowed using a 2-second Hanning window and spectra were represented with 1024 points.

Power spectra were then divided into frequency bands: delta, theta, alpha, beta, and gamma [12].

F. Statistical analysis

VR and no-VR conditions were compared for each task and for each participant by applying a Wilcoxon signed-rank test to the PSD frequency-band arrays through the built-in MATLAB function.

III. Results

Two able-bodied individuals no visually-impaired (P01 and P02, age range = 24–25 years, median age = 24,5 years, both males) without neurological and psychological conditions participated in this study. Both participants conducted 1 session performing the 6 tasks in both conditions. PSD arrays extracted for each frequency band were analyzed, comparing the VR and the no-VR conditions. For the first 5 tasks, p-values showed very high statistically significant differences ($p<0.001$) in beta and gamma bands among most of the channels. Lower or moderate differences ($0.01<p<0.05$) can be detected below 12 Hz. A few channels reported no significant differences but there was no consistency among the 5 tasks for both P01 and P02. As an example, Figure 4 graphically shows the p-value results for the eyes-open task from the P02's recording while the same behavior is confirmed for the other tasks as well.

PSD values extracted while the participants conducted task 6, were used to evaluate fully and semi-immersive scenarios to investigate the effect of immersive VR via HMD on EEG signals. The Wilcoxon Signed-Rank test was applied to compare the VR via HMD mode and the no-VR via Desktop mode showing high statistically significant differences ($p<0.001$) in the occipital and parietal-occipital channels among all the frequency bands and for both participants, demonstrating the impact of the VR visual stimuli on the brain activity.

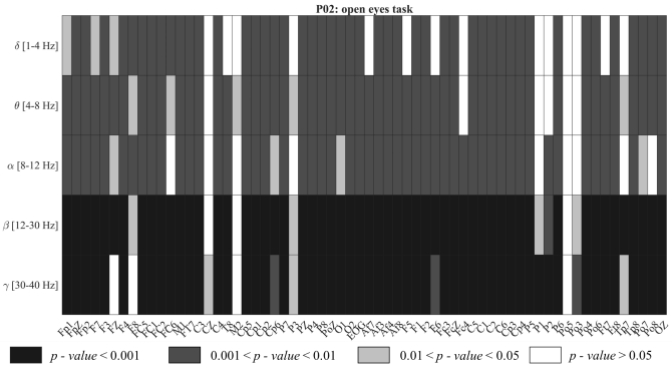


Fig. 4: Graphical representation of the p-values obtained comparing VR and no-VR conditions for participant P02 during the execution of task 2 (eyes-open task).

We compared channels P1-8, Pz, PO3-8, POz, O1, O2, and Oz, focusing on the brain activity of the occipital sulcus, as this is the region known to be involved in the early stages of processing visual stimuli [20] and the parietal area due to its correlation characteristics with the cognitive function considered in this study.

By analyzing the signals from these channels, we were able to gain insights into how immersion level and gaming activity affect the brain's response to visual inputs.

A graphical representation of the results is provided in Figure 5 which demonstrates that the statistically significant p-values were obtained for the isolated channels related to the occipital and parietal brain regions. Figure 5 helps to visually convey the significance of the results and can aid in identifying the impact of immersion level on EEG signals in each channel of the investigated brain regions for each frequency band.

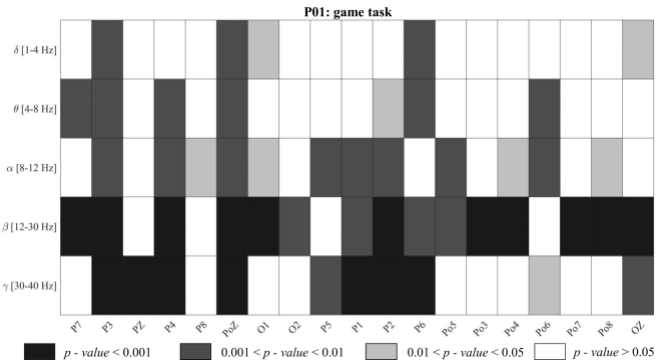


Fig. 5: Graphical representation of the p-values obtained in the occipital and parietal brain regions by comparing VR (HMD mode) and no-VR (Desktop mode) conditions of participant P01 during the execution of task 6 (3D game task).

IV. Discussion

Our preliminary results show that the use of HMDs for VR affect the brain activity measured by EEG caps with a lower impact on the lower frequency bands (<12 Hz) and a higher effect on beta and gamma bands. This is an important finding as the literature was inconclusive on whether the discomfort reported by some users of HMDs or the hardware montage could potentially impact the results. However, our results are in contrast with a previous study [12] where eyes-open and eyes-closed tasks were applied by comparing Oculus Rift and

HTC Vive Pro technologies and 64-channel EEG ANT Neuro system. In fact, Weber et al. [12] showed that HMDs consistently introduced artifacts, but they were negligible below 50 Hz. The different findings may be due to the different technologies applied in our study or to the fact that we used a different protocol pipeline.

We also observed that visual effects in semi-immersive and fully immersive scenarios appear to affect the brain activity differently, specifically in the occipital sulcus, which is responsible for processing visual stimuli.

However, while this study provides valuable insights, it will be necessary to recruit more participants and establish specific inclusion criteria, to validate these findings with a larger dataset. Additionally, while the quality of the signals obtained were deemed acceptable, multiple recordings and sessions of each task should be acquired and compared.

Our results indicate that there are statistically significant differences in beta and gamma frequency bands between fully immersive (HMD mode) and semi-immersive VR (Desktop mode), suggesting that HMDs could potentially raise concerns at these frequency ranges when compared to what is observed in the EEG signals collected while playing desktop 3D game applications. The underlying cause for this phenomenon is currently unclear and further research is needed to investigate this behaviour. One possible approach would be to design a task that gradually increases in difficulty, resulting in a higher cognitive workload. It is expected that as the task demands increase, there will be a corresponding increase in beta and gamma activity. Additionally, a longer acquisition period and an investigation of the time-frequency domain could provide valuable insights as the task progresses, as beta and gamma activity may become more pronounced toward the end of the task.

The comparison between the fully immersive and semi-immersive scenarios served as a foundation for future studies that will implement additional tasks. The main objective of this feasibility study was to establish the feasibility of obtaining valid information from EEG signals when using a BCI to control a 3D game via HMD. Based on our preliminary findings, further investigations are required, and future studies should test the feasibility of combining HMDs and EEG headsets before running EEG brain-computer interface studies.

REFERENCES

[1] Liu, Y., Tan, W., Chen, C., Liu, C., Yang, J., & Zhang, Y. A review of the application of virtual reality technology in the diagnosis and treatment of cognitive impairment. *Frontiers in aging neuroscience*. Vol. 11, 2019.

[2] Voinescu, A.; Sui, J.; Stanton Fraser, D. Virtual Reality in Neurorehabilitation: An Umbrella Review of Meta-Analyses. *J. Clin. Med.* Vol. 10, 2021. https://doi.org/10.3390/jcm10071478

[3] Naomi G., Philippe S. Archambault, Amihai Rigbi & Patrice L. Weiss. Pediatric Powered Mobility Training: Powered Wheelchair Versus Simulator-Based Practice. In Assistive Technology, 2021. 10.1080/10400435.2022.2084183.

[4] Saldana D., Neureither M., Schmiesing A., Jahng E., Kysh L., Roll Shawn C., Liew S.L; Applications of Head-Mounted Displays for Virtual Reality in Adult Physical Rehabilitation: A Scoping Review. In: *Am J Occup Ther*., Vol. 74(5), 2020. https://doi.org/10.5014/ajot.2020.041442

[5] de Sá, A.A.R., Morère, Y. & Naves, E.L.M. Skills assessment metrics of electric powered wheelchair driving in a virtual environment: a survey. *Med Biol Eng Comput*. Vol. 60, 323–335, 2022. https://doi.org/10.1007/s11517-022-02500-8

[6] D. Wen, B. Liang, Y. Zhou, H. Chen and T. -P. Jung, "The Current Research of Combining Multi-Modal Brain-Computer Interfaces With Virtual Reality," in *IEEE Journal of Biomedical and Health Informatics*, vol. 25, no. 9, pp. 3278-3287, 2021, doi: 10.1109/JBHI.2020.3047836.

[7] Leeb R., Friedman D., Müller-Putz G.R., Scherer R., Slater M., Pfurtscheller G., Self-Paced (Asynchronous) BCI Control of a Wheelchair in Virtual Environments: A Case Study with a Tetraplegic. In: *Computational Intelligence and Neuroscience*, 2007, https://doi.org/10.1155/2007/79642

[8] D. Huang, K. Qian, D. -Y. Fei, W. Jia, X. Chen and O. Bai, Electroencephalography (EEG)-Based Brain–Computer Interface (BCI): A 2-D Virtual Wheelchair Control Based on Event-Related Desynchronization/Synchronization and State Control. *IEEE Transactions on Neural Systems and Rehabilitation Engineering*, vol. 20, pp. 379-388, 2012, https://doi.org/10.1109/TNSRE.2012.2190299.

[9] Eidel M. and Kübler A. Wheelchair Control in a Virtual Environment by Healthy Participants Using a P300-BCI Based on Tactile Stimulation: Training Effects and Usability. *Frontiers in Human Neuroscience*. Vol. 14, 2020. https://doi.org/10.3389/fnhum.2020.00265.

[10] Redlinger, E., & Shao, C. Comparing brain activity in virtual and non-virtual environments: a VR & EEG study. *Measurement: Sensors*, Vol. 18, 2021. Doi: https://doi.org/10.1016/j.measen.2021.100062

[11] Tremmel, C., Herff, C., Sato, T., Rechowicz, K., Yamani, Y., & Krusienski, D. J. Estimating cognitive workload in an interactive virtual reality environment using EEG. *Frontiers in human neuroscience*, Vol. 13, 2019.

[12] Weber, D., Hertweck, S., Alwanni, H., Fiederer, L. D., Wang, X., Unruh, F. et al. A structured approach to test the signal quality of electroencephalography measurements during use of head-mounted displays for virtual reality applications. *Frontiers in Neuroscience*, Vol. 15, 2021.

[13] Suchalova, S., Benco, M., & Hudec, R. The Research on Controlling Virtual Reality by EEG Sensor. In *2022 20th International Conference on Emerging eLearning Technologies and Applications (ICETA)*

[14] Cerone G. L., Giangrande A., Ghislieri M., Gazzoni M., Piitulainen H., and Botter A., "Design and Validation of a Wireless Body Sensor Network for Integrated EEG and HD-sEMG Acquisitions" in IEEE Trans. Neural Syst. Rehabil. Eng., vol. 30, pp. 61–71, 2022. doi: 10.1109/TNSRE.2022.3140220

[15] C. He et al., "Diversity and Suitability of the State-of-the-Art Wearable and Wireless EEG Systems Review," in IEEE Journal of Biomedical and Health Informatics, doi: 10.1109/JBHI.2023.3239053.

[16] di Fronso S., Fiedler P., Tamburro G., Haueisen J., Bertollo M. and Comani S. Dry EEG in Sports Sciences: A Fast and Reliable Tool to Assess Individual Alpha Peak Frequency Changes Induced by Physical Effort. *Frontiers in Neuroscience.* 13 (2019). https://doi.org/ 10.3389/fnins.2019.00982

[17] Grégoire Cattan, Anton Andreev, C. Mendoza, Marco Congedo. The Impact of Passive Head-Mounted Virtual Reality Devices on the Quality of EEG Signals. VRIPHYS 2018 - Workshop on Virtual Reality Interaction and Physical Simulation, Apr 2018, Delft, Netherlands. https://doi.org/10.2312/vriphys.20181064ff. ffhal01774915

[18] Welch, P. The use of fast Fourier transform for the estimation of power spectra: a method based on time averaging over short, modified periodograms. *IEEE Transactions on Audio and Electroacoustics*, *15*(2), 70–73. 1967.

[19] Virtanen, P., Gommers, R., Oliphant, T.E. *et al.* SciPy 1.0: fundamental algorithms for scientific computing in Python. *Nat Methods* **17**, 261–272 (2020). https://doi.org/10.1038/s41592-019-0686-2

[20] Lotte, F., Bougrain L., Clerc, M. Electroencephalography (EEG)-based brain – computer interfaces, Wiley Encyclopedia of Electrical and Electronics Engineering, Wiley, pp.44, 2015. https://doi.org/10.1002/047134608X.W8278

Wearable tactile display of softness for virtual reality

G. Frediani, F. Carpi*
*University of Florence, Department of Industrial Engineering, Via di S. Marta, 3 - 50139 Florence, Italy. *Email: federico.carpi@unifi.it*

***Abstract*—Human-machine interfaces are currently challenged by the lack of effective, comfortable and affordable actuation technologies for wearable tactile displays of softness in virtual-reality environments. They are especially needed for applications like virtual reality-based medical training, tele-rehabilitation, tele-manipulation, tele-presence, etc. The state of the art does not offer wearable devices that can combine proper functional properties with simple structure, low weight, low size and electrically safe operation. Recently, we described a tactile display technology that uses fingertip-mounted small inflatable chambers, pneumatically driven by a compact and cost-effective portable unit. Here, we present ongoing investigations on the tactile perception of softness that can be induced by this kind of display when it is used in combination with virtual-reality environments.**

***Keywords*—Wearable, Tactile, Haptic, Softness.**

I. Introduction

MIMICKING the sensation of touching virtual objects that are soft is a major goal for the next generation of multi-sensory human-machine interfaces. Indeed, physically displaying the softness of a computer-generated item is essential to enable a diversity of virtual- or augmented-reality systems, for various possible uses. In the biomedical field, this is especially relevant for a variety of applications, including simulators for training of medical professionals in the palpation of soft tissues [1], tele-operation systems [2] and tele-presence systems for social interactions augmented by the sense of touch [3]

In order to mimic with high accuracy and realism the tactual feeling produced by the indentation of a soft object with a fingertip, so-called haptic displays are needed. They are conceived as interfaces ideally able to provide users with both tactile feedback and kinaesthetic feedback. Nevertheless, Srinivasan and LaMotte have demonstrated that, for the perception of the softness of objects having a deformable surface (and not just being compliant with a rigid surface), tactile feedback alone is sufficient, whilst kinaesthetic feedback alone is insufficient [4]. This has been interpreted as due to the fact that, for any applied force, the object's compliance determines the deformation of the fingertip's skin, and therefore it can adequately be encoded by cutaneous mechanoreceptors [4]. This is consistent with later evidences on the importance of the variation of the contact area between fingertip and object [5]-[7], such that the change in contact area has been proposed as a new proprioceptive cue [8].

As an implication, the softness of virtual objects cannot be rendered using the various existing haptic displays that provide purely kinaesthetic feedback, such as those reviewed in [9]. The simplest effective approach is to rely on purely tactile feedback, using so-called tactile displays.

Furthermore, in order to enable free motions of the hands while performing a virtual- or augmented-reality task, the tactile displays should be wearable, i.e. sufficiently small and light to be arranged on fingers [9].

Another important aspect to be considered for the design of devices capable of realistic tactile feedback is the role played by different tactile cues in the perception of softness. Although this aspect is still a matter of discussion [10], Dhong et al. have demonstrated that, besides the contact area, the indentation depth is another essential tactile stimulus and that they independently concur to the perception of softness [11]. This means that tactile displays that control only the contact area or only the indentation depth are expected to be less effective than devices that could control both of them [11]. Therefore, softness rendering cannot effectively be achieved with the variety of wearable tactile displays that apply forces to fingertips via stiff surfaces, which are however very performing in generating force feedback, especially for shape rendering [12]-[17]. Indeed, such displays just control indentations of the skin and, as discussed by Srinivasan and LaMotte, for an interface that generates a force via a rigid surface, the pressure distribution over the fingertip and the associated deformation of the skin (and so also the contact area) are independent of the interface's compliance; therefore, in this situation, compliance cannot adequately be inferred by the information gathered by the mechanoreceptors [4].

Based on these evidences, the most effective strategy to physically render the softness of a virtual object is to use tactile displays able to deliver quasi-static (non-vibratory) forces, via a soft interface (deformable surface), so as to control both the contact area and the indentation depth.

This can be achieved in different ways. An example is to use rotary motors driving flexible/stretchable structures (e.g. polymer membranes or fabrics), which however typically lead to complex, bulky and heavy mechanisms [18]-[19]. An alternative approach is to use soft materials (elastomers) in a way that allows them to be deformed without complex mechanical transmissions from an actuation source; this concept has been investigated with three technologies: dielectric elastomer actuators (DEAs), electrostatic actuators and pneumatic actuators. DEAs, consisting of electrically deformable elastomeric membranes [20], can be used for non-vibratory fingertip displays suitable for softness rendering, although their main limitation is the need for high driving voltages, which requires challenging future developments [21]. Likewise, high driving voltages are a disadvantage of purely electrostatic actuators [22]. Conversely, electrically safe, compact and lightweight

devices can be designed using pneumatic actuation, as the driving source can be displaced remotely. Recently, we described a wearable pneumatically-driven fingertip display of softness, which combined effective functionality with a simple structure, low weight and low size (not only of the wearable interface but also of its driving unit) [23].

Here, we present ongoing investigations on the tactile perception of softness that can be induced by that kind of display when it is used in combination with virtual-reality environments.

II. Materials and Methods

A. Structure and principle of operation of the softness display

Fig. 1 presents the structure of the device. It consists of a small plastic chamber, which is closed by a thin elastomeric membrane and can be pressurised with air, in order to deform the membrane.

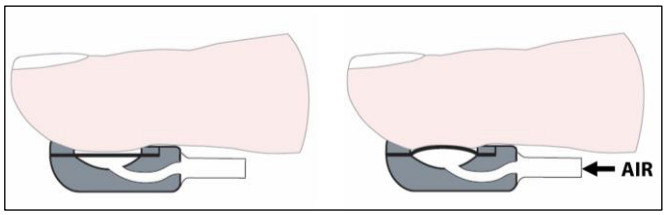


Fig. 1: Schematic drawing of the structure and principle of operation of the softness display.

An ergonomic shape of the plastic chamber allows it to comfortably conform to adult finger pulps. By securing the device to a fingertip, the actuation of the membrane can be used to indent the finger pulp and increase the contact area, as well as the applied force. As recalled in the Introduction, these features make the tactile display suited to mimic contact with soft bodies.

B. Manufacturing of prototype samples of the softness display

A prototype sample of the display is shown in Fig. 2. The internal chamber had a diameter of 12 mm, which was chosen as a (non-optimised) trade-off between the needs for maximising the contact area with the fingertip (so as to maximise the perceivable force) and minimising the device encumbrance. That size was consistent with the average width of thumb and index finger pulps among participants to a psychophysical test described in the following. The display's weight was ~3 g.

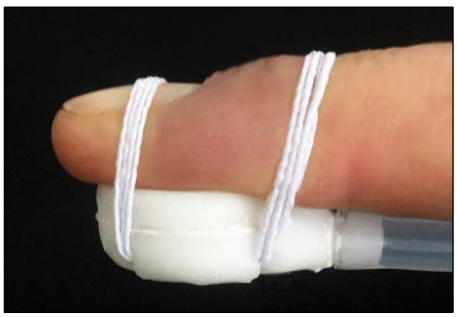


Fig. 2: Prototype sample of the softness display.

The display was manufactured using a commercial PDMS membrane (Elastosil, Wacker, Germany) having a thickness of 70 µm. The plastic parts were 3D printed. A room-temperature-vulcanising silicone was used to fix two plastic parts together (avoiding screws), so as to constrain between them the elastomeric membrane and seal the chamber.

C. Assembly of an electro-pneumatic control unit

An electro-pneumatic control unit was developed with a compact design and a low-cost architecture. It was based on a small pump, six valves and pressure sensors, as well as a microcontroller. It was USB connected to a personal computer, so as to be driven by any external software via serial communication. A custom script for the microcontroller was developed to control the pressure values of up to three fingertip displays independently. The total weight of the unit was 380 g, which made the technology easily portable, as shown in the image presented in the next section (Fig. 3).

D. Psychophysical tests

The system was investigated with psychophysical tests, consisting of an experiment of Just Noticeable Difference (JND). The experiment involved fifteen volunteers and was conceived as a comparison of the softness between two virtual objects, whose compliance was simulated and rendered on three fingertips using the tactile displays. Fig. 3 shows the experimental setup and the virtual environment used to perform the tests.

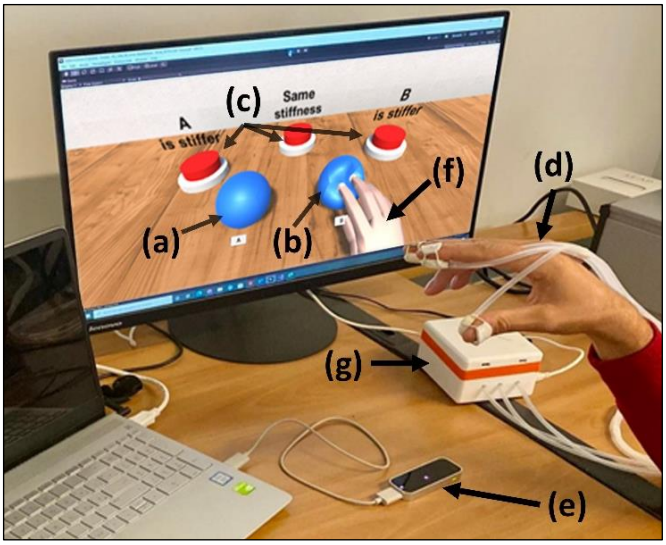


Fig. 3: Experimental setup of the psychophysical tests. The virtual environment showed a reference sphere (a) and a comparison sphere (b), both deformable, and three buttons (c) used to collect the subject's evaluation of the difference in softness between the two spheres. The movements of the real hand wearing three tactile displays (d) were tracked by a commercial optical sensor (e) and mapped within the virtual environment as movements of an avatar hand (f). A custom-made pneumatic control unit (g) supplied independent levels of pressure to the three fingertip-mounted tactile displays.

The participant was asked to wear three displays on three fingers (thumb, index and middle fingertip of their dominant hand) and to interact with a virtual environment, displayed on a computer screen, as described below.

A custom-made virtual environment was developed using the software Unity. It included an avatar hand, which mapped the movements of the real hand wearing the tactile displays. The movements of the real hand were continuously tracked by using a desktop optical sensor (LEAP Motion, USA), arranged below the hand (Fig. 3). The virtual environment showed to the participant two deformable objects (blue spheres) to be compared in terms of softness. In order to avoid a visual bias, the two spheres were identical and intentionally did not represent any specific item which could recall a 'familiar' level of softness.

The three fingers of the avatar hand could interact with each sphere, by deforming it in different ways. As a result of the indentation of the sphere by each finger (Fig. 3), a pressure was rendered on the corresponding real fingertip by the pneumatic control unit, driving the related tactile display. The three levels of pressure applied to the three fingers were independent, according to the actual extent of indentation by each finger.

The subject was asked to comparatively probe the two spheres and to evaluate which of the two was perceived as stiffer, or whether no noticeable difference could be appreciated. The subject had to express the evaluation by pressing, with the avatar hand, one of the three buttons available in the virtual scene (Fig. 3), corresponding to three possible cases: sphere A stiffer; sphere B stiffer; same stiffness.

The pressure provided to each fingertip in response to any given indentation was controlled according to a compressive stress-indentation curve associated to the sphere. Different curves were considered, so as to simulate materials with different softness. In particular, the test used the five stress-indentation curves presented in Fig. 4.

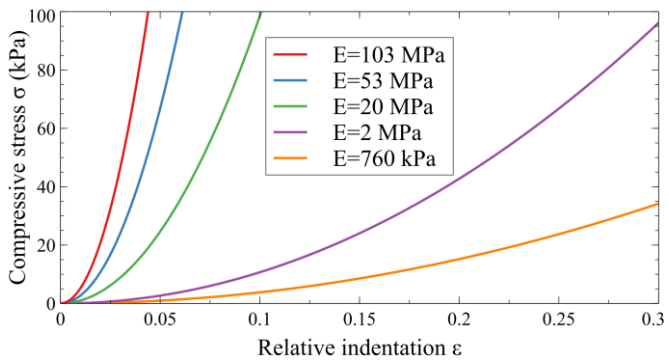


Fig. 4: Stress-indentation curves considered for the JND test, in order to simulate five materials having a different Young's modulus *E*, as indicated in the legend.

The association of any given curve to a sphere was used to create a tactile feedback that mimicked the perceptual experience of touching a real object with those mechanical properties. Indeed, as an avatar finger squeezed the sphere, the occurring variable virtual indentation was continuously monitored by the system, which reacted by driving the related tactile display with pressure levels equal to the corresponding compressive stress values given by the curve.

Each participant performed a sequence of tactile perceptual tasks. Each task was aimed at determining a JND, as the minimum noticeable difference of Young's modulus between the two virtual spheres. The test was accomplished according to the following procedure.

The algorithm initially fixed the reference sphere's Young's modulus E_R, by randomly selecting it among the pre-defined set of five values reported in Fig. 4. The comparison sphere's Young's modulus E_C was randomly selected from the remaining values of the set. The subject was asked to probe the two spheres as many times as needed, in order to evaluate the difference in softness between the two spheres, and finally express the evaluation by pressing with the virtual hand the relevant virtual button available in the scene, as described above.

Following the evaluation, the test proceeded by assigning to the two spheres a new couple of Young's moduli, where E_R was unchanged and E_C was modified according to the following criterion: if the previous comparison sphere had been perceived as stiffer/softer than the reference sphere, the new E_C was respectively decreased/increased by a half of the difference between E_C and E_R. Then, the subject was asked to probe the two spheres again and express the new evaluation. This process continued iteratively, until the subject did not appreciate any noticeable difference; at that step, the difference between E_R and E_C of the preceding iterative step was defined as the JND corresponding to E_R.

Afterwards, a new perceptual task started, with a new E_R, so as to identify the JND related to it. Therefore, at the end of the session, for each volunteer the system gathered five JND values, corresponding to the five values of Young's modulus considered.

The study was conducted according to the guidelines of the Declaration of Helsinki, and approved by the Ethics Commission of the University of Florence (n. 180, 12 October 2021).

III. Results and Discussion

Results of the psychophysical tests for the fifteen volunteers are presented in Fig. 5. It shows the average JND values corresponding to the five values of Young's modulus considered.

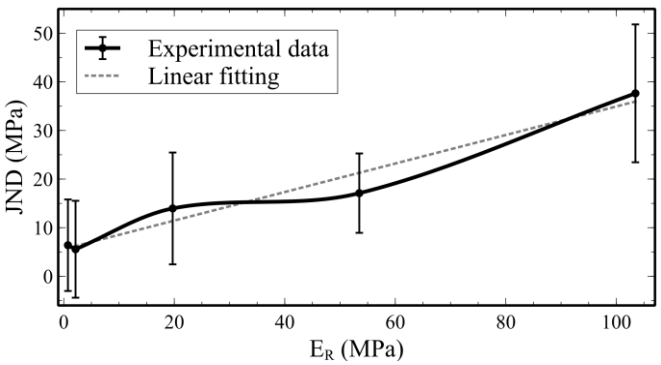


Fig. 5: JND as a function of the Young's modulus of the couple of virtual objects compared with the tactile perception task. The error bars represent the standard deviation among the fifteen volunteers.

The JND trend is consistent with the general Weber's law [24], as it grows with the stimulus intensity (represented in this case in the elastic modulus). The Weber's constant, defined as the slope of the JND curve obtained from a linearisation of the experimental data, was $k = 0.27$. This value is nearly twice the one (k=0.15) that we obtained with the same device in different experimental conditions, as reported in [23]. In that previous work, a JND investigation

was performed with three main differences: i) the test involved only one finger; ii) the experiment did not include any virtual environment; iii) the variable stimulus for the JND assessment was the pressure level, rather than an elastic modulus [23].

Ascertaining whether (and, if so, to which extent) the introduction of visual feedback might have contributed to the higher Weber's constant (e.g. possibly due to a visual distraction) requires more systematic investigations. Nevertheless, the higher Weber's constant might also be significantly caused by the fact that two levels of softness are probably more difficult to distinguish than two levels of pressure. Indeed, estimating softness requires probing the two objects with a similar indentation, so as to avoid any bias while estimating a possible difference in force. This process is even more complex in a virtual environment, owing to the inevitably lower accuracy of visual feedback in comparison to a real scenario.

IV. Conclusion and Future Developments

We described preliminary results of an ongoing study on the tactile perception of softness in a virtual environment, achievable with a custom-made wearable tactile display.

Future developments of this work include the implementation of new kinds of tests, where the virtual environment will include common-life recognisable objects (e.g. jelly), such that the user might predict their compliance prior to the tactile task. This visual bias will be exploited to comparatively assess how experience-based pre-estimates of compliance, purely based on visual cues, can influence the tactile perception. To that aim, confusion tests will also be administered, by varying the compliance in unrealistic ways, in order to evaluate the actual strength of visual bias over tactile perception.

Acknowledgement

Financial support from the European Commission's Marie Skłodowska-Curie Actions Doctoral Networks Programme (HORIZON-MSCA-2021, Project 101072920-SOFTWEAR) and from the projects "HAPTICS" and "REHub" supported by Fondazione Cassa di Risparmio di Firenze, Italy, is gratefully acknowledged.

References

[1] N. E. Seymour, A. G. Gallagher, S. A. Roman, M. K. O'Brien, V. K. Bansal, D. K. Andersen & R. M. Satava, Virtual reality training improves operating room performance: results of a randomized, double-blinded study. *Ann. Surg.* Vol. 236, pp. 458-464, 2002.

[2] I. Sarakoglou, N. Garcia-Hernandez, N. G. Tsagarakis, D. G. Caldwell, A high performance tactile feedback display and its integration in teleoperation. *IEEE Trans. Haptics*, vol. 5, pp. 252-263, 2012.

[3] S. Oh, J. N. Bailenson, & G. F. Welch, A systematic review of social presence: definition, antecedents, and implications. *Front. Robot. AI*, vol. 5, p. 114, 2018.

[4] M. A. Srinivasan, & R. H. LaMotte, Tactual discrimination of softness. *J. Neurophysiol*. vol. 73(1), pp. 88-101, 1995.

[5] A. Bicchi, E. P. Scilingo & D. De Rossi, Haptic discrimination of softness in teleoperation: the role of the contact area spread rate. *IEEE Trans. Rob. & Autom*. vol. 16(5), pp. 496-504, 2000.

[6] K. Fujita, & H. Ohmori, A new softness display interface by dynamic fingertip contact area control. *Proc. 5th World Multiconference on Systemics, Cybernetics and Informatics*, 2001.

[7] W. M. Tiest, & A. M. L. Kappers, Cues for haptic perception of compliance. *IEEE Trans. Haptics.* 2(4), 189-199, 2009.

[8] A. Moscatelli, M. Bianchi, A. Serio, V. Hayward, M. O. Ernst & A. Bicchi, The change in fingertip contact area as a novel proprioceptive cue. *Curr. Biol*. vol. 26, pp. 1159–116, 2016.

[9] C. Pacchierotti, S. Sinclair, M. Solazzi, A. Frisoli, V. Hayward & D. Prattichizzo, Wearable haptic systems for the fingertip and the hand: taxonomy, review, and perspectives. *IEEE Trans. Haptics*, vol. 10(4), pp. 580–600, 2017.

[10] D. Wang, KOhnishi & W. Xu, Multimodal haptic display for virtual reality: a survey. *IEEE Trans. Ind. Electron.* vol. 67(1), pp. 610-623, 2020.

[11] C. Dhong, R. Miller, N. B. Root, S. Gupta, L. V. Kayser, C. W. Carpenter, K. J. Loh, V. S. Ramachandran, & D. J. Lipomi, Role of indentation depth and contact area on human perception of softness for haptic interfaces. *Sci*. *Adv*. vol. 5(8), eaaw8845, 2019.

[12] C. Pacchierotti, A. Tirmizi, & D. Prattichizzo, Improving transparency in teleoperation by means of cutaneous tactile force feedback. *ACM Trans. Appl. Percept.* vol. 11(1), pp. 1-16, 2014.

[13] M. Gabardi, M. Solazzi, D. Leonardis & A. Frisoli, A new wearable fingertip haptic interface for the rendering of virtual shapes and surface features. *Proc. 2016 IEEE Haptics Symposium*, Philadelphia, PA, pp. 140–146, 2016.

[14] E. M. Young, & K. J. Kuchenbecker, Implementation of a 6-DOF parallel continuum manipulator for delivering fingertip tactile cues. *IEEE Trans. Haptics*, vol. 12(3), pp. 295-306, 2019.

[15] A. G. Perez, D. Lobo, F. Chinello, G. Cirio, M. Malvezzi, J. San Martın, D. Prattichizzo, & M. A. Otaduy, Optimization-based wearable tactile rendering. *IEEE Trans. Haptics*, 10(2), pp. 254-264, 2017.

[16] A. Girard, M. Marchal, F. Gosselin, A. Chabrier, F. Louveau, & A. Lécuyer, HapTip: displaying haptic shear forces at the fingertips for multi-finger interaction in virtual environments. *Front. ICT* vol. 3, p. 6, 2016.

[17] H. Kim, H. B. Yi, H. Lee, & W. Lee, HapCube: a wearable tactile device to provide tangential and normal pseudo-force feedback on a fingertip. *Proc. 2018 CHI Conference on Human Factors in Computing Systems*, pp. 1–13, 2018.

[18] T. Endo, A. Kusakabe, Y. Kazama & H. Kawasaki, Haptic interface for displaying softness at multiple fingers: combining a side-faced-type multifingered haptic interface robot and improved softness-display devices, *IEEE/ASME Trans. Mech*., vol. 21(5), pp. 2343-2351, 2016.

[19] S. Fani, S. Ciotti, E. Battaglia, A. Moscatelli, & M. Bianchi, W-FYD: a wearable fabric-based display for haptic multi-cue delivery and tactile augmented reality, *IEEE Trans. Haptics*, vol. 11(2), pp. 304–316, 2018.

[20] F. Carpi, D. De Rossi, R. Kornbluh, R. Pelrine & P. Sommer-Larsen (eds), *Dielectric Elastomers as Electromechanical Transducers. Fundamentals, Materials, Devices, Models and Applications of an Emerging Electroactive Polymer Technology*, Elsevier, Oxford, 2008.

[21] H. Boys, G. Frediani, M. Ghilardi, S. Poslad, J. Busfield & F. Carpi, Soft wearable non-vibratory tactile displays, *Proc. 2018 IEEE Intl Conf. Soft Robotics*, Livorno, Italy, pp. 270-275, 2018.

[22] K. Song, S. H. Kim, S. Jin, S. Kim, S. Lee, J. S. Kim, J. M. Park & Y. Cha, Pneumatic actuator and flexible piezoelectric sensor for soft virtual reality glove system. *Sci. Rep.*, vol. 9, 8988, 2019.

[23] G. Frediani, & F. Carpi, Tactile display of softness on fingertip. *Sci. Rep.*, vol. 10(1), 20491, 2020.

[24] E. H. Weber, *E.H. Weber on the tactile senses - 2nd ed*., H. E. Ross & D. J. Murray (eds), Erlbaum, UK, Taylor & Francis, 1996.

Computational joint action: dynamical models to understand the development of joint coordination

C. De Vicariis[1], L. Bandini[1], V.T. Chackochan[2] and V. Sanguineti[1]
[1] *Dept of Informatics, Bioengineering, Robotics and Systems Engineering, University of Genoa; Italy*
[2] *Odstock Medical Ltd, Salisbury, UK*

***Abstract*—Previous joint action studies using sensorimotor games suggest that human dyads develop coordination strategies which can be interpreted as Nash equilibria. In a previous study, we argued that if players are uncertain about what their partner is doing, they develop a coordination strategy which is more robust to the actual partner actions. This suggested that humans maintain an explicit representation of what the partner will be doing – a partner model – which also accounts for their degree of confidence about it. However, the mechanisms underlying the development of a joint coordination over repeated trials remain unknown. Very much like individual sensorimotor control, dynamical models can be used to understand how joint coordination develops. Here we present a general computational model – based on game theory and Bayesian estimation – to understand the mechanisms underlying the development of a joint coordination. A joint task is modeled as a quadratic game. Each player predicts their partner's next move (partner model) by optimally combining predictions and sensory observations, and selects their actions through a stochastic optimization of its expected cost, given the partner model. We show that the model captures well the temporal evolution of performance in a previous joint action experiment, and the estimated parameters provide a comprehensive characterization of individual participants in a dyad.**

***Keywords*—Joint action, game theory, partner models**

I. INTRODUCTION

Many of our everyday activities take place in social settings and are coordinated with other persons. Even seemingly simple interactions, like a pair of workers sawing timber with back and forth movements, a couple executing complex steps in a dance floor, two children playing badminton or providing physical therapy to a patient, require that two individual minds are somehow connected and their bodies coordinated [1]. The characteristic feature of these interactions is that subjects influence each others' behavior through coupled sensorimotor exchange within continuous action spaces, continuously in time and possibly over repeated trials. Many of those interactions require active coordination, which is manifested by physical and cognitive responses related to explicit knowledge of the interacting partner. For instance, if while walking through a corridor someone is coming towards us, we could move right while the other person passes on the left or vice versa. In our everyday life, we usually tackle these decision-making situations and master it, sometimes with awkward readjustments. Peculiar types of joint action are those in which the two partners are physically coupled through a tool [2] or a pair of haptic interfaces which can be programmed to implement a variety of interaction modalities [3]. This scenario is particularly useful for quantifying various aspects of joint action performance, because it allows to experimentally manipulate all aspects of the interaction. Further, two subjects which are physically connected and have two partly incompatible goals need to negotiate a shared strategy[4]. During the last two decades, discrete-time dynamical models have been used to investigate the mechanisms underlying sensorimotor learning and adaptation [5] and neuromotor recovery through robot-assisted training [6], but have never been used to address the development of joint coordination.

Here we present a general modeling framework for the development of stable coordination strategies in joint action. We specifically focus on situations in which individuals have distinct and possibly conflicting sub-goals, and have minimal or no knowledge of the goals of their counterparts. The model can be used to simulate joint action scenarios, and to analyze joint action experiments. We demonstrate the method in the context of a task where participants are mechanically coupled, have a shared final target, and are instructed to cross a via-point (VP, different for each player) while minimizing the interaction force.

II. METHODS

A. General Computational Framework

We model a joint coordination task as a static non-cooperative infinite game [7]. We assume that players have incomplete information. In particular, each player (i) knows their own goal, but not their partner's; and (ii) has limited information about partner action. We also

assume that learning of a coordination strategy occurs through fictitious play (FP) [8], in which the agents play the game repeatedly, and at every round each agent determines its best response on the basis of their beliefs about how their opponents will play. The overall model is depicted in Figure 1. At each trial t, the i-th player selects an action, $u_i(t)$, on the basis of the partner's expected move (partner model), $x_i(t) = \hat{u}_i(t)$. Once the actions have been carried out, through their sensory systems both players collect information $y_i(t)$ about their partner's action. This information is then used to update their partner model, which will be accounted for when selecting the action on the next trial.

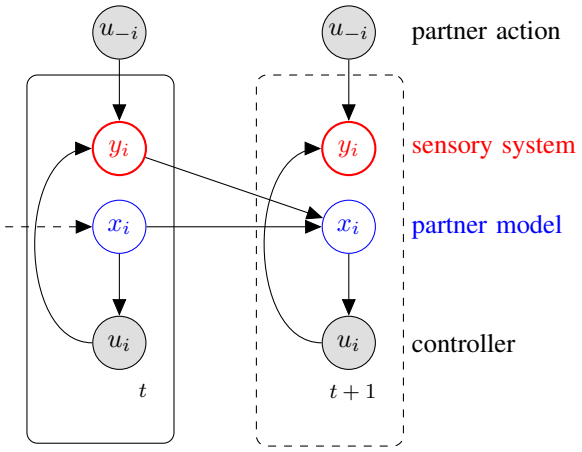


Fig. 1: Computational model. At each time step, each player's partner model (x_i) is used to select the actual action (u_i). Player i receives information about partner action (u_{-i}) through their sensory system (y_i). This information is used to predict the next action (u_i)

1) Joint task as a quadratic game: For each player i the task is specified by a quadratic cost function, which depends on both players' actions:

$$J_i(u_1,u_2) = \begin{array}{l} \frac{1}{2}\left[u_1^T R_{11}^i u_1 + 2\,u_1^T R_{12}^i u_2 + u_2^T R_{22}^i u_2\right] \\ + {r_1^i}^T \cdot u_1 + {r_2^i}^T u_2 + z^i \end{array} \tag{1}$$

where $i = 1, 2$ are the two players. Static games with infinite action space and quadratic costs are known as quadratic games. We assume that all R_{jk}^i are symmetric and positive definite. If this is the case, the Nash equilibrium is uniquely determined [7] as:

$$u^* = -R^{-1} \cdot r \tag{2}$$

where $u = [u_1^T\ u_2^T]^T$, $r = [r_1^1\ r_2^2]^T$ and:

$$R = \begin{bmatrix} R_{11}^1 & R_{12}^1 \\ R_{21}^2 & R_{22}^2 \end{bmatrix} \tag{3}$$

2) Sensory system: At each trial t, the sensory system of each player provides an estimate of the partner's action on that trial:

$$y_i(t) = H^i \cdot u_{-i} + L^i \cdot u_i + v_i(t) \tag{4}$$

where $v_i(t) \sim N(0, \Sigma_y^i)$ is a zero-mean sensory (measurement) noise of the i-th player, and Σ_y^i is its covariance.Parameters H^i and L^i reflect the structure of the sensory system. In particular, H^i and L^i respectively relate partner and own action and their observed features to their sensory consequences.

3) Partner representation: At each trial, t, each player optimally estimates their partner's next action by combining predictions and actual observations into a 'partner model'. Let $\hat{u}_{-i}^-$ and $\hat{u}_{-i}^+$ be the estimates of partner action, respectively before and after the sensory information is available, i.e. after the action has taken place (hereafter, 'prior' and 'posterior' estimates). The posterior estimate combines prior estimate and sensory information. The prior estimate propagates to the next trial by accounting for the player's retention rate. In conclusion, we have:

$$\begin{aligned} \hat{u}_{-i}^+(t) &= \hat{u}_{-i}^-(t) + K_i(t)\left[y_i(t) - H^i\hat{u}_{-i}^-(t) - L^i u_i^*(t)\right] \\ \hat{u}_{-i}^-(t+1) &= A^i \cdot \hat{u}_{-i}^+(t) + w_i(t) \end{aligned} \tag{5}$$

where $K_i(t)$ is calculated iteratively through the Kalman algorithm , which also provides time-varying estimates of the prior and posterior covariance matrices of $\hat{u}_{-i}^-$ and $\hat{u}_{-i}^+$, i.e. $P_i^-(t)$ and $P_i^+(t)$, and $w_i(t) \sim N(0, \Sigma_x^i)$ is a zero-mean process noise of the i-th player, and Σ_x^i is its covariance. Hereafter, we will refer to the prior estimate as the partner model: $x_i(t) \equiv \hat{u}_{-i}^-(t)$.

4) Action selection: The optimal action of player i at time t, $u_i(t)$, is the one which minimizes the expected cost $\bar{J}_i(u_i) = E\{J_i(u_i, u_{-i})\}$, where the average is calculated over the partner's action, u_{-i}. The partner model provides expected value ($x_i(t)$) and covariance matrix ($P_i^-(t)$) of the partner's action, so that the expected cost can be rewritten as:

$$\bar{J}_i(u_i) = \frac{1}{2}\left[u_i - u_i^*(x_i)\right]^T \cdot R_{ii}^i \cdot \left[u_i - u_i^*(x_i)\right] + q(x_i) \tag{6}$$

where

$$\begin{array}{ll} u_i^*(x_i) & = -{R_{ii}^i}^{-1} \cdot \left[R_{i-i}^i \cdot x_i + r_i^i\right] \\ q(x_i) & = -\frac{1}{2}{u_i^*}^T \cdot R_{ii}^i \cdot u_i^* + r_{-i}^i \cdot x_i + z^i + \\ & \frac{1}{2}\mathrm{tr}\left[R_{-i-i}^i \cdot P_i^-\right] + \frac{1}{2}x_i^T \cdot R_{-i-i}^i \cdot x_i \end{array} \tag{7}$$

Each player selects their next action u_i on the basis of the task and on their belief in partner state, x_i. However, a player may not behave in a perfectly optimal and deterministic way. To account for this, we assume that action selection is in fact a stochastic process.

$$p(u_i|\hat{u}_{-i}) \propto e^{-\frac{\bar{J}_i(u_i)}{\lambda^i}} \tag{8}$$

where λ^i reflects the 'temperature' of action selection. With greater λ^i leading to greater randomness – exploration. Eq. 8 implies that the action u_i is calculated as $u_i(t) = u_i^*(x_i) + \eta_i(t)$ where $\eta_i(t) \sim N(0, \Sigma_u^i)$, with $\Sigma_u^i = \lambda^i {R_{ii}^i}^{-1}$. For stable learning to occur, the

'temperature' parameter λ^i should decrease over trials. In the model, we specify the initial temperature, λ_1^i, and assume that it changes gradually over trials according to the following relation: $\lambda^i(t+1) = a^i \cdot \lambda^i(t)$, with $\lambda^i(1) = \lambda_1^i$ and $a^i < 1$.

5) Model identification: The model is completely specified by parameters $b^i = \left\{\Sigma_y^i, A^i, \Sigma_x^i, \lambda_1^i, a^i\right\}$. It can be used to simulate the evolution of a particular dyad, described by one specific parameter vector. It can also be used as analytical tool, to estimate the model parameters which best explain a specific subject behavior. Model parameters for a specific dyad can be estimated from the time series of players' actions $D = \{u_1(t), u_2(t) | t = 1, \ldots, T\}$. For parameter identification purposes, Player i model can be reformulated as

$$\begin{aligned} x_i(t+1) &= F^i(t) \cdot x_i(t) + G^i(t) \cdot u_{-i}(t) + w_i(t) \\ u_i(t) &= u_i^*(x_i) + \eta_i(t) \end{aligned} \tag{9}$$

where the true partner action $u_{-i}(t)$ is the model's external input, $x_i(t)$ is the internal state and $u_i(t)$ is model output. We estimated the model parameters by maximizing the expected log-likelihood of the above model [9].

B. Experimental Data and Statistical Analysis

We applied the model to study the mechanisms of joint coordination in a published study [4], in which two players are mechanically coupled through a pair of haptic interfaces; see Figure 2a. The players were required to perform reaching movements with the same start and end points, but different intermediate via-points. The experiment involved three groups of subjects, which differed for the amount of information available about their partner; see Figure 2c. The 2-VP joint action task can be summarized by the following cost function:

$$\begin{aligned} J_i(p_1, p_2) = \; & w_1 \left\| p_i(t_i) - \mathrm{VP}_i \right\|^2 + \\ & \tfrac{w_2}{N} \textstyle\sum_{n=1}^{N} \left\| p_1(t) - p_2(t) \right\|^2 + \\ & \tfrac{r}{N} \textstyle\sum_{n=1}^{N} \left\| F_i(t) \right\|^2 \end{aligned} \tag{10}$$

where $p_i(t)$ is the position of player i at time $t = T(n-1)/(N-1)$. Body dynamics can be approximated as $m_i \ddot{p}_i(t) + k\left[p_i(t) - p_{-i}(t)\right] = F_i(t)$, where $F_i(t)$ is the motor command. We assume that $p_i(0) = p_{start}$ and $p_i(T) = p_{end}$, and that player i crosses their own via-point, VP_i at time t_i. The whole trajectory $p_i(\cdot)$ can be approximated as a polyharmonic spline $p_i(t) = g(t) \cdot v_i$ where $g(t) = \left[|t-t^1|^3 \; \ldots |t-t^M|^3 \; t \; 1\right]^T$ and the coefficients $v_i = S \cdot u_i$ are specified by a small number M of nodes, $u_i = \left[p_i(t^1) \; \ldots \; p_i(t^M)\right]^T$. In this way, the trajectory of Player i is completely specified as a vector of node coordinates, u_i. Derivatives can be expressed in the same form, so that Eq.10 is transformed into a quadratic function of u_i and u_{-i}. For simulation purposes, we set $t_1 = 0.35 \cdot T$ and $t_2 = 0.65 \cdot T$ where the total movement duration was set to T=2 s. In parameter estimation, for each player, we took their average crossing times. Parameters w_1, w_2, and r were determined by the Bryson rule: $w_1 = 1/r_{VP}^2$, $w_2 = 1/d_{\max}^2$ and $r = 1/F_{max}^2$, where the VP radius is $r_{VP} = 2.5$ mm, the maximum between-subject distance is $d_{\max} = 1.5$ mm and the maximum force is $F_{max} = 0.1$ N. Using these parameters, the Nash equilibrium for this task is a joint trajectory in which both players cross both via-points - see Figure 2b. Further, in Eq. 4 we set $H^i = -L^i = I$ to reflect that what is sensed is the interaction force between the two players. We estimated the model parameters from 120-trial time series of trajectories of 15 dyads (30 participants) – five dyads per group. Parameters describe the learning behavior of each player in all dyads. For each parameter, we used a one-way ANOVA with Group as a factor. In case of a significant group effect, we used post-hoc analysis to identify group differences.

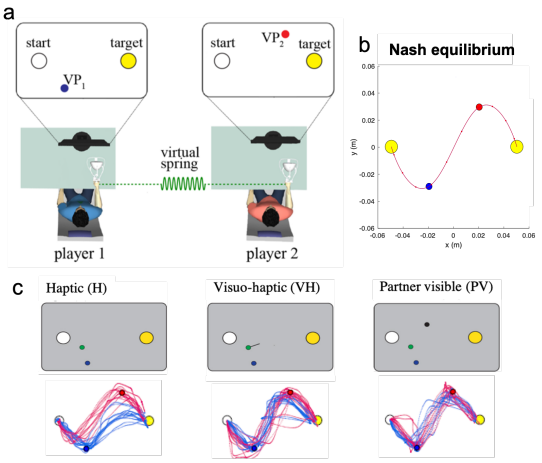


Fig. 2: The 2-VP task. a: Partners in a dyad were connected through a virtual spring. They were instructed to perform reaching movements in between the same start point and the same target point but through different via-points (VP). Each player could only see their own VP, but not their partner's. Both were instructed to keep the interaction force as low as possible during movement. b: Nash equilibrium for the 2-VP task. c: Trajectories at the end training for one representative dyad for each group. Information about partner actions was provided haptically, through the interaction force (Haptic group, H), by additionally displaying the interaction force vector on the screen (Visuo-Haptic group, VH) or by also displaying the partner's cursor (Partner Visible, PV).

III. RESULTS

A. Simulation

We used the model as a generative tool to simulate two dyads, which only differed in the magnitude of the sensory variance, Σ_y: small ($\Sigma_y = 4{\cdot}10^{-4}$ m^2) and large

($\Sigma_y = 4 \cdot 10^{-5}$ m^2). As in the actual experiments, for each model we simulated a sequence of 120 trials. The simulation results are summarized in Figure 3, in terms of the time series of the minimum distances of Player i trajectory to the j-th via-point (MD_{ij}). We observed that

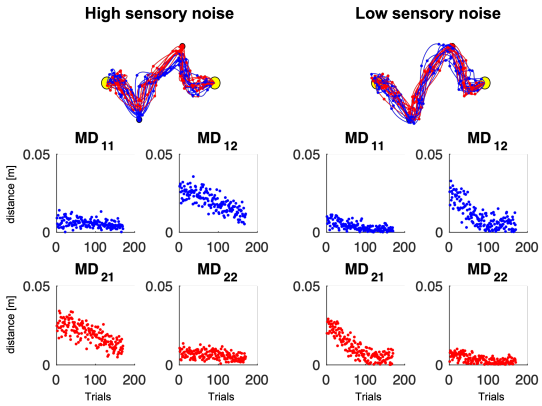


Fig. 3: Simulated trajectories, for large (a) and small sensory noise (b). Top: movement trajectories. Bottom: minimum distances from self and other via-points, for Player 1 (blue) and Player 2 (red).

consistently with experimental findings [4], with lower sensory noise players converged toward a shared solution which is close to the Nash equilibrium - figure 2b.

B. Parameters identification

We estimated the model parameters for each player and each dyad. As expected, and consistent with the experiment design, we found that the estimated sensory variance (Σ_y) decreases as the reliability of partner information increases (p = 0.0098) – see Figure 4. However, a significant group effect was also observed in the parameters which describe the action selection – greater λ_1 (p = 0.0308). Post-hoc analysis revealed a significant H-PV difference for measurement noise (p = 0.0072) and a significant H-VH for the initial exploration rate λ_1 (p = 0.0235).

IV. DISCUSSION

We presented a general computational framework to describe the mechanisms underlying the development of joint coordination. The model can be used to simulate joint action task and to analyze actual experiments. We demonstrated the model in the context of a joint coordination scenario (2-VP task) [4]. The analysis of the experimental observations in terms of the model parameters suggests that (as expected from experimental design), the measurement noise Σ_y decreases from the H to the PV group, consistently with experimental conditions [4]. In addition, the greater initial temperature λ_1 of action selection observed in the VH condition suggests that

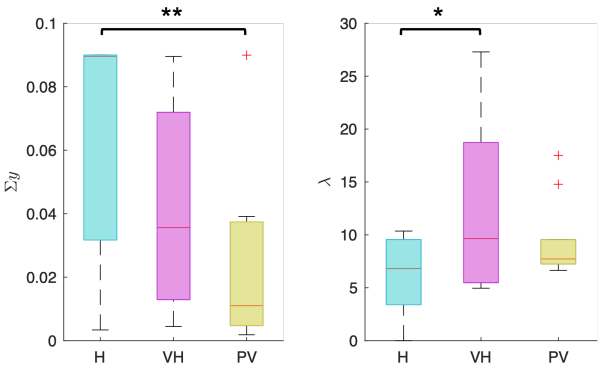


Fig. 4: differences in the estimated model parameters. Boxplots display median, 25th and 75th percentiles of the estimated parameters values, for H (light blue), VH (pink) and PV (yellow) groups. Post-hoc analysis: $*$: p < 0.05; $**$: p < 0.01

displaying interaction force as a vector tends to trigger extra exploration, possibly because the information is not immediately interpretable during movements. Overall, these findings confirm that model-based analysis of joint action experiments may provide valuable information on the underlying mechanisms. The modeling framework is general enough to be usable in a wide variety of joint action scenarios. It can also be used to characterize situations in which social behaviors are defective, as in autism spectrum disorders.

REFERENCES

[1] N. Sebanz, H. Bekkering, and G. Knoblich, "Joint action: bodies and minds moving together," *Trends in Cognitive Sciences*, vol. 10, no. 2, pp. 70–76, 2006.

[2] K. Reed, M. Peshkin, M. J. Hartmann, M. Grabowecky, J. Patton, and P. M. Vishton, "Haptically linked dyads: Are two motor-control systems better than one?," *Psychological Science*, vol. 17, no. 5, pp. 365–366, 2006.

[3] G. Ganesh, A. Takagi, R. Osu, T. Yoshioka, M. Kawato, and E. Burdet, "Two is better than one: Physical interactions improve motor performance in humans," *Scientific Reports*, vol. 4, no. 1, pp. 1–7, 2014.

[4] V. T. Chackochan and V. Sanguineti, "Incomplete information about the partner affects the development of collaborative strategies in joint action," *PLoS Computational Biology*, vol. 15, no. 12, p. e1006385, 2019.

[5] S. Cheng and P. N. Sabes, "Modeling sensorimotor learning with linear dynamical systems," *Neural Comput*, vol. 18, pp. 760–93, Apr 2006.

[6] M. Casadio and V. Sanguineti, "Learning, retention, and slacking: a model of the dynamics of recovery in robot therapy," *IEEE Trans Neural Syst Rehabil Eng*, vol. 20, pp. 286–96, May 2012.

[7] T. Başar and G. J. Olsder, *Dynamic noncooperative game theory*. SIAM, 1998.

[8] D. Fudenberg and D. Levine, "Learning in games," *European Economic Review*, vol. 42, no. 3-5, pp. 631–639, 1998.

[9] N. Gupta and R. Mehra, "Computational aspects of maximum likelihood estimation and reduction in sensitivity function calculations," *IEEE Transactions on Automatic Control*, vol. 19, no. 6, pp. 774–783, 1974.

Fast path replanning in a dynamic environment in percutaneous cardiac interventions

A. Peloso[1], R. Damiano[1], E. Votta[1] and E. De Momi[1]
[1] *Department of Electronics, Information and Bioengineering, Politecnico di Milano, Milan, Italy*

***Abstract*— Percutaneous interventions for structural heart diseases allow for a less invasive approach in elderly or high-risk patients. Great research interest arises in the field, working towards the robotization of current manual procedures. Usually, a catheter is guided by the surgeon from a peripheral vein access towards the relevant intracardiac target. Autonomous intracardiac navigation would require precise planning of the path to safely lead the catheter avoiding collisions. From this standpoint, one of the main challenges is to account for motion of the heart structures. To comply with a dynamic environment, fast replanning needs to be considered to obtain reliable and safe paths in case of moving targets or possible impacts with moving obstacles. In this work Imitation Learning is adopted in a static and dynamic simulation environment. Performances are preliminarily assessed in terms of rate of success in reaching the target and angle of impact against the target. The proposed planner reaches good performances in a dynamic environment, with a success rate of 75% and respecting the maximum bending angle of 20°.**

***Keywords*—dynamic path replanning, imitation learning, structural heart interventions, medical robotics**

I. Introduction

Percutaneous interventions in the frame of mitral valve (MV) repair involve a steerable tendon-driven catheter which is manually advanced from a femoral vein access towards the heart [1]. From the right atrium, through a transeptal puncture, the catheter reaches the left atrium, where it is led to the MV to position a clip to restore MV leaflet coaptation. In this field, reaching autonomous procedures is a matter of great research interest, leading to help surgeons during interventions, as well as reduce the learning curve for new operators and standardize the outcome of the procedure. To reach an autonomous procedure, the actuation must follow a safe trajectory along the way, assuring obstacle avoidance while reaching the target. Indeed, in an intra-operative scenario, the need of a suitable planner able to comply with dynamic anatomical structures and adjust the path in real time is substantial.

Sampling-based approaches have been largely explored for real-time path replanning in a dynamic environment [2]. Although providing a fast and easy to implement approach, traditional methods require further adjustments to find the best trajectory among the possible solutions [3]. Learning based methods, instead, allow for a more comprehensive investigation in complex environments. Reinforcement Learning (RL) has gained credibility in several contexts [4], [5], [6] as a suitable method for estimating the policy that defines the agent's behaviour, such that a reward function is maximized. In the context of path planning, RL enables optimal path definition by directly considering kinematic constraints, path length constraints, and distance to obstacles without any subsequent refinement, thus representing a viable approach for intra-operative dynamic scenarios. Reference [7] implemented a RL algorithm to automatically control a catheter into the heart using Dueling Deep Q-learning method. Another example can be found [8], where robotic trajectories for endovascular procedures are optimized through RL to avoid the contact between catheter's tip and the vessel wall, adapting to complex flow dynamics.

When RL is implemented for complex environments, the design of the reward function becomes very complex. In those cases, Imitation Learning (IL) is a promising technique that might achieve better results [10]. In the framework of IL, the agent learns a policy to perform a task in the environment based on demonstrations by experts. Some methods directly estimate the policy from demonstrations, others instead estimate a reward function and, from there, indirectly estimate the behavioural policy [12]. Reference [13] already adopted this approach to address path replanning in an intra-operative scenario for steerable needles in keyhole neurosurgery.

In this framework, the aim of the present work is to develop an accurate path planner in a dynamic environment, exploiting IL to react to MV motion. We relate to a previous implementation [14], optimizing for a realistic and dynamic intracardiac environment.

II. Materials and Methods

The aim of path planning [15] is to find a set of configurations from a starting pose to a target pose, defining a suitable path for an agent in the free space, i.e., all possible configurations the agent can assume without hitting any obstacle. In the intracardiac environment, we defined as starting configuration a pose in the septum, and we set the target pose along the coaptation line of the MV (Fig 2). A cube encompassing the coaptation line was defined; at each expert demonstration, the target was represented by a point within the cube. This setting allowed for generalizing the problem for any possible site of application of the clip on the MV. The scene was implemented in *Unity3D*, with the main regions of interests derived from the 3D reconstruction of a patient computerized tomography scan.

A. Imitation Learning algorithm

The performed training is based on IL. Two approaches were used together: Generative Adversarial Imitation Learning (GAIL) [12] and Behavioural Cloning (BC) [17]. GAIL algorithm is based on two antagonistic networks: the generator and the discriminator. While the generator proposes new actions, a(t), for the agent on the basis of a RL algorithm (Proximal Policy Optimization), exploiting a given set of

rewards (R_{ext}), a discriminator is embedded to distinguish the generated actions from experts' demonstrations, giving the agent an intrinsic reward (R_{int}). To enhance experts' behaviour mimicking, BC is included: the agent learns a behavioural policy, π, like in a supervised learning problem in which expert's demonstrations represent the ground truth. A descriptive flow is reported in Fig 1. R_{ext} were given based on an empirical analysis: -1 in case of collision with sensible anatomical structures, ending the episode without reaching the target; +0.75 in case of reaching the target point. Since the procedure requires to arrive perpendicularly at the target, a control for the hitting angle was also included, adding a +0.25 reward in case of hitting angle inferior to 20° and -0.25 otherwise. To train the model, the ML-Agents package [18] was integrated in Unity.

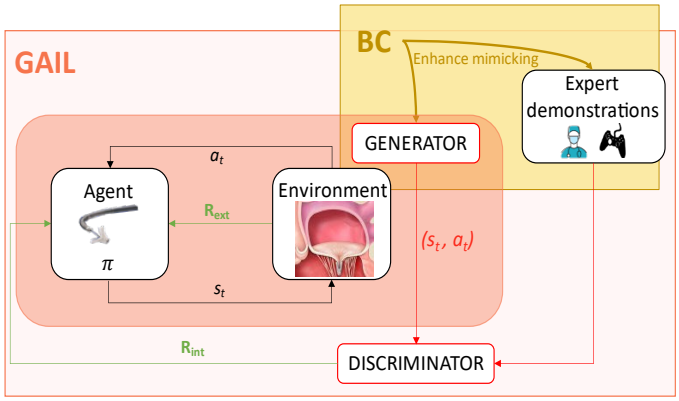


Fig 1 *Description of the algorithm: GAIL and BC*

B. *Mitral valve movement*

To make the environment more realistic, we introduced the dynamics of the MV. We defined the movement by accounting for MV annular plane motion while neglecting leaflet motion, which is not relevant to our specific goal. At each cardiac cycle, the mitral annular plane undergoes a shift towards the apex of the heart due to the contraction of the atria (atrial systole), and then returns to its starting position during the contraction on the ventricles. The motion of the MV annular plane was defined based on typical values of mitral annular plane systolic excursion (MAPSE), which represents the amount of displacement of the mitral annular plane along the heart long-axis towards the apex. As reported in [16], normal values of MAPSE are reported to range from 12 mm to 15 mm. Focusing on MV dysfunctional patients, to train the algorithm we considered 12mm as a reliable estimation of the maximum excursion of the MV annular plane.

The points representing the base and the apex of the heart were manually identified: the base was set in the centre of the MV orifice while the apex as the point of maximum curvature in the left ventricle wall, at the opposite side of the base. The direction of the target's movement was then obtained as the direction of the vector connecting base and apex (green arrow, Fig 2). To define the systolic time-dependent displacement, a *sin* wave was considered for 1/3 of the cardiac cycle duration, while motion was considered absent in diastole, as reported in Eq.1:

$$MV_{shift}(t) = \begin{cases} 12\sin(2\pi f_{systole} t) & 0 < t < t_{systole} \\ 0 & t_{systole} < t < Tcycle \end{cases} \quad (1)$$

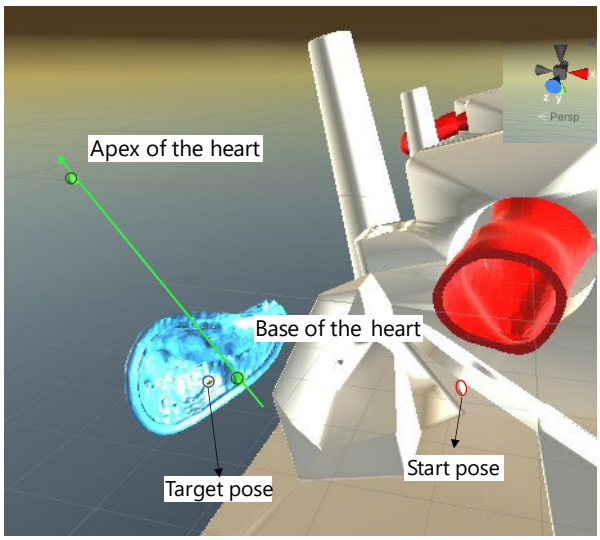


Fig 2 *Intracardiac environment: starting point in the septum and target point in the valve – along coaptation line*

C. *Experimental protocol*

We trained two different models, one with a static environment, and one introducing the movement of the MV. A set of 110 demonstrations was recorded with a joystick both for the static and the dynamic model, with mean reward of 0.85 and 0.8 respectively. 10000 training steps were performed. The model was trained to reach the target sampled from the cube positioned along the coaptation line with a tolerance of 2 mm. The two models were compared in terms of success rate, defined as the number of successful events over 100 attempts and expressed as percentage (SR [%]), of time to compute the path and get to the target (t [s]), and of angle with which the catheter reaches the target ([°]).

III. Results and Discussion

The training in the static environment yielded a SR of 62%, with median time to compute the path and get to the target of 12.8 s and a median angle value of 10.4°. The planner in the dynamic environment, instead, showed a SR of 73% and median values of time and angles equal of 15,8 s and 18.5° respectively. The increase in time metric and in the inaccuracy on target hitting angle in the dynamic setting, compared to the static setting, could be expected, given the higher complexity of the dynamic task. Overall, the time to reach the target is acceptable compared to previous work [14]. On the contrary, the lower SR in the static environment might suggest margins for refinements of the environment setting.

IV. Conclusion

This work investigated the introduction of a dynamic environment for a path planning module in the framework of percutaneous interventions for mitral valve repairment. Although these preliminary achievements showed promising

results of dynamics inclusion in path replanning, several adjustments are needed. One first thing to address is enhancing the training step to assess the stability of the algorithm. Moreover, the model may have suffered sub-optimal demonstrations: the impact of manual dexterity using a joystick might have played a part in the low SR for both models. The unexpected lower SR of the static model with respect to the dynamic one, instead, could be explained given the fact that, thanks to the motion of the valve in different planes, the agent had the possibility of reaching the target in different positions. This increased the possibility of getting to the target (higher SR in dynamic environment), with the consequence of a major angle of impact. One last remark regards the need for physical constraints of the agent: being a tendon-driven catheter, kinematics must be considered in further developments.

Nonetheless, these are the first steps toward a path planning module accounting for the movement of the MV. As a matter of fact, in the real time environment, it becomes extremely important to synchronize the advancement of the catheter inside the left atrium with the MV movement itself. Hence, the need for a continuous correction and replanning to reach the moving target is indispensable to obtain a reliable simulation transposable in real robotics applications.

ACKNOWLEDGEMENT

This work was supported by the European Union's EU Research and Innovation programme Horizon 2020 under the project ARTERY, grant agreement No. 101017140.

REFERENCES

[1] M. Shah, U.P. Jorde, "Percutaneous Mitral Valve Interventions (Repair): Current Indications and Future Perspectives", *Cardiovasc Med*, vol. 6, Jul.2019.

[2] Y.J. Zhao et al., "3D Dynamic Motion Planning for Robot-assisted Cannula Flexible Needle Insertion into Soft Tissue", *International Journal of Advanced Robotic Systems*, vol. 13, pp. 121, May 2016.

[3] S. Patil, J. Burgner, R. J. Webster III, R. Alterovitz "Needle Steering in 3-D Via Rapid Replanning", *IEEE Trans Robot*, ovl.30(4), pp. 853-864, Aug. 2014.

[4] B. Kim, J. Pineau, "Socially Adaptive Path Planning in Human Environments Using Inverse Reinforcement Learning", *International Journal of Social Robotics*, vol. 8(1), pp. 51-66, Jan. 2016.

[5] C. Chen, X. Q. Chen, F. Ma, X. J. Zeng, J. Wang, "A knowledge-free path planning approach for smart ships based on reinforcement learning,", *Ocean Engineering*, 189, 2019.

[6] V. Mnih et al., "Human-level control through deep reinforcement learning", *Nature*, vol. 518, pp. 529-533, Feb. 2015.

[7] H. You, E. Bae, Y. Moon, J. Kweon, J. Choi, "Automatic control of cardiac ablation catheter with deep reinforcement learning method", *Journal of Mechanical Science and Technology* vol. 33, pp. 5415-5423, Nov. 2019.

[8] W. Chi et al., "Trajectory Optimization of Robot-Assisted Endovascular Catheterization with Reinforcement Learning", *International Conference on Intelligent Robots and Systems (IROS)*, 2018.

[9] J. Kumar, C.S. Raut, N. Patel, "Automated Flexible Needle Trajectory Planning for Keyhole Neurosurgery Using Reinforcement Learning", *International Conference on Intelligent Robots and Systems (IROS)*, pp. 4018-1023, 2022

[10] J. Hua, L. Zeng, G. Li, Z. Ju, "Learning for a Robot: Deep Reinforcement Learning, Imitation Learning, Transfer Learning", S*ensors 2021*, 21, 1278, February 2021.

[11] S. Arora, P. Doshi "A survey of inverse reinforcement learning: Challenges, methods and progress", *Artificial Intelligence*, 297(7), March 2021.

[12] J. Ho, S. Ermon, "Generative adversarial imitation learning," *Advances in neural information processing systems*, vol. 29, 2016.

[13] A. Segato et al., "Inverse Reinforcement Learning Intra-Operative Path Planning for Steerable Needle", *IEEE Transactions on Biomedical Engineering*, May 2022.

[14] A.Fortuna et al., "Inverse Reinforcement Learning Algorithm for Intra-Vascular and Intra-Cardiac Catheter's Navigation in Minimally Invasive Surgery", in EasyChair Preprint no.8886, EasyChair 2022.

[15] S. Karman, E. Frazzoli, "Sampling-based algorithms for optimal motion planning", *The International Journal of Robotics Research*, 30(7): pp 846-894, 2011.

[16] K. Hu et al., "Clinical implication of mitral annular plane systolic excursion for patients with cardiovascular disease", *Eur Heart J Cardiovasc Imaging*; 14(3): pp.205-12, Mar. 2013.

[17] T. K. Devi, A. Srivatsava, K. K. Mudgal, R. R. Jayanti, T. Karthick, "Behaviour cloning for autonomous driving.", *Webology*, vol. 17(2), Dec. 2020.

[18] A. Juliani et al., "Unity: A general platform for intelligent agents", *arXiv preprint* arXiv:1809.02627, 2020.

An attention classifier for the evaluation of a robotic therapy in children with Autism Spectrum Disorder

Laura Santos[1,2], Martina Murgo[1], Bárbara Silva[2], Alice Geminiani[1,3], Arianna Caglio[4]
Silvia Annunziata[4], Catarina Barata[2], José Santos-Victor[2], Alessandra Pedrocchi[1]
[1] *NEARLab, Department of Electronics, Information and Bioengineering, Politecnico di Milano*
[2] *Institute for Systems and Robotics, Instituto Superior Técnico, Universidade de Lisboa*
[3] *Department of Brain and Behavioral Sciences, University of Pavia* [4] *IRCCS Fondazione Don Gnocchi*

***Abstract*—Social robots are very promising in therapies with ASD children as they have the potential to promote communication and attention skills of these children. Attention plays a critical role in almost every area of life, allowing people to focus on information. In literature, several authors measured attention through the manual labelling of videos, which is labour-intensive and subjective. However, new algorithms objectively quantify the progress of the child during therapy. This work aims to develop and test an attention measurement system to evaluate a novel robotic therapy for ASD children. First, in cooperation with IRCCS Fondazione Don Carlo Gnocchi, a new protocol focused on eliciting the child's attention through the use of the social robot NAO was developed. The sessions were recorded with a Microsoft Kinect camera for offline analysis. We used Gaze 360 and we implemented a bottom-up solution to compensate for offsets in gaze signal reconstruction caused by subject position, target position, gaze value, and light. The final algorithm included two neural network architectures to classify to which target the subject was looking. In a sample of 5 healthy adults, we obtained a final accuracy of 88%, showing the promising results of our system. In the future, we will test the developed protocol with healthy and ASD children to understand its sensibility to capture the differences between the two groups and to verify its consistency in children.**

***Keywords*—Autism Spectrum Disorder, Deep Neural Networks, Attention classification**

I. INTRODUCTION

Autism spectrum disorder (ASD) is a group of neurodevelopmental disorders characterised by difficulties in social interaction, social communication and the presence of restrictive and repetitive behaviours. There is no standard therapy, but early interventions lead to a better prognosis. Several works showed the advantages of using social humanoid robots for the therapy of ASD children [2]. However, these therapies are still not used in daily practice because the evidence of their impact on children is still missing. One of the principal causes for this lack of evidence is the reduced number of quantitative outcome measures validated with clinical scales, which prevents comparison among studies.

In terms of clinical scales, the ADOS in combination with the Autism Diagnostic Interview-revised are considered the gold standard questionnaires for autism diagnosis [5]. However, since they are diagnostic scales they are not able to collect small changes caused by a therapy. A solution could be the Early Social Communication Scale (ESCS) that was developed to assess individual differences in nonverbal communication skills, namely attention, through 25 semi-structured situations that encourage interactions between the tester and the child [6]. Attention is one of the principal measures analysed in these therapies and can be obtained manually (e.g. therapists analyse the frames recorded during the sessions) or automatically [7], using non-intrusive devices (better for ASD children) such as cameras.

Alnajjar et. al [1] use the camera of a NAO robot to construct an autonomous assessment system of attention based on attention cues. In this study, to generate attention's score, the frequency of detecting a face was analysed during protocol. Instead, Di Nuovo et al. [2] preferred to use a deep learning method to automatically estimate if ASD children focus their visual attention on the robot during a therapy session. They used the facial landmarks extracted from a video recorded by NAO and a Convolutional Neural Networks (CNN) to classify the behaviour of the child. The labelling was considered "Attention" when the child was monitoring the robot and "Distraction" otherwise. In both methods, the children could be facing the camera but looking otherwise, not being a precise measure of attention.

In the context of previous work, we developed a therapy for training of gestures through turn-taking games between a robot, a child and a therapist (IOGIOCO protocol [3]). In the several games, the robot mirrored the participants using a Kinect camera and gave feedbacks about their performance. For measuring the attention of children during this protocol, we developed an automatic system using gaze [7], considered a good proxy of attention. In this system, we used the frames recorded with a Kinect camera to obtain the azimuth gaze angle of the child from an algorithm named Gaze360 [4]. Associating this gaze angle with the positions of our targets, we determined where the subject was looking at, in each moment. The mean accuracy obtained for two ASD children during two sessions was 59%. This low performance was related to the poses that the children and the therapist took during the therapy sessions [7]. Therefore, we had two main

goals: the development of a protocol for a correct evaluation of the improvement of children doing a robotic protocol and the implementation of an objective, accurate and precise attention classifier to evaluate a robotic protocol for ASD children.

II. Methods

A. Robot-mediated evaluation protocol

From a collaboration with Fondazione Don Carlo Gnocchi, we have decided to depart from a Clinical Scale so that we could compare clinical results with the results of our automatic system. We have chosen the Early Social Communication Scale (ESCS) as the starting point for the development of the new evaluation protocol. This scale has as main goal the assessment of nonverbal communication skills which was aligned with ours and it was quite fast to administer (15-25min).

In order to develop our new protocol, we chose three tasks from the ESCS: *object spectacle task*; *gaze following task* and *book presentation task*. Then, we adapted each task to include the robot NAO, obtaining a setup more similar to our therapy protocol (*IOGIOCO* protocol). In this setup, we also included the table of the ESCS and a Microsoft Kinect camera to record our sessions (Figure 1).

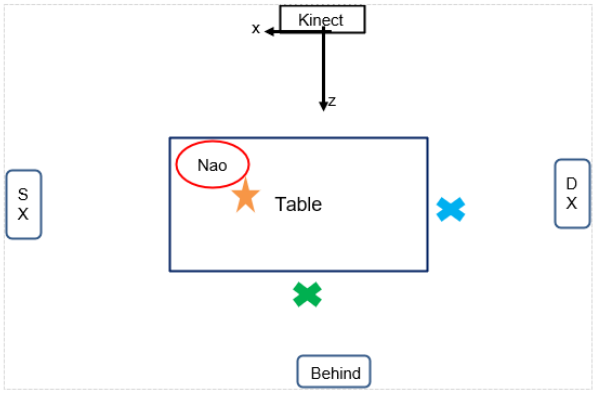


Fig. 1: Protocol setup. The orange star represent the mechanical toy; DX, SX and Behind are the three posters on the wall. The forth poster was below the Kinect camera. The blue x represent the therapist, the green one the child.

The protocol starts with the therapist and child exploring the robot in a kneeling position. After, NAO presents itself and starts the *object spectacle task*, pointing to a small mechanical toy placed in front of it and asking the child if she/he wants to play. As in the ESCS, the therapist shows the toy and then gives it to the child to assess his behaviour during free play. While the child is playing or distracted, the therapist turns on NAO's LEDs, dragging the child's attention to the robot. After the *gaze following task* starts, where first the robot turns its head to one of the four posters present in the room waiting for the child to follow with his/her gaze, and secondly, points and makes a comment on the poster to explicitly call the attention of the child. In the final task (*book presentation task*) NAO points to one of the children's books that the therapist holds. The therapist waits for the answer from the child and then takes one of the books to show it to the child while interacting with him and keeping the child's attention.

B. Attention estimation

After establishing the evaluation protocol, we implemented an attention classifier. As a starting point, we adapted the automatic system described before (Section I), and we chose to test the system in more stable conditions than the ones of the final protocol but with the same setup. We selected five targets that elicit attention behaviours easily: NAO, Kinect and three posters.

In order to have a controlled scenario and to understand the system's performance, we did four tests with four pairs of adults (27 ± 5 years), acting as the child and the therapist of our final protocol. In these tests (protocol S), the subjects sat in the positions represented in Figure 1 and changed the gaze's direction by alternating between the camera and a target every 5s. In all videos, there was one common subject (Subject 1), so in total, we had five subjects.

In order to compute the system's performance, we manually labelled the videos indicating where the subjects were looking. Then, we compared these results with the estimations obtained by the system to calculate the accuracy and precision.

The analysis of protocol S revealed a low precision (18%) for the purpose of the project. Thus, we decided to add the elevation angles, extracted from the Gaze 360 algorithm, to the attention classifier. Following the methodology proposed in the *IOGIOCO* project for the azimuth angle [7], we started by calculating the expected gaze angles (standard angles) for each of the targets and defined an area of interest (AOI) around them, for each frame. Then, we filtered both the azimuth and elevation gaze estimations from the Gaze360 algorithm to reduce the noise. After, if the azimuth estimation was inside the AOI range of angles for a given duration (> 400 ms), we checked the same in the elevation direction. When this occurred, we considered that the subject was looking at the target and we called it a fixation.

Despite the accuracy improvement with this new method, the result was not yet sufficient. We found that this was caused by the presence of offsets between the standard angles and the estimated Gaze360 angle (an example is shown in Figure 2, for the Kinect where the expected gaze value is 0rad, by definition of the Gaze360 algorithm, see [4]). We developed and tested different acquisition protocols to selectively identify the possible different origins of these offsets. From these protocols, we observed that several factors influenced the offsets in a non-linear way, such as light, subjects and targets coordinates, gaze value, and confidence error angle (a measure of the reliability of the gaze outputted by Gaze360).

We developed an explicit and an implicit method for calculating the offsets and then removing them. We tested both solutions on four protocols: protocol S and three other protocols with the same subjects, in which they looked to the same targets as in protocol S but standing. For each protocol (now on called protocol x,y,z), the two adults assumed two

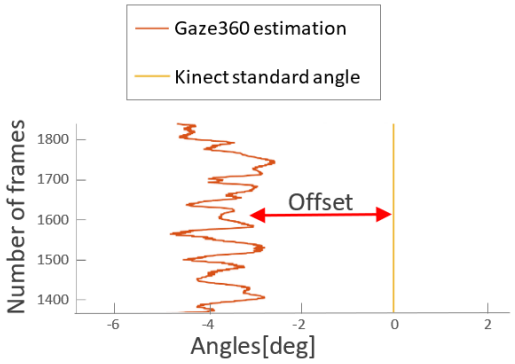


Fig. 2: Example of offset between predicted Gaze360 and standard angle for Kinect camera in azimuth direction

positions and moved only in one direction (x, y, z directions of the Kinect camera, respectively).

1) The explicit method: In this method, we calculated the offset between the estimated gaze and the standard angle explicitly, using the following hypothesis: when the subject looks at a target, the offset for that target is less than for all the other targets. Therefore, the correct offset (O) at each moment could be given by the minimum difference between Gaze360 estimation (γ) and the standard angles (α) of the different targets (Equation 1). This calculation was done separately for the azimuth and the elevation.

$$O(t) = \min_{\forall target} \gamma(t) - \alpha_{target}(t) \quad (1)$$

The chosen offsets were then added to the lower and upper limits of all the AOIs in that frame. Then we computed the fixations as previously mentioned and compared them with our ground truth.

2) The implicit method: Given the wide variety of factors influencing offsets, we decided to apply a bottom-up approach and constructed a deep learning method to predict towards which target the person was looking. In this way, the correction of the offset was implicit in the method.

We chose as input the azimuth and the elevation angles estimated by Gaze360, the x, y, and z coordinates of the head of the subject, the confidence error, the four vertices of the bounding box estimated by Yolo algorithm, and the respective image with the selected face [7]. The output should be a classification in one of the six possible classes corresponding to the different targets: Kinect, NAO, three posters and elsewhere.

In terms of architecture, for extracting the best features of the images, we used a convolutional neural network (CNN), more specifically, a pre-trained EfficientNet architecture [8] associated with two fully connected layers. Regarding the other inputs, we constructed a Multi-Layer Perceptron (MLP) with two fully connected layers. Then three architectures were trained and tested: MLP, CNN and MLP+CNN. In this last architecture, first, there was a pre-training of the weights of each architecture, and then, they were fine-tuned considering the complete network. For the training of the different architectures, we minimised the loss between the predicted and the true class (given by manual labelling of the videos). We tested the MLP and CNN with different hyperparameters keeping the validation set (containing Subject 3 data) fixed. Since we had few subjects, we calculated the mean of the cross-validation process (using four subjects to train and another to test) as a final result.

III. Results and Discussion

From the analysis of protocol S, using just the azimuth, we obtained a mean accuracy of 77% and a mean precision of 18%. With the inclusion of the elevation angle, the mean accuracy improved to 81% and the mean precision to 34%. The improvement was obtained thanks to the fact that some targets (ex: NAO and the Kinect) had similar azimuth directions not distinguishable by the original algorithm. The still low precision was caused by the presence of offsets, as previously mentioned. These offsets are influenced in a non-linear way by several factors. Thus, we developed the two different solutions explained.

In order to have comparable results, we decided to analyze also the protocols x, y, z with the original algorithm and with the addition of elevation (Table I). We verified that the results decreased in relation to protocol S. These lower results can be related to the presence of more noise in these new protocols since the subjects are walking through the room instead of being seated as in protocol S.

TABLE I: Accuracy and precision of the original algorithm and of the original algorithm with the elevation computation

	Original algorithm		**Add of elevation computation**	
Subject	**Precision**	**Accuracy**	**Precision**	**Accuracy**
1	0.09	0.74	0.21	0.78
2	0.17	0.76	0.24	0.78
3	0.20	0.77	0.23	0.78
4	0.11	0.74	0.17	0.76
5	0.18	0.76	0.52	0.86
Mean	0.15	0.76	0.28	0.79
St. deviation	0.05	0.01	0.15	0.04

A. The explicit method

Using an explicit method to correct the offsets, we observed that both precision and accuracy improved (Table II). However, it was not the optimal solution for our system since the lower offset was not always the correct one.

We observed two major problems. First, when two targets had similar coordinates in x or y, their offsets (in azimuth and elevation) were also similar, and the correct offset could not be the chosen one. Second, for the target behind, when the subject looked at that target, his/her face was no longer detectable by the Kinect, which led to a signal with more noise and higher offsets that through this method were not found. However, we decided with therapists not to remove this target, despite a possible decrease in accuracy. Indeed, from a clinical point of view, the child's ability to focus attention even on targets out of his visual field following therapist indications is considered a high-level attention task [6].

TABLE II: Accuracy and precision of explicit method solution

Explicit method		
Subject	**Precision**	**Accuracy**
1	0.58	0.88
2	0.45	0.84
3	0.40	0.83
4	0.44	0.84
5	0.59	0.88
Mean	0.50	0.86
St. deviation	0.04	0.14

B. The implicit method

As explained in II-B2, given the wide variety of factors influencing offsets, we decided to apply a deep learning method to predict towards which target the person was looking.

In terms of hyperparameters, we found that the best loss was the mean square error loss function for both individual architectures. The ideal training time was 80 epochs for the MLP and 30 epochs for the CNN. Regarding the effect of the inputs on the MLP performance, we verified that the head boxes worsened the final precision.

With these parameters, the CNN (precision: 66%) had a lower precision than the MLP (precision: 78%). Thus, we excluded CNN alone from further analysis but added it to the MLP to see if it could improve its performance. In Table III are shown the obtained results for the tests of the MLP and MLP+CNN networks. We noticed that the mean precision and accuracy improved in relation to the explicit method (Table II).

Furthermore, CNN helped to improve model prediction when validating with Subject 1 and Subject 5. The first one was the subject associated with the larger quantity of data. When the data from this subject was used for validation, the training dataset became smaller than the validation set. In the absence of a large quantity of data, the features provided by the CNN were important to improve the overall result. The second one was a subject of the same gender (male) of the subject that we used to determine the best hyperparameters, and, probably, that is why we obtained a good result with him. Nevertheless, in order to take more significant conclusions, the number of subjects should be increased.

TABLE III: Accuracy and precision obtained for all subjects for MLP. In $Subject$ column the additional information of the gender: male (M) and female (F).

Implicit method				
	MLP		**MLP+CNN**	
Subject	**Precision**	**Accuracy**	**Precision**	**Accuracy**
1 F	0.40	0.80	0.48	0.83
2 F	0.60	0.87	0.47	0.82
3 M	0.78	0.93	0.76	0.92
4 F	0.75	0.92	0.67	0.89
5 M	0.64	0.88	0.78	0.93
Mean	0.63	0.88	0.63	0.88
St. deviation	0.15	0.05	0.15	0.05

IV. Conclusion

With this work, we have shown that neural networks are promising to analyse a person's gaze and thus measure his/her attention. Thanks to this method, we achieved an accuracy of 88% improving by 13.7% in comparison to the original algorithm.

One of the major study limitations was the low availability of data for analysis, which prevented the choice of the best architecture. The networks need a large amount of data to train optimally, particularly the CNN. Moreover, we did not include the mechanical toy, which is part of the standard ESCS protocol, in our attention classifier as a target object of attention to simplify the protocol. Therefore, a method for real-time tracking of moving targets should be included so that the position of the mechanical toy could be integrated as input of the deep learning method.

In the future, we will test the developed protocol first with neurotypical children and then with ASD children to understand its sensibility to capture the differences between the two groups. Simultaneously, the attention classifier should be tested to verify its consistency in children. It is anticipated that there will be a minor reduction in accuracy, particularly among children with ASD, due to their inability to remain motionless in fixed postures. Nevertheless, measures similar to the ones used by the clinicians for the ESCS scale should be created to compare our automatic measures with validated clinical measures. In this way, this work will have a two-fold impact: it can be used to test the effect of the $IOGIOCO$ protocol on the improvement of children skills, if any, and it provides a quantitative framework for the qualitative clinical scales being applicable not only for Autism but also for other pervasive developmental disorders.

Acknowledgement

This work was supported by the National Recovery and Resilience Plan *Musa*, the Portuguese Foundation of Science and Technology (projects SFRH/BD/145040/2019) and Associazione Paolo Zorzi (project *IOGIOCO*)

References

[1] Fady Alnajjar, Massimiliano Cappuccio, Abdulrahman Renawi, Omar Mubin, and Chu Kiong Loo. Personalized robot interventions for autistic children: An automated methodology for attention assessment. *International Journal of Social Robotics*, 13:67–82, 2 2021.

[2] Alessandro Di Nuovo, Daniela Conti, Grazia Trubia, Serafino Buono, and Santo Di Nuovo. Deep learning systems for estimating visual attention in robot-assisted therapy of children with autism and intellectual disability. *Robotics*, 7(2), 2018.

[3] Alessia Silvia Ivani, Alice Giubergia, Laura Santos, Alice Geminiani, Silvia Annunziata, Arianna Caglio, Ivana Olivieri, and Alessandra Pedrocchi. A gesture recognition algorithm in a robot therapy for asd children. *Biomedical Signal Processing and Control*, 74:103512, 2022.

[4] Petr Kellnhofer, Adrià Recasens, Simon Stent, Wojciech Matusik, and Antonio Torralba. Gaze360: Physically unconstrained gaze estimation in the wild. *2019 IEEE/CVF ICCV*, 2019.

[5] Juliane E. Medda, Hannah Cholemkery, and Christine M. Freitag. Sensitivity and specificity of the ados-2 algorithm in a large german sample. *Journal of Autism and Developmental Disorders*, 49(2):750–761, 2019.

[6] Peter Mundy, Jessica Goldstein, Meaghan Venezia Parlade, and Anne Hogan. Early social communication scales (escs) view project, 2003.

[7] Laura Santos, Barbara Silva, Filippo Maddaloni, Alice Geminiani, Arianna Caglio, Silvia Annunziata, Ivana Olivieri, Catarina Barata, Jose Santos-Victor, and Alessandra Pedrocchi. Sharing worlds: Design of a real-time attention classifier for robotic therapy of asd children *. pages 1–6, 9 2022.

[8] Mingxing Tan and Quoc V Le. Efficientnet: Rethinking model scaling for convolutional neural networks. *ICML 2019*, pages 6105–6114, 2019.

A safe robot control for semi-autonomous pedicle tapping

C. Lauretti[1], F. Cordella[1], I. Saltarelli[1], and L.Zollo[1]
[1] *Unit of Advanced Robotics and Human-Centred Technologies, Campus Bio-Medico University of Rome*

***Abstract*—The objective of this paper is to propose a novel safe control for robot-aided pedicle tapping that is able to identify the bone layer transition and stop the tool-tip before propulsion of the bone boundaries. The proposed control for pedicle tapping consists of : i) a hybrid position/force control loop that allows the surgeon to move the surgical tool along a pre-planned axis and ii) a velocity control loop that allows him/her to finely tune the tool rotational speed by modulating the tool-bone interaction force along the same axis. The velocity control loop integrates also a bone layer transition detection algorithm that stop the tool bit before propulsion of the the bone last layer. The approach was tested on the Kuka LWR4+ provided with an actuated surgical tapper which was used to tap a wood specimen simulating the bone layer density characteristics. The study demonstrated high capability of the proposed approach to i) promptly detect transition among the specimen layers and ii) stop the tool rotation as the transition to the last bone layer is detected.**

***Keywords*—Robotic Surgery, Spinal Surgery, Tapping Procedure, Human-in-the-Loop Control**

I. INTRODUCTION

In clinical practice, the pedicle screw is the implant of choice for treating patients with spinal deformity or spondylolisthesis [1].

The risk of screw misposition can be considerably decreased by tapping the screw path prior to screw installation [2] also thanks to the use of robotic devices that have been recently employed, in spine surgery, to make the screw fixation more repeatable and increase precision between the preoperative planning and postoperative position of the screws.

Commercial spinal robots are generally used to constrain the orientation and position of the surgical tool providing the surgeon with mechanical guidance [3], [4] during the surgical instrument use.

Although there has been a noticeable improvement in screw placement accuracy, movements along or around the tapping axis are still manually performed by the surgeon, who has to pay great attention while controlling the penetration of the surgical tool into the bone layers and stop its movements based on the visual feedback from the navigation system or, worse yet, on the perceived interaction force.

Therefore, the objective of this paper is to propose a novel safe robot control for pedicle tapping that is based on a bone layer transition detection algorithm [5] and is able to stop the tool rotation before propulsion of the last bone layer, hence preventing the underlying tissues from being damaged and making the procedure safer for the patient.

In addition, the proposed safe robot control for pedicle tapping has the following advantages: i) allows moving the surgical tool along a pre-planned axis, by simply exerting controlled forces on its handle, and ii) allows finely modulating the rotational speed of the surgical tapper by modulating the tool-bone interaction force along the same axis [6].

The proposed control was evaluated, at 6 thrust forces, on a wood specimen made of different materials that simulate the bone layers (i.e. cortical and spongy layer). Moreover, to assess performance in terms of success rate of the tapping execution and the readiness of the control strategy, a volunteer was asked to try the overall platform.

II. MATERIALS AND METHODS

A. The proposed Safe Control for pedicle tapping

The proposed safe control for robot-aided pedicle tapping is shown in the block scheme of Fig. 1. The following steps describe a typical robot-aided pedicle tapping procedure involving the use of the proposed control:

- Robot autonomous positioning: the robot is automatically positioned so as the tapping tool is aligned to the tapping axis, whose orientation is a priori computed based on pre-planned trajectories and thanks to the real-time information provided by an image-guided navigation system.
- Robot-aided tapping: the surgeon manually operate the robot end-effector along the tapping axis and enable the

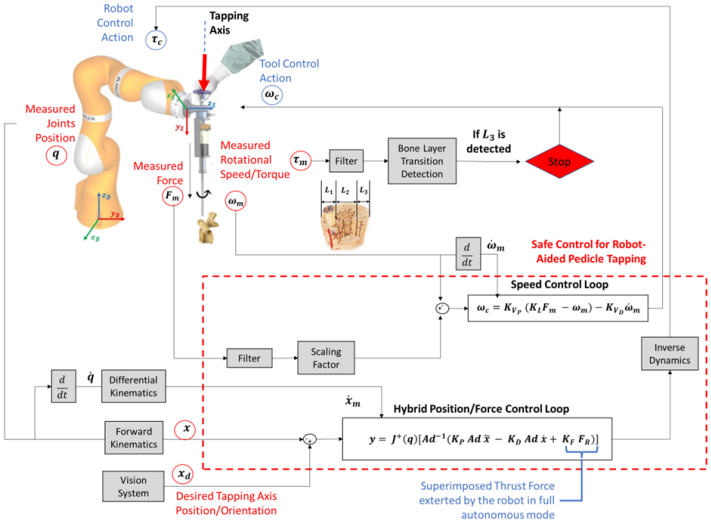


Fig. 1: Scheme of the proposed safe control for robot-aided pedicle tapping

tool rotation by finely tuning the force exerted onto the tool handle.
- Automatic tool stop: During the pedicle tapping, a Bone Layer Transition Detection is used to automatically stop the tool bit before going through the boundaries of the bone.

The following paragraphs report details about i) the robot control loop, ii) the tool motor control loop and iii) the bone layer transition detection algorithm.

B. Robot control Loop

The robot control law is described by the following equations

$$\tau_c = \hat{\mathbf{B}}(\mathbf{q})\mathbf{y} + \hat{\mathbf{C}}(\mathbf{q}, \dot{\mathbf{q}}) + \hat{\mathbf{g}}(\mathbf{q}) \tag{1}$$

$$\mathbf{y} = \mathbf{J}^{\dagger}(\mathbf{Ad}^{-1}(\mathbf{K}_P\mathbf{Ad}\tilde{\mathbf{x}} - \mathbf{K}_D\mathbf{Ad}\dot{\mathbf{x}}_m + \mathbf{K}_F\mathbf{F}_R)] \tag{2}$$

where $\hat{\mathbf{B}}(\mathbf{q})$ is the estimation of robot inertia matrix, $\hat{\mathbf{C}}(\mathbf{q}, \dot{\mathbf{q}})$ accounts for the estimation of the Centrifugal and Coriolis effects, $\hat{\mathbf{g}}(\mathbf{q})$ is the estimation of the gravity contribution, $\mathbf{J}^T$ is the geometric Jacobian transpose, $\mathbf{q}$ and $\dot{\mathbf{q}}$ are the robot joint position and angular velocity, respectively, $\boldsymbol{\phi}$ is the command torque, $\mathbf{J}^{\dagger}$ is the robot geometric [7] Jacobian right pseudo-inverse, $\tilde{\mathbf{x}} = [\tilde{\mathbf{p}}; \tilde{\varphi}]$ is the position error expressed in the base reference frame $[\mathbf{X}_B, \mathbf{Y}_B, \mathbf{Z}_B]$ and $\dot{\mathbf{x}}$ is the robot Cartesian velocity expressed as $\dot{\mathbf{x}} = \mathbf{J}(\mathbf{q})\ \dot{\mathbf{q}}$ (see Fig. 1).

Matrix $\mathbf{Ad}$ in (2) is the adjoint matrix that transforms the velocity error $\dot{\tilde{\mathbf{x}}}$ and the position error $\tilde{\mathbf{x}}$ from the base frame $[\mathbf{X}_B, \mathbf{Y}_B, \mathbf{Z}_B]$ to the end-effector frame $[\mathbf{X}_{ee}, \mathbf{Y}_{ee}, \mathbf{Z}_{ee}]$. It is defined as

$$\mathbf{Ad} = \begin{bmatrix} \mathbf{R}_{ee}^{B} & \hat{\mathbf{p}}_{ee}\mathbf{R}_{ee}^{B} \\ \mathbf{O}_{(3x3)} & \mathbf{R}_{ee}^{B} \end{bmatrix}^T \tag{3}$$

where $\mathbf{R}_{ee}^{B}$ is the rotation matrix that expresses the end-effector orientation with respect to the base frame and $\hat{\mathbf{p}}_{ee}$ is the skew-symmetric matrix of the end-effector Cartesian position $\mathbf{p}_{ee}$.

$\mathbf{K}_P$ and $\mathbf{K}_D$ are the proportional and derivative control gains that are defined as 6×6 positive diagonal matrices $\mathbf{K}_P = diag(k_{P_1}, k_{P_2}, k_{P_3}, k_{P_4}, k_{P_5}, k_{P_6})$ and $\mathbf{K}_D = diag\{k_{D_1}, k_{D_2}, k_{D_3}, k_{D_4}, k_{D_5}, k_{D_6}\}$ where k_{P2} was chosen to be equal to zero so as the position control action has no influence along the Y direction, i.e. the tapping axis.

Conversely, $\mathbf{K}_F$ is a 6×6 identity matrix and $\mathbf{F}_R = [0, f_R, 0, 0, 0, 0]$ is a superimposed force exerted by the robot in an autonomous control mode, or by the surgeon in a semi-autonomous control mode.

C. Tool motor control loop

In the semi-autonomous mode, $\mathbf{f}_R$ is set to zero and the thrust force along the tapping axis is exerted directly by the surgeon. The surgeon can fine-tune the angular velocity of the tool according to the following control law

$$\omega_c = K_{V_P}(K_L F_m - \omega_m) - K_{V_D}\dot{\omega}_m \tag{4}$$

where F_m is the force supplied by the surgeon along the tapping axis (measured by the force/torque sensor put between the tool handle and the motor), K_V is the control gain factor, ω_m is the measured tool rotational speed and K_L is a gain factor used to scale the measured force after filtering.

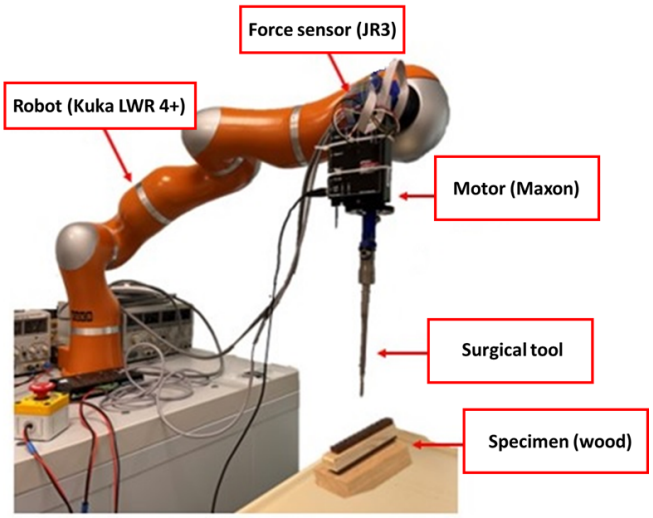


Fig. 2: Experimental setup

D. Bone Layer Transition Detection

Transition among each bone layer is detected on the basis of the the tool torque/current according to the following rules,

$$L = \begin{cases} L_1 & for \quad F(t) < C_1 P \\ L_2 & for \quad C_1 P < F(t) < C_2 P \\ L_3 & for \quad F(t) > C_3 P \end{cases} \tag{5}$$

where C_1, C_2 and C_3 are gain parameters experimentally retrieved, P is a scaling factor that is characteristic for each subject and is the first peak magnitude of the filtered torque and $F(t)$ is a feature function computed on the filtered torque signal as follows,

$$F(t) = \begin{cases} P & for \quad \frac{\tau_F(t) - min(\tau_F)}{P} > 1 \\ P\left(\frac{\tau_F - min(\tau_F)}{P}\right)^3 & for \quad 0 < \frac{\tau_F - min(\tau_F)}{P} < 1 \\ 0 & for \quad \frac{\tau_F(t) - min(\tau_F)}{P} < 1 \end{cases} \tag{6}$$

E. Experimental setup

The experimental setup used to test the proposed safe control for pedicle tapping is shown in Fig. 2. It consists of the following components:

- KUKA LWR 4+: a robotic arm provided with 7 Degrees of Freedom (DoFs) and position and torque sensors enbedded in its joints [8] [9] [10]. Robot Operative System (ROS) ensure the communication between the Kuka controller and a remote PC (UDP communication protocol with a frequency of 500 Hz)
- JR3 force/torque sensor: 6 DoFs force/torque sensor, used to measure the force applied by the surgeon or robot

along the tapping axis. Data acquisition is guaranteed by the DAQ NI USB-6008 device and signal recording and analysis is performed on a workstation under Labview environment
- MAXON EC-max Ø40 mm, brushless, 70W, with Hall sensors: electronically commutated DC motor that is speed-controlled via EPOS2 50/5 which is a modular digital positioning controller. The integrated sensors allow the acquisition of the current signal used for indirect torque measurement
- Surgical tool: used to tap the pedicle screw path. It is provided with a handle on which the user, i.e. the surgeon, can exert a direct force along the tapping axis
- Specimen with similar bone conformation characteristics. The specimen is composed of three layers, namely Upper Layer (UL), Middle Layer (ML) and Lower Layer (LL) whose characteristics are reported below:
  - UL: high density wood material of $8mm$ thickness, reproducing the bone Upper Cortical Layer
  - ML: Low density wood material of $19mm$ thickness, reproducing the bone Middle Spongy Layer
  - LL: high density wood material of $8mm$ thickness, reproducing the bone Lower Cortical Layer

F. Experimental Protocol

The experimental tests were aimed at assessing the capacity of the proposed method to promptly detect transition among different bone layers (measured in terms of time delay between the actual state transition and the detected one) and stop the tool bit before propulsion of the bone.

In a first experimental session, tests were carried out at 6 different thrust forces exerted onto the tool. To guarantee a constant thrust force, the robot again for these trials was piloted in autonomous mode, i.e. the force exerted by the surgeon was simulated by the robot.

In a second experimental session, a human operator was required to perform the specimen tapping by exerting a thrust force along the tapping axis (the orientation of the axis was a priori set to be parallel to the gravity axis). By means of this control modality, the user was able to indirectly tune the tool rotational speed by finely modulating the thrust force. Moreover, thanks to the Bone Layer Transition Detection algorithm, the tool rotation was promptly stopped as the transition between the middle and lower layer was detected.

G. Performance indicators

Three quantitative indicators were computed to assess the system performance in terms of i) capacity of the proposed method to promptly detect transition among different bone layers and ii) capacity of the proposed approach to stop the tool rotation as the transition among the middle and lower layer was detected. They are listed below.

Transition Detection Delay Index: The Transition Detection Delay (TDD) index is calculated as follows

$$TDD = \frac{t_d}{t_p} \tag{7}$$

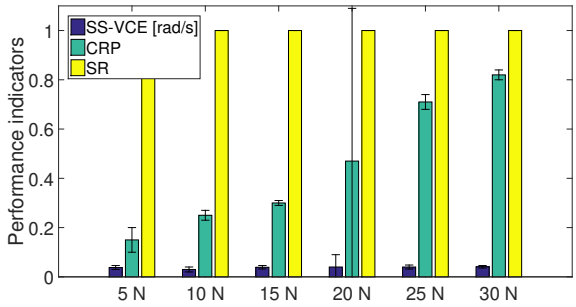


Fig. 3: Results obtained for the 1^{st} experimental session

where t_d is the time elapsed between the time instant when the transition among different specimen layers occurs and the time instant when the proposed Control detects the transition and t_p is the time the tooltip takes to project over the last cortical bone boundaries. t_p is defined as,

$$t_p = \frac{d}{v_t} \tag{8}$$

where d is the thickness of the bone cortical layer (in an adult of medium height this parameter is $2.9mm$ [11]) and v_t is the tool linear velocity.

Control Robustness to Perturbation: The Velocity Control Robustness to Perturbation (CRP) is calculated as follows

$$CRP = \frac{t_c}{t_p} \tag{9}$$

where t_c is the time elapsed between the time instant when a perturbation is given to the control input (i.e. a change in the tool velocity gains due to transition among bone layers) and the time instant when the motor control error reaches $0.05\ \frac{rad}{s}$.

Steady State Velocity Control Error: The Steady State Velocity Control Error (SS-VCE) is used to evaluate the accuracy of the proposed control to track the desired velocity when the thrust force gain parameters are modified according to the bone layer density (in a steady state condition). It is defined as follows,

$$SS - VCE = \|K_L F_m - \omega_m\| \tag{10}$$

Success Rate: The Success Rate (SR) of the tapping execution is evaluated as

$$Success\ rate = \frac{N_{succ}}{N_{tot}} \tag{11}$$

where N_{succ} is the number of trials successfully accomplished and N_{tot} is the number of all the performed trials. A tapping task is considered as successfully accomplished if all the following conditions are satisfied:

- $TDD + CRP < 1$
- $SS - VCE < 0.05\ \frac{rad}{s}$

III. Results and Discussions

Fig. 3 shows the results of the 1^{st} experimental session, i.e. mean value and SD of the CRP, SS-VCE and SR for each of the 6 tested thrust forces. As evident from the figure, the proposed control performance in terms of SS-VCE does not vary significantly as the thrust force increase; comparable errors have been obtained for all the tested forces. Moreover, it is worth noticing that the CRP is always lower than 1, meaning that the time required for the motor to stop is always lower than the time that tooltip takes to project over the specimen boundaries, at a given velocity. Hence, the tapping procedure could be considered successfully accomplished for all the tested forces, resulting in a success rate of 100%.

The results are also confirmed by the ones obtained during the 10 trials performed by the recruited subject ($SS-VCE = 0.06 \pm 0.09\ rad/s$; and $CRP = 0.19 \pm 0.07$) who exerted a mean thrust force of $15 \pm 5N$ during the 10 trials.

IV. Conclusion

In this paper, a Safe Robot Control for pedicle tapping based on bone layers transition detection has been proposed. The proposed approach is able to detect the bone layer density and promptly stop the surgical tool movements before projecting over the bone boundaries.

The ability of the proposed method to detect transition among different bone layers identification has been evaluated in terms of elapsed time between the time instant when the transition is detected and the time instant when the transition actually occurs. This delay has been compared to time that tooltip takes to project over the bone boundaries in order to evaluate the success rate of the tapping execution. A success rate of 100% has been achieved for all the tests.

Acknowledgment

This work was supported in part by the European Union's Horizon 2020 Research and Innovation Program with the Leveraging AI based technology to transform the future of health care delivery in Leading Hospitals in Europe (ODIN) Project under Grant Agreement 101017331 (CUP: C85F21000670006).

References

[1] N Boos and JK Webb. Pedicle screw fixation in spinal disorders: a european view. *European Spine Journal*, 6(1):2–18, 1997.

[2] Serkan Erkan, Brian Hsu, Chunhui Wu, Amir A Mehbod, John Perl, and Ensor E Transfeldt. Alignment of pedicle screws with pilot holes: can tapping improve screw trajectory in thoracic spines? *European Spine Journal*, 19(1):71–77, 2010.

[3] Alexander Ghasem, Akhil Sharma, Dylan N Greif, Milad Alam, and Motasem Al Maaieh. The arrival of robotics in spine surgery: a review of the literature. *Spine*, 43(23):1670–1677, 2018.

[4] Haiyang Jin, Ying Hu, Wei Tian, Peng Zhang, Zhangjun Song, Jianwei Zhang, and Bing Li. Kinematics and cooperative control of a robotic spinal surgery system. *Robotica*, 34(1):226–242, 2016.

[5] Ying Hu, Haiyang Jin, Liwei Zhang, Peng Zhang, and Jianwei Zhang. State recognition of pedicle drilling with force sensing in a robotic spinal surgical system. *IEEE/ASME Transactions On Mechatronics*, 19(1):357–365, 2013.

[6] Clemente Lauretti, Francesca Cordella, Christian Tamantini, Cosimo Gentile, Francesco Scotto di Luzio, and Loredana Zollo. A surgeon-robot shared control for ergonomic pedicle screw fixation. *IEEE Robotics and Automation Letters*, 5(2):2554–2561, 2020.

[7] Clemente Lauretti, Tiberio Grasso, Eliana de Marchi, Stanislao Grazioso, and Giuseppe di Gironimo. A geometric approach to inverse kinematics of hyper-redundant manipulators for tokamaks maintenance. *Mechanism and Machine Theory*, 176:104967, 2022.

[8] Rocco A Romeo, Clemente Lauretti, Cosimo Gentile, Eugenio Guglielmelli, and Loredana Zollo. Method for automatic slippage detection with tactile sensors embedded in prosthetic hands. *IEEE Transactions on Medical Robotics and Bionics*, 3(2):485–497, 2021.

[9] Clemente Lauretti, Francesca Cordella, Francesco Scotto di Luzio, Stefano Saccucci, Angelo Davalli, Rinaldo Sacchetti, and Loredana Zollo. Comparative performance analysis of m-imu/emg and voice user interfaces for assistive robots. In *2017 International Conference on Rehabilitation Robotics (ICORR)*, pages 1001–1006. IEEE, 2017.

[10] Clemente Lauretti, Francesca Cordella, and Loredana Zollo. A hybrid joint/cartesian dmp-based approach for obstacle avoidance of anthropomorphic assistive robots. *International Journal of Social Robotics*, 11(5):783–796, 2019.

[11] SH Zhou, ID McCarthy, AH McGregor, RRH Coombs, and SPF Hughes. Geometrical dimensions of the lower lumbar vertebrae–analysis of data from digitised ct images. *European Spine Journal*, 9(3):242–248, 2000.

Evaluating Spatial Hearing in Virtual Reality Environment

F.Missoni[1] and A.Canessa[1]
[1] *University of Genoa, Department of Informatics, Bioengineering, Robotics and System Engineering-DIBRIS*

***Abstract*—Experimental protocols used in multisensory studies are typically simplified with basic stimuli, in contrast with the complexity of real-world situations. Virtual Reality (VR) and binaural audio technologies pose an opportunity to provide multisensory stimulation in ecological conditions and in a controlled way. The Head-Related Transfer Function (HRTF), which describes the interaction of sound with head and torso, is the most common used binaural spatialization technique. However, non-individual (or generic-) HRTFs are typically used leading to incorrect perception of sound locations. In such context, a common selection procedure of the subjective optimal HRTF is needed. In that work, we investigate the auditory spatial perception with two generic HRTFs in a sound localization task. Moreover, the perceptual similarities between two HRTFs, at individual level, was discussed. Results suggest no statistical significance difference between two chosen HRTFs set in the tested group.**

***Keywords*—Spatial Audio, Binaural Audio, HRTF, Multisensory integration, Virtual Reality.**

I. Introduction

Our brain is able to construct a robust interpretation of the space surrounding us by merging stimuli of different nature (visual, haptic, auditory, etc…). Understanding the underlying mechanisms is one of the key objectives in different fields such as rehabilitation in sensory deficit [1]–[2], neuroscience [3], etc. However, actual experimental paradigms use simplified protocols with basic stimuli, which are unable to capture characteristics of real-world situations that typically are three dimensional, dynamic and complex.

In this context, Virtual Reality (VR) technology represents an opportunity to investigate cross-modal interaction processes that occur in naturalistic environment in a controlled way. More precisely, the use of VR has the advantage to build scalable and reproducible experimental situations with high level of realism and immersivity by employing a relatively low-budget technology [11]-[12]. Recent developments have enriched the virtual experience making use of spatial audio tools (known as Binaural Audio), that allow the creation of three-dimensional soundscapes simply using a pair of headphones as a playback device. A widely used technology consists in the so-called Head Related Impulse Response (HRIR; or its equivalent in frequency domain: Head Related Transfer Function, HRTF), in conjunction with the Binaural Room Impulse Response (BRIR). More in detail, the HRTF is used to describe the change in sound spectrum due to the interaction of sound waves with the listener's torso, head and pinna [5] which embeds localization cues–such as Interaural Time Differences (ITDs), Interaural Level Differences (ILDs), and spectral cues–within the original sound stimuli [6]. The BRIR incorporates in the virtual simulation the acoustical properties of an indoor environment (e.g., reverberation). Because measurements of individual-HRTF are costly and difficult procedures, generic-HRTF are typically used [7], although they provide a worse spatial perception in terms of localization accuracy [8] and confusion over auditory source location [9]. However, the results regarding such limitations are mixed, and other cues, such as reverberation, head movement, and vision, may be more critical factors for robust auditory spatial perception [10].

The aim of this work is the characterization of the individual's auditory spatial perception in a 3D soundscape rendered using binaural audio. In particular, we evaluate the accuracy in localization of a virtual sound source synthesized using non-individual HRTFs: a commonly used evaluation method [13]—[14]. Finally, to select the best HRTF in terms of spatial perception, the perceptual differences within two non-individual HRTFs from IRCAM Listen database (Ircam listen HRTF database, [14]) was investigated.

II. Materials and methods

A. Experimental Setup

The system consists of VR Headset (HTC VIVE Pro), hand VIVE controller and a pair of headphone Sennheiser HD 280 Pro. The VR system is real-time tracked by means of two infrared cameras fixed at the corner of the experimental area. Such tracking system allows to the participant to freely interact in the virtual environment with head and hands movements. The application has been developed by means of Unity 3D; SteamVR 2.0 system was used to define custom behaviour of VIVE controller during the experiment.

As regards the spatial audio engine, the Unity Wrapper of the open-source toolkit 3D Tune-In Toolkit [17] was employed. More in detail, sounds were spatialized using two HRTFs, from the IRCAM Listen database, and a generic BRIR filter synthesized for an empty room of 7x7x3m. Two employed HRTFs correspond to subject IDs IRC0008 and IRC0013 within the database. Active listening is supported by spatial audio engine and real-time tracking system.

Finally, custom-written MATLAB (MATLAB R2021b) scripts were used to generate auditory stimuli.

B. Experimental protocol

Eight participants with normal hearing (mean age 27 y, range 25–29 y) were tested in a sound localization task. During the experiment participants sat on an office chair, in a silent room, listening to the binaural recordings over headphones. Experimental procedure consists in two subsequent sessions: familiarization (see Fig.1) and test, both with no fixed time duration. In the first phase, a set of interactable loudspeakers were located inside the room

around the virtual listener, each one at different location, to familiarize with auditory space. In the next phase, sound localization task with no visual targets was performed. A virtual button positioned in front of the user was used to initiate playback of a complex auditory stimuli, randomly chosen within a set of 19 radio-like communications with time duration of 1.6s. More in detail, the structure of the stimulus consisted in a pink noise burst of 200ms, followed by 1s of female English speech with low level pink noise (SNR equal to 25dB), an another 200ms pink noise burst and, a final, 1kHz tone of 200ms, as described in [16]. Instructions of the experiment was conveyed to the player using a Head-up Display (HUD).

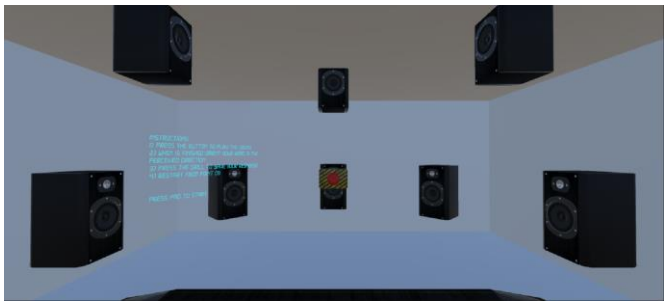


Fig. 1: Screenshot of virtual player view in the virtual reality room during familiarization phase. Virtual button (ahead) initiated playback of spatialized stimulus. Head-up display (HUD) on the left was used to convey instructions to the player

Participants were instructed to start each trial by means of the virtual button and, when the stimulus is finished, orient their head in the perceived direction. Response is saved by pressing a VIVE controller button.

During test block, the two generic HRTFs were switched randomly at each trial. For each one, stimuli were presented in a casual order along twelve different orientations around listener head, each one repeated for $n = 10$ times. Eight were defined at 0° elevation, with azimuths steps of 45°. A further four orientations were defined at 45° elevation with azimuths equal to 45°, 135°, 225° and 315°. Distance from head subject of each trial was chosen randomly between 0.8, 1.4 or 2.0 meters. In summary each subject was tested on $2 * 12 * 10 = 240$ trials.

C. Data Analysis

Data were analysed in MATLAB R2021b, removing outliers meant as trials in which the orientation of the head-mounted display deviated by more than 6° in any direction. Spatial locations are represented in a single-pole coordinate system. More in detail, horizontal location are identified by azimuth θ, defined as the right-handed rotation around vertical axis that passing through the centre of the HMD position with 0° being forward direction; the vertical location are specified by the elevation angle ϕ, that referrers to the angle subtended at the center of the head relative to the horizontal plane, with 0° being horizontal orientation and 90° being vertical orientation.

To evaluate sound localization accuracy two localization unsigned error are used. The former is the **polar error**, defined as the absolute value of the difference between target horizontal location and response horizontal orientation of the head. The rate of trials in which polar error is greater or equal to 60° is defined as *front-back confused* trial. Front-back confusion is the rate of front/back confused trials. The latter, **spherical error**, is defined as the absolute difference between target and response location.

III. Results

Front/back confusion rate is similar within group for two HRTFs (IRC0008, mean = 25.73%, SD = 3.32; IRC0013, mean = 23.44%, SD = 3.71). Fig.2 shows the mean localization error (spherical (a) and polar (b) error) pooled across all participants, as a function of target azimuth, for both conditions (IRC0008 and IRC0013).

The largest accuracy in localization error was observed when the virtual sources were placed laterally, as opposed to the frontal and rear positions resulting in the lowest accuracy, with both HRTFs.

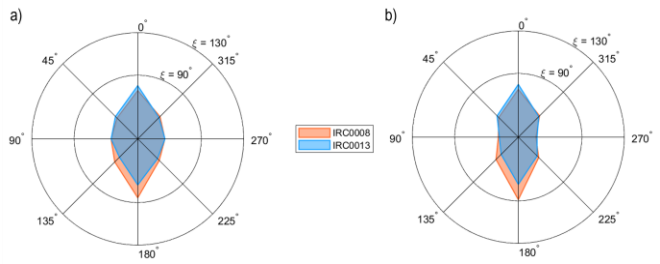


Fig.2: Mean spherical and polar error averaged across participants for the two HRTFs

Subsequently, to investigate individual perceptual dissimilarities with two HRTFs, a one-way ANOVA was conducted. Such analysis indicates no statistically significant difference in localization error distribution within two HRTFs in any subject: F(1,1918) = 2.24, $p = 0.135$ (spherical error) and F(1,1918) = 1.91, $p = 0.167$ (polar error). Fig.3 shows spherical (a) and polar (b) error distribution in both conditions and for each participant.

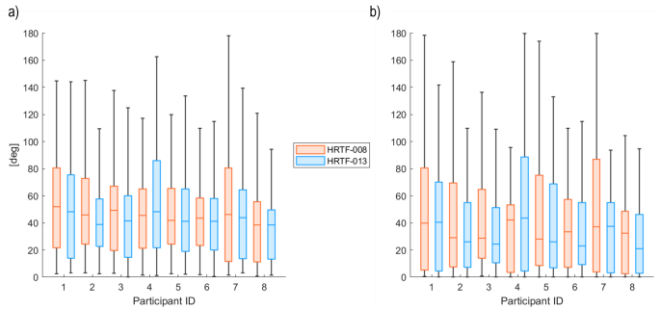


Fig.3 Spherical (a) and polar (b) error distribution for both HRTFs (red: IRC0008, blue: IRC0013) in each participant

IV. Conclusion

A preliminary analysis on sound localization task in virtual reality with two distinct generic-HRTFs has been conducted. Overall, the level of directionality perception and front/back confusion, supports previous findings of several similar studies (see [9]-[16]). Moreover, we investigated the perceptual differences in terms of localization error, within two non-individual HRTFs set from IRCAM Database. No

significant statistical differences were found in any subject suggesting that the two chosen HRTFs are close in terms of perceptual similarities. However, because of the small size of data set, further and more accurate analysis is required. In fact, to investigate the perceptual equality of two HRTFs some metrics can be employed to evaluate spectral differences between two HRTFs such as spectral distortion [20] and auditory models for human sound localization [19].
Moreover, a potential improvement in evaluate sound localization accuracy could be obtained by means of a different coordinate system inspired by binaural hearing (known as interaural-polar coordinate system [16]), that employs coordinates related to localization cues.
Future perspectives consist in improve the acoustic individual realism of the virtual environment. In the recent years, several methodologies have been proposed such as HRTF personalization [7], training paradigms [16] or generic-HRTF recommendation based on perceptual similarities and anthropometric features [18]. The key idea is to employ such technology in a multimodal virtual reality platform to study multisensory integration processes in ecological and controlled situations.

REFERENCES

[1] Tinga, A. M., Visser-Meily, J. M. A., van der Smagt, M. J., Van der Stigchel, S., van Ee, R., & Nijboer, T. C. W. (2016). Multisensory stimulation to improve low-and higher-level sensory deficits after stroke: a systematic review. Neuropsychology Review, 26(1), 73-91.

[2] Bolognini, N., & Vallar, G. (2020). Hemianopia, spatial neglect, and their multisensory rehabilitation. In Multisensory Perception (pp. 423-447). Academic Press.

[3] Stein, B. E. (Ed.). (2012). The new handbook of multisensory processing. Mit Press.

[4] van der Stoep, N., Serino, A., Farnè, A., Di Luca, M., & Spence, C. (2016). Depth: the forgotten dimension in multisensory research. Multisensory Research, 29(6-7), 493-524.

[5] Cheng, C. I., & Wakefield, G. H. (1999, September). Introduction to head-related transfer functions (HRTFs): Representations of HRTFs in time, frequency, and space. In Audio Engineering Society Convention 107. Audio Engineering Society.

[6] Blauert, J. (1997). Spatial hearing: the psychophysics of human sound localization. MIT press.

[7] Li, S., & Peissig, J. (2020). Measurement of head-related transfer functions: A review. Applied Sciences, 10(14), 5014.

[8] Middlebrooks, J. C. (1999). Individual differences in external-ear transfer functions reduced by scaling in frequency. The Journal of the Acoustical Society of America, 106(3), 1480-1492.

[9] Wenzel, E. M., Arruda, M., Kistler, D. J., and Wightman, F. L. (1993). Localization using nonindividualized head-related transfer functions. J. Acoust. Soc. Am. 94, 111–123. doi: 10.1121/1.407089

[10] Rummukainen, O. S., Robotham, T., & Habets, E. A. (2021). Head-Related Transfer Functions for Dynamic Listeners in Virtual Reality. Applied Sciences, 11(14), 6646.

[11] Hohmann, V., Paluch, R., Krueger, M., Meis, M., & Grimm, G. (2020). The virtual reality lab: Realization and application of virtual sound environments. Ear and Hearing, 41(Suppl 1), 31S.

[12] Keidser, G., Naylor, G., Brungart, D. S., Caduff, A., Campos, J., Carlile, S., ... & Smeds, K. (2020). The quest for ecological validity in hearing science: What it is, why it matters, and how to advance it. Ear and hearing, 41(Suppl 1), 5S.

[13] Hofman, P. M., Van Riswick, J. G., & Van Opstal, A. J. (1998). Relearning sound localization with new ears. Nature neuroscience, 1(5), 417-421.

[14] Wightman, F. L., & Kistler, D. J. (1992). The dominant role of low-frequency interaural time differences in sound localization. The Journal of the Acoustical Society of America, 91(3), 1648-1661.

[15] Warusfel, O. (2003). Listen HRTF database. online, IRCAM and AK, Available: http://recherche. ircam. fr/equipes/salles/listen/index. html.

[16] Steadman, M. A., Kim, C., Lestang, J. H., Goodman, D. F., & Picinali, L. (2019). Short-term effects of sound localization training in virtual reality. Scientific Reports, 9(1), 1-17.

[17] Cuevas-Rodríguez, M., Picinali, L., González-Toledo, D., Garre, C., de la Rubia-Cuestas, E., Molina-Tanco, L., & Reyes-Lecuona, A. (2019). 3D Tune-In Toolkit: An open-source library for real-time binaural spatialisation. PloS one, 14(3), e0211899

[18] Pelzer, R., Dinakaran, M., Brinkmann, F., Lepa, S., Grosche, P., & Weinzierl, S. (2020). Head-related transfer function recommendation based on perceptual similarities and anthropometric features. The Journal of the Acoustical Society of America, 148(6), 3809-3817.

[19] Engel, I., Goodman, D. F., & Picinali, L. (2022). Assessing HRTF preprocessing methods for Ambisonics rendering through perceptual models. Acta Acustica, 6, 4.

[20] Jo, H., Park, Y., & Park, Y. S. (2009, August). Analysis of individual differences in Head-Related Transfer Functions by spectral distortion. In 2009 ICCAS-SICE (pp. 1769-1772). IEEE.

A cloud-based mobile platform to monitor and counteract cognitive decline

L. Bandini[1], C. De Vicariis[1], M.C. Novello[2], C. Chiorri[3] and V. Sanguineti[1]
[1] *Department of Informatics, Bioengineering, Robotics and Systems Engineering, University of Genoa, Genoa, Italy*
[2] *Clinical Psychology Unit, Galliera Hospital, Genoa, Italy*
[3] *Department of Educational Sciences, University of Genoa, Genoa, Italy*

***Abstract*—Subjective cognitive decline (SCD) and Mild Cognitive Impairment (MCI) are receiving increasing attention as risk factors for incident dementia. Cognitive training has been reported to delay and/or counteract cognitive decline. During the last years, software applications have been increasingly used to support cognitive training. Here we describe a mobile platform which has been specifically designed for cognitive training and assessment. Subjects use the application to play a variety of exergames and all their actions and performance are recorded into a cloud database. Therapists can monitor subjects performance using the database interface. The application currently focuses on training attention, memory and executive functions, which are some of the functions mostly involved in deterioration. We carried out two preliminary studies. The first study involves healthy subjects of different ages (15-19, 20-30 and 50-65 years old). We also ran a preliminary acceptance study, involving persons with SCD. In all games, performance varies with age. We also found that there is a good acceptance of the application in persons with SCD. We conclude that the application is a promising tool to assess cognitive functions.**

***Keywords*—Cognitive training, mobile health, telehealth.**

I. INTRODUCTION

Dementia is defined as a deterioration of cognitive function – usually of chronic or progressive nature – 'beyond what might be expected as a consequence of biological ageing'. In the last ten years, research has been focused on identifying early predictors of dementia onset.

Persons experiencing a subjective decrease in cognitive functions, with no evidence of objective complaints – Subjective Cognitive Decline (SCD) [1] – exhibit an increased risk of subsequent objective cognitive decline, which may progress into Mild Cognitive Impairment (MCI). From [2], the annual conversion rate from SCD to MCI is 6.6%, while it is 2.3% to dementia, compared with 1% in those without subjective decline. These results have recently been confirmed by [3], a meta-analysis addresses to evaluate the rate of incidence of MCI and dementia in persons with SCD, and also factors which might influence the relationship between SCD and the risk of future decline. After the onset of the COVID-19 pandemic in 2020, the incidence of people with cognitive impairment has been reported to increase [4]. Attention, memory, language and executive functions are the aspects of cognitive functions that are most frequently involved in SCD.

Training strategies have been designed to enhance individual capacity to process and interpret information. While there are no effective treatments for dementia, evidence suggests that cognitive training may have a long-term impact and might enhance cognition in face of future brain changes. For instance, sustained effects of cognitive training have been demonstrated on ageing [5]. As cognitive training programs must be intensive and prolonged over time, information and communication technologies have been increasingly regarded as potentially effective options to support cognitive rehabilitation [6].

Several recent reviews have summarized the most widely used applications. Reference [7] examined different studies on seven commercial training programs within two separate populations: healthy older adults and older adults with MCI. Findings suggest that improvements in cognitive functions using training strategies were limited to tasks similar to the proposed training game. References [7] and [8] analyze individual cognitive domains for healthy subjects and yielded effects for some cognitive functions such as executive functions, memory and processing speed, but not objective measures for attention.

As these applications were not specifically designed for clinical studies, participants' strategies and performance games were not considered in the analysis, which mostly focused on general outcome measures before and after training (for a review see [9], [10]). A more controlled setting may potentially provide information on how cognitive decline affects player performance and evolve over time.

Here we present a novel mobile (Android) application, specifically aimed at telemonitoring of cognitive performance of the outpatients of the Center for Cognitive Disorders and Dementia of the Galliera Hospital, Genoa with SCD episodes. The app – Allenamento Personalizzato Preventivo, or Personalized Preventive Training (APP Galliera) – has been originally developed as a substitute for in-presence periodic assessments during the COVID-19 pandemic, and has been specifically designed to train attention, memory and executive functions. The app makes games available to users and records both game performance and individual moves during each game. This information is stored into a dedicated cloud-based database. Through a custom dashboard, therapists may provide individual users with specific training prescriptions and can monitor game use and ongoing performance, so that changes in performance can be promptly identified. We also present preliminary results from game use in two populations

of subjects: (i) persons with no signs of cognitive decline, stratified by age groups; (ii) persons with SCD.

II. Materials and Methods

A. Platform architecture

The platform consists of an Android application connected to a cloud database where game data is stored; see Figure 1. The application includes different exergames, which are developed to assess – and train through repeated performance – a specific cognitive function. Individual game records are collected into a Cloud Firestore (Firebase) database – a non-relational document database, which allows more flexibility in representing game-specific information. The cloud-based database is compliant with the EU General Data Protection Regulation (GDPR) legal framework. The database keeps track of the list of authorised application users and records performance for each game, and each move within a game. All data are made available to the therapist through the standard web-based interface. Every time the application is run, the user must authenticate through a one-time password (OTP). A cognitive training session typically involves playing different games, possibly multiple times. The application has been developed using Android Studio IDE. The games have been implemented using the LibGDX game engine.

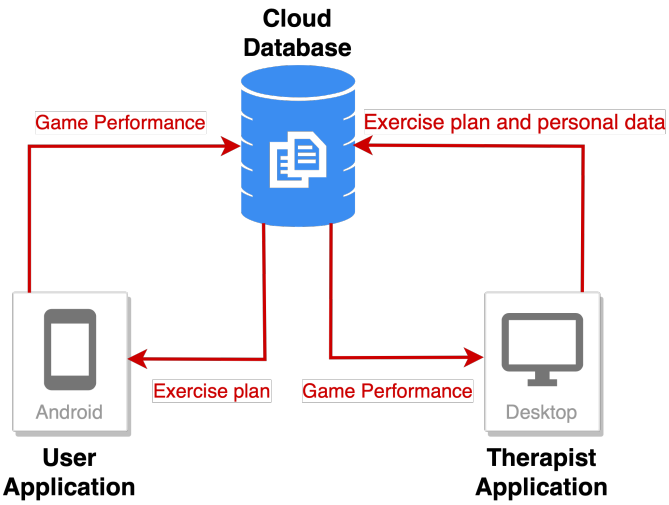


Fig. 1: System architecture. The platform involves a user application, a cloud database and a therapist dashboard

B. Cognitive training games

The application currently offers five games (see Figure 2), each aimed at a specific cognitive domain. Games have been designed to recall daily life activities.

1) Bird: The game focuses on attention and is inspired by the Attention Network Test (ANT)[11]. A flying bird (a swallow) is displayed on the screen. Players must indicate whether the bird is flying by pressing the arrow buttons placed in the bottom region of the screen. There are three difficulty levels: (i) the stimulus (bird) is displayed in isolation, or with other birds (flankers) flying (ii) in the same (congruent) or (iii) opposite (incongruent) direction. The response time (time delay between stimulus onset and user response) is taken as a measure of attention. Errors and flankers are also recorded, so that it is also possible to quantify the effect of flankers on response time.

2) Waste Sorting: In this game – focused on executive functions – the goal is to sort the garbage items that appear on the screen, by putting them into the right trashcan (plastic, glass, paper, and compost waste). There are two levels of difficulty: the garbage items are displayed in the same colour as the correct trashcan, or they are displayed in their natural colour. As before, performance is measured in terms of response time and errors.

3) Key: In this game – also related to executive functions – the goal is to open the door by matching the keyhole with one among the available keys. Response time is taken as a measure of performance; errors are also recorded.

4) Cart: In this game, the action takes place in a supermarket. A list of ingredients is displayed first. The goal is to move a cart in order to catch the items falling down from a shelf. The food items that are not part of the recipe must be ignored. There are different difficulty levels, corresponding to different fall velocities. The game relates to attention and executive functions. Performance is measured by the number of correct catches, which must be put in relation to game difficulty.

5) Memory: The game is an implementation of the popular card game known as Memory or 'concentration' and is related to working memory. A deck of $2n$ cards is displayed (covered) on the screen. Players must turn pairs of cards. If the cards are identical, they are left uncovered and one point is scored. Otherwise, they are covered again. Game performance is related to the number of moves needed to uncover all pairs of cards. Response time is also recorded. Depending on game performance, the number n of card pairs could vary in the next game ($n = 3, 4, 6, 8$). The number of moves required to end the game is related to memory span – the amount of items a player can simultaneously remember. For each move in a game, the application records the value and location (row, column) of the cards selected in a trial, whether the match is correct and the time elapsed from the selection of the first and second cards. It should be noted that different from the other games, performance is not only determined by the skill of the player but also has a chance element – depending on the location of the matching pairs[12].

During a game, game-specific information is saved in the database, which belongs to two broad categories: (i) Context data: all attributes of a single trial of the game, e.g. game modality, difficulty level, etc; (ii) Action data: description of user moves and game performance.

C. Experiments

1) Study 1: age-related differences in game performance: A total of 15 subjects with no evidence of cognitive and motor impairments, were assigned to three age groups: age 15-19 (4M+1F); 20-30 (3M+2F); and 50-65 (2M+3F). Participants



Fig. 2: Game screens. The application includes five games, from the left: bird, waste sorting, cart, key and memory.

were required to play all games once a day for five consecutive days.

2) Study 2: user experience: The study involved seven subjects (2M+5F) with age 59-82 and early signs of cognitive impairment (SCD: 6, MCI: 1). Participants were free to use the application whenever they wanted during the first week from installation.

III. Results

A. Study 1: age-related differences in game performance

One 15-19 subject did not complete the experimental protocol and was excluded from the analysis. In each game, the first answer of the first time playing was excluded from the evaluation.

1) Bird: Game performance (response time of correct answers, in different conditions and age groups) is depicted in Figure 3. Response time is consistently greater when age increases. Inconsistent with ANT outcomes, we observed a decrease in the response time from the simpler (no flankers) to the more complex condition (incongruent flankers). This effect could be explained with the progressive nature of the game – subjects played with the highest level of difficulty always after training with the lower levels.

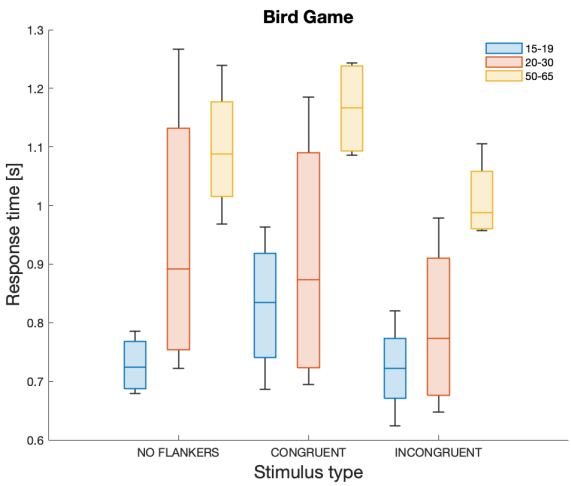


Fig. 3: Bird Game: Response time (correct answers only) for different stimulus types, per age group.

2) Waste Sorting: This game also involved different situations. In trials with no colour cue, the response time was generally shorter – possibly a learning effect as the colour cue was only provided in early trials. Or, colour cues actually made identification of the garbage item more difficult (performance data not shown).

3) Key: We found a degradation of performance (greater response time) in the 50-65 age group; see Figure 4.

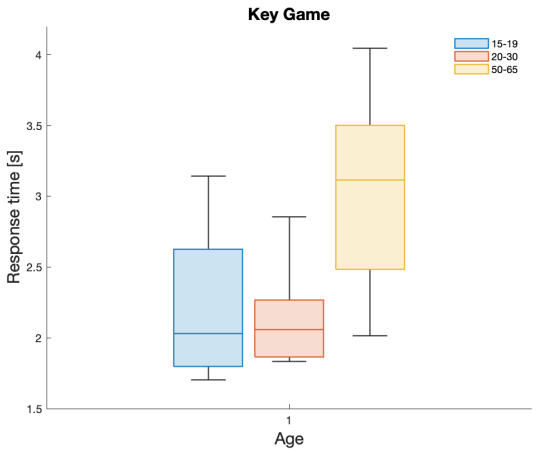


Fig. 4: Key Game: Response time per age group.

4) Cart: Performance (mean number of correct answers, i.e. the number of items that were in the recipe and were taken, plus those that were not in the recipe and were not taken) decreases with age (results no shown).

5) Memory: The mean number of moves suggests no clear group difference when looking at the late performance (the

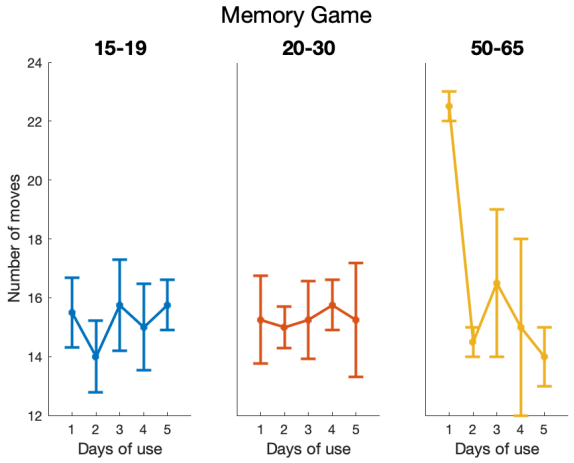


Fig. 5: Memory Game. Number of moves (Mean ± SE) per age group, across days of use.

fifth day of usage). However, across days, a learning effect seems to be only observed in the 50- 65 group (results no shown). Because of the chance element, the number of moves for a given skill (memory span) is a random variable. Theoretical analysis of optimal performance [12] predicts that in the case of perfect memory (infinite memory span), the average number of moves to complete the game is $1.6n$ where n is the number of pairs. In contrast, with no memory (zero memory span) the game is completed on average in n^2 moves. In the experiment, we set $n = 8$, corresponding to a number of moves ranging from 12.8 (perfect memory) to 64 (no memory).

B. Study 2: user experience

Figure 6 summarises the user activity during the first week of use. More than 70% of users actually used the platform at least once (Large and Medium Users), and 57% used it more than three times. This figure suggests that there is an interest in using the platform. A more thorough analysis, involving questionnaires on user experience is currently under way.

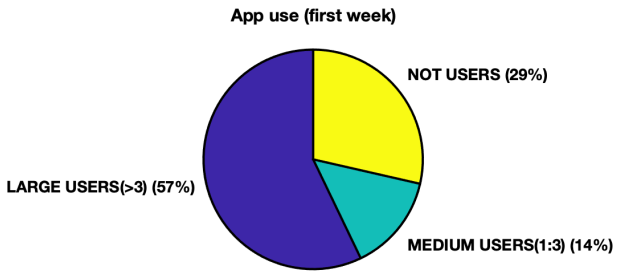


Fig. 6: App use during the first week from installation. Large users played more than three times, medium from one to three times, not users didn't use it.

IV. Conclusion

We have developed a mobile platform for cognitive training, intended for monitoring and counteract cognitive decline. The medical staff at the hospital can monitor the performance of the subjects using the interface of the cloud database where all data is saved. Preliminary results suggest that games developed are able to detect age-dependent differences in cognitive performance. Early results also suggest partly divergent requirements for monitoring and training functionality. While monitoring of multifaceted functions like attention requires randomization of stimulus conditions (i.e. congruent vs incongruent stimuli), promoting engagement requires a gradual increase of exercise difficulty, which may introduce learning effects that need to be acknowledged when interpreting performance. Preliminary results also suggest that the use of the application with persons with SCD/MCI is feasible and well accepted. A full clinical study is under way. The current version of the app has five exercises which target different cognitive functions and a basic therapist interface, but the platform can be easily extended to cover additional cognitive functions, like language processing, and the further development of the therapist interface, equipped with a dashboard to monitor the performance of multiple patients and with the option to set-up personalised exercise schedules.

References

[1] Jessen *et al.*, "The characterisation of subjective cognitive decline," *The Lancet Neurology*, vol. 19, no. 3, pp. 271–278, 2020.
[2] A. J. Mitchell, H. Beaumont, D. Ferguson, M. Yadegarfar, and B. Stubbs, "Risk of dementia and mild cognitive impairment in older people with subjective memory complaints: meta-analysis," *Acta Psychiatrica Scandinavica*, vol. 130, no. 6, pp. 439–451, 2014.
[3] K. E. Pike, M. G. Cavuoto, L. Li, B. J. Wright, and G. J. Kinsella, "Subjective cognitive decline: level of risk for future dementia and mild cognitive impairment, a meta-analysis of longitudinal studies," *Neuropsychology review*, pp. 1–33, 2021.
[4] L. e. a. Crivelli, "Changes in cognitive functioning after COVID-19: A systematic review and meta-analysis.," *Alzheimer's dementia : the journal of the Alzheimer's Association*, vol. 6, pp. 89–106, 2022.
[5] Rebok *et al.*, "Ten-year effects of the advanced cognitive training for independent and vital elderly cognitive training trial on cognition and everyday functioning in older adults," *Journal of the American Geriatrics Society*, vol. 62, no. 1, pp. 16–24, 2014.
[6] E. Mantovani, C. Zucchella, S. Bottiroli, A. Federico, R. Giugno, G. Sandrini, C. Chiamulera, and S. Tamburin, "Telemedicine and virtual reality for cognitive rehabilitation: a roadmap for the COVID-19 pandemic," *Frontiers in Neurology*, vol. 11, p. 926, 2020.
[7] L. Nguyen, K. Murphy, and G. Andrews, "A game a day keeps cognitive decline away? a systematic review and meta-analysis of commercially-available brain training programs in healthy and cognitively impaired older adults," *Neuropsychology Review*, pp. 1–30, 2021.
[8] B. Bonnechère, C. Langley, and B. J. Sahakian, "The use of commercial computerised cognitive games in older adults: a meta-analysis," *Scientific Reports*, vol. 10, no. 1, p. 15276, 2020.
[9] Yousaf *et al.*, "Mobile-health applications for the efficient delivery of health care facility to people with dementia (pwd) and support to their carers: a survey," *BioMed Research International*, vol. 2019, 2019.
[10] Gates *et al.*, "Computerised cognitive training for preventing dementia in people with mild cognitive impairment," *Cochrane Database of Systematic Reviews*, no. 3, 2019.
[11] M. I. Posner and S. E. Petersen, "The attention system of the human brain," *Annu Rev Neurosci*, vol. 13, pp. 25–42, 1990.
[12] D. J. Velleman and G. S. Warrington, "What to expect in a game of memory," *The American Mathematical Monthly*, vol. 120, no. 9, pp. 787–805, 2013.

GNB2023, June 21st-23rd 2023, Padova, Italy

Non-linear dimensionality-reduction approach for powered wheelchair control

E. Misley[1*], F. Rizzoglio[1,2*], A. Bellitto[1,3], A. Massone[3], D. Russo[4], G Carlini[1], M. Casadio[1,3,6] and C. Pierella[1,5,6]
[1] *DIBRIS, University of Genoa, Genoa, Italy*
[2] *Department of Neuroscience, Northwestern University, Chicago, IL*
[3] *Spinal Cord Italian Lab (SCIL), Santa Corona Hospital, Pietra Ligure*
[4] *Ottobock, Genoa, Italy*
[5] *DINOGMI, University of Genoa, Genoa, Italy*
[6] *RAISE Ecosystem, Genova, Italy*

***Abstract*— People with severe body paralysis mainly rely on the use of powered wheelchairs to move autonomously without the assistance of a caregiver. Nowadays powered wheelchairs offer a large variety of controllers, which span from the most common joystick to more sophisticated systems such as the sip-and-puff or the head array. Most of this device use a discrete variable as control inputs, while little effort has been devoted to investigating the possibilities offered by continuous control. Only recently, a powered wheelchair control interface that uses instantaneous upper body-configuration signals to generate powered wheelchair commands was developed, through the application of linear dimensionality reduction (DR) methods. However, DR methods may not be able to capture the non-linear nature of the input data, leading to overestimation of their actual dimensionality. Therefore, in this work we propose a possible solution to overcome the abovementioned restriction based on employing non-linear DR techniques, which could be more efficient in capturing the structure of the input data and, therefore, might improve the control of the devices. In particular, we developed a non linear autoencoder network using the units of its bottleneck as control commands for the powered wheelchair. Such interface was tested with a proof-of-concept experiment involving a single subject successfully performing a variety of tasks while controlling a real powered wheelchair. Our findings suggests that non linear DR methods could lead to a more efficient control for a powered wheelchair interface compared to linear DR methods.**

***Keywords*— Body-Machine Interface, powered wheelchair, Dimensionality Reduction Methods, Autoencoders networks**

I. INTRODUCTION

Body Machine Interfaces (BoMIs) define a way to interact with different types of devices, allowing their users to overcome the limits of their motor abilities by exploring their body's redundancy. Among the many different types of devices that can be controlled through a BoMI, this paper focuses on powered wheelchairs. These represent one of the most effective ways to move autonomously for people who are unable to self-propel a manual wheelchair, for example, people with both lower and upper-body paralysis deriving from a high-level Spinal Cord Injury (SCI). The remaining upper extremity function in these individuals depends on the injury level. For example, people with a cervical lesion between C2 and C4 generally have no arm and hand muscle function, but preserve shoulder elevation and some neck muscle control [1] or in the most severe cases cannot move anything else other than their tongue and face. Therefore, in the former situation, there is still some retainment of movement that can be redirected towards the generation of an efficient control signal. In the latter situation, for the most severe cases a tongue computer interface has been designed to provide real-time discrete and proportional control for computers and for operating a powered wheelchair [2], [3]. While, for SCI people with some residual movements of shoulders and arms it has been previously demonstrated that such signal can be used to successfully control the speed and direction of a powered wheelchair [4]. More specifically, the interface developed in the aforementioned study included Inertial Measurement Unit sensors (IMUs) to detect and measure shoulder movements which were mapped to powered wheelchair control commands for people with cervical SCI. The powered wheelchair commands were obtained by applying a linear DR method to the recorded IMU data: Principal Component Analysis (PCA). PCA reduces the dimensionality of the input creating a map that consists in a low-dimensional, latent space that maximizes the input variance [5], and whose directions are identified by the Principal Components (PCs). Only the first two PCs (which by definition explain the most variance of the input data) were used to control the powered wheelchair velocity.

Although PCA is a computationally straightforward and inexpensive procedure, it presents some limitations imposed by its orthogonality and its ability to only account for linear relationships in the input signals [6]. To account for the non-linear features of shoulder movements, this paper considers a non-linear DR method based on Autoencoder Networks (AEs). The efficacy of AE was previously demonstrated in a study regarding prosthetic hand control [6]. The aim of such research was to find a parsimonious representation of hand kinematics data that could facilitate prosthetic hand control by comparing PCA and AEs in their ability to accurately capture a wide range of hand gestures and actions. According to this study, the AE exhibited higher performance than PCA in its ability to reconstruct hand kinematic data from its latent space, and was able to produce a manifold of more separable movements as well. AEs also showed to be an effective control platform to operate a computer cursor ([6], [7], [8]), or a 4D virtual robotic manipulator [9]. Here, we wanted to extend the use of AEs and verify whether they could also be used as a means to control a powered wheelchair. Therefore, the aim of this study was to test the feasibility of BoMI based on a nonlinear map between the input and output signals to control a power wheelchair.

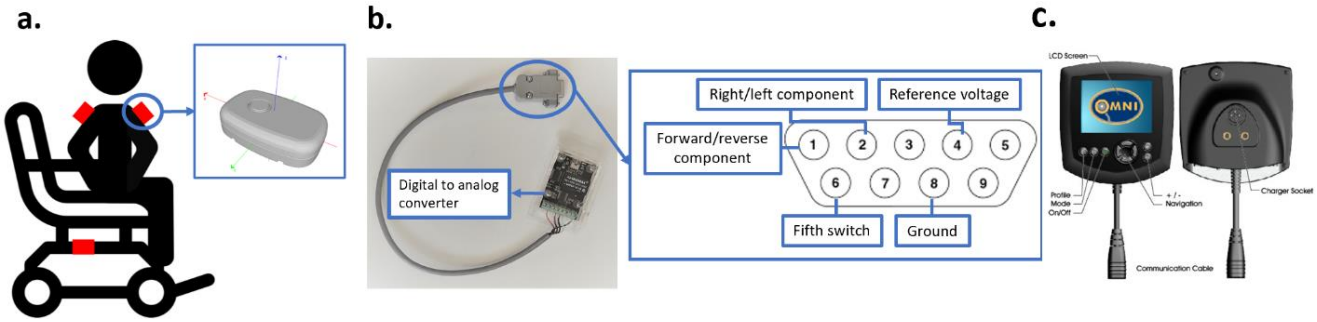


Figure 1: Experimental set up and hardware components: **a.** Experimental set up: Inertial Measurement Unit sensors are represented in red: two are placed on the subject's shoulders and a third one on the wheelchair; **b.** Digital to analog converter connected to 9 way D-Type connector; **c.** OMNI Wheelchair' interface.

II. MATERIALS AND METHODS

A. *General description of the system*

The objective of the BoMI developed in this study was to use high dimensional shoulder movements in order to control, in terms of velocity, a powered wheelchair through the application of non-linear dimensionality reduction methods. In more detail, three IMU sensors (Fig 1a, BNO055 orientation sensors, Bosch Reutlingen, Germany, the same sensors used in [10]) were used to detect the subjects' shoulders movements. The IMUs data was recorded with a sampling frequency of 50 Hz. Similarly to [11], two of the three sensors were placed on the shoulders and attached to a vest, which was worn by the subjects during experimental testing (Fig 1a). The third sensor, was placed on the wheelchair, as a means to subtract the contribution of the wheelchair's acceleration and velocity (during the driving phase) from the signals acquired from the shoulders; and to separate intentional movements (coming from the individuals controlling the wheelchair) from unintentional ones, which could result from uneven surfaces on the road. The data acquired from the IMU was sent via Bluetooth to a computer onboard the wheelchair, which contained the software developed in C#, as a Windows Form Application, to acquire the signals from the IMUs and preprocess them as mentioned above. The processed IMU data recording shoulder movements was then mapped via an AE into a 2D vector that specified the position of a computer cursor, whose coordinates were converted in real time into two digital voltage values. These digital voltage values were finally converted into analog voltages using a digital/analog converter (Phidget Analog 4-Output, Fig. 1b) and were directly sent as input, via a 9 way D-Type Connector, to the wheelchair's interface OMNI (Fig. 1c).

B. *Acquisition and mapping of shoulder kinematics*

Two IMUs were used to acquire shoulder kinematics. Each sensor measured the orientation in quaternions format. Differently from the previous work [11], we did not derive orientation using Euler angles because quaternions are able to overcome the "Gimbal lock effect" [12]; therefore the recorded signal from the body of the subject was a 8-D vector.

The first step of the data acquisition consisted in an initial calibration. Subjects were asked to perform a 1 minute "dance", during which she had to freely move the shoulders within a range of motion that was comfortable for her. The signals acquired during the calibration represented the dataset used to train the AE before using it for operating the BoMI.

The AE is an artificial neural network composed of two networks: an encoder that projects the input data into a latent space, that in the BoMI is the control space for a computer or an external device like the powered wheelchair and a decoder that projects data in the latent space back to the output space, with the same dimensionality as the input. The AE structure used for this project (same as the one found here [6]) included input and output layers of 8 units and a total of three hidden layers, the middle one being the bottleneck layer (Fig.2). The bottleneck layer had two latent units, which were used to control the *x*, *y* coordinates of the computer cursor that would ultimately move the powered wheelchair, respectively; while the first and third hidden layers were composed by 8 units. Similarly to the original AE proposed by Kramer in 1991 [13], we chose a non-linear activation function, a hyperbolic tangent, for the first and third hidden layers, and a linear activation function for the bottleneck. The use of both linear and non-linear activation functions has been shown to help increase the ease with which the network learns linear relationships in the data [14]. In order to train the AE we split the kinematic data recorded during the calibration (3000 samples, 1 minute dance with a sampling frequency of 50 Hz) into 80% of training points (2400) and 20% of test points (600) and a full-batch gradient descent was used.

C. *User interface and Analog powered wheelchair commands*

The screen displayed a circle divided into nine sections by a grid (Fig. 3), corresponding to different wheelchair

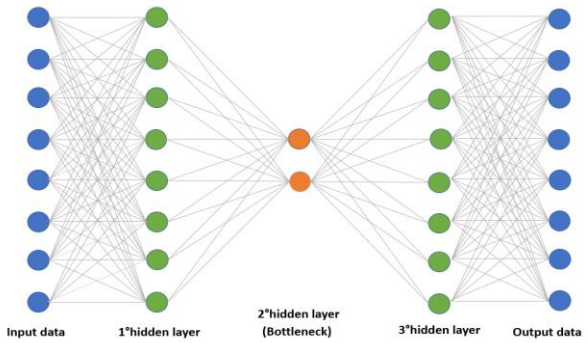


Figure 2: The non-linear Autoencoder (AE) structure used in this study. The AE has an input and output layer of 8 units and a three hidden layers, the middle one is the bottleneck. The bottleneck layer had two latent units, used to control the computer cursor and move the powered wheelchair

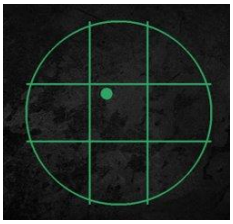


Figure 3: The driving interface shows the circle divided in nine sections in which the subjects can control the cursor on the screen in ordered to move the wheelchair in the desired directions.

commands. We designed such commands to mimic a typical joystick controller. When the cursor was in the center of the screen, the powered wheelchair was stationary. As the cursor moved up or down, the speed increased (wheelchair moving forwards) or decreased (wheelchair moving backwards), respectively. Similarly, as the cursor moved left or right the rotational command changed to cause the powered wheelchair to turn left or right respectively. Therefore, each *x* and *y* cursor's coordinates would be linearly converted into first digital and then analog voltage values compatible with the wheelchair's commands, which ultimately allowed subjects to move the wheelchair. The voltage values assigned varied linearly, progressively increasing as the cursor was moved away from the center of the grid. Overall, the total of voltage values sent to the wheelchair were four (Fig. 1e), corresponding to:

1. Forward/reverse movement component (pin 1);
2. Right/left movement component (pin 2);
3. Reference voltage value (6 V) (pin 3);
4. "Fifth switch" voltage value (pin 6). This output functioned as an emergency button: therefore its value was always maintained at 2.5 V, except in case of an emergency, when it was brought to 0V. In this scenario the wheelchair would stop immediately.

Once the digital voltage values were converted into analog voltage values by the digital/analog converter, such values were sent to the OMNI wheelchair's interface (Fig. 1e). The wheelchair used in this study was provided by Ottobock, Genova, IT

D. Experimental protocol

To assess the correct functioning of the entire system, we designed a protocol that could also be used for potential future experimental testing. In addition to the initial 1-minute initial calibration ("dance" mentioned in section *B*), we included exercises that consisted of a first familiarization phase w BoMI, where the subject was trained to control only a cursor on a computer screen, and a second phase, where the subject was trained to control the powered wheelchair. In the first phase, the subject seated on the non-moving wheelchair performed center-out reaching tasks by controlling the cursor on the laptop's screen using shoulder movements. This exercise was designed to enable the subject to find the best and most comfortable strategy to control the cursor. In this task there were six external targets placed on a circumference centered in the middle of the laptop's screen, with a 5 cm radius, and a central target placed in the center of the screen, corresponding to the "dead zone" of the BoMI wheelchair driving. The subject was required to complete five series of center-out reaching tasks on the screen, with each task consisting of a total of sixteen movements, before proceeding with the second phase of real powered wheelchair driving. In this phase, the subject was instructed to complete different maneuvers with the wheelchair, including: performing a real center-out reaching task, where the subject drove the wheelchair from a starting point to three real targets placed 1.5 meters away (this was repeated three times); going up a ramp with a slight slope (in this case ~5% and 7 m long); perform a slalom around 3 obstacles placed on a straight line every 2 meters. To track the movement of the wheelchair we also integrated an Intel Realsense Depth and Tracking camera, that was attached to one of the armrests of the wheelchair and from which we were able to extract the wheelchair's trajectory.
A preliminary test of the full experimental protocol was conducted on one pilot subject (24 years old unimpaired female).

E. Dimensionality reduction metric

We compared the difference between a linear approach based on PCA and the AE network in terms of variance accounted for (VAF) by the respective 2D latent spaces using as dataset the one of the dance. The VAF measures the difference between the reconstructed output and the original input, therefore it represents a measure of the information preserved by the dimensionality reduction method applied to the original data (equation below, for more details on VAF see [4]).

$$VAF(\%) = \left(1 - \frac{var(Y-\hat{Y})}{var(Y)}\right) * 100$$

Where Y is the original data and $\hat{Y}$ is the reconstructed data.
A VAF of 100% means perfect reconstruction.
First we compared the VAF of the 2D latent space obtained with both PCA and AE, and then we compared the VAF computed on each one of the two dimensions of the latent spaces for PCA and AE.

III. RESULTS

A. Dimensionality reduction methods

In order to compare the performance of PCA and AE we chose to analyze the VAF explained by the above dimensionality reduction methods (as previously mentioned in section *E*). Consistently with the results obtained in the study on hand kinematics [6], we found that AE with 2 latent dimensions was able to account for 95.43% of the input data variance, while PCA was able to account for 86.45 % (Fig. 4).

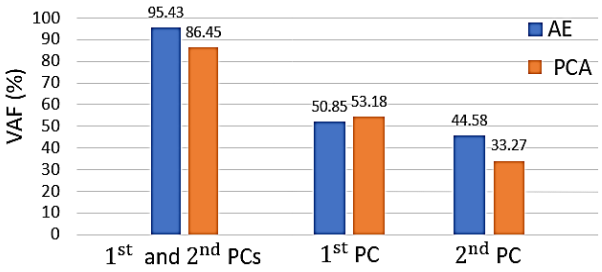


Figure 4: Comparison between Principal Component Analysis (PCA) and the Autoencoder network (AE) in terms of Variance Accounted for (VAF) explained by the latent space.

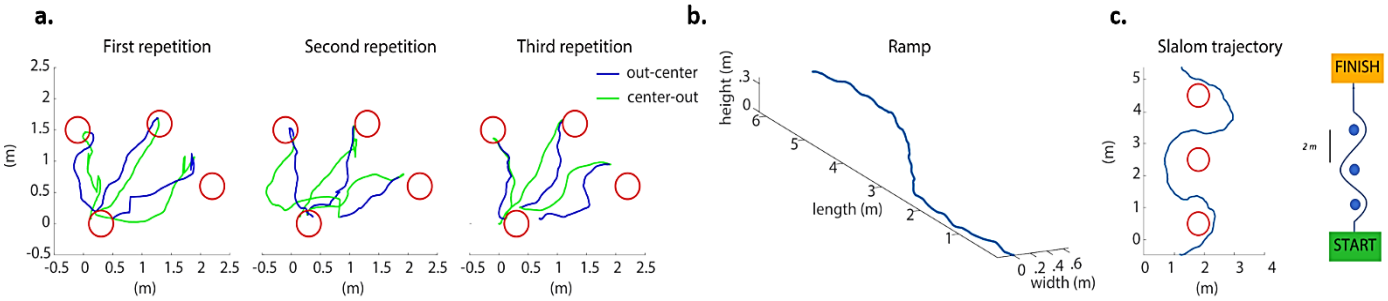


Figure 5: Wheelchair's trajectory during exercises. **a.** wheelchair trajectories while going from the starting point to the external target in green, and in blue the trajectories while going back to the starting target; **b.** wheelchair's trajectory while going up a ramp with a slight slope; **c.** wheelchair's trajectory while doing a slalom.

This result was partially expected due to the fact that AE networks are intrinsically designed to learn both linear and non-linear features from the input data. The more interesting result observed in this study relates to the comparison of the VAF explained by the single dimensions of the latent space obtained with PCA and AE. Fig. 4b, shows that the variance dropped significantly across the first and second PC, while the variance explained by the AE was comparable among the first two latent dimensions. This result demonstrates the limitations imposed by the orthogonality of PCA, and also highlights the benefits deriving from the application of an AE network, which is able to distribute the variance more evenly among its components (in our case we were interested in the first and second components).

B. Driving the wheelchair

The trajectory of the wheelchair extracted by the Intel Realsense sensor can be observed while performing the wheelchair maneuvers mentioned above (section *D*).

The wheelchair was fully tested on one subject. The first task of the real driving was the reaching of three different points in space and the coming back to the starting point. From a visual inspection of the trajectories it is possible to notice how the subject improved in driving a real powered wheelchair, with the trajectories becoming straighter and smoother. In the ramp exercise (Fig. 5b) the subject was able to safely ascend the ramp and stop at the end of it, although the trajectory of the wheelchair seen from above was not comparable to a straight line. More importantly the change of height did not affect the measures of the IMUs, indicating that the correction algorithm that was removing the effects of the wheelchair motion from the subjects body motion was properly working. Moreover, the subject was able to complete the slalom exercise (Fig. 5c) making quite smooth turns not too far from the obstacles and with no need for many corrections.

IV. CONCLUSIONS

The BoMI developed in this study is proof of concept of a powered wheelchair control interface which uses autoencoder networks to map the high dimensional shoulder kinematics into proportional powered wheelchair control commands.

There are two main limitations to this study. First, the powered wheelchair interface control developed was tested on only one subject. Second, we used a specific AE architecture, whereas there are an infinite number of possible AE structures that can be explored, some of which could also be more efficient in our specific application compared to the one used in this study.

Taking into account the limitations mentioned above, some possible future improvements include: the investigation of other AE architectures, the completion of experimental tests of the powered wheelchair control interface on healthy subjects, and if such tests reveal successful the extension of these experiments to subjects with SCI.

REFERENCES

[1] J. Fridén and A. Gohritz, “Tetraplegia Management Update,” *J. Hand Surg. Am.*, vol. 40, no. 12, pp. 2489–2500, Dec. 2015, doi: 10.1016/J.JHSA.2015.06.003.

[2] J. Kim, H *et al.* 2013. The tongue enables computer and wheelchair control for people with spinal cord injury. Science Translational Medicine 5, 213 (2013), 166–187.

[3] E. R. Lontis *et al.* “Wheelchair Control with Inductive Intra-Oral Tongue Interface for Individuals

[4] E. B. Thorp *et al.*, “Upper Body-Based Power Wheelchair Control Interface for Individuals with Tetraplegia,” *IEEE Trans. Neural Syst. Rehabil. Eng.*, vol. 24, no. 2, pp. 249–260, 2016, doi: 10.1109/TNSRE.2015.2439240.

[5] I. T. Jollife and J. Cadima, “Principal component analysis: A review and recent developments,” *Philos. Trans. R. Soc. A Math. Phys. Eng. Sci.*, vol. 374, no. 2065, 2016, doi: 10.1098/rsta.2015.0202.

[6] A. A. Portnova-Fahreeva, F. Rizzoglio, I. Nisky, M. Casadio, F. A. Mussa-Ivaldi, and E. Rombokas, “Linear and Non-linear Dimensionality-Reduction Techniques on Full Hand Kinematics,” *Front. Bioeng. Biotechnol.*, vol. 8, no. May, pp. 1–18, 2020, doi: 10.3389/fbioe.2020.00429.

[7] F. Rizzoglio, M. Casadio, and D. De Santis, “Building an adaptive interface via unsupervised tracking of latent manifolds,” *Neural Networks*, vol. 137, pp. 174–187, 2021, doi: 10.1016/j.neunet.2021.01.009.

[8] I. Vujaklija, *et al.* “Online mapping of EMG signals into kinematics by autoencoding,” *J. Neuroeng. Rehabil.*, vol. 15, no. 1, pp. 1–9, 2018, doi: 10.1186/s12984-018-0363-1.

[9] F. Rizzoglio, M. Giordano, F. A. Mussa-ivaldi, and M. Casadio, “A non - linear body machine interface for controlling assistive robotic arms,” *IEEE Trans. Biomed. Eng.*, vol. PP, pp. 1–11, 2023, doi: 10.1109/TBME.2023.3237081.

[10] G. Marchesi *et al.*, “Robot-based assessment of sitting and standing balance: Preliminary results in Parkinson’s disease,” *IEEE Int. Conf. Rehabil. Robot.*, vol. 2019-June, pp. 570–576, 2019, doi: 10.1109/ICORR.2019.8779387.

[11] A. Farshchiansadegh *et al.*, “A Body Machine Interface based on Inertial Sensors,” pp. 6120–6124, 2014.

[12] E. Engineering *et al.*, “Nominal and observation-based attitude realization for precise orbit determination of the Jason satellites,” no. March, 2019.

[13] E. Lacic *et al. Using autoencoders for session-based job recommendations*, vol. 30, no. 4. Springer Netherlands, 2020.

[14] N. Narisetty, G. R. Kancherla, B. Bobba, and K. Swathi, “Investigative Study of the Effect of Various Activation Functions with Stacked Autoencoder for Dimension Reduction of NIDS using SVM,” *Int. J. Adv. Comput. Sci. Appl.*, vol. 12, no. 5, pp. 152–161, 2021, doi: 10.14569/IJACSA.2021.0120519.

GNB2023, June 21st-23rd 2023, Padova, Italy

A preliminary test of a novel method for the real time estimation of foot displacement using MIMUs attached to the foot

I. G. Porco[1], S. M. G. Solinas[1], A. Lazich[2,3], and U. Della Croce[1]
[1] *Department of Biomedical Sciences, University of Sassari, Italy*
[2] *Italian Joint Veteran Defense Center (Centro Veterani della Difesa), Rome, Italy*
[3] *DIAG, Sapienza University of Rome, Italy*

***Abstract*— The use of virtual reality in motor rehabilitation has gained significant interest in recent years. To track a subject's motion in a virtual reality environment, a real time estimation of his/her movement is necessary. Wearable inertial measurement units represent one of the most suitable technologies to do so. However, it is well known how their recorded signals, once integrated, are affected by unpredictable drift, introducing errors that are hard to cope with. A number of successful methods have been proposed in the recent literature for the reduction of such errors for offline analysis. Unfortunately, those methods may not be used for real-time estimates of the foot displacement.**

In this paper we propose a method to estimate the foot displacement in real-time using an inertial measurement unit attached to it while mitigating integration errors.

***Keywords*—MIMU, Virtual Reality, movement analysis**

I. INTRODUCTION

THE use of virtual-mixed reality (VR/MR) for gait analysis and motor rehabilitation has gained significant interest in recent years.

Studies have shown that VR/MR environments can both ease the motor rehabilitation activities making them part of a more appealing experience and provide an opportunity for monitoring and recording the patient's performance of a task [1]. One potential solution for tracking a subject's motion in a VR/MR environment is the use of Magnetic Inertial Measurement Units (MIMUs). MIMUs are commonly used in gait analysis to estimate temporal and spatial parameters [2].

However, the estimation of such parameters in Real Time (RT), which is necessary in VR/MR applications, hasn't been dealt with as much as the offline estimation, which was developed for evaluation and/or monitoring purposes. In both cases, one of the main challenges in estimating foot displacement from MIMU's measurements is the reduction of the errors introduced by the acceleration double integration.

An approach commonly used to mitigate these errors is the Zero Velocity Update algorithm (ZUPT) [3], which can be combined, in offline applications, with the Direct and Reverse Integration technique (DRI) as suggested in [4], in order to refine the estimate of foot's displacement.

In this paper we present a preliminary study proposing a RT solution for estimating foot displacement from the measurements of a MIMU attached to it and taking advantage of some features of the approach proposed in [4] to mitigate integration errors.

II. MATERIALS AND METHODS

The data used for this study were obtained from a single healthy subject wearing a MIMU (Shimmer, Dublin, Ireland) attached over each foot (Figure 1). The MIMUs acquired linear acceleration and angular velocity with respect to the axes of their Local Reference System (LRS) via Bluetooth, at 100 samples/s in packets of a nominal size of 0.2s (20 samples) using MATLAB R2021a (The MathWorks Inc., Natick, MA, USA). Data were synchronised by identifying the first common timestamp between the two MIMUs.



Fig. 1 Experimental set-up

The subject was asked to walk along a straight line at self-selected speed for about 11 metres.

To reduce the error introduced by the RT double integration of the linear acceleration signals the following was done:

A. a RT identification of Heel Strike (HS) and Toe Off (TO) timings [3];
B. the double integration of the acceleration signals for each gait cycle;
C. the foot displacement is obtained by applying the algorithm proposed in [4] for each gait cycle and used to correct the foot displacement estimation obtained in RT.

For comparison purposes, gait speed and spatio-temporal gait parameters were also determined offline using the method proposed by Trojaniello et al. [4].

For both RT and offline methods, linear acceleration and angular velocity signals were used to provide a reliable

estimate of LRS's orientation with respect to the Global Reference System (GRS) as described in [5]. All linear acceleration signals were first expressed in GRS to remove gravity and then expressed in the LRS instantiated at the first frame of the acquisition.

A detailed description of the RT method is reported below.

A. RT gait events estimation

For each packet of data received, medio-lateral (ML) angular velocity was used to identify a first estimate of gait events as follows:

- The time of the first minimum of amplitude detected (-30 deg/s threshold [6]), was associated with the timing of a TO candidate. If in the following data packet, a maximum was found (50 deg/s threshold [7]), the time between the two could be considered as part of a swing phase, confirming that the ML angular velocity minimum found was in fact a TO.
- The time of the second minimum of amplitude detected (-30 deg/s threshold), was associated with a HS candidate. If in the previous data packet, a maximum was found (50 deg/s threshold), the time between the two could be considered part of a swing phase, confirming that the ML angular velocity minimum found was indeed a HS.

Then, a refinement of the gait events detection based on the technique explained in [4] was made as follows:

- Considering the interval between the first estimate of TO and the beginning of the following swing phase (first value of the ML angular velocity higher than 50 deg/s), the refined TO was identified as "the instant of minimum anterior-posterior (AP) acceleration [...] preceding the instant of the last maximum AP acceleration value" inside the interval.
- Considering the interval between the first estimate of HS and the end of the previous swing phase (first value of the ML angular velocity lower than 50 deg/s), the refined HS was identified as "the minimum value of the ML angular velocity occurring [...] before the instant of maximum AP acceleration" inside the interval.

Since a packet could end with one of the events, so that the latter was not identified as a minimum, an additional control was added:

- If no TO was found after a time interval exceeding the duration of a stance phase of a slow walk (0.7s), then the first value of angular velocity under the threshold (-30 deg/s) was considered as a TO candidate and the same procedure explained above was applied.
- If no HS was found after a time interval exceeding the duration of a swing phase of a slow walk (0.6s), then the first value of velocity under the threshold (-30 deg/s) was considered as a HS candidate and the same procedure explained above was applied.

B. RT foot displacement estimation

To limit the drift due to the double integration of acceleration, the latter was integrated only for a specific interval of time, including swing phase and a portion of the stance phase. Assuming that during the stance phase the displacement is limited, the acceleration signal outside the integration interval was not integrated. The integration interval was identified as the interval between the minimum value of acceleration norm preceding the TO and the first value of acceleration norm under the threshold of 0.2 m/s^2 following the HS. For this purpose, the acceleration norm was filtered (Butterworth filter with cut off frequency of 10 Hz).

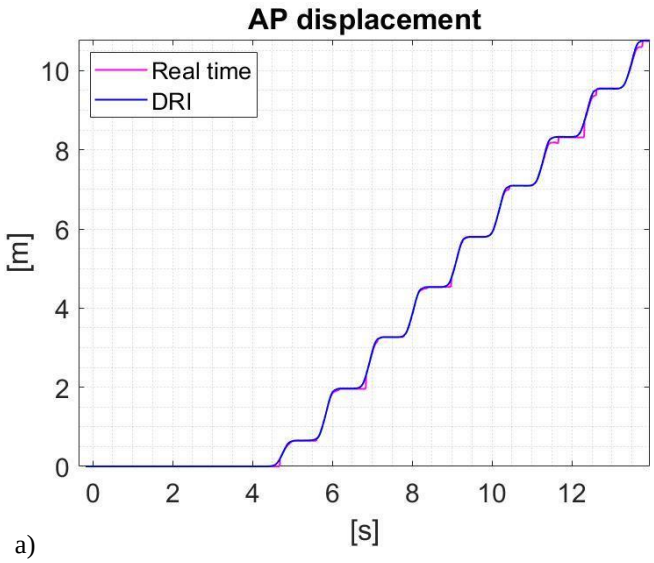
Since at the ends of the interval the foot was considered still, the mean value of the acceleration was removed, a double integration of the acceleration was performed, and the ZUPT-DRI technique was applied ([4]) at the ends of the interval, to limit the drift due to the integration.

C. RT foot displacement correction

The method proposed in [4], which performs a DRI of the acceleration between two instants identified as HS + 40% of stance duration, was used to provide a more reliable estimation of the foot displacement at the end of each gait cycle to correct its RT estimation. For the aforementioned method, a minimum of two complete stance phases is required. For each gait cycle, the correction of the RT foot displacement estimation was made.

III. RESULTS

Only the foot displacement along AP direction is reported given its relevance in determining the stride length. The AP displacement estimates obtained using the proposed RT method and using the offline method are shown in Figure 2a, while the relevant absolute difference in estimating the stride length is shown in Figure 2b. Gait speed absolute difference between the two methods for each gait cycle is shown in Figure 2c.



a)

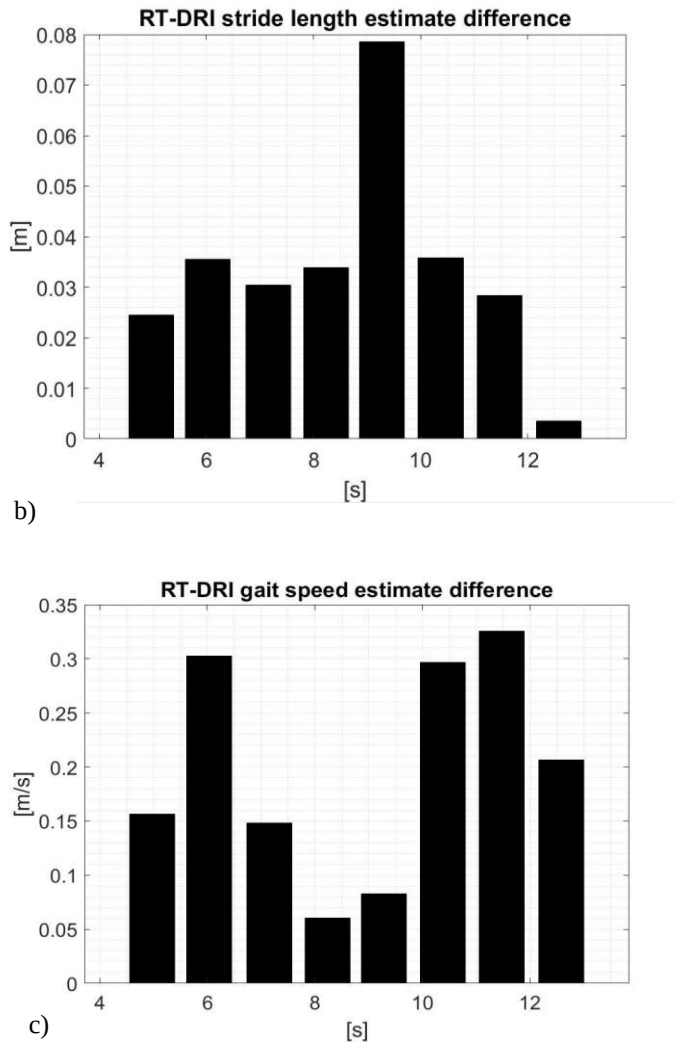


Fig. 2: a) AP foot displacement for both RT and offline methods; b) difference between offline and RT methods estimates of the stride length at each gait cycle; c) difference between offline and RT methods estimates of the gait speed for each gait cycle.

IV. Conclusion

Determining the stride length in RT and tracing foot displacement within the gait cycle is crucial for a suitable use of VR/MR in gait training applications. In this work we attempted to achieve this result uncovering a number of critical issues to be addressed. A validation on additional subjects and walking conditions is needed to validate the proposed method.

Acknowledgement

This research was conducted as part of the project ATLANTICO, founded by Italian Ministry of Defence.

References

[1] T. Massetti et al., "The Clinical Utility of Virtual Reality in Neurorehabilitation: A Systematic Review," J Cent Nerv Syst Dis, vol. 10, p. 117957351881354, Jan. 2018, doi: 10.1177/1179573518813541.

[2] Y. Hutabarat, D. Owaki, and M. Hayashibe, "Recent Advances in Quantitative Gait Analysis Using Wearable Sensors: A Review," IEEE Sens J, vol. 21, no. 23, pp. 26470–26487, Dec. 2021, doi: 10.1109/JSEN.2021.3119658.

[3] H. Prasanth et al., "Wearable sensor-based real-time gait detection: A systematic review," Sensors, vol. 21, no. 8. MDPI AG, Apr. 02, 2021. doi: 10.3390/s21082727.

[4] D. Trojaniello et al., "Estimation of step-by-step spatio-temporal parameters of normal and impaired gait using shank-mounted magneto-inertial sensors: Application to elderly, hemiparetic, parkinsonian and choreic gait," J Neuroeng Rehabil, vol. 11, no. 1, 2014, doi: 10.1186/1743-0003-11-152.

[5] R. Rossanigo, M. Caruso, F. Salis, S. Bertuletti, U. della Croce, and A. Cereatti, "An optimal procedure for stride length estimation using foot-mounted magneto-inertial measurement units," in 2021 IEEE International Symposium on Medical Measurements and Applications, MeMeA 2021 - Conference Proceedings, 2021. doi: 10.1109/MeMeA52024.2021.9478604.

[6] A. M. Sabatini, C. Martelloni, S. Scapellato, and F. Cavallo, "Assessment of walking features from foot inertial sensing," IEEE Trans Biomed Eng, vol. 52, no. 3, pp. 486–494, Mar. 2005, doi: 10.1109/TBME.2004.840727.

[7] A. Salarian et al., "Gait assessment in Parkinson's disease: Toward an ambulatory system for long-term monitoring," IEEE Trans Biomed Eng, vol. 51, no. 8, pp. 1434–1443, Aug. 2004, doi: 10.1109/TBME.2004.827933.

Understanding user needs for robotics assisted cognitive and physical rehabilitation

L. Ferreri[1], E. Parimbelli[1,2], I.G. Aprile[3] and S. Quaglini[1]
[1] *Department of Electrical, Computer and Biomedical Engineering, University of Pavia*
[2] *Telfer school of management, University of Ottawa*
[3] *Department of Neuro-Motor Rehabilitation, Don Gnocchi Foundation, Rome*

***Abstract*— Biorobotics assistance to rehabilitation has the potential to benefit patients and clinicians significantly, helping to improve outcomes and support clinician users in key task while promoting their sustainability. However significant barriers to a widespread adoption of robotics technologies in clinical practice still exist. For these reasons, as one of the kick-off activities of the Fit4MedRob project, we have performed a literature mapping study to inform the design and execution of a large national survey aimed at identifying unmet user needs, barriers of currently available solutions, and key requirements for biorobotics devices supporting physical and cognitive rehabilitation. The survey results will constitute the cornerstone of research, implementation and evaluation activities of the project and significantly contribute to foster the translation of biorobotics from the experimental setting to established practice in the Italian rehabilitation services landscape.**

***Keywords*— biorobotics, cognitive rehabilitation, physical rehabilitation, requirements.**

I. Introduction

BIOROBOTICS, i.e. a melting pot of technologies spanning from bioengineering to robotics, including artificial intelligence, controls, sensors, smart materials, has been proposed as an appealing option to improve the clinical outcome of physical rehabilitation and personal care treatments in a sustainable manner. This because of the unique combination of features offered by robots: they host sensors and computational reasoning to understand and decipher environmental or patient intentions, and they have physical bodies able to perform actions in response to such reasoning. However, significant clinical, organizational and socioeconomical issues still exist for a wide and successful employment of biorobotics in healthcare and rehabilitation. For example, current rehabilitation and assistive models offered by the Italian national healthcare system lack in personalization and adequate continuum of care throughout all the phases of the rehabilitation process. Hence, excluding few exceptions nationwide, rehabilitation outcomes are typically unsatisfactory for the patients albeit expensive to the system.

For these reasons, a large consortium of 11 academic 11 clinical research centres and 3 companies has been created in December 2022 in response to the Italian national initiative on biorobotics, rehabilitation and digital technologies.

A. Background

Fit for Medical Robots - A new generation of biorobotic and digital technologies for a sustainable welfare (F4MR) is the name of the large project consortium, comprising 25 partners, funded by the Italian Ministry of University and Research (MUR), to achieve the above-mentioned goals within a time-horizon of four years.

The project is organized in the Hub and Spokes fashion, with three spokes each corresponding to a project mission. Spoke 1, co-coordinated by the University of Pavia and the Don Gnocchi Foundation, focuses on the pivotal mission of clinical translation and innovation (see Fig.1). Spoke 1 aims to run extensive, in terms of number of patients and/or duration, multi-centric, clinical trials using healthcare or personal care robots that are currently available or developed by the F4MR consortium. Besides identifying their clinical efficacy and evidence (and limits), such treatments will also be assessed in terms of generated value from the perspectives of the involved stakeholders (final users and their families, workers and healthcare professionals, hospital facilities, payers, e.g., insurers, healthcare systems, etc.). In parallel, pivotal actions aimed at understanding and overcoming current legal barriers within the healthcare system will be implemented.

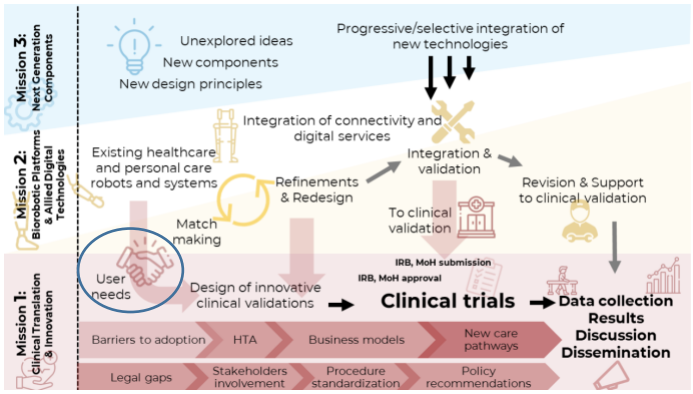


Fig. 1: Overall organization of the F4MR project, its three missions and their inter-relations. This article focuses on the first activity of Mission 1, dedicated to the elicitation of unmet user (both clinician and patient) needs to foster wider adoption.

B. Objective

One of the first objectives of the spoke 1 of Fit4MedRob is to carry out a thorough user (both patients and clinicians) needs elicitation and analysis, to inform development of new systems during the project, improve existing devices, perform sound impact, cost and sustainability evaluation of biorobotics applications, and foster their wider adoption in clinical practice. For this purpose, a literature review of questionnaires used to elicit requirements of robotics-assisted rehabilitation has been performed, in order to develop a F4MR-specific survey instrument to be distributed in the consortium. The overarching objective of the two activities is to collect requirements that can inform the remainder of the F4MR project phases.

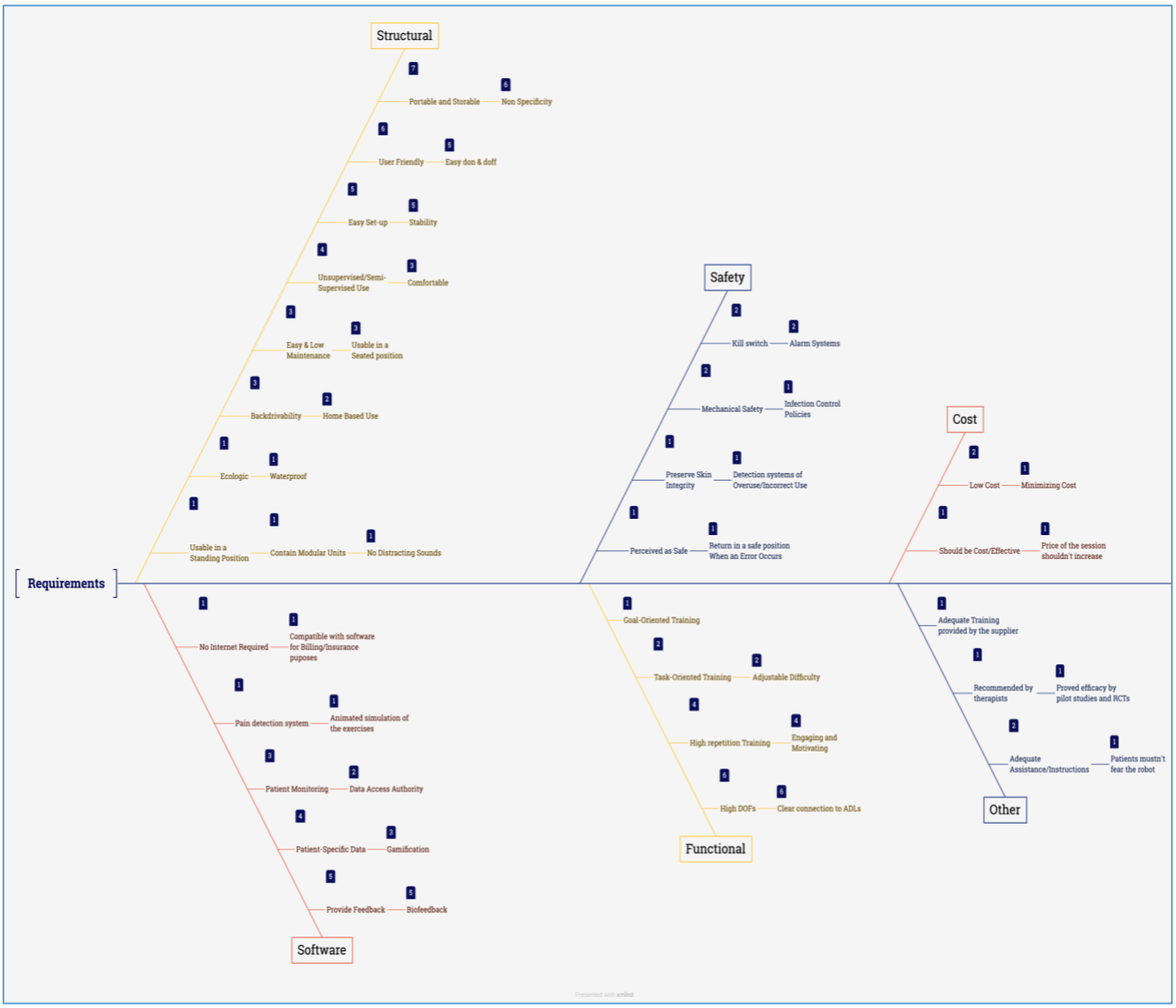


Fig. 2: A conceptual visualization of the user needs and requirements identified in the literature review, organized in 6 macro categories. The figure reports (in blue) the number of articles in our review mentioning/supporting the specific requirement.

In this paper we present the results achieved by the first 2 months of spoke 1 activities, and preview a preliminary version of the formal requirements collection instrument we plan to use for identification of unmet user needs and barriers preventing widespread adoption of currently available device.

METHODS

In order to cover both peer-reviewed as well as grey literature (e.g. industry whitepapers or informal surveys), Google Scholar was searched using the following query: *requirements AND robot AND rehabilitation AND (survey OR questionnaire)*.

Since the retrieved results were quite scarce, we did not apply further filtering based on time of publication.
Additional inclusion criteria consisted in:

- The paper included a requirements analysis aimed at therapists and patients (both or either one)
- The article is not a review of the effectiveness of the rehabilitation robot itself.

Roughly 50 papers were screened by title and abstract, and only 12 were actually selected for full-text analysis and further used to inform our research and F4MR instrument design.

II. RESULTS

A total of 53 requirements, summarized in Fig.2, have been identified from the selected articles. After reviewing the requirements 6 categories were created: Structural (n = 17), Software (n = 12), Functional (n = 6), Safety (n = 8), Cost (n = 4), Other (n = 6). It is worth mentioning that some requirements naturally belong to multiple categories. For

instance, “user friendliness” is meant as a general concept and should also be included in software requirements, on top of the reported categorization in structural requirements that we adopted for Fig.2. In the following we expand on a selection of requirements we identified for the different categories, and discuss the key findings of the review together with their relevance for F4MR.

A. Structural Requirements

A common theme among the interviews conducted in the reviewed articles, is the need for the therapeutic robot to fit the needs of as many patients as possible [1]–[6] (Non-Specificity), this included taking into account the physical characteristics of patients, such as age, weight, disabilities etc., but also to include the specific exercises needed for their therapy (High DOFs[1]–[3], [5], [7], [8],High repetition[2]–[4], [9], Usable in a seated[2], [3], [9] or standing position[3]).

One frequent complaint was about the difficulty of using the robot (User Friendly)[1], [2], [5], [7], [8], [10], but also the long and complex process of set-up[1]–[4], [10], donning and doffing[1], [2], [4], [6], [7]. Many therapists felt that they wouldn’t consider robot therapy if the initial steps required to use it were too time consuming[2], [4].

Other relevant requirements to take into consideration are comfort[1], [2], [6], stability[1]–[3], [7], [9] and focus (No distracting sounds)[6] of patients using the robot.

When it comes to Home-Based robots, there were some conflicting opinions, where some believed that a domicile robot could help with the amount of therapy performed by patients[1], others believed that and independent use wasn’t recommended due to incorrect use, overuse and over reliance[1].

Nonetheless a semi-supervised use was generally seen as positive[1], [3], [4], [10], with some suggesting the possibility of group therapy[4].

B. Functional Requirements

While using the therapeutic robot there should be a clear link to the Activities of Daily Living[2]–[4], [9]–[11] such as grooming, personal hygiene, feeding oneself etc. It is also important to allow for goal-oriented therapy[2] specific to each patient.

C. Software Requirements

Patient monitoring is seen as a critical need by therapists[2], [6], [8]. In order to do so it is mandatory to gather patient-specific data[1], [2], [4], [8] on therapy sessions and configurations for donning. It goes without saying that this data mustn’t be modified by users, therefore data access authority is required[1], [8].

Motivation is also quite important[1], [4], [7], [10], and many believe that robots can help by providing feedback to patients (and therapists alike) [1], [2], [4], [8], [10], gamification[1]–[3] (even though some are against using it[1]) and by making the exterior of the robot attractive[12].

Another somewhat important detail is being compatible with other software, such as notes, billing/insurance [8] etc.

D. Safety Requirements

Obviously, Safety regulations must be followed. The main concerns for safety requirements were about misuse of the device, especially if it allows unsupervised use by patients. In order to make it safer there must be a kill switch[1], [8], alarm systems with sounds and messages[1], [8], and it must slowly return in a safe position whenever an error occurs[8]. Mechanical safety should be guaranteed[1], [6] (no finger traps etc.) at all times.

E. Cost Requirements

Many complained that the devices were too expensive[2], not cost effective[10], and often weren’t even eligible for refund by the public healthcare system[1].

Some papers also investigated how much money the therapist/institutions were willing to spend[1], [3], [9] to acquire or use the device, but the prices were heavily dependent from the country where the study was conducted and the economic situation at the specific times of the survey/interviews.

F. Other Requirements

Providing adequate Assistance[1], [2] and Training[10] should be taken into consideration when developing a robotic device. Some patients weren’t too sure how to feel about the robotic device since they were afraid it might look too technical[6]. Therefore it is important to make sure the patients do not feel scared by the robot[5], and findings suggest that if the use is recommended by therapist[10] himself it helps with patient acceptance and feelings towards the device.

G. F4MR user needs elicitation study

In the immediate future we will implement our own survey instrument using a web-based questionnaire solution, inspired both by the findings of the present literature mapping study and by comparable (albeit more narrow-scoped) studies like ECAD’s RehaTech4Child Survey[13].

The requirements elicitation instrument that will be the basis of the user needs identification study of F4MR has the following structure, and investigates key constructs identified in this review:

- Questions about demographics and work experience. Other than therapists, we will also include engineers as part of our respondents.
- Did you already use robotic devices for therapy purposes?
    - If the answer is yes, questions about their experiences and opinions with robotic devices will follow.
      In particular, for each device listed, a set of questions extrapolated from the present literature mapping study will be asked.
      Although the primary subjects of the F4MR project are patients with certain illnesses, such as CNS and PNS injuries and disorders, people at risk of occupational diseases and the frail elderly are also included.
      Furthermore, it is of special interest the effects that robot therapy has had on paediatric patients.
      Therefore, knowing what kind of patient these machines were subjected to, what the objectives of robotic rehabilitation were and whether they were actually met, will be crucial.

- Otherwise, we will expand on their knowledge and beliefs on robotic devices and if they wish to use them.

III. Conclusions

The aim of this article was to present a list of requirements and unmet user needs for the development, improvement and evaluation of therapeutic robots for rehabilitation. We performed a literature mapping study to inform a project-specific instrument development, and inform subsequent phases of F4MR. Among the most important findings that emerged we highlight the need to fit the needs of as many people as possible while keeping rehabilitation robot devices user friendly. Furthermore, devices should be light weight and easily transportable and storable, especially if home-based use is considered. It is also key to make the robot engaging and motivating for the patients. Finally devices able to perform a wider range of well implemented exercises, instead of a single one, seem preferable.

Based on the results of the literature mapping study a F4MR requirements elicitation instrument is being developed, to be disseminated within the F4MR consortium to gather the largest sample of Italian national respondents to date. Results of such study will be pivotal to inform the following key phases of the project.

Acknowledgement

This work has been funded by the Italian Ministry of University and Research (MUR), under the complimentary plan to the PNRR, initiative proposal Fit4MedRob, in the context of its spoke 1, led by I.G.A. and S.Q. The authors thank Dr. Giuseppina Sgandurra of IRCCS Fondazione Stella Maris and the University of Pisa for bringing the RehaTech4Child Survey to our attention.

References

[1] L. Li, S. Tyson, and A. Weightman, “Professionals’ Views and Experiences of Using Rehabilitation Robotics With Stroke Survivors: A Mixed Methods Survey,” *Front. Med. Technol.*, vol. 3, p. 780090, Nov. 2021, doi: 10.3389/fmedt.2021.780090.

[2] L. Li, Q. Fu, S. Tyson, N. Preston, and A. Weightman, “A scoping review of design requirements for a home-based upper limb rehabilitation robot for stroke,” *Topics in Stroke Rehabilitation*, vol. 29, no. 6, pp. 449–463, Aug. 2022, doi: 10.1080/10749357.2021.1943797.

[3] E. C. Lu, R. H. Wang, D. Hebert, J. Boger, M. P. Galea, and A. Mihailidis, “The development of an upper limb stroke rehabilitation robot: identification of clinical practices and design requirements through a survey of therapists,” *Disability and Rehabilitation: Assistive Technology*, vol. 6, no. 5, pp. 420–431, Sep. 2011, doi: 10.3109/17483107.2010.544370.

[4] J. Zajc and M. Russold, “Elicitation of usability-related Requirements for Upper-Limb Rehabilitation Systems,” in *2019 IEEE 16th International Conference on Rehabilitation Robotics (ICORR)*, Toronto, ON, Canada, Jun. 2019, pp. 477–482. doi: 10.1109/ICORR.2019.8779464.

[5] M. Babaiasl, S. H. Mahdioun, P. Jaryani, and M. Yazdani, “A review of technological and clinical aspects of robot-aided rehabilitation of upper-extremity after stroke,” *Disabil Rehabil Assist Technol*, vol. 11, no. 4, pp. 263–280, 2016, doi: 10.3109/17483107.2014.1002539.

[6] R. Holt *et al.*, “User involvement in developing Rehabilitation Robotic devices: An essential requirement,” in *2007 IEEE 10th International Conference on Rehabilitation Robotics*, Noordwijk, Netherlands, Jun. 2007, pp. 196–204. doi: 10.1109/ICORR.2007.4428427.

[7] M. Iosa, F. Cincotti, I. Pisotta, F. Tamburella, D. Mattia, and M. Molinari, “What users need. Requirements in BNCI-driven robot for gait rehabilitation after stroke: a pilot study”.

[8] M. Lee, M. Rittenhouse, and H. A. Abdullah, “Design Issues for Therapeutic Robot Systems: Results from a Survey of Physiotherapists,” *J Intell Robot Syst*, vol. 42, no. 3, pp. 239–252, Mar. 2005, doi: 10.1007/s10846-004-7194-y.

[9] D. Popescu, F. Manta, L. Rusu, T. E. Avramescu, M. Zavaleanu, and A. Petrisor, “Medical and technical requirements analysis for upper limb rehabilitation system,” in *2017 18th International Carpathian Control Conference (ICCC)*, Sinaia, Romania, May 2017, pp. 539–544. doi: 10.1109/CarpathianCC.2017.7970459.

[10] H. Lakany, “Requirements specification for a wearable robotic exoskeleton for rehabilitation,” presented at the The 20th International Conference on Climbing and Walking Robots and Support Technologies for Mobile Machines: Special session on Wearable Robotics for Assistance and Rehabilitation (WRAR), 2017, pp. 605–612.

[11] P. Maciejasz, J. Eschweiler, K. Gerlach-Hahn, A. Jansen-Troy, and S. Leonhardt, “A survey on robotic devices for upper limb rehabilitation,” *Journal of NeuroEngineering and Rehabilitation*, vol. 11, no. 1, p. 3, Jan. 2014, doi: 10.1186/1743-0003-11-3.

[12] D. Laparidou, F. Curtis, J. Akanuwe, K. Goher, A. Niroshan Siriwardena, and A. Kucukyilmaz, “Patient, carer, and staff perceptions of robotics in motor rehabilitation: a systematic review and qualitative meta-synthesis,” *J Neuroeng Rehabil*, vol. 18, no. 1, p. 181, Dec. 2021, doi: 10.1186/s12984-021-00976-3.

[13] University Hospital, Brest, “Motor REHAbilitation TEChnologies for CHIldren With Disability,” clinicaltrials.gov, Clinical trial registration NCT05176522, Mar. 2022. Accessed: Jan. 12, 2023. [Online]. Available: https://clinicaltrials.gov/ct2/show/NCT05176522

Assessment of Balance disorder and vestibular dysfunction using Mixed Reality

S. Pascucci[1,2], V. Margani[3], M. Franzò[1], M. Curcio[1], A. Polsinelli[1], R. Talamonti[3], M. Barbara[3], F. Marinozzi[1] and F. Bini[1]

[1] *Department of Mechanical and Aerospace Engineering, Sapienza University of Rome Italy*
[2] *Scientific Secretary of the Presidency, Italian national Institute of Health, Rome, Italy*
[3] *ENT Clinic, NESMOS Department, Medicine and Psychology, Sapienza University, Rome, Italy*

***Abstract*— Background: Balance disorder and vestibular dysfunction are related to an increase of the risk of fall related to the ageing of people and to specific pathologies. Mixed Reality is a new tool that could support the clinicians during the hospital activities. The aim of this work is to propose a first version of Mixed Reality application to support the clinicians in fall risk diagnosis. Material and Methods: The application is based on Unity Engine to present the Mixed Reality environment on HoloLens™ 2 used in combination with the Wii Balance Board, managed with Vestlab application, to evaluate the movement of pelvis. The subject must reach with pelvis 8 different target on a 2D plane. Nineteen healthy subjects performed the test. Results and Conclusion. The HoloLens 2 tracks the 3D movement and rotation of the eyes and of the head, meanwhile from the Vestlab application tracks the movement of the pelvis. The evaluation of the application shows the adaptability of Mixed Reality to offer to clinicians a new tool to diagnose the risk of fall by tracking the trajectory and the rotation of the head and of the pelvis.**

***Keywords*—Mixed Reality, Diagnostic, fall prevention, Balance.**

I. Introduction

Balance disorders and vestibular dysfunction are related to the progressive loss of function of sensory systems or the inability to control body movements due to the ageing or due to pathologies [1]. They could be positively treated through physiotherapy and rehabilitation to reduce dizziness and fall risk and improve the gaze stabilization or posture [2].

Mixed Reality (MR) is gaining popularity and academic interest in the medical sector [3] due to the capability to generate a controlled and user-specific environment, and perceptual stimuli that motivate the patient [4]. With MR, the user can freely interact with virtual objects (holograms) while having the possibility of interacting with the real environment, including also the specialist [5]. To use the MR, employment of a Head Mounted Device (HMD) is necessary, a wearable sensor that reproduces the holograms directly on its transparent display. One of the most popular devices is the HoloLens (™) (hereinafter referred as HoloLens), developed by Microsoft in 2016.

In recent studies [6], most of the application related to the use of MR in balance disorders are restricted to the rehabilitation field. MR rehabilitation programmes [7],[8] or similar technologies are shown to produce significant improvements in user outcomes and significantly more effects than alternative rehabilitation programmes with the same duration. In [9], Fung and Perez developed a system that combines visual representation with manipulation of physical environments and haptic feedback to improve balance and mobility after stroke. Pezzera [10] implemented a new software, MIRARTS (Mixed Reality Adaptive Rehabilitation Therapist Station), in HoloLens, which via MR allows the therapist to visualise quantitative values in real time, in form of text or graphs, related to a postural rehabilitation exercise. Qualitative experience supported by the quantitative data enables therapists to come at more appropriate decisions. Miller Koop [11],[12] developed an application aimed at determining the accuracy of HoloLens versus 3D Motion Capture in gait quantification. In [11], the first generation of HoloLens was used on ten healthy adults, while in [12] the second generation of HoloLens, the HoloLens 2 (HL2), was used on 66 healthy adults. In this study, subjects had to perform the continuous walking and the timed up-and-go (TUG) tasks, obtaining a statistically equivalence (error $\leq 5\%$, $p < 0.05$) between HL2 and motion capture system (MoCap).

Due to the totally absence of studies that involve the use of MR in balance diagnostics, the aim of this study is to prove the possibility of applying MR to develop an application for the assessment of balance disorders and to build an endpoints detection system that allows classifying and studying the subject's trajectory.

II. Material and methods

The device used to implement the Mixed Reality application was the HoloLens 2, the Microsoft Head Mounted Device. HoloLens 2 is a stand-alone holographic computer with transparent glasses that displays the holograms directly in front of the eyes of the subject [13] HL2 is equipped with an inertial measurement unit (IMU) sensor that includes a 3D accelerometer and a 3D gyroscope.

A high performing computer was used to manage the communication between HoloLens 2 and the MR application.

A PC equipped with Vestlab OS software (GN Otometrics, Taastrup, Denmark) (Hereinafter reported as Vestlab), a sotfware designed to perform diagnosis tests and procedures for the assessment of the balance disorders, was employed to guarantee the execution of the Limits of Stability (LoS) test in order to obtain the evaluation of pelvis movement. During this test, the user had to stand on a force plate and reach the target displayed on the PC by moving the pelvis. LoS provides an objective measure of displacement of the patient's center of gravity when he is asked to lean to eight different postural position using a force plate. Moreover, it allows the clinician to evaluate the subject risk of fall.

The force plate used was the WII Balance Board-powered by the Nintendo® and it was connected to the PC using the Bluetooth connection.
Nineteen healthy subjects (mean age: 27.21±3,08) performed the LoS test only once. Head trajectories were recorded by using HL2, meanwhile the Vestlab recorded the pelvis movement.

Before starting the test, the subject needed to place himself on the centre of the WII Balance Board and wore the HL2

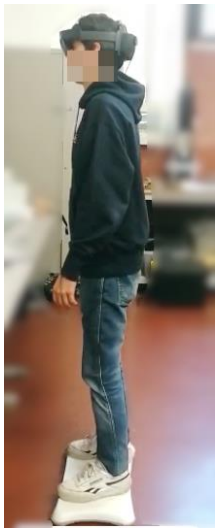


Fig. 1: A subject during the execution of the diagnostic test.

directly on his head. Figure 1 shows the subject during the tests.

After that, the user could start the MR application on HL2 in order to allow the device to record head and eyes' movements.

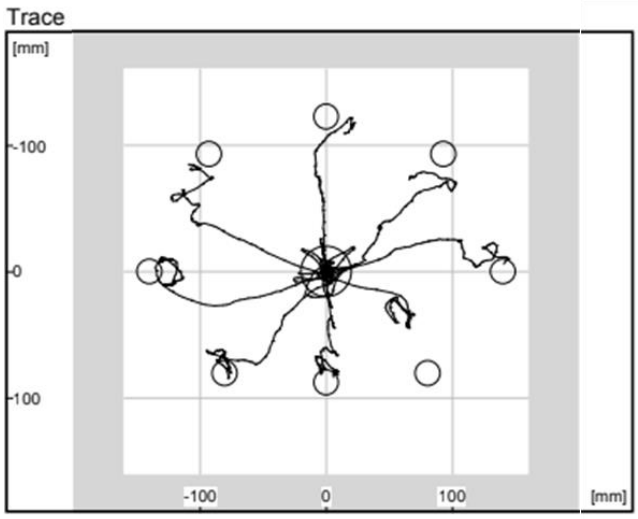


Fig. 2: Pelvis's subject 2D trajectory obtained directly from Vestlab

Lastly, the clinician started the Vestlab application to initialize the LoS test.

During the LoS test, the subject had to reach with the pelvis eight targets one at a time placed in the xy plane. In particular, figure 2 shows the subject's pelvis outward trajectory to reach the eight targets obtained directly from the Vestlab software.

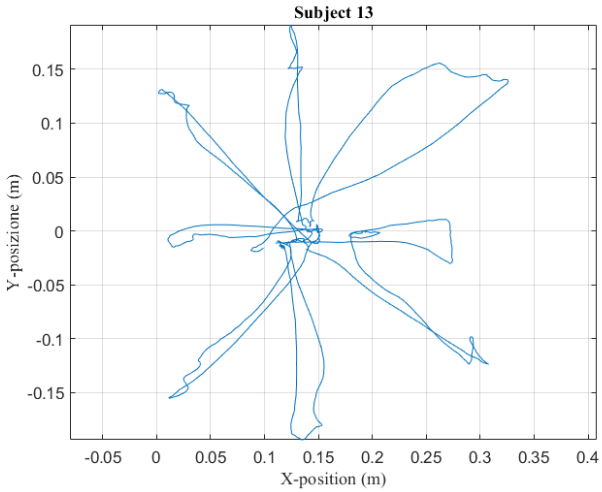
The subject had 20 seconds to reach the target, after that the target disappear and the user had to return at the origin point. If a target is reached, the subject had to return at the origin point.

The HL2 IMU allow to acquire 3D coordinates and 3D angles of head with a sample frequency of 12 Hz. Through our algorithms, data were stored in a txt files and subsequentially download it for the data analyses. The proprietary Vestlab algorithms (not Open Source) compute the following data: reaction time (time in seconds it took the patient to realize they needed to lean toward the target), movement velocity (°/s, how quickly the patient moved toward the target), endpoint (where the target is), maximum excursion (if target was reached initially and whether or not target was reached during the test), and direction control (percentage of movement in direction to the target by the different ~~orientations~~ directions in the space (forward, backward, left and right).

III. Data Analyses

At the beginning, the data were converted from the HoloLens's System of Reference (SoR), a left-handed SoR, into a conventional right-handed SoR.

HoloLens records the test trajectory as a unique track (figure 3), therefore properly cutting the track with an endpoint



detection system is necessary.

Fig. 3: Subject's head 2D trajectory at the end of the test

Subsequently, the reaction time, movement velocity, endpoint, maximum excursion and direction control were evaluated for the head. The mean of x and y positions to obtain the centre of the distribution for each subject. In this final position, a circumference with radius equal to 30 cm was centred.

The circumference was used to virtually divide the overall continuous trajectory of the subject recorded by HL2 in segment based on distance from the centre. So, all the position were divided in inside and outside the circumference. Among all the positions outside the circumference, the algorithm searches for the maximum distance points interpreting them as the final points of the outward movement and consequently the reaching of one of the targets. The opposite process is carried out with the parts inside the circumference finding the final point of the subject's inward movement to reach the return target. Considering the minimum radius that should include not only all the return points, but also the instant in which the

subject starts the trajectory for the next target.
With this characteristic, the circumference can detect and highlight the eight endpoints referred to targets.

These indexes of the points found by the algorithm were exported for the analyses. Coefficient of correlation for the movement velocity (°/s) was computed to evaluate a possible correlation between head and pelvis to idenfity if it is present a potential compensation between the head and pelvis movements during the balance strategy used by the subject to reach each single target.

Wilcoxon-Mann-Whitney test (Mann–Whitney U test) non-parametrical statistical analysis was performed to evaluate the difference between the head and the pelvis.

IV. Results

Figure 4 highlights the results of the trajectory endpoints detection system.

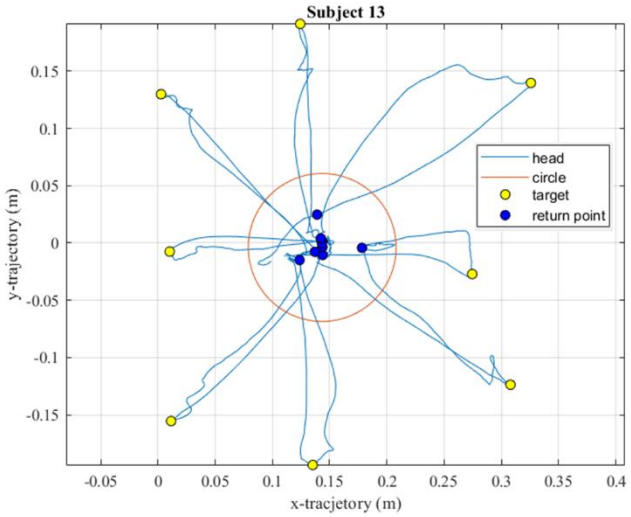


Fig. 4: Subject's Head trajectory with the endpoints of reaching targets

Figure 5 shows the eight endpoints distribution for all the subjects analysed in a polar plane. The coloured areas in the graphic represent the zones in which at least the 95% of subjects reached the targets.

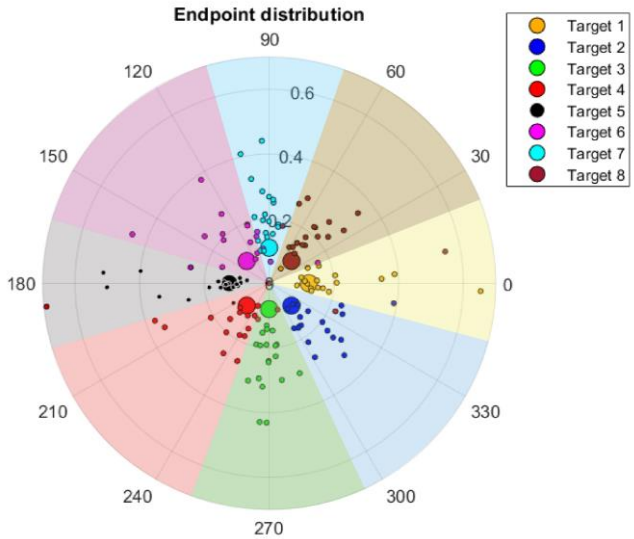


Fig. 5: Eight endpoints distribution for all the subjects in polar plane.

No correlation between the head movement velocity and the pelvis was found (Table I).

TABLE I
COEFFICIENT OF CORRELATION FOR THE MOVEMENT VELOCITY BETWEEN HEAD AND PELVIS

Target to reach	*Coefficient of correlation*
Target 1	0.29
Target 2	-0.13
Target 3	0.11
Target 4	0.25
Target 5	0.11
Target 6	-0.15
Target 7	0.32
Target 8	0.23

The statistical analysis performed is the Wilcoxon-Mann-Whitney test (Mann–Whitney U test) and for the trajectory of target 2, 3, 4 results are statistically significant.

V. Discussion

Even if it is shown no correlation between the head and the pelvis, the head movement reproduces a similar trajectory of the pelvis except for the order of magnitude. This is probably due to the bigger range movement of the head rather than the pelvis joint and also maybe to the instinct of the subjects to move the head together with the rest of the body.

Moreover, there is not a correlation between the head and the pelvis, so the similar movement is probably related to the necessity of the subjects to balance their own body to prevent their falling.

Using an endpoints detection system could be useful to better identify the trajectory the subject executes to reach the eight targets. In addition, this method helps to investigate the track of the head path and to compute specific parameters for each of the eight targets in order to enrich the analysis.

Consequently, an endpoints detection system could be a tool to characterize a healthy subject with important parameters.

Statistical analysis shows no significant results, probably because the movement of the healthy subject are similar, more expected and contained.

Despite the study presents just a first application of HL2, MR in combination with the software Vestlab can be adequate to evaluate the risk of falling.

The introduction of MR could present a benefit for the clinicians. MR is powerful and reliable tool, it is able of reproducing immersive environment and a more realistic space by merging the holographic object directly in the physical room. In this way, the patient is not affected by cybersickness, dizziness or other VR-diseases correlated [14].

The application of MR and innovative technology to decrease the risk of falling mostly in elderly people [15],[16] is particular interesting. However, most of the application use

proper exergames to prevent falls in the elderly, but not to diagnose the level of risk of falling [6].

Considering the results obtained, the MR application could be a resource in order to obtain more measurement that the clinicians could not obtain by only the routinary visit as the movement and rotation of the head and the correlation of their movements.

The system proposed is currently a prototype and it still could be improved. The code could be updated to get it more efficient and the additional software such as Vestlab might be removed in order to have a unity-based MR application for HL2. Moreover, the integration of the new Azure Kinect [17] should increase the useful information of the balance assessment due to the possibility of additionally tracking the lower limbs of the patient.

CONCLUSION

In this work a useful tool for the vestibular dysfunction diagnosis is given to the clinicians in order to allow them to distinguish pathological subject from the healthy ones and to quantify the gravity of their conditions.

REFERENCES

[1] L.Z. Rubenstein, "Falls in older People.epidemiology, risk factors and strategies for prevention", Clinical Risk Assessment, *Age and Ageing*, vol 35, pp. ii37-ii41, 2006.

[2] R.S.M. Bittar, L. Simoncelli, and M.E.B. Pedalini,M.A. Bottino, "The treatment of diseases related to balance disorders in the elderly and the effectiveness of vestibular rehabilitation", *Rev Bras Otorrinolaringol*, vol. 73, pp. 295-298, 2007.

[3] L. Chen, T.W. Day,W. Tang, and N.W. John, "Recent Develoments and future challenges in Medical Mixed Reality", in 2017 IEEE International Symposium on Mixed and Augmented Reality (ISMAR), pp. 123-135, 2017.

[4] M. Franzò, S Pascucci, M Serrao, F Marinozzi, and F Bini, "Exergaming in Mixed Reality for the Rehabilitation of Ataxic Patients", *in Proceedings of the 2022 IEEE International Symposium on Medical Measurements and Applications (MeMeA)*, pp. 1–5.

[5] S. Condino, G. Turini, R. Viglialoro, M. Gesi, and V. Ferrari, "Wearable Augmented Reality Application for Shoulder Rehabilitation", *Electronics*, vol. 8, 2019.

[6] S. Park, S. Bokijonov and Y. Choi, "Review of Microsoft HoloLens Applications over the Past Five Years", *Appl Sci*, vol. 11, 2021.

[7] M.C. Howard and M.M. Davis, "A meta-analysis and systematic literature review of mixed reality rehabilitation programs: Investigating design characteristics of augmented reality and augmented virtuality", Computers in Human Behavior, vol. 130, 2022.

[8] B. Butz, A. Jussen, A. Rafi, G. Lux, J. Gerken, "A Taxonomy for Augmented and Mixed Reality Applications to Support Physical Exercises in Medical Rehabilitation - A Literature Review", *Healthcare (MDPI)*, vol. 10, 2022.

[9] J. Fung and C.F. Perez, "Sensorimotor enhancement with a mixed reality system for balance and mobility rehabilitation", *Annual International Conference of the IEEE Engineering in Medicine and Biology Society. IEEE Engineering in Medicine and Biology Society. Annual International Conference*, pp. 6753-6757.

[10] M. Pezzera, E. Chitti, and N.A. Borghese, "MIRARTS: A mixed reality application to support postural rehabilitation*", in 2020 IEEE 8th International Conference on Serious Games and Applications for Health (SeGAH)*, pp. 1-7.

[11] M. M. Koop, A.B. Rosenfeldt, J.D. Johnston, M.C. Streicher, J. Qu, J.L. Alberts, "The HoloLens Augmented Reality System Provides Valid Measures of Gait Performance in Healthy Adults", *IEEE Transactions on Human-Machine Systems*, vol. 50, pp. 584-592, 2020.

[12] M. M. Koop, A.B. Rosenfeldt, K. Owen, A.L. Penko, M.C. Streicher, A. Albright, J.L. Alberts, "The Microsoft HoloLens 2 Provides Accurate Measures of Gait, Turning, and Functional Mobility in Healthy Adults", *Sensors 2022(MDPI)*, vol. 22, 2009.

[13] Microsoft, (2022, October 14). About HoloLens 2 [Online]. Available: https://docs.microsoft.com/en-us/hololens/hololens2-hardware

[14] D. Saredakis, A. Szpak, B. Birckhead, H. A. D. Keage and A. Rizzo, "Loetscher Tobias Factors Associated with Virtual Reality Sickness in Head-Mounted Displays: A Systematic Review and Meta-Analysis Frontiers", *Human Neuroscience*, vol. 14, 2020.

[15] A. Nishchyk, W. Chen, A. Pripp and A. Bergland, "The Effect of Mixed Reality Technologies for Falls Prevention Among Older Adults: Systematic Review and Meta-analysis ", *JMIR Aging*, vol. 4, pp. e27972, 2021.

[16] A. Castellano-Aguilera, G. Biviá-Roig, F. Cuenca-Martínez, L. Suso-Martí, J. Calatayud, M. Blanco-Díaz, and J. Casaña, "Effectiveness of Virtual Reality on Balance and Risk of Falls in People with Multiple Sclerosis: A Systematic Review and Meta-Analysis", *Int. J. Environ. Res. Public Health 2022*, vol. 19, 2022.

[17] G. Kurillo, E. Hemingway, M. L. Cheng, and L. Cheng "Evaluating the Accuracy of the Azure Kinect and Kinect v2", *Sensors (MDPI)*, vol. 22, 2022.

A Reliable User-Independent Motion Intent Detection from Transient EMG Data for Shoulder Joint

M. Scattolini[1], A. Tigrini[1], F. Verdini[1], S. Fioretti[1], L. Burattini[1], M. Morettini[1], and A. Mengarelli[1]
[1] *Department of Information Engineering, Università Politecnica delle Marche, Ancona, Italy*

***Abstract*—Motion intent detection (MID) through transient surface electromyographic (sEMG) is becoming central for the development of real-time assistive and rehabilitative technologies. However, the adaptation of such myoelectric interfaces in a user-independent framework represents a cutting-edge problem that hampers the practical usage of sEMG based human-machine interfaces. In this study least square canonical correlation analysis (LS-CCA) was employed together with SVM classifier in order to solve a shoulder joint MID problem. A publicly available dataset comprising eight healthy subjects was employed and four shoulder movements were considered. The LS-CCA was used for computing a subject-independent feature space using training data and then the trained SVM model was tested on an unseen subject, eventually implementing a leave-one-subject-out validation. Two window lengths for feature extraction (50 and 150 ms) and three feature sets were also compared. Overall, the best results were obtained using the 50 ms window length (multi-user classification accuracy about 70%), without any significant difference among the three feature sets.**

***Keywords*—Motion intent detection, Transient EMG, Myoelectric control, Cross-user classifier**

I. Introduction

In the last few years, the role of the surface electromyography (sEMG) for pattern-recognition purposes has become more and more important, due to its large range of possible applications regarding the human-machine interactions, in particular in rehabilitation system and prosthetic control [1]. Indeed, many studies presented different ways of using the sEMG to recognize human movements, mainly related to the upper limb and in particular for hand and wrist movements [2]–[4]. However, in more recent years, the recognition of the shoulder joint movements from sEMG data gained significant attention, since it is heavily involved in many upper limb movements and thus it plays a fundamental role in the design of wearable and assistive upper limb devices [5]–[7].

In this scenario, the early recognition of user's motion intent was investigated using transient epochs of sEMG signals [2]. However, the pattern recognition architectures developed using such transient data still maintained the user-specific approach, i.e., calibrated and used with signals recorded from the same user [2]. Nevertheless, it would be a great advantage being able to solve *inter-subject* problems, i.e. training a model through data related to one subject and then apply it to any other different subject, without any long adaptation sessions. Furthermore, the development of sEMG-based human machine interfaces for multi-users applications is important to facilitate the utilization of assistive device, e.g. to aid stroke patients in controlling a wearable lower extremity device [6]. There are some works focused on the motion intent detection (MID) problem using transient data [2], [5], [8], [9] but its extension toward a user-independent framework has not been yet investigated.

Hence, in the present study the identification of the motion intent of the shoulder joint has been investigated for providing a multi-user, calibration-free architectures. The theoretical framework employed was the canonical correlation analysis (CCA), selected for producing a generalized and unified feature space among users, suitable for delivering subject-independent pattern recognition models for shoulder MID problems. Further, a direct comparison between two window lengths for feature computation on transient sEMG data is proposed, together with the evaluation of three different feature sets for classification purposes.

II. Materials and methods

A. Dataset description and signal windowing

For this study, data belonging to a publicly available dataset were used [10]. Eight healthy subjects (four males and four females) aged 25.0 ± 1.8 years were involved. Each subject was instrumented with eight sEMG probes in correspondence of the following muscles: clavicular and sternal heads of pectoralis major, serratus anterior, trapezius descendent, trapezius transversalis, trapezius ascendent, infraspinatus, and latissimus dorsi [10]. Once equipped, they were asked to perform four shoulder movements: i) shoulder flexion by 90°; ii) shoulder hyperextention by -30°; iii) shoulder abduction by 90°; iv) shoulder elevation by 90° in a 45° rotated plane toward the external direction. Each subject repeated all the movements nine times. Bipolar disposable pregelled 26 mm diameter Ag/AgCl surface electrodes (Bielsan, Italy) connected to wireless and miniaturized probes (BTS-FREEEMG 300, Italy) were used. Atlas guideline of muscle innervation zones were considered for electrodes placement, with an inter-electrode distance of 26 mm. More details are reported in [10] and references therein.

Recorded sEMG signals were filtered between 30 and 450 Hz using a zero-phase, 4^{th} order, band-pass digital filter. Then, MID windows of 300 ms were computed on sEMG data, including 150 ms before and 150 ms after the beginning of the movement, thus centered on the movement onset, which

was identified taking into account the shoulder joint kinematics included in the dataset [10], as performed in [8]. At this stage, a total of 9 repetitions $\times$ 8 channels $\times$ 8 subjects sEMG trials for each movement were available for segmentation, feature extraction, and classification.

B. Signal segmentation and feature extraction

The selected MID windows were segmented into sliding windows with an overlap of 50%. In particular, two different window lengths were considered: one of the most used for pattern recognition purposes, 150 ms [11], and one of the shortest, 50 ms [2], [12], with an overlap of 75 ms and 25 ms, respectively. On each sliding window, 10 time-domain and 10 frequency-domain features were extracted and grouped into 3 features sets (Table I): *Hudgins feature set (HUD)*, composed by MAV, WL, SSC and ZC; *Time domain features combined with autoregressive model coefficients (TDAR)*, composed by MAV, SSC, WL, VAR, WAMP, ZC, AR1, AR2, AR3 and AR4; *Frequency feature set (FREQ)*, composed by MNF, MDF, PKF, TTP, SM1, SM2, SM3, FR, PSR and VCF.

C. Canonical correlation analysis

To maximize the correlation between features related to different subjects performing the same task, the canonical correlation analysis (CCA) was employed. Given two different feature matrices $X \in R_{d\times n}$ and $Y \in R_{k\times n}$, with n number of observations and d and k number of features (which could be same or different), the CCA finds two projection matrices, $W_x \in R_d$ and $W_y \in R_k$, able to maximize the following correlation coefficient:

$$\varrho = \frac{W_x^T X Y^T W_y}{\sqrt{((W_x^T X X^T W_x)(W_y^T Y Y^T W_y))}} \tag{1}$$

Since ϱ is invariant with respect to W_x and to W_y, the previous formulation is equivalent to:

$$\max\ W_x^T X Y^T W_y \tag{2}$$

$$\text{subjected to } W_x^T X X^T W_x = 1,$$
$$W_y^T Y Y^T W_y = 1.$$

Once W_x and W_y have been extracted, the new features matrices can be obtained simply by multiplying the original matrices by the projection matrices:

$$M = W_x^T X \tag{3}$$
$$N = W_y^T Y$$

The obtained features matrices M and N have dimension $n \times min(d, k)$ and they are highly correlated in the new space.

This CCA implementation can be simplified by solving a least square problem [13], minimizing the following function:

$$L_2(W, \lambda) = \sum_{j=1}^{k}(\sum_{i=1}^{n}((x_i^T w_j - T_{ij})^2 + \lambda||w_j||_2^2)) \tag{4}$$

TABLE I: LIST OF FEATURES

Domain	Feature name	Abbreviation
Time domain	Mean absolute value	MAV
	EMG Variance	VAR
	Waveform length	WL
	Zero crossing	ZC
	Slope sign change	SSC
	Willison amplitude	WAMP
	Auto-regressive coefficients (4^{th} order)	AR
Frequency domain	Mean frequency	MNF
	Median frequency	MDF
	Peak frequency	PKF
	Total power	TTP
	1^{st} spectral moment	SM1
	2^{nd} spectral moment	SM2
	3^{rd} spectral moment	SM3
	Frequency ratio	FR
	Power spectrum ratio	PSR
	Variance of central frequency	VCF

List of computed time-domain (top) and frequency-domain (bottom) features for the study. Full feature name (central column) and its abbreviation (third column) are reported.

with T defined as:

$$T = (YY^T)^{-\frac{1}{2}}Y \tag{5}$$

To obtain T, feature matrix related to one subject, i.e. *expert user*, constituted the Y matrix. Then, the remaining users, one by one, were made similar to T through (4) to create, at the end, a unified-style-space [14].

D. Experimental framework

Once extracted the feature matrices, projection matrices were computed from 3 repetitions of each movement (calibration subset, CLB-S) by using least-square CCA (LS-CCA). Then, the projection matrices were applied to a subset (training subset, TRN-S) including the remaining repetitions of each movement, i.e. 6 repetitions, and used to train SVM models.

One subject at a time was selected as the expert user [14] and the LS-CCA was applied between the CLB-S belonging to the expert user and that of another subject. The obtained projection matrix corresponding to the other user was then multiplied by the TRN-S of the same subject. Each user in turn was correlated with the expert one in the same way and the obtained projected TRN-S were concatenated to form a unique new feature matrix in the new, highly correlated feature space. One subject was retained from the procedure, since it is used for testing. The same process was applied to all the subjects and thus each subject, in turn, was used as the expert user and for testing. Finally, for dimensionality reduction, the spectral regression algorithm was applied to the new, highly correlated feature matrix, with dimension $n \times (c-1)$, where c represents the number of classes [7]. A graphical representation of the presented framework is reported in Fig.1.

For the classification stage, a support vector machine (SVM) classifier with a linear kernel was employed. The SVM was trained through the reduced matrix obtained after concatenation and dimensionality reduction. Then, it was tested on the

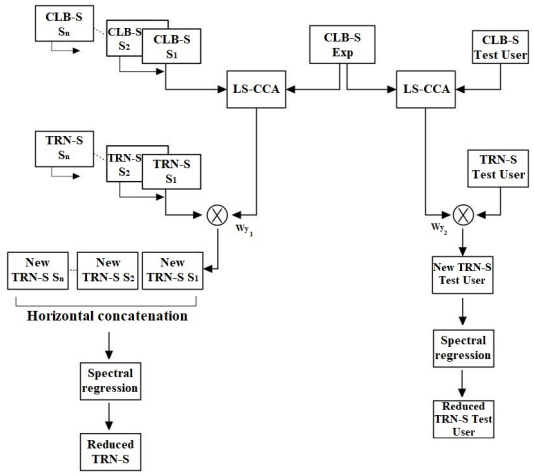


Fig. 1: Schematic representation of the presented framework. n is the maximum number of subject for the correlation (here 6, not considering expert and testing user). CLB-S indicates the calibration subsets of the subjects used to perform the LS-CCA to extract the projection matrix W_y. Reduced TRN-S is the subset used to perform the training of the SVM after the projection, concatenation and dimensionality reduction. Differently, reduced TRN-S test user is used for the testing phase of the classifier. The test user is left out from the concatenation for the training session.

new feature matrix belonging to the test user which was not included in the training session (unseen data). This analysis was repeated for all the three different feature sets and for the two window lengths. Finally, the performance of the framework was evaluated considering classification accuracy and statistically compared through a two-sample t-test with the accuracy obtained performing the same analysis but without applying the LS-CCA based framework. Significance level was set at $p < 0.05$.

III. Results

A. LS-CCA framework

Classification accuracy in all the tested conditions and with and without the application of LS-CCA framework, is reported in Fig. 2 as the average values among all the subjects, each one considered once as expert user and once as testing user. In particular, it can be noted that the accuracy with the LS-CCA ranges between 64% and 71%, except for the FREQ dataset with a 150 ms window (Fig. 2). Conversely, accuracy without the LS-CCA resulted always about 25%. Differences between the results with and without the application of the LS-CCA were statistically significant for each considered case.

B. Window length

In Fig. 3 is reported the comparison between the results obtained with the two window lengths used for feature extraction. In all the conditions, classification performances using a 150 ms window were equal or lower with respect to 50 ms window. However, only for the *FREQ_LSCCA* feature set, the difference between the use of 50 ms or 150 ms was statistically significant.

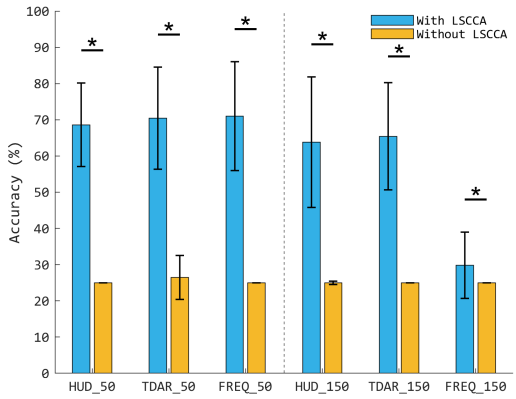


Fig. 2: Classification accuracy for the three feature sets (*HUD*, *TDAR* and *FREQ*) with window length of 50 ms (left side) and 150 ms (right side). Asterisk indicates a significant statistical difference.

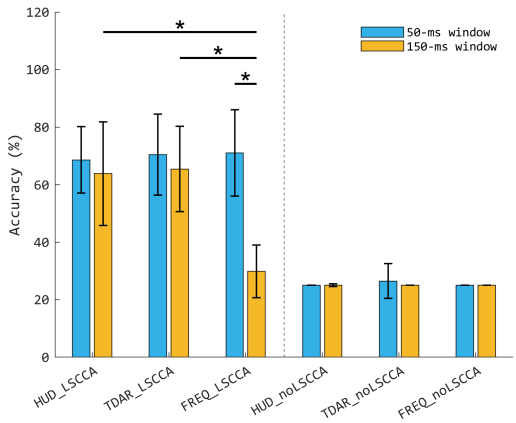


Fig. 3: Classification accuracy for the three feature sets (*HUD*, *TDAR* and *FREQ*) with LS-CCA (left side) and without LS-CCA (right side). Asterisk indicates a significant statistical difference.

C. Feature dataset

The *HUD* and *TDAR* feature sets are composed by time-domain features, while *FREQ* set contains frequency-domain features. Without the LS-CCA, no statistically significant differences were observed between the accuracy obtained with the different feature sets, nor using a 50 ms window, neither with a 150 ms window (Figs. 2 and 3). With the use of LS-CCA, the *FREQ* feature set showed the highest accuracy (71%) with the 50 ms window length, while in the 150 ms condition the *TDAR* feature set presented the highest value (65%). However, significant differences arose only between *HUD* and *FREQ*, and between *TDAR* and *FREQ*, using 150 ms window in both cases (Fig. 3).

IV. Discussion

In the present study, a framework based on the application of the LS-CCA to multi-user MID pattern recognition problems

has been investigated. Nowadays, the topic of motion pattern recognition is largely studied, with particular attention devoted to the multi-user scenario [14], [15]. The MID problem is relatively less studied with respect to the motion recognition, due to its higher intrinsic complexity [6], [9]. However, it represents a research area of interest mainly for medical technology, rehabilitation, and prosthetic, since decoding the intent of motion can aid the use of assistive devices [6]. Hence, in this study, an approach based on the LS-CCA has been applied to the MID problem for multi-user usability. The CCA has been yet employed to solve motion recognition problems [14], [15], i.e. to classify movements having available the entire gesture, with features extracted from a static epoch of the sEMG signal. On the other hand, the recognition of the motion intent deals with transient sEMG epochs: features are computed from a time window relative to the very initial part of the movement, much shorter than the common gesture recognition problem.

The LS-CCA framework proposed in this study proved to be a reliable way for addressing the multi-user problem within a MID context. A significant improvement in the classification accuracy can be appreciated, from 25% up to 71% in the best case (Fig. 2). These outcomes highlighted that the CCA succeeded in enhancing the correlation of the different users with an expert one, providing high classification performances also when a short time window (50 ms) was used for feature computation. Only in the case of the *FREQ* feature set computed with 150 ms window, the improvement of the accuracy was not observed (Fig. 3).

Regarding the use of different window lengths, 150 ms is one of the most used for motion recognition problems [8], [14]. However, the accuracy using 50 ms window are equal or even higher than with respect to those related to 150 ms window (Fig. 3), showing up also a significant difference with *FREQ* feature set together with LS-CCA. Although for motion recognition applications, optimal values for window length are between 150 ms and 200 ms [11], recent studies reported high classification performances also with shorted window lengths, equal or below 50 ms [2], [12].

Finally, in this study, *HUD*, *TDAR* and *FREQ* sets guaranteed similar performances and no significant differences have been observed, except between *HUD* and *FREQ* and between *TDAR* and *FREQ*: the *FREQ* feature set in LS-CCA with 150 ms showed the lowest accuracy (29%). Instead, the *FREQ* feature set reached the highest accuracy in LS-CCA with the 50 ms window, highlighting again the reliability of the 50 ms window for feature computation.

V. Conclusion

In this study, a framework based in LS-CCA is proposed for multi-user myoelectric pattern recognition. The novelty lies in the application of this methodology for motion intent detection, based on transient sEMG data. The LS-CCA allowed the generalization of the feature space among the subjects, with a domain adaptation that provides significant advantages in terms of computational demands with respect to recently introduced techniques such as deep domain adaptation and transfer learning. Moreover, it was observed that features computed from 50 ms window gave similar results, or even better, than those computed from 150 ms window. This, together with the efficient computational methodologies employed, i.e. LS-CCA and SVM, allow possible transfer of such methodology for rehabilitative and assistive technologies.

References

[1] M. Zecca, S. Micera, M. C. Carrozza, and P. Dario, "Control of multifunctional prosthetic hands by processing the electromyographic signal," *Critical Reviews™ in Biomedical Engineering*, vol. 30, no. 4-6, 2002.

[2] A. Tigrini, M. Scattolini, A. Mengarelli, S. Fioretti, M. Morettini, L. Burattini, and F. Verdini, "Role of the window length for myoelectric pattern recognition in detecting user intent of motion," in *2022 IEEE International Symposium on Medical Measurements and Applications (MeMeA)*. IEEE, 2022, pp. 1–6.

[3] A. Mengarelli, A. Tigrini, S. Fioretti, S. Cardarelli, and F. Verdini, "On the use of fuzzy and permutation entropy in hand gesture characterization from emg signals: Parameters selection and comparison," *Applied Sciences*, vol. 10, no. 20, p. 7144, 2020.

[4] F. S. Botros, A. Phinyomark, and E. J. Scheme, "Electromyography-based gesture recognition: Is it time to change focus from the forearm to the wrist?" *IEEE Transactions on Industrial Informatics*, vol. 18, no. 1, pp. 174–184, 2020.

[5] E. Trigili, L. Grazi, S. Crea, A. Accogli, J. Carpaneto, S. Micera, N. Vitiello, and A. Panarese, "Detection of movement onset using emg signals for upper-limb exoskeletons in reaching tasks," *Journal of Neuroengineering and Rehabilitation*, vol. 16, no. 1, pp. 1–16, 2019.

[6] J. V. Kopke, M. D. Ellis, and L. J. Hargrove, "Determining user intent of partly dynamic shoulder tasks in individuals with chronic stroke using pattern recognition," *IEEE Transactions on Neural Systems and Rehabilitation Engineering*, vol. 28, no. 1, pp. 350–358, 2019.

[7] E. Nsugbe and A. H. Al-Timemy, "Shoulder girdle recognition using electrophysiological and low frequency anatomical contraction signals for prosthesis control," *CAAI Transactions on Intelligence Technology*, vol. 7, no. 1, pp. 81–94, 2022.

[8] A. Tigrini, L. A. Pettinari, F. Verdini, S. Fioretti, and A. Mengarelli, "Shoulder motion intention detection through myoelectric pattern recognition," *IEEE Sensors Letters*, vol. 5, no. 8, pp. 1–4, 2021.

[9] D. D'Accolti, K. Dejanovic, L. Cappello, E. Mastinu, M. Ortiz-Catalan, and C. Cipriani, "Decoding of multiple wrist and hand movements using a transient emg classifier," *IEEE Transactions on Neural Systems and Rehabilitation Engineering*, 2022.

[10] D. Rivela, A. Scannella, E. E. Pavan, C. A. Frigo, P. Belluco, and G. Gini, "Analysis and comparison of features and algorithms to classify shoulder movements from semg signals," *IEEE Sensors Journal*, vol. 18, no. 9, pp. 3714–3721, 2018.

[11] L. H. Smith, L. J. Hargrove, B. A. Lock, and T. A. Kuiken, "Determining the optimal window length for pattern recognition-based myoelectric control: balancing the competing effects of classification error and controller delay," *IEEE Transactions on Neural Systems and Rehabilitation Engineering*, vol. 19, no. 2, pp. 186–192, 2010.

[12] A. A. Al Taee, R. N. Khushaba, T. Zia, and A. Al-Jumaily, "The effectiveness of narrowing the window size for ld & hd emg channels based on novel deep learning wavelet scattering transform feature extraction approach," in *2022 44th Annual International Conference of the IEEE Engineering in Medicine & Biology Society (EMBC)*. IEEE, 2022, pp. 3698–3701.

[13] L. Sun, S. Ji, and J. Ye, "Canonical correlation analysis for multilabel classification: A least-squares formulation, extensions, and analysis," *IEEE Transactions on Pattern Analysis and Machine Intelligence*, vol. 33, no. 1, pp. 194–200, 2010.

[14] R. N. Khushaba, "Correlation analysis of electromyogram signals for multiuser myoelectric interfaces," *IEEE Transactions on Neural Systems and Rehabilitation Engineering*, vol. 22, no. 4, pp. 745–755, 2014.

[15] B. Xue, L. Wu, K. Wang, X. Zhang, J. Cheng, X. Chen, and X. Chen, "Multiuser gesture recognition using semg signals via canonical correlation analysis and optimal transport," *Computers in Biology and Medicine*, vol. 130, p. 104188, 2021.

Performance Evaluation of the Gloreha Sinfonia Device in Bimanual Modality

M. Lapresa[1], E.M. Romano[1], L. Zollo[1] and F. Cordella[1]
[1] *Research Unit of Advanced Robotics and Human-Centred Technologies, Department of Engineering, Università Campus Bio-Medico di Roma, Via Alvaro del Portillo 21, 00128 Roma, Italy*

***Abstract*—Hand exoskeleton based devices are widely used to deliver bilateral therapy, and it is worth assessing their performance to evaluate their accuracy in reproducing on the injured hand the configuration recorded on the healthy hand. The aim of this work it to assess the performance of the *Gloreha Sinfonia* device in terms of the accuracy in reproducing the kinematic configuration in bimanual modality and responsiveness, during two types of tasks: a grasping task and a free flexion/extension task. To this purpose, an optoelectronic motion capture system was used to record the position of retroreflective markers positioned on both the sensorized and motorized glove, and the metacarpophalangeal joint angle was estimated. The responsiveness of the system was evaluated through the computation of the activation delay of the motorized glove, and was in the order of 1.5 s. The accuracy was evaluated through the computation of the Mean Absolute Error of the aligned angular trajectories of the two hands. Errors were in the order of 12 deg and 9 deg respectively for the grasping and flexion/extension trials. Nevertheless the magnitude of the errors, the benefits of the use of *Gloreha Sinfonia* in improving the hand function remain undisputable as demonstrated in many clinical studies.**

***Keywords*—Gloreha Sinfonia, Bimanual Therapy, Kinematic Accuracy, Responsiveness, Motion Capture System**

I. INTRODUCTION

Neurological disorders, such as stroke, represent the first cause of long term disability worldwide [1]. More than 12.2 million stroke cases are reported globally each year [2]. Around 60% of people who survive stroke suffers from sensory-motor deficits on the contralateral limb of the affected cerebral area. Main limitations include paresis, spasticity, loss of sensitivity and reduction of Range of Motion (RoM). The administration of a prompt rehabilitative treatment is crucial to allow reeducating the patient to autonomously perform Activities of Daily Living [3]. Robot-mediated therapy allows delivering task-oriented and intensive exercises and quantitatively assessing the patients' improvements [4], therefore representing a valuable support to the traditional therapy.

Numerous examples of robot-mediated rehabilitation applied to the hand can be found in the literature. These applications often involve the use of exoskeletons, devices whose mechanical structure mirrors the skeletal conformation of the limb. Such systems are tipically used to move the paretic hand according to predefined gestures, to deliver task-oriented therapy as well as mirror therapy, which consists in replicating on the injured hand, through a bilateral approach, the movements generated by the healthy hand [5, 6]. The *Gloreha Sinfonia* device [3], the BRAVO exoskeleton [7], the hand exoskeleton developed in [8], the Motion Actuator Glove [9] and the soft gloves-based hand rehabilitation system proposed in [6] are examples of exoskeleton-based devices used to deliver bilateral therapy. All these systems allow reproducing on the affected hand, through a motorized exoskeleton, the movement of the healthy hand recorded through different types of sensors. The performance evaluation of these systems in reproducing the kinematic configuration of the healthy hand on the paretic one is paramount to assess the quality of the rehabilitation therapy. To the best of our knowledge, the performance of the *Gloreha Sinfonia* device was not evaluated yet.

Therefore, the objective of this work is to assess the responsiveness and accuracy of the *Gloreha Sinfonia* in reproducing the hand kinematic configuration in bimanual modality.

The paper is organized as follows: the materials and methods exploited to conduct the analysis are reported in Section II, results are shown and discussed in Section III and conclusions are provided in Section IV.

II. MATERIALS AND METHODS

A. Experimental Setup

The *Gloreha Sinfonia* (Idrogenet, Italy) is a device used to perform hand rehabilitation, which allows restoring the functional hand RoM [3]. It is an exoskeleton capable of independently moving and monitoring the five fingers of the hand. It consists of three modules:

- A glove equipped with five resistive flex sensors (Flexpoint Inc.), that allow evaluating finger flexion and extension range, connected to an electronic board that sends data to the computer via a USB protocol;
- A motorized glove driven by five electric motors (LA12 Actuator, TECHLINE). Each motor, which is placed into a dedicated unit far from the patient, controls the tension of flexible trasmissions that can be mounted on the back of the sensorized glove to assist the user in performing flexion and extension movements of the fingers;
- A software for the data acquisition and motor control, that integrates virtual reality environments to replicate task-oriented daily life activities.

The motorized glove can be used as an independent module for passive hand mobilization or in combination with the sensorized glove to deliver bimanual mirror therapy. In the bimanual modality, the patient wears the sensorized glove on the

healthy hand and the motorized glove on the paretic hand, and performs flexion/extension, grasping or reaching movements with the healthy hand. The angular information measured on the healthy hand is used to control the motorized glove placed on the paretic hand so that the active movement performed by the subject is replicated as efficiently and faithfully as possible on the paretic hand.

Given the architecture of the device, in the bimanual mode it is not possible to record angular information on both hands with the embedded sensors. In fact, the system allows this information to be recorded only on the healthy hand which actively performs the movements.

Therefore, in order to record the angular information from both hands, the BTS Smart-D optoelectronic motion capture system (BTS Bioengineering) was exploited to record the position of retroreflective markers placed on both gloves. The system consists of 8 infrared cameras with a resolution up to 1.4 Mp, an acquisition frequency of 60 Hz, and with an accuracy ≤ 0.2 mm in a volume of $3 \times 2 \times 2$ m^3.

The experimental setup is shown in Figure 1. It consisted of the *Gloreha Sinfonia* system and of the BTS Smart-D optoelectronic system. In particular, both the sensorized and motorized glove were used. Eighteen retroreflective markers were positioned on each glove, as shown in Figure 2 [10, 11]. Markers B1, B2 and B3 allowed defining the hand base reference frame as follows: the x axis was defined as the unit vector pointing from B1 to B2, the y axis as the unit vector obtained by the cross product between $\overrightarrow{B1B3}$ and $\overrightarrow{B1B2}$ and the z axis which completed the frame. For the long fingers, three markers were placed in correspondence of the metacarpophalangeal (MCP) joints, distal interphalangeal (DIP) joints and tip of the fingers (TIP), respectively. For the thumb, three markers (i.e., MCP, IP and TIP) were placed respectively on the metacarpophalangeal joint, interphalangeal joint and tip of the finger. Markers positions were expressed with respect to the hand base reference frame according to Eq. 1

$$M_{hand} = -R^{hand}_{camera} \cdot B1^{camera} + R^{hand}_{camera} \cdot M^{camera} \quad (1)$$

where M^{camera} and M^{hand} were the coordinates of the generic marker expressed with respect to (w.r.t.) the cameras global reference frame and hand base reference frame, respectively, R^{hand}_{camera} was the rotation matrix which expressed the orientation of the cameras global reference frame w.r.t. the hand base reference frame and $B1^{camera}$ was the origin of the hand base reference frame expressed in the camera global reference frame. Then, local reference frames were defined at each joint starting from marker positions. The flexion axis (i.e., the z axis) of each finger was defined as the unit vector normal to the plane defined by markers MCP, DIP and TIP, the x axis was defined as the unit vector pointing from the proximal to the distal marker (i.e., from B2 to MCP for the MCP frame, from MCP to DIP for the DIP frame and from DIP to TIP for the TIP frame), and the y axis as the unit vector which completed the frame.



Fig. 1: Experimental setup: (1) monitor with the virtual reality environment which replicates the hand movements; (2) motor unit; (3) sensorized (left hand) and motorized (right hand) gloves with retrorefletive markers; (4) BTS Smart-D optoelectronic motion capture system.

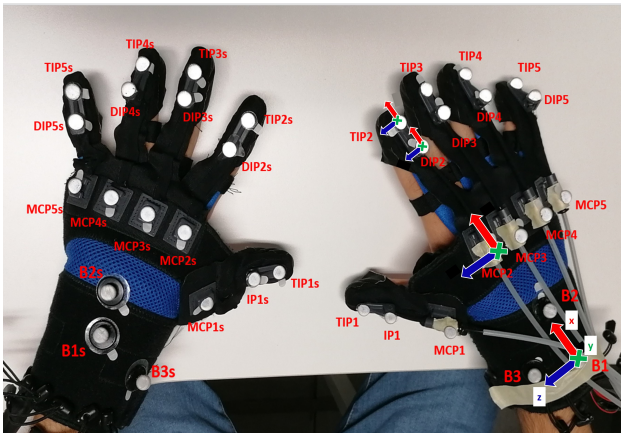


Fig. 2: Retroreflective markers positioned on the gloves.

The underactuated mechanical structure of the motorized glove implies that when the MCP joint flexes, also the other joints flex. Therefore, only the flexion/extension angles of the MCP joints were computed in this work. Angles were extracted as sequences of Euler angles obtained from the rotation of the local reference frame at the DIP w.r.t. the MCP local reference frame. The computed angles were positive for finger flexion and negative for finger hyperextension.

B. Experimental Protocol

One healthy male volunteer aged 21 years was enrolled to perform the experimental acquisitions. He wore the sensorized glove on his left, dominant hand, and the motorized glove on the right hand. He was asked to comfortably sit in front of the table on which the monitor showing the virtual hands was placed (Figure 1). In this experimental protocol, the virtual reality which shows the virtual hands replicating the executed movement is only employed as a built-in functionality of the system, but its therapeutic effects were not taken into account

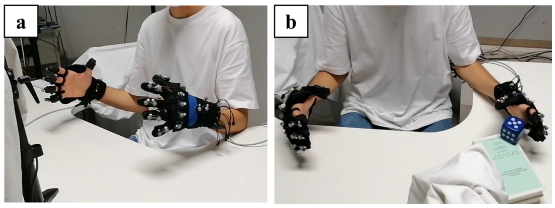


Fig. 3: (a) Initial reference configuration, (b) grasping task of the cube.

as the executed trials were not part of a therapy but they were only technical trials to evaluate the system performance. The volunteer started all the trials from the same reference position, i.e. shoulder adducted, elbow flexed at 90°, wrist in its neutral position and hands completely open, as shown in Figure 3a.

The volunteer performed two types of trials: a free flexion/extension movement of the hand (i.e., flexion of the hand from full extension and return to full extension) and a grasping and release task of a cubic object ($5.5 \times 5 \times 5.5$ cm^3), shown in Figure 3b. For each type of trial, he was asked to perform the movement with the left hand, on which the sensorized glove was placed. The motorized glove placed on the right hand replicated the movement according to the bimanual operation modality. In particular, five repetitions were recorded for each type of movement. We chose to enroll only one volunteer because the aim of this work was to evaluate the accuracy and responsiveness of the system that is independent of the analyzed subject. However, the volunteer performed five repetitions of each type of trial to guarantee a sufficient amount of data to perform the analysis.

C. Data Analysis and Performance Indicators

Angles were extracted through the previously described protocol using the BTS Smart Analyzer software, and then exported as text files to MATLAB R2021b to be post-processed. The MCP flexion/extension angles were filtered with a low-pass Butterworth filter with cutoff frequency of 1 Hz.

The performance of the *Gloreha Sinfonia* device was evaluated by extracting the following performance indicators:

1) Activation delay of the motorized glove (*Delay* [s]), to evaluate the responsiveness of the system, defined as the time from the movement onset of the healthy hand wearing the sensorized glove and the activation of the motorized glove;
2) Mean Absolute Error (*MAE* [deg]) between the angles calculated for the left hand (i.e., the hand with the sensorized glove) and the right hand (i.e., the hand with the motorized glove), to evaluate the accuracy of the system in reproducing angular configurations;
3) Standard Deviation (*SD* [deg]) of the error between the angles of the right and left hand.

The onset of the finger flexion movement, for each hand, was chosen by identifying the first frame for which the movement speed (i.e., the first time derivative of the angular trajectory) exceeded the 10% of the peak movement velocity for each finger. The errors were calculated after aligning the angle tracks by subtracting the activation delay to the right, motorized, hand.

The Kruskal-Wallis test was conducted to evaluate the effect of the finger and of the type of trial (grasping or free flexion/extension) on the computed MAEs. The level of significance was set to 0.05.

III. Results and Discussions

Figure 4 shows the angles computed for a representative grasping trial: the *Delay* is highlighted. The behaviour was similar for all the grasping and flexion/extension trials.

The average delay computed on the five repetitions of each type of movement was 1.48 ± 0.28 s for the grasping trials and 1.51 ± 0.63 s for the free flexion/extension trials. Therefore, the system exhibits a delay in the bimanual modality, due to the activation time of the motors.

The average MAEs are shown in Figure 5 for each finger. As evident, for the grasping trials, the errors ranged between 8.23 ± 3.07 deg for the thumb and 18.5 ± 5.51 deg for the little finger. For the free flexion/extension trials, average errors ranged between 8.26 ± 2.45 deg for the thumb and 10.5 ± 4.06 deg for the little finger.

The Kruskal-Wallis test did not evidence a statistically significant difference between the MAEs computed for the five fingers, for both type of trials ($p - value = 0.06$ and $p - value = 0.84$ for the grasping and flexion/extension trials respectively). The type of trial, instead, influenced the magnitude of the computed MAEs ($p - value = 0.0022$). In fact, errors were in general higher in grasping trials (median error 12.46 deg) w.r.t flexion/extension trials (median error 9.12 deg). This suggests that the interaction with an object could significantly modify the accuracy of the system in reproducing angular configurations, as the movement generated by the motors could be limited by the interaction of the fingers with the object.

Qualitatively, the pattern of the joint angles was slightly different between the two hands (Figure 4). In fact, a smooth trend can be noted for the sensorized glove and a jerky trend for the motorized glove. This behavior is related to the fact that the motors move by discrete steps corresponding to a percentage of the full scale of the motor itself [12]. In addition, the values from which the joint angles replicated by the motorized glove start and at which, in the final phase of motion, stabilize, are greater than those that characterize the joint angles of the sensorized glove. This aspect highlights that, in the bimanual mode, the motorized glove of the *Gloreha Sinfonia* does not allow the paretic hand to assume a configuration of full and maximum finger extension, given the presence of the transmission cables.

The magnitude of the MAEs calculated in this work could be related to the fact that the *Gloreha Sinfonia* motorized glove is an underactuated cable-driven device, therefore it does not allow to precisely control the angular configuration of each joint. Nevertheless, the system allows reproducing the qualitative configuration of the healthy hand on the paretic hand with sufficient accuracy for the considered application,

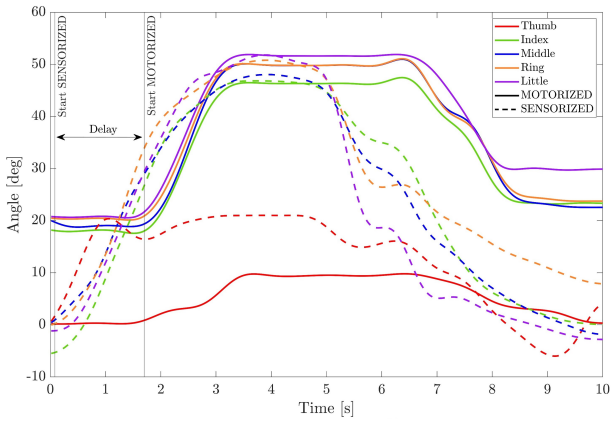


Fig. 4: Grasping trial. The angles calculated on the sensorized and motorized glove are shown with dotted and full lines respectively. The delay between the activation of the sensorized and motorized glove is highlighted.

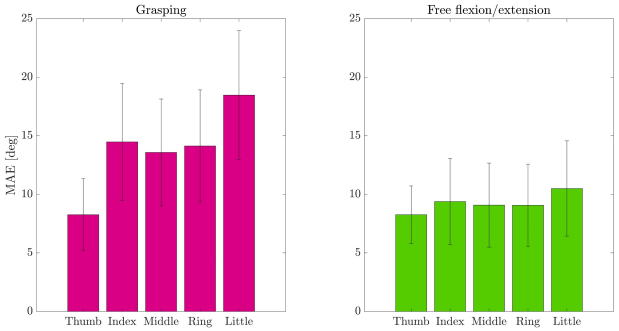


Fig. 5: MAE and SD computed on the five repetitions of each type of movement. For the grasping trials MAE±SD were 8 ± 3, 14 ± 5, 13 ± 4, 14 ± 5, and 18 ± 5 deg for the thumb to little finger, respectively. For the free flexion/extension trials MAE±SD were 8 ± 5, 9 ± 3, 9 ± 3, 9 ± 3, and 10 ± 4 deg for the thumb to little finger, respectively.

which is comparable to the accuracy of other existing systems [8, 9].

IV. Conclusion

In this work, the responsiveness and the accuracy of the *Gloreha Sinfonia* system in reproducing the kinematic configuration in bimanual modality was evaluated. The delay related to the activation of the motors was in the order of 1.5 s. The use of a marker-based motion capture system allowed evaluating the accuracy in reproducing the angular configuration on the contralateral hand through the motors activation. The MAE was in the order of 12.46 and 9.12 deg for the grasping and flexion/extension trials, respectively.

An improvement in motor response time would avoid the initial delay and, thus, make the execution of the exercise in bimanual mode synchronous.

Nevertheless, since the device is developed to administer a rehabilitative therapy to post-stroke patients, these aspects (i.e., motor response time delay of 1.5 s and MAEs in the order of 10 deg) do not negatively affect the effectiveness of the system, as demonstrated by clinical studies [13, 14].

Acknowledgement

This work was supported by the Italian Institute for Labour Accidents (INAIL) with 3D-AID and WiFi-MyoHand projects (CUP: E59E19001460005).

References

[1] Edwin Daniel Oña et al. “Robotics in health care: Perspectives of robot-aided interventions in clinical practice for rehabilitation of upper limbs”. In: *Applied sciences* 9.13 (2019), p. 2586.

[2] Valery L Feigin et al. “World Stroke Organization (WSO): global stroke fact sheet 2022”. In: *International Journal of Stroke* 17.1 (2022), pp. 18–29.

[3] Alberto Borboni, Maurizio Mor, and Rodolfo Faglia. “Gloreha—hand robotic rehabilitation: Design, mechanical model, and experiments”. In: *Journal of Dynamic Systems, Measurement, and Control* 138.11 (2016).

[4] Silvestro Micera et al. “A simple robotic system for neurorehabilitation”. In: *Autonomous Robots* 19.3 (2005), p. 271.

[5] Sivakumar Balasubramanian, Julius Klein, and Etienne Burdet. “Robot-assisted rehabilitation of hand function”. In: *Current opinion in neurology* 23.6 (2010), pp. 661–670.

[6] Xiaoshi Chen et al. “A wearable hand rehabilitation system with soft gloves”. In: *IEEE Transactions on Industrial Informatics* 17.2 (2020), pp. 943–952.

[7] Daniele Leonardis et al. “An EMG-controlled robotic hand exoskeleton for bilateral rehabilitation”. In: *IEEE transactions on haptics* 8.2 (2015), pp. 140–151.

[8] Satoshi Ueki et al. “Development of a hand-assist robot with multi-degrees-of-freedom for rehabilitation therapy”. In: *IEEE/ASME Transactions on mechatronics* 17.1 (2010), pp. 136–146.

[9] Mahdi Haghshenas-Jaryani, Charu Pande, and BJ Muthu Wijesundara. “Soft robotic bilateral hand rehabilitation system for fine motor learning”. In: *2019 IEEE 16th International Conference on Rehabilitation Robotics (ICORR)*. IEEE. 2019, pp. 337–342.

[10] Francesca Cordella et al. “Hand motion analysis during robot-aided rehabilitation in chronic stroke.” In: *Journal of Biological Regulators and Homeostatic Agents* 34.5 Suppl. 3 (2020), pp. 45–52.

[11] Francesca Cordella et al. “A bio-inspired grasp optimization algorithm for an anthropomorphic robotic hand”. In: *International Journal on Interactive Design and Manufacturing (IJIDeM)* 6 (2012), pp. 113–122.

[12] Martina Lapresa et al. “Development and Validation of a System for the Assessment and Recovery of Grip Force Control”. In: *Bioengineering* 10.1 (2023), p. 63.

[13] Jorge H Villafañe et al. “Efficacy of short-term robot-assisted rehabilitation in patients with hand paralysis after stroke: a randomized clinical trial”. In: *Hand* 13.1 (2018), pp. 95–102.

[14] Federica Bressi et al. “Robotic-Assisted Hand Therapy with Gloreha Sinfonia for the Improvement of Hand Function after Pediatric Stroke: A Case Report”. In: *Applied Sciences* 12.9 (2022), p. 4206.

A Safe Reinforcement Learning platform for Autonomous Robotic Tissue Approaching

Ke Fan[1], Giancarlo Ferrigno [1], Elena De Momi[1]
[1] *Department of Electronics, Information and Bioengineering, Politecnico di Milano, Milan*

***Abstract*—Surgical subtask automation in robotics can improve patient throughput, reduce quality-of-care variance among surgeries and relieves surgeons' fatigue. Reinforcement learning (RL) has shown considerable performance in autonomous control in complex environments, which can benefit autonomous surgical subtasks. However, existing RL platforms for surgical robots do not consider any safety requirements since they only allow robots to learn behavior through maximizing rewards based on unsafe trial-and-error interactions with the environment, which is unacceptable in automating surgical subtasks. In this work, we designed a safe RL platform that integrates safety criteria with an RL library and the da Vinci Research Kit (dVRK) for surgical robotic learning. A tissue approaching task under safety constraints is built on this platform, which is common in real-world surgical execution. We evaluate the designed platform using RL algorithms in simulation, provide analysis and show that the robot can learn safe behavior with our platform. Results show the safe RL platform can comply with safe constraints well during the task.**

***Keywords*—Safe RL, autonomous surgical subtasks, dVRK**

I. INTRODUCTION

Robot-Assisted Minimally Invasive Surgery (RAMIS) has obtained considerable achievements in the last two decades e.g. the development of the da Vinci surgical system (Intuitive Surgical, CA, USA). RAMIS allows performing complex surgical operations with high accuracy and flexibility while minimizing the post-operatory impact on the patient [1]. Surgical task automation has become a growing research field, aiming at improving patient throughput, reducing the difference in nursing quality between operations, and possibly providing automated surgery in the future. Nonetheless, substantial specific expertise of individual skills and a complicated development process are required to design the manually-tuned control policies [2], [3].

Learning-based methods, especially RL-based methods, provide a promising alternative to automating surgical tasks. These approaches are able to develop controllers for complex skills and generalize to a broader range of tasks and environments [4]. However, normal RL can not guarantee safe criteria. Agents will sometimes try dangerous or harmful behaviors in the course of learning [5], which is unacceptable, especially in the surgical robotics field. Methods to address the safety in RL have been proposed including Constrained Policy Optimization (CPO) [6] and Primal-Dual Optimization [7]. The latter is based on Lagrangian relaxation and updates parameters in primal and dual spaces in turn, which is proven to have better performance than CPO [8].

To develop safe RL algorithms, an effective learning platform is necessary. Currently, the most popular learning platform is "gym" from openAI [9]. The "satfy-gym" is then proposed based on the concept of safe RL, which is also the only learning platform to validate safe RL algorithms through a set of simple scenarios. There are also many learning platforms that are compatible with the dVRK such as dVRL [10] and UnityFlexML [11]. These learning platforms built the RL simulation environments for dVRK robots on top of Unity3D, integrating mainstream RL algorithms, and trying to endow the robot with standardized surgical skills.

However, The agents trained with these platforms do not consider safe constraints. Moreover, these platforms can not process safety-constrained RL problems which we will introduce in the next section.

In this work, we build a novel simulation platform for da Vinci surgical robot, which is used to accomplish a tissue approaching task. Most importantly, the platform is designed especially for processing safety-constrained RL problems. The platform can collect constraint information during the interaction from the simulation environment and send it to the python RL trainer. Then the safe RL algorithm can exploit this constraint information to endow the agent with safe behaviors. The code is publicly available at https://github.com/fanke1213812138/safe-RL-platform.

II. METHODS

The objective of this work is to approach the tissue under safe constraints, i.e. approaching the target tissue without collision with the nearby tissues or organs. For that, we designed a learning platform for the da Vinci surgical robot. The platform is composed of three parts: 1) a safe RL library for robots to learn behavior considering safe constraints during interaction with the environment; 2) the dVRK robots and surgical contents constructed on top of the physics engine; 3) a side channel is established as the bridge between the simulation and the RL lib to collect and send the constraint information. The system architecture is shown in Fig. 1.

A. Safe RL Lib

The safe RL Lib deals with the problem of training an agent with safe constraints based on constrained Markov Decision Processes (CMDPs)[12]. CMDPs are equipped with a set of cost functions $c_i, \dots c_k$, separate from the reward function. The feasible set in a CMDP is given by

$$\Psi_C = \{\pi : J_{C_i}(\pi) \leq d_i, i = 1, \dots, k\} \tag{1}$$

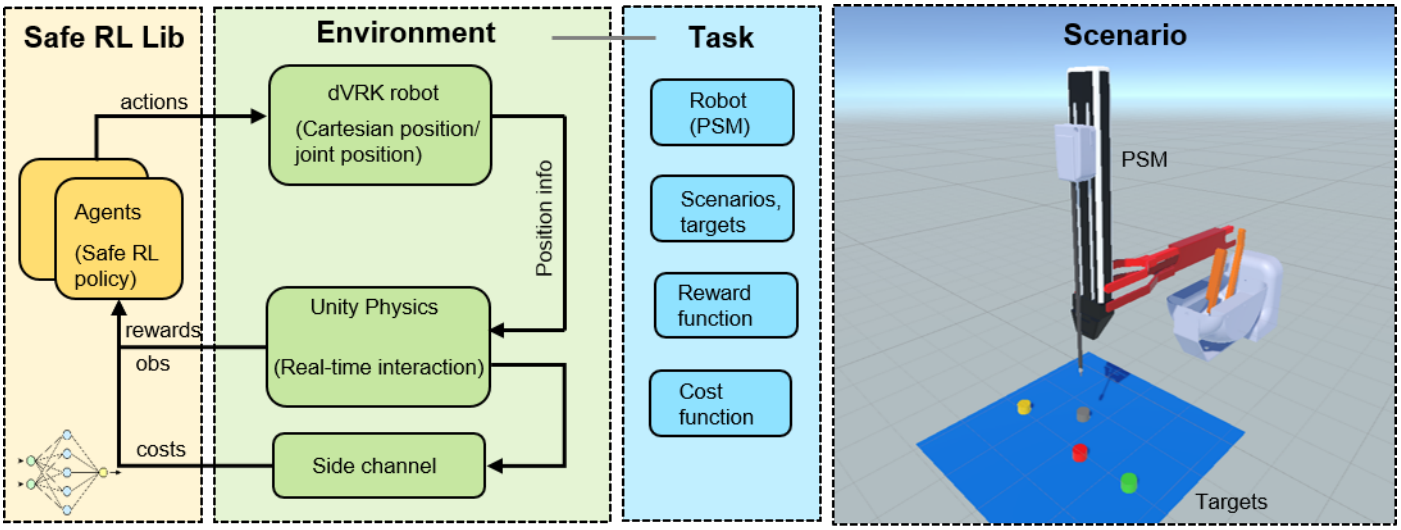


Fig. 1: Platform provides dVRK compatible simulation environments for surgical robot learning, safe RL algorithm and a learning task with a scenario and considering safe constraints in the meantime

where J_{C_i} is a cost function defined in the same way as the reward function, which shows how much the agent violates the constraints. The cost return should be less than a value d_i. Therefore, the constrained RL is to find a set of policies Ψ_C that satisfy the safe constraints. An optimal policy in constrained RL is given by:

$$\pi^* = \arg \max_{\pi \in \Psi_C} J_r(\pi) \tag{2}$$

where $J_r(\pi)$ is the reward function.

The safe RL algorithm aims at solving the above constrained RL problem. We use the PPO-Lagange algorithm [3]. Lagrangian methods use adaptive penalty coefficients to enforce constraints and solve equations (1) and (2) by solving the equivalent max-min optimization problem.

$$\max_{\theta} \min_{\lambda \geq 0} \doteq f(\theta) - \lambda g(\theta) \tag{3}$$

where $f(\theta)$ is the reward objective, $g(\theta)$ is the constraint, λ is the Lagrangian penalty coefficient and θ is the policy parameters.

B. Environment

The simulation environment supporting the patient side manipulator (PSM) of dVRK was built to manipulate various surgical objects. We use Unity3D as the physics engine for interaction. The trajectories (S, A, R, C, P, p_0) for RL training are collected during the interaction between the agent and the unity3d environment. S is the set of state, A is the set of agent actions, R is the reward function, C is the cost function, P is the transition probability function ($P(\acute{s} \mid s, a)$ means the probability of transition from$s$ to $\acute{s}$ by taking action a) and p_0 is the initial state distribution.

The observation space is the low dimensional information such as the object Cartesian positions poses and relative distance. The action space is the six joint positions of PSM or the Cartesian position of the end tip of PSM. In the latter case, the inverse kinematics of PSM is used. We built a side channel to send cost information to Rl trainer in addition to reward information.

C. Task and scenario

The agent which is the PSM in this context accomplishes the tissue approaching task. The task is built as an unity3D scenario. In the tissue approaching task, a dense reward function is designed, which gives a reward making the agent track the target. The cost function is sparse, which means the cost is obtained only when the agent touches constraints.

III. EXPERIMENT

In this section, we validate our safe RL platform by implementing the PPO-Lagange algorithm on a learning task with safe constraints.

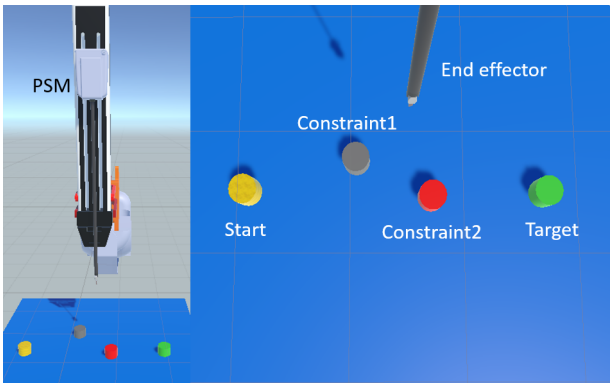


Fig. 2: Experimental setup. PSM is the agent which aims to reach the target without collision.

A. Experimental setup

In our simulation environment, a manipulation workspace was built for PSM and objects to work with as shown in fig.

2. In this task, the aim of the agent (PSM) is to move the end effector from the start position to the target position and avoid collision with constraint objects meanwhile. The end effector should bypass the gray and red objects.

In this context, the state is the Cartesian position of the end effector and the target; the action space is $a \in [-1, 0, 1]^2$ which means the end effector of PSM moves backward/stop/forward along x and y axis. The reward is dense: getting 30 points when reaching the target and $\left(1 - \frac{d}{max(d)}\right)$ points before reaching the target. d is the distance between the end effector and the target and $max(d)$ is the distance between the start position and the target position. The cost is sparse. When the end effector collides with the constraint objects, the agent gets 5 cost points. We also trained a policy based on the normal RL. We make the agent bypass the constraints by implementing punishment on the reward function. The reward function is:

$$\left(1 - \frac{d}{max(d)}\right) - \left(1 - \frac{d(cons)}{max(d)}\right) \tag{4}$$

where $d(cons)$ is the between the end effector and constraints. The training results are shown below.

B. Results

After training the PSM to achieve the goal, we observed two different behavior between the safe RL and the normal RL as shown in Fig. 3. The normal RL policy will act more conservatively trying to avoid collision from start. While the safe RL will learn to bypass the constraint until the action going to be unsafe, which is beneficial in a narrow space. In the approaching process, the distance between the end effector and the target of the safe RL-based agent is always smaller than that of the normal RL-based agent as shown in Fig. 4.

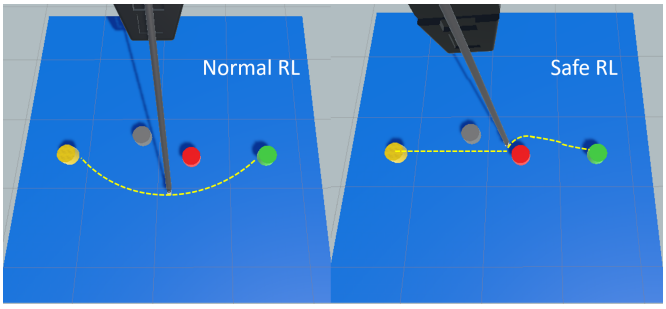


Fig. 3: Trajectory of the normal RL-based agent and the safe RL-based agent after training.

IV. Conclusion

In this work, we took three main steps toward building a safe RL platform for surgical robot learning to accomplish the tissue approaching task. Results show that our platform can confer the agent with safe behavior. We proposed to integrate a constrained RL algorithm into our safe RL library, building a simulation environment for the dVRK robot. We introduced a side channel to send cost information in addition to the normal RL information such as rewards, observation, and termination.

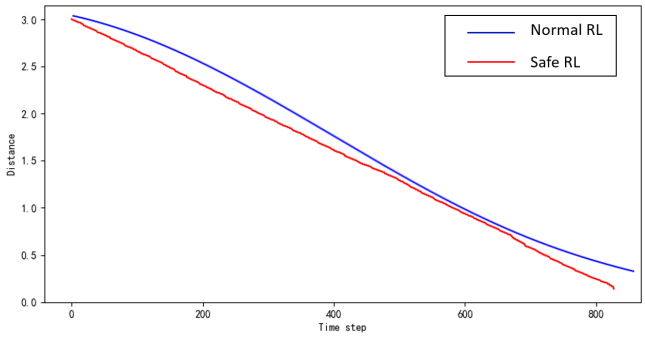


Fig. 4: Distance between the end effector and the target of the normal RL-based agent and the safe RL-based agent.

A task with safe constraints was built to validate the learning platform. We believe safe criteria are very important to surgical robotics. We will develop more effective safe RL algorithms based on the platform to enable the application of RL in surgical robotics in the future.

References

[1] T. Haidegger, "Autonomy for surgical robots: Concepts and paradigms," IEEE Transactions on Medical Robotics and Bionics, vol. 1, no. 2, pp. 65–76, 2019

[2] J. Schulman, A. Gupta, S. Venkatesan, M. Tayson-Frederick, and P. Abbeel, A case study of trajectory transfer through non-rigid registration for a simplified suturing scenario, 2013 IEEE/RSJ International Conference on Intelligent Robots and Systems (IROS). IEEE, 2013, pp. 4111–4117.

[3] S. Sen, A. Garg, D. V. Gealy, S. McKinley, Y. Jen, and K. Goldberg, "Automating multi-throw multilateral surgical suturing with a mechanical needle guide and sequential convex optimization," in 2016 IEEE international conference on robotics and automation (ICRA). IEEE, 2016, pp. 4178–4185.

[4] O. M. Andrychowicz, B. Baker, M. Chociej, R. Jozefowicz, B. McGrew, J. Pachocki, A. Petron, M. Plappert, G. Powell, A. Ray, et al., Learning dexterous in-hand manipulation, The International Journal of Robotics Research, vol. 39, no. 1, pp. 3–20, 2020.

[5] D. Amodei, C. Olah, J. Steinhardt, P. Christiano, J. Schulman, and D. Mané. Concrete Problems in AI Safety. 2016.

[6] J. Achiam, D. Held, A. Tamar, and P. Abbeel, Constrained policy optimization, in Proceedings of the 34nd International Conference on Machine Learning (ICML-17), 2017.

[7] Y. Chow, M. Ghavamzadeh, L. Janson, and M. Pavone, "Risk-constrained reinforcement learning with percentile risk criteria," arXiv preprint arXiv:1512.01629, 2015.

[8] Fujimoto, S., Conti, E., Ghavamzadeh, M. and Pineau, J. Benchmarking batch deep reinforcement learning algorithms. 2019.

[9] Brockman, G., Cheung, V., Pettersson, L., Schneider, J., Schulman, J., Tang, J. and Zaremba, W., 2016. Openai gym. arXiv preprint arXiv:1606.01540.

[10] F. Richter, R. K. Orosco, and M. C. Yip, "Open-sourced reinforcement learning environments for surgical robotics," arXiv preprint arXiv:1903.02090, 2019

[11] E. Tagliabue, A. Pore, D. Dall'Alba, E. Magnabosco, M. Piccinelli, and P. Fiorini, "Soft tissue simulation environment to learn manipulation tasks in autonomous robotic surgery," in 2020 IEEE/RSJ International Conference on Intelligent Robots and Systems (IROS). IEEE, 2020, pp. 3261–3266.

[12] E. Altman. Constrained Markov Decision Processes. page 260, 1999.

[13] D. Amodei, C. Olah, J. Steinhardt, P. Christiano, J. Schulman, and D. Mané. Concrete Problems in AI Safety. 2016.

[14] Fujimoto, S., Conti, E., Ghavamzadeh, M. and Pineau, J. Benchmarking batch deep reinforcement learning algorithms. 2019.

Sensor-based Assessment of Gross and Fine Motor Development in Primary School Children

M.C. Bisi[1], A. Masini[2], S. Toselli[2], S. Marini[2], L. Bragonzoni[3], A. Ceciliani[3], M. Lanari[4], A. Sansavini[5], A. Tessari[5], D. Gori[2], L. Dallolio[2], R. Stagni[1]

[1] *Department of Electrical, Electronic and Information Engineering "G. Marconi", University of Bologna, Italy*
[2] *Department of Biomedical and Neuromotor Science, University of Bologna, Italy*
[3] *Department of Life Quality Studies, University of Bologna, Italy*
[4] *Department of Medical and Surgical Sciences; University of Bologna, Italy*
[5] *Department of Psychology "Renzo Canestrari", University of Bologna, Italy*

***Abstract*— The present study aims to quantitatively assess gross and fine motor development in school children and investigate the influence of possible intrinsic factors. One hundred and fifty children from an Italian primary school participated in the study, which included assessments of anthropometric characteristics and characterization of gross and fine motor performance using wearable inertial sensors. When analysing gross motor development, the results showed that stance and double support duration increased with age, and that overweight was associated with a reduction in the development of automaticity. Quantitative assessment of fine motor skills showed that older children had shorter and less variable cycle durations and less regular and more complex movement patterns. The study highlights the advantages of using sensor-based assessments for monitoring gross and fine motor development in children.**

***Keywords*—motor development, inertial sensor, gross motor control, fine motor control**

I. Introduction

TIMELY motor development in childhood is crucial for a healthy adult life and aging, as it affects not only physical but also mental health and social participation [1]. Assessment of both gross and fine motor development as a part of the overall neuropsychological, and developmental examinations is fundamental to predict possible developmental problems such as developmental delays and disorders [2]. However, the ways in which intrinsic and extrinsic factors influence this development are still not clear.

Several tests have been proposed for the characterization gross and fine motor control, although their evaluation is mainly based on qualitative observation, limiting quantitative assessment to the measure of test durations [2]. Recently, wearable inertial sensors have allowed for the development of a quantitative longitudinal assessment approach for the monitoring of gross and fine motor development that can be used in ambulatory conditions [3].

The present study, which is part of the I-MOVE study [1], a school-based intervention trial, aims at characterizing gross and fine motor performance by exploiting parameters describing temporal performance and its variability, associated to peripheral realization of movement patterns, and nonlinear metrics, characterizing the underlying motor control [3], [4]. In order to investigate the influence of intrinsic factors on motor development, results will be analysed with respect to age, sex, anthropometric characteristics (for gross motor) and handedness (fine motor control).

II. Methods

A. Participants

One hundred and fifty children from an Italian primary school participated in the study, 72 first- (38M, 34F; age 75±5 months) and 78 third grade (48M, 34F; age 108±6 months). The study was approved by the University of Bologna Bioethics Committee, on the 18th of March 2019 (Prot. n. 0054382 of 18/03/2019). The study was conducted following the Declaration of Helsinki and approved by the school board.

B. Experimental protocol

Anthropometric characteristics (height, weight, triceps and subscapular skinfold thicknesses) were collected according to standardized procedures.

Gross motor development: children walked along a 20m straight path 3 times back and forth at self-selected speed (NW) and once in tandem (TW) wearing three synchronized inertial sensors (OPAL, APDM, Usa, sf =128Hz) on the lower back and on the shanks [3], [4].



Fig. 1: Normal walking (NW) and tandem walking (TW)

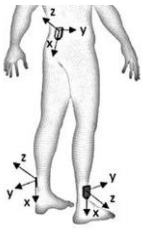


Fig. 2: Sensor positioning during locomotor tasks (NW and TW)

Fine motor development: children performed the Placing Bricks test (PB) [2] while wearing 2 synchronized tri-axial inertial sensors (OPAL, APDM, USA, sampling frequency, 128Hz), one per wrist; both hands were tested.

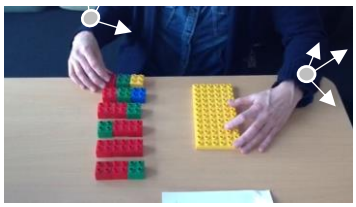


Fig. 3: Placing Bricks (PB) test and sensor positioning (white circles)

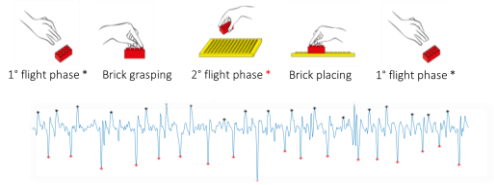


Fig. 4: Placing Bricks (PB) phases. Exemplificative phase segmentation on the measured signal.

C. *Data analysis*

Gross motor development: The following temporal parameters were estimated: stride-, stance-, double support-time. Variability of temporal parameters was calculated using Poicaré plots (short-term and long-term variability). Nonlinear metrics (recurrence quantification analysis and multiscale entropy) were calculated on 3D trunk acceleration to estimate regularity and complexity of movement pattern, respectively [3].

Estimated parameters were statistically analyzed (Kruskal-Wallis test 5%) with respect to age, sex, and anthropometric characteristics (i.e. weight, height, BMI, and triceps and subscapular skinfold thicknesses).

Fine motor development: The following temporal parameters were estimated: cycle duration, brick to board flight time, board to brick flight time [5]. Variability of temporal parameters was calculated using Poicaré plots (short-term and long-term variability). Nonlinear metrics (recurrence quantification analysis and multiscale entropy) were calculated on 3D wrist acceleration to estimate regularity and complexity of movement pattern, respectively.

Estimated parameters were statistically analyzed (Kruskal-Wallis test 5%) with respect to age, sex, and handedness.

III. Results

Gross motor development: Stance and double support duration increased during NW and decreased during TW with age independently from sex, while their variability decreased in both NW and TW. Automaticity (i.e. recurrence indexes) increased with age during NW more in female than in males, while it decreased during TW independently from sex. Complexity (i.e. entropy) increased with age during TW, but not in NW. No dependency on height or weight alone was identified independently from age, while overweight (i.e. BMI and skinfold thicknesses) was associated to a reduction in the development of automaticity during NW independently from age and sex.

Fine motor development: No difference between male and female participants was highlighted and motor performance with the dominant hand was more rapid and less variable, as expected. Older children showed shorter and less variable cycle duration than younger children. With respect to nonlinear measures, older children showed less regular (i.e. recurrence) and more complex (i.e. entropy) movement patterns.

IV. Discussion

Both sex and anthropometry resulted to influence gross motor development in the target population, in particular overweight appears to delay the maturation of automaticity.

When analyzing fine motor skills, older children showed shorter and less variable cycle duration than younger children: these results can be related to the expected maturation and the fine motor skills training during school years. On the other hand, older children showed less regular and more complex movement patterns, showing that their motor control allow the exploration of more flexible movements [4].

The present work highlighted the advantages of sensor-based quantitative assessment and the relevance of nonlinear metrics for assessing motor control development in school-children.

Acknowledgement

Authors would like to thank the School in Imola for agreeing to be part of this project.

References

[1] A. Masini *et al.*, «A Multiple Targeted Research Protocol for a Quasi-Experimental Trial in Primary School Children Based on an Active Break Intervention: The Imola Active Breaks (I-MOVE) Study», *Int. J. Environ. Res. Public. Health*, vol. 17, fasc. 17, Art. fasc. 17, gen. 2020, doi: 10.3390/ijerph17176123.

[2] H. S. Haga Håvard Lorås, Monika, «Assessment of Motor Competence Across the Life Span: Aspects of Reliability and Validity of a New Test Battery - 2016», *SAGE Open*, feb. 2016,

[3] M. C. Bisi, P. Tamburini, e R. Stagni, «A 'Fingerprint' of locomotor maturation: Motor development descriptors, reference development bands and data-set», *Gait Posture*, vol. 68, pp. 232–237, feb. 2019, doi: 10.1016/j.gaitpost.2018.11.036.

[4] M. C. Bisi, «Human motor control: Is a subject-specific quantitative assessment of its multiple characteristics possible? A demonstrative application on children motor development», *Med. Eng. Phys.*, p. 8, 2020.

[5] M.C. Bisi *et al.*, «Sensor based characterization of fine motor control in school children». *Proceedings XXII Congresso SIAMOC 2022.* p.45

Personality Traits Influence the Perception of a Robotic Arm endowed with Social Cues

C. La Viola[1], L. Fiorini[1], G. Mancioppi[1] and F. Cavallo[1]
[1] *Department of Industrial Engineering (DIEF), University of Florence, Via Santa Marta 3, Firenze, Italy*

***Abstract*— When interacting with robots, humans follow similar behavioral patterns as when they interact with other humans. In fact, the personality traits of people have a role in modifying how users perceive a robot that is interacting with them. Similarly, different combinations of social cues on a robot could modify its perception in terms of social aspects. In this context, this paper aims to explore the role of personality in the interaction with a robotic arm and it will investigate how different social cues can affect its perception. The social cues considered in this work are the face, the sound, and 2 different movements (i.e., direct and indirect). Thirty healthy people were included in this experiment. They were requested to perform a robot-to-human handover with different "social" properties. Quantitative feedbacks were collected through a questionnaire to evaluate the perceived emotion, fluidity, likeability, safety, and animacy of the interaction. Participants were divided into 2 clusters based on their Openness personality trait. Results show that when increasing the number of social cues on the robotic arm, the human perception tends to have a similar score for the 2 types of movements, while the differences were higher when comparing the scores of the interaction without social cues.**

***Keywords*—Robotic arm, Social robotics, Laban Movement Analysis, Robots and personality**

I. Introduction

Personality traits explain how people interact with each other [1]; also, when a person interacts with a robot, the human's personality traits play a key role in the perception of the interaction [2]. Researchers have started investigating how the role of personality influences Human-Robot Interaction (HRI) [3], [4], and the role of social interaction is of paramount importance when applied in the field of robotics rehabilitation, where robots are expected to interact with humans [5]. Such HRI in rehabilitation scenarios can be achieved through various social cues, namely robotic sound [6], [7] robotic face [8], [9], and robotic movement [10], [11]. Robotic movement is tackled in literature in different ways, and this work will face it using a theory of movement coming from the classical dance world: Laban Movement Analysis (LMA) [12], [13]. LMA explains movement according to various parameters and the different combinations of such parameters generate movements that carry emotional information. LMA is already used in rehabilitation robotics to make the robots move and interact with children affected by autism spectrum disorders [14], [15]. What was evinced from the literature is the use of LMA especially in humanoid robots (i.e. Nao, Softbank Robotics, Japan), for the execution of cognitive tasks. However, one limitation emerged from the works of rehabilitation and LMA: the social robots used in literature entangle limited capabilities for the execution of physical and manipulation exercises. Therefore, this work aims at establishing a new paradigm, where the manipulation capability of a robotic arm is used to perform cognitive exercises. Particularly, this work explores the interconnection among human perception based on personalities, LMA, and a robotic arm that offers manipulation capabilities. In this way, it would be possible to obtain a rehabilitation session managed by a robot that stimulates the patients in both the physical and the cognitive realms. For this reason, this work focuses on two research questions. The first aims to evaluate how people perceive a robotic arm endowed with different Laban movements in combination with different social cues. The second investigates how the difference in personality traits influences the perception of robotic movements. To evaluate human perception in a cognitive and physical stimulation scenario, the authors designed an experiment involving a robot-human handover. Such exercise can be extended to other kinds of rehabilitation exercises, such as the Tower of London test [16]. The next section will describe the overall procedure to create the experiment.

II. Materials and Methods

A. Robotic Arm and System Architecture

The entire system uses ROS [19] for robotic control. To manage the data collection and the user feedback, a specific web server was implemented and deployed on a Docker container. The networking among the component is done using a local router over the HTTP protocol. The ROS architecture is composed of a controller node, in charge of managing each HRI, 3 nodes, one for each social cue, and 3 utility nodes for the random generation of interaction sequences, for the dispatching of data to the web server, and for the persistence of relevant data. A schema of the proposed architecture is found in Figure 1. The robotic arm used in this experiment is the Panda robot (Franka Emika, Germany). All the user interactions were recorded using a RealSense camera (Intel, USA). Each interaction was triggered by e dedicated ROS service manually called by the experimenter. This allowed control over the duration of the session and management of any unexpected behavior.

B. HRI Design: Movement, Face, Sound

The handover task designed in this work is performed by the robot following two different types of Laban Movement, which will be addressed as Direct and Indirect movements. The first one is based on the LMA definition of angry behavior, while the latter was designed in LMA to trigger happiness. Such movements are generated starting from the authors' previous work [17] and are composed of parameters from the Laban Effort Graph (LEG), which describe the inner attitude towards the use of energy [18], and the Laban Space (LS), or how the person moves in the surrounding space, on the 3 axes [14]. The selected Laban parameters for these movements are explained in Table I. As for the face, it was entirely replicated from a previous work [9] where such a face

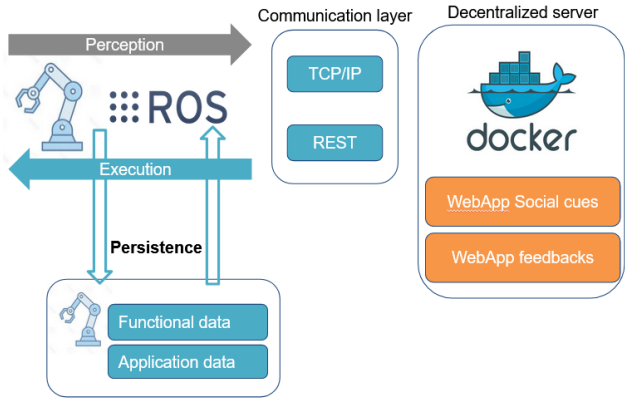


Fig. 1: Architectural schema of robotic components

TABLE I PARAMETERS FOR THE IMPLEMENTATION OF LABAN MOVEMENTS

Movement ID		**Direct (D)**	**Indirect (I)**
Laban Effort Graph (LEG) parameters	*Space*	Direct	Indirect
	Time	Sudden	Sudden
	Weight	Strong	Light
	Flow	Bound	Free
Laban Space (LS) parameters	*Horizontal*	Spreading	Spreading
	Vertical	Ascending	Ascending
	Wheel	Advancing	Advancing

was used on a non-humanoid robot for HRI with older adults. The face is displayed on a tablet at the robotic arm's base. Finally, the sound was designed starting from Zhang et al. [7], reproducing a similar sound pattern. The sound was created using the pygame library (https://www.pygame.org/docs/) and synchronized with the movement of the robotic arm. Each change in the movement triggered a change in the chord played by the sound system.

C. Participants

A total of 31 healthy young people were enrolled in the study. The people enrolled were researchers, medical doctors, psychologists, and nurses that volunteered in the experiment. All volunteers were accepted into the study, with no eligibility criteria. The data of one participant were excluded, for a failure in the technological setup. The group of thirty participants included in the study is composed of 61% female and 39% male; their education level is composed of 3 groups (38.7% Bachelor's Degree, 41.9% Master's Degree, and 19.4% Ph.D.). The mean age of participants is 30.4 years (standard deviation = 3.7). Before starting, all the participants received information on the test and a formal description of the experiment on paper; all of them signed the informed consent.

D. Experimental Procedure

The HRI task consists of the handover of a colored ball from the robot to the user. As the user receives the ball, then should put it in a box of the same ball color.
A single interaction can be divided into 3 main phases, namely Robotic Action, Human Action, and Questionnaires (Figure 2). Before starting with the first phase, the user is asked to fill in demographic and personality information. Then, the *Robotic action phase* takes place, which is composed of 5 sub-phases: i) The robotic arm turns toward the colored balls, ii) The robotic arm gets closer to the balls and picks one of them, iii) The robotic arm turns toward the user, iv) The robotic arm performs a Laban movement and gets closer to the user to handover the ball, v) The robot goes back to the idle position. The choice of the movement and which ball to pick is random. For the *User action phase*, there are 2 sub-phases: i) The user receives the ball from the robot, ii) The user puts the ball in the related box. After each interaction, the user was requested to complete the *Questionnaires phase*. This phase consists of filling the Self-Assessment Manikin [19] questionnaire (i.e. valence, arousal), a subset of the Godspeed questionnaire [20] (i.e. the fields of Animacy and Safety), and two Custom questions related to the Likeability and the Fluidity of the movement. The handover is performed 8 times for each participant, to allow all the combinations of movement and social cues. In the specific, there are 2 possible movements (Direct and Indirect) and 4 possible combinations of social cues (only movement, movement and sound, movement and face, movement, sound, and face); for this reason, the total interactions done per user are 8. At the end of the experiment, the experimenter asks 5 open questions to the participants. In this work only the last question will be evaluated, namely "Imagine bringing the robot home to use for your purpose, which configuration (sound, face, movement) would you like to have?". This experiment is relevant for a rehabilitation scenario because the different colors of the boxes or the balls can be combined to complicate the exercise based on the cognitive load that the therapist wants to reach in the phase of therapy (e.g. place the red ball in the blue box).



Fig. 2: Schema of Interaction Phases

E. Data Analysis

The participants in the experiment were clustered into two groups using a K-mean algorithm based on the results of the personality assessment. Such assessment is based on the BFI10 analysis [21] that classifies personality according to 5 components: Openness, Extraversion, Neuroticism, Conscientiousness, and Agreeableness. Then all the parameters coming from the questionnaire were grouped by personality cluster. For the questionnaire scores, the SAM values were extracted on a scale of 1 to 9; the Godspeed questions, each one evaluated from 1 to 5, were summed up together to obtain an aggregated index with all the scores for the Godspeed elements where the maximum value is 25 for Animacy and 15 for Safety and the minimum values are respectively 5 and 3. The Custom scores of Likeability and Fluidity were evaluated on a scale of 1 to 5. The authors

TABLE II DIVISION OF GROUPS IN CLUSTERS: DISTRIBUTION OF PERSONALITY TRAITS

	O	*E*	*A*	*C*	*N*
LOW-O	5.36	6.00	7.07	7.00	5.21
HIGH-O	8.82	5.88	6.41	7.12	6.35

Legend: O = Openness, E = Extraversion, A = Agreeableness, C = Conscientiousness, N = Neuroticism

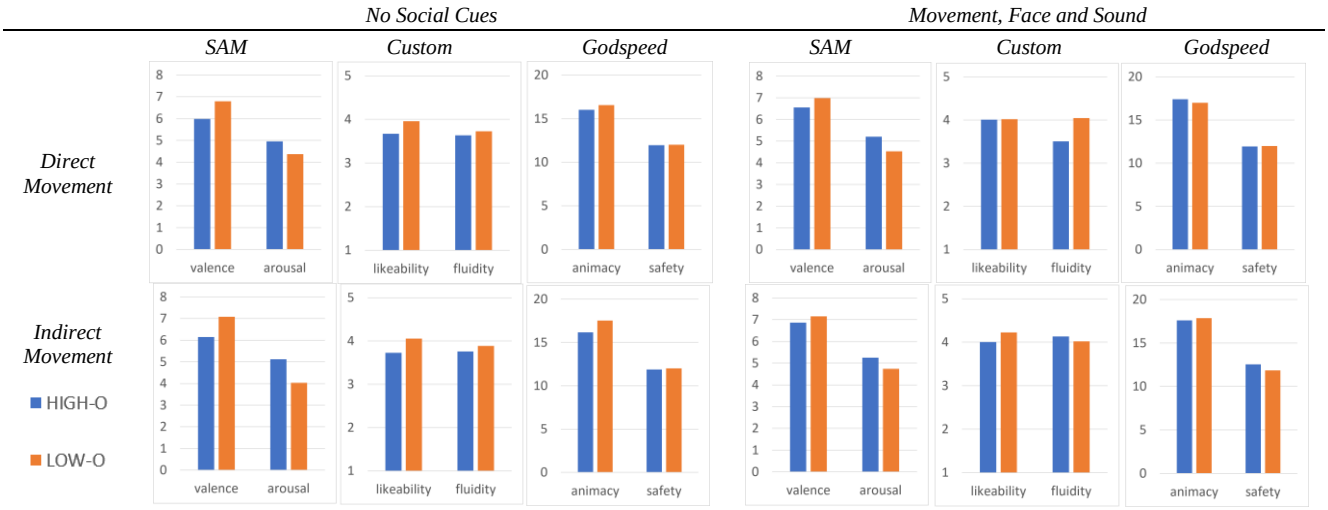


Fig. 3: Different Scoring grouped by Movement and Personality for the two clusters

analyzed the open answers using content analysis [22], and the preferred configuration of social cues and the preferred movement were extracted. This paper reports and compares the questionnaire data of the two cases where users interacted with the robot in presence of all the social cues and without any social cues.

III. Results

The clustering technique of K-mean allowed the authors to identify 2 clusters based on their BFI scores, as depicted in Table II. We can observe that the main difference between the two groups is in the Openness component, so the clusters will be addressed as HIGH-O and LOW-O. Such groups are composed of 13 and 17 people respectively, and their Openness values are 8.82 and 5.36. All the questionnaire scores were aggregated for each cluster and interaction, and the results are plotted in Figure 3. At first glance, the scores obtained by the cluster LOW-O are generally higher than the other one. This difference in scores fades out when compared to the interaction with all the social cues. As for the percentage of the preferred configuration, the one where both face and sound are present was the most voted, with 76.47% of preferences by the HIGH-O group and 53.85% by LOW-O. Related to the preferred movement, both groups preferred the Indirect one, with 52.94% in HIGH-O and 46.15% in LOW-O. It's noticeable that both HIGH-O and LOW-O groups expressed no preference for one specific movement (41.18% and 30.77% respectively). More details are in Table III.

IV. Discussion

The purpose of this study was to find whether personality affects the perception of robotic movements, and the trait of Openness was found suitable to influence human perception. The trait of Openness is defined as the capability of being creative and open to new ideas.

Table III Preferences of Movements By Cluster

	No Preference	*Indirect*	*Direct*
HIGH-O	*41.18%*	*52.94%*	*5.88%*
LOW-O	*30.77%*	*46.15%*	*23.08%*

The two personality clusters of this study show a general trend in all their answers but present a counterintuitive result. For the LOW-O group, the scores are always higher (i.e. more positive perception), while the expectancy was that the higher scores were related to the HIGH-O group. This counterintuitive result should be further investigated, and the correlation between the participant's past experiences with robots and the level of confidence they have in using a robot should be looked into. Only for the Arousal domain of the SAM, the HIGH-O group always has a higher score. As arousal is how strongly the participant perceived the feeling, this could be related to the personality, as more Openness could trigger the increasing emotional perception of a movement.

The results are aligned with findings from other authors that explored the role of Openness in the perception of robots. In [23], [24], Openness was proven to be effective in increasing the positive feeling toward the robot, and in [25] the role of Openness helped the participants in perceiving a robotic voice as positive.

For the Safety dimension, it is possible to notice that there is no fluctuation in its values among the interactions. This is encouraging, as the perceived safety is not changing depending on the movement, social cues, or considering personality. This result suggests for future experiments neglect this component when designing other Laban movements. Another element of contrast among the graphs in Figure 3 is the Fluidity evaluation with all social cues. The variation between the Direct movement and the Indirect is in contrast with the variation in the interaction with no social cues, which is close to 0. These findings suggest two possible implications: i) The interaction with all social cues impacts the perception of fluidity for the HIGH-O cluster, ii) When all the social cues are present, different movements are perceived differently in terms of fluidity.

At last, a general consideration can be extrapolated from the overall graphs. The use of multiple social cues decreases the perception of differences for all the considered parameters (but fluidity); therefore, the personality influences the perception of movement, but when movement is coupled with other social cues the difference gets flattened and the perception is more similar among different movements. The robotic arm employing all the social cues was the preferred configuration

for both groups, suggesting the fact that more social cues imply a higher quality of social communication.

The preference on which movement was the best is not unanimous in the two groups though. While the HIGH-O group has the most scores divided by Indirect and No Preference, such division is less uniform for LOW-O, having a distribution on the 3 possible answers much more balanced without a real polarization (Table II). This is probably due to the intrinsic effect of the Openness personality trait, which influences how people live new experiences. People belonging to LOW-O in fact, show a distribution that does not define a clear preference, enhancing the idea that the LOW-O group has more issues in categorizing robotic arm movements that which are seen for the first time.

V. Conclusion

The designed experiment confirmed the two research questions. The results obtained show how personality, specifically the Openness component, can affect the perception of movement for some parameters. The inclusion of social cues suggests that they have a real impact on the perception; indeed the use of multiple social cues also seems to decrease the difference in movement perception derived from personality traits. In future works, the sample size should be enlarged, and statistical analysis should be computed to verify the trends observed in this study. This work marked a key point in the definition of the best configuration of social cues for a robotic arm that performs exercises with humans and the parameters used in this study (e.g., animacy, fluidity, etc..) are relevant for future implementations because they can be markers for an effective and engaging HRI.

These results can be a starting point in the design of cognitive rehabilitative scenarios with a social robotic arm. For this reason, collaboration with clinicians is necessary, and the design of social cues should be further discussed with psychologists and adapted to HRI rehabilitation scenarios.

Acknowledgment

This publication was produced with the co-funding European Union - Next Generation EU, in the context of The National Recovery and Resilience Plan, PE8 Consequences and challenges of ageing, Project: "A novel public-private alliance to generate socioeconomic, biomedical and technological solutions for an inclusive Italian ageing society" (Age-IT), CUP: B83C22004800006.

References

[1] M. Braun and F. Alt, “Affective assistants: A matter of states and traits,” in *Extended Abstracts of the 2019 CHI Conference on Human Factors in Computing Systems*, 2019, pp. 1–6.

[2] L. P. Robert Jr *et al.*, “A review of personality in human–robot interactions,” *Foundations and Trends® in Information Systems*, vol. 4, no. 2, pp. 107–212, 2020.

[3] S. Rossi, G. Santangelo, M. Staffa, S. Varrasi, D. Conti, and A. di Nuovo, “Psychometric evaluation supported by a social robot: Personality factors and technology acceptance,” in *2018 27th IEEE International Symposium on Robot and Human Interactive Communication (RO-MAN)*, 2018, pp. 802–807.

[4] A. S. Arora, M. Fleming, A. Arora, V. Taras, and J. Xu, “Finding ‘H’ in HRI: Examining human personality traits, robotic anthropomorphism, and robot likeability in human-robot interaction,” *International Journal of Intelligent Information Technologies*, vol. 17, no. 1, pp. 19 – 38, 2021, doi: 10.4018/IJIIT.2021010102.

[5] A. Cook, P. Encarnaço, and K. Adams, “Robots: Assistive technologies for play, learning and cognitive development,” *Technol Disabil*, vol. 22, no. 3, pp. 127–145, 2010, doi: 10.3233/TAD-2010-0297.

[6] E. Frid and R. Bresin, “Perceptual Evaluation of Blended Sonification of Mechanical Robot Sounds Produced by Emotionally Expressive Gestures: Augmenting Consequential Sounds to Improve Non-verbal Robot Communication,” *Int J Soc Robot*, vol. 14, pp. 357–372, 2022, doi: 10.1007/s12369-021-00788-4.

[7] B. J. Zhang, N. Stargu, S. Brimhall, L. Chan, J. Fick, and N. T. Fitter, “Bringing WALL-E out of the Silver Screen: Understanding How Transformative Robot Sound Affects Human Perception,” *2021 IEEE International Conference on Robotics and Automation (ICRA)*, 2021, doi: 10.1109/ICRA48506.2021.9562082.

[8] T. Ariyoshi, K. Nakadai, and H. Tsujino, “Effect of Facial Colors on Humanoids in Emotion Recognition Using Speech,” 2004. doi: 10.1109/ROMAN.2004.1374730.

[9] A. Sorrentino, L. Fiorini, C. la Viola, and F. Cavallo, “Design and development of a social assistive robot for music and game activities : a case study in a residential facility for disabled people *,” 2022, pp. 2905–2908.

[10] J. Xu, J. Broekens, K. Hindriks, and M. A. Neerincx, “Mood contagion of robot body language in human robot interaction,” *Auton Agent Multi Agent Syst*, vol. 29, no. 6, pp. 1216–1248, Nov. 2015, doi: 10.1007/S10458-015-9307-3.

[11] J. Li, M. Chignell, S. Mizobuchi, and M. Yasumura, *Emotions and messages in simple robot gestures*, vol. 5611 LNCS, no. PART 2. 2009. doi: 10.1007/978-3-642-02577-8_36.

[12] R. Laban, *Modern Educational Dance*. London: Macdonald & Evans Ltd, 1948.

[13] D. L. Irmgard Bartenieff, *Body Movement, Coping with the Environment*. 1980.

[14] T. Zhu, Z. Xia, J. Dong, and Q. Zhao, “A Sociable Human-robot Interaction Scheme Based on Body Emotion Analysis,” *Int J Control Autom Syst*, vol. 17, no. 2, pp. 474–485, 2019, doi: 10.1007/s12555-017-0423-5.

[15] M. T. H. van Otterdijk *et al.*, “The effects of long-term child–robot interaction on the attention and the engagement of children with autism,” *Robotics*, vol. 9, no. 4, pp. 1–15, Dec. 2020, doi: 10.3390/robotics9040079.

[16] P. Anderson, V. Anderson, and G. Lajoie, “The tower of London test: Validation and standardization for pediatric populatons,” *Clin Neuropsychol*, vol. 10, no. 1, pp. 54–65, Jan. 1996, doi: 10.1080/13854049608406663.

[17] C. la Viola, L. Fiorini, G. Mancioppi, J. Kim, and F. Cavallo, “Humans and Robotic Arm : Laban Movement Theory to create Emotional Connection *,” in *Ro-MAN*, 2022.

[18] S. J. Burton, A. A. Samadani, R. Gorbet, and D. Kulić, “Laban movement analysis and affective movement generation for robots and other near-living creatures,” in *Springer Tracts in Advanced Robotics*, vol. 111, 2016, pp. 25–48. doi: 10.1007/978-3-319-25739-6_2.

[19] M. Bradley and P. J. Lang, “Measuring Emotion: The Self-Assessment Semantic Differential Manikin and the,” *J Behav Ther Exp Psychiatry*, vol. 25, no. I, pp. 49–59, 1994, [Online]. Available: http://www.sciencedirect.com/science/article/pii/0005791694900639

[20] C. Bartneck, D. Kulić, E. A. Croft, and S. Zoghbi, “Measurement Instruments for the Anthropomorphism, Animacy, Likeability, Perceived Intelligence, and Perceived Safety of Robots,” *Int J Soc Robot*, vol. 1, pp. 71–81, 2009.

[21] B. Rammstedt and O. P. John, “Measuring personality in one minute or less: A 10-item short version of the Big Five Inventory in English and German,” *J Res Pers*, vol. 41, no. 1, pp. 203–212, Feb. 2007, doi: 10.1016/J.JRP.2006.02.001.

[22] K. Krippendorff, *Content analysis: An introduction to its methodology*. Sage publications, 2018.

[23] S. Rossi *et al.*, “The role of personality factors and empathy in the acceptance and performance of a social robot for psychometric evaluations,” *Robotics*, vol. 9, no. 2, 2020, doi: 10.3390/ROBOTICS9020039.

[24] R. Shi and X. Wan, “Human prejudice to the healthcare social robot and the impact of human personality: An experiment of the online mental counseling,” in *27th Annual Americas Conference on Information Systems, AMCIS 2021*, 2021.

[25] S. Schreibelmayr and M. Mara, “Robot Voices in Daily Life: Vocal Human-Likeness and Application Context as Determinants of User Acceptance,” *Front Psychol*, vol. 13, 2022, doi: 10.3389/fpsyg.2022.787499.

A motor-assisted recumbent trike for cycling training in neurological patients

F. Ferrari[1,2], D. Savona[1,2], E. Guanziroli[3], F. Molteni[3], A. Pedrocchi[1,2] and E. Ambrosini[1,2]
[1] *NearLab, Department of Electronics Information and Bioengineering, Politecnico di Milano, Milano, Italy*
[2] *WE-COBOT Lab, Polo territoriale di Lecco, Politecnico di Milano, Lecco, Italy*
[3] *Villa Beretta Rehabilitation Center, Valduce Hospital, Costa Masnaga (LC), Italy.*

***Abstract*—Cycling is a widely used rehabilitative method since it is a safe and intensive exercise that shares several similarities with walking. When practiced outdoors, cycling becomes a model of Sport-Therapy, favoring social inclusion and promoting the psychological well-being of the subjects. The aim of this study is to design a motor-assisted recumbent trike in order to allow even severely impaired people to pedal outdoors. The main novelty of the designed system is in the control strategy which implements an assist-as-needed cooperative approach in order to maximize the residual volitional contribution of the pilot. A commercial recumbent trike (CATRIKE 700) was equipped with a DC brushed motor mounted on a custom-made aluminum support and coupled with a free wheel to transmit torque to the main chain without applying any additional resistance. A Proportional Integral Derivative (PID) controller was implemented in order to modulate the PWM duty cycle to keep a constant target cadence. A feasibility study involving three healthy volunteers and three stroke survivors was conducted. The designed setup proved to be suitable for assisting a fully-active exercise as well as for handling completely passive legs movements. Moreover, it proved to be a good solution in assisting the user in compensating for muscle weakness or fatigue. Future works will combine the voluntary effort of the pilot and the assistance of the motor with the action of Functional Electrical Stimulation (FES) and will verify the feasibility of the hybrid motor-FES approach.**

***Keywords*—Cycling, motor, Hybrid, Stroke, muscular activity, Sport-therapy.**

I. INTRODUCTION

Neurological disorders such as Spinal Cord Injury, stroke, or Multiple Sclerosis are among the main causes of disability and have a significant impact on the quality of life of affected people. A number of studies supported the role of goal-oriented, active and repetitive movement in enhancing motor re-learning, taking advantage of neural plasticity mechanisms.

Cycling represents a pseudo-walking aerobic and periodic exercise, which can improve functional mobility and bring peripheral benefits, such as improvement of muscle strength, bone density, and cardiovascular fitness [1]. Moreover, it provides a safe platform for exercising even at the early stages of the disease and can be maintained for reasonably long periods, maximizing activity-dependent neuroplasticity [2]. Cycling also represents an example of Sport-Therapy, being an accessible form of exercise also for people with disabilities, favoring social inclusion and overall the physiological well-being. Despite the aforementioned benefits, the tendency of severely impaired muscles to early fatiguing and the presence of death areas within the pedaling cycle make difficult to perform a prolonged training in daily life condition, e.g. outdoors. In the last few years, some solutions have been investigated to overcome these issues. Most of these proposed the development of instrumented recumbent trikes instead of stationary cyclo-ergometers, to facilitate cycling exercises outdoors also in highly impaired people and to measure training performances in order to optimize the mechanics of pedaling [3]. Some Authors proposed a motor-assisted cycling system as a solution to prolong the exercise and offer the possibility to train outdoors [4] - [5]. The combination of motor assistance with the residual voluntary contribution of the user may increase the training intensity and duration. Furthermore, to exploit even more the therapeutic benefits of pedaling, such devices should include the possibility to be combined with Functional Electrical Stimulation (FES) [6]. Thus, the aim of this work is to present a novel motor-assisted cycling device to allow even severely impaired people to pedal outdoors, exploiting an assistance-as-needed cooperative approach. The proposed system has been designed to be integrated in the near future with FES to exploit the efficacy of the hybrid FES-motor approach.

II. APPARATUS

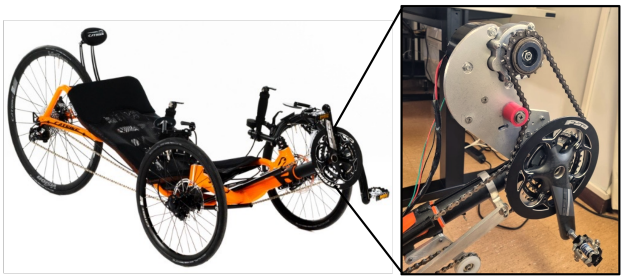


Fig. 1: The commercial recumbent trike with the detail of the structure developed to couple the DC motor

The designed system is shown in Fig.1. A commercial recumbent trike (CATRIKE 700) was chosen for the light but solid vertebrae space frame. Commercial pedals were replaced with sensorized pedals (X-Power, SRM GmbH), in order to measure the tangential and radial forces exerted by the patient's legs, with a sampling frequency of 30Hz. Pedals can be used with cycling shoes equipped with pedals-compatible cleats or with custom-made ankle foot orthoses (AFO), in the

case of disabled users, to keep the ankle angle at 90° and to constrain the leg's movement in the sagittal plane. A brushed motor (24V DC supply, LFaster) was mounted on the trike frame with a custom-made aluminum support which allows for a mid-drive configuration. When the motor is active, it moves the transmission line and the cranks simultaneously, through a second transmission chain mounted on the external chainring, assisting the pedaling action by directly moving the legs. In this way, the motor applies torque at the crank which in turn transmits the rotation to the rear wheel through the main chain. Furthermore, the motor shaft is coupled with a freewheel sprocket that gives the possibility to apply no additional resistance to pedaling when the motor does not support the movement. The motor is controlled via Pulse Width Modulation (PWM), managed through a high current H bridge module (HiLetgo, BTS7960b) by the central control Unit (Raspberry Pi 4 model B). The trike was instrumented with a custom-made tachometer, developed with a Hall sensor (ARCELI, 44e402) mounted on the fixed frame, and a set of 20 50mmx50mm magnets on the internal side of the crankset, used to acquire the pedaling cadence. The control software application was developed in C++ in a Linux-based environment. The motor is controlled in a closed loop to keep a target pedaling cadence. A Proportional Integral Derivative (PID) computes the difference between the measured and the target cadence, given as a set point, and modulates the duty cycle PWM signal accordingly. A trial and error procedure was applied to tune the controller parameters. The following parameters were identified: $K_p = 0.2$, $K_i = 0.001$, $K_d = 0.6$. An intuitive user interface allows one to adjust the target velocity while training.

III. Validation

A feasibility study was conducted in order to verify the performance of the motor-assisted trike in supporting the pedaling exercise under different conditions. The trike was used indoors, placed over a roller and the sixth trike gear was set for all the trials. Three healthy volunteers (2 female, and 1 male, 29 ± 7 y-o, right dominant leg) and three stroke survivors participated in the study. Table I shows the clinical and demographic characteristics of the stroke survivors. The study was approved by the Ethical Committee of Politecnico di Milano (number 31/2021; date: 21/07/2021) and each subject signed the informed consent before participating in the study.

A. Experimental protocol

Each subject performed three consecutive trials, each lasting about 2 minutes. The first trial consisted in a voluntary pedaling trial (VOL), during which the subject was asked to pedal completely voluntarily trying to maintain a constant cadence of 40 rpm, without any motor assistance. The second trial consisted in a partially assisted pedaling trial (VOL+MOT), in which the volitional contribution of the subject was assisted cooperatively by the motor action, i.e. the total power at the crank was exerted by the combination of muscle contractions and motor power. Also during this trial, the subject was asked to maintain a constant cadence of 40rpm. The third trial (MOT) consisted in a passive pedaling trial, in which the legs were moved only by the motor action, controlled to maintain a constant cadence of 40 rpm, and the subject was asked not to voluntarily participate in the exercise. Tangential forces exerted at the pedals were acquired with two commercial MTB/quick release pedals (X-Power, SRM GmbH) with a sampling frequency of 30Hz via a tablet application. Furthermore, the motor output, quantified in terms of duty cycle set by the control algorithm, was acquired with a sampling frequency of 1000Hz.

B. Analysis

Sixty pedaling cycles during each trial were selected for the analysis. Each pedaling cycle were defined as a complete revolution of the left crank and the zero angle corresponded to the left crank up in the vertical axis. All the analyses were performed in Matlab (R2021b version).

IV. Results and discussion

Table II reports the results of the three trials for all subjects who participated in the experimental protocol. All the participants were able to pedal for the entire duration of the voluntary trial maintaining the desired velocity and developed higher forces in the voluntary trial with respect to the cooperative and passive conditions, as expected. During the three trials, an asymmetric pedaling pattern in stroke survivors is suggested by the comparison between the mean values of tangential force exerted by the two legs separately during the voluntary trial. Such high differences were not found in healthy subjects which developed a more symmetrical pedaling pattern. Comparing the two groups of subjects, the healthy subjects developed more similar forces at the pedals in VOL and VOL+MOT trials, while the stroke survivors showed a significant decrease in forces between the VOL and the other two trials. In particular, the two groups show different behavior in the cooperative trial, which reflects the tendency of stroke survivors to let the motor primarily drive the movement. Consequently, the motor output needed to execute the same movement (same target speed of 40 rpm and same gear) for the stroke patients in the VOL+MOT trial was higher with respect to the healthy subject. In this case, the reduced patients' voluntary contribution (indicated by the decrease in mean tangential forces for the same cadence) may be attributed to the onset of muscle fatigue (please consider that the voluntary trial was also performed at first), or due to the slacking effect (i.e. a phenomenon in which the patients remain mainly passive and not engaged in the exercise). Overall, the tangential forces of the three trials were significantly different for all subjects, with a p-value< 0.001 (one-way ANOVA).

Fig.2 shows the data acquired for two stroke survivors (S2, S3), over 60 revolutions, during the three trials (VOL, VOL+MOT, MOT). Comparing the two subjects in terms of symmetry of pedaling it can be appreciated that S3 shows the tendency to compensate for the weakness of the affected side, by developing higher forces with the non-affected leg,

Subj	Gender	Age	Days post-stroke	Type of stroke	Paretic side	6min walking test	Motricity index
1	M	37	273	Hemorrhagic	Left	290	54
2	M	54	216	Ischemic	Left	320	92
3	M	47	287	Hemorrhagic	Right	395	76

Age is expressed in years, 6min walking test in meters

TABLE I: Demographic and clinical characteristics of the stroke survivors

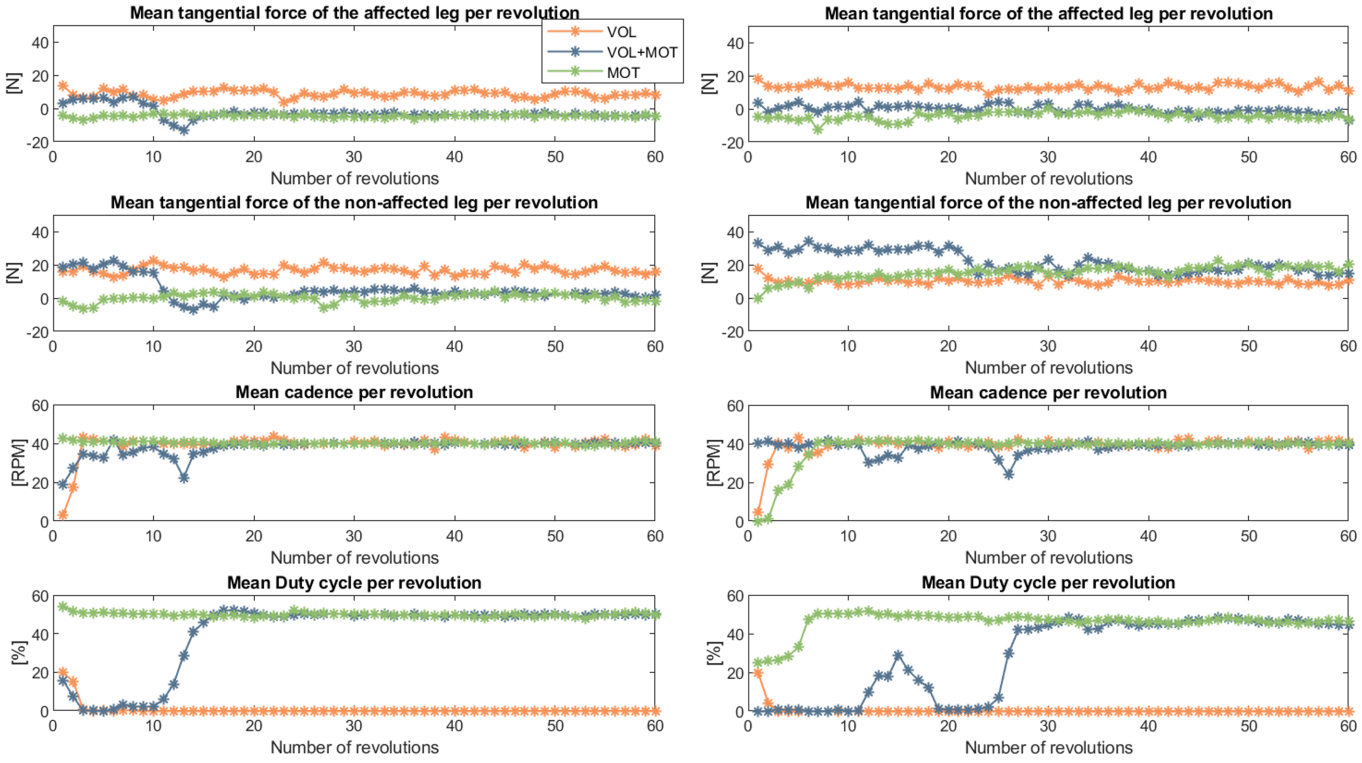


Fig. 2: Mean values of tangential forces, cadence, and duty cycle for two stroke survivors (S2 on the left, S3 on the right) displayed over 60 revolutions, during the three trials (VOL: voluntary, VOL+MOT: cooperative, MOT: passive)

resulting in a highly asymmetric cycling pattern. During the hybrid trial (VOL+MOT) the slacking effect is demonstrated by the behavior of the mean forces and duty cycle over time. During the first part of the hybrid trial, both subjects behave actively developing forces similar to the ones of the voluntary trial, needing no assistance from the motor. After a while, they started decreasing their voluntary contribution, reaching a completely passive state. Overall, the behavior of the control system showed the ability to rapidly compensate for the changes in voluntary contribution to fulfill the desired exercise (i.e. to keep the cadence fixed) in a cooperative way.

V. Conclusions

A motor-assisted cycling system can be considered a good solution to prolong cycling training and allow the practice also in outdoor environments, enhancing the sport-related psychological benefits, even in severily impaired subjects. This study presents the first stages of development of a motor-assisted recumbent cycling system and the results of a series of tests performed by three stroke survivors and three healthy volunteers to verify the feasibility of the approach. Our system is characterized by a motor directly coupled with the crank. This allows both fully-active exercises, meaning that the user is able to pedal also without motor assistance and the mechanical actuation does not introduce any additional friction, and fully passive exercises, even in absence of any voluntary contribution, in case of muscle fatigue or severe impairment. Furthermore, this solution introduces the possibility to perform the exercise in a cooperative way where the motor is in charge of supporting the user to maintain a constant pedaling cadence when she/he is not able to do it autonomously. So far, only feasibility tests were performed to assess the motorized system functioning at different levels of assistance. The designed setup proved to be suitable for the assistance of an active exercise as well as for the handling of completely passive movements. The

Subj		TgF ND/A [N]	TgF D/NA [N]	Mean Cadence [RPM]	Mean Duty-cycle [%]
S1	Vol	-4.5 ± 2.0	24.0 ± 1.9	37 ± 4	0
	Vol+Mot	-6.8 ± 1.8	21.4 ± 5.0	41 ± 4	45 ± 12
	Mot	-6.7 ± 1.0	-2.3 ± 1.1	40 ± 4	50 ± 1
S2	Vol	6.7 ± 1.4	18.3 ± 1.3	40 ± 5	0
	Vol+Mot	-4.6 ± 2.3	2.8 ± 3.7	39 ± 3	49 ± 4
	Mot	-5.4 ± 0.7	1.8 ± 2.2	40 ± 2	50 ± 1
S3	Vol	6.5 ± 2.0	27.0 ± 2.8	40 ± 4	0
	Vol+Mot	-0.1 ± 3.0	18.3 ± 5.0	39 ± 4	39 ± 15
	Mot	-4.0 ± 2.0	17.0 ± 2.4	40 ± 1	47 ± 1
H1	Vol	12.6 ± 1.5	20.0 ± 1.3	42 ± 2	0
	Vol+Mot	12.0 ± 4.1	16.0 ± 3.4	41 ± 3	26 ± 11
	Mot	1.0 ± 5.3	4.8 ± 4.7	41 ± 2	47 ± 1
H2	Vol	13.3 ± 1.9	20.4 ± 2.8	41 ± 3	0
	Vol+Mot	13.6 ± 2.2	19.0 ± 1.3	41 ± 3	33 ± 11
	Mot	0.7 ± 1.7	2.2 ± 4.1	40 ± 4	46 ± 1
H3	Vol	10.3 ± 1.7	13.0 ± 1.5	44 ± 2	0
	Vol+Mot	10.2 ± 3.3	9.0 ± 3.3	40 ± 6	31 ± 11
	Mot	1.0 ± 1.3	2.8 ± 1.6	40 ± 1	48 ± 1

TABLE II: Mean values of tangential force of the non-dominant/affected (Tg F ND/A) and of the dominant/non-affected leg (Tg F D/NA) and mean values of cadence and duty-cycle calculated over 60 revolutions for each subject (S: stroke, H:healthy) under the three modalities..

control software showed stability and precision during cadence tracking and unwanted and potentially dangerous accelerations were avoided. In conclusion, it can be asserted that the motor action can represent a valid assistance, reducing the workload for the subject in active training, and also a valid system for passive training giving the possibility to passively move the patient's legs in the early stages of the rehabilitation program. Based on the results obtained during the validation phase, what is not missing is the ability of the system to enhance users' participation, avoiding patient accommodation. To guarantee a fully cooperative behavior of the system, future insights would consider the development of a torque-based control, given the indirect measure of the power exerted by the motor and the direct assessment of the legs' power developed at the pedals. Future works will also focus on the combination of the motorized system with FES in stroke rehabilitation. The idea behind a hybrid FES-motor approach would be to add to the cycling training the well-known therapeutic benefits of FES, so as to further enhance motor re-learning. The possibility to combine FES with the residual voluntary contribution of the subject maximizes the neuro-plasticity mechanisms, while the motor guarantees a safe and prolonged exercise [7].

ACKNOWLEDGEMENT

This work was performed in collaboration with Centro Protesi INAIL within the project FESleg (PR19-RR-P5) and partially supported by the project Active^3 (Everyone, Everywhere, Everyday) project, funded by Cariplo Foundation and Lombardy Region.

REFERENCES

[1] David Barbosa, Cristina P. Santos, and Maria Martins. The application of cycling and cycling combined with feedback in the rehabilitation of stroke patients: A review. *Journal of Stroke and Cerebrovascular Diseases*, 24:253–273, 2 2015.

[2] Jan W. van der Scheer, Victoria L. Goosey-Tolfrey, Sydney E. Valentino, Glen M. Davis, and Chester H. Ho. Functional electrical stimulation cycling exercise after spinal cord injury: a systematic review of health and fitness-related outcomes. *Journal of NeuroEngineering and Rehabilitation*, 18, 12 2021.

[3] Federica Ferrari, Nicole Sanna, Paolo Brambilla, Francesca Dell'Eva, Simona Ferrante, Marco Tarabini, Alessandra Pedrocchi, and Emilia Ambrosini. Training with a mobile fes-cycling system: A case study with a spinal cord injured pilot to investigate performances optimization. In *Computers Helping People with Special Needs*, pages 437–444, Cham, 2022. Springer International Publishing.

[4] Christian Cousin, Victor Duenas, and Warren Dixon. Fes cycling and closed-loop feedback control for rehabilitative human–robot interaction. *Robotics*, 10, 2021.

[5] Kenneth J. Hunt, Barry Stone, Nils Otto Negård, Thomas Schauer, Matthew H. Fraser, Andrew J. Cathcart, Chiara Ferrario, Susan A. Ward, and Stan Grant. Control strategies for integration of electric motor assist and functional electrical stimulation in paraplegic cycling: Utility for exercise testing and mobile cycling. *IEEE Transactions on Neural Systems and Rehabilitation Engineering*, 12:89–101, 3 2004.

[6] Kenneth Hunt, J Fang, J Saengsuwan, M Grob, and Marco Laubacher. On the efficiency of fes cycling: A framework and systematic review. *Technology and health care : official journal of the European Society for Engineering and Medicine*, 20:395–422, 10 2012.

[7] Antonio del Ama, Angel Gil-Agudo, José Pons, and Juan Moreno. Hybrid fes-robot cooperative control of ambulatory gait rehabilitation exoskeleton. *Journal of neuroengineering and rehabilitation*, 11:27, 03 2014.

An improved method for the characterization of infants' general movements using a RGB-Depth sensor and a deep neural network tracking processing tool

D. Balta[1], I. G. Porco[2], H. H. Kuo[3], J. Wang[3],O. Morozova[4], M. M. Schladen[3,5], A. Cereatti[1], P. S. Lum[3], U. Della Croce[2]

[1] *Department of Electronics and Telecommunications, Politecnico di Torino, Torino, Italy;*
2 Department of Biomedical Sciences, University of Sassari, Sassari, Italy;
3 Department of Biomedical Engineering, The Catholic University of America, Washington (DC), United States of America;
4 Children's National Hospital, Washington (D.C), United States of America;
5 Department of Rehabilitation Medicine, Georgetown University Medical Center, Washington (DC), United States of America;

***Abstract*— Cerebral palsy is often diagnosed through general movements assessment in infancy. However, this tool requires extensive training and is thus difficult to implement on a large scale. Early identification of motor disorders makes possible to leverage the neuroplasticity of infancy for intervening as soon as possible. Computer vision techniques based on a single RGB-D sensor system integrating an RGB camera with a depth sensor in the same device allows to carry out assessments at home or in the clinic. Recently, we published a markerless protocol for studying upper limb movements on infants by using a single RGB-D camera, an open-source markerless motion tracking method (Deep Lab Cut) for estimating estimation of the 2D trajectories of the selected Point of Interest and a purposely developed method for reconstructing their 3D trajectories and extracting nine general movements related metrics. This study aims at proposing a video processing method for improving the robustness of that previously published by limiting the effects of accidental movements of the camera or the infant's seat that could easily occur especially in a non-controlled environment such as the home.**

The above mentioned nine metrics were evaluated with both the original and the improved methods and their values compared. The results demonstrated the improved method limits the detrimental influence of unintentional and unexpected movements.

***Keywords*—Markerless, RGB-D, General movements, Infant movement analysis, Movement disorders.**

I. Introduction

Cerebral palsy (CP) is the clinical description given to a constellation of neuromotor impairments stemming from perinatal brain injuries such as periventricular leukomalacia, intracerebral haemorrhage, infection, and infant stroke [1]. Arguably, the greatest boon to early identification of infants with CP has been the validation and dissemination of the general movements assessment, GMA. This instrument came into being as understanding of the significance of infants' spontaneous movements increased during the latter decades of the 20th century ([2] [3]). Two patterns in particular, predominantly cramped-synchronized movements and the absence of fidgety movements at three to five months of age reliably predict a later finding of CP [4]. Despite the power of the GMA in early identification, its key mechanism of gestalt pattern recognition (from video) requires a significant investment in assessor training and validation [5], making the GMA challenging to implement broadly across clinical practices. Early intervention depends on early identification, which suggests the need for a widely disseminated screening process, which is not found in the current approach to delivering CP care [6]. Families have been identified as the cornerstone of early intervention [7].

Marker-based, multi-camera, 3D analysis of infant movement has been used to detect both upper [8] and lower extremity movements [9] correlated with GMA assessment of CP. Given that marker-based systems typically require multiple cameras and a laboratory setting, an accurate and reliable, markerless, computer vision approach that can be operationalized in either the home or clinic setting may make screening more widely accessible. Markerless, computer vision technology further preserves the non-intrusive character of the GMA, leveraging, as does the GMA itself, video to assess an infant's movements unhampered by markers or other sensing devices [5].

Avoiding markers may be particularly appropriate in the case of infants where they may be poorly tolerated and, as a result, introduce movement patterns that are not part of the infant's typical GM repertoire [5].

Use of a commercial RGB-D sensor system that integrates an RGB camera with a depth sensor in the same hardware is a promising approach which enhances portability and makes it possible to carry out assessment in more confined spaces [10] such as the home or clinic.

Such an integrated system promises to help fill the current gap in infant movement assessment by providing a low-cost, compact platform that can be implemented repeatedly and longitudinally in the infant's naturalistic environment, where movement repertoires are most likely to characterize the actual behaviours of the infant ([11]).

Recently, we published a study proposing a method for assessing infants' GM that features a simplified instrumental setup, suitable for home (or clinic) by recording infants' upper body movements with a single, commercial RGB-D sensor [12].

This study proposes a video processing method aiming at improving the robustness of the previously published method, by limiting the effects of accidental motions of the camera or the seat of the infant.

The improved method was applied to the recordings of a single infant characterized by accidental motion of the camera.

II. MATERIALS AND METHODS

The infant selected for this study was sitting in a baby seat covered with a green cloth to facilitate background exclusion during identification of infant, was positioned on the floor in front of an RGB camera with an integrated depth sensor (Figure 1). The child natural movements were recorded for a target duration of three minutes at 8 months from birth.

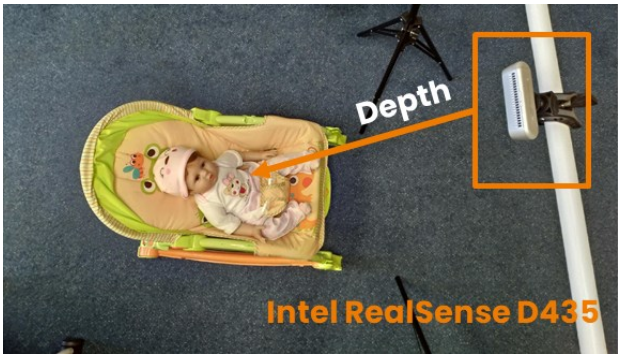


Fig 1. Experimental set-up.

The camera used for the recordings was a commercial RGB-D sensor (Intel RealSense D435 combining a pre-calibrated RGB camera with 1280x720 native resolution and frame rate of ~30fps with a depth sensor generating depth-coded images with 640x480 native resolution and frame rate of ~30fps).

Each pixel of the depth image had an intensity proportional to the distance of the surfaces in the image from the camera. Depth images were generated by the stereo vision of two infrared sensors mounted on the device with the left sensor used as point of view. If a region is seen only by the left sensor, the resulting depth image in that region remains black ("black area"). RGB and depth images were pre-calibrated, however a residual misalignment between the two remained.

The markerless motion tracking software used in this study was DeepLabCut [13], an open-source toolkit for pose estimation in which a training set of images is manually labeled and returns the x,y coordinates of the tracked points along with a confidence level, varying from 0 (lowest confidence) to 1 (maximum confidence). DeepLabCut provides a framework for supervised, deep learning to tune an existing, high-performance convolutional neural network (ResNet) to the features of a specialized dataset to produce a high level of recognition accuracy.

A sequence of steps was implemented to reconstruct the time series of the 3D coordinates of the selected points from the recorded RGB-D videos and to extract the associated GM metrics (Figure 2).

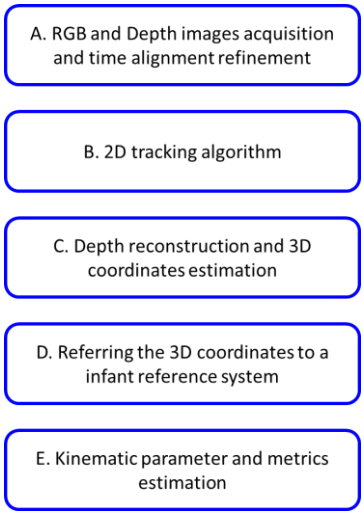


Fig 2. Block diagram of the proposed markerless -based method.

All blocks are explained in the following sections (a more detailed description can be found in [12]).

A. RGB and depth images acquisition and time alignment refinement

The images acquired with the RGB camera and the depth sensor required refinement of the time alignment obtained from the manufacturer's proprietary software, since neither frame rate is exactly constant. The timestamps provided by the acquisition software were used for this purpose [12].

B. 2D Tracking algorithm

RGB images were converted into video files using ImageJ [30] and fed to the DeepLabCut image processing tool. The tracking software was trained to identify seven points on interest (PoIs) on the infant's upper body: left and right shoulders (LS and RS), elbows (LE and RE), and wrists (LW and RW) and belly button (B). All PoIs were manually labeled on 10% of the video frames (540 frames), identified by DeepLabCut using a k-means algorithm that selected frames based on pixel characteristic variability, to create a training set.

After the network was trained and validated, DeepLabCut provided the PoI positions in all RGB frames referred to the image coordinate system(CS_I) , together with their confidence levels. When a PoI was occluded, its position was provided with a low confidence level. A recognition network was trained individually for each infant video to achieve the greatest possible accuracy prior to the association of RGB and depth coordinates of PoI.

C. Depth reconstruction and 3D coordinates estimation

The 3D position of PoIs tracked in the RGB images was obtained by implementing the method which exploits the depth sensor recordings by taking into account PoIs occlusions, lacking of depth information due to the presence of "black areas" and residual spatial misalignment between RGB and depth images [12].

Resulting depth coordinate gaps shorter than 0.2 s were then filled by applying a cubic spline interpolation.

D. Referring the 3D coordinates to an infant reference system

In order to limit the effects of accidental motions of the camera, a new local reference system (infant reference system, CS_{Infant}) was identified as the system having the origin in the centroid (C) of the 3D coordinates of LS, RS and B, with the medio-lateral-axis joining LS and RS, the antero-posterior-axis perpendicular to the plane defined by LS, RS and B and the vertical axis resulting from the cross-product between antero-posterior and medio-lateral axes.

The 3D position of PoIs was referred to the new infant refence system and then their coordinates were low-pass filtered (Figure 3).

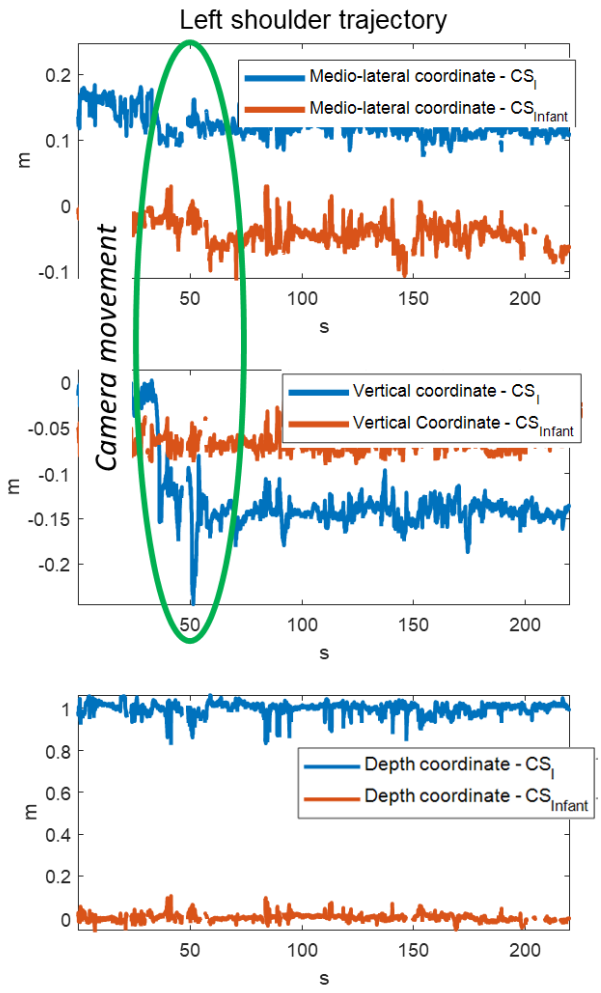


Fig 3. 3D coordinates of left shoulder in both reference systems. The blue line represents the image reference system while the red one represents the new infant reference system. The effects on the shoulder trajectory of the accidental camera movement occurring between frames 40 and 50 are circled in green.

E. Kinematic parameter and metrics estimation

From PoI 3D trajectories the following metrics for quantifying GMs were estimated [9]:

- area in which the trajectories of the wrists differed from the moving average for the same trajectories, normalized with respect to the length of the moving average window (two seconds) (A1_t);
- area in which the trajectories of the wrists were outside of the standard deviation of the moving average for the same trajectories, normalized with respect to the samples in which the trajectories were outside the standard deviation (no information regarding the normalization was provided in the reference work) (A2_t);
- periodicity in the wrist trajectories (PI_t);
- area in which the speed profiles of the wrists differed from the moving average for the velocity profiles, normalized with respect to the length of the moving average window (2 seconds) (A1_v);
- area in which the speed profiles of the wrists were outside of the standard deviation of the moving average for the velocity profiles, normalized with respect to by the length of the moving average window (2 seconds) (A2_v);
- periodicity in the wrist velocities (PI_v);
- the skewness of the velocities of the wrists (SK);
- the cross-correlation of accelerations between left and right wrists (CC).

In addition, we estimated the range of motion (ROM) of the elbow angle (EA).

III. RESULTS

Table 1 shows the values of the nine GM metrics (for left and right sides, both separately and together) estimated from the upper body 3D PoIs obtained by applying the proposed method compared to the estimates obtained applying the original method presented in [12].

For sake of comparison, also the trajectories from the original method were low-pass filtered and only gaps longer than 0.2 s were filled.

TABLE I: COMPARISON BETWEEN METRICS OBTAINED FROM WRIST TRAJECTORIES AND VELOCITIES FOR EACH METHOD.

Metrics		*Balta et al (2022)*	*Improved method*
*A1_t (m*s)*	*R*	2.05	2.51
	L	2.33	2.89
	R+L	4.35	5.40
*A2_t (m*s)*	*R*	0.33	0.29
	L	0.32	0.31
	R+L	0.65	0.60
A1_v (m)	*R*	9.05	13.07
	L	9.32	13.52
	R+L	18.37	26.59
A2_v (m)	*R*	0.56	0.72
	L	0.50	0.61
	R+L	1.06	1.33
PI_t	*R*	0.01	0.02
	L	0.01	0.02
	R+L	0.02	0.04
PI_v	*R*	0.15	0.05
	L	0.24	0.08
	R+L	0.39	0.14
SK	*R*	2.71	3.29
	L	2.65	2.52
	R+L	5.38	5.81
CC	-	0.47	0.67
ROM EA (°)	*R*	173	162
	L	170	173

IV. Conclusion

This work has confirmed that GM metrics can be effectively estimated with a single low cost RGB-D sensor without using markers on the infant's body. The proposed experimental setup allows its use as a screening tool at home, therefore avoiding inconvenient hospital visits therefore facilitating the assessment of true neurodevelopmental performance. This focus could be very beneficial for enhancing screening of neurodevelopmental disorders particularly for infants and families in rural and remote areas, a population with reduced health services.

On the one hand, this method allowed to limit the effects of accidental motions of the camera or the seat of the infant, resulting in a reduced range of the variability of the 3D PoIs coordinates (Figure 3). On the other hand, by introducing B, the 3D coordinates of each PoI referred to CS_{Infant} are noisier than those referred to CS_I.

The above considerations were reflected on A1_t and A1_v obtained from the improved method showing larger values with respect to those obtained from the original method as shown in Table I.

For the same reasons, PI_t and PI_v showed larger values since these are calculated as the number of intersections between the trajectory/velocity and the arithmetic mean.

For what concerns A2_t, on one hand the removal of the artifacts due to the accidental movement of the camera would reduce the standard deviation of the coordinates, on the other hand the noisier signal would increase it resulting in a non-significant change in this metric.

The same reasoning could be applied on A2_v that seems to be more affected by the increase of noise in velocities.

As expected by limiting camera movements, the ROM EA with the improved method shows lower values.

SK shows similar results probably because the improved method has not altered the velocity distribution.

CC estimated with the improved method shows larger values probably because without camera artifacts, the correlation between the limbs could be better estimated.

Although most of the metrics are calculated on the wrist, tracking seven upper-body PoIs allows to limit the detrimental effects on the selected metrics estimation of unintentional and unexpected movements of either the camera or the infant's seat and makes the proposed method suitable also for the calculation of additional metrics based on the movement of the entire upper-body.

Future studies will be devoted to validating the proposed protocol on a higher number of infants for testing its use in clinical practice.

References

[1] C. Metz, M. Jaster, E. Walch, A. Sarpong-Bengelsdorf, A. M. Kaindl, and J. Schneider, "Clinical Phenotype of Cerebral Palsy Depends on the Cause: Is It Really Cerebral Palsy? A Retrospective Study," *J Child Neurol*, vol. 37, no. 2, pp. 112–118, Feb. 2022, doi: 10.1177/08830738211059686.

[2] H. F. R. Prechtl, "Qualitative changes of spontaneous movements in fetus and preterm infant are a marker of neurological dysfunction," *Early Hum Dev*, vol. 23, no. 3, pp. 151–158, 1990, doi: https://doi.org/10.1016/0378-3782(90)90011-7.

[3] P. Heinz *et al.*, "An early marker for neurological deficits after perinatal brain lesions," 1997.

[4] C. Einspieler and H. F. R. Prechtl, "Prechtl's assessment of general movements: A diagnostic tool for the functional assessment of the young nervous system," *Ment Retard Dev Disabil Res Rev*, vol. 11, no. 1, pp. 61–67, Feb. 2005, doi: https://doi.org/10.1002/mrdd.20051.

[5] N. Silva *et al.*, "The future of General Movement Assessment: The role of computer vision and machine learning – A scoping review," *Res Dev Disabil*, vol. 110, Mar. 2021, doi: 10.1016/j.ridd.2021.103854.

[6] A. te Velde, C. Morgan, I. Novak, E. Tantsis, and N. Badawi, "Early diagnosis and classification of cerebral palsy: An historical perspective and barriers to an early diagnosis," *J Clin Med*, vol. 8, no. 10, Oct. 2019, doi: 10.3390/jcm8101599.

[7] M. Hadders-Algra, A. G. Boxum, T. Hielkema, and E. G. Hamer, "Effect of early intervention in infants at very high risk of cerebral palsy: a systematic review," *Dev Med Child Neurol*, vol. 59, no. 3, pp. 246–258, 2017, doi: https://doi.org/10.1111/dmcn.13331.

[8] J. Mazzarella *et al.*, "3d motion capture may detect spatiotemporal changes in pre-reaching upper extremity movements with and without a real-time constraint condition in infants with perinatal stroke and cerebral palsy: A longitudinal case series," *Sensors (Switzerland)*, vol. 20, no. 24, pp. 1–17, Dec. 2020, doi: 10.3390/s20247312.

[9] C. Disselhorst-Klug, F. Heinze, N. Breitbach-Faller, T. Schmitz-Rode, and G. Rau, "Introduction of a method for quantitative evaluation of spontaneous motor activity development with age in infants," *Exp Brain Res*, vol. 218, no. 2, pp. 305–313, Apr. 2012, doi: 10.1007/s00221-012-3015-x.

[10] V. Cimolin *et al.*, "Computation of Gait Parameters in Post Stroke and Parkinson's Disease: A Comparative Study Using RGB-D Sensors and Optoelectronic Systems," *Sensors*, vol. 22, no. 3, Feb. 2022, doi: 10.3390/s22030824.

[11] C. Marcroft, A. Khan, N. D. Embleton, M. Trenell, and T. Plötz, "Movement recognition technology as a method of assessing spontaneous general movements in high risk infants," *Frontiers in Neurology*, vol. 6, no. JAN. Frontiers Media S.A., p. 284, 2015. doi: 10.3389/fneur.2014.00284.

[12] D. Balta *et al.*, "Characterization of Infants' General Movements Using a Commercial RGB-Depth Sensor and a Deep Neural Network Tracking Processing Tool: An Exploratory Study," *Sensors*, vol. 22, no. 19, Oct. 2022, doi: 10.3390/s22197426.

[13] A. Mathis *et al.*, "DeepLabCut: markerless pose estimation of user-defined body parts with deep learning," *Nat Neurosci*, vol. 21, no. 9, pp. 1281–1289, Sep. 2018, doi: 10.1038/s41593-018-0209-y.

Ex Vivo Animal Evaluation of IntraValvular Impedance Sensing Applied to Biological Heart Valve Prostheses

C. Gironi[1], L. Cercenelli[1], B. Bortolani[1], N. Emiliani[1], L. Tartarini[1], and E. Marcelli[1]
[1]*Laboratory of Bioengineering – eDIMES Lab, Department of Medical and Surgical Sciences (DIMEC), University of Bologna, Bologna, Italy*

***Abstract*— We recently demonstrated the feasibility of the application of an electrical impedance measurement (IntraValvular Impedance, IVI) to biological heart valves (BHVs) for the monitoring of the valve condition after implant. In this study, we investigate the IVI sensing applied to a BHV when it is surrounded by biological tissue, similar to what happens in vivo. A commercial model of BHV was sensorized with three miniaturized electrodes embedded in the commissures of the valve leaflets and connected to an external impedance measurement unit. The sensorized BHV was implanted in the aortic position of an explanted porcine heart, which was connected to the LifeTec Group's Cardiac BioSimulator to perform *ex vivo* tests. For each pair of electrodes, the maximum percent variation of the IVI signal was evaluated and compared. The results demonstrate a detectable variation of the IVI signal when the sensorized BHV is surrounded by biological tissue, which is comparable to that we previously obtained in *in vitro* tests using a polymeric housing for the sensorized BHV.**

***Keywords*—Biological heart valve prosthesis, valve thrombosis, electric impedance, implantable sensor.**

I. Introduction

PROSTHESIS Valve Thrombosis (PVT) clinically manifests with the formation of obstructive thrombus on the valve leaflets, resulting in an increase in the transvalvular gradient and sometimes symptoms of heart failure, with consequent dysfunction of the prosthesis itself [1]. Subclinical Leaflet Thrombosis (SLT) is the precursor of PVT and is mainly characterized by hypoattenuating leaflets thickening (HALT) and reduced leaflet motion (RLM) [2]. SLT mainly affects transcatheter Biological Heart Valves (BHVs) rather than surgical BHVs and can be addressed by the assumption of appropriate anticoagulant therapy [3], [4]. The natural history of SLT is not yet fully known; HALT and RLM can develop not only in the first few months following the implantation but also over an extended period (up to one year). Therefore, serial imaging follow-up and proper evaluation of risks and benefits of long-term anticoagulation are extremely important [5]. Given the recent widespread use of heart valve prostheses (HVPs), it is important to identify the risk of SLT in order to be able to tailor an adequate anticoagulant therapeutic strategy for the patient , to ensure an optimal valve hemodynamic [4]

The functionality of HVPs can be evaluated with appropriate imaging following their implantation [6]. The postoperative follow-up includes periodic monitoring by echocardiographic examinations which, however, do not allow to identify the presence of SLT, mainly due to the transvalvular pressure gradients which remain within the physio-logical range [6]. 4D Multi-Detector Computed Tomography (4D-MDCT) is currently the gold standard diagnostic tool for the accurate evaluation of both the thickness and the mobility of the valve leaflets after implantation, therefore for the diagnosis of SLT [7]. Nevertheless, its routine adoption into clinical practice would expose the patient to a high amount of radiation and would introduce logistical constraints for health facilities.

We conceived an innovative sensorized HVP [8] that may open up important perspectives for a system capable of monitoring the functionality of HVPs after implantation. The novelty of the system deals with the application of impedance measurement techniques, currently used in implantable cardiac devices, to HVPs in order to early detect the possible presence of subclinical thrombotic formations that can alter the valve functioning and monitor its progressive deterioration. This would allow for the timely selection of an appropriate anticoagulant therapy prior to compromised cardiac function, resulting in a potential reduction of mortality and improvement in patient quality of life. We have defined this impedance-based technique IntraValvular Impedance (IVI) sensing and we have already designed and tested proof-of-concept prototypes of IVI sensing applied to mechanical HVPs [8].
We also recently presented the conceptual design of IVI sensing applied to BHVs [9]. Different solutions for the sensorization of a commercial BHV model were described and tested on a circulatory mock loop system reproducing both normal and reduced dynamics of the valve leaflets. In that study we found that IVI measurement is sensitive to experimentally-induced changes in valve leaflet motions, specifically for the prototype having small parallelepiped-shaped electrodes embedded in the commissures of the BHV leaflets. Hence, that electrodes configuration has been selected as the optimal one for the IVI measurement.
Furthermore, it is of interest to investigate whether any IVI signal variation is detectable during the opening/closing dynamics of the BHV also when it is surrounded by biological tissue, similar to what happens in vivo. Indeed, this configuration was not reproduced in our previous study since the sensorized valve was inserted inside a circulatory mock loop system by using a customized polymeric housing [9].
The present study aims to *ex vivo* evaluate the IVI measurement applied to BHVs, i.e. with the sensorized BHV implanted inside an explanted porcine heart connected to a cardiac biosimulator platform.

II. Materials and Methods

The IVI measurement is based on embedding miniaturized electrodes in the structure of the BHV, which are used for the

local electric field generation, by injecting sub-threshold currents (I) between each pair of electrodes, and for the recording of potential difference (ΔV) between the same electrodes. Following the Ohm's first law, the impedance measurement (IVI) is obtained as the ratio between the recorded ΔV over the injected I. Since the valve leaflets interfere with the local electric field lines during the valve opening and closing dynamics, IVI variations within the cardiac cycle (ΔIVI) reflect the cyclic movements of the valve leaflets. Thus, it is possible to correlate the alterations of IVI signal with the alteration of the mobility of the valve leaflets which may occur in presence of an obstacle, such as thrombus formations, as shown in Figure 1 [9].

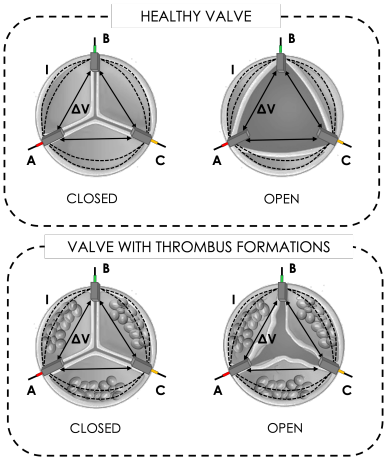


Figure 1. The principle of IntraValvular Impedance (IVI) measurement for a healthy valve (left) and for a valve with a thrombus formation (right): current pulses (I) are injected between each electrodes pair to generate local electric field interfering with leaflets movement and potential difference (ΔV) is recorded.

The *ex vivo* animal evaluation of IVI measurement was performed on a BHV which was sensorized following the optimal electrodes configuration we had previously identified [9]. The prototype was made up of a commercial BHV currently used for surgical aortic valve replacement (Soprano Armonia, LivaNova PCL, London, UK) and was equipped with three electrodes, conventionally called "A", "B" and "C". The three electrodes are visually distinguishable from one another based on the color of the heat shrink which covers the electrode–wire interface: red for electrode "A", green for electrode "B" and yellow for electrode "C" (Figure 2).

The electrodes were manufactured in Pt/Ir which is a biocompatible alloy typically used for implantable electrodes thanks to its biocompatibility and corrosion resistance [10].

The electrodes are small parallelepipeds with the following dimensions: height H=5mm, width W=1mm, thickness T=0.5mm.

Those electrodes, that we called "mini-platelet" electrodes, were positioned in the commissures of the BHV leaflets (Figure 2).

The positions of the electrodes near the valve leaflets were maintained by sewing them to the BHV structure using a suture thread (Figure 2). In addition, a conductor wire was welded in the longitudinal direction of each electrode's structure.

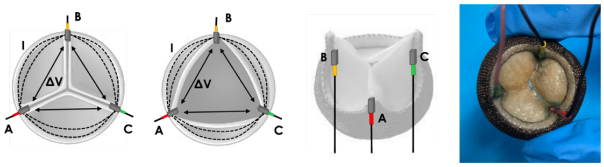


Figure 2. The assembled prototype which includes "mini-platelet" electrodes A (red), B (green) and C (yellow). Local electric field lines (I) and the corresponding potential difference measurement (ΔV) are represented for each pair of electrodes.

For each pair of electrodes ("AB", "BC" and "CA"), an IVI measurement was performed according to the bipolar measurement configuration, which consists of using the same pair of electrodes for both the local electric field generation (source electrodes) and the ΔV recording (receiver electrodes).

The conductor wires welded to the electrodes for signal transmission were connected to a dedicated external impedance measurement unit ("impedance-meter") [9]. The impedance-meter delivers sub-threshold current pulses within the ranges compatible with implantable cardiac devices (biphasic square waveform, 18μA amplitude, 4kHz frequency) to each of the three electrodes embedded in the BHV, thus generating a local electric field near the valve leaflets. Then, the impedance-meter records the potential difference between each pair of electrodes (ΔV_{AB}, ΔV_{BC} and ΔV_{CA}) from which the corresponding IVI measurement is calculated. Hence three IVI signals are obtained (IVI_{AB}, IVI_{BC} and IVI_{CA}), one for each pair of electrodes.

The sensorized BHV was implanted in the aortic position of an explanted porcine heart by a specialized cardiac surgeon. The sensorized prototype was then experimentally evaluated on the Cardiac BioSimulator platform (LifeTec Group™, Eindhoven, Netherlands) [11], shown in Figure 3.

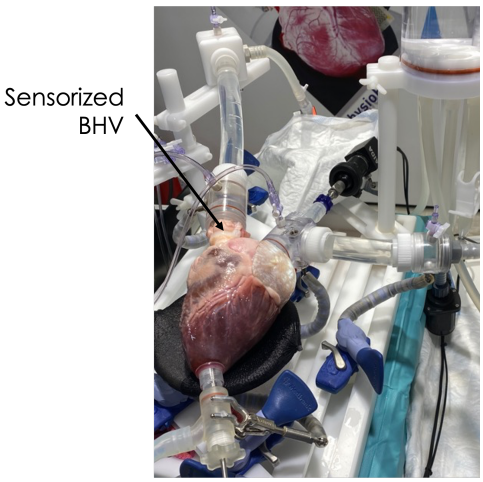


Figure 3. Cardiac BioSimulator platform used for the *ex vivo* animal testing of the sensorized BHV inserted in the aortic position of the porcine heart (indicated by the black arrow).

Two pressure sensors (P10-EX, Becton Dickinson, New Jersey, US) allowed to measure the left atrial and aortic pressure during the tests. IVI measurement was performed connecting the wires, welded to the electrodes, to the impedance-meter. The analog signals (left atrial pressure, aortic pressure, and IVI) were acquired with the MP100 Acquisition System (Biopac System, Galeta, CA, USA) and displayed in real-time using the Acq3.9.1 Software (Biopac

System, Galeta, CA, USA).

We evaluated the IVI measurement by setting the following parameters of the Cardiac BioSimulator platform: cardiac cycle rate of 50 bpm and stroke volume of 80 mL. The IVI signal was recorded between the three pairs of electrodes and IVI variations during the fully opening/closing dynamics of the valve were recorded.

We evaluated the maximum percent variation of the impedance module ($\Delta IVI_{max}\%$), calculated as shown in Equation (1), i.e. as the difference between the maximum and minimum value reached during the opening/closing dynamics, normalized with respect to the minimum value reached during the opening/closing dynamics. For each pair of electrodes, $\Delta IVI_{max}\%$ was reported as $Mean\ Value \pm SD$ calculated over multiple cardiac cycles.

$$\Delta IVI_{max}\% = \frac{=|IVI_{max} - IVI_{min}|}{IVI_{min}} * 100 \quad (1)$$

III. Results

For each pair of electrodes, the recorded atrial and aortic pressures, as well as the IVI signals, are reported in Figure 4, Figure 5 and Figure 6. In the figures, also the calculated $\Delta IVI_{max}\%$ for each pair of electrodes has been identified.

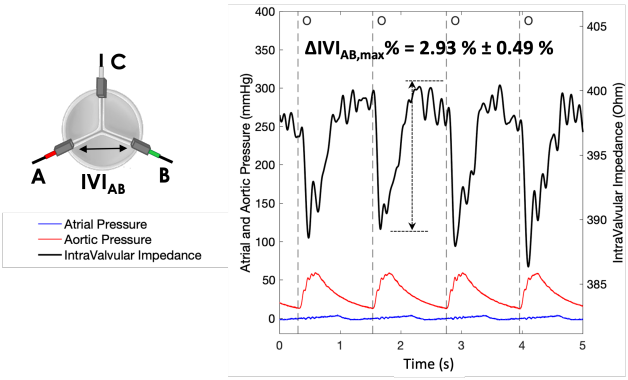


Figure 4. Atrial and aortic pressures and IVI signal recorded inside the porcine heart for the pair of electrodes AB.

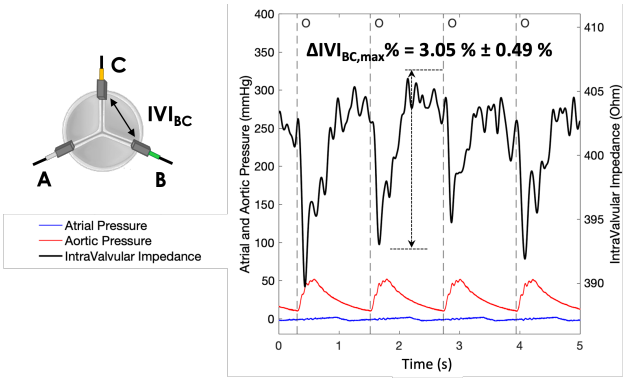


Figure 5. Atrial and aortic pressures and IVI signal recorded inside the porcine heart for the pair of electrodes BC.

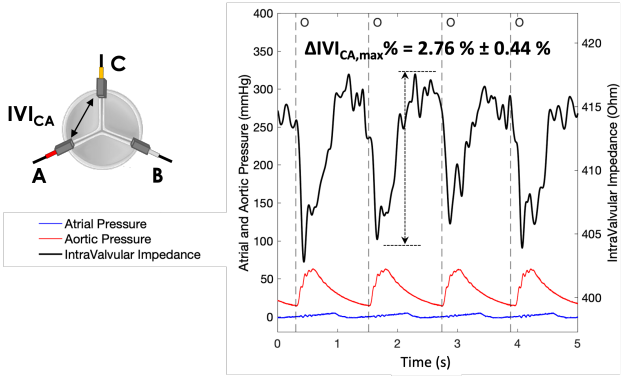


Figure 6. Atrial and aortic pressures and IVI signal recorded inside the porcine heart for the pair of electrodes CA.

The maximum percent variation of the IVI module was obtained in the electrode pair BC ($IVI_{BC,max}\% = 3.05\ \%$), followed by AB ($IVI_{AB,max}\% = 2.93\ \%$) and CA ($IVI_{CA,max}\% = 2.76\ \%$).

IV. Discussion

This study aims to investigate the IVI measurement applied to a sensorized BHV when positioned in a biological environment similar to the real *in vivo* one. This condition has been reproduced by surgically implanting the prototype in the aortic position of an explanted porcine heart. The porcine heart was then connected to the Cardiac BioSimulator platform, which ensures a realistic pulsatile flow through the valve and the pressurization of the cardiac chambers, allowing the evaluation of IVI signal during the valve opening/closing dynamics.

The results confirm the presence of a detectable variation of the IVI signal module within the cardiac cycle following the dynamics of the valve, also when it is surrounded by biological tissue. Moreover, the entity of that excursion is in line to what we previously obtained using a polymeric housing for the valve positioning; indeed, in that case the $\Delta IVI_{max}\%$ obtained for the complete opening/closing dynamics of the valve were in the range $2{,}29\% - 3{,}20\%$for the three pairs of electrodes [9].

The chosen electrodes configuration explains the wave pattern for the IVI signal: there is the maximum IVI signal when the valve is closed, as the valve leaflets close around the electrodes, maximally interfering with the local electric field lines. On the contrary, the IVI signal reaches minimum values when the valve is open, as the valve leaflets stretch outward minimally interfering with the electric field (Figures 4-6).

The intra-prototype variability of the IVI measurement, represented by the differences between IVI_{AB}, IVI_{BC} and IVI_{CA}, may be related to different aspects. First, since it is not possible to carry out simultaneous IVI measurements with the different pairs of electrodes, the signal recorded with each pair refers to a different heartbeat, which has an intrinsic variability. Second, the valve prosthesis does not have perfectly symmetrical leaflets; this determines different opening and closing dynamics for each leaflet, thus introducing a variability in the measured IVI signal between each pair of electrodes. Third, the measuring electrodes positioned inside the valve structure may have variable spatial

orientations and/or inclinations due to the difficulties in their positioning which have been manually executed by sewing. Fourth, even starting from electrodes of the same shape and size, the effective working electrode surface depends on the portion of electrode covered by the heat shrink (applied manually) at the electrode-wire interface; so different electrode surfaces achieved with slightly different portion of applied heat shrink, result in different IVI measurements, as described by Ohm's second law.

The main limitations of the study are related to the use of a working fluid which allows to simulate the electrical conductivity of the blood [8] but not its viscosity, and the absence of a flow sensor inside the Cardiac BioSimulator platform to also detect the transvalvular flow. Another limitation is represented by the missing of the left ventricle pressure sensing, useful for the determination of the closing time of the valve within the cardiac cycle.

Future research should aim to replicate these results in a wider range of working conditions, such as performing a hemodynamically altered situation in which the valve leaflets do not fully open and close due to their reduced mobility induced for example by a simulated "hypotensive" pressure condition.

V. Conclusions

The present study relates the *ex-vivo* evaluation of the IVI measurement applied to a BHV which was inserted in an explanted porcine heart connected to a Cardiac BioSimulator platform which reproduces the complete opening/closing dynamics of the valve. Overall, our results demonstrate the presence of a detectable IVI signal variation following the cardiac cycle phases, also when the valve is surrounded by biological tissue.

These are promising results to further pursue the development of a fully implantable solution of the proposed sensorized BHV.

References

[1] S. Sachdev, N. Bardia, L. Nguyen, e B. Omar, «Bioprosthetic Valve Thrombosis», p. 8.

[2] B. Yanagawa *et al.*, «Subclinical bioprosthetic aortic valve thrombosis: clinical and translational implications», *Current Opinion in Cardiology*, vol. 32, fasc. 2, pp. 137–146, mar. 2017, doi: 10.1097/HCO.0000000000000373.

[3] M. Martín, J. Cuevas, H. Cigarrán, J. Calvo, e C. Morís, «Transcatheter Aortic Valve Implantation and Subclinical and Clinical Leaflet Thrombosis: Multimodality Imaging for Diagnosis and Risk Stratification», *Eur Cardiol*, vol. 16, p. e35, set. 2021, doi: 10.15420/ecr.2021.09.

[4] A. C. Egbe *et al.*, «Bioprosthetic Valve Thrombosis Versus Structural Failure», *Journal of the American College of Cardiology*, vol. 66, fasc. 21, pp. 2285–2294, dic. 2015, doi: 10.1016/j.jacc.2015.09.022.

[5] R. R. Makkar *et al.*, «Subclinical Leaflet Thrombosis in Transcatheter and Surgical Bioprosthetic Valves», *Journal of the American College of Cardiology*, vol. 75, fasc. 24, pp. 3003–3015, giu. 2020, doi: 10.1016/j.jacc.2020.04.043.

[6] S. Kanjanauthai, L. Pirelli, N. Nalluri, e C. A. Kliger, «Subclinical leaflet thrombosis following transcatheter aortic valve replacement», *J Interven Cardiol*, vol. 31, fasc. 5, pp. 640–647, ott. 2018, doi: 10.1111/joic.12521.

[7] O. De Backer *et al.*, «Reduced Leaflet Motion after Transcatheter Aortic-Valve Replacement», *N Engl J Med*, vol. 382, fasc. 2, pp. 130–139, gen. 2020, doi: 10.1056/NEJMoa1911426.

[8] E. Marcelli, B. Bortolani, I. Corazza, e L. Cercenelli, «A Novel Sensorized Heart Valve Prosthesis: Preliminary In Vitro Evaluation», *Sensors*, vol. 18, fasc. 11, p. 3905, nov. 2018, doi: 10.3390/s18113905.

[9] C. Gironi, L. Cercenelli, B. Bortolani, N. Emiliani, L. Tartarini, e E. Marcelli, «Innovative IntraValvular Impedance Sensing Applied to Biological Heart Valve Prostheses: Design and In Vitro Evaluation», *Sensors*, vol. 22, fasc. 21, p. 8297, ott. 2022, doi: 10.3390/s22218297.

[10] K. J. Ely, P. Hall, e Y. Zhou, «Microwelding methods in medical components and devices», in *Joining and Assembly of Medical Materials and Devices*, Elsevier, 2013, pp. 47–79e. doi: 10.1533/9780857096425.1.47.

[11] A. M. Leopaldi, K. Wrobel, G. Speziali, S. van Tuijl, A. Drasutiene, e W. R. Chitwood, «The dynamic cardiac biosimulator: A method for training physicians in beating-heart mitral valve repair procedures», *The Journal of Thoracic and Cardiovascular Surgery*, vol. 155, fasc. 1, pp. 147–155, gen. 2018, doi: 10.1016/j.jtcvs.2017.09.011.

Wearable sensor for in-vivo skin hydration monitoring

A. Cataldo[1], R. Schiavoni[1], A. Masciullo[1] and C. Demitri[1].
[1] *Department of Engineering for Innovation, University of Salento, 73100 Lecce, Italy,*

***Abstract*—Skin hydration is the water content within skin tissues and its monitoring is of crucial importance in many contexts. However, at the current state-of-the-art, there is a lack of objective, non-invasive and wearable monitoring systems for the correct evaluation of skin moisture. To this purpose, in this paper, a new wearable punctual sensing element (SE) was designed and validated to sense variation of skin hydration of the body, even in the case of area as small as a few millimetres. In particular, a truncated customized open-ended coaxial probe was designed. As a matter of fact, the dielectric properties of the skin can be related to the frequency domain (FD) response of the monitoring system. In this regard, full-wave simulations on human phantoms were carried out to demonstrate the feasibility of the system. This strategy, in combination with low-cost miniaturized instrumentation, has potential for achieving a fully wearable system for real-time monitoring of skin hydration.**

***Keywords*—skin hydration, wearable, dielectric permittivity, microwave reflectometry.**

I. INTRODUCTION

Water is a vital element for the skin and the entire body [1]. In particular, maintaining the right level of skin hydration ensures optimal skin health, and improves the skin's appearance. The natural aging process and exposure to factors such as ultraviolet radiation, tobacco smoke [2] and pollution can reduce the amounts of water in the skin, altering its natural function as a protective barrier. The first sign of a compromised skin barrier is properly the dehydration. This can result in symptoms such as redness, itching and peeling. Some of the causes of skin dehydration are related to severe dermatological diseases such as atopic dermatitis [3,4] (very common in children), ichthyosis, psoriasis [5] and eczema. As a matter of fact, skin hydration is an important parameter that is necessary to monitor, especially in the case of dermatological diseases, hormonal alterations [6,7] and for workers in hostile environments [8]. In the literature, most works relate to different methodologies for skin hydration monitoring [9-11]. However, some of these techniques are expensive (e.g., Confocal Raman spectroscopy [12], Near-IR spectroscopy [13], terahertz spectroscopy [14]) or are based on skin impedance [15] or capacitance methods, having a low measurement accuracy. It is worth noting that these types of systems are not wearable, aspect that could improve the patient's experience and the efficiency of the diagnostic process, for example, through real-time remote monitoring with the possibility to send data to the doctor. In addition, such a system needs to implement fully in vivo measurements so it is necessary to make a device that is comfortable for the patient and can provide good adherence to the skin.

For these reasons, this work addresses the design of an innovative wearable device that monitors skin hydration through microwave reflectometry. More in detail, in this paper, which is an extension and continuation of a previous work [16], a new configuration of SE was designed in order to obtain a sensing volume in the subsurface skin region only and to improve the ability to detect the hydration status of small areas, some just a few millimeters. In this regard, it is worth mentioning how some diseases cause punctual excoriations of the skin that need to be monitored over time. For this reason, a system that can detect changes in the moisture status of the skin with good spatial resolution can provide adequate information on the proper functioning of medical therapy.

This paper is organized as follows. Section II describes the theoretical background at the basis of the proposed system. Section III describes the design and the optimization of the new SE and the advancement with respect to the previous work. Section IV addresses the simulation results on human phantom demonstrating the feasibility of the proposed system. Finally, in Section V, conclusions are drawn and the future work is outlined.

II. THEORETICAL BACKGROUND

Microwave reflectometry is a very versatile technique used in several fields [17-22]. More in detail, an electromagnetic test signal is propagated through a sensing element to the target tissue, and useful information can be extracted from the analysis of the reflected signal, in terms of dielectric permittivity. As a matter of fact, the dielectric properties of human tissues can be described in terms of frequency-dependent complex dielectric permittivity $\varepsilon^*(f)$ according to the following equation:

$$\varepsilon^*(f) = \varepsilon'(f) - \varepsilon''(f) \qquad (1)$$

where $\varepsilon'(f)$ is the relative dielectric constant, $\varepsilon''(f)$ is the relative dielectric loss factor and f is the frequency. In particular, in the simulation results described in Section IV, the Cole&Cole model has been adopted. As is well known, Cole&Cole equation is a relaxation model that is often used to extrapolate the measured complex dielectric permittivity of biological tissues. It is given by the equation:

$$\varepsilon^*(f) = \varepsilon_\infty + \frac{\varepsilon_S - \varepsilon_\infty}{1+(j\omega\tau)^{1-\alpha}} \qquad (2)$$

Where ε_s and ε_∞ are the "static" and "infinite frequency" dielectric constants, ω is the angular frequency and τ is a time constant. The exponent parameter α varies between 0 and 1. The adopted Cole&Cole model is that of the reference Gabriel's database [23]. This is one of the most exhaustive and

well-established works in the field of the dielectric properties of biological tissues. As an additional note, it also worth noting that, the adopted model describes accurately the dielectric behaviour of biological tissues through a multiple contribution of a four-terms Cole&Cole expression. The operational strategy of the present work is based precisely on the difference in the dielectric properties of the tissues that can be detected by microwave-based systems and related to different skin hydration level.

III. DESIGN OF THE SENSING ELEMENT

The SE employed in [16] was a planar three-wire transmission line fabricated on a flexible rubber substrate with a layer of Kapton, capable of providing fit, comfort, and high measurement accuracy; however, the SE cannot be used on small areas due to its dimensions (50 mm × 90 mm).
In this work, an enhanced version of the system is presented. More in detail, the basic configuration chosen for the SE is the truncated open-ended coaxial probe, which has been optimized for the purposes of the application. In particular, the objectives to be pursued in the SE design phase were: i) non-invasiveness; ii) a good spatial resolution and capability of detection in the most superficial layer of the skin; iii) ability to analyze even small areas; and v) compatibility for the possible use with low-cost miniaturized FD instrument for in vivo analysis. These requirements have been met through a preliminary feasibility study and a subsequent in-depth simulation analysis which allowed to optimize the geometrical parameters and the configuration of the SE. In the simulation phase, the human tissue has been simulated through a three-layer structure composed by skin, fat and muscle with the frequency-dependent dielectric parameters reported in the "Gabriel&Gabriel" database [23].

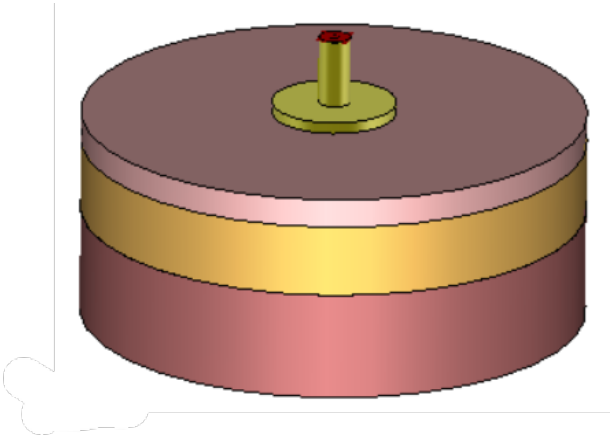


Figure 1: Scheme of the simulated new version of the SE in contact with the three-layer model.

A schematic representation of the proposed SE is shown in Figure 1. As can be seen from the figure, a termination flange was added in order to enhance the sensitivity in terms of the fringing field effect. More in detail, the radiate fringing effects at the probe aperture allow the electric field lines adequately penetrate into the skin portion under test. The fringing fields between outer and inner conductors of the sensor interact with tissues, causing changes in the reflection coefficient measured by the VNA. In addition, in order to optimize the sensitivity in the surface portion, an extremely low input power value of -15 dBm (approximately 32 μW) was chosen. In this way, the EM field is completely confined within the skin layer and decays very quickly, and the variation in the thickness of the skin layer does not affect significantly the response of the system. In addition, the chosen power input level corresponds to a Specific Absorption Rate (SAR) value below the limit imposed by safety regulations. [24, 25]

IV. FULL-WAVE SIMULATIONS WITH DIFFERENT HYDRATION LEVELS

A set of full-wave simulations was carried out through CST Microwave Studio considering the SE in contact with a human phantom with different skin moisture levels, in order to analyse the sensitivity of the system. As explained above, human tissues exhibit a significantly dispersive dielectric behavior in frequency. For this reason, the Cole&Cole model reported in the Gabriel database [23] was used for the implementation of tissue dielectric properties in the simulation software. On such basis, this model has been adopted in describing the dielectric properties of tissues and, consequently, to optimize the full-wave simulation results. More in detail, the database contains dielectric frequency parameters for both dry and wet skin.

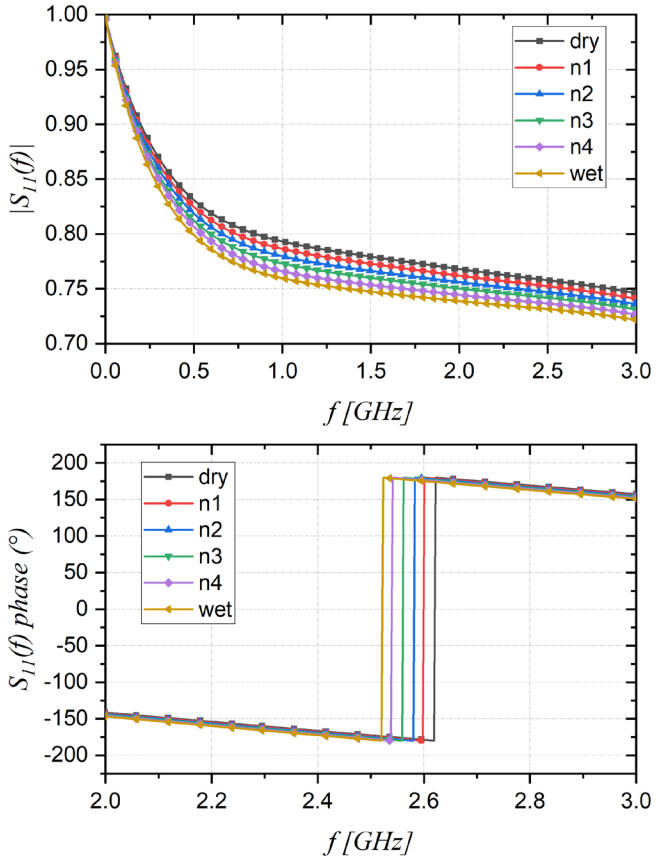


Figure 2: Simulation results for the S11(f)| of the SE in terms of magnitude and phase for 6 skin hydration states (different permittivity).

Accordingly, skin hydration intermediate conditions (from

n1 to n4) were also considered, starting from the dry skin condition and incrementing the dielectric parameters values by 2% for each simulation, until reaching the wet condition. Figure 2 shows the magnitude and the phase of the reflection scattering parameter $S_{11}(f)$. It can be seen that, over the whole considered frequency range, an increase in water in the skin leads to a lower response in terms of magnitude of the reflection parameter. A similar trend is also recognizable in terms of phase of $S_{11}(f)$. This phenomenon is due to changes in the dielectric permittivity of the skin at different hydration states. These results suggest that it could be of interest to relate the values of ε_r to the trend of $S_{11}(f)$.

V. CONCLUSIONS AND FUTURE WORKS

In this paper, the feasibility study of a microwave reflectometry -based portable and low-cost system for in-vivo skin hydration monitoring level is proposed. More in detail, the chosen probe configuration is that of a truncated open-ended coaxial probe equipped with a flange which when in contact with the tissue under test can be sensible to any dielectric variations. As a matter of fact, novelties were introduced compared to previous work [16] since this type of system is more sensitive to local changes in skin hydration compared to a trifilar SE and, consequently, allows more accurate monitoring of the evolution or healing process of dermatologic diseases. Furthermore, this type of system ensures in-vivo and non-invasive measurements and could be used in combination with a miniaturized vector network analyzer in order to ensure full-wearability, portability and low costs. In this regard, further work will be dedicated to validate and test the proposed system on a large-scale measurement campaign on volunteer subjects. Finally, a specific procedure will be implemented in order to extrapolate the dielectric properties of the tissues and its moisture levels from the FD measurements.

REFERENCES

[1] Verdier-Sévrain, S. and Bonté, F. (2007), Skin hydration: a review on its molecular mechanisms. Journal of Cosmetic Dermatology, 6: 75-82.W.-K. Chen, *Linear Networks and Systems* (Book style). Belmont, CA: Wadsworth, 1993, pp. 123–135.

[2] N. Muizzuddin, K. Marenus, P. Vallon, and D. Maes, "Effect of cigarette smoke on skin," Journal of the Society of Cosmetic Chemists, vol. 48, no. 5, pp. 235–242, 1997.

[3] Y. Werner and M. Lindberg, "Transepidermal water loss in dry and clinically normal skin in patients with atopic dermatitis," Acta Derm. Venereol., vol. 65, p. 102–105, 1985.

[4] D. Leung, "A multidisciplinary approach to evaluation and treatment of atopic dermatitis.," Semin. Cutan. Med. Surg., vol. 27, p. 115–127, 2008.

[5] U. M. Thorkar and S. T. Hamde, "Non invasive measurement of skin biophysical parameters in normal, psoriasis, vitiligo affected skin," 2015 International Conference on Industrial Instrumentation and Control (ICIC), pp. 811–815, 2015.

[6] G. Hall and T. J. Phillips, "Estrogen and skin: the effects of estrogen, menopause, and hormone replacement therapy on the skin," Journal of the American Academy of Dermatology, vol. 53, no. 4, pp. 555–568, 2005.

[7] A. P. d. O. M. F. Duarte, G.V.and Trigo, "Skin disorders during menopause.," Cutis, vol. 97(2), pp. 16–23, 2016.

[8] Y. Sunwoo, C. Chou, J. Takeshita, M. Murakami, and Y. Tochihara, "Physiological and subjective responses to low relative humidity," Journal of physiological anthropology, vol. 25, no. 1, pp. 7–14, 2006.

[9] Qassem, M.; Kyriacou, P. Review of Modern Techniques for the Assessment of Skin Hydration. Cosmetics 2019, 6, 19.

[10] Esposito, E., Drechsler, M., Mariani, P., Sivieri, E., Bozzini, R., Montesi, L., Menegatti, E. and Cortesi, R. (2007), Nanosystems for skin hydration: a comparative study. International Journal of Cosmetic Science, 29: 39-47.

[11] Constantin MM, Poenaru E, Poenaru C, Constantin T. Skin Hydration Assessment through Modern Non-Invasive Bioengineering Technologies. Maedica (Bucur). 2014 Mar;9(1):33-8. PMID: 25553123; PMCID: PMC4268288.

[12] P. J. Caspers, H. A. Bruining, G. J. Puppels, G. W. Lucassen, and C. E. A., "In vivo confocal raman microspectroscopy of the skin: Noninvasive determination of molecular concentration profile," Journal of Investigative Dermatology, vol. 116, pp. 434–442, 2001.

[13] E. Attas, M. Sowa, T. Posthumus, B. Schattka, H. Mantsch, and Z. SL, "Near-ir spectroscopic imaging for skin hydration: the long and the short of it," Biopolymers, vol. 67(2), pp. 96–106, 2002.

[14] F. Kadlec, P. Berta, M.and Kuzel, F. Lopot, and V. Polakovic, "Assessing skin hydration status in haemodialysis patients using terahertz spectroscopy: a pilot/feasibility study," Phys Med Biol., vol. 53(24), pp. 7063–71, 2008.

[15] E. Alanen, J. Nuutinen, K. Nickl´en, T. Lahtinen, and J. M¨onkk¨onen, "Measurement of hydration in the stratum corneum with the moisturemeter and comparison with the corneometer," Skin Res. Technol., vol. 10, p. 32–37, 2004.

[16] A. Cataldo, E. De Benedetto, R. Schiavoni, G. Monti, A. Tedesco, A. Masciullo, E. Piuzzi, and L. Tarricone, "Portable microwave reflectometry system for skin sensing," IEEE Transactions on Instrumentation and Measurement, vol. 71, pp. 1–8, 2022.

[17] A. Cataldo, E. De Benedetto, G. Cannazza, E. Piuzzi, and N. Giaquinto, "Embedded TDR wire-like sensing elements for monitoring applications," Measurement, vol. 68, pp. 236–245, 2015.

[18] A. Cataldo, E. De Benedetto, G. Cannazza, E. Piuzzi, and E. Pittella, "TDR-based measurements of water content in construction materials for in-the-field use and calibration," IEEE Trans. Instrum. Meas., vol. 67(5), pp. 1230–1237, 2018.

[19] R. Schiavoni, G. Monti, A. Tedesco, L. Tarricone, E. Piuzzi, E. De Benedetto, A. Masciullo, and A. Cataldo, "Microwave wearable system for sensing skin hydration," in 2021 IEEE International Instrumentation and Measurement Technology Conference (I2MTC), pp. 1–6, 2021.

[20] A. Cataldo, E. De Benedetto, L. Angrisani, G. Cannazza, and E. Piuzzi, "A microwave measuring system for detecting and localizing anomalies in metallic pipelines," IEEE Transactions on Instrumentation and Measurement, vol. 70, pp. 1–11, 2020.

[21] R. Schiavoni, G. Monti, E. Piuzzi, L. Tarricone, A. Tedesco, E. De Benedetto, and A. Cataldo, "Feasibility of a wearable reflectometric system for sensing skin hydration," Sensors, vol. 20, no. 10, 2020.

[22] P. Mehta, K. Chand, D. Narayanswamy, D. Beetner, and V. Zoughi, R.and Stoecker, "Microwave reflectometry as a novel diagnostic tool for detection of skin cancers," IEEE Transactions on Instrumentation and Measurement, vol. 55, no. 4, pp. 1309–1316, 2006.

[23] C. Gabriel, "Compilation of the dielectric properties of body tissues at rf and microwave frequencies.," tech. rep., King's Coll London (United Kingdom) Dept of Physics, 1996.

[24] IEEE Standard C95.1, "Ieee standard for safety levels with respect to human exposure to radiofrequency electromagnetic fields, 3 khz to 300 ghz," 2005.

[25] Guideline ICNIRP, "Guidelines for limiting exposure to time-varying electric, magnetic, and electromagnetic fields (up to 300 ghz)," Health Phys., vol. 74(4), pp. 494–522, 1998.

Establishing Computational Modeling Credibility in Patients Undergoing TAVI

C. Catalano[1], S. Cannata[2], C. Gandolfo[2], and S. Pasta[1,3]
[1]*Dipartimento di Ingegneria, viale delle Scienze Ed.8, University of Palermo, Italy*
[2]*Interventional Cardiology Unit, IRCCS ISMETT via Tricomi, 5, Palermo, Italy*
[3]*Department of Research, IRCCS ISMETT via Tricomi, 5, Palermo, Italy*

***Abstract*—Transcatheter aortic valve implantation (TAVI) is an established treatment for patients with severe aortic valve stenosis ineligible for surgery. Assessing computational modelling credibility is relevant for developing safe and reliable in-silico clinical trials for testing medical devices. The main goal of this work is to present a structural model of TAVI and follow the verification and validation activities suggested by ASME V&V40 standard.**

***Keywords*— TAVI, Finite-Element Analysis, Verification and Validation, ASME V&V40.**

I. Introduction

Transcatheter aortic valve implantation (TAVI) is an established treatment option for patients with aortic valve stenosis at high surgical risk [1, 2]. In the last few years, the success of TAVI is continuously increasing as this procedure is applied to young patients and the bicuspid aortic valve [3].

In this context, several computational models with different aims and model definitions have been proposed to investigate TAVI [4-11]. There is however an implicit risk in computational models for pre-TAVI planning, unless systematic verification and validation activities are performed according to regulatory bodies. The predictive value of computational models is a major concern for the assessment of cardiovascular dysfunction and treatment [12]. Assessing the credibility of computational tools is pivotal towards the development of accurate and realistic personalized approaches. This may also enhance the design process of novel devices, thereby accelerating their development and translation into the clinical practice [13].

This study aims to provide a computational framework for the verification and validation (VV) of TAVI-related patient-specific computer models according to ASME VV40.

II. Materials and Methods

The VV activities were performed on patient-specific computational models of TAVI according to a verification, and validation master plan based on ASME VV40. As the intended use, computer models aim to predict the acute outcome of patients underwent TAVI with the SAPIEN 3 Ultra device (Edwards Lifesciences, USA).

The context of use (COU) and the model risk assessment (relevant parameter changes <1%) were defined. The model form, the model input, the comparator, testing conditions and assessment output comparison were defined. Simulations were carried out for a group of n.20 patients, after signature of informed consent. Clinical workup included ECG-gated CT scans including the systolic and diastolic phases at in-hospital admission, transoesophageal echocardiography during the procedure, and post-TAVI ECG-gated CT done after one month from the procedure. Demographic data and cuff pressure measurement were also collected.

A. FEM Model Development

The workflow for the development of patient-specific modelling of TAVI involves the patient-specific segmentation, including the aortic wall, calcification and native aortic valve leaflets [14]. The aorta and calcification were segmented using the commercial software Mimics (v21, Materialise, BE) using diastolic images. Specifically, semiautomatic thresholding of different levels of grey intensity (Hounsfield units, HU) followed by manual editing was performed. Post processing of anatomic masks was accomplished using smoothing algorithms with factor of 0.4 and 10 iterations in all cases. The resulting masks were then imported as STL (Stereo Lithography Interface) format in Rhino CAD software (v.5.5, McNeel & associates, SP) [15]. Since aortic valve leaflets were not visible at CT scan, a parametric approach using anatomical landmarks was adopted (see Figure 1) [16, 17]. Using standard imaging protocol, 3rd-order NURBS curves lying on the three aortic cusps were developed to model the native valve leaflet attachment to the aortic root. Leaflet free-edges were defined by 3rd-order curves interpolating three points (i.e., anatomic landmarks) describing the commissures in the orthogonal valve plane. The belly of each leaflet was driven by a control point defined at the mid-level in the sagittal view.

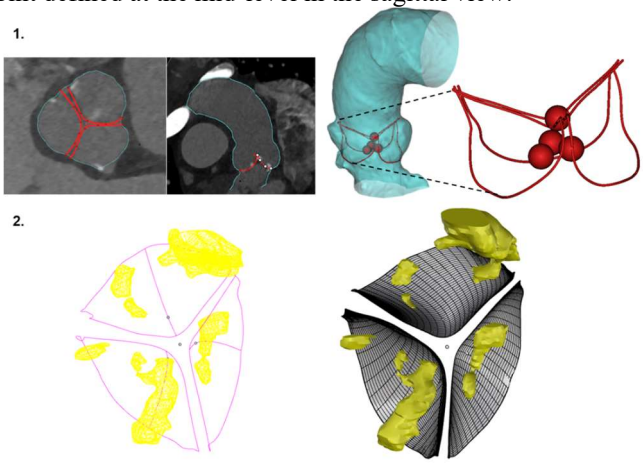


Fig. 1: Patient-specific model for the TAVI simulation.

An aortic wall tissue thickness of 2 mm was assumed while the aortic valve leaflets were 0.5 mm thick. For boundary conditions, a general blood pressure profile was adapted by

scaling the minimum and maximum pressure to those measured at in-hospital admission for each patient. The duration of the pressure profile was scaled to match the cardiac beat. Thus, the pressure profile was then applied to the aortic wall, thereby considering difference from patient-to-patient [18, 19]. Similarly, the transvalvular pressure gradient seen at echocardiography was applied to aortic valve leaflets. The distal and proximal ends of the aortic wall were fixed in all directions. Tie contact condition were used to link the calcification to aortic valve leaflets while different types of contact properties were explored. All simulations were performed with Abaqus\Explicit solver (v.2021hf7, Dassault Systèmes, FR).

B. Verification and Validation Activities

Verification activities were performed to assess the impact of solver parameter and setting while validation against an analytical solution was done to identify any errors of the computer code. Model verification was accomplished according to ASME V&V40 for each structural level accounting for the discretization error (DE), numerical code verification (NCV) and numerical solver errors (NSE). Specifically, the DE is the error associated with the chosen mesh, element type, and the level of mesh refinement. NCV quantifies the code's capability to well solve problems with known solutions while the NSE is the error associated with the type of solver and solver settings.

The relative error (RE) is used for rigor evaluation while the optimal element size was calculated using the convergence index, with errors kept <1% in all cases. The impact of solver parameters on computational time was also evaluated. Simulations were carried out using the same number of CPUs for all simulations (n=60). The investigated solver parameters were i) penalty factor, ii) mass damping (alpha), iii) viscous pressure, iv) bulk viscosity, and v) contact parameter. Comparison with respect to a baseline model is done using the relative error (RE) that was kept <1% in all cases. Output parameters for comparisons were the maximum stress, peak systolic strain, and wall-clock time.

Once the model was verified, a cardiac beat of the pre-TAVI condition of the patient was simulated and results were compared against CT data (i.e., the comparator). Specifically, the aortic wall strain measured as the changes in aortic diameter between systole and diastole divided by the diastolic diameter was considered as output parameter for the aortic wall. For the calcific valve leaflets, the orifice area measured from the CT scan at systole was used for comparison.

III. RESULTS

A. Discretization Error (DE)

1) Aortic Wall

The optimal element size was calculated using convergence analysis using the Mises stress as output parameter. The investigated element sizes and resulting relative errors were 0.5 mm (0.25%), 0.8 mm (0.87%), 1.2 mm (6.4%) and 1.5 mm. We concluded that an element size of 0.8 mm represents a good compromise between accuracy and computational costs. Similarly, the triangular element (S3) versus the quadrilateral element (S4) was tested, with the triangular shell elements resulting the optimal element type (RE=0.76% for S3 vs RE=1.25% for S4). Triangular elements have also better capability to capture the geometric discontinuity of the complex aortic wall shape than the quadrilateral element.

2) Valve leaflets

Meshes were obtained from the extrusion of shell elements with 4 layers through-the-thickness in all cases. For element size analysis, the investigated element sizes (and relative errors) are 0.5 mm (0.29%), 0.6 mm (0.38%), 0.8 mm (5.1%) and 1.0 mm. The element size of 0.6 was therefore selected.

For element types, three types of solid elements were investigated: unstructured prismatic (C3D6), unstructured hex element and structured hex element (C3D8). Due to the complex leaflet morphology, there is a likelihood to observe pronounced element distortion due to geometric discontinuity and high-frequency oscillations for the structured hex mesh.

Simulations demonstrated that both unstructured- and structured hex elements were not appropriate to capture leaflet shapes without providing element with warnings and/or errors. For one representative case, the RE was 0.67% for the unstructured prismatic element, 24.1% for unstructured hex and 23.3% for structured hex element.

3) Calcification

Given the complex and irregular shape of calcifications, the tetrahedron solid element (C3D4) was investigated as this was the only element type that reasonably described the calcific plaques. The investigated element mesh sizes (and relative errors) were 1 mm, 0.8 mm (61.25%), 0.6 mm (20.74%) and 0.5 mm (0.92%), using the principal stress as the output parameters. The element size of 0.5 mm was selected.

B. Numerical Code Verification (NCV)

1) Aortic Wall

On the basis of aortic physiology, the analytical solution of a thin vessel under pressure was considered as the representative problem. The analytical solution is valid for thin structure with isotropic behaviour and under small deformation. Under equilibrium of internal force and pressure condition, the circumferential stress is given from Laplace's law. For the NCV study, a hollow shell vessel was created and meshed with elements size and type defined in the DE section. The neo-Hookean material model was tested as many studies suggested a stiff behaviour for the aortic wall [REF]. After solution, we found a RE of 0.6% between predicted (31.82 kPa) and analytical (31.66 kPa) solutions.

2) Valve Leaflets

For aortic valve leaflets, the choice of an analytical solution was complicated by the multi-axial stress condition of the human aortic valve including tension, compression, bending and shear force. The analytical solution of cantilever beam was proposed assuming the bending as the main loading condition. The plate was modelled with dimensions of 25 mm as length, 0.25 mm as height and 0.5 mm as width, with element type and

size as described in section DE. As for the valve leaflets, the plate was realized starting from a shell mesh model then extruded with 4 layers. One edge of the beam was constrained in all directions, while a concentrated force was applied to the free end. From the simulation, the maximum deflection resulted 7,944 mm. The analytical formula of the maximum deflection gave the value of 8.010 mm, therefore the RE between predicted and analytical solutions was 0.77%, enabling to state that the finite element model can effectively acquire the deformations under these conditions.

3) Calcification

Since calcifications were mainly compressed by the surrounding tissues, the analytical solution was that of a plate subjected to uniform displacement condition in the range of small deformations. The plate was modelled with tetrahedron elements with size of 0.5 mm. Elastic-plastic material properties using literature data were used [REF]. A uniform uniaxial displacement is applied on the surface so that to remain in the elastic field. After solution, the RE between predicted (0.0200) and analytical solutions (0.0198) of the nominal strain developed was 0.77%.

C. Numerical Solver Error (NSE)

1) Aortic Wall

The NSE investigates the influence of numerical solver parameters for the aortic wall with comparison to a baseline (BL) reference simulation. To account for transient effect, the model was initially loaded to systolic pressure (t=0.1s) and then unloaded upon diastolic pressure (t=0.1s) and then a cardiac beat was simulated.

Given the low loading rate for simulating a cardiac beat, the default value of 1 for time increment was selected. Mass scaling of 5.0e-6 and 1.0e-6 led to ratio of kinetic to internal energy lower than 1%, but the value of 1.0e-6 was selected. No remarkable changes (i.e., RE<1%) were observed with alpha damping of 250. The system response is considerable influenced by increasing values of viscous pressure (with deviations leading to RE>1%). In terms of wall-clock time, the model is not appreciably affected by viscous pressure. Changes in the bulk viscosity did not influence the model response, with wall-clock time impacted only for value of 0.6. The default value of bulk viscosity is therefore adopted.

2) Valve Leaflets and Calcification

For the aortic valve, the BL model for NSE considered the interaction of valve leaflets with the calcific plaques and the aortic wall. A mass scaling of 1.0e-6 did not alter the simulation response when using frequency of 10. Since RE was <1%, no effective changes were determined in the system response with material damping. An alpha damping of 250 had minimal effects on output parameters and wall-clock time. As for to the aortic wall, the system response is considerable influenced by increasing values of viscous pressure (with deviations leading to RE>1%) and by bulk viscosity of 0.6. The utilize of friction coefficient (RE < 1%) did not deviate the system responses from output parameters and wall-clock time.

D. Validation

For the comparator (i.e., CT imaging), the test samples consisted of n.20 patients (one-to-one correspondence) with the following range of characteristics: age of 78-89 years; degree of stenosis from mild to severe; calcification volume of 500-1700 mm^3; body surface area of 1.3 to 1.6. CT imaging was performed with the same scanner and an uniformed testing protocol. Blind measurements were taken from an expert radiologist while the simulation output was automatized thanks to element sets taken at mid-ascending aorta for the strain output and leaflet edges for the orifice area. For the pre-aortic wall, the RE in the systolic strain was in the range of 8.6% to 13.6 % for the n.20 patients, with more marked differences in the left ventricular outflow tract region. For the calcific aortic valve, the differences between predicted and measured magnitude of the orifice area were in the range of 0.08% to 11.86% (2.78% ± 4.50%). Figure 2 shows the comparison of the orifice area at systolic peak between the numerical prediction and CT imaging.

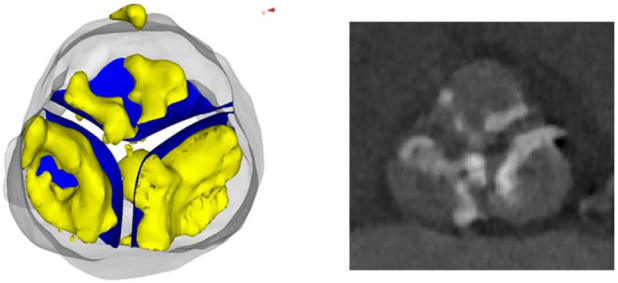


Fig. 2: Comparison between the numerical model (left) and the CT scan (right) at systole for a patient before TAVI.

IV. Discussion

In this study, a workflow for the verification and validation assessment for the TAVI model according to the ASME V&V40 standard was developed. VV activities allow to demonstrate that the credibility of the model is commensurate with the patient risk. In this perspective verified and validated predictive computational models offer the potential to reveal in a robust way the mechanisms of TAVI.

Regulatory agencies are currently evaluating the evidence achieved by simulations to reduce the time-to-market of biomedical devices and the cost related to the device design. There is therefore a growing interest in assessing model credibility [13] before this technique could be effectively implemented as a standard approach .

In this regard, the ASME has published the V&V 40-2018 technical standard “Assessing Credibility of Computational Modeling through Verification and Validation: Application to Medical Devices”, which introduced the model credibility evaluation process and gave the minimum requirements for the qualification with respect to regulatory agencies. Verification, validation, and uncertainty quantification (VVUQ) can be used to establish trust in the predictive capability of a given computational model. Verification assures that a computational model fits the mathematical description. Validation is performed to assess if the model accurately

represents the real-world system. Uncertainty quantification is implemented to determine the impact of numerical and physical parameters variations in the simulation outcome [61,62]. In future study, we propose to quantify the uncertainty of the proposed model of patient undergoing TAVI.

Few studies performed a systematic verification and validation as here proposed. Luraghi et al. [20] implemented a verification approach for the simulation of an idealized tri-leaflet heart valve model by inspecting the impact of element type, formulation, and damping factor. Similarly, Tango et al. [21] validated a FSI model of the aortic valve and root by comparing the predicted velocity field with in-vitro flow data. A similar work was recently proposed by Oks and collaborators [22]. Recently, Bosi et al. [23] validated the computational modeling of TAVI with both Sapien XT and CoreValve devices against post-procedural clinical fluoroscopy and echocardiography images. They found good agreement between predicted and image-based device diameters. However, the study from Bosi et al [23] has adopted the post-TAVI images to verify and validate the model. In this study, we performed the VV activities only using pre-TAVI imaging data with the goal to utilize post-TAVI data as an additional data source to further validate the present findings.

V. Conclusion

This study introduced a systematic verification and validation against CT data of patient-specific computational models replicated pre-TAVI scenario. Such an approach represents a step towards the utilize of accurate and realistic simulations of patients undergoing TAVI.

Acknowledgement

This project has received funding from the European Union's Horizon 2020 research and innovation programme under grant agreement No 101017523.

References

[1] Mas-Peiro S, *et al.* Current issues in transcatheter aortic valve replacement. *Journal of thoracic disease* 2020; 12(4): 1665.
[2] La Grutta L, *et al.* TAVI imaging: over the echocardiography. *La radiologia medica* 2020: 1-19.
[3] Ruparelia N, *et al.* TAVI in 2015: who, where and how? *Heart* 2015; 101(17): 1422-31.
[4] Pasta S, *et al.* Simulation of left ventricular outflow tract (LVOT) obstruction in transcatheter mitral valve-in-ring replacement. *Med Eng Phys* 2020; 82: 40-48.
[5] Pasta S, *et al.* Simulation study of transcatheter heart valve implantation in patients with stenotic bicuspid aortic valve. *Med Biol Eng Comput* 2020.
[6] Finotello A, *et al.* Finite element analysis of TAVI: Impact of native aortic root computational modeling strategies on simulation outcomes. *Medical Engineering & Physics* 2017; 47: 2-12.
[7] Capelli C, *et al.* Patient-specific simulations of transcatheter aortic valve stent implantation. *Med Biol Eng Comput* 2012; 50(2): 183-92.
[8] Luraghi G, *et al.* In silico approaches for transcatheter aortic valve replacement inspection. *Expert Review of Cardiovascular Therapy* 2021; 19(1): 61-70.
[9] Morganti S, *et al.* Prediction of patient-specific post-operative outcomes of TAVI procedure: The impact of the positioning strategy on valve performance. *J Biomech* 2016; 49(12): 2513-9.
[10] Morganti S, *et al.* Simulation of transcatheter aortic valve implantation through patient-specific finite element analysis: Two clinical cases. *Journal of Biomechanics* 2014; 47(11): 2547-55.
[11] Pasta S, *et al.* Transcatheter Heart Valve Implantation in Bicuspid Patients with Self-Expanding Device. *Bioengineering* 2021; 8(7): 91.
[12] Catalano C, *et al.* On the Modeling of Transcatheter Therapies for the Aortic and Mitral Valves: A Review. *Prosthesis* 2022; 4(1): 102-12.
[13] Viceconti M, *et al.* In silico trials: Verification, validation and uncertainty quantification of predictive models used in the regulatory evaluation of biomedical products. *Methods* 2021; 185: 120-27.
[14] Scardulla F, *et al.* Shear stress alterations in the celiac trunk of patients with a continuous-flow left ventricular assist device as shown by in-silico and in-vitro flow analyses. *J Heart Lung Transplant* 2017; 36(8): 906-13.
[15] Pasta S, *et al.* Numerical simulation of transcatheter mitral valve replacement: The dynamic implication of LVOT obstruction in the valve-in-ring case. *Journal of Biomechanics* 2022; 144.
[16] Pasta S, *et al.* Three-dimensional parametric modeling of bicuspid aortopathy and comparison with computational flow predictions. *Artif Organs* 2017.
[17] Cosentino F, *et al.* On the role of material properties in ascending thoracic aortic aneurysms. *Computers in biology and medicine* 2019; 109: 70-78.
[18] Catalano C, *et al.* Atlas-Based Evaluation of Hemodynamic in Ascending Thoracic Aortic Aneurysms. *Appl Sci-Basel* 2022; 12(1).
[19] Catalano C, *et al.* 3D Printing and Computational Modeling for the Evaluation of LVOT obstruction in Transcatheter Mitral Valve Replacement. *Proc Cirp* 2022; 110: 273-78.
[20] Luraghi G, *et al.* Study on the accuracy of structural and FSI heart valves simulations. *Cardiovascular engineering and technology* 2018; 9(4): 723-38.
[21] Tango AM, *et al.* Validation and extension of a fluid–structure interaction model of the healthy aortic valve. *Cardiovascular engineering and technology* 2018; 9(4): 739-51.
[22] Oks D, *et al.* Fluid-structure interaction analysis of eccentricity and leaflet rigidity on thrombosis biomarkers in bioprosthetic aortic valve replacements. *International journal for numerical methods in biomedical engineering* 2022; 38(12).
[23] Bosi GM, *et al.* A validated computational framework to predict outcomes in TAVI. *Scientific reports* 2020; 10(1): 1-11.

Mechanical Properties of Polyamide 12 for the use in Balloon-Expandable Transcatheter Heart Valves

O. Zahalka[1], C. Catalano[2], T. Turgut[1], N. Götzen[1], S. Cannata[3], C. Gandolfo[3], and S. Pasta[2,4]
[1] 4RealSim, Groene dijk 2b Netherlands
[2]Dipartimento di Ingegneria, viale delle Scienze Ed.8, University of Palermo, Italy
[3]Interventional Cardiology Unit, IRCCS ISMETT via Tricomi, 5, Italy
[4]Department of Research, IRCCS ISMETT via Tricomi, 5, Italy

***Abstract*—The SAPIEN 3 Ultra transcatheter heart valve (THV) is implanted in the stenotic aortic valve using an expandable balloon. This study aims to characterize the mechanical behaviour of balloon-related polyamide 12 (PA12) under uniaxial tensile testing at controlled temperatures as well as the viscoplastic response. Three-dimensional (3D) digital image correlation (DIC) was also carried out to determine the strain distribution of the whole device. Data were used to develop a material constitutive model for finite-element analysis. Findings demonstrated the complex mechanical behaviour of PA12 used in balloon catheter, suggesting the need for accurate constitutive modelling.**

***Keywords*—polyamide 12, balloon catheter, transcatheter heart valve, mechanical testing, digital image correlation**

I. Introduction

POLIMERS are widely used in medical devices because of high compliance, low weight and good biocompatibility [1]. Polyamide 12 (PA12) is typically used for the manufacturing of single-use balloons adopted for the deployment of transcatheter heart valves (THV) [2]. PA 12 demonstrates both high strength and compliances as well as low coefficient of sliding friction [3]. However, the mechanical properties of PA12 depends on the surrounding temperature and media, the usage and the fabrication technology.

There is a general lack of knowledge in the mechanical properties for the PA12 balloon material. Some general studies on the material performances were published by several authors and manufacturers [4, 5]. Geith et al [6] stated that an anisotropic behaviour is used to describe the material response only above nominal pressure. However an elastic response is used (no visco, no plasticity) to describe the material. Amstutz at al. [7] demonstrated that the environmental conditions like temperature and humidity can influence the balloon mechanical performance. The viscoelastic and viscoplastic material response was also investigated [8]. However, not any simulation studies of THVs has considered the complex mechanical behaviour of balloon material. The mostly used material model is the linear-elastic model in all simulation studies [9-12].

The purpose of this study is to characterize the PA12 balloon response through extensive material testing, considering temperature and strain rate effects. The strain field of balloons was also quantified using digital image correlation. A constitutive material model suitable for computational analyses is also proposed.

II. Materials and Methods

A. Mechanical Testing

To characterize the mechanical behavior of balloon material, the following testing protocol was used: i) quasi-static uniaxial tensile stress-strain response upon failure at room temperature; ii) uniaxial tensile stress-strain response under steady cyclic conditions at room temperature; iii) uniaxial tensile stress-strain response under 37deg temperature. Both failure and cyclic testing were performed using an ElectroForce 3330 Series II (TA Instrument, Boston, MA), equipped with a 4kN load cell. In a different way, the testing at different temperature was carried out with an ElectroForce TestBench biaxial system (TA Instrument, Boston, MA) with 200N load cell in order to take advantage of the controlled-temperature bath. After cleaning the balloon with isopropyl alcohol, several specimens were cut from the balloon material using a surgical blade as done previously [13]. Rectangular specimens with length of 40 mm and width of 4 mm were obtained where with dimensions ensured by overlaying the transparent balloon material on a graph paper and then using solid line to guide the cut. A total of 15 samples (ie, n.8 for test at different temperature and n.7 for cycling testing) were tested. Balloon thickness was 0.12 mm as measured by a mechanical micrometer. Samples were extrapolated in both longitudinal and circumferential directions, although the PA12 is a isotropic material.

For stress-strain response upon failure, a constant cross-head speed of 0.005 mm/s was. For controlled-temperature testing, the specimen was submerged in water at controlled temperature of 25 C and 37 C for simulating human body temperature.

For cyclic testing, a constant cross-head speed of 0.01 mm/s was used for 10 cycles. The sample was loaded upon 10% deformation and then unloaded to a minimum load of 1 N. The displacement, force and time were recorded with frequency of 1 Hz during the material testing. The strain was calculated as $\varepsilon=\Delta L/Lo$ where ΔL is the change in the length and Lo is the initial specimen length. The stress was calculated as $\sigma=F/(w\cdot t)$ where F is the recorded force, w is the specimen width and t is the tissue thickness

B. 3D Digital Image Correlation

Two intact balloons used for the deployment of both 23 mm and 26 mm SAPIEN 3 Ultra THVs were tested to measure the displacement field under different fluid-filling volume steps. An holding chamber with two cannulas was used to keep the proximal and distal ends of the balloon while allowing free inflation. A random black-speckle pattern on a white uniform layer was used realized on the balloon surface. The 3D DIC system consists of two 50 mm focus cameras mounted on a tripod (VIC3D, Correlated Solution, USA). The balloon was initially inflated with the fluid upon the reference zero-pressure configuration as measured from the pressure gauge. Using a syringe, the fluid volume was gradually increased in steps of 1 ml upon the nominal fluid volume (ie, 17 ml for the 23 mm balloon and 21 ml for the 26mm balloon) and then images were recorded at each increment. During inflation, the fluid pressure was manually recorded. Prior acquisition, the DIC system was calibrated for stereo vision using a calibration table with grid spacing of 3 mm. For displacement analysis, the subset and step sizes were automatically chosen by the VIC3D analysis software. An initial guess of a point in the both the reference image and the deformed images was manually obtained. Rigid translation and rotation were eliminated. Data were transformed in longitudinal (LONG) and circumferential (CIRC) displacement and strain using a cylindrical coordinate system with the origin the middle of balloon axis.

C. Constitutive Modelling

The material response was fit using the Material Calibration App on the 3DEXPERIENCE (R2021 HotFix 8.13, Dassault Systems). Testing results were categorized in specimens obtained from the 23mm balloon versus specimens from the 26mm balloon. Constitutive parameters were assessed for the two specimen groups (ie, the 23 mm vs 26 mm). The material model used to fit the test data was a combination of Yeoh hyperelasticity, Johnson-Cook rate-independent plasticity, and non-linear PRF viscoelasticity (2 networks). This model can capture the “S” shape response typical of hyperelastic material behavior, offers good representation for large strains, and is typically a good choice when limited test data is available . The test data were imported, and the curves were edited (filtered and resamples) to ease the calibration. The curves were shifted so that the loading starts at t=0 seconds (and offset correction). Data sets with a large number of datapoints were reduced while preserving the characteristics of the curvature.

III. Results

Figure 1 shows the stress-strain response for balloon specimens tested at room temperature and controlled temperature. The higher the temperature is, the more compliant the stress-strain response is. No substantial differences were observed from samples extracted in the circumferential balloon direction versus the longitudinal direction. The stress-strain curves were characterized by a steep increase in the stress-strain response upon nearly 7% of strain, followed by a non-linear knee and a linear response uponfailure.

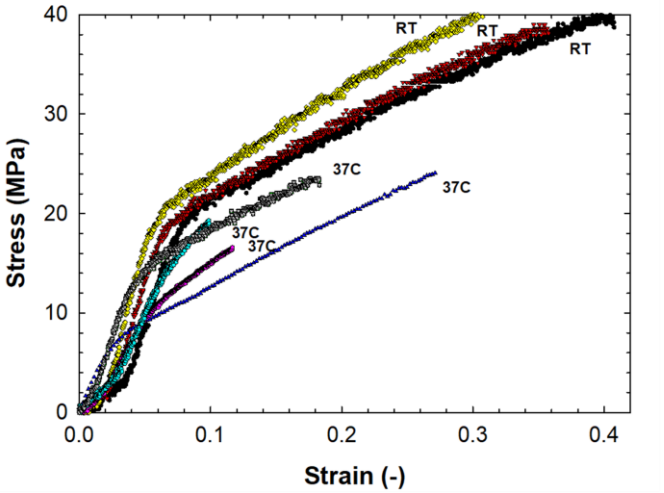


Figure 1. Stress-strain response for n.8 specimens tested at room temperature (RT) and controlled temperature (37C)

Figure 2 shows the stress-strain response for cyclic testing of different samples extrapolated from the 23mm and 26mm balloons. Specimens were loaded and unloaded multiple times during the test to gain insight into the residual deformation developed between different cycles. Cyclic testing was carried out up to ten cycles or specimen rupture during material testing. When all specimens from both the 23 mm and 26 mm balloon were put together, two different material families were observed (see Test1-4 versus Test 5-7).

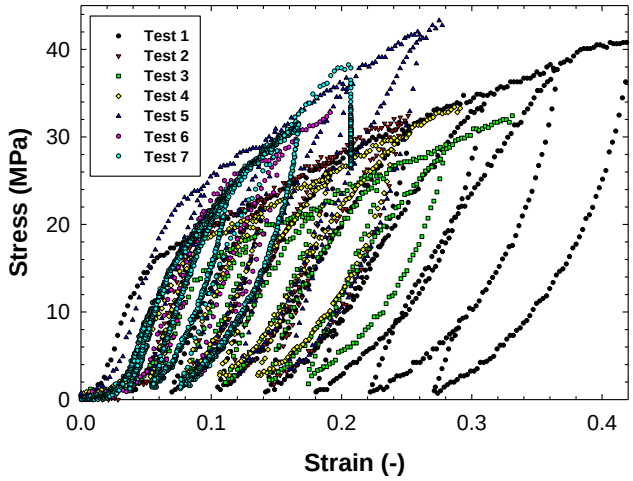


Figure 2. Cyclic stress-strain response for n.7 specimens cut from the 23 mm balloon (Test from 1 to 4) and the 26 mm balloon (Test from 5 to 7)

Figure 3 shows a representative fitting of one sample tested for seven cycles upon rupture. Specifically, the calibrated material model is a combination of Yeoh hyperelasticity with Johnson-Cook rate-independent plasticity and non-linear PRF viscoelasticity as characterized by 2 networks. Fitting was independently performed for the group of specimens from the 23 mm balloon versus those collected from the 26 mm balloon given the response characterized by two material families (see Figure 2).

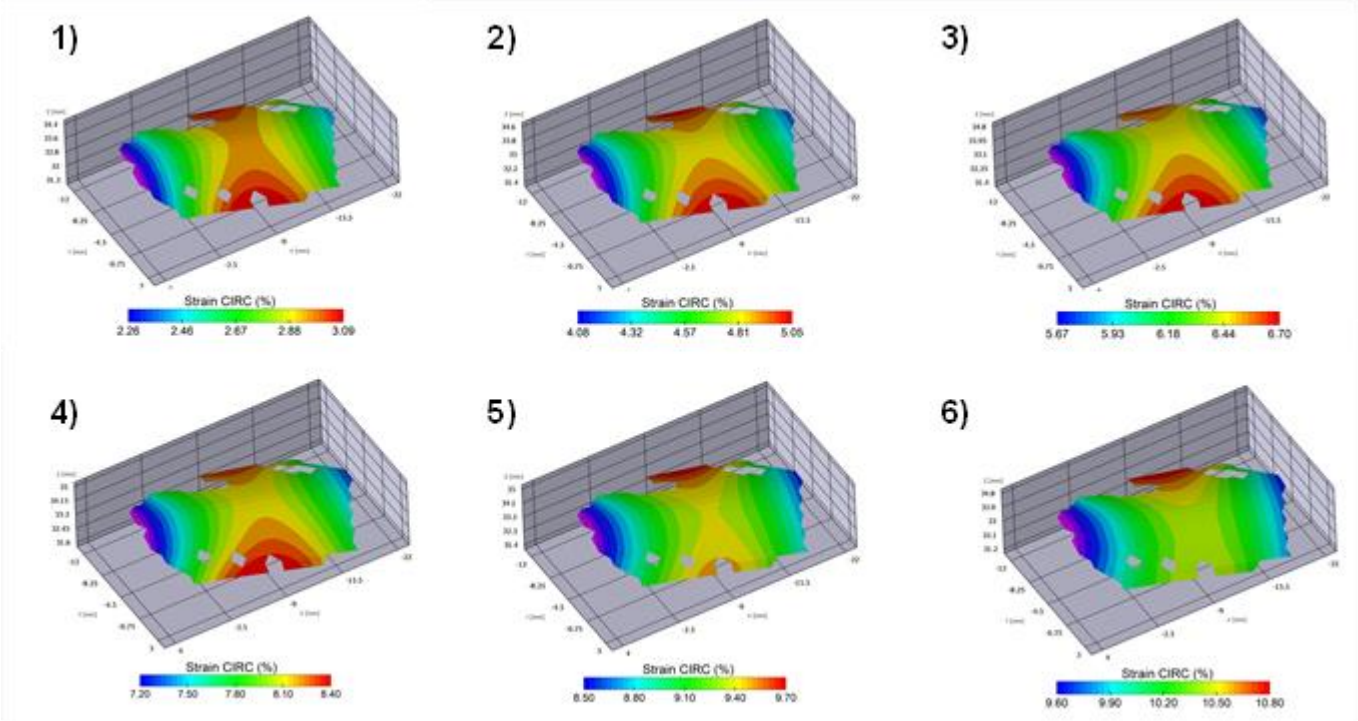


Figure 5. Strain map in CIRC direction at different level of expansion

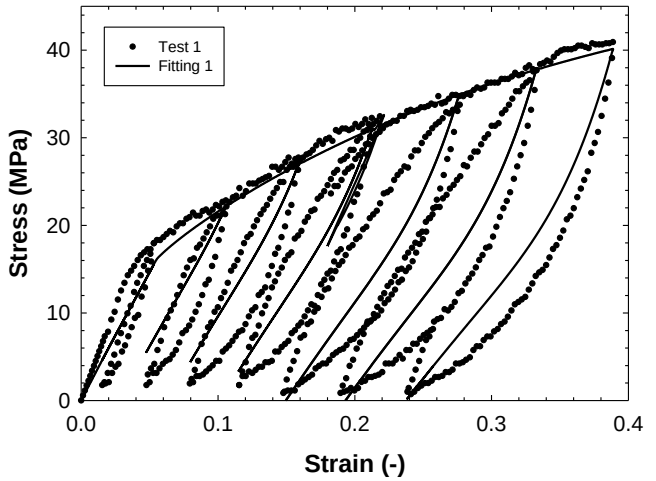


Figure 3. Cyclic stress-strain response for n.7 specimens cut from the 23 mm balloon (Test from 1 to 4) and the

The numerical stability of the constitutive model for the 23 mm balloon was good up to 20% strain which is well above the application strain (see Figure 4). For the 26 mm balloon, the numerical stability was good in all material directions between 0 and 5 strain values.



Figure 4. Range of stability of the constitutive model for the 23 mm balloon

Table 1 summarizes the material parameters for the constitutive model.

	23mm Balloon (MPa)	26mm Balloon (MPa)
Yeoh Hyperelastic material model		
C10	16.38	26.03
C20	2.79	-107.49
C30	-6.75	613.38
D1	0.01	0.01
D2	0.01	0.01
D3	0.01	0.01
Johnson-Cook plasticity hardening material model		
A	28.53	19.30
B	312.8	153.0
n	0.18	0.86
PRF non-linear viscoelasticity – Network 1		
SRATIO	0.610	0.510
Ref stress	121.3	1850.1
n	1.28	1.00
m	-0.64	-0.25
PRF non-linear viscoelasticity – Network 2		
SRATIO	0.298	0.250
Ref stress	29.7	31.2
n	11.33	4.81
m	-0.92	0.00

Figure 5 shows the strain field in the CIRC direction for the 23 mm balloon. As the inflation volume increases, the CIRC

strain increased upon 10% in the mid-section of the balloon.

IV. Discussion

A deep investigation of PA12 material used in balloon-expandable THV was performed to assess mechanical behavior and then develop precise constitutive model. Findings demonstrated that the PA12 mechanical behavior is best described by a combination of hyperelasticity, rate-independent plasticity, and non-linear PRF viscoelasticity. DIC analysis was also used to quantify the circumferential strain field during balloon inflation, and this data can be used to validate computational analysis in the future. Findings demonstrated that the need for accurate constitutive laws when computational models are used to simulate the deployment of balloon-expandable THVs in the human host.

Transcatheter heart valve implantation can be performed using a balloon to support the device deployment. Once the balloon and device assembly have reached the aortic root, the clinician fill the balloon upon a nominal fluid volume indicated by the manufacturer. The procedure is time-dependent and may vary between patient to patient. In borderline cases, the clinician may choose for the over-expansion of the balloon adding one or two milliliters of fluid with respect to the nominal fluid volume. It is however noted that our data demonstrated residual plastic deformation with cyclic inflation [14-17]. It is surprising that a normal clinical usage of the balloon is associated with permanent plastic deformation. Typically, the balloon material should be used (during inflation up to the nominal pressure) only within its linear elastic range.

Cyclic material testing on specimens extracted from 23 mm balloon were found consistent but different from samples obtained by the 26 mm balloon. One group showed a higher yield stress and stronger plastic hardening than the second group. Such differences are likely caused by the fact that we did not test fresh balloons but rather clinically-used devices. Indeed, not much insight was gained into the amount of plasticity developed by the material during the clinical procedure. All balloons had likely a different loading history during their clinical usage (& plastic deformation). It is assumed that fresh balloon device would exhibit a more consistent mechanical response as compared to current findings.

To assess the effect of temperature on the balloon material behavior, a third group of samples was tested. From the test, it can be concluded that temperature has a considerable effect on the balloon material properties leading to visible material softening. Furthermore, the specimens tested at room temperature confirmed the viscoelastic behavior of the balloon material, which was also observed in the second group of samples. As a matter of fact, the failure strain of this batch (~0.12 strain) is lower when compared to the first batch (~0.3 to 0.4 strain), due to the higher loading rate used during testing.

The actual use of a hyperelastic model in combination with Johnson-Cook plasticity and non-linear viscoelasticity for fitting the experimental data showed excellent results. The distinct initial elastic range, the plastic hardening, and the viscoelastic hysteresis were captured very well and appeared to provide a stable mechanical behavior over a wide strain range.

V. Conclusion

This experimental characterization of the material properties of PA12 used in balloon-expandable THVs revealed the importance of appropriate constitutive models. Material testing demonstrated that PA12 has an hyperplastic and viscoplastic response. While findings needs to be confirmed in fresh balloons, such material response needs to be considered in computational analysis and may impact the balloon performance when over-expansion is performed clinically.

Acknowledgement

This project has received funding from the European Union's Horizon 2020 research and innovation programme under grant agreement No 101017523.

References

[1] McKeen L. Introduction to the Properties of Plastic and Elastomer Films. *Pdl Handb Ser* 2012: 19-55.
[2] Binder RK, *et al.* Transcatheter aortic valve replacement with the SAPIEN 3: a new balloon-expandable transcatheter heart valve. *JACC Cardiovascular interventions* 2013; 6(3): 293-300.
[3] Venoor V, *et al.* Understanding the Effect of Water in Polyamides: A Review. *Polym Rev* 2021; 61(3): 598-645.
[4] Menary GH, *et al.* Experimental study and numerical modelling of injection stretch blow moulding of angioplasty balloons. *Plast Rubber Compos* 2006; 35(8): 348-54.
[5] El-Qoubaa Z, *et al.* Characterization and modeling of the strain rate sensitivity of polyetheretherketone's compressive yield stress. *Mater Design* 2015; 66: 336-45.
[6] Geith MA, *et al.* Experimental and mathematical characterization of coronary polyamide-12 balloon catheter membranes. *Plos One* 2020; 15(6).
[7] Amstutz C, *et al.* Temperature-dependent tensile properties of polyamide 12 for the use in percutaneous transluminal coronary angioplasty balloon catheters. *Biomedical Engineering Online* 2021; 20(1).
[8] McFerran NLA, *et al.* Uniaxial tensile viscoelastic and viscoplastic behaviour of Nylon 12 at constant strain rate. *Plast Rubber Compos* 2006; 35(8): 310-16.
[9] Pasta S, *et al.* Simulation of left ventricular outflow tract (LVOT) obstruction in transcatheter mitral valve-in-ring replacement. *Med Eng Phys* 2020; 82: 40-48.
[10] Pasta S, *et al.* Transcatheter Heart Valve Implantation in Bicuspid Patients with Self-Expanding Device. *Bioengineering* 2021; 8(7): 91.
[11] Pasta S, *et al.* Simulation study of transcatheter heart valve implantation in patients with stenotic bicuspid aortic valve. *Med Biol Eng Comput* 2020.
[12] La Grutta L, *et al.* TAVI imaging: over the echocardiography. *La radiologia medica* 2020: 1-19.
[13] Di Giuseppe M, *et al.* Identification of circumferential regional heterogeneity of ascending thoracic aneurysmal aorta by biaxial mechanical testing. *J Mol Cell Cardiol* 2019; 130: 205-15.
[14] Fratini L, *et al.* Residual stresses and FCP prediction in FSW through a continuous FE model. *J Mater Process Tech* 2009; 209(15-16): 5465-74.
[15] Fratini L, *et al.* Residual stresses in friction stir welded parts of complex geometry. *Int J Adv Manuf Tech* 2012; 59(5-8): 547-57.
[16] Scardulla F, *et al.* Shear stress alterations in the celiac trunk of patients with a continuous-flow left ventricular assist device as shown by in-silico and in-vitro flow analyses. *J Heart Lung Transplant* 2017; 36(8): 906-13.
[17] Cosentino F, *et al.* On the role of material properties in ascending thoracic aortic aneurysms. *Computers in biology and medicine* 2019; 109: 70-78.

Patient-specific phantom for home haemodialysis

G. M. Fortunato[1,2], F. Tonelli[2], A. Greco[1,2], N. Carbonaro[1,2], A. Casani[3], C. De Maria[1,2]
[1] *Department of Information Engineering, University of Pisa, Pisa, Italy*
[2] *Research Centre "E. Piaggio", University of Pisa, Pisa, Italy*
[3] *Nephrology and dialysis, NOA Hospital, Massa, Italy*

***Abstract*—The aim of this work is to improve the management of haemodialysis by providing the tools to encourage home treatment. To this end, the design, implementation, and validation of a patient-specific phantom of an arm with arteriovenous fistula, used to train unqualified personnel in the cannulation procedure, is presented. This turns out to be the main obstacle to the transition to home treatment, given the difficulty of performing the dialysis treatment correctly. Through a collaboration with healthcare personnel, the phantom was fabricated using 3D printing technologies and then tested with the cannulation procedure. The test was repeated by expert and non-expert personnel, demonstrating its potential in learning the procedure.**

***Keywords*—home haemodialysis, patient-specific phantom, arteriovenous fistula, cannulation.**

I. Introduction

HAEMODIALYSIS is the most common treatment for renal failure, affecting about 9% of the world's population [1] and occurring with a gradual loss of kidney functions. It involves a blood filtration, which lasts a few hours and is repeated at least three times per week. This causes a clear deterioration in patient's quality of life and even a significant impact on the National Health System since it represents the 2% of the health budget in Europe [2]. By encouraging the transition to home treatment, this work has the aim to improve the patient's management of therapy and cut the costs of in-center haemodialysis. In fact, we propose a novel approach for caregivers' training with personalized phantoms for haemodialysis cannulation, ensuring better outcomes and consequently stimulating this passage. The cannulation procedure represents the main obstacle for home therapy, since the operator in most cases feels unable to act on dialysis treatment [3] as the vessels to cannulate have particular characteristics deriving from an arteriovenous fistula, a surgical anastomosis between a vein and an artery [4]. Indeed, the fistula prevents the collapse of the vessels due to the high cannulation and causes the arterialization of the vessel, which allows to obtain extra pressure and extra blood in lumen as well as an increased wall thickness. In this work the design, fabrication, validation, and cost analysis of a patient-specific phantom to value its effectiveness as well as the feasibility of such training method is presented. The choice of a patient-specific approach is justified by the recipients of the study. Indeed, as caregivers usually are not qualified personnel, it is extremely difficult to learn the cannulation gesture and it is also useless to teach them to cannulate every kind of patients. A typical surgical training approach is used as it is demonstrated to be useful to exercise on the specific model to prevent patients from extra pain and surgeons from excessive stress during the learning phase [5]. To achieve best results, the phantom was developed in a close collaboration with NOA Hospital in Massa, whose Interventional Radiology department provided the image acquisition and the Nephrology and Haemodialysis one followed the development of the phantom and tested the intermediate and final outcomes.

II. Materials and Methods

A. Phantom design and fabrication

Once identified a case study, images of the vessels and fistula were acquired through a phlebography, a computed tomography of the arm with the use of a contrast dye. The resulting sets were inspected and elaborated in itk-SNAP software. An active contour segmentation was carried out to obtain the model of the main structures (Fig. 1). These consisted of bones, blood vessels and the external volume, which were exported and firstly elaborated in Autodesk® MeshMixer to obtain adequate mesh bodies and then imported in Autodesk® Fusion 360™, to handle their design according to the fabrication strategy chosen.

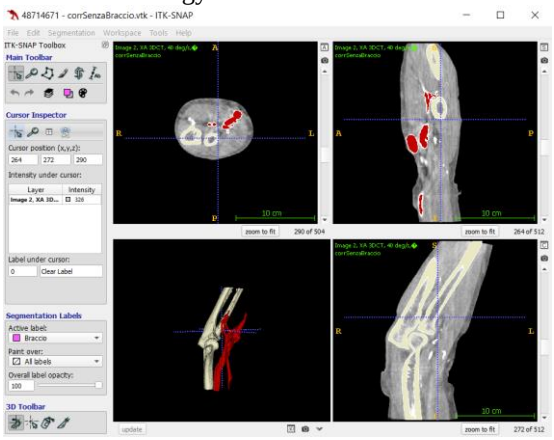


Fig. 1: Segmentation and rendering of bones and vessels in Itk-SNAP software

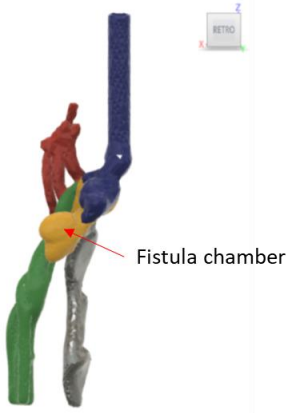


Fig. 2: CAD model of the blood vessels, divided into five components

The blood vessels were divided into five components to reach an almost linear structures and simplify the following fabrication process (Fig. 2). The bones, instead, were filled as they presented an internal cavity and from the whole arm structure a mold design was obtained (Fig. 3). This was divided into two halves (Fig. 3A) as it should allow the placing of bone and vessel before being filled up with the soft-tissues mimicking material. The mold was 3D printed in Acrylonitrile butadiene styrene (ABS) reflecting the negative shape of the arm with some positioning pins to grant the proper pose of the halves. Bones and vessels were placed into the mold to reproduce the correct anatomy of the patient (Fig. 3B) and fixed to the mold walls with adhesive tape to be easily removable after the phantom de-molding.

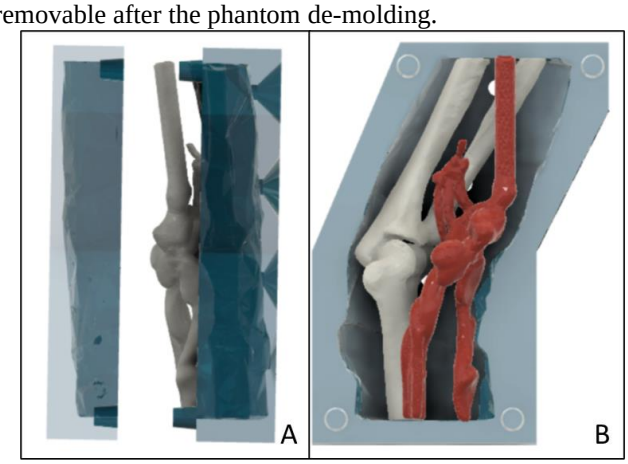


Fig. 3: A) Arm phantom mold design – B) Bones and vessels placed in the mold

At the same time, several trials were carried out in collaboration with the healthcare staff to find the best materials in reproducing target tissues (vessels and soft tissues). To this end, cubic specimens with a cylindrical hole representing an internal vessel (mold for silicone casting shown in Fig. 4) were fabricated using different materials, as shown in Table I, and cannulation tests were performed to identify the most natural feedback.

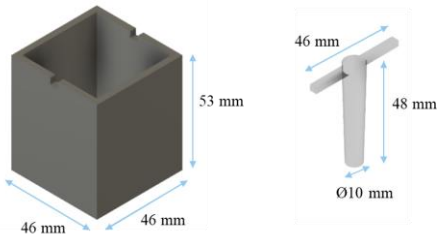


Fig. 4: Mold design for cubic specimens fabrication. The cylindrical hole is obtained placing the core (on the right) in the mold.

TABLE I: MATERIALS TESTED FOR PHANTOM FABRICATION

Vessels	*Soft tissues*
Smooth-On Dragon Skin 10	Smooth-On Ecoflex 0010
Smooth-On Dragon Skin 10 + 0.25 % Thi Vex	Smooth-On Ecoflex 0010 + 50 % Slacker
Smooth-On Dragon Skin 10 + 0.5 % Thi Vex	Smooth-On Ecoflex 0010 + 5 % Thinning
Smooth-On Dragon Skin 10 + 1 % Thi Vex	
Formlabs Elastic 50A Resin (1, 1.2 and 1.4 wall thickness)	

Bones were 3D printed in ABS without joints to avoid any possible movement of the articulation as they only have the role of sustaining the phantom and representing a secondary landmark.

Once selected the proper materials and assembled the mold, it was closed with clamps and the chosen silicone was casted through four countersunk holes and left to cure for 72 hours.

Finally, to mimic the blood and improve the venous return during the cannulation procedure, a 7% w/v alginate solution was used.

B. Phantom validation

Following phantom fabrication, it was validated, in order to evaluate its correctness in terms of geometry and consistency, both in a generic context and in the faithful reproduction of the patient chosen as a case study. It consisted in three phases: an objective, a subjective and an experimental one [6]. The first one was carried out evaluating the reliability, comparing the rendered images of the patient arm and the resulting phantom, since it was not possible to obtain a phantom CT to compare the outcomes in medical images and rendered volumes due to COVID19-pandemic. The second part was about face and content validity and consisted of a questionnaire, which was submitted to the health staff during the final phase of the validation, and which evaluated the morphological and perceptive correctness and the appropriateness of the phantom. In particular, the following four questions were submitted to be scored from 0 to 5:

1. How much the resulting anatomy approximates a generic model of a patient with an arteriovenous fistula?
2. Do the materials properties correctly resemble the real arm?
3. Is the perception returned by the cannulation consistent with the real experience?
4. Can the patient-specific simulation constitute a sufficient training for the caregiver?

The experimental test was used to verify the construct validity and the effectiveness of training and involved an expert and a non-expert group (11 elements) cannulating the phantom. The test was repeated twice.

C. Cost analysis

Finally, a cost analysis was carried out to evaluate the feasibility of this kind of simulators and the eventual impact of a phantom-based training for home haemodialysis on the National Health System. The cost of the phantom includes manufacturing, materials, image acquisition and processing. For a better estimation, the difference between traditional and home treatment, which is valued more than € 40000 per patient per year considering direct, indirect, and social costs, has to be taken into account [7].

III. RESULTS AND DISCUSSION

A. Phantom design and fabrication

Following the preliminary tests outcomes, Smooth-On Ecoflex 0010 was assessed to be the best option in reproducing

soft tissues and Formlabs Elastic 50A Resin for the vessels (1.4 mm wall thickness as shown in Fig. 5), thanks to its capability to reproduce the adequate thickness and a vessel mimicking resistance. Vessel components were thus fabricated using stereolithography with a Formlabs Form 2 printer.



Fig. 5: Vessels internal section with a 1.4 mm wall thickness

After that, they were glued together (Fig. 6) using liquid Elastic 50 Resin, photo-polymerised using a 405 nm lamp. A layer of universal silicone was added on the vessels in order to prevent the liquid from spilling out after cannulation.



Fig. 6: Vessels assembled: the 5 components fabricated by stereolithography were glued together using liquid Formlabs Elastic 50A resin and a 405 nm lamp.

Bones and vessels were then placed in the mold (Fig. 7A), filled up with Ecoflex 0010 silicone (Fig. 7B).

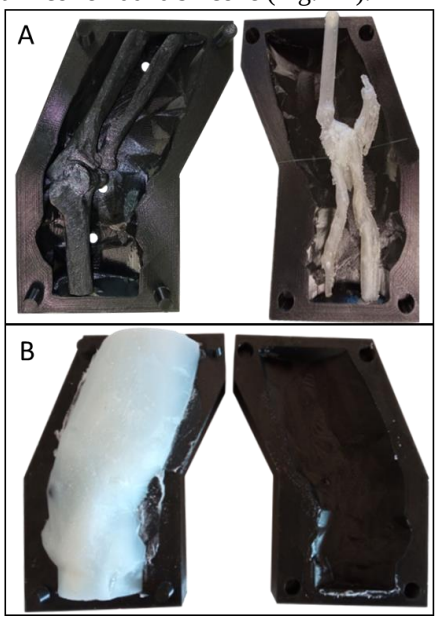


Fig. 7: A) Bones and vessels placed in the mold before silicone pouring – B) Phantom de-molding after 72 h curing

Vessels were then filled up with the alginate solution to add the blood return feedback.

The result of this process returned an anthropomorphic phantom of the interested section of the arm resembling patient's anatomy. To improve the visual perception, a mannequin arm was used to create the upper section of the arm itself as well as hand and wrist (Fig. 8).



Fig. 8: Final assembly of the arm

B. Phantom validation

Considering the objective analysis, it was carried out by comparing the arm images obtained from the phlebography with pictures taken from the assembled phantom. From a qualitatively point of view, the external morphology of the phantom was correspondent to the segmentation obtained in itk-SNAP software, as shown in Fig. 9.

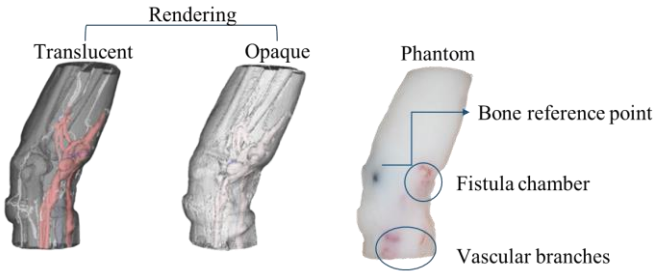


Fig. 9: Comparison between the arm rendering obtained from the phlebography and the real phantom. Correct morphology and pose of the bones are shown.

Looking at the top view (Fig. 10) the bones resulted in a correct position while vessels were subjected to a 36° rotation respect to the target. This is due to the pouring of the silicone that caused the shifting of the soft structures towards the bottom of the mold. This value can be improved by better fixing the vessels in the mold (*e.g.*, using glue) before filling.

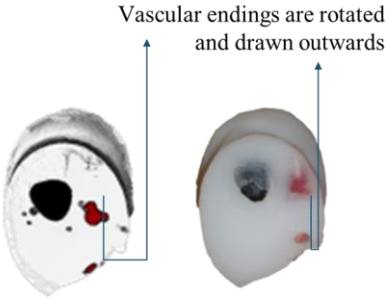


Fig. 10: Comparison between the arm rendering obtained from the phlebography and the real phantom: top view. Vessels are 36° rotated.

Nevertheless, the outcomes allowed to verify the likelihood of the phantom and the validity of the cannulation training carried out (Fig. 11). In fact, the phantom, despite the imperfect positioning of the vessels in relation to the patient's anatomy, was correctly cannulated from the expert staff with a 95% success rate (construct validity), unlike the non-expert group, of which only 20% succeeded. However, the outcomes

of the second trial showed a success rate of 90% for the non-expert group against the 100% of the experts. The differences with their first attempt made thus possible to verify the effectiveness of the training carried on using the phantom.



Fig. 11: Cannulation test on the phantom: the test was repeated twice by an expert and non-expert group proving the effectiveness of the training

Considering the survey taken among experts after the cannulation test, the trend of the answers (Fig. 12) confirmed the morphological correctness and a perception and usability similar to the real arm.

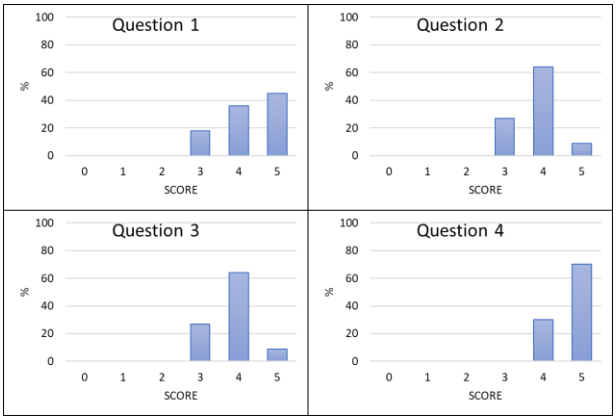


Fig. 12: Answers to the survey taken among experts after the cannulation tests

C. Cost analysis

Due to the importance of the patient-specific approach, a cost-minimising series production is not applicable. Furthermore, the costs of design and manufacturing directly depend on the case study. The total costs for the phantom fabricated in this study are reported in table II.

TABLE II: PHANTOM COSTS

	Info	*Cost*
Image acquisition	Monolateral phlebography of the upper limb	€ 207
Image processing	Image segmentation and CAD design (10 h)	€50/h
Materials	Resin+ABS+silicone	€108.40
Manufacturing	Average cost for manufacturing (11 h)	€30/h
Total		€1145.40

The resulting cost should be related to the health impact of the transition from hospital to home haemodialysis, and it has to be compared to three sessions of treatment. Considering the typical treatment of three services per week, a year of home haemodialysis saves the Italian Health System about €42700 per person [7], compared with traditional in-center handling. This would largely justify the choice of a novel approach to training using patient-specific phantom in the face of a major initial cost. In fact, the phantom should be considered part of a systematic approach to encourage the home haemodialysis. In this way, after just one year the total savings from the new therapy approach would be recognizable.

IV. CONCLUSIONS

In this study we presented the fabrication of a patient-specific phantom for the training of the caregiver towards home haemodialysis. The phantom was fabricated, and cannulation tests were made by both expert and non-expert users. Main limitations of this approach were found in the imperfect positioning of all anatomical components, although this did not compromise the functionality of the phantom. The outcomes achieved during the test phase, in fact, met expectations and with the good response of the health staff demonstrated the feasibility of this new training approach. In addition, the strong economic impact resulting from home haemodialysis saving can justify the initial investment on caregiver training, thanks to its shown effectiveness and the capability of enhancing the transition from in-center to home haemodialysis.

ACKNOWLEDGEMENT

This work was partially supported by the project ENDIADI funded by Tuscany region under the call “Bando Assegni di ricerca anno 2021 – Fondo sviluppo e coesione 2014-2020” and by the European Union by the Next Generation EU project ECS00000017 ‘Ecosistema dell’Innovazione’ Tuscany Health Ecosystem (THE, PNRR, Spoke 4: Nanotechnologies for diagnosis and therapy).

REFERENCES

[1] Carney, E. F. (2020). The impact of chronic kidney disease on global health. Nature Reviews Nephrology, 16(5), 251-251.

[2] Lameire, N., Jager, K., Van Biesen, W. I. M., De Bacquer, D., & Vanholder, R. (2005). Chronic kidney disease: a European perspective. Kidney International, 68, S30-S38.

[3] Walker, R. C., Hanson, C. S., Palmer, S. C., Howard, K., Morton, R. L., Marshall, M. R., & Tong, A. (2015). Patient and caregiver perspectives on home haemodialysis: a systematic review. American Journal of Kidney Diseases, 65(3), 451-463.

[4] Hill, K., Sharp, R., Childs, J., Esterman, A., Le Leu, R., Juneja, R., & Jesudason, S. (2020). Cannulation practices at haemodialysis initiation via an arteriovenous fistula or arteriovenous graft. The Journal of Vascular Access, 21(5), 573-581.

[5] Poorgholami, F., Koshkaki, A. R., Jahromi, M. K., & Parniyan, R. (2016). A study of the influence of group-based learning of stress management on psychology symptoms levels of haemodialysis patients. Global journal of health science, 8(11), 62-68.

[6] McDougall, E. M. (2007). Validation of surgical simulators. Journal of endourology, 21(3), 244-247.

[7] Regione Piemonte, «Potenziamento delle cure domiciliari nei pazienti affetti da insufficienza renale terminale con necessità di trattamento dialitico tramite contributo economico di sostegno alla dialisi domiciliare,» 2009.

A response surface-based approach to predict spinal rod contouring parameters

F. Berti[1], L. Carpenedo[1], C. Boldrin[1], and L. La Barbera[1,2]
[1] *Laboratory of Biological Structure Mechanics, Dept. Chemistry, Materials and Chemical Engineering, Politecnico di Milano, Italy*
[2] *IRCCS Istituto Ortopedico Galeazzi*

***Abstract*— Rod contouring can be intraoperatively performed by surgeons to obtain bent spinal rods that better fit the physiological curvature of the spine. However, this procedure exploits the material plastic deformation, which is known to affect fatigue behavior *in vivo*.**

Numerical models allow the assessment of the residual stress field due to contouring, but at a high computational cost, which is not compatible with the extensive use of *in silico* models in preoperative clinical planning.

For this reason, after preparing a finite element analysis of titanium rod contouring, a response surface-based approach is proposed to correlate contouring-related parameters with residual stress field and rod curvature.

***Keywords*— Spine, spinal fixation, finite element, residual stress, fatigue failure.**

I. Introduction

Spinal rods are commonly used during spine surgery to restore the correct sagittal and coronal alignment in young (i.e. scoliosis) and adult deformity patients. Contouring is the process adopted to achieve the desired spinal profile through a plasticization of the spinal rod. The French Bender is a well-known surgical instrument capable of obtaining very sharp intraoperative contours characterized by a very focused curvature radius. Commercially available pre-contoured rods show a uniform shape characterized by a constant curvature radius.

Several studies demonstrated that the fatigue resistance of spinal rods contoured using several methods is significantly reduced, thus leading to premature rod fracture and revision surgery [1]–[4]. Recent studies also used *in silico* finite element (FE) modeling coupled with *in vitro* experiments both static and dynamic, to demonstrate that deformations in the plastic range involve high residual stresses and, thus, reduce the fatigue resistance of the spinal rods [5], [6].

The usefulness of models relies on their ability to describe the reality of interest and, at the same time, their usability: indeed, models of spinal fixators consist of multiple parts (e.g. rods, screws, connectors), which might be very onerous to simulate due to their interactions [7]. However, long simulation times are not compatible with the intraoperative decision-making process, which would require processing detailed results in the order of tenths of seconds to adjust to real-time surgical planning.

The aim of the present study is twofold:

i) to perform a detailed full-factorial FE analysis describing titanium rod contouring via a four-point bending set-up, which replicates in controlled laboratory conditions the procedure performed by manufacturers (Uniform Contouring). Even though Different rod diameters and applied displacements were simulated as independent parameters to calculate relevant contouring outputs (i.e. residual curvature radius, residual stresses) as dependent parameters;

ii) to extend the validity of the previous discrete FE simulations by preparing a continuous response surface using the dependent parameters as a function of the independent ones.

II. Materials and Methods

All simulations were prepared and run using Abaqus Standard CAE 2022 (Dassault Systemes Ri, Simulia Corp. Providence, RI, USA).

A. Contouring simulations

1) The setup model

A four-point bending setup was chosen for replicating the uniform contouring. This contouring method was prefered over other technique as previous studies already demonstrated that the result in terms of residual compression and tension were similar [5]. The distance between the upper pins (loading pins) was set to 30 mm while that between the lower ones (support pins) was set to 80 mm. Exploiting intrinsic symmetries, the model was reduced to ¼ (Fig. 1a): the model was partitioned along the x and z axes considering half of the length and the cross-section to reduce the computational cost. All pins (d=4 mm) were modeled as linear-elastic material with stainless-steel properties (E=210 GPa, ν=0.3). The rod-pin contacts were described by surface-to-surface interaction with hard normal behavior and a friction coefficient of 0.175, [8]. All the parts of the model are discretized with linear hexahedral elements (C3D8).

2) Titanium spinal rods model

The elastic-plastic material properties of the rods were assessed through experimental tensile tests (E=110 GPa, ν=0.3, σ_Y=886 MPa, σ_U=1134 MPa, ε_U=5.35%) (Fig. 1b) [5].

Three models were prepared according to the rod diameters more often used in clinical practice, namely 5, 5.5, and 6.35 mm. A mesh sensitivity study led to the choice of linear hexahedral elements with incompatible mode formulation (C3D8I), with a global size of 0.45 mm and higher refinement of 0.15 mm in the area of the central rod and rod-pin contacts (Fig. 1c).

1) Simulation and outputs

The contouring step consisted of a loading phase followed by unloading: during the first, the upper pin moved vertically in displacement control, impacting the rod and causing its deformation; then, an opposite displacement was specified to

release the load. The support pin remained fixed during the whole simulation.

Twenty-one simulations were prepared for each of the rods, with different amounts of applied vertical displacements (u), ranging from 0.2 to 9 mm. This allowed to investigate the rod response to elastic loadings and, especially, post-yield conditions.

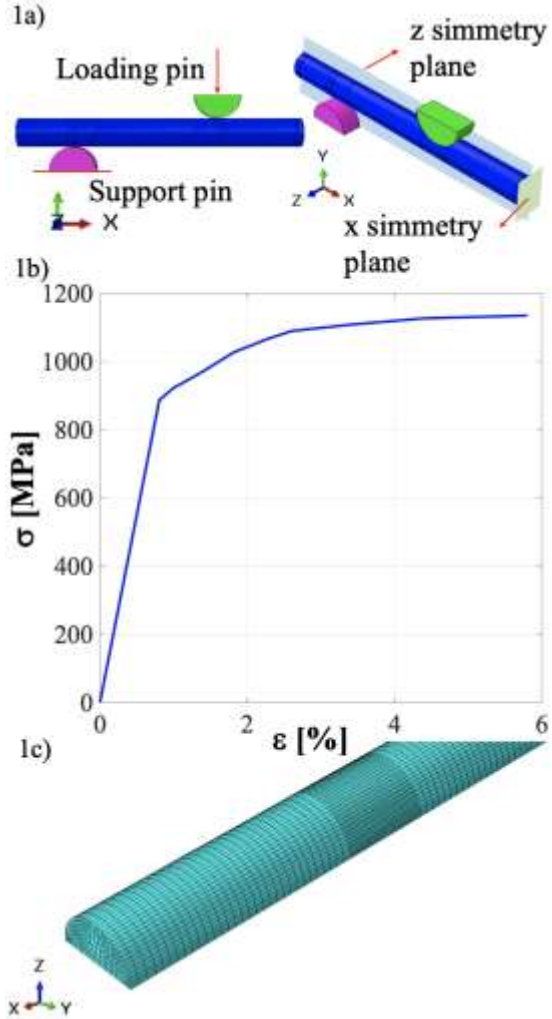


Fig. 1: a) The model of the four-point bending setup, reduced using symmetries; b) elastic-plastic material properties assigned to titanium rods [5]; c) detail of the rod mesh refinement.

In each of the previous cases, the residual curvature radius (RCR) was computed at the end of the unloading phase and stored, together with the residual stress field (σ*) in the central section of the gauge length, according to both radial and circumferential paths.

B. *Generation of the response surfaces*

The response surface-based approach was set starting from the analysis of the FE results, using the Matlab (MathWorks Inc., 2022a) tool *curveFitter*.

In particular, two independent variables, which are relevant input variables that can be chosen by surgeons in the contouring process, were selected:

- rods diameter, D (5, 5.5, and 6.35 mm);
- applied vertical displacement, u (considering only post-yield data).

Five dependent variables, which are the result of the contouring process and the focus of the present work, were identified among the simulation results:

- residual curvature radius, RCR;
- maximum peak tensile residual stress in the central rod section, $\sigma^{*MAX,t}$;
- maximum peak compressive residual stress in the central rod section, $\sigma^{*MAX,c}$;
- radial coordinate of the $\sigma^{*MAX,t}$, $R(\sigma^{*MAX,t})$;
- radial coordinate of the $\sigma^{*MAX,c}$, $R(\sigma^{*MAX,t})$.

The model was in the form of Eq. (1):

$$f(D,u) = p_{00} + p_{10} \cdot D + p_{01} \cdot u + p_{11} \cdot D \cdot u + p_{02} \cdot u^2 \quad (1)$$

where D and u represent the rod's diameter and the applied vertical displacement, respectively.

Notice that polynomial equations up to second order were used to avoid excessive complexity of the response surfaces: the second order appears for u variable only, while the quadratic term was not necessary for D variable. To reduce the effects of outliers, the robust bisquare method was used for the response surface fitting of RCR variable. The coefficients (with 5% and 95% confidence bounds) were then calculated. To quantify the goodness of fit using Eq. 1 (1), coefficient of determination (R^2), root mean square error (RMSE) and Normalised RMSE, computed as in Eq. (2), were used as indicators.

$$Normalised\ RMSE = {}^{RMSE}/_{(\max value - \min value)} \quad (2)$$

The response surfaces were depicted for each dependent parameter as 3D color maps.

III. Results and Discussion

A. *Contouring simulations*

The application of vertical displacements u<2 mm was not sufficient to cause any yield. To reach values in the range of 100÷200 mm, which were compatible with the preformed commercial rods, the vertical displacement had to increase from 5 mm. The higher the rod diameter, the lower the required displacement to get a given curvature radius (Fig. 2).

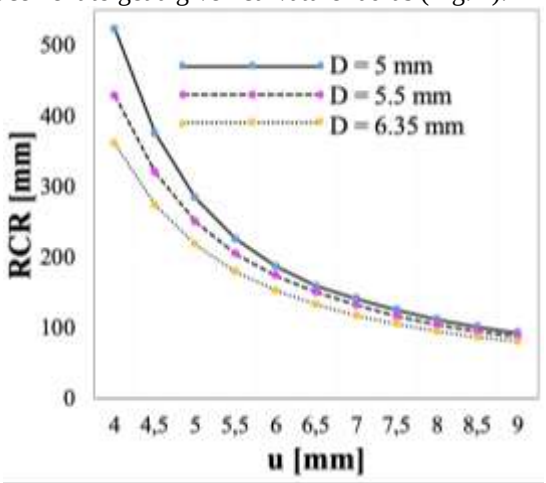


Fig. 2: Residual curvature radius (RCR) in rods having different diameters (D) as a function of the applied vertical displacement (u) in the range 4÷9 mm.

The radial and circumferential paths of residual stresses exhibited similar trends among the different rods, however showing different values and radial coordinates of the peak stresses (Fig. 3).

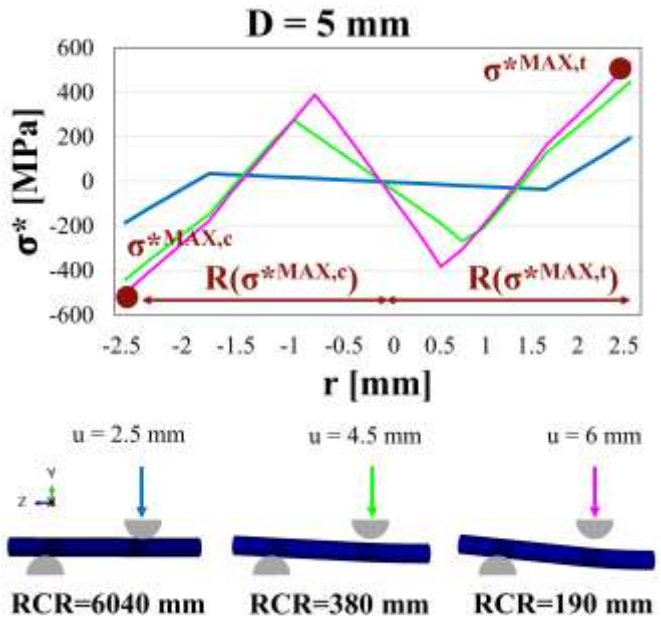


Fig. 3: Computational residual stress fields predicted for a 5 mm diameter rod due to specific applied vertical displacements (u). The dependent variables (RCR, $\sigma^{*MAX,t}$, $\sigma^{*MAX,c}$, $R(\sigma^{*MAX,t})$, $R(\sigma^{*MAX,c})$) used for the generation of the response surface are presented.

B. *Response surfaces*

The resulting response surfaces are depicted in Fig. 4, 5, 6, 7 and 8 for each dependent parameter.

The coefficients for each term of the polynomial response surfaces are summarized in Table I. In the analysis of the residual curvature radius, three points in the range of interest were excluded to avoid analytical biases for very low displacements due to excessively high curvature. This led to a better goodness of fit in the data.

The polynomial terms (Table I) beyond the linear ones only contributed less than 5% for the residual curvature radius, $\sigma^{*MAX,t}$, and $\sigma^{*MAX,c}$. The terms p_{00} and p_{01} contributed, respectively, about 84% and 16% on RCR; while the terms p_{00}, p_{01} and p_{10} contributed, respectively, about 75%, 25% and 10% on the residual stresses. The term p_{10} contributed alone more than 96% on the calculation of the radial coordinate of stresses.

TABLE I: RESPONSE SURFACES COEFFICIENTS

Variable	p_{00}	p_{10}	p_{01}	p_{11}	p_{02}
RCR [mm]	2148 (-1882, 6179)	-121 (-812, 570)	-424 (-1182, 334)	14 (-99, 127)	22 (-14, 57)
$\sigma^{*MAX,t}$ [MPa]	-723 (-979,-468)	99 (55, 143)	233 (185, 282)	-7 (-14, 1)	-12 (-14, -9)
$\sigma^{*MAX,c}$ [MPa]	751 (498, 1004)	-99 (-144,-55)	-261 (-309,-213)	10 (2, 17)	14 (12, 16)
$R(\sigma^{*MAX,t})$ [mm]	-0.020 (-0.023,-0.018)	0.504 (0.504, 0.504)	<<0.001 (-0.001, 0.001)	/	/
$R(\sigma^{*MAX,c})$ [mm]	0.020 (0.018, 0.023)	-0.504 (-0.504,-0.504)	<<-0.001 (-0.001, 0.001)	/	/

Notice that the response surfaces for radial coordinates of both the $\sigma^{*MAX,t}$ and the $\sigma^{*MAX,c}$ are linear planes, as the two peaks are always observed on the outer surfaces of rods. Therefore, for these variables, it might be assumed that their positions will always lie at the maximum radius.

The goodness of fit values are reported in Table II for the sake of completeness.

TABLE II: RESPONSE SURFACES GOODNESS OF FIT

Variable	R^2	*RMSE*	*Normalised RMSE [%]*
RCR [mm]	0.86	407.2	0.2
$\sigma^{*MAX,t}$ [MPa]	0.97	29.9	4.5
$\sigma^{*MAX,c}$ [MPa]	0.96	29.6	5.3
$R(\sigma^{*MAX,t})$ [mm]	1	<0.01	0.1
$R(\sigma^{*MAX,c})$ [mm]	1	<0.01	0.1

The R^2 was higher than 0.96 for most parameters, but for RCR. Although the RMSE showed relatively high absolute errors, the normalized RMSE confirmed that the prediction error in using the response surfaces was satisfactory in general, with maximum residual stress values predicted within 5%.

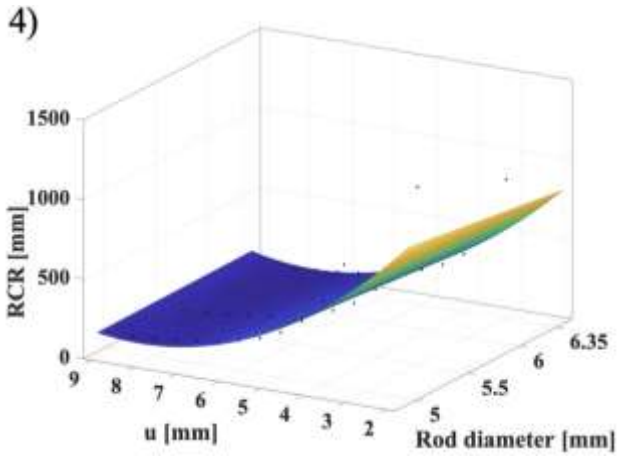


Fig. 4: Results of the response surfaces on RCR. Color map from blue to yellow indicates values from minimum to maximum.

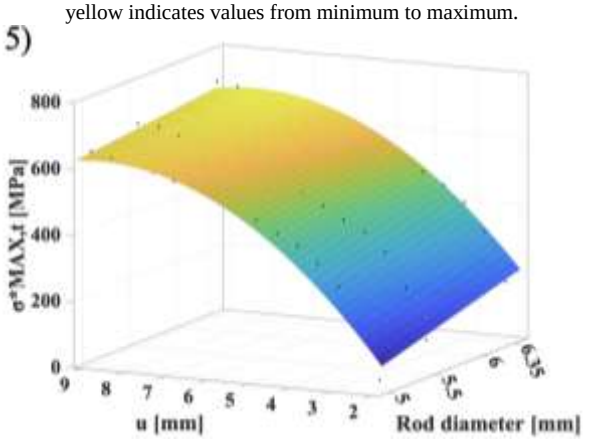


Fig. 5: Results of the response surfaces on $\sigma^{*MAX,t}$. Color map from blue to yellow indicates values from minimum to maximum.

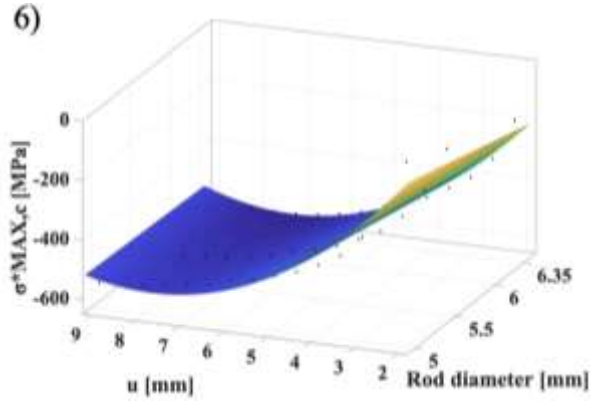


Fig. 6: Results of the response surfaces on $\sigma^{*MAX,c}$. Color map from blue to yellow indicates values from minimum to maximum.

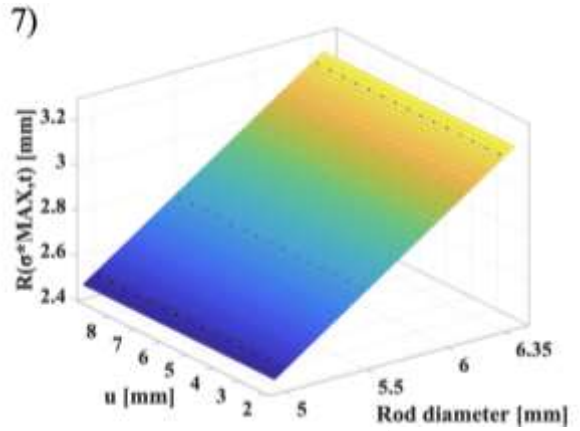


Fig. 7: Results of the response surfaces on $R(\sigma^{*MAX,t})$. Color map from blue to yellow indicates values from minimum to maximum.

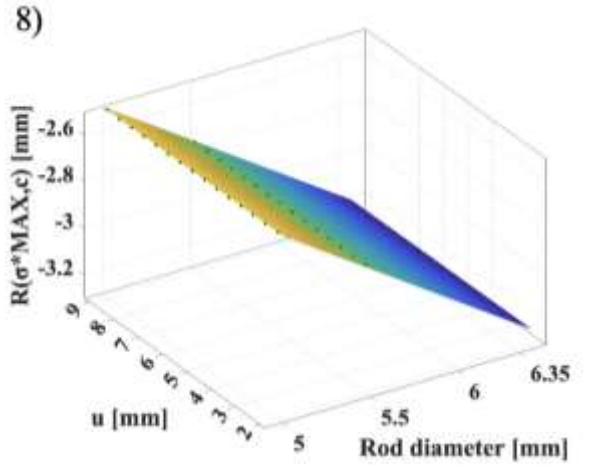


Fig. 8: Results of the response surfaces on $R(\sigma^{*MAX,c})$. Color map from blue to yellow indicates values from minimum to maximum.

IV. Conclusion

The use of FE models allowed for estimating the impact of the contouring process on titanium rods of different diameters. Thanks to the proposed response surface-based approach, data from a reduced number of simulations can be extended to predict the behavior of rods in a larger domain with no need to perform additional computationally demanding simulations. Further developments could be the extension of the approach over different materials and contouring methods to build a complete framework useful for intraoperative strategies. A wider characterization of other contouring processes, such as using the French Bender, could definitely be a future perspective. Moreover, possible cross-correlations between dependent parameters could be evaluated. This first approach was focused on evaluating the effects of the choices made by the surgeon on the mechanical effects due to the contouring process, but a finer analysis could complete the description and supply a total comprehension of how parameters are related.

Acknowledgement

This research was partially supported by MIUR FISR—FISR2019_03221 CECOMES.

References

[1] P. Berjano, R. Bassani, G. Casero, A. Sinigaglia, R. Cecchinato, and C. Lamartina, “Failures and revisions in surgery for sagittal imbalance: Analysis of factors influencing failure,” *Eur. Spine J.*, vol. 22, no. SUPPL.6, pp. 853–858, 2013.

[2] J. S. Smith *et al.*, “Prospective multicenter assessment of risk factors for rod fracture following surgery for adult spinal deformity,” *J Neurosurg Spine*, vol. 21, no. 6, pp. 994–1003, 2014.

[3] C. Lindsey, V. Deviren, Z. Xu, R.-F. Yeh, and C. M. Puttlitz, “The effects of rod contouring on spinal construct fatigue strength.,” *Spine*, vol. 31, no. 15, pp. 1680–7, 2006.

[4] T.-Q. Nguyen, J. M. Buckley, C. Ames, and V. Deviren, “The fatigue life of contoured cobalt chrome posterior spinal fusion rods.,” *Proc. Inst. Mech. Eng. [H]*, vol. 225, no. 2, pp. 194–198, 2011.

[5] F. Berti *et al.*, “Residual Stresses in Titanium Spinal Rods: Effects of Two Contouring Methods and Material Plastic Properties,” *J. Biomech. Eng.*, vol. 140, no. 11, Nov. 2018.

[6] A. Piovesan, F. Berti, T. Villa, G. Pennati, and L. La Barbera, “Computational and Experimental Fatigue Analysis of Contoured Spinal Rods,” *J. Biomech. Eng.*, vol. 141, no. 4, Apr. 2019.

[7] L. Ciriello, F. Berti, L. La, T. Villa, and G. Pennati, “Journal of the Mechanical Behavior of Biomedical Materials Global stiffness and residual stresses in spinal fixator systems : A validated finite element study on the interconnection mechanism,” *J. Mech. Behav. Biomed. Mater.*, vol. 135, no. April, p. 105460, 2022.

[8] S. Eberle, C. Gerber, G. von Oldenburg, F. Högel, and P. Augat, “A biomechanical evaluation of orthopaedic implants for hip fractures by finite element analysis and in-vitro tests.,” *Proc. Inst. Mech. Eng. [H]*, vol. 224, pp. 1141–1152, 2010.

Reducing bone plates standard fatigue test time with an analytical runout load prediction

F.A. Bologna[1,2], A.L. Audenino[1,2], and M. Terzini[1,2]
[1] *Department of Mechanical and Aerospace Engineering, Politecnico di Torino, Turin, Italy*
[2] *Polito^{BIO}Med Lab, Politecnico di Torino, Turin, Italy*

***Abstract*— Mechanical tests on bone plates are mandatory for regulatory purposes but may require very high execution times from the market point of view. Therefore, an accurate prediction of experimental outcomes can reduce test runtime with beneficial costs cut for manufacturers. In this study, an analytical framework for the analytical runout load computation was realised to predict the fatigue behaviour of eleven bone plate models pending certification. The prediction accuracy was verified by performing a fatigue experimental test campaign on each plate. The developed analytical framework shows promising predictive ability, with R^2 above 0.938, with potential impact in reducing the experimental tests needed for the CE marking of bone plates.**

***Keywords*—Bone plate, four-point bending test, runout load, fatigue life prediction.**

NOMENCLATURE

σ_{max} = maximum stress
σ_{min} = minimum stress
R = stress ratio, $R = \sigma_{min}/\sigma_{max}$
σ_a = stress amplitude
σ_m = mean stress
$\Delta\sigma$ = stress range, $\Delta\sigma = 2\sigma_a$
$\sigma^*_{D\text{-}1}$ = specimen stress amplitude for $\sigma_m = 0$ (R = -1)
$\sigma_{D\text{-}1}$ = component stress amplitude for $\sigma_m = 0$ (R = -1)
σ_{UTS} = ultimate tensile strength

I. INTRODUCTION

NOWADAYS, the development of new plates for osteosynthesis, especially in long-bone surgery, has undergone a broad improvement. Their design has changed over the years, from conventional plates with straight linear geometries to implants with irregular shapes that follow the anatomical profile of the healing bone [1]. Indeed, the complexity of clinical procedures and biomechanical characteristics has given rise to a great variety of bone plate concepts (e.g., locking compression plates, dynamic compression plates, variable angle-locking compression plates) intended for specific anatomical regions.

However, modern plates must also meet safety and performance requirements depending on the local biomechanics. For this purpose, manufacturers and research groups are used to evaluate bone plates before commercialization through test methods published as ASTM or ISO standards [2]. ASTM F382 [3] is recognized in full by FDA and MDR, and it is the most widely used test standard for metallic bone plates. This standard presents a four-point bending test setup that allows the evaluation of the bending stiffness, the bending structural stiffness, the bending strength, and the cyclic bending fatigue performance of the bone plate. Quasi-static tests are useful to determine the loading range of fatigue testing, which have a substantial impact on the total runtime of the experimental campaign. The standard suggests for fatigue tests a load frequency of 5 Hz and one million cycles to reach the runout condition. An overall test time per plate has been estimated at around 180 hours without interruption in the best-case scenario [4]. Indeed, the realization of these test campaigns requires a considerable financial outlay on the part of manufacturers, with very long execution times from the market point of view.

Moreover, ASTM F382 provides a test methodology and defines the setup condition, but insufficient knowledge is available to predict the fatigue behaviour of the fixation device. The main goal of ASTM standards is to establish a reference test method that can be performed in any accredited laboratory, thus providing objective results for direct comparison with predicate devices. The first support comes from a recently issued guideline provided by FDA [5] about the performance criteria accepted for each intended anatomical location when ASTM F382 is applied. Nevertheless, this guideline only refers to static tests and does not contain any indication of plate fatigue limits. In this scenario, it would be useful to define a "harmonised testing approach", as highlighted in [2]: a systematic procedure based on standardized criteria for the development of a test procedure. Because of the wide variety of implants and their features, the test procedures shall be developed for each application and must be compliant with the regulatory requirements of ISO 14602, 7.2 [6]. Strategies based on Finite Element (FE) analyses [7] are usually proposed to speed up and simplify the plate testing procedures. FE models allow to predict test outcomes with a high level of detail, but they may require an important computational power to be quickly performed. Moreover, FE analyses are often used for the calculation of the stress distribution in a static condition, to be inserted into commercial software for the evaluation of fatigue life through analytical methods [8].

This work proposes an analytical framework for the direct estimation of the runout load, to speed up the experimental tests campaign for regulatory purposes. An analytical calculation of fatigue properties was implemented starting from the geometrical and material characteristics of the plate to guide the identification of the runout load for fatigue testing. A complete test campaign was then carried out to evaluate static and fatigue bending properties of eleven bone plate models according to ASTM F382 and verify the prediction accuracy of the analytical framework.

II. MATERIALS AND METHODS

A. Bone plates

Eleven different bone plates were evaluated in the present study. Table I lists for each plate the material, the tensile strength, and the anatomical site for which it was designed.

TABLE I: BONE PLATES INVOLVED IN THE STUDY

Plate	*Material*	*Tensile Strength (MPa)*	*Anatomical location*
01	Stainless Steel	900	Malleolus
02	Ti6Al4V	966	Malleolus
03	Pure Titanium	668	Wrist
04	Pure Titanium	652	Wrist
05	Stainless Steel	960	Distal tibia
06	Stainless Steel	910	Distal tibia
07	Ti6Al4V	1012	Distal tibia
08	Stainless Steel	986	Distal femur
09	Ti6Al4V	942	Diaph. tibia
10	Ti6Al4V	968	Distal femur
11	Pure Titanium	991	Diaph. femur

An ad hoc script was implemented on MATLAB R2020b (MathWorks, Natick, MA) to determine the critical section of each plate. The script allows to segment the bone plate following its curvature and returns the thickness (t), width (w), screw hole diameter (d), and moment of inertia (I) of the section with the minimum area.

B. Analytical fatigue evaluation

The analytical evaluation of fatigue behaviour was carried out considering simplified straight plates, derived from the actual geometries by using the characteristics of their critical sections. Plate curvatures were neglected, while the presence of a screw hole was considered by applying the nominal tension Peterson's stress concentration factors (K_t) for transverse bending of a finite-width plate with a circular hole [9]. Indeed, in static loading, the notch effect amplifies all the stress distribution. In fatigue loading, experimental results show that the stress concentration factor decreases at the fatigue limit [10]. In general, a fatigue-notch factor (K_f) is often determined by modifying the value of K_t (Eq. 1) according to a coefficient called notch-sensitivity index (q):

$$K_f = 1 + q(K_t - 1) \tag{1}$$

The notch-sensitivity index depends on both the mechanical and metallurgical characteristics of the material and the absolute dimensions of the notch. Due to the large dispersion of available data, various formulas have been proposed to obtain more precise values of q; the Neuber equation (Eq. 2) can be applied to steel plates:

$$q = \frac{1}{1+\frac{\sqrt{\rho}}{\sqrt{r}}} \tag{2}$$

where ρ is the average grain size and r is the notch radius.

While the Neuber equation is valid only for steels, there is no clear relationship for titanium alloys. In these cases, it is mandatory to carry out fatigue tests on notched and unnotched specimens to determine K_f [11]. Because materials with a uniform fine-grained matrix are very sensitive to notches [12], in titanium plates K_f was considered equal to K_t (q = 1), in a conservative perspective.

Starting from the static strength of the material (σ_{UTS}), K_f was used to estimate the fatigue limit ($\sigma_{D\text{-}1}$) with no average stress (σ_m = 0, corresponding to R = -1) of each bone plate from the following equation (Eq. 3):

$$\sigma_{D-1} = \sigma^*_{D-1} \frac{\prod C_i}{K_f} \tag{3}$$

where σ^*_{D-1} is the fatigue limit of the specimen, while C_i are factors affecting the component fatigue life, such as size (C_S), surface finish (C_F), or loading mode (C_L). In this study, a unit value has been attributed to $\prod C_i$: no correction due to surface finish was applied (all surface roughnesses were less than 0.8 µm) and a reliability of 50% was considered. A fatigue limit equal to $0.5\sigma_{UTS}$ [12] was applied for all bone plates.

Goodman and Gerber failure criteria [13] were implemented to calculate the mean stress effect due to ASTM F382 testing condition (R = 0.1). The traditional Goodman relationship and the Gerber parabola were represented in the Haigh diagram of Fig. 1 for pure titanium of Plate04. From the mean stress, the maximum stress (σ_{max}) and the maximum bending moment (M_{max}) were calculated with both failure criteria using the following relationships (Eq. 4-5):

$$\sigma_m = \frac{\sigma_{max}}{2}(1 + R) \tag{4}$$

$$M = \frac{\sigma_{max}\, I}{(t/2)} \tag{5}$$

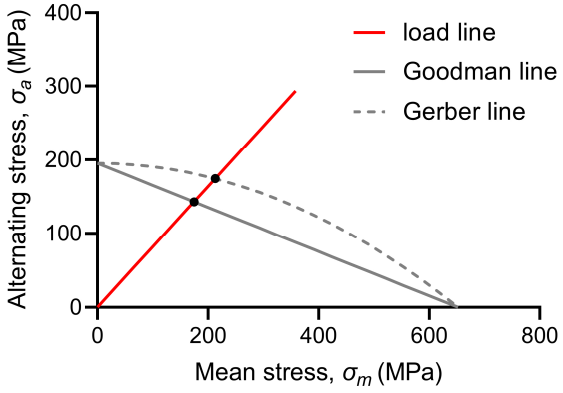


Fig. 1: Haigh diagram of Plate04 in pure titanium. Intersections between the load line and the applied criterion provide the mean stress values for the prediction of the fatigue life.

Finally, two predicted runout loads (L) were determined through Eq. 6 exploiting the loading span of the testing setup (h). These values were used to define the range of the runout load prediction.

$$L = \frac{2M}{h} \tag{6}$$

C. *Standard mechanical testing*

Quasi-static and fatigue bending tests were performed as reported in ASTM F382 to determine the fatigue life of the bone plates. According to A1.6.2.1, rigid extension segments were adopted for plates that did not directly fit into the test configuration, to obtain a sufficiently long section of symmetry.

The testing setup (an example in Fig. 2) was composed of:

- two loading rollers with distance *a* (center span), at least two screw holes must be located between them;
- two support rollers, placed at an equal distance from the loading roller (*h*, loading span); and
- two extension segments (material AISI 630, heat treatment W1.4542 – H900), if required.

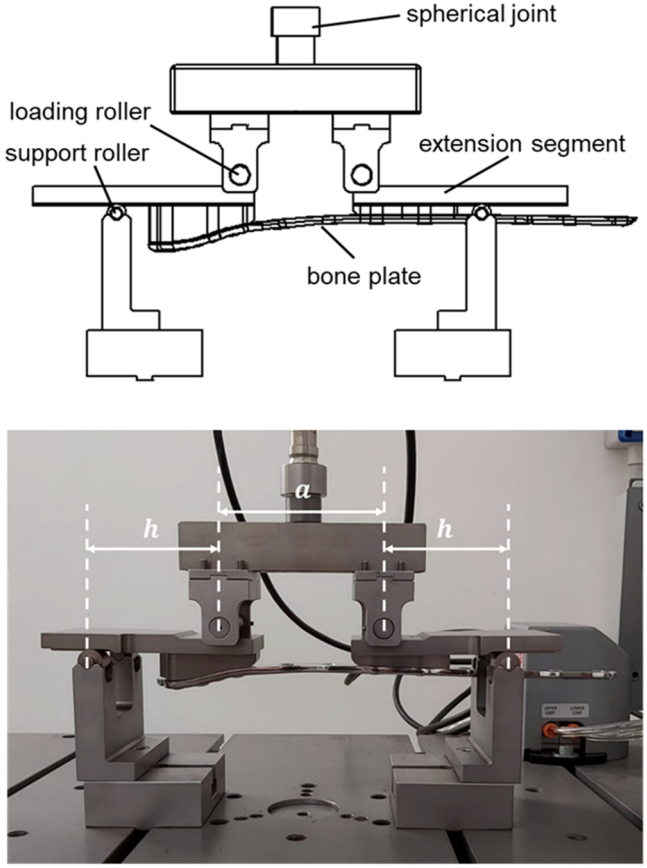


Fig. 2: Testing setup adopted for Plate08: (Top) main components and (Bottom) characterizing distances.

The loading rollers were rigidly connected to a spherical joint, while the support rollers were positioned on holders designed to be used with the testing machine base (Instron E3000). Four plates of each model were tested until failure at 5 mm/min to assess the proof load, obtained from the intersection point of the load-displacement curve and the 0.2% offset displacement line.

The same setup was used for fatigue tests to determine the runout load and the related maximum bending moment of every bone plate. The runout load was determined starting from 75% of the proof load and gradually reducing it until the load that led to one million cycles was identified. The bending moments (M) were computed from the experimental runout load (Eq. 6). The runout condition was repeated on three different samples. As recommended by the ASTM standard, fatigue tests were performed at 5 Hz in load control, adopting an R-ratio of 0.1 (the minimum of the sinusoidal waveform was computed as 10% of the maximum load).

Lastly, predictions realised with the Goodman and Gerber criteria were evaluated with Linear Least Squares (LLS) approach to fit predicted values with experimental results and determine the R^2 coefficients.

III. RESULTS

The prediction of the load required to reach the runout condition for the eleven bone plates was realised and verified through comparison with experimental results obtained by applying the standard methodology described in ASTM F382. Fig. 3 contains the experimental runout loads and their predicted range of values. The predicted range includes in most cases the experimental value of the runout load.

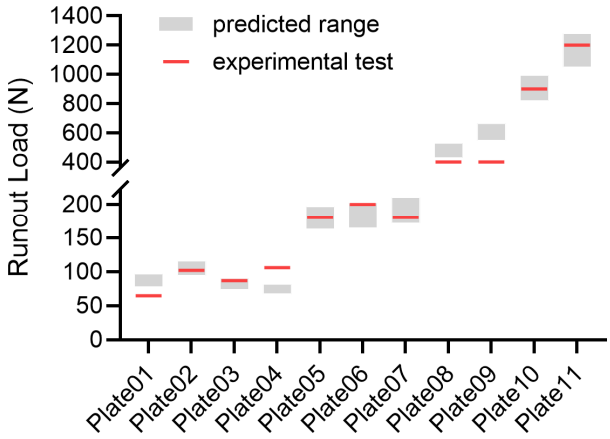


Fig. 3: Experimental and predicted runout loads obtained for each bone plate. Experimental results appear as red transversal lines, while the predicted values are represented by grey boxes.

The Goodman criterion involves a conservative life estimation: values obtained with this approach were considered as the lower limit of range prediction. Indeed, the runout load calculated with the Goodman criterion lay below the experimental load in eight of the tested plates. Runout loads estimated with the Goodman criterion (R^2 = 0.9519) show a better prediction compared to those calculated with the Gerber approach (R^2 = 0.9385). Nonetheless, the latter was useful to estimate the upper limit of the runout load: the experimental runout load fell below the limit estimated with the Gerber criterion for ten bone plates out of eleven.

However, two cases significantly deviate from the expected fatigue values. On the one hand, Plate04 considerably exceeded the expected range: the experimental runout load was approximately 50% higher than the lower limit. On the other hand, the experimental runout load of Plate09 is far below the value predicted by the Goodman criterion. Indeed, the experimental results of this bone plate were rather ambiguous: fifteen fatigue tests were performed and a load equal to approximately 30% of the static proof load was identified to reach the runout condition, suggesting a potential mismatch between the raw material certification and the material actually used to manufacture the batch of tested

plates. Notwithstanding, results reported for Plate09 were useful to analyse the possible implication of fatigue life estimation before starting a test campaign. Although more than 250 hours have been spent testing this bone plate, the runout load was most likely underestimated.

As mentioned before, the analytical methods adopted in this work involve important approximations, which can be reduced, for example, with a specific estimation of the K_f factor for the screw hole on the plate material. Another crucial aspect to be explored is the determination of the fatigue limit, especially for the wide range of multiplication coefficients usually considered for titanium alloys. Beyond these limitations, the implemented procedure can provide a starting point for fatigue testing, and it represents a guideline to avoid the underestimation of the runout load.

IV. Conclusion

In this study, an analytical prediction of the fatigue behaviour of eleven non-certified bone plates was executed.
The analytical predictions of runout loads were then compared with experimental results. Due to the phenomenology of fatigue, it is difficult to estimate a unique fatigue limit with a simple procedure. Indeed, even if the ASTM standard claims the identification of the runout load by gradually decreasing the static proof load, analytical models can be adopted to reduce the range of loads to be investigated in standard fatigue testing. Furthermore, it is important to note that the experimental runout condition does not correspond to a plate fracture at one million cycles, but to the first test where, by gradually reducing the load, one million cycles were reached without breaking. Therefore, in all experimental runouts the load is always underestimated, more or less severely. In this context, a preventive indication of the runout condition could be provided by an analytical framework, which would represent a powerful support to avoid excessive underestimation of the runout load.
In conclusion, this work reported encouraging results showing how the prediction of a runout load range of values could allow the accomplishment of mechanical tests using a limited number of specimens, with a substantial impact on the costs for the manufacturer.

Further works on new bone plates are planned to verify the effective reduction of test execution times through the proposed procedure. Moreover, by calculating the maximum stress through an *in silico* Finite Element replica, it would also be possible to predict the number of cycles of the implanted plate, defining a rationale able to further reduce the regulatory process time.

References

[1] P. Kenedi, L. L. Vignoli, “An osteosynthesis plate analytical model”, *J. Braz. Soc Mech. Sci. Eng*., vol 39, pp. 645-659, 2017.

[2] H. Schorler, F. Capanni, M. Gaashan, R. Wendlandt, and C. Jürgens, “Bone plates for osteosynthesis - a systematic review of test methods and parameters for biomechanical testing,” *Biomed. Eng.-Biomed. Tech.*, pp. 1-9, 2016.

[3] “ASTM F382-17. Standard Specification and Test Method for Metallic Bone Plates,” ASTM International, 100 Barr Harbor Drive, PO Box C700, West Conshohocken, PA 19428-2959, United States, pp. 1-12, 2017.

[4] M. Terzini, G. Serino, A.T. Lugas, G. Dichio, P. Costa and A. L. Audenino, “Strategies to speed up the standardized bone plates mechanical testing for regulatory purposes,” Seventh National Congress of Bioengineering – Proceedings, 2020.

[5] “Orthopedic Fracture Fixation Plates – Performance Criteria for Safety and Performance Based Pathway - Guidance for Industry and Food and Drug Administration Staff,” Food and Drug Administration, 5630 Fishers Lane, Room 1061, (HFA-305), Rockville, MD 20852, 2022.

[6] “ISO 14602. Non-active surgical implants – implants for osteosynthesis – particular requirements,” Geneva, Switzerland: International Organization for Standardization, 2010.

[7] M. Terzini, A. Aldieri, S. Nurisso, G. De Nisco, and C. Bignardi, “Finite Element Modeling Application in Forensic Practice: A Periprosthetic Femoral Fracture Case Study,” *Front. Bioeng. Biotechnol*., vol. 8, art. 619, 2020.

[8] V. Drátovská, R. Sedláček, Z. Padovec, P. Růžička Pavel, A. Kratochvíl, “The mechanical properties and fatigue prediction of a new generation of osteosynthesis devices,” *Journal of Mechanical Engineering*, vol. 71, no. 2, pp. 101-108, 2021.

[9] R.E. Peterson, *Stress concentration factors*, John Wiley & Sons, 1974

[10] M. Rossetto, *Introduzione alla fatica dei materiali e dei componenti meccanici,* Levrotto & Bella, 2000.

[11] M. R. Mitchell, *Foundamentals of Modern Fatigue Analysis for Design*, ASM Handbook, vol. 19, 1996.

[12] R. C. Juvinal, K. M. Marshek, *Fundamentals of Machine Component Design*, Fifth Edit., 2012.

[13] N. E. Dowling, C. A. Calhoun, and A. Arcari, “Mean stress effects in stress-life fatigue and the Walker equation,” *Fatigue Fract. Engng. Mater. Struct.,* vol 32, pp. 163–179, 2009.

Highly controlled ultrasound-mediated drug delivery experiments: an in vitro set-up

S. Sirolli[1,2], L. Ricotti[1,2], and A. Cafarelli[1,2]
[1] *The BioRobotics Institute, Scuola Superiore Sant'Anna, Pisa*
[2] *Department of Excellence in Robotics & AI, Scuola Superiore Sant'Anna, Pisa*

***Abstract*—This work reports the design, development and characterization of a low-intensity pulsed ultrasound (LIPUS) stimulation system to be used for highly controlled ultrasound-triggered drug delivery in vitro experiments. The use of a versatile signal generator and different types of transducers allows the fine tuning of the stimulation parameters over a broad range. Such transducers were carefully characterized in terms of pressure field shape and intensity, guaranteeing a precise estimation and control of the ultrasound dose delivered to the target. Such a system will be used for controlled drug release tests from ultrasound-responsive systems, such as nano and micro carriers, scaffolds and patches, in the context of the REBORN project.**

***Keywords*—Low-intensity pulsed ultrasound, In vitro ultrasound setup, Triggered drug delivery.**

I. Introduction

ULTRASOUND (US) is a mechanical wave, with frequencies higher than 20 kHz [1]. In the clinics, US is widely employed and accepted as an imaging modality for diagnostic purposes, thanks to its ease of use, low cost and non-invasiveness [2]. Besides this well-known use, US, and in particular low-intensity pulsed US (LIPUS), is recently emerging as a therapeutic tool to induce beneficial bioeffects on cells and tissues in the human body, such as bone fracture healing, osteoporosis treatments and soft tissues regeneration, among other applications [3].

Furthermore, US has also been explored in the state-of-the-art as a biophysical trigger for non-invasive targeted drug delivery from US-responsive carriers such as microbubbles (MBs), polymer micelles, liposomes or acoustically-responsive scaffolds (ARSs), exploiting both mechanical and thermal effects [4]-[8]. Ultrasound is indeed an extremely attractive and promising trigger for on-demand drug delivery. In fact, unlike other biophysical triggers such as light and electric fields, it shows highly effective penetration in the majority of body tissues (soft ones) [9]. US, therefore, would allow safe and non-invasive targeting of drug carriers in the vascular network or of implants in most deep tissues [3]-[4]. Furthermore, US also has the advantage of allowing a good spatial resolution within the body thanks to its high focusing capability and controllability [5], also being highly tunable (in terms of frequency, intensity, duty cycle, etc.).

However, advancements towards a clinical translation of this tool is hampered by a lack of accurate control over the US exposure conditions: most existing in vitro US stimulation setups are indeed highly susceptible to calibration errors and lack control on reflection and attenuation phenomena. It has been demonstrated that this kind of errors due to the use of non-standard configurations can lead to uncertainties up to 700% in the estimation of the actual US dose delivered to the target [10]. This results in low repeatability of the stimulation studies and difficulties in understanding the correlation between US dose and materials response, which heavily hinders the development of controllable drug delivery systems. Furthermore, the literature lacks standardized stimulation protocols and an agreement upon the best stimulation parameters for specific applications, which makes it hard to compare different studies, as obtained results are often contradictory.

Herein, we aim to develop a highly controlled US exposure system, where highly controlled means that this system allows to regulate and quantify with a great level of accuracy the US dose actually delivered to the target, reducing to a minimum the uncertainty with which this value is known. In fact, the careful calibration of the US sources and the elimination of sources of uncontrolled phenomena in the acoustic path allows a significant control over the exposure conditions, paving the way for reliable and repeatable release tests from US-responsive drug delivery systems, such as nano and micro carriers, scaffolds and patches. In particular, the setup described here is intended for LIPUS stimulation, a US modality already approved by the Food and Drug Administration (FDA). The developed systems allow to stimulate multiple samples and to explore a wide range of US parameters, offering the possibility to easily vary intensity (0-2000 mW/cm^2), frequency (38 kHz - 5 MHz), duty cycle, pulse repetition frequency and duration at will, thus allowing the researchers to optimize the best stimulation parameters for each specific application.

II. Materials and methods

A. System design

Two systems were developed, one for low-frequency (38 kHz) and one for high-frequencies (500 kHz – 5 MHz) exploration. The overall configuration of the systems is the same, besides some minor differences, and it is carefully designed in order to avoid reflection phenomena, due to materials acoustic impedance differences, unpredictable generation of standing waves and frequency-dependent perturbations of the transmission of US waves.

The high-frequency LIPUS setup (Fig. 1) consists of:

i) a tank (265 × 245 × 490 mm^3) filled with deionized and degassed water;

ii) one acoustic absorber (Aptflex F28P, Precision Acoustics, Dorchester, Dorset, UK) positioned at the top of the tank to prevent reflections;

iii) a sample retaining system, which was previously demonstrated to guarantee transparency to US waves in

correspondence of the samples and also the complete sealing of the three internal chambers [11];

iv) a linear rail that allows the translation of the retaining system along the z-axis in order to modify its distance from the transducers;

v) piezoceramic transducers (Precision Acoustics, Dorchester, Dorset, UK), with different central resonant frequencies, which are used to cover the high-frequency range (i.e. 500 kHz to 5 MHz range) and are fixed at the bottom of the tank;

vi) a multichannel signal generator (IGT, Bordeaux, France), to control the electric input signal to the transducer (20 W maximum power per channel);

vii) an exhaust valve, to fill and empty the tank, and a degassing system (IGT, Bordeaux, France), which includes a vacuum pumped membrane contactor (3M™ Liqui-Cel™, St Paul, Minnesota, USA), to continuously degas water within the tank.

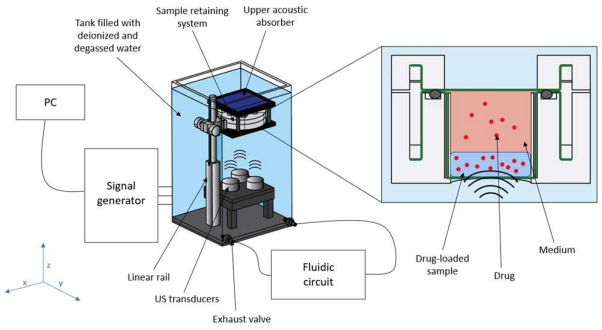


Fig. 1: Scheme of the high-frequency LIPUS stimulation setup, with a zoom on the sample retaining system, to be used for ultrasound-triggered drug release tests

The low-frequency LIPUS setup consists of the same fundamental elements, except for slight variations. Firstly, due to geometrical constraints, only one transducer is fixed at the bottom of the tank, instead of the three employed in the high-frequency system; consequently, the sample retaining system only has one chamber, placed in the center and coaxial with the transducer. Only one type of US transducer (BAC s.r.l., Florence, Italy), centered at a frequency of 38 kHz, was employed and connected to the signal generator (BAC s.r.l., Florence, Italy).

In both systems, the complete immersion of the sample retaining system in deionized and degassed water and the addition of acoustic absorbers in the acoustic path help preventing undesired wave reflections, thanks to the absence of liquid-air interfaces and reflective obstacles along the US propagation direction.

Furthermore, the designed systems allow the investigation of different parameters in the ranges commonly used for LIPUS stimulation, which permits the validation of different stimulation protocols. This is crucial for optimizing the performances of the samples under test, especially considering the general lack of standard protocols and highly contradictory results which can be found in the literature. In this specific case, the setup allows the exploration of frequencies in a broad range (38 kHz - 5 MHz) and intensities varying from few mW/cm^2 up to 2 W/cm^2. The tuning of such parameters can be easily performed by the users thanks to a dedicated software including a user-friendly graphical user interface.

Moreover, temperature control of the water in the stimulation tank can be possible thanks to the use of a heat resistance, thus allowing for example to simulate the in vivo working conditions of the delivery system under test.

In the case of the high-frequency setup, another significant added value of this system is the possibility to simultaneously stimulate three samples in parallel, thanks to the presence of three different transducers aligned with three chambers, which facilitates carrying out the experimental work.

B. Sample holder design and testing

The sample retaining system consists of a polycarbonate disc with three wells (one, in the case of the low-frequency setup) for hosting the samples. Each of these chambers has an open diameter of 16 mm and an open height of 18 mm; their centers are at 7 cm distance from each other in order to prevent possible overlaps between the fields produced by different transducers. At the bottom of each retaining chamber a Stretchlon film of 38 µm thickness was mounted. Elastomeric O-rings were employed to guarantee a hydraulic sealing of the chambers and their compression is guaranteed by an upper polycarbonate plate, which is kept in place through screw nuts and bolts.

The impermeability of the sample retaining system was assessed through a sealing test. It was performed by filling each chamber with deionized water, closing the sample holder and immersing it for 30 minutes in a tank filled with deionized water and fluorescein sodic salt, with the aim to evaluate whether the chamber content was contaminated by fluorescein.

C. Transducers characterization

In order to cover the broad frequency range from 38 kHz to 5 MHz, six different types of unfocused transducers were used: one 50 mm diameter transducer centered at 38 kHz; three 44 mm diameter transducers centered at 600 kHz and used at 500 and 750 kHz; three 23 mm diameter transducers centered at 1 MHz; three 23 mm diameter transducers centered at 2 MHz; three 15 mm diameter transducers centered at 3 MHz; three 15 mm diameter transducers centered at 4 MHz to be used at 4 and 5 MHz.

Calibration of all the transducers was carried out, for each of the aforementioned stimulation frequencies, by means of precise pressure maps and by establishing the relationship between the pressure amplitude at the target and the driving voltage.

The acoustic pressure field was measured using a calibration setup already developed by the authors [12] by means of a hydrophone (Precision Acoustics, Dorchester, Dorset, UK – 2 mm needle; mean sensitivity in the range 0.1 MHz to 10 MHz: 3.5 V/MPa; typical frequency response: flat (4 dB) over the range 100 kHz to 10 MHz).

The intensity calibration was performed by means of the same hydrophone described above for each of the seven stimulation frequencies in the high-frequency range, for finding the relationship between the input voltage and the generated acoustic pressure/intensity. For the 38 kHz transducer, the same calibration procedure was followed, by

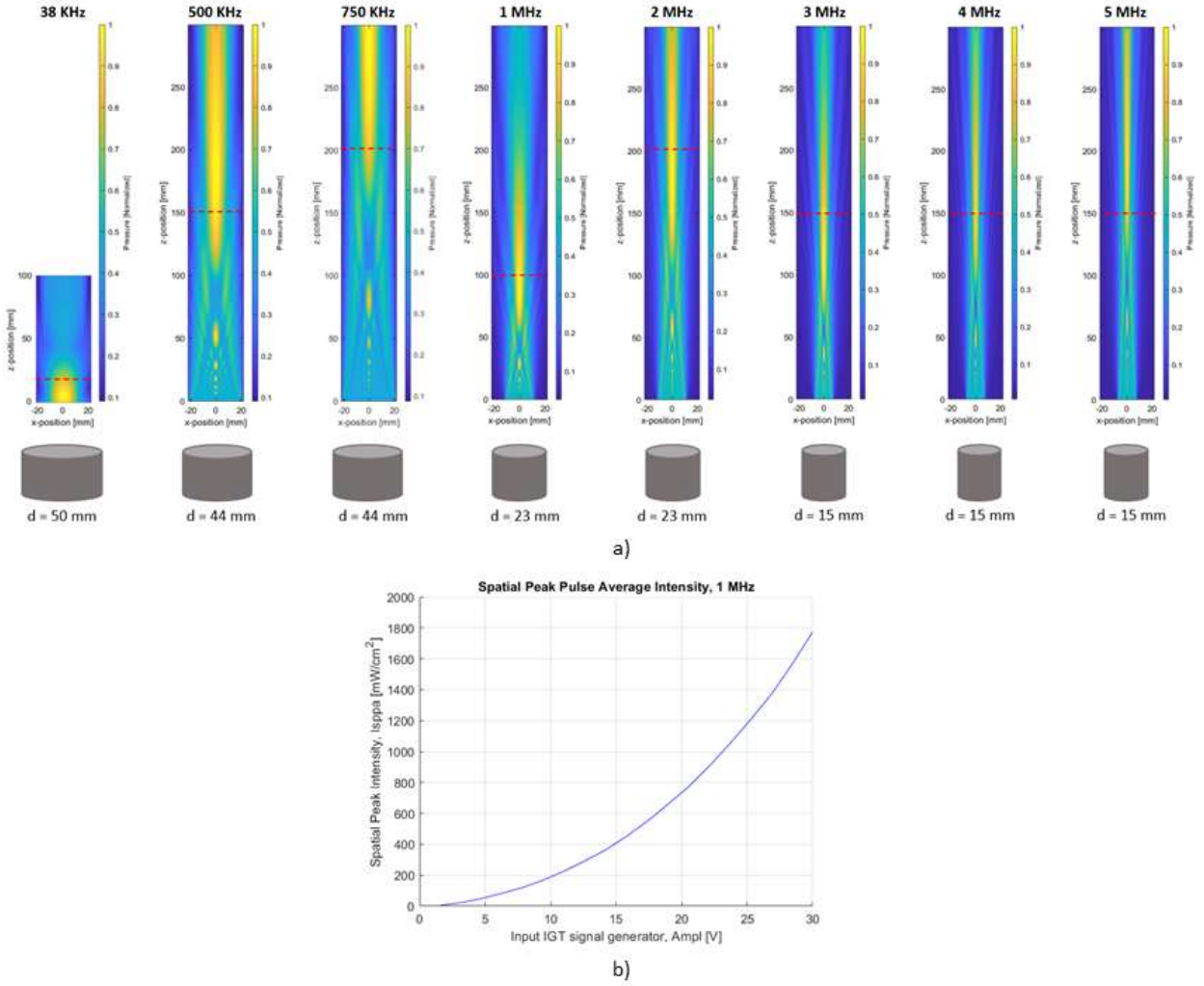


Fig. 2: a) Pressure field maps (in terms of normalized peak-to-peak pressure) for each stimulation frequency in the investigated range. b) Example of a calibration curve expressing the relationship between the applied voltage and the Spatial Peak Pulse Average Intensity (I_{sppa}) measured through a hydrophone

means of an omnidirectional hydrophone (Reson TC 4034, with a frequency response from 1 Hz to 470 kHz (±3 dB)).

III. Results and Discussion

A. Sample holder design and testing

The sample holder was designed and developed to be completely transparent to ultrasonic waves. In fact, the bottom of each retaining chamber was closed through a Stretchlon film of 38 µm thickness, which is smaller than a quarter of the minimum US wavelength employed (i.e. 300 µm, at 5 MHz); this guarantees transparency of the film to the ultrasonic waves, therefore minimizing transmission losses and standing waves formation, which are the typical drawbacks of the commonly used plastic plates.

This US-transparent retaining system prototype was then tested in terms of its sealing ability, performing the test described in paragraph II.*B*. The fluorescence emitted by the liquid inside the chambers resulted to be four orders of magnitude lower than the fluorescence of the liquid filling the tank. Therefore, it was demonstrated that the system possesses an optimal ability to keep the sample chambers isolated from the external environment, and in particular it can effectively avoid water penetration in the wells, which is a crucial requirement for drug release tests, as liquids exchange with the external environment would alter drug concentration assessments.

B. Transducers characterization

The pressure field maps obtained through the hydrophone are shown in Fig. 2a, in terms of normalized peak-to-peak pressure.

The horizontal dashed red lines correspond to planes in the far-field condition, close to the Rayleigh distance, where the pressure field is fully formed and homogeneous, thus representing the optimal distances on the z-axis at which samples under test should be placed during stimulation.

The intensity calibration resulted in the definition of a precise relationship between the voltage provided by the generator to the transducer and the peak-to-peak pressure read by the hydrophone (Fig. 2b), when positioned along the axial direction of the transducer at a distance corresponding to the dashed red lines shown in Fig. 2a.

IV. Conclusion

In this work the design, development and characterization of an innovative system for highly controlled in vitro ultrasonic-mediated drug delivery tests are presented. The setup allows to minimize the typical exposure errors which affect the vast majority of the systems used for in vitro ultrasound experiments, thus allowing to obtain reproducible and reliable results, and providing a precise quantification of the US dose actually delivered to the target. This will enable, in future experiments, a better understanding of the relationship between ultrasound exposure parameters and the effects observed on the tested samples. Furthermore, the system enables the exploration of a broad range of US parameters (i.e. frequency, intensity, duty cycle, pulse repetition frequency) and it can thus be used to investigate different stimulation conditions, allowing parameters optimization for a specific application.

The stimulation setup proposed here could be employed to test a variety of US-responsive drug carriers, such as micro and nanovectors including liposomes and micelles, polymeric particles and perfluorocarbon droplets. Such vectors can be tested in suspension, for intravascular release applications, or embedded in biomaterial structures such as 3D scaffolds and patches constructs with on-demand drug delivery capabilities. Beyond simple carrier testing, this system could also host cells, being able to guarantee the sterility of the internal chambers. This will allow exploring the combined effect of US stimulation and drug release on different cells models.

Acknowledgement

This work received funding from the European Union's Horizon Europe research and innovation program, grant agreement No 101091852, project REBORN (Remodelling of the infarcted heart: piezoelectric multifunctional patch enabling the sequential release of therapeutic factors).

References

[1] A. Cafarelli, A. Marino, L. Vannozzi, J. Puigmartí-Luis, S. Pané, et al., "Piezoelectric nanomaterials activated by ultrasound: the pathway from discovery to future clinical adoption", *ACS Nano*, vol. 15, pp. 11066-11086, July 2021.

[2] E. Cheah, Z. Wu, S. S. Thakur, S. J. O'Carroll, and D. Svirskis, "Externally triggered release of growth factors - a tissue regeneration approach", *Journal of Controlled Release*, vol. 332, pp. 74-95, April 2021.

[3] L. Mei and Z. Zhang, "Advances in biological application of and research on low-frequency ultrasound", *Ultrasound in Medicine & Biology*, vol. 47, pp. 2839-2852, October 2021.

[4] M. Karimi, A. Ghasemi, P. Sahandi Zangabad, R. Rahighi, S. M. M. Basri, H. Mirshekari, et al., "Smart micro/nanoparticles in stimulus-responsive drug/gene delivery systems", *Chemical Society Reviews*, vol. 45, pp.1457-1501, March 2016.

[5] W. Chen and J. Du, "Ultrasound and pH dually responsive polymer vesicles for anticancer drug delivery", *Scientific Reports*, vol. 3, pp. 2162-2170, July 2013.

[6] A. Ranjan, G. C. Jacobs, D. L. Woods, A. H. Negussie, A. Partanen, et al., "Image-guided drug delivery with magnetic resonance guided high intensity focused ultrasound and temperature sensitive liposomes in a rabbit Vx2 tumor model", *Journal of Controlled Release*, vol. 158, pp. 487-494, March 2012.

[7] H. Zhang, H. Xia, J. Wang, and Y. Li, "High intensity focused ultrasound-responsive release behavior of PLA-b-PEG copolymer micelles", *Journal of Controlled Release*, vol. 139, pp. 31-39, October 2009.

[8] A. Moncion, M. Lin, E. G. O'Neill, R. T. Franceschi, O. D. Kripfgans, et al., "Controlled release of basic fibroblast growth factor for angiogenesis using acoustically-responsive scaffolds", *Biomaterials*, vol. 140, pp. 26-36, September 2017.

[9] S. S. Said, S. Campbell, and T. Hoare, "Externally addressable smart drug delivery vehicles: current technologies and future directions", *Chemistry of Materials*, vol. 31, pp. 4971-4989, July 2019.

[10] J. J. Leskinen and K. Hynynen, "Study of factors affecting the magnitude and nature of ultrasound exposure with in vitro set-ups", *Ultrasound in Medicine & Biology*, vol. 38, pp. 777-794, May 2012.

[11] F. Fontana, F. Iberite, A. Cafarelli, et al., "Development and validation of low-intensity pulsed ultrasound systems for highly controlled in vitro cell stimulation," *Ultrasonics*, vol. 116, pp. 106495-106506, September 2021.

[12] A. Cafarelli, A. Verbeni, A. Poliziani, P. Dario, A. Menciassi, et al., "Tuning acoustic and mechanical properties of materials for ultrasound phantoms and smart substrates for cell cultures", *Acta Biomaterialia*, vol. 49, pp. 368-378, February 2017.

Exposure set-up for assessing the far-field electromagnetic immunity levels of active implantable medical devices

C. Vivarelli[1,3], R. Falsaperla[2], G. Burriesci[2], F. Censi[1], G. Calcagnini[1], E. Mattei[1]
[1] *Italian National Institute of Health, Dept. of Cardiovascular, Endocrine-metabolic Diseases and Aging*
[2] *INAIL, Dept. of Occupational and Environmental Medicine, Epidemiology and Hygiene.*
[3] *University of Rome Tor Vergata, Dept. of Civil and Computer Science Engineering*

***Abstract*— This study aims at the development of an exposure set-up to investigate AIMDs immunity under far-field exposure conditions, beyond the General Population Reference Levels, and up to Workers Reference Levels, and at the identification of the worst-case condition in terms of lead path and implant configuration. The proposed set up leverages a G-TEM cell to obtain far-field levels above the general population Reference Levels and, for some frequencies, also above worker's reference levels. The proposed set up was able to properly monitor AIMD activity under electromagnetic disturbance inside GTEM cell. Preliminary findings show that the lead path may affect the immunity level of the device at least at frequencies below 600 MHz, and that interferences may not be excluded above- the general population reference levels but still below occupational exposure.**

***Keywords*— AIMD, immunity, electromagnetic exposure, workers.**

I. INTRODUCTION

Nowadays, electromagnetic (EM) sources are rapidly becoming more and more pervasive and active implantable medical device (AIMD) immunity represents a critical issue, not only for general population, but also for workers. In the international standards for AIMDs, at frequencies above 385 MHz, immunity levels are assessed in near-field conditions and expressed in terms of net power at the antenna input (W) [1]. The international standard ISO 14117:2019 Active implantable medical devices — Electromagnetic compatibility prescribes tests to assess AIMD electromagnetic immunity only in near-field configuration, since it mostly takes into account hand-held terminals (e.g. wireless telephones).

On the other hand, the safety limits for the exposure to electromagnetic fields are given in terms of far-field electromagnetic field strength [2]. Thus, the comparison between these two limits is not immediately possible and the immunity level of AIMDs to far-field exposure above 385 MHz is not known. In addition, the international standard [1] states that near-field immunity guarantees a reasonable protection also from far-field EMF up to General Public Reference Values, but no data are available for workers exposure levels [2].

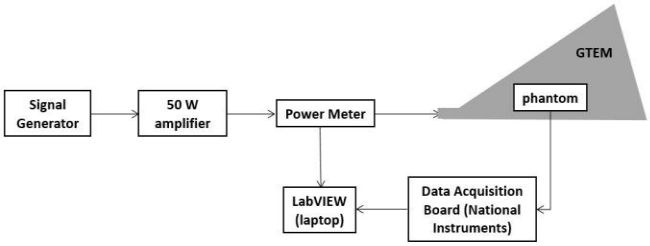
This study aims at the development of an exposure set up able to investigate AIMDs immunity in terms of far-field exposure conditions, beyond the General Population Reference Levels, and up to workers exposure limits, and at the identification of the worst-case condition in terms of lead path and implant configuration.

II. METHODS

A. Exposure set-up

RF signal generator set up (Fig. 1.a) included: GTEM cell (model GTEM 5311 by Emco) (Fig. 1.b); signal generator R&S 9kHz - 3.2GHz; Amplifier KALMUS 116FC-CE 200MHz – 1GHz 50W, ZHL 50 W-63+ MINI-CIRCUIT 700MHz – 6 GHz; directional coupler Amplifier Research DC7144; RF Power meter 4230 Boonton, 10 kHz - 100 GHz.

The proposed exposure set-up also comprehends a rectangular PVC phantom (Fig. 1.c) for the placement of the AIMD and its leads. The phantom was filled with saline solution (σ=0.27 S/m), and equipped with a grid 1 cm apart from the phantom surface. The phantom was also equipped with four electrodes to monitor the AIMD behaviour during the exposure and to inject a simulated ECG signal. AIMD activity signal was acquired using LabVIEW, after passing through a conditioning and A/D conversion board. The board also generated a heart simulated signal able to inhibit the device. Attention was paid to minimize the coupling between the monitoring cables and the RF field generated inside the GTEM cell.



(a)



(b)

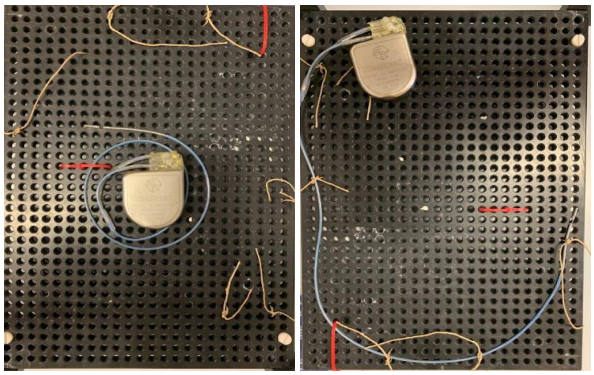


(c)

Fig. 1: (a) schematic representation of the proposed set up; (b) G-TEM cell; (c) rectangular PVC phantom.

B. AIMD implant

An ICD was tested, programmed in DDD mode, at the most sensitive setting (0.2 mV atrial, 0.5 mV both ventricles). Two lead configurations were tested: a spiral configuration (as indicated in [1]) (Figure 2.a) and a loop configuration, forming the loop as large as possible (Figure 2.b). The specific ICD tested allowed also to collect electrograms using real time telemetry, and thus to detect any RF induced malfunctions.



(a) **(b)**

Fig. 2: (a) spiral configuration; **(b)** loop configuration.

C. Test procedure

The following frequencies were tested: 385, 450, 600, 700, 800, 830, 825, 850, 875, 900, 930, 1610, 1850, 1910, 2450, 3000, 3600, 4000 MHz. Both continuous and pulse RF signals were generated. The RF pulsed signal is 100% amplitude modulated at 2Hz (25 ms ON and 475 ms OFF). For each frequency, the unperturbed E-field was measured at 1.4 m from the apex of the GTEM. Then, the phantom was placed where the E-field was measured and the ICD activity was monitored to detect if EMI events occurred (oversensing, undersensing or asynchronous pacing).

Finally, if any EMI event was recorded, injected power was lowered until the EMI was no longer detected. Threshold power level and E field strength at which ICD return to its correct functioning were also collected.

Tests were carried out at the INAIL facilities in Monte Porzio Catone.

III. RESULTS

Table I reports the unperturbed E-field values obtained at the selected frequencies along with the corresponding power injected into the GTEM cell. In the last two columns exposure limits for general public and workers are reported.

The first significant result is that the proposed exposure set allows to obtain EMF levels above general population reference levels, and in some cases even above workers reference levels.

EMI events were detected only at 385 MHz and 450 MHz. The EMI events were oversensing in the atrium channel that triggered inappropriate ventricular pacing. Fig.3 shows the electrograms reporting one of the EMI events observed.

Table II reports the threshold power levels and E field values at which the ICD returns to its correct functioning. Noteworthy, the loop configuration is more susceptible to interference than the spiral configuration.

TABLE I: UNPERTURBED E-FIELD MEASURED VALUES

Frequency [MHz]	*Injected Power [W]*	*E field [V/m]*	*General public exposure limit [V/m]*	*Worker's exposure limit [V/m]*
385	44.4	93.7	28	63.6
450	46.7	76.3	29.2	63.6
600	47.4	60.2	33.7	73.5
800	48.5	88.7	38.9	84.9
825	51.4	110.5	39.5	86.2
850	53.6	96.2	40.1	87.5
875	55.6	100.2	40.7	88.7
900	57.3	112.7	41.3	90
930	58.4	76.1	41.9	91.5
1610	54.0	77.1	55.2	120.4
1850	48.0	90.4	59.1	129
1910	48.8	92.8	60.1	131.1
2450	51.3	87.2	61	140
3000	38.6	81.9	61	140
3600	27.2	63.0	61	140
4000	27.3	78.4	61	140

TABLE II: EMI THRESHOLD POWER LEVEL

Lead configuration	*Frequency [MHz]*	*Threshold Injected Power [W]*	*Threshold E field (unperturbed) [V/m]*
Loop	385	8.8	40.6
Spiral	385	25.9	69.8
Loop	450	19.1	60.4
Spiral	450	>47	>76.3

IV. DISCUSSION

According to international technical standards, AIMDs immunity levels are derived from the European Recommendation 1999/519/EC [2],[3], which set the E-field reference levels for general public at $1.375\sqrt{f}$ V/m in range 400 – 2000 MHz and 61 V/m above 2 GHz. Workers can be exposed to higher values (Directive 2013/35 [2],[4], $3.0\sqrt{f}$ V/m and 137 V/m above 2 GHz). Testing at such high levels is quite challenging.

The proposed set up leverages the use of a G-TEM cell to obtain far-field levels above the general population Reference Levels and, for some frequencies, also above worker's reference levels. Besides the frequencies listed in ISO 14117 standard we include frequencies above 3 GHz, in view of the new RF emitters that are becoming more popular (e.g. 5G systems).

The proposed set up was able to properly monitor AIMD activity under electromagnetic disturbance inside GTEM cell.

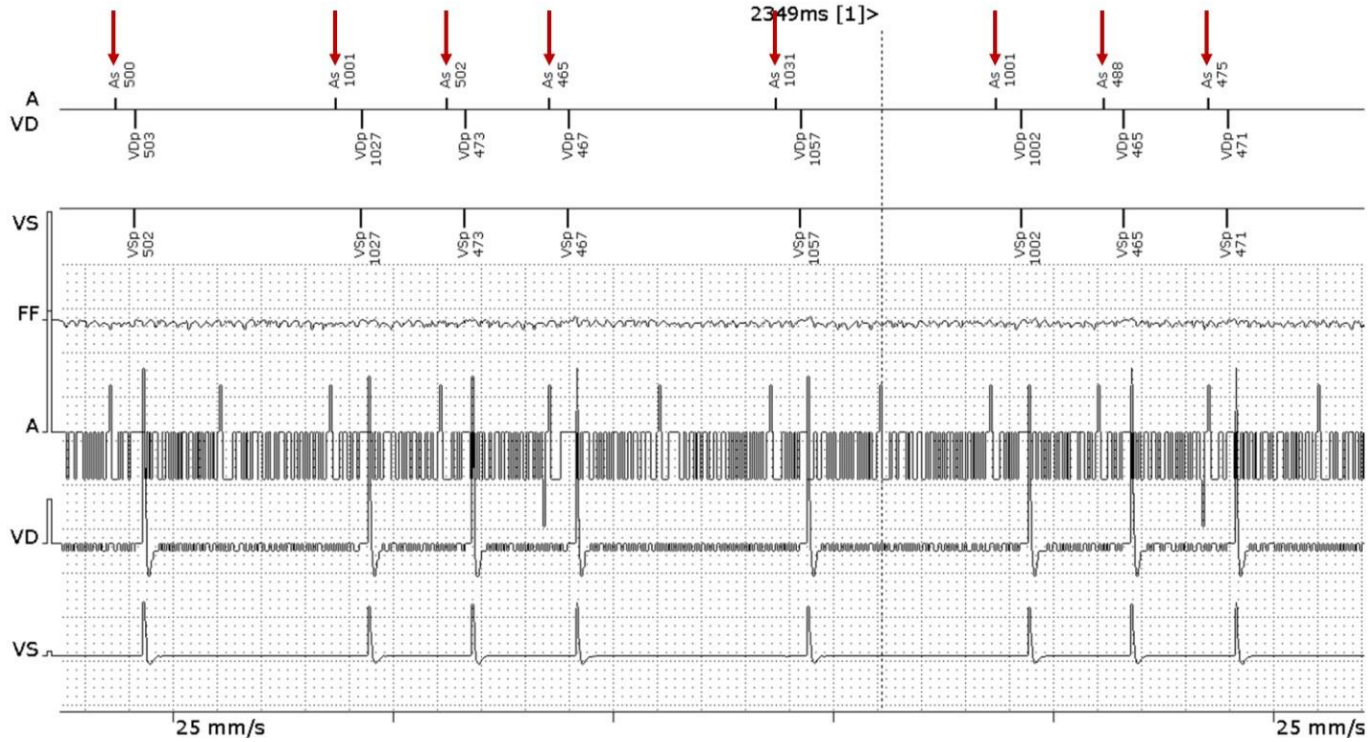


Fig. 3: Electrogram showing the EMI events. Arrows indicate spurious and inappropriate sensing of the atrial activity.

In the specific ICD tested, at 385 MHz and 450 MHz, we observed EMI events at field levels above the general population reference levels but below workers reference levels.

The EMI events observed showed that, at least at these frequencies, the lead path may affect the field level at which the malfunction occurs.

The role of the lead path at higher frequencies could not be assessed since no EMI events were observed.

V. Conclusion

In the international standards for AIMDs, at frequencies above 385 MHz, immunity levels are assessed in near-field conditions. Thus, there is a lack of information about AIMD immunity levels in far-field conditions. This issue is relevant not only for general population but also for workers, since they can be exposed to higher EMF levels. This study proposed a set up to investigate AIMD behavior when exposed to EMF values above general population reference levels.

Preliminary findings show that the lead path may affect the immunity level of the device at least at frequencies below 600 MHz, and that interferences may not be excluded above- the general population reference levels but still below occupational exposure.

Further improvements of the set up are needed to obtain exposure levels up to or above occupational levels for all the frequencies of interest. One limitation of this study is that it was carried out only on a single device and two implant configurations. The main aim of the paper was to propose and demonstrate the feasibility of a novel approach to investigate EMC issues for AIMD in far-field exposure condition. In future studies, a more representative sample of devices and implant configuration will be taken into account, to verify the repeatability of the observed events.

Acknowledgement

This study was funded by INAIL, BRIC 2019 grant.

References

[1] ISO 14117:2019 Active Implantable Medical Devices - Electromagnetic Compatibility.

[2] ICNIRP Guidelines for limiting exposure to time-varying electric, magnetic and electromagnetic fields (up to 300 GHz), Health Physics 74 (4):494-522; 1998

[3] 1999/519/EC Council Recommendation of 12 July 1999 on the limitation of exposure of the general public to electromagnetic fields (0 Hz to 300 GHz).

[4] Directive 2013/35/EU of the European Parliament and of the Council of 26 June 2013 on the minimum health and safety requirements regarding the exposure of workers to the risks arising from physical agents (electromagnetic fields)

Zwitterionic coatings for an implantable artificial pancreas

E. Roventini[1,2], G. Ballardini[1,2], A. Poliziani[1,2], L. Arrico[1,2], and L. Ricotti[1,2]
[1] *The Biorobotics Institute, Scuola Superiore Sant'Anna, Italy*
[2] *Department of Excellence in Robotics & AI, Scuola Superiore Sant'Anna, Italy*

***Abstract*— Type 1 Diabetes is a life-threatening condition for which there is no cure, at the moment. Its treatment consists of multiple daily blood glucose level measurements and insulin injections to keep the blood glucose level in the physiological range. In this scenario, an implantable insulin pump refillable through ingestible insulin-carrying capsules has been proposed. However, successful implantation requires the minimization of the foreign body reaction, a host defense mechanism that ultimately results in the production of a fibrous avascular capsule that isolates the implantable device. In this work, zwitterionic materials are explored as an antifouling coating on the artificial pancreas external case, exploiting the steric hindrance effect of their chains and the formation of a hydration barrier. In particular, the 2-methacryloyloxyethyl phosphorylcholine (MPC) zwitterion was combined with polydopamine to create a coating on poly ether-ether-ketone – PEEK. A novel strategy for the formation of a polydopamine-mediated zwitterionic coating is proposed and compared with other two strategies drawn from the literature. The stability over time of the obtained coating is assessed in a simulated biological environment by measuring the changes in the substrate wettability. The results show that the proposed strategy results in a stable MPC coating on PEEK for up to 8 weeks.**

***Keywords*— MPC, PEEK, implantable device, artificial organs, zwitterionic coating, antifouling.**

I. Introduction

Type 1 Diabetes (T1D) is a life-threatening condition featured by the immune-mediated destruction of insulin-secreting pancreatic β-cells and, consequently, blood glucose regulation [1]. To date, there is no cure for this condition, and its prevalence is dramatically increasing, predicting to reach 13.5-17.4 million people worldwide by 2040 [2].

The mainstay of treatment for T1D is multiple daily glucose level measurements and the injection of appropriate amounts of insulin to maintain the blood glucose level in the physiological range (80-110 mg/dL) [1]. This can be done by the patient with self-injections; however, it results in high glycemic variability that also depends on the patient's ability [3]. Subcutaneous or intraperitoneal closed-loop insulin pumps can decrease this variability [3], [4]. However, on the one hand, subcutaneous insulin delivery has slower pharmacokinetics and dynamics than physiological release [5]. On the other hand, refilling intraperitoneal (ip) pumps is invasive and has to be performed in a clinical setting, increasing the risk of infections [6]. Furthermore, implanted ip pumps (e.g., the Minimed® system from Medtronic) were subjected to a fibrotic reaction, which created a visible bump, raising aesthetic issues [7]. To overcome these limitations, an implantable ip insulin pump refillable through ingestible insulin-carrying capsules has been proposed [7], [8] and tailored for implantation in humans, in an intraperitoneal pouch [9] as shown in Fig. 1a.

In the works published so far on this topic, the possible effects of foreign body reaction (FBR) was not taken into account. FBR is an irrevocable host defense mechanism that starts with the undesired adsorption of non-specific proteins onto the external surface of the implanted device, followed by the arrival of immune system cells and fibroblasts [10]. This process leads to the formation of a fibrous avascular capsule that excludes the device from the rest of the body [10], causing several iatrogenic complications [11] that can result in device failure [12] or aesthetic issues. In particular, in the solution proposed in [8], [9], [13], the device functionality relies on proper positioning and coupling with the intestinal tissue. Thus, an excessive fibrotic reaction can considerably hinder the implant success. Hence, it is critical that the external surface of the device has antifouling properties to decrease the risk of device failure.

II. Selection of Material for the Device Case and Functionalization Strategy

We selected poly ether-ether-ketone (PEEK, Fig. 1a) as the material for the device's external case. Indeed, PEEK has low water permeability, high mechanical resistance, and biocompatibility [14], [15]. Then, we functionalized PEEK with an antifouling coating. We combined the versatility of polydopamine (PDA) with the antifouling potential of zwitterions [16], [17], [18], [19] to create an antifouling coating that could be used on different substrates. Indeed, this approach has already been used to functionalize catheters [20], interfaces for in vivo sensing in the brain [19], and cardiovascular stents [21]. However, because of the different zwitterions and deposition strategies, it is difficult to draw conclusions about the best approach to create an antifouling coating for the polymeric material enclosing an implantable device. In this work, we compared three strategies to form a polydopamine-mediated polymeric zwitterion coating on PEEK to decrease the risk of failure of the artificial pancreas presented in [8], [9]. To this end, we evaluated the wettability of the zwitterionic coating and its stability over time. For this evaluation, the 2-methacryloyloxyethyl phosphorylcholine (MPC), was selected. It is a highly hydrophilic zwitterion that has already been used in several biomedical applications, such as the coating of Ahmed glaucoma valve [22], hip prosthesis [23], and even a glucose monitor device [24].

III. MATERIAL AND METHODS

A. Coating fabrication

Three different strategies to functionalize PEEK were evaluated (Fig. 1b). For each strategy, five independent samples of 3D printed PEEK (Roboze spa, Italy) with a diameter of 12 mm and a height of 1 mm were used, ultrasonicated in a 70% ethanol solution for 15 min [25] and dried overnight.

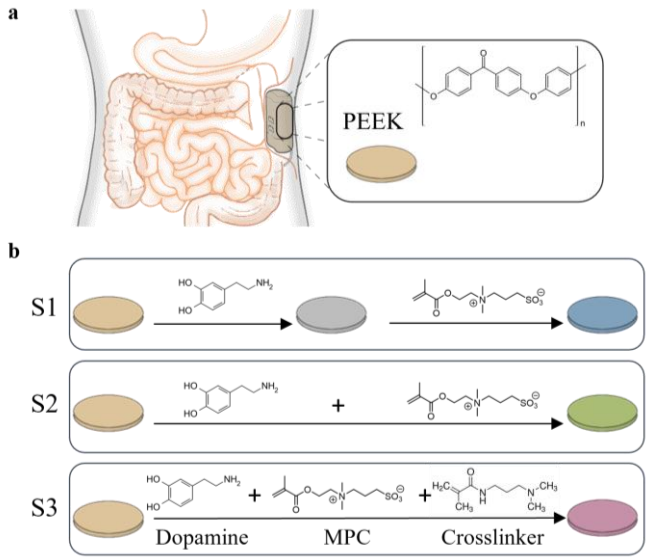


Fig. 1: a) Depiction of the insulin pump implantation site and chemical structure of PEEK, the material selected for the external case of the device. b) Scheme of the three coating strategies (S1, S2, S3) devised for the deposition of the zwitterionic coating on the PEEK substrates and chemical formulas of the components used.

In the *first strategy* (S1 in Fig. 1b), a monomeric zwitterionic layer was obtained in a two-step process. The PDA layer was first deposited onto the surfaces of the substrate, by means of a deep-coating technique [26]. After that, the obtained PDA-coated disks were further functionalized with a zwitterionic layer by Michael addition [16], [19].

Specifically, five cleaned disks of PEEK were immersed in 10 mM Tris buffer solution (8.5 pH) containing dopamine hydrochloride (Sigma-Aldrich) at a concentration of 2 mg/mL at 25°C [16] for 24 h [26]. Then the samples were washed extensively with deionized (DI) water and let dry overnight. After that, the PDA-coated disks were further functionalized by immersing them in a solution of DI water, ethanol, and triethylamine (TEA) with a volume ratio of 400:80:3 and MPC (Sigma-Aldrich) at a concentration of 100 mM. The reaction solution was magnetically stirred at 25°C [18], for 24 h, then the samples were rinsed with DI water and let dry overnight [16], [18].

The *second* and *third strategies* consist of one-step processes, characterized by the co-deposition of a PDA layer functionalized with linear zwitterionic chains and zwitterionic co-polymer respectively, starting from the monomers of dopamine hydrochloride and MPC. In the co-deposition process, the abundant free radicals generated during the oxidative dopamine polymerization trigger the polymerization of zwitterionic monomers [17].

In the *second strategy* (S2 in Fig. 1b), five cleaned disks of PEEK were pre-wetted with ethanol and then immersed in a solution containing 50mM Tris buffer solution (8.5 pH), dopamine hydrochloride, and MPC with a mass ratio of 1:15 [17]. The reaction solution was magnetically stirred at 25°C for 8 h. After that, the samples were washed and soaked in DI water overnight [17].

The *third strategy* (S3 in Fig. 1b), is a novel one that has been devised to create a zwitterionic co-polymer on the substrate. It is based on the same protocol of the second strategy, but with the addition of a co-monomer (N-[3-(dimethylamino)propyl]acrylamide, AmBeed) in the reaction solution, at a concentration of 0.3 mg/mL.

All the coated PEEK samples were stored in Phosphate Buffer Saline (PBS) solution (Sigma-Aldrich) for 8 weeks at 37°C under continuous shaking to mimic a physiological environment and were characterized at different time points (see Section IIIB).

B. Wettability measurements

The antifouling properties of the zwitterionic materials is due to the steric hindrance effect of the polymer chains and the formation of a hydration barrier, preventing the first attachment of molecules on the surface of the implant. For that reason, one well-known indirect method to investigate the presence of a zwitterion coating consists of quantitatively measuring the change in the substrate wettability with static water contact angle (WCA) [19], [27], [28], using a contact angle goniometer (Ossila Ltd., UK).

All samples were tested before and after the coating formation. In the two-step strategy - S1 - the measurements were repeated after each step.

In the WCA measurements, a 7.5 µL droplet of DI water from a microliter syringe was placed on the dried sample, then a camera took a digital photo of the stationary drop. The contact angle of the micro-drop was measured by using the software provided by the company (Ossila Ltd, UK). Then, the sample was stored in PBS solution, as reported in Section IIIA. To investigate the stability of the coating in a simulated physiological environment, the WCA measurements were repeated at different time points (after 1, 2, 3, 4, and 8 weeks).

C. Statistical analyses

A Kruskal-Wallis test was applied to the WCA measurements taken after every time point since the hypothesis of normality was rejected by Kolmogorov-Smirnov's test. Then, the Dunn test was applied as a multiple comparison analysis to compare the changes between the experimental groups. Statistical significance was set at the family-wise error rate of $\alpha = 0.05$.

IV. RESULTS AND DISCUSSION

The functionalization of the PEEK with a polydopamine-mediated zwitterionic monomeric layer (S1) resulted in an increase in hydrophilicity . Indeed, the WCA decreased from 86.5 ± 6.9° (mean ± std) for the PEEK to 46.3 ± 4.0° after the PDA deposition, reaching 42.6 ± 1.9° with the zwitterionic layer (first column of Fig. 2a). This trend is in line with what previously shown on a metal substrate using a similar two-

steps process and the same zwitterion. The wettability measured after each step was lower than the values reported in the literature, which are close to 65° and 51° for the PDA and PDA-MPC layers respectively [21]. However, due to the difference between the substrates, it is difficult to make a direct comparison. After one week in the PBS solution, the WCA significantly decreased ($p<0.05$) to 19.7 ± 7.3°. Thereafter, the hydrophilicity slightly increased over time, reaching the maximum after eight weeks (24.2 ± 6.3°) as shown in the first column of Fig 2b.

The functionalization of PEEK with linear zwitterionic chains (S2) resulted in an increase in hydrophilicity as shown in the second column of Fig. 2a. Specifically, the WCA decreased from 84.6 ± 6.6° to 23.2 ± 6.6°. However, the WCA of the functionalized PEEK resulted slightly higher than the one previously found on a Si wafer [29]. After one week in the PBS solution, the WCA had an initial decrease and then remained stable until week 4, when it significantly increased until week 8 (1-8 weeks: $p=0.047$), as shown in the second column of Fig 2b.

The functionalization of PEEK with zwitterionic co-polymer (S3) resulted in a significant increase in hydrophilicity ($p=0.022$), with a WCA that reached 4.1 ± 0.6 ° (third column of Fig. 2a). Furthermore, this value was stable over time, as shown in the third column of Fig 2b.

In the first and the second strategy, after one week in PBS solution, the PEEK samples functionalized with the zwitterionic coating increased their hydrophilicity. This is probably due to the presence on the surface of salinity left by the PBS solution [30].

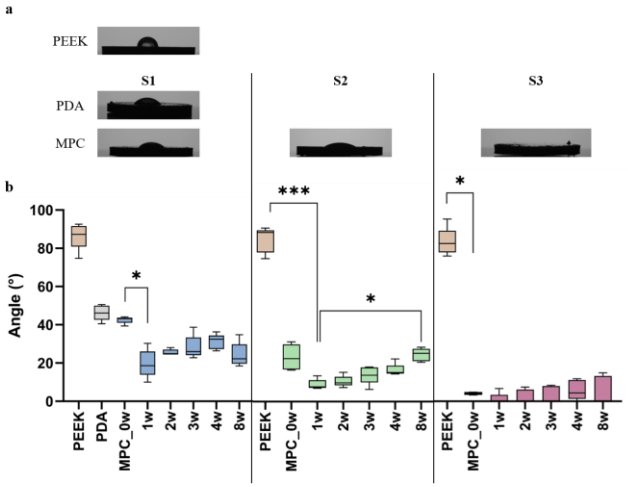


Fig. 2: a) Representative photos taken by the WCA goniometers for the substrate before and after the deposition of the zwitterionic coating with the three strategies. b) Box plots of the WCA measured before (PEEK), after the coating deposition (MPC_0w), and in the intermediate step (PDA) for strategy S1. *=p<0.05, **=p<0.01, ***=p<0.001.

Regarding the comparison of the three strategies for coating formation, the S3 (newly introduced in this work) led to superior results. Indeed, the PEEK functionalized with zwitterionic co-monomer resulted in the highest hydrophilicity, which remained stable up to week 8.

V. Conclusion

In this work, a novel strategy for the formation of a polydopamine-mediated MPC coating was devised and compared with other two strategies drawn from the literature on 3D-printed PEEK. The stability over time of the coated samples in a simulated physiological environment was also investigated. Results show that the newly proposed strategy results in a stable zwitterionic coating for up to 8 weeks, outperforming the other approaches. This strategy can be considered promising for coating the external case of artificial pancreas and other implantable devices. Further chemical and biological analyses will enrich this study. Furthermore, future studies on different substrates could be conducted to further verify the versatility of the poly-dopamine primer and the efficacy of the strategy devised.

Acknowledgement

This work has been funded by the European Union's Horizon-2020 research and innovation program under grant agreement No 951933, project FORGETDIABETES

References

[1] A. L. Burrack, T. Martinov, and B. T. Fife, "T cell-mediated beta cell destruction: Autoimmunity and alloimmunity in the context of type 1 diabetes," *Front. Endocrinol. (Lausanne).*, vol. 8, no. DEC, pp. 1–15, 2017, doi: 10.3389/fendo.2017.00343.

[2] G. A. Gregory *et al.*, "Global incidence, prevalence, and mortality of type 1 diabetes in 2021 with projection to 2040: a modelling study," *Lancet Diabetes Endocrinol.*, vol. 10, no. 10, pp. 741–760, Oct. 2022, doi: 10.1016/S2213-8587(22)00218-2.

[3] J. C. Pickup, "Insulin-Pump Therapy for Type 1 Diabetes Mellitus," *N. Engl. J. Med.*, vol. 366, no. 17, pp. 1616–1624, 2012, doi: 10.1056/nejmct1113948.

[4] P. R. Van Dijk *et al.*, "Continuous intraperitoneal insulin infusion versus subcutaneous insulin therapy in the treatment of type 1 diabetes: Effects on glycemic variability," *Diabetes Technol. Ther.*, vol. 17, no. 6, pp. 379–384, 2015, doi: 10.1089/dia.2015.0001.

[5] R. Hovorka, "Continuous glucose monitoring and closed-loop systems," *Diabet. Med.*, vol. 23, no. 1, pp. 1–12, 2006, doi: 10.1111/j.1464-5491.2005.01672.x.

[6] J. B. Kesavadev Banshi Saboo Meera Krishna Gopika Krishnan, "Evolution of Insulin Delivery Devices: From Syringes, Pens, and Pumps to DIY Artificial Pancreas", doi: 10.6084/m9.figshare.12199748.

[7] L. Ricotti, T. Assaf, P. Dario, and A. Menciassi, "Wearable and implantable pancreas substitutes," *J. Artif. Organs*, vol. 16, no. 1, pp. 9–22, 2013, doi: 10.1007/s10047-012-0660-6.

[8] V. Iacovacci *et al.*, "A fully implantable device for intraperitoneal drug delivery refilled by ingestible capsules," *Sci. Robot.*, vol. 6, no. 57, Aug. 2021, doi: 10.1126/SCIROBOTICS.ABH3328/SUPPL_FILE/SCIROBOTICS.ABH3328_MDAR_CHECKLIST.DOCX.

[9] H. AI-Haddad *et al.*, "Optimizing the Capsule-Based Refilling Strategy for an Implantable Insulin Delivery Device Tailored on Human Anatomy," no. 951933, pp. 1–6, 2022, doi: 10.1109/biorob52689.2022.9925322.

[10] S. R. Meyers and M. W. Grinsta, "Biocompatible and Bioactive Surface Modifications for Prolonged In Vivo Efficacy," pp. 1615–1632, 2012.

[11] D. F. Williams, "On the mechanisms of biocompatibility," *Biomaterials*, vol. 29, no. 20, pp. 2941–2953, 2008, doi: 10.1016/j.biomaterials.2008.04.023.

[12] M. R. Major, V. W. Wong, E. R. Nelson, M. T. Longaker, and G. C. Gurtner, "The Foreign Body Response: At the Interface of Surgery and Bioengineering," *Plast. Reconstr. Surg.*, vol. 135, no. 5, pp. 1489–1498, May 2015, doi: 10.1097/PRS.0000000000001193.

[13] L. Ricotti, "System for controlled administration of a substance from a human-body-implanted infusion device," Patent WO 2 012

011 132 A1 Jan. 26, 2012
[14] R. Pugliese, B. Beltrami, S. Regondi, and C. Lunetta, “Polymeric biomaterials for 3D printing in medicine: An overview,” *Ann. 3D Print. Med.*, vol. 2, p. 100011, 2021, doi: 10.1016/j.stlm.2021.100011.
[15] S. M. Kurtz, *Chemical and Radiation Stability of PEEK*. Elsevier Inc., 2012. doi: 10.1016/B978-1-4377-4463-7.10006-5.
[16] C. Y. Liu and C. J. Huang, “Functionalization of Polydopamine via the Aza-Michael Reaction for Antimicrobial Interfaces,” *Langmuir*, vol. 32, no. 19, pp. 5019–5028, 2016, doi: 10.1021/acs.langmuir.6b00990.
[17] C. Zhang *et al.*, “Dopamine-triggered one-step polymerization and codeposition of acrylate monomers for functional coatings,” *ACS Appl. Mater. Interfaces*, vol. 9, no. 39, pp. 34356–34366, 2017, doi: 10.1021/acsami.7b11092.
[18] X. Chen, Y. Zhai, X. Han, H. Liu, and Y. Hu, “Surface chemistry-dominated underwater superoleophobic mesh with mussel-inspired zwitterionic coatings for oil/water separation and self-cleaning,” *Appl. Surf. Sci.*, vol. 483, no. March, pp. 399–408, 2019, doi: 10.1016/j.apsusc.2019.03.318.
[19] T. Feng *et al.*, “Zwitterionic Polydopamine Engineered Interface for In Vivo Sensing with High Biocompatibility,” *Angew. Chemie - Int. Ed.*, vol. 59, no. 52, pp. 23445–23449, Dec. 2020, doi: 10.1002/anie.202010675.
[20] Z. Zhu *et al.*, “Polydopamine/poly(sulfobetaine methacrylate) Co-deposition coatings triggered by CuSO4/H2O2 on implants for improved surface hemocompatibility and antibacterial activity,” *Bioact. Mater.*, vol. 6, no. 8, pp. 2546–2556, 2021, doi: 10.1016/j.bioactmat.2021.01.025.
[21] W. Ma *et al.*, “Immobilization of poly(MPC) brushes onto titanium surface by combining dopamine self-polymerization and ATRP: Preparation, characterization and evaluation of hemocompatibility in vitro,” *Appl. Surf. Sci.*, vol. 349, pp. 445–451, 2015, doi: 10.1016/j.apsusc.2015.05.035.
[22] H. J. Kee, E. Jung, L. Id, J. C. Han, and C. K. Id, “Ahmed implant coated with poly (2- methacryloyloxyethyl phosphorylcholine) inhibits foreign body reactions in rabbit eyes,” pp. 1–14, 2021, doi: 10.1371/journal.pone.0252467.
[23] S. Ghosh, S. Abanteriba, S. Wong, and S. Houshyar, “Performance analysis of grafted poly (2-methacryloyloxyethyl phosphorylcholine) on additively manufactured titanium substrate for hip implant applications,” *J. Mech. Behav. Biomed. Mater.*, vol. 100, no. August, p. 103412, 2019, doi: 10.1016/j.jmbbm.2019.103412.
[24] X. Xie *et al.*, “Reduction of measurement noise in a continuous glucose monitor by coating the sensor with a zwitterionic polymer,” *Nat. Biomed. Eng.*, vol. 2, no. 12, pp. 894–906, 2018, doi: 10.1038/s41551-018-0273-3.
[25] X. Han *et al.*, “Tailoring the biologic responses of 3D printed PEEK medical implants by plasma functionalization,” *Dent. Mater.*, vol. 38, no. 7, pp. 1083–1098, 2022, doi: 10.1016/j.dental.2022.04.026.
[26] H. Lee, S. M. Dellatore, W. M. Miller, and P. B. Messersmith, “Mussel-Inspired Surface Chemistry for Multifunctional Coatings,” *Science*, vol. 318, no. 5849, p. 426, Oct. 2007, doi: 10.1126/SCIENCE.1147241.
[27] Y. Han *et al.*, “Self-adhesive lubricated coating for enhanced bacterial resistance,” *Bioact. Mater.*, vol. 6, no. 8, pp. 2535–2545, 2021, doi: 10.1016/j.bioactmat.2021.01.028.
[28] B. McVerry *et al.*, “A Readily Scalable, Clinically Demonstrated, Antibiofouling Zwitterionic Surface Treatment for Implantable Medical Devices,” *Adv. Mater.*, vol. 34, no. 20, 2022, doi: 10.1002/adma.202200254.
[29] C. C. Chang *et al.*, “Underwater Superoleophobic Surfaces Prepared from Polymer Zwitterion/Dopamine Composite Coatings,” *Adv. Mater. Interfaces*, vol. 3, no. 6, pp. 1–9, 2016, doi: 10.1002/admi.201500521.
[30] T. J. Plegue, K. M. Kovach, A. J. Thompson, and J. A. Potkay, “Stability of Polyethylene Glycol and Zwitterionic Surface Modifications in PDMS Microfluidic Flow Chambers,” *Langmuir*, vol. 34, no. 1, pp. 492–502, 2018, doi: 10.1021/acs.langmuir.7b03095.

Temperature influence on reflectance photometers for bilirubin measurement

L. Zucchini[1], M. Ajčević[1], A. Accardo[1]
[1] *Department of Engineering and Architecture, University of Trieste, Trieste 34127, Italy*

***Abstract*— An accurate and prompt measurement of unconjugated bilirubin in neonates is fundamental to prevent potentially severe pathological conditions, such as kernicterus which can lead to neurological impairments or death. Several methods were developed to measure bilirubin, in particular direct photometry could be promising and useful both inside and outside clinical facilities. Being applicable to portable devices, it is deemed necessary to investigate how this method is affected by the temperature of air surrounding the device itself, considering the diversity of environments in which a portable device may operate. In this work, a set of eight identical two-wavelength reflectance photometers (blue 465 nm and green 570 nm) were used to execute measurements while heating surrounding air from 15 to 30 °C. The measurements were made on purpose-built paper test strips having eight different absorbances instead of using real bilirubin samples, guaranteeing stability over time and temperature variations. Over 90.000 measurements were performed, and the relation between the reflectance data and external temperature was investigated. A high correlation (R^2>0.95) was identified both for blue and green light showing a significant linear and quadratic relation, respectively. The temperature dependency was more pronounced in case of lower absorbances. In conclusion, we identified the dependency of reflectance on temperature in these devices. The results showed that measurements performed at higher temperatures induced reduction of measured reflectance, leading to potential overestimation of bilirubin.**

***Keywords*—Bilirubin, photometry, temperature, reflectance.**

I. Introduction

Bilirubin is the major product of erythrocytes breakdown; under normal conditions unconjugated bilirubin is released in plasma where bounds to albumin, until it's excreted in bile as conjugate bilirubin [1,2]. In neonates, this metabolism is stronger and unconjugated bilirubin forms in higher concentrations: while a temporary and controlled increase is known to be physiological during the first days of life, an abnormal concentration of unconjugated bilirubin can lead to a pathological condition known as hyperbilirubinemia; due to the neurotoxicity of bilirubin, this condition can lead to kernicterus or death [2–4]. More than half of neonates develops benign hyperbilirubinemia during the first week of life, and roughly one in ten newborns develops clinically significative hyperbilirubinemia [3,4]. In these cases, frequent monitoring of serum bilirubin is needed to establish a proper treatment and reduce chances of neurological damage [5,6].

Several methods were developed to measure bilirubin concentration, both with invasive and non-invasive approaches. Currently used invasive methods are based on diazo reactions or vanadic acid reactions with bilirubin, while non-invasive methods, like transcutaneous bilirubinometers, have been on the market since 1980s [7,8]. An alternative invasive method is direct photometry which presents some advantages: a) it operates directly on plasma or serum without reagents and sample volume can easily be minimized to microliters; b) its complexity and cost are reduced due to the use of visible wavelength; c) it is suitable for compact portable devices. On the other hand, disadvantages are: a) some substances in plasma can interfere with bilirubin, such as oxyhemoglobin; b) any opalescence resulting from sample treatment can limit the accuracy; c) it is only valid for neonates due to the presence of other interfering substances, such as carotenoids, in children and adults [8–11]; d) it is influenced by temperature as stated in the Lambert-Beer law.

The use of direct photometry for bilirubin assay traces back to 1960s [11]; since then several invasive and non-invasive applications of this method have been proposed [9,10,12,13]. However, no literature concerning temperature influence on such systems was found.

Bilirubin measurement devices in clinical settings operate under controlled environment rooms where temperature is almost constant but, as aforementioned, direct photometry can be applied to portable and field instrumentation, which can be used both inside and outside clinical facilities, thus in environments with diverse temperatures.

The aim of this work is to determine the effect of external temperature on the measurement of bilirubin concentration using a simple two-wavelength reflectance photometer.

II. Materials and methods

A. The reflectance photometer

A set of eight identical photometers was used to ensure the repeatability of evidence found during the experiment. Each photometer was composed by an optical chamber, two LEDs (KPHHS-1005QBC-D-V and KPT-1608CGCK, Kingbright Electronic Co., Ltd., Taiwan), a photodiode (TEMD6200FX01, Vishay Intertechnology, Inc., USA), and other electronic components necessary for the acquisition of the signal (Figure 1). The LEDs emitted light at 465 nm and 570 nm, hence blue and green light respectively, and irradiated the sample inserted in the chamber; since no light was transmitted through the sample, the fraction of light not absorbed by the sample was reflected towards the photodiode; the output current of the photodiode was converted to a tension, then digitized with 0 to 3 V range. In this way, the photometer acquired the intensity of reflected light: a high intensity indicated high reflectance, or equivalently low absorption, and vice versa.

A temperature sensor with 0.25 °C resolution (LM73, Texas Instruments, Inc., USA) was placed on the electronic board of each photometer, adequately far from heat sources like microcontrollers or power supplies. Such placement was deemed better than using a single sensor for all instruments: the measurement of "ambient" temperature, intended as the

temperature of the environment in which the instruments were placed, could have differed considerably from the air immediately surrounding the instruments themselves; placing a temperature sensor as near as possible to the optical chamber produces more accurate results [14,15].

Finally, each photometer was provided with a 16-bit ADC and a microcontroller (MKL15Z32VFT4, Freescale Semiconductor, USA) that sent intensity values to a single computer that stored all data.

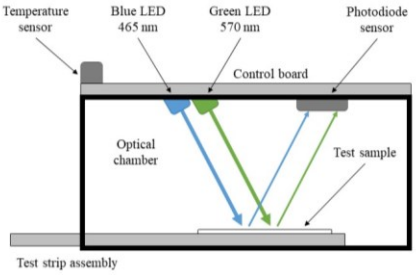


Fig. 1: A schematic representation of one of the photometers used in the experiment. The test strip is inserted into the optical chamber where two LEDs irradiate the sample; a fraction of the light is reflected and detected by the photodiode.

B. The test samples

A set of eight paper test strips was fabricated, simulating different levels of absorption by bilirubin distributed across the input scale of the photometers. Considering that the study is focused on the identification of temperature impact on the measurements, the use of plasma or diluted bilirubin was excluded; this choice allowed to avoid errors due to biological samples preparation, treatment, and conservation. Additionally, "real" samples would not have maintained chemical and physical stability throughout the experiment: bilirubin oxidates when exposed to blue light, bringing further interference to the system [4,6,7].

As demonstrated in Figure 2, eight different patterns were created to form a logarithmic greyscale from an almost white to a very dark shade, then printed with laser printers on normal paper; the patterns were then cut and laid down on test strips assemblies. Since all eight photometers were subjected to the test contemporarily, eight test strips were prepared for each of the eight levels, thus 64 in total. This method had some advantages, two were the most important: a) printing the pattern on paper led to repeatable reflectance values among different strips with the same grey level; b) reflectance values were stable during the whole experiment and any damaged strips could have been replaced easily.

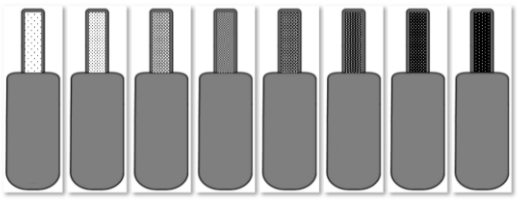


Fig. 2: The greyscale pattern created for the experiment and the test strips, which shape was suitable to fit the optical chamber. The strips were enumerated from 1 to 8 in order of absorbance.

C. Experimental procedure

To measure the influence of external temperature on intensity value, the photometers were placed inside a temperature test chamber. At the beginning of each test, one of the eight groups of test strips was loaded, and the photometers were cooled at 15 °C, maintaining low levels of humidity to avoid condensation of water on the electronic boards and inside the optical chambers. After cooling, they were immediately connected and powered on, and the temperature test chamber was set to 40 °C: in this way, during the heating process, the instruments could reach thermal equilibrium with the test chamber starting from 15 °C or slightly under. Simultaneously, their firmware was started: with a period of 10 s, the instruments executed four consecutive instantaneous readings with the 465 nm LED and another four with the 570 nm LED; the four readings made with each wavelength were arithmetically averaged and sent to the central calculator, as well as timestamp data and temperature data. In other words, every 10 seconds the calculator received eight "rows" of information, one from each instrument, containing timestamp, temperature, blue light intensity, and green light intensity. The experiment was stopped when all temperature sensors provided a temperature above 30 °C. The photometers were consequently powered off and let chill again. This described workflow was repeated eight times, one for each test strip group. To avoid bias errors due to experimental design, such as instruments hysteresis, all the acquisitions for all experimental settings were also performed by starting from 30 °C and cooling the devices until reaching temperatures below 15 °C, hence reversing the described process.

Before and after each test all the test strips and the optical chamber were visually inspected to assess the absence of moisture, condensation, or damages. During the execution of each test both the temperature test chamber and the instruments inside were not moved or handled to avoid producing motion or vibration artifacts.

For each instrument, each test strip, and each wavelength the same procedure was used for the analysis. Any measure below 15.0 °C or above 30.0 °C was excluded from the analysis. Then, 15.0 °C was adopted as reference temperature (T_{ref}): the lower limit of temperature range was set at 15.0 °C as cooling the devices at lower temperatures caused frequent condensation inside the optical chamber of the instruments, or in the paper test strips. For each test, all blue and green measures executed at exactly T_{ref} were averaged in order to find an intensity reference for blue and green data, respectively, identified as $I_{ref,b}$ and $I_{ref,g}$.

As the temperature inside the test chamber increased, each i-th measure was defined by a T_i temperature and an intensity value, $I_{i,b}$ for blue light and $I_{i,g}$ for green light. Consequently, the variation of temperature and blue and green intensity from their respective reference were calculated for each i-th measure:

$$\begin{cases} \Delta T_i = T_i - T_{ref} \\ \Delta I_{i,b} = I_{i,b} - I_{ref,b} \\ \Delta I_{i,g} = I_{i,g} - I_{ref,g} \end{cases} \quad (1)$$

III. RESULTS

Over 90.000 measurements were performed by the eight photometers testing all eight test strip groups. Intensity values for each instrument and each test strip were plotted against time and inspected. The decreasing trend of measured intensity was observed for higher external temperature values, highlighting an increase in absorbance for higher temperatures. Figure 3 shows the temporal trend of intensity and temperature for the lightest strip (Strip 1) irradiated with 465 nm light in one of the eight instruments.

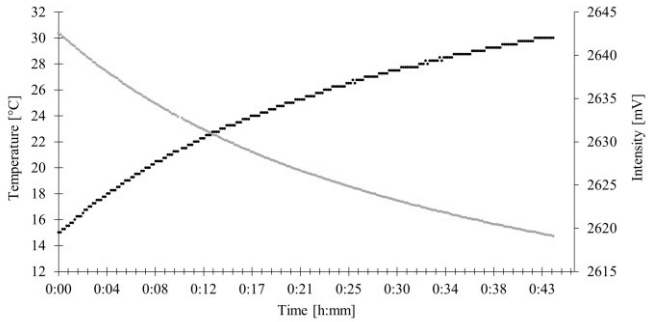


Fig. 3: An example of the typical temporal trend resulting from the experiments, intensity vs. time (grey) and temperature vs. time (black).

In Figure 4 an example of ΔI for blue and green light plotted against ΔT is reported, regarding one of the instruments measuring the lightest strip. A negative relation can be observed between intensity and temperature causing underestimation for temperatures higher than the reference one.

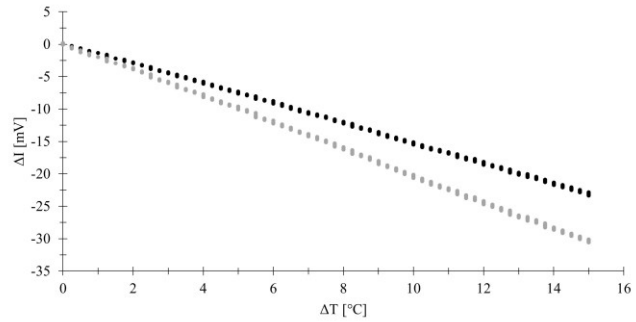


Fig. 4: ΔI_b vs. ΔT (black dots) and ΔI_g vs. ΔT (grey dots). The quadratic behaviour of the relation between green intensity and temperature is noticeable especially in ΔT included in the range 0-4 °C. Data is extrapolated from one of the instruments and refers to the lightest strip.

Blue intensity was differently affected by temperature with respect to the green intensity, with the latter showing a more pronounced quadratic behaviour especially for small ΔT, while the first being linear. Linear functions were then used to approximate the relationship between ΔI_b and ΔT, while quadratic functions were used to approximate the relationship between ΔI_g and ΔT; in every test the approximation resulted in a coefficient of determination R^2 greater than 0.95.

Lighter test strips caused wider deviations from the intensity reference, while darker ones were less influenced by temperature. Table 1 indicates that the relation between ΔI and ΔT depended on the test strip group, hence from the concentration of the sample: for higher concentrations the effect of temperature decreased. This was valid for both blue and green data despite the difference in terms of approximation function degree; the first-grade polynomial coefficient (*m* for blue, *b* for green) exhibited a coherent dependence on strip type.

Finally, the analysis of reversed experiments, therefore with temperature starting at 30 °C until 15 °C, showed no significant differences with the regular setup suggesting the absence of instrument hysteresis effects.

TABLE I: POLYNOMIAL INTERPOLATION RESULTS

	Blue light (465 nm)		*Green light (570 nm)*		
	m	*q*	*a*	*b*	*c*
Strip 1	-681.647	43.862	6.808	-1077.09	0.672
Strip 2	-488.149	64.625	5.915	-811.407	21.209
Strip 3	-421.097	61.836	5.108	-718.362	19.693
Strip 4	-384.226	43.467	3.79	-642.316	52.764
Strip 5	-358.341	33.193	3.913	-607.721	44.35
Strip 6	-351.935	8.435	3.035	-558.412	-17.251
Strip 7	-311.295	39.456	5.058	-564.956	29.77
Strip 8	-335.417	9.1	5.184	-562.882	-13.577
Mean	-416.513	37.997	4.858	-692.893	17.203
±SD	±32.998	±58.271	±1.05	±35.098	±46.433

Strip 1 is the lightest, while Strip 8 is the darkest. For blue light *m* is the first-degree polynomial coefficient, and *q* is the zero-degree one. For green light *a* is the second-degree polynomial coefficient, *b* is the first-degree polynomial coefficient, and *c* is the zero-degree one. Stated values are the result of the average of the values provided by the single photometers.

IV. DISCUSSION

Neonatal hyperbilirubinemia is known as one of the burdens of developing countries, affecting tenths of thousands of newborns and inducing permanent damages to many of them [2]. In developed countries instead, where the incidence is much lower and management protocols are well-established, it is essential to provide effective solutions for reducing costs related to diagnosis and treatment [7].

For these reasons a broad range of methods for the measurement of bilirubin in neonates have been developed, reflectance photometry being one of them. Although being a promising method no evidence was found regarding temperature influence on such systems; this aspect is believed to be fundamental, especially when considering that this method is applicable to portable instruments, which could be used in various environments and not only in clinical laboratories. Previous literature facing temperature influence on optical sensors and spectrometers was found, even though not involving medical systems but agricultural systems [14,16].

The focus of this work was to correlate external temperature and reflectance readings of a series of photometers for bilirubin measurement application. Placing temperature sensors directly on-board allowed to measure the temperature of air immediately surrounding the instruments rather than generic air temperature. Investigating photometers behaviour at temperatures from 15 to 30 °C was necessary to cover different scenarios of use, inside and outside clinical facilities; a large amount of data was consequently produced and allowed a robust analysis.

A first result was how blue and green light were influenced by temperature regardless of the strip type: blue light showed a linear behaviour, while green light was correctly interpolated by quadratic function. In any case, the common feature was a reduction in reflectance for higher temperatures: a reduction of reflectance by the sample is associated to an increase of its

absorbance, hence to greater concentration of bilirubin in the sample itself. In other words, as temperature increases the instrument tends to overestimate bilirubin concentration.

Since blue and green LED measures were executed with a delay of just tenths of a second from each other on the same strip and at identical external conditions, the difference could be traced back to the LEDs characteristics: 465 nm LEDs are less sensitive to temperature than 570 nm LEDs or, in other words, the relative luminous intensity of the first is less dependent from temperature and more linear than the latter.

The second result is how test strips type correlates with temperature, or equivalently how the result of the measurement of a sample varies with temperature. Table I demonstrates how a lighter sample, which reflects most of the incident light, is more temperature dependent than a darker one, producing a steeper relationship. This phenomenon should be associated with the relationship between sample absorbance and temperature: a sample containing a certain concentration of bilirubin provides a certain absorbance dependent to its temperature, as defined by the Lambert-Beer law.

In conclusion, we identified the dependency of reflectance on temperature in these devices. The results showed that measurements performed at higher temperatures induced reduction of measured reflectance, leading to potential overestimation of bilirubin. Future research should be focused to develop mitigating strategies to compensate the effect of temperature on reflectance photometers designed for bilirubin measurements.

ACKNOWLEDGEMENT

The authors acknowledge resources and support from the naME Lab of University of Trieste. The authors also acknowledge Matteo Mottica and MQuadro S.r.l. for providing necessary materials.

REFERENCES

(1) Fevery, J. Bilirubin in Clinical Practice: A Review: Bilirubin in Clinical Practice. *Liver International* **2008**, *28* (5), 592–605. https://doi.org/10.1111/j.1478-3231.2008.01716.x.

(2) Olusanya, B. O.; Kaplan, M.; Hansen, T. W. R. Neonatal Hyperbilirubinaemia: A Global Perspective. *The Lancet Child & Adolescent Health* **2018**, *2* (8), 610–620. https://doi.org/10.1016/S2352-4642(18)30139-1.

(3) Greco, C.; Arnolda, G.; Boo, N.-Y.; Iskander, I. F.; Okolo, A. A.; Rohsiswatmo, R.; Shapiro, S. M.; Watchko, J.; Wennberg, R. P.; Tiribelli, C.; Coda Zabetta, C. D. Neonatal Jaundice in Low- and Middle-Income Countries: Lessons and Future Directions from the 2015 Don Ostrow Trieste Yellow Retreat. *Neonatology* **2016**, *110* (3), 172–180. https://doi.org/10.1159/000445708.

(4) Mitra, S.; Rennie, J. Neonatal Jaundice: Aetiology, Diagnosis and Treatment. *Br J Hosp Med* **2017**, *78* (12), 699–704. https://doi.org/10.12968/hmed.2017.78.12.699.

(5) Bhutani, V. K.; Johnson, L.; Sivieri, E. M. Predictive Ability of a Predischarge Hour-Specific Serum Bilirubin for Subsequent Significant Hyperbilirubinemia in Healthy Term and Near-Term Newborns. *Pediatrics* **1999**, *103* (1), 6–14. https://doi.org/10.1542/peds.103.1.6.

(6) Subcommittee on Hyperbilirubinemia. Management of Hyperbilirubinemia in the Newborn Infant 35 or More Weeks of Gestation. *Pediatrics* **2004**, *114* (1), 297–316. https://doi.org/10.1542/peds.114.1.297.

(7) Muchowski, K. E. Evaluation and Treatment of Neonatal Hyperbilirubinemia. *American Family Physician* **2014**, *89* (11), 873–878.

(8) Ngashangva, L.; Bachu, V.; Goswami, P. Development of New Methods for Determination of Bilirubin. *Journal of Pharmaceutical and Biomedical Analysis* **2019**, *162*, 272–285. https://doi.org/10.1016/j.jpba.2018.09.034.

(9) Penhaker, M.; Kasik, V.; Hrvolova, B. Advanced Bilirubin Measurement by a Photometric Method. *ElAEE* **2013**, *19* (3), 47–50. https://doi.org/10.5755/j01.eee.19.3.3696.

(10) Kazmierczak, S. C.; Robertson, A. F.; Catrou, P. G.; Briley, K. P.; Kreamer, B. L.; Gourley, G. R. Direct Spectrophotometric Method for Measurement of Bilirubin in Newborns: Comparison with HPLC and an Automated Diazo Method. *Clinical Chemistry* **2002**, *48* (7), 1096–1097. https://doi.org/10.1093/clinchem/48.7.1096.

(11) Jackson, S. H.; Hernandez, A. H. A New "Bilirubinometer" and Its Use in Estimating Total and Conjugated Bilirubin Serum. *Clinical Chemistry* **1970**, *16* (6), 462–465. https://doi.org/10.1093/clinchem/16.6.462.

(12) Alla, S. K.; Clark, J. F.; Beyette, F. R. Signal Processing System to Extract Serum Bilirubin Concentration from Diffuse Reflectance Spectrum of Human Skin. In *2009 Annual International Conference of the IEEE Engineering in Medicine and Biology Society*; IEEE: Minneapolis, MN, 2009; pp 1290–1293. https://doi.org/10.1109/IEMBS.2009.5333236.

(13) Javid, B.; Fotouhi-Ghazvini, F.; Zakeri, F. Noninvasive Optical Diagnostic Techniques for Mobile Blood Glucose and Bilirubin Monitoring. *J Med Signals Sens* **2018**, *8* (3), 125. https://doi.org/10.4103/jmss.JMSS_8_18.

(14) Salim, S. G. R.; Fox, N. P.; Theocharous, E.; Sun, T.; Grattan, K. T. V. Temperature and Nonlinearity Corrections for a Photodiode Array Spectrometer Used in the Field. *Appl. Opt.* **2011**, *50* (6), 866. https://doi.org/10.1364/AO.50.000866.

(15) Starks, P. J.; Walter-Shea, E. A.; Schiebe, F. R.; Markham, B. L. Temperature Sensitivity Characterization of a Silicon Diode Array Spectrometer. *Remote Sensing of Environment* **1995**, *51* (3), 385–389. https://doi.org/10.1016/0034-4257(94)00109-Z.

(16) Kipp, S.; Mistele, B.; Schmidhalter, U. The Performance of Active Spectral Reflectance Sensors as Influenced by Measuring Distance, Device Temperature and Light Intensity. *Computers and Electronics in Agriculture* **2014**, *100*, 24–33. https://doi.org/10.1016/j.compag.2013.10.007.

Combination of VR and manikins to improve medical training

M. Coduri[1,2], A. Calandrino[3,4], G. Addiego Mobilio[1], E. Grasso[1], M. Pescio[1], P. Rossi[2], G. Carlini[1], M. Chirico[2], F. Solari[1], M. Chessa[1,2], M. Casadio[1,2], S. Ricci[1,2]

[1] *Department of Informatics, Bioengineering, Robotics and Systems Engineering, University of Genoa, Genoa, Italy*
[2] *Simulation and Advanced Education Center - SimAv, University of Genoa, Genoa, Italy*
[3] *Department of Neuroscience, Rehabilitation, Ophtalmology, Genetics, Maternal and Child Health, University of Genoa, Genoa, Italy*
[4] *Neonatal Intensive Care Unit, IRCCS Giannina Gaslini Institute, Genoa, Italy*

***Abstract*— Medical students must master many different skills prior to starting clinical practice. As practicing on real patients is no longer an option for ethical and working time issues, one possibility medical training can be exploited is through simulations involving manikins. However, manikins need to be surrounded by a fully simulated environment to increase engagement and realism to the simulation. A possible alternative is Virtual Reality (VR); yet, VR applications do not provide realistic haptic feedback, which is fundamental for dexterity training. To overcome these limitations, we designed and developed systems coupling the advantages of VR with those of traditional manikin-based simulations. We developed two educational tools: a Mixed Reality Simulator for Trauma management, MR STEVE, and a Simulator for Newborn Life Support Training, RiNeo MR. Both solutions include a sensorized manikin collecting performance data, a leap motion device to track the users' hands in real time, and a VR headset delivering immersive content. In the virtual environment, the user sees a virtual patient, overlapped with the real one; this way, the user has visual and tactile feedback simultaneously. This is a methodological study highlighting how to combine VR with physical manikins, with the final goal of improving medical training.**

***Keywords*— Virtual Reality, Mixed Reality, Medical Simulation, Trauma Management, Newborn Life Support**

I. Introduction

Patient safety has always been a crucial aspect within the medical field [1]. Historically, students had learned medical skills by practicing on people. However, the learning curve to reach a proficiency level in many medical procedures is steep and strongly subjective [1], and the risk of harming or making patients uncomfortable for lack of practice is no longer being accepted.

For all the reasons mentioned above, medical simulation techniques have been exploited within the last decades [2]. Simulation lets students practice in a riskless and controlled environment [2], and it allows them to practice repeatedly dexterity skills, procedures and soft skills, having the possibility to learn from mistakes [1], [2].

Medical tools include standardized patients, namely, actors who are signed up to teach how to collect clinical history, perform examinations and communicate with the patient. Also, manikins with various levels of fidelity are largely used to teach manual and soft skills [1]. Finally, virtual reality (VR), and augmented reality (AR) applications have garnered more interest in medical training, as they make it possible to create a immersive and realistic experiences in a digital environment [3]. In detail, VR applications are used for procedural training and soft skills training and evaluation; AR is employed for enhancing high-fidelity simulation and to teach basic theoretical skills (i.e., anatomy); mixed reality (MR), namely the combination of virtual and physical elements is typically used in the surgical domain [4].

One of the main limitations of using high-fidelity manikins, is the need for a realistic setting around the manikin. In fact, there are studies reporting that learning and retention are increased if the entire simulation setting is realistic [1]. Also, stress management and communication skills need a realistic and engaging scene to be properly simulated [5]. As opposite, VR lacks of realistic haptic feedback which can affect the learning outcome [4].

To overcome these limitations, a possibility would be to combine a real manikin with a VR application, resulting in an MR system [4].

To date, some research groups are developing MR simulators for adult Cardiopulmonary Resuscitation (CPR) [6]–[8]; however, the works are still at a prototype stage and their use and effectiveness have not been fully investigated yet [4]. Furthermore, to the best of our knowledge, research in other medical fields is even more limited, with several VR applications, but no MR simulators.

Within this framework, we have designed and developed two MR simulators, i.e., coupling VR with a real manikin. This way, one can be immersed in a highly realistic and engaging environment and, at the same time, have haptic feedback. With this approach, manual, procedural and soft skills can be trained with the same tool and at the same time, without the need for a fully equipped simulation centre.

II. Objectives

The goal of the project was to design and develop educational tools which combine the advantages of VR with those of traditional manikin-based simulations. In other words, we aimed at combining different techniques to create simulators which are a fusion between high-fidelity manikins (i.e., full body manikins equipped with sensors to monitor the user's action and provide feedback) and VR applications, that

deliver highly immersive environments.

The proof of concepts presented in this work are the result of a multidisciplinary collaboration between biomedical engineering students, medical students, and paediatric residents. This collaboration has been promoted through the institution of the Joint lab for Emerging Technologies in Simulation (JETS), which is a joint lab between the Department of Informatics, Bioengineering, Robotics and System engineering (DIBRIS), and the Simulation and Advanced Education Centre of the University of Genova, Italy. Indeed, JETS has the goal to (i) implement and test new prototypes of medical simulators; (ii) investigate how disruptive technologies can enhance medical education; (iii) study the processes underlying medical and surgical skills; (iv) carry out feasibility and efficacy studies.

As a first step, we identified domains that could benefit of having both a VR environment and a physical manikin. We selected (i) trauma management and (ii) newborn life support, as they both lack VR-based solutions [4], [9] and require users to both train manual and soft skills [1].

The different points of view of engineers and clinicians led us to define the main features the simulators should have, which can be summarized as follows:

- Train and/or assess manual skills performed on a manikin;
- Monitor the user's actions in real time;
- Provide feedback on the trainee's actions;
- Respond to the learner's maneuver;
- Immerse the user into a realistic scenario;
- Train soft skills (e.g., stress management, time organization);
- Train/Evaluate procedural knowledge;
- Provide a realistic interaction with the elements the trainees should interact with, such as the manikin and the medical instruments.

Additional properties of the simulator are its ease of installation and use by people without specific technical skills, as in the case of healthcare providers; the possibility of having modular systems, usable in different modalities (i.e., VR applications without the manikins, or manikin with a simple screen-based Graphic User Interface), with the possibility of adding additional modules such as a scoring system, additional scenarios, or manoeuvres to be simulated.

III. Solutions

The two systems we realized include (Fig. 1):

- High-fidelity manikins (an adult for the trauma management simulator and a newborn for the NLS one).
- HTC Vive VR setup (HTC Corporation, Taiwan).
- Leap Motion (Ultraleap, UK) device to track the user's hand in real time.
- Sensors to assess trainees' performance.



Fig. 1 System Setup. The simulators include a sensorized manikin, an immersive headset, and a VR application. Data from the manikin are sent in real time to the VR application via Wi-Fi

As we wanted to implement systems usable in different modalities, according to the educational need, we designed two configurations: 2D (non-immersive) to let the user practice manoeuvres on the physical manikin, while receiving real time feedback on a computer screen; 3D (immersive) that allows the user to be immersed in a virtual environment and practice in a realistic setting. With the 3D configuration, the users can physically interact with the some virtual objects of the scene, as the virtual and real worlds are overlapped.

Both 2D and 3D configurations share the same manikin, equipped with sensors to monitor user performance in real time. Sensors acquire data and send them to the VR application in real time via Wi-Fi. The application can either provide performance feedback in real time, as in the case of the training, or saves them to deliver an evaluation at the end of the simulation.

A. MR STEVE: Mixed-Reality Simulator of Traumatic EVEnts

MR STEVE is an educational tool for first aid and trauma management training and evaluation. The VR application of the simulator includes five different scenarios in which the VR simulation can occur (Fig. 2): a helicopter; an outdoor upland scenario; an indoor scenario of a pub; an urban scenario; a hospital setting. Moreover, new scenarios can be easily integrated.

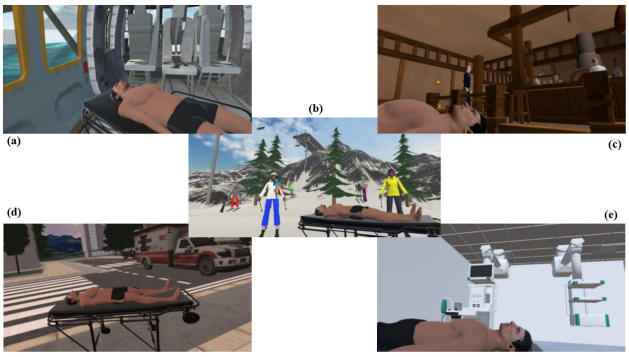


Fig. 2 Scenarios of the MR VR applications. The user can choose from five different scenes: (a) helicopter; (b) outdoor upland scenario; (c) indoor scenario of a pub; (d) urban scenario; (e) hospital setting

The system also includes a sensorized manikin, which monitors the following actions:

- Head and collar positions (through three VR trackers)
- Chest compression (infrared sensor)
- Tourniquet application (using resistive force sensors) [10].

In the immersive version, the trainee is in the same room as the physical manikin. By wearing the VR headset, he/she is immersed into a virtual room and can select a simulation scenario by virtually touching the corresponding button, thanks to the Leap Motion Device. As soon as the simulation starts, the trainee sees the simulation scenario with a virtual patient, which is mapped onto the real manikin (Fig. 3).

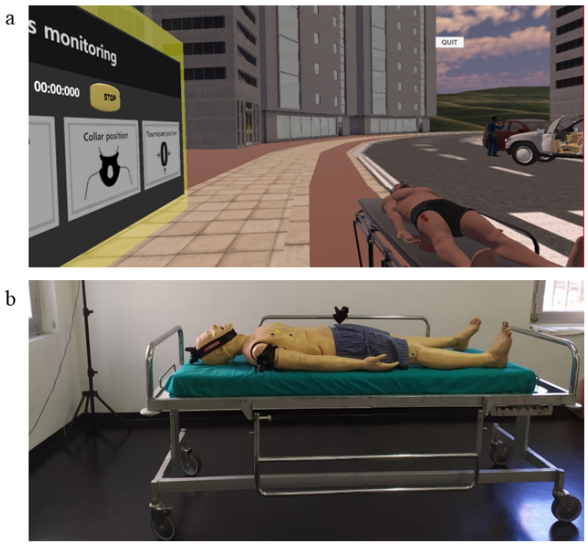


Fig. 3 Setup of MR STEVE. (a) virtual environment that the user can see during the immersive simulation. On the left there is a screen showing the users' performance in real time (b) real high-fidelity manikin that is overlapped with the virtual replica, moving accordingly.

This way, the user can physically touch the real manikin and all their actions are replicated into VR, thus obtaining a coherent mixed reality environment [11]. In other words, the correspondence achieved between the virtual model and the manikin allows the users to have visual and tactile feedback simultaneously. Finally, the instructor can control the simulation (e.g., by selecting different types of wounds). During the training phase the user can see his/her performance in real-time thanks to a screen in the scenario (Fig. 3). Finally, the 2D version shows the information collected by the sensors on a monitor screen, as in the case of traditional high-fidelity simulations.

B. RiNeo MR: Simulator for Newborn Life Support

For NLS simulation, we have created an hospital setting consisting of two rooms: (i) Hallway, which acts as a familiarization scene to help the user become comfortable with the virtual environment (Fig. 4); (ii) Delivery room: which is the place where trainees have to perform NLS [12].



Fig. 4: RiNeo MR, Virtual familiarization environment. The user can explore the hallway to understand how to move in the digital world.

As for MR STEVE, the system is equipped with four different sensors:

- An inertial measurement unit (IMU) to monitor the head position.
- Two magnetic sensors to detect mask position.
- A force sensor to measure positive pressure ventilation.
- An infrared sensor for chest compression.

Even in this case, trainees have coherent virtual and tactile feedback (Fig. 5), and real time feedback is provided on a screen, either inside the virtual environment (3D mode), or on a monitor (2D mode).

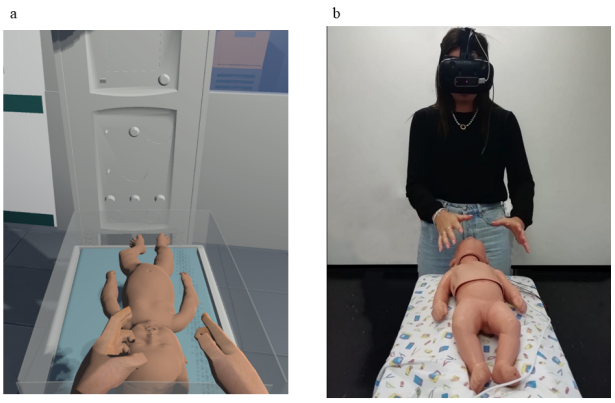


Fig. 5: RiNeo MR steup. (a) user's view of the virtual environment; (b) corresponding real world.

IV. CONCLUSION

This study presents the first steps toward the development of MR simulators for medical training. We developed two preliminary proof-of-concepts: a simulator for first aid training and trauma management and a simulator for newborn life support training and evaluation. Preliminary tests to assess

usability, user experience, and comfort occurrence report that both simulators seem to be promising tools for medical training. Indeed, subjects felt the virtual environment quite realistic and found simulators easy to use. Moreover, no discomfort has been detected after the immersive simulation.

This work is still at a preliminary phase. More data are needed to further investigate simulators usability, and experiments involving healthcare providers will be carried out to assess whether this combination of technologies can be beneficial for medical training.

At the current stage, we have sensorized the manikin to monitor simple tasks, such as chest compression or mask positioning. However, additional manoeuvres can be monitored to have a more complete educational solution.

Similarly, a multi-player version of the two simulators could be developed, such that the systems could be used to train manual skills, as well as team management, communication skills, and stress management.

Finally, once the full development phase is complete, we will compare the effectiveness of the simulators by conducting a comparative study with two groups: one group will follow the training using the proposed solutions, while a control group will use traditional simulation modalities (i.e., manikins). The data collected will be compared to assess the efficacy of MR reality simulation in the training of procedural, manual, and soft skills.

Importantly, indicators and metrics must be used quantitatively assess the proposed solution. One of the possibilities is through validated questionnaires that can provide meaningful information on User Experience, and sense of presence of users inside the virtual environment (e.g., User Experience Questionnaire [13], Igroup Presence Questionnaire IPQ [14]); as well as on the usability of the simulator (e.g., System Usability Scale [15]), also in terms of physical discomfort (e.g., Simulation Sickness Questionnaire, SSQ [16]), and workload (e.g., NASA Task Load Index [17]).

In conclusion, this methodological study, assesses the feasibility of combining two technologies into a single tool, to create complete educational solutions providing both anatomically accurate haptic feedback, and an engaging and immersive scenario which can enhance medical training.

ACKNOWLEDGEMENT

This work was partially supported by the European Union, PON Ricerca e Innovazione 2014-2020 D35F210 0230 0 0 07 (SR) and PON Ricerca e Innovazione 2014-2020 D31B210 0815 0 0 01 (MCo).

The authors thank Ester Issa for helping in the implementation of the virtual scenes.

REFERENCES

[1] A. I. Levine, S. DeMaria Jr, A. D. Schwartz, and A. J. Sim, *The comprehensive textbook of healthcare simulation*. Springer Science & Business Media, 2013.

[2] D. M. Gaba, “The future vision of simulation in health care,” *Qual. Saf. Heal. Care*, vol. 13, no. 1, pp. 2–10, 2004.

[3] Żmigrodzka Małgorzata, “Development of virtual reality technology in the aspect of educational applications.” Marketing of Scientific and Research Organizations, 2017.

[4] S. Ricci, A. Calandrino, G. Borgonovo, M. Chirico, and M. Casadio, “Viewpoint: Virtual and Augmented Reality in Basic and Advanced Life Support Training,” *JMIR Serious Games*, vol. 10, no. 1, p. e28595, 2022.

[5] F. Jaskiewicz, D. Kowalewski, K. Starosta, M. Cierniak, and D. Timler, “Chest compressions quality during sudden cardiac arrest scenario performed in virtual reality: A crossover study in a training environment.,” *Medicine (Baltimore).*, vol. 99, no. 48, p. e23374, Nov. 2020.

[6] O. Almousa *et al.*, “Virtual reality simulation technology for cardiopulmonary resuscitation training: An innovative hybrid system with haptic feedback,” *Simul. Gaming*, vol. 50, no. 1, pp. 6–22, 2019.

[7] F. Buttussi, L. Chittaro, and F. Valent, “A virtual reality methodology for cardiopulmonary resuscitation training with and without a physical mannequin.,” *J. Biomed. Inform.*, vol. 111, p. 103590, Nov. 2020.

[8] F. Semeraro, A. Frisoli, M. Bergamasco, and E. L. Cerchiari, “Virtual reality enhanced mannequin (VREM) that is well received by resuscitation experts.,” *Resuscitation*, vol. 80, no. 4, pp. 489–492, Apr. 2009.

[9] J. Williams, D. Jones, and R. Walker, “Consideration of using virtual reality for teaching neonatal resuscitation to midwifery students.,” *Nurse Educ. Pract.*, vol. 31, pp. 126–129, Jul. 2018.

[10] L. Viola *et al.*, “Design of a system to detect the force applied by tourniquets in a manikin’s limb,” *Proc. Annu. Int. Conf. IEEE Eng. Med. Biol. Soc. EMBS*, pp. 5019–5022, 2021.

[11] E. Girau *et al.*, “A Mixed Reality system for the simulation of emergency and first-aid scenarios.,” *Conf. Proc. 41st Annu. Int. Conf. IEEE Eng. Med. Biol. Soc. IEEE Eng. Med. Biol. Soc. Annu. Conf.*, vol. 2019, pp. 5690–5695, Jul. 2019.

[12] S. Ricci *et al.*, “RiNeo MR: A mixed-reality tool for newborn life support training,” *Proc. Annu. Int. Conf. IEEE Eng. Med. Biol. Soc. EMBS*, pp. 5043–5046, 2021.

[13] B. Laugwitz, T. Held, and M. Schrepp, “Construction and evaluation of a user experience questionnaire,” in *Symposium of the Austrian HCI and usability engineering group*, 2008, pp. 63–76.

[14] T. Schubert, F. Friedmann, and H. Regenbrecht, “Embodied presence in virtual environments,” in *Visual representations and interpretations*, Springer, 1999, pp. 269–278.

[15] R. A. Grier, A. Bangor, P. Kortum, and S. C. Peres, “The system usability scale: Beyond standard usability testing,” *Proc. Hum. Factors Ergon. Soc.*, pp. 187–191, 2013.

[16] P. Bimberg, T. Weissker, and A. Kulik, “On the Usage of the Simulator Sickness Questionnaire for Virtual Reality Research,” *Proc. - 2020 IEEE Conf. Virtual Real. 3D User Interfaces, VRW 2020*, pp. 464–467, 2020.

[17] S. G. Hart and L. E. Staveland, “Development of NASA-TLX (Task Load Index): Results of empirical and theoretical research,” in *Advances in psychology*, vol. 52, Elsevier, 1988, pp. 139–183.

Usability of a multi-sensor array for the application of electro-phonocardiography in home care

N. Giordano[1], G. Balestra[1], S. Rosati[1] and M. Knaflitz[1]
[1] *PoliToBIOMed Lab and Department of Electronics and Telecommunications, Politecnico di Torino, Italy*

***Abstract*—In the latest years, the potentiality of a combined use of electrocardiography (ECG) and phonocardiography (PCG) for the assessment of the electromechanical coupling of the heart has gained interest within the scientific community. The availability of this technology in a home care context would enable the timely monitoring of patients where the electromechanical coupling is impaired, such as in heart failure. Nevertheless, the domiciliary use of electro-phonocardiography is at date prevented by the critical positioning of the electronic stethoscope, which cannot be reliably performed by inexperienced users. In this work, we propose a usability analysis of a multi-sensor array that we developed for this purpose. The multi-sensor array is a flexible pad embedding 3 electrodes and 48 microphones, distributed over the left hemithorax with a high spatial resolution. In our experimental protocol, we simulated a real home care scenario: volunteers with no technical nor clinical skills were enrolled in couples and alternatively performed the recordings on each other, simulating the roles of patient and caregiver. Results show that a Signal-to-Noise Ratio (SNR) higher that 13 dB was always achieved, even before any digital filtering. Moreover, the influence of the body structure of the patient, quantified in terms of Body Mass Index and thoracic circumference, on the quality of the signals was assessed. A moderate significant negative correlation was found, as expected, but in the overall the body structure did not prevent from obtaining reliable signals even in cases of severe overweight. We believe that the presented findings lay the foundations for the use of electro-phonocardiography in telemonitoring applications.**

***Keywords*— usability, telemonitoring, wearable sensors, electro-phonocardiography.**

I. Introduction

PHONOCARDIOGRAPHY (PCG), i.e., the digital recording of heart sounds, and electrocardiography (ECG) are two of the most widely used techniques in the clinical practice for the assessment of the health status of the heart. Due to the nature of the signals, ECG and PCG provide complementary information: whereas ECG is an expression of the electrical behaviour of the heart, PCG reflects its mechanical behaviour [1]. The combination of the two techniques enables the evaluation and monitoring of the status of the electromechanical coupling of the heart, which is difficult to obtain otherwise [2], [3]. The latter can be obtained by estimating the latency of the time of closure of the four cardiac valves in the PCG with respect to the ventricular depolarization event in the ECG [4].

The monitoring of the electromechanical coupling of the heart in a home care setting would open to a range of brand-new possibilities. One of the main possible foreseen applications is the monitoring of the status of compensation of patients affected by chronic heart failure (HF). In fact, both the quality of life and the life expectance of HF patients are mainly affected by the occurrence of acute episodes of decompensation, correlated with a deterioration of the electromechanical coupling of the heart [5], [6]. The availability of a method to timely monitor the patients at their domicile and promptly detect a worsening in their conditions could enable the prevention of the acute episodes and strongly improve the prognosis.

The use of a combination of ECG and PCG looks extremely promising for the scope. In fact, both ECG and PCG can be embedded in low-cost and portable devices, suitable for use outside a clinical setting.

The main technical challenge is posed by their usability by inexperienced users, which is an essential requirement for their application in a home care context. The main problem resides in the recording of heart sounds: it was previously proved that the positioning of the electronic stethoscope over the chest of the subject is critical to obtain a good quality signal, and the best auscultation point depends on the valve of interest [7], [8]. Finding the correct auscultation areas requires trained skills and an inexperienced user cannot be relied on performing an accurate positioning.

We propose a possible solution to the stated problem based on multi-source PCG. Instead of recording a single signal from a specific point of the chest, we propose to record multiple signals, from multiple points of the chest, with a high spatial resolution. In this way, we hypothesize that the positioning of the device can be performed by the patient or a caregiver: the algorithms will be in charge for selecting the most relevant signals, among the multiple recorded ones, for the application of interest. For the purpose, we custom designed a flexible multi-sensor array, embedding electrodes for ECG recording and multiple microphones for PCG recording.

The goal of this study is to validate our work hypothesis that the multi-sensor array is usable by inexperienced users. Moreover, we aim at proving on a sample population that the usability is not affected by the subject's body structure.

II. Materials and Methods

A. Design of the multi-sensor array

Figure 1 proposes a graphical schematic of the architecture of the multi-sensor array.

For PCG recording, the array embeds 48 electret condenser microphones (TOM-1537L-HD-R by PUI Audio), each equipped with an analog front-end for pre-amplification. The microphones are located over a surface of approximately 180 cm^2 which should roughly cover the subject's left hemithorax. The microphones have a diameter of 4 mm and the minimum distance between closest neighbours is 12 mm, to obtain a sufficiently high spatial resolution. The microphones are more

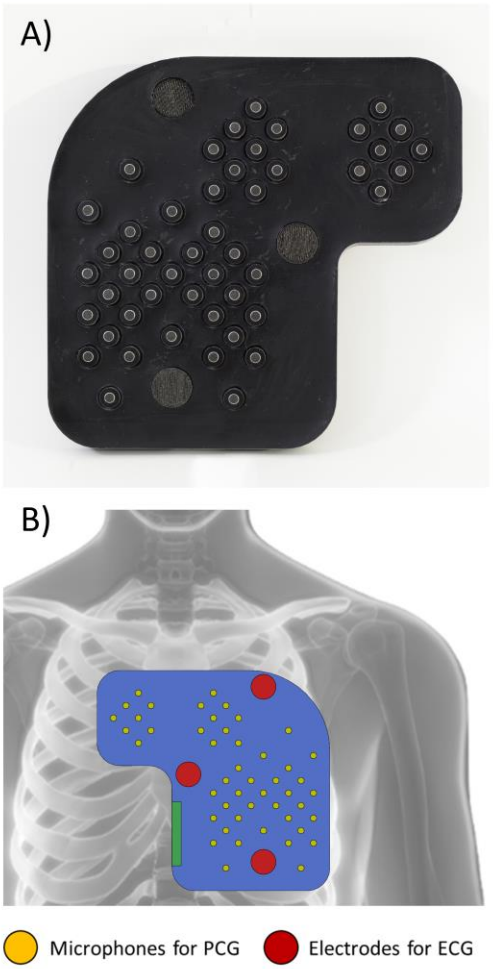


Figure 1. Picture of the designed and realized multi-sensor array (A) and schematic of its positioning over the left hemithorax of the subject.

densely located over the areas corresponding to the traditional auscultation areas. A sensitivity of -37 dB is guaranteed over the bandwidth 20 Hz to 20 kHz.

The recording of a 1-channel ECG relies on 3 custom-made electrodes in stainless steel, conditioned via the well-known Right Leg Driven circuit. The positioning of the electrodes is not critical for the application of interest, which does not involve a morphological analysis of the ECG waveform.

Electrodes and microphones, along with their front-end circuits, are soldered on a flexible PCB realized in Kapton. The flexibility of the array is a key aspect because it enables a good contact between the sensors and the surface of the chest of the subject. The contact is guaranteed by fixing the device to the thorax by means of an elastic band.

Both the ECG and PCG signals are simultaneously sampled at 1 kHz, multiplexed, and transferred to a commercial signal acquisition board (NI USB 6210 by National Instruments). This performs the A/D conversion and the acquisition through a computer, where the following analysis takes place.

B. *Experimental protocol*

The key point to validate the usability of the device in a real-life home care scenario is to have it used by inexperienced users without the help of any clinical nor technical staff. To simulate the latter scenario, we enrolled 12 couples of volunteers, for a total of 24 volunteers. Two exclusion criteria were applied:

1. no known history of cardiovascular disease;
2. no skills in auscultation.

The first criterion is meant to ensure that no pathological condition affects the analysis. In each couple, subjects were assigned the role of subject A and subject B. In the first phase, subject A played the role of the caregiver and subject B played the role of the patient. Subject A was given very simple written instructions on how to use the device (simulating a basic user manual). In the meanwhile, subject B was asked to lay on an examination table in a supine position with a bare thorax. Then, subject A was asked to position the multi-sensor array on the thorax of subject B and fix it with the elastic band. A 5-minute recording was then performed on subject B. At the end, the roles of subject A and subject B were changed, and the experiment was repeated with subject A playing the role of the patient and subject B playing the role of the caregiver. No feedback was given to the subjects concerning the correctness of the use of the device.

The experimental protocol was approved by the Research Ethics Committee of Politecnico di Torino.

C. *Signal processing and quality assessment*

The scope of signal processing is to assess and improve the quality of the heart sounds signals. The ECG signal was first filtered in the bandwidth of interest for the detection of the QRS complex. Filtering involved a moving average filter with a window length of 100 ms to remove baseline wandering, in cascade with a low-pass FIR filter with a cutoff frequency of 35 Hz. Then, the QRS complex was identified by means of a modified version of Pan-Tompkins algorithm [9] and R-waves were taken as reference for heartbeat segmentation.

Each of the 48 PCG signals was filtered with a Chebyshev I filter between 20 Hz and 100 Hz, bandwidth of the two main heart sounds. The signals were then segmented taking R-waves as reference.

The assessment of the quality of the signals was based on the Signal-to-Noise Ratio (SNR), which was computed separately for each of the two heart sounds and for each heartbeat, according to the following formula [10]:

$$SNR = 20 \log \frac{A_S}{4\,\sigma_N} \quad (1)$$

where A_S is a measure of the signal amplitude (peak-to-peak value of the heart sound of interest) and $4\,\sigma_N$ is a measure of the noise amplitude (width of the 95% band of the noise time series, extracted within the 70% and the 85% of the cardiac cycle, when no heart sound is expected to occur).

The assessment of the quality of each recording was based on the mean SNR value over the heartbeats, computed separately for each heart sound (SNR S1 and SNR S2).

D. *Evaluation of the usability*

The proposed evaluation of the usability of the device is two-folded.

On one side, the usability by inexperienced users was assessed. To achieve this, for each subject, we selected the

signal with the highest SNR and compared it to a threshold of 14 dB. The threshold was defined according to the results of a previous study [10], where we experimentally found that a SNR higher than 14 dB for the first heart sound and 13 dB for the second is sufficient to estimate the time of closure of the four cardiac valves with an uncertainty lower than the resolution of the acquisition system (1 millisecond). The metrics used to validate the usability of the device by inexperienced users is the percentage of good-quality recordings, i.e., of recordings with an above-threshold SNR.

On the other side, the usability on patients with a wide range of body structures was assessed. Three anatomical parameters were identified, which can influence the quality of the recordings, namely:

- the biological gender (male or female);
- the Body Mass Index (BMI);
- the thoracic circumference.

To evaluate if either of the abovementioned parameters influences the quality of the recording, we computed the correlation between each parameter and the SNR of the recording (separately for the first heart sound S1 and the second heart sound S2). We used the Pearson correlation coefficient to test the correlation against continuous variables (BMI and thorax circumference), and the point biserial correlation to test the correlation against categorical variables (gender).

III. Results and Discussion

A. *Characteristics of the sample population*

The sample population is composed of 24 healthy subjects who alternatively played the role of the patient and the caregiver. Concerning the gender, 12 males and 12 females were enrolled to ensure gender balance. Figure 2 presents the violin plots of the distribution of BMI and thoracic circumference, separately for female and male subjects, over the sample population.

As it can be observed, enrolled subjects presented all possible body structure from normoweight to obesity (BMI > 30 kg/cm^2). In particular, the presence of subjects with an above-average BMI and thorax circumference is particularly important, since a bigger chest volume may lead to a higher attenuation of the acoustic waves of the heart sounds and hence to signals of lower quality [11], [12]. Therefore, the sample population, despite its rather small size, can be considered representative of the overall population, and in particular of the most critical segment.

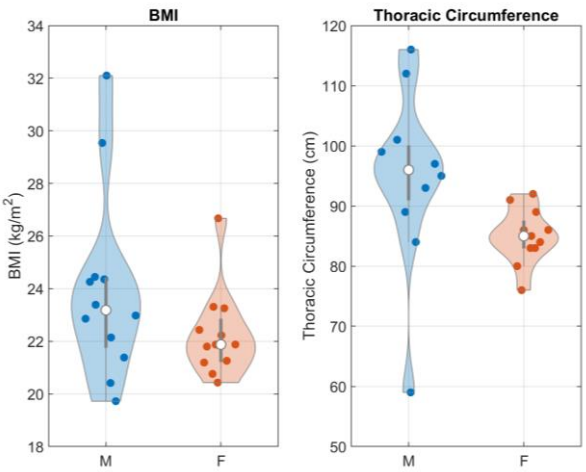


Figure 2. Violin plots of the distributions of BMI and thoracic circumference, separately for female and male subjects, over the sample population.

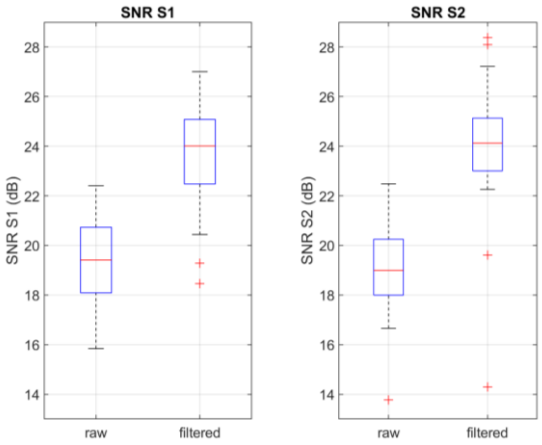


Figure 3. Boxplot of the distributions of the SNR of the recordings, separately for the first and the second heart sounds, before and after digital filtering.

B. *Usability by inexperienced users*

From a qualitative perspective, all the enrolled subjects playing the role of the caregiver could easily perform the positioning of the array according to the instructions. To evaluate if the recordings were of sufficient quality, Figure 3 shows the distribution of their SNR, computed separately for S1 and S2.

It can be observed that all the recordings achieved an SNR higher than 14 dB for S1 and 13 dB for S2, even before any digital filtering is applied. A median SNR of 24 dB was obtained after filtering, which is more than sufficient to reliably carry out any kind of processing. It can be concluded that all subjects were capable of performing a suitable positioning, regardless their inexperience.

C. *Influence of the body structure on the signal quality*

Figure 4 presents a graphical plot of the SNR of the recording in function of respectively a) biological gender, b) BMI and c) thoracic circumference.

Table I summarizes the correlation coefficients computed between each of the three anatomical features and the SNR of the heart sounds.

TABLE I: Correlation between anatomical features and SNR

Anatomical feature	*Correlation with SNR S1*	*Correlation with SNR S2*
Gender	-0.06	0.09
BMI (kg/cm^2)	-0.34	-0.50 *
Thoracic circumference (cm)	-0.38	-0.40

Correlation coefficients computed as Pearson correlation coefficients for continuous variables (BMI and thorax circumference), point biserial correlation coefficients for categorical variables (gender). The * symbol shows what correlations are statistically significant with $\alpha = 0.05$.

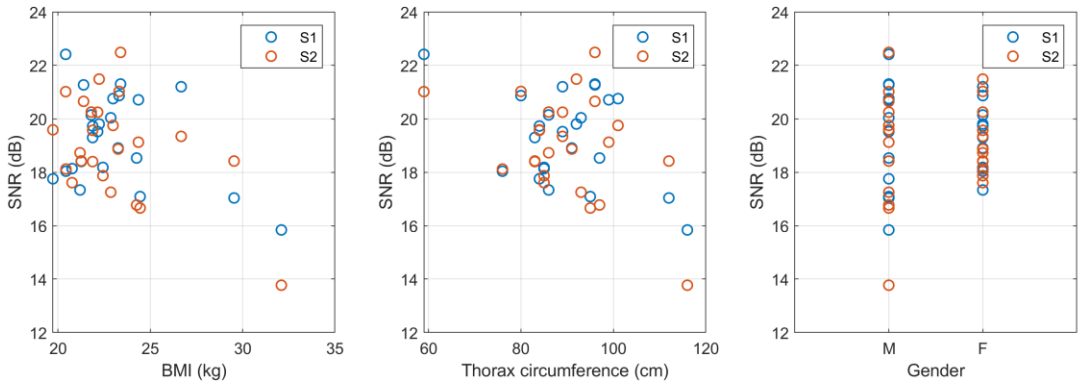


Figure 4. Signal-to-Noise Ratio of the recordings in function of the three anatomical parameters of interest, namely BMI, thorax circumference and gender.

As it can be observed, no correlation was found between the gender and the quality of the recordings. This is a relevant finding because it proves that the shape of the device allows a feasible positioning regardless different shape of the chest which characterizes males and females.

Concerning the body structure, a significant negative correlation was found between the BMI and the SNR, whereas no significant correlation was found between the thoracic circumference and the SNR. Only the correlation between the BMI and the SNR of the second heart sound was found statistically significant at $\alpha = 0.05$.

The presented findings are coherent with the hypothesis that a wider chest can be associated with a lower signal quality. Nevertheless, good-quality recordings could be obtained even with overweight subjects. We can conclude that the body structure may influence the quality of the recording, but it does not prevent the user from obtaining a good-quality recording.

In the overall, the multi-sensor array proved suitable for successfully performing electro-phonocardiography on a wide range of users with a wide range of anatomical characteristics in a simulated home care scenario.

IV. Conclusion

In this work we proposed an analysis of the usability of a multi-sensor array custom designed and realized by our research group. The multi-sensor array embeds electrodes and microphones for the combined recording of ECG and PCG signals. Its main forecasted application is the home monitoring of patients affected by chronic heart failure, or other pathologies where the electromechanical coupling of the heart is impaired. The usability by inexperienced users is critical for the application of interest and distinguishes our proposed device from other available technological solutions.

Our findings demonstrate that users with no technical nor clinical skills can easily use the device and carry out good-quality recordings. In particular, the SNR of the recordings performed by 24 volunteers proved higher than the required SNR for the estimation of the time of closure of the cardiac valves. Moreover, even though a moderate significant negative correlation was found between the body structure of the patients and the quality of the recordings, a high BMI and/or thoracic circumference did not prevent the user from the possibility of obtaining good-quality signals.

The promising findings presented in this work constitute a preliminary validation of the usability of the device in a home care context by the patient or a caregiver. Based on them, a validation on a larger population (including patients affected by a variety of pathologies) will be object of future work. We believe that the availability of a device directly usable by the patients lay the foundations for the application of electro-phonocardiography in telemonitoring in the near future.

References

[1] Y. N. Wen, A. P. W. Lee, F. Fang, C. N. Jin, and C. M. Yu, “Beyond auscultation: Acoustic cardiography in clinical practice,” *Int. J. Cardiol.*, vol. 172, no. 3, pp. 548–560, 2014.

[2] P. Dehkordi *et al.*, “Comparison of Different Methods for Estimating Cardiac Timings: A Comprehensive Multimodal Echocardiography Investigation,” *Front. Physiol.*, vol. 10, no. August, pp. 1–11, 2019.

[3] K. Tavakolian, “Systolic Time Intervals and New Measurement Methods,” *Cardiovasc. Eng. Technol.*, vol. 7, no. 2, pp. 118–125, 2016.

[4] N. Giordano and M. Knaflitz, “A novel method for measuring the timing of heart sound components through digital phonocardiography,” *Sensors (Switzerland)*, vol. 19, no. 8, pp. 1–16, 2019.

[5] J. Shitara *et al.*, “Temporal changes of cardiac acoustic biomarkers and cardiac function in acute decompensated heart failure,” *ESC Hear. Fail.*, vol. 8, no. 5, pp. 4037–4047, 2021.

[6] S. Hu *et al.*, “Model Embraced Electromechanical Coupling Time for Estimation of Heart Failure in Patients With Hypertrophic Cardiomyopathy,” *Front. Cardiovasc. Med.*, vol. 9, no. June, pp. 1–11, 2022.

[7] X. Bao, Y. Deng, N. Gall, and E. N. Kamavuako, “Analysis of ECG and PCG time delay around auscultation sites,” *BIOSIGNALS 2020 - 13th Int. Conf. Bio-Inspired Syst. Signal Process. Proceedings; Part 13th Int. Jt. Conf. Biomed. Eng. Syst. Technol. BIOSTEC 2020*, no. Biostec, pp. 206–213, 2020.

[8] J. Fontecave-Jallon, K. Fojtik, and B. Rivet, “Is there an Optimal Localization of Cardio-microphone Sensors for Phonocardiogram Analysis?,” *2019 41st Annu. Int. Conf. IEEE Eng. Med. Biol. Soc.*, pp. 3249–3252, 2019.

[9] J. Pan and W. J. Tompkins, “A Real-Time QRS Detection Algorithm,” *IEEE Trans. Biomed. Eng.*, vol. BME-32, no. 3, pp. 230–236, 1985.

[10] N. Giordano, S. Rosati, and M. Knaflitz, “Automated assessment of the quality of phonocardographic recordings through signal-to-noise ratio for home monitoring applications,” *Sensors*, vol. 21, no. 21, 2021.

[11] B. S. Larsen, S. Winther, M. Bølttcher, L. Nissen, J. Struijk, and S. E. Schmidt, “Correlations of first and second heart sounds with Age, Sex, and Body Mass Index,” *Comput. Cardiol. (2010).*, vol. 44, pp. 1–4, 2017.

[12] D. H. Lee, J. H. Seo, and R. Mittal, “Quantifying the Effect of Body Habitus on Cardiac Auscultation Via Computational Hemoacoustics,” *J. Biomech. Eng.*, vol. 145, no. 2, pp. 1–8, 2023.

Physiologically relevant in vitro experiments: degradation kinetics of a pool of enzymes

C. Oldani[1,2], N. Bono[1], A. Caldiroli[2], S. A. Riboldi[2] and G. Candiani[1]

[1]*genT_LAB, Department of Chemistry, Materials and Chemical Engineering "G. Natta", Politecnico di Milano, Milan, Italy.*
[2]*Dialybrid S.r.l., Cantù, Italy*

***Abstract*—The validation of a new biodegradable medical device requires the evaluation of its degradative profile. *In vitro* degradation tests are a useful tool to do so, but their protocol needs adequate justification. We propose a method to evaluate the enzymatic degradation kinetics of an enzyme mixture designed to degrade a semi-degradable vascular graft in quasi-physiological conditions.**

***Keywords*—bioresorbable medical device, *in vitro* degradation, enzymatic activity.**

I. Introduction

The use of biodegradable medical devices, meant to be safely absorbed by the body after fulfilling their intended purpose, is becoming increasingly relevant in biomedical research and implantable medical devices' production in particular [1], [2]. Biodegradable medical devices are employed in passive physical support for tissue repair and/or regeneration, e.g., in suture threads, surgical meshes, orthopedic fixation devices, biodegradable stents, and tissue scaffolds [3], [4]. In the case of biodegradable devices, the host response that generally follows implantation is additionally greatly affected by the degradation kinetics of the material composing the device. In particular, by the inflammatory events at the host–implant interface and the degradation products released during the life-cycle of the device [1]. To design a biodegradable device that is functional, but most of all safe, an in-depth understanding of this degradation process and a characterization of the degradation products' release kinetic are needed.

The topic of biodegradation is extensively treated in literature and several methods to test it *in vitro* were proposed, while, on the regulation side, ISO 10993-13:2010 constitutes a standard for the design of *in vitro* degradation tests [5]-[7]. However, since biodegradation is determined by environmental factors, the conditions in which the test is carried out are crucial. In the case of enzymatic degradation tests, non-human enzymes are often used in literature and are proposed as the standard to model hydrolytic mechanisms, e.g., protease XIV, proteinase K, and papain [6]. Additionally, even when human-origin enzymes are used, the concentration used is highly variable in the literature and may be significantly higher than the physiological one. Finally, a crucial factor like the refresh rate of the degradation medium is not regulated and is not always justified in literature. This aspect of the protocol design constitutes a key parameter because the enzyme activity levels should be high enough to steadily degrade the device. In fact, when designing an enzymatic degradation experiment, the activity of the enzymes used can be even more relevant than their concentration. Phenomena such as thermal degradation, aggregation, lysis, and autolysis can alter the enzymes' activity without affecting the protein content. Moreover, the enzymes' activity *in vivo* is further regulated by the presence of physiological inhibitors and proenzymes' activators. For example, in the case of metalloproteinases (MMPs), enzymes that play a key role in wound healing, angiogenesis, and/or fibrotic capsulation of the materials [8], their activity is regulated through the secretion of tissue inhibitors of MMPs (TIMPs) [9], [10].

In light of the above, in this study, we seek to evaluate the enzymatic degradation kinetics of a pool of human-origin enzymes chosen for the degradation of a biodegradable medical device mainly composed of silk fibroin, in physiological conditions, i.e., in the human vascular compartment. Since we sought to characterize the effectiveness of the enzymatic mixture, enzymatic activity and decay were eventually studied using commercially available enzyme activity assays.

The use of a mixture of enzymes is what makes this *in vitro* setup closer to physiological conditions, but the interaction between the different enzymes can potentially alter their activity. We herein describe a methodology to develop an enzymatic mixture in which every enzyme presents the same level of activity in order to easily follow the general activity decay over time. Since the enzyme concentration correlates to the activity measured, enzymes' physiological concentrations were considered, at least initially, as the target ones.

II. Materials and Methods

A. Materials

MMP1, MMP3, MMP9, Chymotrypsin, and Lysozyme were purchased from Merck Life Science (Milan, Italy). MMP activity assay kit (ab112146) and Lysozyme assay kit (ab211113) were purchased from Abcam (Cambridge, UK).

B. Measurement of enzymes' activities

Preliminary studies showed that the MMPs substrate could be used to correctly detect Chymotrypsin activity, thus MMP activity assay kit was used to measure the activity of MMP1, MMP3, MMP9, and Chymotrypsin, while the Lysozyme activity assay kit was used exclusively for Lysozyme.

Each enzyme was first resuspended in Phosphate Buffer Saline (PBS) and tested at different concentrations with the corresponding substrate according to the manufacturer's instructions with slight variations. Briefly, the MMPs and Lysozyme substrates were thawed to room temperature (RT) in the dark, diluted 1:100 and 1:16, respectively, in the specific assay buffer, and vortexed. Substrate control and background control wells were filled with PBS and PBS diluted in assay buffer respectively. Sample wells were filled with each enzyme's dilutions in PBS. Diluted substrates were added to the corresponding sample wells and substrate control wells only right before the measurement.

The activity kinetics was assessed over 1 hr at 37 °C (readings every 5 min) by measuring the fluorescence using a microplate reader (Synergy H1, BioTek, USA). According to the substrate used, the following wavelengths were used: λ_{EX} = 490 nm, λ_{EM} =525 for MMPs substrate and λ_{EX} =360 nm, λ_{EM} =445 nm for Lysozyme substrate.

The quantification of the enzyme activity was, thus, obtained considering the first linear part of the progression curve (generally 30 min - 1 hr), both in terms of the fluorescence emitted at a given time point, expressed in terms of Relative Fluorescence Units (RFUs), and by the velocity of the reaction, expressed in RFU/min. The slope of the linear part of the fluorescence *vs.* time plots was obtained from the linear regression of the values of the first 30 min using GraphPad Prism software.

C. *Effect of temperature on enzyme activity*

To assess the effect of temperature on enzymes activity, an enzymes solution containing MMP-1 (1 µg/mL), MMP-3 (2 µg/mL), MMP-9 (0.4 µg/mL), chymotrypsin (0.05 µg/mL), and lysozyme (20 µg/mL) (hereinafter referred to as enzymes cocktail) was prepared into a 1.5 mL Eppendorf tube and mixed thoroughly with a pipette.

The obtained enzymes cocktail was split into 3 vials and incubated at 3 different temperatures: i) 4 °C, ii) 25 °C (room temperature, RT), and iii) 37 °C under shaking (300 rpm) in a thermomixer for 72 hrs. Following incubation, enzyme activity was evaluated with the 2 substrates as described hereinabove (section II.B) at the corresponding wavelengths.

The activity of the untreated enzyme cocktail was considered a positive control of activity (100 %).

D. *Enzyme inactivation over time*

The enzyme cocktail was prepared in a 1.5 mL Eppendorf tube and mixed thoroughly with a pipette.

The activity measurements were performed after incubation at 37 °C under shaking (300 rpm) in an Eppendorf Thermomixer.

The experiment was iterated multiple times with the following time points: 0, 4, 24, 48, 96, and 168 hrs.

The activity measurements were performed as described in section II.B using both substrates.

The activity of the untreated enzyme cocktail was considered a positive control of activity (100 %).

As a negative control of activity (0 % enzyme activity), the enzymatic mixture was heated at 100 °C for 30 min and subsequently centrifuged for 3 min to obtain the enzymes' denaturation.

Curve fitting on activity decay over time graphs was performed using GraphPad Prism software.

E. *Statistical analysis*

Statistical analysis was carried out with GraphPad Prism software. Comparisons among the three different temperature conditions and positive control of activity were performed by the two-way analysis of variance (ANOVA). Statistical significance was retained when the p-value < 0.05.

III. Results and Description

A. *Design of same level activity enzyme mixture*

The interaction between each enzyme and the MMPs substrate was enzyme-specific. Among them, MMP-9 activity was significantly higher than the others. Therefore, in the enzyme mixture at their physiological concentrations, the MMP-9 activity would conceal any other MMPs and Chymotrypsin (Fig. 1).

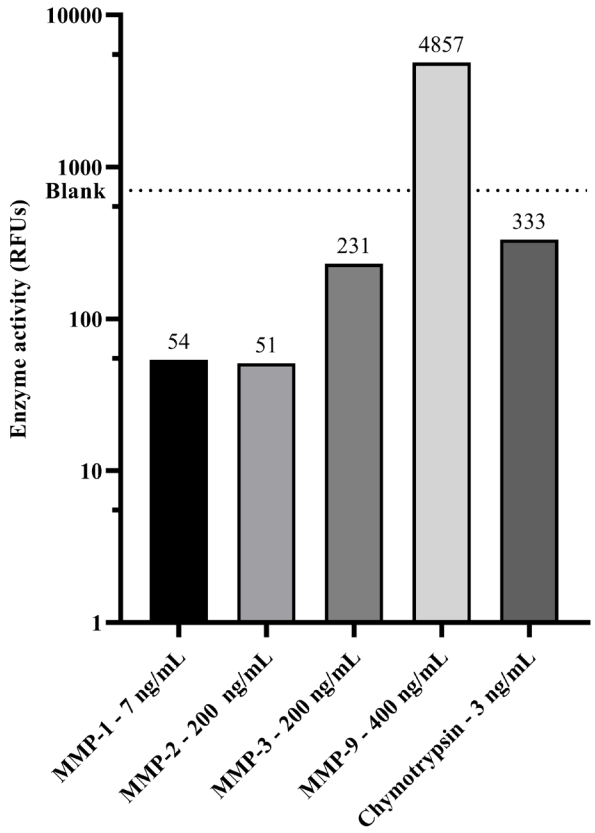


Figure 1: Graph representing the enzymes activity at their physiological concentrations in terms of fluorescence emitted after 30 min (RFU). Among the four enzymes analyzed, MMP9 activity was clearly detectable and produced a fluorescence signal of almost 5000 RFU. Instead, concerning the other three enzymes, their signal was below that of the blank. In particular, MMP-1 activity at its physiological concentration was hardly distinguishable from the blank.

Considering the above results, the MMPs and Chymotrypsin concentrations were purposely varied to give an equal contribution to the overall activity of the enzyme pool. More in detail, as MMP-9 showed the highest activity at its physiological concentration, we decided to increase the concentration of any other enzyme to obtain the same activity level. Enzymes' concentrations were tuned in order to enable an activity level of approximately 4,000 RFU after 30 min, corresponding to the activity of MMP-9. Of note, this value differed sharply from the blank (≈ 700 RFU) and was high enough to monitor the kinetics over time of all the enzymes together.

Concerning Lysozyme, since its activity was detectable at its physiological concentration, this was the concentration selected to carry out the following experimentation.

The final enzymes' concentrations are reported in Table I and compared to the physiological ones [12]-[17].

TABLE I: ENZYMES' CONCENTRATIONS

Enzyme	*Physiological concentration*	*Concentration in same level activity mixture*
MMP-1	7 ng/mL	1 µg/mL
MMP-3	200 ng/mL	2 µg/mL
MMP-9	400 ng/mL	400 ng/mL
Chymotrypsin	3 ng/mL	50 ng/mL
Lysozyme	20 µg/mL	20 µg/mL

Enzymes' physiological concentration and working concentrations of any enzyme in the mixture on the MMP-9 activity.

B. *Effect of temperature on enzymes' activity*

The residual activity of MMPs, chymotrypsin, and lysozyme after a 72 hr-storage at different temperatures is shown in Figure 2. The enzymes' activity of every condition considered resulted to be significantly different from the positive control of 100 % activity. Of note, lysozyme activity decreased over time irrespective of the storage temperature, as at the end-point the residual activity was invariably close to 60 %. On the other hand, the residual activity of MMPs and chymotrypsin in the enzyme cocktail incubated at RT and 37 °C was invariably 30 %, while, when stored at 4 °C, the residual activity of MMPs and chymotrypsin was of 50 %.

Overall, such results demonstrated that the storage temperature plays a significant role in MMPs and chymotrypsin activity, whereas it is less relevant for the maintenance of lysozyme activity.

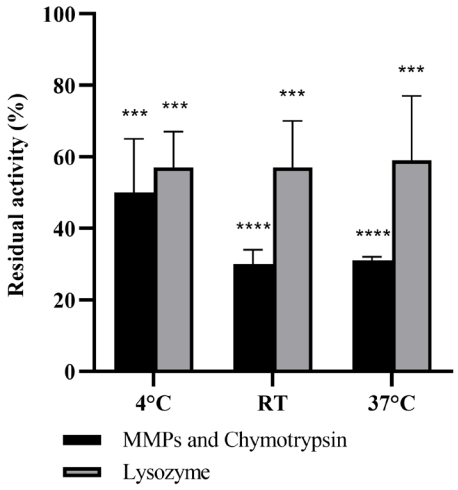


Figure 2: Residual activity of MMPs, Chymotrypsin, and Lysozyme after 72 hrs stored at 4°C, RT and 37 °C. ***p< 0.001, ****p < 0.0001 between every condition and positive control (100 % activity) (two-way ANOVA).

C. *Enzyme inactivation over time - Lysozyme*

The time-dependent decrease of lysozyme's activity is shown in Fig. 3. A one-phase decay curve was fitted to the data obtained suggesting a monophasic inactivation behavior. Following a burst decrease during the first hours of incubation, the enzyme's activity reaches a plateau at approximately 70% of residual activity.

Since it was shown that the activity of this enzyme decreased irrespective of the storage temperature, the lysozyme inactivation might have been caused by the interaction with another enzyme present in the mixture and, thus, by enzyme-induced cleavage. Of note, lysozyme is a known substrate for chymotrypsin [18].

The negative control showed no activity when tested with lysozyme substrate, demonstrating that the residual activities shown here above were not an artifact.

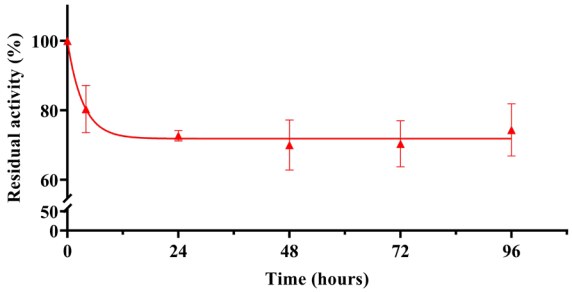


Figure 3: Residual activity over time of the lysozyme in the enzymatic mixture. After a sudden decrease during the first hours of incubation, the residual activity followed a one-phase decay and plateaued at 70 %.

D. *Enzyme inactivation over time – MMPs and Chymotrypsin*

Differently from the decay of Lysozyme, the MMPs and Chymotrypsin combined activity followed a biphasic inactivation behavior (Fig. 4). In fact, after a similarly abrupt decrease in the first hours of incubation, the residual activity further decreased until 30 %. This could be due to the fact that the MMPs substrate was used to observe the inactivation of four enzymes at the same time. Since different mechanisms are involved in this phenomenon, i.e., thermal denaturation, auto-, and cross-hydrolysis, it is reasonable that they elicit a different, time-dependent effect on the enzymatic pool activity. In particular, one acts extremely fast in the very first part of the curve, while the other is slower, resulting in a nearly linear decrease. Moreover, it is important to consider that it was already demonstrated how storage temperature significantly affects MMPs and Chymotrypsin activity.

As for the Lysozyme substrate, the negative control showed no activity when tested with the MMPs substrate.

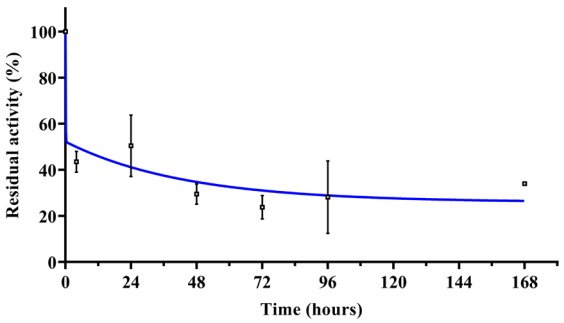


Figure 4: Residual activity over time of the MMPs and Chymotrypsin in the enzymatic mixture. A two-phase decay curve was fitted with GraphPad Prism

to the data obtained. After a sudden decrease during the first hours of incubation, the enzyme's activity slowly decreases until 30 % of residual activity.

IV. Conclusion

The methodology proposed permits easy following the general activity decay over time of a mixture of enzymes designed for the *in vitro* physiological degradation of a medical device. The protocol was developed to evaluate the biodegradation of Dialybrid's Silkothane® Arteriovenous Graft (SAG) a semi-degradable electrospun device manufactured from a new hybrid (natural/synthetic) material, which is a combination of silk fibroin (SF, a biodegradable protein found in silk) and polyurethane (PU, a non-degradable polymer) [19], [20].

Considering the medical device's final purpose, the proposed cocktail was composed through the selection of the enzymes that are known to hydrolyze SF and are present in the human vascular district. Regarding the physiological conditions mentioned in this study, they referred, when available, to renal pathological conditions.

The experimental setup presented represents the worst-case scenario in terms of enzymes' auto-lysis and cross-lysis. First, the increased concentration, with respect to physiological levels, could potentially exacerbate these phenomena [21], [22]. Secondly, an *in vitro* degradation study would obviously be performed in the presence of the graft, which represents a substrate for the enzymes, thus reducing the opportunity for the auto- and cross-lytic process to occur [23], [24]. Nevertheless, even in these conditions, the activity of the enzyme pool was sufficiently high to be detected after 1 week.

The results showed that enzyme cocktail activity decreased significantly in the very first hours of incubation at 37 °C and gradually diminished thereafter. In this light, it is reasonable that in a future degradation experiment, a replacement of the enzyme pool once per week would ensure the degradation of the graft in the long run.

In order to correlate the results obtained *in vitro* with those coming from an *in vivo* study in large animal, the *in vitro* degradation study will last 6 months and include intermediate time points. Large animal models are best for the *in vivo* evaluation of a novel vascular graft and 6 months represent an adequate follow-up time considering the application [25], [26].

References

[1] C. Li et al., "Design of biodegradable, implantable devices towards clinical translation," *Nat. Rev. Mater.*, vol. 5, no. 1, Art. no. 1, Jan. 2020

[2] D. Kai, S. S. Liow, e X. J. Loh, "Biodegradable polymers for electrospinning: Towards biomedical applications," *Materials Science and Engineering: C*, vol. 45, pp. 659–670, Dec. 2014

[3] S. Cassese et al., "Everolimus-eluting bioresorbable vascular scaffolds versus everolimus-eluting metallic stents: a meta-analysis of randomised controlled trials," *Lancet Lond. Engl.*, vol. 387, no. 10018, pp. 537–544, Feb. 2016.

[4] K. S. Devi and P. Vasudevan, "Absorbable Surgical Sutures," *J. Macromol. Sci. Part C*, vol. 25, no. 3, pp. 315–324, Aug. 1985, doi: 10.1080/07366578508081959.

[5] R. L. Horan et al., "In vitro degradation of silk fibroin," *Biomaterials*, vol. 26, no. 17, pp. 3385–3393, Jun. 2005.

[6] [5] C. Guo, C. Li, and D. L. Kaplan, "Enzymatic Degradation of Bombyx mori Silk Materials: A Review," *Biomacromolecules*, vol. 21, no. 5, pp. 1678–1686, May 2020.

[7] *Biological evaluation of medical devices - Identification and quantification of degradation products from polymeric medical devices,* ISO Standard 10993-13, 2010.

[8] Y. Kambe and T. Yamaoka, "Initial immune response to a FRET-based MMP sensor-immobilized silk fibroin hydrogel in vivo," *Acta Biomaterialia*, vol. 130, pp. 199–210, Aug. 2021.

[9] A. H. Baker, D. R. Edwards, and G. Murphy, "Metalloproteinase inhibitors: biological actions and therapeutic opportunities," *Journal of Cell Science*, vol. 115, no. 19, pp. 3719–3727, Oct. 2002.

[10] B. Elsässer and P. Goettig, "Mechanisms of Proteolytic Enzymes and Their Inhibition in QM/MM Studies," *International Journal of Molecular Sciences*, vol. 22, no. 6, Art. no. 6, Jan. 2021

[11] D. H. Manicourt, N. Fujimoto, K. Obata, and E. J. Thonar, "Serum levels of collagenase, stromelysin-1, and TIMP-1. Age- and sex-related differences in normal subjects and relationship to the extent of joint involvement and serum levels of antigenic keratan sulfate in patients with osteoarthritis.," *Arthritis Rheum.*, vol. 37, no. 12, pp. 1774–83, 1994.

[12] E. Rodrigo et al., "Circulating levels of matrix metalloproteinases MMP-3 and MMP-2 in renal transplant recipients with chronic transplant nephropathy," *Nephrol. Dial. Transplant.*, vol. 15, no. 12, pp. 2041–2045, 2000.

[13] M. Lehrke et al., "MMP-1 serum levels predict coronary atherosclerosis in humans," *Cardiovasc. Diabetol.*, vol. 8, p. 50, 2009.

[14] E. Cavusoglu et al., "Relation of baseline plasma MMP-1 levels to long-term all-cause mortality in patients with known or suspected coronary artery disease referred for coronary angiography," *Atherosclerosis*, vol. 239, no. 1, pp. 268–275, 2015.

[15] K. Pawlak, M. Mysliwiec, and D. Pawlak, "Peripheral blood level alterations of MMP-2 and MMP-9 in patients with chronic kidney disease on conservative treatment and on hemodialysis," *Clin. Biochem.*, vol. 44, no. 10–11, pp. 838–843, 2011.

[16] D. J. Prockop and w. D. Davidson, "A study of urinary and serum lysozyme in patients with renal disease.," *N. Engl. J. Med.*, vol. 270, pp. 269–274, Feb. 1964.

[17] S. H. Bharmal et al., "Relationship between circulating levels of pancreatic proteolytic enzymes and pancreatic hormones," *Pancreatology*, vol. 17, no. 6, pp. 876–883, 2017.

[18] L. Derr et al., "Assessment of the Proteolytic Activity of α-Chymotrypsin Immobilized on Colloidal Particles by Matrix-Assisted Laser Desorption Ionization Time-of-Flight Mass Spectrometry", *Anal. Lett.*, vol. 48, fasc. 3, pp. 424–441, Feb. 2015.

[19] S. van Uden et al., "Electrospun fibroin/polyurethane hybrid meshes: Manufacturing, characterization, and potentialities as substrates for haemodialysis arteriovenous grafts," *Journal of Biomedical Materials Research Part B: Applied Biomaterials*, vol. 107, no. 3, pp. 807–817, 2019.

[20] S. van Uden et al., "A novel hybrid silk-fibroin/polyurethane three-layered vascular graft: towards in situ tissue-engineered vascular accesses for haemodialysis," *Biomed Mater*, vol. 14, no. 2, p. 025007, Jan. 2019.

[21] Y. Kawamura, K. Nakanishi, R. Matsuno, and T. Kamikubo, "Stability of immobilized α-chymotrypsin," *Biotechnol. Bioeng.*, vol. 23, no. 6, pp. 1219–1236, 1981.

[22] S. Ray, P. Lukyanov, and J. Ochieng, "Members of the cystatin superfamily interact with MMP-9 and protect it from autolytic degradation without affecting its gelatinolytic activities," *Biochim. Biophys. Acta BBA - Proteins Proteomics*, vol. 1652, no. 2, pp. 91–102, Dec. 2003.

[23] S. Mole and P. G. Waterman, "Tannic acid and proteolytic enzymes: Enzyme inhibition or substrate deprivation?," *Phytochemistry*, vol. 26, no. 1, pp. 99–102, Dec. 1986.

[24] R. P. Guttmann, J. S. Elce, P. D. Bell, J. C. Isbell, and G. V. W. Johnson, "'Oxidation Inhibits Substrate Proteolysis by Calpain I but Not Autolysis," *J. Biol. Chem*., vol. 272, no. 3, pp. 2005–2012, Jan. 1997.

[25] M. Kokozidou et al., "Vascular access animal models used in research," *Ann. Anat. - Anat. Anz.*, vol. 225, pp. 65–75, Sep. 2019.

[26] S. E. Koch et al., "Animal studies for the evaluation of in situ tissue-engineered vascular grafts — a systematic review, evidence map, and meta-analysis," *Npj Regen. Med*., vol. 7, no. 1, Art. no. 1, Feb. 2022.

Multiscale Modelling of Platelet Activation in Membrane Oxygenation Systems

M. Baccarella[1], and S.Pasta[1,2]
[1]*Dipartimento di Ingegneria, viale delle Scienze Ed.8, University of Palermo, Palermo, Italy*
[2]*Department of Research, IRCCS ISMETT via Tricomi, 5, Palermo, Italy*

***Abstract*— One of the most common cause of failure in oxygenator systems consist of the thrombogenic risk associated with the interaction between the blood and the engineering material. For this reason, the use of membrane oxygenators is restricted to only 2-4 weeks in the extracorporeal membrane oxygenation system (ECMO). Using computational fluid dynamics, this study aims to investigate the mechanisms underlying the shear-mediated platelet activation in an oxygenation system. This was accomplished by first developing a multiscale model for the oxygenator system, followed by the estimation of the thrombogenic risk by mathematical modelling. High values of particle stress were found at inlet and outlet of blood flow. Computational flow analysis has revealed important insights into the thrombogenic mechanisms, suggesting that numerical analysis can be an effective tool to improve the design of oxygenator systems and reduce the time-to-market and animal trials.**

***Keywords*—computational fluid dynamic, oxygenation systems, ECMO, thrombogenic risk.**

I. Introduction

The oxygenation system is the main component of extracorporeal membrane oxygenation system (ECMO) and artificial lungs [1-4]. In particular, the oxygenator is the artificial lung of the heart-lung machine and substitutes the biological function of the alveolar membrane, adding oxygen and removing carbon dioxide from the blood. A heat exchanger is usually coupled with the oxygenation system to lead hypothermia to the patient, maintain the correct temperature of the blood's patient and also slow down her/his metabolism to reduce blood and nutrients contribution to tissues. Both oxygenator and heat exchanger are composed by polymeric hollow-fibres membrane, usually polyethylene (PE) or polypropylene (PP).

Computational fluid dynamic (CFD) methods can be used to improve the design process of cardiopulmonary devices such as artificial lung for adult [5] and paediatric patients[6], heart valves [7, 8], ventricular assist device [9-12]. There is however a lack of knowledge in the computational haemodynamic of oxygenator systems. One of the major challenge in the design of oxygenator is represented by the flow-mediated platelet activation at the basis for thrombogenic mechanisms and ultimately device failure. Shear stress is a well-recognized mediator of thrombosis and haemolysis, with physiological values ranging from 0.1 Pa to 10 Pa [13, 14]. The presence of artificial surfaces and hemodynamic disturbances are predisposing factors for thrombosis in oxygenator systems [15]. At the present, the utilize of pharmacological treatments based on anticoagulants and surface-treatment strategies of materials exposed to blood flow are the best options to decrease the risk of thrombosis. However, the flow-mediated mechanism is a complex multifactorial and multilevel mechanisms occurring at different time scale and length [15]. In-vivo animal modelling and in-vitro bench tests may shed insights into the mechanisms underlying the platelet activation. Computational modelling can potentially reduce the need for animal testing and accelerate innovation leading to safer more cost-effective oxygenator devices.

This study aims to understand the flow-induced mechanisms of platelet activation by quantifying the blood cell stress in two commercial oxygenators used for ECMO therapy. Specifically, we developed a multiscale computational fluid dynamic (CFD) model to compute the microscale haemodynamic and then combine the velocity with a macroscale quantifications. The resulting flow parameters were used to quantify the platelet-like stress history and the damage accumulation using a mathematical model.

II. Materials and Methods

Geometric model of oxygenators was developed in the CAD software ANSYS SpaceClaim (ANSYS Inc, Canonsburg, PA, USA) using dimensions from reverse engineering of the original devices (see Figure 1). Two device models (namely A and B) were investigated.

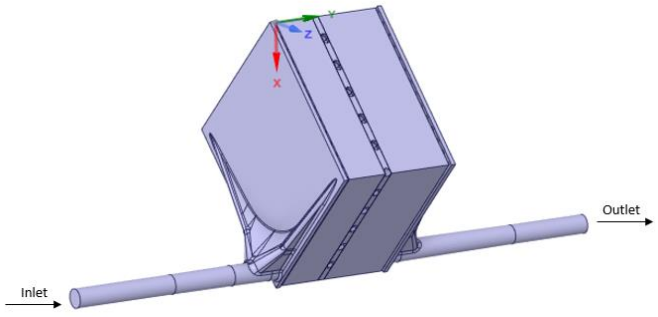


Figure 1: Investigated oxygenators named device (A) and device (B)

For the microscale analysis, the elementary cell unit was obtained considering the orientation, size and fiber package distribution as seen on the oxygenator device. Computational models were developed so that each device had two microscale models. The first one is representative of the flow inlet where the oxygenator cell is followed by heat exchanger cell. The second model considers only the oxygenator cells (see Figure 2)

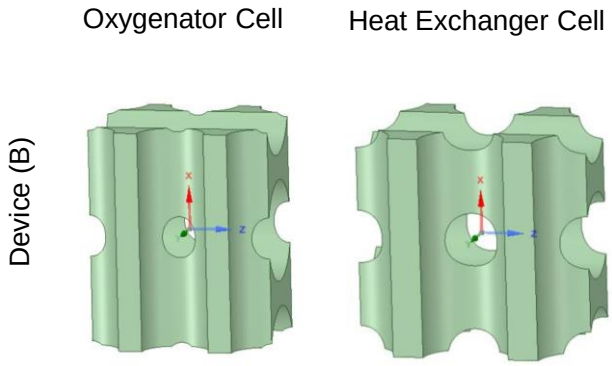


Figure 2: Elementary cell unit for device (A) and device (B)

Both macroscale and microscale simulations were performed with FLUENT (ANSYS Inc, Canonsburg, PA, USA). For the element mesh, we considered n.30 elements for the fiber cell unit while the macroscale models had maximum surface skewness of 0.7 for nearly 4-milion of unstructured tetrahedral elements. The blood was assumed as a Newtonian fluid under laminar flow condition using density of 1052 kg/m^3 and viscosity of 0.00236 Pa×s as done for other studies [16-18]. For the solver, the SIMPLE methods for pressure-velocity coupling with second order upwind scheme was adopted to solve the steady-state Navier-Stokes equations. Microscale simulations were carried out using periodic flow boundary conditions and symmetric flow conditions to account for the presence of surrounding fibers. The mass flow of the elementary cell was calculated from the total device flow of 5 l/min, the inlet area, the ratio of superficial flow velocity and volumetric porosity. Then, the mass flow were imposed as a boundary condition for the cell unit, and the flow dynamic was therefore computed. The solution was used to extrapolate the pressure gradient across the cell unit and thus calculate the anisotropic porosity using the Darcy's law. This allowed us to calculate the boundary inflow and outflow conditions for the macroscale model. Specifically, we imposed a mass flow of 0.087 kg/s at the inlet while a zero-pressure condition was imposed at outflow. Though a turbulence model may result inaccurate and may not influence the blood particle motion, macroscale simulations were carried out using the SST-kϖ turbulence model After solution convergence, a discrete phase model (DPM) with particle tracking to mimic the presence of platelets was carried out. After convergence analysis, a total of n.700 particles with diameter of 3 μm and density of 998 kg/m^3 were considered. To compute the platelet activation state (PAS), the scalar stress history acting on each simulated particle in the oxygenator domain was computed using user-defined-functions. Since simulations included both laminar and turbulent flows, two different UDFs were used to calculate both laminar and turbulent stress using the Boussineq hypothesis.

III. Results

Figure 3 shows flow streamlines and pressure drop for the oxygenator devices, respectively. The device had a pressure drop similar to that of experiments (ie, 50 mmHg).

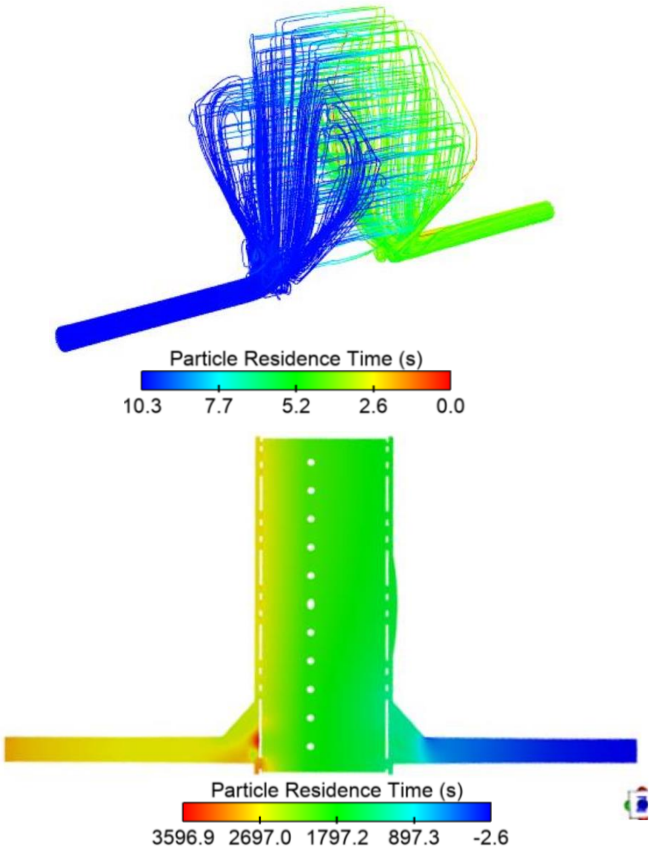


Figure 3 flow streamline as a function of particle residence time and pressure drop for the device A and B

Stress tensor components were used to calculate the total laminar scalar stress and the total turbulent scalar stress acting on each particle using the formulation suggested by Apel et al. [19]. The profile of the variability of particle scalar stress from low (blue lines) to high (green lines) magnitude was computed (Figure 4). Particles with no scalar stress are also shown (red lines).

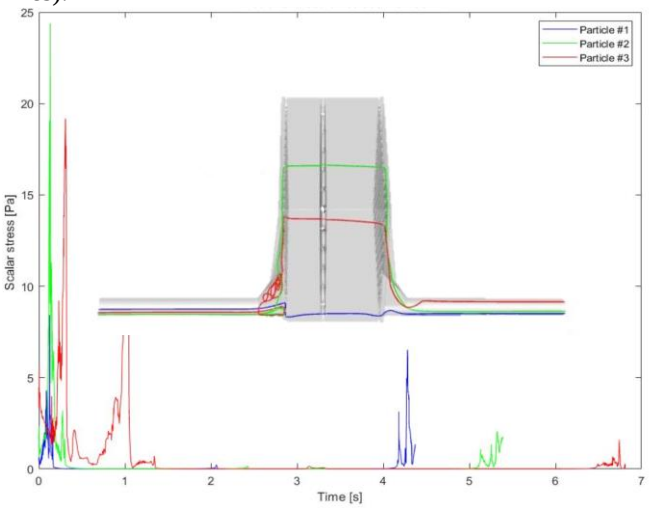


Figure 4: Particle stress as a function of time

Once both the micro- and macroscales were integrated and the particle loading history evaluated, the thrombogenic risk was analyzed using several mathematical models to predict blood damage in terms of platelet activation from the scalar stress and exposure time acting on the platelets. The platelet

activation models considered in this analysis, namely that of Nobili, Soares and Sheriff, are explained in detail in multiple papers [20-23]. Nobili's model [20] for platelet activation uses the PAS metric as dependent variable. PAS is a parameter that varies between 0 and 1 for a population of platelets. "Zero" implies no activated platelets and "One" implies full activation of the platelet population. Both Soares et al. [22] and Sheriff et al. [21] models includes the effects of non-steady stress that may act on the platelets. Thus, Figure 5 shows the boxplot of PAS for the oxygenators systems.

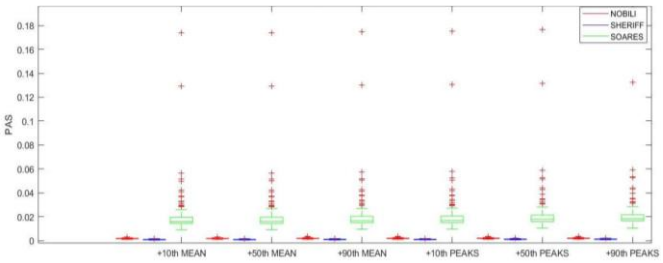


Figure 5: Boxplot of PAS for device (A) and device (B); mean and peak values are shown at 10th, 50th and 90th percentile

IV. Discussion

The aim of this work was to analyze the hemodynamic performance and thrombogenic potential of two commercial oxygenator systems using computational fluid dynamic. Flow analyses allowed us to quantify the flow pattern and pressure drop across the oxygenators. Predictions of the pressure drop were found in agreement with in-vitro data (result not shown). In a different way, the computational analysis overestimated the predicted permeability of porous fiber as compared to in-vitro data. The scalar stress was used to estimate the blood damage and the location where particles are highly stressed. The assessment of scalar stress are fundamental to improve the performance of the oxygenators. The high the scalar stress is, the lower the device permeability is. Using DPM, we computed the thrombogenic risk by computing the platelet activation with several mathematical models. We demonstrated that the Soares et al. [22] model leads to high values of PAS when compared to the mean and peak values estimated by Sheriff et al. [21] and Nobili et al. [20] models. This study extends the use of computational flow simulations to optimize the hemodynamic performance of oxygenators and evaluate their thrombogenic risk.

Despite the abundance of studies on computational flow analysis for assessing the design of cardiopulmonary devices such as heart valves [24, 25], VAD [9-11] and endograft [26], there is limited literature on the mechanical factors initiating platelet activation and thus thrombus formation in oxygenators. Gartner et al. [15] demonstrated that low velocity regions qualitatively matched regions with a high incidence of thrombotic deposition. The computational analysis was however limited to a 2D investigation and not considering the microscale effects. Other studies focused on the experimental quantification of the effects of platelet activation by evaluating the dimension of platelet aggregates [27, 28]. Similar to our study, Pelosi and collaborators [29] determined the thrombogenic potential of a hollow-fiber oxygenator with integrated heat exchanger during extracorporeal circulation. Using computational modeling, both the micro- and macro scales were considered to the order of magnitude of PAS in the device, which was found in agreement with experimental data. The advantage of calculating the PAS was the utilize of a more relevant metric than the scalar stress to quantify the level of platelet activation and ultimately the thrombogenic potential. It should be also considered that the mathematical model proposed by Nobili [20] was validated against experimental data over a range of shear stress obtained in our simulation.

V. Conclusion

In this work, a computational flow method was proposed to quantitatively determine the thrombogenic potential of commercial oxygenators as a result of flow-mediated mechanisms. We estimated the flow velocity and pressure drop at macroscale as well as the hemodynamic of the fiber cell elementary unit at microscale. The thrombogenic risk was evaluated using several mathematical models and revealed that the Sheriff et al. [21] model overestimates the values of platelet activation. This study extends the use of computational flow simulations to optimize the hemodynamic performance of oxygenators to evaluate the thrombogenic device risk.

Acknowledgement

Mrs. Baccarella thanks the RiMED Foundation for supporting her PhD fellowship.

References

[1] Abrams D, *et al.* Emerging indications for extracorporeal membrane oxygenation in adults with respiratory failure. *Annals of the American Thoracic Society* 2013; 10(4): 371-7.
[2] Abrams D, *et al.* Extracorporeal Life Support in Lung Transplantation. *Clinics in chest medicine* 2017; 38(4): 655-66.
[3] MacLaren G, *et al.* Contemporary extracorporeal membrane oxygenation for adult respiratory failure: life support in the new era. *Intensive care medicine* 2012; 38(2): 210-20.
[4] Martin JT, *et al.* Artificial lung and novel devices for respiratory support. *Semin Thorac Cardiovasc Surg* 2013; 25(1): 70-5.
[5] Rinaudo A, *et al.* Development of a self-pumping extracorporeal blood oxygenation device characterized by a rotating shaft with embedded fiber packages. *The International journal of artificial organs* 2020; 43(6): 393-400.
[6] Wu ZJ, *et al.* Computational Fluid Dynamics and Experimental Characterization of the Pediatric Pump-Lung. *Cardiovasc Eng Technol* 2011; 2(4): 276-87.
[7] Pasta S, *et al.* Simulation study of transcatheter heart valve implantation in patients with stenotic bicuspid aortic valve. *Med Biol Eng Comput* 2020.
[8] Xenos M, *et al.* Device Thrombogenicity Emulator (DTE) - Design optimization methodology for cardiovascular devices: A study in two bileaflet MHV designs. *Journal of Biomechanics* 2010; 43(12): 2400-09.
[9] Dimasi A, *et al.* Microfluidic emulation of mechanical circulatory support device shear-mediated platelet activation. *Biomed Microdevices* 2015; 17(6): 117.
[10] Scardulla F, *et al.* Modeling Right Ventricle Failure After Continuous Flow Left Ventricular Assist Device: A Biventricular Finite-Element and Lumped-Parameter Analysis. *Cardiovasc Eng Technol* 2018; 9(3): 427-37.
[11] Scardulla F, *et al.* Particle image velocimetry study of the celiac trunk hemodynamic induced by continuous-flow left ventricular assist device. *Med Eng Phys* 2017; 47: 47-54.
[12] Scardulla F, *et al.* Shear stress alterations in the celiac trunk of patients with a continuous-flow left ventricular assist device as shown by in-silico and in-vitro flow analyses. *J Heart Lung Transplant* 2017; 36(8): 906-13.
[13] Yamaguchi T, *et al.* Particle-Based Methods for Multiscale Modeling of Blood Flow in the Circulation and in Devices: Challenges and Future Directions. *Annals of Biomedical Engineering* 2010; 38(3): 1225-35.
[14] Cunningham KS, *et al.* The role of shear stress in the pathogenesis of atherosclerosis. *Lab Invest* 2005; 85(1): 9-23.

[15] Gartner MJ, *et al.* Modeling flow effects on thrombotic deposition in a membrane oxygenator. *Artif Organs* 2000; 24(1): 29-36.
[16] Cosentino F, *et al.* On the role of material properties in ascending thoracic aortic aneurysms. *Computers in biology and medicine* 2019; 109: 70-78.
[17] Cosentino F, *et al.* Statistical Shape Analysis of Ascending Thoracic Aortic Aneurysm: Correlation between Shape and Biomechanical Descriptors. *Journal of personalized medicine* 2020; 10(2).
[18] Di Giuseppe M, *et al.* Identification of circumferential regional heterogeneity of ascending thoracic aneurysmal aorta by biaxial mechanical testing. *J Mol Cell Cardiol* 2019; 130: 205-15.
[19] Apel J, *et al.* Assessment of hemolysis related quantities in a microaxial blood pump by computational fluid dynamics. *Artif Organs* 2001; 25(5): 341-7.
[20] Nobili M, *et al.* Platelet activation due to hemodynamic shear stresses: Damage accumulation model and comparison to in vitro measurements. *Asaio Journal* 2008; 54(1): 64-72.
[21] Sheriff J, *et al.* Evaluation of Shear-Induced Platelet Activation Models Under Constant and Dynamic Shear Stress Loading Conditions Relevant to Devices. *Annals of Biomedical Engineering* 2013; 41(6): 1279-96.
[22] Soares JS, *et al.* A novel mathematical model of activation and sensitization of platelets subjected to dynamic stress histories. *Biomechanics and modeling in mechanobiology* 2013; 12(6): 1127-41.
[23] Huang PY, *et al.* Aggregation and Disaggregation Kinetics of Human Blood-Platelets .3. The Disaggregation under Shear-Stress of Platelet Aggregates. *Biophys J* 1993; 65(1): 354-61.
[24] Xenos M, *et al.* Patient-Based Abdominal Aortic Aneurysm Rupture Risk Prediction with Fluid Structure Interaction Modeling. *Annals of Biomedical Engineering* 2010; 38(11): 3323-37.
[25] Pasta S, *et al.* Simulation of left ventricular outflow tract (LVOT) obstruction in transcatheter mitral valve-in-ring replacement. *Med Eng Phys* 2020; 82: 40-48.
[26] Rinaudo A, *et al.* Biomechanical implications of excessive endograft protrusion into the aortic arch after thoracic endovascular repair. *Computers in biology and medicine* 2015; 66: 235-41.
[27] Tanaka M, *et al.* Platelet damage caused by the centrifugal pump: Laser-light scattering analysis of aggregation patterns. *Artificial Organs* 2001; 25(9): 719-23.
[28] Linneweber J, *et al.* In vitro comparison of blood pump induced platelet microaggregates between a centrifugal and roller pump during cardiopulmonary bypass. *International Journal of Artificial Organs* 2002; 25(6): 549-55.
[29] Pelosi A, *et al.* Computational evaluation of the thrombogenic potential of a hollow-fiber oxygenator with integrated heat exchanger during extracorporeal circulation. *Biomechanics and modeling in mechanobiology* 2014; 13(2): 349-61.

GNB2023, June 21st-23rd 2023, Padova, Italy

Engineering a smart intrauterine device based on pH-controlled copper release

G. Bertola[2], L. Cacopardo[1,2,3], F. Coro [1,2], Carmelo De Maria [1,2], A. Ahluwalia[1,2,3]
[1] Research Centre "E. Piaggio", University of Pisa, Italy
[2] Department of Information Engineering, University of Pisa, Italy
[3] Centro 3R, Italy

***Abstract*—Traditional contraceptive methods based on intrauterine devices typically results in woman being constantly exposed to hormones or copper. The aim of this study is the design of a copper intrauterine device able to modulate copper ions release thanks to pH-sensitive hydrogels. The working principle exploits physiological pH variations in the vaginal fluids, which increases from 3.5-4.0 up to 7 during intercourse. Medical devices are subject to strict approval processes, thus considering regulatory aspects starting from the device design concept is essential. Using the UBORA platform, the device was classified as Class III. Standards for compliance with the European Medical Device Regulation 745/2017 were identified accordingly. Computational and experimental tests were performed on polyacrylamide and chitosan hydrogels to assess the feasibility of this technological solution.**

***Keywords*— pH sensitive hydrogels, controlled release, intrauterine device, smart medical device**

I. INTRODUCTION

Around 257 million women worldwide do not use modern and safe contraceptive methods; of these, 172 million do not use any method [1]. Moreover, the use of traditional methods results in woman being constantly exposed to contraceptive substances. Intrauterine devices (IUDs) currently on the market are based on the release of copper ions as a spermicidal agent, or of progestin hormone, which causes the thickening the mucous membrane of the cervix. In addition, the presence of a foreign body elicits an inflammatory response which contributes to spermicide action. Copper toxicity and the inflammatory response are also responsible for changes in the lining of the uterus preventing oocyte attachment to the endometrium during fertilization. The copper IUD is also used as an emergency contraceptive because it can prevent up to 99% of pregnancies if inserted within 5 days of unprotected intercourse [2, 3].

For these reasons, the aim of this study is to design of a controlled-release copper IUD, according to relevant standards identified using the tools provided by the UBORA platform (https://platform.ubora-biomedical.org/). The rationale is that the normal vaginal pH of 3.5-4.0 increases up to 7.0 within seconds during intercourse and this value is maintained for up to 48 hours to ensure sperm survival [3,4]. Thus, copper release can be modulated exploiting physiological pH variations.

Different pH-sensitive hydrogels were investigated as possible copper coatings able to reduce the exposure to copper ions and promote ion release only after intercourse. Hydrogels are polymeric materials able to retain a significant fraction of water within their structure. This ability is related to hydrophilic functional groups attached to the polymer backbone, while their resistance to dissolution comes from cross-links between network chains [5, 6]. Alteration of environmental pH changes their ionization leading to their swelling or shrinking. These hydrogels are classified into polyacid (or anionic) and polybasic (or cationic) due to the type of ionic functional groups able to accept or donate H^+ ions in response to changes in environmental pH [5-8].

Among these, polyacrylamide hydrogels (PAAm) and chitosan are widely employed for controlled-release formulations in biomedical applications. PAAm gels are obtained by radical copolymerization of acrylamide monomers (Aam) and N,N-methylenebis (Bis-acrylamide). The molar ratio of the monomer to the crosslinker ranges from 10 to 10^4, and the volume fraction of water ranges from 70 percent to 90 percent. Due to its stability in aqueous environments, polyacrylamide is one of the preferred hydrogels in this field [9-11]. Chitosan is a linear polysaccharide, composed of randomly distributed D-glucosamine and N-acetyl-D-glucosamine units, which is obtained by partial deacetylation of naturally available insoluble chitin obtained from exoskeletons of crustaceans, fungi and insects. Chitosan is nontoxic, stable, biodegradable, and can be sterilized. These properties make it a very versatile material with wide application in the biomedical field [12-15]. Computational simulations and experimental tests were thus performed with these gels to assess the feasibility of the technology.

II. ANALYSIS OF DEVICE RISK CLASSIFICATION AND CONFORMITY TO THE EU MDR REGULATION

IUDs can be classified as class III medical devices in accordance with Rule 15 of Annex VIII of the Medical Device Regulation (MDR) 745/2017 [16].

The regulatory aspects of the device were evaluated using the regulation checklist tool of the UBORA Platform. The following are some of the standards that should be used to ensure compliance with Annex I of MDR 745/2017 [16] regarding safety and performance requirements as required by the CE marking process:

- ISO 14630:2012 NO Active surgical implant [17];
- ISO 7439:2023 Copper-bearing contraceptive intrauterine devices —Requirements and tests [18];
- ISO 14971:2019 Medical devices — Application of risk management to medical devices [19];
- ISO 10993-1:2020 Part 1: Evaluation and testing within a risk management process [20];

TABLE I: List of main risk (R- risks; S severity index; O probability of occurrence; RMC risk mitigation index).

Hazardous situation/ foreseeable sequence of event	*Harm*	*O*	*S*	*RMC*	*RMCindex*	*R*
Wrap damage, non-sterile IUD	*Microbiological contamination*	1	1	*Enclosure condition check*	0.4	0.4
Non-sterile IUD after sterilization process	*Microbiological contamination*	1	1	*Sterility control*	0.4	0.4
Non-biocompatible material	*Uterine cancer or cell death*	1	3	*Use of biocompatible material*	0.2	0.6
	Tumor outside the placement site	1	3	*Use of biocompatible material*	0.2	0.6
	Skin irritation or tissue necrosis	1	2	*Use of biocompatible material*	0.2	0.4
	Genotoxicity	1	3	*Use of biocompatible material*	0.2	0.6

- ISO 10993-3:2014 Part 3: Tests for genotoxicity, carcinogenicity and reproductive toxicity [21];
- ISO 10993-5:2009, Biological evaluation of medical devices - Part 5: Tests for in vitro cytotoxicity [22];
- ISO 10993-10:2023, Biological evaluation of medical devices – Part 10: Tests for skin sensitization [23];
- ISO 10993-11:2018 Part 11: Tests for systemic toxicity [24];
- ISO 13485:2016 Medical devices — Quality management systems —Requirements for regulatory purposes [25];
- ISO 11137-1:2015+A2:2019 Part 1: Requirements for development, validation and routine control of a sterilization process for medical devices [26];
- ISO 11137-2:2015 Part 2: Establishing the sterilization dose [27];
- ISO 13408-1:2015 Aseptic processing of healthcare products [28];
- ISO 15223-1:2021 Medical devices — Symbols to be used with information to be supplied by the manufacturer — Part 1: General requirements [29];
- ISO/TR 24971:2020 Medical devices — Guidance on the application of ISO 14971 [30].

Risk analysis was performed referring to guidelines of standard ISO 14971:2019. The risks (R) associated with hazardous situations were estimated by multiplying the severity index (S) and the probability of occurrence (O) and risk mitigation (RMC) index (Table 1). Then, a 5x5 risk matrix was used. Considering R≤4 as a threshold for risk acceptability, the identified risks resulted acceptable. Only a small excerpt of possible risks related to the use of the medical device are shown in Table I.

III. Materials and Methods

A 15.6% w/v Acrylamide, 0.02% w/v Bis-acrylamide (Bis), 0.086% w/v Ammonium persulfate and 0.056% v/v TEMED solution was prepared and degassed for 2 min. Then, the solution was poured into custom cylindrical molds (diameter = 13 mm, hight = 4mm), and incubated at room temperature for 90 minutes.

1% w/v Chitosan solution in 2% w/v Acetic Acid and 0.5% v/v Glutaraldehyde (GTA) were prepared and poured into the same molds, which were placed in the freezer overnight.

Swelling tests were performed on both polyacrylamide and chitosan samples. Samples were placed pH 4 and 7 buffer solutions based on Sodium Phosphate Dibasique 0.2M and Citric Acid 0.1M (respectively 39%-61% v/v and 82-18 % v/v) and weighed at different time-points. All experiments were performed in triplicate. 4 days cyclic swelling tests were also performed to assess the reversibility of the swelling/deswelling with pH.

Degradation tests were performed on both PAAm and chitosan samples. Samples were placed in pH 4 buffer solution and weighed for 25 days. The 'Curve Fitting' tool was used to derive a mathematical expression for degradation over time, which was used to extrapolate gel degradation considering a 10 year typical device lifetime.

Computational studies were performed on COMSOL Multiphysics® using the Dilute Species Transport Module. A 3D model was developed importing uterus and IUD geometries (Table II) designed using Autodesk Fusion 360®, a CAD (Computer Aided Design) software. A commercial copper IUD (NO-Gravid, kindly gifted by I.r.med S.r.l., Italy) was adopted as a case study. The 515 mm^2 copper surface was covered with a cylindrical hydrogel layer. A parametric study was thus performed to identify the gel thickness which ensure no copper release at pH 4 and a concentration of at least 10^{-6} M at pH 7 (minimum concentration required for contraception), considering a 50 µg/day average ion release [31, 32]. Radial and axial hydrogels variations derived from the experimental swelling tests were also considered (Table IV).

The diffusion coefficients used in the simulation are shown in Table III.

TABLE II: Dimensions of the uterus and IUD [31]

Dimensions		*Values (mm)*
Uterus	*length*	76
	width	45
	thickness	30
IUD	*diameter*	2
	length	20
	wingspan	42

TABLE III: DIFFUSION COEFFICIENTS [33][34]

Material	*Diffusion coefficients at pH 4 (m^2/s)*	*Diffusion coefficients at pH 7 (m^2/s)*
PAAm	$6.3*10^{-12}$	$5.81*10^{-11}$
Chitosan	$3.3*10^{-12}$	$3.3*10^{-13}$

TABLE IV: AXIAL AND RADIAL VARIATION AT PH 7

Material	*Axial variation (%)*	*Radial variation (%)*
PAAm	+27.62	+14.1
Chitosan	-28.57	-18.1

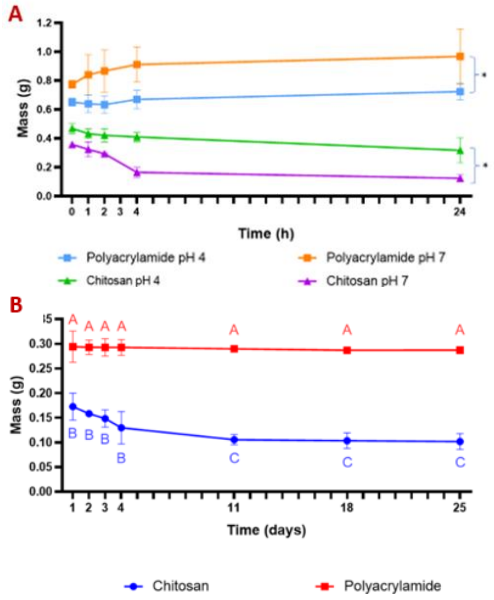
Design and Fabrication: molds for polymer casting were designed on Fusion360®, defining the gel thickness according to computational results. The molds were prototyped in Tough resin 1500 using stereolithography printer Form 3(*Formlabs*).

Copper ion release tests were performed on chitosan hydrogels placed in 10 mL of pH 4 or 7 buffer solution for 4 and 8 hours. The release of cooper ions was measured using the Copper Colorimetric Assay Kit (Elabscience, E-BC-K300-M).

All experiments were performed in triplicate and expressed and mean +/- standard deviation. Statistical analysis was performed using GraphPad Prism software version 8.

IV. RESULTS

As expected, PAAm mass increases with increasing pH, while chitosan mass decreases (Figure 1). The swelling ratios (calculated as the mass variation at pH 7 with respect to pH 4 mass at 24h) were 34 ± 26 % and -61 ± 8% respectively. In particular, the samples start swelling immediately after being in contact with the buffer solution and reach a plateau after 4 hours. Cyclic tests also showed the reversibility of the process. Extrapolating degradation profiles to 10 years resulted in a mass loss of 2.8% for PAAm and 40.8% for chitosan.



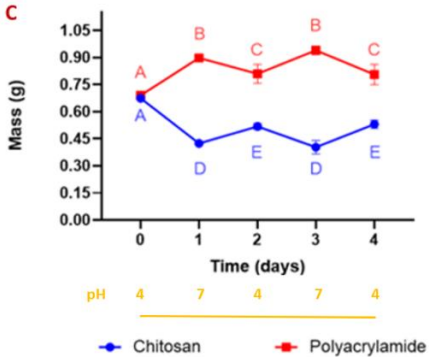


Fig. 1: A - Average mass of the polyacrylamide and chitosan samples at pH 4 and pH 7 at different time points. B - Polyacrylamide and chitosan degradation. C – 4 days cyclic pH variations. * =p<0.05. Different letters indicate statistically significant differences (p<0.05).

Simulations (Figures 2 and 3) suggested that a suitable thicknesses for limiting copper release at pH 4 and for reaching the target concentration for spermicide action at pH 7 is 2 mm.

In particular, at pH 4 the ions are constrained at the copper surface because of the polymer barrier and do not reach high concentrations in the vaginal fluid. On the other hand, at pH 7, the ions pass through the swollen polymer reaching the appropriate concentration for the contraceptive effect in the vaginal fluid. The average concentration of Cu^{2+} in the fluid is indeed equal to $5x10^{-7}$ M at pH 4 and $3.2x10^{-5}$ M at pH 7 in the case of PAAm at to 0 M and $8x10^{-6}$ M in the case of chitosan.

For PAAm, the target concentration was reached after 5h and 30 min; and after 5h and for chitosan. For these reasons, a 2 mm thick mould was design and fabricated (Figure 4).

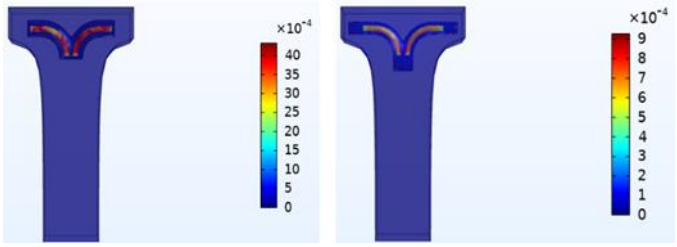


Fig. 2: Copper ion concentration (M) after 24h in the pH 4 (left) and pH 7 solution (right) in the case of 2 mm PAAm layer.

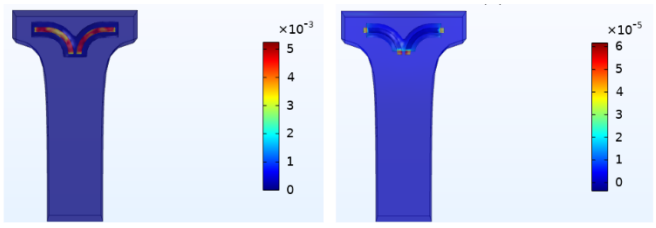


Fig. 3: Copper ion concentration (M) after 24h in the pH 4 (left) and pH 7 solution (right) in the case of 2 mm chitosan layer.

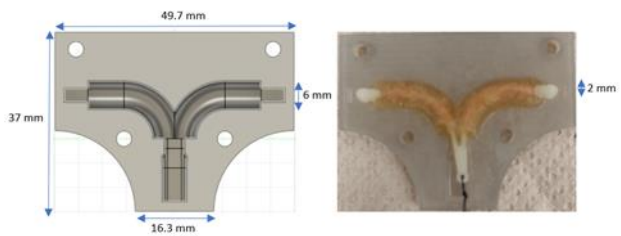


Fig. 4: Left: technical drawing of the mold; Right: 3D printed mold, with IUD and coated with chitosan gel.

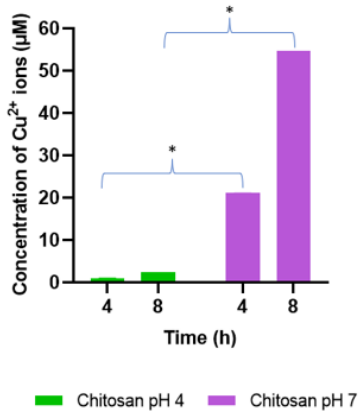


Fig. 5: Cu^{2+} ion concentration released from IUDs wrapped by chitosan in buffer solutions at pH 4 or 7 after 4 and 8 hours. * =$p<0.05$.

V. CONCLUSION

In this work, thanks to experimental tests and simulations, we demonstrated the feasibility of using pH-sensitive gels for the design of a smart IUD able to reduce constant exposure to copper and ensuring ion release after intercourse. A preliminary analysis of the device according to MDR 2017/745 and relevant standards was performed. Although the device has great potential, there are still open challenges to overcome for its commercialisation, such as the long-term stability of the gel and aspects of packaging, sterilisation, and the supply chain to reach the end user.

VI. ACKNOWLEDGEMENT

Thanks to I.r.med S.r.l., Italy, for kindly donating NO-Gravid IUDs.

REFERENCES

[1] United Nations Population Fund Sexual & Reproductive Health Agency. See the unseen (2022) https://www.unfpa.org/sites/default/files/pub-pdf/EN_SWP22%20report_0.pdf [online last access April 2023]
[2] M. E. Ortiz and H. B. Croxatto, "Copper-T intrauterine device and levonorgestrel intrauterine system: biological bases of their mechanism of action", *Contraception* 75, S16 – S30, 15 Jun 2007.
[3] S. Kim, "pH-responsive Biomaterials for Smart Intravaginal Drug Delivery,". A thesis submitted to the *Faculty of Graduate Studies of The University of Manitoba*.
[4] A. K. Mishra, A. Kumar, D. K. Swain, S. Yadav, and R. Nigam, "Insights into pH regulatory mechanisms in mediating spermatozoa functions," *Veterinary World*, vol. 11, no. 6. Veterinary World, pp. 852–858, 2018. doi: 10.14202/vetworld.2018.852-858.
[5] S. Bazban-Shotorbani et al., "Revisiting structure-property relationship of pH-responsive polymers for drug delivery applications," *Journal of Controlled Release*, vol. 253. Elsevier B.V., pp. 46–63, May 10, 2017. doi: 10.1016/j.jconrel.2017.02.021
[6] E. S. Gil and S. M. Hudson, "Stimuli-reponsive polymers and their bioconjugates," *Progress in Polymer Science (Oxford)*, vol. 29, no. 12. pp. 1173–1222, Dec. 2004. doi: 10.1016/j.progpolymsci.2004.08.003.
[7] E. M. Ahmed, "Hydrogel: Preparation, characterization, and applications: A review," *Journal of Advanced Research*, vol. 6, no. 2. Elsevier B.V., pp. 105–121, 2015. doi: 10.1016/j.jare.2013.07.006.
[8] Y. Qiu, K. Park, "Environment-sensitive hydrogels for drug delivery", *Advanced Drug Delivery Revieus*. Aug. 2001.
[9] H. J. Nachash' and O. Okay', "Formation and Structure of Polyacrylamide Gels". *Journal of Applied Polymer Science*. 60(7), 971-979.
[10] C. Yang, T. Yin, and Z. Suo, "Polyacrylamide hydrogels. I. Network imperfection," *J Mech Phys Solids*, vol. 131, pp. 43–55, Oct. 2019, doi: 10.1016/j.jmps.2019.06.018.
[11] S. K. Bajpai, "Swelling-Deswelling Behavior of Poly(acrylamide-co-maleic acid) Hydrogels," 2001. *Journal of Applied Polymer Science*. 80(14), 2782-2789.
[12] M. Gierszewska and J. Ostrowska-Czubenko, "Equilibrium swelling study of crosslinked chitosan membranes in water, buffer and salt solutions," *Prog Chem Appl Chitin Deriv*, vol. 21, pp. 55–62, 2016, doi: 10.15259/PCACD.21.05.
[13] I. Silvestro et al., "Preparation and characterization of TPP-chitosan crosslinked scaffolds for tissue engineering," *Materials*, vol. 13, no. 16, Aug. 2020, doi: 10.3390/MA13163577.
[14] J. Nilsen-Nygaard, S. P. Strand, K. M. Vårum, K. I. Draget, and C. T. Nordgård, "Chitosan: Gels and interfacial properties," *Polymers*, vol. 7, no. 3. MDPI AG, pp. 552–579, 2015. doi: 10.3390/polym7030552J.
[15] M. Gierszewska, J. Ostrowska-Czubenko, M. Pieróg, and M. Gierszewska-Drużyńska, "Effect of ionic crosslinking agents on swelling behaviour of chitosan hydrogel membranes". Chair of Physical Chemistry and Physicochemistry of Polymers, Faculty of Chemistry Nicolaus Copernicus University ul. Gagarina 7, 87-100, 2009.
[16] Regulation (Eu) 2017/745 of the European Parliament and of the Council of 5 April 2017 on medical devices, amending Directive 2001/83/EC, Regulation (EC) No 178/2002 and Regulation (EC) No 1223/2009 and repealing Council Directives 90/385/EEC and 93/42/EEC.
[17] ISO 14630:2012 NO Active surgical implant.
[18] ISO 7439:2023 Copper-bearing contraceptive intrauterine devices — Requirements and tests.
[19] ISO 14971:2019 Medical devices — Application of risk management to medical devices.
[20] ISO 10993-1:2020 Part 1: Evaluation and testing within a risk management process.
[21] ISO 10993-3:2014 Part 3: Tests for genotoxicity, carcinogenicity and reproductive toxicity.
[22] ISO 10993-5:2009, Biological evaluation of medical devices - Part 5: Tests for in vitro cytotoxicity.
[23] ISO 10993-10:2023, Biological evaluation of medical devices – Part 10: Tests for skin sensitization.
[24] ISO 10993-11:2018 Part 11: Tests for systemic toxicity.
[25] ISO 13485:2016 Medical devices — Quality management systems — Requirements for regulatory purposes.
[26] ISO 11137-1:2015+A2:2019 Part 1: Requirements for development, validation and routine control of a sterilization process for medical devices.
[27] ISO 11137-2:2015 Part 2: Establishing the sterilization dose.
[28] ISO 13408-1:2015 Aseptic processing of healthcare products.
[29] ISO 15223-1:2021 Medical devices — Symbols to be used with information to be supplied by the manufacturer — Part 1: General requirements.
[30] ISO/TR 24971:2020 Medical devices — Guidance on the application of ISO 14971.
[31] D. M. Bastidas, B. Valdez, M. Schorr, and J. M. Bastidas, "Corrosion of copper intrauterine devices: Review and recent developments," *Corrosion Reviews*, vol. 37, no. 4. De Gruyter, pp. 307–320, Aug. 01, 2019. doi: 10.1515/corrrev-2019-0012.
[32] D. Elia and J. Belaisch, "[The TCu380 IUD: initial international experimental results with the latest 'T' family IUD].," *Contracept Fertil Sex (Paris)*, vol. 13, no. 9, pp. 973–8, Sep. 1985.
[33] SK Bajpai and S. Dubey. "Modulation of dynamic release of vitamin B2 from a model pH-sensitive terpolymeric hydrogel system". *Polym Int*, 53:2178–2187,2004.
[34] K.H. Chu. Removal of copper from aqueous solution by chitosan in prawn shell: adsorption equilibrium and kinetics. *Journals of Hazardous Materials*,77–95, 2002.

In-flow viscoelastic compression to probe single-cell biomechanical properties

M.I. Maremonti[1], D. Dannhauser[1], V. Panzetta[1], P. A. Netti[1], and F.Causa[1]
[1]*Interdisciplinary Research Centre on Biomaterials (CRIB), Università "Federico II", P.le Tecchio 80, 80125 Naples, Italy.*

***Abstract*—Cell deformability is a well-established marker of multiple cell states for phenotyping and classification purposes. However, the measurement of rheological/mechanical cell properties is often hindered by complex measurement systems and long experimental times. Here, we present a microfluidic approach, as a simple tool to rapidly deform cells in a highly controlled manner, based on tuneable compressive forces. In fact, by simply changing the fluid-flow conditions, we are able to induce variable compression levels at different timescales, depending on the cell line of interest. In particular, we demonstrate how cytoskeletal structures such as actin cortex and microtubule network cooperate to change the overall viscous content of cells. Starting from a completely label-free tracking of dynamic and morphological biophysical parameters, we are able to define inner cell viscosity changes related to actin cortex and microtubule network alterations. Thus, our microfluidic approach is a versatile and easy-to-use way to probe biomechanical cell properties starting from simple in-flow motion parameters.**

***Keywords*—Biomechanics, single-cell, compression, microfluidics.**

I. Introduction

IT is frequently reported how cytoskeletal or nuclear changes are related to cell deformability [1]. In particular, cell phenotype, development, motility and several biological functions are controlled by mechanical loading. In fact, a prolonged or substantial loading can damage cells, eventually leading to their death. Moreover, loading conditions induce specific mechano-structural and mechanobiological responses in different cell types, affecting their internal architecture and morphology as well as the mechanics of the cell components [2]. It is well known that the major cell constituents involved into biomechanical cell responses are the cytoskeletal components of actin cortex and microtubule network. Thus, comprehending the dynamics and mechanics of the cellular components is prerequisite to explain the molecular origins of cell mechanical properties. In particular, in suspension, cells develop a well-defined spherical geometry free of visible stress fibers with the actin cytoskeleton forming a cortex structure which spans the entire cell [3]. Instead, the microtubule network presents as random at the cell interior while with pronounced bundles at the periphery [4]. This aligned peripheral bundling may be due to collective buckling at the cell's boundary. However, it is well known that the actin cortex and microtubules respond differently and then a precise calibration of the mechanical loading is crucial in time and entity.

Over the past years, a variety of microfluidic devices were used to induce cell deformability at high throughput with high-speed bright field imaging techniques, allowing the direct and rapid measurement of several cell biophysical and biomechanical properties such as cell dimension, viscosity and deformability [5]. Recently, a straightforward viscoelastic-based microfluidic approach was used to in-flow compress cells in a controlled and precise manner and to analyse deformed cells by coupling the classical descriptors of morphological and shape alterations with in-flow orientation angles [6], [7]. Inspired by the motion dynamics laws known for RBCs [8]-[13], we already demonstrated that suspended cancer and healthy breast cells with variable cell deformation (CDs) and aspect ratios (ARs) followed multiple in-flow trajectories defined as rolling (R), tumbling (T) and tank-treading (TT) [6]. Of note, we proposed a direct correlation between the measured ARs and trajectories through the inner cell viscosity evaluation [7]. Moreover, by exploitation of in-flow viscoelastic tuneable compression forces, we recently showed that our cell deformability responses are in the range of large deformation (CD > 5%) at which the cell nucleus actively responds by triggering production/remodelling or destruction phenomena of nuclear constituents, such as Lamin-A and Chromatin [14]. For this reason we decided to investigate how actin cortex and microtubule network cooperate to these biomechanical responses. In fact, at large deformation range it is known that actin constituents disrupt while microtubule network elastically responds [4]. Here, we present the possibility to directly correlate the in-flow analysis of compressed single-cells with respect to the biomechanical response of actin cortex and microtubule network of highly metastatic cancer cells. In fact, we demonstrate that changes in the in-flow measured viscosities of cells correspond to different degrees of actin cortex and microtubule deconstruction expressed in terms of inner structural density.

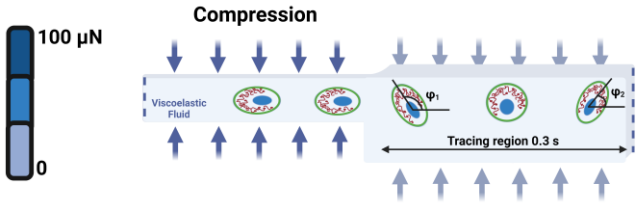


Fig. 1 Sketch representation of the microfluidic device. The exerted viscoelastic compression ranges from 0 to 100 µN, depending on the used PEO concentration. In particular, the final part of the compression region is shown, where deformed cells move before entering into an enlarged region where the brightfield acquisition occurs. The orientation angles (φ_1 and φ_2) are measured at the beginning and the end of the tracing region [6]. Then, after the in-flow measurement, the actin cortex (green) and microtubule compartments (red) are analysed with a confocal microscope after staining procedure. (Created with BioRender.com)

II. Material and Methods

A. Viscoelastic in-flow forces

To induce the compression of single cells under viscoelastic flow conditions, we used a highly biocompatible polyethylene-oxide (PEO 4MDa, Sigma Aldrich). Fluid rheological properties have been previously investigated and properly characterized [6]. We decided to work with two different PEO concentrations, in order to induce two distinct levels of in-flow compressive forces. In particular, we selected PEO 05 and 09 concentrations, which correspond to polymer concentration of

0.53 and 0.88, respectively. A different pressure was fixed for each PEO in order to have the same fluid-flow velocity (~2500 μm/s into the tracing region) to align and compress [6]. To verify the extent of the applied force ($F_{ElMax} \propto U_{Max}^2 \eta_0 \lambda \beta^3$), we tracked cells centroids to estimate such velocity. A good agreement between the measured and the estimated velocity was achieved [6].

B. Experimental setup for the in-flow measurement

The setup includes a pressure pump (P-pump, Dolomite Microfluidics), round shaped flexible fused silica capillary tubing (Molex), an ad hoc designed microfluidic chip, a fluid connector (N-333, IDEX) and an inverted microscope (X81, Olympus) with a CMOS camera (ORCA FLASH 4.0, Hamamatsu Photonics K.K.). Briefly, a pressure pump pushes the sample volume through the capillary in the microfluidic device inlet, while at the end of the chip a reservoir collects the cells. The chip is made of two separate parts made with polymethyl methacrylate, which are placed together by magnetic forces. The main part was machined using a standard CNC based micromilling technique (Minitech Machinery) to develop microfluidic duct sections [6],[7]. of different height, width, and length, while the cover part was simply used to close the chip [6],[7]. In particular, the compression section has the smallest height (W × H: 100 × 25 μm) implying that a well-defined viscoelastic compression over a certain time period on each passing cell is applied, enabling precise cell compression in-flow. Then, a subsequent enlarged section (W × H: 200 × 90 μm) is conceived for the observation and analysis of the compressed cells (Fig.1).

C. Cell culture, immunostaining, and confocal acquisition

We have investigated MDA-MB-231 cells. They were kindly donated by Daidone's group and Dr P. F. Cammarata (Institute of Molecular Bioimaging and Physiology, IBFM-CNR, Cefalù (PA), Italy), respectively. MDA-MB-231 cells are cultured in a 1 : 1 mixture of Dulbecco's modified essential medium (DMEM, Euroclone) and Ham's F-12 medium (Microtech) supplemented with 10% FBS, 1% non-essential amino acid mixture and 100 U ml^{-1} penicillin/streptomycin. Finally, each investigated cell type is diluted in 500 μl of viscoelastic medium to reach a final cell concentration of circa 50 cells per μl. No evidence of mycoplasma infection is present. For immunostaining, cells were fixed with 4% paraformaldehyde (Sigma-Aldrich) for 15 min at room temperature, then rinsed twice with PBS. Permeabilization – with 0.1% Triton X-100 (Sigma-Aldrich) for 5 min– was performed. Thus, the actin cortex was stained at the level of F-actin components with Alexa 488 phalloidin (Invitrogen) at 1 : 200 dilution for 1 h. The microtubule network, instead, was stained with Beta III Tubulin monoclonal antibody overnight at 4 °C with Alexa543 anti-mouse secondary antibody. For the image acquisition of the actin cortex and microtubule network, we used a 63× oil immersion objective (NA 1.4) of a confocal laser scanning microscope (LSM 710, Zeiss) equipped with argon and HeNe laser lines at wavelengths of 488 and 543 nm, respectively. Image resolution was fixed at 512 × 512 square pixels with a 4× zoom factor.

D. Measurement procedure and data analysis

In-flow cell analysis was performed over the full cell tracing length (~0.3 s of measurement in the tracing region), after the compression region (Fig.1). We measured the dynamic in-flow cell parameters, such as the major axis (d_1), minor axis (d_2), circularity (c) and orientation angles (φ) in the range of [−90° to 90°], at each 0.03s. Out of such parameters, the cell deformation (*CD*), cell aspect ratio (*AR*) and angle variation (Δφ, at the beginning and the end of the tracing region) are calculated as follows:

$$AR = \frac{d_1}{d_2} \quad (1)$$

$$CD = 1 - c \quad (2)$$

$$\Delta\varphi = |\varphi_1 - \varphi_2| \quad (3)$$

Where φ_1 and φ_2 are the φ-orientation angles computed at the beginning and the end of the tracing region, respectively. In the specific case of T motion of oblate cells, we computed the variation of the cell orientation angle as function of the viscosity ratio (μ'/μ):

$$tan\big(\varphi(t)\big) = \big(A + B/(A^2 - B^2)^{1/2}\big) \cdot tan(2\pi t/T_{rev}) \quad (4)$$

where,

$$T_{rev} = 2\pi(AR + AR^{-1})\dot{\gamma}^{-1} \quad (5)$$

It indicates a complete period over which a tumbling rotation occurs (0.3 s) and $\dot{\gamma}$ is the shear rate (10 s^{-1} < $\dot{\gamma}$ < 15 s^{-1}). Moreover, $A \propto \dot{\gamma}$ and $B = f(\dot{\gamma}, AR, \mu'/\mu)$ for which μ' and μ are the inner cell viscosity and surrounding fluid viscosity, respectively [13]. Of note, *A* and *B* describe the functional variation of the *AR* of cells with respect to the imposed flow condition in terms of $\dot{\gamma}$.

For a TT cell motion, the equation (4) can be expressed as a stationary angle, only dependent on the fixed $\dot{\gamma}$ and AR:

$$\varphi_{stationary} = 1/2\, arccos(-A/B) \quad (6)$$

Thus, from the known oscillation (φ(t)) of the cell in T or TT motions, we can retrieve the B parameter and then the value of μ'/μ.

For the actin cortex level (Cortex Density) quantification, we normalized the value of the single-channel intensity with respect to the area delimited by the external ring of the cortex itself subtracting it with the nucleus area. Instead, microtubule signal (MT Density) has been computed normalizing the value of the single-channel intensity with respect to the area delimited by the external ring of the cortex itself subtracting it with the nucleus area.

III. Results and Discussion

To in-flow deform cells, we applied a compression ranging from 10^1 to 10^2 μN -05 and 09 conditions- for 5s [6],[7],[14]. Such duration of compression has been established to satisfy time conditions needed to detect viscous behaviour. In fact, since the inner content of suspended cells can be modelled as a viscoelastic fluid, only below a certain length timescale the resulting behaviour is ascribable to purely viscous effects [15],[16]. At stimuli frequencies less than 0.5 s^{-1}, as the ones we used during compression, such viscous behaviour is dominant. Thus, we used an estimation of the inner cell viscosities from the computation of μ'/μ using the T and TT data (equations (4) and (6)).

Here, we decided to test the highly invasive cancer cells MDA-MB-231, for which abnormal expression levels of microtubules and reductions of actin cortex expression have been observed compared to normal cells [18]. In Table 1, we reported the mean values of the biophysical parameter of

interest for the computation of μ'/μ, depending on the identified motion regime [6],[7]. Of note, we indicated the two different T and TT motions which correspond to 05 and 09 compression conditions, respectively.

TABLE I: MDA-MB-231 IN-FLOW RESULTS (N= 31)

Parameter	*Mean ± std. dev.*	*Motion regime*
AR	3.21 ± 1.11	TT, CD ~ (0.15; 0.45)
$\Delta\varphi$	3.39 ± 2.96	TT, CD ~ (0.15; 0.45)
AR	1.43 ± 0.27	T, CD ~ (0.10; 0.21)
$\Delta\varphi$	94.05 ± 25.55	T, CD ~ (0.10; 0.21)

Then, on the viscosity master curve we recently extracted for viscosity computation, we reported the measured *AR*s for which T and TT exist (Fig. 2) describing the resulting μ'/μ variations [7]. The obtained values of μ' are in the order of 10^{-1} Pa·s at T and 10^{-2} Pa·s at TT, meaning a decreasing viscosity after a higher compression (Fig.2).

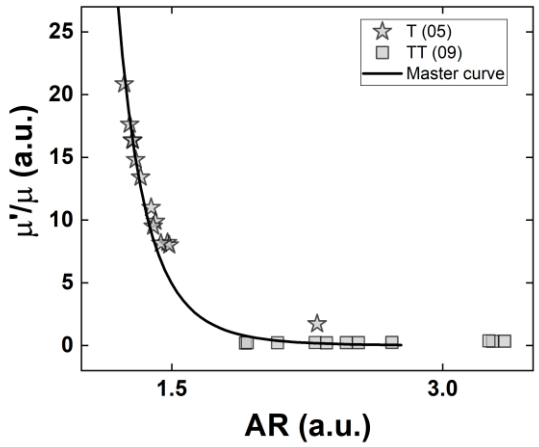


Fig. 2 μ'/μ variations with respect to ARs are shown for the T and TT regimes.

Thus, for such a viscosity decreasing, a possible contribution coming from changes at the actin cortex and microtubule network levels was investigated. A control (Ctrl) condition was investigated to understand the initial states of Cortex and MT densities before the microfluidic compression. Overall, a gradual decreasing of the cortex density is recorded by compression increment (Fig. 3). At the microtubule level, a slight decreasing of the MT density occurs coupled with a spot-like distribution of the relative fluorescence signal into the cell interior like defining a spot accumulation near the nucleus. Of note, microtubule network does not show a relevant change at 05 suggesting a different viscoelastic response to the compression compared to the actin cortex. Instead, the 09 condition results to be critical for both the two compartments. Nevertheless, we already demonstrated that MDA-MB-231 experience a Lamin-A destruction and chromatin de-condensation which lead to a not recovered cell functionality at 09 [12].

IV. CONCLUSION

The proposed microfluidic approach based on viscoelastic compression forces has successfully enabled the possibility to estimate inner cell viscosities in a completely label-free manner, thus correlating such values to alterations of the actin cortex and microtubule networks. Starting from in-flow measured biophysical parameters as AR and $\Delta\varphi$, we extracted inner cell viscosity values. We decided to test the approach on highly metastatic cancer cells (MDA-MB-231). In particular, we demonstrate a gradual decreasing of the inner cell viscosity after an increasing applied loading. Then, we correlated such resulting behaviour with respect to changes in Cortex and MT densities which decrease by increasing the applied compression. Thus, our approach shows how simple motion parameters allow a direct measure of rheological/mechanical properties.

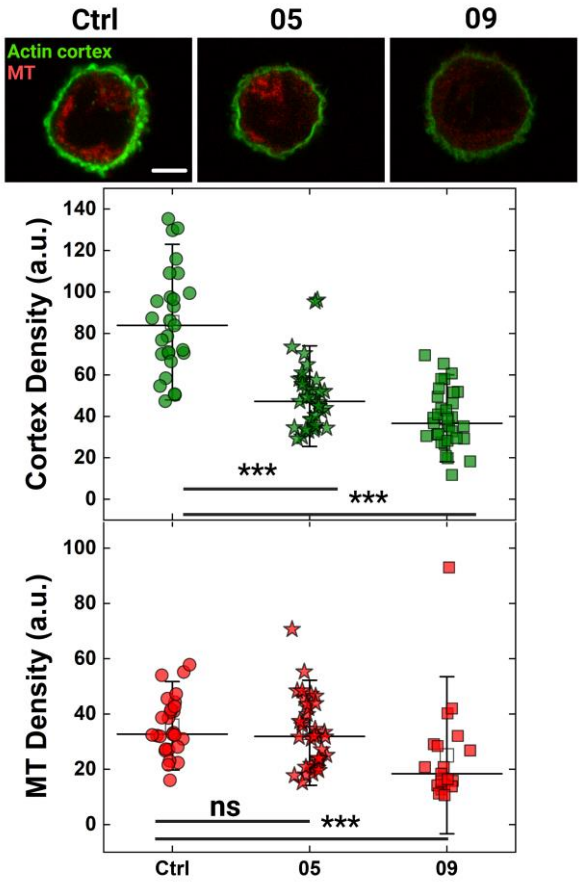


Fig. 3 Actin cortex and microtubule density changes. The 05 and 09 after flow conditions are compared with respect to the Ctrl condition (outflow condition). On the top, the confocal images showing both the two compartments are presented (scale bar 5 μm). On the bottom, the box chart plots of the Cortex and MT density are presented. A Kruskal-Wallis test has been performed for the statistical analysis: $^{ns}p>0.05$, ***$p<0.001$.

REFERENCES

[1] S. Suresh, Biomechanics and biophysics of cancer cells, Acta Biomater., 2007, 3, 413–438.
[2] C. T. Lim, A. Bershadsky, & M. P. Sheetz, Mechanobiology. Journal of The Royal Society Interface, 7(suppl_3), 2010, S291-S293.
[3] G. Salbreux, G. Charras & E. Paluch, Actin cortex mechanics and cellular morphogenesis. Trends Cell Biol. 22, 2012, 536-545.
[4] H. Kubitschke, J. Schnauß, K. D. Nnetu, E. Warmt, R. Stange, & J. Kaes, Actin and microtubule networks contribute differently to cell response for small and large strains. New Journal of Physics, 19(9), 2017, 093003.

[5] Y. Zheng, J. Nguyen, Y. Wei and Y. Sun, Recent advances in microfluidic techniques for single-cell biophysical characterization, Lab Chip, 2013, 13, 2464–2483.
[6] D. Dannhauser & M.I. Maremonti, V. Panzetta, D. Rossi, P.A. Netti & F. Causa, Mechanical phenotyping of breast cell lines by in-flow deformation-dependent dynamics under tuneable compressive forces Lab on a Chip, 20(24):4611–4622 (2020).
[7] M.I. Maremonti, D. Dannhauser, V. Panzetta, P. A. Netti & F. Causa, Cell deformability heterogeneity recognition by unsupervised machine learning from in-flow motion parameters, Lab Chip, 22:4871-4881 (2022).
[8] X. Lu, L. Zhu, R. M. Hua and X. Xuan, Continuous sheathfree separation of particles by shape in viscoelastic fluids, Appl. Phys. Lett., 2015, 107, 264102.
[9] G. D'Avino, M. A. Hulsen, F. Greco and P. L. Maffettone, Numerical simulations on the dynamics of a spheroid in a viscoelastic liquid in a wide-slit microchannel, J. Non- Newton. Fluid Mech., 2019, 263, 33–41.
[10] J. M. Skotheim and T. W. Secomb, Red blood cells and other nonspherical capsules in shear flow: Oscillatory dynamics and the tank-treading-to-tumbling transition, Phys. Rev. Lett., 2007, 98, 078301.
[11] M. Abkarian, M. Faivre and A. Viallat, Swinging of red blood cells under shear flow, Phys. Rev. Lett., 2007, 98, 188302.
[12] C. Dupont, F. Delahaye, D. Barthès-Biesel and A. V. Salsac, Stable equilibrium configurations of an oblate capsule in simple shear flow, J. Fluid Mech., 2016, 791, 738–757.
[13] S. R. Keller and R. Skalak, Motion of a tank-treading ellipsoidal particle in a shear flow, J. Fluid Mech., 1982, 120, 27–47.
[14] M. I. Maremonti, V. Panzetta, D. Dannhauser, P. A. Netti and F. Causa, Wide range viscoelastic compression forces in microfluidics to probe cell-dependent nuclear structural and mechanobiological responses, J. R. Soc., Interface, 2022, 19, 20210880.
[15] T. Kalwarczyk, N. Ziebacz, A. Bielejewska, E. Zaboklicka, K. Koynov, J. Szymanski, A. Wilk, A. Patkowski, J. Gapinski, H. J. Butt and R. Hołyst, Comparative analysis of viscosity of complex liquids and cytoplasm of mammalian cells at the nanoscale, Nano Lett., 2011, 11, 2157–2163.
[16] R. Vaippully, V. Ramanujan, S. Bajpai and B. Roy, Measurement of viscoelastic properties of the cellular cytoplasm using optically trapped brownian probes, J. Phys.: Condens. Matter, 2020, 32, 235101.

Open-source as an enabling approach for the introduction of artificial intelligence in healthcare

F. Coro[1,2], A. F. Bonatti[1,2], G. M. Fortunato[1,2], I. Gulino[1], L. Arcarisi[1,2], M.E. Lippi[3], V. Calderai[3], G. Gallo[1], M. Palmieri[1], P. Ducange[1], C. Bernardeschi[1], G. Tomei[4], P. De Simone[5], A. Ahluwalia[1,2], C. De Maria[1,2]

[1] *Department of Information Engineering, University of Pisa, Pisa, Italy*
[2] *Research Centre 'E. Piaggio', University of Pisa, Pisa, Italy*
[3] *Department of Law, University of Pisa, Pisa, Italy*
[4] *Department of Political Science, University of Pisa, Pisa, Italy*
[5] *Department of Surgical, medical, molecular pathology and Critical Area, University of Pisa, Pisa, Italy*

***Abstract*—Artificial Intelligence (AI) is the ability to make decisions or perform tasks by machines based on a training process. Among the various sectors in which AI is used, healthcare is no an exception, but the risks associated with its use in medical devices may be unacceptable. This work aims to highlight the main barriers to the application of AI in medical devices to date and how open-source design philosophy can be an advantage in overcoming these barriers, through a practical example, named Palpreast, a device for breast self-examination.**

***Keywords*—Open-source medical devices, Artificial Intelligence, breast self-examination.**

I. Introduction

Artificial intelligence (AI) is defined as a machine being able to perform problem-solving and decision-making tasks like any thinking being. Usually, these tasks involve predicting a certain outcome or reasoning a certain question based on a prior learning process carried out by the machine itself on a dataset [1]. In recent years, there has been an inflation in the use of AI in a wide variety of sectors: from aviation to economics, from social sciences to the energy field [2]. Even the healthcare sector has not been spared from the explosion of AI, as this innovative technology supports the skills of professionals and, at the same time, provides more efficient, more sustainable, and higher quality services [3].

In the field of healthcare, four macro-areas can be identified where AI can be potentially employed: i) clinical services (*e.g.*, oncology radiology, home care, surgery, mental health, treatment plans); ii) biomedical research (*e.g.*, drug delivery, personalised medicine); iii) public health (*e.g.*, epidemiological surveillance and event-based surveillance especially for low-middle income countries); and iv) health administration (*e.g.*, coding, patient flow management). Among clinical services, medical devices (MDs) working with AI are particularly critical because of the direct risk related to their use for the patients and healthcare providers [4]. Risks are mainly linked to the limited knowledge about the internal operation of AI algorithms, that often act as a 'black-box' in which no clear explanation is given on how the algorithm computes its output.

In this context, the open-source (OS) philosophy of sharing the entire project is a valuable tool to mitigate the risks [5]. The OS concept foresees the complete sharing of all source material to allow the project to be peer-reviewed, reproduced and eventually upgraded. Open-source medical devices (OSMDs) are therefore devices for which both the design and development documentation must be publicly available to *"study, modify, distribute, make, and sell the medical devices, and their related software or hardware"* [6]. This sharing approach has led to more reliable and appropriate products, although greater attention must be put on safety in the health field. In this context, virtual tools such as the UBORA platform (https://platform.ubora-biomedical.org) can support the design of ISO compliant OSMDs. OS tools for usability analysis of medical devices have been applied with success to identify use errors with infusion devices, as well as with other medical devices [7], [8].

This work aims to highlight how OS design can be the key for overcoming the barriers and the limitation in assessing the regulatory conformity of MDs working with AI. Palpreast, a breast self-examination OSMD, will be described as a case-study of this application.

II. Barriers and Open-source solutions for AI in medical devices

In recent years, some critical issues have been raised among medical services that could be solved by AI applications, as highlighted by the recent COVID-19 pandemic. The enforced isolation, to which a large part of the population has been subjected, has compromised the continuity of essential services mainly for elderly and people with disability. In this context, AI could have been a way of ensuring the continuation of these services and supporting the work of health workers. The lack of personnel within the facilities was another critical issue encountered, although some activities such as checking up basic parameters for hospitalised patients would be possible tasks to be performed automatically by AI.

TABLE I: Summary of the main barriers related to the adoption of AI in MDs.

Barriers	*Description*	*Reference(s)*
Regulatory Barrier	Absence of Regulation focused on AI application on MDs	[9],[10], [11]
Privacy and Data Protection	Data Management: Collection, Storage, Access Protocols and Policy	[12]
Fairness, social and economic impact	Enhancement of societal gaps (e.g., gender, poverty, ethnicity)	[13], [14]
Transparency and explainability	Unknown operation of the AI algorithm and addressing liability	[15]
Reliability and Reproducibility	Necessity of repeatability	[16]

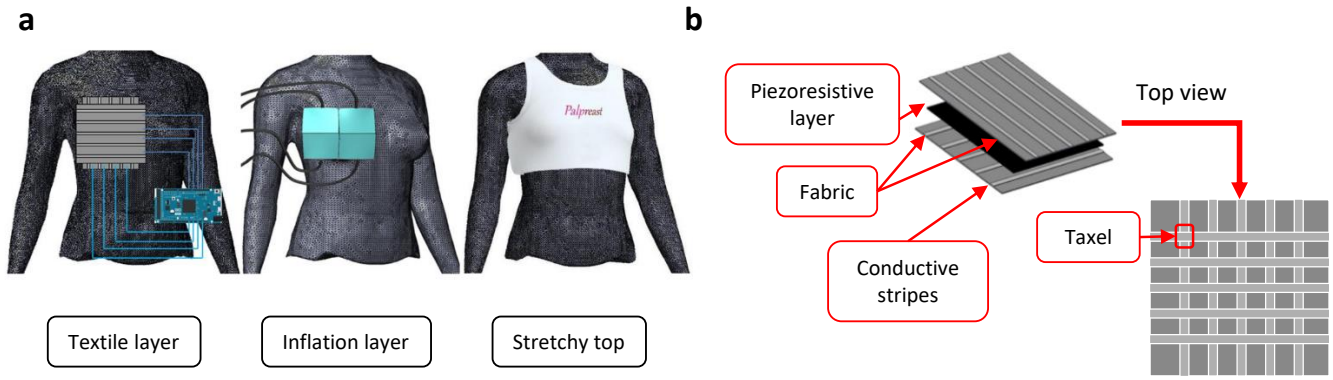


Fig. 1: Overview of the Palpreast OSMD. In (a), the three main elements of the device, including the smart textile layer, the inflation layer (containing the four air chambers per breast), and the stretchy top. In (b), the structure of the smart textile layer, composed of a sandwich structure with two layers of fabric and a piezoresistive material in between. The fabric layers include conductive stripes (with a 90° angle between the top and bottom fabrics) that are used to read the variable resistance of the piezoresistive material. The crossing between two perpendicular stripes forms a taxel, the basic unit during data acquisition.

Despite these potentials in solving relevant clinical needs, there are still gaps to be bridged for these applications to reach the market and guarantee security and reliability, as summarized in Table I. Specifically, the following key points need to be addressed for the adoption of AI in MDs:

- Regulatory barrier: The Medical Device Regulation 745 (MDR 745/2017) [10] and In Vitro Diagnostic Medical Devices Regulation 746 (IVDR 746/2017) [11] enacted by the European Parliament in 2017 do not have specific rules for MDs working with AI. Although compared to previous directives the new ones are more comprehensive, there are no references to this emerging new technology in any of their points. In 2021, the European Commission published a proposal for a regulation on AI. This document is part of a broader plan (Coordinated plan on AI) and divides biomedical applications with AI into tiers based on the associated risk. For these applications, the proposal aims to clear the requirements, the obligations of those who provide the services and those who use them, and includes a draft for conformity assessment. The regulation could enter a transitional period in 2023, while early 2024 is the earliest time for the regulation to be applicable [9]. In US, FDA has provided a risk-based guidance for certifying Software as Medical Device embedding AI [17]. In a regulatory risk-correlated approach divided into four categories (*i.e.*, unacceptable, high, limited, and minimal or no risk), the open and collaborative design approach favours the likelihood of mitigating risks already at the design stage, resulting in safer devices.
- Privacy and Data Protection: The General Data Protection Regulation (GDPR) is the data protection law for citizens of the European Union that regulates the entire management of data, including collection, use, storage, how data are processed, and what protocols are in place to access them. The GDPR should be taken into consideration each time that data flows in AI-based systems, such as i) when input data are entered by users be able to operate, and ii) when countless amount of information is automatically collected to generate the output. The latter, in fact, can be correlated with private aspects of the user, concerning his/her habits, and thus to personal information such as political, sexual, and religious orientation, gender, etc. From a technical point of view, data used in the design stage (i.e., during training and testing of the AI model) must be treated appropriately, as the absence of data integrity would completely change the output of the algorithm [12]. Having access to the source code is an undoubted advantage for ensuring security because it allows i) to control the flow of data (from the collection to the output), ii) to obtain schematics tracing its path (*e.g.* https://www.privado.ai/open-source) and iii) to verify that there are no leakages or any kind of violation of user protection laws.
- Fairness, social and economic impact: The application of AI algorithms must be a step forward for society, not a tool to widen existing gaps. AI must be accessible to all and equally. Starting with the testing of the algorithm, there must be no inquisitiveness, be it gender, ethnicity, disability, poverty, or any possible categorisation [13]. In addition to discrimination, consequences of using unbalanced databases could affect other aspects such as fairness in the market (gaining an advantage over other producers) or consequences on prices [14]. Using open Data for AI training is an advantage on several levels: on the one hand, it limits the monopoly of some companies on datasets, a phenomenon that sometimes severely limits their accessibility and reinforces the bias on *e.g.* gender or race. Open datasets make developers focus on solving problems, rather than on acquiring data, thus mitigating risks and increasing reliability.
- Transparency and explainability: Transparency was set in the ethical guidelines published by the EU Commission's High-Level Expert Group on AI as one of the 7 key requirements for a trustworthy AI. When using an AI system, the user must be aware of how the decision-making system operates and what the predefined rules are. At the same time, the user must always be informed of both the possibilities and limitations of the intelligent system. If the operability of the algorithm is well documented, these requirements are easily fulfilled. However, innovative AI algorithms exploit implicit learning techniques and in this case the transparency requirement for the conformity assessment is difficult to implement because the results of the models are not fully explainable [15]. Article 15 of the GDPR establishes that if automatic decision-making systems are to be employed, the user must have 'meaningful information about the logic involved'. In this context, Explainable AI (XAI) models [18] offer both to designers and users to understand how an AI-based system actually works for generating outputs.
- Reliability and Reproducibility: Reproducibility and reliability are two core concepts for a robust algorithm. An algorithm is robust if it responds correctly to different outputs

and in different situations and under the same conditions it must give the same output. These aspects must always be guaranteed, especially in biomedical applications. The way to guaranteeing this requirement would be to provide a series of appropriate records that allow another research team for instance to reproduce a certain task and verify its reproducibility. However, it is unclear what the appropriate content of these files (called replication files) must be in order for the output to be considered appropriate [16] When designing through an OS approach, the developer shares all source information but also gives the opportunity to study, modify, verify as stated in the definition in the previous paragraph. Having all the resources and being able to study, verify and if necessary, implement changes will make the algorithm more reliable. Reproducibility is the tool to improve the reliability[19].

III. AI IN MDS: THE CASE-STUDY OF PALPREAST

A. Clinical need and device overview

Every year, more than 14 million women are diagnosed with breast cancer, many of them in low- and middle-income settings. Even though substantial treatment advances have been made in recent years, early diagnosis remains the main tool for reducing mortality [20]. Breast self-examination (BSE) is a technique that allows the detection of lumps manually by the patient herself. Although recommended by qualified personnel, a large part of the population does not perform the practice because they do not feel confident to detect the lump.

In this context, in a previous work we presented Palpreast, a non-invasive wearable OSMD, which reproduces BSE procedure [21] is aimed at supporting women in identifying the presence of lumps. As such, the device can be classified as class I medical device, according to the EU MDR 2017/745 as it does not have a diagnostic function, but it only exerts a supportive role. Palpreast, as specified, performs BSE and this practice is not diagnostic. In the event that Palpreast detects any abnormality, this information is not directly related to the presence of a possibly malignant lump, but invites the patient to proceed with more accurate, in this case diagnostic, examinations. The main components of Palpreast are presented in Fig. 1a and include: i) a pressure sensing textile located in direct contact with the skin; ii) an inflation system which uses four air chambers per breast; iii) a stretchy top that covers the two previous elements. The textile consists of a layer of piezoresistive material placed between two layers of fabric with highly conductive stripes. The top and bottom conductive patterns are perpendicular and each intersection between a row and a column corresponds to a sensing element (named taxel), as can be seen in Fig. 1b.

When one of the four air chambers is inflated (herein named ‘quadrant’), a pressure is applied to the textile and thus to the breast, in a similar way to the BSE procedure. By measuring the resistance change in each taxel, a graphic map can be obtained in which the visual information is correlated with the mechanical resistance sensed by the device. The comparison between left and right breast data can be used to infer the presence of the nodule in one of the two breasts [21]. More technical details on the OS device can be found on the UBORA platform, where the project is fully documented [22]. Here we want to explore how AI can assist the identification of lumps, how this support will modify the classification/certification of Palpreast, and how OS can favour the regulatory process.

B. Data collection pipeline

A custom data collection pipeline was implemented to facilitate acquisition, aggregation, and analysis. In particular, after wearing the device, data is collected from the smart textile one quadrant at a time by inflating the corresponding air chamber and reading the voltage difference of each taxel using a voltage divider configuration. The data acquisition is performed by an Arduino Nano 33 BLE board which uses a custom firmware (written in C++). For each quadrant, the Arduino creates two matrices for the two breasts (where each element of the matrix refers to a physical taxel), which are then sent to a computer using serial connection. On the receiving computer, a custom graphical user interface, written in Python using the Streamlit library, allows the visualization of the matrices and their storage to disk with custom identifiers in .csv format for further processing.

C. Development of a preliminary dataset

A preliminary dataset was obtained using the previously described pipeline by mounting the Palpreast device on a mannequin with two breast phantoms. The phantoms were fabricated using Ecoflex 00-10 and Slacker (PartA:PartB:Slacker 1:1:3, Smooth-On, Inc USA) and Dragon Skin 00-10 Medium (PartA:PartB 1:1, Smooth-On, Inc USA) to mimic the mechanical properties of the healthy breast tissue and of the lump, respectively. The phantom was designed in a way that the nodule could be inserted in various positions to ensure greater variability of the data collected. Five lump configurations and one without the lump were tested. For each of the six configurations, multiple repeated acquisitions were performed for a total of 24 acquisitions, which constituted the preliminary dataset for further analysis.

D. Data augmentation using simulated data

Given the large amount of data needed for training the Machine Learning models (see section E), we have planned the implementation of a Digital Twin of Palpreast. A finite element 3D model of Palpreast was implemented in COMSOL Multiphysics. The piezoresistive behaviour of the sensor (*i.e.* the correlation between applied pressure and voltage output), was modelled using an experimentally derived characteristic curve. The model will be interfaced with a virtual model of the data acquisition pipeline of Arduino using Matlab® to fully replicate the entire mechanism from data generation to their processing.

E. Exploratory data analysis

The mixed dataset (simulated and experimental) was preliminarily analyzed to extract relevant per-quadrant metrics, including mean, standard deviation, median, interquartile range (IQR), skewness, kurtosis, and number of outliers (measured as the number of data points outside the IQR). Example plots for these measures can be seen in Fig. 2 for the mean and standard deviation case. These specific measures were chosen as possible explainable variables for further processing using Machine Learning models (e.g., decision tree classifier), which can give insights into the classification process.

F. *Changes in the certification process*

The presence of AI does not change the risk class of Palpreast. The AI algorithm does not modify the intended use of the MD by making it diagnostic, but performs a different data analysis by fusing multiple features of the original signals for highlighting the presence of a lump. However, in the regulatory framework for certifying such MD supported by AI, it is necessary to consider not only the standard benchmarks but also the device's operation with a certain degree of autonomy (DOA) as it is able to generate decision-making outputs. DOA results in an associated risk which have to be reported in the risk management analysis. The IEC TR 60601-4-1:2017 standard offers all the necessary guidelines for identifying the DOA, the associated risk and offers the necessary guidelines for implementing *a detailed risk management and usability engineering processes for medical electrical equipment or systems employing a degree of autonomy* [23].

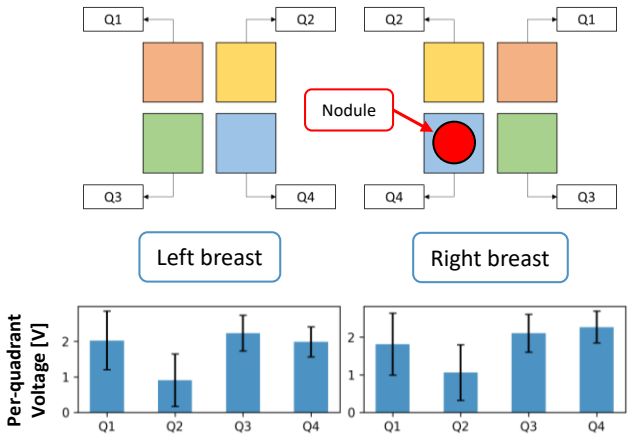


Fig. 2: Example of the measured data during the experiments, alongside a visualization of the per-quadrant mean voltage and its standard deviation, which can be used as an explainable metric for developing AI models. The presented data is related to a nodule placed inside the Q4 quadrant, which corresponds to position 1 in Table II.

IV. Conclusions

This paper highlighted the barriers that currently hind the use of AI in MDs and how the OS approach can help overcome them. The results reported for Palpreast case study are preliminary and still need further investigation in the choice of *e.g.* data analysis metrics and types of comparisons to be made for reliable results. However, it has provided a base for investigating the OS approach applied to AI-based MD.

Acknowledgements

This research has received fundings from the University of Pisa project PRA mOSAIc: Open Source as key enabling approach for AI in healthcare (PRA_2020_38) and has been partially supported by the European Union by the Next Generation EU project ECS00000017 'Ecosistema dell'Innovazione' Tuscany Health Ecosystem (THE, PNRR, Spoke 3: Advanced technologies, methods and materials for human health and well-being and Spoke 4: Nanotechnologies for diagnosis and therapy).

References

[1] S. Miresmailli, D. Badulescu, R. H. Zamar, and M. B. Isman, "A definition of AI: Main capabilities and scientific disciplines," vol. 45, pp. 1–6, 2018.

[2] R. S. Peres, X. Jia, J. Lee, K. Sun, A. W. Colombo, and J. Barata, "Industrial Artificial Intelligence in Industry 4.0 -Systematic Review, Challenges and Outlook," *IEEE Access*, pp. 220121–220139, 2020, doi: 10.1109/ACCESS.2020.3042874.

[3] The Pharmaceutical Group of the European Union, "Position Paper on Digital Health Pharmaceutical Group of the European Union," *Julho*, 2021.

[4] European Commission, "Proposal for a regulation of the European Parliament and of the council laying down harmonised rules on artificial intelligence," *EU Artif. Intell. Act*, vol. 0106, 2022, doi: 10.4324/9781003319436.

[5] J. R. G. Evangelista, R. J. Sassi, M. Romero, and D. Napolitano, "Systematic Literature Review to Investigate the Application of Open Source Intelligence (OSINT) with Artificial Intelligence," *J. Appl. Secur. Res.*, vol. 16, no. 3, pp. 345–369, 2021, doi: 10.1080/19361610.2020.1761737.

[6] C. De Maria, L. Di Pietro, A. Ravizza, A. D. Lantada, and A. D. Ahluwalia, *Open-source medical devices: Healthcare solutions for low-, middle-, and high-resource settings*, Second Edi. Elsevier Inc., 2019.

[7] P. Masci, P. Oladimeji, P. Curzon, and H. Thimbleby, "Using PVSio-web to Demonstrate Software Issues in Medical User Interfaces," 217AD, vol. 34(4), no. December, pp. 312–322.

[8] C. Bernardeschi, P. Masci, D. Caramella, and R. Dell'Osso, "The benefits of using interactive device simulations as training material for clinicians: An experience report with a contrast media injector used in CT," *ACM SIGBED Rev.*, vol. 16, no. 2, pp. 41–45, 2019, doi: 10.1145/3357495.3357500.

[9] "Regulatory framework proposal on artificial intelligence," 2021. https://digital-strategy.ec.europa.eu/en/policies/regulatory-framework-ai.

[10] European Commission, "Regulation (EU) 2017/745 of the European parliament and of the council on medical devices," *Off. J. Eur. Union*, vol. 84, no. 8, pp. 353–359, 2017, doi: 10.1177/2165079915576935.

[11] European Commission, "Regulation (EU) 2017/746 of the European parliament and of the council on in vitro diagnostic medical devices," *Off. J. Eur. Union*, vol. 5, no. 5, pp. 117–176, 2017.

[12] European Commission, "Regulation (EU) 2016/679 of the European Parliament and the council on the protection of natural persons with regard to the processing of personal data and on the free movement of such data," 2016.

[13] "Ethics guidelines for trustworthy AI." https://digital-strategy.ec.europa.eu/en/library/ethics-guidelines-trustworthy-ai.

[14] European Union Agency for Fundamental Rights (FRA), "BigData: Discrimination in data-supported decision making," *FRA Focus*, p. 14, 2018, [Online]. Available: https://fra.europa.eu/sites/default/files/fra_uploads/fra-2018-focus-big-data_en.pdf.

[15] European Commission, "Ethics guidelines for trustworthy AI. High-Level Expert Group on Artificial Intelligence," *Eur. Comm.*, pp. 1–39, 2019.

[16] O. E. Gundersen and S. Kjensmo, "State of the art: Reproducibility in artificial intelligence," *32nd AAAI Conf. Artif. Intell. AAAI 2018*, pp. 1644–1651, 2018, doi: 10.1609/aaai.v32i1.11503.

[17] U. S. F. & D. ADMINISTRATION, "Artificial Intelligence/Machine Learning (AI/ML)-Based Software as a Medical Device (SaMD) Action Plan," no. January, pp. 4023–4024, 2021, doi: 10.1145/3447548.3470823.

[18] "On Artificial Intelligence - A European approach to excellence and trust," *J. Chem. Inf. Model.*, vol. 53, no. 9, pp. 1689–1699, 2013, [Online]. Available: https://ec.europa.eu/commission/sites/beta-political/files/political-guidelines-next-commission_en.pdf.

[19] K. Yu, "The reproducibility issues that haunt health-care AI."

[20] World Health Organization, *Guide to Cancer - Guide to cancer early diagnosis*. 2017.

[21] L. Arcarisi, L. Di Pietro, N. Carbonaro, A. Tognetti, A. Ahluwalia, and C. De Maria, "Palpreast-A new wearable device for breast self-examination," *Appl. Sci.*, vol. 9, no. 3, 2019, doi: 10.3390/app9030381.

[22] "Wearable Device for Breast Self-Examination: Palpreast." https://platform.ubora-biomedical.org/projects/eb95b284-014c-4709-90f4-87a1f07968b9.

[23] *PD IEC/TR 60601-4-1:2017 Part 4-1: Guidance and interpretation – Medical electrical equipment and medical electrical systems employing a degree of autonomy*. 2017.

A method for the evaluation of cervical surgical instrumentation reliability through a computational and experimental approach

L. Ciriello[1], A. Belluzzo[1], A. Grassi[1] and T. Villa[1,2]
[1] *Department of Chemistry, Materials and Chemical Engineering "Giulio Natta" - LaBS, Politecnico di Milano (Italy)*
[2] *IRCCS Istituto Ortopedico Galeazzi (Italy)*

***Abstract* — The use of multi-use Surgical Instrumentation (SI) kits is the standard that is currently used in hospitals for orthopedic and spinal interventions. Nevertheless, this has several disadvantages such as the high cost, the environmental impact of the sterilization, and different problems related to its reliability, including the failure of the SI during the surgery. So, the aim of this work is to develop a method for the mechanical evaluation of a cervical SI through a combined numerical and experimental approach, to redesign it from multi-use to single-use instrumentation, to make up for the previous problems.**

***Keywords*—Spinal surgical instrumentation, mechanical evaluation, finite element model.**

I. Introduction

NOWADAYS multi-use Surgical Instruments (SI) are used for the implantation of orthopedic and spinal devices. Generally, the kits are composed of several instruments made of stainless steel which can be reused for several operations and stored in the hospital only after sterilization to avoid cross-infection among the patients.

Sterilization processes are generally performed internally at the hospital hosting the kit or by subcontractors specialized in performing sterilization processes, either EtO sterilization or moist heat sterilization. These are energy-intense processes, with each load for a medium- to large-sized hospital sterilization requiring about 20kWh of electricity and 500 l of water [1]. These procedures lead also to complications in hospital management, both in terms of costs and organization, as they require (i) a significant time loss due to the necessity of performing the various safety and hygienic protocols (ii) complicated logistic management of the reusable kits in terms of repeated handling in and out of the hospital (or in and out of the operating room) [2].

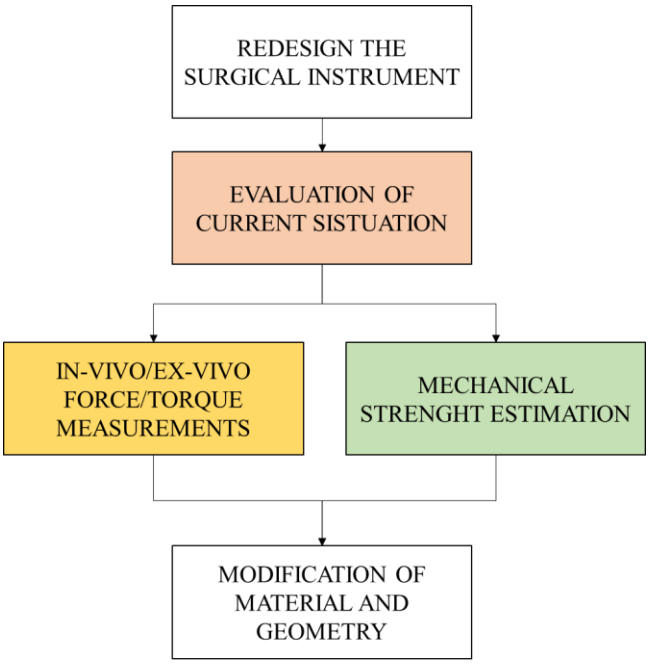


Fig. 1 The workflow for the mechanical evaluation of the SI.

In addition to the high costs due to sterilization, surgical instrumentations can experience a fracture in the operating room, in particular, if used for several procedures.
Dharmashaktu et al. recorded that out of a total of 8132 (6517 major and 1615 minor procedures), 30 (0.36%) cases of intra-operative instrument breakages were noted. The event of an instrument failure may prolong surgery time and add the need for additional procedures such as extra incisions, making fenestration in the bone to remove broken instruments in a destructive and unwanted process [3], [4].

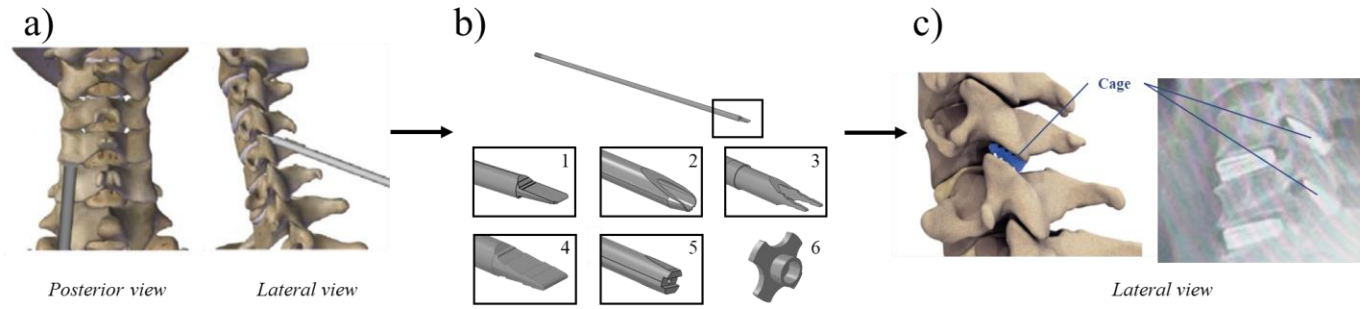


Fig. 2 a) Schematization of a cervical spine section with the instrument inserted between the facet joints, on the left the posterior view and on the right the lateral view; b) the 2B1 kit with in detail the different end tips of the instruments: 1. Chisel; 2. Dilator; 3. Forks; 4. Reamer; 5. Holder; 6. Beat Plug; c) on the left, the schematization of a cervical spine with the cervical cage implanted in detail, on the right, the RX image with in detail the cages.

Tab. 1 Main differences between multi-use and single-use instruments**.**

	Standard SIs	**Single-Use SIs**
Sterilization [1]	500 l every cycle, 327,000 l of leak/year	Save 435 l for every surgery
Always 100% **sterile** [1]	No	Yes
Packaging [5], [7]	↑space and ↑costs	↓space and ↓costs (modular unit)
Logistics in the hospital [1]	Very complicated organization	Not present
More **interventions** per day [4]	Limited kits	Available for immediate use
Transport	↓transport	↑transport
Proper **sizing** of the instrumentation [8]	Not present in the literature	Useful if you change the materials
No damage components and infection [2], [8]	30/8132 cases of intra-operative fractures and more cases of infection	Always new and less % of infections

Within this scenario (Table 1), the introduction of single-use SI can reduce hospital costs, and the risks of breakage of the kit in the operating room and also improve the economic and environmental impact that still occurs with standard instrumentation [1], [3]–[6].

The aim of this work is the development of a workflow able to identify the steps for mechanical redesign from multi-use to single-use SI (Figure 1). For the mechanical design of single-use SI, it is necessary to identify and analyze the current situation of multi-use SI. Instrumentation for cervical cage implantation (Sharkage system manufactured by 2B1 s.r.l, Milan, Italy) was identified as an example for the analysis (Figure 2).

In particular, as reported in Figure 2, the Sharkage kit is composed of several instruments that permit the implantation of the interfacet cage device intended to enhance fusion and mechanical support for the cervical spine (C2-C7 levels).

II. Material and methods

In order to evaluate the current situation of the Sharkage kit in terms of mechanical properties, several activities must be done to identify the various aspect that can be improved.
Firstly, an optical analysis of a used Sharkage SI provided by the manufacturer was carried out to determine the most critical component among those in the kit. Secondly, mechanical strength was evaluated through numerical and experimental analysis of the selected instrument from the previous activity.
Finally, a measurement system was developed to identify under which conditions the instrumentation is used by the surgeon, in terms of forces and torques that are applied to the instruments during surgery.

A. Optical analysis of the Sharkage SI

The Sharkage kit consists of six components used sequentially for the implantation of the vertebral cage. Additionally, a beat plug is also provided in the kit to manipulate the various instruments (Figure 2). An optical analysis on a post-use kit was performed to assess which components were the most critical during surgery. The evaluation was performed using Canon EOS 6D digital camera (20.2 MP) with 2X magnification, to catch any details of geometry. All components were analyzed, with a particular focus on the instrument's end tip, which interfaces with the bone component during implantation (Figure 2b).

B. Evaluation of the strength through a combined numerical and experimental analysis

The mechanical evaluation was carried out only on the most critical component of the Sharkage kit. Specifically, the numerical model was built for the Forks component (Figure 3) using Abaqus 2022 (Dassault Systèmes, SIMULIA Corp., RI), assigning stainless steel material (E=210GPa, υ=0.3) to the instrument according to the manufacturer indications. In order to find the mechanical strength of the device, two types of simulations were carried out: (i) widening of the end spacers (Figure 3a); (ii) shrinkage of the end spacers (Figure 3b). For both configurations an ad-hoc setup was designed and modeled, considering it as undeformable, and an encastre was set on the instrument and on the opposite side as a displacement applied on the surface equal to 7 mm, previously calibrated (Figure 3). A general contact was set between the instrument and the setup, choosing the hard contact (as normal behavior) and the friction coefficient equal to 0.3 (as tangential behavior) [9]. After a mesh sensitivity, 179,467 quadratic tetrahedral elements (C3D10), 5,982 linear quadrilateral elements (R3D4) for the first type of load (Figure 3a) and 8,698 linear quadrilateral elements (R3D4) for the second type of load (Figure 3b), were used for the Forks and the setups respectively.

To validate the FE model in terms of stiffness (K, slope of force-displacement curve) and local strains (ε_{Princ}), specific experimental tests were carried out on prototypes of the Forks component using strain gauge rosette positioned as reported in Figures 3a and 3b and three different experimental tests were performed for each configuration of loading applied to the Forks (Figure 3a and 3b).

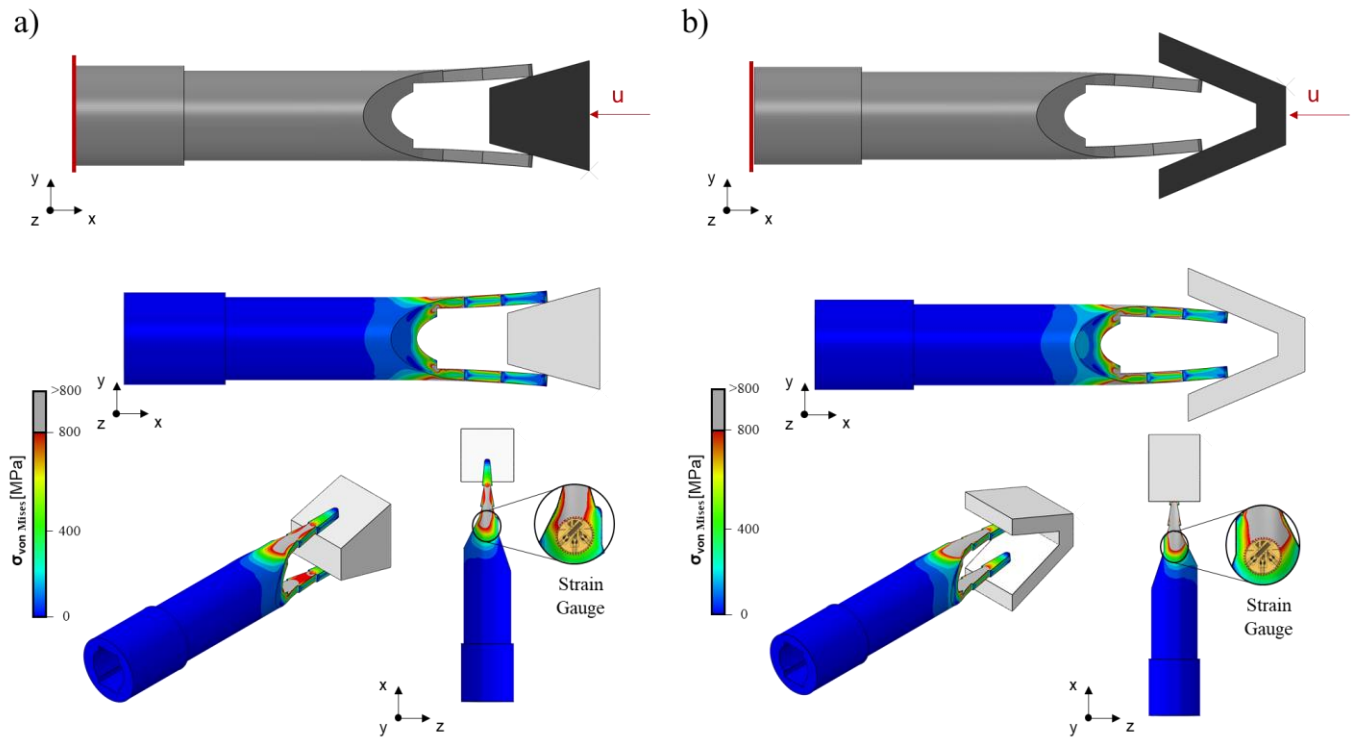


Fig. 3 a) Loading configuration with an ad-hoc setup in order to enlarge the spacer at the end of the instrument. In the bottom part, the results, in terms of von Mises stresses, and in detail the position of the strain gauge applied during the experimental test that matches with the zone where the average value is calculated during the numerical analysis; b) loading configuration with an ad-hoc setup in order to tighten the spacer at the end of the instrument. In the bottom part, the results, in terms of von Mises stresses, and in detail the position of the strain gauge applied during the experimental test that matches with the zone where the average value is calculated during the numerical analysis.

C. Development of the in-vivo measurement system

The Sharkage kit, as described above, consists of several instruments: in particular a beat plug permits and facilitates the insertion and usage of the instruments, including the Forks combined with other components (Figures 2 and 5).

To identify the conditions to which the instruments are subjected during surgery, an *in-vivo* measurement system was developed. In particular, the geometry of the beat plug was modified using Solidworks 2022 (Dassault Systèmes, SIMULIA Corp., RI) and a load cell was purposely designed and realized to be located inside the beat plug in a specific housing (Figure 5).

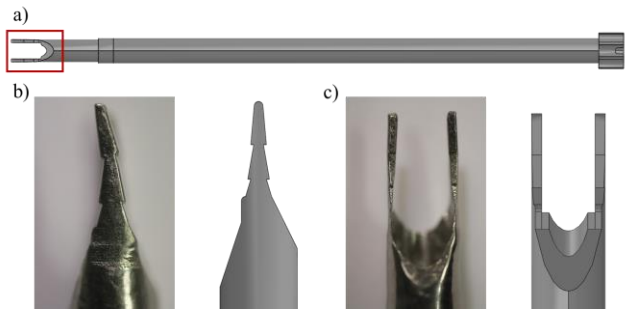


Fig. 4 a) The instrument CAD that shows different plasticized zones, (in the square); b) comparison (lateral view) between optical analysis (2x zoom) vs. CAD model; c) comparison (anterior view) between the optical analysis (2x zoom) vs. CAD model

III. RESULTS

A. Optical analysis of the Sharkage SI

The only instrument, in the Sharkage kit, that presents several deformed parts after use in the operating room is the Forks instrument. That was observed through optical analysis and it is reported in Figure 4a. In particular, it was noticed that the two side spacers of the end part are deformed in both the lateral and anterior planes (Figure 4b and 4c, respectively).

B. Evaluation of the strength through a combined numerical and experimental analysis

As reported in Figure 3, the Forks components have a different zone with von Mises values greater than the yielding stress (equal to 800 MPa) when the force applied is equal to 38 and 32 N for the two configurations respectively (Figure 3a and 3b). The numerical models demonstrated good agreement with experimental static tests with a percentage difference of less than 10% in terms of macroscopic and microscopic behavior (K, stiffness of the system, and ε_{Prin}, local strain respectively).

C. Development of the in-vivo measurement system

The design of the beat plug was modified, in particular, the internal design and the width to permit the housing of the load cell. Indeed, the design was changed to transmit the load from the device to the load cell and to record the data in terms of force and torque (Figure 5). Therefore, the information from the in-vivo measurements will be fundamental in the redesign

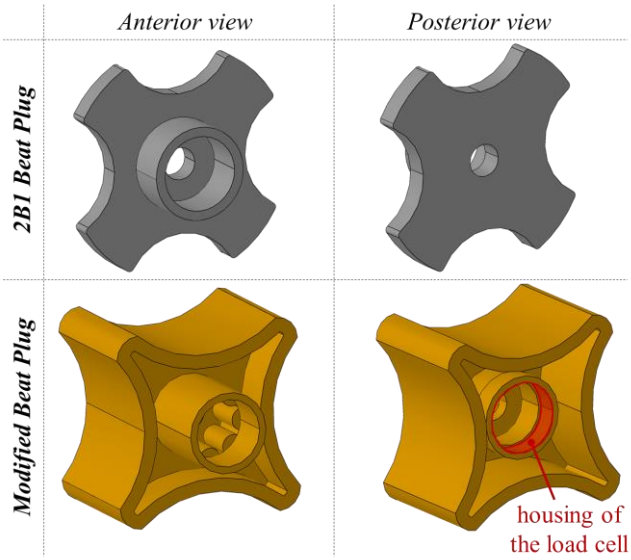


Fig. 5 On the left the anterior view and on the right the posterior view of the 2B1 beat plug and the modified beat plug with in detail the housing of the load cell to recorder the force and torque during the surgery.

and assigning of the new material to the single-use SI. A future step will be to perform the measurement activity during a real surgery or on cadaveric specimens, thus confirming the validity of the simulations in terms of values of applied forces and torques.

IV. Conclusion

This work shows how to mechanically evaluate a surgical instrument with the aim of redesigning it in terms of design and material. In particular, a combined experimental and computation approach was proposed as reported in Figure 1. In addition, the redesign of the instrumentation will reduce the economic and environmental impact associated with the production and life cycle of the current kit [2], [4].

Acknowledgment

The authors gratefully acknowledge Carlo Miglietta (2B1 Srl, Milan, Italy) and Davide Pizzamiglio (Leghe Leggere Lavorate Srl, Milan, Italy) for providing the CAD and the devices useful for the numerical and experimental activity.

References

[1] F. McGain, G. Moore, and J. Black, “Hospital steam sterilizer usage: Could we switch off to save electricity and water?,” *J. Heal. Serv. Res. Policy*, vol. 21, no. 3, pp. 166–171, 2016, doi: 10.1177/1355819615625698.

[2] J. M. Mouritsen, L. Ehlers, J. Kovaleva, I. Ahmad, and K. El-Boghdadly, “A systematic review and cost effectiveness analysis of reusable vs. single-use flexible bronchoscopes,” *Anaesthesia*, vol. 75, no. 4, pp. 529–540, 2020, doi: 10.1111/anae.14891.

[3] G. S. Dharmshaktu, “Intraoperative instrument breakage during the orthopedic elective procedures: A retrospective single-center experience,” *J. Orthop. SPINE*, vol. 8, no. 1, pp. 8–13, 2021, doi: 10.4103/JOASP.JOASP.

[4] A. Leiden, F. Cerdas, D. Noriega, J. Beyerlein, and C. Herrmann, “Life cycle assessment of a disposable and a reusable surgery instrument set for spinal fusion surgeries,” *Resour. Conserv. Recycl.*, vol. 156, no. December 2019, p. 104704, 2020, doi: 10.1016/j.resconrec.2020.104704.

[5] T. D. Goldberg, J. A. Maltry, M. Ahuja, and J. A. Inzana, “Logistical and Economic Advantages of Sterile-Packed, Single-Use Instruments for Total Knee Arthroplasty,” *J. Arthroplasty*, vol. 34, no. 9, pp. 1876-1883.e2, 2019, doi: 10.1016/j.arth.2019.03.011.

[6] C. L. Thiel *et al.*, “Cataract surgery and environmental sustainability: Waste and lifecycle assessment of phacoemulsification at a private healthcare facility,” *J. Cataract Refract. Surg.*, vol. 43, no. 11, pp. 1391–1398, 2017, doi: 10.1016/j.jcrs.2017.08.017.

[7] C. L. Thiel *et al.*, “Minimal Custom Pack Design and Wide-Awake Hand Surgery: Reducing Waste and Spending in the Orthopedic Operating Room,” *Hand*, vol. 14, no. 2, pp. 271–276, 2019, doi: 10.1177/1558944717743595.

[8] K. Nast and K. A. Swords, “Decreasing operating room costs via reduction of surgical instruments,” *J. Pediatr. Urol.*, vol. 15, no. 2, pp. 153.e1-153.e6, 2019, doi: 10.1016/j.jpurol.2019.01.013.

[9] “Friction Coefficient Tables in Air and Vacuum.” https://www.tribonet.org/wiki/friction-coefficients-in-atmosphere-and-vacuum/

Microfluidic platform for cell classification from optical signatures via machine learning

D. Dannhauser[1], M.I. Maremonti[1], P.A. Netti[1,2], and F. Causa[2]
[1] *Centro Interdipartimentale di Ricerca sui Biomateriali (CRIB), Università degli Studi Napoli "Federico II", Italia*
[2] *Center for Advanced Biomaterials for Healthcare@CRIB, Istituto Italiano di Technologia (IIT), Italia*

***Abstract*— Biophysical cell properties are a powerful tool for the label-free classification of cells. Here, we report a single cell investigation approach to detect different peripheral blood cell classes in microfluidics using a machine learning based optical cell signatures detection. The utilized microfluidic platform aligns cells in flow and alternatively allows compression and subsequent investigations of cells in flow. In fact, the presented approach can be interesting for a wide spectrum of clinical and diagnostic single cell investigations, such as the detection of circulating tumour cells in liquid biopsy samples.**

***Keywords*—Single Cell Approach, Microfluidics, Light Scattering, Machine Learning.**

I. Introduction

Cells contain specific biophysical information, that can be useful for their classification as well as for a wide range of therapeutic purposes. To reveal potential cell information in a straightforward manner is challenging. We focus on human peripheral blood mononuclear cells (PBMCs), which can be easily isolated from blood of healthy donors or buffy coats and therefore of valuable interest for diagnostic single cell approaches. Although PBMCs have a different composition, phenotype, and activation status than cells in intestinal tissue, they can be seen as liquid biopsy.
Nevertheless, cancer diagnosis and treatment mostly use solid biopsy from primary or secondary tumours, which has several disadvantages both for patient (time), and for hospital (costs). Such difficulties are particularly of interest when dealing with tumours having difficult surgical access and a high mortality rate [1]. Liquid biopsy can drastically revolutionize the field of clinical oncology, offering the possibility of continuous monitoring. Nowadays, cell discrimination is routinely performed by cytometric analysis based on surface receptor expression, which is also cost and time intensive. Alternatively, a label-free cell classification based on a liquid biopsy is highly demanded.
Therefore, we present a simple microfluidic based approach based on light scattering, and machine learning for single cell class prediction in liquid biopsies (see Fig.1).

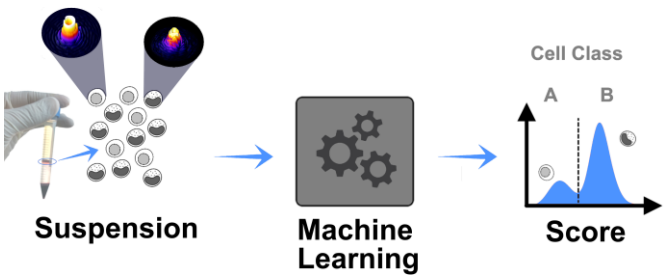


Fig. 1: Working flow of the PBMC type prediction, from optical signatures via machine learning to cell class score.

Briefly, optical signatures of cells (label-free information of biophysical cell information) are recorded by a static light scattering apparatus, which continuously measure scattering profiles of passing living cells. Obtained cell signatures are matched with pre-calculated simulation curves to retrieve the searched for cell properties: dimension of cell and nucleus, optical density of nucleus and cytoplasm. Machine learning uses such cell information as input to predict the searched for cell classes. As proof of concept, a prediction model was trained with ≥100 cells per class covering a wide range of human peripheral blood cell types: Erythrocytes [3], T- and B-lymphocytes [2], Natural Killer cells [4], Monocytes [5], Circulating Tumour Cells (CTC) [6] as well as M0-, M1- and M2-Macrophages [7].
The presented measurement approach allows a distinct classification and selection of single cell types and therefore can be seen as prognostic, easy, accessible, cost saving and accurate pre-screening method useful in clinical routines by searching and detailing CTC from a liquid biopsy sample.

II. Material and Methods

A. Blood samples

We primarily investigated PBMC, which were obtained from healthy donor buffy coats obtained from the blood bank of the medical school of the Federico II University of Naples (Italy). At the time of blood donation, each donor signed an informed consent (model n. 5526 of Azienda Ospedaliera Universitaria "FEDERICO II", Naples, Italy) in which is specified that waste parts of the blood, not useful for medical-therapeutic purposes of blood donation, can be used for scientific research purposes. Moreover, CTC were collected from non-small cell lung cancer patients, which were previously already identified from pathologist examination. The study was conducted according to the guidelines of the Declaration of Helsinki and approved by the ethical committee of AOU Università degli Studi della Campania Luigi Vanvitelli, Protocol number 417 on 22 July 2014. This study was carried out according to the Helsinki declaration and informed written consent was obtained from all patients included in the study. Data regarding medical history and clinical-instrumental work-up were assessed for each patient. Pleural washing collection and storage have been performed during surgical intervention, before any manipulation of the lung and cancer resection, also according, in some aspects of the technique, to previous studies [6], [8].
All the experiments were performed and analysed anonymously, without any biographical reference to donors.

B. Sample preparation

PBMC were collected using standard density gradient centrifugation, with some adaptation to reduce platelet

contaminations [9]. Briefly, the blood sample was gently layered on an equal volume of density gradient fluid (Ficoll) and centrifuged at 300$\vec{g}$ for 45 minutes (without brake). The PBMC ring stratified at the interface between Ficoll and plasma was collected using a Pasteur pipette and washed twice with RBC lysis solution to eliminate possible erythrocyte contaminations of the sample [10], [11]. After separation, the PBMC were washed and diluted in the alignment medium.
A similar procedure was applied for CTC collection. A more detailed description is presented elsewhere [6].

C. *Microfluidic platform*

A microfluidic platform was used for the single cell investigations, assembled by 3D-printer parts, which connect a round shaped glass capillary (alignment section) with a square shaped glass channel (observation section) [2]. The cell alignment in the first section is accomplished by a viscoelastic cell medium (0.2-0.4wt% of Polyethylene-oxide 4MDa) and a pressure driven flow. Thanks to the resulting fluid properties, generated by viscoelastic fluid forces, cells are aligned to the centreline of the round shaped channel and subsequently remain aligned in the centreline of the microfluidic readout channel [12], [13]. Note that fluid forces have been chosen to prevent cell deformation effects, while ensuring sufficient cell focusing in the alignment section. In addition, cross-section of the cell observation section can be tuned to allow precise cell compression in-flow if needed [14], [15]
However, one end of the round shaped channel is immersed in the cell sample: by applying a certain pressure on the sample surface, cell medium is pushed through the channel. Viscoelastic cell alignment can be achieved if the following relationship Eq. (1) is satisfied:

$$\boldsymbol{\Theta} = 3\boldsymbol{Wi}\boldsymbol{\beta}^2 \frac{\boldsymbol{L}}{\boldsymbol{2R}} > -\boldsymbol{ln}\,(\boldsymbol{3.5\beta}), \qquad (1)$$

with $\boldsymbol{Wi} = \boldsymbol{2\lambda\bar{U}\,/\,2R}$, where $\boldsymbol{\lambda}$ is the relaxation time of the fluid, $\boldsymbol{\bar{U}}$ is the average fluid velocity, $\boldsymbol{R}$ is the channel radius, $\boldsymbol{\beta} = \boldsymbol{r_1/R}$, a non-dimensional geometrical channel parameter, with $\boldsymbol{r_1}$ the cell radius and $\boldsymbol{L}$ the channel length [12], [14] The subsequent observation channel allows precise single cell analysis due to is square shape of 400 x 400 µm and preserved centreline alignment. To assure continuity between alignment and observation section, the capillary is collinearly inserted in the squared section and sealed by a soft ferrule. Furthermore, the presented microfluidic concept was applied for barcoded hydrogel readout to detect specific miRNA concentrations in flow to name one alternative application field for single particle alignment [16].
For each investigated cell class, we prepared samples of ~1.25 x10^5 cells mL^{-1} to ensure a throughput rate of ~2 cells sec^{-1} at the readout laser beam. Note that sample concentration and fluid velocities were optimized to avoid possible cell-cell interactions and cell deformation effects. The maximum throughput performance of the presented approach is ~50 cells sec^{-1}. However, at the end of the observation section, cells can be recovered for further studies.

D. *Experimental setup*

We used a static light scattering based measurement approach (see Fig. 2), which can obtain precise optical signature information in a continuous angular range from 2-30°, with an angular resolution of ~0.1°. Briefly, cells aligned in the observation section, pass through a collimated laser beam (λ=633 nm), and the scattered light is collected and mapped on a camera sensor. The hereby-obtained optical scattering signatures (see Fig. 2) are used to retrieve the biophysical information of single cells. In more detail, collected signatures are matched with a look-up table of previously calculated theoretical scattering signatures to retrieve biophysical cell information. Detailed information is shown elsewhere [17], [18]. Machine Learning was implemented with a commercial software (MATLAB, vers. R2020b, MathWorks) to predict different PBMC classes form optical signature information.

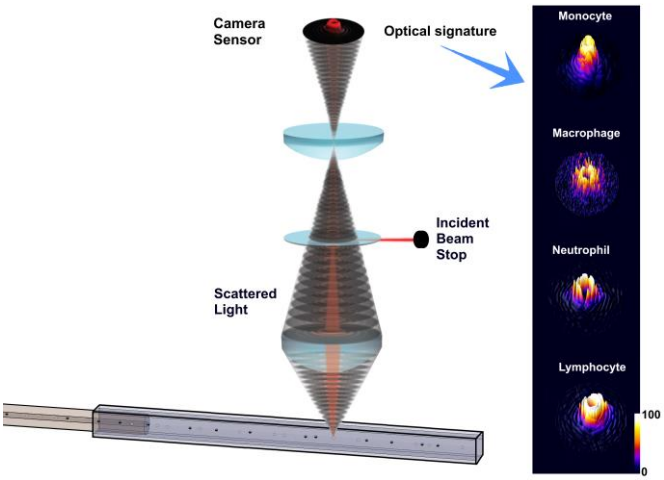


Fig. 2: Experimental setup for the optical signature recording. Illustrative cell signatures are presented for some peripheral blood cell classes.

III. Results and Discussion

First, we analysed previously separated cell types (e.g. Monocytes and M0-, M1-, M2-Macrophage subtypes) with the mentioned light scattering method to obtain single cell based optical signatures. The separate measurement of different cell types allowed us to create a labelled training set (circa 200 cells for each cell type) of cell classes, which is needed for the machine learning based supervised classification. Afterwards, we tested different classification algorithms, regarding single cell type classification accuracy. For instance, a classification accuracy above 80% was obtained using a quadratic Support Vector Machine with one neighbour, euclidean metric distance and equal distance weights. Moreover, we applied a box constraint level of 0.1 and a kernel scale of 1, reducing the penalty imposed on margin-violating observations, and, therefore, preventing overfitting of our test data. We observed the highest misclassification for M1-Macrophages with more than 25%, compared to M0- and M2- Macrophages as well as Monocytes with less than 20%. Indeed, the quadratic Support Vector Machine was found to be the most suitable algorithm according to speed and accuracy (training time ~0.5 sec and a total misclassification cost = 45). Other classifiers resulted into show lower performances: the linear Support Vector Machine trained classifier, fine K nearest neighbour and medium tree, showed an accuracy below 80%. The parallel coordinates plot in Fig. 3 illustrates the correlation between two different cell classes for four extracted biophysical cell features (cell diameter, refractive index of nucleus and cytosol, as well as nucleus over cytosol ratio), where each biophysical cell feature is represented by a vertical line. Due to the different range of each investigated feature, their standard deviations are plotted.

Dashed lines indicate misclassified cells after the model training, while the colour indicate the cell class label. By investigating the highest concentration of misclassified features (dashed lines) the machine learning model performance can be optimized. However, post analyses of cells confirmed that the use of appropriate microfluidics conditions and biocompatible fluids guarantee high cell viability, demonstrating the non-invasiveness of the presented approach.

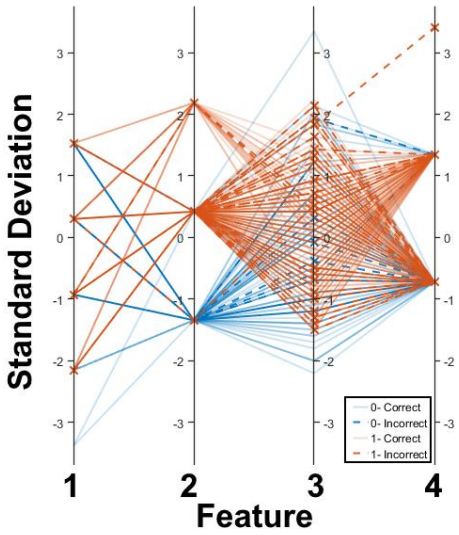


Fig. 3: The parallel coordinates plot indicates the correlation between the four investigates biophysical cell features.

IV. Conclusion

In this work we present an in-flow, non-invasive, label-free approach with supervised machine learning to classify peripheral blood cell subclasses according to their biophysical information. Compared with standard flow cytometric approaches, which are known to have high instrumentation and service costs, the presented optical signature-based method is very simple and cost-effective. Moreover, it permits a classification of cell subtypes without large numbers of cells and resource-intensive labelling. Less than 100 cells of a certain cell PBMC population are needed to precise classify them. More importantly, experiments are realized using a lab-on-a-chip approach permitting the measurement of living cells in suspension, which furthermore are collectable and re-usable for other diagnostic investigations or therapeutic approaches. Measurement times can be drastically reduced with the mentioned measurement approach, while classification accuracy is significantly increased. In fact, by identifying PBMC subsets with high precision our measurement approach could help in accurate pre-screening method useful in clinical routines by searching and detailing cells from a liquid biopsy sample.

References

[1] H. Sung, *et al.* “Global Cancer Statistics 2020: GLOBOCAN Estimates of Incidence and Mortality Worldwide for 36 Cancers in 185 Countries.” CA Cancer J. Clin. 2021, 71, 209–249.

[2] D. Dannhauser, *et al.* “Single-cell screening of multiple biophysical properties in leukemia diagnosis from peripheral blood by pure light scattering." Sci. Rep., 2017, 7, 1-13.

[3] D. Dannhauser, *et al.* “Optical signature of erythrocytes by light scattering in microfluidic flows.” Lab Chip, 2015, 15, 3278-3285.

[4] D. Dannhauser, *et al.* “Non-invasive and label-free identification of human natural killer cell subclasses by biophysical single-cell features in microfluidic flow.” Lab Chip, 2021, 21, 4144-4154.

[5] D. Dannhauser, *et al.* “Biophysical investigation of living monocytes in flow by collaborative coherent imaging techniques." Biomed. Opt. Express, 2018, 9, 5194-5204.

[6] D. Rossi, *et al.* "New Trends in Precision Medicine: A Pilot Study of Pure Light Scattering Analysis as a Useful Tool for Non-Small Cell Lung Cancer (NSCLC) Diagnosis." J. Pers. Med. 2021, 11.10, 1023.

[7] D. Dannhauser, *et al.* "Single cell classification of macrophage subtypes by label-free cell signatures and machine learning." R. Soc. Open Sci. 2022, 9.9, 220270.

[8] G. Kaczmarczyk, *et al.* “Cytological examination of pleural cavity lavage accompanied by the study of gene promoter hypermethylation of p16 and O6-methylguanine-DNA-methyltransferase genes in diagnostics of non-small cell lung cancer metastatic changes into pleura.” Contemp. Oncol. 2012, 16, 322–327.

[9] T. B. Casale and M. A. Kaliner, “Rapid method for isolation of human mononuclear cells free of significant platelet contamination.” J. Immunol. Methods, 1982, 55, 347–353.

[10] C. S. Haas, Participação das proteínas morfogenéticas ósseas no crescimento folicular final, ovulação e função luteal, 2018, 119.

[11] G. Terrazzano, *et al.* “Type 1 diabetes progression is associated with loss of CD3+ CD56+ regulatory T cells that control CD8+ T-cell effector functions.” Nat. Metab., 2020, 2, 142-152.

[12] G. D'Avino *et al.* “Single line particle focusing induced by viscoelasticity of the suspending liquid: theory, experiments and simulations to design a micropipe flow-focuser.” Lab Chip, 2012, 12, 1638-1645.

[13] G. Romeo, *et al.* “Viscoelastic flow-focusing in microchannels: scaling properties of the particle radial distributions.” Lab Chip, 2013, 13, 2802-2807.

[14] D. Dannhauser, *et al.* “Mechanical phenotyping of breast cell lines by in-flow deformation-dependent dynamics under tuneable compressive forces.” Lab Chip, 2020, 20, 4611-4622.

[15] M. I. Maremonti, *et al.* "Wide-range viscoelastic compression forces in microfluidics to probe cell-dependent nuclear structural and mechanobiological responses." J. R. Soc. Interface, 2022, 19, 20210880.

[16] D. Dannhauser, *et al.* "In-flow real-time detection of spectrally encoded microgels for miRNA absolute quantification." Biomicrofluidics, 2016, 10, 064114.

[17] D. Dannhauser, *et al.* “Small angle light scattering characterization of single micrometric particles in microfluidic flows.” Optical Methods for Inspection, Characterization, and Imaging of Biomaterials, 2013. Vol. 8792. International Society for Optics and Photonics.

[18] D. Dannhauser, *et al.* “Multiplex single particle analysis in microfluidics.” Analyst, 2014, 139, 5239–5246.

Remote In-Bed Monitoring of Vital Signs Using Radar Technology

M. Mercuri[1], I. Lorato[2], T. Torfs[3], and F. Crupi[1]
[1] *DIMES, University of Calabria, 87036 Rende (CS), Italy*
[2] *imec – The Netherlands, 5656 AE Eindhoven, The Netherlands*
[3] *imec, 3001 Leuven, Belgium*

***Abstract*—In this work, a radar sensor is proposed and demonstrated *in vivo* for remote vital signs monitoring (measure of respiration rate and heart rate) of a sleeping subject. In addition, a motion artifact rejection signal processing method, based on the wavelet transform, is presented and discussed. A practical setup was implemented in a bedroom with the radar placed on the ceiling above a human volunteer. Experimental results show accurate measurement of the subject's vital signs.**

***Keywords*—Bed monitoring, Doppler, radar remote sensing, vital signs.**

I. Introduction

THE combined senior and geriatric population is expected to increase worldwide, with the total number of people aged 65 years or older projected reach 2 billion in 2050 [1]. Concurrently, in-home care or nursing facilities must scale to support this increase. This will represent an unsustainable burden to society. Technological innovation in *telemedicine* has an important role to play in addressing this problem [2].

Today's devices require sensors that make physical contact and are in the form factor of a wearable device [3]. Current technologies for diagnostics and treatment of chronic diseases typically involve recording of biomedical signals such as brain activity (EEG), heart pattern (ECG), muscle activity (EMG), eye movements (EOG), blood oxygenation saturation (SpO2), and respiration effort [3]. These measurements are made through sensors attached to the patient's skin. Situations exist for which this is not preferable, e. g. patients with severe and extensive burn wounds, premature infants whose skin is easily damaged, or sleep monitoring during which sleep itself can be interfered due to the discomfort caused by the sensing technologies. Commercial alarm systems connecting to medical care units do exist, but they require an action from the person, like pressing a button, e.g., worn as a necklace. However, a person in an emergency situation may no longer have the reflex to press this button or may even no longer be able to do so. One may also forget to put on the necklace or charge the device. Contactless long-term health monitoring is thus preferable. Optical and thermal cameras-based devices represent an option [4], [5]. However, privacy concerns can be present. Furthermore, these solutions can require skin visibility to monitor the vital signs of interest [4] and have typically problems in the case the subjects is (partially) covered by blankets [5]. On the contrary, radar sensors can be mounted in privacy-sensitive areas (e.g., bedroom), being able to monitor vital signs parameters within typical room sizes, also through clothes and blankets [6]. This facilitates a number of highly relevant clinical applications, both in home and clinical environments, such as sleep monitoring, automated nurse call solutions, preventive medicine, etc.

In this work, a radar sensor, based on a frequency-modulated continuous-wave (FMCW) architecture and a signal processing algorithm are proposed for remote in-bed monitoring of the patient's vital signs. Experimental results are shown to demonstrate the ability of the radar in accurately monitoring the vital signs parameters (respiration and heart rates) of a sleeping subject under realistic conditions.

II. Methodology

In Subsection II.A, the FMCW theory is briefly described, while in Subsection II.B, the proposed signal processing method is presented.

A. One-ray Propagation FMCW Model

In this work, it is assumed that there is only a single person lying on the bed at a nominal distance d_0 away from the radar. The FMCW radar transmits, through a transmitting (TX) antenna, a series of *chirps* (Fig. 1) [7]. The *chirps* reach the subject where they are phase modulated by the oscillatory thorax's motion $x(t)$ due to the cardiopulmonary activity [8]. These signals are also reflected back to the radar and collected by the receiving (RX) antenna. After the round trip the delay is equal to $2 \cdot d_0/c$, where c is the speed of the light. Between the transmitted and received *chirps* there is an instantaneous frequency difference Δf which is proportional to the round-trip delay. The *beat signals*, resulting from mixing the transmitted and the received *chirps*, are therefore sinusoidal signals with frequency Δf and a certain initial phase.

The Fast Fourier Transform (FFT) applied to a sine function allows determining its frequency and initial phase information. Thus, it is possible to retrieve Δf and then to determine d_0. The cardiopulmonary activity of a person causes a sub-millimeter motion on the thorax surface which is several orders smaller than the target's nominal distance (i.e., $x(t) << d_0$) [8]. Hence, due to the limited resolution of the FFT, its contribution in estimating Δf is essentially zero. This means that the frequency information cannot be used to monitor the vital signs. The latter operation however can be performed looking at the variation of the initial phases of consecutive beat signals (i.e., Doppler signals). The received chirps are in fact significantly phase modulated by the thorax motion due to the Doppler effect. The instantaneous initial phases of the *M beat signals* are proportional to the instantaneous thorax positions, i.e., $d_0 \pm x(t)/2$, and inversely proportional to the wavelength of the chirps, which is very small in the microwave frequency range. For that reason, even sub-millimeter vibrations involve appreciable Doppler signal. It should be specified that d_0

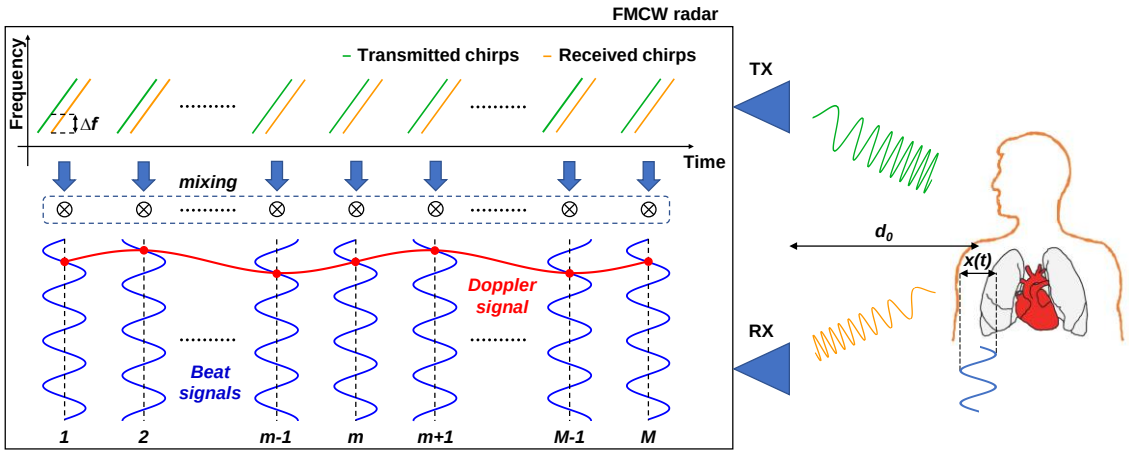


Fig. 1: Block diagram of the FMCW operational principle

involves only a constant phase shift (the subject lies on the bed) whereas, the vital signs involve a variable Doppler (phase) signal.

In order to measure the vital signs parameters, *M chirps* have to be transmitted. The resulting *M beat signals* are acquired, digitized, and arranged in a *N* x *M* matrix, where *N* is the number of samples per beat signal. By applying the FFT per column, a *K* x *M* complex data matrix is obtained (Fig. 2), with *K* being the number of range bins. Calculating the magnitude of the FFT and scanning each column, the spectrum peaks will be only in correspondence of the *k*-th range bin where the subject is present (range bin 4 in the example of Fig. 2). Therefore, the location of the person (distance from the radar) can be determined by multiplying *k* by the predefined radar range resolution. The vital signs information (Doppler signals) can be extracted by determining the *M* phases from the complex FFT samples along the *k*-th row (Fig. 2). However, in real-world room settings, the FFT magnitude cannot be used to locate the target. Furniture and objects (especially if metallic) result in reflections whose magnitudes are much stronger than the reflection from a person. Hence, the subject's peak in the data matrix will be buried by the contributions of furniture and other objects. Further signal processing is hence necessary to extract the weak Doppler information of the subject, rejecting the contributions of static reflectors.

B. Signal Processing

In this work, the variation in the Doppler signal is used to automatically localize the subject (i.e., determining d_0), differencing they from stationary reflectors. The idea is to exploit the evidence that the Doppler information due to the vital signs is a variable signal while furniture/objects involve a constant phase shift. Therefore, the standard deviation is applied to the complex signal per each range bin, i.e., per each row of the data matrix (Fig. 2). The *k*-th range bin with largest variation indicates the location of thorax.

The Doppler information is hence extracted by performing phase demodulation from the complex FFT samples along the *k*-th row. In this work, the linear demodulation technique, proposed in [9], is applied. The respiration and heartbeat signals are finally retrieved after properly bandpass filtering, and the Doppler signal and the corresponding rates are estimated through the FFT.

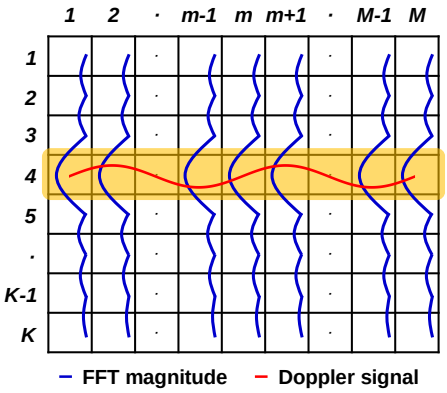


Fig. 2: Data matrix

However, it is expected for subjects to change position or move while sleeping, causing random body movement artifacts. These artifacts, which are several orders of magnitude larger than the sub-millimeter cardiopulmonary motion on the thorax, jeopardize the performance of vital signs monitoring. To address it, the Continuous Wavelet Transform (CWT) is used to locate the artifacts. It provides a time-frequency representation of the signal. Thus, the artifacts, that normally involve signals with a higher frequency content than the ones of the vital sign, can be easily located in time. The artifact episodes can be then discarded from the Doppler signal, avoiding erroneous vital signs estimations. This can be done because, while sleeping, artifacts are expected to be isolated episodes.

III. Bed Monitoring System

A. Radar Signal

The radar transmits linear *chirp* with instantaneous frequency ranging from 7.3 GHz to 8.05 GHz. This total bandwidth of 750 MHz results in a range resolution of 20 cm which is sufficient for localization considering the typical dimensions of the human body. Each *chirp* lasts 102.4 µs. The chirps are not transmitted continuously (i.e., one right after the other) but every 3.027 ms. This results in a sampling rate of the Doppler signal of about 326 Hz, which is higher than the typical vital signs range of 0-3 Hz. The transmitted peak power is of 0 dBm. This, together with the *chirp* configuration (i.e., frequency interval, duration, and duty cycle), allows satisfying

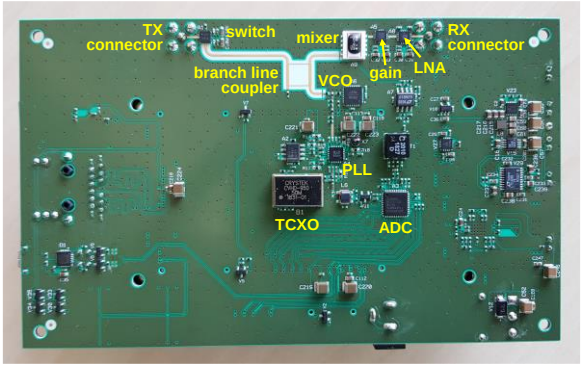


Fig. 3: Radar unit

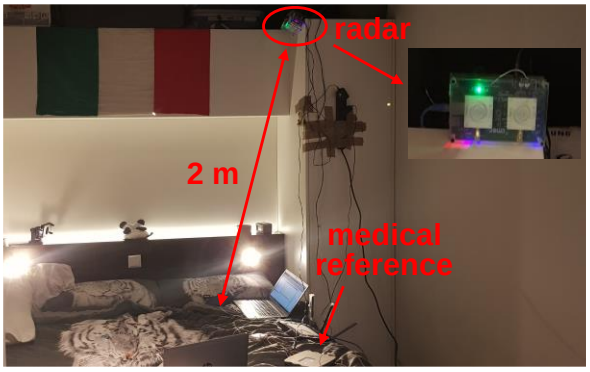


Fig. 4: Experimental set-up

the worldwide UWB indoor radio regulations.

B. Radar Sensor

The radar sensor consists of the radar unit, a processor board and two commercial antennas. A photo of the radar unit is shown in Fig. 3. The FMCW signal is synthesized by the voltage-controlled oscillator (VCO) which is connected to a phase-locked loop (PLL). It feeds a branch line coupler from which two copies of it (with smaller amplitudes) are generated. One is connected to the TX antenna thought its connector and a switch. The latter is used to set the waveform's duty cycle. The other output serves as a local oscillator for the mixer. The reflected signal is received by the RX antenna, amplified by a low-noise amplifier (LNA) and a gain block, before feeding the second port of the mixer. After mixing, the baseband radar signal is filtered, amplified, and acquired by an analog-to-digital converter (ADC). A 50 MHz Temperature Compensated Crystal Oscillator (TCXO) is used to provide the clock reference to the PLL and ADC. This ensures perfect synchronization between chirp generation and acquisition, avoiding phase errors. The processor controls the PLL's synthesizer to generate the *chirps*, controls the switch and sends the ADC's samples to MATLAB by an Ethernet port.

IV. Experimental Results

The experimental protocol was approved by the internal imec – Netherlands Ethical Board. The experiments have been conducted on a human subject in a normal bedroom (Fig. 4). The radar was placed on top of the bed at about 2 m. The volunteer was invited to mimic a realistic sleeping situation, namely lying down on the bed, under the blankets, moving limbs and changing positions (i.e., prone, supine). Different breathing conditions (i.e., holding breath, spontaneous, and paced breathing) have been also mimicked. The g.USBamp device (CE certified and FDA cleared medical device, safety class: II, conformity class: IIa, type of applied part: CF) was used as a reference device to measure heart and respiration activities, through a photoplethysmogram (PPG) finger sensor and a thorax expansion belt, respectively.

Fig. 5 shows the results of an experiment with a spontaneously breathing subject lying on the bed under the blankets. Fig. 5a shows the extracted Doppler signal. It consists of the respiration and heartbeat contributions. The respiration signal is the most dominant. The heartbeat signal is at least one order of magnitude smaller than the respiration

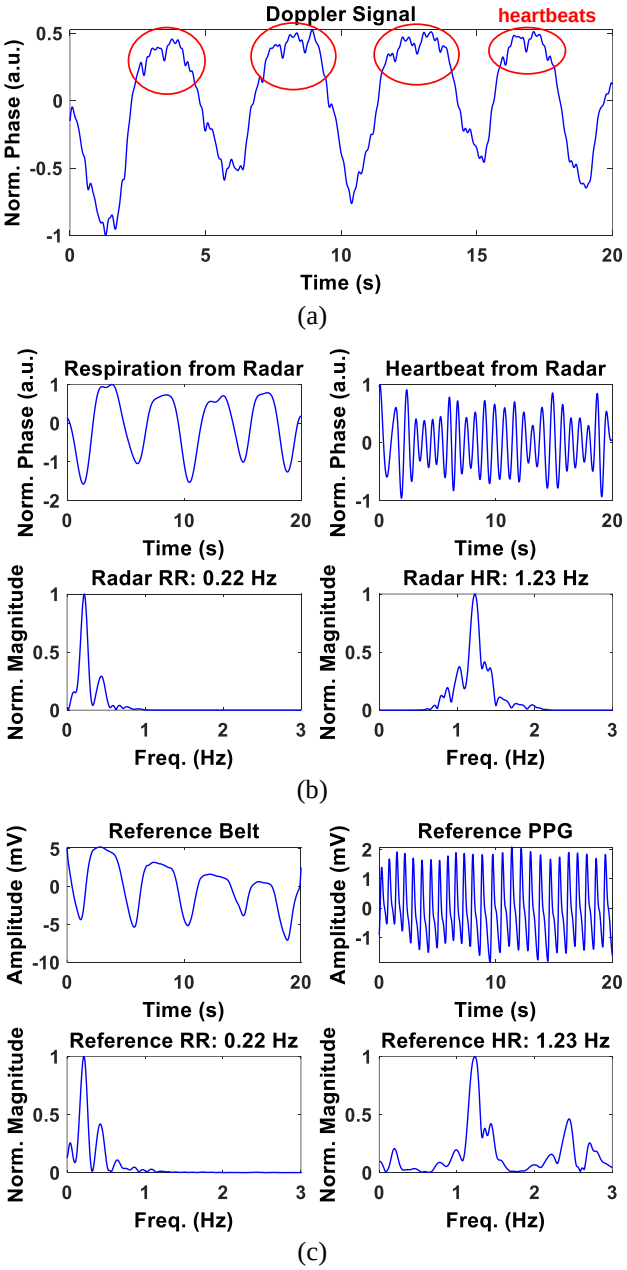


Fig. 5: Experimental results of an asleep (spontaneously breathing) subject. (a) Doppler signal. (b) Respiration and heartbeat signals extracted from the radar and relative spectra. (c) Respiration and PPG signals measured with the reference and relative spectra.

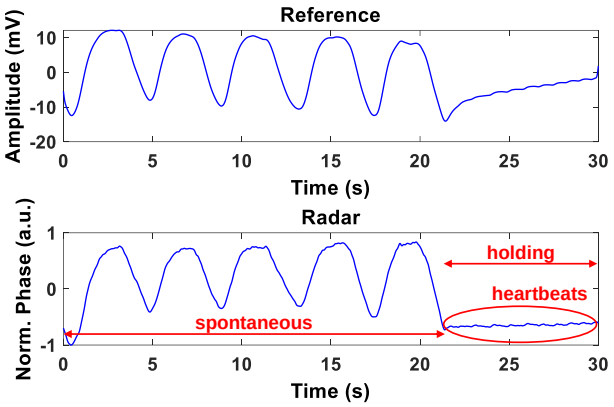


Fig. 6: Breath hold, experimental results. (top) Respiration signal from the belt. (bottom) Doppler signal.

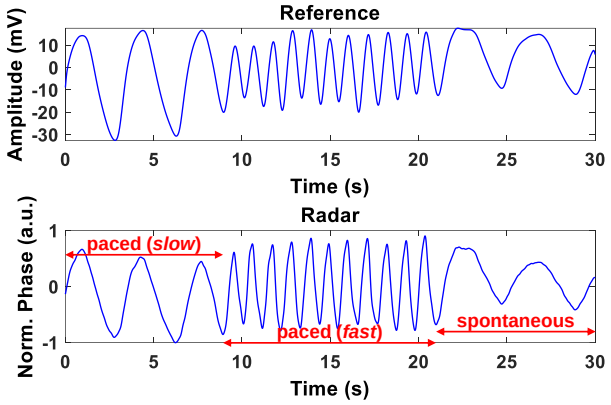


Fig. 7: Paced and spontaneous breathing, experimental results. (top) Respiration signal from the belt. (bottom) Doppler respiration signal.

contribution. For that reason, normally, it is indistinguishable by simply looking at the Doppler signal. It requires, therefore, proper bandpass filtering to be displayed. However, in this example, it can be clearly seen on top of the dominant respiration signal. Figs. 5b and 5c show the respiration and heartbeat signals, together with the relative spectra, extracted from the radar and from the reference device, respectively. It is possible to notice that the radar signals match the respective reference ones.

Figs. 6 and 7 show the results of two experiments during which the subject was invited to mimic different respiratory patterns. Also, in this case, the radar signal fairly matches the reference. In the experiment of Fig. 6, the subject held their breath towards the end of the measurement. In this case, the Doppler signal consists essentially of the heartbeat contribution. The difference in magnitude between the respiration and heartbeat signals is clearly visible in the figure.

Finally, in Fig. 8, an experiment during which the subject was invited to change position from supine to prone is shown. This causes an inevitable motion artifact, corrupting the physiological radar signals. However, this is a temporary effect. In fact, once the movement has ended, the Doppler signal quickly matches fairly the reference and, therefore, the vital signs rates can be accurately estimated. The CWT was used to successfully locate the artifact and the binary mask was built to indicate the segment of the signal to be removed, namely setting 1 if there is an artifact and 0 if not. After this operation, the vital signs can be measured accurately.

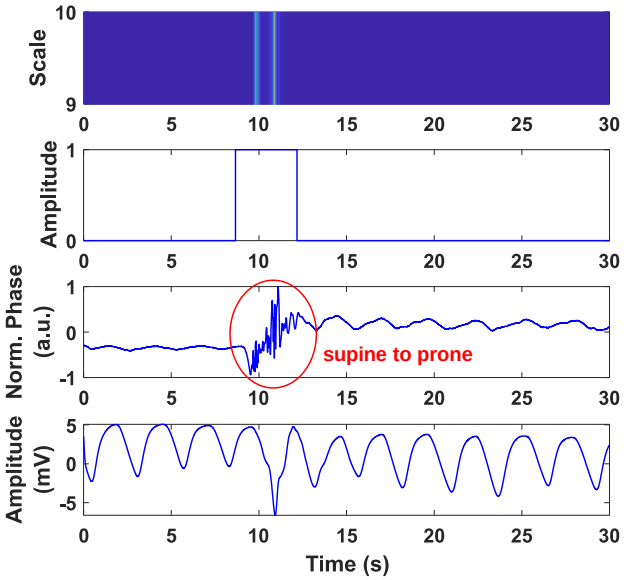


Fig. 8: Experimental results with a subject invited to change position. The first (top) figure shows the CWT result. The second figure is the binary mask indicating the part of the signal to be discarded. The third and the last (bottom) figures show respectively the Doppler signal and the belt reference. The latter was used since the Doppler signal consists mainly of the respiration contribution. In this figure, the parts of Doppler signal containing only the vital sign information (i.e., 0-9 s and 12-30 s) seem small in amplitude. However, this is only due to the normalization operation in a part of the signal containing a large artifact. The amplitude of the signal is sufficiently high and clear for an accurate detection.

V. Conclusion

A radar sensor and a signal processing algorithm have been proposed and *in vivo* demonstrated for remote in-bed monitoring of the vital signs (respiration rate and heart rate) of a single sleeping subject. They enable novel applications in the domain of ambient assisted living, telemedicine, healthcare, geriatric and quarantine medicine. Further works need to be done to confirm the presented finding involving more subjects and including further sleeping conditions and positions.

References

[1] L. Fontana *et al.*, "Medical research: Treat ageing," *Nature*, vol. 511, pp. 405–407, July 2014.

[2] L. S. Wilson and A. J. Maeder, "Recent directions in telemedicine: Review of trends in research and practice,". *Healthc. Inform. Res.*, vol. 21, pp. 213–222, Oct. 2015.

[3] V. Vijayan *et al.*, "Review of Wearable Devices and Data Collection Considerations for Connected Health," *Sensors*, vol. 21, pp. 1-31, Aug. 2021.

[4] W. Wang and A. C. den Brinker, "Modified RGB Cameras for Infrared Remote-PPG," *IEEE Trans. Biomed. Eng.*, vol. 67, pp. 2893-2904, Oct. 2020.

[5] I. Lorato *et al.*, "Towards continuous camera-based respiration monitoring in infants," *Sensors*, vol 21, pp. 1-18, Mar. 2021.

[6] C. Li *et al.*, "Sensing of Life Activities at the Human-Microwave Frontier," *IEEE J. Microw.*, vol. 1, pp. 66-78, Jan. 2021.

[7] M. Mercuri *et al.*, "Automatic radar-based 2-D localization exploiting vital signs signatures," *Sci. Rep.*, vol. 12, pp. 1-11, May 2022.

[8] C. Li *et al.*, "A Review on Recent Advances in Doppler Radar Sensors for Noncontact Healthcare Monitoring," *IEEE Trans. Microw. Theory Tech.*, vol. 61, pp. 2046-2060, May 2013.

[9] M. Mercuri *et al.*, "Analysis of Signal Processing Methods to Reject the DC Offset Contribution of Static Reflectors in FMCW Radar-Based Vital Signs Monitoring," *Sensors*, vol. 22, pp. 1-15, Dec. 2022.

A novel concept of steerable catheters actuated by muscle cells: the BioMeld project

C. Salvatori[1,2], L. Ricotti[1,2], and L. Vannozzi[1,2]
[1] *The Biorobotics Institute, Scuola Superiore Sant'Anna, Italy*
[2] *Department of Excellence in Robotics & AI, Scuola Superiore Sant'Anna, Italy*

***Abstract*—Localized (targeted) therapies allow increasing the efficacy of treatments for several diseases, including cancer. Within this view, the BioMeld project aims at proposing a pipeline to guide the fabrication of an innovative intravascular steerable microcatheter, actuated on its tip by muscle cell contraction. A simulation framework streamlines the process of design quoting, manufacturing, verification, and reporting, thus significantly reducing error-prone manual steps and making the process more efficient. This new generation of steerable microcatheter, fostered by the unconventional kind of actuation provided by muscle cells, will be investigated throughout this project to target localized treatments of deeper and tortuous regions within the cardiovascular systems. In this work we report the overall project vision and we describe some preliminary results on the microcatheter design.**

***Keywords*—catheter, biohybrid actuation, drug release, cancer.**

I. Introduction

Cancer, or neoplasia, is a disease that is spreading more and more in recent years, to the point of being called the "disease of the century". The American Cancer Society has reported that over 1.9 million new cancer cases are expected to be diagnosed only in the US in 2023 [1].

Many therapies are currently available to fight cancers, and several efforts have been conducted by the scientific community to develop more sophisticated treatments to improve patient quality of life and extend life expectancy. Nowadays, chemotherapy, surgery and radiotherapy represent the gold standard. Among them, chemotherapy stands as a treatment based on the administration of drugs, typically injected through catheters by conventional accesses of the cardiovascular system (*e.g.*, in a vein residing in the hand or arm), to fight cancer cells with a cytotoxic action. However, the absorption of a drug at the blood circulation level can cause harmful effects due to the intrinsic toxicity of the chemotherapeutic drug, combined with a non-specific absorption by out-of-target cells, and consequently, a lower therapeutic index.

Alternatively, the use of microcatheters to release the drug locally at the site of interest may enable a local drug release, thus limiting the spread of the drug in healthy organs and tissues. One recent application of local chemotherapy is the hepatic artery infusion (HAI), in which the chemotherapeutic drug is released slowly and steadily into the hepatic artery through a catheter connected with a needle through the skin [2]. In the scientific state of the art, an example of a microcatheter able to locally release drugs has been developed by Sarker *et al.* [3]. Starting from a commercially available catheter, the authors provided a few lateral holes on the catheter wall, and closing the distal end to obtain a localized radial release of drug. The main challenge still remains the guidance of the commercial catheter at increased curvatures and pattern tortuosity.

For this purpose, catheters with a steerable tip have been proposed, recently. Steerable catheters are mainly classified into two groups: those with force generation in the tip and those with force transmitted to the tip [4]. Focusing on the first group, Gopesh *et. al*. developed a hydraulically steerable tip with an outer diameter of 900 µm provided with four channels of 50 µm diameters, filled with a saline solution, symmetrically arranged, and controlled remotely [5]. Regarding the second group, an interesting study was conducted by Kim *et al.* [6]: they developed a remotely-controllable steerable magnetic catheter featured with an outer diameter of 500 µm, remotely controlled, which can navigate through narrow and constrained environments. The magnetic navigation system can assist in approaching the *in vivo* target using magnetic responsive materials within the catheter. However, some restrictions lie on the generation of the torsion movement, which is necessary to facilitate the direction of the tip [7].

In recent years, many advances in manufacturing methods have allowed the production of intravascular catheters with diameters up to 1.8 Fr (500 µm). Such diameter size can potentially enable reaching deep districts, which are intrinsically characterized by a significant tortuosity, thus reaching different targets within the body. However, remotely controlling miniaturized microcatheters on such a small scale remain a challenge. Thus, precise drug release towards hard-to-reach *in vivo* targets still has large margins of improvement.

II. The BioMeld project

BioMeld is a European project funded in the Horizon Europe framework. It aims to develop an intravascular steerable microcatheter actuated by muscle cells to enable drug release in hard-to-reach areas. The development of the microcatheter would benefit from an artificial intelligence-guided modeling and simulation framework to optimize the search for the most efficient design, that will be validated within a validation framework (Figure 1).

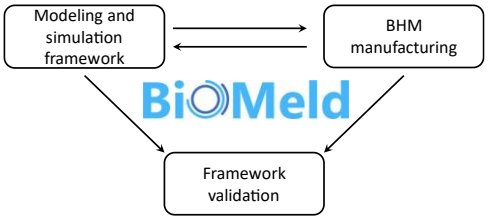


Figure 1: Scheme of a bio-intelligent manufacturing cell for design and production of the microcatheter within the BioMeld project. BHM = biohybrid microcatheter.

A biohybrid actuation paradigm, will be explored for controlling the microcatheter tip.

Biohybrid systems combine living organisms, such as contractile muscle cells, with engineered artificial structures [8]. Biohybrid actuators rely on their ability to convert the chemical energy of the environment into mechanical energy, thus there is no need to supply them when used in *in vivo* environments, avoiding the use of batteries.

One of the most significant challenges affecting current actuation technologies for in vivo applications is represented by the scalability of performance, especially for in vivo applications for which the requirement of biocompatibility is crucial.

Within the BioMeld project, we envisaged a reconfigurable and modular soft catheter bendable by the contractile force generated by the biohybrid actuator. The catheter will be composed of a magnetically-responsive catheter body and a catheter tip, equipped with: (i) a muscle cell-based actuator; (ii) a flexible electronic platform to trigger its activation and receive real-time feedback of catheter motion using flexible strain sensors; (iii) a bioreactor to keep it functional in the long-term.

The catheter body will include magnetically-responsive materials to allow its remote control. A good compromise towards guaranteeing a flexible body but magnetic responsiveness is represented by mixing polymeric materials (*e.g.*, silicones) with magnetic powder, such as NdFeB [9] and orienting them to maximize their responsiveness towards a specific magnetic field direction.

The catheter tip will be designed to host a biohybrid actuator based on skeletal muscle cells, which are controllable through electrical or optical stimuli to generate torque to the catheter tip. Muscle cell-based actuators, as the so-called bio-bots, can generate a relevant force (~100 µN) in the mm-size [10]. As mentioned, the biohybrid system also guarantees the maintenance of the contractile performance while keeping the actuation efficiency high with respect to other actuation technologies when scaled down.

Within the catheter tip, a flexible electronic platform will be integrated to provide muscle cells the electrical stimulation, and able to return the catheter deflection. This platform will exploit a low-voltage organic field-effect transistor fabricated on a polymeric substrate (*e.g.*, Parylene C) acting as a buffer through inkjet printing [11]. Such an electronic platform will also be provided with a deformation sensor to detect the curvature generated on the catheter tip by the muscle cells.

However, a disadvantage of using living materials as a source of actuation is the need to keep the environment parameters controlled with a bioreactor (pH and exchange of nutrients) to maintain muscle cells alive and functional over time [8].

All these components will be integrated inside the microcatheter, while maintaining the tip flexible and soft to be bent. Besides, the catheter will be provided with a hemocompatible coating, a crucial trait for all devices that encounter blood.

III. MATERIALS AND METHODS

A. Selection of the manufacturing techniques and material requirement

For the microcatheter fabrication, we considered molding, additive manufacturing, self-assembly techniques, and dip coating. Soft materials such as silicones (*e.g.*, PDMS, Dragonskin and Ecoflex) will be investigated at first instance. We do not exclude the use of thermoplastic polymers, such as polyurethane or Pebax®, and latex, since these materials represent suitable candidates already used for fabricating commercial devices. Our hypothesis assumes that the soft catheter will offer minimal mechanical resistance. For this purpose, we target materials with a Young's modulus lower than 1.5 MPa. Then, fabrication criteria will be directed to define geometrical parameters to decrease the catheter flexural rigidity.

B. Modeling and estimation of the flexural rigidity and deflection of the catheter

Apart from the magnitude of the force generated by the actuator, the catheter deflection is influenced by several parameters, such as internal and external diameter, wall thickness and elastic modulus [12].

Firstly, we analyzed the catheter mechanical properties in terms of flexural rigidity (*Fl*). For a catheter, such parameter can be calculated as follows:

$$Fl = E * I_0 \quad (1)$$

Where *E* is the Young's modulus of the material used to build the catheter, and *Io* is the moment of inertia that can be expressed for a hollow structure as:

$$I_0 = \frac{\pi(D^4 - d^4)}{64} \quad (2)$$

Where *D* is the external diameter and *d* is the internal diameter. We analyzed the variation of the external diameter *D* (from 2 mm to 10 mm) and, for a specific *D*, the variation of the Young's modulus up to 1.5 MPa.

Then, we estimated the deflection of the catheter by assuming the force generated by the biohybrid actuator equal to 100 µN [10]. According to the Euler-Bernoulli's beam theory [13], the deflection (δ) can be estimated as:

$$\delta = \frac{M * L^2}{2 * E * I_0} \quad (3)$$

Where *L* is the catheter tip length, set at 8 cm, while *M* is the torque generated by the biohybrid actuator, calculated as follows:

$$M = F * \frac{d}{2} \quad (4)$$

Where *F* is the force produced by the biohybrid actuator. Figure 2 shows a schematic representation of model parameters.

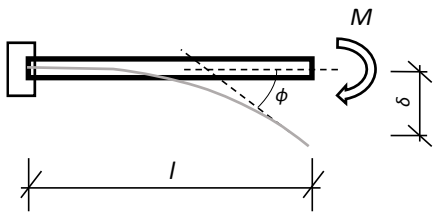


Figure 2: Depiction of the model applied to estimate the catheter deflection.

C. Analysis of the catheter kinking

When a catheter is curved under the application of a moment, the lumen may be occluded if the curvature radius becomes lower than a critical value ($R_{critical}$). This phenomenon is called kinking, and $R_{critical}$ is defined as:

$$R_{critical} = \frac{(1-\nu^2)*R^2}{K*t} \quad (5)$$

Where ν is the Poisson's ratio (set to 0.48, typical value for silicones), R is the external radius of the catheter, t is the wall thickness, and K is a constant (theoretically = 0.99; experimentally 0.72-1.14) [14].

IV. RESULTS AND DISCUSSION

A. Flexural rigidity

Figure 3 shows the influence of the catheter geometrical parameters in the estimation of the flexural rigidity.

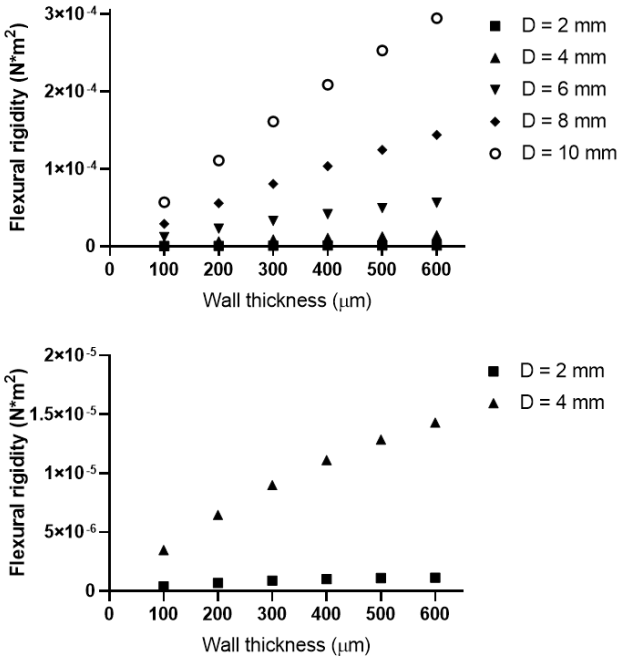


Figure 3: (top) Flexural rigidity estimated by varying the external diameter (D) from 10 to 2 mm, and the catheter wall thickness from 100 to 600 μm, and (bottom) a magnification for the cases D=2 and 4 mm. This estimation was performed by fixing the elastic modulus (E) of the catheter to 1.5 MPa.

Results showed a strong dependence of the flexural rigidity towards the geometrical parameters defined for the catheter, with a difference of two orders of magnitude between the larger (D = 10 mm) and the narrower case (D = 2 mm), for example, from $1.15*10^{-6}$ N*m^2 for D = 2 mm to $2.95*10^{-4}$ N*m^2 for D=10 mm, at a wall thickness of 600 μm. Typical values of flexural rigidity of catheters range from 1 to $50*10^{-4}$ N*m^2, mainly due to the stiffness of the material used to fabricate the catheter [15]. Here, the objective of designing a soft catheter for being actuated by muscle cells implicates the achievement of lower flexural rigidity for the catheter.

We also analyzed the influence of the elastic modulus for a specific case (D = 6 mm) The results are reported in Figure 4.

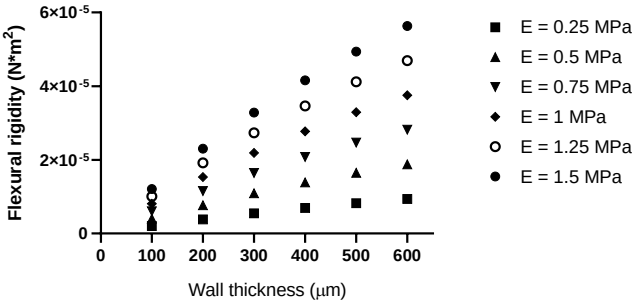


Figure 4: Flexural rigidity estimated by varying the elastic modulus (E) from 0.25 MPa to 1.5 MPa, and the catheter wall thickness from 100 to 600 um. This estimation was performed by fixing the external diameter (D) to 6 mm.

The graphs show that the wall thickness and the elastic modulus influence flexural rigidity. A non-linear trend can be observed with the variation of the external diameter, while a linear trend is noticeable while Young's modulus decreases. As a rule of thumb, flexural rigidity decreases by decreasing the external diameter, wall thickness, and elastic modulus.

B. Deflection

Figure 5 shows the influence of the catheter geometrical parameters in the estimation of the catheter deflection, according to the Euler-Bernoulli's beam theory.

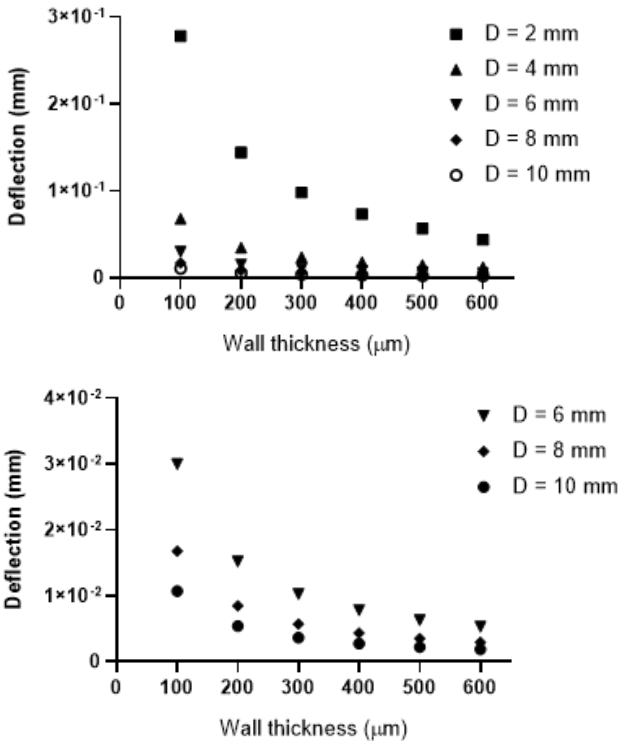


Figure 5: (top) Deflection estimated by varying the external diameter (D) from 10 to 2 mm, and the catheter wall thickness from 100 to 600 μm, and (bottom) a magnification for the cases D=6, 8 and 10 mm. This estimation was performed by fixing the elastic modulus (E) of the catheter to 1.5 MPa.

Results show a strong dependence of the flexural rigidity towards the geometrical parameters defined for the catheter, with a difference of one order of magnitude between the larger (D = 10 mm) and the narrower case (D = 2 mm). The deflection increases by decreasing the wall thickness. For example, for a diameter of 2 mm, and a wall thickness of 0.10 mm, the deflection will be 0.28 mm while for a higher thickness, such

as 600 µm, the deflection becomes less than 100 µm. These results are intuitive since an increase in the wall thickness means an increase in mass, therefore, a higher moment of inertia.

We also analyzed the influence of the elastic modulus for a specific case (D = 6 mm). Results are reported in Figure 6.

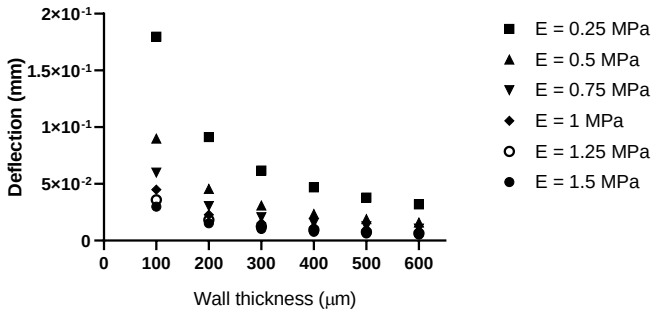


Figure 6: Flexural rigidity estimated by varying the elastic modulus (E) from 0.25 MPa to 1.5 MPa. This estimation was performed by fixing the external diameter to 6 mm.

Results show the effect of the elastic modulus decreasing in the increase of the expected deflection. Indeed, an increase in elastic modulus means a higher material rigidity, which reduces the expected deflection. Such deflections are relatively low and probably not sufficient to navigate vascular branches, and a process of parameter optimization will be necessary to provide a futuristic usage of biohybrid technology.

C. Kinking

Figure 7 shows the influence of the catheter geometrical parameters in the estimation of the critical radius.

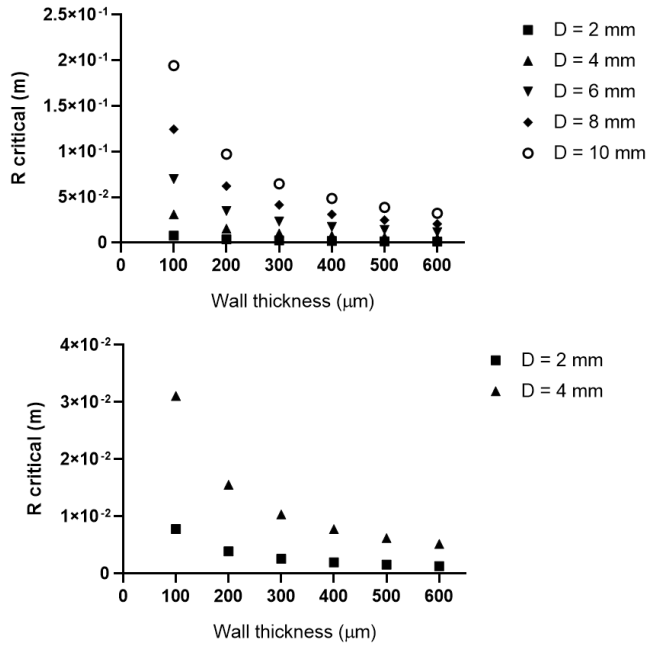


Figure 7: (top) Critical radius estimated by varying the external diameter (D) from 10 to 2 mm, and the catheter wall thickness from 100 to 600 µm, and (bottom) a magnification for the cases D=2 and 4 mm. This estimation was performed by fixing the elastic modulus (E) of the catheter to 1.5 MPa.

Results highlight that the $R_{critical}$ is strongly dependent on the geometrical features of the catheter. From the anatomical point of view, the angle of curvature expected to surpass the first branch of the hepatic artery is equal to ~45° [16], with a radius of curvature ranging between 1-4 cm. Catheter size and wall thickness will be chosen among the cases with the $R_{critical}$ lower than the targeted radius of curvature.

V. CONCLUSION

Within the framework of the BioMeld project, catheter design and manufacturing are encountering the technical challenges of integrating several components. Indeed, it must fit with the integration of an electronic platform and a bioreactor to enable the correct functioning of the biohybrid actuator, while maintaining good flexibility. Beyond the choice of materials and processing techniques, fabricating a soft catheter also involves the investigation of parameter designs. The next steps will be directed towards the definition of suitable geometrical parameters to target components integration, while maximizing the catheter flexibility.

ACKNOWLEDGMENT

This project has received funding from the European Union's Horizon Europe research and innovation programme, BioMeld project, Grant Agreement No. 101070328.

REFERENCES

[1] American Cancer Society. Cancer Facts & Figures 2023. Atlanta: American Cancer Society; 2023.
[2] L. Shi et al., "Initial hepatic artery infusion and systemic chemotherapy for asymptomatic colorectal cancer with un-resectable liver metastasis," Int. J. Clin. Exp. Med., vol. 8, pp. 1000-1008. 2015.
[3] S. Sarker, Y. S. Chatzizisis, S. Kidambi, and B. S. Terry, "Design and development of a novel drug delivery catheter for atherosclerosis," Proceedings of the 2018 Design of Medical Devices Conference. Minneapolis, Minnesota, USA. April 9–12, 2018.
[4] A. Ali, D. H. Plettenburg, and P. Breedveld, "Steerable Catheters in Cardiology: Classifying Steerability and Assessing Future Challenges," IEEE Trans. Biomed. Eng., vol. 63, pp. 679–693, 2016.
[5] T. Gopesh et al., "Soft robotic steerable microcatheter for the endovascular treatment of cerebral disorders," Sci. Robot., vol. 6, 2021.
[6] Y. Kim, G. A. Parada, S. Liu, and X. Zhao, "Ferromagnetic soft continuum robots," Sci. Robot., vol. 4, 2019.
[7] S. Jeon et al., "A Magnetically Controlled Soft Microrobot Steering a Guidewire in a Three-Dimensional Phantom Vascular Network," Soft Robot., vol. 6, pp. 54–68, 2019.
[8] L. Ricotti et al., "Biohybrid actuators for robotics: A review of devices actuated by living cells," Sci. Robot., vol. 2, 2017.
[9] V. Iacovacci et al., "Polydimethylsiloxane films doped with NdFeB powder: magnetic characterization and potential applications in biomedical engineering and microrobotics,", Biomed. Microdev., vol. 17, pp. 1–7, 2015.
[10] M. Guix et al., "Biohybrid soft robots with self-stimulating skeletons," Sci. Robot., vol. 6, 2021.
[11] S. Lai et al., "Ultra-conformable Organic Field-Effect Transistors and circuits for epidermal electronic applications," Org. Electron., vol. 46, pp. 60-67, 2017.
[12] I. Mechanical Properties of Catheters, Acta Radiol. Diag., vol.4, pp. 11-22, 1966.
[13] O. A. Bauchau and J. I. Craig, "Euler-Bernoulli beam theory," Structural analysis. Springer, pp. 173–221, 2009.
[14] R. L. Evans, E. F. Bernstein, E. Johnson, C. Reller, and C. R. Mechancia, "Mechanical properties of the living dog aorta," Am. J. Physiol., vol. 202, pp. 619-621, 1962.
[15] C. M. Hartquist, V. Chandrasekaran, H. Lowe, E. C. Leuthardt, J. W. Osbun, G. M. Genin, and M. A. Zayed, "Quantification of the flexural rigidity of peripheral arterial endovascular catheters and sheaths." J. Mech. Behav. Biomed. Mater., vol. 119, pp. 104459, 2021.
[16] C. A. Basciano, C. Kleinstreuer, A. S. Kennedy, W. A. Dezarn, and E. Childress, "Computer modeling of controlled microsphere release and targeting in a representative hepatic artery system," Ann. Biomed. Eng., vol. 38, pp. 1862-1879, 2010.

Development of a computational model to estimate the hemolysis risk associated with hemodialysis catheters

I. Guidetti[1], F. De Gaetano[1], D. Gallo[2], U. Morbiducci[2], M.L. Costantino[1]
[1] *Department of Chemistry, Material and Chemical Engineering, Politecnico di Milano, Milan, Italy*
[2] *Department of Mechanical and Aerospace Engineering, Politecnico di Torino, Turin, Italy*

***Abstract*— The design and optimization of cardiovascular devices must consider the hemolysis risk associated with their use since excessive hemolysis can lead to severe complications for the patient. Computational fluid dynamics (CFD) integrated with blood damage mathematical models is a powerful tool to evaluate the mechanically-induced hemolysis risk and highlight critical regions of blood contacting devices.**

In this work, a Lagrangian stress-based model is adopted to estimate the blood damage induced by hemodialysis catheters. CFD simulations were performed on two commercially available devices (the Palindrome™ Precision Symmetric Tip by Medtronic and the Arrow-Clark™ VectorFlow® by Teleflex). Technically, the shear stress histories along flow pathlines were computed and processed to quantify the mechanical blood damage associated with the use of the two devices. The computational results were consistent with the experimental findings obtained employing a set-up built in accordance with ASTM F1841, confirming the reliability of the developed hemolysis computational model as a tool supporting the design and optimization of hemodialysis catheters.

***Keywords*—Hemolysis, computational fluid dynamics, ASTM F1841, hemodialysis catheters.**

I. Introduction

An important aspect of the design of cardiovascular devices is the assessment of the mechanically-induced hemolysis risk associated with their use. Indeed, excessive mechanical blood damage can lead to anemia and tissue hypoxia, becoming dangerous to the patient's well-being [1]. Gaining knowledge regarding the hemolysis risk associated with the use of a cardiovascular device is crucial for its optimization and design improvement; therefore, accurate and trustworthy methods to estimate the hemolysis induced are needed.

Nowadays, the degree of mechanical blood damage is assessed experimentally by measuring the increase in the concentration of plasma free hemoglobin (pfHb) using a spectrophotometer, following the international standard ASTM F1841 [2]. Despite the efficacy of this method, it would be useful and cost-effective to be able to determine the hemolysis risk in a purely numerical manner using computational fluid dynamics (CFD) techniques. Various computational models were proposed over the years with this aim. However, there is not a universally accepted model for blood damage prediction yet. This is the consequence of a complex multiscale phenomenon, which is difficult to be simulated properly, and of a lack of a clear definition of the cause-effect relation leading to mechanical hemolysis. Moreover, approximations are needed, in order to reduce the problem complexity and obtain an acceptable computational cost [3].

The aim of this work is the development and the validation of a computational framework able to estimate the risk of mechanical hemolysis associated with cardiovascular devices, in particular with hemodialysis catheters.

II. Methods

The numerical model of hemolysis was implemented considering two central venous catheters for hemodialysis: the Palindrome™ Precision Symmetric Tip (Medtronic, Dublin, Ireland) and the Arrow-Clark™ VectorFlow® (Teleflex, Wayne, Pennsylvania). These are devices currently available on the market and in clinical use. The two devices present a symmetric tip with side openings and a dual-lumen configuration, with the presence of a venous and an arterial line.

In order to define a numerical model able to estimate the hemolysis risk associated with hemodialysis catheters, a geometric model was built for each device using SolidWorks (Dassault Systèmes, Vélizy-Villacoublay, France). Subsequently, the fluid domain was meshed in over 8 million cells employing the open-source software Vascular Modeling Toolkit. Figure 1 shows the geometric model and the mesh built for the Palindrome™ catheter; a similar geometry and mesh were also obtained for the VectorFlow® catheter [4].

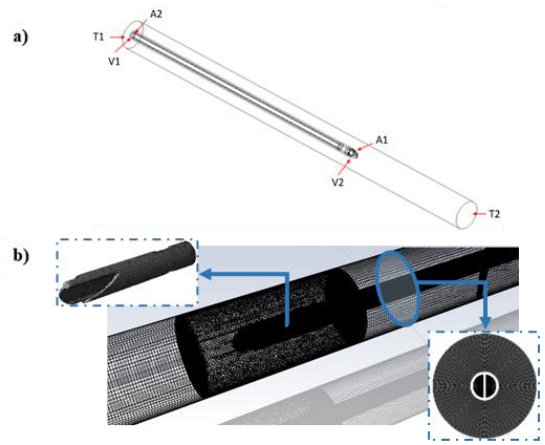


Fig. 1: a) Geometric model consisting of the Palindrome™ catheter coaxially placed into a cylinder representing the superior vena cava (SVC): T1) SVC inlet section, T2) SVC outlet section, V1) venous inlet section, V2) venous outlet section, A1) arterial inlet section, A2) arterial outlet section. **b)** Hybrid mesh created from the geometric model with tetrahedral and hexahedral elements.

The finite volume-based solver Ansys Fluent (ANSYS Inc., Canonsburg, Pennsylvania, USA) was used to solve the

governing equations of fluid motion in discretized form considering blood as a Newtonian fluid and imposing a reference pressure at the outlet of the superior vena cava (T2 in Figure 1). To mimic the working conditions of hemodialysis catheters, a flow rate of 3 L/min was imposed at the inlet section of the superior vena cava while 400 mL/min was imposed at the venous inlet section (T1 and V1 in Figure 1, respectively). Blood flow in the arterial lumen was set prescribing an outflow boundary condition of 400 mL/min in section A2 (Figure 1).

The mechanical hemolysis model adopted in this study employs a stress-based Lagrangian approach, considering the equivalent shear stress ($\bar{\tau}$) formulation proposed by Faghig and Sharp [5], which is based on the von Mises equivalent stress. The equivalent shear stress formulation used is presented in Equation 1, where σ_{xx}, σ_{yy}, σ_{zz} are the normal components of the Cauchy stress tensor and τ_{xy}, τ_{yz}, τ_{xz} are the shear components.

$$\bar{\tau} = \left\{ \frac{1}{3}\left[\sigma_{xx}^2+\sigma_{yy}^2+\sigma_{zz}^2\right] - \frac{1}{3}\left[\sigma_{xx}\sigma_{yy}+\sigma_{yy}\sigma_{zz}+\sigma_{xx}\sigma_{zz}\right] + \left[\tau_{xy}^2+\tau_{yz}^2+\tau_{xz}^2\right] \right\}^{\frac{1}{2}} \quad (1)$$

Equivalent shear stress values were extracted from the particle pathlines. These data, along with the time required by each particle to transit through the fluid domain (namely, the exposure time t), were then imported into MATLAB (MathWorks, Inc., Natick, Massachusetts, USA) to implement the Lagrangian hemolysis model by defining the mechanical damage index (DI in Equation 2). Following the formulation proposed by Grigioni *et al.* [6], the DI is quantified as a function of the magnitude of shear stress ($\bar{\tau}$), exposure time (t), shear history of the red blood cells, and the damage dose D. In Equation 2, χ, α and β are model parameters, firstly introduced by Giersiepen in 1990 [7].

$$DI = \int_{t_0}^{t} \chi\alpha \left[\int_{t_0}^{\phi} \bar{\tau}(\xi)^{\beta/\alpha}\, d\xi + D(t_0)\right]^{\alpha-1} \bar{\tau}(\phi)^{\beta/\alpha}\, d\phi \quad (2)$$

Model parameters are fundamental to the development of affordable models of blood damage; nevertheless, there are currently several sets available in literature, and there is not one universally used. In this work, four different sets were employed (see Table I) [3] – [8].

TABLE I: Parameters sets employed in the development of the hemolysis model [3] – [8].

Research group	χ	A	β
Giersiepen et al. (1990)	3.620 x 10^{-5}	0.7850	2.4610
Heuser and Opitz (1980)	1.800 x 10^{-6}	0.7650	1.9910
Zhang et al. (2011)	1.228 x 10^{-5}	0.6606	1.9918
Ding et al. (2015)	3.458 x 10^{-6}	0.2777	2.0639

The experimental set-up used to validate the hemolysis model was developed in accordance with the international standard F1841. The set-up is shown in Figure 2 and is composed by two volumetric roller pumps able to reproduce the catheter and the systemic flows, the catheter placed in a polymethylmethacrylat tube representing the superior vena cava, a reservoir and a thermostat bath. The test duration was 4 h and blood samples were withdrawn at specific time steps to assess the amount of pfHb.

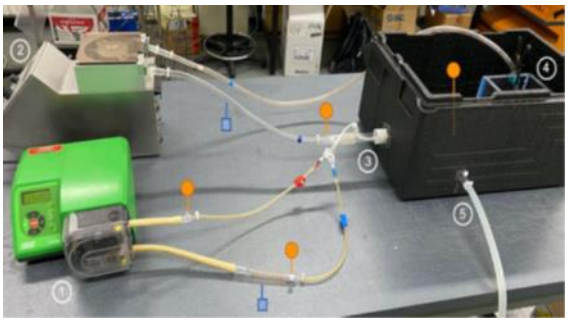


Fig. 2: Experimental set-up: 1) pump reproducing the catheter flow, 2) pump reproducing the systemic flow, 3) catheter, 4) reservoir and 5) thermostat bath. In blue and orange are reported the points where flow and pressure were measured, respectively.

III. Results

The trajectories of blood-like particles are presented in Figure 3, colored according to the value of equivalent shear stress $\bar{\tau}$ experienced along their path within the devices and in the vessel. Equivalent shear stress and velocity values are higher inside the catheters lumens. The hot spots of shear stress are the consequence of the flow disturbances induced in blood flow by the presence of the side holes of the devices, where pathlines undergo a marked deflection (Figure 3).

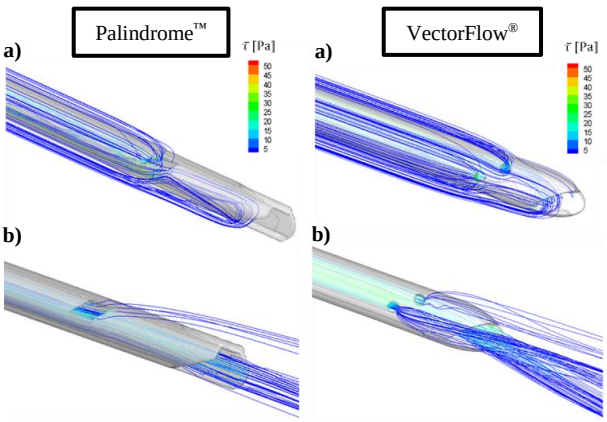


Fig. 3: Trajectories of the seeded particles entering the arterial lumen (**a**) and exiting the venous lumen (**b**) of the catheters.

The pathlines passing through the VectorFlow® catheter are affected by the helical-shaped geometry of its tip, which imparts a spiral motion to blood flowing out of the venous lumen. This feature deflects the flow away from the tip, in the opposite direction with respect to the blood withdrawn by the arterial lumen, theoretically reducing the recirculation and thus improving the device performance [9].

Nevertheless, this improvement is not evident when comparing the estimated mechanical-induced blood damage in the two hemodialysis catheters object of investigation.

Figure 4 shows the mechanical damage index DI (%) related to a passage of blood first into the arterial lumen and then into the venous one, computed by imposing the damage dose obtained at the arterial outlet as the initial damage dose $D(t_0)$ of the venous lumen.

These results highlight a hemolysis risk related to the VectorFlow® catheter double than the Palindrome™. The impact of model parameters on the hemolysis risk estimation is also presented in Figure 4: it emerges that the set of model parameters proposed by Giersiepen *et al.* [7] provides values of mechanical damage considerably higher than those obtained employing the other sets of model parameters available in the literature. This finding is consistent with other studies; in fact, it has been reported that the values of model parameters proposed in [7] tend to overestimate the risk of hemolysis associated with blood contacting devices, in part ascribable to the presence of secondary hemolysis affecting the experimental data used to fit the model [3].

The analysis of the estimated mechanical blood damage allowed also to compare the hemolysis risk related to the two identical lumens of the catheters. Table II shows the values of DI (%) obtained for each lumen of the hemodialysis catheters by employing the four sets of model parameters and considering a null initial damage dose $D(t_0)$. Regardless of the catheter or set of model parameters considered, the mechanical blood damage induced by blood transit into the arterial lumen is always higher than into the venous lumen. This observed difference can be ascribed to the abrupt change in flow direction and acceleration imparted to blood when it is withdrawn inside the arterial lumen. Contrarily, the blood flowing out of the venous side presents more regular trajectories.

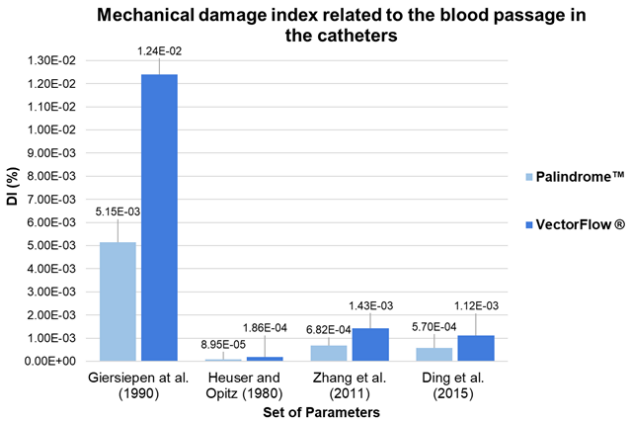


Fig. 4: Comparison of DI (%) related to the passage of blood first into the arterial lumen and then into the venous lumen of the Palindrome™ and the VectorFlow® catheters. DI (%) is reported for the four sets of parameters considered.

TABLE II: Values of DI (%) obtained by considering individually the venous and arterial lumen of the Palindrome™ and the VectorFlow® catheters.

Research Group	***Palindrome™***		***VectorFlow®***	
	DI (%) Venous	*DI (%) Arterial*	*DI (%) Venous*	*DI (%) Arterial*
Giersiepen at al. (1990)	1.77×10^{-3}	3.93×10^{-3}	4.86×10^{-3}	8.82×10^{-3}
Heuser and Opitz (1980)	3.50×10^{-5}	6.44×10^{-5}	7.86×10^{-5}	1.27×10^{-4}
Zhang et al. (2011)	2.46×10^{-4}	5.48×10^{-4}	5.11×10^{-4}	1.10×10^{-3}
Ding et al. (2015)	1.19×10^{-4}	5.68×10^{-4}	2.32×10^{-4}	1.12×10^{-3}

The experimental results are reported in Table III in terms of plasma free hemoglobin [mg/mL] at specific time instants of the in vitro tests. After the first hour, the VectorFlow® catheter presented consistently higher amounts of plasma free hemoglobin that the Palindrome™ and, at the end of the experimental tests a larger number of blood clots in its tip and side holes were observed. These observations are in line with the picture emerging from the CFD-based estimation of blood damage risk.

It must be clarified that the values of plasma free hemoglobin reported in Table III are related to the complete hydraulic circuit and might not accurately reflect the risk of mechanical hemolysis specifically associated with the tested catheter model. In fact, the in vitro tests performed with the set-up presented in Figure 2 did not generate significantly more plasma free hemoglobin than the hydraulic circuits where blood circulates without the presence of the catheters. Since both catheters produced sub-hemolytic blood damage, their specific contribution to the variation of plasma free hemoglobin in the hydraulic circuit is small when compared with other components, in particular the roller pumps, and is challenging to isolate. Therefore, a direct comparison with the numerical predictions is not feasible.

TABLE III: Difference between plasma free hemoglobin [mg/mL] at the various time instants of the in vitro tests and the plasma free hemoglobin of the sample taken before pumping for the Palindrome™ and the VectorFlow® catheters.

	5 min	***30 min***	***60 min***	***120 min***	***180 min***	***240 min***
Palindrome™ [mg/mL]	0*	0*	0	0.03	0.07	0.12
VectorFlow® [mg/mL]	0*	0*	0.01	0.05	0.11	0.16

*cases in which the plasma free hemoglobin before pumping was greater than the plasma free hemoglobin at the time considered.

IV. Conclusion

When used for comparative purposes, the Lagrangian stress-based model here adopted [6] is capable to discriminate among hemodialysis catheters in terms of associated risk of mechanical hemolysis. The findings of this study highlight the potential of the here adopted approach as a tool to improve the design and the optimization of catheters. Indeed, regardless of the set of blood damage model parameters employed, the model correctly predicts the higher degree of blood damage induced by the VectorFlow® catheter and allows the identification of regions characterized by high equivalent shear stresses. Furthermore, the analysis has allowed to discriminate between the intra-device blood damage risk related to the venous and the arterial line, the latter presenting a higher risk of blood damage as a consequence of the associated flow field. In particular, this finding is not affected by the adoption of different sets of model parameters and further supports the robustness and effectiveness of the proposed approach for the design and optimization of hemodialysis catheters.

Nevertheless, the set of model parameters used has great influence on the prediction of hemolysis risk and the results obtained cannot be directly compared with experimental

hemolysis values; therefore, there is a clear need to develop an experimental set-up capable of accurately validating the predictions. The validation of the developed hemolysis model would also pave the way for its application to the design and optimization phases of other cardiovascular devices.

REFERENCES

[1] O. K. Baskurt, M. R. Hardeman, M. W. Rampling, and H. J. Meiselman, *Handbook of hemorheology and hemodynamics*. IOS Press, 2007.

[2] *ASTM standard practice for assessment of hemolysis in continuous flow blood pumps*, ASTM International Standard F1841 – 97, 2017.

[3] H. Yu, S. Engel, G. Janiga, and D. Thévenin, "A review of hemolysis prediction models for computational fluid dynamics", *Artificial Organs*, vol. 41, pp. 603–621, 2017.

[4] T. W. I. Clark, G. Isu, D. Gallo, P. Verdonck, and U. Morbiducci, "Comparison of symmetric hemodialysis catheters using computational fluid dynamics", *Journal of Vascular and Interventional Radiology*, vol. 26, pp. 252–259, 2015.

[5] M. M. Faghih and M. K. Sharp, "Extending the power-law hemolysis model to complex flows", *Journal of Biomechanical Engineering*, vol. 138, 2016.

[6] M. Grigioni, U. Morbiducci, G. D'Avenio, G. Di Benedetto, and C. Del Gaudio, "A novel formulation for blood trauma prediction by a modified power-law mathematical model", *Biomechanics and Modeling in Mechanobiology*, vol. 4, pp. 249–260, 2005.

[7] M. Giersiepen, L. J. Wurzinger, R. Opitz, and H. Reul, "Estimation of shear stress-related blood damage in heart valve prostheses-in vitro comparison of 25 aortic valves", *The International Journal of Artificial Organs*, vol.13, 1990.

[8] J. Ding et al., "Shear-induced hemolysis: species differences", *Artificial Organs*, vol. 39, pp. 795–802, 2015.

[9] T. W. I. Clark, K. Van Canneyt and, P. Verdonck, "Computational flow dynamics and preclinical assessment of a novel hemodialysis catheter", *Seminars in Dialysis*, vol. 25, pp. 574–581, 2012.

Study and characterization of bile acid biosensors in engineered probiotic bacteria

D. Pastorelli[1], D. Dallera[1] , E. Persico[1], M. Bellato[2], G. Cusella De Angelis[3], L. Pasotti[1] and P. Magni[1]
[1] *Department of Electrical, Computer and Biomedical Engineering, University of Pavia, I-27100 Pavia, Italy*
[2] *Department of Information Engineering, University of Padova, I-35122, Padova, Italy*
[3] *Department of Public Health, Experimental and Forensic Medicine, University of Pavia, via Forlanini 8, I-27100 Pavia, Italy*

Abstract— **Recently, the study toward the relationship between microbiota and metabolites is growing to try to understand the complex mechanisms that take place in the gut. Among the metabolites of greatest interest there are bile acids, synthesized in human liver, which interact with the microbial population that inhabits gut. Imbalances of these acids can result in numerous diseases and pathogenic infections. One possible solution to measure these molecules directly *in vivo* is to use synthetic biology techniques to engineer a biosensor into probiotic bacteria. An exploratory work on bile acid biosensors, which are promising tools for future medical and environmental diagnostic applications, is presented here.**

Keywords— **Synthetic biology, biosensor, probiotic bacteria, bile acids**.

I. Introduction

The scientific community interest in gut microbiota is constantly growing as it plays a fundamental role in human physiology due to mutual interactions between microbiota and host organism.

Changes in the microbiota composition lead to alterations in the intestinal metabolites and hence the health of the organism itself. Among the metabolites of greatest interest there are bile acids (BAs) [1], [2].

BAs are first synthesized in liver and, following each meal, released in gut to perform their primary action, i.e. the emulsification of fat-soluble molecules.

The output of cholesterol transformation is primary BAs, conjugated with an amino acid which can be a taurine (T) or a glycine (G). Consequently, in liver we find the conjugated species of the primary acids: taurocholic acid (TCA) and glycolic acid (GCA) are the conjugates of cholic acid (CA), while the taurochenodeoxycholic acid (TCDCA) and glycochenodeoxycholic acid (GCDCA) are those of chenodeoxycholic acid (CDCA) (*Fig. 1*).

When conjugated primary acids transit the gastrointestinal tract, the microbiota carries out a series of transformations that lead to the formation of more than 50 species of chemically different secondary BAs [3]. The predominant ones are deoxycholic acid (DCA) and lithocholic acid (LCA), reaction products from CA and CDCA respectively [3].

The BAs pool and the microbiota influence each other: the former exerts a controlling action on the growth of bacteria coexisting in the gut and the latter transform them into secondary BAs. The pool of BAs is thus the end product between the primary ones synthesized in liver and the secondary ones synthesized by gut microbiome.

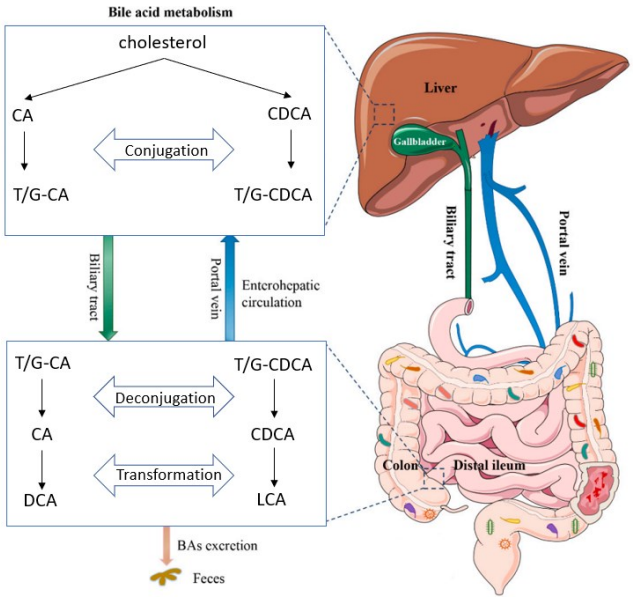


Fig. 1: Bile acid synthesis and metabolism and the major changes in the intestine. Figure adapted from [18].

It is evident how an unbalance of either component can cause a change in the available pool of BAs that results in a metabolic derangement. In fact, BAs are often correlated with numerous pathologies such as obesity, diabetes, colitis, bacterial infections and even colon carcinomas [1], [2].

Moreover, BAs play a fundamental role in the life cycle of *Clostridium difficile*, an enteropathogenic bacteria of considerable medical interest [4], [5]. Some BAs, in fact, inhibit the growth of *C. difficile*, while others promote it. Therefore BAs play a fundamental role in several physiological processes and being able to detect their unbalance is an important factor in recognizing pathologies and intervening with specific treatment [6], [7].

Bacterial biosensors, i.e., engineered bacteria capable of responding to external stimuli or to markers of disease by producing monitorable response signals, constitute promising systems for in vitro but also in vivo diagnostics [8].

In general, bacterial biosensors consist of a sensing module and a transcriptional element that produces a measurable output in response to an exogenous input.

The sensing module consists of a regulated promoter while the regulator is constitutively expressed within the biosensor's genetic circuitry. It is usually a receptor protein that ligates the input of interest and influences the associated promoter [8], [9]. The promoter, in turn, controls the transcriptional activity of the regulated gene, which may be a reporter gene that

translates to a fluorescent protein or an enzyme that performs some function on the input itself. Since model organisms are not always suitable for non-laboratory applications, the interest of the scientific community is shifting towards research and characterization of new engineerable microorganisms by seeking to optimize engineering protocols and the characterization of new parts for gene regulation.
Probiotic organisms, being able to survive in the gut together with the human microbiota, can be engineered with synthetic biology techniques for diagnostics and therapy directly in situ. *Escherichia coli Nissle 1917* (ECN), a Gram-negative bacterium, was chosen as the target probiotic which, compared to other *E. coli* strains, is non-pathogenic. Moreover, it is already used as a drug for the adjuvant treatment of various dysfunctions of the intestinal tract.

II. MATERIALS AND METHODS

ECN competent cells were prepared as described in [10].
A total of 4 different biosensors have been tested, each with its theorical specificity to different set of BAs, as reported in *Table 1*.
The first two tested biosensors, VtrAC and TcpPH, come from the work of Chang et al [11]. There is a regulatory promoter PcadBA, induced by a transcriptional regulator, CadC, and a receptor composed of assembling modules, i.e., the whole part composed of CadC and TcpP and TcpH. The regulated gene in this case encodes the superfolder green fluorescent protein (sfGFP). The other biosensor is identical except that it differs in the receptor modules, called VtrA and VtrC. These two biosensors were tested in the ECN probiotic organism, creating two strains of engineered bacteria inducible by BAs.
Another tested biosensor was *de novo* constructed using the operator sites of the transcriptional inhibitor VFA0359 (*Vibrio fischeri*) from the work of Taketani et al. [12] assembled within a constitutive *E. coli* promoter. The red fluorescent protein (RFP) has been chosen as the reporter gene.
This biosensor was tested in the model organism *Escherichia coli F'*. The last biosensor tested was the plasmid containing CmeR (*Campylobacter jejuni*) from the work of Nasr et al., which was tested by the authors on numerous BAs [13], [14]. The regulated gene encodes the enhanced green fluorescent protein (eGFP). Instead, this biosensor was tested in *E. coli TOP10*.

TABLE I: MAIN CHARACTERISTICS OF THE FOUR BIOSENSORS.

	Regulated promoter	*Transcriptional regulator*	*Reporter gene*
TcpPH	PcadBA	CadC (TcpP+TcpH)	sfGFP
VtrAC	PcadBA	CadC (VtrA+VtrC)	sfGFP
VFA0359	Plac	VFA0359	RFP
CmeR	Ptac	CmeR	eGFP

Biosensors were characterized with the Tecan Infinite F200 Pro instrument, used to incubate bacterial cultures in 96-well plates.
This instrument allows the simultaneous reading of the optical density at 600 nm called OD600, which is a proportional measure of cell growth, and the fluorescence, proportional to the expressed reporter protein.
Collected data are processed by first computing the GFP/OD ratio and then normalizing it by calculating relative promoter unit (RPU). The RPU measurement, shown in Eq. (1), is obtained by normalizing the intensities of fluorescence with those of a reference construct [15].

$$RPU = \frac{GFP/OD(biosensor)}{GFP/OD(reference)} \qquad (1)$$

Each biosensor has been tested at five different concentrations of each BA by measuring the RPU as a quantification of the relative strength of an inducible promoter.
The reference construct is a plasmid containing the same fluorescence protein under the control of a constitutive promoter of known strength. For this reason, the reference construct used for the calculation of RPU of biosensors TcpPH and VtrAC, has a GFP, while for the other two biosensor containing VFA0359 and CmeR, it was used a construct expressing a RFP.

III. RESULTS

Nissle was made competent, i.e. able to be engineered by means of a specially designed and optimized protocol. After establishing that none of the used BAs was toxic to ECN growth, the experimental set-up for the characterization of the four biosensors was defined. The four recombinant strains with the four biosensors were created. The BAs chosen for biosensor characterization have been CA, TCA, CDCA, GCDCA, TCDCA, DCA, GDCA, TDCA and LCA.
While as for concentrations, 10 µM, 40 µM, 80 µM, 120 µM and 200 µM were selected in accordance with physiological levels in the intestine, and at least three replicates were performed for each strain, unless differently indicated.
As mentioned above, the RPU was calculated from the data from the microplate reader, and was fitted to the Hill equation model, shown in Eq. (2), in order to obtain the characteristic parameters; where V_{max} represents the maximum RPU value reached and K_m represents the sensor activation switch point, i.e. the concentration at which it is activated.

$$RPU(V_{max}, K_m, n, C) = V_{max} * \frac{C^n}{K_m^n + C^n} \qquad (2)$$

Overall, the strain engineered with TcpPH senses the expected acids, which were supposed to be all conjugated primaries, i.e., TCA GCA GCDCA and TCDCA [11] although it is actually sensitive to conjugated secondaries as well (Fig. 2A).
The strain engineered with VtrAC senses the same expected acids, i.e., conjugated secondaries GDCA and TDCA, just like previously shown in [11] (Fig. 2B).
The new biosensor containing VFA0359 tested in *Escherichia coli F'* appeared to be insensitive to the selected BAs. Only two replicas were performed for this biosensor (Fig. 2C). Additional promoter engineering will be carried out to address the inducible behavior of this component.
Lastly, the biosensor containing CmeR tested in *Escherichia coli TOP10* also turned out to be not insensitive to the selected BAs (Fig. 2D).

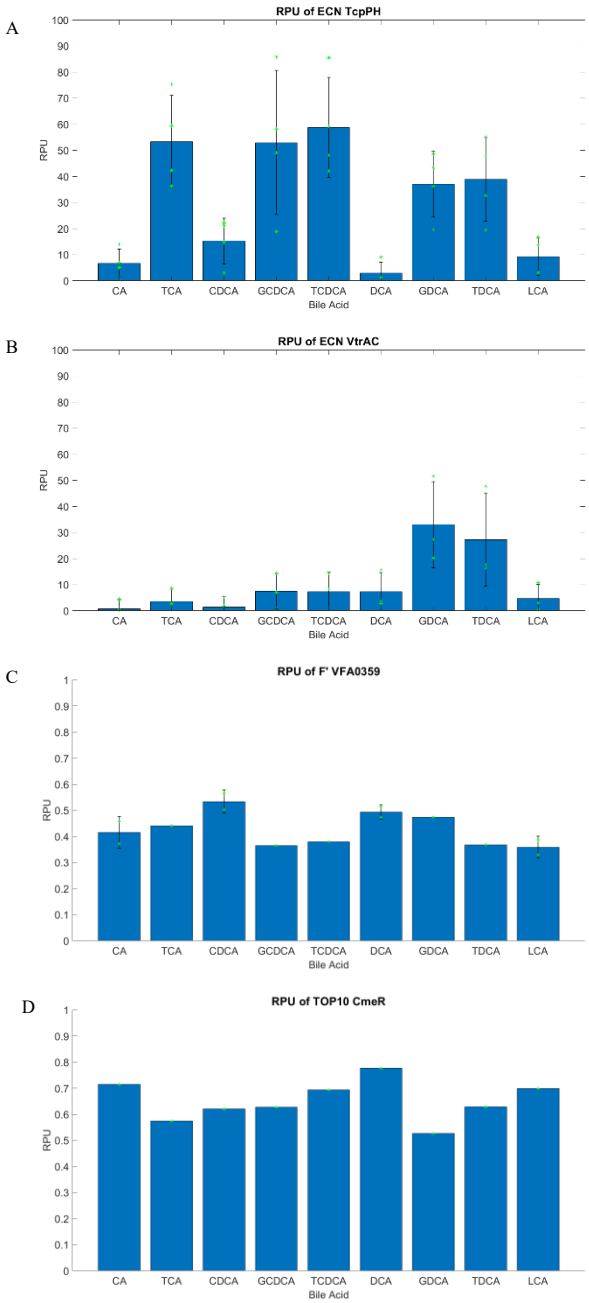


Fig. 2: Bar graphs of mean RPU values related to the four tested biosensors for each BA at the concentration of 80 µM are shown in blue. Individual replicates are shown as green dots. A) TcpPH sensor in ECN. B) VtrAC sensor in ECN. C) VFA0359 sensor in *Escherichia coli F'*. D) CmeR sensor in *Escherichia coli TOP10.*

Another measure for comparing the four different biosensors is Fold Change (FC), calculated as the ratio of two measures of gene expression. In this particular case, the RPU measure was used because it is representative of how much a particular BA activates the expression of the fluorescent protein. Two groups of BAs were distinguished in the 80 µM bar graphs; those that activate the biosensor are identified as on-group, and those that do not activate it are called off-group. The FC measure was calculated as the lowest RPU of the on-group divided by the highest RPU of the off-group. Accordingly, a FC was calculated for every replicate of each biosensor and then averaged across replicates.

The TcpPH and VtrAC biosensors show a FC of 3.49 and 9.05, respectively, while CFA0359 and CmeR exhibit a FC of 0.97 and 0.84, respectively. The latter two have FCs close to 1, which means there are no particular BAs that seem to activate the biosensors. Appropriate tuning of the biosensors, such as changing RBS or promoter strength, can be done to improve these measurements.

As mentioned before, a Hill-type equation model was used to fit the data for biosensors TcpPH and VtrAC since they are the ones sensitive to BAs.

Fig. 3A and 3B shows two fitting examples from which the characteristic parameters V_{max} and K_m can be derived. Fig. 3A shows a fitting example related to TCA, one of those that most activates the TcpPH sensor. Fig. 3B shows a fitting example related to GDCA, one of those that most activates the VtrAC sensor, in this case it looks more like a Michaelis-Menten equation because of the n=1.

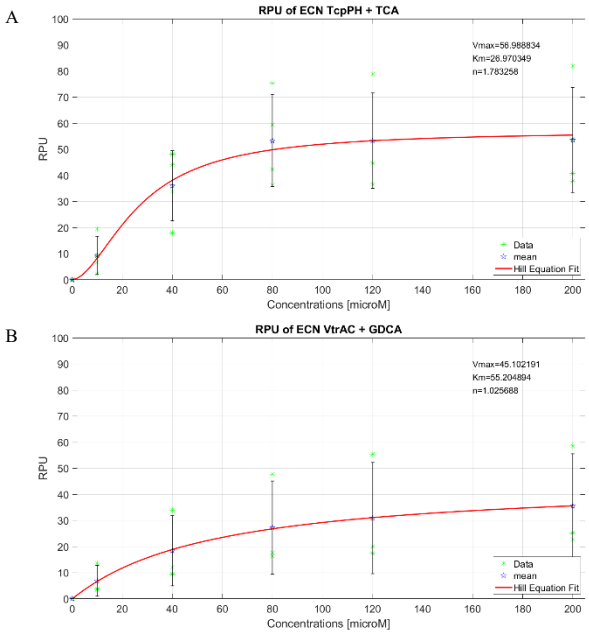


Fig. 3: Fitting of the Hill model to the RPU data from the biosensors. In red it is shown the curve obtained from the model, in blue the averages of the data, and in green dots the data for individual replicates. The characteristic parameters are shown in top left. A) TcpPH sensor in ECN with TCA. B) VtrAC sensor in Escherichia coli Nissle with GDCA.

IV. CONCLUSION

In this study, the TcpPH and VtrAC biosensors are the most suitable to be used for diagnostic purposes, since they are found to be sensitive to different combinations of BAs. As for VFA0359 and CmeR, new studies will be carried out to optimize the response of the biosensors since they currently would not seem to be inducible by BAs. Developments in the short term will include an attempt to expand the number of biosensors available and characterize them in ECN to enrich the number of sensed acids. Although neither biosensor turns out to be specific to a particular BA, a possible approach will be finding combinations of the biosensors that can detect physiological situations of interest. In addition to expanding

the pool of available biosensors, a possible future development is the implementation of a BAs controller in a probiotic organism: for this purpose, in addition to sensors, it will be necessary to develop and couple molecular actuators to them.
An actuator can be a gene that translates for a BA-transforming biosynthetic enzyme(s), exerting control over the target variable, i.e. BA concentration. Assembling a controller means measuring a concentration of a BA by means of a sensor and, if necessary, returning it to an equilibrium state by means of an actuator. It can be done by exploiting genes that implement transformations on BAs, namely bsh gene [16], which deconjugates BAs from amino acids, and bai operon [17], which transforms unconjugated primary conjugated into unconjugated secondaries.
For example, possible scenarios could be:
-sensor of conjugated primary BAs, and sensor of deconjugated primary BAs, with the bsh gene going to inhibit the deconjugation of conjugated BAs;
- deconjugated primary BAs sensor and secondary BAs sensor, with the bai operon going to inhibit the transformation of primary BAs into secondary BAs.
Overall, these platforms can be combined to customize systems able to sense the level of different BAs classes *in vivo*, or interconnecting controller circuits to implement robust regulation tasks, paving the way to for new therapies to interact with microbiota imbalances and restore BAs to normal concentrations.

REFERENCES

[1] J. Y. L. Chiang, "Bile acid metabolism and signaling," *Compr Physiol*, vol. 3, no. 3, pp. 1191–1212, 2013, doi: 10.1002/cphy.c120023.

[2] J. A. Winston and C. M. Theriot, "Diversification of host bile acids by members of the gut microbiota," *Gut Microbes*, vol. 11, no. 2. Taylor and Francis Inc., pp. 158–171, Mar. 03, 2020. doi: 10.1080/19490976.2019.1674124.

[3] J. M. Ridlon, S. C. Harris, S. Bhowmik, D. J. Kang, and P. B. Hylemon, "Consequences of bile salt biotransformations by intestinal bacteria," *Gut Microbes*, vol. 7, no. 1. Taylor and Francis Inc., pp. 22–39, Jan. 02, 2016. doi: 10.1080/19490976.2015.1127483.

[4] J. A. Winston and C. M. Theriot, "Impact of microbial derived secondary bile acids on colonization resistance against Clostridium difficile in the gastrointestinal tract," *Anaerobe*, vol. 41, pp. 44–50, Oct. 2016, doi: 10.1016/j.anaerobe.2016.05.003.

[5] R. Thanissery, J. A. Winston, and C. M. Theriot, "Inhibition of spore germination, growth, and toxin activity of clinically relevant C. difficile strains by gut microbiota derived secondary bile acids," *Anaerobe*, vol. 45, pp. 86–100, Jun. 2017, doi: 10.1016/j.anaerobe.2017.03.004.

[6] T. Dubois *et al.*, "A microbiota-generated bile salt induces biofilm formation in Clostridium difficile," *NPJ Biofilms Microbiomes*, vol. 5, no. 1, Dec. 2019, doi: 10.1038/s41522-019-0087-4.

[7] J. A. Sorg and A. L. Sonenshein, "Inhibiting the initiation of Clostridium difficile spore germination using analogs of chenodeoxycholic acid, a bile acid," *J Bacteriol*, vol. 192, no. 19, pp. 4983–4990, Oct. 2010, doi: 10.1128/JB.00610-10.

[8] A. C. Carpenter, I. T. Paulsen, and T. C. Williams, "Blueprints for biosensors: Design, limitations, and applications," *Genes*, vol. 9, no. 8. MDPI AG, Aug. 01, 2018. doi: 10.3390/genes9080375.

[9] M. Hicks, T. T. Bachmann, and B. Wang, "Synthetic Biology Enables Programmable Cell-Based Biosensors," *ChemPhysChem*, vol. 21, no. 2. Wiley-VCH Verlag, pp. 132–144, Jan. 16, 2020. doi: 10.1002/cphc.201900739.

[10] J. Nzakizwanayo, "Investigation of host-microbe interactions in the probiotic bacteria Escherichia coli Nissle 1917," 2014.

[11] H. J. Chang *et al.*, "Programmable receptors enable bacterial biosensors to detect pathological biomarkers in clinical samples," *Nat Commun*, vol. 12, no. 1, Dec. 2021, doi: 10.1038/s41467-021-25538-y.

[12] M. Taketani *et al.*, "Genetic circuit design automation for the gut resident species Bacteroides thetaiotaomicron," *Nat Biotechnol*, vol. 38, no. 8, pp. 962–969, Aug. 2020, doi: 10.1038/s41587-020-0468-5.

[13] M. A. Nasr, L. R. Timmins, V. J. J. Martin, and D. H. Kwan, "A Versatile Transcription Factor Biosensor System Responsive to Multiple Aromatic and Indole Inducers," *ACS Synth Biol*, p. acssynbio.2c00063, Mar. 2022, doi: 10.1021/acssynbio.2c00063.

[14] J. Lin *et al.*, "Bile salts modulate expression of the CmeABC multidrug efflux pump in Campylobacter jejuni," *J Bacteriol*, vol. 187, no. 21, pp. 7417–7424, Nov. 2005, doi: 10.1128/JB.187.21.7417-7424.2005.

[15] T. Knight, "Idempotent Vector Design for Standard Assembly of Biobricks."

[16] M. H. Foley, S. O'Flaherty, R. Barrangou, and C. M. Theriot, "Bile salt hydrolases: Gatekeepers of bile acid metabolism and host-microbiome crosstalk in the gastrointestinal tract," *PLoS Pathog*, vol. 15, no. 3, Mar. 2019, doi: 10.1371/journal.ppat.1007581.

[17] A. D. Reed, M. A. Nethery, A. Stewart, R. Barrangou, and C. M. Theriot, "Strain-Dependent Inhibition of Clostridioides difficile by Commensal Clostridia Carrying the Bile Acid-Inducible (bai) Operon," 2020, doi: 10.1128/JB.

[18] M. Yang *et al.*, "Bile acid–gut microbiota axis in inflammatory bowel disease: From bench to bedside," *Nutrients*, vol. 13, no. 9. MDPI, Sep. 01, 2021. doi: 10.3390/nu13093143.

Exploring heterogeneity in lymphoid malignancies from mouse to human gene expression profiles

Vescio M.[1*], Bulloni M. [1*], Brendolan A.[2] and Pattini L.[1]
[1] *Department of Electronics, Information and Bioengineering, Politecnico di Milano, Milan, Italy*
[2] *Division of Experimental Oncology, IRCCS San Raffaele Scientific Institute, Milan, Italy*

[*]*These authors contributed equally as co-first authors.*

***Abstract*—Chronic lymphocytic leukemia (CLL) and diffuse large B-cell lymphoma (DLBCL) are two common lymphoid neoplasms, characterized by high heterogeneity among their subtypes. A murine model presenting features of human CLL revealed the existence of two distinct leukemic presentations that differ for their transcriptomic profile. In this study, we used gene expression data from two DLBCL datasets to identify human subjects analogous to the murine and characterize their behaviour in terms of prognosis and microenvironment properties. The results revealed that, despite showing molecular features related to poor prognosis in solid cancers, such as extracellular matrix remodeling and epithelial-mesenchymal transition, group 1 leukemia patients have a significantly better overall and progression-free survival outcome.**

***Keywords*—lymphoid malignancies, tumor microenvironment, gene expression, bioinformatics**

I. Introduction

LYMPHOID neoplasms are a heterogeneous group of diseases arising from the malignant transformation of lymphoid cells. Two common classes of lymphoid malignancies are chronic lymphocytic leukemia (CLL) and diffuse large B-cell lymphoma (DLBCL) [1].

CLL is the most common leukemia among adults in Western countries. The main characteristic of the disease is the progressive accumulation of B lymphocytes in blood, bone marrow, spleen and lymph nodes [2]. The incidence increases with age, with a mean age at diagnosis of 72 years; however, CLL cases in younger subjects are on the rise. Survival times after diagnosis vary greatly, spanning between a few months and decades. The clinical presentation is also extremely heterogeneous: about a third of the patients needs immediate treatment after the diagnosis due to their heavy symptoms, while a similar proportion of subjects are asymptomatic and never require any treatment [2], [3]. DLBCL is the most common lymphoid malignancy in adults and shares some molecular characteristics with CLL, such as the cell of origin [4]. Moreover, it can arise from histologic transformation of CLL in a process called Richter's transformation [5]. It is more frequently observed in elderly patients, but it can also occur in younger subjects and, rarely, in pediatric cases. The majority of patients show a rapidly expanding tumor mass located in one or more lymph nodes and extranodal sites [6].

Similarly to other solid cancers and hematological malignancies, an essential role in survival and proliferation of tumoral B cells is played by the tumor microenvironment, an entity composed by stromal cells that act as an active component of the disease [7], [8]. Within some specialized niches located inside the bone marrow, mesenchymal stromal cells interact with leukemic cells via contact-dependent and soluble factor-dependent mechanisms. This mutual interaction favors cell proliferation, influences their migratory activity and can protect B-cells from cytotoxic agents [9], [10]. For instance, studies conducted in vitro on chronic lymphocytic leukemia (CLL) B-cells demonstrated that direct contact between bone marrow-derived stromal cells and leukemic B-cells is able to protect tumoral cells from apoptosis [11], [12]. As proposed by recent studies regarding tumor microenvironment in lymphomas, its features also play a role in determining the prognostic outcome [13], [14].

In this work, we wanted to analyze the characteristics of two distinct presentations of murine lymphoid neoplasia identified in the Eμ-TCL1 murine model, a mouse model that displays some of the features of human CLL. We utilized gene expression data to investigate the presence of similar transcriptomic profiles in human samples and to examine their properties, in order to investigate molecular mechanisms that could be related to the heterogeneous presentation of the disease. Given their importance in hematological malignancies and their suggested influence on prognosis, we especially focused on molecular mechanisms related to the tumor microenvironment.

II. Materials and Methods

A. Mouse gene expression data

RNA-seq technology was used to measure gene expression in leukemic B-cells samples from the spleen of transgenic mice displaying two distinct transcriptomic profiles. Data were available in 4 replicates for each neoplastic subtype.

B. Human gene expression data

Human microarray gene expression data were downloaded from Gene Expression Omnibus (GEO) [15] for datasets GSE117556 and GSE32918, that include 928 and 172 DLBCL samples, respectively.

C. Mouse data analysis

Gene expression data obtained from mouse models were employed to define a characteristic transcriptomic signature representing the two distinct lymphoid presentations. To this aim, a differential analysis was performed to identify the most distinctive genes for each subtype. The characterizing signature was defined as the 200 genes most upregulated in one subtype with respect to the other.

D. *Human samples classification*

To map the two presentations of leukemia identified in mice to human samples and evaluate their molecular differences, each subject from the selected DLBCL datasets was assigned to group 1 or group 2 according to their expression profile. First, mouse genes included in the signatures representing each type were assigned to their human homologs using the correspondence retrieved from the Mouse Genome Database [16]. After the conversion, the rank-based single sample scoring method Singscore [17] was used to test the enrichment of both signatures in the expression profile of each human sample. Specifically, genes were ranked based on their expression level in the tested sample, then, the mean rank of genes in the signature was calculated and normalized against the theoretical minimum and maximum values. Associated p-values were obtained using a permutation test.

Each sample was assigned to one of the two groups if the corresponding signature had reached the significance level in enrichment analysis ($p<0.05$), otherwise it was considered unclassified.

E. *Characterization of distinct lymphoid presentations*

We performed a log-rank test on follow-up data available for GSE117556 and GSE32918 samples to compare the prognostic outcomes in different lymphoid groups. Both overall survival (OS) and progression-free survival (PFS) were tested.

As for functional characterization of the two subtypes, we tested for differences in enrichment of gene sets representing molecular processes related to tumor microenvironment. Specifically, we selected the signature *Epithelial Mesenchymal Transition* from the Hallmark collection of MSigDB [18] and the signature *STROMAL-1* from Lenz et al. [14]. The enrichment scores were computed using Singscore [17], and the statistical significance of the difference between enrichment scores in group 1 and group 2 was verified using the Mann-Whitney U test.

III. Results

A. *Human samples classification*

To investigate the differences in the molecular presentation of the microenvironment in the two murine preparations in human patients, we assigned each human sample to different groups according to their molecular similarity with murine transcriptomic profiles. Using a single sample enrichment approach, we were able to assign to one of the two classes 34,6% of samples for GSE117556 and 26.2% of samples for GSE32918. In dataset GSE117556, 83 samples were assigned to group 1 and 23 to group 2; for GSE32918, 13 samples were assigned to group 1 and 34 to group 2 (Figure 1).

B. *Survival analysis*

Survival data from patients assigned to one of the two classes were used to test differences in OS times and PFS times between different lymphoid groups (Figure 2). The results showed a significantly better prognosis for group 1 patients, with longer OS times in both datasets (GSE117556: p=0.0168; GSE32918: p=0.0279) and longer PFS times in GSE117556 (p=0.0020). DLBCL patients that were not assigned to any of the groups showed a prognostic outcome intermediate between the two groups (GSE32918, data not shown) or more similar to group 2 (GSE117556, data not shown).

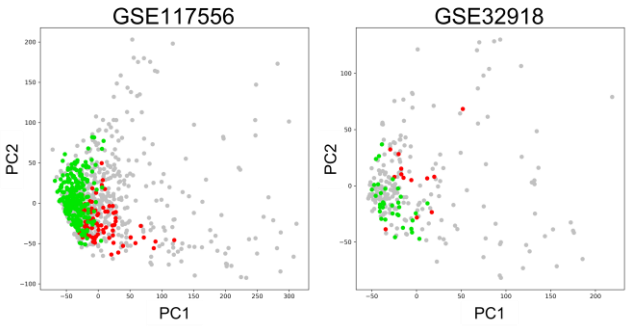


Figure 1: PCA displaying the results of the classification of human samples from GSE117556 and GSE32918. Group 1 samples are shown in red, group 2 samples are shown in green.

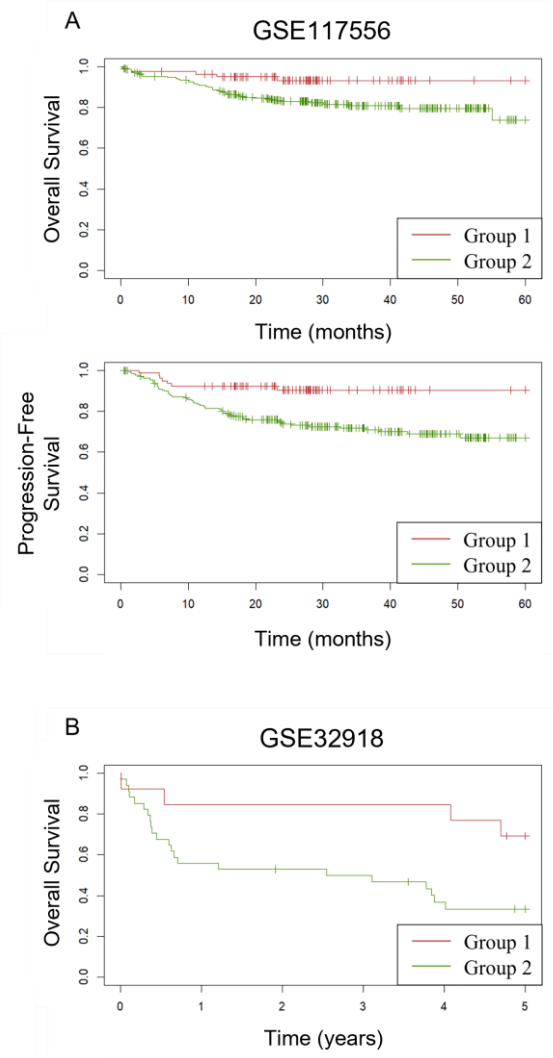


Figure 2: Kaplan-Meier curves comparing OS and PFS times of group 1 and group 2 patients from GSE117556 (A) and GSE32918 (B).

C. *Molecular characterization*

The differences in tumor microenvironment features between patient groups were investigated by evaluating the enrichment of specific gene signatures in each classified sample. The first signature considered included genes involved in epithelial-mesenchymal transition (EMT), a process that disrupts cell adhesion. The signature showed significantly higher enrichment scores in group 1 samples, according to the Mann-Whitney U test (GSE117556: $p=1.12x10^{-17}$, GSE32918: $p=9.30x10^{-7}$).

The second signature tested was defined as *STROMAL-1* in [14] and included genes responsible for the deposition and remodeling of the extracellular matrix. Again, group 1 samples showed significantly higher enrichment scores in both datasets (GSE117556: $p=1.36x10^{-12}$, GSE32918: $p=1.09x10^{-7}$).

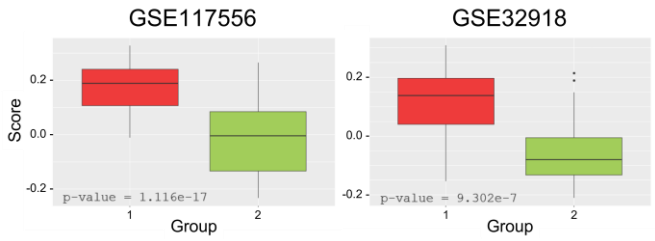


Figure 3: Enrichment scores for the signature *Epithelial-Mesenchymal Transition* in group 1 and group 2 samples.

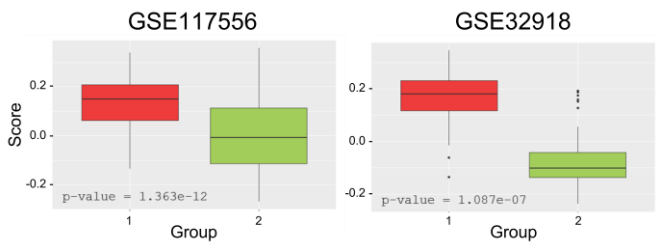


Figure 4: Enrichment scores for the signature *STROMAL-1* in group 1 and group 2 samples.

IV. DISCUSSION

The aim of this study was to explore the molecular characteristics of two subtypes of leukemias identified in the Eμ-TCL1 murine model and showing a different transcriptomic profile. We employed gene expression data from publicly available DLBCL datasets to identify human samples matching murine expression profiles. Then, we used survival data and gene signatures derived from literature to explore the properties of the two leukemias in human patients, with a particular focus on tumor microenvironment.

The mapping of human samples to the two murine lymphoid groups revealed that about one third of the total number of human samples had similar expression profiles to one of the two leukemias, suggesting that the same classes could be translated to humans. Following classification, a survival analysis was conducted to highlight possible differences in patients' prognostic outcome. The results indicated that patients assigned to group 1 had a significantly better prognosis in both datasets. In addition, progression-free survival times were significantly longer in group 1 patients in the largest dataset.

With regard to molecular characterization, we chose to focus on the features of tumor microenvironment, given the increasing amount of evidence demonstrating its vital role in promoting the survival and proliferation of leukemic B-cells [9]–[13]. In solid cancers, extracellular matrix (ECM) remodeling and other processes related to tumor microenvironment are associated to increased aggressiveness and poor prognosis [19]. However, a recent study has proposed the hypothesis that processes traditionally considered as unfavorable in solid tumors could be associated to better survival outcomes in lymphoid neoplasms [14]. There, the authors defined a signature that included components of the extracellular matrix, together with modifiers of collagen synthesis, proteins involved in ECM remodeling and connective-tissue growth factors. In order to comprehend the behavior of these processes within the two distinct lymphoid groups examined in this work, we evaluated the enrichment of the signature proposed by [14], named *STROMAL-1*, in each human sample, together with a signature including only genes related to EMT. The enrichment analysis showed significantly higher expression values in group 1 patients for genes associated to ECM remodeling and EMT.

To summarize, there is a clear distinction in the molecular characteristics of the microenvironment between human samples mirroring murine transcriptomic profiles. Group 1 samples are characterized by the activation of EMT-like programs and an active production and processing of ECM components. Notably, our analysis has further confirmed an unexpected correlation between these features, typical indicators of aggressiveness in solid tumors, and a more favorable outcome of lymphoid neoplasms, with group 1 patients displaying significantly better prognosis with respect to group 2.

REFERENCES

[1] S. H. Swerdlow *et al.*, "The 2016 revision of the World Health Organization classification of lymphoid neoplasms," *Blood*, vol. 127, no. 20, pp. 2375–2390, 2016.

[2] L. Scarfò, A. J. M. Ferreri, and P. Ghia, "Chronic lymphocytic leukaemia," *Crit. Rev. Oncol. Hematol.*, vol. 104, pp. 169–182, 2016.

[3] M. Hallek, "Chronic lymphocytic leukemia: 2020 update on diagnosis, risk stratification and treatment," *Am. J. Hematol.*, vol. 94, no. 11, pp. 1266–1287, 2019.

[4] V. Cherepakhin, S. M. Baird, G. W. Meisenholder, and T. J. Kipps, "Common clonal origin of chronic lymphocytic leukemia and high-grade lymphoma of Richter's syndrome," *Blood*, vol. 82, no. 10, pp. 3141–3147, 1993.

[5] S. A. Parikh *et al.*, "Diffuse large B-cell lymphoma (Richter syndrome) in patients with chronic lymphocytic leukaemia (CLL): A cohort study of newly diagnosed patients," *Br. J. Haematol.*, vol. 162, no. 6, pp. 774–782, 2013.

[6] S. Li, K. H. Young, and L. J. Medeiros, "Diffuse large B-cell lymphoma," *Pathology*, vol. 50, no. 1, pp. 74–87, 2018.

[7] K. Pietras and A. Östman, “Hallmarks of cancer: Interactions with the tumor stroma,” *Exp. Cell Res.*, vol. 316, no. 8, pp. 1324–1331, 2010.

[8] N. A. Bhowmick, E. G. Neilson, and H. L. Moses, “Stromal fibroblasts in cancer initiation and progression,” *Nature*, vol. 432, pp. 332–337, 2004.

[9] L. Raffaghello, A. Vacca, V. Pistoia, and D. Ribatti, “Cancer associated fibroblasts in hematological malignancies,” *Oncotarget*, vol. 6, no. 5, pp. 2589–2603, 2015.

[10] J. A. Burger, “Nurture versus nature: the microenvironment in chronic lymphocytic leukemia.,” *Hematology Am. Soc. Hematol. Educ. Program*, vol. 2011, pp. 96–103, 2011.

[11] P. Panayiotidis, D. Jones, K. Ganeshaguru, L. Foroni, and A. V. Hoffbrand, “Human bone marrow stromal cells prevent apoptosis and support the survival of chronic lymphocytic leukaemia cells in vitro,” *Br. J. Haematol.*, vol. 92, no. 1, pp. 97–103, 1996.

[12] L. Lagneaux, A. Delforge, D. Bron, C. De Bruyn, and P. Stryckmans, “Chronic lymphocytic leukemia (CLL) B-lymphocytes but not normal B-lymphocytes are rescued from apoptosis by contact with bone marrow stromal cells,” *Blood*, vol. 91, no. 7, pp. 2387–2396, 1998.

[13] N. Kotlov *et al.*, “Clinical and biological subtypes of B-cell lymphoma revealed by microenvironmental signatures,” *Cancer Discov.*, vol. 11, no. 6, pp. 1468–1489, 2021.

[14] G. Lenz *et al.*, “Stromal Gene Signatures in Large-B-Cell Lymphomas,” *N. Engl. J. Med.*, vol. 359, no. 22, pp. 2313–2323, 2008.

[15] R. Edgar, M. Domrachev, and A. E. Lash, “Gene Expression Omnibus: NCBI gene expression and hybridization array data repository,” *Nucleic Acids Res.*, vol. 30, no. 1, pp. 207–210, 2002.

[16] C. J. Bult *et al.*, “Mouse Genome Database (MGD) 2019,” *Nucleic Acids Res.*, vol. 47, no. D1, pp. D801–D806, 2019.

[17] M. Foroutan, D. D. Bhuva, R. Lyu, K. Horan, J. Cursons, and M. J. Davis, “Single sample scoring of molecular phenotypes,” *BMC Bioinformatics*, vol. 19, no. 1, pp. 1–10, 2018.

[18] A. Liberzon, A. Subramanian, R. Pinchback, H. Thorvaldsdóttir, P. Tamayo, and J. P. Mesirov, “Molecular signatures database (MSigDB) 3.0,” *Bioinformatics*, 2011.

[19] D. Hanahan and R. A. Weinberg, “Hallmarks of cancer: The next generation,” *Cell*, vol. 144, no. 5, pp. 646–674, 2011.

Modeling metabolic overload effects in bacterial growth rate in synthetic biology

E. Gaetan[1], C. Cimolato[1], L. Schenato[1], and M. Bellato[1]
[1] *Department of Information Engineering, University of Padova, Padova - Italy*

***Abstract*—Modeling growth in bacterial cells is a major issue in systems and synthetic biology. Despite several growth rate functions are proposed in literature, most of them focus on nutrients composition, without explicitly counting for possible perturbation provided by the expression of recombinant genes, an effect called metabolic load or burden. In this work, some already published growth functions are evaluated, highlighting possible disagreements with the biological knowledge, which allow to reject some of them. Furthermore, some alternative functions based on biological evidences are proposed and tested as well, specifically oriented on metabolic load effects. The final aim is to identify a growth rate function that can be applied to models with different levels of complexity, leading to coherent results, which also account for the addition of metabolic burden, decoupled from nutrient composition.**

***Keywords*—Molecular systems biology, metabolic burden, bacterial ribosomes, control systems.**

I. INTRODUCTION

In Synthetic Biology, engineers modify bacterial cells to create novel biological systems with potential therapeutic or biotechnologically-relevant effects. Genetic circuits, realized following a model-driven rational design approach, are added to engineered cells, leading to the production of different proteins than the ones normally synthesized, in a mathematically-predictable manner.

Due to the finite nature of the cells, the limitation in resource availability harness the whole engineering process, often leading to unpredictable outcomes in engineered cells behaviour [1],[2], to the point that extra demand for protein synthesis necessarily affects the cell growth.

While the *growth rate* of the bacterium *Escherichia coli* in its exponential growth phase is typically assumed to be conserved (cells can double every ~ 20 min at $37\,\mathrm{deg}$), it has been observed that this time can be severely reduced [3] or either increased [8] by several factors, such as the amount of available nutrients in the surrounding environment.

While several examples of growth rate functions including temperature or nutrient starvation can be found in literature, unfortunately they do not include metabolic load perturbations, being mostly related to non-engineered systems. Nevertheless, all of them agree that the growth rate function should depend on the ribosomal component.

In [3], [5], the proposed model for the cell growth is a function dependent on the total number of ribosomes: in the first case, the function is linear, while in the second one it is a first order Hill function. In [4], growth rate is a linear function as in [3], but it now depends on the difference between the total active and inactive number of ribosomes and on the total protein mass. Additionally, in [6], the linearity is maintained, but on the ribosome complexes (i.e., a ribosome bound with a mRNA.). Lastly, one more example can be found in [7] where, while a growth rate function was not explicitly defined, the authors provided the ratios of free ribosomes over the total amount of them. Accordingly to this information, the growth rate has been analytically drawn by fitting a Hill function on the available points.

As already stated, all these growth rate functions do not account for the inclusion of metabolic load and therefore they can not be directly applied. Thus, a test phase is needed in order to verify that the chosen growth rate function produces coherent results with the biological evidences.

The following Section 2 describes our mathematical modeling approach to describe the cell system to overcome the existing limitations, Section 3 shows the simulation results and Section 4 resumes the conclusions.

II. MATHEMATICAL MODELING

A. Biological hypothesis and mathematical assumptions

The first assumption to be performed is that RNAP can be considered constant [7]. Consequently, the chemical reaction for the transcription process can be approximated by:

$$\mathrm{D} \xrightarrow{\omega} \mathrm{D} + \mathrm{m} \tag{1}$$

where D is the DNA, ω is the transcription rate and m is the mRNA. In order to limit the number of parameters, assuming equal order of magnitude and over time, the spontaneous decay is considered equal for proteins, ribosomes and ribosomal complexes (regardless of the species) and indicated with δ; analogously, mRNA and rRNA decay is indicated with γ.

Another assumption regards the degradation rate μ. It is defined as the sum between the spontaneous decay γ and the growth rate λ. From [7], it is known that γ is faster than λ for mRNA and rRNA. This leads to the approximation: $\mu_{mRNA,rRNA} = \gamma + \lambda \approx \gamma$. Thus, the degradation rate of mRNA and rRNA can be considered constant.

The last assumption concerns the synthesis of ribosomes R. Indeed the process of formation should involve both rRNA and R-Protein. To simplify further the model structure, the ribosomes are assumed to be derived directly from the DNA with rate β_r:

$$\mathrm{D}_r \xrightarrow{\beta_r} \mathrm{D}_r + \mathrm{R} \tag{2}$$

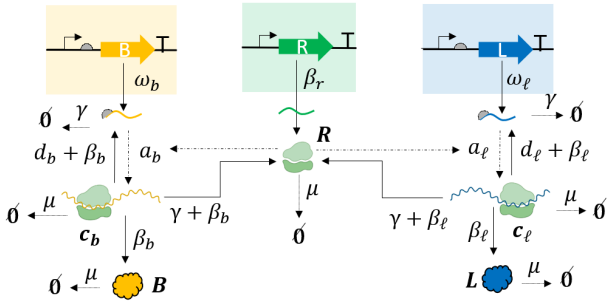


Fig. 1: Model of the cell system.

Additionally, it is possible to identify two different ribosomal species (i.e., components involving free ribosomes in their characteristic chemical reactions): the basal species b, which represents all the components that are fundamental for the survival of the cell and the load species ℓ, which corresponds to extra demand of protein to be synthesized, thus to metabolic burden.

B. Model implementation

The derived model can be represented as in Fig. 1. The structure involves three different types of ribosomal species: the free ribosomes R, the basal c_b and load c_ℓ complexes. Together, they form the total amount of ribosomes of the cell R^{TOT}. Starting from the DNA, the transcription produces the mRNA with RBS (*Ribosome Binding Site*). This can bind the ribosome with rate a_i (where i indicates the species, namely $i = b, \ell$). However, this link can be broken with dissociation rate d_i. In the building phase of the model, an hypothesis is assumed: c_i can release the free ribosome with rate γ. Furthermore, the translation process synthesizes the protein with rate β_i from the ribosomal complex c_i, but also returns the mRNA and the free ribosome used for the bound.This model structure accounts also for the degradation rates (γ for mRNA and μ for ribosomes, ribosomal complexes and protein). Hence, this model is characterized by the following set of chemical reactions (with $i = b, \ell$):

$$\mathrm{D}_i \xrightarrow{\omega_i} \mathrm{D}_i + \mathrm{m}_i \quad (3)$$

$$\mathrm{D}_r \xrightarrow{\beta_r} \mathrm{D}_r + \mathrm{R} \quad (4)$$

$$\mathrm{m}_b + \mathrm{R} \underset{\mathrm{d}_b}{\overset{\mathrm{a}_b}{\rightleftharpoons}} \mathrm{c}_b \xrightarrow{\beta_b} \mathrm{m}_b + \mathrm{R} + \mathrm{B} \quad (5)$$

$$\mathrm{m}_\ell + \mathrm{R} \underset{\mathrm{d}_\ell}{\overset{\mathrm{a}_\ell}{\rightleftharpoons}} \mathrm{c}_\ell \xrightarrow{\beta_\ell} \mathrm{m}_\ell + \mathrm{R} + \mathrm{L} \quad (6)$$

$$\mathrm{m}_i \xrightarrow{\gamma} 0 \quad (7)$$

$$\mathrm{c}_i \xrightarrow{\gamma} \mathrm{R} \quad (8)$$

$$\mathrm{R}, \mathrm{c}_i, \mathrm{B}, \mathrm{L} \xrightarrow{\mu} 0 \quad (9)$$

and mass conservation laws:

$$R^{TOT} = R + c_b + c_\ell \quad (10)$$

$$m_i^{TOT} = m_i + c_i \quad (11)$$

The reactions 3-9 can be translated into a system of differential equations, as it follows (with $i = b, \ell$):

$$\dot{m}_i = \omega_i D_i - a_i m_i R + d_i c_i + \beta_i c_i - \gamma m_i \quad (12)$$

$$\dot{c}_i = a_i m_i R - d_i c_i - \beta_i c_i - \gamma c_i - \mu c_i \quad (13)$$

$$\dot{R} = \beta_r D_r - \sum_i a_i m_i R + \sum_i d_i c_i + \sum_i \beta_i c_i + \gamma \sum_i c_i - \mu R \quad (14)$$

$$\dot{B} = \beta_b c_b - \mu B \quad (15)$$

$$\dot{L} = \beta_\ell c_\ell - \mu L \quad (16)$$

$$\dot{R}^{TOT} = \beta_r D_r - \mu R^{TOT} \quad (17)$$

$$\dot{m}_i^{TOT} = \omega_i D_i - \gamma m_i^{TOT} - \mu c_i \quad (18)$$

A further approximation can be performed. By considering the relation between γ and μ ($\gamma >> \mu$, from [7]) and knowing that $m_i^{TOT} \geq c_i$ (easily derived from Eq. 11), then Eq. 18 become:

$$\dot{m}_i^{TOT} \approx \omega_i D_i - \gamma m_i^{TOT} \quad (19)$$

In the following analysis, this approximated version will be considered. The set of Eqs. 12-17, 19 can be studied in steady state condition. In particular, while Eq. 19 have a closed form solution, namely:

$$m_i^{TOT} = \frac{\omega_i D_i}{\gamma} \quad (20)$$

the others must be solved numerically. However, by exploiting the speed of the reactions, it is possible to find an approximated solution also for the Eqs. 12-14 (and thus for Eq. 17).

Considering the set of differential equations: the fast dynamics are represented by Eqs. 12 and 13, while the slow dynamics is described by 18. Rewriting them by replacing a_i as $\frac{d_i}{K_i}$ (K_i is the dissociation constant) and d_i as $\frac{1}{\epsilon}$:

$$\dot{m}_i = \frac{1}{\epsilon}(-m_i \frac{R}{K_i} + c_i) + \omega_i D_i + \beta_b c_i - \gamma m_i \quad (21)$$

Due to the condition of fast dynamics, $\epsilon \longrightarrow 0$. Consequently, the obtained manifold is:

$$c_i = \frac{R}{K_i} m_i \quad (22)$$

Replacing c_i from Eq. 22 in Eq. 11, one obtains:

$$c_i = \frac{R}{R + K_i} m_i^{TOT} \quad (23)$$

$$m_i = \frac{K_i}{R + K_i} m_b^{TOT} \quad (24)$$

This shows how the evolution of c_i and m_i uniquely depends on the total amount of mRNA and the strength of the bound mRNA-ribosome. Since it is proved that m_i^{TOT} depends on the transcription rate ω_i (by Eq. 20), the only factor which does not influence the mRNA and complex concentration is the translation rate β_i. By replacing Eq. 23 in Eq. 10, one obtains:

$$R^{TOT} = R + \frac{R}{R + K_b} m_b^{TOT} + \frac{R}{R + K_\ell} m_\ell^{TOT} \quad (25)$$

It is worth to notice that this formulation is independent on the growth rate function. Eq. 25 must be solved numerically. However, it is possible to find a closed form solution if the manifolds of c_i (which are Hill functions, according to Eq. 23) are approximated by piece-wise linear functions. Without loss of generality, assuming that $K_b < K_\ell$, then the approximated functions are:

$$c_i \approx \begin{cases} \frac{m_i^{TOT}}{K_i} R & , R \leq K_i \\ m_i^{TOT} & , R > K_i \end{cases} \quad \text{where } i = b, \ell \tag{26}$$

Because of the mass conservation law Eq. 10 and by exploiting Eq. 26, the approximated function of R^{TOT} is:

$$R^{TOT} = \begin{cases} \left(1 + \frac{m_b^{TOT}}{K_b} + \frac{m_\ell^{TOT}}{K_\ell}\right) R & , 0 \leq R \leq K_b \\ \left(1 + \frac{m_\ell^{TOT}}{K_\ell}\right) R + m_b^{TOT} & , K_b < R \leq K_\ell \\ R + m_b^{TOT} + m_\ell^{TOT} & , R > K_\ell \end{cases} \tag{27}$$

Now it is possible to reverse the equations to obtain R as function of R^{TOT}:

$$R = \begin{cases} \frac{1}{\left(1 + \frac{m_b^{TOT}}{K_b} + \frac{m_\ell^{TOT}}{K_\ell}\right)} R^{TOT} & , 0 \leq R^{TOT} \leq \tilde{R}_1^{TOT} \\ \frac{R^{TOT} - m_b^{TOT}}{\left(1 + \frac{m_\ell^{TOT}}{K_\ell}\right)} & , \tilde{R}_1^{TOT} < R^{TOT} \leq \tilde{R}_2^{TOT} \\ R^{TOT} - m_b^{TOT} - m_\ell^{TOT} & , R^{TOT} > \tilde{R}_2^{TOT} \end{cases} \tag{28}$$

where accordingly to the conditions in Eq. 27:

$$\tilde{R}_1^{TOT} = \left(1 + \frac{m_b^{TOT}}{K_b} + \frac{m_\ell^{TOT}}{K_\ell}\right) K_b \tag{29}$$

$$\tilde{R}_2^{TOT} = \left(1 + \frac{m_\ell^{TOT}}{K_\ell}\right) K_\ell + m_b^{TOT} \tag{30}$$

C. Growth Law

Before performing any simulations with the designed ribosomes synthesis model, a growth rate function must be stated. As already explained in the introduction, none of the literature examples can be directly applied, since none of them accounts for the metabolic load. Consequently, one possible strategy is to exploit some of them and verify if they still produce coherent results even with the addition of a burden. The table below resumes all the performed tests.

TABLE I: TESTED GROWTH RATE FUNCTIONS

Growth function	*Variable*	*Data reference*
Linear	c_b	[3]
Linear	$R^{active} = c_b + c_\ell$	[3]
$Hill_{DV}$	c_b	[7]
Hill	c_b	[3]

Furthermore, it is necessary to estimate the initial configuration, which must be the same throughout the tests to perform valid analyses, in which the bacterial cell is before the metabolic burden is applied. We suppose that the cell is in the condition of maximal growth. However, the point of maximal growth varies based on the chosen growth rate function. By assumption, the growth rate formulation in [7] is pursued. As claimed in it, the partition of the ribosomes (in maximal growth) is the following:

$$c_b = \frac{2}{3} R_{max}^{TOT}, \quad R = \frac{1}{3} R_{max}^{TOT} \tag{31}$$

From Eq. 17 at the steady state, the value of $\beta_r D_r$ can be derived simply by substituting R_{max}^{TOT} and μ_{max}. To obtain $\omega_b D_b$, m_b^{TOT} in Eq. 18 at the steady state must be replaced with its value derived from Eq. 23:

$$0 = \omega_b D_b - \gamma \frac{R + K_b}{R} c_b - \mu c_b \tag{32}$$

By replacing c_b and R in Eq. 32 with their values in Eq. 31, the value of $\omega_b D_b$ in the maximal growth condition is obtained:

$$\omega_b D_b = \frac{2}{3} R_{max}^{TOT} (\gamma + \mu_{max}) + 2\gamma K_b \approx 2\gamma \left(\frac{R_{max}^{TOT}}{3} + K_b\right) \tag{33}$$

where the approximation is possible since $\gamma >> \mu_{max}$.

Assuming that the association rate between the ribosome and the mRNA is stronger than the dissociation due to the importance of basal proteins committed to the fundamental processes of the cell, a further approximation is possible, namely:

$$\omega_b D_b \approx 2\gamma \left(\frac{R_{max}^{TOT}}{3} + K_b\right) \approx \frac{2}{3} R_{max}^{TOT} \gamma \tag{34}$$

III. RESULTS

A. Analysis of Total Ribosomes variation

Before studying the load effect, a prior analysis on the distribution of the total amount of ribosomes R^{TOT} among the different ribosomal species (R, c_b and c_ℓ) is required.

The concentration of R^{TOT} is limited in the cell. Because of that, the species must compete for obtaining the needed ribosomes for their reactions. Thus, it is fundamental to understand which parameters regulate the competition for the ribosomes between different species. In Fig. 2, the evolution

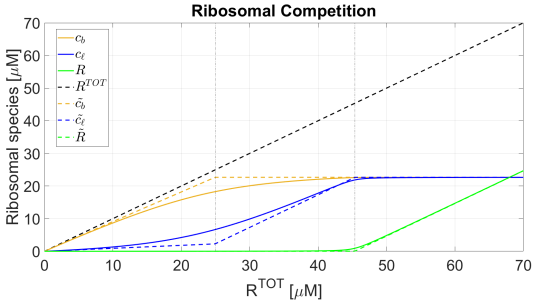


Fig. 2: Competition between species ($K_b < K_\ell$, $m_b^{TOT} = m_\ell^{TOT}$).

of different components is plotted as function of R^{TOT}. The approximate functions are used to predict the behavior of the ribosomal components. Indeed, the study of the breaking points gives information regarding the rise of the complexes. From Eq. 26, it is straightforward that the first complex to reach its maximum value has the smallest K. Thus the order of rising is just regulated by the dissociation constants.

This is consistent with biological knowledge. At the beginning, the amount of available ribosomes is limited; when the species start to compete, only the one with the strongest association rate (which implies the smallest K) can rise, while the others do not have enough strength to bind the needed ribosomes. Furthermore, they are not even able to steal the ribosomes from the already synthesized complex. Thus, when the first complex reaches its maximal value, which means that it does not need other ribosomes, the species with the second smallest dissociation constant can increase.

Moreover, Eqs. 29 and 30 show that the breaking points depend from both the dissociation constants and the total amount of *mRNA*. This is reasonable because, as already explained, the species j starts increasing when the previous one i (with $K_i < K_j$) reaches its maximal value m_i^{TOT}.

B. Analysis of Load effect

Afterwards, it is interesting to extend the analysis in order to better understand the load effects on the system, in particular on the cell growth, starting from the dynamics described by Eqs. 12-17, 19.

Equilibria are studied as function of the burden. This is characterized by three parameters: the dissociation constant K_ℓ, the transcription rate ω_ℓ and the translation rate β_ℓ. From a biochemical point of view, the easiest to adjust is ω_ℓ. Thus, the assumed choice is to vary the transcriptional rate, while the other parameters are kept constant. In particular, the evolution of c_b, c_ℓ, R and R^{TOT} is considered. Despite the concentrations of *mRNAs* and the proteins are changing as well, they do not directly affect the cell growth (indeed, all the growth rate functions in Tab. I depend uniquely on the ribosomal components). Therefore, the study of the evolution of these elements is not fundamental for the aim of the analysis. However, differently from the previous case, the degradation μ is now involved in the equations. In fact, even though the evolution of the complexes can be still derived from the manifolds equations, Eq. 17 at the steady state depends on the growth rate function λ. This means that the results are strongly influenced by the chosen type of growth rate function.

Following the order in Table I, all the growth rate functions were tested. Among all the formulations, the more consistent with the biological evidences is the linear growth rate function dependent on R^{active} (Fig. 3). All the other simulations showed the same critical aspect: the stronger the load, the higher the amount of total ribosomes in the cell. This evidence is used to rule out these growth rate functions, indeed, it is not reasonable to have a potentially infinite concentration of ribosomes in the cell. It is also possible to appreciate the competition between species, which is coherent with the results in Fig. 2. In fact, at first the load species takes the needed ribosomes from the free ribosomes compartment. Once this is empty, it starts stealing them from the basal complex.

IV. Conclusion

In this work, the cell growth was studied, testing different type of functions from literature and it was possible to state

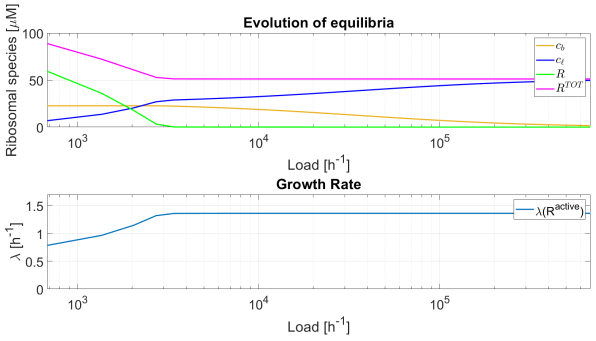


Fig. 3: Evolution of the equilibrium points and the growth rate varying the metabolic load.

that the best growth rate function is the *Linear* dependent on R^{active}. Possible improvements to this work can be performed, especially regarding the model. Its complexity can be increased, reaching a better level of description: in particular, it is possible to add a new species R-Protein, responsible for the synthesis of the ribosomes ([11],[13]), and some biological feedbacks, which are reported in literature ([9]-[12]).

Acknowledgment

This work was funded by Fondazione Cariparo grant "Ricerca Scientifica di Eccellenza 2021 n59576". Authors thank B. Di Camillo and S. Del Favero for helpful discussions.

References

[1] Bellato M, et al. "CRISPR Interference Modules as Low-Burden Logic Inverters in Synthetic Circuits". In *Front. Bioeng. Biotechnol.* 9(743950), 2021. Available: Link.

[2] Huang HH, et al. "dCas9 regulator to neutralize competition in CRISPRi circuits". In *Nat Commun* 12(1692), 2021. Available: Link.

[3] Marr AG. "Growth rate of Escherichia coli". In *Microbiol Rev.* 55(2),316:33, 1991. Available: Link.

[4] Chenhao W, et al. "Cellular perception of growth rate and the mechanistic origin of bacterial growth rate". In *Proceedings of the National Academy of Sciences*. 119(20), 2022. Available: Link.

[5] Levin BR, et al. "A Numbers Game: Ribosome Densities, Bacterial Growth, and Antibiotic-Mediated Stasis and Death". In *mBio*. 8(1):e02253-16, 2017. Available: Link.

[6] Atkinson E, Tuza Z, Perrino G, Stan GB, and Ledesma-Amaro R. "Resource-aware whole-cell model of division of labour in a microbial consortium for complex-substrate degradation". In *Microb Cell Fact*. 21(115), 2022. Available: Link.

[7] Del Vecchio D, and Murray RM. "Biomolecular Feedback Systems". Princeton University Press, 2014.

[8] Bremer H, and Dennis PP. "Modulation of Chemical Composition and Other Parameters of the Cell at Different Exponential Growth Rates". In *EcoSal Plus*. 3(1), 2008. Available: Link.

[9] Condon C, et al. "Control of rRNA transcription in Escherichia coli". In *Microbiol Rev*. 59(4),623:45, 1995. Available: Link.

[10] Srivastava AK, and Schlessinger D. "Mechanism and regulation of bacterial ribosomal RNA processing". In *Annu Rev Microbiol*. 44,105:29, 1990. Available: Link.

[11] Nomura M, Gourse R, and Baughman G. "Regulation of the synthesis of ribosomes and ribosomal components". In *Annu Rev Biochem*. 53,75:117, 1984.Available: Link.

[12] Scott M, Klumpp S, Mateescu EM, and Hwa T. "Emergence of robust growth laws from optimal regulation of ribosome synthesis". In *Mol Syst Biol*. 10(8),747, 2014. Available: Link.

[13] Cerretti DP, Dean D, Davis GR, Bedwell DM, Nomura M. "The spc ribosomal protein operon of Escherichia coli: sequence and cotranscription of the ribosomal protein genes and a protein export gene". In *Nucleic Acids Res*. 11(9):2599:616, 1983. Available: Link.

Network-based integration of clinical, imaging and molecular biomarkers of dementia

C. Alfano[1], L. Farina[2], and M. Petti[2]
[1] *Department of Experimental Medicine, Sapienza University of Rome*
[2] *Department of Computer, Control and Management Engineering, Sapienza University of Rome*

***Abstract*—Biomarkers are measurable characteristics used as indicators for diagnosis, prognosis and therapy-response: they can be of different nature (e.g., clinical, imaging and molecular) and each type captures and describes one or few specific aspects of disease development and progression. However, a single biomarker is rarely enough to operate the high-level characterization needed in a precision medicine scenario. Still, it is not a common practice to study different biomarkers of the same disease at the same time, focusing on their inter-relationships and role in the disease. The common practice is to evaluate pairwise relations. Thus, the definition of comprehensive and integrative biomarkers is an open challenge especially in complex diseases, such as in dementia. Dementia is in fact a multi-factorial condition, with factors related to different domains and whose interactions are not well known. In this study, we applied simple and partial correlation to data of patients and healthy subjects related to a set of relevant features of dementia. Network representation and analysis showed that both approaches provide a clear pattern of interactions among different heterogeneous biomarkers. We found that, even if the two tested methods agree on the strongest edges, partial correlation graphical LASSO can detect more connections and is more sensible to negative correlations providing a more complete description of biomarkers interactions. Comparing the biomarker networks of patients and control cases we also highlighted the changes that can be seen with the development of the disease.**

***Keywords*—Network medicine, biomarker network, partial correlation, dementia**

I. INTRODUCTION

A biomarker is defined as a measurable characteristic that serves as an indicator of normal biological processes, pathogenic processes or responses to an exposure or intervention; there can be many types of biomarkers, depending on what they are derived from (molecular, histological or physiological characteristics) [1]. Molecular biomarkers have recently received particular interest, due to their usefulness in patient stratification, understanding disease etiology, assessing risks, assisting with disease prevention and early detection, and in predicting therapy-response [2]. However, complex diseases are often caused by an intricate network of alterations involving different elements and the way they interact with one another [3], and a single biomarker is not able to capture this complexity. Medical practitioners are stressing the need for more precise and at the same time comprehensive biomarkers, but approaching a disease by considering a multitude of molecular interactions and comprehensively understanding complex biological systems and their link with clinical features is a hard task. However, by using network-based methods is now possible to provide a holistic view to the study of disease complexity, by focusing on more components of the disease at the same time; this is why network-based approaches are successfully used in precision medicine research, for example in disease gene prediction [5] and for the investigation of side effects [6], [7]. Still, common networks analysis approaches rarely include different types of data at the same time [8] and are mostly focused only on gene expression or protein-protein interactions. By creating a biomaker network we are able to integrate different omics and clinical data, and therefore consider the underlying relationships between biomarkers of different nature. In fact, elucidating the inter-dependency and inter-connectivity among different biomarkers and pathways may provide a more comprehensive view of and insight into the pathogenic process [2].

The importance of considering the relationships between different relevant features of a disease has even led to the idea of using a network as a biomarker [3], [4]: this means considering the whole set of disease features and their interaction as a comprehensive biomarker to characterize the patients. This is particularly useful in a dynamic network scenario, where the changes of the biomarkers' network through time can be measured and studied.

Given the fact that this approach is not yet commonly used, no go-to practice has yet been established in the literature. In this work we compare the use of Spearman correlation [9] and partial correlation Graphical Lasso (Glasso) [8], to build a network of different dementia-related biomarkers. Dementia is in fact a multi-factorial condition, that is a major cause of disability and dependency among older people. Nonetheless, risk factors have mainly been researched in isolation. Previous research has identified many factors potentially related to cognitive decline and dementia, some more studied than others. These factors include genetic preconditions, life-style related factors, medical conditions, environmental and social health factors [10].

In this study we will create network biomarkers for both dementia patients and control cases, to describe how the relationships between different dementia-related features changes with the disease development.

II. MATERIALS AND METHODS

A. Data

The data used in this project was taken from the Aging, Dementia and TBI Study, which is available on the Allen Brain

Map webiste [11][12]. This dataset contains neuropathologic and transcriptomic information as well as quantitative image metrics from both people affected by dementia and control cases. All the donors were over 78 years old, but not all of them had suffered traumatic brain injuries (TBIs) before. The available information is of various nature:

- Clinical data (e.g. age, past TBIs, sex, diagnosis etc.)
- RNA sequencing data for temporal cortex, parietal cortex, cortical white matter, and hippocampus isolated by macrodissection
- Protein quantification of neuropathological and immune system targets
- Gas chromatography mass spectrometry (GC/MS) quantitation of isoprostanes
- Histology and immunohistochemistry (IHC) quantitative image metrics

In this study, for each donor more samples were taken from different areas of the brain, depending on analyzed features; for example, quantification of isoprostanoids was only performed on parietal and temporal cortex. We decided to focus on the hippocampus. As for the donors, we only considered the ones that did not present the mutation of the APOE gene, to reduce the differences among the considered cohort.
Among the data available for the chosen region, we selected a group of biomarkers, making sure to avoid both linear dependence between them (tested with the "findLinearCombos" from the caret R package. [13]) and missing values, as well as maintaining a good ratio of cases and control cases. Our final dataset consisted of 50 donors (29 cases and 21 controls) and 20 biomarkers (reported in Table I).

B. Methods

We used and compared two different ways to infer biomarker networks: Spearman correlation and Graphical Lasso (Glasso). Spearman is a non-parametric measure of rank correlation that assesses how well the relationship between two variables can be described using a monotonic function. The Glasso algorithm uses instead partial correlations to infer the connection between each pair of variables, and it estimates sparse graphs through a lasso penalty applied to the inverse covariance matrix.
We created a total of 4 networks: healthy donors with Spearman, dementia patients with Spearman, healthy donors with Glasso and dementia patients with Glasso. For the first ones we used Spearman pairwise correlation and considered only results with an adjusted pvalue (FDR adjustment) lower than 0.05. For the other two we used the "estimateNetwork" function from the bootnet package [14], set on "EBICglasso" with the tuning equal to use regular BIC
Additionally, we performed a pairwise Wilcoxon test with fdr adjustment to check if and which of our variables was significantly different in the two categories of patients.

TABLE I: CONSIDERED BIOMARKERS

Name	*Description*
Age	Age of the donor. Linear for 72-89, binned at 90-94, 95-99, and 100+
Braak	Staging of neurofibrillary tangles (NFTs) from 0 to 6 based on Braak method of staging
ihc_tau2_ffpe	Phospho-tau (mature) immunohistochemistry (formalin fixed, paraffin embedded; labeled by Tau2): areal density
ihc_at8_ffpe	Phospho-tau (immature and mature) immunohistochemistry (formalin fixed, paraffin embedded; labeled by AT8): areal density
ihc_at8	Phospho-tau (immature and mature) immunohistochemistry (fresh frozen tissue; labeled by AT8): areal density
ihc_a_beta	Beta-amyloid immunohistochemistry (fresh frozen tissue): areal density
ihc_a_syn	Alpha-synuclein immunohistochemistry (fresh frozen tissue): areal density
il_10	IL-10 protein quant. by Luminex
ptau	pTau-181 protein quant. by Luminex
tau	Tau protein quant. by Luminex
ab40	Aβ40 protein quant. by Luminex
il_6	IL-6 protein quant. by Luminex
vegf	VEGF protein quant. by Luminex
rantes	RANTES protein quant. by Luminex
mip_1a	MIP-1α protein quant. by Luminex
SLC6A1	Gene expression
MOBP	Gene expression
GFAP	Gene expression
AQP4	Gene expression
SLC17A7	Gene expression

III. Results and Discussion

As a first result, we identified which biomarkers were significantly different among the two groups of donors. We found that braak, ihc_tau2_ffpe, ihc_at8, ptau and GFAP showed a significant increase in people affected by dementia. As far as the first four variables are concerned, this increase

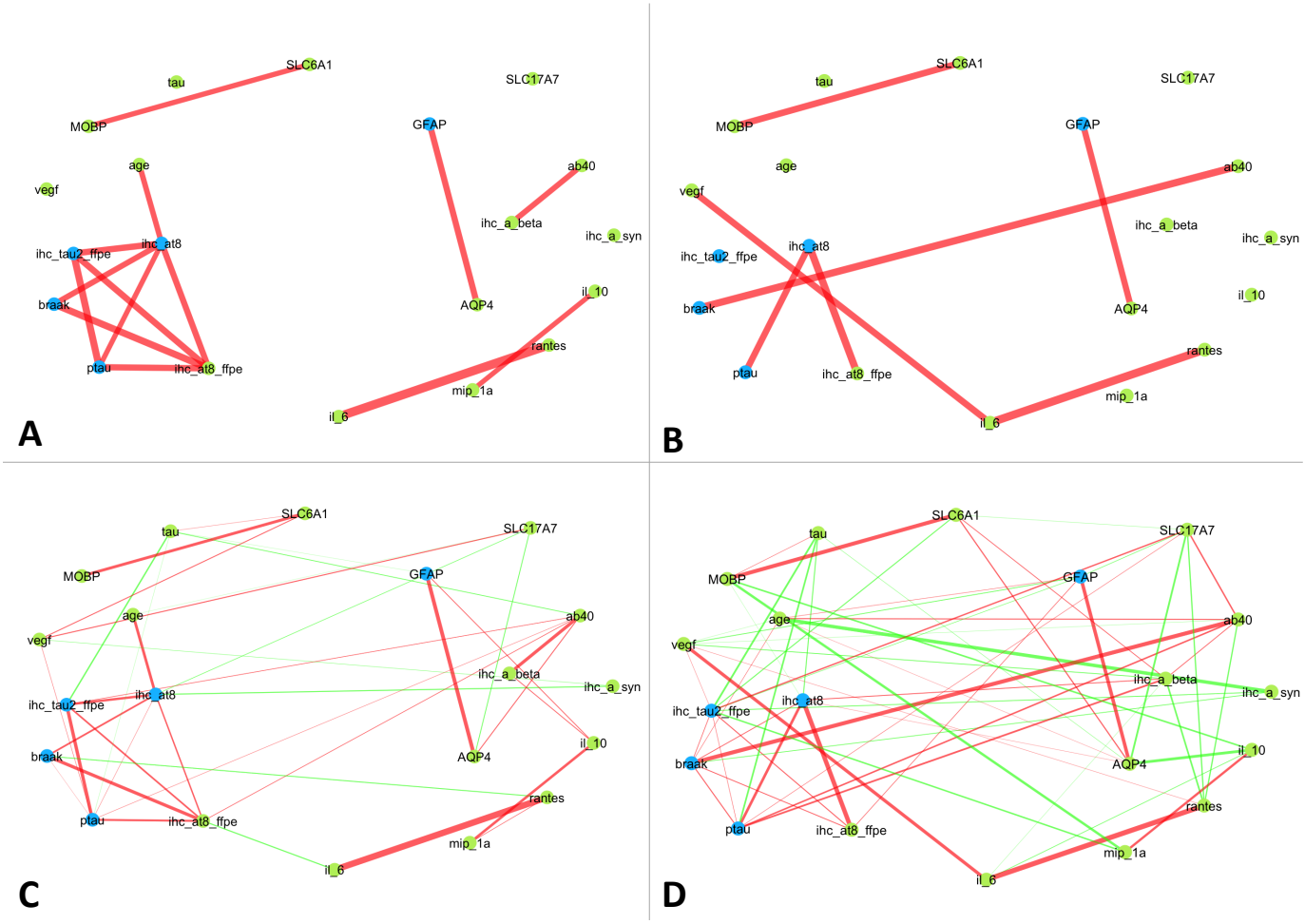


Fig. 1: The four biomarker networks obtained: A) control cases with Spearman correlation, B) dementia patients with Spearman correlations, C) control cases with Glasso, D) dementia patients with Glasso. The biomarkers significantly different in the two conditions (patients vs healthy donors) are displayed with blue nodes. Red edges represent positive correlations, while green ones represent negative correlations. Bigger edges code for bigger weights.

is consistent with the fact that they are all measures linked to brain tangles, which increase with dementia. This result is also consistent with what found by Miller et al. [12] in their first analysis of the dataset.

To carry out the rest of the analyses we used and compared the two methods more commonly used in similar studies: Spearman correlation and Graphical Lasso. Doing so, we obtained four weighted networks: two based on healthy donors and two based on dementia patients (Fig. 1). We found that overall there is a good degree of agreement on the strongest edges between the two methods. However, the Glasso method seems to be better at uncovering more complex underlying interconnections between the biomarkers. Moreover, only the networks created with the Glasso method contain negative correlations.
The general weights of the edges are also smaller in Glasso networks. However, we do find most of the edges detected by Spearman to be among the stronger edges in Glasso networks too (e.g. il-6 and rantes).
Looking at both networks of healthy donors we can find an expected correlation between $A\beta$ IHC density and $A\beta 40$ protein quantification, as well as a correlation between the gene expression of GFAP and AQP4 (both canonical marker genes for astrocytes), SLC6A1 and MOBP, MIP-1α and interleukin10, rantes and interleukin6. However, the Glasso network is also able to detect some interesting negative correlations, like the one between braak and rantes or ihc_tau2_ffpe and tau protein quantification.
Both networks of healthy donors also confirm, as found by Miller et al. [12], a relationship between age and ptau pathology, seen via the at8 immunoistochemistry. Moreover, in the Glasso network we found a negative correlation between age and SCL17A and a positive one between ab40 and APQ4. This caught our attention because Miller et al. [12] searched, without any luck, for module eigengenes (MEs) significantly associated with age, Aβ or α-synuclein pathology. Most of these relationships change when we look

at the network of dementia patients: in this case we found a positive correlation between SCL17A and ab40 as well as between ihc_a_beta and SCL6A1; we also found a positive correlation between GFAP and age.

Depending of the chosen method, we can notice other changes when comparing the relationships between biomarkers in healthy donors and dementia patients. Firstly, we saw a strong correlation between ab40 and braak score, as well as the one between vegf and il-6. Secondly, while the Spearman network mostly highlighted different relationships between metrics of tau pathology (tau, tau2, at8 etc.), Glasso was able to represent a more complex network of correlations, showcasing many interesting negative correlations, like the one between age and α_synuclein or APQ4 and il-10.

IV. Conclusion

We tested and compared two different methods to infer networks of disease biomarkers, and used the results to compare how these networks differ between healthy subjects and dementia patients. By doing so we saw that, in our application, the network obtained with Spearman and Glasso are similar as far as heavier weights are concerned, but that Glasso is better suited to detect negative edges. Through the networks inferred on the chosen dataset were able to confirm some of the findings of the dataset's authors and to extend those information by providing an holistic view of interrelationship between biomarkers of different nature (e.g., ihc_a_beta and rantes in Fig. 1 D) , and how these relationships change once a person has developed dementia. In particular, with Glasso we found correlations between genes of interest and both age and Aβ pathology. This had not been possible with the methodology proposed by Miller et al. [12] or by constructing networks based on Spearman correlations.
A more extensive analysis could reinforce the results illustrated here. Further improvements could include the selection of more biomakers, as well performing test on simulated data or on biomarkers of more varied nature.

Acknowledgement

This work was supported by Sapienza University of Rome, grant number: AR122181684B0183

References

[1] Califf RM. Biomarker definitions and their applications. Exp Biol Med (Maywood). 2018 Feb;243(3):213-221. doi: 10.1177/1535370217750088. PMID: 29405771; PMCID: PMC5813875.

[2] Huang T, Glass K, Zeleznik OA, Kang JH, Ivey KL, Sonawane AR, Birmann BM, Hersh CP, Hu FB, Tworoger SS. A Network Analysis of Biomarkers for Type 2 Diabetes. Diabetes. 2019 Feb;68(2):281-290. doi: 10.2337/db18-0892. Epub 2018 Nov 8. PMID: 30409783; PMCID: PMC6341308.

[3] Wu X, Chen L, Wang X. Network biomarkers, interaction networks and dynamical network biomarkers in respiratory diseases. Clin Transl Med. 2014 Jun 24;3:16. doi: 10.1186/2001-1326-3-16. PMID: 24995123; PMCID: PMC4072888.

[4] Alfano, C.; Farina, L.; Petti, M. Networks as Biomarkers: Uses and Purposes. Genes 2023, 14, 429. https://doi.org/10.3390/genes14020429

[5] Petti M, Bizzarri D, Verrienti A, Falcone R, Farina L. Connectivity Significance for Disease Gene Prioritization in an Expanding Universe. IEEE/ACM Trans Comput Biol Bioinform. 2020 Nov-Dec;17(6):2155-2161. doi: 10.1109/TCBB.2019.2938512. Epub 2020 Dec 8. PMID: 31484130.

[6] Manuela Petti, Caterina Alfano, Lorenzo Farina, Molecular network analysis of hormonal contraceptives side effects via database integration, Informatics in Medicine Unlocked, Volume 36, 2023, 101163, ISSN 2352-9148, https://doi.org/10.1016/j.imu.2023.101163.

[7] E. Guney, Investigating side effect modules in the interactome and their use in drug adverse effect discovery, Complex networks VIII (2017), pp. 239-250

[8] Chu JH, Hersh CP, Castaldi PJ, Cho MH, Raby BA, Laird N, Bowler R, Rennard S, Loscalzo J, Quackenbush J, Silverman EK. Analyzing networks of phenotypes in complex diseases: methodology and applications in COPD. BMC Syst Biol. 2014 Jun 25;8:78. doi: 10.1186/1752-0509-8-78. PMID: 24964944; PMCID: PMC4105829.

[9] Nishihara R, Glass K, Mima K, Hamada T, Nowak JA, Qian ZR, Kraft P, Giovannucci EL, Fuchs CS, Chan AT, Quackenbush J, Ogino S, Onnela JP. Biomarker correlation network in colorectal carcinoma by tumor anatomic location. BMC Bioinformatics. 2017 Jun 17;18(1):304. doi: 10.1186/s12859-017-1718-5. PMID: 28623901; PMCID: PMC5474023.

[10] Seifert, I., Wiegelmann, H., Lenart-Bugla, M. et al. Mapping the complexity of dementia: factors influencing cognitive function at the onset of dementia. BMC Geriatr 22, 507 (2022). https://doi.org/10.1186/s12877-022-02955-2

[11] Dataset: Allen Institute for Brain Science, University of Washington Medicine, and Kaiser Permanente Washington Health Research Institute (2016). Aging, Dementia, and TBI Study [dataset]. Available from aging.brain-map.org. $RRID$: $SCR_0$14554 | Primary publication: Miller J. A., et al. (2017). Neuropathological and transcriptomic characteristics of the aged brain. eLife, 2017;6:e31126. https://doi.org/10.7554/eLife.31126.

[12] Jeremy A Miller et al. (2017) Neuropathological and transcriptomic characteristics of the aged brain eLife 6:e31126. https://doi.org/10.7554/eLife.31126.

[13] https://rdrr.io/cran/caret/ Authors: Max Kuhn [aut, cre] (<https://orcid.org/0000-0003-2402-136X>), Jed Wing [ctb], Steve Weston [ctb], Andre Williams [ctb], Chris Keefer [ctb], Allan Engelhardt [ctb], Tony Cooper [ctb], Zachary Mayer [ctb], Brenton Kenkel [ctb], R Core Team [ctb], Michael Benesty [ctb], Reynald Lescarbeau [ctb], Andrew Ziem [ctb], Luca Scrucca [ctb], Yuan Tang [ctb], Can Candan [ctb], Tyler Hunt [ctb].

[14] Epskamp, S., Borsboom, D. & Fried, E.I. Estimating psychological networks and their accuracy: A tutorial paper. Behav Res 50, 195–212 (2018). https://doi.org/10.3758/s13428-017-0862-1.

Genetic Algorithms for the identification and design of physiologically relevant 3D constructs

F. Fontana[1 *], P. Mancini[1,2, *], E. Botte[1], C. Magliaro[1,2] and A. Ahluwalia[1,2]
[1] *Research Center "E. Piaggio, University of Pisa, Italy*
[2] *Department of Information Engineering, University of Pisa, Italy*
[*] *These authors contribute equally to the work*

***Abstract*— *In vitro* models lack quantitative criteria to determine their extent of physiological relevance. Such criteria could be defined through a bio-inspired methodology, based on the study of how closely *in vitro* models imitate the natural intelligence inherent in biological systems.**

In this work, Genetic Algorithms are used to identify the fittest and hence most physiologically relevant shape and size of 3D constructs, leveraging on fundamental biophysical laws. Preliminary results suggest the feasibility of this approach for providing a predictive tool for identifying robust design criteria for 3D cell aggregates.

***Keywords*—cell cultures, genetic algorithms, optimization, *in-silico* models.**

I. INTRODUCTION

Physiological relevance is defined as the resemblance of a model to its *in vivo* counterpart. Advanced *in vitro* models have been developed for mimicking the functionality, biomechanics and architecture of human tissues. Although they are widely considered a promising technology for different biomedical applications [1,2], quantitative design criteria for determining their physiological relevance and thus their translational potential as functional replicates of their *in vivo* counterpart are still lacking. In this sense, physiological relevance can be considered as the coherence of a construct with biological and biophysical rules. Specifically, it is important to ensure that all the cells within thick constructs have an adequate nutrient supply, due to the lack of vascularisation *in vitro* [14]. Moreover, thermodynamic laws governing energy and mass distribution must be also considered, since all living organisms reach an equilibrium configuration characterised by minimal surface energy [4].

In silico methods have been already exploited as cost-effective and fast tools for guiding the design of more predictive and physiologically relevant *in vitro* models, providing an effective alternative to animals in research [1,2,3,8]. In this scenario, to define biomimetic design criteria, one could rely on the rules governing 'natural selection', *i.e.*, the process through which living organisms adapt to external changes. Mathematically speaking, this process could be described as a global optimization. *Genetic Algorithms (GAs)* [7] have been successfully used in designing reconfigurable organisms with the goal of optimizing cellular characteristics under specific constraints, providing a powerful paradigm for connecting *in silico* and *in vitro* applications [8]. This approach furnishes a starting point to predict the optimal combination of cellular features enabling the emergence of experimentally observable biophysical behaviour.

In this work, we investigated the feasibility of using GAs as an optimization tool for designing physiologically relevant *in silico* cell-laden spheroids, *i.e.*, identifying the optimal biophysical parameters for generating 3D *in vitro* constructs with enhanced predictive and translational power.

II. EXPERIMENTAL PROTOCOL

A. Algorithm overview

The GA workflow (*Figure 1*) is implemented via the COMSOL LiveLink™ for Matlab, which extends the COMSOL modelling environment with an interface between the two platforms. Briefly, a population of individuals is generated. All the individuals are scored through the Fitness Function (FF). The FF allows the identification of the optimal individuals (*Section C*). From this point, all the next generations are obtained through gene recombination, using crossover and mutation operators (*Section D*). The loop of evolution ends once the maximum number of generations is reached, and thus the best score fitting construct is identified. The GA parameters are listed in Table I.

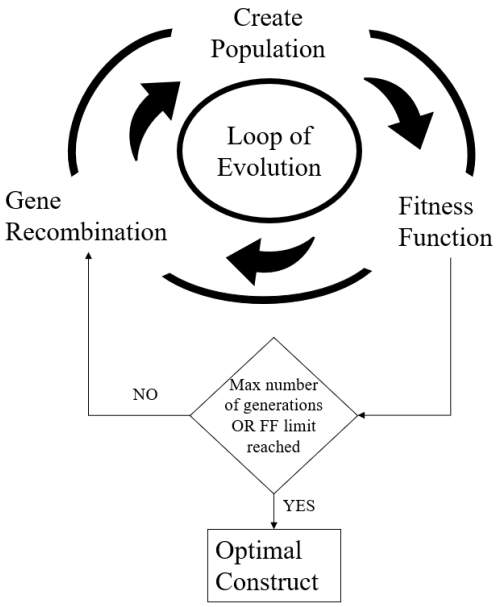


Figure 1 Loop of evolution of the Genetic Algorithm (GAs)

TABLE I: CUSTOMIZED PARAMETER OF THE GA FUNCTION

Parameter	*Description*	*Value*
Crossover fraction	The fraction of the population at the next generation, not including elite children	Γ(γ=4.94) [12]
Elite count	Number of individuals in the current generation	0.05*Population Size

	guaranteed to survive to the next generation.	
Population size	Number of individuals considered	10 – 100
Max Generations	Maximum number of iterations.	3 – 100

B. Generation of the population

A population is a group of individuals, all characterized by a genome, whose genes are described as an array of *morphological* and *biophysical* constraints. While *morphological genes* carry information on shape and dimension of the constructs, the *biophysical* ones deal with surface tension and volume of hypoxic core.

As regards the morphological genes, each individual is modelled as a spheroid with several identical hemispherical protrusions on its surface in order to increase the surface to volume ratio. The different masses so-obtained have an impact on both nutrient supply and surface energy.

Three input parameters are introduced:

i) the *number of protrusions n*, whose formulation is derived according to *Circle Packing Problem* [9] to obtain a maximum number of protrusions uniformly covering the spheroid surface;

ii) the *dimension of the protrusion f*, is defined as the ratio between the radius of the protrusion (r) and that of the central core (R) (*Figure 2*);

iii) the *volume of the whole construct* V_{constr}, a function of R, n and f (Eq. (1)).

$$V_{constr} = \frac{4}{3}\pi R^3 + \frac{n}{2}\frac{4}{3}\pi r^3 = \frac{4}{3}\pi R^3\left(1 + \frac{n}{2}f^3\right) \quad (1)$$

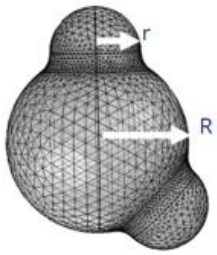


Figure 2 Protrusions' dimension f is the ratio between the protrusions' radius r and the central cores' radius R

The algorithm starts randomly defining the *morphological genes*: the value of *f* and consequently *n*. The first generation of individuals is created from volumes with a lognormal distribution, with means and variances as in [5]. *Morphological genes* are randomly assigned to each construct. and used as input parameters for drawing the computational model geometry.

To determine the oxygen concentration field at the steady state for all the geometries obtained, oxygen transport is modelled via the *Transport of Diluted Species* module in COMSOL Multiphysics (version 6.0, Stockholm, Sweden). The system can be described through the reaction-diffusion equation:

$$\frac{\partial C}{\partial t} = D\nabla^2 C + R \quad (2)$$

Where C $\left[\frac{mol}{m^3}\right]$ is the oxygen concentration field, D $[\frac{m^2}{s}]$ is the diffusion coefficient of oxygen in water and R $[\frac{mol}{m^3 s}]$ describes the cells' oxygen consumption modelled using the Michaelis-Menten (MM) kinetics:

$$R(x,y,z,t) = -\frac{OCR * \rho_{cell} * c(x,y,z,t)}{k_m + c(x,y,z,t)} \quad (3)$$

where ρ_{cell} $[\frac{cell}{m^3}]$ is the volumetric cell density, while OCR $[\frac{mol}{cell\ s}]$ and k_m $\left[\frac{mol}{m^3}\right]$ are the maximum oxygen consumption rate and the MM constant, respectively. All parameters and boundary conditions are listed in Table II.

The 3D models are implemented and solved numerically using the UMFPACK direct solver with a *finer* mesh size. A skewness scale between 0.5 and 0.8 is used to maintain the mesh as regular as possible.

At the end of each computation, the oxygen concentration field is obtained, together with the following derived values:

i) The *fraction of necrotic core NCF*: the percentage of the construct volume in which the oxygen concentration is below the critical threshold for cell viability ($c(x,y,z,t) \leq 0.04$ $[\frac{mol}{m^3}]$)[10];

ii) The *surface area of the construct* S_{constr}*;*

iii) The *sphericity* φ of the construct, defined as:

$$\varphi = \frac{S_{constr}}{S_{sph}} \quad (4)$$

where S_{sph} is the surface area of a sphere with the same volume as the construct considered.

At this point, the whole genome - comprising both *morphological* and *biophysical information* - is determined for each individual.

TABLE II: COMSOL SIMULATION PARAMETERS

Parameter	*Description*	*Value*
k_m	Michaelis-Menten constant	0.201 [mol/m^3] [3]
C_0	Boundary condition oxygen concentration	0.2 [mol/m^3] [10]
OCR	Oxygen Consumption Rate	2.73e^{-17} [mol/s][3]
T_{cell}	Temperature	310.15 [K]
ρ_{cell}	Physiological cell density	5.14e^{14} [1/m^3] [11]
R	Central core radius	R [m]
r	Protrusion radius	f*R [m]
f	Ratio of radii	r / R [∗]
n	Number of protrusions	(π / f) – 2 * π [∗]
D	Diffusion coefficient of oxygen in water	3e^{-9} [m^2/s] [3]

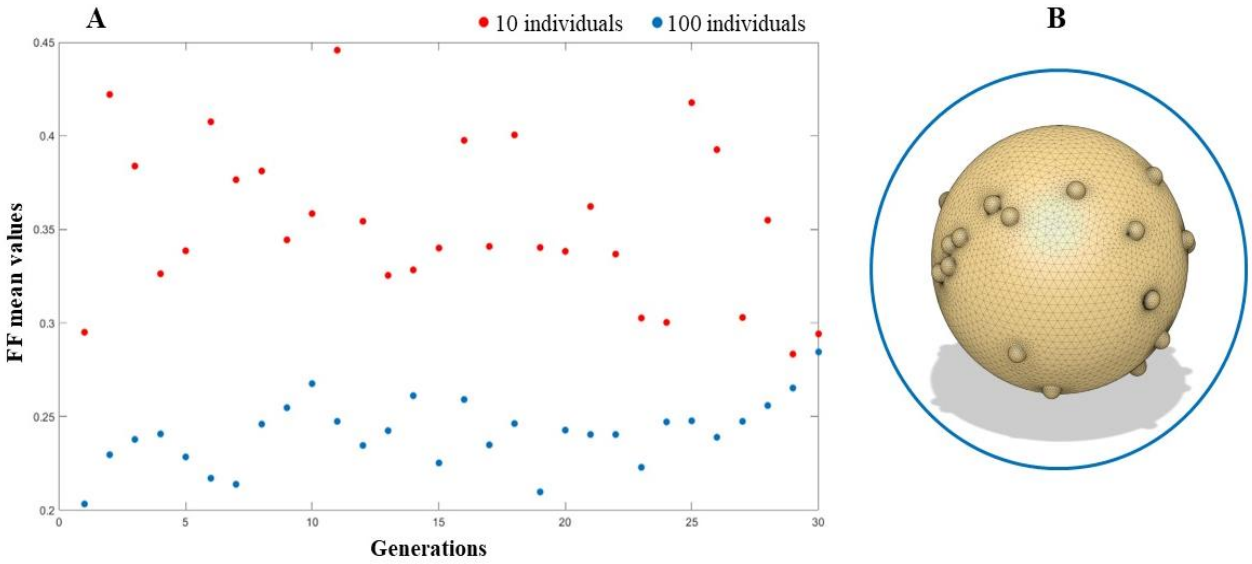


Figure 3 A) Points are the value of the mean fitness function at a given iteration of the algorithm. Blue points represent the GA with 100 individuals per iteration and the red points are that for the GA with 10 individual per iteration. B) The geometrical 3D model of the optimal construct obtained from the convergence of the GA with 100 individuals per iteration

D. *Fitness Function*

The FF scores individuals in every step of creation, crossover and/or mutation. In this work, the FF takes into account both the fraction of necrotic core and sphericity (φ), which are equally weighted ($w_{NCF} = w_{\varphi} = 0.5$) as expressed in Eq. (5):

$$FF = w_{NCF} * NCF + w_{\varphi} * \varphi (5)$$

In such formulation, the FF returns information about how a given morphological arrangement maximizes the cellular viability – a crucial problem in non-vascularized 3D cellular construct – also considering the thermodynamic constraints, i.e., the minimization of the surface tension, which is universally observed in physical systems. Indeed, the FF represents a balance between the number and dimension of the protrusions and the whole constructs' volume.

E. Gene Recombination: Crossover and Mutation Operator

From the second generation onwards, individuals are obtained using gene recombination, which involves only the morphological genes (n, f and V_{constr}). This process takes individuals of the previous generation, called parents, and randomly modifies their morphological genes, obtaining individuals called children.

Gene recombination consists of two operators, namely crossover and mutation. The crossover takes two parents, selects their morphological genes and combines them obtaining the crossover children (*crossover* in Eq. (6)). On the other hand, mutation takes only one parent, randomly selects genes to be changed and modifies their values, obtaining the mutation children (*mutation* in Eq. (6)).

The portion of individuals from the previous generation scored with the highest FF is considered as the elite (*elite* in Eq. (6)). They are not recombined but are directly promoted in the subsequent generation. Its fraction is defined using the *Elite Count* parameter (Table I).

Thus, the total number of children in the next generation is defined by Eq. (6):

$$children = elite + crossover + mutation (6)$$

For better mimicking the stochasticity of natural gene recombination [12], the *Crossover Fraction* of individuals is determined with a Gamma distribution (Table I). The Mutation fraction is automatically defined following the same Gamma distribution. Once these fractions are detected, the algorithm proceeds in varying the genes of individuals. A uniform distribution is used for determining the number of genes (*i.e.*, *n*, *f* and V_{constr}) and which of them are recombined. Once the genes (or the gene) to be recombined have (has) been chosen, their (its) values change according to the principles reported in *Section B*.

At the end, to complete the child's genetic information, the biophysical parameters pertaining to oxygen metabolism are computed. A new offspring population is created, and a new FF ranking is performed. The algorithm proceeds iteratively until the maximum number of generations is reached.

III. RESULTS

Running the GA with a different number of individuals, we noticed that the higher their number, the lower the dispersion of the mean FF against the number of generations (*Figure 3A*), obtained as in [13]. It is worth noting that the two curves appear to converge at the highest number of generations investigated. Thus, optimal biophysical features can hold for different combination of morphological genes.

In *Figure 3B*, the optimal construct geometry (n = 22, f = 0.07444, V_{constr} = 1.8e^{-12} [m^3]) from the GA run with 100 individuals is reported. These "genes" ensure the absence of necrotic core; moreover, since the protrusions are very small, the sphericity is anyway close to 1, so the minimization of surface tension is also respected.

IV. DISCUSSION AND CONCLUSIONS

In this work, GAs were used for identifying the optimal shape and size of cellular aggregates which respect thermodynamic and biophysical criteria for physiological relevance. Having an *in-silico* protocol that automatically predicts the optimal morphology of 3D constructs (based on the evaluation of biophysical parameters) could allow the improvement of experimental protocols for generating engineered tissues. It may also enable the development of high-fidelity computational models, which could, in the future, augment or even substitute costly in vitro models.

Our preliminary results suggest the feasibility of this approach. Further refinements of the algorithm are ongoing, in particular concerning the definition of the FF. Specifically, we are introducing different weighting factors for NCF and φ in Eq. (5) as well as asymmetry which is known to be important in morphogenesis. We will also introduce biological fluctuations as in our previous study [6] and external perturbations for evaluating how the shapes and sizes of optimal constructs adapt to their environment.

In addition, we are currently performing experimental studies to validate the *in-silico* outcomes. As far as we know, this is the first application of genetic algorithms to the study of 3D construct design.

ACKNOWLEDGEMENT

This work has received funding from the Swiss National Science Foundation, through Project SINERGIA 2019 572 CRSII5_186422.

REFERENCES

[1] Theresa E Schnalzger, Marnix HP de Groot, Congcong Zhang, Mohammed H Mosa, Birgitta E Michels, Jasmin Röder, Tahmineh Darvishi, Winfried S Wels, Henner F Farin; "3D Model for CAR-mediated Cytotoxicity Using Patient-derived Colorectal Cancer Organoids", The EMBO Journal, Vol. 38, Jun 2019.

[2] H. Clevers; "Modeling Development and Disease with Organoids", Cell, vol. 165, pp. 1586- 1597, 2016.

[3] C. Magliaro, A. Rinaldo & A. Ahluwalia; "Allometric Scaling of physiologically-relevant organoids", *Sci. Rep.*, Vol. 9, 11890, Aug. 2019.

[4] M. S. Steinberg; "Reconstruction of Tissues by Dissociated Cells: Some morphogenetic tissue movements and the sorting out of embryonic cells may have a common explanation", *Science,* vol. 141, n. 3579, pp. 401-408, 1963

[5] A. Ahluwalia; "Allometric scaling in vitro", *Sci. Rep.*, Vol. 7, 42113, Feb. 2017.

[6] E. Botte et al.; "Scaling of joint mass and metabolism fluctuations in in silico cell-laden spheroids", *PNAS, 118(38),* (2021)

[7] D.E. Goldberg; "Genetic algorithms in search, optimization, and Machine Learning.", Addison-Wesley, 2019

[8] Kriegman et al.; "A scalable pipeline for designing reconfigurable organism", PNAS 117(4), 1853-1859 (2020)

[9] K. Stephenson; "Introduction to circle packing: the theory of discrete analytic functions", Cambridge University Press, 2005

[10] E. Berger et al.; "Millifluidic culture improves human midbrain organoid vitality and differentiation", Lab Chip 18, 3172–3183 (2018)

[11] E. Bianconi et al.; "An estimation of the number of cells in the human body", Ann Hum Biol., 40(6):463–71, Nov-Dec (2013)

[12] T.P. Speed M.S. McPeek; "Model interference in genetic recombination", Genetics, pages 1031–1044, Feb (1995)

[13] Shapiro, J.L; "Statistical Mechanics Theory of Genetic Algorithms" In: Kallel, L., Naudts, B., Rogers, A. (eds) Theoretical Aspects of Evolutionary Computing. Natural Computing Series. Springer, Berlin, Heidelberg (2001).

[14] Zhao X, Xu Z, Xiao L, Shi T, Xiao H, Wang Y, Li Y, Xue F, Zeng W.; "Review on the Vascularization of Organoids and Organoids-on-a-**C**hip", Front Bioeng Biotechnol. 2021 Apr 12;9:637048

A preliminary version of a Genome-Scale Metabolic Model for Induced Human Pluripotent Stem Cells (hiPSCs)

A. Procopio[1,&], E. Parrotta[2,&], S. Scalise[1,&], N. Cortese[1], A. Merola[1], F. Amato[3], G. Cuda[1,†] and C. Cosentino[1,†,*]

[1] *Department of Experimental and Clinical Medicine, Università degli Studi Magna Græcia di Catanzaro*
[2] *Department of Medical and Surgical Sciences, Università degli Studi Magna Græcia di Catanzaro*
[3] *Department of Electrical Engineering and Information Technology, Università degli Studi di Napoli Federico II*
[&] *Equal contribution;* [†] *Joint senior authorship;* [*] *Corresponding author: carlo.cosentino@unicz.it*

***Abstract*—Pluripotent stem cells are undifferentiated cells with the extraordinary capability to differentiate into all cellular types. Based on these characteristics, human induced pluripotent cells (hiPSCs), produced in the laboratory, represent the new frontier of regenerative medicine as an innovative platform for partial or complete regeneration of injured tissues. The metabolic analysis of hiPSCs is fundamental in understanding the mechanisms underlying their functioning and ability to respond to particular environmental conditions, as well as how to develop better strategies for their production. In this context, genome-scale metabolic models (GEMs) offer a powerful tool to model and investigate the metabolism of hiPSCs. In this work, we present hiPSCGEM01, the first version of the context-specific genome-scale metabolic model (GEM) for the hiPSCs, extracted from RECON 3D, [1], as well as a first analysis of the pathways and essential genes reconstructed in the iPSCs specific model. Future developments will focus on the metabolic analysis of the phenotypes resulting from the knockout of the identified essential genes and on the possibility of exploiting the devised metabolic model to design new optimal culture media.**

***Keywords*—genome-scale metabolic model, flux-balance analysis, induced-pluripotent stem cells, reconstruction**

I. INTRODUCTION

Cellular therapies represent the new and promising frontiers for the treatment of several debilitating and degenerative disorders, which result in the gradual deterioration of the involved tissue. These advanced therapies consist of the implantation of selected and laboratory-treated cells into the patient to repair and restore the proper function of the injured organ or tissue. The ideal candidate cells involved in such therapies are pluripotent stem cells (PSCs) due to their proliferation and differentiation capabilities. Every tissue and organ in the human body contains stem cells. During cell division, stem cells originate two types of cells one of which retains the stemness feature while the other becomes committed to a specific cell lineage.

Among the several types of stem cells, the more fascinating ones from a therapeutic standpoint are pluripotent stem cells (PSCs). These cells derive from the early stages of an embryo (ESCs), and they can differentiate into all types of body cells. Ethical issues and the possible post-implantation rejection limit the isolation from embryos and the use of ESCs. To overcome these issues, several studies look for the generation of pluripotent stem cells from differentiated ones. These kinds of induced pluripotent stem cells (iPSCs) are artificially generated in the laboratory from the differentiated cells of the patients by forced expression of a specific set of genes such as Oct3/4, c-Myc, Klf4, and Sox2 (known as Yamanaka factors), [2]. In addition, since iPSCs derived from patient cells, they have the same genotype and hence do not cause rejection issues during cell therapy. For all these reasons, understanding the metabolism of the iPSCs is essential for optimizing their therapeutic efficacy. In this respect, it is critical to look into several issues, including the relevance of particular genes and their effects on metabolic pathways, as well as the potential to enhance the generation of iPSCs in the laboratory by, for example, developing new growth conditions. Despite of the classical mathematical approach to investigate and analyse the behavior of single metabolic pathways, [3], [4], Genome-scale metabolic models (GEMs) represent an easy and attractive systems biology framework able to capture the comprehensive metabolism of different types of cells under different experimental conditions. GEMs consist of a collection of reactions and active enzymes exclusive to a given cellular contest or cellular line. Several strategies have been developed to extract these GEMs from omics data, including transcriptome and proteome data, as well as from all of the literature's accessible knowledge.

In this work, we provide a first version of a dedicated genome-scale metabolic model for the iPSCs. In particular, we focus our attention on the reconstruction, the assessment, and the validation of the model, reported in Section II, as well as, on the analysis of the main reconstructed pathways, and the essential genes, presented in Section III.

II. Materials & Methods

A. Constraint-based model & Flux-Balance Analysis (FBA)

Ordinary differential equations (ODEs) are commonly employed to model the variation of concentration of each metabolite of the observed network, as reported below

$$\frac{dS}{dt} = N \times \nu \tag{1}$$

where $S = (S_1, S_2, ..., S_n)^T$ is the vector of the metabolites of the model, N is $n \times m$ the stoichiometric matrix, composed by n rows (metabolites), and m columns (reactions), and $\nu = (\nu_1, \nu_2, ..., \nu_m)^T$ represents the vector of the reactions rates. The components of a stoichiometric matrix are the stoichiometric coefficients, which represent the ratio of molecules, both substrate, and product, involved in a specific reaction. Stoichiometric coefficient signs assume positive or negative values based on whether a particular metabolite is produced or consumed by a specific reaction. Assuming that the cellular systems can reach their steady-state very quickly (i.e., the metabolic concentrations do not change but reach constant values), we can reduce the complexity of the model (2) by setting $N \times \nu = 0$. In this regard, constraint-based modeling represents the best mathematical framework to describe, in an easy way and with a low computational cost, complex metabolic networks. Since generally, we have more reactions than metabolites, [5], to obtain a unique solution from the devised system, it will be necessary to introduce all the known chemical-physical, spatial or topological constraints useful to determine the metabolic phenotype of the modeled network. These constraints are expressed through the definition of appropriate lower and upper bounds, which are set for each model reaction and allow for the construction of an acceptable range of solutions. Flux-Balance Analysis (FBA), [6], and its variants, are effective methods for determining the best point that maximizes an objective function within a confined space. However, to obtain reliable results, FBA requires the consistency of the model, which can be ensured through several techniques, [7].

B. Experimental Data

To derive the context-specific network for human induced pluripotent stem cells (hiPSCs), we have exploited genome expression data properly selected from Gene Expression Omnibus (GEO). The genome expression dataset used to create the model is shown in Table (I), and it consists of 10 samples acquired using the Affymetrix HG-U133 2 Plus platform. Then, we proceeded with the classification of the processed data by performing detection calls for gene expression: the hybridization of each spot is evaluated by assigning a label Present (P), Absent (A), or Marginal (M), based on the hybridization level, [8]. Before proceeding with the reconstruction of the model, the *ubiquity score*, [11], indicating the frequency with which a gene is expressed in a collection of relevant samples was calculated for each gene. This index was obtained by binarization of the different classes of gene expression levels (1 for the Present call, and 0 otherwise), and, then, by applying to binarized data the following function:

TABLE I: Genome-expression dataset selected from GEO data bank, and employed to reconstruct the iPSC model.

GEO ID	Authors	Description	Series
GSE14711	F. Soldner et al., 2009, [9]	Fibroblasts from 5 Parkinson's patients were successfully reprogrammed, and subsequently differentiated into dopaminergic neurons without the use of viral vectors.	GSM367219 GSM367240 GSM367241 GSM367242 GSM367244 GSM367245 GSM367258
GSE9865	W. E. Lowry et al., 2008, [10]	Dermal fibroblasts are used to generate hiPSCs through different reprogramming and differentiation methods.	GSM249028 GSM249095 GSM249137

$$U_g = \frac{\sum_{n \in N} X_{g_n}}{N} \tag{2}$$

where X represents the binary value associated to the gene *g* in the experiment *n*, while N is the total number of samples. The pre-processing phase, including the labels evaluation, and the computation of the ubiquity score were performed in R by using the Bioconductor package, [12], and in Matlab environment.

C. Reconstruction of the hiPSCGEM01

We obtained the specific GEM for the iPSCs cells by exploiting both the mCADRE (metabolic Context-specificity Assessed by Deterministic Reaction Evaluation), [11], and the COBRA toolbox functions, [13]. Especially, mCADRE requires as input to reconstruct a specific metabolic model i) the gene expression data and ii) the entire metabolic model, RECON 3D, i.e. the most comprehensive and accessible model of the human metabolic network, [1]. The first possible metabolic network for the human iPSCs, hiPSCGEM01, contains 4038 metabolites, 6024 reactions, and 2773 genes. To make the devised hiPSCGEM01 suitable for the FBA, we proceeded to add the metabolites and all the exchange reactions and their constraints necessary to simulate the growth medium for the iPSCs: after this first phase of hiPSCGEM01 refinement, we added to the model 46 new reactions, and 5 new metabolites, for a total of 6070 reactions and 4313 metabolites. Then, we performed the assessment of the model following the protocol reported in [14]. In particular, we proceeded with:

i) the removal of all genes not involved in any reaction;
ii) the analysis of the consistency of the model, evaluated in terms of both flux and stoichiometric matrix, [15];
iii) the analysis of the mass and charge balance;
iv) the removal of all the duplicate reactions in the hiPSCGEM01, and the insertion of transport reactions needed to connect the added metabolites to the remaining model. In this regard, all the missing metabolites, reactions, and charge formulas were added by searching online databases, such as, e.g., Kegg, Reactome, and MetaCyc.

All the analyses performed and described by the protocol previously mentioned, allow us to ensure the consistency of

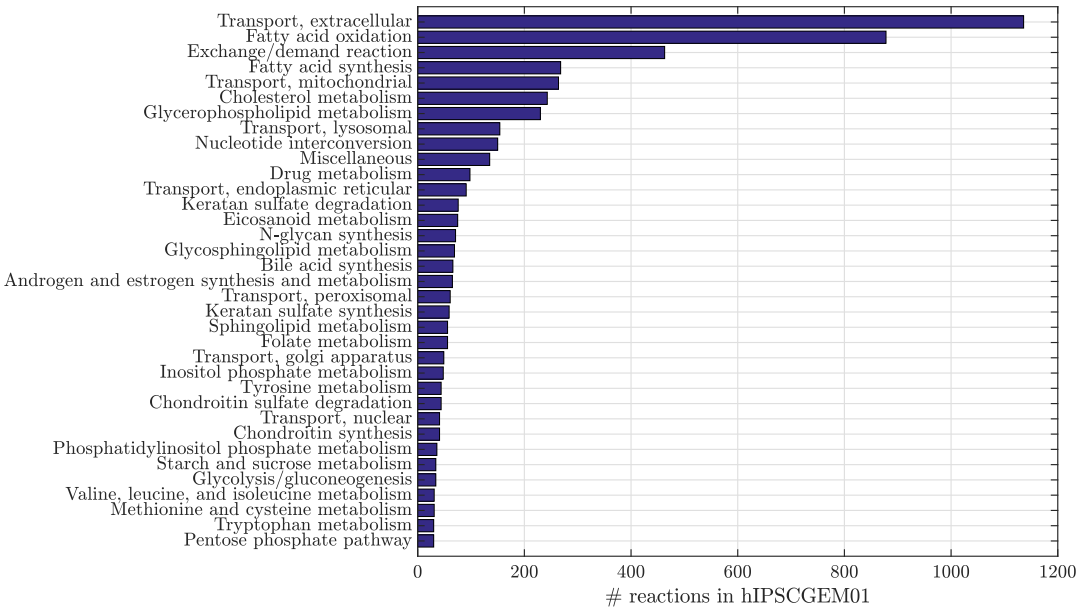


Fig. 1: Distribution of the main pathway reconstructed in hiPSCGEM01 ordered by the number of reactions.

our hiPSCGEM01, as well as make it ready for the FBA. The final hiPSCGEM01 model is composed of 5991 reactions, 4291 metabolites, and 2773 genes.

III. Results & Discussion

Before moving forward with future applications of the hiPSCGEM01 model, we investigated and validated the major pathways and genes involved in the reconstructed network using all the information available in the literature.

A. Analysis of the reconstructed pathways

The hiPSCGEM01 model consists of a total number of 101 pathways. In Figure 1 are reported the first 35 pathways ordered by the number of modeled reactions in hiPSCGEM01. Leaving aside the pathways involved in the transport of metabolites across the several cellular compartments, as well as all the exchange reactions, it is clear from Figure 1 how the most well-modeled seems to be the one related to the oxidation of the fatty acids. In this regard, Lin et al., [16], discovered carnitine palmitoyltransferase (CPT)1B as a regulator of reprogramming mediated by changes in fatty acid oxidation, and identified two of its products, palmitoylcarnitine (PC) and acetyl-CoA, as excellent reprogramming enhancers. Fatty acid synthesis is another fascinating metabolic pathway. A recent study, [17], conducted on the hiPSC-derived differentiated cardiomyocytes (hiPSC-CMs), shows as high levels of enzymes of fatty acid synthesis are expressed in the hiPSCs. In particular, Tanosaki et al. observed a correlation between the inhibition of the fatty acid synthesis pathway and the premature death of these cells following a significant reduction of the PC levels. As outlined in [18], all the pathways involved in energy metabolism are significant during the nuclear reprogramming of differentiated cells into iPSCs, and correctly modeled in hiPSCGEM01, as shown in Figure 1.

B. Analysis of the essential genes

Finally, we focused on the analysis of the essential genes involved in the hiPSCGEM01. Through FBA and knock-out of every single gene of the model, we found 592 different essential genes. Among these genes, we examined those whose removal affected the greatest number of reactions (> 35) in the hiPSCGEM01 model, resulting in a total of 14 selected essential genes. Figure 2 reports the results of the gene ontology enrichment analysis conducted on the set of 14 genes previously selected, for biological process (BP), cellular component (CC), and molecular function (MF). GO enrichment analysis allows screening among the genes identified as essential, those candidates for future in-depth studies. Furthermore, as seen in Figure 2, these genes are also those engaged in the fatty acids metabolic pathways, which, as previously mentioned, are essential to preserving the pluripotency of hiPSC.

IV. Conclusion

Genome-scale metabolic modeling is a powerful tool for studying the metabolism of human induced pluripotent stem cells (hiPSCs). Despite significant advancements in this field, as well as the discovery of the inevitable involvement of cellular metabolism in the expression and maintenance of the pluripotency characteristic, many aspects have not yet been investigated or remain incompletely understood. In this paper, we have presented the reconstruction and assessment phases of the first version of the genome-scale metabolic model specific to the hiPSCs (hiPSCGEM01). Preliminary analyses

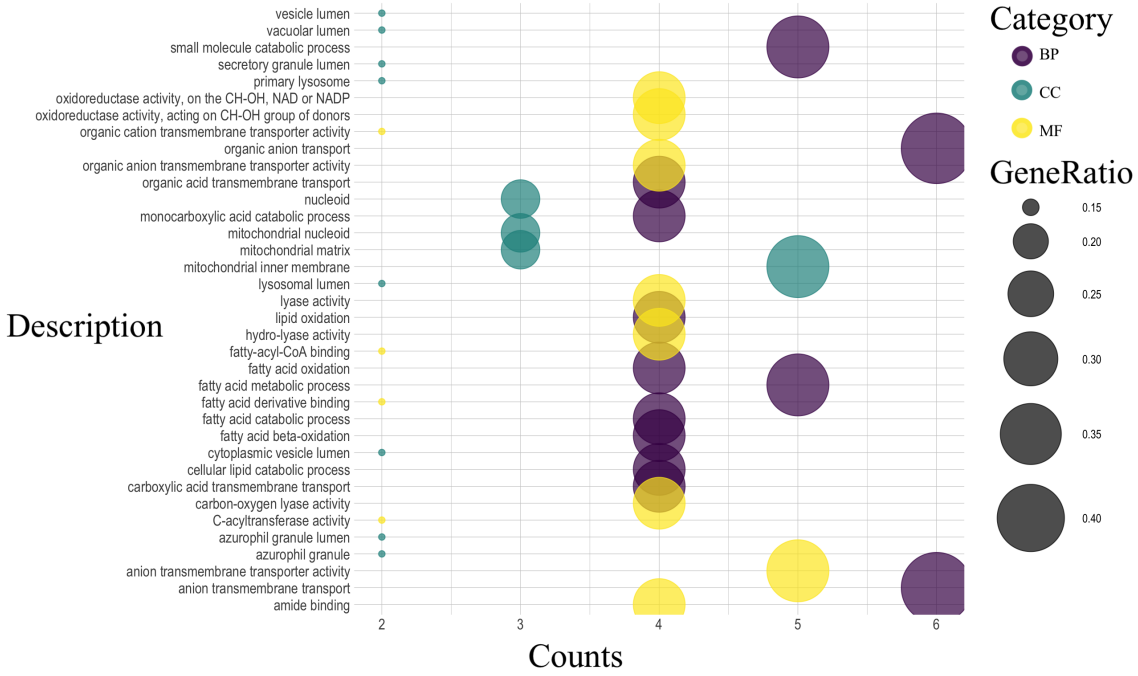


Fig. 2: Gene Ontology (GO) analysis conducted on the 14 most important essential genes, where *Gene Ratio* represents the percentage of total differentially expressed genes (DEGs) in the given GO term, and *Counts* is the number of the annotated genes in the subset of interest.

conducted on the hiPSCGEM0, especially on its pathways and essential genes, allow us to identify a set of genes interesting for future studies. Future studies are focused on investigating the metabolic phenotypes resulting from the knockout of the previously identified set of essential genes. Furthermore, we are interested in studying possible novel and optimal culture media by exploiting the devised model.

References

[1] E. Brunk, S. Sahoo, D. C. Zielinski, A. Altunkaya, A. Dräger, N. Mih, F. Gatto, A. Nilsson, G. A. Preciat Gonzalez, M. K. Aurich, *et al.*, "Recon3d enables a three-dimensional view of gene variation in human metabolism," *Nature biotechnology*, vol. 36, no. 3, pp. 272–281, 2018.

[2] H. Zhou, S. Wu, J. Y. Joo, S. Zhu, D. W. Han, T. Lin, S. Trauger, G. Bien, S. Yao, Y. Zhu, *et al.*, "Generation of induced pluripotent stem cells using recombinant proteins," *Cell stem cell*, vol. 4, no. 5, pp. 381–384, 2009.

[3] L. Salerno, C. Cosentino, A. Merola, D. G. Bates, and F. Amato, "Validation of a model of the gal regulatory system via robustness analysis of its bistability characteristics," *BMC systems biology*, vol. 7, no. 1, pp. 1–14, 2013.

[4] C. Cosentino, L. Salerno, A. Passanti, A. Merola, D. G. Bates, and F. Amato, "Structural bistability of the gal regulatory network and characterization of its domains of attraction," *Journal of Computational Biology*, vol. 19, no. 2, pp. 148–162, 2012.

[5] J. D. Orth, I. Thiele, and B. Ø. Palsson, "What is flux balance analysis?," *Nature biotechnology*, vol. 28, no. 3, pp. 245–248, 2010.

[6] J. M. Lee, E. P. Gianchandani, and J. A. Papin, "Flux balance analysis in the era of metabolomics," *Briefings in bioinformatics*, vol. 7, no. 2, pp. 140–150, 2006.

[7] M. Terzer, N. D. Maynard, M. W. Covert, and J. Stelling, "Genome-scale metabolic networks," *Wiley Interdisciplinary Reviews: Systems Biology and Medicine*, vol. 1, no. 3, pp. 285–297, 2009.

[8] H. Causton, J. Quackenbush, and A. Brazma, *Microarray gene expression data analysis: a beginner's guide*. John Wiley & Sons, 2009.

[9] F. Soldner, D. Hockemeyer, C. Beard, Q. Gao, G. W. Bell, E. G. Cook, G. Hargus, A. Blak, O. Cooper, M. Mitalipova, *et al.*, "Parkinson's disease patient-derived induced pluripotent stem cells free of viral reprogramming factors," *Cell*, vol. 136, no. 5, pp. 964–977, 2009.

[10] W. Lowry, L. Richter, R. Yachechko, A. Pyle, J. Tchieu, R. Sridharan, A. Clark, and K. Plath, "Generation of human induced pluripotent stem cells from dermal fibroblasts," *Proceedings of the National Academy of Sciences*, vol. 105, no. 8, pp. 2883–2888, 2008.

[11] Y. Wang, J. A. Eddy, and N. D. Price, "Reconstruction of genome-scale metabolic models for 126 human tissues using mcadre," *BMC systems biology*, vol. 6, no. 1, pp. 1–16, 2012.

[12] R. C. Gentleman, V. J. Carey, D. M. Bates, B. Bolstad, M. Dettling, S. Dudoit, B. Ellis, L. Gautier, Y. Ge, J. Gentry, *et al.*, "Bioconductor: open software development for computational biology and bioinformatics," *Genome biology*, vol. 5, no. 10, pp. 1–16, 2004.

[13] L. Heirendt, S. Arreckx, T. Pfau, S. N. Mendoza, A. Richelle, A. Heinken, H. S. Haraldsdóttir, J. Wachowiak, S. M. Keating, V. Vlasov, *et al.*, "Creation and analysis of biochemical constraint-based models using the cobra toolbox v. 3.0," *Nature protocols*, vol. 14, no. 3, pp. 639–702, 2019.

[14] I. Thiele and B. Ø. Palsson, "A protocol for generating a high-quality genome-scale metabolic reconstruction," *Nature protocols*, vol. 5, no. 1, pp. 93–121, 2010.

[15] A. Gevorgyan, M. G. Poolman, and D. A. Fell, "Detection of stoichiometric inconsistencies in biomolecular models," *Bioinformatics*, vol. 24, no. 19, pp. 2245–2251, 2008.

[16] Z. Lin, F. Liu, P. Shi, A. Song, Z. Huang, D. Zou, Q. Chen, J. Li, and X. Gao, "Fatty acid oxidation promotes reprogramming by enhancing oxidative phosphorylation and inhibiting protein kinase c," *Stem cell research & therapy*, vol. 9, no. 1, pp. 1–14, 2018.

[17] S. Tanosaki, S. Tohyama, J. Fujita, S. Someya, T. Hishiki, T. Matsuura, H. Nakanishi, T. Ohto-Nakanishi, T. Akiyama, Y. Morita, *et al.*, "Fatty acid synthesis is indispensable for survival of human pluripotent stem cells," *Iscience*, vol. 23, no. 9, p. 101535, 2020.

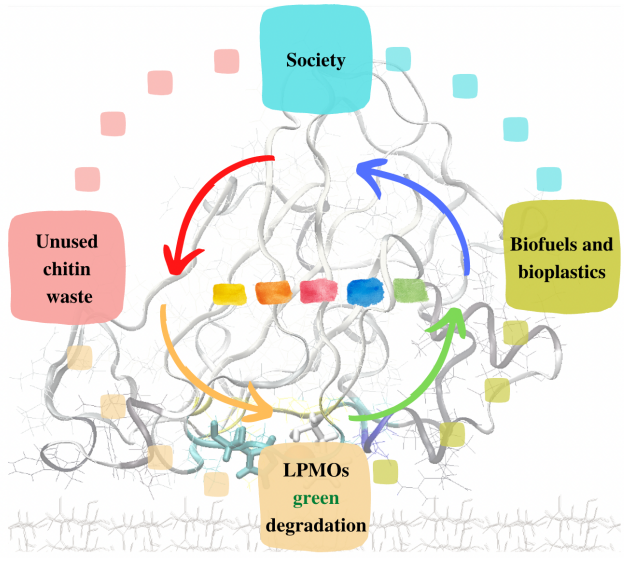
[18] E. Tsogtbaatar, C. Landin, K. Minter-Dykhouse, and C. D. Folmes, "Energy metabolism regulates stem cell pluripotency," *Frontiers in cell and developmental biology*, vol. 8, p. 87, 2020.

Giving new life to seafood waste: *in silico* engineering of a chitinolytic LPMO enzyme

A. Ricci[1], G. Di Rocco[2], C. A. Bortolotti[2], and A. Gautieri[1]
[1] *Biomolecular Engineering Lab, Dipartimento DEIB, Politecnico di Milano, Milan, Italy*
[2] *Università degli Studi di Modena e Reggio Emilia, Modena, Italy*

***Abstract*—Chitin is a recalcitrant, crystalline polysaccharide composed of chained sugar rings of N-acetyl-glucosamine (NAG). This polymer is an unexploited waste product in global seafood industry, a sugar-based waste that could be utilized as an energy resource for a plethora of destinations, from bioplastics to biofuels production. Lytic Polysaccharide Mono-Oxygenases (LPMOs) are newly discovered enzymes with the ability of efficiently degrading molecules like chitin or cellulose, thanks to a redox mechanism. In this study, we predicted and engineered the 3D structure of an LPMO, named PpAA10, acting on the protein sequence and enhancing its stability while preserving its catalytic activity. Studies were carried via molecular dynamics (MD) simulations, selecting the best outcomes for further *in vitro* production and assessment. The best mutants were produced on a lab scale, for *in* vitro testing. Obtaining an operative and stable mutant of PpAA10 could lead to the optimization of a green, sustainable, degradation process to obtain sugars from unutilized chitin waste.**

***Keywords*—LPMO, chitin, molecular dynamics, enzyme engineering.**



I. Introduction

CRUSTACEAN production, in the picture of global seafood economy, has registered up to a 2-3% annual growth rate, reaching 13.7 million metric tons (mmt) in 2015; this resulted in a total of 6 to 8 mmt of lobster, crab and shrimp shells waste [1]. In this framework, chitin represents a widely distributed structural polymer of technological interest, as it can be found unutilized and composing more than 40% in weight of seafood waste materials [2]; more generally, chitin is the most abundant aminopolysaccharide occurring in nature, also being the main structural element for insects (exoskeleton) and fungi (cell walls) [3]. However, its degradation is still a work in progress, as a green and effective process is yet to be found. Lytic Polysaccharide Mono-Oxygenases (LPMOs) are enzymes of recent discovery, now populated by several subfamilies isolated from bacteria, fungi, and insects [4]. The main target of LPMOs are recalcitrant polysaccharides, mostly cellulose or chitin, as the producing organism exploits the activity for nutritional or physiological purposes [5]. LPMOs degrade their target polymer with an oxidative mechanism, based on a copper ion in the active site; this makes them a promising substitute of classic enzymatic cocktails of hydrolytic nature (generally referred as chitinases) [6]. In this work we aim to engineer an LPMO to improve its yield, stability and activity and ultimately improve their usability in waste reconversion. The protein of interest, PpAA10 (UniProtKB – B1J2U9), was isolated from bacterium *Pseudomonas putida* W619, and belongs to the LPMO subfamily named AA10 (Auxiliary Activity 10) on CAZy database [4], [7]. The protein sequence was provided by prof. Giulia Di Rocco's lab (Università degli Studi di Modena e Reggio Emilia) [8].

II. Materials and Methods

A. PpAA10 structure prediction

For the protein of interest there are no experimental structures. Therefore, based on the aminoacidic sequence, structural studies were made via computational modelling. The first step included the prediction of the protein three-dimensional folding. SwissModel online tool was exploited to perform a sequence-based prediction [9]; being able to identify a PDB-deposited protein with a high sequence identity, a chitin-binding domain from *Burkholderia pseudomallei*, we adopted that as a template to perform a structure prediction of PpAA10's folding. RoseTTAFold was also exploited to predict *Pseudomonas putida* LPMO's 3D structure with a different approach, a deep learning-based method for *de novo* structure-from-sequence prediction [10]. Coordinates obtained by both methods (4 structures from SwissModel, 5 from RoseTTAFold) were structurally aligned via PyMOL software to highlight possible differences.

B. Copper ion introduction

Given that the structure prediction was based on the sequence alone, a copper ion had to be included in the PDB file generated. To create a reliable initial structure to use in molecular dynamics simulations, the model proposed by Liao et al. [11] was chosen. This model consisted in a central copper ion surrounded by six so-called "dummy atoms". These dummy atoms, partially charged (+) and covalently bonded to the ion itself, were placed to better simulate its interactions with surrounding atoms. To place the ion and relative dummy atoms in the right place, an alignment was performed between PpAA10 RoseTTAFold predicted structure and *Burkholderia pseudomallei* LPMO, which PDB deposited structure (PDB code: 3UAM) is complete of the copper ion. At this point, PpAA10 and copper coordinates were merged in a separate PDB, hence providing a complete coordinates file for the subject protein.

C. Structure preparation

The complete structure of PpAA10 underwent NAMD simulations to minimize the structure and assess the correct placement and behavior of the metallic ion. To generate the system topology, CHARMM force field was used. Water and counter-ions were added to neutralize the charge of the periodic box.

D. Enzyme equilibration

Starting from the ionized solvation box, three sets of equilibrations were performed. Before the equilibration, 2'000 minimization steps were performed to settle properly the structure. The first equilibration stage was performed at 310 K temperature. 25000 steps were run with a 1 fs timestep, producing a 25 ps simulation. Periodic Boundary Conditions (PBC) and Particle Mesh Ewald (PME) were applied, along with constant pressure (1 atm), applying NPT conditions. For the first equilibration, protein backbone and copper ion were fixed into their original position, with only the residues free to move. In the second equilibration stage, restrains with a 1.0 elastic constant were applied only to backbone and Cu (II) ion. The second equilibration lasted 25000 steps with a 2 fs timestep, producing a 50 ps simulation. In the third equilibration, all parameters were maintained as above, except that the NVT ensemble was used and no restrains were applied. The simulation was run for 1.5 ns. The main target was to produce a functioning model of a structurally unknown protein, to use in further simulations.

E. Chitin model

To replicate chitin fibrils' 3D structure, a VMD tool was exploited, named *Chitin Builder* [12]. The result was a fiber composed by 24 α-chitin chains, organized in 6 parallel columns of 4 layers (Fig. 1). The chains were 24 N-acetyl-glucosamine (NAG) rings each [13] [14] [15].

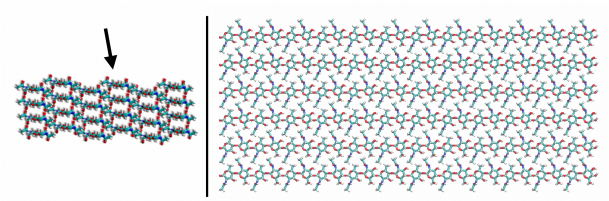


Fig. 1: Front-side and upper view of the small fibril reproduced with *Chitin Builder*. The 24 chains organized in 6 columns of 4 layers each can be seen on the left; the 24-ringed chains can be visualized on the right.

Black arrow represents the most suitable place for PpAA10's structure, in order to simulate the binding on an exposed chitin layer.

This chitin crystal was merged with the LPMO-copper complex previously created. Protein-chitin distance was set at 6 Å, to avoid bad contacts that would crash the simulation. To explore all possible binding geometries, the ion was placed right onto the glycosidic bond's oxygen, without choosing neither C1 nor C4 of the involved NAG rings. Two main systems were generated, distinguished by the 180° rotated orientation of the protein's active planar face. After preparing the crystal with the LPMO on top, the system was equilibrated following a protocol similar to the enzyme alone. Three equilibrations were performed for both orientations of the protein onto the crystal. Subsequently, 100 ns of MD simulation were performed in a water box with 150 mM NaCl. The bottom layer of chitin molecules was restrained (by fixing the positions of C1 atoms).

F. Production MD simulations

Production simulations of 100 ns were performed for the enzyme alone. In the production simulations, no restrains are applied except for three *extrabonds*. *Extrabonds* are additional chemical bonds that were used to prevent copper ion wandering by linking it to its coordination shell: the N terminal free amine (His1) and the two nitrogen atoms of His1 and His100 side chains. *Extrabonds* had distances and energies coherent to the values found in nature [16]. Production simulations were carried in triplicate at two different temperatures (310K and 350 K), to test the enzyme structure in term of stability.

G. PpAA10 mutants library generation

PpAA10 was submitted to two major online tools for designing coupled- or multiple-residue mutations to improve protein stability. PROSS (Protein Repair One-Stop Shop) [17] is an online tool that generates stable mutants based on multi-sequence alignment on known structures (to exclude well conserved regions), followed by filling hydrophobic pockets, pairing H-bonds donors and acceptors, and exposing polar or charged residues on the surface. DbD (Disulfide by Design) [18] is the second online tool that was used for producing the pool of stabilized mutants. DbD introduces coupled mutations, assessing the pairs in terms of distance and geometry coherent to the formation of a disulfide bond (assuming they were mutated into cysteines).

H. MD simulations of engineered enzymes

Molecular Dynamics simulations were performed following the same protocol used for the wild-type protein. Following the equilibrations, a 100 ns, protein-only simulation was performed for each mutant, either at 310 K or at 350 K temperatures. Results were analyzed in terms of Root Mean Square Deviation (RMSD) and Root Mean Square Fluctuation (RMSF).

I. In vitro *production of wild type and mutants*

E. coli BL21 (DE3) was used as a vessel for the lab expression of the studied mutants. Cells were transformed with plasmids containing one of the different variants, and cultures were scaled up to 4 L batches. Proteins were purified and prepared for activity and stability experiments, regarding attenuated total reflectance Fourier transform infrared spectroscopy (ATR-FTIR) for activity (after incubation on crystalline chitin), and circular dichroism (CD) and differential scan calorimetry (DSC) for stability.

III. Results and Discussion

A. PpAA10 structure prediction

After the alignment performed in PyMOL, RMSD values (measuring spatial distance between the atoms, along the chain, belonging to different structures) showed that the prediction was reliable. The average value among all nine structures (4 by SwissModel, 5 by RoseTTAFold) was 0.8 Å, indicating a strong correspondence in the coordinates of the respective atoms in the molecule.

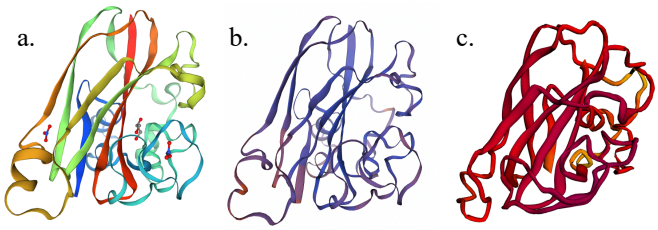


Fig. 2: a) SwissModel 3D representation of *Burkholderia pseudomallei*'s AA10 deposited structure. Color scheme by spectrum. b) SwissModel prediction of Pseudomonas putida AA10 via homology modelling. Colour scheme (purple to orange) based on confidence gradient (high to low). c) RoseTTAFold structure prediction based on a deep learning-based method, working on the sole aminoacidic sequence. Colour scheme (red to yellow) based on confidence gradient (high to low).

B. Chiti-binding residues

Thanks to the previous preparation of a 3D model for chitin layers, we performed production MD simulations of interaction between PpAA10 and chitin, placed in two different, 180°-twisted positions around the vertical axis. This was set to explore possible important residues' behavior, like Glu21, Tyr140 and Trp141 horizontal axis on the planar face (Fig. 2).

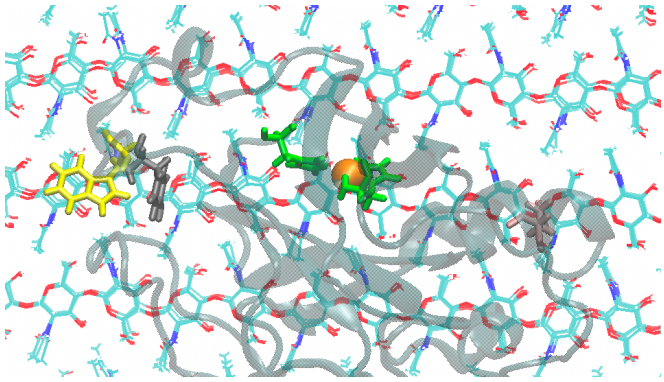


Fig. 3: Detail of the most interesting aminoacids regarding the active planar face of the enzyme: His1 and His100 (green, with copper in orange), Glu21 (pink, on the right), Tyr140 (grey, left) and Trp141 (yellow, left), all in *licorice* visualization. Protein backbone is represented in grey *glassy* cartoon, chitin crystal in *lines* (internally misaligned after equilibration).

From MD runs, aminoacid-chitin distances were calculated, identifying the close contacts as those which remained closer than 6 Å from chitin for at least 33% of the simulation time. Following this criterion, a list of putative positions more likely to be interacting with the substrate was drafted. The interacting aminoacids were excluded during the search of stabilizing mutations. The list of excluded aminoacids comprehended the following positions: 1 (active site), 21-24, 26, 40, 47, 53, 54, 66-68, 99, 100 (active site), 139-142, 143-145, 177-180.

C. *Enzyme mutants libraries*

PROSS and DbD were exploited to produce, via different approaches, stabilized mutants of the query 3D structure. PROSS generates a total of nine protein designs, with a process of cumulative stabilizing mutations (e.g., the second generated structure keeps all the mutations of the first, adding more, and so on). Interactive aminoacids were excluded as an input. From the outputs, six designs were extracted for further evaluation, as the stabilizing mutational process had produced redundant sequences. DbD has a simpler approach (mainly based on distances) and proposed 15 structures with compatible aminoacidic couples substituted into cysteines. Excluding the mutations involving interactive residues (see Section B.), 12 designs were extracted, each with a unique couple of mutated positions.

D. Mutants selection

With a total of 18 designs selected from mutation tools and simulated in the same conditions of the *wild type* protein, RMSD and RMSF data were evaluated. While RMSD certificated the overall stability of the structures, with no critical or terminal anomalies, RMSF was the main indicator for assessing stability along the chain. RMSF is graphed on the *y* axis, with aminoacidic positions on the *x* axis. Its value indicates the average deviation relative to the average position of amino acid during the time of the simulation: the higher the value, the more mobile atoms are, enhancing the probability of misfolding and undermining the overall stability. Three mutants showed significant results after the simulations, that highlighted an improved stability in 350 K high temperature

runs, probably due to the higher stress enhancing differences. Those mutants (1 from PROSS, 2 from DbD) were selected for further *in vitro* production and purification, and named "1", "2", and "3".

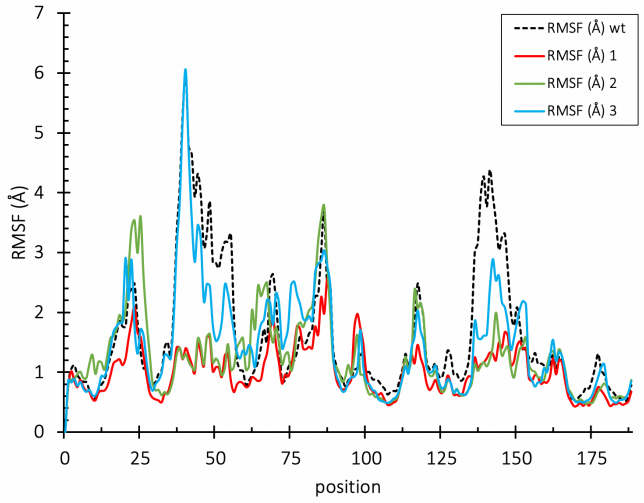


Fig. 4: RMSF (*y* axis) summary comparison between wild type (black, dotted), and mutants 1 (red), 2 (green) and 3 (blue). Aminoacidic positions along the chain are placed on *x* axis. It can be seen how values are mainly under or matching the black dotted line of the wt enzyme, indicating that the stability is always higher (or equal at least). Local matching peaks, in particular, indicate regions of the protein that aren't influenced by mutations.

IV. Conclusion

Starting from the aminoacidic sequence of the LPMO enzyme PpAA10, we predicted its folding with two different computational methods, which converged to a likely structure. Such model was the basis for the production and characterization of possible, more stable mutants, via computational engineering. After determining the best three candidate mutants, the next steps have already included the *in vitro* production and purification, to experimentally assess their effective improvement in stability. These experiments will help the design of an effective, industrial process involving LPMOs and living organisms to efficiently degrade chitin in an environmentally-friendly way. The success of this project could lead to a relevant valorisation of industrial waste-to-resource material, in a true circular economy perspective.

Acknowledgement

We acknowledge the CINECA award under the ISCRA initiative (Grant code IsB26_W2EB and IsCa2_REZYME) for the availability of high-performance computing resources and support.

References

[1] "The State of World Fisheries and Aquaculture 2020. In brief," *State World Fish. Aquac. 2020. Br.*, Jun. 2020, doi: 10.4060/CA9231EN.

[2] N. Yan and X. Chen, "Sustainability: Don't waste seafood waste," *Nat. 2015 5247564*, vol. 524, no. 7564, pp. 155–157, Aug. 2015, doi: 10.1038/524155a.

[3] D. Elieh-Ali-Komi, M. R. Hamblin, and E.-A.-K. Daniel, "Chitin and Chitosan: Production and Application of Versatile Biomedical Nanomaterials," *Int. J. Adv. Res.*, vol. 4, no. 3, p. 411, Mar. 2016, Accessed: Dec. 28, 2022. [Online]. Available: /pmc/articles/PMC5094803/.

[4] P. K. Busk and L. Lange, "Classification of fungal and bacterial lytic polysaccharide monooxygenases," 2011, doi: 10.1186/s12864-015-1601-6.

[5] F. Sabbadin *et al.*, "An ancient family of lytic polysaccharide monooxygenases with roles in arthropod development and biomass digestion," *Nat. Commun. 2018 91*, vol. 9, no. 1, pp. 1–12, Feb. 2018, doi: 10.1038/s41467-018-03142-x.

[6] C. Schmitz, L. G. Auza, D. Koberidze, S. Rasche, R. Fischer, and L. Bortesi, "Conversion of Chitin to Defined Chitosan Oligomers: Current Status and Future Prospects," *Mar. Drugs 2019, Vol. 17, Page 452*, vol. 17, no. 8, p. 452, Aug. 2019, doi: 10.3390/MD17080452.

[7] B. I. Cantarel, P. M. Coutinho, C. Rancurel, T. Bernard, V. Lombard, and B. Henrissat, "The Carbohydrate-Active EnZymes database (CAZy): an expert resource for Glycogenomics," *Nucleic Acids Res.*, vol. 37, no. suppl_1, pp. D233–D238, Jan. 2009, doi: 10.1093/NAR/GKN663.

[8] I. Serra *et al.*, "Activity and substrate specificity of lytic polysaccharide monooxygenases: An ATR FTIR-based sensitive assay tested on a novel species from Pseudomonas putida," *Protein Sci.*, vol. 31, no. 3, pp. 591–601, 2022, doi: 10.1002/pro.4255.

[9] A. Waterhouse *et al.*, "SWISS-MODEL: homology modelling of protein structures and complexes," *Nucleic Acids Res.*, vol. 46, no. W1, pp. W296–W303, Jul. 2018, doi: 10.1093/NAR/GKY427.

[10] M. Baek *et al.*, "Accurate prediction of protein structures and interactions using a three-track neural network," *Science (80-.).*, vol. 373, no. 6557, pp. 871–876, Aug. 2021, doi: 10.1126/SCIENCE.ABJ8754/SUPPL_FILE/ABJ8754_MDAR_REPRODUCIBILITY_CHECKLIST.PDF.

[11] Q. Liao, S. C. L. Kamerlin, and B. Strodel, "Development and Application of a Nonbonded Cu2+ Model That Includes the Jahn-Teller Effect," *J. Phys. Chem. Lett.*, vol. 6, no. 13, pp. 2657–2662, 2015, doi: 10.1021/acs.jpclett.5b01122.

[12] D. C. Malaspina and J. Faraudo, "Chitin builder," Jul. 2019, doi: 10.5281/ZENODO.3274726.

[13] B. Bissaro, I. Isaksen, G. Vaaje-Kolstad, V. G. H. Eijsink, and Å. K. Røhr, "How a Lytic Polysaccharide Monooxygenase Binds Crystalline Chitin," *Biochemistry*, vol. 57, no. 12, pp. 1893–1906, Mar. 2018, doi: 10.1021/acs.biochem.8b00138.

[14] G. T. Beckham and M. F. Crowley, "Examination of the r-Chitin Structure and Decrystallization Thermodynamics at the Nanoscale," *J. Phys. Chem. B*, vol. 115, pp. 4516–4522, 2011, doi: 10.1021/jp200912q.

[15] Z. Střelcová *et al.*, "The structure and dynamics of chitin nanofibrils in an aqueous environment revealed by molecular dynamics simulations," *RSC Adv.*, vol. 6, no. 36, pp. 30710–30721, Mar. 2016, doi: 10.1039/c6ra00107f.

[16] S. Brander *et al.*, "Biochemical evidence of both copper chelation and oxygenase activity at the histidine brace," *Sci. Reports 2020 101*, vol. 10, no. 1, pp. 1–11, Oct. 2020, doi: 10.1038/s41598-020-73266-y.

[17] A. Goldenzweig *et al.*, "Automated Structure- and Sequence-Based Design of Proteins for High Bacterial Expression and Stability," *Mol. Cell*, vol. 63, no. 2, pp. 337–346, Jul. 2016, doi: 10.1016/J.MOLCEL.2016.06.012.

[18] D. B. Craig and A. A. Dombkowski, "Disulfide by Design 2.0: A web-based tool for disulfide engineering in proteins," *BMC Bioinformatics*, vol. 14, no. 1, Dec. 2013, doi: 10.1186/1471-2105-14-346.

Oxygen metabolism in *in vitro* ecosystems

E. Botte[1], P. Mancini[1,2], C. Magliaro[1,2] and A. Ahluwalia[1,2]
[1] *Research Centre 'E. Piaggio', University of Pisa, Pisa, Italy*
[2] *Department of Information Engineering, University of Pisa, Pisa, Italy*

***Abstract* — Modelling down-scaled replicates of biological communities using bioengineering approaches is of interest in life sciences, as it facilitates the investigation of metabolic patterns driven by inter-individual crosstalk across scales. To explore this concept, in this study computational models were used to probe whether multi-spheroid systems can constitute reliable models of coexistence *in vitro* (or *in vitro* ecosystems).**

The results in terms of oxygen metabolism and size-related scaling are consistent with initial predictions, indicating the feasibility of the approach. These models could be employed to better understand cell-cell or organoid-organoid crosstalk and even extended to ecological sciences to assess the impact of resource sharing in the presence of heterogeneities and environmental disturbances.

***Keywords* — coexistence, community dynamics, oxygen metabolism, cell-laden constructs, finite element modelling.**

I. Introduction

COEXISTENCE and resource sharing have been extensively documented to shape individual behaviours across scales, underpinning metabolic patterns which emerge throughout biological communities [1]–[6]. Properly rescaled, these concepts are also likely to hold in cellular systems - such as tissues and organs *in vivo* or corresponding replicates *in vitro* - and should be taken into consideration in the design of human-relevant models. In turn, creating a population of coexisting cell-based constructs might furnish insights into the metabolic behaviour of real communities in biology, providing tractable down-scaled models of ecosystems.

To date, no attempts in quantitatively investigating to what extent the degree of specific inter-individual interaction affects metabolic dynamics at the cellular level have been reported. Recent studies propose allometric scaling [7] as a criterion to assess the physiological relevance of cell-based models [8], [9]. The reasoning is that physiologically relevant *in vitro* systems should obey the Kleiber's law (KL) [10] - which states that the metabolic rate of an organism scales with mass as a power law and holds for over 20 orders of magnitude of size. However, they probe metabolic scaling in isolated cell aggregates but do not investigate whether the presence of multiple consuming individuals modulates cell metabolism. The ability to assess collective metabolic behaviours using *in silico* and *in vitro* models could open up new perspectives, paving the way towards applications to more biologically relevant scenarios. For instance, multi-construct systems containing randomly distributed cell aggregates characterized by variable size and metabolic features or exposed to fluctuating/perturbed environmental conditions could be used to establish a predictive and translational framework for the assessment of mechanisms of coexistence which drive resource management in living systems. Such mechanisms might also play a role in determining scaling coefficients and the size range of cellular models in which KL holds.

This work reports a study designed to evaluate whether and how the oxygen (O_2) metabolism of cell aggregates and the emergence of KL-like behaviours and associated scaling coefficients vary as a function of their coexistence with neighbouring constructs. More in detail, the feasibility of designing, modelling and realizing an *ecosystem* (*i.e.*, a multi-construct model where the crosstalk among cell aggregates coexisting in a shared environment drives metabolic dynamics according to their number and spatial arrangement) was investigated *in silico*. The potential of the approach as down-scaled modelling of community behaviours was tested in simple geometries and ideal conditions, to verify whether computational predictions match expected results. In practice, the influence of community abundance and spatial distribution of coexisting individuals (*i.e.*, cell-laden spheroids) on O_2 uptake and associated scaling characteristics was evaluated in multi-spheroid systems, combining finite element (FE) and statistical analysis.

Albeit preliminary and derived from a simplified model of non-competitive coexistence, the outcome of this work represents a first step towards understanding how multiple cell constructs can interact *in vitro* in terms of resource consumption, with potential applications in diverse fields, such as biomedical sciences and ecology.

II. Materials and Methods

The impact of coexistence on O_2 metabolism and mass-related scaling (*i.e.*, allometric as opposed to isometric mass dependency) was assessed using FE models implemented in Comsol Multiphysics (version 5.6, COMSOL AB, Stockholm, Sweden). O_2 transport and consumption of a population of *in silico* cell-laden spheroids sharing a common resource were simulated to evaluate how metabolic scaling is affected by varying size, abundance and spatial distribution of constructs.

A. Definition of the geometry

For determining how the O_2 metabolism of cellular constructs varies with their number and density, all of them have to be exposed to the same conditions of resource supply, irrespective of their size. To this end, the geometry shown in Fig. 1 was implemented, since it ensures that all spheroids are exposed to the same boundary condition. Spheroids are contained in a toroid, filled with aqueous medium and surrounded by an O_2-saturated environment. Constructs are placed such that their centres constitute the vertices of a regular polygon (Tab. 1) inscribed within a circumference concentric to the toroid (thus, symmetrically distributed with respect to its axis) and having radius $R_{av} = (R_{ext} + R_{int})/2$,

where R_{ext} and R_{int} are the external and internal radii of the toroid, respectively (Fig. 1A).

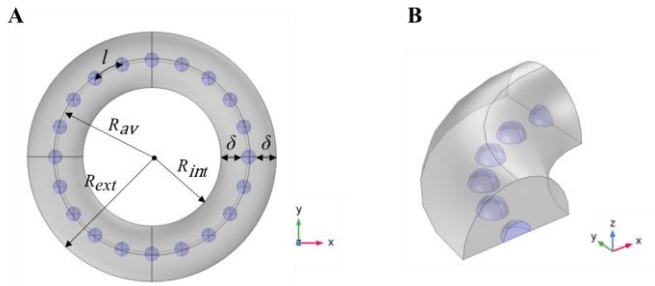


Fig. 1: The toroidal multi-spheroid system in the case of 20 coexisting spheroids. **A)** Top view of the whole designed geometry. **B)** Isometric view of the effectively simulated geometry, accounting for symmetries which hold for the system.

TAB. I: REGULAR POLYGONS USED AS REFERENCES FOR SYMMETRICALLY POSITIONING SPHEROIDS WITHIN THE TOROIDAL ENVIRONMENT ACCORDING TO THEIR ABUNDANCE.

Spheroid abundance (N)	*Regular polygon*
1	-
3	Equilateral triangle
4	Square
6	Hexagon
8	Octagon
12	Dodecagon
20	Icosagon

Hence, spheroid centres are coplanar, and l – intended as the length of the arch joining centres of two adjacent aggregates – is indirectly set through R_{av} depending on the number (or *abundance*, N) of coexisting spheroids. To avoid constructs getting closer to each other while increasing their radius (r_{sph}) and hence decouple coexistence from spheroid size, R_{av} is in turn parametrized as proportional to r_{sph} by means of a constant k, ultimately rendering the expression of l as below.

$$l = \frac{2\pi}{N}\left(k r_{sph} + 2\delta\right) \quad (1)$$

In Eq. (1), δ represents the difference between r_{sph} and the radius of the toroid cross-section (Fig. 1A). Together with the value of k, it determines the relationship between R_{ext} and R_{int}. δ is kept constant and equal to 3 mm, which is in the range of typical thicknesses of hydrogel shells used for organoid cultures [9], [11], [12], to match the requirement of a homogeneous diffusive O_2 supply at the aggregate boundary across sizes. As a result, spheroid cores are increasingly further from the source (and, thus, potentially depleted of O_2) as they increase in radius (r_{sph}), as for studies reported in [8], [9]. As a control, the case of a single construct was also implemented, in which the above-described constraints were maintained by placing the spheroid in the centre of a sphere with radius $R_{ext} = r_{sph} + \delta$.

Regardless of specific values of r_{sph}, N and k, the spatial distribution of constructs results in a geometry with three orthogonal symmetry planes, intersecting each other in the toroid centre. Thus, only the upper (or, equivalently, the lower) half of a toroidal sector corresponding to a 90° angle on the x-y plane (Fig. 1B) needed to be simulated. The parametric sweep on r_{sph}, N and k was performed according to ranges reported in Tab. 2.

B. Simulated biophysical processes and model implementation

The O_2 concentration field c (mol m^{-3}) in the generalized diffusion-reaction equation was solved at the steady state (Eq. (2)), assuming consumption according to the Michaelis-Menten's (MM) kinetics within spheroid domains [8], [9], [13] (then, $D\nabla^2 c = 0$ was the governing equation in the toroid domain).

$$D\nabla^2 c = \frac{\rho_{cell}\, sOCR\, c}{k_M + c} \quad (2)$$

In Eq. (2), D (m^2 s^{-1}) is the O_2 diffusion coefficient in water at 37 °C, ρ_{cell} (cells m^{-3}) the cell density in each construct, while $sOCR$ (mol cells^{-1} s^{-1}) and k_M (mol m^{-3}) denote the maximum rate of single-cell consumption and the MM constant, respectively.

A concentration equal to c_0 (Tab. 2) was set as both the initial and boundary condition on the outer surface of the toroid, while continuity of transport properties and O_2 flux field was assumed on spheroid surfaces. Symmetry held at all the other boundaries. Relevant parameters set for the FE models are listed in Tab. 2. As stem cells are the starting point for organoid generation [14], [15], the consumption parameters are those reported for human mesenchymal stem cells (MSCs) [9], [16]. Each geometry was discretized using a predefined *fine* mesh size.

TAB. II: PARAMETERS USED FOR SIMULATING O_2 DYNAMICS IN THE MULTI-SPHEROID SYSTEM.

Parameter	*Range/Value*	*Description/Reference(s)*
N	[1, 3, 4, 6, 8, 12, 20]	Parametric sweep range
r_{sph}	[31; 5000] µm	Parametric sweep range (log-spaced) [8], [9]
k	[1, 2, 4, 8, 16, 32]	Parametric sweep range
δ	3 mm	[9], [11], [12]
D	3×10^{-9} m^2 s^{-1}	In both culture medium and spheroids [11]
c_0	0.2 mol m^{-3}	O_2 saturation [13]
ρ_{cell}	5×10^{14} cell m^{-3}	*In vivo*-like [9], [19]
$sOCR$	2.75×10^{-17} mol cell^{-1} s^{-1}	Value for human MSCs [9], [16]
k_M	0.201 mol m^{-3}	Value for human MSCs [9], [16]

C. *Post-processing and statistical analysis*

Once convergence was reached, the parametric solution obtained for each possible combination of r_{sph}, N and k was post-processed to estimate the metabolic rate B (mol s^{-1}) of single constructs according to Eq. (3):

$$B = -\oiint \boldsymbol{J}(r_{sph}, t \to \infty) \cdot d\boldsymbol{S} \qquad (3)$$

where $\boldsymbol{J}(r_{sph}, t \to \infty)$ (mol m^{-2} s^{-1}) is the stationary flux field of O_2 through the spheroid surface. Since spheroids are symmetrically distributed in the environment, they all have the same B.

Then, size-related scaling exponents of single-spheroid B were identified as a function of N and k to assess whether these parameters affect metabolic scaling of cell aggregates. Linear fittings were performed in Matlab (The Mathworks Inc., Boston, Massachusetts, USA) on log-log data of construct size (*i.e.*, r_{sph}^3 or, equivalently, mass) and B, applying an approach similar to that proposed by Magliaro *et al.* [9] across the size range studied. However, in this work, the fitting algorithm did not look for a predefined slope (*i.e.*, 3/4 in [9], according to the classical formulation of KL) but determined the optimal stepwise regression of each log-log curve. The best fit was then identified as that in which each size sub-range of the obtained partition covers the most datapoints and displays the highest R^2. Corresponding slopes of regression lines were then extracted, representing the size-related scaling coefficient. Finally, correlation analyses were carried out in GraphPad Prism (version 7, GraphPad Prism Software, California, USA).

III. Results

The results are summarized as interpolated surface plots, to visualize the metabolic rate of single constructs and associated scaling exponents as multivariate functions of r_{sph}, N and k.

Fig. 2A shows values of individual B computed for a single spheroid with respect to r_{sph} and k for the minimum abundance (N = 3). B remains constant with r_{sph} independent of the inter-spheroid distance (*i.e.*, the value of k). Increasing the abundance of the community up to N = 20, B starts depending on k if the construct size increases; a positive correlation is indeed observed for $r_{sph} \geq 466.12$ µm (Spearman coefficient r = 1, significantly different from 0 with p = 0.0028), as evidently shown in the upper-left corner of Fig. 2B. In this region, the spheroids are large (high r_{sph}) and closely packed (since k is small and N equals its maximum). Hence, they are forced to share resources, and the individual B substantially decreases. Overall, this is an expected behaviour. In fact, given that the toroidal configuration avoids the formation of diffusion-limited regions with low O_2 concentration, each spheroid in the system is exposed to near-saturation conditions for high values of k. Then, as k decreases, the constructs are forced to cooperate for resource uptake.

These results suggest that the cooperative coexistence of cell aggregates may also have implications on their size-related scaling. Therefore, for each combination of values of N and k, the power-law behaviour of B versus r_{sph}^3 was analyzed through the stepwise regression procedure described in the previous section. In all cases, three size sub-ranges were identified: *i*) small radii, characterized by isometric scaling behaviour; *ii*) intermediate sizes, where the scaling exponent starts being significantly different from 1 (*i.e.*, *non-isometric* or *allometric* scaling); *iii*) large radii, with a geometry-driven metabolic scaling set by diffusion limitations depending on the system design (*i.e.*, geometric scaling). Construct radii corresponding to the isometric to non-isometric transition as a function of N and k are plotted in Fig. 2C. Irrespective of N, the positive correlation between the transition size and k (Spearman coefficient r = 0.8452, significantly different from 0 with p = 0.0467) indicates that the closer the spheroids are, the smaller their radius triggering non-isometric scaling (Fig. 2C). This result is reasonable for the chosen configuration, since O_2 concentration gradients leading to adaptive and cooperative metabolic behaviour emerge for smaller radii in densely packed constructs, because of limited O_2 availability due to resource sharing. Although the regression coefficients were not constrained, scaling exponents of spheroids in the non-isometric size sub-range were shown to be gathered around the typical value of 3/4 (Fig. 2D), with a coherent decrease when a high number of constructs coexist at low distances. In fact, for $k \leq 8$, correlation analysis between the exponent value and N results in a Spearman coefficient $r \leq$ -0.9429, significantly different from 0 with $p \leq 0.0167$.

IV. Discussion

In this work, a preliminary investigation on the impact of coexistence on O_2 metabolism and the associated size-related scaling of cell aggregates is presented. The aim was to probe the potential of cellular models as down-scaled replicates of ecosystems, to be used for predicting population behaviours in cooperating biological communities.

Metabolic rates (B) of single constructs were computed for MSC-laden spheroids in different configurations, maintaining the same boundary levels of energetic resource for each

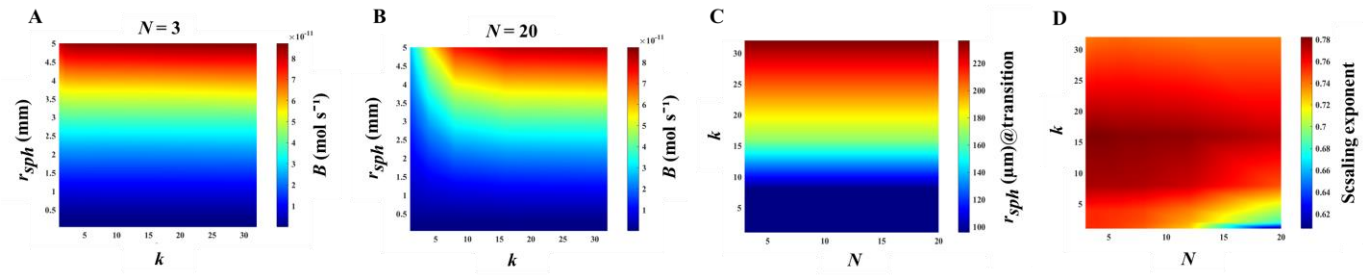


Fig. 2: Impact of coexistence on O_2 metabolism and its size-related scaling in *in silico* cell-laden spheroids. Single-spheroid B estimated as a multivariate function of k and r_{sph} for a toroidal environment hosting **A)** 3 or **B)** 20 constructs. **C)** The spheroid radius corresponding to the isometric to non-isometric transition and **D)** the scaling exponent in the non-isometric size sub-range as multivariate functions of N and k.

population. The *in silico* models show that, for large constructs ($r_{sph} \geq 466.12$ μm), individual *B* decreases when community abundance is high and the inter-spheroid distance small (Fig. 2B). This is in line with the expected behaviour: when coexisting and induced to share resources, cell aggregates tend to adapt their O_2 utilization, giving rise to a metabolic cooperation. Additionally, for widely spaced spheroids (*i.e.*, *k* = 32), the non-isometric size range (Fig. 2C) and associated scaling exponents (Fig. 2D) are similar to those reported in Magliaro *et al*. for single spheroids embedded within a hydrogel shell of thickness comparable to δ [9], even though values for the exponents were not assumed *a priori* in this work. However, when *k* decreases, the isometric to non-isometric transition occurs at smaller size ranges (Fig. 2C). This is because the spheroids approach each other and need to cooperate to share energetic resources. Sharing the same environment also leads – not surprisingly - to the reduction of scaling exponent values in the non-isometric size range when a high number of constructs are densely packed (Fig. 2D).

Even though most of the results reported here are expected, they serve to highlight that computer-based models have the potential for studying cooperative coexistence *in vitro*. In fact, the observed dynamics are analogous to those emerging in cells in both monolayer cultures and 3D spheroids, which have been reported to modulate their individual metabolism as a function of cell density [17]. Although based on specific and simple configurations, these results suggest metabolic adaptation as an inherent feature of any biological system, occurring across scales when multiple biological "units" – be they cells, simple cell aggregates or interconnected organ models – share a finite amount of a fundamental resource (*e.g.*, O_2) within the same environment.

Currently, further analyses on more sophisticated and biologically relevant multi-spheroid systems are being performed. Specifically, we are introducing stochasticity in terms of both construct size - as discussed by our group in [18] - and spatial distribution, accounting for coexisting aggregates laden with different cell phenotypes (*e.g.*, relevant to the composition of a biological tissue or organ). The aim is to identify configurations able to replicate key ensemble behaviours observable among individuals of real non-competitive biological communities. Moreover, experimental tests are ongoing to reproduce and validate the computational models.

To conclude, the outcome of this work is novel, since it represents the first attempt of exploiting coexisting cell aggregates as a down-scaled predictive model of natural cooperative ecosystems. The impacts span from multi-tissue or multi-organ systems in the biomedical field up to heterogeneous communities at the macroscale, which may be of ecological relevance. Taken together with properly designed experimental cell models, the *in silico* tools discussed here could constitute a cost-effective, easy-to-use and sustainable platform to investigate a broad spectrum of coexistence configurations, with a specific focus on how populations adapt to environmental changes.

ACKNOWLEDGEMENT

The work leading to these results has received funding from the Swiss National Science Foundation, through Project SINERGIA 2019 572 CRSII5_186422/1.

Ermes Botte also acknowledges the European Union for his post-doctoral fellowship, funded by the Next Generation EU project CN00000013 'Centro Nazionale 1' HPC, Big Data and Quantum Computing (CN1, PNRR, Spoke 6: Multiscale modelling and engineering applications).

REFERENCES

[1] V. Volterra, "Variations and Fluctuations in the Numbers of Coexisting Animal Species," pp. 65–236, 1978.

[2] A. J. Lotka, *Elements of physical biology*. Williams and Wilkins, Baltimore, Maryland, USA, 1925.

[3] G. F. Gause, *The struggle for existence*. Williams and Wilkins, Baltimore, Maryland, USA, 1934.

[4] R. A. Armstrong and R. McGehee, "Coexistence of species competing for shared resources," *Theor. Popul. Biol.*, vol. 9, no. 3, pp. 317–328, 1976.

[5] R. A. Lankau, "Rapid Evolutionary Change and the Coexistence of Species," *Annu. Rev. Ecol. Evol. Syst*, vol. 42, pp. 335–54, 2011.

[6] J. H. Brown, J. F. Gillooly, A. P. Allen, V. M. Savage, and G. B. West, "TOWARD A METABOLIC THEORY OF ECOLOGY," *Ecology*, vol. 85, no. 7, pp. 1771–1789, Jul. 2004.

[7] J. H. Brown, 1942- Sept. 25, and G. B. West, *Scaling in biology*. Oxford University Press, 2000.

[8] A. Ahluwalia, "Allometric scaling in-vitro," *Sci. Rep.*, vol. 7, no. 1, pp. 1–7, Feb. 2017.

[9] C. Magliaro, A. Rinaldo, and A. Ahluwalia, "Allometric Scaling of physiologically-relevant organoids," *Sci. Rep.*, vol. 9, no. 1, pp. 1–8, Dec. 2019.

[10] M. Kleiber, "Body size and metabolism," *Hilgardia*, vol. 6, no. 11, pp. 315–353, Jan. 1932.

[11] E. Berger *et al.*, "Millifluidic culture improves human midbrain organoid vitality and differentiation," *Lab Chip*, vol. 18, no. 20, pp. 3172–3183, 2018.

[12] R. J. McMurtrey, "Analytic Models of Oxygen and Nutrient Diffusion, Metabolism Dynamics, and Architecture Optimization in Three-Dimensional Tissue Constructs with Applications and Insights in Cerebral Organoids," *Tissue Eng. Part C. Methods*, vol. 22, no. 3, pp. 221–249, Mar. 2016.

[13] G. Mattei, S. Giusti, and A. Ahluwalia, "Design Criteria for Generating Physiologically Relevant In Vitro Models in Bioreactors," *Processes*, vol. 2, no. 3, pp. 548–569, 2014.

[14] H. Clevers, "Modeling Development and Disease with Organoids," *Cell*, vol. 165, no. 7, pp. 1586–1597, Jun. 2016.

[15] M. A. Lancaster and M. Huch, "Disease modelling in human organoids," *DMM Dis. Model. Mech.*, vol. 12, no. 7, Jul. 2019.

[16] E. Curcio, A. Piscioneri, S. Morelli, S. Salerno, P. Macchiarini, and L. De Bartolo, "Kinetics of oxygen uptake by cells potentially used in a tissue engineered trachea," *Biomaterials*, vol. 35, no. 25, pp. 6829–6837, Aug. 2014.

[17] C. Magliaro, G. Mattei, F. Iacoangeli, A. Corti, V. Piemonte, and A. Ahluwalia, "Oxygen Consumption Characteristics in 3D Constructs Depend on Cell Density," *Front. Bioeng. Biotechnol.*, vol. 7, p. 251, 2019.

[18] E. Botte, F. Biagini, C. Magliaro, A. Rinaldo, A. Maritan, and A. Ahluwalia, "Scaling of joint mass and metabolism fluctuations in in silico cell-laden spheroids," *Proc. Natl. Acad. Sci.*, vol. 118, no. 38, p. e2025211118, Sep. 2021.

[19] E. Bianconi *et al.*, "An estimation of the number of cells in the human body," *Ann. Hum. Biol.*, vol. 40, no. 6, pp. 463–471, Nov. 2013.

A bioinformatic pipeline for identifying bacterial constitutive promoters based on transcriptomic data analysis

D. Dallera[1], S. Quaranta[1], D. De Marchi[1], G. Cipriano[1], P. Magni[1] and L. Pasotti[1]
[1] *Department of Electrical, Computer and Biomedical Engineering, University of Pavia, I-27100 Pavia, Italy*

***Abstract*—Promoters are short regions of DNA where RNA polymerase and transcription factor bind to initiate the transcription of target gene sequences. Currently, there is no validated scientific method to predict the total set of promoters within a bacterial genome, especially for non-model chassis. The purpose of this work is the development of an algorithm to support the prediction of bacterial promoters with the desired characteristics, based on genomic and transcriptomic data. The pipeline can allow to expand the toolkit of biological parts implemented in synthetic genetic circuits to enable reliable engineering and gene expression control in model and non-model bacteria. Genome-scale identification of promoters with stable activity in *Escherichia coli* is herein provided as pipeline application.**

***Keywords*—Bioinformatic pipeline, synthetic biology, bacterial promoter, gene expression.**

I. INTRODUCTION

IN bacteria, expression levels are extremely variable between genes. The expression of many genes is subject to variation in response to environmental changes. This regulation is essential for the overall fitness of the bacterial cell. The key regulatory step that modulates gene expression is promoter recognition and transcription initiation which takes place via the enzymatic complex formed by RNA polymerase- *σ-factor* [1]. Different families of *σ-factors* exist. Generally, only one of them (e.g., σ^{70} in *Escherichia coli*) promotes constant transcription of genes in any condition, possibly in combination with specific transcriptional regulators. In contrast, promoters regulated by others are generally modulated by stress and other environmental stimuli [2].

Bacterial promoters are characterized of three elements: Transcription Start Site (TSS), i.e., the position where transcription begins, and two short DNA sequences called "-10" and "-35" because they are located at about 10 and 35 bases upstream TSS, respectively. The nucleotide composition of these two regions mainly determines the strength of the binding between RNA polymerase and DNA [3]. Each sigma factor recognises a specific consensus sequence on the promoter to be regulated. The consensus sequence can be different as a function of the bacterial species.

Inducible promoters alter their transcriptional rate because of external stimuli represented by a physical agent, such as temperature, or a chemical agent, such as a molecule [4]. The quantitative characterization of inducible promoters is a key task in synthetic biology. They are adopted in synthetic circuits as user-controlled transcription initiators. However, some problems can arise using inducible promoters such as hypersensitivity to inducer, the range of activity may be unsuitable to ensure efficient activation or repression of downstream gene expression, the high cost of the inducer may also make the system unusable, and, finally, the levels of expression achieved fluctuate significantly within the population, leading to a large heterogeneity of the transcript. Therefore, in different applications it is preferred to use constitutive promoters with known strength in the construction of synthetic circuits to be inserted inside the host microorganism [5]. Different environments could affect promoter activity unpredictably, due to regulations that are not previously characterized. This motivates further efforts in identifying promoters with robust activity across genomes.

One method that can be used to discriminate between constitutive and regulated promoters is to analyse transcriptomic data. Genes whose transcription is regulated by constitutive promoters have stable level of expression in different experimental conditions. Blount et al. conducted a study to identify a constitutive promoter *in Saccharomyces cerevisiae* and re-engineer it to create a library of promoters by changing the basis of the found promoter sequence [6]. A large data set of microarray experiments in yeast databases was used to identify the promoter whose downstream gene has the least variability under different test conditions.

The identification of the location and function of the promoter regions is challenging as they very often do not reflect certain patterns of sequences and are therefore difficult to determine by analysing the genome with traditional methods of exact research. This becomes an even more difficult test if the objective is to identify promoters in poorly studied species. Most bioinformatic algorithms for promoter identification use research of conserved motives in the regions upstream of genes [7]-[10]. Recently, two bioinformatic tools have been developed using differential RNA sequencing (dRNA-seq) data for the high-throughput screening to examine the precise position of TSS [11],[12].

Here, we present a bioinformatic pipeline, developed in R, to support the prediction of bacterial promoters with desired characteristics, based on genomic and transcriptomic public data. The pipeline is divided into two procedures: the first one analyses transcriptomic data (microarray and RNA-sequencing experiments) to obtain a list of genes with stable transcription level (non-differentially expressed - NDE); the second one predicts TSS upstream of NDE genes from RNA-sequencing (RNA-seq) data. Using expression values from both technologies increases the reliability of the result about NDE genes as many more experimental conditions are considered. The algorithm can be used for any bacteria with

annotated genome and available data from microarray and RNA-seq experiments.

II. METHODS

A. *Identification of NDE genes*

The analysis of transcriptomic data is split up according to the chip technology, RNA-seq vs microarray, and the latter is divided in turn based on the construction of the chip (Affymetrix – one or two channel by other manufacturers). In Fig.1, the overall schema of the procedure is reported.

The experiments, identified by a GSE code, are analysed separately: data are downloaded from the NCBI Gene Expression Omnibus (GEO) database [13]. While for microarray experiments raw expression data are available, for RNA-seq they must be reconstructed through the alignment of the reads along the reference genome and counting how many reads have mapped to each gene. We align along the reference genome because not all the species under study have a well annotated genome.

Then, expression data are processed also making an evaluation of data quality, through standard indices (for microarray Affymetrix data), or evaluating the correlation of expression values among pairs of experiments and removing background noise. If experiments, or some samples, do not pass quality tests, they are discarded from the analysis.

In RNA-seq analysis, *Rockhopper*, i.e., a tool for the identification of operons, is integrated [14]. The information derived from the prediction of operon architecture is stored to eventually eliminate the genes that are not first gene in operon because they are not expected to have specific promoters immediately upstream.

Then, an appropriate *intra-experiment* normalization is applied to remove bias among samples in the same batch (e.g., Robust Multiarray Averaging (RMA) for Affymetrix data, quantile normalization for other microarray data and normalization with DESeq2 for RNA-seq data).

NDE genes are identified using a statistical test with a Bonferroni correction to filter out the genes showing significant differences among the experimental conditions.

For microarray data, the information about the genome of the strain on which the experiment has been performed is not always available. Often therefore the notations, i.e., the locus tag, with which the genes are uniquely identified are not consistent or easily traceable among experiments. As a result, the mapping of all annotated genomes of the species concerned to the reference genome is necessary. A tool implemented in python, *OrthoFinder* [15], is integrated in the procedure: it deals with identifying orthogroups, i.e., groups of orthologous genes, between pairs of genomes, based on the comparison between proteins. A post processing of the *OrthoFinder* output must be done to obtain unique correspondences between pairs of genes of the two compared strains. At the end of the process, all the names by which a gene is annotated in all the strains of the considered species are known.

After the identification of NDE genes commons to all the considered experiments, we proceed with an *inter-experiment* normalization of the expression values using *ComBat* [16], an R function which corrects data to remove *batch-effect*, specifying how many and which batch are present. We considered each experiment as a batch. A sub list of NDE genes of interest can be selected using a threshold on Standard Deviation (SD) or coefficient of variation (CV) of expression. CV is considered equal to SD on the used data because expression values are assumed log-normally distributed, and the data are log-transformed to carry out the analysis.

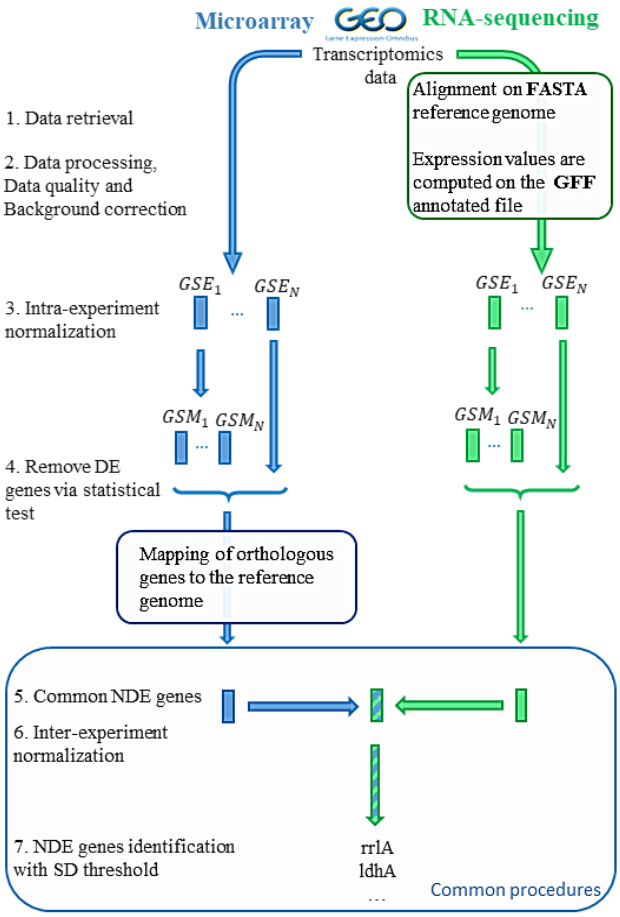


Fig.1: Overall representation of the procedure for NDE genes identification. It has been adapted to handle microarray (blue) and RNA-seq (green) data with different procedures due to the different nature of the transcriptomics data, based on a shared rationale reported in the enumerate list on the left part of the graph. GSE indicates the code of an experiment, while GSM code identifies samples.

B. *Identification of Transcription Start Site*

Coverage is the number of unique reads that include a given nucleotide in the sequence reconstructed during alignment.

This procedure requires the following inputs: files reporting the distribution of reads along the reference genome (coverage and number of reads that starts aligning in each genomic position) for each RNA-seq experiment; a GFF file containing genomic information; a file reporting the level of mean expression, percentiles, and CV of expression of NDE genes identified by the first procedure.

Coverage profiles of every experimental condition are analysed and the TSSs predicted positions are merged to identify the most likely ones (Fig. 2).

For each gene, the genomic region extending from 300 bp upstream starting codon to 300 bp after the gene is extracted. TSS position is searched in the 300 bp upstream of the gene.

First, it is necessary to apply a mathematical transformation to the values of coverage to limit sharp variations in the profiles of genes due to noise. Subsequently, a limitation of the search area is implemented to exclude areas larger than the

length of the reads where there are no pairings between reads and transcripts.

Despite the applied mathematical transformations, coverage profiles are still very noisy: a filter to remove high and low frequency noise must be applied. Coverage values before and after the gene start codon have been differentiated to distinguish the area where the probability to find a TSS position (before the gene start codon) is higher compared to the area where the probability is much smaller (after the gene start codon). The differences of coverage values between one base and the next are calculated and the growth fronts of coverage value are identified both in the area upstream and within the gene. In each sample, each position in the region before gene is selected as a TSS if the probability of belonging to the within-gene distribution of differences is lower than 5%. The probability is computed by comparing each before-gene coverage excursion with the distribution of the within-gene values. At the end of the analysis of all samples, for each gene we get the possible positions of the TSS associated with it.

A post-processing phase of the results is needed to limit the number of false positive TSS due to noisy graphs. Starting from the most identified TSS, called *TSS mode*, we look for the TSS belonging to a range of N bases on the right and left. These are part of the distribution centred in *TSS mode*. It iteratively extends the research area of TSS in the same population by enlarging the same region of N bases starting from extremes. This operation is repeated until in the region under observation there are no more TSS. Once a population is completed, mode is sought among the excluded TSS, and the corresponding population is built. Eventually, a certain number of populations is obtained and each of them is associated to a metric equal to the number of times the population is found multiplied by the number of times the *TSS mode* is found. The *TSS mode* with top metric is considered as the final TSS identified by the pipeline. Putative promoter sequences are the 50 bp upstream the predicted TSSs.

C. Data set

All microarray and RNA-seq experiments have been downloaded from GEO. The organism selected for the analysis is *Escherichia coli* (*E. coli*). It has more than 3000 chassis or version of annotation downloaded from Assembly summary NCBI [17]. Its reference genome is *E. coli str. K12 substr. MG1655* (taxid 511145).

The number of microarrays experiments available on GEO is ~500. A large number has been removed from the analysis because more than one organism was tested, or because there were experimental conditions with single replicate, or because there were problems during the reading of the files. Therefore, only 50 experiments passed this check.

The number of RNA-seq experiment available on GEO is ~170. 16 experiments were excluded because the number of aligned reads on the reference genome was too low.

For the identification of NDE genes were used 206 GSE, i.e., 206 different experimental studies.

Datasets of promoter sequences of *E. coli* have been retrieved from the EcoCyc database [18]. In EcoCyc, 1700 promoter sequences with their relative sigma factors and TSS were present.

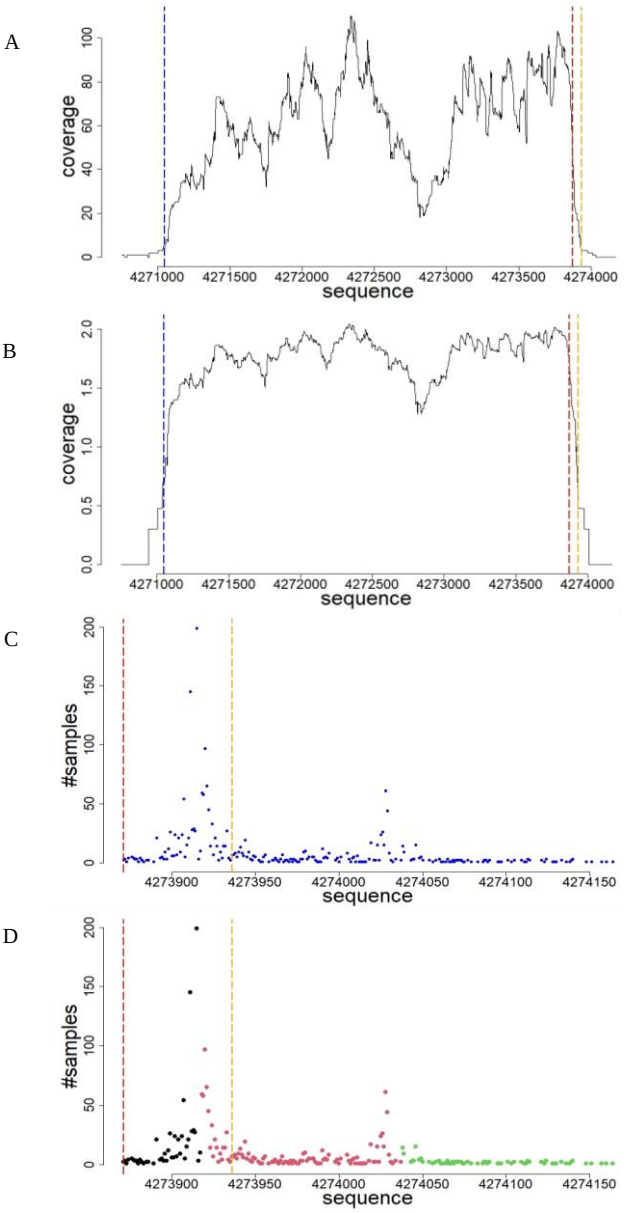


Fig.2: Overall representation of the procedure for the identification of TSS. A. The coverage profile of a gene in the genomic area of interest in a sample. B. The same coverage profile after logarithmic transformation. C. Distribution of TSS identified by the procedure excluding noisy positions. Each dot represents the number of samples in which each TSS is identified. D. Clustering of TSS in subpopulation. Each color represents a different population. Blue line: end of the gene; red line: start of the gene; orange line: TSS annotated.

III. RESULTS

A. Classification of NDE genes

The analysis of microarray experiments identified 1145 NDE genes, while that of RNA-sequencing 2858. Before *inter-experiment* normalization, the genes have been intersected to consider only the common ones, which were 871. NDE genes were sorted according to the mean expression percentile. They were divided into 5 groups, every 20 percentiles. In each group, 5 genes with lowest CV of the expression were selected (Fig.3).

The validation of the first procedure has been based on the genes for which, in the literature, have been demonstrated to be constitutively expressed in different conditions registered. Only the genes with known promoter sequence, sigma factor

and experimental evidence code have been used for the validation process. The data have been collected from EcoCyc. The first procedure detected correctly 19 out 25 genes (~76%). 3 genes were wrongly classified because the molecules that influence their production were present in the considered experimental conditions. The other 3 genes were not well annotated in EcoCyc, so no classification was possible.

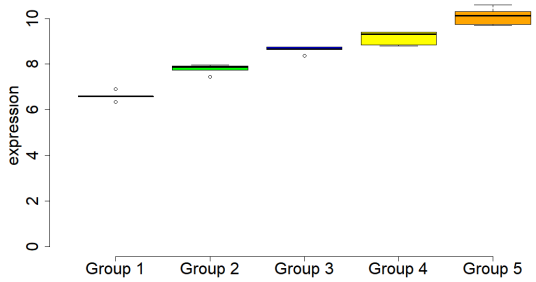


Fig. 3: Distribution of mean expressions of 25 genes selected during the analysis with lowest CV in five groups obtained dividing genes by percentile of expression.

B. Performance of the procedure for the identification of TSS

Although an increasing number of mapped reads to genomic locations downstream of TSS is expected, this may be more or less pronounced depending on the levels of gene expression. So, we limited the analysis on genes with mean percentile of expression higher than 60%.

At the end of the analysis of all samples, the identified TSSs were clustered in populations as described in II.B with N=10. For each gene, the TSS mode of the population with higher metric was identified.

The performance index of the procedure is based on TSS comparison with the literature. In fact, if the annotated TSS is included inside a window of ±5 bp on to the position of the putative TSS then the putative promoter is considered as true positive (TP).

$$performance\ index = \frac{\#\ TP}{all\ putative\ TSSs} \qquad (1)$$

The procedure has been tested in GSE60522 for *E. coli str. K12 substr. MG1655*, reaching a performance index of ~60%.

IV. Discussion and Conclusion

The increasingly demand of expanding the libraries of regulatory parts for non-model microorganisms motivated the development of novel strategies based on bioinformatics approaches for their *in-silico* prediction as an alternative to the high cost and time-consuming *in-vivo* search and characterization.

A new bioinformatics pipeline has been developed with the aim to detect constitutive endogenous promoters in microorganisms with annotated genomes, based on transcriptomics data in different experimental conditions.

Thanks to the RNA-seq resolution, it is possible to reconstruct reads coverage profiles base by base along the genome inferring the TSS genomic coordinate.

The two procedures adopted for promoter sequence detection and for selection of constitutively expressed genes have been tested for the model organism *E. coli* and the results compared with genomics data and scientific literature articles (promoter detection accuracy = ~60%; percentage of putative constitutive genes found = ~76 %).

A method to select RNA-seq experiment for the identification of TSS is needed to avoid the processing of large numbers of samples and to enable quality-based filtering: increasing the collection of experiments with desired characteristics could raise to better performance.

The pipeline performance is expected to depend on the number of experiments and assayed conditions, to sensitively detect NDE genes with robust expression. This may represent an issue when analyzing public data of non-model organisms for which a small number of experiments are available.

In parallel, new applications could be targeted to use the subset of Differentially Expressed (DE) genes. In fact, from the latter it is possible to infer the DNA operator sites linked to a particular perturbation, useful in the synthetic circuit design step to increase the circuit orthogonality from the enzymatic host machinery.

The pipeline can allow to expand the toolkit of biological parts implemented in synthetic genetic circuits to enable reliable engineering and gene expression control in model and non-model bacteria.

References

[1] D. Browning and S. Busby, “Local and global regulation of transcription initiation in bacteria”, *Nature Reviews Microbiology*, vol. 14, pp. 638-650, 2016.

[2] M. C. Davis, C. A. Kesthely, E. A. Franklin, and S. R. MacLellan, “The essential activities of the bacterial sigma factor”, *Canadian Journal of Microbiology*, 63(2), pp. 89-99, 2017.

[3] A. M. Huerta and J. Collado-Vides, “Sigma70 promoters in Escherichia coli: specific transcription in dense regions of overlapping promoter-like signals”, *Journal of Molecular Biology*, 333(2), pp. 261-278, 2003.

[4] A. Feklìstov, B. D. Sharon, S. A. Darst, and C. A. Gross, “Bacterial sigma factors: a historical, structural, and genomic perspective”, *Annual Review of Microbiology*, vol. 68, pp. 357-376, 2014.

[5] J. Gilman and J. Love, “Synthetic promoter design for new microbial chassis”, *Biochemical Society Transactions*, 44(3), pp. 731-737, 2016.

[6] B. Blount, T. Weenink, S. Vasylechko, and T. Ellis, “Rational diversification of a promoter providing fine-tuned expression and orthogonal regulation for synthetic biology”, *PLoS One*, 7(3), 2012.

[7] J. Gilman, et al., “Rapid, Heuristic Discovery and Design of Promoter Collections in Non-Model Microbes for Industrial Applications”, *ACS Synthetic Biology*, 8(5), pp. 1175-1186, 2019.

[8] V. Solovyev and A. Salamov, “Automatic Annotation of Microbial Genomes and Metagenomic Sequences”, *Metagenomics and its Applications in Agriculture, Biomedicine and Environmental Studies*, Ed. R.W. Li, pp. 61-78, 2011.

[9] I. A. Shahamuradov, R. M. Razali, S. Bougouffa, A. Radanovic, and V. B. Bajic, “bTSSfinder: a novel tool for the prediction of promoters in cyanobacteria and Escherichia coli”, *Bioinformatics*, 33(3), pp.334-340, 2017.

[10] S. Burden, Y. Lin, and R. Zhang, “Improving promoter prediction for the NNPP2.2 algorithm: a case study using Escherichia coli DNA sequences”, *Bioinformatics*, 21(5), pp. 601-607, 2005.

[11] F. Amman, et al., “TSSAR: TSS annotation regime for dRNA-seq data”, *BMC Bioinformatics*, 15(89), 2014.

[12] C. M. Sharma, et al., “The primary transcriptome of the major human pathogen Helicobacter pylori”, *Nature 464*, pp. 250-255, 2010.

[13] R. Edgar, M. Domrachev, and A.E. Lash, “Gene Expression Omnibus: NCBI gene expression and hybridization array data repository”, *Nucleic Acids Research*, 30(1), pp. 207-210, 2002.

[14] B. Tjaden, “A computational system for identifying operons based on RNA-seq data”, *Methods*, vol. 176, pp. 62-70, 2020.

[15] D. M. Emms and S. Kelly, “OrthoFinder: phylogenetic orthology inference for comparative genomics”, *Genome Biology*, vol. 20, 238, 2019.

[16] W. E. Jhonson, C. Li, and A. Rabinovic, “Adjusting batch effects in microarray expression data using empirical Bayes methods”, *Biostatistics*, 8(1), pp. 118-127, 2007.

[17] P. A. Kitts, et al., “Assembly: a resource for assembled genomes at NCBI”, *Nucleic Acids Research*, 44, pp. 73-80, 2016.

[18] P. D. Karp, et al., “The EcoCyc Database”, *EcoSal Plus*, 6(1), 2014.

LONGITUDINAL RELATIONSHIPS BETWEEN PROTEOMICS AND BETA-CELL DYSFUNCTION IN TYPE 2 DIABETES: AN IMI DIRECT STUDY

C.A. Rossi[1], A. Viñuela[2], J. M. Schwenk[3], E. R. Pearson[4], A. Mari[1] and R. Bizzotto[1] for the IMI DIRECT Consortium

[1] *Institute of Neuroscience, CNR, Padua, Italy*
[2] *Faculty of Medical Sciences, Biosciences Institute, Newcastle University, Newcastle, UK*
[3] *Science for Life Laboratory, KTH—Royal Institute of Technology, Stockholm, Sweden*
[4] *Population Health & Genomics, School of Medicine, University of Dundee, Dundee, UK*

***Abstract*—β-cell dysfunction is a crucial factor of glycaemic deterioration in type 2 diabetes (T2D), but the role of circulating proteins in its progression is currently not understood.**

We studied the potential associations between β-cell glucose sensitivity progression over 3 years and baseline proteomics in a cohort of recently diagnosed T2D patients (*N* = 653) from the IMI-DIRECT project, through linear regression analysis.

We found that forty-six proteins have a significant association to β-cell glucose sensitivity progression. Subsequent functional analysis showed these proteins belong to functional modules linked to insulin secretion and T2D pathophysiology.

These findings, along with further investigation in longitudinal studies, may point to novel protein markers and processes of β-cell function deterioration.

***Keywords*—β-cell function, T2D, proteomics, glucose sensitivity.**

I. INTRODUCTION

β-cell dysfunction is a key feature of glycaemic deterioration in type 2 diabetes (T2D), alongside reduction in insulin sensitivity and clearance [1]. Recent IMI DIRECT studies highlighted that deteriorating β-cell function is independently associated with glycaemic progression [2].

The role of circulating proteins in β-cell dysfunction is less clear and defined. Many of the available studies on the subject explored the potential association between diabetes and circulating proteins, not specifically β-cell function [3][4]. The few that did so are limited to cross-sectional data [5].

In this study we performed regression analysis to identify possible, significant associations between β-cell glucose sensitivity progression and proteomics and explore the potential biological roles of these associations for T2D physiopathology through functional analysis.

II. METHODS

A. Data

The data utilized in this study were extracted from the prospective multicentre IMI DIRECT cohort of white Nord European T2D patients of recent diagnosis [6].

Mixed meal tests were performed and anthropometric data were collected at 0, 9, 18, and 36 months [6]. β-cell glucose sensitivity (GS) was derived by modelling [7] and chosen as indicator of β-cell function.

Olink targeted proteomics were recorded at month 0 (baseline), from five different panels – Metabolomics, Cardiovascular I and II, Cardiometabolic and Development – for a total of four hundred sixty considered proteins. Proteins concentrations were measured in EDTA plasma samples collected after overnight fasting through multiplex proximity extension assays.

Patients without available progression of glucose sensitivity or with ambiguous T2D (IA2 > 7.5 or GAD > 11) were excluded, reducing the cohort to a total of *N* = 653 individuals.

Only proteins with missing data frequency lower than 0.5 were kept for the study, for a total of four hundreds different proteins.

Protein distributions were adjusted with a linear mixed effects model for plate, centre, seasonality, time of day, and sample age with the R package *lme4* [8]. Lastly, distributions were scaled.

B. *β-cell glucose sensitivity progression*

GS values were modelled with linear functions of time, of which slopes were chosen to represent progression of GS (GSp) [2].

C. *PCA*

Principal component analysis (PCA) was conducted on the proteomics data to identify possible, important principal components that could arise from proteins distributions. PCA was performed through the R *factoMiner* and *factoextra* packages [9].

D. *Regression analysis*

The relationships between GSp and circulating proteins were investigated through linear regression analysis. We employed models that included single proteins from our dataset and several covariates: the first principal component of the proteomics data (21% of data variance explained), medications with reported effects on glycaemia taken or removed within the study, and clinical traits at baseline (sex, age, body mass index, GS, questionnaire-reported moderate physical activity, and glycated haemoglobin).

Influential points in the linear regressions, identified via residuals with excessive Cook's distance (over five times the mean of the Cook's distances), were removed from the dataset to re-run the regressions.

All regressions and influential points analyses were run on R with the *stats* package [10].

To account for multiple testing, regressions p-values were adjusted with the Benjamini-Hochberg procedure (FDR) [11].

E. Functional Analysis

Proteins with statistically significant regression coefficients (FDR-adjusted p-values < 0.1) were used to perform a functional gene enrichment analysis through Over-Representation Analysis (ORA) [12].

We also performed gene set enrichment analysis (GSEA) [13] on the entire proteins set. In this case, proteins were ranked with a score calculated as $-log_{10}(p\text{-}value)*sign_of_coefficient$.

The three gene ontologies Biological Processes, Molecular Functions, and Cell Components [14], and the KEGG [15], WikiPathways [16], and Reactome [17] repositories were used as databases for both analyses. Only results with p-values lower than 0.05 were considered significant.

All functional analyses were run on R with the *clusterProfiler* package [18].

III. RESULTS AND DISCUSSION

A. Proteins identified by linear regression

Linear regression analysis identified forty-six proteins out of the starting four hundreds as statistically significant, with standardized protein coefficients between -0.16 and 0.2 and R-squared higher than 0.27 (Fig.1). The protein with highest significance (FDR = 0.004), SCARF1, showed also the highest positive β-coefficient (0.2).

B. Functional analysis

Among the statistically significant annotations identified by the ORA test, some proved to be more interesting due to their potential role in insulin secretion: Rap1 signalling and MAPK/Ras pathways, involved in β-cell insulin secretion [19] and insulin receptors signal transduction [20], were found to be significant by the analysis on the KEGG database (Fig.2).

GSEA analysis showed many statistically significant terms and pathways describing tyrosine-kinases receptors activity, the class of receptors for insulin signalling and signal transduction [20].

Different terms and pathways related to inflammation signalling, extracellular matrix, cellular membrane organization and transport vescicles were also identified by both ORA and GSEA tests.

IV. CONCLUSION

The application of regression analysis on β-cell glucose sensitivity progression and proteomics allowed to identify a set of markers for β-cell function progression.

The enrichment analyses showed that some of these proteins belong to functional modules already related to insulin secretion or T2D pathophysiology, pointing to the potential role of these proteins and modules in the progression of β-cell dysfunction in T2D.

External and experimental validation of these findings is warranted.

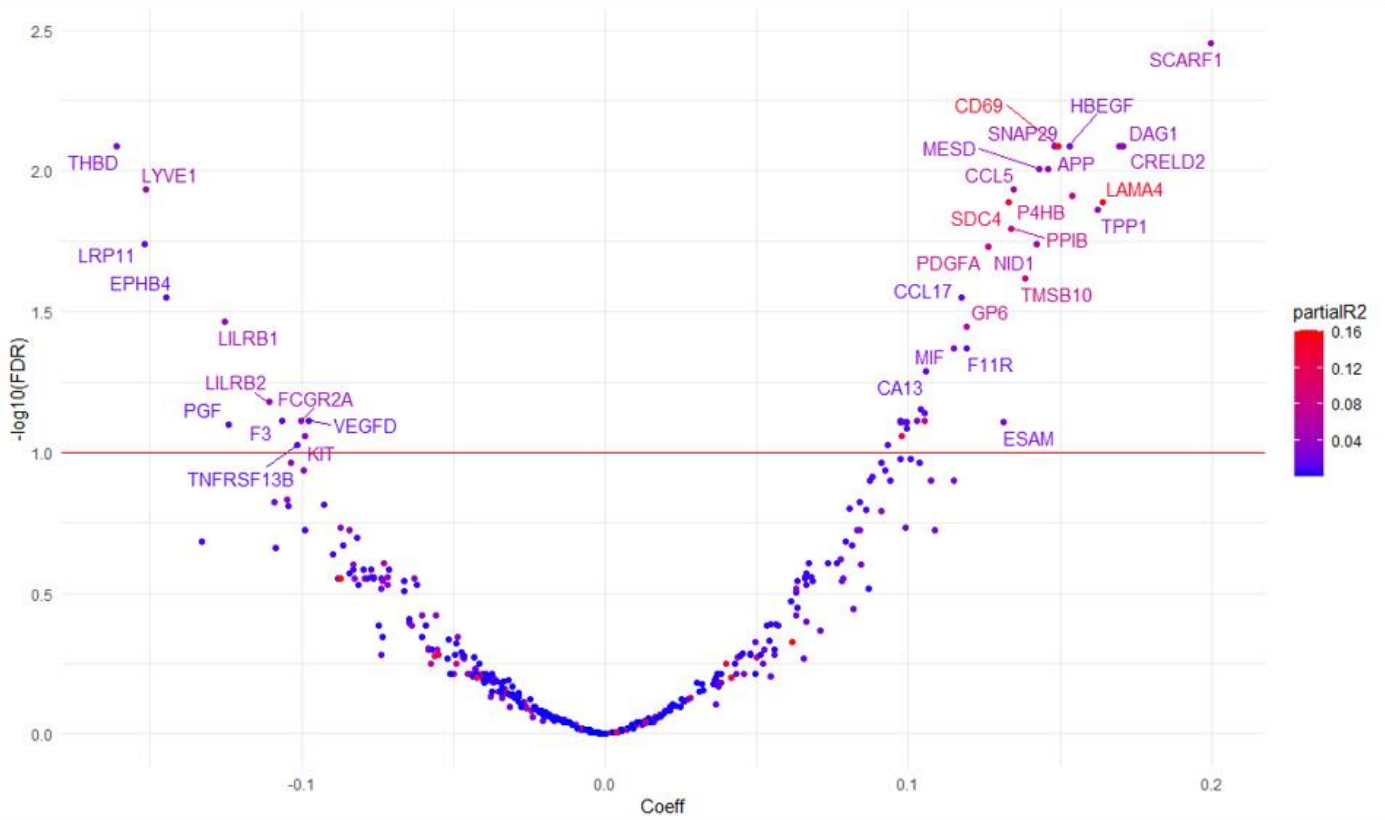


Fig. 1: Linear regressions results as volcano plot showing each protein β-coefficient with its statistical significance (FDR-adjusted p-values), colored by partial R^2 value. Forty-six proteins are above the red line that represents the significance threshold of 0.1.

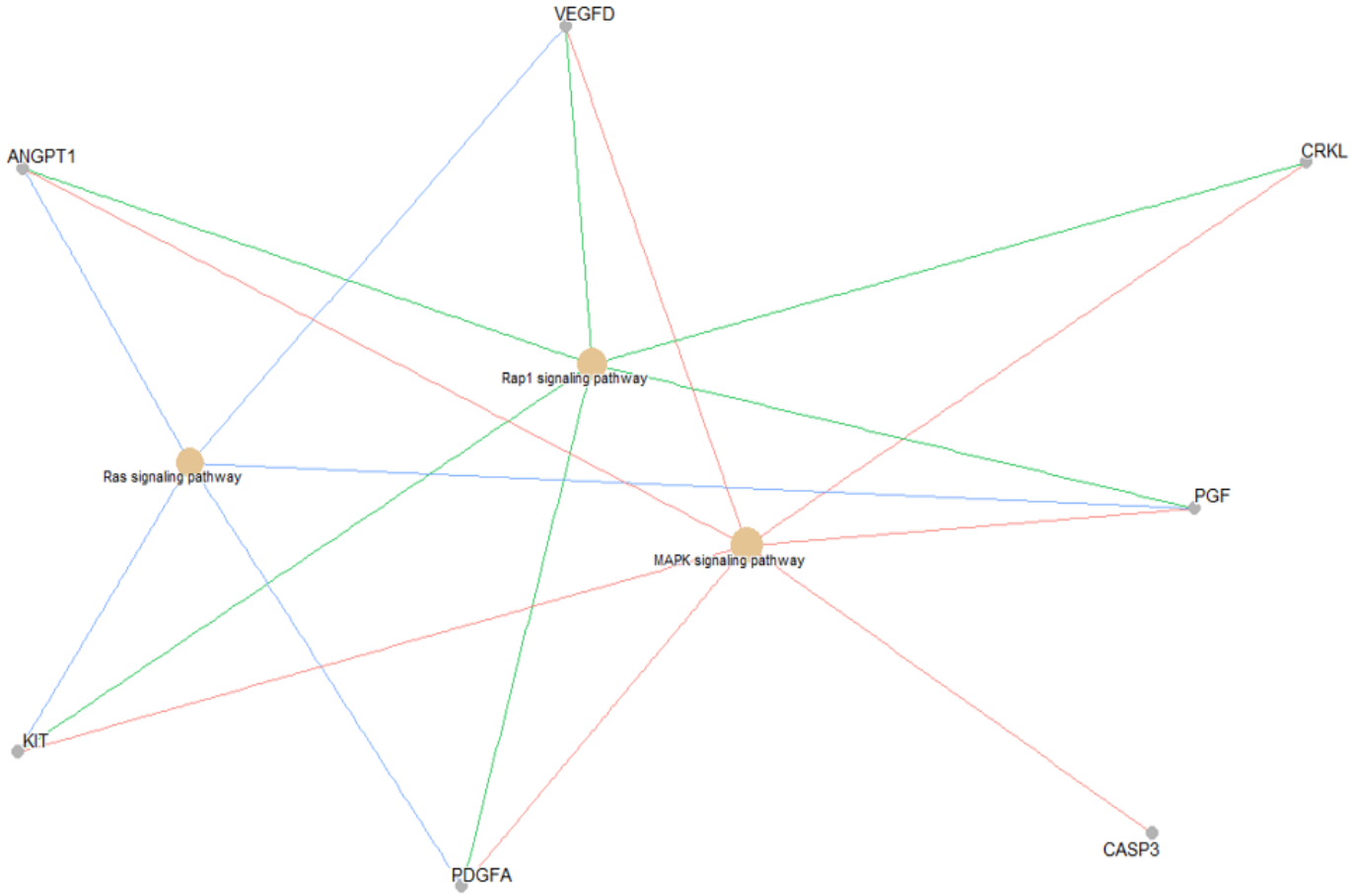


Fig. 2: Gene-concept network of statistically significant (p-value < 0.05) enriched pathways from Over-Representation Analysis on KEGG database, forming a potential functional module for insulin signal transduction and secretion.

ACKNOWLEDGEMENT

The work leading to this publication has received support from the Innovative Medicines Initiative Joint Undertaking under grant agreement 115317 (DIRECT), resources of which are composed of financial contribution from the European Union's Seventh Framework Programme (FP7/2007-2013) and European Federation of Pharmaceutical Industries and Associations companies' in-kind contribution. Information on the project can be found at https://www.directdiabetes.org/.

REFERENCES

[1] J. Levy, *Beta-cell deterioration determines the onset and rate of progression of secondary dietary failure in type 2 diabetes mellitus: the 10-year follow-up of the Belfast Diet Study*, Diabet Med, 1998, 15:290–296.

[2] R. Bizzotto, *Processes Underlying Glycemic Deterioration in Type 2 Diabetes: An IMI-DIRECT Study*, Diabetes Care, 2021.

[3] J. Molvin,, *Using a Targeted Proteomics Chip to Explore Pathophysiological Pathways for Incident Diabetes– The Malmö Preventive Project*. Sci Rep, 2019.

[4] K. Beijer, *In search of causal pathways in diabetes: a study using proteomics and genotyping data from a cross-sectional study*, Diabetologia, 2019.

[5] A.E. Mendham,,*Targeted proteomics identifies potential biomarkers of dysglycaemia, β cell function and insulin sensitivity in Black African men and women*. Diabetologia, 2022.

[6] R.W. Koivula, *DIRECT Consortium. Discovery of biomarkers for glycaemic deterioration before and after the onset of type 2 diabetes: rationale and design of the epidemiological studies within the IMI DIRECT Consortium*, Diabetologia, 2014, 57:1132–1142.

[7] A. Mari, *Assessing Insulin Secretion by Modeling in Multiple-Meal Tests: Role of Potentiation*, Diabetes, 2002, Feb;51 Suppl 1:S221-6

[8] M.M. Bates D, *Fitting linear mixed-effects models using lme4*, J Stat Softw 67 (2015), pp. 1-48.

[9] S. Lê, *FactoMineR: An R Package for Multivariate Analysis*, Journal of Statistical Software, 2008, 25(1). pp. 1-18.

[10] R Core Team (2022), *R: A language and environment for statistical computing. R Foundation for Statistical Computing, Vienna, Austria*. ISBN 3-900051-07-0, URL http://www.R-project.org/

[11] Benjamini, *Controlling the False Discovery Rate: A Practical and Powerful Approach to Multiple Testing*, Journal of the Royal Statistical Society. Series B (Methodological), vol. 57, no. 1, 1995, pp. 289–300. JSTOR.

[12] E. Boyle, *GO::TermFinder–open Source Software for Accessing Gene Ontology Information and Finding Significantly Enriched Gene Ontology Terms Associated with a List of Genes*, Bioinformatics, 2004, 20 (18): 3710–15.

[13] A. Subramanian, *Gene Set Enrichment Analysis: A Knowledge-Based Approach for Interpreting Genome-Wide Expression Profiles*, Proceedings of the National Academy of Sciences of the United States of America, 2005, 102 (43): 15545–50.

[14] Gene Ontology Consortium, *The gene ontology resource: 20 years and still GOing strong*, Nucleic Aids Res, 2019, 47(D1):D330–D338

[15] M. Kanehisa, *KEGG for taxonomy-based analysis of pathways and genomes*, Nucleic Acids Res, 2023, 51, D587-D592.

[16] D.N. Slenter, *WikiPathways: a multifaceted pathway database bridging metabolomics to other omics research*. Nucleic Acids Res, 2018, 46(D1):D661–D667.

[17] B. Jassal, *The reactome pathway knowledgebase*. Nucleic Acids Res, 2020, 48(D1):D498–D503.

[18] G. Yu, *clusterProfiler 4.0: A universal enrichment tool for interpreting omics data*, The Innovation. 2021, 2(3):100141.

[19] P. Kelly, *Rap1 promotes multiple pancreatic islet cell functions and signals through mammalian target of rapamycin complex 1 to enhance proliferation*. J Biol Chem., 2010, May 21;285(21):15777-85.

[20] P. De Metys, *The Insulin Receptor and Its Signal Transduction Network*. Endotext, 2016 Apr 27

Lipid Droplets associated genes link HSV-1 infection to neurodegeneration pathways

V. Zatta[1], M. Bellato[2], A. Pegoraro[1], G. Bernabè[1], S. Letrari[1], A. Stepanyan[3], B. Di Camillo[2], P. Brun[1], and I. Castagliuolo[1]

[1] *Department of Molecular Medicine, University of Padua*
[2] *Department of Information Engineering, University of Padua*
[3] *Department of General Surgery 3, University Hospital of Padua*

***Abstract*— A growing body of evidence support the infectious hypothesis of Alzheimer's Disease (AD) and a possible role of HSV-1. Due to its ability to undergo multiple cycles of latency and reactivation in neurons, HSV-1 is considered a possible agent in triggering neurodegeneration and AD onset.**

In this work we focus on a particular aspect: the connection of lipid droplets (LDs) with viral infection and neurodegeneration. To corroborate this hypothesis, experimental and in-silico approaches have been synergistically adopted, in a rational multimodal framework: *in vivo* and *in vitro* models were exploited, from cytological imaging and flow cytometry to gene expression and protein interaction network analysis.

Our results point out that, after viral infection, not only LDs accumulate in both models, but also that differentially expressed genes can be related to key players, notoriously involved in neurodegeneration. Of note, infected neuronal cells are characterized by an in increase in ROS production, and in particular lipid peroxidation, which is again a known outcome in both viral infection and neurodegeneration.

***Keywords*—HSV1, Lipid Droplets, Neurodegeneration, Networks**

I. Introduction

Alzheimer's Disease (AD) is a neurodegenerative disease characterized by early neuronal death in brain and synaptic loss, events leading to cognitive decline in patients, that exhibit memory and language impairment. Among others, the main hallmarks of AD are the formation of neuronal β-amyloid plaques and neurofibrillary tangles, along with the presence of extensive oxidative stress [1]. Despite several aspects of the pathology have been unraveled, a lot of information are still missing, especially about its etiology: this is reflected in the absence of an effective treatment to date.

In the last decades, a growing body of evidence in literature support the profound link between AD onset and infectious agents. Among others, several suggestive data point out the Herpes simplex virus type 1 (HSV-1) as an extremely attractive putative player: it undergoes latency and it can establish chronic infections through evasion of host immune response and it can be subjected to multiple reactivations from latency during patient's life [2]. It has been demonstrated that HSV-1 infection leads to enhanced AD markers in neurons [3]–[5]; in particular, multiple reactivations from latency are thought to contribute to neuronal dysfunction, thus leading to neurodegeneration.

Lipid droplets (LDs) are intracellular organelles that store neutral lipids. LDs are well characterized in adipocytes where they perform the function of energy storage and their accumulation can be induced by several factors, such as metabolic alterations.

It has been reported that both ageing and neurodegenerating neurons can accumulate LDs in response to inflammation, lipotoxicity and oxidative stress [6], [7]. Interestingly, the increase in these organelles is detected also in several viral infections [8]. In particular, *in vitro* HSV-1 infection is found to induce LDs accumulation in astrocytes and to stimulate an antiviral response [9]. Anyhow, the literature on this topic is very limited and, as far as we know, no data is available regarding the relationship between HSV-1 and LDs in infected neurons.

The aim of this study is to evaluate whether neuronal LDs and ROS production (a proxy for evaluating neuronal degeneration) are affected by HSV-1 infection. A replication-defective mutant of the virus (HSV-MUT) has been used to verify whether the infection per se can lead to the above-mentioned effect. The adopted mutant additionally lacks a specific pattern of viral genes[1], allowing a protein-specific evaluation of the mechanism under study. However, this depth of analysis goes beyond the aim of this study.

II. *In vivo* Hypothesis Validation

A. Mouse Model System

In order to evaluate whether HSV-MUT infection has an impact on LDs in neurons, we decided to exploit a murine model already well characterized by several previous studies that focused on persistent HSV-1 infection in the enteric nervous system [10], [11] (**Fig.1**).



Fig. 1: Mouse model of HSV-MUT infection and subsequent analysis. LMMP: Longitudinal Muscle/Myenteric Plexus

Mice were firstly subjected to intranasal infection with HSV-MUT (1×10^2 PFU) and, 4 weeks later, inoculated via intragastric gavage (1×10^7 PFU). Viral infection obtained in two phases was previously determined to minimize mortality rate among mice [12], [13]. Mice were sacrificed after 4 weeks from intragastric inoculum, and the whole ileum was flushed with PBS and fixed in paraformaldehyde (Whole Mount [WM]

[1] The specific mutant genotype is not reported, due to an existing conflict of interest with another work of the authors that was under revision when this manuscript was submitted.

preparation). Using a stereomicroscope, the Longitudinal Muscle/Myenteric Plexus (LMMP) was separated from the remaining ileal tissue. The same procedure was performed on ileum obtained from control mice (sham infection). To identify enteric neurons, immunofluorescence was performed using a β-III-tubulin primary antibody conjugated with Cy3 fluorophore (diluted 1:400, Millipore). Instead, to detect LDs the LMMP was stained with a green-fluorescent probe recognizing neutral lipids (BODIPY 493/503, diluted 1:1000, ThermoFisher). At least 5 images per sample were captured using Nikon TE200-C1 confocal microscope.

B. Confocal Microscopy Results

In **Fig.2A** enteric neuronal ganglia are clearly identified by β-III-tubulin staining. Interestingly, we detected LDs both in sham uninfected LMMP and in HSV-MUT infected one, with a stronger signal in the latter.

To perform a quantitative evaluation of neuronal LDs, images were analyzed with ImageJ software (n=5 per sample). Only LDs detected in colocalization with neuronal staining were considered and two parameters were measured: the total number of neuronal LDs normalized on β-III-tubulin-defined area and the mean LDs area (**Fig.2B**). While the total number of LDs seem to be comparable between sham and HSV-MUT neurons, there is a clear increase in LDs mean size in presence of infection (p-value <0,05).

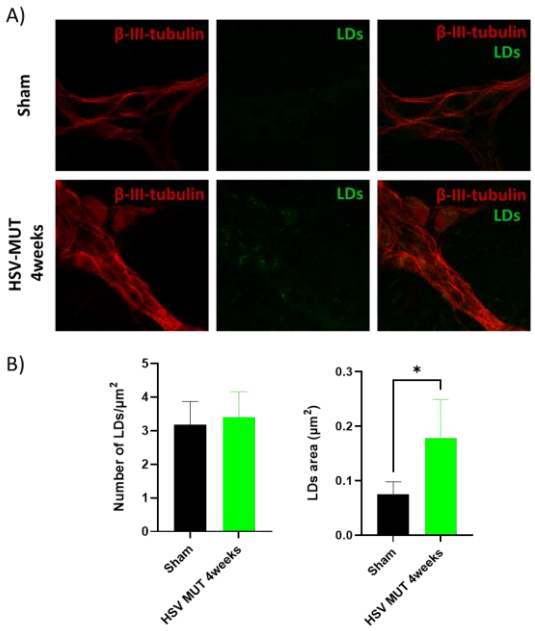


Fig. 2: A) Whole Mount of ileum LMMP from sham and 4-weeks HSV-MUT infected mice (in red: neuronal β-III-tubulin, in green: BODIPY 493/503 staining LDs). **B)** ImageJ quantification of LDs.

III. *IN VITRO* MODEL FOR NEURAL CELL ANALYSIS

A. Murine neuroblastoma cell line

To further explore the relationship between viral infection and LDs formation in the tissue of interest, we moved to an *in vitro* cellular model (**Fig.3**): murine neuroblastoma Neuro2A (N2A) cells are widely used to study neurodegenerative processes and they can be a suitable model to investigate HSV-MUT infection [14].

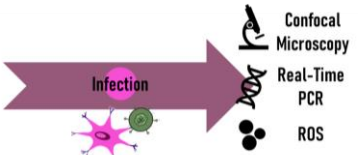


Fig. 3: Murine neuroblastoma model of HSV-MUT infection and subsequent analysis

Briefly, N2A cells were cultured following ATCC guidelines; 10^4 cells were seeded on sterile microscopy glass and cultured for 24 hours. HSV-MUT infection was performed at multiplicity of infection 1:1. Infected cells were maintained in complete culture medium for 48 hours and then processed for the following analysis: (i) confocal microscopy, (ii) gene expression analysis via real-time PCR and (iii) evaluation of oxidative stress with fluorescent probes.

B. Confocal Microscopy Results

For confocal microscopy analysis, cells were fixed with paraformaldehyde and subsequently stained in the same way as the Whole Mount preparations reported in the previous paragraph II-A. As negative control, the same procedure was performed on N2A cells not exposed to virus. At least five images per sample were captured using Nikon TE200-C1 confocal microscope (60X; 488nm and 561nm lasers).

Interestingly, the images obtained from confocal microscopy analysis (**Fig.4A**) show a very low signal for LDs in not infected N2A, while there is an evident increase in LDs after HSV-MUT infection. As previously shown in Whole Mount LMMP, LDs mainly colocalize with neuronal β-III-tubulin staining. ImageJ software was used to quantify the number of LDs per cell (normalized on β-III-tubulin-defined cell area) and the mean LDs area. As we can appreciate in **Fig.4B**, HSV-MUT infection induces an accumulation of LDs, both in terms of number and size. This *in vitro* data confirms the results obtained from the mouse model, in particular as regard the virus-induced increase in LDs dimension.

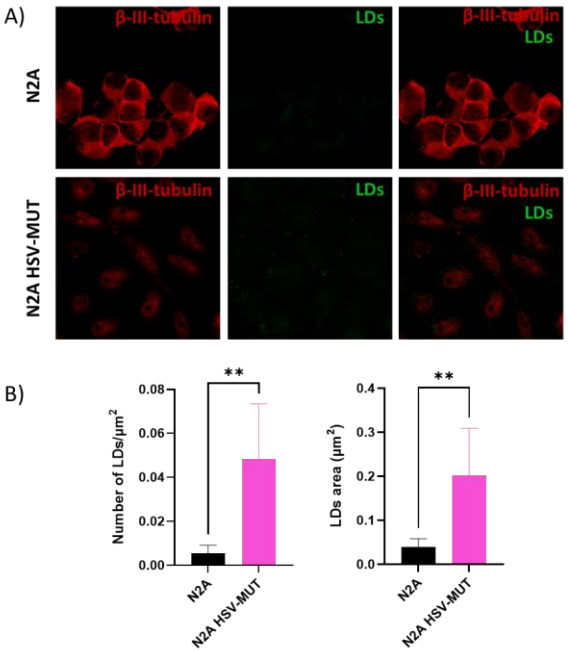


Fig. 4: A) Immunofluorescence analysis of control and HSV-MUT infected Neuro2A cells (in red: neuronal β-III-tubulin, in green: BODIPY 493/503 staining LDs). **B)** ImageJ quantification of LDs.

Nevertheless, LDs number *in vivo* seems to be unaffected during HSV-MUT infection, but this is not surprising, as this difference could be explained with the presence of other cellular types (e.g., glial cells) in LMMP, which could contribute in the response to viral infection.

Clearly, more data are needed to validate this hypothesis.

C. Real-Time PCR

Total RNA was extracted from both control and HSV-MUT infected cells. The expression of 12 genes, selected from literature as LDs-associated genes expressed in the nervous system [15]–[20], was analyzed via real-time PCR, using the iTaq Universal SYBR Green One-Step Kit (Bio-Rad). The expression of mRNA target was normalized to housekeeping GAPDH mRNA and plotted as mean fold expression (**Fig.5**).

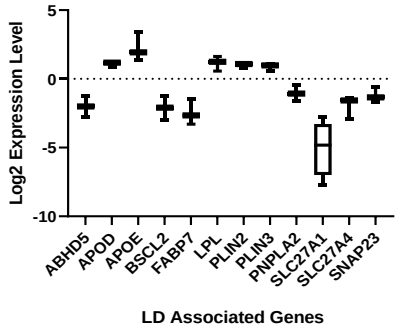


Fig. 5: Real-time PCR analysis of LD associated genes in HSV-MUT infected Neuro2A cells compared to non-infected control cells.

Interestingly, all the chosen genes resulted to be differentially expressed, with up to 5-fold change variation and always with a statistical significance with $p<0.05$ (computed via t-test using GraphPad Prism 8).

D. Oxidative stress and ROS production

To confirm the occurrence of neurodegeneration, an additional validation was performed by evaluating the oxidative stress and detect reactive oxygen species (ROS), as a proxy of neural degeneracy. N2A cells were incubate for 30 minutes with specific fluorescent probes: dichlorodihydrofluorescein diacetate H_2DCFDA, BODIPY 581/591 C11 and MitoSOX. Cells were subsequently analyzed via flow cytometry. This was performed by exploiting 3 different fluorescent probes, to gather information on different compartments, namely: (i) non-specifically localized intracellular free radicals were detected via H_2DCFDA, a compound converted into a fluorescent probe in presence of a broad spectrum of ROS [21]; (ii) lipid peroxidation, explicitly related to LDs, was evaluated through BODIPY 581/591 C11, a lipophilic probe binding cell membranes, which fluorescence emission is shifted from 520 nm to 595 nm in presence of oxidized lipids [22]; (iii) mitochondrial localization of superoxide was assessed with MitoSOX Red mitochondrial superoxide indicator [23]. The measurements were performed with a BD-FACSCalibur using CellQuest software.

Data presented in **Fig.6** clearly show that HSV-MUT infection induces an increase in general ROS production. This analysis highlights a strong raise in lipid peroxidation and the involvement of mitochondria in the establishment of an oxidative stress condition.

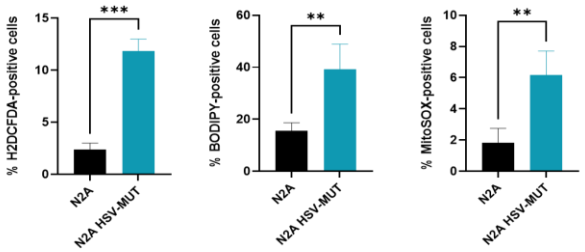


Fig. 6: Flow cytometry analysis of fluorescent probes detecting ROS in HSV-MUT infected Neuro2A cells compared to control cells.

E. Differential expression network analysis

To corroborate our hypotheses and identify further interesting putative proteins of interest, a network analysis was performed to highlight genes directly connected to the ones analyzed in the previous Section II-C.

BIOGRID-ORGANISM-Mus_musculus-4.4.217.psi25 protein, genetic and chemical interactions network (19k nodes, 97k edges) [24] was downloaded from the BioGRID website (https://thebiogrid.org/) and imported in Cystoscape [25] v.3.9.1. A first subnetwork (12.5k nodes, 69.5k edges) was obtained selecting nodes with "containing: Mus musculus" as "Species Full Name", to remove cross-species annotated interaction. Then, a second subnetwork (64 nodes, 142 edges) containing only the first neighborhood of the analyzed genes was generated; after the removal of multiple and looping edges, the latter was transformed into a STRINGfy network (62 nodes, 41 edges), via the Cytoscape-integrated STRING tool, integrating information on associated tissues and cellular compartments to each node. Lastly the nodes were filtered by "Tissue: nervous system" (24 nodes, 24 edges) with a threshold of 4.5 (**Fig.7A**) since a score of 5 (maximum level) resulted in an empty network.

The same pipeline was also performed on the BIOGRID-ORGANISM-Homo_sapiens-4.4.217.psi25 network (42.3k nodes, 1.1M edges), but in this case, the first subnetwork (34.7k nodes, 1M edges) was obtained by selecting nodes for "containing: Human" as "Species Short Label" to include possible Human Herpesvirus related nodes. However, the first neighborhood selection (956 nodes, 20k edges) removed all those nodes; on the other hand, the STRINGfy network (946 modes, 20k edges), obtained setting "Tissue: nervous system" filter at 4.99 resulted to have 35 relevant nodes (159 edges) (**Fig.7B**) and 5 nodes (4 edges) with threshold 5. (**Fig.7C**). Looking at STRINGfy Networks, both the mice and the 4.99-thresholded human ones highlight the APP and PRNP genes: the former is the Amyloid-beta Precursor Protein, the latter a

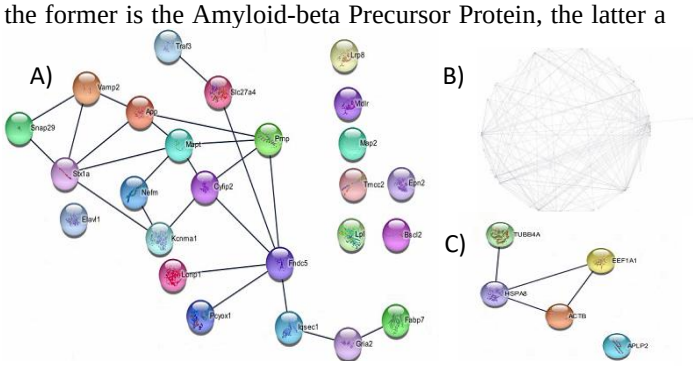


Fig. 7: STRINGfy networks. **A)** Mus musculus, threshold=4.5, **B)** Homo sapiens, threshold=4.99 **C)** Homo sapiens, threshold=5

prion protein involved in neuronal development and synaptic plasticity, required for neuronal myelin sheath maintenance. Additionally, it is worth to notice the presence of heat-shock proteins, associated to neurodegenerative diseases, that correct the folding of toxic misfolded protein under stress conditions.

Lastly, among the genes appearing in the 5-thresholded human network, APLP2 and TUBB4A are an Amyloid beta (A4) precursor-like protein and a Class IVa beta-tubulin, respectively, thus potentially involved in AD-like neurodegenerative processes.

IV. Conclusion and Future Perspectives

All the selected genes analyzed via RealTime PCR were differentially expressed up to a 5-fold in downregulation and 2-fold in upregulation. Of note, the gene APOE is involved in AD and indeed result upregulated. SLC27A1 gene and its homolog SLC27A4, coding for long-chain fatty acid transporter proteins, are both downregulated, thus indicating an impairment in lipid uptake and metabolism. Indeed, both *in vitro* and *in vivo* models highlight the increase of LDs following viral infection compared to the negative controls

Thanks to the network analysis, it was possible to confirm expected biological evidence, such as the APOE wide connection in all the observed networks; moreover, a panel of interesting additional genes that could be revealed as a causative link between LDs formation and AD-like neurodegenerative processes has been highlighted and will be further investigated in future analysis.

Additionally, we demonstrated that lipid peroxidation is linked with LDs accumulation, as the storage of peroxidated lipids can act as a mechanism to counteract lipotoxicity. In addition, oxidative stress and in particular mitochondrial ROS are considered a hallmark of neurodegeneration and AD [1], [26]. Extensive ROS production is well described in wild-type HSV-1 infection [27] and our data indicate that also HSV-MUT provokes a similar outcome. This could suggest that the only genes expressed in the mutant virus, play a fundamental role in oxidative stress.

Overall, these data seem to suggest an intriguing relationship between viral infection, LDs accumulation and oxidative stress in neurons. Being these processes reported in literature to be related to AD, the preliminary results of this work could pave the way to a new perspective aimed to investigate the role of HSV-1 in triggering neurodegeneration.

In this context, we will evaluate whether HSV-MUT infection determines an increase in further AD markers, exploiting both our mouse model and Neuro2A cells. Lastly, to characterize the outcomes' temporal evolution, different viral infection time points will be gathered and evaluated.

Acknowledgement

This study was partially funded by PRID2020 to I. Castagliuolo.

References

[1] Y. Zhao and B. Zhao, "Oxidative Stress and the Pathogenesis of Alzheimer's Disease," *Oxid. Med. Cell. Longev.*, 2013, 2013. Link

[2] P. G. Arduino and S. R. Porter, "Herpes Simplex Virus Type 1 infection: Overview on relevant clinico-pathological features," *J. Oral Pathol. Med.*, 37(2), pp. 107–121, 2008, Link

[3] M. A. Wozniak *et al*. "Herpes simplex virus infection causes cellular β-amyloid accumulation and secretase upregulation," *Neurosci. Lett.*, 429,(2–3), pp. 95–100, 2007, Link

[4] G. De Chiara *et al*., "Recurrent herpes simplex virus-1 infection induces hallmarks of neurodegeneration and cognitive deficits in mice," *PLoS Pathog.*, 15(3), pp. 1–30, 2019, Link

[5] M. A. Wozniak, A. L. Frost, and R. F. Itzhaki, "Alzheimer's disease-specific tau phosphorylation is induced by herpes simplex virus type 1," *J. Alzheimer's Dis.*, 16(2), pp. 341–350, 2009, Link.

[6] B. C. Farmer, A. E. Walsh, J. C. Kluemper, and L. A. Johnson, "Lipid Droplets in Neurodegenerative Disorders," *Front. Neurosci.*, 14(Jul), pp. 1–13, 2020, Link.

[7] E. Islimye, V. Girard, and A. P. Gould, "Functions of Stress-Induced Lipid Droplets in the Nervous System," *Front. Cell Dev. Biol.*, 10(Apr), pp. 1–12, 2022, Link.\

[8] E. A. Monson *et al*., "Lipid droplets and lipid mediators in viral infection and immunity," *FEMS Microbiol. Rev.*, 45(4), pp. 1–20, 2021, Link.

[9] E. A. Monson *et al*., "Intracellular lipid droplet accumulation occurs early following viral infection and is required for an efficient interferon response," *Nat. Commun.*, 12(1), pp. 1–17, 2021, Link.

[10] P. Brun *et al*., "Persistent Herpes Simplex Virus Type 1 Infection of Enteric Neurons Triggers CD8+ T Cell Response and Gastrointestinal Neuromuscular Dysfunction," *Front. Cell. Infect. Microbiol.*, 11(May), pp. 1–18, 2021, Link.

[11] P. Brun *et al*., "Herpes simplex virus type 1 infects enteric neurons and triggers gut dysfunction via macrophage recruitment," *Front. Cell. Infect. Microbiol.*, 8(Mar), pp. 1–18, 2018, Link.

[12] P. Brun *et al*., "Herpes Simplex Virus Type 1 Infection of the Rat Enteric Nervous System Evokes Small-Bowel Neuromuscular Abnormalities," *Gastroenterology*, 138(5), pp. 1790–1801, 2010, Link.

[13] P. Brun and H. I. Akbarali, "Culture of Neurons and Smooth Muscle Cells from the Myenteric Plexus of Adult Mice," *Methods Mol Biol.*, pp. 119–125, 2018, Link.

[14] K. T. LePage *et al.*, "On the Use of Neuro-2a Neuroblastoma Cells Versus Intact Neurons in Primary Culture for Neurotoxicity Studies," *Crit. rev. neurobiol*, 17(1), pp. 2–50, 2005, Link.

[15] L. Liu *et al.*, "The Glia-Neuron Lactate Shuttle and Elevated ROS Promote Lipid Synthesis in Neurons and Lipid Droplet Accumulation in Glia via APOE/D," *Cell Metab.*, 26(5), pp. 719-737.e6, 2017, Link.

[16] C. N. Barber and D. M. Raben, "Lipid metabolism crosstalk in the brain: Glia and neurons," *Front. Cell. Neurosci.*, 13, 2019, Link.

[17] W. Wang *et al.*, "Proteomics analysis of lipid droplets in mouse neuroblastoma cells," *Acta Biochim. Pol.*, 69(2), pp. 399–407, 2022, Link.

[18] K. M. Szymanski *et al*., "The lipodystrophy protein seipin is found at endoplasmic reticulum lipid droplet junctions and is important for droplet morphology," *Proc. Natl. Acad. Sci. U.S.A.*, 104(52), pp. 20890–20895, 2007, Link.

[19] B. A. Loving *et al*., "Lipoprotein lipase regulates microglial lipid droplet accumulation," *Cells*, 10(2), pp. 1–17, 2021, Link.

[20] A. Islam *et al*., "FABP7 Protects Astrocytes Against ROS Toxicity via Lipid Droplet Formation," *Mol. Neurobiol.*, 56(8), pp. 5763–5779, 2019, Link.

[21] M. Oparka *et al*., "Quantifying ROS levels using CM-H2DCFDA and HyPer," *Methods*, 109(2016), pp. 3–11, 2016, Link.

[22] G. P. C. Drummen, et al., "C11-BODIPY581/591, an oxidation-sensitive fluorescent lipid peroxidation probe: (Micro) spectroscopic characterization and validation of methodology," *Free Radic. Biol. Med.*, 33(4), pp. 473–490, 2002, Link.

[23] S. Deshwal *et al*., "Measurement of mitochondrial ROS formation," *Methods Mol. Biol.*, 1782, pp. 403–418, 2018, Link.

[24] C. Stark *et al*., "BioGRID: a general repository for interaction datasets.," *Nucleic Acids Res.*, 34, pp. 535–539, 2006, Link.

[25] P. Shannon *et al*., "Cytoscape: A Software Environment for Integrated Models," *Genome Res.*, 13, pp. 2498–2504, 2003, Link.

[26] S. Manoharan *et al*., "The Role of Reactive Oxygen Species in the Pathogenesis of Alzheimer's Disease, Parkinson's Disease, and Huntington's Disease: A Mini Review," *Oxid. Med. Cell. Longev.*, 2016, 2016, Link.

[27] J. Kavouras *et al*., "Herpes simplex virus type 1 infection induces oxidative stress and the release of bioactive lipid peroxidation by-products in mouse P19N neural cell cultures," *J. Neurovirol.*, vol. 13, no. 5, pp. 416–425, 2007, Link.

Simulating microbial communities' evolution via Agent base modelling: a Python tool

M. Bellato[1], M. Cappellato[1,2], A. Calzavara[1*], A. Lucchiari[1*], S. Rebecca[1*], and B. Di Camillo[1,2,3]
[1] *Department of Information Engineering, University of Padova, Padova - Italy*
[2] *Department of Comparative Biomedicine and Food Science, University of Padova, Padova, Italy.*

** These authors contributed equally to this work.*

***Abstract* — In this work, we blueprint a Dashboard that allows users to simulate the bacterial community's evolution through an intuitive GUI. The underlying Python-coded simulator implements an agent-based model of bacterial species, nutrients, and environment, allowing full customization and upgradability of the tool, due to its intrinsic modularity. Specifically, the model aims to represent discretized spaces, hosting a certain number of bacteria for each species and a defined amount of nutrients characterizing the surrounding environment. Bacteria can migrate from one spatial unit into another, looking for different nutrients (i.e., metabolites) across the whole space path. Growth and survival are governed by bacterial metabolisms, which are in turn functions of the metabolites present in each specific spatial unit at a certain time. Thus, our tool simulates how bacteria consume and produce metabolites, following species-specific metabolism rules, letting the system dynamically evolve through bacterial growth, death, spatial migration, and continuous updates of the available metabolite pool.**

***Keywords* — Microbiome, Agent-based modelling, Systems Biology, Python Dash.**

I. Introduction

HUMAN gut microbiota composition and behavior have been proven to be fundamental for our health; thus, proper modeling of microbial ecology is a hot topic in computational, systems and synthetic biology [1]-[2].

Classical ecological models, such as Generalized Lotka Volterra models (GLVm), describe the absolute abundance of each community mainly as a function of intrinsic growth rate and pairwise interactions with each community member; parameters need to be inferred by co-occurrence networks leveraging on bioinformatic approaches applied on metagenomic data and investigated via topological analysis [3]. The biases and variability in retrieved biological data to be used for training the models, arising from the adoption of different experimental setups and methods between different groups and studies, motivate the need for standardization in data production [4]-[5]. Additionally, these models usually rely on constant parameters to describe microbe-microbe interactions, which are instead determined, among others, by the time-varying biotic and abiotic environment. For this reason, they fail capturing community-level behaviors when the environment changes over time or in space [6]-[7].

Another promising approach relies on flux balance analysis (FBA) methods; in this case, information on bacteria metabolisms is included in the analysis through genome-scale models (i.e., structured information of possible reactions happening in a bacteria species based on annotated transcriptomes through metabolic networks), which are used to implement an optimization problem with biomass production as objective function [8]. While several groups are adopting FBA-derived to develop predictive tools, the lack of sufficiently annotated metabolic models is still a major issue; additionally, similarly to GLVm, this approach need nesting in more complex models to provide spatial information.

Microbe-effector models and, more specifically, agent-based modeling is an inspiring solution to implement efficient and robust methods to describe systems counting for billions of bacterial cells from hundreds of different species. This approach allows to develop mechanistic-level descriptions of simple agents, dynamically interacting with the surrounding environment that can be arbitrarily modeled; then, from agents decoupled behaviors, the complex microbial ecologies should emerge without the need of describing interaction network, which are hard to identify [9]-[10].

In this work we exploit the effectiveness of agent-based modelling to develop a Python-coded bacterial community simulator that is reliable, robust, efficient, reproducible, and scalable. Moreover, for the first time, great effort has been put into developing a functional and usable GUI that allows any user to exploit the full potential of the software setting the simulation parameters, such as bacterial metabolisms, and visualizing interactive summary results.

To date, the technology to characterize bacterial metabolisms in a cheap, reliable, and high-throughput fashion is still under development. However, we demonstrate that the intrinsically modular and incremental structure of our simulator is generalizable enough to be already used for roughly defined communities; indeed, despite the lack of complete information on bacterial metabolisms, it can resemble potentially realistic biological scenarios, potentially allowing computational simulations of mock communities (i.e., an in vitro defined mixture of microbial cells) involving functionally characterized species.

II. Methods

A. System abstraction and general workflow

The space is represented as a series of boxes called *cells*, each one containing a specific set of metabolites, connected with the closest neighborhood cells. This allows representing four different possible scenarios:

- Single cell: a well-mixed space with homogeneous bacteria and metabolites composition (e.g., a stirring bioreactor).
- 1D chain of cells: linear tract where metabolites and bacteria flow in 1 dimension (e.g., gut tract abstraction).
- 2D plane of cells: a surface where movements occur in 2 dimensions (e.g., a Petri dish, layered biofilms).
- 3D geometry of cells: a volume discretized in several cells (e.g., organoids, complex flake-like biofilms, organs).

The definition of neighborhood cells depends on the scenario and on the level of proximity we want to consider. Bacterial agents (i.e., bacteria of different species) can process

the metabolites in a *cell*, grow, die, and move into other neighborhood cells, if existent. In this work we considered a 1D linear tract representing an intestine tract and a neighbourhood proximity of 1 cell and mimic the bacterial evolution for a certain number of iterations, i.e., time points. At each iteration, bacteria can migrate from the i^{th} to the $(i+1)^{th}$ cell (to mimic the direction of chime), grow, die, metabolize the available metabolites, and produce a new set of metabolites for the next iteration (Figure 1).

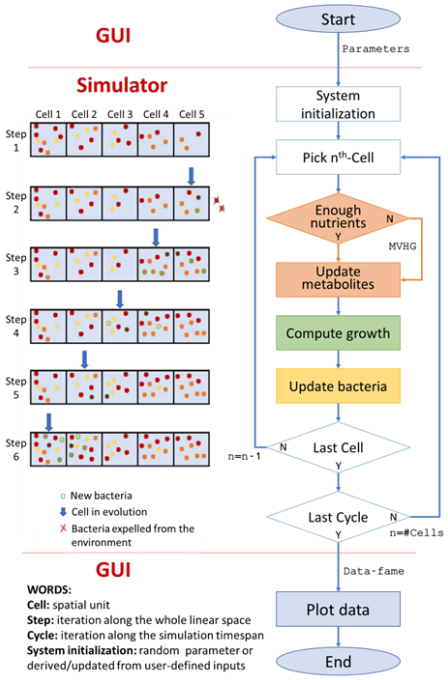


Fig. 1: Example of the simulation framework.

Lastly, after the pipeline has run over all the cells, for the number of iterations required to represent a certain required time window, the resulting data frames are passed to the GUI.

B. System implementation

Our simulator is implemented in Python through two classes: the class *Cell* and the class *Bact*. The class *Cell*, whose instances implement the spatial unity, is defined by:

- A vector $\boldsymbol{f}$ of metabolites available at the current iteration.
- A matrix of metabolites (rows) produced by the bacteria each iteration (columns).
- A dictionary of the bacteria in the cell, with the number of bacterial agents for each *Bact* instance.

The class *Bact*, whose instances implement bacteria species with specific metabolism, is defined by:

- A string with the species name.
- A vector $\boldsymbol{m}$ with the metabolisms, indicating for each metabolite if consumed (positive) or produced (negative).
- A vector $\boldsymbol{t}$ indicating which metabolites lead toxic effects.
- Two integers $\mu_{i,j}^{max}$ and $\mu_{i,j}^{t,max}$ describing the maximum growth rate and the toxicity level, to be adopted in the Hill equations for the population growth and death.

In addition to the accessor and set methods – which are fundamental for the interface between the simulator model and the GUI – the Cell class includes methods to update the concentration of metabolites and the number of bacteria in each cell at each iteration. Analogously, methods for the class *Bact* include methods to compute the variation in each species' abundance, depending on the nutrients available in a certain cell and the presence of toxic metabolites. The food update involves the sampling of the nutrients from a multivariate hypergeometric distribution so to model the propensity of remaining nutrients to be consumed by the most abundant and highly metabolizing species. As concerns the chain of cell implementation, a method describing the flux of microbes at each interaction from one cell to the next one is implemented by fixing the number of bacteria flowing as proportional to the species abundance and used to realize the system evolution.

C. Mathematical details

When computing the system evolution, for each j^{th} cell, the first evaluation considers whether the amount of nutrients $\boldsymbol{f_j}$ is enough to fulfil the whole metabolic request for all the bacteria $n_{i,j}^{bac}$ of all the i^{th} species in the space, as in Eq. (1). If the condition is true, each bacteria species access to all the requested nutrients and, in turn, produce a novel set or metabolites $\boldsymbol{p_{i,j}}$ through its species' metabolism $\boldsymbol{m_i}$, as in Eqs. (2-3). If the amount of nutrients is not overabundant, the metabolites are randomly distributed among the different species through a multivariate hypergeometric distribution (MVHG), as in Eq. (4); this is to prioritize the access to nutrients to the bacterial species that are more abundant and greedier for a specific resource. Then, the novel metabolic composition of the cell is computed as in Eq. (5).

$$IF \quad \boldsymbol{f_j} > \sum_i \left(n_{i,j}^{bac} \cdot \boldsymbol{m_i}|_{k>0}\right) \tag{1}$$

$$\boldsymbol{f_{i,j}} = n_{i,j}^{bac} \cdot \boldsymbol{m_i}|_{\boldsymbol{k>0}} \tag{2}$$

$$\boldsymbol{p_{i,j}} = n_{i,j}^{bac} \cdot |\boldsymbol{m_i}||_{\boldsymbol{k<0}} \tag{3}$$

$$ELSE \quad \{\mathbf{f_{i,j}}, \boldsymbol{p_{i,j}}\} \sim \mathbf{MVHG}(\boldsymbol{f_j}, \boldsymbol{m_i}, n_i^{bac}) \tag{4}$$

$$\boldsymbol{f_j} = \boldsymbol{f_j} - \sum_i (\boldsymbol{f_{i,j}}) + \sum_i (\boldsymbol{p_{i,j}}) \tag{5}$$

The second step involve the computation of the growth and death rates $\mu_{i,j}$ and $\mu_{i,j}^t$, respectively. These two values are computed as Hill's functions of the total amount of the processed nutrients $\boldsymbol{f_{i,j}^{tot}}$ and toxic metabolites $\boldsymbol{t_{i,j}^{tot}}$ in the cell, as in Eqs. (6-9).

$$\mu_{i,j} = \frac{\mu_i^{max}}{1+\left(\frac{k_i \cdot n_{i,j}^{bac}}{f_{i,j}^{tot}}\right)^{\eta_i}} \tag{6}$$

$$f_{i,j}^{tot} = \sum_k f_{i,j} \tag{7}$$

$$\mu_{i,j}^t = \frac{\mu_i^{t,max}}{1+\left(\frac{k_i^t \cdot n_{i,j}^{bac}}{t_{i,j}^{tot}}\right)^{\eta_i^t}} \tag{8}$$

$$t_{i,j}^{tot} = \boldsymbol{f_j} \cdot \boldsymbol{t_i} \tag{9}$$

The half saturation constant is multiplied by the number of bacteria $n_{i,j}^{bac}$ composing a population, so that the bigger is the population, the higher will be the required number of metabolites to expand or kill it. It is worth noting that, despite the definition of Hill's equation to model bacterial growth as a function of the processed metabolites is purely empirical (with only the maximum growth rates μ_i^{max} computed from doubling times randomly sampled from a log-normal distribution, with *E.coli* average doubling time as mean, while $k_i = 0{,}5$ and $\eta_i = 1$ where empirically chosen as default values) the modularity of the class allows to easily change this function into an alternative, more physiological, one.

The new bacterial composition $n_{i,j}^{new}$ is computed for each cell as in Eq. 10, proportional to the existent number of bacteria $n_{i,j}^{bac}$ and the related growth rate $\mu_{i,j}$. Analogously, the

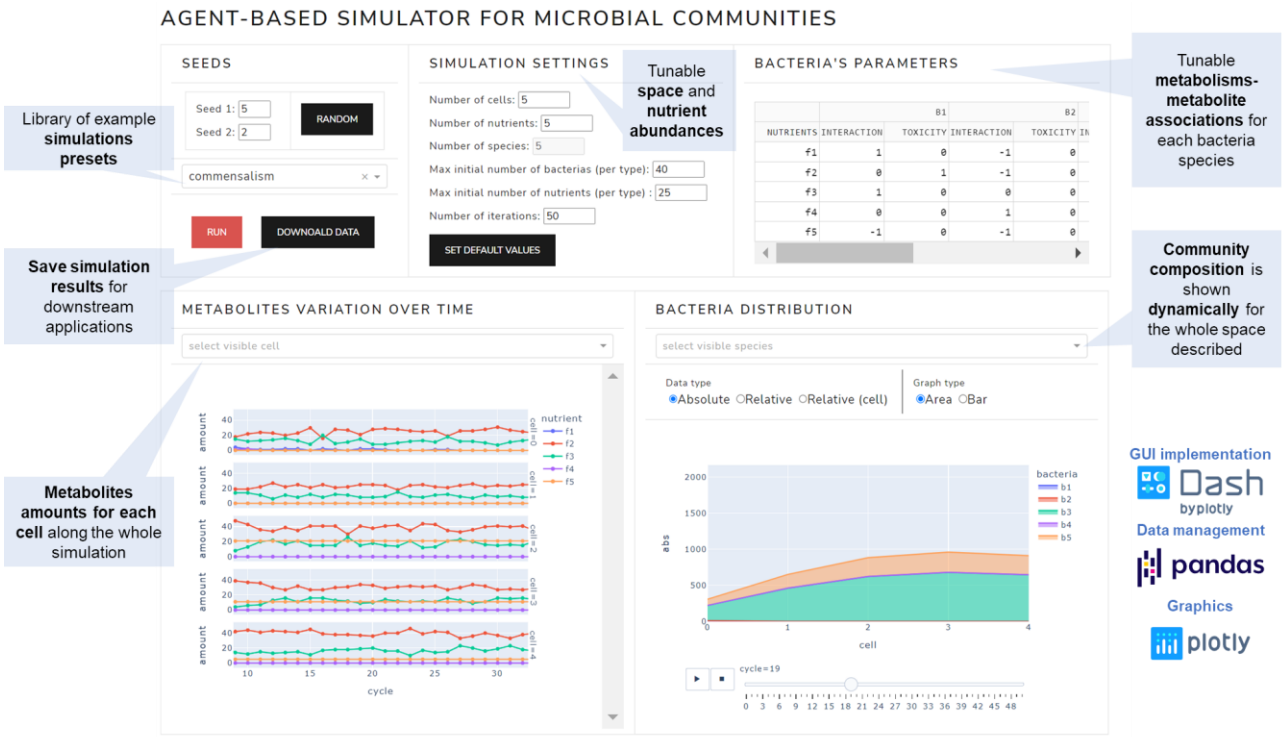


Fig. 2: Dashboard GUI schema.

number of dying bacteria is computed as in Eq. 11, including basal death and toxicity rates, while the bacteria migrating from the j^{th} cell to the $(j+1)^{th}$ are computed in in Eq. 12 as proportional to the migration rate ρ. Lasty, the new vector of bacteria is updated considering all the contributions, as reported in Eq. 13.

$$n_{i,j}^{new} = \lceil \mu_{i,j} \cdot n_{i,j}^{bac} \rceil \quad (10)$$

$$d_{i,j} = \lceil (\lambda + \mu_{i,j}^{t}) \cdot n_{i,j}^{bac} \rceil \quad (11)$$

$$n_{i,j}^{flow} = \lceil \rho \cdot n_{i,j}^{new} \rceil \quad (12)$$

$$n_{i,j}^{bac} = n_{i,j}^{bac} + (n_{i,j}^{new} - n_{i,j}^{flow}) - d_{i,j} + n_{i,j-1}^{flow} \quad (13)$$

Model parameters are summarized in Tab. I.

TABLE I: MODEL PARAMETERS

Symbol	*Meaning*	*Symbol*	*Meaning*
$\mathbf{f}_j$	Nutrients	μ_i^{max}, k_i, η_i	Hill parameters for growth rate
$\boldsymbol{m}_i$	Metabolism	$\mu_i^{t,max}, k_i^t, \eta_i^t$	Hill parameters for toxicity rate
$\boldsymbol{t}_i$	Toxicity	λ	Basal death rate
$\boldsymbol{f}_{ij}$	Nutrients consumed by the i^{th} bacteria	$\boldsymbol{p}_{ij}$	Metabolites produced by the i^{th} bacteria
$f_{i,j}^{tot}$	Consumed metabolites	ρ	Migration rate
$t_{i,j}^{tot}$	Toxic molecules	$MVHG(\boldsymbol{f}_j, \boldsymbol{m}_i, n_i^{bac})$	Nutrients multivariate hypergeometric distribution
$n_{i,j}^{bac}$	Number of bacteria		

D. Graphical User Interface

The GUI, implemented by adopting the Python Dash framework (in particular, Plotly and Pandas libraries for graphics and data frames management, respectively), allows simple setup and visualization of the simulation. Parameters defining the spatial structure and both initial nutrients and bacterial composition can be set on the Dashboard (Figure 2), also exploiting a table-like interface to modify the metabolisms for each bacterial species.

Additionally, the user can download simulation results as .xls tables and choose from a panel of preloaded parameter sets to start new simulations from relevant scenarios. Possible interesting random simulations, once obtained by casual selection of random seeds, can be re-called by selecting the previously adopted seed, automatically saved when downloading the data.

Metabolites and bacterial evolution over time can be observed in the bottom panels of the Dashboard, where the user can select the preferred visualization modality and graphical representation, by selecting the cell of interest for the metabolites and changing the view of the bacteria as absolute or relative, either as stack plot or histogram.

Moreover, the interactive graphs allow zooming, display information on mouseover and selection of the metabolites and species to be shown. All graphs can also be exported in a ready-to-publish format.

III. RESULTS

Starting from the same space definition (i.e., 5 bacterial species, able to interact with 5 different metabolites, migrating from left to right in a 5-unit linear space) but with differently distributed initial metabolites concentration and bacterial abundances along the whole space, the model is able to simulate different notable conditions and relevant scenarios, peculiar of natural bacterial communities (Figure 3) such as:

- Perfect fitness: most of the nutrients are highly metabolized by a single specific species (violet bacteria).
- Bad fitness: no nutrient in a cell is metabolized by any of the species causing a particularly hostile environment (only the nutrients in cell 0 allow a brief survival, consuming the present metabolites and producing the metabolite f1 as waste; migrating bacteria are not able to metabolize the

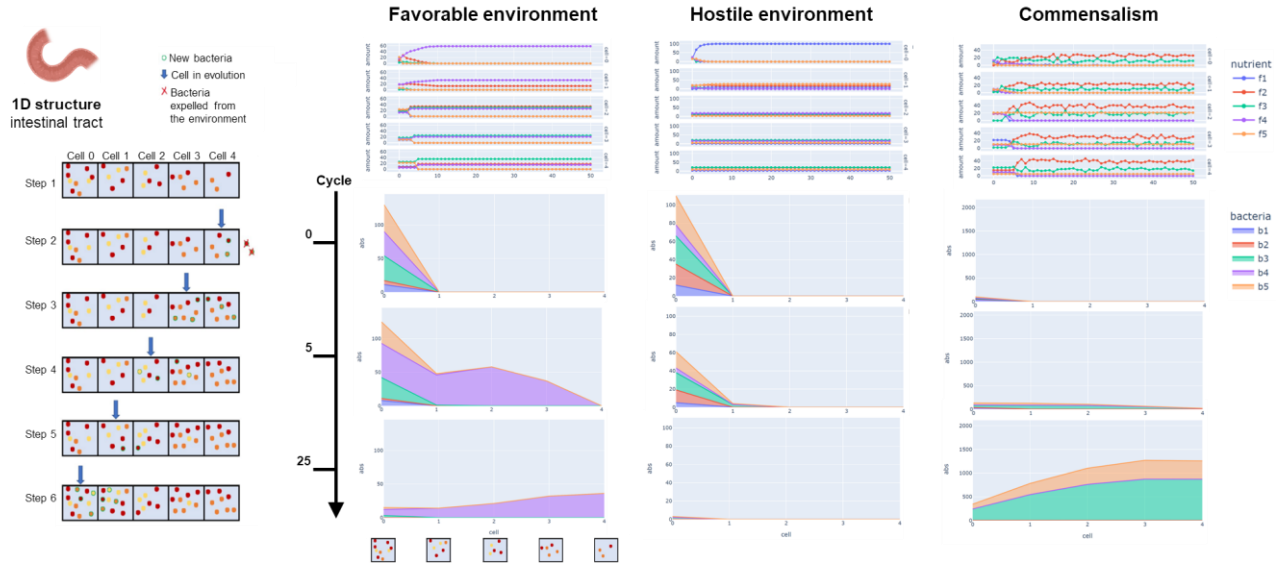


Fig. 3: Simulation of three significant scenarios in a gut-like environment.

nutrients in the following cells).

- Commensalism: most of the metabolites produced by a certain species are metabolized by another specific one and vice versa, i.e., bacteria b3 and b5 (green and orange) and metabolites f2 and f3 (red and green), creating a pseudo-periodic pattern in metabolite consumption and production.

IV. Conclusion

Despite the naive implementation of some features (e.g., migration, growth rate, etc.) of the current implementation, which is still undergoing significant enrichments and refinements, the simulator is already able to provide meaningful results; indeed, biologically sound characteristic and behaviors of the bacterial community emerge from random metabolic patterns and nutrient distribution, mimicking a natural evolution. The Python package implementing the model for a stand-alone use and the GUI will be available on our GitLab page (https://gitlab.com/sysbiobig).

So far, our model allows the description of bacterial communities growing on linear space (e.g., a gut tract), however, a 2D evolution framework is currently under development. In addition to spatial evolution refinements, ongoing activities are focused on the integration of specific nutrient lists and presets of known media composition from curated databases [11]-[12]. Moreover, information on actual bacterial species and related metabolisms are being added based on data contained in genome-scale metabolic models.

Lastly, a methodology to include and describe features related to bacterial communication (i.e., *quorum sensing*) is still under evaluation, to be exploited both in design and characterization in those studies where bacterial signaling significantly drives the overall community behavior [13]-[15].

Obviously, the GUI will also undergo changes in relation to the new features such as the possibility of selecting information from the database to automatically fill in the parameters which are now set by hand; or the possibility of visualizing space in 2D over time, always maintaining the interactivity characteristic. The ultimate goal will always be to maintain the characteristics of reliability, robustness, efficiency, reproducibility and scalability to allow a user to simulate, save and visualize the results in a single dashboard without necessarily writing code.

Acknowledgements

Funds: Fondazione Cariparo grant “Ricerca Scientifica di Eccellenza 2021 n59576”, University of Padova – Dept. of Information Engineering “type B Research Grant”. The authors want to thank G. Baruzzo, L. Schenato and S. Del Favero for the precious discussions, and N. Venturini Degli Esposti for his preliminary work on database integration.

References

[1] Davar D, et al. “Fecal microbiota transplant overcomes resistance to antiPd1 therapy in melanoma patients”. *Science,* 371(6529), 2021. Link
[2] Zheng P, et al. “Gut microbiome remodeling induces depressive-like behaviors through a pathway mediated by the host’s metabolism”. *Mol Psychiatry*, 21(6), 2016. Link
[3] Bucci V, et al. “MDSINE: Microbial Dynamical Systems INference Engine for microbiome timeseries analyses”. *Gene Biol*, 17, 2016. Link
[4] Barlow JT,et al. “A quantitative sequencing framework for absolute abundance measurements of mucosal and lumenal microbial communities”. *Nat Commun*, 11(2590), 2020. Link
[5] Tourlousse DM, et al. “Synthetic spike-in standards for high-throughput 16S rRNA gene amplicon sequencing”. *Nucleic Acids Res*, 45(e23), 2017. Link
[6] McGregor K, Labbe A and Greenwood CMT. “MDiNE: a model to estimate differential co-occurrence networks in microbiome studies”. *Bioinformatics*, 36(6), 2020. Link
[7] Ren Z, et al. “Bacterial Communities Present Distinct Co-occurrence Networks in Sediment and Water of the Thermokarst Lakes in the Yellow River Source Area”. *Front Microbiol*, 2021. Link
[8] Edwards J, Ibarra RU and Palsson BO. “In silico predictions of Escherichia coli metabolic capabilities are consistent with experimental data”. *Nat Biotech*, 19(2), 2001. Link
[9] Qian Y, Lan F and Venutrelli OS. “Towards a deeper understanding of microbial communities: integrating experimental data with dynamic models”. *Cur Op Microbiol*, 62, 2021. Link
[10] Bauer E, Zimmermann J, Baldini F, Thiele I and Kaleta C. “Bacarena: Individual-based metabolic modeling of heterogeneous microbes in complex communities”. *PLoS Comp Biol*, 13(5), 2017. Link
[11] Söhngen C, et al. “BacDive-the Bacterial Diversity Metadatabase”. *Nucleic Acids Res*, 42, 2014. Link
[12] Magnúsdóttir S, et al. “Generation of genome-scale metabolic reconstructions for 773 members of the human gut microbiota”. *Nat Biotechnol*, 2017. Link
[13] Pasotti L, et al. “A synthetic close-loop controller circuit for the regulation of an extracellular molecule by engineered bacteria”. *IEEE TBioCAS*, 13(1), 2018. Link
[14] Usai F. et al. “Design and biofabrication of bacterial living materials with robust and multiplexed biosensing capabilities”. *Mat Today Bio* 18, 2023. Link
[15] Bernabè G, et al. “A novel phenolic derivative inhibits AHL-dependent quorum sensing signaling in Pseudomonas aeruginosa” *Front Pharmacol*, 13, 2022. Link

Automated control of bioreactors: An hardware-in-the-loop proof of concept test towards an experimental facility

A. Bernardi[1], M. Bellato[1], R. Antonello[2], B. Di Camillo[1,3,4], L. Schenato[1], and S. Del Favero[1]
[1] *Department of Information Engineering, University of Padova, Padova - Italy*
[2] *Department of Management and Engineering, University of Padova, Padova - Italy*
[3] *Department of Comparative Biomedicine and Food Science, University of Padova, Padova - Italy*
[4] *CRIBI Innovative Biotechnology Centre, University of Padova, Padova - Italy.*

***Abstract*—Ensuring controlled environmental conditions during bacterial growth in a bioreactor is often crucial for the success of an experiment or to grant efficiency in an industrial procedure. For instance, in some experiments, temperature, oxygen and pH levels should be kept constant to achieve a good yield. Commercial bioreactors commonly provide proprietary automation systems for the regulation of some of the above mentioned variables, but the possibility to personalize the control algorithm, to jointly control multiple variables or to modify the control task, is usually rather limited. To surpass this limitation we aim to build an Arduino-based bioreactor, controlled by a PC and capable of running customized, possibly advanced, control algorithms. As a preliminary step toward this goal, in this contribution we present the design of a simple Arduino-based reactor for the control of the concentration of a substance (coffee) in a tank, by automatically pumping a concentrated solution of the same substance or pure water. The optimal command of the pumps is computed with a nonlinear model predictive control (MPC) by using a model of the mass balance occurring within the reactor. The controller is implemented in Simulink. The system is tested via hardware-in-the-loop (HIL) simulation. The controller proved to be able to drive the simulated concentration of caffeine to the desired value, and it was verified that the pumps were correctly commanded. Similarly, sensor readings were also successfully transferred to the Simulink scheme. Future experiments with the physical system will complete the validation and demonstrate the possibility of creating controller prototypes in Matlab for this toy problem.**

***Keywords*—Arduino-Based Bioreactor, Model Predictive Control, Simulink, Hardware-in-the-loop Simulation**

I. INTRODUCTION

In a bioreactor, automatic control systems are used to monitor and control various parameters, such as temperature, pH, dissolved oxygen, dissolved carbon dioxide and kinetic metabolic rates, in order to maintain optimal conditions for microorganisms growth and product production. Off-the-shelf equipment usually offers proprietary control systems to regulate these key parameters, for instance by using pumps to inject acids and bases to control pH, using heating jackets and coils to exchange heat and control temperature, blowing air or oxygen and managing stirring speed to control dissolved oxygen. Finally, by adjusting the amount of nutrients that are supplied in fed-batch and continuous bioreactors, one can affect the microorganisms metabolic activity and thus control their growth rate. Proprietary bioreactor systems do not always allow complete manipulation of the actuators and, in particular, of the peristaltic pumps adjusting the feed and uptake rates. Moreover, these setups are expensive and not easily affordable in low budget experiments or for teaching purposes.

On the contrary, do it yourself (DIY) projects are emerging as a low-cost alternative with the advantage of offering complete control of process variables through inexpensive components managed by microcontrollers such as Arduino boards [1], as well as allowing the manipulation of the feed rates with Arduino, via dedicated customized algorithms [2].

As a first step toward the construction of a fully customizable bioreactor, this paper will present a simple system for the automatic control of the concentration of a substance (coffee) by pumping either water, to dilute the solution, or a concentrated solution of the same substance. Specifically, the inflow rate of two peristaltic pumps is calculated in real-time with a nonlinear MPC on the basis of the concentration measured by an optical sensor. The non-linear control unit is implemented on a laptop computer and can interact with the peristatic pumps and the optical sensor thanks to an Arduino board that serves input-output interface. In this work, we present an hardware-in-the-loop (HIL) validation of the system, where the physical system is replaced by a model simulated in a different unit (another Arduino board). The controller and the simulation unit communicate via the input-output interfaces, so their functioning can also be verified.

Even if of limited practical impact by itself, this toy problem retains non-trivial control challenges, as it will be illustrated below. Furthermore, as a further step, one could use the same equipment to control bacterial growth in a bioreactor by controlling the concentration of a key nutrient (e.g. carbon sources or nitrogen sources). This second, more relevant problem, shares various analogies with the toy problem presented here, despite an higher complexity due to the dynamical interaction of biomass, substrates and products/by-products.

The advantages of using Arduino to build the above illustrated system lies in the fact that it offers a cheap and flexible platform to read data from the the sensor and to

control the peristaltic pumps. Moreover, there are affordable Arduino-compatible sensors (temperature, pH and dissolved gas concentration), as well as several Arduino-compatible actuators, that can be added in future stages of the project, to enable the control of additional process parameters. Moreover, Arduino allows an easy interaction with a PC via serial port and a library of Arduino real-time control algorithms and functions is available in Matlab Simulink, allowing rapid implementation of, arbitrarily advanced, control schemes.

As far as the control technique is concerned, MPC is an appealing strategy in the control of bioreactors requiring feed rate manipulation, since it can manage multi-input multi-output systems, account for the strong saturation of the actuators and permits custom cost function to be minimized, making the controller versatile for different strategies. Several examples in the literature show the use of MPC in different cultures with different organisms, ranging from bacteria, mammalian cells, and microalgae [3], with the aims that include maximizing product concentration [4], minimizing by-product formation [5], maximizing productivity and biomass concentration [6], tracking of biomass and substrate concentration [7], [8] or regulation of kinetic rates, i.e., uptake and growth [9].

II. System description

A. Problem formulation

As discussed above, in this paper we consider the toy problem of steering the concentration $C(t)$ in $[mg/mL]$ of a single substance (coffee) in a tank, following a piece-wise constant target profile $C_{\text{ref}}(t)$ from an arbitrary initial value.

The system architecture is depicted in Fig. 1. It consists of three containers, namely the reactor in which mass exchange takes place, and two feeding reservoirs. Two peristaltic pumps are used to feed the reactor with the liquids contained in the two reservoirs, i.e., the highly concentrated coffee solution with concentration $C_{in,1}$, and pure water with caffeine concentration $C_{in,2} = 0mg/mL$ (i.e., no caffeine dissolved).

The control of the coffee concentration in the reactor is performed by adjusting the inflow of the two pumps, denoted respectively with $F_{\text{in},1}$ and $F_{\text{in},2}$, both in $[mL/min]$. We consider a continuous reactor framework where the volume in the bioreactor is kept constant by applying an harvest outflow F_{out} such that $F_{\text{out}} = F_{\text{in},1} + F_{\text{in},2}$.

The outflow is obtained thanks to an harvest pump, connected to the main reactor. All the three pumps are wired to an Arduino board, to turn power on and off as required, to achieve the commanded average flows during one sample time ($\tau = 10s$).

B. System modeling

The mathematical model can be derived directly from the mass balance on the system. In fact, the amount of mass in the reactor can increase if liquids are introduced with feed rates and can decrease due to dilution effect of introduced liquids [10]. Under assumptions of homogeneity (well mixed system), the concentration of caffeine in the reactor is perturbed according to the net balance of mass:

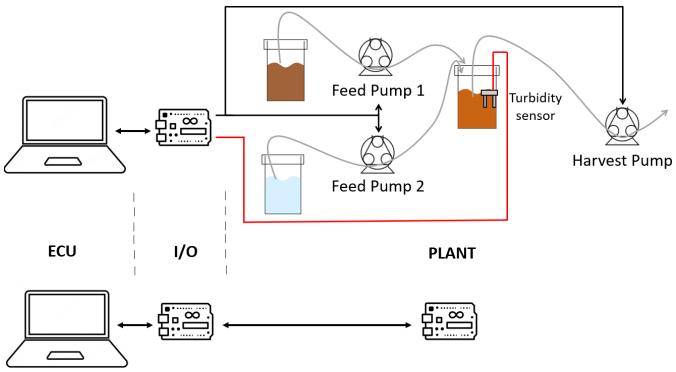


Fig. 1: Architecture of the system. Upper half: physical set-up, the control algorithm running on the PC interacts with pumps and sensor via the Arduino board. Bottom half: hardware in the loop simulation, the physical system is simulated on a second Arduino board.

$$\dot{C} = \frac{F_{in,1}(t)}{V} C_{in,1} - \frac{F_{in,1}(t)}{V} C(t) - \frac{F_{in,2}(t)}{V} C(t) \qquad (1)$$

where V $[mL]$ is the total volume of the reactor. Since the second feed bottle solution has no caffeine, there is no mass increase by pumping the solution but only mass decrease given by dilution effect. Since we set $F_{\text{out}} = F_{\text{in},1} + F_{\text{in},2}$ (continuous bioreactor), the volume does not change

$$\dot{V} = F_{in,1}(t) + F_{in,2}(t) - F_{out}(t) = 0 \qquad (2)$$

and thus can be treated as a parameter rather than as a state. The final model has a single state, two inputs and one output:

$$x = [C], \quad \bar{u} = \left[F_{in,1},\ F_{in,2}\right]^T, \quad y = x \qquad (3)$$

All the parameters, variables and constants involved in the model are reported in table I. The state is directly measured with a sensor based on optical absorbance and we will neglect the noise affecting the sensor. Therefore, the construction of an observer is superfluous.

As a final comment, it should be stressed that this simple dual-input-single-output system is strongly nonlinear, as the inputs are both multiplied by the state in Eq.(3). This makes this toy problem non trivial. For the physical implementation and software methodologies used, see Section II-D.

C. Control design

The nonlinear MPC was implemented in Matlab via *nlmpc* function and based on model described in the previous section. The differential Eq.(1) was solved numerically using the Matlab routine ODE45 (implementing a Runge-Kutta integration). The objective function J for the optimization include a penalty term based on the deviation between the target reference for coffee concentration and the model prediction. In addition, a nominal input value of zero was imposed to ensure that the pumps were turned-off once the set-point was reached.

$$J = \sum_{j=0}^{p} (q(\hat{C}((k+j+1)\tau) - C_{\text{ref}}((k+j+1)\tau))^2 + \bar{u}((k+j)\tau))^T \bar{u}((k+j)\tau))$$

where $C_{\text{ref}}(k\tau)$ is the reference value for caffeine concentration at time instant $k\tau$, p is the prediction horizon and q is the

weight on control aggressiveness. A suitable tuning for q was found trough trial and error in simulation and set to $q = 10$. Similarly, the prediction horizon was set to $p = 10$. The control horizon m was instead set to $m = 2$. The constraints are dictated by the physical flow rate limitations of the pumps. The maximum flow rate of each pump is $62\ mL/min$, so the maximum and minimum constraint value assigned for the input are:

$$0\frac{mL}{min} \leq F_{in,i}(k\tau) \leq 62\frac{mL}{min} \quad \text{with } i \in \{1,2\} \qquad (4)$$

TABLE I: SYSTEM PARAMETERS and THEIR VALUES

Symbol	*Description*	*Value*	*Unit*
τ	sampling time	10	s
C	caffeine concentration in the main reactor	*var*	mg/mL
$C_{in,1}$	caffeine concentration in first feed reservoir	2	mg/mL
V	volume of the reactor	35	mL
$F_{in,1}$	flow rate of coffee solution	*var*	mL/min
$F_{in,2}$	flow rate of water	*var*	mL/min
F_{out}	flow rate for the exhaust pump	*var*	mL/min
$\hat{C}$	model prediction	*var*	mg/mL
C_{ref}	reference for caffeine concentration	*var*	mg/mL
q	control aggressiveness weight	10	[-]
p	prediction horizon	10	[-]
m	control horizon	2	[-]

D. Control implementation

1) Hardware: Data storage and control algorithms were performed using a HP laptop running Windows 10, equipped with an Intel Core i3-8145U processor $2.1GHz$ frequency, $8GB$ of RAM and integrated graphics.

The computer was connected to an *Arduino Mega2560 board* via USB cable, to provide power supply and serial communication for data exchange. A second Arduino Mega2560 board, was used to simulate the system in the HIL scheme. The pumps used were the *12V peristaltic pump* (Adafruit ID:1150), powered by a $12V$ *Switching Power Supplies* (Delta Eletronics). Three digital output ports were used to command the pumps flow rates, using pulse width modulation (PWM) through three *Motor driver board* (Adafruit ID:3190), one for each pump. Lastly, an *Analog turbidity sensor* for Arduino (SKU:SEN0189 DFRobot) was also tested, to be used for future measures of turbidity, assumed proportional to the caffeine concentration.

The reading of the model output implemented by the Arduino board was accomplished by building a RC low pass filter circuit that extract the mean value of PWM digital output that could be read by the analog input pin of the I/O board. A $10k\Omega$ resistor and a $10\mu F$ capacitor were used for the circuit. The same type of circuit was used in the unit in charge of simulating the system to read the voltage commands sent to the pumps by the controller.

TABLE II: HARDWARE COMPONENTS USED (WITH LINK TO THE WEBSITE USED TO PURCHASE THEM)

Hardware	*Quantity*
Analog turbidity sensor	1
12V peristaltic pump	3
12V Switching Power Supplies	1
Arduino Mega2560 board	1
Motor driver board	3

2) Software: The controller was implemented using the MathWorks' Simulink programming environment, integrated in Matlab, see Fig.2. Specifically, the Simulink Desktop Real-Time and Arduino Support from Simulink packages were used for reading and writing of Arduino analog inputs and outputs, as well as for digital inputs and outputs in real time.

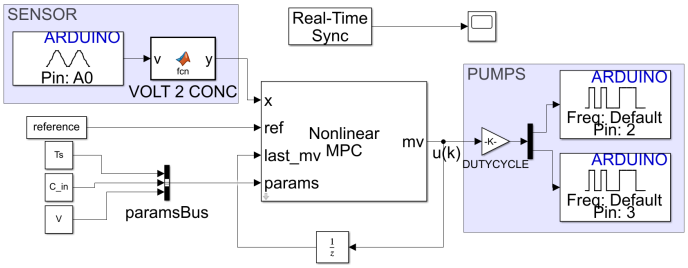


Fig. 2: Simulink control scheme for the HIL simulation.

The control scheme in Fig.2 is structured as follows:

- The area SENSOR reads the sensor data and converts the voltage value into the corresponding coffee concentration;
- The MPC block receive this value and computes the optimal flow rates value of the peristaltic pumps. For the creation of the MPC object and the MPC block, the Model Predictive Control Toolbox was used.
- In the PUMPS area, the value provided by the MPC is used to compute the dutycycle for the PWM blocks of digital output of Arduino.
- The real-time execution is ensured by the *real-time sync* block for which the sampling time must be provided.

Also the simulation unit was programmed using Simulink and porting the code on the Arduino Board. The plant simulated using *ode4* integration see Fig.3.

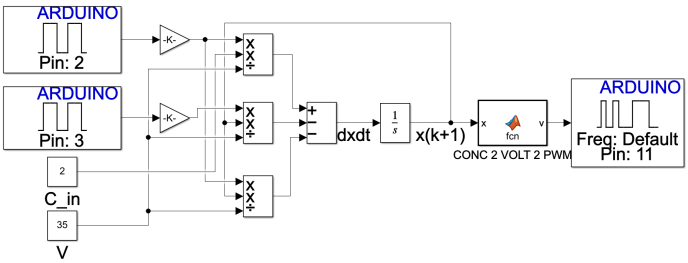


Fig. 3: Simulink model of the plant running on the Arduino board.

III. SIMULATION RESULTS

We show the results for a 3 minutes experiment in which the coffee concentration reference profile $C_{\text{ref}}(t)$ changes 3 times. It starts at $1.3mg/mL$, then drops to $0.7mg/mL$ after $30s$ and finally rises again to $1.7mg/mL$ at $90s$. The initial concentration is $C(0) = 1mg/mL$

Fig.4 shows that the control by nonlinear MPC is consistent with the physical understanding of the system: when the concentration in the bioreactor is higher than the reference value, the water is pumped to dilute the coffee concentration, while the pump connected to the solution with coffee is not

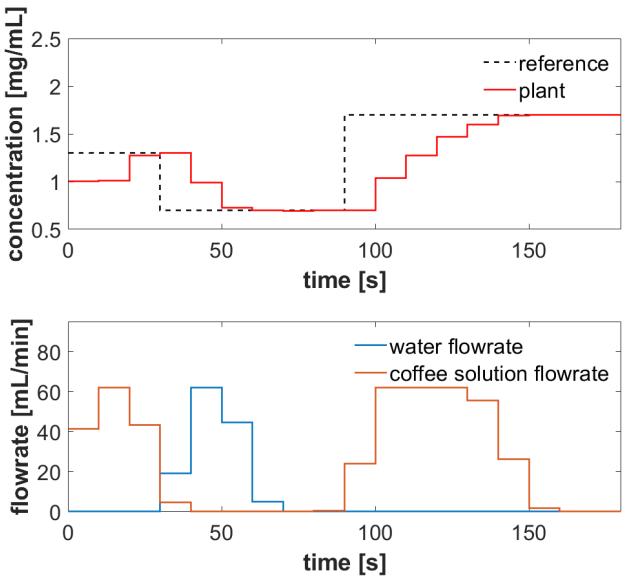


Fig. 4: Simulation results. Caffeine concentration tracking of the reference profile and pump commands computed by MPC.

activated. On the other hand, the opposite occurs when the state is below the reference value. Finally, it can be seen that when the concentration has reached the set-point, both pumps are switched off and the system dynamic becomes zero.

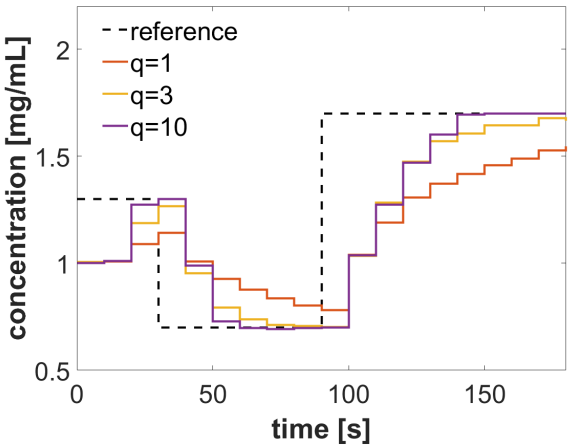


Fig. 5: Caffeine concentration tracking of the reference obtained for different values of the tuning parameter q in the cost function.

In Fig. 5 it is shown the output of the plant for different values of the weight $q \in \{1, 3, 10\}$. When the weight is small, the controller is less aggressive, causing the rise time to be slower. Increasing the weight, on the other hand, results in a faster response, as expected. Lastly, in these experiments, we verified that the activation time of the pump correctly satisfy the MPC requests.

IV. Conclusion and future perspectives

In this manuscript, we illustrated the design and testing of simple system for the automatic control of the concentration of a substance in a simple reactor, achieved by modulation of the inflow of two pumps. A non linear model predictive controller was developed in Matlab Simulink to track a reference trajectory for the concentration of a substance. The MPC leveraged a model built taking into account the mass balance in the reactor. Arduino support from Simulink package made it possible to use block diagrams to communicate with Arduino board and implement physical activation of input pumps for a HIL simulation. The MPC proved helpful in handling a single concentration and two manipulated variables.

Future works will include the physical realization of this simple system and its experimental validation.

Once the system will be validated on this toy problem, the same hardware will be used for a more practically relevant task: the control of the growth of a microorganism population by administration of a key nutrient. This objective will be pursued by equipping the MPC with a model capable to link the consumption of nutrients with bacterial growth.

We then envision, by leveraging the modularity offered by Arduino and the flexibility of the MPC framework, to build a customizable facility to control biomass concentrations and metabolic activity by exploiting different input substrates and input substances.

Acknowledgement

This work was funded by: Fondazione Cariparo grant “Bando Ricerca Scientifica di Eccellenza 2021 n 59576.

References

[1] P. R. Marinescu GC, “Open-source bioreactor controller for bacterial protein expression.,” *PeerJ Preprints*, 2018.

[2] A. Juneja and G. S. Murthy, “Model predictive control coupled with economic and environmental constraints for optimum algal production,” *Bioresource Technology*, vol. 250, pp. 556–563, 2018.

[3] L. Mears, S. M. Stocks, G. Sin, and K. V. Gernaey, “A review of control strategies for manipulating the feed rate in fed-batch fermentation processes,” *Journal of Biotechnology*, vol. 245, pp. 34–46, 2017.

[4] K. Kovárová-Kovar, S. Gehlen, A. Kunze, T. Keller, R. von Däniken, M. Kolb, and A. P. van Loon, “Application of model-predictive control based on artificial neural networks to optimize the fed-batch process for riboflavin production,” *Journal of Biotechnology*, vol. 79, no. 1, pp. 39–52, 2000.

[5] A. Merouane, L. Dewasme, S. Tebbani, D. Dumur, and A. Vande Wouwer, “Experimental validation of a nonlinear model predictive controller regulating the acetate concentration in fed-batch escherichia coli bl21 (de3) cultures,” *Advanced Control for Applications*, vol. 4, 2022.

[6] S. Yoo, D. Jeong, J. Kim, and J. Lee, “Optimization of microalgal photobioreactor system using model predictive control with experimental validation,” *Bioprocess and Biosystems Engineering*, vol. 39, 2016.

[7] A. Kuprijanov, S. Schaepe, R. Simutis, and A. Lübbert, “Model predictive control made accessible to professional automation systems in fermentation technology,” *Biosystems and Information technology*, vol. 2, pp. 26–31, 2013.

[8] S. Craven, J. Whelan, and B. Glennon, “Glucose concentration control of a fed-batch mammalian cell bioprocess using a nonlinear model predictive controller,” *Journal of Process Control*, vol. 24, no. 4, pp. 344–357, 2014.

[9] S. Ulonska, D. Waldschitz, J. Kager, and C. Herwig, “Model predictive control in comparison to elemental balance control in an e. coli fed-batch,” *Chemical Engineering Science*, vol. 191, pp. 459–467, 2018.

[10] G. Bastin and D. Dochain, *On-line Estimation and Adaptive Control of Bioreactors*. Contributions to Economic Analysis, Elsevier, 1990.

The long story of SWIM methodology: from grapevine to personalised medicine

Paola Paci[1,2]
[1] *Department of Computer, Control and Management Engineering, Sapienza University of Rome, Rome, Italy*
[2] *Karolinska Institutet, 17177 Stockholm, Sweden*

***Abstract*—SWIM is a recently developed network-based tool that fulfils the criteria of the new quickly emerging field of Network Medicine in finding disease-associated genes, called switch genes. The phenotype-specific applications of SWIM are broad and include the identification of switch genes in grapevine berry maturation as well as in complex diseases, including but not limited to human cancers.**
Here, a brief summary of the promising results obtained by applying SWIM in different biological contexts is presented.

***Keywords*—Network Medicine, Network Theory, Disease genes.**

I. INTRODUCTION

Recently, I developed a new promising methodology, called SWIM (SWItch Miner), which integrates different network-based methods to analyse the correlation network arising from large-scale gene expression data [1]. Considering the topological properties of the nodes and assessing their functional roles according to their ability to convey information within and between modules in the network, SWIM identifies a small pool of genes (called switch genes) that are associated with intriguing patterns of molecular co-abundance and play a crucial role in the observed phenotype.

The phenotype-specific applications of SWIM are broad and include the identification of switch genes in grapevine berry maturation (*Vitis vinifera*) as well as in human cancers, including Glioblastoma (Fig. 1).

In viticulture, SWIM has been gainfully applied to the global gene expression atlas of grapevine in order to identify switch genes between immature and mature phase of the developmental program of grapevine [2]. In cancer research, SWIM network analysis has been gainfully applied to a large panel of TCGA (The Cancer Genome Atlas) cancer datasets in order to characterise disease etiologies and identify potential therapeutic targets [1]. SWIM has also been used to investigate glioblastoma multiforme (GBM) and to uncover new insights into the molecular mechanism determining the stem-like phenotype of glioblastoma cells [3], [4].

Recently, SWIM methodology has been successfully applied to the chronic obstructive pulmonary disease (COPD), a severe lung disease characterized by progressive and incompletely reversible airflow obstruction [5]. The results of this study would both support known pathways and provide evidence for novel pathways in COPD pathogenesis. In the last two years, SWIM has been applied within the framework of Network Medicine to study the interplay between switch genes and human diseases in the human interactome (i.e., the cellular network of all physical molecular interactions) [6].

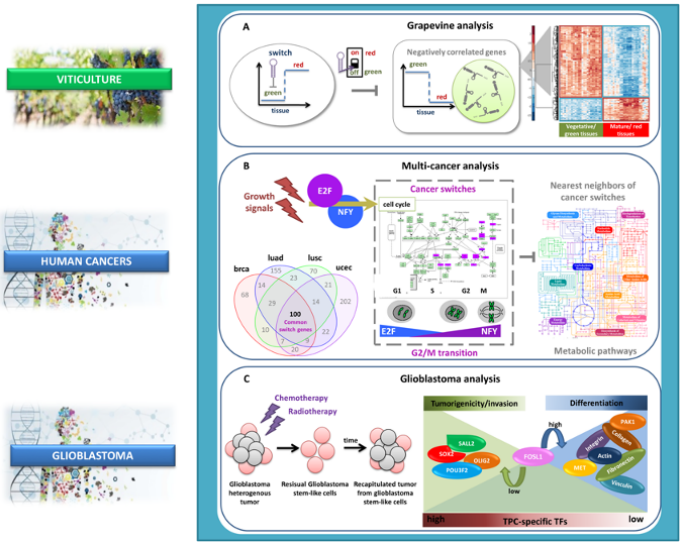


Fig. 1: Phenotype-specific applications of SWIM methodology.

In the following, a detailed description of the more recent applications of SWIM to complex diseases is provided.

II. METHODS

SWIM is a freely downloadable network-based tool, developed both in MATLAB [1] and in R language [7], which predicts important (switch) genes that are strongly associated with drastic changes in cell phenotype. SWIM first computes the differentially expressed genes (DEGs) between two conditions of interest (e.g., normal state versus tumor state) and then builds a gene correlation network (GCN) by calculating correlations (positive and negative) between the expression profiles of each gene pair. Specifically, SWIM implements a hard thresholding approach to build a GCN where nodes are DEGs, and a link occurs if their expression profiles are highly correlated or anti-correlated (according to a defined threshold). Then, SWIM classifies each network hub (i.e., nodes with degree at least equal to 5 according to [8]) as date, party, or fight-club on the basis of the Average Pearson Correlation Coefficient (APCC) between its expression profile and that of its first nearest neighbours. Date hubs show a positive and mild APCC value; party hubs show a positive and high APCC value; fight-clubs hubs show a negative APCC

value. To assign a role to each node in the GCN, SWIM firstly searches for clusters (or modules) using the k-means algorithm and evaluates the quality of clusters by minimising the Sum of the Squared Error (SSE), depending on the distance of each object to its closest centroid. The position of an elbow (i.e., change of the slope) in the behaviour of the SSE as function of the number of clusters (scree plot) indicates the number of clusters to use. Then, SWIM draws the heat cartography map by evaluating two coordinates related to their intra- and inter-modular connections: the clusterphobic coefficient, which is a measure the fear of each node to be confined in its own cluster and measures the links of each node to nodes outside its own cluster; the within-module degree, which measures how "well-connected" each node is within its own cluster. In the heat cartography map, dots (i.e., nodes of the correlation network) are distributed across seven regions (R1 to R7) according to their clusterphobic coefficient (x-axis), and to their within-module degree (y-axis). Each node is coloured according to its APCC value. Nodes having much more external than internal links present high values of the clusterphobic coefficient and are called connectors, whereas high values of the within-module degree denote nodes that are hubs within their community and are called local hubs. Switch genes are defined as a subset of fight-club nodes with the following features: i) they are network connectors that mainly interact outside their own cluster (very high value of the clusterphobic coefficient); ii) they are not local hubs (very low value of the within-module degree); iii) they are mainly anti-correlated with their interaction partners (negative value of the APCC).

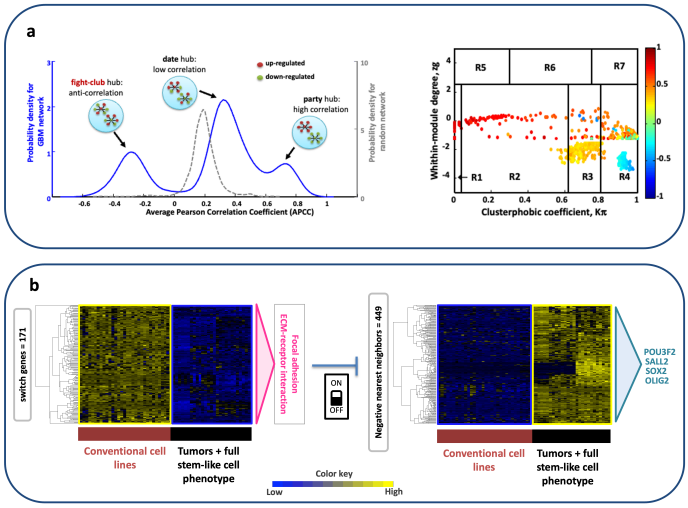


Fig. 2: SWIM application to the GBM dataset of [13]. (a) Left: probability distribution of APCC for hubs identified in the GBM correlation network (blue solid line) and in its randomized counterpart obtained by shuffling the edges but preserving the degree of each node (grey dashed line). Differently from the randomized case, the true APCC distribution shows a clear trimodal pattern where peaks correspond to previously reported hub categories (such as party and date hubs) but also to the new category of hubs, the fight-club hubs. Right: heat cartography maps where dots correspond to network nodes colored according of APCC. (b) Dendrogram and heat map of switch genes (left) and of their negative nearest neighbors (right) with their corresponding enriched pathways The expression profiles of the switch genes and their negative nearest neighbors are clustered according to genes (rows) and GBM cell lines (columns), using Pearson correlation distance as metrics. Heat map colors represent different expression levels increasing from blue to yellow.

III. Results and Discussions

A. Glioblastoma

Glioblastoma is the most aggressive and frequent brain tumour, with a median survival time of 12–15 months from diagnosis [9], [10], [11]. The mortality rate is extremely high with the 5-years survival rate achieved for only 5% of patients. This tumour is resistant to the standard therapies like radio and chemotherapy. Its aggressiveness is due to the presence of cancer stem-like cells that sustain tumour growth and are hence named "tumour fuel". Cancer stem-like cells are cancer cells that have characteristics typical of normal stem cells: i) self-renewal that is the ability to maintain their undifferentiated state; ii) potency that is the ability to differentiate into specialised cell types. Cancer stem-like cells are resistant to many conventional cancer therapies and cause relapse and metastasis by giving rise to new tumours [12]. Thus, targeting cancer stem-like cells could pave the way for new therapeutic strategies.

A recent study identified 19 neurodevelopmental transcription factors (TFs) that are selectively expressed in glioblastoma stem-like cells to maintain their stem-like phenotype and prevent differentiation [14]. A subset of only four of them (named 4-core TFs), SOX2, OLIG2, POU3F2, and SALL2, has been shown to be sufficient to fully reprogram differentiated cells into glioblastoma stem-like cells [14].

In order to identify switch genes related to the stem-like phenotype, SWIM was applied to glioblastoma dataset of [14] and then the further dataset of [13] was used to validate the results [3], [4]. In Fig. 2 the results obtained by applying SWIM to the GBM dataset obtained in [13] are shown. The APCC behaviour (blue solid line) shows a clear peak for negative values indicating the fight-club hubs (Fig. 2a left). The APCC randomised counterpart (grey dashed line), obtained by shuffling the edges but preserving the degree of each node, indicates that fight-club hubs are not a random event. A subset of the fight-club hubs falling in the region of connectors (R4) of the heat cartography map corresponds to switch genes (Fig. 2a right, blue dots). The expression profiles (z-score normalised) of the switch genes (Fig. 2b left) and their negative nearest neighbours (Fig. 2b right) indicates that switch genes are all up-regulated in differentiated cells, and their activation strongly correlates with the inhibition of their first network interactors, including the 4-core TFs. By performing a functional enrichment analysis, switch genes were found to be involved in cell-cell communication pathway. Thus, while their activation could promote differentiation and restrain tumour growth, their repression could promote tumour invasiveness due to the loss of cell-cell adhesion.

Among the common switch genes obtained by running

SWIM on the two GBM datasets of [13] and [14], there is FOSL1. It is up-regulated in differentiated glioblastoma cells and this up-regulation highly correlates with the over-expression of genes involved in cell-cell communications (Fig. 3 top left/middle). It is down-regulated in stem-like cells and this down-regulation highly correlates with the up-regulation of the 4-core of TFs (Fig. 3 top right). In order to investigate possible co-regulation of the 4-core of TFs, their promoter regions were inspected to search for enriched motifs and they were found to harbour a consensus binding site for FOSL1 (Fig. 3 bottom right).

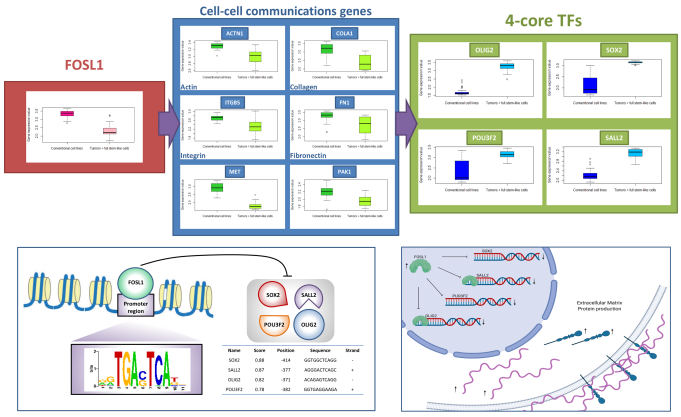


Fig. 3: FOSL1 mode of action. Upper panel: from left to right, boxplot of the expression of FOSL1, its positive and negative nearest neighbours in the GBM correlation network, in conventional GBM cell lines with respect to cancer stem-like cells in GBM dataset of [13]. Lower panel: logo plot for the statistically significant enriched motif found by using JASPAR to analyse the promotore regions of the 4-core of TFs (left). This motif corresponds to a consensus binding site for FOSL1. A schematic representation of the FOSL1 mode of actions: it acts as putative repressor of the 4-core of TFs and its activation reduces the cells' ability to generate aggregates increasing the extracellular matrix component.

Altogether these findings suggest FOSL1 as possible therapeutic biomarker of glioblastoma, which could promote the differentiation of cancer stem-like cells by repressing the 4-core TFs. This hypothesis has been partially experimentally validated in [15], where the NTERA-2 and HEK293T cells where selected for an in-vitro study to investigate the role of FOSL1 in the reprogramming mechanisms (Fig. 3 bottom right). The two cell lines where transfected with a constitutive FOSL1 cDNA plasmid. This study showed that FOSL1 i) directly regulates the 4-core of TFs binding their promoter regions and reducing their expression; ii) is involved in the deregulation of several stemness markers; iii) reduces the cells' ability to generate aggregates increasing the extracellular matrix component FN1. Although further experiments are necessary, these findings support the hypothesis that FOSL1 may reprograms the stemness by regulating the 4-core TFs.

This result could have a significant impact on personalized healthcare, since promoting differentiation and thus restraining tumor growth may support rational, personalized planning of disease prevention or treatment.

B. COPD

COPD is a heterogeneous and complex syndrome influenced by both genetic and environmental determinants, and is one of the main causes of morbidity and mortality worldwide.

By applying SWIM on COPD [5], the correlation network turned out to be formed by three well-characterised modules (data not shown, see [5]): i) one (module 3) populated by switch genes, all up-regulated in COPD cases and involved in COPD-related pathways, like B cell receptor signalling pathway; ii) one (module 1) populated by negative interactors of switch genes, down-regulated in COPD cases, including well-known GWAS genes like AGER and CAVIN1; iii) one (module 2) populated by well-recognised immune signature genes, all up-regulated in COPD cases. Switch genes appear to form localised connected subnetworks displaying an intriguingly common pattern of up-regulation in COPD cases compared with controls. A more sophisticated analysis revealed that they were not only topologically related, but also functionally relevant to the observed phenotype as witnessed by their enrichment in the regulation of inflammatory and immune responses.

In order to demonstrate the disease specificity of switch genes, SWIM was applied on another COPD dataset and on the acute respiratory distress syndrome (ARDS), another severe lung disease with an inflammatory component. The two lists of COPD switch genes were found to form overlapping modules in the human interactome that are topologically separated with the ARDS switch genes (data not shown, see [5]). This observation demonstrates that even though different diseases can share similar endophenotypes, the molecular network determinants responsible for them are disease-specific.

Interestingly, ARDS switch genes were different from COPD switch genes, but the major pathways affected in the two diseases were similar, emphasising that different diseases often have common underlying mechanisms and share intermediate endophenotypes (convergent phenotypes) [16].

C. Network Medicine

Network Medicine is a new emerging paradigm in medicine, where disease proteins are assumed not to be randomly scattered, but agglomerate in specific regions of the molecular interactome, suggesting the existence of specific disease network modules for each disease [17], [18], [19].

To quantify the interplay between switch genes and human diseases in the human interactome, the results obtained by the pan-cancer [1] and COPD [5] SWIM-based analysis were complemented with the application of SWIM tool on two cardiac disorders (i.e., ischemic and non-ischemic cardiomyopathy) and on Alzheimer's disease (AD) [6]. Switch genes associated with specific disorders were found to be not randomly scattered but they form localised connected subnetworks (Fig. 4a). These subnetworks overlap between similar diseases (like cancers or cardiac disorders) and are situated in different neighbourhoods for pathologically distinct phenotypes (like AD and COPD), showing a direct relation between the pathobiological similarity of diseases and their

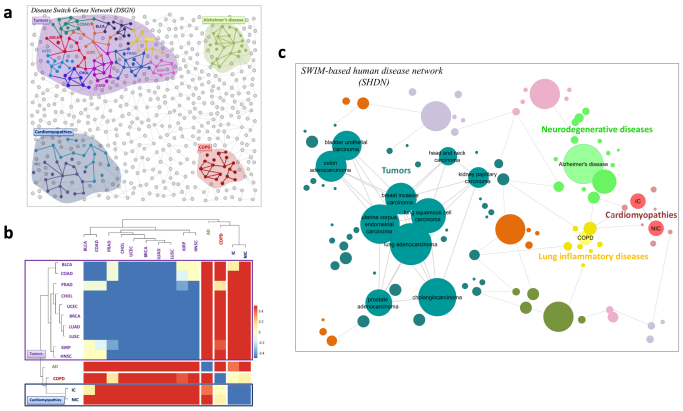


Fig. 4: SWIM and Network Medicine. (a) Switch genes mapping on the human interactome. (b) Hierarchical clustering where the network-based separation measure was used as a distance metric: blue color corresponds to overlapping modules, red color corresponds to non-overlapping modules. (c) SHDN where nodes are the disorders and the size of each node is proportional to the number of switch genes involved in the corresponding disorder. Nodes are coloured based on the disorder class to which they belong. Labeled nodes correspond to the diseases analysed, while unlabelled nodes are artificial.

relative distance in the human interactome (Fig. 4a). These results were confirmed by the hierarchical clustering where two main clusters were found: one including all tumour datasets and one including the two cardiomyopathies along with AD and COPD datasets as isolated branches (Fig. 4b). Finally, the first SWIM-informed Human Disease Network (SHDN) was built (Fig. 4c), where nodes correspond to distinct disorders and a link occurs between two diseases if they share a substantial number of switch genes. Clustering of nodes of similar color (denoting the same disease class) means that similar pathophenotypes have a higher probability of sharing switch genes than do pathophenotypes that belong to different disease classes.

These findings support the hypothesis that SWIM-based correlation network analysis can serve as a useful tool for efficient screening of potentially new disease gene associations. When integrated with an interactome-based network analysis, it not only identifies novel candidate disease genes, but also may offer testable hypotheses by which to elucidate the molecular underpinnings of human disease and reveal commonalities between seemingly unrelated diseases.

Acknowledgement

This work was partially funded by BiBiNet project (grant n: H35F21000430002) within the POR-Lazio FESR 2014-2020, by PRIN 2017 (grant n: 20178L3P38), and by Progetto di Ricerca di Ateneo 2021 of Sapienza University of Rome (grant n: RM12117A34663A2C).

References

[1] P. Paci, T. Colombo, G. Fiscon, A. Gurtner, G. Pavesi, and L. Farina, "SWIM: a computational tool to unveiling crucial nodes in complex biological networks," *Scientific Reports*, vol. 7, p. srep44797, Mar. 2017.

[2] M. C. Palumbo, S. Zenoni, M. Fasoli, M. Massonnet, L. Farina, F. Castiglione, M. Pezzotti, and P. Paci, "Integrated Network Analysis Identifies Fight-Club Nodes as a Class of Hubs Encompassing Key Putative Switch Genes That Induce Major Transcriptome Reprogramming during Grapevine Development," *The Plant Cell Online*, p. tpc.114.133710, Dec. 2014.

[3] G. Fiscon, F. Conte, and P. Paci, "SWIM tool application to expression data of glioblastoma stem-like cell lines, corresponding primary tumors and conventional glioma cell lines," *BMC bioinformatics*, vol. 19, p. 436, Nov. 2018.

[4] G. Fiscon, F. Conte, V. Licursi, S. Nasi, and P. Paci, "Computational identification of specific genes for glioblastoma stem-like cells identity," *Scientific Reports*, vol. 8, p. 7769, May 2018.

[5] P. Paci, G. Fiscon, F. Conte, V. Licursi, J. Morrow, C. Hersh, M. Cho, P. Castaldi, K. Glass, E. K. Silverman, and L. Farina, "Integrated transcriptomic correlation network analysis identifies COPD molecular determinants," *Scientific Reports*, vol. 10, pp. 1–18, Feb. 2020. Number: 1 Publisher: Nature Publishing Group.

[6] P. Paci, G. Fiscon, F. Conte, R.-S. Wang, L. Farina, and J. Loscalzo, "Gene co-expression in the interactome: moving from correlation toward causation via an integrated approach to disease module discovery," *npj Systems Biology and Applications*, vol. 7, pp. 1–11, Jan. 2021. Number: 1 Publisher: Nature Publishing Group.

[7] P. Paci and G. Fiscon, "SWIMmeR: an R-based software to unveiling crucial nodes in complex biological networks," *Bioinformatics*, vol. 38, pp. 586–588, Jan. 2022.

[8] J.-D. J. Han, N. Bertin, T. Hao, D. S. Goldberg, G. F. Berriz, L. V. Zhang, D. Dupuy, A. J. Walhout, M. E. Cusick, F. P. Roth, and others, "Evidence for dynamically organized modularity in the yeast protein–protein interaction network," *Nature*, vol. 430, no. 6995, pp. 88–93, 2004.

[9] M. Jansen, S. Yip, and D. N. Louis, "Molecular pathology in adult gliomas: diagnostic, prognostic, and predictive markers," *The Lancet Neurology*, vol. 9, no. 7, pp. 717–726, 2010.

[10] R. M. Young, A. Jamshidi, G. Davis, and J. H. Sherman, "Current trends in the surgical management and treatment of adult glioblastoma," *Annals of translational medicine*, vol. 3, no. 9, 2015.

[11] K. Anjum, B. I. Shagufta, S. Q. Abbas, S. Patel, I. Khan, S. A. A. Shah, N. Akhter, and S. S. U. Hassan, "Current status and future therapeutic perspectives of glioblastoma multiforme (GBM) therapy: A review," *Biomed Pharmacother*, vol. 92, pp. 681–689, Aug. 2017.

[12] R. C. Gimple, S. Bhargava, D. Dixit, and J. N. Rich, "Glioblastoma stem cells: lessons from the tumor hierarchy in a lethal cancer," *Genes & Development*, vol. 33, no. 11-12, pp. 591–609, 2019.

[13] A. Schulte, H. S. Günther, H. S. Phillips, D. Kemming, T. Martens, S. Kharbanda, R. H. Soriano, Z. Modrusan, S. Zapf, M. Westphal, and K. Lamszus, "A distinct subset of glioma cell lines with stem cell-like properties reflects the transcriptional phenotype of glioblastomas and overexpresses CXCR4 as therapeutic target," *Glia*, vol. 59, pp. 590–602, Apr. 2011.

[14] M. L. Suva, E. Rheinbay, S. M. Gillespie, A. P. Patel, H. Wakimoto, S. D. Rabkin, N. Riggi, A. S. Chi, D. P. Cahill, B. V. Nahed, and others, "Reconstructing and reprogramming the tumor-propagating potential of glioblastoma stem-like cells," *Cell*, vol. 157, no. 3, pp. 580–594, 2014.

[15] V. Pecce, A. Verrienti, G. Fiscon, M. Sponziello, F. Conte, C. Durante, L. Farina, S. Filetti, and P. Paci, "FOSL1 in the stemness mechanism: An in vitro study," *Scientific Reports*, 2021.

[16] S. D. Ghiassian, J. Menche, D. I. Chasman, F. Giulianini, R. Wang, P. Ricchiuto, M. Aikawa, H. Iwata, C. Müller, T. Zeller, A. Sharma, P. Wild, K. Lackner, S. Singh, P. M. Ridker, S. Blankenberg, A.-L. Barabási, and J. Loscalzo, "Endophenotype Network Models: Common Core of Complex Diseases," *Scientific Reports*, vol. 6, pp. 1–13, June 2016.

[17] A.-L. Barabási, N. Gulbahce, and J. Loscalzo, "Network medicine: a network-based approach to human disease," *Nature Reviews. Genetics*, vol. 12, pp. 56–68, Jan. 2011.

[18] M. Caldera, P. Buphamalai, F. Müller, and J. Menche, "Interactome-based approaches to human disease," *Current Opinion in Systems Biology*, vol. 3, pp. 88–94, June 2017.

[19] A. R. Sonawane, S. T. Weiss, K. Glass, and A. Sharma, "Network Medicine in the Age of Biomedical Big Data," *Frontiers in Genetics*, vol. 10, Apr. 2019.

A workflow for the construction of reproducible living biosensors built by printing bacterial materials

F. Usai[1], G. Loi[2], F. Scocozza[2], M. Bellato[3], P. Magni[1], M. Conti[2] and L. Pasotti[1]
[1] *Department of Electrical, Computer and Biomedical Engineering, University of Pavia, I-27100 Pavia, Italy*
[2] *Department of Civil Engineering and Architecture, University of Pavia, I-27100 Pavia, Italy*
[3] *Department of Information Engineering, University of Padua, I-35131 Padua, Italy*

The dissemination of synthetic biology into materials science allows to realize engineered living materials (ELMs). By being alive, ELMs represent a radically different paradigm compared to traditional materials, enabling new functionalities, with decreased costs and environmental impact. This work aims to set up a bioprinting workflow to reproducibly fabricate bacteria-laden materials with biosensing capabilities, to address field-relevant applications.

***Keywords*— Bioprinting, synthetic biology, engineered living materials, biosensors.**

I. Introduction

ELMs are rapidly emerging as an innovative class of materials with tailored morphologies and functions. Born at the intersection of synthetic biology and materials science, the field of ELMs allows to realize 3D structures composed by living and non-living components [1]. These systems can take advantage of the broad range of modalities now readily achievable with modern genetic engineering, including sensing and responding functions, molecule production, and self-assembly.

Whole-cell biosensors are generally confined in vials into which the sample to be tested is added manually. In contrast to the liquid culture, there has been an increasing interest in trying to trap cells into abiotic materials. This advanced system allows to exploit biological properties to perform a specific functionality, leveraging non-living matter for structural mechanical characteristics and enabling portability of sensing devices. Bioprinting brings advantages of reproducibility, spatial control, customization of the product in terms of shape, and automation. Functional bacteria-laden structures in the form of ELMs are considered as a transformative technology as they can address real life challenges, e.g., in therapeutics [2], [3], diagnosis, pollutant detection [4], [5], and industrial manufacturing [6], [7]. The genetic circuits of this type of devices are designed to emit fluorescence, luminescence or pigmentation upon detection of the specific contaminant, creating low cost biological sensors compatible with remote detection [8]. In contrast to systems with additional substrates for activation, the ease of use and visualization may allow ELMs biosensors to be employed for rapid, on-site use. Furthermore, some examples of multi-strain materials are reported in the literature [1], [9], [10], [11], which can contribute to increase the complexity of the device functionality and to multiplexed sensing. Finally, these materials with the addition of appropriate biocontainment strategies avoid ethical, safety, and acceptance issues of using living biosensors in the field.

Here, the idea is to establish a workflow to create bacteria-laden biosensor materials. To realize and validate this platform, bioprinting and synthetic biology techniques were used and the reproducibility of fabricated structures as well as their functions were addressed. We anticipate that ELMs can be used for prototyping and automation of a new generation of smart materials, relevant for real-world biosensing purposes.

II. Materials and Methods

Non-pathogenic *Escherichia coli* strains were engineered to carry out biosensing functions via synthetic circuits including a signaling molecule (*Vibrio fischerii* autoinducer, VAI) inducible promoter and a reporter gene providing visible pigmentation as readout.

Engineered bacteria suspended in 2-fold concentrated LB media were mixed with a sodium alginate (SA)- and gelatin-(GEL) based hydrogel (1:10 ratio) to obtain the bioink. The living materials were printed using the INKREDIBLE+ bioprinter (Cellink AB, Sweden) and crosslinked with $CaCl_2$. The structures can be used immediately and incubated the overnight at 37 °C on LB agar plate with or without inducers, or stored in the refrigerator for future use. Variations of hydrogel composition (e.g., concentration of SA, removal of GEL, concentration of LB), incubation protocol (e.g., LB media, no media), crosslinking procedure (e.g., supplementation of $CaCl_2$ in LB medium) were also tested to screen for the optimal bioprinting workflow.

Viability tests of bacteria within the material, using the colony forming units method (CFUs), were performed for two weeks by dissolving the ELM with sodium citrate.

In this work, we used engineered bacteria that express the red fluorescent protein (RFP), also allowing observation of red color development at naked eye. Protein expression was verified by fluorescence microscopy (Eclipse 80i microscope, Nikon), and image analysis of ELMs, taking the only red component through the CIELAB space. Color data derived from pictures were confirmed by fluorescence measurements in the microplate reader (Infinite F200Pro, Tecan), by transferring cut pieces of ELMs into 96-well plates and measuring red fluorescence in 3-by-3 square-filled acquisitions per well (RFP gain = 30) and averaging the obtained values.

For biosensing experiments, after the construction of the libraries of interest, we first characterized the biosensors with liquid assays in the microplate reader, then we studied printed ELMs incubated under optimal laboratory conditions (LB agar plates containing chemical inducers).

Finally, experiments in more realistic environments under non-optimal incubation conditions (e.g., soil and clinical samples as matrices), were carried out. Non-optimal incubation conditions refer to incubation of the structures on plastic or cut LB agar, both by inducing with a 200 µl drop of inducer pipetted on the ELMs. For sensing tests in environmentally relevant samples, VAI was added to the soil by adding about 10% (w/w) water containing the autoinducer at a 400 nM concentration, and structures were placed in the induced soil (incubation at RT). For experiments with clinical samples the structures were tested by pipetting 200 µl the sample on the ELMs, incubating the structures overnight at 37 °C on a cut LB agar.

III. Results and Discussion

A. *ELM bioprinting*

A workflow for printing living bacterial materials was established and optimized to create tailored shapes and single/multi-strain structures. In order to obtain the optimal workflow for bacterial printing, we first investigated the bioink composition in terms of hydrogels and nutrients, growth conditions, printing support, and crosslinking procedure (Fig. 1).

For the composition of the hydrogels we tested 6% SA, 8% SA, 10% SA, and 8% SA + 4% GEL (w/v). The first confirmed to give the weakest structure, while among the last two, the one with the addition of gelatin was chosen due to reliable handling and to avoid any breakage of the structures over time.

We also investigated how incubate the ELMs, testing solid LB, liquid LB medium, plastic, or PBS. The conditions with LB proved to be the best, allow a naked eye color development (using a constitutive bacterial strain of RFP, named MCred), suggesting that these external nutrients provide the necessary support for growth and gene expression. Furthermore, solid LB led to better results in terms of viability than the liquid condition, avoiding also situations as the collapse of the constructs.

In addition, incubation in liquid media caused a rapid contamination of the liquid by planktonic growth, probably depleting some nutrients.

The addition of nutrients directly into the bioink was also studied, comparing the viability of the bacteria inside the structures with LB, 2-fold and 4-fold concentrated LB. Since there were only differences with the first option, between 2-fold and 4-fold the former was selected as there were no significant improvements with 4-fold concentrated nutrients.

For the crosslinking procedure, we tested the traditional one, i.e., the addition of $CaCl_2$ to the structure after printing in a plastic support, and the alternative with the crosslinking agent in the culture medium by printing directly over the LB agar. The latter showed problems such as clogging of the nozzle with agar, due to non-perfectly flat media surfaces, so we chose the traditional method.

Bioprinting reproducibility was demonstrated analyzing print fidelity parameters in terms of coefficient of variation, both for filament size and filament distance in at least 30 values measured from grid-like structures (Fig. 2A). In addition, reproducibility was also proven in terms of weight of the printed structures, both for 20x20x2.5 mm grids (CV = 18%) and 10x10x0.7 mm (CV = 1%).

B. *ELM functionality*

The first step to validate the platform from a biological point of view was to study cell viability of bacteria within the material. The results demonstrated that, without changing culture media, after two days there is a decrease in viability probably due to nutrient deficiency and accumulation of waste products. Cell viability of ELMs is reported after being printed and after one day of overnight incubation at 37 °C (Fig. 2B), demonstrating the bacterial growth in the bioink.

Gene expression investigation, by analyzing sections of printed structures with fluorescence microscopy, confirmed what emerged in the literature. In fact the fluorescence resulted greater in the surface rather than the core, probably related to the different oxygenation and therefore a different viability of the bacteria between the outside and inside, and a different

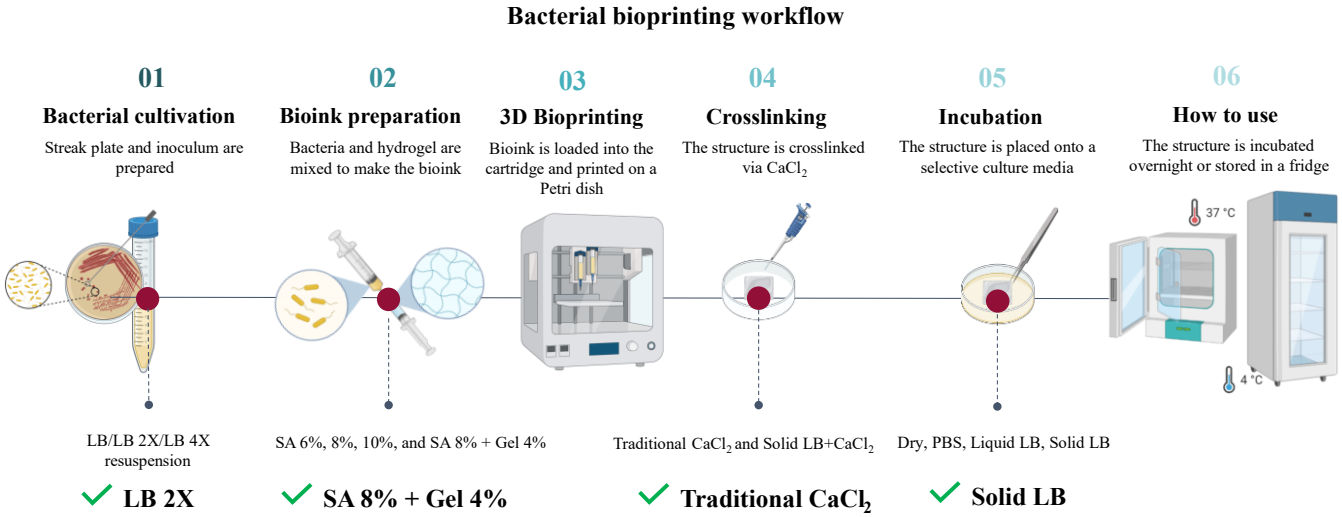


Fig. 1: Optimized bacterial bioprinting workflow. An INKREDIBLE+ bioprinting platform (Cellink AB, Sweden) was used to fabricate the bacteria-laden materials. Starting from a saturated culture, the biosensing strain was mixed (1:10 ratio) with an alginate- and gelatin-based hydrogel with LB nutrients, obtaining a bioink that was extruded on a Petri dish. The structure was crosslinked via $CaCl_2$ and moved to selective agar plates. The printed structure can be incubated overnight at 37 °C or stored in a regular fridge for future use. Red circles refer to the main variables screened during the development of the protocol: nutrients concentration included in the bioink, composition of hydrogel, crosslinking method, and type of incubation. Green single ticks refer to the screening outcomes.

O_2-dependent maturation of the RFP protein (Fig. 2C).

To further explore the capabilities of our bacterial bioprinting workflow, we used bacterial biosensors of signal molecules (e.g., bacterial hormone), first analyzing their dose-response profiles in liquid assays, and then printing them to evaluate the performance and the reproducibility of the output.

Functionality of biosensing ELMs was successful in optimal lab conditions exploiting a VAI biosensor (named LUX_{lac}-MCred), characterized in previous works [12], [13], [14], [15], and it exhibited promising stability up to 1 month of refrigerated storage conditions.

C. *ELM robustness*

In addition, we extended the characterization of ELMs in optimal and non-optimal incubation, starting from batches of different materials by printing 8 biological replicates in three different days.

A first experiment was carried out in optimal lab conditions evaluating the a* values of the images, confirmed by the reading on the microplate reader (Fig. 2D). These results demonstrated not only the correlation between the two measures adopted (r = 0.97), but also a good reproducibility of the output among different bacterial culture batches (average CV = 26% among replicates in the same day), and among different days (average CV = 27% among the mean outputs obtained in different days). A second experiment was designed to study the VAI-sensing response under non optimal conditions. From these data it emerged that a variation of the experimental condition corresponds to a variation of the output of the device (Fig. 2E). The biosensor readout can be deeply influenced by factors such as temperature (RT or 37 °C) or nutrient deficiency.

D. *ELM application*

Finally, to demonstrate that our ELMs biosensors can function in a real-world setting, we used the LUX_{lac}-MCred-based ELMs in soil containing VAI, either by covering them completely or by placing them on top. The induced materials reported a distinguishable color compared to the negative controls without VAI, but the color was less intense than that under optimal conditions, probably due to the lower amount of nutrients in the soil compared to LB and the lower concentration of VAI.

By exploiting the non-specific activation of the lux-based machinery, we were able to use the same biosensor also to detect PAI (*Pseudomonas aeruginosa* autoinducer) and not just as a laboratory molecule, but in clinical-derived complex matrices. The sterile-filtered supernatants of 4 clinical isolates of *P. aeruginosa* grown to saturation were collected and applied to biosensing patches. The a∗ values were examined to quantify the red pigmentation, reporting a successful result for two samples (Fig. 2F), confirming the capability of such ELM to detect molecules directly produced by pathogenic

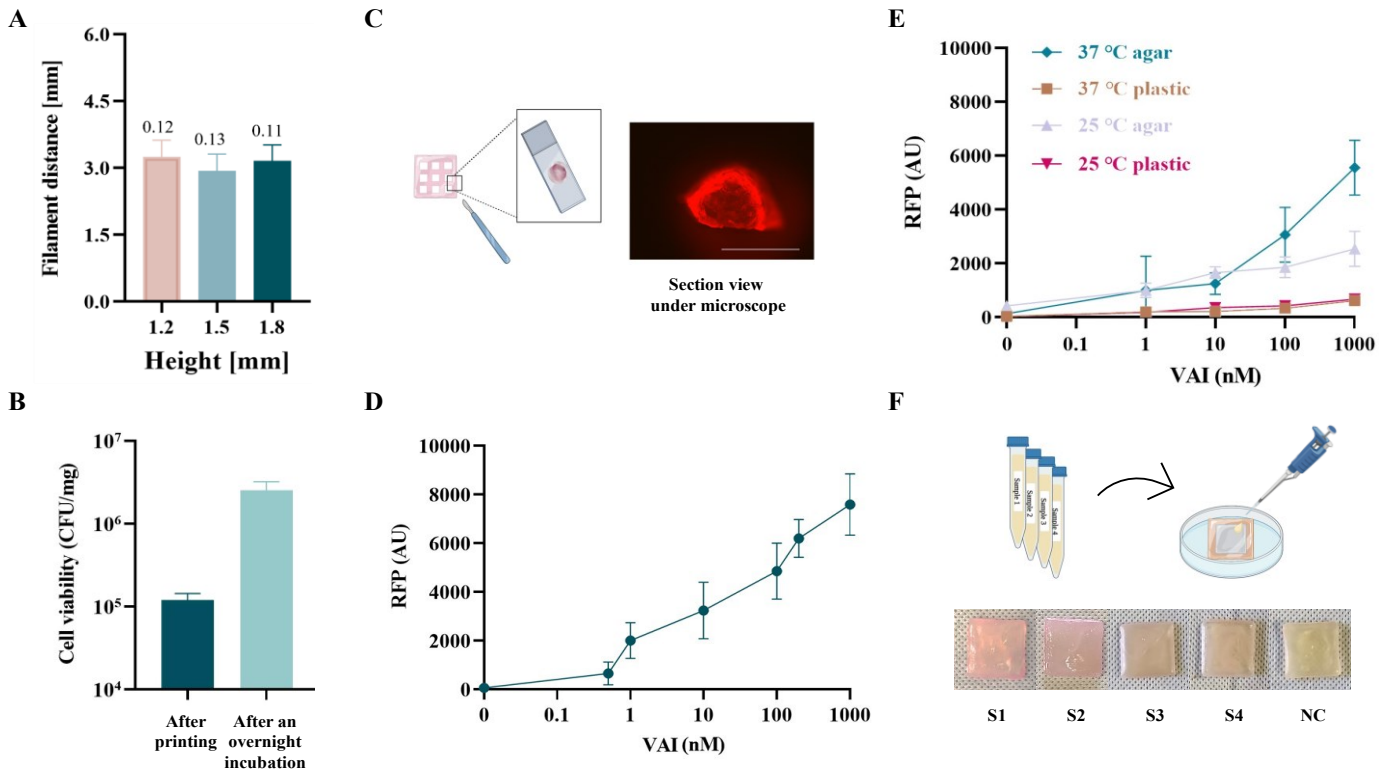


Fig. 2: A) Bar showing filament distance for grid structures printed at different heights (1.2, 1.5, 1.8 mm). Bars represent the average values, and error bars represent standard deviations (N > 30). The CV is reported above each bar. B) Bar chart showing bacterial viability obtained just after printing and after an overnight incubation at 37 °C. Data refer to biological triplicate, and error bars represent standard deviations. C) Microscopic image of the section of a strand in a 20x20x1 mm grid structure with MCred strain. The microscopy picture was acquired using the TRITC filter channel, 150 ms exposure. D) Dose-response curves of bioprinted ELMs tested in optimal laboratory conditions, in terms of RFP (AU) as a function of VAI concentrations. Data points represent mean values with the relative standard deviations as error bars (N=8). E) Dose-response curves of bioprinted ELMs, in terms of RFP (AU) as a function of VAI concentration, in different non-optimal conditions tested. Data points represent mean values with the relative standard deviations as error bars (N=3). F) ELM response upon PAI sensing from filter-sterilized supernatants of four *P. aeruginosa* clinical isolates (S1–S4). Negative control (NC) refers to the supernatant of an MG1655-Z1 strain grown at 37 °C, 220 rpm overnight, not producing PAI. ELMs were stored at 2–8 °C for 1 day before use.

bacteria. Taken together, these results demonstrated the sensing efficiency for environmentally- and clinically-relevant applications.

IV. Conclusions

A workflow for bacterial printing has been established to make biosensors reproducible in output and shape, usable for realistic conditions of use, such as environmental and clinical settings.

The preliminary step of protocol optimization led us to choose SA and GEL (8% (w/v) + 4% (w/v)) to have robust and easy to handle constructs. The extrusion was set on solid support (e.g., on a petri dish), and for the nutrients we chose the condition in which they are supplied both by the presence of LB agar, and by including within the bioink itself.

Then, we demonstrated how bacterial viability and gene expression are compatible with our printing platform, moving on to biosensing experiments demonstrating the feasibility and success in realizing biosensing materials, functional up to one month if stored in fridge.

We then focused on the reproducibility of the biosensor intended as robustness of the output, in laboratory and non-optimal set-ups by tuning conditions such as temperature and nutrient supply, not yet addressed in literature. This has allowed us to establish good reproducibility even in prints of different days, and to understand how the environment can dramatically affect the output, to consider for the use in realistic settings.

We next demonstrated that our biosensor ELMs can be used even in complex matrices, such as soil and clinical samples. In the last point, the biosensor was tested in the presence of supernatants and it was capable of sensing a molecule directly produced by a pathogen.

These results, taken together have demonstrated how our platform can be used for bacterial printing, leading to the creation of low-cost, customizable and user-friendly biosensor devices significant in real world challenges.

Acknowledgement

We want to thank Angelica Frusteri and Debora Dallera (UniPV) for their support in strain construction, Anca Macovei (UniPV) for helpful discussion on biosensing in soil, Ignazio Castagliuolo, Giulia Bernabè, and Shirin Asa'Ad (UniPD) for providing clinical samples.

References

[1] B. A. Lehner, D. T. Schmieden, and A. S. Meyer. A straightforward approach for 3D bacterial printing. *ACS synthetic biology*, vol. *6*, pp. 1124-1130, 2017.

[2] A. M. Duraj-Thatte, et al., Programmable microbial ink for 3D printing of living materials produced from genetically engineered protein nanofibers. *Nature communications*, 12(1), 1-8, 2021.

[3] J. Huang, et al., Programmable and printable Bacillus subtilis biofilms as engineered living materials. *Nature chemical biology*, 15(1), 34-41, 2019.

[4] M. Schaffner, P. A. Rühs, F. Coulter, S. Kilcher, & A.R. Studart. 3D printing of bacteria into functional complex materials. *Science advances*, 3(12), eaao6804, 2017.

[5] T. C. Tang, et al., Hydrogel-based biocontainment of bacteria for continuous sensing and computation. *Nature Chemical Biology*, 17(6), 724-731, 2021.

[6] A. Majerle, D.T. Schmieden, R. Jerala, & A.S. Meyer. Synthetic biology for multiscale designed biomimetic assemblies: from designed self-assembling biopolymers to bacterial bioprinting. *Biochemistry*, 58(16), 2095-2104, 2019.

[7] C. Gilbert, et al., Living materials with programmable functionalities grown from engineered microbial co-cultures. *Nature materials,* 20(5), 691-700, 2021.

[8] S. Belkin, et al., Remote detection of buried landmines using a bacterial sensor. *Nature biotechnology*, 35(4), 308-310, 2017.

[9] L. Wang, et al., Engineering consortia by polymeric microbial swarmbots. *Nature Communications*, 13(1), 1-13, 2022.

[10] X. Liu, et al., 3D printing of living responsive materials and devices. *Advanced Materials*, 30(4), 1704821, 2018.

[11] T. G. Johnston, et al., Cell-Laden Hydrogels for Multikingdom 3D Printing. *Macromolecular Bioscience*, 20(8), 2000121, 2020.

[12] L. Pasotti, et al. Re-using biological devices: a model-aided analysis of interconnected transcriptional cascades designed from the bottom-up. *Journal of Biological Engineering,* 11, 50, 2017.

[13] M. Bellato, et al., CRISPR Interference Modules as Low-Burden Logic Inverters in Synthetic Circuits. *Frontiers in Bioengineering and Biotechnology,* 9:743950, 2022.

[14] L. Pasotti, et al., A Synthetic Close-Loop Controller Circuit for the Regulation of an Extracellular Molecule by Engineered Bacteria. *IEEE Transactions on Biomedical Circuits and Systems*, vol. 13, no. 1, pp. 248-258, 2019.

[15] L. Pasotti, M. Bellato, D. De Marchi, P. Magni. Mechanistic Models of Inducible Synthetic Circuits for Joint Description of DNA Copy Number, Regulatory Protein Level, and Cell Load. *Processes*, 7, 119, 2019.

Uncovering quorum sensing and quenching structural properties: a systems biology approach

C. Cimolato[1], G. Selvaggio[2], M. Bellato[1], L. Marchetti[2,3], and L. Schenato[1]
[1] *Department of Information Engineering, University of Padova - Padova, Italy*
[2] *Fondazione The Microsoft Research - University of Trento COSBI - Rovereto, Italy*
[3] *Department of Cellular, Computational and Integrative Biology (CIBIO), University of Trento - Trento, Italy*

***Abstract*—Bacteria have the ability to coordinate their behavior in a cell density-dependent manner by using diffusible signal molecules. The mechanism, known as quorum sensing, is a cell-to-cell communication process exploited either by pathogens to regulate the expression of virulence and antimicrobial resistance-related genes and by synthetic biologists to engineer bacterial density-dependent functions. Using a systems biology approach, we developed a novel quorum sensing mathematical model and performed a comprehensive study of the equilibrium properties of this communication process. This analysis highlighted crucial structural properties as a result of bistability in the genetic circuit and underlined that bacteria exploit feedback control strategies to produce a unified and robust response. Due to increased antibiotic-resistant infections, researchers investigated enzymatic methods to interfere with quorum sensing. In this paper, we simulated two quorum quenching strategies. Using a modeling approach, we discovered core parameter values which guarantee the effectiveness of these strategies and could be exploited in rational design of synthetic biology based engineered bacteria.**

***Keywords*—Quorum sensing modeling, Molecular systems biology, Equilibrium analysis, Quorum quenching.**

I. INTRODUCTION

The Food and Agriculture organization of the United nations and the World health organization raked antimicrobial resistance (AMR) among the major alarming global threats to medicine and public health [1]. Up to 60% of current hospital infections are caused by AMR strains [2]. In this respect, in many pathogens, physiological processes related to AMR have proven to be strongly dependent on the population size. As a consequence, during an infection, when the population density is low, the immune system is not able to detect their presence, but, when bacterial density reaches a critical level, they exploit their communication mechanisms to coordinate their response and switch on the expression of antimicrobial resistant genes (ARGs). This unanimous response enables bacteria to overcome the immune defenses. This phenomenon is known as quorum sensing (QS). It is a cell-to-cell communication system by which bacteria can modify the expression of several ARGs based on microbial population density and consequently coordinate their response, acting together in the same manner through positive feedback regulation. Most of Gram-negative bacteria exploit similar QS networks, which are homologous to the *Vibrio Fischeri*'s LuxI/R system (hereinafter referred as Lux system). We focused on this system, not for its clinical relevance, but to leverage on the many experimental data that already exist in the literature [3].

The key element of the communication process is enclosed in the signal molecule, also called autoinducer, which is a small molecule able to quickly diffuse inside and outside the cell through the bacteria membrane. At a low cell density, communication system is in its off-state and bacteria produce the autoinducer at a basal level. As the population size grows, the autoinducer reaches a critical concentrations that moves the state of the system to the on-state, by activating the expression of ARGs and by further increasing the autoinducer synthesis.

State of the art: In light of the crucial role that QS plays in antibiotic resistance of bacteria, in the last decades, the interest of researchers focused on the development of QS mathematical models, using either a deterministic or a stochastic approach [4], and on the study of different strategies to control this cell-to-cell communication processes. The increasing threat prompted researchers to develop a new research area, focused on studying the so called quorum quenching (QQ) mechanisms, which aims to discover QS inhibitors to treat bacterial infections [5].

Contributions: In this paper, we carried out a detailed mathematical and computational analysis of the equilibrium behavior and structural properties of a deterministic mathematical model representing the proposed system, showing that bistability plays a crucial role. We then investigated two QS inhibition strategies, performing computational simulations to infer the possible system response and variations in its equilibria. To conclude, we identified key threshold parameters crucial to design and perform QQ experiments.

II. LUX QUORUM SENSING SYSTEM MODELING

A. Quorum sensing system description

Most of the QS systems are comprised of three principal elements: (i) A gene encoding for a synthase, which is an enzyme able to synthesize a specific signal molecule (autoinducer); (ii) A gene encoding for a receptor, which is a protein able to bind the same signal molecule creating an active complex; (iii) A regulated promoter inducible by the above mentioned active complex, which drives the expression of the synthase itself.

This structure implements a positive feedback loop which, up-regulating the concentration of the receptor-autoinducer complex, leads to a further increment in synthase production. Interestingly, this latter activation often involves other AMR-, pathogenic- and biofilm- related genes, thus strictly correlating

QS thresholds with the enhancement of bacterial virulence and resistance to therapies.

As an example of prototypical QS mechanism, in the Lux system (reported in Fig. 1), the gene *luxI* encodes the synthase LuxI, an enzyme which synthesizes a small signal molecule called acyl-homoserine-lactone (AHL), which can rapidly diffuse across the membrane and accumulate in and out of the cell. When it spreads inside bacteria, AHL can be detected and bounded by the dimerized form of the receptor LuxR, encoded in the gene *luxR*, constitutively expressed by the promoter (P_R); the resulting LuxR-AHL complex is able to induce the regulated promoter P_{lux}, driving the expression of *luxI* and thus closing the positive feedback loop. Previous studies suggested that the activated complex has a hetero-tetrameric structure in which two molecules of LuxR are bound to two molecules of AHL [6].

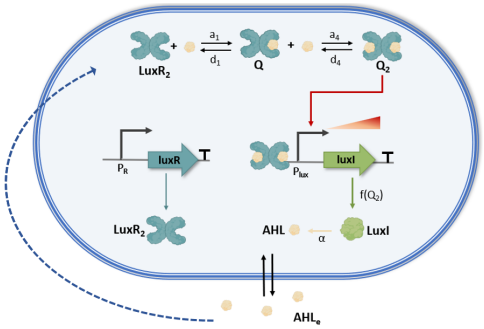


Fig. 1: Schematic of Lux quorum sensing network.

B. The model

We developed a novel cell-based dynamical model for a engineered system of Lux quorum sensing mechanism implemented in host strains of *Escherichia Coli* [6], [8] (Fig. 1):

$$\frac{dI}{dt} = \beta_{lux} + \frac{\alpha_{lux} - \beta_{lux}}{1 + \frac{K_{lux}}{Q_2}} - \gamma_I I \quad (1)$$

$$\frac{dL}{dt} = \alpha_I I - \gamma_L L + d_1 Q - K_1 d_1 R_2 L + \quad (2)$$
$$+ d_4 Q_2 - K_4 d_4 Q L + K_{15}(L_e - L)$$

$$\frac{dL_e}{dt} = K_{15}\frac{NV_I}{V - NV_I}(L - L_e) - \gamma_{L_e} L_e \quad (3)$$

$$\frac{dR_2}{dt} = d_1 Q - K_1 d_1 R_2 L \quad (4)$$

$$\frac{dQ}{dt} = K_1 d_1 R_2 L - d_1 Q - K_4 d_4 Q L + d_4 Q_2 \quad (5)$$

$$\frac{dQ_2}{dt} = K_4 d_4 Q L - d_4 Q_2 \quad (6)$$

whose parameters are summarized in Table I, where I denotes the concentration of protein LuxI, L and L_e are the intracellular and extracellular concentrations of AHL, respectively, and R_2 indicates the concentration of LuxR homodimer. Finally, Q and Q_2 define the concentrations of LuxR dimer bound to one or two molecules of AHL, respectively.

TABLE I: MODEL PARAMETERS

Symbol	*Description*	*Value*	*Units*	*Ref.*
β_{lux}	Basal LuxI synthesis rate per cell regulated by P_{lux}	0.08	$[AUmin^{-1}]$	[8]
α_{lux}	Maximum LuxI synthesis rate per cell regulated by P_{lux}	4.99	$[AUmin^{-1}]$	[8]
K_{lux}	Concentration of Q_2 corresp. to half-maximum induction of P_{lux}	194	$[nM]$	[8]
α_I	Synthesis rate of AHL	1.826	$[nMAU^{-1}min^{-1}]$	[9],[6]
R_2^{TOT}	Total concentration of dimer R_2 per cell	499.66	$[nM]$	[6]
$K_1 = \frac{a_1}{d_1}$	Equilibrium constant	0.0055	$[nM^{-1}]$	[6]
$K_4 = \frac{a_4}{d_4}$	Equilibrium constant	0.001375	$[nM^{-1}]$	[6]
K_{15}	AHL permeability rate	30	$[min^{-1}]$	[7]
γ_I	Degradation rate of LuxI	0.0173	$[min^{-1}]$	[8]
γ_L	Degradation rate of intracellular AHL	$2 \cdot 10^{-4}$	$[min^{-1}]$	[8]
γ_{L_e}	Degradation rate of extracellular AHL	$2 \cdot 10^{-4}$	$[min^{-1}]$	[8]
V_I	*E.coli* volume	1.1	$[\mu m^3]$	[12]
V	Culture environment volume	1	$[mL]$	[-]

The LuxI rate equation (Eq. 1) is composed by β_{lux}, which corresponds to the basal synthesis rate at the off-state, an inducible synthesis term which depends on the concentration of the complex Q_2, and a degradation term with spontaneous degradation rate γ_I. The Q_2-dependent synthesis rate is described as a Hill equation where α_{lux} is the maximum synthesis rate per cell and K_{lux} corresponds to the AHL concentration to reach the half-maximum synthesis rate.

In Eq. 2, α_I is the AHL synthesis rate and γ_L denotes its degradation rate. a_1 and d_1 are, respectively, the forward and reverse rate constants for the binding and unbinding reactions of the first AHL molecule to the LuxR homodimer. The equilibrium constant for this reaction is defines as $K_1 = a_1/d_1$. The forward and reverse rates describing the second AHL binding reaction are defined by a_4 and d_4, respectively. We assumed that the AHL binding and unbinding probability to the sites of R_2, Q and Q_2 are equal, therefore $a_4 = \frac{a_1}{2}$ and $d_4 = 2d_1$ implies that $K_4 = \frac{a_4}{d_4} = \frac{K_1}{4}$, where K_4 is the equilibrium constant of the second binding reaction. The last term in Eq. 2 counts the diffusion process of the autoinducer across the membrane and K_{15} is the AHL permeability rate of the *E. coli* wall [7]. Eq. 3 describes the dynamics of extracellular AHL, where N is the number of spatially homogeneous bacteria in the culture, V_I is the volume of a single *E.coli* and V is the entire culture environment volume. The degradation rate of L_e is described by γ_{L_e}.

Since LuxR is constitutively produced, we assumed R_2 has already reached its steady-state concentration. For this reason, its synthesis and degradation terms were omitted from Eq. 4. Moreover, in Eqs. 5 and 6 degradation terms for Q and Q_2 are neglected since the binding of AHL on the LuxR homodimer stabilizes the latter.

Below are the R_2 and L conservation of mass laws:

$$R_2^{TOT} = R_2 + Q + Q_2 = R_2^{TOT}(0) \quad (7)$$

$$L^{TOT} = L + Q + 2Q_2 \quad (8)$$

It is worth noticing that, since LuxR is produced at a constant basal rate, once it reaches its steady-state level, its total concentration can be assumed unchanged.

C. Deciphering the equilibrium properties of a QS system

In this section, we performed the analysis of the equilibrium behavior of the set of Eqs. 1-6. The following assumptions were made: reactions to form complexes Q and Q_2 and vice versa are reasonably much faster than the others. Under this assumption, Q and Q_2 immediately reach their steady state values and, exploiting the quasi-steady state approximation and the conservation law in Eq. 7, the model Eqs. 1-6 can be reduced to the following system:

$$\frac{dI}{dt} = \beta_{lux} + \frac{\alpha_{lux} - \beta_{lux}}{1 + \frac{K_{lux}}{Q_2}} - \gamma_I I \tag{9}$$

$$\frac{dL}{dt} = \alpha_I I - \gamma_L L + K_{15}(L_e - L) \tag{10}$$

$$\frac{dL_e}{dt} = K_{15}\frac{NV_I}{V - NV_I}(L - L_e) - \gamma_{L_e} L_e \tag{11}$$

$$Q_2 = \frac{\frac{K_1^2}{4}L^2}{1 + K_1 L + \frac{K_1^2}{4}L^2} R_2^{TOT}. \tag{12}$$

To investigate the equilibrium behavior, we assumed the steady state of all intracellular processes of the above system, by setting Eqs. 9-11 equal to 0. After some manipulations, this leads to the following equilibrium conditions:

$$L_e = \frac{\Delta}{\Delta + \gamma_{L_e}} L, \qquad L = \underbrace{\frac{\alpha_I}{\gamma_L - \Psi}}_{=:\chi} I, \tag{13}$$

where $\Delta = K_{15}\frac{NV_I}{V - NV_I}$ and $\Psi = K_{15}(\frac{\Delta}{\Delta + \gamma_{L_e}} - 1)$. Now, rewriting Q_2 as a function of LuxI:

$$Q_2 = \frac{\frac{K_1^2}{4}\chi^2 I^2}{1 + K_1 \chi I + \frac{K_1^2}{4}\chi^2 I^2} R_2^{TOT}, \tag{14}$$

where $\chi = \frac{\alpha_I(\frac{K_{15}NV_I}{V - NV_I} + \gamma_{L_e})}{(\frac{K_{15}NV_I}{V - NV_I} + \gamma_{L_e})\gamma_L + K_{15}\gamma_{L_e}}$, and substituting Eq. 14 into Eq. 9, the steady state levels of LuxI are obtained by solving the following equation:

$$\frac{dI}{dt} = \beta_{lux} + \frac{(\alpha_{lux} - \beta_{lux})(\frac{K_1}{2}\chi I)^2}{(\frac{K_1}{2}\chi I)^2 + \frac{K_{lux}}{R_2^{TOT}}(1 + \frac{K_1}{2}\chi I)^2} - \gamma_I I = 0. \tag{15}$$

It is worth noting that the equilibria of the system strongly depend on the number N of cells inside the culture environment. For this reason, we computed the solution pairs (I, N) of Eq. 15 for different values of N. Fig. 2 displays the bifurcation diagram of the steady state LuxI concentration per cell against the population density.

For low values of cell density, the system has one stable equilibrium point corresponding to a the basal concentration of LuxI (off-state). Increasing the population density, the system exhibits three different steady states, two of them stable and one unstable. The further increase in cell density brings the system back to a single stable equilibrium point, this time corresponding to a high LuxI concentration per cell (on-state).

Moreover, the bacteria colony exhibits hysteretic behavior: the system response is not simply a function of the cell density, but it also depends on its history. Indeed, the cell density level at which the communication process switches on is higher than the one at which switches off, conferring robustness to the communication process.

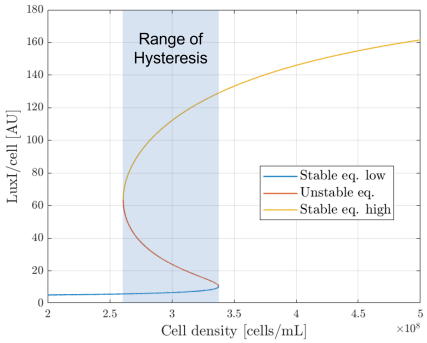


Fig. 2: Bifurcation diagram of LuxI.

III. Quorum Quenching

To address the problem of increasing antimicrobial resistant bacteria, researchers developed novel therapeutic techniques, some of which based on QQ i.e., the inhibition of bacterial communication [2]. In the QS pathway, there are several possible sites where it is possible to interfere. In this work, we explored the following two strategies to destroy AHL communication system: (i) Degradation of the extracellular AHL molecule, exploiting AHL-degrading enzymes which prevent the accumulation of extracellular AHL, as exploited in [8]; (ii) Sequestration of the AHL-receptor protein via antagonist compounds, as studied in [10].

A. QQ simulation via parameter sensitivity analysis

We exploited the developed model and the equilibrium analysis just performed to evaluate the effectiveness of these two therapeutic strategies. We addressed the problem from a parametric point of view, increasing or decreasing specific parameters which resembled the possible effect of the intended therapeutic strategy. Indeed, the degradation of the extracellular AHL can be numerically simulated by increasing the degradation rate γ_{L_e} of Eq. 3. On the other hand, the sequestration of LuxR dimer antagonizes its interaction with AHL to form complexes Q and Q_2 and it is equivalent to reduce binding rates a_1 and a_4 or, equivalently, the equilibrium constants K_1 and K_4. Results are reported in Fig. 3.

B. Critical parameter thresholds identification

Our goal is to simulate the effect of the described inhibition mechanisms and to find the key threshold values of γ_{L_e} and $K_{1,4}$ that prevent the activation of quorum sensing, even at high population sizes. In nature, there is an upper limit on the cell density that can be reached in the culture environment. Therefore, to destroy QS communication, it is sufficient to require that the autoinducer synthesis remains at the basal level until the maximum density is reached. In this way, the QS system cannot be activated at any feasible cell density.

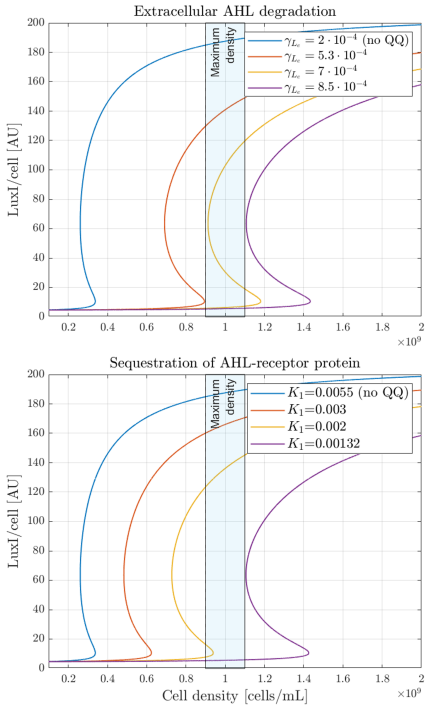


Fig. 3: QQ simulation highlighting critical parameter values forcing off-states. Top: AHL degradation. Bottom: receptor sequestration.

In literature, the maximum value of *E.coli* cell density found is around $1.1 \cdot 10^9$ cells/mL [11] and, using a conservative approach, this is the upper limit that we considered in our analysis. We simulated the two QS blocking strategies described above varying the corresponding parameters and, in Fig. 3 the resulting LuxI bifurcation diagrams are illustrated. Note that, with the parameter values corresponding to the purple curves, we reached our goal: at all feasible cell densities the system has a unique stable equilibrium which corresponds to the basal level of autoinducer. Therefore, $\gamma_{L_e} > 8.5 \cdot 10^{-4}$ min^{-1} or $K_1 < 1.32 \cdot 10^{-3}$ nM^{-1} guarantee the inhibition of QS.

These simulations clearly indicate that QS switching from off-state to on-state strictly depends on the population size: while each bacterium must produce a sufficiently low amount of AHL to avoid self-activation of QS, on the other they must produce enough autoinducer to switch on QS once the threshold cell density has been reached. This behavior strongly depends on the hysteretic curve displayed in Fig. 2 and is a consequence of the underlying positive feedback loop.

The effort required to activate the communication process is considerable, and hysteresis ensures that once triggered, it is more difficult to reverse it by a cell density decrease. Indeed, our analysis proved that the system requires a significantly lower level of cell density to reset the autoinducer production to the basal level, compared to the QS activating threshold one. This finding confirms that bacteria exploit control strategies to perform disturbance rejection to cell density variations. In this case, the positive feedback ensured robustness to autoinducers perturbations and reduced susceptibility to noise.

Lastly, while higher *E.coli* cell density thresholds could be considered (e.g., for bioreactors), this would only imply that a stronger QQ action would be required to achieve the same results in that type of systems. Despite some parameters could be affected by unmodeled aspects, e.g., pH-dependant AHL stability [13] or altered synthase/receptor degradation rates, a sensitivity analyses on those parameters is beyond the aim of this study and will be addressed in future works.

IV. Conclusion

Due to the rise in antibiotic resistance and the need to prevent new emergence of such strains, there will be in the near future a progressive application of synthetic biology studies exploiting QQ enzymes and CRISPR interference [14], [15]. This will enable the development of new therapeutic approaches against AMR bacteria and a better understanding of the structural properties of QS mechanisms. In this regard, this work identified key threshold parameters that are essential for designing and carrying out quorum quenching experiments, highlighting design requirement for pharmacological- and synthetic biology-based therapeutic approaches.

Acknowledgement

Funds: Fondazione Cariparo grant “Ricerca Scientifica di Eccellenza 2021 n59576”, Dept. of Information Engineering - UniPD PhD Grant PON-RI 2014-20 (CCI2014IT16M2OP005) on FSE REACT-EU funds. The authors thank B. Di Camillo and S. Del Favero for the helpful discussions.

References

[1] FAO, Drivers, dynamics and epidemiology of antimicrobial resistance in animal production, 2016. Link
[2] P. Williams, Quorum sensing: an emerging target for antibacterial chemotherapy?, *Expert Opin Ther Targets*, 6(3):257–274, 2002. Link
[3] M. E. Taga, B. L. Bassler, Chemical communication among bacteria, *Proc Natl Acad Sci*, 100:14549-14554, 2003. Link
[4] J. Pérez-Velazquez, M. Golgeli, Mathematical modelling of bacterial quorum sensing: A review, *Bull Math Biol*, 78:1585–1639, 2016.Link
[5] S. Zhong, S. He, Quorum sensing inhibition or quenching in Acinetobacter baumannii: the novel therapeutic strategies for new drug development, *Front Microbiol*, 12:558003, 2021. Link
[6] L. Pasotti, M. Bellato, D. De Marchi, P. Magni, Mechanistic models of inducible synthetic circuits for joint description of DNA copy number, regulatory protein level, and cell load", *Processes*, 7(3):119, 2019. Link
[7] X. Li, J. Jin, X. Zhang, F. Xu, J. Zhong, et al., Quantifying the optimal strategy of population control of quorum sensing network in Escherichia coli, *npj Systems biology and applications*, 7(1):1-16, 2021. Link
[8] L. Pasotti, et al., A synthetic close-loop controller circuit for the regulation of an extracellular molecule by engineered bacteria, *IEEE Trans Biomed Circuits Syst*, 13(1):248-258, 2019. Link
[9] A. L. Schaefer, D. L. Val, B. L. Hanzelka, J. E. Cronan, E. P. Greenberg, Generation of cell-to-cell signals in quorum sensing: acyl homoserine lactone synthase activity of a purified Vibro fischeri LuxI protein, *Proc Natl Acad Sci*, 93(18):9505-9509, 1996. Link
[10] G. Bernabè, et al., A novel phenolic derivative inhibits AHL-dependent QS signaling in P. aeruginosa, *Front Pharmacol*, 13:996871, 2022. Link
[11] P. Mira, P. Yeh, B. G. Hall, Estimating microbial population data from optical density, *Plos one*, 17(10):e0276040, 2022. Link
[12] H. E. Kubitschek, J. A. Friske, Determination of bacterial cell volume with the Coulter Counter, *J Bacteriol*, 168(3):1466-1467, 1986. Link
[13] N. Politi, et al., Half-life measurements of chemical inducers for recombinant gene expression, *J Biol Eng* 8(5), 2014. Link
[14] H. H. Huang, et al., dCas9 regulator to neutralize competition in CRISPRi circuits, *Nat Commun*, 12(1):1-7, 2021. Link
[15] M. Bellato, et al., CRISPR Interference Modules as Low-Burden Logic Inverters in Synthetic Circuits, *Front Bioeng Biotech*, 9:1513, 2022. Link

Bioinformatics analyses to identify molecular gene signatures associated with breast cancer phenotypes

Federica Conte[1], Giulia Fiscon[1,2] and Paola Paci[1,2,3]
[1] *Institute for Systems Analysis and Computer Science "A. Ruberti" (IASI) National Research Council (CNR) of Rome, Rome, Italy*
[2] *Department of Computer, Control and Management Engineering, Sapienza University of Rome, Rome, Italy*
[3] *Karolinska Institutet, 17177 Stockholm, Sweden*

***Abstract*— Breast cancer is a heterogeneous and complex disease as witnessed by the existence of different subtypes with distinct morphologies and clinical implications. Despite the remarkable advances in understanding the mechanisms underlying breast cancer, this disease is still a major public health problem worldwide and poses significant open challenges. Here, we show how a multi-omics data integration analysis may provide useful insights in the identification of promising molecular signatures associated with the different breast cancer subtypes.**

***Keywords*— breast cancer subtypes, bioinformatics, computational medicine, gene signature**

I. Introduction

BREAST CANCER (BC) is the most common female cancer and, despite important advances in early detection and research development, it continues to be the second leading cause of death in women worldwide [1]. BC is a heterogeneous pathology as witnessed by the existence of different subtypes with distinct morphologies and clinical implications [2]. These subtypes are usually defined by using the immunohistochemical (IHC) classification, which is based on immunoprofile (i.e., Estrogen Receptor-ER, Progesterone Receptor-PR and Human Epidermal growth factor Receptor2-HER2 status) and Ki67 index [3]; or by using the genetic (PAM50) classification, based on the expression of a 50-gene signature [4], [5]. According to the IHC classification, breast cancers are stratified into four subtypes, i.e. luminal A, luminal B, Her2 positive and triple negative. According to the PAM50 classification, they are classified into four molecular intrinsic subtypes that are luminal A, luminal B, Her2 positive and basal-like. The most aggressive BC pathophenotypes are the triple-negative and the basal-like for the two classifications, respectively. Although triple-negative and basal-like are not the same by definition, these two terms are often used interchangeably, since most basal-like breast cancers also have a triple-negative phenotype (i.e., ER-negative, PR-negative, HER2-negative) [6] and since triple-negative breast cancers overlap with the molecular entity of basal-like [7], [8]. The identification of BC-associated biomarkers and the development of effective therapeutic strategies for the different subtypes are ongoing challenges to be faced.

Here, we present a bioinformatics approach for the integration of multi-omics data (e.g., transcriptomics, genomics, epigenomics, clinical) that can offer promising insights for understanding BC-related molecular mechanisms.

II. Materials and Methods

A. Data retrieval

Transcriptomic, clinicopathological, Copy Number Variations (CNVs) and DNA methylation data of patients affected by breast cancer were retrieved from The Cancer Genome Atlas (TCGA) repository [9]. Male samples, as well as samples undergoing a neoadjuvant treatment, were removed from the TCGA-BC cohort. The Human Protein Atlas (HPA) website [10] was leveraged to retrieve immunohistochemistry images and to evaluate changes in the proteins expression patterns.

B. SWIM algorithm

SWIM (SWItch Miner) is a recently developed tool able to unveil key (switch) genes within gene co-expression networks strongly associated with drastic changes in cell/tissue phenotype [11], [12]. SWIM algorithm has been implemented both in Matlab and in R language and encompasses a series of steps described in details in [11], [12].

C. In vitro and ex vivo experiments

To validate the common gene signature found to be altered in all BC subtypes, in vitro and ex vivo experiments were performed by using BC model cell lines and tissue specimens. The detailed description of these experiments was provided in [13].

D. Survival analysis

To analyze the correlation between the expression level of the basal-like specific switch genes and patient overall survival and therefore to evaluate their prognostic value, we used the RNA-sequencing data from TCGA to split the entire cohort of BC patients (1049 samples) into two groups (called low-expression and high-expression group) according to the upper and lower expression quartile. Low- and high-expression groups refer to patients with expression levels of the given switch gene lower and greater than the 50th percentile (i.e., median), respectively. For each patient cohort, the cumulative survival rates were computed for each switch gene according to the Kaplan-Meier (KM) method [14] on the clinical metadata provided by TCGA. For each switch gene, the survival outcomes of the two patients' groups were compared by the log-rank test. Switch genes with log-rank p-values less than 0.05 were suggested as candidate prognostic biomarkers.

E. Gene regulatory network analysis

To investigate putative transcription factor activities on the regulation of the basal-like specific switch genes, we built a gene regulatory network by integrating information from Pscan web tool [15], TRRUST database [16] and the human interactome assembled by Cheng and coauthors [17]. In particular, we firstly exploited Pscan web tool to predict TFs putatively able to bind the promoter regions of the selected switch genes. Then, we filtered the Pscan predictions keeping only the TFs known to physically interact with at least one switch genes in the human interactome. These TF-target relationships were finally complemented with those experimentally validated from TRRUST database.

III. Results and Discussion

A. Identification of a common gene signature altered in all BC subtypes

In our recent study [13], we applied SWIM methodology on the transcriptomic data of TCGA-BC patients stratified according to two different subtype classification (i.e., PAM50 and IHC classification) in order to identify switch genes both shared among all subtypes and specific for each subtype (Fig. 1). We focused on switch genes common to all subtypes of both classifications and we found a common gene signature composed of 11 genes.

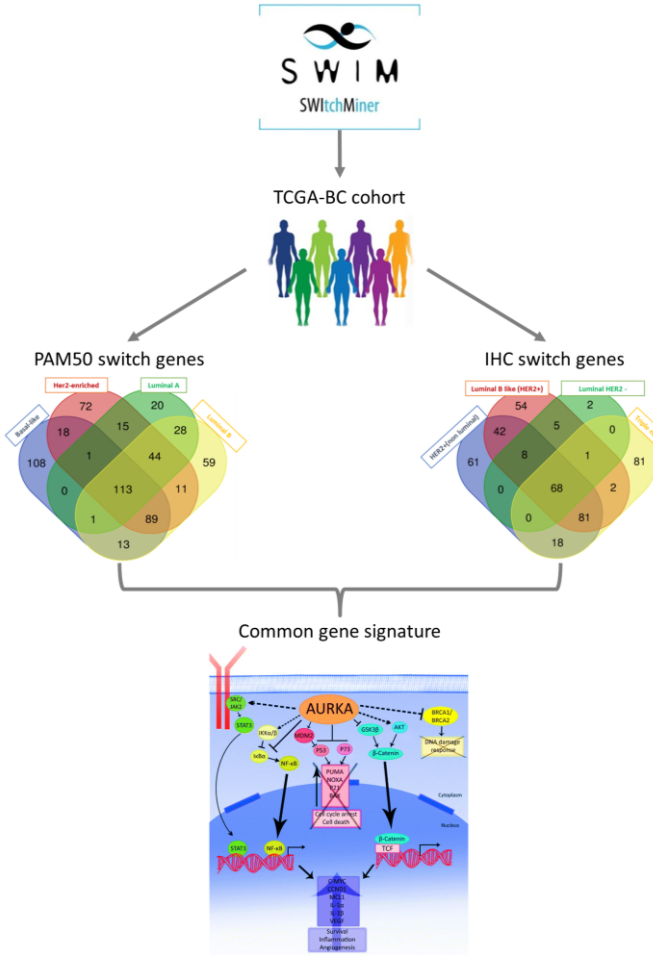


Fig. 1: Workflow for the identification of a common gene signature altered in all BC subtypes

Among them, Aurora Kinase A (AURKA) appears to be very promising since: i) it is a kinase known to have a key role in cell division and cell-cycle progression; ii) it plays a critical role in regulation of mitotic events like spindle assembly and chromosomal segregation; iii) it is deregulated in many human cancers; iv) it collaborates with several tumor suppressors like P53, BRCA1 and BRCA2; v) it is suggested as a pharmaceutical target for the treatment of various cancers [18].

The key role of AURKA in the context of BC subtypes was experimentally validated by showing that the encoded protein is always over-expressed both in BC cell lines (Fig.2A) and tissues (Fig.2B).

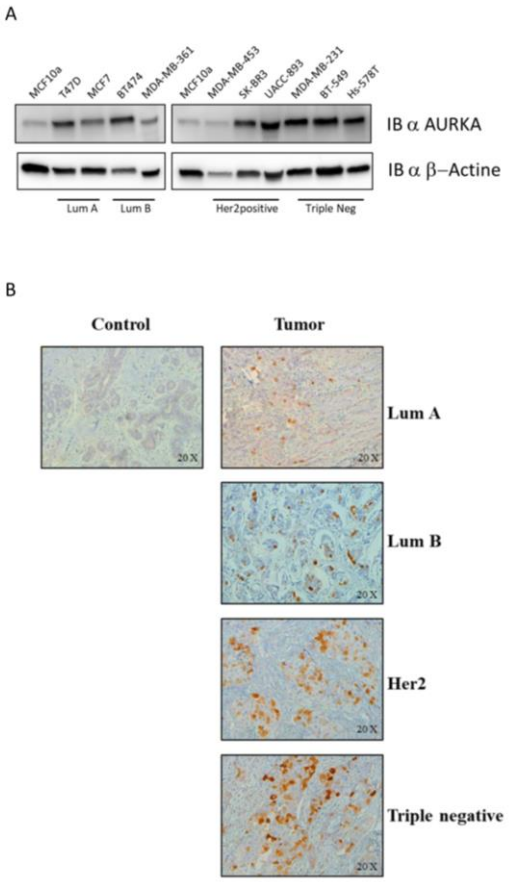


Fig. 2: AURKA protein expression examined in vitro by immunoblotting on BC subtype cell lines (A) and ex vivo by immunohistochemical analysis on surgical BC tissue specimens (B).

Moreover, we demonstrated that the AURKA inhibition by using alisertib drug led to a reduction in the cell growth of all BC subtype cell lines (Fig.3A) and to arrest their cell cycle (Fig.3B) up to 72 h after the treatment.

Taken together, all these findings supported the hypothesis that AURKA pathway could be a common mechanism univocally altered in all BC subtypes.

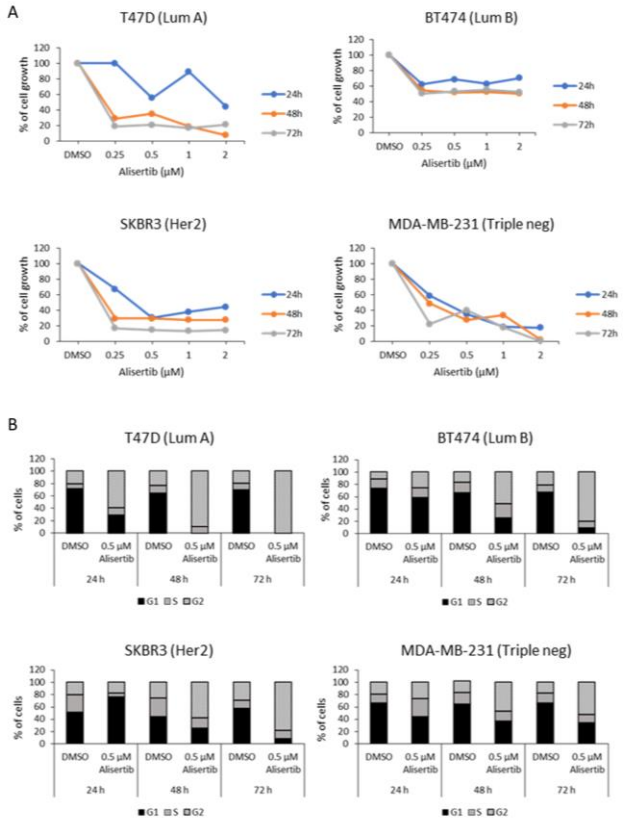


Fig. 3: Effect of AURKA's inhibitor (alisertib) assessed on cell growth (A) and cell cycle (B) of BC subtype cell lines.

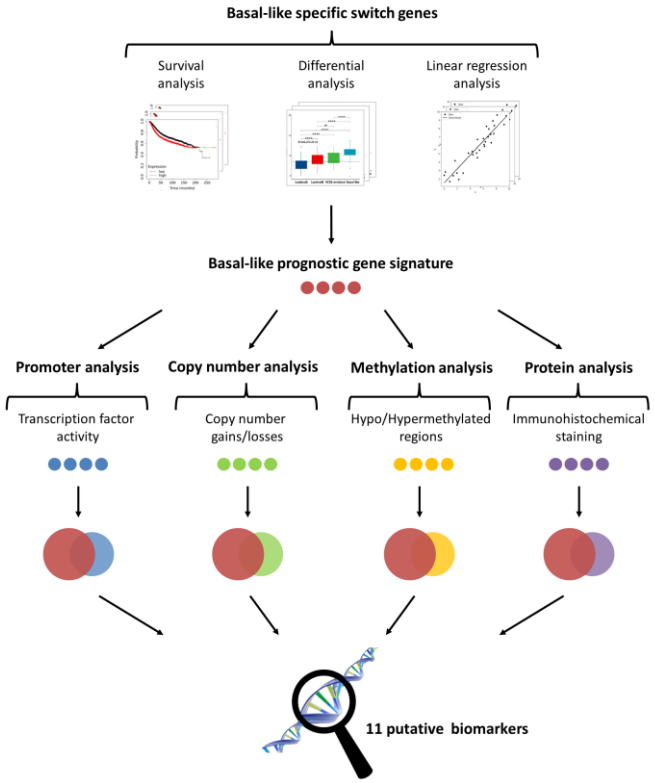


Fig. 4: Workflow for the identification of a prognostic gene signature for basal-like subtype.

B. Identification of a prognostic gene signature for basal-like subtype

Among the various recognized BC subtypes, basal-like is the most aggressive with a poor prognosis, a high risk of relapse and a high resistance to pharmacological treatments [19]. Currently, there are not available widely accepted prognostic biomarkers to predict the outcomes of basal-like patients. Therefore, in our recent study [20], we carried out a bioinformatics pipeline integrating transcriptomic, genomic, epigenomic, and clinical data in order to identify a prognostic gene signature for the basal-like subtype (Fig.4).

Our pipeline started from the 108 basal-like specific switch genes identified in [13] and performed a Kaplan-Meier (KM) survival analysis in order to explore their clinical relevance with respect to BC patients' overall survival (OS). This first step allowed us to identify 11 basal-like specific switch genes, i.e., CENPN, LRP8, DSCC1, CTPS, RCOR2, GINS4, TUBA1C, PRAME, SLC7A11, CDCA7, GSDMC, acting as unfavourable prognostic biomarkers (i.e., their higher expression was significantly associated with poorer BC patients' OS). The clinical relevance of these 11 switch genes was also confirmed using other larger BC datasets collected in the KM plotter website [21].

Next, we evaluated the gene expression of these 11 putative basal-like prognostic biomarkers demonstrating that they always reached the highest level in the basal-like condition.

To statistically quantify the increasing trend of their expression values as the phenotype varies from physiological to pathological condition passing across the different BC subtypes, we performed a linear regression analysis, where the index R-squared estimates the goodness-of-fit. We found that all of them showed a very strong straight-line relationship (R-squared >= 0.7) with respect to the tumor aggressiveness. These results were mostly confirmed also by performing the same analysis with respect to the pathological staging of the BC patients.

Moreover, we explored the expression patterns of the proteins encoded by the 11 prognostic switch genes through the HPA. We found that six of these proteins were overexpressed in BC tissues compared to normal breast tissues. For the remaining ones, there are pending cancer and normal tissue analysis on the HPA and the immunohistochemistry images are not currently available.

Eventually, we investigated if the overexpression of the 11 basal-like prognostic biomarkers may depend on the action of important transcription factors (TFs) as well as basal-like specific genomic alterations (CNVs) and/or epigenomic alteration (DNA methylation changes). In particular, to provide some hints on which TFs could regulate the expression of the 11 basal-like switch genes, we built a gene regulatory network by combining information on both computationally predicted and experimentally validated TF-target relationships (see Materials and Methods). The final gene regulatory network was composed of seven switch genes and twelve TFs, including well-known TFs that, if deregulated, contribute to neoplastic transformation as MYC, TP53 and NFKB. By performing hierarchical clustering analyses, we highlighted different CNVs (copy number gain/loss) and DNA methylation (hypo/hypermethylated

regions) status of the 11 putative prognostic biomarkers in basal-like subtype with respect to the less aggressive BC subtype, i.e., luminal A [20].

Taken together, all these findings prompted us to propose the 11 basal-like specific switch genes as a specific gene signature to evaluate the prognosis of basal-like BC patients.

IV. Conclusion

In the present work, we showed how bioinformatics may be exploited to provide a contribution in the identification of putative gene signatures associated with one of the most heterogeneous and widespread disease, i.e. breast cancer, thus helping in the discovery of effective therapies as well as prognostic biomarkers.

Acknowledgement

This work has been partially funded by BiBiNet project (grant number: H35F21000430002) within the POR-Lazio FESR 2014-2020 and by Progetto di Ricerca di Ateneo 2021 (grant n: RM12117A34663A2C).

References

[1] J. Ferlay *et al.*, "Estimating the global cancer incidence and mortality in 2018: GLOBOCAN sources and methods," *Int. J. Cancer*, vol. 144, no. 8, pp. 1941–1953, 2019, doi: 10.1002/ijc.31937.

[2] Z. D, I. A, S. C, and P. M, "Clinical management of breast cancer heterogeneity," *Nat. Rev. Clin. Oncol.*, vol. 12, no. 7, Jul. 2015, doi: 10.1038/nrclinonc.2015.73.

[3] A. Goldhirsch *et al.*, "Personalizing the treatment of women with early breast cancer: highlights of the St Gallen International Expert Consensus on the Primary Therapy of Early Breast Cancer 2013," *Ann. Oncol.*, vol. 24, no. 9, pp. 2206–2223, Sep. 2013, doi: 10.1093/annonc/mdt303.

[4] D. C. Koboldt *et al.*, "Comprehensive molecular portraits of human breast tumours," *Nature*, vol. 490, no. 7418, Art. no. 7418, Oct. 2012, doi: 10.1038/nature11412.

[5] J. S. Parker *et al.*, "Supervised risk predictor of breast cancer based on intrinsic subtypes," *J. Clin. Oncol. Off. J. Am. Soc. Clin. Oncol.*, vol. 27, no. 8, Art. no. 8, Mar. 2009, doi: 10.1200/JCO.2008.18.1370.

[6] A. C. Garrido-Castro, N. U. Lin, and K. Polyak, "Insights into Molecular Classifications of Triple-Negative Breast Cancer: Improving Patient Selection for Treatment," *Cancer Discov.*, vol. 9, no. 2, pp. 176–198, Feb. 2019, doi: 10.1158/2159-8290.CD-18-1177.

[7] P. Alluri and L. A. Newman, "Basal-like and triple-negative breast cancers: searching for positives among many negatives," *Surg. Oncol. Clin. N. Am.*, vol. 23, no. 3, pp. 567–577, Jul. 2014, doi: 10.1016/j.soc.2014.03.003.

[8] P. Gazinska *et al.*, "Comparison of basal-like triple-negative breast cancer defined by morphology, immunohistochemistry and transcriptional profiles," *Mod. Pathol. Off. J. U. S. Can. Acad. Pathol. Inc*, vol. 26, no. 7, pp. 955–966, Jul. 2013, doi: 10.1038/modpathol.2012.244.

[9] K. Tomczak, P. Czerwinska, M. Wiznerowicz, and others, "The Cancer Genome Atlas (TCGA): an immeasurable source of knowledge," *Contemp Oncol Pozn*, vol. 19, no. 1A, pp. A68–A77, 2015.

[10] A. Asplund, P.-H. D. Edqvist, J. M. Schwenk, and F. Pontén, "Antibodies for profiling the human proteome-The Human Protein Atlas as a resource for cancer research," *Proteomics*, vol. 12, no. 13, pp. 2067–2077, Jul. 2012, doi: 10.1002/pmic.201100504.

[11] P. Paci, T. Colombo, G. Fiscon, A. Gurtner, G. Pavesi, and L. Farina, "SWIM: a computational tool to unveiling crucial nodes in complex biological networks," *Sci. Rep.*, vol. 7, p. srep44797, Mar. 2017, doi: 10.1038/srep44797.

[12] P. Paci and G. Fiscon, "SWIMmeR: an R-based software to unveiling crucial nodes in complex biological networks," *Bioinformatics*, vol. 38, no. 2, pp. 586–588, Jan. 2022, doi: 10.1093/bioinformatics/btab657.

[13] A. M. Grimaldi *et al.*, "The New Paradigm of Network Medicine to Analyze Breast Cancer Phenotypes," *Int. J. Mol. Sci.*, vol. 21, no. 18, Art. no. 18, Jan. 2020, doi: 10.3390/ijms21186690.

[14] J. T. Rich, J. G. Neely, R. C. Paniello, C. C. J. Voelker, B. Nussenbaum, and E. W. Wang, "A practical guide to understanding Kaplan-Meier curves," *Otolaryngol. Neck Surg.*, vol. 143, no. 3, pp. 331–336, Sep. 2010, doi: 10.1016/j.otohns.2010.05.007.

[15] F. Zambelli, G. Pesole, and G. Pavesi, "Pscan: finding over-represented transcription factor binding site motifs in sequences from co-regulated or co-expressed genes," *Nucleic Acids Res.*, vol. 37, no. suppl_2, pp. W247–W252, Jul. 2009, doi: 10.1093/nar/gkp464.

[16] H. Han *et al.*, "TRRUST v2: an expanded reference database of human and mouse transcriptional regulatory interactions," *Nucleic Acids Res.*, vol. 46, no. D1, pp. D380–D386, Jan. 2018, doi: 10.1093/nar/gkx1013.

[17] F. Cheng *et al.*, "Network-based approach to prediction and population-based validation of in silico drug repurposing," *Nat. Commun.*, vol. 9, no. 1, Art. no. 1, Jul. 2018, doi: 10.1038/s41467-018-05116-5.

[18] R. Du, C. Huang, K. Liu, X. Li, and Z. Dong, "Targeting AURKA in Cancer: molecular mechanisms and opportunities for Cancer therapy," *Mol. Cancer*, vol. 20, no. 1, p. 15, Jan. 2021, doi: 10.1186/s12943-020-01305-3.

[19] N. U. Lin *et al.*, "Clinicopathologic features, patterns of recurrence, and survival among women with triple-negative breast cancer in the National Comprehensive Cancer Network," *Cancer*, vol. 118, no. 22, pp. 5463–5472, 2012, doi: 10.1002/cncr.27581.

[20] F. Conte, P. Sibilio, A. M. Grimaldi, M. Salvatore, P. Paci, and M. Incoronato, "In silico recognition of a prognostic signature in basal-like breast cancer patients," *PLOS ONE*, vol. 17, no. 2, p. e0264024, Feb. 2022, doi: 10.1371/journal.pone.0264024.

[21] B. Győrffy *et al.*, "An online survival analysis tool to rapidly assess the effect of 22,277 genes on breast cancer prognosis using microarray data of 1,809 patients," *Breast Cancer Res. Treat.*, vol. 123, no. 3, pp. 725–731, Oct. 2010, doi: 10.1007/s10549-009-0674-9.

A network-based algorithm for identifying drug repurposing opportunities for complex diseases

G. Fiscon[1,2], F. Conte[2], and P. Paci[1,2,3]
[1] *Department of Computer, Control and Management Engineering "A. Ruberti", Sapienza University of Rome;*
[2] *Institute for Systems Analysis and Computer Science "A. Ruberti", National Research Council of Rome;*
[3] *Karolinska Institutet, Stockholm, Sweden*

***Abstract*— SAveRUNNER is a recently developed network-based tool to efficiently identify novel medical indications for currently approved drugs (known as drug repurposing strategy). Up to now, SAveRUNNER has been gainfully applied to unveil repurposable solutions for several diseases, including viral infection (e.g., SARS, COVID-19, HIV, Malaria, Ebola), breast cancer, progressive disorders of central nervous system (e.g., Amyotrophic Lateral Sclerosis, Multiple Sclerosis), and other neurodegenerative diseases (e.g., Alzheimer's Disease). Here, SAveRUNNER algorithm and its main applications are described.**

***Keywords*— Network Theory, Network Medicine, Drug Repurposing.**

I. Introduction

Drug repurposing represents an effective drug discovery strategy to find new uses from existing drugs out of the scope of their original medical indication, which can shorten the time, reduce the cost, and increase the success rate of molecular entities compared to the traditional de novo drug discovery [1].

In this context, we recently developed a network-based algorithm, called SAveRUNNER (Searching off-lAbel dRUg aNd NEtwoRk) [2], [3], which predicts new uses for already approved drugs by exploiting concepts from the emerging field of Network Medicine [4]. According to the Network Medicine paradigm, the human interactome network (i.e., the cellular network of all physical molecular interactions) [5] can be considered as map, where the molecular determinants of a given disease (*disease genes*) tend to co-localize and agglomerate in specific regions (*disease modules*), whose perturbation can contribute to the manifestation of the pathophenotype [4]. In this perspective, even the action of a drug can be considered as a local perturbation of the human interactome and thus, for a drug to be effective against a specific disease, its target proteins should be in the immediate vicinity of the corresponding disease module [6]. Following these principles, SAveRUNNER predicts drug-disease associations by quantifying the interplay between the drug targets and the disease-associated genes in the human interactome through the computation of a novel network-based similarity measure, which prioritizes associations between drugs and diseases located in the same network neighbourhoods.

In the last two years, SAveRUNNER has been acknowledged as promising tool to find drugs repurposable opportunities for several diseases (Fig. 1). In particular, the pioneer application was for predicting repurposable drugs against COVID-19 [3], [7]. In the same study, we also analyzed other related diseases linked to the COVID-19 infection as genetic similarity (i.e., Severe Acute Respiratory Syndrome - SARS), as risk factors (e.g., cardiovascular diseases, diabetes mellitus), or other viral infections (i.e., malaria, HIV and Ebola), and immune disorders (i.e., rheumatoid arthritis) [3]. More recently, it has been successfully applied to identify candidate repurposable drugs also for Amyotrophic Lateral Sclerosis (ALS) [8], Multiple Sclerosis (MS) [9], breast invasive carcinoma subtypes [10], and neurodegenerative diseases, such as Alzheimer's Disease (AD) [11] (Fig. 1). In all these studies, SAveRUNNER turned out as a novel promising tool for an efficient screening of the repurposable opportunities, outlining where looking at for further ad-hoc experimental validations.

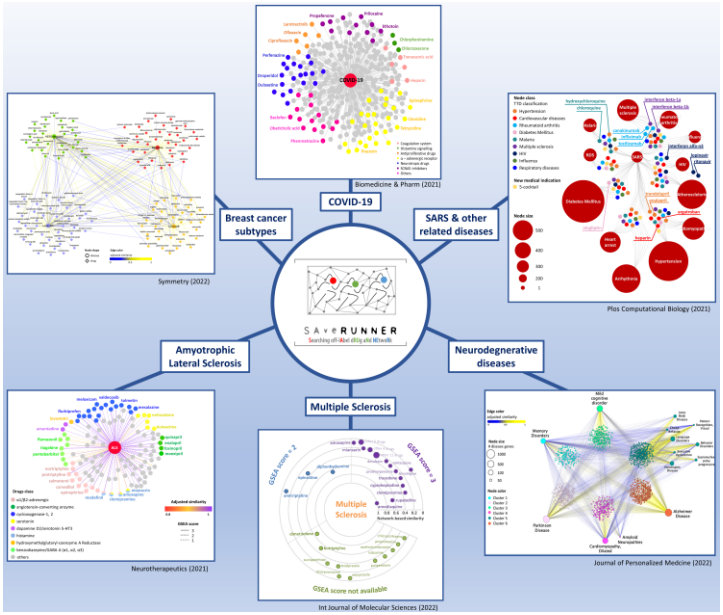


Fig. 1. Overview of SAveRUNNER applications. Each panel corresponds to a different study, where the drug-disease network computed by SAveRUNNER was shown. In these networks, nodes refer to drugs (smaller nodes) and diseases of interest (bigger nodes), and a link occurs between a drug and a disease if their corresponding drug-target proteins and disease-associated genes are proximal in the human interactome more than by chance. The link is weighted according to the novel network-based similarity measure implemented by SAveRUNNER [3].

II. Methods

A. Input data

1) Human interactome network

The human interactome used in all the SAveRUNNER applications was downloaded from [6], including 217,160 interactions connecting 15,970 unique proteins.

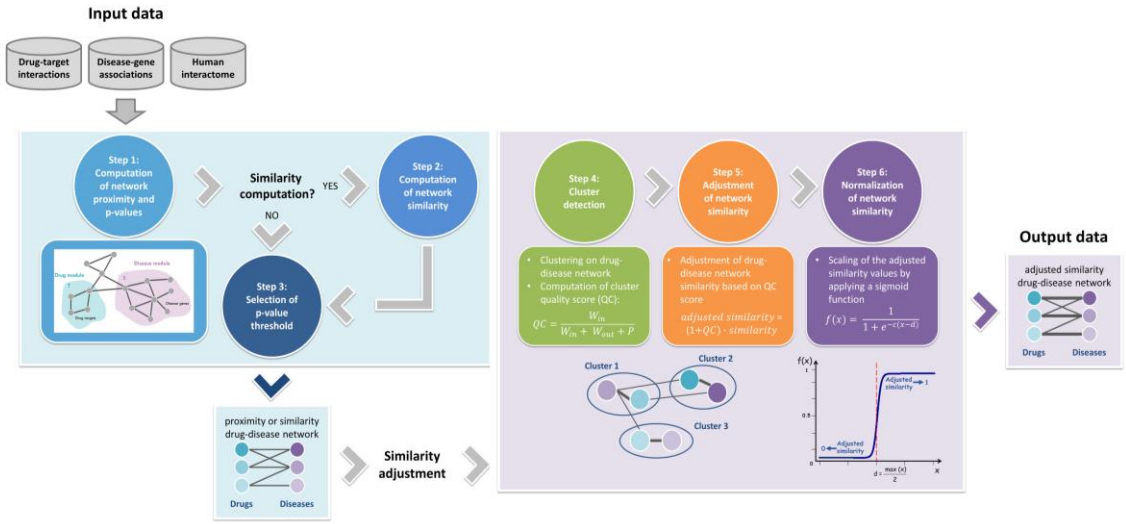


Fig. 2. Overview of SAveRUNNER algorithm [2], [3]**.** Taking as input a list of disease genes, drug targets, and the human interactome, SAveRUNNER releases a drug-disease network via six steps. In steps 1-3, it builds a proximity-based bipartite drug-disease network, where nodes are both drugs and diseases and edges are the statistically significant drug-disease associations. In steps 4-7, it builds a similarity-based bipartite drug-disease network, where the weights represent the adjusted similarity measure computed to prioritize the predicted drug-disease associations by rewarding the associations between drugs and diseases belonging to the same network cluster.

2) Disease gene associations

Disease-associated genes were retrieved from Phenopedia (last release April 2020) [12] and DisGeNET (last release October 2021) [13], two of the most popular and largest publicly available collections of disease genes obtained by integrating and homogeneously annotating data from expert-curated repositories and GWAS catalogues. For one of SAveRUNNER application to COVID-19 [7], transcriptomic data from whole blood cells of patients with COVID-19 was retrieved from GEO repository (GSE152641) and differentially expressed genes between infected cells and heathy controls were used as *disease genes*. Yet, for SAveRUNNER application to breast cancer subtypes [10], due to a poor knowledge of the genes associated with each subtype, transcriptomic data from patients affected by breast invasive carcinoma was retrieved from The Cancer Genome Atlas (TCGA) repository and stratified according to PAM50 classification [14]. Then, a list of genes (known as *switch genes*) previously identified by SWIM software [15] as likely associated to each subtype were used as *disease genes* [14].

3) Drug-target interactions

Drug-target interactions were retrieved from DrugBank [16] (5.1.6 release of April 2020), the most acknowledged database about drugs information and drug-target interactions. The targets' Uniprot IDs provided by DrugBank were mapped to Entrez gene IDs by using the BioMart – Ensembl tool (https://www.ensembl.org/), obtaining a total of 2,165 genes interacting with 1,873 drugs.

B. Algorithm

SAveRUNNER algorithm takes as input the human interactome, a list of disease-gene associations related to disease(s) of interest, and the list of drug-target interactions and, via the implementation of several steps depicted in Fig. 2 and detailed in [2], [3], gives as output a weighted drug-disease bipartite network.

In the network released by SAveRUNNER, nodes are drugs and diseases, and a drug and a disease are connected if the corresponding drug targets and disease genes are closer in the interactome than expected by chance (p-value ≤ 0.05). The weight of their association is based on the implementation of a novel network-based similarity measure, known as *adjusted similarity* (AS), defined in Eq. (1).

$$AS(p) = \frac{1}{1+e^{-c\left[\frac{(1+QC)(m-p)}{m} - d\right]}} \quad (1)$$

In Eq (1), p refers to the network proximity measure described in Eq. (2) [6].

$$p(T,S) = \frac{1}{\|T\|}\sum_{t\epsilon T} \min_{s\epsilon S} d(t,s) \quad (2)$$

where $p(T,S)$ represents the average shortest path length between drug target t in the drug module T and the nearest disease gene s in the disease module S; QC is a quality cluster score that rewards associations between drugs and diseases located in the same network cluster; m is max(p); c and d are the steepness and the midpoint of AS(p), respectively. A comprehensive description of SAveRUNNER methodology can be found in [2], [3].

C. GSEA

To test whether the repurposable drugs predicted by SAveRUNNER could counteract the gene expression perturbations caused by the disease of interest (i.e., up-regulate genes down-regulated by the disease or vice versa), the so-called gene set enrichment analysis (GSEA) was downstream performed [3] in most of the studies. This analysis takes as input: (i) differentially expressed genes of the understudied disease (generally obtained by GEO or TCGA repository) to use as *disease signature*; (ii) differentially expressed genes of drug-treated human cell lines (obtained by Connectivity Map (CMap) database [17]) to use as *drug signature*. For each drug both included in the CMap database and predicted by SAveRUNNER, an enrichment score (ES) was computed to evaluate whether the effect of the drug could counteract the effect of the disease (ES < 0, drug and disease signature negatively correlated) or

not (ES > 0, drug and disease signature positively correlated) [17]. For each tested drug, a GSEA score equal to 1 was assigned if that drug was found to have ES < 0 with respect to a given disease, or equal to 0, otherwise. By repeating this procedure for several independent disease signatures, the final GSEA score ranges from 1 to *n* (with *n* is the total number of disease signatures tested): the greater the GSEA score, the greater the number of disease datasets satisfying this criterion.

III. Results

A. COVID-19, SARS, and other related diseases

SAveRUNNER was first applied to COVID-19 and a panel of 14 diseases COVID-related for genetic similarity, comorbidity, or for their association to drugs with ongoing clinical trials for treating COVID-19 patients [3]. In particular, we tested: SARS, as it is caused by the coronavirus with the highest sequence identity with SARS-CoV-2 [18] and there existed a well-established knowledge of its associated disease genes; diabetes, cardiovascular diseases, and hypertension, whose comorbidity in COVID-19 patients was observed; and finally other viral infections (i.e., malaria, HIV and Ebola) and immune disorders (i.e., rheumatoid arthritis), since drugs approved for their treatment were investigated for their potential effect to fight coronavirus disease [19]. In this study, SAveRUNNER prioritized 282 potential anti-SARS repurposable drugs and 98 anti-COVID-19, including ACE-inhibitors, monoclonal antibodies, and thrombin inhibitors that were further in-silico corroborated by GSEA, considering drug-treated cell lines from CMap and coronaviruses-induced transcriptomics data from GEO repository.

SAveRUNNER was also used to study COVID-19 starting from differentially expressed genes obtained by exploiting transcriptomic data from COVID-19 infected patients and healthy control samples [7]. In this study, SAveRUNNER identified 399 repurposable drugs for COVID-19, whose top-ranked ones were molecules involved in the modulation of the coagulation system (e.g., *heparin* and *tranexamic acid*), antihistaminic drugs, mast cell stabilizers (e.g., *chlorzoxazone* and *chlorpheniramine*), anti-proliferative drugs including tyrosine kinase (TRK) inhibitors and antibiotics (e.g., *larotrectinib* and *ciprofloxacin*), alpha-adrenergic receptor agents (e.g., *clonidine* and *prazosin*); drugs affecting the central nervous system (e.g., *perfenazine* and *droperidol*), and inhibitors of the sodium voltage-gated channel alpha subunit 5 (SCN5A) involved in cardiac rhythm control (e.g., *propafenone* and *prilocaine*).

B. Amyotrophic Lateral Sclerosis and Multiple Sclerosis

SAveRUNNER was applied to study ALS [8] and MS [9]. In both cases, by prioritizing the network-predicted drugs according to the decreasing value of their network similarity with ALS and MS, SAveRUNNER highlighted some interesting drug modulators of histamine receptors. The expression of histamine receptors were shown to increase in cortical tissues of patients affected by MS [9], thus suggesting that histamine-related molecules can be potential therapeutic strategies for the disease. Moreover, it has been shown that the histaminergic modulation might participate to the mechanisms of ALS insurgence, progression, and therapy as well, since other studies found that histamine-related genes could be modifiers in ALS, and thus supporting their role as candidate biomarkers and therapeutic targets [20]. The histaminergic compounds predicted by SAveRUNNER were also in-silico-validated by GSEA analysis, considering drug-treated cell lines from CMap as drug signatures, and three different datasets of transcriptomics data of cortex tissues from patients affected by ALS [8] and MS [9] collected from GEO repository as disease signatures for ALS and MS, respectively.

C. Breast cancer subtypes

SAveRUNNER was applied to study four subtypes of breast invasive carcinoma stratified based on PAM50 classification (i.e., luminal A, luminal B, Her2-enriched, and basal-like) [10]. In this study, SAveRUNNER predicted: (i) 74 repurposable drugs for luminal A, including as top-ranked *teniposide* that has been studied as suppressor of the growth of subcutaneous cell lines of luminal A (MCF-7) [21]; (ii) 54 repurposable drugs for luminal B, including as top-ranked *ivabradineI*, recently repurposed as a novel therapy for breast cancer [22]; (iii) 79 repurposable drugs for HER2-enriched, including as top-ranked several compounds for the treatment of bacterial infections; and (iv) 77 repurposable drugs for basal-like, whose top-ranked one was *metergoline*, acting as antagonist of certain subtypes of 5-HT receptor, which has been showed to induce cell proliferation of triple-negative breast cancer via 5-HT7 receptor signaling [23]. Yet, the 20% of the total predicted drugs have also an indication originally related to cancer treatment, including *dexrazoxane*, *ixabepilone*, *capecitabine* already approved for fighting breast cancers. Most of the predicted repurposable drugs were also in-silico-validated by GSEA, considering breast cancer drug-treated cell lines from CMap as drug signatures and transcriptomics data of breast cancer patients from TCGA as diseases signature.

D. Neurodegenerative diseases

SAveRUNNER was applied to study AD and other 13 AD-related disorders, including Mild Cognitive Impairment (MCI), which is the stage between the expected cognitive decline of normal aging and the more serious decline of dementia, other neurological diseases (i.e., Parkinson's disease, Huntington disease, supranuclear palsy progressive, and Lewy body disease), and other diseases that can be symptoms, risk factors, or consequences of AD (i.e., language disorders, memory disorders, visual pattern recognition, executive dysfunction, choice behavior, cardiomyopathy, amyloid neuropathies). SAveRUNNER predicted some interesting compound belonging to the family of: (i) beta-blockers, including *betaxolol*, originally used for hypertension treatment and already linked to a lower risk of developing AD [24]; (ii) multi-kinase inhibitors, including *regorafenib*, whose beneficial effects were recently investigated on neuroinflammation and AD pathology in vitro and in vivo [25]; (iii) anti-platelet inhibitors, including *clopidogrel*, whose therapy has been associated with lower risk of developing AD and whose anti-inflammatory effect has been recently studied in in-vivo model of AD [26]; and mTOR inhibitors, including *sirolimus*, an immunosuppressant drug used in transplantation medicine to prevent organ rejection, whose modulation could have

potential application to delay memory loss and age-related neurodegenerative diseases [27]. All these compounds were also corroborated by GSEA, considering neural drug-treated cell lines available from CMap as drug signatures and three different datasets of transcriptomic data from brain tissues of patients affected by AD from GEO as disease signature.

IV. Conclusion

We presented an overview of SAveRUNNER, a network-based approach that offers a promising framework to efficiently detect putative novel uses for marketed drugs against diseases of interest. We reviewed its main applications, including but not limited to viral infections, breast cancer, and neurodegenerative progressive disorders.

Acknowledgments

This work was partially funded by PON Ricerca e Innovazione 2014-2020 – DM 1062/202, BiBiNet project (grant n: H35F21000430002) within the POR-Lazio FESR 2014-2020, by Finalizzata Giovani Ricercatori 2021 (grant n.: GR-2021-12372614, CUP: B83C22007560001), by Progetto di Ricerca di Ateneo 2021 (grant n: RM12117A34663A2C) and 2022 (grant n: RP12218139131053) of Sapienza University of Rome.

References

[1] S. Pushpakom *et al.*, «Drug repurposing: progress, challenges and recommendations», *Nat. Rev. Drug Discov.*, vol. 18, fasc. 1, pp. 41–58, gen. 2019, doi: 10.1038/nrd.2018.168.

[2] G. Fiscon e P. Paci, «SAveRUNNER: an R-based tool for drug repurposing», *BMC Bioinformatics*, vol. 22, fasc. 1, p. 150, mar. 2021, doi: 10.1186/s12859-021-04076-w.

[3] G. Fiscon, F. Conte, L. Farina, e P. Paci, «SAveRUNNER: A network-based algorithm for drug repurposing and its application to COVID-19», *PLOS Comput. Biol.*, vol. 17, fasc. 2, p. e1008686, feb. 2021, doi: 10.1371/journal.pcbi.1008686.

[4] A.-L. Barabási, N. Gulbahce, e J. Loscalzo, «Network medicine: a network-based approach to human disease», *Nat. Rev. Genet.*, vol. 12, fasc. 1, pp. 56–68, gen. 2011, doi: 10.1038/nrg2918.

[5] M. Caldera, P. Buphamalai, F. Müller, e J. Menche, «Interactome-based approaches to human disease», *Curr. Opin. Syst. Biol.*, vol. 3, pp. 88–94, giu. 2017, doi: 10.1016/j.coisb.2017.04.015.

[6] F. Cheng *et al.*, «Network-based approach to prediction and population-based validation of in silico drug repurposing», *Nat. Commun.*, vol. 9, fasc. 1, p. 2691, 12 2018, doi: 10.1038/s41467-018-05116-5.

[7] P. Sibilio *et al.*, «In silico drug repurposing in COVID-19: A network-based analysis», *Biomed. Pharmacother.*, vol. 142, p. 111954, ott. 2021, doi: 10.1016/j.biopha.2021.111954.

[8] G. Fiscon, F. Conte, S. Amadio, C. Volonté, e P. Paci, «Drug Repurposing: A Network-based Approach to Amyotrophic Lateral Sclerosis», *Neurotherapeutics*, mag. 2021, doi: 10.1007/s13311-021-01064-z.

[9] S. Amadio, F. Conte, G. Esposito, G. Fiscon, P. Paci, e C. Volonté, «Repurposing Histaminergic Drugs in Multiple Sclerosis», *Int. J. Mol. Sci.*, vol. 23, fasc. 11, Art. fasc. 11, gen. 2022, doi: 10.3390/ijms23116347.

[10] F. Conte, P. Sibilio, G. Fiscon, e P. Paci, «A Transcriptome- and Interactome-Based Analysis Identifies Repurposable Drugs for Human Breast Cancer Subtypes», *Symmetry*, vol. 14, fasc. 11, Art. fasc. 11, nov. 2022, doi: 10.3390/sym14112230.

[11] G. Fiscon, P. Sibilio, A. Funari, F. Conte, e P. Paci, «Identification of Potential Repurposable Drugs in Alzheimer's Disease Exploiting a Bioinformatics Analysis», *J. Pers. Med.*, vol. 12, fasc. 10, Art. fasc. 10, ott. 2022, doi: 10.3390/jpm12101731.

[12] W. Yu, M. Clyne, M. J. Khoury, e M. Gwinn, «Phenopedia and Genopedia: disease-centered and gene-centered views of the evolving knowledge of human genetic associations», *Bioinformatics*, vol. 26, fasc. 1, pp. 145–146, gen. 2010, doi: 10.1093/bioinformatics/btp618.

[13] J. Piñero *et al.*, «DisGeNET: a comprehensive platform integrating information on human disease-associated genes and variants», *Nucleic Acids Res.*, vol. 45, fasc. D1, pp. D833–D839, gen. 2017, doi: 10.1093/nar/gkw943.

[14] A. M. Grimaldi *et al.*, «The New Paradigm of Network Medicine to Analyze Breast Cancer Phenotypes», *Int. J. Mol. Sci.*, vol. 21, fasc. 18, Art. fasc. 18, gen. 2020, doi: 10.3390/ijms21186690.

[15] P. Paci e G. Fiscon, «SWIMmeR: an R-based software to unveiling crucial nodes in complex biological networks», *Bioinformatics*, vol. 38, fasc. 2, pp. 586–588, gen. 2022, doi: 10.1093/bioinformatics/btab657.

[16] D. S. Wishart *et al.*, «DrugBank 5.0: a major update to the DrugBank database for 2018», *Nucleic Acids Res.*, vol. 46, fasc. Database issue, p. D1074, gen. 2018, doi: 10.1093/nar/gkx1037.

[17] J. Lamb *et al.*, «The Connectivity Map: using gene-expression signatures to connect small molecules, genes, and disease», *Science*, vol. 313, fasc. 5795, pp. 1929–1935, set. 2006, doi: 10.1126/science.1132939.

[18] Y. Zhou, Y. Hou, J. Shen, Y. Huang, W. Martin, e F. Cheng, «Network-based drug repurposing for novel coronavirus 2019-nCoV/SARS-CoV-2», *Cell Discov.*, vol. 6, fasc. 1, pp. 1–18, mar. 2020, doi: 10.1038/s41421-020-0153-3.

[19] A. R. Sahin *et al.*, «2019 Novel Coronavirus (COVID-19) Outbreak: A Review of the Current Literature», *EURASIAN J. Med. Oncol.*, vol. 4, fasc. 1, pp. 1–7, 2020.

[20] C. Volonté, S. Apolloni, e S. Amadio, «The Histamine and Multiple Sclerosis Alliance: Pleiotropic Actions and Functional Validation», *Curr. Top. Behav. Neurosci.*, ago. 2021, doi: 10.1007/7854_2021_240.

[21] B. Chu *et al.*, «Preparation and evaluation of teniposide-loaded polymeric micelles for breast cancer therapy», *Int. J. Pharm.*, vol. 513, fasc. 1, pp. 118–129, nov. 2016, doi: 10.1016/j.ijpharm.2016.09.005.

[22] K.-C. Mok *et al.*, «Repurposing hyperpolarization-activated cyclic nucleotide-gated channels as a novel therapy for breast cancer», *Clin. Transl. Med.*, vol. 11, fasc. 11, p. e578, nov. 2021, doi: 10.1002/ctm2.578.

[23] V. Cınar, Z. Hamurcu, A. Guler, N. Nurdinov, e B. Ozpolat, «Serotonin 5-HT7 receptor is a biomarker poor prognostic factor and induces proliferation of triple-negative breast cancer cells through FOXM1», *Breast Cancer Tokyo Jpn.*, ago. 2022, doi: 10.1007/s12282-022-01391-9.

[24] E. E. Beaman *et al.*, «Blood–brain barrier permeable β-blockers linked to lower risk of Alzheimer's disease in hypertension», *Brain*, p. awac076, feb. 2022, doi: 10.1093/brain/awac076.

[25] K.-M. Han *et al.*, «Regorafenib Regulates AD Pathology, Neuroinflammation, and Dendritic Spinogenesis in Cells and a Mouse Model of AD», *Cells*, vol. 9, fasc. 7, p. 1655, lug. 2020, doi: 10.3390/cells9071655.

[26] D. Pan *et al.*, «Anti-platelet Therapy Is Associated With Lower Risk of Dementia in Patients With Cerebral Small Vessel Disease», *Front. Aging Neurosci.*, vol. 14, 2022.

[27] R. X. Santos, S. C. Correia, S. Cardoso, C. Carvalho, M. S. Santos, e P. I. Moreira, «Effects of rapamycin and TOR on aging and memory: implications for Alzheimer's disease», *J. Neurochem.*, vol. 117, fasc. 6, pp. 927–936, giu. 2011, doi: 10.1111/j.1471-4159.2011.07262.x.